REPORT DOCUMENTATION PAGE

Form Approved
OMB NO. 0704-0188

Public reporting burden for this collection of information is estimated to average 1 hour per response, including the time for reviewing instructions, searching existing data sources, gathering and maintaining the data needed, and completing and reviewing the collection of information. Send comment regarding this burden estimates or any other aspect of this collection of information, including suggestions for reducing this burden, to Washington Headquarters Services, Directorate for information Operations and Reports, 1215 Jefferson Davis Highway, Suite 1204, Arlington, VA 22202-4302, and to the Office of Management and Budget, Paperwork Reduction Project (0704-0188), Washington, DC 20503.

1. AGENCY USE ONLY *(Leave blank)*	2. REPORT DATE	3. REPORT TYPE AND DATES COVERED
	April 1997	Final

4. TITLE AND SUBTITLE	5. FUNDING NUMBERS
Twenty-Sixty Symposium (International) on Combustion, Volume II	DAAH04-96-1-0020
6. AUTHOR(S)	
Robert F. Sawyer (principal investigator)	
7. PERFORMING ORGANIZATION NAMES(S) AND ADDRESS(ES)	8. PERFORMING ORGANIZATION REPORT NUMBER
The Combustion Institute Pittsburgh, PA	
9. SPONSORING / MONITORING AGENCY NAME(S) AND ADDRESS(ES)	10. SPONSORING / MONITORING AGENCY REPORT NUMBER
U.S. Army Research Office P.O. Box 12211 Research Triangle Park,, NC 27709-2211	ARO 35111.2-EG-CF

11. SUPPLEMENTARY NOTES

The views, opinions and/or findings contained in this report are those of the author(s) and should not be construed as an official Department of the Army position, policy or decision, unless so designated by other documentation.

12a. DISTRIBUTION / AVAILABILITY STATEMENT	12 b. DISTRIBUTION CODE
Approved for public release; distribution unlimited.	

13. ABSTRACT *(Maximum 200 words)*

NO ABSTRACT FURNISHED

14. SUBJECT TERMS	15. NUMBER IF PAGES
	16. PRICE CODE

17. SECURITY CLASSIFICATION OR REPORT	18. SECURITY CLASSIFICATION OF THIS PAGE	19. SECURITY CLASSIFICATION OF ABSTRACT	20. LIMITATION OF ABSTRACT
UNCLASSIFIED	UNCLASSIFIED	UNCLASSIFIED	UL

NSN 7540-01-280-5500

Standard Form 298 (Rev. 2-89)
Prescribed by ANSI Std. 239-18
298-102

DISCLAIMER NOTICE

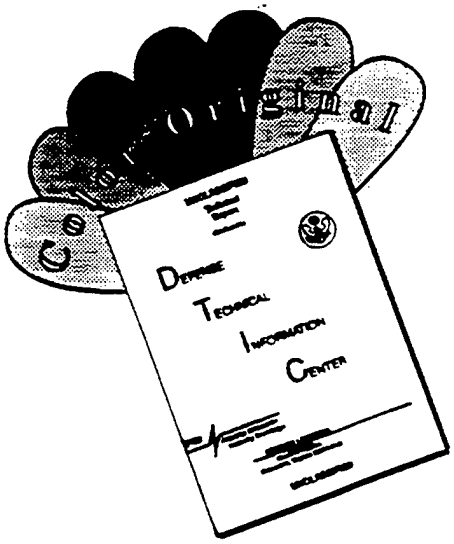

THIS DOCUMENT IS BEST QUALITY AVAILABLE. THE COPY FURNISHED TO DTIC CONTAINED A SIGNIFICANT NUMBER OF COLOR PAGES WHICH DO NOT REPRODUCE LEGIBLY ON BLACK AND WHITE MICROFICHE.

The following corrections to the printed volumes of the *26th International Symposium on Combustion*, which had been made by the publisher and typesetter, were mistakenly not incorporated by the printer. The errors do not appear in the CD-ROM, which is correct.

P. xxxii (xviii in Volume Two): Quantitative 2D Single-Shot Imaging of NO Concentrations and Temperatures in a Transparent SI Engine — change author "V. Siek" to "V. Sick"
P. xxxiii (xix in Volume Two): Heterogeneous/Homogeneous Reaction and Transport Coupling During Flame-Wall Interaction — change authors to "P. Popp, M. Smooke, and M. Baum"
P. xxxiii (xix in Volume Two): The Effects of Fuel-Air Mixing on NO_X Formation in Non-Premixed Swirl Burnerd — change "Burnerd" to "Burners"
P. xxxv (xxi in Volume Two): Experimental Investigation of a scramjet Model Combustor with Injection Through a Swept Ramp Using Lazer-Induced Fluorescence with Tunable Excimer Lasers — change "scramjet" to all caps: "SCRAMJET"
P. xxxvii (xxiii in Volume Two): Modeling of Premixed Gas Combustion in Porous Media Composed of Coarse-Sized Particles: 1-D Description with Discrete Solid Phase — change author "A. V. Feflov" to "A. V. Fefelov"
P. 3391: Andresen entry — should read "Andresen, P., **153**, **2589**, **2827**, **2949**"
P. 3391: add entry — "Baum, M., **2693**"
P. 3391: add entry — "Boesl, U., **2859**"
P. 3391: Bowman entry — should read "Bowman, C. T., **481**, **799**, **2803**"
P. 3392: Choi, J. Y. entry — should read "Choi, J. Y., 2883, **2925**, **2957**"
P. 3393: Dietrich entry — should read "Dietrich, D. L., **1201**, 1619"
P. 3394: Halsbeck entry — should read "Haslbeck, J., **2091**"
P. 3394: Hancock entry — should read "Hancock, R. D., 35, **1087**"
P. 3394: Hu entry — should read "Hu, I. Z., **307**"
P. 3395: Kenedy entry — should read "Kennedy, I. M., **1953**"
P. 3395: Kohse Höinghaus entry — should read "Kohse-Höinghaus, K., 48, **153**, 982, 1824, 1832, 2284"
P. 3395: Lafleur entry — should read "Lafeur, A. L., **2319**"
P. 3397: Mullholland entry — should read "Mulholland, G. W., **1445**, 2429"
P. 3398: add entry — "Saso, Y., **2413**"
P. 3398: Schreiber, I. entry — should read "Shreiber, I., **1557**"
P. 3399: Sinkovits entry — should read "Sinkovits, R. S., 91, **899**"
P. 3399: Stairkovskii entry — should read "Starikovskii, A. Yu, **2999**"
P. 3399: Theinel entry — should read "Thienel, Th., **2303**"
P. 3399: Togan entry and Toqan entry — combine to read "Toqan, M., 2302, 2453, 3160"
P. 3400: Van Tiggelen entry and Van Tigglen entry — combine to read "Van Tiggelen, P. J., 479, 626, **1009**, 1393"
P. 3400: Vlachos entry — should read "Vlachos, D. G., 1070, 1754, **1763**, 1778, 2292"
P. 3400: Wornat, J. entry and Wornat, M. J. entry — combine to read "Wornat, M. J., 2107, **3075**, 3160, **3287**"

TWENTY-SIXTH SYMPOSIUM
(International)
ON
COMBUSTION
Volume Two

At Università Frederico II
Napoli, Campi Phlegraci, Italy
July 28–August 2, 1996

Organized By

THE COMBUSTION INSTITUTE
Pittsburgh, Pennsylvania
1996

Program co-chairs:
Norbert Peters and Charles K. Westbrook
Co-editors:
Anthony R. Burgess and Frederick L. Dryer

19970422 090

COPYRIGHT © 1996 BY THE COMBUSTION INSTITUTE

ALL RIGHTS RESERVED

No part of this book may be reproduced in any form
by photostat, microfilm, or any other means,
without written permission from the publishers.
Brief quotations from this book for purposes of scientific
discussion will be permitted.

THE COMBUSTION INSTITUTE
5001 Baum Boulevard
Suite 635
Pittsburgh, Pennsylvania 15213-1851 USA

ISSN 0082-0784

Type composed at Impressions Book and Journal Services, Inc., Madison, Wisconsin
Printed by Edwards Brothers, Inc., Ann Arbor, Michigan

PRINTED IN THE UNITED STATES OF AMERICA

CONTENTS

Preface iii
The Combustion Institute v
Technical Program Committee ix
Session Chairs xvi
Introduction xxxix

VOLUME ONE

HOTTEL PLENARY LECTURE

The Challenge of Turbulent Combustion. *K. N. C. Bray* 1

NON-PREMIXED TURBULENT COMBUSTION

A Numerical Study on Flame Stability at the Transition Point of Jet Diffusion Flames. *H. Yamashita, M. Shimada and T. Takeno* 27
Direct Numerical Simulation Analysis of Flame Surface Density Equation in Non-premixed Turbulent Combustion. *E. Van Kalmthout, D. Veynante and S. Candel* 35
An Integrated PDF/Neural Network Approach for Simulating Turbulent Reacting Systems. *F. C. Christo, A. R. Masri, E. M. Nebot and S. B. Pope* 43
A Mixing Model to Improve the PDF Simulation of Turbulent Diffusion Flames. *A. R. Masri, S. Subramaniam and S. B. Pope* 49
Subgrid Mixing and Molecular Transport Modeling in a Reacting Shear Layer. *S. Menon and W. H. Calhoon Jr.* 59
Simulation of Detailed Chemistry in a Turbulent Combustor Flow. *H. C. Magel, U. Schnell and K. R. G. Hein* 67
Interaction of Turbulence and Radiation in Confined Diffusion Flames. *J. W. Hartick, M. Tacke, G. Früchtel, E. P. Hassel and J. Janicka* 75
Computational and Experimental Investigation of a Turbulent Non-premixed Methane Flame. *M. Nau, W. Neef, U. Mass, E. Gutheil and J. Warnatz* 83
Exothermicity and Three-Dimensional Effects in Unsteady Propane Square Jets. *F. F. Grinstein and K. Kailasanath* 91
Measurements of the Detailed Flame Structure in Turbulent H_2-Ar Jet Diffusion Flames with Line-Raman /Rayleigh/LIPF-OH Technique. *Y.-C. Chen and M. S. Mansour* 97
Conditioned Dissipation and Average Consumption Maps in a Turbulent Nonpremixed Flame Using Planar Laser-Induced Fluorescence of O_2. *S. Guerre, R. Bazile and D. Stepowski* 105
Extinction of Counterflow Diffusion Flames under Velocity Oscillations. *J. S. Kistler, C. J. Sung, T. G. Kreutz, C. K. Law and M. Nishioka* 113
Characteristics of Lifted Flames in Nonpremixed Turbulent Confined Jets. *M. S. Cha and S. H. Chung* 121
Images of the Strained Flammable Layer Used to Study the Liftoff of Turbulent Jet Flames. *D. A. Everest, D. A. Feikema and J. F. Driscoll* 129

Experimental Investigation of the Flame Structure and Extinction of Turbulent Counterflow Nonpremixed Flames. *A. Kitajima, T. Ueda, A. Matsuo and M. Mizomoto* 137
Vortex-Flame Interactions and Extinction in Turbulent Jet Diffusion Flames. *F. Takahashi, W. J. Schmoll, D. D. Trump and L. P. Goss* 145
Contribution to the Analysis of Temporal and Spatial Structures near the Lift-Off Region of a Turbulent Hydrogen Diffusion Flame. *A. Brockhinke, P. Andresen and K. Kohse-Höinghaus* 153
A Study of Turbulent Diffusion Flames Formed by Planar Fuel Injection into the Wake Formation Region of a Slender Square Cylinder. *P. Koutmos, C. Mavridis and D. Papailiou* 161
Study of Swirling Recirculating Hydrogen Diffusion Flame Using UV Raman Spectroscopy *M. M. Tacke, T. C. Cheng, E. P. Hassel and J. Janicka* 169
Simulation of a Bluff-Body-Stabilized Diffusion Flame Using Second-Moment Closure and Monte Carlo Methods. *H.A. Wouters, P. A. Nooren, T. W. J. Peeters and D. Roekaerts* 177
Swirl-Induced Intermittency: A Novel Effect Modifying the Turbulence Structure of Swirling Free Jets. *F. Holzäpfel, B. Lenze and W. Leuckel* 187
Turbulent Length Scales in a Swirling Flame. *G. Früchtel, E. P. Hassel and J. Janicka* 195
Mixing and Chemical Reaction in an Idealized Swirl Chamber. *O. M. Knio, A. S. Worlikar and H. N. Najm* 203
Predicting the Near-Burner-Zone Flow Field and Chemistry of Swirl-Stabilized Low-NO_x Flames of Pulverized Coal Using the RNG-k-ε, RSM and k-ε Turbulence Models. *F. Breussin, F. Pigari and R. Weber* 211

INVITED PLENARY LECTURE

Using Direct Numerical Simulations to Understand Premixed Turbulent Combustion. *T. Poinsot* 219

PREMIXED TURBULENT COMBUSTION

Triple Flames and Partially Premixed Combustion in Autoignition of Non-Premixed Turbulent Mixtures. *P. Domingo and L. Vervisch* 233
Large Eddy Simulation of Unsteady Combustion. *S. I. Möller, E. Lundgren and C. Fureby* 241
A Test of an Engineering Model of Premixed Turbulent Combustion. *V. Karpov, A. Lipatnikov and V. Zimont* 249
Study of Premixed Turbulent Combustion Including Landau-Darrieus Instability Effects. *R. N. Paul and K. N. C. Bray* 259
Computation of Premixed Turbulent Combustion Using the Probability Density Function Approach. *A. Sadat Sakak and M. Schreiber* 267
Probability Density Function Modeling of Premixed Turbulent Opposed Jet Flames. *W. P. Jones and Y. Prasetyo* 275
Three-Dimensional Spatial Flamelet Statistics for Premixed Turbulent Combustion Modeling. *S. S. Shy, R. H. Jang, W. K. I and K. L. Gee* 283
Effect of Density Ratio on Flame Propagation along a Vortex Tube. *T. Hasegawa amd K. Nishikado* 291

Model Simulations of Freely Propagating Turbulent Premixed Flames. *T. Smith and S. Menon* 299
Calculations of Turbulent Flames Using a PSR Microstructural Library. *I. Z. Hu and S. M. Correa* 307
Spectral Model of Premixed Flame Propagation. *L. R. Collins and M. Ulitsky* 315
Negative Flame Speed in an Unsteady 2-D Premixed Flame: A Computational Study. *I. R. Gran, T. Echekki and J. H. Chen* 323
Spatial and Temporal Dynamics of Flamelets in Turbulent Premixed Flames. *C. Ghenaï, C. Chauveau and I. Gökalp* 331
Flamelet Behavior in a Turbulent Diffusion Flame Measured by Rayleigh Scattering Image Velocimetry. *M. Komiyama, A. Miyafuji and T. Takagi* 339
Effects of Unsteady Stretch on the Strength of a Freely-Propagating Flame Wrinkled by a Vortex. *C. J. Mueller, J. F. Driscoll, D. L. Reuss and M. C. Drake* 347
The Time Evolution of a Vortex-Flame Interaction Observed via Planar Imaging of CH and OH. *Q. V. Nguyen and P. H. Paul* 357
Turbulent Premixed Flame Propagation in a Cylindrical Vessel. *M. Fairweather, S. S. Ibrahim, H. Jaggers and D. G. Walker* 365
Flame Surface Density and Burning Rate in Premixed Turbulent Flames. *I. G. Shepherd* 373
Combustion Intensity and Burning Rate Integral of Premixed Flames. *F. C. Gouldin* 381
Burning Velocity of Turbulent Premixed Flames in a High-Pressure Environment. *H. Kobayashi, T. Tamura, K. Maruta, T. Niioka and F. A. Williams* 389
Extinction of Turbulent Premixed Flames by Small-Scale Turbulence at Kolmogorov Microscale. *A. Yoshida, H. Kakinuma and Y. Kotani* 397
Turbulence Characteristics within the Local Reaction Zone of a High-Intensity Turbulent Premixed Flame. *J. Furukawa, K. Okamoto and T. Hirano* 405
Experimental Analysis of Flame Surface Density Models for Premixed Turbulent Combustion. *D. Veynante, J. Piana, J. M. Duclos and C. Martel* 413
Experimental and Numerical Investigation of the Structure of Flames under Engine Conditions. *H. Wassenberg and G. Adomeit* 421
Surface Density Measurements of Turbulent Premixed Flames in a Spark-Ignition Engine and a Bunsen-Type Burner Using Planar Laser-Induced Fluorescence. *B. M. Deschamps, G. J. Smallwood, J. Prieur, D. R. Snelling and O. L. Gülder* ... 427
Measurement of the Instantaneous Detailed Flame Structure in Turbulent Premixed Combustion. *A. Buschmann, F. Dinkelacker, T. Schäfer and M. Schäfer, J. Wolfrum* 437
Experimentally Measured Burning Rates of Premixed Turbulent Flames. *E. Bourguignon and L. W. Kostiuk, Y. Michou and I. Gökalp* 447
Highly Turbulent Premixed Flames Stabilized in a Co-Axial Jet Flame Burner. *T.-W. Lee and A. Mitrovic* 455

INVITED PLENARY LECTURE

Theory and Modeling in Combustion Chemistry. *J. A. Miller* 461

ELEMENTARY REACTION KINETICS

Measurement of the Rate Coefficent of $H + O_2 + M \rightarrow HO_2 + M$ for M = Ar and N_2 at High Pressures. *D. F. Davidson, E. L. Petersen, M. Röhrig, R. K. Hanson and C. T. Bowman* 481
Absolute Reactive Cross Sections for the Reaction $OH + CO \rightarrow H + CO_2$. *S. Koppe, T. Laurent, H.-R. Volpp, J. Wolfrum and P. D. Naik* 489
Kinetic and Mechanistic Studies of the Reaction of Hydroxyl Radicals with Acetaldehyde over an Extended Temperature Range. *P. H. Taylor, M. S. Rahman, M. Arif, B. Dellinger and P. Marshall* 497
Elementary Reactions of the Methoxymethyl Radical in the Gas Phase: $CH_3OCH_3 + F$, $CH_2OCH_3 + CH_2OCH_3$, $CH_2OCH_3 + O_2$, and $CH_2OCH_3 + O$. *K. Hoyermann and F. Nacke* 505
Kinetics of the Reaction of Vinyl Radicals with Acetylene. *V. D. Knyazev, S. I. Stoliarov and I. R. Slagle* 513
The $CH_3 + C_5H_5$ Reaction: A Potential Source of Benzene at High Temperatures. *L. V. Moskaleva, A. M. Mebel and M. C. Lin* 521
The Reactions of $O(^3P)$ Atoms with Aromatic Hydrocarbons with Unsaturated Side Chains. *M. Eichholtz, S. Kohl, A. Schneider, J.-T. Vollmer and H. Gg. Wagner* 527
Kinetics and Mechanism of the Reaction of $S(^3P)$ with O_2. *A. Miyoshi, H. Shiina, K. Tsuchiya and H. Matsui* 535
High-Temperature Reactions and Thermodynamic Properties of Phenyl Radicals. *E. Heckmann, H. Hippler and J. Troe* 543
A Shock Tube Study of $H + HNCO \rightarrow H_2 + NCO$ and the Thermal Decomposition of NCO. *J. D. Mertens and R. K. Hanson* 551
A Kinetic Study of the Reactions of $NH(X^3\Sigma^-)$ with O_2 and NO in the Temperature Range from 1200 to 2200 K. *H.-J. Römming and H. Gg. Wagner* .. 559
Measurement of the Branching Ratio of NCO + NO into N_2O at 1100–1400 K. *S. A. Flatness and J. C. Kramlich* 567
Direct Measurement of the Reaction Pair $C_6H_5NO \leftrightarrow C_6H_5 + NO$ by a Combined Shock Tube and Flow Reactor Approach. *C. Horn, P. Frank, R. S. Tranter, J. Schaugg, H.-H. Grotheer and Th. Just* 575
A Shock Tube Study of the Reaction of S-Atoms with NO. *D. Woiki and P. Roth* .. 583

KINETIC MECHANISMS—MODELS AND EXPERIMENTS

The Mutually Sensitized Oxidation of Ethylene and NO: An Experimental and Kinetic Modeling Study. *A. Doughty, F. J. Barnes, J. H. Bromly and B. S. Haynes* 589
A Kinetic Study of the Oxidation of Acetonitrile: A Model for NO Formation from Fuel-Bound Nitrogen. *E. Ikeda and J. C. Mackie* 597
The Thermal Decomposition of C_2H_5I. *S. S. Kumaran, M.-C. Su, K. P. Lim and J. V. Michael* 605
The Ignition and Oxidation of Allene and Propyne: Experiments and Kinetic Modeling. *H. Curran, J. M. Simmie, P. Dagaut, D. Voisin and M. Cathonnet* 613
The Formation of C_2 during High Temperature Pyrolysis of Fullerene C_{70}. *T. Sommer and P. Roth* 621

Chemical Kinetic Study of Dimethylether Oxidation in a Jet Stirred Reactor from 1 to 10 ATM: Experiments and Kinetic Modeling. *P. Dagaut, J.-C. Boettner and M. Cathonnet* 627
Chemical Kinetic Modeling of High-Pressure Propane Oxidation and Comparison to Experimental Results. *D. N. Koert, W. J. Pitz, J. W. Bozzelli and N. P. Cernansky* 633
An Intermediate Temperature Modeling Study of the Combustion of Neopentane. *H. J. Curran, W. J. Pitz, C. K. Westbrook, M. W. M. Hisham and R. W. Walker* 641
Dissociation and Chain Reaction in the Pyrolysis of Pyrazine. *J. H. Kiefer, Q. Zhang, R. D. Kern, H. Chen, J. Yao and B. Jursic* 651
Thermal Decomposition of Benzonitrile A Combined Single-Pulse Shock Tube–ARAS Investigation. *A. Lifshitz, Y. Cohen, M. Braun-Unkhoff and P. Frank* 659
Thermal Decomposition of Benzene. Single-Pulse Shock-Tube Investigation. *A. Laskin and A. Lifshitz* 669
A Detailed Comprehensive Kinetic Model for Benzene Oxidation Using the Recent Kinetic Results. *Y. Tan and P. Frank* 677
Reaction Mechanisms in Aromatic Hydrocarbon Formation Involving the C_5H_5 Cyclopentadienyl Moiety. *C. F. Melius, M. E. Colvin, N. M. Marinov, W. J. Pitz and S. M. Senkan* 685
Experimental and Modeling Investigation of Aromatic and Polycyclic Aromatic Hydrocarbon Formation in a Premixed Ethylene Flame. *M. J. Castaldi, N. M. Marinov, C. F. Melius, J. Huang, S. M. Senkan, W. J. Pitz and C. K. Westbrook* .. 693
Benzene Formation Chemistry in Premixed 1,3-Butadiene Flames. *R. P. Lindstedt and G. Skevis* 703
Destruction of Benzene in High-Temperature Flames: Chemistry of Benzene and Phenol *R. A. Shandross, J. P. Longwell and J. B. Howard* 711
Detailed Kinetic Reaction Mechanism for Ignition and Oxidation of α-Methylnaphthalene. *H. Pitsch* 721
Reduced *n*-Heptane Mechanism for Non-premixed Combustion with Emphasis on Pollutant-Relevant Intermediate Species. *M. Bollig, H. Pitsch, J. C. Hewson and K. Seshadri* 729
Experimental Data and Kinetic Modeling of Primary Reference Fuel Mixtures. *C. V. Callahan, T. J. Held, F. L. Dryer, R. Minetti, M. Ribaucour, L. R. Sochet, T. Faravelli, P. Gaffuri and E. Ranzi* 739
Comparison of Oxidation and Autoignition of the Two Primary Reference Fuels by Rapid Compression. *R. Minetti, M. Carlier, M. Ribaucour, E. Therssen and L. R. Sochet* 747
Computer-Aided Design of Gas-Phase Oxidation Mechanisms—Application to the Modelling of *n*-Heptane and Iso-Octane Oxidation. *G. M. Côme, V. Warth, P. A. Glaude, R. Fournet, F. Battin-Leclerc and G. Scacchi* 755
Numerical and Asymptotic Studies of the Structure of Premixed *iso*-Octane Flames. *H. Pitsch, N. Peters and K. Seshadri* 763
Kinetic Modeling of the Oxidation of Large Aliphatic Hydrocarbons. *M. Nehse, J. Warnatz and C. Chevalier* 773
Self-Ignition of Diesel-Relevant Hydrocarbon-Air Mixtures under Engine Conditions. *U. Pfahl, K. Fieweger and G. Adomeit* 781
Combustion-Like Pyrolysis of Organic Polymers: Species and Kinetic Details by *T*-Jump/FTIR Spectroscopy. *T. B. Brill, H. Arisawa and P. E. Gongwer* 791

High-Pressure Methane Oxidation behind Reflected Shock Waves. *E. L. Petersen, M. Röhrig, D. F. Davidson, R. K. Hanson and C. T. Bowman* 799
Analysis of Wet CO Oxidation under Turbulent Non-premixed Conditions Using a PDF Method and Detailed Chemical Kinetics. *M. Kraft, E. Stöckelman and H. Bockhorn* 807
Ignition of Hydrogen and Oxygen in Counterflow at High Pressures. *B. T. Helenbrook and C. K. Law* 815
A Broader Definition of Symmetry Number and Its Application to a Kinetic Model Describing Polyarene Growth. *M. C. Masonjones and A. F. Sarofim* 823

Invited Topical Review

Multistep Asymptotic Analyses of Flame Structures. *K. Seshardi* 831

LAMINAR PREMIXED FLAMES

The Phenomena of Flame Propagation in a Rotating Tube. *Y. Sakai and S. Ishizuka* 847
The Mechanism of Mutual Annihilation of Stoichiometric Premixed Methane-Air Flames. *T. Echekki, J. H. Chen and I. R. Gran* 855
Extinction Mechanisms of Near-Limit Premixed Flames and Extended Limits of Flammability. *C. J. Sung and C. K. Law* 865
Markstein Lengths of CO/H_2/Air Flames, Using Expanding Spherical Flames. *M. J. Brown, I. C. McLean, D. B. Smith and S. C. Taylor* 875
A Numerical Study of Large Amplitude Baroclinic Instabilities of Flames. *J. Chomiak and G. Zhou* 883
Shock Wave Interaction with a Fast Convection-Reaction Driven Flame. *R. G. Johnson, A. C. McIntosh, J. Brindley, M. R. Booty and M. Short* 891
A New Time-Dependent, Three-Dimensional Flame Model for Laminar Flames. *G. Patnaik, K. Kailasanath and R. S. Sinkovits* 899
Numerical Study of Premixed Laminar Flame Propagation in a Closed Tube with a Full Navier-Stokes Approach. *F. S. Marra and G. Continillo* 907
Two-Dimensional Mathematical Modeling of Laminar, Premixed, Methane-Air Combustion on an Experimental Slot Burner. *D. Bradley, P. H. Gaskell, K. C. Kwan and M. J. Scott* 915
Experimental and Numerical Study of a Premixed Flame Stabilized by a Rectangular Section Cylinder. *P. Bailly, D. Garréton, O. Simonin, P. Bruel, M. Champion, B. Deshaies, S. Duplantier and S. Sanquer* 923
Flame Propagation along 90° Bend in an Open Duct. *K. Sato, Y. Sakai and M. Chiga* 931
On the Use of Light Sheet Methods in the Presence of Refraction by Flames. *F. Weinberg* 939
Temperature Field Measurements in a Sooting Flame by Filtered Rayleigh Scattering (FRS). *D. Hofmann and A. Leipertz* 945
The Optical Band Gap Model in the Interpretation of the UV-Visible Absorption Spectra of Rich Premixed Flames. *P. Minutolo, G. Gambi and A. D'Alessio* 951
Quantitative CH Determinations in Low-Pressure Flames. *J. Luque, G. P. Smith and D. R. Crosley* 959
CH_3 Detection in Flames Using Photodissociation-Induced Fluorescence. *P. Desgroux, L. Gasnot, B. Crunelle and J. F. Pauwels* 967

Degenerate Four-Wave Mixing Measurements of Methyl Radical Distributions in Hydrocarbon Flames: Comparison with Model Predictions. *R. L. Farrow, M. N. Bui-Pham and V. Sick* 975
Initiation of Laminar Flames in Near-Limit $H_2/O_2/H_2O$ Mixtures. *A. Yu. Kusharin, O. E. Popov and G. L. Agafonov* 985
Acetylene and Ethylene Mole Fractions in Methane/Air Partially Premixed Flames. *L.-K. Tseng, J. P. Gore, I. K. Puri and T. Takeno* 993
Experimental and Computational Investigation of Concentration Profiles of C_1-C_4 Hydrocarbon Radicals and Molecules in Low-Pressure C_2H_2/O/H Atomic Flames at 600 K. *J. Peeters and K. Devriendt* 1001
Experimental Study of the Structure of Rich Ethane Flames. *R. Ancia, J. Vandooren and P. J. Van Tiggelen* 1009
Experimental and Numerical Studies of Two-Stage Methanol Flames. *S. C. Li and F. A. Williams* 1017
Laminar Flame Speeds and Oxidation Kinetics of Benzene-Air and Toluene-Air Flames. *S.G. Davis, H. Wang, K. Brezinsky and C. K. Law* 1025
Hydrogen-Oxygen Flame Doped with Trimethyl Phosphate, Its Structure and Trimethyl Phosphate Destruction Chemistry. *O. Korobeinichev, V. Shvartsberg, A. Chernov and V. Mokrushin* 1035
Molecular Beam Mass Spectrometric and Modeling Studies of Neat and NH_3-Doped Low-Pressure H_2/N_2O/Ar Flames: Formation and Consumption of NO. *R. C. Sausa, G. Singh, G. W. Lemire and W. R. Anderson* 1043

LAMINAR DIFFUSION FLAMES

Instability of Diffusion Flames. *A. Lingens, K. Neemann, J. Meyer and M. Schreiber* 1053
Heat Loss and Lewis Number Effects on the Onset of Oscillations in Diffusion Flames. *S. Cheatham andM. Matalon* 1063
Effects of Multi-Dimensionality on a Diffusion Flame. *M. Nishioka, Y. Takemoto, H. Yamashita and T. Takeno* 1071
Structure of a Non-Premixed Flame Interacting with Counterrotating Vortices. *D. Thévenin, J. C. Rolon, P. H. Renard, D. W. Kendrick, D. Veynante and S. Candel* 1079
Thermal Diffusion Effects and Vortex-Flame Interactions in Hydrogen Jet Diffusion Flames. *R. D. Hancock, F. R. Schauer, R. P. Lucht, V. R. Katta and K. Y. Hsu* 1087
Ignition Delay Associated with a Strained Fuel Strip. *T. J. Gerk and A. R. Karagozian* 1095
Studies on Strained Non-premixed Flames Affected by Flame Curvature and Preferential Diffusion. *T. Takagi, Y. Yoshikawa, K. Yoshida, M. Komiyama and S. Kinoshita* 1103
Response of Counterflow Premixed and Diffusion Flames to Strain Rate Variations at Reduced and Elevated Pressures. *C. J. Sun, C. J. Sung, D. L. Zhu and C. K Law* 1111
The Sensitive Structure of Partially Premixed Methane-Air vs. Air Counterflow Flames. *M. A. Tanoff, M. D. Smooke, R. J. Osborne, T. M. Brown and R. W. Pitz* 1121
Effects of Pressure Diffusion on the Characteristics of Tubular Flames. *K. Yamamoto, T. Hirano and S. Ishizuka* 1129

The Effects of Flame Structure on Extinction of CH_4-O_2-N_2 Diffusion Flames. *J. Du and R. L. Axelbaum* 1137
Edge-Flame-Holding. *J. Buckmaster and R. Weber* 1143
Unsteady Extinction Mechanisms of Diffusion Flames. *F. Takahashi and V. R. Katta* 1151
Quantitative Two-Photon Laser-Induced Fluorescence Imaging of CO in Flickering CH_4/Air Diffusion Flames. *D. A. Everest, C. R. Shaddix and K. C. Smyth* 1161
Thin-Filament Pyrometry in Flickering Laminar Diffusion Flames. *W. M. Pitts* 1171
Tunable Diode Laser Absorption Measurements of Carbon Monoxide and Temperature in a Time-Varying, Methane/Air, Non-Premixed Flame. *R. R. Skaggs and J. H. Miller* 1181

Invited Topical Review

Current State of Combustion Research in Microgravity. *M. Kono, K. Ito, T. Niioka, T. Kadota and J. Sato* 1189

MICROGRAVITY COMBUSTION

Droplet Combustion Experiments in Spacelab. *D. L. Dietrich, J. B. Haggard Jr., F. L. Dryer, V. Nayagam, B. D. Shaw and F. A. Williams* 1201
Microgravity Combustion of Methanol and Methanol/Water Droplets: Drop Tower Experiments and Model Predictions. *A. J. Marchese, F. L. Dryer, R. V. Colantonio and V. Nayagam* 1209
Hydroxyl Radical Chemiluminescence Imaging and the Structure of Microgravity Droplet Flames. *A. J. Marchese, F. L. Dryer, V. Nayagam and R. Colantonio* 1219
An Unsteady-State Analysis of Porous Sphere and Droplet Fuel Combustion under Microgravity Conditions. *M. K. King* 1227
Characterization of Spherical Hydrocarbon Fuel Flames: Laser Diagnosis of the Chemical Structure through the OH Radical. *J. König, C. Eigenbrod, M. Tanabe, H. Renken amd H. J. Rath* 1235
Investigation of Sooting in Microgravity Droplet Combustion. *M. Y. Choi and K.-O. Lee* 1243
Observation of Sooting Behavior in an Emulsion Droplet Flame by Planar Laser Light Scattering in Microgravity. *M. Tsue, D. Segawa, T. Kadota and H. Yamasaki* 1251
High-Pressure Droplet Burning Experiments in Microgravity. *B. Vieille, C. Chauveau, X. Chesneau, A. Odeïde and I. Gökalp* 1259
Experimental Study on High-Pressure Droplet Evaporation Using Microgravity Conditions. *H. Nomura, Y. Ujiie, H. J. Rath, J. Sato and M. Kono* 1267
Influence of Gravity on the Propagation of Initially Spherical Flames. *J. Daou and B. Rogg* 1275
Experimental Study on Methane-Air Premixed Flame Extinction at Small Stretch Rates in Microgravity. *K. Maruta, M. Yoshida, Y. Ju and T. Niioka* 1283
Soot-Field Structure in Laminar Soot-Emitting Microgravity Nonpremixed Flames. *C. M. Megaridis, D. W. Griffin and B. Konsur* 1291
Gravitational Effects on Sooting Diffusion Flames. *C. R. Kaplan, E. S. Oran, K. Kailasanath and H. D. Ross* 1301

Influence of Gravity and Pressure on Pool Fire-Type Diffusion Flames. *J.-M. Most, P. Mandin, J. Chen, P. Joulain, D. Durox and A. C. Fernandez-Pello* 1311
Opposed-Flow Flame Spread across *n*-Propanol Pools. *D. N. Schiller, W. A. Sirignano* 1319
Detailed Experiments of Flame Spread across Deep Butanol Pools. *H. D. Ross and F. J. Miller* 1327
Quiescent Flame Spread over Thick Fuels in Microgravity. *J. West, L. Tang, R. A. Altenkirch, S. Bhattacharjee, K. Sacksteder and M. A. Delichatsios* 1335
Effects of Slow Wind on Localized Radiative Ignition and Transition to Flame Spread in Microgravity. *T. Kashiwagi, K. B. McGrattan, S. L. Olson, O. Fujita, M. Kikuchi and K. Ito* 1345
Model Calculation of Steady Upward Flame Spread over a Thin Solid in Reduced Gravity. *C.-B. Jiang, J. S. T'ien amd H.-Y. Shih* 1353
Small-Scale Smoldering Combustion Experiments in Microgravity. *D. P. Stocker, S. L. Olson, D. L. Urban, J. L. Torero, D. C. Walther and A. C. Fernandez-Pello* 1361
An Experimental Study on Particle-Cloud Flames in a Microgravity Field. *Y. Okuyama, Y. Ohtomo, K. Maruta, H. Kobayashi and T. Niioka* 1369

CHEMICAL FLAME INHIBITION

Effect of Halogenated Flame Inhibitors on C_1-C_2 Organic Flames. *T. Noto, V. Babushok, D. R. Burgess Jr., A. Hamins, W. Tsang and A. Miziolek* 1377
The Effect of CF_3I Compared to CF_3Br on OH· and Soot Concentrations in Co-flowing Propane/Air Diffusion Flames. *K. C. Smyth and D. A. Everest* 1385
Chemical Effects of CF_3H in Extinguishing Counterflow CO/AIR/H_2 Diffusion Flames. *G. S. Fallon, H. K. Chelliah and G. T. Linteris* 1395
Extinction of Non-premixed Methane- and Propane-Air Counterflow Flames Inhibited with CF_4, CF_3H, and CF_3Br. *P. Papas, J. W. Fleming and R. S. Sheinson* 1405
Suppression of a Baffle-Stabilized Spray Flame by Halogenated Agents. *A. Hamins, C. Presser and L. Melton* 1413
Experimental Study of the Inhibition of Premixed and Diffusion Flames by Iron Pentacarbonyl. *D. Reinelt and G. T. Linteris* 1421

FIRE SAFETY

Global Properties of Gaseous Pool Fires. *A. Hamins, K. Konishi, P. Borthwick and T. Kashiwagi* 1429
Flame Base Structure of Small-Scale Pool Fires. *S. Venkatesh, A. Ito, K. Saito and I. S. Wichman* 1437
The Effect of Pool Diameter on the Properties of Smoke Produced by Crude Oil Fires. *G. W. Mulholland, W. Liggett and H. Koseki* 1445
Measurements and Prediction of Air Entrainment Rates of Pool Fires. *X. C. Zhou, J. P. Gore and H. R. Baum* 1453
Effect of the Fuel Boiling Point on the Boilover Burning of Liquid Fuels Spilled on Water. *J. P. Garo, J. P. Vantelon and A. C. Fernandez-Pello* 1461
Study of the Thermocapillary Layer Preceding Slow Steadily-Spreading Flames over Liquid Fuels. *P. L. Garcia-Ybarra, J. L. Castillo, J. C. Antoranz, V. Sankovitch and J. San Martin* 1469

Determination of the Spread Rate in Opposed-Flow Flame Spread over Thick Solid Fuels in the Thermal Regime. *S. Bhattacharjee, J. West and R. A. Altenkirch* 1477
The Dependence of the Flame Spread Rate over Solid Fuel on Damköhler Number and Heat Loss. *S. S. Rybanin* 1487
Creeping Flame Spread: Energy Balance and Application to Practical Materials. *M. A. Delichatsios* 1495
Controlling Mechanisms in the Transition from Smoldering to Flaming of Flexible Polyurethane Foam. *S. D. Tse, A. C. Fernandez–Pello and K. Miyasaka* 1505
Two-Regime Global Kinetics of Cellulose Pyrolysis: the Role of Tar Evaporation. *E. M. Suuberg, I. Milosavljevic and V. Oja* 1515
Numerical Simulation of Combustion in Fire Plumes. *W. E. Mell, K. B. McGrattan and H. R. Baum* 1523
Numerical Simulation of the Dynamics of Large Fire Plumes and the Phenomenon of Puffing. *A. F. Ghoniem, I. Lakkis and M. Soteriou* 1531
The Transport of Carbon Monoxide from a Burning Compartment Located on the Side of a Hallway. *B. Y. Lattimer, U. Vandsburger and R. J. Roby* 1541
Burning Regimes for the Finite-Duration Releases of Fuel Gases. *G. Makhviladze, J. Roberts and S. Yakush* 1549
Effect of Liquid Drops on the Thermal Explosion of a Gas Mixture. *V. Goldshtein, I. Goldfarb, A. Zinoviev and I. Shreiber* 1557
Propagation Limits of Dust/Air Flames Diluted by Additions of Inert Solid Particles. *R. Blouquin and G. Joulin* 1565
The Role of Radiation Absorption in Defining Explosibility of Coal/Rock Dust Mixtures. *C. D. Litton and R. F. Chaiken* 1571
Numerical Investigation on the Influence of Carbonaceous Particles on the Ignition Behavior of Methane/Air Mixtures. *T. Ludwig and P. Roth* 1579
Characterization of the Chaotic Dynamics in the Spontaneous Combustion of Coal Stockpiles. *G. Continillo, G. Galiero, P. L. Maffettone and S. Crescitelli* 1585

INVITED PLENARY LECTURE

Spray Combustion Phenomena. *G. M. Faeth* 1593

SPRAY COMBUSTION

Surface Tension Influences on Methanol Droplet Vaporization in the Presence of Water. *H. A. Dwyer, I. Aharon, B. D. Shaw and H. Niazmand* 1613
Characteristics of Supercritical Droplet Gasification. *A. Umemura and Y. Shimada* 1621
Statistical Analysis on Onset of Microexplosion for an Emulsion Droplet. *M. Tsue, H. Yamasaki, T. Kadota and D. Segawa* 1629
Spontaneous Ignition of Liquid Droplets from a View of Non-Homogeneous Mixture Formation and Transient Chemical Reactions. *M. Tanabe, T. Bolik, C. Eigenbrod, H. J. Rath, J. Sato and M. Kono* 1637
Gas Property Effects on Droplet Atomization and Combustion in an Air-Assist Atomizer. *R. Aftel, A. K. Gupta, C. Cook and C. Presser* 1645
Anomalous Group Combustion of Premixed Clusters. *H. H. Chiu and C. L. Lin* ... 1653
Structure of an Acoustically Forced Turbulent Spray Flame. *E. Haile, O. Delabroy, F. Lacas, D. Veynante and S. Candel* 1663

Droplet Size Distribution Effects in Spray Combustion. *J. A. Bossard and R. E. Peck* 1671
Droplet and Vapor Transport in a Turbulent Jet. *J. Ye and C. D. Richards* 1679
PLIF Imaging Measurements of a Co-axial Rocket Injector Spray at Elevated Pressure. *U. Brummund, A. Cessou and A. Vogel* 1687
Flame Propagation in Planar Droplet Arrays and Interaction Phenomena Between Neighboring Droplet Streams. *N. Roth, A. Karl, K. Anders and A. Frohn* 1697
Polydispersity and Reaction Zone Structure in Partially Premixed Spray Flames. *J. B. Greenberg and N. Sarig* 1705
Electrostatic Dispersion and Evaporation of Clusters of Drops of High-Energy Fuel for Soot Control. *J. Bellan and K. Harstad* 1713
Measurement of the Local Group Combustion Number of Droplet Clusters in a Premixed Spray Stream. *F. Akamatsu, Y. Mizutani, M. Katsuki, S. Tsushima and Y. D. Cho* 1723
Modeling of Turbulent Spray Diffusion Flames Including Detailed Chemistry. *C. Hollmann and E. Gutheil* 1731
Quantitative Comparison of Detailed Numerical Computations and Experiments in Counterflow Spray Diffusion Flames. *L. P. Gao, Y. D'Angelo, I. Silverman, A. Gomez and M. D. Smooke* 1739

CATALYTIC COMBUSTION

Numerical Modeling of Catalytic Ignition. *O. Deutschmann, R. Schmidt, F. Behrendt and J. Warnatz* 1747
Gas Temperature above a Porous Radiant Burner: Comparison of Measurements and Model Predictions. *M. D. Rumminger, N. H. Heberle, R. W. Dibble and D. R. Crosley* 1755
Homogeneous Ignition of Hydrogen-Air Mixtures over Platinum. *P.-A. Bui, D. G. Vlachos and P. R. Westmoreland* 1763
Catalytic Oxidation of Natural Gas over Supported Platinum: Flow Reactor Experiments and Detailed Numerical Modeling. *T. C. Bond, R. A. Noguchi, C.-P. Chou, R. K. Mongia, J.-Y. Chen and R. W. Dibble* 1771
Pd on Low-Surface-Area α-Alumina System: Is Metallic Pd Active for Methane Combustion? *M. Lyubovsky, R. Weber and L. Pfefferle* 1779
Catalytic Combustion of Carbon Particulate at High Values of the Carbon/Catalyst Mass Ratio. *P. Ciambelli, M. D'Amore, V. Palma and S. Vaccaro* 1789
Ignition of Catalytic Reactions in a Vertical Wall Immersed in a Combustible Gas. *C. Treviño and F. Méndez* 1797

VOLUME TWO

Invited Topical Review

Gas-Phase Combustion Synthesis of Materials. *K. Brezinsky* 1805

MATERIALS SYNTHESIS

Diamond Thin Film Deposition in Low-Pressure Premixed Flames. *D. G. Goodwin, N. G. Glumac and H. S. Shin* 1817
Temperature Profile Measurements in Stagnation-Flow, Diamond-Forming Flames Using Hydrogen CARS Spectroscopy. *K. E. Bertagnolli and R. P. Lucht* 1825

The Controlling Chemistry in Flame Generated Surface Deposition of Na_2SO_4 and the Effects of Chlorine. *M. Steinberg and K. Schofield* 1835
A Mathematical Model of Laser-Induced Synthesis of Ultra Fine SiC Powders. *S. S. Khartchenko and A. I. Kuzmin* 1845
Controlled Combustion Synthesis of Nanosized Iron Oxide Aggregates. *Z. Zhang and T. T. Charalampopoulos* 1851
The Formation of SiO_2 from Hexamethyldisiloxane Combustion in Counterflow Methane-Air Flames. *H. K. Chagger, D. Hainsworth, P. M. Patterson, M. Pourkashanian and A. Williams* 1859
Pulsating Instability in the Nonadiabatic Heterogeneous SHS Flame: Theory and Experimental Comparisons. *A. Makino and C. K. Law* 1867
Supercritical Combustion Synthesis of Titanium Nitride. *K. Brezinsky, J. A. Brehm, C. K. Law and I. Glassman* 1875
Metal-Sulfur Combustion. *S. Goroshin, A. Mizera, D. L. Frost and J. H. S. Lee* 1883
Gas-Phase Combustion Synthesis of Aluminum Nitride Powder. *R. L. Axelbaum, C. R. Lottes, J. I. Huertas and L. J. Rosen* 1891

METALS COMBUSTION

Flame Structure Measurement of Single, Isolated Aluminum Particles Burning in Air. *P. Bucher, R. A. Yetter, F. L. Dryer, T. P. Parr, D. M. Hanson-Parr and E. P. Vicenzi* 1899
A Comprehensive Physical and Numerical Model of Boron Particle Ignition. *W. Zhou, R. A. Yetter, F. L. Dryer, H. Rabitz, R. C. Brown and C. E. Kolb* 1909
Evolution of Particle Temperature and Internal Composition for Zirconium Burning in Air. *I. E. Molodetsky, E. L. Dreizin and C. K. Law* 1919
Ignition and Combustion of Bulk Titanium and Magnesium at Normal and Reduced Gravity. *A. Abbud–Madrid, M. C. Branch and J. W. Daily* 1929
Modeling of Solid Particle Interaction in a High-Velocity, Hot Gas Stream. *M. M. Elkotb, N. Salama and I. Nassef* 1937
Combustion Characteristics of Mg-CO_2 Counterflow Diffusion Flames. *A. Fukuchi, M. Kawashima and S. Yuasa* 1945
The Behavior of Chromium in Laminar Hydrogen and Ethene Diffusion Flames. *Y. Yoon, C. Reyes, A. D. Jones, P. Kelly, D. P. Y. Chang and I. M. Kennedy* 1953
Burning Velocities in Fuel-Rich Aluminum Dust Clouds. *S. Goroshin, I. Fomenko and J. H. S. Lee* 1961

PROPELLANTS

Combustion of Porous Energetic Materials in the Merged-Flame Regime. *S. B. Margolis, F. A. Williams andA. M. Telengator* 1969
Solid Propellant Diffusion Flame Structure. *T. P. Parr and D. M. Hanson-Parr* 1981
A Three-Phase Model of HMX Combustion. *J. E. Davidson and M. W. Beckstead* 1989
Simplified Chemical-Kinetic Mechanisms for Characterizing the Structure of the Dark Zones of Double Base and Nitramine Propellants. *N. Ilincic, W. R. Anderson, K. Seshadri and N. E. Meagher* 1997
Oscillatory Combustion of Aluminized Composite Propellants. *S. R. Hickman and M. Q. Brewster* 2007

Propellant Dark Zone Concentrations via Multichannel IR Absorption. *S. H. Modiano and J. A. Vanderhoff* 2017
Laser Recoil Combustion Response of N5 Propellant from 1 to 9 Atmospheres. *J. C. Finlinson* 2025
Convective Ignition of a Granular Solid Propellant Bed: Influence of Propellant Composition. *D. E. Kooker, S. L. Howard and L.-M. Chang* 2033
Flame Stabilization in Cryogenic Propellant Combustion. *G. Herding, R. Snyder, P. Scouflaire, C. Rolon and S. Candel* 2041

Invited Topical Review

Impacts and Control of Air Toxics from Combustion. *C. P. Koshland* 2049

NO_X FORMATION AND CONTROL

Pressure Effects on the Thermal $DeNO_x$ Process. *K. Kjærgaard, P. Glarborg, K. Dam-Johansen and J. A. Miller* 2067
Reburning Promoted by Nitrogen- and Sodium-Containing Compounds. *V. M. Zamansky, L. Ho, P. M. Maly and W. R. Seeker* 2075
Flow Reactor Studies and Testing of Comprehensive Mechanisms for NO_x Reburning. *D. Stapf and W. Leuckel* 2083
Control of NO_x Emission by NO_x Recycle Approach. *C. Q. Zhou, L. G. Neal, R. Bolli, J. Haslbeck and A. Chang* 2091
Isotopic Labeling Studies of the Selective Non-Catalytic Reduction of NO with NH_3. *B. L. Duffy and P. F. Nelson* 2099
Thermal Reduction of NO by NH_3: Kinetic Modeling of the NH_2 + NO Product Branching Ratio. *M. J. Halbgewachs, E. W. G. Diau, A. M. Mebel, M. C. Lin and C. F. Melius* 2109
A Model for Prediction of Selective Noncatalytic Reduction of Nitrogen Oxides by Ammonia, Urea, and Cyanuric Acid with Mixing Limitations in the Presence of CO. *J. Brouwer, M. P. Heap, D. W. Pershing and P. J. Smith* 2117
Gas Phase Reactions of Hydrogen Peroxide and Hydrogen Peroxide/Methanol Mixtures with Air Pollutants. *V. M. Zamansky, L. Ho, P. M. Maly and W. R. Seeker* 2125
Evidence for a New NO Production Mechanism in Flames. *J. E. Harrington, G. P. Smith, P. A. Berg, A. R. Noble, J. B. Jeffries and D.R. Crosley* 2133
Behavior of Key Reactions on NO Formation in Methane-Air Flames. *M. Nishioka, Y. Kondoh and T. Takeno* 2139
A LIF and CARS Study of the Effects of Upstream Heat Loss on NO Formation from Laminar Premixed Burner- Stabilized Natural-Gas/Air Flames. *A. V. Mokhov and H. B. Levinsky* 2147
NO_x Formation in Turbulent Lean-Premixed Combustion with Minimum Heat Losses. *L. Xie, S. Hayashi and K. Hirose* 2155
Computational and Experimental Study of *NO* in an Axisymmetric Laminar Diffusion Flame. *M. D. Smooke, A. Ern, M. A. Tanoff, B. A. Valdati, R. K. Mohammed, D. F. Marran and M. B. Long* 2161
Reduced Mechanisms for NO_x Emissions from Hydrocarbon Diffusion Flames. *J. C. Hewson and M. Bollig* 2171
The Effect of Changes in the Flame Structure on the Formation and Destruction of Soot and NO_x in Radiating Diffusion Flames. *A. Atreya, C. Zhang, H. K. Kim, T. Shamim and J. Suh* 2181

Measurements of NO in Turbulent Nonpremixed Flames Stabilized on a Bluff Body. *B. B. Dally, A. R. Masri, R. S. Barlow, G. J. Fiechtner and D. F. Fletcher* 2191
Oxygen Atom Concentrations and NO Production Rates in a Turbulent H_2/N_2 Jet Flame. *R. S. Barlow, G. J. Fiechtner and J.-Y. Chen* 2199
Flamelet and PDF Modeling of CO and NO_x Emissions from a Turbulent, Methane Hydrogen Jet Nonpremixed Flame. *J.-Y. Chen and W.-C. Chang* 2207
Analysis of Turbulence-Chemistry Interaction with Respect to NO Formation in Turbulent, Nonpremixed Hydrogen-Air Flames. *M. Schlatter, J. C. Ferreira, M. Flury and J. Gass* 2215
Impact of Mixing Model on Predicted NO Formation in a Nonpremixed, Partially Stirred Reactor. *W.-C. Chang and J.-Y. Chen* 2223
Impact of Temperature and Fuel-Nitrogen Content on Fuel-Staged Combustion with Coal Pyrolysis Gas. *U. Greul, H. Spliethoff, H.-C. Magel, U. Schnell, H. Ruediger, K. R. G. Hein, C.-Z. Li and P. F. Nelson* 2231
Measurements and Predictions of Nitric Oxide and Particulates Emissions from Heavy Fuel Oil Spray Flames. *M. A. Byrnes, E. A. Foumeny, T. Mahmud, A. S. A. K Sharifah, T. Abbas, P. G. Costen, S. Hassan and F. C. Lockwood* 2241
Effects of CaO and Burnout on the Kinetics of NO Reduction by Beulah Zap Char. *F. Guo and W. C. Hecker* 2251

SOOT FORMATION AND DESTRUCTION

PAH and Aromers: Precursors of Fullerenes and Soot. *M. Bachmann, W. Wiese and K.-H. Homann* 2259
Soot Precursor Material: Visualization via Simultaneous LIF-LII and Characterization via TEM. *R. L. Vander Wal* 2269
Comprehensive Two-Dimensional Soot Diagnostics Based on Laser-Induced Incandescence (LII). *S. Will, S. Schraml and A. Leipertz* 2277
On Surface Growth Mechanism of Soot Particles. *M. Frenklach* 2285
Soot Surface Growth by Polycyclic Aromatic Hydrocarbon and Acetylene Addition. *S. Macadam, J. M. Beér, A. F. Sarofim and A. B. Hoffmann* 2295
Soot Formation in the Pyrolysis of Benzene/Acetylene and Acetylene/Hydrogen Mixtures at High Carbon Concentrations. *V. G. Knorre, D. Tanke, Th. Thienel and H. Gg. Wagner* 2303
A Simplified Phenomenological Model for Soot Growth Based on Plug Flow Reactor Experiments. *B. Bartenbach and W. Leuckel* 2311
C_2H_2 and PAH as Soot Growth Reactants in Premixed C_2H_4-Air Flames. *T. G. Benish, A. L. Lafeur, K. Taghizadeh and J. B. Howard* 2319
The Effect of Temperature on Soot Inception in Premixed Ethylene Flames. *A. Ciajolo, A. D'Anna, R. Barbella, A. Tregrossi and A. Violi* 2327
Polycyclic Aromatic Hydrocarbon and Soot Formation in Premixed Flames of CH_3Cl/CH_4 and CH_4. *J. Huang and S. M. Senkan* 2335
Re-Initiation of Soot Surface Growth in Premixed Counter-Flow Flames. *M. Marquardt, F. Mauß, B. Jungfleisch, R. Suntz and H. Bockhorn* 2343
Influence of Hydrogen Addition to Fuel on Temperature Field and Soot Formation in Diffusion Flames. *Ö. L. Gülder, D. R. Snelling and R. A. Sawchuk* 2351
Experiments and Numerical Simulation on Soot Formation in Opposed-Jet Ethylene Diffusion Flames. *H. Wang, D. X. Du, C. J. Sung and C. K. Law* 2359

Flamelet Modeling of Soot Formation in Laminar Ethyne/Air-Diffusion Flames. *M. Balthasar, A. Heyl, F. Mauß, F. Schmitt and H. Bockhorn* 2369
CFD Prediction of Coupled Radiation Heat Transfer and Soot Production in Turbulent Flames. *N. W. Bressloff, J. B. Moss and P. A. Rubini* 2379
Assessment of Soot Volume Fractions from Laser-Induced Incandescence by Comparison with Extinction Measurements in Laminar, Premixed, Flat Flames. *J. Appel, B. Jungfleisch, M. Marquardt, R. Suntz and H. Bockhorn* 2387
Investigation of Sooting in Normal-Gravity Droplet Combustion Using Light Extinction and Gravimetric Techniques. *K.-O. Lee, K. A. Jensen and M. Y. Choi* 2397

OTHER POLLUTANTS

The Reaction of Phenoxy Radicals with Mono-Chlorobenzene and Its Meaning for Gas-Phase Dioxin Formation in Incineration. *H.-H. Grotheer and R. Louw* 2405
Effects of Ambient Water in the Combustion Enhancement of Heavily Chlorinated Hydrocarbons: Studies on Droplet Burning. *H. Wang, D. L. Zhu, Y. Saso and C. K. Law* 2413
The Effect of the Bulk Equivalence Ratio on the PAH Emissions from the Combustion of PVC, Poly(styrene), and Poly(ethylene). *T. Panagiotou, Y. A. Levendis, J. Carlson and P. Vouros* 2421
Influence of Turbulent Mixing on the Pyrolysis of Chloroform Using Detailed Chemical Kinetics. *M. Kraft, E. Stöckelmann and H. Bockhorn* 2431
Adsorption of Metallic Mercury on Activated Carbon. *D. Karatza, A. Lancia, D. Musmarra and F. Pepe* 2439
Mechanisms Governing Trace Sodium Capture by Kaolinite in a Downflow Combustor. *P. O. Mwabe and J. O. L. Wendt* 2447
A Real-Time Monitor for Toxic Metal Emissions from Combustion Systems. *S. G. Buckley, C. P. Koshland, R. F. Sawyer and D. Lucas* 2455

INCINERATION AND FUEL SUBSTITUTION

Effects of External Acoustic Excitation on Enhanced Transport in a Resonant Incinerator. *G. Pont, J. W. Willis, A. R. Karagozian and O. I. Smith* 2463
Compact Incinerator Afterburner Concept Based on Vortex Combustion. *T. P. Parr, E. Gutmark, K. Wilson, D. M. Hanson-Parr, K. Yu, R. A. Smith and K. C. Schadow* 2471
Combustion Studies on Concentrated Distillery Effluents. *N. M. Patel, P. J. Paul, H. S. Mukunda and S. Dasappa* 2479
The Energy and Environmental Implications of Using Sewage Sludge as a Co-Fired Fuel Applied to Boilers. *T. Abbas, P. Costen, G. De Soete, K. Glaser, S. Hassan and F. C. Lockwood* 2487
Transformations of Sludge Waste During Combustion in a Low-High-Low Temperature Reactor. *J. A. Koziński, R. Saade and G. Zheng* 2495

Invited Topical Review

Modern Tools for Diesel Engine Combustion Investigation. *W. Hentschel* 2503

DIESEL ENGINES

Application of a Reduced Kinetic Model for Soot Formation and Burnout in Three-Dimensional Diesel Combustion Computations. *P. Belardini, C. Bertoli, C. Beatrice, A. D'Anna and N. Del Giacomo* 2517
Analysis of Pyrolysis Process in Diesel-Like Combustion by Means of Laser-Induced Fluorescence. *R. Ragucci, M. de Joannon and A. Cavaliere* 2525
Spectral Extinction Measurements of Spray Combustion in a Divided-Chamber Diesel Engine System. *F. E. Corcione, G. Mazziotti and B. M. Vaglieco* 2533
An Experimental Database for Diesel Spray Combustion. *E. Winklhofer* 2541
Near-Field Entrainment in Unsteady Gas Jets and Diesel Sprays: a Comparative Study. *R. Andriani, A. Coghe and G. E. Cossali* 2549
Flame Liftoff in Diesel Sprays. *J. Chomiak and A. Karisson* 2557
A Simple Model of Ignition Modes of Dense Droplet Clouds. *D. Thibaut and S. Candel* 2565
Self-Ignition of Hybrid (H_2 + Atomized Liquid Hydrocarbon Fuel + Gaseous Oxidizer) Mixtures at Engine Relevant Conditions. *B. E. Gelfand, A. M. Bartenev, S. V. Khomik, S. P. Medvedev and A. N. Polenov* 2573

SPARK IGNITION ENGINES

Advanced Diagnostics for Minimizing Hydrocarbon Emissions from a Direct-Injection Gasoline Engine. *M. C. Drake, D. T. French and T. D. Fansler* 2581
Polarization Separated Spatially Resolved Single Laser Shot Multispecies Analysis in the Combustion Chamber of a Realistic SI Engine with a Tunable KrF Excimer Laser. *M. Knapp, A. Luczak, V. Beushausen, W. Hentschel, P. Manz and P. Andresen* 2589
Quantitative 2D Single-Shot Imaging of NO Concentrations and Temperatures in a Transparent SI Engine. *C. Schulz, V. Siek, J. Wolfrum, V. Drewes, M. Zahn and R. Maly* 2597
An Experimental Study on Quenching Crevice Widths in the Combustion Chamber of a Spark-Ignition Engine. *S. Ishizawa* 2605
A Fiber-Optic Probe to Measure Precombustion In-Cylinder Fuel-Air Ratio Fluctuations in Production Engines. *M. J. Hall and M. Koenig* 2613
Time-Resolved Investigation of Hot Spots in the End Gas of an S.I. Engine by Means of 2-D Double-Pulse LIF of Formaldehyde. *B. Bäuerle, J. Warnatz and F. Behrendt* 2619
Modeling Turbulent Combustion and Pollutant Formation in Stratified Charge SI Engines. *T. A. Baritaud, J. M. Duclos and A. Fusco* 2627
Relation Between Flame Propagation Characteristics and Hydrocarbon Emissions Under Lean Operating Conditions in Spark-Ignition Engines. *N. Hadjiconstantinou, K. Min and J. B. Heywood* 2637
Oxidation of Hydrocarbons from Lubricant Oil Layers in Spark-Ignition Engines. *M. G. Norris, W. Bauer and S. Hochgreb* 2645
Heat Release Rates Due to Autoignition, and Their Relationship to Knock Intensity in Spark Ignition Engines. *D. Bradley, G. T. Kalghatgi, M. Golombok and J. Yeo* 2653
Heat Transfer Modeling During Knock and Flame Quenching in an Engine Chamber. *O. A. Ezekoye* 2661

Autoignition Chemistry in a Motored Engine: An Experimental and Kinetic Modeling Study. *H. J. Curran, P. Gaffuri, W. J. Pitz, C. K. Westbrook and W. R. Leppard* 2669

Deflagration-to-Detonation Transition in End Gases. *C. K. Chan and W. A. Dewit* 2679

Extents of Alkane Combustion During Rapid Compression Leading to Single- and Two-Stage Ignition. *A. Cox, J. F. Griffiths, C. Mohamed, H. J. Curran, W. J. Pitz and C.K. Westbrook* 2685

Heterogeneous/Homogeneous Reaction and Transport Coupling During Flame-Wall Interaction. *P. Popp andM. Smooke* 2693

1-D Simulation of a Spark Discharge in Air. *M. Schäfer, R. Schmidt and J. Köhler* 2701

Analytical Study on Flame Stabilization in Reciprocating Combustion in Porous Media with High Thermal Conductivity. *J. G. Hoffmann, R. Echigo, S. Tada and H. Yoshida* 2709

Interpretation of k-ε Computed Turbulence Length-Scale Predictions for Engine Flows. *Z. Han, R. D. Reitz, F. E. Corcione and G. Valentino* 2717

GAS TURBINES

Effect of Hardware Alignment on Fuel Distribution and Combustion Performance for a Production Engine Fuel-Injection Assembly. *V. G. McDonell, L. Arellano, S. W. Lee and G. S. Samuelsen* 2725

The Effects of Fuel-Air Mixing on NO_x Formation in Non-Premixed Swirl Burnerd. *T. Terasaki and S. Hayashi* 2733

A Numerical and Experimental Study of Fuel Evaporation and Mixing for Lean Premixed Combustion at High Pressure. *M. Rachner, M. Brandt, H. Eickhoff, C. Hassa, A. Bräumer, H. Krämer, M. Ridder and V. Sick* 2741

Use of an Optical Probe for Time–Resolved *in Situ* Measurement of Local Air–to–Fuel Ratio and Extent of Fuel Mixing with Applications to Low NO_x Emissions in Premixed Gas Turbines. *R. K. Mongia, E. Tomita, F. K. Hsu, L. Talbot and R. W. Dibble* 2749

Influence of Air and Fuel Flows on Gas Turbine Sprays at High Pressures. *Q. P. Zheng, A. K. Jasuja andA. H. Lefebvre* 2757

Effect of Temperature and Concentration Fluctuations on Radiative Heat Transfer in Turbulent Flames. *W. Krebs, R. Koch, B. Ganz, L. Eigenmann and S. Wittig* 2763

Stability and Emissions Characteristics of a Lean Premixed Gas Turbine Combustor. *W.-P. Shih, J. G. Lee and D. A. Santavicca* 2771

Fluorescence Imaging of NO and O_2 in a Spray Flame Combuster at Elevated Pressures. *B. L. Upschulte, M. G. Allen and K. R. McManus* 2779

Visualization of Fuel Distribution in Premixed Ducts in a Low-Emission Gas Turbine Combustor Using Laser Techniques. *C. Löfström, H. Kaaling and M. Aldén* 2787

Fiber-Optic Sensors for Long-Wavelength Pyrometry and Thermometry in Gas Turbines. *A. S. Bonanno, W. W. Smith, R. Bassilakis and M. A. Serio* 2795

ACTIVE COMBUSTION CONTROL

Real-Time Adaptive Feedback Control of Combustion Instability. *A. Kemal and C. T. Bowman* 2803
Experimental Demonstration of Active Control of Combustion Instabilities Using Real Time Modes Observation and Secondary Fuel Injection. *Y. Neumeier and B. T. Zinn* 2811
Optimization of Gas Turbine Combustor Performance Throughout the Duty Cycle. *N. T. Davis and G. S. Samuelsen* 2819
Spatially Selective Chemistry Control in an Oil-Burning Furnace: a New Method to Reduce NO_x Emissions Developed Through Combined Three-Dimensional Laser Diagnostics. *A. Luczak, S. Eisenberg, M. Knapp, H. Schlüter, V. Beushausen and P. Andresen* 2827
Active Instability Control with Direct-Drive Servo Valves in Liquid-Fueled Combustion Systems. *C. Hantschk, J. Hermann and D. Vortmeyer* 2835
Active Control of Liquid-Fueled Combustion Using Periodic Vortex-Droplet Interaction. *K. H. Yu, T. P. Parr, K. J. Wilson, K. C. Schadow aqnd E. J. Gutmark* 2843
Combustion Control Using a Multiplexed Diode-Laser Sensor System. *E. R. Furlong, D. S. Baer and R. K. Hanson* 2851
On-Line Emission Control of Combustion Processes by Laser-Induced Resonance-Enhanced Multi-Photon Ionization/Mass Spectrometry. *R. Zimmermann, D. Lenior, A. Kettrup, H. Nagel and U. Boesl* 2859
Industrial Combustion Control Using UV Emission Tomography. *A. Leipertz, R. Obertacke and F. Wintrich* 2869

HIGH SPEED COMBUSTION

Numerical Simulation of a Counterflow Diffusion Flame in Supersonic Airflow. *K. Takita and T. Niioka* 2877
On Strained Flames with Hypergolic Reactants: The $H_2/NO/F_2$ System in High-Speed, Supersonic and Subsonic Mixing-Layer Combustion. *F. N. Egolfopoulos, P. E. Dimotakis and C. Bond* 2885
Observations of H_2O Formation in the Supersonic Combustion of H_2 by High-Enthalpy Air. *M. F. Miller, W. T. Rawlins, M. G. Allen and T. E. Parker* 2895
Experimental Observation of Unsteady H_2-O_2 Combustion Phenomena Around Hypersonic Projectiles Using a Multiframe Camera. *J. Kasahara, T. Horii, T. Endo and T. Fujiwara* 2903
PLIF Imaging of Hypersonic Reactive Flow Around Blunt Bodies. *M. R. Kamel, C. I. Morris, I. G. Stouklov and R. K. Hanson* 2909
Quenching of Reaction in Gas-Sampling Probes to Measure Scramjet Engine Performance. *T. Mitani* 2917
Dimensional Analysis of the Effect of Flow Conditions on Shock-Induced Combustion. *J.-Y. Choi, I.-S. Jeung and S. Lee* 2925
Shock-Wave-Enhancement of the Mixing and the Stability Limits of Supersonic Hydrogen-Air Jet Flames. *H. Huh and J. F. Driscoll* 2933
Numerical Simulation of Flame-Stabilization and Combustion Promotion by Plasma Jets in Supersonic Air Streams. *R. Kato and I. Kimura* 2941

Experimental Investigation of a scramjet Model Combustor with Injection Through a Swept Ramp Using Lazer-Induced Fluorescence with Tunable Excimer Lasers. *R. Hönig, D. Theisen, R. Fink, R. Lachner, G. Kappler, D. Rist and P. Andresen* 2949
Transient Simulation of Superdetonative Mode Initiation Process in Scram-Accelerator. *J.-Y. Choi, I.-S. Jeung and Y. Yoon* 2957

DETONATIONS

Critical Conditions for Detonation Propagation Through Mixture with Decreasing Reaction Rate. *S. I. Kryuchkov, S. B. Dorofeev and A. A. Efimenko* 2965
The Influence of Initial Temperature on Flame Acceleration and Deflagration-to-Detonation Transition. *G. Ciccarelli, J. L. Boccio, T. Ginsberg and H. Tagawa* ... 2973
On the Evolution of Cellular Detonation. *D. S. Stewart, T. D. Aslam and J. Yao* ... 2981
Detailed Structure and Propagation of Three-Dimensional Detonations. *D. N. Williams, L. Bauwens and E. S. Oran* 2991
Ignition and Detonation in N_2O-CO-H_2-He Mixtures. *A. Y. Starikovskii* 2999
Detonation Supported by Combustible Dust Deposit. *B.-C. Fan and H.-Z. Li* 3007
Oblique Detonation Stabilized on a Hypervelocity Projectile. *M. J. Kaneshige and J. E. Shepherd* 3015
Onset of Oblique Detonation Waves: Comparison Between Experimental and Numerical Results for Hydrogen-Air Mixtures. *C. Viguier, L. F. Figueira da Silva, D. Desbordes and B. Deshaies* 3023
Numerical Simulations of the Diffraction of Planar Detonations in H_2-O_2 Mixtures. *N. A. Tonello, M. Sichel and E. S. Oran* 3033

INVITED PLENARY LECTURE

Solid Fuel Utilization: From Coal to Biomass. *F. C. Lockwood* 3041

COAL AND CHAR COMBUSTION

A Transient Two-Dimensional Chemically Reactive Flow Model: Fuel Particle Combustion in a Nonquiescent Environment. *J. Lee, A. G. Tomboulides, S. A. Orszag, R. A. Yetter and F. L. Dryer* 3059
Flame Structure and Combustion Rate of Burning Graphite in the Stagnation Flow. *A. Makino, I. Kato, M. Senba, H. Fujizaki and N. Araki* 3067
Single-Particle Combustion of Two Biomass Chars. *M. J. Wornat, R. H. Hurt, K. A. Davis and N. Y. C. Yang* 3075
Influence of Pressure on the Combustion Rate of Carbon. *R. H. Essenhigh and A. M. Mescher* 3085
The Influence of Pressure on Char Combustion Kinetics. *E. Croiset, C. Mallet, J.-P. Rouan and J.-R. Richard* 3095
Transient High-Temperature Thermal Deactivation of Monomaceral-Rich Coal Chars. *T. Beeley, J. Crelling, J. Gibbins, R. Hurt, M. Lunden, C. Man, J. Williamson and N. Yang* 3103
Structural Changes of Char Particles During Chemically Controlled Oxidation. *X. Zhang, A. Dukhan, I. I. Kantorovich, E. Bar-Ziv, A. Kandas and A. F. Sarofim* .. 3111
Surface Heterogeneity in the Formation and Decomposition of Carbon Surface Oxides. *M. C. Ma and B. S. Haynes* 3119

A New Approach to Studying Pore Diffusivity During Char Combustion at FBC Conditions. *S. Goel, A. F. Sarofim and J. Lu* 3127
The Impact of Fragmentation on Char Conversion During Pulverized Coal Combustion. *R. E. Mitchell and A. E. Jacob Akanetuk* 3137
A General Model for Devolatilization of Large Coal Particles. *Y. Zhao, M. A. Serio and P. R. Solomon* 3145
Chemical Structure of Coal Tar During Devolatilization. *M. Watt, T. H. Fletcher, S. Bai, M. S. Solum and R. J. Pugmire* 3153
Conversion of Coal Tar to Soot During Coal Pyrolysis in a Post-Flame Environment. *J. Ma, T. H. Fletcher and B. W. Webb* 3161
Statistical Kinetics for Pulverized Coal Combustion. *R. H. Hurt, M. M. Lunden, E. G. Brehob and D. J. Maloney* 3169
Measurements of Coal Particle Shape, Mass, and Temperature Histories: Impact of Particle Irregularity on Temperature Predictions and Measurements. *R. Sampath, D. J. Maloney, J. W. Zondlo, S. D. Woodruff and Y. Yeboah* 3179
Laser Ignition and Flame Propagation of Pulverized Coal Dust Clouds. *M. Taniguchi, H. Kobayashi and S. Azuhata* 3189
Sodium Partitioning in a Pulverized Coal Combustion Environment. *N. B. Gallagher, T. W. Peterson and J. O. L. Wendt* 3197
An Experimental Study of the Release of Nitrogen from Coals Pyrolysed in Fluidised-Bed Reactors. *C.-Z. Li, P. F. Nelson, E. B. Ledesma and J. C. Mackie* 3205
Fundamental Study on N_2O Formation/Decomposition Characteristics by Means of Low-Temperature Pulverized Coal Combustion. *I. Naruse, Y. Yamamoto, Y. Itoh and K. Ohtake* 3213
Fundamental Experiment on the Combustion of Coal-Water Mixture and Modeling of the Process. *K. Takeno, K. Tokuda, T. Ichinose and S. Kaneko* 3223

Invited Topical Review

Fluidized Bed Combustion: Achievements and Problems. *B. Leckner* 3231

FLUIDIZED BEDS

The Fate of Fixed Carbon During the Fluidized-Bed Combustion of a Coal and Two Waste-Derived Fuels. *U. Arena, R. Chirone and P. Salatino* 3243
Progress of Combustion in the Furnace of a Circulating Fluidised Bed Boiler. *A. Lyngfelt, L.-E. Åmand and B. Leckner* 3253
Coal Combustion and Gasification in a Compartmented, Fluidised-Bed Coal Gasifier. *H. Yan, V. Rudolph and D.-K. Zhang* 3261
Fragmentation of Small Coal Particles Under Fluidised-Bed Combustor Conditions. *B. R. Stanmore, A. Brillard, P. Gilot and L. Delfosse* 3269
Prediction of Coal-Water Slurry Dispersion in a Fluidized Bed Combustor. *F. Okasha and M. Miccio* 3277
The Effects of Pyrolysis Temperature and Ion-Exchanged Metals on the Composition of Brown Coal Tars Produced in a Fluidized-Bed Reactor. *B. A. Vernaglia, M. J. Wornat, C.-Z. Li and P. F. Nelson* 3287
Scattering of Thermal Radiation in the Freeboard of a 1 MW_t Fluidized Bed Combustor with Coal and Limestone Feeding. *M. Filla, A. Scalabrin and C. Tonfoni* 3295

In Situ Alkali Concentration Measurements in a Pressurized, Fluidized-Bed Coal Combustor by Excimer Laser Induced Fragmentation Fluorescence. *F. Greger, K. T. Hartinger, P. B. Monkhouse, J. Wolfrum, H. Baumann and B. Bonn* 3301
Pollutant Formation During Coal Combustion in a CFB Test Furnace. *A. Reidick and H. Kremer* 3309
Emissions of Nitrogen Oxides from Circulating Fluidized-Bed Combustors: Modeling Results Using Detailed Chemistry. *S. Goel, A. Sarofim, P. Kilpinen and M. Hupa* 3317
The NO and N_2O Formation Mechanism During Devolatilization and Char Combustion Under Fluidized-Bed Conditions. *F. Winter, C. Wartha, G. Löffler and H. Hofbauer* 3325
Nitrogen Chemistry in FBC with Limestone Addition. *A. Jensen, J. E. Johnsson and K. Dam-Johansen* 3335

Invited Topical Review

Scaling Characteristics of Aerodynamics, Heat Transfer, and Pollutant Emissions in Industrial Flames. *R. Weber* 3343

POROUS MEDIA, FIXED-BED COMBUSTION, AND FURNACES

Studies of Helmholtz Resonance in a Swirl Burner/Furnace System. *D. Froud, A. Beale, T. O'Doherty and N. Syred* 3355
The Effect of Heat Content and Composition of Fuel on Pulse Combustor Performance. *A. Kushari, L. J. Rosen, J. I. Jagoda and B.T. Zinn* 3363
Structures of Multiple Combustion Waves Formed Under Filtration of Lean Hydrogen-Air Mixtures in a Packed Bed. *A. V. Saveliev, L. A. Kennedy, A. A. Fridman and I.K. Puri* 3369
Superadiabatic Combustion Wave in a Diluted Methane-Air Mixture Under Filtration in a Packed Bed. *S. I. Foutko, S. I. Shabunya, S. A. Zhdanok and L. A. Kennedy* 3377
Modeling of Premixed Gas Combustion in Porous Media Composed of Coarse-Sized Particles: 1-D Description with Discrete Solid Phase. *O. S. Rabinovich, A. V. Feflov and N. V. Pavlyukevich* 3383

Index of Authors and Discussors 3391
Subject Index 3401

Twenty-Sixth Symposium (International) on Combustion/The Combustion Institute, 1996/pp. 1805–1816

INVITED TOPICAL REVIEW

GAS-PHASE COMBUSTION SYNTHESIS OF MATERIALS

K. BREZINSKY
Princeton University
Department of Mechanical and Aerospace Engineering
Princeton, NJ 08544, USA

To emphasize the scientific and technological challenges still remaining in combustion synthesis, this review highlights three classes of combustion processes for nonoxide refractory solids, especially ceramics, that involve the gas phase during synthesis. In one synthesis process, where the reactants are all gases, simultaneous control of powder particle size, size distribution, and microstructure is still an elusive goal but one that may be on the verge of achievement. A second class of process, gas-phase-assisted solid-solid combustion synthesis, reveals the often hidden role that gases play in facilitating and catalyzing the reactions that yield refractories and ceramics, and raises the prospect of tailoring reaction chemistry through judicious selection of additives. A third class of process, the much studied synthesis reaction between a gas and a condensed phase, demonstrates the need for an understanding of both equilibrium and kinetic processes to achieve microstructural control of solid product phases.

Introduction

The term, gas-phase combustion synthesis, often raises the image of a synthesis process in which all the reactants are gases. That image is consistent with many mature, industrial, gas-phase combustion processes, especially for the production of oxides such as TiO_2 and SiO_2 [1]. However, a broader interpretation of the term could allow it to include all combustion synthesis processes that involve the gas phase during some part of the synthesis. This broader view is used in this review as a context for examining the application of gas-phase combustion synthesis to the generation of nonoxide, refractory solids, especially ceramics. Nonoxide ceramics are defined as those inorganic compounds comprising metallic elements and the nonmetals carbon, nitrogen, phosphorous, and sulfur [2]. These covalent ceramic compounds, especially the nitrides and carbides, have been the subject of special symposia (see, for example, Ref. 3) because they are extremely hard, chemically resistant, and refractory—having higher melting points than their metallic constituents and, therefore, resistant to high-temperature environments that would damage materials made of metals or metal alloys [4]. Since these ceramic properties of high temperature, chemical resistance, and hardness are shared by many of the metal hydrides, borides, silicides, and selenides [5], these species can also be considered desirable products of gas-phase combustion synthesis. The synthesis of nonoxide refractories through such gas-phase methods is a much less developed area than the synthesis of oxides, and consequently, still offers a variety of fascinating scientific and technical challenges. In order to highlight these challenges, three classes of "gas-phase" combustion synthesis processes, especially for ceramics, are discussed: (1) the more traditional process exemplified by gas-gas reactions, such as between silane and hydrazine to produce silicon nitride; (2) solid-solid synthesis reactions catalyzed by chemical transport through the gas phase, such as the reaction between tantalum and carbon facilitated by the formation of TaI_5 gas; and (3) the self-propagating high-temperature synthesis (SHS) reaction between a gas and a condensed phase, exemplified by the reaction between nitrogen gas and titanium powder.

Gas-Gas Synthesis

Background

In this combustion process, the ceramic particles form directly from the gas phase through the self-sustaining reaction of gaseous species. Selection of the gas-phase environment to achieve control over particle size, shape, and composition is the primary challenge.

Control over particle characteristics is important since powders composed of small particles with a narrow size distribution and high purity are preferred for transforming a porous, powder-compacted structure into a dense, strong ceramic product by heat treatment [4,6,7]. The high-temperature transformation process of sintering has been shown to proceed at a rate inversely proportional to the initial particle radius; small particles, with diameters less than 1 μm, sinter faster. The driving force for the sintering of the particles is the decrease in free

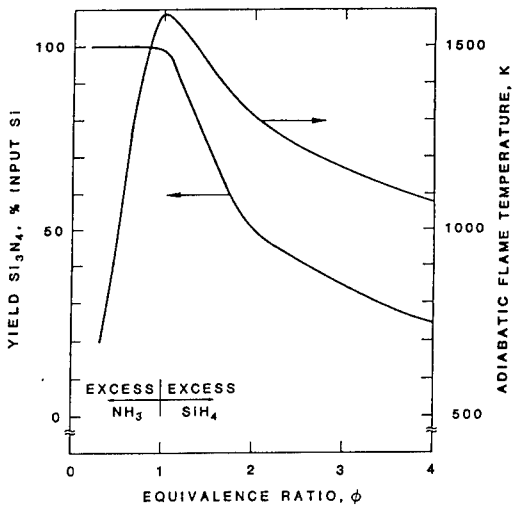

FIG. 1. Yield and adiabatic flame temperature for the reaction $3SiH_4$ and $4NH_3 \rightarrow Si_3N_4 + 12H_2$ at 100 kPa; $\phi = 4/3\ (SiH_4/NH_3)$ [8].

energy across the curved surfaces as the sintered particles join together. The joining forces can become very large when the radius of curvature is small, as it would be for small-diameter spherical particles, making them desirable for their increased rate of sintering. Also, small, spherical particles with a narrow diameter distribution can be packed together with a uniform pore size distribution and concentration that facilitates densification by sintering. The removal of pores is less successful if small-diameter particles form agglomerates which do not pack to give a uniformity of pores sizes. During sintering, the variation in pores leads to large holes and residual porosity, making it is essential, for complete densification, to avoid agglomeration. Also to be avoided are impurities which, by collecting at grain boundaries, interfere with grain boundary diffusion, leading to grain growth and sintering.

Given that the densification of powders is facilitated by small, uniform-diameter, spherical particles of high chemical purity, the goal of gas-gas combustion syntheses has been to provide these types of powders for further processing. Developers [8–10] of the most representative of gas-gas combustion processes, flame synthesis, argue that the sharp thermal gradient and controlled reagent concentrations existing in a flowing reactant mixture are conducive to the rapid reactions necessary for particle formation. Rapid reactions lead to the minimization of nucleation and growth times so that small particles with a narrow distribution of sizes could be achieved. This advantage of flames is offset by the coupling of reactant concentrations, thermodynamics, kinetics, and transport, which may constrain both the ability to sustain the synthesis process and the optimum conditions for high yield, purity, or particle size/morphology. Mitigation of the constraints is possible through the selection, as guided by thermodynamic calculations, of reactants and their relative concentrations, dilution, and pressure, and by the type of flame. In the following section, a selective review is given of some partially successful attempts at control within synthesis flames. The selective review will help define the additional research challenges that must be addressed before flames can be optimally configured as material synthesis high-temperature chemical reactors.

Partial Control

Flame synthesis control of particle size and shape of oxide particles, especially silica, has been the subject of many studies, with important insight into the theoretical and experimental aspects of premixed flame processes provided by Ulrich [11–14] and by Katz et al. [15,16] for counterflow diffusion flames. In both premixed and diffusion flames, the precursor to the oxide product is added as a dopant to the flame reactants. For the formation of nonoxide powders, a different but prototypical gas-phase combustion process has been described by Calcote and Felder at the 23rd Combustion Symposium [8]. In this process, which avoids oxygen entirely, gaseous premixed combinations of silane, ammonia, and hydrazine, all of which are contributors to the self-sustaining nature of the flame, are burned in a flat flame burner. The flame produces silicon nitride particles that are captured in the postflame region by entrainment in a hydrocarbon liquid spray.

Calcote et al. [8] demonstrated the value of thermodynamic calculations in selecting reactants for the control of product composition by mapping out the yield of Si_3N_4 and the adiabatic flame temperature for a range of equivalence ratios defined by the reactions

$$3SiH_4 + 4NH_3 = Si_3N_4 + 12H_2$$

$$3SiH_4 + 2N_2H_4 = Si_3N_4 + 10H_2$$

$$3SiH_4 + (4 - 2a)NH_3 + aN_2H_4 = Si_3N_4 + (12 - a)H_2,$$

where a is the hydrazine-ammonia ratio.

The results demonstrating the dependence of the yield and adiabatic flame temperature on various ratios of reactants are shown in Figs. 1 and 2. The calculations reveal that 100% conversion to silicon nitride is possible if an excess of ammonia is available and equilibrium is attained (Fig. 1). For the pure hydrazine system, the highest yields are obtained at equivalence ratios in which the hydrazine is in excess. A more practical combination of reactants that still provides high yields can be obtained with

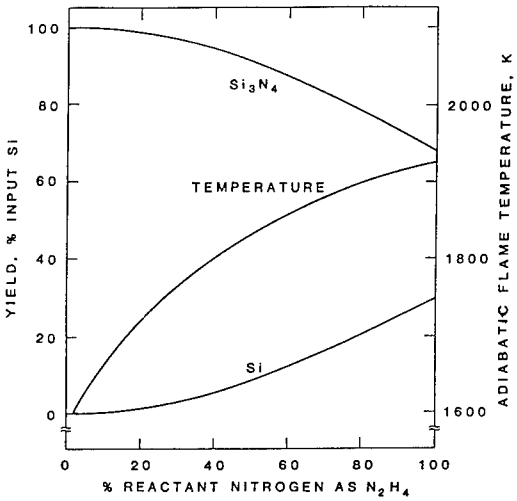

FIG. 2. Yield and adiabatic flame temperature for the reaction $3SiH_4 + (4\text{-}2a)NH_3 + aN_2H_4 \rightarrow Si_3N_4 + (12\text{-}a)H_2$. Stoichiometric mixtures at 100 kPa [8].

mixtures of hydrazine and ammonia, as revealed by Fig. 2.

The thermodynamics calculations, of course, do not reveal the time-dependent processes that affect particle morphology or microstructure. However, for those systems in which the kinetics are fast and equilibrium conditions are indeed attained, the thermodynamic calculations play a key role in the selection of both the combination of reactants and also their relative proportions. For the silicon nitride flame synthesis process, the thermodynamic values necessary for the calculation are readily available and afforded the clearly useful results indicated above. However, other reactant combinations suffer from a paucity of complete data, limiting the ability to calculate the formation of complex condensed phases, although some progress in adapting numerical techniques to do so has been achieved [17–20].

When the thermodynamic data are available and the adiabatic flame calculation is promising, other factors may determine if the flame can actually be sustained. Therefore, the promising combinations of silane, ammonia, and hydrazine as sources of silicon nitride were subjected to a series of static ignition bomb tests to establish if the thermodynamically determined ranges of operation were experimentally feasible. A surprising result of the tests was that the silane/ammonia mixtures that seemed to have the greatest potential as a nitride source could not be ignited over the pressure range of 10–1400 kPa and equivalence ratio range of 0.4–1.5. There was no obvious reason for this result and it highlighted a little studied but additional area of importance in flame synthesis: the conditions necessary for sustaining the synthesis flame. Further ignition experiments did reveal that mixtures containing hydrazine could be ignited and sustained, possibly because of its intrinsic exothermic decomposition.

The combination of thermodynamic calculations and ignition experiments were sufficient to define feasible flame synthesis conditions. Calcote et al. established synthesis flames for $SiH_4/NH_3/N_2H_4/N_2$ combinations that spanned an equivalence ratio range of 0.1–1. Flame temperatures ranged from 900 to 2000 K, and flame speeds were from about 20 to 150 cm/s. The silicon nitride initially formed at these conditions was an amorphous material that could be crystallized to a single alpha phase (see Ref. 4 for structure) by heating to 1870 K. Both the amorphous and crystalline product showed trace quantities of oxygen-containing silicon species. Primary particles were spherical and particle diameters were in the range of 10–50 nm. There was evidence of clustering of the primary particles but no indication of the strength of the bonding between the particles. Despite the wide range of equivalence ratios, temperatures, and flame speeds, the surprising conclusion reached was that there was no *obvious* controlling relationship between the experimental conditions and the product properties of phase, purity, size, and shape, although the achieved properties were desirable.

A flame process with the control of product composition as the goal was presented at the last Symposium by Gerhold and Inkrott [21]. The process differs from that of Calcote et al. [8] because the product, silicon carbide, was generated in a two-stage flame reactor. The primary stage of the reactor burned ethene and ethene/acetylene mixtures in oxygen, and in the secondary stage, tetramethyl silane carried by ethene was injected into the postflame region of the primary flame. Placement of the secondary stage injector in the burner assembly was optimized so as to minimize heat loss yet still maintain staging.

Using this two-stage flame configuration, the researchers focused their attention primarily on product composition as a function of overall equivalence ratio. Composition, calibrated against commercially available beta silicon carbide, was determined by powder X-ray diffraction, infrared absorption, and elemental analyses. These techniques revealed that the degree of conversion to silicon carbide was a sensitive and complex function of the total equivalence ratio that could not be accounted for simply through thermodynamic calculations. Measurements (Fig. 3), appeared to indicate that other factors, especially kinetics, influenced the observed yield. The influence of path-dependent irreversible kinetics was dramatized by operating the flame reactor both in one and two stages for the identical reactant concentrations. In two-stage operation, addition of tetramethyl silane produced silicon carbide, while in one-stage operation, silicon dioxide and

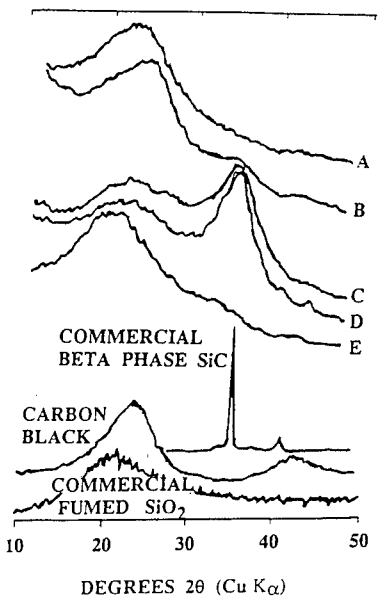

FIG. 3. X-ray diffraction patterns of produced powders collected during two-stage operation. The flame reactants are C_2H_4 and O_2 (0.61 gmol/min) with C_2H_4 sweep gas and TMS silicon reactant. The following summarizes the equivalence ratio (including silicon as SiO_2), C/O for the flame, C/O for the ceramic formation zone (including TMS and sweep gas): curve A, 4.0, 1.10, 1.31; curve B, 3.8, 1.02, 1.22; curve C, 3.4, 0.92, 1.10; curve D, 3.2, 0.85, 1.02; curve E, 2.9, 0.77, 0.93. Patterns of fine particle commercial beta-phase SiC, carbon black, and commercial fumed silica are shown for reference. The abscissa designation defines the scattering angle and the incident radiation (0.154 nm wavelength) [21].

carbon particles were formed. The authors argued that even though thermodynamic calculations predict that at the given temperature and gas composition silicon carbide formation was favored for both one- and two-stage operation, the formation of silicon dioxide in the one-stage operation was essentially irreversible on the time scale of the experiment.

It appears that the goal of achieving simultaneous control over particle size, size distribution, and morphology is not yet completely accomplished for nonoxide ceramics. For oxides, there has been considerably more success by varying initial conditions [11–16,22]. This may be due to the inherently different nature of the nucleation and particle growth process of oxides and nonoxides. The nucleation and growth of oxides produced from gas-gas flame processes have been ascribed to the formation of a monomer species that chemically resembles the final oxide composition. For example, SiO is the monomer for formation of silica particles, SiO_2 [23]. Control of monomer formation, its nucleation, and the growth of nuclei to larger particles has been demonstrated through variation of the monomer precursor, such as silane (SiH_4) that has been added as a dopant to the oxidizing flame [15,16,24]. The processes of nucleation and growth of oxide particles from the monomer in oxygen-containing flames has been amenable to relatively successful modeling [11,13,14,25–27]. A comparable understanding of nonoxide ceramics nucleation and particle growth does not appear to be available, in part because of a lack of comparable in-depth studies, in part because of the nature of the flames themselves (in most cases the precursors are the primary reactants, not dopants), and in part because the nucleation process may not proceed through the formation of a gas-phase monomer of the type found in many oxide-forming flames. For example, in a gas-gas synthesis for titanium nitride, the gas-phase reactions may first produce condensed titanium, and subsequent surface reactions with nitrogen gas may then lead to the nitride in a sequence that is very different from that in oxide-forming flames. Similar titanium nitride processes have already been ascribed to its formation by chemical vapor deposition [28]. Heterogeneous reaction processes of this type are very different from ones involving the condensation of monomer species, and consequently, understanding how to achieve simultaneous control over particle size, distribution, and morphology for nonoxides requires significant additional study. Achieving control, if possible, seems to be approachable at this time through phenomenological approaches. One such approach that has been successful at controlling agglomeration is based on metal exchange reactions.

Metal Exchange Reactions

Metal exchange reactions have been successfully used to produce commercially desirable nonceramics such as solar-grade silicon [29], have been demonstrated to be a feasible source of oxidation-resistant boron particles [34], and in the form of a classical thermite reaction have been used to produce oxide ceramics [35]. For the production of a nonoxide ceramic, a typical metal exchange reactions is

$$4Na + TiCl_4 + 1/2N_2 \rightarrow TiN + 4NaCl$$

This highly exothermic reaction generates enough heat that under the proper conditions it is self-sustaining. The proper conditions require careful selection of reactants which, again, can be screened with thermodynamic calculations [32]. For example, because the change in reaction entropy is small for these exchange reactions, the free energy of reaction is dominated by the reaction enthalpy. The reaction enthalpy is then a simple screening criterion for the selection of metals that will react spontaneously and

TABLE 1
Materials formed and reaction environment

Product	Environment constituent species	T_{flame} (K)
TiN	$TiCl_4$ and N_2	2450
TiB_2	$TiCl_4$ and BBr_3	2600
TiC	$TiCl_4$ and CCl_4	2950
$TiSi_2$	$TiCl_4$ and $SiCl_4$	[a]
SiC	$SiCl_4$ and CCl_4	2750
B_4C	BBr_3 and CCl_4	2700

[a]Flame temperatures were calculated using the NASA chemical equilibrium code. For $TiSi_2$, a convergent solution could not be obtained [32].

perhaps hypergolically with metal chlorides. The product of such a thermodynamically favored reaction is a high-temperature metal species, the one previously bound to the chloride, that is now available for subsequent reaction, often in the gas phase.

Glassman, Davis, and Brezinsky [32,33] have used the metal halogen chemistry described above to produce the refractories TiN, TiB_2, TiC, and $TiSi_2$. A variety of gaseous chlorides were used including $TiCl_4$, $SiCl_4$, and, for the carbide syntheses, CCl_4. Boron tribromide was used in the synthesis of TiB_2 and B_4C. A summary of these reactants is provided in Table 1.

As an example of the quality of product obtained from this type of exchange reaction process, the collected titanium nitride solid was composed of particles with diameters, as measured from selected scanning electron micrographs, of the order 100 nm or smaller. Particles within this size range are preferred for sintering but some less desirable large agglomerates on the order of a few microns were also found. Product purity as determined by X-ray diffraction measurements of the lattice parameter was excellent.

The advantages of higher temperatures suggest that a self-sustaining, high-temperature flame process may still be a more desirable route to the formation of high purity small powder particles if control over particle size and distribution is achievable. A flame technique that delivers both particle size and composition control has been reported by Dufaux and Axelbaum at the last Symposium [34]. This flame technique uses the well-known chemistry of the reaction of sodium with metal halides, as described above, to produce elemental titanium. In the presence of BCl_3, subsequent reaction produces TiB_2. By using a variation of the diffusion flame of Glassman et al. [33], this experiment not only permits the reactants to mix and react at the high temperature of a diffusion flame but also permits coating of the nanosized particles with the sodium chloride by-product to prevent agglomeration.

The burner utilized for the coating process has a coflow, annular configuration. External heating is used to vaporize the sodium but, in principle, the heat released from the flame could be used. The halides exit a central tube mix and then react with sodium vapor exiting from another tube separated from the first by a tube supplying only argon. The intermediate argon source is essential to the process since the reactants are hypergolic and, without the argon, particles near the base of burner would collect and interfere with the burner operation. The particles that form higher in the flow break through the flame top in a plume which can be sampled. The sampling reveals that the ceramic particles are sodium chloride coated by vapor released during the exchange reaction that has condensed on the particle surfaces in process described by the Kelvin equation [35]. When this condensation occurs, the particle sizes are of the order of ten nanometers. These highly desirable small particles can be cleaned of their encapsulating sodium chloride matrix by vacuum sublimation or washing with water or glycerin.

In the flame process of Dufaux and Axelbaum, the chemical reactions proceed unabated by the sodium chloride, as do the nucleation processes, whatever they may be. It is only after the nuclei have grown to nanometer size but before they collide to produce much larger particles that the precipitation of the coating interferes with the sticking and coalescence of two titanium or titanium diboride particles. Particles neither grow further in diameter nor agglomerate to form secondary structures of fused primary particles. Control of agglomeration is thus achieved.

Summary

Gas-gas combustion synthesis as epitomized by flame syntheses processes have clearly demonstrated the capability of yielding small-diameter, high-purity, high-yield refractory particles with narrow size distributions. Recent flame syntheses of crystalline silicon carbide and mixed silicon carbide/nitride powders [9,10] add further evidence to the potential of flame processes as a source of sinterable powder particles, if agglomeration can be avoided. Prevention of agglomeration and even oxidation appears possible with the advent of the self-coating process described above. The remaining, but nontrivial, challenge is to couple controlled and selected coating techniques with parametric control of nucleation and particle growth, so that spherical particles of a selected and adjustable diameter range can be synthesized without agglomeration.

Gas-Phase-Facilitated Solid-Solid Synthesis

Background

The antithesis of the gas-gas processes discussed above is solid-solid combustion synthesis. Aside from

the novelty of a combustion wave propagating in condensed media, this type of process has been the subject of study because of its potential for yielding dense, near-final-shape objects through self-sintering during the combustion process [5]. Nominally, the synthesis occurs when solid reactants are mixed and heated until reaction transpires. The enthalpy released by the reaction makes the further supply of external heat unnecessary and can lead to an adiabatic flame temperature higher than the melting temperature of one of the reactants. When this occurs, a liquid film of the melted reactant coats the solid particles of the other reactant. The liquid-phase coating facilitates transport of one reactant to the other, and the whole process proceeds at a faster rate than would be expected if diffusion transport among solids were the only form of mass transport. Combustion synthesis facilitated by the melting of the components has been treated in depth theoretically by Law and Makino [36,37].

The most intriguing aspect of solid-solid combustion synthesis occurs when the flame temperature is below the melting point of either reactant and of the products. The progress of the synthesis would then appear to depend on the solid-phase diffusion of reactants through their interfacial contact points. It has been argued [38] that solid-phase diffusion is so slow that nominally solid-solid reactions are actually facilitated by the presence of trace impurities such as adsorbed oxygen that actually create a gas-phase, catalytically assisted, combustion synthesis process. The facilitation of the synthesis process both by the presence of unintentionally present gas-phase-producing species, impurities, and by deliberately selected additives provides insight into product control strategies that capitalize on chemical transport reactions [39].

Trace Oxygen

Two relatively recent research efforts support the argument that trace species can catalytically enhance a self-propagating, high-temperature synthesis (SHS) process through gas-phase intervention.

The tantalum-carbon SHS process was the subject of a study by Merzhanov and coworkers [40] on the effect of an oxygen impurity contained in the tantalum (0.3% impurity by mass) and in the carbon (0.4 to 2 mass%). The working hypothesis was that this oxygen was released during the combustion synthesis process to form CO. The CO acted as a gas-phase transport agent as it diffused to the tantalum metal surface.

An examination by scanning electron microscopy of the TaC product demonstrated flaky, hollow shells of tantalum carbide that are similar to the hollow shells observed from the reactions of aluminum with oxygen and carbon dioxide and are associated with lower-temperature gas-phase syntheses. At higher temperatures, globule structures form. These microstructural observations raise the prospect of control of product morphology—a reoccurring goal of researchers working in combustion synthesis.

The study by Merzhanov et al. increases the appreciation of the role volatile oxides can play. A more complete thermodynamic and experimental study of the role of oxides, which may permit better control of product composition and particle morphology, was discussed by Kashireninov and coworkers at the 24th and 25th Combustion Symposia [38,41]. These researchers performed a complex set of equilibrium calculations for oxygen and the combinations molybdenum/boron, tungsten/boron, and tantalum/carbon. All these combinations in the absence of oxygen would, in principle, react in the solid-solid mode without melting of the reactants or products. For these reactant combinations, the calculations revealed that there were critical values of the partial pressure of oxygen for which the oxides of the reactants can play a major role in the gas-phase transport of one species to the other. For example, MoB(s) formation involving gas-phase oxides is shown to be possible through global equilibrated reactions such as

$$MoO_2(g) + B(s) = MoB(s) + O_2(g)$$

and

$$2B_2O_3(g) + 4Mo(s) = 4MoB(s) + 3O_2(g).$$

Similar reactions exist for the W/B and Ta/C systems. However, these reactions, though necessary, are not sufficient for the formation of MoB(s), since very low critical partial pressures of oxygen are required for the above reactions to be effective without the occurrence of back reactions that oxidize the MoB. Very low oxygen partial pressure implies that additional reactions that form a catalytic sequence are necessary for a high level of conversion. Subsequent experimental measurements [41] of the boron oxides vapor over the surface of a pressed sample of stoichiometrically mixed Mo and B confirmed that the solid-solid combustion synthesis of MoB in fact proceeds predominantly through the catalytic intervention of boron oxides.

The results described suggest that oxygen-containing additives deliberately introduced with the reactants may accelerate the combustion synthesis in a controlled manner.

Controlled Addition for Chemical Transport

The explicit catalytic role of non-oxygen-containing species deliberately added to enhance the combustion synthesis process has been addressed by Shtessel and coworkers [42,43]. In the catalytic process investigated by Shtessel, the gaseous additive reacts with a metal reactant to form a gaseous intermediate which is transported by diffusion to the

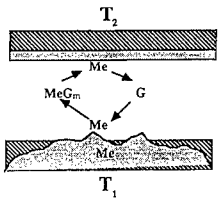

$$Me_{sol} + m/n\ G_{n\,gas} = Me\ G_{m\,gas}$$

$$T_1,\ T_2 < T_{melt}, T_{evap}$$

FIG. 4. Schematic representation of the gas-phase chemical transport reaction [61].

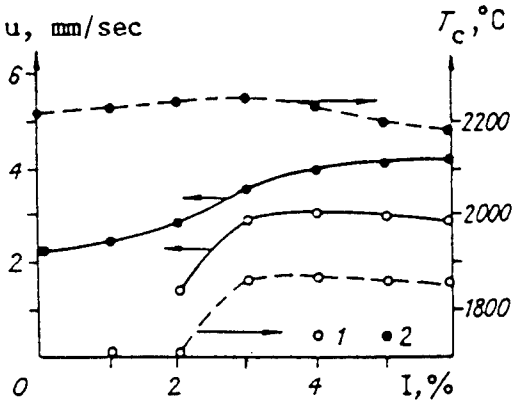

FIG. 5. Dependencies of the combustion velocity and temperature on the mass content of iodine in the systems 2Ta-C (1) and Ta-C (2) [42].

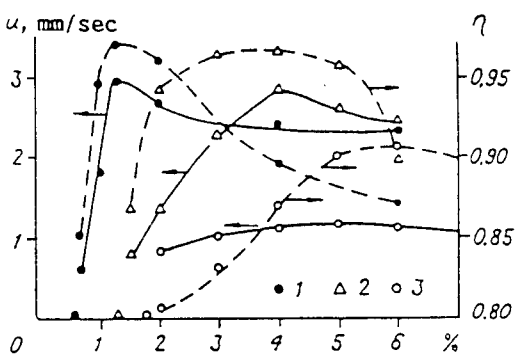

FIG. 6. Variation of the combustion velocity and the degree of conversion with the amount of carrier in the Nb-C system. Carriers: (1) C_2F_4, (2) C_6Cl_6, (3) I_2 [42].

other reactant surface. At the surface of the second reactant, the intermediate decomposes to regenerate the gaseous additive and to deposit the transported metal onto the particle surface. The process is represented schematically in Fig. 4. The direction of species transport will be determined primarily by the thermodynamics of the reaction. For the exothermic formation of the intermediate, transport will be from the lower temperature surface to the higher temperature one where heat will drive the endothermic decomposition. The temperature differential that drives the above process need not be only as depicted. As the combustion wave passes through the mixture, the gas-phase intermediate may form ahead of the thermal wave, and then decompose during the passage of the highest temperature portion. It is conceivable that the cycle of formation and decomposition could occur many times during the passage of the wave. The process would truly be a catalytic means of increasing the transport of one material to the surface of the other for greater extent and faster reaction.

Faster reaction, as manifested by an increase in flame speed, has indeed been demonstrated by Shtessel and coworkers. Tantulum and carbon, and niobium and carbon were chosen as test cases for gas-phase-facilitated combustion synthesis since neither of these systems will undergo any species melting at the adiabatic flame temperature. Mixtures of tantalum and carbon in both stoichiometric, 1:1, and nonstoichiometric, 2Ta and 1C, ratios were tested in the presence of added iodine. Without the iodine, 2Ta + C would not even sustain a combustion wave. In the presence of the easily volatilized iodine, the propagation velocity increased for both the stoichiometric and tantalum rich mixture as shown in Fig. 5. Similarly, the measured temperature increases with the addition of iodine, especially for the rich mixture. The transfer process responsible for the increase in velocity and temperature is presumed to be the reversible overall reaction

$$2Ta(solid) + 5I_{2(gas)} = 2TaI_{5(gas)}$$

since volatile carbon/iodine combinations would not exist at these conditions.

For the Niobium/C system, the effects of a variety of transfer agents on both the speed and degree of conversion are even more dramatic than those for the tantalum system. The additives C_2F_4, C_6Cl_6, and I_2 were introduced into the reacting mixture of stoichiometric combinations of niobium and carbon black. At temperatures in the range of 350–450 K the hexachlorobenzene and tetraflouroethylene decompose to release halogens that can enter into reaction with the niobium to form volatile compounds. The general, reaction is the same as above for tantalum and iodine except the halogens Cl_2, F_2, and I_2 are all available. The effect on flame speed is shown in Fig. 6. Even a small amount of tetraflouroethylene greatly increases the flame speed. The range of increases for all the reactants is approximately 1.5 to 5 for these conditions. The effect of additives on the extent of conversion is equally dramatic (Fig. 6). Both the tetraflouroethylene and the hexachlorobenzene bring the extent of conversion from approximately 85 to more than 95%.

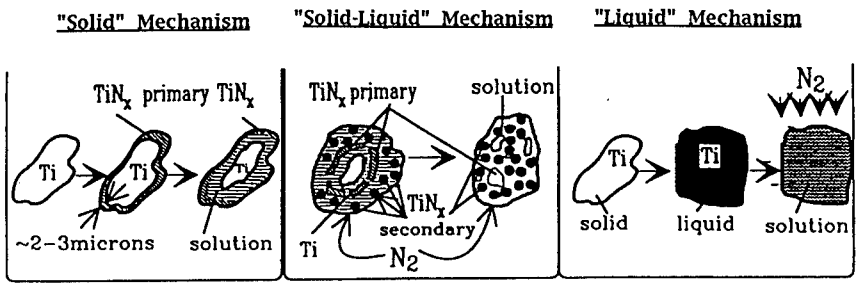

FIG. 7. Mechanisms of Ti-N interaction during SHS. (Adapted from Ref. 56)

Summary

The enhanced flame speed and conversion of "solid-solid" combustion synthesis in the presence of gas-producing additives is clear, as is the potential for control of product microstructure. Nevertheless, significant open-ended questions remain, among which, the most important are:

1. Can microstructure be controlled or even influenced?
2. How can additives be systematically selected, especially for the control of product morphology?
3. What are the detailed chemical mechanisms of the catalytic processes?
4. Does trapping of a trace amount of additive form an impurity in the product thereby reducing its quality?

Gas-Condensed-Phase Combustion Synthesis

Background

In this self-propagating, high-temperature synthesis (SHS) process, one of the reactants is recognizably a gas such as nitrogen or hydrogen, and the other reactant is initially a solid. The solid may melt during the course of the combustion synthesis process but because the adiabatic flame temperature is below the boiling point of the unreacted metal, the reactant will remain a liquid. These types of liquid-gas and solid-gas combustion synthesis processes are considered a type of SHS process and have been studied extensively. There is a vast literature on the subject, focusing mostly on the reaction of packed powders. This literature examines the conditions that influence the speed of propagation [44], the role of filtration of gas through a porous compact of metal powder [45–47], the influence of initial particle size on final product morphology [48], the retarding effects of melted reactant [45,49,50], the role of capillary action [45], thermodynamic constraints [51], and other issues as well [52–54]. Because of the wealth of literature already available and because some the critical issues are discussed in a companion article in this volume [55], only one of the most important issues that surround the subject will be profiled, and only briefly: the mechanism of conversion of the metal to a nitride or hydride.

Mechanisms

A discussion of this subject is facilitated by concentrating on the mechanism of nitrides formation because of the greater number of studies of these important compounds. Mukasyan and Borovinskaya [56] succinctly identify the challenge of understanding the mechanisms of nitride formation by reaction of nitrogen with different condensed-phase species. Depending on the choice of solid reactant, the combustion temperature can be higher or lower than the melting point of the solid. The phase of the condensed material affects the solubility of nitrogen in it, and the conditions that affect the melting of the reactant have implications for the mechanism and product composition. Potential variation in product composition can be illustrated with the titanium nitride phase diagram [57]. Titanium nitride can be formed with a wide range of nitrogen content, from roughly 28 to 50 atomic percent. The desirable product contains 50% nitrogen. Achieving this level of nitrogen in the product depends on the details of the mechanism of formation, as represented in Fig. 7 [56].

In the solid-state mechanism, which is characteristic of conditions that lead to only surface nitridation, the titanium does not get hot enough, because of heat loss, to melt. A time-resolved X-ray diffraction study of this nitridation process, shown in Fig. 8 [58], revealed that the nitrogen dissolves in the surface titanium to form a solid alpha solution. A structural change to a different solid solution, beta titanium, and the formation of titanium nitride follow. Saturation of the beta solution phase leads to further formation of titanium nitride and an alpha solid solution, all on the surface of the titanium. The nitride that forms will most likely not be stoichiometric, and a related study [50] indicated that the interior of the reacting solid is a low-nitrogen-content solid solution. The sequence of phase transitions

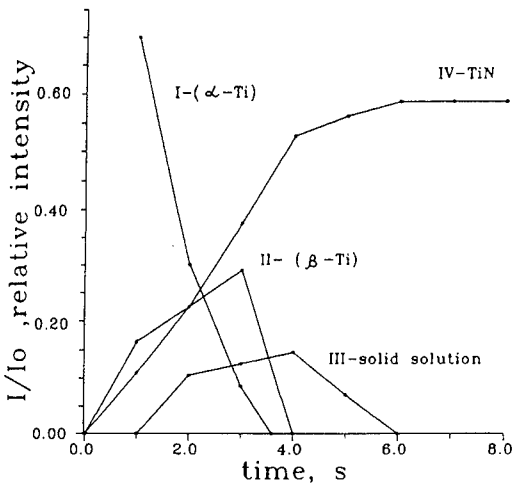

FIG. 8. Kinetic curves of phase formation during titanium combustion in nitrogen [58].

that were revealed by these studies cannot be explained by a reaction path along the titanium/nitrogen equilibrium phase diagram which clearly indicates that an understanding of the nonequilibrium temperature time history of the process, the kinetics, is critical to controlling the phase composition of the final product.

If the reaction between titanium and nitrogen is controlled so that heat is retained, then the underlying titanium melts. Any previously formed surface TiN cracks, allowing the liquid to spread, and the "solid-liquid" mechanism of Fig. 7 is followed. In this mechanism, the formation of a liquid titanium/nitrogen solution leads to encapsulation of the primary titanium nitride. The encapsulating liquid solution, as it becomes saturated with nitrogen, yields a secondary titanium nitride product which may have a different composition than the primary nitride. Subsequent quenching may create a three-phase system with a nonequilibrium mixture of nitrides of two different stoichiometries imbedded in a titanium/nitrogen solid solution. Again, knowledge of the kinetics of the process is required for composition control.

Under the most extreme conditions, the titanium undergoes significant melting [59] and the reaction proceeds primarily through a liquid solution mechanism. If equilibrium conditions can be maintained, then product composition can be predicted from the reaction path (the change in composition and temperature) followed across the phase diagram.

In some cases, the solubility of the gases in the transition metal leads to the formation of metastable states not predictable from equilibrium phase diagrams and to non-equilibrium synthesis processes not predictable from a reaction path analysis of the phase diagram. Such nonequilibrium synthesis processes have been revealed by real-time measurements during the passage of the combustion wave and have been found as well for "nongas" reactions such as for Ti-C, Mo-Si, and others [58,60].

Summary

This brief discussion of the mechanism of nitride formation through gas-condensed-phase combustion synthesis reveals that a knowledge of time-dependent processes is important and suggests that more of the mechanistic questions can be answered if combustion synthesis are subjected to more dynamic, time-resolved measurements.

Conclusions

The gas-phase combustion synthesis of materials, defined in this article to encompass three different modes of gas involvement in the production of nonoxide ceramics, can be a source, under separate sets of conditions, of submicron spherical particles, with a narrow size distribution, high purity, and well-defined composition. The challenge described in this article is to find a process and a set of conditions to provide particles with these characteristics simultaneously. To meet this challenge, it is first necessary, as revealed by the discussions of the three different gas-phase combustion synthesis processes, to develop an increased understanding of (1) particle nucleation and growth in flames so that particle size, shape and size distribution can be selected; (2) nucleation and growth of particle coatings for protection against agglomeration and oxidation; (3) the catalytic chemistry that accelerates the slow solid-solid synthesis process so that control of microstructure may be obtained; and (4) time dependent processes to determine regimes of equilibrium and kinetic control so that stable and metastable phases may be selected to give a tailored microstructure and composition.

Acknowledgments

The support of the National Aeronautics and Space Administration, Microgravity Materials Science program under grants NAG3-1418 and NAG 8-1261 is gratefully acknowledged.

REFERENCES

1. Rosner, D. E., *Class Notes—ChE/ME 622a: Combustion Synthesis and Materials Processing (CS/MP)*, Yale University Graduate School, New Haven 1995.
2. Shackelford, J. F., *Introduction to Materials Science for Engineers*, 3rd ed., Macmillan Publishing, New York, 1992.

3. Barron, A. R., Fischman, G. S., Fury, M. A., and Hepp, A. F. (Ed.), *Proceedings, Materials Research Society,* 1993, Vol. 327.
4. Chiang, Y.-M., Birnie, D. P., III, and Kingery, W. D., *Physical Ceramics, Principles for Ceramic Science and Engineering,* John Wiley & Sons, New York, 1997.
5. Merzhanov, A. G. and Borovinskaya, I. P., *Combust. Sci. Technol.* 10:195–201 (1975).
6. Kingery, W. D., Bowen, H. K., and Uhlmann, D. R., *Introduction to Ceramics,* 2nd ed., John Wiley & Sons, New York, 1960.
7. Readey, D. W., *Proceedings of the First International Conference on Advanced Synthesis of Engineered Materials,* (Moore, J. J., Lavernia, E. J., and Froes, F. H., Eds.), ASM International, Menlo Park, CA, 1993, pp. 109–117.
8. Calcote, H. F., Felder, W., Keil, D. G., and Olson, D. B., *Twenty-Third Symposium (International) on Combustion,* The Combustion Institute, Pittsburgh, 1990, pp. 1739–1744.
9. Keil, D. G., Calcote, H. J., and Gill, R. J., "AeroChem TP-540," *Mater. Res. Soc. Proc.* 410:161–166 (1996).
10. Keil, D. G., Calcote, H. J., and Gill, R. J., "AeroChem TP-540," *Mater. Res. Soc. Proc.* 410:167–172 (1996).
11. Ulrich, G. D., *Combust. Sci. Technol.* 4:47–57 (1971).
12. Ulrich, G. D., Milnes, B. A., and Subramanian, N. S., *Combust. Sci. Technol.* 14:243–249 (1976).
13. Ulrich, G. D. and Subramanian, N. S., *Combust. Sci. Technol.* 17:119–126 (1977).
14. Ulrich, G. D. and Riehl, J. W., *J. Coll. Interface Sci.* 87:257–265 (1982).
15. Chung, S.-L. and Katz, J. L., *Combust. Flame* 61:271–284 (1985).
16. Hung, C.-H. and Katz, J. L., *J. Mater. Res.* 7:1861–1869 (1992).
17. Kubaschewski, O., Alcock, C. B., and Spencer, P. J., *Materials Thermochemistry,* 6th ed., Pergamon Press, New York, 1993.
18. Lupis, C. H. P., *Chemical Thermodynamics of Materials,* North-Holland, New York, 1983.
19. Allendorf, M. D., Janssen, C. L., Colvin, M. E., Melius, C. F., Nielsen, I. M. B., Osterheld, T. H., and Ho, P., in *Process Control, Diagnostics, and Modeling* in *Semiconductor Manufacturing,* I, 95(2):393 (1995).
20. Allendorf, M. D., Melius, C. F., Ho, P., and Zachariah, M. R., *J. Phys. Chem.,* 99:15285–15293 (1995).
21. Gerhold, B. W. and Inkrott, K. E., *Combust. Flame* 100:144–152 (1995).
22. Zachariah, M. R., Chin, D., and Semerjian, H. G., *Combust. Flame* 78:287–298 (1989).
23. Zachariah, M. R. and Tsang, W., *Aerosol Sci. Technol.* 19:499–513 (1993).
24. Xing, Y., Koylu, U. O., and Rosner, D. E., *Combust. Flame* 107:85–102 (1996).
25. Xing, Y., Koylu, U. O., Tandon, P., and Rosner, D. E., *Proceedings of the Fifth World Congress of Chemical Engineering,* AIChE 5:43–48 (1996).
26. Zachariah, M. R. and Semerjian, H. G., *AIChE J.* 35(12):2003–2012 (1989).
27. Zachariah, M. R. and Dimitriou, P., *Aerosol Sci. Technol.* 13:413–425 (1990).
28. Larson, R. S. and Allendorf, M. D., *Proceedings of Thirteenth (International) Conference on Chemical Vapor Deposition* (Beman, T. M., Allendorf, M. D., Robinson, McD., and Ulrich, R. K., Eds.), Journal of Electrochemical Society Inc., Pennington, NJ, 1996, pp. 41–45.
29. Calcote, H. F. and Felder, W., *Twenty-Fourth Symposium (International) on Combustion,* The Combustion Institute, Pittsburgh, 1992, pp. 1869–1876.
30. Calcote, H. F., Gill, R. J., Berman, C. H., and Felder, W., AeroChem TP-493, *Proceedings of Third ONR Propulsion Meeting/Contractors Review* (Gabriel, R., Ed.), Middletown, RI, 1990.
31. Moore, J. J., *AIAA 31st Aero. Sci. Mtg. & Exhibit,* 1993, paper no. AIAA-93-0830.
32. Glassman, I., Davis, K. A., and Brezinsky, K., *Twenty-Fourth Symposium (International) on Combustion,* The Combustion Institute, Pittsburgh, 1992, pp. 1877–1882.
33. Davis, K. A., "A New Gas-Phase Combustion Synthesis Process for the Formation of Nanoscale Nonoxide Ceramic Powders," Ph.D. Thesis, Princeton University, Princeton, NJ, 1992.
34. Dufaux, D. P. and Axelbaum, R. L., *Combust. Flame* 100:350–358 (1995).
35. Seinfeld, J. H., *Atmospheric Chemistry and Physics of Air Pollution,* John Wiley & Sons, New York, 1986.
36. Makino, A. and Law, C. K., *Twenty-Fourth Symposium (International) on Combustion,* The Combustion Institute, Pittsburgh, 1992, pp. 1883–1891.
37. Makino, A. and Law, C. K., *Twenty-Fifth Symposium (International) on Combustion,* The Combustion Institute, Pittsburgh, 1994, pp. 1659–1667.
38. Kashireninov, O. E., Yuranov, I. A., and Fomin, A. A., *Twenty-Fourth Symposium (International) on Combustion,* The Combustion Institute, Pittsburgh, 1992, pp. 1899–1906.
39. Schafer, H., *Chemical Transport Reactions,* Academic Press, New York, 1964.
40. Merzhanov, A. G., Rogachev, A. S., Mukas'yan, A. S., Khusid, B. M., Borovinskaya, I. P., and Khina, B. B., *J. Eng. Phys.* 59:809–816 (1990).
41. Kashireninov, O. E. and Yuranov, I. A., *Twenty-Fifth Symposium (International) on Combustion,* The Combustion Institute, Pittsburgh, 1994, pp. 1669–1675.
42. Shtessel, E. A. and Dorozhevets, I. N., *Combust. Explos. Shock Waves* 26:52–59 (1990).
43. Kostogorov, E. P. and Dorozhevets, I. N., *Int. Self-Propagating High-Temp. Synth.* 1(1):55–63 (1992).
44. Merzhanov, A. G. and Borovinskaya, I. P., *Dokl. Phys. Chem.* 204:429–432 (1972).
45. Mukas'yan, A. S., Martynenko, V. M., Merzhanov, A. G., Borovinskaya, I. P., and Blinov, M. Y., *Combust. Explos. Shock Waves* 22:534–540 (1987).
46. Dandekar, H. W., Puszynski, J. A., and Hlavacek, V., *AIChE J.* 36(11):1649–1660 (1990).

47. Agrafiotis, C. C., Puszynski, J. A., and Hlavacek, V., *Combust. Sci. Technol.* 76:187–218 (1991).
48. Agrafiotis, C. C., Puszynski, J. A., and Hlavacek, V., *J. Am. Ceram. Soc.* 74(11):2912–2917 (1991).
49. Munir, Z. A., Deevi, S., and Eslamloo-Grami, M., *High Temp. High Pressures* 20:19–24 (1988).
50. Deevi, S. and Munir, Z. A., *J. Mater. Res.* 5(10):2177–2183 (1990).
51. Davis, K. A., Brezinsky, K., and Glassman, I., *Combust. Sci. Technol.* 77:171–178 (1991).
52. Hirao, K., Miyamoto, Y., and Koizumi, M., *Adv. Ceram.* 21:289–300 (1987).
53. Munir, Z. A. and Holt, J. B., *J. Mater. Sci.* 22:710–714 (1987).
54. Varma, A. and Lebrat, J.-P., *Chem. Eng. Sci.* 47(9–11):2179–2194 (1992).
55. Brezinsky, K., Brehm, J. A., Law, C. K., and Glassman, I., *Twenty-Sixth Symposium (International) on Combustion,* The Combustion Institute, Pittsburgh, 1996, pp. 1875–1881.
56. Mukasyan, A. S. and Borovinskaya, I. P., *Int. J. Self-Propagating High-Temp. Synth.* 1(1):55–63 (1992).
57. Wriedt, H. A. and Murray, J. L., *Bull. Alloy Phase Diagrams* 4(4):412 (1987).
58. Khomenko, I. O., Mukasyan, A. S., Ponomaryev, V. I., Borovinskaya, I. P., and Merzhanov, A. G., *Combust. Flame* 92:201–208 (1993).
59. Brehm, J. A., Jr., "Self-Propagating High-Temperature Synthesis of Titanium Nitride in Supercritical Nitrogen," M.S.E. Thesis, Princeton University, Princeton, NJ, 1995.
60. Merzhanov, A. G., Borovinskaya, I. P., Khomenko, I. O., Mukasyan, A. S., Ponomarev, V. I., Rogachev, A. S., and Shkiro, V. M., *Ann. Chim. Fr.* 20:123–138 (1995).
61. Shtessel, E., Exotherm Corporation, Camden, NJ, 1996.

COMMENTS

John W. Daily, University of Colorado, USA. How have time dependent composition measurements been carried out?

Author's Reply. The time dependent measurements were made by allowing the combustion synthesis event to take place within the x-ray diffractometer sampling chamber and obtaining spectra at sequential time intervals.

•

Prof. D. E. Rosner, Yale University, USA. Your emphasis on the use of the soluble coating technique (eg. NaCl(s) in the work of Axelbaum et. al.) to prevent nanoparticle aggregation may lead many readers to conclude that aggregates (formed by the coagulation of "primary" spherules) are to be avoided in most situations of industrial interest. But, even apart from applications like fumed silica additives for viscosity modification and carbon black for improving the properties of rubber tires, in which tenuous aggregates are actually desirable, there are many situations (eg., titania pigment production) in which aggregate formation is not a problem provided the *bond strength* between spherules is low enough to facilitate rupture in post-processing. For this reason the control of spherule bond strength, and the *morphological stability* of aggregates [1] are important issues in flame-synthesized nano-materials.

Your remarks on the sparcity of relevant phase-diagram information to help describe the equilibrium thermodynamics of multicomponent condensed materials brought to my mind the importance of adding at least a comment on the fact that nano-materials will normally have "shifted" or "unusual" phase diagrams (including the lowering of melting points) in view of the importance of *interfacial* free energies. This phenomenon, well-known in the field of supported metal alloy catalysis, evidentally influences the stability of even pure alumina aggregates in high temperature flames [2].

REFERENCES

1. Tandon, P. and Rosner, D. E., "Sintering Kinetics and Transport Property Evolution of Large Multi-particle Aggregates", *Chem. Eng. Communi.* (S. K. Friedlander issue), 1996, in press.
2. Xing, Y., Koylu, U. O., Tandon, P., and Rosner, D. E., "Measuring and Modelling the Synthesis and Morphological Evolution of Particles in Laminar Counterflow Diffusion Flames," *Proc. 5th World Congress of Chemical Engineering,* AIChE, Vol. V, July 1996, pp. 43–48.

Author's Reply. As you emphasize, it is the control of particle properties that is the major challenge in synthesis. In the case of aggregates, control over the bonds between particles and particle stability requires more examination.

As you point out, the unusual properties of nano-materials have been ascribed to the importance of interfacial free energies and their effect on the thermodynamics. This area too requires further examination.

•

H. F. Calcote. We have used a silane/acetylene flame to synthesize an extremely pure, white, crystalline silicon carbide powder with a particle diameter of 40 ± 7 nm (Keil, D. G., Calcote, H. F., Gill, R. J., Mat. Res. Soc. Proc. 410 (1996). In this work and in our synthesis of Si_3N_4 there was no real effort to determine the effect of flame conditions on product properties. Both products had excellent properties as produced.

The most important research opportunities in these systems are in developing an economically useful process. This means developing burner/product collection technologies for continuous operation, minimizing complications due to thermophoresis, buoyancy and agglomeration. In the more scientific realm, the challenge is to model a flame in which 90 wt% of the product is a solid powder and the remainder is hydrogen.

In hypergolic sodium vapor/metal halide mixtures, the reactions are very fast and the products are close to equilibrium. Separation techniques are the main challenge for making such processes practical. We have invented two such processes, both based upon expanding the combustion products in a supersonic nozzle to produce a supersonic stream that is caused to impact a surface producing a standing shock wave. This separates the product aerosol from gaseous sodium chloride to produce either a solid boule [1] or to collect a fine powder [2].

REFERENCES

1. Calcote, H. F. and Felder, W., *Twenty-Fourth Symposium (International) on Combustion,* The Combustion Institute, Pittsburgh, 1992, p. 869.
2. Felder, W., U.S. Patent 5, 183; 481, February 1993.

Author's Reply. Thank you for your informative comment.

Twenty-Sixth Symposium (International) on Combustion/The Combustion Institute, 1996/pp. 1817–1824

DIAMOND THIN FILM DEPOSITION IN LOW-PRESSURE PREMIXED FLAMES

D. G. GOODWIN, N. G. GLUMAC AND H. S. SHIN
Division of Engineering and Applied Science
California Institute of Technology
Pasadena, CA 91125, USA

A study of combustion synthesis of diamond films has been carried out using low-pressure, fuel-rich hydrocarbon/oxygen flames. Diamond growth results are reported for acetylene/oxygen, propylene/oxygen, and propane/oxygen flames. The best results are achieved with acetylene/oxygen flames, in which we have grown uniform, 5-cm-diameter polycrystalline films at up to 2.3 μm/h. The deposition rate in propane/oxygen is much lower (0.15 μm/h), and the diamond film quality is also lower.

The experimental results are compared to the predictions of a numerical model that includes both detailed flame chemistry and simplified diamond surface chemistry. The comparison of the experimental conditions with the simulation results shows that diamond growth occurs for stoichiometries where a small amount of hydrocarbon (<1%) is present at the substrate location, and the H/CH_3 ratio is of order 10. These conditions are quite similar to those found in other diamond chemical vapor deposition methods. Both experiment and simulation show that under some conditions oxidation of diamond can occur simultaneously with diamond deposition. However, oxidation is negligible for the best diamond film growth conditions.

The model correctly predicts the variation of film growth rate with changes in pressure, substrate temperature, and fuel type. For all flames, the absolute predicted growth rate is somewhat higher than measured, but the agreement is reasonable considering the modeling uncertainties associated with the high peak flame temperatures and incompletely understood diamond surface kinetics.

Introduction

Ever since the demonstration by Hirose and Mitsuizumi in 1988 [1] that diamond could be deposited using a simple oxygen-acetylene welding torch, combustion methods for diamond synthesis have attracted great interest. While the original method usually produces small, nonuniform deposits, by using multiple nozzles [2] or substrate-stabilized flat flames [3,4], uniform polycrystalline diamond films a few square centimeters in area may be grown at rates exceeding 20 μm/h at atmospheric pressure. However, these methods require very large flows of acetylene and oxygen and elaborate substrate cooling techniques.

An alternative approach to combustion synthesis of diamond films is to use a low-pressure flat flame [5–12]. While this results in a lower growth rate than achieved at atmospheric pressure, large area (~20 cm^2 [8]), uniform films are easily grown, and substrate temperature control is greatly simplified. Also, low-pressure flat flames are well-suited to diagnostics and modeling of combustion synthesis of diamond [13].

Some basic requirements of any technique to grow diamond films from the gas phase are the ability to supply the substrate with a large flux of atomic hydrogen (which plays important roles in the surface chemistry, including suppression of nondiamond sp^2 carbon deposition) and to provide a flux of hydrocarbons (particularly CH_3) as a carbon source, while maintaining a reducing environment to suppress diamond oxidation. In order to deposit a diamond film, rather than a graphitic or amorphous film, the carbon deposition rate must be small compared to the rate at which H impinges on the surface. In standard diamond chemical vapor deposition (CVD) reactors, which typically employ a dilute hydrocarbon/hydrogen gas mixture, diamond growth requires the H/CH_3 ratio at the substrate to be approximately 10 or greater [14–16].

For a combustion technique, these conditions can be satisfied by using a fuel-rich, presooting flame, which results in a reducing postflame environment with a small level of residual hydrocarbons. Using pure O_2 as the oxidizer results in a hot flame (>3000 K), leading to a high H flux at the substrate.

However, the gas-phase environment the substrate is exposed to in a flame differs significantly from a conventional diamond CVD environment in several respects. For example, it has been suggested that OH in a flame may play a role similar to H, creating surface radical sites and suppressing sp^2

carbon [17]. The high CO and H_2O levels might also conceivably alter the diamond surface chemistry.

In the present paper, we present a comparison of experimental diamond growth results we have obtained in several different low-pressure flames [6–8,10,18,19], with predictions of a numerical model which includes detailed flame chemistry and a surface mechanism known to describe diamond growth kinetics in noncombustion CVD environments. Despite the uncertainties inherent in the simulation, we find that the model is able to account semiquantitatively for the experimental diamond growth observations, and therefore we conclude that diamond growth chemistry in flames is essentially the same as that in other CVD environments.

For several of the cases discussed here (A, C, F), we have previously presented SEM images and Raman spectra of the diamond films [6,7,10]. A complete discussion of these experiments, including additional diagnostics and modeling of these flames is given in the reports by Glumac [18] and Shin [19].

Experimental

The experiments were carried out using a flat-flame burner contained in a water-cooled bell-jar vacuum chamber. The burner faces downward above a horizontal substrate [13], which consisted of a molybdenum plate or disk in most cases, although silicon wafers were also used.

The burner is designed for work with hot, premixed, fuel-rich hydrocarbon/oxygen flames, and is based loosely on the design of Bittner [20]. Most of the results discussed here were obtained with a water-cooled burner constructed from a 6-cm-diameter tellurium copper rod, with an 4-cm-diameter array of 1-mm-diameter holes spaced 2.5 mm apart in one end, through which the fuel/oxygen mixture flows. The earliest experiments (case A) were carried out in a different burner, which was limited to low flow rates by cooling limitations. For some experiments (case F), the flame area had to be reduced to 2 cm in diameter due to limitations of our mass flow controllers. This was done by attaching to the burner a faceplate with a smaller drilled area.

Electronic mass flow controllers meter the input gas flows to the burner, and the pressure is regulated with a feedback-controlled throttle valve in the exhaust line. Depending on flame conditions, the substrate is either heated or cooled to maintain the desired temperature. Heating is accomplished by passing current through the silicon wafer substrate or by using a resistively heated nichrome coil in the substrate holder. Cooling is provided by a helium flow in a narrow gap (~1 mm) between the back of the substrate and a water-cooled copper cooling block. The gap between the substrate and the cooling block can be varied during a run, and this capability was used to maintain a constant temperature in the initial period of film growth, as the substrate emissivity changed due to the diamond film deposition.

The substrate temperature was measured using a two-color pyrometer. Calibration against a thermocouple indicated a temperature uncertainty of approximately $\pm 35°C$.

In all experiments below 60 torr, the flame appeared visually flat, and little if any structure due to the individual holes in the burner face was obvious. However, in some of the higher-pressure runs (particularly at 180 torr) the flame appeared convoluted and the burner hole pattern was apparent in the film deposited on the substrate, indicating the presence of distinct jets impinging on the substrate. The burner was designed primarily for the lower pressure range; a more suitable burner for the higher pressures would require more tightly spaced, smaller holes.

Typically, each run lasted 5 h or longer. The diamond growth rate was estimated as the film thickness divided by the run duration, which may underestimate the true growth rate somewhat since it does not account for the time required for nucleation. The carbon film deposited was characterized by scanning electron microscopy and by Raman spectroscopy. A sharp line at 1332 cm^{-1} in the Raman spectrum is a clear signature of the presence of diamond in the sample.

Numerical Model

The numerical model we have developed is described in more detail elsewhere [13]. The model solves the continuity, radial momentum, energy, and species equations for axisymmetric flow in the gap between the burner and substrate for the limiting case of large D/L, where D is the burner (and substrate) diameter and L the burner/substrate separation. In this limit, a similarity solution holds for low Mach number, such that the temperature, axial velocity, and species profiles are functions only of axial distance [21,22]. This limit is approximately valid for our experiments, for which D/L is of order 4–6.

The conservation equations are solved in similarity form by first finite-differencing them, and then solving the resulting set of algebraic equations using the Sandia hybrid Newton/time-integration boundary-value-problem solver (TWOPNT [23]), refining the grid as necessary. The solution is found in a manner very similar to the Sandia premixed flame code [24]. All chemical and thermodynamic terms in the equations are evaluated using the Chemkin subroutine library [25], and all transport properties are evaluated using the package of Kee et al. [26] in the multicomponent formulation. Thermal diffusion is included, and is found to be important in the boundary layer above the substrate.

TABLE 1
Gas-phase reactions used in the propane and propylene simulations in addition to the 218 reactions of Miller and Melius [27][a]

	Reaction	A	n	E	Reference
(219)	$C_2H_5 + CH_3 \rightleftharpoons C_3H_8$	2.83 E 13	0.0	0.0	34
(220)	$H + C_3H_8 \rightleftharpoons H_2 + n\text{-}C_3H_7$	1.33 E 6	2.54	6756.0	35
(221)	$H + C_3H_8 \rightleftharpoons H_2 + i\text{-}C_3H_7$	1.3 E 6	2.4	4471.0	35
(222)	$O + C_3H_8 \rightleftharpoons OH + n\text{-}C_3H_7$	1.93 E 5	2.68	3716.0	35
(223)	$O + C_3H_8 \rightleftharpoons OH + i\text{-}C_3H_7$	4.77 E 4	2.71	2106.0	35
(224)	$OH + C_3H_8 \rightleftharpoons H_2O + n\text{-}C_3H_7$	3.16 E 7	1.8	934.0	36
(225)	$OH + C_3H_8 \rightleftharpoons H_2O + i\text{-}C_3H_7$	7.08 E 6	1.9	−159.0	36
(226)	$C_2H_4 + CH_3 \rightleftharpoons n\text{-}C_3H_7$	2.11 E 11	0.0	7353.0	34
(227)	$C_3H_6 + H \rightleftharpoons n\text{-}C_3H_7$	1.3 E 13	0.0	3261.0	37
(228)	$C_3H_6 + H \rightleftharpoons i\text{-}C_3H_7$	1.3 E 13	0.0	1560.0	37
(229)	$C_3H_6 + O \rightleftharpoons CH_3 + CH_3CO$	5.0 E 12	0.0	597.0	28
(230)	$C_3H_6 + OH \rightleftharpoons CH_3 + CH_3CHO$	7.0 E 12	0.0	0.0	28
(231)	$H + CH_3CHO \rightleftharpoons H_2 + CH_3CO$	4.0 E 13	0.0	4207.0	38
(232)	$O + CH_3CHO \rightleftharpoons OH + CH_3CO$	5.0 E 12	0.0	1792.0	38
(233)	$OH + CH_3CHO \rightleftharpoons H_2O + CH_3CO$	3.37 E 12	0.0	−616.0	39
(234)	$CH_3CO(+M) \rightleftharpoons CH_3 + CO(+M)$				
	High pressure limit	2.5 E 13	0.0	16382.0	40
	Low pressure limit	3.95 E 16	0.0	13753.0	40

[a]Rate constants are of the form $k = AT^n \exp(-E/RT)$. Units: cm^3, mol, s, cal.

The gas-phase mechanism must be capable of simulating fuel-rich, presooting flames ($\phi \approx 2$). For the acetylene/oxygen simulations, we use the rich flame mechanism of Miller and Melius [27] (218 reactions). For the propylene and propane flames, we add 16 reactions, listed in Table 1, to describe the oxidation of C_3H_8 and C_3H_6. These reactions are taken from Warnatz [28] but we use updated rate constants.

Surface chemistry is included in the model to simulate diamond film growth and oxidation, and is listed in Table 2. Reactions s1–5 are a reduced mechanism for diamond growth, which we have described elsewhere [13]. This reduced mechanism is a simplification of a CH_3 growth mechanism [29,30] which is known to reproduce experimental growth rates to within a factor of 2 over a range of two orders of magnitude.

Abstraction of surface H by OH is accounted for by reaction s6, with a rate constant estimated from that for the analogous gas-phase reaction [31] $OH + i\text{-}C_4H_{10} \rightarrow H_2O + t\text{-}C_4H_9$. Reactions s7 and s8 are global reactions that implement the oxidation rate of CVD diamond measured by Sun and Alam [32]. The oxidation rate expression they report is proportional to $[O_2]^{0.6}$. We include this nonintegral reaction order for this reaction only. Their data extend to 1073 K, requiring an extrapolation to higher temperatures. We estimate an uncertainty in the calculated oxidation rate of at least a factor of 2.

We do not include oxidation of the diamond film by OH or other species, since no rate data exists. We will return to this question later.

Results and Discussion

Diamond Growth

Diamond was successfully deposited for a variety of different flame conditions, summarized in Table 3. Case A is similar to the flame conditions of Cooper and Yarbrough [5], who first deposited isolated diamond particles in a low-pressure flame. Cases B–E are much hotter, higher-flow-rate acetylene/oxygen flames. Cases F and G have conditions that deposit diamond in propylene and propane flames, respectively.

Case A

Under the low-flow-rate conditions of case A, only isolated diamond particles could be grown [6]. The

TABLE 2
Reduced diamond surface mechanism[a]

	Reaction[b]	A	n	E
(s1)	$C_dH + H \rightarrow C_d^\circ + H_2$	7.8E13	0	7.3
(s2)	$C_d^\circ + H \rightarrow C_dH$	2.2E11	0.5	−2.1
(s3)	$C_d^\circ + CH_3 \rightarrow C_dM$	1.0E15	0	18.0
(s4)	$C_dM + H \rightarrow C_dM^\circ + H_2$	2.8E7	2.0	7.7
(s5)[c]	$C_dM^\circ + H \rightarrow C_dH + H_2$	1.E17	0	0
(s6)	$C_dH + OH \rightarrow C_d^\circ + H_2O$	5.73E10	0.51	0.064
(s7)[d]	$C_dH + O_2 \rightarrow CO_2 + C_dH$	2.1E16	0	54.7
(s8)[d]	$C_d^\circ + O_2 \rightarrow CO_2 + C_d^\circ$	2.1E16	0	54.7

[a]The surface site density is assumed to be 3×10^{-9} moles/cm^2. Rate constants are of the form $k = AT^n \exp(-E/RT)$. Units: cm^3, mol, s, kcal.

[b]C_dH denotes a chemisorbed surface hydrogen, C_d° an open surface radical site, C_dM a surface methyl group, and C_dM° a surface methylene group.

[c]Rate chosen to be large enough that (s4) is rate limiting.

[d]0.6 reaction order in O_2 [32].

TABLE 3
Experimental conditions for which diamond deposition was observed[a]

Case	Fuel	P (torr)	V_u (m/s)	L (cm)	T_s (°C)	Fuel/oxygen	Growth rate (μm/h)	Notes
A	C_2H_2	40	2.2	0.8	965	0.71–0.77	0.3	b
B	C_2H_2	52	4.6	1.0	850	0.86	1.0	c
C	C_2H_2	52	4.6	1.0	800	0.86	0.6	c
D	C_2H_2	30	8.3	1.0	800	0.84	1.5	c
E	C_2H_2	30	8.3	1.0	870	0.84	2.3	c
F	C_3H_6	180	2.6	0.425	800	0.47	0.9	d
G	C_3H_8	90	1.6	1.05	700	0.42	0.15	e

[a]V_u is the unburned gas velocity, L is the substrate/burner separation, and T_s is the substrate temperature.

[b]Isolated particles

[c]High quality continuous film

[d]Nonuniform film

[e]Low quality continuous film

deposits were similar to those reported by Cooper and Yarbrough [5], except that we were able to achieve a uniform nucleation density due to the stagnation flow geometry. Diamond deposition required bringing the substrate very close to the edge of the luminous flame, 7–9 mm from the burner. Moving the substrate to 6 mm resulted in flame extinction, and moving it further away led only to nondiamond carbon deposition.

Faceted diamond was deposited only in a narrow stoichiometry window that depended on burner/substrate distance [18]. The diamond particles deposited exhibit etch pits characteristic of diamond that has been partially oxidized. For slightly leaner flame conditions ($C_2H_2/O_2 = 0.71$, $\phi = 1.78$), no deposition occurred, and the silicon substrates appeared oxidized after the run. For slightly richer conditions ($C_2H_2/O_2 = 0.83$, $\phi = 2.1$), a carbon film was deposited, but it had no diamond content detectable by Raman spectroscopy. These results suggest that oxidation is occurring simultaneously with carbon deposition under these diamond deposition conditions.

Attempts were made to allow the isolated diamond particles to grow together in long-duration runs. However, the diamond quality inevitably degraded as the film became continuous. We interpret this as due to depletion of atomic hydrogen, since the recombination coefficient of H on diamond is higher than that on silicon or silicon dioxide.

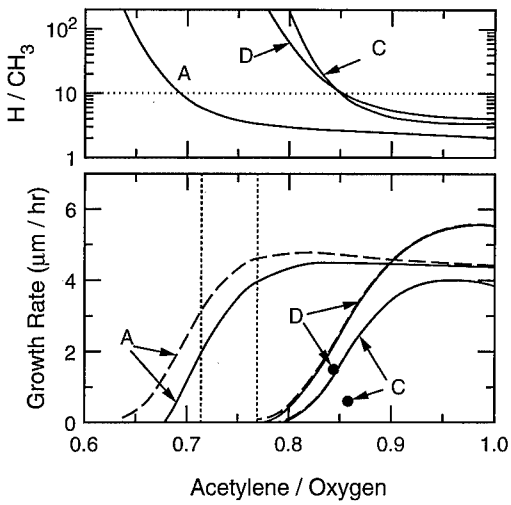

FIG. 1. Model predictions for growth rate and H/CH_3 ratio compared to experiment for cases A, C, and D. Calculations are done both using full surface mechanism (solid curves) and neglecting diamond oxidation (dashed curves). Filled circles, experimental growth rates for cases C and D; shaded region, stoichiometry range for diamond particle deposition for case A.

Cases B–E

The high-flow-rate acetylene/oxygen flames (cases B–E) proved much better suited to diamond film growth, and large-area continuous films could be routinely grown [7,8]. The mass flow rate for all of these cases was close to 0.02 g/cm²/s, only a factor of 2–3 below the mass flow rate calculated for an adiabatic, freely propagating flame.

For the runs at 52 torr, diamond films were deposited on molybdenum substrates that were essentially the same diameter as the flame (4 cm). At 30 torr, the deposition was done on 5-cm-diameter disks and the diamond film completely covered the top of the disk, extending somewhat beyond the burner diameter. In all cases where large-area films were grown, the film thickness was very uniform, typically ±3%, due to the stagnation flow geometry. No evidence of diamond oxidation was observed on any of the films deposited under these conditions.

Cases F and G

For case F at 180 torr, the flame was convoluted, as already discussed. The best diamond was generally deposited directly below the burner holes. This may be due to the flame front being closest to the substrate at these points. High-quality, continuous diamond films were deposited in small regions on the molybdenum substrate [10].

The propane/oxygen conditions (case G) resulted in a large-area, continuous, uniform polycrystalline film. The crystallites, approximately 0.5–1.0 μm in size, are less sharply defined than expected for high-quality diamond. The diamond peak in the Raman spectrum is weak, but distinctly observable above the amorphous carbon background [19]. The polycrystalline morphology indicates this film is primarily sp^3 diamond, but sp^2 carbon is present as well.

Simulation Results

Cases A–E

The model predictions for the diamond growth rate and H/CH_3 ratio at the substrate are shown in Fig. 1 for the conditions of cases A, C, and D, except that the acetylene/oxygen ratio is allowed to vary from 0.6 to 1.0 (ϕ = 1.5 to 2.5). The simulations were done with both the full surface mechanism (solid curves) and neglecting diamond oxidation (dashed curves). Since the growth rate is assumed to be first order in CH_3, for a given substrate temperature the growth rate neglecting oxidation is simply proportional to the methyl concentration at the surface.

Considering first cases C and D (both at 800°C), the results show that the experimental diamond growth conditions correspond to conditions where hydrocarbons just barely survive to the substrate. For case C, the calculated acetylene mole fraction (the predominant hydrocarbon) at C_2H_2/O_2 = 0.86 is 0.25%, while for case D it is 0.37%. These results are very reasonable in light of the standard gas composition of < 1% hydrocarbon in H_2 for diamond CVD in other environments.

For both cases C and D, the predicted H/CH_3 ratio is of order 10 at the experimental growth conditions, and the oxidation rate is insignificant. Both the simulation and experiment show that the 30-torr flame produces a higher growth rate than the 52-torr flame. This results since both have essentially the same mass flow rate, leading to a higher velocity and flame temperature (3892 K for case D vs. 3420 for case C) for the lower pressure case. This in turn results in more H delivered to the substrate (2.86×10^{-9} mol/cm³ for case D; 1.75×10^{-9} mol/cm³ for case C) despite the lower pressure.

The absolute calculated growth rate is higher than that measured, but considering the uncertainties in diamond surface kinetics, the predicted CH_3 concentration, and the experimental induction time, the agreement is reasonable. The simulations indicate that the chemical environment the substrate is exposed to under these conditions is very similar to conventional plasma or hot-filament diamond chemical vapor deposition conditions. Diamond film growth in these flames can therefore be accounted for in terms of the standard picture of diamond CVD.

For richer flame conditions, the calculated growth

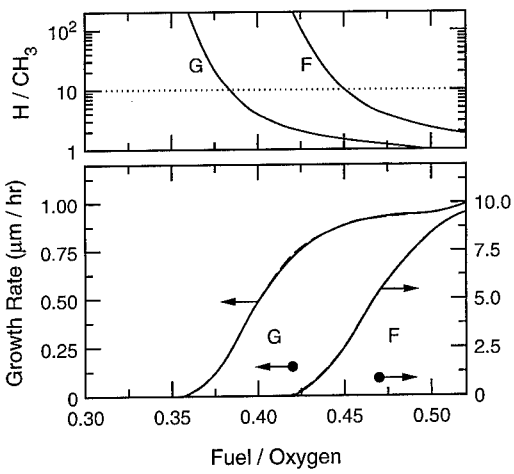

FIG. 2. Model predictions for growth rate and H/CH_3 ratio compared to experiment for cases F and G. Calculations are done both using full surface mechanism (solid curves) and neglecting diamond oxidation (dashed curves). Filled circles, experimental growth rates.

rate saturates as the methyl concentration levels off and heavier hydrocarbons are formed. The H/CH_3 ratio falls to a level of 2–3, insufficient to suppress sp^2 carbon deposition required to maintain diamond growth. The simulations thus predict that richer flames will result in nondiamond carbon films, in agreement with experiment.

If chemical equilibrium existed in the postflame gas at the substrate, no hydrocarbons would be present for acetylene/oxygen ratios below 1.0. The appearance of hydrocarbons at the substrate for the C/D conditions at $C_2H_2/O_2 \approx 0.8$ is therefore due to kinetics, and the agreement between model and experiment is an indication that the model is at least semi-quantitatively-correct.

Cases B and E differ from C and D, respectively, only in substrate temperature. The calculated growth rate ratio at 52 torr $G_B/G_C = 1.5$ is essentially identical to the measured ratio of 1.7. For cases D and E at 30 torr, the calculated ratio $G_E/G_D = 1.9$, while the measured ratio is 1.5.

The simulations for case A show, not surprisingly, that this flame is significantly different than the flames of cases B–E. The case A flame is highly burner stabilized, with a mass flow rate 13 times lower than the calculated value for an adiabatic freely propagating flame (0.046 g/cm²/s). The calculated peak flame temperature is 2076 K, which agrees well with temperature profile measurements we have recently reported using OH LIF in a flame very similar to this one [13].

In this much cooler flame, oxidation kinetics are slower and some hydrocarbons survive to the substrate position even at $C_2H_2/O_2 = 0.7$ ($\phi = 1.75$). Under these conditions, there is still enough oxygen present (10^{-4} mole fraction at $C_2H_2/O_2 = 0.75$) to result in significant diamond oxidation. The H/CH_3 ratio is well below 10 throughout the range where isolated diamond particle deposition is observed. However, the simulation assumes a diamond surface, in contrast to the experimental situation of isolated particles on a silicon substrate. The level of H at the diamond particle surface may have been greater than that calculated, due both to the lower recombination rate on silicon, and to the enhanced diffusive transport of H to the small diamond nuclei. It is also possible that oxygen is playing an enabling role under these conditions, assisting H in suppressing sp^2 carbon deposition.

The simulation predicts a lean boundary for diamond growth under case A conditions of $C_2H_2/O_2 = 0.68$. The experimental boundary is closer to 0.72, but the uncertainties in both the oxidation and diamond growth kinetics could easily account for this difference.

Cases F and G

The simulation results for cases F and G are shown in Fig. 2. The comparison to experiment can be made only qualitatively, since for case F the flame and diamond film are nonuniform, while for case G the film quality is low.

For case F, the simulations suggest that $H/CH_3 = 10$ occurs at a C_3H_6/O_2 ratio of 0.45, at which point the growth rate should be ~2 μm/h. The experimental C_3H_6/O_2 ratio for diamond growth was 0.47. The qualitative trend is the same as for the acetylene/oxygen cases: diamond film deposition occurs when residual hydrocarbons are present in dilute amounts at the substrate, adequate H is present, and the oxygen concentration is low enough that film oxidation is negligible.

The simulations predict that H/CH_3 is only 2–3 under the case G experimental conditions. This is consistent with the low film quality observed. By moving to a slightly leaner flame ($C_3H_8/O_2 = 0.38$), it appears possible to achieve an H/CH_3 ratio adequate for high-quality diamond growth. However, the growth rate would be expected to fall by a factor of 3–4 from the already low experimental value of 0.15 μm/h. It is likely that this could be increased somewhat by using a substrate temperature closer to 800°C, but it still appears unlikely that propane/oxygen flames will be an attractive environment for diamond film deposition.

Effects of OH

Although we include the possibility of OH contributing to surface radical site production, in practice, the OH concentration at the surface is too low for this to be important. For example, for case D, which had one of the highest OH mole fractions at

the surface other than case A, the radical surface site coverage with reaction s6 is 0.1175, while without this reaction it is 0.1157. We conclude that OH does not appreciably contribute to surface activation for these conditions.

While we do not include diamond oxidation by OH, we can estimate an upper bound on the rate. For case D, the OH mole fraction at the surface is 5.6×10^{-5}, and no evidence of oxidation is apparent in the film morphology. If we assume that the OH oxidation rate is at most one-tenth the measured growth rate, then the number of carbons removed per incident OH is at most 2×10^{-3}.

Superadiabatic flame temperatures

For all of the flames except cases A and G, the peak flame temperature is predicted to be greater than the adiabatic flame temperature. For cases C, D, and F, the peak calculated temperatures are 3420, 3892, and 2986 K, compared to their respective adiabatic flame temperatures of 3012, 2941, and 2739 K. These temperature overshoots result from the high level of thermal dissociation (particularly the high atomic hydrogen level) at the final equilibrium state. Since slow, pressure-dependent reactions such as

$$H_2 + M \rightarrow H + H + M \qquad (1)$$

are required to achieve this equilibrium dissociation level in the postflame region, the temperature overshoots the equilibrium value and then decays as H is produced beyond the flame. Similar (but smaller) temperature overshoots have been predicted [22] and verified experimentally [33] in atmospheric-pressure, substrate-stabilized acetylene/oxygen flames.

Summary and Conclusions

A study of diamond film deposition in low-pressure hydrocarbon/oxygen flames has been presented. Comparison of experimental results with a detailed model clearly shows the flame conditions needed for diamond deposition. Good diamond films may be grown for conditions where the H/CH_3 ratio is of order 10 at the substrate, which in turn requires a low residual hydrocarbon level (<1%). Under conditions well-suited to high-quality diamond deposition, no effects of oxidation are observed or predicted, although for cases where diamond growth is otherwise marginal, oxygen may play an enabling role. In general, these results are in good agreement with standard ideas and growth mechanisms for diamond CVD in other environments.

Acknowledgments

Financial support from the National Science Foundation and the Naval Research Laboratory is gratefully acknowledged.

REFERENCES

1. Hirose, Y. and Mitsuizumi, M., *New Diamond* 4:34 (1988).
2. Ravi, K. V., Koch, C. A., and Olson, D., *Proc. 2nd Int. Conf. Appl. Diamond Films and Related Materials*, MYU, Tokyo, 1993, p. 491.
3. Murayama, M. and Uchida, K., *Combust. Flame* 91:239 (1992).
4. McCarty, K. F., Meeks, E., Kee, R. J., and Lutz, A. E., *Appl. Phys. Lett.* 63:1498 (1993).
5. Cooper, J. A., Jr. and Yarbrough, W. A., *Diamond Optics III, SPIE Proceedings*, SPIE, Bellingham, Washington, 1990, Vol. 1325, p. 41.
6. Glumac, N. G. and D. G. Goodwin, *Thin Solid Films* 212:122 (1992).
7. Glumac, N. G. and Goodwin, D. G., *Mater. Lett.* 18:119 (1993).
8. Shin, H. S., Glumac, N. G., and Goodwin, D. G., *Proc. 4th Intl. Conf. New Diamond Science and Technology*, Materials Research Society, Pittsburgh, 1995, p. 27.
9. Harris, S. J., Shin, H. S., and Goodwin, D. G., *Appl. Phys. Lett.* 66:891 (1995).
10. Shin, H. S. and Goodwin, D. G., *Appl. Phys. Lett.* 66:2909 (1995).
11. Kim, J. S. and Cappelli, M. A., *Appl. Phys. Lett.* 65:2786 (1994).
12. Kim, J. S. and Cappelli, M. A., *J. Mater. Res.* 10:149 (1995).
13. Glumac, N. G. and Goodwin, D. G., *Combust. Flame* 105:321 (1996).
14. Hsu, W. L., *Appl. Phys. Lett.* 59:1427 (1991).
15. Hsu, W. L., *J. Appl. Phys.* 72:3102 (1992).
16. Harris, S. J. and Weiner, A. M., *J. Appl. Phys.* 75:5026 (1994).
17. Hiroso, Y., Amanuma, S., and Komaki, K., *J. Appl. Phys.* 68:6401 (1990).
18. Glumac, N. G., Ph.D. Thesis, California Institute of Technology, Pasadena, CA, 1994.
19. Shin, H. S., Ph.D. Thesis, California Institute of Technology, Pasadena, CA, 1995.
20. Bittner, J. D., Ph.D. Thesis, Massachusetts Institute of Technology, Cambridge, MA, 1981.
21. Kee, R. J., Miller, J. A., Evans, G. H., and Dixon-Lewis, G., *Twenty-Second Symposium (International) on Combustion*, The Combustion Institute, Pittsburgh, 1988, p. 1479.
22. Meeks, E., Kee, R. J., Dandy, D. S., and Coltrin, M. E., *Combust. Flame* 92:144 (1993).
23. Grcar, J. F., Report No. SAND91-8230, Sandia National Laboratories, 1985.
24. Kee, R. J., Grcar, J. F., Smooke, M. D., and Miller, J. A., Report No. SAND85-8240, Sandia National Laboratories, 1985.
25. Kee, R. J., Rupley, F. M., and Miller, J. A., Report No. SAND89-8009, Sandia National Laboratories, 1989.
26. Kee, R. J., Dixon-Lewis, G., Warnatz, J., Coltrin, M. E., and Miller, J. A., Report No. SAND86-8246, Sandia National Laboratories, 1986.

27. Miller, J. A. and Melius, C. F., *Combust. Flame* 91:21 (1992).
28. Warnatz, J., *Eighteenth Symposium (International) on Combustion,* The Combustion Institute, Pittsburgh, 1981, p. 369.
29. Harris, S. J., *Appl. Phys. Lett.* 56:2298 (1990).
30. Harris, S. J. and Goodwin, D. G., *J. Phys. Chem.* 97:23 (1993).
31. Tsang, W., *J. Phys. Chem. Ref. Data* 19:1 (1990).
32. Sun, Q. and Alam, M., *J. Electrochem. Soc.* 139:933 (1992).
33. Bertagnolli, K. E. and Lucht, R. P., *Twenty-Sixth Symposium (International) on Combustion,* The Combustion Institute, Pittsburgh, 1996, p. 1825–1833.
34. Baulch, D. L., Cobos, C. J., Cox, R. A., Esser, C., Frank, P., Just, Th., Kerr, J. A., Pilling, M. J., and Troe, J., *J. Phys. Chem. Ref. Data* 21:411 (1992).
35. Tsang, W., *J. Phys. Chem. Ref. Data* 17:887 (1988).
36. Cohen, N., *Int. J. Chem. Kinet.* 23:397 (1991).
37. Tsang, W., *Ind. Eng. Chem.* 31:3 (1992).
38. Warnatz, J., *Combustion Chemistry,* Springer-Verlag, New York, 1984, p. 197.
39. Atkinson, R., Baulch, D. L., Cox, R. A., Hampson, R. F., Jr., Kerr, J. A., and Troe, J., *J. Phys. Chem. Ref. Data* 21:1125 (1992).
40. Benosura, A., Knyazev, V. D., Slagle, I. R., Gutman, D., and Tsang, W., *Ber. Bunsenges. Phys. Chem.* 96:1338 (1992).

COMMENTS

Jerry Finlinson, NAWL, USA. In these experiments you quote a substrate surface temperature near 1100 K. How is it measured and what is the accuracy of the measurement? Does the temperature change significantly when diamond is coating the surface? Is it possible to measure temperature on surface of diamond film after formation begins?

Author's Reply. The temperature was measured using a two-color pyrometer; we estimate an uncertainty of +/− 35 K. If no cooling is provided, the substrate temperature initially overshoots the final steady-state value, since the initial substrate emissivity is much lower than that obtained once a diamond film is present. We varied the helium-jet cooling in real time to minimize the temperature overshoot. Techniques exist to measure the diamond film temperature directly, such as Stokes/Anti-Stokes Raman Scattering. However, this is far from a straightforward measurement and may have experimental uncertainties at least as large as pyrometry. For deposition on massive substrates (e.g. thick molybdenum disks) perhaps the most accurate technique would be simply to instrument the substrate with multiple embedded thermocouples, from which the surface temperature and substrate heat flux could be inferred.

•

Jay Jeffries, SRI International, USA. What produces the rapid drop of OH concentration near the surface? Does surface chemistry of OH play an important role or does the OH concentration simply follow the rapid drop of atomic hydrogen in an attempt to maintain a steady state?

Author's Reply. Both gas-phase and surface chemistry contribute to the drop in OH near the substrate. For example, for the Case D experimental conditions, if surface reaction (s6) is neglected, the predicted OH mole fraction at the surface is a factor of 5 higher than the value obtained when this reaction is included (5.6×10^{-5}). However, the OH profile is affected by surface chemistry only within 0.5 mm of the substrate. Further away (out to 2 mm from the substrate), the decay in OH is closely coupled to the decay of H, primarily through $OH + H_2 \rightleftharpoons H + H_2O$, which is close to partial equilibrium.

•

Katharina Kohse-Höinghaus, Universitat Bielefeld, Germany. What is the role of nucleation in your system? Do you have experimental evidence for this phase of growth? How does the model account for nucleation? Do you grow basically on diamond for that?

Author's Reply. Our substrates are pretreated by polishing them with diamond grit to provide nuclei and allow film growth without a significant induction time. We do not explicitly account for nucleation, which, as stated in the paper, introduces some small uncertainty in the experimental diamond growth rate. The model assumes the existence of a flat, continuous diamond surface. While this is an oversimplification, we feel that it is adequate considering the uncertainties associated with the calculated species concentrations at the surface and the diamond growth kinetics, both of which are uncertain by a factor of at least 2 or 3.

•

Bernhard Ruf, University Heidelberg IWR, Germany. What reactions are involved in the surface oxidation mechanism and do oxygen atoms play a role in that mechanism?

Author's Reply. The surface oxidation mechanism is a global one, which only seeks to implement the experimental oxidation rate measured in Ref. 32. Since the oxidation rate was measured in heated O_2, the atomic oxygen level was presumably negligible. In environments with higher O levels, such as a flame, the oxidation rate may be higher. However, there is no experimental data on oxidation of diamond by O (or OH) and this was therefore not included in the model.

Twenty-Sixth Symposium (International) on Combustion/The Combustion Institute, 1996/pp. 1825–1833

TEMPERATURE PROFILE MEASUREMENTS IN STAGNATION-FLOW, DIAMOND-FORMING FLAMES USING HYDROGEN CARS SPECTROSCOPY

KEN E. BERTAGNOLLI AND ROBERT P. LUCHT
University of Illinois at Urbana-Champaign
Urbana, IL, USA

Gas-phase temperature profiles were measured near the deposition substrate in atmospheric-pressure, stagnation-flow, diamond-forming flames. In these flames, an acetylene–oxygen–hydrogen mixture accelerates through a nozzle and impinges on a water-cooled molybdenum substrate, stabilizing a flat flame approximately 1 mm below the substrate. A thin, polycrystalline diamond film is deposited on the substrate under appropriate conditions of flame stoichiometry and substrate temperature. Coherent anti-Stokes Raman scattering (CARS) spectroscopy of H_2 was used to determine the temperature at various points between the substrate and the incoming premixed jet. The CARS measurements show that the boundary layer (the region between the premixed flame reaction zone and the substrate) is approximately 0.6–0.8 mm thick along the stagnation streamline, depending on the velocity of the incoming jet. The CARS measurements also show peak flame temperatures ~200–300 K above the adiabatic equilibrium temperature—an effect of the short residence times in the flame. Measured temperature profiles are in good agreement with a theoretical calculation of the profile performed by Meeks and coworkers at Sandia National Laboratories, except that the measured distance between the substrate and the reaction zone is much less than predicted. H_2 CARS was also compared to N_2 CARS in a calibration burner and found to be in good agreement, with the H_2 CARS temperatures an average of 3.6% higher than the N_2 CARS results. The estimated H_2 CARS temperature accuracy is $\pm 4\%$ in the diamond-forming flames, and the estimated spatial resolution is $\pm 50\ \mu m$ perpendicular to the deposition surface.

Introduction

The deposition of polycrystalline diamond film has been demonstrated using a wide variety of flames and plasmas. Uniform diamond deposition was recently demonstrated in a rich acetylene–oxygen–hydrogen (C_2H_2–O_2–H_2) flat flame stabilized in the stagnation region of a molybdenum substrate [1,2]. Stagnation-flow, diamond-forming flames are of great interest because of the high growth rates that can be achieved, the uniformity and high quality of the deposited polycrystalline films, and the potential for scaling the flame systems for the deposition of large-area films [3]. Current attention is focused on how to increase the area of diamond deposition, reduce the required substrate temperatures without sacrificing growth rate, and deposit diamond film on surfaces with complex geometry. Progress in these areas depends on increased understanding of the diamond growth process through both experimental and theoretical studies [4].

In addition to issues associated with diamond deposition, these stagnation-flow flames are of fundamental interest in combustion science because of their high strain rates. They also pose a challenging test of current flame models. The stagnation-flow, diamond-deposition flames of Murayama and Uchida have been modeled recently by Meeks et al. at Sandia National Laboratories [3]. The numerical results show a steep temperature gradient near the substrate and, strikingly, peak flame temperatures that exceed calculated adiabatic equilibrium flame temperatures by 200 K. Meeks et al. speculated that the primary reason for the occurrence of the superadiabatic flame temperatures was that unreacted acetylene did not have time to fully dissociate to its equilibrium concentration. Acetylene oxidation occurs quickly, but in the model, a significant amount of acetylene remains unreacted in the fuel-rich environment. Endothermic dissociation of acetylene is required to reach equilibrium concentrations, and the superequilibrium acetylene concentration results in superadiabatic flame temperatures [3].

We have constructed a combustion apparatus similar to the Murayama and Uchida burner [2] and have begun a series of laser diagnostic measurements to improve fundamental understanding of these flames and to provide experimental data for comparison with numerical models. We have demonstrated diamond film formation in our apparatus under various run conditions. The measurement of accurate temperature and species-concentration profiles in these flames is challenging because of the high temperatures and spatial gradients. In this paper, we discuss coherent anti Stokes Raman scattering (CARS) temperature measurements near the

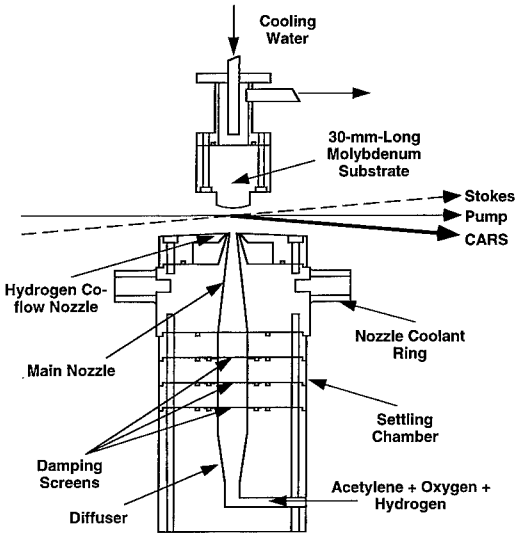

FIG. 1. Schematic diagram of the stagnation-flow, diamond-forming flame with the high-growth-rate (15-mm–diameter, 30-mm–long) substrate. The low-growth-rate substrate has a diameter of 15 mm and a length of 15 mm. Also shown is the position of the hydrogen CARS laser beams relative to the deposition substrate.

deposition substrate. CARS is well suited for probing these stagnation-flow flames because of its excellent spatial resolution and the coherent nature of the signal beam. We chose to use CARS spectroscopy of diatomic hydrogen for the temperature measurements because hydrogen is present in major concentrations throughout the flame, its Raman cross section is large, and the widely spaced vibrational Q-branch transitions ($\Delta v = \pm 1$, $\Delta J = 0$) are within the spectral working range of a broadband dye laser.

Experimental Methods

Burner Apparatus

Figure 1 is a schematic of the atmospheric-pressure, diamond-forming flame apparatus. A rich, premixed mixture of acetylene, oxygen, and hydrogen is accelerated through a converging nozzle with an exit diameter of 3 mm. An annular flow of hydrogen gas shields the premixed gases. This flow impinges on the bottom of 15-mm-diameter molybdenum substrate, and a rich, premixed flat flame is stabilized approximately 1 mm below the substrate surface. Polycrystalline diamond film is deposited on the bottom of the substrate under appropriate conditions of flame stoichiometry and substrate temperature.

The top surface of the substrate is cooled by a water flow of 3.4–3.8 L/min. The substrate surface temperature was estimated ($\pm 10\%$ uncertainty) by assuming one-dimensional conduction between two embedded thermocouple probes. Constant cooling-water flow rates kept the substrate temperature nearly constant over the course of an experiment. Two substrates with different lengths were used in the study. A 30-mm-long substrate produced surface temperatures ranging from 1000 to 1200 K, leading to the deposition of a high-quality diamond film at growth rates up to $\sim 70\ \mu$m/h. Surface Raman scattering analysis and scanning electron microscopy (SEM) images of the freestanding diamond films have confirmed their quality. We also constructed a 15-mm–long substrate to study the case where the substrate temperature was too low for high–growth-rate deposition of polycrystalline diamond. The 15-mm–long substrate maintains the surface temperature between 800 and 900 K, which reduces the growth rate to $\sim 1.5\ \mu$m/h. Both substrates were designed with a slight end curvature to allow the diagnostic laser beams to approach closer to the surface.

The burner apparatus is mounted on a three-axis positioner, which allows movement of the flame relative to the CARS laser probe with resolution of $\pm 2.54\ \mu$m. Tylan FC-280 mass flow controllers control the flow rates for each gas with an accuracy of ± 0.3 standard liters per minute (SLM). Oxygen and hydrogen are supplied from pressurized gas bottles at 99.95% purity. Absorption-grade acetylene (99.6% pure) is supplied in a commercial gas cylinder and passed through an activated charcoal filter to reduce the amount of acetone in the gas stream.

Hydrogen CARS Instrument

The 532-nm pump beams for the hydrogen CARS process were provided by a 10-Hz Continuum NY-81C injection-seeded Nd:YAG laser with a pulse length of 5–7 ns. This laser is nearly monochromatic, with a line width of 0.0045 cm^{-1}. A portion of the Nd:YAG output was used to pump a Mode-X System-2 modeless, broadband dye laser [5]. This laser generates a broadband Stokes beam with a frequency spectrum centered around 680 nm using a mixture of LDS-698 and DCM dye in ethanol. The concentrations of LDS-698 in the oscillator and amplifier were 4×10^{-4} and 5×10^{-5} M, respectively. The concentrations of DCM in the oscillator and amplifier were 2×10^{-4} and 3×10^{-5} M, respectively. The pump and Stokes beams were arranged in a folded BOXCARS fashion and focused into the combustion medium, generating a fourth coherent CARS beam. The CARS signal was directed into a SPEX-1000M single-grating, 1-m focal length spectrometer. A Photometrics blue-sensitive, unintensified charged couple device (CCD) camera with a 512-by-512 pixel array was used to detect the dispersed CARS signal. An unintensified CCD camera

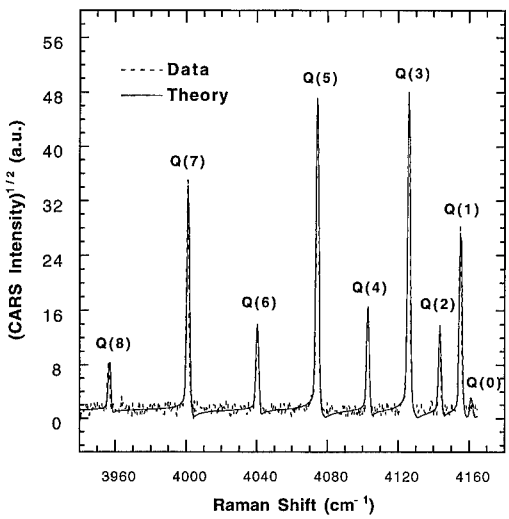

FIG. 2. Comparison of a theoretical CARS spectrum at 3290 K to an experimental H_2 CARS spectrum obtained 0.56 ± 0.05 mm below the substrate. The experimental spectrum was accumulated for 20 s on the CCD and has been divided by the nonresonant CARS spectrum, thus accounting for variations in the dye laser spectral profile.

was used for signal collection because of its excellent linearity, dynamic range, and spectral resolution [6]. The spectral resolution of the CARS instrument is 1.0 cm^{-1}, as determined by the spectrometer grating, the exit-slit relay lenses, and the CCD pixel size. A high-speed mechanical shutter (Vincent Associates Uniblitz LS6T2) was placed in front of the spectrometer entrance slit to reduce the amount of unwanted flame emission recorded by the CCD array.

Results and Discussion

Hydrogen CARS Thermometry

The CARS spectrum reflects the internal energy partitioning among the various vibrational-rotational states of the molecule being excited. Normally—as in nitrogen CARS—temperature is determined from a least-squares fit of a theoretical CARS spectrum to an experimental spectrum. We initially attempted to use the Sandia CARSFT code [7] to analyze our data but encountered problems due to slight variations in spectral dispersion across the CCD array. Figure 2 shows a comparison of an experimental spectrum obtained 0.56 ± 0.05 mm below the substrate and a theoretical spectrum generated by CARSFT at 3290 K. There is a slight difference between the location of the experimental and theoretical Q-branch line centers, preventing the CARSFT program from automatically fitting the theory to the data. Visually, however, the theory and data appear to agree well at a temperature of 3290 K.

Because the Q-branch transitions of hydrogen are isolated spectrally, temperature can also be determined by comparing the relative integrated line intensities using a Boltzmann analysis [8]. Assuming that the nonresonant susceptibility of the gas is negligible (valid for fuel-rich conditions) and that the pump beams are monochromatic, the integrated intensity for each isolated Q-branch transition j is given by

$$I_j \propto \frac{(n_a - n_b)_j^2\, \omega_3^2}{\Gamma_j \omega_2^8} \left(\frac{\partial\sigma}{\partial\Omega}\right)_j^2 I_{2\omega} \qquad (1)$$

where Γ_j is the Raman line width (full width at half-maximum, FWHM) (s^{-1}), n_a and n_b are the number densities (m^{-3}) of the lower ($v = 0, J$) and upper ($v = 1, J$) transition levels, $I_{2\omega}$ is the spectral intensity [$W/(s^{-1}\cdot m^2)$)] of the broadband Stokes beam, and ω_2 and ω_3 are the Stokes laser frequency and the CARS signal frequency (cm^{-1}), respectively [9]. Mean spectral intensity variations in the broadband Stokes beam are accounted for by dividing the hydrogen CARS spectrum by a nonresonant background spectrum generated in room air. The $(\partial\sigma/\partial\Omega)_j$ term is the differential Raman cross section (cm^2) for each Q -branch transition,

$$(\partial\sigma/\partial\Omega)_j \propto (\omega_2^4/\omega_j)\, [1 + (4/45)\, b_{J,J}\, (\gamma'/a')^2]$$
$$[1 - 6J(J + 1)\, (B_e/\omega_e)^2] \qquad (2)$$

where ω_j is the vibrational frequency (cm^{-1}), $b_{j,j}$ is the Placzek–Teller coefficient, B_e and ω_e are Herzberg molecular parameters (cm^{-1}), and γ'/a' is the ratio of the anisotropy of the polarizability derivative to the mean polarizability derivative. The ratio γ'/a' is equal to 0.855 for diatomic hydrogen. The rightmost bracketed term in Eq. (2) is a centrifugal force correction [7].

The population of a particular rotational level J is proportional to the rotational degeneracy $2J + 1$ and the nuclear spin statistical weight g_{nuc} (1 for even J, 3 for odd J). To determine temperature, the rotational energy $F(J)$ (cm^{-1}) is plotted versus the product of $-k/hc$ and the natural log of β, where

$$\beta = \frac{\omega_2^4 \sqrt{I_j \Gamma_j}}{g_{nuc}(2J + 1)\omega_3(\partial\sigma/\partial\Omega)_j} \qquad (3)$$

The slope of a linear least-squares fit through the data points is equal to the temperature.

Figure 3 shows the corresponding Boltzmann plot for the $Q(1)$-to-$Q(7)$ transitions of the experimental spectrum shown in Fig. 2. The line-integrated Boltzmann temperature is 3290 ± 60 K, the same temperature used to generate the theoretical CARS spectrum in Fig. 2. For the data in Fig. 3, the average uncertainty in the measurement of the integrated line intensities is ±0.8% (corresponding to

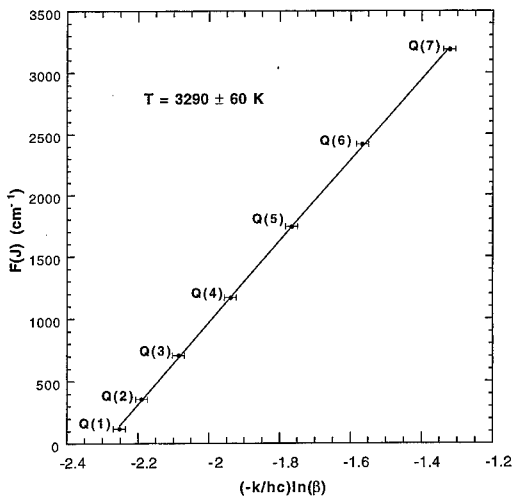

FIG. 3. Line-integrated Boltzmann plot for the experimental CARS spectrum shown in Fig. 2. The slope of the line fit to the $Q(1)$-to-Q (7) transitions gives a temperature of 3290 K with an uncertainty in the slope of ± 60 K. The error bars correspond to a $\pm 0.8\%$ uncertainty in the measurement of the integrated line intensities.

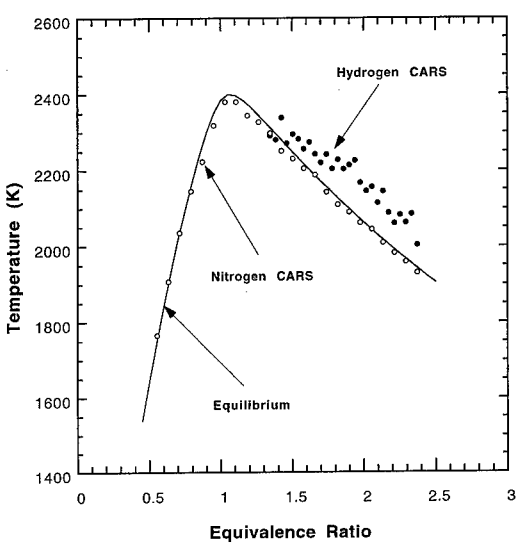

FIG. 4. Comparison of measured H_2 CARS (●) and N_2 CARS (○) temperatures in a Hencken burner. The solid line (—) represents the calculated adiabatic equilibrium temperature.

the error bars), and the resulting uncertainty in the linear least-squares-fit slope (i.e., temperature) is $\pm 1.8\%$. The average uncertainty in the slope for all of the data presented in this paper is 2.0%, providing a measure of the random error or precision of the hydrogen CARS measurements.

As a check of the Boltzmann method accuracy, the Sandia CARSFT code was used to generate theoretical H_2 CARS spectra at specified temperatures, and then these spectra were analyzed as if they were experimental data. The temperatures calculated using the Boltzmann analysis varied by only $\pm 1\%$ relative to the theoretical temperatures.

It is assumed in writing Eq. (1) that the CARS lines are collisionally broadened. In fact, the CARS lines are primarily Doppler broadened in atmospheric pressure flames. Using the measured collisional parameters of Bergmann and Stricker [10], we calculate that the collisional width is less than 10% of the Doppler width in the diamond-forming flame. This is indeed fortunate because their line-width measurements show a pronounced decrease of the collisional line width with increasing rotational quantum number J. Dicke narrowing of the Doppler profile due to velocity-changing collisions is probably significant, but the rate of velocity-changing collisions is likely to be independent of J. Since the H_2 CARS lines are neither purely Doppler broadened nor purely collisonally broadened, a Voigt line shape model is used to compute the Raman line-width Γ_j.

To assess hydrogen CARS thermometry accuracy, we used both hydrogen and nitrogen CARS to measure temperature in a surface-mixing, flat-flame calibration burner—a so-called Hencken burner. Temperatures were measured at a central position approximately 3.8 cm above the burner in a hydrogen-air flame at various equivalence ratios. Temperatures measured using hydrogen and nitrogen CARS and calculated adiabatic equilibrium flame temperatures are plotted versus the flame equivalence ratio in Fig. 4. Comparison of nitrogen CARS data and the equilibrium code calculations confirm that for sufficiently high flow rates, the Hencken burner produces nearly adiabatic flames [11].

Hydrogen CARS data could only be obtained under fuel-rich conditions because of the CARS signal diminishing as the hydrogen concentration decreased. The scatter in the data is due primarily to variations in the Stokes beam spectral profile.

On a percentage basis, the difference between the measured hydrogen CARS temperatures and the equilibrium calculations is $\pm 3.6\%$, with a standard deviation of $\pm 2\%$. The $\pm 3.6\%$ difference is a measure of the systematic error of the measurements. The difference between the H_2 CARS results and the equilibrium calculations is probably due to the assumption of purely Doppler-broadened lines. The fact that the temperatures calculated from the H_2 CARS spectra are high compared to the N_2 CARS temperatures may indicate that low-J Q-branch lines are actually broader than high-J Q-branch lines, a result that would be consistent with the reported J dependence of the high-pressure, collision-broadened line widths [10]. High-resolution measurements of H_2 CARS line shapes in atmospheric

TABLE 1
Experimental conditions for the stagnation-flow, diamond-forming flame hydrogen CARS temperature measurements

Parameter	Flame 1A	2A	1B	2B
Mean exit velocity (m/s)	40	55	40	55
Substrate temperature (K)	1050 ± 110	1150 ± 120	800 ± 50	900 ± 55
Premixed C–O ratio	1.05	1.02	1.05	1.02
Premixed H–O ratio	0.5	0.5	0.5	0.5
Premixed equivalence ratio	2.9	2.8	2.9	2.8
Adiabatic flame temperature (K)	3082	3109	3082	3109

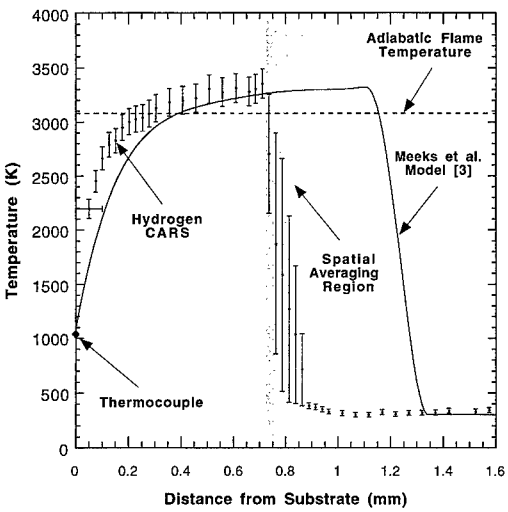

FIG. 5. Measured H_2 CARS temperatures (●) in the diamond-forming flame for flame 1A (40-m/s mean flow, 1050 K substrate). The solid line (—) represents the computational results of Meeks et al. [3]. The dashed line (---) represents the adiabatic equilibrium temperature for this gas mixture, and the solid diamond (♦) is the estimated substrate surface temperature. Temperatures in the shaded region are a spatial average across the steep temperature gradient due to the finite size of the CARS probe volume. The accuracy of the temperature measurements between the substrate and 0.8 mm is ±4%.

pressure combustion environments are needed to resolve this issue. However, temperature measurement errors associated with this assumption should be reduced in the diamond-forming flames, since the ratio of Doppler to collisional width scales linearly with temperature.

Temperature Profiles

CARS temperature profiles were obtained in the diamond-forming flame under four different conditions, summarized in Table 1. The substrate was located 4.5 mm away from the nozzle for each run. An annular flow of hydrogen gas surrounded the core gas flow at 3.5 SLM for all cases.

CARS spectra were obtained along the central stagnation streamline between the nozzle exit and the substrate surface. The spatial resolution of the CARS probe volume was measured to be ~50 μm normal to the substrate and 1.5 mm long (FWHM). Radial temperature profile measurements showed the diamond-forming flame temperature was uniform over the center 4 mm of the flame, thus minimizing the effect of the probe volume length. Temperature probability density functions obtained from single-shot CARS spectra confirmed that the flame was steady. Therefore, each CARS spectrum was accumulated for 20 s (200 laser shots) on the CCD array. Two spectra were obtained at each location, and their temperatures were averaged.

A measured hydrogen CARS temperature profile obtained along the stagnation-point streamline for the base-case flame 1A (40 m/s mean flow, 1050 K substrate) is shown in Fig. 5. The computational results of Meeks et al. [3] are included in the plot for comparison. The model calculations were performed using a mean exit velocity of 37.6 m/s, a C–O ratio of 1.16, an H–O ratio of 0.5, and a substrate temperature of 1073 K. These exact conditions could not be matched in our experiments due to slight instabilities in the flame at the model conditions, but they are close to the flame 1A conditions. The plot also shows the calculated adiabatic flame temperature and the substrate surface temperature as measured by the embedded thermocouples (±10%).

For flame 1A, the hydrogen CARS temperature data points measured within 0.75 mm from the substrate are accurate to within ±4%, based on a root-mean-squared sum of the random and systematic errors. The relative positions of each data point are accurate to within ±2.5 μm, with a ±50-μm uncertainty in the position of the first data point. In the region approximately 0.8 mm below the substrate,

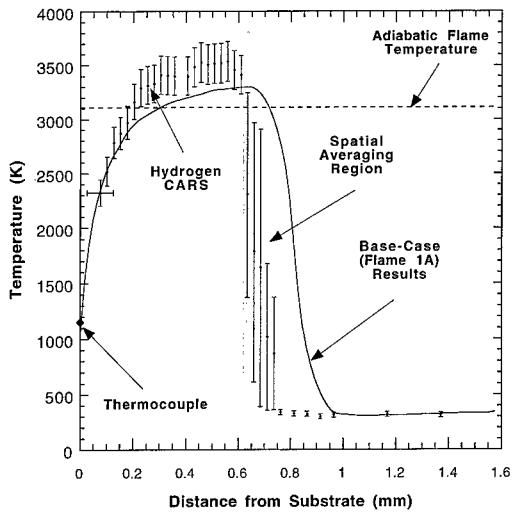

FIG. 6. Measured H_2 CARS temperatures (●) in the diamond-forming flame for flame 2A (55-m/s mean flow, 1150 K substrate). The results from the base-case flame 1A (—), the adiabatic flame temperature (---), and the estimated substrate surface temperature (◆) are plotted for comparison. The temperatures in the shaded region are a spatial average across the steep temperature gradient. The accuracy of the temperature measurements below 0.6 mm is ±5.2%.

the temperatures are a mixture of both cold and hot gases, since the CARS probe volume spans a portion of the steep temperature gradient. The relatively high-energy spacing of the rotational states in the ground vibrational state of hydrogen leads to a very rapid decrease in population density with increasing rotational quantum number at room temperature. Thus, cool gas produces a CARS signal only for the first four resonances of the hydrogen Q-branch [$Q(0)$ to $Q(3)$]. The higher-energy levels [$Q(4)$ to $Q(7)$] are populated only at high temperature. The error bars associated with the temperature measurements in this region correspond to a separate Boltzmann analysis of lines $Q(0)$ to $Q(3)$ and lines $Q(4)$ to $Q(7)$. The actual temperature is assumed to lie somewhere between these extremes. For data obtained at distances greater than 0.95 mm from the substrate, the uncertainty associated with the temperature is ±7%. The error is larger in this region because only four lines are available for the least-squares fit. The hydrogen CARS measurements in this region are on average 315 ± 20 K, close to the actual measured, premixed gas temperature of 300 K.

The hydrogen CARS temperature profile agrees well with the general model profile in the region less than 0.75 mm below the substrate. Peak measured temperatures in this region are on the order of 200 K above the adiabatic flame temperature, a feature predicted by the model. The hydrogen CARS technique also provided the spatial resolution necessary to measure temperatures near the substrate. The temperatures very near the substrate (<100 μm) are a spatial average of the temperatures contained in the CARS probe volume.

However, there is a significant difference between the measured and computed flame standoff distance (the distance between the substrate surface and the steep temperature gradient indicating the location of the reaction zone). The model predicts a standoff distance of nearly 1.2 mm, while the measurements show a distance of about 0.8 mm. The difference between computed and measured flame standoff distance is a matter for conjecture at this point. Hot-film anemometer measurements showed that the velocity profile at the nozzle exit was uniform for the conditions found in the diamond-forming flame, eliminating this as a possible source of discrepancy. The difference between predicted and measured flame standoff distances is probably due to differences between the actual and calculated velocity fields [12], although in these high-temperature flames, the accuracy of the chemistry and transport models must be examined also.

A hydrogen CARS temperature profile obtained in flame 2A (55 m/s mean flow, 1150 K substrate) is shown in Fig. 6. The base-case (flame 1A) temperature profile is shown for comparison. The accuracy of each data point is ±5.2%, slightly higher than for the flame 1A measurements because the dye laser spectral profile was not as well behaved. For this 55-m/s mean flow condition, the boundary layer is thinner than for the 40-m/s case, scaling approximately as $1/\sqrt{R_e}$. The peak temperatures are also higher for this case. The temperature overshoot is consistent with the results in the well-stirred reactor model of Meeks et al. [3]. The residence time for the premixed gases is on the order of 100 μs for the 40-m/s mean flow and 80 μs for the 55-m/s mean flow. Reducing the residence time increases the peak temperature because now there is even less time for equilibrium acetylene dissociation. The temperature gradient near the substrate is also greater for this case than for the base case, a result expected with a thinner boundary layer.

A hydrogen CARS temperature profile measured in flame 1B (40-m/s mean flow, 800 K substrate) is shown in Fig. 7. The 30-mm–long substrate was replaced with the 15-mm–long substrate to produce much lower substrate surface temperatures. For this case, the CARS temperature accuracy is ±3.8%. Overall, the temperature profile is very similar to the base case (flame 1A). The boundary-layer thickness and peak flame temperature are approximately the same for both flames. The temperature gradient near the substrate surface is also nearly the same, even though the substrate surface temperature is

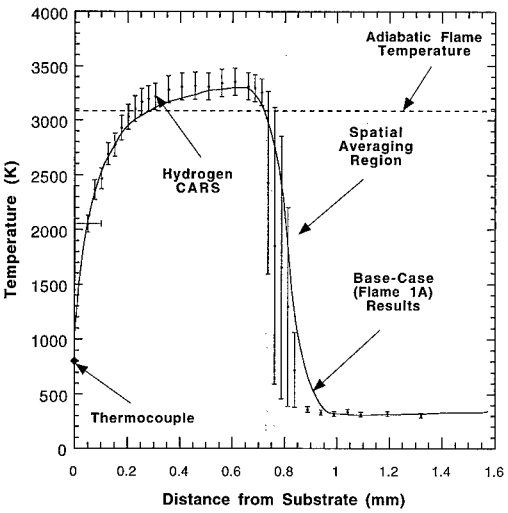

FIG. 7. Measured H_2 CARS temperatures (●) in the diamond-forming flame for flame 1B (40-m/s mean flow, 800 K substrate). The results from the base-case flame 1A (—), the adiabatic flame temperature (---), and the estimated substrate surface temperature (◆) are plotted for comparison. The temperatures in the shaded region are a spatial average across the steep temperature gradient. The accuracy of the temperature measurements below 0.8 mm is ±3.8%.

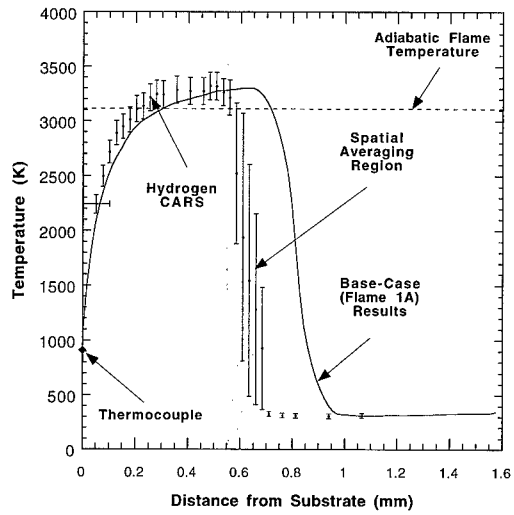

FIG. 8. Measured H_2 CARS temperatures (●) in the diamond-forming flame for flame 2B (55-m/s mean flow, 900 K substrate). The results from the base-case flame 1A (—), the adiabatic flame temperature (---), and the estimated substrate surface temperature (◆) are plotted for comparison. The temperatures in the shaded region are a spatial average across the steep temperature gradient. The accuracy of the temperature measurements below 0.6 mm is ±3.8%.

roughly 300 K less. This is probably a result of the spatial averaging near the substrate by the 50 μm–diameter CARS probe volume.

Upon increasing the mean premixed gas flow velocity to 55 m/s with the 15-mm–long substrate (flame 2B), a temperature profile as seen in Fig. 8 results. As in the results for flame 2A, the boundary-layer thickness for this higher-velocity case is less than that for the base case. However, the peak temperatures are only slightly higher than for the base case where we saw a significant increase in peak temperature for flame 2A. The peak temperatures appear to rise faster than in the base case in the region between 0.2 and 0.4 mm below the substrate, indicating a higher-temperature gradient into the substrate.

Conclusions

In conclusion, we have successfully measured temperature profiles in the region near the deposition surface in a diamond-forming flame using H_2 CARS. We were able to measure temperatures to within approximately 50 μm of the deposition surface with a spatial resolution of 50 μm. A comparison of measured hydrogen and nitrogen CARS temperatures and calculated adiabatic equilibrium flame temperatures in a calibration flat-flame burner showed good agreement. The temperatures measured in the diamond-forming flame are estimated to be accurate within ±4% based on the results of this calibration and linear-regression analysis of the Boltzmann plots. The measured diamond-forming flame temperature profile results are in good agreement in many respects with the numerical computations of Meeks et al. [3]. Peak measured temperatures are up to 300 K above the adiabatic flame temperature, as predicted by the model. However, the measured flame standoff distances are much less than the calculated distances. This difference may result from differences between the actual and calculated velocity fields.

Acknowledgments

This research is supported by the National Science Foundation, Combustion and Thermal Plasma Program, Chemical and Transport Systems Division Grant #CTS-9313829 under the supervision of Dr. Milton J. Linevsky. The authors also gratefully acknowledge Dr. Roger Farrow and Dr. Robert Kee at Sandia National Laboratories, Livermore, CA, for helpful suggestions and stimulating discussions.

REFERENCES

1. Murayama, M., Kojima, S., and Uchida, K., *J. Appl. Phys.* 69:7924–7926 (1991).

2. Murayama, M. and Uchida, K., *Combust. Flame* 91:239–245 (1992).
3. Meeks, E., Kee, R. J., Dandy, D. S., and Coltrin, M. E., *Combust. Flame* 92:144–160 (1993).
4. Goodwin, D. G., *J. Appl. Phys.* 74:6888–6894 (1993).
5. Ewart, P., *Optics Comm.* 55:124–126 (1985).
6. Rakestraw, D. J., Lucht, R. P., and Dreier, T., *Appl. Optics* 28:4116–4120 (1989).
7. Palmer, R. E., *The CARSFT computer code for calculating coherent anti-Stokes Raman spectra: User and programmer information*, Sandia National Laboratories Report No. SAND89-8206, 1989.
8. Chen, K.-H., Chuang, M.-C., Penney, C. M., and Banholzer, W. F., *J. Appl. Phys.* 71:1485–1493 (1992).
9. Eckbreth, A. C., *Laser diagnostics for combustion temperature and species*, Abacus Press, Cambridge, MA, 1988, pp. 220–300.
10. Bergmann, V. and Stricker, W., *Appl. Phys. B* 61:49–57 (1995).
11. Hancock, R. D., Bertagnolli, K. E., and Lucht, R. P., *Combust. Flame*, submitted.
12. Sick, V., Arnold, A., Diebel, E., Dreier, T., Ketterle, W., Lange, B., Wolfrum, J., Thiele, K. U., Behrendt, F., and Warnatz, J., *Twenty-Third Symposium (International) on Combustion*, The Combustion Institute, Pittsburgh, 1990, pp. 495–501.

COMMENTS

D. E. Rosner, Yale University, USA. In view of your evident concern with accurate local temperature measurements and their importance for future modeling efforts, it may be relevant to point out that the conditions for diamond film growth from atmospheric (or subatmospheric) pressure flames seem to be those that will inevitably be associated with non-negligible temperature "jumps" at gas/solid interfaces [1]. The high energy fluxes, small dimension gas gaps, large disparities between the molecular weights of the participating gases (e.g., mixtures "rich" in H atoms and CH_3-radicals) and the solid substrates (Mo(s)), and/or the vibrational frequency mismatch (between adatoms and C-atoms within the diamond film itself), all seem to "conspire" to produce an expected systematic difference between the gas temperature evaluated at the growth surface and the (colder) solid surface itself. Does the spatial resolution of your present near-deposition-surface measurements permit you to comment on this?

REFERENCE

1. See, e.g., the recent invited paper: Rosner, D. E. and Papadopoulos, D. E., "Jump, Slip and Creep Boundary Conditions at Non-Equilibrium Gas/Solid Interfaces," *Industrial Eng. Chem. Res. (Am. Chem. Soc.)*, September 1996.

Author's Reply. At this point it is not possible to comment definitively on this question. Our estimate of a spatial resolution of 50 micrometers in a direction perpendicular to the surface is based on burn patterns observed when the 532-nm beam from our Nd:YAG laser is brought to a line focus. The actual spatial resolution of the CARS measurements should be somewhat better than this because the signal is proportional to the square of the 532-nm intensity. However, the temperature gradients near the surface are very large, on the order of 10 K per micrometer, and we cannot resolve the near-surface gradient accurately. It is interesting to note, though, that if significant spatial averaging in the CARS probe volume is occurring for measurements near the wall, the measured temperatures would tend to be weighted towards lower temperatures because cold gases generate more CARS signal than hot gases. In addition, we might expect to see a significant deterioration in the quality of our Boltzmann fits, but we do not. The lowest temperatures that we observe are approximately 2000 K, and the Boltzmann fits even for the measurement points closest to the wall are still quite good. Based on these results, it is certainly possible that there is a significant temperature jump at the gas/solid interface. We may be able to address this question more definitively in future experiments in low-pressure diamond-forming flames in a facility that has just become operational in our laboratory.

•

Katharina Kohse-Höinghaus, Universitat Bielefeld, Germany. Based on you current understanding of the deposition process and with semiconductor quality diamond in mind, how well does the flame CVD process compete with other CVD methods? And will the answer differ for high (atmospheric) pressure or low-pressure flames?

Author's Reply. Our paper did not focus on the economics of diamond-forming flames. We asked Prof. David G. Goodwin of Caltech and Dr. Jay B. Jeffries of SRI International for their answers to these questions and they were kind enough to reply.

Prof. Goodwin:

A cost analysis carried out recently by IBIS Associates, Inc. (Wellesley, MA) concluded that the microwave plasma and DC arcjet methods are currently the most economical techniques for production of 1-mm thick diamond thermal management substrates for electronic cooling applications. The combustion technique suffers currently from high gas cost and low carbon conversion efficiency ($< 10^{-5}$). A combustion method using a fuel cheaper than acetylene could

become competitive, but only if the conversion efficiency, which is directly related to how much atomic hydrogen the flame can deliver to the substrate, were also increased. So far, using alternative fuels has been found to lower the conversion efficiency. Nevertheless, there may well be other applications for which combustion-grown diamond has a cost advantage. Depending on the application, the high growth rate of an atmospheric-pressure process or the large area coverage of a low-pressure process may be desirable.

For active electronic applications, the economics are much less certain, since state-of-the-art CVD diamond is not yet close to semiconductor grade, and significant problems with single-crystal growth, twinning, and n-type doping remain to be solved.

Dr. Jeffries:

It is not at all clear that flame grown diamond will have sufficiently low defect densities to be useful for semiconductor devices; in fact control of defects is currently the biggest challenge to semiconductor device quality CVD diamond. Both atmospheric and low-pressure flames produce good thermal management diamond material; however, the fuel costs are significantly higher than arcjet and microwave CVD methods.

•

Jerry Finlinson, NAWL, USA. In these experiments you quote a substrate surface temperature near 1100 K. How is it measured and what is the accuracy? Does it change significantly when diamond is coating the surface? Is it possible to measure temperature on the surface of diamond film after formation begins?

Author's Reply. The surface temperature was estimated from the measured temperature difference between thermocouples imbedded in the molybdenum substrate at distances of 5 mm and 8 mm from the surface. We assume one-dimensional heat conduction and estimate the uncertainty of the measurement as $\pm 10\%$. The substrate surface temperature typically varied by only about 10 K during an experimental run as the diamond film was depositing, indicating that there was little temperature drop across the diamond film. It would be possible to measure the diamond film surface temperature by optical pyrometry as the film is growing, and a number of groups have measured the film temperature in this fashion.

Twenty-Sixth Symposium (International) on Combustion/The Combustion Institute, 1996/pp. 1835–1843

THE CONTROLLING CHEMISTRY IN FLAME GENERATED SURFACE DEPOSITION OF Na_2SO_4 AND THE EFFECTS OF CHLORINE

M. STEINBERG AND K. SCHOFIELD
Materials Research Laboratory, University of California
Santa Barbara, CA, USA 93106

This paper examines the behavior of sodium/sulfur flame deposition on cooled probe surfaces for cases where the sulfur concentration is equal to or in excess of that of sodium. In all cases, Na_2SO_4 is the predominant component deposited, quite pure in most cases, but occasionally indicating the presence of several percent of Na_2CO_3 and implying possible thermodynamic control by the surface. Rates of deposition are exactly first order with respect to sodium concentrations, and zero order with respect to sulfur. The surface shows a total indifference to the atomic or molecular state of the flame sodium, be it Na, NaOH, or NaCl. Moreover, it is indifferent to the nature of the flame, its fuel type, stoichiometry, temperature, or state of equilibration. The surface adsorption rate of sodium is very efficient for probes at 640–780 K (35–60%) and appears to be the rate-controlling kinetic step and is not governed by normal boundary layer or laminar/turbulent flow considerations. Deposition displays a linear growth rate with negligible incubation time and is irreversible. Up to at least the 100-ppm concentration level, salts such as Na_2SO_4, Na_2SO_3, $Na_2S_2O_3$, and $NaNO_3$ are shown to be equivalent sources of sodium or sulfur. For the range of probe temperatures (640 to 780 K) and with Inconel-600 probe material, negligible differences were noted for rates of deposition in a wide range of propane and hydrogen flames. Rather surprising, however, was the fact that deposits formed on top of the burner (350 K) reflected closely those on the probe and were not mixtures of other possible sodium/sulfur compounds. Preliminary experiments incorporating chlorine into the system indicate, for high levels of chlorine (0.4% Cl_2), that the deposit consists of one-third Na_2SO_4 and two-thirds NaCl. At lower levels of chlorine no such halide component has been reported.

Introduction

High temperature corrosion is a major factor that controls the useful life of hot section components in boilers, gas turbines, and other types of fossil-fueled combustion systems [1,2]. Since the identification of alkali sulfates, primarily Na_2SO_4, as the major culprits in catalyzing corrosion, attempts have concentrated on developing materials and coatings to minimize the effects. Current efforts are aimed at reducing sodium and sulfur levels. Also, considerable efforts are now centered on understanding the role played by chlorine [3]. Details of the parameters controlling the chemical aspects remain scant and have emerged largely from the significant efforts of the NASA Lewis Research Center Group utilizing burner rigs [4,5]. As a result of our earlier work on the chemistry of sulfur [6], sodium [7], and sodium/sulfur interactions in flames [8,9], we have extensively characterized the gas-phase aspects of the problem. Moreover, it was felt that we could manipulate the gas-phase distributions in such a manner as to resolve the controlling deposition chemistry and identify the specific gas-phase sodium form involved.

This is the first in a series of papers concerning deposition of sodium compounds. It represents the first accurately controlled quantitative study of a well-understood series of rich and lean propane- and hydrogen fueled flames. This paper emphasizes the behavior when sulfur concentrations are equal to or are in excess of those of sodium. Subsequent papers will cover the additional conditions of when sodium is in excess of sulfur, and for the case when sulfur is absent altogether.

Experimental System

Most of the measurements were made utilizing a flat-flame shielded burner. This was redesigned with 1-mm-diameter stainless steel hypodermic tubing, with facilities for heating the whole burner to minimize sodium deposition within the burner. The flame gases are nearly isothermal, one-dimensional, and with laminar vertical flows having Reynolds numbers in the range 36–65 for propane flames and 150–180 for hydrogen flames. Several studies also used a drilled plate, shielded Meker-type burner with similar 1-mm-diameter hole sizes. This produced, as was desired, turbulent burnt gases. All flames were premixed and at atmospheric pressure.

C_3H_8/air flames with equivalence ratios of 0.8 to 1.2 were burnt as were $H_2/O_2/N_2$ flames with lean to rich ratios of 1/1/3, 1.4/1/5, 1.8/1/5, 2.2/1/6, and 4/1/6. Additions of 1–2% C_2H_2 were made to some hydrogen flames to test for its effect. All the hydrogen flames, however, used air as a source of O_2, which contained 360 ppm CO_2 and so had some slight carbon content. Hydrogen flames give better spatial resolution than propane flames. The time scale, for example, for the 4/1/6 flame corresponds to about 1.6 ms/cm. That for stoichiometric C_3H_8/air approximates to 5 ms/cm. As a result, hydrogen flames can be better used to examine nonequilibrium and kinetic aspects whereas atmospheric pressure propane flames equilibrate over much shorter distances. Flame temperatures varied from 1680 to 2285 K.

In order to obtain measurable probe deposition in a reasonable length of time, sodium flame concentrations on the parts-per-million scale are required. In the present work, sodium was introduced as an aqueous aerosol generated by an ultrasonic nebulizer. This was extensively calibrated absolutely using both spectroscopic curve of growth and physical liquid N_2 trap collection methods. Functioning at almost its upper limit of operation, with 0.1 N solution strengths, this produced sodium burnt gas concentrations in the 30–60 ppm range (by volume) for propane flames, and 8–10 ppm for hydrogen flames. Solutions of $NaNO_3$, NaI, Na_2SO_3, Na_2SO_4, and $Na_2S_2O_3$ have been examined. Added aerosol H_2O content is negligible. A small mixing vessel (100 cm^3) and a flexible tube connected the nebulizer output to the burner inner core and were wrapped with heating tape and kept hot. Even so, measurements of sodium aerosol loss in the delivery line and in the burner indicated that only 70–80% reached the burnt gases. Sodium aqueous solutions were spiked with a trace of potassium (1% that of sodium). In this way, by spectrally monitoring the optically thin resonance line of potassium, it was possible to monitor the system constancy with time.

Sulfur was added to the premixed gases in the form of SO_2 at levels of 500 ppm to 0.8%. Very low levels of sulfur were obtained by nebulizing salt solutions containing sulfur, such as Na_2SO_3 or $Na_2S_2O_3$. Chlorine was added as Cl_2.

Various probes were used, constructed of Inconel-600 and air cooled through a central core channel. A thermocouple was incorporated into their design and measured the surface temperature. Probe temperatures over the range 640–780 K were used. Probe shapes varied from a wedge to circular to blunt, and the probe was placed horizontally through the vertical flow burnt gases at a particular downstream distance. In all cases, the probes at their widest dimension (12.7 mm) corresponded to the 12-mm-diameter inner burner core flame flow and so intercepted at some point the full seeded flow. Boundary layers were modified, however, by the differing shapes and flame conditions.

Probe deposits were characterized with laser Raman techniques as elegantly illustrated previously [10]. A frequency-doubled cw Nd-YAG laser with a power of about 250 mW, coupled to a double-pass spectrometer, provided in situ measurements. In the majority of cases, however, samples were removed from the probe, sealed in capillary glass tubes, and analyzed with a Nicolet Fourier transform Raman spectrometer that uses a 1.06-μm excitation source. The analysis of sodium/sulfur salts is well suited to Raman spectroscopy in that they display very characteristic sharp banded spectra, making for easy molecular identifications [11,12]. For such compositional analysis, deposits generally were collected for about 3 h. Rates of deposition were measured by dissolving the sample from the probe with distilled water and analyzing for total sodium with a flame photometric Beckman analytical burner. Sodium delivery line loss was also analyzed by this means. Sensitivity was such that highly accurate and reproducible values could be obtained from experiments lasting only 1 h.

Results and Discussion

Deposit Composition

As illustrated by Figs. 1 and 2, the Raman spectra of flame-generated probe deposits show a consistent behavior for all the flames examined. Sodium predominantly forms Na_2SO_4 in a relatively pure state. For comparison, the spectrum of pure anhydrous Na_2SO_4 is included in Fig. 2. The distribution of peaks is very characteristic and not shown by any other Na/H/S/O salt. For $\phi = 0.9$ to 1.1, a small peak at 1078 cm^{-1} reflects a very small contribution from this, the strongest line of Na_2CO_3, and indicates the presence of only a few percent, maximum at around a stoichiometric flame mixture. It is not present in the $\phi = 0.8$ spectrum, possibly due to the slightly lower probe temperature of 687 K, whereas the others were at 744 K. The only other feature in these spectra is the small peak at 1202 cm^{-1}. This is a somewhat rare frequency magnitude and remains unidentified. It does require the presence of sulfur but is insensitive to sulfur concentration and is not present on cooler temperature probes. As to whether it is associated with the stainless steel probe materials, which is suspected, will become clear in future work. It is not listed as an Na/S compound frequency. The sand-colored deposit evident from the $\phi = 1.1$ flame of Fig. 1 clearly indicates some corrosive interaction with the probe even at these temperatures. This level of corrosion increased more so for richer C_3H_8 flames, and spec-

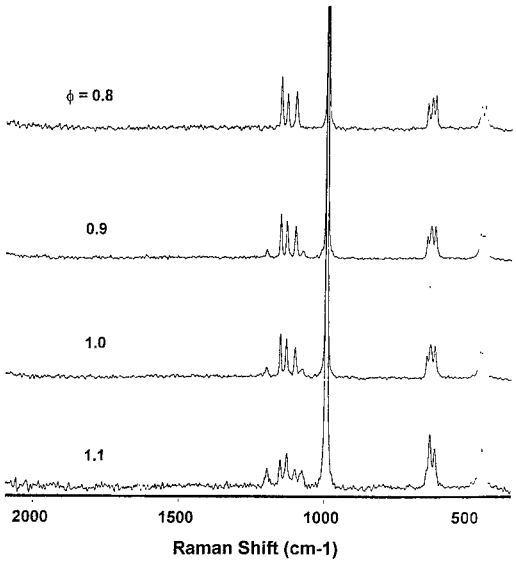

FIG. 1. Raman spectra of probe deposit material for various C_3H_8/air flames. These flames contained sodium concentrations (from $NaNO_3$ aqueous aerosols) of 60 to 36 ppm, respectively, and 500 ppm SO_2. The probe was located 5–7 ms downstream and maintained at 687 K (ϕ = 0.8) and 744 K for the other flames. No other spectral features are apparent in the 100–3600 cm^{-1} range, outside of that illustrated, for any of the Raman spectra displayed in this paper.

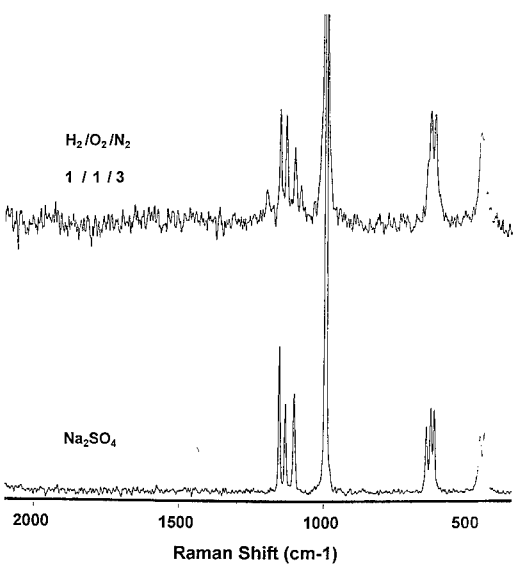

FIG. 2. Raman spectra of pure anhydrous Na_2SO_4 and of the probe deposit material for a fuel-lean hydrogen flame. The flame contained 10 ppm sodium (from $NaNO_3$) and 500 ppm SO_2. The probe was located 4 ms downstream and maintained at 744 K.

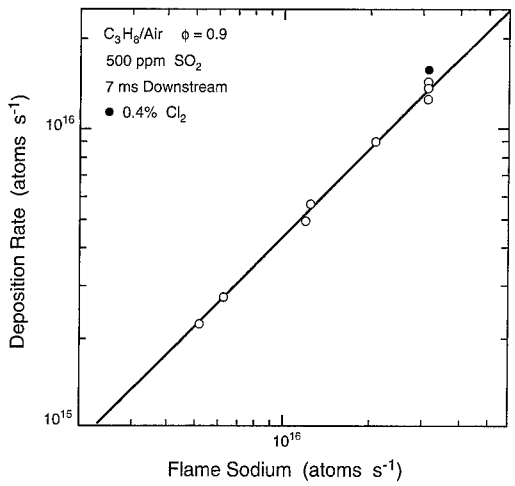

FIG. 3. First-order dependence of the rates of deposition of Na_2SO_4 on flame sodium concentration (from $NaNO_3$) for a fuel-lean C_3H_8 flame with the probe at 745 K. The effect of added Cl_2 is indicated.

tra were difficult to obtain due to contaminant absorption with resultant blackbody radiation that prevented the recording of the weaker Raman features. Similar increased corrosion/oxidation was also noted with fuel-rich hydrogen flames. Future analyses for these cases will utilize an inert probe material.

Sodium Dependence

Measurements of deposit formation rates indicated a linear growth rate, confirming previous data [10,13,14], and gave no indication of incubation times. Typical deposition rates are about 6×10^{-3} gm Na_2SO_4/h-cm^2. Figure 3 indicates the dependence of the rate of deposition on flame sodium concentration. The dependence is exactly first order and was found to be thus for ϕ = 0.8 to 1.2 with C_3H_8/air stoichiometries. Figure 4 shows that exactly the same behavior is seen for hydrogen flames, rich or lean. Such a first-order dependence was also implied by the more difficult burner rig experiments [14,15] burning gas-oil and jet A-1 fuels and is predicted by the chemically frozen multicomponent boundary layer diffusion theory of Rosner [16].

In hydrogen flames, measurements were made both upstream, closer to the reaction zone, and downstream to examine nonequilibrium effects. As illustrated in Fig. 4, there is very little difference between the two locations, and the first-order dependence is observed in all cases. Radical levels in the two probe locations differ 5-fold for OH and H, and 25-fold for O and O_2. The small splitting of the data is consistent solely with the diffusional spread with time of the sodium concentration in the flame, reducing its concentration and, hence, deposition

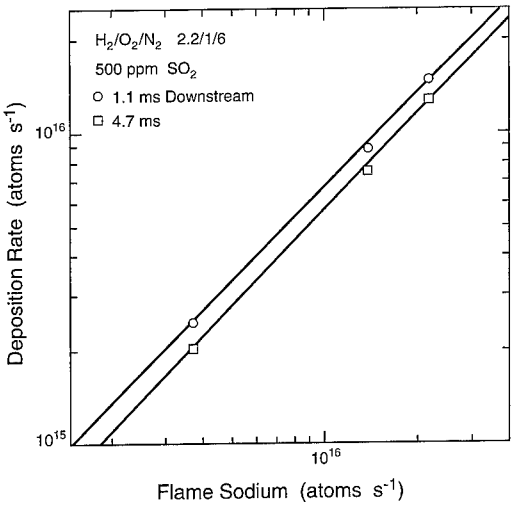

FIG. 4. First-order dependence of the rates of deposition of Na_2SO_4 on flame sodium concentration (from $NaNO_3$) for a fuel-rich hydrogen flame. The effect of flame downstream location on the 730 K probe is indicated.

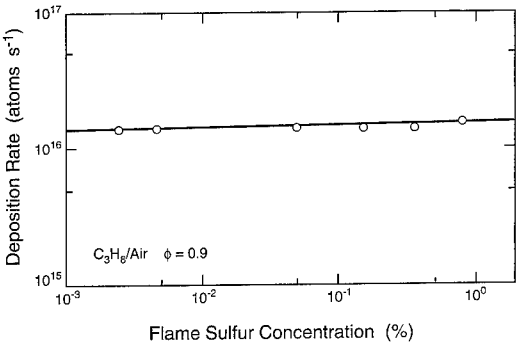

FIG. 5. Zero-order dependence of the rates of deposition of Na_2SO_4 on flame sulfur content for a fuel-lean propane flame. Sodium flame flux (3.1×10^{16} atoms s^{-1}) with a probe located 7 ms downstream and maintained at 745 K.

rate slightly. Similar data were obtained for an $H_2/O_2/N_2$, 1/1/3 flame at 0.9 and 3.6 ms locations. Clearly, deposition is not affected by the state of equilibration in the flame gases.

As established in our earlier work [7–9], although NaOH is the dominant flame gas species under fuel-lean conditions, atomic Na becomes dominant for fuel-rich cases. Deposition rates are essentially identical for the differing stoichiometries. Moreover, on the addition of 0.4% Cl_2 to a $\phi = 0.9$, C_3H_8/air flame, the situation changed from one in which NaOH is dominant to one in which NaCl is dominant (60:1 ratio relative to NaOH). As indicated in Fig. 3, no pronounced change occurs in the sodium

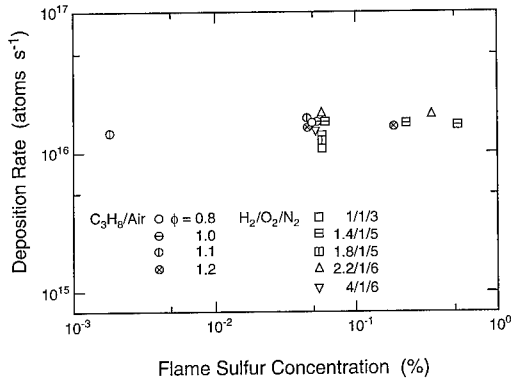

FIG. 6. Zero-order dependence of the rates of deposition of Na_2SO_4 on flame sulfur content for a variety of rich and lean, propane and hydrogen flames. Sodium flame flux (3.1×10^{16} atoms s^{-1}) with the probe located 4–10 ms downstream and maintained at 700–775 K for the various flame cases.

deposition rate. Consequently, it is very clear that the surface is nonselective with regard to sodium. It adsorbs Na, NaOH, or NaCl at equivalent rates and treats them as equivalent sodium sources. The formation of Na_2SO_4 is unambiguously a heterogeneous process, and it appears that the rate-determining step that reflects the first-order dependence is the initial efficient adsorption.

After careful calibration of the nebulizer delivery and transmission line losses, it is apparent in Fig. 3 and 4 that deposition rates are large. Collection efficiency is 43% for the propane flame, and 67% (upstream) and 57% (downstream) in the hydrogen flame of Fig. 4. Calibration errors are not expected to be in excess of 20%. The surface acts like a sticky fly paper and extracts a significant fraction of the sodium from the intercepted flow streams. Deposition appears not to be a boundary layer diffusion phenomena, which is a much slower, less efficient process. Previous work [4,5] invoked the presence of particles in the burnt flame and the concept of inertial impact, in which the particle momenta carries the particles directly through the boundary layer. Current conditions in this work tend to guarantee homogeneous burnt gases, and alternate fluid mechanistic explanations for such high rates of deposition now appear to be needed. Consequently, it is difficult to accept recent claims that agreement exists between a boundary layer diffusion theory and experimental measurements of Na_2SO_4 deposition rates on a complex burner rig system [15].

Sulfur Dependence

As illustrated in Fig. 5 for a $\phi = 0.9$, C_3H_8/air flame, Na_2SO_4 formation is zero order with respect

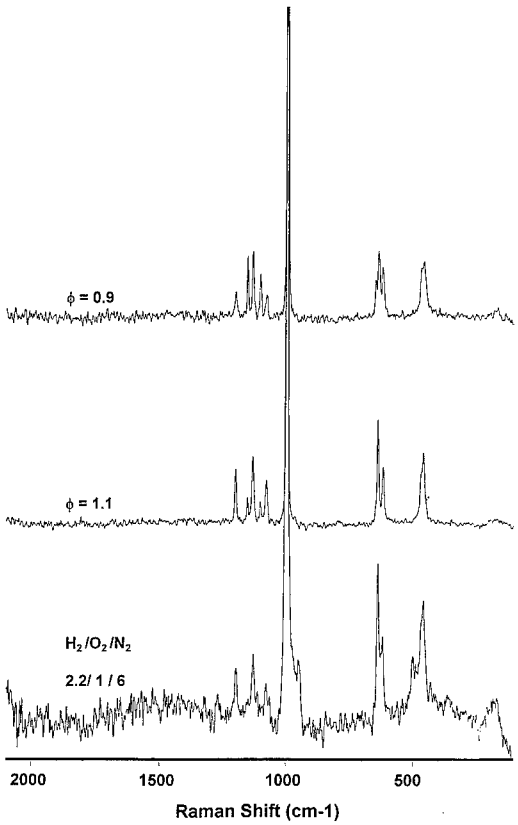

FIG. 7. Raman spectra of probe deposit material for various flames in which sodium and sulfur concentrations were identical (from $Na_2S_2O_3$ aqueous aerosols) and at about 97, 72, and 20 ppm, respectively, in the three flames. Probe locations were 7, 5, and 4 ms downstream and maintained at about 725–740 K.

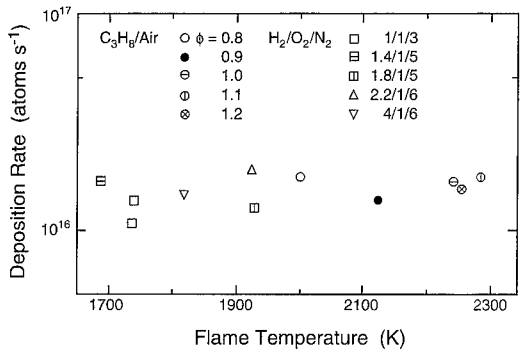

FIG. 8. Rates of deposition of Na_2SO_4 as a function of flame temperature for a wide variety of propane and hydrogen flames. Flames contain 500 ppm SO_2, refer to a similar sodium flame flux (3.1×10^{16} atoms s^{-1}, from $NaNO_3$), and are collected on probes located 4–10 ms downstream, maintained at temperatures in the range 700–770 K.

to sulfur flame concentrations. The data lie within 1% of such a zero trend over several orders of magnitude. Figure 6 shows the generality of this observation for a wide variety of rich and lean propane and hydrogen flames. The data show more scatter due to the difficulties arising from making such comparisons between very different flames. This independence appears not to have been reported previously. It extends over the full range for sulfur concentrations that are equal to or in excess of the flame sodium concentrations. As indicated in Fig. 7, deposits obtained in cases where sodium and sulfur have equal concentrations are identical to those obtained with larger excesses of SO_2 (Fig. 1) and confirm the formation of quite pure Na_2SO_4 with just a trace of Na_2CO_3 and the slight impurity that generates the 1202 cm^{-1} Raman line.

Obviously, attempts to lower the sulfur content of fuels will have no influence on the Na_2SO_4 deposition rates and the attendant Na_2SO_4 high-temperature corrosion rates.

Equivalence of Differing Sources of Sodium or Sulfur

Although flame techniques are widely accepted for total sodium analyses, there still remain skeptics as to the efficiency with which flames can atomize molecules. In the present program, numerous salts have been used as sources of both Na and S. $NaNO_3$, Na_2SO_3, and $Na_2S_2O_3$ are all known to dissociate at low temperatures. Na_2SO_4, however, is thermodynamically more stable and thermally vaporizes and dissociates above its melting point (1157 K) [17]. Because of the uncertainties associated with this stability, deposition comparisons were made for nebulized Na_2SO_4 and Na_2SO_3 solutions. In $\phi = 0.9$ and 1.1, C_3H_8/air flames, there was exact agreement. Present results confirm that for concentrations up to 100 ppm, certainly, and in flames hotter than 1700 K, all the salts used were totally equivalent sources of sodium or sulfur, and reflected their formula ratios.

A necessary conclusion, supported by our previous work [8,9], is that under normally experienced conditions, $Na_2SO_4(g)$ is not present in the burnt gases even if Na_2SO_4 is used as the source of sodium.

Dependence of Deposition Rates on Flame Temperature, Stoichiometry, or Fuel Type

Figure 8 summarizes Na_2SO_4 deposition rates for equivalent amounts of sodium in the various flames examined. The scatter of the data is not regarded as significant. It is concluded that the probe surface appears to be indifferent as to the type of flame, its

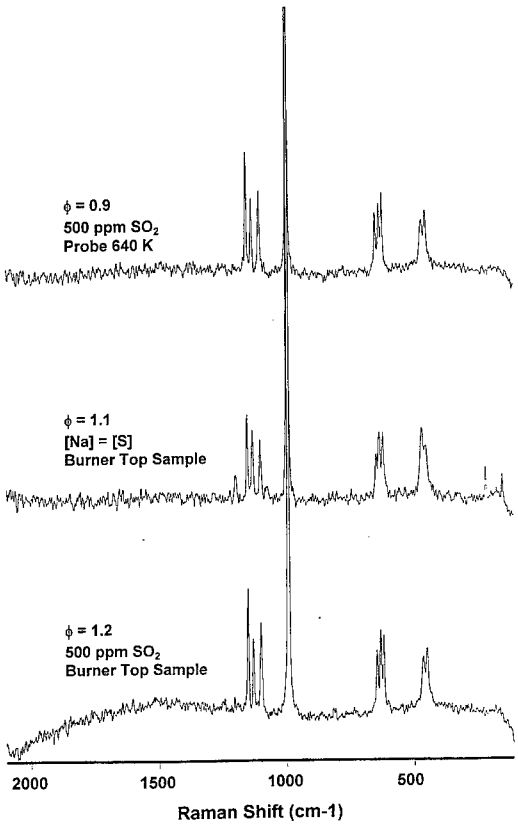

FIG. 9. Raman spectra of a lower temperature probe sample and some burner top samples for various C_3H_8/air flames containing 49, 72, and 31 ppm of sodium, respectively.

temperature, fuel type, or state of equilibration. The surface appears to regard the flame solely as a source of gaseous sodium (and is equally indifferent to its atomic or molecular state) and will process this to Na_2SO_4 if adequate sulfur exists.

This constancy of deposition rate was also reported by Deadmore et al. [18]. On a burner rig utilizing jet A fuel, two lean flames of 0.50 and 0.76 equivalence ratios formed equivalent amounts of Na_2SO_4 but displayed significantly different extents of corrosion. Factors other than rates of deposition of Na_2SO_4 are clearly also involved in corrosion mechanisms.

Irreversibility

Numerous experiments examined whether the Na_2SO_4 deposition process was reversible or not. Deposits were collected on the probe, after which the sodium and sulfur sources were turned off but the clean flame gases were still allowed to impinge on the deposit. It was found that even after several hours no change occurred and the Na_2SO_4 deposit was unaffected. Even if the probe was relocated to a position very close to the reaction zone of an $H_2/O_2/N_2$ flame and placed in the highly nonequilibrated region rich in radical species, no burning off of the deposit was at all evident. Indications are that due to its thermodynamic stability and high melting point (1157 K), once deposited, Na_2SO_4 remains and is not susceptible to chemical attack (except possibly by chlorine).

Probe Temperature Effects and Burner Top Samples

Probe surface temperatures were maintained in the range 640–780 K. Many of the possible sodium/sulfur salts that can exist are unstable and dissociate at these temperatures, namely $NaHSO_3$, $NaHSO_4$, Na_2SO_3, $Na_2S_2O_3$, $Na_2S_2O_4$, $Na_2S_2O_5$, $Na_2S_2O_6$, and $Na_2S_2O_8$. Other than Na_2SO_4, the only other stable salts are the pyrosulfate, $Na_2S_2O_7$ (674 K melting point, dissociation on boiling at 733 K), and Na_2S (1193 K melting point). As indicated in Fig. 9, however, even with probe temperatures at 640 K there is no indication of formation of these salts. The lower temperatures also appear to remove the slight presence of Na_2CO_3 (1123 K melting point) and the 1202 cm^{-1} frequency peak and show only the Raman spectrum of pure Na_2SO_4. There is no indication of Na_2O (sublimes at 1548 K) or NaCN (835 K melting point), and NaOH deposits are not expected (591 K melting point). $NaHCO_3$ also is unstable at these temperatures (dissociating on melting at 543 K). For this range of probe temperatures, rates of deposition remained essentially constant for both the propane and hydrogen series of flames. The high collection efficiency with respect to sodium also remained unaltered. The physical state of the probe surface, however, did seem to be affected. At higher temperatures, the surface blackened significantly and greater levels of probe surface oxidation were evident. Nevertheless, whether the probe surface was cleansed of oxide deposit or utilized without cleaning for numerous experiments, rates of deposit were insensitive to the exact quality of the stainless steel surface.

Srinivasachar [19] has carried out a series of long-term deposition experiments very similar to our own. Utilizing a $\phi = 0.8$, CH_4/air flame at 1650 K, and a 3.2-mm-diameter air-cooled tubular probe maintained at 1050–1100 K (close to the melting point of Na_2SO_4), his data imply a 2–4.3% sodium collection efficiency by the surface. The surface collection efficiency may become a function of temperature at higher temperatures. This, however, is in conflict with NASA data which indicate constant rates of deposition from 770 K to the melting region of 1150 K, but for Mach 0.3 flows at much higher Reynolds numbers [5].

On burning the present flames, deposits not only formed on the cooled probe surface but also started building up on the capillary honeycomb matrix of the top of the burner. This was most pronounced with the slower burning velocity propane flames but was also evident, although quite slight, for the hydrogen flames. Samples were removed from the top of the burner and analyzed. Typical Raman spectra are indicated in Fig. 9 for two extreme cases of sulfur concentrations. Surprisingly, their analysis reflected the probe samples. Even though the burner top is only at about 350 K, none of the other numerous sulfur compounds that could exist are formed. Formation of Na_2SO_4 appears to be the dominant channel and must occur with minimal if any activation energy. Although there is a slight indication of the 1202 cm^{-1} peak when [Na] = [S], it is not present for an excess of sulfur. Back diffusion of pyrolyzing $NaNO_3$ in the preheating gases that constitute the short stand-off distance above the burner top, or of sodium atoms from the reaction zone appears to provide the required sodium source.

Laminar/Turbulent Effects

As already described, the probe surface extraction of sodium from these flames appears not to be a boundary layer–controlled process. A reasonable fraction (35–60%) of the gaseous atomic or molecular sodium that is physically intercepted was adsorbed onto the surface. This was illustrated by a series of experiments with different-shaped probes and by comparing laminar and turbulent flow flames. Deposition results from a V-wedge, a circular, and a totally flat surface directed against the burnt gas flow were identical. Moreover, changing the laminar flow burner to a drilled plate design that created turbulent flames also produced similar results. At the relatively low levels of sodium, the burnt gases are homogeneous and sodium salt condensation appears impossible. The mechanism by which the sodium is drawn through the boundary layer so effectively requires explanation.

Chlorine Effects

At present, we have done only several preliminary experiments on Na/S/Cl flame systems and all with significant levels of chlorine addition. As already discussed, whether Na, NaOH, or NaCl is the dominant form of sodium in the burnt gases, all show similar sodium deposition rates and a first-order dependence on sodium concentration. An initial analysis of a deposit from a $\phi = 0.9$, C_3H_8/air flame containing 50 ppm Na, 500 ppm SO_2, and 0.4% Cl_2 has been made. This shows a composition of 37% Na_2SO_4 and 63% NaCl and indicates, at sufficiently high levels of chlorine, that NaCl formation can compete with that of Na_2SO_4, but that the overall rate of deposition of sodium remains unchanged. Unpublished results of Srinivasachar [19] also confirm the insensitivity of sodium deposition rates to the presence of chlorine. However, in a $\phi = 0.8$, CH_4/air flame containing 33 ppm Na, 250 ppm SO_2, and 200 ppm HCl, his analyses indicate that NaCl $< 10\%$ Na_2SO_4 in the deposit. In practical systems, NaCl is almost never found on corroded turbine blades [1,3] or mixed with normal Na_2SO_4 deposits [19]. Consequently, it presently appears, at normally encountered levels of chlorine, that Na_2SO_4 deposition is dominant but is controllable by the flame Cl content. Whether NaCl formation can compete at substantially lower levels of sulfur has to be seen, as also whether Na_2SO_4 and NaCl deposits may be interconvertible.

Concluding Remarks

The present program has revealed numerous unexpected results, some of which need explanation and some further study. Overall, we now see a consistent behavior for conditions when sulfur is equal to or in excess of the sodium concentration. Among the questions remaining is whether the probe surface is controlled solely by thermodynamic equilibrium considerations. The very high collection efficiency of the probe is an unexplained surprise. The observation that Na_2SO_4 deposition rates are first order in sodium and zero order in sulfur indicates that sodium concentration levels are the most important controlling parameter with regard to high-temperature corrosion.

Acknowledgments

The authors gratefully acknowledge the support of this work by the Chemical and Transport Systems Section of the National Science Foundation, Grant Number NSF CTS-9020355, monitored by Dr. M.J. Linevsky, and by the Electric Power Research Institute, Grant Number EPRI RP8005-15, monitored by Dr. A. Mehta. We are also indebted to Dr. V. Srdanov for help in obtaining spectra on the Nicolet Fourier transform Raman spectrometer.

REFERENCES

1. Stringer, J., *High Temp. Technol.* 3:119–141 (1985).
2. Gupta, A. K., Immarigeon, J.-P., and Patnaik, P. C., *High Temp. Technol.* 7:173–186 (1989).
3. Stringer, J., and Banerjee, D. D., Eds., *Chlorine in Coal: Proceedings of an International Conference, Coal Science Technology Series*, Elsevier, Amsterdam, 1991.
4. Stearns, C. A., Kohl, F. J., and Rosner, D. E., in *High Temperature Corrosion* (R. A. Rapp, Ed.), NACE, Houston TX, 1983, NACE-6, pp. 441–450.
5. Santoro, G. J., Gokoglu, S. A., Kohl, F. J., Stearns,

C. A., and Rosner, D. A., in *High Temperature Corrosion in Energy Systems* (M. F. Rothman, Ed.), Metallurgical Society of AIME, 1985, pp. 417–434.
6. Muller III, C. H., Schofield, K., Steinberg, M., and Broida, H. P., *Seventeenth Symposium (International) on Combustion,* 1979, The Combustion Institute, Pittsburgh, pp. 867–879.
7. Hynes, A. J., Steinberg, M., and Schofield, K., *J. Chem. Phys.* 80:2585–2597 (1984).
8. Steinberg, M., and Schofield, K., *Prog. Energy Combust. Sci.* 16:311–317 (1990).
9. Schofield, K., and Steinberg, M., *J. Phys. Chem.* 96:715–726 (1992).
10. McCarty, K. F., and Anderson, R. J., *Combust. Sci. Technol.* 54:51–60 (1987).
11. Sato, S., Higuchi, S., and Tanaka, S., *Appl. Spectrosc.* 39:822–827 (1985).
12. Degen, I. A., and Newman, G. A., *Spectrochim. Acta* 49A:859–887 (1993).
13. Brown, T. D., *J. Inst. Fuel* 39:378–385 (1966).
14. Hart, A. B., Laxton, J. W., Stevens, C. G., and Tidy, D., in *High Temperature Alloys for Gas Turbines* (D. Contsouradis et al., Eds.), Applied Science Publishers, Ltd., London, 1978, pp. 81–107.
15. Gokoglu, S. A., and Santoro, G. J., in *High Temperature Alloys for Gas Turbines and Other Applications* (Betz, W. et al., Eds.), Reidel, Dordrecht, 1986, pp. 1117–1126.
16. Rosner, D. E., Chen, B.-K., Fryburg, G. C., and Kohl, F. J., *Combust. Sci. Technol.* 20:87–106 (1979).
17. Lau, K. H., Brittain, R. D., Lamoreaux, R. H., and Hildenbrand, D. L., *J. Electrochem. Soc.* 132:3041–3048 (1985).
18. Deadmore, D. L., Lowell, C. E., and Kohl, F. J., *Corrosion Sci.* 19:371–378 (1979).
19. Srinivasachar, S., private communication, 1994.

COMMENTS

Prof. D. E. Rosner, Yale University, USA. The experimental observations you report, especially on Raman-inferred solid deposit compositions well below the Na_2SO_4 melting point, are refreshing additions to this recently dormant field. Many of your observations, especially those on alkali capture fraction and insensitivity to "normal boundary layer considerations", are provocative and must be accounted for in a generally useful theoretical framework. As you point out, this framework has been under intensive development in the last 2 decades, with emphasis on "boundary layer (BL) considerations" rather than the detailed interfacial chemistry of what is really a chemical vapor deposition (CVD) process (since the material deposited is not present in the mainstream vapor mixture). Among my immediate comments and questions are the following:

Our earlier work, in which NaOH(g) was the dominant Na-carrier, was deliberately focused on the liquid deposit surface temperature interval between the dew-point (dp) and the deposit melting point (mp) because hot corrosion rates of turbine blade alloys usually peak within this interval. Have you examined dp-temperatures in your experiments, and deposition rates in the immediate vicinity of this interesting and important surface temperature [1–3]? We have shown that provided the interfacial chemistry is fast enough, deposition rates far below T_{dp} are quite insensitive to vapor phase speciation and were nearly the same in the two asymptotic limits of "chemically frozen" and "local equilibrium" BLs [2].

However, if the interfacial chemistry (adsorption + reaction) were rate-controlling then deposition rates far below T_{dp} should be insensitive to mainstream velocity as well as target shape, and sensitive to surface temperature. Moreover, vapor capture fractions should be much lower than 2 $Nu_m/(Re^{\bullet}Sc)$ [4]. Is this the case in your experiments?

REFERENCES

1. Rosner, D. E. and Nagarajan, R., "Transport-Induced Shifts in Condensate Dew Points and Composition in High Temperature Multi-component Systems With Chemical Reaction," *Chem Eng. Sci.* (Pergamon) 40 (2):177–186 (1985).
2. Rosner, D. E. et al., "Maximum Effect of Vapor Phase Chemical Reactions on CVD Rates and Deposition Onset Conditions in the Absence of Interfacial Chemical Kinetic Barriers," *Proc. 10th CVD Conf., Electrochem. Soc.*, 87-8:61–80 (1987).
3. Rosner, D. E., "Experimental and Theoretical Research on the Deposition Dynamics of Inorganic Compounds from Combustion Gases," *Physico-chemical Hydrodynamics (PCH)* 10(5/6):663–674 (1988).
4. See, eg., Rosner, D. E., *Transport Processes in Chemically Reacting Flow Systems,* Butterworth-Heinemann, 1st. ed., 1986, Eq. 6.3-6 (Second Ed. in prep.).

Author's Reply. We are familiar with your interesting analyses of transport phenomena, particularly in interpreting the data obtained at the NASA Lewis Research Center. Their results were obtained at much higher Reynolds numbers with turbulent boundary layers and under much more difficult experimental conditions. The possible shift in expected dew point temperatures due to boundary layer compositional modifications by transport is intriguing. In our fuel-rich flames, however, the predominant sodium species in the burnt gases is atomic sodium and the probe temperatures were always well above its dew point. For fuel-lean flames the probe was below the dew point of NaCl but in cases where NaOH was predominant the probe was in the very vicinity of the dew point region in numerous

cases. The constancy of deposition rates does tend to suggest that dew point considerations cannot be paramount.

Although our current measurements have been with probe temperatures below the melting point of Na_2SO_4, corrected NASA data [5] do indicate a constancy of deposition from 773 to 1240 K. This connects our temperature range to above the Na_2SO_4 melting point, which is about 1157 K, and indicates that the presence of the liquid phase on the surface does not significantly modify the process. We do plan to confirm this in the near future.

Our sodium vapor capture rates are high (35–60%). Based on your equation above for the predicted upper limits, we have calculated these values for our conditions using an average temperature in the boundary layer. This indicates that capture rates should be lower than 9–21% for the hydrogen flames and 37–50% for the propane flames, based on these transport considerations.

The indifference of the surface to the atomic or molecular state of the alkali in the flame is intriguing. This will be tested further by using cesium-seeded flames in which the cesium is essentially fully ionized.

Twenty-Sixth Symposium (International) on Combustion/The Combustion Institute, 1996/pp. 1845–1849

A MATHEMATICAL MODEL OF LASER-INDUCED SYNTHESIS OF ULTRAFINE SiC POWDERS

S. S. KHARTCHENKO AND A. I. KUZMIN
Russian Scientific Center "Applied Chemistry"
14 Dobrolyubova, St.-Petersburg, 197198, Russia

Introduction

Ultrafine ceramic powders are of considerable interest at present as components in the fabrication of structural ceramics. The laser-induced synthesis may be the most promising method for producing such powders. The small reaction volume and the steep temperature gradients permit the formation of very fine, nearly monodispersed, and extremely pure particles.

There are a number of works to date where the numerical investigation of some aspects of the process has been carried out [1,2]. This paper seeks to describe a simple model of SiC powder synthesis in gas phase with a CO_2 laser as a heat source, including all important aspects of the process, and on the basis of the model seeks to investigate the principal relations in the system. The model couples the hydrodynamics, the simplified chemical kinetics, and the equations describing the nucleation and particle growth. The model is used to get some basic relationships between the process parameters. The schematic of the problem is shown in Fig. 1.

Model Description

The description of the gas flow is based on the following assumptions:

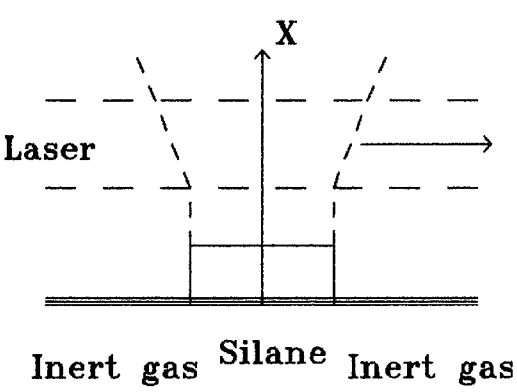

FIG. 1. Schematic of the problem.

a. The process is stationary.
b. The one-dimensional approach is used. Thus, the jet expansion due to mixing is disregarded and the heat expansion is modeled.
c. The pressure is assumed to be constant.
d. The gas viscosity is disregarded.
e. The carbide particles being very small are assumed to move at the local gas speed.
f. In order to simplify the calculations, the sections of the laser beam and the gas jet are treated as square instead of circular.

The chemical kinetics is described by the summarized reactions, and the effective reaction rates are used. In this work, the following process is considered:

$$2\ SiH_4 + C_2H_4 \rightarrow 2\ SiC + 6\ H_2$$

The reactions are assumed to proceed by a purely thermal mechanism, i.e., the molecules of SiH_4 and C_2H_4 absorb the laser energy, and due to V-T relaxation, the gas heats up. Under certain conditions, the reactions between the vibrationally excited molecules may be a factor, yet, apparently, the thermal mechanism is dominant [1].

The system of equations is described as follows:

- Mass and momentum of the gas-powder mixture are

$$d(\rho uF)/dx = 0 \quad (1)$$

$$d(\rho u^2F)/dx = 0 \quad (2)$$

(As follows from Eqs. (1) and (2), $\rho uF = G =$ const. and $u = u_0 =$ const.)

- Energy of the gas-powder mixture is

$$d(\rho uhF)/dx = J_0 \min(L, D)\,[1 - \exp(-\alpha PD)] - Q_\sigma \quad (3)$$

- Energy of the solid phase is

$$d(\rho_c u h_c F)/dx = 4\pi r^2 N_p F\, u\, C_Q - Q_\sigma \quad (4)$$

- Heat radiation of carbide particles is

$$Q_\sigma = 4\pi r^2 N_p F \sigma_0 (T_c^4 - T_w^4)$$

(An expression for the term C_Q for the tiny particles is given in Ref. 4.)

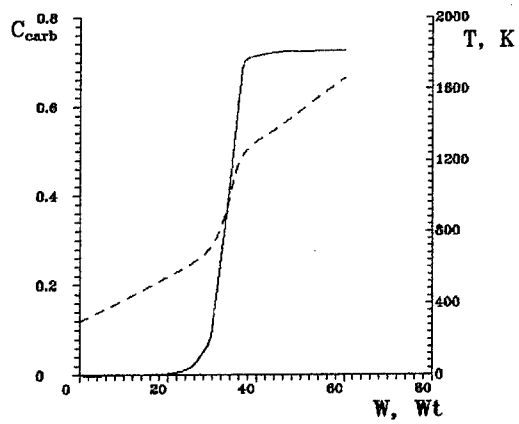

FIG. 2. Mass fraction of carbide powder (solid line) and temperature of gas after it leaves the laser beam (dashed line) as functions of laser power.

- Species of gas phase is

$$d(\rho u C_i F)/dx = W_i(C_i, T) \quad (5)$$

(where C_i are the mass fractions of SiH_4, C_2H_4, H_2, and SiC).

- Mass fraction of solid phase is

$$d(\rho u C_e F)/dx = (4\pi/3)\rho_{SiC} F \left(I_0 r^{*3} + \int_0^x I_0\, dr^3/dx\, dx\right) \quad (6)$$

The nucleation and growth of carbide particles are described within the scope of the Zel'dovich–Frenkel theory [3]:

$$I_0 = \alpha_k (P_{SiC}/kT)^2 (1/\rho_c)(2\sigma\mu_{SiC}/\pi N_A)^{1/2} \exp(-4\pi\zeta\sigma r^{*2}/3kT)$$

$$dr/dx = (\alpha_k/\rho_{SiC})\,[P_{SiC}/(2\pi RT)^{1/2} - P_\infty/(2\pi RT_c)^{1/2}]$$

$$r^* = 2\,\sigma\mu_{SiC}/[\rho_{SiC} RT \ln(P_{SiC}/P_\infty)]$$

where α_k is the condensation factor and ρ_{SiC}, μ_{SiC}, and P_{SiC} are carbide density, molecular weight, and partial pressure, respectively. The correction factor ζ is introduced according to Ref. 4.

The system of equations is closed by the state equation

$$P = \rho_g R T_g/\mu$$

and the relations

$$\rho = \rho_g + \rho_c$$
$$h = C_g h_g + C_c h_c$$
$$C_g + C_c = 1$$

The specific enthalpies of species are approximated by polynomials of the third power based on the tables in Ref. 5. The saturated vapor pressure is approximated, based on the same tables, as

$$p_\infty = A \exp(-E/RT_g)$$

It is assumed that the vaporized silicon carbide condenses immediately into the solid phase because the melting temperature of α-SiC is 3100 K.

The absorption coefficients are calculated as

$$\alpha = \gamma_{C_2H_4}\,\alpha_{C_2H_4} + \gamma_{SiH_4}\,\alpha_{SiH_4}$$

The absorption coefficient of silane is approximated, based on [1], as

$$\alpha_{SiH_4} = [\alpha_0 + a \exp(-b(P - P_0)^2]\ (Pa^{-1}m^{-1})$$

where $\alpha_0 = 3.66\ 10^3$, $a = 9.8\ 10^{-3}$, $b = 1.38\ 10^{-7}$, and $P_0 = 3.4\ 10^3$ Pa.

The absorption coefficient of ethylene is assumed to be constant and equal to $1.1\ 10^{-3}\ Pa^{-1}\ m^{-1}$ [1].

The reaction mechanism of silane decomposition may be described as follows [6]:

$$SiH_4 \rightarrow SiH_2 + H_2 \rightarrow \text{products}$$

The rates of many multistep reactions are controlled by the first step where the formation of active radicals occurs. The evaluation of reaction rates shows that in this case, the decomposition reaction $SiH_4 \rightarrow SiH_2 + H_2$ is a factor. The results of the work [6] corroborate the conclusion. Thus, the total reaction rate is taken equal to the controlling reaction rate:

$$K_{SiH_4} = 5.0\ 10^{12} \exp(-26\ 800/T)\ (s^{-1})$$

In order to examine the effect of variables for which the precise values are unknown (surface tension, reaction rates), the preliminary calculations were carried out. The value of the surface tension was varied by a factor of 100. This variation has no impact on the powder output (it changes within 10%) but affects the particle size (from 1 to 100 nm). The reaction rate also was varied by a factor of 100. The powder output changes within 20% and the particle size within 10%. Thus, the obtained results for powder output depend weakly on inaccuracy of the model parameters.

Results

The following calculations were carried out to compare model and experiments. The starting values are as follows: the flow velocity is 1 m/s, the pressure is 0.2 atm, the initial temperature is 300 K, the initial jet diameter is 2 mm, and the mass fractions are SiH_4 (0.55) and C_2H_4 (0.45). The calculations start after gas flow enters the laser beam. The laser beam diameter is 7 mm. These data correspond to the conditions of the experiment [7].

In Fig. 2, the SiC powder output and the gas temperature after the flow leaves the laser beam are

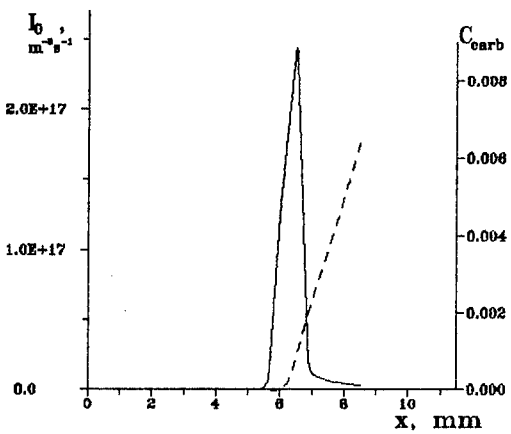

FIG. 3. Nucleation rate and mass fraction of carbide powder as functions of distance, $W = 33$ Wt.

plotted against laser power. The threshold is clearly displayed on the plot. As can be seen from Fig. 2, the reaction is initiated upon heating to 900 K, which corresponds to the experiment [7]. Under reference conditions, the gas absorbs about 10% of the laser energy. The gas temperature is growing monotonically down the stream. When the laser power exceeds the threshold value, the temperature growth beyond the laser beam is slowed down but is not stopped completely because the heterogeneous reaction of silane and ethylene is exothermic and does not need the external heating after the initiation.

The particle sizes rather weakly depend on the laser intensity and are 20–22 nm. The experimental value [7] was 23 nm. The agreement between the model and the experiment is excellent with a correction factor $\zeta = 5$ and a condensation factor $\alpha_k = 0.9$.

Figure 3 presents the plot of nucleation rate and mass fraction of carbide powder as functions of distance, for the threshold value of laser intensity. The figure shows that the nucleation rate has a distinctive maximum at the point where active condensation starts. Behind this point, the condensation causes mainly the growth of existing particles, which evidently provides the monodispersed properties of carbide powder.

The model predicts the closeness of the particle temperature and the given ambient temperature due to the heat radiation. Thus, the total losses by radiation are small (under 1% from the absorbed laser energy). If the ambient temperature is higher, the particle temperature also rises and the condensation of vaporized carbide is slowed.

The investigation of effects of model parameters on the particle size indicates that when the laser intensity exceeds the threshold value, the particle size weakly depends on the intensity and the temperature and the value is 19–22 nm.

It should be noted that due to the lack of data on chemical kinetics and several important parameters (for example, condensation factor, absorptivity as a function of temperature and pressure), the results require further verification.

Discussion

On the basis of the calculation results and an understanding of the process, an expression for the threshold power can be obtained. The gas phase reaction has negative heat balance (-31.55 mJ/kg) and is endothermic. During the condensation process, the heat is released and the total heat balance is 9.49 mJ/kg. Thus, the reaction becomes exothermic and the process becomes self-increasing when the heat of carbide formation in the gas phase and the heat of its condensation are equal. Because at the initiation of active condensation the nucleation is predominant, the condensation rate is determined by the rate of nucleation, and so, the ignition condition can be written as

$$\Delta Q_{\text{cond}} A_{\text{cond}} C_{\text{SiC}}^2 / T \exp(-E_{\text{cond}}/RT) = -\Delta Q_{\text{form}} A_{\text{form}} \exp(-E_{\text{form}}/RT)$$

or

$$C_{\text{SiC}} = [(\Delta Q\, A)_{\text{form}}/(\Delta Q\, A)_{\text{cond}}]^{1/2}\, T^{1/2} \exp[-(Ez_{\text{form}} - E_{\text{cond}})/2RT] \qquad (7)$$

where subscript *form* corresponds to gas-phase reaction and subscript cond corresponds to condensation. Actually, E_{cond} depends on a critical nucleus radius r^*, but, as the calculations show, r^* changes weakly (about 1–2%), and E_{cond} may be taken as constant.

It should be noted that this condition is very close to that of quasi-stationary condensation (i.e., the equality of the carbide formation and condensation rates), which is correct as the calculations show. On the other hand, before the initiation of active condensation, the mass fraction of carbide in the gas phase is determined by the gas-phase reaction rate and is governed by the equation

$$d\, C_{\text{SiC}}/dx = A_{\text{form}} \exp(-E_{\text{form}}/RT)$$

As the gas temperature in the laser beam increases monotonically, the temperature may replace the coordinate as the independent variable. Also, the diameter of gas flow increases as the square root of the temperature. Taking into account that the laser emission gives the main contribution to the temperature growth and assuming that the fraction of absorbed laser energy is small (a few percent), the following equation for the temperature gradient can be obtained:

$$dT/dx = W_{abs}(0)/H_0T$$

where $W_{abs}(0) = J_0\,\alpha\,P\,D_0^2$ and $H_0 = G\,h(T_0)$.

Then, the connection between the mass fraction of carbide in the gas phase and the gas temperature is

$$dC_{SiC}/dx = A_{form}H_0/W_{abs}(0)\,\exp(-E_{form}/RT)/T$$

The equation integrates to the following expression:

$$C_{SiC} = A_{form}H_0/W_{abs}(0)\,[Ei(-E_{form}/RT_0) - Ei(-E_{form}/RT)]$$

Because $E_{form}/RT > 1$, the expansion of $Ei(x)$ into a series can be used. Retaining only the first term of the series, the following expression can be obtained:

$$C_{SiC} = A_{form}H_0/W_{abs}(0)\,[\exp(-E_{form}/RT)\,RT/E_{form} - \exp(-E_{form}/RT_0)RT_0/E_{form}]$$

The temperature equation gives the temperature after the flow leaves the laser beam as a function of the laser intensity:

$$T = T_0\,\exp(W_{abs}(0)/H_0\,L) \tag{8}$$

Finally, the expression connecting the mass fraction of vaporized carbide and the gas temperature after the flow leaves the laser beam was obtained:

$$C_{SiC} = A_{form}L/\ln(T/T_0)\,[\exp(-E_{form}/RT)\,RT/E_{form} - \exp(-E_{form}/RT_0)\,RT_0/E_{form}] \tag{9}$$

Equating (7) and (9), the equation can be obtained that gives the temperature of process initiation and the corresponding laser intensity (8).

The final equation under the conditions of this work

$$[(\Delta Q\,A)_{form}/(\Delta Q\,A)_{cond}]^{1/2}\,T^{1/2}\,\exp[-(E_{form} - E_{cond})/2RT] = A_{form}L/\ln(T/T_0)\,[\exp(-E_{form}/RT)\,RT/E_{form} - \exp(-E_{form}/RT_0)\,RT_0/E] \tag{10}$$

gives the following values: the initiation temperature $T = 1095$ K and the threshold laser power about 40 W. These values are somewhat higher than those obtained in the numerical calculations. Nevertheless, Eq. (10) allows us to evaluate the threshold intensity quickly and rather correctly without full-scale numerical investigations.

The above-mentioned expressions are valid over a wide range of laser-induced processes with heat excitation of exothermic reactions. For endothermic reactions, the energy consumption for sustaining reaction should be included.

Conclusions

1. On the basis of the described model, the numerical investigation of the laser-induced synthesis of very fine silicon carbide powder from the reactions of silane with ethylene was carried out. Some parameters are in good agreement with experiment. The model indicates that the necessary laser power under the examined conditions is about 35 W. The threshold behavior of the powder output as a function of laser power is shown.
2. At or near the threshold value, the outlet characteristics (powder output, particle size) depend strongly on laser intensity. Further augmentation of intensity changes the characteristics weakly. Within the examined range of parameters, the particle size depends weakly on gas temperature and composition and is equal to 19–22 nm when the laser intensity exceeds the threshold value.
3. The analysis of the process shows that the threshold value of laser power corresponds to the heating of the gas to ignition temperature. The formulas for evaluation of these values have been obtained.

Nomenclature

C	species mass fraction
D	gas stream diameter
F	gas stream section area
h	specific enthalpy
I_0	nucleation growth
J_0	laser intensity
L	diameter of laser beam
N_p	particles concentration
P	pressure
P_∞	pressure of saturated carbide vapor
r	particles (mean) size
r^*	critical nucleus size
T	temperature
u	velocity
W	laser power
W_i	rate of consumption/production of gaseous components

Greek symbols

α	absorptivity
ρ	density
σ	surface tension
σ_0	Stephan–Boltzmann constant

Subscripts

c	condensed phase
g	gas
w	wall

REFERENCES

1. Haggerty, J. S., and Cannon, W. R., in *Laser-Induced Chemical Processes* (J. I. Steinfeld, Ed.), Plenum Press, New York, 1981, p. 183.
2. Akmandor, I. S., Szekely, J., and Haggerty, J. S., *Int J Heat Mass Transfer* 31:2239–2249 (1988).
3. Pirumov, U. G., and Ryzhov, Yu. A., *Voprosy Mekhaniki i Protsessov Upravleniya* 13:153–159 (1990) (in Russian).
4. Pirumov, U. G., and Roslyakov, G. S., *Gas Dynamics of Nozzles,* Nauka, Moscow, 1990, pp. 312–332 (in Russian).
5. *Thermodynamic Properties of Individual Materials* (V. P. Glushko, Ed.), Nauka, Moscow, 1979, Vols. 1 and 2 (in Russian).
6. Coltrin, M. E., Kee, R. J., and Miller, J. A., *J. Electrochem. Soc.* 131:425–434 (1984).
7. Cannon, W. R. et al., *J. Am. Ceram. Soc.* 65:324–335 (1982).

Twenty-Sixth Symposium (International) on Combustion/The Combustion Institute, 1996/pp. 1851–1858

CONTROLLED COMBUSTION SYNTHESIS OF NANOSIZED IRON OXIDE AGGREGATES

Z. ZHANG AND T. T. CHARALAMPOPOULOS
Mechanical Engineering Department
Louisiana State University
Baton Rouge, LA 70803, USA

Nanosized chainlike aggregates were synthesized in an iron pentacarbonyl–carbon monoxide–air diffusion flame system. The size and shape of the chainlike aggregates and primary particles were characterized in terms of measurable morphological parameters such as diameter of primary particles and aspect ratio. The influences of operating conditions on the parameters have been investigated systematically by employing thermophoretic sampling and transmission electron microscopy (TEM). The morphological parameters were found to be strong functions of operating conditions, residence time, and locations within the flame and could be controlled by adjusting the concentration of $Fe(CO)_5$ seeded in the flame through the variation of carrier gas flow rate and/or temperature of additive.

X-ray diffraction measurements coupled with thermodynamic equilibrium composition predictions were used to identify the chemical states of the particulate components. The results indicated that the aggregates formed in this flame consisted predominantly of primary particles of Fe_2O_3. In addition, the physical and chemical mechanisms of formation of chainlike aggregates are reviewed. Our observations suggest that, while the magnetic forces are necessary for providing a self-alignment mechanism, the flame temperature may also be critical for the formation of chainlike aggregates.

Introduction

Knowledge of the shape and size of aggregates formed in flames is significant in many areas of research and practical applications. Information about the size and shape of both isotropic and anisotropic particulates is important (1) for predicting growth and oxidation of particulates in the combustion systems, (2) for identifying the agglomeration mechanisms of particulates, (3) for efficient control of fibrous aerosols in the industrial hygiene, (4) for quality control of materials synthesized in flame reactors, and (5) for air pollution–control applications [1]. On the other hand, the study of the iron oxide and its properties under formation conditions is particularly useful in ferrofluids applications.

Several studies have been carried out for determining the morphological features of aggregates formed in combustion processes; see Refs. 1–5 and references therein. A number of studies have dealt specifically with the mechanisms of formation of chainlike aggregates in combustion processes [6–11]. The formation of chainlike iron oxide aggregates in a CO-air diffusion flame was studied more recently [2–5], employing both ex situ and in situ techniques. The characteristics of the chain aggregates were determined for samples taken in the postflame region of the flame at different concentrations of the seeding vapor and variable O_2:CO mixing ratio. However, the effects of operating conditions on the morphology variation within the flame were not addressed. In addition, the physical and chemical mechanisms governing the formation of chainlike aggregates remain unclear [6].

Thus, the objectives of the present study were (a) to synthesize chainlike aggregates in an iron pentacarbonyl vapor seeded CO/air diffusion flame, (b) to identify the most critical operating parameters among temperature, feeding flow rate, and feeding ratio of the metal additive to fuel for the dominant generation of chainlike aggregates, (c) to characterize the primary particle size and aspect ratio of the aggregates as a function of residence time and of additive concentration, (d) to determine the chemical compositions of the particulates from experimental measurement and theoretical simulation, and (e) to investigate the mechanism for the formation of chainlike aggregates both from physical and chemical perspective.

Experimental

The experimental system consists of a diffusion-type carbon monoxide–air flame centered around a concentric stainless steel tube. Regulated fuel, carbon monoxide (CO), is supplied through the inner tube (1/4 inch in diameter). The metal additive, iron pentacarbonyl vapor $Fe(CO)_5$, is introduced into the CO-air flame by diverting a small fraction of bulk

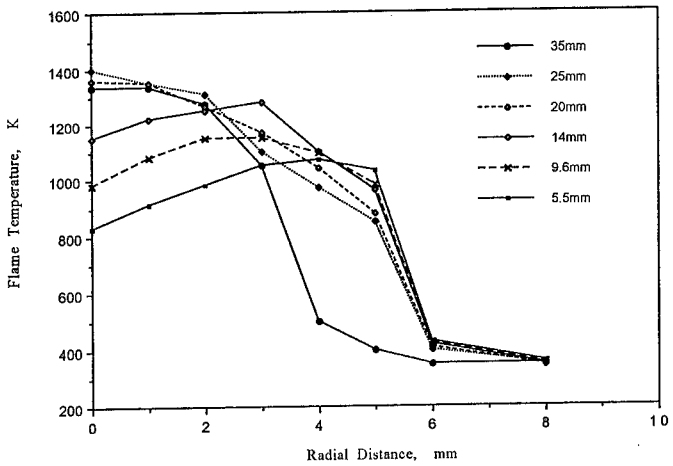

FIG. 1. Radial temperatures for CO-air diffusion flame as function of position above the burner surface.

fuel flow through a column of liquid $Fe(CO)_5$ stored in a temperature-regulated stainless steel cylinder. At the outlet of the cylinder, partially saturated vapor is diluted by main fuel flow and directed to the burner for combustion. The concentration of iron pentacarbonyl vapor introduced into the flame may be controlled by adjusting either the cylinder temperature or the carrier gas flow rate. The system is calibrated so that the actual mass flow rate of iron pentacarbonyl vapor delivered to the fuel, corresponding to different carrier flow rates and cylinder temperature, is known before it enters the flame with an accuracy of $\pm 3.6\%$.

The particulates produced in the flame were extracted through a thermophoretic sampling system, which eliminates the potential postsampling agglomeration of particles [12,13] and were deposited on a 200-mesh copper grid coated with carbon film that is stable under electron beam and can withstand relatively higher temperature conditions. The thermophoretic sampling system consists of a double-acting pneumatic cylinder, a solenoid-controlled directional four-way valve, and a computer-controlled variable time-delay relay circuit. A hall effect switch mounted on the pneumatic cylinder is used to calibrate the position and motion of the piston/probe assembly. A piston speed of 0.86 m/s and a transition time 4 ± 1 ms for the entry of the probe into the flame were achieved with the present system. The vertical position of the probe is fixed, whereas the burner system can be translated in the vertical direction. A pulse generator attached to the gear of the burner translation mechanism monitors the vertical displacement of the burner so that the height of the probe with respect to the burner surface can be controlled to within 1/10 of a millimeter. A slotted plate is placed between the flame and probe to deflect the air current induced by the motion of the probe and to block the heat transfer from the flame to the probe. A platinum versus platinum–10% rhodium (S type) thermocouple with a bead diameter of 0.3 mm was used to measure the flame temperature at various axial and radial locations. Figure 1 shows the radiation-corrected radial temperature profiles of the unseeded CO/air diffusion flame at various heights above the burner surface. Each point on these curves represents an average value of three measurements. A maximum deviation of 2.7% from the average value occurred at a radial position of 4 mm and a height of 35 mm above the burner surface. A detailed description of the experimental system, its components, control, and calibration procedures are presented in Ref. 14.

Results and Discussion

Morphology Characterization

Experiments for the synthesis of chainlike aggregates and the determination of size and morphology of primary particles and chainlike aggregates were performed. Chainlike aggregates were produced in the CO-air diffusion flame seeded with $Fe(CO)_5$ vapor. The configurations of the flame under unseeded and seeded conditions are shown in Figs. 2a and 2b. Seeding the flame with $Fe(CO)_5$ causes bright yellow emissions, which is thermal radiation from the iron oxide particles formed within the flame. The unseeded flame is a predominantly blue flame with a distinct conical white flame front. Yellow regions occurring in the upper portions of the unseeded flame may be attributed to formerly deposited solids in the honeycomb stabilizer of the flame. Nevertheless, the occurrence of such emissions was very sporadic and thus could not influence the measurements of the results in any way.

The size and shape of the chainlike aggregates and primary particles were characterized in terms of the diameter of primary particles and aspect ratio. The

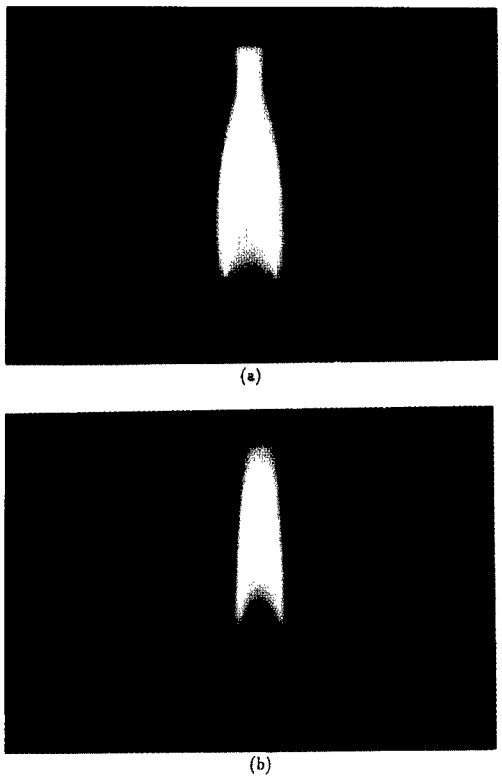

FIG. 2. (a) CO-air diffusion flame. (b) Flame seeded with $Fe(CO)_5$ vapor.

sampled particles and aggregates were grouped and analyzed statistically employing TEM technique so that quantitative results on the primary particle size distribution and aggregate size distribution as a function of position in the flame for various concentrations of $Fe(CO)_5$ were obtained. Typical structures of primary particles and aggregates are shown in the TEM photograph (see Fig. 3). The image of the iron oxide primary particles appears to be hexagonal or polyhedric, which is consistent with the microstructure of Fe_2O_3 [15]. On the other hand, the aggregates exhibit for the most part straight-chain configuration.

The variation of the morphological parameters of iron oxide aggregates with concentrations of iron pentacarbonyl vapor seeded in the flame was investigated by adjusting the cylinder temperature and the carrier flow rate. The first set of experiments was performed by fixing a total fuel flow rate 450 cc/min and a carrier flow rate 20 cc/min and by setting the cylinder temperatures at 23°, 35°, 45°, and 55°C, respectively. A higher cylinder temperature corresponds to a higher mass flow rate of $Fe(CO)_5$ vapor, resulting in a higher concentration of additive in the flame. Under the operating conditions, the frequency distributions of diameters of the primary particles and aspect ratio of chainlike aggregates for samples collected from the center of the flame at 35 mm above the burner surface are presented in Fig. 4. The differential frequency distributions of diameter and aspect ratio are roughly bell-shaped in the linear plot. As cylinder temperature increases, the frequency distributions shift toward larger values of diameter and aspect ratio. It should be noted that at cylinder temperature 45° and 55°C, branched chainlike aggregates were observed.

Note that an alternate way to vary the concentration of $Fe(CO)_5$ vapor seeded into the flame is by adjusting the carrier gas flow rate. The experiments were also performed at a fixed cylinder temperature of 23°C. The carrier gas flow rates were 15, 20, 25, and 35 cc/min, corresponding to 0.5, 0.9, 1.5, and 2.6% of $Fe(CO)_5$ vapor to fuel by weight for a total fuel flow rate of 450 cc/min. Analysis of the results for samples collected from the center of the flame at a height of 25 mm above the burner surface for distributions of diameters and aspect ratios yielded the same trends as those discussed previously. These trends are consistent with the expectation that increasing both cylinder temperature and carrier gas flow rate in turn increased the concentration of seed-

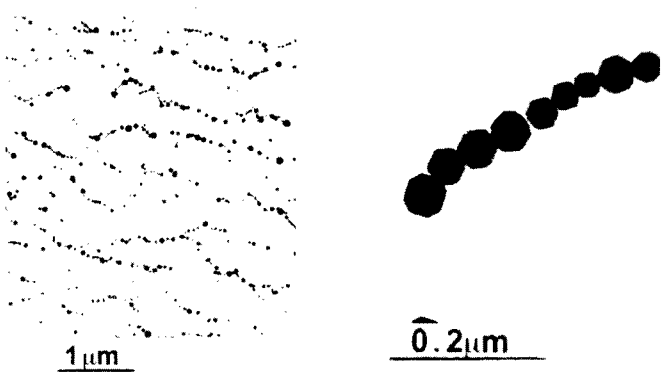

FIG. 3. TEM photographs.

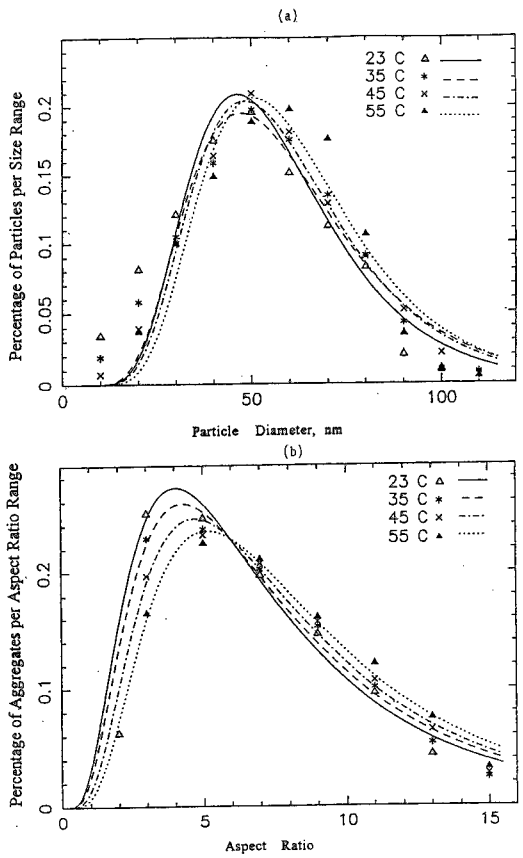

FIG. 4. Frequency distributions of measured diameter (a) and aspect ratio (b) along with ZOLD predictions (Eqs. [1]–[3]) as functions of heated cylinder temperature.

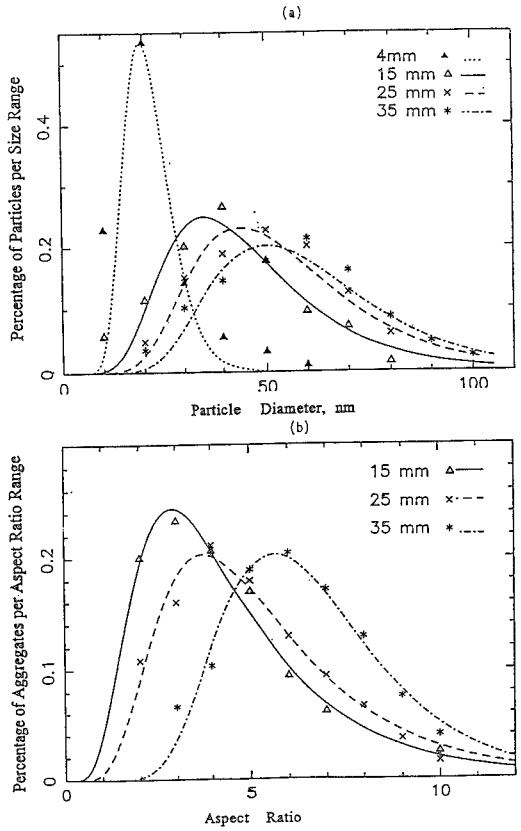

FIG. 5. Frequency distributions of measured diameter (a) and aspect ratio (b) along with ZOLD predictions (Eqs. [1]–3]) as functions of height above the burner surface.

ing vapor. Higher concentrations of $Fe(CO)_5$ vapor result in increased concentration of primary particles. Therefore, the collision probabilities between particles for particle growth and interparticle aggregation are also expected to increase, yielding larger primary particles and longer chainlike aggregates.

The variations of morphological parameters with residence time were assessed by collecting samples within the flame along the centerline at heights of 4, 15, 25, and 35 mm above the burner surface under operating conditions of a total fuel flow rate of 450 cc/min and a carrier flow rate of 25 cc/min with evaporator cylinder temperature maintained at 23°C. The distributions of the sizes of primary particles and aggregates are shown in Fig. 5. At lower positions in the flame, all primary particles possess smaller diameters and the distribution is narrower. As the residence time increases, the particles grow, while the distribution becomes broader as a result of the continuous formation of new primary particles and subsequent aggregation. Because of the magnetic nature of Fe_2O_3 [15], chainlike aggregates were observed at short residence times (about 4 mm above the burner surface). However, the ill-defined aggregate shapes precluded any reliable quantification of the aspect ratio distribution in the range of 4–15 mm above the burner surface. It should also be noted that when the flame temperature at 4 mm above the burner surface was above the Curie point of Fe_2O_3 ($\approx$950 K) [16], no chains were observed throughout the flame. On the other hand, for positions higher than 15 mm above the burner surface, more well-defined chainlike structures were observed.

The experimental data were curve fitted using the method of least squares to a zero-order logarithmic distribution (ZOLD) function [1], which is defined as

$$P(\alpha) = \frac{\exp\left(-\frac{\sigma_o^2}{2}\right)}{\alpha_m \sigma_o (2\pi)^{1/2}} \exp\left(-\frac{\left(\ln\frac{\alpha}{\alpha_m}\right)^2}{2\sigma_o^2}\right) \quad (1)$$

The parameter α_m is the modal value of α, which

TABLE 1
Calculated average diameter, aspect ratio, and standard deviation using ZOLD function with variable additive concentration and height above the burner surface

Variable Temperature				Variable Carrier Flow Rate				Variable Height			
T (°C)	d (nm)	l/d	σ	Q (cc/min)	d (nm)	l/d	σ	H (mm)	d (nm)	l/d	σ
23	57.4	7.08	4.0	15	45.89	4.93	2.6	4	21.7	—	—
35	60.97	8.16	6.0	20	51.03	5.52	2.6	15	45.61	4.17	2.5
45	61.31	8.63	6.1	25	55.13	—	—	25	54.76	5.93	3.2
55	62.16	9.09	6.2	35	59.56	6.38	2.4	35	60.52	6.75	2.4

represents d in the case of particle diameter distribution and (l/d) in the case of aspect ratio distribution. The parameter σ_o is a measure of the width and skewness of the distribution. The calculated ZOLD curves based on the inferred α_m and σ_o values from the least-squares analyses are also shown, along with the experimental data as determined by sampling and TEM analyses. The parameters α_m and σ_o are related to the mean value through the equation [17]:

$$\ln\alpha = \ln\alpha_m + 1.5\sigma_o^2 \tag{2}$$

whereas the standard deviation is given by

$$\sigma = \alpha_m(\exp(4\sigma_o^2) - \exp(3\sigma_o^2)^{1/2}) \tag{3}$$

The mean diameters of primary particles, mean aspect ratio of chainlike aggregates, and standard deviations were calculated for all operating and sampling conditions mentioned previously, and are summarized in Table 1. The results revealed a definite increase in both the mean primary particle diameter and the mean aspect ratio with increasing height above the burner surface and with increasing concentration of $Fe(CO)_5$ vapor seeded into the flame. Note that the largest increase of mean values was encountered at lower positions in the flame (short residence times) and lower concentrations of the additive.

The experimental data of aspect ratio distributions show excellent agreement with the ZOLD function representation, whereas the diameter distributions, for the most part, follow closely the ZOLD function with maximum deviations occurring at the lower and upper portions of the distributions. The somewhat large values of σ exhibited by all distributions may be attributed to any one or combination of the following reasons: (a) The flame is of diffusion type and continuous formation of small particles and aggregates is possible at both radial and axial locations of the flame. (b) The particles formed in the reaction zone, within which the particle volume fraction is high, may be transported to the central portions of the flame through thermophoresis since temperature gradients exist in radial direction (approximately 750 K/mm). (c) The thermophoretic probe could have been contaminated at high particle volume fraction locations during the insertion and/or extraction of the sampling assembly.

Chemical Composition

Although knowledge of chemical states of particle components under flame condition is important for complete understanding of physical and chemical mechanisms through which the chainlike aggregates are formed, it was not possible, at this time, to identify the chemical composition of combustion products under in situ conditions.

Powder X-ray diffraction (XRD) has been proven to be an important standard tool for identification of material compositions. As part of the study, the chemical composition of the particulates collected from $Fe(CO)_5$-seeded flame was identified using X-ray diffraction. The measured X-ray diffraction pattern and characteristic peaks from database (International Unit for Diffraction Data, Powder Diffraction File) are presented in Fig. 6. It was found that the composition of the particulates is Fe_2O_3 with two different microstructures: hematite and maghemite. The sample used for X-ray testing was collected at 35 mm above the burner surface. The equipment used was SIEMENS D5000 X-ray diffraction machine, which has a resolution on the order of 0.5% by weight. It also distinguishes coating material with thickness on the order of 5 nm or even lower, provided that the atoms of mixture are known. However, the shortcoming of the approach may be that the samples could not be isolated entirely from air during the sampling and transportation. Thus, particle oxidation might have taken place before and during the measurement. Nevertheless, since it is generally thought that local thermodynamic equilibrium exists at various points throughout a flame [18], the thermodynamic equilibrium calculations of chemical composition were carried out to predict the distributions of possible chemical species in this flame. Specifically, the computer code developed by

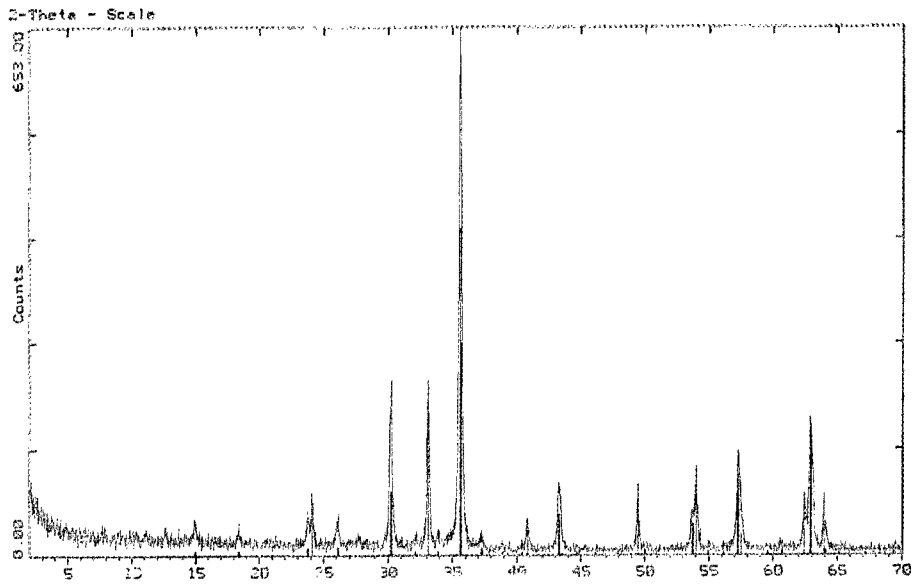

FIG. 6. Measured powder X-ray diffraction pattern for particulates collected from $Fe(CO)_5$ seeded CO-air diffusion flame at 35 mm above the burner surface. Blue lines: hematite; green lines: maghemite. Wavelength used was 1.5406 Å.

Gordon and McBride [19] was employed for the prediction of chemical compositions of particles formed in the $Fe(CO)_5$-seeded CO-air diffusion flame.

Chemical equilibrium compositions of carbon monoxide flames seeded with 1.5% iron pentacarbonyl by weight were calculated for a range of fuel equivalence ratios and over a range of flame temperatures. The predicted fractional distribution of iron species as a function of temperature has been presented in Ref. 20 and demonstrates that nonsignificant ionic iron exists (whereas the dominant iron-containing species is Fe_2O_3 within the flame temperature range studied). It should be noted that the equilibrium calculations are from thermodynamic viewpoint, which gives no indication of the kinetics of such reactions. Moreover, there may be a number of potential pathways through which iron or iron oxides may be formed and a number of factors, such as fuel-equivalence ratio, temperature, concentration of iron additive, flame configuration, type of fuel, and/or other combustion operating conditions, by which the chemical states of iron species may be affected. Thus, the precise chemical composition of all pertinent reaction products may not be precisely predictable at this time.

Mechanism of Chain Formation

As noted earlier, a few studies have addressed specifically the formation of chainlike aggregates. It may be argued that most flame-generated aggregates are formed from thermal coagulation, leading to randomly structured aggregates [9]. However, under certain conditions and specific types of materials, the random motion may be ordered by other forces such as electrostatic and/or magnetic to form well-defined, straight chainlike aggregates. So far, chainlike aggregates have been observed at later stages of the formation or postflame region, and it is believed that the origin of their formation was the result of electrostatic interactions [6–11].

In this study, chainlike aggregates were observed at short residence times (approximately 4 mm above the burner surface) for temperatures lower than about 950 K, which is considered the Curie point for Fe_2O_3 [16]. Since Fe_2O_3 is magnetic material, this observation suggests that the magnetic properties may play a relatively more important role during the particle interactions and chain formation. Nevertheless, as will be explained in the section that follows, other system parameters such as flame temperature may play a role in the formation.

The magnetic properties of Fe_2O_3 are complex in that its fundamental antiferromagnetism superimposed by a weak parasitic ferromagnetism results most likely from defects of cystallization. When the iron-oxide particle sizes are below 3 μm with an aspect ratio of 10, they are magnetized as single-domain particles in the presence of a magnetic field [21]. The mean diameter of particles produced in this flame ranges from 20 to 65 nm, or even smaller at early stages of formation; thus, they possess a net magnetic moment. If each particle is treated as a

dipole of magnetic moment, apparently the magnetic dipole interactions between particles are stronger than thermal interactions in this flame particle system such that the particles are aligned by the magnetic forces through a self-alignment mechanism. This implies that the most stable configuration of three magnetic dipoles energetically is a chain, and the end of the chain is the energetically most favorable position for an approaching fourth particle to be attached, provided there is no mechanism for deforming the chain. Still, as the flame temperature increases, thermal interactions may prevail and provide a mechanism to deform the chain. Thus, aligned chains may no longer constitute the most stable configuration. Instead, either branched chains are formed or the chains break up to form clusters, depending on the relationship of combustion temperature and Curie temperature of the particles. It is noteworthy that in the present study, when the flame became turbulent, only clusterlike aggregates were observed.

Currently, the effects of magnetic forces or dipole moments are not understood well enough to permit a quantitatively precise assessment. Clearly, further studies are required to elucidate the interactions of magnetic and temperature effects and their influence on the morphology and dynamics of the aggregates. Work is underway in this laboratory to study the effects of magnetic fields and temperature on particle interaction/growth.

Summary

The results of the present study may be summarized as follows:

a. The CO-air diffusion flame seeded with $Fe(CO)_5$ vapor was tested and dominantly chainlike aggregates were produced. The size and shape of chainlike aggregates and primary particles were characterized in terms of measurable morphological parameters under different operating conditions. The average diameter of primary particles and average aspect ratio of chainlike aggregates can be controlled by varying the concentration of iron pentacarbonyl vapor seeded into the flame.
b. For the concentration range investigated, namely 0.75–2.8% iron pentacarbonyl vapor to fuel by weight, the average diameter of primary particles and aspect ratio increased by about 30% at 25 mm above the burner surface.
c. The average diameter of primary particles increased by 8.0% and the average aspect ratio by 28% as the temperature of the heated cylinder increased from 23 to 55°C. The total increase of average diameter was about 179% from 4 to 35 mm and the aspect ratio 62% from 15 to 35 mm.
d. Higher concentrations and residence times favor the formation of longer chainlike aggregates. The preceding observations were repeated with identical results with maximum deviation of 5% from the mean values by performing the same measurements. The data, statistically analyzed for the average 1000 particles and 500 aggregates from each run, are expected to provide representative picture of the particulate morphology of iron oxide aggregates formed in this type of flame reactor.
e. Both X-ray diffraction measurements and thermodynamic equilibrium calculations showed that the chemical composition of the particles formed in the flame is consistent with Fe_2O_3. In addition, our observations indicated that, while magnetic forces are essential for providing a self-alignment mechanism, the flame temperature may also be critical for the formation of chainlike aggregates.

Acknowledgment

This research was supported by the Air Force Office of Scientific Research Grant F49620-0477 and the National Science Foundation Grant CTS-9528598.

REFERENCES

1. Charalampopoulos, T. T., *Prog. Energy Combust. Sci.* 18:13–45 (1992).
2. Kasper, G., Shon, S.-N., and Shaw, D. T., *J. Am. Ind. Hyg. Assoc.* 41:288–296 (1980).
3. Kasper, G. and Shaw, D. T., *Aerosol Sci. Technol.* 2:369–381 (1983).
4. Fu, T. H., Cheng, M. T., Wong, F. C. H., and Shaw, D. T., *Aerosol Sci. Technol.* 15:19–29 (1991).
5. Cheng, M. T., Xie, G. W., and Shaw, D. T., *Aerosol Sci. Technol.* 14:74–81 (1991).
6. Jacobs, I. S. and Bean, C. P., *Physical Review* 100:1060–1067 (1955).
7. Green, H. L. and Lane, W. R., *Particulate Clouds: Dust, Smokes and Mists,* Wiley, New York, 1964, p. 33.
8. Zebel, G., in *Aerosol Science,* Vol. 1 (Davies, C. N., Ed.), Wiley, New York, 1966, p. 45.
9. Howard, J. B., *Twelfth Symposium (International) on Combustion,* The Combustion Institute, Pittsburgh, 1954, pp. 877–887.
10. Wersborg, B. L., Howard, J. B., and Williams, G. C., *Fourteenth Symposium (International) on Combustion,* The Combustion Institute, Pittsburgh, 1954, pp. 929–940.
11. Whitby, K. T. and Liu, Y. H., in *Aerosol Science,* Vol. 1 (Davies, C. D., Ed.), Wiley, New York, 1966, p. 83.
12. Dobbins, R. A. and Megaridis, C. M., *Langmuir* 3:254–266 (1987).
13. Rosner, D. E. and Mackowski, D. W., *Combust. Sci. Technol.* 80:87–101 (1991).
14. Zhang, Z., Waguespack, G., and Charalampopoulos, T. T., submitted to *Rev. Sci. Instrum.* (1996).

15. *CRC Handbook of Chemistry and Physics,* Vol. 60, CRC Press Inc., Boca Raton, FL, 1979, p. E121.
16. Niel, L., *Rev. Modern Phys.* 25:58–63 (1953).
17. Kerker, M., *The Scattering of Light and Other Electromagnetic Radiation,* Academic Press, New York, 1969, p. 356.
18. Alkemade, C. T. J. and Zeegers, P. J. T., Wiley-Interscience 9:3–125 (1972).
19. Gorden S. and McBride, J., NASA SP-273, 1976, p. 1.
20. Zhang, Z., M.S. Thesis, Mech. Eng. Dept., Louisiana State University, 1995.
21. Morrish, A. H. and Yu, S. P., *J. Appl. Phys.* 26:1049–1055 (1955).
22. Beischer, D. and A. Winkel, *Naturwissenschaften* 26:27–420 (1937).

Twenty-Sixth Symposium (International) on Combustion/The Combustion Institute, 1996/pp. 1859–1865

THE FORMATION OF SiO_2 FROM HEXAMETHYLDISILOXANE COMBUSTION IN COUNTERFLOW METHANE-AIR FLAMES

H. K. CHAGGER, D. HAINSWORTH, P. M. PATTERSON, M. POURKASHANIAN AND A. WILLIAMS
Department of Fuel and Energy
University of Leeds
Leeds, LS2 9JT, UK

Silica formation from hexamethyldisiloxane (HMDS) oxidation was studied by means of a CH_4–N_2/air opposed diffusion flame technique to which vaporized HMDS was added to the fuel flow. The CH_4–N_2/air flame changed color from a pale-blue flame to whitish pink color when small amounts of HMDS were introduced in the flame. Increasing concentrations (1.3 mol %) made the flame more luminous, and a second thin-flame zone, orange in color, appeared on the fuel side. Emission spectroscopy revealed the existence of Si–H and Si–O species. SiO_2 particles were observed only in the postcombustion gases, and the analysis of solid materials suggested the formation of fused silica particles, which were initially about 10 nm in size, forming outside the flame zone in these experiments. The overall mechanism in addition to that for methane oxidation is suggested as follows:

$$C_6H_{18}Si_2O + OH = 2C_3H_9SiO + H$$

$$C_6H_{18}Si_2O + O_2 = 2C_3H_9SiO + O$$

$$C_6H_{18}Si_2O + HO_2 = 2C_3H_9SiO + OH$$

$$C_3H_9SiO + M = 3CH_3 + SiO + M$$

$$SiO + HO_2 = HSiO + O_2$$

$$SiO + OH = SiO_2 + H$$

$$SiO + O + M = SiO_2 + M$$

$$SiO + O_2 = SiO_2 + O$$

together with the formation of SiOH and SiO(OH) species. The agreement between the model predictions using Sandia code OPPDIF and the experimental data was found to be satisfactory. The model appears to be a useful tool in elaboration of chemistry of formation of SiO_2 in flames used to synthesize pure silica in this way.

Introduction

Flame synthesis is a useful technology for the synthesis of oxide powders like TiO_2, Al_2O_3, and SiO_2. Fumed silica obtained from this process has numerous commercial applications and is used as a precursor material in the fiber-optic, ceramic, semiconductor, pigment, and dye industries. For the production of high-purity nanometer-sized particles (nanoparticles in the 2–100 nm size range), gas-phase flame synthesis is particularly attractive to the material industry as this process can be scaled up and is economically advantageous [1]. However, the role of flame species, such as OH, and carbon compounds may determine the purity of the final product.

The synthesis of silica by the oxidation of silane and silicon tetrachloride in hydrogen or hydrocarbon flames has been studied both experimentally and theoretically [2–4]. The study showed that both the final silica aggregate and primary particle size were strongly affected by flame temperature and residence time, whereas the nucleation and surface reaction did not affect particle dynamics. These studies were extended to show that coalescence was a rate-controlling step in the growth of silica [2–4]. The basic flame chemistry, such as kinetics, and thermodynamic properties of simple silicon compounds like SiH_4 and $SiCl_4$ are fairly well documented [5–9] as a consequence of their use in chemical vapor deposition (CVD) and semiconductor manufacturing. Currently, industrial interest has been directed to the use of organosiloxanes as a precursor for these silica synthesis processes because of their ease of availability and economic advantage. These compounds include the highly methylated siloxanes and disiloxanes and the cyclic siloxanes ($[-(CH_3)_2SiO-]_n$).

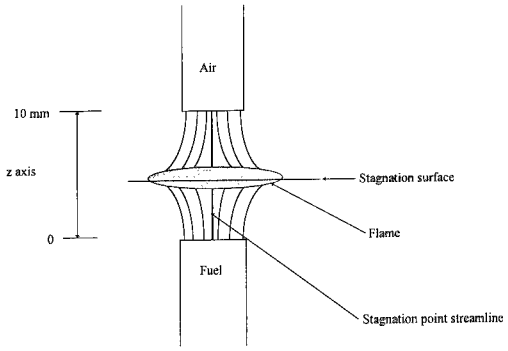

FIG. 1. Schematic representation of an opposed diffusion flame. The fuel outlet corresponds to zero on the z-axis distance scale, and the air outlet corresponds to 10 mm.

In this paper, the formation of SiO_2 from the organodisiloxane, hexamethyldisiloxane (HMDS), $(CH_3)_3Si–O–Si(CH_3)_3$, is reported. The oxidation of HMDS has been studied by the addition of small amounts to a counterflow methane-air diffusion flame; a process that is similar to that used in industry where the production of high-purity fused silica formation occurs through the diffusion flame oxidation of a vaporized silicon-containing compound. A number of previous studies have been undertaken in opposed diffusion flames of silane-air or of silane decomposition in opposed H_2–O_2 diffusion flames, and some of these cases have been numerically modeled [5–9]. In addition, the growth processes leading to formation of silica particles have been investigated [2–4]. Although the general features of these flames have been described, there has been little validation of the detailed chemical models, and there are uncertainties about both the reaction kinetics and the thermochemistry. To our knowledge, there have been no studies of HMDS combustion in opposed diffusion flames to date, and in this paper, we report the results of such a study.

Numerical Model

Calculations were carried out to simulate the counterflow diffusion flame, as shown diagrammatically in Fig. 1, by means of the Sandia OPPDIF code. The distance between the two burners in the theoretical model can be varied. The distance chosen between the two opposing burners in this model was 1 cm to reproduce the actual experimental conditions; this made the solution more difficult to converge than the conventional distance of several centimeters. The model was applied to a fuel stream containing methane and nitrogen/HMDS on one side and an oxidizer stream consisting of air on the other. The methane combustion mechanism was modified to incorporate an oxidation mechanism for HMDS. The computations were conducted such that the gradient of axial velocity dV/dx was constant on both sides of the flame, and Eq. (i) held [10]

$$\left(\frac{dV}{dx}\right) = \left(\frac{\rho_{\text{air}}}{\rho_{\text{fuel}}}\right)^{1/2} \left(\frac{dV}{dx}\right)_{\text{air}} \qquad \text{(i)}$$

where ρ is the density, and this allows the use of Eq. (ii):

$$\frac{U}{r} = \frac{V}{2(x - X_{\text{stag}})} \qquad \text{(ii)}$$

where U is the radial velocity, r is the radius to any point in the flow defined by (x,r), and X_{stag} is the abscissa of the computed stagnation point. The stretch rate selected to characterize the flame was defined by the expression $(-J/\rho_{\text{fuel}})^{1/2}$, where J is the constant eigenvalue of the experimental flow configuration, which is equal to

$$\left[\left(\frac{1}{r}\right)\cdot\left(\frac{dP}{dr}\right)\right]$$

where P is the pressure.

The chemical mechanism used for the methane oxidation is the natural gas oxidation scheme given by GRI version 2.11 [11]. The Miller and Bowman reaction scheme [12] was also tried, and it gave similar results. Table 1 lists the additional reactions added to the mechanism to describe HMDS decomposition and the subsequent production of SiO and SiO_2. The area of greatest uncertainty relates to the decomposition of the HMDS. In previous modeling studies [5,13], silane was taken to react in an analogous manner to methane with allowance made for the difference in bond energies of Si–H and C–H. Similarly, in this study, HMDS was assumed to behave as a typical higher molecular weight hydrocarbon in the initial stages of the flame. The SiO and SiO_2 reactions have been taken from the Britten et al. mechanism [13]. The reactions of the product CH_3 are incorporated into the methane oxidation reaction scheme, which consists of 190 reactions in total.

The rate constants are expressed in modified Arrhenius form

$$k = AT^n \exp(-E_a/RT) \qquad \text{(iii)}$$

Reverse rate constants are calculated from the forward rates, and the appropriate equilibrium constants are computed from available or estimated thermochemical data. Thermochemical data for Si intermediates such as HSiO were assumed to be identical to that of C-analogs. SiO_2 was assumed to be formed initially in the gaseous state.

The model was used to compute temperature and species concentration profiles for a counterflow CH_4–N_2/air diffusion flame doped with HMDS. The

TABLE 1
HMDS oxidation mechanism, the units are cm^3, mol, s, and cal

	Reaction	Rate Constant		
		A	n	E_a
1	$C_6H_{18}Si_2O + OH = 2C_3H_9SiO + H$	9.6 E 12	2	100
2	$C_6H_{18}Si_2O + O_2 = 2C_3H_9SiO + O$	6.0 E 13	0	261
3	$C_6H_{18}Si_2O + HO_2 = 2C_3H_9SiO + OH$	1.3 E 13	0	103
4	$C_3H_9SiO + M = 3CH_3 + SiO + M$	8.7 E 12	0	0
5	$SiO + HO_2 = HSiO + O_2$	5.27 E 12	0	34,300
6	$SiO + H_2O = HSiO + OH$	2.84 E 15	0	105,000
7	$SiO + OH = HSiO + O$	2.88 E 14	0	87,900
8	$SiO + H_2 = HSiO + H$	1.31 E 15	0	90,000
9	$SiO + H + M = HSiO + M$	1.74 E 11	0	11,600
10	$SiO + OH = SiO_2 + H$	4.0 E 12	0	5,700
11	$SiO + O_2 = SiO_2 + O$	1.0 E 13	0	6,500
12	$SiO + O + M = SiO_2 + M$	2.5 E 15	0	4,370

$k_f = AT^n \exp(-E_a/RT)$.

model studied here is far from a complete HMDS combustion mechanism, as it does not fully consider nucleation of SiO_2 to form solid particulates or the full reactions of silicon-containing intermediate species.

Experimental Methods

The oxidation of HMDS is studied in a counterflow CH_4–N_2/air diffusion flame to obtain some experimental measurements with which the results of the model may be compared quantitatively. The advantage of using a counterflow geometry is that, to a first approximation, flow along the stagnation streamline can be described as one-dimensional. The basic characteristics of the flow field of such a flame are illustrated in Fig. 1. The experimental arrangement consists of two circular burners (d = 2.5 cm), containing wire mesh screens as flow straighteners and mounted in square steel plates (10 × 10 cm) to reduce external air entrainment, aligned vertically opposite to each other. The burners are separated by a distance of 10 mm. Air (43.3 $cm^3\ s^{-1}$) flowed downward from the top burner, while the fuel mixture, methane diluted with nitrogen (11.7 $cm^3\ s^{-1}\ CH_4$ + 10 $cm^3\ s^{-1}\ N_2$) flowed upward from the bottom burner. The flow rates of all components of the oxidizer and fuel stream were controlled using mass flowmeters. A flame was generated in the region where the two opposing gas streams impinged. The fuel and air are mixed with each other within a narrow zone near the stagnation point mainly due to diffusion and can hold a stable diffusion flame, provided the air and fuel velocities do not exceed certain critical values. The flame, approximately 2.5 cm in diameter, was reasonably flat, stable, and uniform in the horizontal plane. A known vapor pressure of the HMDS was added to the fuel stream by bubbling the nitrogen through a bottle containing HMDS at room temperature. This gave a typical maximum concentration of 1.3 mol % of HMDS in the flame gases. All experimental measurements were made along the stagnation streamline (z axis), as shown in Fig. 1, where 0 mm corresponds to the fuel outlet and 10 mm is the air outlet. Temperature profiles were obtained using a platinum–platinum 13% rhodium thermocouple and corrected for radiation losses using Kaskan's method [14]. The composition of flame gases was obtained by microprobe sampling and gas chromatography (GC) analysis using flame ionization detection (FID) or thermal conductivity detection. The HMDS disappearance in the flame was monitored by Fourier transform infrared (FTIR). Visible, UV, and FTIR emission spectroscopy were used to detect flame species. The visible emission from the flame was focused using a monochromator with a resolution of ±1 nm. Surface-area measurements were obtained using N_2 adsorption at liquid nitrogen temperature (Quantasorb instrument).

Results and Discussion

Study of the Flame with Added HMDS

The CH_4–N_2/air diffusion flame with no HMDS is mainly blue with a pale-yellow zone on the rich side. As small amounts of HMDS were added to the fuel stream, the flame changed color to whitish pink and became more luminous. On increasing the

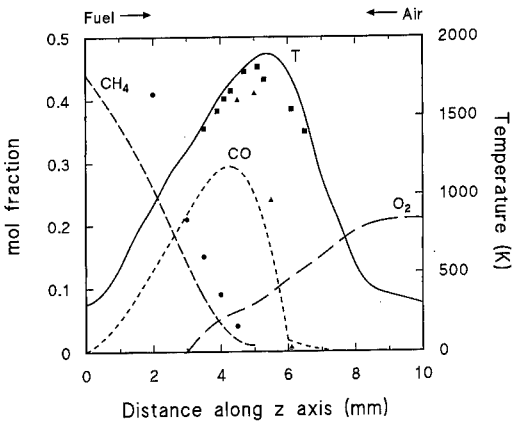

FIG. 2. Temperature and composition profiles along the z axis of the CH_4–N_2/air opposed diffusion flame with added HMDS. Calculated profiles are represented by lines and experimental profiles as data points; ● CH_4, ▲ CO, and ■ T.

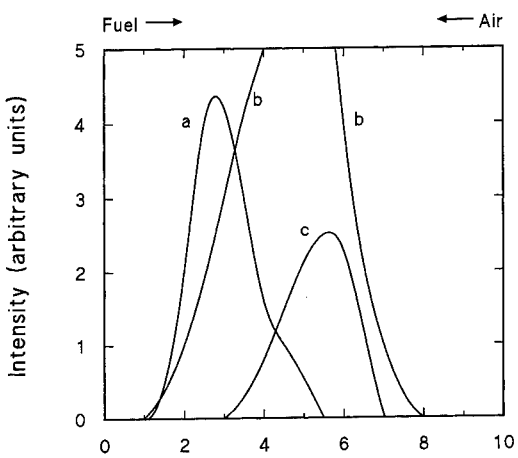

FIG. 3. Emission profiles obtained along the z axis of the CH_4–N_2/air opposed diffusion flame with added HMDS. Line a, 441.4 nm emission; line b, carbon emission, and line c, visible light emission.

concentration of the HMDS further, a secondary flat flame, orange in color, appeared on the fuel side, and a stronger blue emission was observed on the lean side. These effects are similar to those previously observed for silane combustion in H_2–O_2 counterflow flames [7,8]. A white smoke is seen clearly to rise from the diffusion flame, and significant particle deposition was observed on the plates surrounding the burners. Laser light was found to be scattered only in the postcombustion gases, indicating the presence of silica particles. No particles were observed in the flame zone using this technique. The SiO_2 particles collected in the postcombustion gases were white in color, but those collected nearer to the flame were slightly brown, indicating the presence of SiO_x [8]. The particles collected in the postcombustion gases and deposited on the surrounding plates had a surface area of 130 ± 10 $m^2\ g^{-1}$, compared with a value of 200–250 $m^2\ g^{-1}$ for the particles produced by an analogous H_2–N_2/air diffusion flame also doped with HMDS [15].

The temperature profile and concentration profiles of some stable species obtained along the z axis for the CH_4–N_2/air diffusion flame with added HMDS are shown in Fig. 2. The data points represent the experimental measurements, and the lines are the calculated results from the model, which will be discussed later. Figure 3 shows the overall visible light emission and the continuum emission (at 441.4 nm) profiles [8]. The flame emission at 441.4 nm was scanned along the z axis, with the methane flame alone and with added HMDS. The latter case gave an enhanced signal (20%) compared with methane alone, which was associated with visible enhancement of the yellow zone to become a reddish yellow zone. The methane-air flame exhibited the characteristic emissions of OH^* (310 nm), CH^* (431 nm), and C_2^* (516.5 nm), with visible yellow and blue zones. When HMDS was added, an orange color zone appeared on the fuel side, and the intensity increased with further addition of HMDS, and the blue emission on the lean side also intensified in the same way. These emissions have previously been observed [8,9]; the red emission is apparently a continuum, while the blue emission is unidentified specifically in this flame but thought to be due to SiO blue band (420 nm) and SiO_2 bands (421–430 nm), although the most distinctive SiO lines appeared at 284 and 254 nm [16]. The FTIR emission studies of the flame indicated that the gas in the flame zone exhibited the expected emissions for C–H (4.55 μm), O–H (2.73–2.79 μm), Si–H (4.35–4.76 μm), and Si–O (9.15–9.77 μm) and that the HMDS rapidly decomposed in the initial stages of the flame [17].

Modeling of HMDS Decomposition

Decomposition of HMDS is proposed to proceed via the following reactions:

$$C_6H_{18}Si_2O + OH = 2C_3H_9SiO + H \quad (1)$$

$$C_6H_{18}Si_2O + O_2 = 2C_3H_9SiO + O \quad (2)$$

$$C_6H_{18}Si_2O + HO_2 = 2C_3H_9SiO + OH \quad (3)$$

$$C_3H_9SiO + M = 3CH_3 + SiO + M \quad (3)$$

Table 1 lists the kinetic values used for the decomposition of HMDS, which involves the attack of O_2, HO_2, and OH, on the HMDS molecule resulting in the formation of a short-lived organosilicon species.

TABLE 2
Bond dissociation energies of carbon and silicon

Bond	Bond Energy (kcal mol^{-1})
C–H	99.1
Si–C	68.3
Si–O	108.1

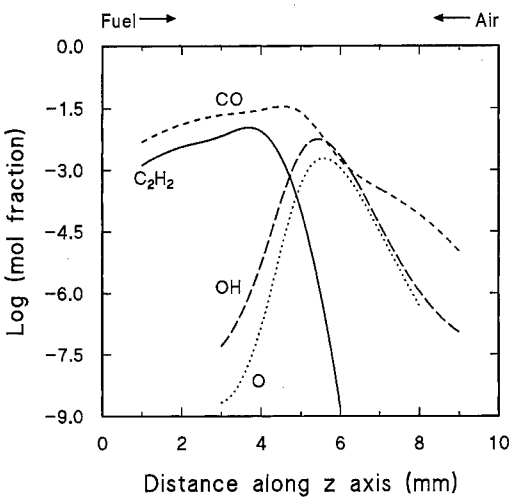

FIG. 4. Some computed species profiles along the z axis of the CH_4–N_2/air opposed diffusion flame with added HMDS.

The values were chosen, by analogy with similar reactions of hydrocarbons, to account for the disappearance of HMDS by approximately 3 mm in the flame. The destruction of the intermediate species $(CH_3)_3SiO$ depends upon the bond strengths, which are given in Table 2. The Si–C bond is weaker and breaks first, leaving the SiO species [18]. The use of reactions (1)–(4) for HMDS seem to be valid and shows that the HMDS decomposes rapidly, which is consistent with experimental observation. Some computed profiles obtained for the methane flame species are shown in Fig. 2 together with some experimental data for CH_4 and CO, and the agreement between experimental and calculation is quite satisfactory. The calculated profiles of O_2 are shown for illustrative purposes. Figure 4 shows computed profiles of representative radical species calculated using OPPDIF. This model is further validated by the position of the yellow and blue reaction zones (Fig. 3); The yellow zone coincides with the calculated acetylene concentration, and the blue zone coincides with the product of [CO] and [O] (Fig. 4). Computed profiles for some silicon species are shown in

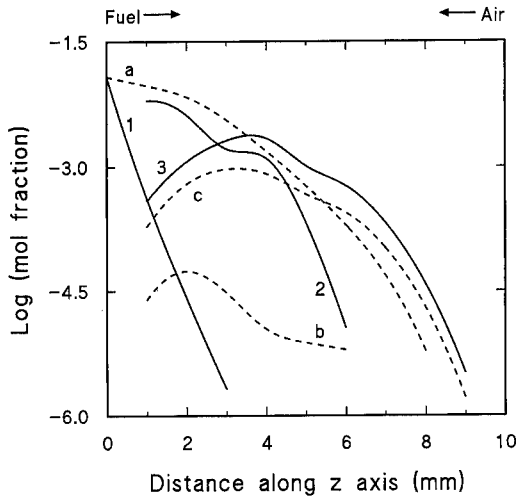

FIG. 5. Calculated profiles for some silicon species along the z axis of the CH_4–N_2/air opposed diffusion flame with added HMDS. Solid lines represent fast kinetics, and dashed lines represent slower kinetics for HMDS decomposition. Lines 1 and a, HMDS; lines 2 and b, SiO; and lines 3 and c, SiO_2.

Fig. 5. The computed HMDS disappearance shown in these figures demonstrates how sensitive it is to the decomposition rate. The species SiO is formed rapidly and undergoes further reaction to form SiO_2. The model at this stage is not complete in that the calculated SiO_2 profiles represent SiO_2 in the gaseous state and does not take nucleation or particle formation into consideration. One interesting aspect of the variation of the rate of HMDS decomposition is that the ultimate SiO_2 production appears relatively insensitive to its initial value.

The reactions that are postulated involving SiO are given below, where the data for the heats of formation at 298.15 K have been taken from the literature [19–21].

On the Lean Side of the Reaction Zone

$$SiO + OH = SiO_2 + H$$
$$\Delta H = -0.1 \text{ kcal mol}^{-1} \quad (10)$$
$$SiO + O_2 = SiO_2 + O$$
$$\Delta H = 16.7 \text{ kcal mol}^{-1} \quad (11)$$
$$SiO + O\,(+M) = SiO_2\,(+M)$$
$$\Delta H = -102.5 \text{ kcal mol}^{-1} \quad (12)$$

SiO is electronically analogous with CO. On this basis, it is possible to expect the reaction

$$SiO + O = SiO_2^g \quad (13)$$

to occur in a similar way to $CO + O = CO_2^*$ and may possibly explain the enhanced blue emissions and the blue SiO_2 bands.

On the Rich Side of the Reaction Zone

In the reducing atmosphere on the fuel side of the flame, other reactions of SiO are possible. The brownish particles that were observed were assumed to be a mixture of SiO_2 and SiO and/or Si [8]. These particles, called SiO_x, could be responsible for the red continuum emission and could be produced via

$$SiO + SiO_2 = 2\ SiO_{1.5} \qquad (14)$$

In addition, SiO may react with hydrogen atoms that lead to the formation of HSiO. The overall reactions can be given as

$$SiO + H + (M) = HSiO + (M)$$
$$\Delta H = -20 \text{ kcal mol}^{-1} \qquad (9)$$

followed by

$$HSiO + OH = SiO + H_2O$$
$$\Delta H = -64 \text{ kcal mol}^{-1} \qquad (-6)$$

SiO_2 Particle Growth

Silica particles are formed when HMDS is added to the CH_4–N_2/air diffusion flame; however, different views prevail regarding the process of nucleation and the actual formation of the first particles. Chong and Rogg [22] have stated that if the nuclei are formed with a radius smaller than a critical radius, then they re-evaporate, and only those having radii larger than the critical radius grow. This phenomenon results in the formation of nanosized particles because of differential limit growth rates; these then coagulate, forming a floc [23]. A difficulty is the calculation of the size of the critical nucleus, as the equilibrium vapor consists not only of SiO but also of some hydroxylated products such as SiO(OH) or HSiO(OH) [24].

The species SiO is a relatively stable entity that reacts with O, OH, or O_2 to form SiO_2 in the gas phase. The SiO_2 then condenses to produce liquid drops, and it has been proposed that the molten oxide droplets grow by Brownian collisions according to [2]

$$N = (BcT^{1/2}C_o^{1/6}t)^{-6/5} \qquad \text{(iv)}$$

where N is the particle concentration per cm^3, B is a constant dependent on the density and molecular weight of silica (equal to 6.8×10^{-12}), c is the sticking coefficient (ratio of successful to actual collisions), T is absolute temperature, C_0 is the number of silica molecules per cm^3 in the combustion gases, and t is the growth time. Likewise, the surface area may be expressed as

$$SA(\text{m}^2\ \text{g}^{-1}) = 1.81 \times 10^8 (T^{1/2}\ cC_0t)^{-2/5} \qquad \text{(v)}$$

where $SA = 3/(\rho R)$, R is the radius of the particle, and ρ is the density of silica. This Brownian growth can be illustrated using some recent data for particle formation in premixed H_2–O_2–N_2 flames with added HMDS [25]. For a lean flame with $T = 2414$ K ($v = 18.5$ m s^{-1}), $C_0 = 5 \times 10^{16}$ molecules SiO_2 per cm^3, and employing a sticking coefficient of 0.3, the following particle dimensions were computed: At $t = 5.4 \times 10^{-4}$ s, there are 3.8×10^{12} particles cm^{-3} with a surface area of 262 $m^2\ g^{-1}$, yielding a radius of 5.2 nm, and the number of SiO_2 molecules per particle is 1.3×10^4. At $t = 4.9 \times 10^{-3}$ s, there are 2.7×10^{11} particles cm^{-3} with a surface area of 108 $m^2\ g^{-1}$, yielding a radius of 12.6 nm, and the number of SiO_2 molecules per particle is 1.85×10^5. Butler and Hayhurst [25] found that samples taken early in the flame had small diameters (5–10 nm), whereas those sampled farther downstream had diameters of the order of 20–30 nm, which agrees quite well with the Brownian growth model using a sticking coefficient of 0.3.

There are also important reactions involving OH, as these reactions can result in the formation of silica-containing hydroxyl bonds. Among all the intermediate and final products, SiO_2 is considered to be the major one, but the species OSiOH and OHSiOH are thermodynamically favored, especially in the flame zone by the reactions [20]

$$SiO_2 + H = OSiOH$$
$$\Delta H = -58.1 \text{ kcal mol}^{-1} \qquad (15)$$
$$SiO + OH = OSiOH$$
$$\Delta H = -58.2 \text{ kcal mol}^{-1} \qquad (16)$$

These reactions may explain the experimental observation that the particulate SiO_2 is not present in the flame zone. However, once the concentration of OH and H decay, these species will also decline to yield SiO_2 particles in an oxygen-containing burned gas zone.

Conclusions

Hexamethyldisiloxane (HMDS) was added to a CH_4–N_2/air counterflow diffusion flame. The Sandia OPPDIF code was used to formulate a mechanism for HMDS oxidation in this flame. Good agreement was obtained between experimental measurements and computed results. The model illustrates that HMDS decomposes rapidly to yield SiO, which is subsequently oxidized to SiO_2. The model, however, does require further refinement in the future to include nucleation of the product SiO_2 to form solid particles.

Acknowledgments

This work was supported by the EPSRC. In addition, we thank Drs. C. J. Butler, V. Dupont, A. N. Hayhurst, and I. G. Sayce and Prof. R. Walsh for their helpful discussions.

REFERENCES

1. Stamatakis, P., Natalie, C. A., Palmer, B. R., and Yuil, W. A., *Aerosol Sci. Technol.* 14:316–321 (1991).
2. Ulrich, G. D., *Combust. Sci. Technol.* 4:47–57 (1971).
3. Ulrich, G. D., Milnes, B. A., and Subramanian, N. S., *Combust. Sci. Technol.* 14:243–249 (1976).
4. Ulrich, G. D. and Subramanian, N. S., *Combust. Sci. Technol.* 17:119–126 (1976).
5. Koda, S., *Prog. Energy Combust. Sci.* 18:513–528 (1992).
6. Zachariah, M. R., Chin, D., Semerjian, H. G., and Katz, J. L., *Combust. Flame* 78:287–298 (1989).
7. Koda, S. and Fujiwara, O., *Twenty-First Symposium (International) on Combustion,* The Combustion Institute, Pittsburgh, 1986, pp. 1861–1867.
8. Chung, S.-L., Tsai, M.-S., and Lin, H.-D., *Combust. Flame* 85:134–142 (1991).
9. Chung, S. L. and Katz, J. L., *Combust. Flame* 61:271–284 (1985).
10. Dupont, V., Pourkashanian, M., Richardson, A., and Williams, A., *Proc. of the Eighth International Conf. on Transport Phenomenon,* 1995.
11. Gas Research Institute, Natural Gas Oxidation Mechanism Version 2.11, Taylor and Francis, in press.
12. Miller, J. A. and Bowman, C. T., *Prog. Energy Combust. Sci.* 15:287–338 (1989).
13. Britten, J. A., Tong, J., and Westbrook, C. K., *Twenty-Third Symposium (International) on Combustion,* The Combustion Institute, Pittsburgh, 1990, pp. 192–202.
14. Kaskan, W. E., *Combust. Flame* 2:229–286 (1958).
15. Chagger, H. K., Hainsworth, D., Pourkashanian, M., Patterson, P. M., and Williams, A., *Joint Meeting of the Portuguese, British, Spanish and Swedish Sections of the Combustion Institute,* April 1–4, Funchal, 1996.
16. Pearse, R. W. B. and Gaydon, A. G., *The Identification of Molecular Spectra,* Chapman and Hall Ltd, London, 1963.
17. Cross, A. D. and Jones, R. A., *An Introduction to Practical Infra-Red Spectroscopy,* Butterworths, London, 1969.
18. Walsh, R., *The Chemistry of Organic Silicon Compounds* (S. Patai and Z. Rappoport, Eds.), Pt. 1, Wiley, Chichester, 1989, pp. 371–391.
19. Chase, Jr., M. W., Davies, C. A., Downey, Jr., J. R., Frurip, D. J., McDonald, R. A., and Syverud, A. N., *JANAF Thermochemical Tables,* 3rd ed., *J. Phys. Chem. Ref. Data,* Vol. 14, Suppl. No. 1 (1985).
20. Hildenbrand, D. L. and Lau, K. H., *J. Chem. Phys.* 101:6076–6079 (1994).
21. Darling, C. L. and Schlegel, H. B., *J. Phys. Chem.* 97:8207–8211 (1993).
22. Chong, K. H. and Rogg, B., *Joint Meeting of the British and German Sections,* The Combustion Institute, 29 March–2 April, Queen's College, Cambridge, 1993.
23. Wright, P. G., *Proc. R. Soc. Edinburgh* 64:65–80 (1962).
24. Horton, J. H. and Goodings, J. M., *Can. J. Chem.* 70:1069–1081 (1992).
25. Butler, C. J. and Hayhurst, A. N., *Joint Meeting of the Portuguese, British, Spanish and Swedish Sections of the Combustion Institute,* April 1–4, Funchal, 1996.

Twenty-Sixth Symposium (International) on Combustion/The Combustion Institute, 1996/pp. 1867–1874

PULSATING INSTABILITY IN THE NONADIABATIC HETEROGENEOUS SHS FLAME: THEORY AND EXPERIMENTAL COMPARISONS

ATSUSHI MAKINO
Department of Mechanical Engineering
Shizuoka University, Hamamatsuv 432, Japan

CHUNG K. LAW
Department of Mechanical and Aerospace Engineering
Princeton Materials Institute
Princeton University, Princeton, NJ 08544, USA

Linear pulsating instability of the nonadiabatic heterogeneous self-propagating, high-temperature synthesis (SHS) flame is analyzed based on a premixed mode of propagation for the bulk flame supported by the non-premixed reaction of dispersed nonmetals in the liquid metal. The formulation allows for volumetric heat loss in the bulk flame and temperature-sensitive Arrhenius mass diffusion in the liquid with infinitely fast surface reaction in the diffusion limit, as is the case for most SHS processes. Neutral stability boundary, which separates the regime of steady combustion from that of pulsating combustion, has been obtained by determining the critical heat-loss parameter as functions of the Zeldovich number, melting parameter, and melting point of the metal. Results show that the instability is promoted by increasing the heat generation rate at the bulk flame and/or reducing the heat-transfer rate from the flame, particularly by increasing the mixture ratio, decreasing the degree of dilution, decreasing the size of the nonmetal particles, increasing the compact diameter, and decreasing the thermometric conductivity of the compacted mixture. The theoretical results are found to agree well with available experimental data, in trend and in approximate magnitude, indicating that the heterogeneous theory for the SHS flame propagation captures the essential features of this unstable SHS combustion process.

Introduction

There has been increasing interest in the combustion synthesis of new materials. In particular, the self-propagating high-temperature synthesis (SHS) process, proposed by Merzhanov and co-workers [1] and characterized by flame propagation through a matrix of compacted particles, holds the practical significance of producing novel solid materials. The relevant theoretical and experimental results have been reviewed in Refs. 2–6.

Concerning the theoretical developments, almost all such studies have been based on the concept of premixed flame propagation in a homogeneous medium. Recognizing the fundamental heterogeneous nature of the SHS flame propagation, a heterogeneous theory has been formulated [7]. This theory describes a premixed mode of bulk flame propagation supported by the non-premixed mode of surface reaction for the dispersed nonmetal particles or the particles that have higher melting points in the compacted matrix. While the theory allows for the finite rate of the surface reactions, it has been demonstrated [7] that the surface reactions can usually be considered to be infinitely fast such that diffusion is the rate-limiting process. By further recognizing that mass diffusion varies sensitively with temperature [8] in an Arrhenius manner, extinction of the SHS flame under heat loss conditions has also been described [9]. Explicit, analytical expressions have been obtained for the flame propagation speed [10] and the extinction limit [11]. The theoretical predictions have been found to agree well with a variety of experimental results [7,9,12], including a bimodal dispersion system [13] with respect to the radii of nonmetal particles. The ability of the heterogeneous theory to describe the experimental dependence of the various flame responses on the particle size of the nonmetal component is particularly noteworthy because such a description at the fundamental level is inherently absent from the homogeneous theories.

Having established the viability of the heterogeneous theory, we now extend our study to perhaps the most complex fundamental phenomenon observed in SHS flame propagation, namely, the existence of the pulsating flame propagation mode [1]. Specifically, we aim to determine the neutral stability boundary in heterogeneous flame propagation by applying and extending the linear stability analysis of Margolis [14,15] and Kaper et al. [16], developed for

premixed flame propagation in the homogeneous medium, and compare the predictions with the available experimental results. We shall show in due course that the instability is sensitively affected by the mixture ratio, the degree of dilution, the size of the nonmetal particles, the compact diameter, the thermophysical properties of the compacted mixture, and as such, the instability can be suppressed by enhancing heat transfer from the flame and/or by reducing the heat generation rate at the bulk flame. We shall also show that predictions from the stability analysis yield fair agreement with the experimental results.

Governing Equations and Boundary Conditions

The problem of interest (*cf.* Fig. 1 in Ref. 7) is the one-dimensional, planar, heterogeneous SHS flame propagation in the doubly infinite domain of a condensed medium, originally consisting of a mixture of particles of nonmetal (or higher-melting-point metal) N, lower-melting-point metal M, and an inert I that can be the product P of the reaction between N and M according to

$$\nu_M M + \nu_N N \rightarrow \nu_P P$$

where ν_i is the stoichiometric coefficient. Monodisperse-size distribution is considered for the N particles, which have an initial radius of R_0 and number density of n_0. Reaction between N and M is suppressed until the mixture is heated to the melting point T_m of the metal, at which all the M particles instantaneously melt. The reaction between solid N and molten M then takes place at the particle surface at an infinite rate in the diffusion limit and proceeds until all the nonmetal N particles or the molten M are consumed. The enthalpy of phase change is neglected because it is much smaller than the heat of combustion. The propagation considered here is nonadiabatic, with heat loss to the ambience occurring throughout the entire flame structure.

Using the nondimensional and reduced parameters defined as

$$\theta = \frac{\tilde{T} - \tilde{T}_0}{\tilde{T}_\infty - \tilde{T}_0}, \quad \zeta = \frac{\tilde{Y}_M - \tilde{Y}_{M0}}{\tilde{Y}_{M\infty} - \tilde{Y}_{M0}}$$

$$\xi = \frac{Z - Z_0}{Z_\infty - Z_0}, \quad \tau = \frac{(Z_\infty - Z_0)^2 m_a^2 t}{(\lambda/c)\rho_t}$$

$$\sigma = \frac{(Z_\infty - Z_0) m_a x}{(\lambda/c)}$$

$$\Phi(\theta) = \frac{(\lambda/c)L}{m_a^2 q(\tilde{T}_\infty - \tilde{T}_0)}, \quad Le_0 = \frac{(\lambda/c)}{(\rho_t D)_0}$$

$$\tilde{T}_\infty = Z_\infty - Z_0 + \tilde{T}_0, \quad \tilde{Y}_{M\infty} = (\tilde{Y}_{M0} + 1)\frac{Z_0}{Z_\infty} - 1$$

$$Z_\infty = \begin{cases} 1 & (\mu \le 1) \\ Z_0 + \dfrac{1 - Z_0}{\mu} & (\mu \ge 1) \end{cases}$$

$$\tilde{\chi} = \ln\left[1 + \left(\frac{A}{1 + A}\right)\tilde{Y}_M\right]$$

$$A = Da \cdot \exp\left(-\frac{\tilde{T}_a}{\tilde{T}}\right)$$

$$Da = \frac{B \cdot R}{D}, \quad D = D_0 \exp\left(-\frac{\tilde{T}_d}{\tilde{T}}\right)$$

$$\tilde{T} = cT/q, \quad \tilde{Y}_M = Y_M/f$$

$$f = (\nu_M W_M)/(\nu_N W_N), \quad Z = \rho_f/(\rho_f + \rho_s)$$

where Z is the mass fraction of the fluid, T the temperature, Y_M the mass fraction of M in the fluid, $\tilde{\chi}$ the surface regression rate, Da the Damköhler number for the surface reaction, D the mass diffusivity, u the velocity along the x-coordinate, λ the thermal conductivity, c the specific heat, q the heat of reaction per unit mass of N, f the stoichiometric mass ratio, W the molecular weight, and μ the mixture ratio. The conservation equations for total energy and the concentration of the nonmetal are as follows [7,9]:

$$\frac{\partial}{\partial\tau}(\xi - \theta) + \frac{(m/m_a)}{(Z_\infty - Z_0)}\frac{\partial}{\partial\sigma}(\xi - \theta) + \frac{\partial^2\theta}{\partial\sigma^2} = \frac{\Phi(\theta)}{(Z_\infty - Z_0)^2} \tag{1}$$

$$\frac{\partial\xi}{\partial\tau} + \frac{(m/m_a)}{(Z_\infty - Z_0)}\frac{\partial}{\partial\sigma}\left(\xi + \frac{Z_0}{Z_\infty - Z_0}\right) = \frac{\tilde{\chi}}{(Z_\infty - Z_0)A_0(\rho_{t0}/\rho_t)\exp(\tilde{T}_d/\tilde{T})}\left[1 - \left(\frac{Z_\infty - Z_0}{1 - Z_0}\right)\xi\right]^{1/3} \tag{2}$$

$$\sigma \rightarrow -\infty: \quad \theta = 0, \quad \xi = 0 \tag{3}$$

$$\sigma = 0: \quad \theta = C \tag{4}$$

$$\sigma \rightarrow \infty: \frac{\partial\theta}{\partial\sigma} = -\frac{\Phi(\theta)}{(m/m_a)(Z_\infty - Z_0)}, \quad \frac{\partial\xi}{\partial\sigma} = 0 \tag{5}$$

Here, $\partial^2\theta/\partial\sigma^2$, $-[(m/m_a)/(Z_\infty - Z_0)](\partial\theta/\partial\sigma)$, and $[(m/m_a)/(Z_\infty - Z_0)]\ (\partial\xi/\partial\sigma)$ are the diffusion, convection, and consumption terms, respectively; the right-hand side (RHS) of Eq. (1) is the heat loss term, which is assumed to be Newtonian such that $\Phi(\theta) = \Psi \cdot \theta$. In addition, we have the relation, $\zeta \approx (Z_\infty\xi)/[(Z_0 + (Z_\infty - Z_0)\xi]$, obtained from the assumption of large Lewis number (say, $Le > 10^4$) in the reaction zone. We also note that since

$[A/(1 + A)] \rightarrow 1$ in the diffusion limit, the mass diffusivity in the Arrhenius fashion exerts a nonlinear influence on flame propagation and extinction. Then, the mass burning rate m $(= \rho_t u)$ subject to heat loss L would emerge from the solution as an eigenvalue, with m_a and

$$\Lambda_0 = \left[\frac{(Z_\infty - Z_0)^2 m_a^2}{4\pi(\rho_M D_0)(\lambda/c)n_0 R_0}\right] \tag{6}$$

being respectively the mass burning rate and the mass burning rate eigenvalue in the steady-state, adiabatic limit. A particle-size-weighted flame propagation speed, $F_0 = u_0 R_0$, is obtained from this eigenvalue.

Asymptotic Solution for Steady, Planar Propagation

In the limit of large Zeldovich number β $(= \tilde{T}_d(\tilde{T}_\infty - \tilde{T}_0)/\tilde{T}_\infty^2)$, melting, diffusion, and consumption/convection are confined to a thin layer in the neighborhood of $\sigma = 0$. Outside this layer, the diffusion and consumption/convection terms are exponentially small, as shown in Ref. 9. Following Kaper et al. [16], we first obtain an asymptotic solution in the steady state, with the outer solution given by

$$\theta = C \exp\left\{-\frac{(m/m_a)}{2(Z_\infty - Z_0)}\left[1 + \sqrt{1 + \frac{4\Psi}{(m/m_a)^2}}\right]\sigma\right\}$$

$$\xi = 0, \qquad (\sigma < 0) \tag{7}$$

$$\theta = C \exp\left\{-\frac{(m/m_a)}{2(Z_\infty - Z_0)}\left[1 - \sqrt{1 + \frac{4\Psi}{(m/m_a)^2}}\right]\sigma\right\}$$

$$\xi = 1, \qquad (\sigma > 0) \tag{8}$$

where m/m_a and the maximum temperature C are to be determined. By matching this outer solution with the inner solution [11], we have the relation

$$(m/m_a)^2 = \frac{\exp[\beta(C - 1)] - M}{k(1 - M)} \tag{9}$$

where

$$k = \frac{2}{1 + \theta_m}, \quad (1 - M) = \beta I_\theta \exp\left(\frac{\beta}{\alpha}\right)$$

$$\alpha = \frac{\tilde{T}_\infty - \tilde{T}_0}{\tilde{T}_\infty}$$

$$I_\theta = \int_{\beta(1-\theta_m)}^{0} \exp\left[-\left(\frac{3\beta}{4\alpha}\right) - \left(\frac{\beta}{\alpha}\right)\left(\frac{1}{2} - \frac{\alpha t_1}{\beta}\right)^2\right]\frac{dt_1}{\beta}$$

$$\approx \frac{\sqrt{\pi}}{2\sqrt{\alpha\beta}} \exp\left(-\frac{3\beta}{4\alpha}\right) \times$$

$$\left[erfc\left(\frac{\sqrt{\beta}}{2\sqrt{\alpha}}\right) - erfc\left\{\frac{\sqrt{\beta}}{2\sqrt{\alpha}}[1 + 2\alpha(1 - \theta_m)]\right\}\right] \tag{10}$$

cf. Ref. 11. Here, θ_m is the nondimensional melting point for metal, and M is the melting parameter first introduced by Margolis [14,15]. We also have the relation

$$C\sqrt{1 + \frac{4\Psi}{(m/m_a)^2}} = 1 \tag{11}$$

from the jump in $d\theta/d\sigma$ at $\sigma = 0$.

Linear Stability of Steady Planar Burning

The preceding model for the nonadiabatic heterogeneous SHS flame may be extended to allow for nonsteady effects. In the limit of large Zeldovich number, the first-order inner solution is identical to that for the adiabatic combustion because the volumetric heat loss term is a higher-order effect. The outer problem, however, is affected by both heat loss and unsteadiness, and is given by

$$\frac{\partial\theta}{\partial\tau} + \frac{(m/m_a)}{(Z_\infty - Z_0)}\frac{\partial\theta}{\partial\sigma} = \frac{\partial^2\theta}{\partial\sigma^2} - \frac{\Psi\cdot\theta}{(Z_\infty - Z_0)^2} \tag{12}$$

$$\theta = 0 \quad \text{as} \quad \sigma \rightarrow \pm\infty \tag{13}$$

The linear stability of the steady planar SHS flame may be determined in the standard fashion by linearizing the nonlinear problem [Eqs. (1)–(5)] about the basic solution [Eqs. (7)–(9) and (11)] and seeking harmonic solutions. Introducing the perturbation quantities $\theta_1(\sigma, \tau)$ and $\alpha_1(\tau)$ according to

$$\theta = \theta_0(\sigma) + \theta_1(\sigma, \tau) \tag{14}$$

$$m/m_a = a_0 + a_1(\tau)$$

and substituting them into Eq. (12), we obtain

$$\frac{\partial\theta_1}{\partial\tau} + \frac{a_0}{(Z_\infty - Z_0)}\frac{\partial\theta_1}{\partial\sigma}$$

$$+ \frac{a_1}{(Z_\infty - Z_0)}\frac{d\theta_0}{d\sigma} = \frac{\partial^2\theta_1}{\partial\sigma^2} - \frac{\Psi\cdot\theta_1}{(Z_\infty - Z_0)^2} \tag{15}$$

$$\theta_1 = 0 \quad \text{as} \quad \sigma \rightarrow \pm\infty \tag{16}$$

where

$$a_1 = B\theta_1(0, \tau), \quad \frac{B}{a_0} = \frac{B}{2}\left[1 + \frac{M}{a_0^2 k(1 - M)}\right] \tag{17}$$

Note that, since $(1 - M)$ is the normalized driving force for the flame propagation [11], B/a_0 is a measure of the energy generated at the flame zone compared to the driving force for the nonadiabatic flame propagation, that is, a measure of the driving force for instability.

It is found that there exists a normal mode solution that is a scalar multiple of

$$\theta_1(\sigma, \tau) = \exp(i\omega\tau)\left\{-\frac{1}{i\omega}\frac{BC\lambda_+}{(Z_\infty - Z_0)}\exp(\lambda_+\sigma)\right.$$

$$\left. + \left[1 + \frac{1}{i\omega}\frac{BC\lambda_+}{(Z_\infty - Z_0)}\right]\exp(p_+\sigma)\right\}, \ (\sigma < 0) \tag{18}$$

$$\theta_1(\sigma, \tau) = \exp(i\omega\tau)\left\{-\frac{1}{i\omega}\frac{BC\lambda_-}{(Z_\infty - Z_0)}\exp(\lambda_-\sigma) + \left[1 + \frac{1}{i\omega}\frac{BC\lambda_-}{(Z_{in} - Z_0)}\right]\exp(p_-\sigma)\right\}, (\sigma < 0) \tag{19}$$

where

$$\lambda_+ = \frac{1}{2}\left(\frac{a_0}{Z_\infty - Z_0}\right)\left(1 + \sqrt{1 + \frac{4\Psi}{a_0^2}}\right), \quad p_+ = \frac{1}{2}\left(\frac{a_0}{Z_\infty - Z_0}\right)\left[1 + \sqrt{1 + \frac{4\Psi}{a_0^2} + 4\left(\frac{Z_\infty - Z_0}{a_0}\right)^2 (i\omega)}\right] \tag{20}$$

$$\lambda_- = \frac{1}{2}\left(\frac{a_0}{Z_\infty - Z_0}\right)\left(1 + \sqrt{1 + \frac{4\Psi}{a_0^2}}\right), \quad p_- = \frac{1}{2}\left(\frac{a_0}{Z_\infty - Z_0}\right)\left[1 - \sqrt{1 + \frac{4\Psi}{a_0^2} + 4\left(\frac{Z_\infty - Z_0}{a_0}\right)^2 (i\omega)}\right] \tag{21}$$

If we further use the jump condition with respect to $\partial\theta/\partial\sigma$ at $\sigma = 0$, the dispersion relation that $i\omega$ satisfies is

$$4(i\omega)^2 + \left(\frac{a_0}{Z_\infty - Z_0}\right)^2\left[\frac{1}{C^2} - \left(\frac{B}{a_0}\right)^2 + 4\left(\frac{B}{a_0}\right)C\right](i\omega) + \left(\frac{a_0}{Z_\infty - Z_0}\right)^4\left(\frac{B}{a_0}\right)C\left[\frac{1}{C^2} - \left(\frac{B}{a_0}\right)\left(\frac{1}{C} - C\right)\right] = 0 \tag{22}$$

which yields

$$i\omega = \frac{1}{8}\left(\frac{a_0}{Z_\infty - Z_0}\right)^2\left\{-\left[\frac{1}{C^2} - \left(\frac{B}{a_0}\right)^2 + 4\left(\frac{B}{a_0}\right)C\right] \pm \left(\frac{1}{C} - \frac{B}{a_0}\right)\sqrt{\left(\frac{1}{C} + \frac{B}{a_0}\right)^2 - 8\left(\frac{B}{a_0}\right)C}\right\} \tag{23}$$

The imaginary part of $i\omega$ exists when

$$4C - \frac{1}{C} - 4C\sqrt{1 - \frac{1}{2C^2}} < \left(\frac{B}{a_0}\right) < 4C - \frac{1}{C} + 4C\sqrt{1 - \frac{1}{2C^2}} \tag{24}$$

with $1 \leq (1/C) < \sqrt{2}$, while the real part of $i\omega$ becomes negative when

$$0 \leq \left(\frac{B}{a_0}\right) < 2C\left(1 + \sqrt{1 + \frac{1}{4C^4}}\right) \quad \left(1 \leq \frac{1}{C} < \frac{\sqrt{6}}{2}\right) \tag{25}$$

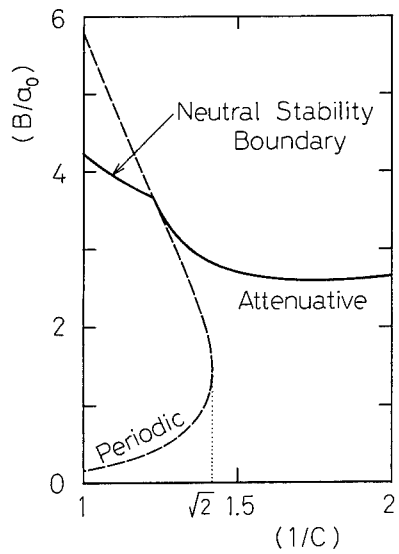

FIG. 1. Stable region for planar flames.

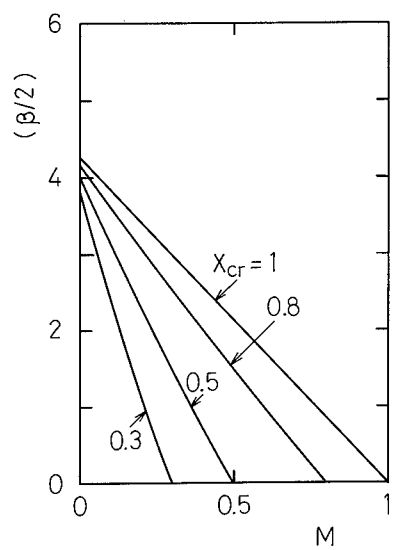

FIG. 2. Neutral stability boundary for planar flames.

$$0 \leq \left(\frac{B}{a_0}\right) < \frac{1}{C(1 - C^2)}, \quad \left(\frac{\sqrt{6}}{2} < \frac{1}{C}\right) \tag{26}$$

Figure 1 shows the stable region for the SHS flame propagation; the abscissa is $1/C$ and the ordinate B/a_0. Here, C is the maximum temperature, and B/a_0 is the driving force for instability. The flame propagation speed changes periodically in the region enclosed by the ordinate and the dashed curve, as indicated by Eq. (24). In the region enclosed by the

abscissa and the solid curves, the flame propagation speed attenuates and, hence, is stable, as indicated by Eqs. (25) and (26). We see that the upper limit of the stable regime with respect to B/a_0 decreases with increasing $1/C$ and that a part of the upper boundary $1 \leq 1/C \leq \sqrt{6}/2$ is the neutral stability boundary, on which there is no attenuation and/or no amplification in the flame propagation speed.

The critical value at which the pulsating mode of propagation occurs is given by

$$(a_0)_{cr}^2 = \frac{X_{cr} - M}{k(1 - M)} \tag{27}$$

$$\Psi_{cr} = -\frac{(a_0)_{cr}^2}{2\beta} \ln X_{cr} \tag{28}$$

$$\theta_{cr} = 1 + \frac{\ln X_{cr}}{\beta} \tag{29}$$

where X_{cr} is determined by solving the neutral stability condition

$$\frac{\beta}{2}\left(\frac{X}{X - M}\right) = \frac{2}{\sqrt{1 - \frac{2}{\beta}\ln X}\left[1 + \sqrt{1 + \frac{1}{4}\left(1 - \frac{2}{\beta}\ln X\right)^2}\right]} \tag{30}$$

with $X = a_0^2 k(1 - M) + M$; Eqs. (11) and (17) have also been used to obtain Eq. (30). Figure 2 shows the neutral stability boundary in the $\beta - M$ plane, with X being taken as a parameter. The region lower than the boundary is stable, whereas that above it is unstable. For a certain β and/or M, values of X in the stable region are smaller than X_{cr}, which depends on β and M. Since $\Psi \propto -\ln X$, an increase in heat loss tends to suppress the occurrence of instability.

Knowing the critical values of the heat-loss parameter Ψ_{cr} and the flame temperature θ_{cr}, the critical size of the N particle and the compact diameter for the SHS flame instability are determined through

$$\left(\frac{R_0^2}{2r}\right)_{cr} = \frac{\Psi_{cr}(\rho_t c)(u_0 \cdot R_0)^2}{[\lambda/(\rho_t c)]4\,\varepsilon\sigma(T_{cr}^2 + T_0^2)(T_{cr} + T_0)} \tag{31}$$

where only the thermal radiative heat loss from the cylindrical surface of the compact with radius r is considered [9]. We also note that the particle-size-weighted flame propagation speed, $F_0 = u_0 R_0$, is given by

$$F_0^2 = 3Le_0 D_0^2 \left(\frac{\rho_M}{\rho_N}\right)\left(\frac{1 - Z_0}{Z_\infty - Z_0}\right)\left(\frac{I_\theta}{I_\xi}\right) \tag{32}$$

obtained by rearranging Eq. (6). Here, I_ξ is expressed as

$$\begin{aligned} I_\xi \approx \left(\frac{1 + \theta_m}{2}\right)(\phi + \gamma)\Bigg\{2 - \frac{1}{5(\phi + \gamma)} &+ \frac{(\phi - 1)}{2a}\left[\ln\frac{(1 + a)^3}{\phi} - 2\sqrt{3}\tan^{-1}\left(\frac{2 - a}{\sqrt{3}\,a}\right) - \frac{\sqrt{3}}{3}\pi\right] \\ &+ \frac{(\phi + 2\gamma + 1)}{6b}\left[\ln\frac{(b - 1)^3}{\phi + 2\gamma} + 2\sqrt{3}\tan^{-1}\left(\frac{2 + b}{\sqrt{3}\,b}\right) - \frac{\sqrt{3}}{3}\pi\right]\Bigg\}, \quad (\mu \leq 1) \end{aligned} \tag{33}$$

$$\begin{aligned} I_\xi \approx \left(\frac{1 + \theta_m}{2}\right)\left(\frac{\phi + \gamma}{\phi^2}\right)\Bigg\{2(1 - a^2) &+ \frac{(3 - 5\phi) - 3(1 - \phi)a^2}{10(\phi + \gamma)} + \frac{(\phi + \gamma)}{3b} \\ &\left[\ln\frac{2(\phi + \gamma)}{\phi + 2\gamma}\left(\frac{b - 1}{a + b}\right)^3 + 2\sqrt{3}\tan^{-1}\left(\frac{2 + b}{\sqrt{3}\,b}\right) - 2\sqrt{3}\tan^{-1}\left(\frac{-2a + b}{\sqrt{3}\,b}\right)\right]\Bigg\}, \quad (\mu \geq 1) \end{aligned} \tag{34}$$

where

$$\phi = \frac{1}{\mu}, \quad \gamma = \frac{Z_0}{1 - Z_0}$$
$$a^3 = \phi - 1, \quad b^3 = \phi + 2\gamma + 1 \tag{35}$$

Comparisons

Analytical results are compared with the experimental data of Makino et al. [17–19] for the Ti–C system. For consistency, values of the physicochemical parameters are the same as those in previous work [13]:

$$\begin{aligned} (q/c) &= 1.5 \times 10^4 \text{ K} \\ \rho_M &= 4.50 \times 10^3 \text{ kg/m}^3 \\ \rho_N &= 2.25 \times 10^3 \text{ kg/m}^3 \\ W_M &= 47.9 \times 10^{-3} \text{ kg/mol} \\ W_N &= 12.0 \times 10^{-3} \text{ kg/mol} \\ T_m &= 1973 \text{ K} \\ D &= 2 \times 10^{-7} \exp(-1.66 \times 10^4/T) \text{ m}^2/\text{s} \\ c &= 1.0 \text{ kJ/(kg}\cdot\text{K)} \\ \varepsilon &= 0.4 \\ \lambda/(\rho_t c) &= 2.5 \times 10^{-6} \text{ m}^2/\text{s} \\ \sigma &= 5.67 \times 10^{-11} \text{ kJ/(m}^2\cdot\text{s}\cdot\text{K}^4) \end{aligned}$$

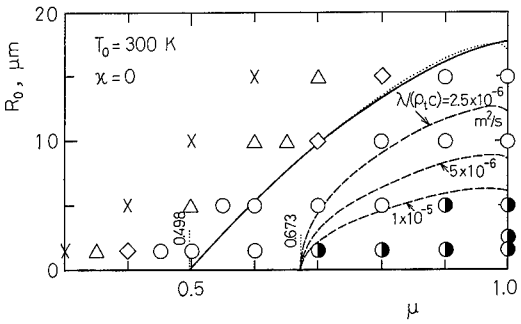

FIG. 3. Ranges of flammability and instability for the Ti–C system as functions of the mixture ratio μ and the radius R_0 of N particles for the initial temperature T_0 of 300 K and the compact diameter $2r$ of 18 mm, with $\lambda/\rho_t c$ taken as a parameter. In the region below the dashed curve, pulsating combustion proceeds. In the region between the solid (or dotted) and dashed curves, stable and steady propagation occurs. Data points are experimental [17], indicating (○) steady propagation, (◑) pulsating combustion, (◇) multipoint or spinning combustion, (△) flame extinction during the propagation, and (×) non-ignition.

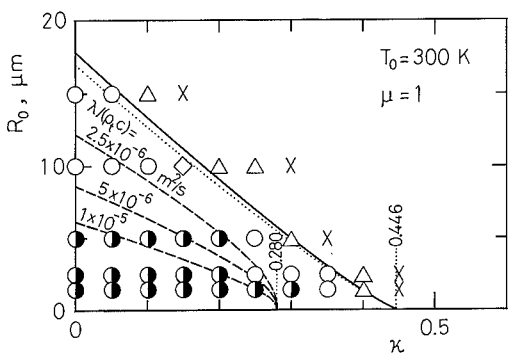

FIG. 4. Ranges of flammability and instability for the Ti–C system as functions of the degree of dilution κ and the radius R_0 of N particles for initial temperature T_0 of 300 K and compact diameter $2r$ of 18 mm, with $\lambda/\rho_t c$ taken as a parameter. Data points are experimental [17,18].

Figure 3 shows the ranges of flammability and instability with respect to the mixture ratio μ and the radius R_0 of N particles for an initial temperature T_0 of 300 K. In accordance with the experiments, the compact diameter is $2r$ = 18 mm. The solid and dotted curves are respectively the numerically [9] and analytically [11] obtained extinction limits. The dashed curves are the neutral stability boundaries, with $\lambda/\rho_t c$ taken as a parameter. Results show that, except near stoichiometry (μ = 1), the range of instability with respect to R_0 is reduced with decreasing mixture ratio. When $\mu < 0.673$, instability is suppressed, even for $R_0 \to 0$, because of the decrease

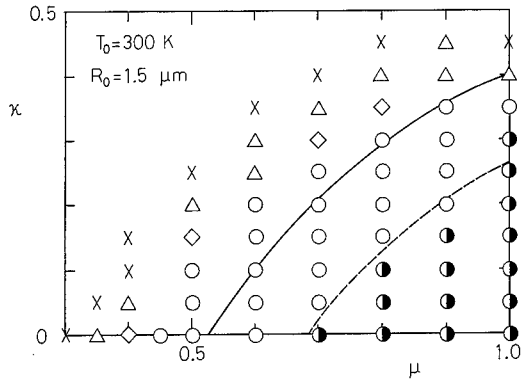

FIG. 5. Ranges of flammability and instability for the Ti–C system as functions of the mixture ratio μ and the degree of dilution κ, for particle radius R_0 of 1.5 μm, initial temperature T_0 of 300 K, and compact diameter $2r$ of 18 mm. Data points are experimental [17].

in the volumetric heat generation with decreasing μ. We also see that the instability can be suppressed with increasing $\lambda/\rho_t c$. This is attributed to the fact that the heat transferred from the flame zone increases with increasing $\lambda/\rho_t c$. By the same token, a reduction of T_0 is also expected to suppress instability, although the range of flammability is reduced. The slight increase in the range of instability with decreasing μ near stoichiometric is attributed to the overestimation in I_ξ in Eqs. (33) or (34), as noted in previous work [10].

Experimental results [17] also show that the range of pulsating combustion extends with decreasing R_0. The decrease in R_0 increases the total surface area for surface reactions in the SHS flame zone and, hence, makes the mixture more energy intensive. Since instability is invariably dependent on the burning intensity, mixtures with small particles have wider ranges for pulsating combustion. Experimental results suggest that the limit of instability predicted by the present analytical result is fair.

Figure 4 shows the ranges of flammability and instability with respect to the degree of dilution κ and the radius R_0 of N particles at 300 K. We see that the range of instability with respect to R_0 is narrowed with increasing κ. When $\kappa > 0.280$, instability is suppressed even at $R_0 \to 0$. Comparing with the experimental results [17,18], we see that there is again fair agreement.

Figures 3 and 4 show that the predicted limit of instability with $\lambda/\rho_t c = 5 \times 10^{-6}$ m^2/s fairly represents the experimental results, whereas the limit of extinction has been obtained with $\lambda/\rho_t c = 2.5 \times 10^{-6}$ m^2/s. This difference may be caused by the different temperatures at which these two phenomena occur; that is, the temperature at which the instability ceases to occur is about 200 K higher than that for flame extinction.

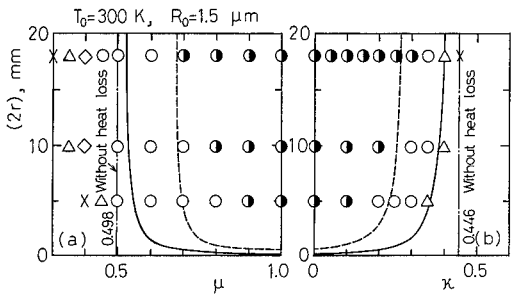

FIG. 6. Ranges of flammability and instability for the Ti–C system for particle radius R_0 of 1.5 μm and initial temperature T_0 of 300 K; (a) as functions of the mixture ratio μ and the compact diameter $2r$; (b) as functions of the degree of dilution κ and the compact diameter $2r$. Data points are experimental [19].

Figure 5 shows the ranges of flammability and instability with respect to the mixture ratio μ and the degree of dilution κ, with $R_0 = 1.5\,\mu$m at $T_0 = 300$ K. The limit of instability is obtained with $\lambda/\rho_t c = 5 \times 10^{-6}$ m^2/s. We see that the instability can be suppressed with decreasing μ and/or increasing κ because of the decrease in the volumetric heat generation. Fair agreement is again demonstrated between the prediction and the experimental results [17]. Figure 6(a) shows the ranges of flammability and instability with respect to the mixture ratio μ and the compact diameter $2r$, with $R_0 = 1.5\,\mu$m at $T_0 = 300$ K. We see that the range of instability is extended with increasing $2r$ because the effect of heat loss is reduced due to the increase in the volume-to-surface ratio. Figure 6(b) shows a similar plot for the degree of dilution κ and the compact diameter $2r$.

Figures 7(a) and (b) show the ranges of flammability and instability with respect to the mixture ratio μ, the degree of dilution κ, and the ratio of the square of the particle radius to compact diameter, $R_0^2/(2r)$, at $T_0 = 300$ K. Since this ratio is a measure of the heat loss rate to the heat generation rate in the SHS flame zone, it is expected to be useful in arranging experimental results. Experimental data are for various particle radii (1.5, 5, 10, and 15 μm) and various compact diameters (3, 5, 7, 10, and 18 mm). It is seen that fair agreement exists between the predicted and the experimental results.

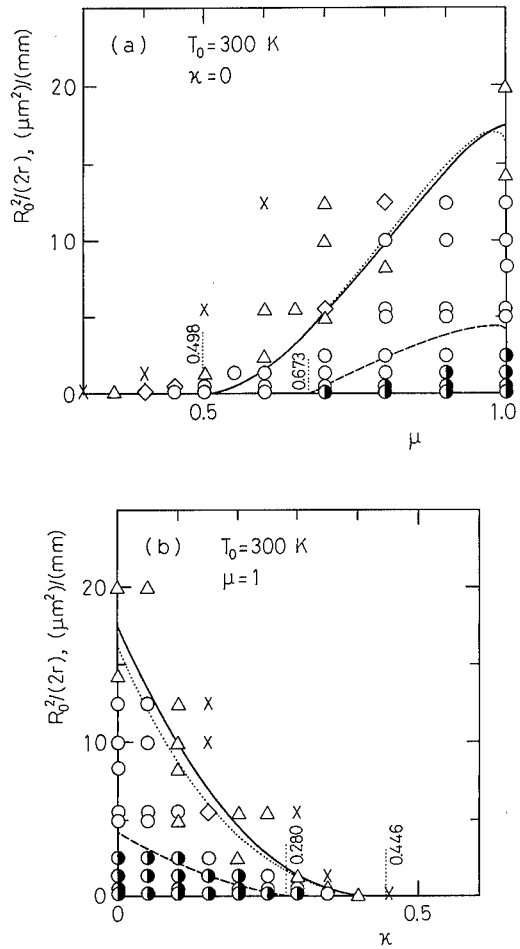

FIG. 7. Ranges of flammability and instability for the Ti–C system for initial temperature T_0 of 300 K; (a) as functions of the mixture ratio μ and the parameter $R_0^2/(2r)$; (b) as functions of the degree of dilution κ and the parameter $R_0^2/(2r)$. Data points are experimental for various particle radii and compact diameters [17–19].

Concluding Remarks

In the present study, we have analyzed the linear pulsating stability of SHS flame propagation, allowing for volumetric heat loss, temperature-sensitive Arrhenius mass diffusion, and infinitely fast surface reaction. Neutral stability boundary, which separates the regime of steady combustion from that of pulsating combustion, has been obtained by determining the critical heat loss parameter as functions of the Zeldovich number, melting parameter, and melting point of the metal. It is shown that the neutral stability boundary, that is, the limit of instability, depends on the mixture ratio, the degree of dilution, the size of nonmetal particles, and the compact diameter, as well as the thermophysical properties of the compacted mixture. Suppression of the instability can be achieved by reducing the heat generation rate at the bulk flame and/or enhancing the heat transfer rate from the flame. Fair agreement between the predictions and the experimental results is demonstrated, as far as the trend and the approximate magnitude are concerned. It is suggested that

the heterogeneous theory for the SHS flame propagation has captured the essential features of the neutral stability boundary in the SHS processes.

Nomenclature

A	reduced Damköhler number
a	normalized mass burning rate or constant
B	driving force for instability
b	constant
c	specific heat
D	mass diffusivity
Da	Damköhler number
F	particle-size-weighted flame propagation speed
f	stoichiometric mass ratio
I	integration
k	constant
M	melting parameter
m	mass burning rate
n	number density
p_+, p_-	exponent
q	heat of reaction
R	particle radius
r	specimen radius
T	temperature
u	velocity
W	molecular weight
Y	mass fraction of species
Z	mass fraction of fluid
α	temperature rise
β	Zeldovich number
γ	fluid-to-solid mass ratio
ε	emissivity
ζ	normalized mass fraction of species
θ	normalized temperature
κ	degree of dilution
λ	thermal conductivity
λ_+, λ_-	exponent
μ	mixture ratio
ν	stoichiometric coefficient
ξ	normalized mass fraction of fluid
ρ	density
σ	nondimensional distance
τ	nondimensional time
Φ	heat loss
ϕ	$=1/\mu$
χ	surface regression rate
Ψ	heat loss parameter
ω	frequency

Subscripts

M	metal or lower-melting-point metal
m	melting point
N	nonmetal or higher-melting-point metal
P	product
0	zeroth order
1	first order
ξ	with respect to ξ
θ	with respect to θ

Acknowledgments

AM and CKL were respectively supported by the Grant-in-Aid for Scientific Research of the Ministry of Education, Japan, and the US NASA Microgravity Program. We thank Dr. S. B. Margolis for his interests and helpful suggestions during the course of this investigation.

REFERENCES

1. Merzhanov, A. G. and Borovinskaya, I. P., *Combust. Sci. Technol.* 10:195–201 (1975).
2. Frankhouser, W. L., Brendley, K. W., Kieszek, N. C., and Sullivan, S. T., *Gasless Combustion Synthesis of Refractory Compounds,* Noyes, Park Ridge, NJ, 1985.
3. Munir, Z. A. and Anselmi-Tamburini, U., *Mater. Sci. Rep.* 3:277–365 (1989).
4. Merzhanov, A. G., *Combustion and Plasma Synthesis of High-Temperature Materials* (Z. A. Munir and J. B. Holt, Eds.), VCH, New York, 1990, pp. 1–53.
5. Varma, A. and Lebrat, J.-P., *Chem. Eng. Sci.* 47:2179–2194 (1992).
6. Margolis, S. B., *Prog. Energy Combust. Sci.* 17:135–162 (1991).
7. Makino, A. and Law, C. K., *Twenty-Fourth Symposium (International) on Combustion*, The Combustion Institute, Pittsburgh, 1992, pp. 1883–1891.
8. Margolis, S. B. and Williams, F. A., *Combust. Flame* 83:390–398 (1991).
9. Makino, A. and Law, C. K., *Twenty-Fifth Symposium (International) on Combustion*, The Combustion Institute, Pittsburgh, 1994, pp. 1659–1667.
10. Makino, A. and Law, C. K., *Combust. Flame* 101:551–555 (1995).
11. Makino, A. and Law, C. K., *J. SHS* 4:25–34 (1995).
12. Makino, A. and Law, C. K., *J. Am. Ceram. Soc.* 77:778–786 (1994).
13. Makino, A. and Law, C. K., *Combust. Sci. Technol.* 106:193–201 (1995).
14. Margolis, S. B., *SIAM J. Appl. Math.* 43:351–369 (1983).
15. Margolis, S. B., *Combust. Sci. Technol.* 43:197–215 (1985).
16. Kaper, H. S., Leaf, G. K., Margolis, S. B., and Matkowsky, B. J., *Combust. Sci. Technol.* 53:289–314 (1987).
17. Makino, A., Yamada, T., and Araki, N., *Nensho no Kagaku to Gijutsu (Combust. Sci. Technol., Jpn.)* 3:41–52 (1995) (in Japanese).
18. Makino, A., Kita, K., and Araki, N., *Nensho no Kagaku to Gijutsu (Combust. Sci. Technol., Jpn.)* 1:165–174 (1993) (in Japanese).
19. Makino, A., Sugiyama, K., and Araki, N., *Nensho no Kagaku to Gijutsu (Combust. Sci. Technol., Jpn.)*, 93–102, (1996).(in Japanese).

Twenty-Sixth Symposium (International) on Combustion/The Combustion Institute, 1996/pp. 1875–1881

SUPERCRITICAL COMBUSTION SYNTHESIS OF TITANIUM NITRIDE

K. BREZINSKY, J. A. BREHM, C. K. LAW AND I. GLASSMAN
Department of Mechanical and Aerospace Engineering
Princeton University, Princeton, NJ 08544, USA

To increase the interstitial mass loading of nitrogen for enhanced product yield in the self-propagating, high-temperature synthesis (SHS) of metallic nitrides, the synthesis was conducted in cryogenic nitrogen at supercritical states just above the critical point. This state regime has the unique characteristic that the density increases significantly with pressure. The viability of this concept has been experimentally substantiated for loosely packed titanium powders. Results show that the bubbling that characterized the synthesis process in liquid nitrogen was avoided and that liquidlike initial densities were maintained. Yields of titanium conversion to titanium nitride of almost 75% were achieved. This level of conversion is comparable to the highest of previously reported values obtained for titanium in gaseous nitrogen at ultrahigh pressures. Analysis of the present supercritical and literature data on high-pressure gas synthesis shows that the yield does not correlate well with pressure in accordance with the previous concept that filtrational transport is the controlling mechanism, especially for the after-burn condition. The data, however, were satisfactorily correlated against fluid density. Mass diffusion is the apparent relevant process for after-burn in low-nitrogen-density environments, and nitrogen loading in the interstices of the powdered titanium controls the yield at high-initial-nitrogen densities.

Introduction and Concept

In self-propagating, high-temperature synthesis (SHS), materials are synthesized strictly by the energy released from the exothermic reaction between the starting materials. Various approaches involving solid–solid reactions [1], gas-phase reactions [2], and fluid–solid reactions [3] have been proposed for SHS. The process under investigation in the present study considers an initial mixture of a reactant gas and loose powders, ignited by a heating element, usually a tungsten filament. The subsequent release of heat from the initially reacted "layer," of mixture ignites the adjacent "layer," and a thermal wave is propagated until the entire mixture has reacted. This self-sustaining reaction is observed as a flame passing through the condensed phase. If the reactants are comprised of a metal powder and nitrogen gas, then passage of the flame can lead to the formation of a metallic nitride of various elements such as titanium, silicon, or tantalum.

An inherent difficulty with SHS as a method of producing nitrides is the necessity to "pack in" the stoichiometric mass of nitrogen required within the pores of the powder bed so that the metal can be completely reacted by the nitrogen in the vicinity of the individual particles. Because of the significant disparity between the metal and nitrogen densities at, say, atmospheric conditions, it is clear that such a condition cannot be readily met.

The problem of nitrogen availability can be circumvented by performing the synthesis under extremely high pressures at which the density of nitrogen in the interstices between metal particles can reach the value necessary for stoichiometric conversion of the metal. An alternate and perhaps less physically demanding solution is to immerse the compact or powder in liquid nitrogen; however, as recent experiments [4] have shown, bubble formation during the passage of the combustion wave interferes with the direct contact between the particles and liquid nitrogen, and as a consequence, the efficient formation of products is adversely affected.

In view of the above considerations and the experimental results obtained with liquid nitrogen [4], a nitride synthesis technique was initiated in which the nitride product would be generated from a flame propagating through a controlled density of titanium particles in supercritical fluid nitrogen, at temperatures and pressures just above the critical point of nitrogen, 126.26 K and 3.39 MPa, respectively. For states just above the critical point, often defined to mean temperatures from 1.01 to 1.10 times the critical temperature and pressures from 1.01 to 1.50 times the critical pressure [5], the isothermal compressibility, which designates the change of density with changing pressure at constant temperature, is almost infinite. This behavior can be observed in Fig. 1 in which nitrogen density is plotted as a function of pressure near the critical point [4]. Doubling the pressure from 2 to 4 MPa leads to an almost 10-fold increase in the density, to approximately 0.5 g/cc. To obtain this magnitude of change in density in room-temperature nitrogen, the pressure of the gas would

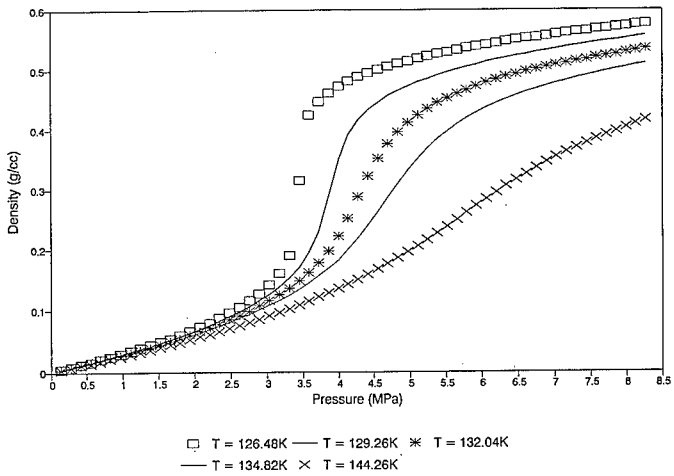

FIG. 1. Pressure-versus-density curves for nitrogen along various isotherms: 126.48, 129.26, 132.04, 134.82, and 144.26 K obtained from "NIST Thermophysical Properties of Pure Fluids Database," Version 3.1 [4].

have to be increased almost 10-fold, from 6.2 to 60 MPa. Taking advantage of this unique behavior of a fluid near its critical point has been one of the goals of the experimental approach.

It becomes evident that the approach of forming nitride through SHS in supercritical fluid nitrogen therefore offers the significant advantage of providing an adequate and more convenient supply of nitrogen, without bubble formation, for the potentially complete reaction of the metal powders at high (approximately 40 atm), but not extremely high, pressures. At these near-supercritical pressures, the density, and therefore the concentration, of nitrogen is "tailorable" because of the almost infinite isothermal compressibility near the critical point and, as such, raises the possibility of increased product formation.

On the basis of the concept advanced above, an experiment has been designed and conducted on the synthesis of titanium nitride in supercritical nitrogen. In the next section, the experimental aspects of the investigation are presented, and the results are discussed. It will be demonstrated in due course that the concept of supercritical SHS proposed is indeed viable, that a high degree of product yield is achievable, and that there appears to be a fundamental relationship between yield and the initial nitrogen density.

Experimental

The low-temperature (126.26 K) and high-pressure (3.4 MPa) values of the critical point of nitrogen required the design of a unique apparatus for investigating the formation of nitrides in the supercritical nitrogen regime. The details of the design are given in Ref. 4 and hence will only be outlined here.

The design was centered around the construction of a vessel that could be used to obtain temperatures and pressures near the critical point of nitrogen simply through cooling and temperature control with liquid nitrogen. Thus, the vessel and its components were designed to withstand temperatures as low as 77 K, the boiling point of liquid nitrogen. Similarly, the vessel, while cold, had to withstand at least twice the critical pressure of nitrogen, 6.8 MPa. A vessel with these capabilities was constructed from austenitic stainless steel 304L for all weldable parts and with 304 stainless steel for all other parts; a schematic of the apparatus is shown in Fig. 2. Incorporated into the end portions of the vessel were sight windows that could withstand both low temperature and high pressure and permit viewing of the combustion event. Associated liquid nitrogen delivery controls, electrical input to provide current for the ignition source, and safety devices were also attached to the vessel. The entire apparatus met ASME test standards for a maximum working pressure of 8.28 MPa at 305.4 K and a minimum temperature of 77.6 K at this same pressure.

The interior cylindrical working space of the cryogenic vessel had a nominal diameter of 12 cm and a length of 15 cm. Into this space was placed a sample of powdered titanium. Although the powdered titanium as specified by the manufacturer had an average particle diameter between 10 and 15 μm, with 10% of the particles below 5 μm and 10% above 20 μm, scanning electron microscope examination of the powder indicated that the average diameter was more likely in the 25-μm range.

For most experiments, the loosely packed, undiluted* samples were contained in a 5-cm-long quartz cylinder into which a tungsten igniter filament was

*The term "diluted" is used to describe the technique of adding the nitride product to the initial mixture to control the reaction temperature generally to prevent the melting of the reacting metal during synthesis. "Undiluted" means no product is added.

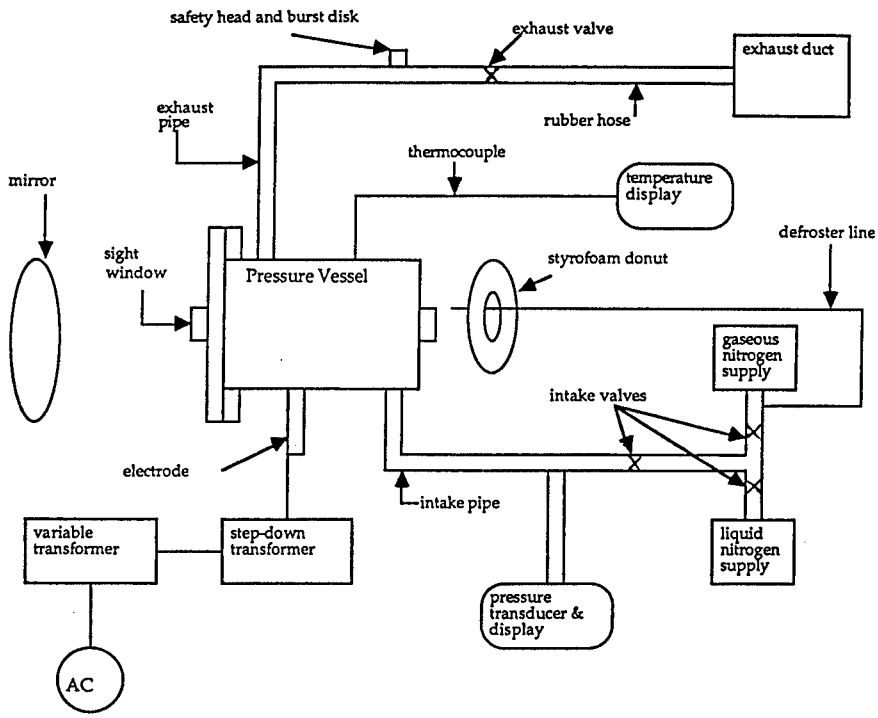

FIG. 2. Schematic of the entire system: pressure vessel, electrical hookups, and pressure and temperature equipment.

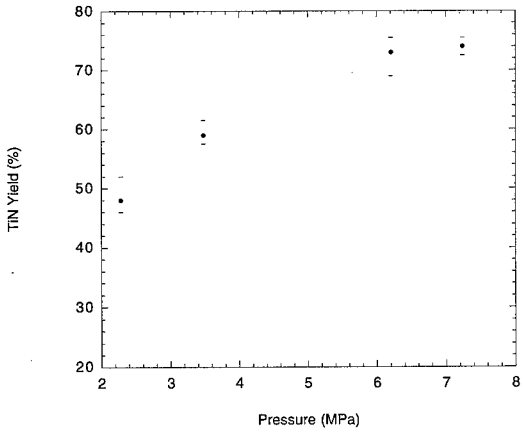

FIG. 3. The yield of titanium nitride produced from the combustion synthesis conducted with supercritical nitrogen and different pressure. The solid circles are the average yields. The horizontal bars represent the high and low ranges of values. The temperature of supercritical nitrogen at the pressures 2.28, 3.48, and 6.21 MPa was 132.04 K, and at 7.20 MPa it was 134.82 K.

positioned. Upon ignition, two flames propagated from the centrally located filament toward the ends of the cylinder, which were sealed with a stainless steel wire cloth that quenched the flames. The conversion yield was then determined from a comparison of the weights of material before and after passage of the flames.

For the experiments conducted at 2.28 and 3.48 MPa, the pressure rise during the combustion synthesis was no greater than 2.5 MPa and consequently did not approach the high-pressure limit of the reaction vessel. For experiments with higher initial pressures, a 2–3 MPa pressure rise during the combustion phase would lead to a total pressure greater than that specified for the vessel. In order to prevent such an occurrence, the pressure was regulated to remain at the initial pressures of 6.48 and 7.24 MPa during the higher-pressure experiments. As discussed below, the differences between the pressure conditions after passage of the combustion wave appear to be less important than the differences in the initial nitrogen density. Further details of the operational procedure are provided in Ref. 4.

Results

Figure 3 presents the extent of conversion of titanium to titanium nitride as a function of the su-

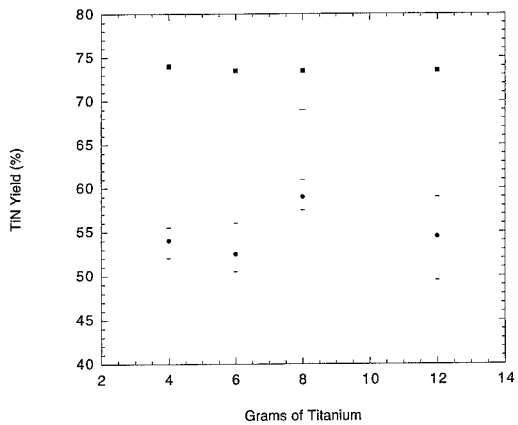

FIG. 4. The variation in titanium nitride yield with the mass of titanium at 3.48 MPa (solid circles) and at 6.21 MPa (solid squares). Points represent average values when high- and low-range bars are present.

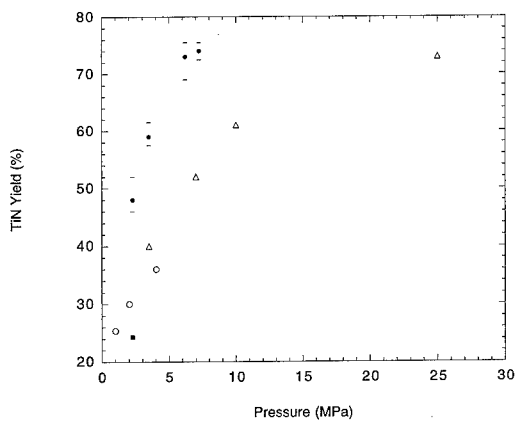

FIG. 5. The percent of TiN yield with respect to pressure obtained in the present supercritical nitrogen work (solid circles with bars representing high and low values), by Hirao et al. [6] (open triangles) and Agrafiotis [7] (open circles), and in room-temperature nitrogen at 2.28 MPa (solid square).

percritical nitrogen pressure. At each pressure, the experiment was repeated several times so that the data represent an average value and the range of values obtained for the yield. It is seen that the yield increases with nitrogen pressure so that at 134.82 K and 7.24 MPa, an asymptotic average conversion of 74% was achieved. This conversion, together with those of the ultrahigh-pressure experiments of Hirao et al. [6], are the highest reported SHS conversions for pure, undiluted titanium.

Examination of the product sample revealed that, even at these high yields, the nitride product exhibited a heterogeneous microstructure. Specifically, the microstructure of the top layer of the nitride product, which had been mostly in direct contact with nitrogen, was ascertained to be stoichiometric TiN through X-ray diffraction measurements, while most of the interior consisted of a fine, rigid, sponge-like structure of fine pores surrounded by thin titanium walls coated with titanium nitride.

Figure 4 presents the yield of titanium nitride as a function of the mass of titanium contained in the quartz cylinder at two different pressures. It appears that the yield is insensitive to the total mass within the range of the scatter in the data.

Discussion

The results of Fig. 3 clearly demonstrate that using supercritical nitrogen is a viable technique for the combustion synthesis of titanium nitride. It would also appear from these results that the yield of titanium nitride formed by the reaction of titanium with supercritical nitrogen is simply a function of pressure as has been observed for the same reaction with room-temperature nitrogen at high pressure. Specifically, Hirao et al. [6] conducted a set of experiments in which loose titanium powders of similar size to those of the present experiments were reacted with room-temperature nitrogen over the pressure range of approximately 3.5–25 MPa. An increase in yield with pressure from 40% to over 70% was observed. In a similar set of experiments, Agrafiotis [7] nitrided undiluted loose powders of small titanium particles at pressures of 1.01, 2.03, and 4.05 MPa and found that the yield increased from 25% to 36%. It has been suggested and demonstrated through modeling [8,9] that this kind of pressure dependence of nitride yield is a consequence of the flow of nitrogen through the porous reacting medium resulting from the pressure gradient between the external nitrogen and that which is being consumed at the reaction front. This filtration process, which can be described by Darcy's law, could also control the eventual nitride yield through the extensive after-burn period that has frequently been observed by others as well as in the present experiments.

In order to investigate the role of pressure in determining nitride yield, the present results on the TiN yield, together with those of Agrafiotis [7] and Hirao et al. [6], for undiluted titanium powder are plotted as a function of pressure in Fig. 5. Two observations are apparent. First, Fig. 5 clearly displays in a quantitative manner that for a given pressure, the yields obtained with the present technique of using supercritical nitrogen are substantially higher than those obtained by using high-pressure nitrogen alone. Second, in contrast to the suggestion of the central role of pressure in the synthesis process, Fig. 5 shows that the yields are not correlated when plot-

ted versus pressure. This lack of correlation, in turn, suggests that, even though the present results appear to exhibit the pressure dependence that might be associated with filtration-limited yields, filtration actually may not be the controlling process in the synthesis. Indeed, there are additional factors that appear to support this possibility, to be discussed next.

First, note that at the high pressures of the present experiments, there is more nitrogen available than is necessary for the yield obtained; for example, at an initial titanium/nitrogen equivalence ratio of 1.16 at 6.2 MPa, a yield of 86% titanium nitride would be expected instead of 73% as was observed. Calculations analogous to those of Munir and Holt [10] were conducted, at the initial temperature and pressure conditions, to compare the amount of nitrogen contained within the pores of an ensemble of powder particles with that necessary for the stoichiometric conversion of the titanium to the nitride. At the high-pressure end of the supercritical nitrogen experiments described above, the initial nitrogen density in the pores was approximately 0.49 g/cc, which is 86% of the value needed for complete conversion. Therefore, no filtration of nitrogen would be necessary to obtain the yield observed at the high pressures, assuming that the initial amount of nitrogen remained available during the conversion process.

The observed high yield at lower pressures, however, does imply that additional nitrogen must have been transported to the reacting titanium after passage of the flame. For example, at 2.28 MPa, the amount of nitrogen in the pores is only 20% of that needed for complete conversion, although a yield of approximately 50% was nevertheless obtained. This difference, however, cannot be explained by filtration transport, for the following reason. Figure 4 demonstrates that within the experimental accuracy defined by the precision of the measured yield at a given pressure, the yield is independent of the amount of titanium placed in the reaction cylinder. By changing the mass of titanium powder contained in a fixed length of tube, the depth of the bed is changed, as is the surface-to-volume ratio. Despite these changes, the yield remains the same even though the bed height increases from approximately 4 mm at 4 g to 9 mm at 12 g. These results are therefore contrary to those limited by filtration barriers of the type associated with percolation of nitrogen through the porous powder, which have been shown to be dependent on the bed height [9].

An additional argument against filtration control of yield is that despite the pressure sensitivity shown in Fig. 3 for the present results, a comparison with the results of Hirao et al. indicates that for similar levels of porosity, very different pressures have only a small effect; for example, yields of approximately 70% can be obtained at the present 7.2-MPa pressure and the 25-MPa pressure of Ref. 6. This is contrary to results obtained from computational simulation that differing pressures usually have a dramatic effect when filtration is *assumed* to be the controlling mechanism [9].

The above observations then suggest that pressure, with its associated implications for filtration limitations on the supply of nitrogen, may not be a universal correlating parameter for the yield of nitride formed from loosely packed small particles of titanium, especially for the present experiments. Recognizing that transport is not needed for the high-pressure, high-yield situations in which there is sufficient nitrogen for the yield obtained, a more appropriate fundamental thermodynamic parameter would appear to be the density. This hypothesis is supported by comparison of the conversions obtained in the present work and those reported by Hirao et al. for particles of similar sizes. The conversion yield of 48.7% reported here for initially subcritical conditions of 132.04 K and 2.28 MPa is nearly equal to the value of 50% obtained by Hirao et al. for initial conditions of room temperature and 7 MPa. At these sets of conditions, the density of nitrogen was nearly identical: 0.076 g/cc and 0.079 g/cc, respectively. At initial conditions just above the critical point of nitrogen, 132.04 K and 3.48 MPa, a conversion of 59.0% was achieved and was found to be about equal to the value of 60% reported by Hirao et al. at conditions well into the supercritical regime (room temperature and 25 MPa); to be noted in particular is that even though the pressure of Hirao's experiments was 7 times higher than the present value, the densities at the experimental condition, 0.26 g/cc and 0.15 g/cc, respectively, differ by only a factor of 1.7. Furthermore, it was found in the present work that at an initially subcritical nitrogen pressure of 2.28 MPa, conversion of 48.7% was achieved at an initial temperature of 132.04 K, while a conversion of only 24.3% was obtained at room temperature. At constant pressure, the density at 132 K is 0.076 g/cc, which is a factor of 3 higher than the 0.026 g/cc density at room temperature. Furthermore, Agrafiotis [7] conducted a similar set of experiments using undiluted 29-μm titanium particles loosely packed in room-temperature nitrogen at 1.01, 2.03, and 4.05 MPa. The yields at these conditions were 25.4, 30.0, and 36.0%, with the corresponding densities of 0.011, 0.023, and 0.046 g/cc. Thus, the increase in yield is again associated with the increased density.

A plot of the results of Agrafiotis [7], Hirao et al. [6], and those from the present investigation against density, Fig. 6, reveals a very satisfactory correlation and thus substantiates the postulate posed above. The seemingly disparate high yields from the present supercritical nitrogen experiments are now seen to be simply a consequence of the high density of the working fluid. Furthermore, it is significant to note that the correlation not only captures the high-pressure gas results of Hirao et al. but also the lower-

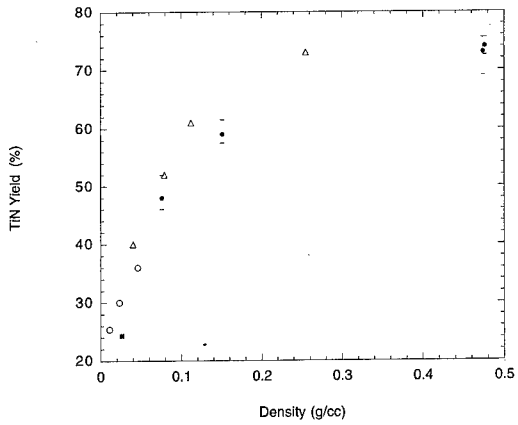

FIG. 6. The percent of titanium nitride yield with respect to the initial density of nitrogen for the present work (solid circles with high- and low-range bars), the data of Hirao et al. [6] (open triangles), the data of Agrafiotis [7] (open circles), and in room-temperature nitrogen at 2.28 MPa (solid square).

pressure gas results of Agrafiotis. In contrast, Fig. 5 demonstrates that even the high- and low-pressure results from the gas experiments do not correlate well with pressure.

The possibility that density instead of pressure could be the fundamental parameter also implies that the controlling transport process in the porous medium of the powdered bed, especially during the after-burn process, is one that depends on the density and density gradient instead of on filtration, which depends on the pressure gradient. A logical choice for a mass transport process that depends on the density gradient is mass diffusion, whose rate is significantly elevated at the high temperatures of SHS. Indeed, a recent study on zirconium particle combustion [11] has experimentally demonstrated that during burning, the particle composition is perpetually uniformized due to diffusion. The diffusion is affected by the chemical depletion of nitrogen as well as the invariably multicomponent nature of the fluid in the powdered sample due to either melting and/or dissolution of the reactants and products. Note that a large nitrogen concentration gradient could potentially still be established at the surface of the titanium particles even in the presence of a small amount of solute [12].

Therefore, a rational interpretation of the density-correlated results is that in the high-density regime, the extent of conversion is simply related to the fluid density, whereas in the lower-density regime, the controlling transport process is mass diffusion, which, in turn, depends on the bulk density of the fluid. Filtration driven by a pressure gradient does not appear to be a dominant process for the systems analyzed herein, despite a nominal dependence on initial nitrogen pressure.

Finally, Fig. 6 also reveals that the yield at the highest densities appears to reach an asymptotic limit for these undiluted powders. To explore the implications of this result, adiabatic flame temperature calculations were performed using STANJAN [13], which is particularly suited for the calculation of equilibrium concentrations when condensed phases are present. At the asymptotic limit of density, the calculation was performed assuming that the only nitrogen available for reaction was the amount originally present in the pores, approximately 86% of the stoichiometric value. For this titanium-rich condition, the adiabatic flame temperature calculation yields an equilibrium liquid TiN concentration of 79%, which is surprisingly close to the experimentally observed yield. As expected from related adiabatic flame temperature calculations [14], the computed flame temperature, even after accounting for the initial low temperature, was 3958 K. At this high temperature and at the pressure of the calculation, 6.21 MPA, not only are the TiN and the excess Ti liquid, but some TiN product also dissociates to create an equilibrium concentration of nitrogen and nitrogen atoms. In reality, heterogeneity and radiation would modify both the flame temperature and composition as calculated based on an adiabatic homogeneous mixture. The concept of product dissociation, which could place an upper limit on the yield of SHS refractory products, is, however, still applicable and could possibly be controlled by product dilution but, obviously, merits further study.

Concluding Remarks

Three significant contributions have evolved from the present study. First, the utility of supercritical nitrogen as a means of increasing the product yield in the SHS of metallic nitrides has been promoted. Specifically, by working in slightly supercritical states, the fluid density and hence the interstitial mass loading can be significantly increased without the need for ultrahigh pressures as needed for the synthesis in gaseous nitrogen. Second, this approach has been applied to the synthesis of titanium nitride and has resulted in yields up to 74%, which even slightly exceed the highest value previously obtained by using high-pressure gaseous nitrogen. Third, it has been demonstrated that previous and present data on high-pressure TiN SHS can be correlated in terms of the fluid density, instead of the system pressure, which implies that mass diffusion instead of filtration is the controlling process for after-burn in low-density environments and that nitrogen loading in the interstices of the powdered titanium controls the yield at high-initial-nitrogen densities.

Acknowledgments

This research has been supported by the National Aeronautics and Space Administration, Microgravity Materials Science program, under grant number NAG3-1418. We thank Mr. J. Sivo and Mr. D. L. Zhu for their assistance and advice in the experimentation.

REFERENCES

1. Merzhanov, A. G., "Solid Flames: Discoveries, Concepts, and Horizons of Cognition," *Combust. Sci. Technol.* 98:307 (1994).
2. Glassman, I., Davis, K. A., and Brezinsky, K., "A Gas-Phase Combustion Synthesis Process for Non-Oxide Ceramics," *Twenty-Fourth Symposium (International) on Combustion,* The Combustion Institute, 1992, p. 1877.
3. Merzhanov, A. G. and Borovinskaya, I. P., "Self-Propagated High-Temperature Synthesis of Refractory Inorganic Compounds," *Dokl. Akad. Nauk. USSR* 204:366 (1972).
4. Brehm, J. A., "Self-Propagating High-Temperature Synthesis of Titanium Nitride in Supercritical Nitrogen," Master's Thesis, Princeton University, Princeton, NJ, June 1995.
5. Brennecke, J. F. and Eckert, C. A., "Phase Equilibria for Supercritical Fluid Process Design," *AIChE J.* 35:1409 (1989).
6. Hirao, K., Miyamoto, Y., and Koizumi, M., "Combustion Synthesis of Nitride Powders Under High Nitrogen Pressure," *Adv. Ceram.* 21:287 (1987).
7. Agrafiotis, C. C., "Self-Propagating High-Temperature Synthesis of Nitrogen Ceramics," Ph.D. Thesis, State University of New York at Buffalo, 1991.
8. Agrafiotis, C. C., Puszynski, J. A., and Hlavacek, V., "Experimental Study on the Synthesis of Titanium and Tantalum Nitrides in the Self-Propagation Regime," *Combust. Sci. Technol.* 76:187 (1991).
9. Dandekar, H. W., Puszynski, J. A., and Hlavacek, V., "A Numerical Study of the Combustion Synthesis of Transition Metal Nitrides," *AIChE J.* 36:1649 (1990).
10. Munir, Z. A. and Holt, J. B., "The Combustion Synthesis of Refractory Nitrides," *J. Mater. Sci.* 22:710 (1987).
11. Molodetsky, I. E., Dreizin, E. L., and Law, C. K., "On the Evolution of Particle Temperature and Internal Composition for Zirconium Burning in Air," *Twenty-Sixth Symposium (International) on Combustion,* The Combustion Institute, Pittsburgh, 1996, pp. 1919–1927.
12. Glassman, I. and Law, C. K., "Sensitivity of Metal Reactivity to Gaseous Impurities in Oxygen Environments," *Combust. Sci. Technol.* 80:151 (1991).
13. Reynolds, W. C., "STANJAN, The Element Potential Method for Chemical Equilibrium Analysis," Department of Mechanical Engineering, Stanford University, 1986.
14. Glassman, I. and Papas, P., "Determination of Enthalpies of Volatilization for Metal Oxides/Nitrides Using Chemical Equilibrium Combustion Temperature Calculations," *J. Mater. Syn. Proc.* 2:151 (1994).

COMMENTS

Robert V. Kee, Colorado School of Mines, USA. Your micrographs show a very smooth molten-type appearance. Could you comment on the crystallographic microstructure of the TiN material?

Author's Reply. The x-ray diffraction spectra of bulk samples were identical with those of commercially available TiN. Such a match of spectra does not preclude microscopic regions being other than TiN especially those that showed the smooth molten type appearance you mention. The composition of the microstructural features requires further examination.

Twenty-Sixth Symposium (International) on Combustion/The Combustion Institute, 1996/pp. 1883–1889

METAL-SULFUR COMBUSTION

S. GOROSHIN, A. MIZERA, D. L. FROST, AND J. H. S. LEE
Department of Mechanical Engineering, McGill University
817 Sherbrooke Street West
Montreal, Quebec, H3A 2K6, Canada

A number of metal-sulfur compounds have been synthesized in the present investigation via self-propagating, high-temperature synthesis (SHS) process. Equilibrium calculations indicate that a large number of metals react with sulfur energetically, yielding adiabatic flame temperatures sufficiently high to support self-sustained flame propagation. To permit the combustion process to proceed entirely in the condensed phase, the pressure of the environment has to be kept at elevated levels (1–20 MPa) for most of the metal-sulfur mixtures studied. Computed adiabatic flame temperatures of some of the metal-sulfur reactions exceed 5000 K (Ca–S, Sr–S, Ba–S). The present experimental investigation was carried out to verify the equilibrium calculations. Seven metals have been studied (i.e., Mg, Si, Ti, Mn, Cr, Zn, and Mo). Samples are prepared by melting the metal-sulfur precursor mixture, which eliminates any trapped gas so that the density of the sample approaches the theoretical value. X-ray diffraction analysis of the products shows that the synthesized samples have a high purity and that the reactions are close to completion. Ignition temperatures for the metal-sulfur mixtures were found to be in the range of 350–600 °C. Flame speeds measured for several of the metal-sulfur mixtures ranged from 5 to 10 mm/s. The large-energy-release, low-ignition temperatures and high adiabatic flame temperatures associated with metal-sulfur combustion make this process also promising for a variety of "energetic" applications.

Introduction

Elemental sulfur reacts readily with almost all elements, except for iodine, gold, platinum, and the noble gases. Sulfur is situated directly below oxygen in the periodic table, and its properties as a reactant resemble many of the oxygen characteristics. In particular, it reacts exothermically with many metals to form stable refractory compounds. Metal-sulfur reactions are sufficiently energetic to support the self-sustained propagation of a combustion front if the small metal particles are mixed with sulfur to provide a sufficiently large surface area for the reaction. This was first demonstrated in Ref. 1 with the synthesis of ZnS when a cold-pressed mixture of sulfur and zinc powders was reacted in the self-propagating, high-temperature synthesis (SHS) mode. However, it was found that the synthesized samples were porous and that the purity was not sufficiently good, particularly for electronics applications.

A novel method for the preparation of the metal-sulfur precursor charge, i.e., mixing of the metal powder with molten sulfur, was proposed in Ref. 2. This permitted, for the first time, the complete elimination of trapped gases in the precursor SHS charge, which is the major shortcoming of the traditional cold-pressing method. Using this new charge preparation technique, high-purity ZnS samples with a density close to the theoretical value were synthesized [2].

In the present study, the technique developed for ZnS is extended to other metal-sulfur compounds (for example, MgS, SiS, etc.). These compounds have a variety of practical applications (for example, CrS is used as a catalyst, MoS_2 as a solid lubricant, MnS as an additive in steel production, etc.). The simple, environmentally benign and energetic SHS method is attractive when compared with traditional techniques for metal-sulfide synthesis, such as the precipitation with hydrogen sulfide from an aqueous solution of the corresponding salts or the heating of elemental reactant powders in a resistive furnace [3].

The unique properties of metal-sulfur combustion, including high flame temperatures (up to 5000 K), low ignition temperatures, liquid combustion products, nonporous precursor charges, and gasless combustion (for some charges at elevated pressures), also make it attractive in traditional "energetic" applications, which utilize the heat release in combustion phenomena (for example, pyrotechnics [4], closed energy propulsion systems [5], etc.).

In the present paper, the thermodynamics of metal-sulfur combustion is investigated to predict the adiabatic flame temperatures and the yields of

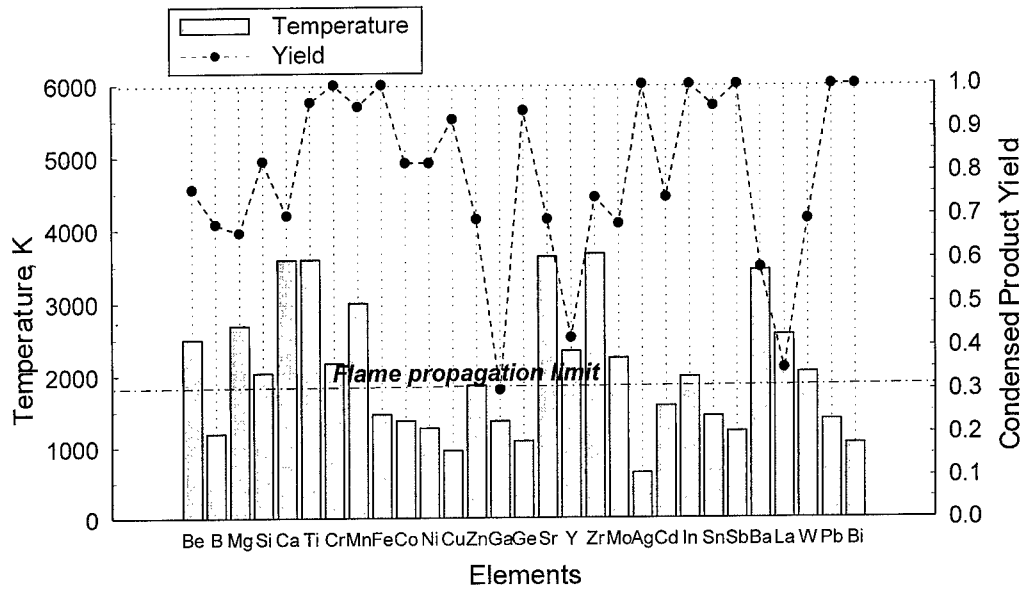

FIG. 1. Flame temperature and yield of condensed product in combustion of elemental sulfur with different metals. Constant-pressure equilibrium calculations, $P = 0.1$ MPa.

various reactions as a function of ambient pressure. Various high-quality metal sulfides were obtained for the first time by combustion synthesis in the present work. Finally, some characteristics of the metal-sulfur combustion process (ignition temperature and flame speed) have also been investigated.

Thermodynamics

To select the metal-sulfur mixtures that would most likely support self-sustained flame propagation, thermodynamic calculations of the adiabatic flame temperature and product composition were performed. The thermodynamic software package "Thermo," developed by Dr. A. Shiryaev at the Institute of Structural Macrokinetics (Moscow), was used [6]. The package includes a thermodynamic database, a program for the calculation of the coefficients of thermodynamic functions for new compounds, and a program for the calculation of equilibrium characteristics based on minimizing the thermodynamic potential.

The equilibrium characteristics for constant pressure combustion of stoichiometric compositions were calculated for about 30 different metal-sulfur mixtures. If more than one stable metal-sulfur compound may be formed in the reaction, the stoichiometric composition was chosen to consider the formation of the most energetic and stable compound at normal conditions (i.e., $P = 0.1$ MPa, $T = 300$ K).

The results of the calculated adiabatic flame temperatures and the yields of the corresponding metal-sulfur compound in a condensed form (at the flame temperature) are presented in Fig. 1 (for constant pressure combustion, $P = 0.1$ MPa). The empirically established flame temperature limit in SHS systems at which a self-sustained combustion wave can be observed is about 1800 K [7]*. It can be seen from Fig. 1 that at normal pressure conditions, the flame temperature of the stoichiometric mixture of 15 elements, i.e., Be, Mg, Si, Ca, Ti, Cr, Mn, Sr, Y, Zr, Mo, In, Ba, La, and W, exceeds the minimum value required for the flame propagation. However, the thermodynamic calculations predict a 100% yield of the final product in a condensed phase for two elements: chromium and indium. For the rest of the compounds, although the amount of gas product in terms of mass percent is relatively small, the volume of the gas products exceeds the volume of the condensed product by orders of magnitude due to the low gas density and high flame temperatures.

The total pressure has to be increased to suppress the evaporation and dissociation of the product. The

*Strictly speaking, the flame propagation limit is a function of heat losses and therefore depends on the charge size and geometry, initial and ambient temperature, and for the samples with liquid products, on the gravity condition and sample orientation [2]. For example, it can be decreased using a thermal blanket consisting of another energetic SHS mixture around the charge.

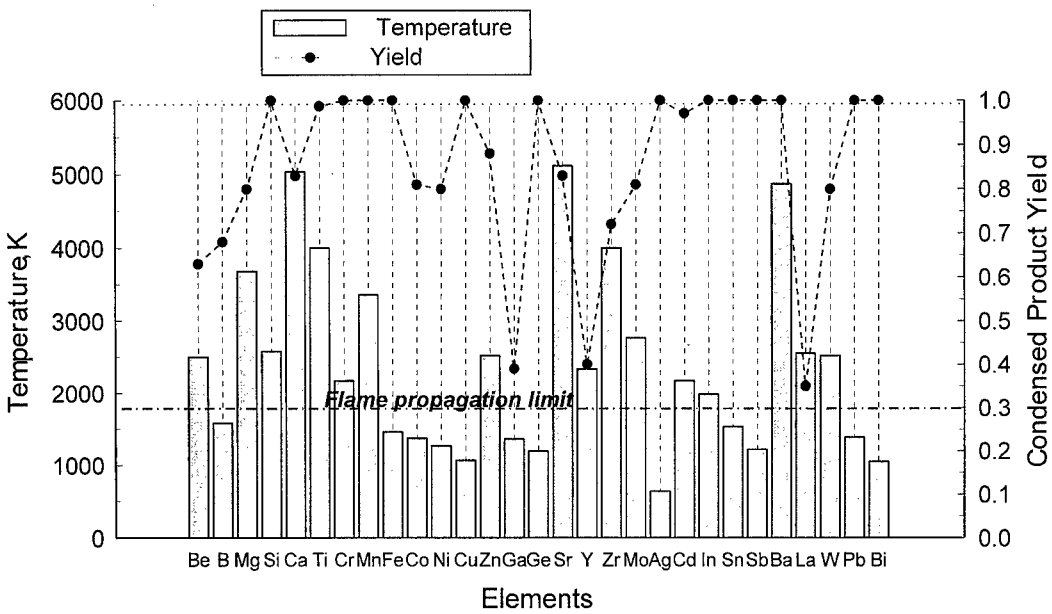

FIG. 2. Flame temperature and yield of condensed product in combustion of elemental sulfur with different metals. Constant-pressure equilibrium calculations, $P = 5$ MPa.

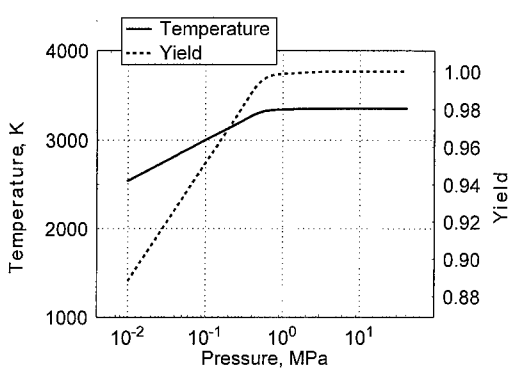

FIG. 3. Dependence of flame temperature and yield of condensed product on pressure in Mn–S constant-pressure combustion.

combustion at elevated pressure increases the yield of the condensed products as well as the adiabatic flame temperatures. The results of the thermodynamic constant pressure combustion calculations at an elevated pressure of 5 MPa are shown in Fig. 2. The number of elements able to react in a self-sustained combustion mode, according to the 1800-K limit, does not seem to increase significantly with pressure. Only Cd crossed the flame temperature propagation limit at elevated pressure. However, the flame temperatures and the yield of condensed reaction products changed significantly for many elements at elevated pressures. Three elements, Ca, Sr, and Ba, show combustion temperatures close to or exceeding 5000 K. The combustion temperatures of three other elements, Mg, Ti, and Zr, are close to 4000 K. In addition to chromium and indium, two more elements, namely, Mn and Ba, also show a 100% yield of the condensed product. The condensed product yield of the Ti–S reaction is also very close to 100% at $P = 5$ MPa. The influence of the ambient pressure on the flame temperature and the condensed product yield, for a wide range of pressures, is given in more detail for the Mn–S and Zn–S mixtures in Figs. 3 and 4.

SHS Synthesis of Metal-Sulfur Compounds

Although the thermodynamic equilibrium calculations indicate that about 15 metals will react with sulfur in a self-sustained combustion mode, only 7 metals were chosen for the present experimental study, namely, Mg, Si, Ti, Cr, Mn, Zn, and Mo. This choice was mostly dictated by practical considerations. Some of the metals are highly toxic (Be, Cd), requiring special handling procedures; some are not available commercially in a powdered form (Ca, Sr, Ba); some are spontaneously flammable in open air (Zr); and others are simply too expensive (Y, In) for the present feasibility study.

High-purity (99.5% on average) metal powders with a particle size in the 1–5-μm range (produced by Atlantic Equipment Engineering Company, Bergenfield, NJ) were used. The high-purity (99.5%),

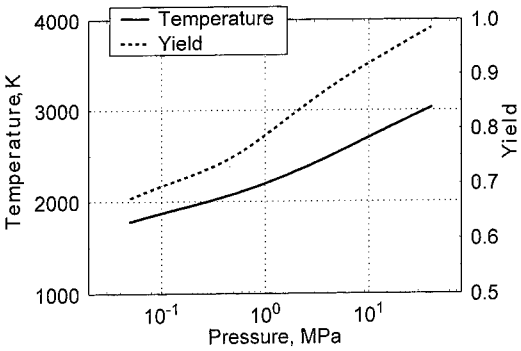

FIG. 4. Dependence of flame temperature and yield of condensed product on pressure in Zn–S constant-pressure combustion.

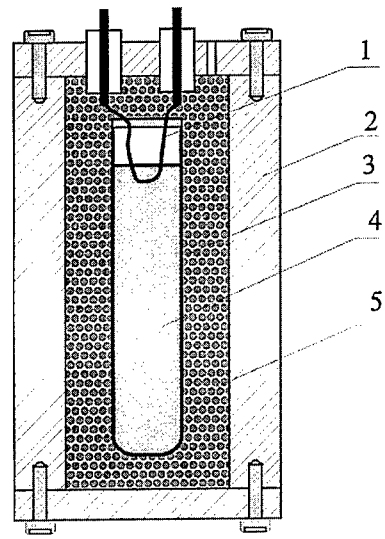

FIG. 5. Arrangement of the sample for SHS synthesis of metal-sulfur compounds: 1, tungsten ignition wire; 2, heavy-walled aluminum container; 3, quartz ampoule; 4, metal-sulfur precursor mixture; 5, ceramic alumina beads.

resublimed sulfur powder was supplied by A & C American Chemicals Company, Montreal, Canada. The powders were mixed in a bench-top laboratory roller mill with stainless steel metal balls for 12 h prior to carrying out an experiment. Mixing of the powders was done in stoichiometric proportions according to the following reactions:

$$Cr + S \rightarrow CrS$$

$$Mn + S \rightarrow MnS$$

$$Mg + S \rightarrow MgS$$

$$Mo + 2S \rightarrow MoS_2$$

$$Si + S \rightarrow SiS$$

$$Ti + S \rightarrow TiS$$

$$Zn + S \rightarrow ZnS$$

As mentioned earlier, the traditional method of sample preparation is by cold pressing of the powder mixture in a hydraulic press. In the present investigation, the mixture is heated to the melting point of sulfur. Then, the molten mixture is poured into a mold to form a charge of the desired shape. To ensure a uniform distribution of the metal particles in the sulfur melt, the mixture was carefully stirred during the melting process and then maintained at a temperature of about 200 °C, which corresponds to maximum viscosity of the molten sulfur. Phase separation is negligibly small at such a high viscosity. The charges were solidified in silica test tubes (20 mm ID, 150 mm length), and a 0.25-mm tungsten wire (for ignition) was embedded into the sample during the casting process. The silica tube containing the sample mixture was then placed in a heavy-walled aluminum container but isolated from the container walls with several layers of 2-mm alumina ceramic beads, as shown in Fig. 5. During synthesis, the ampoule sometimes melts under the high temperatures, but the beads allow the specimen to retain its original form until the products cool down and solidify. The synthesis was performed under a constant pressure of 14 MPa of pure argon in the high-pressure reactor apparatus, which is described in detail in Ref. 2.

The X-ray diffraction analysis of the synthesized samples was provided with an automated Nicolet-Stoe Powder Diffractometer with a graphite monochromator and CuK_α radiation. The data were interpreted using a software package for comprehensive X-ray analysis (Dr. E. Shelechov, Institute of Steel and Alloys, Moscow) with a data base from Ref. 8. Thin, polished sections of synthesized samples were also prepared in order to determine their crystal structure.

Qualitative Features of the Compounds and X-ray Analysis

MgS

The sample synthesized has a porous, central core. The bulk of the sample is a yellow-green color and with a very thin pink layer, which is in contact with the wall of the test tube. The pink color is probably evidence of an amorphous MgS structure [9]. Thin, polished sections are transparent to light and demonstrate a uniform sample structure. The bulk of the sample consists of small, rectangular crystals (50–300 μm) with their size decreasing from the center of the sample toward the periphery. Analysis of the X-ray scattering pattern demonstrates that all strong

peaks belong to the cubic MgS structure (type NaCl). However, weak peaks with an intensity less than 0.9% that were not identified cannot be attributed to elemental Mg or S. The estimated maximum volumes of unreacted Mg and S that are presented in the sample are 0.3 and 1.1%, respectively. The estimated completeness of the reaction is more than 99%.

SiS

This sample is light gray, is highly porous, and has a strong odor of H_2S. The high porosity of the sample is consistent with the thermodynamic calculations that predict a low yield of condensed product (see Figs. 1 and 2). X-ray analysis was not carried out.

TiS

Synthesis of TiS produced a uniform, but porous, golden brown sample. All the strong peaks in the X-ray scattering pattern belong to a rhombohedral TiS phase. The intensities of the weak peaks do not exceed 6% and were not identified, although they cannot be attributed to different modifications of Ti or S. The estimated minimum volumes of unreacted Ti and S detected in the mixture are 0.3–0.7% (Ti) and 0.7% (S), and therefore, the completeness of the chemical reaction is probably more than 98.6%. It is also interesting to note that by adding an excess of sulfur in the precursor, the crystal structure of the synthesized sample is changed from the rhombohedral phase TiS (structure *h*R6) to the rhombohedral phase $Ti_{16}S_{21}$ (structure *h*R14).

CrS

This monolithic, nonporous sample is very hard and is a uniform dark-gray color. Thin (40–50 μm) cuts of the sample are not transparent. However, thin, radially oriented, columnar crystals are visible when viewing the sample in reflected light. The qualitative X-ray analysis shows that the sample is a mixture of several crystal phases: hexagonal CrS (type NiAs), monoclinic CrS (structure *m*C8), rhombohedral Cr_2S_3 (structure *h*R10), and rhombohedral Cr_5S_6 (structure *h*P22). The quantitative analysis does not demonstrate a good fit of the theoretical program, which may be due either to some metastable phase that is absent in the database or to the predominant orientation of the crystals in the powder sample used for the X-ray analysis.

MnS

This sample is very uniform and nonporous and is a dark-green color. Thin cuts are not transparent and exhibit a weak pattern of columnar crystals when viewed in reflected light. Qualitative X-ray analysis shows that all the strong peaks belong to the cubic phase of MnS (type NaCl). The estimated maximum volume fraction of Mn in the sample is less than 0.2%. The volume fractions of MnS and Mn_2O_3 are 94.7 ± 0.2% and 5.1 ± 0.2%, respectively. Taking into account that oxidized Mn is most probably present in the metal reactant powder, the reaction yield is very high, i.e., more than 99.8%. This also is consistent with the thermodynamic predictions (see Fig. 3) that show that the yield of the condensed product in the Mn–S reaction reaches unity at pressures higher than 0.4 MPa.

ZnS

The description of the crystal structure of the ZnS synthesized by SHS was given in detail previously [2]. More careful quantitative analysis of X-ray scattering spectra provided in the present work shows that the SHS-synthesized ZnS samples contain both the wurtzite and the sphalerite modification of ZnS (as compared to the pure wurtzite structure reported previously [2]), although the percentage of the sphalerite modification is relatively small (11–15%).

MoS_2

The SHS-synthesized sample of molybdenum disulfide has a uniform, nonporous structure and a slippery, graphite-like texture, and is light gray with a characteristic metallic luster. The X-ray pattern for this sample has one very strong peak at $2\Theta = 4.8°$ and many weak peaks (the strongest has an intensity of about 11%). The automated search shows that all strong peaks belong to the rhombohedral MoS_2 modification, although the presence of some quantities of other phases such as monoclinic Mo_2S_3 and rhombohedral Mo_3S_4 was also indicated. An accurate quantitative analysis of this spectra is not possible at present due to the strong texture of the MoS_2 phase. This is due to the layered structure of MoS_2, which breaks mostly along the (001) plane to form long, flat particles, and hence, it is very difficult to achieve the random orientation required for the X-ray analysis.

Combustion Characteristics of Metal-Sulfur Mixtures

An understanding of the combustion characteristics of metal-sulfur mixtures (i.e., ignition temperature, flame propagation speed, etc.) is important for controlling the purity of the products and "energetic" applications of metal-sulfur combustion. Ignition and flame propagation data are also the major source of information about the unknown high-temperature kinetics of the metal-sulfur reactions. The ignition temperature is only a weak function of the geometry of the sample, and hence, it is often considered to be a physicochemical constant for practical applications.

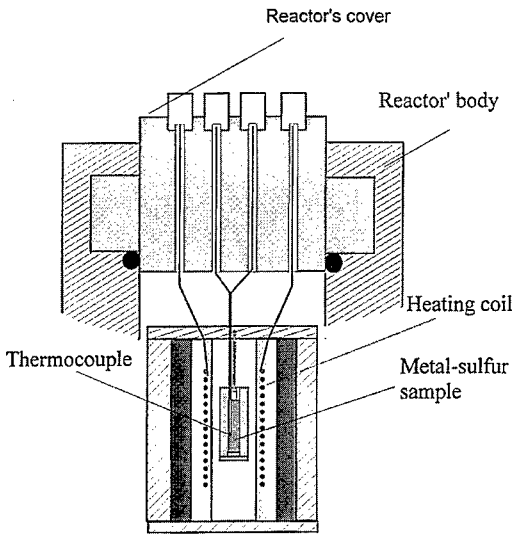

FIG. 6. Schematic of the experiment for measurement of the ignition temperature of metal-sulfur mixtures.

TABLE 1
Ignition temperatures of metal-sulfur mixtures

Mg + S	522 ± 20 °C
Si + S	508 ± 15 °C
Ti + S	453 ± 7 °C
Mn + S	355 ± 6 °C
Cr + S	423 ± 7 °C
Zn + S	499 ± 15 °C
Mo + 2S	584 ± 10 °C

A schematic of the experimental apparatus used for the ignition experiments with metal-sulfur mixtures is shown in Fig. 6. The samples were cast in small, cylindrical copper containers (8 mm ID, 30 mm long), which were suspended in the center of a cylindrical ceramic fiber heater (Wattlow Inc., MO). A fine-gauge, unsheathed thermocouple (chromel-alumel, $d = 50\,\mu$m) was embedded in the cylindrical sample. The signal from the thermocouple was amplified ($\times 100$) and recorded with a PC-based data acquisition system (R.C. Electronics). The boiling point of sulfur at normal pressure is 445 °C. To suppress the evaporation of sulfur at the ignition temperatures (which may be up to 600 °C), an ambient pressure of about 7 MPa is required. Therefore, the ignition experiments were performed in the same high-pressure reactor that was used for the material-synthesis experiments. The heater assembly was enclosed in a thick-walled, stainless steel, cylindrical container that acts as a heat sink to minimize the heating of the argon gas inside the reactor. The samples were heated slowly (typically for 5–7 min) to minimize the thermal gradient within the sample. A sharp rise in the sample temperature indicated the point of ignition. The average ignition temperature and the standard temperature deviation found from 5–7 experimental trials for each different substance are shown in Table 1.

It is interesting to note that replacing the Mn powder having a particle size in the range of 1–5 μm with a coarser powder having a size distribution in the range of 1–15 μm increases the ignition temperature from 355 to 384 °C. This is a reflection of the heterogeneous character of the chemical reaction prior to and during the ignition process.

Linear flame propagation speeds were measured using a modified ion-probe technique. The hardware and experimental procedure is described in detail in Ref. 2. Samples with a diameter of 1 cm and a length of 12 cm were used in the present experiments. Although the experiments were performed in a high-pressure environment (with an ambient pressure of up to 10 MPa), it was found that for samples that produced a significant amount of gas during the combustion, the measurement technique was not reliable. Thus, only results for the pure, gasless reacting mixtures of Mn–S and Cr–S (cf. earlier thermodynamic results) are reported in the present work. The value of the flame speed for the Mn–S mixture was found to be 5.4 ± 0.7 mm/s and for the Cr–S mixture, 8.4 ± 0.8 mm/s. The flame speed for the Zn–S mixture reported previously [2] was found to be 4.5 mm/s for a sample with a diameter of 10 mm. Note that the measured flame speeds do not correlate with the energetic potential of the reaction. The highest speed is observed for the Cr–S mixture, which has the lower adiabatic flame temperature of the two mixtures.

Conclusions

Equilibrium calculations suggest that the energy of the reaction of a large number of metals with sulfur is sufficiently high to permit self-sustained flame propagation. The present study has demonstrated experimentally that high-purity metal-sulfur compounds of Mg, Si, Ti, Cr, Mn, Zn, and Mo can readily be synthesized by the SHS method. X-ray analysis of the products indicates that the reactions are close to completion in the SHS process. The precursor mixture is prepared in a novel scheme where the sulfur is melted. Theoretical density can thus be achieved with the absence of trapped gases in the precursor mixture. Ignition temperatures of the metal-sulfur mixtures measured in the present study are in the range of 350–600 °C. The flame speeds are found to be in the range of 5–10 mm/s. The high-flame temperatures, low-ignition temperatures, and large energy release associated with metal-sulfur combustion make this process promising for a variety of practical applications.

Acknowledgments

This work is supported by Canadian Space Agency under contract #9F007-3-6019/01SW, and the authors are grateful to Dr. M. Koknayeva (Department of Physics, McGill University) for her help in the interpretation of the results of the X-ray scattering data.

REFERENCES

1. Kozitskiy, S. V., Pisarskiy, V. P., and Polischuk, D. D., *Izv. Acad. Nauk SSSR* 10:2472–2475 (1990) (in Russian).
2. Goroshin, S. V., Lee, J. H. S., and Frost, D. L., *Twenty-Fifth Symposium (International) on Combustion*, The Combustion Institute, Pittsburgh, 1994, pp. 1651–1657.
3. Moh, G. H., in *Topics in Current Chemistry* (F. L. Boschke, Ed.), Springer-Verlag, New York, 1978, Vol. 26, pp. 107–151.
4. Coukling, J. A., *Chemistry of Pyrotechnics*, Marcell-Dekker, New York (Basel), 1985.
5. Huges, T. G., Smith, R. B., and Kiely, D. H., *J. Energy* 7:28–133 (1982).
6. Merzhanov, A. G., *Int. J. SHS* 2:133–156 (1993).
7. Merzhanov, A. G., in *Combustion and Plasma Synthesis of High-Temperature Materials* (L. A. Munir and B. Holt, Eds.), VCH, New York, 1990, pp. 1–53.
8. *Pearson's Handbook of Crystallographic Data for Intermetallic Phases* (P. Villars and L. D. Calvert, Eds.), American Society for Metals, Metal Park, OH, 1986, Vols. 1–3.
9. *Handbook of Inorganic Chemicals* (D. L. Perry, S. L. Phillips, Eds.), CRC Press, Boca Raton, FL, 1995.

COMMENTS

S. Dasappa, Indian Institute of Science, India. Are there any emissions in the gas phase because of sulphur combustion? If so can you quantity them?

Author's Reply. Thermodynamic calculations of constant pressure combustion show that at flame temperatures some of the metal sulfides will be in a gaseous phase or will dissociate as S_n-gas and metal-gas. The amount of gas products strongly depends on pressure and is also very different for various metals. For example, the gas phase products in Zn-S combustion are ZnS-gas, S_n-gas and Zn-gas. The amount of gas gradually decreases if the pressure increases, however gas products are present even at pressure as high as 100 MPa. At the same time, gas products are present in Mn-S combustion only at pressures bellow 0.5 MPa. For some metals, combustion is gasless even at normal pressure. Our qualitative experimental observations basically confirm the results of thermodynamic calculations, however quantitative measurements of gas emissions in metal-sulfur combustion have not yet been performed.

•

Atsushi Makino, Shizuoka University, Japan. Generally speaking, burning velocity and the range of flammability for the NHS process depend on particle size of the higher melting-point metal of the system. How does the burning velocity depend on the particle size of the metal? How large is the particle size when the combustion wave ceases to propagate? Is the combustion mode unchanged with increasing particle size?

Author's Reply. This is a very interesting question. However, we are not ready to answer it yet because we just started the experiments on influence of the metal particles size on flame propagation and ignition. At present, we can only mention that increasing of the specific surface area of metal powder in Mn-S mixture from 2.33 to 3.12 $\mu m^2/\mu m^3$ decreases ignition temperature from 385°C to 306°C.

Twenty-Sixth Symposium (International) on Combustion/The Combustion Institute, 1996/pp. 1891–1897

GAS-PHASE COMBUSTION SYNTHESIS OF ALUMINUM NITRIDE POWDER

R. L. AXELBAUM, C. R. LOTTES, J. I. HUERTAS AND L. J. ROSEN
Department of Mechanical Engineering
Washington University, St. Louis, MO 63130, USA

Due to its combined properties of high electrical resistivity and high thermal conductivity, aluminum nitride (AlN) is a highly desirable material for electronics applications. Methods are being sought for synthesis of unagglomerated, nanometer-sized powders of this material, prepared in such a way that they can be consolidated into solid compacts having minimal oxygen content. A procedure for synthesizing these powders through gas-phase combustion is described. This novel approach involves reacting $AlCl_3$, NH_3, and Na vapors. Equilibrium thermodynamic calculations show that 100% yields can be obtained for these reactants with the products being AlN, NaCl, and H_2. The NaCl by-product is used to coat the AlN particles in situ. The coating allows for control of AlN agglomeration and protects the powders from hydrolysis during post-flame handling. On the basis of thermodynamic and kinetic considerations, two different approaches were employed to produce the powder, in co-flow diffusion flame configurations. In the first approach, the three reactants were supplied in separate streams. In the second, the $AlCl_3$ and NH_3 were premixed with HCl and then reacted with Na vapor. X-ray diffraction (XRD) spectra of as-produced powders show only NaCl for the first case and NaCl and AlN for the second. After annealing at 775 °C under dynamic vacuum, the salt was removed and XRD spectra of powders from both approaches show only AlN. Aluminum metal was also produced in the co-flow flame by reacting $AlCl_3$ with Na. XRD spectra of as-produced powders show the products to be only NaCl and elemental aluminum.

Introduction

Background on AlN

Due to its unique physical properties, aluminum nitride (AlN) has been considered for many applications, from piezoelectric materials to matrix materials for a composite uranium nitride nuclear fuel. The largest market for AlN is in the electronics industry. This interest stems from the need to develop electronics substrates with high thermal and low electrical conductivities. Few materials possess such properties. Of those that do, AlN is the most desirable for reasons of safety and cost [1]. As a ceramic, AlN has a high electrical resistivity ($r > 10^{13}\ \Omega \cdot \mathrm{cm}$) while possessing a theoretical thermal conductivity comparable to copper ($k = 319\ \mathrm{W/m \cdot K}$). The potential market for AlN in electronics applications alone is predicted to be $550 million by the year 2000 [2].

The current commercial methods for producing AlN—carbothermal reduction and direct nitridation [3]—yield fine powders that can be further processed by, for example, sintering or hot-pressing to produce solid compacts. Carbothermal reduction is a batch process involving a high-temperature (1400–1800 °C), solid–solid reaction between alumina and carbon powders in a nitrogen atmosphere, yielding AlN powders with particle diameters of 0.01–3.0 μm [1,3]. AlN production via direct nitridation is also a batch process and involves reacting aluminum powder with nitrogen gas at temperatures in excess of 1200 °C, to produce powders with particle diameters in the range of 0.3–12 μm [3,4].

Challenges in AlN Production

There is a great need for new synthesis routes for the production of AlN due to the inherent limitations of present production processes. Both carbothermal reduction and direct nitridation employ precursors that contain oxygen: aluminum oxide and aluminum powders, respectively (aluminum powders inherently contain oxygen in the surface layer and lattice). Furthermore, both processes include steps that expose the AlN product powders to oxygen and other contaminants: excess carbon is burned off during carbothermal reduction, whereas direct nitridation employs at least one grinding step, which introduces oxygen and metallic impurities [3]. Oxygen impurities dramatically decrease the thermal conductivity of AlN. For example, the thermal conductivity of AlN with 300 ppm oxygen is 280 W/m · K, whereas with 0.8 wt % oxygen, it reduces to 80 W/m · K [5].

Another challenge in the production of AlN is the reduction of particle size in order to exploit superplastic-forming (SPF). Since SPF rates increase with decreasing grain size, it is desireable to identify commercially viable methods of synthesizing nanometer-

sized (2–100 nm) powders of AlN. However, the high surface-to-volume ratio for these powders has heretofore resulted in excessive oxygen contamination due to surface hydrolysis via

$$AlN + 3H_2O \rightarrow Al(OH)_3 + NH_3 \quad (1)$$

which occurs when AlN is exposed to moisture. To produce AlN powder that is useful in high thermal conductivity applications, the process must yield powders that are free of impurities and not susceptible to surface hydrolysis during subsequent handling.

Another important criterion for AlN applications is that the starting powders be unagglomerated or weakly agglomerated to ensure that the resulting compacts can be sintered to near-theoretical density. Flames generally produce powders composed of long-chain, hard agglomerates. These powders are not easily compacted, resulting in materials with high void fractions and greatly diminished properties. Recently, Axelbaum et al. have developed a flame process, applicable to a broad class of materials, for synthesizing *unagglomerated, unoxidized* nanometer-sized particles [6]. In this paper, the process is extended to the synthesis of AlN.

Particle-Coating to Prevent Agglomeration and Oxygen Contamination

The approach to prevent agglomeration in flames is to allow nucleation and growth of *primary particles* to proceed normally, until they have grown to a desired size, and then encapsulate these particles with an appropriate material before they excessively agglomerate. Upon subsequent collisions, the coated particles will agglomerate, but the primary particles within them will not. When the coating is later removed, the resulting powder will contain unagglomerated or weakly agglomerated particles of the specified size.

In addition to controlling size, the particle coating also protects oxygen- and moisture-sensitive primary particles during post-flame handling. Thus, ultrafine, nonoxide particles produced in an oxygen-free environment can be handled without extreme precautions.

This flame and coating procedure has been demonstrated in a sodium halide flame for the synthesis of titanium metal powders [6]. The reaction employed is given by

$$TiCl_4 + 4Na \rightarrow Ti + 4NaCl \text{ [7]} \quad (2)$$

Sodium halide reactions such as this can be applied to produce a variety of materials, including metals, intermetallics, ceramics, and composites. Calcote and Felder have produced high-purity solid silicon [7], and Glassman et al. have produced TiN, TiB_2, TiC, $TiSi_2$, SiC, and B_4C [8]. Axelbaum et al. have extended these works and produced Ti, TiB_2, W, and W-Ti [6,9,10], with emphasis on producing unagglomerated, nanometer-sized powders by employing the coating procedure described above. The coating material for particles produced in sodium halide flames is conveniently the sodium chloride by-product. Sodium chloride is an effective coating because its boiling point is 1410 °C, which allows condensation to be triggered in the flame by controlling temperature and NaCl concentration. Furthermore, it is possible to exploit the Kelvin effect to control the onset of coating and attain control of particle size for particles <40 nm in diameter [6]. Finally, the NaCl coating can be easily removed by washing with an appropriate solvent or through vacuum sublimation at moderate temperatures (~800 °C).

The sodium halide flame and coating process should be well suited for production of AlN powders with low oxygen content. The reaction precursors are oxygen free, and the salt by-product is produced in the reaction zone simultaneously with the primary-product particles, with coating occurring on a millisecond time scale. The coating should then allow the particles to be conveniently handled without acquiring the oxygen impurities that can be so deleterious to the thermal conductivity of AlN.

Thermodynamics

One approach to producing AlN that has received considerable attention recently is the gas-phase reaction of $AlCl_3$ with NH_3. Kimura et al. [11], Park et al. [12], and Riedel and Gaudl [13] produced AlN powders with this reaction, and Lewis [14], Nickel et al. [15], and Riedel and Gaudl [13] produced films by chemical vaper deposition (CVD). There are a number of difficulties associated with this endothermic (35.5 kJ/mole) reaction, as can be seen from the equilibrium composition for

$$AlCl_3 + NH_3 + 50Ar \rightarrow \text{products} \quad (3)$$

shown in Fig. 1. These results were obtained using commercial software and verified with the NASA equilibrium code. The yields for this chemistry are only modest, typically <30% with stoichiometric NH_3. Yields increase with increasing NH_3 or N_2; however, over 50 times stoichiometric NH_3 is needed to approach 100% yields [16]. Nickel et al. have shown that the primary reason for the low yield of Eq. (3) is the decomposition of NH_3 [15]. With no decomposition, near-perfect yields are achieved thermodynamically. Physically, it is possible to reduce the extent of ammonia decomposition by proper selection of reactor materials and formation of stable $AlCl_3 \cdot (NH_3)_n$ (n = 1–6) adducts [12]. By employing these measures, yields of up to 70% have been achieved with 6 times stoichiometric NH_3 at moderate temperatures (1000 °C) [14]. An inherent limitation of this chemistry is that the reactor tem-

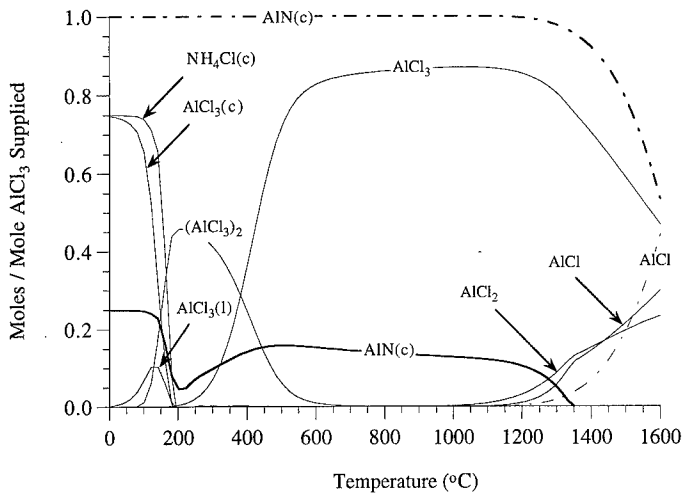

FIG. 1. Equilibrium compositions as functions of temperature for mixtures of $AlCl_3$ + NH_3 + 50Ar (solid lines) and $AlCl_3$ + NH_3 + 3Na + 50Ar (dashed lines).

perature must be high to obtain reasonable production rates; however, high temperature promotes NH_3 decomposition, which limits yield [12]. Also, Riedel et al. have shown that the resulting fine powders contain ~3 wt % oxygen due to hydrolysis [13].

The addition of Na to the $AlCl_3$-NH_3 system can greatly enhance thermodynamic yield, with or without NH_3 decomposition. Adding stoichiometric Na to the reaction in Eq. (3) results in

$$AlCl_3 + NH_3 + 3Na + 50Ar \rightarrow \text{products}. \quad (4)$$

The equilibrium products for this reaction are shown in Fig. 1. The adiabatic flame temperature for Eq. (4) is 1225 °C when the reactant temperature is 650 °C. Nonetheless, radiative heat transfer can be so significant in these flames that the product temperature can be controlled by the temperature of the combustion chamber. Thus, product composition is reported as a function of temperature in Fig. 1. The results reveal that 100% yields are achieved with this system over a wide range of temperatures. In addition to high yield, Eq. (4) has many other practical advantages over Eq. (3). First, the by-product NaCl can be incorporated as a coating material, as discussed above, to avoid agglomeration and oxygen contamination during post-synthesis handling. Second, it is overall exothermic (−1244 kJ/mole), resulting in lower energy costs. And third, the gaseous by-product is hydrogen, which can be used for its high heating value, as compared to HCl, which must be scrubbed.

Experimental Considerations

For the three reacting species shown in Eq. (4), two possible schemes exist for mixing: either the reactants can be supplied in three separate co-flowing streams or two of the reactants can be premixed and then this mixture can be reacted with the third. The second scheme presumes that the two premixed reactants will not react to form an unacceptable product, for example, a solid phase that will either plate out on the walls or lead to inhomogeneities in the final product. $AlCl_3$ and NH_3 will react below 225 °C to form AlN(s) and NH_4Cl(s), as shown in Fig. 1. Above 225 °C, the only condensed phase is AlN(s). Thus, mixing $AlCl_3$ and NH_3 would not appear promising because condensed phases would form in the supply lines. Similarly, $AlCl_3$ reacts hypergolically with Na to form Al and NaCl, thereby making this mixture infeasible. The possibility of mixing NH_3 and Na has been considered, but preliminary studies revealed that NH_3 decomposition is excessive and that a solid phase, possibly NaH, is formed.

Thus, it would appear that the three reactants have to be supplied to the burner in separate jets, and this approach, referred to as case A, is considered. However, an alternative approach, wherein the reaction of $AlCl_3$ and NH_3 is suppressed, is also examined. When $AlCl_3$ and NH_3 are mixed at 400 °C, stable $AlCl_3 \cdot (NH_3)_n$ adducts are formed [17], and these adducts decompose into AlN and HCl above 700 °C [14]. Incomplete conversion to the adduct results in AlN(s) and HCl(g) production as shown in Fig. 1, which is not acceptable. Nonetheless, by adding HCl to the reactants, the forward reaction, which produces AlN, can be suppressed. Following this reasoning, it is possible to supply a purely gaseous mixture of $AlCl_3$, NH_3, and HCl that will then react with Na. This approach is considered and will be referred to as case B.

The basic characteristics of the co-flow sodium flame used in this study have been described previously for the production of titanium and titanium diboride [6]. Only modifications and improvements will be described. Configuration 1, shown in Fig. 2,

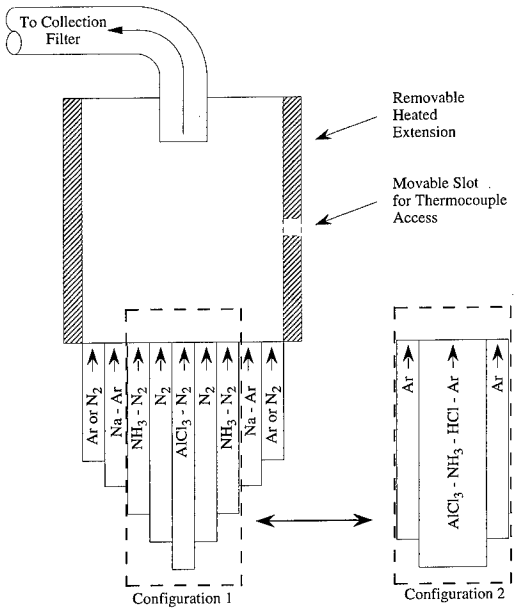

FIG. 2. Schematic diagram illustrating two different burner configurations employed to produce AlN and Al.

is for case A, where all three reactants are supplied separately. It consists of five heated, concentric tubes, all stainless steel, except for the innermost tube, which is quartz. The tubes have outside/inside diameters of 3.1/1.9, 6.4/4.6, 12.7/10.9, 25.4/19.1, and 75/70 mm, respectively. All reactants are introduced in the vapor phase. The halide is introduced through the central tube, followed by inert, then NH_3, and then Na. An inert shroud gas is supplied in the outermost annular section. The reaction zone occurs in the mixing layer of the reactants, with the inner inert stream acting as a diffusion barrier near the base to avoid particle deposition at the burner mouth. The outer shroud ensures a uniform flow and isolates the flame from room air. Honeycomb is placed at the exits to ensure uniform laminar flows.

The configuration for case B, where $AlCl_3$, NH_3, and HCl are premixed, is as shown in the inset of Fig. 2. In this configuration, the 3.1/1.9-mm quartz tube is removed, and the 6.4/4.6-mm stainless steel tube is replaced with a graphite tube with outside/inside diameters of 7.5/5.0 mm, respectively.

Sodium is metered in the liquid phase with a stainless steel syringe pump. Supplying sodium with a positive displacement pump is necessary to ensure that a line failure would not lead to an uncontrolled release of liquid sodium. The liquid sodium is fed to the interior of a sintered, stainless steel tube where it wicks through and wets the outer walls. Argon, supplied to the exterior of the porous tube, carries the sodium vapor to the burner.

Aluminum chloride powder is stored in a temperature-controlled monel reservoir. Nitrogen or argon carrier gas is metered by a mass flow controller and then bubbled through the aluminum chloride powder, after which it is assumed to be saturated with aluminum chloride vapor.

A heated, insulated, stainless steel extension is attached to the outermost tube of the burner. The extension acts to minimize heat loss from the burner surface and the flame and to prevent entrainment of oxygen. The extension contains a slot in the axial direction to allow for thermocouple measurements.

The plumes emanating from these flames are well-defined streams of particles akin to soot emanating from an inverse–co-flow hydrocarbon flame [18]. The particles are collected into a 1.2-cm-diameter stainless steel tube located approximately 6 cm above the burner rim. The particles are extracted under near-isokinetic conditions and collected on a 10-μm porous stainless steel filter. After collection, the particles are scraped from the filter and placed in storage vials under an inert atmosphere.

Flame temperatures are obtained with Pt-6%Rh/Pt-30%Rh thermocouples (type B). The wire size is 0.05 mm, and the thermocouple wires and bead are bare. The rapid insertion technique is employed to minimize particle buildup on the thermocouple and to limit exposure to the hostile environment. Due to the relatively low temperatures in these flames, radiation corrections were not made.

Particle composition is analyzed with a Rigaku horizontal X-ray diffractometer (XRD). The Scherrer formula, which is based on the inverse relationship between XRD peak width and particle size, is used to determine nominal particle size.

Experimental Results

Prior to synthesizing AlN, elemental aluminum was produced via

$$AlCl_3 + 3Na \rightarrow Al + 3NaCl \qquad (5)$$

The burner was configured as shown in Fig. 2 for configuration 2. The $AlCl_3$ vapor with Ar carrier gas was introduced in the innermost graphite tube, followed by a co-flow of Ar, and then the Na–Ar mixture. The shroud gas in the outermost annulus was Ar.

Operating conditions, shown in Table 1, were chosen to ensure the flame was overventilated in Na; i.e., Na vapor was present along the centerline above the luminous flame tip. In accord with thermodynamic calculations, this mode of operation ensures nearly 100% yields because the local stoichiometry will ultimately be sodium-rich along the centerline. The Na-$AlCl_3$ flame is similar in appearance to that of Na-$TiCl_4$ [6]. The apparent reaction zone is evident as a thin, yellow luminous zone. The shape of the flame is typical of the Burke–Schumann flame.

TABLE 1
Run conditions and configuration for specified product

Product	Burner Temp (°C)	Species	Total Flow Rate (sccm)	Reactant Concentration
		$AlCl_3$/Ar	38	0.48/0.52
Al	800	Ar (inner co-flow)	1100	—
		Na/Ar	1600	0.10/0.90
		$AlCl_3/N_2$	160	0.44/0.56
AlN	710	N_2 (inner co-flow)	960	—
(case A)		NH_3/N_2	2290	0.22/0.78
		Na/Ar	2830	0.10/0.90
		$AlCl_3/NH_3$/HCl/Ar	235	0.12/0.15/0.17/0.56
AlN	650	Ar (inner co-flow)	350	—
(case B)		Na/Ar	2750	0.07/0.93

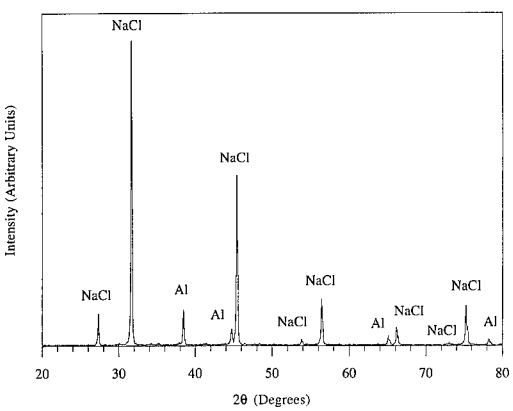

FIG. 3. X-ray diffraction spectra of as-produced powder from an $AlCl_3$–Na flame under conditions shown in Table 1 and in configuration 1 of Fig. 2.

Buoyancy is negligible in these heavily diluted flames because the flame temperature is only 300–500 °C higher than the reactant and co-flow temperatures.

The as-produced aluminum powder is light gray. A characteristic XRD of the as-produced powders is shown in Fig. 3. XRD peaks index to only Al and NaCl. The nominal diameter of the particles in Fig. 3, as estimated by the Scherrer formula, are 60 nm for Al and 80 nm for NaCl.

Nitrogen was then substituted in place of Ar for the $AlCl_3$ carrier gas and inner and outer co-flows to determine if AlN might be produced by in situ nitridation of the aluminum particles. Nitridation of Al by N_2 has been reported to begin at temperatures as low as 800 °C but to be very slow at these temperatures. For 15-μm-diameter aluminum particles at 1550 °C, nitridation occurs within 2 s [2]. For nanometer-sized particles, the time would be expected to be considerably less. For the run conditions investigated, the flame temperatures did not exceed 1100 °C, and temperatures quickly decreased downstream of the flame due to radiative heat loss and heat loss to the outer shroud gas. Under these conditions, the nitridation reactions appear to be too slow to effectively produce AlN because no AlN peaks were observed in XRD spectra of either the as-produced or the annealed samples.

Employing the chemistry of Eq. (4) and considering the thermodynamic results, AlN was then synthesized using configuration 1 shown in Fig. 2 and experimental conditions of case A. Under these conditions, two reaction zones are expected: an inner reaction zone where NH_3 reacts with $AlCl_3$ and an outer reaction zone where the products of the inner zone react with Na. Indeed, two thin, distinct particle-formation zones were observed by laser light scattering. Quantitative scattering measurements were not made because of the broad and strong absorption cross section of Na_2 [19].

Powders were collected from the $AlCl_3$–NH_3–Na flames under various operating conditions. The as-produced powders contain NaCl, with certain run conditions also producing NH_4Cl. As shown in Fig. 1, NH_4Cl is a low-temperature product of the $AlCl_3$–NH_3 system, and with the addition of stoichiometric Na, NH_4Cl is not present. Thus, if the flame is operated underventilated in Na, NH_4Cl may be produced when the products reach the cooler regions of the sampling system. Unlike the $AlCl_3$–Na flame, it is difficult to ensure that this flame is overventilated in Na. Samples obtained from runs with Na in excess of the stoichiometric amount show no NH_4Cl peaks in the XRD spectra.

XRD spectra of as-produced powders do not indicate the presence of crystalline AlN. This may be

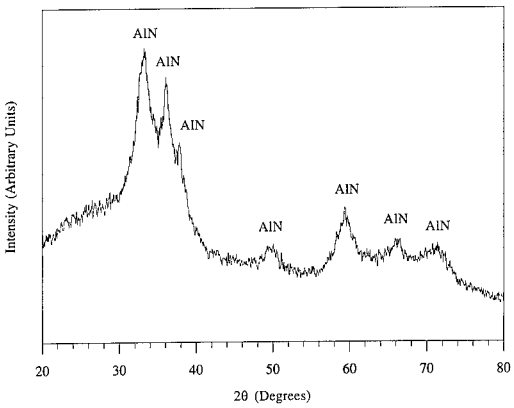

FIG. 4. X-ray diffraction spectra of heat-treated powder produced in an $AlCl_3$-NH_3-Na-N_2 flame under conditions of case A in Table 1 and in configuration 1 of Fig. 2.

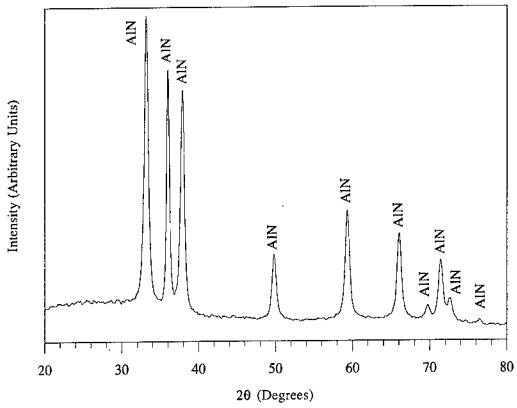

FIG. 6. X-ray diffraction spectra of heat-treated powder produced in an $AlCl_3$-NH_3-HCl-Na flame under conditions of case B in Table 1 and in configuration 2 of Fig. 2.

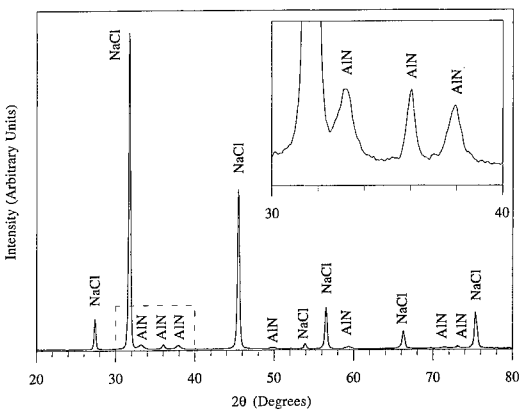

FIG. 5. X-ray diffraction spectra of as-produced powder from an $AlCl_3$-NH_3-HCl-Na flame under conditions of case B in Table 1 and in configuration 2 of Fig. 2.

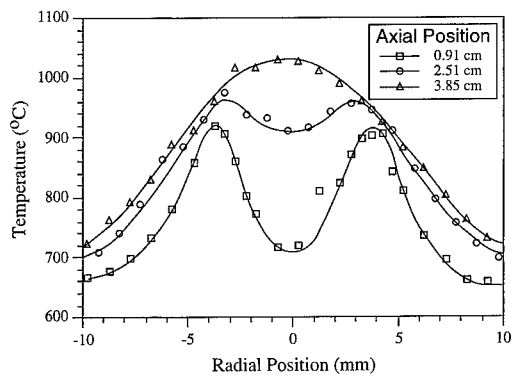

FIG. 7. Radial temperature profiles of an $AlCl_3$-NH_3-HCl-Na flame at three different axial locations above the burner exit under conditions of case B in Table 1 and in configuration 2 of Fig. 2.

because the AlN is amorphous or the peaks are too small and broad to be detected against the large background of NaCl. As shown in Fig. 4, XRD patterns of powder that were produced under the conditions in Table 1 and heat-treated for 4 h at 775 °C under dynamic vacuum show AlN peaks. The broad peaks indicate that the AlN particles are very small, 6 nm in diameter as estimated by the Scherrer formula.

The two reaction zones associated with separate mixing of the three reactants can potentially lead to a broad range of morphologies because AlN is formed in both zones and under very different conditions—one zone being endothermic and the other exothermic. Uniformity of product is often, though not always, desirable from a materials perspective.

Case B, which results in a single, exothermic reaction zone, can potentially lead to a more uniform product. Figure 5 shows the XRD spectra of as-produced powders for configuration 2 with operating conditions of case B. The only phases detected are NaCl and AlN. The Scherrer formula predicts a crystal size of 40 nm for the NaCl and 20 nm for the AlN. The taller NaCl peaks are a result of the stoichiometry, which leads to about 4 times as much NaCl as AlN on a molar basis, and the fact that larger-sized particles have taller, narrower peaks. The AlN may also not be fully crystalline. After heat treatment at 775 °C for 4 h under dynamic vacuum, the salt is removed and, as shown in Fig. 6, the only phase present is AlN. No special precautions were necessary to obtain this sample. Prior to heat treatment, the as-produced powders were stored for 4 days in vials filled with Ar. Nonetheless, no oxide, hydroxide, or oxynitride phases are observed.

Radial temperature measurements at three different axial locations are shown in Fig. 7. The basic profiles are consistent with the Burke–Schumann flame, except that the maximum temperatures near the base are significantly lower than at the tip. This result is a consequence of the inert co-flow between the reactant streams. This co-flow is added to avoid particle buildup at the rim by minimizing formation rates of condensed phases in this region. Since the reactants are hypergolic, the burner would rapidly clog if the inner co-flow were not employed.

Due to the significant dilution in this flame, the increase in temperature is only modest, about 400 °C. Accounting for the inner co-flow, the stoichiometric adiabatic flame temperature is 1145 °C, which is consistent with the maximum-measured temperature of 1050 °C.

Conclusions

Nanocrystalline aluminum and aluminum nitride powders have been successfully synthesized for the first time in sodium-halide flames. Aluminum was synthesized by the reaction of $AlCl_3$ with Na. Aluminum nitride was synthesized by adding Na to the well-known $AlCl_3$–NH_3 system. Thermodynamic yields of this system are dramatically improved by the addition of Na, with the by-products of the reaction being NaCl and H_2. The NaCl has been used to encapsulate the metal and ceramic particles in situ. XRD spectra suggest that the particles are indeed nanoscale, as desired. Despite having handled these high-surface-area powders in air, indications are that the coating has protected them from oxygen contamination, a problem that has plagued AlN production. The Al and AlN powders appear to be single phase, as detected by XRD.

By keeping the AlN particles encased in NaCl until just before consolidation, it is believed that the final compacts will have low oxygen impurities. Thus, this process holds promise as a commercially viable method of producing large quantities of nanocrystalline AlN materials with high thermal conductivities.

Acknowledgments

The authors gratefully acknowledge the support of the Office of Naval Research and the National Science Foundation. LJR was also supported by a Lowy Fellowship and gratefully acknowledges this support. The authors are also grateful to Dr. S. M. L. Sastry for helpful discussions and Dr. S. Hariprasad for performing the XRD analyses.

REFERENCES

1. Bachelard, R. and Joubert, P., *Mater. Sci. Eng.* 109A:247–251 (1989).
2. Sheppard, L. M., *Am. Ceram. Soc. Bull.* 68:1801–1812 (1990).
3. Selvaduray, G. and Sheet, L., *Mater. Sci. Technol.* 9:463–473 (1993).
4. Weimer, A. W., Cochran, G. A., Eisman, G. A., Henley, J. P., Hook, B. D., Mills, L. K., Guiton, T. A., Knudsen, A. K., Nicholas, N. R., Volmering, J. E., and Moore, W. G., *J. Am. Ceram. Soc.* 77:3–18 (1994).
5. Huseby, I. C. and Bobik, C. F., High Thermal Conductivity Aluminum Nitride Ceramic Body, U.S. Patent No. 4,547,471, 1985.
6. DuFaux, D. P. and Axelbaum, R. L., *Combust. Flame* 100:350–358 (1995).
7. Calcote, H. F. and Felder, W., *Twenty-Fourth Symposium (International) on Combustion*, The Combustion Institute, Pittsburgh, 1992, pp. 1869–1876.
8. Glassman, I., Davis, K. A., and Brezinsky, K., *Twenty-Fourth Symposium (International) on Combustion*, The Combustion Institute, Pittsburgh, 1992, pp. 1877–1882.
9. Axelbaum, R. L., DuFaux, D. P., Frey, C. A., Kelton, K. F., Lawton, S. A., Rosen, L. J., and Sastry, S. M. L., *J. Mater. Res.* 11:948–954 (1996).
10. Axelbaum, R. L., Huertas, J. I., and Lottes, C. R., Hariprasad, S., and Sastry, S. M. L., in *Mater. Manuf. Process, submitted.*
11. Kimura, I., Hotta, N., Nukui, H., Saito, N., and Yasukawa, S., *J. Mater. Sci.* 24:4076–4079 (1989).
12. Park, J., Rhee, S., and Lee, K., *J. Mater. Sci.* 28:57–64 (1993).
13. Riedel, R. and Gaudl, K., *J. Am. Ceram. Soc.* 74:1331–1334 (1991).
14. Lewis, D. W., *J. Electrochem. Soc.* 117:978–982 (1970).
15. Nickel, K. G., Riedel, R., and Petzow, G., *J. Am. Ceram. Soc.* 72:1804–1810 (1989).
16. Hashman, T. W. and Pratsinis, S. E., *J. Am. Ceram. Soc.* 75:920–928 (1992).
17. Klemm, W. and Tanke, E., Z. *Anorg. Allgem. Chem.* 200:343–384 (1931).
18. Sidebotham, G. W. and Glassman, I., *Combust. Flame* 90:269–283 (1992).
19. Steffens, K. L., Zachariah, M. R., DuFaux, D. P., and Axelbaum, R. L., *Chem. Mater.* 8:1871–1880 (1996).

Twenty-Sixth Symposium (International) on Combustion/The Combustion Institute, 1996/pp. 1899–1908

FLAME STRUCTURE MEASUREMENT OF SINGLE, ISOLATED ALUMINUM PARTICLES BURNING IN AIR

P. BUCHER, R. A. YETTER AND F. L. DRYER
Department of Mechanical and Aerospace Engineering
Princeton University
Princeton, NJ 08544-5263, USA

T. P. PARR AND D. M. HANSON-PARR
Combustion Diagnostics Laboratory, Propulsion Research Section, Code 474320D
Naval Air Warfare Center, China Lake, CA 93555-6001, USA

E. P. VICENZI
Princeton Materials Institute
Princeton University
Princeton, NJ 08544-5263, USA

Spatially resolved measurements of the flame structure about single, isolated aluminum particles burning in air were made using planar laser-induced fluorescence (PLIF) and electron probe microanalysis (EPMA). Spherical aluminum particles of 210 μm diameter were generated continuously by mechanical chopping of wire strands and laser heating, which also ignited the particles. After ignition, combustion was found to occur in two stages consisting of an initial steady burning phase, characterized by a spherical flame positioned off the surface, and a second violent, unsteady burning phase, during which gaseous ejections occurred from the particle surface. PLIF was used to measure the radial profiles of gaseous AlO and AlO vibrational temperature during the steady burning stage of particle free fall. The radial distribution of condensed-phase Al_2O_3 was measured by impaction and rapid quenching of individual particles and their associated oxide clouds on silicon plates. Analysis of the impacted cloud distribution was performed off-line with EPMA and Abel transform techniques. Results indicate a flame structure of finite thickness, wherein AlO is a gas-phase intermediate. Relative peak concentrations of AlO and Al_2O_3 were measured at $r/r_s = 2.8$ and $r/r_s = 3.5$, respectively. The temperature rose from ~2350 K at the particle surface to a nearly constant value of ~3800 K between $5 < r/r_s < 6$. The surface temperature agrees well with previously reported ignition temperatures, while the plateau temperature is ~300 K higher than the theoretically predicted adiabatic flame temperature for a stoichiometric Al-air mixture. The species and temperature measurements support previously proposed models where gasification can occur by both vaporization and heterogeneous surface reactions. Transport of Al outward and reaction with inward-diffusing molecular oxygen yields AlO. Subsequent heterogeneous reactions involving AlO yield condensed-phase Al_2O_3 at even greater radii.

Introduction

Aluminum particles are routinely used as a fuel ingredient in solid propellants, primarily to increase the motor-specific impulse and to facilitate damping of oscillatory combustion instabilities by aerodynamic particle drag. Experimental observations of aluminum behavior in solid propellant environments, and single, isolated particle studies in controlled atmospheres, have provided understanding of macroscopic burning behavior. A good summary of the current state of knowledge of aluminized solid propellant combustion may be found in Ref. 1.

Currently, little is known about the temperature and chemical composition fields surrounding and within burning particles as suitable diagnostic techniques for probing the particle-laden microscopically thin flame region have emerged only recently. There are two studies in which emission spectroscopy has been used to identify intermediate species in flames of aluminum samples. Driscoll et al. [2] recorded time-dependent AlO emission intensities at a single point in a reaction zone off the surface of a thin sheet of aluminum foil behind a reflected shock wave at 40 atm and at temperatures up to 5150 K. AlO was found to be a gas-phase intermediate.

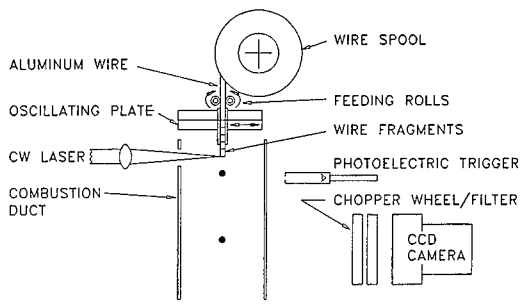

FIG. 1. Schematic of the droplet generator.

Yuasa and Sakurako [3] measured spatial emission intensity distributions of Al and AlO in the flame above heated aluminum pellets burning in counterflow CO_2 streams at pressures of 0.1–1 bar. Peak concentrations of AlO and Al_2O_3 were observed in the gas phase positioned away from the pellet surface. However, these measurements are difficult to interpret because the emission signal was line-of-sight integrated over a curved surface and a stagnation-type flow field was imposed on the problem. More recently, in a study related to the present one, planar laser-induced fluorescence (PLIF) and Mie scattering were used to study aluminum particle combustion in AP and nitramine-based propellants [4].

Characterization of primary combustion species, as well as that of time-dependent, two-dimensional species and temperature distributions, is important for formulating and calibrating detailed numerical descriptions of the ignition and burning process of isolated single particles. In particular, knowledge of the flame structure will contribute to addressing such questions as (1) What are the primary kinetic pathways leading to the formation of refractory products? (2) Are surface reactions important, in other words, are Al_2O and AlO surface products? (3) Is there a critical particle diameter at which a transition from diffusive to kinetically controlled burning occurs? (4) What are the effects of halogens on flame structure and the burning process? Furthermore, measurement and model development of the combustion of single particles in well-controlled environments is important to understanding the combustion of aluminized propellants where the flow fields are more complex and the surrounding chemical environment is less defined. Improved understanding of the gas-phase chemistry of aluminum particle combustion is particularly important for characterizing the dynamic burning-rate response of new aluminized propellant formulations containing mixed nitramines and difluoroamines.

This paper reports on the measurement of species and temperature profiles in the combustion zone surrounding a 210-μm-diameter isolated aluminum particle during free fall through a combustion duct. PLIF was used to map out the radial structure of AlO and AlO gas-phase vibrational temperature. The successful application of PLIF depended largely on the development of a novel technique for repetitive production and deployment of metal particles in a well-controlled environment [5], which is briefly described in the next section. An electron probe microanalyzer was used for determination of condensed-phase Al_2O_3 profiles by off-line analysis of smoke clouds deposited on substrates during particle quenching. While the oxidizer was room air at 1 atm pressure for experimental simplicity in this study, these measurements could be carried out on particles burning in simulated products of solid propellant flames and at variable pressure.

Although the interpretation of measured relative AlO and Al_2O_3 radial concentration and temperature profiles will ultimately depend on comparison with numerical model solutions, some qualitative observations on the combustion mechanism are discussed using literature thermochemical and kinetic rate data for the oxidation of Al to Al_2O_3.

Experimental

Droplet Generation

An experimental technique for producing a stream of monodisperse burning particles with reproducible size was developed for this study using continuous mechanical chopping of wire strands and laser ignition [5]. The particles are formed with zero initial velocity and accelerate to Reynolds numbers on the order of 0.1 during free fall. These conditions greatly simplify analysis and numerical modeling of the combustion system as a result of spherical symmetry. As shown in Fig. 1, the raw metal, in the form of thin wires, is fed from a spool to a chopping mechanism. The chopping blade produces small cylinders by periodically shearing a metal wire (99.99% pure aluminum obtained from Aldrich). The length of the cylindrical particles formed is determined by the chopping frequency in relation to the wire feeding rate. A sequence of cylinders, attracted to each other, end-to-end, by electrostatic and van der Waals forces, is moved into densely focused (0.1-mm beam diameter) radiation from either a 20-W argon ion or a 150-W CO_2 laser. Upon contact with the laser beam, the temperature of the cylinder with a free end rapidly increases above the metal's melting temperature. While exposed to laser radiation, the small cylinder contracts into a spherical particle, ignites, and begins to traverse vertically downward through a glass column filled with air. The sequence of events is repeated for each cylinder at a rate of typically one particle per second, resulting in a highly dispersed stream of monosized burning particles.

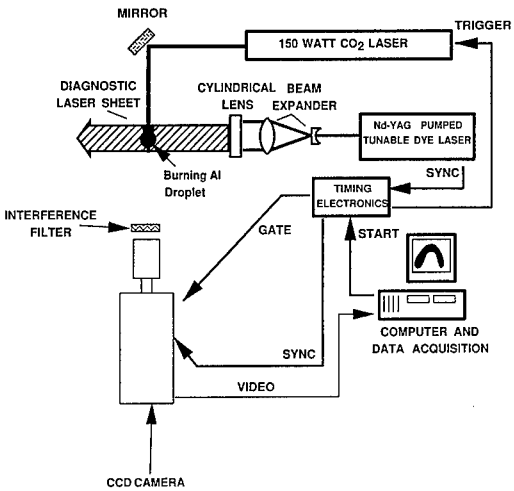

FIG. 2. Apparatus used for PLIF experiments.

The experimental arrangement reflects an effort to closely emulate assumptions underlying idealized particle-burning theories. Burning particles are generated with zero initial velocity and released into a quiescent atmosphere, minimizing the effect of forced convection on combustion.

Time-exposed, natural-luminosity images of burning particles were obtained using a gated charge coupled device (CCD) computer camera in conjunction with a chopper wheel. Rotation speed and slot arrangement of the chopper wheel were chosen to expose the CCD camera to the flame luminosity at intervals of 3 ms and for the duration of 0.3 ms each. Luminosity traces between ignition and extinction were measured using an amplified photo detector and a digital oscilloscope.

AlO and Temperature Measurements

Planar laser-induced fluorescence was used for in situ high (spatial)-resolution imaging of AlO in the flame around individual droplets. The experimental setup for the optical measurements is shown in Fig. 2 [6]. AlO laser-induced fluorescence (LIF) was excited from the blue-green ($X^2\Sigma^+ - B^2\Sigma^+$) band systems by using a Nd:Yag-pumped dye laser and Coumarin 460. The PLIF image was recorded by a gated image-intensified CCD camera (Xybion, model ISG-250-U-2) with 752 by 480 pixels. The camera was gated on for 25 ns during the diagnostic laser pulse to discriminate against natural flame emission and to monitor LIF during the period in which the laser saturates the transition. A set of interference filters was used to block Mie-scattered light, the $\Delta v = 0$ LIF and thermal radiation from the condensed phases (droplet and oxide particles).

In order to measure radial temperature profiles in the diffusion flame envelope, a large number of PLIF images were obtained from pumping both the (1,0) and the (2,1) band heads of the (B–X) vibronic transitions of AlO at 4648.1 and 4671.9 Å, respectively. Because much is known about the spectroscopy of the AlO molecule [7,8], the AlO ($B^2\Sigma^+ - X^2\Sigma^+$) LIF was simulated to obtain the relationship between predicted relative LIF signal and temperature. This is critical for proper analysis of the vibrational temperature from ratios of the LIF signal strength because the efficiency of the imager in capturing the emitted fluorescence directly impacts the temperature calculation. The (B–X) system involves transitions from a $^2\Sigma^+$ to a $^2\Sigma^+$ electronic state, the same as for CN. Therefore, a program previously developed for detailed spectroscopic modeling of the CN molecule [4] was modified using the spectroscopic constants, energy levels, and transition dipole moments of the AlO molecule. Reference 9 details the equations used in the absorption part of the spectrum simulations. For saturation, the equations found in Ref. 10 were used to simulate the relative LIF signal dependence on temperature. Because collisional broadening parameters for AlO were not found in the literature, those for CN were used, scaled by the ratios of the reduced mass and diameters for AlO and CN, respectively.

Al_2O_3 Measurement

Particles were quenched at various positions (burn times) along the particle trajectory by impacting them on solid plates made from single-crystal silicon wafers. Electron Probe Micro Analysis (EPMA) was conducted on the planar smoke pattern surrounding the particles. It has been shown previously [11] that the three-dimensional (spherical) configuration is rapidly quenched, yielding a relatively undistorted two-dimensional (planar) projection of the condensate around the droplet. Spherical oxide intensity distributions were reconstructed using an inverse Abel transform algorithm.

EPMA on the condensate around quenched particles was performed with a CAMECA SX50. High spectral resolution X-ray measurements were performed using wavelength dispersive spectroscopy (WDS). The excitation volume for a point analysis was approximately 2.0 μm^3 for a 15-kV acceleration voltage and a 20-nA beam current. Standard materials [oxygen, K_α (Al_2O_3), AlK_α (Al)] were used to calibrate X-ray lines for quantitative analysis, and standard methods were used to subtract background radiation from the AlK_α peak intensities.

Results

Figure 3 shows typical multiple exposure sequences of 210-μm-initial-diameter burning alumi-

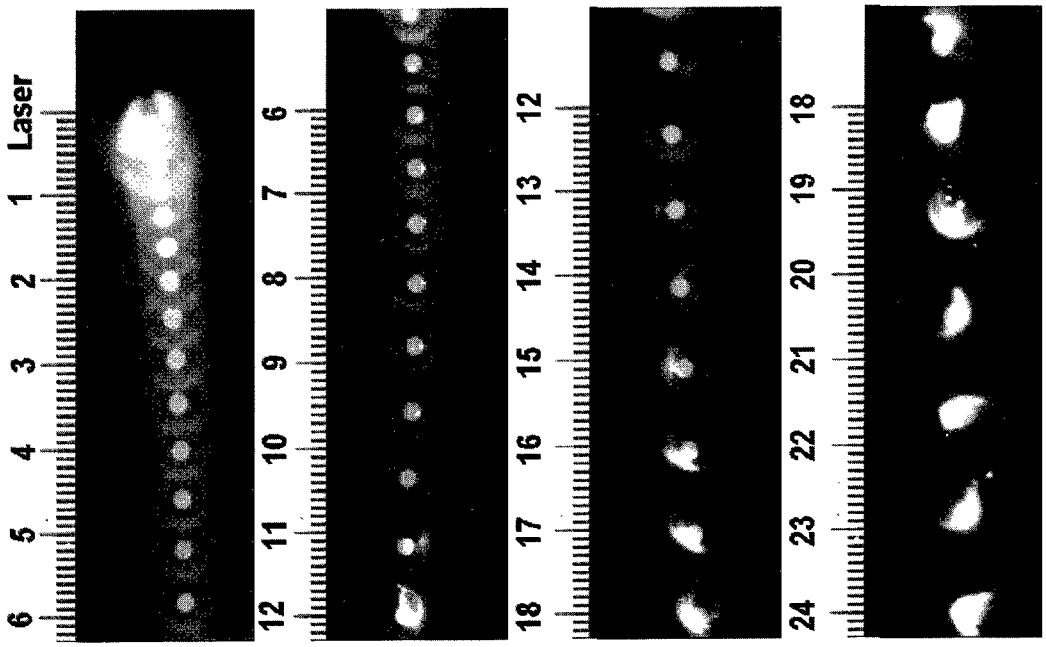

FIG. 3. Luminosity multiexposure images of 210-μm-initial-diameter aluminum particles burning in ambient air. The scale indicates distance (mm) from laser ignition.

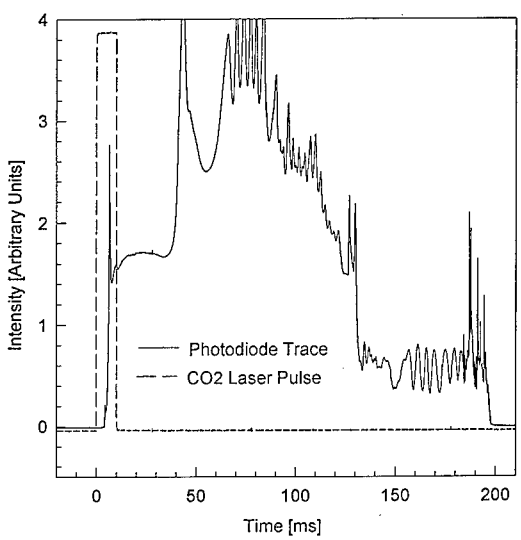

FIG. 4. Photodiode trace of 210-μm-initial-diameter aluminum particle and CO_2 laser pulse timing.

num droplets in free fall through the combustion duct. Because of field-of-view constraints, each of the four columns corresponds to a different particle burning under identical conditions. Immediately following ignition by the focused radiation of a 20-W argon-ion laser (488 nm wavelength), a spherically symmetric diffusion flame forms at ca. 3.0 times the particle diameter. The particle accelerates during free fall, as indicated by the increasing distance between images (the time elapsed between consecutive images is 0.3 ms). After traversing 8–15 mm (t = 50–75 ms) vertically downward through the combustion duct, the brightness of the flame envelope decreases slightly, and the particle diameter remains nearly unchanged. Toward the end of this period, gaseous jets are observed to emanate from the particle surface [12]. Jet position and curvature in a number of successive images indicate random particle spin. Subsequently, the presence of jets gives rise to disruptive events in which the flame luminosity is sharply increased, and numerous burning particle fragments appear in the vicinity of the initial parent droplet. Processes responsible for departure from the steady, spherically symmetric burning mode were investigated [5,12] by using a series of back-lighted particle images and microprobe analysis of the internal structure of quenched particles. The findings were indicative of chemical processes within the burning particle, and fragmentation was attributed to gas-phase oxides, which were produced and trapped in bubbles just beneath a surface oxide layer.

Figure 4 shows a photodiode trace for a droplet burned under the same conditions as in Fig. 3, except now a 150-W CO_2 laser was used as an ignition source instead of the argon-ion laser. The square

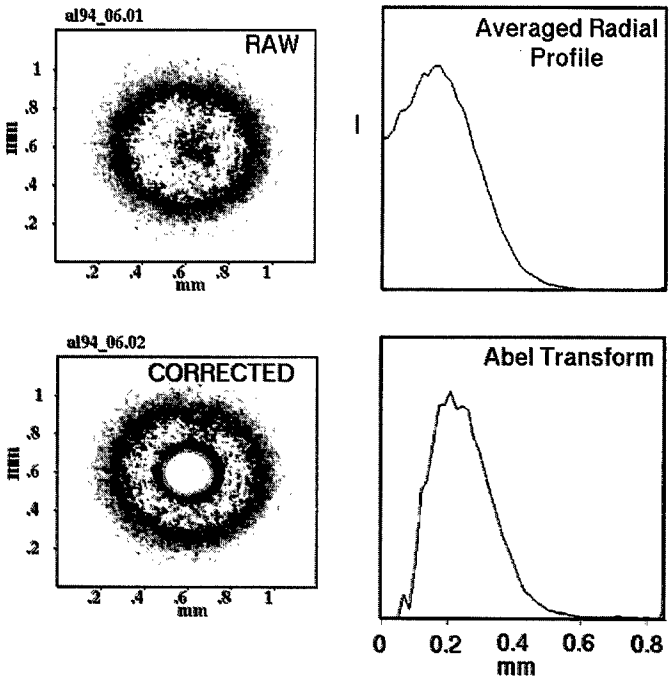

FIG. 5. Typical particle image when using a thick laser sheet for AlO PLIF. The raw line-of-sight integrated image is shown at top left with corresponding average radial profile to its right. The image below shows the same image after applying an inverse Abel transform with corresponding cross-sectional AlO profile.

pulse in Fig. 4 indicates the time of laser radiation, the low-to-high edge of the pulse was used to trigger the laser. The luminosity rose above the detection limit after the droplet was exposed to radiation for a duration of about 5 ms. Because heating is slow relative to a characteristic time for thermal diffusion, heating occurs uniformly throughout the droplet. After a brief period of laser-assisted combustion (initial luminous spike), the droplet traverses out of the radiation field and reaches a constant-intensity burning phase, as indicated by the relatively constant signal between 10 and 40 ms. During this period, a spherically symmetric diffusion flame envelope prevails (Fig. 3). The luminosity greatly increases thereafter and possesses a fluctuating component. This burning mode corresponds to the disruptive burning phase identified in Fig. 3; the fluctuating component of the signal likely arises from gaseous jetting and combustion combined with particle spinning. During the remaining lifetime, which varies between 200 and 300 ms, combustion is characterized by increasing and decreasing flame luminosity and frequent changes in direction of the particle trajectory. For reasons of steadiness and spherical symmetry, the measurement of species profiles were conducted at a burning time of 28 ms in the steady burning regime.

The PLIF images of AlO were recorded during the initial spherical burning period (the small spike seen in Fig. 4 at 28 ms is due to electrical interference from Nd:Yag flashlamps firing). The PLIF signal was confirmed to originate from AlO by varying the dye laser wavelength in increments of 0.01 nm. The average PLIF signal tracked the (1,0) vibrational band head structure, and tuning away from resonance greatly decreased the PLIF signal. A separate set of experiments confirmed that the AlO transitions were saturated. The PLIF output signal was found to be relatively insensitive to laser power variations, as measured with neutral density filters.

Initially, attempts were made to measure AlO LIF from a plane that intersected the particle center, using a laser sheet of 50 μm thickness. Such measurements, which would have directly yielded radial AlO distributions at this cross section, were not possible because the surrounding Al_2O_3 cloud scattered the laser sheet, and LIF resulted from regions much broader than the initial sheet width. Alternatively, a pump sheet of 3 mm thickness was used to ensure that the entire flame envelope of the burning particle resided within the radiation field and that cross-sectional distributions were obtained from the line-of-sight–integrated LIF signals using the flame symmetry. The center of each of the particle PLIF images was found using centroid determination algorithms, and an averaged radial profile was determined from each image. A one-dimensional, three-point Abel transform [13] was performed on each averaged radial profile to extract true relative cross-sectional vibrational populations (Fig. 5). For each vibrational band, these profiles were then averaged over 30 experiments, and only those profiles for

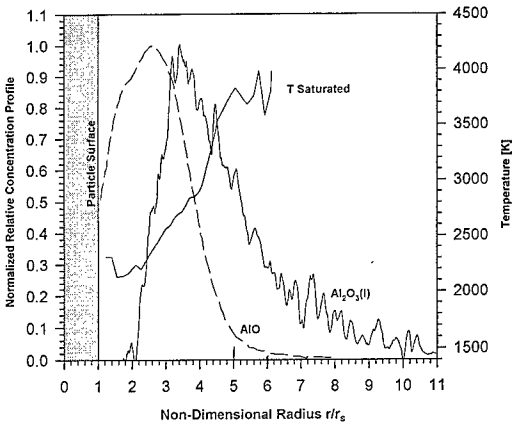

FIG. 6. Abel transform-recovered relative radial AlO and Al_2O_3 concentration profiles and AlO vibrational temperature versus nondimensional radius.

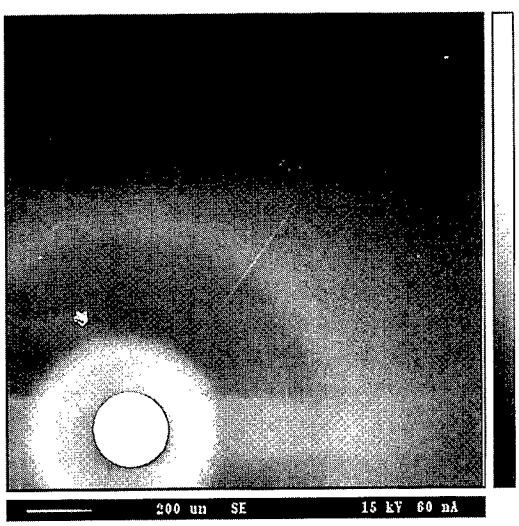

FIG. 7. Secondary electron image of a quenched 210-μm-initial-diameter particle with surrounding circular Al_2O_3 (smoke) pattern. The particle was silicon-plate intercepted after a burning time of 28 ms.

which the maximum intensity was within one standard deviation of the ensemble-averaged maximum were retained for final analysis. Fig. 5 shows gray-scale, raw, and Abel-inverted AlO PLIF images with corresponding averaged radial profiles for a single experiment.

For the purpose of estimating radial temperature profiles, the ratio of the averaged LIF signals from the (1,0) and (2,1) bands was formed as a function of distance from the particle center. Radial temperatures were assigned by comparison of calculated ratios with the locally measured LIF ratios. The resulting temperature profiles, which are shown in Fig. 6, are marked with a high statistical uncertainty because population ratios were calculated using ensemble averages. Simultaneous monitoring of population distribution in two vibrational states requires a two-camera, two-laser system, and such measurements will substantially enhance the accuracy and measurement precision. Additional errors are expected to originate from the assumption of rotational and vibrational equilibrium in the excited state [14]. In the future, temperature measurements can be further refined by accounting for the dynamic evolution of the rotational- and vibrational-level populations. However, the present measurements remain noteworthy because they are the first such measurements performed in metal-particle–burning experiments, and the results are qualitatively significant.

The measured temperature close to the particle surface is between 2300 and 2400 K, which is below the aluminum boiling temperature of 2723 K, but corresponds well with the melting point temperature of Al_2O_3 (2315 K) and with previously reported ignition temperatures [1]. The temperature rises with increasing distance from the particle surface, as expected from theory, and eventually reaches a nearly constant value of ca. 3800 K between $5 < r/r_s < 6$. Relative radial AlO concentrations were calculated from the ensemble-averaged vibrational population using the experimental temperature profile and the Boltzmann equation. The normalized relative AlO profile, which is shown in Fig. 6, exhibits a maximum away from the particle surface at $r/r_s = 2.8$.

Measurements of condensed-phase Al_2O_3 were carried out by impacting particles on silicon wafers after 28 ms burning time. Figure 7 shows a secondary electron image of a typical 210-μm-initial-diameter particle. The symmetric, circular smoke pattern surrounding the particle is consistent with the photographic and luminosity observations of Figs. 3 and 4. The smoke pattern, as determined by WDS scans, consists of stoichiometric Al_2O_3 particles. Both aluminum and oxygen K_α X-ray relative measurements were made along radial traces from the particle center outward (see track in Fig. 7). The excitation depth (determined by the electron-accelerating voltage of the instrument) was maintained greater than the oxide layer thickness so that the signal intensity was always proportional to the number of Al and O atoms present on the silicon substrate at the probing sight. Spherical oxide intensity distributions were reconstructed using an inverse Abel transform algorithm. The reconstructed relative Al_2O_3 profile for the particle in Fig. 7 is shown in Fig. 6. The oxide distribution between 1 and 1.5 nondimensional radii could not be measured because of detector obstruction. Relatively small amounts of oxide are seen between 1.5 and 2 radii. The profile shows a distinct peak outside the location of the AlO peak at about 3.5 radii and gradually decays radially outward.

TABLE 1
Reaction enthalpies and rate constants (Units are KJ-mol-K-cm^3-s)

Al and AlO Reactions	$\Delta H_{R\,298}$	**Rate Constant**
$Al + O + M \leftrightarrow AlO + M$	−512	
$Al + O_2 \leftrightarrow AlO + O$	−14	$k = 9.76 \times 10^{13} \exp(-80\ K/T)\ cm^3 mol^{-1} s^{-1}$
AlO_2 Reactions		
$AlO + O + M \leftrightarrow AlO_2 + M$	−402	
$AlO + O \leftrightarrow AlO_2 + O$	96	$k = 4.63 \times 10^{14} \exp(-10008\ K/T)\ cm^3\ mol^{-1} s^{-1}$
$AlO + AlO \leftrightarrow AlO_2 + Al$	110	
Al_2O Reactions		
$Al + AlO + M \leftrightarrow Al_2O + M$	−542	
$Al_2O + O \leftrightarrow AlO + AlO$	30	
$Al_2O + O_2 \leftrightarrow AlO + AlO_2$	126	
Al_2O_2 Reactions		
$AlO + AlO + M \leftrightarrow Al_2O_2 + M$	−528	
$AlO_2 + Al + M \leftrightarrow Al_2O_2 + M$	−638	
$Al_2O + O + M \leftrightarrow Al_2O_2 + M$	−499	
$Al_2O + O_2 \leftrightarrow Al_2O_2 + O$	−0.2	
$AlO + Al_2O \leftrightarrow Al_2O_2 + Al$	13	
$Al_2O_2 + AlO \leftrightarrow Al_2O + AlO_2$	96	
Surface Gasification		
$Al(l) \leftrightarrow Al$	318	
$Al(l) + AlO \leftrightarrow Al_2O$	−224	
Overall Al_2O_3 Formation		
$2Al + 3/2\ O_2 \rightarrow Al_2O_3(l)$	−2280	
$2AlO + 1/2\ O_2 \rightarrow Al_2O_3(l)$	−1754	
$AlO_2 + AlO \leftrightarrow Al_2O_3(l)$	−1601	
$Al_2O + O_2 \rightarrow Al_2O_3(l)$	−1475	
$Al_2O_2 + 1/2\ O_2 \rightarrow Al_2O_3(l)$	−1226	

Thermochemical Properties

Species	Structure	$\Delta H_{f\,298}$	S_{298}
Al		329.7	164.6
AlO	Al–O 1.62 Å	66.9	218.4
AlO_2	O–Al–O 1.69 Å, 180°	−86.2	251.8
Al_2O	Al–O–Al 1.73 Å, 180°	−145.2	252.3
Al_2O_2	O–Al | Al–O 1.8 Å, 90°, 90°	−394.6	281.0
$Al_2O_3(l)$		−1620.6	67.3

Discussion

Although the overall burning behavior under the condition studied is inherently transient due to frequent particle fragmentation, there exists an initial quasi-steady burning phase suitable for high-resolution optical measurements. During this period, the flame envelope exhibits spherical symmetry due to small relative velocities of particles [small Re (<0.1) and Gr numbers] typical for the experimental technique used. The thin-laser-sheet approach usually employed for PLIF imaging failed as a result of scattering caused by the condensed-phase products of the metal-oxygen system. However, relative radial species profiles could be calculated from thick-laser-sheet excitation and line-of-sight–integrated LIF signals using the inverse Abel transform and exploiting the spherical symmetry of the flame. Thus, isolated particle experiments in idealized environments are complementary to experiments conducted in actual propellant environments [4], in which the flame symmetry around individual particles is destroyed by convective motion.

In the present experiments, the laser ignition process destroys a significant portion of the initial oxide layer, and combustion in the steady-burning phase begins with little or no oxide on the particle surface. During the steady-burning phase, measurements show AlO to be a true gas-phase intermediate product, most likely formed in a thin reaction sheet from gaseous aluminum and oxygen. Table 1 lists possible reactions for the formation and consumption of AlO, corresponding heats of reaction, and kinetic rate data for the reactions experimentally studied. The reaction between Al and O_2 is slightly exothermic (−14 kJ/mol) and proceeds without an energy barrier [15]. The fast rate of this reaction and the absence of any significant heat release in the vicinity of AlO formation (Fig. 6) also supports this reaction as a major production route for AlO formation. Alternative gas-phase mechanisms for AlO production are a recombination of Al with O atoms (which is extremely exothermic and thus may readily dissociate) or reactions of Al_2O, which requires a mechanism for its own production.

As indicated by the slope of the AlO profile at the particle surface (Fig. 6), AlO diffuses from the region of its production to the particle surface.

Consumption of AlO at the Al(l) surface (Table 1) has been proposed by others as a means to produce Al_2O [3] and gasify aluminum via other mechanisms than pure vaporization. However, the nonzero value of AlO at the surface suggests that during the quasi-steady burning phase of combustion, the rate of this reaction is kinetically and not diffusively limited.

Wilson [16] and others have experimentally observed the accumulation of condensed-phase products on the particle surface. Oxide lobes that have been observed on particle surfaces in higher Reynolds number experiments were not observed to form during the steady combustion stage, or even during the subsequent, more violent combustion stage. Because the vaporization–decomposition temperature of pure Al_2O_3 is considerably higher than the temperature at the droplet surface, $Al_2O_3(l)$ formed in the surrounding gas can be transported back to the surface by thermopheresis [17] and deposited on the surface. In addition, gas-phase oxides such as AlO, which are present close to the surface in relatively high concentrations, may continuously accumulate on the relatively cold surface by means of condensation [18]. The presence of oxygen on the surface, in the form of either a liquid Al_2O_3 film or gas-phase oxides, gives rise to the possibility of producing AlO and Al_2O via heterogeneous reactions directly on the surface. Whereas reactions involving condensed-phase Al, Al_2O_3, and soluble species are believed to be important in later (disruptive) burning stages [12], aluminum gasification in the present work appears to mainly undergo a pure phase change at the liquid–gas interface, and chemical reactions producing AlO occur predominantly in the gas phase.

In the gas phase, AlO is likely consumed by reaction with O_2, by self-reactions, and through heterogeneous reactions that lead to condensed phase Al_2O_3 [19,20]. The reaction with O_2 is 96 kJ/mol endothermic and about an order of magnitude slower than the rate of Al with O_2 at flame temperatures [21]. The aluminum-containing product of this reaction is AlO_2, which could also diffuse inward to oxidize Al to AlO. Reactions of AlO with itself will also produce AlO_2 and Al_2O. These species along with AlO can yield the dimer of AlO, all of which are candidate species involved in the production of condensed-phase Al_2O_3, with AlO acting as an important growth species [20].

At the high flame temperatures of the aluminum–oxygen reaction, much of the chemistry will be in local equilibrium and the burning process will be diffusion-controlled. In the equilibrium limit, the combustion temperature is controlled by the decomposition temperature of the condensed-phase oxide [22]. The combustion system appears to have reached a nearly constant flame temperature over some radial distances as shown qualitatively in Fig. 6, consistent with the overall energy considerations of Ref. [22]. Within the temperature plateau region, a fraction of the oxide dissociates into AlO, AlO_2, or Al_2O and the reaction-sheet limit typically observed in diffusion flames is not formed. Rather, the oxide is produced over a distributed region as inferred by the gradual decrease of the Al_2O_3 profiles radially outward. Detailed modeling with estimates for the rate constants of reactions not experimentally studied will be required to further address mechanistic issues.

In view of the statistical error associated with the temperature profiles, thermodynamic equilibrium calculations were performed to establish theoretical bounds on the plateau temperature. Glassman and Papas [22] show that the plateau temperature of Al_2O_3 is shifted downward with increasing partial pressure of the inert species. In the present case of particles burning in an O_2–N_2 mixture, the flame temperature will be between 4000 and 3500 K, depending on the local mole fraction of N_2 and the enthalpy of the mixture. Unlike hydrocarbon droplet diffusion flames where enthalpy losses due to non-equilibrium radical concentrations, diffusive losses, and radiation losses lower the flame temperature from that predicted by an adiabatic flame temperature calculation, similar losses in the present system initially decrease the amount of Al_2O_3 (l) dissociation before lowering the flame temperature. The relative AlO concentration profiles, which were calculated from the temperature-corrected LIF signals, are insensitive to temperature variations within the theoretical limits.

In summary, new diagnostic techniques have been applied for measuring relative radial distributions of AlO and Al_2O_3, and temperature profiles of aluminum particles burning in air. These techniques can be applied to characterize additional species of the aluminum-air system or, more generally, to describe the vapor-phase combustion of metal particles in simulated products of solid propellant flames. In the future, the temperature measurements can be refined using a two-camera, two-laser system for simultaneously monitoring LIF from two band systems. These structural measurements will aid the development of detailed numerical models and will further facilitate a fundamental understanding of the combustion properties of metals.

Acknowledgments

This work was supported by the Office of Naval Research under contracts N00014-93-1-0732 and N00014-95-1-1339, subgrant 96-184. PLIF measurements were conducted collaboratively at the Naval Air Warfare Center, China Lake, CA. EPMA analysis was performed at the PMI, by using MRSC Shared Facilities.

REFERENCES

1. Price, E. W., Kraeutle, K. J., Prentice, J. L., Boggs, T. L., Crump, J. E., and Zurn, D. E., *Behavior of Alu-*

minum in Solid Propellant Combustion, NWC TP 6120, 1982.
2. Driscoll, J. F., Nicholls, J. A., Patel, V., Shahihi, B. K., and Liu, T. C., *AIAA* 24:856–858 (1986).
3. Yuasa, S. and Sakurako, S., *Twenty-Fourth Symposium (International) on Combustion,* The Combustion Institute, Pittsburgh, 1992, p. 1871.
4. Parr, T. P., Hanson-Parr, D. M., Bucher, P., Yetter, R. A., and Dryer, F. L., 32nd JANNAF Combustion Subcomittee Meeting, 1995.
5. Bucher, P., Yetter, R. A., Dryer, F. L., and Vicenzi, E. P., *Combust. Sci. Technol.* (1996), submitted.
6. Hanson-Parr, D. M. and Parr, T. P., *Twenty-Fifth Symposium (International) on Combustion,* The Combustion Institute, Pittsburgh, 1994, p. 1635.
7. Coxon, J. and Naxakis, S., *J. Mol. Spectrosc.* 111:102–113 (1985).
8. Partridge, S., Langhoff, B., Lengsfield, III, and Liu, B., *J. Quant. Spectrosc. Rad. Transfer* 30:449–462 (1983).
9. Colket, III. M. *J. Quant. Spectrosc. Rad. Transfer* 31:7–13 (1984).
10. Lucht, R. P., Laurendeau, N. M., and Sweeney, D. W., *Appl. Optics* 21:3729–3735, (1982).
11. Prentice, J. L. and Nelson, L. S., *J. Electrochem. Soc.* 15:809–812 (1968).
12. Bucher, P., Yetter, R. A., Dryer, F. L., and Vincenzi, E. P., Fall Technical Meeting, The Combustion Institute, Clearwater, FL (1994).
13. Dasch, C., *Appl. Opt.* 31:1146–1152 (1992).
14. Crosley, D. R., *Optical Eng.* 20:511–521 (1981).
15. Garland, N. L. and Nelson, H. H., *Chem. Phys. Lett.* 191:269–272 (1992).
16. Wilson, R. P. Jr., Paper 69-3, Spring Meeting, Western States Section, The Combustion Institute, China Lake, CA (1969).
17. Macek, A., Friedman, R., and Semple, J. M., *Heterogeneous Combust.* 15:3–16 (1964).
18. Christensen, H. C., Knipe, R. H., and Gordon, A. S., *Pyrodynamics* 3:91–119 (1965).
19. King, M. K., *Seventeenth Symposium (International) on Combustion,* The Combustion Institute, Pittsburgh, 1979, pp. 1317–1328.
20. Henderson, C. B., *Combust. Sci. Technol.* 1:275–278 (1970).
21. Belyung, D. P. and Fontijn, A., *J. Phys. Chem.* 99:12225–12230 (1995).
22. Glassman, I. and Papas, P., Fall Meeting, Eastern States Section, The Combustion Institute, Clearwater Beach, FL (1994).

COMMENTS

Herman Krier, Univ. Of Illinois at Urbana-Champaign, USA. I'm concerned that at elevated pressures, where aluminum particles will burn, i.e., 10–100 atmospheres, that the distribution of the AIO (relative to the Al_2O_3) will be significantly different than what you've measured a 1 atm. Would you please comment?

Also for aluminum particles that will be burning in various zones of a solid propellant the aluminum will be reacting with dissociated H_2O, and with O_2 concentrations (much) less than the $X_{O2} = 0.21$ that you studied. Again, thanks, in advance.

Author's Reply. It is unlikely that the techniques presently used can be applied to study aluminum particle combustion at pressures up to 100 atmospheres. At such pressures it is likely that diagnostic techniques for the combustion process only yield more global characterizations such as induction and total burn time measurements. However, it should be pointed out that the combination of detailed measurements at pressures at which they can be performed together with global measurements at high pressures can yield insight into the combustion process through numerical modeling comparisons using techniques similar to work published here [1].

It is certainly true that the combustion environment of a rocket motor is considerably different from air. These were preliminary studies. As emphasized in the paper, future work will be done in H_2O, CO, CO_2, etc. atmospheres to separate the effects of differing oxidizing environments, and in simulated products of solid propellant flames.

REFERENCE

1. Zhou, W., Yetter, R. A., Dryer, F. L., Rabitz, H., Brown, R. C., and Kolb, C. E., *Twenty-Sixth Symposium (International) on Combustion,* The Combustion Institute, Pittsburgh, 1996, pp. 000–000.

•

Edward L. Dreizin, AeroChem Research Laboratories, Inc., USA. Results of your measurements appear to enable one to correlate shape and size of luminous zones surrounding burning aluminum particles with the shape and size of the traces observed when a particle is quenched on a substrate. Such a comparison would be interesting and it would help to identify primary radiators in the flame zone around the particle.

Author's Reply. The luminosity distribution on multi exposure images of burning aluminum particles (Fig. 3.) could be correlated with the WDS measured relative oxide distribution on quenching plates (Fig. 5.) as proposed by Dreizin. However, on the quenching plate, one measures the relative oxide distribution directly, whereas in the

luminosity images one measures the thermal radiation which originates from both, the hot oxide particles in the flame envelope and the aluminum droplet. In order to correlate the temperature and luminosity measurements with the AL_2O_3 distribution on the quenching plate one would have to (1) account for the temperature dependant spectral emissivities for both, liquid aluminum and liquid Al_2O_3, (2) discriminate between radiation originating from the particle surface and condensate in the flame envelope, and (3) account for the spectral transmissivity of the optical components as well as the spectral efficiency of the camera used. The most important aspect is that the radiation emitted is extremely dependant on temperature (i.e. T^4), therefore a precise independent temperature measurement is needed to attempt such correlation. Because of the complexity involved, we have not pursued such a correlation in the present work.

•

John W. Daily, Univ. of Colorado at Boulder, USA. Did you experience a problem with radiative trapping of either the laser sheet or LIF in making the AIO concentration or temperature measurements? If so, what procedure did you follow to correct for the effects?

Author's Reply. In these experiments the (1,0), (2,1), and (3,2) bands of AlO were pumped and fluorescence imaged near the (0,0), (1,1), (2,2), ect. bands. The transitions were determined to be saturated, so laser sheet absorption was not a problem (also the images had no upstream/downstream asymmetry). However, emitted fluorescence could have been trapped by high AlO concentration in the flame, especially if it came from the (0,0) transition. Spectral simulation indicated that the vibrational energy redistribution in the excited (B) electronic state was quick relative to emission or quenching, so the emission was probably thermalized and a large fraction came from the (0,0) transition that could show radiation trapping problems. Since imaging requires relatively broad-band spectral selection, it would be difficult to monitor a transition not subject to radiative trapping. It might be possible, using an iterative application of a modified Abel transformation, to correct the measured results for radiative trapping (assuming, as usual, spherical symmetry). We have not done this because it would require an absolute concentration measurement, rather than the relative profile measured in the experiments. The effect of radiative trapping would be to reduce the apparent AlO concentration at small radial distances.

Twenty-Sixth Symposium (International) on Combustion/The Combustion Institute, 1996/pp. 1909–1917

A COMPREHENSIVE PHYSICAL AND NUMERICAL MODEL OF BORON PARTICLE IGNITION

W. ZHOU, R. A. YETTER AND F. L. DRYER
Department of Mechanical and Aerospace Engineering
Princeton University
Princeton, NJ 08544, USA

H. RABITZ
Department of Chemistry
Princeton University
Princeton, NJ 08544, USA

R. C. BROWN AND C. E. KOLB
Center for Environmental and Atmospheric Physics
Aerodyne Research, Inc.
Billerica, MA 01821, USA

A comprehensive spherosymmetric numerical model has been developed to study the ignition of an isolated boron particle with a thin boron oxide layer. This model includes detailed chemistry and multicomponent molecular transport in the surrounding gas phase, heterogeneous reactions, and physical absorption on the boron oxide/gas interface, as well as transport of the dissolved gas in the oxide layer and heterogeneous reactions at the boron oxide/boron interface. The calculated times required to gasify the oxide layer are in good agreement with published experimental data, with greater disparity for small particle cases at high temperatures. The desorption of complexes (at low surface temperature) and the adsorption of gas-phase species (at high surface temperature) at the boron oxide/gas interface are found to be rate controlling during the gasification of the oxide layer, with little sensitivity to species transport within the oxide layer. The gasification rate of the oxide layer increases with gas temperature and water vapor mole fraction, but is independent of the mole fraction of oxygen. The onset of oxide layer removal also occurs at lower temperatures with moisture present. Consistent with experiment, the presence of moisture is computationally shown to lead to a reduction in the particle ignition temperature.

Introduction

With the recent development of new difluoroamino/nitramino-based oxidizers and new difluoroamino/azido oxetane binders, boron is receiving renewed interest as a solid fuel ingredient. Conceptually, these new oxidizers have substituted $-NF_2$ groups for $-NO_2$ groups. For example, the fluorinated analog of RDX (FRDX) is shown below.

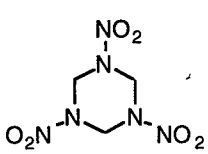

RDX

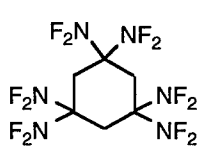

FRDX

In air-breathing propulsion devices, the use of boron has never achieved its theoretical potential as a high energy density component because of poor ignitability and performance characteristics. The poor ignition characteristics result from the presence of an oxide layer on the particle surface. The poor combustion efficiency results from an inability to achieve the maximum theoretical heat release because the formation of liquid boron oxide (as a final product) is both thermodynamically and kinetically limited. The potential advantages of combined fluorine-oxygen oxidation of boron-solid propellant mixtures include elimination of condensed-phase boron oxides and oxyhydrides as final products, greater overall heat of reaction, and shorter over all burn times, primarily from faster removal of the oxide shell covering the boron particles.

The combustion of boron is known to occur in several stages, often referred to in the literature with different terminology. Physically, these stages

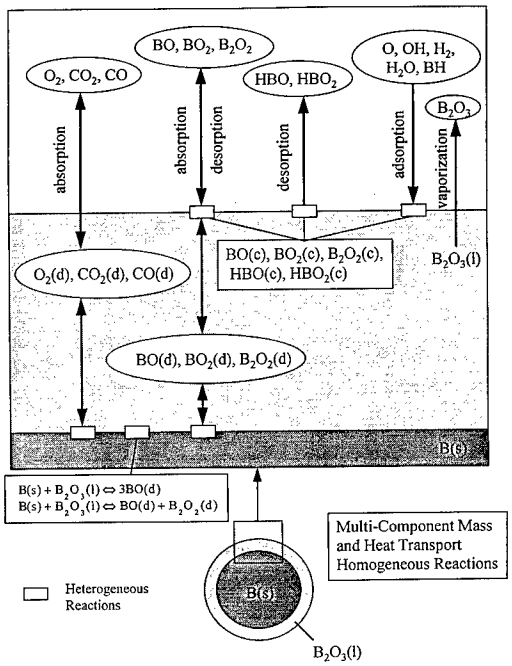

FIG. 1. Schematic of kinetic processes used to model boron/boron oxide combustion.

include an initial stage in which the particle heats up with little or no net oxide removal, a second stage in which the liquid oxide shell is gasified to expose the boron substrate, and finally, a stage in which the pure boron particle burns vigorously following the removal of the oxide layer. Here, we will refer to those stages as the particle heat up, the oxide layer removal, and the combustion stage, respectively.

To investigate the effects of fluorine on boron particle oxidation, we have been developing various numerical submodels to separately study the effects of fluorine on the homogeneous gas-phase kinetics of boron oxidation [1], the chemically assisted gasification of liquid boron oxide droplets [2], and the combustion of "clean surface" boron particles [3]. These studies have been extensions of our earlier works on oxidation of boron in hydrocarbon combustion environments [4–9].

The objective of the present work has been to combine the modeling aspects of Refs. 1–9 into a comprehensive particle model for the ignition and combustion of a spherical boron particle initially covered with a thin oxide shell. Of special interest is the comparison of the combustion characteristics for single particles placed instantaneously into a high temperature environment of combustion products generated by oxygen- and/or fluorine-containing oxidizers. Here, we present results for the ignition process in hydrocarbon/air combustion-product environments. This work concentrates on oxygen systems because of the availability of experimental data with which to compare model predictions [10,11]. Furthermore, significant controversy exists in previous models regarding the mechanisms occurring within the oxide layer and at the boron substrate/boron oxide and boron oxide/gas interfaces during ignition in air environments [12–15]. Experimental data currently do not exist for fluorine-enriched environments, but experiments to produce such data are underway [16,17]. Studies on the effects of fluorine will be presented in a future paper [18].

Model

The problem considered here is the transient spherosymmetric combustion of an isolated boron particle, coated with a liquid oxide layer, placed instantaneously into a hot, quiescent, gaseous ambient. This problem is described by the coupling of classical equations of conservation of mass, momentum, species, and energy [19] in all three phases, and with transport and homogeneous chemical kinetics in the fluids (liquid oxide and gas), heterogeneous kinetics at the two fluid interface boundaries (liquid oxide/gas and liquid oxide/boron substrate interfaces), and thermal conduction in the boron substrate.

The numerical model is divided into two parts: gas-phase and condensed-phase which are coupled by a time-splitting technique. For instance, the fluxes of species or energy on the liquid side of the liquid oxide/gas interface are "frozen" while the gas-phase conservation equations are solved. The updated boundary conditions on the gas side are then used to obtain the solution on the condensed phase in the next time step. The movements of the interface boundaries are governed by

$$\frac{dr_{lg}(t)}{dt} = -\left.\frac{\sum_{i=1}^{n_g} M_i(R_{lg,i} + R''_{lg,i})}{\rho_l}\right|_{r=r_{lg}} \quad \text{and} \quad \frac{dr_{sl}(t)}{dt} = -\left.\frac{\sum_{i=1}^{n_l} M_i R_{sl,i}}{\rho_s}\right|_{r=r_{sl}}$$

which are implemented as boundary conditions for the nodal control equations. Radiative heat transfer is given by a Stefan-Boltzman relation. The particle emissivity is 0.43, based on the study of Turns et al. [20] on boron oxide droplet combustion. Numerical methods based on the moving finite element method and stiff time integration were employed to solve the gas-phase and condensed-phase components. Detailed description of these methods are given elsewhere [21].

The kinetic processes used to model the boron particle ignition have been schematically shown in Fig. 1. In the gas phase, transport processes are described by the mixture-fraction formulation [22],

TABLE 1
Reaction mechanism for the liquid oxide/gas interface

Reactions	$K_f = K_0 \sqrt{T} S_0 e^{(-E_a/RT)}$			$K_b = A_b e^{-(E_b/RT)}$	
	K_0 (cm/s)	S_0	E_a (Kcal/mole)	A_0 (cm²/complex-s)	E_b (Kcal/mol)
LG_1 $B_2O_3(l) + O(g) \Leftrightarrow BO_2(c) + BO_2(c)$	910	0.1	0	3.0×10^{-5}	5
LG_2 $B_2O_3(l) + H_2(g) \Leftrightarrow HBO_2(c) + HBO(c)$	2571	0.001	10	3.0×10^{-5}	5
LG_3 $B_2O_3(l) + OH(g) \Leftrightarrow BO_2(c) + HBO_2(c)$	882	0.1	0	3.0×10^{-5}	5
LG_4 $B_2O_3(l) + H_2O(g) \Leftrightarrow 2HBO_2(c)$	857	0.05	10	3.0×10^{-5}	10
LG_5 $B_2O_3(l) + BH(g) \Leftrightarrow HBO(c) + B_2O_2(c)$	1058	0.001	30	3.0×10^{-5}	5
LG_6 $BO_2(g) \Leftrightarrow BO_2(c)$	556	0.1	0	$0.2T_s \exp\left(-\frac{\Delta H_{LG9,f}}{RT}\right) ps^{-1}$	
LG_7 $HBO(g) \Leftrightarrow HBO(c)$	690	0.005	10	$0.2T_s \exp\left(-\frac{\Delta H_{LG7,f}}{RT}\right) ps^{-1}$	
LG_8 $HBO_2(g) \Leftrightarrow HBO_2(c)$	549	0.001	10	$0.02T_s \exp\left(-\frac{\Delta H_{LG8,f}}{RT}\right) ps^{-1}$	
LG_9 $B_2O_2(g) \Leftrightarrow B_2O_2(c)$	497	0.0001	10	$0.2T_s \exp\left(-\frac{\Delta H_{LG9,f}}{RT}\right) ps^{-1}$	
LG_{10} $BO(g) \Leftrightarrow BO(c)$	702	0.2	10	$0.2T_s \exp\left(-\frac{\Delta H_{LG10,f}}{RT}\right) ps^{-1}$	

while in the liquid oxide phase, variable transport coefficients are correlated as [23],

$$D = 7.5 \times 10^{-8} \frac{T(XM)^{1/2}}{\mu V^{0.6}} \text{ [cm}^2/s]$$

where X is an association factor that is introduced to define the effective molecular weight of the solvent with respect to the diffusion process. In the estimation of D, the diffusion coefficient equation was used as a scaling relationship with data from reference [13].

The gas-phase chemistry is described by a comprehensive model which includes 20 species (H, O, OH, H_2, O_2, H_2O, HO_2, H_2O_2, CO, CO_2, HCO, B, BO, BO_2, B_2O_2, B_2O_3, HBO, HBO_2, BH, and N_2) and 77 reversible reactions [4–7]. This limited number of species was defined by equilibrium considerations and subsequent kinetic calculations [3–5]. Homogeneous kinetics in the liquid oxide layer have been neglected in the present model.

The gasification of the liquid boron oxide layer and the oxidation of a solid boron substrate forming dissolved gases are both described by finite rate heterogeneous kinetics. The vaporization of $B_2O_3(l)$ is described by an equilibrium process $B_2O_3(l) \Leftrightarrow B_2O_3(g)$. The liquid oxide/gas interface kinetics model used here (Table 1) is an extension of a previously described model [6,9], which has been further extended here to include reactions for H_2 and BH with $B_2O_3(l)$, using elemental adsorption and desorption reactions, and two additional surface complexes, HBO(c) and BO(c). The reactions between gas-phase species and the oxide surface (which are endothermic) are first order in gas reactants. Higher-order reactions involving gas-phase species with complexes are also possible and will be included in our future work [18]. These reactions are not expected to be important in the present calculations where the ambient temperature is high and energy input is almost entirely generated by transport from the gas to condensed phase. Determinations and sources of the rate constant data are described elsewhere [6].

The current model assumes that the surface complexes, BO(c), BO_2(c), and B_2O_2(c), can be physi-absorbed into the liquid oxide layer, forming the dissolved species, BO(d), BO_2(d), and B_2O_2(d), respectively, i.e., $Z(g) \Leftrightarrow Z(c) \Leftrightarrow Z(d)$. The concentration of HBO(c) at the liquid oxide and gas interface was found to be negligible, and the dissolution of HBO(c) was neglected. Based on the estimated solubility, HBO_2(d) was also neglected. The gas-phase species O_2(g), CO(g), and CO_2(g) do not form surface complexes at the liquid oxide/gas interface, but are physi-absorbed and dissolved into the liquid oxide layer, i.e., $Z(g) \Leftrightarrow Z(d)$. The corresponding physi-absorption rates are determined by the partial pressure of the gas species at the liquid oxide/gas interface and the diffusion coefficient of the gas species dissolved in the liquid oxide layer [24], i.e., $R''_Z = D_Z(A^0_Z - A^e_Z)/\delta$, where the Nerst boundary layer thickness, δ, is chosen to be the order of magnitude of the diameter of one B_2O_3 molecule. The physi-absorption of other species are neglected here since

TABLE 2
Reaction mechanism for the boron substrate/liquid oxide interface

	B(s) + Z(d) reactions	$\Delta H_{r,298}$ (Kcal/mol)	$K = K_0 S_0 \exp(-E_a/(RT_s))$ K_0 (cm/s)	S_0	E_a (Kcal/mol)
SL_1	$2B(s) + O_2(d) \rightarrow 2BO(d)$	0.0	643	0.001	0.0
SL_2	$B(s) + O_2(d) \rightarrow BO_2(d)$	−68.0	643	10^{-7}	0.0
SL_3	$2B(s) + O_2(d) \rightarrow B_2O_2(d)$	−109.0	643	0.064	3.0
SL_4	$B(s) + BO_2(d) \rightarrow 2BO(d)$	68.0	556	0.001	4.6
SL_5	$B(s) + BO_2(d) \rightarrow B_2O_2(d)$	−41.0	556	0.005	5.0
SL_6	$B(s) + CO_2(d) \rightarrow BO(d) + CO(d)$	67.7	548	0.0013	4.5
	Substrate-oxide reactions				
SL_7	$B(s) + B_2O_3(l) \Leftrightarrow BO(d) + B_2O_2(d)$		partial equilibrium		
SL_8	$B(s) + B_2O_3(l) \Leftrightarrow 3BO(d)$		partial equilibrium		

we assume that atomic boron does not exist as a distinct chemical entity within the oxide layer. Boron from the boron substrate is transported to the oxide surface only in the form of the suboxides BO, BO_2, and B_2O_2. Finally, the gas-phase species H_2, OH, H_2O, BH, and H are consumed at the liquid oxide/gas interface by adsorption.

The six species dissolved in the liquid oxide layer (O_2(d), CO(d), CO_2(d), BO(d), BO_2(d), and B_2O_2(d)) transport from the liquid oxide/gas interface to the liquid oxide/boron substrate interface and react with boron substrate at the boron/boron oxide interface producing CO(d), BO(d), and B_2O_2(d). In turn, these dissolved species diffuse toward the liquid oxide/gas interface and either vaporize or desorb as surface complexes.

The heterogeneous kinetics model which describes the oxidation of the boron substrate is summarized in Table 2. At the interface of boron substrate and boron oxide, the reactions between dissolved gases and the boron substrate are analogous to the reactions of the corresponding gases reacting with boron reported earlier [3], neglecting those reactions that would involve species for which the absorption rate has been assumed to be zero based on the general approximation discussed above. The reverse reactions are very slow and, thus, are neglected. Note that reactions of the liquid oxide with the boron substrate (SL_7 and SL_8) are replaced by the partial equilibrium conditions due to the lack of rate data.

A "clean surface" boron particle is exposed to the ambient when the oxide layer is completely removed. The heterogeneous reaction mechanism including elementary adsorption and desorption at the interface of boron and gas have been reported previously [3]. Here we study only the heat-up and oxide layer removal stages of particle burning, and thus, the "clean surface" boron reactions are not considered.

Results

Calculations for the combustion of a 34.5 μm diameter particle with an initially 0.2 μm-thick oxide layer were performed to compare with the experimental data of Macek [10]. Particle ignition was studied by injection of particles into the postcombustion gases of premixed CO–air and CH_4–air flames. The gas temperatures and compositions for the various experiments that we modeled are summarized along with the numerical results in Table 3. The gasification rate of the oxide layer is sensitive to gas temperature and ambient moisture content. For example, if 19% of water vapor is in the ambient gases, the ignition time decreases by a factor of 2 and the temperature at the onset of the oxide layer removal decreases from about 1520 K to about 1470 K. As a result, the surface temperature of the boron substrate, when the oxide layer disappears, is lower than when no moisture is present.

The calculated thickness and surface temperature of the oxide layer as functions of time for conditions 1, 2, and 6 in Table 3 are shown in Fig. 2. The linear variation of the oxide layer thickness during gasification is indicative of kinetically controlled removal. The duration of both the particle heating and oxide layer gasification stages decrease with increasing gas temperature and ambient water concentration.

The radial gas-phase species distributions at two different times (t = 2.12 and 4.55 ms) for condition 6 are shown in Fig. 3. The principal gas-phase products are HBO_2(g) and BO_2(g), and the concentrations of these species, as well as those of B_2O_3(g) and BO(g), increase monotonically with time. It should be noted that the surface temperature of the

TABLE 3
Calculated liquid oxide layer removal times compared with the experimental data of Macek [10][a]

No.	T_g (K)	Mole fractions, X, of components							t_1 (ms)	
		O_2	H_2O	CO_2	CO	N_2	O	OH	Measured	Calculated
1	2280	0.23	0	0.30	0	0.45	0.01	0	4.4	6.4
2	2430	0.20	0	0.33	0.01	0.43	0.01	0	4.8	5.2
3	2870	0.23	0	0.44	0.20	0.09	0.03	0	3.4	2.0
4	2240	0.19	0.16	0.11	0.01	0.50	0	0.01	4.0	3.3
5	2330	0.21	0.16	0.12	0.01	0.47	0	0.01	3.5	3.1
6	2430	0.19	0.19	0.13	0.02	0.45	0	0.02	3.8	2.7
7	2640	0.20	0.21	0.15	0.03	0.35	0.01	0.04	2.6	1.7
8	2490	0.28	0	0.35	0.03	0.32	0.01	0	3.6	3.9
9	2450	0.37	0	0.34	0.02	0.25	0.01	0	2.1	4.0

[a]$d = 34.5\ \mu m$, $h = 0.2\ \mu m$.

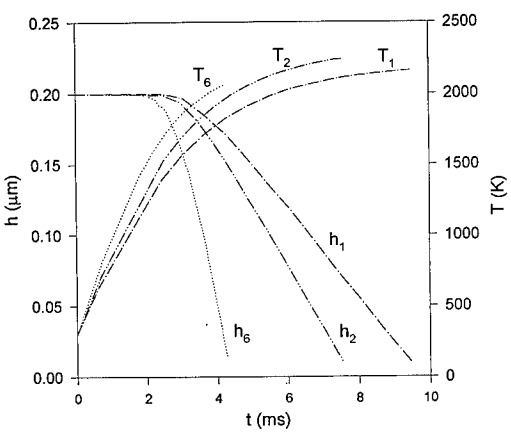

FIG. 2. The thickness and surface temperature of the oxide layer as a function of time. The calculation conditions are those of numbers 1, 2, and 6 in Table 3.

liquid oxide/gas interface rises substantially during oxide layer removal. Both conductive heating and gas-phase chemical reaction near the surface are contributing sources of energy.

The species distributions within the oxide layer at two different times (t = 2.12 ms and t = 3.55 ms) for condition 6 are shown in Fig. 4. Reactions of O_2(d) and CO_2(d) at the boron substrate/liquid oxide interface and the desorption of B_2O_2(d) at the liquid oxide/gas interface are diffusion limited.

Comparisons of numerical predictions with the experimental data of Yeh and Kuo [11] for a particle diameter of 3 μm are given in Table 4. Boron particles were injected into the postcombustion gases of a premixed flat flame burner fired with various $CH_4/O_2/N_2$ mixtures. The calculated oxide layer removal times are in good agreement with the measured data for low temperatures, but are considerably shorter than experimental data at high temperatures. This time is independent of the oxygen mole fraction and decreases with increasing gas temperature.

Discussion

During the heat-up period, the complex desorption rate at the oxide surface is much slower than the gaseous species adsorption rate because of the low surface temperature and the high activation energy of desorption (≈55.7 Kcal/mole). A layer of surface-bound complexes initially develops to occupy a significant fraction of the available reactive surface sites. In oxidizing environments without water, the adsorption of oxygen atoms is rate controlling and BO_2(c) is found to be the dominant surface-bound complex. In contrast, when moisture is present, the adsorption of water competes with that of oxygen atoms, resulting in the formation of HBO_2(c). The slow reactions of the dissolved molecular oxygen, carbon dioxide, and boron dioxide at the boron substrate/liquid oxide interface produce some CO(d), BO(d), and B_2O_2(d), resulting in a slow growth of the liquid oxide layer thickness (too small to be observed in Fig. 2).

With the onset of the liquid oxide layer removal, the desorption rates of HBO_2(c) and BO_2(c) become comparable to the physi-absorption and chemi-adsorption rates of gaseous species, and the gasification rate increases significantly. Numerical results indicate that the characteristic transport time in the liquid oxide layer and the heterogeneous reaction time at the boron and boron oxide interface are much longer than those in the surrounding gas phase. Consequently, when a cold boron particle is injected into an environment with a gas temperature greater than the ignition temperature, the mechanisms within the

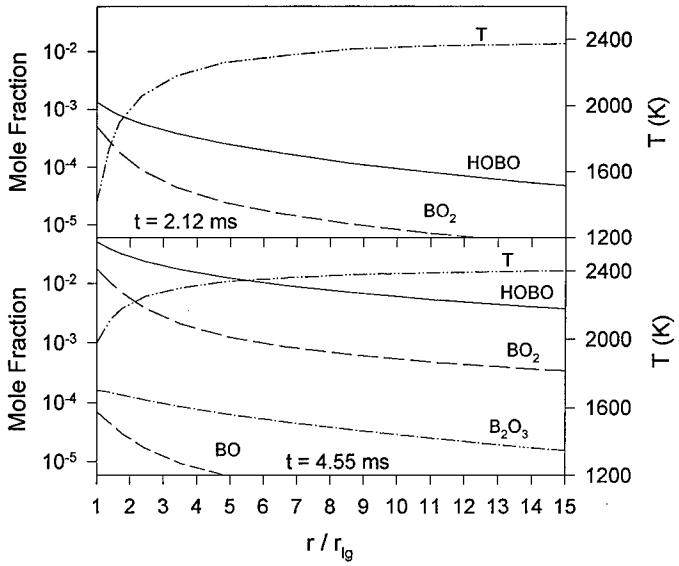

FIG. 3. The gas-phase species and temperature distribution as a function of the nondimensional distance from the oxide surface at two instances. The calculation conditions are those of number 6 in Table 3; r_{lg} is the outer radius of the oxide layer.

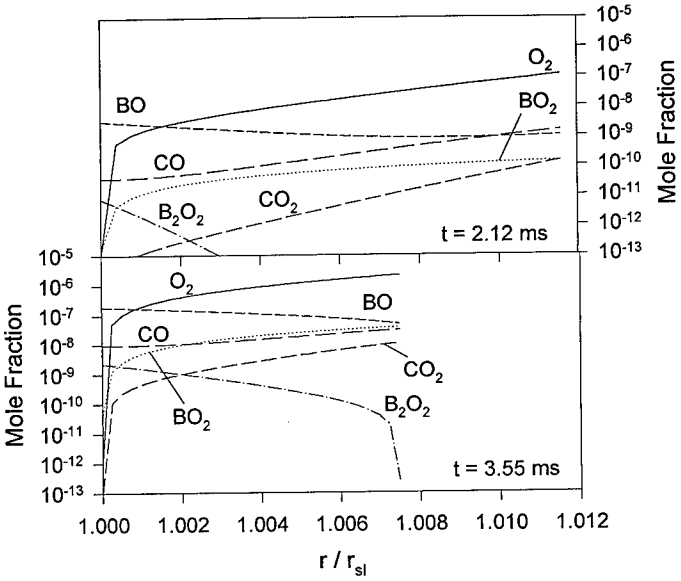

FIG. 4. The species profiles within the oxide layer as a function of the nondimensional distance from the boron surface at two instances. The calculation conditions are those of number 6 in Table 3; r_{sl} is the inner radius of the oxide layer.

oxide layer are unimportant in terms of controlling ignition.

When the temperature at the liquid oxide/gas interface layer is less than 1800 K, the desorption of complexes is rate controlling and gasification is slow. Without moisture, the desorption rate of $BO_2(c)$ approximates the liquid oxide gasification rate, and the oxide layer removal time can be estimated as

$$t_1 \approx \frac{4\pi r^2 h \rho_{B_2O_3(l)}}{4\pi r^2 R_{BO_2(c),de} M_{BO_2}} = \frac{h \rho_{B_2O_3(l)}}{R_{BO_2(c),de} M_{BO_2}}$$

For a 34.5-μm diameter particle, with a 0.2-μm-thick oxide layer, the estimated removal time, t_1, is in good comparison with experiments. With water vapor present, both desorption of $HBO_2(c)$ and $BO_2(c)$ must be considered. However, when the surface temperature rises above 1800 K, the rate-controlling steps are the adsorption of various gases.

Under all cases, surface kinetics are controlling, and the gasification rate increases with the temperature at the liquid oxide/gas interface. In the present studies, particles are burning in high temperature

TABLE 4
Calculated liquid oxide layer removal times compared with the experimental data of Yeh and Kuo [11][a]

Test condition	T_g (K)	Mole fraction, X		Measured t_1 (ms)		Calculated t_1 (ms)
		O_2	H_2O	Cryst.	Amor.	
A	1962	0.182	0.184	1.54 ± 0.07	1.55 ± 0.16	0.44
B	1988	0.234	0.185	1.48 ± 0.12	1.56 ± 0.24	0.37
C	1993	0.126	0.192	—	2.14 ± 0.18	0.36
D	1782	0.185	0.152	2.16 ± 0.12	1.56 ± 0.15	1.60
E	1784	0.228	0.153	2.08 ± 0.11	1.57 ± 0.10	1.58
F	1772	0.277	0.145	2.04 ± 0.06	1.45 ± 0.13	1.69

[a]$d = 3\ \mu m$, $h = 0.02\ \mu m$.

ambient, and the ignition of a particle is driven by the heat transport from the surrounding hot gas instead of self-heating from surface reactions. Thus, the particle surface temperature increases at a higher rate in a high gas temperature ambient than at lower ambient gas temperatures, as shown in Fig. 2. In the cases with the same ambient gas temperature, however, the surface temperature of a boron particle in an environment containing moisture increases at a faster rate than that in a dry environment, because the heat of reaction for the formation of HBO_2(g), which is the main gaseous product in a high-temperature wet ambient ($\Delta H_{r,298} = -133.99$ Kcal/mole), is higher than the heat of reaction that yields BO_2(g), which is the dominant product in a dry environment ($\Delta H_{r,298} = -68.00$ Kcal/mole). In a fluorinated environment, the surface temperature of the particle would increase at an even larger rate compared with that in a moisture environment because of the higher heat of fluorination for the overall reaction that forms gaseous OBF and BF_3 ($\Delta H_{r,298} = -143.99$ Kcal/mole for HBO_2(g) and -271.42 Kcal/mole for BF_3(g)) [3].

The calculated temperatures when oxide layer removal begins (1520 K in dry environments and 1470 K in wet environments) are much lower than the measured ignition temperature data of Macek where ignition was found to occur at 1950 K and 1880 K in dry and wet environments, respectively. However, the experimental temperature corresponds to the measured gas temperatures surrounding the boron particle. The measured gas temperature is likely to be several hundred degrees higher than the surface temperature of the particle due to radiation losses, endothermic surface reactions, and even from the nonadiabatic character of the burner postcombustion gases.

The measured and calculated oxide layer removal times listed in Tables 3 and 4 are in generally good agreement with the experiment. However, the calculated oxide layer removal times for small boron particles at high gas temperatures are much shorter than the corresponding experimental data [11]. This result raises some concern with regard to the present estimation of the temperature dependence of the adsorption rate associated with water vapor. Further modeling is required to address the source of this disparity. Finally, Yeh and Kuo [11] performed experiments using both crystalline and amorphous boron particles. Although the experimental results do show some dependence on the boron structure, the current calculations do not consider the solid-phase characteristic of the boron substrate.

Most of the previous experimental and analytical work focused on studying the effect of water vapor and oxygen on the ignition of boron particles. This work also shows that the gasification rate of a boron particle is very sensitive to the concentration of O(g) and OH(g) in the ambient, which is consistent with previous results for the gasification of liquid oxide droplets [2,6].

Conclusions

A comprehensive physical and numerical model has been developed and utilized to investigate the ignition of a boron particle coated with an oxide layer. BO_2(c) and HBO_2(c) have been identified as the dominant surface complexes formed at the oxide layer/gas interface in hydrocarbon combustion environments, and the surface desorption and adsorption rates were found to be controlling oxide layer removal. Transport within the oxide layer and chemical reaction at the boron substrate/oxide layer interface were found to be unimportant to the removal of the oxide layer, since diffusion time scales were found to be very long in comparison to the oxide layer removal time.

The numerical results are generally in good agreement with the experimental results of Macek [10] and Yeh and Kuo [11], including the noted experimental effects of water vapor addition and the insensitivity of particle ignition to ambient oxygen

concentration. The oxide surface mechanism will be extended in future work to include the reactions between the complexes and gas-phase species in order to evaluate the effects that self-heating may have on particle ignition. Finally, the present work provides a reference case for comparison of boron particle ignition properties with those yet to be investigated for environments containing both oxygen- and fluorine-containing combustion products.

Nomenclature

A^0	average concentration of dissolved gas, mole/cm^3
A^*	equilibrium concentration for the partial pressure of the gas at the liquid/gas interface
c	complex
d	particle diameter, μm
D	diffusion coefficient, cm^2/s
de	desorption
g	gas
h	thickness, μm
l	liquid
lg	the interface of liquid oxide and gas
M	molecular weight, g/mole
n	number of species
X	association factor, constant
r	radius
R	heterogeneous reaction rate, mole/cm^2-s
R''	physi-absorption rate, mole/cm^2-s
sl	the interface of boron substrate and liquid oxide
t	time, sec
T	temperature, K
V	molar volume, cm^3/g-mole
Z	species
δ	Nerst boundary layer thickness, cm
μ	viscosity, cp
ρ	density, g/cm^3

Acknowledgments

This work was supported by the office of Naval Research under contract *N* 00014-95-C-0083. The authors gratefully acknowledge the support of Dr. Richard Miller at ONR.

REFERENCES

1. Brown, R. C., Kolb, C. E., Yetter, R. A., Dryer, F. L., and Rabitz, H., *Combust. Flame* 101:221–238 (1995).
2. Yetter, R. A., Dryer, F. L., Rabitz, H., Brown, R. C., and Kolb, C. E., *Combust. Flame,* to be submitted, 1996.
3. Zhou, W., Yetter, R. A., Dryer, F. L., Rabitz, H., Brown, R. C., and Kolb, C. E., "Effects of Fluorine on the Combustion of "Clean" Surface Boron Particles," Paper No. 7, Eastern States Sectional Meeting of the Combustion Institute, Clearwater, FL., 1994.
4. Yetter, R. A., Rabitz, H., Dryer, F. L., Brown, R. C., and Kolb, C. E., *Combust. Flame* 83:43–62 (1991).
5. Yetter, R. A., Cho, S. Y., Dryer, F. L., Rabitz, H., Brown, R. C., and Kolb, C. E., *Twenty-Second Symposium (International) on Combustion,* The Combustion Institute, Pittsburgh PA, 1988, p. 919–929.
6. Brown, R. C., Kolb, C. E., Yetter, R. A., Dryer, F. L., and Rabitz, H., *Int. J. Chem. Kinet.* 23:957–970 (1991).
7. Brown, R. C., Kolb, C. E., Cho, S. Y., Yetter, R. A., Rabitz, H., and Dryer, F. L., in *Gas-Phase Metal Reactions,* (A. Fontijn, Ed.), Elsevier Science Publishers, B. V., The Netherlands, 1992, p. 643.
8. Brown, R. C., Kolb, C. E., Cho, S. Y., Yetter, R. A., Rabitz, H., and Dryer, F. L., *Int. J. Chem. Kinet.* 26:319–332 (1994).
9. Cho, S. Y., Yetter, R. A., Dryer, F. L., Rabitz, H., Brown, R. C., and Kolb, C. E., *Int. J. Chem. Kinet.,* in review.
10. Macek, A. and Semple, J. M., *Combust. Sci. Technol.* 1:181–191 (1969).
11. Yeh, C. L. and Kuo, K. K., "Experimental Studies of Boron Particle Combustion", 8th International Symposium on Transport Phenomena in Combustion, July, 1995.
12. King, M. K., *J. Spacecraft Rockets* 19:294–306 (1982).
13. Glassman, I., Williams, F. A., and Antaki, P., *Twentieth Symposium (International) on Combustion,* The Combustion Institute, Pittsburgh, 1984, pp. 2057–2064.
14. Li, S. C. and Williams, F. A., in *Combustion of Boron-Based Solid Propellants and Solid Fuels,* (K. K. Kuo, Ed.), p. 248.
15. Yeh, C. L. and Kuo, K. K., "Theoretical Model Development and Verification of Diffusion/Reaction Mechanisms of Boron", 8th International Symposium on Transport Phenomena in Combustion, July, 1995.
16. Krier, H., Burton, R. L., Pirman, S. R., and Spalding, M. J., "Shock Initiation of Crystalline Boron in Oxygen and Fluorine Compounds," AIAA Paper No. 95-2120, 30th AIAA Thermophysics Conference, San Diego, CA, June 1995.
17. Bucher, P., Yetter, R. A., Dryer, F. L., Parr, T. P., Hanson-Parr, D. M., Vincenzi, E. P., "Flame Structure Measurement of Single, Isolated Aluminum Particles Burning in Air," *Twenty-Sixth Symposium (International) on Combustion,* The Combustion Institute, Pittsburgh, 1996, pp. 1899–1908.
18. Zhou, W., Yetter, R. A., Dryer, F. L., Rabitz, H., Brown, R. C., and Kolb, C. E., "Effects of Fluorine on Boron Particles Ignition," Eastern States Sectional Meeting of the Combustion Institute, Hilton Head, SC, 1996, submitted.
19. Williams, F. A., *Combustion Theory,* 2nd ed., Benjamin/Cummings Publishing, Menlo Park, CA, 1985.
20. Turns, S. R., Holl, J. T., Solomon, A. S. P., and Faeth, G. M., *Combust. Sci. Technol.* 43:287–300 (1985).
21. Cho, S. Y., Yetter, R. A., and Dryer, F. L., *J. Comput. Phys.* 102:160–179 (1992).
22. Kee, R. J., Warnatz, J., and Miller, J. A., SAND 83-8209, Sandia National Laboratory, Livermore, CA, 1983.
23. Wilke, C. R. and Chang, P., *A.I.Ch.E J.* June, 1955, pp. 264–270.
24. Nernst, W. Z., *Phys. Chem.* 47:52 (1904).

COMMENTS

Merril King, NASA Headquarters, USA. I would suggest that the authors run their model against the thermogravimetric data published by Safaneev 10–15 years ago in *Combustion, Explosion, and Shockwaves* as a further test.

Author's Reply. We were aware of your reference to this work in your publication [1]. Here, we constrained our work to the ignition problem leading to full fledged combustion. We will consider your suggestion in our future work.

REFERENCE

1. King, M. K., in *Combustion of Boron-Based Solid Propellants and Solid Fuels,* K. K. Kuo, (Editor), p. 1.

•

Herman Krier, University of Illinois at Urbana, USA. I commend you and your co-authors for developing a very detailed heterogeneous and homogeneous chemical and transport model for this energetic metal ignition. My concerns are as follows:

a. How sensitive is the *assumed* oxide layer thickness (h) for the B_2O_3 layer to the ignition time delay?
b. Is this thickness independent of initial boron particle size?
c. Finally, how accurate one the various (I assume, over 20) kinetic rates for the heterogeneous reactions?

Author's Reply. The oxide layer removal time (the ignition delay time) is not only a function of the oxide layer thickness, but the rate at which it is removed. In the high temperature environment of interest, the current model indicates that the layer gasification rate is controlled by the surface kinetics at the boron oxide/gas interface for small particles or by gas phase species transport for large particles. The formation of boron oxide at the boron/boron oxide interface is negligible. The oxide layer regression rate was insensitive to the initial oxide layer thickness as long as the thickness is much smaller compared to the particle radius. Thus, the oxide layer removal time is proportional to the thickness. If we were to have limited the gas phase oxidation species to dry oxygen, at low temperatures, the growth or regression rate of the oxide layer will be determined by the transport of species in the oxide layer itself. It is therefore likely that the overall removal rate may become a function of the thickness. In the comparison of our model with the experimental data, we utilize the experimental data reported by Yeh and Kuo [1,2] and for Macek's data [3], we use the estimated oxide layer thickness reported by King [4].

According to the analysis of Glassman et al. [5], the ratio of the oxide layer thickness and the particle radius is determined by the thermal chemical properties of a metal particle and is approximately a constant. Although the analyses the authors perform is not specific to boron, the general conclusion to be drawn from their work was that the oxide layer thickness depends on the particle size.

The sources of kinetic data for these heterogeneous reactions can be found in Ref. 6 in the paper. These rate parameters are obtained under best estimation based on limited experimental data, and thus, are highly uncertain. The purpose of the work is to identify the controlling reactions, thus guiding kineticists to those rate parameters which need further study.

REFERENCES

1. Yeh, C. L. and Kuo, K. K., "Experimental Studies of Boron Particle Combustion," *8th International Symposium on Transport Phenomena in Combustion,* July, 1995.
2. Yeh, C. L. and Kuo, K. K., "Theoretical Model Development and Verification of Diffusion/Reaction Mechanisms of Boron," *8th International Symposium on Transport in Combustion,* July, 1995.
3. Macek, A. and Semple, J. M., *Combustion Science and Technology,* 1:181–191 (1969).
4. King, M. K., in *Combustion of Boron-Based Solid Propellants and Solid Fuels.* K. K. Kuo (Editor), p. 1.
5. Glassman, L., Papas, P., and Brezinsky, K., "A New Definition and Theory of Metal Pyrophoricity," *Combust. Sci. Technol.* 83:161–165 (1992).

•

Prof. Alon Gany, Tecnion-Israel Inst. of Technology, Israel. From the paper it seems that transport phenomena in the liquid B_2O_3 layer are insignificant. However, I believe that at lower particle temperatures diffusion of species within the liquid layer might play an important role. Could you please comment on this?

Author's Reply. The current model was developed and exercised here specifically to compare with experiments on boron-ignition that typically occurred in environments above 1700 K. Because of the low volatility of liquid B_2O_3 layer at the lowest temperatures studied, the transient thickness of the layer results primarily from a competition of chemical reactions at the boron/boron oxide interface and the boron oxide/gas interface. For a gas phase which includes hydrocarbon combustion products, the gaseous species surface reaction rate is much greater than the diffusion-controlled rate at the boron/boron oxide interface even at a low particle temperature. If the gas phase oxidants are limited to oxygen without the presence of H-containing species, it is plausible that there are situations in which at a low particle temperature, the reaction rates at the boron oxide/gas interface may become slower than those at the boron/boron oxide interface. In this particular case, the transport phenomena in the liquid B_2O_3 layer may become significant. It should also be noted that the current model excludes chemical reactions within the oxide layer, a phenomena which may also be important at low temperatures.

Twenty-Sixth Symposium (International) on Combustion/The Combustion Institute, 1996/pp. 1919–1927

EVOLUTION OF PARTICLE TEMPERATURE AND INTERNAL COMPOSITION FOR ZIRCONIUM BURNING IN AIR

I. E. MOLODETSKY[1], E. L. DREIZIN[2] AND C. K. LAW[1]
[1]*Princeton University*
Department of Mechanical and Aerospace Engineering
Princeton, NJ 08544, USA

[2]*AeroChem Research Laboratories, Inc.*
Princeton, NJ 08542-0012, USA

An experimental study of single zirconium particle combustion in air is presented, with emphasis on understanding the mechanism causing particle temperature jumps and the subsequent explosions. The experiment involved generating uniform, ~200 μm-size particles of controlled initial temperature by a pulsed micro-arc, letting them burn in air in free fall, measuring their instantaneous temperatures with a three-wavelength optical pyrometer, quenching the burning particles during various stages of burning, and subsequently analyzing the particles' internal compositions using a high-resolution X-ray electron microprobe. Special techniques were developed to separate out the radiation from the gas-phase luminous zone in the temperature determination, and to rapidly quench the particles in order to freeze their internal composition. Results show that during combustion, the particle temperature first increases and then decreases; oxygen and nitrogen are dissolved in the particle interior whereas no oxide (or nitride) shells or inclusions have been detected. The maximum particle temperature is considerably less than the boiling temperatures of Zr and ZrO_2. It is demonstrated that the occurrence of the particle temperature jumps and explosions is due to the attainment of the eutectic state within the particle interior, which leads to the precipitous formation of solid αZr and ZrO_2 from supersaturated Zr-O solution, with simultaneous heat release and nitrogen gas release.

Introduction

Studies on metal particle combustion in oxidizing environments have been primarily motivated by fire safety issues and by metal used as additives in solid and liquid propellants [1–3]. For zirconium particle combustion, most of the research was conducted in the sixties and seventies by Nelson and coworkers [4–7]. A distinguishing feature of Zr particle combustion which emerged from such studies was the appearance of sudden brightness and temperature jumps or "spearpoints," on the particle streaks, as well as possible explosions that terminated the particle burning. It was suggested [5,6] that these spearpoints were associated with the crystallization of supercooled molten ZrO_2 particles, while the particle explosions were caused by the nitrogen release from the zirconium oxynitride formed during the combustion process. The possibility that the particle explosion was caused by zirconium solidification was ruled out based on the very high values of the measured brightness temperatures [4–6].

It is significant to note that while processes occurring within the particle interior were suggested to be responsible for the spearpoints and explosions, there have not been any direct quantitative measurements of the temporal variations of the particle internal composition. Furthermore, it appears that the brightness temperature measurements reported previously [4–7] were obtained with inadequate pyrometer calibration, and were also not corrected for radiation from the external gas-phase luminous zone surrounding the particle. Since this external luminous zone significantly increases the radiating surface, the measured value could imply a higher particle temperature. In particular, since the maximum measured temperature was found to be higher than the melting point of ZrO_2, it became a crucial element in the proposed supercooling mechanism responsible for the occurrence of spearpoints [4,5].

The phenomena of temperature jumps and particle explosions were recently also observed in the combustion of Mo, W, Ta, Cu, and steel particles in oxidizing environments [8,9]. It was proposed that these phenomena could be caused by oxygen dissolution into the burning metal particle and the subsequent transformation of the metal-gas solution into stoichiometric oxide.

In view of the above considerations, we have performed an experimental investigation on Zr particle combustion in oxidizing environments with the following focuses. First, since the temporal evolution

of the particle composition is a crucial feature in the phenomena of interest, we have performed careful experimentation in acquiring the quenched samples whose internal composition was subsequently determined using state-of-the-art analytical instrumentation. Second, since the processes occurring within the particle interior and, consequently, the particle composition are intimately coupled to the particle temperature, we have also accurately determined the particle temperature history by properly accounting for the interference effects from the luminous zone surrounding the particle. We shall demonstrate in due course that such a close coupling between the particle temperature and composition indeed exists, and that a coherent mechanism for the observed phenomena of temperature jump and explosion can be offered based on these measurements.

Experimental

A schematic of the apparatus for the production and ignition of uniform metal particles can be found in Ref. 10. The experimental procedure includes generating and igniting a freely falling molten metal particle, measuring the temporal evolution of its temperature and velocity, quenching and collecting the particle by various means, measuring its size, and analyzing its interior composition. The specifics of the different components of the experimentation are briefly discussed in the following. Details can be found in Ref. 11.

Particle Generation

Metal particles were formed and ignited using a pulsed micro-arc that melts the edge of a consumable wire electrode and separates molten particles from the wire as described elsewhere [10]. An argon flux (approximately 0.5 cc/s) was directed perpendicular to the particle trajectory in order to shield the electrode unit and prevent wire ignition. Extensive experiments and analysis were performed for particles with an initial size of 240 μm, with $\pm 4\%$ standard deviation. The initial temperature of the particles can be adjusted over a wide range above the metal melting point, hence providing a means to ignite particles instantly upon entering an oxygen-containing environment. Instabilities in ignition caused by the nonuniformity of the oxide layer on the wire surface were circumvented by electroplating a thin copper coating of thickness less than 1 μm on the wire surface. There was no noticeable difference in the combustion behavior, including the particle temperature and composition histories, by using either uncoated or copper-coated wire electrodes.

Temperature Measurements

Color temperatures of burning particles were measured in real time using a three-wavelength pyrometer which included an iris, a fiber optics trifurcated bundle, three interference filters, and three HC120-01 Hamamatsu photomultipliers. The wavelengths of the interference filters were chosen so that no bands observed in the Zr-O and Zr-N spectra [12] could contribute to the measured signals. The pyrometer has been calibrated using a tungsten strip-lamp providing a maximum blackbody temperature of 2377°C. Two filter sets were used: (a) 589, 532, and 510 nm; and (b) 589, 458, and 510 nm. These provided two experimental series, during which two different color temperatures were measured independently. A comparison between the two simultaneously measured temperatures provided a criterion for the correctness of the measurements: their agreement indicated that the radiation spectrum was close to that of a graybody.

Preliminary experiments found a significant disagreement (~350°C) between the two color temperatures for burning Zr particles. Additional testings on copper particle combustion, which did not have an external luminous zone of gas-phase combustion, indicated that the observed difference for the Zr particles was caused by the presence of this luminous zone. In order to spatially resolve the optical signals produced by a burning particle and its surrounding external luminous zone, we used a slot array positioned between the burning particle trajectory and the pyrometer. These slots were 205 μm wide, equally spaced, and perpendicular to the particle velocity vector so that the radiation of a burning particle moving behind the slots was registered as a series of pulses. The form of the pulses revealed separate peaks due to radiation from the particle surface and from the external luminous zone (insert in Fig. 1). Detailed temperature curve analysis then showed that a period existed when the two inferred temperatures agreed well for each radiation pulse produced by the surface of a burning particle crossing a single slot (Fig. 1). This temperature was taken to be equal to that of the burning particle surface and, hence, the burning particle, because it is reasonable to assume temperature uniformity within the metal particle interior.

Particle Quenching

In physical quenching, it is essential to ensure that the composition of the particle does not change during quenching, especially if a phase transition could occur during this period. Previously, particles were quenched by introducing them into an inert gas [9]. Because of the low cooling rate, a significant redistribution of oxygen over the particle interior and the formation of different oxide modifications could

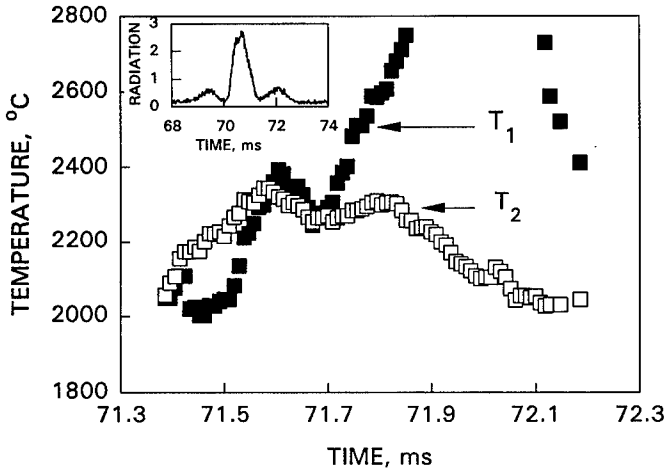

FIG. 1. Two color temperatures independently measured for a 240 μm diameter Zr particle crossing a 205 μm slot at a velocity of 0.94 m/s. Insert: radiation pulse produced by a 240 μm diameter Zr particle crossing a 205 μm slot at a velocity of 0.94 m/s.

have occurred during quenching. This possibility is confirmed by recognizing that, for a diffusion coefficient of oxygen in zirconium, $D \sim 3 \cdot 10^{-8}$ m^2/s (estimated as $D = 5.2 \exp(-25{,}577/T)$ [13] at the combustion temperature of 2350°C), the characteristic diffusion time within a 200-μm particle is 0.3 s, which is comparable to the quench time in the inert gas as determined from the measured particle temperature history. Thus, much faster quenching is needed to preserve the internal structure of the burning particle during quenching. Following but modifying the well-known "splat" methods of rapid cooling of metal droplets [14] used to produce metal glasses, which could have cooling rates as high as 10^6 K/s due to the high heat conductivity of metals, we have quenched the particles on an aluminum foil (12 μm thick) which has the additional advantage of not distorting the particle shape. The interaction between the burning particle and the foil resulted in welding the particle into the foil upon impact. Usually, the particle penetrated approximately half of the way through the foil and was "frozen" there without apparent shape distortion. Diameters of the particles quenched at different combustion times were measured with an accuracy of $\pm 5\%$ using an optical microscope. Quench times measured from particle radiation curves recorded using the three-wavelength pyrometer varied in the range of 0.6–5ms, depending on the particle temperature and composition. These times are considerably smaller than that needed for oxygen to diffuse through the particle interior. The actual diffusion length is of the order of $L = (Dt)^{1/2}$ which is ~4–12 μm for the experimental range of quench times. This is comparable to the spatial resolution of the electron microprobe analyzer and, thus, is adequate for our experiment.

For comparison, particles were also quenched in an inert (Ar) environment separated from air by a thin soap-bubble film [9]. Adjusting the film height and monitoring the radiation of the particle moving in the inert gas allowed us to predetermine and measure the time of quenching and the cooling rate in each experiment. The cooling time of the metal particles in Ar varied from 50 to 150 ms. In several experiments, nitrogen was used as an inert gas to address the role of metal-nitrogen interactions.

Electron Microprobe Analysis

An electron microprobe analyzer (Cameca SX50) was used to examine the particle cross sections, and an energy-dispersive spectroscopy (EDS) detector (Princeton Gamma Tech.) and a wavelength-dispersive spectroscopy (WDS) scan were utilized to determine the internal composition of the particles. Calibration of the X-ray spectrometer used pure metal samples, metal oxides, and nitrides as standards. Special consideration was given to account for the "background" oxygen level which is always measured in metal samples due to the thin surface oxide film formed in atmospheric air [11].

Results

General Observations

Experiments were conducted with 180- and 240-μm initial diameter particles burning in air, with combustion times of 150 and 250 ms, respectively. No qualitative difference in the combustion behavior was observed for particles of different sizes. While radiation measurements were conducted for particles of both sizes, only the quenched samples of the 240-μm particles were cross-sectioned and studied using the electron microprobe analyzer.

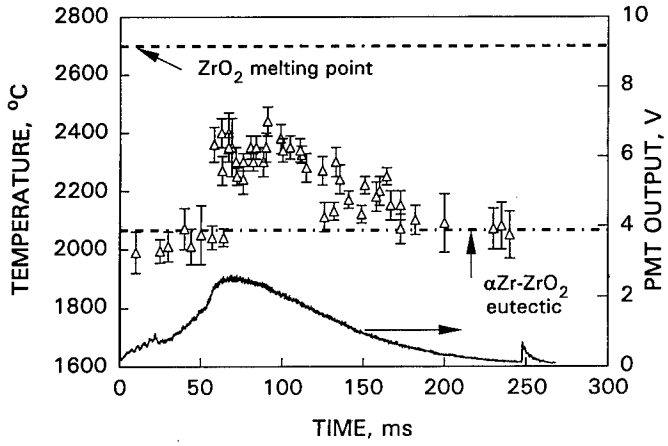

FIG. 2. Radiation and temperature histories of 240 μm diameter Zr particles burning in air.

Visual observations of the present burning sequence agreed well with those reported earlier (e.g., Refs. 4–7) in that particle ignition was followed by gradually increasing and then decreasing radiation output, and termination of the combustion event by spearpoints and strong explosions. Residues collected after the particle explosion consisted of white and transparent ZrO_2 microspheres (~1–50 μm diameter).

Spatially resolved radiation measurements using the slot array and photographs of particle streaks consistently showed a luminous zone surrounding the burning Zr particle, similar to that observed in Ref. 7. The size of the luminous zone correlated well with the size of the smoke clouds observed on traces of particles quenched on foil or glass slides. The cloud was spherically symmetric upon ignition but lost its symmetry as combustion progressed. During the entire particle combustion period, the radiation intensity from the luminous zone was considerably less than that from the particle surface.

No significant change in the particle diameter was observed during combustion. The particle diameter seemed to be slightly increased (ca. 10%), although the extent was close to the experimental scatter, including the ±4% initial particle size nonuniformity. The particles could have also suffered minor deformation upon quenching.

Particle Temperature

Figure 2 shows the trace of the radiation from a burning Zr particle, as well as its temperature history (triangles) which was determined, reproducibly, from several particles crossing the slot array. Each experimental point shows where the two simultaneously measured temperatures became consistent for different pulse sequences recorded for single particles crossing the slots.

Results show that the initial temperature was close to 2000°C, which is above the Zr melting point of 1852°C. The maximum particle temperature of 2380 ± 80°C was well below the ZrO_2 melting point (2700°C). It is of particular significance to note that the particle temperature approached the temperature for the eutectic αZr formation, 2065°C [15], shortly before particle explosion at 250 ms, indicated by the spike in the radiation trace. The particle temperature itself, however, could not be meaningfully determined at the state of explosion.

These measured temperatures are considerably lower than the particle temperatures reported earlier [4–7] through brightness measurements in which no correction for the external luminous zone radiation was made, but based on which the mechanism of particle explosion was proposed [5,6].

Internal Structure and Composition

The internal structure of the particles quenched on Al foil was homogeneous at early combustion times, but consisted of two mixed and finely divided phases near the end of combustion. The WDS measurements revealed the presence of dissolved oxygen and nitrogen in the particle interior, while no oxide or nitride shells, or inclusions, were observed with the ~1-μm resolution defined by the microprobe electron beam diameter.

Figure 3a shows an example of the cross section of a particle quenched on Al foil at 180 ms after ignition. The phase distribution in the particle of Fig. 3a is shown in Fig. 4a. It is seen that the local oxygen and nitrogen concentrations varied in opposite phases, that is, the oxygen concentration was higher in regions where the nitrogen concentration was lower, and vice versa. Furthermore, the average total concentration of dissolved oxygen and nitrogen was nearly constant across the particle interior, indicating uniformity of the particle internal composition. The measured concentrations of oxygen and

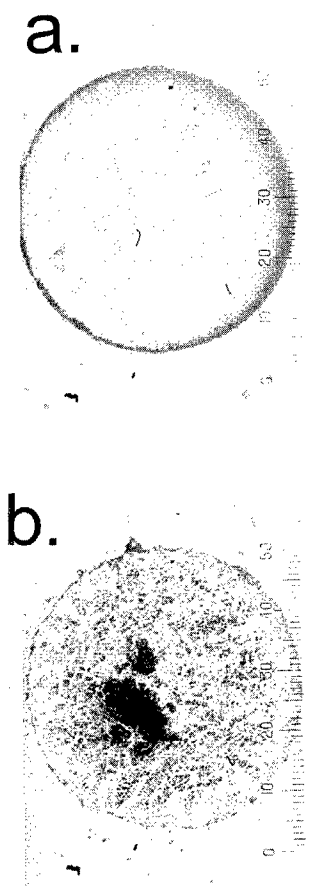

FIG. 3. Cross sections of partially burned Zr particles of 240 μm initial diameter. (a), A particle rapidly quenched in aluminum foil at 180 ms; (b), a particle slowly quenched in argon at 120 ms.

nitrogen did not correspond to either the stoichiometric oxide or the nitride of zirconium.

Because of spatial uniformity of the particular composition, we could readily determine its temporal variation as burning progressed. Figure 5 shows that the average concentration of dissolved oxygen gradually increased, while the average nitrogen concentration increased to almost 20% and then slightly decreased to about 10%.

Particle Internal Structure and Temperature in an Argon Environment

The internal structure and composition of particles quenched in an Ar atmosphere differed significantly from those quenched rapidly on Al foil. Internal voids were observed (Fig. 3b) when the time of particle combustion in air exceeded ~60 ms. Further, the particle interior always consisted of two distinct phases, namely, stoichiometric ZrO_2 and a ZrO_xN_y solution, with $0.1 < x < 0.9$ and $0.1 < y < 0.3$. The phase distributions for the particle of Fig. 3b are shown in Fig. 4b. One can see that there is a greater radial variation in the concentrations of the dissolved gases for the present slowly quenched sample than that obtained with rapid quenching (Fig. 4a). This shows clearly that, given enough time, some phase separation process had occurred and significantly transformed the internal structure of the particle. However, the average dissolved gas concentrations measured for particles quenched after different combustion times in argon agreed well with those measured for particles quenched rapidly after the same combustion times. These average concentrations were determined using particle cross-section images produced with the electron backscattering technique. In such images, the darkness is proportional to the concentration of the dissolved gas. The details of the image processing are discussed in Ref. 11.

Color temperatures were also measured for burning particles introduced in Ar. They showed that when the particle combustion time in air exceeded ~100 ms (for 240-μm diameter particles), brightness and temperature jumps occurred during cooling. The amplitude of the temperature jumps varied from 20 to 130°C, and no particles exploded. The temperature at which the jumps were initiated was repeatable and was close to 2065°C (±50°C), the temperature of the eutectic formation of αZr in a binary Zr-O system.

The introduction of burning particles into the N_2 environment resulted in combustion quenching similar to that observed in Ar.

Discussion

Summarizing the results reported above, we have experimentally shown that the burning of zirconium particles in air is characterized by (1) absence of surface oxide or nitride layers and internal oxide inclusions; (2) progressive increase of oxygen concentration in the particle interior; (3) gradual increase and then saturation of nitrogen concentration in the particle interior; (4) the occurrence of brightness and, by implication from the quenching results in the argon atmosphere, temperature jumps when the particle temperature reached about 2065°C while the internal oxygen concentration reached about 60%; and (5) some form of gas-phase reaction as evidenced by the external luminous zone. The present study did not address the nature of the gas-phase and surface reactions, the coupling between them, and the mechanism through which oxygen enters the particle interior. Some preliminary progress has been made [11] but substantially more work is

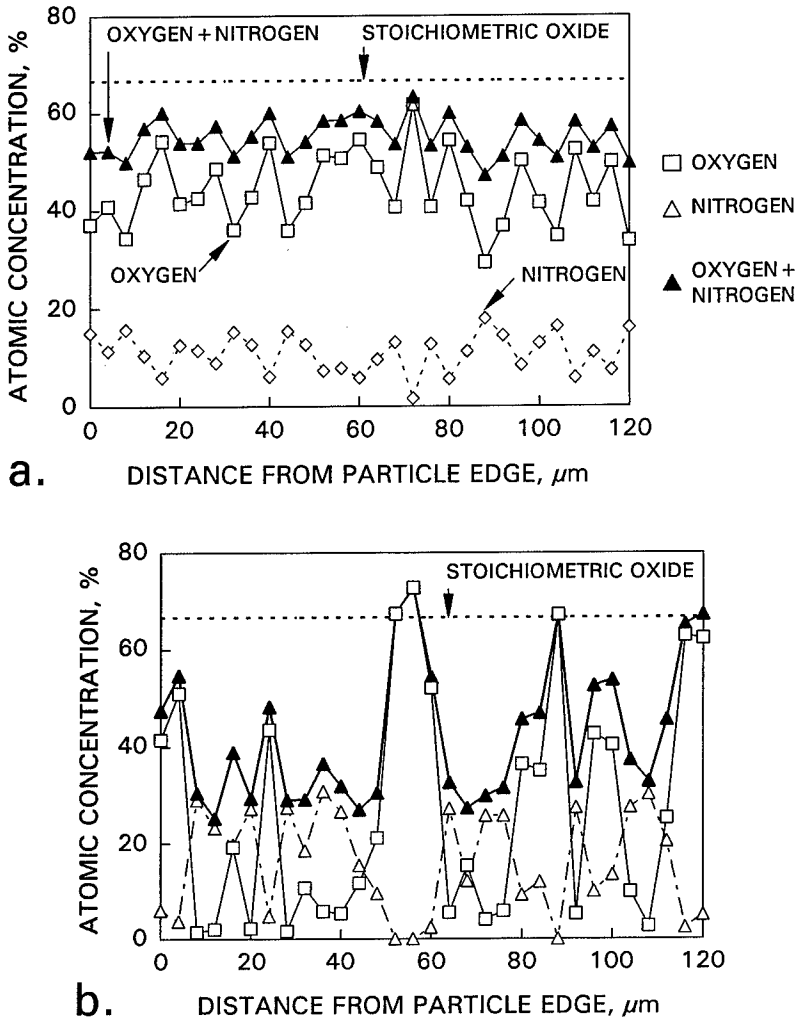

FIG. 4. Distribution of species over the radius of quenched Zr particles of 240 μm initial diameter. (a), A particle rapidly quenched in aluminum foil at 180 ms; (b), a particle slowly quenched in argon at 120 ms.

needed. On the other hand, the present study has provided sufficient evidence to suggest a new mechanism for the interaction between liquid zirconium and oxygen, as well as factors leading to the occurrence of spearpoints and explosions, to be discussed in the following.

The discussion can best be carried out by considering the phase diagram of the Zr-O-N system. Unfortunately, there is no reliable reference data characterizing a ternary system of Zr-O-N at high temperatures, although binary Zr-O and Zr-N phase diagrams have been described and are, in fact, quite similar [15]. Zr is able to dissolve significant amounts of both oxygen and nitrogen, and the structures of solid Zr-O and Zr-N solutions are similar: both O and N atoms are accommodated by octahedral interstices of the metal lattice [16]. Since higher oxygen (as compared to nitrogen) contents have been measured in Zr particles, and since Zr-O interaction is expected to be the key process, we shall base our discussion on the Zr-O phase diagram, shown in Fig. 6, with the assumption that the presence of the small amount of nitrogen would not significantly affect the validity of our discussion.

In Fig. 6, we have superimposed a pathline for the evolution of the Zr particle temperature and oxygen concentration as given by Figs. 2 and 5, respectively. Since experimental sampling could be performed only up to 200 ms, while the particle explosion occurred at about 250 ms, the concentration of atomic oxygen at 250 ms was estimated through linear extrapolation. Referring to Fig. 6, we see that when

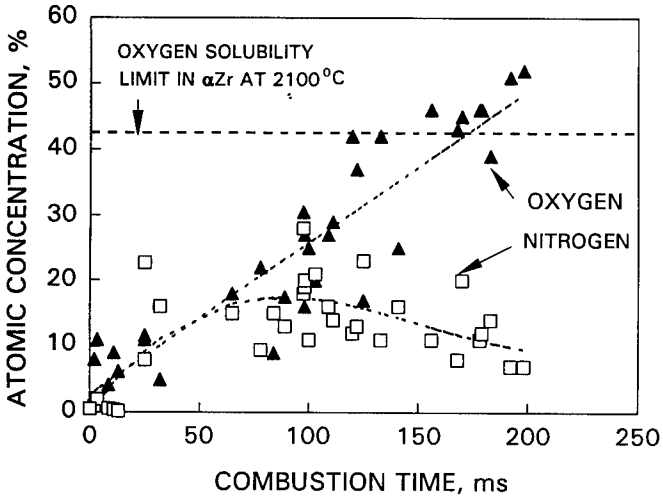

FIG. 5. Internal composition history of 240 μm diameter Zr particles burning in air.

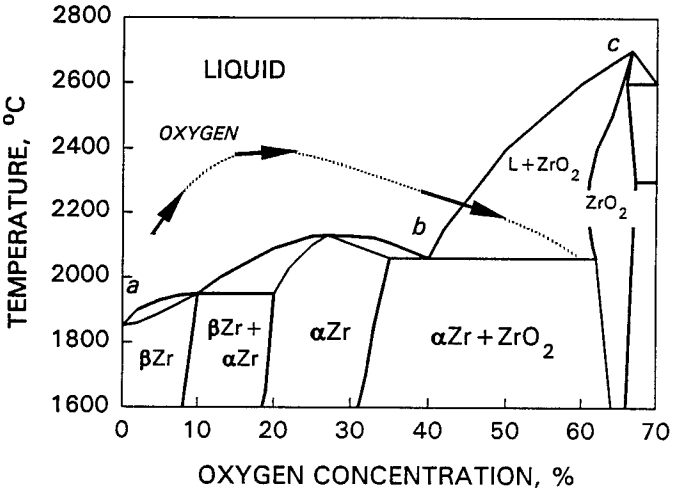

FIG. 6. Zr-O phase diagram [15] and the pathline showing changes in experimental dissolved oxygen concentration and temperature for a burning Zr particle (240 μm diameter).

the molten pure Zr particle is initially exposed to oxygen, it has a temperature higher than the melting point of Zr, 1852°C, and is therefore thermodynamically situated above the *ab* line on the phase diagram. The particle temperature subsequently increases and then decreases, forming the pathline as shown. Before the particle crosses the *bc* line, the equilibrium state of the particle is a liquid Zr-O solution. Stoichiometric oxide can be formed only after the oxygen concentration exceeds the solubility limit, varying from 40 to 66%, along the line *bc*, depending on temperature. Note that if oxygen diffusion in liquid zirconium were slow compared to its uptake, a gradient of the oxygen concentration would have been established in the burning particle. This would have resulted in the rapid saturation of the solution near the particle surface and the subsequent formation of an oxide surface layer. However, since our experiments did not reveal either an oxide layer or any noticeable dissolved gas concentration gradient in the rapidly quenched particles (Fig. 3a), it is reasonable to suggest that diffusion of the dissolved gas in the liquid metal was faster than the oxygen uptake, and a homogeneous metal-gas solution formed and existed in the burning particle.

When the *bc* line is crossed, the system will consist of two phases, namely, a saturated solution and solid stoichiometric oxide, provided it attains thermodynamic equilibrium. This composition was, indeed, observed for particles quenched in Ar because there was sufficient time for the system to reach equilibrium. The stoichiometric oxide, however, was not observed for particles rapidly quenched on the Al foil, as shown in Fig. 3a, indicating that thermodynamic equilibrium was not actually attained in the particle interior even at a burning time of 200 ms.

Instead, a supersaturated Zr-O solution was formed, in which the dissolved oxygen concentration was greater than the solubility limit but lower than that of the stoichiometric ZrO_2. Such a phase is metastable.

At the burning time of 250 ms, brightness jumps and particle explosions were observed. At this instant we see that (Fig. 6) the particle temperature reached the eutectic transition level (~2065°C) at which the equilibrium solubility limit of oxygen in zirconium is sharply decreased and the solid solution (αZr) starts to form. Additional oxygen is freed and, thus, the rest of the liquid instantly becomes even more supersaturated, causing the formation of stoichiometric oxide. This is an exothermic reaction and is, therefore, associated with heat release sufficient to cause a temperature jump [17]. Furthermore, nitrogen gas is released and voids are formed in the particle when the stoichiometric ZrO_2 oxide precipitates out of the ZrO_xN_y solution. When these processes occur in an oxygen-containing atmosphere, fresh αZr surface is instantly produced and further reacts with the ambient oxygen. The attendant temperature increase then leads to expansion of the gas in the voids and, consequently, explosion. The above mechanism, therefore, provides a viable link between the observed temperature jumps, production of voids in the particle interiors, and particle explosions with the attainment of the eutectic state in the particle interior.

Concluding Remarks

The present investigation has resulted in two specific aspects of contribution. First, we have developed special experimental techniques for the accurate and meaningful determination of the instantaneous particle temperature and internal composition. It is clear that without using the three-wavelength pyrometry with slotted blockage we would have obtained temperatures that would lead to completely erroneous interpretation of the mechanism for particle explosion—a difficulty that caused earlier studies to attribute this event to the supercooling of molten ZrO_2. By the same token, without using aluminum foil for rapid quenching, we might not have recognized the existence of Zr-O solution, including the metastable, supersaturated solution. These techniques are expected to be useful for future studies of metal particle combustion.

Second, we have experimentally shown that a liquid Zr-O solution forms in burning Zr particles, and the concentration of dissolved oxygen eventually exceeds the solubility limit. It was identified that the mechanism for the onset of temperature jumps and particle explosions is the attainment of the supersaturated Zr-O solution to the eutectic state, with the attendant precipitous formation of the stoichiometric oxide, release of nitrogen gas, and further reaction of zirconium with the ambient oxygen to cause explosion.

Acknowledgments

The work at AeroChem and Princeton University were, respectively, funded by the NASA Lewis Research Center under Contract NAS3-27259 and by the Office of Naval Research under Contract No. N00014-94-1-0613. The authors wish to thank Dr. H. F. Calcote of AeroChem, and Mr. D. Johnson, Dr. E. Vicenzi, and Mr. D. L. Zhu of Princeton University for technical discussions and assistance.

REFERENCES

1. Hertzberg, M., Zlochower, I. A., and Cashdollar, K. L., *Twenty-Fourth Symposium (International) on Combustion,* The Combustion Institute, Pittsburgh, 1992, pp. 1827–1835.
2. Price, E. W., in *Fundamentals of Solid Propellant Combustion,* (K. K. Kuo and M. Summerfield, Eds.), AIAA, New York, 1984, pp. 479–514.
3. King, M. K., in *Combustion of Boron-Based Solid Propellants and Solid Fuels,* (K. K. Kuo and R. Pein, Eds.), CRC Press, Ann Arbor, pp. 1–80.
4. Nelson, L. S., *Eleventh Symposium (International) on Combustion,* The Combustion Institute, Pittsburgh, 1967, pp. 409–416.
5. Nelson, L. S., Rosner, D. E., Kurzius, S. C., and Levine, H. S., *Twelfth Symposium (International) on Combustion,* The Combustion Institute, Pittsburgh, 1968, pp. 59–70.
6. Levine, H. S., *High Temp. Sci.* 3:237–243 (1971).
7. Marshall, R. L., Nelson, L. S., and Richardson, N. L., *Combust. Flame* 13:216–219 (1969).
8. Dreizin, E. L., Suslov, A. V., and Trunov, M. A., *Combust. Sci. Technol.* 87:45–58 (1992).
9. Dreizin, E. L., Suslov, A. V., and Trunov, M. A., *Combust. Sci. Technol.* 90:79–99 (1993).
10. Suslov, A. V., Dreizin, E. L., and Trunov, M. A., *Powder Technol.* 74:23–30 (1993).
11. Molodetsky, I. E., M.S. Thesis, Department of Mechanical and Aerospace Engineering, Princeton University, 1996.
12. Pearse, R. W. B. and Gaydon, A. G., *The Identification of Molecular Spectra,* Halsted Press, New York, 1976.
13. Kofstad, P., *High-Temperature Oxidation of Metals,* John Wiley & Sons, New York, 1966.
14. Duwez, P., Willens, R. H., and Klement, W., *Nature* 187:189–199 (1960).
15. Massalski, T. B., Okamoto, H., Subramanian, P. R., and Kacprzak, L. (Eds.), *Binary Alloy Phase Diagrams,* ASM Publ., Materials Park, OH, 1990.
16. Fast, J. D., *Interaction of Metals and Gases,* Academic Press, New York, London, 1965.
17. Molodetsky, I. E. and Dreizin, E. L., in *Decomposition, Combustion, and Detonation Chemistry of Energetic Materials,* MRS Symp. Proceedings, (T. B. Brill, T. P. Russel, W. C. Tao, and R. B. Wardle, Eds.), MRS, Pittsburgh, 1996, Vol. 418, pp. 195–200.

COMMENTS

F. A. Williams, UCSD, USA. I do not believe the error bars on your temperature measurements. You are trying to interpret pyrometric results obtained in an environment having very large temperature variations and gradients in two-phase flow. It is unreasonable to expect accuracies better than 500 K, irrespective of reproducibility of agreement of three-wavelength results. You have not analyzed radiation transport in two-phase flow, which you need to do if you are to try to interpret your results.

Author's Reply. The authors agree that the temperature measurement of burning zirconium particles was not trivial due to the presence of external luminous zone, or, a two-phase system which was seen by the pyrometer. However, since that was understood, special care was taken to account for this additional radiation. In addition to the description of experimental technique and results given in the paper, we reiterate two major points. First, the intensity of the external zone radiation was considerably smaller than that of particle surface, as was indicated by photo and video images. This difference in the radiation intensities could be seen even better from the radiation signals measured for particles crossing the slots (Fig. 1, insert). A simple estimate shows that the radiation of external luminous zone contributed less than 5% of the total radiation measured by the pyrometer when a burning particle filled a slot, i.e., when the temperature measurements were actually taken. Thus, particle surface was the primary source of the radiation signal used to determine the particle temperature. The second, and in our opinion, the most important argument is that using six different wavelengths chosen specifically to eliminate possible Zr-O and Zr-N radiation bands yielded repeatable color temperatures. This is direct evidence that the spectrum of the signal measured was similar to that of a gray body, and thus was characterized by a definitive temperature. This temperature was measured and the accuracy of these measurements is shown by the error bars in Fig. 2.

Twenty-Sixth Symposium (International) on Combustion/The Combustion Institute, 1996/pp. 1929–1936

IGNITION AND COMBUSTION OF BULK TITANIUM AND MAGNESIUM AT NORMAL AND REDUCED GRAVITY

ANGEL ABBUD-MADRID, MELVYN C. BRANCH AND JOHN W. DAILY
Center for Combustion Research
Mechanical Engineering Department
University of Colorado
Boulder, CO 80309-0427, USA

An investigation of the effect of gravity on ignition and combustion of metals has been conducted with bulk titanium and magnesium samples. A 1000-W xenon lamp irradiates the top surface of cylindrical specimens, 4 mm in diameter and 4 mm high, in a quiescent, pure-oxygen environment at 1 atm. Reduced gravity is obtained from an aircraft flying parabolic trajectories. Values of critical and ignition temperatures are obtained from thermocouple records. Qualitative observations and propagation rates are extracted from high-speed cinematography. Emission spectra of gas-phase reactions are obtained with an imaging spectrograph/diode array system. High applied heating rates and large internal conduction losses generate critical and ignition temperatures that are several hundred degrees above the values obtained from isothermal experiments. Because of high conduction and radiation heat losses, no appreciable effect on ignition temperatures with reduced convection in low gravity is detected. Lower propagation rates of the molten interface on titanium and of ignition waves on magnesium are obtained at reduced gravity. These rates are compared to theoretical results from heat conduction analyses with a diffusion/convection controlled reaction. The close agreement found between experimental and theoretical values indicates the importance of the influence of natural convection-enhanced oxygen transport on combustion rates. Lower oxygen flux and lack of oxide product removal in the absence of convective currents appear to be responsible for longer burning times of magnesium diffusion flames at reduced gravity. The accumulation of condensed oxide particles in the flame front at low gravity produces a previously unreported unsteady explosion phenomenon in bulk magnesium flames. This spherically symmetric explosion phenomenon seems to be driven by increased radiation heat transfer from the flame front to an evaporating metal core covered by a porous, flexible oxide coating.

Introduction

Recently, metal combustion studies at the University of Colorado have focused on the effects of gravity (g) on the ignition and burning behavior of bulk metals. The impetus behind this effort is the understanding of the ignition conditions and flammability properties of structural metals found in oxygen (O_2) systems for space applications. Since spacecraft are subjected to higher-than-1 g loads during launch and reentry and to a zero-gravity environment while in orbit, the study of ignition and combustion of bulk metals at different gravitational accelerations is of great practical concern. From the scientific standpoint, studies conducted under low gravity conditions provide simplified boundary conditions, since buoyancy is removed, and make possible the identification of fundamental ignition and combustion mechanisms.

The influence of microgravity on the burning of bulk metals has been investigated by Steinberg et al. [1] in a drop tower simulator. All metals and alloys tested (including titanium and magnesium) supported combustion in the absence of gravity. In general, the study found that in microgravity, the upward regression rate of the melting surface of a metal rod is significantly faster than in normal gravity.

From a review of some of the theoretical models of bulk metal combustion [2–4], it is believed that gravity plays an important role in heat and mass transport processes that dominate metal-oxygen reactions. The possible significance of convection on mass transfer rates and on the outward transport of condensed oxides in vapor-phase metal diffusion flames was first mentioned by Brzustowski and Glassman [5].

This investigation is intended to provide experimental verification of the influence of natural convection on the burning behavior of metals. In addition, the study offers the first findings of the influence of gravity on ignition of bulk metals and on the combustion mechanism and structure of metal-oxygen, vapor-phase diffusion flames.

Titanium (Ti) and magnesium (Mg) metals were chosen because of their importance as elements of

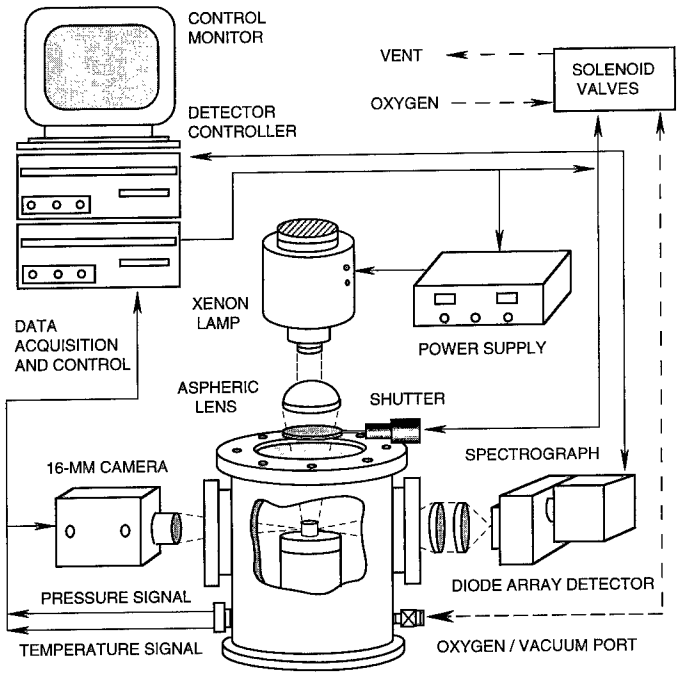

FIG. 1. Schematic diagram of the experimental system.

structural materials and their simple chemical composition—pure metals instead of multicomponent alloys to simplify chemical and spectroscopic analyses. In addition, these elements present the two different combustion modes observed in metals: heterogeneous or surface burning (Ti) and homogeneous or gas-phase reaction (Mg). Finally, Mg, Ti, and their oxides exhibit a wide range of thermophysical and chemical properties.

Metal surface temperature profiles, critical and ignition temperatures, propagation rates, and burning times are obtained under normal and reduced gravity. Visual evidence of all phenomena is provided by high-speed photography. A qualitative description of the unique behavior of homogeneous, vapor-phase metal flames in low gravity is presented with a discussion of the possible controlling mechanisms.

Experimental System and Procedures

A schematic of the experimental system used is shown in Fig. 1. The ignition source consists of a 1000-W xenon lamp that generates a highly collimated beam (4° half angle) with broadband radiation (300–1100 nm). An aspheric lens focuses the beam to provide a 1.75-MW/m^2 power density on the top surface of a 4 mm-diameter and 4 mm-high metal specimen that sits on an alumina holder. An electric shutter permits effective control of heating time. A 4.5-L, stainless steel, cylindrical combustion vessel houses the lens, metal specimen, and alumina holder. Optical access for the movie camera and spectrograph is provided through two fused-silica side windows, while a third window is used for sample replacement. Ti and Mg metal specimens (99.95% purity) are placed in an oxygen environment (99.6% min.) at an absolute pressure of 1 atm. Evacuation and filling of the vessel is accomplished with a series of computer-controlled solenoid valves. The chamber pressure is monitored with a solid-state piezoresistive transducer. The surface temperature is measured with a 0.125 mm diameter, Type *R* thermocouple attached to the outer wall of the sample. A second thermocouple is sometimes used in different locations to measure temperature gradients within the sample.

A high-speed, 16 mm movie camera provides surface and flame visualization; the images are also used for measurement of propagation rates. With a 7.5° shutter and speeds up to 500 frames/s, exposure times as short as 1/20,000 s are obtained. A 50 mm lens and various extension tubes are used for image magnification. In addition to visible light imaging, time- and space-resolved spectral information on gas-phase reactants and products is obtained with an imaging spectrograph and a 1024-element diode array detector. Various spectral ranges are covered with two motorized gratings (300 and 2400 grooves/mm). The output signal from the detector is processed by an external controller that delivers a 15-bit dynamic range and a 150-Hz readout rate with direct memory access.

The experiment is controlled entirely by a computer, a digital/analog data acquisition board, and an interface code written in graphical programming software. In a typical run, the complete sample assembly (clean metal specimen mounted in alumina holder with attached thermocouple) is introduced into the chamber. Five evacuation and filling cycles are executed to provide a pure-oxygen atmosphere inside the vessel. The lamp is adjusted to the desired output power and the computer signals the shutter to open when the target gravity level (measured from a three-axis accelerometer located near the chamber) is achieved. Data acquisition starts (with 1-ms resolution), and the signal from the thermocouple is used to trigger all events. Immediately after ignition, the shutter is closed to remove all external heating to the sample. Temperature, pressure, energy input, gravity level, high-speed photography, and emission spectra are monitored throughout the experiment. After complete combustion, the final pressure is recorded to quantify oxygen consumption, and the burned or quenched samples are stored for chemical composition studies.

The low-gravity experiments were conducted onboard the NASA-Lewis DC-9 Research Aircraft in Cleveland, Ohio. Up to 20 s of reduced gravity ($+/-0.01\ g$) were available in a single parabolic maneuver. Ten tests were conducted for each metal and gravity level to ensure experimental repeatability.

Results and Discussion

Heating and Ignition Behavior

Figure 2 shows temperature profiles of Ti and Mg samples heated in O_2 at 1 atm. During the heating phase, all curves exhibit an increasing temperature with an intermediate plateau corresponding to the α–β solid-phase transition in Ti and the solid–liquid phase change in Mg. Occurrence of the critical temperature (T_{crit}) marks the point at which heat generation from surface oxidation equals heat losses from the sample. A short time after T_{crit} is exceeded, a sudden change in the heating rate at the ignition temperature (T_{ign}) coincides with the appearance of a luminous reaction front. The limit on the maximum operating temperature of thermocouples (2000 K) makes it impossible to measure combustion temperatures (above 3000 K).

In the case of Ti, a significant increase in the heating rate following the phase transformation near 1100 K signals the transition from a parabolic to a linear oxidation rate. Soon after, enhanced external oxidation produces rapid visible changes in surface texture and coloration, as seen in Fig. 3a. As T_{crit} is exceeded (around 1700 K), the metal specimen undergoes thermal runaway (even if the heat source is removed), leading to ignition on the upper surface

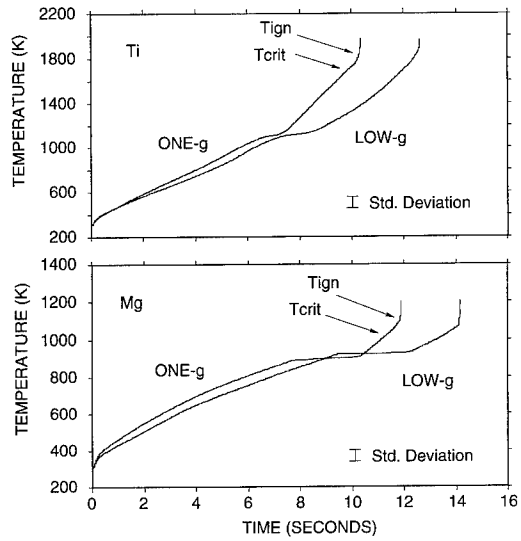

FIG. 2. Surface temperature profiles of bulk Ti (top) and Mg (bottom) specimens in pure O_2 at 1 atm during the heating and ignition stages under normal and low gravity conditions.

at a few degrees below the melting temperature of Ti, 1933 K.

For Mg, the transition from a parabolic to a linear oxidation rate occurs before melting (around 800 K), as evidenced by the rapid formation of a white layer of magnesium oxide (MgO) around the outer surface of the sample (Fig. 4a). At normal gravity, the sample collapses after melting of the inner metal. The outer MgO layer remains in the solid phase and continues its growth as the temperature resumes its rise. Once T_{crit} is reached (near 1050 K), the oxide coating turns black and rapidly stretches in one direction until ignition occurs in the hottest spot (Fig. 4b). In the low gravity case, the specimen slowly grows upward, raising the high-temperature upper surface as a result of volumetric expansion after melting. As T_{crit} is exceeded, the top surface temperature rises exponentially as predicted by a kinetic-controlled oxidation rate. Vapor pressure increases and the sample rapidly stretches upward as the metal temperature approaches the boiling point of Mg (1380 K). Ignition occurs when enough Mg vapor reacts with oxygen to generate a visible flame on the sample top (Fig. 4b). In both the normal and low gravity cases, the thermocouple (not seen in Fig. 4) is located at the bottom of the sample to prevent its detachment from the continuously distorting upper surface. Therefore, T_{ign} shown in Fig. 2 is approximately 200 K below the actual T_{ign} (1300 K) in the top surface—as measured by a second thermocouple used in probing tests. The lag is caused by the rapid rise in temperature after T_{crit} compared to the longer diffusion time in the metal.

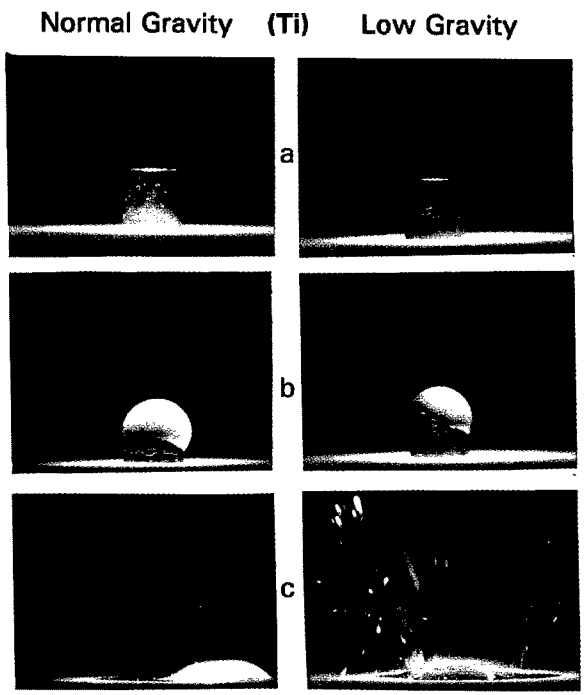

FIG. 3. Sequence of high-speed photographs of the heating, ignition, and combustion events of bulk Ti specimens in pure O_2 at 1 atm under normal and low gravity conditions. (a) Heating and surface oxidation (around 1400 K); (b) steady-state propagation (200 ms after ignition); (c) particle shower and fragmentation during combustion.

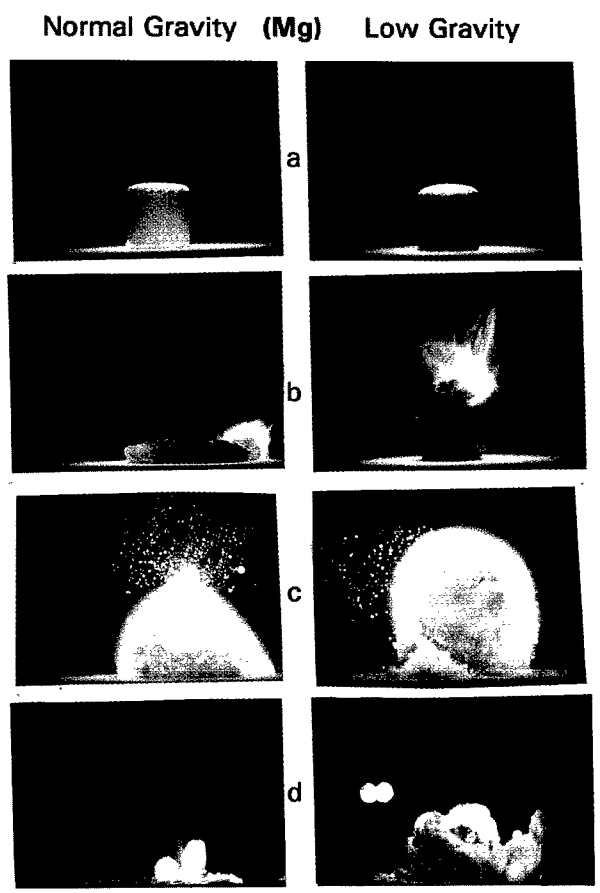

FIG. 4. Sequence of high-speed photographs of the heating, ignition, and combustion events of bulk Mg specimens in pure O_2 at 1 atm under normal and low gravity conditions. (a) Beginning of melting stage (around 923 K); (b) ignition wave propagation (7 ms after ignition); (c) fully developed combustion; (d) end of combustion.

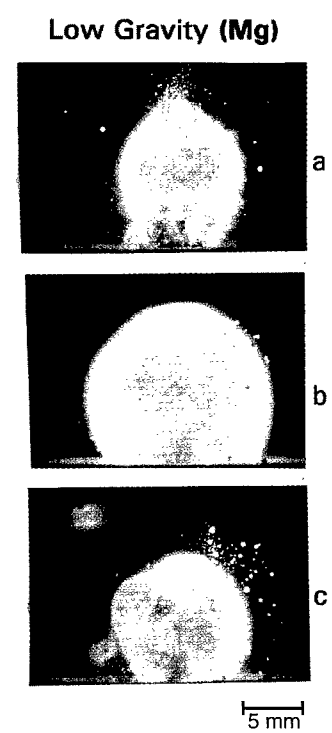

FIG. 5. Radiation-Induced Metal Explosion (RIME) in a bulk Mg specimen at low gravity. (a) Start of cycle; (b) maximum flame diameter; (c) oxide layer explosion.

For both metals under normal and low gravity conditions, higher critical and ignition temperatures are obtained than the values reported in the literature [6,7]—more than 200 K above the highest measured temperatures for bulk metals. The disparity stems from the high heating rates applied in this investigation (above 100 K/s in the early stages), which are required for fast ignition during the low gravity time available in the aircraft. Although the applied heating rate is only 15% higher than the experimentally determined minimum ignition heat flux, it exceeds by two orders of magnitude the linear heating rates used for near-isothermal studies. The high heating rate applied to the top surface of the metal creates a significant temperature difference within the specimen (around 40 K in Mg and 150 K in Ti). In addition, the surrounding gas and vessel walls remain at a temperature close to ambient during the fast heating phase. As a result, higher T_{crit} and T_{ign} values are obtained as the large increase in internal conduction and radiation heat losses overcomes the phase-change contributions to heat generation that generally determine ignition of Mg and Ti in isothermal experiments.

The apparent lack of influence of gravity on T_{crit} and T_{ign} is another consequence of the high value of conduction (for Mg) and radiation (for Ti) heat losses versus natural convection heat loss present at these temperatures. A general theoretical model was developed to calculate the effect of low gravity on T_{crit} for a metal sample subjected to conduction, convection, and radiation heat losses, as well as heat generation by oxidation. For our experimental conditions, the model shows a reduction of approximately 10 K on T_{crit} at low gravity, a small value that is within experimental uncertainty.

Combustion Behavior

Titanium

After ignition at a point on the top outer rim of the sample, a molten mass consisting of a mixture of metal and oxides starts traveling across the upper surface of the specimen. Steady-state downward propagation of a spherical mass follows in a smooth, nonexplosive fashion until reaching the alumina base. The average steady-state propagation rates measured for the normal and low gravity cases are 16.2 mm/s and 8.7 mm/s, respectively. A steady regression behavior during this period at 1 g suggests that the propagation velocity has not been altered significantly by the influence of the gravity force on the molten mass—as confirmed by its spherical shape in Fig. 3b. Furthermore, a calculation of the Bond number (Bo = gravitational force/surface tension force) under these conditions results in values below 0.1. Evaluating the ratio of propagation velocities at normal (V_n) and low (V_l) gravity gives a value of 1.86.

Following a theoretical approach similar to the one used for gaseous flame propagation, several studies [3,4] have obtained an expression of the form $V \sim (w)^{1/2}$ to calculate the propagation velocity V along metal cylinders undergoing heterogeneous surface burning with a rate of reaction w. Considering the diffusion and convection of O_2 to the sample as the rate-limiting step, the reaction rate becomes proportional to $w \sim (Gr)^{1/4}$, where Gr is the Grashof number. The propagation velocity then depends on Gr as $V \sim (Gr)^{1/8}$, so that $V \sim (g)^{1/8}$. Evaluating V_n/V_l for the normal (1 g) and low gravity ($+/-0.01$ g) cases, a theoretical ratio of 1.78 is obtained. The close agreement between experimental and theoretical ratios of propagation velocities indicates the importance of the influence of natural convection-enhanced oxygen transport on combustion rates.

Upon reaching the end of steady-state propagation, the spherical molten mass is destroyed by the liquid-solid interfacial force as it touches the alumina holder. Once in the alumina base, Ti exhibits a more vigorous reaction with random outward expelling of small particles undergoing gas-phase reactions and multiple fragmentation (Fig. 3c).

Magnesium

Following the first flash generated by the Mg-O_2 homogeneous reaction, an ignition wave runs through the sample driven by the difference between the flame temperature (near 3430 K, the vaporization-decomposition point of MgO [8]) and the temperature of the unreacted metal, which is near the Mg boiling point. The average ignition wave speeds measured for the normal (V_n) and low (V_l) gravity cases are 220 mm/s and 115 mm/s, respectively. If the approximation used to compare propagating velocities in Ti rods is used to evaluate the V_n/V_l ratio of ignition wave speeds of Mg (similarly assuming a diffusion/convection controlled reaction rate), close agreement is again found between the experimental (1.91) and the theoretical (1.78) values. Owing to the irregularly shaped, porous oxide layer surrounding the sample—a consequence of metal melting before ignition—no attempt was made to calculate surface regression rates. Instead, an evaluation of burning times and a qualitative discussion of important phenomena is given.

From the visible images and emission spectra measurements, the structure of the luminous flame that engulfs the sample after the passage of the ignition wave is in general agreement with the extended reaction zone model from Glassman et al. [2]. An inner region of Mg-O_2 vapor-phase reaction is followed by MgO condensation in the bright white flame front observed in the photographs. However, a thin green emission band and a wider outer diffuse blue zone are visible in addition to the prescribed features from the model (Fig. 4c). This radiation

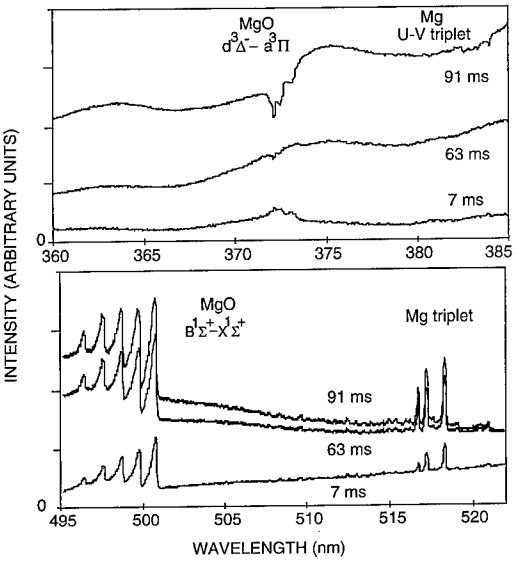

FIG. 6. Time-resolved emission spectra from the UV (top) and green (bottom) systems of the Mg-O_2 gas-phase reaction at 1 atm in low gravity at 7 ms (start of ignition), 63 ms (end of ignition wave propagation), and 91 ms (fully developed combustion) after ignition.

may come from excited metal vapor created by oxide dissociation in the high-temperature front, by fine oxide particles, and possibly by Mg-O_2 heterogeneous reactions occurring in the oxide surface in a lower temperature region [9].

The spectroscopic measurements show similar behavior in the normal and low gravity cases. The familiar UV and green systems of MgO and Mg appear as the major radiation contributors. However, an interesting feature was captured by time-resolved spectroscopic measurements during the ignition wave propagation. Figure 6 shows the sequence of spectra for the UV and green systems from the onset of ignition to fully developed combustion in a low gravity experiment. The UV bands of MgO and the UV Mg triplets appear in emission during the early stages of the ignition process, followed by an absorption and emission equilibrium toward the end of the ignition phase. The line and band systems later exhibit reversal to absorption against an intense continuum background during fully developed combustion. In contrast, the green system of MgO and the green triplets of Mg appear in emission at all times. Although no conclusive explanation can be given at this time, it is believed that the reversal may be caused by the transition from chemiluminescence from early ignition reactions to thermal excitation of products in an extended reaction zone with background radiation from condensed oxides.

During fully developed combustion, buoyancy-generated convection currents are responsible for the main differences observed in the two cases investigated. At 1 *g*, high convection currents enhance burning by increasing O_2 flux to the reaction zone and by removing oxide products that may constitute a barrier to O_2 diffusion (Fig. 4c). The proximity of the resulting flame front to the metal sample is an indication of fast burning rates. In comparison, at low gravity conditions, the severe reduction of convection—threefold by the $(Gr)^{1/4}$ dependence—and the increased resistance to O_2 diffusion by combustion products diminish the oxygen transport. Figure 4c shows a broader, particle-laden outer blue zone (undisrupted by convection currents) and a larger flame front detachment.

While in 1 *g* the products are swept upward by buoyancy-induced currents, condensed oxides rapidly accumulate and agglomerate in the reaction front at low gravity, producing a highly radiant flame front. Sporadic removal occurs only for large-diameter particles expulsed by inertial forces and residual accelerations during the reduced-gravity trajectory (*g* jitter). Particle accumulation may account for the unique unsteady, spherically symmetric explosion phenomenon observed at low gravity—which we refer to as Radiation-Induced Metal Explosion (RIME). As shown in Fig. 5, a high particle density in the flame front generates a large heat flux to the sample. This effect raises the surface temperature and increases metal evaporation; the flexible oxide membrane that keeps Mg at temperatures below its boiling point expands as vapor pressure builds up inside the metal core. As evaporation increases, so does the flame front diameter to accommodate greater oxygen flux and maintain the stoichiometry. At the peak of the cycle, the amorphous specimen is transformed into a spherical core with twice the size of the original cylinder (Fig. 5b). Finally, the oxide layer explodes and breaks in multiple points (creating small jets), relieving its internal pressure and reducing its size while ejecting a large number of particles in the process (Fig. 5c). The RIME cycle may repeat several times during the burning stage. Although RIMEs are not observed at normal gravity, explosions and jets are still induced at 1 *g* by localized pressure bursts where the flame gets too close to the sample.

Burning times vary widely depending on the number of jets and explosions that accelerate combustion. Nevertheless, the average burning time at low gravity (4 s) is around twice the average value at 1 *g*. In some cases, longer burning times at low gravity may also result from the reduced reaction area produced by oxide walls surrounding the sample. These large oxide structures are built from condensed particles in the flame front using the alumina holder as an anchoring point (Fig. 4d).

Conclusions

An investigation of the effects of reduced gravity on the ignition and combustion of radiatively ignited

Ti and Mg bulk metals has been conducted in pure O_2 at 1 atm pressure. Reduced gravity is obtained from an aircraft flying parabolic trajectories.

High applied heating rates and large internal conduction losses into the metal sample generate critical and ignition temperatures that are several hundred degrees above the values obtained from isothermal experiments. Because of high conduction and radiation heat losses, no appreciable effect on ignition temperatures with reduced convection in low gravity is detected. These findings are important from a fire-safety standpoint, since a large number of practical situations involve ignition by fast external heating.

Lower regression rates of the molten interface on Ti rods and slower propagation rates of the gas-phase ignition wave on Mg specimens are observed at reduced gravity. These rates are compared to theoretical results from heat-conduction analyses with a diffusion/convection controlled reaction. The close agreement found between experimental and theoretical values indicates the importance of the influence of natural convection-enhanced oxygen transport on combustion rates.

The lower propagation rates observed at low gravity in this study differ from the higher regression rates in microgravity given by Steinberg et al. [1]. The disagreement arises from the different experimental configurations used. In Ref. 1, propagation rates are measured for cylindrical rods ignited at the bottom. The increase in regression rates in microgravity is attributed to an increase in the temperature of the retained molten mass; cyclical detachment of this mass occurs during upward propagation at 1 g. The influence of the gravity force on the molten mass (whose detachment subsequently reduces heat transfer to the unreacted metal) is apparently greater than the influence of buoyancy-induced convection on oxygen transport to the reaction zone. In our investigation, only the latter influence is evaluated by comparing the propagation rate at low gravity with the 1 g steady-state downward propagation rate at low Bond numbers.

Convection currents also affect the burning of Mg diffusion flames. Lower oxygen flux and increased resistance to O_2 diffusion by oxide products appear to be responsible for the longer burning times observed at reduced gravity. The formation of oxide walls around the sample may also contribute to prolonged burning by reduction of the reaction area. The accumulation of condensed oxide particles in the flame front at low gravity produces a unique, unsteady, spherically symmetric explosion phenomenon in bulk Mg termed Radiation-Induced Metal Explosion (RIME). The explosions seem to be driven by increased radiation heat transfer from the flame front to an evaporating metal core covered by a porous, flexible oxide coating.

Acknowledgments

This work was supported by the National Aeronautics and Space Administration, Grant NASA-NAG3-1685. Special thanks go to Wesley Ramm and David Bunting, both senior undergraduate students from the University of Colorado, who helped with the structural design and software development of the ICOM project.

REFERENCES

1. Steinberg, T. A., Wilson, D. B., and Benz, F. J., in *Flammability and Sensitivity of Materials in Oxygen-Enriched Atmospheres,* Vol. 6, ASTM STP 1197 (Janoff, D. D. and Stoltzfus, J. M., Eds.), American Society for Testing and Materials, Philadelphia, 1993, pp. 133–145.
2. Glassman, I., Mellor, A. M., Sullivan, H. F., and Laurendeau, N. M., *AGARD Conference Proceedings,* Vol. 52, Paper 19, 1970.
3. Leibowitz, L., Baker, L. Jr., Schnizlein, J. G., Mishler, L. W., and Bingle, J. D., *Nuclear Sci. Engineering* 15:395–403 (1963).
4. Hirano, T., Sato, K., Sato, Y., and Sato, J., *Combust. Sci. Technol.* 32:137–159 (1983).
5. Brzustowski, T. A. and Glassman, I., in *Heterogeneous Combustion: AIAA Progress in Astronautics and Aeronautics,* Vol. 15 (Wolfhard, H. G. et al., Eds.), Academic Press, New York, 1964, pp. 75–116.
6. Mellor, A. M., Ph.D. Thesis, Princeton University, Department of Aerospace and Mechanical Sciences, 1968.
7. Breiter, A. L., Mal'tsev, V. M., and Popov, E. I., *Combust. Explosion Shock Waves* 13:475–485 (1977).
8. Glassman, I. and Papas, P., *J. Mater. Synthesis Proc.,* 2:151–159 (1994).
9. Markstein, G. H., *Eleventh Symposium (International) on Combustion,* The Combustion Institute, Pittsburgh, 1967, pp. 219–234.

COMMENTS

Robert F. Chaiken, DOE/Pittsburgh Research Center, USA. I do not understand what you mean by ignition in this experiment. Is it the start of self-propagation? It seems to me you are forming a coherent surface oxide which heats the solid metal until it melts and vaporizes, bursting the coating.

Author's Reply. The ignition process described in this study begins when the critical temperature, T_{crit}, is reached, i.e., when the heat generated by the oxidation reaction equals the heat losses from the metal surface. After a delay time (during which self-heating occurs) the ignition temperature, T_{ign}, is achieved. This temperature is identified as the point where a visible flame appears or where a temperature runaway is detected by the thermocouple. The ignition process ends when self-propagation (combustion) begins (see Fig. 2).

The coherent surface oxide that forms prior to ignition may become porous or non-protective at a temperature (known as the transition temperature, T_{trans}) lower than T_{crit} (as in the case of Mg and Ti). After T_{trans}, ignition is then solely controlled by the competition between heat losses and heat generation at the surface.

•

Prof. Alon Gany, Technion-Israel Inst. of Technology, Israel. The paper reveals some interesting phenomena during the ignition of bulk metals. However, it seems the ignition process as described was very much dependent on the experimental setting and procedure, and the results might not yield universal conclusions. For instance, what would be the ignition sequence when applying very high heat flux? Could ignition take place prior to a total melting of the sample?

Author's Reply. Since the ignition of metals is a process controlled by the competition between heat generation vs. heat losses, T_{crit} and T_{ign} are therefore strongly dependent on the experimental setting. These temperatures are not an absolute property of the metal and their value is a function of variables such as sample size and heating technique. In experiments performed with Mg in pure O_2 at 1 atm under near-isothermal conditions [6] (or slow linear temperature rise), the critical temperature (in the order of 850 K) and ignition take place before the melting of the sample (T_{melt} = 923 K). In the present investigation, the high heating rate (two orders of magnitude higher than in the aforementioned experiments) applied to bulk Mg samples in O_2 at 1 atm generates a large internal conduction heat loss that results in critical and ignition temperatures above the melting point of Mg (see Fig. 2).

•

I. Glassman, Princeton University, USA. I do not see any difference in the ignition characteristic in gravity of μg experiments. What your video shows is that the destruction of the growing oxide layer on the surface of the Mg configuration controls the ignition process. When this layer is destroyed combustion begins in the vapor phase as Mellor proposed in 1968. The reason for the difference in burning of Mg is due to the physical configuration chosen and how gravity affects this configuration as it melts. Thus a flat plate or pool of Mg would show no effect of gravity on burning.

The Ti burning is also not controlled by gravity but surface tension as you stated; however the size of the Ti cylinder chosen determines the burning rate as an uninhibited solid propellant strand and has a burning rate determined by size. The larger the size Ti cylinder chosen the slower the overall consumption rate because the ratio of the cylinder surface area to the cross-section decreases.

Overall, then microgravity affects the physical characters of the Mg melt and not the vapor-phase combustion.

Author's Reply. There was indeed no appreciable difference in the critical and ignition temperatures between normal and reduced gravity. This is due to the small contribution of the convective heat loss to the total heat losses from the metal surface—which are dominated by the internal conduction heat transfer. As Mellor stated in 1968 [6], since "... the critical and ignition temperatures are defined in terms of heat losses from the reaction surface, these temperatures are expected to depend strongly on the environment experienced by the metal sample". Therefore, in an experiment where convection heat losses were the dominant heat loss mechanism, their elimination in microgravity (μg) would noticeably affect T_{crit} and T_{ign}. As for the vapor-phase burning of Mg, we believe that regardless of the gravity effects on the physical configuration of the melt, convection plays a significant role on the transport of O_2 to the reaction zone. Not only does the lower O_2 flux reduce the burning rate in μg, but the accumulated condensed oxides act as a barrier for O_2 diffusion to the reaction zone. These effects may explain the longer burning times of Mg in μg. In addition, RIMEs (observed exclusively at μg) also appear to be caused by oxide accumulation in the absence of convective currents.

For Ti under our experimental configuration, the spherical shape (and the reaction surface) of the molten mass is maintained at normal gravity by the dominance of surface tension over gravity. However, the lack of convective transport of O_2 to the surface in μg is responsible for the lower propagation speeds. It is true that the size of the sample determines the burning rate, and that is the reason why Ti samples of the same size were used in both the normal and low gravity experiments.

Twenty-Sixth Symposium (International) on Combustion/The Combustion Institute, 1996/pp. 1937–1944

MODELING OF SOLID PARTICLE INTERACTION IN A HIGH-VELOCITY, HOT GAS STREAM

M. M. ELKOTB
Faculty of Engineering
Cairo University, Egypt

N. SALAMA AND I. NASSEF
Arab Industrial Authority
Sakr Factory, Egypt

A detailed mathematical model for predicting ignition characteristics of an accelerated solid-particle parcel of various loading ratios in the gas flow behind shock waves in an actual motor environment is developed using the moving coordinate system. The model incorporates the effect of evaporation, radiation, and loading ratio on the drag and heat transfer to the solid particles and their effect on the ignition delay period. Moreover, it considers momentum wall losses, heat transfer to the wall, and viscous work done by the wall on the fluid. The present model responds to the shock wave intensity, loading ratio, and metal powder size. The solid particles investigated include magnesium, aluminum, and solid propellant. A parametric study has been carried out to study the factors affecting the ignition delay of metal powder. Results show that for shock intensities ranging between 2.5 and 4, magnesium and aluminum powder of sizes 30 and 14-μm are ignited by the thermal explosion mechanism. Small particles have also been found to accelerate up to the induced gas velocity behind the shock wave, resulting in higher ignition delay periods. Results have also been validated from experimental data in the literature, and reliable chemical kinetic constants have been deduced for Mg and Al, respectively: $A = 2.4 \times 10^4$ and 1×10^6 cm^2/s, $E = 2.0 \times 10^2$ and 3.7×10^2 kJ/mole, and $Q = 4.7 \times 10^4$ and 1.67×10^4 kJ/kg.

Introduction

Modeling of a reactive gas-solid mixture flow is important for solid propellant metallized admixture, air-breathing rockets, and pyrotechnic igniters. Such metallized solid propellant is used to improve the ignition and combustion quality.

Analytical and experimental studies of pure and binary alloys [1–16] have been conducted to clarify and improve the ignition and combustion processes of metal particles. These efforts have not proved entirely satisfactory because most of the experimental results have been strongly affected by the experimental conditions under which most authors deduced that their experimental results are far from the real conditions for solid propellant combustion in a rocket motor.

Baek et al. [17] have investigated theoretically the shock-wave ignition of dust particles, considering particle acceleration, subsequent convective heating, and chemical exothermic surface reaction in the pores and on the particle surface. Asymptotic analysis for a limit of large activation energy was carried out for spherical particles, with constant average values of the gas recovery temperature and the convective heat transfer coefficient. Klement et al. [18] and Gordon [19] have investigated flux dust mixed with quartz as inert gas and found that the addition of inert particles caused a linear decrease of the detonation wave velocity. Volyan [20] gave a brief review of ignition and combustion of organic dusts. Researches on shock-wave ignition of particles carried out at the University of Michigan during the last two decades have been summarized by Kauffman et al. [21]. Lee et al. [22] studied the detonability of RDX dust in air/oxygen mixtures and showed that detonation can be induced with particles 37 μm in size in an 88% air–12% O_2 mixture. A theoretical model was developed to explain the effect of particle size on the detonability of a dust/oxidizer mixture. Elkotb et al. [23] studied ignition of organic dust behind a shock wave and found that the particle concentration has a great effect on the ignition pressure and the ignition delay. Shtertser [24] showed that the oxide thickness on the particle surface for aluminum-based alloy granules has a significant effect on the magnitude of the shock wave pressure. Exact analytical solutions for particular values of the dust loading ratio and heat capacity were obtained by Pike [25] for the flow of a gas carrying dust particles through a shock wave, neglecting temperature variations within the particle.

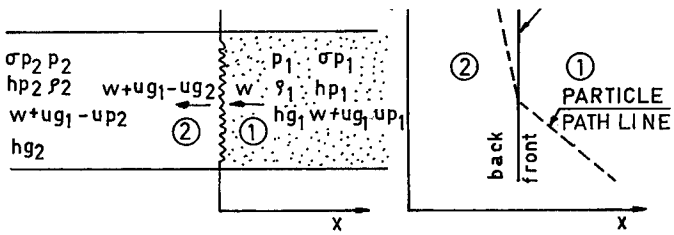

FIG. 1. Transformation to a moving coordinate system and shock wave flow.

There have been successful attempts [3,5,26] to model solid-gas interaction. However, analysis has been reduced to the consideration of a single, accelerating, spherical particle without considering the surrounding effect on the drag and heat transfer. Increase of the loading ratio decreases the shock-wave velocity and pressure, which directly affect the ignition delay period. Moreover, momentum wall losses, heat transfer to walls, and viscous work done by the wall on the fluid have not been considered. Neglecting these factors together with the particle size, surrounding particles, and temperature gave conditions quite far from the real case in an actual motor environment. It is also noted that all theoretical studies suffer from a lack of reliable chemical kinetics data.

The present work deals with a more comprehensive theoretical study for metal powder ignition under dynamic conditions. A prediction model has been built to detect the ignition delay period of accelerated, spherical, metal particles behind a shock wave, considering all the mentioned parameters. Equations for unsteady particle heat transfer, and particle equations of motion coupled with the conservation equations are developed. Parametric study has been carried out to identify factors affecting the ignition delay of metal powder. Reliable kinetic data have been obtained for the ignition of aluminum and magnesium powder.

Basis for the Model

The propagation of shock through the gas-particle mixture creates a relaxation zone behind the shock where momentum and heat transfer occurs. This is followed by the equilibrium zone and the nonequilibrium (frozen) zone where there are lags for velocity and temperature between the gas and particles.

Immediately after the shock passage, each particle is in supersonic flow, and bow shocks stand ahead of the particles, introducing a recovery temperature T_f. The resultant convective heating causes a rapid increase in the particle surface temperature. At the same time, drag forces cause the particle to accelerate with an accompanying reduction in the relative velocity and rate of convective heating. Thermal explosion occurs whenever the heat evolved from the chemical reaction is greater than the dispersed heat to the gas and it reaches a critical ignition temperature. The following assumptions are involved:

1. A dilution two-phase flow is considered and, consequently, uniformly distributed, discrete, spherical particles with constant loading ratio are dealt with.
2. The particle cloud is considered a continuum that is one dimensional without mutual interaction, as the particle density is much greater than the gas density interaction and the average local mean quantities are calculated. In this case, the conservation equations of continuity and momentum are in complete agreement with the gas dynamical equations.
3. Turbulent fluctuations of solid particles are neglected.
4. The particle relaxation time is long enough that the particles are unaffected when passing through the constant-speed shock.
5. Chemical reaction takes place at the particle surface and its rate is described by an overall, one-step reaction.

Mathematical Formulation and Solution Method

Considering a constant-speed plane wave with constant strength, and employing a moving coordinate system (Fig. 1), the governing conservation equations supplemented by the addition of wall effect have been detected. The explicit equations [27,28] describing the gas-phase velocity and thermodynamic properties for the initial stagnant mixture in the driven section are extracted.

$$U_{p1} = U_{g1} = 0$$

$$A_1 U_{g2} + B_1 U_{g2} = C_1 \qquad (1)$$

where, $A_1 = 0.5 - (C_p/R)_2$

$$B_1 = (C_p/R)_2\,(W\{1 - 1(C_p/R)_2\} - D_1)$$

$$D_1 = h_{g1}/[W(C_p/R)_1] - W_L/(\rho_1 W) + K\,U_{p2}$$

$$C_1 = h_{g1}\,[1 - (C_p/R)_2/(C_p/R)_1] + K[(h_{p1} - h_{p2}) + U_{p2}(W - U_{p2}/2 - W(C_p/R)_2)] - (Q_w - Q_s - WW_L(C_p/R)_2)/(\rho_1 W)$$

$$h_{g2} = h_{g1} + 0.5\, U_{g2}(2W - U_{g2}) + K[(h_{p1} - h_{p2}) + U_{p2}(W - U_{p2}/2)] - (Q_w - Q_s)/(\rho_1 W) \quad (2)$$

$$P_2 = P_1 + \rho_1 W(U_{g2} + KU_{p2} - W_L/(\rho_1 W) \quad (3)$$

The losses due to wall effects are defined as:

1. momentum losses,

$$W_L = (2X/D_h)\,(C_f\rho_2\,(W - U_{g2})^2)$$

2. heat transfer losses to the wall,

$$Q_w = 2X/D_h(C_f\rho_2)\,(W - U_{g2})\,(h_{g2} + (W - U_{g2})^2/2 - h_w) \text{ and}$$

3. viscous work done by the wall on the fluid

$$Q_s = (2X/D_h)\,(C_f\rho_2\, W(W - U_{g2})^2)$$

and $C_f = 0.079\,(Re)^{-0.25}$

Particle Momentum Equation

Knowing that each particle is independent of other particles in the cloud, the analysis reduces to a single, accelerating, spherical particle moving in a supersonic flow. The particle momentum equation can be written as follows:

$$dU_{p2}/dt = -3\, C_D\rho_2/(8r\rho_s)(U_{p2} - U_{g2})(U_{p2} - U_{g2}) - (F_m + F_B)/m_s \quad (4)$$

The drag coefficient C_D is given by [29]

$$C_D = C_{D,C} + (C_{D,FM} - C_{D,C})\exp(-ARe^N)$$

where, $C_{D,C}$ and $C_{D,FM}$ are continuum and free molecular values of drag coefficient, respectively, while A and N are empirical functions of the particle Mach number. The apparent mass force acceleration of the fluid around the particle, F_m, and the Basset force, F_B, are small and can be neglected.

Particle Thermal Balance Equation

For shock-induced ignition, there is insufficient time for diffusion to occur, and a heterogeneous reaction at the particle surface causes ignition. Then, the equation describing the heating process of the metal particle can be written as

$$dT/dt = 3\, Q/Cr(d\delta/dt) + 1.5\,\lambda_g\, Nu(T_f - T)/(\rho_s Cr^2) + 3\sigma\varepsilon(T_f^4 - T^4)/\rho_s C - Q_{vap}/m_s C \quad (5)$$

where the change in oxide layer thickness is given by [5]

$$d\delta/dt = AC_{ox}\exp(-E/RT)/\delta^n$$

$n = 0$ for Mg and $n = 1$ for Al, and the Nusselt number [12] is described by

$$Nu = 2\alpha_1 + 0.459\alpha_2 Re^{0.55}Pr^{0.33}$$

where, $\alpha_1 = e^{-M_{sh}}/(1 + 17M_{sh}/Re)$ and $\alpha_2 = 2/3\,(1 + 0.5e^{-17M_{sh}/Re})$.

The effect of the evaporation losses on the calculation can be estimated from the ratio $Q_{vap}/Q_{conv} = L_v Le 10^5 \exp(-L_v/RT)/(C_p PNu(T_f - T))$.

Taking the following values for Mg: $Le = 1$, $L_v = 132$ kJ/mole, $C_p = 28.9$ kJ/mole, $R = 8.313$ kJ/mole, and P in the range 2–10 bars, the evaporation losses were found to be maximum. These losses did not exceed 2% at lower shock Mach numbers, i.e., at lower $(T_f - T)$ and at higher values of particle temperature (of more than 800 K) and can therefore be neglected. For Al, the protective oxide layer yields no evaporation from the metal.

Regarding the radiation losses, it is estimated from the ratio

$$Q_{rad}/Q_{conv} = 2\sigma\varepsilon\Psi T_f^3 r/\lambda_g Nu$$

where $\Psi = 1 + T/T_f + (T/T_f)^2 + (T/T_f)^3$. Taking $\varepsilon = 0.4$, $\lambda_g = 8.37 \times 10^{-2}$ W/m K, the shock Mach number in the range 2–6, $Nu = 15$–5, then Ψ will be in the range 1.5–3, and $(T/1000)^3$ in the range 10–1 K, so the term Q_{rad}/Q_{conv} will be in the range $(0.5{:}3)\,10^{-3}\,r$, and can be neglected for particles less than 100 μm.

Whenever the thermal conductivity of solid propellant particles is relatively low, the temperature within the particle will not be uniform and, in this case, the thermal balance equation is reduced to the heat conduction equation

$$\partial T/\partial t = (\alpha/r^2)\,(\partial r^2/\partial r)\,(\partial T/\partial r)$$

subjected to the boundary condition

$$\lambda_p \partial T/\partial t_{r=R} = h(T_f - T_R) + Q\rho_s d\delta/dt + \sigma\varepsilon(T_f^4 - T_R^4) \quad (6)$$

Initial and Boundary Conditions

The initial values for gas flow properties behind the shock, U_{g2}, P_2, and h_{g2}, and the shock speed W are required for the solution of the problem. For the shock-tube flow (Fig. 1), it is assumed that the flow pattern has properties immediately after the diaphragm is broken, and the traveling rarefaction wave $U_3 = 0$ [28], $U_{g2} = U_{g4}$, and $P_2 = P_4$, considering the flow is isentropic, then

$$U_{g2}/C_3 = 2/(\gamma - 1)\,(1 - (P_2/P_3)^{(\gamma-1)/2\gamma}) \quad (7)$$

initially, the particles start to move from zero velocity so that $U_{p2} = 0$ and $h_{p2} = h_{p1}$, and momentum heat and shear losses W_L, Q_w, and Q_s are negligible. The initial gas properties and shock speed can be determined from the following equations:

TABLE 1
Thermal and chemical properties of metals and solid propellant powder used in parametric study

Properties	Composite solid propellant	Aluminum	Magnesium
Density (g/cm^3)	1.6	2.7	1.74
Heat capacity (J/g K)	1.26	1.17	1.13
Thermal conductivity (J/cm s)	3.6×10^{-3}	1.26	1.26
Heat of combustion (kJ/kg)	4.1×10^3 [30]	16.7×10^3 [31]	22.2×10^3
Oxidation law $d\delta/dt =$	$AC_{ox} \exp(-E/RT)$;	$A\delta^{-n}(P/P_0)^{0.45} \exp(-E/RT)$	$AC_{ox} \exp(-E/RT)$
Pre-exponential factor (cm^2/s)	1×10^{12} (s^{-1}) [30]	0.77×10^8 [31]	2.4×10^6
Activation energy (J/mole)	12×10^4 [30]	42×10^4 [31]	16.7×10^4

$$A_1 U_{g2} + B_1 U_{g2} = C_1 \tag{1a}$$

where

$$A_1 = 0.5 - (C_p/R)_2$$

$$B_1 = (C_p/R)_2 \, (W\{1 - 1(C_p/R)_2\} - D_1)$$

$$D_1 = h_{g1}/[W(C_p/R)_1]$$

$$C_1 = h_{g1} \, [1 - (C_p/R)_2/(C_p/R)_1]$$

$$P_2 = P_1 + \rho_1 W U_{g2} \tag{2a}$$

and the properties C_p, R, and γ for the gas-solid mixture are estimated from

$$C_{p\,mix} = (C_p + KC_s)/(1 + K)$$

$$R_{mix} = R/(1 + K)$$

$$\gamma_{mix} = \gamma/(1 + (KC_s/C_p/(1 + KC_s/C_p)) \, (\gamma - 1)$$

Solution Method

The unknowns W, P_2, and U_{g2} can be evaluated by solving equations 1, 2, and 3, while the enthalpy of the gas behind the shock is calculated from the equation

$$h_{g2} = h_{g1} + 0.5U_{g2} \, (2W - U_{g2}) \tag{3a}$$

Equations 4 and 5 contain the derivatives of two independent variables of particle velocity and temperature. These two differential equations are solved using the Runge Kutta fourth-order method. The solution of the partial differential equations 6a and 6b is obtained by the finite difference technique to evaluate the temperature distribution within the solid propellant particle. At each time step, the particle velocity and temperature are calculated and then introduced into equations 1–3 to obtain the gas-phase properties of velocity, temperature, and pressure at the same time step. Calculations are then repeated until a very large value for the particle temperature gradient is obtained. The delay period is estimated from the moment of bursting of the diaphragm up to this moment. The input into the model includes the physical properties of the powder and oxidizer, particle size, shock Mach number, and loading ratio. The outputs are the ignition delay time, time histories of the thermodynamic properties of the gas phase, and particle velocities.

Results and Discussion

The model has been used to explain the effect of various parameters on the ignition delay of magnesium, aluminum, and composite solid propellants; the thermal and chemical properties of these propellants are given in Table 1. Moreover, the model is used to obtain the histories of particle temperature and velocity as well as gas velocity.

Parametric study, using data in Table 1, has been carried out to examine the effect of shock Mach number, loading ratio, and particle size, ranging between 3:5, 0.1:1, and 5:50 μm, respectively. The relation between the ignition delay time and shock Mach number for different loading ratios and metal powder is shown in Fig. 2. The results show that this relation has exponential shape where it decreases with increasing M_{sh}. The effect of the loading ratio is to decrease the ignition delay time with its increase, and has a small effect as M_{sh} approaches a value of 5. On the other hand, a notable effect on loading ratio is clear for a value of M_{sh} beyond 4, especially for loading ratios of 0.4 and 0.1. The increase of ignition delay time with the increase of particle diameter and with the decrease of M_{sh} may be attributed to the decrease of heat transfer to the droplet due to the decrease of the particle relative velocity. This also decreases with time as the particle velocity decreases until it reaches the gas velocity. Thus, as the rate of heat transfer to large particles is less than that for small particles; large particles need long heating time and have more ignition delay time than small particles (Fig. 3). Immediately after the

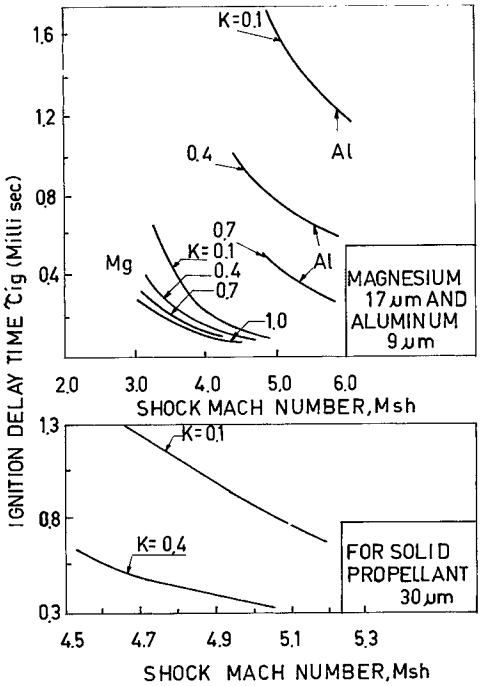

FIG. 2. Effect of shock intensity on ignition delay at different loading ratios.

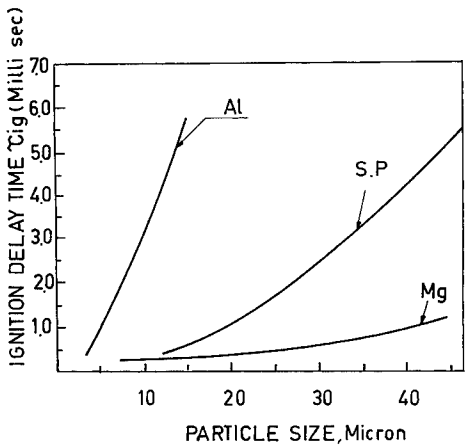

FIG. 3. Effect of particle size on ignition delay time for aluminum, solid propellant, and magnesium particles at loading ratio 0.1 and shock Mach number 4.0.

shock passes the particle, the resultant convective heating causes a rapid increase in the particle surface temperature (Fig. 4). At the same time, the drag force causes the particles to accelerate with an accompanying reduction in the relative velocity and the rate of convective heating. With increasing

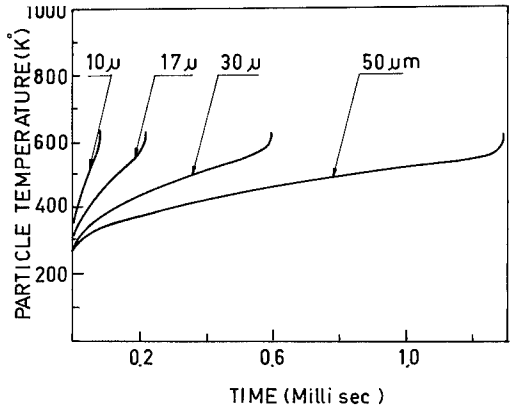

FIG. 4. Temperature particle history for magnesium with different sizes at loading ratio 0.1 and shock Mach number 4.0.

particle temperature, the rate of gaseous oxidation and required action increases until ignition occurs.

Thus, the ignition delay is governed by two characteristic time scales: thermal time, in which convective heating is the main cause of particle heating, and chemical time due to heat evolved from chemical reaction. The calculated particle temperature history with time illustrates the two distinct times, where the thermal period is denoted by the gradual increase of temperature while the chemical period starts from the point of inflection and ends with ignition. It is clear that the thermal period is the predominant one and, therefore, the convective heating is a key feature of particle ignition behind incident shocks, and its duration depends on the particle acceleration time. Thus, small particles rapidly accelerate to reach the local gas velocity (Fig. 5), so that the time available for convective heating is short. This results in shorter ignition delay than for larger particles.

Initially the particle is in supersonic flow induced by the shock wave, and bow shock results in a recovery temperature, T_f, that is higher than the gas temperature. The recovery temperature contributes in the convective heating process in the early stage of the thermal period. Sudden decrease of recovery temperature is observed at the beginning, corresponding to changing the particle relative Mach number from supersonic to subsonic, until reaching the gas temperature.

A comparison between the experimental results [15] using the shock tube and the theoretical results for a particle size of 17 μm is shown in Fig. 6. Good agreements are observed for M_{sh} ranging between 4.85 and 5 at a loading ratio of 0.3. Deviations at greater or less M_{sh} may be attributed to the use of inaccurate kinetic data, Nusselt, and drag coefficient formulas.

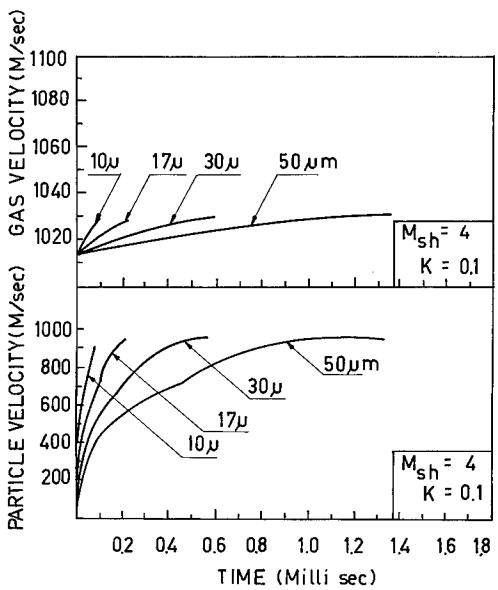

FIG. 5. Gas and particle velocities of various magnesium particle sizes.

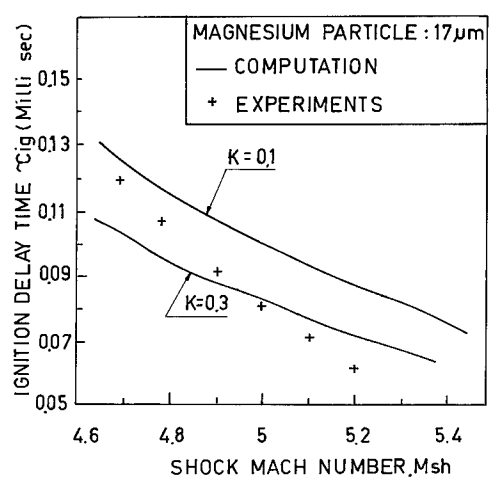

FIG. 6. Comparison between predicted results and experimental results of Ref. 15.

The prediction model is used also to calculate the ignition time delay of Al for different loading ratios and particle sizes ranging between 0.1:0.7 and 5:9 μm, respectively, and the results are shown in Fig. 2. Ignition of aluminum is difficult and it is clear that it needs a higher shock intensity than magnesium. It is clear also from Fig. 3 that the size increase from 5 to 15 μm increases the ignition time delay by a factor of 9, which assures the difficulty of ignition of aluminum compared to magnesium. The decrease of the loading ratio, as in the case of Mg, increases the ignition delay time, and the slope decreases when K is increasing. This may be attributed to the decrease of the shock intensity for the same pressure ratio as the wave propagates into a more condensed medium, but the gas enthalpy and pressure are increased, resulting in shorter delay periods.

The prediction calculation of the behavior of solid propellant (composite type) particles was carried out and the results are given in Fig. 2. The decrease of the ignition time delay with the loading ratio increase is larger for Mg and smaller for Al. Aluminum can be used as an additive to composite propellants to improve their performance. However, efficient combustion can be obtained whenever both powders ignite and burn at the same time without time lag. This condition could be achieved when using Al powder of 5 μm for mixing with propellant ingredients of 30 μm for $M_{sh} = 5$ and $K = 0.4$ with a corresponding gas temperature 1400 K, as this gives the same ignition delay of about 400 μs for both powders. Regarding the effect of the particle size increase on the ignition delay time (Fig. 3), it is noted that it increases by a factor of 13 when the size is increased from 10 to 50 μm.

The gas velocity and particle velocity distribution are shown in Fig. 5 for various sizes. They increase until the moment of ignition with a rate depending upon the size of the particle. Such increase of gas velocity of about 20 m/s is very small compared to the initial gas velocity of 1020 m/s. Regarding the particle velocity, there is a rapid increase in its value for small sizes, and the particle may not attain equilibrium with the gas before ignition takes place, while large particles of 50 μm reach an equilibrium state with the gas before ignition. This does not change for various powders. Decreasing the shock intensity increases the time needed for the particle to reach equilibrium with the gas, while for higher shock intensity, the particle may ignite before reaching equilibrium with the gas.

The effect of radiative heat transfer on ignition delay was found to be negligible for particle sizes of less than 25 μm, while the error reaches 30% for 50-μm-diameter particles.

Comparing the kinetic constants given by various investigators for loading ratios 0.1 and 0.9, shown in Fig. 7, it is found that the predicted ignition delay time with kinetic constants from Ref. 3 is compatible with the present research at $K = 0.9$ and M_{sh} range 4.0–4.5. As M_{sh} decreases, the discrepancy is noticed, especially at $K = 0.1$. On the other hand, kinetic constants of Ref. 9 have results far from the present research results for the two loading ratios 0.1 and 0.9.

In the present work, validation of the prediction model using experimental results of Ref. 27, shown in Fig. 8, for Mg powder 30 μm in diameter and Al at various shock Mach numbers and loading ratios

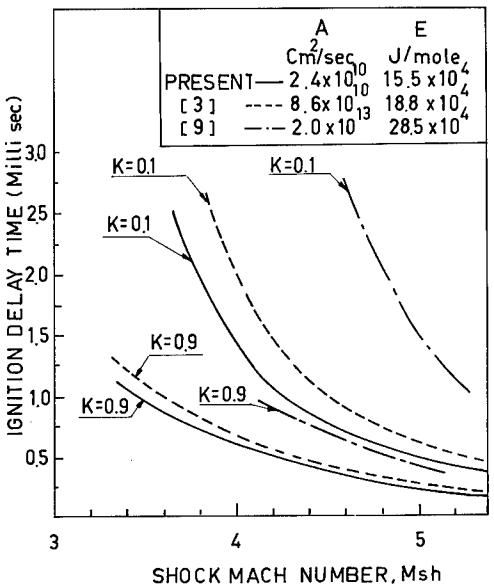

FIG. 7. Effect of kinetic data on the ignition delay time for magnesium with a size of 50 μm.

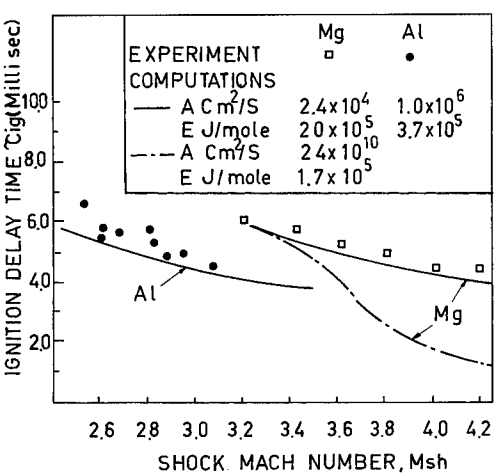

FIG. 8. Validation of prediction model for magnesium with a size of 30 μm and aluminum with a size of 14 μm and loading ratio 0.15.

shows that the most suitable kinetic constants are the following: Preexponential factor, $A = 2.4 \times 10^4$ cm²/s; activation energy, $E = 2.0 \times 10^2$ kJ/mole; and heat of combustion, $Q = 4.7 \times 10^4$ kJ/kg. For aluminum these are: $A = 1 \times 10^6$ cm²/s; $E = 3.7 \times 10^2$ kJ/mole; and $Q = 1.67 \times 10^4$ kJ/kg.

Conclusions

A mathematical model to predict the ignition characteristics of metal powders was developed using the moving coordinate system to transform the moving shock to a stationary one. The conservation equations of continuity, momentum, and energy for both phases in integral form, as well as the particle momentum and energy equations and the perfect gas law for the gas phase have been derived and solved. The model is fully validated from the data of Refs. 15 and 27, and the following chemical kinetic constants have been deduced for magnesium and aluminum: $A = 2.4 \times 10^4$ and 1×10^6 cm²/s, $E = 2.0 \times 10^2$ and 3.7×10^2 kJ/mole, and heat of combustion $Q = 4.7 \times 10^4$ and 1.67×10^4 kJ/kg, respectively.

A parametric study has been carried out for accerated powders of Mg, Al, and solid propellants behind incident shock, and the following results have been obtained. Ignition delay time decreases with increasing shock Mach number and loading ratio and with decreasing particle size. Magnesium and solid propellant powders are more easy to ignite than aluminum powder, and the following values at $M_{sh} = 5$, $K = 0.1$ and particle size 15 μm are an indication of the ignition characteristics of these powders, respectively: $\tau_{ig} = 100$ μs, 250 μs, and 5500 μs. The temperature distribution inside the particle should be taken into account for solid propellants due to their low thermal conductivity for particles larger than about 100 μm.

Nomenclature

A	preexponential factor cm²/s
C_D	drag coefficient
C_{OX}	oxidizer concentration
C_f	mean friction coefficient
C_p	gas specific heat at constant pressure kJ/mole
C	heat capacity kJ/kg K
D_h	hydraulic diameter m
E	activation energy kJ/mole
h	enthalpy kJ/kg
K	loading ratio (particle mass/mixture mass)
L_e	Lewis number
L_v	heat of evaporation kJ/mole
M_{sh}	shock Mach number
m	mass kg
Nu	Nusselt number
P	medium pressure bar
Pr	Prandtl number
Q	heat of combustion kJ/kg
Q_L	heat losses kJ/sec.m
U_p	particle velocity m/s
R	gas constant kJ/mole
r	particle radius μm
Re	Reynolds number
T	particle temperature K
t	time s
W	shock speed m/s

W_L momentum losses kJ/s
X relaxation length m

Suffix

g gas
p particle
R particle radius
s solid particle
w wall
f recovery due to bow shock

Greek Letters

α heat transfer coefficient kJ/m^{2}h K
δ thickness μm
λ thermal conductivity kJ/m h K
ε emissivity coefficient
μ dynamic viscosity kg/m s
ρ density kg/m^3
τ_{ig} ignition delay time μs
σ Boltzmann's constant 5.6688×10^{-8} W/m^2 K^4

Acknowledgment

The authors wishes to thank the Arab Industrial Authority Sakr Factory, Egypt, for their financial support.

REFERENCES

1. Gurevich, M. A. and Stepanof, A. M., *Combust. Explos. Shock Waves* 4:109–112 (1968).
2. Belyaev, A. F., Frolov, Yu. V., and Korotkov, A. J., *Combust. Explos. Shock Waves* 4:182–185 (1968).
3. Gurevich, M. A. and Stepanov, A. M., *Combust. Explos. Shock Waves* 4:188–192 (1968).
4. Channapragada, R. S. and Anderson, R., *AIAA J.* 7:1581–1587 (1969).
5. Khaikin, B. I., Bloshjenko, V. N., and Merzhanov, A. G., *Combust. Explos. Shock Waves* 4:412–432 (1970).
6. Gal'chenko, Yu. A., Grigorev, Yu. M., and Merzhanov, A. G., *Combust. Explos. Shock Waves* 9:96–98 (1973).
7. Aldushin, A. P., Bloshenko, V. N., and Seplyarskii, B. S., *Combust. Explos. Shock Waves* 9:423–428 (1973).
8. Breiter, A. L., Mal'tsev, V. M., and Popov, E. I., *Combust. Explos. Shock Waves* 13:475–485 (1977).
9. Ezhovskii, G. K., Ozerov, E. S., and Roshenya, Yu. V., *Combust. Explos. Shock Waves* 13: 716–721 (1977).
10. Ryzhik, A. B., *Combust. Explos. Shock Waves* 14:258–260 (1977).
11. Derevyaga, M. V., Stesik, L. N., and Fedorin, E. A., *Combust. Explos. Shock Waves* 14:731–735, (1977).
12. Fox, T. W., Rackett, C. W., and Nickholls, J. A., *Eleventh International Symposium on Shock Tubes and Waves,* University of Washington Press, Seattle, WA, 1977, pp. 262–268.
13. Ezhovskii, G. K., Ozerov, E. S., and Roshenya, Yu. V., *Combust. Explos. Shock Waves* 15:194 (1979).
14. Ermakov, V. A., Razdsobreev, A. A., Skorik, A. K., Pozdeev, V. V., and Smolyakov, S. S., *Combust. Explos. Shock Waves* 18:256–257 (1981).
15. Medvedev, A. E., Fedorov, A. V., and Fomin, V. M., *Combust. Explos. Shock Waves* 19:261–265 (1982).
16. Gremyachkin, V. M., *Combust. Explos. Shock Waves* 19:259–263 (1983).
17. Beak, S. W., Kauffman, C. W., and Sichel, M., *Combust. Flame* 81:219–228 (1990).
18. Klemens, R., Kapuscinski, M., Wolanski, M., Wolanski, P., and Sichel, M., *Combust. Flame* 99:742–748 (1994).
19. Gordon, S. and McBride, B. J., NASA, SP-273, 1971.
20. Volyan, Ski, P., *J. Combust. Explos. Shock Waves* 20:500–506 (1984).
21. Kauffman, C. W., Sichel, M., and Wolanski, P., *Powder Technol.* 71:119–134 (1992).
22. Lee, F. P., Kauffman, C. E., Sichel, M., and Niccholls, J. A., *AIAA J.* 24:1811–1816 (1986).
23. Elkotb, M. M., Saad, A. E., El-Taher, R. M., Abdel-Latif, A. M., 9th International Symposium on Transport Phenomena, Singabor, Paper No. A290, 1996.
24. Shertser, A. A., *Combust. Explos. Shock Waves* 29:500–506 (1993).
25. Jack Pike, *AIAA J.* 32:979–986 (1994).
26. Merzhanov, A. C., *AIAA J.* 13:209–214 (1975).
27. Nasef, I. M., "Ignition Study of Metal Powder in a Shock Tube," Ph.D. Thesis, Cairo University, Dept. of Mechanical Engineering, Cairo, 1989.
28. Shapiro, A. H., in *The Dynamics and Thermodynamics of Compressible Fluid Flow,* Ronald Press, New York, 1954, Vol. 11, Chap. 25, pp. 994–1004.
29. Walsh, M. J., *AIAA J.* 13:1526–1528 (1975).
30. Mcalevy, R. F., Cowan, P. L., and Summerfield, M., *Solid Propellant Rocket Research,* Academic Press, New York, 1960, pp. 623–652.
31. Nechitailio, J. N., *Combust. Explos. Shock Waves* 14:175–178 (1977).

COMMENTS

Dr. Igor G. Assovskii, Semenov Inst. of Chemical Physics, Russia. You used the parameters of heat and mass transfer which are averaged over the particle surface. Meanwhile, at a high value of the Mach number the condition of heat transfer changes rather significantly over the surface. So, could you estimate the exactness of your model at the high values of Mach number?

(No response received from author.)

Twenty-Sixth Symposium (International) on Combustion/The Combustion Institute, 1996/pp. 1945–1951

COMBUSTION CHARACTERISTICS OF Mg-CO_2 COUNTERFLOW DIFFUSION FLAMES

APORO FUKUCHI, MASARU KAWASHIMA AND SABURO YUASA
Tokyo Metropolitan Institute of Technology
Asahigaoka 6-6, Hino-shi, Tokyo 191, Japan

To examine the details of the Mg-CO_2 combustion consisting of the gas-phase reactions and the surface reactions, we tried to separate the Mg-CO_2 flame from the surface reactions. For this purpose, we formed a stable Mg-CO_2 counterflow diffusion flame between the Mg vapor and a CO_2 stream by using a Mg vaporizer with many small ejection holes.

The Mg-CO_2 counterflow diffusion flames contained two types of flames: the luminous flame and the dark flame. In the luminous flame, the homogeneous reaction of Mg with CO_2 forming gaseous MgO and CO occurred, as well as the condensation of MgO. The dark flame was observed when the Mg ejection velocity was small. The heterogeneous reaction of Mg with CO_2 forming condensed MgO and C occurred. The change from the luminous flame to the dark flame was caused by the heat loss to the Mg vaporizer.

The flame stability limits diagram of Mg-CO_2 counterflow diffusion flame was obtained, in which the Mg ejection velocity is plotted against the stagnation stream velocity gradients. There exists a critical value of the Mg ejection velocities, below which the flame can never be stabilized. This limit is due to the thermal quenching of the flame near the Mg vaporizer. Also, the critical value of the stagnation stream velocity gradients exists and is due to the chemical limitations on the combustion rate in the flame zone. This flame stability limits diagram was similar to those of the ordinary gaseous fuel-oxidizer counterflow diffusion flames.

Introduction

We have proposed a CO_2-breathing engine using metal fuels for a future aircraft vehicle in the atmosphere of Mars consisting of CO_2 [1]. One of the most attractive metal fuels is Mg. Some experimental studies on the ignition and combustion of Mg in CO_2 and CO_2/CO streams have been performed. Yuasa and Isoda found that Mg ignited easily and had a fast burning rate, and, during combustion, intermittent flames appeared sporadically over the surface of the Mg to produce CO by gas-phase reactions [2]. Shafirovich and Goldshleger studied the combustion of Mg in high-temperature CO_2/CO mixtures and concluded that the heterogeneous reaction of Mg with CO occurred during combustion in CO_2, along with the homogeneous reaction of Mg with CO_2 [3]. Yuasa and Fukuchi found that on the nonflame surface, the reactions of Mg with CO diffusing from the flames generated condensed MgO and C that built up the porous layers. The pulsation the flames can be explained in terms of the abrupt breaking of the layer followed by its blockage caused by the surface reaction with CO [4].

These results show that the reaction film formed on the Mg surface complicates the combustion phenomena of Mg combustion in CO_2. To design a combustor for the CO_2 breathing engine, an understanding of the combustion mechanism, in particular Mg-CO_2 flames, is required. To our knowledge, no work has been reported on the details of the structure and stability of Mg-CO_2 flames.

Here, it is desirable to separate the Mg-CO_2 flame from the surface reactions of Mg with CO. We tried to form a stable counterflow diffusion flame using a Mg vaporizer with many small ejection holes, which may be useful to examine the details of the Mg-CO_2 diffusion flame structure. The present study investigated the flame stability and the structure of the counterflow diffusion flame.

Experimental Apparatus and Procedure

Figure 1 shows a schematic of the experimental apparatus used in this study, which is basically the same as that used in the previous paper [4]. It consisted of a CO_2 and Ar supply system, a combustion chamber, a Mg vaporizer, a heating device, and several measuring devices. CO_2 at room temperature issued through a nozzle (25 mm in diameter) into the combustion chamber, then impinged on the surface of the Mg vaporizer situated 18 mm downstream of the nozzle exit. The vaporizer consisted of a crucible and a multihole plate (14 mm in diameter, 6 mm in height) with 21 holes (0.8 mm in diameter, at 2 mm intervals) made of stainless steel. A Mg sample (0.6 g in weight, purity: 99.9%) mounted in the

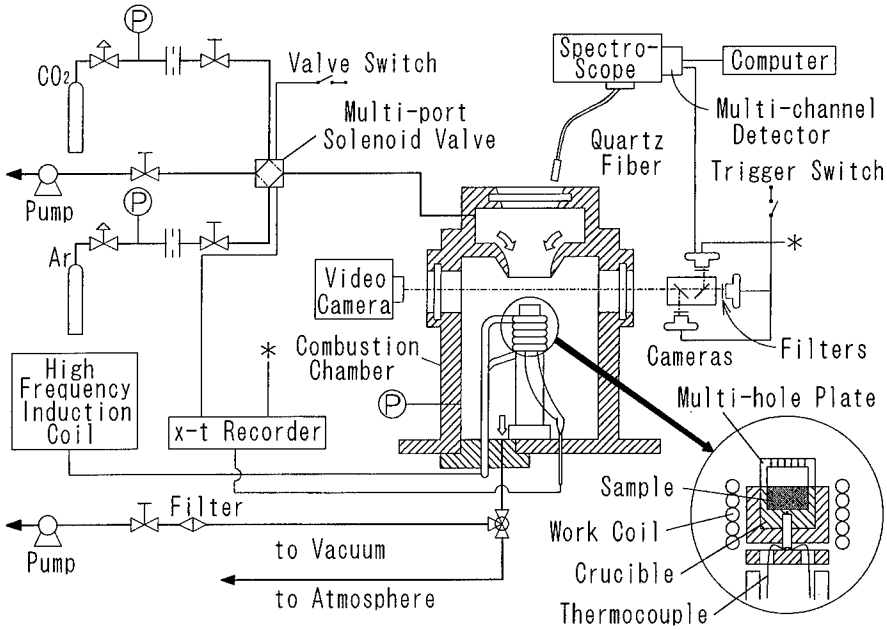

FIG. 1. Schematic of experimental apparatus.

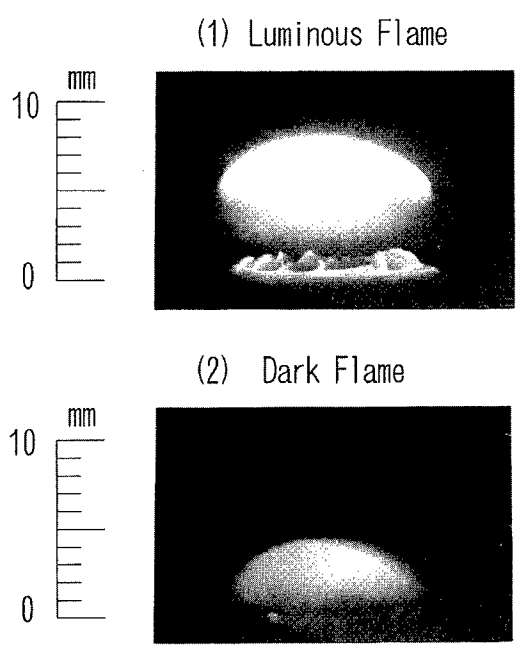

FIG. 2. Direct photographs of Mg-CO_2 counterflow diffusion flames. (1) Luminous flame: P = 21 kPa, V_{CO_2} = 0.3 m/s, V_{Mg} = 0.41 m/s; (2) dark flame: P = 21 kPa, V_{CO_2} = 0.3 m/s, V_{Mg} = 0.19 m/s.

crucible was heated by the high-frequency induction heater. The crucible temperature was measured by a chromel-alumel thermocouple.

The experiments were performed at the combustion chamber pressure of 21 kPa, while varying the nozzle exit velocity V_{CO_2} from 0.3 to 4 m/s. Before each test run, the heated Mg sample ejected Mg vapor against the Ar stream at a predetermined pressure and flow rate. When the crucible temperature reached a predetermined value, the test run was started by changing Ar to CO_2 of the same pressure.

Changes in the flame appearance were continuously recorded by a video camera. Emission spectra through a quartz fiber were measured by using a multichannel detector. Also, three motor-driven cameras with filters corresponding to Mg, MgO, and continuum emissions took photographs simultaneously. Condensed combustion products gathered after the experiment were analyzed chemically.

Experimental Results

Counterflow Diffusion Flame

Under appropriate conditions of velocity V_{CO_2} of the CO_2 and the crucible temperature, a counterflow diffusion flame of Mg with CO_2 stream was formed over the multihole plate like ordinary counterflow diffusion flames [5]. Figure 2(1) shows a typical flame observed in the present study. The flame is very luminous and dome-shaped. Here, we call

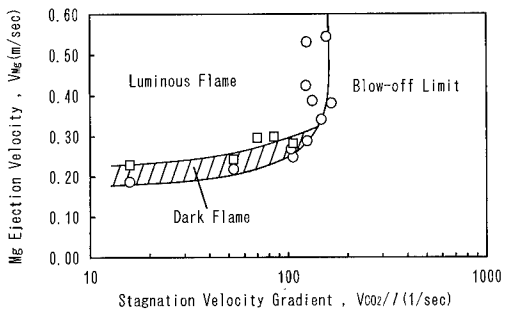

FIG. 3. Flame-stability diagrams for Mg-CO_2 at a pressure of 21 kPa.

this type of flame *luminous flame.* The outer region of the flame is white–blue and the inner region of the flame is green or blue. White smoke, which is the condensed combustion product MgO, is generated vigorously. The figure shows the combustion products that piled up on the multihole plate during combustion.

When the crucible temperature was decreased at a constant V_{CO_2}, the flame approached the surface of the multihole plate and its thickness decreased. Its lightness decreased somewhat, but the flame was still very luminous. As the crucible temperature was decreased further, the color of the flame changed to red and became dark suddenly. Corresponding to this, the height of the most luminous region in the flame from the multihole plate decreased sharply. It retained the dome shape of the luminous flame. We call this type of flame *dark flame.* Figure 2(2) shows a typical dark flame formed close to the multihole plate. The dark flame never generated the white smoke. As the crucible temperature was decreased further, at a certain critical value the dark flame quenched suddenly.

For the luminous flame, at less than $V_{CO_2} = 0.5$ m/s the flame was very stable. With increasing V_{CO_2} at a constant crucible temperature, the flame became unstable and approached the multihole plate; its thickness was decreased. As V_{CO_2} was increased further, at a certain critical value of V_{CO_2}, the luminous flame blew off suddenly.

In this study, the Mg ejection velocity V_{Mg} against the CO_2 stream could not be measured directly. We estimated V_{Mg} in Ar streams using the following method: In Ar streams, the Mg vaporizer ejected Mg vapor that condensed and formed some white smoke consisting of condensed small Mg particles. Since a stagnation stream line between the Ar stream and Mg vapor was formed at the stream line, the stream line of the white smoke forms a stagnation stream line. V_{Mg} was estimated as a function of the crucible temperature by measuring the height of the stagnation point and the temperature of the crucible using the following equation [6]:

$$V_{Mg} = V_{Ar} \times (l_{Mg}/l_{Ar}) \times (\rho_{Ar}/\rho_{Mg})^{0.5}$$

where V_{Ar} is the Ar ejection velocity, l_{Ar} is the distance between the nozzle exit and the stagnation point, and l_{Mg} is the distance between the surface of the multihole plate and the stagnation point. ρ_{Ar} is the density of Ar at room temperature, and ρ_{Mg} is the density of Mg vapor at the measured crucible temperature. l_{Ar} and l_{Mg} depend on the crucible temperature.

Figure 3 shows the measured stability limits of the Mg-CO_2 counterflow diffusion flames in this study. In the figure, the estimated Mg ejection velocity V_{Mg} is plotted against the stagnation velocity gradient V_{CO_2}/l (l is the distance between the nozzle exit and the surface of the multihole plate). Also, the border line separating the luminous flame from the dark flame is plotted in the figure. The value of V_{Mg} at the flame stability limit increases slightly with an increase of V_{CO_2}/l over a wide range. However, when V_{CO_2}/l becomes large, V_{Mg} at the stability limit increases steeply and a critical stagnation velocity gradient exists, beyond which the flame can never be stabilized. The dark flame was only seen in the narrow region of V_{Mg}. It is important to note that this tendency of the flame stability limit is very similar to the well-known flame stability diagrams for the counterflow diffusion flame of air/city-gas and air/C_3H_8 researched by Tsuji and Yamaoka [7,8].

Spectroscopic Analysis

Figure 4 shows the emission spectra of burning Mg-CO_2 counterflow diffusion flames in this study. Figure 4(1) is for the luminous flame and Fig. 4(2) for the dark flame. For the luminous flame, the atomic lines of Mg, the bands of MgO gas, and the continuum emission are visible. The result suggests that the homogeneous overall reaction of $Mg(g) + CO_2 \rightarrow MgO(g) + CO$ occurred in the luminous flame. This spectrum agrees with the other observations for Mg flames in oxygen [9–11] and CO_2, CO_2/CO atmospheres [3,4]. On the other hand, for the dark flame, only the weak emission spectra of Mg were recognized and the bands of MgO were not observed in spite of much longer exposure time of the spectroscopy photographs and a wider slit width than those for the luminous flame. The continuum emission is very strong due to this photographic condition, suggesting that the reaction mechanism changes drastically when the luminous flame turns into the dark flame.

Filtered Photographs

To investigate the structure of the Mg-CO_2 counterflow diffusion flame, photographs of a Mg flame having a wide emission zone were taken on infrared films through interference and high-pass filters

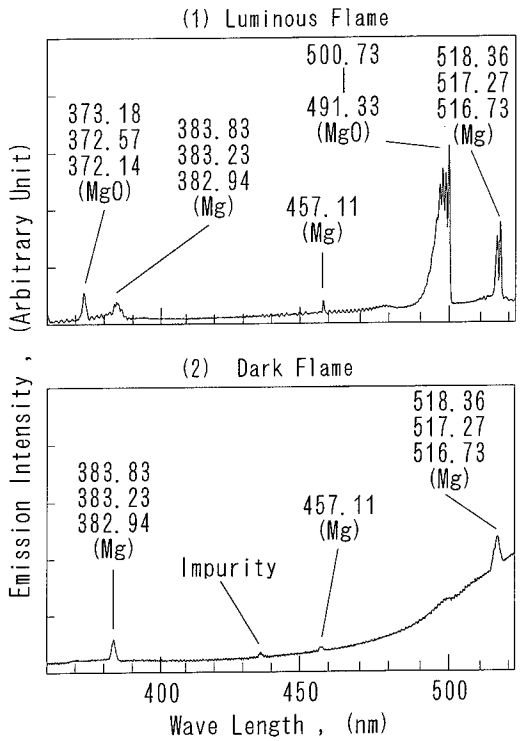

FIG. 4. Emission spectrum of Mg-CO_2 counterflow diffusion flames. (1) Luminous flame: P = 21 kPa, V_{CO_2} = 2.32 m/s, V_{Mg} = 0.92 m/s; (2) dark flame: P = 21 kPa, V_{CO_2} = 0.3 m/s, V_{Mg} = 0.23 m/s.

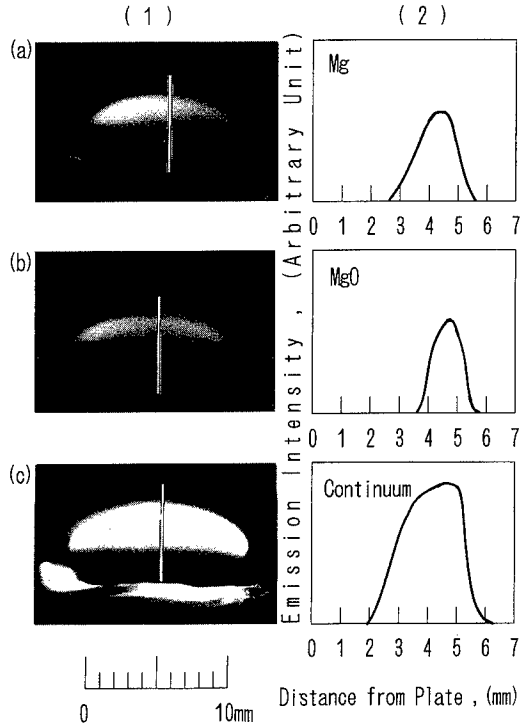

FIG. 5. Filtered photographs of Mg-CO_2 counterflow diffusion flames (1) and emission intensity distributions (2). P = 21 kPa, V_{CO_2} = 0.3 m/s, V_{Mg} = 0.34 m/s. (a) Mg emission = 517 nm, $\Delta\lambda/2$ = 1.7 nm. (b) MgO emission = 498 nm, $\Delta\lambda/2$ = 15 nm. (c) Continuous emission > 700 nm.

simultaneously. The center wavelengths of interference filters were 517 nm for the Mg triplet and 498 nm for the MgO band, respectively. The threshold wavelength of the high-pass filter was 700 nm for the continuum. For wavelengths greater than 700 nm, only the continuous emission was observed except for the weak emission spectrum of K as an impurity.

Figure 5(1) shows typical filtered photographs of the luminous flame, and Fig. 5(2) shows the corresponding emission intensity distributions along the paths drawn in the photographs. The continuum emission was attributed to the condensed particles of MgO and C and the heated multihole plate surface. Since the condensed MgO and C small particles emitting continuous light are convected away by the bulk gas flow in the region, the outer edge of the flame forms as a stagnation stream line [12]. In the filtered photographs, the emission intensities passing through the filters for the Mg lines and the MgO bands contained continuum emission. However, the spectroscopic analysis of this flame shown in Fig. 4(1) shows that the emission intensities of the Mg lines and the MgO bands are much stronger than those of the continuum emission at the same wavelengths. Thus, the filtered photographs for the Mg lines and the MgO bands essentially represent the profiles of Mg and MgO emission intensity. Since the dome-shaped flame as shown in the photographs and was not one-dimensional, an emission intensity in which light in the depth direction had been integrated was recorded on the photographs. Therefore, the three-dimensional property of the flame influenced the emission profiles. In this experiment, the influences caused by the three-dimensional property were not corrected.

The filtered photographs for the luminous flame show that the Mg and MgO emissions exist in the gas phase away from the surface of the multihole plate. The positions of the peak and the inner edge of the Mg profile are closer to the surface of the multihole plate than those of the MgO profile. This indicates that the reaction of gaseous Mg with CO_2 produces gaseous MgO. The continuum profile is distributed over a wide area and the Mg and MgO profiles lie inside the continuum profile. In the overexposed photographs for the filtered photographs, the luminous area consisting of the emissions of

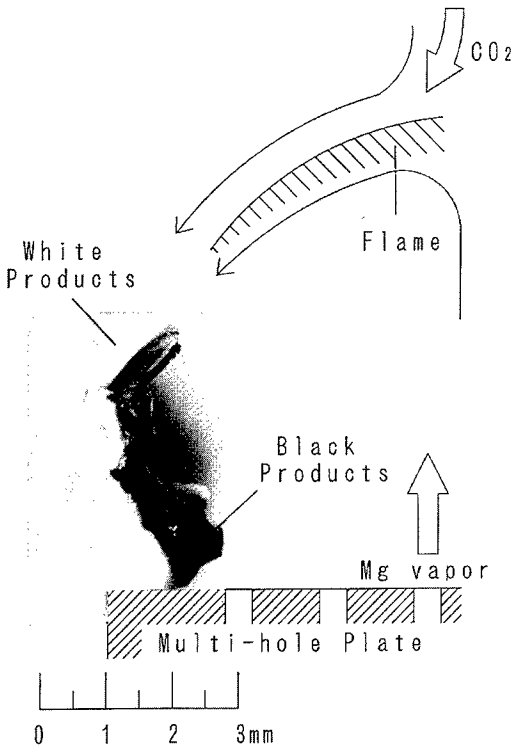

FIG. 6. Cross section of combustion products and illustration of the luminous flame: P = 21 kPa, V_{CO_2} = 0.3 m/s, V_{Mg} = 0.38 m/s.

gaseous MgO and the condensed MgO was recognized outside the stagnation stream line. In this area, no Mg emission was recognized outside the stagnation stream line. This suggests that the gaseous MgO diffuses through the stagnation point to the CO_2 stream and condenses there to produce the white smoke that was observed. Since metal atomic spectra often occur because of thermal processes [13], the distribution of the Mg emission represented the concentration of excited Mg atoms, which was associated with the temperature in the flame and the concentration of Mg vapor.

For the dark flame, filtered photographs were taken in the same manner as for the luminous flame. Only the thin flame was taken through the filter for the continuum emission and the Mg and MgO signals were negligible through the filters for Mg and MgO, respectively. This result agrees with the spectroscopic analysis of the dark frame (see Fig. 4(2)).

Combustion Products

As combustion progressed, the combustion products piled up on the surface of the multihole plate. Figure 6 shows a cross section of the combustion products with an illustration of a luminous flame. For the luminous flame, the combustion products were found to consist of black and white. The inside of the combustion products that were produced in the luminous flame was black and the outside was white. During the combustion, the black products were produced inside the flame and piled up on the surface of the multihole plate. The white products were the condensate of the white smoke generated outside the flame that convected by the bulk flow and piled up on the outer edge of the multihole plate.

The combustion products were analyzed chemically. The mole fraction of carbon, defined as X_C = molC/(molC + mol MgO), was 0.319 in the black products and 0.016 in the white products for the luminous flames.

For the dark flame, the inside of the combustion products was black and the outside was gray. The X_C of the combustion products was 0.175 in the black products and 0.079 in the gray products. The value of X_C of 0.319 of the black products for the luminous flame is about twice that of 0.175 of the black products for the dark flame. This result suggests that the reaction that forms carbon in the luminous flame is clearly distinguished from the reaction in the dark flame.

Discussion

Chemical Mechanics

Two types of flames (luminous and dark) were observed in the present experiment and were clearly distinguishable. For the luminous flame, the flame location over the multihole plate was higher than that of the dark flame and gaseous MgO was observed. On the contrary, the dark flame formed near the multihole plate and gaseous MgO was not observed. The different flame luminosity and its location between the luminous flame and the dark flame suggest that the flame temperature of the luminous flame was higher than that of the dark flame. The reaction of gaseous Mg with CO_2 produces gaseous MgO in the luminous flame and condensed MgO in the dark flame. The difference of flame temperature may be explained easily by the heat loss to the multihole plate, and the increase of heat loss may change the reaction that occurs in the luminous flame with respect to that in the dark flame.

Figure 7 shows the equilibrium compositions and the temperatures of the Mg-CO_2 mixture considering the heat loss by reducing the enthalpy of reactants Mg and CO_2 that was calculated using the NASA-SP-273 equilibrium computer program [14]. The initial condition of reactants was [Mg]:[CO_2] = 1:1 in mole base. In this figure, the calculated flame temperature and the mole fractions of the

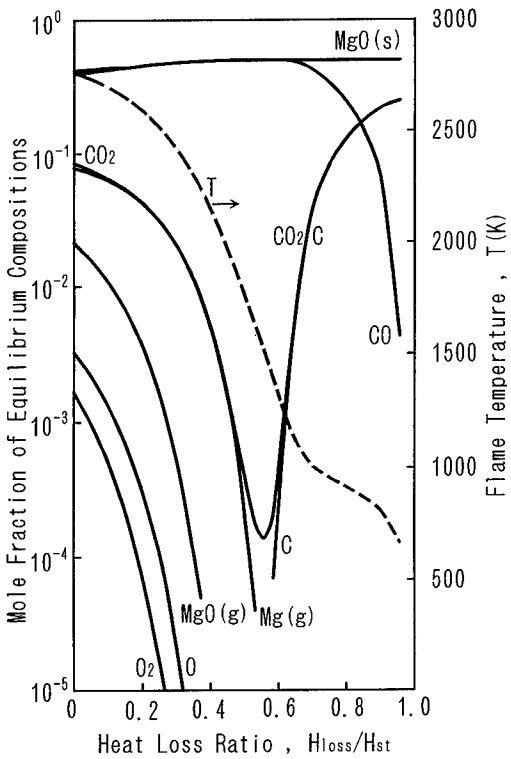

FIG. 7. Equilibrium compositions and flame temperature with heat loss at a pressure of 21 kPa.

equilibrium compositions are plotted against the heat-loss ratio defined as H_{loss}/H_{st} (H_{st} being the standard enthalpy of the reactants and H_{loss} the reduced enthalpy). As the heat-loss ratio increases, the flame temperature and the mole fractions of MgO(g), Mg(g) and CO_2 decrease. When the heat-loss ratio exceeds the disappearance point of Mg(g), the mole fraction of CO_2 increases again and C appears. Finally, the mole fractions of C, CO_2, and MgO(s) converge to 0.25, 0.25, and 0.5, respectively.

The calculated compositions suggest that at small heat-loss ratios, the following overall reactions are predominant:

$$Mg + CO_2 \rightarrow MgO(g) + CO \qquad (1)$$

and

$$MgO(g) \rightarrow MgO(s) \qquad (2)$$

On the other hand, when the heat-loss ratio is large, the possible overall reaction is

$$Mg + 1/2CO_2 \rightarrow MgO(s) + 1/2C \qquad (3)$$

In this case, half of the initial CO_2 amount does not react and thus remains.

For the luminous flame regime, the possible reactions that could produce the preceding results are the reactions in Eqs. (1) and (2). The white combustion products of the luminous flame consisted mainly of MgO that was produced by the reaction in Eq. (2) and convected from the flame area directly, piling up on the outside of the mound of combustion products by the bulk flow (see Fig. 6). The black products of the luminous flame consisted of MgO(s) caused by the reaction in Eq. (2) at the flame and of C. One possible explanation for the formation of C in the black products of the luminous flame is the reaction of CO with Mg. Some of the CO, produced at the flame by the reaction of Eq. (1), diffuses inside the flame and is convected toward the combustion product surface, and the reaction

$$Mg + CO \rightarrow MgO(s) + C \qquad (4)$$

occurs with Mg from the vaporizer to form MgO(s) and C there. It is suggested that the reaction in Eq. (4) occurs only at the surface where the temperature is low [4].

On the contrary, in the dark flame regime only the reaction in Eq. (3) occurs at the inner area of the flame. X_C of black products caused by the reaction in Eq. (4) of the luminous flame must be just twice as much as that caused by the reaction in Eq. (3) of the dark flame. Analysis of the black products showed that X_C of the luminous flame is theoretically 1.93 times that of the dark flame. This analytical result supports the reaction mechanisms discussed here.

Flame Stability Limits

The present experimental results show that the Mg-CO_2 counterflow diffusion flame has a flame stability limit similar to ordinary gaseous fuel oxidizer counterflow diffusion flames [5–7]. According to the reports by Tsuji and Yamaoka [6–7], the quenching of the flame at small values of stagnation velocity gradient is mainly due to thermal quenching of the flame near the surface of the fuel-ejecting device. The blow off at a critical value of the stagnation velocity gradient is mainly due to chemical limitations on the combustion rate in the flame zone.

This consideration may be applied to the explanation of our stability limits; that is, the change from the luminous flame to the dark flame is determined by the increase of heat loss to the reaction zone. The disappearance of the dark flame at a critical V_{Mg} with a small values of V_{CO_2}/l is due to thermal quenching. The blow off at a critical value of V_{CO_2}/l that is changed little with increase of V_{Mg} is due to the chemical limitation of the overall reaction of Mg and CO_2 in the flame.

The present experimental results show a critical value of V_{CO_2}/l of 140 s^{-1} in the Mg-CO_2 counterflow diffusion flame. According to the flame stability diagrams for the counterflow diffusion flames of

air/C_3H_8, one of the typical critical values of velocity gradient is 340 s^{-1} for air/C_3H_8 at 1 atm [7]. The order of critical value of velocity gradient for Mg-CO_2 in this experiment is nearly equal to that of air/C_3H_8. This suggests that the order of total reaction rate for Mg-CO_2 is the same order as that for air/C_3H_8.

Conclusion

1. A counterflow diffusion flame of Mg-CO_2 was formed by using a Mg vaporizer. The blow-off limits were caused by thermal quenching or chemical limitations on the combustion rate in the flame zone. These properties are very similar to those of the ordinary counterflow diffusion flames of gaseous fuels-oxidizers.
2. A luminous flame and a dark flame were observed over the multihole plate. In the luminous flame region, the reaction of

$$Mg + CO_2 \rightarrow MgO(g) + CO$$

occurred, and in the dark flame region, the reaction of

$$Mg + 1/2CO_2 \rightarrow MgO(s) + 1/2C$$

occurred. This difference is due to the heat loss to the surface of the multihole plate.
3. This experimental method using the counterflow diffusion flame is useful for investigating the overall reactions of gaseous metal fuel with an oxidizer.

Acknowledgments

This work was supported by the Grants-in-Aid for Special Project Research of Tokyo Metropolitan Government and Scientific Research of the Ministry of Education, Japan. The authors would like to express their thanks to Prof. H. Tsuji for his suggestions concerning the experiment results.

REFERENCES

1. Yuasa, S. and Isoda, H., AIAA 25th Joint Propulsion Conference, AIAA Paper 89-2863, 1989.
2. Yuasa, S. and Isoda, H., *Twenty-Second Symposium (International) on Combustion,* The Combustion Institute, Pittsburgh, 1989, pp. 1635–1641.
3. Shafirovich, E. Ya. and Goldshleger, U. I., *Combust. Sci. Technol.* 84:33–43 (1992).
4. Yuasa, S. and Fukuchi, A., *Twenty-Fifth Symposium (International) on Combustion,* The Combustion Institute, Pittsburgh, 1994, pp. 1587–1594.
5. Potter, A. E. Jr. and Butler, J. N., *ARS J.* 29:54–56 (1959).
6. Kim, J. S., Libby, P. A., and Williams, F. A., *Combust. Sci. Technol.* 87:1–25 (1992).
7. Tsuji, H. and Yamaoka, I., *Eleventh Symposium (International) on Combustion,* The Combustion Institute, Pittsburgh, 1967, pp. 979–984.
8. Tsuji, H. and Yamaoka, I., *Twelfth Symposium (International) on Combustion,* The Combustion Institute, Pittsburgh, 1969, pp. 997–1005.
9. Brzustowski, T. A. and Glassman, I., *Heterogeneous Combustion* (Wolfhard, H. G. et al., Eds.) Academic Press, New York, 1964, p. 117.
10. Sullivan, H. F. and Glassman, I., *Combust. Sci. Technol.* 4:41(1972).
11. Takeno, T. and Yuasa, S., *Combust. Sci. Technol.* 21:109 (1980).
12. Yuasa, S., Sogo, S., and Isoda, H., *Twenty-Fourth Symposium (International) on Combustion,* The Combustion Institute, Pittsburgh, 1992, pp. 1817–1825.
13. Gaydon, A. G., *The Spectroscopy of Flames,* Chapman and Hall, London, 1974.
14. Gordon, S. and Mcbride, B., Computer Program for Calculation of Complex Chemical Equilibrium Compositions, Rocket Performance, Incident and Reflected Shocks, and Chapman–Jouguet Detonations, NASA Report No. NASA SP-273, 1971.

Twenty-Sixth Symposium (International) on Combustion/The Combustion Institute, 1996/pp. 1953–1959

THE BEHAVIOR OF CHROMIUM IN LAMINAR HYDROGEN AND ETHENE DIFFUSION FLAMES

YOUNGBIN YOON[1], CHRISTOPHER REYES[1], A. DANIEL JONES[2], PETER KELLY[3], DANIEL P. Y. CHANG[4] AND IAN M. KENNEDY[1]

[1]*Department of Mechanical and Aeronautical Engineering*
University of California at Davis
Davis, CA 95616, USA

[2]*Facility for Advanced Instrumentation*
University of California at Davis
Davis, CA 95616, USA

[3]*Department of Chemistry*
University of California at Davis
Davis, CA 95616, USA

[4]*Department of Civil and Environmental Engineering*
University of California at Davis
Davis, CA 95616, USA

The fate of chromium has been studied in laminar hydrogen and ethene diffusion flames. Nitrogen was added in order to vary the flame temperature in hydrogen flames. Ethene flames were used in order to investigate the potential for interaction between the soot aerosol that is formed in these flames and the chromium aerosol. Two sources of chromium compounds were introduced: chromium nitrate and chromium hexacarbonyl. Samples of the vapor and particle phases of chromium compounds emitted from the flames were collected by an isokinetic dilution sampling probe. The amounts of Cr(VI) and total Cr were determined by a spectrophotometric method and by X-ray fluorescence spectrometry, respectively.

Results of Cr(VI) analysis in the hydrogen flame showed that the emission of Cr(VI) from the undiluted H_2 flame was more than 10 times larger than in the 50% H_2/50% N_2 flame on a mass basis. Approximately 50% of the total chromium emission from the pure H_2 flame was in the form of Cr(VI). This fraction dropped to about 1% in the heavily diluted H_2 flames. The relative amount of Cr(VI) in the vapor phase decreased by adding N_2 to the flame. The results indicated that flame temperature is an important factor with regard to emission of Cr(VI). In the ethene flame, the fraction of Cr(VI), which was found in the condensed phase, decreased slightly with increasing soot levels. It was not possible to detect chromium as a separate particle phase within the soot matrix.

Introduction

The disposal of hazardous waste has become a major issue as public concern over human and environmental exposures to toxic compounds has grown. Thermal treatment systems, such as incineration, can be useful methods for the disposal of toxic chemicals. However, pollutant emissions, such as the toxic products of incomplete combustion, fly ash, and bottom ash [1], from combustion processes are of great concern. Toxic metal aerosols emitted as a result of the incineration process are composed of micron and submicron particles [2] which can stay airborne for long periods of time and penetrate deep within the lung, causing mutagenic and carcinogenic effects [3].

Chromium, identified as a carcinogenic metal [4], has been widely used in alloys, refractories, and dyes. The toxicity of chromium depends on the valence of the metal; the hexavalent form of chromium (Cr[VI]) is known to be highly carcinogenic, whereas the trivalent form of chromium (Cr[III]) is noncarcinogenic and an essential nutrient for humans [4,5]. Almost all the hexavalent chromium in the environment comes from human activities. A major source of concern is from chrome-plating operations, although Cr may also be emitted from incineration, partly in the form of Cr(VI). In this hexavalent oxidation state, chromium is relatively stable in air and pure water, although it is reduced to the trivalent state over time. Consequently, it is very important that incinerators be designed to minimize the generation of the toxic metal emissions [6,7].

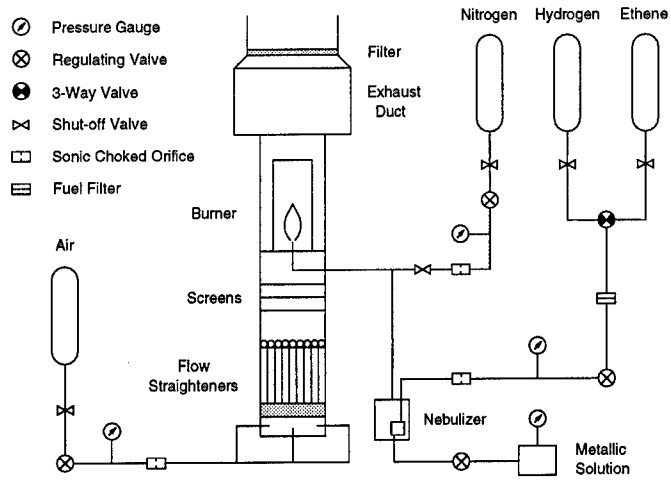

FIG. 1. Schematic of experimental apparatus.

TABLE 1
Experimental conditions of hydrogen flames using chromium nitrate

	100% H_2	67% H_2/33% N_2	50% H_2/50% N_2	33% H_2/67% N_2
H_2 flow rate (L/min)	1.30	1.30	1.30	1.30
N_2 flow rate (L/min)	0	0.65	1.30	1.95
Air flow rate (L/min)	315	315	315	315
Max. adiabatic flame temperature (K)	2450	2224	2032	1873
Flame height (mm)	65	75	85	95
Feed rate of chromium nitrate solution (mg/min)	31.6	31.6	31.6	31.6
Concentration of chromium nitrate solution (g/L of nano-pure H_2O)	200	200	200	200

Investigators have developed various methods to determine the speciation of chromium and its compounds in samples that are obtained from incinerators [8–10]. Information relating to the kinetics of chromium oxidation has been obtained at realistic incinerator temperatures by Fontijn et al. [11]. The thermodynamics of gas-phase chromium species have also been assessed for application to chromium volatility calculations [12]. However, there is little information available on the emissions of hexavalent chromium from flames with varying flame temperature, residence time, concentration of soot, etc. In this study, laminar diffusion flames of hydrogen and ethene have been used to provide a well-controlled model of non-premixed combustion. The hydrogen flame has been used to examine the effect of temperature on the formation of chromium compounds by adding nitrogen gas to the flame. In addition, the amount of soot produced from the ethene flame was varied in order to investigate interaction of soot with chromium particles. A fundamental understanding of the fate of chromium in these flames will facilitate the development of reduction technologies and predictive capabilities for the toxic metal emissions from incinerators.

Experimental Methods

Apparatus

The coflow, laminar, diffusion flame system is shown in Fig. 1. The 5-mm burner nozzle was positioned in the center of a 100- × 100-mm duct containing flow straighteners and a series of fine-mesh screens to ensure air-flow uniformity. Two fuels were used in this experiment: hydrogen and pure ethene. In the hydrogen flame, nitrogen was added to vary the flame temperature; the hydrogen was also used to atomize the chromium solution. The flow rate of hydrogen was fixed at 1.3 L/min, and the feed rate of chromium nitrate solution was constant, as shown in Table 1. The fuel and entrained aerosol were mixed with nitrogen gas and injected at the fuel

TABLE 2
Experimental conditions of ethene flames using chromium nitrate

	Nonsooting	Incipient Sooting	Sooting	Heavily Sooting
C_2H_4 flow rate (L/min)	0.20	0.28	0.33	0.50
Air flow rate (L/min)	315	315	315	315
Flame height (mm)	75	120	150	180
Feed rate of chromium nitrate solution (mg/min)	10.4	15.2	15.7	17.8
Concentration of chromium nitrate solution (g/L of nano-pure H_2O)	200	200	200	200

TABLE 3
Properties of chromium compounds

	Valence	Toxicity	Melting Point (°C)	Boiling Point (°C)	Color	Solubility in Water
$Cr(NO_3)_3 \cdot 9H_2O$	III	noncarcinogenic	60	dec. @ 100	purple	soluble
$Cr(CO)_6$	zero	noncarcinogenic	dec. @ 110	expl. @ 210	white	insoluble
Cr_2O_3	III	noncarcinogenic	2435	4000	green	insoluble
CrO_3	VI	carcinogenic	197	dec. @ 250	orange-red	soluble

Abbreviations: dec. = decomposes; expl. = explodes.

nozzle. In ethene flames, the fuel was the carrier gas, and the flow rate of ethene was varied to achieve different types of sooting flames, as shown in Table 2. All flow rates were controlled by calibrated sonic orifices.

Two different sources of chromium compounds were introduced: chromium nitrate and chromium hexacarbonyl. Their properties are shown in Table 3. Chromium nitrate ($Cr(NO_3)_3 \cdot 9H_2O$) is soluble in water and has an oxidation state of Cr(III). A 0.5-M chromium nitrate solution was atomized by a Lovelace nebulizer and introduced into the flame. Chromium hexacarbonyl ($Cr(CO)_6$) was used as a source of zero oxidation state of chromium. A 13-mm-diameter glass cartridge containing 0.5 g of chromium hexacarbonyl was plugged with glass wool at both ends and connected to the fuel lines. Since chromium hexacarbonyl is volatile at room temperature, its vapor was carried by the fuel and then introduced directly to the flame.

Sampling

Samples of vapor and particle phases of chromium compounds emitted from the flame were obtained using a stainless steel sampling probe positioned 20 mm above the flame tip at the centerline. The 200-mm-long, 22-mm outer diameter sampling probe contained a 150-mm-long, 13-mm-diameter inner sintered metal tube. The sintered metal tube formed the inner wall of the probe. Nitrogen dilution gas was provided to the sampling probe through the sintered metal part and mixed with the sample in order to quench reactions and the development of aerosols through the sampling lines [13]. The flow of N_2 was radially inward in order to minimize the transport of particles and vapors to the probe wall. Dilution of the sample with N_2 served to reduce the partial pressure of condensable compounds and hence minimized conversion of vapor to particulates. Because some interphase conversion is unavoidable, the reported vapor fractions of chromium represent a lower limit estimate of the actual fraction present at the sampling location above the flame. Furthermore, the cooling of the sample by dilution was a reasonably realistic representation of the process encountered by emissions from the flame zone of a combustion system as they mix with excess air. The flow rate of nitrogen dilution gas was fixed at 1.5 L/min; this corresponded to about 25% of the total flow rate of sample. Variation of the N_2 flow rate verified that the chemical compositions of chromium compounds were not sensitive to the quenching conditions. Furthermore, tests with unseeded flames showed that no detectable chromium was introduced into the samples from the metal in the probe itself. The sampling probe was grounded in order to avoid electro-

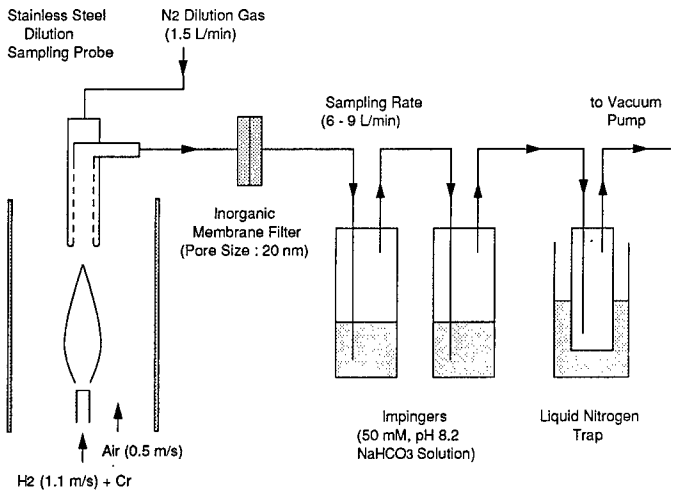

FIG. 2. Schematic of chromium sampling system.

static deposition of charged chromium particles along the sampling line wall.

Figure 2 shows the chromium sampling system. The particle phase of chromium was captured on a 47-mm-diameter alumina membrane filter with 20-nm pores. The sampling rate was measured with a flowmeter and was controlled to achieve an isokinetic condition. Tygon™ was used in all the sampling lines to reduce the problem of electrostatic deposition [14]. The sampling lines between the sampling probe and the filter were heated with heating tapes to prevent condensation in the lines. Thus, the temperature of the sampled gas at the filter was 105°C, which was high enough to prevent water from being condensed along the sampling lines and was low enough to avoid the conversion between Cr(VI) and Cr(III). Hence, the chromium particles were collected in an environment free of liquid water.

The impinger and liquid nitrogen trap were designed to capture the vapor phase of the chromium compounds. This sampling method was based upon a modified version of the Method 0013 train prescribed by the EPA [15,16] with the inclusion of alumina filters for particulate collection. It was important to choose an impinger solution in which chromium oxides were soluble and stable. NaOH(0.1N) solution, which has been used for chromium sampling [17], was not suitable for sampling Cr(III) because Cr(III) was precipitated as $Cr(OH)_3$ in the NaOH solution. It was also found that Cr(VI) reactivity was pH dependent: at pH 8.0, the Cr(VI) reaction was sufficiently slow that Cr(VI) concentrations remained relatively unchanged [17]. Therefore, 100-mL $NaHCO_3$ (0.05 M, pH 8.2) was chosen as a buffer solution for each impinger after a validation test that confirmed that Cr(III) and Cr(VI) were stable in the buffer solution. The impinger captured the vapor phase of the chromium compounds, which was soluble in $NaHCO_3$. Any vapor phase of chromium compounds passing through the impinger was captured in a condensed state by the liquid nitrogen trap. The liquid nitrogen trap consisted of an Erlenmeyer flask placed in an insulated container; the container was surrounded by liquid nitrogen at 77 K.

Sample Analysis

Two different sampling times were used for each source of chromium compounds, because the feed rates of chromium compounds were different: 4-h sampling times for chromium nitrate and 30 min for chromium hexacarbonyl. Measurable amounts of chromium were captured in the filter, impinger, and liquid nitrogen trap during these periods. The weights of the filters were measured before and after sampling. The filters were then extracted with 10-mM $NaHCO_3$ solution for 20 h. The sampling probe and sampling line in front of the filter were rinsed with nano-pure water and collected in sampling bottles. These samples were considered to contribute to the measured particle phase of chromium. Samples collected in the sampling lines after the filter, the impingers, and the liquid nitrogen trap were considered to represent the vapor phase of chromium.

A spectrophotometric method was used for Cr(VI) analysis. A 1.7-mL sample was mixed with 200-mL 6N H_2SO_4 and 100-mL diphenyldicarbazide (0.5 g in 100-mL acetone), and absorbance was measured at 540 nm in a quartz cuvette using a Shimadzu PC-2101A spectrophotometer. An X-ray fluorescence (XRF) method was used to measure the total chromium with a Kevex 0700/8000 energy-dispersive XRF spectrometer; solutions were analyzed by loading 100 mL of solution onto alumina filters. Cr(III)

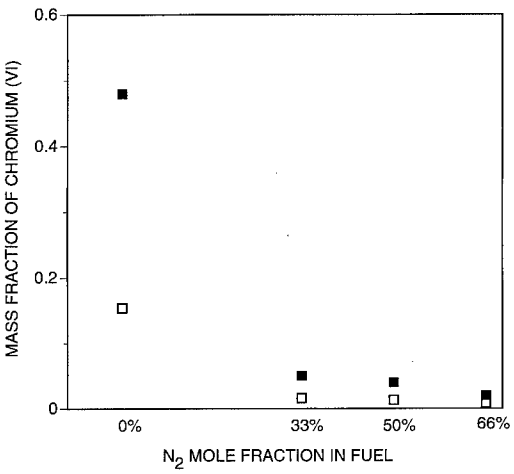

FIG. 3. Fractions of total chromium emitted as Cr(VI) from hydrogen flames with varying N_2 dilution: chromium nitrate (open symbols) and chromium hexacarbonyl (solid symbols).

was determined by subtracting Cr(VI) concentration from total chromium [10].

Results

One of the significant factors in the destruction of hazardous wastes and in the formation of chromium compounds is the flame temperature. The temperature could affect not only the formation of chromium species but also the phases of species, as shown below. Thus, the adiabatic flame temperature was varied in the hydrogen flames; as the addition of nitrogen inert gas increased from 0 to 67% on a mole basis, the maximum adiabatic flame temperatures, which were calculated with STANJAN code [18], decreased from 2450 to 1873 K, as shown in Table 1.

The results of Cr sample analysis showed the effect of N_2 addition to the flame and the importance of the form in which chromium was added to the flame. When the chromium was added in the form of nitrate solution, filter samples revealed the presence of micron-sized cenospheres in SEM images. The cenospheres were composed of many spherules, which may have been formed from a melt of the nitrate as it was heated in a manner similar to that described by Mulholland and Sarofim [19,20]. The size distribution of the aerosol sample was bimodal with a distinct submicron mode. Samples obtained by seeding with hexacarbonyl were quite different. A shiny yellow-orange color filter was obtained from the pure-hydrogen flames, which was consistent with the color of CrO_3(Cr(VI)oxide), whereas a dark green color was observed with the hydrogen flames diluted by N_2 gas. This color corresponded to the color of Cr_2O_3(Cr(III) oxide), as shown in Table 3. These two chromium oxides are expected to be the major Cr compounds formed from nonchlorinated chromium waste flames [21,22].

The recovery efficiency of total chromium added to the flame was estimated from knowledge of the vapor pressure of hexacarbonyl as a function of temperature. Use of the vapor pressure estimate was necessary because of the difficulty in measuring accurately the very small differences in carbonyl masses at different times. At room temperature, the saturation pressure of chromium carbonyl was equivalent to a concentration in the flow through the nozzle of 500 ppm. Further assuming that all the flame gases entered the sampling probe, the recovery of total chromium was about 12% for the 33% H_2/67% N_2 flame, a typical result. This was a lower limit to the recovery of chromium. The fuel stream was unlikely to have been saturated with carbonyl vapor. Subsequent analysis of actual samples for which total chromium input was measured showed that the recovery of total Cr was 27% for the ethene flames and 46% for the hydrogen flames. Although the recovery was low, sampling and analysis of metals from flames is notoriously difficult. The results are presented in the form of ratios of Cr(VI) to total Cr, so that the uncertainty resulting from low recoveries is minimized. It was found from the sample analysis that the emission of Cr(VI) from the H_2 flame decreased as N_2 was added to the flame (Fig. 3); high temperatures favored the formation of Cr(VI) although this was not expected to be an equilibrium product at the low sampling temperatures above the flame. For example, Cr(VI) emissions from the 100% hydrogen flame with chromium hexacarbonyl addition was 15 times larger on a mass basis than those from the 50% H_2/50% N_2 flame. Although less Cr(VI) was produced in the 100% hydrogen flame using chromium nitrate, the trend was similar to that of the chromium hexacarbonyl case. These observations were consistent with the results reported by Steinsberger et al. [17]. They found that higher incinerator temperatures and longer residence times led to an increase in the ratio of Cr(VI) to total chromium in the incinerator emissions. Their results indicated that improved combustion actually exacerbated the Cr(VI) problem, posing something of a dilemma when hazardous wastes need to be destroyed to very low levels. Chemical equilibrium calculations [21,22] also offer some insight into the chromium behavior. These calculations predict that over a wide range of temperatures (500–1500 K), the formation of the condensed phase of Cr_2O_3 (Cr(III)) is favored thermodynamically and that at higher temperatures (above 1500 K), the formation of the vapor phase of CrO_3 (Cr(VI)) becomes significant. As noted above, Cr(VI) is not an equilibrium product at low temperatures and results from frozen

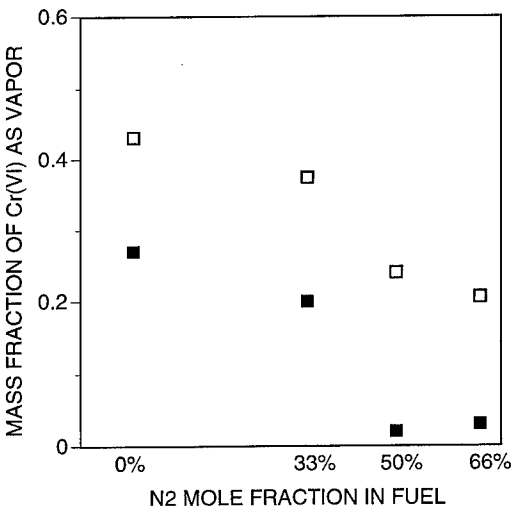

FIG. 4. Fractions of chromium (VI) emitted as vapor and condensed phases from hydrogen flames with varying N_2 dilution: chromium nitrate (open symbols) and chromium hexacarbonyl (solid symbols).

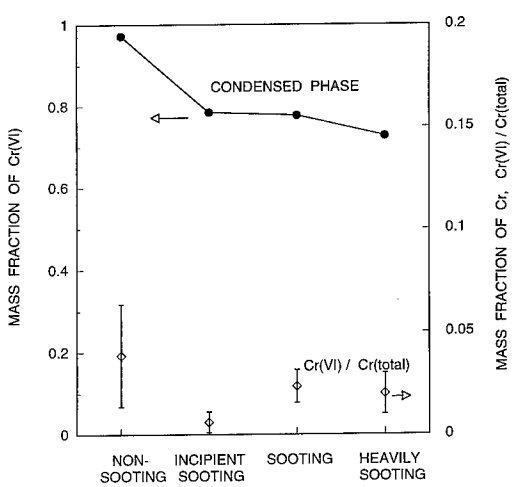

FIG. 5. Partitioning of chromium(VI) between vapor and condensed phase and Cr(VI) fraction of total chromium in ethene flames using chromium hexacarbonyl: ● condensed-phase fraction of total Cr(VI) emissions, ◇ Cr(VI) fraction of total chromium.

reactions in the post-flame region. These results indicate that flame temperature is a dominant factor in the formation and conversion of chromium compounds. Kinetics and the temperature history of metal species in post-flame gases are important in determining the ultimate nature of the metal emissions.

It should be noted that the form of the chromium feed had an impact on the emissions. The fraction of total chromium emitted as Cr(VI) from the 100% hydrogen flame using chromium hexacarbonyl was larger by a factor of 3 than the Cr(VI) fraction using chromium nitrate feed, that is, Cr(III). It is possible that the formation of a melt of the nitrate preserved the initial oxidation state of the chromium and inhibited further reactions through slow diffusion into the pores of the cenospheres.

The partitioning of Cr(VI) between condensed and vapor phases is shown in Fig. 4 for nitrate and carbonyl feeds. It was found that the amount of vapor phase Cr(VI) was reduced by adding N_2 to the flame; the vapor phase of Cr(VI) decreased by a factor of 2 by adding N_2 to the hydrogen flame using chromium nitrate. A greater decrease in the vapor phase of Cr(VI) was observed with the chromium hexacarbonyl feed. Most of the vapor phase chromium was found in the impinger solutions with very little reaching the N_2 trap. For example, sampling from the pure H_2 flame seeded with chromium carbonyl for 30 min produced 26 mg of chromium in the impinger solution and only 2.5 mg in the N_2 trap; the lower-temperature 67% N_2/33% H_2 flame yielded 1 mg in the impinger and 0.3 mg in the trap. The mass of chromium collected from the sampling probe and lines was significantly greater than the amount collected in the impinger, typically 4 to 10 times greater than the impinger figures quoted above. Although the ratio of vapor phase to condensed phase chromium was dependent on the source of chromium, the trend with respect to temperature was the same for both sources of chromium. Lower temperatures would be expected to lead to more conversion of the chromium to the condensed form. Furthermore, it is noted that the Cr(VI) appears mainly as an aerosol over the entire temperature range.

Ethene flames were operated in nonsooting, incipient sooting, and sooting modes by varying the flow rate of the fuel. The mass fractions of condensed-phase and vapor-phase chromium (VI) are shown in Fig. 5; the chromium source was hexacarbonyl. The fractions of total chromium that were recovered as Cr(VI) are also shown in Fig. 5. These numbers are similar to the Cr(VI) yields from the lower-temperature H_2 flames. The yield of Cr(VI) from the ethene flames was almost constant (within experimental uncertainties) at around 1–3% of the total chromium. As the soot yield from the flame increased, the fraction of the Cr(VI) in the condensed phase decreased. It is not possible to offer a firm explanation for the apparent impact of soot on the partitioning of Cr (VI) between condensed and vapor phases. Although the soot-laden filters were allowed to leach in the bicarbonate solution for 1 week, it is possible that some Cr(VI) was retained within the soot after this time. It is also possible that the soot may act as a sink for Cr (VI) via reduction reactions between the chromium aerosol and the

carbon. Resolution of these important issues will require further investigation.

Summary

Chromium sampling in hydrogen and ethene flames has been performed using a N_2 dilution sampling probe, an inorganic membrane filter, an impinger, and a liquid nitrogen trap. All the samples were analyzed by a spectrophotometric method and X-ray fluorescence spectrometry to quantify the amounts of Cr(VI) and Cr(III), including the partitioning of Cr(VI) phases. The results of Cr sample analysis showed the emission of large amounts of Cr(VI) in a pure H_2 flame (up to 50% of the total chromium). The fraction of Cr(VI) in the post-flame gases decreased as N_2 was added to the flame; the amount of Cr(VI) emitted from the 100% hydrogen flame was more than 10 times larger than that of the 50% H_2/50% N_2 flame on a mass basis. This shows the strong effect of the flame temperature on the nature of chromium emissions. In fact, the temperature dependence of the chromium oxidation state poses something of a dilemma for incinerator operators, who require high temperatures in order to ensure complete destruction of hazardous wastes. It was found that the vapor phase of Cr(VI) decreased by decreasing the flame temperature in the hydrogen flames. Although the general trends with two different Cr sources, namely, chromium nitrate (Cr III) and chromium hexacarbonyl (Cr 0), were similar to each other, the Cr(VI) emissions from H_2–N_2 flames seeded with chromium hexacarbonyl were more sensitive to the variations of the flame temperature, possibly as a result of the heterogeneous nature of chromium nitrate decomposition. Soot emissions from ethene flames did not have a measurable impact on the Cr(VI) fraction that was emitted. The chromium in the aerosol form was found by electron microscope examination to be intimately bound up with the soot. There was no evidence of chromium appearing as a separate phase.

Acknowledgment

This research was supported by the NIEHS Superfund Basic Research Program, P42ES04699.

REFERENCES

1. Linak, W. P. and Wendt, J. O. L., *Prog. Energy Combust. Sci.* 19:145–185 (1993).
2. Davidson, R. L., et al., *Environ. Sci. Technol.* 8:1107–1113 (1974).
3. Smith, R. D., *Prog. Energy Combust. Sci.* 6:53–119 (1980).
4. Health Assessment Document for Chromium, U.S. EPA, EPA-600/8-83-014F, 1983.
5. Environmental Health Criteria 61 for Chromium, World Health Organization, Geneva, 1988.
6. Linak, W. P., Srivastava, R. K., and Wendt, J. O. L., *Combust. Sci. Technol.* 101:7–27 (1994).
7. Oppelt, E. T., *J. Air Poll. Control. Assoc.* 37:557–583 (1987).
8. Winter, R. M., Mallepalli, R. R., Hellem, K. P., and Szydlo, S. W., *Combust. Sci. Technol.* 101:45–58 (1994).
9. Axner, O. and Rubinsztein-Dunlop, H., *Appl. Opt.* 32:867–883 (1993).
10. The Sources, Chemistry, Fate, and Effects of Chromium in Aquatic Environments, American Petroleum Institute, Ecological Analysts, Inc., 1981.
11. Fontijn, A., Blue, A. S., Narayan, A. S., and Bajaj, P. N., *Combust. Sci. Technol.* 101:59–73 (1994).
12. Ebbinghaus, B. B., *Combust. Flame* 101:311–338 (1995).
13. Heinsohn, R. J., Davis, J. W., Anderson, G. W., and Kopetz, Jr., E. A., Paper No. 76-37.3, Annual Meeting, Air Pollution Control Association, 1976.
14. Willeke, K. and Baron, P. A., *Aerosol Measurement,* Van Nostrand Reinhold, New York, 1993, p. 103.
15. Method 0013, Code of Federal Regulations, EPA SW-846, Title 40, Part 266, Appendix IX, pp. 546–557.
16. Draft Method 0013, EPA/530-SW-91-010 (NTIS PB91-120006), pp. 3-49–3-69, Washington, D.C., 1990.
17. Steinsberger, S. C., DeWees, W. G., Bell, A. C., Finken, R. A., Knoll, J. E., and Midgett, M. R., *Fuel Processing Technol.* 39:265–276 (1994).
18. Reynolds, W. C., STANJAN, The Department of Mechanical Engineering, Stanford University, Stanford, CA, 1986.
19. Mulholland, J. A. and Sarofim, A. F., *Environ. Prog.* 10:83–88 (1991).
20. Mulholland, J. A. and Sarofim, A. F., *Environ. Sci. Technol.* 25:268–274 (1991).
21. Rizeq, R. G., Hansell, D. W., Clark, W., and Seeker, W. R., 93-TP-63.03, 86th Annual Meeting & Exhibition, AWMA Denver, CO, 1993.
22. Wu, C. Y. and Biswas, P., *Combust. Flame* 93:31–40 (1993).

Twenty-Sixth Symposium (International) on Combustion/The Combustion Institute, 1996/pp. 1961–1967

BURNING VELOCITIES IN FUEL-RICH ALUMINUM DUST CLOUDS

S. GOROSHIN, I. FOMENKO AND J. H. S. LEE
Department of Mechanical Engineering
McGill University, 817 Sherbrooke Street West
Montreal, Quebec, H3A 2K6, Canada

A new experimental apparatus that can produce Bunsen-type premixed dust flames stabilized on a water-cooled ring has been constructed. The burning velocities in rich aluminum dust clouds of particle size $d_{32} = 5.4\ \mu m$ have been measured by determining the surface area of the inner flame cone and the total volumetric flow rate. It was found that in rich Al-O_2-N_2 mixtures, the burning velocity is a weak function of dust concentration. At the same time, the dependence of the burning velocity on the oxygen concentration is considerably stronger in rich mixtures than that reported in literature for the fuel-lean aluminum dust clouds. The burning velocity changes from 12–13 cm/s to about 32 cm/s when the oxygen content in the mixture increases from 11% to 30%. The burning velocity was also found to be a strong function of the molecular transport properties of the carrier gas. Thus, replacing the argon in an Al-O_2-Ar mixture with helium increases the burning velocity from 20 to 65 cm/s. The oxygen limit for the flame propagation (9.5 ± 0.5%) was also found by measuring the minimal oxygen concentration in the dust carrier gas when a premixed flame cone is formed inside the diffusive dust flame. A simple model of the dust flame with molecular heat transfer that has been proposed is based on the assumption that the particle burning rate in the flame front is controlled by the oxygen diffusion. It was shown that the weak dependence of the flame speed on dust concentration is a direct result of the weak dependence of the particle burning rate in the diffusive regime on the flame temperature. The model also predicts dependence of the burning velocity in rich dust mixtures on the Lewis number in accordance with the experimental observations.

Introduction

Combustion of a suspension of solid-fuel particles in a gaseous oxidizing medium (premixed dust flame) is important for many areas of modern technology (e.g., coal combustion, dust explosion hazards, propulsion systems). However, the understanding of dust combustion phenomena is still in a rudimentary state compared with gas flames. This is due mostly to the lack of reliable fundamental data on dust combustion such as burning velocity. (A large amount of experimental data accumulated on constant volume [closed bomb] dust explosions cannot be converted into fundamental combustion parameters because of unknown flame temperature and often incomplete and nonsymmetrical combustion caused by dust dispersion problems.)

With the exception of coal dust flames [1], very limited data are available in the literature on the combustion of dusts, particularly pure, nonvolatile, nonorganic substances such as metals.* Cassel, in his pioneering works [2,3], measured burning velocities in aluminum-air suspensions using Bunsen-type and flat-dust flame burners. Ballal obtained burning velocities in magnesium, aluminum, and carbon dust-air clouds, observing the propagation of flat flames in tubes under microgravity conditions [4]. Both investigators worked with lean dust mixtures and the dust concentration range investigated was relatively narrow, between B = 120–150 and B = 270–300 g/m^3 (the stoichiometric fuel concentration in aluminum-air suspension is about 305 g/m^3). Both investigators found that for atomized aluminum dust (particle size <10 μm), the burning velocity increases with dust concentration from 20–25 cm/s near the lean limit to about 40 cm/s for dust concentrations close to stoichiometric level. Cassel also found that the burning velocity for lean mixtures increases approximately proportionally to $\sqrt{Y_{O_2}}$ when the oxygen content (Y_{O_2}) in the O_2-N_2 mixture is increased from 21% to 100% of oxygen.

It is well-known from constant-volume dust combustion experiments that dust mixtures demonstrate a peculiar behavior in the region of fuel-rich mixtures. Many investigators [5,6] have found that during the constant volume dust explosion, the rate of the pressure rise reaches its maximum value and correspondingly the time to peak pressure reaches a minimum for very rich mixtures (e.g., 800–1000 g/m^3 for aluminum-air mixtures [6]). The burning rate then levels off in a wide range of dust concentrations after the maximum. The value of the rich concen-

*Strictly speaking, coal burning is not a pure solid combustion phenomenon but a combination of a gaseous flame [combustion of volatile] and heterogeneous solid char combustion.

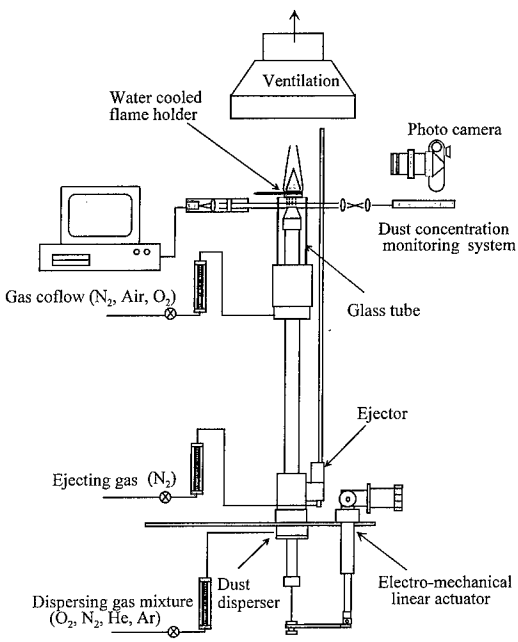

FIG. 1. Schematic of the experimental setup–dust burner.

tration limit of flame propagation is probably extremely large and is still unknown [7]. One can expect that the burning velocity will follow the same trend as the rate of the pressure rise.

Our recent measurements of the flame propagation speed in rich dust mixtures using the laminar stage of flame propagation in vertical tubes [8] have confirmed the weak dependence of the flame speed on dust concentration. Thus, this behavior appears to be a fundamental feature of the dust flame. However, it should be noted that the flame speed data obtained in a flame tube cannot be converted to the laminar burning velocity because of the difficulties of defining the flame shape and particle velocity in the unburned mixture ahead of the flame.

In the present work, a new experimental apparatus that can produce Bunsen-type premixed dust flames stabilized on a water-cooled ring has been constructed to permit accurate measurements of burning velocity in fuel-rich aluminum dust clouds over a wide range of dust concentrations. The influence of oxygen concentration and the type of inert carrier gas on the burning velocity are also studied in the present investigation.

Experimental Details

The burning velocity in homogeneous gas mixtures has been studied extensively in Bunsen-type burners. Most of the existing experimental data available have been obtained with this technique [9]. However, the curvature effect at the flame tip, heat losses at the flame base, and the stretch effects have restricted the accuracy of burning velocity measurements by Bunsen flame to about 25% [10]. Recently, novel methods, such as the counterflow opposed-jet technique, have been developed to eliminate the disadvantages posed by the Bunsen-burner method [11]. The use of the counterflow burner for dust combustion posed considerable technical difficulties in obtaining identical opposite uniform dust flows of the same dust concentration. Therefore, the Bunsen-burner method is used in the present study. However, we expect that the accuracy of the burning velocity measurements is still in the range of 25% according to an analysis provided by Andrews and Bradley for homogeneous gas flames [10]. This is because an estimation of the thickness of aluminum dust flames of small particle sizes ($d_{32} = 5\ \mu$m) based on our quenching distance measurements [8] show the flame width to be about 1.5–2 mm. This is about an order of magnitude less than the diameter of the burner used in present experiments.

Dust Burner

The schematic of the present experimental setup–dust burner is shown in Fig. 1. The dust dispersion system includes a syringe-type dust feeder and a circular, annular, high-velocity gas jet sheet for dispersing the dust. The dispersion technique has been used recently in our quenching distance experiments and is described in detail in Refs. 8 and 12. The system has been demonstrated an ability to produce a uniform dust flow for a wide range of dust concentrations for a duration of up to 4–6 min. The gas flow through the dispersion system is maintained constant, and the variation of the dust concentration is achieved by changing the dust feeding rate. To regulate the dust flow rate to the burner, a calibrated ejection system is used to eject the required part of the dust flow from the main stream to a side tube. A long, stainless steel tube of 70 cm length and inner diameter 25 mm is connected to the dispersion chamber through a small-angle conical diffuser. This provides laminarization of the initially turbulent dust flow as it exits the dust disperser. The dust flow exits the combustion tube through a small-angle conical nozzle ($D = 1.8$ cm). A water-cooled brass ring with a triangular cross section ($ID = 20$ mm, $H = 5$ mm) is used as a flame holder and is located 1 cm above the nozzle exit. An auxiliary stream of N_2, concentric to the dust stream, is used to maintain the cylindrical configuration of the dust cloud issuing from the burner.

The dust concentration is monitored by a light extinctiometer using an expanded parallel He-Ne laser beam ($d = 8$ mm) crossing the dust flow along the diameter in the space between the nozzle exit and

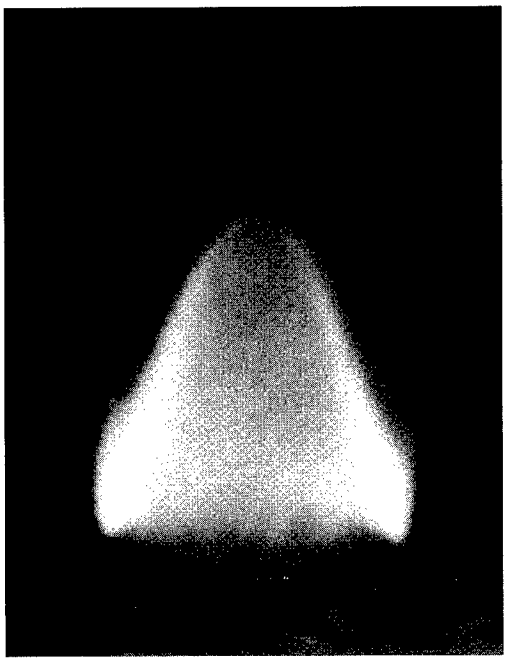

FIG. 2. Photograph of aluminum Bunsen dust flame in the oxygen-nitrogen mixture. Oxygen concentration in the mixture: 16%; dust concentration: 410 g/m^3.

the flame holder. The photodetector with a focusing lens is placed inside a narrow channel to minimize the collection of scattered laser light; it is also protected by a narrow bandwidth interference filter (λ = 632.8 nm, $\Delta\lambda$ = 1 nm) from the light emitted by the flame and scattered by aluminum particles. The signal from the photodetector is amplified and registered by a computer data-acquisition system (R.C. Electronics). The optical dust concentration monitoring system was first calibrated. A set of fine synthetic filters attached to a vacuum pump (see Ref. 8 for details) is used to collect all of the dust from the flow for a known period of time (usually several seconds).

Experimental Procedure

Atomized aluminum powder (produced by Ampal Inc., NJ) with an aluminum content not less than 99.5% is used in present experiments. The aluminum particles are of spheroidal or nodular shape and the Sauter mean diameter d_{32} is found to be 5.4 μm. The differential distribution of particle size is relatively narrow: 90% of the total powder mass is located in the range of particle sizes between 2 and 10 μm. The powder was dried at 120–140°C for 24 h before an experiment to improve its dispersion characteristics.

Once the steady dust flow has been established, it is ignited by a small, remotely operated propane-air torch. The torch is immediately turned off after a stabilized dust flame is achieved. The flame shapes were recorded with a Canon single-lens reflex camera with a bellows macrophoto attachment at a scale of 3:1. The aluminum dust flame is extremely bright, and a neutral filter with an optical density of about 3 had to be used to attenuate the flame radiation. The time-synchronization marks produced by the camera at the moment of recording are registered on the computer data-acquisition system. This allows the dust concentration in the flow at the moment of the image recording to be determined.

To obtain the total flame surface area, the flame photo image is magnified (10×) and the coordinates of the inner boundaries of the luminous flame cone are then measured at 12–15 points. A third-degree polynomial approximation taken from standard curve fitting software (KaleidaGraph) is used to approximate the shape of the projection of the flame boundaries. The surface area of the corresponding rotational figure was then found by numerical integration. The burning velocity is determined as a product of division of the total flow rate through the nozzle by the measured flame surface area.

Experimental Results

General Observations

A typical photograph of the aluminum dust flame in oxygen-nitrogen atmosphere is shown in Fig. 2. The flame base is usually lifted about 1–2 mm above the flame holder; it has a rounded tip, and the inner boundary of the luminous cone is usually well defined in comparison with the outer flame boundary. This is probably due to the scattering of the emitted light by the condensed combustion products (ultrafine aluminum oxide particles) in the postflame zone. Because of this scattering and the curvature effects, the visible thickness of the flame front (2–3 mm) as shown in the photograph is probably larger than the real thickness of the combustion zone. It is also interesting to note that the tip of the flame is often open for very rich flames (in homogeneous gas combustion this effect is usually observed only for very lean mixtures [13]). The size of the opening (1–2 mm), however, is not large enough to affect the results of the burning velocity measurements.

Burning Velocity Measurements in Oxygen-Nitrogen Mixtures

The results of the burning velocities measurements as a function of dust concentration in mixtures of nitrogen with different oxygen content are shown in Fig. 3. In general, the minimum dust concentration in which a stabilized flame can be observed (i.e.,

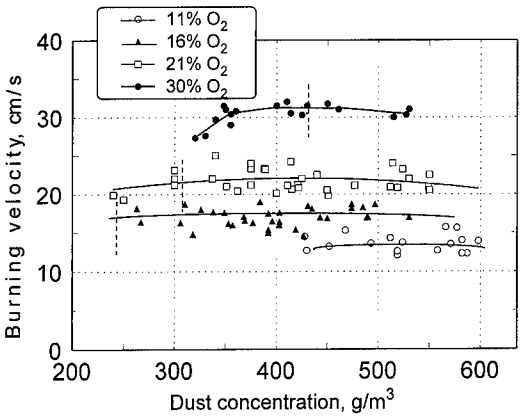

FIG. 3. Dependence of burning velocity on dust concentration in Al-O_2-N_2 mixtures with a different oxygen content. Dotted lines indicate the stoichiometric concentrations.

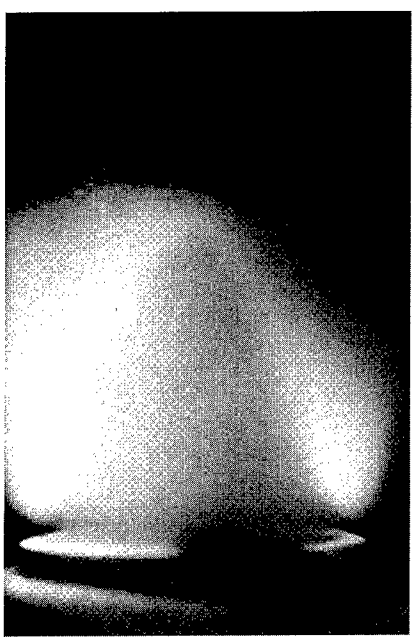

FIG. 4. Photograph of aluminum dust Bunsen flame in Al-O_2-He mixture. Oxygen concentration in the mixture: 21%; dust concentration: 360 g/m^3.

stability limit) increases with decreasing oxygen concentration in the mixture. However, the flames demonstrate poor symmetry and a strong tendency toward flashback at low dust concentrations in mixtures with the highest initial oxygen content (30% O_2). Thus, the burning velocity could not be determined with an acceptable accuracy for these lean mixtures with the present method.

The range of dust concentrations (B, g/m^3) studied in terms of the fuel equivalence ratio ($\phi = B/B_{st}$, B_{st} is a stoichiometrical dust concentration) is rather high and reaches the value of $\phi = 2.5$ for the mixture with 16% O_2 and $\phi = 3.7$ for the mixture with 11% O_2. As can be seen from Fig. 3, the value of the mass concentration of fuel in rich mixtures does not affect the flame speed for a whole range of investigated dust concentrations. The observed effect is in contrast to the relatively strong dependence of burning velocity on the fuel concentration observed by Cassel [2,3] and Ballal [4] for lean aluminum dust mixtures. This result is also in contrast to the dependence of the burning velocity on fuel concentration usually observed for premixed gas flames (which is approximately symmetrical around stoichiometry [9]). The present results are in agreement with our recent measurements of quenching distance in aluminum dust clouds [8]. The dependence of the quenching distance on dust concentration mirrors the behavior of the flame speed. The quenching distance also reaches a minimal value at concentrations close to stoichiometric and then levels off in a wide range of dust concentrations. As will be shown later, both effects are direct consequences of the diffusive mechanism of aluminum particle combustion.

The initial oxygen content has a much stronger influence on burning velocity for rich mixtures (see Fig. 3) than was observed by Cassel for lean dust mixtures [3]. This is because the higher oxygen content in rich mixtures not only leads to an increase in the speed of diffusive particle combustion ($W \sim Y_{O_2}$) but also produces higher flame temperatures because of the larger amount of burned fuel. The initial oxygen concentration has no influence on the adiabatic flame temperature in lean mixtures.

Burning Velocity Measurements in Argon-Oxygen and Helium-Oxygen Mixtures

The carrier gas (nitrogen) used in the mixture was replaced by the inerts argon or helium to investigate the role of the gas molecular transport properties such as thermal heat conductivity (a [cm^2/s]) and oxygen diffusivity (D [cm^2/s]) on the dust flame propagation phenomena. The visible flame structure and flame speeds in argon-oxygen-aluminum dust clouds are very close to those observed for the air-aluminum dust flames (see Fig. 5). The only noticeable difference is that the flame with argon appears to be considerably brighter than the air flame. This observation is in agreement with thermodynamic equilibrium calculations that show that the replacement of the two-atom molecular nitrogen by a single-atom inert gas such as argon or helium increases the flame temperature from 3540 to 3650 K. The higher flame temperature probably compensates a somewhat lower value of molecular transport coefficient in argon-oxygen mixtures compared to those in air. Thus,

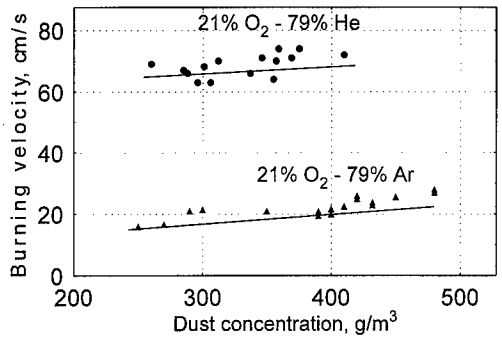

FIG. 5. Experimental data on burning velocity in Al-O_2-He and Al-O_2-Ar mixtures at different dust concentrations.

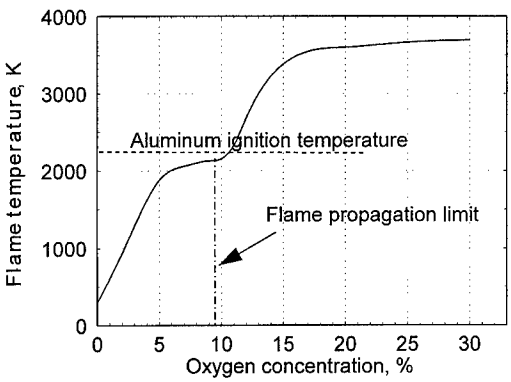

FIG. 6. Dependence of calculated adiabatic flame temperature in Al-O_2-Ar mixtures on the concentration of oxygen. Dust concentration: 350 g/m^3.

the flame speeds in argon-oxygen mixtures and in air are almost identical.

In contrast, the flames in helium-oxygen mixtures are not only more than three times faster than the Al-air or Al-O_2-Ar flames (see Fig. 4) but the flame structure is also different for flames with helium (Fig. 5). As can be seen from Fig. 5, only the inner boundary of the flame (dark cone) is visible and a luminous zone of gradually diminishing brightness stretches for more than a centimeter above the inner dark cone.

Direct interferometric temperature measurements in the small-scale Bunsen-type aluminum dust flames [14] have demonstrated the negligible role played by radiation in heat transfer from the flame to a preheat zone. For flames whose propagation mechanism is controlled by the molecular heat transfer, the burning velocity v (cm/s) depends on thermal heat conductivity and characteristic time of chemical reaction τ_c (s) as $v \sim \sqrt{a/\tau_c}$ [15]. However, if the particle combustion is controlled by the process of oxygen diffusion toward the particle surface (or some flame zone that envelops the particle), the characteristic combustion time is inversely proportional to the oxygen diffusivity ($\tau_c \sim 1/D$) and therefore $v \sim \sqrt{a \cdot D}$. If we take into account that the flame temperatures in both helium and argon mixtures are identical, the flame speeds in Al-O_2-Ar and Al-O_2-He mixtures should be related as

$$v_{He}/v_{Ar} = \sqrt{(a \cdot D)_{He}/(a \cdot D)_{Ar}} \qquad (1)$$

Eq. (1) predicts that the flame speed with helium should be about 3.9 times higher than with argon, while the experiment shows only a 3.2 times difference. This discrepancy (as will be shown later) is the result of dependence of the flame structure and therefore the flame speed on the Lewis number, which is considerably different in O_2-He and O_2-Ar mixtures. (According to thermodynamic calculations, most of the molecular oxygen in Ar-O_2 and He-O_2 mixtures at flame temperature is dissociated. Therefore, the diffusivity and heat conductivity of the atomic oxygen should be taken into account when calculating average gas molecular transport coefficients.)

Oxygen Concentration Limit of the Flame Propagation

An experiment has also been performed to measure the oxygen concentration limit of the flame propagation, which is an important parameter for practical applications. For this, nitrogen in an auxiliary shroud flow surrounding the dust stream was replaced by pure oxygen and the dust in the disperser was dispersed and carried initially by pure argon. The stable diffusive dust flame was first established after ignition at the exit of the nozzle (the diffusive aluminum dust flame was investigated in detail in Ref. 16). Then, oxygen was added slowly to the dispersing gas (argon) until a premixed dust flame cone was formed inside the diffusive flame. The procedure was then reversed and oxygen was slowly removed from the dust-dispersing flow until the inner premixed flame cone disappeared. It was found that the premixed flame appears at an oxygen concentration of 10 ± 0.5% and disappears at an oxygen concentration of 8.5 ± 0.5%. It was also found that these critical oxygen concentrations do not actually depend on the value of dust concentration. The observed hysteresis effect is surprising and may be explained by the inertia of the gas delivery system. The absolute average value of the critical oxygen concentration (9.5%), however, is very close to the point at which the dependence of the adiabatic flame temperature on oxygen concentration (Fig. 6) reaches the value of 2300 K (the melting point of aluminum oxide), which is also generally considered the ignition temperature of micron-size aluminum particles [17]. (The small plateau in the dependence of adiabatic flame temperature on

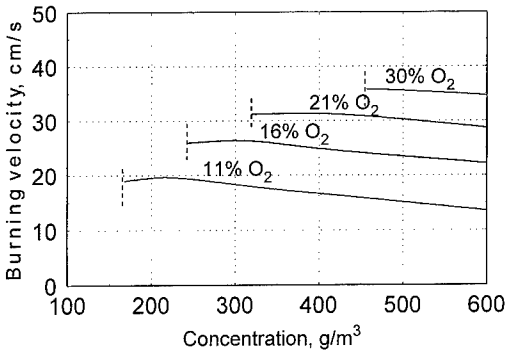

FIG. 7. Theoretically predicted dependence of burning velocity on dust concentration in Al-O_2-N_2 mixtures with different oxygen contents. Dotted lines indicate the stoichiometric concentrations.

oxygen concentration in Fig. 6 stretches from 6 to 10% O_2 and also can be the additional cause of the hysteresis effect mentioned.)

Theoretical Considerations and Discussion

In the present theoretical analysis, we will basically follow the simple one-dimensional model of the dust flame that has been developed recently for the analysis of the flame quenching phenomena in fuel-rich aluminum dust clouds [8]. For the purpose of the calculation of laminar flame burning velocities, we assume that the flame is adiabatic and the heat losses by radiation and conduction from the flame are negligible. We also assume that aluminum particles burn individually in the flame front. The rate of particle combustion is controlled by the diffusion of oxygen toward the particle surface or to some flame zone enveloping each particle close to its surface. To simplify the analysis, we also assume that the particle temperature at the moment of ignition is close to the melting point of the aluminum oxide protective film on the particle surface (2300 K) and does not depend on the local oxygen concentration and gas temperature.

Formally, the combustion time of the particle in the diffusive regime tends to infinity in stoichiometric or fuel-rich mixtures. However, with the depletion of oxygen, the particle burning rate decreases rapidly and becomes negligible shortly after ignition. Because of the weak dependence of the diffusive oxygen transport on the average local gas temperature in the combustion zone, the particle burning rate in the flame front is fundamentally controlled only by the value of local oxygen concentration and can be written as

$$W \sim kY(x)/Y_u \tag{2}$$

where $Y(x)$ is the local and Y_u the initial oxygen concentration and k (s/cm^2) is a constant of the diffusive particle combustion at the initial oxygen concentration in the unburned mixture. With a source term of the form of Eq. (2), the governing equations describing heat and oxygen transfer in a flame front are linear in both the preheat and combustion zones and can be integrated easily. By matching heat and oxygen fluxes on the border between these zones, the algebraic equation for the flame burning velocity can be obtained (as in Ref. 8):

$$3\mu\phi\bar{R} = 2(1 + \phi\nu)(\phi\nu + A)\cdot A\kappa^2 \text{ where} \tag{3}$$

$$A = 1 - \frac{Le}{2} + \sqrt{\frac{Le^2}{4} + \frac{3}{2}Le\frac{\phi}{\kappa^2}\bar{R}}$$

$\bar{R}$ in Eq. (3) is the average nondimensional particle size during combustion, which can be expressed through the fuel equivalence ratio ϕ in rich mixtures in the form

$$\bar{R} = \frac{r_u + r_f}{2r_u} = 0.5\cdot(1 + \sqrt[3]{1 - 1/\phi})$$

where r_u is the initial particle radius and r_f is the particle radius after combustion.

Other "natural" nondimensional parameters in Eq. (3) also have a definite physical meaning. Thus, $\kappa = v_u^2\tau_c/a_u$ is the nondimensional burning velocity (an unknown quantity) and also the ratio of the single particle combustion time τ_c at initial oxygen concentration to the particle heating time in the flame preheat zone, a_u/v_u^2 (index u indicates the initial cold mixture). The relative heat productivity of the chemical reaction is defined by the parameter $\mu = B_{st}Q/c_g\rho_g(T_{si} - T_u)$. Here, Q is the heat of reaction, c_g and ρ_g are the specific heat and the density of the carrier gas, T_{si} is the particle ignition temperature, and T_u is the initial dust temperature. Le in Eq. (3) is the Lewis number of the gas in suspension.

The results of a numerical solution of Eq. (3) are shown in Fig. 7 in dimensional form. The constant for the diffusive aluminum particle burning rate, $-k$(s/cm^2), which is used in calculating the value of the flame speed from the nondimensional parameter κ, was derived from the experimental data of Fridman and Macek [17,18].

Both the qualitative and quantitative correlation between experimental data and theoretical predictions can be considered satisfactory taking into account an estimated 25% accuracy of the burning velocity measurement by the Bunsen-cone method. The theory also predicts very weak dependence of burning velocity on dust concentration, which can be considered a distinguishing feature of fuel-rich dust combustion. The main factor responsible for this is the independence of the particle burning rate on flame temperature in the diffusive regime. In addition, the decline in adiabatic flame temperature in

the poststoichiometric region (rich mixtures) is very gentle in dust mixtures compared with homogeneous combustion. This is because the volume occupied by condensed fuel is negligible and therefore the amount of oxygen that can be burned (the amount of energy released) remains constant in spite of an increase in fuel concentration. The adiabatic dust flame temperature declines slowly with an increase of dust concentration due only to an increase in the average specific heat of the mixture. At the same time, this decline is compensated for by an increase in the rate of oxygen consumption caused by a higher specific surface area in the richer dust suspension.

The dependence of the flame speed on the Lewis number (as is reflected in Eq. [3]) is the result of the global oxygen diffusion in the rich dust flame in relation to the thermal flame thickness. It shows that the nondimensional flame speed κ is a function of the *Le* number $\kappa = f(Le)$ and that it also decreases with an increase of the *Le* number. Correspondingly, the dimensional flame speed depends to a somewhat lesser extent on the gas molecular transport properties (as $v \sim f(Le)\sqrt{a \cdot D}$) in comparison with the heuristically derived prediction ($v \sim \sqrt{a \cdot D}$). The value of the Lewis number in an Ar-O_2 mixture is close to unity, whereas in a He-O_2 mixture it is about 2. Consequently, the theory predicts only 3.1 times increase in burning velocity in helium mixtures (experimental value is about 3.2) compared with the prediction of 3.9 times increase that follows from the heuristically derived expression, Eq. (1).

Acknowledgments

This work was partially supported by the Canadian Space Agency under contract # 04SW.9F007-3-6017.

REFERENCES

1. Smoot, L. D., Hedman, P. O., and Smith, P. J., *Prog. Energy Combust. Sci.* 10:359–441 (1984).
2. Cassel, H. M., Das Gupta, A. K., and Guruswamy, S., *Third Symposium on Combustion and Flame and Explosion Phenomena,* Baltimore, Williams & Wilkins, 1949, pp. 185–190.
3. Cassel, H. M., U.S. Bureau of Mines, Report of investigation 6551, 1964.
4. Ballal, D. R., *Proc. R. Soc. London, Ser. A* 385:21–51 (1983).
5. Jacobson, M., Cooper, A., and Nagy, J., U.S. Bureau of Mines, Report of Investigation 6516, 1964.
6. Ishihama, W. and Enomoto, H., *Fifteenth Symposium (International) on Combustion,* The Combustion Institute, Pittsburgh, 1974, pp. 474–487.
7. Mintz, K. J., *Combust. Flame* 94:125–130 (1993).
8. Goroshin, S., Bidabadi, M., and Lee, J. H. S., *Combust. Flame* 105:147–160 (1996).
9. Lewis, B. and von Elbe, G., *Combustion, Flames, and Explosions of Gases,* Academic Press, New York, 1961.
10. Andrews, G. E. and Bradley, D., *Combust. Flame* 18:133–153 (1972).
11. Wu, C. K. and Law, C. K., *Twentieth Symposium (International) on Combustion,* The Combustion Institute, Pittsburgh, 1985, pp. 1941–1950.
12. Goroshin, S., Kleine, H., Lee, J. H. S., and Frost, D., *Third International Microgravity Combustion Workshop,* NASA Conference Publication 10174, Cleveland, 1995, pp. 141–146.
13. Katta, V. R. and Roquemore, W. M., *Combust. Flame* 102:21–39 (1995).
14. Goroshin, S., Shoshin, Yu., Ageyev, N., and Poletayev, N., *Proceedings of the Third International Conference on Flame Structure* Vol. 2, Novosibirsk, NAUKA, 1991, pp. 213–218.
15. Landau, L. D. and Lifshitz, E. M., *Fluid Mechanics,* Addison-Wesley, New York, 1966.
16. Ageyev, N., Vovchuck, Ya., Goroshin, S., Poletayev, N., and Zolotko, A., *Combust. Explos. Shock Waves* 26:668–677 (1991).
17. Fridman, R. and Macek, A., *Ninth Symposium (International) on Combustion,* The Combustion Institute, Pittsburgh, 1963, pp. 703–709.
18. Fridman, R. and Macek, A., *Combust. Flame* 6:9–19 (1962).

Twenty-Sixth Symposium (International) on Combustion/The Combustion Institute, 1996/pp. 1969–1979

COMBUSTION OF POROUS ENERGETIC MATERIALS IN THE MERGED-FLAME REGIME

STEPHEN B. MARGOLIS
Combustion Research Facility
Sandia National Laboratories
Livermore, California 94551, USA

FORMAN A. WILLIAMS AND ALEXANDER M. TELENGATOR
Department of Applied Mechanics and Engineering Sciences
University of California, San Diego
La Jolla, California 92093, USA

The structure and burning rate of an unconfined deflagration propagating through a porous energetic material is analyzed in the limit of merged condensed and gas-phase reaction zones. A global two-step reaction mechanism, applicable to certain types of degraded nitramine propellants and consisting of sequential condensed and gaseous steps, is postulated. Taking into account important effects due to multiphase flow and exploiting the limit of large activation energies, a theoretical analysis based on activation-energy asymptotics leads to explicit formulas for the deflagration velocity in a specifically identified regime that is consistent with the merged-flame assumption. The results clearly indicate the influences of two-phase flow and the multiphase, multi-step chemistry on the deflagration structure and the burning rate, and define conditions that support the intrusion of the primary gas flame into the two-phase condensed decomposition region at the propellant surface.

Introduction

There is increasing interest in the combustion behavior of systems characterized by significant two-phase flow. Examples include filtration combustion, smoldering, and the deflagration of porous energetic materials, where the latter, the focus of the present work, is of interest in propulsion and pyrotechnics. In such problems, the porous nature of the material arises from a certain degree of metastability which, after either a prolonged existence and/or exposure to an abnormal thermal environment, leaves the material in a chemically degraded, porous state. As a result, two-phase-flow effects associated with different velocities and properties of the condensed and gaseous species have a pronounced effect on the structure and propagation velocity of the combustion wave.

Although relatively complete formulations have been proposed for analyzing combustion phenomena involving multiphase flow [1], they are difficult to analyze because of the wide range of physical phenomena associated with such systems, and the highly nonlinear nature of the problem. Accordingly, early two-phase work in this area tended to alleviate some of the difficulties by treating the two-phase medium as a single phase with suitably averaged properties [2,3]. Unfortunately, such models effectively require the velocity of each phase to be the same, precluding any analysis of two-phase-flow effects. More recently, however, it has proven possible to analyze deflagration models for porous energetic materials that explicitly involve multiphase flow [4–9]. These studies have largely been applicable to nitramine propellants, such as HMX and, in some cases, RDX, that are characterized by a liquid melt region in which extensive bubbling in an exothermic foam layer occurs. In some cases [4–6], two-phase-flow effects were confined to this layer, while in others [7–9], the solid material was assumed to be porous, with two-phase flow occurring throughout the preheat region. In order to focus on the effects of multiphase flow, chemistry was generally confined to a single-step overall reaction $R(c) \rightarrow P(g)$ representing direct conversion of condensed (melted) propellant to gaseous products. A generalization [5] in which a separate (primary) gas flame follows the initial multiphase decomposition region is given by $R(c) \rightarrow P(g)$, $R(c) \leftrightarrow R(g)$, $R(g) \rightarrow P(g)$, where $R(g)$ is a gaseous reactant. This scheme was applied to a nonporous problem to determine the structure and propagation velocity of a steady, planar nitramine deflagration, while stability results for these models have thus far been confined to single-step mechanisms [6,8,9].

The present work analyzes the limiting case in which the primary gas flame intrudes upon the

multiphase decomposition region, a tendency that is often observed experimentally as the pressure increases. Thus, the single-step analysis [7] is extended by incorporating both condensed- and gas-phase reactions in the thin multiphase reaction region. In particular, a global sequential reaction mechanism is assumed, consisting of an overall condensed-phase reaction that produces gas-phase intermediates, and a gas-phase reaction that converts these intermediates to final products. While this mechanism is still an extreme approximation to actual nitramine chemistry [10,11], it enables us to fully incorporate two-phase flow into the analysis, and to assess its effect on the structure and propagation speed of the deflagration. The merged-flame analysis presented here is thus a multiphase-flow analog to single-phase studies of propagating combustion waves that are also governed by sequential reactions occurring in a single thin reaction zone [12–15].

The Mathematical Model

We consider an unconfined, steady, planar deflagration, propagating from right to left into a degraded (porous) energetic solid. Melting of the solid occurs at a moving location $\tilde{x} = \tilde{x}_m(t)$ where the solid temperature equals its melting point $\tilde{T}_m$. Subsequent to melting, gas-phase intermediates are assumed to be produced directly by liquid-phase reactions, and these, in turn, react to form final combustion products according to the mechanism $R(c) \rightarrow I(g)$, $I(g) \rightarrow P(g)$, where $R(c)$, $I(g)$, and $P(g)$ denote the condensed (melted) reactant material, the intermediate gas-phase species, and the final gas-phase products, respectively. The pores within the solid are assumed to be filled with a mixture of $I(g)$ and $P(g)$, with the mass-fraction ratio ϕ of the two specified far upstream. The present analysis considers a merged regime in which both reactions occur within a single reaction zone, and thus, the deflagration wave consists of a solid/gas preheat region, the melting surface, a liquid/gas preheat region, a thin reaction zone in which all reactive species are converted to gaseous products, and the burned region. The latter typically corresponds to a dark zone that separates the primary flame from a secondary gas flame that has little effect on the burning rate.

A model describing a multiphase deflagration was derived previously for a single-step reaction mechanism $R(c) \rightarrow P(g)$ [7]. For two gas-phase species (I and P), an additional species conservation equation is thus required. For simplicity, we consider the single-temperature limit in which the rates of interphase heat transfer are large so that all phases have the same local temperature, but since a complete derivation of the full two-temperature model is given elsewhere [7,16], we provide only a brief explanation of the origin of each equation. Thus, we introduce, in terms of dimensional quantities (denoted by tildes) defined in the nomenclature, the nondimensional variables $x = \tilde{\rho}_s\tilde{c}_s\tilde{U}\tilde{x}/\tilde{\lambda}_s$, $t = \tilde{\rho}_s\tilde{c}_s\tilde{U}^2\tilde{t}/\tilde{\lambda}_s$, $T = \tilde{T}/\tilde{T}_u$, $u_{l,g} = \tilde{u}_{l,g}/\tilde{U}$, and $\rho_g = \tilde{\rho}_g/\tilde{\rho}_g^u$, where $\tilde{U} = -d\tilde{x}_m/d\tilde{t}$ is the (unknown) propagation speed of the melting front, and constant heat capacities and thermal conductivities have been assumed. We also define the parameters

$$r = \tilde{\rho}_l/\tilde{\rho}_s, \quad \hat{r} = \tilde{\rho}_g^u/\tilde{\rho}_s, \quad l = \tilde{\lambda}_l/\tilde{\lambda}_s, \quad \hat{l} = \tilde{\lambda}_g/\tilde{\lambda}_s$$

$$b = \tilde{c}_l/\tilde{c}_s, \quad \hat{b} = \tilde{c}_g/\tilde{c}_s, \; \gamma_s = \tilde{\gamma}_s/\tilde{c}_s\tilde{T}_u$$

$$w = \tilde{W}_I/\tilde{W}_P, \quad Le = \tilde{\lambda}_g/\tilde{\rho}_g\tilde{D}\tilde{c}_g$$

$$Q_{l,g} = \tilde{Q}_{l,g}/\tilde{c}_s\tilde{T}_u, \; N_{l,g} = \tilde{E}_{l,g}/\tilde{R}^\circ\tilde{T}_b \tag{1}$$

$$\Lambda_l = \tilde{\lambda}_s\tilde{A}_l e^{-N_l}/\tilde{\rho}_s\tilde{c}_s\tilde{U}^2$$

$$\Lambda_g = \tilde{\lambda}_s\tilde{A}_g(\tilde{\rho}_g^u)^n\, e^{-N_g}/\tilde{\rho}_s^2\tilde{c}_s\tilde{U}^2 \tag{2}$$

where n is the reaction order of the gas-phase reaction and Le is the gas-phase Lewis number. Here, $\tilde{\lambda}_g$, $\tilde{\rho}_g\tilde{D}$, and hence Le are assumed constant, r and $\hat{r}$ are density ratios (liquid-to-solid and upstream gas-to-solid), l and $\hat{l}$ are thermal conductivity ratios, b and $\hat{b}$ are heat-capacity ratios, w is the ratio of molecular weights of the two gas-phase species, γ_s is a heat-of-melting parameter (negative when melting is endothermic), $Q_{l,g}$ are heat-release parameters associated with the condensed and gas-phase reactions, $N_{l,g}$ are the activation energies, and $\Lambda_{l,g}$ are rate coefficients, or Damköhler numbers. Since $\Lambda_g/\Lambda_l = \hat{r}(\tilde{A}_g/\tilde{A}_s)\,(\tilde{\rho}_g^u)^{n-1}e^{N_l-N_g}$, we may regard Λ_l as the burning-rate eigenvalue.

For a steadily propagating deflagration, it is convenient to transform to the moving coordinate $\xi = x + t$ whose origin is defined to be $x_m(t)$. In the solid/gas region, the volume fraction α of gas is assumed constant ($\alpha = \alpha_s$), the solid phase is assumed to have constant density and zero velocity with respect to the laboratory frame of reference, and gas-phase continuity is given by

$$\frac{d}{d\xi}[\rho_g(u_g + 1)] = 0$$

$$\frac{d}{d\xi}[\hat{r}\rho_g Y(u_g + 1)] = (\hat{l}/\hat{b}Le)\frac{d^2Y}{d\xi^2}$$

$$\xi < 0 \tag{3}$$

representing overall continuity for the gas phase and mass conservation for the mass fraction Y of the gas-phase intermediates. In the liquid/gas region $\xi > 0$, overall continuity, continuity of the liquid phase, and continuity of the intermediate gas-phase species are given as

$$\frac{d}{d\xi}[r(1-\alpha)(u_l+1)+\hat{r}\alpha\rho_g(u_g+1)]=0 \quad (4)$$

$$(d/d\xi)[(1-\alpha)(u_l+1)] = -\Lambda_l(1-\alpha)\,e^{N_l(1-T_b/T)} \quad (5)$$

$$\frac{d}{d\xi}[\hat{r}\alpha\rho_g Y(u_g+1)+r(1-\alpha)(u_l+1)] = (\hat{l}/\hat{b}Le)\frac{d}{d\xi}\left[\alpha\frac{dY}{d\xi}\right]-\Lambda_g(\alpha\rho_g Y)^n\,e^{N_g(1-T_b/T)} \quad (6)$$

where equation 5 has been used to eliminate the condensed-phase reaction-rate term that would have otherwise appeared in equation 6. Finally, overall energy conservation is given in the single-temperature limit by

$$(1-\alpha_s)\frac{dT}{d\xi}+\hat{r}\hat{b}\alpha_s\frac{d}{d\xi}[\rho_g(u_g+1)T] = \frac{d}{d\xi}\left[(1-\alpha_s+\hat{l}\alpha_s)\frac{dT}{d\xi}\right],\quad \xi<0 \quad (7)$$

$$\frac{d}{d\xi}[r(1-\alpha)(u_l+1)(Q_l+Q_g+bT) + \hat{r}\alpha\rho_g(u_g+1)(Q_gY+\hat{b}T)] = \frac{d}{d\xi}\left\{[l(1-\alpha)+\hat{l}\alpha]\frac{dT}{d\xi}+(Q_g\hat{l}/\hat{b}Le)\,\alpha\frac{dY}{d\xi}\right\},\quad \xi>0 \quad (8)$$

where equations 5 and 6 have been used to eliminate the reaction-rate terms in the latter.

The above system of equations is closed by adding an equation of state (assumed to be that of an ideal gas) and an expression for the liquid velocity u_l. An approximate analysis of gas-phase momentum conservation implies, for an unconfined, small Mach-number deflagration, that pressure is constant, thereby allowing the former to be expressed as $\rho_g T[Y + w(1-Y)] = \phi + w(1-\phi) \equiv \bar{\phi}$, where ϕ is defined below. An analysis of condensed-phase momentum and the assumption of zero velocity for the solid phase, on the other hand, leads to the kinematic approximation $u_l = (1-r)/r$ in the limit of small viscous and surface-tension-gradient forces [4,7]. The problem is then completely defined by imposing the boundary conditions $\alpha = \alpha_s$ for $\xi \le 0$, $u_g \to 0$, $Y \to \phi$ $(0 \le \phi \le 1)$, $T \to 1$ as $\xi \to -\infty$ and $\alpha \to 1$, $Y \to 0$, $T \to T_b$ as $\xi \to +\infty$, and the melting-surface conditions, which are continuity of $T = T_m$, u_g, Y and $dY/d\xi$ at $\xi = 0$ and the jump condition

$$[l(1-\alpha_s)+\hat{l}\alpha_s]\left.\frac{dT}{d\xi}\right|_{\xi=0^+} - (1-\alpha_s+\hat{l}\alpha_s)\left.\frac{dT}{d\xi}\right|_{\xi=0^-} = (1-\alpha_s)[-\gamma_s+(b-1)T_m] \quad (9)$$

Here, the final burned temperature T_b is to be determined, as is the burning-rate eigenvalue Λ_l, which determines the propagation velocity of the deflagration according to equation 2.

Expressions for T_b and the burned gas velocity $u_g^b \equiv u_g|_{\xi=\infty}$ are obtained from the above model as follows. From equations 3, 4, and the boundary conditions, we have the first integrals

$$\rho_g(u_g+1) = 1,$$

$$Y-\phi = (\hat{l}/\hat{r}\hat{b}Le)\frac{dY}{d\xi},\quad \xi<0 \quad (10)$$

$$(1-\alpha)+\hat{r}\alpha\rho_g(u_g+1) = \hat{r}\rho_g^b(u_g^b+1),\quad \xi>0 \quad (11)$$

where $\rho_g^b = \bar{\phi}/wT_b$ is the burned gas density. Thus, evaluating equation 11 at $\xi = 0$ using the first of equations 10 and continuity across the melting surface, we obtain

$$u_g^b = [1+\alpha_s(\hat{r}-1)]/\hat{r}\rho_g^b - 1 = [1+\alpha_s(\hat{r}-1)]\,wT_b/\hat{r}\bar{\phi} - 1 \quad (12)$$

Using these results, first integrals of the overall energy equations 7 and 8 are given by

$$(1-\alpha_s+\hat{r}\hat{b}\alpha_s)(T-1) = (1-\alpha_s+\hat{l}\alpha_s)\frac{dT}{d\xi},\ \xi<0 \quad (13)$$

$$[b(1-\alpha)+\hat{b}(\alpha-\alpha_s+\alpha_s\hat{r})]T + (\alpha-\alpha_s+\alpha_s\hat{r})\,Q_gY = [l(1-\alpha)+\hat{l}\alpha]\frac{dT}{d\xi} + (Q_g\hat{l}/\hat{b}Le)\alpha\frac{dY}{d\xi} - (1-\alpha)(Q_l+Q_g) + \hat{b}(1-\alpha_s+\alpha_s\hat{r})T_b,\quad \xi>0 \quad (14)$$

Thus, subtracting equation 13 evaluated at $\xi = 0^-$ from equation 14 evaluated at $\xi = 0^+$ and using the melting-surface condition 9, we obtain

$$T_b = [(1-\alpha_s)(Q_l+Q_g+1+\gamma_s) + \hat{r}\alpha_g(\phi Q_g+\hat{b})]/\hat{b}[1+\alpha_s(\hat{r}-1)] \quad (15)$$

This result, which can be derived from a more general two-temperature model [16], is independent of the particular form of the gas-phase equation of state. In the limit $Q_g \to 0$, equation 15 collapses to the result obtained for the single-step model [7]. Equations 10, 13, and 14, being first integrals of equations 3, 7, and 8, now take the place of the latter in our model.

Equations 12 and 15 imply that there are significant variations in T_b and u_g^b with the upstream

gas-to-solid density ratio $\hat{r}$, which in turn is proportional to the pressure $\tilde{p}_g^0$ according to $\hat{r} \equiv \tilde{p}_g^u/\tilde{\rho}_s = \tilde{W}_l\tilde{p}_g^0/\tilde{\rho}_s\tilde{R}^0\tilde{T}_u\bar{\phi}$. This important effect arises from the thermal expansion of the gas, the two-phase nature of the flow in the solid/gas and liquid/gas regions, and the fact that, for nonzero α_s, some of the heat released by combustion must be used to help raise the temperature of the gas-phase species within the porous solid from unity to T_b [7]. Consequently, both T_b and u_g^b are typically decreasing functions of $\hat{r}$. An additional effect, revealed by the two-step reaction analysis, is that T_b does not depend just on the total heat release $Q_l + Q_g \equiv Q$ associated with the complete conversion of the energetic solid to final gas products, but also on the heat release Q_g specifically associated with the gas-phase reaction. This, too, is a two-phase-flow effect that arises from the fact that reactive intermediate species exist within the voids in the porous solid, and the heat released by these intermediates affects the final burned temperature, which, for a given total heat release Q, increases as the fractional heat release associated with the gas-phase reaction increases.

The Asymptotic Limit and the Outer Solution

Further analytical development leading to the determination of Λ_l requires an analysis of the reactive liquid/gas region $\xi > 0$. Equations 5, 6, and 14 constitute three equations for Y, T, and α in this region, with u_g then determined from equation 11 and the equation of state, and the eigenvalue Λ_l determined by the boundary conditions. In order to handle the Arrhenius nonlinearities in equations 5 and 6, we exploit the largeness of the activation energies $N_{g,l}$ and consider the formal asymptotic limit $N_{g,l} \gg 1$ such that $N_g/N_l = \nu \sim O(1)$ and $\beta \equiv (1 - T_b^{-1})N_l \gg 1$, where β is the Zel'dovich number. This ordering of the activation energies, along with a corresponding order relation for the ratio Λ_g/Λ_l to be introduced shortly, helps to insure that both the condensed and gas-phase reactions are active in a single thin reaction zone, since departures from these orderings can result in separated reaction zones [17].

In the limit $\beta \to \infty$, the Arrhenius terms are exponentially small unless T is within $O(1/\beta)$ of T_b. Consequently, all chemical activity is concentrated in a zone whose thickness is $O(1/\beta)$. On the scale of the (outer) coordinate ξ, this thin region is a sheet whose location is denoted by $\xi_r = x_r - x_m$, where $x_r > x_m$. Hence, the liquid/gas region is comprised of a preheat zone ($0 < \xi < \xi_r$) where chemical activity is exponentially small, the thin reaction zone where the two chemical reactions are active and go to completion, and a burned region $\xi > \xi_r$. Denoting the outer solutions on either side of the reaction zone by a zero superscript, we conclude from equations 5, 10–12, and the equation of state,

$$\alpha^0 = \begin{cases} \alpha_s, & \xi < \xi_r \\ 1, & \xi > \xi_r \end{cases},$$

$$u_g + 1 = [(\alpha - \alpha_s + \hat{r}\alpha_s)/\hat{r}\alpha\bar{\phi}][Y + w(1 - Y)]\,T \tag{16}$$

where the latter is valid for all ξ. Thus, there is a jump in α^0, and hence in u_g^0, across the reaction zone. Similarly, in obtaining the complete outer solution for Y and T, it is necessary to connect the solutions on either side of the reaction zone by deriving appropriate jump conditions across $\xi = \xi_r$. This will entail an analysis of the inner reaction-zone structure, whereupon an asymptotic matching of the inner and outer solutions will yield these jump conditions and an expression for Λ_l. In connection with this procedure, it is convenient, and physically appealing, to attempt a representation of the reaction-rate terms in equations 5 and 6 as delta-function distributions with respect to the outer spatial variable ξ [12,13]. Using the results from equation 16, the system of equations for the outer variables Y^0 and T^0 thus become

$$\hat{r}(Y^0 - \phi) = (\hat{l}/\hat{b}Le)\frac{dY^0}{d\xi}, \quad \xi < 0;$$

$$(1/r)\frac{d\alpha^0}{d\xi} = P_l\delta(\xi - \xi_r), \quad \xi > 0 \tag{17}$$

$$\frac{d}{d\xi}[(\alpha^0 - \alpha_s + \hat{r}\alpha_s)Y^0 - \alpha^0] = (\hat{l}/\hat{b}Le)\frac{d}{d\xi}\left(\alpha^0\frac{dY^0}{d\xi}\right) - P_g\delta(\xi - \xi_r - H), \quad \xi > 0 \tag{18}$$

$$(1 - \alpha_s + \hat{r}\hat{b}\alpha_s)(T^0 - 1) = (1 - \alpha_s + \hat{l}\alpha_s)\frac{dT^0}{d\xi}, \quad \xi < 0 \tag{19}$$

$$[b(1 - \alpha^0) + \hat{b}(\alpha^0 - \alpha_s + \alpha_s\hat{r})]T^0 + (\alpha^0 - \alpha_s + \alpha_s\hat{r})Q_gY^0 = [l(1 - \alpha^0) + \hat{l}\alpha^0]\frac{dT^0}{d\xi} + (Q_g\hat{l}/\hat{b}Le)\alpha^0\frac{dY^0}{d\xi} - (1 - \alpha^0)(Q_l + Q_g) + \hat{b}(1 - \alpha_s + \alpha_s\hat{r})T_b, \quad \xi > 0 \tag{20}$$

where P_l and P_g are the source strengths of the distributions at $\xi = \xi_r$ and $\xi = \xi_r + H$. Here, P_l, P_g, and H are to be determined, where the $O(1/\beta)$ width of the merged reaction zone implies that H is of this order (or smaller) as well.

The solution of equations 17–20 subject to the melting and boundary conditions is given by

$$P_l = (1 - \alpha_s)/r, \quad P_g = 1 - \alpha_s + \hat{r}\alpha_s\phi,$$

$$Y^0(\xi) = \begin{cases} \phi + [(1-\phi)(1-\alpha_s) - (1 - \alpha_s + \hat{r}\alpha_s\phi) \\ \quad \times e^{-(1-\alpha_s+\hat{r}\alpha_s)\hat{b}LeH/\hat{l}}]e^{\hat{r}\hat{b}Le(\xi-\xi_r)/\hat{l}}/(1 - \alpha_s + \hat{r}\alpha_s), \\ \quad \xi < \xi_r \\ [(1 - \alpha_s + \hat{r}\alpha_s\phi)/(1 - \alpha_s + \hat{r}\alpha_s)] \\ \quad \times [1 - e^{(1-\alpha_s+\hat{r}\alpha_s)\hat{b}Le(\xi-\xi_r-H)/\hat{l}}], \\ \quad \xi_r < \xi < \xi_r + \mathrm{H} \\ 0, \ \xi > \xi_r + \mathrm{H} \end{cases} \tag{21}$$

$$T^0(\xi) = \begin{cases} 1 + (T_m - 1)\, e^{[(1-\alpha_s+\hat{r}\hat{b}\alpha_s)/(1-\alpha_s+\hat{l}\alpha_s)]\xi}, \\ \quad \xi < 0 \\ B + (T_m - B)\, e^{\{[b(1-\alpha_s)+\hat{r}\hat{b}\alpha_s]/[l(1-\alpha_s)+\hat{l}\alpha_s]\}\xi}, \\ \quad 0 < \xi < \xi_r \\ B_1 + (T_b - B_1)\, e^{\hat{b}(1-\alpha_s+\hat{r}\alpha_s)(\xi-\xi_r-H)/\hat{l}}, \\ \quad \xi_r < \xi < \xi_r + H \\ T_b = B_1 + (1 - \alpha_s + \hat{r}\alpha_s\phi)Q_g/\hat{b}(1 - \alpha_s + \hat{r}\alpha_s), \\ \quad \xi > \xi_r + H \end{cases} \tag{22}$$

where

$$B = [(1 - \alpha_s)(1 + \gamma_s) + \hat{r}\hat{b}\alpha_s]/[b(1 - \alpha_s) + \hat{r}\hat{b}\alpha_s],$$

$$B_1 = [(1 - \alpha_s)(Q_l + 1 + \gamma_s) + \hat{r}\hat{b}\alpha_s]/\hat{b}(1 - \alpha_s + \hat{r}\alpha_s),$$

$$\xi_r = \{[\hat{l}(1 - \alpha_s) + \hat{l}\alpha_s]/[b(1 - \alpha_s) + \hat{r}\hat{b}\alpha_s]\} \times \ln\{[B_1 - B + (T_b - B_1)e^{-\hat{b}(1-\alpha_s+\hat{r}\alpha_s)H/\hat{l}}]/(T_m - B)\} \tag{23}$$

A sketch of the outer solution is shown in Fig. 1. Since the interval $\xi_r < \xi < \mathrm{H}$ lies within the merged reaction zone, only that portion of equations 21 and 22 for $\xi < \xi_r^-$ and $\xi > \xi_r + \mathrm{H} \approx \xi_r^+$ actually represents the outer solution. Consequently, there is an $O(1/\beta)$ jump in Y^0 and T^0 across this region. Alternatively, for small H, an expansion of $\delta(\xi - \xi_r - H)$ in equation 18 about $H = 0$ introduces the derivative $\delta'(\xi - \xi_r)$ [13], which implies discontinuities in Y^0 and T^0 at $\xi = \xi_r$. These discontinuities are determined by H, which, like Λ_l, is an eigenvalue. Both are calculated by matching the outer solution to that of the inner reaction-zone problem.

Reaction-Zone Solutions

To analyze the chemical boundary layer at ξ_r, we introduce a stretched inner variable $\eta = \beta(\xi - \xi_r)$ and a normalized temperature $\Theta = (T - 1)/(T_b - 1)$. We then seek solutions in this region as $\alpha \sim \alpha_0 + \beta^{-1}\alpha_1 + \cdots, u_g \sim u_0 + \beta^{-1}u_1 + \cdots, Y \sim \beta^{-1}y_1 + \beta^{-2}y_2 + \cdots, \Theta \sim 1 + \beta^{-1}\theta_1 + \cdots, \Lambda_l \sim \beta(\Lambda_0 + \beta^{-1}\Lambda_1 + \cdots)$ and $H \sim \beta^{-1}h_1 + \beta^{-2}h_2 + \cdots$, where the u_i are calculated in terms of the α_i, y_i and θ_i from equation 16, which is valid in the reaction zone. We also order the rate-coefficient ratio $\Lambda_g/\Lambda_l = \hat{r}(\tilde{p}_g^n)^{n-1}(\tilde{A}_g/\tilde{A}_l)e^{(1-\nu)N_1} \equiv \beta^n\lambda$, where λ is an $O(1)$ parameter. This scaling, along with the previous ordering of the activation energies, partly defines one regime that is consistent with a merged reaction-zone structure.

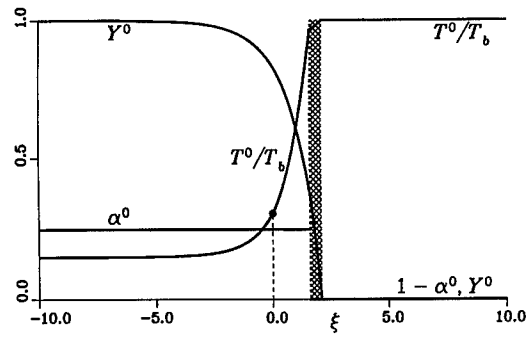

FIG. 1. Outer structure of the leftward-propagating deflagration wave. The solid/gas region lies to the left of $\xi = 0$, and the liquid/gas region to the right. The shaded area denotes the region $\xi_r < \xi < \xi_r + H$, which, despite the explicit representation afforded by the outer delta-function formulation, actually lies within the inner reaction zone. The region to the right of the reaction zone consists of purely gaseous products. Parameter values used were $b = r = Le = l = \phi = 1$, $\hat{b} = \hat{r} = \hat{l} = .8$, $a_s = .25$, $Q_l = 5$, $Q_g = H = .5$, $\gamma_s = -.2$, $T_m = 2$.

Substituting these expansions into equations 5, 6, and 14, the leading-order inner variables α_0, y_1, and θ_1 are governed by

$$\frac{d\alpha_0}{d\eta} = r\Lambda_0(1 - \alpha_0)e^{\theta_1} \tag{24}$$

$$[l + (\hat{l} - l)\alpha_0]\frac{d\theta_1}{d\eta} + [\hat{l}Q_g/\hat{b}Le(T_b - 1)]\alpha_0\frac{dy_1}{d\eta} = \{[(b - \hat{b})T_b + Q_l + Q_g]/(T_b - 1)\}(1 - \alpha_0) \tag{25}$$

$$(\hat{l}/\hat{b}Le)\frac{d}{d\eta}\left(\alpha_0\frac{dy_1}{d\eta}\right) = -\frac{d\alpha_0}{d\eta} + \lambda\Lambda_0(\alpha_0 y_1\bar{\phi}/wT_b)^n e^{\nu\theta_1} \tag{26}$$

Solutions to these equations as $\eta \to \pm\infty$ must match with the outer solution as $\xi \uparrow \xi_r^-$ and as $\xi \downarrow (\xi_r + H)^+$, leading to the matching conditions

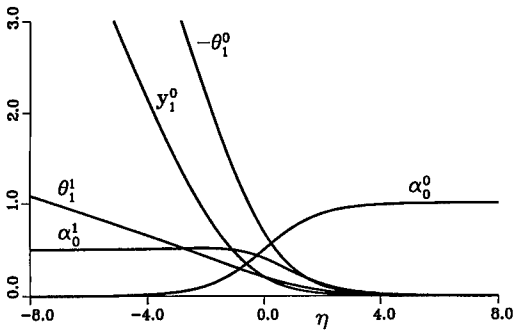

FIG. 2. Inner structure of the leftward-propagating deflagration wave for the case $\lambda_0 = 4$. The curves were drawn for the parameter regime analyzed in the paper, based on the parameter values used in Fig. 1 (choosing $\varepsilon = .5$, the latter imply that the scaled parameters $a_s^1 = a_s/\varepsilon = .5$, $Q_g^1 = Q_g/\varepsilon = 1$ and $\hat{l}^1 = (\hat{l} - l)/\varepsilon = -.4$).

$$\alpha_0 \to 1,\ \theta_1 \to 0,\ y_1 \to 0 \text{ as } \eta \to +\infty \tag{27}$$

$$\alpha_0 \to \alpha_s,\ \theta_1 \sim E_1\eta + E_2 h_1,$$

$$y_1 \sim (\hat{b}Le/\hat{l})[-\hat{r}\eta + (1 - \alpha_s + \hat{r}\alpha_s\phi)h_1]$$

$$\text{as } \eta \to -\infty,$$

$$E_1 = [(T_b - B)/(T_b - 1)]\,\frac{b(1 - \alpha_s) + \hat{r}\hat{b}\alpha_s}{l(1 - \alpha_s) + \hat{l}\alpha_s},$$

$$E_2 = -[(T_b - B_1)/(T_b - 1)]\,\frac{\hat{b}}{\hat{l}}\,(1 - \alpha_s + \hat{r}\alpha_s) \tag{28}$$

Solution of the complete inner problem given by equations 24–28 will only be possible for certain values of h_1 and Λ_0, the leading-order coefficients in the expansions of H and Λ_l.

Employing α_0 as the independent variable, equations 25 and 26 take the form

$$[l + (\hat{l} - l)\alpha_0]e^{\theta_1}\frac{d\theta_1}{d\alpha_0} + [\hat{l}Q_g/\hat{b}Le(T_b - 1)]\alpha_0 e^{\theta_1}\frac{dy_1}{d\alpha_0} = [(b - \hat{b})T_b + Q_l + Q_g]/(T_b - 1)r\Lambda_0 \tag{29}$$

$$(r\Lambda_0\hat{l}/\hat{b}Le)\frac{d}{d\alpha_0}\left[\alpha_0(1 - \alpha_0)e^{\theta_1}\frac{dy_1}{d\alpha_0}\right] = -1 + (\lambda/r)(\alpha_0 y_1\bar{\phi}/wT_b)^n e^{(\nu-1)\theta_1}/(1 - \alpha_0) \tag{30}$$

A closed-form solution to this system is not readily apparent, and thus further analytical development is restricted to a perturbation analysis of equations 29 and 30 in the limit that Q_g is small relative to Q_l. Since this implies that most of the heat release occurs in the first stage of the two-step reaction process, at least some of the initial exothermic gas-phase decomposition reactions should be lumped with the overall reaction (1a), regarding the resulting decomposition products as the gas-phase intermediates $I(g)$. Thus, we formally introduce a small bookkeeping parameter ε, where $O(\beta^{-1}) \ll \varepsilon \ll O(1)$, and write $Q_g = \varepsilon Q_g^1$, where $Q_g^1 \sim O(1)$. We now seek solutions to the leading-order inner problem in the form $\alpha_0 \sim \alpha_0^0 + \varepsilon\alpha_0^1 + \cdots$, $y_1 \sim y_1^0 + \varepsilon y_1^1 + \cdots$, $\theta_1 \sim \theta_1^0 + \varepsilon\theta_1^1 + \cdots$, $\Lambda_0 \sim \Lambda_0^0 + \varepsilon\Lambda_0^1 + \cdots$, and $h_1 \sim h_1^0 + \varepsilon h_1^1 + \cdots$.

Substituting these latest expansions into equations 24, 29, and 30, a closed subsystem

$$[l + (\hat{l} - l)\alpha_0^0]\,e^{\theta_1^0}\frac{d\theta_1^0}{d\alpha_0^0} = [(b - \hat{b})B_1 + Q_l]/(B_1 - 1)r\Lambda_0^0,$$

$$\frac{d\alpha_0^0}{d\eta} = r\Lambda_0^0(1 - \alpha_0^0)\,e^{\theta_1^0} \tag{31}$$

is obtained, subject to $\alpha_0^0 \to 1$, $\theta_1^0 \to 0$ as $\eta \to +\infty$, and $\alpha_0^0 \to \alpha_s$, $\theta_1^0 \sim E_1^0\eta$ as $\eta \to -\infty$, where E_1^0 is given by E_1 in equation 28 with T_b replaced by its leading-order approximation B_1. The first of equations 31 is readily integrated from $\alpha_0^0 = \alpha_s$ (at $\eta = -\infty$) to any $\alpha_0^0 \le 1$ ($\eta \le +\infty$) to give

$$e^{\theta_1^0(\alpha_0^0)} = [(b - \hat{b})B_1/(B_1 - 1)r\Lambda_0^0] \times \int_{\alpha_s}^{\alpha_0^0} d\bar{\alpha}/[l + (\hat{l} - l)\bar{\alpha}] \tag{32}$$

Evaluating equation 32 at $\alpha_0^0 = 1$ (at which $\theta_1^0 = 0$) thus determines Λ_0^0 as

$$\Lambda_0^0 = \begin{cases} \{[(b - \hat{b})B_1 + Q_l]/(B_1 - 1)r(\hat{l} - l)\} \\ \quad \times \ln\{\hat{l}/[l + (\hat{l} - l)\alpha_s]\},\ l \neq \hat{l} \\ (1 - \alpha_s)[(b - \hat{b})B_1 + Q_l]/(B_1 - 1)rl, \\ \quad l = \hat{l} \end{cases} \tag{33}$$

Substituting this result into equation 32 for arbitrary α_0, we thus obtain

$$\theta_1^0(\alpha_0^0) = \begin{cases} \ln\{\ln[l + (\hat{l} - l)\alpha_0^0] - \ln[l + (\hat{l} - l)\alpha_s]\} \\ \quad - \ln\{\ln\hat{l} - \ln[l + (\hat{l} - l)\alpha_s]\},\ \hat{l} \neq l \\ \ln(\alpha_0^0 - \alpha_s) - \ln(1 - \alpha_s),\ \hat{l} = l \end{cases} \tag{34}$$

The determination of $\alpha_0^0(\eta)$, and hence $\theta_1^0(\eta)$, then follows directly from the second of equations 31. For example, when $\hat{l} = l$ (equal gas and liquid thermal conductivities), we obtain

$$\alpha_0^0(\eta) = \{\alpha_s + e^{[(b-\hat{b})B_1+Ql](1-\alpha_s)\eta/l(B_1-1)}\}/\{1 + e^{[(b-\hat{b})B_1+Ql](1-\alpha_s)\eta/l(B_1-1)}\} \quad (35)$$

where the matching condition at $\eta = -\infty$ has been used to evaluate the constant of integration.

From equation 33, the leading-order expression for Λ_l is independent of the effects of the second reaction, which has been assumed to have a relatively small thermal effect. Consequently, the first effects of the two-step mechanism on the burning rate appear at $O(\varepsilon)$, which requires the calculation of Λ_0^1. We proceed by first calculating y_1^0, which is determined from the leading-order version of equation 30. For simplicity, we consider the parameter regime $\alpha_s = \alpha_s^1\varepsilon$, $\hat{l} = l + \varepsilon\hat{l}^1$ and $v = 1 + \varepsilon v^1$, corresponding to $O(\varepsilon)$ porosities, $O(\varepsilon)$ differences in the conductivities of the condensed and gaseous phases, and $O(\varepsilon\beta)$ differences in the activation energies of the two reaction steps. Also, we consider only a first-order gas-phase reaction ($n = 1$), and assume that $(\lambda\bar{\phi}/rw\Lambda_0^0T_b^0)(\hat{b}Le/rl) = \lambda_0 + \varepsilon\lambda_1$, where $T_b^0 = (Q_l + 1 + \gamma_s)/\hat{b}$ is the leading-order approximation to T_b with respect to ε. The parameter group $(\lambda\bar{\phi}/rw\Lambda_0^0T_b^0)(\hat{b}Le/rl)$ is a gas-to-liquid ratio of diffusion-weighted reaction rates, referred to as consumption rates [12,13], which represent relative rates of depletion, taking into account both chemical reaction and, for the gas phase, species diffusion. The fact that larger Lewis numbers are associated with higher rates of depletion of the gaseous reactant stems from the higher concentration of this species in the reaction zone that results from a smaller mass diffusivity.

In the parameter regime just outlined, θ_1^0 and Λ_0^0 simplify to

$$\theta_1^0 = \ln \alpha_0^0, \quad \Lambda_0^0 = [bQ_l + (b - \hat{b})(1 + \gamma_s)]/rl(Q_l + 1 + \gamma_s - \hat{b}),$$
$$\alpha_0^0(\eta) = e^{r\Lambda_0^0\eta}/[1 + e^{r\Lambda_0^0\eta}] \quad (36)$$

or $\eta = (1/r\Lambda_0^0)\ln[\alpha_0^0/(1 - \alpha_0^0)]$. Hence, the leading-order version of equation 30 for y_1^0 is given by

$$\frac{d^2y_1^0}{d\alpha_0^{0^2}} + \left(\frac{2}{\alpha_0^0} - \frac{1}{1 - \alpha_0^0}\right)\frac{dy_1^0}{d\alpha_0^0} - \frac{\lambda_0 y_1^0}{\alpha_0^0(1 - \alpha_0^0)^2} = -\frac{(\hat{b}Le/rl\Lambda_0^0)}{(\alpha_0^0)^2(1 - \alpha_0^0)} \quad (37)$$

subject to $y_1^0 \to 0$ as $\alpha_0^0 \to 1$. An appropriate matching condition as $\alpha_0^0 \to 0$, however, cannot be obtained directly from equation 28 because that equation was derived under the assumption that $\alpha_s \neq 0$, whereas to leading order in ε, α_s is zero. Indeed, at this level of approximation, the outer variable Y^0 has no meaning for $\xi < 0$, since there is essentially no gas in this region. To derive proper matching conditions on y_1^0 and, for later use, y_1^1, we consider the local mass fraction Z of the intermediate gas-phase species with respect to the total mass of all species, gaseous and condensed [16]. Thus, $Z = \hat{r}\alpha\rho_g Y/[\hat{r}\alpha/\rho_g + r(1 - \alpha)] = \hat{r}\bar{\phi}\alpha Y/\{\hat{r}\bar{\phi}\alpha + r(1 - \alpha)[Y + w(1 - Y)]T\}$ is unambiguous as $\alpha \to 0$, where it must vanish. From the outer solution written in terms of η, the required behavior of Z as $\eta \to -\infty$ is $Z \sim \varepsilon\beta^{-1}(\hat{r}\bar{\phi}\alpha_s^1\hat{b}Le/rwT_b^0l)(-\hat{r}\phi\eta + h_1^0)$. Hence, substituting the inner expansions into the definition of Z and imposing this asymptotic behavior implies

$$\alpha_0^0y_1^0 \to 0, \quad \alpha_0^0y_1^1 \sim -\alpha_s^1y_1^0 + \alpha_s^1(\hat{b}Le/l)[-(\hat{r}\phi/r\Lambda_0^0)\ln\alpha_0^0 + h_1^0] \text{ as } \alpha_0^0 \to 0 \quad (38)$$

where we have written these conditions in terms of α_0^0, using the fact that $\alpha_0^1 \to \alpha_s^1$ as $\alpha_0^0 \to 0$.

Formal solutions to equation 37 can be expressed in terms of hypergeometric functions, but since we desire explicit representations for use in the next-order problem, we focus on such solutions that may be obtained for certain values of λ_0. In particular, solutions for $\lambda_0 = 1$ [16] and $\lambda_0 = 4$ that satisfy the matching conditions are given by

$$y_1^0 = -(\hat{b}Le/2rl\Lambda_0^0)\cdot \begin{cases} 1 + [(1 - \alpha_0^0)/\alpha_0^0]\ln[(1 - \alpha_0^0)/\alpha_0^0] + \ln\alpha_0^0/\alpha_0^0(1 - \alpha_0^0), & \lambda_0 = 1 \\ (3 - \alpha_0^0)/(1 - \alpha_0^0) + 2\ln\alpha_0^0/(1 - \alpha_0^0)^2, & \lambda_0 = 4 \end{cases} \quad (39)$$

We observe that although $\alpha_0^0y_1^0 \to 0$ as $\alpha_0^0 \to 0$, y_1^0 itself is unbounded, exhibiting the behavior

$$y_1^0 \sim -(\hat{b}Le/rl\Lambda_0^0)\cdot \begin{cases} \ln\alpha_0^0 & \lambda_0 = 1 \\ \ln\alpha_0^0 + 3/2, & \lambda_0 = 4 \end{cases} \text{ as } \alpha_0^0 \to 0 \quad (40)$$

Profiles of the leading-order inner variables as functions of η are shown in Fig. 2.

The reaction-zone problem at the next order in ε determines α_0^1, y_1^1, θ_1^1 and Λ_0^1, as well as h_1^0, which is still unknown. As before, the problem for α_0^1 and θ_1^1 decouples and is given by

$$\frac{d\alpha_0^1}{d\eta} = r[\Lambda_0^0(1 - \alpha_0^0)\theta_1^1 + \Lambda_0^1(1 - \alpha_0^0) - \Lambda_0^0\alpha_0^1]e^{\theta_1^0} \quad (41)$$

$$l\frac{d\theta_1^1}{d\eta} + l^1\alpha_0^0\frac{d\theta_1^0}{d\eta} + [lQ_g^1/\hat{b}Le(T_b^0 - 1)]\alpha_0^0\frac{dy_1^0}{d\eta} = -C_0\alpha_0^1 + C_1(1 - \alpha_0^0) \quad (42)$$

$$\alpha_0^1 \to 0,\ \theta_1^1 \to 0 \text{ as } \eta \to +\infty;$$
$$\alpha_0^1 \to \alpha_s^1,\ \theta_1^1 \sim E_1^1\eta + E_2^1 h_1^0 \text{ as } \eta \to -\infty \quad (43)$$

where

$$C_0 = [(b - \hat{b})T_b^0 + Q_l]/(T_b^0 - 1) = rl\Lambda_0^0,$$
$$C_1 = [Q_g^1(T_b^0 - 1) - T_b^1(Q_l + b - \hat{b})]/(T_b^0 - 1)^2,$$
$$E_1^1 = \alpha_s^1(\hat{r}\hat{b} - b)/l + [\alpha_s^1(T_b^0 - 1) + T_b^1](1 + \gamma_s - b)/l(T_b^0 - 1)^2,$$
$$E_2^1 = -Q_g^1/l(T_b^0 - 1) \quad (44)$$

and $T_b \sim T_b^0 + \varepsilon T_b^1 + \cdots$, with $T_b^0 = (Q_l + 1 + \gamma_s)/\hat{b}$ and $T_b^1 = Q_g^1/\hat{b} - \hat{r}(T_b^0 - 1)\alpha_s^1$. We observe that T_b^1, and hence C_1 and E_1^1, all depend on α_s^1, reflecting, to this order of approximation, a linearly decreasing dependence of the burned temperature on the porosity of the solid.

Transforming to α_0^0 as the independent variable, equations 41 and 42 become

$$\frac{d\alpha_0^1}{d\alpha_0^0} + \frac{\alpha_0^1}{1 - \alpha_0^0} = \theta_1^1 + \Lambda_0^1/\Lambda_0^0 \quad (45)$$

$$rl\Lambda_0^0\alpha_0^0\frac{d\theta_1^1}{d\alpha_0^0} + C_0\frac{\alpha_0^1}{(1 - \alpha_0^0)} = C_1 - r\hat{l}^1\Lambda_0^0\alpha_0^0 - [Q_g^1 rl\Lambda_0^0/\hat{b}Le(T_b^0 - 1)]\,(\alpha_0^0)^2\frac{dy_1^0}{d\alpha_0^0} \quad (46)$$

subject to equation 43 expressed in terms of α_0^0. Rewriting equation 45 as $(d/d\alpha_0^0)\,[\alpha_0^1/(1 - \alpha_0^0)] = (\theta_1^1 + \Lambda_0^1/\Lambda_0^0)/(1 - \alpha_0^0)$ and substituting this result into the derivative of equation 46, we obtain

$$\frac{d^2\theta_1^1}{d\alpha_0^{0\,2}} + \frac{1}{\alpha_0^0}\frac{d\theta_1^1}{d\alpha_0^0} + \frac{\theta_1^1}{\alpha_0^0(1 - \alpha_0^0)} = -\frac{Q_g^1}{\hat{b}Le(T_b^0 - 1)}\frac{1}{\alpha_0^0}\frac{d}{d\alpha_0^0}\left[(\alpha_0^0)^2\frac{dy_1^0}{d\alpha_0^0}\right] - \frac{\Lambda_0^1/\Lambda_0^0}{\alpha_0^0(1 - \alpha_0^0)} - \frac{\hat{l}^1/l}{\alpha_0^0} \quad (47)$$

where y_1^0 is given by equation 39. Homogeneous solutions of equation 47 are $(1 - \alpha_0^0)\ \ln\,[\alpha_0^0(1 - \alpha_0^0)^{-1}] + 1$ and $1 - \alpha_0^0$, so that the general solution for θ_1^1 may be constructed by reduction of order and substituted into equation 45 to determine α_0^1. Thus, for example,

$$\theta_1^1 = c_1\left[1 + (1 - \alpha_0^0)\ln\left(\frac{\alpha_0^0}{1 - \alpha_0^0}\right)\right] + c_2(1 - \alpha_0^0) - \frac{\Lambda_0^1}{\Lambda_0^0} + \frac{\hat{l}^1}{2l}(1 - \alpha_0^0)\ln\alpha_0^0 + \frac{Q_g^1}{rl\Lambda_0^0(T_b^0 - 1)}\left\{\frac{11 - 9\alpha_0^0}{2(1 - \alpha_0^0)} + \frac{\ln\alpha_0^0}{(1 - \alpha_0^0)^2} - \frac{5\ln\alpha_0^0}{2(1 - \alpha_0^0)} - 2\ln\alpha_0^0 + \frac{13}{2}(1 - \alpha_0^0)\ln\left(\frac{\alpha_0^0}{1 - \alpha_0^0}\right) + 2(1 - \alpha_0^0)\left[\frac{\pi^2}{6} + \mathrm{Li}_2(\alpha_0^0)\right]\ln\alpha_0^0 + 2\mathrm{Li}_2(1 - \alpha_0^0) - 2(1 - \alpha_0^0)\,[2\mathrm{Li}_3(\alpha_0^0) + \mathrm{Li}_3(1 - \alpha_0^0)]\right\} \quad (48)$$

$$\alpha_0^1 = c_3(1 - \alpha_0^0) + (1 - \alpha_0^0)\left[c_1\alpha_0^0\ln\left(\frac{\alpha_0^0}{1 - \alpha_0^0}\right) + c_2\alpha_0^0 + \frac{\hat{l}^1}{2l}(\alpha_0^0\ln\alpha_0^0 - \alpha_0^0)\right] + \frac{Q_g^1(1 - \alpha_0^0)}{rl\Lambda_0^0(T_b^0 - 1)}\left\{\frac{1}{2(1 - \alpha_0^0)}\left(1 + \frac{\ln\alpha_0^0}{1 - \alpha_0^0}\right) - \left[\frac{1 + 4\alpha_0^0}{2(1 - \alpha_0^0)} - \left(\frac{\pi^2}{3} + \frac{13}{2}\right)\alpha_0^0\right]\ln\alpha_0^0 - \frac{13}{2}\alpha_0^0\ln(1 - \alpha_0^0) + 2\alpha_0^0\mathrm{Li}_2(\alpha_0^0)\ln\alpha_0^0 - 2\mathrm{Li}_2(1 - \alpha_0^0) - 4\alpha_0^0\mathrm{Li}_3(\alpha_0^0) - 2\alpha_0^0\mathrm{Li}_3(1 - \alpha_0^0)\right\} \quad (49)$$

for $\lambda_0 = 4$, where c_1, c_2 and c_3 are integration constants, and the polylogarithms $\mathrm{Li}_n(\alpha)$, $n \geq 2$, are defined recursively for all complex α by $\mathrm{Li}_2(\alpha) = -\int_0^\alpha \hat{\alpha}^{-1}\ln(1 - \hat{\alpha})d\hat{\alpha} = \sum_{j=1}^\infty \alpha^j/j^2$, $\mathrm{Li}_{n>2}(\alpha) = \int_0^\alpha \hat{\alpha}^{-1}\,\mathrm{Li}_{n-1}(\hat{\alpha})d\hat{\alpha} = \sum_{j=1}^\infty \alpha^j/j^n$, where the series representation is convergent for $|\alpha| \leq 1$ [18]. For $0 \leq \alpha \leq 1$, $\mathrm{Li}_2(\alpha)$ and $\mathrm{Li}_3(\alpha)$ are monotonic functions that range from $\mathrm{Li}_2(0) = \mathrm{Li}_3(0) = 0$ to $\mathrm{Li}_2(1) = \pi^2/6$ and $\mathrm{Li}_3(1) \doteq 1.20205690$. Also, $\mathrm{Li}_2(\alpha) + \mathrm{Li}_2(1 - \alpha) = \pi^2/6 - \ln\alpha\ln(1 - \alpha)$, which was used to obtain equations 48 and 49. Application of the matching conditions then determines Λ_0^1, c_1, $c_2(h_1^0)$, and c_3 as

$$
\begin{aligned}
\Lambda_0^1 &= Q_g^1(21 - 2\pi^2)/6rl(T_b^0 - 1) \\
&\quad + E_1^1/r - \Lambda_0^0\hat{l}^1/2l, \\
c_2 &= Q_g^1([3 - \pi^2 + 6\mathrm{Li}_3(1)]/3r\Lambda_0^0 \\
&\quad - h_1^0)/l(T_b^0 - 1), \\
c_1 &= -Q_g^1(9 + \pi^2)/3rl\Lambda_0^0(T_b^0 - 1) \\
&\quad + E_1^1/r\Lambda_0^0 - \hat{l}^1/2l, \\
c_3 &= \alpha_s^1 + Q_g^1(2\pi^2 - 3)/6rl\Lambda_0^0(T_b^0 - 1)
\end{aligned} \tag{50}
$$

An expression for h_1^0 may be determined by continuing with the perturbation analysis, but it can be deduced directly from the second matching condition (equation 38) which, for $\lambda_0 = 4$, gives

$$
\begin{aligned}
y_1^1 \sim \alpha_s^1(\hat{b}Le/rl\Lambda_0^0)[(1 - \hat{r}\phi) \ln \alpha_0^0 \\
+ r\Lambda_0^0 h_1^0 + 3/2]/\alpha_0^0 \text{ as } \alpha_0^0 \to 0
\end{aligned} \tag{51}
$$

Since $1/\alpha_0^0 \sim \exp(-r\Lambda_0^0\eta)$ as $\eta \to -\infty$, equation 51 implies that y_1^1 grows exponentially as $\eta \to -\infty$ unless the right-hand side is identically zero. Since only algebraic growth of the inner solution is compatible with an asymptotic matching with the outer solution, as indicated in equation 28, we conclude from equation 51 that $\hat{r}\phi = 1 + O(\varepsilon)$ and $h_1^0 = (-3/2)/(r\Lambda_0^0)$. This required restriction of $\hat{r}$ to values that are relatively close to $1/\phi \geq 1$ corresponds to high upstream gas-phase densities, or pressures, and may be interpreted as a compatibility condition, required for the existence of a merged-flame solution, that accompanies our ordering of the activation energies and consumption rates when gas-phase heat release is small. According to equation 16 for u_g, it essentially limits the two-phase-flow effect to that associated with thermal expansion of the gas. Larger rates of gas-phase transport relative to the condensed phase would cause the gas-phase reaction to occur increasingly downstream of the condensed reaction, leading to a breakdown in the merged-flame structure analyzed here, but it is anticipated that larger gas-phase consumption rates would allow for larger gas-phase convective transport arising from smaller upstream gas densities. Profiles of α_0^1 and θ_1^1 for $\lambda_0 = 4$ are shown in Fig. 2.

Discussion of the Burning Rate and Conclusions

The dimensional propagation speed $\tilde{U}$, from the definition of Λ_l given in equation 2, is given by

$$
\begin{aligned}
\tilde{U}^2 &\sim (\tilde{\lambda}_s\tilde{A}_l/\tilde{\rho}_s\tilde{c}_s)\beta^0[1 + \varepsilon T_b^1(2 - T_b^0)/T_b^0(T_b^0 - 1) \\
&\quad + \cdots](\Lambda_0^0 + \varepsilon\Lambda_0^1 + \cdots)^{-1}e^{-N_l^0(1 - \varepsilon T_b^1/T_b^0 + \cdots)} \\
&\sim (\tilde{\lambda}_s\tilde{A}_l/\tilde{\rho}_s\tilde{c}_s)(\beta^0/\Lambda_0^0)\, e^{-N_l^0}\, e^{\varepsilon\beta^0 T_b^1/(T_b^0 - 1) + \cdots} \\
&\quad \times \{1 + \varepsilon[T_b^1(2 - T_b^0)/T_b^0(T_b^0 - 1) \\
&\quad - \Lambda_0^1/\Lambda_0^0] + \cdots\}
\end{aligned} \tag{52}
$$

where T_b, which appears in the definitions of the nondimensional activation energy N_l and the Zel'dovich number β, has been expanded according to the expansion given below equation 44, and we have introduced the ε-independent definitions $N_l^0 \equiv \tilde{E}_l/\tilde{R}^0\tilde{T}_b^0$ and $\beta^0 \equiv (T_b^0 - 1)N_l^0/T_b^0$. Substituting the expressions obtained in the previous section for Λ_0^0 and Λ_0^1 and setting the bookkeeping parameter ε equal to unity (implying $\alpha_s^1 \equiv \alpha_s$, $\hat{l}^1 \equiv \hat{l} - l$ and $Q_g^1 = Q_g$), we obtain the asymptotic expression for the burning rate, in the specific merged-flame parameter regime considered here, as

$$
\begin{aligned}
\tilde{U}^2 &\sim (\tilde{\lambda}_s\tilde{A}_l/\tilde{\rho}_s\tilde{c}_s)[rl(T_b^0 - 1)/(bT_b^0 - 1 - \gamma_s)] \\
&\quad \times \beta^0 e^{-N_l^0}\, e^{\beta^0[Q_g/\hat{b}(T_b^0 - 1) - \alpha_s/\phi] + \cdots} \\
&\quad \times \{1 + (\hat{l} - l)/2l + [Q_g/(T_b^0 - 1)(bT_b^0 - 1 - \gamma_s)] \\
&\quad \times [(2 - T_b^0)(bT_b^0 - 1 - \gamma_s)/\hat{b}T_b^0 \\
&\quad - (21 - 2\pi^2)(T_b^0 - 1)/6 - (1 + \gamma_s - b)/\hat{b}] \\
&\quad - [\alpha_s/(bT_b^0 - 1 - \gamma_s)\phi][(2 - T_b^0)(bT_b^0 - 1 - \gamma_s)/T_b^0 \\
&\quad + (T_b^0 - 1)(\hat{b} - \phi b) - (1 - \phi)(1 + \gamma_s - b)] + \cdots\}
\end{aligned} \tag{53}
$$

for $\lambda_0 = 4$, with a similar expression for $\lambda_0 = 1$. The first effects of heat release associated with the second step of the reaction model are determined by the terms proportional to Q_g in equation 53.

The dominant effects associated with gas-phase heat release are determined by the second exponential factor in equation 53, which is exponentially large unless $\alpha_s/Q_g \approx \hat{b}^{-1}(T_b^0 - 1)^{-1}\phi$. Values of α_s/Q_g less (greater) than this critical value thus produce a significant increase (decrease) in the burning rate over that of a nonporous material governed solely by the condensed reaction, corresponding to whether or not the perturbation in the burned temperature, which arises from nonzero porosity and the additional heat release associated with the gas-phase reaction, is positive or negative. Since Q_g is positive, the additional heat release associated with the gas-phase reaction enhances the burning rate, but decreasing amounts of solid material that correspond to increasing porosities lead to a lower overall heat release associated with the condensed-phase reaction, resulting in a critical value of porosity for which

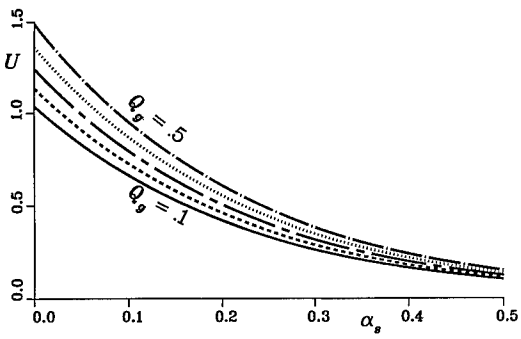

FIG. 3. Approximate nondimensional propagation speed $U = \tilde{U}(Q_g, \alpha_s)/\tilde{U}(0,0)$, corresponding to the case $\lambda_0 = 4$, as a function of α_s for $Q_g = .1$ (solid), .2 (dash), .3 (chain-dash), .4 (dot), and .5 (chain-dot), where the remaining parameter values were taken to be the same as those used in the previous figures.

these counteracting effects balance. Plots of $U = \tilde{U}(Q_g, \alpha_s)/\tilde{U}(0,0)$ are shown in Fig. 3.

Although the primary effect associated with nonzero porosity and a second gas-phase reaction step is thus thermodynamic in nature, additional effects are revealed by those terms arising from the correction Λ_0^1 to the leading-order burning-rate eigenvalue Λ_0^0, which give rise to the last two terms proportional to both Q_g and α_s and the term proportional to $\hat{l} - l$ within the curly brackets in equation 53. For example, it is readily seen that a value of the gas-phase thermal conductivity greater (less) than that of the liquid phase tends to increase (decrease) the propagation speed, since larger values of $\hat{l} - l$ allow for greater heat transport from the reaction zone back to the preheat region, providing a type of "excess enthalpy" effect for the condensed-phase portion of the reaction. The result for the case in which $\lambda_0 = 1$, corresponding to a smaller preexponential reaction-rate coefficient for the gas-phase reaction, is identical to equation 53, except for the fact that the numerator $21 - 2\pi^2 \doteq 1.26$ is replaced by $\pi^2 - 6 \doteq 3.87$ in the second term proportional to Q_g in that equation. Thus, as expected, a smaller gas-phase consumption rate results in a smaller overall burning rate when the corresponding rate for the condensed-phase reaction is unchanged.

In conclusion, the present analysis has sought to describe some of the effects associated with the deflagration of porous energetic materials arising from two-phase flow in the presence of a multiphase sequential reaction mechanism. In contrast to previous work in which the condensed and gas-phase reactions were spatially separated, a merged-flame parameter regime, in which both reactions are operative and proceed to completion in a single thin reaction zone, was considered in the present study. Although additional parameter constraints were required to support a merged-flame structure, such a structure was calculated for the case of a high-pressure deflagration in which the relative flow of gas with respect to the condensed material arises primarily from thermal expansion of the former. This result is consistent with typical experiments involving the nitramine propellants HMX and RDX that show the tendency of the primary gas flame to move closer to the propellant surface as the pressure increases. Further parametric studies are in progress and will be reported in future publications.

Nomenclature

$\tilde{A}$	preexponential rate coefficient
$\tilde{D}$	mass-diffusion coefficient
$\tilde{c}$	heat capacity
$\tilde{E}$	activation energy
$\tilde{Q}$	heat release
$\tilde{R}^\circ$	gas constant
$\tilde{t}$	time
$\tilde{T}$, Θ, θ	temperature variable
$\tilde{u}$	velocity variable
$\tilde{U}$	propagation speed
$\tilde{W}$	molecular weight
$\tilde{x}$, ξ, η	spatial coordinate
Y, y	gas-phase mass-fraction variable
α	gas-phase volume fraction
$\tilde{\gamma}_s$	heat of melting
$\tilde{\lambda}$	thermal conductivity
$\tilde{\rho}$	density
ϕ	gas-phase mass-fraction ratio

Subscripts, Superscripts

g, l, s	gas, liquid, solid phase
b	downstream burned value
m	melting-surface value
u	upstream unburned value

Acknowledgments

This work was supported by the U.S. Department of Energy under Contract DE-AC04-94AL85000 and by a Memorandum of Understanding between the Office of Munitions (Department of Defense) and the Department of Energy. A.M.T. was supported by a President of Russia Scholarship for Study Abroad.

REFERENCES

1. Baer, M. R., and Nunziato, J. W., *Int. J. Multiphase Flow* 12:861–889 (1986).
2. Maksimov, E. I., and Merzhanov, A. G., *Combust. Explos. Sh. Waves* 2:25–31 (1966).

3. Merzhanov, A. G., *Combust. Flame* 13:143–156 (1969).
4. Margolis, S. B., Williams, F. A., and Armstrong, R. C., *Combust. Flame* 67:249–258 (1987).
5. Li, S. C., Williams, F. A., and Margolis, S. B., *Combust. Flame* 80:329–349 (1990).
6. Margolis, S. B., and Williams, F. A., *Combust. Flame* 79:199–213 (1990).
7. Margolis, S. B., and Williams, F. A., *J. Propulsion Power* 11:759–768 (1995a).
8. Margolis, S. B., and Williams, F. A., *Combust. Sci. Technol.* 106:41–68 (1995b).
9. Margolis, S. B., and Williams, F. A., *Int. J. Multiphase Flow,* 22:69–91 (1996).
10. Prasad, K., Yetter, R. A., and Smooke, M. D., Yale University Report ME-101-95, Yale University, New Haven, CT 1995.
11. Li, S. C., and Williams, F. A., *J. Propulsion Power* 12:302–309 (1996).
12. Margolis, S. B., and Matkowsky, B. J., *SIAM J. Appl. Math.* 42:1175–1188 (1982a).
13. Margolis, S. B., and Matkowsky, B. J., *Combust. Sci. Technol.* 27:193–213 (1982b).
14. Peláez, J., and Liñán, A., *SIAM J. Appl. Math.* 45:503–522 (1985).
15. Booty, M. L., Holt, J. B., and Matkowsky, B. J., *Q. J. Mech. Appl. Math.* 43:224–249 (1990).
16. Margolis, S. B., *Int. J. Eng. Math.*, (1997), in press.
17. Peláez, J., *SIAM J. Appl. Math.* 47:781–799 (1987).
18. Lewin, L., *Polylogarithms and Associated Functions,* Elsevier North Holland, New York, 1981.

COMMENTS

Jerry Finlinson, NAWC, USA. It would be very useful if you would compare your model against some real data, such as the HMX porous bed data generated for DDT experiments. It seems that having the burn rate decrease with decreasing porosity is different from DDT data. HMX will transition to detonation in approx 1 cm. Could you comment on that?

Author's Reply. The analysis and results presented in the paper were for the case of an unconfined deflagration, and thus the DDT experiments to which you refer are not directly applicable to the present study. In a DDT scenario, the (weak) deflagration structure described here breaks down, giving rise to nonnegligible pressure gradients that result in a fundamentally different structure in which convective processes assume a much more significant role. In particular, the strong convective influences force hot gases into the pores of the unburned material, providing, among other things, a significant preheating effect. In such a strongly convective regime, it is not surprising that, as the porosity increases, this convective preheating can dominate the thermal loss associated with a diminished amount of energetic material, thereby increasing the burning rate. In contrast, in the deflagration regime analyzed here, diffusive effects are insufficient to overcome the thermal loss associated with increasing porosity, and the burning rate decreases. In continuing work, we are looking further into the aforementioned effects associated with convective burning, and thus hope to be able to compare future results with some of the DDT data that is currently available.

Twenty-Sixth Symposium (International) on Combustion/The Combustion Institute, 1996/pp. 1981–1987

SOLID PROPELLANT DIFFUSION FLAME STRUCTURE

T. P. PARR AND D. M. HANSON-PARR
Combustion Diagnostics Laboratory, Research Division, Naval Air Warfare Center
China Lake, CA 93555-6100, USA

Laser-supported deflagration of ADN, AP, HNF, TNAZ, RDX, or HMX in sandwich configurations with various energetic and nonenergetic binders was studied. Planar laser–induced fluorescence (PLIF) was used to measure the two-dimensional NH, OH, and CN species profiles for these sandwiches. For the HNF sandwiches, obvious diffusion flames were present at low pressure, but they were weak, further from the surface than the HNF monopropellant flame, and not expected to be burn-rate controlling. ADN was found to have diffusion flames with energetic binders at low pressures, but they were very far from the surface. The high burn rate of ADN at pressures above 3 atm left the binder behind, and the diffusion flames became weak. AP showed clear evidence for strong close diffusion flames with binders and even with other oxidizers. The combination of HMX or TNAZ with AP leads to obvious diffusion flame interactions: the highly reactive AP-decomposition products accelerated the nitramine dark zone kinetics and caused the secondary flame to hold on the interface region. This leads to higher heat feedback in the interface region and a somewhat faster nitramine regression rate. TNAZ, RDX, and HMX were not found to have any diffusion flames with energetic or nonenergetic binders: the monopropellant flame was lifted in the region around the binder. These results imply that ADN, HNF, TNAZ, RDX, and HMX propellants will not have the clear particle size ballistic tailorability seen with AP propellants, because diffusion flames appear to be strong and close to the surface (and therefore burn-rate controlling) only in AP propellants.

Introduction

Nearly all solid rocket propellants are composite mixtures of several ingredients, some acting more like fuels and others more like oxidizers. Since particle sizes can be the same scale as or larger than flame lengths, diffusion flames between ingredients are important in some propellant systems. Understanding the interaction between ingredients, as well as diffusion flame structure, is important to understanding the effects of particle size on propellant ballistic properties. For example, most AP (ammonium perchlorate)–based composite propellants are thought to have diffusion flames between the AP and fuel decomposition products, and such propellants show particle size effects on ballistic properties [1,2]. Changing the AP particle size can lead to a factor of nearly 8 change in burn rate. The smallest particles lead to the highest burn rate, because the hot primary diffusion flame between AP and fuel dominates the heat feedback to the AP and leads to a high regression rate. Large AP particles see mostly the cooler AP monopropellant flame, leading to a lower burning rate [2].

A solid propellant flame is a complex system, and it is necessary to understand the decomposition processes and the kinetic mechanisms of the diffusionally mixed products of the materials that comprise the propellant to understand the system as a whole. Once understood, the system can be modeled, and the models used for a priori prediction of global ballistic properties. Techniques with adequate spatial and temporal resolution must be employed so that species and temperature profiles can be measured and mechanisms deduced.

Substantial work has been done in our laboratory and others to characterize the flame zone of neat RDX (cyclotrimethylene trinitramine) laser-supported deflagration and self-deflagration [3–14]. RDX was seen to have a two-stage flame structure under laser-supported deflagration. The secondary and primary flames collapse together without the extra flux from the laser, however [3]. A combustion model based on detailed kinetics [15] has been able to adequately predict the temperature and most of the species profiles measured. The model also predicts the merging of flame zones with removal of laser flux and very closely predicts the burning rate, pressure exponent, and temperature sensitivity measured experimentally [14].

HMX (cyclotetramethylene tetranitramine) is a monopropellant similar to RDX. A combustion model has also been developed for HMX [16], and it predicts measured species and temperature profiles and the global ballistic properties. HMX was found to undergo more condensed phase decomposition so that the gas species fed to the flame are different from RDX, which makes the flame structure different.

It is a continuing effort of this laboratory to study

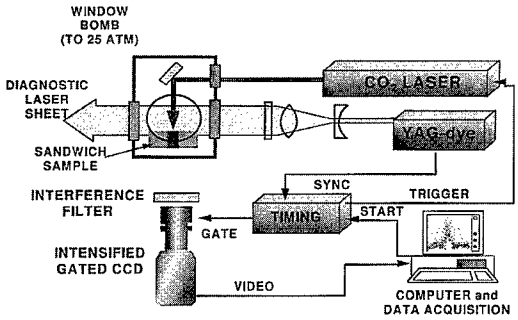

FIG. 1. Apparatus diagram for planar laser–induced fluorescence experiments.

new oxidizers, such as ADN (ammonium dinitramide). Work has also been done with neat HNF (hydrazinium nitroformate or $(N_2H_5)^+(C(NO_2)_3)^-$ [4] and sandwiches of HNF and other materials with energetic binders and other oxidizers such as HMX and RDX. These and other recent two-dimensional diffusion flame structure results from our laboratory will be discussed.

Experimental

The oxidizer samples used in the experiments were either pressed neat from powders (ADN, AP, HNF, TNAZ [1,3,3-trinitroazetidine]) or pressed from powders using 1 drop of spectrophotometric grade methanol (HMX, RDX) at about 80,000 PSI to between 96% to 97% theoretical maximum density (TMD, or crystal density). The methanol was dried out of the HMX and RDX samples before use. These solid pellets were right circular cylinders. The laser used to ignite the samples and subsequently aid in the deflagration was a 150-W CW CO_2 laser.

Binder sandwiches generally consisted of 2-mm-thick slabs of oxidizer with a thinner piece of binder in between. If an oxidizer were used as the binder, that is, the center lamina, the thickness was generally 0.5–1 mm with 2-mm slabs of other oxidizer on the outside. The energetic polymeric binders (BAMO [bis(azidomethyl)oxetane]/NMMO [3-nitratomethyl-3-methyl oxetane] and GAP[glycidylazide polymer]) and the wax were sliced from a large already-cured piece using a razor blade. The BAMO/NMMO and GAP were high energy (high plasticizer-to-polymer ratio). Other polymers, such as HTPB (hydroxyl-terminated polybutadiene) or PU (polyurethane), were obtained from cured sheets as thin as 50 μm. As will be seen in the results section, the use of the terms *binder* and *oxidizer* is continued for historical reasons. However, some compounds normally classified as oxidizer are actually fuel rich and act as fuels in some of the sandwich configurations.

Sandwich construction was by manual means. Pellets were cut in half with a razor blade and the bottoms sanded flat. Thin slices of binder were placed between two half pellets in a miniature vise. No glue was used. Excess binder was cut off and the semicylinders planed flat using a sharp razor blade. A microscope was used to measure the lamina thickness for the soft binders or measured with calipers if the material was stiff enough.

Previous work in our laboratory on neat nitramines showed that laser-supported deflagration is a good method to study flame structure. It allows the study of systems below their pressure deflagration limit, yet does not drastically alter the flame chemistry or structure. In the sandwich work, the low average power laser flux of 50 cal/cm^2 s (reasonably flat unfocused beam) was kept on during the entire experiment.

The flame structure was measured using planar laser–induced fluorescence (PLIF) imaging [3–5,17–21]. The apparatus diagram for the PLIF setup is shown in Fig. 1. The CO_2 laser irradiated the sandwich surface at about 15° from normal to prevent absorption by plume gases. The laser used to excite PLIF was a Nd-Yag^{3+} pumped tunable dye laser with nonlinear crystal mixing and doubling into the ultraviolet. The ultraviolet beam was expanded and formed into a sheet and passed across the sandwich laminae, perpendicular to their surfaces, through the center of the flame. The camera used to image PLIF for recent tests was a gated image intensified CCD with 752 × 480 pixels. For PLIF work, the camera was gated on for about 80 ns only during or just after the diagnostic laser pulse; this discriminated against natural flame emission and monitored only the laser-induced fluorescence. The camera imaged the PLIF signal at 90° with respect to the diagnostic laser sheet. The pressure vessel (bomb) was essentially a stainless steel box with four windows in it. The three largest were 50-mm-diameter sapphire windows and the fourth a 25-mm-diameter ZnSe window for the CO_2 laser. Before each pressure test, N_2 gas flowed into the bomb, and the desired pressure was established by adjusting the flow out of the outlet valve. The N_2 flow was from the bottom of the bomb to the top, but the propellant flames were in the dead zone downstream of the vise and the N_2 flow velocity was quite low.

PLIF imaging monitors the ground electronic state of flame species, whereas chemiluminescence comes only from excited electronic states formed in low probability energetic reactions. Thus, it is often not a good idea to use chemiluminescence to monitor flame structure because it tracks low probability secondary reactions rather than the main flame chemistry pathways. For OH radicals, for example, the chemiluminescence does not track ground state OH concentrations at all [22]. This is why we chose to use PLIF. In addition, PLIF provides a narrow

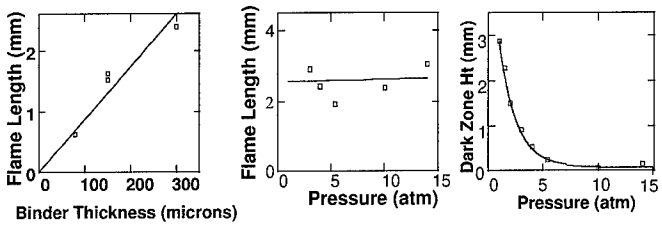

FIG. 2. Effect of binder thickness and pressure on diffusion flame characteristics: (left) flame length versus central lamina thickness, (center) flame length versus pressure, and (right) dark zone length versus pressure.

planar slice through the flame, while emission imaging is a line of sight average technique. The thickness of the laser sheet was less than 150 μm, and the resolution of the camera system was about 9 microns per pixel for the HNF sandwich tests.

CN radicals were monitored using PLIF by exciting the (0, 0) *B-X* bandhead at 388.34 nm (all wavelengths reported here are in air, not vacuum) while imaging (0, 1) emission using a 420-nm interference filter. The laser power used saturated the CN transition, thereby partially limiting problems caused by quenching. The CN PLIF image profiles are therefore expected to be a good relative image of CN-radical concentration profiles. NH PLIF was obtained by tuning the laser to the Q_3 (1, 0) (*A-X*) bandhead near 305 nm and monitoring LIF from the $\Delta v = 0$ spectral region around 336 nm using a combination of WG335 and UG11 filters. OH PLIF was done by either tuning the laser to the $R_1(10)$ line of the (1, 0) (*A-X*) transition, which has low temperature sensitivity, or to a bandhead, and monitoring the LIF using a combination of two WG305 with one UG11 filters. Verification of signal for each of these species was made by tuning off resonant of the molecular absorption and observing the disappearance of the PLIF image.

Results and Discussion

To study the interaction between ingredients, sandwiches [4,17,23–29] consisting of planes or slabs of two ingredients in close contact were used. This allowed imaging of the diffusive flame structure from known geometries. The approach in this laboratory was to use PLIF to get a two-dimensional image of a particular species in the flame of a sandwich and study the effects of lamina thickness, lamina type, and pressure on the flame structure. How much kinetic delay there is to significant heat release can be seen by the length of the dark zone. If the decomposition products of the oxidizer and fuel react with fast kinetics, then the flame standoff seen will be short. If the kinetics are slow, the standoff will be tall. By comparing these standoffs with the neat material flame standoffs, one can judge whether there is any positive diffusion flame interaction between the ingredients that might lead to a particle-size control of ballistics. By laminar jet theory [30] for a slot burner configuration, the flame length should be proportional to $d \times U/D$, where d is the central slot dimension (the binder thickness here), U is the fuel flow velocity (central slot), and D is the diffusion coefficient. (This contrasts with the more common axisymmetric case for which the dependence is $d^2 \times U/D$.) Laminar theory is used because the Reynolds number for these sandwich experiments is only about 7.

Extensive measurements have been made in our laboratory of diffusion flame structure of nitramines [17,27], ammonium dinitramide (ADN) [17,28–29], and AP composite sandwich solid propellants [17]. The slot burner diffusion flame height relationship has been tested for sandwich propellants. Figure 2 shows flame length and dark zone height (measured from CN PLIF) for an energetic binder sandwiched between ADN laminae. The binder was N5, a double-base propellant, and the deflagration was laser supported. Because of the external CO_2 laser flux used, the burning rate and "fuel" velocity, U, were probably about constant, independent of fuel lamina thickness and pressure. The flame length was found to increase linearly with lamina thickness (Fig. 2, left) and remain constant with increasing pressure (Fig. 2, center), in agreement with laminar jet theory. The dark zone height decreased with pressure as a result of the increase in kinetic rates (Fig. 2, right).

It is important to do these sandwich studies as a function of pressure. The diffusion flames that gave rise to the data of Fig. 2 became weak as pressure rose and the binder pyrolysis could not keep up with the ADN regression. The diffusion flames seen were too weak and much too far from the surface to be burn-rate controlling [29]. The regression rate is largely defined by the ADN self-rate. Thus, ADN propellants are not expected to have the particle-size ballistic tailorability of AP propellants. This has been confirmed by recent information on Russian ADN propellants [31].

Work done with AP has shown strong diffusion flames close to the surface that have persisted at elevated pressures. Work with nitramines has shown no diffusion flames. An example of these results is shown in Fig. 3. The center image shown is CN PLIF from laser-supported deflagration of neat HMX. (The flame exhibits a bell shape because of

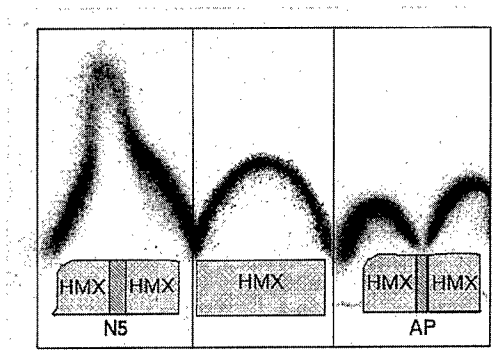

FIG. 3. Effect of diffusional mixing between products of HMX decomposition and other materials: (left) with N5, (center) neat HMX, and (right) with AP. If the diffusion flame between the reaction products slows the kinetics from that of the pure material (center), the flame becomes lifted (left), and if the kinetics are enhanced, the flame anchors on the interface region (right).

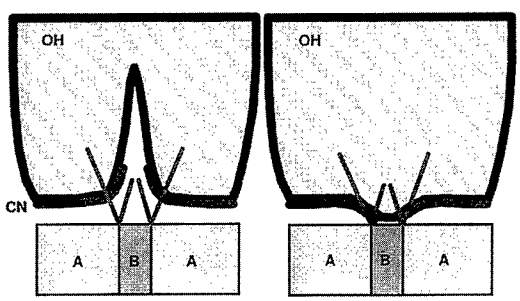

FIG. 4. Schematic drawing of various flame interactions. The diffusional mixing fan is shown as a dotted line. In the left picture, the *B* products poison the *A* flame and lift it; in the right picture, the *B* products enhance the *A* combustion in the mixing fan and shorten the flame height.

both the CO_2 laser energy spatial geometry and edge heat losses.) The left image shows what happens when an energetic binder lamina (again N5) is added to HMX. Even with an energetic binder, the HMX secondary flame sheet is lifted in the diffusive mixing layer, not shortened. Other work done in our laboratory showed that HMX also has no diffusion flame with various nonenergetic binders [17]. On the other hand, the combination of AP with HMX leads to obvious diffusion flame interactions. The AP decomposition products accelerated the nitramine dark zone kinetics in the diffusive mixing fan and the flame holds very close to the surface on the interface regions. These physical processes are illustrated in Fig. 4 (with the bell shape flattened for clarity). In the left picture, the products of the binder (*A*) dilute or poison the products of the oxidizer (*B*) and the

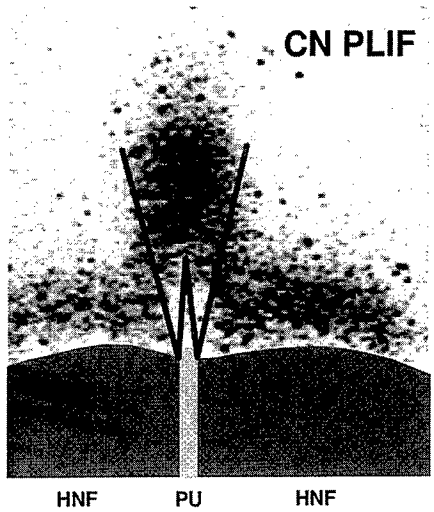

FIG. 5. CN PLIF image of diffusion flame at 1 atm between HNF (outer lamina) and polyurethane binder (center). The polyurethane is 190 microns thick.

flame lifts in the diffusive mixing fan. Figure 4 shows the CN flame sheet extinguishing in the center of the mixing region. This happens for nonenergetic binders in HMX; energetic binders merely lift and weaken the flame (Fig. 3). In the right-side picture, the products of component (*A*) react with those of (*B*) and accelerate the flame in the mixing fan. This causes a shorter flame standoff, increased heat feedback, and enhanced burning rate. The right-side images of Figs. 3 and 4 are really both "inverse" diffusion flames in the sense that the center lamina is acting as oxidizer, not fuel, and the outer as fuel, not oxidizer.

The OH and NH PLIF results mirrored those from CN PLIF. OH was seen in the high-temperature areas of the flame, rising about where the CN appeared and staying almost constant in the high-temperature region above the CN flame sheet (as shown schematically in Fig. 4). The OH PLIF is not shown for space reasons (combining PLIF images without color capability is impossible). The NH sheet was generally somewhat narrower than the CN sheet and almost coincided with it. CN PLIF is far easier to do than NH PLIF because the NH-absorption transition strength is very small (poor Franck–Condon factor). For these reasons, only the CN results are presented here.

PLIF measurements were most recently made on the diffusion flame structure between HNF and various energetic and nonenergetic binders including HTPB, wax, PU, GAP, and BAMO/NMMO in sandwich configurations. Unlike ADN, HNF entirely consumes even nonenergetic binders for low-flux laser-supported deflagration at 1 atm. ADN did not

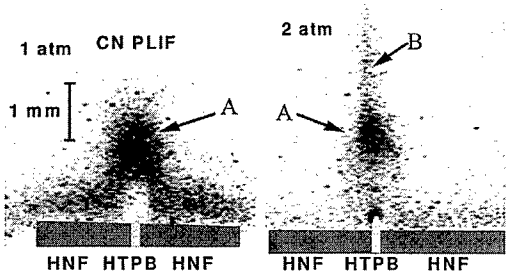

FIG. 6. HNF/HTPB sandwich combustion at 1 atm (left) and 2 atm (right). Arrows marked *A* point to CN PLIF signal, while *B* points to HTPB binder decomposition products (determined by tuning off resonance for CN). Note that the HTPB sticks up above the HNF in the 2-atm image.

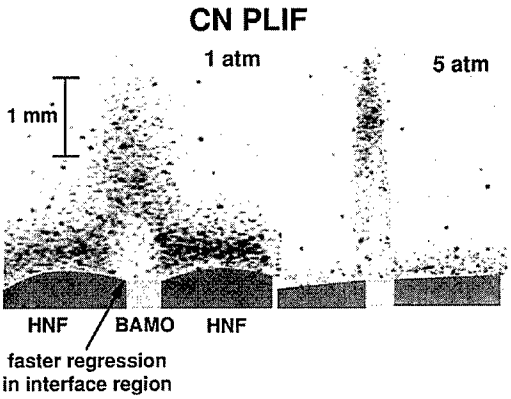

FIG. 7. CN PLIF from HNF/BAMO sandwiches at 1 atm (left) and 5 atm to the same scale.

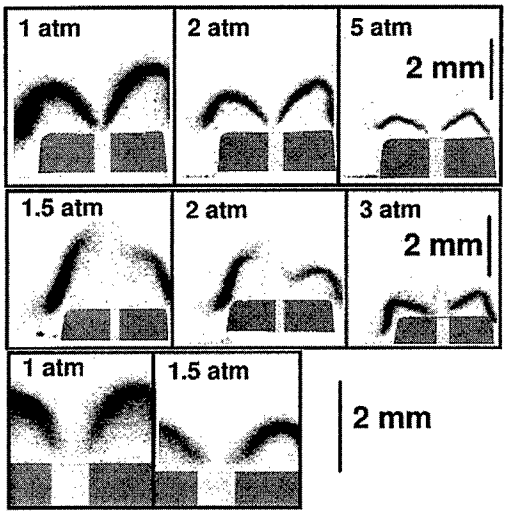

FIG. 8. CN PLIF images for HMX/X/HMX sandwiches at various pressures where X = AP in the top three frames, X = ADN in the middle three, and X = HNF in the bottom three.

even consume energetic binders, at 10 atm, for a laser heating flux nearly nine times as large as for the HNF tests [17]. Diffusion flames between the HNF and binder were clearly evident in the emission and PLIF imaging experiments, and these flames had much lower kinetic standoff distances than those seen with ADN sandwiches (Fig. 5). The HNF self-deflagration flame, however, is also very close to the surface [32], as can be seen in the regions to the left and right of the binder lamina in Fig. 5.

The HNF and binder regression rate was highest in the interface region where the diffusion flame heat is localized. This behavior is understandable: neat HNF has a relatively hot reactive flame extremely close to the surface, whereas ADN has no visible flame. PLIF measurements of CN, NH, and OH were undertaken for the various binder combinations and binder length scales. These experiments were then extended to elevated pressure to determine whether the diffusion flames seen are also important at higher pressures.

It was found that, as with ADN, as the pressure increases the burn rate of the HNF increases and it starts to leave nonenergetic binders behind. Even at 2 atm, the HTPB lamina sticks up above the HNF. At 10 atm, HTPB lamina of 200 microns were recovered only charred. The PLIF images showed weaker diffusion flames at elevated pressures, and some HTPB decomposition products seemed to pass through the diffusion flame (Fig. 6).

When HNF was used with energetic binders, such as BAMO/NMMO, the binder was able to keep up with the increasing HNF regression rate at higher pressures and obvious diffusion flames were seen even at elevated pressures. Figure 7 compares the flame structure of HNF/BAMO-NMMO sandwiches at 1 and 5 atm. Notice that, as predicted by laminar jet flame theory [30], the diffusion flame's length is approximately independent of pressure. On the other hand, the HNF self-flame standoff height decreases dramatically because of faster gas kinetics. The diffusion flame height is much taller than the neat HNF flame, so even in this case it is probably not burn-rate controlling. Any particle size controllability of HNF composite propellant ballistics will likely be much weaker than seen for AP.

HNF with either RDX or HMX as the outer laminae was also studied (Fig. 8). In comparison, ADN somewhat accelerated the HMX dark zone chemistry and shortened the HMX secondary flame, while AP greatly accelerated it. HNF had the same effect on both RDX and HMX secondary flames and

appeared closer to AP's effectiveness than ADN's. The dark zone of HMX and RDX is caused by the slow reduction of NO. The N_xH_y decomposition products of ADN, HNF, and AP probably accelerate the reduction of NO. For example, NH_3 is a well-known de-NO_x agent.

Summary

Planar laser–induced fluorescence (PLIF) images of flame structure were done for CO_2 laser-supported deflagrating sandwich propellants. Two-dimensional NH, OH, and CN species profiles were obtained. For some combinations, the diffusional mixing between ingredient products enhanced combustion, while for others there was no obvious positive diffusion flame. Of the oxidizers studied, only AP appeared to have burn-rate controlling diffusion flames close to the surface. Nitramines showed no positive diffusion flame at all. ADN and HNF showed weak diffusion flames that are too far from the surface to be burn-rate controlling.

Acknowledgments

The authors gratefully thank Dr. May Chan, Jerry Finlinson, and Vicki Brady of NAWC and Dr. Jerry Manser of Aerojet for supplying us with binders, Dr. David Vanderah for supplying us with ADN, Dr. Jay Levine of Phillips Laboratory/Edwards for the HNF, and especially Dr. Richard Miller of ONR for funding this work.

REFERENCES

1. Beckstead, M. N., "Combustion Calculations for Composite Solid Propellants," *Proceedings of the 13th JANNAF Combustion Meeting,* CPIA Publication 281, Vol. II, 1976, p. 299.
2. Blomshield, F. S., "Nitramine Composite Solid Propellant Modeling," Naval Weapons Center Report No. NWC TP-6992, 1989.
3. Parr, T. P. and Hanson-Parr, D. M., "RDX, HMX, and XM39 Self-Deflagration Flame Structure," *Proceedings of the 32nd JANNAF Combustion Subcommittee Meeting,* CPIA Publication 631, 1995.
4. Parr, T. P. and Hanson-Parr, D. M., "HNF Diffusion Flame Structure," *Proceedings of the 32nd JANNAF Combustion Subcommittee Meeting,* CPIA Publication 631, 1995.
5. Hanson-Parr, D. M. and Parr, T. P., "RDX Laser Assisted Flame Structure," *Proceedings of the 31st JANNAF Combustion Subcommittee Meeting,* CPIA Publication 620, Vol. II, 1994, p. 407.
6. Parr, T. P. and Hanson-Parr, D. M., "Solid Propellant Flame Structure," in *Non-Intrusive Combustion Diagnostics* (Kuo, Kenneth K. and Parr, Tim, Eds.), Begell House, Inc., New York, 1994, pp. 571–599.
7. Lee, Y. J., Tang, C. J., and Litzinger, T. A., "A Study of the Gas-Phase Processes of RDX Combustion Using a Triple Quadrupole Mass Spectrometer," *Proceedings of the 31st JANNAF Combustion Subcommittee Meeting,* CPIA Publication 620, Vol. II, 1994, pp. 425–430.
8. Fetherolf, B. L. and Litzinger, T. A., "Chemical Structure of the Gas Phase above Deflagrating RDX: Comparison of Experimental Measurements and Model Predictions," *Proceedings of the 30th JANNAF Combustion Committee Meeting,* CPIA Publication 606, Vol. II, 1993, p. 15.
9. Korobeinichev, O. P., "Dynamic Flame Probe Mass Spectrometry and Condensed-System Decomposition," *Combust. Expl. Shock Waves* 23:565–576 (1988).
10. Ermolin, N. E., Korobeinichev, O. P., Kuibida, L. V., and Fomin, V. M., "Processes in Hexogen Flames," *Combust. Expl. Shock Waves* 24:400–407 (1989).
11. Aron, K. and Harris, L. E., "CARS Probe of RDX Decomposition," *Chem. Phys. Lett.* 103:413–417 (1983).
12. Stufflebeam, J. H. and Eckbreth, A. C., "CARS Diagnostics of Solid Propellant Combustion at Elevated Pressures," *Combust. Sci. Technol.* 66:163–179 (1989).
13. Zhao, X., Hintsa, E., and Lee, Y. T., "Infrared Multiphoton Dissociation of RDX in a Molecular Beam," *J. Chem. Phys.* 88:801–810 (1988).
14. Atwood, A. I., Curran, P. O., and Price, C. F., "Laboratory Ignition and Combustion Data and the Determination of Global Kinetics and Energetic Parameters of RDX," *Proceedings of the 32nd JANNAF Combustion Subcommittee Meeting,* CPIA Publication 631, 1995.
15. Prasad, K. and Smooke, M., "An Eigenvalue Approach for Computing the Burning Rate of RDX Propellants," *32nd JANNAF Combustion Subcommittee Meeting,* CPIA Publication 631, 1995; *Combust. Sci. Technol.* (1996). Accepted.
16. Prasad, K., Yetter, R. A., Smooke, M. D., Parr, T. P., and Hanson-Parr, D. M., "An Eigenvalue Approach for Computing the Burning Rate of HMX Propellants," *AIAA 34th Aerospace Sciences Meeting,* Reno, January 1996, AIAA Paper 96-0880, 1996.
17. Parr, T. P. and Hanson-Parr, D. M., "Advanced Oxidizers Diffusion Flame Structure," *Proceedings of the 31st JANNAF Combustion Subcommittee Meeting,* CPIA Publication 620, Vol. II, 1994, pp. 333–344.
18. Parr, T. P. and Hanson-Parr, D. M., "Advanced Diagnostic Techniques for NonSteady Burning of Solid Propellants," in *Progress in Astronautics and Aeronautics* Vol. 143 (De Luca, L., Price, E. W., and Summerfield, M., Eds.), AIAA, Washington, D.C., 1992, pp. 261–324.
19. Parr, T. P. and Hanson-Parr, D. M., "Nitramine Flame Structure as a Function of Pressure," *Proceedings of the 26th JANNAF Combustion Committee Meeting,* CPIA Publication 529, Vol. I, 1989, p. 27.
20. Parr, T. P. and Hanson-Parr, D. M., "Temperature and Species Profiles in Propellant Ignition and Combustion," *Proceedings of the 24th JANNAF Combustion*

Committee Meeting, CPIA Publication 476, Vol. I, 1987, p. 367.

21. Parr, T. P. and Hanson-Parr, D. M., "The Application of Imaging Laser Induced Fluorescence to the Measurement of HMX and Aluminized Propellant Ignition and Deflagration Flame Structure," *Proceedings of the 23rd JANNAF Combustion Committee Meeting*, CPIA Publication 457, Vol. I, 1986, p. 249.
22. Dyer, M. J. and Crosley, D. R., "Rapidly Sequenced Pairs of Two-Dimensional Images of OH Laser Induced Fluorescence in a Flame," *Opt. Lett.* 9:217 (1984).
23. Price, E. W. et al., "Combustion of Ammonium Perchlorate—Polymer Sandwiches," *Combust. Flame* 63:381 (1986).
24. Price, E. W. and Sambamurthi, J. K., "Dependence of Burning Rate of AP-Polymer Sandwiches on Thickness of Binder Laminae," *Proceedings of the 20th JANNAF Combustion Subcommittee Meeting*, CPIA Publication 383, 1983.
25. Price, E. W., Markou, C., and Sigman, R. K., "Effect of Types of Binder and Burning Rate Catalysts on Edge Burning AP-Binder-AP Sandwiches," *Proceedings of the 26th JANNAF Combustion Subcommittee Meeting*, CPIA Publication 529, Vol. II, 1989, p. 93.
26. Price, E. W. et al., "Role of the Leading Edge of the Diffusion Flame in Combustion of Solid Propellants," *Proceedings of the 27th JANNAF Combustion Subcommittee Meeting*, CPIA Publication 557, Vol. III, 1990, p. 31.
27. Parr, T. P. and Hanson-Parr, D. M., "Propellant Diffusion Flame Structure," *Proceedings of the 28th JANNAF Combustion Subcommittee Meeting*, CPIA Publication 573, Volume III, 1991, pp. 359–368.
28. Parr, T. P. and Hanson-Parr, D. M., "ADN Propellant Diffusion Flame Structure," *Proceedings of the 29th JANNAF Combustion Subcommittee Meeting*, Hampton, VA, October 1992, CPIA Publication 593 Vol II, 1992, p. 313.
29. Parr, T. P. and Hanson-Parr, D. M., "ADN Diffusion Flame Structure at Elevated Pressure," *Proceedings of the 30th JANNAF Combustion Subcommittee Meeting*, CPIA Publication 606, Vol. II, 1993, p. 1.

Twenty-Sixth Symposium (International) on Combustion/The Combustion Institute, 1996/pp. 1989–1996

A THREE-PHASE MODEL OF HMX COMBUSTION

JEFFREY E. DAVIDSON AND M. W. BECKSTEAD
Brigham Young University
350 CB BYU
Provo, UT 84602, USA

The solid rocket propellant ingredient RDX has received a lot of research attention in recent years by both experimentalists and modelers. There has been fairly good agreement between predictions by models and experimental data. In this paper, the three-phase, one-dimensional RDX model is extended to a similar ingredient, HMX. All model inputs were determined independent of the model except for the heat capacity and thermal conductivity of HMX_{liquid} for which no experimental data was found. Reasonable correlation with experimentally determined burn rate, surface temperature, adiabatic flame conditions, melt layer thickness, and some gas-phase species concentration profiles was made using this model. Sensitivity analysis indicates that the adiabatic flame conditions are controlled by the specification of the thermodynamic properties of the solid and liquid phases. The surface temperature is controlled by the vapor pressure correlation, and the burn rate is largely controlled by the heat feed back from the gas-phase flame, or in other words, the gas-phase mechanism. Sensitivity analysis indicates that differences noted in combustion characteristics of HMX and RDX are likely caused by differences in vapor pressure and melting temperature, while the similarity of burn rate data is attributed to the similarity of the gas-phase flames. The sensitivity analysis also indicates which model inputs require further study.

Introduction

The cyclic nitramines RDX (cyclotrimethylenetrinitramine, $C_3H_6N_6O_6$, hexogen) and HMX (cyclotetramethylenetetranitramine, $C_4H_8N_8O_8$, octogen) are important ingredients in gun and solid rocket propellants [1]. Because of the large quantity of gas and the high energy of these compounds, high values of specific impulse and impetus can be achieved. The exhaust gases of these propellants are less corrosive and less visible than chlorine-containing propellants (such as AP). RDX ($\Delta H_{f,298}$ = 61.42 J/mol) and HMX ($\Delta H_{f,298}$ = 74.94 J/mol) are very similar compounds. The molecular structure consists of a cyclic chain of $(H_2CNNO_2)_n$ where n equals 3 for RDX and 4 for HMX.

Background

The combustion of nitramines (particularly HMX and RDX) has been the focus of much research for many years. In recent years, the focus has been primarily on RDX. It is hoped that by thoroughly understanding and accurately modeling this monopropellant, a model (and kinetic mechanisms) can be established that could be extended to other propellants for a priori calculations. Although this is not a review paper, a brief summary of progress in nitramine modeling is given. In 1979, Ben-Reuven et al. modeled RDX and HMX combustion in three regions (solid, liquid, and gas) [2]. Using global kinetics, the authors were able to show good agreement (or at least the correct trends) between their model's predictions and experimental data for RDX. In 1985, Ermolin et al. [3] used a detailed elementary-step mechanism to model the gas-phase RDX flame. Their predicted species concentration profiles agreed very well with their experimental results at 0.5 atm. In 1987, Hatch [4] used a similar mechanism for HMX combustion but linked it to a condensed phase. This model failed to give the correct burn rate versus pressure correlation. In 1990, Melius [5] modeled RDX ignition with a detailed gas-phase mechanism. His condensed phase and burn rate calculations were dominated by an evaporation/condensation model. Yetter et al. [6] have made many additions and improvements to Melius' gas-phase mechanism. Their RDX gas-phase mechanism has been used in almost all subsequent RDX models that include elementary reactions. In 1995, Liau and Yang [7] modeled RDX steady-state combustion in three regions (solid, two-phase (i.e., liquid/gas), and gas). The condensed-phase mechanism included three subsurface reactions and evaporation. In 1994, Hanson-Parr and Parr [8] published experimental results of laser-assisted RDX combustion, which showed a two-flame structure separated by a dark zone that had not appeared without the laser augmentation. Ben-Reuven et al. [1] and Bizot and Beckstead [9] showed dark zones in their models with global mechanisms but were not considering any laser augmentation. However, based on experi-

mental data, there should not be a dark zone unless there is a laser spreading out the flame. Recently, models by Davidson and Beckstead [10] and Prasad et al. [11] have shown a dark zone under laser assisted conditions for RDX. The models of Liau [7] and Davidson [10] are based on similar assumptions, while the model of Prasad differs from those of Liau and Davidson only in the treatment of propellant evaporation, the calculation of the surface temperature, and method of numerical convergence. All three of these models show very reasonable agreement with a variety of experimental data (burn rate as a function of pressure and initial temperature, melt layer thickness, surface and final flame temperatures, and species and temperature profiles). After briefly reviewing the model, this paper will discuss the process and results of extending the RDX model of Davidson and Beckstead to HMX and explore the sensitivity of model predictions to model inputs. This sensitivity analysis will explain the similarity and differences noted in the combustion of HMX and RDX.

Description of Combustion Model

A detailed description of the model is published elsewhere [10] but will be briefly reviewed here. The model is based on the assumption that the combustion is one dimensional and at steady state. These assumptions make the mass burning rate ($\dot{m}$) constant in x but because $\dot{m}$ is unknown and all the governing equations have $\dot{m}$ in at least one term, it becomes the eigenvalue of the system. The mass burning rate is determined by matching boundary conditions between different regions of calculations (see later).

Three regions of the combustion process are considered: solid, two-phase (liquid and gas), and gas. As in several other propellant models [2,4,5,7,10,11], it is assumed that any reactions occurring in solid phase are negligible. In the solid region, only the energy equation is solved analytically to give the temperature profile.

Once the propellant melts, several steps are considered. The propellant can evaporate or decompose into gas and/or liquid fragments, creating a frothy melt layer. As a gas-phase develops in this two-phase region, bubbles form. The approach followed in this model for the two-phase region is similar to that taken by Liau [7]. The bubbles are represented by the void fraction (ϕ, the fraction of the original propellant liquid volume that has been converted to gas by either evaporation or decomposition). As in many models [7,10,11], mass diffusion is neglected in this two-phase region. Because the melt layer thickness and the surface boundary conditions are unknown until the solution is complete, the energy and species equations are integrated as a system of initial boundary value problems. The energy and species (liquid and gas) equations in the two-phase region are the following:

$$\dot{m}\frac{dT}{dx} - \frac{1}{c_{p,gl}}\frac{d}{x}\left(\lambda A\frac{dT}{dx}\right) + \frac{A}{c_{p,gl}}\sum_{k=1}^{\#\text{ of species}} \dot{w}_k H_k = 0 \quad (1)$$

$$\frac{d}{dx}\left[(1-\phi)\,\rho_l v_l Y_{l,k}\right] = \dot{w}_k \quad (2)$$

$$\frac{d}{dx}\left(\phi\rho_g v_g Y_{g,k}\right) = \dot{w}_k \quad (3)$$

The void fraction (ϕ) is calculated by keeping track of the volume of liquid changing to gas. By assuming $T_g = T_l$ and $v_l = \dot{m}/\rho_l$, the groups of variables in equations 2 and 3 can be separated. (See Ref. 10 for more detail.) Gas transport and thermodynamic properties are calculated via Chemkin [12] and Transport [13] subroutines. Liquid mixture properties are mass averaged and calculated from temperature-dependent correlations discussed later. For the two-phase mixture, heat capacity is mass averaged and thermal conductivity is volume averaged.

The initial boundary conditions at the solid/liquid interface for equations 1–3 are the following:

$$\frac{dT}{dx} = \frac{\dot{m}}{\lambda_l}\left(\frac{\Delta H_{\text{melting}}}{W_{\text{propellant}}} + c_{p,s1}(T_{\text{melt}} - T_{\text{init}}) + \frac{c_{p,s2}}{2}(T_{\text{melt}}^2 - T_{\text{init}}^2)\right) \quad (4)$$

$$\phi = 0, \quad T = T_{\text{melt}}$$

$$Y_{g,k} = 0 \text{ for all gas species}$$

$$Y_{l,k} = 0 \text{ for all liquid species except the monopropellant}$$

$$Y_{l,\text{propellant}} = 1$$

The system of ODEs describing the two-phase region are integrated in x until the liquid mass flux times area is equal to the rate of evaporation $(1 - \phi)\,\rho_l v_l \cdot area = q_{evap}$. This defines the surface, and all remaining liquid is mathematically evaporated. The evaporation rate is calculated following the work of Liau and Yang [7]. The surface temperature and mass flux fractions serve as boundary conditions for the gas region.

The gas region calculations are handed by a modified version of PREMIX [14] in the "burner-stabilized mode." The equations describing the gas phase are the following:

$$\dot{m} = \rho u A \quad \rho = \frac{p\bar{W}}{RT} \quad (5)$$

$$\dot{m}\frac{dT}{dx} - \frac{1}{c_p}\frac{d}{dx}\left(\lambda A\frac{dT}{dx}\right) + \frac{A}{c_p}\sum_{k=1}^{kk}\rho Y_k V_k c_{pk}\frac{dT}{dx} + \frac{A}{c_p}\sum_{k=1}^{kk}\dot{w}_k h_k W_k = 0$$

$$\dot{m}\frac{dY_k}{dx} + \frac{d}{dx}(\rho A Y_k V_k) - A\dot{w}W_k = 0 \quad (k = 1, \ldots, kk)$$

This system of equations (equation 5) is solved using finite difference discretization and Newton's method. The solution is first converged on a coarse grid and then the grid is refined to obtain the desired resolution. Further details can be found in reference [14].

The eigenvalue $\dot{m}$ is determined by iteration between the two-phase and gas region calculations. The correct $\dot{m}$ will satisfy the energy balance at the two-phase/gas interface:

$$\lambda_{gl}\frac{dT}{dx}\bigg|_{s-} + [\rho_l v_l(1 - \phi)\,\Delta H_{vap}]_{s-} = \lambda_g\frac{dT}{dx}\bigg|_{s+} + Q_{\text{laser}} \quad (6)$$

Equation 6 says that the heat flux back from the gas phase flame plus any heat flux from a laser must equal the heat flux into the gas phase plus the energy flux required to vaporize any remaining liquid. In short, $\dot{m}$ is solved by using a "shooting method" for the initial boundary value problem in the two-phase region to give the first-order boundary conditions and match the second-order boundary conditions of the finite-difference boundary value problem in the gas region.

Model Inputs

This model was developed with the objective to be able to predict as many characteristics of the propellant combustion process as possible while limiting the required model inputs to those available in the literature or obtainable by either experiment or calculation. The inputs, pressure and initial temperature of the propellant are determined by the condition of the system. Ideally, all other inputs should be determined independently of the model. These independent inputs include the thermodynamic and physical properties of solid, liquid, and gas phases as well as the reaction mechanisms describing the decomposition and combustion of the propellant. If the inputs and the model are correct, then the model's predictions should agree with correct measured results. Unfortunately, uncertainty in the model's inputs causes uncertainty in the model's predictions.

C_p, λ, ρ and ΔH_f for the solid can be measured in the laboratory. Similar properties for gas-phase species can either be measured or determined by ab initio calculations or statistical mechanics. But because rapid decomposition commences at the melting point of HMX, the properties of the melted phase are difficult to find. Assuming all the required inputs can be determined, the model will predict the burn rate, temperature profile, species concentration profiles, surface temperature, melt layer thickness, void fraction profile, adiabatic flame conditions, and the heat feedback to the condensed phases from the gas region. A discussion of the inputs for HMX follows.

HMX Solid Properties

The ΔH_f of HMX_{solid} (298 K) is 74.9 kJ/mol [15]. Unlike RDX, HMX can exist in several phases before melting. The β phase (ρ = 1.903 g/cm^3) is most stable from room temperature to about 388 K. From 388 to 429 K, the α phase (ρ = 1.87 g/cm^3) is stable. Above 429 K exists the unstable γ phase and the stable δ phase (ρ = 1.78 g/cm^3) [1]. In the model, the α phase is lumped in with the β phase. Hall reported a β-to-δ phase transition at 460 K ($\Delta H_{\beta\to\delta}$ = 9840 J/mol) [16]. Shoemaker measured the heat capacities of the β and δ phases which could both be fit by $C_p(T) = 0.215 + 0.00272 \cdot T$ (J/g·K) [17]. The heat of melting ($\Delta H_{melting}$) was estimated to be the same as that for RDX (160.7 J/g) on a mass basis [18].

HMX Liquid Properties

The ΔH_f of HMX_{liquid} (298 K) was calculated by adding the ΔH_f of HMX_{solid} plus the $\Delta H_{\beta\to\delta}$ $\Delta H_{melting}$, giving 132.5 kJ/mol. The density of HMX_{liquid} was estimated at 1.72 g/cm^3 (same density reported by Fogelzang [19] for pressed HMX pellets). No values for the λ_{liquid} nor the $c_{p,liquid}$ were found in the literature. As an initial guess, the same correlations used for the solid δ phase were extrapolated to the liquid phase but this resulted in the model failing to predict the correct adiabatic flame temperature and melt layer thickness. The correlation $C_{p,liquid}(T) = 0.6115 + 0.00146 \cdot T$ (J/g·K), and $\lambda_{liquid} = 0.006$ (J/cm·sec·K) were chosen for these two inputs. The reasoning for these choices is discussed here.

In the model, HMX was allowed to either decompose or evaporate to form the gas-phase species. The HMX_{liquid} decomposition mechanism proposed by Brill [20] was slightly modified (the prefactors, A's, were multiplied by WT_{HMX}/ρ, and A_2 was optimized to fit Brill's measured N_2O to NO_2 ratio):

$$HMX \rightarrow 4(CH_2O + N_2O)\; A_1 = 5.81 \times 10^{10}\; E_a = 34{,}000 \text{ cal/mol} \quad (7)$$

$$HMX \rightarrow 4(H_2CN + NO_2)\; A_2 = 1.66 \times 10^{14}\; E_a = 44{,}100 \text{ cal/mol} \quad (8)$$

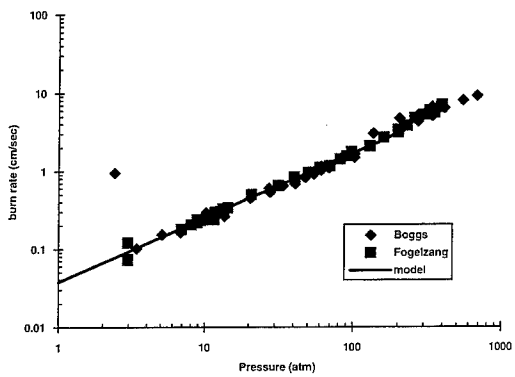

FIG. 1. HMX burn rate as a function of pressure, $T_{initial}$ = 298.

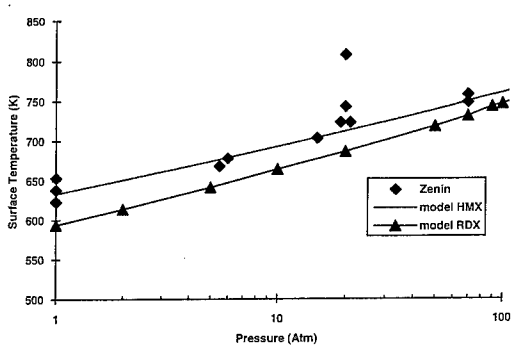

FIG. 2. HMX and RDX surface temperature as a function of pressure.

Although the vapor pressure of HMX is believed to be significantly lower than that of RDX, we included it in the model. The evaporation model of Liau and Yang [7] is used with the sublimation pressure correlation measured by Taylor [21]: $\log_{10}$ [P (torr)] = 14.73 − 8296/T (K). No vapor pressure correlations were found in the literature for HMX. (For RDX, using a sublimation pressure correlation rather than a vapor pressure correlation gave much more reasonable results from the model [10].)

HMX Gas Properties

As previously mentioned, Melius [5], and Yetter, et al. [6] have developed a gas-phase mechanism (232 reactions) for RDX with thermophysical properties for 45 species. Because of the similarity between RDX and HMX, this mechanism (August 1995 version) was adapted with little difficulty. Although some stoichiometic coefficients had to be adjusted, all rate constants were assumed to be the same. The thermodynamic properties of HMX_{vapor} were estimated to be the same as those of RDX_{vapor} on a mass basis. The properties of species HMXR and HMXRO (see Refs. 5 or 6 for their definitions) were estimated to have the same difference on a mole basis from HMX_{vapor} as the difference between RDX_{vapor} and RDXR and RDXRO, respectively.

Results

Using the inputs described above, the model was able to agree with much of the available experimental data. As described above, all inputs were determined or estimated independently of the model except for the heat capacity and thermal conductivity of HMX_{liquid}. In the sensitivity analysis that follows, the effects that these parameters have on model predictions will be discussed.

For an initial temperature of 298 K, the model agreement with experimentally determined burn rate data [19,22] as a function of pressure is very reasonable (see Fig. 1). It is significant to note that the burn rates of HMX and RDX are essentially the same (within the data scatter). The predicted adiabatic flame conditions agree to within 0.2% with the NASA–Lewis equilibrium code [23] from 1 to 200 atm.

The predicted surface temperatures for HMX and RDX are plotted with the experimental HMX data from Zenin [24] in Fig. 2. The model predictions fall within the scatter of the data. The surface temperature of HMX is approximately 40 K greater than that of RDX at 1 atm, but this difference decreases as pressure increases. The higher surface temperature of HMX is apparently due primarily to the lower vapor pressure of HMX. (See Sensitivity Analysis Section.) According to the correlations used, as temperature increases, the difference in vapor pressure between these two nitramines decreases, thus explaining the approaching surface temperatures. It should be noted that although the vapor pressure of HMX is much lower than that of RDX at atmospheric conditions, the model indicates that evaporation is a significant factor in HMX combustion at all pressures. At 1 atm, approximately 77% of the RDX evaporates compared to 52% for HMX. This difference is much less at 100 atm (89 and 84%, respectively).

Model predictions for HMX and RDX melt layer thicknesses are compared to Zenin's HMX data in Fig. 3. Again there is very reasonable agreement. The melt thickness of RDX is approximately 100 μm thicker than that of HMX at 1 atm but both approach the same value as pressure increases. This difference at 1 atm can be attributed to the lower melting temperature of RDX. The similarity at higher pressures can be attributed to the increased and dominating effect of the heat feedback from the gas-phase flame. (See Sensitivity Analysis section.)

Litzinger et al. [25] have used their triple quadrupole mass spectrometer to probe the laser-assisted

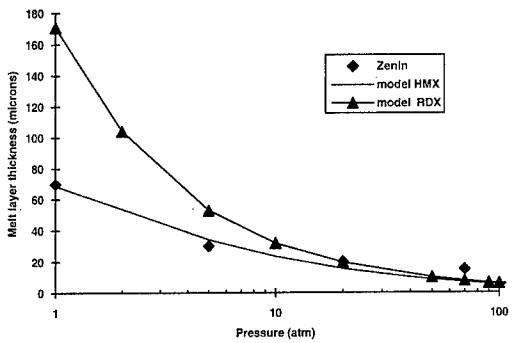

FIG. 3. HMX and RDX melt layer thickness as a function of pressure.

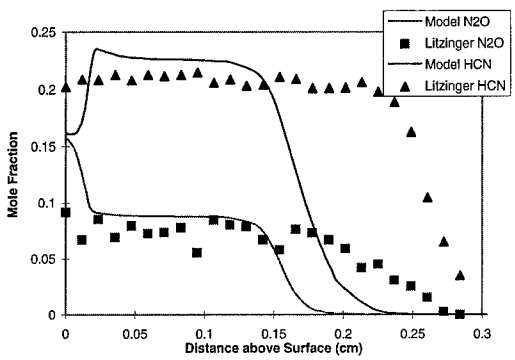

FIG. 4. Comparison of calculated N_2O and HCN species profiles with experimentally determined values under laser-assisted conditions.

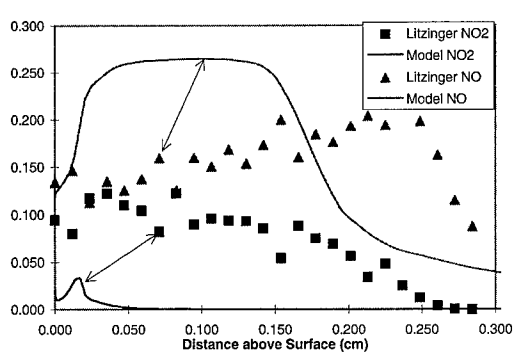

FIG. 5. Comparison of calculated NO_2 and NO species profiles experimentally determined values under laser-assisted conditions.

HMX flame structure at 1 atm. At a burn rate of 0.09 cm/s, the model predicts a two-stage flame (as also seen in modeled [10] and experimental [8] laser-assisted RDX combustion), whereas the experiment shows a one-stage flame that is detached from the surface. Comparisons between the model and some of the measured mole fractions are shown in Figs. 4 and 5. Although the model's predictions for HCN and N_2O agree reasonably well with experiment, the model underpredicts NO_2 and overpredicts NO mole fractions. Similar trends for NO_2 and NO were also observed when comparing the model's predictions with laser-assisted RDX results [10,26] and self-deflagrating HMX results [27] by Hanson-Parr and Parr. Although some of this disagreement can be attributed to the one-dimensionality of the model and the three dimensionality of the experiments, further refinement of the gas-phase mechanism is needed.

Sensitivity Analysis

In modeling, a very important question to ask is How does model input A affect model output B? Sensitivity analysis is a tool that can be used to identify the controlling parameters. Use of the normalized sensitivity coefficient

$$s = \frac{A}{B}\left(\frac{\partial B}{\partial A}\right) \tag{9}$$

permits the comparison of the effects that a variety of model inputs have on a particular output. By considering these effects along with the level of uncertainty associated with each input, the researcher is guided to those inputs or model assumptions that should be investigated further. For example, Fig. 6 shows the sensitivity coefficients for the surface and adiabatic flame temperatures. Pressure is the dominating factor but there is no uncertainty associated with pressure. The same is true for the initial temperature. When the model failed to predict the correct adiabatic flame temperature, the thermal properties ($c_{p,\text{solid}}$, $c_{p,\text{liquid}}$, $\Delta H_{\text{melting}}$, $\Delta H_{f,\text{liquid}}$) were investigated. No literature values were found for $c_{p,\text{liquid}}$, therefore, until independently determined values for $c_{p,\text{liquid}}$ can be attained, this input is estimated by "back calculation" from the model. Also from this figure, one observes that the surface temperature is largely controlled by the vapor pressure (as was also noted for RDX [10]).

Figure 7 shows those parameters that control the burn rate and melt layer thickness of HMX at 1 atm. The burn rate and melt layer thickness are both strongly affected by the heat feedback from the gas-phase flame (i.e., gas-phase mechanism) and the melting temperature. As pressure increases, these parameters become more dependent upon the heat feedback. The similarity between HMX and RDX in

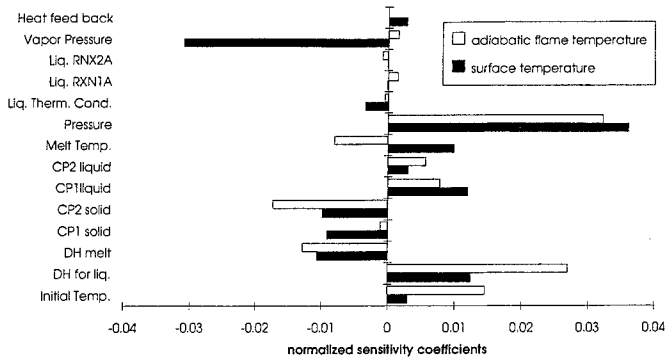

FIG. 6. Parameters controlling the adiabatic flame and surface temperatures of deflagrating HMX at 1 atm.

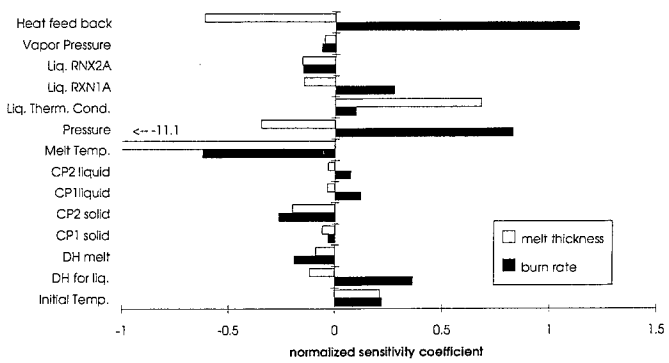

FIG. 7. Parameters controlling the burn rate and melt layer thickness of deflagrating HMX at 1 atm.

burn rate as a function of pressure can be attributed to the similarity in the gas-phase flame.

As noted above, when using the solid δ-phase thermal conductivity for the liquid phase, the model greatly under predicted the melt layer thickness. We choose to "back calculate" the liquid thermal conductivity rather than investigate the other inputs for two reasons. First, no values for the liquid thermal conductivity were found in the literature, and second, the uncertainty associated with the melt temperature could not explain this discrepancy.

Conclusions

The three-phase, one-dimensional model developed for RDX has been applied to HMX. Wherever possible, model inputs were taken from the literature, independent of model results. Little experimental data exist pertaining to liquid HMX. Where model inputs could not be found in the literature, they were "back calculated" from the model. Model predictions of burn rate, surface temperature, melt layer thickness, adiabatic flame temperature, and some species concentration profiles show reasonable agreement with experiment. Sensitivity analysis indicates that the adiabatic flame temperature is controlled by the thermodynamic properties assigned to the liquid phase. The surface temperature is controlled by the vapor pressure. The melt layer thickness is a function of melting temperature, heat feedback from the gas flame, and the liquid thermal conductivity. The burn rate is largely controlled by the heat feedback from the gas flame. The differences noted in experimental combustion data between HMX and RDX can be explained by the differences in vapor pressure and melting temperature, while the similarity in burn rate data is attributed to similarities in the gas-phase flames. Further investigation of the liquid phase properties and gas-phase mechanism is needed. As uncertainty in model inputs is reduced, better agreement between model predictions and experimental data is expected.

Nomenclature

A	area
c_p	heat capacity
H	heat of formation
$\dot{m}$	mass flux
T	temperature
u	gas phase velocity
V	diffusion velocity
$\dot{w}$	mass production rate
W	molecular weight
x	distance from liquid/gas surface
Y	mass fraction

λ thermal conductivity
ρ density
v two-phase velocity
ϕ void fraction
ΔH Enthalpy change

Acknowledgment

This work was funded by the Air Force Office of Scientific Research under contract AFOSR F496209-93-1-0420. The support is much appreciated.

REFERENCES

1. Boggs, T. L., in *Fundamentals of Solid-Propellant Combustion* (K. K. Kuo and M. Summerfield, Eds.), AIAA, New York, 1984, Vol. 90, p. 121.
2. Ben-Reuven, M., Caveny, L. H., Vichnevetsky, R. J., and Summerfield, M., *Sixteen Symposium on Combustion,* The Combustion Institute, Pittsburgh, 1976, pp. 1223–1233.
3. Ermolin, N. E., Korobeinichev, O. P., Kuibida, L. V., and Fomin, V. M., *Fizika Goreniya i Vzryva* 22:544–553 (1986).
4. Hatch, R. L., *Twenty-Fourth JANNAF Combustion Meeting,* CPIA # 476, 1987, Vol. 1, pp. 383–391.
5. Melius, C. F., in *Chemistry and Physics of Energetic Materials,* Kluwer, Netherlands, 1990, pp. 51–78.
6. Yetter, R. A., Dryer, F. L., Allen, M. T., and Gatto, J. L., *J. Propulsion Power* 11:683–697 (1995).
7. Laiu, Y.-C. and Yang, V., *J. Propulsion Power* 11:729–739 (1995).
8. Hanson-Parr, D. and Parr, T., *Thirty-First JANNAF Combustion Meeting,* CPIA, 1994, Vol. 2, pp. 407–423.
9. Bizot, A. and Beckstead, M. W., in *Flame Structure* (O. P. Korobeinichev, Ed.), NAUKA Novosibirsk, Russia, 1991, pp. 230–235.
10. Davidson, J. E. and Beckstead, M. W., *Thirty-Second JANNAF Combustion Meeting,* CPIA Publication 638 Vol. 1, Columbia, MD, 1995, pp. 41–56. See also *Improvements to RDX combustion Modeling,* AIAA Paper No. 96-0885, 1996.
11. Prasad, K., Yetter, R., and Smooke, M., *Thirty-Second JANNAF Combustion Meeting,* CPIA Publication 638, Vol. 1, 1995, pp. 69–84. *Combust. Sci. Technol.*, 1997. In press.
12. Kee, R. J., Rupley, R. M., and Miller, J. A., *Chemkin-II: A Fortran Chemical Kinetics Package for the Analysis of Gas-Phase Chemical Kinetics,* Sandia National Laboratories Report No. SAND89-8009B•UC-706, Sandia National Laboratories, 1992.
13. Kee, R. J., Dixon-Lewis, G., Warnatz, J., Coltrin, M. E., and Miller, J. A., *A Fortran Computer Code Package for the Evaluation of Gas-Phase Multicomponent Transport Properties,* Sandia National Laboratories Report No. SAND86-8246•UC-401, Sandia National Laboratories, 1992.
14. Kee, R. J., Grear, J. F., Smooke, M. D., and Miller, J. A., *A Fortran Program for Modeling Steady Laminar One-Dimensional Premixed Flames,* Sandia National Laboratories Report No. SAND85-8240•UC-401, Sandia National Laboratories, 1992.
15. Kubota, N., in *Fundamentals of Solid-Propellant Combustion* (K. K. Kuo and M. Summerfield, Eds.) AIAA, New York, 1984, Vol. 90, pp. 1–52.
16. Hall, P. G., *Trans. Faraday Soc.* 67:556–562 (1971).
17. Shoemaker, R. L., Stark, J. A., and Taylor, R. E., High Temperatures High Pressures 17:429–435 (1985).
18. Ben-Reuven, M., Ph.D. Thesis, Princeton University, Princeton, NJ, 1980.
19. Fogelzang, A. E., *Combustion of Explosives and Propellants Database,* Moscow, Russia, Version 2.43, 1994.
20. Brill, T. B., *J. Propulsion Power* 11:740–751 (1995).
21. Taylor, J. W. and Crookes, R. J., *J. Chem. Soc.* 3:723–729 (1976).
22. Boggs, T. L., personal communication.
23. McBride, B., *Computer Program for Calculation of Complex Chemical Equilibrium Compositions, Rocket Performance, Incident and Reflected Shocks, and Chapman-Jonquet Detonations,* NASA Report Nos. SP-273, TM-86885, and TM-100785, 1996.
24. Zenin, A., *J. Propulsion Power* 11:752–758 (1995).
25. Tang, C., Lee, Y., Kudva, G., and Litzinger, T. A., *Thirty-Second JANNAF Combustion Meeting,* CPIA Publication 638, Vol. 1, Columbia, MD, pp. 107–118, 1995.
26. Hanson-Parr, D., and Parr, T., *Twenty-Fifth Symposium (International) on Combustion,* Combustion Institute, Pittsburgh, 1994, pp. 1635–1643.
27. Parr, T., and Hanson-Parr, D., *Thirty-Second JANNAF Combustion Meeting,* CPIA Publication 631 Vol. 1, Columbia, MD, 1995, pp. 429–437.

COMMENTS

Oleg P. Korobeinichev, Institute of Chemical Kinetics and Combustion, Russia. Did you take into account that the composition of decomposition products and kinetics in condensed phase may change with pressure? Could that change your results?

Author's Reply. The current condensed phase decomposition mechanism model has a small, indirect dependence on pressure. As the pressure increases, there is an increase in surface temperature which results in a slight shift toward the second decomposition step (equation 8). According to the model, this effect is probably insignificant because evaporation plays a more dominate role in the conversion of HMX_{liquid} to gas phase species (even more so for RDX) than the two condensed phase decomposition reactions. According to the model, the percent of the ni-

tramines evaporating increases with pressure. This is the opposite conclusion reached by Zenin [24]. There is already enough uncertainty in other model inputs that we felt that until more is known about the liquid phase decomposition, additional complexity in the condensed phase mechanism would generate more questions than answers.

•

H. S. Mukunda, Indian Institute of Science, India. The predictions on liquid layer thickness vs. pressure seem to have higher slope than experimental data seem to show. Can you comment on the accuracy of experimental data (w.r.t. pressure index of liquid thickness) and what model parameters affect the predictions of the pressure index of liquid layer thickness?

Author's Reply. By plotting the data shown in Figure 3 on Log-Log scale, the model predicts a greater slope than the experimental data indicate for both HMX and RDX. The data come from Zenin [24] who used microthermocouples to measure temperature profiles from which he calculated the melt layer thickness. No error bounds were given. For comparison, the scatter in the reported surface temperature measurements (Fig. 2) is significant. The relatively thin melt layer (15 microns) at high pressure (>70 atm), the rapid surface regression rate (1.0 cm/sec), and the thickness of the thermocouples (3–5 microns) make these measurements very difficult. It is likely that the model falls within the error bounds of the experimental data. According to the model, the heat feedback from the gas-phase flame (a strong function of pressure) has a strong effect on the melt layer thickness (Fig. 7) and is likely the dominating factor determining the pressure index of the liquid thickness.

•

Alexander Telengator, University of California, San Diego, USA. Other authors have recently addressed very similar problems involving solid, liquid/gas, and gas regions in the combustion process. The approach here appears to give satisfactory surface temperature dependences on pressure as well as burn rate, which is rather noteworthy.

Author's Reply. The models recently published by Liau and Yang [7] and Prasad and Smooke [11] for RDX are similar to this model in the assumptions that are made and equations that are solved. The differences in predictions made by the three models can be largely attributed to differences in the values of model inputs. The model of Prasad and Smooke differ from the other two models in their treatment of the two-phase region though the effect this has on model predictions appears to be minimal. As noted, our model does do a reasonable job of predicting the surface temperature. Liau and Yang used a different (higher) vapor pressure correlation (for RDX) which resulted in lower surface temperature predictions. The surface temperature is a required input for model of Prasad and Smooke.

Twenty-Sixth Symposium (International) on Combustion/The Combustion Institute, 1996/pp. 1997–2006

SIMPLIFIED CHEMICAL-KINETIC MECHANISMS FOR CHARACTERIZING THE STRUCTURE OF THE DARK ZONES OF DOUBLE BASE AND NITRAMINE PROPELLANTS

N. ILINCIC[1], W. R. ANDERSON[2], K. SESHADRI[1] AND N. E. MEAGHER[2]

[1]*Center for Energy and Combustion Research*
Department of Applied Mechanics and Engineering Sciences
University of California at San Diego
La Jolla, CA 92093-0411, USA

[2]*U.S. Army Research Laboratory*
Aberdeen Proving Ground, MD 21005-5066, USA

Simplified chemical-kinetic mechanisms were employed to calculate the structure of the dark zone formed over the burning surface of double base and nitramine propellants. It is believed that ignition delays in large-caliber-gun ballistic cycles are related to the chemistry taking place in the dark zone. Skeletal chemical-kinetic mechanisms comprising 22 elementary reactions among 15 species and 23 elementary reactions among 17 species were used to calculate the structure of the dark zone of double base and nitramine propellants, respectively. These skeletal chemical-kinetic mechanisms were previously extracted from a detailed chemical-kinetic mechanism incorporating 190 elementary reactions involving 41 species. Ignition-delay times are calculated using these mechanisms in homogeneous mixtures in which the initial concentrations of various reactants are similar to those found at the beginning of the dark zones of double base and nitramine propellants. These calculations were performed for various initial pressures and temperatures. The ignition-delay times calculated using the skeletal chemical-kinetic mechanisms are found to agree reasonably well with those calculated using the detailed chemical-kinetic mechanism. Reduced chemical-kinetic mechanisms were derived from the skeletal mechanisms by introducing steady-state approximations for a number of species. For double base propellants, a reduced mechanism of three global reactions is obtained. Reduced mechanisms using six and four global reactions are deduced for nitramine propellants. The ignition-delay times and structures of the dark zones calculated using the reduced three-step mechanism for double base propellants and six-step mechanism for nitramine propellants are in agreement with calculations made using the skeletal mechanisms. The ignition-delay times calculated using the four-step reduced mechanism for nitramine propellants are found to be significantly smaller than those calculated using the skeletal mechanism. The reduced chemical-kinetic mechanisms are expected to be useful in interior ballistics calculations.

Introduction

Many double base and nitramine propellants exhibit a two-stage flame zone during combustion. In this process, a nonluminous region separates the primary reaction zone, near the surface of the propellant, from the luminous secondary flame zone. The nonluminous region is commonly referred to as the dark zone. In the primary reaction zone, decomposition of the solid propellant takes place and moderately reactive intermediate species are formed. These intermediate species are convected away from the surface and ignite after a short delay. Recent experiments show that chemical effects caused by the use of propellants of differing chemical composition can lead to major differences in ignition-delay times during typical large-caliber-gun ballistic cycles [1–4] (note that the ignition-delay times in guns are not the same as the dark zone chemical delays). For some propellants, these delays are undesirably long. It is believed that the range of ignition-delay times for various propellants arises from differences in the chemistry taking place in the dark zone [3,4].

It has been established that the dark zone of solid propellants contains large amounts of NO, which is a rather weakly reactive oxidizer. The low reactivity of NO is the principal reason for dark zone formation. This weakly reactive mixture is rapidly converted to equilibrium products at the end of the dark zone. In particular, NO is converted to N_2, and the temperature at the end of the dark zone is much higher than at the beginning.

The temperature and species concentrations change very slowly with distance in the dark zone. Sharp gradients in these profiles are observed only at its boundaries. It is therefore reasonable to as-

sume that the structure of the dark zone is one dimensional, adiabatic, and isobaric and that diffusion of heat and mass are negligibly small.

The ignition-delay time (τ_{ig}) for any reactive mixture is defined in this work as the delay time from the initiation of the reaction (time zero) to the time of maximum heat release associated with the thermal runaway. It is possible, in unusual situations, to obtain an incorrect value for τ_{ig} if there is rapid heat release from the reaction mixture that is not connected with the steep temperature gradient generated at ignition. All ignition-delay times reported in this work were compared with temperature profiles to ensure validity of the result. Measured dark zone thickness is directly related to the ignition delay through mass conservation and gas velocity in the dark zone [5,6].

A detailed chemical-kinetic mechanism has been developed describing the time-dependent chemistry for reactive mixtures with initial compositions at temperature and pressure conditions similar to those at the beginning of the dark zone of double base and nitramine propellants [7,8] (the first-stage propellant combustion is not modeled). These reactive systems were presumed to be homogeneous, adiabatic, and isobaric. Results of calculations performed using this detailed mechanism have also been compared with experimental measurements [7–9].

In this work, skeletal mechanisms comprising fewer elementary reactions than those in the detailed mechanisms are developed for use in modeling the structure of the dark zone of propellants. Reduced chemical-kinetic mechanisms for both propellant types are also presented. Ignition-delay times were calculated under isobaric and adiabatic conditions using the skeletal and reduced mechanisms; the results are compared with those calculated using the detailed mechanism. These calculations were done for differing values of pressure (p) and initial temperature (T^0). Pressure was held constant for all calculations.

Skeletal Mechanisms

The skeletal chemical-kinetic mechanisms employed to calculate the structure of the dark zone over the burning surface of double base and nitramine propellants are shown in Table 1. All elementary reactions are reversible. In Table 1, the elementary reactions (1) through (22) among 15 species were used to model the structure of the dark zone of double base propellants, and reactions (1) through (12) and (23) through (33) among 17 species were used to model the structure of the dark zone of nitramine propellants. These skeletal mechanisms were derived from a detailed mechanism comprising 190 elementary reactions among 41 species [9] by removing those reactions found to have negligible influence on the calculated values of the ignition-delay times. The skeletal mechanisms were used in the development of the reduced mechanisms.

For each elementary reaction n, Table 1 presents the values of the frequency factor A_n, the temperature exponent b_n, and the activation energy E_n that appear in the parametric expression $k_n = A_n T^{b_n} \exp[-E_n/(\hat{R}T)]$ for the specific reaction rate constant k_n, where $\hat{R}$ represents the universal gas constant and T the gas temperature. The symbol M in reactions (1); (12), (13), (14), (18), (24), and (33) represents any third body, and the catalytic efficiencies, η_i, of various species, i, acting as the third body in these reactions are shown. The catalytic efficiency of those species omitted in Table 1 is assumed to be unity. The concentration of the third body, C_M, is calculated from the expression $C_M = [p/(\hat{R}T)]\Sigma_{i=1}^{N} X_i\eta_i$, where X_i is the mole fraction of species i. The rate of the elementary reactions 1, 12, 13, and 14 depend on pressure and are calculated using the expression [10] $k = F \cdot k_\infty \cdot k_L$, where $k_L = k_0 C_M/(k_\infty + k_0 C_M)$, $\log_{10}F = \log_{10}F_C/\{1 + [\log_{10}(k_0 C_M/k_\infty)]^2\}$, $F_C = a_0 + a_1 T$. The values of k_∞, k_0, a_0, and a_1 are shown in Table 1.

The dark zones of typical double base propellants are known to include large amounts of NO, CO, H_2, N_2, H_2O, and CO_2 [6,11]. Traces of CH_4 and C_2H_4 have also been observed. In addition to these species, large amounts of HCN and trace amounts of N_2O are also observed in the dark zones of common nitramine propellants [6]. Calculations with the detailed chemical-kinetic mechanism have shown that the trace amounts of CH_4 and C_2H_4 have negligible influence on the ignition-delay times [8]. Inclusion of their chemistry would unnecessarily complicate the skeletal mechanism; therefore, these species are omitted from the initial mixture. The main difference between the skeletal mechanism for double base and nitramine propellants is the inclusion of HCN chemistry in the latter. Typical conditions of interest are values of p between 1 and 30 atm and values of T^0 between 1000 and 1800 K. These ranges of values for p and T^0 were used to guide the choice of reactions in the detailed and skeletal mechanisms and the initial conditions for the numerical problem described.

Computations were performed using the SENKIN computer code written at Sandia National Laboratories [12]. A minor modification was made to the code to allow input of the functional form for pressure-dependent rate constants (presented earlier) used by Tsang and Herron [10]. A number of chemical details of the solutions from SENKIN were investigated using a postprocessing code written at the Army Research Laboratory (ARL) [13]. Heat-release rate, chemical pathways, and logarithmically normalized sensitivities of the calculated species and temperature profiles to the rate constants were obtained in this manner. The temperature sensitivities

TABLE 1

Skeletal chemical-kinetic mechanisms for modeling the dark zone of double base and nitramine propellants and associated rate constants. Units are kilocalories, moles, seconds, and cubic centimeters. Reactions (1) through (22) are for double base propellants and reactions (1) through (12) and (23) through (33) for nitramine propellants.

No.	Reaction		A_n	b_n	E_n
1.	N_2O (+M) = N_2 + O (+M)	k_∞	1.26E + 12	0.0	62.62
		k_0	5.97E + 14	0.00	56.64
	a_0 = 1.0, a_1 = 0 third-body efficiencies/N_2O 5.0/H_2O 7.5/N_2 1.0/CO_2 3.2/				
2.	HNO + NO = N_2O + OH		8.51E + 12	0.0	29.59
3.	CO + OH = CO_2 + H		1.51E + 07	1.3	−0.758
4.	OH + H_2 = H_2O + H		2.16E + 08	1.5	3.43
5.	O + H_2 = OH + H		5.06E + 04	2.67	6.29
6.	NH + NO = N_2O + H		3.50E + 14	−0.46	0.016
7.	N_2O + H = N_2 + OH		2.23E + 14	0.0	16.75
8.	H + HNO = NH + OH		3.00E + 14	0.0	18.00
9.	H + HNO = H_2 + NO		4.46E + 11	0.72	0.655
10.	N_2O + NO = N_2 + NO_2		4.29E + 13	0.0	47.13
11.	HNO + HNO = N_2O + H_2O		3.63E + 03	3.98	1.19
12.	H + NO (+M) = HNO (+M)	k_∞	1.52E + 15	−0.41	0.0
		k_0	8.96E + 19	−1.32	0.735
	a_0 = 0.82, a_1 = 0 third-body efficiencies/N_2O 5.0/H_2O 5.0/N_2 1.0/CO_2 1.3/				
13.	NO_2 (+M) = NO + O (+M)	k_∞	7.60E + 18	−1.27	73.29
		k_0	2.47E + 28	−3.37	74.80
	a_0 = 0.95, a_1 = −0.0001 third-body efficiencies/N_2O 1.5/H_2O 4.4/N_2 1.0/CO_2 2.3/				
14.	NO + OH (+M) = HONO (+M)	k_∞	1.988E + 12	−0.05	−0.721
		k_0	5.08E + 23	−2.51	−0.0676
	a_0 = 0.62, a_1 = 0 third-body efficiencies/N_2O 5.0/H_2O 8.3/N_2 1.0/CO_2 1.5/				
15.	H_2 + NO_2 = HONO + H		3.21E + 12	0.0	28.81
16.	HNO + NO_2 = HONO + NO		6.00E + 11	0.0	1.987
17.	2OH = O + H_2O		6.00E + 08	1.3	0.0
18.	H + OH + M = H_2O + M		1.60E + 22	−2.0	0.0
	third-body efficiency/H_2O 5.0/				
19.	NO_2 + H = NO + OH		1.30E + 14	0.0	0.361
20.	N_2O + O = NO + NO		6.92E + 13	0.0	26.60
21.	N + NO = N_2 + O		3.27E + 12	0.3	0.0
22.	NO + H = N + OH		1.70E + 14	0.0	48.80
23.	NH_2 + NO = N_2O + H_2		5.00E + 13	0.0	24.64
24.	CO + O + M = CO_2 + M		2.36E + 15	0.0	4.34
	third-body efficiencies/CO 1.77/CO_2 2.7/H_2O 5.0/N_2O 5.0/				
25.	HCN + O = NH + CO		3.45E + 03	2.64	4.98
26.	NH_2 + H = NH + H_2		4.00E + 13	0.0	3.65
27.	NH_2 + NO = N_2 + H + OH		9.30E + 11	0.0	0.0
28.	NH_2 + NO = N_2 + H_2O		2.00E + 20	−2.6	0.924
29.	HNC + O = NH + CO		5.44E + 12	0.0	0.0
30.	HNC + OH = HNCO + H		2.80E + 13	0.0	3.696
31.	HNCO + H = NH_2 + CO		2.25E + 07	1.7	3.80
32.	CO + NO_2 = NO + CO_2		9.04E + 13	0.0	33.78
33.	HCN + M = HNC + M		4.36E + 26	−3.34	50.194

TABLE 2
Comparison of the values of the ignition-delay times calculated using the various mechanisms for double base propellants. The initial mole fractions of NO, CO, H_2, N_2, H_2O, and CO_2 are set equal to 0.24, 0.33, 0.08, 0.04, 0.20, and 0.10, respectively.

Initial conditions	Detailed mech. (41 sp., 190 r.)	Skeletal mech. (15 sp., 22 r.)	Reduced mech. (3 steps)
1 atm, 1000 K	52.59 s	51.47 s	50.49 s
1 atm, 1400 K	1.035 s	1.046 s	1.042 s
1 atm, 1800 K	$3.738 \cdot 10^{-2}$ s	$3.843 \cdot 10^{-2}$ s	$3.684 \cdot 10^{-2}$ s
5 atm, 1000 K	8.297 s	8.062 s	7.769 s
5 atm, 1400 K	$1.142 \cdot 10^{-1}$ s	$1.147 \cdot 10^{-1}$ s	$1.142 \cdot 10^{-1}$ s
5 atm, 1800 K	$7.517 \cdot 10^{-3}$ s	$7.774 \cdot 10^{-3}$ s	$7.624 \cdot 10^{-3}$ s
10 atm, 1000 K	3.994 s	3.887 s	3.725 s
10 atm, 1400 K	$4.383 \cdot 10^{-2}$ s	$4.375 \cdot 10^{-2}$ s	$4.346 \cdot 10^{-2}$ s
10 atm, 1800 K	$3.448 \cdot 10^{-3}$ s	$3.571 \cdot 10^{-3}$ s	$3.503 \cdot 10^{-3}$ s
30 atm, 1000 K	1.274 s	1.255 s	1.194 s
30 atm, 1400 K	$9.90 \cdot 10^{-3}$ s	$9.75 \cdot 10^{-3}$ s	$9.63 \cdot 10^{-3}$ s
30 atm, 1800 K	$9.31 \cdot 10^{-4}$ s	$9.64 \cdot 10^{-4}$ s	$9.49 \cdot 10^{-4}$ s

were quite useful because they qualitatively reflect the sensitivity of the calculated ignition-delay time to the various rate coefficients (information not directly available). The pathway and sensitivity analyses were used to identify reactions that have a significant influence on the solution, indicating those that must be retained in the skeletal mechanisms.

The approximations introduced in the numerical model of the structure of the dark zone are described in detail elsewhere [5–9]. Therefore, only a brief description is given here. The system is considered to be spatially homogeneous, adiabatic, and isobaric. Calculations were performed with the initial mole fractions of NO, CO, H_2, N_2, H_2O, and CO_2 set equal to 0.24, 0.33, 0.08, 0.04, 0.20, and 0.10, respectively, for double base propellants. For nitramine propellants, the initial mole fractions of NO, CO, H_2, N_2, H_2O, CO_2, N_2O, and HCN are set equal to 0.13, 0.22, 0.07, 0.06, 0.20, 0.09, 0.02, and 0.22, respectively. The results presented in Table 2 demonstrate that τ_{ig} calculated using the skeletal mechanism agrees well with the values obtained from calculations using the detailed mechanism [8] for the double base propellants. Values of τ_{ig} calculated for the nitramine propellants using the skeletal mechanism are in good agreement with those of the detailed mechanism [8]. (There are differences with those in Ref. 8 because of minor revisions of the detailed mechanism.)

Reduced Chemical-Kinetic Mechanisms

Procedures for deriving reduced chemical-kinetic mechanisms are described in detail elsewhere [14,15]. The skeletal mechanisms were reduced by introducing steady-state approximations for a number of species. For any species, the time derivative of its concentration is the difference between production and consumption rates for that species. A steady-state approximation is justified if either the species' production or consumption rate, which of course are nearly equal at steady state, is much larger than the time derivative of its concentration [16].

For the reduced mechanisms, the concentrations of the steady-state species were calculated using the nonlinear algebraic equations resulting from the differential rate equations for these species by making the steady-state assumptions. That is, algebraic equations are obtained simply by setting these species' concentration time derivatives to zero. The steady-state species' concentrations are then specified in terms of the other species' concentrations. However, the initial steady-state species' concentrations are no longer arbitrary. For example, setting them to zero is internally inconsistent, which causes numerical difficulties. In the calculations with the reduced mechanisms, the steady-state species' initial concentrations were therefore first calculated numerically using the algebraic equations. For all cases investigated, the initial steady-state species' concentrations were found to be negligibly small and to have no significant influence on the calculated ignition-delay times.

Double Base Propellants

In Fig. 1, the ratios of the time derivatives of concentration to production rates for N, NH, HNO, HONO, H, OH, and O are plotted as a function of time (t). The calculations were performed using the skeletal mechanism for double base propellants for

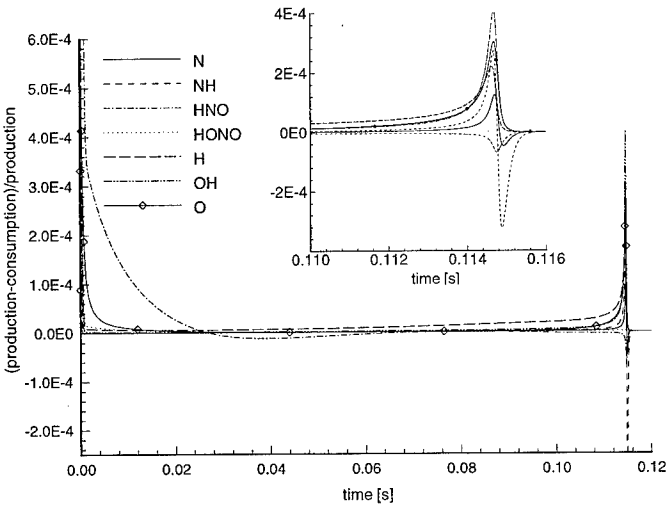

FIG. 1. The ratio of the difference between the rates of production and the rates of consumption to the rates of production for the species N, NH, HNO, HONO, H, OH, and O plotted as a function of time. The calculations are performed using the skeletal mechanism for double base propellants for $p = 5$ atm and $T^0 = 1400$ K.

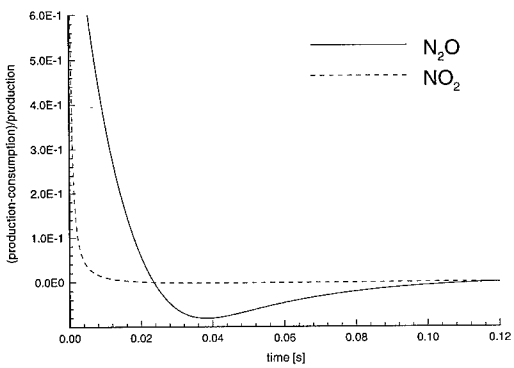

FIG. 2. The ratio of the difference between the rates of production and the rates of consumption to the rates of production for the species N_2O and NO_2 plotted as a function of time. The calculations are performed using the skeletal mechanism for double base propellants for $p = 5$ atm and $T^0 = 1400$ K.

$p = 5$ atm and $T^0 = 1400$ K. Figure 1 reveals that at all conditions, except those close to $t = 0$ and $t = \tau_{ig}$, the value of this ratio is very small. Therefore, it is reasonable to introduce steady-state approximations for these species. In Fig. 2, the ratios of the time derivatives of concentration to production rates for N_2O and NO_2 are plotted as a function of time. These results were also obtained using the skeletal mechanism for double base propellants for $p = 5$ atm and $T^0 = 1400$ K. Comparison of the results in Fig. 2 with the results in Fig. 1 indicates that the concentration of N_2O is not in steady state, but it is still reasonable to introduce a steady-state approximation for NO_2. In view of the results presented in Figs. 1 and 2, steady-state approximations are introduced for N, NH, HNO, HONO, H, OH, O, and NO_2. The steady-state relations provide eight nonlinear algebraic equations used to calculate the concentration of the steady-state species in terms of the concentrations of the remaining species. The source terms of the species that are not in steady state are rearranged and collected in three groups such that each group represents the rate of one of the three overall steps of the reduced mechanism, which is written as

$$2\,NO + H_2 \rightleftharpoons N_2O + H_2O \qquad \text{(I)}$$

$$N_2O + H_2 \rightleftharpoons N_2 + H_2O \qquad \text{(II)}$$

$$CO + H_2O \rightleftharpoons CO_2 + H_2 \qquad \text{(II)}$$

The rates of the overall steps w_k, $k = \text{I, II, III}$ expressed in terms of the rates of the elementary reactions are

$$\left.\begin{aligned} w_{\text{I}} &= w_2 + w_8 + w_{11} - w_{20} + w_{22} \\ w_{\text{II}} &= w_1 - w_7 + w_{10} + w_{22} \\ w_{\text{III}} &= w_3 \end{aligned}\right\} \qquad (1)$$

where w_n is the net reaction rate of the elementary reaction n shown in Table 1.

Nitramine Propellants

Reduced chemical-kinetic mechanisms for nitramine propellants were obtained using the same procedure employed for double base propellants. The rates of production and consumption of various species were calculated using the skeletal mechanism for nitramine propellants. The results of these calculations demonstrate that it is reasonable to introduce steady-state approximations for NH, HNO, HNC, NH_2, NO_2, OH, and O. The steady-state assumptions provide seven nonlinear algebraic equations that can be used to calculate the concentrations

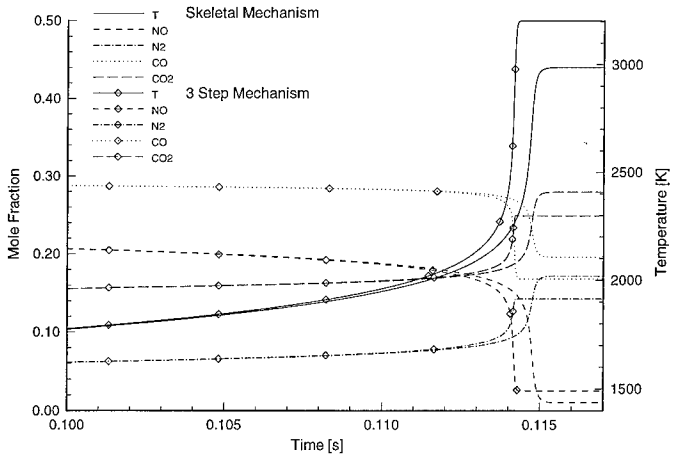

FIG. 3. Profiles of temperature T and mole fractions of NO, N_2, CO, and CO_2 plotted as a function of time. The calculations are performed using the skeletal mechanism and the reduced three-step mechanism for double base propellants for p = 5 atm and T^0 = 1400 K.

of the steady-state species in terms of the concentration of the remaining species. The reduced mechanism has six overall steps that can be written as

$$2\,NO + 2\,H_2 \rightleftharpoons N_2O + 2\,H + H_2O \quad \text{(I)}$$

$$H_2O + HCN \rightleftharpoons H_2 + HNCO \quad \text{(II)}$$

$$N_2O + 2\,H_2 \rightleftharpoons N_2 + 2\,H + H_2O \quad \text{(III)}$$

$$CO + H_2O \rightleftharpoons CO_2 + H_2 \quad \text{(IV)}$$

$$2\,H + M \rightleftharpoons H_2 + M \quad \text{(V)}$$

$$NO + H + HNCO \rightleftharpoons N_2O + CO + H_2 \quad \text{(VI)}$$

The rates of the overall steps w_k, k = I–VI expressed in terms of the rates of the elementary reactions are

$$\left.\begin{aligned} w_{\mathrm{I}} &= w_2 + w_8 + w_{11} \\ w_{\mathrm{II}} &= w_{25} + w_{33} \\ w_{\mathrm{III}} &= w_1 + w_7 + w_{27} + w_{28} + w_{32} \\ w_{\mathrm{IV}} &= w_3 + w_{24} + w_{32} \\ w_{\mathrm{V}} &= w_7 + w_{12} + w_{24} + w_{28} + w_{32} \\ w_{\mathrm{VI}} &= w_{25} + w_{29} + w_{31} \end{aligned}\right\} \quad (2)$$

To further simplify the mechanism, steady-state approximations were introduced for the species H and HNCO, yielding four overall steps that can be written as

$$2\,NO + H_2 \rightleftharpoons N_2O + H_2O \quad \text{(I}'\text{)}$$

$$NO + H_2O + HCN \rightleftharpoons N_2O + CO + 1.5\,H_2 \quad \text{(II}'\text{)}$$

$$N_2O + H_2 \rightleftharpoons N_2 + H_2O \quad \text{(III}'\text{)}$$

$$CO + H_2O \rightleftharpoons CO_2 + H_2 \quad \text{(IV}'\text{)}$$

The rates of the overall steps of the four-step mechanism w_k, k = I′–IV′ are identical to the rates for the overall steps I–IV in the six-step mechanism shown in Eq. (2).

Results and Discussions

Calculations with the reduced mechanisms were performed by multiplying time derivative terms in the differential equations for the steady-state species by a small number. In the limiting case in which the value of this number is zero, the differential equations are transformed to algebraic equations. The value of the multiplier was chosen such that any further decrease in its value had no influence on τ_{ig}.

In Fig. 3, the profiles of temperature, T, and the mole fractions of NO, N_2, CO, and CO_2 are plotted as a function of time. The calculations were performed using the skeletal mechanism and the reduced three-step mechanism for double base propellants for p = 5 atm and T^0 = 1400 K. The profiles from the reduced mechanism agree closely with those calculated using the skeletal mechanism, except for times close to ignition. The maximum value of temperature and the final values of the mole fractions of various species after ignition calculated with the reduced mechanism differ from those calculated using the skeletal mechanism; these differences occur because the concentrations of the steady-state species are not included in the atom-conservation equations in calculations with the reduced mechanism. The concentrations of the steady-state species represent excess mass in the system. Therefore, in the calculations with the reduced mechanism, the mass fractions of the various atoms change with time and the final mass fractions of these atoms are different from their initial values. However, these differences become noticeable only at times close to τ_{ig}. In fact, calculations prove that the differences between the initial mass fractions of the atoms and their mass fractions at times approximately 90% of τ_{ig} are very small.

Figure 4 shows profiles of temperature, T, and the mole fractions of NO and N_2 plotted as a function of time. Figure 5 shows profiles of T and mole frac-

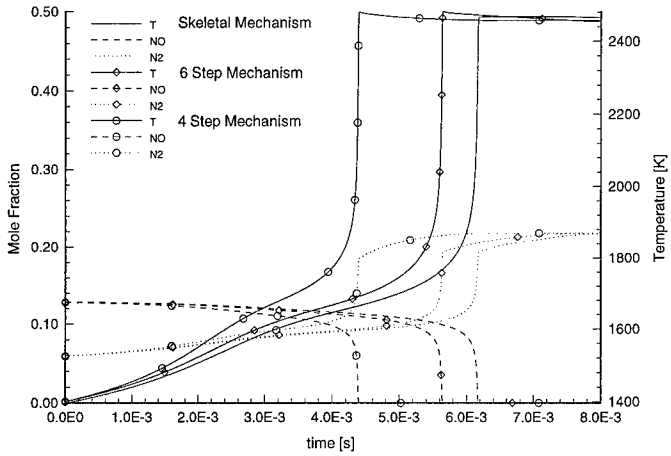

FIG. 4. Profiles of temperature T and mole fractions of NO and N_2 plotted as a function of time. The calculations are performed using the skeletal mechanism and the reduced six-step and four-step mechanism for nitramine propellants for $p = 10$ atm and $T^0 = 1400$ K.

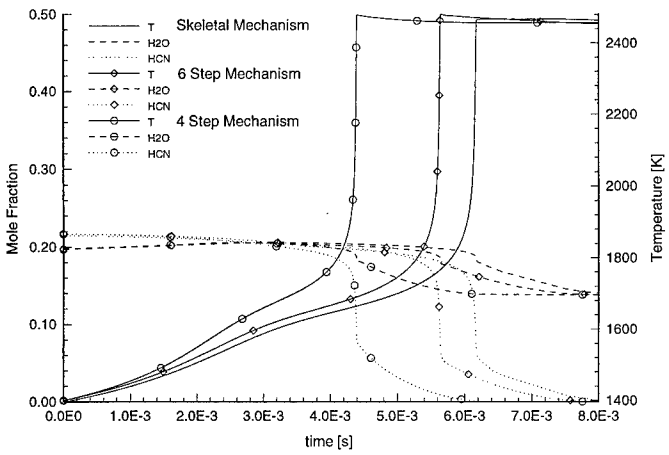

FIG. 5. Profiles of temperature T and mole fractions of H_2O and HCN plotted as a function of time. The calculations are performed using the skeletal mechanism and the reduced six-step and four-step mechanism for nitramine propellants for $p = 10$ atm and $T^0 = 1400$ K.

tions of H_2O and HCN. These profiles are calculated using the skeletal mechanism and the reduced six-step and four-step mechanisms for nitramine propellants for $p = 10$ atm and $T^0 = 1400$ K. The profiles in Figs. 4 and 5 calculated using the reduced mechanisms agree closely with those calculated using the skeletal mechanism, except near ignition.

Table 2 shows that the values of the ignition-delay times calculated using the reduced three-step mechanism for double base propellants agree well with those calculated using the skeletal mechanism. The differences in the values of τ_{ig} are less than 10%, with τ_{ig} from the reduced mechanism smaller than that obtained using the skeletal mechanism. If a steady-state approximation is introduced for N_2O, a reduced two-step mechanism is obtained. The value of τ_{ig} calculated using this two-step mechanism at $p = 1$ atm and $T^0 = 1000$ K is found to be 50% lower than calculated with the three-step mechanism. This result illustrates that a steady-state approximation for N_2O is not justified (although at other conditions the agreement is better).

Table 3 compares the values of the ignition-delay times calculated using the six-step and four-step mechanisms for nitramine propellants with those calculated using the skeletal mechanism. The values of τ_{ig} calculated using the reduced six-step mechanism agree very well with those calculated using the skeletal mechanism. The differences are less than 18%. However, the maximum differences in the values of τ_{ig} calculated using the reduced four-step mechanism and the skeletal mechanism are about 50%. The large differences between the values of τ_{ig} calculated using the reduced four-step mechanism and the skeletal mechanism are attributed to inaccuracies introduced by the steady-state approximations for H and HNCO.

Pyrolysis experiments have demonstrated that lower temperatures favor production of CH_2O and N_2O, whereas higher temperatures cause more HCN and NO_2 to be formed for nitramines and nitramine propellants [17,18]. Clearly, the former intermediates reacting near the propellant surface are expected to favor formation of N_2 and N_2O at the

TABLE 3

Comparison of the values of the ignition-delay times calculated using the various mechanisms for nitramine propellants. The initial mole fractions of NO, CO, H_2, N_2, H_2O, CO_2, N_2O, and HCN are set equal to 0.13, 0.22, 0.07, 0.06, 0.20, 0.09, 0.02, and 0.22, respectively.

Initial conditions	Detailed mech. (41 sp., 190 r.)	Skeletal mech. (17 sp., 23 r.)	Reduced mech. 6 steps	Reduced mech. 4 steps
1 atm, 1000 K	17.20 s	17.34 s	16.92 s	16.60 s
1 atm, 1400 K	$2.062 \cdot 10^{-2}$ s	$1.995 \cdot 10^{-2}$ s	$1.790 \cdot 10^{-2}$ s	$1.322 \cdot 10^{-2}$ s
1 atm, 1800 K	$3.056 \cdot 10^{-4}$ s	$2.602 \cdot 10^{-4}$ s	$2.160 \cdot 10^{-4}$ s	$1.319 \cdot 10^{-4}$ s
10 atm, 1000 K	2.754 s	2.265 s	2.185 s	2.171 s
10 atm, 1400 K	$5.723 \cdot 10^{-3}$ s	$6.162 \cdot 10^{-3}$ s	$5.632 \cdot 10^{-3}$ s	$4.388 \cdot 10^{-3}$ s
10 atm, 1800 K	$7.573 \cdot 10^{-5}$ s	$6.669 \cdot 10^{-5}$ s	$5.590 \cdot 10^{-5}$ s	$3.066 \cdot 10^{-5}$ s
30 atm, 1000 K	1.241 s	1.145 s	1.099 s	1.103 s
30 atm, 1400 K	$3.122 \cdot 10^{-3}$ s	$3.283 \cdot 10^{-3}$ s	$3.037 \cdot 10^{-3}$ s	$2.492 \cdot 10^{-3}$ s
30 atm, 1800 K	$4.903 \cdot 10^{-5}$ s	$4.474 \cdot 10^{-5}$ s	$3.803 \cdot 10^{-5}$ s	$2.125 \cdot 10^{-5}$ s

TABLE 4

Comparison of the values of the ignition-delay times calculated using the various mechanisms for nitramine propellants. The initial mole fractions of NO, CO, H_2, N_2, H_2O, CO_2, and HCN are set equal to 0.133, 0.224, 0.071, 0.061, 0.204, 0.091, and 0.224, respectively.

Initial conditions	Detailed mech. (41 sp., 190 r.)	Skeletal mech. (17 sp., 23 r.)	Reduced mech. 6 steps	Reduced mech. 4 steps
1 atm, 1800 K,	$2.035 \cdot 10^{-3}$ s	$1.446 \cdot 10^{-3}$ s	$1.204 \cdot 10^{-3}$ s	$5.738 \cdot 10^{-4}$ s
10 atm, 1800 K,	$5.858 \cdot 10^{-4}$ s	$5.233 \cdot 10^{-4}$ s	$4.452 \cdot 10^{-4}$ s	$3.026 \cdot 10^{-4}$ s
30 atm, 1800 K,	$3.270 \cdot 10^{-4}$ s	$3.090 \cdot 10^{-4}$ s	$2.671 \cdot 10^{-4}$ s	$1.944 \cdot 10^{-4}$ s

leading edge of the dark zone, while the latter favor NO. Because a higher initial dark zone temperature would be expected to produce a steeper temperature gradient near the propellant surface, temperatures near the high end of the range studied might lead to initial dark zone mixtures that contain little N_2O. Therefore, it was deemed prudent to ensure that if future experimental data become available exhibiting this trend, the reduced mechanisms would still properly predict the chemical behavior for such mixtures. For this reason, ignition-delay time calculations for an initial temperature of 1800 K were repeated with N_2O removed from the initial mixture. The results are shown in Table 4. The differences in the values of τ_{ig} calculated using the skeletal mechanism and the six-step reduced mechanism are less than 17%, and the maximum difference in the values of τ_{ig} calculated using the skeletal mechanism and the four-step reduced mechanism is about 60%.

The data in Tables 3 and 4 highlight the importance of the trace of N_2O in the initial mixture. Comparison of results in these tables shows that, in general, the presence of the N_2O decreases τ_{ig} by nearly a factor of 2 at 1800 K. The effect is even greater at lower temperatures (not shown). Addition of N_2O to the mixtures results in an increase in the rate of the reaction $N_2O + M = N_2 + O + M$ (elementary step 1 in Table 1), an important radical source.

Summary and Conclusions

Skeletal and reduced chemical-kinetic mechanisms are derived for predicting the structure of the dark zones formed over the burning surface of typical double base and nitramine propellants. In the calculations with the reduced mechanisms, the final mass fractions of the atoms after ignition differ from their initial values because the concentrations of the steady-state species are not included in the atom-conservation equations. Therefore, the reduced mechanisms are suitable for calculating the values of ignition-delay times, but, in some applications, the errors introduced in the final temperature and species concentrations may not be acceptable. Attempts to improve the accuracy of the predictions of the final concentrations of these species in the reduced mechanisms are in progress. It is hoped that these skeletal and reduced chemical-kinetic mechanisms will be suitable for use in interior ballistics calculations.

Note Added in Paper Revision

Recently, we have performed further updates to the detailed chemical mechanism from which the skeletal and reduced mechanisms are derived. We have discovered that three important reactions involving two additional species were overlooked for the detailed mechanism. These changes have pronounced effects at low temperatures, especially at high pressures, resulting in shortening of predicted ignition delays by up to a factor of 3. The effects are, unfortunately, negligible in regions in which experimental data are available for testing. Reduced mechanisms have been developed from the newest detailed mechanism in a way entirely analogous to that used herein. The results are qualitatively similar in terms of accuracy compared to the detailed mechanism. The number of reactions in both skeletal mechanisms increases by three and the steady-state species increase by two. These new results, as well as comparisons to our previous results, will be presented in future papers.

Acknowledgments

The research at UCSD was supported by the U.S. Army Research Office through Grant # ARO DAAH-95-1-0108. Dr. N. E. Meagher was supported by the ASEE/ARL postdoctoral fellowship program. Dr. W. R. Anderson's travel to the symposium was partially supported by ERO (Dr. Roy Reichenbach). The authors acknowledge helpful discussions with S. W. Bunte, A. M. Dean, J. W. Bozzelli, R. A. Yetter, F. L. Dryer, and M. C. Lin about their recent research. The authors are also grateful to J. W. Bozzelli for providing kinetic estimates for the HCN = HNC reaction.

REFERENCES

1. Kooker, D. E., Chang, L. M., and Howard, S. L., Technical Report ARL-TR-80, Army Research Laboratory, 1993.
2. Kooker, D. E., Chang, L. M., and Howard, S. L., Technical Report ARL-TR-446, Army Research Laboratory, 1994.
3. Kooker, D. E., Chang, L. M., and Howard, S. L., *32nd JANNAF Combustion Subcommittee Meeting,* CPIA Publication 631, Vol. 1, 1995, pp. 397–408.
4. Kooker, D. E., private communication, 1995.
5. Fifer, R. A., Kotlar, A. J., Miller, M. S., and Morris, J. B., *27th JANNAF Combustion Subcommittee Meeting,* CPIA Publication 557, Vol. 1, 1990, p. 95.
6. Vanderhoff, J. A., Anderson, W. R., and Kotlar, A. J., *29th JANNAF Combustion Subcommittee Meeting,* CPIA Publication 593, Vol. 2, 1992, p. 225.
7. Anderson, W. R., Ilincic, N., and Seshadri, K., *31st JANNAF Combustion Subcommittee Meeting,* CPIA Publication 620, Vol. 2, 1994, p. 387.
8. Anderson, W. R., Ilincic, N., Meagher, N. E., Seshadri, K., and Vanderhoff, J. A., *32nd JANNAF Combustion Subcommittee Meeting and 1995 Propulsion Systems Hazards Subcommittee Meeting, Joint Sessions,* CPIA Publication 638, Vol. 1, 1995, p. 197.
9. Anderson, W. R., Meagher, N. E., Ilincic, N., Seshadri, K., and Vanderhoff, J. A., "Chemical Kinetic Mechanisms for Characterizing the Structure of the Dark Zone of Double Base and Nitramine Propellants," 1996, in preparation.
10. Tsang, W. and Herron, J. T., *J. Phys. Chem. Ref. Data* 20:609 (1991).
11. Heller, C. A. and Gordon, A. S., *J. Phys. Chem.* 59:773 (1955).
12. Lutz, A. E., Kee, R. J., and Miller, J. A., Technical Report SAND87-8248, Sandia National Laboratories, 1988.
13. Anderson, W. R., Haga, S. W., Nuzman, J. F., and Kotlar, A. J., in preparation.
14. Peters, N., in *Reduced Kinetic Mechanisms and Asymptotic Approximations for Methane-Air Flames* (Smooke, M. D., Ed.), Springer Verlag, Berlin and Heidelberg, 1991, Chapter 3, pp. 48–67.
15. Göttgens, J. and Terhoeven, P., in *Reduced Kinetic Mechanisms for Applications in Combustion Systems* (Peters, N. and Rogg, B., Eds.), Springer Verlag, Berlin and Heidelberg, 1993, Appendix B, pp. 345–349.
16. Williams, F. A., *Combustion Theory,* 2d ed., Addison-Wesley Redwood City, CA, 1985, pp. 565–570.
17. Fifer, R. A., in *Fundamentals of Solid-Propellant Combustion* (Kuo, K. K. and Summerfield, M., Eds.), American Institute of Aeronautics and Astronautics, New York, 1984, Chapter 4, pp. 177–237.
18. Schroeder, M. A., Technical Report BRL-TR-2659, AD-A159 325, U.S. Army Research Laboratories, Aberdeen Proving Grounds, Maryland, 1985; see also *Proceedings of the 18th JANNAF Combustion Meeting,* CPIA Publication 347, Vol. 2, Pasadena, California, October, 1981, pp. 395–413.

COMMENTS

O. P. Korobeinichev. Institute of Chemical Kinetics and Combustion Russia. What data for concentration of free radicals did you use in your calculations of the structure of the dark zones of propellants? What was the influence of the choice of radical concentrations on results of the calculations?

Author's Reply. For calculations with the detailed and skeletal mechanisms, we assumed initial radical concentrations are zero. Steady-state assumptions are valid and were used in the reduced mechanisms for several species, including most radicals (but not all, see text; those for which the steady-state assumption was unacceptable were assumed to have zero initial concentrations). For a steady-state species, the derivative equation for the species' concentration becomes algebraic when the steady-state assumption is made. The resulting system of equations is solved for steady-state species' concentrations. Initial values of these species' concentrations are no longer variable, but are specified by the system's initial conditions. The initial steady-state concentrations can no longer be set to zero; this choice is mathematically inconsistent (does not solve the algebraic equations) and causes the numerical algorithm to fail. Instead, the algebraic equations were solved for the initial steady-state species' concentrations; this procedure is equivalent to assuming these species are at their steady-state concentrations upon entering the dark zone. Using steady-state concentrations for initial values in the finite rate mechanisms yields results virtually identical to using zero, proving initial steady-state concentrations are negligibly small.

Two facts lead to an important new insight concerning the assumption of zero initial radical concentrations. First, even for those radicals for which the steady-state assumption yielded unacceptable errors, if the assumption is used, the ignition delays are only in error by, at worst, a factor of two (see text). Thus, the concentrations must be fairly close to their steady-state values for *all* radicals. Second, using our detailed mechanism and assuming a large initial mole fraction of 0.001 for H atoms, the change in calculated ignition delays is small. We found the steady-state species' concentrations will *very* rapidly shift toward their steady-state values (within confines of conservation laws). This behavior explains previous observations of simultaneous, minor, rapid, early changes in temperature, heat release, and/or other species' concentrations for cases using arbitrary choices for initial concentrations of steady-state species. (See, e.g., [5,8]. Rapid shifts in assumed trace species concentrations toward steady-state values explain the observed early time results.) The kinetics *compels* concentrations of radical species at the leading edge of the dark zone to be close to their steady-state values. Therefore the assumption of zero initial radical concentrations, which has been made by all dark zone modelers, is excellent.

•

D. R. Crosley. SRI International, USA. When you altered the initial temperatures to examine sensitivity and comparison with experiment, did you just choose a new fizz zone initial temperature and use the calculated heat release, or did you alter the entire temperature profile?

Author's Reply. This question refers to calculations we did using the detailed mechanism so that predicted dark zone ignition delays could be compared with experimental results. This was introductory material used in the oral presentation to clarify the basic concepts used in the modeling and present tests of the detailed mechanism. These results are discussed in [8,9]. The present paper concerns only the reduced mechanisms which were developed to reproduce predictions of the detailed mechanism over a variety of conditions. In [8,9] and in the presentation, we showed that the detailed mechanism (and, by inference, the reduced mechanisms) agrees only modestly well with experiment using the measured dark zone temperature as initial temperature for nitramines; however, the agreement could be made very good by adjusting the initial temperatures used in the calculation within the experimental tolerances.

In response, we used the adiabatic assumption for all mechanism variations. Therefore, the heat release upon chemical reaction determines the temperature profiles; that is, it is indeed calculated. Of course, the entire temperature profile is affected by changes in the assumed initial temperature. (Here, we think you are asking whether we used the measured temperature profiles as fixed input parameters, as is frequently done in burner stabilized premixed flame modeling. This procedure is unnecessary because many measurements have shown propellant flames generally reach the adiabatic limit.) However, a change in the initial temperature, within experimental limits, does not strongly affect the rest of the profile, especially the adiabatic temperature.

Twenty-Sixth Symposium (International) on Combustion/The Combustion Institute, 1996/pp. 2007–2015

OSCILLATORY COMBUSTION OF ALUMINIZED COMPOSITE PROPELLANTS

S. R. HICKMAN AND M. Q. BREWSTER
Department of Mechanical and Industrial Engineering
University of Illinois
Urbana, Illinois 61801, USA

The unsteady combustion of aluminized composite propellants (Al/AP/HTPB) was studied using laser recoil and other measurements. It was found that propellants with fine aluminum (<15 μm) and high aluminum loading (>15%) produced large aluminum agglomerates and a strong low-frequency (<100 Hz) oscillatory combustion response with burning rate oscillations at the same frequency and in phase with departure of large aluminum agglomerates at the propellant surface. Coarser aluminum propellants produced only moderate-sized agglomerates and minimal oscillatory combustion response. The frequency of the burning rate oscillations increased (approximately linearly) with increasing mean burning rate and aluminum loading, and decreased with increasing aluminum ingredient particle size. The oscillatory burning response appears to be related to periodic accumulation, agglomeration, ignition, and departure of aluminum at the burning surface of the propellant. Both the oscillatory burning and agglomerate particle size data are consistent with Gany and Caveny's model of aluminum accumulation in a mobile surface melt layer. These observations confirm that aluminum can have a significantly stronger influence on the combustion of AP/HTPB propellants than that indicated by the normally small changes observed in macroscopically steady burning rate or the mean burning rate during macroscopically unsteady (oscillatory) combustion. The proposed mechanism linking aluminum behavior and propellant burning rate is that of cyclic heat sink and source effects associated with the periodic aluminum accumulation and departure.

Introduction

Aluminum has been used extensively as an additive in solid rocket propellants for two distinct reasons: increased performance [1] and damping of high-frequency acoustic oscillations [2]; however, the effect of aluminum on solid propellant combustion is still not well understood. Several recent studies have reported abnormally high combustion response functions for highly aluminum loaded AP/HTPB propellants (compared with nonaluminized analogs) in the 300–500 Hz range. T-burner measurements at NAWC [3] of a high burning rate (catocene catalyzed) 20% Al/AP/HTPB propellant at 225 atm showed a response peak at a relatively low frequency (300–500 Hz) that was not present in the corresponding nonaluminized propellant and could not be explained in terms of classical quasi-steady, homogeneous, one-dimensional (QSHOD) theory. The aluminum effect was attributed to distributed combustion of aluminum, although the reported observations are also consistent with a modified propellant combustion response. Recent measurements of Ariane solid booster propellant combustion response indicated a strong aluminum effect on the propellant response. Using microwave and interrupted exhaust techniques, investigators at ONERA observed a previously undetected 200- 300-Hz response peak at 40 atm [4] that was not present in the nonaluminized propellant. Additional evidence that aluminum can significantly modify the propellant combustion response in the 0- 500-Hz frequency range comes from recent studies using the laser recoil technique [5–7]. In that work, certain highly aluminum loaded AP/HTPB propellants were found to exhibit pronounced low-frequency (<100 Hz) oscillatory burning when perturbed by unsteady laser radiation at 1 atm. These oscillations in propellant burning rate were thought to be related to aluminum behavior, particularly the periodic accumulation, agglomeration, and departure of aluminum at the surface. The results of these various independent techniques (T-burner, laser recoil, microwave, and modulated exhaust—the latter three of which are not influenced by distributed combustion) suggest that aluminum can significantly alter propellant combustion response, and factors that affect aluminum agglomeration might also affect propellant combustion response.

Aluminum agglomeration has been shown to be affected by both gas-phase flame conditions and condensed-phase packing and accumulation considerations. The primary gas-phase observation [8–10] is that a hot, partially premixed AP/HTPB leading-edge flame in close proximity is necessary if aluminum is to ignite before it leaves the propellant

surface. AP particle size and pressure play important roles in this regard. The primary condensed-phase packing consideration is that the volume between coarse AP particles determines the amount of aluminum that is available to form an agglomerate via cracking and "oxidative welding" of neighboring aluminum particles at the surface [11]. The primary accumulation observation is that if a melt layer (e.g., HTPB) exists on the surface of the propellant, ingredient aluminum particles that are smaller than this layer thickness can accumulate in the layer, leading to more extensive agglomeration [12]. In this paper, the factors related to condensed phase accumulation (prior to agglomeration, ignition, and departure) were investigated.

Experimental Procedure

The laser recoil technique measures the dynamic burning rate of propellants and energetic materials using small (gram) quantities of material. The principle of the technique is to perturb the propellant burning rate with laser radiation, measure the recoil force associated with the momentum flux of the combustion gases, and infer the instantaneous burning rate. The plume, which can be rather optically dense in metalized propellants, is kept sufficiently optically thin by ample ventilation, and the laser flux absorbed by the propellant is determined by measuring the transmissivity of the plume and reflectivity of the propellant. A fraction of the laser energy is split off and monitored simultaneously. This signal is calibrated to give the instantaneous absorbed laser flux. In this study, both YAG and CO_2 lasers were used. Most tests were conducted at 1 atm using a Kistler 9207 force transducer. The force transducer and laser flux data were spectrally analyzed using standard FFT algorithms to give the complex thrust frequency response function $H(f)$. For small amplitude perturbations, $H(f)$ is independent of the radiant flux amplitude, Δq, and $H(f)$ is the linear frequency response function for recoil force. Since the recoil force is related to the momentum flux of the gases leaving the propellant surface, the thrust response is a good indicator of the propellant burning rate response. Further discussion of momentum considerations can be found in Ref. 5.

Formulations of the most-studied propellants are shown in Table 1. A complete list of investigated formulations can be found in Ref. 6.

Aluminum agglomerate sizes were measured to investigate the correlation between agglomerate size and oscillatory burning behavior. The agglomerates from a burning propellant sample were captured in a beaker containing an ethanol bath that had been buffered with ammonium acetate. The propellant was located 1 cm above the surface of the ethanol, with the surface facing downward (gravity acting to pull agglomerates from the surface), whereas in all other tests (laser recoil and strand burning rate) the surface faced upward. This method of capturing particles was similar to the method used in Ref. 13. Particle size distributions were measured with a sedimentation analyzer based on light scattering.

Luminosity of the region near the burning propellant surface was measured with a fiber optic (7° half angle) that viewed the propellant surface and the gas region just above it, and a photodiode.

Results

Mean Burning Rates

Mean burning rates for zero laser flux at 1 atm are listed in Table 1. The A-0, A-20, R-18-1, and R-0-1 results exemplify the well-known observation that aluminum addition does not greatly alter the steady burning rate; the addition of a relatively large percentage (16 or 17%) of aluminum (keeping the AP/HTPB ratio constant) increases the steady burning rate only 10–30%. The AP size distribution has a much stronger effect on mean burning rate than the presence of aluminum; fine AP increases burning rate significantly.

The effect of a steady radiant heat flux on burning rate is shown in Fig. 1. Mean burning rate increased monotonically (no apparent plateau region) with mean flux. In addition to the steady tests, Fig. 1 shows the mean burning rate when oscillatory (pulsed and sinusoidal) laser flux was used. Some of the oscillatory results exhibit nonlinear effects, i.e., deviations in mean burning rate from the constant flux values.

The effect of aluminum ingredient size on mean burning rate is shown in Table 2. Mean burning rate decreased slightly with increasing ingredient aluminum size. This trend is possibly related to changes in agglomeration (see the following agglomeration results).

Agglomerate Sizes

The mass mean agglomerate size results are given in Table 2. Most of the preoxidized aluminum samples (U/P was an exception) produced smaller agglomerates than their nontreated counterparts, as previously observed by others [1,11]. The R-18-1, H-3, and H-5 propellant samples contained large, flake-shaped agglomerates. Their characteristics spanwise dimension was usually over a millimeter. It should be noted that the flakes occurred only in the propellants that also exhibited strong oscillatory burning behavior. In contrast to the small ingredient aluminum, the large ingredient aluminum produced no flakes, just smaller, round agglomerates. The results of Table 2 show that the smallest, untreated

TABLE 1
Propellant formulations

Propellant	Primary metal	% Metal	% AP	% HTPB	% Carbon	$\bar{r}_b$ (cm/s) $q = 0$
R-18-1	Al (Reynolds)	17.75 (5 μm average size)	42.83 (<90 μm) 21.42 (20 μm)	17.0[a]	1.0	0.18
R-18-2	Al (Reynolds)	17.75 (5 μm average size)	42.83 (90 μm) 21.42 (20 μm)	17.0[a]	1.0	0.11
R-0-1	–	0.0	52.07 (<90 μm) 26.04 (20 μm)	20.67[a]	1.22	0.14
A-20	Al	16.7 (5 μm)	34.2 (200 μm) 34.2 (25 μm)	14.9	0.0	0.14
A-10	Al	9.1 (5 μm)	37.3 (200 μm) 37.3 (25 μm)	16.3	0.0	0.12
A-5	Al	4.9 (5 μm)	39.0 (200 μm) 39.0 (25 μm)	17.1	0.0	0.11
A-0	–	–	41.0 (200 μm) 41.0 (25 μm)	18.0	0.0	0.11
QCZ-1	Al	20.0 (5 μm)	44.0 (200 μm) 20.0 (20 μm) 4.0 (10–20 μm)	12.0	0.0	0.23
U ad P	Al (ALCOA)	17.75 (14–18 μm)	42.83 (<90 μm) 21.42 (20 μm)	17.0[a]	1.0	0.13
H-3 to 95[b]	Al (Valley Met)	17.75 (spherical) (3–95 μm)	42.83 (<90 μm) 21.42 (20 μm)	17.0[a]	1.0	see Table 2

[a]Binder, 84.0% HTPB, 10.0% DOA, and 6.0% IPDI by mass.
[b]H-Xp (e.g., H-5p) designates pretreated aluminum, heated in oxygen to increase oxide coating thickness.

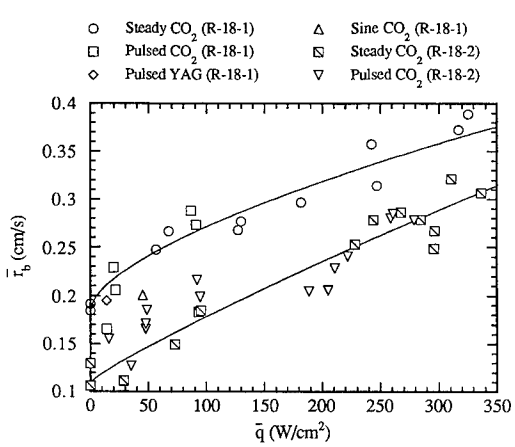

FIG. 1. Mean burning rate as a function of mean heat flux for constant, pulsed, and sinusoidal heat flux for R-18-1 and R-18-2 propellants (CO_2 laser).

ingredient aluminum sizes (R-18-1, H-3, and H-5) produced the largest agglomerates. The intermediate-sized ingredient aluminum produced the smallest agglomerates. With the largest ingredient aluminum size, agglomerate size increased again, probably due to the larger ingredient size, and not necessarily because of more extensive agglomeration relative to the intermediate case.

Oscillatory Burning: Time-Domain Response

Several of the propellants (R-18-1, R-18-2, H-3, H-5, A-20, and QCZ-1) exhibited pronounced oscillatory burning when perturbed by periodic laser radiation while others did not. Those that burned in an oscillatory fashion also displayed synchronous oscillatory accumulation and departure of aluminum at the propellant surface. Figure 2 shows force transducer and luminosity traces for R-18-1 and R-0-1 propellants subjected to 10 Hz, 5 ms of pulsed YAG

TABLE 2
Zero flux burning rates and agglomerate size results

Propellant	R-18-1	H-3	H-5	H-5p	H-15	H-15p	H-30	H-60	H-60p	H-95	U	P
Burning rate (cm/s)	0.18	0.19	0.18	0.17	0.16	0.15	0.14	0.14	0.13	0.13	0.13	0.13
Agglomerate size (μm)	218	143	277	56	78	42	51	113	78	152	84	88

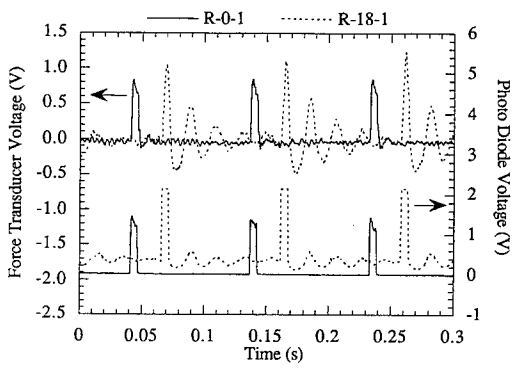

FIG. 2. Recoil force and luminosity traces for R-18-1 and R-0-1 propellants (10 Hz, 5 ms pulsed YAG radiation, 14 W/cm^2 mean absorbed flux).

radiation at 14 W/cm^2 mean absorbed flux. The large, initial peak in the traces corresponds to the periodic pulse of the laser. The force traces indicate a strong oscillatory burning rate response (at 47 Hz) following the laser pulse for R-18-1 propellant but essentially no response for nonaluminized R-0-1. Similarly, the luminosity traces show a strong oscillatory signal following the laser pulse for R-18-1, which is nearly in phase with the force (burning rate) signal. That this oscillatory luminosity was due to periodic accumulation, agglomeration, ignition, and departure of aluminum at the propellant surface was verified by high-speed video imaging. These results suggest a causal relationship between aluminum behavior on the propellant surface and the dynamic burning rate of the propellant.

Oscillatory Burning: Frequency Response Function

Time-domain responses were converted to the frequency domain as discussed previously, assuming linearity of the combustion response. Nonlinear effects are evident in some of the data, such as mean burning rate shifts. However, the primary effects of nonlinear behavior on the linearly computed response function [14] are to reduce the response function magnitude near the peak (i.e., to shift some of the response to higher frequencies) and, for pulsed input, to create false secondary peaks at frequencies corresponding to integer multiples of the inverse pulsewidth. Since the reduction in primary response peak magnitude is never enough to obscure its general characteristics and identity, and since the first false secondary peak frequency is beyond the range of interest in this study (>200 Hz), the linearly computed frequency response functions are a useful indicator of the linear combustion response and the general combustion behavior.

Figure 3 shows the thrust frequency response for aluminized R-18-1 and nonaluminized R-0-1 using both YAG and CO_2 lasers with pulsed input (10 Hz, 5 ms, 14 W/cm^2 mean flux). For both lasers,

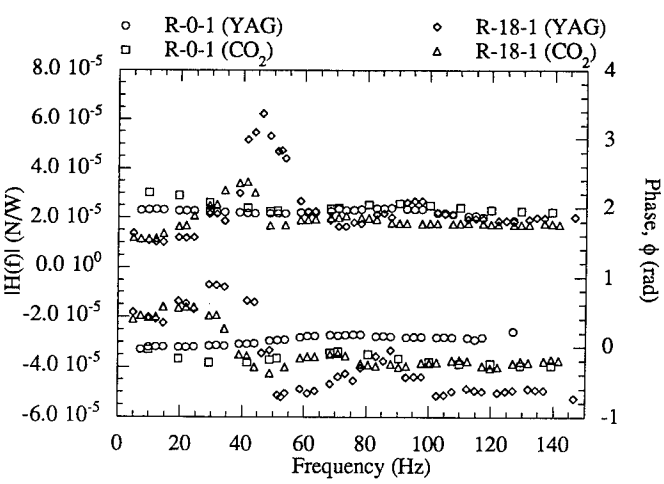

FIG. 3. Thrust frequency response function for R-18-1 and R-0-1 propellants (10 Hz, 5 ms pulsed radiation, 14 W/cm^2 mean absorbed flux).

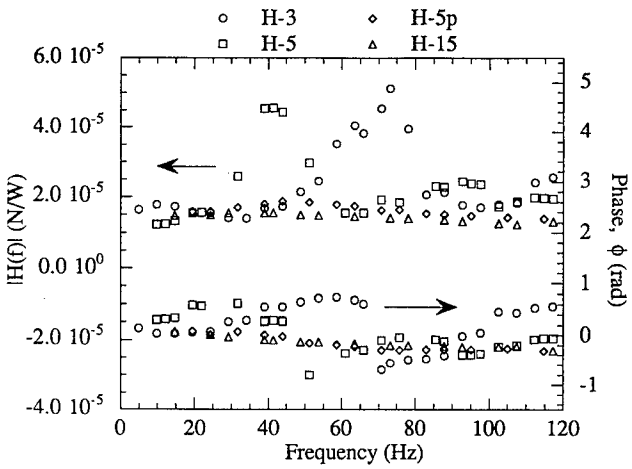

FIG. 4. Thrust frequency response function for H propellants (10 Hz, 5 ms pulsed CO_2 radiation, 14 W/cm^2 mean absorbed flux): effect of ingredient aluminum size.

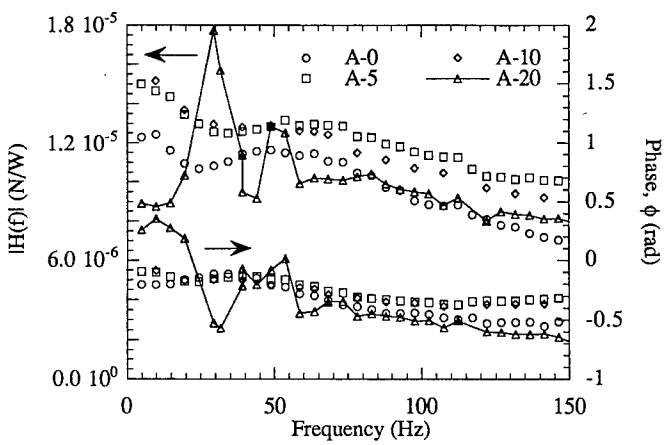

FIG. 5. Thrust frequency response function for A propellants (10 Hz, 5 ms pulsed CO_2 radiation, 14 W/cm^2 mean absorbed flux): effect of aluminum loading.

a strong peak in the 40- 50-Hz range is observed with R-18-1. The flat response for R-0-1 confirms that the oscillatory response in R-18-1 (which has the same AP/HTPB ratio) is probably not due to combustion of the fuel-rich AP/HTPB mixture but is related to the aluminum behavior. Previous studies have shown that some nonmetalized, fuel-rich AP/hydrocarbon mixtures exhibit strong oscillatory burning responses when excited periodically [15–17]. However, this effect seems to correspond to quasi-homogeneous mixtures with fine AP (<20 μm) [18] and therefore would not be applicable in the present propellants.

The effect of aluminum ingredient particle size was investigated with the H-propellant series. Ingredient aluminum sizes included 3, 5, 15, 30, 60, and 95 μm. Out of all the H propellants, only the 3- and 5-μm aluminum powders produced strong oscillatory responses. As shown in Fig. 4, the 3-μm aluminum response peaked at 74 Hz and the 5-μm aluminum response at 42 Hz, thus showing a decrease in peak frequency with increasing ingredient aluminum size. The 5-μm pretreated aluminum propellant H-5p had a very weak peak at the same frequency as H-5 but the magnitude was greatly reduced; presumably, this was related to a much lower degree of agglomeration and smaller agglomerates (Table 2). The propellants with larger ingredient aluminum (H-15 and larger) did not produce an oscillatory response. It should be noted that all the nonoscillatory burning propellants (H-5p, H-15, etc.) produced much smaller agglomerates than the oscillatory propellants (see Table 2).

The effect of aluminum loading was investigated with the A-propellant series. A-20 produced the strongest oscillatory response of the A propellants. As shown in Fig. 5, the A-20 response peaked at 30 Hz. The A-5 and A-10 propellants had weaker oscillatory responses that peaked at <10 Hz.

The relationship between the frequency of the characteristic aluminum agglomeration response peak and mean burning rate was explored by varying the mean heat flux with pulsed CO_2 laser input. The peak frequency was found to increase linearly with

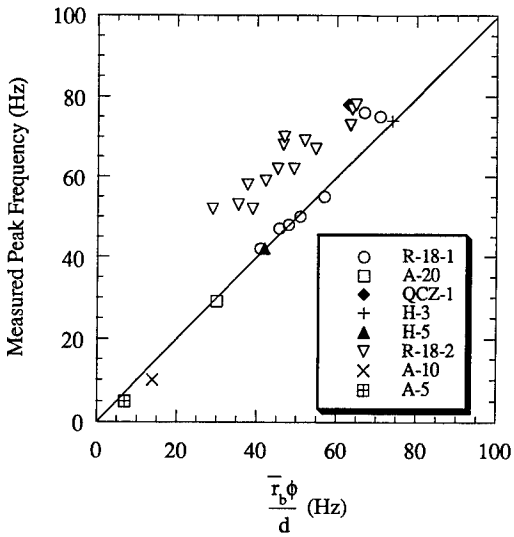

FIG. 6. Approximate correlation between experimental oscillatory burning frequency and theoretical replenishment frequency for accumulating one monolayer of aluminum particles in surface melt layer.

mean burning rate, as shown in Fig. 6 for R-18-1 and R-18-2. In Fig. 6, the measured peak frequency is plotted versus $\bar{r}_b\phi/d$ (which has units of frequency) for reasons discussed later. For the R-18-1 and R-18-2 data in Fig. 6, the aluminum volume fraction ($\phi = 0.114$) and particle size ($d = 5\ \mu$m) are constant parameters. The linear relationship between peak frequency and mean burning rate confirms that the characteristic aluminum agglomeration peak is not the classical, inert thermal conduction response peak for which peak frequency varies as the square of mean burning rate.

Mechanism of Aluminum Accumulation and Agglomeration

The mechanism of aluminum accumulation and agglomeration suggested by Gany and Caveny [12] seems to explain many of the results observed in this study. The key feature of Gany and Caveny's model is a "mobile" melt layer on the propellant surface wherein ingredient aluminum particles smaller than this layer thickness ($d < \delta$) would be free to move relative to the surrounding molten binder. Particles arriving at the melt layer–gas interface would be retained there by surface tension while the surrounding binder flowed past and decomposed to vapor. As more particles arrived, they would push aside or be pushed aside by previously accumulated particles; the molten binder would continue flowing past the particles. This would continue at least until a densely packed monolayer of particles was formed. After that point, new arrivals would tend to fill in the holes, choking off binder flow to the surface. This would create additional viscous drag force and a tendency to push particles into the gas phase. If gas flame conditions were conducive (i.e., many hot, leading-edge flames near the propellant surface), the probability of protruding aluminum encountering a hot flame would be high, and rapid heating, coalescence, and ignition of all the neighboring aluminum particles would occur. The accumulated aluminum would leave the surface as a large, burning agglomerate, and the cycle would begin again. The cycle time for this process would be approximately the time to accumulate one monolayer of aluminum particles in the melt layer surface, which from mass conservation is

$$t_{\text{mono}} = \frac{d}{\bar{r}_b\beta\phi}(1 - \beta\phi) \tag{1}$$

If gas flame conditions were not conducive (i.e., fewer hot leading-edge flames near the surface), aluminum ignition would not occur until more aluminum particles had accumulated in the melt layer, thereby exerting greater force and/or pushing more particles into the gas phase. In the limit, if the melt layer became saturated with aluminum without ignition and departure having occured, the newly arriving wave of aluminum particles from the solid binder phase would force all the accumulated aluminum into the gas phase, resulting in either ignition and departure of burning agglomerates (if flame conditions were conducive for ignition) or just departure of nonburning agglomerates. Then the cycle would begin again. The cycle time for this process would be approximately the time to saturate the melt layer of thickness, δ, with aluminum particles, as given by

$$t_{\text{sat}} = \frac{\delta}{\bar{r}_b\beta\phi}(1 - \beta\phi) \tag{2}$$

The foregoing description applies to small ingredient aluminum ($d < \delta$) and gives the limiting scenarios corresponding to the shortest (equation 1) and longest (equation 2) accumulation/departure cycle times.

The situation for ingredient aluminum particles larger than the melt layer thickness ($d > \delta$) would be quite different. These particles would protrude through the melt layer into the gas phase where they would have opportunity to be heated to ignition without undergoing extensive accumulation and agglomeration with neighboring particles, providing gas flame conditions were conducive (i.e., close in spatial proximity and relatively hot). If near-surface gas flame conditions were not conducive to ignition, these large ingredient aluminum particles would be carried into the gas stream unignited and relatively unagglomerated.

This mechanistic description explains many of the agglomeration results observed both in Ref. 12 and

in this study. It accounts for the much more extensive agglomeration observed with smaller ingredient aluminum (see Table 2). It also accounts for the observed variation in aluminum accumulation/departure frequency with ingredient aluminum size, loading, and mean burning rate according to equation 1 (see Figs. 4–6).

A semiquantitative test of the Gany and Caveny model can be made by comparing the predictions of equation 1 with the measured peak (oscillatory) frequencies, as shown in Fig. 6. The horizontal axis in Fig. 6 corresponds to the inverse of t_{mono}, with $\beta\phi$ neglected relative to unity, and β set equal to unity. The value of ϕ used is the total aluminum volume fraction. It might be argued that this value underpredicts the effective value in an AP composite propellant if the aluminum accumulation is viewed to occur in the molten binder layer. In addition, there is uncertainty about the correct effective aluminum particle accumulate layer thickness necessary before ignition occurs. Equations 1 and 2 indicate that this value could vary between d and δ; the value of d is probably a lower limit. Thus, the effective values of both d and ϕ in equation 1 could conceivably be increased, but reliable means for more accurate estimates are not known. Further information about the microstructure of both the condensed-phase and gas-phase combustion zones is needed. Nevertheless, the agreement between the experimentally measured peak frequencies and the "theoretical" peak frequency (as indicated by the diagonal line in Fig. 6) are noteworthy. Particularly significant are the following: (1) both R-18-1 and R-18-2 data show a linear increase with mean burning rate; (2) H-3 and H-5 data, for which both mean burning rate and ingredient aluminum size vary, show good correlation; and (3) A-5, A-10, and A-20 data, for which both aluminum loading and mean burning rate vary, show good correlation. All the propellants that demonstrated oscillatory burning are plotted in Fig. 6 and all show reasonable correlation with the Gany-Caveny model.

Relation between Agglomeration and Propellant Burning Rate

The most important new information obtained in this study is evidence of the link between aluminum agglomeration behavior and dynamic propellant burning rate, particularly the correlation between extensive agglomeration and pronounced oscillatory burning. The mechanistic connection might be as follows. Aluminum is an inert heat sink from the time it begins accumulating in the melt layer until it ignites and leaves the surface; after departing the surface (assuming it ignites at the surface) it becomes a heat source both by radiative and conductive heat feedback. As a heat sink, aluminum takes energy from the primary leading-edge flames that would have gone to augmenting the propellant burning rate. As a heat source, aluminum transfers energy back to the propellant, both by conduction and radiation while it is close to the propellant surface, and by radiation after it is too far from the surface to conduct, thus providing additional heat feedback to augment the propellant burning rate. Thus, the cycle of periodic accumulation and departure of aluminum represents an oscillating heat sink/source effect which influences the dynamic burning rate. Averaged over a long period (relative to the accumulation/departure cycle), the aluminum sink/source effects tend to cancel, resulting in only a modest net effect on the mean burning rate. But the dynamic burning rate effect can be quite significant, particularly when agglomeration is extensive. Larger agglomerates have larger inertia-to-drag ratios ($\sim d^3/d^2$). Thus, they have longer residence times near the propellant surface after ignition and can provide more effective conductive heat feedback. This effect seems to be evident as a weak trend in the steady burning rate and agglomerate size data for the H propellants, (Table 2) and a strong trend in the oscillatory burning rate data (Fig. 4).

Conclusions

Although gas-phase leading-edge flame effects are clearly important in determining aluminum agglomeration behavior, the results of this study and those of Gany and Caveny show that the accumulation process at the propellant surface also plays an important role. Furthermore, this work shows that the agglomeration process can significantly affect dynamic propellant burning rate behavior. Future studies should consider this effect more carefully.

Nomenclature

β	reciprocal of packing factor for spherical particles (e.g., simple cubic, face centered cubic, etc.), of order one
δ	melt layer thickness
ϕ	volume fraction of aluminum in propellant, or response function phase
d	mean diameter of ingredient aluminum particles
f	frequency (Hz)
F_t	recoil force per unit area
$H(f)$	complex thrust frequency response function, $H(f) = F_t'/q'$
q	absorbed radiant heat flux
r_b	propellant burning rate
t	time (s)
$\bar{}$	(over bar) denotes average or steady values
$'$	denotes oscillatory values

Acknowledgments

The support of the Office of Naval Research (N00014-91-J-1977), Dr. Richard S. Miller scientific officer, is gratefully acknowledged.

REFERENCES

1. Price, E. W., in *Fundamentals of Solid-Propellant Combustion,* Progress in Astronautic and Aeronautics, (K. K. Kuo and M. Summerfield, Eds.), AIAA, Washington, DC, 1984, Vol. 90, pp. 479–513.
2. Price, E. W., in *Nonsteady Burning and Combustion Stability of Solid Propellants,* Progress in Astronautic and Aeronautics, (L. De Luca, E. W. Price, and M. Summerfield, Eds.), AIAA, Washington, DC, 1992, Vol. 143, pp. 1–16.
3. Bloomshield, F. S. and Stalnaker, R., *Proceedings of the 30th JANNAF Combustion Subcommittee Meeting,* CPIA, 1993, Pub. 606, Vol. 3, pp. 197–207.
4. Traineau, J. C., Prevost, M., and Tarrin, P., *30th AIAA/ASME/SAE/ASEE Joint Propulsion Conference,* AIAA paper 94-3043, 1994.
5. Brewster, M. Q., Hites, M. H., and Son, S. F., *Combust. Flame* 94:178–190 (1993).
6. Hickman, S. R. and Brewster, M. Q., *Proceedings of the 30th JANNAF Combustion Subcommittee Meeting,* CPIA, Pub. 1993, 606, Vol. 1, pp. 317–326.
7. Hickman, S. R. and Brewster, M. Q., *Proceedings of the 31st JANNAF Combustion Subcommittee Meeting,* CPIA, 1994, Pub. 620, Vol. 2, pp. 51–61.
8. Price, E. W., Sambamurthi, J. K., Sigman, R. K., and Sheshadri, T. S., *Proceedings of the 20th JANNAF Combustion Meeting,* CPIA, 1983, Pub. 383.
9. Sambamurthi, J. K., Price, E. W., and Sigman, R. K., *AIAA J.* 22:1132–1138 (1984).
10. Price, E. W., *J. Prop. Power* 11:717–728 (1994).
11. Boggs, T. L., Kraeutle, K. J., and Zurn, D. E., *Proceedings of the 9th JANNAF Combustion Meeting,* CPIA, 1972.
12. Gany, A. and Caveny, L. H., *Seventeenth Symposium (International) on Combustion,* The Combustion Institute, Pittsburgh, 1978, pp. 1435–1461.
13. Hardt, B. E. and Brewster, M. Q., *J. Prop. Power* 7:1076–1078 (1991).
14. Zebrowski, M. A. and M. Q. Brewster, *J. Prop. Power,* 12:564–573 (1996).
15. Simonenko, V. N., Svit, A. G., and Fomenko, V. M., *Joint Meeting of the Soviet and Italian Sections of the Combustion Institute,* Tacchi Editore, Pisa, Italy, 1990, p. 7.6.
16. Simonenko, V. N. and Chertishchev, V. V., *Fiz. Goreniya Vzryva* 29:53–55 (1993).
17. Son, S. F. and Brewster, M. Q., *Combust. Flame* 100:283–291 (1995).
18. Hickman, S. R. and M. Q. Brewster, *Proceedings of 32nd JANNAF Combustion Meeting,* CPIA, 1995. Publ. 631, Vol. 1, 297–302.

COMMENTS

I. Gökalp, CNRS LCSR, France. Oscillatory burning of single aluminum particles is a well documented phenomenon by Dreizin in Russia and Mavion and Gökalp (CST, 1996, forthcoming) and others. Do you think that your observations on aluminized propellants can be explained by the oscillatory burning behavior of aluminum agglomerates?

Author's Reply. The oscillatory propellant burning reported here is related to the oscillatory burning behavior of aluminum but not in the way you suggest. Oscillatory aluminum combustion in propellants has to do with periodic accumulation in the binder melt layer, agglomeration, ignition, and departure from the surface. This is a sequence of events unique to propellants and different from oscillatory burning of isolated aluminum droplets, which of course can also occur for a variety of reasons.

•

Robert F. Chaiken, DOE/Pittsburgh Research Centre, USA. In a rocket motor chamber, pressure oscillations related to chamber configuration are coupled to the burn rate. In your experiment you replace the pressure-burn rate effect with laser oscillations. While the Al may be responsible for the force results you see, how do you relate the Aluminum mechanisms to what would occur in a rocket chamber?

Author's Reply. The key to relating these results to a motor environment is the coupling between aluminum combustion behavior and propellant burning rate response, which these results demonstrate exists under certain conditions. Although pressure has a significant effect on the flame zone structure near the propellant surface, it is quite possible that a strong coupling may exist in rocket motors at elevated pressures. The laser is merely a convenient perturbing influence in these experiments. In a motor pressure would be the primary perturbing influence. Still, if a strong coupling mechanism existed a pronounced, relatively low frequency response could be expected due to the metal/propellant combustion coupling.

•

Jerry Finlinson, Naval Air Warfare Center, USA. In your paper you explained the mechanism based upon the fact that the particles diameters were less than the melt layer

thickness. What was the melt layer thickness at 1 atm pressure? At much higher pressures the melt layer is thinner. At what pressure does the melt layer become less than 3 microns thick?

Author's Reply. Based on the observation that aluminum 15 μm and larger did not agglomerate we would estimate the binder melt layer thickness to have been approximately 15 μm. However, no independent measurements of binder melt layer thickness were attempted. We would agree that in general the binder melt layer thickness would decrease with increasing pressure, but further studies are needed to quantify the thickness better.

•

Joseph M. Powers, University of Notre Dame, USA. Have you examined the force response of the propellant to a single pulse and do you observe a long time-scale amplitude decay?

Your results suggest there may be an underlying second order differential equation, based on fundamental physics, which models your system well. Have you identified such a system?

Author's Reply. We have examined the response to a variety of pulse conditions. The response for a single pulse (or series of widely spaced pulses) for a propellant that exhibited oscillatory behavior would be similar to that shown in Fig. 2; the amplitude would continue to decay as shown.

The burning rate can be determined in theory by solution of the conservation equations, mass, energy, and species. For this system a rigorous formulation would be exceedingly complex, but perhaps there is a simplified approach that would capture the essential physics that has the general character you describe. We haven't identified such a description.

•

John A. Vanderhoff, Army Research Laboratory, USA. Different frequency oscillations were shown for aluminized propellant when changing the driving source from a CO_2 laser to a YAG laser. Could you comment on the source of this difference?

Author's Reply. Differences are probably due to the different optical properties of the various ingredients at the two wavelengths. At 10.6 μm both AP and binder have intrinsic absorption coefficients on the order of several hundred cm^{-1}, which corresponds to mean free photon paths on the order of tens of μm. At 1.06 μm both AP and binder are very transparent (photon mean free paths on the order of cm). Only aluminum and carbon (for R-18) are relatively absorptive and they exist in the binder, not the AP. Their effect is to increase the binder absorption coefficient to several cm^{-1}, reducing the mean free path in that region to tens of μm. Still the 90 μm AP allows deeper penetration of the YAG laser radiation. These differences in spatial distribution of absorption and selective absorption probably account for the observed difference in response.

Twenty-Sixth Symposium (International) on Combustion/The Combustion Institute, 1996/pp. 2017–2023

PROPELLANT DARK ZONE CONCENTRATIONS VIA MULTICHANNEL IR ABSORPTION

S. H. MODIANO AND J. A. VANDERHOFF
U.S. Army Research Laboratory
Aberdeen Proving Ground, MD 21005-5066, USA

A multichannel infrared absorption technique has been developed and applied to the study of steady-state, self-sustained combustion of solid propellant flames at elevated pressure. An infrared light source, windowed pressure chamber, and spectrometer-diode array detector formed the basic experimental setup with which in situ absorption measurements were made. Spectra were obtained over the wavenumber range of 2300 to 6000 cm^{-1}. Within this range, absorptions for HCN, H_2O, N_2O, CO, CO_2, and CH_4 have been detected through the use of a 1024-element platinum silicide array detector with the ability to read complete spectra in 10 ms. Experimental dark zone results for a nitramine propellant (XM39) and a double-base-like propellant (JA2) have been obtained, and these absorption spectra analyzed with a full spectrum, multivariate, nonlinear, least-squares-fitting pc program that makes use of the HITRAN database for the required molecular information. In some cases, the absorption spectra of the molecule had sufficient detail and fidelity to allow determination of both temperature and absolute concentration. This occurred for HCN and H_2O in XM39 propellant and for H_2O and CO in JA2 propellant. Dark zone temperatures (1185 K for XM39 and 1433 K for JA2) obtained in this fashion are in good agreement with reported values. All six of the species were found in XM39, and absolute concentration or upper limits are given. No evidence of HCN or N_2O absorption was observed in the dark zone of JA2, thus, four dark zone species concentrations are reported for this propellant. Comparisons of species concentration and dark zone temperature measurements are made with other published measurements under conditions of steady-state, self-sustained propellant combustion.

Introduction

Delayed ignition events that occur in gun firings are thought to be related to detailed chemistry effects of the solid propellant propulsion charge. At moderate pressure (~2 MPa), where the transition from ignitor burning to the main propellant burning occurs, many solid propellants burn with a clearly observable two-stage flame structure [1]. These two flames are separated by a nonluminous region called the dark zone whose spatial extent is governed by pressure. The length of this dark zone increases with decreasing pressure, and for sufficiently low pressure the second stage "luminous flame" does not form. At high pressures the two stages merge. Overall, these dark zones appear because of the slow conversion of NO to N_2. The chemistry involved in this conversion process is relevant to delayed ignition. Hence, a research effort to supply interior ballistic codes with detailed chemistry for the conversion of the propellant dark zone to the second-stage flame is underway. One of the beginning steps is to probe the dark zone for temperature and species concentration information. This information can be used to develop and test detailed chemical reaction mechanisms.

Absorption spectroscopy with full spectrum least squares data analysis has been developed and used for this purpose. This technique, applied to the UV/visible spectral region, has been used to obtain temperature and NO and OH concentration profiles through the dark zones and luminous flame zones of single-base, double-base, and nitramine propellants [2–6]. Many of the major dark zone species (CO, CO_2, N_2O, H_2O, HCN, CH_4) have no easily accessible transitions in the UV/visible region of the spectrum, thus, absorption spectroscopy in the infrared region has been recently investigated. Two full-spectrum, in situ techniques have been reported: an FTIR method [7] and a multichannel method [8,9]. Here, in addition to experimental improvements, a larger set of species concentrations have been determined by using the HITRAN database [10] as input into a program for data analysis.

Experimental

The absorption experiment and windowed pressure chamber have been described previously [2,3,6,8,9], thus, only pertinent improvements will be discussed here. A sketch of the experiment is shown in Fig. 1. The primary light source was a 250-W quartz-tungsten-halogen lamp. At wavenumbers

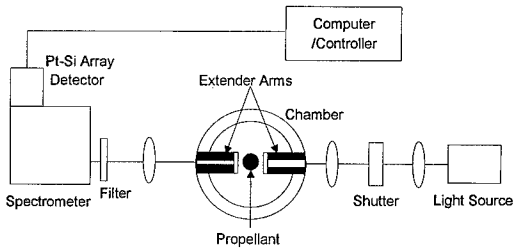

FIG. 1. Sketch of experimental setup. The windowed pressure chamber is shown in cross section to display the minimal chamber path length obtained with added extender arms.

less than 3300 cm^{-1}, a silicon carbide Globar provided greater intensity and was employed for some experiments. CaF_2 lenses directed light through the chamber and focused it onto the entrance slit of a 0.32-m spectrometer containing a 75-groove/mm grating blazed at 2500 cm^{-1}. A liquid nitrogen–cooled focal plane array detector (Princeton Instruments) composed of 1024 platinum-silicide (Pt-Si) elements in a linear configuration was used to detect the dispersed light. When operated in first order, the system has a total spectral window of about 1100 cm^{-1} when centered on 3000 cm^{-1} with a spectral resolution of about 6 cm^{-1} using a 125-μm entrance slit. Spectral calibrations were performed using a low-pressure argon lamp. This array detector is sensitive from about 2250 to 11,000 cm^{-1}, and when used with the Princeton Instruments ST-120 controller, a scan rate of 10 μs/diode (i.e., 10.24 ms is needed to read out the entire diode array) is obtained with a dynamic range of 14 bits.

An IR longpass filter was used between the sample chamber and spectrometer to remove any higher-order light, as well as visible radiation emanating from the burning propellant. Radiation emitted from the flame is more of a problem in the IR region than in the UV region, and a fast shutter with a minimum opening time of 1.8 ms (Vincent Associates Model LS6) was placed between the light source and the chamber. Thus, a spectrum consisting of the background, the dark charge, and any emission from the sample was available for subtraction from the spectrum of the transmitted light. In order to compensate for the finite time required by the shutter to open or close, the frequency of the shutter was set to one-fourth of the frequency of a master clock controlling the readout of the diode array. This allows every other spectrum to be acquired while the shutter is either fully opened or fully closed. The time to acquire one data pair (two spectra) is 42 ms when signal averaging is required, or 32 ms for a single-shot experiment. The ability to acquire both IR absorption and emission spectra sequentially at a fast acquisition rate and with low noise provides advantages over other diagnostic techniques applied to solid propellant flames.

Although the space surrounding the cylindrical propellant sample is purged with flowing nitrogen [3], combustion products may still migrate into this region. Concentrations of these products were minimized by reducing the path length to about 0.4 cm larger than the propellant sample diameter. This was accomplished by extender arms terminated with sapphire windows. When possible, propellant samples with a larger diameter were used (1.08 cm vs. 0.64 cm) to increase the ratio of the sample length to the total path length. The overall spatial resolution of 0.25 cm was set by the inside diameter of the extender arm on the spectrometer side. Spectra obtained in this study were acquired in the dark zone at an average height of 0.15 cm directly above the propellant burning surface.

Data Analysis

The governing equations for absorption have been discussed previously [2,3] and are based on the differential absorption law where $I(\nu)$, the transmitted intensity of light at frequency ν, is attenuated along a path of length l according to

$$I(\nu) = I_0 \exp[-k_\nu l]$$

If a background absorption occurs over the path-length and is only weakly dependent on ν, then

$$I(\nu) = I_0 B(\nu) \exp[-k_\nu \nu l]$$

where I_0 is the incident light intensity, k_ν is the absorption coefficient for the molecule of interest, and $B(\nu)$ is the baseline correction factor for any broadband attenuation along the path length. For conditions where the light source and spectrometer bandwidths are much larger than the width of the absorption line, an instrument function, $S(\nu, \nu_0)$, centered at ν_0, is introduced to give

$$I_t = \int S(\nu, \nu_0) I(\nu) d\nu$$

where I_t is the integrated light transmitted.

A nonlinear, multivariate, least-squares-fitting-program using a Simplex algorithm [11] has been written for use within the Galactic Industries' GRAMS/386 environment. Molecular parameters and transition line strengths needed for the calculation of k_ν are obtained from the HITRAN [10,12] database. The linewidths for the instrument function were obtained from a low-pressure argon lamp whose shape was well approximated by a Gaussian function.

The data analysis procedure has been tested previously [13] by fitting experimental spectra obtained from a pressure- and temperature-controlled test cell. These results showed temperature and concentration agreement to 2% and 6%, respectively.

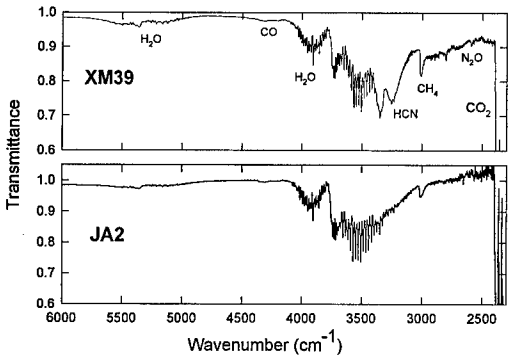

FIG. 2. Transmittance spectra taken in the dark zones of XM39 and JA2 propellants undergoing self-sustained combustion in 1.0 MPa nitrogen. The wavenumber range for the detection system at one spectrometer setting was such that it was necessary to piece four spectra together to provide this coverage.

Results

The transmission spectra of XM39 and JA2 propellants taken in the dark zone region during steady-state combustion conditions in 1 MPa nitrogen are shown in Fig. 2. Major ingredients for XM39 propellant are (by weight percent): cyclotrimethylenetrinitramine, 76%; cellulose acetate butyrate, 12%; acetyl-triethyl-citrate, 7.6%; and nitrocellulose, 4% (12.6% nitration). Major ingredients for JA2 propellant are (by weight percent): nitrocellulose, 58.2% (13.04% nitration); nitroglycerin, 15.8%; and diethyleneglycoldinitrate, 25.2%. Six species labeled on the XM39 spectrum have been identified as exhibiting absorption over this region. Prominent absorptions for H_2O are found in the 4000- to 3200-cm^{-1} region and can be assigned to the ν_1 (3657 cm^{-1}) and ν_3 (3756 cm^{-1}) fundamental vibrational bands. A combination band, $\nu_2 + \nu_3$ (5332 cm^{-1}) for H_2O has smaller absorption features in the 5600- to 4800-cm^{-1} region. The largest absorption observed starts around 2350 cm^{-1} and is the asymmetric stretch of CO_2. Other readily identifiable absorption features are the fundamental CH stretch of CH_4 at 3020 cm^{-1} and the fundamental CH asymmetric stretch of HCN at 3311 cm^{-1}. Two overtone bands at 4292 cm^{-1} and 2563 cm^{-1} are identified as CO and N_2O, respectively. When comparing the spectra of XM39 with JA2, the absence of HCN in the JA2 spectrum is apparent. Looking at the data in more detail, there is no identifiable N_2O absorption for JA2, and the broader shape of the CH_4 absorption indicates the JA2 spectrum is hotter. Each of these features for the six species has been examined more closely by least-squares fitting to extract temperature and concentration information. Fitting of the CO and N_2O overtone spectra has been discussed in detail previously [13] and, thus, only the results are reported in Table 1.

Least-squares fits of H_2O structure in the fundamental and combination band regions for XM39 propellant burning in 1 MPa nitrogen are shown in Figs. 3 and 4, respectively. The amount of absorption and thus the signal-to-noise ratio is greater for the fundamental absorptions shown in Fig. 3. Fits are represented by solid or dashed lines while the data are represented by points. Two different experiments (propellant burns) were required to obtain the data of Figs. 3 and 4; in addition, another pair of experiments was performed for XM39. The temperatures and H_2O concentrations obtained from these four experiments were averaged and these values are reported in Table 1. In all cases, the averaged values are reported in Table 1 and thus may differ slightly from the fitted value given in the figure caption. Figure 5 illustrates a least-squares fit for CO_2 in the combustion of XM39. This is the end of the

TABLE 1
Major dark zone species concentrations and temperatures obtained from least-squares-fitting IR transmittance spectra of XM39 and JA2 propellants undergoing self-sustained combustion in 1.0 MPa nitrogen

	XM39		JA2	
Species	Mole fraction	T (K)	Mole fraction	T (K)
CO	0.13	[a]	0.38	1448
N_2O	≤0.02	[a]	n.a.[b]	n.a.[b]
H_2O	0.15	1217	0.23	1418
CO_2	0.045	[a]	0.11	[c]
HCN	0.13	1153	n.a.[b]	n.a.[b]
CH_4	~0.005	[a]	~0.005	[c]

[a]Temperature fixed to 1150 K.
[b]No absorption feature observed.
[c]Temperature fixed to 1450 K.

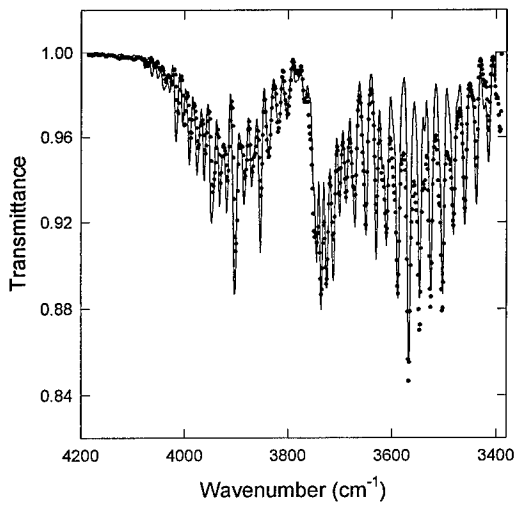

FIG. 3. Transmittance spectrum of the ν_1 and ν_3 stretches of water. Spectrum taken in the dark zone of XM39 burning in 1.0 MPa nitrogen. Best fit gives a temperature of 1204 K and a 0.12 mole fraction water.

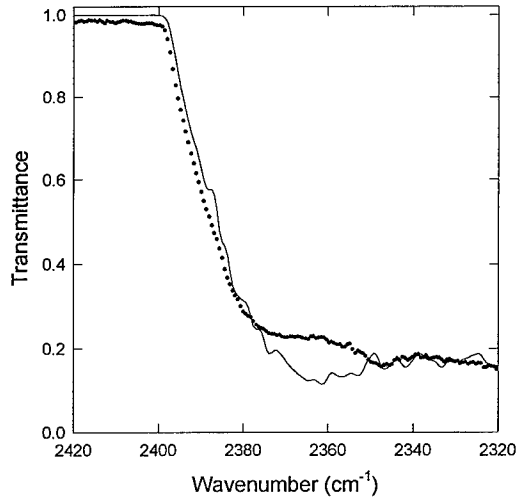

FIG. 5. Transmittance spectrum of the ν_3 stretch of CO_2. Spectrum taken in the dark zone of XM39 burning in 1.0 MPa nitrogen. The temperature was held fixed at 1150 K and the best fit gives a 0.04 mole fraction CO_2.

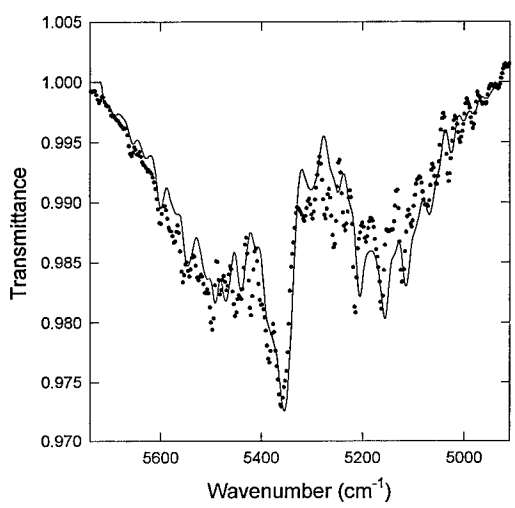

FIG. 4. Transmittance spectrum of the $\nu_2 + \nu_3$ combination band of water. Spectrum taken in the dark zone of XM39 burning in 1.0 MPa nitrogen. Best fit gives a temperature of 1204 K and 0.17 mole fraction water.

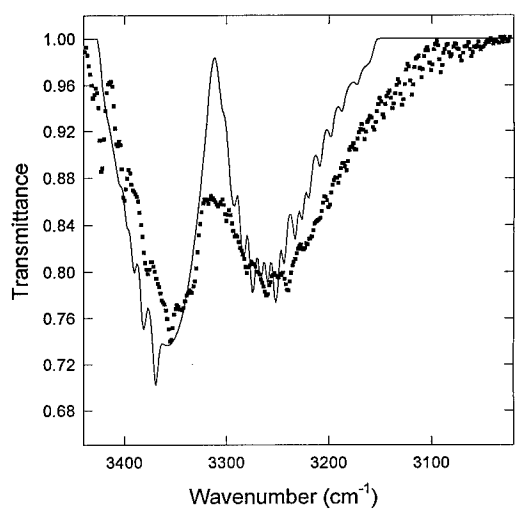

FIG. 6. Transmittance spectrum of the ν_3 stretch of HCN. Spectrum taken in the dark zone of XM39 burning in 1.0 MPa nitrogen Best fit to the data gives a temperature of 1173 K and 0.14 mole fraction HCN.

sensitivity range for the Pt-Si array detector, and when combined with the absence of detailed features, it is difficult to reliably fit for both concentration and temperature. Thus, the temperature was fixed to 1150 K and the only fitting variable was concentration.

A substantial absorption for HCN is observed in the dark zone of XM39, and Fig. 6 displays a least-squares fit for steady-state combustion at 1.0 MPa nitrogen pressure. The fit to the data deviates the most around 3310 cm^{-1}, showing a much more pronounced separation of the P and R branches. Additionally, significant deviation appears in the 3100- to 3200-cm^{-1} region. Recently, it has been reported [7] that a significant amount (3–4%) of C_2H_2 is present in the dark zone of this propellant flame. Acetylene

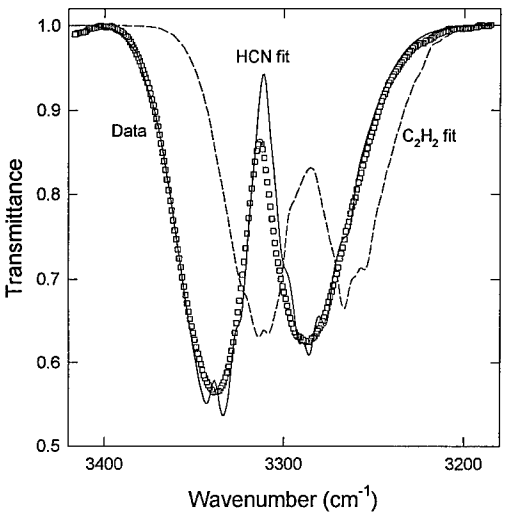

FIG. 7. Transmittance spectrum of the ν_3 stretch of HCN in windowed chamber after flame extinguishment. The open squares are the data, the solid line a least-squares fit, assuming the species is HCN, and the dashed line assuming the species is C_2H_2. Assuming the spectrum is HCN, the fitted temperature is 314 K.

does have absorption features in this wavelength range, so C_2H_2 contributions could be present in the data shown on Fig. 6, and/or the HITRAN database for HCN is not accounting for all of the high-temperature effects. Evidence suggesting that the absorption features displayed in Fig. 6 are predominantly HCN is concluded from the results shown in Fig. 7. The data of Fig. 7 come from the transmittance obtained after the XM39 propellant has been consumed, but prior to the chamber being completely purged by the flowing nitrogen gas. Both HCN and C_2H_2 should remain in the gas phase at close to room temperature while gas-phase H_2O absorptions disappear because of condensation. A least-squares fit to the data, assuming the species is HCN, is shown as a solid line. The dashed line represents a fit assuming the species is C_2H_2. Clearly, the HCN fit follows the experimental data much more closely than the C_2H_2 fit. The HCN fit gives a quite reasonable value of 314 K for temperature. A meaningful concentration value is not available since, in this case, the path between the chamber windows is occupied with a nonuniform mixture of gases.

While least-squares fitting the CH_4 absorption feature at room temperature resulted in excellent fits, when applied to the dark zone spectra of XM39 and JA2, some of the high temperature effects in the Q branch could not be well represented. Consequently, concentration values for CH_4 given in Table 1 contain larger uncertainty, estimated as a factor of 2.

Discussion

Table 1 contains the present results which indicate that the determined dark zone temperatures of XM39 and JA2 are consistent and agree well with previous work [3,6], where the dark zone temperature was determined from fitting NO ultraviolet absorption spectra, giving temperatures of 1150 K for XM39 burning in 1.2 MPa nitrogen, and 1450 K for JA2 burning in 1.6 MPa nitrogen. The pressure dependence of the dark zone temperature is small, decreasing slightly with decreasing pressure. Although the dark zone is a steady-state region where temperatures and concentrations are not a strong function of spatial position or pressure, the situation is far from equilibrium. Thermochemical equilibrium codes cannot be expected to predict species and concentrations in this region, and so experimental measurements are needed to determine this information. Table 1 contains concentration information for five major dark zone species. A substantial amount of HCN fuel has been identified in the dark zone of the nitramine propellant as well as evidence for the presence of a small amount of N_2O oxidizer. Accurate values for these species are very important to detailed chemical modeling of the major reaction paths that lead to the establishment of the final flame.

Table 2 has been constructed in order to place the present data in context with published work. Mallory and Thynell [7] investigated the dark zone of XM39 under the conditions of self-sustained combustion, and their results are included. Reasonable agreement is observed for CO, CO_2, N_2O, CH_4, and temperature. Differences occur for HCN and H_2O. As discussed previously, we believe that the spectral absorptions in the 3300-cm^{-1} region are predominantly from HCN. Mass spectrometric sampling studies of XM39, under conditions of laser-assisted combustion and 0.1 MPa pressure, report HCN mole fractions of about 0.2 [14]. These same studies also report H_2O mole fractions of about 0.2.

Lengelle et al. [15] have obtained dark zone concentrations from a double base propellant [18] (DB) under self-sustained combustion conditions. Major ingredients for DB propellant are (by weight percent): nitrocellulose, 52% (11.6% nitration); and nitroglycerin, 43%. The reported gas composition was renormalized to include 0.2 mole fraction H_2O. This propellant has energy content similar to JA2 and these results are given in Table 2 for comparison. Good agreement is observed for CO, CO_2, and temperature. No comparison can be made for water since the experimental technique of Ref. 15 does not detect this species. Differences are observed for CH_4, and these may be due, in part, to differences in the propellant composition.

Uncertainties in the reported data are estimated in the following fashion. It is assumed that no large

TABLE 2
Comparison of dark zone species and temperatures with published results for self-sustained combustion conditions[a]

Parameters	XM39[b]	XM39[c]	JA2[b]	DB[d]
P (MPa)	1.0	2.2	1.0	0.9
Ht (cm)	0.15	0.10	0.15	0.2
T (K)	1185	1125	1433	1500
CO	0.13	0.10	0.38	0.38
N_2O	≤0.02	0.03	n.a.[e]	—
H_2O	0.15	0.09	0.23	—
CO_2	0.04	0.04	0.11	0.09
HCN	0.13	0.04	n.a.[e]	—
CH_4	~0.005	0.004	~0.005	0.03

[a]Concentrations in mole fraction.
[b]Present data.
[c]Data of Mallory and Thynell [7].
[d]Data of Lengelle et al. [17].
[e]No absorption feature observed.

systematic error is present in either the determination of path length or in the molecular database used to least squares fit the experimental absorption spectra. The largest variations come from the run-to-run repeatability of the experiment and include changes in the flatness of the burning surface and combustion intensity. Run-to-run variations in the concentration are in the ±20% range, except for CH_4, and about ±5% for the temperature.

Summary

A nonintrusive optical absorption technique has been developed and applied to the extremely hostile environment of self-sustained solid propellant combustion. Quantitative data for species concentrations and temperature have been obtained in the dark zone of two classes of solid propellants by a least-squares analysis of multifeatured spectra.

Acknowledgment

This work was made possible by funding from the Army Capital Investment Program.

REFERENCES

1. Kubota, N., *Eighteenth Symposium (International) on Combustion,* The Combustion Institute, Pittsburgh, 1980, pp. 187–194.
2. Vanderhoff, J. A. and Kotlar, A. J., *Twenty-Third Symposium (International) on Combustion,* The Combustion Institute, Pittsburgh, 1990, pp. 1339–1344.
3. Vanderhoff, J. A., Teague, M. W., and Kotlar, A. J., *Twenty-Fourth Symposium (International) on Combustion,* The Combustion Institute, Pittsburgh, 1992, pp. 1915–1922.
4. Hanson-Parr, D. and Parr, T., *Twenty-Eighth JANNAF Combustion Meeting,* CPIA Publ. No. 573, II, 1991, pp. 369–378.
5. Lu, Y. C., Freyman, T. M., Kuo, K. K., *Combust. Sci. Technol.* 104:193 (1995).
6. Teague, M. W., Singh, G., and Vanderhoff, J. A., "Spectral Studies of Solid Propellant Combustion IV: Absorption and Burn Rate Results for M43, XM39 and M10 Propellants," Army Research Laboratory Technical Report, Aberdeen Proving Ground, MD, ARL-TR-180, 1993.
7. Mallory, C. F. and Thynell, S. T., "Further Improvements to FTIR Absorption Spectroscopy of Propellant Flames for Profiling of Species and Temperature", *32nd JANNAF Combustion Meeting,* CPIA Publ. No. 631, I, 1995, pp. 449–460.
8. Modiano, S. H. and Vanderhoff, J. A., *Combust. Flame* 99:187–189 (1994).
9. Modiano, S. H. and Vanderhoff, J. A., "Multichannel Infrared Absorption Spectroscopy Applied to Solid Propellant Flames," ARL-TR-900, 1995.
10. Rothman, L. S., Gamache, R. R., Tipping, R. H., Rinsland, C. P., Smith, M. A., Benner, D. C., Malathy Devi, V., Flaud, J. M., Brown, L. R., and Toth, R. A., *J. Quant. Spectrosc. Radiat. Transfer* 48(5/6): 469 (1992).
11. Daniels, R. W., *An Introduction to Numerical Methods and Optimization Techniques,* North Holland Publ., Amsterdam, 1978.
12. An updated HITRAN database was obtained for the CO molecule. This database was developed to be able to better represent higher temperature conditions. HITRAN 1992 was used for the other molecules.
13. Modiano, S. H. and Vanderhoff, J. A., "Multichannel

IR Spectroscopy of Solid Propellant Flames: CO and N_2O Concentration Measurements", 32nd JANNAF Combustion Meeting, CPIA Publ. No. 631, I, 1995, pp. 439–447.

14. Tang, C., Lee, Y., and Litzinger, T. A., *31st JANNAF Combustion Meeting*, CPIA Publ. No. 620, II, 1994, p. 307.
15. Lengelle, G., Bizot, A., Duterque, J., and Trubert, J. F., "Steady State Burning of Homogeneous Propellants," in *Fundamentals of Solid Propellant Combustion,* (K. Kuo and M. Sommerfield, Eds.), AIAA Progress in Astronautics and Aeronautics Series, Vol. 90, American Institute of Aeronautics and Astronautics, Inc., New York, 1984.

Twenty-Sixth Symposium (International) on Combustion/The Combustion Institute, 1996/pp. 2025–2031

LASER RECOIL COMBUSTION RESPONSE OF N5 PROPELLANT FROM 1 TO 9 ATMOSPHERES

JERRY C. FINLINSON
Naval Air Warfare Center Weapons Division
Research Code 474320D
China Lake, CA 93555, USA

The combustion response of N5-catalyzed double-base propellant was experimentally measured at 1, 2, 3, 4, 6, and 9 atm using the laser recoil technique. Tests were done using a logarithmic frequency sweep controller to gain maximum data from each test. Sample burn rate at a mean heat flux of 35 W/cm^2 and 1 atm was 1.3 mm/s. The CO_2 laser power was monitored in real time using a fast response HgCdTe room temperature detector. The effects of pressure (1–9 atm) and oscillation amplitude ($\pm$9, 15, and 25 W/cm^2) on the response function were measured. Steady-state burn rate data at low pressure was measured.

The slight pressure rise inside the combustion tank caused an upward drift in the force transducer signal. Light oscillations generally changed from lead to a lag of over 100 degrees as frequency changed from 10 to 50 Hz. At a constant pressure, thrust oscillation levels increased as the laser power oscillation level was increased. The cross from phase lead to lag seemed to decrease in frequency as the power oscillation amplitude increased. At constant pressure, the light amplitude response broadened as the power oscillation amplitude increased and the phase crossover moved to a slightly lower frequency. Thrust oscillation amplitudes decreased as the pressure increased to 75 psi, above which they became insignificant at these low heat flux levels. Thrust phase lead increased as the pressure was increased. Light oscillations increased as the pressure increased, due to the flame zone moving closer to the propellant surface.

Introduction

The purpose of this work is to increase our understanding of mechanisms affecting combustion resonance which cause combustion oscillations in solid propellant rocket motors. Using the laser recoil technique allows us to measure the influence of heat feedback on the combustion response. Experimental measurements using the laser recoil technique were done on N5 propellant at atmospheric and elevated pressures. N5 is a readily available, catalyzed, double-base propellant, which is well characterized and exhibits a large combustion response. The specific objective of this paper was to determine the laser recoil response of N5 as a function of flux oscillation amplitude ($\pm$9, 15, and 25 W/cm^2) and pressure (1–9 atm). Understanding the effect of pressure assists in relating the results to pressure-coupled combustion oscillations, which is what occurs in a real rocket motor.

The laser recoil technique with an oscillating radiant heat flux has been used by several experimenters [1–13]. Since the propellant burn rate and thrust respond to laser radiation, sinusoidal modulation of the CO_2 laser power results in sinusoidal thrust oscillations which are measured by a force transducer. Laser recoil has the advantage of requiring smaller sample sizes than T-burner, which is important for new ingredients that are very expensive and difficult to obtain. However, instead of measuring the pressure-coupled combustion response, the device measures the radiant heat flux response. Collaboration with Brewster and Son at the University of Illinois is furthering our theoretical understanding by allowing us to compare data from previously developed flame models [1–4,10,11]. A transfer function between the heat flux response, R_q, and the more useful pressure response, R_p, has been developed and is being verified.

Apparatus

A schematic of the laser and data acquisition equipment is shown in Fig. 1. Tests were done using the 114-L surge tank filled with nitrogen. The recirculation fan pulls smoke away from the mirrors during tests. Combusting an N5 sample with a diameter of 12.5 cm, thickness of 2.04 mm, and a mass of 0.4 g resulted in a pressure increase of 0.3 psi. A Melles Griot 240-W continuous CO_2 laser was modulated sinusoidally by a function generator that controlled the modulation frequency (10–100 Hz) and amplitude (35 $\pm$ 9, 15, and 25 W/cm^2) of the heat flux oscillations. SPAWR beam integration was used to spread the laser beam energy distribution into a flat profile. A HgCdTe fast-response room temperature IR detector (BSA PEM-L-3 with 481-1 preamp) was

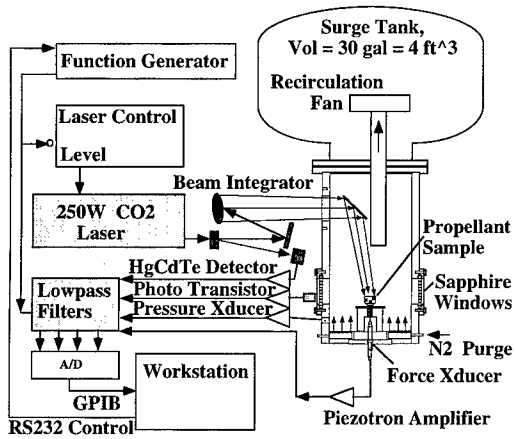

FIG. 1. Schematic of the laser and data acquisition system on the laser recoil apparatus.

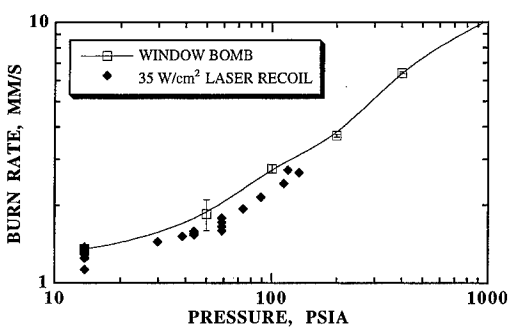

FIG. 2. N5 burn rate as a function of pressure for strand burn rate data compared to 35 W/cm^2 laser augmented data.

installed with a GENTEC holographic beam sampler to monitor the laser power on-line. This corrects for laser response amplitude and phase lag by allowing the actual laser power waveform to be compared to the pressure and light oscillations. Light emission from the flame was monitored by a photosensor with no filter. The NRC Model 815 photosensor has a spectral response of 350–1100 nm. The light emission signal was lowpass filtered at the same settings as the laser power signal and force transducer. Data was sampled at least 50 times per cycle to allow for at least 7-degree resolution on the phase cross correlation. The rms amplitude and phase relation of the imposed heat flux and the propellant thrust signal were determined using digital cross correlation.

The laser was operated at an average power of 160 W. The optical train that absorbed and reflected about half the power included 8 mirrors, a zinc selenide lens, a window, and a holographic sampler. Power measured at the target area was 87 W over a 2.25-cm^2 area or 39 W/cm^2. Additional energy losses arose from soot particle scattering and CO_2 gas absorption in the flame. Estimation of exhaust plume transmission of 0.90 yielded 35 W/cm^2 at the sample [8,11,12].

To increase the amount of data obtained from each laser recoil test, tests were done using a logarithmic frequency sweep controller. The laser power oscillation frequency was varied logarithmically from 5 to 100 Hz during a test to allow the entire response function to be generated from one test. The log-sweep data has been compared against single frequency sine tests and found to agree within 15%. Frequency sweep was especially valuable for pressurized tests which are more time consuming.

Preparation for each test involved calibrating the power, fastening the sample to the aluminum sample holder with silicon grease and placing it on the pedestal inside the combustion bomb, bolting the window, purging and pressurizing with nitrogen, and adjusting the laser control signal sweep time and amplitude, the lowpass filters, and the A/D sampling rate. A timing control restarted the log sweep when the test trigger was fired.

Experimental Results

Figure 2 is a plot of the mean burn rate as a function of pressure for data measured in the window strand burner by coworker Curran with no irradiation and in the laser recoil experiments under laser irradiation of 35 W/cm^2. The laser flux data had a lower burn rate than the window burner data, which was unexpected. The laser flux added extra energy and should have increased the rate. The difference is likely due to differences in technique. We plan to measure the nonirradiation burn rate in the same combustion device for accurate comparison at different test pressures. N5 with no irradiation exhibits a plateau at a burn rate of 11 mm/s and 1000 psi. Steve Son's data shows a burn rate mesa at 5 mm/s and atmospheric pressure under heat fluxes of 100–300 W/cm^2 [4]. This heat flux of 35 W/cm^2 is below the plateau.

Laser recoil tests on N5 propellant were done at atmospheric pressure and 30, 45, 60, 75, 90, 100, and 120 psig using sinusoidal heat flux oscillations from 20 to 50 W/cm^2. Figure 3 is a plot of the chamber pressure, force transducer, and light emission signals with a log-sweep of 2–90 Hz at atmospheric pressure (13.7 psi). The tank was closed and pressure increased 0.3 psi during the test, while the thrust signal showed maximum oscillation amplitude at 40 Hz. Unfortunately, the pressure increase affected the force transducer, making it difficult to measure the average thrust for pressurized tests. Figure 4 is a plot of the laser power detector, force transducer, and light emission signals during a test with a log-sweep of 10–100 Hz at 44 psia. Light

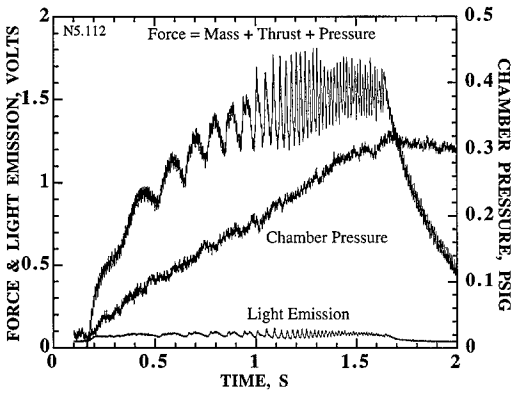

FIG. 3. N5.112 closed volume test record for N5 propellant using 2–90 Hz log-sweep under CO_2 laser radiation of 34 ± 15 W/cm^2 at 13.7 psia, showing force, pressure rise, and light emission signals. Pressure increased 0.3 psi.

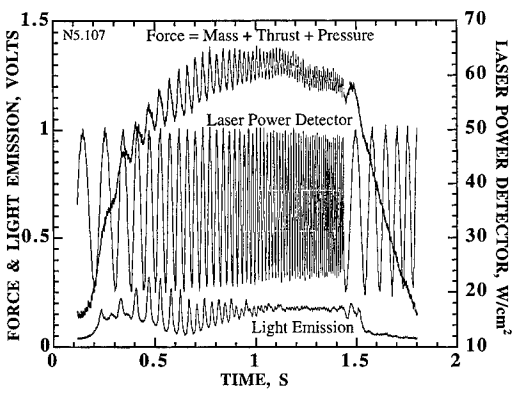

FIG. 4. N5.107 baseline test record for N5 propellant using log-sweep technique under CO_2 laser radiation of 35 ± 15 W/cm^2 at 44 psia, showing force, laser power detector, and light emission signals.

oscillation levels increased by a factor of 4 compared to Fig. 3 at 13.7 psia. Thrust oscillation levels decreased by a factor of 3. Both thrust and light emission show a peak near 25 Hz, and light oscillations were very small above 50 Hz. Useful calibration values are 3.5 V/Vrms (from cross correlation) and 1.86 g/Vrms.

Experimental Analysis

For the log-sweep data, the cross correlation was performed one cycle at a time and a new frequency computed for each cycle, then amplitude and phase was determined. An amplitude plot shows the rms amplitude of the thrust or light emission as a function of frequency. Phase lead was determined by comparing the thrust or light signal to the normal-

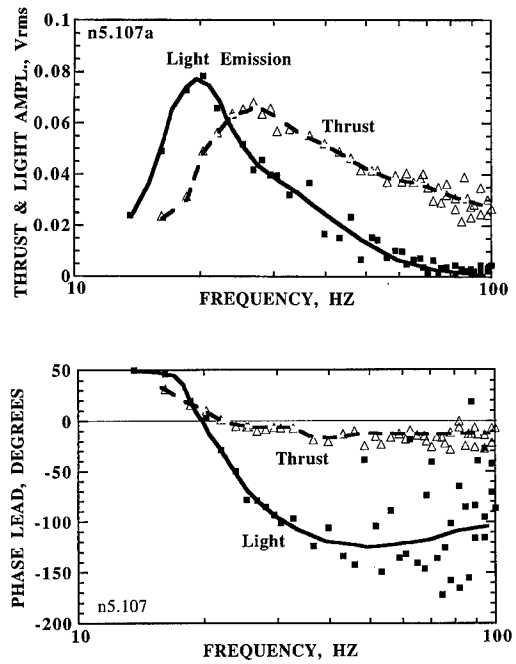

FIG. 5. a., Comparison of thrust and light rms amplitude for N5 propellant using log-sweep technique under CO_2 laser radiation of 35 ± 15 W/cm^2 at 44 psia. Amplitude cross-correlation results for test N5.107. b., Comparison of thrust and light phase lead for N5 propellant using log-sweep technique under CO_2 laser radiation of 35 ± 15 W/cm^2 at 44 psia. Phase cross-correlation results for test N5.107.

ized laser detector signal. Data in Fig. 4 at 44 psia and a flux of 35 ± 15 W/cm^2 was analyzed and the results are shown in Fig. 5a, b. Figure 5a is a plot of the rms amplitude of the light and thrust signals compared against the laser detector signal. The light peak occurred at a lower frequency, 20 Hz, and dropped to very low levels at 100 Hz. It was surprising that relatively high amplitude thrust oscillations from 70 to 100 Hz were not accompanied by oscillations in light emission. Figure 5b is a plot of the phase lead of the light and thrust signals compared against the laser detector signal. The light phase led 50 degrees at low frequency and changed to a lag of 130 degrees at frequencies above 40 Hz. As the signal level dropped for frequencies above 60 Hz, the scatter of the phase correlation increased. The thrust signal led about 30 degrees at 13 Hz and lagged about 15 degrees above 30 Hz.

The effects of laser power oscillation amplitude on thrust and light oscillation response levels are shown in Figs. 6 and 7. The tests were done under 44 psia nitrogen atmosphere using log sweep from 10 to 100 Hz, a mean flux of 35 W/cm^2, with power oscillations of ±9, 15, and 25 W/cm^2. Figure 6a shows that the

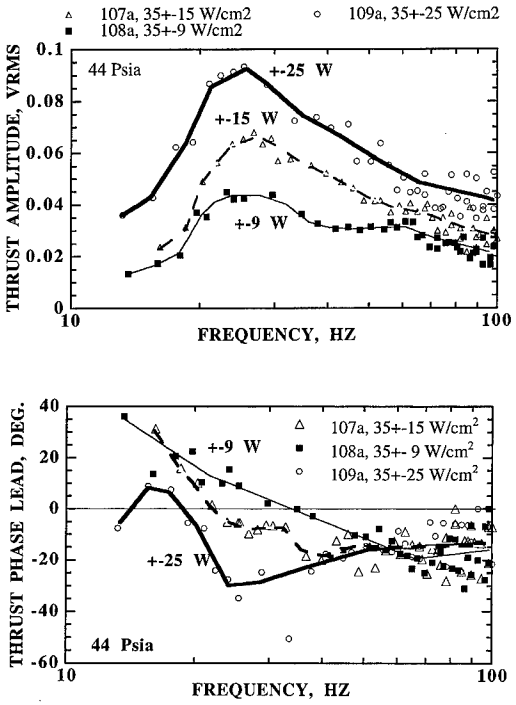

FIG. 6. a., Effect of laser power oscillation on thrust amplitude. Comparison of thrust oscillation amplitudes for N5 propellant using log-sweep technique under CO_2 laser radiation of 35 W/cm^2 ± 9, 15, and 25 W/cm^2 at pressure 44 psia. b., Effect of laser power oscillation on thrust phase lead. Comparison of thrust oscillation phase lead for N5 propellant using log-sweep technique under CO_2 laser radiation of 44 W/cm^2 ± 9, 15, and 25 W/cm^2 at pressures 44 psia.

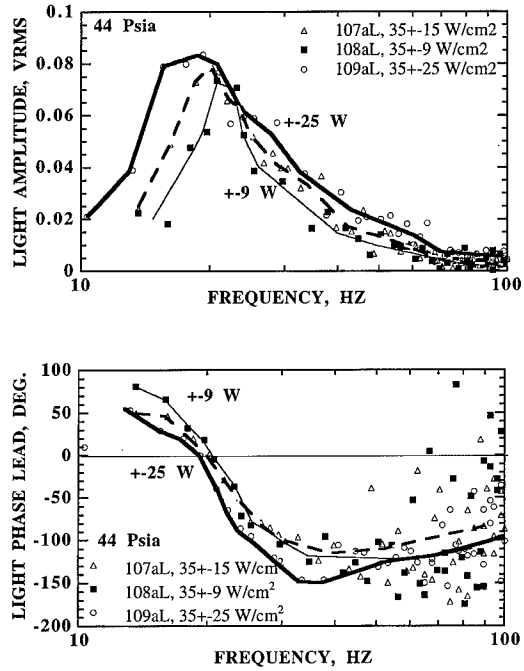

FIG. 7. a., Effect of laser power oscillation on light amplitude. Comparison of light oscillation amplitudes for N5 propellant using log-sweep technique under CO_2 laser radiation of 35 W/cm^2 ± 9, 15, and 25 W/cm^2 at pressure 44 psia. b., Effect of laser power oscillation on light phase lead. Comparison of light oscillation phase lead for N5 propellant using log-sweep technique under CO_2 laser radiation of 35 W/cm^2 ± 9, 15, and 25 W/cm^2 at pressures 44 psia.

response amplitude increased as the laser oscillation amplitude increased. In Fig. 6b, the phase crossed from lead to lag at about 32 Hz for the 9-W/cm^2 oscillation and crossed at 18 Hz for the 25-W/cm^2 oscillation. In Fig. 6a, the peaks appeared at the same frequency, so we expected the phase cross over to occur at the same frequency, but they did not. It is unknown why the frequency of crossing from lead to lag should decrease as the amplitude increased. Figure 7 shows the corresponding light response peaks at 44 psia. In Fig. 7a, the light response peak near 20 Hz broadened as the oscillation amplitude increased. However, the peak amplitude increased only slightly. Figure 7b shows the phase crossing from lead to lag at about 20 Hz and decreasing slightly in frequency as the power level increased. The light emission levels were less affected by power level than was the thrust.

The effects of pressure on thrust and light oscillations are shown in Figs. 8 and 9. Tests were done with mean flux of 35 W/cm^2 and oscillation levels of ± 15 W/cm^2, while the pressure was increased from 13.7 to 114 psia. Figure 8a is a plot of the thrust amplitude as a function of frequency and pressure. Notice two tests at 13.7 psia that demonstrate repeatability of within 10%. The thrust amplitude decreased by a factor of 8 as the pressure increased to 74 psia. Above 75 psia, the thrust oscillations became so small that they were difficult to separate from transducer noise. Flux oscillation power levels must be increased to produce significant oscillations at higher pressures. This was as expected, for we showed previously that increasing the mean flux with the same oscillation amplitude tended to decrease the response [10]. Zarko has shown that the response of catalyzed, double-base propellant decreases with pressure [8]. As pressure increased, the flame moved closer to the surface and caused the burn rate to increase. This is similar to adding additional mean flux with the laser.

Figure 8b shows the corresponding thrust phase versus pressure. Above 50 Hz, the phase lead increased from −40 degrees to a lead of 15 degrees

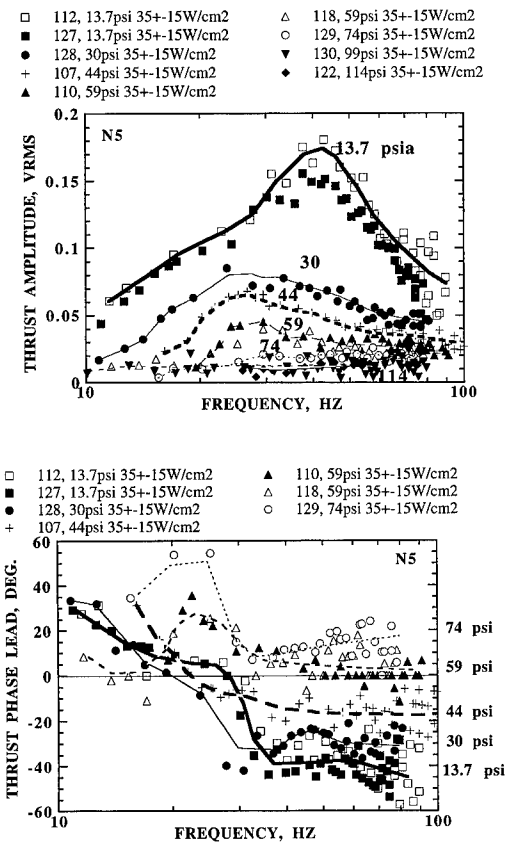

FIG. 8. a., Effect of pressure on thrust amplitude. Comparison of thrust oscillation amplitudes for N5 propellant using log-sweep technique under CO_2 laser radiation of 35 ± 15 W/cm^2 at pressures 13.7, 30, 44, 59, 74, 99, and 114 psia. b., Effect of pressure on thrust phase lead. Comparison of thrust phase lead for N5 propellant using log-sweep technique under CO_2 laser radiation of 35 ± 15 W/cm^2 at pressures 13.7, 30, 44, 59, and 74 psia.

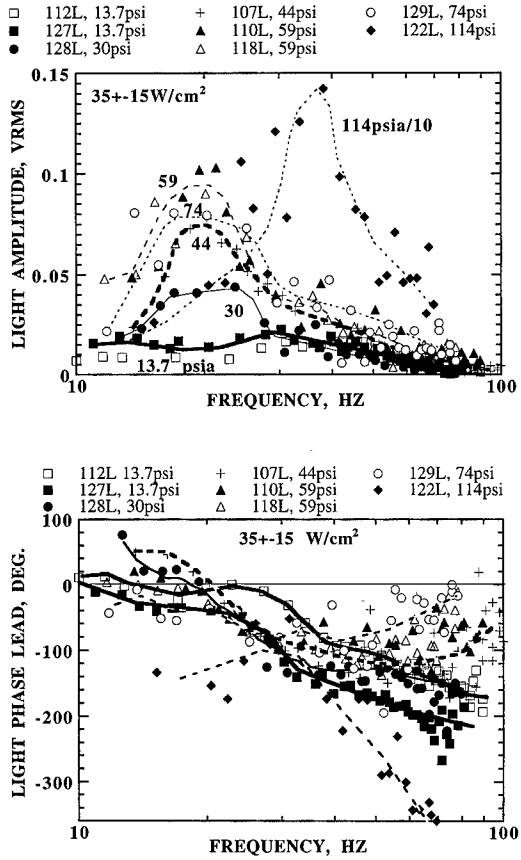

FIG. 9. a., Effect of pressure on light amplitude. Comparison of light oscillation amplitudes for N5 propellant using log-sweep technique under CO_2 laser radiation of 35 ± 15 W/cm^2 at pressures 13.7, 30, 44, 59, 74, 99, and 114 psia. b., Effect of pressure on light phase lead. Comparison of light phase lead for N5 propellant using log-sweep technique under CO_2 laser radiation of 35 ± 15 W/cm^2 at pressures 13.7, 30, 44, 59, and 74 psia.

as the pressure increased. It is unknown why the phase lead should increase as the pressure increased. Theoretically, the thrust response peak should move to a higher frequency as the burn rate increases. However, the peaks in the thrust do not show the response peak moving to a higher frequency as the pressure was increased in Fig. 8a. This effect must be further investigated. Figure 9a is a plot of the corresponding light amplitude oscillations as a function of frequency and pressure. Note that the signal level for 114 psia has been divided by 10 due to its large magnitude. The general trend was for the light signal level to increase as pressure increased. This is because the dark zone compresses and the flame moves closer to the surface and the field of view of the photodetector. Above 100 psia, the flame was in view of the photodetector and light oscillations were much larger, but with a significant phase lag since gases convect from the surface about 3/4 inch up to the flame zone. Figure 9b shows the corresponding phase plot. There are no general trends noticed except that phase generally changes over 100 degrees during the frequency change from 10 to 100 Hz.

Summary

Tests were done using the logarithmic frequency sweep technique at pressures from 1 to 9 atm. The slight pressure rise inside the combustion tank caused an upward drift in the force transducer signal. Light oscillations generally changed from a lead to a lag of over 100 degrees as frequency changed from 10 to 50 Hz. At constant pressure, thrust

oscillation levels increased as the laser power oscillation level increased. The cross from phase lead to lag seemed to decrease in frequency as the power oscillation amplitude increased. At constant pressure, the light amplitude response broadened as the power oscillation amplitude increased and the phase crossover moved to a slightly lower frequency. Thrust oscillation amplitudes decreased as the pressure increased to 75 psi, above which they became insignificant at these low heat flux levels. Thrust phase lead increased as the pressure was increased. Light oscillations increased as pressure increased due to the flame zone moving closer to the propellant surface.

From this, we know that to cause combustion oscillations at high pressures, large thermal oscillations are required. Continued research needs to be done on the mechanisms in a high pressure motor that cause these large thermal oscillations. The data presented here is valuable for understanding the role of heat feedback on combustion oscillations in solid propellants. It can be used to calibrate models for converting heat flux response to the more useful pressure response. This is part of an ongoing investigation of the combustion instability fundamentals of different propellants.

Acknowledgments

Thanks to Tim Parr and Donna Hanson-Parr for assistance with electronics, data acquisition, and laser detector. Thanks to Pat Curran for burn rate measurements, to Richard Stalnaker for machining, and to Ken Yu for assistance with video editing. I thank Dr. Richard Miller at ONR for funding this work.

REFERENCES

1. Brewster, M. Q. and Son, S. F., *Combust. Flame* 103:11–26 (1995).
2. Brewster, M. Q., Zebrowski, M. A., Schroeder, T. B., and Son, S. F., 31st AIAA/ASME/SAE/ASEE Joint Propulsion Conf., AIAA-95-2859, July 1995.
3. Brewster, M. Q., Hites, M. H., and Son, S. F., *Combust. Flame* 94:178–190 (1993).
4. Son, S. F., Ph.D. Thesis, University of Illinois at Urbana-Champaign, October, 1993.
5. Mihlfeith, C. M., Baer, A. D., and Ryan, N. W., *AIAA J.* 10(10):1280–1285 (1972).
6. Mikheev, V. F., Zarko, V. E., Borin, S. M., Kutsenogii, K. P., and Simonenko, V. N., AIAA 14th Aerospace Sciences Meeting, AIAA-76-102, Jan. 1976.
7. Zarko, V. E., Simonenko, V. N., and Kiskin, A. B., *Fiz. Goreniya Vzryva* 23(5):16–26 (1987).
8. Zarko, V. E., Simonenko, V. N., and Kiskin, A. B., in *Nonsteady Burning and Combustion Stability of Solid Propellants,* (L. De Luca, E. W. Price, and M. Summerfield, Eds.) Progress in Astronautics and Aeronautics, 1992, Vol. 143, pp. 363–398.
9. Finlinson, J. C., Parr, T., and Hanson-Parr, D., *Twenty-Fifth Symposium (International) on Combustion,* The *Combustion Institute, Pittsburgh,* 1994, pp. 1645–1650.
10. Finlinson, J. C., Hanson-Parr, D., Son, S. F., and Brewster, M. Q., 29th Aerospace Sciences Meeting, AIAA-91-0204, Jan. 1991.
11. Son, S. F., Burr, R. F., and Brewster, M. Q., 27th Joint Propulsion Conference, AIAA/SAE/ASME/ASEE, AIAA-91-2194, 24–26 June 1991.
12. Mikheev, V. F., Zhdanov, V. F., and Khlevnoi, S. S., *Fiz. Goreniya Vzryva* 7(2):257–260 (1971).
13. Summerfield, M., Caveny, L. H., Ohlemiller, T. J., and DeLuca, L., BRL Report 1707, April 1974.

COMMENTS

Merril K. King, NASA, USA. How do you plan to convert your data to pressure-coupled or velocity-coupled combustion response functions?

Author's Reply. We understand that the pressure- and velocity-coupled response functions are the most useful, because they are used in motor stability codes, such as SSP. The data we generate using the laser recoil technique is the heat-flux response and must be converted to pressure- and velocity-coupled response to be used in such codes.

An approximate conversion can be done using the radiation response function models developed by Prof. Brewster and Dr. Son and students at UIUC. However, they rely on assuming a simplified flame model and on knowing the optical properties, which have not been measured at combustion temperatures. So there is room for significant error there. Currently, our data attempts to get the same burn rate on the propellant sample as would be achieved by operating at high pressure. The ideal case is to operate at higher pressure and have as small laser power oscillations as necessary to get the linear response.

Since there is no information for pressure-coupled and laser-recoil data at the same pressure, we plan to extend the range of laser-recoil data to higher pressures. Experimentally, we will be doing laser-recoil tests at pressures up to 150 psi, so that we can observe the effect of mean pressure on the laser recoil response and so that we are closer in pressure to existing T-burner data. Most current T-burner data does not go below 1000 psi, but we could generate more data at lower pressures for comparison against the laser-recoil data. Horton's initial T-burner data was nearly all at 200 psi, because propellants oscillated so nicely at that pressure.

We also have scheduled in FY97 to perform T-burner tests on pure AP, HMX, RDX, ADN and other oxidizers, so that we will have their pure pressure-coupled responses. This will likely be done at lower pressures. These data will allow a better calibration of Beckstead's pure ingredient transient combustion models currently under development. It can also be used to verify the response function predictions based on temperature sensitivity.

Lastly, we are attempting to design an apparatus that would measure the thrust recoil caused by pressure oscillations. This is a very tricky problem, because the pressure oscillations will likely pick up on the force transducer. This would allow us to measure the pressure-coupled response directly with small sample sizes under similar conditions to the laser-recoil tests.

Twenty-Sixth Symposium (International) on Combustion/The Combustion Institute, 1996/pp. 2033–2040

CONVECTIVE IGNITION OF A GRANULAR SOLID PROPELLANT BED: INFLUENCE OF PROPELLANT COMPOSITION

DOUGLAS E. KOOKER, STEPHEN L. HOWARD AND LANG-MANN CHANG
U.S. Army Research Laboratory
Aberdeen Proving Ground, MD 21005-5066, USA

In previous work, the authors designed and built a laboratory apparatus that subjects a confined bed of granular propellant to essentially a planar hot-gas ignition wave. Diagnostics include wall-mounted pressure transducers to monitor the time history of the pressure field, and fast-response thermocouples protected within custom sting-mounted steel holders which protrude into the propellant bed to measure gas temperature. The present investigation examines convective ignition behavior of five different granular solid propellants under nearly identical flow conditions. This was made possible by employing special lots of M10 (single-base), JA2 (double-base), M30 (triple-base), M43, and XM39 (nitramine composites), each as identical-sized 7-perf grains. Since the initial flow characteristics of these propellant beds are the same, differences in chamber ignition response are the direct result of propellant composition. Ignition delays for M10, JA2, and M30 are essentially within the range of 2.3–6 ms; the response is independent of composition. However, the nitramine composite M43 (energetic binder) exhibits delays of 220–300 ms, during which the gas-phase temperatures within the bed drop from 1100 K to below 400 K before a runaway reaction finally ruptures the shear disc in the chamber. It is more difficult to ignite the nitramine composite XM39 (inert binder); time delays can exceed 600 ms. The data also suggest an inverse dependence on pressure, which is consistent with the hypothesis that gas-phase chemical reactions are controlling chamber response. When the chamber configuration is altered to promote a rapidly rising pressure field, ignition delays for both nitramine propellants are reduced to less than 1 ms.

Introduction

The convective ignition process in most solid propellant gun systems is dominated by a complicated three-dimensional flow field as the result of the combustion chamber geometry, a combination base-pad/centercore ignition system, protrusion of the projectile afterbody into the chamber, etc. When simple design changes unwittingly lead to an ignition process accompanied by excessive time delay [1], as can happen with nitramine composite solid propellants, it is virtually impossible to isolate and examine fundamental aspects of the ignition process. Unless eliminated, these delays in flamespreading can foster combustion chamber conditions that promote large amplitude pressure waves [2] and possible system failure. Diagnosing and correcting anomalous ignition behavior would benefit from additional insight into the fundamental process.

This investigation is a deliberate attempt to study convective ignition of granular solid propellant in a simplified flowfield. The ignition environment is created by a laboratory device that subjects the confined bed of granular propellant to essentially a planar hot-gas ignition wave. The objective is straightforward: monitor the differences in ignition behavior between single-base, double-base, triple-base, and nitramine composite solid propellants under nearly identical initial flowfield conditions and ignition stimulus. Five propellant compositions were chosen. The single-base is M10 (98% NC), the double-base is JA2 (58.2% NC, 15.8% NG, 25.2% DEGDN), the triple-base is M30 (28.7% NC, 22% NG, 47.3% NQ), and the two nitramine composites are XM39 (76% RDX, 12% CAB, 4% NC, 7.6% ATC) and M43 (76% RDX, 12% CAB, 4% NC, and energetic plasticizer). The nitramine composites are of interest from a vulnerability standpoint because they exhibit a higher threshold for thermal ignition, and once ignited, burn at slower rates at low pressure. However, both properties may create difficulties in the ignition sequence of a gun system. All five propellants (taken from the BRL Research Series) have identical geometry. Each grain is a right-circular cylinder with 7 perforations parallel to the longitudinal axis; nominal length is 15.2 mm, diameter is 7.62 mm, and diameter of each perforation is 0.762 mm. Thus, to the degree the igniter system can be held constant, each propellant bed will experience the same initial flowfield (convective heat transfer, gas/solid drag, etc.). Differences in chamber response will be directly traceable to propellant composition.

The last two decades have witnessed a number of experiments [3–10] devoted to exploring the behavior of convective ignition of solid propellant—both as single grains and compacted aggregates. A

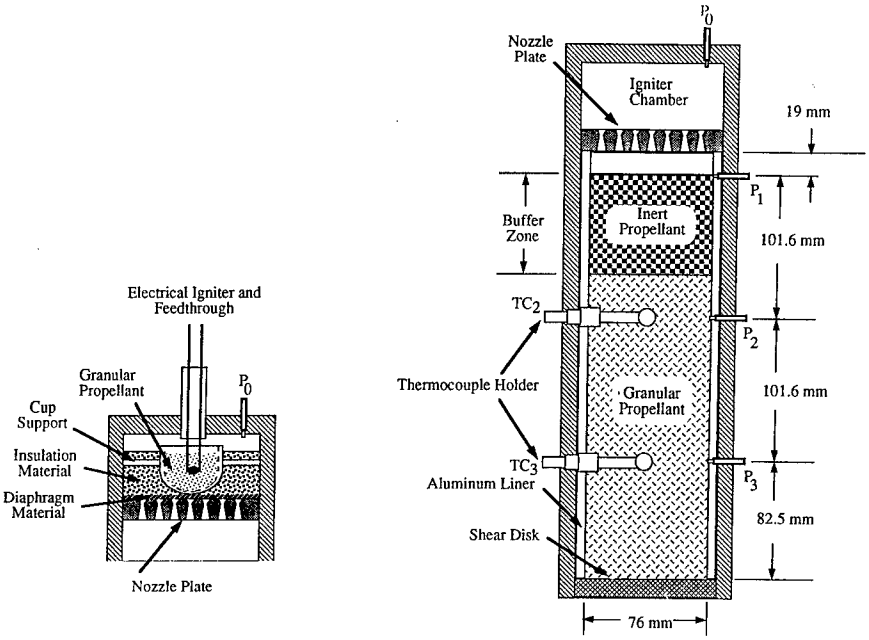

FIG. 1. Schematic of flamespreading chamber with igniter system detail.

discussion can be found in Refs. 11 and 12. A unique aspect of the present experiment is the attempt to vary only propellant composition. The experiment also combines several other potentially important features. The test chamber intentionally includes a closed volume (as opposed to a flow-through device) to simulate conditions in the gun combustion chamber, which will trap and retain all pyrolysis products from the solid propellant. The design attempts to provide an ignition stimulus composed of only gas-phase products, where the composition of the igniter gases could be altered. Although certain condensed-phase products are known to be effective ignition aids, they are difficult to describe in a theoretical model. The present experiment employs wall-mounted pressure transducers to monitor pressure time-history. Furthermore, gas temperature is monitored by fast-response thermocouples protected within custom sting-mounted steel holders which protrude into the propellant bed. Time-history of gas temperature may give important clues into the mechanism responsible for the anomalous ignition delay. Finally, to recreate the marginal ignition environment suggested by previous tank gun simulator experiments [1], the hot-gas igniter wave should have a rise time of 2–4 ms and maintain a chamber pressure level within the range 1–3 MPa.

Flamespreading Chamber Experiment

Figure 1 is a schematic of the dual chamber apparatus in which a nozzle plate partitions the chamber into the igniter section and the flow or test section which contains the sample granular material. A similar dual chamber design was first used by Kuo [5]. The operation commences by burning a small quantity of ball powder in the igniter chamber which is sealed by a diaphragm covering the multiple-nozzle plate. When the diaphragm bursts, combustion gases initially confined in the igniter chamber are driven through the nozzle plate, forming an approximately planar wave of hot gas which propagates through the flow chamber. The rise time and strength of the ignition wave [11,12] are functions of the amount of ball powder consumed in the igniter chamber, the burst pressure of the diaphragm covering the nozzle plate, the size of the nozzle holes, and so forth.

The flow chamber contains an aluminum liner with an i.d. of 76 mm and a length of 304.8 mm. A 9.5-mm-thick acrylic blowout disc at the far end of the flow chamber limits the maximum chamber pressure. The 12.7-mm-thick steel nozzle plate contains 101 holes (2.38 mm diameter) flared into nozzles. Pressure sealing is accomplished with two layers of mylar film which initially cover the nozzle plate. In the igniter chamber (Fig. 1), 5 g of Olin ball powder (undeterred sieved WC-870, average particle diameter of 0.775 mm) are placed within a 38-mm-diameter aluminum cup and ignited near the top with a bridge wire; the cup is thermally insulated to minimize heat loss. The other material surrounding the cup is consumable thermal insulation acting

as a thermal shield to prevent hot particles which may escape the cup from burning through the mylar layers before they reach their burst pressure (2 layers produce ~16 MPa). Pressure time-history of the chamber event is recorded by four wall-mounted Kistler 211B1 pressure transducers. P_0 is in the igniter chamber, and the other three are in the flow chamber, separated by 101.6 mm; P_1 is located 19 mm into the flow chamber, P_2 is located at 120.6 mm, and P_3 is at 222 mm.

Measurement of gas temperature within the propellant bed necessarily involves some compromise. Of the measurement options available (e.g., Ref. 13), we chose to use a type S thermocouple (platinum vs. platinum–10% rhodium) in a special holder. The maximum temperature limit of a type S thermocouple is approximately 2040 K, which provides an adequate upper limit for an ignition and/or incomplete combustion event. Of course, the thermocouple is sacrificed upon successful ignition of the solid propellant. An important problem is how to protect the structural integrity of a thermocouple placed within the packed bed. The scheme adopted (see Fig. 1) was to mount the thermocouple inside a hollow steel cylinder (o.d., 8 mm; length, 11 mm; wall thickness, 0.9 mm) that has dimensions slightly smaller than the solid propellant grain. The thermocouple is "strung across" the inside diameter of the hollow cylinder with the junction placed near the cylinder axis; this configuration is held in place by applying a coating of clear NC-based lacquer with polyester resin to the inside walls of the hollow cylinder. The lacquer also electrically insulates the thermocouple leads from the steel walls. The lead wires are fed through a ceramic insulator internal to the sting mount which positions this assembly so that the thermocouple junction is located near the flow chamber centerline axis (additional details in Ref. 14). The adequacy of the response time of the thermocouple in a transient flowfield can be an issue. The strategy adopted here was to evaluate thermocouples of various diameters in the identical transient environment. Paired combinations (1-mil with 2-mil, and 2-mil with 3-mil) were mounted within the same holder and the response compared [11,12,14] during a typical operation of the experiment. These comparisons suggest that, except for submillisecond excursions involving large amplitudes, a 1-mil-diameter (0.025 mm) thermocouple reports with minimal distortion. However, a 1-mil thermocouple does not have the structural integrity to survive the mechanical forces associated with the hot-gas igniter wave when the hollow cylindrical holder is aligned parallel to the chamber axis. The compromise was to turn the holder 90 degrees to the chamber axis, which allows the cylindrical walls to shield the thermocouple from the blast. As indicated in Fig. 1, the chamber experiment includes two thermocouple holders, each containing a single 1-mil type S thermocouple. Each holder assembly is colocated with a pressure gauge; TC_2 is opposite the pressure gauge P_2, and TC_3 is opposite P_3.

Once the mylar diaphragms burst, flow through the multiple nozzle plate remains choked for approximately 2 ms; the supersonic flow exiting the nozzle system negotiates a complicated shock-diamond/Mach-disc pattern in order to adjust to the pressure level in the flow chamber, which is rising rapidly. The 19-mm void region just below the nozzle plate (see Fig. 1) is intended to keep propellant grains out of this harsh flowfield environment. When the nozzle system unchokes, the rise in chamber pressure is nearly arrested (see solid line in Fig. 2), leaving a plateau behavior which decays primarily due to heat loss. The strength of the ignition system is held constant by burning 5 g of ball powder in the igniter chamber. However, to modulate the influence of the igniter gases on the granular propellant, a column of granular inert material (grain is solid cylinder, L = 24.3 mm, D = 10.7 mm, PVC filled with $CaCO_3$) is added as a "buffer zone" between the nozzle plate and the beginning of the live propellant bed. The combined length of the buffer zone and live propellant bed is held constant. Increasing the length of the buffer zone increases convective heat losses, thus cooling the igniter gases before they reach the live propellant bed. An additional important but more subtle effect is to lower the level of the pressure plateau region because the porosity of the inert bed (~0.55) is greater than that of the live propellant bed (~0.45), and hence the igniter gases expand into a greater volume.

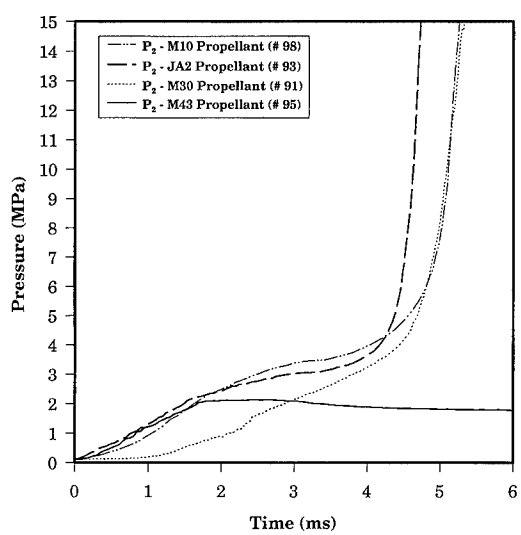

FIG. 2. Data from flamespreading chamber with 82.5-mm buffer zone. Comparison of pressure time-history monitored by transducer P_2 for granular propellants M10, JA2, M30, and M43.

TABLE 1
Ignition delay time from flamespreading chamber runs[a]

Research propellant	Full-up (No buffer zone)	38.1-mm buffer zone	82.5-mm buffer zone
M43	0.6 ms (#104)	110.5 ms (#89) 40.5 ms (#90) 69.1 ms (#96) 57.8 ms (#97)	251.5 ms (#88) 224.5 ms (#95) 292.2 ms (#103)
XM39	0.5 ms (#102)	557 ms (#100) 843.6 ms (#101)	660 ms (#99)
M30			5.7 ms (#87) 2.36 ms (#91)
JA2			12.65 ms (#92) 3.4 ms (#93) 2.75 ms (#94)
M10			2.95 ms (#98)

[a]Ignition delay time = time (4 MPa) − time (1 MPa), from transducer P_2; run numbers in parentheses.

Experimental Results

Three of the solid propellants exhibited very similar ignition behavior in the flamespreading chamber: the single-base M10, the double-base JA2, and the triple-base M30. Figure 2 compares chamber pressure time-history from gauge P_2 (see Fig. 1) for typical runs involving these three propellants, where the length of the inert buffer zone was 82.5 mm (longest used here). Considering the differences in composition, their ignition/transient combustion responses are remarkably similar. For comparison purposes, we define an ignition delay time to be the time interval between attaining 1 MPa (⇒ the igniter has functioned) and 4 MPa (⇒ runaway combustion is imminent), as reported by gauge P_2. Then, all but one ignition delay time (JA2) is within the range 2.3–6 ms (data in Table 1). Although JA2 will be discussed later, none of these three propellants gave an indication of susceptibility to excessive ignition delay. This finding is also consistent with gun system behavior.

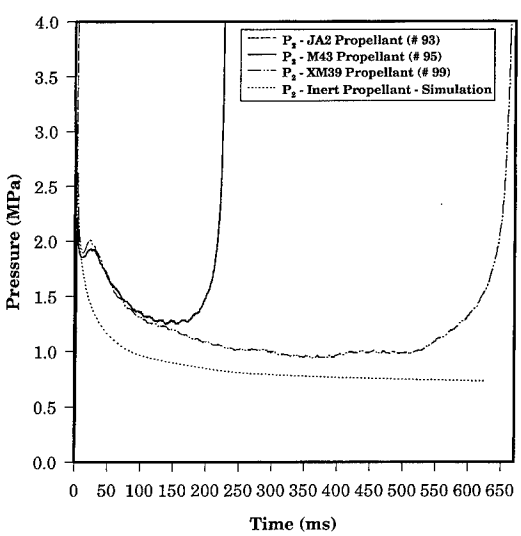

FIG. 3. Data from flamespreading chamber with 82.5-mm buffer zone. Comparison of pressure time-history monitored by transducer P_2 for granular propellants JA2, M43, and XM39. Dotted line is from model simulation assuming inert propellant bed.

The pressure time-history shown as a solid curve in Fig. 2 was not generated by an inert material. Indeed, this curve represents the chamber response of M43 (nitramine with an energetic plasticizer) which ignited successfully but on a much longer time scale. The continuation of the solid curve is shown in Fig. 3 (along with the JA2 curve from Fig. 1 for reference), indicating an ignition delay time of 224 ms. The chain-double-dot curve in Fig. 3 was produced by XM39 (nitramine with inert binder) which exhibits a delay of over 600 ms. The ignition delays with the nitramine propellants are essentially two orders of magnitude greater than those observed with M10, JA2, and M30. Delayed ignition sequences have been noted before [1,6–10], although not time delays of these magnitudes. However, the present results are the first to isolate the effect under controlled conditions. Apparently, significant differences exist in completing the ignition process and establishing full combustion of the nitramine composite propellants. And, clearly, the inert binder in

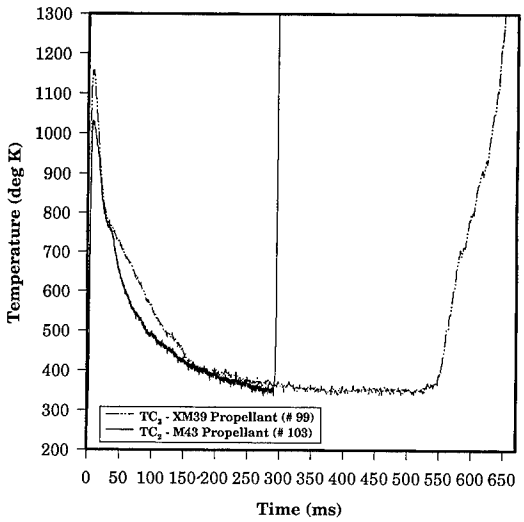

FIG. 4. Data from flamespreading chamber with 82.5-mm buffer zone. Comparison of gas temperature time-history reported by 1-mil thermocouple TC_2 for granular propellants M43 and XM39.

XM39 serves to retard the ignition process. Note that as the chamber pressure level decreases from 2 to 1 MPa, both nitramine pressure time-histories follow a similar curve, until the onset of runaway. A model [15] based on two-phase mixture theory was used to simulate the chamber response for the limiting case when the igniter functions and the propellant is assumed inert. The pressure history predicted at P_2, shown by the dotted line in Fig. 3, is the result of heat loss and forms a plausible lower bound to the measured values. One interpretation of the comparison is that some exothermic heat release occurs before a time of 40 ms, but then subsides to a lower level where heat loss governs the shape of the curve.

Some additional insight into what happens in the propellant bed during this long time delay may be provided by the 1-mil thermocouples. Figure 4 is a comparison of the gas temperature time-history monitored at TC_2 (opposite P_2) from the XM39 run shown in Fig. 3 (#99, ignition delay over 600 ms), with an M43 run (#103, ignition delay of 292 ms); both had an 82.5-mm buffer zone. Again, both temperature histories follow a similar path, until runaway. As the chamber pressure decreases through the range of 2 to 1 MPa, the gas-phase temperature decreases from approximately 1100 K (the igniter wave) to approximately 350 K before the reaction accelerates. Once underway, the runaway reaction in M43 requires only 2–3 ms while in XM39 it consumes over 100 ms; both runs blew the shear disc out of the chamber. It is rather remarkable, and certainly unexpected, that gas-phase temperatures can fall below 400 K and yet the reaction does not die.

Because of the length of these delays and the fact that the wall-mounted transducers report virtually identical pressures, it might be assumed that the reaction process is proceeding uniformly throughout the propellant bed. This is apparently not the case. The lower thermocouple, TC_3, indicates a maximum temperature of approximately 600 K from the igniter wave, and then an asymptotic approach to the values from TC_2 over a time interval of 200–300 ms. The lower maximum temperature seen by TC_3 is a plausible result of the significant heat loss experienced by convective flow through a compacted aggregate. However, the model simulation mentioned above was prompted by concern over the persistence of the temperature difference. The model, which assumes an inert propellant bed, predicts a similar but lower-magnitude axial temperature distribution that remains almost suspended in time (convective heat transfer is minimal) as the oscillatory flow generated by the igniter wave dies away. Furthermore, the predictions suggest that gases within the buffer zone just upstream from TC_2 are 200–400 K hotter than those at the location of TC_2. Thus, it is entirely possible that the runaway reaction begins in this region where no thermocouple was located, and at temperatures above those reported by TC_2. It is also prudent to question the accuracy of the thermocouple measurement. The design [14] of the hollow steel cylinder that protects the thermocouple was motivated by the expected transient environment within the initial 20–30 ms. However, at later times, if the chamber flow stagnates, conductive losses to the steel walls could influence the thermocouple response. Consider the limiting case of an infinite cylinder of gas with the circumferential boundary (i.e., steel) held at constant temperature. Assuming a uniform initial gas temperature, the solution [16] predicts that the thermal wave from the cold wall reaches the centerline in 100–200 ms, depending upon the value of thermal diffusivity. However, when this limiting case accounts for the 4 coats (~0.3 mm) of NC lacquer applied to the inside of each steel holder (before mounting the thermocouple), then the centerline temperature does not sense the cold wall for 600 ms. This provides reasonable assurance that the thermocouple readings were not corrupted. Additionally, the two-phase model simulation discussed above predicts a low amplitude oscillation in the chamber for times up to 600 ms. Typical peak velocities are 6 cm/s, which implies that the contents of the hollow cylinder would be flushed every 200 ms, before heat loss to the thermocouple holder could compromise the measured gas temperature.

To the authors' dismay, the current investigation encountered some difficulties with reproducibility. However, the data obtained with less than perfect control inadvertently demonstrate an important trend. Results for M43 subjected to a 38.1-mm buffer zone {see Table 1} illustrate the problem; the

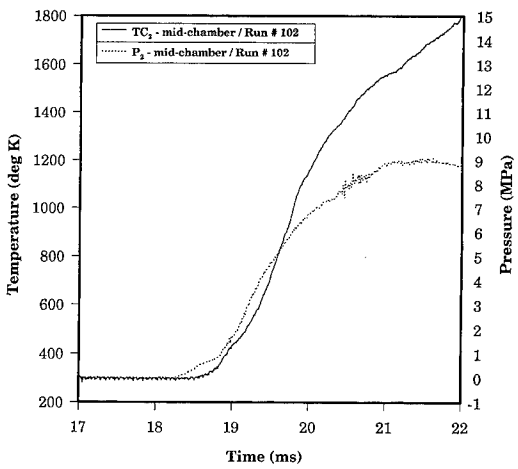

FIG. 5. Data from flamespreading chamber with no buffer zone. XM39 granular propellant. Comparison of pressure time-history from P_2 and gas temperature time-history from TC_2. Ignition delay time is 0.5 ms; hang-fire ignition has vanished.

delay times for four runs are within the range 40–110 ms. This disappointingly large spread in time delay is attributable to the inability to get the mylar diaphragms to burst the same way each time. Although not a structural integrity problem, the mylar diaphragms are especially vulnerable to burning ball powder particles that have escaped the confinement of the aluminum cup. The thermal insulation material surrounding the cup is not always successful in keeping these hot particles off the diaphragm surface. Premature burn-through of the mylar diaphragm results in a lower maximum pressure in the igniter chamber, and hence a reduced driving "force" into the flow chamber. These differences in diaphragm behavior appear in the flow chamber as variations in the pressure plateau level. These variations actually provide additional information because ignition delay time correlates inversely with pressure level. For example, the average chamber pressure level in run #97 is approximately 2.25 Mpa, leading to an ignition delay of 57.8 ms. While run #89, with an average pressure level of 1.75 MPa, showed a delay time of 110 ms. Such a trend would be consistent with the hypothesis that gas-phase chemical reactions are controlling the chamber response. A future goal, however, is to devise a method to open the igniter chamber within a closer tolerance.

Decreasing the length of the buffer zone which consists of granular inert simulant has two effects: (a) less convective heat loss means the igniter gases that reach the leading edge of the live propellant bed will be hotter, and (b) a reduction in void volume in the chamber (i.e., porosity) means the pyrolysis/combustion products will pressurize the chamber at a faster rate. If gas-phase chemical reactions are controlling the chamber behavior, then both influences should shorten the ignition delay time. Removing the buffer zone altogether and loading the chamber with XM39 provides the most serious test of this hypothesis. Such a test was conducted. Figure 5 displays both the pressure time-history from P_2 and temperature time-history from thermocouple TC_2; under these conditions, the ignition delay for XM39 is 0.5 ms! These diagnostics are reporting the passage of a full combustion wave at midchamber (the shear disc ruptured shortly after the indicated time of 20 ms); the hang-fire ignition process has vanished. Repeating this run with no inert buffer zone, but substituting M43 propellant for the XM39, produced virtually the same result—an ignition delay of 0.6 ms.

Observations of constant-pressure combustion of both M43 and XM39 indicate that they share a distinct flame zone characteristic [17]. At pressures up to approximately 4 MPa, the visible final flame zone appears to stand above the propellant surface, separated by a "dark zone" [17,18]. Double-base solid propellants such as JA2 also exhibit this general characteristic. The implication of the dark zone, of course, is a staged energy release process, i.e., a large percentage of gases leaving the propellant surface are reactive intermediates that must undergo further decomposition to complete their energy release. If the ignition process is just a transient flowfield to establish the flame zone, *where* these reactions occur is important. A convective flow environment may easily carry these reactive species a considerable distance from their origin. By contrast, in the same pressure range, M30 shows evidence [17] of a vigorous visible flame zone at or close to the propellant surface, suggesting the energy release process is nearly complete as the gases leave the propellant surface.

Concluding Remarks

The present study investigated the convective ignition behavior of five different granular solid propellants under nearly identical flow conditions. The results support the hypothesis that convective ignition of nitramine composite solid propellant is significantly influenced by the low-pressure flame zone structure together with the slow burning rate. Before the final flame zone has a chance to form, the partially reacted pyrolysis products evolving from the propellant surface can be swept away into a cooler part of the chamber (i.e., a Damkohler number argument). This reactive mixture must wait for the gas-phase decomposition mechanism to accelerate before ignition is successful. The time delay may be appreciable unless the low-pressure mass generation

rate (e.g., pyrolysis) is sufficient to raise the chamber pressure. However, at pressures above 4 MPa, dark zone formation is minimal, with energy release virtually complete at the propellant surface. The present results strongly suggest that anomalous and/or long ignition delays can be eliminated by designing the ignition system to quickly raise the pressure above 4 MPa. Note, however, that existence of a dark zone at low pressures is not sufficient evidence to predict difficult convective ignition. For example, the low-pressure flame zone of JA2 propellant also exhibits a dark zone but JA2 is not susceptible to excessive ignition delays in the normal gun chamber environment. The explanation is the difference in mass generation rate: the burning rate of JA2 at 2 MPa is more than five times greater than that of XM39. The higher mass generation rate will pressurize the chamber much faster.

Acknowledgments

The authors appreciate the many insightful comments offered by Dr. M. S. Miller (ARL) during the course of this investigation. We would also to thank M. B. Ridgely and T. E. Rosenberger of the U.S. Army Research Laboratory (ARL) for their special assistance to this program at the ARL Indoor Range facility. The authors are grateful to H. A. McElroy of the Olin Ordnance Corporation who, under the provisions of an ARL-Olin unfunded study agreement, supplied the ball powder propellant used in the igniter chamber.

REFERENCES

1. Chang, L. M. and Rocchio, J. J., "Simulator Diagnostics of the Early Phase Ignition Phenomena in a 105-mm Tank Gun Chamber," BRL-TR-2890, U.S. Army Ballistic Research Laboratory, Aberdeen Proving Ground, MD, March 1988. (See also Chang, L. M., *21st JANNAF Combustion Meeting,* CPIA, Columbia, MD, 1984, Pub. 412, Vol. II, pp. 301–311.)
2. Horst, A. W., "Multiphase Flow Analysis of the Ballistic Performance of an Anomalous LOVA Propellant Mix," 20th JANNAF Combustion Meeting, CPIA, Columbia, MD, 1983, Pub. 383, Vol. I, pp. 557–570.
3. Birk, A. and Caveny, L. H., *AIAA J.* 18(11):1363–1403 (November 1980). (See also MAE Report 1486, Dept. of Mechanical and Aerospace Engineering, Princeton University, September 1980.)
4. Ritchie, S. J., Hsieh, W. H. and Kuo, K. K., *AIAA J. Propul. Power* 8(3):570–577. (See also *26th AIAA/SAE/ASME/ASEE Joint Propulsion Conference,* 16–18 July 1990, AIAA Paper 90-2194; *27th JANNAF Combustion Meeting,* CPIA, Columbia, MD, 1990, Pub. 557, Vol. I, pp. 287–298; and *26th JANNAF Combustion Meeting,* CPIA, Columbia, MD, 1989, Pub. 529, Vol. I, pp. 1–12.)
5. Kuo, K. K., Koo, J. H., Davis, T. R., and Coates, G. R., *Acta Astronaut* 3:573–591 (1976). (See also Kuo, K. K. and Koo, J. H., Contract Report 346, U.S. Army Ballistic Research Laboratory, Aberdeen Proving Ground, MD, August 1977.)
6. Varney, A. M., Keeser, J. W., and Brandstadt, R., *16th JANNAF Combustion Meeting,* CPIA, Columbia, MD, 1979, Pub. 308, Vol. I, pp. 653–672.
7. Varney, A. M., Martino, J., and Henry, R., *20th JANNAF Combustion Meeting,* CPIA, Columbia, MD, 1983, Pub. 383, Vol. I, pp. 547–556.
8. Varney, A. M., Martino, J., and Peters, S., *24th JANNAF Combustion Meeting,* CPIA, Columbia, MD, 1987, Pub. 476, Vol. III, pp. 235–249.
9. Messina, N. A., Ingram, L. S., and Tricarico, S. A., *25th JANNAF Combustion Meeting,* CPIA, Columbia, MD, 1988, Pub. 498, Vol. IV, pp. 379–396.
10. Messina, N. A., Ingram, L. S., and Konig, G. F., *26th JANNAF Combustion Meeting,* CPIA, Columbia, MD, 1989, Pub. 529, Vol. III, pp. 145–164.
11. Kooker, D. E., Chang, L. M., and S. L. Howard, "Flamespreading in Granular Solid Propellant: Design of an Experiment" ARL-MR-80, U.S. Army Research Laboratory, June 1993. (See also *29th JANNAF Combustion Meeting,* CPIA, Columbia, MD, 1992, Pub. 593, Vol. I, pp. 1–13.)
12. Kooker, D. E., Howard, S. L., and L. M. Chang, *30th JANNAF Combustion Meeting,* CPIA, Columbia, MD, 1993, Pub. 606, Vol. I, pp. 241–258. (See also ARL-TR-446, U.S. Army Research Laboratory, June 1994.)
13. McClure, D. R., "Measurements of Gas Temperature and Convective Heat Flux in a Reacting Granular Propellant Bed," Ph.D. Thesis, Department of Mechanical Engineering, The Pennsylvania State University, University Park, PA, August 1984.
14. Howard, S. L., Chang, L. M., and D. E. Kooker, *Rev. Sci. Instrum.* 66(8):4259–4266 (1995).
15. Gough, P. S., "The XNOVAKTC Code," BRL-CR-627, Contractor Report to U.S. Army Ballistic Research Laboratory, Aberdeen Proving Ground, MD, February 1990.
16. Carslaw, H. S. and Jaeger, J. C., *Conduction of Heat in Solids,* Oxford University Press, London, 1959, p. 199.
17. Miller, M. S., personal communications concerning extensive strand-burner experiments at ARL, Aberdeen Proving Ground, MD, 1993. (See also Miller, M. S., *23rd JANNAF Combustion Meeting,* CPIA, Columbia, MD, 1986, Pub. 457, Vol. II, pp. 329–335.
18. Vanderhoff, J. A., Anderson, W. R., and Kotlar, A. J., *29th JANNAF Combustion Meeting,* CPIA, Columbia, MD, 1992, Pub. 593, Vol. II, pp. 225–237.

COMMENTS

Dr. Igor G. Assovskii, Semenov Inst. of Chemical Physics, Russia. The effect of delayed ignition is very important for large caliber artillery systems. So, the question is how the experimental conditions for the ignition (for example, the loading density) correspond to the real conditions in a gun chamber.

Author's Reply. The initial conditions in our laboratory apparatus are similar to those in large-caliber gun systems. For example, with no inert buffer zone in the flamespreading chamber, the loading density (weight of propellant/chamber volume) is approximately 0.83 g/cc. This is considerably higher than typical closed vessel tests conducted at a loading density of 0.2 g/cc.

Twenty-Sixth Symposium (International) on Combustion/The Combustion Institute, 1996/pp. 2041–2047

FLAME STABILIZATION IN CRYOGENIC PROPELLANT COMBUSTION

G. HERDING, R. SNYDER, P. SCOUFLAIRE, C. ROLON AND S. CANDEL
Laboratoire E.M2.C., Ecole Centrale Paris et C.N.R.S.
F-92295 Châtenay-Malabry, France

Cryogenic combustion is of considerable technological interest in propulsion applications. Cryogenic propellants used in rocket engines provide the high performance needed for spacecraft launching and have operated safely for a number of years, but the processes that control combustion in such devices are still not well understood. Among the many important issues, flame stabilization constitutes one basic problem. This question is investigated in this article by imaging the flame originating from a single, coaxial injector fed with liquid oxygen and gaseous hydrogen. Results of experiments carried out on a facility for cryogenic propellant combustion research operated by ONERA are used to characterize the mechanisms that control the flame-holding process at atmospheric pressure, 5, and 10 bars. Data acquired correspond to elastic scattering by the spray, emission of *OH* radicals, and planar laser-induced fluorescence of these radicals. Fluorescence is obtained by pumping the $X^2\Pi(v'' = 0) \rightarrow A^2\Sigma(v' = 1)$ band of *OH*, and off-resonance light radiation is observed. This database provides the general structure of the flame in the injector near-field, and may be used to determine the position of the flame stabilization region. Simultaneous acquisition of laser-induced fluorescence and elastic scattering was used to locate the flame in respect to the liquid. It is shown that in all cases investigated the flame is initiated at a close distance from the injector exhaust plane.

Introduction

While cryogenic combustion has found important application in rocket propulsion, design of rocket engines has remained essentially empirical [1]. Recent efforts [2] have been made to develop modeling tools but their validation is lagging because data from controlled experiments are not available. Basic processes controlling cryogenic combustion are in fact not well understood because few experiments were carried out in simplified injection geometries. The data generated in such experiments could be used to guide modeling. Considerable effort is now being expended in this direction using modern optical diagnostics [3–7]. The objective of the present research is to examine one of the many issues in cryogenic combustion, that of flame stabilization. We specifically consider the case of a single coaxial injector operating with liquid oxygen and gaseous hydrogen. This injector is placed in a rectangular chamber equipped with transparent side walls and an ejection nozzle. While the geometry and operating conditions are similar to those prevailing in real engines, there are also notable differences. In the present test series, the operating pressure does not exceed 10 bar, to be compared with the 100 bar of the Ariane 5 Vulcain engine. Our study concerns a single injector while real engines comprise a few hundred coaxial units covering the motor back plane and feed the chamber with propellants as a "showerhead." The confinement effect provided by the chamber wall only imperfectly replaces the aerodynamic confinement experienced in the real geometry. Despite these differences inherent to model-scale testing, the experimental geometry may be used to identify the mechanisms that control the stabilization process. One may also examine the flame structure in the near-field and consider effects of operating parameters.

This study is focused on stabilization mechanisms, deals with the structure of the nascent reaction sheet, and considers the influence of injection parameters and operating pressure. Three types of visualization are used [5,8]: spontaneous emission, and planar-induced fluorescence for the OH radical, as well as elastic laser light scattering to map the liquid phase of the oxygen. In this article, we use induced fluorescence images to investigate the flame structure. We wish further to locate the flame with respect to the liquid core of oxygen and consider its response to liquid jet breakup and atomization. To do so, we analyze simultaneously acquired induced fluorescence and elastic scattering images. Other aspects of the problem are treated in Refs. 5 and 8. Additional data on supercritical conditions may be found in Ref. 4.

Combustion and Flame Stabilization Processes

In typical cryogenic combustion applications, propellants are introduced through a coaxial injector.

The liquid oxygen flows in the inner tube while the gaseous hydrogen is delivered by the outer annular duct. In the present case, we consider flush-mounted LOx and hydrogen ducts with no swirl. Atomization begins at the confluence of the two streams. The size of the liquid core diminishes progressively as the spray is formed. Liquid ligaments are torn away by the high-speed hydrogen stream. The ligaments break into droplets which may still be too large to sustain the large stresses induced by the velocity difference between the gaseous stream and the liquid droplets. This leads to secondary atomization. The droplets vaporize and the gaseous oxygen and hydrogen react in a highly turbulent flowfield.

Among the many dimensionless groups that govern the previous processes it is possible to sort out the controlling factors. In what concerns atomization, one may conclude from systematic experiments on coaxial injectors operating at large Reynolds numbers that the main dimensionless groups are the momentum flux ratio J and the relative gaseous Weber number We_g, respectively, defined by

$$J = \frac{\rho_g u_g^2}{\rho_l u_l^2}, \; We_g = \frac{\rho_g (u_g - u_l)^2 d_l}{\sigma} \tag{1}$$

These expressions involve the initial liquid diameter d_l and injection velocities, where indices g and l designate gas and liquid. The Weber number compares inertial and surface tension forces acting on the liquid sheet. If the Reynolds numbers are sufficiently large, the two streams of propellant are turbulent. The disintegration of the liquid jet into ligaments is then governed by the momentum flux ratio J [9]. This ratio determines the breakup of the liquid core and sets the core length. The size of the droplets formed by secondary atomization is then mainly controlled by the Weber number.

Another set of dimensionless groups may be formed by considering characteristic times of vaporization, mixing and combustion processes t_v, t_m and t_c respectively. These three characteristic times define a chemical Damköhler number which compares the mixing time to the chemical time and a vaporization Damköhler number which compares the mixing time to the vaporization time:

$$Da_c = \frac{t_m}{t_c}, \; Da_v = \frac{t_m}{t_v} \tag{2}$$

Estimates of the characteristic times may be obtained under some simple assumptions [5,8]. In these experiments, the Damköhler numbers belong to the following ranges: $10^{-2} \leq Da_v \leq 2$ and $10 \leq Da_c \leq 100$. This indicates that the chemical reaction is much faster than mixing which is also faster then vaporization in most regions of the flow. Vaporization appears as the controlling process, which in turn is governed by atomization.

Two other operating parameters should be added to this list. The initial ratio of oxygen to hydrogen mass flow rates $E = \dot{m}_O/\dot{m}_F$ determines the global level of heat release and influences the chemical time. The operating pressure p plays an important role. This variable influences the characteristic times, thermodynamics, and transport phenomena.

The experimental design is based on the previous analysis. It is important to set the mass flow rates at levels that are typical of the real conditions. This assures that the Reynolds and Weber numbers are in the proper ranges. As atomization appears to be a key process, it is important to see if changes in the momentum flux ratio J will influence flame stabilization. Cold test flows indicate a critical value for J above which the quality of atomization becomes acceptable. It was then decided to change J around this value and compare the resulting flame patterns.

One important issue in nonpremixed combustion is that of flame stabilization. Among the possible patterns of stabilization one may distinguish four situations [8]. The stabilization process has been studied extensively in the case of a fuel jet injected into an ambient oxidizing atmosphere at rest (see Refs. 10–14 and the review by Pitts [15]). These experiments indicate that when the fuel jet velocity is low, the flame is anchored on the injector rim. The flame lifts off when the jet velocity is increased beyond a certain value. The flame is then established at a standoff distance from the injection plane. If the jet velocity is increased further, there comes a point where the flame is blown out [14]. The cryogenic injector configuration differs in some notable ways from this case. The oxygen is delivered in liquid form and heat has to be provided for vaporization. The oxidizer stream is injected at low speed while the outer hydrogen stream flows at high speed. Under these circumstances the inner jet acts like a wake producing a velocity "defect" in the central region.

The stabilization point will then lie in the low velocity region. One may however imagine different possibilities. The flame may be anchored on the injector lip, lifted and stabilized at a distance or it may be stabilized as a premixed front anchored downstream on the liquid core breakup region. One may also imagine a combination of a weak reaction region in the immediate vicinity of the injector followed by an initiation region which after a certain distance allows a runaway of the reaction producing a stabilization region. We will try to identify the mechanism of stabilization from the images obtained in this investigation.

Experimental Configuration

The Mascotte facility operated by ONERA allows investigations of cryogenic propellant combustion. The facility comprises a single element combustor

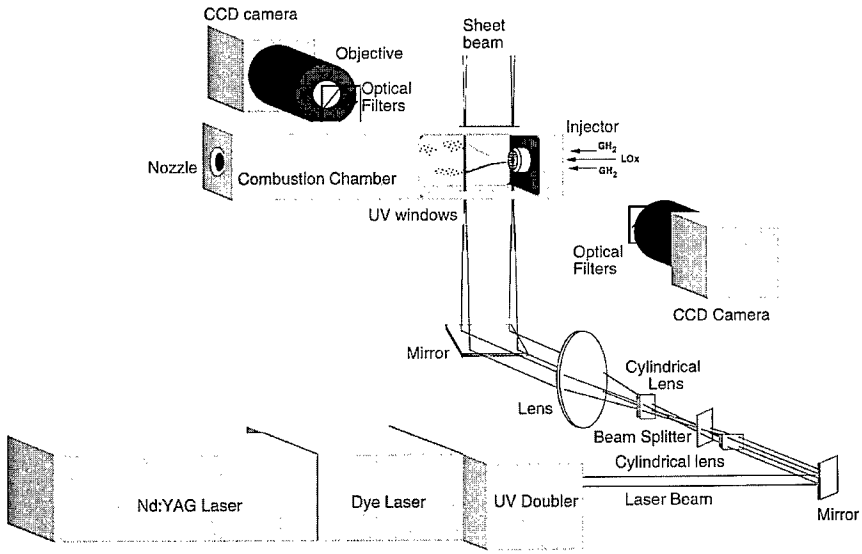

FIG. 1. The combustion chamber comprises a single injector, allows optical access through the lateral walls, and includes upper and lower windows for laser sheet transmission.

(there are more than 500 elements in the Vulcain engine). Liquid oxygen is subcooled to a temperature of 80 K and enters the chamber at a similar temperature that is typical of real engines. Hydrogen is injected at room temperature which differs from values of 100 K found in the Vulcain engine. The LOx mass flow rate used for the experiments were 40 and 50 g/s. The gaseous hydrogen mass flow rate varied between 10 and 24 g/s. The mixture ratio is set between 2 and 5 in the model. It is around 5 in engine main chambers and around 1 in gas generators. The momentum flux ratio takes values in the experiments that are of the same order as those found in the real devices. Weber numbers in the experiment take values between 8.8 and 19.7×10^3, of the same order as in gas generators, but three times less than in motor chambers. Pressures investigated are 1, 5, and 10 bar.

The combustion chamber features a square cross section with an inner dimension of 50 mm. The 100×50 mm^2 lateral windows allow optical access for the CCD cameras. The 80×3 mm^2 upper and lower windows are used to introduce an axial laser sheet into the cavity. Three different types of visualization have been applied: spontaneous emission of OH, induced fluorescence (LIF) of this radical, and elastic scattering on the liquid oxygen. Frequency shifted fluorescence was obtained by pumping the $Q_1(6)$ absorption line of OH. This allows separation of the elastic scattering by using optical filters. Four highpass filters (WG305) and one glass filter (UG5) were used for the experiments. The laser sheet thickness was less than 0.6 mm inside the combustion chamber. A schematic view of the experimental setup and the combustion chamber is provided in Fig. 1. The cylindrical light beam originates from a frequency-doubled dye laser pumped by a Nd:YAG laser. The beam is converted into a sheet by a set of UV lenses, passing the combustion chamber from bottom to top. Two CCD cameras are used to image the combustion chamber. The visualized area is 50×60 mm^2, one pixel measures 0.27×0.27 mm^2, and the optical resolution is better than 0.5 mm.

Experimental Results and Interpretation

While images over a wide range of parameters were recorded, only results for two sets of flow conditions are shown. Indeed, the analysis holds for all initial flow conditions examined, but the flame will depart earlier from the core region if the relative velocity of hydrogen to oxygen is increased further. Pressure is 5 bar, mass flow rates of gaseous hydrogen $\dot{m}_{H_2}$ and liquid oxygen $\dot{m}_{\mathrm{LOx}}$ are 11.2 and 50 g/s, respectively. For the simultaneous acquisition images, $\dot{m}_{\mathrm{LOx}}$ is reduced to 40 g/s. The resulting Weber number is $We_g = 10.5 \times 10^3$, momentum flux ratio is either $J = 6.5$ or $J = 10.2$. Figure 2 shows a LIF image with the injector to scale. Above the axis, the fluorescence signal fades out at a distance where the elastically diffusing spray becomes too dense and laser light is scattered before reaching the upper flame front. Signal near the axis and close to the injection plane is either due to Raman scattering—frequency shifted to 298 nm—or fluorescence from impurities in the liquid oxygen. Henceforth, the signal will be

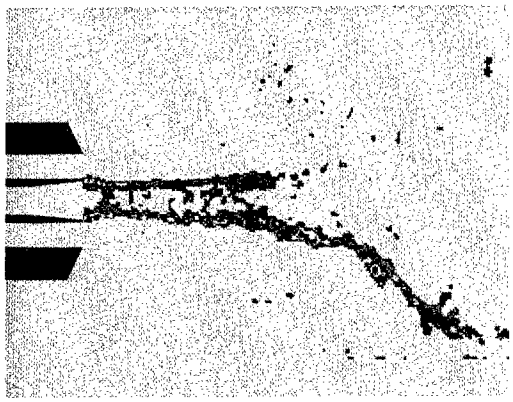

FIG. 2. Induced fluorescence imaging at 5 bar. $\dot{m}_{LOx}$ = 50 g/s, $\dot{m}_{H_2}$ = 11.2 g/s. v_{LOx} = 2.23 m/s, v_{H_2} = 292 m/s, J = 6.5, We_g = 12.6 × 10^3, E = 4.5.

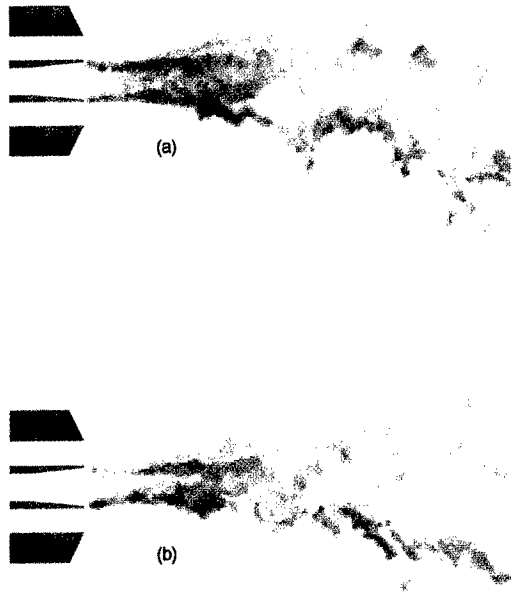

FIG. 3. Simultaneous acquisition of LIF and elastic scattering images. The background is white, elastic scattering is shown in blue, laser-induced fluorescence in red. $\dot{m}_{LOx}$ = 40 g/s, $\dot{m}_{H_2}$ = 11.2 g/s, v_{LOx} = 1.78 m/s, v_{H_2} = 292 m/s, J = 10.2, We_g = 12.6 × 10^3, E = 3.6.

referred to Raman scattering. It is seen that the flame stays close to the central axis over a certain distance x_d, before it departs from it. The expansion rate in the near-field of the injector is then closely coupled to the atomization and breakup of the liquid jet. The interaction between the liquid oxygen and the flame may be examined by simultaneous acquisition of elastic scattering and induced fluorescence images. Two of such image couples are represented superimposed in Fig. 3. One clearly notices that the flame is intimately close to the liquid phase especially in the near-field. In Fig. 3b, the flame follows the contours of the liquid phase over a longer distance. In Fig. 3a, the flame departs from the dense spray region at a certain distance and has probably been pushed out by vaporized liquid, leaving a hole behind. It thus appears that the flame is oxygen starved in the near-field of the injector and, therefore, is situated close to the liquid phase where equilibrium between consumption and evaporation is established. It is worth noting that under other flow conditions, the rate of expansion may be controlled by other phenomena. At higher relative velocities, one observes, for instance, that the flame expands earlier at an axial distance $x_d/d_l < 2$ (compared to $2 < x_d/d_l < 7$). This is due to better atomization resulting in increased vaporization, burning, and heat release rates.

To further investigate the structure of the flame near the injector, the radial fluorescence distributions are plotted as a function of axial distance in Fig. 4. While the maximum value of fluorescence in an axial section may vary, complete extinction is not often found. The slices are quite symmetric and may be represented as Gaussian fits. Toward the center, however, data points deviate from symmetry due to the presence of Raman scattering. The Raman signal distribution is also provided in the same figure. It

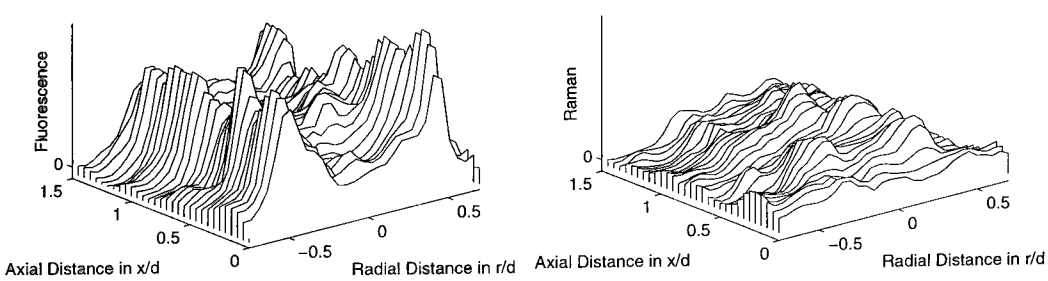

FIG. 4. Fluorescence (left) and Raman scattering (right) distributions as a function of axial distance from the injection plane. Flow conditions are as in Fig. 2.

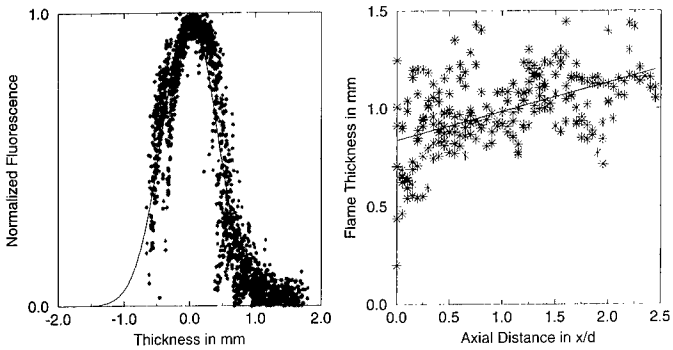

FIG. 5. Fluorescence data from 10 images in axial slices located between the injection plane and $x = 2.5d_{LOx}$ downstream. Left: The data is reorganized and normalized according to Gaussian fits of the radial distributions. Right: Width deduced from these Gaussian fits and its evolution with axial distance. Flow conditions are as in Fig. 2.

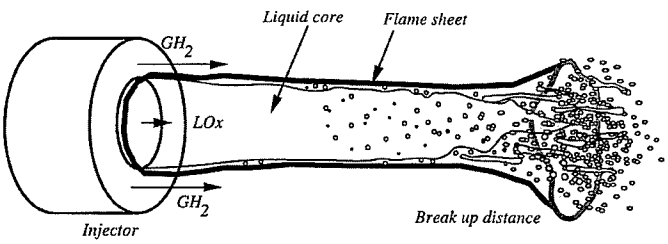

FIG. 6. Schematic representation of the flame in near-field showing the stabilization geometry encountered in the experiments.

was obtained in another test run under the same flow conditions and with the same optics by shifting the laser wavelength to a nonabsorbing region. While the Raman distributions are quite regular, they vary in time and it is, thus, not possible to correct the instantaneous fluorescence images by simply subtracting the Raman image. This is, however, feasible for time-averaged distributions, and one essentially suppresses the parasitic signal due to the liquid spray. To explore the instantaneous flame structure, we processed the lower half of 10 fluorescence images. For all images, Gaussian curves have been fitted to the data in each transverse slice from the injection plane up to 2.5 d_l downstream. To avoid problems, we did not consider pixels where the Raman signal was found to be important. The fitted parameters for height and position are used to normalize the data. The ensemble of data points corresponding to the region $0 < x/d_l < 2.5$ is shown in Fig. 5. In this range, one finds an average fluorescence distribution width at half height of about 1 mm. The width evolution is shown in the same figure. The mean value changes from 0.8 mm, close to the injector, to 1.2 mm at 2.5 d_l. Taking into account the optical transfer function, a rough deconvolution provides estimates for the real widths of 0.6 and 1.1 mm, respectively. The previous data show that the reaction layer is weakly wrinkled and quasi-laminar. Considering a laminar diffusion flame, one may interpret the flame thickening as indicative of a consumption rate decreasing with axial distance.

In summary, the previous data and all our results indicate that the flame is anchored on the LOx injector rim. No lift-off is observed in the range of parameters explored. In general the initial flame ($x \leq 2d_l$) is located on the border of the liquid core.

Initial Rates of Oxygen Vaporization and Consumption

The data gathered in this experiment suggest that in the range of parameters explored, the flame initiated in the vicinity of the LOx tube develops into a roughly cylindrical shell surrounding the liquid core. The corresponding flow structure is sketched in Fig. 6.

To back up this view, it is worth estimating the rates of vaporization and consumption of oxygen in the initial region. A comparison of these rates will then indicate if a balance may be achieved to sustain the nascent reaction sheet. The rough estimates obtained in this section are based on many simplifications. To evaluate the rate of consumption of oxygen in the flame sheet, we assume a single-step reaction between fuel (hydrogen) and oxidizer (oxygen) $F + sO \rightarrow P$, that the chemistry is infinitely fast, that reaction takes place between pure oxygen $Y_{O0} = 1$ and pure hydrogen $Y_{F0} = 1$, corresponding to a global mixture ratio $\phi = sY_{F0}/Y_{O0} = 8$. For a plane *time-evolving* diffusion flame formed under these conditions, the mass consumption rate of oxidizer per unit flame surface is given by [16]:

$$\dot{m}''_{O_2} \simeq \rho Y_{O0} \frac{(1 + \phi)}{2} \left[\frac{D}{\pi t}\right]^{1/2} \exp(-\eta_f^2) \qquad (3)$$

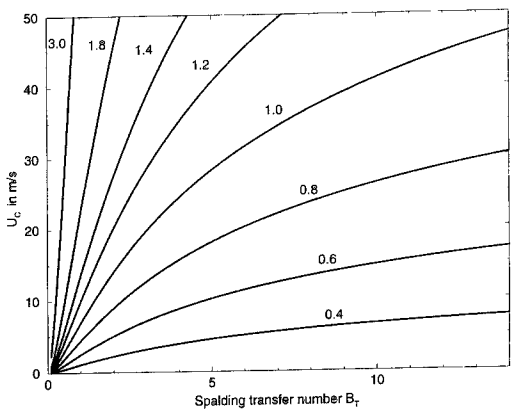

FIG. 7. Ratio of oxygen consumption to vaporization rates ($\dot{m}_{O_2}$) as a function of the transfer number B_T and flow velocity at the flame sheet, U_c. Operating velocities $v_{LOx} = 2$ m/s, $v_{H_2} = 300$ m/s.

where $\eta_f = \mathrm{erf}^{-1}[(1 - \phi)/(1 + \phi)]$ and D is the species diffusion coefficient. It is possible to estimate the rate of consumption of the *spatially evolving* flame by assuming that the reaction layer is convected at a velocity U_c. Physically, this velocity is bounded by the liquid core and hydrogen stream velocities $v_l < U_c < v_g$. The time variable that appears in equation 3 may then be related to the spatial variable by $t \simeq x/U_c$. The consumption rate of oxygen is then found to be proportional to $(DU_c/x)^{1/2}$.

To estimate the vaporization rate, one may use results established in studies of burning surfaces in convective streams [17]. Assuming that the Schmidt number is equal to one and that the boundary layer surrounding the liquid core is initially laminar, one finds

$$\dot{m}''_v \simeq \frac{\rho}{C}\left[\frac{D(v_g - v_l)}{x}\right]^{1/2} \frac{\ln(1 + B_T)}{B_T^{0.15}} \tag{4}$$

where $C \simeq 3.67$ and B_T designates the Spalding heat transfer number. The mass rates of consumption and vaporization are then easily compared by taking the ratio of the previous expressions. One obtains

$$\frac{\dot{m}''_{O_2}}{\dot{m}''_v} \simeq \frac{CY_{O0}(1 + \phi)\exp(-\eta_f^2)}{2\pi^{1/2}}\left[\frac{U_c}{v_g - v_l}\right]^{1/2} \frac{B_T^{0.15}}{\ln(1 + B_T)} \tag{5}$$

For fixed injection conditions, this ratio is a function of B_T and U_c and does not depend on the axial coordinate x. One may note, however, that the expressions used to derive this result are not strictly valid near $x = 0$. While the consumption and vaporization rates increase with pressure as $p^{1/2}$, their ratio is not affected by this variable. The ratio $\dot{m}''_{O_2}/\dot{m}''_v$ is plotted in Fig. 7 as contour lines. When this ratio is less than unity, vaporization exceeds consumption and a sufficient amount of oxygen is provided to sustain the flame. This condition is satisfied for a broad range of parameters indicating that the flame may be established as expected. For typical values of B_T around 10, the velocity U_c should be less than 40 ms^{-1}, indicating that the flame will develop on the low-velocity side of the shear layer formed near the liquid jet. This result is in agreement with measurements already described, indicating that the flame spreads in the vicinity of the liquid surface. The value of the velocity U_c is in agreement with a rough estimate deduced from the measured flame thickness. For this purpose, one uses standard expressions combining flame thickness and velocity U_c, taking the diffusion coefficient at 1000 K. The consumption is then found to decrease with axial distance in the initial region as indicated in equations 3 and 4. Reality is, however, more complicated, and derivation of previous equations assumed that a laminar boundary layer develops and does not account for atomization processes. Experiments and theory indicate that ripples on the liquid surface will grow with axial distance and thus create surface for heat transfer. Area will be increased by droplets torn apart from the core. Also, the laminar boundary layer may be broken by ejected filaments and droplets. All these effects will favor the stabilization process. There may also be an influence of the wake region of the LOx injection tube, and the initial turbulence of the streams. Liquid turbulence should decrease vaporization as it favors heat transfer into the interior of the subcooled oxygen and increase it by corrugation of the surface.

Conclusions

Research reported in this article addresses fundamental issues in cryogenic propellant combustion. It focuses on the flame stabilization mechanisms and the structure of the flame in the injector near field. Because the flow involves two phases, it is necessary to simultaneously image the liquid core and the reaction layers. This is achieved in the present study by collecting data with combined diagnostics. Images obtained from laser-induced fluorescence of OH radicals and elastic light scattering are used to locate the flame inception point and describe the flame structure in the stabilization region. It is shown for a single injector and in the range explored (pressure ≤ 10 bar, $6.5 \leq J \leq 14$, etc.) that the flame is anchored in the vicinity of the liquid oxygen injection tube. Composite images displaying elastic scattering and LIF signals indicate that the flame

sheet is established on the boundary of the liquid core. The flame appears as a thin corrugated sheet closely following the liquid core border. At a distance from the injector, the liquid jet breaks down into a spray of ligaments and droplets. The flame spreads away from the axis and forms a shell around the spray. The data collected suggest that the initial flame anchoring is achieved by a detailed balance between vaporization from the liquid core and the reaction of the oxygen made available in the gas phase. Estimates of vaporization and consumption rates confirm this interpretation. While momentum flux ratio influences the general structure of the flame further downstream [5,7], it has little effect on stabilization. High Weber numbers, We_g, assure early atomization and as a consequence vaporization from shed off droplets may no longer be neglected.

Acknowledgments

This study was supported in part by SEP and CNES. GH is supported jointly by CNES and DLR. Technical support was provided by G. Coeur-Joly, Y. Le Teno and G. Lucas. Help of the ONERA "Mascotte" team is gratefully acknowledged.

REFERENCES

1. Burick, R. J., *Spacecraft* 9:326–331 (1972).
2. Liang, P. Y., Fisher, S., and Chang, Y. M., "Comprehensive Modeling of a Liquid Rocket Combustion Chamber," *AIAA* 1985, Paper 85-0232.
3. Pal, S., Moser, M. D., Ryan, H. M., Foust, M. J., and Santoro, R. J., "Drop Size Measurements in a LOX/GH_2 Propellant Rocket," in Central and Eastern States Sections of the Combustion Institute, New Orleans, 1993.
4. Mayer, W. and Tamura, H., "Flow Visualization of Supercritical Propellant Injection in a Firing LOX/gh_2 Rocket Engine," in *Thirty-First AIAA Joint Propulsion Conference,* 1995. *AIAA* 95-2433, San Diego, CA.
5. Herding, G., Snyder, R., Scoufflaire, P., Rolon, C., and Candel, S. M., "Emission and Laser Induced Fluorescence Imaging of Cryogenic Propellant Combustion," in *Conference on Propulsive Flows in Space Transportation Systems,* 1995. Bordeaux, France.
6. Vogel, A., "Investigations on Atomization of a Coaxial Injected h_2/lo_x under Hot Fire Conditions," in *Sixth International Conference on Liquid Atomization and Spray Systems,* 1994. Rouen, France.
7. McManus, K., Aguerre, F., Yip, B., and Candel, S., in "Analysis of the Ignition Sequence of a Multiple Injector Combustor Using PLIF Imaging," *Third International Symposium on Special Topics in Chemical Propulsion: Non-Intrusive Combustion Diagnostics,* 1993.
8. Snyder, R., Herding, G., Rolon, C., and Candel, S. M., *Combust. Sci. Technol.* 1996, submitted.
9. Hopfinger, E. J. and Lasheras, J. C., "Breakup of a Water Jet in High Velocity Co-Flowing Air," in *Sixth International on Liquid Atomization and Spray Systems,* ICLASS, Rouen, France, 1994, pp. 110–117.
10. Eikhoff, H., Lenze, B., and Leuckel, W., *Twentieth Symposium (International) on Combustion,* The Combustion Institute, Pittsburgh, 1984, pp. 331–318.
11. Miake-Lye, R. C. and Hammer, J. A., *Twenty-Second Symposium (International) on Combustion,* The Combustion Institute, Pittsburgh, 1988, pp. 817–824.
12. Dahm, W. J. and Dibble, R. W., *Twenty-Second Symposium (International) on Combustion,* The Combustion Institute, Pittsburgh, 1988, pp. 801–808.
13. Takahashi, F., Mizomoto, M., Ikai, S., and Futaki, N., *Twentieth Symposium (International) on Combustion,* The Combustion Institute, Pittsburgh, 1984, pp. 295–302.
14. Broadwell, J. E., Dahm, W. J., and Mungal, M. G., *Twentieth Symposium (International) on Combustion,* The Combustion Institute, Pittsburgh, 1984, pp. 303–310.
15. Pitts, W. M. *Twenty-Third Symposium (International) on Combustion,* The Combustion Institute, Pittsburgh, 1990, pp. 661–668.
16. Carrier, G. F., Fendell, F. E., and Marble, F. E., *J. Appl. Math.* 28:463;–500 (1975).
17. Glassman, I., *Combustion,* Academic Press, New York, 1987.

Twenty-Sixth Symposium (International) on Combustion/The Combustion Institute, 1996/pp. 2049–2065

INVITED TOPICAL REVIEW

IMPACTS AND CONTROL OF AIR TOXICS FROM COMBUSTION

CATHERINE P. KOSHLAND
University of California, Berkeley
School of Public Health, and the Energy and Resources Group
Berkeley, California 94720, USA

The debate over the contribution of air toxics to adverse human and ecosystem health effects continues in both scientific and policy arenas. While the primary concern in the 1970s and 80s was the criteria pollutants and the nonmethane volatile organics which contribute to ozone formation, concern in the late 1980s was directed to air toxics as well. Major changes in regulatory legislation occurred in the early 1990s resulting in increased demand for emissions reductions. Air toxics in combustion emissions include volatile and semivolatile organics such as benzene, dioxins, and furans, as well as inorganic species such as HCl, many metals (including metal oxides and chlorides), and aerosols with particles less than 10 μm in diameter. Air toxics are of concern for their potential to impact both human and ecosystem health. While carcinogenic potential was of greatest concern initially, other health impacts including reproductive effects and endocrine system disruption are receiving increasing attention. Within the combustion community, research efforts focused initially on air toxics emissions from incinerators. More recently, air toxics emissions from other combustion processes have come under scrutiny. The relationships among the feedstock, the combustion process, and postcombustion processes all influence the emissions of air toxics and the distribution or transfer of pollutant species among environmental media. This paper reviews impacts by air toxics from combustion on human health and ecosystem health, reviews the factors that contribute to the formation of air toxics, and considers how the impacts can guide combustion research to focus on those factors most crucial to control of air toxics.

"We are uniquely fire creatures on a uniquely fire plant, and through fire the destiny of humans has bound itself to the destiny of the planet"

(Stephen Pyne)

Introduction

Fire and combustion emissions, have shaped the earth's atmospheric chemical composition and its climate [1]. Combustion air toxics (Table 1) are those species emitted from combustion processes, often in trace amounts, that are associated with adverse human health or environmental impacts. Originally identified as carcinogens, air toxics are now associated with other health endpoints as well. (For the purposes of this paper, the criteria pollutants CO, NO_x, SO_x, O_3, and greenhouse gases [CO_2, CH_4] are excluded.)

The association between combustion products and cancer has long been recognized. In 1775, Sir Percival Pott observed the association between the incidence of scrotal cancer in adolescent chimney sweeps and high soot exposures [2]. Diseases that correlate with high occupational exposures to compounds such as lead or mercury were reported by Alice Hamilton and others in the early twentieth century [3]. In 1930, benzo[a]pyrene was the first pure chemical found to be carcinogenic; other PAHs were identified as carcinogenic, and their extent in the environment recorded by 1954 [4]. What was not anticipated was that low levels of such substances distributed to the environment via emissions might have human health or environmental impacts. Dramatic evidence of a widespread, low-level combustion exposure is provided by the blood lead levels of the U.S. population in 1976–1980, when all gasoline contained tetra-ethyl lead; 4% of U.S. children had blood lead levels high enough to induce health effects [5]. Lead in gasoline is banned in the United States, and blood lead levels dropped 93% from 1979 to 1988 [6], while emissions dropped 97% [5].

The designation of "Superfund" sites in the late 1970s intensified research on environmental effects of xenobiotic compounds. Combustion research focused on incinerators, since the waste feedstocks were often hazardous, with high potential for toxic emissions [7]. Recently, toxics emissions from other combustion processes have come under scrutiny. Common issues include the influence that the feedstock and combustion and postcombustion processes have in the formation of air toxics, and the distribution of air toxics among environmental media.

Air toxics include volatile and semivolatile organics such as benzene and dioxins as well as inorganic species such as HCl, many metals, and particulates less

TABLE 1
Air toxics associated with combustion processes

HAPs[a,8]		Median or ranges ($\mu g/m^3$)[b]	Lifetime[c] (days)	Products	Biological impacts[8],f
Hydrocarbons					
Aliphatics	Acetonitrile		> 5	**Alkanes (C_{18} and less):** Aldehydes, alkyl nitrates, ketones, O_3 precursors with NO_x	R
	1,3-Butadiene	0.4	< 1		
	Hexane	3.8	< 1		
	Diethyl Sulfate		< 1(W)		
	Dimethyl Sulfate	8.1	< 1(W)	**Alkenes (C_4 and less):** Aldehydes, keytones, O_3, precursors with NO_x	
Aromatics	Benzene	5.1	> 5	phenol	C (leukemia)
	o-Cresol	1.5	< 1		
	m-Cresol		< 1		
	p-Cresol	0.5–20	< 1	**Monocyclic aromatics:** Hydroxylated & hydroxylated–nitro derivatives	C, M
	Nitrobenzene	ND	> 5		
	4-Nitrophenol	3–34 ng/m^3	1–5 to > 5		
	Phenol	17	< 1		
	Toluene	8.6	1 to 5		
	n-Xylene	2.2	< 1		
	m-Xylene	4.2	< 1		
	p-Xylene	4.3	< 1 to 1–5		
PAHs	Naphthalene	1.2	< 1	**PAHs (4 rings and more):** Nitro-PAHs, quinones & hydroxylated-nitro derivatives, nitro-PAH lactones	M, AL, R, suspected carcinogen
	Polycyclic Organic Matter[c]	ND–100 ng/m^3	< 1 to 1–5		

TABLE 1 (*Continued*)
Air toxics associated with combustion processes

HAPs[a,[8]]		Median or ranges ($\mu g/m^3$)[b]	Lifetime[c] (days)	Products	Biological impacts[[8],f]
Halogenated HCs					
Aliphatics	Bis(chloromethyl)ether		< 1 to 1–5 (W)	**Chlorinated alkanes/ alkenes:** carbinal dihalides, formyl dihalides, halogenated, ketones, HCl, aldehydes, and alcohols	Highly persistent if nonreactive with OH; reduces concentration of Stratospheric O_3
	Bromoform	ND			
	Carbon tetrachloride	0.8	> 5 (Ph)		
	Chloroform	0.2	> 5		
	Ethyl chloride	ND	> 5		BA, SK, E, R, A
	Ethylene dichloride	0.04	> 5		
	Hexachloroethane	ND	> 5		C_1 compounds are less likely to be carcinogenic
	Methyl chloride	1.3	> 5		
	Methyl chloroform	2.3	> 5		
	Methylene chloride	0.5	> 5		
	1,11,2,2-Tetrachloroethane	ND	> 5		C_3 compounds: M, G, C
	Tetrachloroethylene	1.7	> 5		
	1,1,2-Trichloroethane	ND	> 5		
	Trichloroethylene	0.4	> 5		
	Vinyl bromide		< 1 to 1–5		
	Methyl bromide	ND	> 5		
	Ethylene dibromide	ND	> 5		
	Vinyl chloride	ND	< 1 to 1–5	CO, formaldehyde, formic acid, formyl chloride, HCl	known carcinogen
	Phosgene	0.08	1 to 5 (W)	not well known	M, G, R
Aromatics	Bis(2-ethylhexy)phthalate	ND–17 ng/m^3	< 1	**Halogenated Monocyclic Aromatics:** products not well known	Many monocyclic, chlorinated aromatics are probable or suspected carcinogens, cause mutations and cancer in laboratory animals, and are general irritants.
	Chlorobenzene		> 5		
	1,4-Dichlorobenzene(p)	ND	> 5		
	Hexachlorobenzene	ND–13 ng/m^3	> 5		
	Pentachlorophenol[c]	1 ng/m^3	> 5		
	Phthalic anhydride	< 6	> 5		
	2,4,5-Trichlorophenol	ND–0.3 ng/m^3	> 5		
	2,4,6-Trichlorophenol	ND–0.3 ng/m^3	> 5		
	1,2,4-Trichlorobenzene	ND	> 5		SK, R

TABLE 1 (*Continued*)
Air toxics associated with combustion processes

HAPs[a,[8]]		Median or ranges ($\mu g/m^3$)[b]	Lifetime[c] (days)	Products	Biological impacts[[8],f]
PAHs[a]	Dibenzofurans (PCDF)	ND	< 1	**PCDD & PCDF**	C, M, E, R, N, BA, AL, RP
	2,3,7,8-TCDD	ND–0.05 pg/m^3	1 to 5		
	PCBs	1–36 ng/m^3	> 5	**PCBs:** UV reactions form toxic compounds	R, E, LV, AP, RP, C
Oxygenated Organics	Formaldehyde	3.3	1 to 5 (Ph)	**Formaldehyde:** CO, hydroperoxy radicals, O_3 with NO_x	C, AL, R
	Acetaldehyde	2.7	< 1	**Higher Aldehydes:** Peroxyacyl nitrates precursor to formaldehyde breaks down easily in environment, soluble in water	R, E, A, AL
	Acrolein	ND	< 1		
	Methanol	6–60	1 to 5		E, N, not well known
	Methyl Ethyl Ketone		< 1 (Ph)		E, R, SK, N
Metals	Arsenic compounds	ND–12 ng/m^3	> 5 (Dep)	Organisms can uptake and methylate metals. Metals never degrade entirely. The threat of remobilizations remains.	BA, Many metals are suspected carcinogens. Some metals have health benefits. Long-term exposure to metal dusts ⇒ R.
	Beryllium compounds	ND–0.5 ng/m^3	> 5 (Dep)		
	Cobalt compounds	ND–23 ng/m^3	> 5 (Dep)		
	Manganese compounds	ND–20 ng/m^3	> 5 (Dep)		
	Nickel compounds	ND–600 ng/m^3	> 5 (Dep)		
	Phosphorus		< 1 (Oxygen)		
	Antimony compounds	< 3 ng/m^3	> 5 (Dep)		C (lung & skin)
	Lead compounds	ND–300 ng/m^3	> 5 (Dep)		N, K, RP, C, BA
	Cadmium compounds	ND–200 ng/m^3	> 5 (Dep)		C, HD, IS, K, BA, LV, AS
	Chromium compounds	ND–120 ng/m^3	> 5 (Dep)	**Cr(VI):** Transforms quickly to Cr (III)	Cr(VP: C, AL, R, Cr: AO, AS
	Mercury compounds	ND–20 ng/m^3	> 5 (Aq. O_3)	**Mercury:** methyl mercury, increases rain acidification	BA, methyl mercury: N,
	Selenium compounds	ND–8 ng/m^3	> 5 (Dep)	**Selenium:** reduces human toxicity of other metals	BA, AT

TABLE 1 (*Continued*)
Air toxics associated with combustion processes

HAPs[a,[8]]		Median or ranges ($\mu g/m^3$)[b]	Lifetime[c] (days)	Products	Biological impacts[[8],f]
Other inorganics & mixtures	Chlorine		> 5	Removes O_3 in the stratosphere–ClO_x cycle	E, R, SK, A
	Coke oven emissions			not well known	not well known
	Hydrogen Fluoride	1–8	1 to 5 (Dep)	not well known	not well known
	Hydrogen Chloride	ND–4	1 to 5 (Dep)	Reaction with OH forms Cl atoms.	SK, R, E, C, A

Compounds of concern in combustion, but not on HAPs list

Aluminum	Benzo(a)pyrene (byproduct)	Chrysene	Hydrogen	Radium 226
Ammonia	Benzo(e)pyrene	Copper	Indeno(1,2,3-c,d)pyrene	In organic sulfates
Anthracene	Benzo(g)pyrylene	Dibenzo(a)aOnthracene	Methane	Sulfur
Barium	Benzo(h)pyrylene	Dibenzo(h)anthracene	Molybdenum	Thalium
Benz(a)anthracene	Benzo(i)pyrylene	Dibutylphthalate	Particulate Matter	Tin
Benzo(b)fluoranthene	Butylbenzylphthalate	Diethylphthalate	Particulate organic carbon	1,1,1-Trichlorethane
Benzo(k)fluoranthene	Carbon (elemental—black soot)	Fluoranthene	Phosphate	Vanadium
Benzo(j)fluoranthene	2-Chloronapthalene	Fluoride	Pyrene	Zinc
		Fluorine	Pyrylene	

RP, reproductive effects; C, probable human carcinogen; M, mutagen; G, genotoxic; N, nervous system effects; L, lung damage; LV, liver damage; K, kidney damage; HD, heart disease; IS, immune system effects; AL, allergen; AS, asthmategen; B, anemia; AP, abdominal pain; SK, skin irritant; E, eye irritant; R, respiratory irritant; BA, bioaccumulate in some plants and animals; A, agricultural or plant damage; AT, animal toxin.

[a]Hazardous Air Pollutants as defined by the EPA in the 1990 Clean Air Act.

[b]Ambient air concentration in vg/m^3, unless otherwise noted. ND, Nondetectable.

[c]Lifetimes are the estimated time required for the toxin to decrease 1/e (or 37%) its original value. The primary reaction is with OH, unless otherwise stated: Dep, dry or wet deposition; W, reaction with liquid water; Oxygen, reaction with O_2; Ph, photolysis; Aq. O_3, reaction with aqueous phase O_3.

[d]Likely to be present in both gas and particle phases in ambient air; lifetime calculated for gas phase, OH reaction.

[e]Toxicity information: Nauss et al. [96], Leikauf et al. [18], Watson et al. [85], and Harte et al. [6].

[f]Impact results from both the emission components and the atmospheric reaction products.

than 10 μm in diameter (PM_{10}). Air toxics in the United States are identified in Title III of the 1990 Clean Air Act Amendments (CAAA) as hazardous air pollutants (HAPs): 189 individual compounds, classes of compounds, or mixtures emitted by over 100 regulated source categories. Atmospheric levels of air toxics are not well characterized; for 74 of the HAPs, there are no reported values. Table 1 lists those HAPs found in combustion emissions and their median ambient air levels in the United States [8].

Air toxics regulations in the United States and Europe mandate emissions reporting, set allowable emission levels, and may define control measures. Title III requires maximum achievable control technology standards and establishes a goal of 75% reduction in cancer incidence risk by HAPs. The CAAA includes motor vehicle emission and fuel standards which govern emissions and control of air toxics as well. Emissions reporting is required under the CAAA and for certain facilities via the Toxic Release Inventory (TRI) (173 of the 300 TRI chemicals are also HAPs). Because many emissions inventories exclude sources, the U.S. Environmental Protection Agency (EPA) is developing National Screening Inventories (NSI) that include virtually all anthropogenic sources and major biogenic sources for 13 specific pollutants or pollutant categories; draft inventories for 12 species were published in 1995 [9]. Similar standards are set by the member countries of the Organization of Economical Cooperation and Development (OECD). Germany and Switzerland list 160 pollutants and source categories; other OECD countries set emissions or ambient air quality standards for specific air toxics [10].

No national air quality standards for air toxics exist in the United States. Attempts by states to establish ambient air level standards (AALs) have met with mixed success because of the difficulty in establishing no-effect levels. AALs for benzene exposure, standardized to a 24-h averaging time, range from 1718 $\mu g/m^3$ in New York to 1.2 $\mu g/m^3$ in Massachusetts; the former was based on an occupational standard; the latter was determined by a quantitative risk assessment [11].

This paper reviews the current knowledge on human health and environmental impacts to identify what aspects of four major classes of air toxics (volatile and semivolatile organics, dioxins and halogenated hydrocarbons, metals, and particulates) present current challenges to combustion science. In addition, it reviews the sources of combustion air toxics to identify the source or source characteristics whose modifications are critical to reducing emissions of air toxics from combustion systems.

Combustion Air Toxics: Sources and Impacts

Determining contributions by air toxics to rates of morbidity and mortality in human populations is complicated by the lack of information on atmospheric levels, the difficulty in assessing the risk from low-level exposures, and the lack of information on synergistic effects of exposure to multiple trace chemicals. Mass emissions information alone does not reveal the degree of hazard, nor do emissions inventories include effects of chemical and physical transformations. The toxicity of a compound is related to the exposure (duration and pathway), possible metabolic transformations, and the subsequent dose received by the target tissue.

Impacts (Table 1) may be associated with a single chemical, a class of chemicals, or combinations of chemicals, and range from short-term effects associated with direct exposure (irritancy or respiratory effects) to long-term effects (cancer, other chronic diseases, and reproductive impacts) [12]. While experiments show that over 50 air pollutants or mixtures are carcinogens in animals [13], data on carcinogenicity or genotoxicity exist for only about 10% of identified air pollutants (Graedel et al., 1986 as cited in Lewtas et al. [14]). Whether the level of carcinogens in urban air is significant is disputed [11]. Estimates of excess lung cancer cases attributed to air pollution range from 11 to 2% [13,15,16]. Other chronic and acute effects may be more important [17]. Chronic obstructive pulmonary disease (COPD) is the third leading cause of death, and accounts for 13–15% of all hospitalizations [18]. Increased incidence of asthma has been associated with air pollution, and several air toxics are asthmagens [19]. European studies show evidence of short-term effects and possible chronic effects from criteria pollutants at or below current standards [20,21].

Concern has escalated about exposures leading to disruption of the endocrine system and impacts on reproductive endpoints including male and female fertility, pregnancy loss, and fetal and postnatal development. Effects depends on the stage of development; each stage integrates several biological events that are potentially at risk when exposure to xenobiotics occurs [22]. For example, children's bones accumulate lead more rapidly than adults' [23]. High exposure during rapid development may explain scrotal cancer in adolescent chimney sweeps. Acute effects are a primary concern for children's health: respiratory diseases rank as the second highest cause of death in developing countries [24], and there is evidence that particulate exposures from cooking fires, especially using coal, contributes [25]. Increased asthma in children is associated with fine particulate pollution in developed countries [24]. The capacity for human milk to contain high levels of dioxin and other toxics means that nursing infants can receive higher doses; whether these exposures lead to health effects is not clear [26].

The relationship between the emission sources and the pollutant species that are toxic to human or

TABLE 2
Classes and characteristics of metals in combustion processes [138–140]

Grouped Classes of Metal Emissions
Class 1: Al, Ba, Be, Ca, Co, Fe, K, Mg, Mn, Si, Sr, and Ti • Do not easily volatilize, make up the matrix of fly ash and prevalent in bottom ash • Undergo mainly mechanical transport • If oxide more stable than chloride: mechanical transport is dominant, and the species is present in the matrix of fly ash
Class II: As, Cd, Cu, Ga, Pb, Sb, Zn, and Se • Easily volatilize, condense and found on the flyash surface; less in bottom ash • Transport mechanism is a combination of volatilization and condensation • If oxide stability = chloride stability: transport is by both volatilization-condensation and mechanical mechanisms
Class III: Hg, Cl, and Br • Volatilize but do not condense; found only in the gas phase • Transport mechanism is mainly volatilization with no condensation • If chloride is more stable than oxide: transport mechanism is volatilization-condensation and the compounds are deposited mainly on the surface of the fly ash

ecosystem receptors has been recognized as complex. What is experienced by the receptor often differs from the direct emissions [27]. The transformation of compounds, their deposition, and interaction in soil, water, and air affects their roles as contaminants [28]. Exposures may occur directly, or after the combustion emissions have been aged or transformed in the atmosphere (ozone, nitrates, sulfates, and particles), or because a compound persists in the environment [28].

Risk assessments suggest that it is persistent compounds (metals, polychlorinated aromatics, dioxins, dioxin like compounds, PCBs, and pesticides) that pose the greatest risk [29,30]. "Global pollutants" are persistent compounds that are atmospherically stable, can be revolatilized and redeposited, transported long distances, and accumulated through food chains, thus disrupting ecosystem services and, ultimately, adversely affecting human health [31]. In the environment, "individually minor stress can be significant when aggregated through space and time" [32]. Thus, the restricted spatial scale of many risk assessments is a problem; by not considering long-range transport and chemical and physical transformation, the adverse impacts are underestimated. Impacts associated with long-range transport may be more significant than previously believed [33] as suggested by a cross-media modeling study of the Chesapeake Bay. The study shows that the "geographical air shed" from which air is transported and from which material is ultimately deposited in the Bay is 5.5 times larger than the watershed [34]. Transport from major point sources is influenced by stack height; 70% of emissions exit tall stacks (>480 ft) compared to 1900 when 70% of emissions exited stacks less than 120 ft [33].

Assessing exposure requires knowledge of the atmospheric reactions, the reaction products, and the atmospheric lifetime. Table 1 lists the removal rates largely for daytime reactions with OH [8], and products for several combustion HAPs. Atmospheric transformation products may be more or less toxic than the original emitted species. Atmospheric lifetimes determine the spatial distribution and persistence of toxics: short lifetimes (<1 day) = local/regional (<200 km), midrange lifetimes (a few days) = continental (1000–5000 km), and long lifetimes (> week) = global [35], with persistent compounds lasting for over five days.

Sinks are important to the transport, transformation, and fate of pollutant species. Deposition in bodies of water or in soils may result in transformation. Studies of bioaccumulation of hydrophobic chemicals in the agricultural food chain are important for identifying exposure [36]. Vegetation may be a significant sink for lipophilic organic pollutants and can occur directly through uptake of gas-phase substances from the air, deposition of substances from the air on the plant, or uptake from the soil through the root system [37]. In many recent risk assessments, the ingestion of food, including fish, vegetables, and milk, accounts for close to 90% of the risk associated with particular compounds [30].

Organics: Volatile and Semivolatile Nonhalogenated

Impacts

Volatile (VOC) and semivolatile (SVOC) organics contribute to ozone and photochemical smog, may be adsorbed onto particle surfaces, and may directly expose humans or ecosystems (Table 2). Many organics cause acute effects at high doses. Chronic and/or high-level exposures are associated with cancer but the impacts of chronic, low-level exposures are not well understood. Differences in species sensitivity to organic compounds have been observed and evidence of different metabolic pathways suggests that understanding mechanisms is critical to determining whether a compound is a carcinogen in given species [38].

Benzene is a human leukemogin; other benzene-induced cancers are less probable in humans. Human reproductive/developmental effects have not been observed [39] although benzene has been shown to be embryo- and/or fetotoxic in animals [40]. Exposures to other gasoline components show varying effects among species; ethanol is a reproductive toxin for most [22]. Other combustion mixtures (coal tars and pitches, soots, and shale oil) are associated with cancer in humans [41]. Aromatic hydrocarbon solvents (e.g., toluene, xylene, and trichloroethylene) found in combustion emissions have induced neurotoxic effects in humans and animals, and PAHs have been associated with immune system [12], and reproductive effects as well [42]. At low doses, 1,3-butadiene is carcinogenic in mice; rats require high doses. Some epidemiological data suggests butadiene may be carcinogenic in humans [43].

Mobile/Area Sources

Vehicle exhausts contribute about one-half of the VOC emissions including over 50% of benzene emissions, about 75% of 1,3-butadiene emissions, and almost 50% of direct formaldehyde emissions [9]. In addition, 90% of formaldehyde and 40–60% of acetaldehyde in the atmosphere are formed photochemically from other organic precursors [44,45]. A respeciation study in Los Angeles, which found almost twice the level of unburned gasoline in the ambient air than previously estimated, suggests that the current inventory "understates emissions of unburned gasoline relative to combustion-derived hydrocarbons" [44]. The high levels of benzene and 1,3-butadiene in urban air correlate with gasoline formulations. Evidence is mounting that malfunctioning vehicles contribute disproportionately to tailpipe emissions [46].

In the United States, the National Screening Inventory (NSI) reports that about three-fifths of the 488,591 tons/year of emitted benzene were from mobile combustion sources in 1990. Mean personal exposure to benzene in the United States is 15 $\mu g/m^3$; mean atmospheric levels are 6 $\mu g/m^3$ [47]; cigarette smoking and driving in automobiles explain the difference in personal vs. ambient levels. In Paris, commuting in cars contributes 20–30% of daily inhaled benzene exposure [48], 2–6 times higher than ambient air levels, and is attributed to exhaust from surrounding vehicles. Similar exposures were observed in Taiwan [49,50].

Biomass burning is used extensively for land clearing, agricultural purposes, and to provide domestic and community fuels; little biomass burning is non-anthropogenic [25,51–53]. Biomass burning annually contributes 22% of the methyl chloride, 24% of the NMHC, and 39% of the particulate organic carbon, and probably 38% of the tropospheric ozone over the last 100 years [1]. Permanent removal of biomass (such as deforestation) eliminates critical sinks for heavy metals and other toxic compounds.

One of the highest sources of exposures internationally is stoves burning biomass or coal indoors in rural households. About 50% of the world's households rely on burning biomass for heating and cooking, accounting for up to 10% of global fuel usage. This may produce a dose of certain pollutants comparable to that of all other fuels combined. Emissions of hydrocarbons and CO per unit of delivered energy from biomass can exceed those of coal and other fossil fuels. Actual exposures depend on stove design and household ventilation as well as the feedstock [25].

Major Point Sources

Although the mass of VOC emissions associated with major combustion point sources (utilities, incineration, furnaces, and industrial boilers) is relatively small (2% of the U.S. total of 23 × 106 tons of VOCs in 1994) [9], the significance of these sources to total exposure is controversial [54–59]. A study on low-emission boiler systems suggests that polycyclic organic material (POM) is the most probable organic emission, although benzene, formaldehyde, 1,3-butadiene, and several chlorinated organics also have a probability of being emitted [56]. Concerns remain about direct, local impacts caused by mixtures of organics, and long-range impacts of persistent compounds from tall stacks.

Dioxins and Halogenated Organics

Impacts

Halogen-containing compounds may be present in feedstocks or may be generated during combustion. Volatile chlorinated hydrocarbons have high lipid solubility which contributes to rapid absorption in humans [60]. The persistence and atmospheric stability of other halocarbons contributes to stratospheric ozone loss and greenhouse effects; evidence of damage due to uptake by plants and animals also exists [60]. The estimated average human intake of dioxins in the United States and Europe is about 50 times the virtually safe level estimated by the EPA. Most exposure is from diet, with negligible intake via inhalation [61]. Fifty percent of exposures are attributed to local sources and about 50% reflect advective inflow from outside sources [62].

Halocarbons such as CH_3Cl, HFCs, or CH_3CCl_3 react slowly with OH to form carbinal dihalides, formyl dihalides, or halogenated ketones, aldehydes, and alcohols [60]. In general, C_1 compounds have low carcinogenic potential; saturated C_2 compounds (e.g., 1,2-dichloroethylene) are potential carcinogens. Unsaturated C2 compounds include vinyl chlo-

ride which is carcinogenic, and trichloroethylene and tetrachloroethylene which are suspected carcinogens. C_3 compounds are directly genotoxic and mutagenic as are oxygen-containing CHCs [63].

Persistent bioaccumulative organohalogen compounds are considered potential "environmental hormone disrupters" or xenoestrogens [64]. Xenoestrogens are most likely the coplanar halogen-substituted multiring structures such as PCDDs, PCDFs, and some PCBs [65]. The working hypothesis is that these compounds bind to the Ah receptor and act as endocrine disruptors, impacting the immune, neurobehavioral, endocrine, and reproductive systems [66]. However, there is recent evidence that TCDD and other like compounds may actually inhibit certain estrogen-induced responses [67]. That xenoestrogens are present in the environment at concentrations substantially lower than natural levels of estrogens found in plants or in humans suggests to some that they are unlikely to produce the observed effects [65,68]. One new study, however, indicates that certain pesticides, when combined, show up to 1000 times higher estrogenic activity than when evaluated alone, a finding that if replicated may change the evaluation of potential xenoestrogens [69], and has implications for evaluating synergistic effects of combustion emissions.

Sources

Environmental levels of dioxins have been estimated to be several times higher than can be accounted for by source emissions estimates [70]. Several studies have attempted to reconcile the estimated mass emissions of dioxins and the apparent rate of deposition in the environment. Rigo et al., and Hattemeyer-Frey and Travis argue that there is a significant unknown dioxin source based on their assessment of deposition versus source emissions [59,71]. Gribble argues that global forest fires contribute a larger fraction than previously estimated [72], and Thomas and Sprio conclude that there are no missing sources [73]. The latter argue that although deposition data are scarce, the distributions correlate with historical patterns of production and use, and reductions are observed with improved controls. U.S. dioxin deposition is estimated at 10–20 kg toxic equivalency (TEQ)/year of dioxins; source emissions are estimated between 9 kg TEQ/year (EPA) and 6 kg TEQ/year [73]. These results appear consistent with a recent global study examining deposition and sources that show a factor of 4 difference [70].

The distributions of dioxins and furans (the homologue profiles) found in soil samples are often different from the source profiles [70], raising questions about vapor-phase versus particle transport, the behavior in the environment of different congeners, and the potential for reentrainment of congeners. Vapor-phase dioxins (usually less chlorinated and more toxic) react with OH, photolize, or are removed by vegetation; deposition from point and area sources is dominated by particles less than 2.5 μm, estimated to account for 0.5–10% of deposited dioxin. The resuspension and subsequent redeposition of dioxin-containing soil dust (dp $>$ 2.5 μm) may account for significant fractions of soil deposition (upward of 90% in urban areas) which could explain the missing source discrepancy. These estimates, however, need to be verified in the field [74].

There is a remarkable consistency in the rank ordering of dioxin sources although there is high uncertainty, particularly on the upper bounds [73]. The two major sources in the United States appear to be medical waste incineration (Thomas and Spiro estimate 700 g TEQ/year; EPA estimates 5000 g TEQ/year; range including uncertainty is 200–10,000 g TEQ/year), and municipal waste incineration (2000–3000 g TEQ/year, range 900–9000) [73]. Cement kilns and boilers, industrial wood burning, secondary copper smelting, and forest fires each contribute about 200 g TEQ/year, although the cement kiln upper bound is much higher. In Germany, steel reclamation plant contributions appear comparable to municipal waste incineration [75]. Several studies observe that burning metal scrap containing high levels of organics leads to higher levels of dioxins [76,77]. Globally, it is estimated that leaded gasoline contributes about 11 kg/year dioxin, and unleaded gasoline about 1 kg/year [70].

Metals

Impacts

Metals in the environment participate in geological and biological cycles; mobility occurs naturally or is induced by anthropogenic actions. Long-range transport and acid deposition play key roles in the exposure process [78]. Of the 80 metal or metallic-like elements, about 30 have known impacts on humans [79]. Metals of concern are transition-state metals and, in some cases, alkali metals, and the ancient metals (lead, iron, tin, and copper). Certain metals are biologically essential and protect cells at low levels of exposure; protection fails at higher levels [80]. The speciation of a metal, that is, its chemical form and oxidation state and/or the metal complex in a biological system, determines the degree of toxicity [81]. Oxidation-reduction reactions are important factors in metal toxicity; as the oxidation state changes, the toxicity of the metal species changes. For example, chromium (VI) is carcinogenic in humans; chromium (III) is not. Although the mechanisms of reaction for methylation are similar, the outcomes depend on the methyl donors, reaction conditions, and the original metal form.

Methylation of Sn and Hg increase toxicity; methylation of As reduces it [82].

Human exposure to metals occurs primarily through ingestion (80–90%), although inhalation exposures also occur. Cd, Cr, Se, Ni, and As affect the kidney, liver, and skin. Pb, methyl mercury, Sn, and Al can affect the central nervous system. Methyl mercury and Pb can impair fetal development. Cancer is associated with Ar, Be, Cd, Cr, and Ni.

Ecosystems are also affected by metals. Recent studies have evaluated the uptake of metals into vegetation and the bioconcentration and bioaccumulation of metal species that may be consumed by humans or other organisms. Plants have significant uptake of cadmium which accumulates in the food chain. Arsenic affects plant fertility. Forest decline, attributed in part to acids and oxidants, may be a function of metal exposure as well. Recent work on phytochelatins (intracellular metal-binding peptides) shows higher levels in trees in decline than in those that are healthy [83].

Sources

Metals are found in feedstocks. The manner in which metals are bound to organic material influences their distribution in the emissions. Combustion sources contribute virtually all the anthropogenic cadmium and mercury [9]. Although mercury emissions are largely biogenic (a result of degassing from the lithosphere or the hydrosphere), about two to five times more anthropogenic mercury is deposited now compared to preindustrial times, and can affect the global cycle of mercury. Eighty percent of the anthropogenic emissions are from fossil fuel combustion, mining, and smelting, and 80% are released to the air.

Recent studies estimate metal emissions and associated health risks from specific utilities, industrial boilers, and incinerators. Consideration of long-range transport and multiple exposure pathways, and the appropriate values for emissions estimates are sources of debate. Two studies suggest that the most likely metals released from industrial or utility boilers are arsenic, beryllium, cadmium, lead, chromium, manganese, mercury, and selenium [54,56]. One study found cumulative carcinogenic risks from utilities are less than one in a million, although the metal contributing the highest mass emission or the highest risk tends to be site specific [54]. Metal emissions are a concern in waste incineration as well [84].

Lead and manganese are the two metals released from mobile sources. Lead emissions are a major source of exposure in those countries that continue to permit leaded gasoline [85].

Particulates

Impacts

Particulates are composed in part of polycyclic organic matter (POM), which includes polycyclic aromatic hydrocarbons (PAHs), heterocyclic aromatic compounds (e.g., aza-arenes), and substituted aromatic hydrocarbons (e.g., nitrated-PAHs). Particulates are a means for transporting semivolatile air toxics and metals. Primary particulates are emitted directly; secondary particulates are formed by atmospheric chemical reactions.

Lung cancer and cardiovascular and respiratory diseases are positively associated with air pollution exposures. Recent studies show strong associations between outdoor concentrations of TSP, PM_{10}, or smaller particles, and increased human mortality and morbidity [86–89]. Although the weight of the evidence appears strong, a few studies do not show the reported effects [90,91]. Questions have been raised about the data analysis techniques, why the association is observed with outdoor measurements, and because a biologically plausible hypothesis for the association has been lacking [92,93]. A comprehensive reevaluation of data from six cities suggests that "daily mortality from all causes combined, and from cardiovascular and respiratory causes in particular increased as levels of particulate air pollution indexes increased." The reanalysis shows that the results are not dependent on the analytic approach; however, the association does not yet support an independent effect of either TSP or SO_2 alone [94]. Another comprehensive review that considered TSP, PM_{10}, $PM_{2.5}$, PM_{10}–$PM_{2.5}$ (coarse particles), COH, SO_x, H^+, and CO shows that one can attribute about 5% mortality to air pollution. The role of other air toxics was not directly considered [86].

The current working hypothesis argues that ultrafine particles (0.01–0.1 μm) penetrate and remain in the alveolar regions of the human lung, causing local reactions and long-term chronic damage. These submicron particles (often enriched with metals) are not easily controlled, are easily transported, and persist in the atmosphere. A recent study examining the penetration indoors of outdoor VOCS, PM_{10}, and $PM_{2.5}$ suggests that the protective effect of being indoors was less strong than expected [95], lending support to the association between outdoor particle measurements and human mortality and morbidity.

Diesel exhaust, consisting of low molecular weight gases and carbonaceous particles to which higher molecular weight compounds are absorbed, is classified as a hazardous air pollutant and is under consideration as a human carcinogen [96]. Effects are associated with the combination of soot particles, particle-associated organics, and the gas phase compounds, including odor, eye irritation, chronic lung function decrements, cardiovascular symptoms, lung cancer, and bladder cancer, although new evidence suggests that the carbon core may be more important than the associated organic mutagens or carcinogens [97]. Evidence suggests a relative risk of about 1.5 for diesel exhaust carcinogenicity [38,98].

Area and Point Sources

Particle composition varies regionally and seasonally; crustal matter often dominates in rural areas (up to 90% total PM_{10} mass); urban particles are generated from vehicles, biomass burning, and other activities [74,99,100]. EPA emission inventories show total combustion sources contributing only about 5% annually to the 40 million tons of PM_{10} [9]. Stationary source combustion and metals processing contribute a similar fraction as mobile sources; residential and commercial sources contribute slightly less. However, virtually all the reported emissions of extractable organic matter (almost 700,000 tons/year) come from combustion sources [9].

In Los Angeles, contemporary carbon sources (fireplace use, cooking, cigarette smoke, paved road dust, and brake dust) contribute up to one-third of the fine carbon aerosol (particles $< 2.5\ \mu m$) [101]. Evaluation of fine particle emissions rates from residential and high-priority commercial natural gas combustion suggests that these sources could contribute as much PAH and oxy-PAH as that contributed by diesel vehicles, and about one-half that contributed by catalyst equipped vehicles [102].

Stoves burning biomass or coal indoors can produce high levels of TSP and PM_{10}. Data from several studies show that total suspended particulate levels in rural developing countries are several times the accepted standards in the United States, Europe, and Japan [25,103].

Mobile Sources

In the San Joaquin Valley, mobile sources contribute only 5–10% of the PM_{10} mass [99]. However, in Los Angeles, 62% of the fine particulate primary fossil carbon aerosol is attributed to motor vehicles; fossil aerosols are about 50% of the total fine carbon aerosol [101]. The fraction of extractable organic matter (EOM) found in urban air particles apportioned to motor vehicles often contributes a high fraction of the sample mutagenicity [14]. Emitted particles from vehicles are in the range suspected of contributing to adverse health effects. Whether mobile sources are a significant source of particulate exposure leading to adverse effects remains a question.

Intervention and Control: Research Directions

The above review of sources and impacts of combustion-generated air toxics demonstrates that damage caused by emissions is not a function of the combustion process alone. Understanding interactions among the fuel or feedstock, the combustion process, and the postcombustion environment is crucial to prevention and, if understood, may be exploited as means for control. This review also suggests that toxicity is complex: rather than being an inherent characteristic of the structure of a chemical compound or element, it depends on the character of the receptor and the way the chemical structure is modified by the environment or by the receptor's metabolism. In addition, a compound's reactivity in different media and its persistence and stability determine the impacts. Decisions about control depend not only on the direct emissions from combustion processes, but also on the postcombustion environment. The following considers three cases where an understanding of these interactions will contribute to reducing air toxics.

Vehicles and Fuels: A Critical Partnership

That mobile combustion sources contribute significantly to air toxics has been shown in this review. Modification of vehicle combustion technologies and fuels has been guided by knowledge of the contributions that emitted compounds make to the production of ozone and photochemical smog, as well as other environmental and human health impacts [104,105]. Vehicle technology improvements such as fuel injectors, exhaust gas recirculation, computer control, and three-way catalysts reduce unburned fuel or combustion emissions; tailpipe HC emissions dropped from 7.25 g/mile to 0.39 g/mile for cars built in the United States after 1982 [106]. Considerable information is available on the chemistry of the troposphere and the impact of anthropogenic emissions on that chemistry. By understanding the complex chemistry, automotive fuels can be tailored to reduce emissions that contribute to photochemical smog, CO emissions, or immediate or long-term health effects; oxygenated fuels reduce CO, and reformulated gasoline reduces emissions of toxics and components that contribute to ozone production and photochemical smog [107]. Tunnel studies in the San Francisco Bay area show oxygenated fuel use reduces CO by 21% ($\pm 7\%$), benzene by 25% ($\pm 17\%$), and VOCs by 18% ($\pm 10\%$), with an increase of 13% of formaldehyde ($\pm 6\%$) [108].

In addition to fuel modifications, improvements in cold start, warm-up control, and catalysts can influence the specific reactivity and mass of toxic air pollutants. This requires improved understanding of hydrocarbon oxidation in the postflame exhaust [109], coupled with the knowledge of what species persist or react to form more toxic compounds.

Postcombustion Chemistry: The Case of CHCs

Koshland and coworkers, and others have studied the flame and postflame regions of combustion processes to understand what increases or reduces the production of air toxics even under conditions in which sufficient time, temperature, and mixing of

feedstock and oxidizer are presumed to occur [110–121]. Studies have focused on C_1–C_4 chlorinated compounds because of their presence in waste incineration, and their environmental stability and persistence. Substantial progress in identifying the basic reaction mechanisms for C_1–C_4 CHCs has been made and these mechanism are summarized in Senkan [116]. More important for the future, however, may be studies of the interactions of hydrocarbons, chlorinated species, and metals, which lead to higher emissions of CO and the formation of air toxics including polychlorinated aromatics. The picture presented by halogenated compounds is complex—the many congeners and the vast differences in impacts make control decisions difficult.

Dioxin illustrates the importance of postcombustion chemistry. It is proposed that dioxin formation occurs through two principal mechanisms: (1) PCDD/F formation from direct chloroorganic precursors in heterogeneous catalysis reactions in the presence of fly ash surfaces; and (2) PCDD/F de novo synthesis from simple organocarbon sources (active carbon particulates) and inorganic chlorine at temperatures between 200 and 500°C in the presence of metal catalysts [122], although there is evidence that, given appropriate conditions of time and temperature, any combination of C, H, O, and Cl may yield dioxin or dioxin-like compounds [123]. The role of products of incomplete combustion in the formation of simple chlorinated aromatics at $T \geq 400$°C may be fundamental to dioxin formation and the formation of other toxic, persistent, chlorinated and nonchlorinated aromatics. Several pathways from short-chain C_2 aliphatics to simple chlorinated aromatics have been demonstrated experimentally [123–125]. Recent observations have shown that O_2 is required for de novo synthesis [126,127]. The most important parameter for formation of PCDDs, PCDFs, BCBzs, and PCBs may be the residence time in the postcombustion zone [128].

The evidence suggests that reducing the opportunity for chlorinated species (organic and inorganic) to interact with metals, especially in the temperature range between 200 and 800°C, is critical. Products that may ultimately be incinerated or reprocessed (as in steel reclamation) should be designed so that metals and plastics can be separated prior to exposure to elevated temperatures, and combustion systems designed to minimize the residence times at those temperatures.

Exploiting Interactions: Metals Control

The combustion process can determine the extent to which any particular combination of toxic metals may distribute into the three environmental media—and that challenges us to devise methods to modify combustion and air pollution control equipment to minimize multimedia impact. Knowledge of metal speciation and partitioning is necessary to develop control strategies [79]. Similarly, advances in control may come from exploiting the interaction of various species of metals with volatile or semivolatile organics or other compounds; less reactive metal may reduce environmental impacts. Studies of metals' interactions with O_2, sorbents, chlorine, or sulfur are providing new insights into ways of reducing metals emissions. Several factors that influence metal behavior, including residence time, temperature, metal speciation, vapor pressure of the metal species, metal concentration, and the role of nonmetallic chemicals, are summarized in Table 2 [138–140].

It is the metal in the vapor phase that appears to be of greatest concern, and preventing vaporization is the challenge. Vaporized metals may nucleate and/or condense, then coagulate [79]. Vapor pressures of pure metals do not predict species formation [131]. Some species such as NiO have low vapor pressures [130] and are not readily vaporized. Metal chlorides such as $NiCl_2$ vaporize at combustion temperatures. Even in trace amounts, chlorine can increase vaporization and affect speciation, causing less mature aerosols [79,129–131,133,135,141,143]. Sulfur may inhibit formation of metal chlorides.

Equilibrium calculations do not accurately predict field measurements [133,141]. A bimodal particle size distribution (PSD) with micron and submicron particles can be used to represent emissions from incinerators, boilers, and industrial furnaces [143]. Detailed kinetic models may be necessary in determining PSD, since various metallic species possess different physical properties (i.e., surface tension) that are important in aerosol formation calculations. Various species and PSDs require different control strategies [145].

Metals could be a key factor in the increased use of biomass fuels. Biomass is as variable as coal and ranges from solids to sludges and biomass wastes from paper and wood processing. The presence of alkali metals, essential for plant growth, contribute to fouling and slagging and to air pollution [147]. On the other hand, combining biomass with other feedstocks may lead to prevention: heavy trace metals are distributed differently in burned coal and incinerated biosludge. One study found that the outer surface of fly ash from burned biosludge was composed of light metals layers (Si, Ca, Al, NA, K), while the heavy metals were located near the center [136]. Glassy fly ash particles may reduce the leachability of fly ash. Genetically engineered plants have been proposed to take up metals from soils; in some cases, the metals are reduced to less toxic forms by the plants [148]. Volatile metals would be released into the air from the plants; other metals would be recovered by harvesting and burning the vegetation.

Assessing Impacts During Design

Recent work has investigated compounds that may affect reproduction or development, and are persistent and environmentally mobile. Reducing simultaneous exposures to several compounds that may give rise to synergistic or antagonist effects has received less attention. Researchers are attempting to develop indices for design and research guidance as well as for risk assessment that include these concepts [28,149,150–151]. It is hoped that these green design tools will aid in evaluating the tradeoffs associated with different environmental or health impacts, leading to an overall reduction of the entire mass emission or selective control. One such index is a proposed modification to the DRE (which is based on mass throughput of POHCs only) to include product and byproducts weighted by toxicity factors derived from carcinogenic potential and noncarcinogenic hazard index [150]. The relative change in the toxicity of the emissions for different substances under different technologies was easily discerned. This approach, however, neglected pathways other than inhalation, and considered only direct emissions. Development of green design tools is constrained by lack of information about sources of emissions, their transformation and fate in the environment, and the relative toxicity associated with routes of exposure and characteristics of the receptor such as species, age, or sex. Nevertheless, efforts to modify combustion processes or feedstocks using green design approaches may have advantages over relying solely on mass emissions estimates and air pollution control technologies to reduce toxics.

Conclusions

The preferred strategy in the combustion research community has been to address questions about emissions by directly influencing the combustion process [152]. But the combustion process alone does not determine the emissions. The coupling of the combustion process with a particular feedstock is a major determinant of toxic byproduct production. The coupling of the flame processes with downstream events, either in the postflame region of the combustor or in the air pollution control system, also plays a critical role. Emissions, once released, may be transformed in the atmosphere and, depending on their stability and persistence, may be transported over a wide region before wet or dry deposition removes them. Previous control efforts have been based either on a compound's toxicity, usually with respect to one health endpoint, or have involved condemnation of a class of compounds, or even a process. This review demonstrates that combustion science's efforts should extend to reducing exposures to those compounds or mixtures that are persistent, bioaccumulate, have reproductive or developmental impacts, or that affect ecosystem health. By focusing research on the interactions of emitted compounds with the environment and applying that knowledge to design combustion or post-combustion processes or to modify feedstocks, more effective control and reduced exposures to combustion air toxics can be expected.

Acknowledgments

Without the considerable efforts of Lee Anne Sgro, this paper would not have been completed. Thanks also to Don Lucas and Steve Buckley for reading and critiquing the manuscript. Partial support for this work is from the University of California Toxic Substances Research and Teaching Program, and the Wood-Calvert Chair in Engineering. This publication was made possible in part by grant number P42-ES04705 from the National Institute of Environmental Health Sciences, NIH, and its contents are solely the responsibility of the author and do not necessarily represent the official views of the NIEHS, NIH.

REFERENCES

1. Levine, J. S., et al., *Env. Sci. Technol.* 29:121A (1995).
2. Sawyer, R. F., *Eighteenth Symposium (International) on Combustion,* The Combustion Institute, Pittsburgh, 1981, p. 1.
3. Sicherman, B., *Alice Hamilton: A Life in Letters,* Harvard University Press, Cambridge, MA, 1984.
4. Finlayson-Pitts, B. J. and Pitts, J. N., Jr., *Atmospheric Chemistry: Fundamentals and Experimental Techniques,* John Wiley and Sons, New York, 1986.
5. Godish, T., *Air Quality,* 2nd ed., Lewis Publishers, Chelsea, MI, 1991.
6. Harte, J., et al., *Toxics A to Z, a Guide to Everyday Pollution Hazards,* University of California Press, Berkeley, CA, 1991.
7. Koshland, C. P., *Combust. Sci. Technol.* 101:1 (1994).
8. Kelly, T. J., et al., *Environ. Sci. Technol.* 28:378A (1994).
9. EPA, *National Air Pollutant Emission Trends, 1900–1994,* US EPA, Research Triangle Park, NC, 1995.
10. Wiederkehr, P., in *Managing Hazardous Air Pollutants, State of the Art,* (W. Chow and K. K. Connor, Eds.), Lewis Publishers, Boca Raton, FL, 1993, p. 29.
11. Calabrese, E. J. and Kenyon, E. M., *Air Toxics and Risk Assessment,* Lewis Publishers, Boca Raton, 1991.
12. Bailey, B. J. and Grupenhoff, J. T., *National Conference on Air Pollution Impacts on Body Organs and Systems,* National Association of Physicians for the Environment (NAPE), Bethesda, MD, 1994.
13. Tomatis, L., *Air Pollution and Human Cancer,* Springer-Verlag, Berlin, 1990.
14. Lewtas, J., et al., *Pharmacogenetics* 2:288 (1992).
15. Karch, N. J. and Schneiderman, M. A., *Explaining the Urban Factor in Lung Cancer Mortality,* Clement

Associates, Report to the Natural Resources Defense Council, Washington, DC, 1981.
16. Doll, R. and Peto, R., *J. Natl. Cancer Inst.* 66:1191 (1981).
17. Sexton, K., *Environ. Health Perspect.* 103:213 (1995).
18. Utell, M., Personal Communication, 1996.
19. Leikauf, G. D., et al., *Environ. Health Perspect.* 103:253 (1995).
20. Katsouyanni, K., *Environ. Health Perspect.* 103:23 (1995).
21. Brunekreef, B., Dockery, D. W., and Krzyzanowski, M., *Environ. Health Perspect.* 103:3 (1995).
22. Skalko, R. G., *Environ. Health Perspect.* 101:143 (1993).
23. Bearer, C. F., *Environ. Health Perspect.* 103:7 (1995).
24. Bates, D. V., *Environ. Health Perspect.* 103:49 (1995).
25. Smith, K. R., *Biofuels, Air Pollution, and Health: A Global Review,* Plenum Press, New York, 1987.
26. Sonawane, B. R., *Environ. Health Perspect.* 103:197 (1995).
27. Cass, G., "Physical and Chemical Characteristics of Airborne Particulate Matter," *Fourth International Conference on Toxic Combustion Byproducts,* Berkeley, CA, 1995.
28. Horvath, A., et al., *Environ. Sci. Technol.* 29:86A (1995).
29. Eitzer, B. D. and Hites, R. A., *Chemosphere* 18:593 (1989).
30. Smith, A. H. and Goeden, H. M., *Combust. Sci. Technol.* 74:51 (1990).
31. Halsall, C. J., et al., *Env. Sci. Technol.* 29:2368 (1995).
32. Cairns, J., Jr. and Niederlehnen, B. R., *Environ. Health Perspect.* 102:936 (1994).
33. Pahl, D. A., Zimmerman, D., and Ryan, R. (eds.), *An Overview of Combustion Emissions in the United States,* Lewis Publishers, Ann Arbor, MI, 1990.
34. Appleton, E. E., *Environ. Sci. Technol.* 29:550A (1995).
35. Winer, A. M. and Busby, W. F., Jr., in *Diesel Exhaust: A Critical Analysis of Emissions, Exposure and Health Effects,* Health Effects Institute, Cambridge, MA, 1995, p. 83.
36. McLachlan, M. S., *Environ. Sci. Technol.* 30:252–259 (1996).
37. Simonich, S. L. and Hites, R. A., *Environ. Sci. Technol.* 29:2905 (1995).
38. Mauderly, J. L., *Toxicol. Environ. Chem.* 49:167 (1995).
39. Raabe, G. K., *Environ. Health Perspect.* 101:35 (1993).
40. Paustenbach, D. J., Bass, R. D., and Price, P., *Environ. Health Perspect.* 101:177 (1993).
41. Vainio, H., Wilbourn, J., and Tomatis, L., in *Advances in Modern Environmental Toxicology, The Identification and Control of Environmental and Occupational Diseases: Hazards and Risks of Chemicals in the Oil Refining Industry,* (M. A. Mehlman and A. Upton, Eds.), Princeton Scientific Publishing Co., Princeton, NJ, 1994, p. 1.
42. Seppalainen, A. M., in *The Identification and Control of Environmental and Occupational Diseases: Hazards and Risks of Chemicals in the Oil Refining Industry,* (M. A. Mehlman and A. Upton, Eds.), Princeton Scientific Publishing Co., Princeton, NJ, 1994, p. 223–233.
43. Lang, L., *Environ. Health Perspect.* 102:282–285 (1994).
44. Harley, R. A., Hannigan, M. P., and Cass, G. R., *Environ. Sci. Technol.* 26:2395 (1992).
45. Loscutoff, W. V. and Poore, M. W., (Eds.), *Ambient Air Toxics Data from California's Toxic Air Contaminant Monitoring Program,* Lewis Publishers, Boca Raton, FL, 1993.
46. Zhang, Y., et al., *Environ. Sci. Technol.* 29:2286–2294 (1995).
47. Wallace, L. A., *Environ. Health Perspect.* 82:165 (1989).
48. Dor, F., Le Moullec, Y., and Festy, B., *J. Air Waste Manage. Assoc.* 45:103 (1995).
49. Chan, C.-C., et al., *J. Air Waste Manage. Assoc.* 45:116 (1995).
50. Chan, C. C., Lin, S. H., and Her, G. R., *J. Air Waste Manage. Assoc.* 43:1231 (1993).
51. Pyne, S. J., *Chemosphere* 29:889 (1994).
52. Andrea, M. O., in *Global Biomass Burning,* (J. S. Levine, Ed.), The MIT Press, Cambridge, MA, 1991.
53. Levine, J. S. (Ed.), *Global Biomass Burning,* The MIT Press, Cambridge, MA, 1991.
54. Lamarre, L., *EPRI J.* 6 (1995).
55. Jones, C., *Power* 138:51 (1994).
56. Wesnor, J. D., in *Combustion Modeling, Scaling, and Air Toxics,* (Gupta, K., Moussa, A., Presser, C., Rini, M. J., Weber, R., and Woodward, G., Eds.), ASME FACT, 18, ASME, New York, p. 155 (1994).
57. Dempsey, C. R., *Air Waste* 43:1374 (1993).
58. Travis, C. C., et al., *Inhalation Pathway Risk Assessment of Hazardous Waste Incineration Facilities,* Oak Ridge National Laboratory, Oak Ridge, TN, 1984.
59. Hattemer-Frey, H. A. and Travis, C. C., in *Emissions From Combustion Processes: Origin, Measurement, Control,* (R. Kagel and R. Clement, Eds.), Lewis Publishers, Ann Arbor, MI, p. 439.
60. Zabel, F., *Toxicol. Environ. Chem.* 46:153 (1994).
61. Schecter, A., et al., *Environ. Health Perspect.* 102:962 (1994).
62. Paterson, S., et al., in *Emissions From Combustion Processes: Origin, Measurement, Control,* (R. Kagel and R. Clement, Eds.), Lewis Publishers, Inc., Ann Arbor, MI, 1990, p. 405.
63. Eder, E., *Toxicol. Environ. Chem.* 46:137 (1994).
64. McKinney, J. D. and Wallen, C. L., *Environ. Health Perspect.* 102:290 (1994).
65. Rhomberg, L., in *Risk in Perspective,* Harvard Center for Risk Analysis, Cambridge, MA, 1996, p. 1.
66. Lindström, G., et al., *Environ. Health Perspect.* 103:135 (1995).
67. Safe, S. and Krishnan, V., *Toxicol. Lett.* 82:731 (1995).
68. Simons, S. S. J., *Science* 272:1451 (1996).

69. Arnold, S. F., et al., *Science* 272:1489–1492 (1996).
70. Brzuzy, L. P. and Hites, R. A., *Environ. Sci. Technol.* 30:1797–1804 (1996).
71. Rigo, H. G., *Solid Waste Technol.* Jan/Feb:36 (1995).
72. Gribble, G. W., *Environ. Sci. Technol.* 28:310A (1994).
73. Thomas, V. M. and Spiro, T. G., *Environ. Sci. Technol.* 30:82A (1996).
74. Kao, A. S. and Vankataraman, C., *Chemosphere* 31:4317 (1995).
75. Jager, J., *Toxicol. Environ. Chem.* 40:201 (1993).
76. Alawi, M. A., et al., *Chemosphere* 32:907 (1996).
77. Gonzalez, M. J., et al., *Toxicol. Environ. Chem.* 33:169 (1991).
78. Nordberg, G. F., *Toxicol. Environ. Chem.* 49:131 (1995).
79. Linak, W. P. and Wendt, J. O. L., *Prog. Energy Combust. Sci.* 19:145 (1993).
80. Clarkson, T., *Environ. Health Perspect.* 103:9 (1995).
81. Carter, D. E., *Environ. Health Perspect.* 103:17 (1995).
82. Hamasaki, T., et al., *Crit. Rev. Environ. Sci. Technol.* 25:45 (1995).
83. Gawel, J. E., et al., *Nature* 381:64 (1996).
84. Travis, C. C. and Blaylock, B. P., *Toxicol. Environ. Chem.* 49:203 (1993).
85. Watson, A. Y., Bates, R. R., and Kennedy, D. (Eds.), *Air Pollution, the Automobile, and Public Health,* National Academy Press, Cambridge, MA, 1988.
86. Lipfert, F. W. and Wyzga, R. E., *J. Air Waste Manage. Assoc.* 45:949 (1995).
87. Dockery, D. W. and Pope III, C. A., *Annu. Rev. Public Health* 15:107 (1994).
88. Dockery, D. W., et al., *New Engl. J. Med.* 329:1753 (1993).
89. Pope III, C. A., et al., *Am. Rev. Respir. Dis.* 144:668 (1991).
90. Moolgavkar, S. H., et al., Colloquium on Particulate Air Pollution and Human Mortality and Morbidity, (Phalen, R. J., Ed.), Air Pollution Health Effects Laboratory, Community and Environmental Medicine, University of California, Irvine, CA, 1994, pp. 235–251.
91. Styer, P., et al., *Environ. Health Perspect.* 103:490 (1995).
92. Utell, M. J. and Frampton, M. W., Colloquium on Particulate Air Pollution and Human Mortality and Morbidity, (Phalen, R. J., Ed.), Air Pollution Health Effects Laboratory, Community and Environmental Medicine, University of California, Irvine, CA, 1995, pp. 386–406.
93. Utell, M. J. and Samet, J. M., *Am. Rev. Respir. Dis.* 147:1334–1335 (1993).
94. HEI, Particulate Air Pollution and Daily Mortality, Health Effects Institute, Cambridge, MA, 1995.
95. Wallace, L., *J. Air Waste Manage, Assoc.* 46:98 (1996).
96. Nauss, K. M., et al., in *Diesel Exhaust: A Critical Analysis of Emissions, Exposure, and Health Effects,* Health Effects Institute, Cambridge, MA, 1995, p. 11.
97. Scheepers, P. T. J. and Bos, R. B., *Int. Arch. Occup. Environ. Health* 64:163 (1992).
98. Cohen, A. J. and Higgens, M. W. P., in *Diesel Exhaust: A Critical Analysis of Emissions, Exposure, and Health Effects,* Health Effects Institute, Cambridge, MA, 1995, p. 251.
99. Chow, J. C., et al., *Atmos. Environ.* 26A:3335–3354 (1992).
100. Li, C.-S., *Atmos. Environ.* 28:3139–3144 (1994).
101. Hildeman, L. M., et al., *Environ. Sci. Technol.* 28:1565–1576 (1994).
102. Rogge, W. F., et al., *Environ. Sci. Technol.* 27:2736 (1993).
103. Brauer, M., et al., *Environ. Sci. Technol.* 30:104–109 (1996).
104. Sawyer, R. F., *Twenty-Fourth Symposium (International) on Combustion,* The Combustion Institute, Pittsburgh, 1992, p. 1423.
105. Calvert, J. G., et al., *Science* 261:37 (1993).
106. Johnson, in *Air Pollution, the Automobile, and Public Health,* (A. Y. Watson, Bates, R. R. and Kennedy, D., Eds.), National Academy Press, Washington, DC, 1988, p. 39–76.
107. Bowman, F. M. and Seinfeld, J. H., *J. Prog. Energy Combust. Sci.* 21:387 (1995).
108. Kirchstetler, T. W., et al., *Environ. Sci. Technol.* 30:661 (1996).
109. Maly, R. R., *Twenty-Fifth Symposium (International) on Combustion,* The Combustion Institute, Pittsburgh, 1994, p. 111.
110. Fisher, E. M. and Koshland, C. P., *J. Air Waste Manage. Assoc.* 40:1384 (1990).
111. Koshland, C. P., Fisher, E. M., and Lucas, D., *Combust. Sci. Technol.* 82:49 (1992).
112. Thomson, M. J., et al., *Combust. Flame* 98:155–169 (1994).
113. Kim, T. J., Yetter, R. A., and Dryer, F. L., *Twenty-Fifth Symposium (International) on Combustion,* The Combustion Institute, Pittsburgh, 1994, p. 759.
114. Roesler, J. F., Yetter, R. A., and Dryer, F. L., *Combust. Sci. Technol.* 101:199 (1994).
115. Roesler, J. F., Yetter, R. A., and Dryer, F. L., *Comb. Sci. Technol.* 85:1 (1992).
116. Senkan, S. M., in *Combustion Chemistry,* 2nd Edition, publication pending, (J. W. C. Gardiner, Ed.), Springer-Verlag, New York, 1993, p. 56.
117. Yildirim, R. and Senkan, S. M., *Ind. Eng. Chem. Res.* 34 (1995).
118. Ho, W., Yu, Q.-R. and Bozelli, J. W., *Combust. Sci. Technol.* 85:23 (1992).
119. McKinnon, J. T. and Howard, J. B., *Combust. Sci. Technol.* 74:175 (1990).
120. Ritter, E. R. and Bozzelli, J. W., *Combust. Sci. Technol.* 74:117 (1990).
121. Taylor, P. H., Tirey, D. A., and Dellinger, B., *Combust. Flame* 104:260 (1996).

122. Gullet, B. K., Lemieux, P. M., and Dunn, J. E., *Environ. Sci. Technol.* 28:107 (1994).
123. Froese, K. L. and Hutzinger, O., *Environ. Sci. Technol.* 30:998 (1996).
124. Froese, K. L. and Hutzinger, O., *Environ. Sci. Technol.* 30:1009 (1996).
125. Addink, R. and Olie, K., *Environ. Sci. Technol.* 29:1425 (1995).
126. Addink, R. and Olie, K., *Environ. Sci. Technol.* 29:1586 (1995).
127. Milligan, M. S. and Altwicker, E., *Environ. Sci. Technol.* 27:1595 (1993).
128. Fängmark, I., et al., *Environ. Sci. Technol.* 27:1602 (1993).
129. Linak, W. P., Srivastava, R. K., and Wendt, J. O. L., *Combust. Sci. Technol.* 101:7 (1994).
130. Linak, W. P., Srivastava, R. K., and Wendt, J. O. L., *Combust. Flame* 100:241 (1995).
131. Linak, W. P., Ryan, J. V., and Wendt, J. O. L., *Combust. Sci. Technol.* (1996).
132. Karimanal, K. V. and Hall, M. J., *J. Hazard. Waste Hazard. Mater.* 13:63 (1996).
133. Ho, T. C., et al., "Effect of Additives on Metal Volatilization during Thermal Treatment," *Fourth International Congress on Toxic Combustion By-Products.* Berkeley, CA, 1995.
134. Ho, T. C., et al., *Hazard. Waste Hazard. Mater.* 11:53 (1994).
135. Ebbinghaus, B. B., *Combust. Flame* 110:311 (1995).
136. Eddings, E. G. and Lighty, J. S., *Combust. Flame* 85:375 (1992).
137. Huang, H. S., Wu, J. M., and Livengood, C. D., *J. Hazard. Waste Hazard. Mater.* 13:107 (1996).
138. Klein, D. H., et al., *Environ. Sci. Technol.* 9:973 (1975).
139. Cahill, C. A. and Newland, L. W., *Environ. Anal. Chem.* 11:227 (1982).
140. Fernández, M. A., et al., *Environ. Sci. Technol.* 26:1040 (1992).
141. Verhulst, D., et al., *Environ. Sci. Technol.* 30:50 (1996).
142. Meij, R., *Water Air Soil Pollut.* 56:21 (1991).
143. Lin, W.-Y. and Biswas, P., *Combust. Sci. Technol.* 101:29 (1994).
144. Winter, R. M., et al., *Combust. Sci. Technol.* 101:45 (1994).
145. Fontijn, A., et al., *Combust. Sci. Technol.* 101:59 (1994).
146. Hall, B., Schager, P., and Lindqvist, O., *Water Air Soil Pollut.* 56:3 (1991).
147. Dayton, D. C. and Chum, H. L., *Energy Fuels* 10:267 (1996).
148. *Chemical and Engineering News,* April 2, 1996, p. 34.
149. Jia, C. Q., DiGuardo, A. D., and Mackay, D., *Environ. Sci. Technol.* 30:87A (1996).
150. Thomson, M., Lucas, D., and Koshland, C. P., *Hazard. Waste Hazard. Mater.,* submitted.
151. Hertwich, E. G., Sheng, P. S., and Koshland, C. P., *Proceedings of the 4th IEEE International Symposium on Electronics and the Environment,* IEEE International Symposium on Electronics and the Environment, Piscataway, NJ, 1996, pp. 269–274.
152. Wendt, J. O. L., *Twenty-Fifth Symposium (International) on Combustion,* The Combustion Institute, Pittsburgh, 1994, p. 277.

COMMENTS

A.E. Jacob Akanetuk, Stanford University, USA. A few years ago while trying to develop a framework for air toxics research, I noticed that utility emissions data in open literature was scant. Has the situation changed? If not, how can utilities and incinerator operators be encouraged to provide more emissions data to the public domain?

Author's Reply. One of the challenges in air toxics research is developing data bases of source emissions and of concentration distributions in the ambient air. In some cases, there is a disincentive to sample since increased sampling leads to an increased probability of obtaining a measurement that might be a violation of an emission standard. In other cases, the emission factors used to estimate emissions based on level of activity of a source are highly uncertain, and can lead to gross over (or under) estimates of emissions, particularly for trace species. Recent studies in the US for both utilities and incinerators, prompted by requirements in the 1990 Clean Air Act, contain more information than previously available. Incentives could include more flexibility on the part of EPA to enable actual measurements to be made to assess both current emissions, and future reductions; improvements in sampling methods; possible tax breaks or other incentives based on open assessment of emissions and subsequent reductions.

•

Robert F. Chaiken, DOE/Pittsburgh Research Center, USA. Are epidemiological studies being coordinated into environmental statistical studies to insure or correlate decreases in specific toxic gases with decreases in specific health problems? Are we directing our scientific and engineering resources to solving the proper problems?

Author's Reply. Epidemiological studies which assess patterns of human disease are key components of environmental exposure and risk assessment. However, general population studies that would be conducted to assess decrease in deleterious health outcomes with decreases in exposures to air toxics are difficult to conduct. Assessments of interventions or applications of controls to reduce ex-

posure are most easily conducted when a single agent is involved, when the effect shows up with sufficient frequency in a reasonable study population and when the intervention can be adequately controlled, and reductions in exposure observed. In the case of air toxics, inadequate monitoring data, inadequate exposure data, lack of dose-response information, and the lack of information on synergistic or antagonistic effects of various air toxics, make it difficult to assess changes in disease patterns with reductions. Nevertheless, efforts are being made to determine which exposures should be controlled, and to assess whether such interventions are effective. Methods which link exposure assessment with some form of economic valuation of control effectiveness in terms of reduced exposures are being developed.

•

Wm. J. McLean, Sandia National Laboratories, USA. Probabalistic risk assessment is being offered as a rational method for choosing which compounds/sources to regulate, yet there are always possibilities for statistical "outlyers." For example, small numbers of automobiles may be responsible for a large fraction of the emissions. Can you please comment on the applicability of risk assessment tools?

Author's Reply. Risk assessment methods applied to environmental problems have steadily improved since there origins as regulatory decision making tools. The underlying science and the mathematical sophistication have improved. Probablistic methods, that incorporate both variability and uncertainty, have the potential to improve the assessment of risk over methods that use single (default) values to build a worst case scenario.

•

Ivan Milosavljevic, Air Liquide, France. I have just one comment: Many toxical products from combustion processes can be eliminated and/or reduced by replacing air by oxygen.

Contrary to the popular belief, *air is not always free* in combustion processes. For example, replacing air by oxygen results in lower investment costs (separation unit belongs to us), better thermal efficiency and higher profits. There are many cases in the industry where oxygen helped achieve or exceed emission standards and, at the same time, increase profits.

Thus, it is obvious that replacing air by oxygen results in a more "environmentally friendly" process. It is also obvious that, in some cases, "free" air can be very expensive in terms of, both, environmental policy and the process economics itself.

Author's Reply. Replacing air with oxygen reduces those toxic species that contain nitrogen derived from the air. Eliminating N_2 may enable processes to operate at higher temperatures with greater thermal efficiency. However, pure oxygen does not necessarily reduce pollutants formed as a consequence of fuel or feedstock constituents, and some species like phosgene are more likely to be formed in oxygen rich environments.

•

Jozef Peeters, University of Leuven, Belgium. You presented a graph showing that the amounts of VOC, CO an NO_x emitted by cars per mile have been decreasing markedly over the last few decades. On the other hand you referred to the finding by Stedman that the 10 to 20% badly timed cars actually on the roads cause 60 to 80% of the total emissions. Does your graph take into account these "non-statistical", highly polluting cars? Shouldn't controls and regulations in the first place have to be directed toward reducing the numbers of such cars on the roads?

Author's Reply. The graph (1) is that of total vehicle emissions and includes the highly polluting vehicles. Certainly reducing the total number of vehicles on the road as well as reducing the total vehicle miles traveled, increasing the fuel economy and decreasing cold starts would contribute to emissions reductions of toxics from vehicles. In some regions, regulations and incentive programs to induce travelers to car-pool and use mass transit are in place. However, without flexible, affordable, reliable and frequent mass-transit alternatives, the necessity remains to make vehicles less polluting. Determining the best approach to reducing the 10–20% of gross polluters is both a technical and political problem.

REFERENCE

1. Calvert, J. G. et al., *Science* 261:37 (1993).

Twenty-Sixth Symposium (International) on Combustion/The Combustion Institute, 1996/pp. 2067–2074

PRESSURE EFFECTS ON THE THERMAL DE-NO_x PROCESS

KARSTEN KJÆRGAARD, PETER GLARBORG AND KIM DAM-JOHANSEN
Department of Chemical Engineering
Technical University of Denmark
2800 Lyngby, Denmark

JAMES A. MILLER
Combustion Research Facility
Sandia National Laboratories
Livermore, CA 94551-0969, USA

The effect of pressure on the thermal de-NO_x process has been investigated in flow reactor experiments. The experiments were performed at pressures from 1 to 10 bar and temperatures ranging from 925 to 1375 K. The inlet O_2 level was varied from 1000 ppm to 10%, while NH_3 and NO were maintained at 1000 and 500 ppm, respectively. At the highest pressure, CO was added to shift the regime for NO reduction to lower temperatures.

The results show that the pressure affects the location and the width of the temperature window for NO reduction. As the pressure is increased, both the lower and the higher boundaries for the process are shifted toward higher temperatures. Overall, the temperature range for NO reduction appears to be slightly broadened. The shift in chemistry toward higher temperatures is most pronounced at low oxygen concentrations. High oxygen levels act to counterbalance the inhibiting effect of the pressure but also cause a slight decrease in the NO reduction potential.

The results are consistent with recent atmospheric pressure experiments of thermal de-NO_x covering a wide range of reactant partial pressures. Comparisons of the experimental data with the recent chemical kinetic model of Miller and Glarborg show satisfactory agreement. The implications of the results for application of thermal de-NO_x in high-pressure systems, such as pressurized fluidized bed combustion and gas turbines, are discussed.

Introduction

Attempts to apply the thermal de-NO_x process [1] for NO_x control in high-pressure combustion systems such as gas turbines and pressurized fluidized bed (PFBC) systems have so far been hampered by the lack of reliable information on process performance at high pressures. No laboratory experiments have been published. Some results from tests in PFBC systems [2,3,4] are available, but these data are obtained under complicated flow conditions with temperature gradients and significant concentrations of solids. Furthermore, only a limited parameter variation was reported.

Modeling extrapolations to high-pressure conditions have been uncertain, because the commonly used mechanisms [5,6] have been developed for a narrow range of pressure and concentrations. The laboratory experiments used for model validation [5,7,8,9] were typically obtained at atmospheric pressure and 1—4% vol O_2.

Two recent studies have contributed to characterizing the thermal de-NO_x process over a wider range of conditions, thereby improving the understanding of the process chemistry. Kasuya et al. [10] extended significantly the experimental database by varying the reactant partial pressures in the ranges 0–50% O_2 and 200–1400 ppm NO (NH_3/NO = 2). Based on these results, as well as new data on amine/NO_2 interactions [11], Miller and Glarborg [12] formulated a revised mechanism that provided a better prediction than previous models of the effect of initial oxygen concentration on the thermal de-NO_x process. The new feature of this mechanism is that NO_2 appears as an essential intermediate in the reaction scheme.

In the present work, the effect of pressure on the thermal de-NO_x process is investigated systematically. The objective is partly to assess the potential of the process for high-pressure applications and partly to obtain data important for further development and validation of the chemical kinetic model. The experiments are carried out at pressures from 1 to 10 bar in a specially designed flow reactor system. The effects of pressure, temperature, and oxygen concentration are investigated and the implications

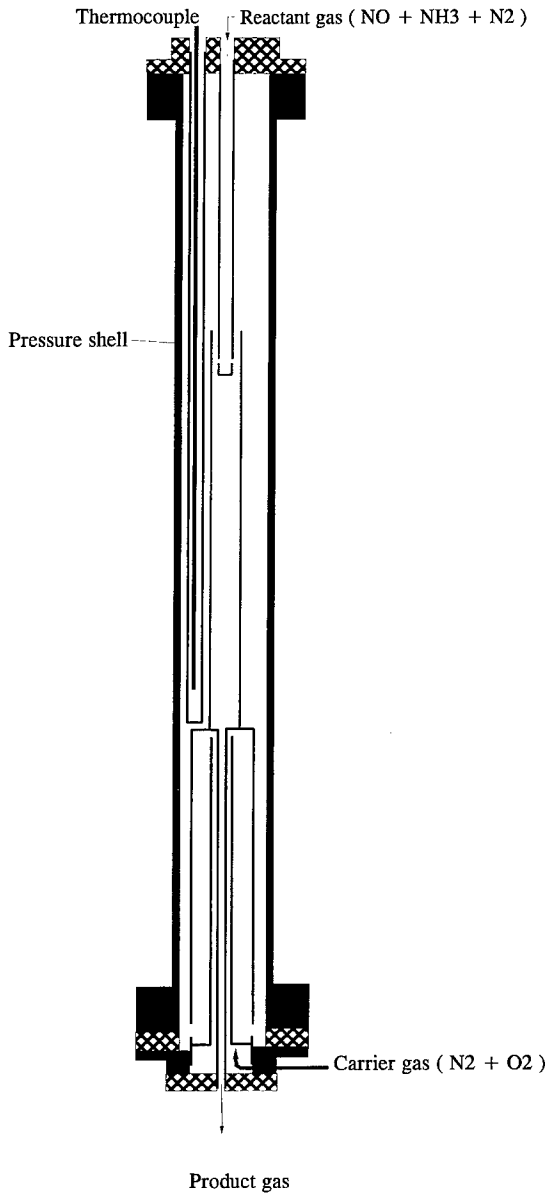

FIG. 1. Schematic of the high-pressure flow reactor.

of the results in terms of high-pressure applications, as well as the understanding of the detailed chemistry, are discussed.

Experimental

The main components of the experimental apparatus are a flow reactor, a gas mixing system, and a data collecting/control system. The setup is a modification of a system developed to study high-pressure gas–solid reactions [13], drawing on the experience from an atmospheric pressure flow reactor for homogeneous reactions [8,9,14].

The feed gas is supplied from gas cylinders and regulated by mass flow controllers. Depending on the position of a three-way valve, the reaction gas can either enter the top of the reactor or bypass the reactor. The pressure in the reactor is controlled by a back-pressure regulator, through which the gas is expanded to atmospheric pressure.

The reactor is made of quartz and enclosed in a pressure vessel (Fig. 1). The vessel is able to stand simultaneously pressures and temperatures of up to at least 10 bar and 1400 K. It is heated in a three-zone electrical oven, which can maintain a constant temperature over the reaction zone within ± 5 K.

The reaction gas is divided into two streams, a reactant stream and a bulk flow, that are heated separately. The bulk flow, which enters the reactor at the bottom of the vessel, is in contact with the walls of the pressure vessel. This stream must be noncorrosive and usually contains nitrogen and oxygen. After heat exchange with the product gas, the bulk flow passes upward between the steel wall and the exhaust tube.

The reactant gas contains ammonia, nitric oxide, and water vapor, delivered by an HPLC evaporator. The pipe connecting the evaporator and the reactor vessel is heated electrically to prevent condensation of water vapor. The reactant gas stream, which usually constitutes about 20% of the total flow, enters the pressure shell through an opening in the top. It is led through a quartz tube and mixed in cross flow with the bulk gas at the entrance to the reaction zone. The separate heating of the reactants secures a well-defined reaction volume. The reaction zone has a volume of 10 mL. After reaction, the products are cooled rapidly by the incoming bulk gas. The product gas is then led to a water condenser and finally to the gas analyzers.

Continuous gas analyzers were used to measure the concentrations of NO, O_2, CO, and CO_2. Before each series of experiments, the analyzers were calibrated using span gases. The concentrations detected were within a relative range of $\pm 3\%$ but with an absolute accuracy not higher than ± 5 ppm. Ammonia was measured by an automated wet method, bubbling it through an NH_4Cl solution, where the pH was kept constant by an autotitrator adding HCl. For NH_3, the uncertainty is $\pm 10\%$ but not less than ± 10 ppm.

Reaction Mechanism

The reaction mechanism used in the present investigation is the same as that described by Miller and Glarborg [12], which in turn contains only a few changes from that given by Glarborg, Dam-Johan-

TABLE 1
Selected rate coefficients from the mechanism $k = AT^{\beta} \exp(-E/RT)$. Units are mol cm^3, s, K, and cal/mol. Reactions (R126) and (R127) were not included in the mechanism of Ref. 11.

	A	β	E_a
12. $H_2NO + O \rightleftharpoons NH_2 + O_2$	2.5E14	0.00	0
18. $NH_2 + NO \rightleftharpoons NNH + OH$	8.9E12	−0.35	0
19. $NH_2 + NO \rightleftharpoons N_2 + H_2O$	1.3E16	−1.25	0
$NH_2 + NO \rightleftharpoons N_2 + H_2O$	−8.9E12	−0.35	0
Duplicate reaction			
90. $NNH \rightleftharpoons N_2 + H$	1.0E07	0.00	0
126. $NNH + O_2 \rightleftharpoons N_2 + HO_2$	2.0E14	0.00	0
127. $NNH + O_2 \rightleftharpoons N_2 + H + O_2$	5.0E13	0.00	0

sen, and Miller [11]. These changes are listed in Table 1, and a reaction path diagram for the process is shown in Fig. 2. The reaction numbering refers to the listing in Ref. 11, except where noted. Thermodynamic data are taken from the Sandia Thermodynamic Database [16]. Miller and Glarborg [12] discuss the key features of the mechanism in detail, including its historical development.

The most important consequence of the present mechanism compared with that of Miller and Bowman [6] is that NO_2 is now an essential intermediate in the process. To allow a short lifetime for NNH and still predict the results of laboratory experiments on thermal de-NO_x, it is necessary to have a fast reaction between NNH and O_2, $NNH + O_2 \rightleftharpoons N_2 + HO_2$ (R126), to compete with spontaneous dissociation of NNH (R90) and thus avoid an unconstrained branched-chain explosion [6,12]. A consequence of a large value for k_{126} is that NO_2 is formed readily by the reaction $HO_2 + NO \rightleftharpoons NO_2 + OH$ (R38). However, under normal thermal de-NO_x conditions, NO_2 does not accumulate appreciably, because the rapid reaction $NH_2 + NO_2 \rightleftharpoons H_2NO + NO$ (R21) followed by the $H_2NO \rightarrow HNO \rightarrow NO$ sequence shown in Fig. 2 converts the NO_2 back to NO [12]. Only with very high initial oxygen levels do appreciable quantities of NO_2 accumulate [10,12].

As has been discussed previously [6,12,17,18], the predictions of the mechanism are very sensitive to the mix of chain-branching and chain-terminating reactions. In the present mechanism, chain branching comes primarily from the reaction $NH_2 + NO \rightleftharpoons NNH + OH$ (R18) and the dissociations of H_2NO and HNO, which occur as a consequence of reaction (R21). Chain termination comes from the step $NH_2 + NO \rightleftharpoons N_2 + H_2O$ (R19) and radical reactions (particularly those of OH) with H_2NO and HNO. The competition of the latter reactions with H_2NO and HNO dissociation as the OH concentration rises produces the self-inhibiting effect [6,12].

There are four features of the mechanism that could be affected by increased pressure:

1. The competition between $H + O_2 \rightleftharpoons O + OH$ and $H + O_2 + M \rightleftharpoons HO_2 + M$. As pressure is increased this competition should result in a slight inhibition of the NO removal.
2. The competition between $NNH \rightleftharpoons N_2 + H$ and $NNH + O_2 \rightleftharpoons N_2 + HO_2$. This competition also should result in inhibition of the NO removal as the pressure is increased. Note that a thermal distribution of NNH is assumed to exist at all times in the model, with dissociation occurring by tunneling from all vibrational states. The only effect of increased pressure is the establishment of thermal distribution more readily. On this basis, we expect no pressure dependence for k_{90} to exist, although more subtle effects could conceivably introduce some pressure dependence.

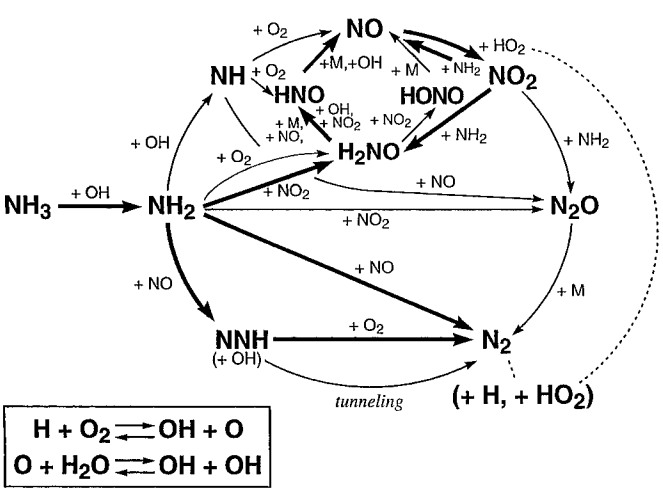

FIG. 2. Reaction path diagram for the thermal de-NO_x process [12]. The bold arrows represent the dominant paths.

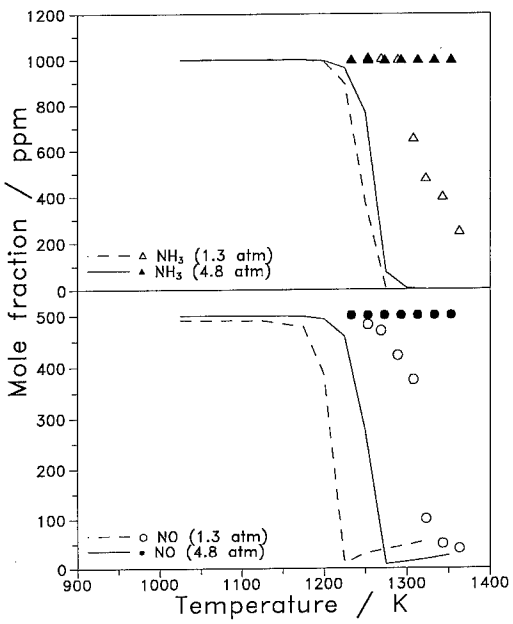

FIG. 3. Effect of pressure and temperature on NH_3 and NO outlet concentrations at low oxygen concentration. Symbols denote experimental data, while lines denote model predictions. Inlet concentrations, 1.3 bar: NH_3 = 1000 ppm, NO = 490 ppm, O_2 = 1010 ppm, H_2O = 1.0%, balance N_2; 4.8 bar: NH_3 = 1000 ppm, NO = 500 ppm, O_2 = 1000 ppm, H_2O = 1.0%, balance N_2. Residence time at 1200 K (constant mass flow) is 126 ms (1.3 atm) or 122 ms (4.8 bar).

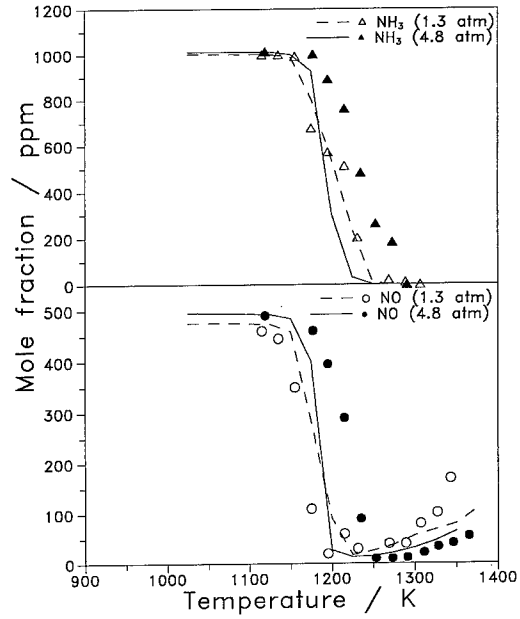

FIG. 4. Effect of pressure and temperature on NH_3 and NO outlet concentrations at medium oxygen concentration. Symbols denote experimental data, while lines denote model predictions. Inlet concentrations, 1.3 bar: NH_3 = 1000 ppm, NO = 475 ppm, O_2 = 1.0%, H_2O = 1.0%, balance N_2; 4.9 bar: NH_3 = 1010 ppm, NO = 500 ppm, O_2 = 1.0%, H_2O = 1.0%, balance N_2. Residence time at 1200 K (constant mass flow) is 118 ms (1.3 atm) or 122 ms (4.9 bar).

3. Initiation. The principal initiation reaction in the mechanism is $O_2 + H_2O \rightleftharpoons HO_2 + OH$, whose total rate increases with pressure. Increased pressure could then reduce the induction time for NO removal and thus result in a more efficient process, particularly at the low-temperature end of the effective temperature range. However, our experience indicates that this is a minor effect, because the chain-branching reactions begin to dominate the process very early in the reaction.
4. The dissociation of H_2NO and HNO. Early in the reaction (i.e., before the OH concentration has had a chance to build up), these dissociation reactions have no competing paths. Thus, increased pressure should increase the rate of H-atom formation and thus enhance the NO removal at lower temperatures.

It is impossible to tell a priori which of these pressure effects are dominant in practice. Consequently, we have initiated this combined experimental and modeling study.

Results and Discussion

The flow reactor experiments were carried out in the temperature range 925–1375 K with a constant stoichiometric ratio between NH_3 and NO of β = 2. Oxygen mole fractions were varied between 0.1% and 10%. In the range 1–5 bar, it was possible to maintain a constant residence time, independent of pressure. Because of limitations in the total flow rate, experiments at 10 bar were conducted at longer residence times.

The experimental data were interpreted in terms of the detailed reaction mechanism discussed previously. Calculations were performed using Senkin [19], a plug-flow code that runs in conjunction with the Chemkin library [20].

Figures 3, 4, and 5 show the effect of pressure (1.3 and 4.8 bar) and inlet oxygen mole fraction (0.1%, 1%, 10%) on the thermal de-NO_x process. Symbols denote experimental data, while lines denote model predictions.

Several interesting features of the process are notable from these figures. From comparison of Figs. 3, 4, and 5, and from the results of Kasuya et al. [10], one can see that at constant pressure the "initiation temperature" for the process (i.e., the temperature for onset of reaction) decreases with increasing initial oxygen concentration. It is also apparent that as

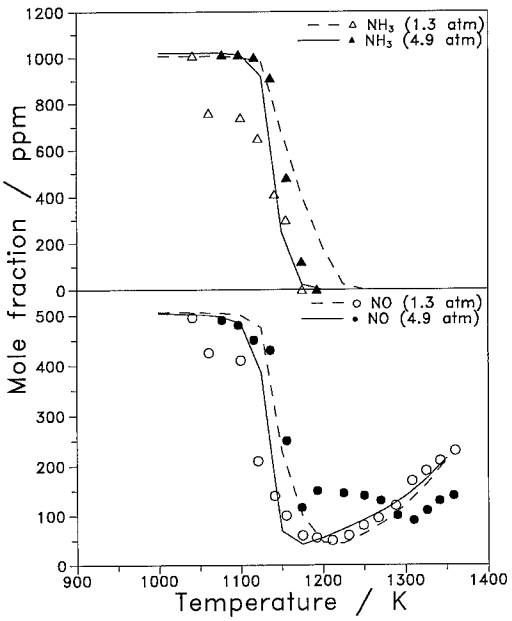

FIG. 5. Effect of pressure and temperature on NH_3 and NO outlet concentrations at high oxygen concentration. Symbols denote experimental data, while lines denote model predictions. Inlet concentrations, 1.3 bar: NH_3 = 1010 ppm, NO = 510 ppm, O_2 = 10.2%, H_2O = 1.0%, balance N_2; 4.8 bar: NH_3 = 1020 ppm, NO = 500 ppm, O_2 = 10.1%, H_2O = 1.0%, balance N_2. Residence time at 1200 K (constant mass flow) is 126 ms (1.3 atm) or 128 ms (4.8 bar).

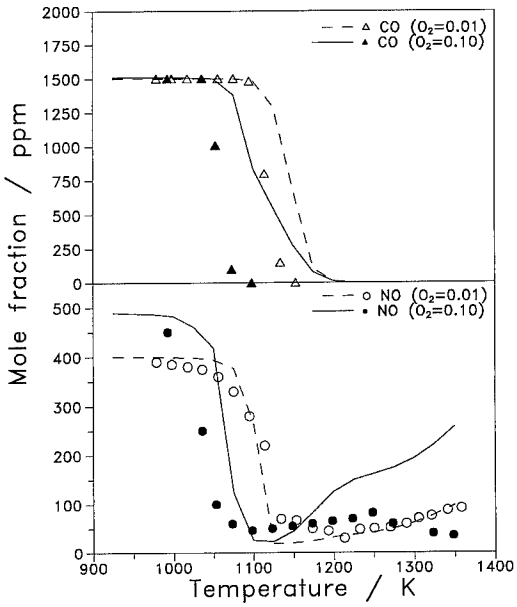

FIG. 6. Effect of inlet CO and O_2 level and temperature on NH_3 and NO outlet concentrations at high pressure (10 bar). Symbols denote experimental data, while lines denote model predictions. Inlet concentrations, low O_2; NH_3 = 1010 ppm, NO = 400 ppm, CO = 1500 ppm, O_2 = 1.0%, H_2O = 1.0%, balance N_2; high O_2: NH_3 = 990 ppm, NO = 490 ppm, CO = 1510 ppm, O_2 = 10.1%, H_2O = 1.0%, balance N_2. Residence time at 1200 K (constant mass flow) is 261 ms (1% O_2) or 268 ms (10% O_2).

the oxygen level increases, the temperature range for NO reduction is widened but the NO reduction potential decreases. However, due to the smaller variation in O_2, these trends are less pronounced in the present data (Figs. 3–5) than in Ref. 10.

When the pressure is raised from 1 to 5 bar, reaction is inhibited and the initiation temperature is increased. This effect is most pronounced at low initial oxygen concentration. At 0.1% O_2 (Fig. 3), the increase in pressure causes a shift in the initiation temperature from about 1300 K to more than 1360 K, the high-temperature limit of the reactor system. As the oxygen level increases, the effect of pressure on the initiation temperature is reduced; at 10% O_2, the corresponding shift is only about 30 K (Fig. 5).

The NO reduction potential is apparently unaffected by pressure at 1% O_2 (Fig. 4), whereas it is slightly reduced at elevated pressure at 10% O_2 (Fig. 5). Kasuya et al. [10] showed that an increase in NH_3/NO partial pressures increased the NO reduction potential while an increased O_2 partial pressure had the opposite effect. Thus, it appears that these effects cancel at lower oxygen levels; however, at high O_2 concentrations, a slight negative impact of pressure on the maximum NO reduction occurs.

The effect of pressure on the width of the temperature window is difficult to assess from the present experiments because of the experimental temperature limitation. The results of Figs. 4 and 5 may indicate that higher pressures cause a widening of the temperature window toward higher temperature, but the results are not conclusive.

To explore this issue further, a number of high-pressure thermal de-NO_x experiments were conducted with addition of CO. The effect of CO is similar to that of H_2 and other combustibles [5,6,8] in that it shifts the reaction regime to lower temperatures by replenishing the radical pool. Figure 6 shows results obtained at 10 bar with 1500 ppm CO and O_2 concentrations of 1% and 10%, respectively.

The results show that NO is reduced over a wide temperature range, more than 300 K at 10% O_2. Comparison of the results of Fig. 6 with atmospheric pressure kinetic calculations indicates that the pressure change from 1 to 10 bar causes a widening of the temperature window of more than 100 K, significantly moving the upper boundary toward higher temperatures. The suggestion of a wider temperature window is supported by comparison of the results of Fig. 6 with those of Figs. 4 and 5 for 5 bar

and similar O_2 levels. Despite the higher pressure, the presence of CO and the longer reaction times (compared to the data of Figs. 4 and 5) cause a shift of more than 100 K toward lower values in the initiation temperature, apparently without altering the high-temperature boundary.

The suggestion of a widening of the temperature window for the process at elevated pressure is in agreement with the observations of Kasuya et al. [10]. Their data showed that an increase in reactants' partial pressures, both NH_3/NO and O_2, was accompanied by a broadening of the temperature range for NO reduction.

An interesting phenomenon occurs at high pressure and high oxygen concentration (Figs. 5 and 6). Under these conditions, the NO concentration exhibits a double minimum. This behavior was observed also by Kasuya et al. [10] at very high O_2 concentrations (50%) and by Bregendahl [15] in preliminary high-pressure experiments performed in this laboratory. The phenomenon appears to be characteristic for the thermal de-NO_x process at high molar concentrations of oxygen. The first minimum is located close to the initiation temperature, while the second one appears roughly in the middle of the temperature window, separated from the first minimum by 100–200 K, depending on the conditions.

No changes in the mechanism of Miller and Glarborg [12] have been made in the present work to improve model performance. The predictions are generally in good agreement with the experimental data (Figs. 3–6). The model predicts the major effects of variations in the oxygen mole fraction and the pressure correctly, that is, the following are true:

- An increase in the oxygen mole fraction at constant pressure leads to a lower initiation temperature.
- An increase in pressure at a fixed oxygen level inhibits the reaction at low temperatures.
- The effect of pressure is most pronounced at low O_2 levels.

Even though the trends are described qualitatively correctly by the model, some deviations are apparent. At 10% O_2, the model predicts a slightly enhanced reaction rate at elevated pressure, in contrast with the experimental observations. This suggests that the balance in the model between the enhancing effect of an increased oxygen molar concentration and the inhibiting effect of increased total pressure needs to be adjusted slightly.

The double minimum in NO occurring at high oxygen molar concentrations is not predicted by the model (Figs. 5 and 6). The previous data [10,15] show that the low temperature minimum occurs under conditions with significant NO_2 concentrations but that the NO_2 peaks at slightly higher temperatures. We attribute the discrepancy to uncertainties in the description of amine–NO_2 interactions in the mechanism.

Another difference occurs at 0.1% O_2 (Fig. 3), where the model, at both low and high pressure, predicts too low an initiation temperature for the process. At these conditions, with very low O_2 mole fractions, the predicted onset of reaction is very sensitive to the branching ratio for the NH_2 + NO reaction, $\alpha = k_{18}/(k_{18} + k_{19})$, while other uncertain parameters in the mechanism, including the NNH lifetime, are of little significance [12]. The present value of α was chosen to match the 0.1% O_2 data of Kasuya et al. [10], obtained at atmospheric pressure and shorter reaction times. The current discrepancy could be caused by a small inaccuracy in the temperature dependence of α; efforts are presently undertaken to reconcile this issue.

Despite these discrepancies, we consider the overall agreement between the experimental data and the modeling to be good. A number of parameters in the mechanism are still uncertain [12], including the NH_2 + NO branching ratio, the NNH lifetime, the NH_2 + O_2 rate coefficient and products, and details of the NO/NO_2 interconversion. However, that the major properties of the thermal de-NO_x process are described well over a large range of conditions suggests that the important kinetic features of the process are now understood.

Analysis of the calculations allows us to identify the effects of pressure on the detailed kinetics of the process. As described previously, increased pressure may act to inhibit reaction by favoring the two steps, $H + O_2 + M \rightleftharpoons HO_2 + M$ (R114, R115) and $NNH + O_2 \rightleftharpoons N_2 + HO_2$ (R126), over the reactions $H + O_2 \rightleftharpoons O + OH$ (R103) and $NNH \rightleftharpoons N_2 + H$ (R90). Our analysis confirms that the increased importance of (R114)/(R115) and (R126) is responsible for the predicted inhibition at elevated pressure.

The inhibiting effect of pressure is partly counterbalanced by effects that promote reaction at low temperatures. The results of Kasuya et al. [10] show that the initiation temperature is very sensitive to the oxygen partial pressure but not to the partial pressures of NH_3/NO. The increased oxygen molar concentration at increased pressure may thus act to promote reaction at low temperatures. Also, a faster dissociation of H_2NO and HNO at higher pressures acts to enhance reaction at low temperatures, while the impact of pressure on induction time for the process is minor under the present conditions.

Overall, the pressure effects on the thermal de-NO_x process tend to cancel, particularly at the oxygen mole fractions of interest in most practical applications (i.e., 1–10%). The most interesting feature is the indicated shift of the upper boundary for the process toward higher temperatures.

Practical Implications

Because of difficulties in implementing conventional nitrogen oxide abatement methods, manufac-

turers of gas turbines and pressurized fluidized bed combustors have shown interest in applying thermal de-NO_x or alternate selective noncatalytic reduction techniques for NO_x control. The results of the present study allow us to provide some estimate of the thermal de-NO_x potential in these systems.

The operating conditions for thermal de-NO_x in PFBC systems will typically be a temperature of approximately 1150 K, a pressure of 12–16 bar, and an O_2 level of about 5%. In the absence of combustibles, this combination of low temperature and high pressure appears to be unfavorable for the process. However, modest amounts of CO would shift the temperature regime for reaction into the operating region for PFBC. The results in Fig. 5 indicate a significant NO_x reduction potential, provided the proper location for NH_3 injection is chosen.

Test results for thermal de-NO_x in pressurized fluidized bed systems, obtained at 6–8 bar in pilot scale [2,3] and 12 bar in full scale [4], are not conclusive. However, the observations [3] that higher temperatures are favorable for the process performance and that there exists a close coupling between combustion conditions and SNCR performance is in agreement with our expectations.

Thermal de-NO_x is not usually taken into consideration for application in gas turbines. A major concern is that the accessible ammonia injection temperatures are too high for SNCR processes to work. The turbine rotor inlet temperatures for heavy-duty industrial gas turbines are currently 1350–1500 K and may approach 1700 K as more heat-resistent materials are developed for the turbine vanes. While such temperatures would be prohibitive for NO reduction by thermal de-NO_x at atmospheric pressure, the high pressure in the gas turbine, at present 12–20 bar, may make SNCR feasible for some turbine applications by moving the upper boundary for NO reduction to higher temperatures. However, the pressure effect on the high-temperature limit may be reduced by high oxygen concentrations or by the presence of combustibles in the flue gas. Therefore, the combination of an O_2 level of typically 15% together with the potential presence of CO may prevent a successful application of thermal de-NO_x in these systems.

Conclusions

In the present work, the effect of pressure and oxygen concentration on the thermal de-NO_x process has been investigated. It is observed that an increase in the O_2 mole fraction at constant pressure leads to a lower initiation temperature, whereas an increase in pressure at fixed oxygen level inhibits the reaction at low temperatures. The effect of pressure is most pronounced at low O_2 levels. There are some indications that an increase in pressure extends the NO reduction regime for the process significantly toward higher temperatures, but this effect could not be quantified because of experimental limitations.

Model predictions performed with the newly proposed mechanism by Miller and Glarborg [12] are generally in good agreement with the experimental data. The model predicts the major effects of variations in the oxygen mole fraction and the pressure correctly. Analysis of the calculations indicates that the inhibiting effect of pressure is due to the increased importance of the reactions $H + O_2 + M \rightleftharpoons HO_2 + M$ and $NNH + O_2 \rightleftharpoons N_2 + HO_2$ compared to $H + O_2 \rightleftharpoons O + OH$ and $NNH \rightleftharpoons N_2 + H$. However, this effect is partly counterbalanced by the increasing oxygen molar concentration, which promotes reaction at low temperatures. Overall, the pressure effects on the thermal de-NO_x process in the 1000–1400 K range tend to cancel, particularly at the oxygen mole fractions of interest in most practical applications (i.e., 1–10%).

Acknowledgments

This work is supported by the CHEC research program and by the U.S. Department of Energy, Office of Basic Energy Sciences, Division of Chemical Sciences. The research program CHEC (Combustion and Harmful Emission Control) is cofunded by the Danish Technical Research Council, Elsam (the Jutland–Funen Electricity Consortium), Elkraft (the Zealand Electricity Consortium), and the Danish Energy Research Program.

REFERENCES

1. Lyon, R. K., U.S. Patent 3,900,554, 1975.
2. Jahkola, A., Lu, Y., and Hippinen, I., *Proceedings of the 1991 International Conference on Fluidized Bed Combustion,* ASME, New York, 1991, pp. 725–730.
3. Andries, J., Verloop, C. M., and Hein, K. R. G., *Proceedings of the 1993 International Conference on Fluidized Bed Combustion,* ASME, New York, 1993, pp. 795–802.
4. Dahl, A., *Proceedings of the 1993 International Conference on Fluidized Bed Combustion,* ASME, New York, 1993, pp. 931–935.
5. Lyon, R. K., *194th Ann. ACS Meet., Div. Fuel Chem.* 32:433 (1987).
6. Miller, J. A. and Bowman, C. T., *Prog. Energy Combust. Sci.* 15:287 (1989).
7. Lyon, R. K. and Hardy, J. E., *Ind. Engng. Chem. Fund.* 25:19 (1986).
8. Duo, W., Dam-Johansen, K., and Østergaard, K., *Twenty-Third Symposium (International) on Combustion,* The Combustion Institute, Pittsburgh, 1990, pp. 297–303.
9. Hulgaard, T. and Dam-Johansen, K., *AIChE J.* 39:1342 (1993).

10. Kasuya, F., Glarborg, P., Johnsson, J. E., and Dam-Johansen, K., *Chem. Eng. Sci.* 50:1455 (1995).
11. Glarborg, P., Dam-Johansen, K., and Miller, J. A., *Int. J. Chem. Kin.* 27:1207 (1995).
12. Miller, J. A. and Glarborg, P., "Modeling the Formation of N_2O and NO_2 in the Thermal De-NO_x Process," accepted by Springer Series in Chemical Physics (1996).
13. Illerup, J. B., Dam-Johansen, K., and Lundèn, K., *Chem. Eng. Sci.* 48:2151 (1993).
14. Kristensen, P. G., Glarborg, P., and Dam-Johansen, K., "Nitrogen Chemistry during Burnout in Fuel-Staged Combustion," accepted by *Combust. Flame*, (1996).
15. Bregendahl, M., M. Sc. Thesis, Department of Chemical Engineering, Technical University of Denmark, 1995.
16. Kee, R. J., Rupley, F. M., and Miller, J. A., "The Chemkin Thermodynamic Data Base," Sandia Report SAND87-8215, 1991.
17. Miller, J. A., Branch, M. C., and Kee, R. J., *Combust. Flame* 43:81 (1981).
18. Glarborg, P., Dam-Johansen, K., Miller, J. A., Kee, R. J., and Coltrin, M. E., *Int. J. Chem. Kin.* 26:421 (1994).
19. Lutz, A., Kee, R. J., and Miller, J. A., "SENKIN: A Fortran Program for Predicting Homogeneous Gas Phase Chemical Kinetics with Sensitivity Analysis," Sandia Report SAND87-8248, 1987.
20. Kee, R. J., Rupley, F. M., and Miller, J. A., "CHEMKIN-II: A Fortran Chemical Kinetics Package for the Analysis of Gas-Phase Chemical Kinetics," Sandia Report SAND89-8009, 1989.

COMMENTS

J. Wolfrum, Universität Heidelberg, Germany. As shown in our paper at the 25th Symposium, low concentration of hydrocarbons can lower significantly the on set temperature of NO reduction by NH_3. Did you study this effect at higher pressures?

Author's Reply. We have not in the present work investigated the effect of hydrocarbon addition on the Thermal DeNO_x process. However, we anticipate that the effect would be similar to that of CO addition; i.e. that the presence of hydrocarbons acts to replenish the radical pool and shift the regime for NO reduction to lower temperatures.

•

William R. Anderson, U.S. Army Research Laboratory, USA. Comparisons of your model to experiment for most observables revealed good agreement. However, the effect of added CO was not modeled well. Was the reaction $CO + N_2O = CO_2 + N_2$ included in the modeling, and with what rate coefficient? Is enough N_2O formed for this to matter?

Author's Reply. The reaction $CO + N_2O \rightleftharpoons CO_2 + N_2$ with the rate coefficients recommended in the recent evaluation by Tsang and Herron [1] is too slow to affect the current modeling results.

REFERENCE

1. Tsang and Herron, *J. Phys. Chem. Ref. Data* 20:609 (1991).

Twenty-Sixth Symposium (International) on Combustion/The Combustion Institute, 1996/pp. 2075–2082

REBURNING PROMOTED BY NITROGEN- AND SODIUM-CONTAINING COMPOUNDS

VLADIMIR M. ZAMANSKY, LOC HO, PETER M. MALY AND W. RANDALL SEEKER
Energy and Environmental Research Corporation
18 Mason, Irvine, CA 92618, USA

Experiments in a 300-kW combustor and kinetic modeling demonstrate a strong effect of N-agents (ammonia and urea) and sodium salts on NO removal in the reburning process. The NO reduction process is more effective if the N-agents appear in the gas mixture with a delay time (0.1–0.5 s) after injection of the reburning fuel. By this time, the concentration of oxygen from the main combustion zone has been significantly depleted by the reburning fuel, thus preventing oxidation of the N-agents into NO. Sodium compounds, such as sodium carbonate, do not affect NO concentrations without N-agents but do significantly promote the effect of N-agents. The deeper NO reduction in the presence of promoters can be explained by reactions of additional active radicals formed in the reburning zone via interaction of sodium compounds with water molecules. About 80–90% NO_x control was achieved by 10–20% natural-gas reburning in the presence of ammonia or urea and sodium carbonate in comparison with 45–65% NO_x reduction by 10–20% reburning only. Kinetic modeling qualitatively describes the chemical processes responsible for NO_x reduction. The following factors primarily control process efficiency: stoichiometric ratio in the reburning zone, delay time between injection of the reburning fuel and formation of NH_i radicals in the reburning zone, oxygen concentration at the time of N-agent injection, concentration of N-agent, and overfire air (OFA) injection location.

Introduction

Reburning, a fuel-staging method for NO_x control, was suggested by Wendt et al. [1]. This is a three-stage method that involves combustion of a fuel in two stages. In the main combustion zone, 80–90% of the fuel is burned with a normal amount of air (about 10% excess). The combustion process forms a definite amount of NO_x. Then, in the second stage, the rest of the fuel (reburning fuel) is added at temperatures of about 1400–1700 K into the secondary combustion zone, called the reburning zone, to maintain a fuel-rich environment. In a specific range of conditions (stoichiometric ratio, temperature, and residence time in the reburning zone), the NO_x concentrations can typically be reduced by 50–70%. In the third stage, the overfire air (OFA) is injected at a lower temperature to complete combustion. The chemical mechanism of reburning was investigated in many publications (e.g., [2–4]). Addition of the reburning fuel leads to its rapid oxidation to CO and hydrogen. The reburning fuel provides a fuel-rich mixture with certain concentrations of carbon-containing radicals: CH_3, CH_2, CH, HCCO, etc. These active species can convert NO into N_2 via formation of intermediate products, such as HCN, NH_3, NH_2, NH, etc. The OFA added on the last stage of the process oxidizes existing CO, H_2, HCN, and NH_3. Reburning is currently a commercial NO_x control technology for boilers and furnaces. In recent demonstrations in three industrial boilers, 60–70% NO removal was achieved [5].

Since fossil fuels contain nitrogen, several studies have been conducted to evaluate influence of N-compounds on reburning efficiency. Wendt and Mereb [3] used ammonia-doped natural-gas reburning to evaluate the effect of nitrogen content in the reburning fuel. The presence of nitrogen produced higher levels of HCN, NH_3, and NO (total fuel nitrogen, TFN) within the first 0.4 s, but at greater residence times, the level of TFN was about the same as without ammonia. Rudiger et al. [6] reported a positive effect of nitrogen in the reburning fuel on NO reduction.

This paper examines, via experiments in a 300-kW combustor and kinetic modeling, the effect of N-agents (ammonia and urea) on NO removal in the reburning process. Results demonstrate that NO reduction is enhanced if N-agents are injected into the reburning zone with a delay time after injection of the reburning fuel. Furthermore, the presence of sodium compounds, such as sodium carbonate, promote the effect of N-agents. About 80–90% NO_x control was achieved by injection of 10% reburning fuel in the presence of ammonia and Na_2CO_3 in comparison with 45–50% NO_x reduction by 10% reburning alone. Kinetic modeling qualitatively describes the chemical processes responsible for NO_x reduction.

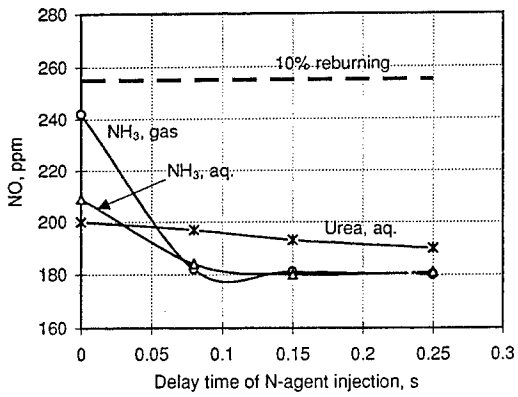

FIG. 1. NO removal by 10% reburning and with injections of N-agents (ammonia and urea, NSR = 1.5) into the reburning zone at various delay times from 0 to 0.25 s. OFA was added at 1422 K. Initial NO concentration is 530 ppm.

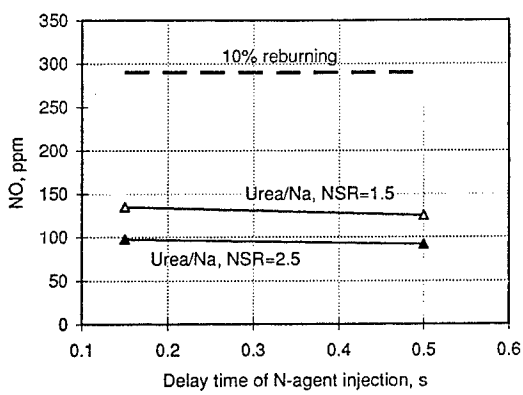

FIG. 2. NO removal by 10% reburning and with injections of urea (NSRs = 1.5 and 2.5) and 100-ppm Na into the reburning zone at various delay times. OFA was added at 1422 K. Initial NO concentration is 530 ppm.

Experimental

Experiments were conducted in a 300-kW boiler simulator facility (BSF), firing natural gas as main and reburning fuels. The BSF is a downfired combustor consisting of a vertical radiant furnace and a horizontal convective pass. The radiant furnace is a refractory-lined cylinder with a 56-cm inside diameter and 6.7-m height. It is equipped with numerous ports to allow introduction of sampling and injection probes. The furnace is also configured with movable water-cooled panels to allow control of facility residence time–temperature history. The BSF is equipped with a variable swirl-distributed mixing burner, a continuous emissions monitoring (CEM) system, and a personal computer–based data acquisition system. The CEM system includes a chemiluminescent NO/NO_x analyzer, infrared CO and CO_2 analyzers, a flame ionization total hydrocarbon analyzer, a paramagnetic O_2 analyzer, and an infrared N_2O analyzer. Furnace temperatures are measured using a suction pyrometer. Temperature gradient in the furnace was −170 K/s at 1700–1800 K and about −300 K/s at 1200–1600 K. Flue gas was sampled at different locations and analyzed by the CEM system. In all experiments, the initial stoichiometric ratio (SR) in the main combustion zone was $SR_1 = 1.1$. Ammonia was added to the main fuel to provide an initial NO concentration of 530 ppm in all tests. The reburning fuel was injected at 1700 K at two injection rates, 10 and 20% of heat input, providing stoichiometries in the reburning zone ($SR_2 = 0.99$ and 0.90). Ammonia and urea were injected in the form of aqueous solutions with different nitrogen stoichiometric ratios (NSRs); ammonia was also injected in gas form. The NSR is a molar ratio of N-agent to the NO concentration at the time of injection. N-agents were injected with a delay time, 0–0.5 s, after injection of the reburning fuel. Sodium salts were diluted in N-agent solutions. Sodium carbonate, sodium formate, and sodium gluconate were tested. Since the process was not particularly sensitive to the amount of sodium (within a range of 50–100 ppm) and the type of sodium salt, most experiments were conducted with 100-ppm Na in flue gas. OFA was injected at different locations to provide a final stoichiometry of $SR_3 = 1.2$.

Results

Reburning with heat inputs of 10 and 20% reduced NO concentrations by 45–50% and 60–65%, respectively, almost independently on location of OFA injection (in a range of 1255–1533 K). Injection of N-agents into the reburning zone caused NO reduction and was more efficient in the presence of sodium. When no N-agent was present, sodium had no effect on NO emissions. Blank water injection tests confirm the effect of N and Na compounds. Results presented in each figure are compared with average baselines obtained in the same test day. Figure 1 demonstrates results of consecutive injections of 10% natural gas, N-agent with a delay time from 0 (co-injection with reburning fuel) to 0.25 s, and OFA at 1422 K. Reburning alone reduced the NO level from 530 to 255 ppm. In the presence of N-agents (NSR = 1.5), NO was further reduced to about 180 ppm. In all cases, the delayed injection of N-agents decreased NO emissions: slightly for injection of water solutions and substantially for injection of gaseous ammonia. Figure 2 presents NO emissions after 10% reburning (OFA at 1422 K) and injection of urea (NSRs = 1.5 and 2.5) along with 100 ppm sodium. In these tests, reburning reduced NO concentration from 530 to 290 ppm, and injection

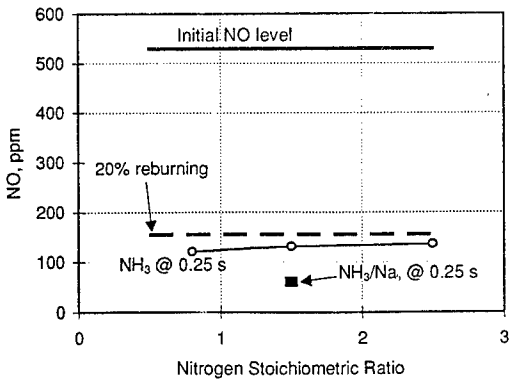

FIG. 3. NO removal by 20% natural-gas reburning and with 0.25-s delayed injections of aqueous ammonia (in the presence and in the absence of 100-ppm Na) into the reburning zone at various NSR with OFA added at 1255 K.

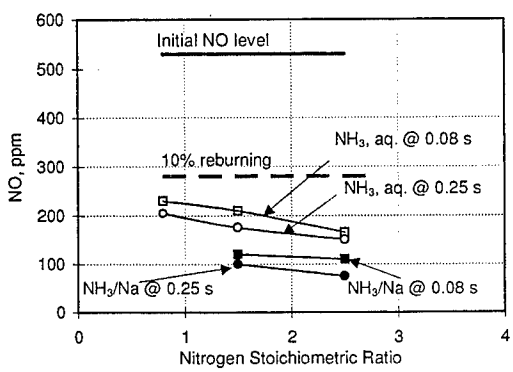

FIG. 4. Effect of NSR and the delay time (0.08 and 0.25 s) of aqueous NH_3/Na_2CO_3 injection on NO removal by 10% reburning. OFA added at 1255 K.

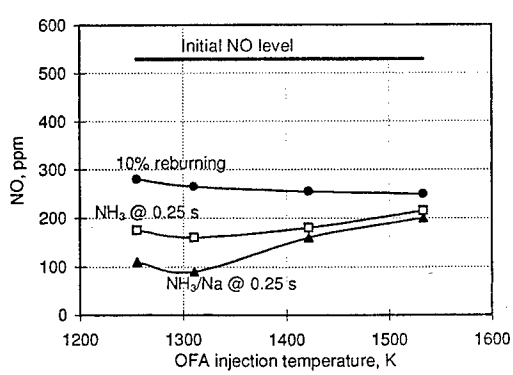

FIG. 5. Effect of OFA location on NO removal by 10% reburning with injections of aqueous ammonia (NSR = 1.5) and sodium carbonate at a 0.25-s delay time.

of the urea/sodium mixture further removed NO to 70–130 ppm, depending on conditions. Similar results were obtained for injection of ammonia.

Figure 3 demonstrates that at 20% reburning (SR_2 = 0.90), ammonia injection minimally decreased NO emissions, but if sodium was added with a N-agent, the NO level was decreased by more than 50%.

Figure 4 shows the impact of NSR and the delay time of N-agent injection on NO removal via 10% reburning with injection of ammonia and Na_2CO_3. As expected, NO reduction increased with increasing NSR. NO removal was higher at longer delay times of ammonia injection. After 45% NO reduction by reburning, ammonia with Na_2CO_3 (injected with a 0.25-s delay time) gave incremental NO reduction of about 48 and 52%, respectively, at NSR = 1.5. Maximum overall NO reduction was about 85% for the combined process.

Performance of the process depends on OFA injection temperature. Figure 5 shows the effect of OFA location on NO removal with injections of ammonia and sodium carbonate at a 0.25-s delay time. The optimum OFA injection temperature appears to be about 1300 K. Similar results to Figs. 3–5 were obtained for injection of urea.

Concentration of N_2O in exhaust flue gas after OFA injection was about 6 ppm for most of the tests.

Kinetic Modeling

The Chemkin-2 code [7] and the reaction mechanism based on the GRI-Mech version 2.11 [8] were used for modeling. Thermal $DeNO_x$ reactions (Table 1), which are absent in the GRI-Mech, were selected from the scheme [9] and added to the mechanism. Modeling was performed without variation of rate constants for a plug flow reactor with a temperature decrease of 300 K/s in the reaction zone and for the following mixture entering the reburning zone: 8% CO_2 – 15% H_2O – 1.74% O_2 – 600 ppm NO. Concentrations of reburning fuel and ammonia and delay times of ammonia injection were varied.

Modeling does not quantitatively describe the experimental results. Observed discrepancies demonstrate the potential need for model improvement and are explained by (1) poor understanding of the chemical reactions between NO and carbon-containing radicals (HCCO, CH_2, CH_3, and CH) and (2) differences in mixing conditions: instantaneous in modeling and within about 50 ms in experiments. Therefore, the goal of the modeling effort was to provide insight into the controlling chemical factors of the process and qualitatively describe the experimentally observed main reaction trends, such as the chemical effects of delayed N-agent injection and Na promotion.

Experiments demonstrated (Fig. 1) that addition

TABLE 1
Additional reactions [9] included in GRI-Mech 2.11 mechanism [8]. Reactions are in Chemkin format with rate constants in the form $k_i = AT^n\exp(-E/RT)$.

Reaction	A(cm/mol/s)	n	E, cal
$NH_2 + O = NO + H_2$	0.50 E 14	0.0	0.
$NH_2 + NO = NNH + OH$	0.28 E 14	−0.55	0.
$NH_2 + NO = N_2 + H_2O$	0.13 E 17	−1.25	0.
DUPLICATE			
$NH_2 + NO = N_2 + H_2O$	−0.28 E 14	−0.55	0.
DUPLICATE			
$NNH + NO = N_2 + HNO$	0.50 E 14	0.0	0.
$NNH + NH_2 = N_2 + NH_3$	0.50 E 14	0.0	0.
$NNH + NH = N_2 + NH_2$	0.50 E 14	0.0	0.
$NNH + O = N_2O + H$	0.10 E 15	0.0	0.
$HNO + NH_2 = NH_3 + NO$	0.20 E 14	0.0	1,000.
$HNO + HNO = N_2O + H_2O$	0.395 E 13	0.0	5,000.
$HNO + NO = N_2O + OH$	0.20 E 13	0.0	26,000.
$NH_2 + NH = N_2H_2 + H$	0.15 E 16	−0.5	0.
$NH + NH = N_2 + H + H$	0.25 E 14	0.0	0.
$NH_2 + N = N_2 + H + H$	0.72 E 14	0.0	0.
$N_2H_2 + M = NNH + H + M$	0.50 E 17	0.0	50,000.
$H_2O/15/O_2/2/N_2/2/H_2/2/$			
$N_2H_2 + H = NNH + H_2$	0.50 E 14	0.0	1,000.
$N_2H_2 + O = NH_2 + NO$	0.10 E 14	0.0	0.
$N_2H_2 + O = NNH + OH$	0.20 E 14	0.0	1,000.
$N_2H_2 + OH = NNH = H_2O$	0.10 E 14	0.0	1,000.
$N_2H_2 + NO = N_2O + NH_2$	0.30 E 13	0.0	0.
$N_2H_2 + NH = NNH + NH_2$	0.10 E 14	0.0	1,000.
$N_2H_2 + NH_2 = NH_3 + NNH$	0.10 E 14	0.0	1,000.
$NH_2 + NH_2 = N_2H_2 + H_2$	0.50 E 12	0.0	0.
$NH_2 + O_2 = HNO + OH$	0.45 E 13	0.0	25,000.
$NCO + NO_2 = N_2O + CO_2$	0.58 E 15	−0.7	0.
$NH + HNCO = NH_2 + NCO$	0.30 E 14	0.0	23,700.
$NH_2 + HNCO = NH_3 + NCO$	0.10 E 13	0.0	6,955.
$HO_2 + HNCO = NCO + H_2O_2$	0.3 E 12	0.0	29,000.
$NH_3 + HO_2 = NH_2 + H_2O_2$	0.3 E 12	0.0	22,000.
$NH_2 + NO_2 = N_2O + H_2O$	0.284 E 19	−2.2	0.
$NH + NO_2 = N_2O + OH$	0.1 E 14	0.0	0.
$NH_2 + NH_2 = NH + NH_3$	0.5 E 14	0.0	10,000.
$NH_2 + HO_2 = NH_3 + O_2$	0.43 E 14	0.0	0.

of N-agents into the reburning zone improves NO_x reduction if the N-agent is injected in the form of solution shortly after introduction of the reburning fuel. Modeling shows that addition of the fuel to the reburning zone results in very fast oxygen consumption to form CO and H_2. If N-agents are injected into the reburning zone, they form NH_i radicals (NH_2, NH, N) that are active in NO removal reactions. The NH_i radicals can react either with O_2 into NO or with NO into N_2. The NO reduction process is effective if the NH_i precursors (N-agents) appear in the gas mixture when concentration of oxygen has been significantly depleted by the reburning fuel, thus preventing oxidation of N-agents into NO. Calculated characteristic times for O_2 disappearance after the injection of the reburning fuel are less than 0.01 s at 1700 K and about 0.1 s at 1450 K. The delay time between injection of a reburning fuel and the formation of NH_i species should exceed these times for effective NO reduction.

Results of calculations that demonstrate the effect of NO reduction by CH_4 reburning in the presence of NH_3 are presented in Fig. 6 (curves 1–4). Curve 1 is the initial uncontrolled NO level of 600 ppm. Curve 2 models 10% reburning when CH_4 is added to the reburning zone at 1700 K. The NO concentration decreases to 412 ppm in 1.5 s (the time of OFA addition at 1255 K), or about 31% NO reduc-

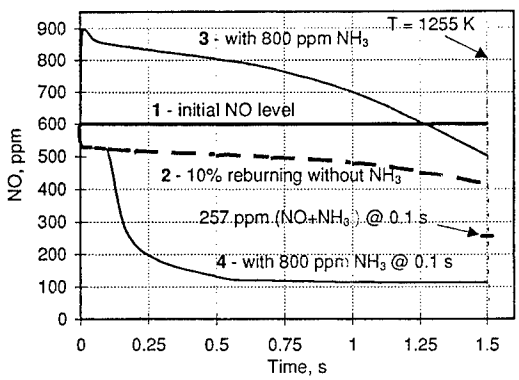

FIG. 6. Modeling the effect of ammonia in the reburning zone (without OFA): 1, initial NO level; 2, 10% reburning without ammonia; 3, 800-ppm NH_3 is added simultaneously with the reburning fuel; 4, 800-ppm ammonia is added into the reburning zone with a 0.1-s delay time. TFN concentration ($NO + NH_3 = 257$ ppm) is shown at 1.5 s (the time of OFA injection at 1255 K).

tion (about 45% was achieved in experiments, Fig. 4).

Curve 3 shows that if 800 ppm NH_3 is added simultaneously with the reburning fuel, the NO concentration is rapidly increased to 900 ppm and then reduced to 500 ppm in 1.5 s. Thus, the addition of NH_3 in the presence of oxygen initially increases the NO concentration, but by the time of OFA injection, [NO] is close to the level achieved by 10% reburning. Oxygen prevents NO reduction because the added NH_3 burns rapidly in the presence of O_2 to form additional NO.

Therefore, it is logical to add ammonia not with the reburning fuel, but after the O_2 concentration has decreased through reaction with the reburning fuel: NSR = 1.5 with 0.1-s delay in curve 4. In 1.5 s of the reaction time, the NO concentration drops to 113 ppm, but 144 ppm NH_3 is left in the reaction media, and thus, TFN = 257 ppm, as shown in Fig. 6. Concentration of HCN was below 1 ppm under all process conditions with 10% reburning (SR_2 = 0.99). Injection of OFA at 1255 K resulted in 230 ppm final NO concentration, 62% NO reduction (approximately as that in experiments, Fig. 4).

At higher reburning fuel concentration (20% reburning, SR_2 = 0.90), modeling shows formation of 229 ppm TFN in 1.5 s (70 ppm HCN, 115 ppm NH_3, and 44 ppm NO). Injection of OFA at 1255 K results in a 200 ppm final NO level, corresponding to 67% NO reduction (experimentally 71% NO reduction was achieved, Fig. 3). Injection of ammonia (NSR = 1.5) into the fuel-rich zone at SR_2 = 0.90 with a 0.1-s delay time, followed by OFA injection, does not significantly change the final NO level in modeling, and the same was shown experimentally (Fig. 3). Thus, injection of N-agents into the reburning zone is more efficient under near-stoichiometric conditions. At higher reburning fuel levels, concentrations of active radicals are lower, most of the fuel nitrogen is present in the form of NH_3 and HCN, and the NO reduction rate is slower. However, Na promoters are effective even at SR_2 = 0.90 (Fig. 3).

As follows from the experimental results with Na promoters (Figs. 2–5), sodium can promote the effect of N-agents under fuel-rich conditions. A similar effect of reducing NO levels and broadening the temperature window for effective N-agent injection was demonstrated earlier under fuel-lean conditions [10]. One can suggest several hypothetical sodium reactions with flue gas components to promote NO reduction:

1. Sodium atoms and oxides react with H_2O; for instance, $Na + H_2O \rightarrow NaOH + H$ and $NaO + H_2O \rightarrow NaOH + OH$ followed by formation of NH_2 radicals from ammonia, $OH + NH_3 \rightarrow NH_2 + H_2O$, and NO–$NH_2$ interaction: $NH_2 + NO \rightarrow N_2 + H_2O$.
2. Sodium atoms formed during Na_2CO_3 decomposition react with ammonia [11] followed by dissociation of $NaNH_2$: $Na + NH_3 \rightarrow NaNH_2 + H$ and $NaNH_2 + M \rightarrow Na + NH_2 + M$.
3. Na_2CO_3 dissociates at high temperatures to form oxides, for example, to $NaO + Na + CO_2$ or $Na_2O + CO_2$. The oxides then react with ammonia via equations: $NaO + NH_3 \rightarrow NaOH + NH_2$ and $Na_2O + NH_3 \rightarrow NaOH + NaNH_2$, followed by the sodium-amide decomposition.

Although it is unknown which of the sodium reactions are most important, the effect of all reactions is formation of active radicals (NH_2 or OH) at a faster rate than that of ammonia decomposition without sodium additives. It was assumed for modeling that an interaction of Na promoters with water is responsible for the formation of the additional OH radicals. The following empirical reaction was added to the mechanism: $[(Na)HOH] + M \Rightarrow (Na) + OH + H + M$. This equation simulates fast interaction of sodium compounds with water molecules with formation of a complex [(Na)HOH], which dissociates into OH and H. The initial concentration of [(Na)HOH] was assumed to be 100 ppm in modeling. The rate constant for [(Na)HOH] decomposition was selected in the form $A \exp(-20{,}000/T)$ cm^3/mol s, where the pre-exponential factor A was varied in the range from 10^9 to 10^{12}. These values of the rate constant provided decomposition of the complex with characteristic times between approximately 0.1 and 100 s. Injection of the promoter caused slightly higher H and OH concentrations in the reaction media than those in the absence of the promoter.

Figure 7 compares the results of modeling NO

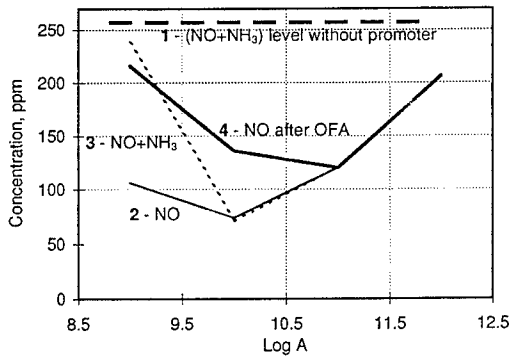

FIG. 7. Modeling of the promotion effect at different pre-exponential factors A. NO and NH_3 concentrations are shown at $t = 1.5$ s for injection of 800-ppm ammonia and 100-ppm promoter into the reburning zone with a 0.1-s delay time. 1, TFN level without promoter; 2, NO concentration before OFA injection; 3, TFN concentration (NO + NH_3) before OFA injection; 4, NO level after OFA injection.

and NH_3 concentrations at $t = 1.5$ s (the same conditions shown by curve 4 in Fig. 6 at $T = 1255$ K) at different values of the pre-exponential factor A. The promoter [(Na)HOH] was added into the reburning zone along with ammonia at a 0.1-s delay time. The level of TFN without promoter (257 ppm) is shown in Fig. 7 for comparison. In a wide range of the promoter decomposition rate, NO and TFN concentrations are substantially lower than their values without promoter. In the presence of the promoter, there is a minimum of the final NO concentration at log $A = 10.5$. Thus, there exists an optimum rate constant for formation of additional radicals that cause minimum NO emissions. Figure 7 compares NO and (NO + NH_3) concentrations at $T = 1255$ K before OFA injection and the final NO concentration after OFA injection. In the OFA zone, some NO reacts with NH_3 due to the thermal $DeNO_x$ reactions, and the minimum level of NO at log $A = 10.5$ after OFA injection is about 120 ppm. Experimental data indicate that under similar conditions, NO is reduced to 100–120 ppm by injection of N-agents with Na_2CO_3 into the reburning zone (Figs. 4 and 5). Hence, additional formation of radicals in the reburning zone can explain deeper NO reduction in the presence of Na promoters.

Modeling also shows that small concentrations of oxygen in the reburning zone can promote NO–NH_3 interaction. Oxygen reacts with CO and H_2 to form radicals that accelerate the reaction between NO and NH_3. Thus, high oxygen concentrations burn NH_3 to form NO, but low [O_2] concentrations do not form radicals to promote NO reduction. An optimum oxygen concentration (20 ppm–1%) depends on process conditions (temperature, concentrations of CO, H_2, NO, N-agent, etc.) and provides maximum NO_x control.

Discussion

In the reburning zone, the initial NO_x reduction reactions occur rapidly once the reburning fuel and furnace gases are contacted. Following an initially rapid NO_x reduction, the subsequent NO_x decay rate is slow since the radical pool has been depleted. If a N-agent is injected after a suitable delay time following the reburning fuel, it can restart the NO_x reduction reactions and increase the overall level of NO_x reduction beyond that of reburning alone.

The delayed introduction of N-agent into the reburning zone can be accomplished either by physically separating the injection of N-agents from that of the reburning fuel or by utilizing aqueous solutions of urea or ammonia injected in the form of a droplet cloud together with the reburning fuel. The evaporation time of the aqueous droplets and N-agent decomposition time can provide the delay time necessary for the significant consumption of oxygen in the reburning zone. This delay time can be controlled by adjusting the droplet size to vary the rate of evaporation of the droplets.

Sodium additives can be added along with solutions of N-agents to promote the chemical reactions between NO and N-agents in the reburning zone. As a result, the NO_x control achieved with a given N-agent injection rate is increased. The promoters are sodium salts that are added in small quantities, in comparison with NO concentration. Sodium carbonate is one example that is nontoxic, readily available, and very effective. Most likely, promoters do participate in the process, but their role is to provide radical pool that will initiate the NO–NH_3 interaction. Small amounts of oxygen in the reburning zone can also help for promoting NO_x reduction.

Fuel N and sodium compounds that are constituent parts of various fuels can serve as the precursors of ammonia, NH_i radicals, and active sodium species in the reburning zone. For instance, coal, biomass, and various waste streams can contain nitrogen and alkali compounds. These compounds can be released or formed from different fuels by pyrolysis, gasification, physical or chemical separation, or by other techniques. N-agents and promoters can also be formed from the reburning fuel directly in the reburning zone with a time delay that is defined by the rates of their release or formation from the reburning fuel.

The location of OFA injectors is an important factor that affects process efficiency. Depending on temperature profiles, the residence time in the reburning zone should be kept as long as possible to complete the NO_x reduction process. However, too low of an OFA injection temperature will increase

concentrations of CO and other combustibles in flue gas. Maximum NO removal with N-agent injection into the reburning zone can be achieved with OFA injection at about 1300 K. This temperature is high enough to reduce CO emissions and low enough to provide higher NO removal.

Arand et al. [12] and Brogan [13] presented results on NO reduction by interaction with urea and ammonia, respectively, under fuel-rich combustion. They considered the presence of N-agents in the fuel-rich main combustion zone. Reburning provides firing most of the fuel under fuel-lean conditions, and only a small portion of the fuel is fired under fuel-rich conditions in a relatively small part of the furnace. This process can substantially reduce corrosion and burner deposits simultaneously providing high efficiency NO_x control.

Conclusions

The results of this study demonstrate a significant influence of nitrogen- and sodium-containing compounds on NO removal via reburning. Delayed appearance of N-agents in the gas mixture provide the time that is necessary for depletion of the oxygen from the main combustion zone by the reburning fuel, thus preventing oxidation of the N-agents into NO. Sodium compounds, such as sodium carbonate, promote the effect of N-agents. The promotion effect can be explained by reactions of additional active radicals formed in the reburning zone via interaction of sodium compounds with water molecules. The following factors primarily control process efficiency: stoichiometric ratio in the reburning zone, delay time between injection of the reburning fuel and formation of NH_i radicals in the reburning zone, oxygen concentration at the time of N-agent injection, concentration of N-agent, and OFA injection location. Over 80% NO reduction was achieved in a 300-kW combustor by injection of only 10% natural gas as reburning fuel (SR_2 = 0.99) at 1700 K, followed by 0.1–0.5-s delayed injection of aqueous ammonia or urea (NSR = 1.5) with sodium carbonate (100-ppm Na in gas mixture) and injection of OFA at 1300 K. Under similar conditions, injection of 20% reburning fuel results in about 90% NO_x control.

Acknowledgment

This work was supported by EER Corporation and the U.S. Department of Energy under Contract No. DE-AC22-95PC95251; DOE Project Manager is William P. Barnett.

REFERENCES

1. Wendt, J. O. L., Sterling, C. V., and Matovich, M. A., *Fourteenth Symposium (International) on Combustion,* The Combustion Institute, Pittsburgh, 1973, p. 897.
2. Chen, S. L., Cole, J. A., Heap, M. P., Kramlich, J. C., McCarthy, J. M., and Pershing, D. W., *Twenty-Second Symposium (International) on Combustion,* The Combustion Institute, Pittsburgh, 1988, pp. 1135–1145.
3. Wendt, J. O. L. and Mereb, J. B., *Nitrogen Oxide Abatement by Distributed Fuel Addition,* Report to DOE, Contract No. AC22-87PC79850, 1991.
4. Glarborg, P., Dam-Johansen, K., and Kristensen, P. G., *Reburning Rich-Lean Kinetics,* Report to GRI, Contract No. 5091-260-2126, 1993.
5. Folsom, B. A., Sommer, T., Ritz, H., Pratapas, J., Bautista, P., and Facchiano, T., *EPRI/EPA 1995 Joint Symposium on Stationary Combustion NO_x Control,* Kansas City, MO, 1995, Book 4, Session 8.
6. Rudiger, H., Greul, U., Spliethoff, H., and Hein, K. R. G., *3-d International Conference on Combustion Technologies for a Clean Environment,* Lisbon, Portugal, 1995, pp. 27.2(9–16).
7. Kee, R. J., Rupley, F. M., and Miller, J. A., *Chemkin-II: A Fortran Chemical Kinetics Package for the Analysis of Gas-Phase Chemical Kinetics,* Sandia National Laboratories Report No. SAND89-8009, 1989.
8. Bowman, C. T., Hanson, R. K., Davidson, D. F., Gardiner, W. C., Jr., Lissianski, V., Smith, G. P., Golden, D. M., Frenklach, M., and Goldenberg, M., http://www.me.berkeley.edu/gri_mech/.
9. Bowman, C. T., in *Physical and Chemical Aspects of Combustion: A Tribute to Irvin Glassman* (F. L. Dryer and R. F. Sawyer, Eds.), Gordon and Breach, New York, 1996.
10. Ho, L., Chen, S. L., Seeker, W. R. and Maly, P. M., U.S. Patent 5,270,025, 1993.
11. Lappert, M. F., *Metal and Metalloid Amides,* Ellis Horwood Ltd., 1982.
12. Arand, J. K., Muzio, L. J., and Telxelra, D. P., U.S. Patent 4,325,924, 1982.
13. Brogan, T. R., U.S. Patent 4,335,084, 1982.

COMMENTS

P. Glarborg, Technical University of Denmark, Denmark. In your present work you have investigated the effect of sodium on reduction of NO by NH_3 (thermal De-NOx) under overall reducing conditions. Have you looked at the interaction of sodium with the thermal de-NO_x chemistry under overall lean conditions?

Author's Reply. Yes, we studied the effect of sodium on de-NO_x chemistry under fuel lean conditions [1]. It was shown that small amounts of sodium salts injected with N-agents (ammonia or urea) can also enhance NO reduction. In particular, the temperature window of the de-NOx reaction becomes deeper and wider in the presence of sodium. In our recent studies [2] we considered the combined injection of N- and Na-compounds in the advanced reburning process [3] under both fuel-rich and fuel-lean conditions. This multiple injection advanced reburning has the potential to achieve about 90–95% NOx control in all types of utility boilers.

REFERENCES

1. Ho, L., Chen, S. L., Seeker, W. R., and Maly, P. M., U.S. Patent 5,270,025, 1993.
2. Zamansky, V. M., Ho, L., Maly, P. M., and Seeker, W. R., Second Generation Advanced Reburning for High Efficiency NOx Control, American Flame Research Committee 1996 Intern. Symp., September 30–October 2, Baltimore, MD.
3. Seeker, W. R., Chen, S. L., and Kramlich, J. C., U.S. Patent 5,139,755, 1992.

•

William C. Hecker, Brigham Young University, USA. How do other promoters/catalysts such as potassium or calcium behave in this process? Have they been tested and how do they compare?

Author's Reply. In this work we studied the efficiency of several sodium salts on NO reduction by reburning in the presence of ammonia and urea. These salts are carbonate, formate and gluconate. They show a strong promotional effect which almost does not depend on the nature of the compound. In recent experiments we also tested several other sodium and potassium compounds. Sodium bicarbonate and sodium hydroxide had similar NO reduction effect. This supports the conclusion that either Na atoms or its oxides or hydroxide are responsible for the promotion reaction. Although potassium carbonate demonstrated some NO reduction, the effect was smaller than the effect of sodium.

•

F. Temps, Institut f Physikaliscke Chemie, Germany. Regarding your outlook of advanced NO_x reburning schemes, can you comment on the emission of hydrocarbons and especially CO?

Author's Reply. Injection of ammonia or urea into the reburning zone does not substantially affect the concentrations of CO and hydrocarbons in exhaust flue gas. However, in our recent experiments performed after submitting this paper, we noticed an increase in the final CO concentration, measured by an IR analyzer, in the presence of even small sodium additives. This CO concentration depends on the amount of sodium and the location of the overfire air injector. We continue to study this effect which currently can be explained either by a specific chain mechanism of Na interaction with flue gas components or by formation of unidentified species which have an absorption band overlapping with the CO band.

Twenty-Sixth Symposium (International) on Combustion/The Combustion Institute, 1996/pp. 2083–2090

FLOW REACTOR STUDIES AND TESTING OF COMPREHENSIVE MECHANISMS FOR NO_x REBURNING

DIETER STAPF AND WOLFGANG LEUCKEL

Engler-Bunte-Institut
der Universität Karlsruhe (T.H.)
Lehrstuhl und Bereich Feuerungstechnik
76128 Karlsruhe, Germany

A plug flow reactor has been set up to study NO_x reburning kinetics under conditions comparable to those in industrial boilers. The overall situation corresponds to low radical concentrations. Therefore, mixtures of natural gas and nitrogen were injected into a flow of flue gas containing 1000 ppm NO_x and varying levels of residual oxygen. The reduction of nitric oxide by attack of hydrocarbon radicals was investigated for equivalence ratios Φ between 1.1 and 1.6 and at temperatures of 1200, 1300, and 1400°C. Plug flow calculations were performed with three comprehensive mechanisms taken from recent literature.

A comparison of measured and computed concentration profiles showed that consumption of NO and production of HCN are overestimated by all models, especially when the initial oxygen content of the rich mixtures is increased. Analysis of the calculated NO production rates identified the attack of NO by the HCCO radical with a temperature independent rate coefficient to be the dominating pathway of NO consumption. Reactions of nitric oxide with other hydrocarbon radicals exercise only a minor influence. However, recently measured data for the reactions of CH_3 with NO underlines the importance of this pathway in reburning kinetics. If this reaction is emphasized in the calculations, the reaction of NO with HCCO has to become very slow in order to achieve good agreement with experimental data.

One of the mechanisms from the literature was modified by means of sensitivity analysis and critical revisions of kinetic data for important reactions under rich conditions. Usage of this modified mechanism is leading to significantly improved agreement for NO profiles with experimental data. Nevertheless, there still remains some uncertainty in the description of HCN consumption and concerning the reaction pathways and rate coefficients of NO-consuming reactions under rich conditions with low levels of radicals.

Introduction

Reburning is a powerful technique of reducing NO_x emission of boilers. In a secondary stage, reburn fuel is injected into the NO-containing flue gas of the primary stage, turning the stoichiometry into one that is fuel-rich. Under these conditions, NO_x is reduced by the attack of hydrocarbon radicals. The main product of the NO_x reduction is HCN which subsequently is converted into NH_i and N_2 under rich conditions. The aim of reburning must be to minimize the total fixed nitrogen, TFN, which represents the concentrations of all stable N species, as most TFN leaving the reburn stage is oxidized to NO in the third stage where required air for complete burnout is injected. Extensive laboratory and pilot-scale experiments have shown the effectiveness of NO_x reburning (Wendt et al. [1], Kolb et al. [2]).

Reactions of N species in combustion have been studied for many years in order to reduce pollutant formation by optimizing these kinetically controlled processes. As a result, there now exists a detailed knowledge of the elementary reactions producing and consuming NO, HCN, and NH_3, and with regard to their coupling with combustion chemistry in general, as summarized by Miller and Bowman [3]. However, there is still a lack of qualitative understanding of the interaction between hydrocarbon and NO_x chemistry, especially under fuel-rich conditions important for modeling staged combustion processes as shown, for example, by Glarborg and Hadvig [4].

A variety of investigations have been performed in order to develop a comprehensive C/H/O/N mechanism for natural gas combustion. Focusing on NO removal reactions, Glarborg et al. [5] suggested the attack of C, CH, and CH_2 on NO represents the essential NO recycle reactions that lead to CN and HCN, either directly or via the HCNO radical that has a very short lifetime under practical conditions. Miller and Bowman [3] introduced the reaction of NO with CH_3, which has two product channels, one to HCN and H_2O and the other to H_2CN and OH. They also took into account the reduction of NO by the ketenyl radical HCCO, which leads to HCNO and CO. They estimated its rate coefficient by means of a comparison with the isoelectronic reaction $NO + NCO \leftrightharpoons N_2O + CO$.

TABLE 1
Rate coefficients of NO recycle reactions of the form

$$k = A_0 \cdot T^{\beta} \cdot \exp\left\{-\frac{E_A}{R \cdot T}\right\}$$

		Miller and Bowman (1989)			Glarborg and Hadvig (1991)			Bockhorn et al. (1991)		
		A_0 [cm³/(mol·s)]	β	E_A (J/mol)	A_0 [cm³/(mol·s)]	β	E_A (J/mol)	A_0 [cm³/(mol·s)]	β	E_A (J/mol)
$NO + C \rightleftharpoons CN + O$	(R1)	$6.60 \cdot 10^{13}$	0	0	$1.90 \cdot 10^{13}$	0	0			
$NO + CH \rightleftharpoons HCN + O$	(R2)	$1.10 \cdot 10^{14}$	0	0	$1.10 \cdot 10^{14}$	0	0	$1.10 \cdot 10^{14}$	0	0
$NO + CH_2 \rightleftharpoons HCNO + H$	(R3)	$1.39 \cdot 10^{12}$	0	−4600						
$NO + CH_2 \rightleftharpoons NCO + H_2$	(R4)				$3.50 \cdot 10^{12}$	0	−4600	$2.90 \cdot 10^{12}$	0	−2500
$NO + CH_2(s) \rightleftharpoons HCN + OH$	(R5)	$2.00 \cdot 10^{13}$	0	0	$1.00 \cdot 10^{14}$	0	0			
$NO + CH_3 \rightleftharpoons HCN + H_2O$	(R6)	$1.00 \cdot 10^{11}$	0	62850	$5.30 \cdot 10^{11}$	0	62850	$5.00 \cdot 10^{12}$	0	0
$NO + CH_3 \rightleftharpoons H_2CN + OH$	(R7)	$1.00 \cdot 10^{11}$	0	62850	$5.30 \cdot 10^{11}$	0	62850			
$NO + HCCO \rightleftharpoons HCNO + CO$	(R8)	$2.00 \cdot 10^{13}$	0	0	$2.00 \cdot 10^{13}$	0	0			
$H_2CN + M \rightleftharpoons HCN + H + M$	(R9)	$3.00 \cdot 10^{14}$	0	92180	$3.00 \cdot 10^{14}$	0	92180			
$HCNO + H \rightleftharpoons HCN + OH$	(R10)	$1.00 \cdot 10^{14}$	0	50160	$1.00 \cdot 10^{14}$	0	50160			

Several improvements of the Miller/Bowman mechanism have been suggested on the basis of more reliable determinations of rate parameters of important reactions. The revision of Glarborg and Hadvig [4] concerns the C/H/O system and prompt NO formation. With respect to some experimental data relevant to NO_x reburning, they added an additional product channel to the NO + CH_2 reaction leading to NCO. They also took into account a reaction of singlet methylene with NO. Both reactions of CH_3 with NO were enhanced by a factor of 5.

Another group [6] developed a prompt NO mechanism which was added to the C/H/O system based on the mechanism of Warnatz [7]. It is referred to as mechanism #3 in this paper. Table 1 gives an overview of the rate coefficients of the recycle reactions included in these three comprehensive mechanisms.

Recently, direct or indirect measurements of several NO recycle reactions have been performed at temperatures relevant to combustion. Methylene chemistry in particular is very complicated because of the difference in behavior of singlet and triplet CH_2. Atakan et al. [8], for example, investigated the CH_2 + NO reaction at moderate temperatures and found a broad product distribution. Braun-Unkhoff et al. [9] performed shock-tube measurements of the CH_3 + NO reactions; the derived rate data are in good agreement with the measurements of Gardiner et al. [10]. The rate coefficient of the CH_3 + NO $\leftrightharpoons$ HCN + H_2O reaction found by those groups is significantly higher than in all comprehensive mechanisms from the literature. When simulating NO_x reburning processes, the concentrations of hydrocarbon radicals must be known, as must the rate coefficients of the NO recycle reactions.

Unfortunately, there is very limited experimental data for testing comprehensive mechanisms against NO_x reburning. Thorne et al. [11] studied reburning reactions in low pressure H_2/O_2-Ar flames seeded with NO and acetylene. Flow reactor experiments in a small tube were performed by Myerson [12] for different hydrocarbon fuels. Chen and Malte [13] used a jet-stirred reactor to investigate the reactions of NO in $CH_4/O_2/N_2$ mixtures at high temperatures and high NO input concentrations. Glarborg and Hadvig simulated the data of Refs. 12 and 13 and found good agreement with the measured NO and HCN profiles for the stirred reactor. Finally, Etzkorn et al. [14] reported a kinetic study on a stoichiometric low pressure CH_4/O_2 flame seeded with 1.8% NO. Using a modified version of the mechanism from Ref. 8, they achieved fair agreement between measured and calculated CN concentrations, whereas observed NO consumption within the flame front could not be reproduced by their model.

The aim of the present study was to provide kinetic data for NO_x reburning under conditions typical for industrial boilers, i.e., at relatively low radical concentrations due to little excess oxygen in the flue gas, and moderate temperatures. The second objective was the comparison of three comprehensive mechanisms by testing them against measured concentration profiles. By means of detailed analysis of the numerically calculated results in combination with rate data revision, the main reaction pathways for NO_x removal under reburning conditions are identified. Additional work on C/H/O reaction schemes under rich conditions is not included in this paper but will be reported elsewhere [15].

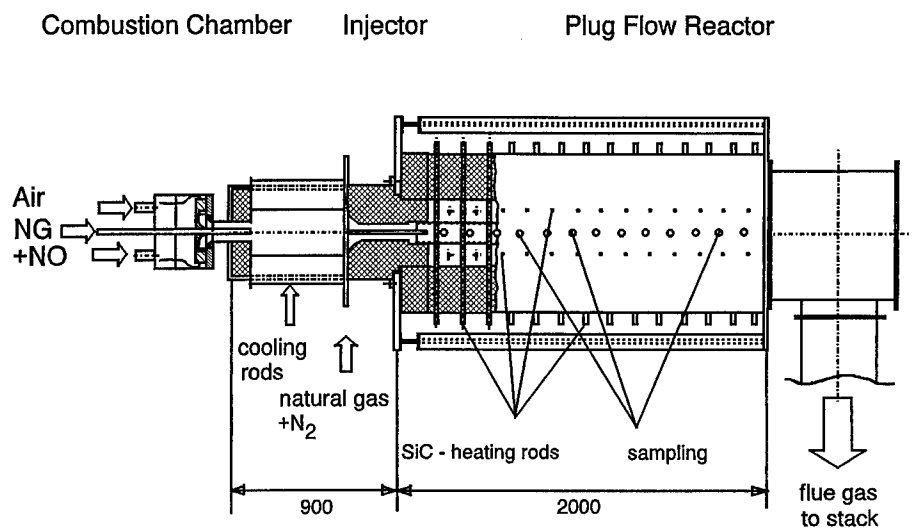

FIG. 1. Schematic of the plug flow reactor.

Experimental

A flow reactor was chosen because it can reproduce overall diluted reburning conditions with low radical concentrations. Furthermore, such a reactor provides high spatial resolution. It was set up on a semitechnical scale rather than a laboratory scale to justify applying probe sampling techniques and to avoid wall effects. Figure 1 shows a schematic of the flow reactor which consists of the primary combustion chamber, the mixing system, and the reaction tube which is 100 mm in diameter. The flue gas temperature of the refractory-lined combustion chamber can be adjusted by means of postflame cooling rods. A quarter-circle-shaped nozzle between the combustion chamber and reaction tube accelerates the flow smoothly into the ceramic tube to velocities of about 15 m/s. At this point, natural gas is injected radially through a multihole nozzle. Number and momentum of the near sonic jets were optimized for very fast mixing. In order to keep the mixing constant it is important to add nitrogen to the natural gas, which varies in dependence on the equivalence ratio Φ in the primary combustion chamber and in the flow tube. By variation of the equivalence ratio in the primary combustion chamber and of the injected natural gas flow, it is possible to control the initial oxygen content and the equivalence ratio in the reaction tube independently.

Depending on temperature and stoichiometry, the reaction starts before homogeneous mixing and the plug-flow situation are achieved, though the mixing time scale is very short, as reported before [15]. Thus, homogeneity of the mixture was checked at the beginning of every experiment by means of radial measurements of the equivalence ratio Φ and time-resolved temperatures using the compensated thermocouple technique.

The axial temperature and concentration profiles in the plug flow were measured by means of water-cooled stainless steel probes introduced through side-stream ports. Besides conventional analyzers for O_2, H_2, CH_4, CO, CO_2, and NO/NO_x, an FTIR was used to determine the concentrations of HCN, NH_3, N_2O, NO_2, C_2H_2, and C_2H_4 in the wet flue gas. The tube was electrically heated to avoid significant heat losses, and so the temperature of the reacting flow was almost constant; variations were within a range of $\pm 30°C$.

Results and Discussion

The measured temperature profile was imposed for the numerical calculations. All concentrations measured at the first position after injection and homogenous mixing were taken as input. The Senkin solver [16] was used to compute concentration profiles, production rates, and sensitivity coefficients in the frame of the Chemkin-II package. Several comparisons were conducted in the present study. The focus of the following discussion is the N species reactions and the effects of initial oxygen concentrations as the most important parameter.

Figure 2 gives a comparison of measured and calculated concentration profiles of stable N species as a function of residence time at $\Phi = 1.25$, $T = 1300°C$, and an oxygen concentration of 1.13% by volume at the first measuring point. Within the recorded 100 ms, the NO concentration decreased gradually because NO was consumed by reaction with hydrocarbon radicals forming HCN. HCN was

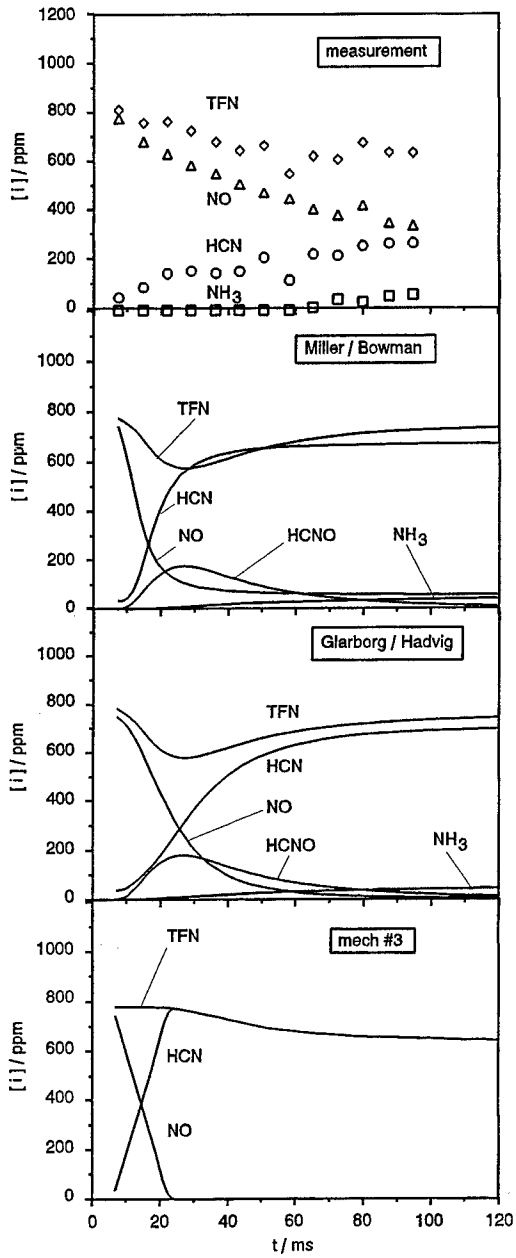

FIG. 2. Measured and calculated concentrations of N species as a function of residence time. Conditions: $p = 1$ atm, $T = 1300°C$, $\Phi = 1.25$, and $[O_2]_{initial} = 1.13\%$.

partly consumed forming NH_3 which was mostly converted to N_2 under the prevailing fuel-rich conditions. Formation and consumption of HCN lead to the observed moderate increase of its concentration. Overall, the measured TFN concentration decreased slightly. Gradients at 100 ms were generally smaller than at the beginning because the radical pool depleted as all the oxygen was consumed.

The numerical results computed with the Miller/Bowman and the Glarborg/Hadvig schemes show principally the same tendencies. Obviously, NO consumption is too fast, resulting in a significantly higher conversion of NO to HCN. As mentioned before, HCNO is an intermediate of NO recycle reactions leading to hydrogen cyanide. According to our definition of the TFN value (which does not include the HCNO species), the calculated TFN concentration shows a minimum due to the HCNO storage. Our measurements do not confirm this behavior. After consumption of the radical pool, only small concentrations of NO and NH_3 are calculated, in contrast to our measurements. Mechanism #3, in particular, predicts total NO-to-HCN conversion due to the high rate coefficient of reaction R6 in the model (see Table 1).

In order to provide a ranking of all recycle reactions that contribute more than 5% to the total NO consumption, the NO production rates are plotted in Fig. 3. According to the Miller/Bowman mechanism, nearly all NO is consumed by reaction with the ketenyl radical, forming intermediary HCNO. For the Glarborg/Hadvig case, where the two reactions of NO with methyl were enhanced slightly, the CH_3 + NO reactions provide a small contribution to NO consumption. In both cases, other radicals are of minor importance. The prompt NO mechanism (#3) is a more global model. For all experiments investigated, NO is completely recycled to HCN by reaction R6. Since that model does not seem to be adequate under rich conditions, we will focus on the two other detailed mechanisms with regard to N species reactions. Despite this, mechanism #3 contains HCN consumption chemistry different from the two other models.

Figure 4 is a comparison of measured and computed N species concentrations at the same temperature and stoichiometry as before ($\Phi = 1.25$, $T = 1300°C$). However, the initial oxygen concentration was decreased by an order of magnitude to $[O_2] = 0.12\%$. The measured profiles of the two experiments do not show significant difference except for the initial TFN level, which was 200 ppm higher than in the first experiment. However, the calculated results are in much better agreement with measurements of both total NO consumption and moderate concentration gradients. This is a result of the smaller NO destruction rate predicted by reaction R8 (Fig. 5) because the oxygen pool that is needed to form HCCO is smaller. Therefore, the relative importance of the CH_3 + NO reactions increases. More NO is recycled by CH_3 than by HCCO, as per the Glarborg/Hadvig model.

The same behavior of the kinetic schemes was found at all stoichiometries and all temperatures investigated, considering both the steepness of the

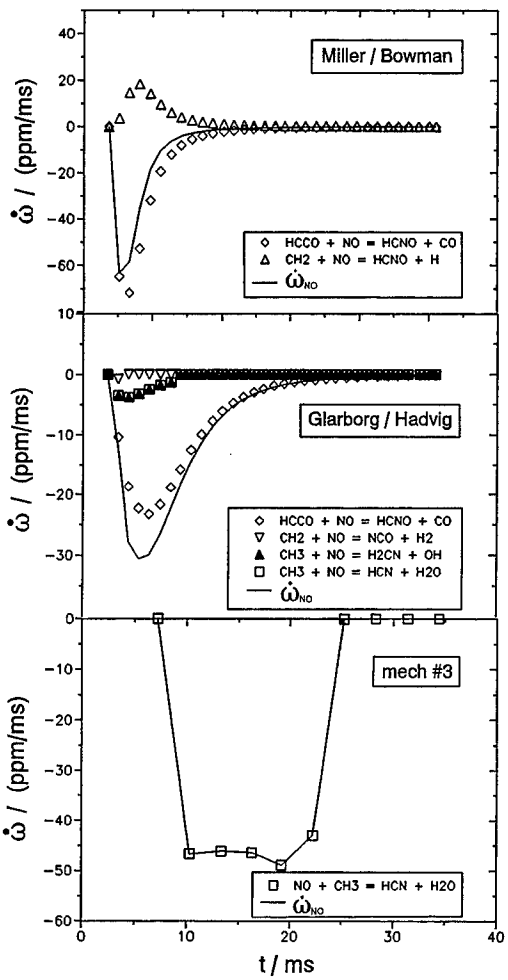

FIG. 3. Computed NO production rates as a function of residence time. Conditions: p = 1 atm, T = 1300°C, Φ = 1.25, and $[O_2]_{initial}$ = 1.13%.

gradients and the importance of the recycle reactions R6–8. The reaction behavior depends more on the initial oxygen content that controls the radical pool than on stoichiometry. With a generally small radical pool where [H] > [OH] > [O], measurements and calculations are in fair agreement, whereas NO consumption is overestimated if $[O_2]$ > 1%. At very rich conditions with low radical concentrations, calculated time scales were larger than measured ones. This behavior clearly shows that incomplete micromixing, which reduces the radical pool, cannot be held responsible for the observed discrepancies between experiments and computations.

Modified Mechanism

Changes in the most reliable mechanism were made to abolish the two main discrepancies observed: the strong dependence of reaction time scales on initial oxygen content in an overall diluted situation, and overestimated NO-to-HCN conversion.

An evaluation of relevant reaction rate data was carried out. Braun-Unkhoff et al. [9] derived the following Arrhenius expressions for reactions R6 and R7:

$$k_6 = (1.66 \pm 0.8)\cdot 10^{12}\cdot \exp\{(-8100 \pm 1400)/T\}\ (\mathrm{cm^3/mol/s})$$

$$k_7 = (7.13 \pm 1.3)\cdot 10^{12}\cdot \exp\{(-12140 \pm 610)/T\}\ (\mathrm{cm^3/mol/s})$$

These expressions provide significantly higher reaction rates than those assumed in the models of Miller/Bowman and Glarborg/Hadvig. Including this data into the Glarborg/Hadvig model, the HCCO + NO reaction becomes nearly insignificant with respect to overestimated NO consumption, as shown before. Therefore, we decided to eliminate this reaction from the mechanism. Until now, rate data of R8 was derived only at ambient conditions [17]. Product distribution and branching ratios could not be identified clearly.

Figure 6 shows a comparison of measured and calculated N species profiles for the first experiment (Φ = 1.25, T = 1300°C, $[O_2]$ = 1.13%). The mechanism used here includes only the changes in R6–8. All the other data are from Glarborg/Hadvig. The diagram shows a better agreement of measured and calculated NO profiles than achieved with the original mechanism. All NO reduction now proceeds through the NO + CH_3 channel. For unchanged HCN chemistry, HCN-to-N_2 consumption remains underestimated.

For lower radical concentrations (Φ = 1.25, T = 1300°C, $[O_2]$ = 0.12%), the modifications result in minor changes of concentration profiles. Nevertheless, total NO consumption proceeds through R6 and R7, in contrast with the former importance of the HCCO + NO reaction.

Again, this behavior was found at all temperatures and stoichiometries we investigated in this study. Using the modified Glarborg/Hadvig model, measured and calculated reaction time scales as well as NO profiles are in better agreement.

It should be pointed out that computed and observed TFN and HCN concentrations do not fit well. While NO consumption seems to be better understood by introducing those modifications, the HCN-to-N_2 consumption network is still not elucidated sufficiently under rich conditions. Therefore, calculated HCN concentrations are too high. New modifications of the HCN submechanisms were proposed by Glarborg and Miller [18] and Glarborg et al. [19] on the basis of flow reactor data under slightly lean conditions. Introducing those

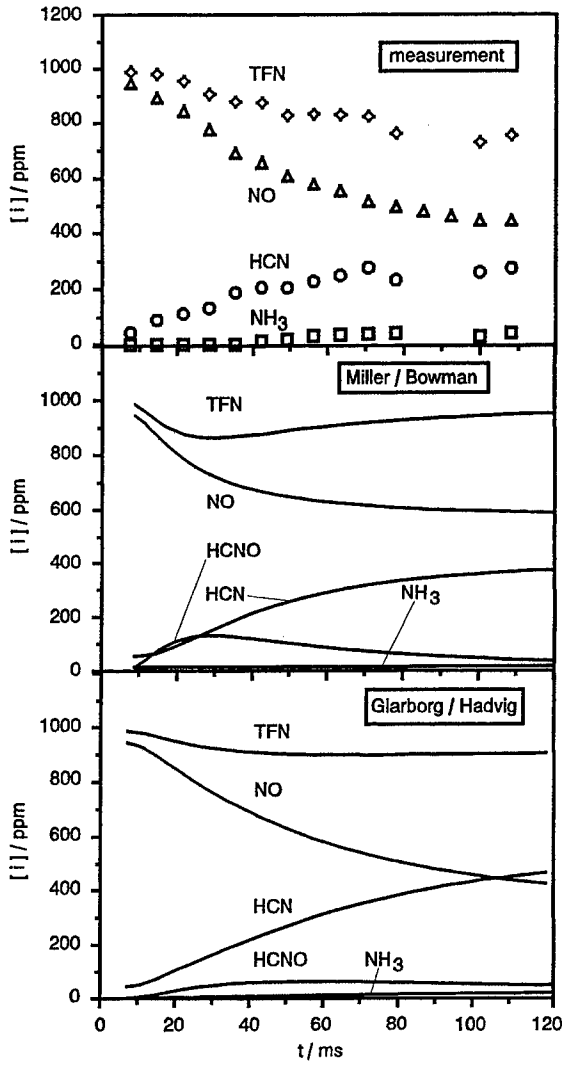

FIG. 4. Measured and calculated concentrations of N species as a function of residence time. Conditions: p = 1 atm, T = 1300°C, Φ = 1.25, and $[O_2]_{initial}$ = 0.12%.

modifications into our calculations did not significantly improve the calculated results for the reburning case.

Recently, Braun-Unkhoff et al. published a study on NO reburning elementary reactions [20], introducing a new pathway for NO reduction by the $CH_3 + NO \leftrightharpoons NH_2 + HCO$ reaction. They also estimated a rate coefficient for this pathway. Reactions of this type would compete with HCN production from NO. HCN-to-NH_i conversion is rather slow, whereas N_2 production from NH_i proceeds very fast. Thus, HCN concentrations would become smaller and N_2 production would be enhanced. When including this reaction rate data into our modified model, we found only small improvements in HCN and TFN concentration profiles.

Analysis of the C/H/O kinetics which were part of our investigations are not reported here. Production and destruction rates of HCCO as well as sensitivity analysis in combination with rate data revision of C_2 species reactions have been performed to determine uncertainties in hydrocarbon radical formation under rich conditions. Calculated HCCO concentrations vary within ±50% [15].

Conclusions

Under reburning conditions, as when natural gas is injected into NO-containing flue gas, the radical pool is controlled by excess oxygen in the flue gas. Current comprehensive mechanisms show strong dependence on the initial oxygen content and predict shorter global reaction time scales than found

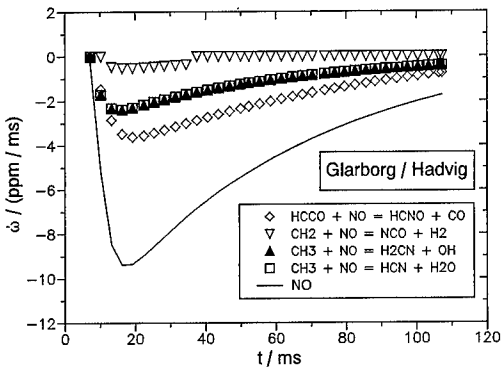

FIG. 5. Computed NO production rates as a function of residence time. Conditions: p = 1 atm, T = 1300°C, Φ = 1.25, and $[O_2]_{initial}$ = 0.12%.

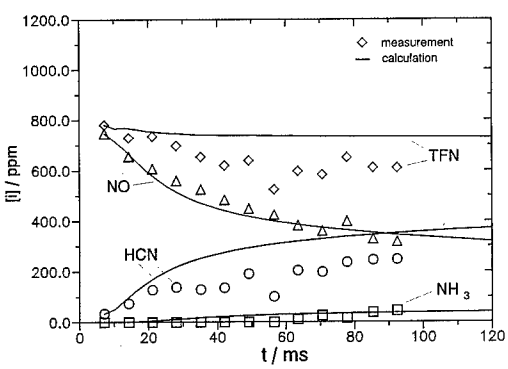

FIG. 6. Comparison of measured and computed (modified mechanism) concentrations of N species as a function of residence time. Conditions: p = 1 atm, T = 1300°C, Φ = 1.25, and $[O_2]_{initial}$ = 1.13%.

in the flow reactor experiments. By introduction of carefully revised data of important elementary reactions into the model of Glarborg and Hadvig, the accuracy of the mechanism was improved significantly with respect to NO.

All mechanisms investigated here overestimate the conversion of NO to HCN, which is dominated by the HCCO + NO reaction. However, the CH_3 + NO pathway is emphasized by the introduction of recent rate data for this reaction into the models. To obtain good agreement between measured and calculated concentration profiles, it was necessary to eliminate the ketenyl + NO reaction with its temperature-independent rate coefficient. Direct or indirect measurements of this reaction under high temperature conditions are needed to derive reliable rate coefficients. Further investigations are necessary to clarify whether the NO + CH_i pathways are sufficiently understood and if HCN consumption under rich conditions must be enhanced.

Acknowledgments

The authors gratefully acknowledge the financial support by the Deutsche Forschungsgemeinschaft, Bonn, Germany in the frame of the SFB 167 joint research program. Also, the authors are grateful to Mr. A. Hoffmann, Mr. M. Kopp, Mr. R. Espinagosa, and Mr. N. Elm for their computational and experimental studies performed during their diploma theses.

The experimental data including temperature and concentration profiles of stable C/H/O/N species as well as the modified mechanism in Chemkin-II format can be received by e-mail from the authors (dieter.stapf@ze.basf-ag.de).

REFERENCES

1. Wendt, J. O. L., Sternling, C. V., and Matovich, M. A., *Fourteenth Symposium (International) on Combustion,* The Combustion Institute, Pittsburgh, 1972, pp. 897–904.
2. Kolb, T., Jansohn, P., and Leuckel, W., *Twenty-Second Symposium (International) on Combustion,* The Combustion Institute, Pittsburgh, 1988, pp. 1193–1203.
3. Miller, J. A. and Bowman, C. T., *Prog. Energy Combust. Sci.* 15:287–338 (1989).
4. Glarborg, P. and Hadvig, S., *Development and Test of a Kinetic Model for Natural Gas Combustion,* Nordic Gas Technology Centre, DK, ISBN 87-89309-44-8, (1991).
5. Glarborg, P., Miller, J. A., and Kee, R. J., *Combust. Flame* 65:177–202 (1986).
6. Bockhorn, H., Chevalier, Ch., Warnatz, J., and Weyrauch, V., 15. *Deutscher Flammentag,* VDI-Verlag, Düsseldorf, Germany, 1991, VDI-Berichte 922, p. 171.
7. Warnatz, J., in *Combustion Chemistry,* (W. C. Gardiner, Ed.), Springer-Verlag, New York, 1984, p. 197.
8. Atakan, B., Kocis, D., Wolfrum, J., and Nelson, P., *Twenty-Fourth Symposium (International) on Combustion,* The Combustion Institute, Pittsburgh, 1992, pp. 691–699.
9. Braun-Unkhoff, M., Naumann, C., Wintergerst, K., and Frank, P., *16. Deutscher Flammentag,* VDI-Verlag, Düsseldorf, Germany, 1993, VDI-Berichte 1090, p. 287.
10. Gardiner, W.; Lissianski, V., Okoroanyanwu, U., Yang, H., and Zhao, M., *Phys. Chem.* 97:10042 (1993).
11. Thorne, L. R., Branch, M. C., Chandler, D. W., Kee, R. J., and Miller, J. A., *Twenty-First Symposium (International) on Combustion,* The Combustion Institute, Pittsburgh, 1986, pp. 965–977.
12. Myerson, A. L., *Fifteenth Symposium (International) on Combustion,* The Combustion Institute, Pittsburgh, 1975, pp. 1085–1092.
13. Chen, A. T. and Malte, P. C., 84–86 Presented at the 1984 Fall Meeting of Western Sates Section, The Combustion Institute, 1984.
14. Etzkorn, T., Muris, S., Wolfrum, J., Dembny, C., Bock-

horn, H., Nelson, P. F., Attia-Shahin, A., and Warnatz, J., *Twenty-Fourth Symposium (International) on Combustion,* Pittsburgh, 1992, pp. 925–932.
15. Stapf, D., Ph.D. Dissertation, Universität Karlsruhe (TH), Germany, in preparation.
16. Kee, R. J. and Miller, J. A., *Senkin: A Fortran Program for Predictiing Homogeneous Gas-Phase Chemical Kinetics With Sensitivity Analysis,* Report No. SAND86-8841, Sandia National Laboratories, Livermore, CA, 1988.
17. Boullart, W., Nguyen, M. T., and Peeters, J., *J. Phys. Chem.* 98:8036–8043 (1994).
18. Glarborg, P. and Miller, J. A., *Combust. Flame* 99:475–483 (1994).
19. Glarborg, P., Kristensen, P. G., Jensen, S. H., and Dam-Johansen, K., *Combust. Flame* 98:241–258 (1994).
20. Braun-Unkhoff, M., Nauman, C., Wintergerst, K., and Frank, P., *Proceedings of the Twentieth International Shock Wave Symposium,* Pasadena, 1995.

COMMENTS

Th. Just, DLR—Institut für Physikalische Chemie d. Verbrennung, Germany. We definitely have deficits in appropriate modeling of the HCCO forming and destruction reactions. Therefore, further research into these important reactions would be valuable for better understanding of reburning processes.

Author's Reply. The authors agree with this opinion. It was shown [1] that introduction of revised rate data of important acetylene consuming reactions leads to significantly better agreement between plug flow data and calculated stable C_2-species profiles than provided by the three comprehensive schemes. Discrepancies concerning rate coefficients and branching factor e.g. for HCCO formation from C_2H_2 can be found, when comparing the revised submechanism with recently published low temperature data for acetylene consumption [2]. Further modifications of rate data would as a matter of course have an impact on calculated HCCO profiles.

REFERENCES

1. Stapf, D., Ph.D. Dissertation, Universität Karlsruhe, Germany (in prep.).
2. Peeters, J., Devriendt, K., *Twenty-Sixth (International) Symposium on Combustion,* The Combustion Institute, Pittsburgh, 1996, pp. 000–000.

Vladimir Zamansky, Energy and Environmental Research Corporation, USA. This work is very important for the understanding of the reburning mechanism. Since the mechanism is not clear to date, efforts directed to comparison of kinetic and gas dynamic modeling with reliable experimental data should be continued. Did you try to compare your results with calculations using GRI-Mech?

Author's Reply. Recently, the current release 2.11 of GRI-Mech [1] has been tested against the plug flow data to complete the analysis of C/H/O/N reburning schemes [2]. Generally, GRI-Mech shows qualitatively better agreement with the experimental data with respect to C/H/O species profiles and reaction time scales. This is not the case for NO consumption and HCN formation because GRI-Mech still includes the Miller and Doverman rate expression for HCCO + NO reaction with HCNO as the only product channel.

REFERENCES

1. Bowman, C. T., Hanson, R. K., Davidson, D. F, Gardinier, W. C., Lissianski, Jr., Smith, G. P., Golden, D. M., Frenklach, M., and Goldberg, M., GRI-Mech 2.11, http://www.berkeley.me.edu/qui mech/ (1996).
2. Braun-Unkehoff, M., Frank, P., Stapf, D., and Leuckel, W., paper presented at 3rd Workshop on Modelling of Chemical Reaction Systems, Heidelberg, Germany (1996).

Twenty-Sixth Symposium (International) on Combustion/The Combustion Institute, 1996/pp. 2091–2097

CONTROL OF NO_x EMISSIONS BY NO_x RECYCLE APPROACH

CHENN Q. ZHOU
Purdue University Calumet
Department of Engineering
Hammond, IN 46323, USA

L. G. NEAL, RITA BOLLI, JOHN HASLBECK AND ALEX CHANG
NOXSO Corporation
2414 Lytle Road
Bethel Park, PA 15102, USA

NO_x recycle is an alternative approach for the control of NO_x emissions from combustion. It uses regenerable sorbent to adsorb NO_x in the flue gas from a combustor followed by desorption, producing a highly concentrated NO_x-laden stream containing both NO and NO_2. This stream is then sent back to the same combustor or to a separate combustor, where the NO_x is reduced in the flame and NO_x formation is inhibited. Experimental studies have been performed to investigate the effect of NO_x recycle on the reduction of NO_x emissions. Highly concentrated NO, NO_2, or NO/NO_2 mixtures were recycled into a combustor at different locations. It has been found that a range of 50–90% of NO_x reduction efficiency could be achieved depending on experimental conditions. The NO_x reduction efficiency in the combustor is affected by the recycle location, the amount of exit air, and the composition of recycle gases. The most favorable recycle location is at the primary air duct. When NO_x is recycled into the secondary air duct, the lower the exit O_2, the better for the NO_x destruction in the flame. The experimental results also indicated higher NO_x reduction efficiency for the NO_2 recycle in comparison with the NO recycle. The concept of the NO_x recycle approach has been implemented in the NOXSO process, which is a dry, postcombustion flue gas treatment technology for fossil-fueled boilers that can remove more than 90% of NO_x/SO_2. The NO_x recycle approach is expected to be a new alternative for NO_x removal from flue gas, especially for integrated systems that use regenerable sorbent to simultaneously remove NO_x, SO_2, and other pollutants emitted from combustion.

Introduction

Nitrogen oxides (NO_x), including both nitric oxide (NO) and nitrogen dioxide (NO_2), are known to be primary precursors to acid deposition and photochemical smog. The control of NO_x emissions from utility boilers is required under the acid rain provisions of the 1990 Clean Air Act Amendments.

Currently, there are three general types of NO_x control approaches: precombustion fuel treatment, combustion modification, and postcombustion flue gas treatment [1–4]. Fuel treatment reduces the amount of fuel-bound nitrogen. It is not cost-effective and can only reduce fuel NO_x. Combustion modification techniques inhibit the formation of NO_x in combustors through changes in combustor design and operation. These techniques have been used widely by utility companies to accomplish the emission reductions in the Phase I compliance. However, they all impose penalties in other areas of the power station's performance, such as efficiency and heat rate, reliability of components, operating flexibility, fuel flexibility, and increases in other emissions [5]. Problems also exist in postcombustion flue gas treatment techniques, which remove NO_x from the flue gas. For example, the selective catalytic reduction (SCR) can achieve high NO_x reduction [6]. It is very costly, however, and may produce secondary pollutants, such as ammonia and nitrous oxides and solid-waste discharges. To meet stringent regulations from government agencies and local legislatures, effort is needed to search for new solutions or improvements to existing approaches.

Among the postcombustion flue gas treatment processes, a number of technologies are under development that use regenerable sorbent to adsorb NO_x emitted from a combustor followed by desorption to produce a highly concentrated NO_x-laden stream. This stream can then be sent back as part of combustion air to the same combustor or to a separate combustor, where the NO_x is reduced in the flame and the NO_x formation is inhibited. This concept is called NO_x recycle and has been developed by NOXSO Corporation and employed in the

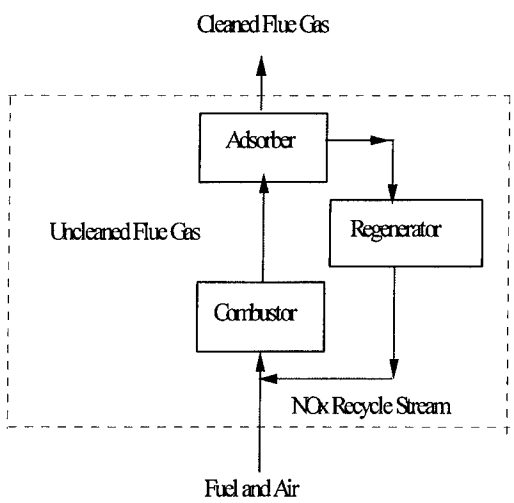

FIG. 1. NO_x recycle scheme.

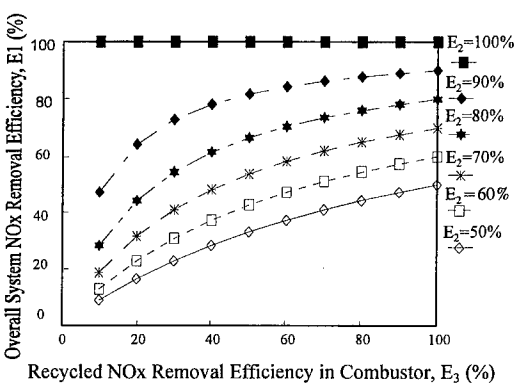

FIG. 2. NO_x removal efficiency.

NOXSO Process [7,8]. It is expected to be a simple, secondary-pollutant-free, and cost-effective approach for NO_x removal from flue gas, especially for integrated systems that use regenerable sorbent to simultaneously remove NO_x, SO_2, and other pollutants emitted from combustion.

Experiments have been conducted to investigate the effect of NO_x recycle on the reduction of NO_x emissions. The results are presented in the following sections. The description of the NO_x recycle concept and its implementation in a practical device are also included.

Concept of NO_x Recycle

The concept of NO_x recycle stream is illustrated in Fig. 1. The NO_x recycle stream contains highly concentrated NO and NO_2, which are reduced in the flame. The overall system NO_x removal efficiency (E_1) is dependent mainly on the NO_x adsorption efficiency in the adsorber (E_2) and the recycled NO_x reduction efficiency in the combustor (E_3). The relationship between these three efficiencies can be derived as shown in Eq. (1) and Fig. 2.

$$E_1 = \frac{E_2 E_3}{1 - E_2(1 - E_3)} \tag{1}$$

Figure 2 is a plot of the overall system NO_x removal efficiency versus the recycled NO_x reduction efficiency in the combustor with varied NO_x adsorption efficiency. It shows that, for a given NO_x adsorption efficiency, the more recycled NO_x reduced in the combustor, the higher the NO_x removed from the overall system. In a practical system, if the design of the adsorber is unchangeable, the increase of the recycled NO_x reduction efficiency in the combustor will improve the overall system NO_x removal efficiency.

The NO_x recycle approach has its unique features in comparison with the other NO_x reduction techniques, such as the reburning process [9–11] and flue gas recirculation (FGR) [12]. First, the NO_x recycle stream, which is less than 25% of the combustion air flow, is sent to the main combustion zone and the recycle location is adjustable; it can be at the primary air duct, the secondary air duct, or other favorable locations. Second, the NO_x concentration in the NO_x recycle stream is very high, in the range of 0.3–2.0 vol. %, while NO_x concentration in the flue gas is normally 0.06–0.1 vol. %. Thirdly, in the NO_x recycle stream, the NO_2 could be as high as 70 vol. % of total NO_x, depending on the nature of the sorbent and regeneration conditions. The effects of highly concentrated NO_2 in a combustor have not been found in any literature yet, since NO_x generated from combustion generally contains only 5 vol. % NO_2 or less. Because of these unique features, an investigation of recycled NO_x reduction in combustors is needed.

There are two postulated general mechanisms for NO reduction in the NO_x recycle approach: thermodynamic-kinetic conditions and reducing atmospheres. The thermal NO is formed by the following reactions [13]:

$$O + N_2 \Leftrightarrow NO + N \tag{2}$$

$$N + O_2 \Leftrightarrow NO + O \tag{3}$$

If these equations are combined, the formation of NO can be described by

$$N_2 + O_2 \Leftrightarrow 2NO \tag{4}$$

As indicated in the equations, these reactions are reversible and controlled by chemical kinetics [14,15]. If NO is present at concentrations greater than equilibrium values, it will be decomposed into

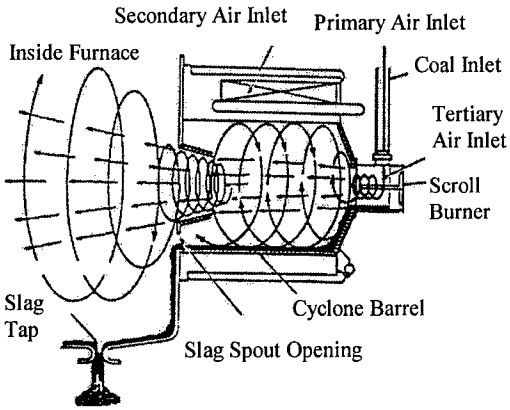

FIG. 3. B&W's cyclone burner.

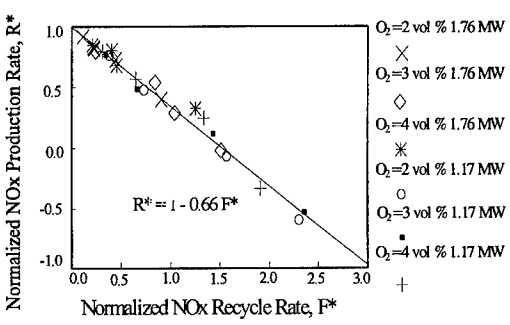

FIG. 4. NO recycle into primary air stream.

N_2 and O_2 because of the high reverse reaction rates. Consequently, the net NO_x production rate from combustion is reduced. Therefore, the thermodynamic-kinetic conditions could play a very important role in the NO_x recycle approach. In addition, free radicals, such as CH^+, NH^+, and NH_2^+, generated in the flame (especially in the fuel-rich zone), might also serve to reduce NO_x by their reactions with NO or NO_2 [11,14,15]. The detailed mechanisms need to be investigated in further studies.

Reduction of Recycled NO_x in a Combustor

To investigate the reduction of recycled NO_x in a combustor, an experimental study was performed on a 1.76-mW (6 mmbtu/h) cyclone furnace at the Babcock & Wilcox (B&W) Research Center, funded by the U.S. Department of Energy (DOE) and the NOXSO Corporation. The schematic of the cyclone burner is shown in Fig. 3. In this study, the NO_x recycle stream was simulated by a gas stream prepared from bottled gases and then injected into the combustion air stream, reducing NO_x in the combustor. Although the NO_x was provided from bottled gases, the NO_x concentrations and compositions in the combustion air represented very realistic conditions in the NO_x recycle approach. The NO_x concentrations in the combustion air and in the stack were measured to determine the recycled NO_x reduction efficiency. The parametric effects were investigated. The parameters included the NO_x recycle rate; the recycle location including the primary air (PA) alone, the secondary air (SA) alone, and PA and SA simultaneously; the gas compositions including NO, NO_2, and a mixture of NO/NO_2; the furnace load; and the exit O_2 concentration. A typical experimental condition was at furnace load of 1.76-mW (6 mmbtu/hr), exit O_2 concentration of 3 vol. % and flue gas flow of 0.69 kg/s (5500 lb/h). Typical experimental results are presented in the following sections.

NO Recycle into Primary Air Stream

Figure 4 shows the experimental results for NO gas recycle into the primary air stream at two different furnace loads and three different exit O_2 concentrations. It is a plot of the normalized NO_x production rate, R^*, versus the normalized NO_x recycle rate, F^*. The definition of R^* is given in Eq. (5). It is the difference between the stack NO_x (NO_{xs}) and recycled NO_x (NO_{xi}), which can be considered as the NO_x produced from combustion, divided by the stack NO_x without NO_x recycle, which is the baseline NO_x (NO_{xb}). The definition of F^* is the ratio of recycled NO_x to the baseline NO_x as indicated in Eq. (6);

$$R^* = \frac{NO_{xs} - NO_{xi}}{NO_{xb}} \tag{5}$$

$$F^* = \frac{NO_{xi}}{NO_{xb}} \tag{6}$$

where, NO_{xs} and NO_{xb} are stack NO_x with and without NO_x recycle, respectively (mol/s); NO_{xi} is the NO_x recycle rate into the combustor (mol/s).

This plot provides two types of basic information. One is the relationship between the NO_x production rate and the NO_x recycle rate, which can be used directly in the design program of the process. As shown in Fig. 4, the NO_x production rate decreases with an increase of NO recycle rate. All the data fall in a straight line that can be described by a correlation $R^* = 1 - aF^*$, where a is the slope of the line and equals 0.66. This correlation is very useful for the calculations of the mass flows in the design program of the process.

The other information provided by Fig. 4 is the conventional reduction efficiency of recycled NO_x in the combustor. It is defined as the percentage of the recycled NO_x reduced in the combustor as indicated in Eq. (7):

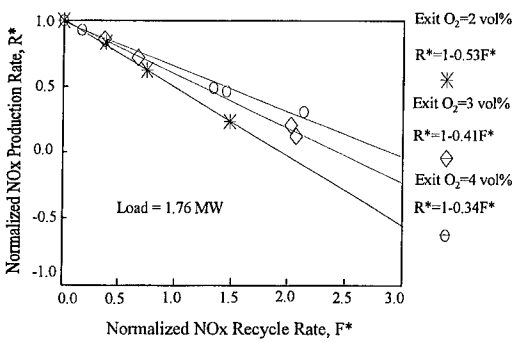

FIG. 5. NO recycle into secondary air stream.

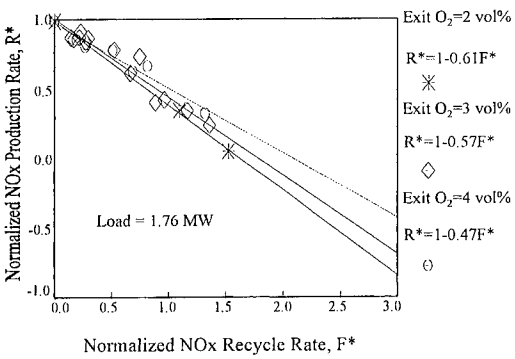

FIG. 6. NO_2 recycle into secondary air stream.

$$\eta\% = \left(1 - \frac{NO_{xs} - NO_{xb}}{NO_{xi}}\right) \times 100 \qquad (7)$$

It can be derived that the slope a in the correlation mentioned earlier actually represents the average recycled NO_x reduction efficiency. The value of 0.66 in Fig. 4 means that 66% of the recycled NO_x is reduced in the combustor. It is not affected by the exit O_2 concentration and the furnace load in the experimental conditions.

NO Recycle into Secondary Air Stream

Experimental results for NO recycle into the secondary air stream at one furnace load and three different exit O_2 concentrations are displayed in Fig. 5. It shows that the NO_x reduction efficiency is varied with the exit O_2 concentrations. The average reduction efficiencies are 53%, 41%, and 34% corresponding to the exit O_2 concentration of 2 vol. %, 3 vol. %, and 4 vol. %, respectively, which are lower than those of the NO recycle into the primary air stream. This is attributed to the less-reducing atmosphere in the secondary air region that causes fewer radicals serving for NO_x reduction and lower temperatures unfavorable for reaction rates.

NO Recycle into PA and SA Streams Simultaneously

A few experiments were conducted for NO recycle into both primary and secondary air streams simultaneously. The ratio of the amount of NO recycled into the PA stream to the amount of NO recycled into the SA stream was varied. As expected, the greater the percentage of NO recycled into the PA stream, the higher the NO_x reduction efficiency. The favorable recycle location is at the PA duct, which provides good mixing between the recycled NO_x and the reducing atmosphere.

NO_2 Recycle into Secondary Air Duct

The NO_x recycle stream may contain a large portion of NO_2. The investigation of the fate of highly concentrated NO_2 in a combustor has not been found in the literature. Experiments were conducted to recycle NO_2 into the secondary air stream. The results are shown in Fig. 6. The data demonstrate a consistent trend similar to the NO recycle tests. The effect of exit O_2 is also similar. The lower the exit O_2, the higher the NO_x reduction efficiency because of the increased reducing atmosphere. Average NO_x reduction efficiencies were 61%, 57%, and 47% for exit O_2 concentrations of 2 vol. %, 3 vol. %, and 4 vol. %, respectively. These values are higher than those for NO recycle at the corresponding conditions. This is positive to the overall NO_x reduction efficiency, because the percentage of NO_2 is higher than NO in the NO_x recycle stream of the NOXSO Process. However, the mechanisms need to be explored. Generally, when NO_2 is recycled into the combustor, it is expected to be converted first to NO at high temperatures; then NO will be reduced in the flame. In addition to this, the experimental results implied that some other reactions contributed to the reduction of NO_2 directly. As mentioned previously, the free radicals could serve for the NO_2 reduction, which is the topic of future studies.

NO/NO_2 Mixture Recycle

Figure 7 shows experimental data of NO/NO_2 mixture recycled into the secondary air stream in comparison with NO and NO_2 recycle data. As expected, the data points of NO/NO_2 mixture recycle fall between the separate NO and NO_2 recycle data. The NO_x reduction efficiency for NO/NO_2 mixture recycle is higher than that for NO recycle and lower than that for NO_2 recycle.

One of the concerns of the NO_2 recycle is the emission of NO_2 in the stack. If high NO_2 emissions result from the NO_2 recycle, additional problems

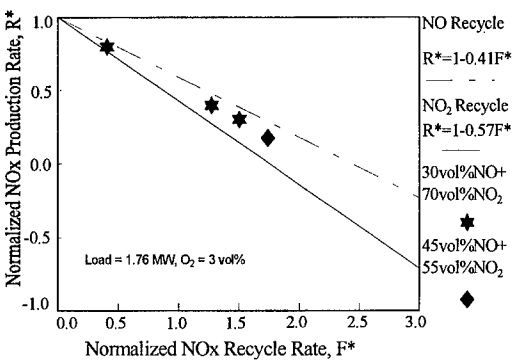

FIG. 7. NO/NO_2 mixture recycle into secondary air stream.

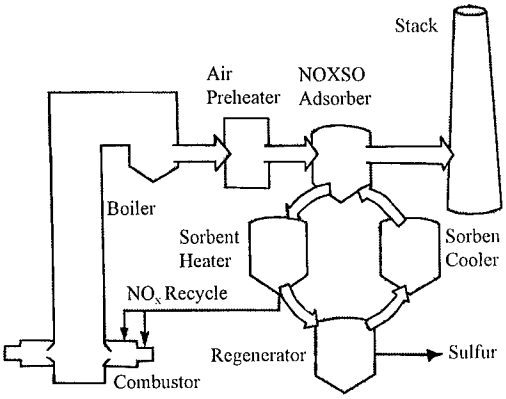

FIG. 8. Schematic of NOXSO Process.

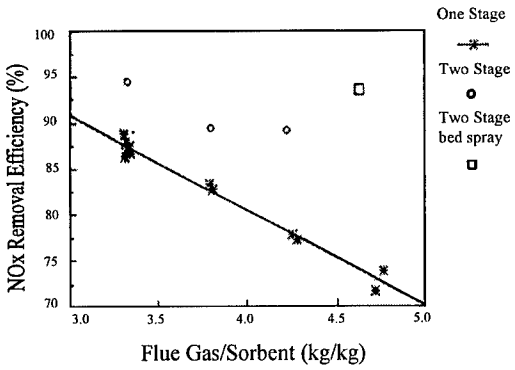

FIG. 9. NOXSO pilot test results (one-stage versus two-stage adsorber).

can be created. This effect was investigated by measuring both NO_x and NO in the stack, which gave NO_2 as the difference between the NO_x and NO. It was found that although very high NO_2 concentrations were measured in the combustion air during NO_2 or NO/NO_2 recycle, almost no NO_2 was found in the stack. This implies that the recycled NO_2 was partially destroyed and partially converted to NO in the combustor.

Implementation of NO_x Recycle in a Practical System—The NOXSO Process

The concept of NO_x recycle has been employed in the NOXSO Process. The NOXSO Process is a dry, postcombustion flue gas treatment technology that can simultaneously remove more than 90% NO_x/SO_2 by using a dry and regenerable sorbent. The sorbent, developed and patented by NOXSO Corporation, is a γ-alumina sphere impregnated with sodium carbonate, Na_2CO_3. It is stable, inert, nontoxic, and noncombustible. Both sodium and alumina contribute to the NOXSO sorbent's capacity to adsorb NO_x and SO_2 from flue gas.

In the NOXSO Process, NO_x and SO_2 are adsorbed in a fluidized bed of sorbent in an adsorber at a temperature of 120°C. The NO_x is then desorbed by heating the sorbent in a heater and recycled back to the boiler to be reduced. The volume of NO_x recycle stream is small since only a small amount of air is used to heat the sorbent in the sorbent heater. Consequently, the recycle stream can easily be sent back to the main combustion zone with little effects on the combustion process. SO_2 is desorbed at 620°C using a reducing gas and converted to a sulfur by-product in a Claus plant. After sulfur regeneration, the sorbent is cooled and transported to the adsorber for reuse. The NOXSO Process has completed pilot-scale (POC) tests and is currently at the stage of commercialization [16]. The schematic of the NOXSO Process is shown in Fig. 8.

The POC tests have indicated that more than 90% NO_x from a combustor could be adsorbed in the adsorber. A plot of NO_x adsorption efficiency versus the flue-gas-to-sorbent-mass ratio obtained during the POC tests is depicted in Fig. 9. It shows that the NO_x adsorption efficiency is affected by the number of stages in the adsorber and the operating temperature in the fluidized bed. For the one-stage adsorber, the NO_x adsorption efficiency decreases in proportion to the increase in mass ratio. For the two-stage adsorbers (two fluidized beds in series) with or without in-bed water spray, experimental data show the same trend; however, NO_x adsorption efficiencies are higher by 5–10 absolute percentage points. This improvement is due to (1) better gas distribution with the addition of the second grid plate and (2) counter-current flow of flue gas and

sorbent so that in the bottom bed of the adsorber, partially spent sorbent is in contact with the highest concentration of pollutants. During the experiments, it was also observed that over an adsorber bed temperature range of 120–180°C, there is a definite trend of increasing NO_x adsorption efficiency with decreasing bed temperature. Further improvement is anticipated at bed temperatures lower than 120°C. A NO_x adsorption efficiency of 95% at a flue-gas-to-sorbent ratio of 4.6 was achieved with the two-stage fluidized bed including in-bed water spray for reducing the bed temperature.

The POC tests have also indicated that all the adsorbed NO_x was desorbed in the sorbent heater, producing both NO (30 vol. %) and NO_2 (70 vol. %). The complete desorption could also take place in a fixed bed reactor around 370°C as found in laboratory studies.

As discussed earlier, the NO_x removal efficiency in the NOXSO system is affected by the recycled NO_x reduction efficiency and the NO_x adsorption efficiency. From all the experimental data, more than 80% of NO_x can be removed from the flue gas by the NOXSO Process.

Conclusions and Future Work

The NO_x recycle approach has been proven to be a new alternative for control of NO_x emission from combustion. It is simple, secondary-pollutant-free, and cost-effective. Experiments for investigation of the recycled NO_x reduction in a combustor indicate that:

1. High NO_x reduction efficiency can be obtained depending on experimental conditions.
2. The NO_x recycle location had a significant effect. The highest NO_x reduction efficiency was achieved when NO_x was recycled into the primary air stream.
3. The exit O_2 concentration affected NO_x reduction when NO_x was recycled in the secondary air stream.
4. Higher NO_x reduction efficiency was obtained for the NO_2 recycle in comparison with the NO recycle.

The experimental results indicate that good mixing between recycled NO_x and a reducing atmosphere and a long resident time in high-temperature fuel-rich zones will be favorable for the recycled NO_x reduction in combustors. Studies on detailed mechanisms of the recycled NO_x reduction in combustors, especially for NO_2 recycle, are topics of future work.

Acknowledgments

The support for this research from the U.S. Department of Energy's Pittsburgh Energy Technology Center and NOXSO Corporation is appreciated. The efforts made by Cliff Eckhart and Jennifer Lyden of the B&W Research Center, which was NOXSO's subcontractor for the NO_x recycle tests, are also acknowledged.

REFERENCES

1. EPA Office of Air and Radiation, "Summary of NO_x Control Technologies and Their Availability and Extent of Application," EPA-450/3-92-004, 1992.
2. Kokkinos, A., Cichanowicz, J. E., Eskinazi, D., Stallings, J., and Offen, G., "NO_x Controls for Utility Boilers: Highlights of the EPRI July 1992 Workshop," *J. Air Waste Manage. Assoc.* 42(11):1498–1505 (1992).
3. Rhodes, T. W., Marks, J. R., and Siebert, P. C., "Overview of Industrial Source Control for Nitrogen Oxides," Environmental Progress, 9(2):126–130 (1990).
4. Energy and Environmental Analysis, Inc., "NO_x Control for Gas-Fired Industrial Boilers and Combustion Equipment: A survey of Current Practices," Topical Report for Gas Research Institute, October 1992.
5. Makansi, J., ;"Reduction of No_x Emmissions from Today's Powerplants," *Power* 137(5):11–26 (1993).
6. Behrens, E. S., "SCR Operating Experience on Coal-Fired Boilers and Recent Progress," *Joint Symposium on Stationary Combustion NO_x Control,* EPA/EPRI, Washington, D.C., 1991, Section 4B, pp. 1–20.
7. Haslbeck, J. L., Ma, W. T., and Neal, L. G., "A Pilot-Scale Test of the NOXSO Flue Gas Treatment Process," NOXSO Report, Pittsburgh, June 1988.
8. Zhou, Q., Haslbeck, J. L., and Neal, L. G., "An Experimental Study of NO_x Recycle in the NOXSO Flue Gas Cleanup Process," Final Report to U.S. Department of Energy, Pittsburgh Energy and Technology Center, March 1993.
9. Wendt, O. L., Sterling, C. V., and Matovich, M. A., "Reduction of Sulfur Trioxide and Nitrogen Oxides by Secondary Fuel Injection," *Fourteenth Symposium (International) on Combustion,* The Combustion Institute, Pittsburgh, 1973, p. 897.
10. Smart, J. P. and Morgan, D. J., "Multi-Fuel Reburning in a Coal Fired Internally Fuel Staged Burner for NO_x Reduction," *Joint Symposium on Stationery Combustion NO_x Control,* EPA/EPRI, Washington, D.C., March 1991, Section 3B, pp. 1–20.
11. Chen, W. and Lester, T. W., "Effects of Reburning Fuel Type on NO_x Reduction," *Proceedings of the Eighth Coal Preparation, Utilization, and Environmental Control Contractor Conference,* DOE-PETC, Pittsburgh, July 1992, pp. 231–239.
12. Michel, Y. and Belles, F. E., "Effects of Flue Gas Recirculation on NO_x Production and Performance of Pulse Combustion Hot-Water Boilers," *Combust. Sci. Technol.* 94(1–6):447–468 (1993).
13. Zeldovich, Y. B., "Oxidation of Nitrogen in Combustion and Explosion," *Comput. Rend. Acad. Sci. USSR.* 51:417 (1946).
14. Miller, J. A. and Bowman, C. T., "Mechanism and

Modeling of Nitrogen Chemistry in Combustion," *Prog. Energy Combust. Sci.* 15:287–338 (1989).
15. Flagan, R. C. and Seinfeld, J. H., *Fundamentals of Air Pollution Engineering,* Prentice Hall, Englewood Cliffs, NJ, 1988.
16. Bolli, R., Browning, J. P., and Halslbeck, J. L., "The NOXSO Project/Incorporating Lessons Learned from a Pilot into a Full-Scale Demonstration," *88th Annual Meeting of Air Waste & Management Association,* Paper No. A-201, June, 1995, pp. 1–16.

COMMENTS

Vladimir Zamansky, Energy and Environmental Research Corporation, USA. Please comment on two aspects of the NO_x recycle approach: (1) What compounds are used in the adsorber and can you give a reference which describes the adsorber characteristics? (2) Could you compare costs, in particular capital expenses, for the NO_x recycle approach and SCR?

Author's Reply. The compounds used in the adsorber of the NOXSO process are sodium deposited on an alumna substrate. Reference 16 listed in the paper has good descriptions of the adsorber characteristics.

The cost of the NO_x recycle approach depends on how the approach is incorporated in a real system. In the NOXSO process, which removes both NO_x and SO_2 simultaneously, it is extremely difficult to separate capital costs of the NOXSO system to identify separate costs of NO_x and SO_2 reductions. When compared to current US costs for an advanced scrubber with an SCR, the capital costs are 25% less for a NOXSO system. Evaluating a levelized cost of NO_x reduction (capital cost levelized over 30 years plus annual operating costs) in the NOXSO system, it is 35% less (in $/ton) than the SCR system.

•

Th. Just, DLR - Institut für Physikalische Chemie d. Verbrennung, Germany. The degree of NO_x reduction by recycling the flue gases is likely burner specific. Can you comment on that?

Author's Reply. The experimental data on the cyclone furnace showed that the NO_x reduction was highly affected by the recycle location. This indicates that the degree of NO_x reduction by the NO_x recycle approach is likely burner specific. Future test data should develop specific values for various burner designs. However, cyclone furnace represents a case which is on the most conservative side on the degree of NO_x reduction because there is no suspension type of flame and well defined reducing zone, which is favorable for high NO_x reduction, within the cyclone.

In the most recent project, NO_x recycle process was employed in the NOXSO's pilot plant at the Technical University of Denmark. The NO_x recycle stream was directed to a newly designed separate low NO_x burner in the regeneration system and test data showed over 80% total reduction of NO_x [1]. NOXSO has also incorporated the NO_x recycle in the first commercial design of the NOXSO process at the ALCOA's plant in Indiana, USA, which has a wall-fired pulverized coal boiler. The test data will be collected and reported in the future.

REFERENCE

1. B. H. Jensen, S. B. Lading and K. Daub, "Implementation of Novel Combined deNO_x and deSO_x process to Power Plants", presented at the 3rd NORDIC Conference on SO_x and NO_x, March 13–14, 1996, Copenhagen, Denmark.

Twenty-Sixth Symposium (International) on Combustion/The Combustion Institute, 1996/pp. 2099–2108

ISOTOPIC LABELING STUDIES OF THE SELECTIVE NON-CATALYTIC REDUCTION OF NO WITH NH_3

B. L. DUFFY AND P. F. NELSON
CSIRO Division of Coal and Energy Technology
North Ryde, Australia 2113

The reaction of NO and NH_3 in the presence of excess O_2 has been investigated using ^{15}N-isotopic labeling techniques under selective noncatalytic reduction (SNCR) conditions. Experiments were conducted with and without added H_2. The results show that $^{14}N^{15}N$ is always the predominant nitrogen-containing product. Conversion of NH_3 to ^{14}NO is a prerequisite for the formation of both $^{14}N_2$ and $^{14}N_2O$. Experiments conducted in the presence of added H_2 result in higher selectivities to N_2O; at temperatures above the maximum NO conversion, a large proportion (43%) of the nitrous oxide is $^{14}N_2O$. In general, the experimentally determined isotopic product distributions were in good agreement with model predictions based on accepted detailed kinetic schemes for the SNCR process. However, under some conditions, the model predicted significant concentrations of $^{15}N_2$ and $^{15}N_2O$, but these doubly labeled species were not observed experimentally. Measured concentrations of $^{15}N_2O$ never exceeded the detection limit (0.05 ppm). Sensitivity and rate-of-progress analyses show that these doubly labeled ^{15}N species are produced via channels in which the first steps are reactions of the NNH species with H radicals. An NNH lifetime of less than 10^{-8} s decreased the predicted amounts of these species. However, this lifetime would imply that H atoms should be produced in kinetic studies of the NH_2 + NO reaction, but this has not been observed. Alternately, the kinetics of the reaction involving the N_2H_i species should be reviewed. The source of HCN produced from the propane-promoted SNCR reaction has also been investigated using labeling techniques. Both $HC^{14}N$ and $HC^{15}N$, in similar concentrations, are produced from an equimolar mixture of ^{15}NO and $^{14}NH_3$, under conditions in which ammonia oxidation to NO is insignificant. The results therefore imply that both NO-propane and NH_3-propane interactions are important in HCN formation under competitive conditions.

Introduction

The removal of NO_x emissions from the flue gases of stationary combustors, by the conversion of nitric oxide into molecular nitrogen, is commonly achieved by either selective catalytic reduction (SCR) or selective noncatalytic reduction (SNCR). Considerable effort has been applied to developing a kinetic model of the SNCR process to predict NO conversion over a range of conditions. The key step in the SNCR process is the reaction of the NH_2 radical with nitric oxide:

$$NH_2 + NO \rightleftarrows N_2 + H_2O \qquad \text{(R1)}$$

Current understanding of the process requires that there be an additional reaction channel leading to chain branching with a fractional yield of around 25% at 1200 K. However, the nature of the chain-branching reaction is still unclear. Miller and coworkers [1,2] have presented a model in which the following reaction has been assumed to be responsible for the chain-branching character:

$$NH_2 + NO \rightleftarrows NNH + OH \qquad \text{(R2)}$$

with subsequent additional reactions of the NNH species such as

$$NNH \rightleftarrows N_2 + H \qquad \text{(R3)}$$

$$NNH + NO \rightleftarrows N_2 + HNO \qquad \text{(R4)}$$

$$NNH + H + M \rightleftarrows N_2H_2 + M \qquad \text{(R5)}$$

The extent of NO reduction with increasing temperature is governed by the rate of chain branching to create and maintain sufficient concentration of NH_2 (or OH). However, with increasing temperature, NO reduction becomes less effective because of the negative temperature dependence of reaction (R1) and increasing amounts of ammonia being oxidized to nitric oxide. Hence, NO reduction occurs only within a narrow temperature window. The increase in chain-branching reactions at elevated temperatures, and consequently larger O and OH concentrations, result in the following reactions becoming competitive:

$$NH_2 + O \rightleftarrows HNO + H \qquad \text{(R6)}$$

$$NH_2 + O \rightarrow NH + OH \qquad \text{(R7)}$$

Subsequent reactions of HNO and NH lead to NO formation:

$$HNO + M \rightleftarrows H + NO + M \quad (R8)$$

$$HNO + OH \rightleftarrows H_2O + NO \quad (R9)$$

$$NH + O \rightleftarrows NO + H \quad (R10)$$

$$NH + O_2 \rightleftarrows NO + OH \quad (R11)$$

Another reaction that leads to NO reduction at higher temperatures results in the formation of minor amounts of nitrous oxide, with the dominant reaction thought to be

$$NH + NO \rightleftarrows N_2O + H \quad (R12)$$

Other reactions potentially leading to the formation of N_2O included in the model [1,2] are

$$HNO + NO \rightleftarrows N_2O + OH \quad (R13)$$

$$HNO + HNO \rightleftarrows N_2O + H_2O \quad (R14)$$

$$N_2H_2 + NO \rightleftarrows N_2O + NH_2 \quad (R15)$$

There are some significant problems with this mechanistic description, mostly concerning the production of OH from the NH_2 + NO reaction. Experimental observations [3–5] of OH from this reaction give rise to a branching ratio (to the chain-branching reaction, R2), α, of 0.11 at room temperature and values between about 0.15 and 0.2 at higher temperatures. For values of the branching ratio less than about 0.3 at 1150 K, poor agreement is observed between previous flow reactor data and modeling predictions [2], and, as Glarborg et al. [2] state, "the only way the low value of α could be consistent with available flow reactor data was if an important chain branching mechanism was missing or under-predicted in presently used kinetic models."

The majority of previous experimental studies have been conducted in N_2 bulk gas, where it is difficult to measure the quantities of N_2 produced by the reaction unless all other N-containing products can be identified and measured with reasonable accuracy. In addition, conversions of NH_3 have not previously been widely reported. Thus, testing of the modeling predictions have been restricted largely to comparing the overall NO conversion and the quantities of N_2O produced.

In this study, model predictions are tested more rigorously by performing experiments using He as the bulk gas and by measuring the NH_3 conversion. To further investigate the products and pathways of this process, we have also used isotopic labeling techniques. Isotopic labeling is a powerful tool for identifying the most important pathways in complex reaction systems operating under competitive conditions (in the present case between NO coupling with NH_3 and ammonia oxidation). We have used these techniques to great advantage in studies of the SCR process [6]. Apart from an initial study [7] of the products of the NH_2 + NO reaction, isotopic labeling experiments have not been used previously to verify the product distribution of the SNCR reaction.

The products of the SNCR reaction have been determined in both the absence and presence of H_2. The effect of adding hydrocarbons (HCs) on the product distribution has also been investigated. Some problems with the use of HCs as additives have emerged recently from laboratory studies [8]; formation of HCN was reported when hydrocarbons were used as additives at low oxygen concentrations. Here, we investigate the source of HCN produced when propane is used to promote the SNCR reaction.

Experimental

The gas mixing, reaction apparatus, and analysis techniques have been described elsewhere [6]. Briefly, experiments were performed at atmospheric pressure in a tubular microreactor (quartz, 5-mm i.d.) by maintaining a constant mass flow rate and varying the temperature within the range 850–1350 K. Nominal reactant gas compositions used were ≈300 ppm nitric oxide (^{14}NO or ^{15}NO), ≈500 ppm $^{14}NH_3$, and 1.5% O_2 in a He balance. For some experiments, 1000 ppm H_2 was added. The residence time depended on the temperature and was estimated to be 0.25 s at 1173 K for reaction without H_2 and 0.19 s at 973 K for reaction in the presence of H_2. The reaction of NO and NH_3 in the presence of propane and small oxygen concentrations was also investigated. Reactant feed concentrations were ≈800 ppm NO and NH_3, ≈905 ppm C_3H_8, and 0.61% O_2, and the residence time was estimated to be 0.18 s at 1100 K. The steady-state products at each condition were first determined using unlabeled reactants before substituting ^{14}NO with ^{15}NO to obtain the isotopic product distribution. Analytical equipment used in this study included a quadrupole mass spectrometer (MS) (VG SX-200), two Fourier-transform infrared (FTIR) spectrometers (a Digilab and a Nicolet Magna 550), and a gas chromatograph (GC) (Hewlett Packard HP-5890). The ^{14}N and ^{15}N mass balances were accurate to less than ±5%.

The chemical-kinetic scheme used to model the SNCR reaction was the gas-phase mechanism for thermal de-NO_x developed by Glarborg et al. [2]. Calculations were performed using Senkin [9], a kinetics code that runs in conjunction with the Chemkin library [10].

The standard reaction mechanism of Glarborg et al. [2] was modified to incorporate all possible ^{15}N and ^{14}N isotopic isomers of the reactants, products, and reaction intermediates. Where necessary, kinetic parameters were also adjusted to compensate for duplicated reactions, and it was assumed that thermodynamic properties were unaffected by isotopic substitution. The modified mechanism consisted of 333

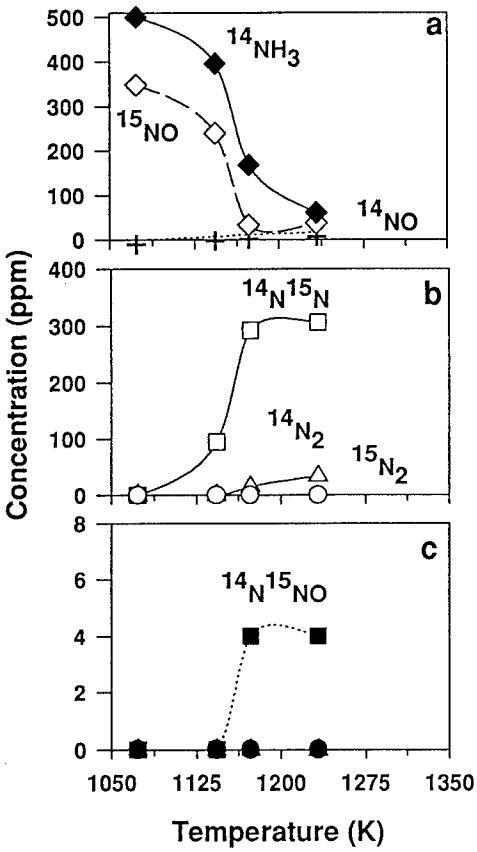

FIG. 1. Concentrations of the isotopic isomers of (a) nitric oxide and ammonia, (b) diatomic nitrogen, and (c) nitrous oxide for the reaction of ^{15}NO and $^{14}NH_3$ in the absence of added H_2 as a function of temperature. Conditions: 500 ppm $^{14}NH_3$, 350 ppm ^{15}NO, 1.5% O_2 in a He balance; $p = 1$ atm; residence time of 0.25 s at 1173 K (constant mass flow). Symbols: (◆, $^{14}NH_3$; ◇, ^{15}NO; +, ^{14}NO; △, $^{14}N_2$; □, $^{14}N^{15}N$; ○, $^{15}N_2$; ▲, $^{14}N_2O$; ■, $^{14}N^{15}NO$; ▼, $^{15}N^{14}NO$; ●, $^{15}N_2O$).

equations and 46 reaction species. The output of the modified model was verified by comparing the sum of the concentrations of the isotopic isomers of a given molecule (NO, NH_3, N_2, and N_2O) with that predicted by the original model using unlabeled reactants.

Results and Discussion

Reaction of ^{14}NO and $^{14}NH_3$ with and without Added H_2

Experimental Observations

The homogeneous reaction of ^{14}NO and $^{14}NH_3$ in excess O_2 was studied in both the absence and presence of hydrogen. The results are not presented graphically but are similar to those reported previously [1,2]. As expected, the addition of molecular hydrogen shifted the onset of NO reduction toward lower temperatures (from 1200 K to 1000 K). However, it should be mentioned that for experiments without H_2, the typical temperature window profile for the NO conversion was not observed. The rated maximum operating temperature of the reactor used in these experiments was only about 1275 K, and there was some evidence that significant heat loss occurred at the ends of the heated reaction zone at set point temperatures above about 1250 K. Hence, the results for the higher temperatures should be regarded with caution because it is possible that considerable reaction occurs in the gas phase before the mixture reaches the maximum temperature region within the furnace.

There are several other differences in the reaction profiles. Without hydrogen, nitrogen is the dominant product, with negligible amounts (<5 ppm) of nitrous oxide produced at all temperatures. However, with added H_2, nitrous oxide is a significant reaction product at higher temperatures, the selectivity to nitrous oxide increasing to about 10% of the products at 1133 K.

Model Predictions

The agreement between model predictions and experimental observations is good for the reaction without H_2. The temperature for maximum NO conversion is well predicted at ≈1150 K, but the decrease in the NO conversion and the accompanied decrease in the nitrogen production predicted by the model was not observed experimentally (probably because of the reactor limitations already discussed). In the H_2 promoted case, NO conversion is overpredicted, with almost complete consumption of the NO at 100 K below the maximum NO conversion observed experimentally. A similar overprediction is also observed by Glarborg et al. [2] for H_2-promoted SNCR.

Reaction of ^{15}NO and $^{14}NH_3$ with and without Added H_2

Experimental Observations

SNCR experiments are typically conducted in a N_2 balance, making it difficult to report with certainty the relative product distribution between N_2 and N_2O. Ammonia conversions are also rarely reported. Figure 1 presents the experimentally determined isotopic distributions of the reactant and product species in the effluent stream for the unpromoted reaction of ^{15}NO and $^{14}NH_3$ in excess (1.5%) O_2. Similarly, Fig. 2 presents the results for the H_2-promoted case.

The combination reaction to form $^{14}N^{15}N$ is the

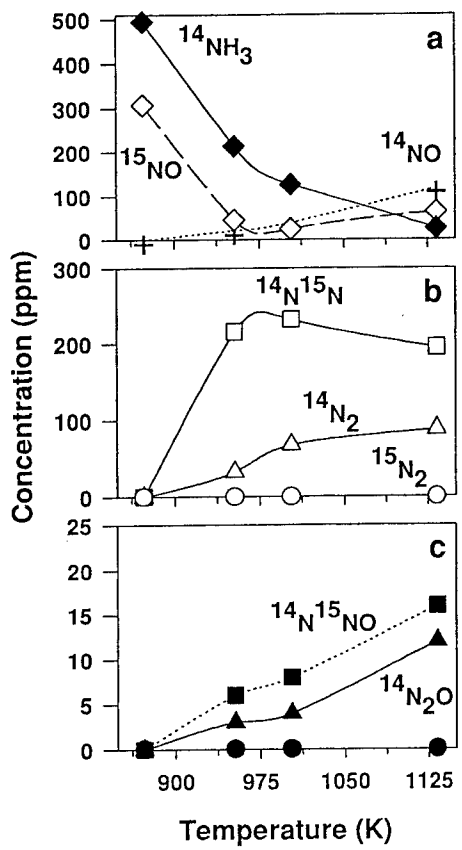

FIG. 2. Concentrations of the isotopic isomers of (a) nitric oxide and ammonia, (b) diatomic nitrogen, and (c) nitrous oxide for the reaction of ^{15}NO and $^{14}NH_3$ in the presence of added H_2 as a function of temperature. Conditions: 450 ppm $^{14}NH_3$, 350 ppm ^{15}NO, 1000 ppm H_2, 1.5% O_2 in a He balance; $p = 1$ atm; residence time of 0.19 s at 973 K (constant mass flow). Symbols: (◆, $^{14}NH_3$; ◇, ^{15}NO; +, ^{14}NO; △, $^{14}N_2$; □, $^{14}N^{15}N$; ○, $^{15}N_2$; ▲, $^{14}N_2O$; ■, $^{14}N^{15}NO$; ▼, $^{15}N^{14}NO$; ●, $^{15}N_2O$.).

major source of nitrogen at all temperatures, both with and without added H_2. There appears to be a greater propensity for ammonia oxidation to nitrogen in the presence of H_2. In the absence of added hydrogen, ammonia oxidation to $^{14}N_2$ represents about 10% of the total nitrogen species at the highest temperature studied (1233 K). With added H_2, the corresponding value is markedly higher at 31%. Figures 1b and 2b indicate that negligible amounts of nitrogen arising from the interaction of two ^{15}NO molecules (i.e., $^{15}N_2$), were produced under all conditions. At this point, it is instructive to highlight some of the experimental difficulties or uncertainties involved in the quantitative determination of the $^{15}N_2$ species. Mass spectral data alone cannot be used to determine the $^{15}N_2$ produced because both $^{15}N_2$ and ^{14}NO have signals at *m/e* 30. An additional interference is caused by the oxidation of $^{14}NH_3$ to ^{14}NO, which is known to occur on the MS filament [6]. Thus, concentrations of ^{14}NO produced by the SNCR reaction were determined from FTIR spectra after subtraction of the ^{15}NO features. These values for the ^{14}NO concentration showed good agreement with values calculated from MS data assuming all the signal at *m/e* 30 was attributable to ^{14}NO (after correction for ammonia oxidation on the MS filament). This indicated that negligible amounts of $^{15}N_2$ are produced under these conditions.

There are four possible isotopic isomers of nitrous oxide: $^{14}N_2O$, $^{14}N^{15}NO$, $^{15}N^{14}NO$, and $^{15}N_2O$. FTIR spectroscopy has been used previously to distinguish between $^{14}N^{15}NO$ and $^{15}N^{14}NO$ [6]. This technique was again used to show that $^{14}N^{15}NO$ was the dominant form of nitrous oxide produced for all conditions studied. Thus, the nitrogen-oxygen bond of the ^{15}NO molecule is preserved during the formation of the "mixed" nitrous oxide species. Additionally, larger amounts of the nitrous oxide species arising from ammonia oxidation ($^{14}N_2O$) are observed in the presence of added hydrogen. Indeed, at 1133 K, with added H_2, $^{14}N_2O$ represents about 43% of the total nitrous oxide produced. The uncertainties associated with the quantitative determination of the $^{15}N_2$ species are not experienced in the case of $^{15}N_2O$. The parent fragment for the $^{15}N_2O$ species in the MS is at *m/e* 46. Under these conditions, the background signal at *m/e* 46 is so low that the detection limit for this species is about 0.05 ppm. Even so, the production of $^{15}N_2O$ was never observed, supporting the earlier inference that no $^{15}N_2$ is produced.

At elevated temperatures, ammonia oxidation to ^{14}NO also becomes significant. Again, this is far more pronounced in the presence of added H_2. Note also that $^{14}N_2O$ is only observed in significant amounts when large amounts of ^{14}NO are produced.

Model Predictions

Figure 3 presents the model-predicted concentrations of the reactant and product species for the unpromoted ^{15}NO-labeled SNCR reaction. These modeling results can be compared with the experimentally determined isotopic distributions presented in Fig. 1. The only obvious discrepancy between the experimental and the predicted concentrations occurred for the nitrous oxide species. Firstly, the model predicts about double the quantity of $^{14}N^{15}NO$ than is actually produced and also predicts the formation of small but measurable amounts of $^{14}N_2O$ at higher temperatures. The model also predicts about 0.1 ppm $^{15}N^{14}NO$; however, this amount is below the FTIR detection limit.

Figure 4 shows the modeling results in the presence of H_2, which can be compared with the

experimentally determined distributions shown in Fig. 2. On the whole, there is reasonable agreement; however, at lower temperatures, the model predicts significant amounts of doubly labeled nitrogen and nitrous oxide arising from the combination of two ^{15}NO molecules. Peak concentrations of these species (≈5.6 ppm $^{15}N_2$ and ≈1 ppm $^{15}N_2O$) are predicted at around 950 K. As discussed previously, this amount of $^{15}N_2O$ is well above the detection limit of ≈0.05 ppm of this species by the MS. By inference, it is unlikely (although cannot be unequivocally stated) that $^{15}N_2$ is produced during the reaction. Implications of the nonobservation of these doubly labeled species is discussed later.

Mechanistic Implications

The mixed nitrogen species $^{14}N^{15}N$ is both the major product and the major form of nitrogen at all temperatures, both with and without added H_2. These results are consistent with reaction (R1). Additionally, FTIR spectroscopy has been used to confirm that $^{14}N^{15}NO$ is the dominant form of mixed nitrous oxide produced, indicating that the N—O bond of the reactant nitric oxide molecule is retained during the SNCR reaction. Added H_2 is thought to dramatically increase the OH concentration that in turn promotes hydrogen abstraction from the ammonia species to form, in this case, ^{14}NH. The ^{14}NH produced can then react with ^{15}NO via reaction (R12) to form $^{14}N^{15}NO$:

$$^{14}NH + {}^{15}NO \rightleftarrows {}^{14}N^{15}NO + H. \quad \text{(R12b)}$$

While the amount of $^{14}N^{15}NO$ as a percentage of the mixed species ($^{14}N^{15}N$ + $^{14}N^{15}NO$) increases with both temperature and hydrogen addition, this value is always relatively small (<10%). A rate-of-progress (ROP) analysis at a residence time of 10 ms for conditions with added H_2 at 1125 K showed that hydrogen abstraction from the NH_2 species by oxygen (reaction [R7]) is still about five times slower than the reaction of NH_2 with available nitric oxide (reaction [R1]).

The mechanism for the formation of the ammonia oxidation products also needs to be identified. At 1133 K, in the presence of added H_2, the concentration of ^{14}NO (117 ppm) in the effluent stream is approximately double the ^{15}NO concentration (64 ppm). A ROP analysis at 1125 K showed that the dominant routes for ammonia oxidation are, as expected, reactions (R6) through (R11). However, oxidation via the $H^{14}NO$ intermediate (reaction [R6] followed by reaction [R9]) occurs at a significantly faster rate than oxidation via the ^{14}NH intermediate.

Note that the $^{14}N_2O$ was observed only at significant concentrations when large amounts of ^{14}NO are also present. ROP and sensitivity analyses showed that ^{14}NO produced by ammonia oxidation reacts further with ^{14}NH via reaction (R12) to produce the $^{14}N_2O$ species:

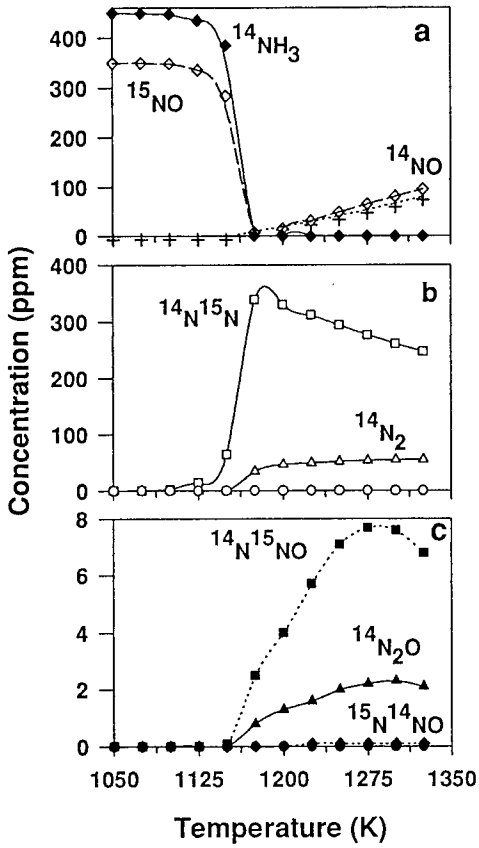

FIG. 3. Model-predicted concentrations of the isotopic isomers of (a) nitric oxide and ammonia, (b) diatomic nitrogen, and (c) nitrous oxide for the reaction of ^{15}NO and $^{14}NH_3$ in the absence of added H_2 as a function of temperature. Conditions: 500 ppm $^{14}NH_3$, 350 ppm ^{15}NO, 1.5% O_2 in a He balance; p = 1 atm; residence time of 0.25 s at 1173 K (constant mass flow). Symbols: (♦, $^{14}NH_3$; ◇, ^{15}NO; +, ^{14}NO; △, $^{14}N_2$; □, $^{14}N^{15}N$; ○, $^{15}N_2$; ▲, $^{14}N_2O$; ■, $^{14}N^{15}NO$; ▼, $^{15}N^{14}NO$; ●, $^{15}N_2O$).

$$^{14}NH + {}^{14}NO \rightleftarrows {}^{14}N_2O + H \quad \text{(R12c)}$$

A similar process occurs for the formation of the $^{14}N_2$ species. Product ^{14}NO reacts with $^{14}NH_2$ via reaction (R1) to form $^{14}N_2$:

$$^{14}NH_2 + {}^{14}NO \rightleftarrows {}^{14}N_2 + H_2O \quad \text{(R1b)}$$

As discussed, for the mixed nitrogen and nitrous oxide species, the rate of reaction (R1) is significantly faster than reaction (R12). Hence, the amount of $^{14}N_2$ formed always exceeds that of the $^{14}N_2O$ species. However, note that large amounts of $^{14}N_2$ were sometimes produced when only small amounts of ^{14}NO were present. It is only at higher temperatures, where the rate of reaction (R6) becomes

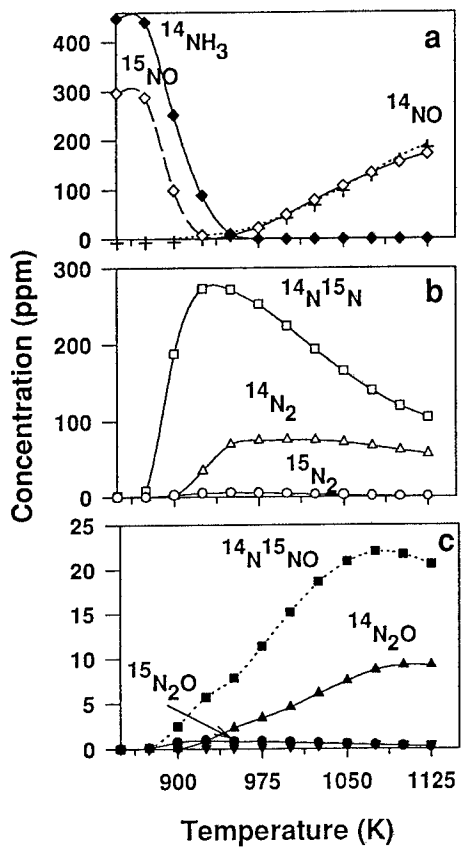

FIG. 4. Model-predicted concentrations of the isotopic isomers of (a) nitric oxide and ammonia, (b) diatomic nitrogen, and (c) nitrous oxide for the reaction of ^{15}NO and $^{14}NH_3$ in the presence of added H_2 as a function of temperature. Conditions: 450 ppm $^{14}NH_3$, 350 ppm ^{15}NO, 1000 ppm H_2, 1.5% O_2 in a He balance; $p = 1$ atm; residence time of 0.19 s at 973 K (constant mass flow). Symbols: (◆, $^{14}NH_3$; ◇, ^{15}NO; +, ^{14}NO; △, $^{14}N_2$; □, $^{14}N^{15}N$; ○, $^{15}N_2$; ▲, $^{14}N_2O$; ■, $^{14}N^{15}NO$; ▼, $^{15}N^{14}NO$; ●, $^{15}N_2O$).

comparable to that of reaction (R1), that ^{14}NO is observed concurrently with $^{14}N_2$.

The preceding discussions indicate that there are always larger amounts of the nitrogen species compared to the corresponding nitrous oxide species. An additional contributing factor may be the subsequent reduction of nitrous oxide species in the reactor. ROP analyses indicated that the rate of any reaction for direct reduction of nitrous oxide is at least an order of magnitude lower than the formation of the corresponding nitrogen species via reaction (R1). Additionally, a modeling run was performed in which 50 ppm labeled nitrous oxide ($^{15}N_2O$) was introduced with unlabeled reactants (^{14}NO and $^{14}NH_3$) in the presence of 1.5% O_2 at 1125 K. Results show that only 20% of the $^{15}N_2O$ was reduced to form $^{15}N_2$.

The ammonia oxidation products and the products of the selective reactions are fairly easily accounted for in terms of the reaction mechanism. However, in the presence of H_2, the model by Glarborg et al. [2] also predicts significant quantities of products derived from the interaction of two ^{15}NO molecules ($^{15}N_2$ and $^{15}N_2O$) at 950 K. Formation of doubly labeled species requires incorporation of ^{15}N, derived from ^{15}NO, into N_iH_j or HNO species. Reactions (R13) through (R15) indicate possible routes of formation for the $^{15}N_2O$ species. Using labeled species, the following pathways for $^{15}N_2O$ formation are possible:

Pathway 1:

$$^{14}N^{15}NH + {}^{15}NO \rightleftarrows {}^{14}N^{15}N + H^{15}NO \quad \text{(R4b)}$$

$$H^{15}NO + {}^{15}NO \rightleftarrows {}^{15}N_2O + OH \quad \text{(R13b)}$$

Pathway 2:

$$^{14}NH_2 + {}^{15}NO \rightleftarrows {}^{14}N^{15}NH + OH \quad \text{(R2b)}$$

$$^{14}N^{15}NH + H + M \rightleftarrows {}^{14}N^{15}NH_2 + M \quad \text{(R16)}$$

$$^{14}N^{15}NH_2 + {}^{15}NO \rightleftarrows {}^{15}N_2O + {}^{14}NH_2 \quad \text{(R17)}$$

ROP and sensitivity analyses show that the second pathway is the major route to $^{15}N_2O$ formation.

Similarly, the major steps for $^{15}N_2$ formation have been identified as the following:

$$^{14}N^{15}NH_2 + H + M \rightleftarrows {}^{14}N^{15}NH_3 + M \quad \text{(R18)}$$

$$^{14}N^{15}NH_3 + O \rightleftarrows {}^{15}NH_2 + H^{14}NO \quad \text{(R19)}$$

$$^{15}NH_2 + {}^{15}NO \rightleftarrows {}^{15}N_2 + H_2O \quad \text{(R1c)}$$

The model predicts that more $^{15}N_2$ is formed than $^{15}N_2O$ because the rate of reaction (R18) is faster than that of (R17).

There are two alternatives for modifying the model so that the prediction of the doubly labeled species can be eliminated to make the product distribution consistent with that observed experimentally. One is to revise the kinetics of the reactions in which the N_2H_i species are formed and in which they subsequently participate; the second is to reduce the NNH lifetime so that the subsequent reactions of NNH with H are not competitive.

To investigate the effect of the lifetime of the NNH species on the model predictions, we have varied the kinetic rate of the NNH $\rightleftarrows$ N_2 + H reaction in the range from 10^4 to 10^8 s^{-1}. The results given in Table 1 show that a lifetime at least as short as 10^{-8} s is required to reduce the modeled predictions for $^{15}N_2$ to less than 1 ppm and for $^{15}N_2O$ to less than 0.1 ppm.

Although the changes to the model parameters cause the predicted product distributions to be more consistent with experimental isotopic product

TABLE 1
The effect of changing the lifetime of the NNH species (by varying the rate of the reaction NNH ⇄ H + N_2) on the isotopic product distribution for the reaction of ^{15}NO (350 ppm) and $^{14}NH_3$ (450 ppm) in the presence of H_2 (1000 ppm) and excess O_2 (1.5%) at 950 K.

NNH ⇄ H + N_2 Reaction rate	Effluent concentrations (ppm)										
	^{14}NO	^{15}NO	$^{14}NH_3$	$^{15}NH_3$	$^{14}N_2$	$^{14}N^{15}N$	$^{15}N_2$	$^{14}N_2O$	$^{14}N^{15}NO$	$^{15}N^{14}NO$	$^{15}N_2O$
10^4	5.0	30.8	178.5	1.0	10.0	237.0	9.5	0.2	4.8	0.2	2.1
10^6	13.9	6.8	11.1	0.1	69.5	271.6	5.6	2.3	7.8	0.1	0.8
10^8	19.3	19.9	2.5	0.0	72.3	266.5	0.7	2.5	10.9	0.0	0.1
Expt.-this study at 953 K	21	46	213	0	33	216	[a]	3	6	<2	<0.05

[a]Indicates that this value is difficult to determine experimentally.

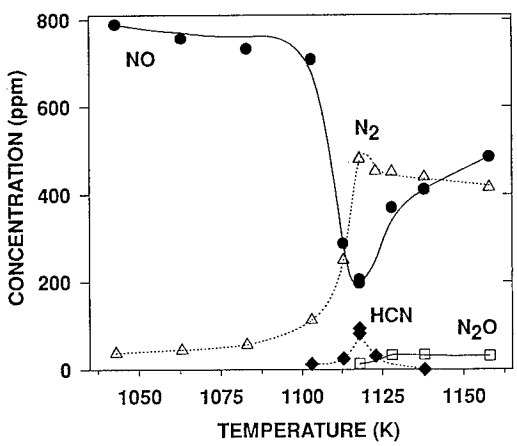

FIG. 5. Concentration of some reactant and product species as a function of temperature for the reaction of NO and NH_3 in the presence of propane at low O_2 concentrations. Conditions: 630 ppm ^{14}NO, 610 ppm $^{14}NH_3$, 905 ppm C_3H_8, and 0.61% O_2; p = 1 atm; residence time is 0.18 s at 1100 K (constant mass flow).

distributions, this raises some problems with the mechanism [2] and the agreement between experiment and model. The NNH species was originally invoked to explain experimental observations of the production of OH from the reaction of NH_2 + NO without concomitant production of H. Miller and Bowman [1] initially modeled the SNCR reaction using a lifetime for the NNH species of 10^{-4} s. However, theoretical calculations and experiments [4,11] have indicated that NNH is unstable with respect to dissociation to H and N_2 with a lifetime between 10^{-11} and 10^{-8} s. The most realistic estimate of the NNH lifetime in its electronic ground state is 3×10^{-9} s [4,11]. As Stephens et al. [4] indicate, such a short lifetime of the NNH species would necessarily result in the appearance of H atoms (see reaction [R3]) that have not been observed experimentally. Additionally, Unfried et al. [12] did not find any evidence for the HNO species.

SNCR of NO by NH_3 in the Presence of Hydrocarbons at Low Oxygen Concentrations

SNCR in the presence of HCs is industrially attractive because, like hydrogen, HCs have been shown to cause a decrease in the temperature window for NO reduction. HCs are preferable to H_2 from a safety aspect but can lead to the formation of undesirable by-products. For example, HCN formation has been observed during the reaction of NO and NH_3 in the presence of ethane [8]. The absolute concentration of HCN produced was found to depend strongly on the oxygen-to-HC ratio in the feed stream: no HCN was formed in the absence of O_2 and with inlet concentration ratios of O_2 to C_2H_6 greater than 5.

Figure 5 shows the NO, N_2, N_2O, and HCN concentration profiles as a function of temperature for the SNCR reaction in the presence of propane and small amounts of oxygen. The maximum NO conversion, the peaks in the N_2 (≈500 ppm) and HCN (≈100 ppm) formation, and the onset of the N_2O formation all occur at around 1120 K. For these particular conditions, the formation of HCN occurs in a narrow temperature window, and the concentration of N_2O rapidly reaches a plateau concentration of ≈40 ppm. No HNCO was produced (detection limit of 1 ppm). Concentrations of NH_3 have not been included in Fig. 5 in the interest of clarity.

Hemberger et al. [8] found that HCN was formed using $NH_3/C_2H_6/O_2$ and $NO/C_2H_6/O_2$ mixtures. The origin of the N atom in the HCN produced under competitive SNCR conditions can be determined easily by isotopic labeling.

Figure 6a shows the features due to the C—H stretching mode of the $HC^{14}N$ molecule in the 3280–3340 cm^{-1} region of the product spectrum for

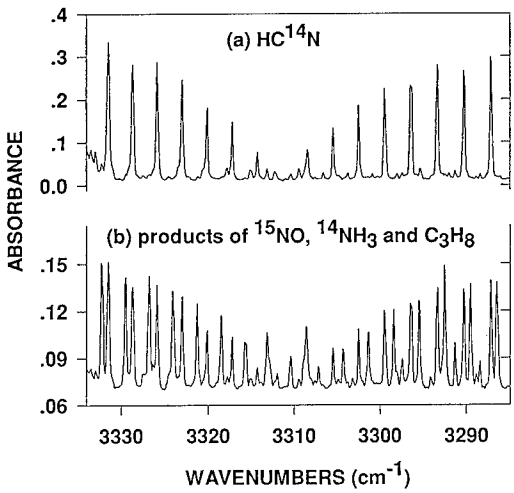

FIG. 6. Features due to the C—H stretching vibration of HCN in the 3280–3340 cm^{-1} region of the gas-phase FTIR spectrum of (a) the products of the homogeneous reaction of ^{14}NO (630 ppm) and $^{14}NH_3$ (610 ppm) in the presence of propane (905 ppm) and O_2 (0.61%) at 1120 K, and (b) the products of the reaction under conditions identical to that of (a) but with substitution of ^{15}NO for ^{14}NO. Spectra recorded at 0.25 cm^{-1} with the co-addition of 16 scans.

the reaction of unlabeled NH_3 and NO in the presence of propane. Figure 6b is the same region of the product gas spectrum for the reaction under otherwise identical conditions but after substituting ^{15}NO for ^{14}NO. Taking into account that there will be some interference from ammonia and water absorption lines, the spectrum of Fig. 6b clearly shows that roughly equal amounts of $HC^{14}N$ and $HC^{15}N$ are formed. Note that the quantity (also determined by FTIR) of ^{14}NO formed via ammonia oxidation is <5 ppm at this temperature. Because the concentration of ^{14}NO is more than an order of magnitude lower than the ^{15}NO concentration, the HCN must be produced from interactions of both NO and NH_3 with the products of propane oxidation. However, at ≈1160 K, the formation of ^{14}NO from ammonia oxidation is approximately 160 ppm, but there is no evidence for HCN formation at the higher temperature.

Other information on the distribution of the isotopic isomers of nitrogen and nitrous oxide is limited because of interference from CO and CO_2 in both the MS and the FTIR spectra.

Hemberger et al. [8] suggested that the HCN formation from the interaction of NO and ethane may be attributable to the reaction of HCCO with NO:

$$HCCO + NO \rightleftarrows HCNO + CO \quad (R20)$$

$$HCNO + H \rightleftarrows HCN + OH \quad (R21)$$

However, they concluded that an additional route to HCN formation must be possible from the interaction of the HC with ammonia and suggested the reaction of an NH_2 species with an unsaturated HC such as C_2H_2 or C_2H_4.

Conclusions

1. ^{15}N-isotopic labeling techniques have shown that $^{14}N^{15}N$ is always the predominant nitrogen-containing product of the reaction of ^{15}NO and $^{14}NH_3$ in the presence of excess O_2, both with and without added H_2.
2. H_2-promoted SNCR results in higher selectivities to N_2O; at temperatures above the maximum NO conversion, a large proportion (43%) of the nitrous oxide is $^{14}N_2O$. Rate-of-progress and sensitivity analyses have confirmed that conversion of NH_3 to ^{14}NO is a prerequisite for the formation of both $^{14}N_2O$ and $^{14}N_2$.
3. In general, the experimentally determined isotopic product distributions were in a reasonable agreement with the model predictions based on a detailed kinetic model of the SNCR process [2]. However, under some conditions, the model predicted significant concentrations of $^{15}N_2$ and $^{15}N_2O$, but these doubly labeled species were not observed experimentally (measured concentrations of $^{15}N_2O$ never exceeded the detection limit of 0.05 ppm). Modifying the model such that the lifetime of the NNH species is less than 10^{-8} s was sufficient to stop the prediction of either $^{15}N_2$ or $^{15}N_2O$.
4. The source of HCN produced from the propane-promoted SNCR reaction has also been investigated using labeling techniques. Both $HC^{14}N$ and $HC^{15}N$, in similar concentrations, are produced from an equimolar mixture of ^{15}NO and $^{14}NH_3$, under conditions in which ammonia oxidation to NO is insignificant. Therefore, both NO-propane and NH_3-propane interactions are important in HCN formation under competitive conditions.

REFERENCES

1. Miller, J. A. and Bowman, C. T., *Prog. Energy Combust. Sci.* 15:287–338 (1989).
2. Glarborg, P., Dam-Johansen, K., Miller, J. A., Kee, R. J., and Coltrin, M. E., *Int. J. Chem. Kinet.* 26:421–436 (1994).
3. Atakan, B., Jacobs, A., Wahl, M., Weller, R., and Wolfrum, J., *Chem. Phys. Lett.* 155:609–613 (1989).
4. Stephens, J. W., Morter, C. L., Farhat, S. K., Glass, G. P., and Curl, R. F., *J. Phys. Chem.* 97:8944–8951 (1993).
5. Bulatov, V. P., Ioffe, A. A., Lozovsky, V. A., and Sarsikov, O. M., *Chem. Phys. Lett.* 161:141–146 (1989).

6. Duffy, B. L., Curry-Hyde, H. E., Cant, N. W., and Nelson, P. F., *J. Phys. Chem.* 98:7153–7161 (1994).
7. Gehring, M., Hoyermann, K., Schacke, H. J., and Wolfrum, J., *Fourteenth Symposium (International) on Combustion,* The Combustion Institute, Pittsburgh, 1973, pp. 99–105.
8. Hemberger, R., Muris, S., Pleban, K. U., and Wolfrum, J., *Combust. Flame* 99:660–668 (1994).
9. Lutz, A., Kee, R. J., and Miller, J. A., Sandia National Laboratories Report No. SAND87-8248, 1987.
10. Kee, R. J., Rupley, F. M., and Miller, J. A., Sandia National Laboratories Report No. SAND89-8009, 1989.
11. Koizumi, H., Schatz, G. C., and Walch, S. P., *J. Chem. Phys.* 95(6):4130–4135 (1991).
12. Unfried, K. G., Glass, G. P., and Curl, R. F., *Chem. Phys. Lett.* 173:337–342 (1991).

COMMENTS

Alan Doughty, The University of Sydney, Australia. In order to predict the observed isotopic mixture of the products from selective non-catalytic reduction of NO, your reaction mechanism requires a specific lifetime of NNH. You state this as being a consequence of competition between unimolecular decomposition of NNH and the reaction of NNH with H atoms. To what extent could other aspects of the mechanism, such as the predicted concentration of H-atoms during reaction, affect your conclusions concerning the lifetime of NNH?

Author's Reply. When using labelled reactants (^{15}NO and $^{14}NH_3$) the model by Glarborg et al. [1], modified to include all possible isotopic isomers, predicted doubly labeled species ($^{15}N_2O$ and $^{15}N_2$) in the presence of added H_2. These species were not observed experimentally, and in the paper we suggest two possible ways to modify the mechanism to force the model to limit the prediction of these species. One was to reduce the lifetime of the NNH species, and the other was to modify the kinetics of the reactions involving N_2H_2 species, including the reaction of NNH and H. We investigated the former and found that an NNH lifetime of less than 10^{-8} s was sufficient to force the model predicted isotopic product distribution to agree with that observed experimentally. As you suggest, it is possible that the predicted concentration of H atoms is overestimated. However, it is probable that the H atoms concentration would have to be overpredicted by several orders of magnitude to account for the modeled prediction of the doubly labeled species.

REFERENCE

1. Glarborg, P., Dam-Johansen, K., Miller, J. A., Kee, R. J., and Coltrin, M. E., *Int. J. Chem. Kinet.* 26:421–436 (1994).

•

A. M. Dean, Exxon Research & Engineering Co., USA. Your conclusion that the lifetime of NNH is less than 10^{-8} sec is consistent with the calculations of Koizumi et al. [1]. This short lifetime of NNH implies that H addition to N_2 is rapid, which can lead to rapid onset of a low partially-equilibrated NNH concentration in flames. NNH in turn, can react with 0 in a new route to NO_x production [2]. Recent NO measurements of Harrington et al. [3] are consistent with the Bozzelli–Dean mechanism.

REFERENCES

1. Koizumi et al., *J. Chem. Phys.* 95:4130 (1991).
2. Bozzelli, J. W. and Dean, A. M., *Int. J. Chem. Kinet.* 27:1097 (1995).
3. Harrington et al., *Twenty-Sixth (International) Symposium on Combustion,* The Combustion Institute, Pittsburgh, 1996, pp. 000–000.

Author's Reply. Firstly, a slight clarification needs to be made. Our conclusion was not that the NNH lifetime is less than 10^{-8} s, but that an NNH lifetime of less than 10^{-8} s was sufficient to force the model predicted isotopic product distribution to agree with that observed experimentally, i.e., limit the prediction of doubly labelled species ($^{15}N_2O$ and $^{15}N_2$) in the presence of added H_2. We used the model by Glarborg et al. [1] to model the system, and there may be other ways to modify this mechanism to produce a similar result. The other obvious possibility that we eluded to in the paper is the kinetics of the reactions involving N_2H_2 species, including the reaction of NNH with H. It should also be noted that the effect of changing the NNH lifetime on the overall model outcomes (NO and NH_3, conversions as a function of temperature) was not considered in detail.

REFERENCE

1. Glarborg, P., Dam-Johansen, K., Miller, J. A., Kee, R. J., and Coltrin, M. E., *Int. J. Chem. Kinet.* 26:421–436 (1994).

•

Judy Wornat, Princeton University, USA. Could you please describe the difference in the FTIR spectra between $^{15}N^{14}NO$ and $^{14}N^{15}NO$?

Author's Reply. The center band of the ν_3 N = N stretching vibration for $^{14}N^{14}NO$, $^{14}N^{15}NO$, $^{15}N^{14}NO$, and $^{15}N^{15}NO$ occur at 2223.756 cm^{-1}, 2177.6581 cm^{-1}, 2201.605 cm^{-1} and 2154.730 cm^{-1} respectively. The use of FTIR spectroscopy to distinguish these species has been demonstrated previously [1,2].

REFERENCES

1. Duffy, B. L., Curry-Hyde, H. E., Cant, N. W., and Nelson, P. F., *J. Catal.* 149:11–22 (1994).
2. Duffy, B. L., Curry-Hyde, H. E., Cant, N. W., and Nelson, P. F., *J. Phys. Chem.* 98:7153–7161 (1994).

Twenty-Sixth Symposium (International) on Combustion/The Combustion Institute, 1996/pp. 2109–2115

THERMAL REDUCTION OF NO BY NH_3: KINETIC MODELING OF THE NH_2 + NO PRODUCT BRANCHING RATIO

M. J. HALBGEWACHS, E. W. G. DIAU, A. M. MEBEL AND M. C. LIN
Department of Chemistry
Emory University
Atlanta, GA 30322, USA

C. F. MELIUS
Combustion Research Facility
Sandia National Laboratories
Livermore, CA 94550, USA

The product-branching ratio for the reaction $NH_2 + NO \rightarrow HN_2 + OH$ (1) and $N_2 + H_2O$ (2) has been determined in the temperature range of 950–1200 K by pyrolysis of Ar-diluted NH_3 + NO mixtures and at 1173 and 1200 K by pyrolysis of Ar-diluted NH_3-NO-CO mixtures. Analysis of the pyrolyzed and unpyrolyzed mixtures was carried out by the FTIR spectrometric method. Kinetic modeling of the decay rates of NH_3 and NO and the production rate of CO_2 by varying the branching ratio, $\alpha_1 = k_1/(k_1 + k_2)$, and keeping the known total rate constant ($k_t = k_1 + k_2 = 9.6 \times 10^{14}\, T^{-0.85}$ cm^3 mol^{-1} s^{-1}) unchanged at each temperature allows determination of the value of α_1 with good reproducibility. Kinetic modeling of α_1, using previously measured H_2O formation data [28] from the NH_3 + NO reaction in the temperature range of 1123–1273 K was also carried out. The branching ratio was found to increase rapidly from 0.27 at 950 K to 0.58 at 1273 K, which is fully consistent with the sharply rising trend recently reported from NH_3-NO flame studies, in which $\alpha_1 \approx 0.5$ at 1500 K and rose to 0.9 at 2000 K. These new findings cast doubt on the much lower values, $\alpha_1 \leq 0.17$ at $T \leq 1173$ K, obtained by laser kinetic measurements.

Introduction

The reaction of NH_2 with NO has been shown to greatly affect the overall NO_x-reduction efficiency of NH_3 and the burning velocity of the NH_3-NO flame [1–6]. The reaction takes place primarily by the following two product channels [1–15]:

$$NH_2 + NO \rightarrow HN_2 + OH \qquad (1)$$

$$\rightarrow N_2 + H_2O \qquad (2)$$

The relative importance of these reaction paths, as measured by the branching ratio $\alpha_1 = k_1/(k_1 + k_2)$, strongly influences the overall kinetics of the NH_3-NO system. The thermal-neutral reaction, Eq. (1), generates two key chain carriers, H and OH, because HN_2 is unstable under combustion conditions. However, reaction (2), producing N_2 and H_2O, is an exothermic chain-termination step that releases as much as 120 kcal mol^{-1} energy. Therefore, these two reactions are highly competitive. Reaction (1) enhances the efficiency of NH_3 for NO_x reduction and the overall NH_3 + NO reaction rate, whereas reaction (2) reduces the efficiency and reaction rate.

On the basis of the results of recent kinetic modeling on the structure of a quasi-equimolar NH_3-NO flat flame by Vandooren et al. [5] and on the burning velocity data of Andrew and Gray [16] by Brown and Smith, [6] the branching ratio for reaction (1), α_1, has been determined to be $\geq$0.5 above 1500 K. This value is significantly higher than that deduced from laser kinetic measurements, most notably by Wolfrum and co-workers [11] and by Stephens et al. [12], who found α_1 to be $\leq$0.2 at $T \leq 1200$ K. In a recent kinetic modeling of the NH_3 de-NO_x process by Glarborg et al. [15], the temperature-dependent expression, $\alpha_1 = 2.2 \times 10^{-3}\, T^{0.70}$, was employed by fitting $\alpha_1 = 0.11$ at 300 K and 0.3 at 1150 K. A large gap exists between the low-temperature (300–1000 K) kinetic data and the results of high-temperature (1500–2000 K) flame studies. The objective of the present work is to bridge the gap by presenting kinetic data in the temperature range of 950–1200 K using the pyrolysis-FTIR spectrometric method [17–19].

Experimental

The pyrolysis of two mixtures, one of NH_3 and NO, the other of NH_3, NO, and CO, both diluted with Ar, was carried out in a quartz reactor of volume

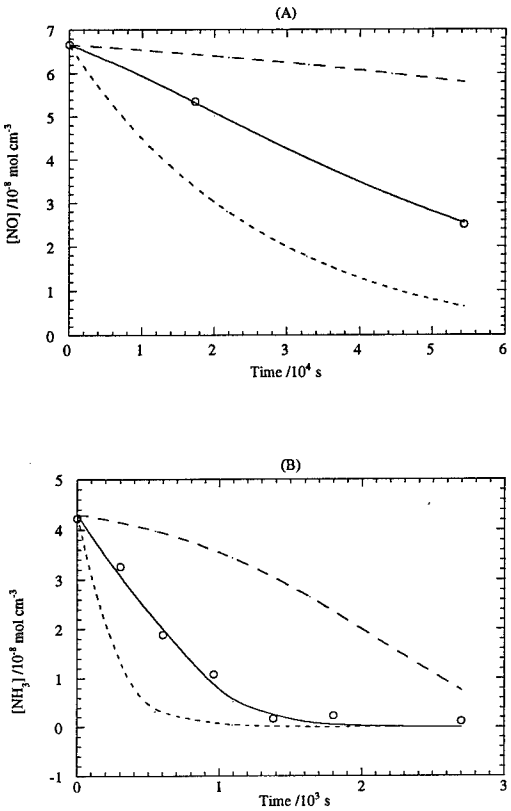

FIG. 1. Typical concentration versus time profile of NO (A) and NH_3 (B) for the reaction conditions and the α_1 values shown in Table 2 (Nos. 4 and 9, respectively), with kinetically modeled results shown by a solid curve, a short dash curve, and a long dash curve representing α_1, α_1 + 0.1, and α_1 − 0.1, respectively.

270 cm^3 with a surface-to-volume ratio of 0.748 cm^{-1}. The reactor was heated by a double-walled cylindrical oven. Concentrations of the NH_3 and NO mixtures ranged from 0.6 to 3.7% NO and 0.3 to 0.9% NH_3. The concentrations of the NH_3, NO, and CO mixtures ranged from 2.0 to 2.7% NO, 0.8 to 1.0% NH_3, and 4.9 to 6.3% CO. The reactor was heated to temperatures ranging from 950 to 1200 ± 1 K for the NH_3 and NO mixtures and at 1173 and 1200 ± 1 K for the NH_3, NO, and CO mixtures.

Unpyrolyzed and pyrolyzed samples were analyzed by a Mattson Instrument Polaris Fourier Transform Infrared (FTIR) spectrometer with a resolution of 2 cm^{-1}. Concentrations of NO, NH_3, and CO_2 were determined by calibration curves of concentration versus absorbance at 1900 cm^{-1}, 993 cm^{-1}, and 668 cm^{-1}, respectively. The calibration curves were plotted using data from samples of various appropriate concentration combinations of NO, NH_3, CO, and CO_2 that were expanded into the FTIR absorption cell at pressures ranging from 150 to 200 torr, corresponding to the pressures at which the pyrolyzed samples were analyzed. The curves were of good quality with little scatter of the data points, and the estimated error in our concentration measurements is smaller than 2–3%.

NH_3 was purified by degassing at 77 K and distillation at 228 K, attained by ethanol cooled with liquid N_2. NO, which often contains NO_2 impurities, was purified by passing the gas through a silica gel trap, held at 195 K by an ethanol–dry ice slush, and then condensing it at 77 K by means of a liquid N_2 trap. Occasional pumping was also carried out to remove noncondensables. CO was purified by passing it through Cu/CuO filings at about 423 K and two liquid N_2 traps. FTIR spectra were taken to ascertain the purity of the gases. Ar of 99.999% purity, obtained from Specialty Gases, was used without further purification. Care was always taken to adequately purge and evacuate the vacuum lines while making the mixtures and expanding the gases into the reactor and the FTIR analysis cell.

Results

Typical time-resolved concentration profiles of NO and NH_3 are shown in Fig. 1. The data were kinetically modeled via CHEMKIN [20] and SENKIN [21], using a mechanism composed primarily of reactions recently used in our simulation of the kinetics of the NH_3-NO system initiated by a pulsed ArF (193 nm) laser near 1000 K [10] and reactions studied by others [22–24,26,27]. The total rate constant, $k_t = k_1 + k_2 = 9.6 \times 10^{14}\, T^{-0.85}$ cm^3 mol^{-1} s^{-1}, previously measured [10] for the NH_2 + NO reactions (1) and (2), was used and held constant at each temperature, and k_1 was varied until the best fit with $\alpha_1 = k_1/k_t$ was found.

In this system, NO reduction is initiated by NH_3 + NO → NH_2 + HNO, reaction (3), but because of the unavailability of an experimentally determined rate constant for this reaction, the value of k_3 was obtained by variational transition state theory (VTST) calculation based on a high level ab initio MO result [25]: $k_3 = 1.04 \times 10^7\, T^{1.73}\, e^{-28{,}454/T}$ cm^3 mol^{-1} s^{-1}. Because of the high temperatures involved, the decay of NO and NH_3 was found to be controlled to a much greater extent by the mutually competitive reactions (1) and (2) than by reaction (3), as can be seen by the result of representative sensitivity analyses in Fig. 2. The reliability of the modeled α_1 values can also be seen in Fig. 1, where predicted profiles of NO and NH_3 with the branching ratio values of ±0.1 from best fit values of α_1 are plotted. Our branching ratio results for seven other temperatures and NH_3 and NO concentrations are summarized in Table 1. These results will be compared with other branching ratio data later.

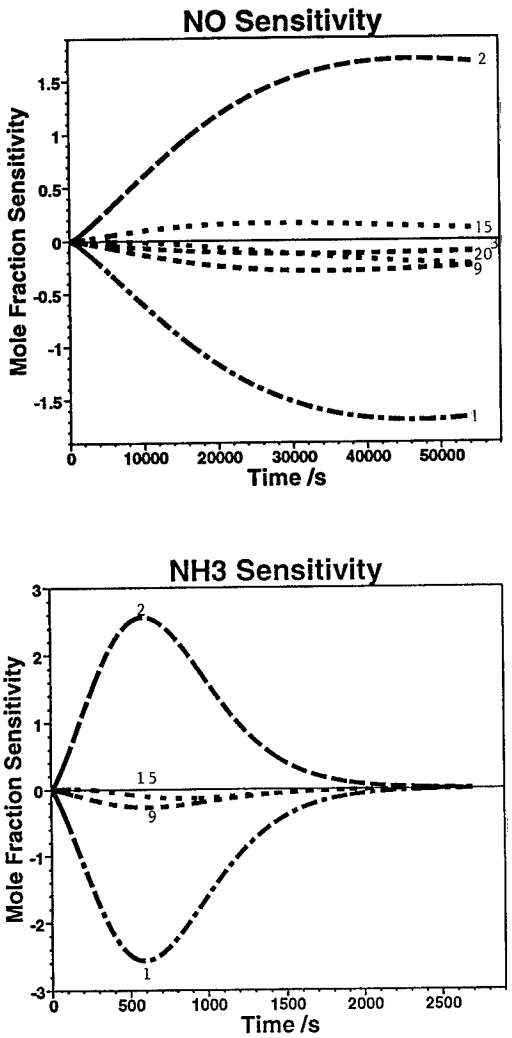

FIG. 2. Plot of normalized sensitivity coefficients for NO (A) and NH_3 (B) with the initial conditions and α_1 values presented in Table 2 (Nos. 4 and 9, respectively). The rate constants of the reactions identified in the figure are given as follows in units of $cm^3\ mol^{-1}s^{-1}$:

$$NH_2 + NO \xrightarrow{1} HN_2 + OH \qquad k_1 + k_2 = 9.6 \times 10^{14}\ T^{-0.85}$$

$$NH_2 + NO \xrightarrow{2} N_2 + H_2O$$

$$NH_3 + NO \xrightarrow{3} NH_2 + HNO \qquad k_3 = 1.0 \times 10^7\ T^{1.73} e^{-28454/T}$$

$$HNO + NO \xrightarrow{9} N_2O + OH \qquad k_9 = 8.5 \times 10^{12} e^{-14920/T}$$

$$H + NH_3 \xrightarrow{15} NH_2 + H_2 \qquad k_{15} = 1.3 \times 10^{14} e^{-10820/T}$$

$$H + HNO \xrightarrow{20} H_2 + NO \qquad k_{20} = 4.5 \times 10^{11} T^{0.72} e^{-327/T}.$$

Reactions were also carried out in the temperature range of 900–1200 K using CO as the OH-radical scavenger. As in the NH_3-NO system, modeling of the NH_3-NO-CO system was also carried out with CHEMKIN [20] and SENKIN [21]. Under our reaction conditions, however, CO_2 formation was found to be sensitive to the NH_2 + NO branching reactions only at 1173 K and higher temperatures. Reaction conditions and modeled branching ratio values are presented in Table 1.

As discussed later, in addition to modeling our own kinetic data, we carried out computer simulation of data published earlier by Poole and Graven [28] for H_2O formation and briefly studied the work of Wise and Frech [29] for the rate of total pressure change.

Poole and Graven's H_2O-Formation Data

Poole and Graven [28] used a flow technique for gravimetric measurement of H_2O production from mixtures with varying amounts of NO and NH_3 diluted in N_2 or He to a total pressure of 800 torr. Two flow vessels were used: vessel I and vessel II of volumes 42.6 cm^3 and 324 cm^3 and surface-to-volume ratios of 5.6 cm^{-1} and 2.3 cm^{-1}, respectively. The temperature range was 1123–1273 K. The measured H_2O-formation rate was found to follow the relationship

$$\frac{\Delta H_2O}{\Delta t} = \frac{k_a(NH_3)^{1/2}\,(NO)}{1 - k_b(NH_3)^{1/2}\,(NO)}$$

Poole and Graven noted that at 1223 K, vessel I, which had an S/V ratio twice as large, yielded a 20% larger value of k_a and concomitantly a smaller value of k_b than vessel II, resulting in an effective rate difference between the two vessels by less than 10%. This compensating effect resulted in an even smaller (3%) difference between the NH_2 + NO product branching ratios (see Table 2) that we modeled for the two vessels. In Fig. 3, the quantity $NO/(\Delta H_2O/\Delta t)$ is plotted against $NH_3^{-1/2}$, as presented originally by Poole and Graven. Each of these data points was employed to model the NH_2 + NO product branching ratio, and the average value for each temperature was used to calculate the rate of H_2O production; the result is shown as the solid curve in the figure. Table 2 summarizes the resulting average modeled branching ratio for the temperatures and conditions noted. The result of a sensitivity analysis for H_2O production shows that reaction (1) is the dominant reaction and that the initiation process has little effect on H_2O formation.

Wise and Frech's Total Pressure Measurement

Wise and Frech [29] pyrolyzed mixtures of 29.6–64.6% NH_3 and 31.6–70.4% NO in a quartz reaction vessel of 1560 cm^3 with a surface-to-volume ratio of 1.12 cm^{-1} in the temperature range of 990–1150 K.

TABLE 1
Summary of the present experimental conditions and modeled values of α_1 for the NH_3/NO pyrolysis system

No.	T/K	P/torr	No of exp.	$[NO]_0^a$	$[NH_3]_0^b$	$[CO]_0^a$	$t/10^2$s[c]	$\alpha_1 \pm \sigma$[d]
1	950	706	3	4.39	9.85	—	844.2	0.272 ± 0.011
2	1000	705	3	1.07	4.53	—	684.9	0.297 ± 0.011
3	1000	704	3	3.70	9.48	—	287.4	0.267 ± 0.005
4	1050	706	2	0.666	8.73	—	543.6	0.398 ± 0.001
5	1100	708	5	0.904	3.93	—	110.4	0.291 ± 0.004
6	1100	703	5	3.38	7.84	—	48.0	0.398 ± 0.004
7	1150	704	3	0.848	8.92	—	43.8	0.449 ± 0.013
8	1173	708	8	2.18	2.43	—	7.20	0.345 ± 0.005
9	1200	709	6	0.869	4.22	—	2.70	0.458 ± 0.012
10	1100	708	6	2.89	9.41	6.64	36.0	0.69[e]
11	1173	705	7	1.96	7.81	4.52	3.00	0.505 ± 0.011
12	1200	707	5	2.59	9.28	5.95	8.40	0.511 ± 0.009

[a]Concentrations of NO and CO are given in units of 10^{-7} mol cm^{-3}.
[b]Concentration of NH_3 is given in units of 10^{-8} mol cm^{-3}.
[c]The time given is the longest pyrolysis time for each set of conditions.
[d]For each set of conditions, $\alpha_1 = k_1/(k_1 + k_2)$ is the average of the branching ratios from NH_3 or NO (whichever was most sensitive for each set of conditions) decay modeled for each data point. σ is the mean of the deviations of the branching values modeled using each of the individual data points from α_1.
[e]This point is not reliable because of the relatively low sensitivity indicated by the result of a sensitivity analysis.

TABLE 2
Summary of the our kinetic modeling values of α_1 by using Poole and Graven's [28] experimental conditions and H_2O-formation data

No./ vessel	T/K	P/torr	No of exp.	$[NO]_0^a$	$[NH_3]_0^b$	t/s	$\alpha_1 \pm \sigma$[d]
1/II	1123	800[c]	10	1.07–5.32	5.35	7.995–11.26	0.494 ± 0.017
2/II	1223	800	9	1.30–5.30	5.24	0.895–1.205	0.517 ± 0.011
3/II	1223	800	10	5.24	1.08–5.40	0.840–1.177	0.521 ± 0.007
4/I	1223	800	7	4.91	1.13–4.94	0.806–1.056	0.538 ± 0.003
5/I	1273	800	12	4.88	0.49–4.89	0.187–0.308	0.581 ± 0.009
6/I	1273	800	8	1.22–4.88	4.88	0.282–0.381	0.528 ± 0.031

[a]Concentration is given in units of 10^{-6} mol cm^{-3}.
[b]$\alpha_1 = k_1/(k_1 + k_2)$ is the average of the branching ratios modeled for each point.
[c]All mixtures were diluted in Ar to 800 torr except for the last one, in which the mixture, consisting solely of NO and NH_3, was slightly more than 800 torr.
[d]σ is the average deviation of each data point from α_1.

They monitored the progress of the reaction by observing the change in the total pressure of the system via a differential manometer filled with Fluorolube S. Wise and Frech found the following relationship between the total pressure change ΔP of the system and the initial partial pressures of NH_3 and NO: $\Delta P/\Delta t = A \exp(-54,700/RT)(NH_3)(NO)^{1/2}$, which, interestingly, is totally different from that of Poole and Graven's H_2O-formation measurements as presented in the preceding section.

Since the rate of total pressure change is a global quantity, we only briefly modeled Wise and Frech's $\Delta P/\Delta t$ data, which were presented in their Figs. 1 and 2. The result of this modeling gave $\alpha_1 = 0.41$ at both 994 and 1056 K, which is in reasonable agreement with the values given in Tables 1 and 2.

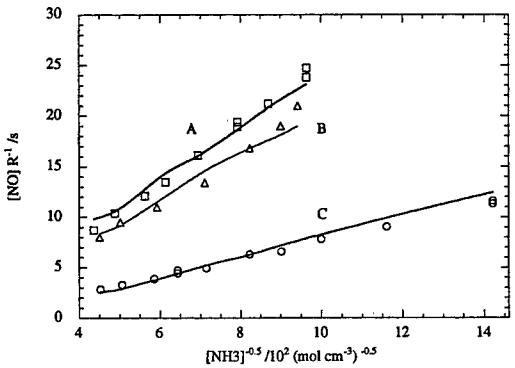

FIG. 3. Comparison of experimental and modeling results. The points are $[NO]/(\Delta H_2O/\Delta t)$ versus $[NH_3]^{-0.5}$ experimental results of Poole and Graven [28] with conditions as outlined in Table 2 (Nos. 3, 4, and 5, corresponding to A, B, and C, respectively); the solid curves are our modeled results.

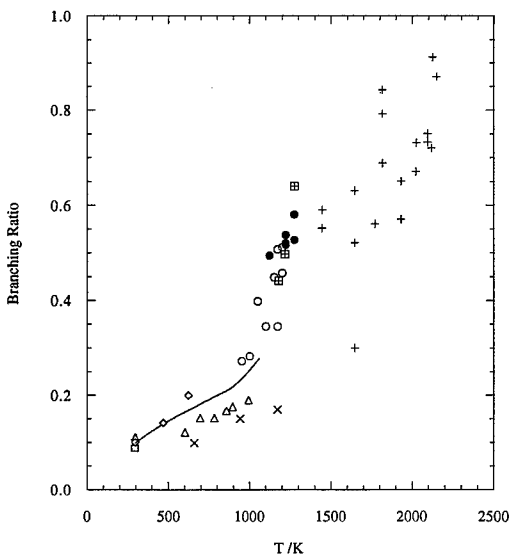

FIG. 4. Summary of the branching ratio α_1 as a function of temperature. O: This work; modeling of NH_3, NO, and CO_2 concentration profiles. ●: Our modeling of Poole and Graven's [28] data. ●: Ref. 3. +: Ref. 5. Δ: Ref. 11. X: Ref. 12. ◇: Ref. 14. □: Ref. 9. solid curve: Ref. 30.

Discussion

Our result, evaluated in the temperature range of 950–1200 K, although effectively bridging the gap between the low- ($T \leq 1000$ K) and high- ($T \geq 1500$ K) temperature data, strongly favors the higher values of the branching ratio reported by Bulatov [14], Hanson [3], Vandooren et al. [5], and that employed by Glarborg et al. in their recent modeling of the (NH_3 – NO – O_2) NH_3 de-NO_x process [15]. It casts severe doubt on the lower values, $\alpha_1 \leq 0.2$ at $T \leq 1200$ K, obtained by Atakan et al. [11], as well as by Stephens and co-workers [12]. The greater OH-production efficiency in the low-temperature (300–1000 K) range has also been confirmed recently by measuring the yields of H_2O and CO_2 in a laser-initiated reaction of NH_3, NO, and CO by mass spectrometry [30], as shown in Fig. 4, which summarizes all experimentally determined α_1 values.

The low OH-production efficiencies at $T \leq 1173$ K reported by Wolfrum et al. [11] and by Stephens co-workers [12], using laser-induced fluorescence and IR laser resonance absorption, respectively, although somewhat puzzling, could be attributed to the common difficulty in providing exact concentrations of a radical species for quantitative calibration over a wide range of temperatures. At high temperatures, the lack of accurate absorption cross-section data and the thermal instability of the OH-calibration source molecules such as H_2O_2 may also become severe problems. Our direct determination of the rates of reactant (NH_3 and NO) decay and product (CO_2 and H_2O) formation by FTIR spectrometry and/or mass spectrometry [30], aided by accurate calibrations, allowed us to circumvent the difficulty and minimize the uncertainty.

As can be seen in Fig. 4, our average values of α_1, 0.278 ± 0.011 and 0.289 ± 0.009, at 950 and 1000 K, respectively, agree closely with the branching ratio values measured mass spectrometrically by Park and Lin [30], as well as with those employed by Glarborg et al. [15], $\alpha_1 = 2.2 \times 10^{-3}\ T^{0.70}$, in their modeling of experimental de-NO_x data [31–33]. These authors [15] also concluded that the effect of the quartz reactor surface on the overall NO_x-reduction kinetics is negligible under low surface-to-volume (S/V) conditions used in typical pyrolytic experiments. In fact, our branching ratio modeling of Poole and Graven's [28] H_2O-formation rates in the NH_3 + NO reaction indicates that an increase of S/V from 2.3 to 5.6 cm^{-1} has only a negligible (3%) effect on α_1 for the NH_2 + NO reactions, which strongly affect the rates of H_2O production. Under our temperature and pressure conditions with S/V = 0.5 cm^{-1}, which is much smaller than either of the S/V ratios of the vessels used by Poole and Graven [28], the effect of the quartz reactor surface on the modeled values of α_1 is believed therefore to be negligible.

The values of α_1 determined in the present study appear to be insensitive to the lifetime or the magnitudes of the rate constants of the HN_2 radical assumed in the mechanism. Under the conditions employed ($T \geq 940$ K, $P = 700$ torr Ar), an increase or decrease in the rate constants assumed for the following reactions involving HN_2:

$$HN_2 + M = N_2 + H + M$$

$$k = 1.0 \times 10^{14}\, e^{-1510/T}\ \mathrm{cm^3\ mol^{-1}\ s^{-1}}$$

$$HN_2 + NO = N_2 + HNO$$

$$k = 7.2 \times 10^{13}\, T^{-0.4}\ \mathrm{cm^3\ mol^{-1}\ s^{-1}}$$

by two orders of magnitude separately resulted in no noticeable effect on the calculated concentration profiles of the reactants or products. In fact, the assumption of the direct production of the H atom in reaction (1), by using $NH_2 + NO = H + N_2 + OH$, resulted in no change in the modeled α_1 values. The same conclusion was reached in our recent mass spectrometric study of the $NH_2 + NO$ reaction [30].

The sharp increase in the value of α_1 with temperature is challenging theoretically. The prediction of the branching ratio and the effect of temperature on its value quantitatively requires not only the full knowledge of the intermediates and transition states for the isomerization reactions involving these intermediates (as has been acquired by Melius [7], Walch [8], and Durant [9]), but also a full understanding of the interaction potential for the reactants (NH_2 and NO) and the radical products (HN_2 and OH) for a reliable calculation of the capturing and fragmenting processes, respectively. To more reliably calculate the rate constants for reactions (1) and (2) at different temperatures, an elaborate statistical approach such as variational RRKM theory should be used in conjunction with the multiple-reaction intermediates involved.

Acknowledgment

The authors gratefully acknowledge the support of this work by the Office of Naval Research through contract no. N00014-89-J-1949 to Emory University under the direction of Dr. R. S. Miller.

REFERENCES

1. Lyon, R. K. U.S. Patent 3, 900, 554, *Int. J. Chem. Kinet.* 8:315–318 (1976).
2. Miller, J. A., Branch, M. C., and Kee, R. J., *Combust. Flame* 43:81–98 (1981).
3. Kinball-Linne, M. A. and Hanson, R. K., *Combust. Flame* 64:337–351 (1986).
4. Dean, A. M., Chou, M. S., and Stern, D., *Int. J. Chem. Kinet.* 16:633–653 (1984).
5. Vandooren, J., Bian, J., and van Tiggelen, P. J., *Combust. Flame* 98:402–410 (1994).
6. Brown, M. J. and Smith, D. B., *Twenty-Fifth Symposium (International) on Combustion,* The Combustion Institute, Pittsburgh, 1995, pp. 1011–1018.
7. Melius, C. F. and Binkley, J. S., *Twentieth Symposium (International) on Combustion,* The Combustion Institute, Pittsburgh, 1985, pp. 575–583.
8. Walch, S. P., *J. Chem. Phys.* 99:5295–5300 (1993).
9. Durant, J. L. Jr., *Proc. Seventeenth Combustion Contractors Meeting,* May 31–June 2, 1995, Lake Geneva, WI, pp. 84–87.
10. Diau, E. W. G., Yu, T., Wagner, M. A. G., and Lin, M. C., *J. Phys. Chem.* 98:4034–4042 (1994).
11. Atakan, B., Jacobs, A., Wahl, M., Weller, R., and Wolfrum, J., *Chem. Phys. Lett.* 155:609–613 (1989).
12. Stephens, J. W., Morter, C. L., Farhat, S. K., Glass, G. P., and Curl, R. F., *J. Phys. Chem.* 97:8944–8951 (1993).
13. Silver, J. A. and Kolb, C. E., *J. Phys. Chem.* 86:3240–3246 (1982).
14. Bulatov, V. P., Ioffe, A. A., Lozovsky, V. A., and Sarkisov, O. M., *Chem. Phys. Lett.* 161:141–146 (1989).
15. Glarborg, P., Dam-Johansen, K., Miller, J. A., Kee, R. J., and Coltrin, M. E., *Int. J. Chem. Kinet.* 26:421–436 (1994).
16. Andrews, D. G. R. and Gray, P., *Combust. Flame* 8:113–125 (1964).
17. He, Y., Kolby, E., Shumaker, P., and Lin, M. C., *Int. J. Chem. Kinet.* 21:1015–1027 (1989).
18. Aldridge, K. H., Liu, X., Lin, M. C., and Melius, C. F., *Int. J. Chem. Kinet.* 23:947–956 (1991).
19. He, Y., Liu, X., Lin, M. C., and Melius, C. F., *Int. J. Chem. Kinet.* 25:845–863 (1993).
20. Kee, R. J., Rupley, F. M., and Miller, J. A., "CHEMKIN-II: A Fortran Chemical Kinetics Package for the Analysis of Gas-Phase Chemical Kinetics," Sandia National Laboratories Report SAND89-8009, 1989.
21. Lutz, A. E., Kee, R. J., and Miller, J. A., "SENKIN: A Fortran Program for Predicting Homogeneous Gas-Phase Chemical Kinetics with Sensitivity Analysis," Sandia National Laboratories Report SAND87-8248, 1988.
22. Diau, E. W. G., Lin, M. C., He, Y., and Melius, C. F., *Prog. Energy Combust. Sci.* 21:1–23 (1995).
23. Hanson, R. K. and Salimian, S., "Survey of Rate Constants in the N/H/O System," in *Combustion Chemistry* (Gardiner, W. C. Jr., Ed.), Springer Verlag, New York, 1984, pp. 361–421.
24. Baulch, D. L., Cobos, C. J., Cox, R. A., Esser, C., Frank, P., Just, T., Kerr, J. A., Pilling, M. J., Troe, J., Walker, R. W., and Warnatz, J., *J. Phys. Chem. Ref. Data* 21:411–734 (1992).
25. Mebel, A. M., Diau, E. W. G., Lin, M. C., and Morokuma, K., *J. Phys. Chem.* 100:7517–7525 (1996).
26. Wu, C. H., Wang, H.-T., Lin, M. C., and Fifer, R. A., *J. Phys. Chem.* 94:3344–3347 (1990).
27. Diau, E. W., Halbgewachs, M. J., Smith, A. R., and Lin, M. C., *Int. J. Chem. Kinet.* 27:867–881 (1995).
28. Poole, D. R. and Graven, W. M., *J. Am. Chem. Soc.* 83:283–287 (1961).
29. Wise, H. and Frech, M. W., *J. Chem. Phys.* 22:1463–1464 (1954).
30. Park, J. and Lin, M. C., *J. Phys. Chem.* 100:3317–3319 (1996).
31. Lyon, R. K. and Hardy, J. E., *Ind. Eng. Chem. Fundam.* 25:19–24 (1986).
32. Lyon, R. K., *Div. Fuel Chem.* 32:433–443 (1987).
33. Hulgaard, T. and Dam-Johansen, K., *A. I. Chem. Eng. J.*, 39:1342–1354 (1993).

COMMENTS

W. Gardiner, Jr., University of Texas—Austin, USA. Could you please comment on the pressure dependence of the branching ratio of the NH_2 + NO reaction?

Author's Reply. On the basis of the results of our previous RRKM calculations [1], the overall rate constant for NH_2 + NO and those for the two product channels, N_2H + OH and N_2 + H_2O, are pressure-independent under $deNO_x$ conditions (1200 K $\leq$ T $\leq$ 1400 K, P $\leq$ 1 atm).

REFERENCE

1. Diau, E. W. G., Yu, T., Wagner, M. A., and Lin, M. C., *J. Phys. Chem.* 98:4034 (1994).

Twenty-Sixth Symposium (International) on Combustion/The Combustion Institute, 1996/pp. 2117–2124

A MODEL FOR PREDICTION OF SELECTIVE NONCATALYTIC REDUCTION OF NITROGEN OXIDES BY AMMONIA, UREA, AND CYANURIC ACID WITH MIXING LIMITATIONS IN THE PRESENCE OF CO

J. BROUWER AND M. P. HEAP
Reaction Engineering International
77 West, 200 South, Suite 210
Salt Lake City, UT 84101, USA

D. W. PERSHING AND P. J. SMITH
University of Utah
Salt Lake City, UT 84112, USA

A reduced chemical kinetic mechanism for the prediction of selective noncatalytic reduction (SNCR) chemistry has been developed and incorporated into a three-dimensional, CFD-based turbulent reacting flow model. The model can be used for prediction and investigation of thermal and mixing effects as well as the influence of CO on the SNCR process in practical systems. The model accurately describes the SNCR chemistry as indicated by comparisons of NO reduction efficiency, ammonia slip, and N_2O emissions with predictions using a complete chemical mechanism (70 species, 327 reactions) and experimental measurements from independent investigators. The reduced mechanism (6 species, 7 reactions) and individual rate constants are provided so that the mechanism could be incorporated into any CFD-based computer code.

The effects of thermal environment (injection temperature and quench rate), reactant ratios (initial NO and NH_3/NO), and reagent mixing on NO reduction by ammonia were investigated in the presence and absence of CO using a pilot-scale facility. Comparison with the coupled CFD/chemistry model predictions indicated good agreement, and both suggest that SNCR effectiveness is critically influenced by (1) finite-rate chemistry, (2) imperfect reagent dispersion, (3) mixing delay times, (4) local CO concentrations, and (5) nonisothermal temperature profile.

Introduction

Twenty years after Lyon's patent [1] defining the conditions for selective noncatalytic NO reduction to N_2 by ammonia (excess air conditions, 850–1100°C), there is continuing industrial interest in its use as a low-cost, effective, and retrofittable NO_x control technique. Current applications include utility boilers, waste incinerators, and other stationary combustion equipment; however, the NO_x removal efficiency is equipment specific and depends on the time available for contacting the selective reducing agent within the appropriate temperature range.

There has been considerable other laboratory and pilot-scale work performed to identify the controlling process parameters. Muzio et al. [2] first demonstrated the effectiveness of urea and other amines. A temperature range for selective reduction under fuel-rich conditions was also identified [3,4]. Perry and Siebers [5] found that cyanuric acid could be an effective, selective reducing agent, and Heap et al. [6] noted that these reactions could be catalyzed by stainless steel at temperatures as low as 600°C. Chen et al. [7] suggested a hybrid NO_x control scheme using selective reducing agents with combustion modifications like reburning. Lyon and Hardy [8] characterized the interactions with hydrogen and CO. Teixeira et al. [9] evaluated the effect of trace combustion species, and others have tested proprietary compounds for NO reduction in practical applications. Under well-mixed, plug flow conditions, selective noncatalytic reduction (SNCR) can provide excellent reduction efficiencies [8] (>90% at NH_3/NO ratios around 1.2), but such performance has not been achieved in practical applications where typical reduction efficiencies are often less than 50% for various boiler types and fuels [11–14].

SNCR is effective over a very narrow temperature range (or "window"). Reduction at higher temperatures is poor because the reducing agent itself oxidizes to NO. Below the optimum temperature, the selective reduction reactions are too slow, and unreacted reagent can be emitted (e.g., ammonia slip). In existing combustion systems, the spatial location of the optimum temperature window may vary with operating conditions or occur in regions of large

thermal gradients, e.g., convective heat exchangers. This places severe design constraints on the reagent injection system, which must disperse the reagent throughout the entire combustion product stream and mix the reagent with the NO while the gases are within the appropriate temperature window.

Although reactant mixing and injection location optimization have been evaluated [8,10,13], few studies have quantified the impact of mixing limitations on SNCR performance. Muzio et al. [15] defined the effects of residence time and identified three characteristic times: (1) mixing of the reducing reagent with combustion products, (2) reactive nitrogen compound release from the reagent (maybe an aqueous solution), and (3) chemical reaction times.

Improved computational tools are needed for SNCR design and optimization because of tightened emissions standards and the desire for lower cost control techniques in developing nations. Unfortunately, SNCR effectiveness at full scale is governed by rate-limiting processes, including turbulent mixing, heat transfer, spray droplet evaporation, devolatilization, and others. Since these processes are coupled, incorporation of fully detailed chemistry in a turbulent reacting flow computation is prohibitive, hence a reduced chemical kinetic mechanism is needed. The specific objectives of this study were to accomplish the following:

- Develop a reduced chemical mechanism and verify that it was capable of accurately predicting the chemical behavior of ammonia, urea, or cyanuric acid in SNCR.
- Incorporate the reduced mechanism into a comprehensive, three-dimensional, combustion model.
- Compare the resulting predictions with existing and new pilot-scale data quantifying interactions of reagent composition, injection temperature, thermal quench rate, mixing rates, and the impact of trace species such as CO to validate the model for practical applications.

Model Development

Mixing/Reacting Flow Code

The base computer models [16,17] (JASPER and GLACIER) are steady-state, two- and three-dimensional, computational-fluid-dynamics codes that fully couple reacting gases, solids, and liquids with turbulent mixing and radiative heat transfer. Coupling turbulence and heat transfer with reaction chemistry requires the number of chemical kinetic steps be small. These codes use partial equilibrium to compute local instantaneous chemistry from a set of reduced kinetic steps for slow reactions and minimize Gibbs free energy for all other species. Mean values for species concentrations, temperature, and density are obtained from computed probability density functions consistent with a κ-ε turbulence model. The discrete ordinates method is used for radiation and is also fully coupled with the turbulent fluid mechanics and reaction chemistry. This model can be distinguished from other CFD-based SNCR models [19,20] in that it fully couples and incorporates the chemistry into the CFD calculation. The resulting model is directly applicable to industrial equipment.

Fully Detailed Chemical Kinetic Model

The kinetic rates of Miller and Bowman [21], with recent literature modifications [22,23], were applied in SENKIN [24] to model the complete SNCR chemistry under quenched or isothermal conditions. The simplified SNCR mechanism and its rates were derived from this same database through sensitivity analyses and curve fitting, as described below. The reduced SNCR chemistry was incorporated into the CFD code to model the coupled turbulent mixing, radiation, and chemical kinetic problem.

Reduced Chemical Mechanism Development

Principle reaction pathways for NO reduction in the SNCR process have been suggested in the literature [21,25]. With cyanuric acid ($(HNCO)_3$) or iso-cyanic acid (HNCO), N_2O is a major intermediate species and product [26]. Ammonia injection results indicate very little N_2O formation [1,2]; NH_2 and HNO are the key intermediates. Sensitivity analyses applied to the complete chemical mechanism agreed with this view; the principle NO reduction pathways occur by reaction with NH_2 to form N_2 for ammonia and by reaction with NCO, forming N_2O as an intermediate for the cyanuric acid case. With urea, both pathways are important.

This understanding was used to develop a reduced mechanism for the homogeneous chemistry of the SNCR process with ammonia, urea, and cyanuric acid reagents (Fig. 1). Ostberg and Dam-Johansen developed a similar reduced kinetic model for ammonia only [18]. Vaporization and devolatilization for liquid or solid reagents is simulated by submodels described elsewhere [16,17]. The mechanism assumes instantaneous reagent break down into ammonia (NH_3) and iso-cyanic acid (HNCO) in the gas phase. Breakdown of urea into equal parts of NH_3 and HNCO and cyanuric acid into 3 moles of HNCO has been suggested in the literature [21,26]. However, to account for the HNCO that subsequently reacts along the ammonia pathway, the reduced mechanism assumes that 10% of the isocyanic acid is converted to ammonia (based on full chemistry calculations). This produces 1.1 moles of NH_3 and 0.9 moles of HNCO per mole of urea, and 0.3 moles

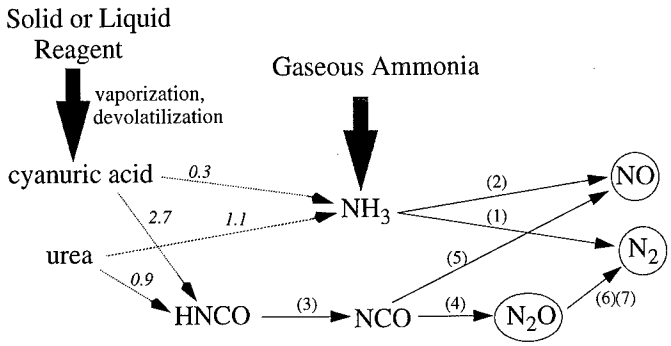

FIG. 1. Schematic of the reduced SNCR model (numbers in parentheses correspond to reaction numbers in Table 1).

of NH_3 and 2.7 moles of HNCO per mole of cyanuric acid.

The reduced SNCR mechanism consists of seven irreversible, finite-rate reactions describing the ammonia and iso-cyanic acid reactions, given in Table 1. The first two reactions describe the ammonia pathway. Reaction 1 dominates NO reduction at lower temperatures; reaction 2 produces NO from NH_3 and oxygen at higher temperatures. Rate parameters for these equations were determined through detailed sensitivity analyses performed with the full chemical kinetic mechanism for conditions spanning typical SNCR operation. Parameters that were varied included initial NO, reagent nitrogen-to-NO ratio, injection temperature, and quench rate in the SNCR zone. The rate parameters from the sensitivity analyses were fit to a modified Arrhenius form with a pre-exponential factor, temperature exponent, and activation energy.

Reactions 3 through 7 describe the iso-cyanic acid pathway. Reaction 3 describes the decomposition of HNCO to NCO, the reactant responsible for NO reduction in this pathway. This rate was determined to match the observed HNCO decomposition with the complete chemical mechanism. Reaction 4 is the desired NO reduction reaction producing N_2O; the complete mechanism indicated that this was the primary NO destruction pathway, accounting for more than 90% of the NO reduction over a wide range of conditions. The rate parameters for reactions 4 through 7 were all obtained from the literature[21] without modification. However, when applied in the reduced mechanism without radical chemistry, the rates for reactions 5 and 6 would not match the complete mechanism due to the assumption of equilibrium OH.

The mechanism presented above compares well with the fully detailed chemical kinetic mechanism as indicated in Fig. 2 for isothermal, homogeneous conditions at various temperatures. The reduced mechanism accurately predicts the decay of ammonia and iso-cyanic acid as well as the NO reduction and N_2O emissions of the fully detailed model. In general, reduced chemistry schemes do not work well over a wide range of conditions. However, since the applicable range of SNCR is limited to a temperature window, as described above, reduced chemical kinetic mechanisms for SNCR are not required for a broad range of conditions. As indicated in Fig. 2, the reduced mechanism accurately represents the fully detailed mechanism in the temperature range of interest.

Effects of CO

Several studies have shown the influence of CO on the selective reduction process [8–10], indicating

TABLE 1
Rate parameters for the reduced SNCR model

Reaction	A	b	E_a
1. $NH_3 + NO \rightarrow N_2 + H_2O + H$	$4.24E+08$	5.30	83,600
2. $NH_3 + O_2 \rightarrow NO + H_2O + H$	$3.500E+05$	7.65	125,300
3. $HNCO + M \rightarrow H + NCO + M$	$2.400E+14$	0.85	68,000
4. $NCO + NO \rightarrow N_2O + CO$	$1.000E+13$	0.00	−390
5. $NCO + OH \rightarrow NO + CO + H$	$1.000E+13$	0.00	0
6. $N_2O + OH \rightarrow N_2 + O_2 + H$	$2.000E+12$	0.00	10,000
7. $N_2O + M \rightarrow N_2 + O + M$	$6.900E+23$	−2.50	64,760

Units are A = cm–mol–s–K; E_a = cal/mol.

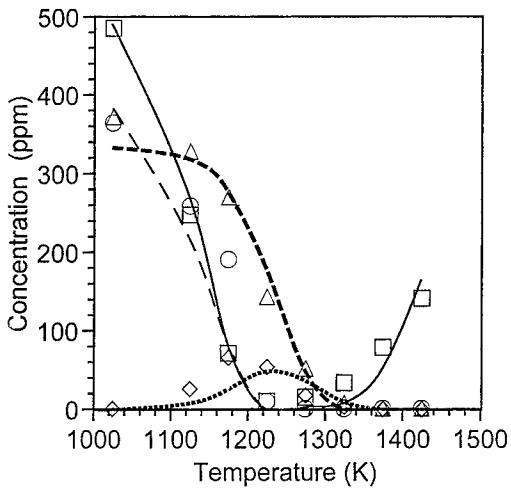

FIG. 2. Comparison of the reduced SNCR model to fully detailed chemical kinetic predictions for homogeneous, isothermal conditions at various temperatures. Symbols are fully detailed chemistry (□ = NO, ○ = NH_3, △ = HNCO, ◇ = N_2O), and lines are reduced chemistry (—— = NO, — — = NH_3, ---- = HNCO, ···· = N_2O).

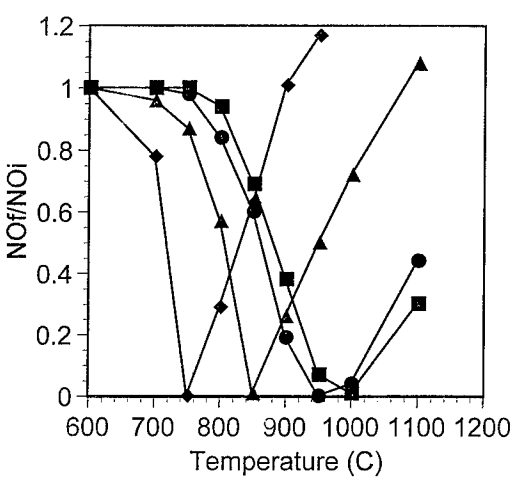

FIG. 3. Effect of CO on SNCR with ammonia for homogeneous conditions with NO_i = 500 ppm, NH_3/NO_i = 1.5, and a thermal quench rate of 260 K/s (■ = without CO, ● = 100 ppm CO, ▲ = 1000 ppm CO, ◆ = 5000 ppm CO).

that the presence of CO shifts the selectivity by increasing the rate of NH_2 formation and the rate of NH_3 oxidation to NO. Figure 3 shows results of detailed chemical kinetic calculations showing the effect of various CO levels on SNCR in a thermally quenched reactor. As the injected CO level increases, the optimal temperature for NO reduction shifts to lower temperatures due to enhanced chemical rates in the presence of CO. The shift in selectivity is accomplished by two mechanisms: increasing local temperatures and increasing net production of OH radical. The first effect is due to the exothermicity of the main CO burnout reaction, CO + OH $\rightarrow CO_2$ + H, while the second effect is due to chain-branching reactions that result from the H produced in this reaction.

The contribution of CO oxidation to the local temperature is accounted for in the model. Without including details of radical chemistry, an empirical adjustment to the rates must be included to account for the effect of CO on radical concentrations. This empirical adjustment was determined by detailed chemical kinetic calculations over a wide range of SNCR conditions (100 < NOi < 1000 ppm, 0.5 < N/NO_i < 3.0, and 0 K/s < quench rates < 2500 K/s) at specified temperatures. The empirical adjustment is applied in the form of a shift in the effective temperature to account for the radical chemistry effects of CO. For example, the rate of reaction 1 of Table 1 is calculated as follows:

$$k_1 = [NO][NH_3](4.24 \times 10^8)[T + S(CO)]^{5.3} \exp\left\{-\frac{83{,}600}{[T + S(CO)]}\right\} \quad (8)$$

where k_1 is the rate of NO + $NH_3 \Rightarrow N_2$, and $S(CO)$ is the shift in temperature required to achieve the same NO reduction and reagent decomposition compared to the case without CO. In the current model, the empirical adjustment, $S(CO)$, is given by

$$S(CO) = 17.5 \times \ln([CO]) - 68.0 \quad (9)$$

where $[CO]$ is the concentration of CO in ppm. This adjustment is applied to reactions 1–3, 5, and 6 of Table 1 since the rates of each of these reactions were developed to fit reactions or groups of reactions that involved OH radical chemistry. Reactions 4 and 7 are assumed to be unaffected by the presence of CO.

Verification of Model Predictions—Alternative Reagents

To verify the predictive capability of the reduced mechanism, model calculations were compared with experimental measurements from the literature for ammonia, cyanuric acid, and urea.

Ammonia Reagent

Figure 4 compares the reduced mechanism applied in JASPER to the premixed ammonia data of Lyon [27] and to calculations with the complete mechanism. Initial conditions for the data and model are 225 ppm NO, 1.23% O_2, 450 ppm NH_3, balance

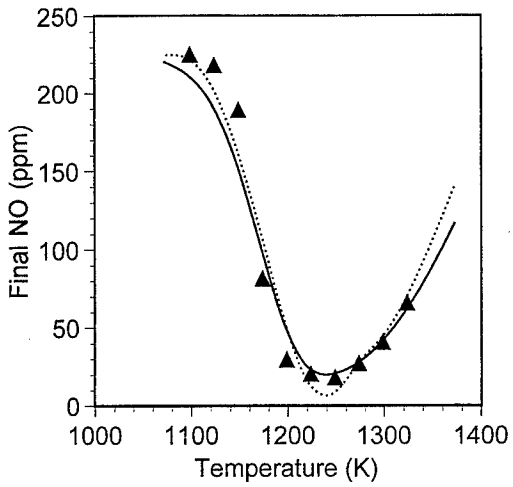

FIG. 4. Comparison of the reduced SNCR chemistry in JASPER with the full chemistry set and the data of Lyon for homogeneous conditions (···· = full chemistry, —— = JASPER calculations with reduced chemistry, ▲ = data of Lyon [27]).

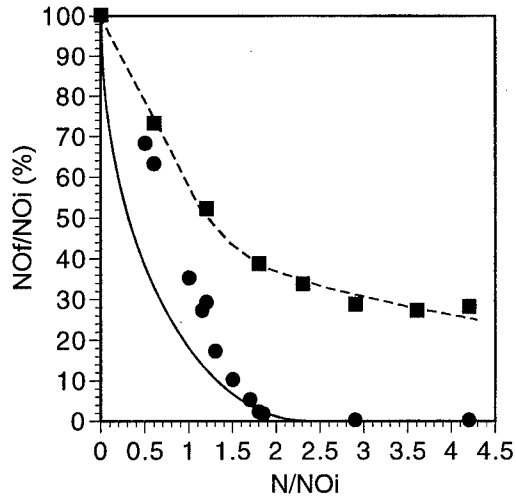

FIG. 5. Comparison of the reduced SNCR model to the data of Caton and Siebers [26] for homogeneous conditions with and without CO. Symbols are data (■ = with CO, ● = without CO), and lines are results from mixing and reduced chemistry model (----- = with CO, —— = without CO).

helium. The reduced mechanism predicts both the absolute reduction and the temperature dependence equally as well as the complete mechanism for this premixed condition.

Cyanuric Acid Reagent

Figure 5 compares predictions of the reduced mechanism to the data of Caton and Siebers [26] for cyanuric acid. The data were obtained in a 1.6-cm-ID quartz reactor that flowed simulated exhaust gases into which was injected vaporized cyanuric acid (at nominally 740 K) through an orifice. The mixing limitations were considered small for this experiment, so the model was applied to conditions of premixed reactants. Notice that the reduced model accurately predicts the NO reduction observed by Caton and Siebers for both cases with and without CO.

Urea Reagent

Application of the SNCR model for urea reagent was accomplished for the conditions of Teixeira et al. [9]. The data were obtained by injecting a 2.4 wt. % urea/water solution through an atomizer into the throat of a furnace with controlled injection temperature and a temperature profile that drops at a nominal rate of 250 K/s. Figure 6 presents the results obtained from modeling these experiments using the coupled turbulent-flow model (JASPER) and chemical kinetic mechanism of Table 1 for conditions of liquid urea/water injection into combustion products

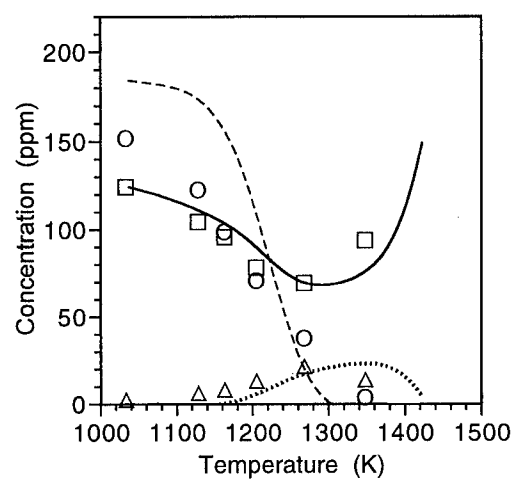

FIG. 6. Comparison of the measurements of Teixeira et al. [9] to predictions of the turbulent-reacting flow model with the simplified SNCR chemical model for urea injection. Symbols are data (□ = NO, ○ = NH_3, △ = N_2O), and lines are results from mixing and reduced chemistry model (—— = NO, ---- = NH_3, ···· = N_2O).

as in the experiment. The predictions show good agreement with data, except for a slight over prediction of NH_3 slip at lower temperatures and a slight shifting of the peak NO reduction and N_2O emission levels to higher temperatures. With mixing limitations and a quenched thermal profile, one would

expect the peak reduction to shift to higher temperatures than those predicted by homogeneous kinetics. The fully detailed chemistry applied to premixed, quenched (−250 K/s) conditions predicts a minimum NO level of 20 ppm at 1260 K, which severely overpredicts NO reduction compared to the experiment and the coupled model.

Practical System Constraints—Impacts of CO, Mixing, and Decaying Thermal Profiles

To provide SNCR performance data under typical industrial conditions (discrete jet injection into an actual flue gas with decreasing temperatures), the authors performed small pilot-scale experiments [28] in a 29 kW, refractory-lined furnace (16 cm in diameter by 7.3 m in length). Ammonia was injected through a water-cooled stainless steel injector located on the chamber axis at the beginning of the SNCR section (centerline axial injection). The ammonia was injected with nitrogen to allow variation of the reagent stream momentum and thus reagent/product mixing characteristics. The product stream entering the SNCR section contained 2.5% O_2, 8.4% CO_2, 16.7% H_2O, and 500 ppm NO in nitrogen. The injected ammonia level corresponded to 750 ppm with various amounts of nitrogen and CO injected with the reagent. NO was measured by chemiluminescence and ammonia slip by FTIR.

In practical systems, imperfect mixing and inadequate residence time at temperature can lead to emissions of the reagent, which is a major concern. Figure 7 presents a comparison of ammonia slip measurements and JASPER model predictions for a low quench rate (~200 K/s), and 1267 K injection temperature as a function of the amount of CO that was injected with the reagent. The model predicts the data well, except at low CO levels (where the measured data are believed to be low because the FTIR was not calibrated for such high NH_3 concentrations.) The model predictions suggest that the ammonia slip decreases at higher CO concentrations because the CO oxidation increases local radical concentrations that enhance ammonia reactions.

Figure 8 summarizes comprehensive measurements and predictions of SNCR effectiveness ($NO_{final}/NO_{initial}$) for 1267 K injection as a function of

1. local CO concentration (none vs. 750 ppm),
2. temperature decay rate at the injection point (200 vs. 1200 K/s), and
3. momentum ratio of ammonia jet/combustion product flow (0.5:1 to 7:1).

The turbulent reacting flow model with the reduced chemistry mechanism correctly predicts the four complex trends:

- SNCR performance is much worse in rapidly

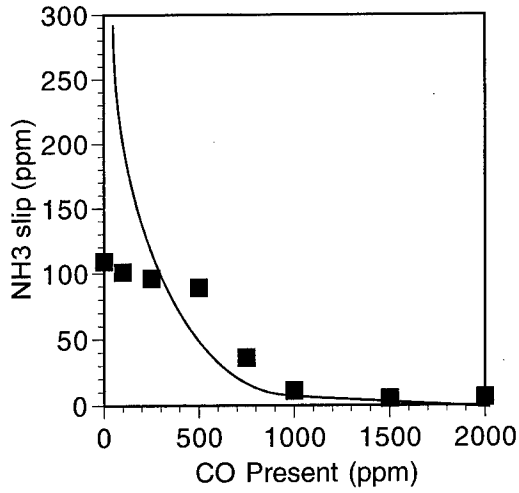

FIG. 7. Comparison of measurements and model predictions of ammonia slip for low quench rate (~200 K/s), an injection temperature of 1267 K, NO_i = 500 ppm, and NH_3/NO_i = 1.5 (■ = NH_3 slip data, —— = NH_3 slip model results).

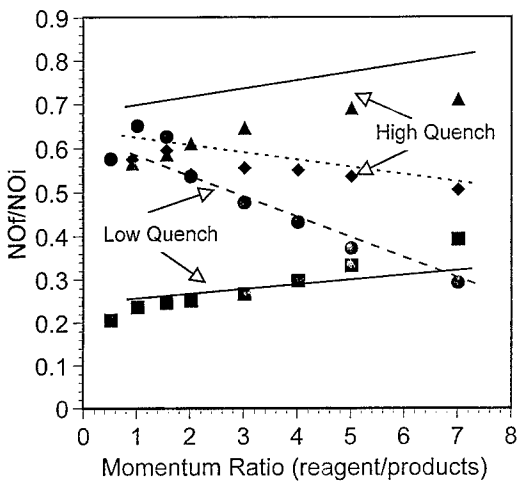

FIG. 8. Measurements and predictions of the effect of reagent jet/product stream momentum ratio on SNCR with and without CO at high and low quench rates. Symbols are data (■ = low quench with 0 ppm CO; ● = low quench with 750 ppm CO; ▲ = high quench with 0 ppm CO; ◆ = high quench with 750 ppm CO), and lines are results from mixing and reduced chemistry model (—— = low quench with 0 ppm CO; ---- = low quench with 750 ppm CO; —— = high quench with 0 ppm CO; ···· = high quench with 750 ppm CO).

quenched systems due to decreased reaction rates downstream of the injection point.

- Without CO, increasing the momentum ratio (reagent/bulk mixing rate) decreases SNCR effectiveness because the reactants pass through the temperature window before they can react.
- The presence of CO is beneficial under rapid quench conditions because it enhances the radical pool at the lower temperature conditions.
- The presence of CO is detrimental under slow quench conditions, particularly with slow mixing rates, because the radical pool is enhanced at higher temperatures, which favors ammonia oxidation to NO (see also Fig. 3).

Conclusions

A reduced mechanism to describe the finite-rate chemistry of SNCR reactions with ammonia, urea, or cyanuric acid injection has been developed and is suitable for incorporation into turbulent reacting flow models. The reduced mechanism has been validated for each of the three reagent types by comparison to a complete, detailed, chemical kinetic mechanism and experimental data from independent investigators. Incorporation of the reduced mechanism into existing CFD-based turbulent flow codes and subsequent application to experimental conditions proved the capabilities of the model for predicting NO reduction, ammonia slip, and N_2O emissions during SNCR. Comparison of model predictions for conditions of practical concern (which include mixing constraints and quenched thermal profiles in the presence of CO) indicate good agreement between model and data.

More importantly, both the model and the data demonstrate that SNCR effectiveness is critically influenced by practical constraints that reduce the reductions achieved in most full-scale systems. Optimization of SNCR must properly account for (1) finite-rate chemistry, (2) imperfect reagent dispersion, (3) mixing delay times, (4) local CO concentration, and (5) nonisothermal temperature profile. Hence, a fully coupled chemical reaction/turbulent mixing/radiant heat-transfer model is needed to help achieve maximum NO reduction efficiency.

Acknowledgments

Financial support for this program was provided by the U.S. EPA under Contract No. 68D20121. The authors would like to acknowledge the help of Dr. Adel Sarofim in the development of the SNCR mixing model and Messrs. Dana Overacker, Dale Inkley, Dave Wagner, and Dave Warren for the construction and operation of the test facility.

REFERENCES

1. Lyon, R. K., U.S. Patent No. 3,900,554 (1975).
2. Muzio, L. J., Arand, J. K., and Teixeira, D. P., *Sixteenth Symposium (International) on Combustion,* The Combustion Institute, Pittsburgh, 1977, p. 199.
3. Arand, J. K., U.S. Patent No. 4,325,924 (1982).
4. Brogan, T. R., U.S. Patent No. 4,335,084 (1982).
5. Perry, R. A. and Siebers, D. L., *Nature* 324:657 (1986).
6. Heap, M. P., Chen, S. L., McCarthy, J. M., and Pershing, D. W., *Nature* 335:691 (1988).
7. Chen, S. L., Lyon, R. K., and Seeker, W. R., *AFRC Fall International Symposium on NO_x Control, Waste Incineration and Oxygen Enriched Combustion,* Paper #32, San Francisco, CA, 1990.
8. Lyon, R. K. and Hardy, J. E., *Ind. Eng. Chem. Fundam.* 25:19 (1986).
9. Teixeira, D. P., Muzio, L. J., and Montgomery, T. A., *AFRC/JFRC International Conference on Environmental Control of Combustion Processes,* Honolulu, HI, 1991.
10. Chen, S. L., Ho, L., Maly, P. M., Payne, R., and Seeker, W. R., *Joint EPRI/EPA Symposium on Stationary NO_x Control,* Bal Harbor, FL, 1993.
11. Jodal, M., Nielsen, C., Hulgaard, T., and Dam-Johansen, K., *Twenty-Third Symposium (International) on Combustion,* The Combustion Institute, Pittsburgh, 1990, pp. 237–243.
12. Jodal, M., Lauridsen, T. L., and Dam-Johansen, K., Environment. Progr. 11(4):296–301 (1990).
13. Teixeira, D. P., Lin, C. J., Muzio, L. M., Jones, D. G., and Okazki, *Joint EPRI/EPA Symposium on Stationary NO_x Control,* Bal Harbor, FL, 1993.
14. Shore, D. E., Buening, H. J., Prodan, Teetz, R. D., Muzio, L. M., Quartucy, G. C., Sun, W. H., Carmignani, P. G., Stallings, J. W., and O'Sullivan, R. C., *Joint EPRI/EPA Symposium on Stationary NO_x Control,* Bal Harbor, FL, 1993.
15. Muzio, L. J., Montgomery, T. A., Quartucy, G. C., and Texeira, D. P., *Joint EPRI/EPA Symposium on Stationary Combustion NO_x Control,* Bal Harbor, FL, 1993.
16. Smith, P. J. and Eddings, E. G., *User Guide for JASPER 1.3,* Reaction Engineering International, 1993.
17. Smith, P. J., Adams, B. R., and Eddings, E. G., *User Guide for GLACIER 2.5,* Reaction Engineering International, 1995.
18. Ostberg, M. and Dam-Johansen, K., *Chem. Eng. Sci.* 49(12):1897–1904 (1994).
19. Sun, W. H., Michels, W. F., Stamatakis, P., Comparato, J. R., and Hofmann, J. E., *AFRC Fall International Symposium,* Cambridge, MA, 1992.
20. Sun, W. H., Hoffman, J. E., and Pachaly, R., Post combustion NO_x control with Urea: Theory and practice, *Seventh Annual International Pittsburgh Coal Conference,* Pittsburgh, PA, 1990.
21. Miller, J. A. and Bowman, C. T., Mechanism and modeling of nitrogen chemistry in combustion, *Prog. Energy Combust. Sci.* 15:287–338 (1989).
22. Miller, J. A. and Melius, C. F., *Twenty-First*

Symposium (International) on Combustion, The Combustion Institute, Pittsburgh, 1986, pp. 919–927.
23. Dean, A. J., Hanson, R. K., and Bowman, C. T., *J. Phys. Chem.* 95:3180–3189 (1991).
24. Lutz, A. E., Kee, R. J., and Miller, J. A., *SENKIN: A FORTRAN Program for Predicting Homogeneous Gas Phase Chemical Kinetics with Sensitivity Analysis*, Sandia National Laboratories, Albuquerque, NM, Sandia Report SAND87-8248, 1987.
25. Kramlich, J. C., Cole, J. C., McCarthy, J., Lanier, S. W., and McSorely, J. A., *Combust. Flame* 77:375 (1989).
26. Caton, J. A. and Siebers, D. L., *Combust. Sci. Technol.* 65:277–293 (1989).
27. Lyon, R. K., 194th Annual ACS Meeting, *Div. Fuel Chem.* 32:433 (1987).
28. Heap, M. P., Brouwer, J., and Pershing, D. W., *Prototype Demonstration of the Augmented Selective Reduction Process*, Final Report, EPA Contract No. 68D20121, July, 1995.

COMMENTS

Kim Dam-Johansen, Technical University of Denmark, Denmark. Have you compared your model to the work performed at the Technical University of Denmark, i.e. The Empirical Kinetic Model of Duo et al. [1] and The Empirical Mixing Model of Ostberg and Dam-Johansen [2]?

REFERENCES

1. Duo et al., *Can. J. Chem. Eng.* 709 (1992).
2. Ostberg and Dam-Johansen, *Chem. Eng. Sci.* 49 (1994); 50 (1995).

Author's Reply. We have compared our model to that developed at the Technical University of Denmark for the limited cases of homogeneous conditions and ammonia reagent. The temperature window and ammonia reductions obtained with each of these models is comparable to that obtained with fully detailed chemical kinetic mechanisms as shown in Figure 4. Further comparisons for the urea and cyanuric acid reagent are not possible since the kinetic model of Duo et al. is for ammonia only.

The empirical mixing model of Oestberg and Dam-Johansen accounts for micromixing limitations using a droplet diffusion model which is coupled to the reduced chemistry for SNCR with ammonia. They assume that macromixing is instantaneous. The model presented here uses an assumed probability density function approach to model turbulent fluctuations and solves the macromixing problem through solution of the Favre averaged Navier-Stokes equations with a k-ε closure.

•

Vladimir Zamansky, Energy and Environmental Research Corporation, USA. You demonstrated by diagram of the reduced mechanism. Could you show the real reactions which you took into account and, in particular, comment on how you can reach balance for N, O, and C atoms?

Author's Reply. The reactions which are included in the mechanism are presented in Table 1. Each of these reactions is balanced.

•

William R. Anderson, U.S. Army Research Laboratory, USA. I noticed in your figure of the mechanism pathways for the additive urea that the initial step was not exactly 1:1 decomposition into NH_3 and HNCO, which seems mildly surprising. Why is this the case?

Author's Reply. The breakdown of urea into 1.1 parts NH_3 and 0.9 parts HNCO, as well as the breakdown of cyanuric acid into 2.7 parts HNCO and 0.3 parts NH_3 is explained in the section of the paper entitled Reduced Chemical Kinetic Mechanism. The split was determined by detailed chemical kinetic calculations which indicated a fraction of the HNCO which reacted along the NH_3 pathway ranging from about 6% to over 12% for a wide range of SNCR conditions. Instead of including another reaction to account for this fraction, 10 percent of the HNCO is assumed to reaction along the NH_3 path.

Twenty-Sixth Symposium (International) on Combustion/The Combustion Institute, 1996/pp. 2125–2132

GAS PHASE REACTIONS OF HYDROGEN PEROXIDE AND HYDROGEN PEROXIDE/METHANOL MIXTURES WITH AIR POLLUTANTS

VLADIMIR M. ZAMANSKY, LOC HO, PETER M. MALY AND W. RANDALL SEEKER
Energy and Environmental Research Corporation
18 Mason, Irvine, CA 92618, USA

Hydrogen peroxide and its mixtures with methanol are capable of removing multiple air pollutants, NO, SO_3, and carbon-containing compounds from combustion-generated flue gas. Chemical kinetic calculations and experimental data demonstrate that hydrogen peroxide can be injected into flue gas at temperatures of 700–1100 K to convert unreactive NO and corrosive SO_3 to NO_2 and SO_2. Nitrogen dioxide is much more reactive than NO and can be removed downstream simultaneously with SO_2 by wet or dry scrubbing systems that are currently required for SO_2 control. Hydrogen peroxide also promotes the oxidation of organic compounds to CO and CO_2 and the oxidation of CO to CO_2. The H_2O_2 molecules dissociate into two OH radicals, and four chain reactions of different types are involved in the pollutant emission removal process with the following main reactions:

NO-to-NO_2 conversion: $OH + H_2O_2 \rightarrow H_2O + HO_2$; $HO_2 + NO \rightarrow NO_2 + OH$
SO_3-to-SO_2 conversion: $OH + H_2O_2 \rightarrow H_2O + HO_2$; $HO_2 + SO_3 \rightarrow HSO_3 + O_2$; $HSO_3 + M \rightarrow SO_2 + OH + M$
RH oxidation: $OH + RH \rightarrow H_2O + R$; $R + O_2 \rightarrow$ oxidation
CO oxidation: $OH + CO \rightarrow CO_2 + H$; $H + O_2 \rightarrow OH + O$

Methanol is also capable of converting NO and SO_3 to NO_2 and SO_2, respectively. However, injection of methanol generates CO emissions. Therefore, H_2O_2/CH_3OH mixtures might be injected into combustion flue gas with the amount of CH_3OH controlled to satisfy CO requirements and with the H_2O_2 concentration controlled to obtain target NO conversion. Experimental data describing chemical reactions of H_2O_2 and H_2O_2/CH_3OH mixtures with NO, SO_3, CO, CH_4, C_6H_6, and CH_2Cl_2 were obtained in a 300-kW combustor firing natural gas. Up to 98, 85, and 80% removal efficiencies were achieved for NO, SO_3, and CH_4, respectively. The results are explained by kinetic modeling.

Introduction

Along with traditional catalytic and noncatalytic methods for postcombustion removal of NO_x and SO_x, another air pollution control strategy is currently under development: NO-to-NO_2 and SO_3-to-SO_2 conversion followed by simultaneous scrubbing of NO_2 and SO_2 from combustion flue gas. Lyon et al. [1] described a method of NO-to-NO_2 and SO_3-to-SO_2 conversion by injection of methanol into flue gas at temperatures 900–1300 K. In this method, methanol forms hydroxyl radicals that can react with CH_3OH molecules: $OH + CH_3OH \rightarrow H_2O + CH_2OH$. The CH_2OH radicals formed are oxidized by oxygen into CH_2O and HO_2: $CH_2OH + O_2 \rightarrow CH_2O + HO_2$, and the HO_2 radicals can react rapidly with NO to form NO_2. $NO + HO_2 \rightarrow NO_2 + OH$. In pilot-scale experiments [2], 87% NO-to-NO_2 conversion was achieved by injecting methanol. Unfortunately, a problem with using methanol is the formation of CO as a by-product. Each CH_3OH molecule forms one molecule of formaldehyde that is oxidized to CO, and, at relatively low methanol injection temperatures, CO is not oxidized to CO_2. Another method for NO-to-NO_2 conversion is addition of yellow phosphorus in wet scrubber systems [3]. Although a high level of NO oxidation was achieved, yellow phosphorus is a dangerous substance, and this can prevent its commercial application for NO control.

Nitrogen dioxide formed from NO in these processes is much more reactive and soluble in water than NO, and can be more easily removed by wet or dry scrubbing processes [4,5] for simultaneous SO_2/NO_2 control.

Zamansky et al. [6] have recently performed experiments in a flow system in which hydrogen peroxide was added to simulated flue gas at temperatures of 700–1100 K and was capable of converting NO to NO_2 and also removing other combustion-generated pollutants. The existence of the chemical reaction between NO and H_2O_2 had been proven earlier by Azuhata et al. [7] in a flow system with long residence times of ~12 s, which is not applicable to air pollution control. Most of the experiments [6] were performed in a 2.5-cm-i.d. quartz

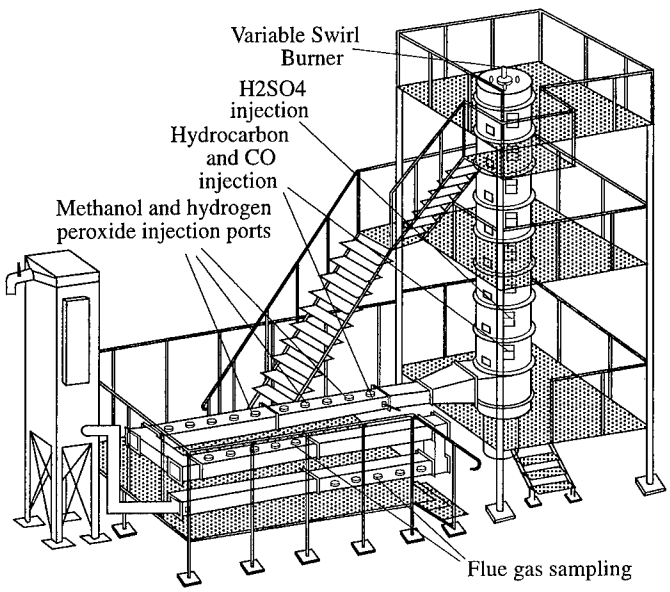

FIG. 1. Boiler simulator facility (BSF) schematic.

flow reactor with residence times of 0.4–1.6 s, but the results were affected by heterogeneous H_2O_2 decomposition.

This paper presents experimental study of H_2O_2 and H_2O_2/CH_3OH reactions with NO, SO_3, CO, and toxic organic compounds in a 300-kW combustor in which the effect of H_2O_2 heterogeneous decomposition was negligible. A range of residence times from 0.5 to 3.2 was examined. The results are explained by kinetic modeling. The H_2O_2 molecules dissociate into two OH radicals, and four chain reactions are involved in the pollutant emission removal process.

Experimental

Experiments were conducted at a 300-kW boiler simulator facility (BSF) firing natural gas. The BSF (Fig. 1) is a downfired combustor consisting of a vertical radiant furnace and a horizontal convective pass. The furnace is a refractory-lined cylinder with a 56-cm inside diameter and 6.7-m height. It is equipped with numerous ports to allow introduction of sampling and injection probes. The furnace is also configured with movable water-cooled panels to allow control of residence time–temperature history. The convective pass is refractory lined and square in geometry, having inside dimensions of 20 × 20 cm and length of 14.2 m. It is configured with movable air-cooled tubes for heat extraction, simulating the economizer and superheater sections of a full-scale boiler. The BSF is equipped with a variable swirl distributed mixing burner, a baghouse, a continuous emissions monitoring (CEM) system, and a personal computer–based data acquisition system. The CEM system includes a chemiluminescent NO/NO_x analyzer, infrared CO and CO_2 analyzers, a fluorescence SO_2 analyzer, a flame ionization total hydrocarbon analyzer, and a paramagnetic O_2 analyzer. Furnace temperatures are measured using a suction pyrometer. Convective pass temperatures are measured by thermocouples.

Solutions of hydrogen peroxide and/or methanol (15% in water) were injected by a pressure nozzle into the convective pass at different locations. The rate of temperature decrease in the reaction zone (600–1100 K) was about 188 K/s. In most experiments, flue gas was sampled downstream at a temperature of about 500 K and analyzed by the CEM system. Preliminary tests indicated that stainless steel could promote reconversion of NO_2 to NO. To minimize stainless steel surface area of the convective pass, all cooling coils and heat exchanger surfaces were coated with high-temperature ceramic boron nitride paint. The sampling system consisted of a water-cooled quartz probe, heated sample line with filter, and vacuum pump.

The performance of SO_3-to-SO_2 conversion was examined while injecting sulfuric acid into the high-temperature furnace zone. At high temperatures, sulfuric acid is converted to SO_3 and H_2O. However, if the temperature is too high, the SO_3 is reduced to SO_2. Preliminary experiments were conducted by injecting sulfuric acid at different temperatures with downstream measurements of SO_2 concentration. When H_2SO_4 was injected into the upper furnace zone at temperatures of 1700 K and higher, recovery of SO_2 was 86%. The remaining 14% sulfur was attributed to H_2SO_4 or SO_3 capture by furnace walls.

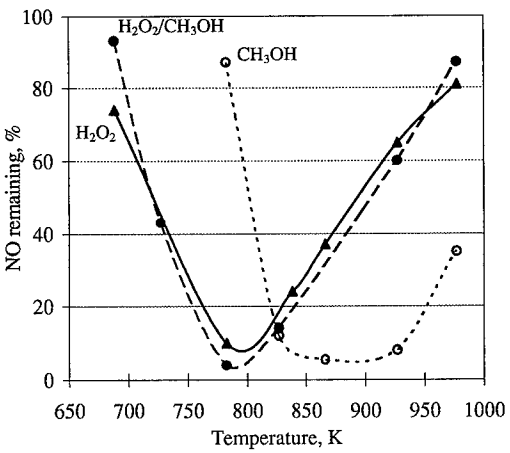

FIG. 2. Temperature windows of NO removal by injection of H_2O_2, CH_3OH, and their mixture of 1:1 molar ratio. $[NO]_i$ = 200 ppm, additive/$[NO]_i$ = 1.5, $[O_2]$ = 3.8%.

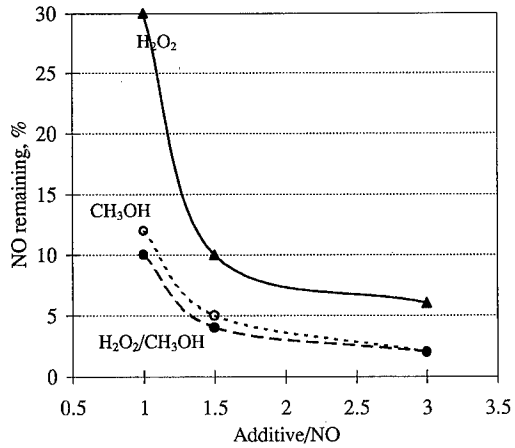

FIG. 4. Effect of the additive/NO molar ratio on NO removal at optimum injection temperatures for injection of H_2O_2, CH_3OH, and their mixture of 1:1 molar ratio. $[NO]_i$ = 200 ppm, $[O_2]$ = 3.8%.

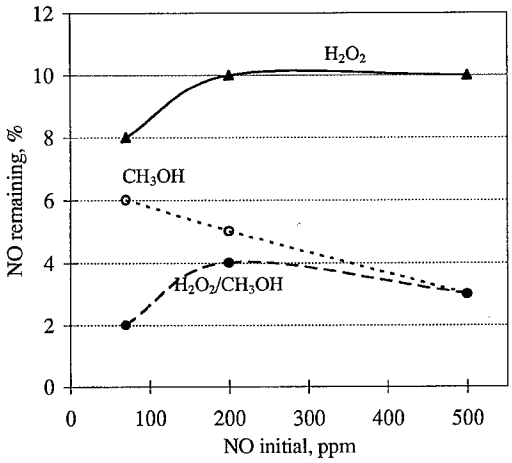

FIG. 3. Influence of initial NO concentration on NO removal at optimum injection temperatures for injection of H_2O_2, CH_3OH, and their mixture of 1:1 molar ratio. Additive/$[NO]_i$ = 1.5, $[O_2]$ = 3.8%.

When H_2SO_4 was injected at 1144 K, recovery of SO_2 was near zero since H_2SO_4 was converted to SO_3. In the SO_3-to-SO_2 conversion tests, H_2SO_4 was injected at 1144 K, and a 14% SO_3 loss in the system was assumed.

Results

In most tests, three additives were used: hydrogen peroxide, methanol, and their mixture at 1:1 molar ratio. Mixtures of H_2O_2 and CH_3OH of other composition show similar performance, and some results with different H_2O_2/CH_3OH mixtures were presented elsewhere [6]. All graphs present percentage of remaining air pollutants defined as a ratio of pollutant exhaust level to its initial concentration, for instance $[NO]_{ex}/[NO]_i 100\%$.

NO-to-NO_2 Conversion

The three additives were tested as a function of injection temperature at three initial NO levels of 70, 200, and 500 ppm. Maximum NO removal performance was achieved at 750–820 K for injection of H_2O_2 and the H_2O_2/CH_3OH mixture and at 850–930 K for CH_3OH injection. Figure 2 shows results at $[NO]_i$ = 200 ppm. From 90 to 96% NO-to-NO_2 conversion was achieved with an additive/NO molar ratio (MR) of 1.5. Maximum performance, about 96%, was observed with the H_2O_2/CH_3OH mixture: NO level was reduced from 200 to 8 ppm. Methanol gave slightly greater maximum NO conversion than H_2O_2. Figure 3 demonstrates that the NO removal efficiency for the three additives depends only slightly on initial NO concentration. Figure 4 shows the NO control efficiency for the three additives at MR = 1.0–3.0. Conversion increased with increasing additive/NO_i ratio. About 70 and 90% NO were removed after injection of H_2O_2 and the H_2O_2/CH_3OH mixture at MR = 1.0, respectively. At MR = 3.0, from 94 to more than 98% NO removal was achieved by injection of the three additives.

Oxygen concentration in flue gas affected the NO control performance as demonstrated in Fig. 5. By variation of air/fuel ratio, oxygen level was varied from 0.48 to 8%. Initial NO concentration was 200 ppm, and the experiments were performed at optimum temperatures for each additive and at

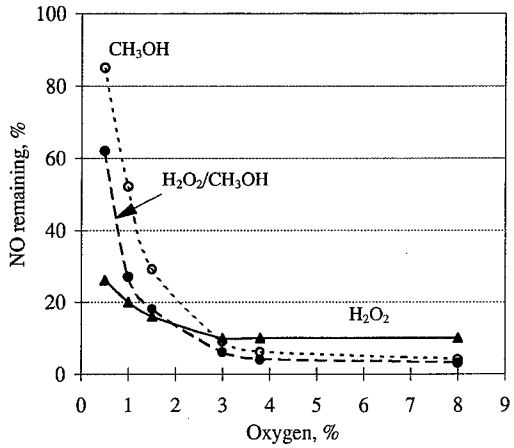

FIG. 5. Effect of oxygen concentration on NO removal at optimum injection temperatures for injection of H_2O_2, CH_3OH, and their mixture of 1:1 molar ratio. $[NO]_i$ = 200 ppm, additive/$[NO]_i$ = 1.5.

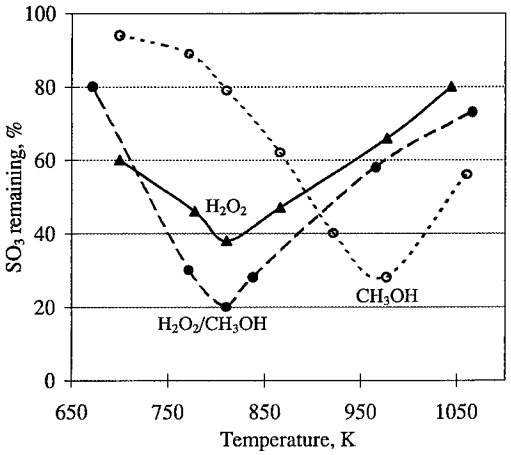

FIG. 6. Temperature windows of SO_3 removal by injection of H_2O_2, CH_3OH and their mixture of 1:1 molar ratio. $[NO]_i$ = 200 ppm, $[SO_3]_i$ = 100 ppm, additive/$[NO + SO_3]_i$ = 1.5, $[O_2]$ = 3.8%.

MR = 1.5. At oxygen concentrations between 3 and 8%, there were no significant differences in NO removal. Performance decreased at O_2 levels below 3%. Below about 1% oxygen, NO removal by methanol injection was not effective. Hydrogen peroxide injection showed a relatively small difference in NO control for the different O_2 levels. The H_2O_2/CH_3OH mixture had intermediate behavior.

It was noticed that a small amount of NO_2 is reconverted to NO, which reduces effective NO control performance. Reconversion efficiency was defined by NO/NO_x measurements at two locations of

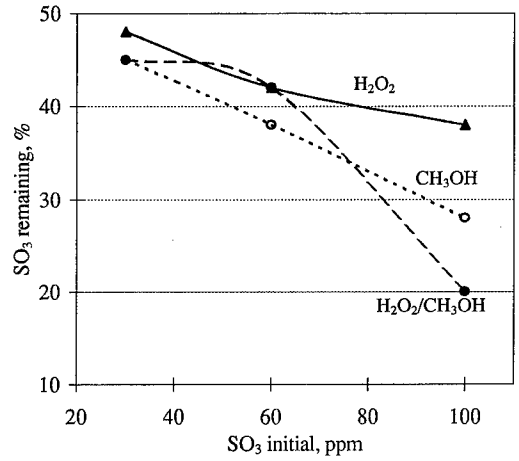

FIG. 7. Influence of initial SO_3 concentration on SO_3 removal at optimum injection temperatures for injection of H_2O_2, CH_3OH, and their mixture of 1:1 molar ratio. Additive/$[NO + SO_3]_i$ = 1.5, $[O_2]$ = 3.8%.

the sampling probe. The sampling was performed at 755 and 500 K, corresponding to residence times of 0.5–0.8 s and 1.9–2.2 s, respectively. These reconversion measurements demonstrated that the NO control performance was decreased–but not substantially–by about 2–3% for all additives. This small effect could be explained by heterogeneous NO_2 reduction on the walls of the convective pass.

SO_3-to-SO_2 Conversion

Measurements of SO_3-to-SO_2 conversion were conducted for three initial SO_3 levels in flue gas (30, 60, and 100 ppm) at $[NO]_i$ = 200 ppm, $[O_2]$ = 3.8%, and additive/([NO] + $[SO_3]$) = MR = 1.5 and 3.0. Sulfuric acid was injected and SO_3 removal was quantified by measuring the SO_2 concentrations formed from SO_3. No sulfur dioxide was formed when additives were absent in the flue gas. Maximum SO_3-to-SO_2 conversion was achieved at about 810 K for H_2O_2 and H_2O_2/CH_3OH injection and about 980 K in the presence of methanol. Thus, optimum temperature for SO_3 control is slightly shifted to higher temperatures in comparison with NO removal. Figure 6 presents the results of the experiments for injection of the three additives into flue gas containing 100 ppm SO_3 at MR = 1.5. Under optimum injection conditions, the additives provided about 60–80% SO_3 control. Figure 7 demonstrates SO_3 control for the three additives (MR = 1.5) at optimum injection temperatures and at SO_3 initial levels of 30, 60, and 100 ppm. This range of SO_3 is of practical importance for firing oil and Orimulsion in utility boilers. Removal efficiency is higher at higher SO_3 concentrations. At MR = 3.0

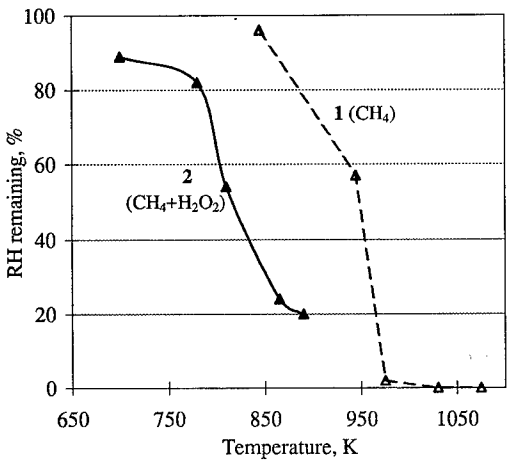

FIG. 8. Effect of H_2O_2 injection on CH_4 removal. $[NO]_i$ = 200 ppm, $[CH_4]_i$ = 45 ppm, $[H_2O_2]/[NO + CH_4]_i$ = 1.5, $[O_2]$ = 3.8%. Curve 1: injection of CH_4 at different temperatures without H_2O_2; curve 2: injection of H_2O_2 at different temperatures with CH_4 injected at 895 K.

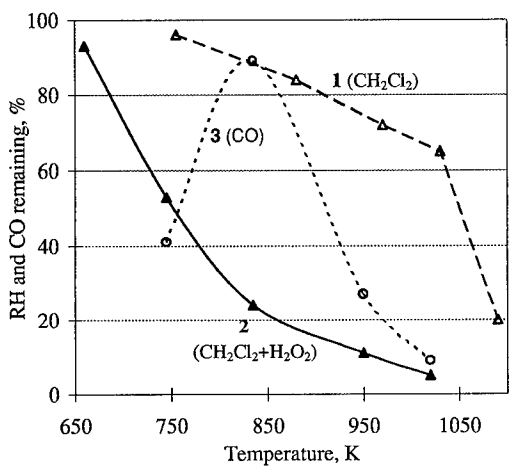

FIG. 9. Effect of H_2O_2 injection on CH_2Cl_2 removal. $[NO]_i$ = 200 ppm, $[CH_2Cl_2]_i$ = 37 ppm, $[H_2O_2]/[NO + CH_2Cl_2]_i$ = 1.5, $[O_2]$ = 3.8%. Curve 1: injection of CH_2Cl_2 at different temperatures without H_2O_2; curve 2: injection of H_2O_2 at different temperatures with CH_2Cl_2 injected at 1020 K; curve 3: formation of CO during injection of H_2O_2.

and $[SO_3]_i$ = 100 ppm, SO_3 removal efficiencies of 83, 74, and 89% were achieved by injecting H_2O_2, CH_3OH, and the H_2O_2/CH_3OH mixture, respectively. The performance of H_2O_2 is significantly improved at higher H_2O_2 levels, but the CH_3OH performance depends minimally on its concentration. The H_2O_2/CH_3OH mixture provided 55–89% SO_3

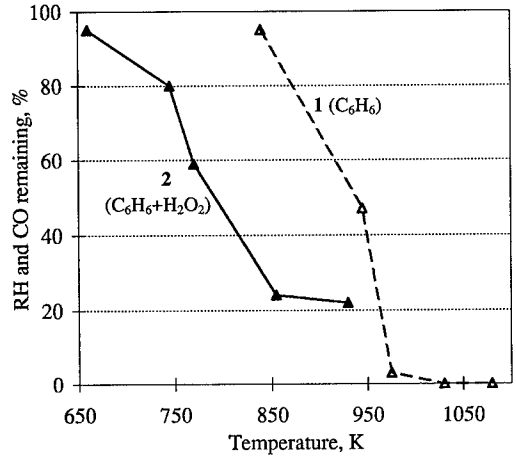

FIG. 10. Effect of H_2O_2 injection on C_6H_6 removal. $[NO]_i$ = 200 ppm, $[C_6H_6]_i$ = 17 ppm, $[H_2O_2]/[NO + C_6H_6]_i$ = 1.5, $[O_2]$ = 3.8%. Curve 1: injection of C_6H_6 at different temperatures without H_2O_2; curve 2: injection of H_2O_2 at different temperatures with C_6H_6 injected at 930 K.

control under different conditions with a higher performance and a wider temperature window than those for individual components.

Oxidation of CO

The goal of this set of experiments was to show the improvement of the CO oxidation in the presence of H_2O_2. Hydrogen peroxide injected at 866 K was capable of removing about 20% CO. The exhaust CO concentration was 25 ppm. For comparison, injection of 300 ppm of the H_2O_2/CH_3OH mixture and pure CH_3OH at optimum temperatures caused formation of about 125 and 300 ppm CO, respectively. Thus, the presence of H_2O_2 in the H_2O_2/CH_3OH mixture, injected at 866 K, decreases by 15–20% the CO amounts formed by CH_3OH injection.

Oxidation of Organic Compounds

Interaction of three organic compounds (methane, dichloromethane, and benzene) with H_2O_2 was studied by injection of the reagents at different temperatures and at $[NO]_i$ = 200 ppm, $[O_2]$ = 3.8%, and $[H_2O_2]/[NO + RH]$ = 1.5. To evaluate the effect of H_2O_2, it was assumed that each C-containing fragment has equal sensitivity in the flame ionization detector. In the presence of H_2O_2, the temperature limit for removal of the organics is shifted to lower temperatures by 100–150 K for CH_4 and C_6H_6 and by 200–300 K for CH_2Cl_2. This is demonstrated in Figs. 8–10, which present experimental data on

TABLE 1
Additional reactions included in both mechanisms. The rate constants in the form $k_i = AT^n \exp(E/RT)$ are from the NIST chemical kinetics database (1994).

Reaction	A (cm/mol/s)	n	E, cal
$SO_2 + O + M = SO_3 + M$	0.145E + 17	0.00	2,000
$SO_2 + OH + M = HSO_3 + M$	2.120E + 25	−3.30	0
$HSO_3 + O_2 = HO_2 + SO_3$	0.783E + 12	0.00	656
$O + SO_3 = SO_2 + O_2$	1.320E + 12	0.00	6,100
$NO_2 + SO_2 = NO + SO_3$	6.310E + 12	0.00	27,000
$NO_2 + OH + M = HNO_3 + M$	5.800E + 32	−5.40	2,186
$CH_3 + O_2 = CH_3O_2$	9.020E + 58	−15.00	17,027
$CH_3O_2 + HO_2 = CH_3O_2H + O_2$	4.630E + 10	0.00	−2,583
$CH_3O_2 + CH_4 = CH_3O_2H + CH_3$	1.810E + 11	0.00	18,481
$CH_3O_2 + CH_3 = CH_3O + CH_3O$	2.410E + 13	0.00	0
$CH_3O_2 + O = CH_3O + O_2$	3.610E + 13	0.00	0
$CH_3O_2 + OH = CH_3OH + O_2$	6.030E + 13	0.00	0
$CH_3O_2 + H = CH_3O + OH$	9.640E + 13	0.00	0
$CH_3O_2 + CH_3OH = CH_3O_2H + CH_2OH$	1.810E + 12	0.00	13,712
$CH_3O_2 + NO = CH_3O + NO_2$	2.530E + 12	0.00	−358
$CH_3O_2 + C_2H_6 = CH_3O_2H + C_2H_5$	2.950E + 11	0.00	14,944
$CH_3O_2 + CH_2O = CH_3O_2H + HCO$	1.990E + 12	0.00	11,665
$CH_3O_2 + H_2O_2 = CH_3O_2H + HO_2$	2.410E + 12	0.00	9,936
$CH_3O_2H = CH_3O + OH$	4.000E + 15	0.00	42,924
$CH_3O_2H + OH = CH_3O_2 + H_2O$	7.230E + 11	0.00	−258

injection of CH_4, CH_2Cl_2, and C_6H_6, respectively, at different temperatures with and without H_2O_2. Curve 1 in Fig. 8 shows remaining concentrations of organic products at different CH_4 injection temperatures without H_2O_2 injection. In these tests, methane reacted with available oxygen at temperatures higher than 970 K. Curve 2 was obtained by CH_4 injection at 895 K with variation of the H_2O_2 injection temperature. About 80–90% of CH_4 removed was converted to CO and the rest to CO_2. Thus, injection of H_2O_2 can cause CO formation from CH_4 if it is present in flue gas in the temperature range of 800–950 K. The efficiency of CH_4 oxidation was 40–80%.

Dichloromethane injected without H_2O_2 at different temperatures (Fig. 9, curve 1) was decomposed at temperatures higher than 1030 K. However, when CH_2Cl_2 was injected at 1020 K and H_2O_2 was added at 750–1020 K, about 50–90% CH_2Cl_2 was removed (Fig. 9, curve 2). Curve 3 in Fig. 9 shows that from 30 to 90% CO is formed from CH_2Cl_2 while the rest of CH_2Cl_2 is converted to CO_2.

Similar tests on the reaction between C_6H_6 and H_2O_2 (Fig. 10) also demonstrate promotion of C_6H_6 oxidation in the presence of H_2O_2. In these tests, C_6H_6 was first injected without H_2O_2 (curve 1) and then injected at 930 K with variation of H_2O_2 injection temperature (curve 2). Near 100%, CO was formed from C_6H_6.

Kinetic Modeling

The Chemkin-2 kinetic code [8] and two sets of reaction mechanisms were used for kinetic modeling. The first mechanism was presented by Miller and Bowman [9]. The second mechanism was a combined scheme consisting of the GRI-Mech 1.1 [10] and the N-chemistry mechanism by Glarborg et al. [11]. Twenty reactions of SO_2/SO_3, HNO_3, CH_4O_2, and CH_4O_2H were added to both mechanisms (Table 1). Detailed results of kinetic modeling are presented in the poster session [12]. The objective of the modeling work was to determine the most important elementary reactions responsible for air pollutant removal and to provide insight into the controlling factors of the process. Both models demonstrate similar results that qualitatively describe all substantial features of H_2O_2 reactions with NO, SO_3, CO, and CH_4. The GRI-Glarborg mechanism includes CH_3OH species and can model reactions of methanol. Modeling was performed without variation of rate constants, and, in general, it gave satisfactory qualitative description of the process, though it showed some quantitative problems. For instance, calculated temperature windows of NO removal show higher maximum level of NO control and a shift to higher temperatures by about 50–70 K in comparison with experiments. Additionally, modeling does not show a decrease in NO control with H_2O_2 injection at low oxygen concentrations,

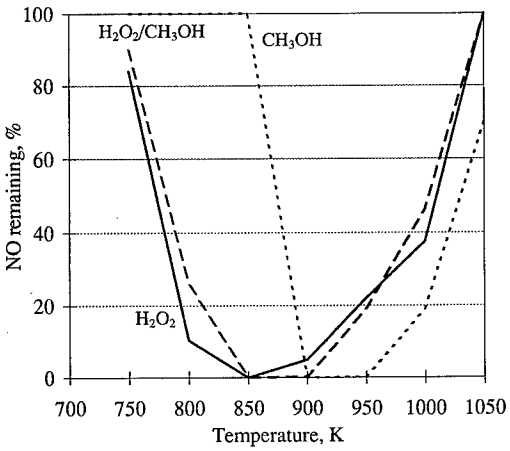

FIG. 11. Kinetic modeling of NO removal by injection of H_2O_2, CH_3OH, and their mixture of 1:1 molar ratio. Conditions of Fig. 2.

and modeling predicts a wider temperature window for SO_3 control than was found experimentally. These discrepancies demonstrate the potential need for model improvement. As an example, Fig. 11 shows application of the GRI-Glarborg mechanism to modeling the efficiency of NO removal under the same conditions as those in experiments presented in Fig. 2.

Modeling predicted some homogeneous NO_2-to-NO reconversion at higher temperatures. This reconversion had higher efficiency for CH_3OH than for H_2O_2 injection. Main reactions responsible for NO-to-NO_2 conversion and reconversion can be seen from sensitivity analysis. NO sensitivity coefficients were calculated for conditions of Fig. 2 by using SENKIN code [13]. Sensitivity calculations demonstrate the main elementary reactions that are presented in the following section and define NO and NO_2 concentrations during injection of H_2O_2 and H_2O_2/CH_3OH in flue gas.

Discussion and Conclusions

The results of this study demonstrate homogeneous gas-phase interaction of air pollutants with H_2O_2 and H_2O_2/CH_3OH mixtures in combustion gases at high temperatures. In the presence of H_2O_2, the total amount of OH radicals increases because of dissociation: $H_2O_2 + M \rightarrow 2OH + M$. The following four chain reactions are responsible mainly for air pollutant removal.

NO removal: $OH + H_2O_2 \rightarrow H_2O + HO_2$
$HO_2 + NO \rightarrow NO_2 + OH$
SO_3 removal: $OH + H_2O_2 \rightarrow H_2O + HO_2$
$HO_2 + SO_3 \rightarrow HSO_3 + O_2$
$HSO_3 + M \rightarrow SO_2 + OH + M$
RH oxidation: $OH + RH \rightarrow H_2O + R$
$R + O_2 \rightarrow$ oxidation
CO oxidation: $OH + CO \rightarrow CO_2 + H$
$H + O_2 \rightarrow OH + O$.

The reaction $OH + HO_2 \rightarrow H_2O + O_2$ removes the active species and is the main chain termination process.

Hydrogen peroxide also enhances the oxidation of heptane and isopropanol in dilute air mixtures at $T = 910–1073$ K [14]. One can conclude that injection of H_2O_2 is a general method for removing NO and SO_3 and for conversion of toxic organic compounds into CO and CO_2 in flue gas.

Injection of H_2O_2 and H_2O_2/CH_3OH mixtures can be used for tail-end NO removal in combination with other upstream NO control methods, as, for example, in a hybrid process [2] that includes reburning, urea injection, methanol injection, and SO_2/NO_2 scrubbing. Assuming 90% NO-to-NO_2 conversion by H_2O_2 injection and taking into account pilot-scale results [2] in other steps, the total process will reduce NO_x emissions by 96–98%.

The efficiency of methanol in reactions with NO and SO_3 is about the same or higher than that of H_2O_2. However, the efficiency of H_2O_2/CH_3OH mixtures is higher than that of each component individually because of easier formation of OH radicals from H_2O_2. As soon as OH radicals are formed, they can initiate chain reactions interacting with both H_2O_2 and CH_3OH. The presence of H_2O_2 in mixtures with CH_3OH is capable of (1) promoting the efficiency of NO and SO_3 removal, (2) shifting the temperature windows for NO and SO_3 control to lower temperatures, and (3) decreasing the amount of CO formed from CH_3OH. If CO emissions are considered the primary drawback of CH_3OH injection, one strategy might be to add as much CH_3OH as possible within CO limits and then add enough H_2O_2 to obtain target NO and SO_3 conversion.

Acknowledgment

This work was supported by the U.S. Department of Energy under Grant No. DE-FG05-93ER81538.

REFERENCES

1. Lyon, R. K., Cole, J. A., Kramlich, J. C., and Chen, S. L., *Combust. Flame* 81:30–39 (1990).
2. Pont, J. N., Evans, A. B., England, G. C., Lyon, R. K., and Seeker, W. R., *Environ. Prog.* 12:140–145 (1993).
3. Chang, S. G. and Lee, G. C., *Environ. Prog.* 11:66–73 (1992).
4. Zamansky, V. M., Lyon, R. K., Evans, A. B., Pont, J. N., Seeker, W. R., and Schmidt, C. E., 1993 SO_2 Control

Symposium, EPRI/EPA/DOE, Boston, 1993. Vol. 3, Session 7.
5. O'Dowd, W. J., Markussen, J. M., Pennline, H. W., and Resnik, K. P., *Ind. Engineer. Chem. Res.* 33:2749–2756 (1994).
6. Zamansky, V. M., Ho, L., Maly, P., and Seeker, W. R., *Third International Conference on Combustion Technologies for a Clean Environment*, Vol. 2, Lisbon, Portugal, 1995, pp. 26.4(24–32).
7. Azuhata, S., Akimoto, H., and Hishimura, Y., *AIChE J.* 28:7–11 (1982).
8. Kee, R. J., Rupley, F. M., and Miller, J. A., Sandia National Laboratories Report No. SAND89-8009, 1989.
9. Miller, J. A. and Bowman, C. T., *Prog. Energy Combust. Sci.* 15:287–338 (1989).
10. GRI-Mech Ver. 1.1 at CRVAX.SRI.COM released 3/15/94.
11. Glarborg, P., Dam-Johansen, K., and Kristensen, P. G., Report to GRI, Contract No. 5091-260-2126, 1993.
12. Zamansky, V. M., Presented as Work-in-Progress Poster at Twenty-Sixth International Symposium, Naples, Italy, 1996, Poster 264.
13. Lutz, A. E., Kee, R. J., and Miller, J. A., Sandia National Laboratories Report No. SAND87-8248, 1987.
14. Cooper, C. D., Clausen, C. A., Tomlin, D., Hewett, M., and Martinez, A., *J. Hazard Mat.* 27:273–285 (1991).

COMMENTS

A. E. Jacob Akanetuk, Stanford University, USA. Values of fractional NO remaining have been reported, the assumption being that all depleted NO is converted to NO_2. Were NO_2 values measured; if so, what was the extent of closure on N species balance?

Author's Reply. A standard chemiluminescent NO/NO_x analyzer was used in this study. The analyzer makes it possible to measure separately NO and $NO_x = NO + NO_2$. Most measurements were performed in the NO mode of the analyzer, and it was assumed that the decrease of the NO concentration after H_2O_2/CH_3OH injection is explained by NO-to-NO_2 oxidation. The NO_2 concentration was measured in several experiments as the difference between NO and NO_x modes of the analyzer. These measurements shown about 20–30% lower NO_2 concentrations than was dictated by the N-species balance. However, estimations show that this amount of NO_2 can be removed by water in the sample preparation line. In the past, we measured the NO-to-NO_2 conversion due to methanol injection using a more precise method for NO_2 monitoring. We first measured the NO concentration and then passed the gas mixture containing $NO + NO_2$ through a NO_2-to-NO converter and measured the resulting NO concentration in the same NO mode of the analyzer. The NO_2 concentration measured as the difference between these two measurements was in balance on N-species within a few percentage points. The mechanisms of CH_3OH and H_2O_2 reactions with NO are similar. Therefore, we believe that most of NO is converted to NO_2. Kinetic modeling predicts that under optimum conditions about 1% of the initial NO is converted to HNO_2 and HNO_3 and the rest of the NO is oxidized to NO_2.

Twenty-Sixth Symposium (International) on Combustion/The Combustion Institute, 1996/pp. 2133–2138

EVIDENCE FOR A NEW NO PRODUCTION MECHANISM IN FLAMES

JOEL E. HARRINGTON, GREGORY P. SMITH, PAMELA A. BERG, ALISON R. NOBLE, JAY B. JEFFRIES AND DAVID R. CROSLEY

Molecular Physics Laboratory
SRI International
Menlo Park, CA 94025, USA

Bozzelli and Dean [1] recently proposed a new mechanism for NO production via the reaction O + NNH ⇔ NH + NO that predicts formation of significant amounts of NO in flames burning in air. To test the predictions of this new NNH mechanism, we designed low-pressure flame experiments to minimize the amount of NO made through other, more established mechanisms and to yield measurable amounts of NO through NNH chemistry. We used laser-induced fluorescence (LIF) to measure NO in 38 and 78 torr, $\Phi = 1.5$, hydrogen/air flames. NO is observed in both flames at ~0.3 ppm, consistent with model predictions using the Bozzelli and Dean mechanism. We also measured OH and temperature profiles and tested thoroughly for potential contamination sources. Though agreement of experiment and model is imperfect, the NNH mechanism provides a viable explanation for the presence of ppm levels of NO in these flames. The NNH mechanism should therefore be included in NO_x combustion models and may be a significant route to NO in many flames.

Introduction

Recent environmental regulation of NO_x emissions has increased emphasis on understanding the chemical kinetics that control NO_x production. Bozzelli and Dean [1] have proposed a new mechanism for NO production that predicts formation of significant amounts of NO in flames burning in air. This mechanism could pose limits on the lowest NO emission levels achievable. They argue that the reaction O + NNH ⇔ NH + NO can be an important route to NO formation under specific conditions. In their model, significant quantities of NNH must form from the reaction H + N_2 ⇔ NNH. In the Miller–Bowman mechanism [2], which is often used for calculating nitrogen chemistry, the rate given for the reverse NNH dissociation reaction is too slow, $\sim 10^4$ s^{-1}, to account for significant concentrations of NNH through microscopic reversibility. However, Bozzelli and Dean estimate a tunneling-enhanced NNH dissociation rate that is five orders of magnitude higher than the Miller–Bowman rate. Furthermore, they assert that NNH concentrations are thermodynamically controlled in a 1-atm methane/air flame if the NNH dissociation rate is above 1×10^7 s^{-1}: even if their proposed rate were two orders of magnitude too high, the derived NNH concentrations would be unaffected. If Bozzelli and Dean's kinetic arguments are correct, the O + NNH route to NO should be added to any combustion chemistry model that is intended to predict NO_x emissions. To test the predictions of this new NNH mechanism, we designed low-pressure flame experiments to minimize the amount of NO made through other, more established mechanisms and to yield measurable amounts of NO through NNH chemistry.

The presence of NNH in flames was first proposed as a product of the NO_x destruction reaction of NH_2 with NO [3]. NNH is metastable with respect to N_2 + H by about 6 kcal/mol, and has a 6 kcal/mol barrier to dissociation according to calculations [4,5]. A rapid quantum mechanical tunneling rate constant was computed for dissociation, and thus also for formation by microscopic reversibility [5]. The second part of the Dean and Bozzelli mechanism, the O + NNH reaction path to form NO + NH, is supported by recent shock tube measurements on a fast reverse reaction of NO and NH where the products were not detected [6]; Bozzelli and Dean argue that the observation of a positive activation energy for the NH + NO reaction strongly suggests that, of the possible products, the endothermic product channel that forms O and NNH is the most likely. Hence, if the shock tube products are O and NNH, the rate constant for O + NNH ⇒ NH + NO should also be fast.

Cool, rich, low-pressure, premixed hydrogen/air flames satisfy the experimental design requirements. We used laser-induced fluorescence (LIF) to measure NO and OH as well as temperature profiles in 38- and 78-torr premixed hydrogen/air flames. NO is observed in both flames at ~0.3 ppm, consistent with the Bozzelli and Dean mechanism. Barring contamination, hydrogen flames produce no prompt [7] NO, which requires a source of CH radicals.

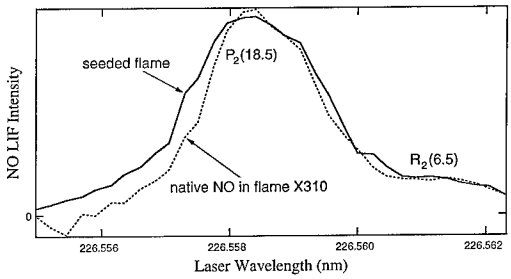

FIG. 1. Nitric oxide measured by LIF of the NO A-X (0-0) P_2 (18.5) and R_2 (6.5) lines. The native NO signal (dotted line) has been scaled up by a factor of 310 to overlay with the seeded NO spectrum (solid line). The difference in line shape between the two traces does not reproduce on duplicate measurements.

Thermal [8] NO is insignificant at temperatures below 1700 K [9] and certainly not a consideration at the ~1200 K peak temperatures attained in our low-pressure flames. Rich, low-pressure flames minimize the potential for the reaction $O + N_2 + M \Leftrightarrow N_2O + M$ [10], where the N_2O may subsequently react with O or H to form NO in trace concentrations. Rich flames also provide many H atoms for the $H + N_2$ reaction, step one of the Bozzelli and Dean mechanism. There are no odd nitrogen compounds (e.g., NO_2, NH_3) present in the fuel or oxidizer at levels that could form significant NO.

Experimental

Two premixed hydrogen/air flames were burned, with total flow rates of 6 L/min of hydrogen and air at an equivalence ratio of $\Phi = 1.5$. An argon shroud surrounds the flames on a 6-cm-diameter McKenna burner with a shroud flow rate of 1.2 L/min. These flows create stable flames at pressures of 38 and 78 torr; an exhaust gas butterfly valve regulates the chamber pressure through a feedback controller. Propane/air flames were lit at atmospheric pressure and the fuel was gradually switched to hydrogen as the chamber pumped down. Great care was taken to ensure that there was no remaining hydrocarbon in the hydrogen fuel during the NO measurements.

The burner translates vertically to allow collection of spatially resolved fluorescence profiles, while the laser beam and optics remain fixed in the chamber. LIF signals are collected at 90° from the laser beam axis. For the OH temperature profiles, a high-intensity Bausch & Lomb monochromator was set for trapezoidal bandpass giving uniform transmission over 20 nm centered at 309 nm. For NO fluorescence, the monochromator was replaced with a UG-5 filter in front of a solar-blind R431 photomultiplier. Photomultiplier output was averaged over a short, 15-ns gate in an SRS boxcar integrator to avoid quenching corrections. A high-precision laser energy meter measures the laser power simultaneously for signal normalization.

LIF excitation scans in the OH *A-X* (0-0) band provide temperature profiles as a function of distance above the burner. These are needed as input for the flame model and in the conversion of the LIF data to concentration profiles. Kiton Red dye in an excimer-pumped dye laser produces light near 614 nm, which is scanned and frequency doubled to excite OH in a short section of *R*-branch lines between 306.5 and 307.1 nm. Scans are typically averaged over 40 shots per point, with laser power maintained at less than 0.5 μJ per pulse in a 0.1-mm-diameter beam cross section to avoid optical saturation. This short OH excitation scan is an excellent spectroscopic thermometer for premixed flames [11]. OH concentration profiles were obtained by exciting the A-X (0-0) $R_2(6)$ transition and translating the burner. Profiles were corrected for Boltzmann fraction using the temperature profiles.

Nitric oxide was measured by LIF of the NO A-X (0-0) $P_2(18.5)$ and $R_2(6.5)$ lines in a very short excitation scan near 226.5 nm, shown in Fig. 1. Because signal levels were so low, these lines were chosen as a distinctive signature of the presence of NO within a small scan range; precise measurements required as many as 1000 shots averaged per wavelength step of the dye laser, so the practical scanning range was limited. The LIF signal was then calibrated by adding NO (in He buffer) at 0.015% of the total flow and measuring relative signal strengths within the flame. After calibration runs, the system was purged with nitrogen for at least two days until the background NO in the chamber was undetectable. Measurements of native flame NO were then repeated and showed no change.

Impurity Checks

As reported later, NO mole fractions are less than 1 ppm in the hydrogen/air flames. Because the native NO levels are low, measurements would be especially sensitive to any contamination in the chamber or impurities in the reactant gases. To rule out nonnative sources of NO, an extensive set of tests and precautions were taken.

The most obvious possible nonflame NO source is NO present as a contaminant in the reactant gases or the chamber. The results presented here make a convincing case for a source of NO within the flame: no NO is detected in the cold gas flows in the early part of the flame. In addition, all three gases introduced into the chamber, hydrogen, synthetic air, and argon, were analyzed by GC-MS and showed no detectable NO (<0.1 ppm), NH_3, NO_2, or N_2O. Frequency modulation infrared absorption measurements on the synthetic air show <0.1 ppm N_2O. Identical flame NO levels were measured using

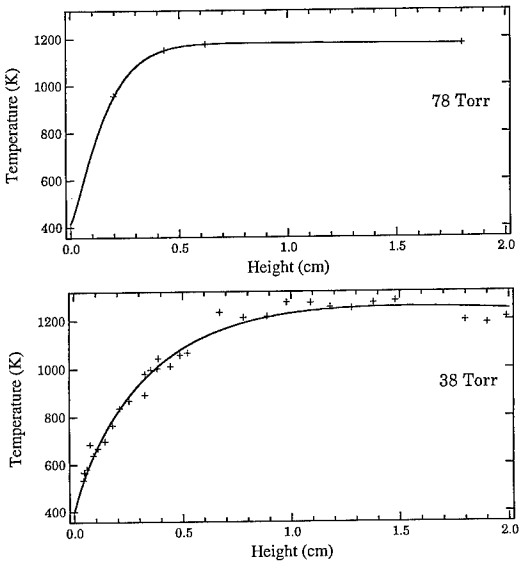

FIG. 2. Temperature profiles for the 38- and 78-torr flames as a function of distance above the burner. Temperatures are a Boltzmann fit to LIF intensities from OH A-X (0-0) *R*-branch lines. The smooth line through the data points is a fit to an empirical function.

standard purity gases and using ultrahigh purity hydrogen and argon (99.999%, <1 ppm hydrocarbon) and automotive standard "Zero" air with <0.1 ppm NO. NO could not be detected in the feed gas at operating pressure with the flame off. Burning a flame with Ar replacing the nitrogen removed all NO signal. The chamber had zero detectable background NO when evacuated and purged for two days.

Hydrocarbon impurities in the reactant gases might produce NO in the flame through the prompt mechanism. Formation of prompt NO would exhibit a flame profile similar to the experimental profiles, so hydrocarbon impurities are of concern. Analyses of the bottled reactant gases showed no detectable hydrocarbons (<1 ppm). Because the flames were lit with propane, residual propane in the gas lines is another conceivable source of hydrocarbon contamination. The flames burned for at least an hour before any measurements were made, and NO levels were identical after 1 h and after 8 h of burning. If propane were slowly diffusing through the gas plumbing, some change in the NO level would be expected over 8 h. Because prompt NO requires the presence of CH, the flame was probed for excited-state OH chemiluminescent emission (produced by the reaction of O_2 with CH), CH excited state emission, and CH LIF. No CH was detected. In addition, the 1200-K peak temperatures in these flames would suppress the prompt mechanism. Calculations suggest that several ppm of CH, a clearly detectable amount, would be required to produce the observed tenths of ppm of NO. To produce several ppm of CH, hydrocarbon contamination would have to be several percent of the feed gases. Similar arguments eliminate concerns about possible pump oil contamination of the burner chamber.

Model

The flames were modeled using the Sandia laminar flame code Premix [12], with the measured temperature values input into the calculations, multicomponent diffusion option, and recombination of hydrogen atoms at the burner surface. Measured total flow rates and temperature profiles constrain the calculations. The H—O—N thermodynamics and kinetics from the GRI-Mech 2.11 mechanism [13] were employed to describe the chemistry. All carbon-containing species were removed from the calculation. This mechanism has 69 reactions involving 18 species, with all accepted known mechanisms for NO formation, and the proposed Bozzelli and Dean kinetics for NO production from NNH [1]. Radial expansion of the flame was estimated based on CCD camera line images of seeded NO in the flame at three heights. The ratio of intensities in line images of A-X O_{12} (19.5) and O_{12} (1.5) gives a radial temperature profile. The integrated intensity in the line image was corrected for Boltzmann fraction and density, and the diameter of the flame was estimated as the diameter of a top-hat profile with the same integrated intensity. The area of the 38-torr flame appears to increase 10% over the burner exit cross section 3 mm into the flame and shows a 40% expansion 4 cm above the burner. The 78-torr flame expands similarly.

Experimental and Model Results

Excitation scans as shown in Fig. 1, taken in the burned gases of the 38-torr flame, are unambiguous evidence that NO is present in our hydrogen/air flames. Using the calibration procedure described earlier, we measure 0.3 and 0.4 ppm NO in the burned gases of the 38- and 78-torr flames, respectively. Because the calibration NO is introduced into the flame and measured at the same position in the flame as the native NO, the ratio of native to seeded NO is simply the ratio of the fluorescence signals scaled by the calculated dilution of the seeded NO in the flame as calculated by the model. In replicate measurements, absolute mole fractions are reproducible to within about 25%.

Temperature profiles for the two flames are shown in Fig. 2. The smooth line through the data points is a fit to an empirical function that is used for input into the model calculations, partition function corrections, and concentration-to-mole fraction conver-

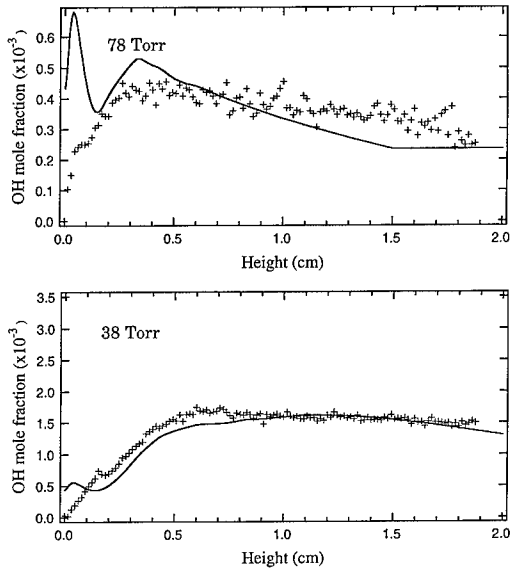

FIG. 3. OH vertical profiles for the 38- and 78-torr flames. Signal from the A-X (0-0) R_2 (6) transition is corrected for Boltzmann fraction and converted to mole fraction using the experimental temperature profiles. Solid lines are the results of the model calculations; a single scaling factor has been applied to both experimental profiles to best match the calculated OH mole fraction in the burned gases.

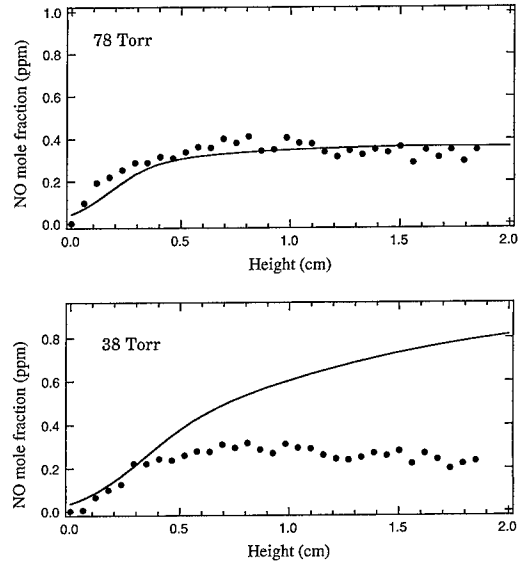

FIG. 4. NO vertical profiles for the 38- and 78-torr flames. LIF signal from the NO A-X (0-0) P_2 (18.5) transition is corrected for Boltzmann fraction and converted to mole fraction using the experimental temperature profiles. All the flames show a clear onset of NO within the flame. Solid lines are the results of the model calculations.

sions of the OH and NO species profiles. The OH spectroscopic temperatures presented are reproducible to within 40 K.

OH height profiles (Fig. 3) were taken using a single rotational transition, corrected for partition function and converted to mole fraction using the temperature profiles. The solid lines in Fig. 3 are the results of the model calculations incorporating radial expansion of the flowing gases. The experimental data have been scaled using a single constant for both flames to match the burned gas OH mole fractions from the calculations. The relative burned gas OH levels agree nicely with the calculations, but there are obvious problems with the agreement for OH low in the 78-torr flame.

NO height profiles (dots in Fig. 4) are corrected for partition function and converted to mole fraction in similar fashion. The burned gas calibrations described previously place the profiles on an absolute scale. All the flames show a clear onset of NO within the flame, further eliminating concerns about spurious NO signal from contamination. Solid lines in Fig. 4 are the model predictions, incorporating radial expansion of the flame. The peak mole fractions and profile agree for the 78-torr flame. The amount of NO predicted for the 38-torr flame is within the expected error of the measurement. The 38-torr model NO profile continues to increase in the burned gases past where the experimental profile levels off.

Model Results

We modeled both low-pressure flames with the Sandia flame code, the GRI-Mech 2.11 mechanism, and the imposed experimental temperature profiles. NO levels of 1.0 and 0.4 ppm are predicted for the burned gas regions of the 38- and 78-torr flames, respectively (see Fig. 4). This NO is almost entirely due to the Bozzelli and Dean NNH mechanism in the model; when it is removed, the predicted level of NO in the 38-torr flame from the thermal and N_2O mechanisms is only 0.7 ppb. The observed NO is within the likely error limits of the critical rate constants of the NNH mechanism–NNH formation which is thermodynamically controlled, and NO production from the O + NNH reaction. A change of 1.5 kcal/mol in the NNH heat of formation, whose value currently relies solely on quantum mechanical computations, will alter NO concentrations by a factor of 2.

The 78-torr experimental OH profile is in significant disagreement with the model prediction near the burner, whereas the 38-torr results agree. While this discrepancy is not understood, the OH production in the model low in the flame is only sensitive to reactions of H atoms with HO_2 and O_2 and the

TABLE 1
NO sensitivity coefficients at 2 cm, 38 Torr, $\Phi = 1.5$, H_2-air flame $S = d[NO]/[NO]/dk/k$

Reaction	S	Reaction	S
$O + H_2 \Rightarrow OH + H$	−0.41	$H + N_2 \Leftrightarrow NNH$	+0.005
$H + O_2 + M \Rightarrow HO_2 + M$	−0.51	$H + NNH \Rightarrow H_2 + N_2$	−0.005
$2H + M \Rightarrow H_2 + M$	−0.33	$O + N_2 \Rightarrow N + NO$	−0.000
$O + NNH \Rightarrow NO + NH$	+1.00	$O + N_2 + M \Leftrightarrow N_2O + M$	+0.001

code already includes 100% recombination of H atoms at the burner. Possible explanations of the discrepancy might include occlusion of the experimental OH profile near the burner or improperly modeled hydrogen atom transport.

Sensitivity analysis was applied to the 38-torr flame model for NO to determine which rate constants control NO production. Table 1 shows the results for the most important reactions. A sensitivity of 1.0 means that changing the rate constant a certain percentage will increase the NO concentration by an equal percentage. The prominence of the O + NNH reaction and the absence of the other NO mechanisms is clearly evident. The low sensitivity to NNH formation and destruction reactions is consistent with thermodynamic control of the NNH concentration. The predicted burned gas NNH concentrations of 1 ppb match what is expected from partial equilibrium with H atoms. Hence, those reactions controlling the H-atom concentration also show up prominently in the sensitivities.

Two approaches were used to determine the NO sensitivity to the NNH heat of formation. From the Sandia code, the sensitivity coefficient was directly computed to give $S = d[NO]/[NO]/\{d\Delta H\} = -0.45/(\text{kcal/mol})$ This agrees with the results of computations with ΔH (NNH) adjusted by ± 1 kcal/mol in the 38-torr flame model, which gave a decrease (or increase) in predicted NO of a factor of 0.62 (1.48). It appears from the model that equilibrium concentrations of NNH are established in our flames and likely in other flames. When the rapid tunneling process for NNH formation is removed, so that only collisionally stabilized formation above the barrier remains ($H + N_2 + M \Rightarrow NNH + M$), the model still predicts about 80% of the NO. Above a threshold at which the NNH formation rate is fast enough to reach equilibrium, the model is insensitive to the value of the rate constant.

We also used modeling to examine one other alternate explanation for the observed NO. H-atom recombination occurs at the burner surface [14] and is included in our model. This suggests the remote possibility that O atoms diffusing to the burner surface could combine with N_2 to produce N_2O. Later in the flame front, this N_2O would react to produce some NO. We recalculated the 78-torr model with a starting N_2O concentration of 8.5 ppm, the surface O concentration from the original model calculation, and without the NNH mechanism active. This model predicted an upper limit of 0.2 ppm NO (we observe 0.4 ppm), assuming all of the O atoms undergo efficient catalytic recombination with N_2. The gas-phase reaction is spin forbidden and has a 20-kcal/mol barrier; thus, complete conversion of O atoms to N_2O on the burner surface is unlikely.

Additional modeling runs on atmospheric pressure hydrogen/air flames with the current NNH mechanism predict ~2 ppm of NO production at $\Phi = 0.5$, and levels of ~10 ppm for stoichiometric and rich flames. This mechanism would also be important for other hydrogen-containing fuels burned in air. In a stoichiometric 40-torr propane/air flame [15], for example, 5 ppm of NO (40% of the total) is predicted to form through the NNH route. This mechanism is less pressure and temperature dependent than other NO formation mechanisms, making it potentially more difficult to circumvent by controlling flame conditions.

Conclusions

We have presented strong evidence for NO production at 0.2–0.5 ppm in low-temperature, low-pressure hydrogen/air flames that cannot be predicted from previously established NO chemistry. The flames are too cool to produce more than ppb levels of thermal NO. There is no CH to produce prompt NO, and production of significant quantities of N_2O is unlikely. Bozzelli and Dean's newly proposed NNH mechanism successfully predicts the ppm level NO mole fractions seen in these flames.

Discrepancies remain between experimental and model profiles of OH and NO. The model NO continues to increase in the burned gases of the 38-torr flame, where the experimental data levels off. The 78-torr model OH profile is in significant disagreement with the experiment low in the flame. Though agreement of experiment and model is imperfect, Bozzelli and Dean's new mechanism remains a viable explanation for the presence of ppm levels of NO in our flames. Their mechanism should be included in NO_x combustion models. The NNH

intermediate may be a significant route to NO in many flames.

Acknowledgments

This work was funded by the Basic Research Group of the Gas Research Institute. A.R.N. was supported by the National Science Foundation Physics Research Experiences for Undergraduates Program.

REFERENCES

1. Bozzelli, J. W. and Dean, A. M., *Int. J. Chem. Kinet.* 27:1097 (1995).
2. Miller, J. A. and Bowman, C. T., *Prog. Energy Combust. Sci.* 15:287 (1989).
3. Miller, J. A., Branch, M. C., and Kee, R. J., *Combust. Flame* 43:81 (1981).
4. Melius, C. F., BAC-MP4 Heats of Formation and Free Energies, 1993.
5. Koizumi, H., Schatz, G. C., and Walch, S. P., *J. Chem. Phys.* 95:4130 (1991).
6. Mertens, J. D., Chang, A. Y., Hanson, R. K., and Bowman, C. T., *Int. J. Chem. Kinet.* 13:173 (1991).
7. Fennimore, C. P., *Thirteenth Symposium (International) on Combustion,* The Combustion Institute, Pittsburgh, 1971, p. 373.
8. Zeldovich, Y. B., *Acta Phisicochim URSS* 21:577 (1948).
9. Miller, J. A. and Bowman, C. T., *Combust. Sci.* 15:287 (1989).
10. Malte, P. C. and Pratt, D. T., *Combust. Sci. Technol.* 9:221 (1974); Wolfrum, J., *Chem. Ing. Tech.* 44:656 (1972).
11. Weiland, K. J. R., Wise, M. L., and Smith, G. P., *Appl. Opt.* 32:4066 (1993); Crosley, D. R. and Jeffries, J. B., in *Temperature: Its Measurement and Control in Science and Industry* Vol. 6 (Schooley, J. F., Ed.), AIP, New York, 1992.
12. Kee, R. J., Grcar, J. F., Smooke, M. D., and Miller, J. A., "A Fortran Program for Modeling Steady Laminar One-Dimensional Premixed Flames," Sandia National Laboratories Report SAND85-8240, 1985.
13. Bowman, C. T., Hanson, R. K., Davidson, D. F., Gardiner, W. C. Jr., Lissianski, V., Smith, G. P., Golden, D. M., Frenklach, M., Wang, H., and Goldenberg, M. "GRI-Mech 2.11 Home Page," access via http://www.me.berkeley.edu/gri_mech/, 1995.
14. Jeffries, J. B., Smith, G. P., Heard, D. E., and Crosley, D. R., *Ber. Bunseges. Phys. Chem.* 96:1410 (1992).
15. Luque, J., Smith, G. P., and Crosley, D. R., *Twenty-Sixth Symposium (International) on Combustion,* The Combustion Institute, Pittsburgh, 1996, pp. 000–000.

COMMENTS

Th. Just, DLR—Institut für Physikalische Chemie d. Verbrennung, Germany. The H and, to a lesser extent, the OH profiles might have been influenced under your experimental conditions by radial diffusion. This makes difficult the application of an one-dimensional flame program to an intrinsic two-dimensional flame when quantitative conclusions are to be drawn.

My former co-worker Kohse-Höinghaus did experiments on $H_2/O_2/Ar$ flames (6cm McKenna burner, 20 to 50 Torr). She showed, by measuring OH and H by LIF or two-photon-LIF respectively, that in particular the H-profiles were strongly disturbed by radial diffusion.

Author's Reply. Thank you for reminding us of this reference [1]. If the H atoms in the burnt gases of the 38-Torr flame are severely depleted by radial diffusion, as you indicated, this could explain the absence of NO growth beyond 0.5 cm. It would resolve the discrepancy with the one-dimensional flame model in Fig. 4.

REFERENCE

1. Bittner, J., Kohse-Höinghaus, K., Meier, U., Kelm, S., and Just, T., *Combust. Flame* 71:41–50 (1988).

•

Hans-Robert Volpp, Universität Heidelberg, Germany. What is the lifetime you assume in your model for the NNH compared to the theoretical estimate [1] and what rate coefficient do you use for the NNH + O_2 reaction? Wouldn't it be very interesting to replace the H_2 in your flame by D_2?

REFERENCE

1. Koizumi, H., Schatz, G. C., and Walch, S. P., *J. Chem. Phys.* 95:4130–4235 (1991).

Author's Reply. The model NNH lifetime of 3 ns is sufficiently rapid by several orders of magnitude in these flames to maintain an equilibrium concentration, even with our rate constant of 5×10^{12} cm^3 mol^{-1} s^{-1} for the oxygen reaction. We have thought about burning D_2, and chiefly from zero point energy differences we would expect about 60% more NO formation. However, it is probably more likely that transport changes will dominate the comparison of the isotopically substituted flames.

Twenty-Sixth Symposium (International) on Combustion/The Combustion Institute, 1996/pp. 2139–2145

BEHAVIOR OF KEY REACTIONS ON NO FORMATION IN METHANE-AIR FLAMES

M. NISHIOKA, Y. KONDOH AND T. TAKENO
Department of Mechanical Engineering, Nagoya University
Chikusa-ku, Nagoya, 464-01 Japan

The behavior of three key elementary reactions on NO formation in methane air flames of fundamental or generic type has been studied numerically to understand the effects of general flame type and flame parameters on NO-emission characteristics. The flame types are the normal premixed flame, the pure diffusion flame, and the so-called double flame. The counterflow flame geometry was used in the study of the latter two flames. The reaction scheme adopted to describe combustion reactions and NO formation was that compiled by Miller and Bowman. A sensitivity analysis of the emission index has revealed that the key elementary reactions are the initiation reactions of thermal NO and Fenimore NO and the initiation reaction of the HCN recycle route. The effects on the behavior of the three reactions of equivalence ratio in the premixed flame, and of velocity gradient in the diffusion and double flames, were studied in detail. The study has revealed that these reactions behave in a different manner in the respective flames and that their behavior is closely related to their inherent flame structures.

Introduction

Nitrogen oxides are one of the major pollutants from fossil fuel combustion, and the recent concern for environmental protection has resulted in increasingly stringent NO_x-emission regulations in a number of industrialized countries [1]. There is an urgent need to develop low-emission combustion devices. Our fundamental knowledge of the combustion reaction of hydrocarbon fuels, especially of methane, and the reaction mechanisms leading to NO_x formation has reached a certain level [2–4]. However, the complicated interacting processes between flow and chemistry make it difficult to understand the NO_x-formation process in flames.

In a series of studies, we have studied numerically the emission characteristics of fundamental methane air laminar flames [5–10]. The fundamental flames are the normal premixed flame, the pure diffusion flame, and the so-called double flame. The last one is very popular in gas appliances and consists of a rich premixed flame that produces CO and H_2 as the main intermediate products and a diffusion flame in which the intermediate products burn with surrounding air [5]. The counterflow flame was used to study the behavior of the pure diffusion flame and the double flame. The emission characteristics were evaluated quantitatively in terms of the emission index [6], and the contribution of the four NO-formation mechanisms (thermal, Fenimore, N_2O, and NO_2) in the total production has been identified.

A comparison was made of the characteristics of the three flames, and their dependence on the flame parameters was studied [7]. In addition, to understand the different emission behaviors, a new method was proposed to evaluate the significance of specified elementary reactions in the whole NO-formation processes in terms of a quantitative reaction path diagram (QRPD). The effects of general flame type and of flame parameters on QRPD were studied [8,9]. Furthermore, a sensitivity analysis of elementary reactions has been made to find the key reactions in NO formation in the three flames. The detailed discussions of the results, especially of the correlation with the results of QRPD analysis, are described elsewhere [10]. Here, we simply notice that the key elementary reactions common to the three flames are the initiation reactions of thermal NO and Fenimore NO and the initiation reaction of the HCN recycle route. The latter route was found to play a significant role in reducing the emission index of the diffusion flame. In the present work, further numerical studies have been made to elucidate the behavior of these key reactions in the three flames to understand the effects of general flame type and of flame parameters on the NO emission behavior. The most important question to be answered should be why the contribution of the HCN recycle route is so significant in the diffusion flame, whereas in the premixed flame the contribution is almost negligible.

Numerical Model

The numerical model, as well as the assumptions and the formulation, are identical to previous ones [5–10] and, hence, will not be described here. The

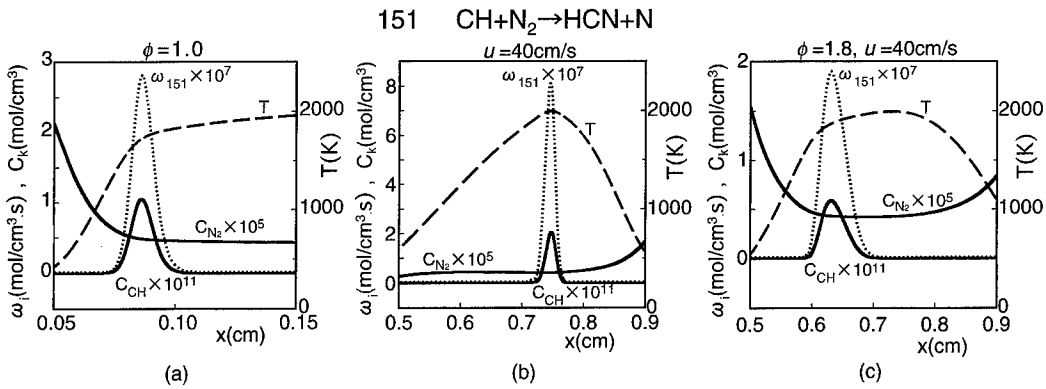

FIG. 1. Typical flame structures of (a) premixed, (b) diffusion, and (c) double flame as related to reaction (151).

adopted reaction scheme to describe combustion reactions in the flames was the so-called C2 chemistry and was compiled by Miller and Bowman [2]. Some preliminary calculations have also been done using the new GRIMECH [4], and some quantitative differences in the predictions have been observed. However, the derived qualitative conclusions remain unchanged, and, in the present study, the original Miller and Bowman mechanisms have been adopted throughout the calculations so as to maintain consistency with the previous studies. To describe NO formation, prompt and thermal mechanisms compiled by Miller and Bowman [2] were used. The former includes the mechanism through N_2O, in addition to the Fenimore mechanism [11,12]. The reactions leading to NO_2 formation are also included. The resulting scheme involves 52 species and 235 elementary reactions. The species involved and the elementary reactions with their reaction rate constants are the same as those described in Appendix A of Ref. 2. The number of reactions in parentheses is also the same. The necessary thermochemical and transport properties were obtained from the CHEMKIN database [13–15].

Initiation Reaction of Fenimore Mechanism (151)

To study the behavior of the initiation reaction of Fenimore NO, reaction (151) shown in Fig. 1, we introduce the representative temperature and concentrations. Figure 1 shows some typical flame structures of the three flames as related to (151). In the figures, temperature T and mole concentrations of CH, C_{CH}, and mole production rate of product, HCN or N, through reaction (151) ω_{151} are plotted against space coordinate x. In the stoichiometric premixed flame, the CH profile is located in the upstream region of the main reaction zone, where the temperature is still relatively low. On the contrary, in the diffusion flame, the position of maximum reaction rate is located in the vicinity of the temperature peak, where the CH concentration is very high as well. In the double flame, the reaction rate is determined mostly by the CH distribution and the maximum reaction rate is located in the rich premixed flame region, where the temperature is relatively low. Now we give attention to the position at which ω_{151} becomes a maximum. The temperature and CH concentration at this position are very important, since they determine the maximum reaction rate. The rate depends on the N_2 concentration as well, but there is a plentiful amount of N_2 present and hence the latter dependence is not crucial. Therefore, we may take the temperature and CH concentration at the maximum reaction rate as the representative temperature and concentration for this reaction and designate them by T_ω and $C_{CH,\omega}$, respectively. Now we can study the behavior of this reaction in terms of these quantities when general flame type and parameters are varied.

Figure 2 shows how the representative temperature and concentration, and the maximum reaction rate, depend on the flame parameters. In the premixed flame, the maximum reaction rate increases with ϕ because of increases in temperature and CH concentration on the lean side. On the far rich side, the temperature attains a gradual maximum whereas the CH concentration decreases with ϕ. As a result, the maximum reaction rate has a maximum at around $\phi = 1.3$ and decreases for a further increase of ϕ. In the diffusion flame, the temperature decreases while the CH concentration increases slightly with the injection velocity u. The resultant maximum reaction rate increases with u at first, attains a gradual maximum, and then decreases for a further increase in u. The behavior in the double flame is simple. For an increase in u, the temperature remains almost constant while CH concentration increases monotonically. Then the reaction rate increases with u monotonically.

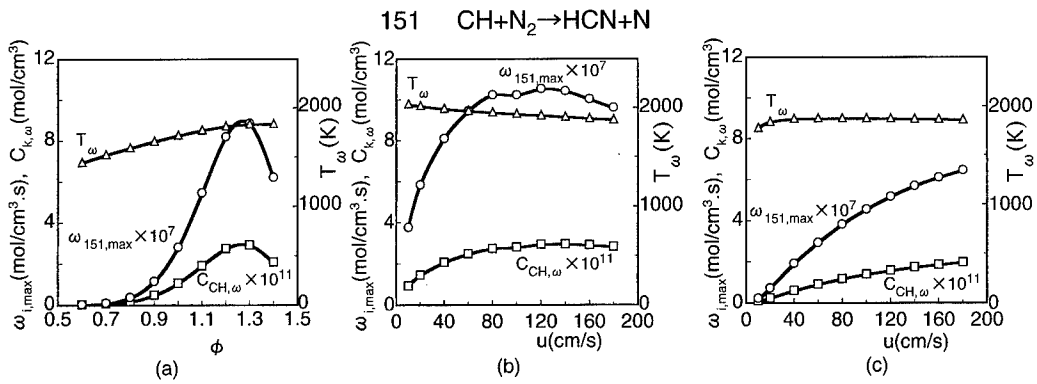

FIG. 2. Dependence on flame parameters of representative temperature and concentration and maximum reaction rate of (151) for (a) premixed, (b) diffusion, and (c) double flame.

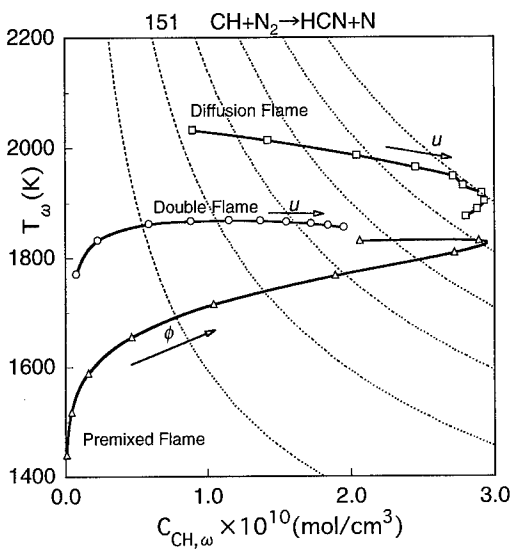

FIG. 3. Comparison of behavior of representative quantities of (151) in three flames.

Figure 3 illustrates effects of general flame type on the representative temperature and CH concentration. The figure shows how they change with an increase in ϕ in the premixed flame and in u in the diffusion and double flames. The fine dotted curves represent contours of constant maximum reaction rate of (151) divided by $C_{N2,\omega}$. As u is increased in the diffusion flame, the CH concentration increases but the temperature decreases slightly and then the resultant reaction rate increases to a certain maximum value. Then the rate decreases because of decreases in temperature and CH concentration. In the premixed flame, on the other hand, both the temperature and CH concentration increase with ϕ to produce the rapid increase in the reaction rate. CH concentration and hence the reaction rate decrease at the far rich side. The temperature is always higher for the diffusion flame in the whole range of ϕ and u. In this way, we understand that the contribution of the Fenimore mechanism is much more significant in the diffusion flame simply because the representative temperature is higher. In addition, we understand that in lean premixed flames, not only the temperature but the CH concentration is too low to have an appreciable contribution of this mechanism. In the double flame, the temperature and thus the reaction rate is in the middle of the diffusion and premixed flames.

Initiation Reaction of HCN Recycle Route (161)

Figure 4 shows some typical flame structures as related to the initiation reaction of HCN recycle route, reaction (161). In the stoichiometric premixed flame, HCCO is distributed in the upstream region of the main reaction zone where temperature and NO concentration are still relatively low. In the diffusion flame, the position of maximum reaction rate is located in the vicinity of the temperature peak, where NO and HCCO concentrations are very high. In the double flame, the reaction rate is determined mostly by the HCCO distribution, and the maximum reaction rate is located in the rich premixed flame region. Now, we take the concentrations of HCCO and NO at the position where ω_{161} becomes maximum as the representative concentrations. Please note that the activation energy and the temperature exponent of the frequency factor are zero for this particular reaction and hence the rate is independent of temperature.

Figure 5 shows how the representative concentrations depend on ϕ and u. The dependence of maximum reaction rate is also shown. In the left figure, we see that in the premixed flame, the maximum reaction rate increases with ϕ because both HCCO

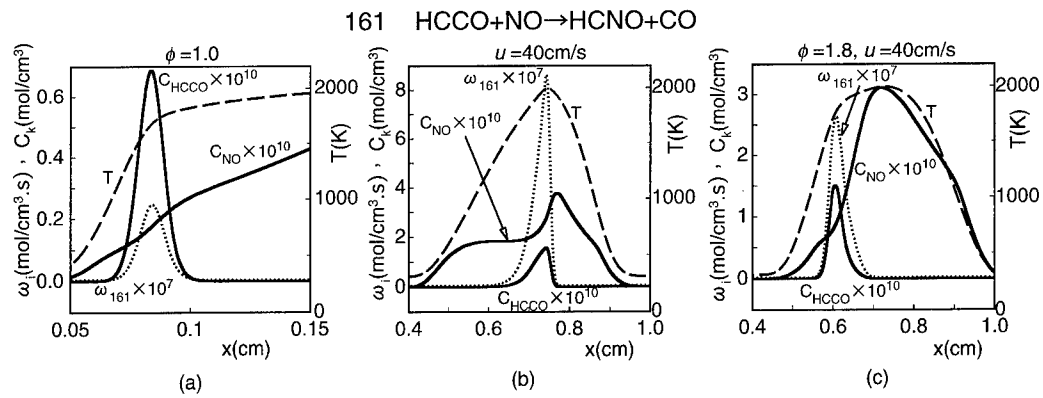

FIG. 4. Typical flame structures of (a) premixed, (b) diffusion, and (c) double flame as related to reaction (161).

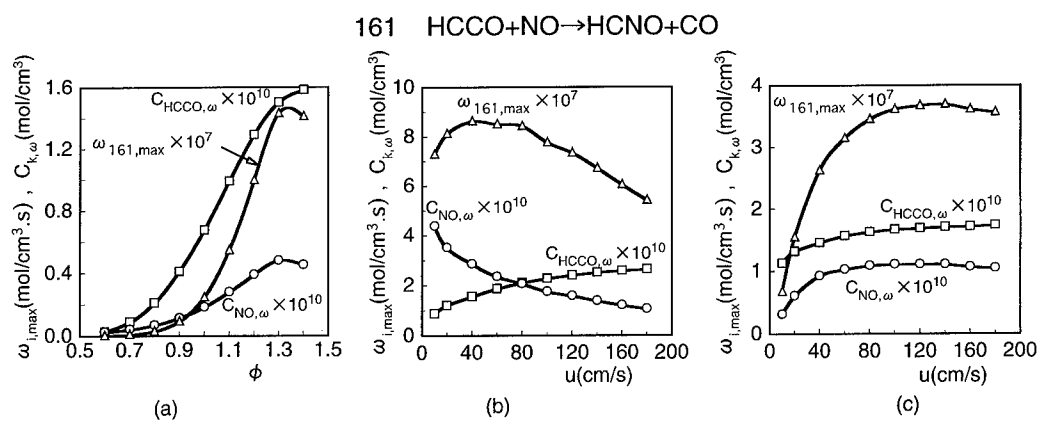

FIG. 5. Dependence on flame parameters of representative concentrations and maximum reaction rate of (161) for (a) premixed, (b) diffusion, and (c) double flame.

and NO concentrations increase with ϕ. The slight decrease in the far rich side is due to the decrease in NO concentration. As u is increased, in the diffusion flame, the NO concentration decreases whereas the HCCO concentration increases. As a result, the reaction rate increases first, takes a maximum, and then decreases for a further increase in u. It should be noticed that the NO concentration is one order of magnitude larger than in the premixed flame. The behavior in the double flame is simpler. Both concentrations increase with u when u is small and approach quickly to constant values. When u is very large, the NO concentration decreases slightly with u to cause a slight decrease in the reaction rate.

Figure 6 shows how the concentrations change with an increase in ϕ in the premixed flame and in u in the diffusion and double flames. The fine dotted curves represent contours of maximum reaction rate. The figure explains why the contribution of the HCN recycle route is so significant in the diffusion flame while it is negligible in the premixed flame. As u is increased in the diffusion flame, NO decreases but HCCO increases and the resultant reaction rate decreases slightly to keep the rather high rate. On the other hand, both NO and HCCO and thus the reaction rate increase with ϕ in the premixed flame. The NO concentration, however, is too small to have a significant reaction rate. That is, the NO concentration at the region where HCCO is produced is so low that the HCN recycle route does not come into play in the premixed flame. Again, the double flame is just in the middle of the premixed and diffusion flames here.

Initiation Reaction of Thermal Mechanism (−232)

The behavior of the initiation reaction of thermal NO, reaction (−232) shown in Fig. 7, is somewhat different from that of the previous two reactions; consequently, we have to study it differently. The

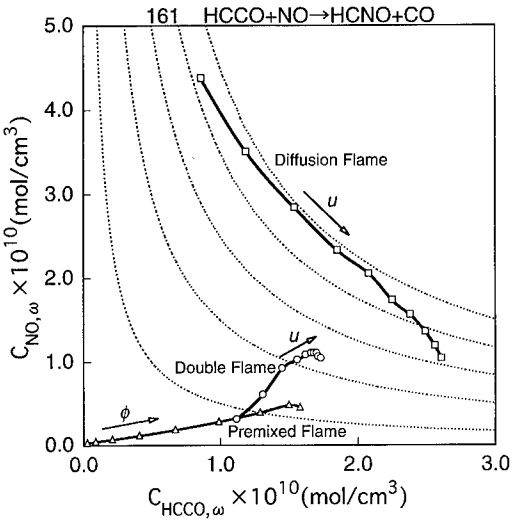

FIG. 6. Comparison of behavior of representative quantities of (161) in three flames.

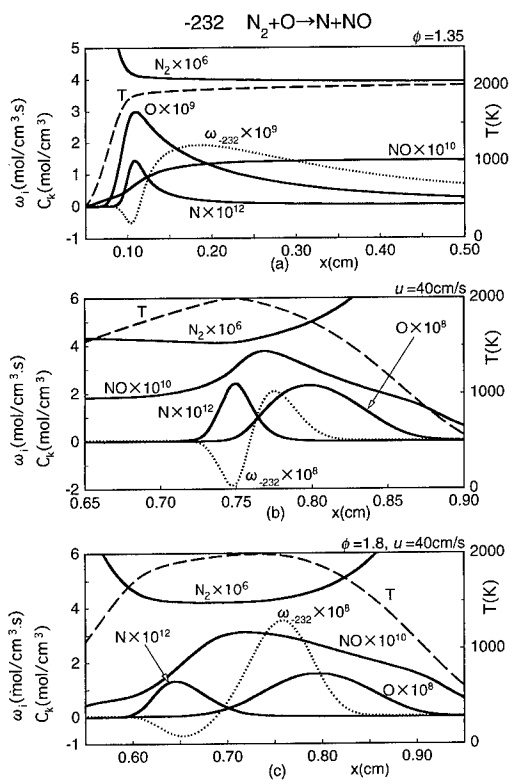

FIG. 7. Typical flame structures of (a) premixed, (b) diffusion, and (c) double flame as related to reaction (−232).

flame structures shown in Fig. 7 reveal that there are regions in the flames where the reaction rate becomes negative. Please note that in the figure the abscissa is enlarged so as to show the detailed distributions of the related quantities in the vicinity of the positive and negative regions. The negative reaction rate is rather large in the diffusion and double flames, whereas it is small in the premixed flame. In the former two flames, the distributions of N and O are separated; N is on the fuel side and O is on the air side. Detailed analysis of the distributions has revealed that N is produced mostly through (151) and (211) [9]. Thus, an appreciable amount of N is present in the region where the NO concentration is rather high and causes reaction (−232) to proceed backwards. The direction of the reaction depends mostly on the concentration ratio of N to O. The critical ratio C_N/C_O, where the direction changes, remains between 2 and 3×10^{-4} for the varied range of u of two flames. On the other hand, the N and O distributions overlap in the premixed flame. N is produced, in this particular rich flame, through (211) and (151) again [9]. However, O is also produced in the same region. In addition, the NO concentration in this region is so low as to make it unlikely that (−232) proceeds backwards, except in a small upstream region.

To assess the significance of the backwards reaction, we introduce the following space-integrated reaction rate Ω_{-232}:

$$\Omega_{-232} = \int_0^L \omega_{-232} dx = \int_{\omega_{-232} \geq 0} \omega_{-232} dx + \int_{\omega_{-232} < 0} \omega_{-232} dx = \Omega^+ + \Omega^-$$

where Ω^+ represents the integration of the positive region while Ω^- represents that of the negative region. This quantity will represent the net production rate of N or NO per unit flame surface area through this reaction. The dependence of the respective three terms of the preceding equation on flame parameters in the three flames has been studied to reveal that the contribution of the backwards reaction is negligible in the premixed flame but is significant in the diffusion flame. In the latter flame, the net production rate is reduced significantly by the presence of the backwards reaction, especially when u is small. This partly explains why the thermal mechanism is not as important in the diffusion flame. In the double flame, the backwards reaction has some small contribution in reducing the role of the thermal mechanism.

Discussion

In a series of studies, we have so far developed a numerical analysis to understand NO-emission characteristics and formation mechanisms of methane air

flames. This kind of approach might be somewhat controversial, since the kinetics to describe combustion and NO-formation reactions has not yet been established. Some may think that there is still much uncertainty in the kinetics and that it is too early to adopt this kind of approach. The derived results may depend on the different kinetics. However, we believe that the qualitative results should remain unchanged for future modified kinetics. In addition, we believe it is very important at this stage to understand why the emission behavior is different according to the general flame type. In a recent study [16], we have found that the emission characteristics of a diffusion flame are rather insensitive to the flow field in which the flame is stabilized. This means that the general flame type is much more important than flow field in the emission behavior. Therefore, it must be more important than had been imagined to elucidate the effects of the general flame type.

The foregoing analysis has shown that the behavior of key elementary reactions is related closely to the inherent flame structure. In the diffusion flame, everything happens in the narrow reaction zone. CH, HCCO, N, and NO are produced in this region to give high concentrations in the vicinity of the temperature peak. Then the Fenimore mechanism produces a large amount of NO in this region, but the destruction of NO through the HCN recycle route is also very large. In addition, the presence of a large amount of NO and N on the fuel side forces NO to reduce to N_2 and O. This prevents the thermal mechanism from playing a significant role. The combination of all these processes results in the ultimate NO-emission index, which is comparable to that of the premixed flame [7].

On the other hand, in the premixed flame, NO is produced in two separate regions. Fenimore NO is produced in the upstream low-temperature region, whereas thermal NO is produced in the downstream high-temperature region. The low temperature in the former region decelerates NO production rate through the Fenimore mechanism. And because of the resultant low NO concentration in this region, the HCN recycle route will not come into play in the premixed flame. In the double flame NO is also produced in two separate regions. Fenimore NO is produced in the rich premixed flame region, whereas thermal NO is produced mostly in the diffusion flame region. The temperature of the former region is higher than that of a normal premixed flame to accelerate the Fenimore mechanism. However, the NO concentration in this region is higher and HCN recycle is more effective. The net result is an ultimate emission index that is comparable to those of the premixed and diffusion flames [7].

Acknowledgments

The authors would like to express their sincere thanks to Profs. C. T. Bowman, P. Van Tiggelen, and K. N. C. Bray for their helpful discussions. The financial support by Toho Gas Co. and Rinnai Co. are gratefully acknowledged.

REFERENCES

1. Bowman, C. T., *Twenty-Fourth Symposium (International) on Combustion,* The Combustion Institute, Pittsburgh, 1992, p. 859.
2. Miller, J. A. and Bowman, C. T., *Prog. Energy Combust. Sci.* 15:287–338 (1989).
3. Baulch et al., *Combust. Flame* 98:59–79 (1994).
4. GRIMECH 2.11 (Nov. 4, 1995), available from www.gri.org.
5. Nishioka, M., Nakagawa, S., Ishikawa, Y., and Takeno, T., *Prog. Astronaut. Aeronaut.* 151:141 (1993).
6. Takeno, T. and Nishioka, M., *Combust. Flame* 92:465–468 (1993).
7. Nishioka, M., Nakagawa, S., Ishikawa, Y., and Takeno, T., *Combust. Flame* 98:127–138 (1994).
8. Nishioka, M., Kurita, A., Kondoh, Y., and Takeno, T., *Nensho Kenkyu* (in Japanese) (*Combust. Res.*) 104:75–90 (1996).
9. Takeno, T., "NO Emission Characteristics and Formation Mechanisms of Methane Air Flames," *Proceedings of The 8th International Symposium on Transport Phenomena in Combustion,* Taylor & Francis, in press.
10. Kondoh, Y., Nishioka, M., and Takeno, T., "A Sensitivity Analysis of NO Formation of Methane Air Flames," submitted to *Nensho Kenkyu* (in Japanese).
11. Fenimore, C. P., *Thirteenth Symposium (International) on Combustion,* The Combustion Institute, Pittsburgh, 1971, p. 373.
12. Drake, M. C. and Blint, R. J., *Combust. Flame* 83:185–203 (1991).
13. Kee, R. J., Miller, J. A., and Jefferson, T. H., Sandia Report SAND80-8003, 1980.
14. Kee, R. J., Dixon-Lewis, G., Warnatz, J., Coltrin, M. E., and Miller, J. A., Sandia Report SAND86-8246, 1986.
15. Kee, R. J., Rupley, F. M., and Miller, J. A., Sandia Report SAND87-8215, 1987.
16. Nishioka, M., Takemoto, Y., Yamashita, H., and Takeno, T., "Effects of Multidimensionality on Diffusion Flame," *Twenty-Sixth Symposium (International) on Combustion,* The Combustion Institute, Pittsburgh, 1996, pp. 00–00.

COMMENTS

Prof. Jozef Peeters, University of Leuven, Belgium. This paper and a few others in this symposium emphasize the importance of the HCCO + NO reaction to NO_x chemistry in fuel-rich flames and to reburning in particular. In the current mechanisms, one adopts a rate coefficient of 2×10^{13} $cm^3mol^{-1}s^{-1}$, independent of temperature, and assumes HCNO + CO as products. Two years ago, we measured the rate coefficient over the 290 to 670 K range, finding $k(T) = (6 \pm 2) \times 10^{13} \exp[-(350 \pm 150)/T]$ $cm^3mol^{-1}s^{-1}$ [1]. In our product analysis at 700 K we observed two reaction channels, one yielding CO + HCNO (or HNCO), and the second CO_2 + HCN, with a branching ratio of approximately 3 to 1 [1]. The isoelectronic reaction NCO + NO also proceeds via two similar channels. Given the importance of HCCO + NO, I suggest that the mechanisms used in NO_x modeling be updated accordingly. In a complementary ab initio study [2] we suggested that the first channel could yield HNCO rather than HCNO. This would have important implications given the different reactivities expected for fulminic acid and isocyanic acid; however, the identity of the isomer needs confirmation.

REFERENCES

1. Boullart, W., Nguyen, M. T., and Peeters, J., *J. Phys. Chem.* 98:8036–8043 (1994).
2. Nguyen, M. T., Boullart, W., and Peeters, J., *J. Phys. Chem.* 98:8030–8035 (1994).

Twenty-Sixth Symposium (International) on Combustion/The Combustion Institute, 1996/pp. 2147–2154

A LIF AND CARS STUDY OF THE EFFECTS OF UPSTREAM HEAT LOSS ON NO FORMATION FROM LAMINAR PREMIXED BURNER-STABILIZED NATURAL-GAS/AIR FLAMES

A. V. MOKHOV AND H. B. LEVINSKY
Gasunie Research
N.V. Nederlandse Gasunie
P.O. Box 19
9700 MA Groningen, The Netherlands

Measurements of NO concentration and temperature in laminar, premixed, natural-gas/air flames stabilized on a water-cooled sinter burner at atmospheric pressure are reported. The NO concentration and temperature, determined by laser-induced fluorescence and coherent anti-Stokes Raman scattering, respectively, are seen to vary with exit velocity of the fuel-air mixture and thereby with the degree of heat transfer upstream to the burner. For lean and stoichiometric flames, the NO concentration decreases rapidly with increased stabilization, as the contribution from the Zeldovich mechanism is diminished. Further, near extinction, these flames exhibit a finite NO concentration (12 ± 2 ppm at $\Phi = 1$ and 2 ± 2 ppm at $\Phi = 0.85$), ascribed to the Fenimore mechanism that form a lower limit to NO_x control strategies based on upstream heat loss, such as radiant surface combustion. Measurements on fuel-rich flames at equivalence ratios of 1.3 and 1.4 also show a strong dependence on exit velocity, allowing for the possibility of operating low-NO_x radiant surface burners under fuel-rich conditions. The results are compared with those from one-dimensional flame calculations to gain more insight into the processes involved. Whereas the fuel-lean and stoichiometric flames appear to be well understood, the origin of the decrease in NO concentration with increasing stabilization in the fuel-rich flames is unclear. In addition, the practical implications of the results are discussed.

Introduction

Recently, a great deal of effort has been spent designing burner systems to meet the increasingly stringent regulations for the emissions of nitrogen oxides (NO_x) from natural-gas–fired equipment. This has led to several combustion strategies that, to a greater or lesser extent, have been successful in achieving this aim. A serious challenge to the equipment designer lies in the fact that emission requirements are becoming *progressively* more stringent. As a result, the existing techniques are being pushed ever closer to their operational limits, generally determined by flame stability and/or unacceptably high CO emissions, and new methods of combustion are being sought. While the initial, substantial gains in reducing NO_x emissions were based on the empirical approach, further emissions reductions will require insight into the underlying physical and chemical phenomena.

This drive toward continually lower emissions has also renewed interest in the possibility of a fundamental lower limit to NO formation, that is, the lowest emission possible with a given technique. The existence of fundamental limits is of practical consequence for two reasons. First, if a given method is shown fundamentally incapable of satisfying the expected requirements, an equipment developer would be wasting his or her time pursuing it. Thus, this information increases the efficiency of the design process. Second, knowledge of the limitations of the state of the art provides a sound basis for the rational choice of future allowable emissions by regulatory agencies.

A particularly effective method of obtaining low NO_x emissions is fully premixed radiant surface combustion (see, for example, Ref. 1 and references therein). This type of combustion employs a porous or perforated burner deck fired with a fully premixed (equivalence ratio $\Phi \leq 1$) fuel-air mixture. When the exit velocity of the mixture is lower than the corresponding free flame velocity, the laminar, stabilized flame transfers heat to the burner surface, which reduces the flame temperature (as well as the burning velocity), lowering the NO emission. The often-incandescent burner surface radiates the transferred heat to the surroundings: a heat exchanger in domestic appliances or a "load" in process applications. This description of the radiant burner [2] is identical to the mode of operation of a water-cooled flat-flame burner [3], with the exception of the manner in which the burner surface transfers the heat removed from the flame—through radiation rather than into the cooling water.

TABLE 1
Adiabatic flame temperatures and laminar burning velocities of Groningen natural gas. The values of laminar burning velocities are taken from Ref. 9

φ	0.85	1.00	1.15	1.30	1.40
T_{ad}, K	2066	2222	2168	2048	1970
S_u, cm/s	30	39	36	25	16

For this example of NO_x abatement through "upstream" heat loss, one can speculate, at least qualitatively, about the processes that will govern the NO_x emissions and their possible limits. This conjecture can be based on the current understanding of the routes to NO formation in methane-air flames [4]. Under fuel-lean conditions, we expect substantial contributions from the Fenimore-prompt mechanism [5] in the flame front and from the Zeldovich mechanism, both in the postflame gases (if the temperature is ≥2000 K [6]) and in the flame front (through reaction with superequilibrium oxygen atoms [7]). Given the differences in activation energy of the rate-limiting steps involved [4,8], one is tempted to speculate (perhaps naively) that the reduction in temperature caused by reducing the exit velocity will eventually freeze out both Zeldovich contributions, leaving a constant Fenimore contribution. If this reasoning is true, at constant equivalence ratio, the prompt contribution forms a fundamental lower limit for the NO_x emission from this burner. We remark here that for practical purposes, ascertaining *whether* a limit to the NO_x reduction potential of a particular technique exists is less important than determining what this potential is.

In this paper, we examine the effects of upstream heat loss on the NO formation from atmospheric-pressure, natural-gas/air flames stabilized on a water-cooled, flat-flame burner, under both fuel-lean and fuel-rich conditions. Toward this end, the gas temperatures have been measured using coherent anti-Stokes Raman scattering (CARS), and the NO concentration has been determined quantitatively using laser-induced fluorescence (LIF). The inclusion of fuel-rich flames in this study extends the validity of the results to many real devices that operate in this region, while the choice for natural gas is made to ensure the practical validity of the results. In addition, the results are compared to those calculated using a one-dimensional flame code to gain insight into the underlying mechanisms. Further, possible fundamental limitations for this type of burner as an NO_x control strategy are discussed.

Experimental Method

The measurements were performed on a flat flame stabilized above a water-cooled, sintered–stainless steel McKenna Products burner. To prevent interaction of the combustion products with ambient air, the inner flame with a diameter of 6 cm was surrounded by a shroud of nitrogen. Groningen natural gas (~81% CH_4, ~14% N_2, ~3.5% C_2H_6, ~1% CO_2, <1% C_3 and higher alkanes) was used as a fuel. We remark that the thermochemical properties for this gas, such as adiabatic flame temperatures and burning velocities, differ little from those of pure methane; for the equivalence ratios used in this study, these properties are listed in Table 1. For calibration purposes, N_2 with or without 4500 ppm NO was added to the gas-air mixture. The composition of the fuel-air mixture used, with equivalence ratio Φ, can be presented formally as

$$\Phi \cdot \text{Fuel} + 8.42 \cdot \text{Air} + \beta \cdot N_2$$

The measurements of the NO concentrations reported later were performed in flames without added N_2, that is, $\beta = 0$. The fuel-air mixture with $\beta = 0.5$ was used for calibration. This composition provides a substantial seeded NO concentration (~200 ppm) at relatively high flame temperatures. The flow rates of gases were measured by Brooks mass flow meters. Special attention was paid to ensure the reproducibility of flame conditions. The equivalence ratio was determined from measurements of the methane concentration in the fuel-air mixture by a Maihak Unor 610 infrared analyzer, which provides better accuracy and flame reproducibility than deriving Φ from the measured gas and air flows.

The flame temperature and NO concentration were measured "simultaneously" (within minutes of each other) by CARS and LIF, respectively. The flame temperature was determined using broadband planar BOXCARS for nitrogen thermometry. The optical scheme was similar to that reported in Refs. 10 and 11. The reproducibility of the evaluated flame temperatures was of the order 20 K. The accuracy of the temperature measurements, evaluated from comparison of the measured and adiabatic temperatures for free burning (just stabilized) flames, was better than 30 K; as a rule, the measured temperatures are always higher than the adiabatic temperatures. The flame temperature at fixed Φ was changed by varying the flow rate of the gas-air mixtures; as described in the introduction, varying the degree of stabilization varies the upstream heat loss.

For LIF measurements, a Nd:YAG-pumped dye laser with a wavelength extender (Continuum Powerlite 8010/ND6000/UVX) was used as a source of ultraviolet radiation. The energy of the laser radiation at 226 nm was roughly 3 mJ per pulse. The laser beam was focused by a quartz lens (f = 850 mm) into the flame, giving a beam waist of ≤0.5 mm. Fluorescence was collected at right angle by a quartz lens (f/4.5). An interference filter, centered at 250

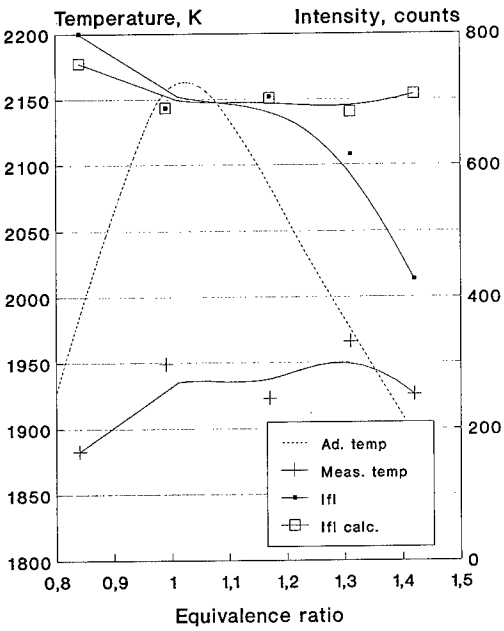

FIG. 1. NO fluorescence intensity and temperature as a function of equivalence ratio for seeded (~200 ppm NO) flames. Dashed line represents the adiabatic flame temperature.

nm with a bandwidth of approximately 45 nm, was installed in front of the camera lens, providing substantial rejection of the Rayleigh-scattered signal. The fluorescence was imaged onto a gated intensified diode array (EG&G 1420HQ). The linearity of the detection system was checked by measuring the intensity of the Rayleigh scattering in air as a function of laser intensity. The laser pulse energy was measured by a pyroelectric joulemeter (Molectron Model J3-05). The temperature and NO fluorescence profiles were measured for every equivalence ratio and exit velocity by moving the burner vertically with a precision positioner (Daedal Corp.). Each profile consisted of 20 steps of 1 mm, starting at the closest possible position (2–3 mm) of the laser beam relative to the burner surface. For all but the highest exit velocities, this limitation precluded measurement of most of the rise in temperature and NO concentration through the flame front.

The excitation spectra of the NO fluorescence at different flame temperatures and equivalence ratios were calculated using the procedure described in Refs. 12 and 13. The calculations resulted in choosing the spectral line at 225.965 nm (air). This line is a combination of the P_{11} (23.5) + Q_{11} (14.5) + $^{Q}P_{21}$ (14.5) + Q_{22} (20.5) + $^{Q}R_{12}$ (20.5) rotational lines (notation according to Ref. 14). This line is well separated from other transitions and has high intensity and modest temperature dependence, in the cases of both linear and saturated fluorescence. The same spectral line was used in Ref. 13.

The measured dependence of the NO fluorescence intensity on laser power clearly showed saturation behavior for high laser power (>2 mJ) both in lean and rich flames. Although rotational relaxation can result in a substantial quenching correction being necessary, even when the absorption transition is saturated, both the temperature and composition dependence of the fluorescence indicated behavior closer to saturation. (A more detailed discussion of this and other aspects of the calibration procedure are found in Ref. 15). An example of this behavior is discussed later.

The fluorescence excitation spectrum in the region close to the line chosen for diagnostic purposes was measured for every equivalence ratio with and without seeded NO. The excitation spectrum in the nonseeded flame has a distinct background. The magnitude of the background was determined by comparison of ratios of intensities at the center of the spectral line and in the wings for seeded and nonseeded flames [15]. This background signal arises partially from Rayleigh scattering and partially from scattering of the laser radiation from the optical elements and nonresonant emission from other flame molecules. In the analysis of the experimental data, the background was subtracted from the measured intensity of the NO fluorescence. We point out here that the background determines the accuracy of the concentration measurement at low (single-ppm) levels.

As described previously, calibration of the LIF measurements was performed by adding a known amount of NO to the air-gas mixture [16,17]. Earlier work [15] has shown that for lean, stoichiometric, and slightly rich flames, the seeded NO concentration is substantially preserved in the postflame gases. This was further supported by calculations performed using a laminar one-dimensional flame code [18], using a prompt-NO mechanism [19]. These calculations indicate, however, that a substantial amount of reburning of the seeded NO can occur at richer ($\Phi \geq 1.2$) equivalence ratios. The calibration is performed by subtracting the fluorescence intensity in nonseeded flames from the intensity in the seeded flames, under otherwise identical conditions (Φ, exit velocity, and β). Since the subtraction eliminates the contributions from both the naturally occurring NO present in the flame and the fluorescence background to the LIF intensity, the resulting intensity *difference* is then ascribed to the amount of seeded NO. The differences in fluorescence intensities thus measured as a function of equivalence ratio at nearly constant exit velocity are presented in Fig. 1. In addition to the measured intensities, the calculated fluorescence intensities, assuming saturated fluorescence and a constant concentration of added nitric oxide, are shown. The calculated

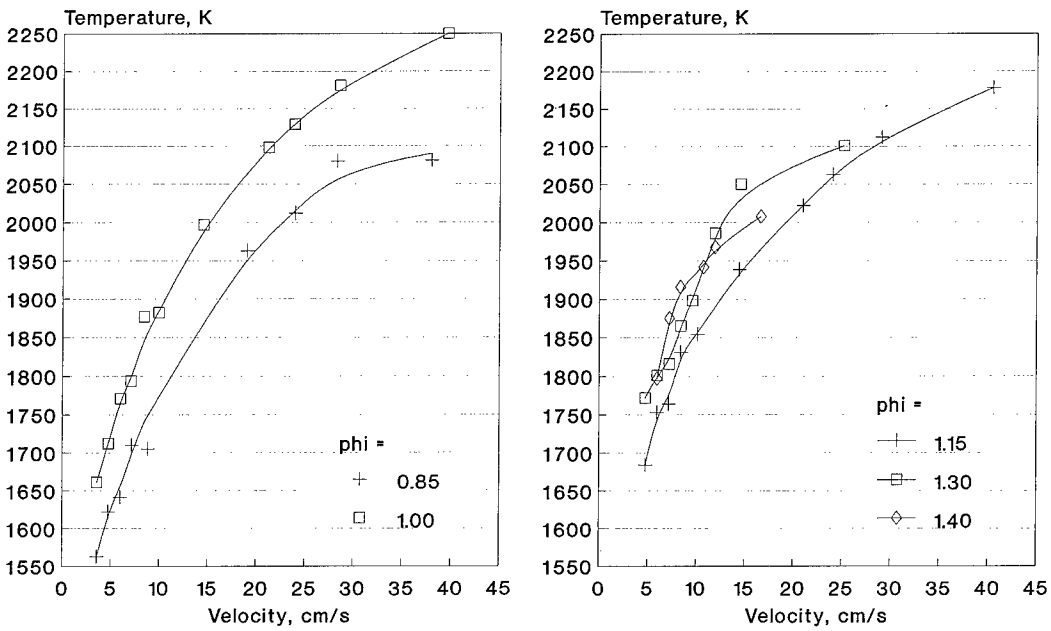

FIG. 2. Temperature at a distance of 5 mm above burner as a function of the exit velocity of the air-gas mixture: (a) fuel-lean and stoichiometric flames; (b) fuel-rich flames.

intensity is normalized to the measured intensity for the stoichiometric flame. The calculated adiabatic and measured flame temperatures are presented in Fig. 1, as well. As can be seen, the measured temperature is practically independent of the equivalence ratio. Since the hotter flames (when adiabatic) have higher burning velocities, they are stabilized more strongly at a fixed exit velocity; this tends to smooth out the variation in actual temperature with equivalence ratio.

There is good agreement (better than 10%) between the calculated and measured fluorescence intensities for lean and rich flames up to $\Phi = 1.3$. For $\Phi \geq 1.3$, the measured values are much lower than calculated, although the trend is apparent from the data for $\Phi \geq 1.2$. We are disinclined to attribute this effect to collisionally induced effects such as quenching and/or effects associated with rotational relaxation processes [15], since the variation in composition between the lean and slightly rich flames, where there is excellent agreement, is much larger than the change on going from $\Phi = 1.2$ to $\Phi = 1.4$. We therefore ascribe the "anomalous" decrease in fluorescence intensity to the conversion of the added nitric oxide to N_2 in the flame front, as suggested by the flame code calculations. Based on these arguments, the absolute NO concentrations in the measurements reported later were extracted from the measured fluorescence intensities using calibration with the added nitric oxide in a stoichiometric flame and assuming the temperature dependence of saturated NO fluorescence. This procedure resulted in a relative accuracy of ~5% for higher concentrations, governed essentially by the flow measurement; as mentioned previously, for concentrations on the order of 2 ppm, the uncertainty is a factor of 2.

Results and Discussion

As stated earlier, profiles of temperature and NO concentration through the flame front were only measurable in the flames with the highest exit velocities (essentially adiabatic flames). Lowering the exit velocity to the point at which heat transfer occurred resulted in moving the entire flame front into the optically inaccessible region. Therefore, the results presented are taken at 5 mm above the burner for the stabilized flames. The temperature and NO profiles are essentially flat at this point for all flames whose maximum temperatures are below 2000 K. To obtain equivalent information for the nearly adiabatic flames, the temperature and NO concentration are reported at ~4 mm above the point at which the temperature is 90% of its maximum value. (The profiles measured for these flames are available from the authors upon request.)

Temperatures

Figures 2a and 2b show the measured temperature at 5 mm as a function of exit velocity for the

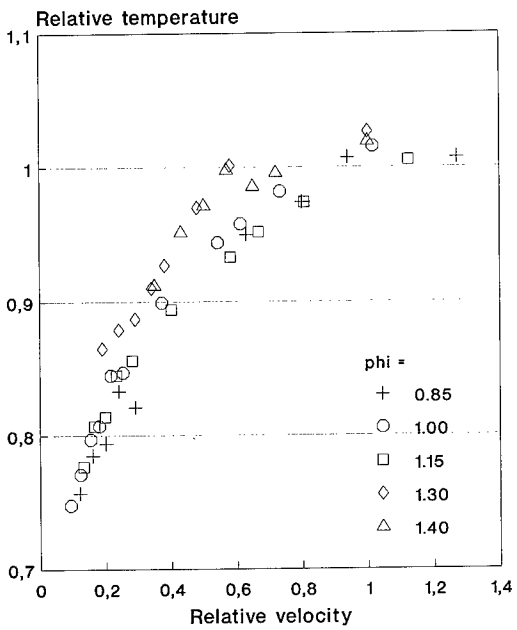

FIG. 3. Relative flame temperature as a function of relative exit velocity for different equivalence ratios. The flame temperatures and exit velocities are normalized to the adiabatic flame temperatures and laminar burning velocities, respectively, taken from Table 1.

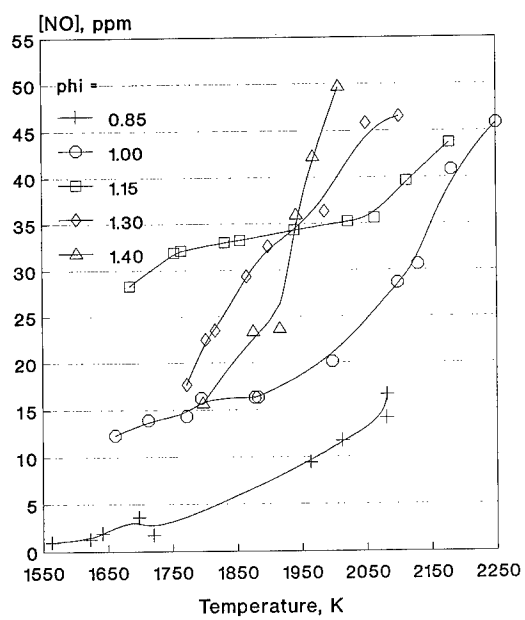

FIG. 4. Measured NO concentration at a distance of 5 mm above burner as a function of flame temperature for fuel-lean, stoichiometric, and fuel-rich flames.

lean/stoichiometric and rich flames, respectively. At higher velocities, the temperatures approach the adiabatic values and become essentially constant. This is best illustrated by the curve for $\Phi = 0.85$ in Fig. 2a. As is well known for flames stabilized on sinters [3], the flame is no longer flat in the near-adiabatic region of exit velocity. However, this was the case only for the highest velocities studied here, and the vast majority of the results were obtained on flames without discernible multidimensional structure. Further, although we have explored higher exit velocities, these results are practically identical to those presented at the highest velocities reported here.

The lowest obtainable flow velocities were determined by the stability of the flames themselves; the flames were close to extinction. This allowed a variation in flame temperature at constant equivalence ratio from more than 200 K at $\Phi = 1.4$ to nearly 600 K for the stoichiometric flame.

It is interesting to note that the temperature change caused by upstream heat loss in the process of stabilization scales with the fraction of the free flame burning velocity. This is illustrated in Fig. 3, where the measured temperature normalized by the adiabatic temperature is plotted as a function of the exit velocity normalized to the free flame burning velocity (see Table 1 for the data used in the normalization). The apparent "super-adiabatic" temperatures close to unity relative velocity are due to the accuracy of the CARS measurements, which, as discussed previously, appear to be systematically 30 K too high. As can be seen, the variation observed in Figs. 2a and 2b collapse well to one curve. (Parenthetically, choice of another set of burning velocities for the two richest flames results in an even better similarity.)

NO Measurements: Fuel-Lean Flames

The measured NO concentrations (in ppm) at 5 mm above the burner are presented in Fig. 4, plotted as a function of the measured flame temperature. The very strong dependence of the NO concentration at the higher temperatures ($T \geq 2000$ K) for the lean and stoichiometric flame is clearly the result of the high-temperature Zeldovich mechanism, as will also be shown later. The NO concentration in ppm in the lean flame drops quickly to single digits, which is indicative of the behavior seen in practical devices [1,7]. The NO concentration at this location in the stoichiometric flame appears to decrease only slowly between ~1900 K and extinction, remaining on the order of 15 ppm; this NO probably arises via the Fenimore mechanism.

To shed further light on this matter, we have performed one-dimensional flame calculations of the type described earlier, for both free and burner-stabilized (obtained by solving the energy equation) conditions; the results are shown in Fig. 5. The

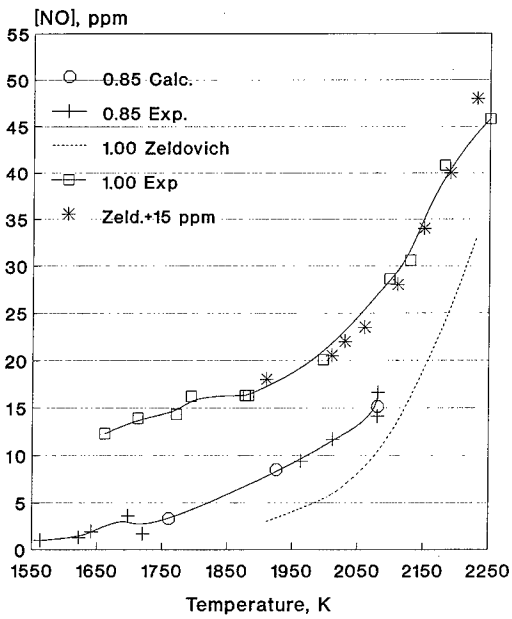

FIG. 5. Measured and calculated NO concentration for the lean and stoichiometric flames as a function of equivalence ratio. For further description of the curves, see the text.

calculations for the lean flame were performed using the mechanism with "full" nitrogen chemistry (Zeldovich and Fenimore; preliminary calculations using an N_2O mechanism [4] yielded only an additional 0.5 ppm NO). The calculated points have been shifted by 30 K, allowing for the estimated systematic error in the CARS measurements. The excellent agreement is due to the dominant role of the Zeldovich mechanism at this equivalence ratio, the degree to which it is understood, and the adequacy of the flame model to account for superequilibrium concentrations of flame radicals. The model predicts ~2.5 ppm Fenimore NO in this flame. Relying on the correct prediction of thermal NO formation, we have performed calculations for the stoichiometric case, *without* the Fenimore mechanism. These results (also shifted by 30 K) are shown as the dashed line in Fig. 5. This curve demonstrates the strong decrease in the Zeldovich NO with increasing stabilization described previously. For the purposes of comparison, we have added a constant 15 ppm Fenimore NO to the calculated thermal contribution. The resulting agreement with the experimental data, even allowing for uncertainties in measurement position (± 0.5 mm), accuracy in NO measurement (better than 10%), and mechanism, is more than adequate to lend credence to the preceding interpretation. The origin of the slow decrease below 1800 K is not clear.

We point out here that for both the lean and stoichiometric mixtures, the flame extinguishes at a finite value of the NO concentration: roughly 12 ppm under stoichiometric conditions and ~2 ppm for the lean case. Since the flame temperatures under these conditions are low enough to freeze out any postflame NO formation, these concentrations, when corrected to a standard oxygen concentration, will form the basis for the emissions from a practical device fired under these conditions. Whereas 2 ppm can scarcely be considered a limitation from a practical standpoint, it will be clear that the concentration near extinction is the fundamental limit for the emission behavior from this type of burner; it is impossible to obtain less than 10 ppm NO for stoichiometric premixed firing using upstream heat loss as a control strategy.

NO Measurements: Fuel-Rich Flames

Examining the results for $\Phi = 1.15$ in Fig. 4, we observe a decrease in the NO concentration between ~2150 K and ~2050 K, again most likely [7] due to the slowing of the Zeldovich mechanism at these high temperatures, both in the flame front and in the postflame gases. Similar to the stoichiometric case, this drop is followed by a large region in which the NO concentration changes only slowly with temperature. When close to extinction, the NO concentration in this flame is still close to 30 ppm, probably all from the Fenimore mechanism. We remark here that the measured concentration of NO under these conditions is three times higher than that estimated by Miller and Bowman [4,7] for the Fenimore contribution from an equivalent methane-air flame.

Substantially more interesting are the results for $\Phi = 1.3$ and 1.4. Inasmuch as we expect a negligible contribution from the thermal mechanism at these equivalence ratios [4,7], one would anticipate that the NO concentration would remain more or less constant with temperature. However, both curves decrease dramatically with decreasing temperature, particularly at $\Phi = 1.4$, which shows a decrease in NO by a factor of 2 with a temperature change of only 100 K. One-dimensional flame calculations, as described previously, overpredict the magnitude of the NO concentration by a factor of 2 and predict the *expected* constancy of the concentration with temperature. The absolute magnitude of the measured NO concentration at the highest exit velocities (the highest temperatures), which are comparable to the conditions calculated in Ref. 4, are a factor of 2 higher than those calculated. The wide range of values predicted for these flames (varying over a factor of 4) seems to point to the necessity of a closer look at the chemical mechanism for fuel-rich flames and its response to stabilization.

Given the small activation energy of the CH + N_2 reaction as compared to O + N_2, it is difficult to

ascribe the decrease in NO with temperature, which is *steeper* than that from the stoichiometric flame, to a simple reduction in the velocity of the rate-limiting step in the Fenimore mechanism. In our opinion, there are two other possibilities within the framework of the current general ideas concerning NO formation in natural gas flames [4,7]. One possibility is that the stabilization process results in a slower conversion of HCN to NO, through a decreased concentration of the necessary flame radicals as a result of the lower temperature. The second possibility is that there is a shift in the relative positions of the profiles of temperature and CH upon stabilization; the relative locations of these profiles have been shown [20] to be crucial to the NO formation rate. (From a theoretical standpoint, it is somewhat distressing that the calculations appear to fail to account correctly for either alternative.) Although from a practical point of view the latter possibility would be the most fortunate (low NO emissions for fuel-rich flames), it will be necessary to rule out the former mechanism before drawing conclusions concerning the limiting NO emissions under these conditions. Since any residual HCN will be oxidized to NO in the burnout region of a practical flame (practical devices use secondary air to oxidize the CO and H_2 derived from the fuel-rich combustion zone), a shift from NO to HCN upon stabilization will clearly not help lower NO_x emission. Experiments are currently in progress to ascertain whether residual HCN is present.

Conclusions and Further Practical Implications

As mentioned previously, since current devices using premixed surface combustion are operated fuel lean, the results for the limiting NO concentrations from the lean and stoichiometric flames are expected to be representative for practical systems. In addition, given the observation [6] that postflame NO formation is negligible at temperatures below ~2000 K, the results for these two flames between 2000 K and extinction are anticipated to reflect the emissions from practical devices in this operating region as well.

An interesting complication in the practical interpretation of the results for the fuel-rich flames is that of the extant chemical enthalpy in the hot combustion gases. This enthalpy is released during the burnout process upon mixing with secondary air. For example, at $\Phi = 1.4$, the residual enthalpy allows for an ultimate flame temperature during burnout above 2000 K, despite a decrease in the fuel-rich flame temperature by 100 K through stabilization. Although the actual maximum temperature realized during burnout will depend on the details of the mixing process, one cannot rule out the possibility that additional NO will be formed by the Zeldovich mechanism. This phenomenon is also a current subject of study in our laboratory.

Whereas the discussion thus far has focused on the effects of stabilization on NO formation, we point out that, at least in principle, the NO concentrations measured in the fuel-rich flames under nearly adiabatic conditions should be indicative of those produced in the primary combustion zones of bunsen-type flames, such as are used in the vast majority of domestic appliances. In this regard, the concentrations measured in our experiments under near-adiabatic conditions are all in excess of 40 ppm, a proposed future limit for equipment using these burners in many countries. The promise of obtaining NO emissions below this value by means of upstream heat loss in and of itself merits further investigation.

Acknowledgments

We gratefully acknowledge a grant from the Gas Research Institute, R. V. Serauskas, contract manager, for partial support of this work. We also thank D. R. Crosley, for helpful discussions on the importance of the relative positions of the temperature and CH profiles in Fenimore-NO formation, and C. E. van der Meij, H. de Vries, and R. Pieters, for experimental assistance. Further, we thank J. Warnatz for the use of his flame codes.

REFERENCES

1. Williams, A., Woolley, R., and Lawes, M., *Combust. Flame* 89:157–166 (1992).
2. Levinsky, H., *1989 International Gas Research Conference,* Government Institutes, Inc., Rockville, MD, 1990, pp. 1026–1034.
3. Botha, J. P. and Spalding, D. B., *Proc. R. Soc. London, Ser. A* 225:71–96 (1954).
4. Miller, J. A. and Bowman, C. T., *Prog. Energy Combust. Sci.* 15:287–338 (1989).
5. Fenimore, C. P., *Thirteenth Symposium (International) on Combustion,* The Combustion Institute, Pittsburgh, 1971, pp. 373–379.
6. Levinsky, H., *Proceedings of the 35th Eurotherm Seminar,* Leuven (Belgium), 1994, pp. 1–14.
7. Bowman, C. T., *Twenty-Fourth Symposium (International) on Combustion,* The Combustion Institute, Pittsburgh, 1992, pp. 859–878.
8. Dean, A. J., Hanson, R. K., and Bowman, C. T., *Twenty-Third Symposium (International) on Combustion,* The Combustion Institute, Pittsburgh, 1991, pp. 259–265.
9. Van Oostendorp, D. L. and Levinsky, H. B., *J. Inst. Energy* 63:160–166 (1990).
10. Kroll, S., Alden, M., Bengtsson, P.-E., and Lofstrom, C., *Appl. Phys. B* 49:445–453 (1989).
11. van der Meij, C., Mokhov, A. V., Jacobs, R. A. A. M.,

and Levinsky, H. B., *Twenty-Fifth Symposium (International) on Combustion,* The Combustion Institute, Pittsburgh, 1994, pp. 243–250.
12. Reisel, J. R., Partridge, W. P. Jr., and Laurendeau, N. M., *JQSRT* 53:165–178 (1995).
13. Battles, B. E. and Hanson, R. K., *JQSRT* 54:521–537 (1995).
14. Reisel, J. R., Carter, C. D., and Laurendeau, N. M., *JQSRT* 47:43–54 (1992).
15. Mokhov, A. V., Levinsky, H. B., and van der Meij, C. E., in manuscript.
16. Reisel, J. R., Carter, C. D., Laurendeau, N. M., and Drake, M. C., *Combust. Sci. Technol.* 91:271–295 (1993).
17. Reisel, J. R. and Laurendeau, N. M., *Energy Fuels* 8:1115–1122 (1994).
18. Warnatz, J., *Ber. Bunsenges. Phys. Chem.* 87:1008–1022 (1983).
19. Bockhorn, H., Chevalier, C., Warnatz, J., and Weyrauch, V., *Heat Transfer in Fire and Combustion Systems,* HTD-Vol. 166, ASME, 1991, pp. 11–16.
20. Heard, D. E., Jeffries, J. B., Smith, G. P., and Crosley, D. R., *Combust. Flame* 88:137–148 (1992).

COMMENTS

Wolfgang Meier, DLR Stuttgart, Germany. What is the material of the burner plate? Are you sure that the doped NO for calibration is not consumed in the reaction zone or at the burner plate?

Author's Reply. The sinter was made of stainless steel. Flame calculations show substantial conversion of seed NO to HCN in the flame front, with reconversion to NO in the hot gases. For the near-adiabatic, stoichiometric flames used for calibration, independent measurements using suction probing and chemiluminescent analysis show that the seed concentration is preserved in the hot gases to better than 5%. As stated in the paper, we suspect substantial reburning of the seed NO (conversion to N_2) in the flame under fuel-rich conditions.

•

Marc Rumminger, University of California, Berkeley, USA. In my modeling of lean premixed porous radiant burners that have a flame stabilized on the surface, I have found that the properties of the porous medium have a moderate influence on NO_x at high exit velocity and conditions near $\emptyset = 1$ (i.e. where Zeldovich NO is important). As the upstream heat propagation increases, the NO_x goes down by up to 40%. Did the porous plug in the McKenna Products burner allow any heat to propagate upstream in the porous plug? Or was the cooling water flow high enough to maintain a nearly isothermal porous plug?

Author's Reply. The flow of water through the burner was such that the burner surface was maintained at room temperature.

Twenty-Sixth Symposium (International) on Combustion/The Combustion Institute, 1996/pp. 2155–2160

NO_x FORMATION IN TURBULENT LEAN-PREMIXED COMBUSTION WITH MINIMUM HEAT LOSSES

LIN XIE
Research Laboratory
Noritz Corporation
Tokyo, Japan

SHIGERU HAYASHI
Thermofluid Dynamics Division
National Aerospace Laboratory
Tokyo, Japan

KOHICHI HIROSE
Department of Mechanical Engineering
Faculty of Engineering
Tokyo Denki University
Tokyo, Japan

The formation of NO_x in turbulent combustion of lean-premixed methane/air mixtures and hydrogen/air mixtures was investigated at various levels of turbulent intensity using an impinging jet reactor. Much attention was paid to minimizing heat losses from the combustion field to the ambient. Experiments were carried out at atmospheric pressure and an inlet temperature of 323 K. The equivalence ratio ranged from 0.5 to 1.0 for CH_4/air mixtures and from 0.6 to 0.7 for H_2/air mixtures. Detailed results obtained at combustion gas temperatures (T_g) of 1390–2200 K with complete combustion are presented.

It was found that a change in the level of turbulence intensity did not result in a change in NO_x emissions. At $T_g > 1700$ K, the NO_x formation was contributed primarily by the thermal mechanism. The NO_x emissions were proportional to the reactor residence time and sensitive to the combustion gas temperature. The NO_x concentration for CH_4/air can be expressed as follows:

$$[NO_x] = \tau(5.96 \times 10^7) \exp(-31{,}500/T_g) \text{ (ppm)}$$

where τ is the mean residence time in ms and T_g in K. At $T_g < 1700$ K, however, the NO_x concentrations were independent of residence time and were only slightly sensitive to T_g. The NO_x concentrations for CH_4/air mixtures were in agreement with those for H_2/air mixtures. This implies that the NO_x was formed by a mechanism without hydrocarbon–nitrogen path. The nitrous oxide mechanism is expected to be an important mechanism for NO_x formation in the present impinging jet reactor.

Introduction

The emissions of oxides of nitrogen (NO_x) from combustion processes cause environmental pollution. An understanding of NO_x-formation mechanisms is essential for reducing the emissions levels. The chemistry of NO_x formation in a laminar laboratory flame has been studied for a long time, and the major reaction mechanisms are well understood [8]. In most practical combustors and engines, however, combustion proceeds in turbulent flow fields. The NO_x formation in turbulent combustion has been studied in many aspects [1–7]. An investigation of the NO_x formation in impinging jet combustion of premixed mixtures in a closed chamber demonstrated that a significant reduction of NO_x emissions (up to 88%) was attained at high turbulence levels [7]. However, the reduction cannot be fully attributed to the enhanced mixing of burned and unburned gases since heat losses to the walls of the chamber should be increased with the increased turbulence levels. In contrast with the considerable reduction of NO_x emissions, H. Semerjian et al. [2] reported that the rates of NO_x formation in fuel-lean, turbulent flames were higher when compared with those found for laminar flames at the same temperature. At present, the effect of turbulence on NO_x formation remains unclear.

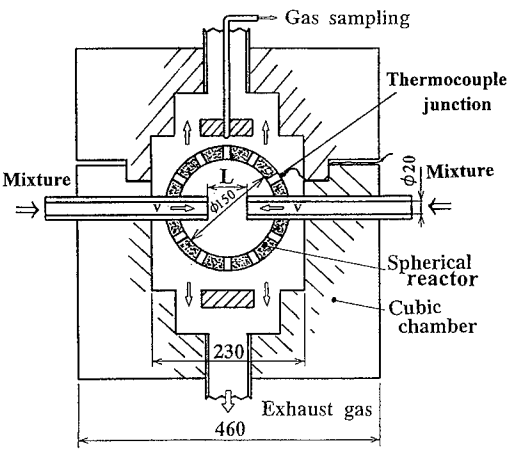

FIG. 1. Schematic of impinging jet reactor.

The application of the lean combustion concept to combustor design is an area of active investigation because of the potential benefit of ultra-low NO_x emissions [1]. In fuel-lean combustion, the contribution of the Zeldovich mechanism and the Fenimore mechanism to NO_x formation becomes small when the combustion temperature is below 1800 K [6]. It is proposed that most of the NO_x is formed by the nitrous oxide mechanism [5,6]. However, little experimental data are available on evaluation of the mechanisms.

In this study, the characteristics of NO_x formation in lean-premixed combustion were investigated in an impinging jet reactor made of ceramics. Much attention was paid to minimizing heat losses from the combustion field to the ambient. Detailed results obtained at combustion gas temperatures of 1390–2200 K with complete combustion are presented in this paper. The effects of turbulent intensity on NO_x emissions are examined.

Experimental Apparatus

The impinging jet reactor used in this study is shown in Fig. 1. The spherical ceramic reactor, 150 mm in inner diameter, is fed by two ceramic tubes of 20 mm in diameter. The reactor has 40 holes with diameters of 12 mm equally spaced on its wall. Inside the reactor, the two jets of premixed mixture impinge at the same velocity and form a turbulent flow field where combustion takes place. The burned gas goes through the holes and the space between the reactor and the heat-insulating firebrick chamber, of 230-mm cube, and finally is exhausted. The heat losses from the reactor are reduced greatly since the reactor is surrounded by hot, burned gases.

Experiments were conducted at atmospheric pressure for CH_4/air and H_2/air mixtures heated electrically to a temperature of 323 K. The equivalence ratio (ϕ) ranged from 0.5 to 1.0 for CH_4/air mixtures and from 0.6 to 0.7 for H_2/air mixtures. For H_2/air mixtures, flashback into the tubes occurred at combustion gas temperatures higher than 1700 K. Thus, the range of combustion gas temperatures was narrowly limited in the present measurement. The reactor mean residence time (τ) changed from 5.3 to 35.0 ms. H_2/air mixtures were used to examine the contribution of hydrocarbon–nitrogen paths to NO_x formation at lower combustion gas temperatures. The characteristics of NO_x formation for H_2/air mixtures were compared with those for CH_4/air mixtures.

To generate various levels of turbulence in the reactor, the jet velocity (V) and the distance between the exit planes of the two tubes (L) were varied. Data were collected for L = 20, 40, and 150 mm, and V = 20, 40, and 80 m/s, corresponding to mass flow rates of mixture (Q_m) of 13.8, 27.6, and 55.2 g/s, respectively.

Combustion gas temperatures were measured with Pt-Rh 20%/Pt-Rh 40% thermocouples coated with silicate-based zirconia at the center of several holes on the reactor wall. The measured temperatures were not found to differ significantly from each other. The averaged values of the measured temperatures were referred to as combustion gas temperature (T_g). The temperatures of the inner and outer surfaces of the reactor and those of cubic chamber walls were also measured. On the basis of these surface temperatures, the heat loss from the reactor was estimated to be less than approximately 8% of the heat release in the reactor. The combustion gas temperatures measured were only 50–110 K lower than the corresponding adiabatic temperatures. The turbulence characteristics of the impinging jet flow were measured under nonburning conditions by using a hot-wire anemometer. A 5-μm wire probe, calibrated in an orifice wind tunnel, was used.

Burned gas was withdrawn using a water-cooled stainless steel gas sampling probe with a 1-mm-diameter orifice and then fed to a gas analyzer to determine the concentrations of NO, NO_x, CO, CO_2, O_2, and total hydrocarbons. In the analyzer, NO and NO_x were detected by a chemiluminescence analyzer, CO and CO_2 by nondispersive infrared detectors, the total hydrocarbons by a flame ionization detector, and O_2 by a paramagnetic detector. The sampling line that connected the probe to the gas analyzer was heated electrically to prevent condensation of water vapor. The temperature and concentration data presented in this paper were collected after the establishment of thermally steady states at each reactor condition. The values of NO_x emissions, obtained in this study and derived from published papers, were expressed in terms of ppm corrected to 0% O_2, wet basis.

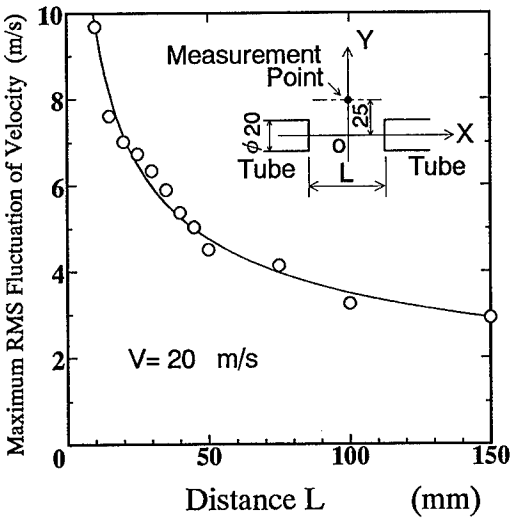

FIG. 2. Variation of maximum rms fluctuation of velocity with separation distance L.

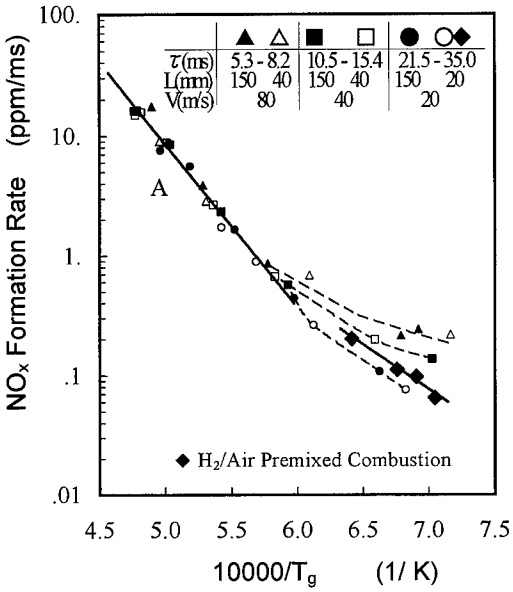

FIG. 3. Dependence of NO_x formation rate for CH_4/air and H_2/air on combustion gas temperature.

Experimental Results

In this work, the impingement strength of the two counterflow jets in the reactor was changed by varying L and V. The results of turbulence measurements revealed that an increase in V and a decrease in L intensified the turbulence in the bulk of the impinging flow field. In addition, it was found that the root-mean-square fluctuations of gas velocity (u') gradually increased from the tube exit toward the stagnation plane perpendicular to the axis of the tubes. On the stagnation plane, u' reached a peak value at a radial position of 1.25 times the tube diameter. Figure 2 illustrates the variation of u' at the peak with respect to L. A decrease in L from 150 to 10 mm resulted in an increase in the peak value from 2.9 to 9.7 m/s when V was equal to 20 m/s.

Figure 3 shows the dependence of NO_x formation rates on combustion gas temperatures for various turbulence levels. The NO_x formation rate on the vertical axis was defined as the ratio of NO_x concentration to τ. The values of τ can be divided into three groups in terms of V. Each test condition specified by V and L is labeled with a symbol in the figure corresponding to a level of turbulence intensity. The data corresponding to those in the figure are listed in Table 1.

Figure 3 shows that when $T_g > 1700$ K ($10^4/T_g < 5.88$), the NO_x-formation rate for CH_4/air mixtures depended primarily on T_g and was independent of V and L. Under the operating conditions in this study, therefore, the turbulence intensity generated by the impinging jets did not change the rate of NO_x formation.

The linear line (A) fitted to the data of NO_x emissions at temperatures higher than 1700 K was represented by the following equation:

$$[NO_x] = \tau\,(5.96 \times 10^7)\,\exp(-31{,}500/T_g)\ \text{(ppm)}$$

where τ is in ms and T_g in K. The overall activation energy for NO_x formation was estimated to be 63 kcal/mol by the expression based on the Arrhenius relationship.

Line A was compared with the data for NO_x-formation rates derived from published papers. H. Semerjian et al. investigated NO_x formation in lean-premixed, turbulent flames of prevaporized Jet-A fuel stabilized by perforated plate flame holders [2]. The NO_x was found to be formed more quickly in the recirculation zone behind the flame holders than in the postflame zone. The NO_x-formation rates, derived with respect to the residence time in the combustion reaction zone, are shown in Fig. 4. The data on line A were found to be very close to those of H. Semerjian et al., as well as those obtained in a jet-stirred combustor burning CH_4/air mixtures by C. J. Jachimowski et al. [4]. Figure 4 also shows another set of data (line B) for the NO_x-formation rates obtained by R. C. Steele et al. in a fuel-lean, jet-stirred reactor [6]. Although the NO_x-formation rates were greater by a factor of 3 to 4 when compared with line A, the overall activation energy of 55 kcal/mol, obtained by fitting to the data, was close to that for line A.

The data for the fuel-lean combustion with intense back mixing, shown in Fig. 4, are in agreement on the NO_x-formation rates being proportional to the

TABLE 1
Emissions data for combustion of CH_4/air and H_2/air mixtures

	T_g (K)	τ (ms)	NO_x (ppm)	CO (ppm)	$EI(NO_x)$ (g/kg)		T_g (K)	τ (ms)	NO_x (ppm)	CO (ppm)	$EI(NO_x)$* (g/kg)
	1395.6	8.22	1.8	82	0.09		1422.9	15.36	2.1	71	0.11
	1445.2	7.82	1.9	72	0.10		1517.3	14.57	2.9	73	0.16
	1473.0	7.44	1.6	76	0.08		1686.9	12.98	7.4	120	0.34
	1731.7	6.35	5.5	82	0.25		1715.8	12.93	8.6	102	0.40
CH_4	1883.9	6.10	17.6	104	0.71	CH_4	1844.3	11.92	28.0	180	1.09
V = 80 m/s	1891.7	5.82	22.8	170	0.88	V = 40 m/s	1863.6	11.90	31.8	156	1.30
	2016.1	5.69	51.5	584	1.85		1985.2	11.05	94.0	380	3.26
	2041.0	5.39	94.6	840	3.24		1994.7	11.14	98.0	740	3.61
	1465.2	35.01	2.7	4	0.15		2074.5	10.69	168.0	2340	5.59
	1509.0	28.84	3.1	30	0.15		2087.8	10.52	171.0	2580	5.41
	1633.0	31.75	8.3	23	0.40		2093.2	10.59	158.0	5180	5.19
	1673.5	26.03	11.4	71	0.49		2096.2	10.45	168.0	4620	5.20
CH_4	1758.4	29.57	26.2	37	1.11		1418.2	33.23	2.2		
V = 20 m/s	1809.1	24.10	39.9	120	1.46	H_2	1446.0	29.17	2.9		
	1842.7	28.87	49.8	113	1.93	V = 20 m/s	1477.8	26.35	2.9		
	1926.7	22.72	126.0	322	4.17		1556.2	26.48	5.4		
	2013.1	21.47	161.6	3050	4.98						

*$EI(NO_x)$: NO_x emission index

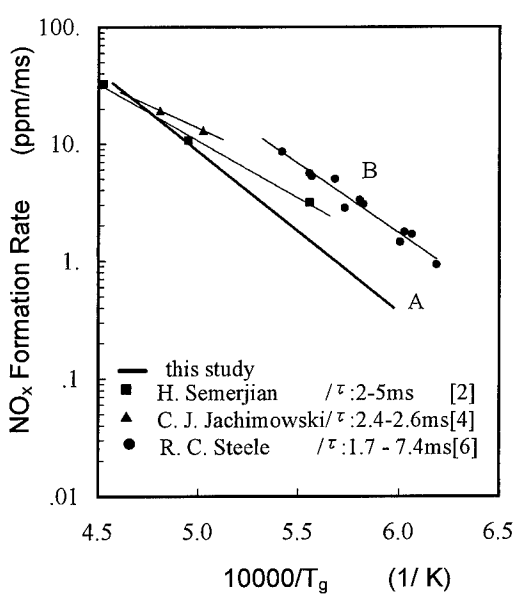

FIG. 4. NO_x formation rate for CH_4/air compared with data from previous experimental studies.

residence time and the values of the overall activation energy of NO_x formation approximately cover the range of 40–65 kcal/mol. These values were much lower than 134 kcal/mol for the thermal NO_x formation in a pure oxygen/nitrogen system but close to the heat of formation of atomic oxygen (59 kcal/mol) [10].

The mechanism of NO_x formation in laminar premixed combustion has been well understood [8] as a result of numerous experimental and modeling studies. Generally, NO_x formation by the thermal mechanism is proportional to its production time and depends heavily on the combustion gas temperature. The prompt NO_x formation occurs because of the superequilibrium concentrations of radicals (such O and OH) in regions near flame zone [8] or because of the Fenimore mechanism, especially at fuel-rich conditions [9]. In the present fuel-lean, turbulent, impinging jet combustion, the NO_x formation at the higher temperatures was primarily by the thermal mechanism; the Fenimore mechanism was not an important source of NO_x. In the turbulent flames, the intense back mixing between the burned and unburned gases occurred, which may lead to the rapid mixing of the excessive radicals from burning gases with unburned gases and then accelerate NO_x formation by the thermal mechanism at higher temperatures [8]. The difference between the overall activation energies for the turbulent flames and those for the pure oxygen/nitrogen system is prob-

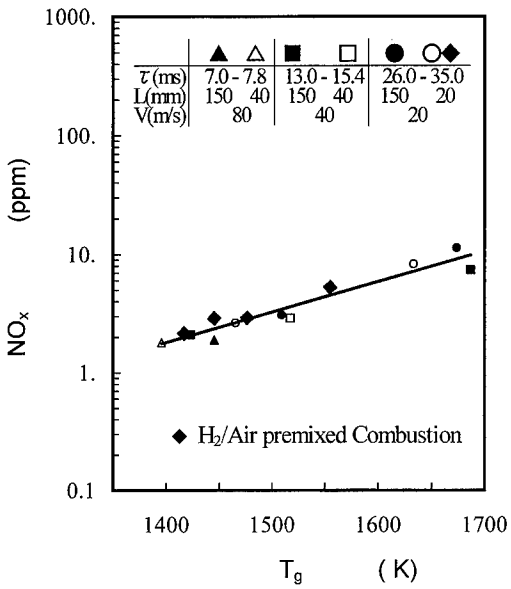

FIG. 5. NO_x emissions for CH_4/air and H_2/air at low-combustion gas temperatures.

ably accounted for by the rapid radical mixing in the flames. However, it is difficult to recognize essentially how the mixing affected the NO_x formation on the basis of the present experimental data.

The data for the NO_x-formation rates at temperatures below 1700 K deviated from line A, as shown in Fig. 3. The formation rates depended on the residence time in the reactor: The shorter the residence time, the greater the formation rate at a given T_g. The measured NO_x concentrations, rather than the NO_x formation rates, were plotted versus combustion gas temperature in Fig. 5. It is clear that the NO_x concentrations were independent of the residence time and only slightly dependent on the combustion gas temperature. Therefore, the thermal NO_x mechanism was thought to be largely suppressed and not a major contributor at the lower combustion temperatures. An alternate mechanism for NO_x formation is necessary to account for the observed behavior, including residence-time independence and very weak temperature dependence.

The NO_x concentrations for H_2/air mixtures plotted in Fig. 5 are found to be in agreement with those for CH_4/air mixtures. This implies that the NO_x in CH_4/air was formed by a mechanism without hydrocarbon reactions at $T_g < 1700$ K. As mentioned previously, P. C. Malte et al. proposed the nitrous oxide mechanism as an important mechanism of NO_x formation in lean-premixed combustion and suggested that the mechanism is a significant source, especially at temperatures below 1800 K [5,6]. They reported that their experimental data for NO_x emissions at combustion gas temperatures of 1650–1850 K in the jet-stirred combustion, shown in Fig. 4, could be accounted for by the modeling predictions, including the mechanism. Their predictions indicated that the dependence of NO_x formation on residence time becomes weak with decreasing temperature. This mechanism is expected to be an alternate mechanism for NO_x formation at $T_g < 1700$ K in the present impinging jet reactor.

Concluding Remarks

The mechanism of NO_x formation in lean-premixed, turbulent combustion of CH_4/air and H_2/air mixtures was investigated in an impinging jet reactor with minimum heat losses. The conclusions under the present operating conditions are as follows:

A change in the level of turbulence intensity did not result in a change in NO_x emissions.

At $T_g > 1700$ K, the NO_x formation was contributed primarily by the thermal mechanism. The NO_x emissions were proportional to the reactor residence time and sensitive to the combustion gas temperature. NO_x concentration for CH_4/air can be expressed as follows:

$$[NO_x] = \tau(5.96 \times 10^7) \exp(-31{,}500/T_g) \text{ (ppm)}$$

where τ is in ms and T_g in K.

At $T_g < 1700$ K, however, the NO_x concentrations were independent of residence time and only slightly sensitive to the combustion gas temperature. The NO_x concentrations for CH_4/air were in agreement with those for H_2/air. This implies that the NO_x was formed by a mechanism without hydrocarbon–nitrogen path. The nitrous oxide mechanism is expected to be an important mechanism for NO_x formation in the present impinging jet reactor.

REFERENCES

1. Tacina, R. R., "Low NO_x Potential of Gas Turbine Engines," NASA Report No. TM-102452, 1990.
2. Semerjian, H. and Vranos, A., *Sixteenth Symposium (International) on Combustion,* The Combustion Institute, Pittsburgh, 1977, pp. 169–179.
3. Xie, L. and Hayashi, S., "Effects of Jet Strength on NO_x Formation in Premixed Impinging Jet Combustion with Minimum Heat Losses," National Aerospace Laboratory Report No. TR-1237T, 1994.
4. Jachimowki, C. J. and Wilson, C. H., "Chemical Kinetic Models for Combustion of Hydrocarbons and Formation of Nitric Oxide," NASA Report No. TP-1794, 1980.
5. Malte, P. C. and Pratt, D. T., *Combust. Sci. Technol.* 9:221–231 (1974).
6. Steele, R. C., Malte, P. C., Nicol, D. G., and Kramlich, J. C., *Combust. Flame* 100:440–449 (1995).

7. Fujimoto, S., Kaneko, Y., and Tsuruno, S., *Twentieth Symposium (International) on Combustion*, The Combustion Institute, Pittsburgh, 1985, pp. 61–66.
8. Miller, J. A. and Bowman, C. T., *Prog. Energy Combust. Sci.* 15:287–338 (1989).
9. Fenimore, C. P., *Thirteenth Symposium (International) on Combustion*, The Combustion Institute, Pittsburgh, 1971, pp. 373–380.
10. Gaydon, A. G. and Wolfhard, H. G., *Flames*, Chapman and Hall, London, 1979.

COMMENT

Dr. Gregory Smith, SRI International, USA. If the N_2O mechanism is responsible for the low temperature NO, one might expect more NO at leaner stoichiometry. Do you have information on how the NO varies with stoichiometry?

Author's Reply. Your comment and question are very interesting. In our experiments, the decrease in stoichiometric ratio of the premixture of CH_4/air or H_2/air resulted in a decrease in combustion gas temperature, leading to smaller NO_x emissions. We believe that the information on variation of NO_x emissions with stoichiometric ratio at a constant temperature would be more helpful to understanding of NO_x formation, particularly at leaner stoichiometric ratio.

Twenty-Sixth Symposium (International) on Combustion/The Combustion Institute, 1996/pp. 2161–2170

COMPUTATIONAL AND EXPERIMENTAL STUDY OF NO IN AN AXISYMMETRIC LAMINAR DIFFUSION FLAME

M. D. SMOOKE,[1] A. ERN,[2] M. A. TANOFF,[1] B. A. VALDATI,[1] R. K. MOHAMMED,[1] D. F. MARRAN[1] AND M. B. LONG[1]

[1]*Department of Mechanical Engineering*
Yale University,
New Haven, CT 06520-8284, USA

[2]*CERMICS-ENPC, 93167 Noisy-le-Grand cedex, France.*
CMAP-CNRS, Ecole Polytechnique, 91128 Palaiseau cedex, France.

In this study, we extend the results of previous combined numerical/experimental investigations of an axisymmetric laminar diffusion flame in which spontaneous Raman spectroscopy, laser-induced fluorescence, and a multidimensional flame model were used to generate profiles of the temperature and major and minor species. We discuss issues related to the computation and measurement of NO in an unconfined laminar flame in which a cylindrical fuel stream is surrounded by a co-flowing oxidizer jet. Computationally, the governing conservation equations of mass, momentum, species, and energy were solved with detailed transport and finite-rate chemistry submodels to predict the velocity, species mass fractions, and temperature fields as functions of the two independent spatial coordinates. A discrete solution was obtained on a two-dimensional grid by employing Newton's method with adaptive mesh refinement. The computations were performed in both serial and parallel using up to 32 processors of an IBM SP2. Experimentally, NO radical concentrations were measured using laser-induced fluorescence. The associated results of the computational study clearly indicate that the prompt production path is the dominant formation route of NO. Thermal NO and the N_2O submechanism play minor roles in total NO production. Excellent agreement was obtained for the structural features of the computed and measured NO. The peak NO mole fractions agreed to within 30% of the experimental value. Additional quantitative CH computations and measurements are essential for further study of this problem.

Introduction

In recent years, we have witnessed a shift in the main thrust of combustion research. The push for higher combustion efficiency in propulsion applications that dominated much of combustion research in the past few decades is gradually being replaced by a drive toward *cleaner* combustion. This is a direct result of environmental consciousness, and it has been translated into stricter air quality legislation. Although it originated as a reaction to regulatory pressure, research in the area of pollutant formation and control will become economically indispensable to the export of combustion-related technologies and products worldwide. In addition, environmental concerns will become increasingly important in nations with strong growth potential.

As emissions legislation becomes more restrictive, a detailed understanding of pollutant formation in flames (e.g., soot, NO_x, unburned hydrocarbons) will be critical for the design of pollutant abatement strategies and for the preservation of the competitiveness of combustion-related industries. In particular, it is clear that there will be increasing pressure to lower NO_x emission indices of practical combustion devices. While catalytic combustion is one potential candidate for achieving this reduction, much work is still needed in understanding the detailed heterogeneous kinetic processes as well as in developing low-cost practical catalysts.

From a chemical viewpoint, computations of methane-air flames with C_2 chemistry represent the most complex multidimensional flame study to date [1]. From an environmental perspective, these studies are seriously lacking from the neglect of nitrogen-based chemistry. To address the issue of NO formation, we include a full NO_x reaction mechanism in a multidimensional axisymmetric model and compare the results of the calculations for NO with experimental measurements. An optically thin radiation model is also included. From an experimental viewpoint, laser-induced fluorescence measurements are combined with detailed information on the temperature and species concentrations in the flame and with a recent NO quenching model to obtain quantitative NO concentrations. Based on the success of this study, the model and diagnostic techniques could then be applied in the design of small,

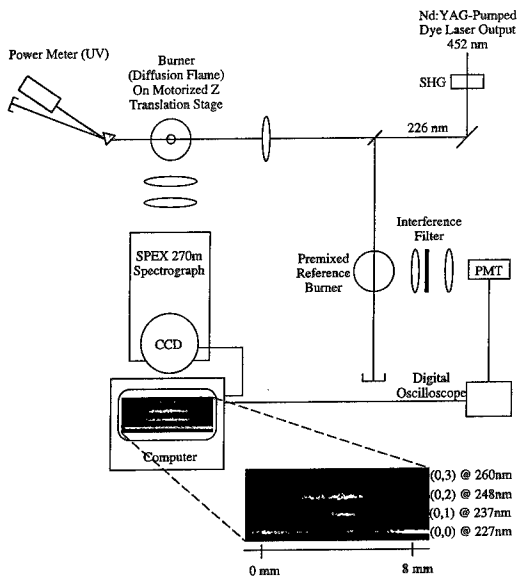

FIG. 1. Schematic of the LIF experimental setup.

practical natural gas burners. These burners often contain partially premixed flames and eventually will be subject to regulatory restrictions. In the next section, the experimental procedure is described. The solution method is discussed in the third section and the results of the study in the fourth section.

Experimental Procedure

The experimental configuration used for the linear NO fluorescence measurement is shown schematically in Fig. 1. The third harmonic of a Nd:YAG laser pumped a dye laser (coumarin 450 dye), producing a beam at 452 nm. A BBO crystal doubled the dye laser output to produce the 225.8-nm ultraviolet (UV) radiation used in the experiment ($\approx$40 μJ per 8-ns pulse at 10 Hz repetition rate). The residual 452-nm beam did not interfere with the measurement in any way and was not separated from the UV until after the beam passed through the flame, where a quartz prism separated the two wavelengths and allowed the measurement of the UV energy during the experiment. The main beam was focused using a 25-cm-focal-length quartz lens. To ensure that the fluorescence was in the linear regime, with no partial saturation, the measurements were made 10 cm beyond the primary focus of the UV beam and resulted in a beam diameter of 0.6 mm in the measurement region. The measured bandwidth of the 452-nm beam was 1 cm^{-1}, which corresponds to a UV spectral intensity of $\approx 10^6$ $W/cm^2/cm^{-1}$. This is well below the saturation value [2].

A portion of the main beam was separated and passed 6.2 cm above a premixed reference burner. The NO fluorescence from the lean propane flame was separated from other scattering by an interference filter (peak at 259 nm, 12.5-nm bandwidth) and detected with a PMT (Hamamatsu R166UH) connected to a digital oscilloscope. This signal was used to monitor laser energy and to ensure that the laser wavelength did not shift off of the peak of the NO transition being pumped. The PMT was also used to obtain an excitation spectrum to identify the various NO spectral features. Features over a spectral range from 225.4 to 226.8 nm were matched with the data of Engleman [3]. The Q_1 (18) transition of the NO $A^2\Sigma^+ - X^2\Pi$ (0, 0) band (44,275.684 cm^{-1}) was selected for this work. This transition is reasonably well separated from neighboring transitions and has significant population from room temperature to the flame temperatures investigated. In addition, no significant spectral interferences were encountered in the laminar flames investigated [4].

For measurement of the NO fluorescence in the diffusion flame, a pair of quartz lenses (8- and 10-cm focal lengths) imaged the scattered light onto the 300-μm entrance slit of a spectrograph (SPEX 270M). The fluorescence was dispersed with a 300-groove/mm grating (250-nm blaze angle) and imaged with an intensified CCD detector (consisting of a gated Gen II microchannel plate intensifier optically coupled to a cooled Photometrics STAR I CCD). A microcomputer controlled the experiment and recorded data from both the CCD and the digital scope. The CCD image contained information in one spatial and one spectral dimension. Spatially, a line extending from the centerline to 8.6 mm in the radial direction was imaged, and spectrally the region from 220 to 265 nm was recorded. The spectral region included Rayleigh scattering (overlapped with the [0, 0] fluorescence) as well as the (0, 1), (0, 2), and (0, 3) vibrational fluorescence bands. The fluorescence signal was integrated on the detector for 25 s and then read out and stored in the computer. During the integration time, the signals from the PMT and the energy meter were also integrated and stored. To generate a two-dimensional image of the NO fluorescence distribution, a series of spatial/spectral images was recorded at different heights above the burner. The burner was moved vertically in 0.25-mm steps using a computer-controlled stepping motor. Measurements were made from 0.35 cm above the burner surface (less than the liftoff height of the flame) to 5.8 cm downstream.

The final fluorescence image was obtained by summing the fluorescence intensity over a 7.5-nm spectral region centered on the (0, 2) transition [5]. No significant difference was noted, however, when the detection band was centered on the (0, 1) transition. The fluorescence image compiled from the series of spatial/spectral images was corrected for detector background and for nonuniform detector

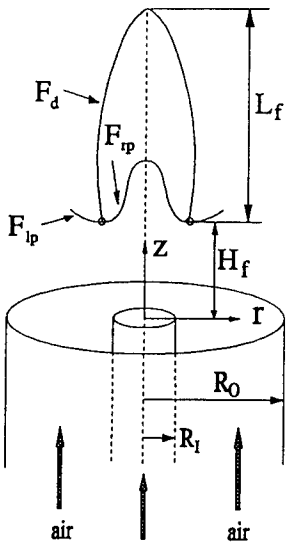

FIG. 2. Schematic of an unconfined axisymmetric laminar diffusion flame.

gain and optical throughput. This latter "response" correction was obtained by imaging a nonreacting flow of 46 ppm NO in N_2 through the burner's co-flow, which resulted in a uniform NO concentration field in the imaged region. Changes in the laser energy and any slight drift of the laser wavelength were normalized using the averaged output of the NO fluorescence from the premixed reference burner detected by the PMT. The final corrected fluorescence image had a signal/noise ratio of ≈40 in the downstream region where the NO signal was highest and a pixel volume of $0.3 \times 0.3 \times 0.6$ mm^3.

For linear fluorescence, the scattered intensity is dependent on the total number density in the ground electronic state, N_g, as well as a variety of other variables in the flame as follows:

$$I_f = CN_g f_B B_{12} I \frac{A_{21}}{(A_{21} + Q)} \quad (1)$$

C is an instrumental constant, f_B is the Boltzmann population fraction, A_{21} and B_{12} are the Einstein coefficients, and I is the laser intensity. Q represents the total collisional quenching rate. For NO, the quenching term is particularly important and varies significantly with temperature and quenching partners. Fortunately, a good deal of information is available on NO quenching in the form of experimental measurements and models. Drake and Ratcliffe [5] have measured quenching cross sections as a function of temperature for a number of different species important in combustion research. More recently, Paul et al. [6] have developed a model for temperature-dependent NO quenching that is in general agreement with the experimental work by a number of groups. Because the flame we are studying has been well characterized in terms of temperature and major species [7], we can use our previous data on this flame along with the quenching models to quantitatively determine the NO concentration. The major species and temperature measured with Raman scattering were seen previously to be in good agreement with the calculated values [7], so the computed values were used for the quenching and Boltzmann corrections in the results presented here. By using the computed values, we avoided adding the noise that was present in the Raman measurements. In calculating the NO mole fraction of our flame, we have used the results of Paul's model to account for the temperature-dependent quenching of CO_2, H_2O, O_2, N_2, and CO. The instrumental constant was determined from the known NO concentration (46 ppm) in the NO/N_2 mixture used in the response correction.

The quantitative value obtained for NO concentration in the laminar diffusion flame is critically dependent on the quenching and Boltzmann corrections. As a check to the accuracy of the NO measurements, an additional set of experiments was performed in the postflame region of premixed CH_4/N_2/O_2 flames. In these experiments, NO fluorescence measurements were made with CH_4/O_2 and pure N_2 and then repeated with a mixture of 46 ppm NO in N_2 replacing the pure N_2. By ratioing these measurements, the amount of NO in the undoped premixed flame can be determined without the need for Boltzmann or quenching corrections. (The assumption that the additional NO does not significantly affect the flame seems to be borne out in other experiments [8,9].) The NO concentration from the undoped flames was then determined using the same quenching and Boltzmann correction approach used in the diffusion flame results. Calculated equilibrium values of temperature and major species were used for the corrections. For flames of stoichiometric ratios of 0.87 and 1.0, the values of NO concentration obtained in the two different ways agreed to within 7% and 2%, respectively.

Problem Formulation and Method of Solution

Our model of an axisymmetric laminar diffusion flame considers an unconfined laminar flame in which a cylindrical fuel stream is surrounded by a co-flowing oxidizer jet (see Fig. 2). Computationally, the full set of elliptic two-dimensional governing equations—mass, momentum, species, and energy—are discretized on a two-dimensional mesh. The resulting nonlinear equations are then solved by a combination of time integration and Newton's method. The Newton equations are solved by a preconditioned Bi-CGSTAB iteration. We determine the grid points of the two-dimensional mesh by

equidistributing positive weight functions over mesh intervals in both the r and z directions. The size of each time step is chosen by monitoring the local truncation error of the time discretization process (see also Ref. 10). Because of the cost of forming the Jacobian matrices with detailed transport and finite-rate chemical kinetics, a modified Newton method is implemented along with several theoretical estimates that determine when a new Jacobian should be formed. These theoretical results help increase the overall efficiency of the algorithm. The binary diffusion coefficients, the viscosity, the thermal conductivity of the mixture, the chemical production rates, and the thermodynamic quantities were evaluated using vectorized and highly optimized transport and chemistry libraries [11].

Anticipating that radiative losses could have a significant influence on NO levels compared to a nonradiative system, we have included an optically thin radiation model in our calculations. We assume that for methane-air mixtures, the only significant radiating species are H_2O, CO, and CO_2. By using an optically thin limit in which self-absorption of radiation is neglected, the divergence of the net radiative flux can be written

$$\nabla \cdot q_R = 4\pi \sum_i \rho_i \alpha_i B_i (T) \tag{2}$$

where $B_i(T)$ is the Planck function evaluated at the band centers of the contributing vibration-rotation or pure rotational bands whose integrated intensities are given by α_i [12,13].

As the number of grid nodes required to resolve the dependent variables increases, the size of the problem grows dramatically. A full NO_x problem (e.g., temperature, 48 elementary species, and three fluid dynamic variables) on a 12,000-node mesh requires the solution of more than half a million nonlinear algebraic equations. The nonzero entries of the blocked nine-diagonal Jacobian matrix require more than 2GB memory. Previous studies illustrate that while field-by-field solution methods could be used at lower memory cost, their convergence rate is significantly slower than by fully coupling the dependent variables [14]. In addition, techniques that do not require a copy of the Jacobian are extremely inefficient computationally when performing sensitivity analyses.

Problems of this size are difficult to solve on even the most powerful high-speed workstations. As a result, we have modified the serial implementation of the solution algorithm so as to be applicable to a distributed memory parallel computer. Specifically, the time-dependent/Newton solution algorithm is divided into two computationally intensive portions—the formation of the Jacobian matrix and the subsequent iterative solution of the Newton equations. Formation of the Jacobian requires $9K + 1$ function evaluations where K represents the number of dependent solution variables and where each function evaluation requires the formation of the residual function. Given a solution estimate U, each function evaluation can be performed independent of the others. We partitioned the $9K + 1$ function evaluations across $N = 1, 2, \ldots, 32$ wide nodes of the IBM SP2 at the Cornell Theory Center. In this way, each processor was able to compute a portion of the Jacobian matrix in parallel with the other processors. Once the Jacobian was formed, the linear Newton equations were solved iteratively using a preconditioned Bi-CGSTAB iteration across each of the N domains. CPU times were reduced by a factor of 20–25 over serial times on a 32-node machine. Serial computations were performed on an IBM RS/6000 Model 590 computer.

Numerical Results

NO can be formed in hydrocarbon flames by several different mechanisms [15,16]. The "thermal" (Zeldovich) path involves reactions between atmospheric nitrogen and atomic oxygen. It is significant at temperatures above ≈1850 K. Thermal NO formation can also be enhanced by superequilibrium free radical concentrations. The expression *prompt NO* was coined [17] to describe an apparently instantaneous formation of NO when the axial profile of NO in a flat-flame burner was extrapolated to the surface. The nonzero intercept was termed the

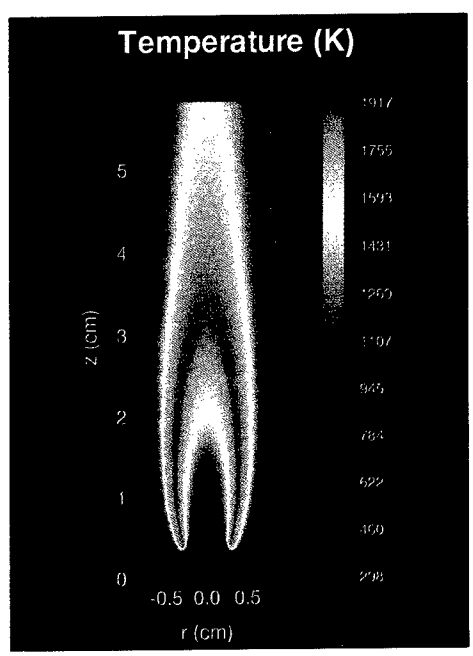

FIG. 3. Computed temperature isotherms for the unconfined methane-air diffusion flame.

prompt contribution. This arises through reactions between alkyl species and atmospheric nitrogen, in particular, via the reaction

$$CH + N_2 = HCN + N \qquad (I)$$

NO can also be formed via the N_2O intermediate. The rate of formation of NO through this path increases at higher pressures. In this section, we present the results of a joint experimental and computational study of a diluted methane-air laminar diffusion flame. The calculations employed the 48-species, 275-reaction GRI-Mech version 2.11 [18]. We also considered a combined mechanism using the C_2 reaction set of Ref. 1 with the NO_x submechanism of Drake and Blint [16].

The experimental configuration was such that the radius of the inner fuel jet $R_I = 0.2$ cm and the radius of the outer oxidizer jet $R_O = 2.5$ cm. Fuel and nitrogen are introduced through the center tube and air through the outer co-flow. The boundary conditions at the inlet are given by

Inlet ($z = 0$):

$r < R_I$

$$T = 298 \text{ K} \qquad (3)$$

$$Y_{CH_4} = 0.5149,\ Y_{N_2} = 0.4851$$

$$Y_k = 0,\ k \neq CH_4, N_2$$

$$v_r = 0.0 \text{ cm/s},\ v_z = 35.0 \text{ cm/s}$$

$R_I < r < R_O$

$$T = 298 \text{ K} \qquad (4)$$

$$Y_{O_2} = 0.232,\ Y_{N_2} = 0.768,\ Y_k = 0,\ k \neq O_2, N_2$$

$$v_r = 0.0 \text{ cm/s},\ v_z = 35.0 \text{ cm/s}$$

For reference purposes, the temperature isotherms are illustrated in Fig. 3. As has been pointed out in earlier studies [1,7], the high-temperature region has a wishbone-type structure. The highest energy release rate occurs in a thin region above the inlet. The temperature rapidly rises from 298 to nearly 1900 K in approximately 4.0 mm. It is in the vicinity of this region that the fuel and the oxidizer first meet in stoichiometric proportion. The methane and oxygen co-exist in only a very small domain. Most of the methane disappears within 1.0 cm of the fuel jet. Large quantities of H_2O, CO, and H_2 are produced soon after the methane has been consumed. It is in this region that the methane is attacked by O, H, and OH radicals and CH_3 is formed. Only small amounts of OH, H, and O exist because of the high affinity of methane for these radicals.

In Fig. 4, we compare computed and experimental NO mole fraction isopleths. The region illustrated corresponds to the section of the flame imaged by the detector. The calculated results include radiation and are based on GRI-Mech. From a structural point of view, there is excellent agreement among the various features of the two plots. NO increases along the centerline and peaks at approximately 3.2 cm; the wishbone regions extending along the edges of the flame front begin at the same height and close on the centerline at approximately 2.9 cm. Computationally, we determine a peak NO mole fraction of 67 ppm compared to 100 ppm determined via LIF. The peak computed temperature is 1917 K. If radiation is neglected, we find that the peak temperature rises to about 2000 K and NO levels increase by a few ppm.

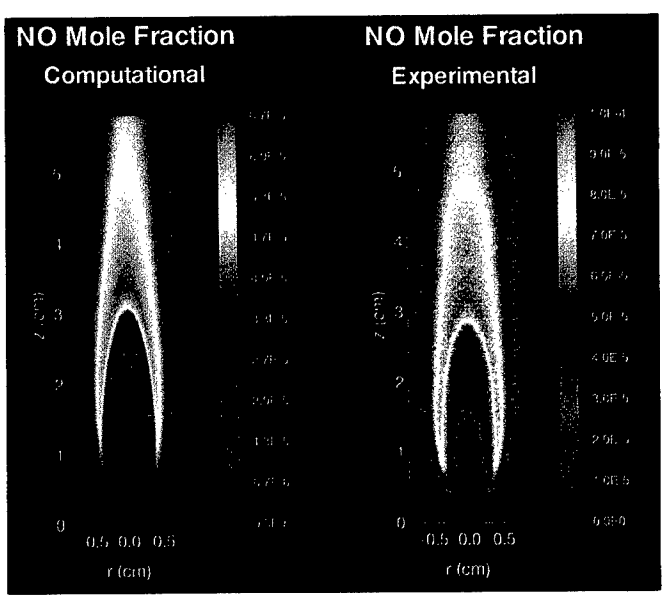

FIG. 4. Computed and experimental NO isopleths for the unconfined methane-air diffusion flame. The computations were made with GRI-Mech and an optically thin radiation model. The region illustrated corresponds to the domain imaged by the detector.

The CH radical is important in prompt NO production in both premixed and non-premixed methane-air systems. As has been pointed out by several authors [19], uncertainty in the rate of (*I*) can lead to disagreement in NO levels. Moreover, even if the value of the rate used is "correct," it is still critical that CH levels be predicted accurately. Accurate computation of CH radicals poses a difficult numerical problem. The CH profile has the highest spatial activity of any of the 48 species (45 species using the mechanism from Refs. 1 and 16) considered in this study. It can change by an order of magnitude within 0.1 mm. This requires that the adaptive grid be refined to an extremely small mesh size. Underresolution of the profile can lead to inaccuracies in CH values. The extremely thin CH "shell" is observable in the numerical (see Fig. 5), as well as in the experimental profile found in Ref. 1. Peak CH levels are 3.3 ppm. In addition, the HCN precursor peaks along the CH shell but further downstream from the CH peak.

To determine the relative contributions of the other two NO formation pathways, several additional computations have been performed. Starting with the hydrocarbon reaction set of Ref. 18, we included only the thermal portion of the NO_x mechanism, that is,

$$N_2 + O = NO + N \qquad \text{(II)}$$

$$N + O_2 = NO + O \qquad \text{(III)}$$

$$N + OH = NO + H \qquad \text{(IV)}$$

This reaction set will be important at high temperatures and long residence times in the flame. As we mentioned earlier, the peak temperature in this flame is only 1917 K. In addition, because of the acceleration of the gases due to buoyancy, the residence time τ along the centerline from where the temperature first reaches $\approx$1850 K to where it finally falls below this value is small. In particular, by computing

$$\tau = \int_{z_{min}}^{z_{max}} \frac{dz}{v_z(0, z)} \qquad (5)$$

where z_{min} and z_{max} are the minimum and maximum flame heights where the centerline temperature is above 1850 K, respectively, and where we have made specific reference to the fact that the axial velocity is taken along the centerline $r = 0$, we find the residence time equal to 5.1 ms. It is interesting to point out that in previous studies of lean stirred reactors [20], short (1–5 ms) residence times precluded significant yields of NO via the thermal pathway. The prompt mechanism was the most important path to NO formation. In these studies, total NO concentrations were small. In the current study, however, residence times are short but total NO is high. Thermal NO isopleths are presented in Fig. 6. The peak

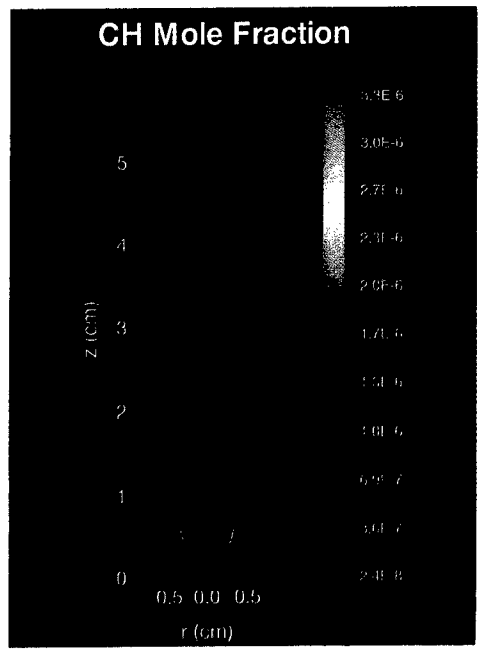

FIG. 5. Computed CH radical isopleths for the unconfined methane-air diffusion flame.

NO mole fraction is only 10.1 ppm and the region of highest thermal NO occurs nearly 10 mm above the peak NO mole fraction for the full mechanism calculation.

Using the hydrocarbon portion of the reaction set plus reactions (II) through (IV), we next included the N_2O submechanism

$$N_2 + O + M = N_2O + M \qquad \text{(V)}$$

$$O + N_2O = NO + NO \qquad \text{(VI)}$$

$$O + N_2O = N_2 + O_2 \qquad \text{(VII)}$$

$$H + N_2O = NO + NH \qquad \text{(VIII)}$$

$$H + N_2O = N_2 + OH \qquad \text{(IX)}$$

in our calculations. As pointed out by Drake and Blint [16], this submechanism becomes more important in NO formation as the pressure increases. As a result, we do not expect it to be a major contributor in this study. Inclusion of reactions (V) through (IX) raises the peak NO mole fraction by less than 1 ppm. Based on these results, we find that prompt NO accounts for nearly 85% of total NO with thermal NO and the N_2O pathway accounting for the rest.

In previous computational and experimental studies, we employed a C_2 methane-air reaction mechanism containing 26 species. Excellent agreement

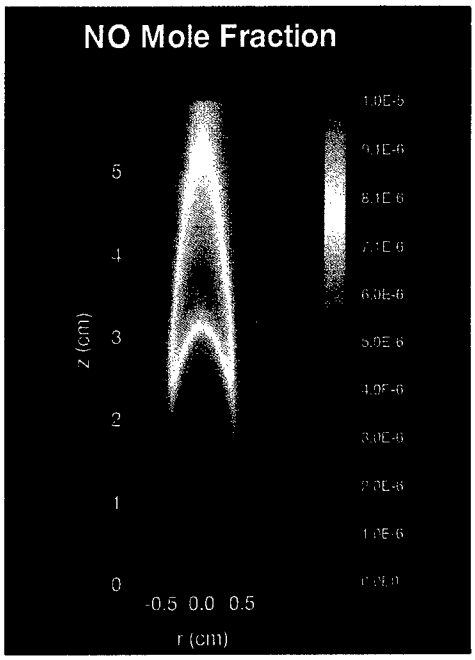

FIG. 6. Computed thermal NO isopleths for the unconfined methane-air diffusion flame. The computations were made with the hydrocarbon portion of GRI-Mech with reactions (II) through (IV) and an optically thin radiation model.

was found to exist between computational and experimental profiles of the temperature [7,21], velocity at extinction [22], major species [7,21], and the OH radical [1]. Only structural comparisons were made between computed and measured CH profiles [1]. Using this mechanism and the NO_x submechanism of Drake and Blint [16], we recomputed the axisymmetric methane-air flame structure. In Fig. 7, we illustrate computed and experimental NO isopleths obtained with the joint mechanism. While the general structure of the computed results looks similar to that in Fig. 4, peak mole fraction values are significantly different. This mechanism predicted a peak NO value of 176 ppm (11 ppm thermal NO). If the higher rate reported in Ref. 16 for reaction (I) is used, the peak NO mole fraction increases to 180 ppm. To illustrate specific structural similarities and differences among the experiments and computations with the two mechanisms, we plot in Fig. 8 NO mole fractions along the centerline of the flame. Both the experimental and the GRI-Mech computations illustrate a very rapid increase in NO values around 2.9 cm and a gradual falloff as we enter the postflame region. The combined mechanism from Refs. 1 and 16 significantly overpredicts NO levels and does not show as sharp an increase in NO near the tip of the flame. The shape of the postflame decline in NO is similar to the other two cases.

Uncertainties in the quenching correction represent the largest source of uncertainty in the quantitative measurement of the NO mole fraction. For example, if an empirical fit to Drake's data is used for the NO quenching cross section (rather than the Paul et al. model), the peak NO concentration determined from the measurements decreases by

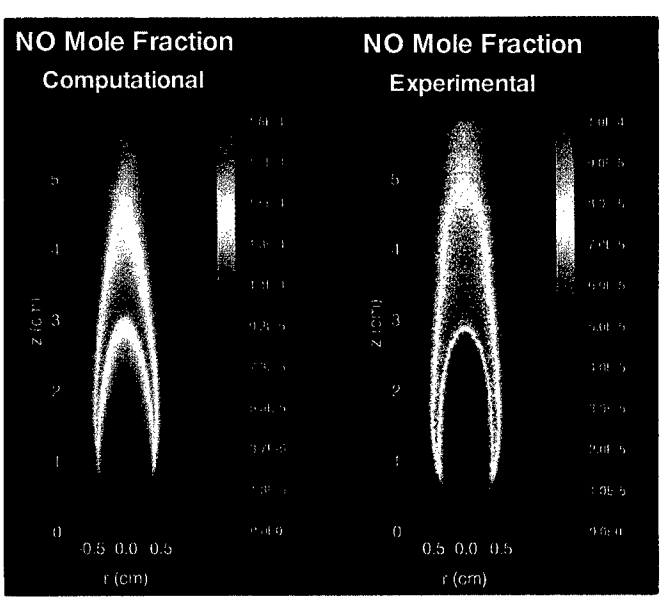

FIG. 7. Computed and experimental NO isopleths for the unconfined methane-air diffusion flame. The computations were made with the combined hydrocarbon mechanism from Ref. 1 and the NO_x submechanism from Ref. 16 with an optically thin radiation model. The region illustrated corresponds to the domain imaged by the detector.

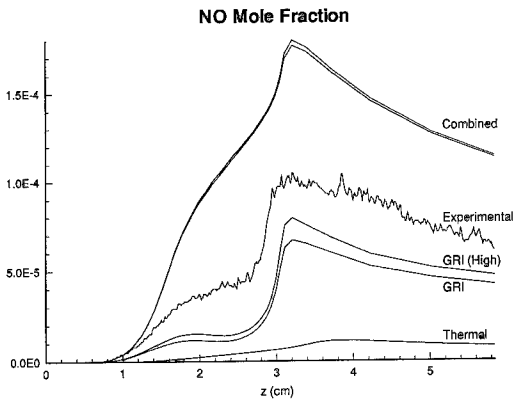

FIG. 8. NO mole fractions as a function of distance along the centerline. We illustrate the total (prompt + thermal + N_2O) NO mole fraction obtained with GRI-Mech, the experimental NO profile, the thermal portion of GRI-Mech, and the total NO from combined mechanism [1,16]. The two GRI curves illustrate results for the original rate of (I) reported in Ref. 18 and the higher rate reported in Ref. 16. The two curves for the combined mechanism indicate computations for the high and low rate of reaction (I) reported in Ref. 16.

roughly 20%. While this would bring the peak NO very close to that calculated using GRI-Mech, the agreement with the doped/undoped premixed flame would be poorer. Even with an experimental uncertainty on the order of 20% for the peak value of the NO concentration, the agreement between experiment and computation is extremely encouraging.

Conclusions

In this study, we extended the results of previous combined numerical/experimental investigations of an axisymmetric laminar diffusion flame in which spontaneous Raman spectroscopy, laser-induced fluorescence, and a multidimensional flame model were used to generate profiles of the temperature and major and minor species. We discussed issues related to the computation and measurement of NO in an unconfined laminar flame in which a cylindrical fuel stream is surrounded by a co-flowing oxidizer jet. The computations were performed in both serial and parallel using up to 32 processors of an IBM SP2. Experimentally, NO radical concentrations were measured using laser-induced fluorescence.

The results of the study clearly indicate that the prompt production path is the dominant formation route of NO for this type of axisymmetric laminar diffusion flame. Thermal NO and the N_2O submechanism play minor roles in total NO production. Excellent agreement was obtained for the structural features of the computed and measured NO profiles using GRI-Mech, with good agreement for peak mole fraction values. Significant variations in NO levels were obtained by using a different mechanism—though one that had predicted very good agreement in temperatures, velocities, and major and some minor species in various flame configurations. Additional quantitative CH and CH_2 measurements are needed to complete our understanding of this problem.

Acknowledgments

This work was supported in part by the U.S. Department of Energy, Office of Basic Energy Sciences, and by the Office of Naval Research. The authors would like to express their appreciation to Drs. M. C. Drake, M. B. Colket, and R. Yetter for their comments and input regarding this work.

REFERENCES

1. Smooke, M. D., Xu, Y., Zurn, R., Lin, P., Frank, J., and Long, M. B., *Twenty-Fourth Symposium (International) on Combustion,* The Combustion Institute, Pittsburgh, 1992, p. 813.
2. Verdieck, J. F. and Bonczyk, P. A., *Eighteenth Symposium (International) on Combustion,* The Combustion Institute, Pittsburgh, 1981, p. 1559.
3. Engleman, R. Jr., Rouse, P. E., Peek, H. M., and Baiamonte, V. D., "Beta and Gamma Systems of Nitric Oxide," Los Alamos Scientific Laboratory Report LA-4364, Los Alamos, NM, 1970.
4. Carter, C. D. and Barlow, R. S., *Opt. Lett.* 19(4):299 (1994).
5. Drake, M. C. and Ratcliffe, J. W., *J. Chem. Phys.* 98(5):3850 (1993).
6. Paul, P. H., Gray, J. A., Durant, J. L. Jr., and Thoman, J. W. Jr., *Appl. Phys.* B 57:249 (1993).
7. Smooke, M. D., Lin, P., Lam, J. K., and Long, M. B., *Twenty-Third Symposium (International) on Combustion,* The Combustion Institute, Pittsburgh, 1990, p. 575.
8. Reisel, J. R., Carter, C. D., Laurendeau, N. M., and Drake, M. C., *Combust. Sci. Technol.* 91:271 (1993).
9. Barlow, R. S. and Carter, C. D., *Combust. Flame* 97:261 (1994).
10. Smooke, M. D., Mitchell, R. E., and Keyes, D. E., *Combust. Sci. Technol.* 67:10 (1989).
11. Giovangigli, V. and Darabiha, N., "Vector Computers and Complex Chemistry Combustion," Proceedings of the Conference on Mathematical Modeling in Combustion, Lyon, France, NATO ASI Series, 1987.
12. Hall, R. J., *J. Quant. Spectros. Radiat. Transfer* 49:517 (1993).
13. Hall, R. J., *J. Quant. Spectros. Radiat. Transfer* 51:635 (1994).
14. Xu, Y., Ph.D. Thesis, Yale University, New Haven, CT, 1991.

15. Miller, J. A. and Bowman, C. T., *Prog. Energy Combust. Sci.* 15:287 (1989).
16. Drake, M. C. and Blint, R. J., *Combust. Sci. Technol.* 75:261 (1991).
17. Fenimore, C. P., *Thirteenth Symposium (International) on Combustion,* The Combustion Institute, Pittsburgh, 1971, p. 373.
18. Bowman, C. T., Hanson, R. K., Davidson, D. F., Gardiner, W. C. Jr., Lissianski, V., Smith, G. P., Golden, D. M., Frenklach, M., Wang, H., and Goldenberg, M., GRI-Mech version 2.11, http://www.gri.org, 1995.
19. Drake, M. C. and Blint, R. J., *Combust. Flame* 83:185 (1991).
20. Correa, S. M. and Smooke, M. D., *Twenty-Third Symposium (International) on Combustion,* The Combustion Institute, Pittsburgh, 1990, p. 289.
21. Puri, I., Seshadri, K., Smooke, M. D., and Keyes, D. E., *Combust. Sci. Technol.* 56:1 (1987).
22. Smooke, M. D. and Giovangigli, V., *Twenty-Third Symposium (International) on Combustion,* The Combustion Institute, Pittsburgh, 1990, p. 447.

COMMENTS

Kermit C. Smyth, NIST, USA. Your results show that both the peak NO concentrations and the maximum NO production rates occur very close to the locations of the peak temperatures for a range of axial locations, yet the prompt route dominates NO formation. This situation is somewhat counter-intuitive and occurs because the fastest NO consumption reactions involve hydrocarbons and act to mask prompt NO formation [1,2].

REFERENCES

1. Nishioka, M., Nakagawa, S., Ishikawa, Y., and Takeno, T., *Combust. Flame* 98:127–138 (1994).
2. Smyth, K. C., "NO Production and Destruction in a Methane/Air Diffusion Flame," *Combust. Sci. Technol.,* in press.

Author's Reply. As we illustrated in the paper, the prompt route dominates NO formation in the flame. We agree that this is not what one would first expect considering that the peak NO concentrations and production rates occur very close to the region of the peak temperature as you move upward in the flame. However, in portions of these high production rate regions the temperature is actually below 1850 K. Also, as you point out, the fastest NO consumption reactions involve hydrocarbon species which can "hide" the prompt formation route.

•

Robert S. Barlow, Sandia National Laboratories, USA. With the laser system we use for NO measurements, we have found that it is important to account for changes in the overlap integral between room temperature and flame temperatures [1]. This is one of the reasons which has led us to perform NO calibrations in flames, rather than cold gases. Is this an issue for your measurement system? Also, is the statement that there is no interference from O_2 fluorescence based on the use of narrow-band detection of NO at ~248 μm? With broadband detection there will certainly become O_2 interference, though it may only be important for measurements of low NO concentrations (say, below 20 ppm).

REFERENCES

1. Carter, C. D. and Barlow, R. S., *Opt. Lett.* 19:299 (1994).

Author's Reply. With our laser linewidth and measurement system, the difference between room-temperature and flame-temperature calibration was not significant. This was verified by the agreement in NO concentration between the room-temperature-calibrated results and the doped/undoped results in the premixed flame.

Regarding interference from O_2, the $Q_1(18)$ transition in NO was selected based on Cater and Barlow, Optics Letters, 1994 (Ref. 9 in paper) which stated that "the $Q_1(18)$ transition of NO (λ = 225.9) is isolated from neighboring NO lines and does not overlap distinct O_2 lines." Because a spectrograph was used for detection of the NO signal, we were able to spectrally resolve the fluorescence signal. Distinct spectral interferences (such as those from oxygen) would be expected to have a different fluorescence signature than that of NO, and no such interferences were observed in our data. We found that the measured NO concentration was not significantly different when the detection band was centered at either the (0,1) or (0,2) transitions. We did not, however, determine the NO concentration using broadband detection, which could be influenced by a broadband background.

•

Yung-cheng Chen, Tsinghua University, Taiwan. In your oral presentation, high CH_2 concentration along the lean and rich premixed flame fronts of the triple flame structure can be seen at the flame stabilization point. However, such tri-branch structure can't be seen in the CH concentration distribution, which should also exist along the premixed flame fronts. Could you please explain why? Can you see the tri-branch structure in OH concentration distribution?

Author's Reply. Observation of the tribrachial structure of the flame is difficult unless there is significant resolution of the flame structure in the region in question. While the structure is clearly visible in the CH_2 concentration, it is

somewhat less visible (though still there) in the CH mole fraction contour. For OH, the structure is not visible due to the "broadened" structure at the base of the flame compared to CH_2 and CH.

•

Jay Jeffries, SRI International, USA. How large is the effect of the radiative losses on the NO production? When you calibrate the NO signal with NO added to the flame, is reburning an important effect?

Author's Reply. Radiative losses account for about an 80–85 K lowering of the peak temperature value. If radiative losses are not included in the model, peak NO levels increase to 83 ppm.

Other studies (Refs. 8 and 9 in the paper) have shown that doping the premixed flame with a small amount of NO can be used to provide an additive NO concentration of a known amount in the post-flame region. The measurements were performed well downstream of the flame to avoid any chemistry effects at the flame front.

Twenty-Sixth Symposium (International) on Combustion/The Combustion Institute, 1996/pp. 2171–2179

REDUCED MECHANISMS FOR NO_x EMISSIONS FROM HYDROCARBON DIFFUSION FLAMES

J. C. HEWSON
Center for Energy and Combustion Research
University of California, San Diego
La Jolla, CA 92093-0411, USA

M. BOLLIG
Institut für Technische Mechanik
RWTH Aachen
D-52056 Aachen, Germany

Reduced mechanisms are used to study the importance of various NO_x production and consumption mechanisms in non-premixed hydrocarbon-air flames. It is found that the prompt, thermal, and nitrous oxide mechanisms for NO production can each be important under conditions realistic for practical combustion devices. Further, the reburn process contributes significantly to NO consumption under certain conditions. In general, the prompt mechanism is the dominant production mechanism when the residence time is shortest and NO_x emissions are correspondingly low; in these flames, radical concentrations are high and the flame temperatures are relatively low. As the pressure or residence time increases, radical concentrations are reduced and flame temperatures rise; these changes lead to an increase in the importance of the thermal mechanism with respect to the prompt mechanism. Under these conditions, the reburn process is also important. Because of the pressure dependence of nitrous oxide concentrations, the nitrous oxide mechanism is a significant contributor only at high pressures.

Introduction

To address problems of global air pollution, it is necessary to understand the mechanisms of formation and destruction of pollutants such as oxides of nitrogen in flames. Numerous works have been directed toward the development of detailed kinetic mechanisms [1–7] and the application of these mechanisms to well-stirred reactors [1–3,8,9] and premixed flames [4,5,10,11]. However, with a few exceptions [12–15], very little work has been directed toward understanding nitrogen chemistry in non-premixed flames. Since most practical combustion devices operate under conditions of imperfect mixing, consideration of varying stoichiometries is essential to the understanding of pollutant formation in realistic combustors. Reduced mechanisms, derived through the successive application of the steady-state assumption to judiciously selected species, which focus on the global processes in the flame, are ideal for developing this understanding. Despite this fact, the applications of reduced mechanisms to nitrogen chemistry has been very limited [8,13,15,16].

There are several possible means of producing nitric oxide in diffusion flames. For all of the paths, the relevant timescales are large with respect to the overall timescale for combustion of the primary fuel. Thus, in calculating emissions, it is necessary to take into account the finite rates of the associated reactions. Furthermore, the NO production is strongly influenced by flame temperature and radical concentrations, so these must be modeled carefully. In the current work, three routes to NO formation are considered: the thermal mechanism, prompt mechanism, and nitrous oxide mechanism. If NO concentrations are significant enough, reburn reactions that lead from NO back to N_2 can become important, and these are also considered herein.

In addition to nitric oxide, nitrous oxide and nitrogen dioxide are also important pollutants arising from the reactions of nitrogen-containing species. It is known that nitrous oxide emissions are usually small from hydrocarbon diffusion flames [17], and this result is found herein. Nitrogen dioxide is formed from nitric oxide on the lean side of the flame, and it is a significant emission. Generally, however, emissions are reported in terms of the sum of NO_2 and NO emissions. Since the NO_2 is formed through NO, its formation does not alter the total pollutant emissions, and therefore this process will not be emphasized here.

Emissions are reported in terms of the emission index, which describes the grams of NO_x produced

per kilogram of fuel consumed after all NO_x has been converted by convention to NO_2. This is found computationally by integrating the appropriate reaction rates across the flame as

$$E_{NO_x} = \frac{1000 \times W_{NO_2} \int_{-\infty}^{\infty} (\omega_{NO} + \omega_{NO_2}) dy}{W_F \int_{-\infty}^{\infty} \omega_F dy} \quad (1)$$

where W_i and ω_i are the molecular weight and molar production rate of species i, and F represents the fuel.

Diffusion flame structure is described conveniently in terms of the mixture fraction variable, Z. There are numerous definitions of the mixture fraction [18]; in the numerical calculations, it is carried as a hypothetical conserved scalar with unity Lewis number. All computations are made for planar, counterflow diffusion flames, but the use of Z enables the results to be applied to other configurations. The measure of the timescale for the flame is the scalar dissipation rate, defined as $\chi_{st} = 2D|\nabla Z|^2$, where D is the self-diffusion coefficient of nitrogen and the gradient is evaluated at the stoichiometric mixture fraction.

In the present study, methane is considered because it is probably the best understood of hydrocarbon fuels that produce significant quantities of those radicals involved in prompt NO_x formation. Its study, therefore, is of fundamental significance and provides information useful for developing an accurate understanding of chemical mechanisms involved in NO_x production. Moreover, results from investigating methane can be applied as submodels in analysis of larger hydrocarbon oxidation.

A Starting Mechanism

Recent advances in the knowledge of elementary rate constants important in the production and consumption of oxides of nitrogen [2–7,19–21] have led to the development of an improved detailed mechanism [22,23] from which a starting mechanism for the nitrogen chemistry was derived. The rates retained in the starting mechanism are determined by considering both sensitivity and flux analyses for a variety of conditions. These conditions included non-premixed counterflow configurations at pressures of 1–40 bar, with boundary temperatures ranging from 298 to 860 K, and with scalar dissipation rates ranging from 0.1 s^{-1} to near extinction. The C_1 and C_2 submechanism consisting of the first 61 elementary reactions given in Ref. 24 is used to describe the oxidation of methane and also provides a basis from which to build larger mechanisms. The starting mechanism for the nitrogen chemistry is described by the additional 52 reactions and 13 species given in Table 1. The starting mechanism is still long but maintains excellent agreement with the detailed mechanism for all retained species.

While most experimental studies have concentrated on well-stirred reactors and low-pressure premixed flames, it is important to compare the starting mechanism with diffusion flame experiments. To this end, measurements of NO_x emissions from methane-air laminar co-flow diffusions flame were performed [14]. The exit velocities and nozzle diameter were varied, and the fuel stream was diluted with nitrogen to obtain a wide range of conditions. The measured emission indices are plotted in Fig. 1 against a calculated scalar dissipation rate averaged over the co-flow flame surface [25]; the scalar dissipation rate is calculated using a boundary layer approximation and a flame sheet model as done by Li [26]. Also plotted in Fig. 1 is the emission index calculated for a counterflow flame using the starting mechanism; this crude comparison indicates that the levels of emissions are of the proper magnitude, the shallow slope of the experimental values coming from the fact that scalar dissipation rates vary by a couple orders of magnitude within the co-flow flames, and thus each point representing an average over the calculated curve. Inclusion of radiant heat losses would result in lower calculated emissions for small χ.

Five-Step Reduced Mechanism for Methane Oxidation

Previous two-, three-, and four-step mechanisms for methane combustion were found to model diffusion flame extinction and premixed flame burning rates well. However, these mechanisms are insufficient for modeling fuel-derived radicals, in particular CH and $^3CH_2$, which are important in the prompt and reburn chemistry. Using as a starting mechanism the C_1 and C_2 chemistry from Bollig et al. [24] with CH_3, CH_2O, CH_2OH, CH_3O, $^1CH_2$, $^3CH_2$, CHO, CH, OH, O, HO_2, C_2H_6, C_2H_5, C_2H_4, C_2H_3 in steady state, a five-step reduced mechanism can be derived:

$$3H_2 + O_2 \rightleftharpoons 2H + 2H_2O \quad \text{(F-I)}$$

$$2H \rightleftharpoons H_2 \quad \text{(F-II)}$$

$$CO + H_2O \rightleftharpoons CO_2 + H_2 \quad \text{(F-III)}$$

$$2CO + H_2 \rightleftharpoons C_2H_2 + O_2 \quad \text{(F-IV)}$$

$$CH_4 + 2H + H_2O \rightleftharpoons CO + 4H_2 \quad \text{(F-V)}$$

Because of space limitations, the reader is referred to a report [27] for the explicit global rate and steady-state expressions employed. Except for reaction F-IV, this mechanism is identical to that presented more than a decade ago [28] in one of the early reduced mechanisms for fuel chemistry. Reaction F-IV represents the effect of methyl

TABLE 1
Reaction mechanism for nitrogen chemistry

Number	Reaction				A	n	E	Ref.
N1f	NH_3 + M3	→	NH_2 + H + M3		2.200E+16	0.00	391	[2]
N2f	NH_3 + H	→	NH_2+H_2		6.400E+05	2.39	42.6	[2,5]
N3f	NH_3 + O	→	NH_2 + OH		9.400E+06	1.94	27.1	[2]
N4f	NH_3 + OH	→	NH_2 + H_2O		2.040E+06	2.04	2.37	[2,5]
N5f	NH_2 + H	→	NH + H_2		4.000E+13	0.00	15.3	[2,5]
N6f	NH_2 + O	→	HNO + H		9.900E+14	−0.50	0	[5]
N7f	NH_2 + OH	→	NH + H_2O		4.000E+06	2.00	4.19	[2]
N8f	NH_2 + NO	→	N_2 + H_2O		2.000E+20	−2.60	3.87	[4,5]
N9f	NH_2 + NO	→	N_2H + OH		9.300E+11	0.00	0	[4]
N10f	NH + H	→	N + H_2		1.000E+13	0.00	0	[5]
N11f	NH + O	→	NO + H		9.200E+13	0.00	0	[2]
N12f	NH + OH	→	HNO + H		4.000E+13	0.00	0	[5]
N13f	NH + OH	→	N + H_2O		5.000E+11	0.50	8.37	[2]
N14f	NH + O_2	→	HNO + O		4.600E+05	2.00	27.2	[2]
N15f	NH + NO	→	N_2O + H		2.940E+14	−0.40	0	[2]
N15x	NH + NO	→	N_2O + H		−2.200E+13	−0.23	0	[2]
N16f	NH + NO	→	N_2 + OH		2.200E+13	−0.23	0	[2]
N17f	HNO + M1	→	H + NO + M1		1.500E+16	0.00	204	[2]
N18f	HNO + H	→	NO + H_2		4.400E+11	0.72	2.72	[2]
N19f	HNO + OH	→	NO + H_2O		3.600E+13	0.00	0	[2]
N20f	N + O_2	→	NO + O		6.400E+09	1.00	26.3	[2]
N21f	N + OH	→	NO + H		3.800E+13	0.00	0	[2]
N22f	N + NO	→	N_2 + O		3.300E+12	0.30	0	[2]
N23f	N_2H	→	N_2 + H		1.000E+08	0.00	0	[2]
N24f	N_2H + H	→	N_2 + H_2		1.000E+14	0.00	0	[2]
N25f	N_2 H + O	→	N_2O + H		1.000E+14	0.00	0	[2]
N26f	N_2H + OH	→	N_2 + H_2O		5.000E+13	0.00	0	[2]
N27f	N_2O	→	N_2 + O	k_0	3.980E+14	0.00	237	[21]
				k_∞	1.600E+12	0.00	262	
N28f	N_2O + H	→	N_2 + OH		2.230E+14	0.00	70.1	[20]
N29f	N_2O + O	→	2NO		2.900E+13	0.00	96.9	[2]
N31f	NO_2 + M3	→	NO + O + M3		1.000E+16	0.00	276	[2]
N32f	NO + HO_2	→	NO_2 + OH		2.100E+12	0.00	−2.01	[2]
N33f	NO_2 + H	→	NO + OH		3.500E+14	0.00	6.28	[2]
N34f	NO_2 + O	→	NO + O_2		1.000E+13	0.00	2.51	[2]
N35f	HNCO + M4	→	NH + CO + M4		1.100E+16	0.00	360	[3]
N36f	HNCO + H	→	NH_2 + CO		2.200E+07	1.70	15.9	[3]
N37f	HNCO + O	→	NCO + OH		2.200E+06	2.11	47.9	[3]
N38f	HNCO + O	→	NH + CO_2		9.600E+07	1.41	35.7	[3]
N39f	HNCO+OH	→	NCO + H_2O		6.400E+05	2.00	10.7	[3]
N40f	NCO + M4	→	N + CO + M4		3.100E+16	−0.50	201	[3]
N41f	NCO + H	→	CO + NH		5.000E+13	0.00	0	[3]
N42f	NCO + O	→	NO + CO		4.700E+13	0.00	0	[3]
N43f	NCO + H_2	→	HNCO + H		7.600E+02	3.00	16.7	[3]
N44f	N_2 + CH	→	HCN + N		4.400E+12	0.00	92	[7]
N45f	NO + CH_3	→	HCN + H_2O		8.300E+11	0.00	67.3	[34]
N46f	NO + $_3$-CH_2	→	HNCO + H		2.900E+12	0.00	−2.5	[10]
N47f	NO + CH	→	HCN + O		1.100E+14	0.00	0	[19]
N48f	HCN + O	→	NCO + H		1.400E+06	2.10	25.6	[19]
N49f	CN + H_2	→	HCN + H		3.600E+08	1.55	12.6	[19]
N50f	CN + H_2O	→	HCN + OH		7.800E+12	0.00	31.2	[6]
N51f	CN + OH	→	NCO + H		4.200E+13	0.00	0	[6]
N52f	CN + O_2	→	NCO + O		7.200E+12	0.00	−1.75	[19]

Rate Constants are $k = AT^n \exp(-E/RT)$; units are mol, cm, s, kJ.
Reverse rates from equilibrium constants. Reaction N28 is in Lindeman form.
Third-body efficiencies are
[M1] = 2.0[H_2] + 2.0[N_2] + 10.0[H_2O] + 2.0[O_2] + 1.0[other]
[M3] = 1.0[other]
[M4] = 1.5[N_2] + 1.5[O_2] + 18.6[H_2O] + 1.0[other].

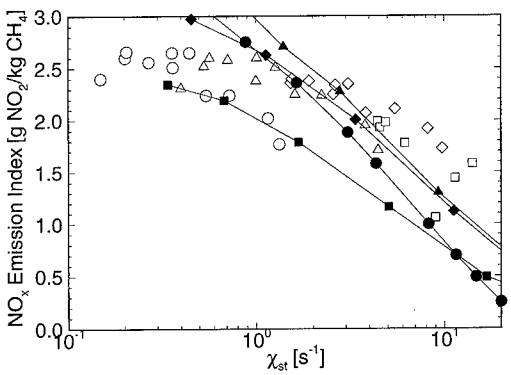

FIG. 1. Measured NO_x emission indices for co-flow laminar methane-air diffusion flames (open symbols) compared with results for calculations with the counterflow flame (solid symbols and lines). The fuel stream is diluted with nitrogen; fuel mass fractions are circles, $Y_F = 1.0$; triangles, $Y_F = 0.6$; diamonds, $Y_F = 0.3$; and squares, $Y_F = 0.2$.

recombination producing C_2 hydrocarbons, and, in reverse, the consumption of these C_2 species.

Efforts to simplify the fuel chemistry by introducing further steady-state relations will meet with problems for various reasons. An acetylene steady state giving the more traditional four-step mechanism results in $^3CH_2$ and CH existing over the entire region where methyl radicals exist rather than the known [29] very thin layer where acetylene and oxygen atoms coexist (which is roughly an order of magnitude smaller). Similarly, steady state for H underpredicts penetration of radicals into the fuel consumption layer, thereby greatly underpredicting all fuel-derived radicals.

To adapt the model for methane to other hydrocarbon diffusion flames, for example, *n*-heptane, it is only necessary to change the fuel-consumption steps to reflect the conversion of the fuel molecules to smaller C_1 and C_2 species. Doing this for heptane requires two additional steps [24].

Six-Step Reduced Mechanism for Nitrogen Chemistry in Diffusion Flames

The mechanics of developing a reduced mechanism involve identifying the fastest consumption reaction for each species eliminated from the mechanism with a steady-state approximation. Naturally, the reaction identified may vary for different conditions. The present work is concerned with conditions characteristic of diffusion flames with high temperatures and a large radical pool. Under these conditions, nitrogen-containing radicals react most frequently with radicals of the hydrogen-oxygen system, leading to the formation of NO. A different series of reactions would be eliminated for conditions related to, for example, exhaust-gas treatment.

Assuming the radicals NH_2, NH, N_2H, HNO, NCO, CN, and N to be in steady state, a six-step mechanism is obtained to describe the nitrogen chemistry, namely,

$$N_2 + O_2 \rightleftharpoons 2NO \qquad \text{(N-I)}$$

$$HCN + H + 2H_2O \rightleftharpoons NO + CO + 3H_2 \qquad \text{(N-II)}$$

$$HNCO + O_2 + H_2 \rightleftharpoons NO + CO + H + H_2O \qquad \text{(N-III)}$$

$$NH_3 + H + H_2O \rightleftharpoons NO + 3H_2 \qquad \text{(N-IV)}$$

$$N_2 + H_2O \rightleftharpoons N_2O + H_2 \qquad \text{(N-V)}$$

$$NO + H_2O \rightleftharpoons NO_2 + H_2 \qquad \text{(N-VI)}$$

with global rates given by

$$\begin{aligned}
\omega_{\text{N-I}} &= \omega_{\text{N9b}} + \omega_{\text{N15b}} + \omega_{\text{N16b}} + \omega_{\text{N22b}} \\
&\quad + \omega_{\text{N29f}} + \omega_{\text{N44f}} - \omega_{\text{N8f}} \\
&\quad - \omega_{\text{N9f}} - \omega_{\text{N15f}} - \omega_{\text{N15x}} \\
&\quad - \omega_{\text{N16f}} - \omega_{\text{N22f}} - \omega_{\text{N29b}} - \omega_{\text{N44b}} \\
\omega_{\text{N-II}} &= \omega_{\text{N44b}} + \omega_{\text{N45b}} + \omega_{\text{N47b}} + \omega_{\text{N48f}} \\
&\quad + \omega_{\text{N51f}} + \omega_{\text{N52f}} - \omega_{\text{N44f}} \\
&\quad - \omega_{\text{N47f}} - \omega_{\text{N48b}} - \omega_{\text{N51b}} \\
&\quad - \omega_{\text{N52b}} \\
\omega_{\text{N-III}} &= \omega_{\text{N35b}} + \omega_{\text{N36b}} + \omega_{\text{N37b}} + \omega_{\text{N38b}} \\
&\quad + \omega_{\text{N39b}} + \omega_{\text{N43f}} + \omega_{\text{N46f}} \\
&\quad - \omega_{\text{N35f}} - \omega_{\text{N36f}} - \omega_{\text{N37f}} \\
&\quad - \omega_{\text{N38f}} - \omega_{\text{N39f}} - \omega_{\text{N43b}} \\
&\quad - \omega_{\text{N46b}} \\
\omega_{\text{N-IV}} &= \omega_{\text{N1f}} + \omega_{\text{N2f}} + \omega_{\text{N3f}} + \omega_{\text{N4f}} \\
&\quad - \omega_{\text{N1b}} - \omega_{\text{N2b}} - \omega_{\text{N3b}} - \omega_{\text{N4b}} \\
\omega_{\text{N-V}} &= \omega_{\text{N15f}} + \omega_{\text{N15x}} + \omega_{\text{N25f}} + \omega_{\text{N27b}} \\
&\quad + \omega_{\text{N28b}} + \omega_{\text{N29b}} - \omega_{\text{N15b}} \\
&\quad - \omega_{\text{N25b}} - \omega_{\text{N27f}} - \omega_{\text{N28f}} - \omega_{\text{N29f}} \\
\omega_{\text{N-VI}} &= \omega_{\text{N31b}} + \omega_{\text{N32f}} + \omega_{\text{N33b}} + \omega_{\text{N34b}} \\
&\quad - \omega_{\text{N31f}} - \omega_{\text{N32b}} - \omega_{\text{N33f}} - \omega_{\text{N34f}}
\end{aligned} \qquad (2)$$

Evaluation of these rate expressions requires use of steady-state relations that may be derived from the balance equations [27]. With this mechanism, the net formation of NO_x is described by the global rate

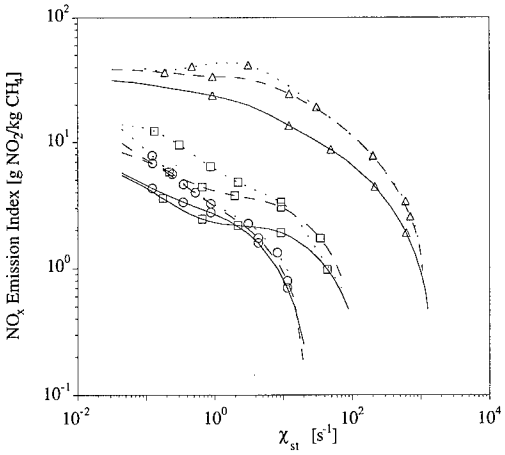

FIG. 2. Comparison between NO_x emissions calculated using the starting mechanism (solid lines) and the reduced mechanism with five-step nitrogen chemistry (dashed lines) and one-step nitrogen chemistry (dotted lines) for methane-air diffusion flames. Circles represent calculations at $p = 1$ bar and $T_O = T_F = 298$ K, squares at $p = 40$ bar and $T_O = T_F = 298$ K, triangles at $p = 40$ bar and $T_O = 855$ K, $T_F = 700$ K.

N-I, which includes the elementary rates corresponding to the thermal, prompt, and nitrous oxide mechanisms. Step N-I also includes those reactions between nitrogen-containing radicals and nitric oxide that ultimately are responsible for converting NO back to N_2; of course, these rates are directed backward. Global rates N-II, N-III, and N-IV describe the shuffle of bound nitrogen between various undesirable species. This generally occurs on the rich side of the flame, and HCN, HNCO, and NH_3 are not emitted from the air side of the flame. Step N-II is involved in the prompt mechanism, step N-III in reburn, and step N-IV in the so-called thermal de-NO_x process; these last three processes are combinations of the cited global step with others. Nitrous oxide is formed through step N-V, and in diffusion flames it is found to nearly equilibrate within the flame. The near-equilibration of step N-V indicates that nitrous oxide emissions, like CO emissions [14], are controlled by the freezing of the pollutant consumption reactions on the air side through radical depletion. A small fraction of the nitrous oxide formed is converted to NO; this phenomenon is included in step N-I. The formation of NO_2 from NO described in step N-VI occurs mainly in the low-temperature regions outside the reaction zone where steady states are poor for radicals, resulting in poor prediction of the conversion from NO to NO_2. Since the NO-to-NO_2 conversion is a well-studied phenomenon that can affect measurements but not the ultimate NO_x emissions, step N-VI is omitted in the calculations.

A One-Step Mechanism for the Nitrogen Chemistry

As a further simplification, a one-step description of the nitrogen chemistry is obtained if steps N-II, N-III, N-IV, and N-V are placed in partial equilibrium, corresponding to steady states for HCN, HNCO, NH_3, and N_2O, and the conversion of NO to NO_2 in step N-VI is neglected. The steady-state assumptions for HCN, HNCO, NH_3, and N_2O are questionable, but within the flame where nitric oxide chemistry occurs they are reasonable. The only significant exception is that NH_2 is not well predicted because of breakdown of the steady states for HNCO and NH_3 on the rich side of the flame. As a result, reburn is underpredicted, leading to an overprediction of emissions at low strain rates and high pressures.

NO_x Emissions from Diffusion Flames

The "FlameMaster" code [30] was employed to calculate flame structure and NO_x emissions with the starting and reduced mechanisms described in preceding sections. Computations were performed for methane-air flames with reactants at normal atmospheric conditions, at normal temperature but at 40 bar, and at 40 bar with fuel and air temperatures increased to 700 K and 855 K as would occur in adiabatic compression from normal conditions. Comparison of these three cases serves to illustrate the influences of changes in pressure and temperature. A detailed transport mechanism derived from the Chemkin package [31] is included in "FlameMaster." In the present calculations, thermal diffusion and radiant energy loss are excluded; more realistic results are obtained if these effects are included, in particular at low strain rates where radiation is significant, and results including these effects are available [32]. However, to remove uncertainties and focus on kinetic effects, simplified transport without radiative heat loss is adopted here. The emission indices for the counterflow flames, calculated according to Eq. (1), are shown in Fig. 2.

The rates of production of NO_x by the various mechanisms are influenced primarily by the flame temperature and the concentrations of various radicals. These are in turn functions of such factors as the composition and temperature of the fuel and oxidizer streams, the pressure, and the scalar dissipation rate.

The flame temperature is determined by considering first the temperature that corresponds to infinitely fast chemistry, the Burke–Schumann limit, and then the decrement below that temperature that is a result of finite-rate heat release. The temperature in the Burke–Schumann limit is a function of the total enthalpy at the flame that is a function of the enthalpy in the fuel and oxidizer streams and is

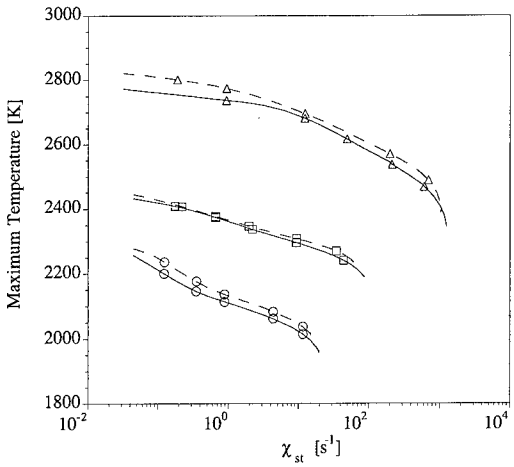

FIG. 3. Peak temperatures in methane-air flames as a function of the scalar dissipation rate, pressure, and ambient temperature. Symbols as in Fig. 2.

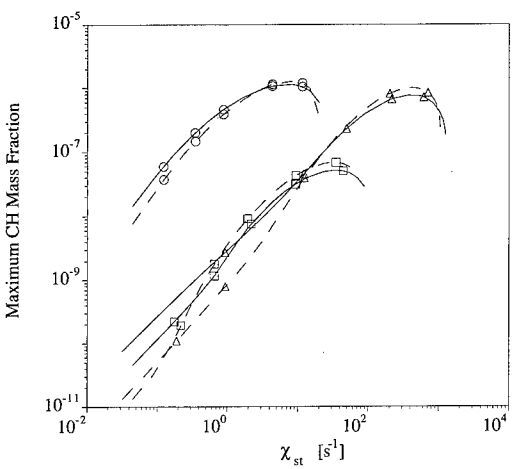

FIG. 4. Maximum mass fractions of CH, a representative radical, in methane-air flames as a function of the scalar dissipation rate, pressure, and ambient temperature. Symbols as in Fig. 2.

also significantly affected by effects of differential diffusion and radiant losses. The effects of finite-rate chemistry arise from the fact that intermediates such as H_2 and CO are not immediately converted into final products in the flame. In Fig. 3, the peak flame temperatures are plotted as a function of scalar dissipation rate for the three different methane flames. For conditions in which the timescale is short, as is desired to minimize NO_x formation, it is seen that the temperature decrement due to finite-rate effects can be greater than 400 K. Since the rate of heat release in flames is essentially limited by the rates of three-body recombination reactions, in particular the reaction $H + O_2 + M \rightleftharpoons HO_2 + M$, increasing pressure leads to an increase of the rate of heat release relative to the rates of other reactions, increasing the flame temperature as seen comparing the circles and squares in Fig. 3. The flame temperature is slightly overpredicted by the reduced mechanism; this is due to reduced heat capacity and diffusivity associated with many species being in steady state. The result is that the production by the thermal mechanism and consequently overall emissions will be overpredicted by the reduced mechanism as seen in Fig. 2.

Three radicals play particularly important roles in the production and consumption of oxides of nitrogen: O, CH, and $^3CH_2$. In the reduced mechanism, all three are linked to hydrogen concentrations through the steady-state relations. For O, the link is primarily through the hydrogen-oxygen shuffle reactions, while $^3CH_2$ and CH come primarily through reactions of C_2H_2 with O. Within the flame, the qualitative behavior of radicals can be understood by assuming that H is in steady state, reducing the order of the reduced mechanism by one, and that this steady state is described by partial equilibrium of the shuffle reactions [33]. Superequilibrium radical levels exist because radical consumption is limited by the relatively slow three-body reactions such as $H + O_2 + M \rightleftharpoons HO_2 + M$. Thus, as the scalar dissipation rate increases, radical concentrations will increase, as seen in Fig. 4. Conversely, as the pressure rises the rates of the three-body reactions increase preferentially to those of the two-body reactions and radical concentrations decrease.

The Importance of Various Mechanisms in Determining the NO_x Emissions

Figure 5 shows the reaction rates of the thermal, prompt, and nitrous oxide mechanisms, as well as the reburn for four different flames. Figures 5b and 5c demonstrate the effects of isothermal and adiabatic compression when compared with Fig. 5a. While $\chi = 3.0\ s^{-1}$ is a moderate dissipation rate for flame (a), it is an extremely low rate for flame (c); correspondingly, comparison of parts (c) and (d) serves to illustrate the effects of residence time on the various mechanisms.

The thermal or Zeldovich mechanism is perhaps the best understood of the mechanisms that produce nitric oxide. The reaction $O + N_2 \rightarrow NO + N$, with its extremely large activation energy, is responsible for initiating a sequence of reactions that produces a pair of NO molecules. Because the mechanism is so strongly dependent on temperature, it is relatively easy to control. Methods such as exhaust-gas recirculation, which reduce the adiabatic flame temperature, and shortening the local residence time, which reduces the peak flame temperature through finite-

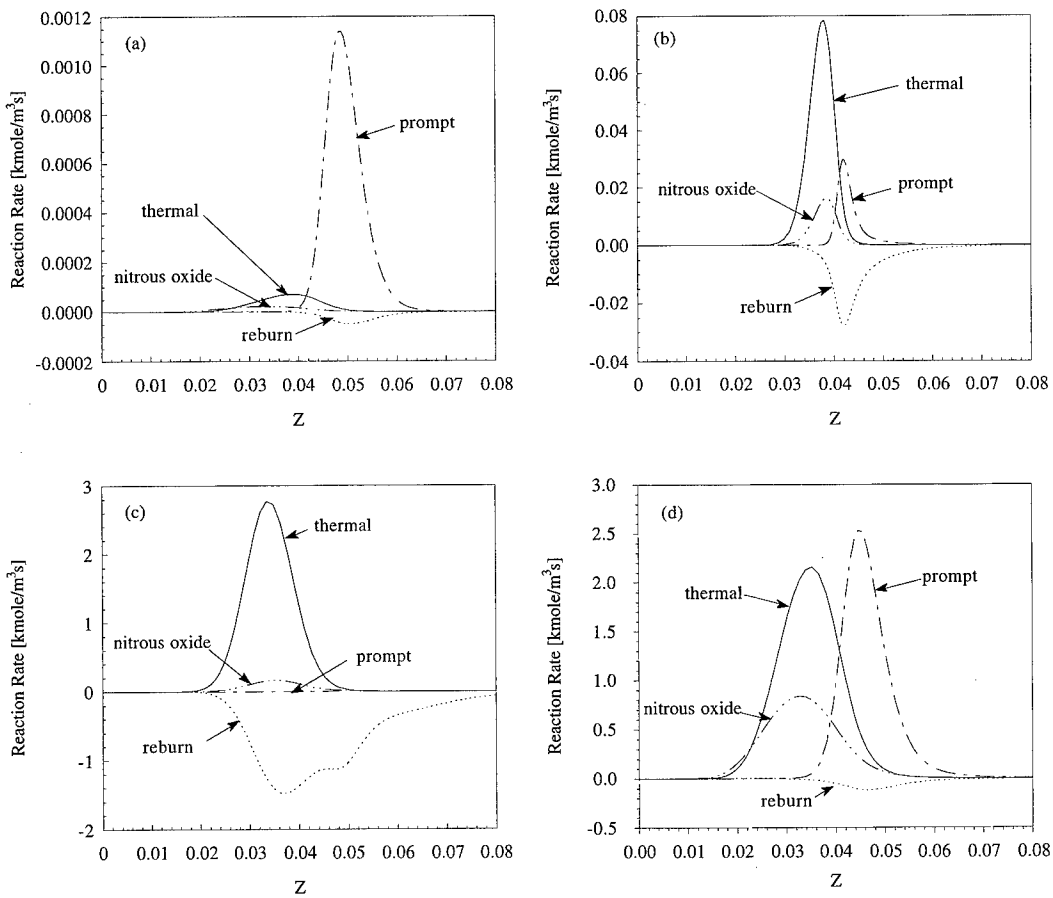

FIG. 5. Reaction rates corresponding to the various mechanisms of NO production and consumption for pressures, fuel and oxidizer temperatures, and scalar dissipation rates at the flame surface of (a) $P = 1$ bar, $T_O = T_F = 298$ K, $\chi = 3\ s^{-1}$, (b) $P = 40$ bar, $T_O = T_F = 298$ K, $\chi = 3\ s^{-1}$, (c) $P = 40$ bar, $T_O = 855$ K, $T_F = 700$ K, $\chi = 3\ s^{-1}$, and (d) $P = 40$ bar, $T_O = 855$ K, $T_F = 700$ K, $\chi = 600\ s^{-1}$ for methane-air diffusion flames at $T_O = T_F = 298$ K.

rate chemistry effects, are both effective in reducing the contribution of the thermal mechanism. Still, in diffusion flames with long residence times as in Fig. 5c or high flame temperatures as in Figs. 5b, 5c, and 5d, the thermal mechanism is a major contributor to the formation of NO_x.

The production via the prompt mechanism is controlled by the rate of $CH + N_2 \rightarrow HCN + N$. This rate is not strongly dependent on temperature but relies heavily on radical concentrations. As a result, increasing χ leads to a rise in the relative rate of the prompt mechanism as is seen comparing Figs. 5c and 5d; however, because the residence time is reduced, the emission index still decreases with χ [14]. Similarly, the effect of pressure on radical levels leads to a decrease in the importance of the prompt mechanism as the pressure rises for a fixed χ. It is seen in Fig. 5a that prompt is the dominant production mechanism in diffusion flames at atmospheric conditions. At elevated pressure in parts (b) and (c), reduction in radical levels and rise of peak flame temperatures result in the thermal mechanism gaining in relative importance, although at high scalar dissipation rates, part (d), the prompt mechanism is always important.

It has been demonstrated that nitrous oxide is formed in measurable quantities within diffusion flames, but emissions are negligible, at least at atmospheric conditions [17]. Because N_2O is present in the flame, it is necessary to consider the possibility that it leads to nitric oxide. Nitrous oxide is formed primarily through reactions N27b, which is at the low-pressure limit for $P < 40$ bar, or from N_2H after N23b, while consumption is through two-body reactions. Thus, N_2O concentrations tend to increase with pressure. Most consumption is through thermal decomposition or reaction with H to reform N_2, but some (less than 4%) reacts via $N_2O + O \rightarrow 2NO$.

The fraction of N_2O reacting to form NO tends to decrease somewhat as pressure increases and χ decreases since radical levels decrease and the thermal decomposition becomes faster; thus, the increase in the nitrous oxide mechanism is not as great as the increase in nitrous oxide concentrations. Still, as is evident in Figs. 5b–5c the contribution is not negligible at elevated pressures.

Of particular importance when nitric oxide concentrations are high, the reburn process is responsible for converting NO back to N_2. While reactions such as $^3CH_2 + NO \rightarrow HNCO + H$ are often referred to as reburn reactions, these only indirectly affect the conversion of NO back to N_2. Actually, reburn depends on the competition between reactions such as N7f, N13f, N21f, and N41f that ultimately lead to NO formation and reactions such as N8f, N9f, N15f, N16f, and N22f where N-containing radicals react with NO to form N_2. The reburn reactions are important when NO concentrations are large relative to radical concentrations, and rates of these appear in the backward direction for the global rate N-I. As pressure and temperature rise, the increased production of NO from the thermal mechanism combined with the significant reduction in radical levels leads to an increase in the importance of reburning shown in Fig. 5c. As the scalar dissipation rate is decreased, similar effects are observed. Unfortunately, these conditions correspond to high NO_x emissions and are not a viable means to control emissions when low indices are required.

Conclusions

Reduced mechanisms have been used to demonstrate the primary features of the formation of oxides of nitrogen in non-premixed hydrocarbon flames. The number of steps in the reduced mechanisms and its complexity depend on the number of phenomena to be modeled accurately. To accurately model the formation and destruction of all stable species in methane flames required a six-step nitrogen mechanism along with a five-step mechanism for the methane chemistry. However, a one-step mechanism for the nitrogen chemistry is sufficient to estimate the NO_x emissions.

When flame residence times are short and peak temperatures are reduced, nitric oxide production is minimized and the prompt mechanism is generally the dominant route to formation of NO_x. Longer residence times and higher ambient pressures result in higher flame temperatures; hence, the thermal mechanism becomes important. Radical concentrations are also reduced in high-pressure flames and those with long residence times, leading to a reduction in the production via the prompt mechanism. Elevated pressures also lead to an increase in the contribution of the nitrous oxide mechanism, and it is seen to be significant at sufficiently elevated pressures. The reburn chemistry is significant in flames with relatively large concentrations of NO, such as those flames in which the thermal mechanism is important. Thus, neglect of the prompt and reburn chemistry will lead to underprediction of emissions at short residence times and overprediction for long residence times.

Acknowledgments

This work took shape while J. Hewson was at RWTH-Aachen in the fall of 1994 with the support of Professor N. Peters. The authors would like to acknowledge the support and guidance of Professors N. Peters and F. A. Williams. This work is partially supported by the Office of Naval Research under contract number N00014-94-1-0679.

REFERENCES

1. Miller, J. A. and Bowman, C. T., *Prog. Energy Combust. Sci.* 15:287–338 (1989).
2. Glarborg, P., Dam-Johansen, K., Miller, J. A., and Kee, R. J., *Intl. J. Chem. Kinetics* 26:421–436 (1994).
3. Glarborg, P., Kristensen, P. G., Jensen, S. H., and Dam-Johansen, K., *Combust. Flame* 98:241–258 (1994).
4. Vandooren, J., Bian, J., and van Tiggelen, P. J., *Combust. Flame* 98:402–410 (1994).
5. Lindstedt, R. P., Lockwood, F. C., and Selim, M. A., *Combust. Sci. Technol.* 99:253–276 (1994).
6. Tsang, W., *J. Phys. Chem. Ref. Data* 21:753 (1992).
7. Dean, A. J., Hanson, R. K., and Bowman, C. T., *Twenty-Third Symposium (International) on Combustion,* The Combustion Institute, Pittsburgh, 1990, pp. 259–262.
8. Glarborg, P., Lilleheie, N. I., Byggstøyl, S., Magnussen, B., Kilpinen, P., and Hupa, M., *Twenty-Fourth Symposium (International) on Combustion,* The Combustion Institute, Pittsburgh, 1992, pp. 889–898.
9. Miller, J. A. and Bowman, C. T., *Int. J. Chem. Kinetics* 23:289–313 (1991).
10. Bockhorn, H., Chevalier, C., Warnatz, J., and Weyrauch, V., *Heat Transf. Fire Combust. Systems* 166:11–16 (1991).
11. Lindstedt, R. P., Lockwood, F. C., and Selim, M. A., Thermofluids Report TF/95/3, Imperial College, Thermofluids Section, Exhibition Road, London SW7 2BX, UK, 1995.
12. Drake, M. C. and Blint, R. J., *Combust. Flame* 83:185–203 (1991).
13. Røkke, N. A., Hustad, J. E., Sonju, O. K., and Williams, F. A., *Twenty-Fourth Symposium (International) on Combustion,* The Combustion Institute, Pittsburgh, 1992, pp. 385–393.
14. Hewson, J. C. and Williams, F. A., Western States Sec-

tion/The Combustion Institute, Paper No. WSS/CI 94-046, 1994.
15. Card, J. M., Rydén, R., and Williams, F. A., *Combust. Flame* (1996), in press.
16. Lindstedt, R. P. and Selim, M. A., *Combust. Sci. Technol.* 99:277–298 (1994).
17. Hayhurst, A. N. and Lawrence, A. D., *Prog. Energy Combust. Sci.* 18:529–552 (1992).
18. Liñán, A. and Williams, F. A., *Fundamental Aspects of Combustion,* Oxford University Press, 1993.
19. Baulch, D. L., Cobos, C. J., Cox, R. A., Frank, P., Hayman, G., Just, T., Kerr, J. A., Pilling, M. J., Troe, J., Walker, R. W., and Warnatz, J., *Combust. Flame* 98:59–79 (1994).
20. Röhrig, M., Petersen, E. L., Davidson, D. F., and Hanson, R. K., *Int. J. Chem. Kinetics* (1996), in press.
21. Marshall, P., Ko, T., and Fontijn, A., *J. Chem. Phys.* 93:1922–1927 (1989).
22. Bollig, M. and Hewson, J. C., to be published (1996).
23. Bollig, M., Hewson, J. C., Rogg, B., and Peters, N., Technical report, Institut für Technische Mechamik, RWTH-Aachen, 1995.
24. Bollig, M., Pitsch, H., Hewson, J. C., and Seshadri, K., *Twenty-Sixth Symposium (International) on Combustion,* The Combustion Institute, Pittsburgh, 1996, pp. 729–737.
25. Williams, F. A., Seventh ONR Propulsion Meeting, 1994.
26. Li, S. C., Gordon, A. S., and Williams, F. A., *Combust. Sci. Technol.* 104:75–91 (1995).
27. Hewson, J. C. and Williams, F. A., Technical report, CECR Report No. 95-01, 1995.
28. Peters, N., in *Numerical Simulation of Combustion Phenomenon* (Glowinski, R., Larrouturou, B., and Temam, R., Eds.), *Lecture Notes in Physics,* Vol. 241, Springer Verlag, New York, 1985, pp. 90–109.
29. Norton, T. S., Smyth, K. C., Miller, J. H., and Smooke, M. D., *Combust. Sci. Technol.* 90:1–34 (1993).
30. Bollig, M., Pitsch, H., Göttgens, J., and Terhoeven, P., *Flame Master,* Institut für Technische Mechanik, RWTH-Aachen, 1994.
31. Kee, R. J., Warnatz, J., and Miller, J. A., Technical Report UC-32, Sandia Report, SAND83-8209, Livermore, CA, 1983.
32. Bollig, M., Technical report, Institut für Technische Mechamik, RWTH-Aachen, 1995.
33. Seshadri, K. and Peters, N., *Combust. Flame* 73:23–44 (1988).
34. Peters, N. and Just, T., personal communication, (1994).

Twenty-Sixth Symposium (International) on Combustion/The Combustion Institute, 1996/pp. 2181–2189

THE EFFECT OF CHANGES IN THE FLAME STRUCTURE ON THE FORMATION AND DESTRUCTION OF SOOT AND NO_x IN RADIATING DIFFUSION FLAMES

A. ATREYA, C. ZHANG, H. K. KIM, T. SHAMIM AND J. SUH
Combustion and Heat Transfer Laboratory
Department of Mechanical Engineering and Applied Mechanics
The University of Michigan
Ann Arbor, MI 48109-2125, USA

In this study, soot and NO_x production in four counterflow diffusion flames with different flame structures is examined both experimentally and theoretically. The distance between the maximum temperature zone and the stagnation plane is progressively changed by changing the inlet fuel and oxidizer concentrations, thus shifting the flame location from the oxidizer side to the fuel side of the stagnation plane. One flame located at the stagnation plane is also examined. Detailed chemical, thermal, and optical measurements are made to experimentally quantify the flame structure, and supporting numerical calculations with detailed chemistry are also performed by specifying the boundary conditions used in the experiments. Results show that as the radical-rich, high-temperature reaction zone is forced into the sooting zone, several changes occur in the flame structure and appearance. These are the following: (1) The flames become very bright due to enhanced soot-zone temperature. This can cause significant reduction in NO formation due to increased flame radiation. (2) OH concentration is reduced from superequilibrium levels due to soot and soot-precursor oxidation in addition to CO and H_2 oxidation. (3) Soot-precursor oxidation significantly affects soot nucleation on the oxidizer side, while soot nucleation on the fuel side seems to be related to C_2H_2 concentration . (4) Soot interacts with NO formation through the major radical species produced in the primary reaction zone. It also appears that the Fenimore NO initiation mechanism becomes more important for low-temperature flames and when N_2 is added to the fuel side, due to higher N_2 concentrations in the CH-rich zone.

Introduction

The production of soot and NO_x in combustion processes is of considerable practical interest because of the need to control pollutant formation. Industrial furnaces that employ nonpremixed natural gas burners use several methods of reducing NO_x. These are based upon decreasing the gas temperature and/or controlling the combustion process via staged introduction of fuel or air. Bowman [1] and Sarofim and Flagan [2] present excellent reviews of these NO_x control strategies and their underlying chemical mechanisms. One method of reducing the combustion gas temperature, and hence the NO_x production rate, is via enhanced flame radiation [3]. For industrial furnaces, this method has additional advantages because radiation is the primary mode of energy transfer in these systems. Thus, increasing the flame radiation also increases the efficiency of energy transfer to the objects in the furnace, and hence the furnace productivity.

Enhanced flame radiation can be accomplished by increasing the soot production rate in such a way that it is completely oxidized before leaving the flame zone. Thus, an important question is: How should the nonpremixed flames be configured to increase flame radiation, reduce NO_x, and oxidize all the soot and hydrocarbons produced in the process? In search of such flame configurations, a detailed experimental and theoretical study on a basic unit of a turbulent diffusion flame (a radiating laminar flamelet) was conducted. The objective was to explore the interrelationships between soot, NO_x, transport processes, and flame radiation. Experimentally, methane counterflow diffusion flames (CFDF) were used to represent these flamelets, and their thermal, chemical, and radiation structure was measured and modeled.

Clearly, if soot can be forced into the high-temperature reaction zone, then flame radiation will be enhanced and soot and other hydrocarbons will be simultaneously oxidized. Our previous experimental work [4] shows that this can be accomplished by bringing the CFDF to the fuel side of the stagnation plane (SP). To realize such flame configurations, we note the following: (1) In CFDFs, all particulate matter (such as soot) is essentially convected toward the SP. Thus, bringing the soot zone closer to the reaction zone implies bringing the peak temperature region closer to the SP. (2) The location of the SP is

determined by momentum balance, and the location of the flame is determined by stoichiometry. In an ideal diffusion flame, fuel and oxidizer diffuse into the flame in stoichiometric proportions. Thus, by adjusting the diffusive mass flux of fuel and oxidizer, flame location can be altered relative to the SP. While the diffusive mass flux can be changed by changing the "ρD" product, the most convenient method is to adjust the inlet fuel and oxidizer mass fractions. To examine the benefits of changing the flame location relative to the SP, comparisons of the detailed flame structure measurements and calculations are needed for flames on the fuel side, on the oxidizer side, and at the stagnation plane. While there have been several previous experimental and theoretical studies of CFDF structure [5–7], they have been limited to normal flames that lie on the oxygen side of the SP. Recently, Du and Axelbaum [8] have investigated limiting strain rates for soot suppression in CFDFs as a function of the stoichiometric mixture fraction, and numerically examined the structure of two flames on the fuel and the oxidizer side of the SP. Similar studies in coflow flames have been presented by Sugiyama [9] and Faeth and coworkers [10]. However, flame structure measurements and comparisons for sooting flames are not available in the literature. This study provides such measurements and comparisons and investigates the effect of changes in the flame structure on formation and destruction of soot and NO_x.

Experimental Methods

The experiments were conducted in a unique, high-temperature, low strain rate CFDF burner. Various diffusion flame conditions were obtained by changing the inlet fuel and oxidizer concentrations and flow rates. Low strain rates were maintained to facilitate measurements of the flame structure. All measurements were made along the axial streamline of a flat axisymmetric diffusion flame roughly 8 cm in diameter. One dimensionality of scalar variables in the flame was confirmed by radial temperature measurements. All gases used in the experiments were obtained from chemical purity gas cylinders, and their flow rates were measured using calibrated critical flow orifices. The complete experimental apparatus including the optical and the gas chromatography setup is described in detail elsewhere [7].

The soot volume fraction and the number density were measured by using an Ar-ion laser. The soot aerosol was assumed monodispersed with a complex refractive index of $1.57 - 0.56i$. These measurements were highly repeatable (within $\pm 3\%$). OH concentration was measured by laser saturated fluorescence [11,12]. The relative OH measurements were calibrated using detailed chemistry calculations for a nonsooty (blue) methane flame. OH measurements were repeatable to within $\pm 10\%$.

Other chemical species were measured by gas chromatographs (GCs). A quartz microprobe (~ 100 μm in diameter) was used for extracting the gas sample from the flame. The gas sample was then distributed via heated lines and valves to the GCs and the NO_x analyzer. Gasses measured were CO, CO_2, H_2O, H_2, CH_4, He, O_2, and N_2; light hydrocarbons from C_1 to C_6; and PAHs up to C_{18}. The GC and NO_x measurements were accurate to within $\pm 5\%$, except for H_2O which had variations larger than $\pm 10\%$.

Temperatures in the flame were measured by a Pt/Pt–10% Rh thermocouple (0.076-mm wire diameter). The thermocouple was coated with SiO_2 to prevent possible catalytic reactions on the platinum surface. It was traversed across the flame in the direction of decreasing temperature at a rate fast enough to avoid soot deposition and slow enough to obtain negligible transient corrections. These temperature measurements were estimated to be accurate to within ± 30 K after radiation corrections. However, the repeatability was within ± 10 K.

The experimental flame conditions used for the measurements are summarized in Table 1. These flames were measured three times on separate days to check for overall repeatability. This was found to be within the repeatability of the individual measurements. Table 1 also lists the measured locations of the peak flame temperature (and its value) and the locations of the SP. Note that very low strain-rate flames (5–8 s^{-1}; defined as half the velocity gradient at the SP) were used to facilitate flame structure measurements. In flames 1 and 2, N_2 was used as the diluent for O_2, whereas in flames 3 and 4, N_2 was used as the diluent for CH_4. This was done to simulate the effect of fuel-side N_2 on NO formation. Helium was used as the other diluent to help experimentally stabilize these low strain-rate flames. Flame 1 was a very sooty flame located, significantly, on the air side of the SP, whereas, flame 4 was on the fuel side. The mixture fraction Z listed in the table was calculated as the sum of elemental carbon and hydrogen mass fractions [13].

Numerical Calculations

To better understand the experimental results, numerical calculations with detailed chemistry were performed by specifying the experimental boundary conditions listed in Table 1. An experimental burner separation of 29 mm was used and the measured boundary temperatures and species mass fluxes were specified as boundary conditions. Like the experiments, the model considers a steady axisymmetric CFDF established between impinging fuel and oxidizer streams. The governing equations for the conservation of mass, momentum, species, and energy were solved in the boundary layer form, assuming

TABLE 1
Experimental Flame Conditions

Flame Number		Inlet species con.(%)		Burner inlet conditions Vel. (cm/s)	Burner inlet conditions Temp (K)	Strain rate (1/sec) [1/2 Velocity gradient @ SP]	Distance from the fuel side (mm) SP (T)	Distance from the fuel side (mm) T_{max} (T)	Comments and visual observations (Mix. fra.)
1	Fuel	CH_4	28.86	11.01	565	5.6	12.3 (1260 K)	19.3 (2130 K)	Very sooty Flame on O_2 side (Z = 0.129)
		He	71.14						
		N_2	57.40						
	Oxy	O_2	42.60	4.96	668				
2	Fuel	He	84.50	15.23	704	7.8	12.1 (1743 K)	15.7 (2209 K)	Bright Flame on O_2 side (Z = 0.297)
		CH_4	15.50						
		N_2	18.23						
	Oxy	O_2	81.77	5.42	722				
3	Fuel	N_2	74.95	7.88	677	7.4	14.5 (2198 K)	14.3 (2236 K)	Bright Flame at the stagnation plane (Z = 0.48)
		CH_4	25.05						
		O_2	43. 54						
	Oxy	He	56.46	10.09	708				
4	Fuel	CH_4	21.23	7.78	667	6.8	15.6 (1967 K)	12.5 (2263 K)	Bright Flame on the fuel side (Z = 0.584)
		N_2	78.77						
		He	47.82						
	Oxy	O_2	52.18	9.31	689				

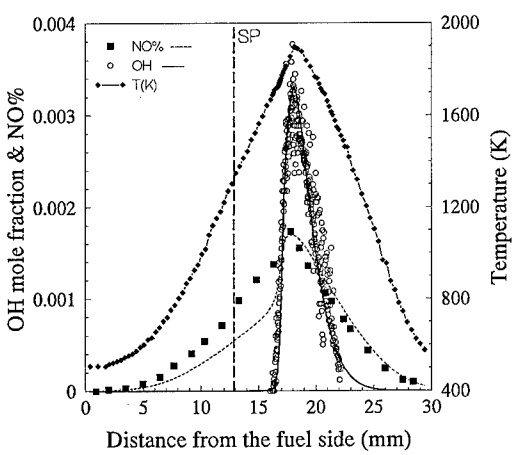

FIG. 1. Measurements and calculations for the nonsooty, blue reference flame. Calculations of NO and OH were done using measured (and radiation-corrected) temperatures and detailed kinetics (276 reactions and 50 species). The calculated OH concentration was used to calibrate the fluorescence measurements.

potential flow at the boundary [6]. The GRIMECH 2.11 mechanism (276 reaction equations and 50 species) with realistic multicomponent transport was used in the numerical model. The numerical code used in this work was provided by A. E. Lutz and R. J. Kee [14]. The calculations were done using the measured temperature profiles to eliminate uncertainties caused by the flame radiation model. Some calculations were also done by solving the energy equation without the radiative heat loss term to evaluate the effect of flame radiation on NO_x production.

Results and Discussion

Detailed flame structure measurements and calculations for the four flames are presented in this section. Figure 1 shows the measured temperature and the measured and calculated NO and OH concentrations for the low strain-rate ($\sim 6s^{-1}$) blue reference flame. This flame was chosen to represent a typical, nonsooty blue flame studied in the literature [5,6] with the hope that the kinetics employed would adequately represent the flame chemistry. The relative OH fluorescence measurements were calibrated using these calculations. The measured and calculated NO results show good agreement, except on the fuel side. The discrepancy on the fuel side appears to be due to the chemical mechanism employed. In sum, this figure represents the expected

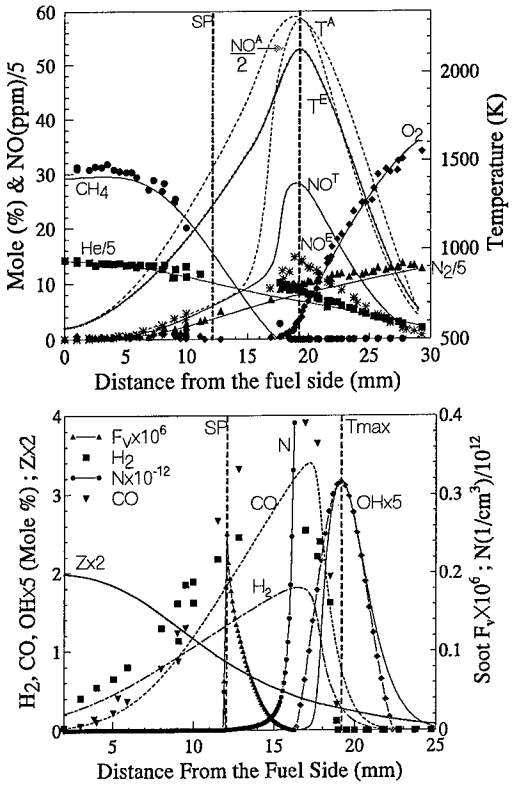

FIG. 2. Measured and calculated (using measured temperatures) structure of flame 1. The upper graph shows the mole fractions of burner inlet species , temperature, and measured and calculated NO concentrations. Measured NO represented by *, NO^T calculated using the measured temperatures, and NO^A calculated by using the energy equation with zero radiative heat loss. Bottom graph shows the sooting structure. Measured soot volume fraction and number density are plotted along with measured and calculated H_2, CO, and OH concentrations. The locations of the maximum flame temperature (T_{max}) and the stagnation plane (SP) are marked on both the graphs. Note that this flame lies on the oxidizer side of the stagnation plane. The mixture fraction Z is also plotted.

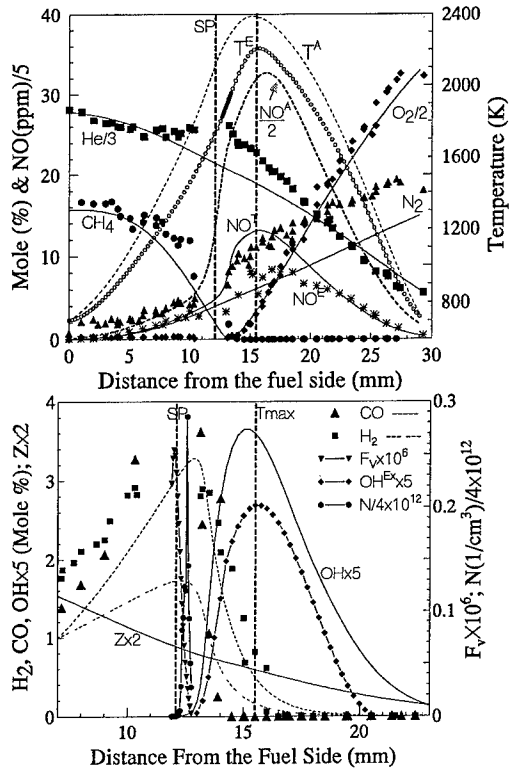

FIG. 3. Measured and calculated (using measured temperatures) structure of flame 2. The upper graph shows the mole fractions of burner inlet species, temperature, and measured and calculated NO concentrations. Measured NO represented by *, NO^T calculated using the measured temperatures, and NO^A calculated by using the energy equation with zero radiative heat loss. Bottom graph shows the sooting structure. Measured soot volume fraction and number density are plotted along with measured and calculated H_2, CO, and OH concentrations. The locations of the maximum flame temperature (T_{max}) and the stagnation plane (SP) are marked on both the graphs. Note that this flame lies on the oxidizer side of the stagnation plane. The mixture fraction Z is also plotted.

level of agreement between the measured and calculated NO and OH concentrations. Any significant differences between measurements and calculations for sooting flames may then be attributed to the difference between assumed and real chemistry.

Figures 2–5 show flame structure measurements and calculations for the four flames listed in Table 1. The upper graph in these figures shows the measurements of mole fractions for burner inlet species, temperature, and NO concentrations. The lower graph in these figures shows the sooting structure. Measured soot volume fraction and number density are plotted along with the measured and calculated H_2, CO, and OH concentrations. H_2 and CO were chosen because they are the primary species oxidized by OH. The locations of the maximum flame temperature (T_{max}) and SP are marked on all the graphs. The mixture fraction Z is also plotted to enable conversion from physical distance to mixture fraction coordinate. Individual aspects of this data are compared and discussed in the following sections.

Major Chemical Species

The calculated and measured burner inlet species profiles, presented in the upper graphs of Figs. 2–5,

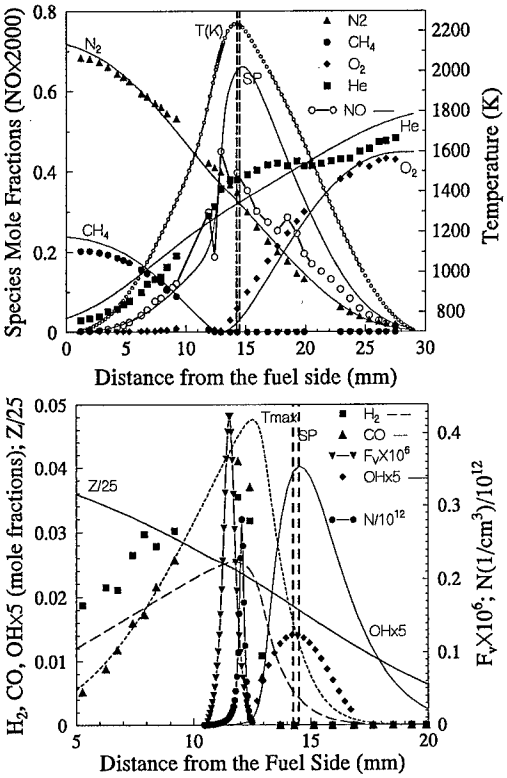

FIG. 4. Measured and calculated (using measured temperatures) structure of flame 3. The upper graph shows the mole fractions of burner inlet species, temperature, and measured and calculated NO concentrations. The bottom graph shows the sooting structure. Measured soot volume fraction and number density are plotted along with measured and calculated H_2, CO, and OH concentrations. The locations of the maximum flame temperature (T_{max}) and the stagnation plane (SP) are marked on both graphs. Note that this flame lies at the stagnation plane within measurement accuracy. The mixture fraction Z is also plotted.

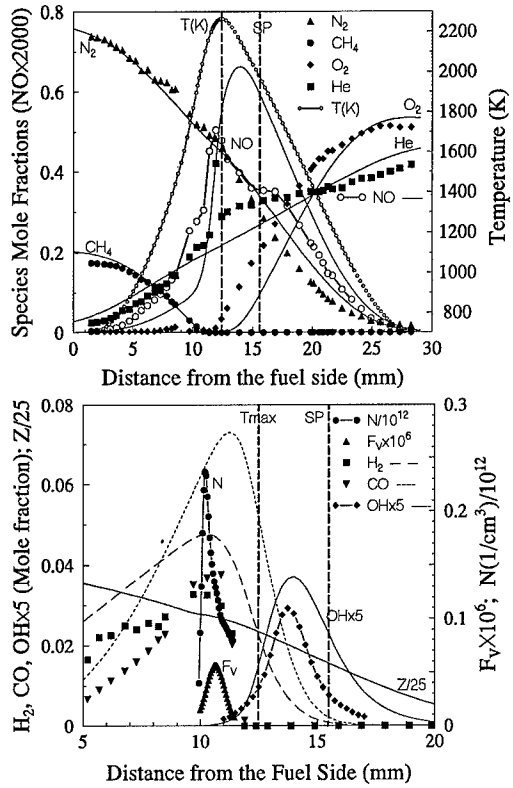

FIG. 5. Measured and calculated (using measured temperatures) structure of flame 4. The upper graph shows the mole fractions of burner inlet species, temperature, and measured and calculated NO concentrations. The bottom graph shows the sooting structure. Measured soot volume fraction and number density are plotted along with measured and calculated H_2, CO, and OH concentrations. The locations of the maximum flame temperature (T_{max}) and the stagnation plane (SP) are marked on both graphs. Note that this flame lies on the fuel side of the stagnation plane. The mixture fraction Z is also plotted.

show good agreement for all four flames. Since the calculations were done by using measured temperatures and experimental boundary conditions, the differences between measured and calculated CO, H_2, OH, and NO profiles may be attributed to the soot formation and oxidation process which is not represented in the chemical mechanism employed. It is expected that the relative rates of soot formation and oxidation will change significantly with the position of the flame relative to the SP. In earlier work [8], similar calculations with C-2 chemistry were used to infer soot nucleation propensity, while Faeth et al. [10] have correlated measured soot nucleation rates with C_2H_2 concentration. Thus, C_2H_2 was chosen for comparison between measurements and calculations. These comparisons are presented in Fig. 6 for all four flames. Since the C_2H_2 measurements in the sooting region (which is expected to have the maximum concentration) could not be obtained due to probe clogging difficulties, comparisons with the acetylene concentration on the fuel side (before the sooting region) are meaningful. In this region, flames 1 and 2 show reasonable agreement, whereas, predictions for flames 3 and 4 are off by an order of magnitude. Likewise, CO and H_2 measurements (Figs. 2–5) also show disagreement. Measured CO and H_2 are higher than calculated for flames 1 and 2, and lower than calculated for flame 4. Recall that flames 1 and 2 were on the oxidizer side, flame 3 was at the SP, and flame 4 was on the fuel side of SP. While the reasons for this discrepancy are unclear, it seems to be related to the soot formation

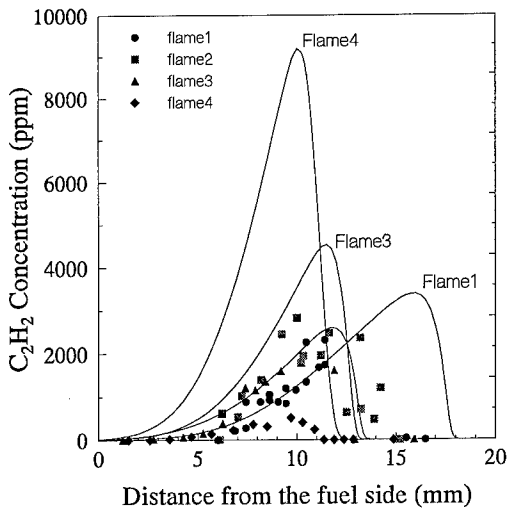

FIG. 6. Calculated and measured concentrations of acetylene for all four flames. Lines indicate calculations; symbols indicate measurements.

and oxidation process which changes significantly with the location of the flame relative to the SP. These results also show that it is difficult to infer sooting tendencies of diffusion flames with C-2 chemistry.

Sooting Structure

As these flames were moved closer to the SP, they become visibly very different. Flame 1 had a thick, yellow-orange sooting zone, whereas, flames 2, 3, and 4 were very bright yellow with narrow sooting zones. The thickness of the sooting zone can be inferred from Figs. 2–5, and the brightness from the average temperature of the sooting zone. Since soot is primarily convected toward the SP, the higher the temperature at the SP, the brighter the flame becomes. Measured temperatures at SP, listed in Table 1, show that this difference can be as large as 1000 K, making a significant difference in flame radiation. Essentially, as the distance between the flame and SP is changed, soot is constrained between the OH oxidizing zone and the location on the fuel side that satisfies appropriate conditions for soot nucleation. These conditions are not uniquely identified by temperature alone. The temperatures at zero f_v and N on the fuel side vary from 1250 K for flame 1 to 1750 K for flame 2 to 1650 K for flame 3 to 1900 K for flame 4.

These flames have very different sooting structures. In flame 1, the soot volume fraction (f_v) monotonically increases toward SP, and the number density (N) monotonically decreases. In flame 2, while f_v monotonically increases toward SP, N first increases and then decreases, indicating that soot nucleation is severely affected by the presence of OH. For flames 3 and 4, both f_v and N first increase and then decrease, and unlike for flames 1 and 2, maximum f_v does not occur at the SP. Interestingly, while the maximum value of f_v is about the same in flames 1 and 2, the maximum N in flame 2 is about three times larger. Also, the maximum value of N correlates with the measured C_2H_2 concentration (not the calculated C_2H_2), whereas the maximum value of f_v does not. Flame 3 shows the largest f_v, probably because of the increased residence time in the acetylene-rich zone, being close to the SP.

The most interesting aspect of these flames is that as the radical-rich zone (identified by peak temperature and OH concentration) is forced into the soot zone, large discrepancies between the measured and calculated OH concentration occur. For flame 1, measured and calculated OH show good agreement and OH is essentially being used to oxidize CO and H_2. As evidenced by monotonically increasing N, there seems to be little soot oxidation. OH, however, does seem to control the soot inception location. This behavior is very different in flames 2 and 3. A considerable reduction in the measured OH occurs, signifying that soot competes for OH along with CO and H_2. This is evident from the sharp decrease in N on the oxidizer side. Similar conclusions were obtained by Santoro [15] in coaxial flames, however, a corresponding increase in the CO concentration is not observed in the present flames. In flame 4, soot and OH coexist, perhaps due to larger velocities that carry the soot particles into the OH zone. Also, less reduction in the OH concentration occurs due to lower f_v and N. From these results, it appears that OH plays an important role in determining the soot inception location on the oxidizer side. As noted earlier, the soot inception location on the fuel side seems to be controlled by the C_2H_2 concentration.

NO Structure

Figures 2–5 show the measured and calculated NO for the four flames. Figures 2 and 3 correspond to the flames where N_2 was added to O_2, whereas Figs. 4 and 5 correspond to the flames where N_2 was added to CH_4. In Figs. 2 and 3, the results of adiabatic calculations (i.e., without flame radiation) are also plotted to determine the effect of flame radiation on NO production. There is approximately a 200-K increase in the maximum flame temperature for the adiabatic calculations which significantly increases the NO concentration (difference between NO^A and NO^T in Figs. 2 and 3). While this difference can be directly attributed to the radiative heat loss, measured NO is still lower than NO^T by 70 ppm for flame 1 and by 40 ppm for flame 2. Yet, a good comparison was obtained for the blue flame. A possible explanation is the effect of soot on the major

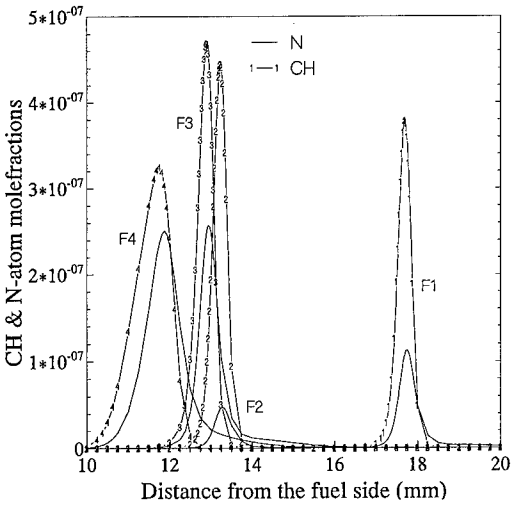

FIG. 7. Calculated mole fractions of N atoms and CH radicals in the four flames. These calculations were done using the experimental boundary conditions, measured temperatures, and GRIMECH-211.

radical species produced in the primary reaction zone and their subsequent effect on NO production. In flame 2, the OH concentration was significantly reduced due to soot/soot-precursor oxidation. Thus, the O atom concentration will also be reduced since, at least approximately, partial equilibrium may be assumed [16]. Thus, even if significant contribution to N atoms comes from the Fenimore initiation reaction [17] ($CH + N_2 = HCN + N$), the corresponding contribution from the Zeldovich initiation reaction ($O + N_2 = N + NO$) is reduced. Another possibility is that the 40-ppm difference for flame 2 is due to low N_2 concentration in the primary reaction zone. Calculations show that N_2 concentration difference is responsible for giving peak $NO^T = 75$ ppm for flame 2 and peak $NO^T = 145$ ppm for flame 1 despite about an 80-K higher temperature for flame 2. Thus, it appears that the 70- and 40-ppm reductions in NO in flames 1 and 2, respectively, are due to soot-NO interactions through the radicals in the primary reaction zone.

Figures 4 and 5 show measured and calculated NO for flames 3 and 4. These flames show much higher NO concentration than flame 2, despite only a small increase in the flame temperature. Both flames 3 and 4 show a good agreement (similar to the blue flame) on the fuel side in the sooting zone, but a substantial discrepancy between the measured and calculated NO exists in the radical-rich primary reaction zone. Thus, it seems that the NO formation mechanism has changed. Two questions arise. (1) Why is NO so much higher in flames 3 and 4? (2) What are the possible mechanisms? We first note that in flames 3 and 4, N_2 was added to CH_4, making higher N_2 available in the fuel rich region. Thus, the Fenimore initiation mechanism is likely to become more effective. To check this hypothesis, calculated N and CH concentrations are plotted in Fig. 7 for all four flames. (Note: These calculations do not contain the effect of soot.) The calculated peak NO concentrations are directly related to the calculated N atom concentrations, and a direct correspondence between OH and O atom profiles exists. While the CH peak for flame 2 is higher than for flame 1, the N peak is lower due to lower N_2 at the CH peak (~7% N_2 for flame 2 and ~35% N_2 for flame 1). For flames 1 and 2, the N peaks do not correlate well with the CH peaks, whereas flames 3 and 4 show much better correlation. This implies that for flames 1 and 2, N atoms are produced primarily by the Zeldovich initiation mechanism, whereas for flames 3 and 4, the Fenimore mechanism is more effective. Since a large amount of NO is produced by the Fenimore mechanism in flames 3 and 4, the effect of the reduction in the radical population due to soot (corresponding to the discrepancy between the measured and calculated OH concentrations) appears only in the primary reaction zone or the Zeldovich NO zone. For flame 4, the difference in OH is less, and a corresponding smaller difference in NO is also seen. Although more work is needed, it seems that soot has a large influence on NO through the radical pool in the reaction zone affecting the Zeldovich initiation mechanism, and the Fenimore mechanism becomes much more important when N_2 is added to the fuel side, due to higher N_2 concentrations. Thus, the relative importance of the Zeldovich mechanism shifts as N_2 is shifted from the O_2 side to the fuel side.

Conclusions

In this work, soot and NO production in four diffusion flames with different structures was examined both experimentally and theoretically. The distance between the primary reaction zone and the stagnation plane was progressively changed to bring the flames from the oxidizer side to the fuel side, including one flame located at the stagnation plane. Although more work is needed to understand the soot and NO structure of these flames, the following may be concluded:

1. C-2 chemistry does not adequately describe the minor species and radical concentrations in sooting flames.
2. As the radical-rich, high-temperature reaction zone is forced into the sooting zone, the flames become very bright due to enhanced soot-zone temperature.
3. OH concentration is significantly reduced due to soot and soot-precursor oxidation in addition to CO and H_2 oxidation.

4. The presence of OH significantly affects soot nucleation on the oxidizer side, while soot nucleation on the fuel side seems to be related to C_2H_2 concentration.
5. A significant reduction in NO formation occurs due to a reduction in the flame temperature caused by flame radiation.
6. It seems that soot interacts with NO formation through the major radical species produced in the primary reaction zone.
7. It appears that the Fenimore mechanism becomes more important when N_2 is added to the fuel side, due to higher N_2 concentrations in the CH zone. The relative importance of the Zeldovich mechanism shifts as N_2 is shifted from the O_2 side to the fuel side.

Acknowledgments

This work was supported by GRI under the contract number GRI 5087-260-1481 with the technical direction of Drs. R. V. Serauskas and J. A. Kezerle; by NSF under the grant number CBT 8552654, and by NASA under the grant number NAG3-1460.

REFERENCES

1. Bowman, C. T., *Twenty-Fourth Symposium (International) on Combustion,* The Combustion Institute, Pittsburgh, 1992, pp. 859–878.
2. Sarofim, A. F. and Flagan, R. C., *Prog. Energy Combust. Sci.* 2:1–25 (1976).
3. Turns, S. R. and Myhr, F. H., *Combust. Flame* 87:319–335 (1991).
4. Atreya, A., Wichman, I., Guenther, M., Ray, A., and Agrawal, S., Second International Microgravity Workshop, NASA Lewis Research Center, Cleveland OH, 1992.
5. Tsuji, H., *Prog. Energy Combust. Sci.* 8:93 (1982).
6. Smooke, M. D., Seshadri, K., and Puri, I. K., *Combust. Flame* 73:45 (1988).
7. Zhang, C., Atreya, A., and Lee, K. *Twenty-Fourth Symposium (International) on Combustion,* The Combustion Institute, Pittsburgh, 1992, p. 1049.
8. Du, J. and Axelbaum, R. L., *Combust. Flame* 100:367–375 (1995).
9. Sugiyama, G., *Twenty-Fifth Symposium (International) on Combustion,* The Combustion Institute, Pittsburgh, 1994, p. 601.
10. Sunderland, P. B., Koylu, U. O., and Faeth, G. M., *Combust. Flame* 100:310 (1995).
11. Reisel, J. R., Carter, C. D., Laurendeau, N. M., Drake, M. C., *Combust. Sci. Technol.* 91:271–295 (1993).
12. Carter, C. D., King, G. B., and Laurendeau, N. M., *Appl. Opt.,* 31:1511 (1992).
13. Peters, N., *Twenty-First Symposium (International) on Combustion,* The Combustion Institute, Pittsburgh, 1986, pp. 1231–1250.
14. Lutz, A. E. and Kee, R. J., personal communications.
15. Puri, R., Santoro, R. J., and Smyth, K. C., *Combust. Flame* 97:125 (1994).
16. Smyth, K. C. and Tjossem, P. J. H., *Twenty-Third Symposium (International) on Combustion,* The Combustion Institute, Pittsburgh, 1990, pp. 1829–1837.
17. Drake, M. C. and Blint, R. J., *Combust. Flame* 83:185 (1991).

COMMENTS

J. Jurng, Korea Institute of Science & Technology, Korea. In the laser extinction measurement of soot volume fraction, the spatial resolution will not be higher than 0.2 due to the beam width. This will make the measured peaks of soot concentration broaden. So especially in a very-thin soot layer, there may be complications. What is your opinion on this problem?

Author's Reply. We agree with the difficulties cited in experimentally resolving the soot volume fraction peaks. The narrowest soot layer in our flames is about 1.5 mm thick. Thus, the laser probe width of 0.2 mm is not entirely satisfactory in resolving the magnitude of the soot volume fraction peak. The peak value is somewhat reduced. However, the location and the width of the peak are not significantly affected.

•

Jay Jeffries, SRI International, USA. Could you please comment on the calibration uncertainties for the OH and NO measurements? How do you account for quenching changes between the sooting and calibration blue flame for OH? What is the NO uncertainty?

Author's Reply. Quenching corrections were not made in the reported results. However, to minimize the sensitivity of OH measurements to quenching, laser-saturated fluorescence was used and the laser power was held constant for all the flames. The frequency doubled Nd:Yag-pumped dye laser output of 4–5 mJ/pulse at 282.7 nm was used to excite the $Q_1(5)$ line of the (1,0) band. The resulting fluorescence signal was measured in a narrow band around 312 nm by an ICCD spectrograph. Also, as recommended by Laurendeau and coworkers [11,12], only the 5 ns long peak of the temporal fluorescence pulse was collected and 200 pulses were averaged. Another important aspect of the

structure of these flames, that is in our favor, is that the OH and soot zones do not occur at the same location. Thus, interference due to soot is minimized.

Repeated tests with NO calibration gas (60 ppm) resulted in a maximum variation of ± 2 ppm. There may be some additional unquantified errors in the sooting region of the flame where measurements were difficult due to probe clogging. Fortunately, the sooting region is quite narrow and does not coincide with the location of maximum NO.

Twenty-Sixth Symposium (International) on Combustion/The Combustion Institute, 1996/pp. 2191–2197

MEASUREMENTS OF NO IN TURBULENT NON-PREMIXED FLAMES STABILIZED ON A BLUFF BODY

B. B. DALLY AND A. R. MASRI
Department of Mechanical and Mechatronic Engineering
The University of Sydney
NSW 2006, Australia

R. S. BARLOW AND G. J. FIECHTNER
Combustion Research Facility
Sandia National Laboratories
Livermore, CA 94551, USA

D. F. FLETCHER
Department of Chemical Engineering
The University of Sydney
NSW 2006, Australia

Spontaneous, single-point measurements of nitric oxide, NO, are made jointly with temperature, OH, and the major species using the Raman/Rayleigh/LIF technique. Turbulent non-premixed flames stabilized on a bluff body are studied with fuels ranging from simple H_2/CO to complex H_2/CH_4 and gaseous methanol. The fuel jet velocity is varied to investigate the Damköhler number effects on the formation of NO. Data are presented for different axial and radial locations along the full length of most flames. It is found that the NO is generated either in the recirculation zone or further downstream of the neck zone. When the stoichiometric contour lies within the outer vortex, NO is produced mainly within the recirculation zone. Within the neck zone of the flame, the NO index levels are either constant or decreasing. This is due to the lower production of NO and the higher contribution of the consumption mechanisms such as NO reburn to N_2. The overall NO emission level in flames of CH_3OH fuel is about a quarter of that measured in H_2/CO and H_2/CH_4 flames.

Introduction

Growing environmental concerns have led regulatory authorities to impose much stricter control on emissions from combustion systems. This in turn has led to renewed research interests in polluting species such as NO_x, SO_x, and CO. NO_x emission, in particular, has attracted special attention because of its contribution to acid rain and depletion potential of the stratospheric ozone layer. A summary of the emission regulations and control of combustion-generated nitrogen oxide can be found elsewhere [1]. The main constituents of NO_x are NO and NO_2 gases. NO is formed first in all the diffusion-type flames, while NO_2 is a by-product and forms at temperatures in the range of 700–800K. The fraction of NO that converts into NO_2 is believed to be very sensitive to fluid mechanical mixing and basically to the rapid cooling of NO [2]. NO emission from flames is thought to be controlled by four different mechanisms: thermal, prompt, nitrous, and NO reburn mechanisms. The relative contribution of each of these mechanisms depends on the fuel type, temperature, pressure, and residence times [3,4].

There have been many experimental studies in turbulent jet diffusion flames investigating the effects of fuel type, Reynolds number, Damköhler number (Da), and radiation heat loss on NO_x formation [4–11]. Bilger and Beck [5] found a shift in the NO peak toward the rich zone and a dependence on the jet exit Reynolds number, $Re^{-1/2}$. Drake et al. [6] suggested that the rich shift of the NO peak is due to probe sampling effects and that the super-equilibrium (O) radical concentration leads to higher NO_x formation rate covering a broader mixture fraction on both lean and rich sides of stoichiometric. Driscoll et al. [7] studied the dependence of the NO_x-emission index ($EINO_X$) on *Re* and *Da* numbers and proposed alternate correlations. Turns et al. [8,9] looked at the effects of radiation losses on NO formation and found them to be significant even in nonsooting flames.

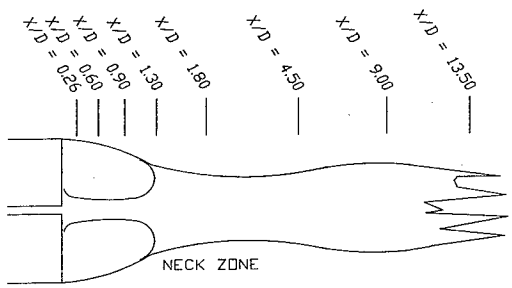

FIG. 1. Sketch of a typical bluff-body-stabilized flame and the measurement locations.

In all of these investigations, the experimental results were mostly obtained using a water-cooled sampling probe positioned downstream of the visible flame tip. These data were used mainly to calculate the NO_x-emission index ($EINO_X$) normalized by a global residence time that is generally defined, using the similarity assumption, as the length of the flame divided by the bulk jet velocity. This technique suffers from averaging effects and falls short of giving details on the effects of turbulence-chemistry interaction on NO_x and the instantaneous relation between NO concentration and other scalars. Barlow and Carter [12,13] recently have used laser-induced fluorescence (LIF) to make instantaneous and quantitative measurements of NO jointly with temperature and other species using the Raman/Rayleigh/LIF technique. The measurements were made in a H_2 flame diluted with helium. They demonstrated that peak NO occurs at stoichiometric levels and that the rich shift detected by others [5,7] is due to averaging effects. Such nonintrusive and spontaneous measurements of NO in flames are very revealing and extremely important for understanding the evolution of NO in flames.

Fewer attempts have been made to model NO_x formation in turbulent diffusion flames using realistic chemistry. Such efforts must account for all the relevant NO_x-formation mechanisms. This involves many species and reactions and necessitates the use of reduced mechanisms such as those produced recently by Hewson and Williams [4]. A further complication associated with the computation of NO_x is the need to account for the effects of radiation heat losses. Smith et al. [14] recently have tackled such problems using the PDF and CMC approaches for jet diffusion flames with H_2/He fuel.

The purpose of this paper is to present instantaneous measurements of NO jointly with temperature, mixture fraction, and the hydroxyl radical OH in turbulent diffusion flames stabilized on a bluff body. Such measurements are made using the same Raman/Rayleigh/LIF technique used by Barlow and Carter [12]. The novelty here is threefold. First, fuels with complex chemical kinetics such as methanol and methane are used. Second, the flow pattern is more complex and includes a recirculation zone of fluid just downstream of the jet exit plane. Third, a detailed map of the flame structure is obtained from the recirculation zone to the flame tip. Bluff-body-stabilized flames are of significant practical importance and are being studied extensively. They present an immense challenge to modelers of turbulent combustion.

Experimental Setup

The bluff-body burner has an outer diameter of 50 mm with a concentric jet diameter of 3.6 mm. The wind tunnel has an exit cross section of 254 × 254 mm. The co-flow air velocity is fixed at 40 m/s for all the flames and the free stream turbulence level in the tunnel is at ~2%. The single-point Raman/Rayleigh/LIF technique is used to measure temperature and the concentration of stable species as well as the concentration of two minor species: OH and NO. Figure 1 shows a schematic of the flame and the corresponding measurement locations. The Raman/Rayleigh measurements use two Nd:YAG lasers in which the successive pulses are stretched from ~8 to ~40 ns to avoid excessive energy in the probe volume and hence gas breakdown. The energy delivered to the probe volume is ~700 mJ. The combined Nd:YAG (532-nm) beams are reflected back through the probe volume using a collimating lens and a 180° turning prism, which effectively doubles the Raman and Rayleigh energy to ~1.4 J.

The OH and NO fluorescence measurements are accomplished using two separate Nd:YAG–pumped dye laser systems. The OH excitation beam is tuned for the $O_{12}(8)$ transition in the $A^2\Sigma^+ - X^2\Pi$ (1, 0) band (λ = 287.9 nm), and the OH signal is collected through broadband colored glass filters, Schott WG-295 and Hoya U-340 (both 3 mm thick). This allows the capture of the fluorescence in both the (1, 0) and (0, 0) band. The NO excitation beam has a wavelength of 225.9 nm, and the signal is collected from the system of bands at 236, 247, 259, and 271 nm. The Raman and Rayleigh scattered light is collected using a six-element achromat and later focused onto the entrance slit of a 0.75-m polychromator. The OH and NO signals are collected using a Cassegrain mirror at the opposite side of the test section from the Raman/Rayleigh lens. A dichroic beam splitter directed the NO fluorescence onto one detector, while the OH fluorescence passed through to another detector. Calibration for the Rayleigh, OH, and the Raman species is done using a laminar premixed flame established on a Hencken burner. A premixed CH_4/air flame stabilized on a McKenna burner is used for the NO calibration. The quantitative OH and NO concentrations are obtained by correcting the

TABLE 1

U_J is the jet velocity (m/s), U_{CO} is the co-flow air velocity (m/s), Re_J is the jet Reynolds number, % *BO* is the percentage ratio of jet velocity over the blow-off velocity, and T_{IN} is the temperature of the fuel at the jet exit plane

Flame	Symbol	U_J/U_{CO}	Re_J	% *BO*	T_{IN} (K)
CH_3OH	ML1	80/40	23,700	55	373
CH_3OH	ML2	121/40	35,900	84	373
H_2/CO (2:1)	HC1	134/40	17,500	22	298
H_2/CO (2:1)	HC2	321/40	41,990	53	298
H_2/CH_4(1:1)	HM1	118/40	15,800	50	298
H_2/CH_4(1:1)	HM2	178/40	23,900	75	298
H_2/CH_4(1:1)	HM3	214/40	28,700	91	298

fluorescence signals on a shot-to-shot basis for the variations in the Boltzmann fraction and the collisional quenching rate that are determined from the measured temperature and species concentration. Quenching cross sections of NO and OH are obtained from Paul [16–18]. These procedures are described in detail by Barlow and Carter [12].

Three different fuels are investigated: CH_3OH, H_2/CO (2:1), and CH_4/H_2 (1:1) by volume. The first and second fuels have a stoichiometric mixture fraction of 0.135, while the third has a stoichiometry of 0.050. Methanol is evaporated and delivered through heated line before being released at 100°C from the jet. A list of the flames investigated is given in Table 1. The fuel jet velocity is varied to investigate the Damköhler number effect on NO_x formation. The measurements are taken at different axial locations in the flame. Typically, 800 shots are collected at each radial location covering the whole width of the flame.

Results and Discussion

The bluff-body-stabilized flames investigated here are characterized by three distinct zones, shown schematically in Fig. 1. The first is referred to as the recirculation zone. It establishes downstream of the bluff body and extends to ~1.0 bluff-body diameter. It has an outer larger vortex close to the air side and, depending on the flow, an inner vortex adjacent to the central jet [15]. Generally, the outer vortex has a nearly uniform mixture and its strength depends on the fuel and flow conditions. The stoichiometric mixture fraction contour is found to shift from the outer vortex to the inner vortex with increasing jet velocity. Beyond the recirculation zone is the neck zone, which is a region of intense mixing in which local extinction and blow off occur at high enough jet velocity. The third zone is the rest of the flame, which spreads in a jetlike manner.

Although detailed measurements have been made in all the flames listed in Table 1, results are only presented here for flames of methanol fuel. The detailed data for the rest of the fuels will appear elsewhere [19]. Scatter plots of temperature, NO, and OH mole fractions versus the mixture fraction are shown in Fig. 2 for flames ML1 and ML2. Each of these plots corresponds to a different axial location. In flame ML1, the peak NO mole fraction drops from 50 to 20 ppm as the axial location increases from $X/D_B = 0.26$ to 1.8. Further downstream and outside the neck zone ($X/D_B > 1.8$), the flame slows down and the NO peak increases back to ~40 ppm. Flame ML2 shows a similar trend for NO, albeit with lower peak values that generally are due to higher jet velocity and hence shorter residence time. Unlike OH concentrations that decrease to zero for mixture fractions greater than ~0.25, the measured NO profile covers almost the entire mixture fraction range. Peak temperature and OH levels in flame ML1 are similar right across the flame length, except at $X/D_B = 0.26$, where lower peak OH is observed. Flame ML2, which is closer to blow off, shows significant local extinction in the neck zone at $X/D_B = 1.6$ with full reignition occurring further downstream at $X/D_B = 4.5$. The intense mixing at the neck zone leads to temperature depression, lower residence time, and hence a decrease in the production of NO. The lower peak NO near stoichiometric is also due to the rapid mixing of NO away from these regions. Peak temperature, OH, and NO occur around stoichiometric for both flames. The average length of these flames, determined as the location at which the average value of the mixture fraction on the centerline reaches the stoichiometric value, is about 9 bluff body diameters, which is much shorter than the visible length.

NO Index

The emission index $EINO_X$ is a nondimensional quantity often used when comparing the NO_x emission from different fuels. Since NO_2 is not measured here and since the measurements cover the whole

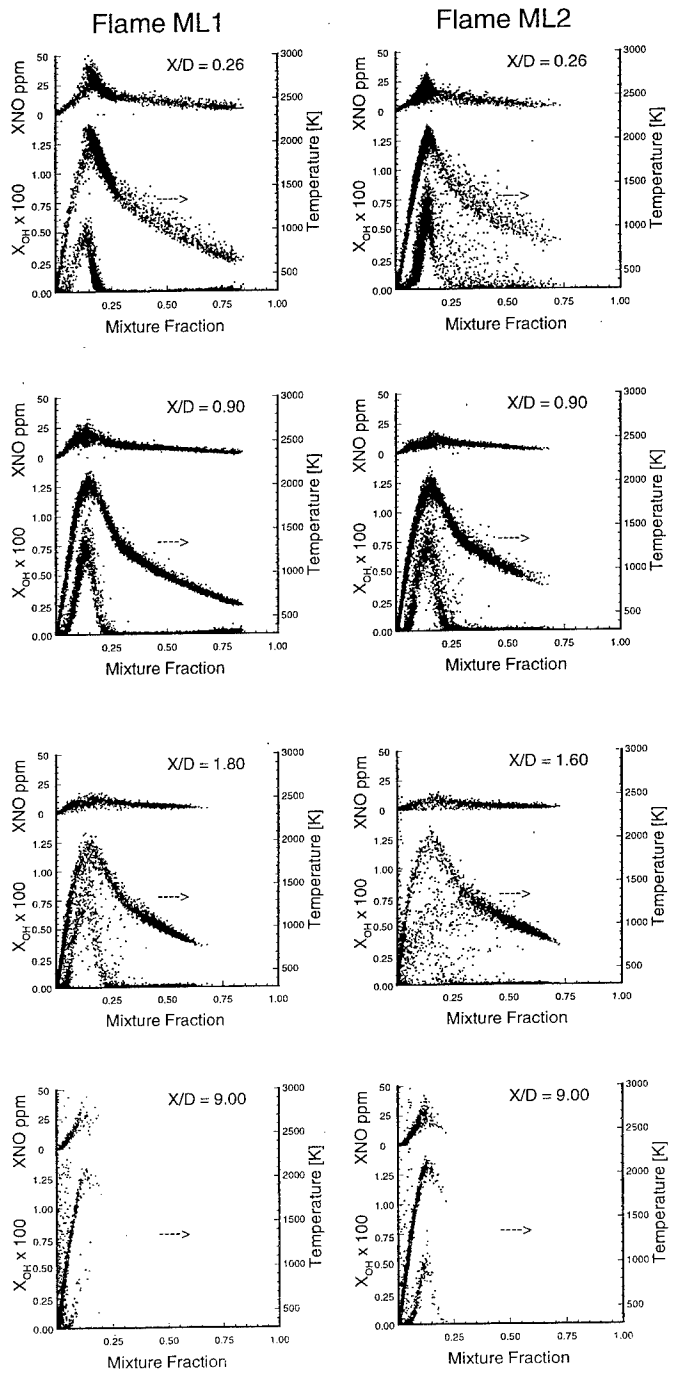

FIG. 2. Scatter plots of temperature and the mole fractions of NO and OH plotted versus mixture fraction for a range of axial locations in the CH_3OH flame with U_j/U_{BO} = 0.55 (ML1) and U_j/U_{BO} = 0.84 (ML2).

flame length rather than just one location downstream of the tip, a new NO index (NOI) is defined as the net mass of NO convected downstream at a given axial location in the flame per unit mass of jet fuel:

$$NOI = \frac{2\pi W_{NO}}{A\dot{m}_{JET}} \int_0^\infty [N_{NO}(r)]U(r)rdr \qquad (1)$$

where W_{NO} is the molecular weight of NO, A is Avogadro's number, $\dot{m}_{JET}$ is the mass flow rate of the

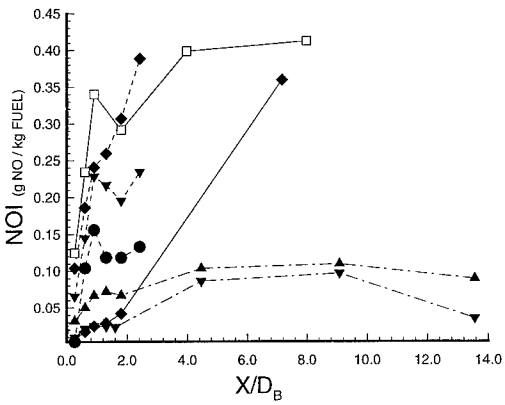

FIG. 3. Axial plot of the NO index (NOI) obtained for bluff-body-stabilized flames with a range of fuels: ---◆--- H_2/CH_4 fuel with U_j/U_{BO} = 0.50 (HM1); ---▼--- H_2/CH_4 fuel with U_j/U_{BO} = 0.75 (HM2); ---●--- H_2/CH_4 fuel with U_j/U_{BO} = 0.91 (HM3); —□— H_2/CO fuel with U_j/U_{BO} = 0.22 (HC1); ---◆--- H_2/CO fuel with U_j/U_{BO} = 0.53 (HC2); ---▲--- CH_3OH fuel with U_j/U_{BO} = 0.55 (ML1); ---▼--- CH_3OH fuel with U_j/U_{BO} = 0.84 (ML2)

fuel, $[N_{NO}(r)]$ is the measured mean number density of NO, and $U(r)$ is the computed mean axial velocity at radial location (r). The calculated velocities are used here because measurements are not available at all the axial locations of interest. The flow field is calculated using the CFDS-FLOW3D package [20]. The modified k-ε turbulence model and the "mixed is burnt" combustion model are used in the calculations. More information about these calculations is provided in Ref. [21].

At each axial location, the net mass flow rate of NO is normalized by the fuel mass flow rate at the jet exit plane. Figure 3 shows the NOI for all flames listed in Table 1, plotted against the normalized distance above the burner. It should be noted here that although this index is an approximation (since it uses the mean values of the measured NO concentration and computed velocity), it reveals valuable information about the NO formation or destruction at different locations in the flame. In the H_2/CH_4 flames, measurements are presented down to X/D_B = 2.4 only, while the entire flame length is covered for the H_2/CO and CH_3OH fuels. The general trend observed for all flames is an increase in NOI in the recirculation zone followed by a region in the neck zone in which NOI decreases or remains constant. NOI then increases further to a maximum that occurs well downstream of the neck zone. The decrease in NOI at the tip of the methanol flames ML1 and ML2 is largely due to conversion of NO to NO_2. The decrease in NOI observed at the neck zone of the H_2/CO and H_2/CH_4 flames suggests that the production of NO has dropped considerably and that NO reburn to N_2, which is enhanced by the combination of a short residence time and high concentration of NO, may be active. The NOI decrease at the neck zone is smaller for lower jet velocity flames.

The following points should be noted:

1. Methanol fuel is a lower NO pollutant with peak NOI being about a quarter that of H_2/CH_4 and H_2/CO fuel mixtures.
2. As the jet velocity is increased and blow off approaches, the NOI level decreases right across the flame, especially in the neck zone where the temperature decreases and local extinction occurs. This is illustrated clearly in the H_2/CO and H_2/CH_4 flames. Further downstream of the neck zone, NOI levels increase again because of reignition and relaxed turbulent mixing rates.
3. The increase in the NOI within the recirculation zone is controlled by the location of the stoichiometric contour with respect to the stabilizing vortices. The vortices' shape and strength are determined by the geometry and jet momentum. At high jet momentum, the outer vortex is shortened and the inner vortex disappears because of the jet expansion. As a consequence, the residence time inside this inner zone is much shorter than in the outer vortex and hence a smaller amount of NO is produced. This implies that for flows in which stoichiometric mixtures are largely within the inner zone, the levels of NO produced in the recirculation zone will be much lower. This is the case for flames HC2 and ML2. The calculations of the flow field [15,21], described above, show

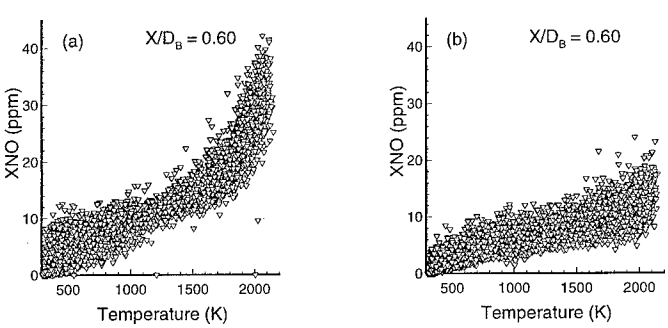

FIG. 4. Scatter plots of NO mole fraction plotted versus temperature at axial location X/D_B = 0.60 in flames (a) ML1 and (b) ML2.

that for these flames, the stoichiometric contours are within the inner zone. However, in the H_2/CH_4 flames and the low-velocity HC1 and ML1 flames, the stoichiometric contours are within the outer vortex and hence the levels of NOI within the recirculation zone are much higher.

Analysis of the relative contribution of the various mechanisms to the overall production of NO is beyond the scope of this paper. It is known, however, that this is affected by a range of factors including temperature, residence time, and species concentrations in the radical pool. Figure 4 shows scatter plots of NO mole fraction versus temperature measured at $X/D_B = 0.6$ in the recirculation zones of flames ML1 and ML2. The correlation between NO and temperature changes as the jet velocity is increased and the stoichiometric contour shifts from the outer vortex to the inner zone. The lower peak mole fraction of NO measured in flame ML2 reflects the shorter residence time experienced at this location in the flame. Further analysis of the correlations between temperature, NO, OH, and other scalars coupled with calculations of flames with similar fuel mixtures and detailed or reduced kinetics will be useful in determining the sources of NO.

Conclusions

Single-point measurements of NO made in bluff-body-stabilized flames indicate that peak levels of NO occur at stoichiometric mixture fraction regardless of the fuel mixture, the Damköhler number of the flame, and the axial location in the flame. As the residence time decreases, the correlation between temperature and NO changes, reflecting the lower levels of NO produced. The amount of NO produced in the recirculation zone is very high if the stoichiometric contour lies within the outer vortex and decreases sharply if the stoichiometric contour moves to the inner zone. Within the neck zone of the flame, NOI levels are either constant or decrease because of temperature depression and the low residence time, which decreases the production of NO and increases the contribution of the consumption mechanisms such as the NO reburn to N_2. The overall NO emission level in flames of CH_3OH fuel is about quarter of that measured in H_2/CO and H_2/CH_4 flames.

Acknowledgments

The authors acknowledge the support of the Australian Research Council and the U.S. Department of Energy, Office of Basic Energy Sciences, Division of Chemical Sciences.

REFERENCES

1. Bowman C. T., *Twenty-Fourth Symposium (International) on Combustion,* The Combustion Institute, Pittsburgh , 1992, pp. 859–878.
2. Hori, M., *Twenty-First Symposium (International) on Combustion,* The Combustion Institute, Pittsburgh, 1986, pp. 1181–1188.
3. Fenimore, C. P., *Thirteenth Symposium (International) on Combustion,* The Combustion Institute, Pittsburgh, 1971, pp. 373–380.
4. Hewson, J. C. and Williams, F. A., *Proceedings of the 8th ONR Propulsion Meeting,* La Jolla, CA, 1995, pp. 52–59.
5. Bilger, R. W. and Beck R. E., *Sixteenth Symposium (International) on Combustion,* The Combustion Institute, Pittsburgh, 1976, pp. 541–551.
6. Drake, M. C., Correa, S. M., Pitz, R. W., Shyy, W., and Fenimore, C. P., *Combust. Flame* 69:347–365 (1987).
7. Driscoll, J. F., Chen, R. H., and Yoon, Y., *Combust. Flame* 88:37–49 (1992).
8. Turns, S. R. and Myhr, F. H., *Combust. Flame* 87:319–335 (1991).
9. Turns, S. R., Myhr, F. H., Bandaru, R. V., and Maund, E. R., *Combust. Flame* 93:255–269 (1993).
10. Chen, R.-H. and Driscoll, J. F., *Twenty-Third Symposium (International) on Combustion,* The Combustion Institute, Pittsburgh, 1990, pp. 281–288.
11. Correa, S. M., *Combust. Sci. Technol.* 87:329–362 (1993).
12. Barlow, R. S. and Carter, C. D., *Combust. Flame* 97:261–280 (1994).
13. Barlow, R. S. and Carter, C. D., *Combust. Flame* (in press).
14. Smith, N. S. A., Bilger, R. W., Carter, C. D., Barlow, R. S., and Chen, J.-Y. *Combust. Sci. Technol.* 105(4,6):357–375 (1995).
15. Dally, B. B., Masri, A. R., and Fletcher, D. F., *Twelfth Australasian Fluid Mechanics Conference,* Vol. 1, Sydney, Australia, 1995, pp. 529–532.
16. Paul, P. H., *J. Quant. Spectrosc. Radiat. Transfer* 51:511–524 (1994).
17. Paul, P. H., Gray, J. A., Durant, J. L. Jr., and Thoman, J. W. Jr., *AIAA J.* 32:1670–1675 (1994).
18. Paul, P. H., Private communication on quenching of OH and NO by methanol; Sandia National Laboratories, Livermore, CA, 1995.
19. Dally, B. B., Masri, A. R., Barlow, R. S., and Fiechtner, G. J., Submitted to *Combust. Flame* (1996).
20. CFDS-FLOW3D release 3.3: user manual; Computational Fluid Dynamics Services, AEA Technology, Harwell Laboratory, Didcot, Oxon, UK, 1995.
21. Dally, B. B., Fletcher, D. F., and Masri, A. R., *Proc. First Asian CFD Conference,* Hong Kong, 1995, pp. 177–182.

COMMENTS

J. P. Gore, Purdue University, USA. Would you comment on the effects of neglecting the cross correlation between NO number density and axial velocity? What is your justification for calculating the emission index without considering this effect?

Author's Reply. The effects of the correlation between NO number density and the velocity are not known and require a joint instantaneous measurement of these scalars. This has not been done and forms an interesting and challenging project. The NOI presented here is an approximate measure of the NO flux which serves as a basis for comparison of the evolution of NO in flames with similar flow field structure and different fuels.

•

A. Ghoniem, MIT, USA. Previous experiments by Namazian et al [1] and by Roquemore et al [2] showed the presence of strong oscillations near the bluff body over a wide range of velocity ratios. Numerical simulations by Martins and Ghoniem [3] and others have shown that these oscillations are related to vortex sheddings and interactions within the recirculation zone, 1–2 bluff-body diameters. Have you detected similar oscillations in your experiments and can strain related effects near the jet flame base be used to interpret some of your observations.

REFERENCES

1. Namazian, M., Kelly, J. T., and Schafer, R. W., *Twenty-Second Symposium (International) on Combustion,* The Combustion Institute, Pittsburgh, 1988, pp. 627–634.
2. Roquemore, W. M., Britton, R. L., and Sandhu, S. S., "Investigation of the dynamic behavior of a bluff-body diffusion flame using flame emission," AIAA-82-0178, AAIA 20th Aerospace Sciences Meeting.
3. Martins, L. T. and Ghoniem, A. F., *ASME J. Fluids Eng.* 115:474–484 (1993).

Author's Reply. The flames investigated in this paper are stable and do not exhibit the oscillations or the vortex shedding referred to in the question. This is mainly due to the fact that the jet and the coflow momentum and hence the Reynolds numbers of these flames are higher than those for the flames referred to by Prof. Ghoniem. For example the Schefer/Namazian methane flame has a coflow and fuel jet momentum of 750 and 300 (N/m^2) respectively, as opposed to 1920 and 5200 (N/m^2) for the CH_4/H_2 flames presented in this paper. The corresponding Reynolds number is 7000 for the Schefer/Namazian flame and 16,000 and above for the flames discussed in this paper.

Twenty-Sixth Symposium (International) on Combustion/The Combustion Institute, 1996/pp. 2199–2205

OXYGEN ATOM CONCENTRATIONS AND NO PRODUCTION RATES IN A TURBULENT H_2/N_2 JET FLAME

R. S. BARLOW AND G. J. FIECHTNER
Combustion Research Facility
Sandia National Laboratories
Livermore, CA 94551-0969, USA

J.-Y. CHEN
Department of Mechanical Engineering
University of California
Berkeley, CA 94720, USA

An experimental procedure is demonstrated that allows determination of instantaneous oxygen-atom concentrations and thermal NO production rates in turbulent flames. This is accomplished without direct measurement of O atoms by laser-induced fluorescence, a technique that has been shown to be problematic. Simultaneous point measurements of temperature, the major species, OH, and NO are performed in a non-premixed turbulent jet flame of nitrogen-diluted hydrogen fuel. The O-atom concentration for each laser shot is derived from these data, based on the assumption of partial equilibrium of the reaction OH + OH = O + H_2O. The derived O-atom concentration is then used with the measured N_2 concentration and temperature to calculate the instantaneous thermal (Zeldovich) NO production rate. The partial equilibrium assumption is shown to be appropriate in this flame for conditions relevant to thermal NO formation. The maximum conditionally averaged O-atom mole fraction is about 6.5 times the maximum value for full chemical equilibrium. The width in mixture fraction coordinates of the conditionally averaged NO production rate curve is roughly twice that calculated from adiabatic equilibrium values of temperature, [O], and N_2. Experimental results are compared with predictions obtained using the Monte Carlo PDF model with detailed chemistry. With some exceptions, there is good agreement between experiment and prediction when results are plotted against mixture-fraction (scatter plots and conditional averages). Agreement is not as good when radial profiles of averaged scalar quantities are compared. This indicates that the present PDF model predicts the hydrogen and nitrogen chemistry with good accuracy but that improvements are needed in the modeling of the turbulent fluid dynamics and mixing. A comparison of experimental results with steady strained laminar flame calculations shows that the turbulent flame conditions cannot be represented by a combination of the laminar flames.

Introduction

Thermal NO formation is a significant mechanism in many combustion applications. Considerable research has been carried out using gas-sampling probes to determine the effects of various parameters on NO_x formation in turbulent jet flames [1–6]. More recently, simultaneous laser-based measurements of multiple species have been used to investigate NO formation in hydrogen jet flames [7–10], in laminar CH_4-air Bunsen flames [11], and in bluff-body-stabilized flames [12]. In much of this work, there has been speculation regarding the effects of turbulence-chemistry interactions on superequilibrium levels of O atoms, which contribute to NO production. Experimental O-atom concentrations and thermal NO production rates would be useful in developing a better understanding of the influence of turbulence-chemistry interactions on NO formation and in evaluating various modeling approaches. Investigations of laser-induced fluorescence (LIF) detection of O atoms in laminar flames [13,14] suggest that quantitative single-shot measurements of O-atom concentrations in turbulent flames would be a difficult challenge because the 226-nm laser that excites the O atoms produces additional O atoms by photolysis.

In the present study, we demonstrate an experimental alternative to direct LIF measurements of O-atom concentrations. Pulsed-laser diagnostics are used to obtain simultaneous point measurements of temperature, the major species, OH, and NO. The instantaneous O-atom concentration is derived from the measured temperature, [OH], and [H_2O], based on the assumption of partial equilibrium of the reaction:

$$OH + OH \Leftrightarrow O + H_2O \quad (R1)$$

such that

$$[O] = K_{EQ,1}\,[OH]^2/[H_2O] \quad (1)$$

The thermal NO production rate is then calculated on a shot-to-shot basis from the extended Zeldovich mechanism:

$$N_2 + O \rightarrow N + NO \quad (R2)$$

$$N + O_2 \rightarrow O + NO \quad (R3)$$

$$N + OH \rightarrow H + NO \quad (R4)$$

Here, the first reaction is rate limiting, and because the NO levels are far below equilibrium in the flames of interest, the overall production rate may be calculated as twice the forward rate of the first reaction [15]:

$$d[NO]/dt = 2k_2[N_2][O] \quad (2)$$

where

$$k_2 = 1.84 \times 10^{11} \exp(-38{,}370/T) \text{ mol/L s}$$

To demonstrate this approach, we consider results of measurements along a single radial profile in a non-premixed turbulent jet flame of 80% H_2 and 20% N_2 by volume. Experimental data are compared with steady strained laminar flame calculations and with a Monte Carlo PDF simulation of the turbulent flame.

Experimental Methods

The flow facility, diagnostic systems, and calibration procedures have been described previously [7,8,11]. Spontaneous Raman scattering of the beams from two Nd:YAG lasers (532 nm) was used to measure concentrations of the major species. Pulse-stretching optics were used to avoid breakdown at the focus [11], and the energies in the beams were measured by two pyroelectric joulemeters. The Rayleigh scattering signal was converted to temperature using a species-weighted scattering cross section based on the Raman measurements. Linear LIF was used to measure OH and NO, and the fluorescence signals were corrected on a shot-to-shot basis for variations in the Boltzmann fraction and the collisional quenching rate. These corrections were determined from the measured species concentrations and temperature and from published correlations for collisional quenching cross sections [16,17]. The spatial resolution for all measurements was ~750 μm in each direction.

The temperature-dependent calibration functions for each of the Raman channels were determined through an extensive series of measurements in the flow above a gas heater and in flat flames above a Hencken burner [8]. Radiative losses from the calibration flames were accounted for in this procedure. Additional Raman/Rayleigh calibrations were performed immediately before and after the turbulent flame measurements. OH measurements were referenced to a H_2-air flat flame, in which the OH number density had been measured previously by laser absorption [7]. The NO calibration factor was determined by doping a lean premixed CH_4-air laminar flat flame (McKenna burner) with four known concentrations of NO. Detailed flame calculations have shown that destruction of the seeded NO in this flame is negligible [11]. The NO calibrations were also performed immediately before and after the turbulent flame measurements.

Derivation of O-atom concentrations and NO production rates depends on precision and accuracy of the measured scalars, particularly [OH] and temperature. Estimates of random errors at temperatures relevant to thermal NO production were based on the standard deviations of measured and derived scalars in steady premixed flat flames. These estimates are listed in Table 1 along with the conditions at which they were determined. Estimates of potential systematic errors are also listed in Table 1. Systematic uncertainties for [O] and $d[NO]/dt$ were determined from Eqs. (1) and (2) as worst-case products of the contributing potential systematic errors in the measured scalars. The estimated systematic uncertainty of ±80% in the NO production rate may seem high. However, we shall see that this level of quantitative information may be sufficient to distinguish between modeling approaches.

The burner was a straight tube (inner diameter, d = 4.58 mm; outer diameter, 6.34 mm; squared-off end) centered at the exit of a 30-cm by 30-cm vertical wind tunnel contraction. The co-flow air

TABLE 1
Relative standard deviations of scalars measured or derived at the listed conditions in steady flat flames and potential systematic uncertainties estimated from the calibration procedures

Scalar	σ(rms)	Conditions (mole frac., T)	Systematic Uncertainty
N_2	3%	0.71, 2140 K[a]	2%
H_2O	5%	0.18, 2140 K[a]	3%
OH	7%	0.0023, 2140 K[a]	10%
NO	10%	26, 1740 K[b]	10%
T	1%	2140 K[a]	2%
O	14%	2140 K[a]	35%
$d[NO]/dt$	21%	2140 K[a]	80%

[a] Premixed CH_4/air, ϕ = 0.96, uncooled burner
[b] Premixed $CH_4/O_2/N_2$, ϕ = 0.72, cooled (McKenna) burner

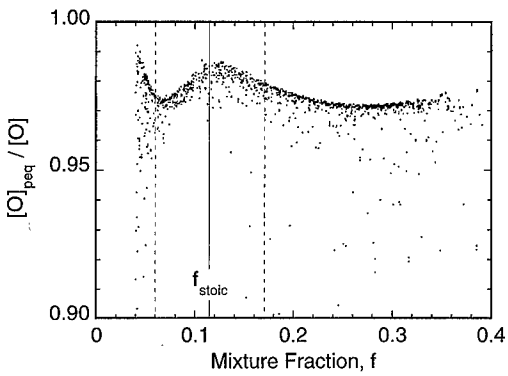

FIG. 1. Scatter plot of the ratio $[O]_{peq}/[O]$ versus mixture fraction from the PDF model simulation at $x/d = 30$, indicating the degree of departure from partial equilibrium of the reaction $OH + OH = O + H_2O$. The dashed lines bracket the region of interest for thermal NO formation. Data below 1200 K are not plotted.

conditions were 0.75 ± 0.05 m/s velocity, 290 K temperature, and 0.0116 H_2O mole fraction. The fuel composition was 80% H_2 and 20% N_2, by volume. The jet velocity was 151 ± 3 m/s, the exit temperature was 294 K, and the Reynolds number was 14,000, based on a mixture viscosity of $\upsilon = 4.85 \times 10^{-5}$ m²/s. Laboratory pressure was 0.977 atm.

Measurements were made along a radial profile through the jet centerline at a streamwise distance of 30 nozzle diameters ($x/d = 30$), with 600–800 shots taken at each location. These experimental conditions were selected for several reasons. First, the spatial resolution of the system is sufficient to resolve the smallest scales at this location, as estimated following Smith et al. [18]. Second, N_2 dilution reduces the OH levels such that fluorescence trapping effects are small. Third, differential diffusion effects are not expected to be significant at this Reynolds number and streamwise location [18]. Finally, N_2 dilution reduces radiative loss, which is not included in the PDF simulation.

Monte Carlo PDF Prediction

The mean flow field was modeled by a Reynolds stress closure with a downstream marching algorithm [19]. The joint scalar PDF was solved by its modeled transport equation using the Monte Carlo technique [20]. The turbulent transport term was modeled by a gradient diffusion model using the turbulence time and fluctuating velocities from the Reynolds stress model. A modified Curl's mixing model was used to simulate the effect of turbulent stirring on the molecular diffusion process. The amount of mixing was modeled through a characteristic mixing time, which is related to the turbulence timescale. In the Monte Carlo simulation of the joint scalar PDF, the jet flame is assumed to be axisymmetric and adiabatic. Forty grid points across half of the jet were used, each containing 400 stochastic elements. The time evolution of chemical kinetics for each element was directly computed using a detailed mechanism for hydrogen combustion with NO_x chemistry that includes 14 species and 48 steps [21]. The CPU time was about 200 h on an SGI workstation for calculations up to $x/d = 150$, demonstrating that the inclusion of detailed chemistry in the PDF model is computationally expensive but not prohibitive. This simulation was based on the experimental boundary conditions of nozzle diameter, fuel composition, jet velocity, and co-flow velocity; the model was not tuned to match any aspect of the measured scalar data.

Results and Discussion

The Partial Equilibrium Assumption

Strained laminar flame calculations and perfectly stirred reactor (PSR) calculations of H_2/N_2 reacting with air were performed to assess the validity of the partial equilibrium assumption. The detailed mechanism cited previously was used, and results show that for temperatures above ~1500 K and mixtures fractions between about 0.06 and 0.17, the O-atom concentration determined from Eq. (1) differs from the actual O-atom concentration by less than 5%.

The PDF calculation can also be used to examine the partial equilibrium assumption. Figure 1 shows a scatter plot of the ratio of the partial-equilibrium O-atom concentration determined from Eq. (1) to the actual O-atom concentration predicted by the PDF simulation. For mixture fractions relevant to thermal NO formation in this flame ($0.06 < f < 0.17$), the deviation of the O-atom concentration from partial equilibrium is only 1.5–3% for the great majority of samples. We conclude that the partial equilibrium assumption is reasonable for the experimental application described here, except for determining O-atom concentrations in fuel-lean mixtures below ~1500 K.

Scatter Plots and Conditional Means

The relationships among scalars in reacting flows can be interpreted effectively when results are plotted in mixture fraction coordinates. For both experiment and prediction, the mixture fraction was calculated following the method of Bilger et al. [22] as:

$$f = \frac{(Y_H - Y_{H,2})/w_H - 2(Y_O - Y_{O,2})/w_O}{(Y_{H,1} - Y_{H,2})/w_H - 2(Y_{O,1} - Y_{O,2})/w_O}$$

where Y are elemental mass fractions, w_H and w_O

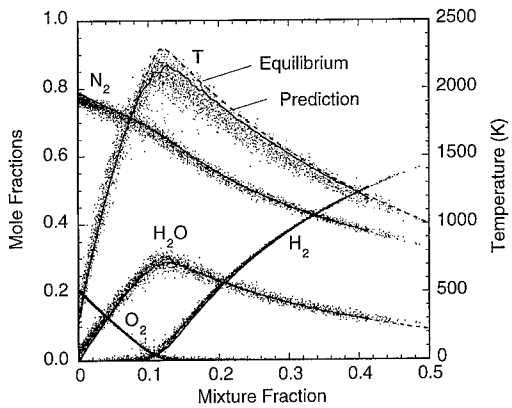

FIG. 2. Comparison of measured temperature and major species mole fractions (scatter points) with conditional averages from the PDF model prediction (———) for the streamwise location of $x/d = 30$. Equilibrium curves (- - - -) are included for temperature and H_2O.

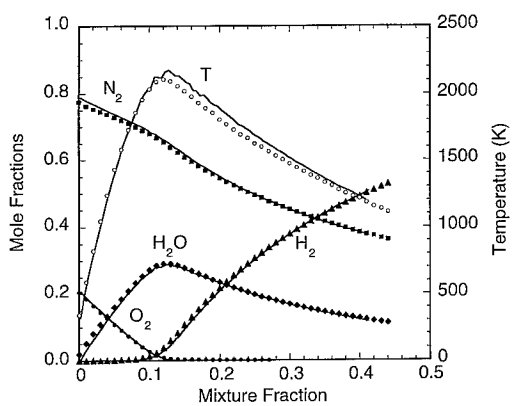

FIG. 3. Comparison of conditional averages of measured temperatures and major species mole fractions (symbols) with the corresponding predicted conditional means (———) as in Fig. 2.

are atomic weights, and the subscripts 1 and 2 refer to the fuel stream and co-flowing air stream, respectively.

Figure 2 shows scatter plots of measured temperature and the major species mole fractions. Conditional averages (conditional on mixture fraction) from the PDF calculation are shown as solid lines, and adiabatic equilibrium curves are included for H_2O and temperature. In this flame, the temperature and major species are close to equilibrium, except near the stoichiometric mixture fraction, where temperatures and H_2O mole fractions are depressed because of finite-rate chemistry. Here, results from the full radial profile are included for both experiment and prediction. In Fig. 3, conditional averages

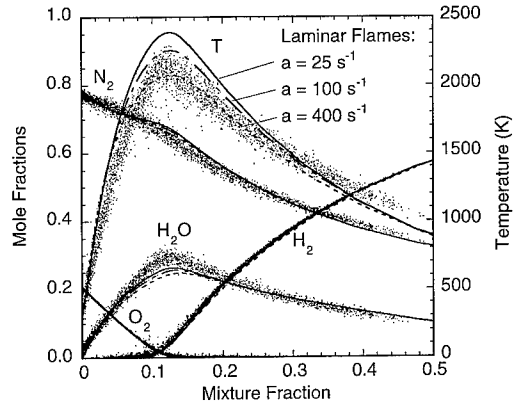

FIG. 4. Comparison of measured temperature and major species mole fractions (scatter points) with results from steady laminar flame calculations for values of the strain parameter, a, of 25 s^{-1} (———), 100 s^{-1} (— — —), and 400 s^{-1} (- - - - -).

of the measured scalars are compared with the prediction. Agreement for the major species mole fractions is very close, except for differences near $f = 0$, which arise because the calculation does not include ambient levels of H_2O and argon. The peak in the experimental temperature curve is about 50 K lower than the prediction, and the two temperature curves appear to be shifted slightly in mixture fraction relative to each other.

In Fig. 4, the experimental scatter data are compared with strained laminar flame calculations at three values of the strain parameter, a, for the Tsuji geometry. These calculations were performed using the same chemical mechanism as in the PDF simulation. They are included to illustrate that temperatures and some species mole fractions in the laminar calculations can be quite different from the turbulent flame measurements. These differences are believed to be due in part to the effects of differential diffusion being more pronounced in laminar flames [18].

Experimental and predicted results for OH mole fraction, O-atom mole fraction, NO production rate, and NO mole fraction are compared in Fig. 5. Measurements and PDF results are plotted as scatter points and conditional averages. To minimize the effect of OH fluorescence trapping, we have included only the measurements from the half of the flame profile that was closest to the fluorescence collection optics. The average fluorescence trapping effect near the center of this reaction zone was about 3%, and this correction has been applied to the OH results in this figure. Curves for the laminar flame calculations and for full adiabatic equilibrium are also included, except for NO mole fraction. NO mole fractions at equilibrium and in the laminar flames are much higher than in the turbulent flame.

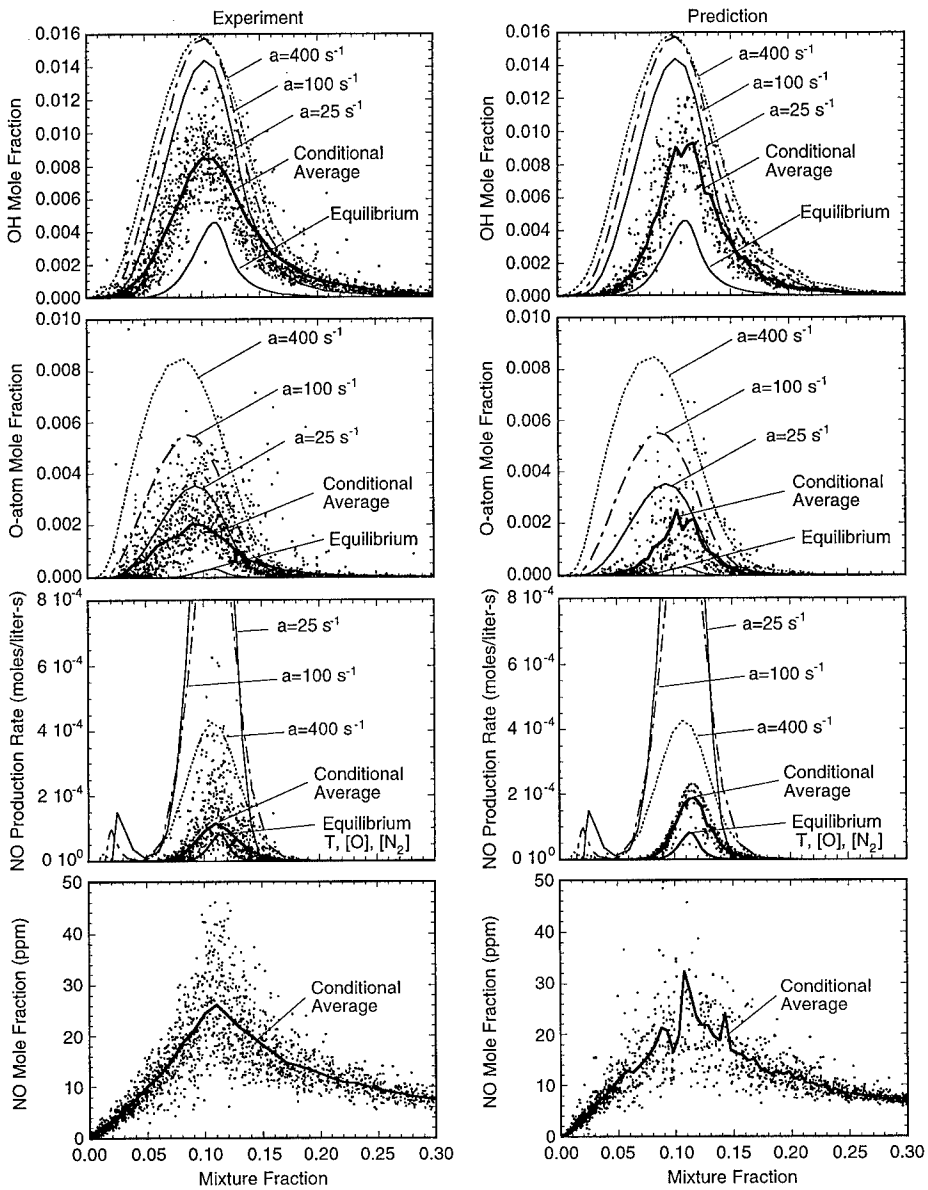

FIG. 5. Scatter plots and conditional means of experimental (left side) and predicted (right side) results for OH mole fraction, O-atom mole fraction, thermal NO production rate, and NO mole fraction at $x/d = 30$. Adiabatic equilibrium curves and results of laminar flame calculations at $a = 25\ s^{-1}$, $100\ s^{-1}$, and $400\ s^{-1}$ are included. Note that the jaggedness in the conditional averages for the prediction results from statistical noise in the Monte Carlo simulation.

There is good agreement between experiment and PDF prediction on OH mole fractions. Experimental O-atom mole fractions are significantly above equilibrium and show greater scatter than OH. The maximum in the conditionally averaged curve of experimental O-atom mole fraction is about 6.5 times that for full chemical equilibrium. The PDF prediction yields a peak value of the conditionally averaged O-atom mole fraction that is consistent with the experiment, but the experiment yields higher O-atom levels on the fuel-lean side of the peak. For mixture fractions less than about 0.06, the measured temperatures begin to drop below the range where the partial equilibrium assumption is valid and the experimental O-atom results become unreliable. This is not a problem in the context of thermal NO

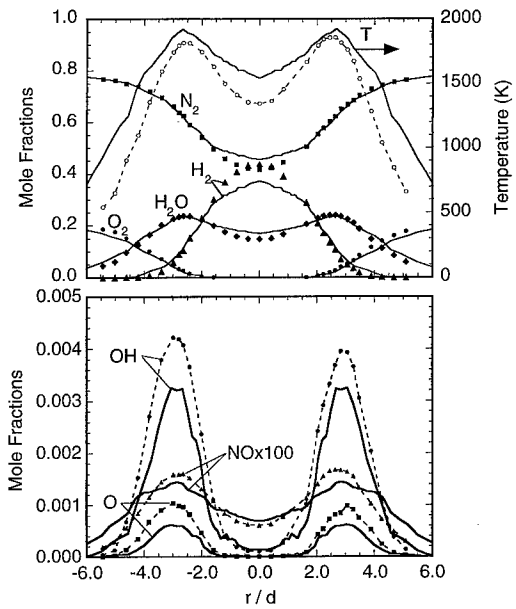

FIG. 6. Radial profiles of ensemble-average temperature and species mole fractions from the experiment (symbols) and the prediction (———) at $x/d = 30$.

production because the production rate becomes negligibly small before the partial equilibrium assumption breaks down.

The experimentally derived instantaneous NO production rates are generally greater than the curve calculated from Eq. (2) and adiabatic equilibrium values of temperature, [O], and $[N_2]$. The small fraction of samples that falls below this equilibrium curve may correspond to highly strained conditions in the flame, where temperature depression counters the superequilibrium O-atom levels. The widths in mixture fraction of the measured and predicted conditional average NO production curves are roughly twice that of the equilibrium curve. The experimental and predicted curves have peak values approximately 40% and 90%, respectively, above the equilibrium curve. The difference between experiment and prediction is within the estimated uncertainty in the experiment. We note that inclusion of ambient water vapor and flame radiation in the simulation is expected to decrease the predicted NO production rate, bringing it closer to the experiment.

The PDF prediction yields NO mole fractions that are close to the measurements. However, inclusion of ambient water and radiation will also reduce the predicted NO mole fraction. Firm conclusions regarding the accuracy of the PDF model in predicting NO production rates and mole fractions should not be drawn until ambient water vapor and radiation are included in the simulation, experiment and prediction may be compared at several streamwise locations, and data on the velocity field are available.

A comparison of steady laminar flame calculations with the experimental results in Fig. 5 reveals that it would not be possible to represent the turbulent flame using a combination of these laminar flames. OH levels in the laminar flames are significantly higher than both the measurements and the PDF model predictions. O-atom levels for strain rates below $a = 25\ s^{-1}$ would be consistent with the experimental results. However, the NO production rates for these weakly strained flames would greatly exceed the experimental production rates.

Radial Profiles

Radial profiles of ensemble-average temperature and species mole fractions are shown in Fig. 6. Agreement between experiment and prediction is not as good for these spatial profiles as when results are plotted against mixture fraction. The predicted temperature profile is broader than the measured profile. The predicted H_2 mole fraction on the centerline is lower than measured, and the predicted centerline temperature is higher. Within the reactions zones (near $r/d = \pm 2.5$), the predicted OH-, NO-, and O-atom mole fractions are all below the measured curves. These results show that, while the model predicts most aspects of the chemistry, it overpredicts the turbulent mixing rates such that the flame spreads too rapidly and the PDFs of mixture fraction in the reaction zones are too broad.

Conclusions

1. An experimental procedure for determining oxygen atom concentrations and instantaneous thermal NO production rates in turbulent flames was demonstrated. This procedure is based on simultaneous point measurements of temperature, the major species, and OH, and it may be applied wherever the assumption of partial equilibrium of the reaction $OH + OH \Leftrightarrow O + H_2O$ is valid.
2. Measurements were made across a radial profile at a single streamwise location, 30 nozzle diameters from the base of a turbulent jet flame of nitrogen-diluted hydrogen. The partial equilibrium assumption was shown to be valid in this flame for temperatures greater than about 1500 K. Instantaneous and conditionally averaged O-atom mole fractions at this measurement location are significantly greater than equilibrium levels. The conditional mean of the experimentally derived thermal NO production rate has a peak value 40% greater than the peak rate calculated from adiabatic equilibrium conditions of temperature, [O], and $[N_2]$.

3. Experimental results were compared with predictions by the Monte Carlo PDF model using detailed chemistry. With some exceptions, there is good agreement between measurements and predictions when results are plotted against mixture fraction. Agreement is less good when radial profiles of ensemble-average scalars quantities are compared. This indicates that the present PDF model predicts the hydrogen and nitrogen chemistry well but that improvements are needed in the modeling of the turbulent fluid dynamics and mixing.
4. A comparison with steady strained laminar flame calculations showed that the turbulent flame measurements cannot be represented by a combination of these laminar flames.

Acknowledgments

The partial equilibrium approach was inspired in part by the insightful comments of one of the reviewers of Ref. 9. This research was supported by the U.S. Department of Energy, Office of Basic Energy Sciences. The laboratory technical support of T. Prast is gratefully acknowledged.

REFERENCES

1. Bilger, R. W. and Beck, R. E., *Fifteenth Symposium (International) on Combustion,* The Combustion Institute, Pittsburgh, 1976, pp. 541–552.
2. Drake, M. C., Correa, S. M., Pitz, R. W., Shyy, W., and Fenimore, C. P., *Combust. Flame* 69:347–365 (1987).
3. Vranos, A., Knight, B. A., Procia, W. M., and Chiapetta, L., *Twenty-Fourth Symposium (International) on Combustion,* The Combustion Institute, Pittsburgh, 1992, pp. 377–384.
4. Turns, S. R. and Lovett, J. A., *Combust. Sci. Technol.* 66:233–249 (1989).
5. Turns, S. R. and Myhr, F. H., *Combust. Flame* 87:319–335 (1991).
6. Driscoll, J. F., Chen, R.-H., and Yoon, Y., *Combust. Flame* 88:37–49 (1992).
7. Carter, C. D. and Barlow, R. S., *Opt. Lett.* 19:299–301 (1994).
8. Barlow, R. S. and Carter, C. D., *Combust. Flame* 97:261–280 (1994).
9. Barlow, R. S. and Carter, C. D., *Combust. Flame* 104:288–299 (1996).
10. Meier, W., Vyrodov, V., Bergmann, W., and Stricker, W., "Simultaneous Raman/LIF Measurements of Major Species and NO in Turbulent H_2/Air Diffusion Flames," accepted by *Appl. Phys. B.*
11. Nguyen, Q. V., Dibble, R. W., Carter, C. D., Fiechtner, G. J., and Barlow, R. S., *Combust. Flame* 105:499–510 (1996).
12. Dally, B. B., Masri, A. R., Barlow, R. S., Fiechtner, G. J., and Fletcher, D. F., *Twenty-Sixth Symposium (International) on Combustion,* The Combustion Institute, Pittsburgh, 1996, pp. 000–000.
13. Goldsmith, J. E. M., *Appl. Opt.* 26:3566–3572 (1987).
14. Smyth, K. C. and Tjossem, P. J. H., *Appl. Phys. B* 50:449–511 (1990).
15. Correa, S. M., *Combust. Sci. Technol.* 87:329–362 (1992).
16. Paul, P. H., *J. Quant. Spectrosc. Radiat. Transfer* 51:511–524 (1994).
17. Paul, P. H., Gray, J. A., Durant, J. L. Jr., and Thoman, J. W. Jr., *AIAA J.* 32:1670–1675 (1994).
18. Smith, L. L., Dibble, R. W., Talbot, L., Barlow, R. S., and Carter, C. D., *Combust. Flame* 100:153–160 (1995).
19. Chen, J.-Y., Kollmann, W., and Dibble, R. W., *Combust. Sci. Technol.* 64:315–346 (1989).
20. Pope, S. B., *Combust. Sci. Technol.* 25:159–174 (1981).
21. Gutheil, E., Balakrishnan, G., and Williams, F. A., in *Reduced Reaction Mechanisms* (Peters, N. and Rogg, B., Eds.), Springer Verlag, 1993, pp. 177–195.
22. Bilger, R. W., Starner, S. H., and Kee, R. J., *Combust. Flame* 80:135–149 (1990).

COMMENTS

A. Mokhov, N. V. Nederlandse Grasunie, The Netherlands. Did you observe partial equilibrium between the measured concentrations of OH, H_2O and O_2 on lean side and between OH, H_2O and H_2 on rich side?

Author's Reply. We have not looked for this in our data. However, based upon several papers in the literature, including work by Graham Dixon-Lewis, Jim Miller, and others, one might expect partial equilibrium of these species to be satisfied in hydrogen flames for temperatures above about 1500 K. In the present paper we have been able to extract useful information on O-atom concentrations because OH and H_2O, the measured species in the reaction $OH + OH = H_2O + O$, can be measured with useful accuracy on a single-shot basis. Our present laser systems cannot provide comparable single-shot accuracy for the Raman measurements of O_2 or H_2 because their concentrations are low in the interesting parts of the flames. In general, any evaluation of partial equilibrium in these experimental data or use of the partial equilibrium assumption in deriving new results from these data should be preceded by careful consideration of uncertainties. Unfortunately, the limitations of the O_2 and H_2 measurements also restrict our ability to derive any useful single-shot information on H-atom concentrations in these flames.

Twenty-Sixth Symposium (International) on Combustion/The Combustion Institute, 1996/pp. 2207–2214

FLAMELET AND PDF MODELING OF CO AND NO_x EMISSIONS FROM A TURBULENT, METHANE HYDROGEN JET NONPREMIXED FLAME

J.-Y. CHEN AND WEI-CHEN CHANG
Department of Mechanical Engineering
University of California at Berkeley
Berkeley, CA 94720, USA

Modeling of NO formation in a turbulent, nonpremixed jet flame with a fuel mixture of 31% methane and 69% hydrogen has been performed using the joint scalar probability density function (PDF) approach and the traditional flamelet model. The importance of various effects such as transients, flame interaction, preferential diffusion, and radiative heat loss on NO formation is evaluated by comparisons of predictions with experimental data. The radiative heat loss is included in the PDF approach using the optically thin limit model. A simple model to account for the effect of temperature decrease on thermal NO formation is used in the flamelet model. The model results suggest that radiative heat loss becomes increasingly important for NO predictions in the far field, and it can lower the predicted values by a factor of 3 leading to a better agreement with the experimental data. Preferential diffusion, which is not included in the PDF model, is found to be insufficient to account for the overprediction in the NO levels by the flamelet approach. Comparisons of the predicted CO concentrations from the two models indicate that transient and flame interaction may be important for describing the flame behavior in the near field.

Introduction

Modeling of turbulent flames is a challenging task due to computational constraints. Models for the interaction between turbulence and chemical kinetics are necessary to make the computation tasks possible. The flamelet approach is an attractive way for modeling turbulent flames, because chemical kinetics is eliminated from the calculations. Although many questions have been raised about the validity of the flamelet approach for modeling nonpremixed turbulent flames (e.g., Bilger [1]), the potential of the flamelet approach has not been critically assessed against other modeling approaches. As delineated recently by Turns [2], NO formation in turbulent flames is a complex process that requires accurate modeling of chemistry, turbulence, and their interactions. The study of Vranos et al. [3] showed large discrepancies between their flamelet model results and the measured NO levels. It was speculated that the steady-state flamelet approach is inadequate, and transients as well as flame interactions may be significant in describing the flame behavior. The importance of transient flame behaviors was asserted in an early study by Haworth et al. [4]. However, the effect of radiation heat loss on NO was considered by Vranos et al. [3] to be insignificant based on counterflow laminar flame calculations at a scalar dissipation rate of 1 s^{-1}. Since the scalar dissipation rate decreases rapidly as x^{-4} for turbulent jet flames, a scalar dissipation rate of 1 s^{-1} corresponds roughly to a location of $x/D = 30$, based on our model results. Since the predicted flame height is about 140 diameters, the potential of radiative heat loss on NO can be important and will be explored in this study. Because transients and flame interactions are naturally included in the joint scalar PDF method [5], predictions with the PDF method using a newly developed nine-step reduced chemistry are performed for assessing these effects and for comparison with the flamelet results.

Modeling Approaches

PDF Simulation with a Nine-Step Reduced Chemistry

A nine-step reduced chemistry including prompt and thermal NO production routes has been developed by Chang [6], based on the detailed mechanism of Miller and Bowman [7] as summarized in the Appendix. Detailed expressions for the steady-state species can be found in Ref. 6. Evaluation of the performance of the nine-step reduced chemistry has been conducted extensively for perfectly stirred reactors (PSRs), Tsuji-type opposed-flow flames, and transient flamelets. The evaluation indicates that the maximum errors are within 10% in NO_x predictions for flames with equivalence ratios from 0.7 to 1.3. Since our development of the above nine-step mechanism, a detailed mechanism with NO reactions (GRI-2.1) [8] became available. Based on PSRs, the differences in NO predictions between these two

mechanisms are noticeable only at temperatures below 2000 K, with lower NO levels predicted by the Miller and Bowman mechanism. However, the differences are not large enough to explain the discrepancies seen between predictions and data for the flame studied here. Since there are 13 species in the nine-step reduced mechanism, it is impractical to construct look-up tables as has been done in past studies. The stiff chemical kinetics are solved directly for every stochastic representation.

For the mean turbulent flow field, a Reynolds stress model with the Favre average (density-weighted) statistics was solved [9]. The turbulent flow field model provides the mean velocity and turbulence time scale to the scalar PDF method. The scalar PDF model then returns the mean density for each grid point that is required for the Reynolds stress model. Equal diffusivity of species and heat was assumed and the molecular mixing process was simulated by the modified Curl's model. Forty grids across half of the jet were used and each grid point had 400 statistics representations. Typically, 1500–2000 steps are needed to complete the calculations up to one-and-one-half times the flame height. To assess the potential of radiative heat loss on NO formation, an optically thin limit radiation model [9] was employed for each statistics. The Planck mean absorption coefficient is obtained by a linear combination of the respective coefficients for H_2O and CO_2 weighted by their partial pressures.

Flamelet Model

The flamelet model follows the traditional approach in expressing thermo-chemical properties in terms of mixture fraction and its dissipation rate (e.g., Peters [10]). The detailed methane combustion mechanism of Miller and Bowman [7] was used for generation of the flamelet library. Using Sandia's Tsuji-type opposed-flow flame code [11], we have performed calculations for strain rates ranging from 0.1 s^{-1} up to 2500 s^{-1}, which is near the flame extinction point. The corresponding scalar dissipation rate, χ, at the stoichiometric point changes from 1.73×10^{-3} s^{-1} to 37.4 s^{-1}. The low-strain-rate flames are needed in the library since the predicted centerline scalar dissipation rate varies from 2.3 at $x/D = 23$ to 9.8×10^{-4} at $x/D = 160$, following closely the x^{-4} scaling relation. When the scalar dissipation rate is below the lowest limit in the flamelet library, thermo-chemical properties are obtained by a linear interpolation between the flame at the lowest strain rate and the equilibrium state. At the equilibrium state, a zero value is assigned to the scalar dissipation rate, as its reciprocal represents a diffusion time scale. The chemical source term for NO is obtained directly from the flamelet library. The PDF of the scalar dissipation rate is assumed to have the log-normal distribution with $\sigma = 1.0$ [3]. In order to keep the differences between the flamelet and the PDF simulations at minimum, the same stochastic simulation used in the scalar PDF approach is applied to the flamelet approach [4].

Inclusion of radiative heat loss into the flamelet approach would require substantial efforts since one additional parameter of radiation heat loss is needed to determine the thermal-chemical properties. Since the major NO production path in the present flame is dominated by the Zeldovich thermal route, as will be presented later, we have adopted a simple method for estimating the importance of radiative heat loss without direct inclusion of heat loss effect into the flamelet library. For each particle, radiative heat loss is computed based on the optically thin limit model. The decrease in mixture enthalpy due to radiative heat loss is computed for each particle, and due to molecular mixing, it is redistributed among the statistics by the modified Curl's mixing model. During the simulation, the NO source term is corrected for the radiative heat loss by the ratio $\exp(-38{,}400/T)/\exp(-38{,}400/T_{\text{adiabatic}})$, where the flame temperature T is computed based on the mixture enthalpy for each particle. This method provides a reasonable estimate of the decrease in NO formation rate due to temperature decrease only.

Flame Conditions

Simulations have been performed to study the nitric oxide formation in a turbulent, nonpremixed jet flame with a fuel mixture of 31% methane and 69% hydrogen by volume. This flame has been investigated in the past by Vranos et al. [3] both experimentally and numerically using a k-ε-g model coupled with a flamelet library approach. The major difference in the current flamelet approach is in the flamelet library which includes flames computed at low strain rates and the equilibrium limit. The jet nozzle has an internal diameter of 6.22 mm, and the jet Reynolds number was 10,000 based on the jet exit velocity of 67 m/s. The coflowing air has a velocity of 1.52 m/s to shield the central fuel from drafts. Species measurements were obtained with a gas sampling probe, and the temperatures were measured by a coated thermocouple. Temperature corrections for catalytic effects were made at peak flame temperatures. Details can be found in Ref. 3.

Results and Discussion

Measured and predicted radial profiles of mean mixture fraction with the flamelet model are compared in Fig. 1. Similar results are obtained from the PDF model. The agreement between the predictions and the measurements is reasonably good. Evaluation of model performances will be made by comparisons of measured and predicted mean

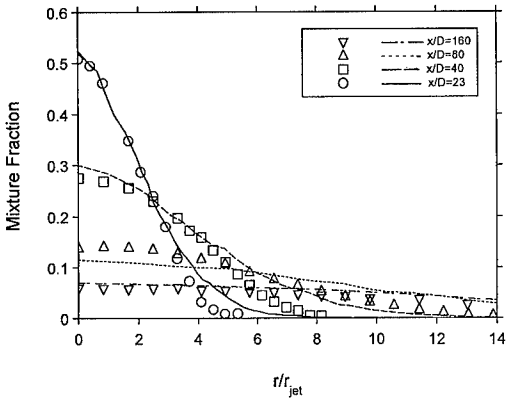

FIG. 1. Measured and computed radial profiles of mean mixture fraction for a turbulent, nonpremixed jet flame with a fuel mixture of 31% methane and 69% hydrogen showing reasonable agreement. Symbols indicate experimental data; lines indicate predictions.

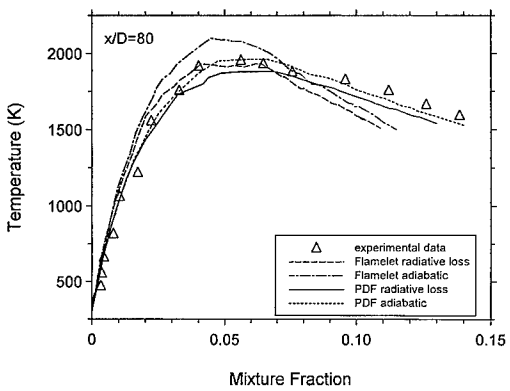

FIG. 2. Measured and computed mean temperature profiles versus mean mixture fraction for a turbulent, nonpremixed jet flame with a fuel mixture of 31% methane and 69% hydrogen at 80 diameters downstream, indicating that radiative heat loss becomes important in the far field.

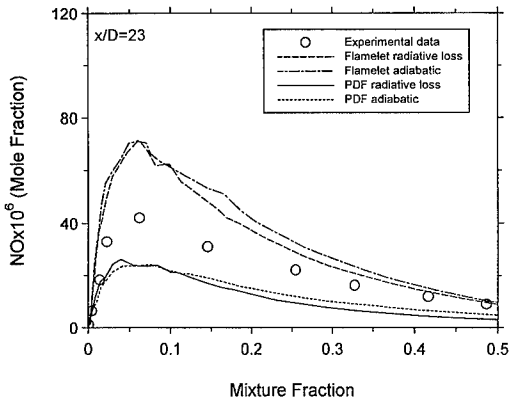

FIG. 3. Measured and predicted radial profiles of NO mole fraction for a turbulent, nonpremixed jet flame with a fuel mixture of 31% methane and 69% hydrogen at 23 diameters downstream. Radiative heat loss is seen to have negligible effect on the predicted NO levels. Flamelet model predicts about twice the amount of NO as compared to the PDF model.

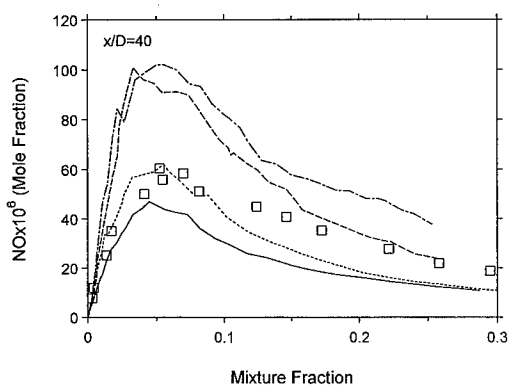

FIG. 4. Measured and predicted radial profiles of NO mole fraction for a turbulent, nonpremixed jet flame with a fuel mixture of 31% methane and 69% hydrogen at 40 diameters downstream. Radiative heat loss starts to have impact on the predicted NO levels. Symbols indicate experimental data; legends for predictions are the same as in Fig. 3.

distributions in the mixture fraction space to remove spatial dependence, as done by Vranos et al. [3]. A comparison of measured and predicted mean temperatures versus the mixture fraction at 80 diameters downstream ($x/D = 80$) is presented in Fig. 2. Unweighted temperatures are computed by the same method used in Ref. 3. The predicted peak values are in reasonable agreement with the measurements. The flamelet model with/without radiative heat loss predicts higher peak values than its counterpart from the PDF model. Inclusion of radiative heat loss in the model lowers the peak flame temperatures by about 110–200 K in both models. The computed radiant fraction is about 0.05–0.07. The corresponding predictions at $x/D = 23$ (not shown) exhibit little impact of radiative heat loss as the flame residence time at this location is too short to be important.

Figures 3–6 present comparisons of the modeling results and the experimental data for NO mole fraction profiles at four downstream locations. First we compare the modeling results without radiative heat loss. Compared to the flamelet model, the PDF simulation predicts lower NO levels by about half throughout the entire flame. Compared to the experimental data at $x/D = 23$ in Fig. 3, the flamelet

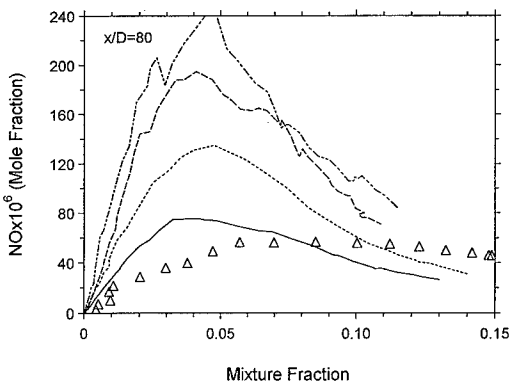

FIG. 5. Measured and predicted radial profiles of NO mole fraction for a turbulent, nonpremixed jet flame with a fuel mixture of 31% methane and 69% hydrogen at 80 diameters downstream. Inclusion of radiative heat loss in the model lowers the predicted NO levels by 30%. Symbols indicate experimental data; legends for predictions are the same as in Fig. 3.

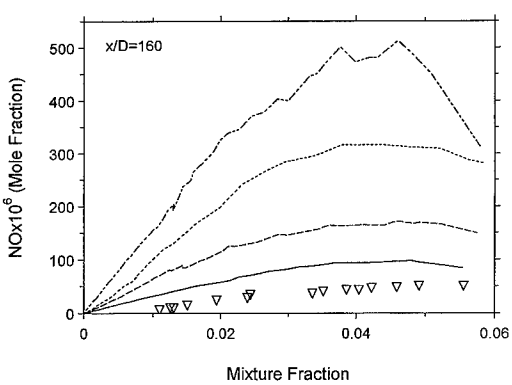

FIG. 6. Measured and predicted radial profiles of NO mole fraction for a turbulent, nonpremixed jet flame with a fuel mixture of 31% methane and 69% hydrogen at 160 diameters downstream. Radiative heat loss is seen to have a significant effect on the predicted NO concentrations, lowering them by a factor of 3. Symbols indicate experimental data; legends for predictions are the same as in Fig. 3.

model overpredicts the NO levels while the PDF approach underpredicts the NO levels. Both the flamelet and the PDF models predict a strong dependence of NO concentration on axial location, while the experimental data exhibit nearly similar profiles with the same peak value of about 60 ppm. The measured NO levels are significantly lower than model predictions at $x/D = 160$. The predicted peak NO values are 500 ppm and 300 ppm from the flamelet and the PDF models, respectively. Compared to the flamelet model results obtained by Vranos et al. [3], the present flamelet model gives lower NO levels in the near field but twice the NO values at $x/D = 160$. The differences are caused by the different implementations of the flamelet approach as well as by the differences in the flamelet libraries. The measured peak NO concentration is rich-shifted from the stoichiometric point (~0.0456). This is especially profound at $x/D = 80$. Recent laser-based measurements by Barlow and Carter [12] indicated that the rich shift is due to the average of fluctuating mixtures. When the instantaneous NO data are averaged by conditioning on a given mixture fraction, the peak NO concentration locates right at the stoichiometric point. When conventional Favre averaging of NO statistics is performed, the average NO concentration starts to show the rich shift. However, both model predictions have peak NO values located near the stoichiometric. Since the PDF modeling is capable of treating effects of premixing, transients, and flame interactions by solving a time-dependent chemical kinetics equation with the mixing model, the model's failure in predicting the rich shift is unlikely to be attributed to these effects, as speculated by Vranos et al. [3].

Next, we consider the influence of radiative heat loss on NO formation. As seen in Figs. 3–6, the radiative heat loss has a significant impact on the predicted NO levels, especially at downstream locations beyond $x/D = 40$. From comparisons of the model predictions, a factor of 3 reduction in the predicted NO levels is seen at $x/D = 160$. Due to radiative heat loss, the predicted NO concentration increases with the axial distance at a much slower rate than for the adiabatic case. Although the NO levels are still overpredicted at the far field by a factor of 2, the agreement between predictions and the experimental data is substantially improved. Compared to the predicted results from the PDF approach, the present flamelet model predicts twice the amounts of NO. As speculated by Vranos et al. [3], one possible cause for the overprediction is the overpredicted preferential diffusion effects of hydrogen and hydrocarbon species by the flamelet approach. This possibility was evaluated using an equal diffusivity flamelet library which was generated with diffusivities of all species set equal to that of nitrogen. Compared to the traditional flamelet library, the predicted NO levels with equal diffusivity increase by 25% at $x/D = 23$, but decrease by 15% at $x/D = 80$ and 160. Consequently, the overprediction of NO levels seen in the flamelet calculations cannot be explained simply by the preferential diffusion effect.

One of the main objectives in developing the nine-step reduced chemistry is to better capture the NO_x formation in methane flames as other reduced mechanisms, an eight-step and a seven-step reduced chemistry, have been tested by Chang [6] and found to be inaccurate. We have included all the important chemistry paths leading to NO_x formation in the

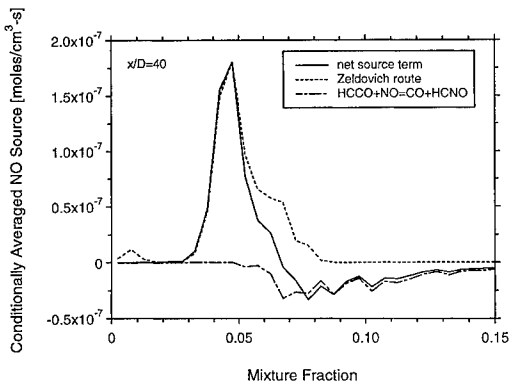

FIG. 7. Predicted contributions of NO formation routes at 40 diameters downstream of a turbulent, nonpremixed jet flame with a fuel mixture of 31% methane and 69% hydrogen, showing that most NO is formed via the Zeldovich mechanism.

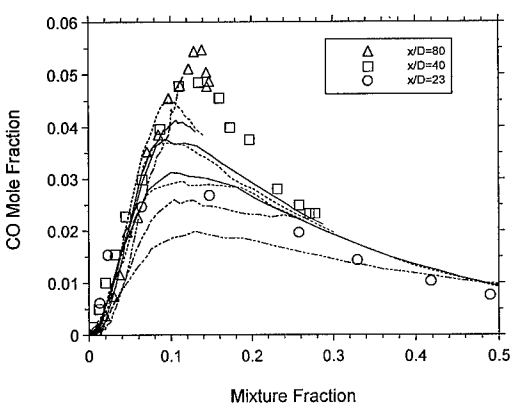

FIG. 8. Measured and predicted radial profiles of CO mole fraction for a turbulent, nonpremixed jet flame with a fuel mixture of 31% methane and 69% hydrogen at 23, 40, and 80 diameters downstream. The PDF modeling is shown to be in best agreement with the data, and inclusion of radiative heat loss in the model lowers the predicted CO levels by 10% at 80 diameters downstream. Symbols indicate experimental data; solid lines indicate PDF with radiative heat loss; dashed lines indicate PDF, adiabatic; dash-dotted lines indicate flamelet, adiabatic.

nine-step reduced chemistry. It is interesting to examine the importance of the Zeldovich mechanism relative to other pathways from the PDF model. Figure 7 presents the computed net NO production rate and the contributions from the Zeldovich steps as well as from the step HCCO + NO = CO + HCNO. Conditionally averaged source terms versus mixture fraction are plotted in this figure to remove spatial dependence. As evident from the comparison, the Zeldovich mechanism is dominant for the production of NO near the stoichiometric. However, in the rich parts of the flame, the net production of NO becomes negative because NO is consumed by fuel-rich mixtures. As examined by Miller and Bowman [7], in rich combustion systems, NO is converted to molecular nitrogen through HCN and CN intermediate species. The prediction indicates that HCCO + NO = CO + HCNO is the major reaction step for removing NO in fuel-rich zones. Similar analysis has been performed for other axial locations revealing a similar trend.

Carbon monoxide is another important species for exploring the effect of turbulence on chemical kinetics. Figure 8 presents the predicted and the measured CO mole fractions versus mixture fraction. As the present flamelet model does not include the radiative heat loss effect on CO, only results from the adiabatic calculations are presented. Among these model predictions, the PDF predictions agree best with the experimental data. However, the predicted peak CO values by the PDF model are slightly lower than the measurements, and they exhibit a stronger dependence on axial location than the experimental data. The computed radiative heat loss has minor influence on CO levels, causing them to be slightly lower than the adiabatic calculations in the far field. Compared to the flamelet results obtained from Vranos et al. [3], the present model gives higher CO levels at $x/D = 40$ and 80. The differences are caused by the differences in the flamelet libraries used in the two flamelet models. Vranos et al. [3] constructed a flamelet library with strain rates ranging from 200 to 1000 s^{-1}, and the flame properties outside this range were obtained by extrapolation. Based on their flamelet library, the maximum extrapolated (zero strain rate) CO mole fraction is 3.3%. In the present flamelet library, the computed peak CO value at a strain rate of 0.1 s^{-1} is about 4.2%. The scalar dissipation at this strain rate is $1.73 \times 10^{-3}\ s^{-1}$. Flame properties below this scalar dissipation rate are obtained by interpolation with the equilibrium value at $\chi = 0$. Since the present library contains more details for low-strain flames, the predictions are higher than those obtained by Vranos et al. [3] in the far field.

Conclusions

Extensive comparisons have been made among the results obtained with a traditional flamelet model and the joint scalar PDF model for a turbulent, nonpremixed jet flame of 31% methane and 69% hydrogen. The potential effect of radiative heat loss on the predicted NO levels is explored using the optically thin limit radiation model in the PDF model. A simple model to reflect the effect of temperature decrease on thermal NO production is included in the flamelet model. Comparisons of model predictions

and experimental data reveal that radiative heat loss plays an important role in the predicted NO levels, especially at downstream portions of the jet flame. Although both models overpredict NO levels, the agreement with the experimental data is substantially improved when radiative heat loss is included in the models. Compared to the results obtained from the PDF model, the flamelet model predicts twice the amount of NO. However, this discrepancy is not attributed to the overpredicted preferential diffusion effects by the flamelet approach. The CO concentrations predicted by the PDF model are in better agreement with the data than those of the flamelet model, especially in the near field, suggesting that the transients and flamelet interactions may be significant in describing the flame behavior.

Appendix: A Nine-Step Reduced Mechanism for Methane-Air Combustion

$$CH_4 + O = H_2 + CO + 2H \quad \text{(R1)}$$

$$CO_2 + H = CO + OH \quad \text{(R2)}$$

$$4H + 2CO + O_2 = 2O + 2OH + C_2H_2 \quad \text{(R3)}$$

$$2CO + OH + H + N_2 = 3O + 2HCN \quad \text{(R4)}$$

$$CO + OH + NO = O_2 + O + HCN \quad \text{(R5)}$$

$$H + H + M = H_2 + M \quad \text{(R6)}$$

$$H + OH = H_2O \quad \text{(R7)}$$

$$OH + M = O + H + M \quad \text{(R8)}$$

$$O + OH = H + O_2 \quad \text{(R9)}$$

with the following global reaction rates:

$$\omega_{R1} = \omega_{24} + \omega_{25} - \omega_{32} + \omega_{35} - \omega_{37} + \omega_{40} + \omega_{41} + \omega_{43} + \omega_{44} + \omega_{45} + \omega_{47} + \omega_{48} + \omega_{49} + \omega_{50} + \omega_{51} + \omega_{52} + \omega_{53} + \omega_{69} + \omega_{70} + \omega_{71} - \omega_{76} - \omega_{79} + \omega_{80} + \omega_{83} - \omega_{89} - \omega_{90} - \omega_{91} + \omega_{95} + \omega_{97} - \omega_{101} + \omega_{109} + 2\omega_{114} + \omega_{121} + 2\omega_{128} + \omega_{129} + \omega_{155} + \omega_{159} - \omega_{161} + \omega_{162} + \omega_{163}$$

$$\omega_{R2} = \omega_{30} + \omega_{42} - \omega_{45} - \omega_{47} - \omega_{59} - \omega_{61} - \omega_{62} - \omega_{64} - \omega_{93} + \omega_{166}$$

$$\omega_{R3} = \omega_{33} + \omega_{34} + \omega_{35} + \omega_{36} + \omega_{40} + \omega_{41} + \omega_{69} + \omega_{71} - \omega_{76} - \omega_{82} - \omega_{90} - \omega_{93} - \omega_{94} - \omega_{98} - \omega_{99} - \omega_{101} - \omega_{102} - \omega_{103} - \omega_{112} + \omega_{114} - \omega_{118} + \omega_{121} + \omega_{128} + \omega_{129} - \omega_{161}$$

$$\omega_{R4} = \omega_{151} - \omega_{152} - \omega_{197} - \omega_{207} + \omega_{212} - \omega_{221} - \omega_{222} - \omega_{237}$$

$$\omega_{R5} = \omega_{156} + \omega_{157} + \omega_{159} + \omega_{160} + \omega_{162} + \omega_{163} - \omega_{166} - \omega_{193} + \omega_{197} - \omega_{206} + \omega_{207} - 2\omega_{212} + 2\omega_{221} + \omega_{222} - \omega_{226} - \omega_{228} - \omega_{229} - \omega_{232} - \omega_{233} - \omega_{234} - \omega_{235} + \omega_{237} - \omega_{238} - \omega_{239}$$

$$\omega_{R6} = \omega_4 + \omega_{13} + \omega_{16} + \omega_{17} - \omega_{25} + \omega_{31} + \omega_{32} - \omega_{35} + \omega_{37} - \omega_{40} - \omega_{41} - \omega_{43} - \omega_{45} - \omega_{48} - \omega_{49} - \omega_{50} - \omega_{51} - \omega_{53} + \omega_{57} + \omega_{66} - \omega_{70} - \omega_{71} + \omega_{76} - \omega_{78} + \omega_{79} - \omega_{83} + \omega_{89} + \omega_{90} + \omega_{91} - \omega_{97} + \omega_{101} - \omega_{109} - \omega_{110} - \omega_{114} - \omega_{121} - \omega_{128} - \omega_{129} - \omega_{130} - \omega_{131} - \omega_{133} + \omega_{139} + \omega_{141} + \omega_{146} + \omega_{149} - \omega_{155} - \omega_{159} + \omega_{161} - \omega_{162} - \omega_{163} - \omega_{179} - \omega_{198} + \omega_{216} + \omega_{220} + \omega_{224} + \omega_{228} + \omega_{235}$$

$$\omega_{R7} = \omega_5 + \omega_{12} + \omega_{18} + \omega_{19} + \omega_{25} - \omega_{32} + \omega_{48} + \omega_{51} + \omega_{55} + \omega_{68} + \omega_{71} + \omega_{83} + \omega_{87} + \omega_{97} + \omega_{121} + \omega_{131} + \omega_{135} + \omega_{138} + \omega_{143} + \omega_{150} + \omega_{159} + \omega_{171} + \omega_{172} + \omega_{173} + \omega_{177} + \omega_{192} + \omega_{198} - \omega_{206} - \omega_{207} - \omega_{216} + \omega_{219} + \omega_{223} - \omega_{226} - \omega_{228} - \omega_{232} - \omega_{233} - \omega_{235}$$

$$\omega_{R8} = \omega_8 - \omega_{11} + \omega_{15} + \omega_{17} + \omega_{19} - \omega_{20} + \omega_{23} + \omega_{26} + \omega_{31} + \omega_{32} + \omega_{34} + \omega_{35} + \omega_{42} + \omega_{46} - \omega_{50} - \omega_{51} - \omega_{52} - \omega_{53} + \omega_{55} + \omega_{56} + \omega_{57} + \omega_{60} - \omega_{61} - \omega_{64} - \omega_{67} - \omega_{70} - \omega_{76} - \omega_{77} - \omega_{79} + \omega_{80} + \omega_{83} - \omega_{92} - \omega_{93} - \omega_{112} + \omega_{114} - \omega_{116} - 2\omega_{118} + \omega_{120} + 2\omega_{121} - \omega_{124} - \omega_{126} + \omega_{128} - \omega_{130} - \omega_{133} - \omega_{136} - \omega_{137} + \omega_{138} - \omega_{144} - \omega_{148} - \omega_{155} - \omega_{159} - \omega_{162} - \omega_{163} + \omega_{171} + \omega_{172} + \omega_{173} + \omega_{177} - \omega_{179} - \omega_{189} + \omega_{192} + \omega_{196} + \omega_{197} - \omega_{206} - \omega_{209} - \omega_{212} + \omega_{219} + \omega_{220} + \omega_{223} + \omega_{224} - \omega_{240}$$

$$\omega_{R9} = \omega_9 - \omega_{10} - \omega_{11} + \omega_{26} - \omega_{27} - \omega_{31} +$$

$$\omega_{32} + \omega_{34} + \omega_{35} + \omega_{36} + \omega_{39} + 2\omega_{40} + 2\omega_{41} + \omega_{42} - \omega_{45} - \omega_{47} - \omega_{48} - \omega_{49} - \omega_{50} - \omega_{51} - \omega_{52} - \omega_{53} - \omega_{64} + \omega_{69} + \omega_{71} - \omega_{76} - \omega_{82} - \omega_{90} - \omega_{93} - \omega_{94} - \omega_{98} - 2\omega_{99} - \omega_{101} - \omega_{102} - 2\omega_{103} - \omega_{109} - \omega_{112} + \omega_{114} - \omega_{116} - 2\omega_{118} + 2\omega_{120} + 2\omega_{121} - \omega_{124} - \omega_{126} + \omega_{128} + \omega_{129} - \omega_{130} + \omega_{132} - \omega_{136} - \omega_{148} - \omega_{152} - \omega_{157} - \omega_{159} - \omega_{160} - \omega_{161} - \omega_{162} - \omega_{163} + \omega_{166} - \omega_{181} - \omega_{188} + \omega_{193} - \omega_{197} - \omega_{205} - \omega_{207} + \omega_{208} + 2\omega_{212} - 2\omega_{221} - \omega_{222} + \omega_{226} + \omega_{228} + \omega_{229} + \omega_{232} + \omega_{233} + \omega_{234} + \omega_{235} - \omega_{237} + \omega_{239}$$

where ω_i are the elementary reaction rates taken from the detailed methane mechanism by Miller and Bowman [7].

Acknowledgments

This work was supported partially by the NASA Lewis Research Center under Contract NAS3-26613 through a subcontract with Quest Integrated, Inc. The computing resources provided by the Sandia National Laboratories at Livermore are greatly appreciated.

REFERENCES

1. Bilger, R. W., *Twenty-Second Symposium (International) on Combustion,* The Combustion Institute, Pittsburgh, 1988, pp. 475–488.
2. Turns, S. R., *Prog. Energy Combust. Sci.* 21:361–385 (1995).
3. Vranos, A., Knight, B. A., Proscia, W. M., Chiappetta, L., and Smooke, M. D., *Twenty-Fourth Symposium (International) on Combustion,* The Combustion Institute, Pittsburgh, 1992, pp. 377–384.
4. Haworth, D. C., Drake, M. C., Pope, S. B., and Blint, R. J., *Twenty-Second Symposium (International) on Combustion,* The Combustion Institute, Pittsburgh, 1988, pp. 589–597.
5. Pope, S. B., *Prog. Energy Combust. Sci.* 11:119–192 (1985).
6. Chang, W.-C., "Modeling of NO_x Formation in Turbulent Flames: Development of Reduced Mechanisms and Mixing Models," Ph.D. Thesis, University of California at Berkeley, 1995.
7. Miller, J. A. and Bowman, C. T., *Prog. Energy Combust. Sci.* 15:287–338 (1989).
8. Bowman, C. T., Hanson, R. K., Davidson, D. F., Gardiner, W. C., Lissianski, V., Smith, G. P., Golden, D. M., Frenklach, M., and Goldenberg, M., http://www.gri.org, 1995.
9. Chen, J.-Y. and Kollmann, W., *Combust. Flame* 79:75–99 (1990).
10. Peters, N., *Prog. Energy Combust. Sci.* 10:319–339 (1984).
11. Miller, J. A., Kee, R. J., Smooke, M. D., and Grcar, J. F., "The Computation of the Structure and Extinction Limit of a Methane-Air Stagnation Point Diffusion Flame," Western States Section Spring Meeting, The Combustion Institute, Paper number WSS/CI 84-10, 1984.
12. Barlow, R. S. and Carter, C. D., *Combust. Flame* 97:261–280 (1994).

COMMENTS

S. B. Pope, Cornell University, USA. Which mixing model was used in the PDF calculations, and was the sensitivity of the calculated results to the choice of mixing model studied?

Author's Reply. Only the modified Curl's mixing model was used in the present PDF calculations. Since NO is formed mostly at far downstream locations where fluids are close to the well-mixed state, we expect negligible changes in our NO predictions if different mixing models were used.

Robert S. Barlow, Sandia National Laboratories, USA. In comparing predictions with experiments it is important to know something about the uncertainties in the measurements. Is it possible to provide some information on the experimental uncertainties in the Vranos NO and CO measurements? Two particular concerns are that (1) the nearly constant NO levels measured over the length of the flame are suspicious and (2) the paper of Nguyen and Dibble in the 25th Symposium indicated that CO probe measurements can have significant errors.

Author's Reply. A sampling probe was used in the experiments by Vranos et al. [1] and no information on ex-

perimental uncertainties was given in their paper. It is important to know the uncertainties in the measurements; however, they are difficult to quantify for probe measurements without non-intrusive measurements. The results by Nguyen et al. [2] suggested that probe sampling of CO may be increasingly inaccurate at temperatures above 1000K. The predicted results by our modeling as well as by Vranos et al. [1] show strong dependence of NO and CO levels on downstream position, contrary to the experimental observation. Further experiments using non-intrusive measurement techniques would be of great value in clarifying the discrepancies between the experimental data and the predictions.

REFERENCES

1. Vranos, A., Knight, B. A., Proscia, W. M., Chiappetta, L., and Smooke, M. D., *Twenty-Fourth Symposium (International) on Combustion,* The Combustion Institute, Pittsburgh, 1992, pp. 377–384.
2. Nguyen, Q. V., Edgar, B. L., Dibble, R. W., and Gulati, A., *Combust. Flame* 100:395–406 (1995).

Twenty-Sixth Symposium (International) on Combustion/The Combustion Institute, 1996/pp. 2215–2222

ANALYSIS OF TURBULENCE-CHEMISTRY INTERACTION WITH RESPECT TO NO FORMATION IN TURBULENT, NONPREMIXED HYDROGEN-AIR FLAMES

MARTIN SCHLATTER, JORGE C. FERREIRA, MATTHIAS FLURY AND JÜRG GASS
Institute of Energy Technology
ETH Zurich, Switzerland

The formation of thermal nitrogen oxides (NO_x) in turbulent, nonpremixed hydrogen-air flames is analyzed on the basis of experimental and numerical data. Detailed measurements of the mean velocities and the Reynolds stress tensor were performed, which in combination with the species and temperature measurements of Barlow and Carter, now form a complete data set. Earlier experimental studies showed that the ratio of the NO_x emission index and the residence time is proportional to the square root of a Damköhler number. This scaling law implies a strong dependence of NO formation on turbulence-chemistry interaction which must be considered by any modeling approach. Two combustion models, a Lagrange IEM model and a laminar flamelet model, were used for the numerical simulation of these flames in order to identify the relevant parameters that lead to the observed NO scaling law. The expected trend of the NO emission was obtained only with the Lagrange IEM model, despite similar predictions of global properties of the flames. The analysis revealed that the scaling law is a consequence of different radical concentration levels. The radical concentration levels are controlled by the slow recombination reactions. These slow chemical reactions must be modeled separately with some kind of reaction progress variable. This was shown to be successful with the Lagrange IEM combustion model.

Introduction

The chemical mechanisms responsible for the formation of nitrogen oxides (NO_x) in gaseous combustion are reasonably well understood [1]. However, the knowledge of NO_x formation in turbulent flames is still far from complete [2]. This is because in turbulent flow, NO_x formation is influenced by various effects such as turbulence-chemistry interaction, radiation, buoyancy, and so forth which are far less well understood. As NO_x formation is a kinetically limited process, its analysis offers the possibility to improve our general knowledge of turbulence-chemistry interaction. To investigate this interaction in an isolated manner, it is necessary to select a system where the other processes mentioned have a minor influence. Nonpremixed, hydrogen-air jet flames are a good candidate due to the relatively simple flow field in which buoyancy and local extinction effects may be excluded by selecting an appropriate Reynolds number. Furthermore, only thermal NO formation has to be considered, which is well described by the extended Zeldovich mechanism. Finally, there is no soot formation; hence, radiative heat losses have a minor influence, which may be further suppressed by the addition of an inert gas such as helium [3].

To compare the NO_x emissions of different flames it is useful to introduce the global NO_x emission index $EINO_x$, which is defined as the total mass of NO_x formed per unit mass of fuel, assuming a full conversion of NO to NO_2. From the analysis of their extensive gas sampling probe experiments, Driscoll et al. [3] showed that the ratio between $EINO_x$ and the residence time is proportional to the square root of the fuel jet velocity divided by the fuel jet diameter, which may be interpreted as a dependence on a Damköhler number. This observed half-power scaling law seems to be a pertinent characteristic of the NO emissions from turbulent hydrogen jet flames and is believed to be strongly related to turbulence-chemistry interaction. Because of the continuously strong interest in this subject, sophisticated experimental techniques have been used during recent years to establish a profound data set for the analysis of NO formation in hydrogen flames [4].

In the past, models based on the fast chemistry assumption have been used for the numerical analysis of such flames [5], and good results concerning global properties such as mean temperature and mean main species concentrations were obtained. However, predictions of NO formation using chemical equilibrium assumptions [6] did not yield the observed scaling dependence. In an attempt to model NO with the flamelet approach, it seems that Sanders and Gökalp [7] did not produce the half-power trend either. From a scaling analysis, they observed a wrong trend of the NO production rate. The half-power scaling law was obtained by Chen and Kollmann [8] who used a probability density

function (PDF) method [9]. Smith et al. [10] have compared the conditional moment closure method with the PDF method and concluded that both methods are capable of providing reasonable predictions, although the overall emission of NO was overpredicted with both models. Recently, Chen et al. [11] analyzed the influence of different reduced chemical reaction mechanisms with the PDF method. They found that the more detailed mechanisms gave better results. Despite the success of the PDF method, it is still not clear why some models fail and others succeed in the prediction of the NO scaling law. In the present analysis, we use two rather simple turbulent combustion models, namely a Lagrange IEM model and a laminar flamelet model, to predict NO formation. The advantage is that the local flame structure provided by both models is governed by just a few parameters. Hence, it is possible in combination with scaling analysis to identify the relevant parameters that lead to the observed scaling behavior of NO formation.

Experimental Setup

The burner for the investigated nonpremixed H_2/He flames was a straight tube with an inner diameter of 3.75 [mm] which was mounted in a small wind tunnel that provided the coflowing air at a constant velocity of 1 m/s. The three-dimensional laser doppler anemometer consisted of a 5-W argon-ion laser at wave lengths of 514.5 nm, 488 nm, and 476.5 nm. Using cross scattering, the diameter of the measurement volume was reduced to 80 μm. Signal processing was done with FFT analysis. The flames were seeded with ZrO_2 in the fuel and in the coflow simultaneously. To prevent bias errors due to velocity fluctuations, density fluctuations, and conditional sampling, a reconstruction algorithm from Veynante and Candel [12] was used for the postprocessing. The inlet conditions of the measured flames were: flame A with 0% helium at $Re = 10{,}000$, flame B with 20% helium dilution at $Re = 10{,}000$, and flame C with 40% helium dilution and $Re = 8300$.

This setup and the inlet conditions were identical to the ones used by Barlow and Carter [4] who performed combined Raman/Rayleigh/LIF measurements and reported on simultaneous, time-resolved measurements of major species, mixture fraction, temperature, OH, and NO concentrations. Thus, a complete experimental data set for these flames now exists, and will be used throughout this paper.

Turbulent Combustion Modeling

Thermal NO formation depends strongly on the instantaneous temperature and radical species composition. Hence, any modeling approach must provide this information and, in addition, must take into account the fluctuations of the respective quantities. The Lagrange IEM and the laminar flamelet concept, which are both discussed here, fulfill these requirements. Both models use a joint PDF of the mixture fraction, which represents the mixing state, and a second scalar that represents the influence of the flow field on the chemistry. They provide the information on temperature and radical species that is required to compute the instantaneous NO source term with the extended Zeldovich mechanism. The mean NO source term is then obtained by integration over the joint PDF.

Both models assume that the turbulent fluctuation of the mixture fraction is described by a presumed shape PDF (beta function), which is defined by the mean and the variance of the mixture fraction. However, the modeling concepts are based on different viewpoints of the interaction between chemistry and turbulence, and therefore, the obtained joint PDFs represent different aspects. In the following, we will highlight this difference and the main features of the two modeling concepts.

The Lagrange IEM Concept

Borghi [13] proposed a concept that is based on a Lagrangian description of a fluid particle. Two model versions exist for nonpremixed flames, namely the MIL (modele intermittent Lagrangien) model [14] and the PEUL (probabilistic Euler Lagrange) model [15] which will be used here. The PEUL model provides the PDF of a reactive species Y_i conditioned on the mixture fraction Z, which is then used to calculate the mean chemical source term

$$\bar{\dot{\omega}}_i = \iint \dot{\omega}_i(Z, Y_i)P(Z, Y_i)dZdY_i = \int P(Z)dZ \int \dot{\omega}_i(Z, Y_i)P(Y_i|Z)dY_i \quad (1)$$

In a Lagrangian frame work, the mass fraction of species i changes due to molecular mixing and reaction, yielding

$$\frac{\partial Y_i}{\partial t} = \frac{\tilde{Y}_i - Y_i}{\tau_e} + \dot{\omega}_i \quad (2)$$

where molecular mixing is modeled with the interaction by exchange with the mean (IEM) model, and $\dot{\omega}_i$ represents the instantaneous source term for species i. For hydrogen combustion, a two-step reduced mechanism [16] is used to calculate the chemical source term $\dot{\omega}_i$ and the instantaneous radical concentrations. Using a similar equation for the mixture fraction, without source term, equation 2 is transformed into composition space. Thus, for a given mixing time scale, this equation yields the evolution of the mass fraction Y_i as a function of mixture fraction Z. Mixing in a turbulent flow is not governed only by one time scale but rather by a spectrum of mixing times. This spectrum is approximated with an intermediate time scale $\tau_e = C_t\tilde{k}/\tilde{\varepsilon}$ as well as a

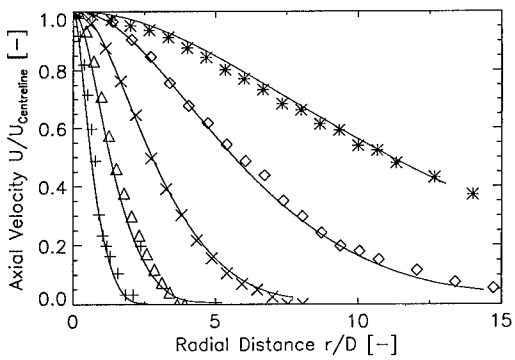

FIG. 1. Radial profiles of the normalized axial velocity for flame B. LDA measurements at: +, $x = 1/16\ L_v$; △, $x = 1/8\ L_v$; ×, $x = 1/4\ L_v$; ◇, $x = 1/2\ L_v$; *, $x = 1\ L_v$; and ——, predictions with the PEUL model at the corresponding locations. L_v is the visible flame length which is about 150 nozzle diameters, D.

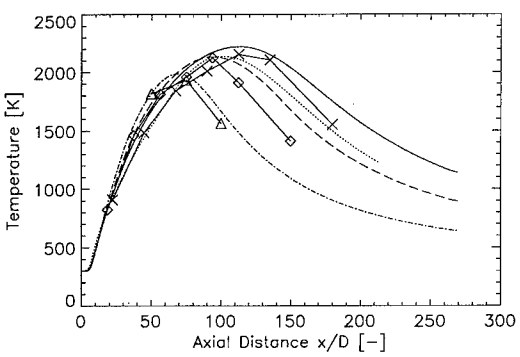

FIG. 2. Mean temperature distribution along the centerline of the flames A, B, and C. Measurements: ×, flame A; ◇, flame B; and △, flame C. Predictions with the PEUL model: ——, flame A; - - -, flame B; and -·-, flame C; ····, predictions for flame B with the flamelet model.

very large and a very small time scale, with respect to chemical time scales. These considered time scales lead to three possible traces of the species i and its chemical source term in the composition space. The position of these traces depends on the mean value of $\tilde{Y}_i$ (equation 2) which represents a mean reaction progress variable. Hence, the computation of the local flame structure is affected by the mean reaction progress. The conditional PDF is zero in the whole composition space, except on these traces, where it is represented by delta functions.

The Laminar Flamelet Concept

Within the laminar flamelet concept, a turbulent flame is regarded as an ensemble of stationary laminar diffusion flamelets [17] that are stretched and distorted by the turbulent flow. A main assumption of this concept is that the local turbulent flame structure is similar to a representative laminar flame. A common laminar flow configuration is the counterflow diffusion flame, for which the flame structure is defined by the mixture fraction and the strain rate K. The main advantage is that a complex hydrogen chemistry including detailed transport phenomena such as preferential diffusion are taken into account, and hence, no simplifying assumptions concerning the chemistry are required. The coupling between the laminar subsystem and the turbulent flow is governed by a single aerodynamic parameter, namely the strain rate K for which in the turbulent flow the common modeling assumption $\tilde{K} = C_q\tilde{\varepsilon}/\tilde{k}$ is used. Note that the strain rate K is an aerodynamic parameter and hence no information concerning the mean reaction progress affects the local flame structure.

The one-dimensional governing equations of the laminar subsystem were solved with the OPPDIF code [18] and stored in libraries. The instantaneous radical concentrations and the temperature, which are required for the NO computation, are obtained from those flamelet libraries. The mean species mass fractions are obtained from

$$\tilde{Y}_i = \int_0^\infty \int_0^1 Y_i(Z, K)P(Z)P(K)dZdK \qquad (3)$$

where $Y_i(Z, K)$ are the results of the laminar counterflow diffusion flame and $P(K)$ is represented by a delta function.

Results and Discussion

Mean Flow Properties

Figures 1–3 exhibit mean properties of the flames A, B, and C. For flame B, Fig. 1 shows radial profiles of the axial mean velocities at different downstream locations. The flow field was modeled with the Favre averaged Navier-Stokes equations, and the turbulent Reynolds stress tensor was closed with a modified k-ε model to account for the correct spreading rate in a round jet [19]. The measured Reynolds stresses, not shown here, reveal the anisotropic behavior of the turbulence in the jet. Fortunately, the spreading of the jet is governed mainly by the off-diagonal elements in the Reynolds stress tensor, which are in good agreement with the k-ε model results.

For the three flames, the temperature distributions along the centerline are shown in Fig. 2. Increasing dilution of helium reduces the mean peak temperature and shortens the flame length. The temperature decrease due to the entrainment of surrounding air in the postflame zone is underpredicted for all flames. Both combustion models are equally capable of predicting the measured temperatures with reasonable accuracy. Despite similar predictions of the mean temperature, the predicted NO

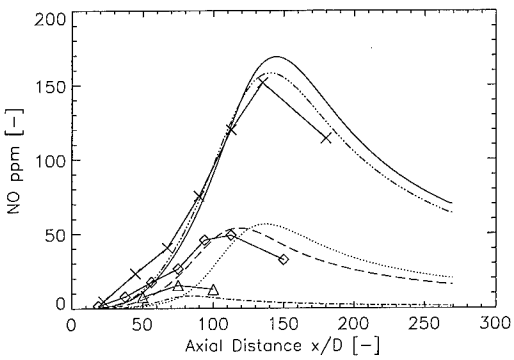

FIG. 3. Mean NO concentration in ppm along the centerline of the flames A, B, and C. Measurements: ×, flame A; ◇, flame B; and △, flame C. Predictions with the PEUL model: ——, flame A; -···-···, flame A with radiative heat losses; - - -, flame B; and -·-, flame C; ····, prediction for flame B with the flamelet model which is reduced by a factor of 10.

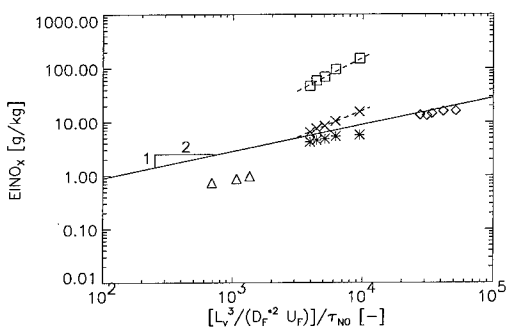

FIG. 4. Emission index, $EINO_x$, for different diluted flames plotted against the Damköhler number $[L_V^3/(D_F^{*2}U_F)]/\tau_{NO}$. The experimental scaling relation from Chen et al. [11], straight line (——), is compared with several computations. Predictions for flames with 20% He dilution using equilibrium chemistry for all species except for NO are denoted with (×). PEUL predictions are: ◇, 0% He dilution;•, 20% He dilution; and △, 40% He dilution. Flamelet predictions for 20%-He-diluted flames are denoted with (□).

concentration is far too high for the flamelet model (Fig. 3). The slow temperature decrease in the post-flame zone results in a slight downstream shift of the maximum mean NO concentration. For flames A and B, the absolute levels of NO are well predicted with the PEUL model, whereas in the case of flame C, the NO formation is underpredicted, which can be attributed to the failure of the steady-state assumptions for the radical concentrations in such highly diluted flames. This is in line with the observation of Chen et al. [11].

The influence of radiative heat losses was investigated for flame A using a simple total emissivity model with a gray gas assumption [20]. Radiative heat losses reduce the total NO emission by roughly 5% (Fig. 3) compared to the emissions calculated without considering radiation. However, we believe that the influence of radiation on the scaling behavior of $EINO_x$ is small. This may be concluded from the observation that dilution of the flames with helium reduces the radiative heat losses significantly but does not alter the scaling law. Hence, radiation was neglected for the present analysis.

Analysis of Thermal NO Formation

Based upon an extensive set of experimental data, Driscoll et al. [3] proposed a scaling relation for $EINO_x$ that includes a half-power dependence on a global Damköhler number. Chen et al. [11] extended the scaling for diluted flames, leading to

$$EINO_x = 0.09\,\{L_V^3/(U_F D_F^{*2})/\tau_{NO}\}^{1/2} \approx Da^{1/2} \quad (4)$$

where L_V is the visible flame length, $D_F^* = (\rho_F/\rho_{Air})^{1/2} D_F$ the effective nozzle diameter [3], and τ_{NO} a chemical time scale that characterizes NO formation under equilibrium chemistry conditions for the given dilution [11].

Analytically, $EINO_x$ is obtained by integrating the mean source term for the NO formation over the flame volume V, which is then multiplied with the ratio of the molecular weights of NO_2 and NO and divided by the fuel mass flow, equation 5. As thermal NO is formed only in a very narrow zone around stoichiometry [6,8], it is a good approximation to consider only the source term conditioned on stoichiometric mixture fraction $\tilde{\omega}_{NO}(\underline{x}) \approx \dot{\omega}_{NO}(\underline{x}|Z = Z_{st})P(\underline{x}|Z = Z_{st})$. $EINO_x$ is thus approximated by

$$EINO_x = \frac{W_{NO_2}}{W_{NO}} \frac{4\int \tilde{\omega}_{NO}(\underline{x})dV}{\pi U_F \rho_F D_F^2} \approx \frac{W_{NO_2}}{W_{NO}} \frac{\int \dot{\omega}_{NO}(\underline{x}|Z = Z_{st})P(\underline{x}|Z = Z_{st})dV}{U_F \rho_F D_F^2} \quad (5)$$

where U_F, ρ_F, and D_F are the velocity, density, and diameter of the fuel jet, and W_i is the molecular weight of species i.

Under the assumption of chemical equilibrium for all species, except for NO, the conditional source term of NO, $\dot{\omega}_{NO}(\underline{x}|Z = Z_{st})$, is constant and yields $EINO_x \sim V/(U_F \rho_F \bar{D}_F^2)$. This suggests a constant ratio between $EINO_x$ and the residence time in the flame, resulting in a slope of 1 in Fig. 4. The comparison with the experimental scaling relation of equation 4 shows that the assumption of chemical equilibrium does not exhibit the observed Damköhler number dependence, and therefore, the observed

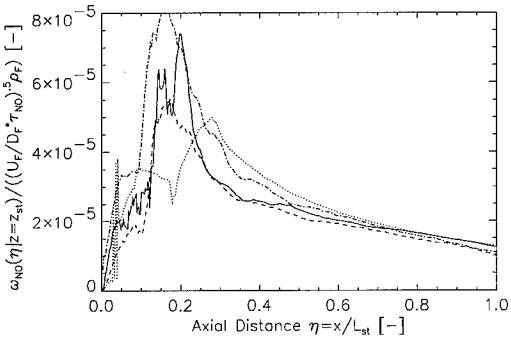

FIG. 5. Normalized NO source terms conditioned on stoichiometric mixture fraction for different dilutions and Reynolds numbers. PEUL predictions: ····, 0% He dilution, Re = 6000; ——, 0% He dilution, Re = 10,000; -·-·, 20% He dilution, Re = 6800; and - - -, 20% He dilution, Re = 11,400.

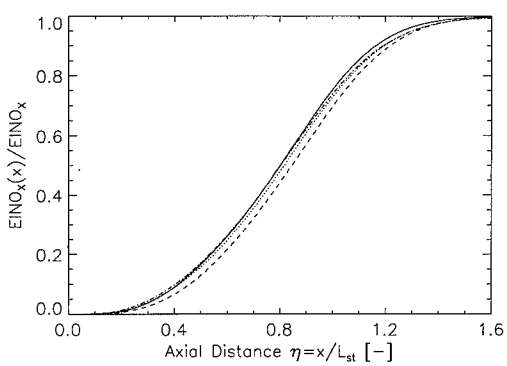

FIG. 6. Growth of the normalized emission index $EINO_x$ along the flame for different dilutions and Reynolds numbers. PEUL predictions: ····, 0% He dilution, Re = 6000; —, 0% He dilution, Re = 10,000; - · - ·, 20% He dilution, Re = 6800; and - - -, 20% He dilution, Re = 11,400.

dependence must originate from the source term $\dot{\omega}_{NO}(\underline{x}|Z = Z_{st})$ itself. Good agreement with the experimental scaling is obtained with the PEUL model, which reveals the half-power dependence on the Damköhler number for all cases. In line with Fig. 3, the absolute NO level is underpredicted for the 40%-He-diluted flames. The flamelet model predicts too high absolute levels and a slope of approximately 1.3, which can be interpreted as a reduced emission index with decreasing residence time. Obviously, the two combustion models yield completely different trends for NO formation, despite the agreement of the mean properties. To analyze $\dot{\omega}_{NO}(\underline{x}|Z = Z_{st})$, we assume that the characteristic of the NO source term along the flame is similar for all flames, which can be expressed by $\dot{\omega}_{NO}(\eta|Z = Z_{st}) = \dot{\omega}_{NO}^{max}(Da)f(\eta)$, where $\eta = x/L_{st}$ is a dimensionless

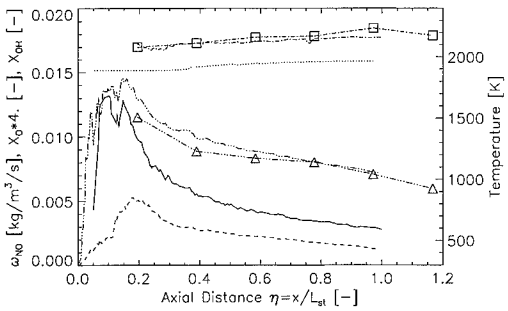

FIG. 7. Different properties, which are all conditioned on stoichiometric mixture fraction, along flame B. Left axis: ····, predicted OH mole fraction with the flamelet model; -····-, OH mole fraction with the PEUL model; -···Δ-···, measured OH mole fraction; ——, predicted O mole fraction (PEUL model), magnified by a factor 4; - - -, NO source term (PEUL model). Right axis: -·-·, predicted temperature (PEUL model); and -·□-·, measured temperature.

distance and L_{st} the stoichiometric flame length. This relation is verified by Fig. 5, where the source terms $\dot{\omega}_{NO}(\eta|Z = Z_{st})$ for different Reynolds numbers and dilutions are scaled with equations 4 and 5:

$$\dot{\omega}_{NO}(\eta|Z = Z_{st}) = \dot{\omega}_{NO}^{max}(Da)f(\eta)$$

$$\approx EINO_x \frac{U_F \rho_F D_F^2}{L_{st}^3} f(\eta) \approx \left(\frac{U_F}{\tau_{NO} D_F^*}\right)^{1/2} \rho_F f(\eta) \quad (6)$$

Up to $\eta \approx 0.4$, the source terms vary strongly due to the different levels of the superequilibrium O radical concentrations, whereas for $\eta > 0.4$, the source terms show a nearly linear decrease with downstream distance. The deviations from the scaling in the first part can be neglected because the contribution to the total emission of NO is small for $\eta < 0.4$. This is illustrated in Fig. 6 where the axial growth of $EINO_x$ is shown. When $0 < \eta < 0.4$, less than 10% of the total NO is formed. An important result of this analysis is that the assumption of a similar characteristic of the NO source term is valid and that the magnitude scales with equation 6.

In the following, the parameters that influence the NO source term $\dot{\omega}_{NO}(\eta|Z = Z_{st})$ will be analyzed in more detail. For flame B, Fig. 7 shows the experimental data and the PEUL results conditioned on the stoichiometric mixture fraction for temperature and radicals. The temperature rises from 2100 K to 2200 K along the flame, and therefore, the kinetic NO formation should increase by a factor of 2. Hence, to obtain the observed reduction of the NO source term by a factor of 4, the O radical concentration must decrease by a factor of 8. These factors show the relative importance of the radical concentrations compared with the temperature influence. Because experimental measurements for O radicals

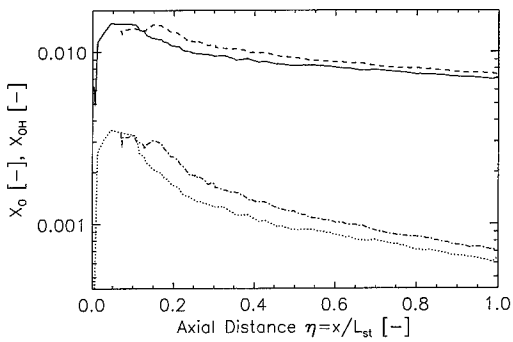

FIG. 8. Radical concentrations for two flames (20%-He-diluted) at different Reynolds numbers. Results from the PEUL model: ——, OH mole fraction, Re = 6800; ---, OH mole fraction, Re = 11,400; ····, O mole fraction, Re = 6800; and - · - ·, O mole fraction, Re = 11,400.

are not available, the OH radicals are taken as a representative for the radical behavior. They show a peak due to superequilibrium and the expected continuous reduction along the flame. In contrast to the O radicals, the concentration of OH is reduced by only a factor of 3, which is in line with the PEUL predictions. With the flamelet model, this radical decay is not predicted because the radical concentrations are rather insensitive to strain rate variations. Hence, the strain rate is not the relevant parameter for the radical decay toward chemical equilibrium.

Figure 8 shows the radical concentrations of OH and O conditioned on the stoichiometric mixture fraction for the 20% diluted flame at two different Reynolds numbers. For $\eta > 0.4$, a higher radical concentration is obtained for the higher Reynolds number. This tendency is similar for OH and O radicals, therefore, OH can be taken again as a representative for O. The magnitude of the peak concentration of OH remains nearly constant, which is consistent with experimental findings of Drake et al. [21], but the location of the peak moves downstream with increasing Reynolds number. After the peak, the decay of the OH radicals from superequilibrium to the equilibrium values begins. This decay is determined by the relatively slow recombination reactions [22]. The time that is needed to consume the OH radicals is approximately constant. However, the convective time scale depends on the Reynolds number and, thus, the point where the radical decay starts is shifted downstream for higher Reynolds numbers. As a consequence of this shift, the level of the radical concentrations is higher for higher Reynolds numbers, which in turn enhances the NO production. Thus, the observed half-power scaling law of $EINO_x$ is a result of the recombination reactions. This process has its own history which is affected by the convective time scale of the fluid flow. Therefore, it may be concluded that the local flame structure of any model to be used successfully for the prediction of thermal NO must include information concerning the mean reaction rate that governs the slow radical concentration decay. The flamelet model does not include such information because the only coupling between the turbulent flow and the chemistry is the strain rate. This explains the inaccurate predictions of NO formation. In contrast, the inclusion of a simple reaction progress variable, as used in the PEUL model, is sufficient to give the correct trend.

Conclusions

The numerical analysis of turbulent, nonpremixed hydrogen-air flames with two simple combustion models revealed an inaccurate trend of the scaling law for the NO emission index $EINO_x$ with the laminar flamelet model, and the expected trend for the PEUL model, despite their similar predictions of global properties of the flames. It was shown that the $EINO_x$ half-power scaling law, equation 4, is a consequence of different radical concentration levels. The radical concentration levels are controlled by the slow recombination reactions. This chemical process must be modeled separately with some kind of reaction progress variable, which was shown to be successful with the PEUL combustion model.

Acknowledgments

The authors would like to thank Dr. Robert Barlow who provided the species and temperature measurements, and Dr. Andrew Lutz for a prerelease of the OPPDIF code. This work was financed by the Bundesamt fuer Energiewirtschaft of the Swiss Federal Government under the coordination of Dr. A. Hintermann.

REFERENCES

1. Miller, J. A. and Bowman, C. T., *Prog. Energy Combust. Sci.* 15:287–338 (1989).
2. Correa, S. M., *Combust. Sci. Technol.* 87:329–362 (1992).
3. Driscoll, J. F., Chen, R. H., and Yoon, Y., *Combust. Flame* 88:37–49 (1992).
4. Barlow, R. S., Carter, C. D., *Combust. Flame* 97:261–280 (1994).
5. Kent, J. H., Bilger, R. W., *Sixteenth Symposium (International) on Combustion,* The Combustion Institute, Pittsburgh, 1977, pp. 1643–1656.
6. Peters, N. and Donnerhack, S., *Eighteenth Symposium (International) on Combustion,* The Combustion Institute, Pittsburgh, 1981, pp. 33–42.
7. Sanders, J. P. H. and Gökalp, I., *Eighth International Symposium on Transport Phenomena in Combustion,* Taylor and Francis, San Francisco, 1995.

8. Chen, J. Y. and Kollmann, W., *Combust. Flame* 88:397–412 (1992).
9. Pope, S. B., *Twenty-Third Symposium (International) on Combustion,* The Combustion Institute, Pittsburgh, 1990, pp. 591–612.
10. Smith, N. S. A., Bilger, R. W., Carter, C. D., Barlow, R. S., and Chen, J. Y., *Combust. Sci. Technol.* 105:357–375 (1995).
11. Chen, J. Y., Chang, W. C., and Koszykowski, M., *Combust. Sci. Technol.,* to be published, 1996.
12. Veynante, D. and Candel, S., *Exp. Fluids* 6:534–540 (1988).
13. Borghi, R., *Prog. Energy Combust. Sci.* 14:245–292 (1988).
14. Obounou, M., Gonzalez, M., and Borghi, R., *Twenty-Fifth Symposium (International) on Combustion,* The Combustion Institute, Pittsburgh, 1994, pp. 1107–1113.
15. Vervisch, L., Ph.D. Thesis, University of Rouen, France, 1991.
16. Trevino, C. and Mauss, F., in *Reduced Kinetic Reaction Mechanisms for Applications in Combustion Systems,* (N. Peters, B. Rogg, Ed.), Springer, Berlin (1993), pp. 165–182.
17. Peters, N., *Prog. Energy Combust. Sci.* 10:319–339 (1984).
18. Lutz, A. E., Kee, R. J., and Grcar, J. F., *OPPDIF: A Fortran Program for Computing Opposed-Flow Diffusion Flames,* Sandia National Laboratories Report, SAND96-8243, Livermore, CA, 1995.
19. Pope, S. B., *AIAA J.* 16(3):279–281 (1978).
20. Smith, T. F., Shen, Z. F., and Friedman, J. N., *J. Heat Transfer* 104:602–608 (1982).
21. Drake, M. C., Pitz, R. W., Lapp, M., Fenimore, C. P., Lucht, R. P., Sweeny, D. W., and Laurendau, N. M., *Twentieth Symposium (International) on Combustion,* The Combustion Institute, Pittsburgh, 1984, pp. 327–335.
22. Barlow, R. S., Dibble, R. W., Chen, J. Y., and Lucht, R. P., *Combust. Flame* 82:235–251 (1990).

COMMENTS

J. P. Gore, Purdue University, USA. Please comment on the wiggles and non-monotonic, highly Re number dependent behavior of O atom concentrations in the near injector region. Why did you not start the graph at the injector exit? The resulting upstream concentrations may affect downstream development and the velocity scaling you propose would be more convincing if these wiggles and "artifacts of grid resolution" were absent.

Author's Reply. In the present calculations the radical concentrations are obtained from a reduced chemical mechanism, i.e. no transport equation is solved for the radicals. For the reaction progress variable the profiles are smooth, even in the very near nozzle region, because a transport equation is solved. It is clear, that the steep gradients of the mixture fraction near the nozzle lead to some difficulties to extract the conditional values of the reaction progress variable and then to calculate the radical concentrations invoking steady state assumptions. Thus the observed wiggling is mainly due to these numerical difficulties. However, the radicals are always closely tied to the reaction progress variable. Thus these wiggles will not influence values downstreams. Grid resolution was checked, by refining the grid in each direction by a factor of two. Only minor changes of the mean reaction progress variable were found.

•

S. B. Pope, Cornell University, USA. Haworth et al. [1] reported flamelet calculation in which transient effects were accounted for to some extent. In particular, the flight time from the jet exit played a role. It might be useful to contrast the results and conclusion of Haworth et al. with yours.

Author's Reply. In the mentioned paper from Haworth et al. [1] the influence of a change in the PDF for the scalar dissipation due to the response time of a flamelet was investigated. They observed a slower approach to chemical equilibrium, as a consequence of the different scaling for the dissipation rate, which changed from $(x/D)^{-4}$ to $(x/D)^{-1}$ along the flame. The present work emphasizes not a different scaling of the dissipation rate, but a change of the reaction structure along the flame, which is not recovered by the flamelet model using the counterflow diffusion flame and the strain rate. Such a change in reaction structure due to mixing with products, which is also discussed by Haworth et al., may lead to improved results [2].

REFERENCES

1. Haworth, D. C., Drake, M. C., Pope, S. B., and Blint, J., *Twenty-Second Symposium (International) on Combustion,* The Combustion Institute, Pittsburgh, 1990, pp. 589–597.
2. Ferreira, J. C., Gass, J., and Suter, P., Work in Progress Poster 02-87, *Twenty-Sixth Symposium (International) on Combustion,* The Combustion Institute, Pittsburgh, 1996.

•

J. P. H. Sanders, LCSR-CNRS, France. I agree with your conclusion that the strain rate may not be the correct pa-

rameter to describe chemical non-equilibrium effects in the laminar flamelet model. However, in recent work [1] we found that with the scalar dissipation rate as the non-equilibrium parameter, the correct 0.5 slope of emission index vs. Da-number can be reproduced. The reason is the faster decay of the scaler dissipation rate with axial distance in a jet flame ($\sim x^{-4}$) with respect to the strain rate ($\sim x^{-2}$). The analysis can be found in Ref. 1.

REFERENCE

1. Sanders, J. P. H., Chen, J.-Y., and Gökalp, I., Flamelet Based Modeling of NO Formation in Turbulent Hydrogen Jet Diffusion Flames, submitted to *Combust. Flame* (1996). Also Work-in-Progress Poster 4-021 *Twenty-Sixth Symposium on Combustion,* Naples.

Author's Reply. The scalar dissipation rate in a turbulent jet flame scales as $\chi \approx (U/D)(x/D)^{-4}$. From the analysis of $EINO_X$ in eq. (6) it follows that $\dot{\omega}_{NO}(\eta|Z = Z_{ST}) \approx (U_F/\tau_{NO}D_F^*)^{1/2}$ and thus $\dot{\omega}_{NO}(\eta|Z = Z_{ST}) \approx \chi^{1/2}$. Provided that your laminar flamelet model fulfills this scaling, you will obtain the right scaling for $EINO_X$. But this is not yet a proof that the model is valid, as other quantities such as the absolute values for $EINO_X$ and mean temperatures should be predicted in a correct manner.

Looking at the temperatures for low strain rates in Ref. 1, they will lead to far too high mean values compared to the experiments. Furthermore, the effect of preferential diffusion would become more pronounced along the flame, which stands also in contrast to the measurements. Another question is the validity of the one dimensional calculation of the counter flow diffusion flame for low strain rate, as this simplification makes use of the assumption that the axial gradients are much bigger than the radial ones. Finally, the boundary conditions of the laminar one-dimensional flamelet configuration may have a strong influence on the radical concentrations as shown in Ref. 2. Hence, we refer to our conclusion that in order to obtain a correct level of $EINO_X$ and its scaling the underlying flame structure cannot be simply described by one single parameter such as the strain rate or the scalar dissipation rate.

REFERENCES

1. Sanders, J. P. H., Chen, J. Y., and Gökalp, I., *Combust. Flame,* submitted.
2. Ferreira, J. C., Gass, J., and Suter, P., Work in Progress Poster 02-87, *Twenty-Sixth Symposium (International) on Combustion,* The Combustion Institute, Pittsburgh, 1996.

Twenty-Sixth Symposium (International) on Combustion/The Combustion Institute, 1996/pp. 2223–2229

IMPACT OF MIXING MODEL ON PREDICTED NO FORMATION IN A NONPREMIXED, PARTIALLY STIRRED REACTOR

W.-C. CHANG AND J.-Y. CHEN
Department of Mechanical Engineering
University of California at Berkeley
Berkeley, CA 94720, USA

Stochastic simulations of non-premixed, partially stirred reactors (PaSRs) with three mixing models have been carried out for investigating the influence of unmixedness and differential diffusion on predicted NO levels. The three mixing models considered here include the modified Curl's model, the interaction-by-exchange-with-the-mean (IEM) model, and the linear-eddy model (LEM). The first two mixing models lack the ability in modeling the detailed diffusion process at the molecular level. The potential impact of differential diffusion on predicted NO levels is explored by using the LEM with/without differential diffusion. Comparisons of the predicted mean temperatures and NO levels indicate that at a given unmixedness level, the IEM model gives highest NO and temperatures due to its deterministic nature. Differential diffusion is found to have little impact on the predicted mean temperatures by the LEM, but it increases the predicted NO levels by a factor of 2. The modified Curl's mixing model predicts temperatures and NO levels lying between those given by the IEM and the LEM. Comparisons of detailed statistics have been performed to gain better understanding of these mixing models, especially the importance of the subtle features of mixing processes embedded in the LEM. The results suggest that superequilibrium temperatures seen in the predictions by the LEM with differential diffusion are the cause of the increase in the predicted NO levels. The predicted differential diffusion effect is found to scale with $Re^{-1/2}$ in agreement with the predictions for nonreacting flows. At a given unmixedness level, the mixing times computed by $\tau_{\text{mix}} = C_m\langle\xi''\xi''\rangle/\tilde{\chi}$ based on the LEM correlate reasonably well with the prescribed mixing times for the modified Curl's model or the IEM model.

Introduction

Modeling of the conditional scalar dissipation rate remains a research issue for the probability density function (PDF) approach [1]. Traditional mixing models, such as the Curl's mixing model [2], do not have the capability to predict the diffusion process at the molecular level. Often, this type of model is justified by the high-Reynolds number argument of turbulent flows for which equal diffusivity is considered to be a reasonable assumption. Therefore, there is no need to consider detailed molecular diffusion processes in turbulent flows. Several experimental investigations [3–5] raised concerns about the above argument, as combustion can decrease local Reynolds number by an order of magnitude. Recently, an experimental investigation by Smith et al. [6] showed that differences in species molecular diffusivities could have significant impacts on fluid composition and thus on chemical evolution in turbulent-reacting flows. Consequently, the differential diffusion effect may have an important impact on NO formation and chemical reactions for turbulent-reacting flows with moderate Reynolds number.

Unlike the traditional mixing models, the linear-eddy model (LEM) proposed by Kerstein [7,8] has the unique feature of being capable of modeling the molecular diffusion process in a projected one-dimensional domain. We have further refined this model and incorporated it into a stochastic model of a partially stirred reactor (PaSR) [9] to study the potential impacts of differential diffusion on predicted NO formation for stoichiometric hydrogen-air combustion. As detailed in Ref. 9, the conditional scalar dissipation rate is the only term that needs modeling in the PDF transport equation for the PaSR. Hence, the PaSR provides an ideal platform for studying different mixing models. The predicted results with/without differential diffusion are compared with those obtained with two widely used mixing models. One is the modified Curl's model [10–12], and the other is the interaction-by-exchange-with-the-mean (IEM) model [13–15]. The influence of the unmixed nature of fluids on the temperature and NO formation is explored by performing a parametric study over a wide range of mixing conditions. Examination of the statistical properties predicted by different mixing models is carried out to explain the computed results and to provide better understanding of the different mixing models.

Numerical Simulation of PaSR

The modeled joint scalar PDF equation for the PaSR is solved by the Monte Carlo technique using 1000 statistical events [16]. A time-marching scheme with fractional steps is used and statistically stationary solutions are obtained when the variation of time-averaging mean thermochemical properties is small. The mass fluxes of input streams are set to produce an overall stoichiometric mixture. The unmixedness parameter is used for quantifying the unmixed state of the fluids, and it is computed as $\langle \xi'' \xi'' \rangle / [(1-\tilde{\xi})\tilde{\xi}]$, where $\tilde{\xi}$ is the density-weighted mixture fraction and $\langle \xi'' \xi'' \rangle$ is the corresponding variance. The unmixedness is bounded by 1 and 0 corresponding respectively to the completely segregated state and the fully mixed state.

According to our previous studies [17,18], the results obtained with a five-step reduced mechanism agreed very well with those from the detailed hydrogen mechanism for both laminar and turbulent flames. Hence, in the current PaSR simulations, the five-step hydrogen reduced mechanism is used to save computational time. Thermochemical properties and chemical kinetics are computed by using the Chemkin-II subroutines [19], and the stiff chemical kinetics equations are solved by the VODE package [20].

The Mixing Models

Modified Curl's Mixing Model

The modified Curl's mixing model can be classified under the general pair-exchange model [10]. The stochastic simulation of this mixing model is implemented by randomly selecting two particles and mixing them up to random degree. The amount of mixing is modeled through a characteristic mixing time, τ_{mix}, and its reciprocal can be considered as the mixing frequency, ω_{mix}. Since the present PaSR model does not contain modeling of the fluid dynamics, the mixing frequency will be an input parameter for the PaSR model. Consequently, there are two characteristic fluid mechanics times in the PaSR model. The mean residence time, τ_{res}, corresponds to the through flow, and mixing time corresponds to the molecular mixing process. When the mixing time is relatively small compared to the residence time and chemical kinetics times, the PaSR approaches the perfectly stirred reactor (PSR) limit.

IEM Mixing Model

Different from the modified Curl's model, the IEM mixing model is a deterministic model. As time proceeds, the stochastic event moves toward the mean at a rate proportional to its distance from the mean. Therefore, the shape of the PDF remains unchanged. As derived in Ref. 9, the theoretical unmixedness for the PaSR with either the modified Curl's model or the IEM model can be expressed as $1/(1 + C_\phi \tau_{res} \omega_{mix})$, where C_ϕ is an adjustable constant in each model. By assigning a common value of 1/3 to C_ϕ, the predicted unmixedness at the statistically stationary state will be the same using these two traditional models.

Linear-Eddy Mixing Model

The LEM proposed by Kerstein [7,8] contains more physically sound representations of the molecular diffusion and fluid motion compared with the previous two mixing models. To resolve molecular diffusion processes, the model relies on a one-dimensional representation of the fluid motion. For the turbulent stirring process, a random process of rearranging the fluid particles, for example, the triplet mapping, is used to mimic the effect of an individual eddy on the scalar field along this linear domain. The location of the eddy is selected randomly from the domain, and the rate of this process is governed by an event-frequency parameter λ, where λ has the units of 1/(length $\times$ time). The eddy size is selected according to a PDF $f(l)$. The sequence of rearrangement events induces a random walk of a fluid particle, and the associated diffusivity is set to be the turbulent diffusivity D_T. The PDF $f(l)$ is chosen to satisfy the Kolmogorov inertial-range cascade so that D_T is proportional to $l^{4/3}$. The eddy size is bounded by the integral length scale L and the Kolmogorov length scale L_K of the turbulent flow. The stirring time step τ_s is calculated by $1/\lambda X$, where X is the length of the one-dimensional domain. The molecular diffusion is directly implemented by solving the diffusion equation. Details of implementation of the LEM into the stochastic PaSR simulation can be found in Ref. 21.

Parameters for PaSR Simulations

A mean residence time of 1 ms was chosen for the PaSR with input streams set to give an overall stoichiometric mixture of hydrogen and air. The prescribed mixing frequencies were adjusted from 70 to 10 kHz for both the modified Curl's and the IEM models so that the predicted unmixedness falls between 0.01 and 0.23. Stochastic simulations with the LEM are carried out with/without differential diffusion for Reynolds numbers from 50 to 2000. The Reynolds numbers were chosen in such a way that the LEM predicts the same level of unmixedness as IEM or modified Curl's models. The integral length scale was set to 5 cm, and the total length for the one-dimensional array is chosen so that the total number of cells is at least 1000, to be comparable with the other two mixing models. In the LEM, the

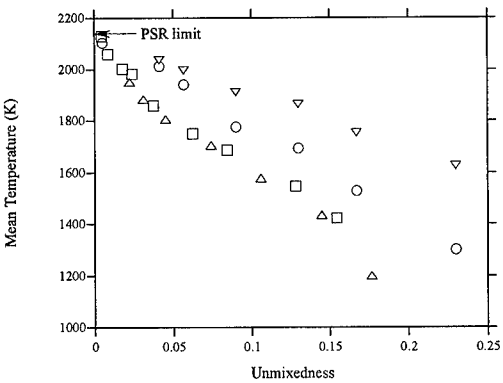

FIG. 1. Predicted mean temperatures versus unmixedness for a PaSR of stoichiometric hydrogen-air mixture with 1-ms residence time. Three different mixing models are used with the five-step hydrogen-air reduced mechanism for the PaSR simulation. ▽, the IEM model; ○, the modified Curl's model; △, the linear-eddy model with equal diffusivity; □, the linear-eddy model with differential diffusion.

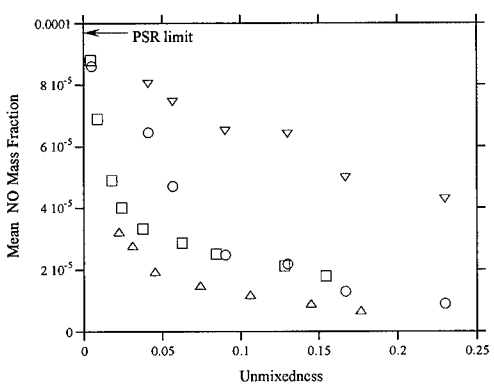

FIG. 2. Predicted mean NO mass fractions versus unmixedness for a PaSR of stoichiometric hydrogen-air mixture with 1-*ms* residence time. Three different mixing models are used with the five-step hydrogen-air reduced mechanism for the PaSR simulation. ▽, the IEM model; ○, the modified Curl's model; △, the linear-eddy model with equal diffusivity; □, the linear-eddy model with differential diffusion.

diffusion coefficients are computed using a mixture-average formula that takes into account the effect of heat release. For equal diffusivity runs, the diffusion coefficients for all species were assigned a value of 0.2 cm^2/s. Due to the extra information needed in specifying the molecular diffusion process in the LEM, comparing different models at the same level of unmixedness serves to explore the sensitivity of predicted results to higher moment statistics.

Results and Discussions

Mean Temperature and NO Mass Fraction

Figures 1 and 2 present comparisons of the predicted mean temperatures and NO mass fractions versus the unmixedness obtained with different mixing models. As the unmixedness decreases, the predicted mean temperatures and NO mass fractions with each model approach the PSR limits as one expects. As seen in Fig. 1, the predicted mean temperatures with the IEM model are higher than those obtained with other mixing models, and the temperature differences increase with unmixedness. Consequently, the IEM predicts higher levels of NO concentration than other models, as shown in Fig. 2. The differences among the results obtained with the modified Curl's model and those with the LEM with/without differential diffusion effect are noticeable. Overall, the LEM predicts lower mean temperatures than those given by the modified Curl's model; hence, lower levels of NO have been computed using the LEM. Inclusion of differential diffusion into the LEM has little impact on the predicted mean temperatures, but it increases the predicted NO levels by a factor of 2. This difference is attributed to the superequilibrium temperatures caused by the differential diffusion among species and heat [22–25]. The differential diffusion effect is expected to become less important as the Reynolds number increases. This expectation is consistent with the predicted results shown in Fig. 2; the differences among predicted NO levels decrease as unmixedness decreases or as the Reynolds number increases.

Scatter Plots and Probability Density Functions of Temperature

To provide further insight into the nature of the predicted statistics, we compare the temperature scatter plots versus mixture fraction and the PDFs obtained with different models. As an example, comparisons are made for the cases with unmixedness about 0.04, and the results are presented in Figs. 3–10. Also shown in these figures are the equilibrium temperatures without differential diffusion. As anticipated, the temperatures obtained with mixing models of equal diffusivity are bounded by the equilibrium temperatures. Since the IEM model is deterministic, the predicted temperatures follow a single trajectory without scatter, as shown in Fig. 3. Comparison of Figs. 5 and 9 indicates that the predicted temperatures by the modified Curl's model exhibit less scatter than those by the LEM with equal diffusivity. As seen from Fig. 7, the LEM with the differential diffusion predicts a number of statistics with superequilibrium temperatures near the stoichiometric and some for the rich mixtures. Since

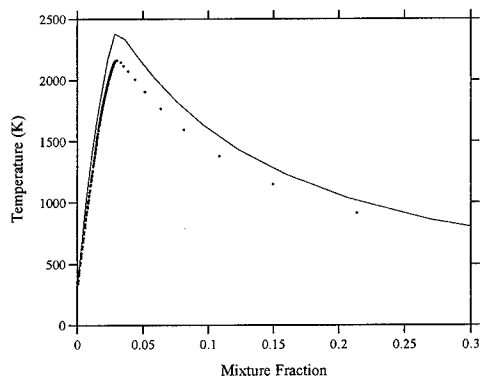

FIG. 3. A scatter plot of predicted temperature for a PaSR of stoichiometric hydrogen-air mixture with mixing frequency 70 kHz of the IEM mixing model. Solid line denotes the equilibrium temperatures, and the dots are obtained from the Monte Carlo simulation.

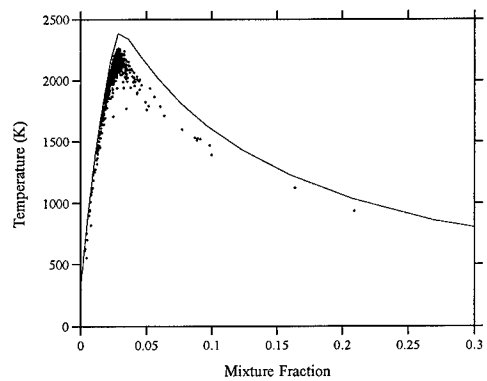

FIG. 5. A scatter plot of predicted temperature for a PaSR of stoichiometric hydrogen-air mixture with mixing frequency 70 kHz of the modified Curl's mixing model. Solid line denotes the equilibrium temperatures, and the dots are obtained from the Monte Carlo simulation.

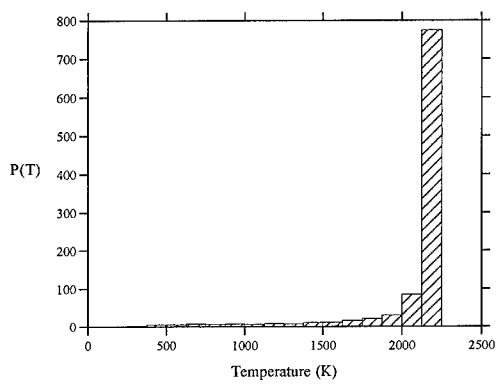

FIG. 4. Probability density functions of the predicted temperature for a PaSR of stoichiometric hydrogen-air mixture with mixing frequency 70 kHz of the IEM mixing model.

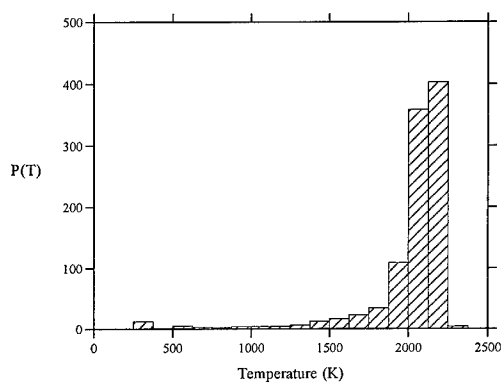

FIG. 6. Probability density functions of the predicted temperature for a PaSR of stoichiometric hydrogen-air mixture with mixing frequency 70 kHz of the modified Curl's mixing model.

NO is formed mainly via the Zeldovich mechanism in the present hydrogen flames, the predicted superequilibrium temperatures can have profound impact on the predicted NO levels.

Comparison of the predicted temperature PDFs provides us with information on the differences in the predicted distributions by the different models. As shown in Fig. 4, the temperature distribution given by the IEM model is narrower than those given by other models. This is attributed to the deterministic nature of the IEM model, and it explains the higher temperature predictions by the IEM model, as noted in Fig. 1. Compared to the distribution obtained with the modified Curl's mixing model (Fig. 6) or the IEM model (Fig. 4), the LEM with/without differential diffusion (Figs. 8 and 10) predicts a much broader temperature distribution. Although the noted difference is caused by the specific mixing conditions assigned to the LEM, the comparison shows a strong sensitivity of temperature prediction to the mixing model.

Differential Diffusion

We now examine the predicted differential diffusion effect obtained with the LEM. As suggested by Bilger [26], the degree of differential diffusion may be quantified by a variable z defined as $z = \xi_H - \xi_O$, where ξ_H is the mixture fraction based on the atomic element H and ξ_O is the mixture fraction based on the atomic element O. Accordingly, z is zero when the equal diffusion condition is achieved. Deviation of the z value from zero serves as an indicator of the existence of differential diffusion.

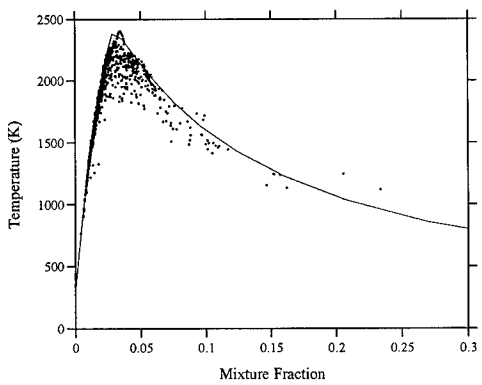

FIG. 7. A scatter plot of predicted temperature for a PaSR of stoichiometric hydrogen-air mixture at Reynolds number 160 of the linear-eddy mixing model with differential diffusion. Solid line denotes the equilibrium temperatures, and the dots are obtained from the Monte Carlo simulation.

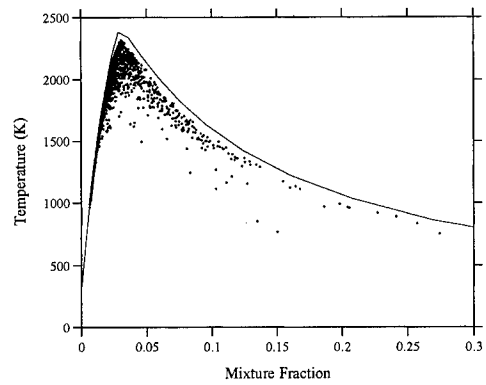

FIG. 9. A scatter plot of predicted temperature for a PaSR of stoichiometric hydrogen-air mixture at Reynolds number 1500 of the linear-eddy mixing model with equal diffusivity. Solid line denotes the equilibrium temperatures, and the dots are obtained from the Monte Carlo simulation.

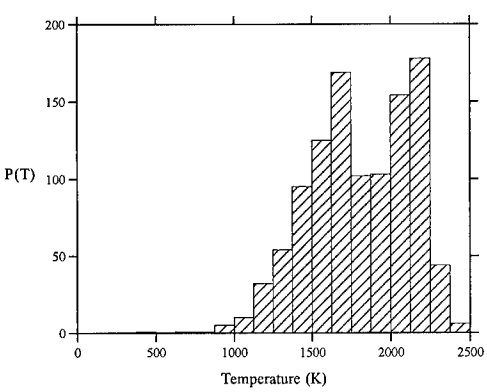

FIG. 8. Probability density functions of the predicted temperature for a PaSR of stoichiometric hydrogen-air mixture at Reynolds number 160 of the linear-eddy mixing model with differential diffusion.

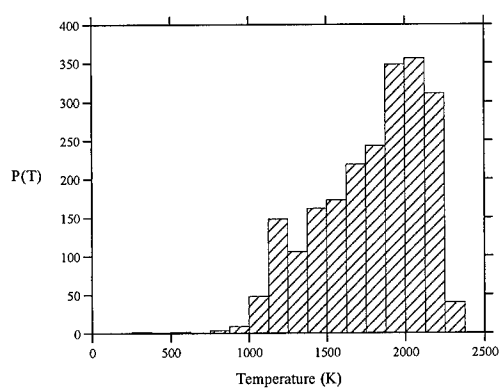

FIG. 10. Probability density functions of the predicted temperature for a PaSR of stoichiometric hydrogen-air mixture at Reynolds number 1500 of the linear-eddy mixing model with equal diffusivity.

Shown in Fig. 11 is a scatter plot of ξ_O versus ξ_H for the case with a Reynolds number of 80. The diagonal straight line with a unity slope indicates the equal diffusion condition. The dashed line represents the predicted results for an opposed laminar flame at a strain rate of 100 s^{-1}, and the predicted differential diffusion effect is not sensitive to the strain rate [6]. The points above the straight line represent fluids with excessive H content, compared to the fluids under the equal diffusivity condition. The predicted differential diffusion effect for the PaSR is seen to follow the similar trend observed in the opposed laminar flame. The excursion and scatter from the trend predicted for the laminar flame are caused by the turbulent stirring, which is absent in laminar flows. Near the stoichiometric condition (ξ = 0.0283), there are more points scattering above the equal diffusivity line, indicating that lean mixtures have more H content than rich mixtures. Figure 12 presents the predicted dependence of the variance of z, z_{rms}, on the Reynolds number. A negative one-half power dependence seems to fit well for the range of Reynolds numbers studied here, and it agrees with the results obtained by Kerstein et al. [27] for the nonreacting flows. The predicted dependence of differential diffusion effect on the Reynolds number remains to be verified by future experimental data.

Timescales for Mixing

Mixing time is an extremely valuable quantity in understanding the interaction between chemistry

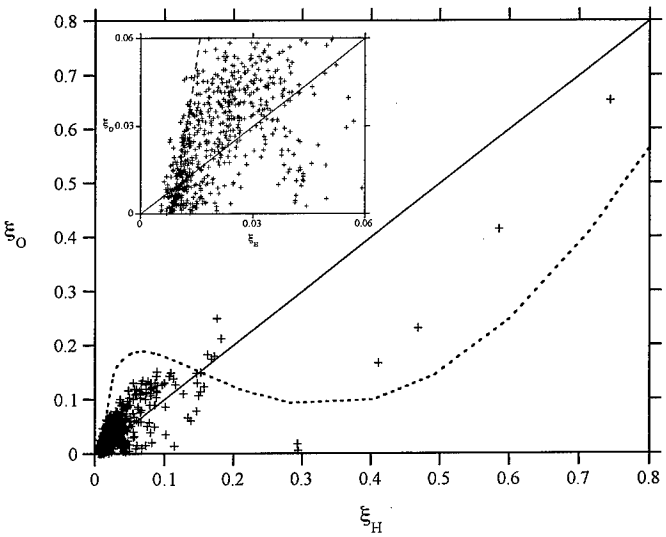

FIG. 11. A scatter plot of ξ_O versus ξ_H for the case with Reynolds number = 80. The linear-eddy model with differential diffusion is used with the five-step hydrogen-air reduced mechanism for the PaSR simulation. The solid diagonal line denotes the line of equal diffusivity. The dashed line is calculated from laminar, opposed flow in Tsuji geometry at strain rate equal to 100 s^{-1}.

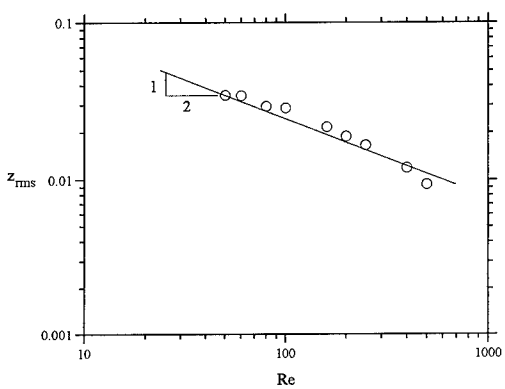

FIG. 12. Dependence of Z_{rms} on the Reynolds number. The linear-eddy model with differential diffusion is used with the five-step hydrogen-air reduced mechanism for the PaSR simulation.

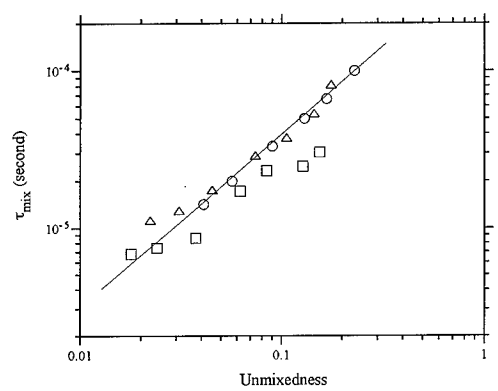

FIG. 13. Comparison of the mixing timescales for the modified Curl's model and the linear-eddy model with/without differential diffusion. ○, the modified Curl's model; ▽, the linear-eddy model with equal diffusivity; □, linear-eddy model with differential diffusion.

and turbulence. However, prediction of mixing time remains an unsettled area in current turbulent combustion models. In the IEM and modified Curl's mixing models, the mixing time is specified usually through a k-ε–type model. Since the LEM contains spatial information in one-dimensional form, we may use the predicted results to estimate the mixing time for scalars. One possible way for computing the mixing time is $\tau_{mix} = C_m\langle\xi''\xi''\rangle/\tilde{\chi}$, where C_m is a constant, $\tilde{\chi}$ is the density-weighted scalar dissipation rate given by $2 < \rho D(d\xi/dx)\,(d\xi/dx) > /\bar{\rho}$, and the angle brackets mean ensemble average over many realizations. In Fig. 13, the results with $C_m = 0.4$ are plotted against unmixedness along with those prescribed for the Curl's mixing model. The results from the IEM model are not presented as they are the same as those from the Curl's mixing model. For a given residence time, the predicted unmixedness with the modified Curl's model is proportional almost linearly with the prescribed mixing time when the value of $C_\phi\tau_{res}/\tau_{mix}$ is larger than 1, as in the present study. At a given unmixedness, the computed mixing times from the LEM with equal diffusivity show a good correlation with the prescribed mixing times. Differential diffusion causes some deviations from the linear relation. This suggests that for predictions of the unmixed nature of turbulent flows, the modified Curl's mixing model or the IEM model will give comparable results as those from the LEM when the mixing times are computed by $\tau_{mix} = C_m\langle\xi''\xi''\rangle/\tilde{\chi}$. When used as a subgrid scalar model

for CFD codes, the LEM has the advantage over other mixing models since modeling of mean scalar dissipation rate is not needed.

Conclusions

Numerical simulations of the PaSR with a mean-stoichiometric hydrogen-air mixture have been performed to study the differences in the predicted NO levels by three mixing models, including the modified Curl's mixing model, the IEM model, and the LEM. At the same degree of unmixedness, the predicted thermal NO levels are found to be quite sensitive to the mixing model. This high sensitivity implies the importance of higher moments of the mixture fraction to NO prediction. Due to its deterministic nature, the IEM model predicts the highest NO level. On the other hand, the LEM gives the lowest NO values under the present specific molecular diffusion conditions. The results by the modified Curl's model fall between the above two models. With the LEM, the effect of differential diffusion was found to increase the predicted NO levels by a factor of 2. This increase is attributed to the super-equilibrium temperatures caused by differential diffusion among species and heat. The predicted differential diffusion effect scales with $Re^{-1/2}$, which remains to be verified by experiments. The mixing time determined from the LEM correlates well with the prescribed mixing times for the Curl's mixing model or the IEM model.

Acknowledgment

This work was supported partially by NASA Lewis Research Center under Contract NAS3-26613 through a subcontract with Quest Integrated Inc.

REFERENCES

1. Pope, S. B., *Twenty-Third Symposium (International) on Combustion,* The Combustion Institute, Pittsburgh, 1990, pp. 591–612.
2. Curl, R. L., *AIChE J.* 9:175–181 (1963).
3. Drake, M. C., Lapp, M., Penney, C. M., Warshaw, S., and Gerhold, B. W., *Eighteenth Symposium (International) on Combustion,* The Combustion Institute, Pittsburgh, 1981, pp. 1521–1531.
4. Bilger, R. W. and Dibble, R. W., *Combust. Sci. Technol.* 28:161–172 (1982).
5. Drake, M. C., Pitz, R. W., Lapp, M., *AIAA J.* 24:905–917 (1986).
6. Smith, L. L., Dibble, R. W., Talbot, L., Barlow, R. S., and Carter, C. D., *Combust. Flame* 100:153–160 (1995).
7. Kerstein, A. R., *J. Fluid Mech.* 231:361–394 (1991).
8. Kerstein, A. R., *J. Fluid Mech.* 240:289–314 (1992).
9. Chen, J.-Y., Western States Section of the Combustion Institute, Fall Meeting, paper no. WSS/CI93-071, Oct. 18–19, Menlo Park, CA, 1993.
10. Janicka, J., Kolbe, W., and Kollmann, W., *J. Non-Equilib. Thermodyn.* 4:47–56 (1979).
11. Pope, S. B., *Combust. Sci. Technol.* 28:131–145 (1982).
12. Dopazo, C., *Phys. Fluids* 22:20–30 (1979).
13. Dopazo, C. and O'Brien, E. E., *Acta Astronaut* 1:1239 (1974).
14. Villermaux, J., in *Encyclopedia of Fluid Mechanics,* Gulf Publ. Co., New Jersey, 1986, pp. 707–768.
15. Yamazaki, H. and Ichikawa, A., *Intl. Chem. Eng.* 10:471–478 (1970).
16. Pope, S. B., *Prog. Energy Combust. Sci.,* 11:119–192 (1985).
17. Chang, W.-C., Chen, J.-Y., and Herr, C., Western States Section of the Combustion Institute, Fall Meeting, paper no. WSS/CI93-113, Oct. 18–19, Menlo Park, CA, 1993.
18. Chen, J.-Y., Chang, W.-C., and Koszykowski, M., *Combust. Sci. Technol.,* 110–111: 505–529 (1995).
19. Kee, R. J., Rupley, F. M., and Miller, J. A., *Chemkin-II: A FORTRAN Chemical Kinetics Package for the Analysis of Gas-Phase Chemical Kinetics,* Sandia National Laboratories Report No. SAND 89-8009, 1989.
20. Brown, P. N., Byrne, G. D., and Hindmarsh, A. C., *SIAM J. Sci. Stat. Comput.* 10:1038–1051 (1989).
21. Chang, W.-C., Ph.D. Thesis, University of California, Berkeley, 1995.
22. Katta, V. R., Goss, L. P., and Roquemore, W. M., *Combust. Flame* 96:60–74 (1994).
23. Takagi, T. and Xu, Z., *Combust. Flame* 96:50–59 (1994).
24. Drake, M. C., Correa, S. M., Pitz, R. W., Shyy, W., and Fenimore, C. P., *Combust. Flame* 69:347 (1987).
25. Drake, M. C. and Blint, R. J., *Combust. Sci. Technol.* 61:187–224 (1988).
26. Bilger, R. W., *AIAA J.* 20:962–970 (1982).
27. Kerstein, A. R., Cremer, M. A., and McMurtry, P. A., *Phys. Fluids* 7:1999–2007 (1995).

Twenty-Sixth Symposium (International) on Combustion/The Combustion Institute, 1996/pp. 2231–2239

IMPACT OF TEMPERATURE AND FUEL-NITROGEN CONTENT ON FUEL-STAGED COMBUSTION WITH COAL PYROLYSIS GAS

U. GREUL, H. SPLIETHOFF, H.-C. MAGEL, U. SCHNELL, H. RUEDIGER AND K. R. G. HEIN
Institut für Verfahrenstechnik und Dampfkesselwesen, IVD
Universität Stuttgart, Germany

C.-Z. LI AND P. F. NELSON
CSIRO Division of Coal & Energy Technology
PO Box 136, North Ryde, Australia

At an experimental facility of the Stuttgart University, the process of fuel splitting and staging is investigated with a view to lower NO_x emissions. Raw coal is introduced into either an electrically heated, entrained flow reactor or a fluidized bed reactor where it is split into pyrolysis gas and residual char. In a following staged combustion, the remaining char or raw coal is used as primary fuel and the pyrolysis gas as reburn fuel. The test facility allows a systematic study to evaluate the effect of different parameters on NO_x reduction independently of each other. Pyrolysis experiments, combustion studies, and calculations have been performed to explain the effective NO_x reduction with coal pyrolysis gas.

To compare the results and show the advantage of this process, investigations with fuel staging were carried out. With gaseous reburn fuels and residence times higher than 1.5 s, minimum NO_x emissions below 200 mg/m^3 at 6% O_2 could be achieved independently of the coal type (200 mg/m^3 is approximately equivalent to 100 ppmv). Reburning with coal pyrolysis gas increases the optimum air/fuel ratio from 0.75 to 0.9, yielding the same or even lower NO_x emissions. The main parameters are stoichiometry and residence time in the fuel-rich secondary zone. The results also show an increase of the reduction efficiency with increasing reburning temperatures in the reburn zone. The tar components in the reburn fuel and the fuel-N content are very important parameters in achieving excellent results when using coal pyrolysis gas. These appear to have a positive effect on the reduction of NO_x emissions. To explain this effect, the model of the perfectly stirred reactor (PSR) was employed. The modeling results agree well with the experimental investigations.

Introduction

New developments and investigations of research laboratories led more and more to applying in-furnace measures to coal-fired utility boilers to reduce NO_x emissions in the combustion chamber. Low NO_x combustion with air or fuel staging is very effective and cuts the need to apply expensive SCR technology.

The background of these measures is that emissions of nitrogen oxides from the combustion of coals are a major environmental problem because they have been proven to contribute to the formation of acid rain and photochemical smog. For these reasons, German NO_x emission standards are among the most stringent.

Because there is no causal relationship between coal nitrogen and NO_x emissions, the combustion conditions are of major influence on NO_x emissions, and their control by modifying the combustion process is a challenging goal. To limit NO_x emissions to 200 mg/m^3_n only by primary measures has proved to be successful for brown coal–fired boilers. For the combustion of bituminous coal, this level has not yet been achieved.

Fuel staging, or reburning, is therefore an effective method to reduce NO_x emissions in the combustion chamber. One part of the applied fuel is used to establish a fuel-rich zone after the main combustion zone. In this substoichiometric zone, NO_x can be reduced, for example, by hydrocarbon or NH radicals. The delay in supplying the burnout air provides the residence time for NO_x reduction, but the necessary high amount of reburn fuel and the substoichiometric conditions may result in corrosion or burnout problems if the reburn fuel is pulverized coal. To limit these effects, additional measures must be taken in the coal preparation and combustion process. With fuel staging, NO_x emissions of 400 mg/m^3 can be achieved with bituminous coal firing in large-scale applications [1].

Investigations with reburning using methane [2], natural gas [3], oil [4], or coal [4,5] in bench- and pilot-scale facilities have been published by several

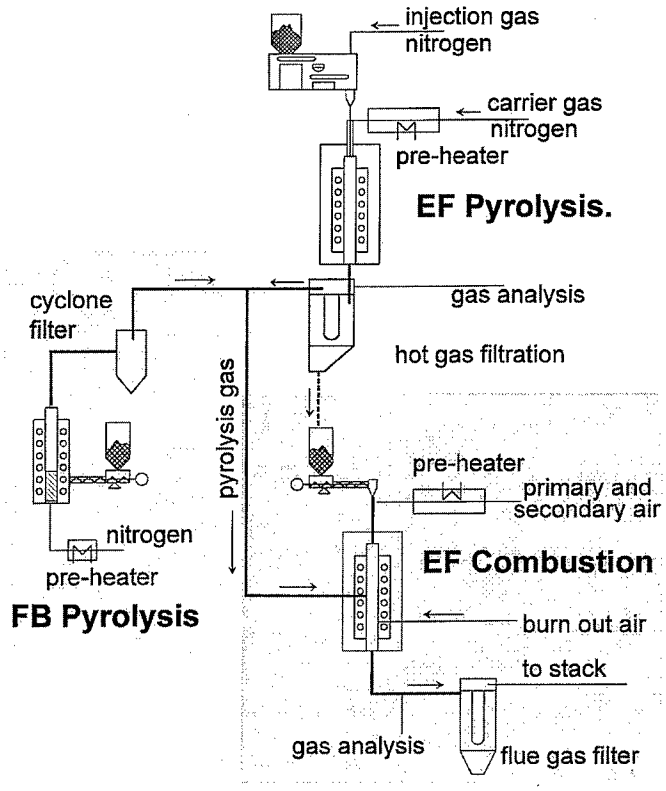

FIG. 1. Scheme of the BTS test facility at IVD. The main parts include the EF, entrained flow pyrolysis reactor; the FB, fluidized bed pyrolysis reactor; and the EFC, entrained flow combustion reactor.

authors. The principal conclusions of these studies indicate that the conditions in the reburn zone should include high temperatures (those higher than 1400°C are not useful [3]) and long residence times (from 0.4 s [6] up to 2 s [7]) to increase the reburn efficiency.

The discrepancies observed for the optimum air ratio in the reduction zone between 0.7 [2] and 0.9 [6] could be due to the impact of different process parameters such as mixing, oxygen content in the primary zone [3], primary NO_x levels [5,6], reburn temperature, reburn fuel used, N content of the reburn fuel [4,8], and scale of the facility. The optimum reburn fuel has not yet been evaluated.

NO_x emissions lower than 200 mg/m^3 without SCR technology may be reached by a recently proposed technology called *reburning with coal pyrolysis gas.* This process, also called *fuel splitting and staging* (Brennstoff–Trenn–Stufung [BTS]); is based on the production of a reburn gas by coal pyrolysis, the separation of pyrolysis gas and remaining char, the combustion of char (or coal) as primary fuel, and the fuel-staged combustion with pyrolysis gas as reburn fuel. This advanced fuel-staging process avoids the disadvantages of the fuel staging with coal (poor burnout, low reduction efficiency) or with natural gas (high quantities of gas needed, very costly). A further advantage is the possibility of adjusting pyrolysis conditions to the specific coal properties and thus producing an optimum reburn fuel with maximum NO_x reduction efficiency.

Description of the Test Facility

A scheme of the test facility is shown in Fig. 1. It is composed of three main parts: the entrained flow (EF) pyrolysis reactor, the fluidized bed (FB) pyrolysis reactor, and the entrained flow combustion (EFC) reactor. Detailed descriptions of the EF and FB pyrolysis reactors and the EFC reactor are given in Ref. 9. For baseline investigations, each reactor can be operated separately. For the process of fuel splitting and staging, the EFC reactor and a pyrolysis reactor, either the EF or FB, were operated simultaneously.

The electrically heated, entrained flow pyrolysis reactor (ca. 30 kW_{el}, total height 2400 mm) has a 2-m reaction tube with a diameter of 100 mm made of CrNi steel. The maximum furnace temperature is 1300°C. The second pyrolysis plant is an electrically heated fluidized bed reactor. The reactor can be heated up to temperatures of 1100°C with three regulated heating zones. The total height is 3 m, the

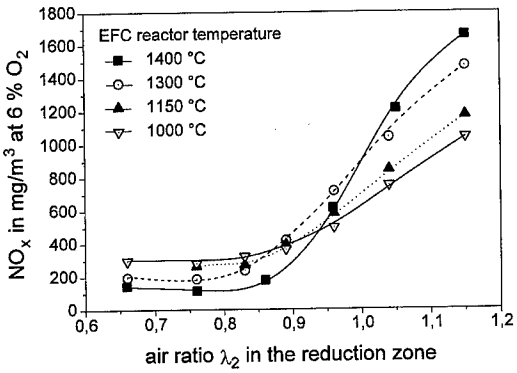

FIG. 2. Effect of EFC temperatures on NO_x reduction with Göttelborn hard coal as primary fuel, methane as reburn fuel, and residence time in the reduction zone of 2 s.

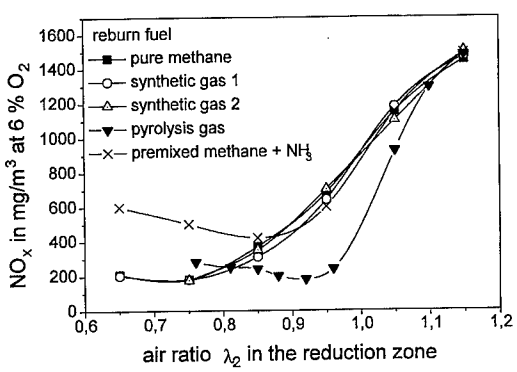

FIG. 3. Reduction efficiencies of different gaseous reburn fuels at an EFC reactor temperature of 1300°C were compared.

bed diameter 108 mm, and the freeboard diameter 135 mm.

The electrically heated, entrained flow combustion reactor has five regulated heating zones with a maximum temperature of 1400°C. For the separate investigation of individual parameters concerning their effect on pollutant formation, the temperature can be regulated along the combustion process. The combustion air can be heated up to ca. 400°C. Air staging at the burner and swirled secondary air are possible. A gravimetric screw conveyor (0.5–5 kg/h) supplies a constant coal-feeding rate. The ceramic tube has a length of 2.5 m and an internal diameter of 200 mm. Fuel and air staging in the furnace with different residence times in each zone can be investigated. The flue gas composition (NO, NO_2, CO, CO_2, SO_2, O_2) in the different combustion zones can be measured with a gas probe.

Results

Within this project, investigations were carried out on the pyrolysis of five coals and four temperatures between 600 and 900°C in the FB and of five coals and six temperatures between 600 and 1200°C in the EF reactor. The analysis of gas, tar, and char and the distribution of fuel-N was the main goal of the pyrolysis experiments. Detailed information about the composition of the pyrolysis gas, tar, and char are given in Refs. 9 and 10 for the EF and FB reactors at IVD and for the test facility at CSIRO in Ref. 11.

Investigations on staged combustion were conducted with a German hard coal (Göttelborn) as primary fuel and with various reduction fuels, including methane (with and without NH_3 addition), various gas mixtures, and pyrolysis gas produced with EF or FB. The standard conditions for all reburn test runs can be summarized as follows: the same reactor wall temperature for all combustion zones, Göttelborn raw coal (1 kg/h) as primary fuel and a residence time of 2 s in the reduction zone to ensure the optimum reduction potential and air ratios in the primary and burnout zone $\lambda_1 = \lambda_3 = 1.15$ (ca. 3% O_2 in the flue gas). The NO_x emissions shown in the figures are calculated as mg/m³ NO_2 at 6% O_2 in the flue gas under standard conditions.

The influence of different combustion reactor temperatures with Göttelborn coal as primary fuel and methane as reburn fuel is shown in Fig. 2. Unstaged combustion in conjunction with high temperatures in the combustion zone results in high NO_x emissions. The NO_x values in the primary combustion zone increase from 1000 to 1700 mg/m³ at reactor temperatures between 1000 and 1400°C. With air/fuel ratios $\lambda_2 < 0.85$ and high temperatures (1400°C) in the reduction zone, NO_x emissions can be reduced by ca. 94%. Despite a higher initial NO_x concentration, the lowest emission values are achieved at the highest temperature.

With the variation of the primary-zone NO_x concentration from 1000 to 1500 mg/m³ at a constant reburn temperature, the reburn efficiency increases from 85% to 90%, although the emission values are higher. These results agree with findings of other authors [5,6].

The same positive influence of the reactor temperature was found for air-staged combustion [12]. Further investigations [9] show the effect of the residence time in the reduction zone for reburning. Residence times higher than 1.2 s do not improve the NO_x reduction further, whereas NO_x emissions strongly increase with residence times below 0.7 s. The optimum residence time for fuel staging is ca. 1.2 s.

At substoichiometric air ratios above 0.9, up to 10% of the NO_x reduction can be due to the dilution, with the addition of burnout air, to achieve the overall air ratio of 1.15. At lower air ratios, the remaining N species of the reduction zone can form up to 30% of the total NO_x emissions at the burnout air addition, despite the dilution with air [12].

There is only a small difference in NO_x reduction

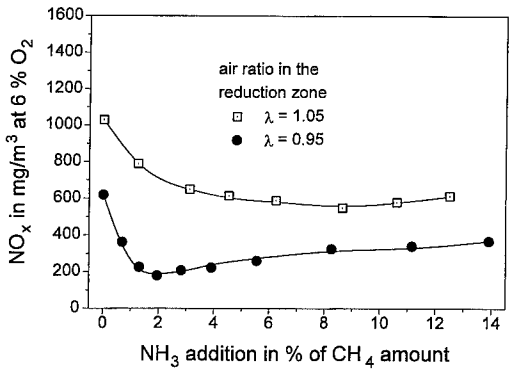

FIG. 4. Effect of ammonia addition to the reburn zone (created with methane) with a total residence time of 1.5 s at an EFC reactor temperature of 1300°C.

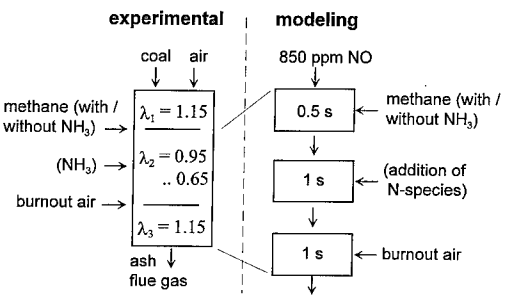

FIG. 5. Scheme of the experimental and modeling investigations.

efficiency between methane and synthetic gas mixtures as reburn fuel, in spite of the different compositions (gas blend 1:8% H_2, 25% CO, 61% hydrocarbons; gas blend 2: 38% H_2, 41% CO, 21% hydrocarbons). NO_x emissions differed by less than 10% at all investigated stoichiometries (see Fig. 3). Also, the variation of the reactor temperature did not change the comparable reduction efficiency of these three gaseous reburn fuels. With a pyrolysis gas generated in the EF pyrolysis reactor, lower NO_x emissions can be achieved at rather air-rich conditions. The composition of the synthetic gas mixtures and the uncondensable pyrolysis gas fraction of hard coal is quite similar [9]. In addition to the analyzed components, tar vapors (ca. 140 g/kg), such as benzene and naphthalene, are contained in the pyrolysis gas (ca. 400 g/kg daf coal at 800°C), and N species are contained in the pyrolysis gas (ca. 10% coal-N) and in the tar (ca. 17% coal-N). This seems to positively affect NO_x reduction. The tar vapors, which are assumed to be still in the gas phase, are the condensable share of the pyrolysis gas.

To determine the most effective components for NO_x reduction, premixed methane and ammonia was used as reburn fuel. Test runs were done with a NH_3 admixture from 1% up to a maximum of 10% of the prevailing CH_4 amount. The NO_x emissions increase with increasing NH_3, especially for fuel-rich conditions ($\lambda_2 < 0.95$) in the reburn zone. Profile measurements showed NO formation after addition of the burnout air so that the overall emissions are higher because of an increased conversion of remaining NH_i to NO in the burnout zone. These findings showed that the amount of N in the gas phase of the pyrolysis gas does not bring about the excellent NO_x reduction [13].

Nevertheless, there are contradictory results on this important issue published in literature. Whereas Smart and Morgan [4] have shown that the fuel-N content has only little effect on NO_x reduction, Knill et al. [8] published results of a positive effect at 1400°C and a residence time of 1 s. Our results show that the use of pyrolysis gas improves the reburn efficiency and shifts the optimum air ratio from $\lambda_2 = 0.75$ for methane to 0.9 for pyrolysis gas with tar. The lowest NO_x emissions of ca. 200 mg/m^3 are attained at air ratios that are very suitable for technical applications.

A positive effect of N species in the reburn fuel can be obtained if NH_3 is injected in the substoichiometric reburn zone. The results of this configuration are shown in Fig. 4. With increasing NH_3, the NO_x emissions decrease at the investigated air ratios $\lambda_2 = 1.05$ and 0.95. The optimum NH_3 addition is ca. 8 or 2% of the methane amount, for $\lambda_2 = 1.05$ and 0.95, respectively. This result may explain the good reduction efficiency of pyrolysis gas as reburn fuel (see Fig. 3). The major reduction effect is caused by the tar released during pyrolysis. The decomposition of tar and N components takes place after the pyrolysis gas components (e.g., H_2, CH_4) have consumed the available oxygen. The released N species of the tar can reduce the existing NO, depending on the temperature in the reburn zone and, primarily, the oxygen concentration at the addition point. Comparable results were found for NH_3 added under substoichiometric conditions in air-staged combustion [12].

For a more detailed explanation of this advantageous effect of fuel-N addition, the model of the perfectly stirred reactor (PSR) was employed [14]. A series of PSRs is used as an approximate approach for modeling turbulent combustion in the EFC. The full reaction mechanism is adopted from Miller and Bowman [15], and the major conditions are depicted in Fig. 5. The reburn zone is split into two PSRs to allow the staged addition of fuel-N components. Following the experimental test runs, the residence times were selected and three different reburn fuel cases calculated: (a) pure methane, (b) premixed methane and N species, and (c) methane and staged N species.

The results are given in Fig. 6 for the predicted

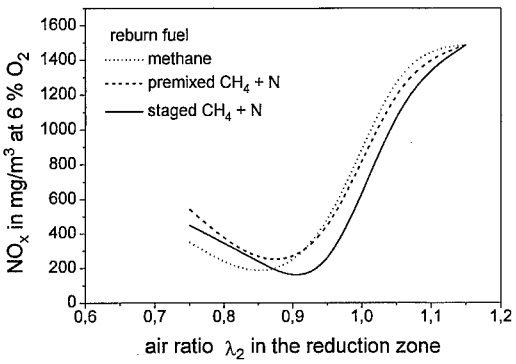

FIG. 6. Predicted NO_x emissions for different reburn gas compositions of PSR modeling at an EFC reactor temperature of 1300°C.

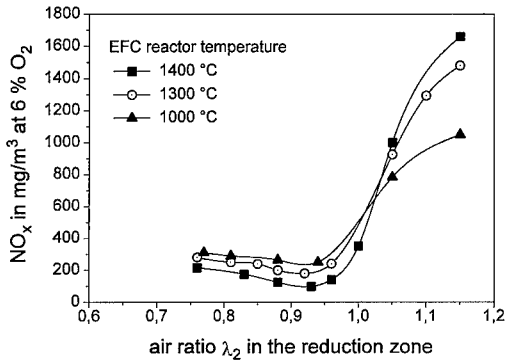

FIG. 7. Effect of EFC reactor temperatures on NO_x reduction, given a residence time of 2 s, with Göttelborn as primary fuel and EF-produced coal pyrolysis gas at 800°C as reburn fuel.

NO_x emissions and in Table 1 for the concentration of different N species in the second PSR. NO_x emissions only showed a marginal dependence on the addition of premixed methane and ammonia at air ratios of 1.05 and 0.95, compared to pure methane as reburn fuel. At $\lambda_2 = 0.75$, even higher NO_x emissions are predicted. The addition of HCN or NH_3 to the substoichiometric reburn zone works very well at air ratios between 0.9 and 0.95. The NO_x emissions can be further reduced from 500 to 260 mg/m^3. These predicted values are equivalent to a reduction efficiency of 82%.

Although the phenomena occurring during the admixture of reburn fuel in the substoichiometric reburn zone and of burnout air in the burnout zone are strongly idealized using the PSR code, the calculated profiles in Fig. 6 agree well with the experimental data in Fig. 3. This supports the theory about the effectiveness of coal pyrolysis gas as reburn fuel.

The increasing NO_x emissions with NH_3 added at $\lambda_2 = 0.75$ can be explained by the concentrations of N species given in Table 1. In the second PSR, only minimal NO concentrations exist in all three cases, contrasted with high concentrations of HCN and NH_3. The remaining N species would be partially oxidized after the addition of burnout air in the third PSR at temperatures of 1300°C. Thus, it is useless to add more ammonia for better NO_x reduction in this area.

The experimental results in Figs. 7 and 8 were obtained using raw coal as the primary fuel in the EFC and pyrolysis gas from the EF as reburn fuel. The influence of EFC reactor temperatures on NO_x reduction is similar to the findings with pure methane (see Fig. 7). Higher temperatures accelerate the nitrogen oxide decomposition under reducing conditions in the reduction zone. Even though NO_x emissions of the primary zone are higher at 1400°C than at 1000°C, the lowest NO_x emissions of ca. 120 mg/m^3 are achieved at 1400°C. The optimum

TABLE 1
Concentration of N species in the reburn zone (2nd PSR) in ppm, predicted with Refs. 14 and 15

λ_2	Gas composition	Reburn fuel: Pure methane	Reburn fuel: Premixed methane + N	Reburn fuel: Methane + staged N
	NO	801	750	674
1.05	HCN	0	0	0
	NH_3	0	0	0
	NO	334	321	157
0.95	HCN	0	3	44
	NH_3	0	0	14
	NO	9	7	8
0.75	HCN	423	765	409
	NH_3	237	741	551

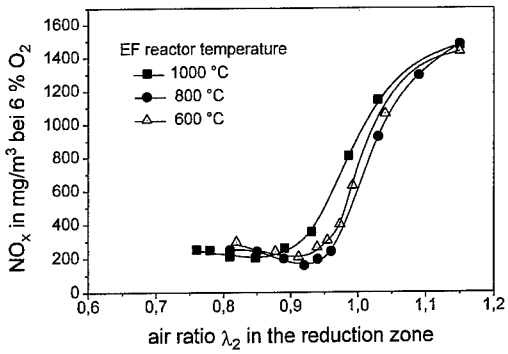

FIG. 8. Effect of EF pyrolysis reactor temperatures on NO_x reduction at an EFC reactor temperature of 1300°C and a residence time of 2 s, with Göttelborn hard coal as primary and pyrolysis fuel.

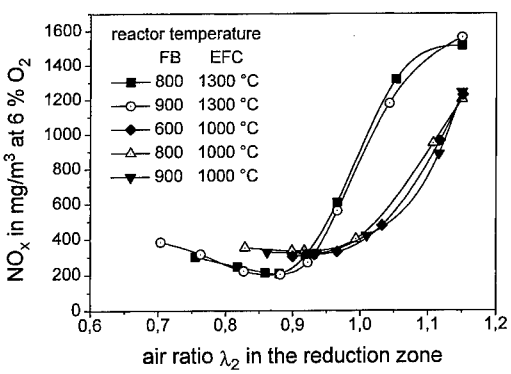

FIG. 9. NO_x emissions at different FB and EFC temperatures for hard coal Göttelborn as pyrolysis and combustion fuel.

air ratio in the reduction zone is independent at the reactor temperature at $\lambda_2 = 0.93$.

In the EF, pyrolysis gas with optimum NO_x reduction potential is generated at temperatures between 600 and 800°C (Fig. 8). A certain share of gaseous components is needed to establish a substoichiometric zone, and a certain share of tar is crucial for effective reduction of NO. At lower pyrolysis temperatures, the yields of tar and pyrolysis gas are not sufficient. There is not enough gas yield for $\lambda_2 < 1$, so the tar becomes oxidized in the reduction zone of the EFC. At higher temperatures in the EF, the tar is partially cracked and so the pyrolysis gas is not as effective for NO_x reduction. These test runs also showed that the N species in the gas phase are not the reason for excellent NO_x reduction because, otherwise, pyrolysis temperatures of 1000°C producing a high gas yield and a high N content in the gas [10] would result in lower NO_x emissions. The best NO_x reduction was obtained with a reburn fuel

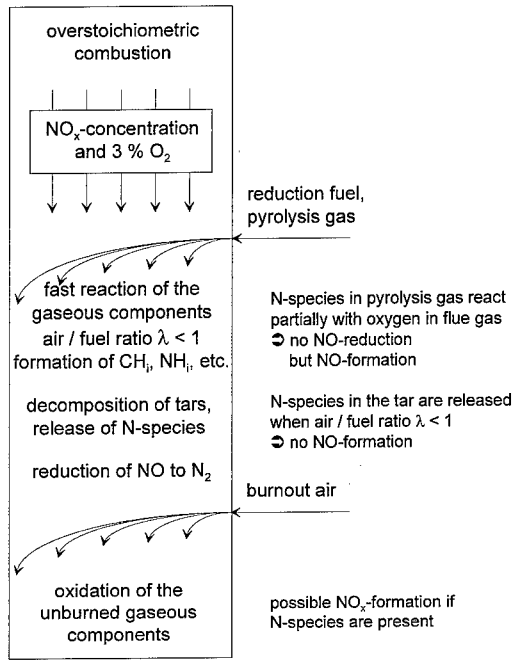

FIG. 10. Explanation of the excellent reduction efficiency of pyrolysis gas as reburn fuel.

produced between 600 and 800°C with high tar yield and high N content in the tar.

Using pyrolysis gas produced in the fluidized bed gasifier gives similarly promising results. The influence of the gasification temperature in the FB and the impact of the temperature in the reduction zone of the EFC are shown in Fig. 9. There is only a small deviation in NO_x reduction between different pyrolysis temperatures. Pyrolysis gas produced in the FB is a less effective reburn fuel than EF pyrolysis gas. This is due to the lower yield of tar from coal pyrolysis in the FB in contrast to yields in the EF. The tar yield decreases from 10% of the coal at 600°C to 5% at 900°C for the FB and from 20% at 600°C to 6% at 1000°C for EF pyrolysis of the hard coal Göttelborn [10]. The optimum air ratio is shifted to a lower value of 0.88, and the NO_x emissions are ca. 200 mg/m^3. The effect of EFC temperature is comparable to the results with pure methane or EF pyrolysis gas as reburn fuel.

A comparison of coke oven tar and fuel oil [9] demonstrated that the nitrogen-containing tar played a key role in NO_x reduction. Figure 10 gives an explanation for the more effective NO_x reduction with coal pyrolysis gas compared to other reductives. Because of the delayed release of tar nitrogen, an unwanted oxidation during the injection of the reburn fuel does not happen and the N species can further reduce, selectively, nitrogen oxides in the reduction zone.

Conclusions

Fuel staging, or reburning, is an efficient method to reduce NO_x emissions from lignite- and hard coal-fired utility boilers. The NO_x reduction efficiency increases with higher EFC temperatures. The lowest NO_x emissions were achieved at 1400°C with values of 150 mg/m^3 for pure methane and 120 mg/m^3 for coal pyrolysis gas as reburn fuel. The impact of the composition (H_2, CH_4, C_2H_4, CO) of gaseous reburn fuels is small. With pyrolysis gas as reburn fuel containing tar and N species, NO_x can be further reduced. The main advantages are higher air ratios in the reduction zone and lower NO_x emissions, as well as the reburn fuel being produced from the primary fuel coal.

The experimental and modeling results have shown that the N species in the gas phase are not the reason for the obtained excellent NO_x reduction. The most important component of the pyrolysis gas is the nitrogen-containing tar. The uncondensable components of the pyrolysis gas create the substoichiometric zone in which the tar vapors are cracked. The released N-species out of the tar are able to reduce nitrogen oxides selectively. For hard coals, the process of fuel splitting and staging has been found to be a promising option to reach NO_x emissions below 200 mg/m^3 without SCR.

Acknowledgments

The research was funded in part by the Bundesministerium für Bildung, Wissenschaft, Forschung, and Technologie (Federal German Ministry of Education, Science, Research, and Technology), Förderkennzeichen 0326766A and the Saarbergwerke AG, Saarbrücken, Germany. The award of a Rothmans Foundation Fellowship to C.-Z. Li is gratefully acknowledged.

REFERENCES

1. Spliethoff, H., "Großtechnische Untersuchung der Stickstoffoxidminderung mit dem Schwerpunkt Brennstoffstufung an einer Schmelzkammerfeuerung," *VDI-Fortschrittsberichte,* Reihe 6, Nr. 276, 1993.
2. Mechenbier, R., *Experimentelle Untersuchung der Stickoxid-Reduktion durch Brennstoff-stufung mit Methan bei der Kohlenstaubverbrennung,* Dissertation Universität Bochum, 1989.
3. Bilbao, R., Alzueta, M. U., and Millera, A., *Third International Conference on Combustion Technologies for a Clean Environment,* Lisbon/Portugal, July 1995, p. 27.1.
4. Smart, J. P. and Morgan, D. J., *Fuel* 73:1437–1442 (1994).
5. Liu, H., Hampartsoumian, E., and Gibbs, B. M., *Second International Conference on Combustion & Emissions Control,* The Institute of Energy, London, 1995, pp. 17–27.
6. Chen, S. L., McCarthy, J. M., Clark, W. D., Heap, M. P., Seeker, W. R., and Pershing, D. W., *Twenty-First Symposium (International) on Combustion,* The Combustion Institute, Pittsburgh, 1988, pp. 1159–1169.
7. Wendt, J. O. L., Pershing, J., Lee, J. W., and Glass, J. W., *Seventeenth Symposium (International) on Combustion,* The Combustion Institute, Pittsburgh, 1979, pp. 77–87.
8. Knill, K. J., Dekker, J. S., and Morgan, M. E., "Evaluation of the Effect of Process Variables on NO_x and Nitrogen Species Reduction in Coal Fuel Staging," IFRF Doc. Nr. F037/a/20.
9. Spliethoff, H., Rüdiger, H., Greul, U., Spliethoff, H., and Hein, K. R. G., *NO_x-Minderung mit Reduktionsbrennstoffen aus der Steinkohle,* VGB TW 207, 1995.
10. Spliethoff, H., Greul, U., Rüdiger, H., Magel, H.-C., Schnell, U., Hein, K. R. G., Li, C.-Z., and Nelson, P. F., *Coal Sci. Technol.* 2:1775–1778 (1995).
11. Nelson, P. F., Buckley, A. N., and Kelly, M. D., *Twenty-Fourth Symposium (International) on Combustion,* The Combustion Institute, Pittsburgh, 1992, pp. 1259–1267.
12. Greul, U., Spliethoff, H., and Hein, K. R. G., *Twenty-First International Technical Conference on Coal Utilization & Fuel Systems,* CSTA, Clearwater, FL, March 1996.
13. Greul, U., Spliethoff, H., and Hein, K. R. G., "Investigation of Advanced Reburning in a Bench Scale Test Facility," Joule IIe 0331, 2nd progress report, October 1994–September 1995.
14. Glarborg, P., Kee, R. J., Grcar, J. F., and Miller, J. A., *"PSR: A Fortran Program for Modeling Well-Stirred Reactors,"* Sandia Report SAND86-8209, Sandia National Laboratories, Livermore, CA, 1986.
15. Miller, J. A. and Bowman, C. T., *Prog. Energy Combust. Sci.* 15:287 (1989).

COMMENTS

A. E. Jacob Akanetuk, Stanford University, USA. Minima in NO_x were reported with respect to air-to-fuel ratio. Was the air-to-fuel ratio changed by adjusting the air input or the fuel input? (The question is motivated by the observation that the exact numerical value of air-to-fuel ratio at the NO_x minimum is dependent upon residence time.)

Author's Reply. The air-to-fuel ratio was changed by adjusting the reburn fuel input.

The primary fuel mass flow (1 kg/h) and the primary air ratio (λ_1 = 1.15) were kept constant for all presented results. Lower air ratios in the reburn zone were achieved by increasing the reburn fuel volume flow. The residence time in the reburn zone was kept constant by adjusting the burnout air injection. In order to establish a defined and reproducible mixing a certain amount of nitrogen was used to enhance the momentum.

For the investigations with coal pyrolysis gas as reburn fuel, the mass flow of the pyrolysis feed stock was increased. Previous investigations [1] had shown that the mass flow to the pyrolysis reactor in the range up to 3 kg/h, corresponding to an air-to-fuel ratio of approximately 0.7, had no effect on the pyrolysis product composition. The amount of pyrolysis gas and tar increases linearly with an increasing coal mass flow. So higher fuel-to-air ratios in the reduction zone of the combustion reactor were gained with higher mass flows entering the pyrolysis reactors.

For the presented results the desired residence time in the reduction zone was 2 s in order to achieve the maximum NO_x reduction efficiency for all reburn fuels. Previous investigations [2] with methane or pyrolysis gas as reburn fuel had shown that the optimum air-to-fuel ratio is dependent on the residence time in the reburn zone. For residence times higher than 1.2 s an optimum air ratio of 0.75, for residence times shorter than 1.2 s, values of 0.85 were determined with methane as reburn fuel.

REFERENCES

1. Rüdiger, H., Greul, U., Spliethoff, H., and Hein, K. R. G., "Pyrolysis Gas of Biomass and Coal as a NO_x-Reductive in a Coal-Fired Test Facility," *Proc. of the Thirrd Int. Conf. on Combustion Technologies for a Clean Environment,* Lisbon, July 1995.
2. Spliethoff, H., Greul, U., Maier, H., and Hein, K. R. G., "Low-NO_x Combustion for Pulverized Coal—A Comparison of Air Staging and Reburning," *Proc. of the Second Int. Conf. on Combustion and Emission Control,* London, December 1995.

•

L. Douglas Smoot, Brigham Young University, USA.

1. Did you compare your reburning test results using pyrolysis gas with published results or your own results using coal directly as a reburning fuel?
2. Was the percentage of N-species in your pyrolysis gas comparable to that in the CH_4-NH_3 mixtures which you used for comparison?

Author's Reply. Yes, we compared the reburning test results using pyrolysis gas with our own results using coal as reburning fuel. With comparable conditions in the primary and reburn zone (reactor wall temperature 1300 °C, primary coal mass flow 1 kg/h, primary air ratio 1.15) minimum NO_x emissions of 600 mg/m^3 (compared with 150 mg/m^3 for coal pyrolysis gas) were achieved using coal as reburn fuel. With a primary air ratio of 1.05 the NO_x emissions were reduced from 1000 mg/m^3 baseline to values of approximately 400 mg/m^3.

This effect can be explained by the ratio of volatile to available oxygen. After the injection of the reburn fuel coal, the pyrolysis and decomposition of the volatiles takes place. The released volatiles deplete the remaining oxygen from the primary combustion zone. At a higher primary air ratio a higher amount of the released volatiles is oxidized (approx. 50% at 1.15 and only 20% at 1.05). The remaining char is less effective for NO_x reduction.

These investigations have shown that the volatiles of coal are very effective for NO_x reduction if the oxygen is minimized before decomposition. Using coal as reburn fuel there is a major effect of the primary zone stoichiometry due to the different NO_x reduction efficiency of char and volatiles.

Yes, the percentage of the N-species in the pyrolysis gas was in the same range as in the methane-ammonia mixtures for reburning. The nitrogen content of the synthetic gas mixtures can easily be adjusted and was desired in a range of 1 to 10% of the hydrocarbon amount. For the pyrolysis of the hard coal Göttelborn (1.5% N daf) at temperatures between 600 and 1100 °C the N in tar was between 11.5 and 15% with a maximum at 800 °C and the sum of NH_3 and HCN in the gas phase was between 6 and 20% of the coal nitrogen. So a nitrogen amount in the gaseous pyrolysis products of 1 to 3.5% of the hydrocarbon content and a nitrogen yield of 1 to 4% in the tar products was determined. Both ratios depend on the pyrolysis temperature.

•

Vladimir Zamansky, Energy and Environmental Research Corporation, USA. This is a very interesting and significant piece of work which describes the coal pyrolysis gas as an effective reburning fuel. I would like to point out the importance of not only nitrogen compounds, but also the sodium species on reburning efficiency. In our work presented at this symposium [1] we studied experimentally and via kinetic modeling the effect of both N- and N_a compounds on reburning in a 300 kW. Boiler Simulator Facility. Since N_a compounds are present in coal and may be present in coal pyrolysis gas, they may also affect the reburning efficiency in your experiments.

REFERENCE

1. Zamansky, V. M., Ho, L., Maly, P. M., and Seeker, W. R., Reburning Promoted by Nitrogen- and Sodium-Containing Compounds, *Twenty-Sixth Symposium (International) on Combustion,* The Combustion Institute, Pittsburgh, 1996.

Author's Reply. Although there are Na components in the coal, our current investigations in coal combustion and further publications concerning gasification [1] showed that the concentration of Na in the flue gas or in the pyrolysis gas is very low, in most cases below 0.3 ppm.

In our electrically heated entrained flow combustion reactor, at reactor wall temperatures between 1000 and 1300 °C, the Na concentrations were determined below 150 ppb for the combustion of Göttelborn coal. The sodium (Na_2O) content in the ash analysis (DIN 51729) of Göttelborn coal was 1.2 wt%. This value is quite high, although only very little concentrations were found in the gas phase.

So we believe that the low concentrations of Na components (compared with 100 ppm in your experiments) did not affect the reburning efficiency in our investigations.

REFERENCE

1. Kurkela, E., Stahlberg, P., and Laatikainen, J., Pressurized fluidized-bed gasification experiments with wood, peat and coal at VTT in 1991–1992, VTT Publications 161.

Twenty-Sixth Symposium (International) on Combustion/The Combustion Institute, 1996/pp. 2241–2250

MEASUREMENTS AND PREDICTIONS OF NITRIC OXIDE AND PARTICULATES EMISSIONS FROM HEAVY FUEL OIL SPRAY FLAMES

M. A. BYRNES, E. A. FOUMENY, T. MAHMUD AND A. S. A. K SHARIFAH
Department of Chemical Engineering
The University of Leeds
Leeds LS2 9JT, UK

T. ABBAS, P. G. COSTEN, S. HASSAN AND F. C. LOCKWOOD
Department of Mechanical Engineering
Imperial College of Science, Technology, and Medicine
London SW7 2BX, UK

The results of extensive experimental and predictive studies of nitric oxide (NO) and particulates (unburned coke) emissions from a large-scale laboratory furnace, fired by a heavy fuel oil (HFO) swirl burner with a rotary cup air blast atomizer are presented. A detailed in-flame data archive of gas temperature and O_2, CO, CO_2, and NO concentrations has been obtained for five flames for differing excess air levels (15% and 20%), swirl numbers (1.05 and 1.2), primary air-to-fuel ratios (2.5 and 3.0), and atomizer cup speeds (1.0×10^4 and 2.0×10^4 rpm). A wider range of operating parameters has been established to quantify their effects on NO and particulate concentrations at the exit of the furnace. In a parallel modeling study, a two-dimensional computational fluid dynamics code for the prediction of HFO spray combustion and NO and particulates emissions has been constructed. Validation of the code against the experimental data reveals reasonably good quality predictions in the near burner region. The code is capable of simulating the measured trends of flue-gas NO and particulates emissions with useful precision for a wide range of atomizer/burner operating conditions. A scrutiny of the in-flame and flue-gas data, with the aid of the predictions, has provided an enhanced understanding of combustion and combined NO/particulate emissions characteristics of the HFO flames generated by the rotary cup atomizer and establishes the foundation for future work in optimizing combustion and emissions performance.

Introduction

To meet the increased demand for light distillate products, refineries have moved toward the production of "heavier" fuel oil. This oil has a high asphaltene content, typically about 15%, which has a strong influence on the amount of coke formed and hence the particulates emissions. Unfortunately, most methods of ameliorating the particulate burden favor an increase in NO_X production and vice versa. The ideal oil burner design should be capable of producing a high turn-down, stable flame with minimal NO_X and particulates emissions from these lower-cut fuels.

The combustion and emissions performance of a heavy fuel oil (HFO) flame is established by the initial spray characteristics of the atomization method used in the burner and the aerodynamics inherent in the near burner region (NBR) of the furnace in which it is located. Performance optimization, therefore, requires a thorough knowledge of the relevant physical and chemical processes. To gather such information in a full-scale plant is both difficult and expensive, with the resulting data being specific to that furnace rather than having a universal application. An alternative is the use of a large-scale laboratory furnace in which the turbulence levels, radiation heat transfer, and residence timescales of the full-scale plant are replicated under well-controlled conditions. By allying such data to a validated mathematical model, the performance of any full-scale oil-fired furnace can be predicted with confidence.

Comprehensive combustion data sets, including NO_X and particulate concentrations, for HFO flames in such furnaces are, however, very rare; some notable data sets have been collected in earlier studies, for example by the authors' group [1] and by other groups [2,3]. This same dearth of information is also true regarding the applications of generalized computational fluid dynamics (CFD) models to predict the combustion performance, particularly the NO and particulates emissions, of HFO-fired furnaces. Previous relevant modeling studies include, for example, predictions of combustion performances of HFO-fired furnaces [4,5] and NO emissions from medium fuel oil flames [6]. In a relatively recent

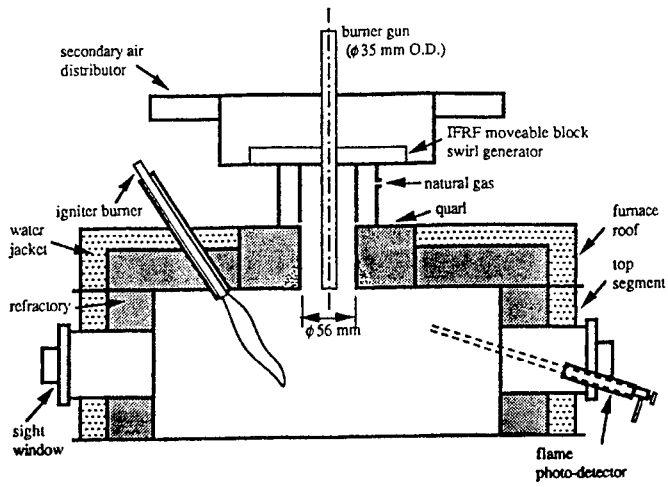

FIG. 1. Schematic diagram of the furnace roof and burner arrangement.

study [7], a one-dimensional model, based on prescribed O_2 concentration and residence time distributions, for the prediction of particulates emissions from residual fuel oil fired utility boilers has been presented. To the authors' knowledge, no CFD-based modeling study pertaining to combined NO and particulates emissions from HFO-fired furnaces has been reported in the open literature.

In the initial investigations in this work, isothermal measurements of droplet size distribution in the hollow-cone sprays generated by the rotary cup atomizer were obtained using a Malvern particle-size analyzer. The flames of several of the spray distributions were established in the large-scale laboratory furnace at Imperial College (ICSTM), where detailed in-flame measurements of NO and major species (O_2, CO, CO_2) concentrations and gas temperature, as well as NO and particulates emissions in the flue-gas, were recorded. The experimental data supplement that previously collected [1,8] for a twin-fluid atomizer giving a solid-cone distribution included detailed in-flame combustion but only flue-gas NO and particulate measurements. A complementary CFD model of HFO spray combustion capable of predicting the emissions of NO and particulates was constructed at the University of Leeds.

The Experiments

The Atomizer/Burner Gun Assembly and Spray Test Rig

The burner gun consisted of the rotary cup atomizer, along with oil and air (primary) supply conduits within a support pipe of external diameter 35 mm. The atomizer design was a necessary compromise between the accuracy of replicating an existing full-scale unit and operational reliability and durability; the cup drive was provided by an electric motor normally found in a dentist's drill.

The HFO-spray characterization tests were carried out under nonreacting conditions in a vertical, cylindrical chamber [8], 0.6 m in diameter and 1.5 m in height. The droplet size distributions at different radial and axial locations were recorded using the Malvern 2600 Particle Size Analyser for various changes in the input parameters, such as the atomizer cup speed, primary air-to-fuel ratio (PAFR), and oil viscosity. PAFR refers to the ratio of the mass flow rate of the primary air jet surrounding the atomizer cup to the mass flow rate of fuel. The measurement techniques are described fully in Ref. 8.

The Furnace and Instrumentation

A detailed description of the ICSTM furnace and its instrumentation and oil supply system can be found in many previous publications, e.g., [1,8]. The vertical furnace is of modular construction comprised of 10, 0.6 m internal diameter, cylindrical water-cooled steel sections, each of a height 0.3 m. The burner is mounted in the roof section and fires downward (see Fig. 1). The five uppermost sections and the roof have an internal lining of castable silicon carbide refractory. The burner consists of a gun and a secondary combustion air nozzle in a conventional double-concentric configuration. Swirl is imparted to the secondary air using a movable-block swirl generator developed by the International Flame Research Foundation. In-flame gas temperatures were measured using 40 μm Pt/Pt:13%Rh thermocouples. The uncertainty in temperature measurements caused by radiation losses was about 10% in the regions of highest temperatures. The sampling for gas species concentration was achieved through the use of a water-cooled, water-quenched, stainless

TABLE 1
Fuel properties and the atomizer/burner operating conditions

Property	
% Composition by mass	
Carbon	86.9
Hydrogen	10.3
Sulphur	2.35
Nitrogen	0.36
Oxygen	0.037
Ash	0.053
Density at 288 K (kg/m^3):	988
Gross calorific value (MJ/kg):	42.54

Atomizer/burner operating conditions Flame	A	B	C	D	E
Fuel flow rate (kg/h)	12	12	12	12	12
Air flow rate (kg/h)	187.6	195.8	187.6	187.6	187.6
Secondary air temperature (K)	573	573	573	573	573
Swirl number	1.2	1.2	1.05	1.2	1.2
Excess air (%)	15	20	15	15	15
PAFR	2.5	2.5	2.5	2.5	3.0
Cup speed ($\times$1000, rpm)	20	20	20	10	20

steel probe of 22 mm overall diameter. A Land Ltd. probe was used to sample back-end solids concentrations. Reproducibility of the data was, on average, within 10%.

Test Conditions and Experimental Data

The properties of the HFO and burner operating conditions are given in Table 1. For all experiments, an oil flow rate of 12 kg/h at 368 K was used. Detailed in-flame measurements of gas temperature, NO, and major species concentrations were carried out for five flames, referred to as Flames A–E, for different excess air level, swirl number, PAFR, and atomizer cup speed. Measurements of NO and particulate concentrations at the furnace exit were also carried out to quantify the effects of atomizer/burner operating parameters on the pollutants' emissions.

The Mathematical Modeling of HFO Combustion

A parallel study for the prediction of the data was effected at the University of Leeds. An existing two-dimensional CFD code [9,10] for pulverized-coal combustion was adapted by incorporating relevant physical models to handle HFO spray combustion. This included modeling of the droplet heating and evaporation, coke and soot particle formation, and the coke and soot burnout. A NO postprocessor, simulating the thermal-, prompt- and fuel-NO mechanisms, was developed.

The Aerodynamics and Combustion Models

The gas-phase conservation equations are solved in a conventional finite-volume Eulerian treatment, while Lagrangian calculations resolve the particulate-phase equations. The turbulence is handled by the standard k-ε model [11], without any swirl-related modification. The QUICK scheme [12] is used for the discretization of the convective terms in the gas-phase momentum equations, while the hybrid scheme [13] is employed for the scalar equations. The continuity and momentum equations are solved using the PISO algorithm [14].

The modeling of the turbulent combustion of droplet evaporation products presents a major difficulty in the prediction of HFO flames. This is also the case for the gas-phase volatiles combustion of pulverized-coal flames [9,10]. The evaporation products are represented by a single chemical species and their combustion processes are simulated by a two-step reaction mechanism. The time–mean burning rate of the fuel vapor is obtained using the widely employed eddy-dissipation combustion model [15]. The CO formed from the fuel vapor combustion is oxidized to CO_2 and the time–mean oxidation rate

is taken as the smaller of the turbulent mixing rate [15] and an Arrhenius chemical kinetic rate [16].

The radiation heat transfer is simulated by a nonequilibrium diffusion model [17]. The presence of soot has been accounted for. A global Arrhenius-type rate expression [18] has been used to model the soot formation, and a turbulent mixing rate expression [15] is employed to determine its burning rate. This approach has been found adequate for HFO and hydrocarbon flames [4,19]. The absorption coefficient of the medium is determined using the mixed gray gas model of Ref. 20.

The Coke Formation and Burnout Models

The emission of coke particles from HFO-fired systems involves the formation of coke, following the rapid evaporation of the low-boiling components of the oil, and the subsequent combustion of these particles. The processes involved in coke formation are extremely complex and the mechanism is far from established [21]. A simple model has been formulated to predict the coke formation and burnout and is fully described in Ref. 22. It is assumed that a single coke particle is formed from each oil droplet after evaporation is completed [23]. The portion of the initial mass of an oil droplet converted to coke has been correlated in terms of the Coke Formation Index (CFI), defined as the ratio of the initial mass of coke particle to the initial mass of oil droplet [24]. By assuming a spherical shape, this correlation allows the calculation of the initial mass and diameter of an individual coke particle to be made. The value of CFI used in the calculation was obtained from measurements [24] for residual fuel oils with similar asphaltene contents to that of the oil used in this study.

The coke burnout has been handled in a manner similar to pulverized-coal char combustion. The heterogeneous combustion rate of the coke particles with O_2 is controlled by the rate of external diffusion of O_2 to the particle surface and by the rate of chemical reaction at the external surface. The apparent reaction order with respect to O_2 partial pressure is taken as unity [25]. The kinetic parameters recommended by Northrop et al. [25] have been employed.

The NO Postprocessor

NO emissions from HFO flames arise from both atmospheric (thermal- and prompt-NO) and fuel-bound nitrogen (fuel-NO). The relative contributions of each to the total NO emission depend on the nitrogen content of the fuel and on the operating conditions of the atomizer/burner. The NO postprocessor [22,26] employed in this study accommodates all three mechanisms.

The thermal-NO model is that of Zeldovich [27] and includes the effect of the reverse reactions. The rate constants were obtained from Ref. 28. The contribution of prompt-NO to the total formation is relatively small under fuel-lean or near stoichiometric conditions [29]. Hence, the global rate expression proposed by DeSoete [30] is employed. The formation and destruction of fuel-NO involve a complex series of radical reactions. A simple chemical scheme, again suggested by DeSoete [30], has been adopted here. In this approach, the assumed first product of the evolved fuel-bound nitrogen in the gas phase is HCN, which is subsequently either oxidized by an oxygen-containing species to NO or reduced by NO to N_2. The kinetic parameters are those of DeSoete except for the preexponential factor for the HCN oxidation reaction, which, in common with other studies [31,32], was adjusted to achieve best overall agreement with the data. Following numerical experiments [22], the preexponential factor was assigned a value of $0.15 \times 10^{11}\ s^{-1}$, which is within the range of values (0.1×10^{11} to $1.0 \times 10^{11}\ s^{-1}$) reported in the literature [30–32].

Computational Details

The computations were performed on a two-dimensional, nonuniform 61×37 grid. This specification is the result of extensive experience of predicting the ICSTM furnace [9,10]. The inlet boundary conditions for the predictions were specified, wherever possible, using the measured atomizer/burner operating parameters as given in Table 1. The inlet axial and swirl velocities were obtained from the measured flow rate and swirl number, and the radial velocity was taken as zero. In the absence of measurements, the shapes of the inlet velocity profiles and turbulence levels were specified based on previous sensitivity studies [9,10] of these parameters. The measured droplet size distributions were represented by four discrete sizes, and the droplets were injected at the measured spray cone angle from the periphery of the atomizer cup. In the absence of measurements, the droplet injection velocities were estimated from the rotational speed of the cup, assuming that the liquid discharged at a velocity corresponding to the cup speed [33]. The sensitivity of the predictions to the number of discrete droplet sizes and their injection velocities was examined, and these parameters were optimized with data to achieve best overall predictions.

Discussion of Experimental and Predicted Results

Although an extensive in-flame data archive was compiled from the experimental investigation, only selected results are presented because of space limitations. Additional isothermal atomization and com-

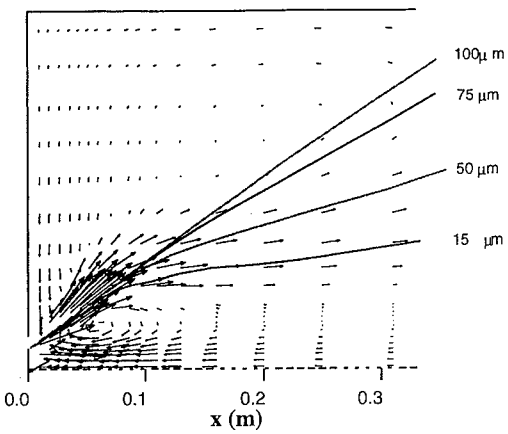

FIG. 2. Predicted gas flow pattern and droplet/particle trajectories in the NBR.

bustion data and predictions are reported in Ref. 34 and 22, respectively.

General Aerodynamic Characteristics

Figure 2 shows typical predictions of the gas flow pattern and trajectories of the oil droplets/coke particles in the NBR for Flame A. The gas flow pattern reveals the formation of an internal recirculation zone (IRZ) caused by the high level of swirl imparted to the secondary air and a large external recirculation zone resulting from the flow separation due to the sudden expansion of the furnace configuration. As the spray droplets emerge from the periphery of the atomizer cup, they are entrained by the secondary air jet and travel around the boundary of the IRZ. Evaporation is completed within an axial displacement of 0.03–0.13 m from the burner throat, depending on the droplet size, which is in general agreement with the experimental observations. The coke particles penetrate further into the furnace with particles produced from the smaller droplets ($<100\ \mu$m) being completely burned before the furnace exit.

It is important to note that in the absence of gas velocity data, a deficiency common to many two-phase reacting flow experiments, the quality of the predicted flow field cannot be evaluated quantitatively. However, nonreacting swirling flow measurements in sudden expansion configurations (see, for example, Ref. 35) suggest that the general features of the predicted flow pattern are correct. The predictions for Flames B–E (not shown here) reveal that the basic aerodynamic characteristics of this burner are rather insensitive to the inlet conditions.

Flame Characteristics

The measured and predicted radial profiles of O_2 and CO concentrations and gas temperature for Flame A are presented in Figs. 3 and 4. As can be seen, the predictions are, generally, in good agreement with the measurements and match the general trends. However, at the first station, $x/D = 0.71$ (where x is the axial distance from the burner throat and D is the diameter of the secondary nozzle), fairly uniform measured O_2 concentration near the furnace axis suggests that the width of the IRZ is somewhat underpredicted. As a consequence, the radial location of the predicted peak is nearer to the axis compared with the measured one. The predicted droplets' trajectories and the measured peaks in the CO concentration profiles suggest that the droplet evaporation and subsequent combustion of fuel vapor occur in the shear region around the boundary of the IRZ. The measured high CO concentrations at and about the furnace axis in the NBR also reveal that a proportion of droplets, generated in the hollow-cone distribution by the action of the rotary cup, diffuse into the IRZ, and the evaporation products combust there. This feature is not replicated in the prediction, possibly because of the droplets/turbulence interaction being neglected in the model. At $x/D = 6.6$, the uniform O_2 concentration and temperature profiles indicate that the fuel vapor combustion has already been completed. At this location and further downstream, the measured and predicted CO concentrations are both negligible. The gas temperature predictions also show a reasonable correlation with the experimental data. The lack of data at $x/D = 0.71$ is due to unacceptable errors caused by droplets impinging on the fine-wire thermocouples.

In-flame NO Formation

The measured and predicted radial profiles of NO concentration for Flame A are presented in Fig. 4b. The overall agreement is reasonably good. The measured level of NO emission at the furnace exit is well reproduced by the prediction. In the NBR, the measured peak values of NO concentration at the furnace axis are also well predicted. However, the discrepancy observed between the measured and predicted O_2 concentrations near the axis at $x/D = 0.71$ is also reflected in the NO concentrations. At the next two downstream stations ($x/D = 1.25$ and 1.79), differences between the measurements and predictions are evident in the forward flow region, which is dominated by the secondary air flow. This may be attributed to the overestimation of the secondary air jet spreading and the rate of mixing by the existing physical models. The steep gradients of the measured and predicted NO concentrations near the axis suggest that the NO formation occurs mainly within the IRZ and the surrounding forward flow zone. In this region, the gas temperatures are high and sufficient O_2 is available, as shown in Figs. 3a

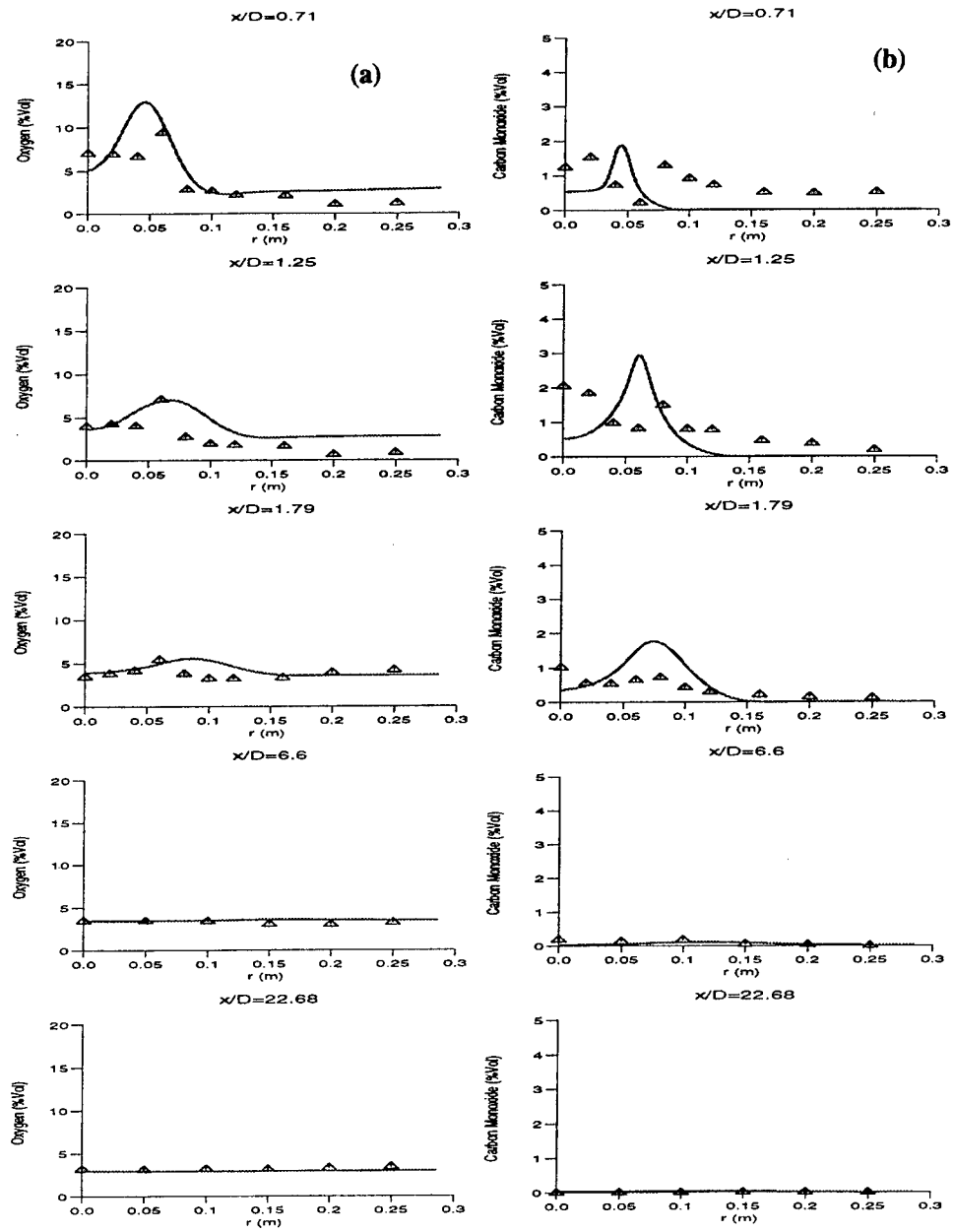

FIG. 3. Measured and predicted (a) O_2 and (b) CO concentration profiles (△ experimental; —— prediction).

and 4a, to encourage the formation of NO by both the thermal and fuel mechanisms. The calculated rates of NO formation indicate that the main reaction zone extends up to an axial distance of about $x/D = 3.5$. In the downstream region of this zone, the NO concentration distribution is fairly uniform, as shown by the measured and predicted radial profiles at $x/D = 6.6$.

Effects of Operating Conditions on NO and Particulates Emissions

The measured and predicted furnace-exit NO and particulate concentrations for a range of the operating conditions are shown in Fig. 5. As can be seen, the measured trends of NO emissions are well simulated, whereas the particulates emissions are qualitatively reproduced by the model.

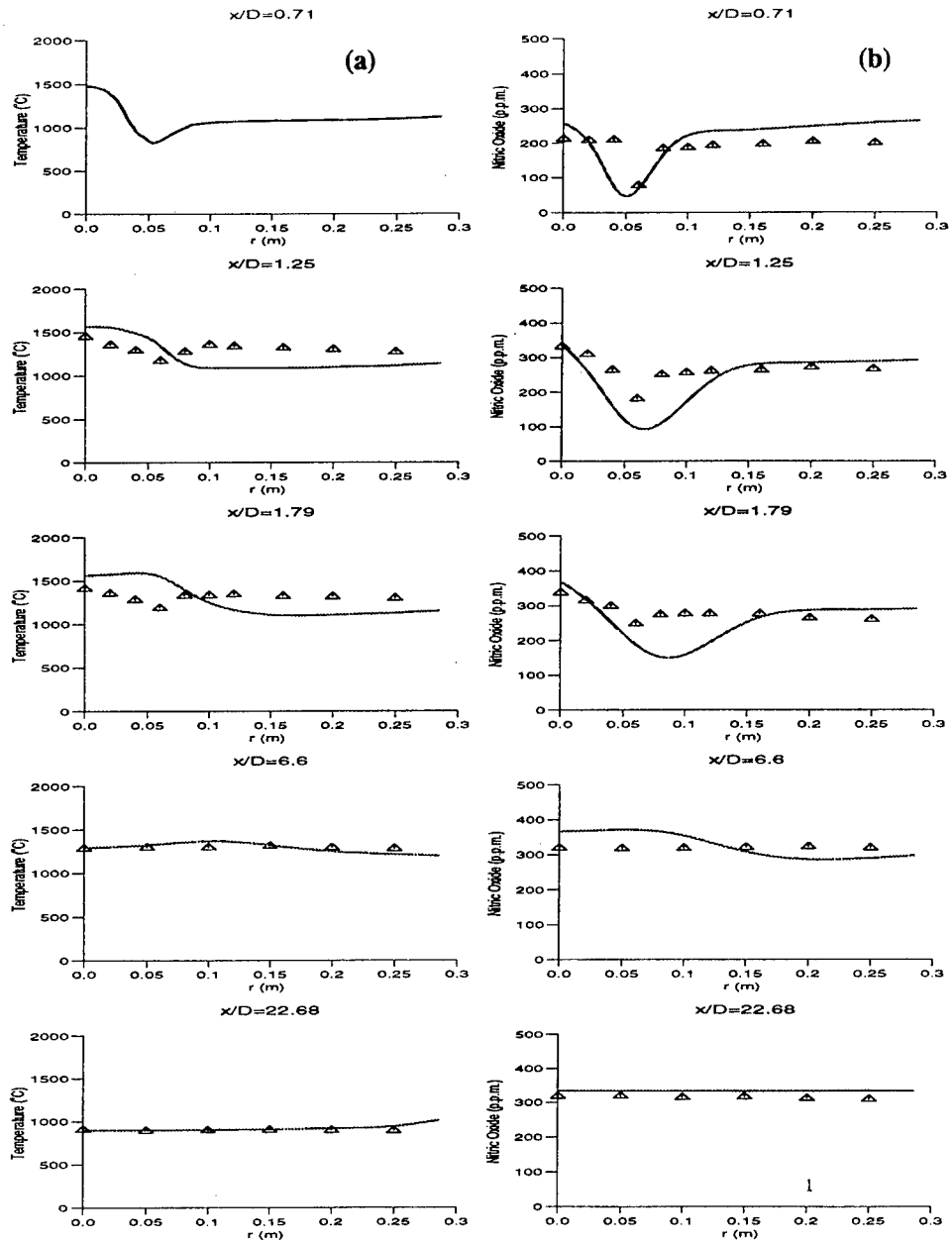

FIG. 4. Measured and predicted (a) gas temperature and (b) NO concentration profiles (△ experimental; —— prediction).

The improvement in spray quality with primary air is reflected in an initial decrease in the particulate burden and a corresponding increase in NO. Beyond a PAFR of 2.5, no further improvement in spray quality was observed in the isothermal spray characterization experiments. The consequence in the flame is a leveling off of the particulate emissions at approximately 55 mg/m^3. The further increase in NO emissions with PAFR is due to the increased availability of O_2 in the evaporation region.

The effect of increased O_2 availability, on this occasion due to the increase in excess air, is shown in Figs. 5aii and 5bii. In this instance, the reduction in particulates burden is due to the augmented heter-

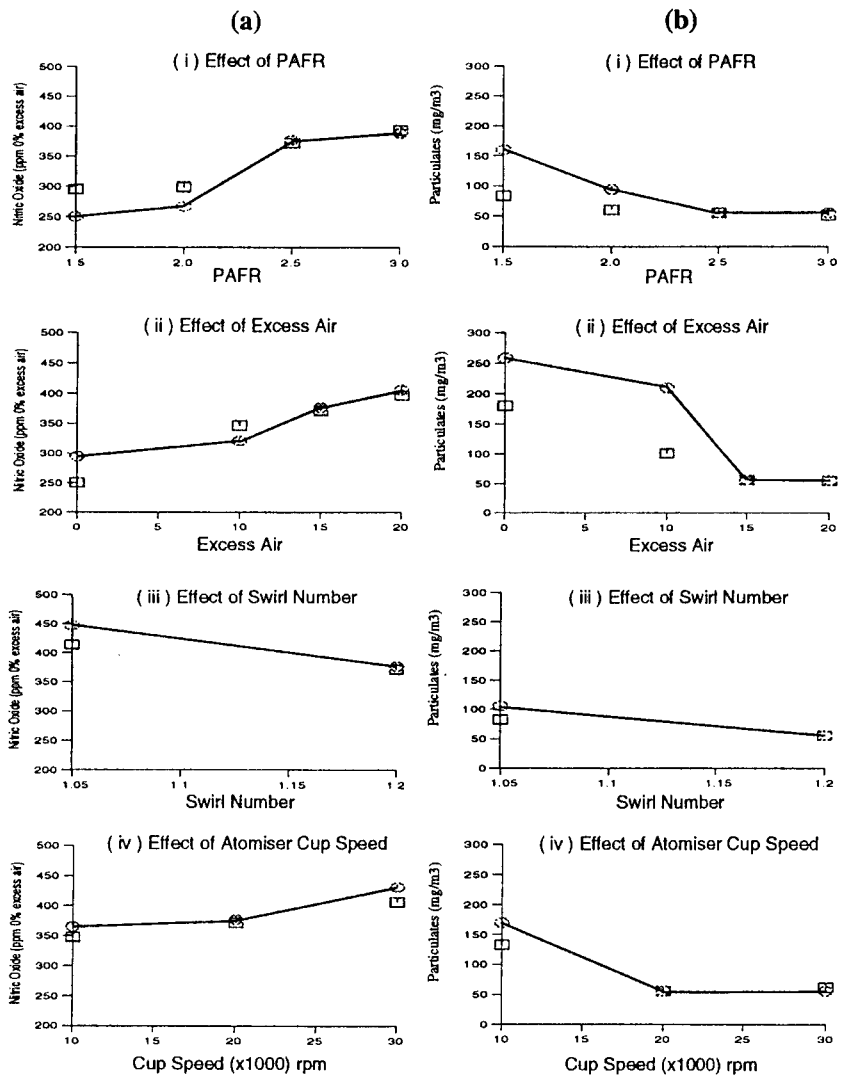

FIG. 5. Measured and predicted (a) NO and (b) particulates emissions at the furnace exit (□ experimental; —○— prediction).

ogeneous oxidation of the coke particles. Beyond 15% excess air, there is no further reduction in the particulate concentration because of the complete burnout of carbon in the particles. It should be noted that a particulate concentration of about 55 mg/m^3 corresponds to complete carbon burnout. Additional O_2 leads, however, to a further increase in the NO emissions.

The effect of secondary air swirl on NO and particulates emissions is shown in Figs. 5aiii and 5biii . As can be seen, both the NO and particulate concentrations decrease slightly between swirl numbers of 1.05 and 1.2. The effect of this parameter is not readily apparent, as a larger range of swirl settings were not possible due to flame stability problems.

The final effect is that of rotating cup speed, which is shown in Figs. 5aiv and 5biv. As expected, increasing cup speed enhances the spray fineness, which leads to a more intense flame resulting in an increased level of NO emissions. However, this has an opposite effect on particulates emissions, which decrease because of the enhanced coke burnout rate of smaller-size particles.

Concluding Remarks

The experimental data collected for HFO swirling flames, generated by a rotary cup atomizer, comple-

ment and extend the data previously gathered for a twin-fluid atomizer at ICSTM. The additional computational input from the University of Leeds further enhances the value of the work, with the code being validated against the axisymmetric experimental data. The resulting code is capable of simulating with useful precision the measured trends of NO and particulates emissions for a wide range of operating conditions of the atomizer and the burner. It is readily apparent from this work, and the work of others using different types of atomizers (e.g., pressure-jet, twin-fluid), that the "holy grail" of low-NO and low-particulates emissions appears to be mutually exclusive, and only a compromised operation is possible.

A minimum particle concentration of about 55 mg/m^3, achieved by increasing the quality of the atomization and using high levels of excess air, corresponds to the desired complete burnout of carbon in the fuel. Unfortunately, this is only achieved at the expense of high NO emissions. From the predicted oil droplets' trajectories and our knowledge of low NO_x technologies used for solid fuels, the atomization and evaporation must be established in an O_2-lean atmosphere if NO emissions are to be reduced. Although the rotary cup, and to a greater extent the pressure-jet atomizer, can separate atomization quality from primary air-to-fuel ratio, low NO emissions demand that the droplets penetrate into the rich IRZ. Unfortunately, the fine droplets are more likely to follow the gas stream readily and diffuse into the O_2-rich secondary air stream.

A fundamental rethinking of the design of conventional atomizers is implied to achieve the target of combined low NO and particulates emissions. To this end, further modification of the present atomizer is being undertaken, while the furnace and the CFD code are being adapted to accommodate non-ambient air concentrations prevalent in flue-gas recirculation or oxygen injection as a means of satisfying the dual demands of high efficiency and low emissions per unit energy input.

Acknowledgment

The authors are indebted to the Engineering and Physical Sciences Research Council of the United Kingdom for financial support (GR/H 15585) of this research project.

REFERENCES

1. Costa, M., Costen, P., and Lockwood, F. C., *Combust. Sci. Technol.* 77:1–26 (1991).
2. Sayre, A. N., Dugue, J., and Weber, R., "Development of Multi-Fuel Low NO_x Burner Technology," IFRF Doc. No. F10/y/6, 1992.
3. Ballester, J. M. and Dopazo, C., *Combust. Sci. Technol.* 103:235–263 (1994).
4. Abbas, A. S., Lockwood, F. C., and Koussa, S. S., ASME Paper No. 81-WA/HT-48, 1981.
5. Barreiros, A., Carvalho, M. G., Costa, M., and Lockwood, F. C., *Combust. Flame* 92:231–240 (1993).
6. Hampartsoumian, E., Nimmo, W., Pourkashanian, M., Williams, A., and Missaghi, M., *Combust. Sci. Technol.* 93:153–172 (1993).
7. Walsh, P. M. and Olen, K. R., *J. Inst. Energy* 66:140–146 (1993).
8. Costa, M., Costen, P., and Lockwood, F. C., *Combust. Sci. Technol.* 75:129–154 (1991).
9. Lockwood, F. C. and Mahmud, T., *Twenty-Second Symposium (International) on Combustion,* The Combustion Institute, Pittsburgh, 1988, pp. 165–173.
10. Costa, M., Costen, P., Lockwood, F. C., and Mahmud, T., *Twenty-Third Symposium (International) on Combustion,* The Combustion Institute, Pittsburgh, 1990, pp. 973–980.
11. Launder, B. E. and Spalding, D. B., *Comp. Meth. Appl. Mech. Engineer.* 3:269–289. (1974).
12. Leonard, B. P., *Comp. Meth. Appl. Mech. Engineer.* 19:59–89 (1979).
13. Spalding, D. B., *Int. J. Numerical Meth. Engineer.* 4:551–559 (1972).
14. Issa, R. I., *J. Comput. Phys.* 62:40–65 (1986).
15. Magnussen, B. F. and Hjertager, B. H., *Sixteenth Symposium (International) on Combustion,* The Combustion Institute, Pittsburgh, 1978, pp. 719–730.
16. Howard, J. B., Williams, G. C., and Fine, D. H., *Fourteenth Symposium (International) on Combustion,* The Combustion Institute, Pittsburgh, 1972, pp. 975–986.
17. Arscott, J. A., Gibb, J., and Jenner, R., *European Symposium,* The Combustion Institute, 1973, pp. 674–679.
18. Khan, I. M. and Greeves, G., in *Heat Transfer in Flames* (Afgan, N. H. and Beer, J. M., Eds.), Scripta Books Co., Washington, D.C., 1974, pp. 389–404.
19. Abbas, A. S. and Lockwood, F. C., *J. Inst. Energy* 58:112–115 (1985).
20. Truelove, J. S., "A Mixed Grey Gas Model for Flame Radiation," UK AERE Harwell report HL 76/3448, 1976.
21. Lawn, C. J., Cunningham, A. T. S., Street, P. J., Matthews, K. J., Sergeant, M., and Godridge, A. M., in *Principles of Combustion Engineering for Boilers* (Lawn, C. J., Ed.), Academic Press, London, 1987, pp. 61–196.
22. Byrnes, M. A., Mahmud, T., and Sharifah, A. S. A. K., "Mathematical Modelling of NO and Particulates Emissions from a Heavy Fuel Oil Fired Furnace," Department of Chemical Engineering Report, The University of Leeds, March, 1995.
23. Gollahalli, S. R., *Combust. Sci. Technol.* 19:245–250 (1979).
24. Urban, D. L., Huey, S. D. C., and Dryer, F. L., *Twenty-Fourth Symposium (International) on Combustion,* The Combustion Institute, Pittsburgh, 1992, pp. 1357–1364.
25. Northrop, P. S., Gavalas, R., and Levendis, V. A., *Energy Fuels* 5:587 (1991).

26. Byrnes, M. A., Foumeny, E. A., and Mahmud, T., *Proceedings of 3rd Asia-Pacific International Symposium on Combustion and Energy Utilization,* Hong Kong, 1995, pp. 19–25.
27. Zeldovich, Y. B., Sandovnikov, P. Y., and Frand-Kamenetskii, D. A., *Academy of Sciences of USSR,* Inst. Chem. Phys., Moscow-Leningrad, 1947.
28. Baulch, D. L., Drysdale, D. D., Horne, D. G., and Lloyd, A. C., *Evaluated Kinetic Data for High Temperature Reactions,* Vol. 1–3, Butterworth, London, 1973.
29. Hayhurst, A. N. and Vince, I. M., *Prog. Energy. Combust. Sci.* 6:35–51 (1980).
30. DeSoete, G. G., *Fifteenth Symposium (International) on Combustion,* The Combustion Institute, Pittsburgh, 1975, pp. 1093–1102.
31. Smith, P. J., Hill, S. C., and Smoot, L. D., *Nineteenth Symposium (International) on Combustion,* The Combustion Institute, Pittsburgh, 1982, pp. 1263–1270.
32. Lockwood, F. C. and Romo-Millares, C. A., *J. Inst. Energy* 65:144–152 (1992).
33. Lefebvre, A. H., *Atomisation and Sprays,* Hemisphere Publishing, New York, 1989.
34. Hassan, S., Ph.D. Thesis in preparation, ICSTM, University of London, 1996.
35. Hagiwara, A., Bortz, S., and Weber, R., "Theoretical and Experimental Studies on Isothermal, Expanding Swirling Flows with Application to Swirl Burner Design," IFRF Doc. No. F259/a/3, 1986.

COMMENTS

Dr. Josette Bellan, Jet Propulsion Laboratory, USA. During combustion of asphaltene—containing oils, cenospheres are formed. These cenospheres have a central "blow hole" and burn very differently from coal particles, with transport processes being very important. We have published about 10 years ago a model (Lowenberg, Bellan and Gavales in Chemical Eng. Communications) describing precisely cenosphere combustion. Why are you using a coal-burning model? You certainly cannot hope to obtain a predictive model with a model that is so far from reality.

Author's Reply. Comprehensive simulation of heavy fuel oil spray combustion in a practical system requires modelling of a large number of physical and chemical processes. In order to construct an economical model for engineering predictions we have chosen to incorporate simple yet realistic models for these processes where possible. We agree in general with you that it would be more realistic to use a detailed coke combustion model which accounts for the evolution of the coke structure and intricate transport processes within the porous particle during combustion. However, to date, studies on coke oxidation have been rather limited, and it is extremely difficult to quantify these effects. As a consequence, we have adopted a simplified model, as described in the text, where the kinetic rate constants are those evaluated for coke [25] and not for coal chars. A similar approach has also been used in Ref. 7 to model coke emissions from residual fuel oil fired boilers. It is of interest to note that the present coke combustion model is able to predict the measured trends of particulates emissions for a wide range of operating conditions of the atomizer and the burner. We shall bear your comments in mind and try your coke combustion model when time permits.

Twenty-Sixth Symposium (International) on Combustion/The Combustion Institute, 1996/pp. 2251–2257

EFFECTS OF CaO AND BURNOUT ON THE KINETICS OF NO REDUCTION BY BEULAH ZAP CHAR

FENG GUO AND WILLIAM C. HECKER
Department of Chemical Engineering and
Advanced Combustion Engineering Research Center (ACERC),
Brigham Young University,
350 CB, Provo, Utah 84604, USA

The heterogeneous reaction of NO with char is important in understanding the formation and reduction of NO_x from coal combustion processes. The kinetics of NO reduction by North Dakota lignite char (NDL), its acid-washed char (NDW), and its calcium-reloaded char (NCa) were investigated in a packed-bed reactor at temperatures from 723 to 1073 K. The results show that the reaction rate of NO with char increases significantly as the CaO content of the char increases. They also indicate clearly that the reaction is first order with respect to NO pressure and that there is a sharp increase in the apparent activation energy with increasing temperature. In the low temperature regime, the activation energies for all three char types are essentially the same (22–26 kcal/mol); in the high temperature regime, they are all higher, but decrease from 60 to 45 kcal/mol as the CaO content increases. The temperature at which the shift takes place also decreases as the CaO content increases.

Using a series of six NDL chars, the effect of char burnout level on the reaction of NO with char was also studied. The transition temperatures and apparent activation energies were found to be independent of char burnout, but both the reaction rate constant and CaO surface area (determined by CO_2 uptake at 573 K) decreased as char burnout level increased from 0 to 80%. When the reaction rates are normalized by CaO surface area, they become essentially independent of burnout level, which suggests the importance that CaO sites play in the reduction process. The correlation of rate with CaO surface area is quantitative and also holds for the three char types (NDL, NDW, and NCa) in the low-temperature regime. It does not hold for the three char types in the high-temperature regime.

Introduction

The reduction of NO emissions from combustion processes has become increasingly important in protecting the world's environment. It has been shown that selective catalytic reduction (SCR) with ammonia is an effective commercial technique to remove NO_x from combustion flue gas. However, the implementation of this technique is limited by high investment and operating costs, "ammonia slip," and SO_x poisoning, which motivate the search for alternatives [1]. Carbon (activated carbon or char) is a promising reducing agent for NO_x reduction with many potential advantages, such as low cost, easy availability, high efficiency, simplicity of process, and no secondary pollution [1–7]. Moreover, the heterogeneous reaction of NO with char is very important for the understanding and modeling of the formation of NO_x from coal combustion processes. The reaction may significantly destroy the NO_x formed earlier in coal combustion, which partially contributes to low NO emission from fluidized-bed combustion [2,3]. Therefore, the reaction of NO with char is receiving significant attention in the literature.

Previous investigations of the reaction of NO with char involve the kinetics and mechanism [6–23], the effects of char surface area [24,25], the effects of feed gas composition [10,7,25], and the catalytic effects of metals [5,10,22,26–29]. The reaction of NO with char has generally been reported to be first order with respect to NO partial pressure [7,13–16], but reaction orders between 0.42 and 0.73 have also been reported [30]. A sharp shift in the activation energy has been observed in the temperature range of 873–973 K, which suggests a complex reaction mechanism [6,7,15–18]. Several mechanisms have been proposed [5,6,12,16,18,19,31]. However, questions concerning N_2 formation, the surface complexes, the nature of active surface sites, and the effects of minerals in char are still not well understood. In most previous studies, chars were taken to be pure carbon, thus the effects of char ash and its composition on the kinetics and mechanism of the reduction reactions are not well known. Although the catalytic effects of certain metals or metal oxides on the reactions have been investigated [5,10,22,26–29], little is known about their effects on the kinetics of the reaction. Moreover, the effect of burnout level on the reaction have not been reported previously. Therefore, the objectives of this study are to

TABLE 1
Properties of North Dakota lignite and chars

	ND lignite	NDL	NDW	NCa	ND21	ND26	ND24	ND17	ND9
Ash content (%)	6.0	13.6	5.4	7.0	14.4	18.8	21.9	27.2	42.8
Char burnout (%)	N/A	0.0	N/A	N/A	6.5	31.8	43.9	57.8	79.0
CaO content (%)	1.3	3.5	1.1	2.4	3.7	4.8	5.6	7.0	11.0
App. density (g/cc)	1.41	0.63	0.62	0.74	0.51	0.59	0.61	0.63	0.82
True density (g/cc)	1.43	1.88	1.74	1.75	1.93	2.00	2.02	1.80	2.07
Porosity (%)	1.2	66	64	58	74	70	70	65	61
Particle diam. (μm)	75	66	65	64	70	61	57	52	41
N_2 S.A. (m^2/g)	0.32	190	116	128	134	163	87	118	56
CO_2 S.A. (m^2/g)	267	543	526	543	567	540	511	517	401
CaO S.A. (m^2/g)	9.0	17.8	3.2	4.8	17.2	13.1	12.1	11.1	7.0
CaO dispersion (%)	54	41	24	17	36	24	18	15	6

investigate the kinetics of the reaction of NO with Beulah Zap chars, to study the effects of CaO on the kinetics, and to determine the effects of char burnout level (or conversion) on the reaction.

Experimental Methods

Char Properties

The parent char used in this study was prepared from 63/74 km particles of North Dakota Beulah Zap lignite in a methane flat-flame burner (FFB) at a high heating rate (10^4–10^5 K/s) and high temperature (peak gas temperature was 1900 K). The resulting parent char (dubbed NDL), a portion of the NDL that was washed with HCl to remove mineral matter (dubbed NDW), and a portion of NDW *reloaded* with calcium oxide (dubbed NCa) were used. In addition, a series of chars made by burning out NDL char to various extents with 3–5% oxygen in a drop tube reactor (DTR) at about 1800 K were also used in this study. All of these chars were made previously in our laboratory, and details of their preparation have been reported elsewhere [32,33]. The properties of these chars, along with those of the lignite, are shown in Table 1.

Reactor Operation

The reduction of NO by char was carried out for all chars at 5–6 temperatures between 723 and 1073 K in a 10-mm-i.d. VYCOR glass, vertical packed-bed reactor with a fritted quartz disc of medium porosity as a support. For each run, 0.2 g char mixed with 2 g silicon carbide (inert for NO reduction) was packed in the reactor and heated in He to the maximum temperature desired using an electric furnace. NO diluted with He (3130 ppm NO) was then fed downward through the reactor until the outlet NO concentration reached a quasi-steady-state value. The transient usually lasted about 1 h and was probably due to the build-up of adsorbed species on the char. Once the quasi-steady-state was reached, data were collected at 5–6 flow rate settings (between 100 and 500 ml/min (NTP)) at each of the 5–6 temperatures studied. For each run, it took about 4 h to collect all the data, and the burnout of the char was about 10% during that period of time. Accompanying the slow loss of char, the outlet NO concentration increased very slightly with time, and thus we have used the term quasi–steady state. In the calculation of rates and kinetic parameters (described later), the small loss in char mass was accounted for by normalizing by the char mass *available*.

The inlet gas pressure in the reactor was controlled at 300 kPa (3 atm). The outlet pressure at each run condition was measured to determine the pressure drop cross the packed bed. The average pressure was used in calculation of concentrations.

Gas Analysis

The composition of the outlet gas was continuously monitored for N_2, CO, CO_2, N_2O, and O_2 by a GC (Perkin-Elmer, 3920B) with TCD and two columns (one packed with Chromosorb 106, the other packed with molecular sieve 5A), and for NO and NO_2 by a Chemiluminescence NO_x analyzer (Thermo Environmental, 42H). Nitrogen and oxygen mass balances were determined between inlet and outlet streams for each run, and variations always fell within $\pm 5\%$.

Mass Transfer Influences?

The calculation of film mass transfer and pore diffusion resistances for a worst-case scenario (the maximum particle diameter, the minimum flow rate, and the maximum reaction rate observed) indicated that

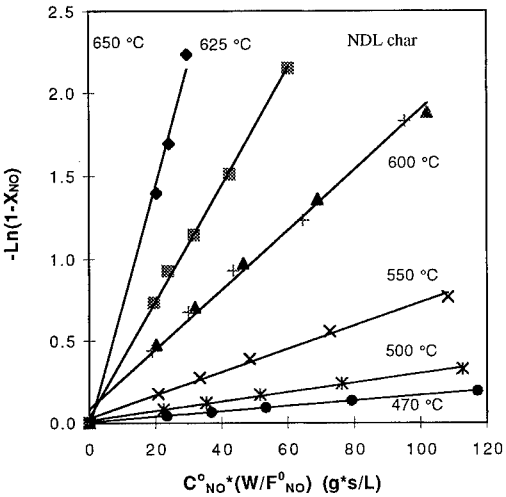

FIG. 1. Experimental data for NDL char plotted in form of first-order integrated rate expression.

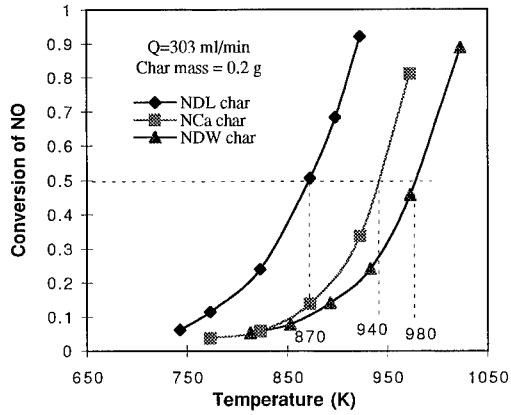

FIG. 2. The variation of NO conversion with temperature for three char types.

film mass transfer (maximum MT resistance, $(C_g - C_s)/C_g = 2.7\%$) and pore diffusion (minimum effectiveness factor, $\eta = 0.99$) were negligible in this study.

Results

Kinetics

Because a broad range of NO conversion was observed in this study, the reactor was modeled as an integral plug flow reactor. The reaction rate constants and reaction order were obtained by integral analysis [38] of the experimental data.

The experimental data for NDL char plotted as: $-\ln(1 - X_{NO})$ vs. $C^0_{NO}\, W/F^0_{NO}$ (X_{NO} is NO conversion, F^0_{NO} is inlet molar flow rate of NO (mol/s), W is char mass available (g), C^0_{NO} is inlet NO concentration (mol/L)) are shown in Fig. 1. The data for all six temperatures are very linear, which is consistent with the reaction being first order with respect to NO partial pressure. Attempts to fit the data to other orders were made, but straight lines were not obtained for all temperatures. Table 2 lists values for the reaction rate constants, their lower and upper 95% confidence limits, and statistical analysis parameters for NDL char data obtained at six different temperatures. The correlation coefficients, t-test values, and F-test values all show that the experimental data were excellently fit by first-order kinetics under the experimental conditions. The standard error was typically less than 5%. Similar first-order behavior was observed for the other two char types, NDW and NCa.

The Effect of CaO

The variations of NO conversion with temperature at a flow rate of 303 ml/min (NTP) are shown in Fig. 2 for the three char types. The results for other flow rates are similar. The conversion of NO increases

TABLE 2
Reaction rate constants and statistical anaysis parameters for NO reduction by NDL char

T °C	k_1 L/s-g-Char	k_1 Low 95%	k_1 Up 95%	Std error	Corr coef r^2	t-Test	t-Distrib $\alpha = 0.01$	F-Test	F-Distrib $\alpha = 0.01$
650	0.0736	0.0562	0.0909	4.03E-03	0.994	18.2	9.925	333	199
625	0.0353	0.0333	0.0373	7.29E-04	0.998	48.5	4.604	2348	26
600	0.0182	0.0161	0.0202	7.40E-04	0.993	24.6	4.604	457	26
600	0.0181	0.0158	0.0205	8.48E-04	0.991	21.4	4.604	604	26
550	0.0070	0.0063	0.0078	2.66E-04	0.994	26.5	4.604	701	26
500	0.0029	0.0026	0.0032	1.10E-04	0.994	26.2	4.604	686	26
470	0.0016	0.0016	0.0017	2.56E-05	0.999	64.1	4.604	4103	26

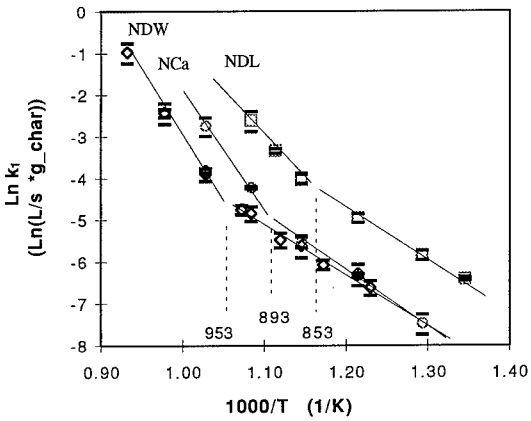

FIG. 3. Arrhenius plots of the reaction rate constants for NO reduction with char for three char types.

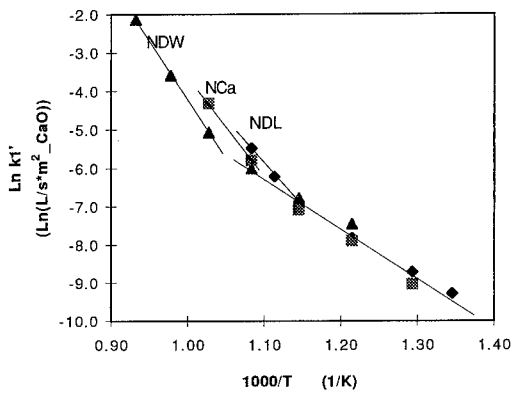

FIG. 4. Arrhenius plots of the reaction rate constants normalized by CaO surface area for three char types.

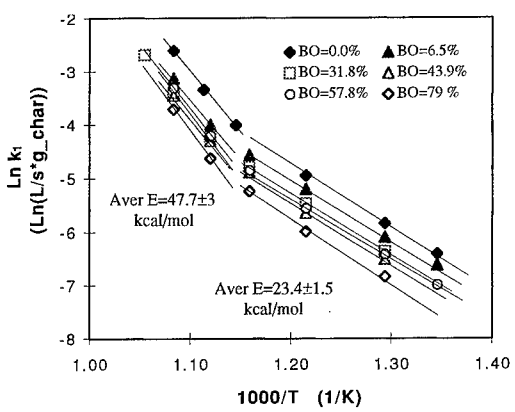

FIG. 5. Arrhenius plots of the reactions rate constants for NO reduction by NDL chars with different burnout levels.

noticeably in the order NDL > NCa > NDW. For example, the temperatures for 50% conversion are 870, 940, and 980 K for NDL, NCa, and NDW, respectively. This is in the same order as the CaO content of the three chars, 3.5% > 2.4% > 1.1%. Therefore, the effect of CaO on the reaction of NO with char appears to be significant.

Figure 3 is an Arrhenius plot of the rate data for the NDL, NDW, and NCa chars. The bars around points in the figure show the variation of the reaction rate constants within a 95% confidence interval. A sharp shift in the apparent activation energy with increasing temperatures was observed for three char types, as has also been reported in the literature [6,7,15–18]. The temperature at which the transition takes place increases from 823 to 973 K as the CaO content decreases. This shift to higher activation energy with increasing temperature is opposite to that expected if a reaction is changing from chemical rate control to mass transfer control, and suggests different mechanisms or rate-determining steps at high and low temperatures. It is also noted that at low temperatures the apparent activation energies for all three char types are essentially the same (22–26 kcal/mol); at high temperatures, however, the activation energies vary from 45 to 60 kcal/mol, increasing as the CaO content of the chars decreases.

In most heterogeneous and catalytic reactions, it is not the gross amount or *mass* of catalyst or solid that is proportional to the reaction rate, but rather the amount of active *surface area* that the given material contains. CaO surface area can be measured by selective CO_2 chemisorption at 573 K using a thermogravimetric analyzer [32,33]. This was done for the NDL, NDW, and NCa chars, and the resulting values were 17.8, 3.2, and 4.8 m^2/g of char, respectively (see also Table 1). If the rate constants shown in Fig. 3 are then normalized by the appropriate CaO surface area, the Arrhenius plot shown in Fig. 4 results. This indicates quite definitively that for the low-temperature regime the rate constant is independent of char type, while in the high-temperature regime it still varies as a function of char type with the high-CaO-containing chars still showing higher values. This seems to indicate a direct first-order dependence on CaO surface area in the low-temperature regime, and possibly an even higher order dependence on CaO surface area in the high-temperature regime.

The Effect of Char Burnout

The Arrhenius plot of rate data for six NDL chars with different burnout levels is shown in Fig. 5. The transition temperatures and apparent activation energies in both temperature regimes are apparently independent of char burnout level. The reaction rate constants decrease (by about a factor of 3) as char burnout level increases from 0 to 80% over the en-

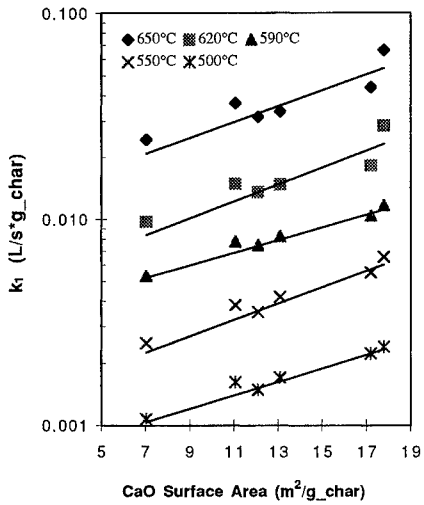

FIG. 6. The dependence of the reaction rate constants for NO reduction by NDL char on CaO surface area.

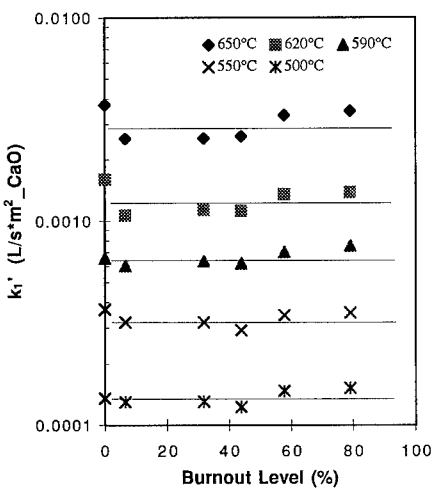

FIG. 7. The effect of char burnout level on the rate constants normalized by CaO surface area for NO reduction by NDL chars.

tire temperature range. Note that these rate constants are already per gram of *available* (or residual) char, and thus the decrease is real. (If they were per gram of *initial* char, the differences would be even greater, by an additional factor of 5.)

It has also been shown by previous work in this laboratory [32,33] that the CaO surface area for these same chars decreases with burnout level. A cross plot (Fig. 6) shows that the rate constants increase as CaO surface area increases. When the rate constants are normalized by CaO surface area, they become essentially independent of char burnout

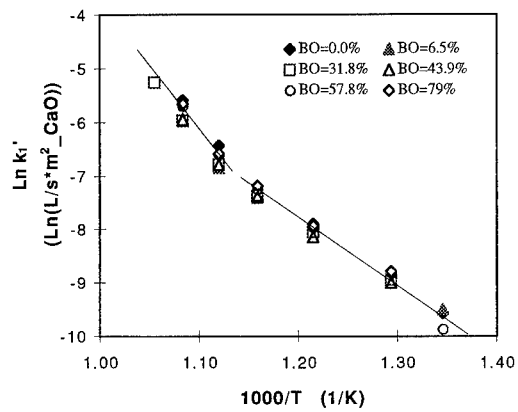

FIG. 8. Arrhenius plot of the rate constants normalized by CaO surface area for NO reduction by NDL chars with six different burnout levels.

level for all five measured temperatures as shown in Fig. 7. When the data of Fig. 5 are replotted using the CaO-normalized rate constants instead of the mass-based rate constants, all points for six different burnout levels fall on one line (Fig. 8), again confirming that the reaction rate of NO reduction by NDL chars normalized by CaO surface area is independent of char burnout level. These results suggest strongly that CaO is involved directly in the reaction process, probably as a catalyst.

Discussion

The fact that the CaO surface area correlates the data in both the low- and high-temperature regimes for this NDL series of chars is in contrast to the behavior of the three char types shown in Figs. 3 and 4, in which the low-temperature regime was correlated but the high-temperature regime was not. The reasons for this difference are not clear at this time. The behavior suggests that there is a difference between the three char types that does not exist between the members of the NDL series that is important for determining reactivity in the high-temperature regime, but not in the low-temperature regime. Possibilities would include char organic structure or other inorganic constituents. Other inorganic constituents besides CaO were removed in the washing process (see ash content values in Table 1), while in the NDL series, the ratio of inorganic constituents would have remained fairly constant.

One crude measure of organic structure would be N_2 BET surface area. Attempts to correlate the rate constant data for the NDL chars with N_2 BET surface areas of the chars (see Table 1) have been made. For the NDL series, a moderate correlation was observed [34], albeit less definitive than that with CaO surface area. However, for the three char types no

clear correlation was observed at either high or low temperature. Thus, BET surface area does not appear to explain the differences between the two series.

Conclusions

The kinetics of the reaction of NO with char have been determined for three kinds of char with different CaO contents. The results show that the reaction rate increases significantly as the CaO content of the char increases. The reaction is first order with respect to NO partial pressure and has a sharp shift in the activation energy with temperature for all char types studied. In the low-temperature regime, the activation energies for all three char types are essentially the same (22–26 kcal/mol); in the high-temperature regime, they are all higher but decrease from 60 to 45 kcal/mol as the CaO content increases. The temperature at which the shift takes place also decreases as the CaO content increases.

The effect of char burnout level on the reaction was also studied. The transition temperatures and apparent activation energies were found to be independent of char burnout, but both the reaction rate constant and CaO surface area decreased as char burnout level increased from 0 to 80%. When the reaction rates are normalized by CaO surface area, they become essentially independent of burnout level, which suggests the important part that CaO sites play in the reduction process.

Finally, the data in the low-temperature regime for both char series were correlated very well by CaO surface area. Data in the high-temperature regime for the burnout series of similar NDL chars were again correlated well by CaO surface area, but data for the three char types were not. The difference is not yet understood.

Acknowledgments

This work was sponsored by the Advanced Combustion Engineering Research Center at Brigham Young University. Funds for this center are received from the National Science Foundation, the State of Utah, the U.S. Department of Energy, and a number of industrial participants. We also thank Richard F. Cope for char preparation and Troy Ness for technical assistance.

REFERENCES

1. Bosch, H., Janssen, F., *Catalysis Today* 2:369–521 (1988).
2. Pereira, F. J., Beer, J. M., Gibbs, B., Hedley, A. B., *Fifteenth Symposium (International) on Combustion,* The Combustion Institute, Pittsburgh, 1975, pp. 1149–1155.
3. Johnson, J. E., *Fuels* 73:1398–1415 (1994).
4. Illan-Gomez, M. J., Linares-Solano, A., Salinas-Martinez de Lecea, C., *Energy Fuels* 7:146–154 (1993).
5. Yamashita, H., Tomita, A., *Energy Fuels* 7:85–89 (1993).
6. Teng, H., Suuberg, E. M., Calo, J. M., *Energy Fuels* 6:398–406 (1992).
7. Furusawa, T., Tsunoda, M., Tsujimura, M., Adschiri, T., *Fuel* 64:1306–1309 (1985).
8. Furusawa, T., Kunii, D., Osuma, A., Yamada, N., *Int. Chem. Eng.* 20:239–289 (1980).
9. Wendt, J. O. L., Pershing, D. W., Lee, J. W., Glass, J. W., *Seventeenth Symposium (International) on Combustion,* The Combustion Institute, Pittsburgh, 1979, pp. 77–85.
10. Levy, J., Chan, L. K., Sarofim, A. F., Beer, J. M., *Eighteenth Symposium (International) on Combustion,* The Combustion Institute, Pittsburgh, 1981, pp. 111–120.
11. Watts, H., *Trans. Faraday Soc.* 54:93–105 (1958).
12. Smith, R. N., Swinehart, J., Lesnini, D., *J. Phys. Chem.* 63:544–547 (1959).
13. Richthofen, A. V., Wendel, E., Neuschiitz, D., *Fresenius' J. Anal. Chem.* 346:261–264 (1993).
14. Edwards, H. W., *AIChE Symp. Ser. No. 126* 68:91–104 (1972).
15. Song, Y. H., Beer, J. M., Sarofim, A. F., *Combust. Sci. Technol.* 25:237–240 (1981).
16. Chan, L. K., Sarofim, A. F., Beer, J. M., *Combust. Flame* 52:37–45 (1983).
17. Radovic, L. R., Walker, P. L., Jr., *Fuel Process Technol.* 8:149–154 (1984).
18. Suuberg, E. M., Teng, H., Calo, J. M., *Twenty-Third Symposium (International) on Combustion,* The Combustion Institute, Pittsburgh, 1990, pp. 1199–1205.
19. Teng, H., Suuberg, E. M., *J. Phys. Chem.* 97:478–483 (1993).
20. Teng, H., Suuberg, E. M., *Ind. Eng. Chem. Res.* 32:416–423 (1993).
21. Chu, X., Schmidt, L. D., *Ind. Eng. Chem. Res.* 32:1359–1366 (1993).
22. Lai, C.-K. S., Peters, W. A., Longwell, J. P., *Energy Fuels* 2:586–588 (1988).
23. Matos, M. A. A., Pereira, F. J. M. A., Ventura, J. M. P., *Fuel* 69:1435–1439 (1990).
24. Shimizu, T., Sazawa, Y., Adschiri, T., Furusawa, T., *Fuel* 71:361–365 (1992).
25. Yamashita, H., Yamada, H., Tomita, A., *Appl. Catalysis* 78:L1–L6 (1991).
26. Furusawa, T., Koyama, M., Tsjimura, M., *Fuel* 64:413–414 (1985).
27. Illan-Gomez, M. J., Linares-Solano, A., Radovic, L., Salinas-Martinez de Lecea, C., *Energy Fuels* 9:97–103 (1995).
28. Illan-Gomez, M. J., Linares-Solano, A., Radovic, L., Salinas-Martinez de Lecea, C., *Energy Fuels* 9:104–111 (1995).
29. Illan-Gomez, M. J., Linares-Solano, A., Radovic, L., Salinas-Martinez de Lecea, C., *Energy Fuels* 9:112–119 (1995).

30. Johnson, J. E., Dam-Johansen, K., *Eleventh International Conference on Fluidized-Bed Combustion,* American Soc. Mech. Eng., New York, 1991, pp. 1389–1396.
31. De Soete, G. C., *Twenty-Third Symposium (International) on Combustion,* The Combustion Institute, Pittsburgh, 1990, pp. 1257–1264.
32. Cope, R. F., Arrington, C. B., Hecker, W. C., *Energy Fuels* 8:1095–1099 (1994).
33. Cope, R. F., Ph.D. Dissertation, Brigham Young University, Provo, Utah, 1995.
34. Guo, F., Hecker, W. C., Western States Section/The Combustion Institute, Stanford, California, Oct. 1995, Paper WSS/CI 95F-178.
35. Illan-Gomez, M. J., Linares-Solano, A., Radovic, L., Salinas-Martinez de Lecea, C., *Coal Science* (Pajaves, J. A. and Tascon, J. M. D., Eds.), *Coal Sci. Technol.,* 24, Elsevier, Amsterdam, 1995, pp. 1911–1914.
36. Yang, R. T., Wong, C., *J. Chem. Phys.* 75:4471–4476 (1981).
37. Ben-Aim, R. I., *Int. Chem. Eng.* 27:70–75 (1987).
38. Levenspiel, O., *Chemical Reaction Engineering,* 2nd ed., Wiley and Sons, New York, 1972.

Twenty-Sixth Symposium (International) on Combustion/The Combustion Institute, 1996/pp. 2259–2267

PAH AND AROMERS: PRECURSORS OF FULLERENES AND SOOT

M. BACHMANN, W. WIESE AND K.-H. HOMANN
Institut für Physikalische Chemie
Technische Hochschule Darmstadt
Petersenstr. 20, D-64287 Darmstadt, Germany

Positively and negatively charged flame ions in flat laminar low-pressure benzene/oxygen flames were analyzed by means of mass spectrometry. A rectangular burner consisting of two neighboring sintered plates was used to analyze concentration profiles of the ions, as well as concentrations at different lateral positions, by moving the burner vertically and horizontally. Polycyclic aromatic hydrocarbons (PAH) were detected in their thermodynamically most stable forms; very hydrogen-rich PAH were also found in the oxidation zone of the flame. In the mass spectra of the negative ions, a new class of high-mass species has been observed. These species are formed through combination reactions of PAH with masses beyond about 300 u and are given the name *aromers*. The formation of fullerenes in the center and of soot at the rim of a benzene flame is explained. In this context, a detailed formation mechanism of fullerenes from PAH via aromers is discussed with respect to the temperature dependence of unimolecular reactions during this process. Besides the PAH concentration, the flame temperature determines whether soot or fullerenes are formed in fuel-rich low-pressure benzene flames.

Introduction

The three classes of high molecular–weight material in flames (i.e. PAH, fullerenes, and soot) have been studied best with benzene as a fuel. There might be more investigations on soot formation from ethylene, but there are very few studies on polycyclic aromatic hydrocarbons (PAH) and none on fullerenes with this fuel. In benzene flames, concentration profiles of PAH have been measured [1], and fullerenes have been analyzed both on-line [2] and after extraction from soot [3]. However, there are some strange observations concerning soot formation in low-pressure benzene/oxygen for which an explanation is lacking, because each study concentrated on one of the classes and did not deal with the others in the respective flames.

Morgeneyer measured a continuous absorption at 518.4 nm of about 1.5% in the burned gas of a flat benzene oxygen flame (C/O = 0.89, p = 2.7 kPa), which he attributed to soot, stating that it was comparable to that of a very strongly sooting acetylene/oxygen flame (C/O = 1.7) [4]. However, electrically charged soot, which is normally a sensitive indicator for soot particles in flames, was not found along the axis in such a benzene flame [5]. Only at C/O > 0.935 could a small fraction of charged soot be detected. Grayish deposits out of a molecular beam from the middle of the benzene flames indicated soot particles that were much smaller than those from acetylene flames and hardly grew at greater flame heights in contrast to soot from other fuels [6]. Nevertheless, an extrapolation of both the continuous absorption and emission to zero values indicated a C/O threshold for soot formation of about 0.72 (p = 2.7 kPa), which was widely accepted and compatible with the beginning of visual yellow luminosity [4].

It has long been known that soot formation in flat flames is strongly reinforced at the rim; consequently, it was penetrated in the optical experiments with so-called window pipes [7]. More recently, it was found that for ethylene flames the threshold C/O (not only visually) is dependent on temperature [8]. In the present work on flat benzene flames, in which profiles were also taken horizontally, we show that the temperature dependence of the soot threshold and the strong soot formation at the rim gets a new meaning in connection with fullerene formation and that the threshold C/O is far from 0.72 in the middle of a flat flame.

Experimental

The experiments have been performed on the natural positive and negative ions of PAH and fullerenes and with positively charged soot particles. The positive ions serve as a good and very sensitive probe (ppt range) for the respective uncharged species that can usually be analyzed in the ppb range with online methods [9]. Moreover, the experiments with large negative ions reveal a new class of aromatic species and the direct precursors of the fullerenes.

Premixed flames were stabilized at a pressure of p = 2.7 kPa on a water-cooled burner that consisted of two sintered plates (70 × 50 mm), divided by a

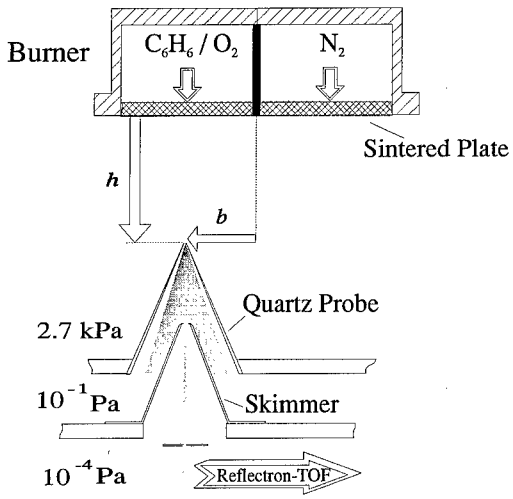

FIG. 1. Experimental setup of the vertically and horizontally movable, rectangular two-side burner and the molecular beam sampling system. h: vertical distance between burner plate and probe tip; b: horizontal distance between the probe tip and the plane of the dividing strip ($b < 0$ $\hat{=}$ inside the flame)

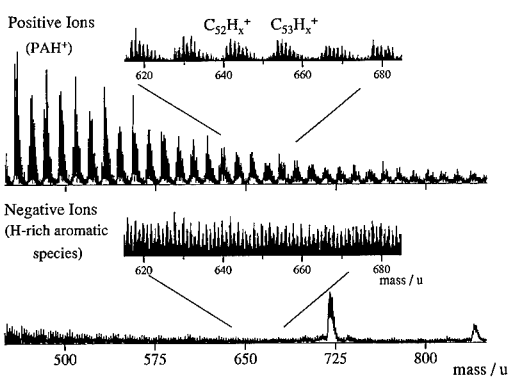

FIG. 2. Upper part: mass spectrum of positively charged ions; lower part: mass spectrum of negatively charged ions. Insets shown with higher resolution. $h = 7$ mm; (benzene/oxygen flame: C/O = 0.8, $v_u = 42$ cm/s, $p = 2.7$ kPa).

2-mm strip (see Fig. 1). The burner was also movable horizontally (b) in addition to the usual vertical mode (h) [10]. On the one side, a fuel-rich benzene/oxygen flame (C/O = 0.8, $v_u = 42$ cm/s) was burning, while nitrogen was streaming through the other plate, $v_{N_2} \approx 100$ cm/s. The nitrogen flow prevented the formation of eddies at the rim of the flame formed by the recirculation of burned gas. The reinforced soot formation also occurred at the side of the nitrogen flow and could clearly be seen because of the rectangular shape of the burner.

On-line analysis of the flame ions was performed as described previously [11,12]. In addition, the time-of-flight mass spectrometer was equipped with an ion reflector, increasing the mass resolution. Ions with masses up to about 6000 u could be detected. In addition to the ion profiles in vertical direction, they were also determined across the flame. Mass distributions of small charged soot particles were obtained by means of a Wien filter mass spectrometer described previously [13].

Results

Overview Mass Spectra

Figure 2 shows the mass spectra of large positive and negative flame ions in the mass region between 450 and 850 u. Both spectra were taken from the center of a benzene/oxygen flame at $h = 7$ mm (C/O = 0.8, $v_u = 42$ cm/s, $p = 2.7$ kPa). There is a significant formation of broad groups spaced by 12 u in the positive ion mass spectrum. They are due to PAH with the same number of C atoms but different numbers of H atoms as revealed through higher mass resolution shown for the part of the spectrum from 620 to 680 u. To obtain the relative abundances, the peak heights have been corrected with respect to the ^{13}C isotope contributions. From GC analysis of smaller flame PAH, it is known that there are numerous isomers. This must also be assumed for every peak in the mass spectrum of the larger PAH. Positive fullerene ions appear at larger distances from the burner (see Fig. 3).

In contrast to the positively charged PAH in groups, the mass spectrum of the negative ions has a completely different intensity distribution of the signals. The peaks occupy each mass of the region shown that is the same as for the positive ions. There is hardly a variation in intensity of the peaks and if so, it is an odd–even variation. That is, any grouping caused by the increase in carbon number is smeared out through a variation in the hydrogen content of the PAH, which is distinctly larger than that of the PAH that form preferentially positive ions, at least +/−6 H with reference to a medium H content.

This means that there are PAH in the flame with any number of C atoms. For a certain number of C atoms per PAH, there is a very broad variation in the hydrogen content. However, it is not only the hydrogen content that makes them differ but the two classes of PAH. In one, the hydrogen content does not vary much and forms preferentially positive ions. The PAH of the other class, with the much larger variation in H, have a different quality expressed through their tendency to form negative ions. The early appearance of fullerene ions, C_{60}^- and C_{70}^-, in the negative ion mass spectrum is an indication that the latter class of PAH also contains five-membered rings that increase their electron affinity.

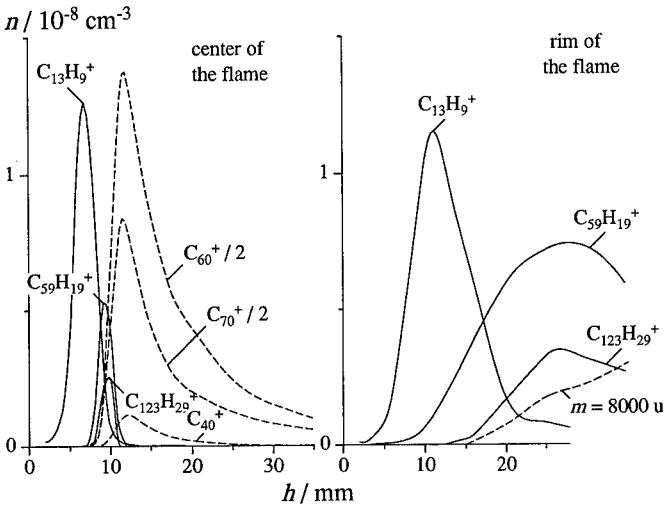

FIG. 3. Left: concentration profiles of PAH^+ (solid lines) and fullerene ions (dashed lines) in the center of the flame. Right: concentration profiles of PAH^+ (solid lines) and charged soot particles (for example, $m = 8000$ u; dashed line) at the rim of the flame ($b = 0$ mm).

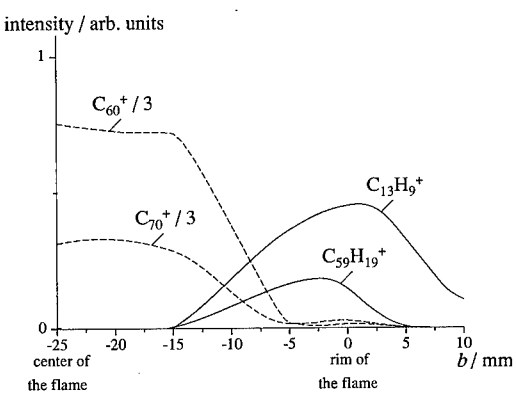

FIG. 4. Lateral intensity profiles of PAH^+ and fullerene ions at $h = 15$ mm. The parameter b represents the distance between the probe tip and the rim of the flame.

Vertical Profiles

Qualitatively, the mass spectra of positive PAH ions look similar when taken from the center or the rim of the flame, but their axial profiles do not. On the left-hand side of Fig. 3, concentration profiles of three positively charged PAH (solid lines) and fullerene ions (dashed lines) from the center of the flame ($b = -25$ mm) are shown. The profiles of the PAH ions are from some of those mass peaks that have a relative maximum intensity within the respective groups after ^{13}C isotope correction. These are also called *main PAH* in the following discussion. Each of the PAH profiles reaches a maximum, followed by a steep decrease that is due mainly to oxidation. With increasing molecular mass, both the first rise and the maximum, h_{max}, are shifted to larger distances from the burner. However, these h_{max} converge to an upper limit. Even PAH with masses of more than 1500 u ($C_{123}H_{29}^+$) reach their maximum concentration at this distance, which is $h \approx 10$ mm from the burner. The mass region of PAH extends up to 2000 u. Afterwards, PAH do not grow further and no soot is formed in the center of the flame [14].

The right-hand side of the figure shows profiles at the rim of the flame, $b = 0$ mm. The PAH profiles are much broader and their decrease after the maxima is less steep. Each individual PAH reaches its maximum concentration at a greater distance than in the center of the flame. There is also a limit h_{max}, but it lies at a larger value, $h \approx 27$ mm. That means that both the rate of formation and consumption of PAH is slower. In contrast to the flame center, the PAH grow up to a mass of approximately 4000 u. Although the maximum concentrations of low-mass PAH (for example $C_{13}H_9^+$) are comparable in the center and at the rim, there is a steady increase of the maximum concentrations at the rim with increasing mass or a respective decrease in the center. However, the greatest difference is that there are no fullerenes at the rim of the flame, regardless of the distance h from the burner the sample was taken. Instead, soot is formed in this extreme part of the flame, illustrated by the increasing profile of charged soot particles with $m = 8000$ u.

Lateral Profiles

The retarded PAH formation and the absence of fullerenes at the rim are also shown with the aid of lateral profiles. Several such profiles were taken at different distances from the burner. For $h = 15$ mm, the intensities of C_{60}^+ and C_{70}^+, as representatives for all fullerenes (see, for example, Ref. 15), and of two PAH^+ are shown in Fig. 4. In the center of the flame at $b = -25$ mm, only fullerenes (dashed lines) are

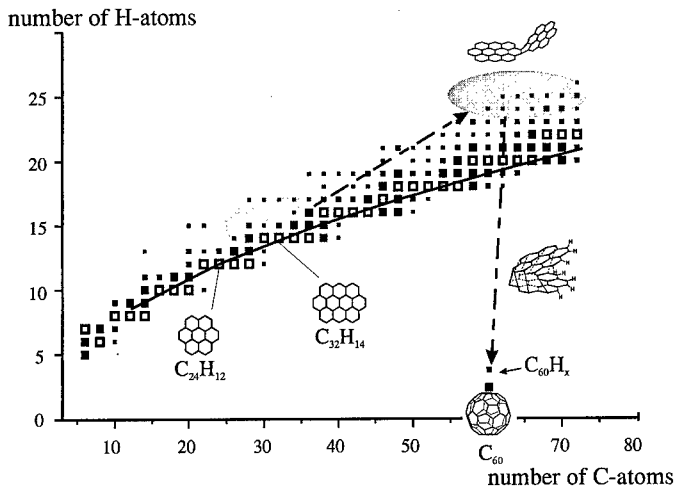

FIG. 5. H–C diagram of PAH analyzed in the center of a benzene/oxygen flame. Solid line: most pericondensed PAH; dashed line: path to fullerenes. C/O = 0.8, v_u = 42 cm/s, p = 2.7 kPa at h = 10 mm.

detectable. Their lateral profiles exhibit a plateau between $b = -25$ mm and $b = -15$ mm. Toward the rim of the flame is a relatively steep decline of these profiles to $b = -5$ mm, where they have nearly vanished.

In the center of the flame, the PAH (full lines) have already disappeared in the burned gas at h = 15 mm. Because of their retarded formation toward the rim, the lateral profiles of the PAH show a smooth rise, beginning at $b = -15$ mm and maximizing near the rim of the flame ($b = 0$ mm). They extend somewhat into the nitrogen stream ($b > 0$).

Discussion

Growth and Hydrogen Content of PAH

Large PAH have long been recognized as precursors of soot particles, and there is also good evidence that PAH over a certain size play an important role, at least for a part of the fullerenes formed in fuel-rich flames [16]. However, the strong dependence on the burning conditions, whether soot or fullerenes are formed from a flame that contains a relatively large intermediate PAH concentration, is a new result [14]. Also new is that flame PAH occur with such a large variation in their hydrogen content.

Since very few of the PAH larger than coronene have been identified, their occurrence shall be illustrated with the aid of a C/H diagram. The groups in the mass spectrum (see Fig. 3) are represented by the vertical lines of squares in Fig. 5, in which PAH with up to 72 C atoms per molecule with different numbers of H atoms are plotted. Each square stands for a molecular formula. For reasons of clarity, only groups with even numbers of C atoms have been included. The odd-numbered PAH do not change the picture. Unfilled squares represent the main PAH of a group. The size of the filled squares in a vertical line indicates qualitatively the intensity of the PAH of the respective group relative to that of the main PAH. The solid line connects the most pericondensed PAH, such as pyrene, coronene, ovalene, and circum-coronene, which only contain six-member rings. It also serves as a standard to distinguish hydrogen-rich (above) from hydrogen-poor PAH (below the line).

An increase in the number of H atoms, while the number of C atoms stays constant, could be due to a progressive hydrogenation retaining the carbocyclic structure. However, a detailed GC/MS analysis of PAH from benzene and naphthalene flames has shown recently that this occurs to a small extent (1–3%) only with small PAH, for example, with dihydronaphthalene/naphthalene [17]. In the case of larger PAH, a variation in the hydrogen content always signifies a different carbocyclic aromatic structure that is thermodynamically more stable than a partially hydrogenated ring. For hydrogen-rich PAH, this means a more open, less condensed structure with "bays" [18] as in phenanthrene ($C_{14}H_{10}$, H/C = 0.714) in contrast to a pericondensed PAH without bays, for example, pyrene ($C_{16}H_{10}$, H/C = 0.625). Most of these PAH contain extended regions of condensed six-member rings without pentagons. This causes low ionization potentials and consequently the tendency to become positively ionized [19]. Hydrogen-poor PAH must contain one or more five-member rings within a maximum condensed structure, as in cyclopenta(cd)pyrene ($C_{18}H_{10}$, H/C = 0.555), or ethynyl/poly-ynyl side chains. The C/H diagram shows that there are relatively few hydrogen-poor PAH below the full line.

That there is a relatively broad C/H band shows that the growth mechanism does not follow a simple path such as along the most pericondensed structures. These six-member ring structures are the most

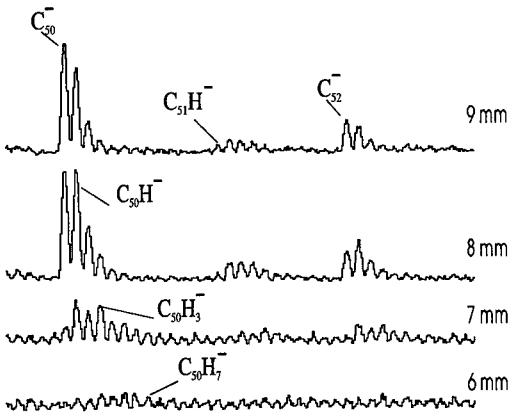

FIG. 6. Hydrogen-containing carbon cages precede the formation of fullerenes (see text).

thermodynamically stable species, and they occur in the relatively largest concentrations. However, there are certainly many ways to grow via hydrogen-rich PAH. During this growth, the average hydrogen content of the PAH decreases smoothly and seldom leads to PAH below the full line in the diagram. This is compatible with a growth mechanism through repetitive addition of small, unsaturated hydrocarbons such as acetylene and/or benzene [20]. Hydrogen is split off at the sites where these growth species form C–C bonds with the PAH. Few five-member rings may be formed at the periphery, such as in acenaphthylene or in a position as in fluoranthene. But these stepwise reactions do not alter the carbon skeleton in such a way that reactions can be started that lead to a drastic loss of that hydrogen, which is already bound in the PAH. However, a rapid loss of hydrogen has to take place for fullerene formation. By such a mechanism, the region below the solid line in Fig. 5 is crossed so rapidly that most of the H-poor intermediates are too short-lived to be detected.

Negative Ions and "Aromer" Formation

The way this can happen may be deduced from the negative ion mass spectrum. The exact number of carbon and hydrogen atoms belonging to a certain mass peak of this spectrum (see Fig. 2) cannot be determined with certainty because of superposition of ions $C_xH_y^-$ and $C_{(x-1)}H_{(y+12)}^-$. However, it is highly probable that this spectrum is also composed of aromatics with any number of C atoms. Groups of these species with the same number of C cannot be distinguished because of their greater variation in hydrogen content (or H/C, respectively) than for those groups of PAH that form positive ions. The combination of two PAH molecules creates products with a larger electron affinity [19], since they may contain five-member rings. These products are less condensed and therefore have a relatively larger H content. This is indicated by the upward dashed arrow and a combination of, for example, coronene and ovalene in the right upper corner of Fig. 5. The shaded areas at the ends of the arrow indicate that combination to form products that have 60 C atoms is possible starting from many different reactants. In this way, very hydrogen-rich PAH species with a relatively low degree of structural condensation are formed. This kind of combination can take place with any two PAH. Therefore, it is clear that a grouping with respect to the number of C is no longer found in the mass spectrum.

Since these compounds form a distinct class, which is discernible by mass spectrometry, and because they are the expected products of a different reaction mechanism, we call them *aromers*, although they are still PAH in principle. For the latter reason and since their individual molecular formulas are not always known, they are not indicated separately in Fig. 5. The word *aromer* indicates the *aro*matic nature of the oligo*mers* formed through combination of PAH. Besides growth by addition of small hydrocarbons, combination of PAH is a second very effective growth process. The aromers are nonplanar molecules (or ions, respectively) with a large flexibility for bringing near peripheral C atoms to each other for unimolecular dehydrogenation. On the other hand, they may grow further by both mechanisms and are still potential precursors of soot particles. It is the structure of these aromers that offers an explanation that either soot or fullerenes may be formed from them, depending on the burning conditions and the chemical environment in the flame.

Fullerene Formation Mechanism

From the upper shaded area in Fig. 5, a downward arrow toward C_{60} has tentatively been drawn. Together with the first arrow, it should indicate that fullerene formation must be preceded by aromer formation with a subsequent rapid loss of hydrogen. Most of the intermediates between a hydrogen-rich aromer and a fullerene cannot be observed. But the last stages with very little hydrogen in the molecule and their development to a fullerene can be seen from the negative ion mass spectra. To illustrate this, the development of the negative ion mass spectra in the region of C_{50}^- to C_{52}^-, for example, from h = 6–9 mm, is shown in Fig. 6. The mass spectrum of h = 6 mm shows signals with nearly the same intensity spaced by one mass unit. These signals represent a pool of aromers as possible precursors of fullerenes. Closing of the cage by a kind of zipper mechanism [16], by which most of the peripheral H atoms of the two parts of the aromer are split off and pentagons are formed, is first observed in the spectrum from 7 mm. It still carries 6 to 7 H atoms, probably

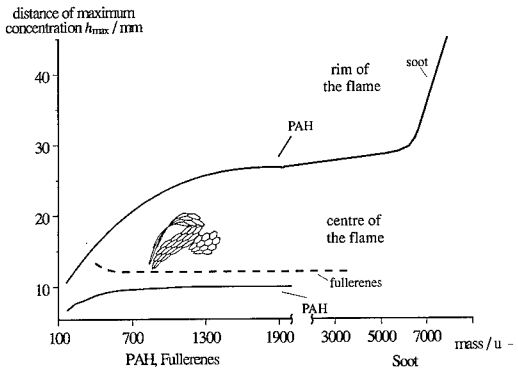

FIG. 7. Distance of maximum concentration of PAH^+, fullerene ions, and charged soot particles plotted versus their respective masses.

with carbon atoms that are shared by a pair of adjacent pentagons. These H atoms are split off in consecutive reactions until C_{50}, which is hardly discernible at 7 mm, is complete with its isotopic peak pattern at 9 mm.

These residual H atoms are split off less rapidly than all the others of the original aromer. This may be because their removal requires simple C–H bond breaking to take place while the majority of H atoms is lost as H_2 in concerted reactions of ring formation during the cage closure. The same development can also be seen for C_{60} and C_{70}. In fact, the $C_{60}H_x$ group is the first to appear from the aromer mass spectrum. From the number of just 60, 70, or 50 C atoms, we conclude that these cages are already closed. The zipper mechanism of ring closure and pentagon formation must be accompanied by a shifting of the pentagons to energetically favorable positions to avoid too much bond tension during the closure of the cage.

Fullerenes smaller than C_{60} have been extracted from neither soot of flames [21] nor soot of graphite evaporation [22]. Nevertheless, these small fullerenes are clearly detectable with on-line mass spectrometry. The smallest fullerene detectable as positively charged ion is C_{32}^+, which was formed in benzene flames, while the smallest negatively charged fullerene has 30 carbon atoms and occurs in naphthalene flames [23]. The formation of these small fullerenes starts a little later with respect to the formation of C_{60} and other large fullerenes (see Fig. 3 and Fig. 7 dashed line). This indicates the possibility that small fullerenes are formed by partly oxidative decomposition of large fullerenes that have not achieved their thermodynamically favored structure.

The possible role of partial oxidation in the fullerene formation mechanism is not yet clear. The overall reaction to fullerenes by combination of PAH and subsequent total loss of hydrogen is very endothermic [24]. Probably the cage closure is partly promoted by an oxidative removal of some extra carbon and hydrogen atoms. However, oxygenated incomplete fullerenes have not been detected by mass spectrometry.

Fullerenes and Soot in the Center and at the Rim of the Flame

Whether aromers react finally to give soot or to produce fullerenes is a question of temperature and of the concentration of growth species such as acetylene. In other words, for fullerene formation, unimolecular reactions (cage closure reactions, breaking of C–H bonds, intramolecular rearrangements) are important steps. These kinds of reactions have comparatively large activation energies and are favored by a higher flame temperature. In the center of the benzene flame, the temperature is considerably higher (maximum 2200 K) [7] than at the rim of the flame. Therefore, the unimolecular reactions to produce fullerenes are fast enough. On the other hand, oxidation of PAH is also fast enough to prevent the PAH from growing to more than about 2000 u. Consequently, no soot is formed in the center of the flame.

Conversely, growth reactions of PAH and of aromers are slower at the rim of the flame than in the center of the flame, because the temperature is lower at the rim. However, fullerene formation is much slower because its steps have a larger activation energy than the growth reactions. Therefore, fullerenes are not noticeably formed. Oxidation reactions of PAH are also slower at the rim so that growth can continue and soot is formed.

The different situations in the center and at the rim can also be illustrated in a diagram in which the location of maximum concentration h_{max} (see Fig. 3) of a PAH is plotted versus the mass of the PAH (Fig. 7). The upper solid curve represents the rim of the flame ($b = 0$ mm), while the lower curve shows the situation in the center of the benzene flame ($b = -25$ mm). At both lateral positions, the distance of maximum concentration h_{max} at first increases with increasing mass up to 500 u in the center and about 1300 u at the rim. Then both curves show a plateau at a constant distance h_{max}. All masses between 500 u and about 2000 u and between 1300 u and about 5000 u, respectively, maximize at the same distance from the burner plate, depending on the lateral position. This distance is $h \approx 10$ mm in the center and $h \approx 27$ mm at the rim of the benzene flame.

However, at the rim there is more growth of the soot particles. The concentration maxima of particles with a certain mass are again shifted to larger distances with increasing mass. In the center of the flame, no second slope of the curve is detected. The curve shows a plateau at the respective maximum value h_{max} and stops at about 2000 u. There is no

formation of soot particles in the center of the flame. The corresponding curve of h_{max} of fullerene concentrations in the center of the flame is indicated by the dashed line. It is horizontal from C_{50} to about C_{300}. That is, these fullerenes reach their maximum simultaneously. For fullerenes with less than 50 C atoms, the respective h_{max} are shifted toward higher values. This means that the smaller fullerenes are formed a little later.

Conclusions

A new class of particles has been detected in flames to be precursors to both fullerenes and soot particles. This new class has been named *aromers* because of their structural properties. The products of these particles are determined by the flame temperature and the concentration of growth species such as acetylene. At a high temperature in the center of the flame and with a relatively low concentration of acetylene, these particles form fullerenes, while at low temperature and/or high concentration of small growth species, mainly soot is formed.

Acknowledgments

We gratefully acknowledge the financial support extended by the Fonds der Chemischen Industrie, the Deutsche Forschungsgemeinschaft, and the Land Hessen for this research.

REFERENCES

1. Bittner, J. D. and Howard, J. B., *Eighteenth Symposium (International) on Combustion,* The Combustion Institute, Pittsburgh, 1981, p. 1105.
2. Ahrens, J., Kovacs, R., Shafranovskii, E. A., and Homann, K.-H., *Ber. Bunsenges. Phys. Chem.* 98:265–268 (1994).
3. Howard, J. B., *Twenty-Fourth Symposium (International) on Combustion,* The Combustion Institute, Pittsburgh, 1992, p. 933.
4. Homann, K.-H., Morgeneyer, W., and Wagner, H. G., *Combustion Institute European Symposium 1973,* London, 1973, pp. 394–399.
5. Homann, K.-H. and Ströfer, E., *Soot in Combustion Systems and Its Toxic Properties,* Plenum Press, New York, 1983, pp. 217–242.
6. Homann, K.-H. and Wolf, H., *Ber. Bunsenges. Phys. Chem.* 87:1073–1077 (1983).
7. Bonne, U. and Wagner, H. G., *Ber. Bunsenges. Phys. Chem.* 69:35–48 (1965).
8. Bönig, M., Feldermann, B., Jander, H., Luers, B., Rudolph, G., and Wagner, H. G., *Twenty-Third Symposium (International) on Combustion,* The Combustion Institute, Pittsburgh, 1990, pp. 1581–1587.
9. Keller, A., private communication, 1995.
10. Bachmann, M., Wiese, W., and Homann, K.-H., *Twenty-Fifth Symposium (International) on Combustion,* The Combustion Institute, Pittsburgh, 1994, pp. 635–643.
11. Gerhardt, P., Löffler, S., and Homann, K.-H., *Twenty-Second Symposium (International) on Combustion,* The Combustion Institute, Pittsburgh, 1988, pp. 395–401.
12. Gerhardt, P. and Homann, K.-H., *Combust. Flame* 81:289–303 (1990).
13. Wegert, R., Wiese, W., and Homann, K.-H., *Combust. Flame* 95:61–75 (1993).
14. Bachmann, M., Wiese, W., and Homann, K.-H., *Combust. Flame* 101:548 (1995).
15. Löffler, S. and Homann, K.-H., *Twenty-Third Symposium (International) on Combustion,* The Combustion Institute, Pittsburgh, 1990, pp. 355–362.
16. Baum, T., Löffler, S., Löffler, P., Weilmünster, P., and Homann, K.-H., *Ber. Bunsenges. Phys. Chem.* 96:841–857 (1992).
17. Griesheimer, J., private communication, 1995.
18. Mukherjee, J., Sarofim, A. F., and Longwell, J. P., *Combust. Flame* 96:191–200 (1994).
19. Lias, S. G., Bartmess, J. E., Liebman, J. F., Holmes, J. L., Levin, R. D., and Mallard, W. G., "Gas Phase Ion and Neutral Thermochemistry," *J. Phys. Chem. Ref. Data* 17:1 (1988).
20. Frenklach, M., Clary, D. W., Gardiner, W. C., and Stein, S. E., *Twentieth Symposium (International) on Combustion,* The Combustion Institute, Pittsburgh, 1984, pp. 887–901.
21. Howard, J. B., McKinnon, J. T., Makarovsky, Y., Lafleur, A. L., and Johnson, M. E., *Nature* 352:139–141 (1991).
22. Krätschmer, W., Lamb, L. D., Fostiropoulos, K., and Huffman, D. R., *Nature* 347:354 (1990).
23. Bachmann, M., Griesheimer, J., and Homann, K.-H., *Chem. Phys. Lett.* 223:506–510 (1994).
24. Hites, R. A. and Simonick, W. J., *Calculated Molecular Properties of Polycyclic Aromatic Hydrocarbons,* Elsevier, Amsterdam, 1987.

COMMENTS

Vadim G. Knorre, University MADI, Russia. It is well known that different investigators mean different things while speaking about soot. Are you sure or do you believe that soot formed at a pressure 27 mbar is quite the same as soot formed at a pressure 27 bar? In other words, did you compare the properties of soot (structure, chemical composition) formed in your experiment with soot described in other work? I think this should be done before your work could be generalized.

Author's Reply. In this work the pressure was not varied. It is known that the fullerene yield decreases with pressure so that in flames even at atmospheric pressure fullerene formation is negligible. As a consequence, there are practically no fullerenes in commercial carbon black. It is true that the properties of soot change when going to very high burning pressure. But this has nothing to do with the absence of fullerenes. Increasing the pressure also increases the absolute concentration of unsaturated aliphatic and aromatic hydrocarbons and enhances the bimolecular growth reactions towards soot, but not the unimolecular reactions necessary for fullerene formation. These can be slowed down by decrease in temperature due to strong soot radiation.

•

J. B. Howard, MIT, USA. How high can the C/O ratio become while still obtaining the very interesting condition of solely fullerenes formation with no soot?

Author's Reply. Judging from the formation of charged soot particles, which is always a sensitive indication of the presence of particles of some thousand u, soot formation starts in the center of a flat benzene/oxygen flame (27 mbar, v_u = 45 to 50 cm/s) at C/O $\geq$ 0.92 to 0.93 [1]. This ratio decreases with decreasing maximum flame temperature, if the unburned gas velocity is lowered. Since the charged soot particles had been withdrawn through a conical probe which cools the flame by about 200 K, this figure might change in undisturbed flames. Absorption in the center of benzene flames with C/O $<$ 0.92 which has been reported in earlier work [2] must be due to large PAH and fullerenes. It can be assumed that this ratio also decreases with increasing burning pressure. The influence of temperature on the ratio fullerenes/soot has also been observed with acetylene flames [3].

REFERENCES

1. Homann, K.-H. and H. Wolf, *Ber. Bunsenges. Phys. Chem.* 87:1073 (1983).
2. Homann, K.-H., Morgeneyer, W., and Wagner, H. Gg., *Combustion Institute European Symposium 1973*, London, 1973, pp. 394–399.
3. Bachmann, M., Wiese, W., and Homann, K.-H., *Twenty-Fifth Symposium (International) on Combustion, The Combustion Institute, Pittsburgh, 1994, pp. 635–643.*

•

A. J. E. Akanetuk, Stanford University, USA. Is the functional dependence of soot/fullerene partition on temperature path independent? For instance, after soot is formed at low temperature, could it be converted to fullerene by increasing the temperature? If the answer is no, how high must the heating rate for reaching high temperature be for fullerene to be formed without soot intermediate?

Author's Reply. The possibility of producing fullerenes from soot in flames has been discussed [1]. From comparing fullerene profiles with the development of mass distributions of very small soot particles in a low-pressure acetylene/oxygen flame it was concluded that, if any fullerenes were formed from soot, this could only happen from particles which had not gained a mass larger than approximately $2 \cdot 10^4$ u. If this really occurs, it would mostly concern very large fullerenes $> C_{200}$ which have only been detected in the presence of soot. However, in these flames the temperature was higher than at the rim of the benzene flame reported in this work.

Increasing the temperature of soot particles in the same pre-mixed flame in which they have been formed can practically only be accomplished by external means, for example a laser beam. It is known that soot particles can thus be evaporated to form C_1, C_2 and possibly other small carbonaceous particles. But it can be excluded that fullerenes are formed from these species in flames. As soot is not formed from fullerenes there is no reverse reaction in a thermodynamical sense from soot to fullerenes. Heating the peripheral zone of a benzene flame by a neighboring fuel-rich flame, which does not just burn the soot, creates the same situation as in the middle of the single flame. Soot is not formed, but the fullerene concentration increases [2].

REFERENCES

1. Baum, Th., Löffler, S., Löffler, Ph., Weilmünster, P., and Homann, K.-H., *Ber. Bunsenges. Phys. Chem.* 96:841–857 (1992).
2. Bachmann, M., Wiese, W., and Homann, K.-H., *Twenty-Fifth Symposium (International) on Combustion,* The Combustion Institute, Pittsburgh, 1994, pp. 635–643.

•

H. F. Calcote. You report a large concentration of $C_{13}H_9^+$ in benzene/oxygen flames in agreement with our 1981 results. In previous work you reported that $C_{13}H_9^+$

could not be measured in benzene/oxygen flames. What has changed?

Here, and in many papers since 1987, you measure ions and interpret them as neutral PAH. Ions and neutral PAH react very differently, with no coupling between them: (1) At soot threshold there is no change in the concentration of PAH or any other neutral species, but there is a dramatic change in ion concentration and mass distribution. (2) The change in concentration with increasing mass and size is different for ions and PAH. (3) The peak concentration for individual ions shifts position downstream with increasing mass very little compared with neutral PAH shifts. (4) Ion—molecule growth reactions are much faster than PAH growth reactions, and ions require fewer reaction steps in current reaction mechanisms for the same increase in mass.

Why not interpret your results in terms of an ionic mechanism? Wherever you refer to a neutral species, you would call it what you actually measure—an ion. Your results support the ionic mechanism of soot formation.

Author's Reply. Concerning the formation of $C_{13}H_9^+$ you are right. This is formed in benzene/oxygen flames as in acetylene flames. The reason why the species $C_{12}H_9O^+$ was reported instead [1] is the following: Later work (not yet published) using a reflection TOF-MS showed that PAH^+ appear in groups with the same number of C but different numbers of H. Furthermore, the spectra of these groups C_xH_y are superimposed by ions $C_{x-1}\ H_{y-4}\ O^+$ in the oxidation zone. This led to the erroneous identification in the former work.

Work is in progress to determine absolute concentration profiles of neutral PAH larger than coronene and to compare them with those of ions with the same mass. Preliminary results from benzene flames which relate to the questions are the following: Up to a mass of about 300 u the maximum neutral PAH concentrations decrease strongly with increasing mass. In the mass range beyond there is only a very smooth decrease when the PAH grow larger. The concentration of large ions still increases with increasing mass in this range, since their ionization potential decreases. However, the position of the maxima in the profiles of PAH and the respective ions coincide. This indicates that there is no extra fast growth rate of the large ions over that of the neutral PAH. That ion/molecule growth reactions are much faster than those of the respective neutrals is only true for very small hydrocarbon radical ions, not for the very large PAH ions where the charge is delocalized.

There are many studies much more suitable for the discussion of the role of large ions in soot formation than this work. Here we wanted to show that, depending on the burning conditions and the temperature profile in a flat flame, precursors can either go to soot or to fullerenes.

REFERENCE

1. Löffler, S. and Homann, K.-H., *Twenty-Third Symposium (International) on Combustion,* The Combustion Institute, Pittsburgh, p. 355, (1990).

Twenty-Sixth Symposium (International) on Combustion/The Combustion Institute, 1996/pp. 2269–2275

SOOT PRECURSOR MATERIAL: VISUALIZATION VIA SIMULTANEOUS LIF-LII AND CHARACTERIZATION VIA TEM

RANDALL L. VANDER WAL
Nyma@ NASA-Lewis
Cleveland, OH 44135, USA

Simultaneous combined laser-induced fluorescence and laser-induced incandescence (LIF-LII) images are presented for both a normal and inverse diffusion flame. The excitation wavelength dependence distinguishes the LIF and LII signals in images from the normal diffusion flame while the temporal decay distinguishes the signals in images of the inverse diffusion flame. Each flame presents a minimum in the combined LIF-LII intensity in a region separating the fuel pyrolysis and soot containing regions. Opacity, geometric definition, and extent of crystallinity measured through both bright and dark field transmission electron microscopy (TEM) characterizes the thermophoretically sampled material from within this minimal LIF-LII intensity region. TEM analysis reveals rather different soot processes occurring within the normal and inverse diffusion flame. In the normal diffusion flame, rapid chemical and physical coalescence of PAHs results in initial formation of soot precursor particles that are highly crystalline and evolve toward fully formed soot. In the inverse diffusion flame, rapid coalescence of pyrolysis products occurs, producing tarlike, globular structures equivalent in size to fully formed soot aggregates but with markedly less crystallinity than normal-appearing soot. These different material properties are interpreted as reflecting different relative rates of chemical and physical coalescence of fuel pyrolysis products versus carbonization. Significantly, these TEM images support qualitative photophysical arguments suggesting that, in general, this "dark" region observed in the LIF-LII images demarcates a transitional region in which a fundamental change in the material chemical/physical properties occurs between solid carbonaceous soot and condensed or gaseous molecular growth material.

Introduction

The intrinsic connection between polycyclic aromatic hydrocarbons (PAHs) and soot production within both diffusion [1–3] and premixed flames [4–7] suggests an intermediate stage or process whereby the molecular species are transformed to solid particulate matter. An early theory of soot formation held that large liquid droplets formed by rapid condensation of fuel pyrolysis products (mainly PAHs) subsequently transformed into soot [8]. Fuel pyrolysis studies in shock tubes [9], flow reactors [10], and premixed flame studies [5,11] provide varying degrees of support for this mechanism. An alternate soot-formation process begins with small (1–5 nm), individual entities called soot-precursor particles [12]. The existence of soot-precursor particles has been inferred based on light-scattering measurements in premixed flames [13], diffusion flames [14], and direct visualization via transmission electron microscopy (TEM) of sampled material in diffusion flames [12,15,16] and low-pressure premixed flames [4].

Although both soot formation mechanisms begin with the coalescence of fuel pyrolysis products, the difference between these mechanisms depends on the relative rates of subsequent mass growth versus carbonization and will be highly dependent on the combustion process. Carbonization in this context is understood to represent a complex series of chemical processes including but not limited to processes involving dehydrogenation and polymerization. In the former mechanism, soot mass growth is mainly completed before carbonization [8,10], whereas in the latter mechanism, carbonization appears to occur faster than mass growth [12,15]. Support for the latter process is based on the observations of continued growth of individual primary particles before significant agglomeration producing aggregates [14,17], the similar appearance of these individual primary particles (with diameter >10 nm) to those within soot aggregates [18], and laser microprobe mass analysis of soot-precursor particles revealing a hydrogen mole fraction similar to that of fully aged soot [12,15].

Given the critical link soot-precursor material (either as coalescing liquid droplets or soot-precursor particles) provides between molecular fuel pyrolysis products such as PAHs and carbonaceous soot, both spatial location and characterization of their chemical/physical properties is essential in understanding soot-formation and growth processes [8–12,15]. No reported measurements using in situ optical techniques have identified the spatial location of soot

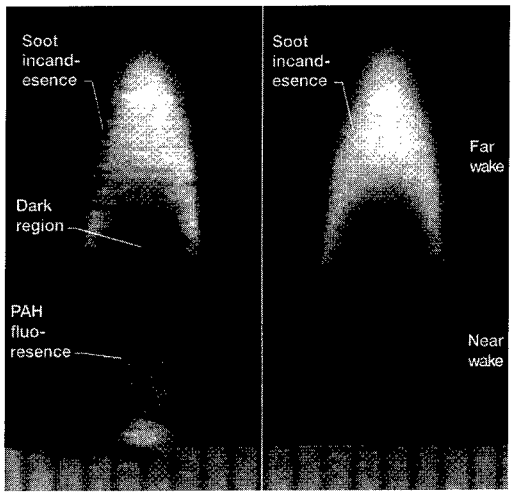

FIG. 1. (a) Simultaneous LIF-LII image of a fiber-supported burning fuel droplet (*n*-decane) produced by 266-nm excitation and (b) LII image of a similar droplet using 1064-nm excitation light. Each image was obtained 300 ms after ignition. The spatial scale is in millimeters. In each image, the droplet is spatially located just below the ruler top edge.

precursor material and characterized the material transformation processes via laser-induced fluorescence (LIF) measurements of PAHs (soot-inception species) and laser-induced incandescence (LII) measurements of soot (final product) within soot-containing diffusion flames.

Thus, the purpose of this paper is to combine LIF-LII measurements to identify the spatial location of the chemical and physical transformation of material toward solid carbonaceous material. Then this transformation is optically characterized with these optical measurements. LIF has successfully monitored PAHs within both premixed [11,13] and diffusion flames [1–3,16,19,20]. Similarly, LII has revealed soot concentrations in both one- and two-dimensional imaging configurations [21–25]. Previous combined LIF-LII measurements did not examine the transition between the LIF and LII signals along a well-defined streamline such as exists along the axial centerline of a gas-jet diffusion flame [1,24]. In this paper, simultaneous two-dimensional LIF-LII images of both a normal and inverse diffusion flame (IDF) are presented and characterized by the excitation wavelength dependence and temporal decay characteristics of the signals. The spatial identification provided by the combined LIF-LII images allows precise thermophoretic sampling measurements to be made with detailed characterization of the sampled material via both bright- and dark-field TEM.

Experimental

Light at 1064 and 266 nm was used for LII and combined LIF-LII measurements, respectively. An 8× Galilean telescope of spherical UV fused silica lenses followed by a pair of cylindrical lenses formed the laser beam into a sheet of 20 mm height. The intensity for the 1064 nm light sheet was estimated to be 2.5×10^7 W/cm^2 based on a 10 ns laser pulse and sheet thickness of 750 μm. Using a 5 ns pulse width (FWHM) and 300-μm sheet thickness for the 266-nm light yielded an approximate intensity of 9×10^6 W/cm^2. For two-dimensional images, a gated intensified camera fitted with an ultraviolet *f*4.5/105-mm (adjustable) focal length camera lens and extension tube captured the LII and/or LIF images. A bandpass filter centered at 400 nm with 70 nm FWHM bandwidth preceded the gated intensified array camera for both the LII and simultaneous LIF-LII measurements. The spatial resolution was approximately 27 pixels per millimeter. A frame grabber was used to digitize the images for transfer to the host computer.

The first flame system studied was a fiber-supported burning fuel droplet that presents a (normal) diffusion flame where the entire fuel source and pyrolysis region is enclosed within the flame front, preventing oxidative pyrolysis. The small spatial scale associated with such an envelope flame is well matched to the spatial dimensions of the TEM grid. Individual 5 μL droplets of *n*-decane ignited by a spark served as the fuel for the droplet flame. A beam block shielded the droplet from the laser light to prevent potential laser-droplet interactions.

The second flame system chosen was an inverse diffusion flame. An oxidizer flow rate of 470 sccm with an O_2/N_2 ratio of 22.5 issued from a 17-mm (i.d.) tube while a fuel-N_2 flow rate of 5.0 slpm with a C_2H_4/N_2 ratio of 0.4 flowed from a surrounding annulus of 47 mm (i.d.). Hastalloy honeycomb (0.064 cell size × 1.25 cm thick) preceded by a layer of glass beads (3 cm thick) served as flow straighteners. An outer shroud (73 mm inner ring diameter) of N_2 at roughly 25 slpm stabilized the flame and also served to dilute unburned fuel gas before venting. To eliminate the effects of room drafts, a 70 mm O.D. quartz tube fitted with slots for sampling access sat atop the outer portion of the burner. With the fuel source surrounding the central oxidizer jet, thermophoretic sampling within the fuel-rich side of the diffusion flame is readily accomplished without penetrating the flame front, thereby minimizing probe-induced disturbance of the flame. Thermophoretic sampling was accomplished using an air-actuated piston driving a rod holding the TEM grid holder and grid [26].

Observations

Figure 1a presents a simultaneous LIF-LII image of a fiber-supported burning fuel droplet using 266

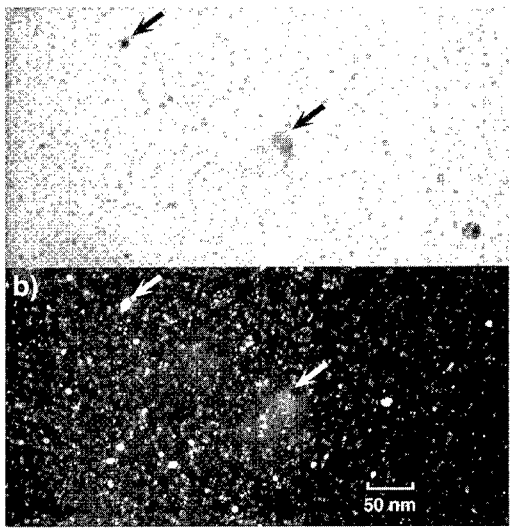

FIG. 2. (a) Bright-field TEM and (b) dark-field TEM of thermophoretically sampled material from within the dark region illustrated in Fig. 1a. The markers indicate common reference points in each panel.

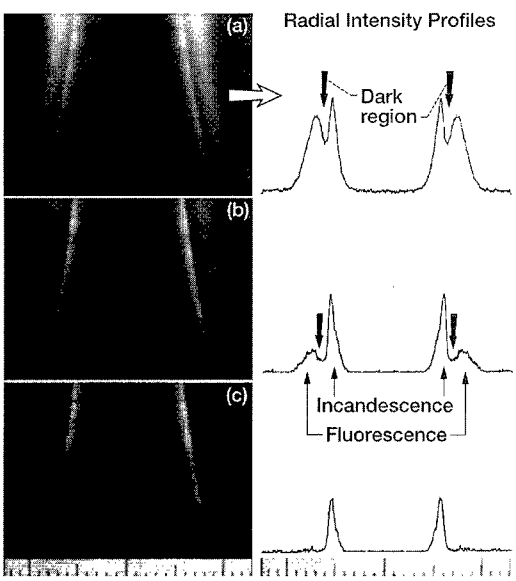

FIG. 3. Simultaneous LIF-LII images of an inverse diffusion flame of C_2H_4 with radial intensity profiles obtained at a height of 13.5 mm above the burner. The spatial scale is in millimeters. Ten individual LIF-LII images were averaged together to obtain the panels shown in the figure. Each image was obtained using the same camera intensifier gain and gate duration. The different images correspond to different signal collection time delays after the excitation laser pulse and are (a) 40 ns, (b) 80 ns, and (c) 160 ns.

nm excitation light, while Fig. 1b presents a LII image obtained using 1064-nm light. This excitation wavelength dependence can be used to distinguish molecular fluorescence and soot incandescence as discussed later. The laser-induced emission (LIE) intensity in Fig. 1a decreases with increasing distance (or equivalently residence time) above the droplet, passes through a minimum, hereafter referred to as a dark region, and then increases, whereas only LIE intensity in the far wake region is seen in Fig. 1b.

Figure 2a shows a bright-field TEM image of the thermophoretically collected material from within the dark region illustrated in Fig. 1a. Numerous small, individual particles are observed. From the indicated magnification, the particle sizes range from 1–4 nm with an average size of 3 nm. Figure 2b shows the corresponding dark-field image of the same material shown in Fig. 1a. The dark-field TEM image shows that each individual particle consists of two to three bright points, hereafter referred to as crystallites.

Figure 3 shows a sequence of LIF-LII images of the inverse diffusion flame along with radial intensity profiles where for each image, the burner surface lies 1 mm below the lower edge of the image. As shown by both the images and the corresponding radial intensity profiles (corresponding to the arrow location in Fig. 3a); a minimum in the LIE intensity exists between the inner and outer annular regions. Similar to the droplet flame, this minimum in the combined LIF-LII intensity is also hereafter referred to as the dark region.

Figure 4a shows a bright-field TEM image of thermophoretically sampled material from within the dark region of Fig. 3. The low magnification provides an overview of the material variation along the indicated radial direction within the flame. Figure 4b shows a higher magnification of material seen in Fig. 4a. A distinct contrast in both the shape definition and opacity to the electron beam is observed between the two structures shown in Fig. 4b. Interestingly, while the less-opaque object seems to possess a larger diameter than the other structure, it appears more transparent to the electron beam despite presenting more material in the electron beam path. Figure 4c shows the corresponding dark-field TEM image of the structures seen in Fig. 4b. The more-opaque structure in the bright-field image contains many more crystallites in the dark-field image compared to the other structure. The fuzziness surrounding the less-bright object is not due to focusing (both structures lie within 200 nm of each other) but represents less-dense or less-crystalline material.

Discussion

LIF-LII Signals

Both the excitation wavelength dependence and radiative lifetime distinguish the LIF signal from the

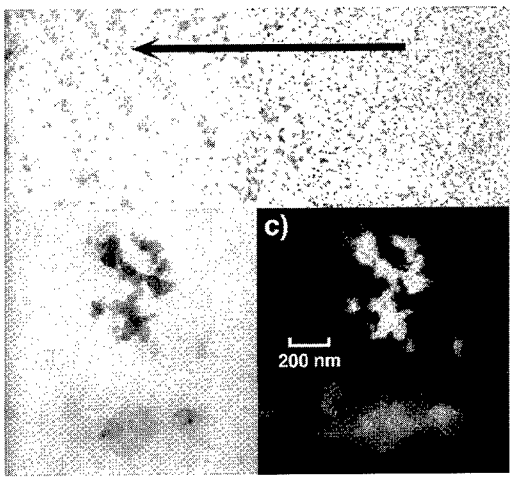

FIG. 4. (a) Bright-field TEM at low magnification illustrating the variation in soot morphology across the soot-containing region. The arrow is directed radially outward. The image is meant to convey the range of particle morphologies observed. (b) Bright-field TEM contrasting the soot morphologies observed in (a). (c) Dark-field TEM of the corresponding structures observed in (b). For each image, the sampling height was 13.5 mm above the burner.

LII signal in the images in Figs. 1 and 3, respectively. Light at 1064 nm will not produce molecular fluorescence in the visible, whereas 266 nm light is known to readily excite electronic transitions in a variety of combustion intermediates resulting in fluorescence [27,28]. To excite visible fluorescence, multiphoton absorption of 1064 nm light that could occur through a nonresonant multiphoton absorption process is necessary. Not only is infrared multiphoton absorption improbable given the laser intensities used, but even if it did occur, it would likely result in molecular dissociation from the ground electronic state, which generally does not lead to photofragment emission [29]. Thus, the presence of signal in the near-wake region using 266 nm excitation and its absence when using 1064-nm light indicates that this signal is LIF, likely arising from PAH fluorescence. Since both 1064 and 266 nm light is readily absorbed by soot, at sufficient intensities, each excitation wavelength is capable of producing LII [16]. Thus, the similar spatial extent of the laser-induced emission signal in the far-wake region of Figs. 1a and 1b using either 266 or 1064 nm light indicates that this LIE signal is LII.

While fluorescence from PAHs within diffusion flames is generally detectable only tens of nanoseconds after laser excitation [3,16], LII is detectable hundreds of nanoseconds after the laser pulse at moderate laser intensities [16,21–25]. The slower temporal decay of LII compared to fluorescence results from cooling processes, which determine the LII signal decay, being slower than collisional quenching, which determines the fluorescence decay rate within atmospheric pressure flames [16]. Thus, the rapid temporal decay of the LIE signal in the outer annular region of the inverse diffusion flame shown in Fig. 3 indicates that this signal is molecular fluorescence (LIF). Conversely, the long temporal decay of the signal within the annular extending hundreds of nanoseconds (in contrast to tens of nanoseconds for the fluorescence) confirms the identity of this signal as soot incandescence (LII).

TEM Images

Droplet

The small size (1–4 nm) of the particles seen in Fig. 2a is characteristic of those observed by other researchers as indicating the first incipient soot particles [4,12,15,16]. The intermediate spatial location of these particles between the PAH- and soot-containing regions confirms the transitional role of soot-precursor particles in the soot-formation process. At slightly higher axial heights within the dark region shown in Fig. 1a, larger individual particles of greater than 5 nm diameter were found, indicating further mass growth.

Despite their small size and close temporal origin to molecular PAHs, the soot-precursor particles observed in Fig. 2 are crystallized. The bright points in the dark-field TEM image of Fig. 2b are interpreted as crystallites appropriately oriented to diffract a portion of the electron beam into the viewing angle. In fully formed carbon black particles, X-ray diffraction has shown each particle to be made up of a large number of crystallites ($\sim 10^{+4}$) [30]. Each crystallite consists of 5–10 sheets of carbon atoms with each sheet having a length or breadth of 20–30 Å. A random packing of such crystallites is commonly considered amorphous carbon [30]. Diffraction from ordered carbon layer planes indicates carbonization of these precursor particles has occurred, with the chemical/physical structure no longer resembling a "clump" of condensed hydrocarbons but rather a disorganized solid. Such a rapid material transformation is feasible because LMMA analysis of soot precursor particles collected within an ethylene-air diffusion flame indicates that graphitization of soot-precursor particles can occur rapidly, ($\sim$10 ms), resulting in a particle hydrogen mole fraction, X_H, of 0.15, typical of mature soot released from flames [12]. As the transparency of these structures increased in the bright field TEM images, the number of crystallites within these structures decreased, as observed in the dark-field TEM images. In summary, these results indicate that carbonization proceeds rapidly compared to mass growth for the soot-precursor particles in the droplet flame.

Inverse Diffusion Flame

Numerous soot-formation/growth studies have used shock tubes [9,31,32], flow reactors [8,10], and *in situ* probe sampling within premixed [4–7] and diffusion flames [2,20,33]. With the exception of the carbon black industry, few fuel pyrolysis studies have used TEM for product morphological analysis. One particularly revealing study, however, sampled the exhaust within a flow tube reactor of 2% benzene in N_2 at 1383 K at different positions (residence times) [10]. With increasing residence time, the rapid decrease in the extractable tar content coincided with an equally rapid increase in the carbonaceous residue content of the sampled material. TEM micrographs of the sampled material at early residence times (<50 ms) revealed a condensed phase of semitransparent tarlike material existing in large "globs," far different than the usual chainlike structures normally associated with soot. Hereafter, the term *tar-like* is used to denote a disorganized, unstructured solid material (potentially a highly viscous "liquid" at flame temperatures) with both a lower degree of crystallinity and C/H ratio compared to ordinary soot commonly observed.

The TEM observations in the inverse diffusion flame shown in Fig. 4 are consistent with these results. As seen in the bright-field TEM image of Fig. 4b, the decreased opacity despite the larger size indicates that the tar-like material appears less dense to the electron beam. The relatively uniform opacity of the tarlike material suggests a rather uniform composition. Far less crystallinity of the tarlike substance is revealed by the markedly lower intensity in the dark-field TEM image of Fig. 4c compared to the normal-appearing soot aggregate. The chainlike resemblance of the tar-like substance indicates that agglomeration of the pyrolytic material has occurred before carbonization [8,10]. The poorer geometrical outline is consistent with the formation of the tarlike aggregate via pyrolytic deposition.

Just as for normal diffusion flames, the fuel-rich side of the inverse diffusion flame closely resembles a pyrolytic system with the flame front presenting an oxygen barrier. In this context, the present results indicate that rapid deposition of pyrolytic material (mass growth) occurs before significant carbonization [8,10]. This accounts for the rather uniform tar-like appearance of the structures shown in Fig. 4, the lack of opacity in the bright-field TEM images (Figs. 4a and 4b), and the lack of crystallinity in the dark-field TEM image (Fig. 4c). While the images in Fig. 4 do not prove soot formation occurring via carbonization of large tar-like structures, they do indicate that significantly different relative rates of soot-precursor material nucleation, coalescence, and growth occur relative to carbonization in this flame system compared to the droplet flame (normal diffusion flame), resulting in very different material properties compared to normal carbonaceous soot as discussed next.

The Dark Region

As seen in Figs. 1a and 3, a minimum occurs in the combined LIF and LII intensity spatially located between the PAH- and soot-containing regions. The fluorescence intensity decrease is likely due to three factors: (a) an increase in the size of PAHs through molecular growth, (b) a decrease in the gas-phase PAH concentration, and (c) PAH coalescence into soot-precursor particles. As PAHs grow in size, the number of rovibrational and electronic quantum states increases dramatically [34]. With an increased quantum state density, nonradiative transitions between electronic states increases because of increased coupling between these states [34]. Thus, the fluorescence quantum yield decreases. Secondly, as the PAHs coalesce into particles, the gas-phase number concentration of PAHs decreases since large PAHs presumably serve as building blocks for soot-precursor particles, while small PAHs serve as initial mass growth material for the precursor particles [35,36]. Thirdly, as carbonization continues, the PAH "molecules" lose their individual identity and become assimilated into an object that is becoming more solid in form. With increasing solid structure, the probability for nonradiative decay increases dramatically because of the far higher quantum state density [37]. Thus, while the particle readily absorbs light and may still fluoresce because the constituent "molecules" possess highly absorbing chromophoric groups, with increasing carbonization, the fluorescence quantum yield decreases relative to isolated gas-phase molecules, eventually becoming negligible. These three factors account for the decrease in fluorescence intensity with increasing axial height seen in Fig. 1a. Similarly, the probability for nonradiative decay is greatly increased in condensed and/or partially carbonized tar-like material relative to gaseous species, thus accounting for the fluorescence intensity decrease with decreasing radial distance seen in Fig. 3.

With increasing solid character of the particle, rapid internal dissipation of energy deposited through multiphoton absorption occurs [38]. If a sufficient number of photons is absorbed, the particle will be heated to incandescence temperatures. The detailed chemical and physical structure of the particle will determine the fate of the particle upon rapid, high-energy deposition. Very small soot-precursor particles are thought to possess a high number of reactive radical sites accounting for the rapid mass growth [35]. This large number of reactive sites indicates that the extent of bonding of the aromatic structures within the compound is very incomplete. Upon rapid energy deposition, bonds linking aromatic units to the solid structure may sever, leading

to fragmentation. Until bonding of adjoining molecular units is substantially complete, fragmentation of the particle will likely occur during the energy deposition process, resulting in minimal or no incandescence. Similarly, the tar-like objects that are only partially carbonized may be intermediate between molecular and solid structures [9–11,32]. If enough energy accumulates within the particle through absorption of multiple photons (not necessarily simultaneously), molecular fragmentation rather than incandescence would more likely occur given the largely molecular structure. Thus, during this transitional period in which significant chemical and physical material transformation processes are occurring, both nonradiative transitions and/or fragmentation are likely to result from laser excitation. Consequently, minimal intensity is observed in either the LIF or LII signals, thereby accounting for the dark region observed in the simultaneous LIF-LII images.

These changes in the photophysical properties reflect the chemical and physical transformation in material properties occurring between molecular material (condensed or gaseous) and solid carbonaceous soot. This transformation appears general despite the very different apparent relative rates of soot-precursor material growth and coalescence versus carbonization within the normal and inverse diffusion flames. Both the decreasing opacity with increasing radial distance (or increasing tar-like appearance) of the soot structures seen in the bright-field TEM images of Figs. 4a and 4b and decreasing crystallinity seen in the dark-field TEM image of Fig. 4c reveal a consistent physical/chemical change in the material composition. With increasing radial distance from the centerline in the inverse diffusion flame, the material changes from a disorganized yet highly crystalline solid to barely visible condensed molecular matter. A similar material transformation is suggested by the soot-precursor particles observed in Fig. 2. In contrast to the large structures observed in Fig. 4, the initial small structures and subsequent growth suggest a soot-formation process proceeding through chemical and physical condensation of large molecules (PAHs) followed by mass addition concurrent with carbonization. Irrespective of the relative rates, surface mass growth, coalescence, and carbonization are all critical processes leading to solid carbonaceous soot.

The observed optical properties of the soot structures also vary in a spatially similar manner. With decreasing radial distance, the LIF intensity (with no apparent contributing LII signal) decreases from a maximum reaching a minimum spatially overlapped with an intensity minimum in the LII signal as seen in Fig. 3. At smaller radial distances, the LII intensity increases, reaching a maximum still on the fuel-rich side of the diffusion flame. Analogous behavior is observed in the normal diffusion flame with increasing axial distance above the burning droplet. At small axial heights within the normal diffusion flame and large radial distances within the IDF, no material was collected via thermophoretic sampling as would be expected if only gaseous species were present. In these regions, only fluorescence is observed. At high axial heights in the normal diffusion flame or small radial distances in the IDF flame, only solid carbonaceous soot was found through TEM analysis of thermophoretically sampled material. In these regions, only incandescence is observed.

Thus, the postulated variation in material photophysical properties suggested by the spatial variation in the LIF and LII intensities is supported by the spatial variation in the material composition as revealed by both the bright- and dark-field TEM images. Most significantly, the minimum in the combined LIF-LII intensities is indicative of the chemical and physical changes accompanying the transformation of molecular matter into solid carbonaceous soot regardless of the specific soot formation route. On this basis, the dark region illustrated in the simultaneous LIF-LII images spatially locates the region containing soot-precursor material.

Conclusions

Simultaneous LIF-LII images are valuable for visualizing both PAH and soot-containing regions within both transitory (droplet) flame and steady-state IDF flames. The LIF and LII signals may be distinguished either by the excitation wavelength dependence or the temporal decay following the laser pulse. As revealed in the LIF-LII images, a dark region appears juxtaposed between the PAH and soot-containing regions. TEM measurements of thermophoretically sampled material from within this dark region suggest very different rates of soot-precursor material growth and coalescence versus carbonization within the normal and inverse diffusion flame. Postulated photophysical properties accounting for the minimal LIF and LII intensity (the "dark" region) observed in the LIF-LII images are supported by both bright- and dark-field TEM measurements of the sampled material. Both the spatial position of the dark region and TEM measurements indicate that the dark region represents a transformation region. In this region, the chemical and physical material conversion between gaseous or condensed molecular species (soot-precursor material) and solid carbonaceous soot particles occurs.

Acknowledgments

Support under NASA contract NAS3-27186 with Nyma Inc. for this work is acknowledged. The author extends special thanks to Mr. David Hull of NASA-LeRC for perform-

ing the TEM measurements and for helpful discussions regarding TEM.

REFERENCES

1. Ni, T., Gupta, S. B., and Santoro, R. J., *Twenty-Fifth Symposium (International) on Combustion,* The Combustion Institute, Pittsburgh, 1994, pp. 585–592.
2. Prado, G., Garo, A., Ko, A., and Sarofim, A., *Twentieth Symposium (International) on Combustion,* The Combustion Institute, Pittsburgh, 1984, pp. 989–996.
3. Gomez, A., Littman, M. G., and Glassman, I., *Combust. Flame* 70:225–241 (1987).
4. Wersborg, B. L., Fox, L. K., and Howard, J. B., *Combust. Flame* 24:1–10 (1975).
5. Ciajolo, A., D'Anna, A., Barbella, R., and Tregrossi, A., *Twenty-Fifth Symposium (International) on Combustion,* The Combustion Institute, Pittsburgh, 1994, pp. 679–685.
6. Bittner, J. D. and Howard, J. B., *Eighteenth Symposium (International) on Combustion,* The Combustion Institute, Pittsburgh, 1981, pp. 1105–1116.
7. McKinnon, J. T. and Howard, J. B., *Twenty-Fourth Symposium (International) on Combustion,* The Combustion Institute, Pittsburgh, 1994, pp. 965–972.
8. Lahaye, J. and Prado, G., *Carbon* 12:24–31 (1974).
9. Graham, S. C., Homer, J. B., and Rosenfeld, J. L. J., *Proc. R. Soc. London, Ser. A* 344:259–285 (1975).
10. Lahaye, J., in *Particulate Carbon Formation during Combustion,* (Siegla, D. C. and Smith, G. W., Eds.), Plenum Press, New York, 1981, p. 143.
11. D'Alessio, A., Gambi, G., Minutolo, P., Russo, S., and D'Anna, A., *Twenty-Fifth Symposium (International) on Combustion,* The Combustion Institute, Pittsburgh, 1994, pp. 645–651.
12. Dobbins, R. A., Fletcher, R. A., and Lu, W., *Combust. Flame* 100:301–309 (1995).
13. Haynes, B. S., Jander, H., and Wagner, H. G., *Ber. Bunsenges. Phys. Chem.* 84:585–592 (1980).
14. Santoro, R. J. and Semerjian, H. G., *Twentieth Symposium (International) on Combustion,* The Combustion Institute, Pittsburgh, 1994, pp. 997–1006.
15. Dobins, R. A. and Subramaniasivam, H., in *Soot Formation in Combustion,* (Bockhorn, H., Ed.), Springer Verlag, Heidelberg, 1994, p. 290.
16. Vander Wal, R. L., Jensen, K. A., and Choi, M. Y., *Combust. Flame,* 1996, accepted.
17. Megaridis, C. M. and Dobbins, R. A., *Twenty-Second Symposium (International) on Combustion,* The Combustion Institute, Pittsburgh, 1988, pp. 353–362.
18. Megaridis, C. M. and Dobbins, R. A., *Combust. Sci. Technol.* 71:95–109 (1990).
19. Petarca, L. and Marconi, F., *Combust. Flame* 78:308–325 (1989).
20. Smyth, K. C., Miller, J. H., Dorfman, R. C., Mallard, W. G., and Santoro, R. J., *Combust. Flame* 62:157–181 (1985).
21. Vander Wal, R. L. and Weiland, K. J., *J. Appl. Phys. B* 59:445–454 (1994).
22. Vander Wal, R. L. and Dietrich, D. L., *Appl. Opt.* 34:1101–1107 (1995).
23. Shaddix, C. E., Harrington, J. E., and Smyth, K. C., *Combust. Flame* 99:723–732 (1995).
24. Cignoli, F., Benecchi, S., and Zizak, G., *Appl. Opt.* 33:5778–5782 (1994).
25. Ni, T., Pinson, J. A., Gupta, S., and Santoro, R. J., *Appl. Opt.* 34:7083–7091 (1995).
26. Vander Wal, R. L., Choi, M. Y., and Lee, K.-O., *Combust. Flame* 102:200–204 (1995).
27. Bengtsson, P.-E. and Alden, M., *Combust. Sci. Technol.* 77:307–318 (1991).
28. Beretta, F., D.'Alessio, A., D'Orsi, A., and Minutolo, P., *Combust. Sci. Technol.* 85:455–470 (1992).
29. Letokhov, V. S., *Nonlinear Laser Chemistry: IRMPD,* Bristol, New York, 1985.
30. Palmer, H. B. and Cullis, C. F., in *Chemistry and Physics of Carbon,* Vol. 1 (Walker, P. L., Ed.), Marcel Dekker, New York, 1965, p. 265 (and references therein).
31. Frenklach, M., Taki, S., and Matula, R. A., *Combust. Flame* 49:275–282 (1983).
32. Graham, S. C., *Sixteenth Symposium (International) on Combustion,* The Combustion Institute, Pittsburgh, 1976, pp. 663–669.
33. Hepp, H., Siegmann, K., and Sattler, K., *Chem. Phys. Lett.* 233:16–22 (1995).
34. Steinfeld, J. I., *Molecules and Radiation: An Introduction to Modern Molecular Spectroscopy,* The MIT Press, Cambridge, 1981, pp. 169–225.
35. Howard, J. B., *Twenty-Third Symposium (International) on Combustion,* The Combustion Institute, Pittsburgh, 1990, pp. 1107–1127.
36. Marr, J. A., Giovane, L. M., Longwell, J. P., Howard, J. B., and Lafleur, A. L., *Combust. Sci. Technol.* 101:301–309 (1994).
37. Turro, N. J., *Modern Molecular Photochemistry,* Benjamin/Cummings Menlo Park, CA, 1978, pp. 153–195.
38. Parker, S. P., Ed., *The Solid State Physics Source Book,* McGraw Hill, New York, 1988, pp. 95–198.

Twenty-Sixth Symposium (International) on Combustion/The Combustion Institute, 1996/pp. 2277–2284

COMPREHENSIVE TWO-DIMENSIONAL SOOT DIAGNOSTICS BASED ON LASER-INDUCED INCANDESCENCE (LII)

STEFAN WILL, STEPHAN SCHRAML AND ALFRED LEIPERTZ
Lehrstuhl für Technische Thermodynamik (LTT)
Universität Erlangen-Nürnberg
Am Weichselgarten 8, D-91058 Erlangen, Germany

A strategy for a comprehensive description of soot sizes and concentrations is described, which relies on various two-dimensional techniques based on laser-induced incandescence (LII) and elastic scattering. Time-resolved LII (TIRE-LII) is an important tool in this process, it allows a direct measurement of primary particle size d_p as a central quantity for the description of soot. The paper discusses the essential features of the method which is based on the acquisition of the LII signals at two delay times after an initial laser pulse, where monomer size can be deduced from the local signal ratio. Delays of about 100 and 800 ns should be chosen as moments of observation in order to obtain precise information for a wide range of primary particle sizes. Local soot volume fractions f_v may be directly obtained from the prompt LII signal, where a necessary calibration factor can be deduced from a simple line-of-sight extinction measurement. In combination with elastic scattering, this technique can also be used to give relative values for the volume-equivalent diameter D of soot clusters. Additionally, the local mean number n of monomers within a cluster and number concentrations N_p and N_a of primary particles and aggregates, respectively, can be determined. Although some uncertainties persist regarding the absolute monomer sizes measured, and some data can be given only on a relative basis, experimental results obtained for the upper region of a laminar ethene diffusion flame are in good agreement with the established models of soot oxidation and aggregation.

Introduction

The understanding of soot formation and oxidation in combustion processes relies heavily on suitable diagnostic techniques for the measurement of the soot volume fraction f_v, the diameter d_p of primary particles, the volume-equivalent diameter D of the aggregates formed, the number n of primary particles within a cluster, and other quantities derivable from these, as the number concentration of primary particles N_p and that of the aggregates N_a. For the measurement of these quantities, optical techniques are of major importance [1], for example, dynamic light scattering [2] for the cluster size, and various scattering and extinction methods [3,4], to yield information on both cluster size and structure and soot volume fraction. These methods are pointwise or show a line-of-sight character. In the latter case they are often combined with a tomographic reconstruction in order to recover distributions at a given plane above a burner [5]. Besides the considerable effort necessary to gain full information on the soot distribution, these well-established optical techniques suffer from two substantial drawbacks. One disadvantage is that it is not possible to obtain data on the whole combustion field simultaneously, which limits the utility for nonstationary processes. Another limitation is that they most often require input data for the size of primary particles, which are not accessible directly by these techniques and are usually gained by a sample probe and subsequent electron microscopy [3], even though a scheme for indirectly recovering the monomer size from optical structure-factor measurements has been described [6].

Alternatively, laser induced incandescence (LII) techniques have been used successfully for two-dimensional soot diagnostics, especially on the soot volume fraction [5,7]. In the present contribution, we continue our recent approach [8] to the measurement of primary particle sizes by time-resolved LII (TIRE-LII) and demonstrate a strategy to obtain comprehensive information on soot properties by the combination of various LII techniques with scattering and extinction methods.

Theory

LII and Soot Volume Fraction

The basic principle of LII is to increase the temperature of the soot particles to slightly above vaporization temperatures by means of a highly energetic laser pulse and to detect the enhanced thermal radiation. The differential equation for the temperature of the primary particles, assumed as spherical

with diameter d_p, follows from the conservation of energy and reads

$$Q_{abs} \cdot \frac{\pi d_p^2}{4} \cdot E_i - A \cdot (T - T_0) \cdot \pi d_p^2 - \frac{\Delta H_V}{M} \cdot \frac{dm}{dt} - \bar{\varepsilon}(T) \cdot \sigma_{SB} T^4 \cdot \pi d_p^2 - \frac{\pi d_p^3}{6} \rho C \frac{dT}{dt} = 0 \quad (1)$$

The individual terms denote absorption of the laser irradiation (absorption efficiency, Q_{abs}; irradiance, E_i), heat transfer to the surrounding medium (heat transfer coefficient, A; temperature, T_0, of surrounding gas), vaporization of soot particles (heat of vaporization, ΔH_v; molar mass, M, of carbon; loss of mass, dm/dt), thermal radiation (mean emission coefficient, $\bar{\varepsilon}$; Stefan-Boltzmann constant, σ_{SB}), and rise of internal energy (density, ρ; specific heat, C, of carbon). In setting up equation 1, we have assumed a sufficiently loose structure of soot aggregates, which is justified with the typical fractal dimension of soot aggregates in the range of 1.5–1.8 [4], resulting the absorption of energy and the heat transfer, including radiation, to the surrounding medium being essentially governed by the size of the primary particles.

According to Melton [9], the radiative emission for a given wavelength λ_{em}, and thus the detected signal S in the moment of maximum temperature ($dT/dt = 0$), can be calculated to give

$$S \propto N_p d_p^x \quad (2)$$

where the exponent is

$$x = 3 + 154 \text{ nm}/\lambda_{em} \quad (3)$$

with emission wavelength λ_{em}. Thus, the LII technique may be used for the approximate determination of soot volume fraction, f_v, in spite of a slight overestimation and a bias toward larger particles, which may be tolerated for most practical applications. The proportional constant, which is given by the optical system, may be obtained by calibration measurements of flames with a known volume fraction or by a data point acquired by an independent technique.

TIRE-LII and Primary Particle Size

The basic idea of the time-resolved LII technique is based on the fact that, after the initial laser pulse, smaller particles cool down faster than larger ones due to their larger specific surface [7,9]. There are three paths for energy loss: vaporization, heat conduction to the surrounding gas, and radiation. Provided with high enough initial laser power, vaporization is the dominant path for a period of order 100 ns, after which heat conduction is the most important heat transfer mechanism. The calculations of heat transfer must take into account that typical particle sizes are smaller than the mean free path length and result in corrections to continuum heat transfer expressions [9,10]. It should be pointed out that radiative heat transfer contributes little (less than 5% for all times) to the total temperature decrease, although there exists a detectable signal, and that all three paths are included in the heat transfer calculations.

From a numerical integration of equation 1, a model for the particle temperature as a function of time can be set up. The LII signal S (apart from a calibration constant for the optical system) can then be calculated with the help of Planck's radiation function, where the emissivity, which equals the absorption efficiency, can be obtained from the usual Mie formulae [11].

From the ratio of the LII signals taken at two moments after the laser pulse, the size of primary particles can be deduced. Strictly speaking, this ratio is built up as a mean value from various primary particle sizes when there is a size distribution. As the connection between the signal ratio and particle size is roughly linear to a first approximation, and primary particle sizes may be assumed as rather narrowly distributed at a given location in a flame [12], the averaging process is not expected to be heavily biased.

Combined Techniques and Other Quantities of Interest

Besides information about primary particle sizes, knowledge about cluster size is also highly desirable. This may be achieved through a combination of LII and elastic scattering (ES). With the relationships for the signals of either technique,

$$S_{LII} \propto N_a n d_p^3 \quad (4)$$

for the prompt LII signal and

$$S_{ES} \propto N_a n^2 d_p^6 \quad (5)$$

for elastic scattering in the Rayleigh approximation, a relative value for the volume equivalent diameter D of a soot cluster may be obtained:

$$\left(\frac{S_{ES}}{S_{LII}}\right)^{1/3} \propto \left(\frac{N_a n^2 d_p^6}{N_a n d_p^3}\right)^{1/3} = n^{1/3} d_p = D \quad (6)$$

Note that aggregate sizes are not expected to exhibit a narrow distribution in most systems of interest; thus, the signal combination obviously yields a mean diameter D_{63}, where the kind of averaging is determined by the sixth and the third moment [14]. Also note that in equation 4 the deviation of the exponent from three is neglected. It is possible, however, to use the exact exponent from equation 3 for the calculation of the diameter D; for the actual calculations, a value of 3.35 was taken. Furthermore, similar to the determination of the volume fraction, the combination of LII and ES yields only a relative

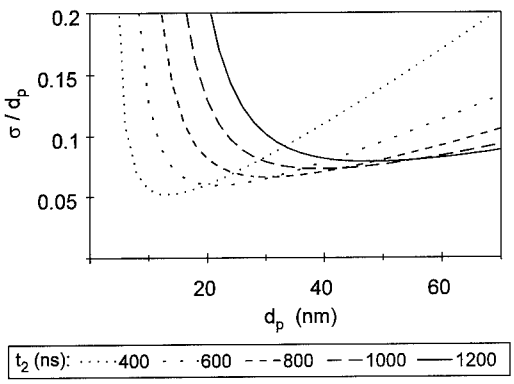

FIG. 1. Theoretical standard deviation of the particle diameter, d_p, measured as it is obtained from photoelectron statistics.

value for the cluster size. For either quantity it is therefore necessary to obtain at least one calibration point.

In the case of f_v, this may be most easily accomplished by extinction measurements, where a laser beam with wavelength λ and incident energy flux I_0 is attenuated to a value I along the total length L of the combustion zone. For the determination of the soot volume fraction, a common approach is to approximate the extinction efficiency by the absorption efficiency, thus neglecting scattering, and to calculate absorption in the Rayleigh approximation, which results in the relationship [15]

$$\ln\left(\frac{I_0}{I}\right) = \int_0^L 6\pi f_v E(\tilde{m})\lambda^{-1} dl \tag{7}$$

where

$$E(\tilde{m}) = -Im\left(\frac{\tilde{m}^2 - 1}{\tilde{m}^2 + 2}\right) \tag{8}$$

follows from the complex index of refraction given by $\tilde{m} = n - ik$. In an axisymmetric flame, the volume fraction at each point may be achieved by scanning the laser beam through the whole flame and applying a subsequent tomographic reconstruction [5]. In order to obtain a calibration constant for the LII measurements, it is sufficient, however, to compare the total absorption along a line of sight according to equation 7, preferably through the center of the flame in an axisymmetric case, with the corresponding integral of the LII values.

A calibration value for the aggregate size may be obtained from a combination of extinction and scattering measurements [15], which yields a D_{63} value, too. A tempting alternative approach for the determination of cluster sizes is based solely on extinction measurements at two different wavelengths, where from the ratio of extinction efficiencies a volume-equivalent sphere diameter is to be obtained on the basis of Mie calculations. It has been shown, however, (see, e.g., Dobbins et al. [16] and references therein) that this concept is not appropriate for the fractal structure of soot particles, where specific absorption is essentially independent of the number of monomers within a cluster. Until a calibration value by a suitable independent technique (scattering/extinction or dynamic light scattering) is available, both the diameter D as obtained by the combination ES/LII, and properties derived from that must be of relative character.

With the volume fraction and the cluster size calibrated, it is a straightforward task to calculate other quantities required for the individual volume elements. The average number n of monomers in an aggregate follows directly from equation 6, the number concentrations of primary particles and aggregates, N_p and N_a, respectively, can be derived from the soot volume fraction and the corresponding sizes.

Aspects of TIRE-LII Performance

Moment of Observation and Signal Considerations

Time-resolved LII relies on the measurement of the LII signals at two times after the laser pulse. As laid down in previous work [8], the first point chosen favorably in a way to avoid the first tens of nanoseconds of the decay; 100 ns is a reasonable selection. In order to choose a suitable value for the second point of observation, several arguments have to be taken into consideration. One aspect is how sensitively the ratio

$$r = \frac{S(t_2)}{S(t_1)} \tag{9}$$

of the obtained LII signals at times t_1 and t_2 depends on the particle size. The analysis must also take into account experimental noise (i.e., signal statistics). With the use of an intensified CCD-camera, the predominant source is photoelectron noise, which shows a relative increase with larger delay times due to the signal drop. Figure 1 depicts the relative uncertainty obtained in particle size according to signal-to-noise considerations for the individual acquisition times. The figure is based on a value of 3000 effective photoelectrons at a time delay of 100 ns, with the resulting values for other times calculated according to the theoretical signal decrease and the background signal due to natural flame luminosity set to 10% at t_1. The figure may help to choose a favorable delay time, depending on the range of particle sizes to be expected in the system under investigation. Short times appear advantageous for small particles, but only marginally suitable for larger ones. On the other hand, a value of around 800 ns seems to be a reasonable choice for a rather broad spec-

trum of particle sizes. Additionally, it should be pointed out that signal statistics could be improved for long decay times if it is possible to change the characteristics of the detecting system for the second point of observation. This may be performed in stationary combustion if one sets the luminous gain in a way to achieve saturation at t_1 and then decreases the f-number of the detection optics to obtain a higher luminous flux at t_2.

Parameters of Influence on Monomer Size Determination

The accurate determination of absolute values for monomer size relies heavily on the models used for the heat transfer mechanism and the LII signal, and on correct physical data for the quantities involved therein. Our calculations are based mainly on the data given by Melton [9], in which we have corrected two typographic errors (heat of vaporization of carbon and thermal conductivity of air; the latter had regrettably not been corrected in our earlier paper) and chosen more commonly used values for the refractive index (1.57–0.56i) and density (1.8 g cm^{-3}) of soot. Yet, these data form a major source of uncertainty for TIRE-LII calculations. One point to be considered is a possible change of soot properties, and thus cooling effects due to intense laser irradiation, as recently reported by other researchers [17,18]. As a consequence, irradiation should be chosen as small as possible, avoiding an irradiance in excess of 10^8 W cm^{-2}. Since the model calculations take into account particle shrinkage, the influence of parameters such as refractive index or laser irradiance on the determination of original monomer size is present, yet not dominant. In general, because the energy transfer after some 100 ns is determined mainly by the internal energy of the soot particles and the heat transfer to the surrounding gas, the density and heat capacity of soot and the heat transfer coefficient Λ gain major importance. If one avoids a very high laser irradiance, and thus a substantial change of soot properties, it is possible to determine the density and the heat capacity with a reasonable degree of accuracy; yet, major problems arise in the calculation of the heat transfer term.

Following Melton's model, our calculations are also based on air as the surrounding medium, due to a lack of knowledge on local gas composition. A differing thermal conductivity of the local gas mixture may result in a considerable error in particle size, where the relative error in the latter is of a similar magnitude as that in the first one. Despite the fact that an error in thermal conductivity may in part be compensated for a corresponding change in the mean free path length, it is obvious that even a rough description of local gas composition might help to improve the accuracy of TIRE-LII significantly. Yet, it should be pointed out that relative sizes, at least, can be obtained more reliably in systems with smooth variations of local composition.

Similar to the considerations above, errors regarding local gas temperatures must be taken into account. Model calculations are based on a combustion temperature of 1800 K. A deviation in the true gas temperature of +200 K (−200 K) amounts to an error of about +15% (−9%) in particle size for a 30-nm particle and a detection time, t_2, of 800 ns. The error decreases for conditions under which the temperature difference between the particles and the surrounding gas is large, because then a deviation in the true absolute temperature results only in a small relative error in the cooling rate. Thus, the error becomes smaller for larger particles and earlier detection times (t_2). Generally, it is less, as may be deduced from the deviating temperature alone, since the dependence of the thermal conductivity on temperature in part compensates for the effect of a wrong assumption of the gas temperature. Again, the local variation of monomer size may be determined more reliably in systems with moderate local temperature changes, and TIRE-LII performance may be significantly improved by providing information on local gas temperature.

Experimental

The diagnostic techniques described above have been applied to a laminar ethene diffusion flame. The burner was constructed from plans similar to those of Gülder [19], where the fuel flow in an inner stainless steel tube 13 mm in diameter is stabilized by an air coflow in an outer steel tube 89 mm in diameter. Experimental flow rates were 2.4 mg/s for ethene and about 50 mg/s for air.

Both prompt and TIRE-LII experiments were performed with irradiation from a frequency-doubled Nd:YAG laser with a Gaussian temporal profile and a pulse duration of 8 ns (FWHM). A light sheet was formed with a height of approximately 15 mm and a minimum thickness of about 300 μm by expanding the beam parallel to the burner axis and weakly focusing it in the perpendicular direction with cylindrical lenses. For better definition of the light sheet, rectangular stops were employed close to the burner. Laser irradiances of up to 10^8 W/cm^2 were used with deviations across the light sheet of less then ±5% from the mean value. Observation of the LII signal was performed by an intensified two-dimensional CCD-camera aligned perpendicularly to the light sheet and operated with a gate width of 20 ns. Both a shortpass filter with a cutoff wavelength of 450 nm and an additional mirror for 532 nm were placed in front of the camera objective, resulting in a complete suppression of elastic scattering. The nominal resolution of the detection system was 0.15 × 0.15 mm^2. TIRE-LII experiments

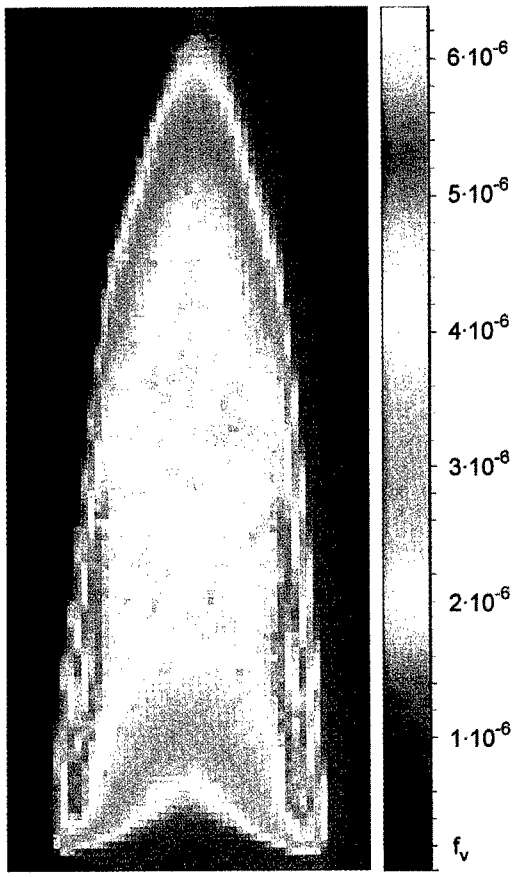

FIG. 2. Map of soot volume fractions, f_v, in the upper region of a laminar ethene diffusion flame.

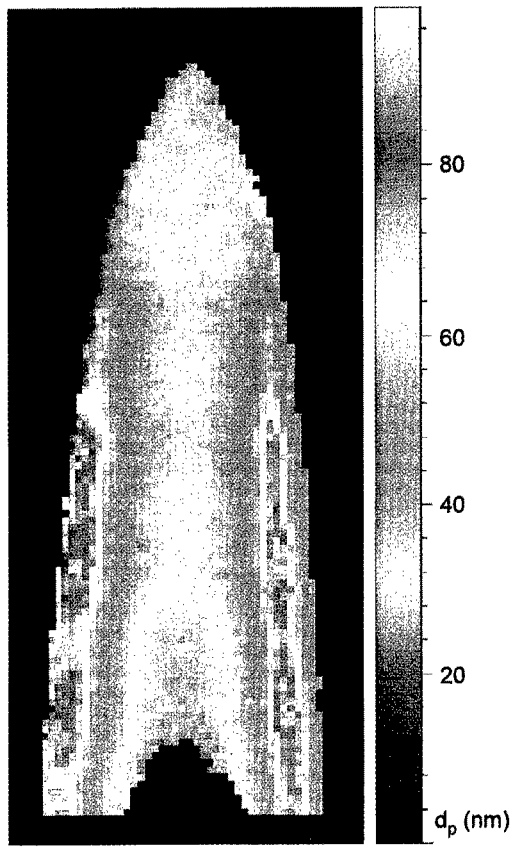

FIG. 3. Primary particle sizes, d_p, from TIRE-LII measurements.

were carried out with delay times of 100 ns and 800 ns, respectively. For either LII technique, 30 frames were averaged at a given time in order to reduce noise, and an averaged picture without laser irradiation was subtracted in order to account for the natural flame luminosity.

For elastic scattering, images were taken with the help of an interference filter with a center wavelength of 532 nm and a width of 8 nm (FWHM) instead of the filters used for LII. Extinction measurements were carried out with a HeNe laser at 633 nm for which the beam waist was reduced to approximately 0.2 mm. In order to compensate for fluctuations in laser intensity, an additional reference photodiode was used. The accuracy of the transmission values obtained in this way is estimated to be about 0.2–0.3%.

Results and Discussion

Figure 2 shows the soot volume fraction f_v for a height of 19–34 mm above the burner exit, as it was obtained from the prompt LII signal with a calibration by comparison to the integral extinction signal at 20 mm. In agreement with the expected behavior for a laminar diffusion flame, an annular region of maximum soot concentration and a decrease of f_v due to oxidation processes with increasing height can be observed. Primary particle sizes determined by TIRE-LII at acquisition times of 100 and 800 ns are depicted in Fig. 3, which, in the annular region of high soot concentration, exhibit a fairly constant plateau value and the expected decrease with an increasing residence time due to oxidation processes. There remains some uncertainty, however, regarding the absolute values which are in a range of approximately 20–80 nm, and thus slightly larger than reported for other ethene diffusion flames [12]. This may be due to the lack of knowledge about local gas composition and temperature, which results in considerable uncertainty, as already discussed. In order to reduce uncertainties due to local temperature variations, a measurement series for the temperature field has been started at our laboratory, based on the pure rotational CARS technique [20]. First results

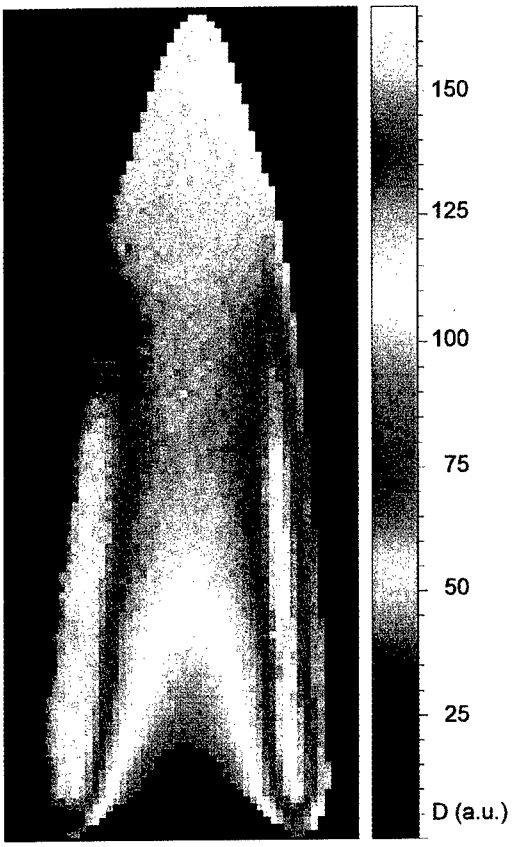

FIG. 4. Relative aggregate sizes, D, from the combination of prompt LII and elastic scattering.

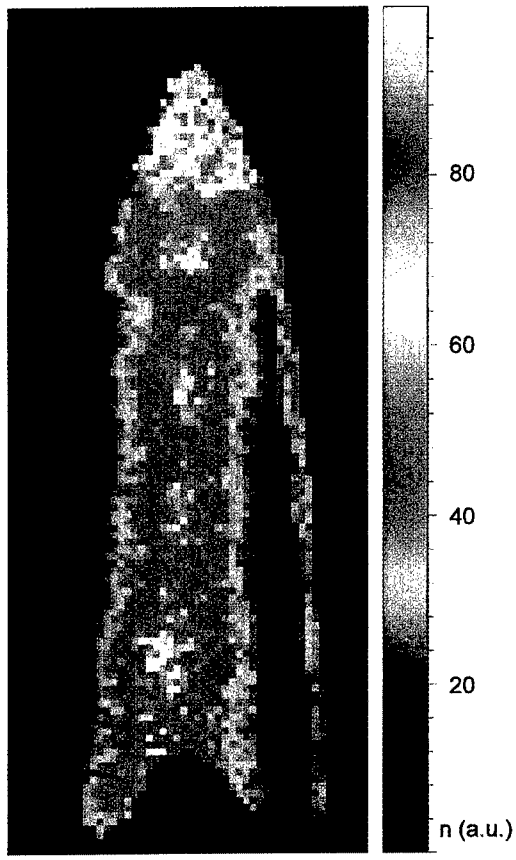

FIG. 5. Relative distribution of the average number, n, of monomers within a cluster.

indicate that the temperature in the upper region of the flame and in the annular zone of high soot concentration are in part well above the 1800 K assumed throughout, and these corrections may result in reductions of particle size of order of 20% in some instances.

Combining prompt LII and elastic scattering, information on aggregate size, D, may be deduced, which is shown in Fig. 4. Due to the fact that an independent calibration has not yet been performed, cluster sizes can be given only on a relative basis, though a decrease of cluster size can be observed with increasing residence time. This observation is consistent with the concept of a decrease of primary particle size which is only partly balanced by an increase of the mean number, n, of monomers within a cluster. This quantity may be derived from the size information obtained by the combination of LII/ES and TIRE-LII, but is again limited to relative information due to the lack of an absolute calibration standard for D. Although there might be considerable experimental error in this quantity, as two pictures both for TIRE-LII and the LII/ES combination and a third power are involved, the expected increase can be observed in Fig. 5. Figure 6 shows various profiles for the number concentrations of primary particles and aggregates, N_p and N_a, respectively, which were deduced from a combination of soot volume fraction and the corresponding sizes.

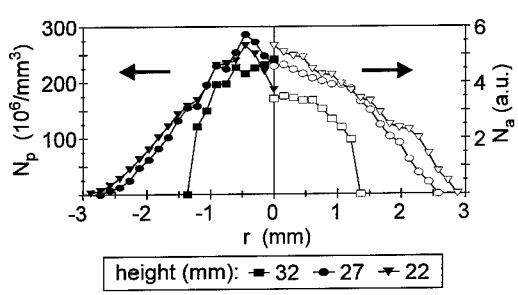

FIG. 6. Number concentrations, N_p and N_a, of primary particles (left) and aggregates (right), respectively, for various heights above the burner; N_a can be given only on a relative basis.

Since it is necessary to combine several pictures to obtain this information, there is considerable noise and uncertainty. The profiles indicate that there is a low concentration of both primary particles and aggregates in the annular zone of maximum soot concentration. Obviously, the large monomer size in these regions outweighs the low number of particles, to result in the high volume fractions observed. The number concentration of aggregates, N_a, changes more strongly with residence time than that of the monomers, N_p, which backs the idea that the number of monomers is essentially unchanged after formation and that there are fewer aggregates because there are more primary particles per cluster. Still, more extensive experimental data, where even a larger number of individual frames are employed for the mean values, or with a more advanced detection system, are needed to give a more detailed and accurate description of changes in number concentrations.

Conclusions

It has been shown that laser-induced incandescence data may form the basis for a comprehensive description of soot in combustion processes where two-dimensional information of soot volume fractions and particle sizes is required. Time-resolved LII offers the chance of obtaining a complete map of monomer sizes, which is not easily possible by any other known technique. Although experimental investigations in a laminar ethene diffusion flame indicate reasonable results, uncertainties in the physical data and especially in local gas composition and temperature pose limits for obtaining highly accurate information. Detailed tests should be carried out to validate size information on the basis of comparisons with TEM data. Despite these limitations, the advantages of the LII techniques prevail, and further experiments could yield an even larger range of information on the interactions between both monomer and cluster sizes and concentrations in combustion processes. Future work should also include the use of supplementary techniques for the calibration of aggregate size and the determination of local gas temperature and composition.

Acknowledgments

The authors would like to thank A. Thumann for performing temperature measurements by the CARS technique. Burner plans from Gülder have been made available by the Institute for Physical Electronics of the University of Stuttgart.

REFERENCES

1. Charalampopoulos, T. T., *Prog. Energy Combust Sci.* 18:13–45 (1992).
2. Scrivner, S. M., Taylor, T. W., Sorensen, C. M., and Merklin, J. F., *Appl. Opt.* 25:291–297 (1986).
3. Bockhorn, H., Fettig, F., Meyer, U., Reck, R., and Wannemacher, G., *Eighteenth Symposium (International) on Combustion,* The Combustion Institute, Pittsburgh, 1981 pp. 1137–1147.
4. Puri, R., Richardson, T. F., Santoro, R. J., and Dobbins, R. A., *Combust. Flame* 92:320–333 (1993).
5. Shaddix, C. R., Harrington, J. E., and Smyth, K. C., *Combust. Flame* 99:723–732 (1994).
6. Sorensen, C. M., Cai, J., and Lu, N., *Appl. Opt.* 31:6547–6557 (1992).
7. Quay, B., Lee, T.-W., Ni, T., and Santoro, R. J., *Combust. Flame* 97:384–392 (1994).
8. Will, S., Schraml, S., and Leipertz, A., *Opt. Lett.* 20:2342–2344 (1995).
9. Melton, L. A., *Appl. Opt.* 23:2201–2208 (1984).
10. McCoy, B. J. and Cha, C. Y., *Chem. Eng. Sci.* 29:381–388 (1974).
11. Bohren, C. F. and Huffman, D. R., *Absorption and Scattering of Light by Small Particles,* Wiley, New York, 1983.
12. Dobbins, R. A., Santoro, R. J., and Semerjian, H. G., *Twenty-Third Symposium (International) on Combustion,* The Combustion Institute, Pittsburgh, 1990, pp. 1525–1532.
13. Dec, J. E., "Soot Distribution in a D.I. Diesel Engine Using 2-D Imaging of Laser-Induced Incandescence, Elastic Scattering, and Flame Luminosity," SAE Paper No. 920115 (1992).
14. Pinson, J. A., Mitchell, D. L., Santoro, R. J., and Litzinger, T. A., "Quantitative Planar Soot Measurements in a D.I. Diesel Engine Using Laser-Induced Incandescence and Light Scattering," SAE Paper No. 932650 (1993).
15. Santoro, R. J., Semerjian, H. G., and Dobbins, R. A., *Combust. Flame* 51:203–218 (1983).
16. Dobbins, R. A., Mulholland, G. W., and Bryner, N. P., *Atmos. Environ.* 28:889–897 (1994).
17. Vander Wal, R. L., Choi, M. Y., and Lee, K.-O., *Combust. Flame* 102:200–204 (1995).
18. Ni, T., Pinson, J. A., Gupta, S., and Santoro, R. J., *Appl. Opt.* 34:7083–7091 (1995).
19. Gülder, Ö. L., *Combust. Flame* 92:410–418 (1993).
20. Seeger, T. and Leipertz, A., *Appl. Opt.,* 35:2665–2671 (1996).

COMMENTS

Ö. L. Gülder, National Research Council of Canada, Canada. In a similar ethylene diffusion flame, Megaridis and Dobbins [1] measured primary soot particle sizes by a thermophoretic sampling technique. The maximum mean particle size measured was about 35 nm at the mid-flame height. Your 80 nm maximum diameter is more than a factor of two larger than reported [1]. Could you please comment on the reason for this discrepancy?

REFERENCE

1. Megaridis, C. M. and Dobbins, R. A., *Twenty-Second Symposium (International) on Combustion,* The Combustion Institute, Pittsburgh, 1989, pp. 353–362.

Author's Reply. As set out in our contribution the calculations for primary particle size are based on simplifying approximations both for the heat transfer model and the underlying physical data, especially for the composition and the temperature of the surrounding gas.

As you know, the temperatures in such a type of flame may be well above the 1800 K laid down for the model calculations, especially near the regions, where a large monomer size is found. Temperatures in excess of 2000 K may lead to corrections of particle size of order −20%.

Another possible reason for discrepancies observed are the simplifying assumptions of point contact between monomers and unhindered heat transfer. If the surface of primary particles effective for heat transfer was reduced by 10%, the size of large particles would have to be corrected by about −20%.

Thus, the technique may well be improved by providing a better data base for the surrounding gas and refined models for the heat transfer from particle clusters. These and other related questions like that for deviations from spherical form will be addressed in more detail in future work.

•

Katharina Kohse-Höinghaus, Universitat Bielefeld, Germany. I am somewhat puzzled by the 40 nm size you quote for your primary particles. How would your cooling curves be affected if the particles were not spherical? Did you perform calculations on that subject?

Author's Reply. The accuracy of particle size measurements is addressed in some detail in our reply to Dr. Gülder's question. Non-spherical particles exhibit an increased specific surface as compared to spherical particles. Such an effect would result in the determination of larger particle sizes. Results of thermophoretic sampling with subsequent TEM analysis published in the literature show, however, that the particles for such a type of flame are nearly spherical and therefore the resulting error is negligible.

•

Kermit C. Smyth, NIST, USA. In moderately to heavily sooting flames, attenuation of the LII signal from its point of origin to the detector can lead to significant errors (underestimates) of the soot volume fraction. How do you account for varying signal attenuations, depending upon local values of the soot volume fraction, in your measurements?

Author's Reply. Signal attenuation between the sample volume and the detector may lead to an underestimation of the volume fraction by LII, but our way of calibration, comparing a line-of-sight extinction with the corresponding cross section through the incandescence image, accounts for a mean signal attenuation. The maximum attenuation for any laser beam passing through the given flame horizontally was measured to be about 15% and only weakly dependent on the exact radial position. The local deviations from the average calibration factor resulting in errors in local soot volume fraction are thus small, with a maximum error estimated to be less than 5%.

If desired, an exact way to take into account signal attenuation in axisymmetric flames is to perform a tomographic reconstruction on the LII-image itself, which includes all the information necessary.

Finally, it should be pointed out that the determination of primary particle sizes by TIRE-LII is essentially unaffected by signal attenuation, as only the signal ratio at two delay times is employed.

•

E. Winklhofer, AVL-List, Austria. Applicability of the technique to high pressure-density diffusion flames: the examples given in the presentation show good transparency of the flame for both the input beam as well as for the incandescence signal. Above which soot density levels is this high transparency affected by absorption within the flame?

Author's Reply. A favorable property of LII is that both for volume fractions and especially for primary particle sizes results are not heavily dependent on laser fluence; therefore an attenuation of the incident laser beam only results in small errors as long as the laser fluence is high enough to initiate particle vaporisation. Signal attenuation between the sample volume and the detector is addressed in detail in the reply to Dr. Smyth's question.

Twenty-Sixth Symposium (International) on Combustion/The Combustion Institute, 1996/pp. 2285–2293

ON SURFACE GROWTH MECHANISM OF SOOT PARTICLES

MICHAEL FRENKLACH
Department of Mechanical Engineering
University of California
Berkeley, CA 94720-1740, USA

A sterically resolved kinetic Monte Carlo technique was applied to model surface growth of soot particles under conditions typical of flame environments. The employed elementary surface reaction mechanism was based on analogous reactions of gaseous aromatic species. The simulations indicated that the growth rate of soot particle surface *increases* rather than decreases with temperature, even when the reaction reversibility is fully accounted for. This implies that the decreasing thermal stability of surface intermediates is unlikely to be responsible for the decline in surface reactivity of soot particles. In contrast, the growth of gaseous aromatics by the same reaction mechanism is impeded by the reversibility of cyclization reactions and was shown to result in zigzag edges, inconsistent with the armchair substrate assumed for the particle surface growth. The inconsistency was resolved by invoking the formation of five-member rings that serve as surface nuclei for the subsequent growth. The computational results also showed that the surface growth rate is proportional to the C_2H_2 concentration and independent of H at high H concentrations but declines with the decrease in the abundance of hydrogen atoms. This concurs with the previous analysis identifying the decreasing H concentration as one of the primary causes for the decay in the surface reactivity of soot particles.

Introduction

Mechanistic understanding of soot formation in hydrocarbon flames has advanced significantly in recent years, shifting the focus of discussion from conceptual possibilities to specifics of reaction kinetics [1]. One of the key aspects of soot formation phenomena, identified from experiment [2–4] and confirmed by detailed modeling [5–9], is the deposition of soot mass through reactions of gaseous species with the soot particle surface. Although responsible for the formation of most of the soot mass, surface growth is not understood in sufficient detail. Therefore, it is imperative to establish a fundamental nature of the surface growth reactions.

Experimental studies with laminar premixed flames concluded that surface growth rate is proportional to the acetylene concentration [3]. Employing the first-order kinetics law for the analysis of surface growth in laminar diffusion flames identified empirical growth constants similar to those determined for the premixed flames [4].

Frenklach and Wang [5] suggested a detailed reaction mechanism for surface growth of soot particles. This mechanism is based on the postulate of chemical similarity between analogous surface and gas-phase reactions of carbonaceous species [10]. In the case of soot, this postulate states that chemical reactions of soot particle surface are similar to those of large polycyclic aromatic hydrocarbons (PAHs). In other words, the principle of chemical similarity postulates a specific *physical* nature of surface active sites (as opposed to typically considered *generic* active sites [11–15]).

Faced with many uncertainties, the initial reaction set proposed by Frenklach and Wang [5] for the surface growth of soot particle surface was a minimal mechanism capturing the bare essence of the H-abstraction–C_2H_2-addition (HACA) growth for the armchair edge of PAHs,

$$C_s\text{–H} + \text{H} \rightarrow C_s\bullet + H_2$$

$$C_s\bullet + \text{H} \rightarrow C_s\text{–H}$$

$$C_s\bullet + C_2H_2 \rightarrow \text{cyclization} + \text{H}$$

where C_s denotes a carbon atom on an edge of the soot surface. Mauss, Schäfer, and Bockhorn [8,9] adopted this approach but argued that the last reaction, the acetylene addition step, should be represented by

$$C_s\bullet + C_2H_2 \rightleftarrows C_s\text{–CH=CH}\bullet \rightleftarrows \text{cyclization} + \text{H}$$

that is, with the inclusion of reaction reversibility (although in order to match the experimental results, the authors had to use the low-pressure limit for the addition of acetylene while from physical considerations such reaction should be in its high-pressure limit). These authors asserted that the reaction reversibility substitutes for the need to use a steric multiplier to the surface rates, α, introduced earlier by Frenklach and Wang [5]. A similar suggestion was

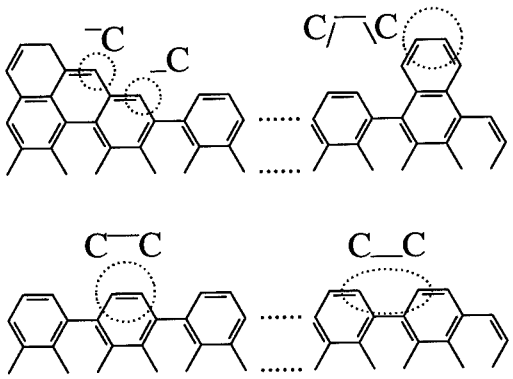

FIG. 1. A schematic diagram of the initial surface model (bottom) and identification of reaction sites.

made by Colket and Hall [7], who compared several reaction schemes.

While reversibility of HACA reaction steps is indeed a distinctive feature of aromatic growth [16], analysis of more complete reaction schemes requires consideration of not only the reactive site itself but also its surface neighbors. The present study reports a kinetic Monte Carlo (KMC) model, in which the outcome of a specific elementary chemical reaction depends not only on the collision frequency and nominal reaction probability, both being consistent with the standard kinetic approach, but also on the environment of the aromatic reactive site determined by the nature of the surrounding sites. The developed model is applied to a set of conditions testing the effects of temperature and species concentrations on the growth rate and dominant reaction channels. A comparison between the growth of a surface and a similar gaseous aromatic revealed an inconsistency, which is resolved by a new proposal invoking the formation of five-member rings.

Model

Surface Model

The initial surface was modeled by a one-dimensional armchair substrate, shown on the bottom of Fig. 1. Periodic boundary conditions were applied throughout the calculations on the left and right sides of the substrate. The present calculations employed substrates 100 carbon atoms long. For simulations of gaseous PAH growth, pyrene was assumed to be the initial structure with no limitations imposed on growth in any direction.

Gas-Phase Composition

The gas contacting the substrate was assumed to have the same temperature as the surface and to be composed of H, H_2, and C_2H_2—the principal gaseous species of the HACA mechanism. The gas-phase species concentrations and temperature were maintained unchanged during an individual simulation, however, they differ from run to run. For the "base" case, the pressure was chosen to be 1 atm and the mole fractions of the respective species $x_H = 0.01$, $x_{H_2} = 0.1$, and $x_{C_2H_2} = 0.1$, typical of laminar premixed flame simulations of past studies [5,6].

Stochastic Procedures

The process of growth is modeled as a Markovian sequence of reaction events [17]. There are two types of reaction events that comprise the present model: bimolecular reactions between gaseous species and surface sites, and unimolecular decompositions of some surface species.

The bimolecular reactions were modeled following collisions of gas-phase species—H, H_2, and C_2H_2—with the growing surface. The outcome of an individual collision between a given gaseous species, j, with a given surface site, i, is determined by the product of the conditional probability of reaction to occur upon this collision and the probability of the (i, j) collision to occur.

Let ν_j be the frequency of collisions of gaseous species j with the model surface, defined in the present study as

$$\nu_j = Sz_jC_j = Ns\left(\frac{k_BT}{2\pi M_j}\right)^{1/2} C_j$$

where k_B is the Boltzmann constant, T the temperature, M_j the molecular weight, C_j the molar concentration of species j, z_j the molecular flux of species j toward the substrate surface, S the total surface area of the substrate, N the total number of surface sites, and s the area of one surface site. The value of s was assumed equal to 1.42×3.5 Å^2, where 1.42 Å is the length of an aromatic C–C bond and 3.5 Å the interplanar distance in soot [18].

Given that t_n is the instant of a current collision, the next collision occurs at $t_{n+1} = t_n - (\ln x)/\nu$, where ν is the total frequency of collisions, $\nu = \nu_H + \nu_{H_2} + \nu_{C_2H_2}$, and x is a random number distributed uniformly from 0 to 1. Which gaseous species arrives at the surface (i.e., H, H_2, or C_2H_2) is chosen at random, according to $p_j = \nu_j/\nu$, that is, the probability that the colliding gaseous species is j. The surface site of collision is also determined randomly, assuming all substrate sites to be equiprobable. A possible reaction outcome for the chosen pair of a gaseous species and a surface site is determined on the basis of the specific reaction probability assigned to each such combination and the status of the neighboring surface sites (see below). For example, a collision between H_2 and a hydrogenated carbon site, C_s–H, does not lead to any reaction; and reac-

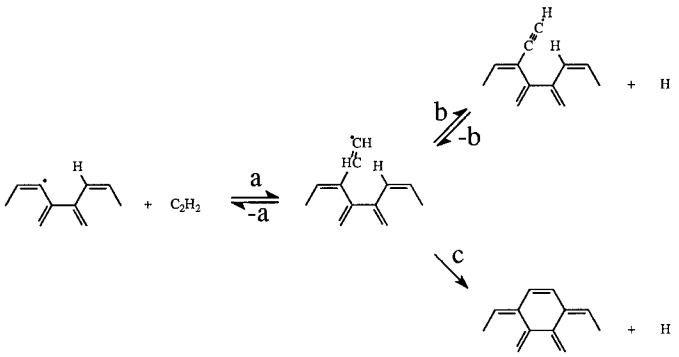

FIG. 2. A diagram illustrating the system of reactions 4, 5, 7, and 8.

tion between an incoming C_2H_2 and a surface radical, C_s•, depends on whether aromatic cyclization is at all possible.

If a reaction does occur the states of all affected sites are adjusted accordingly. Irrespective, however, of whether reaction took place or not, the stochastic process moves to the next collision event, and so on, unless it is "interrupted" by a unimolecular event. When a surface species, formed at time t, can undergo a unimolecular decomposition, the instant of such an event is determined by $t_d = t - (\ln x)/k_d$, where k_d is the corresponding rate coefficient. At time t_n satisfying the condition $t_n < t_d < t_{n+1}$, the stochastic process first executes the unimolecular reaction (at time t_d) before moving to the next collision event at t_{n+1}.

Reaction Mechanism

The gas-surface reaction set employed in the present simulations is given in Table 1; the nomenclature used for identification of the surface sites is illustrated in Fig. 1. The reaction probabilities of bimolecular gas-surface reactions were calculated by $\gamma = k_g/(sz_j)$ [21], where k_g is the rate coefficient of the corresponding gas-phase reaction, or guessed otherwise. For instance, in the case of H combination with a surface radical, reaction 3 in Table 1, the value of γ in access of unity is obtained using the given equation; therefore, this value was limited to unity.

Many steps of the assumed reaction mechanism proceed through formation of relatively unstable intermediate species, whose decomposition rates are orders of magnitude faster than the gas-surface collision rates. Inclusion of such short-lived intermediates would substantially increase the computational time, to the extent that stochastic simulations may become impractical. As common to this situation, the small reaction time scales were removed by assuming the short-lived intermediates to be in the steady state. The overall expressions resulted from this assumption were then used as k_g in the calculations of reaction probabilities. Computer tests fully confirmed the validity of this approximation.

Figure 2 illustrates a reaction set that involves short-lived intermediates, and the bottom group of reactions in Table 1 summarizes the corresponding elementary reactions. The rate coefficients of these elementary surface reactions were taken from analogous reactions of one-, two-, and three-ring aromatics [19], in their respective high-pressure limits whenever appropriate.

The first three reactions in Table 1 are those between surface sites and gaseous hydrogen, with the rate coefficient of reaction 1 taken from Kiefer et al. [20] and that of reaction 2 calculated via detailed balancing. Reactions 4–10 describe the formation of an aromatic ring over the "boat" site of the armchair surface and reactions 11–13 over the "chair" site. The cyclization step for the former reaction set was assumed irreversible on the basis of recent data [19], while the latter reaction sequence is highly reversible and hence slow—it could be safely eliminated from the calculations of surface growth but played a critical role in the simulations of gaseous PAH growth. It should also be noted that some surface reactions are differentiated between the boat and chair sites, because the two have different rate coefficients [19] and the latter cannot in principal lead to the immediate formation of an aromatic ring according to the HACA mechanism.

Computational Details and Initial Tests

The computations were carried out on an IBM RISC 6000-550 computer. To collect sufficient statistics, a typical run took about 1–2 h, with up to 10^8 gas-surface collisions and 10^3–10^4 carbon atoms deposited.

A series of initial test runs were performed using only a small subset of the mechanism, namely reactions 1, 3, 7, and 9. The results of these computations were compared to those obtained with the same reaction mechanism but using the standard (i.e., nonstochastic) kinetic calculations. The results of the two methods compared favorably with each other, thus confirming the stochastic algorithm. The scatter in the computed growth rates, as determined

TABLE 1
Reaction set

Number	Reaction[a]	Rate Coefficient[b]	Comments
1	$C_s\text{–}H + H \rightarrow C_s\bullet + H_2$	$(2.5 \times 10^{14}/6)\ e^{-66.9/RT}$	c
2	$C_s\bullet + H_2 \rightarrow C_s\text{–}H + H$	$3.4 \times 10^9\ T^{0.88}\ e^{-32.9/RT}$	c
3	$C_s\bullet + H \rightarrow C_s\text{–}H$	$p = 1.0$	d
4	$_C\bullet + C_2H_2 \rightarrow _C\text{–}C_2H + H$	$\dfrac{k_a k_b}{k_{-a} + k_b + k_c}$	e
4′	$^{-}C\bullet + C_2H_2 \rightarrow {}^{-}C\text{–}C_2H + H$	$\dfrac{k_{a'} k_{b'}}{k_{-a'} + k_{b'}}$	e
5	$_C\text{–}C_2H + H \rightarrow _C\bullet + C_2H_2$	$\dfrac{k_{-a} k_{-b}}{k_{-a} + k_b + k_c}$	e
5′	$^{-}C\text{–}C_2H + H \rightarrow {}^{-}C\bullet + C_2H_2$	$\dfrac{k_{-a'} k_{-b'}}{k_{-a'} + k_{b'}}$	e
6	$\bullet C_C\text{–}C_2H \rightarrow HC{=}C\bullet$	$p = 1.0$	d
7	$HC_C\bullet + C_2H_2 \rightarrow HC{=}CH + H$	$\dfrac{k_a k_c}{k_{-a} + k_b + k_c}$	e
8	$HC_C\text{–}C_2H + H \rightarrow HC{=}CH + H$	$\dfrac{k_{-b} k_c}{k_{-a} + k_b + k_c}$	e
9	$\bullet C_C\bullet + C_2H_2 \rightarrow HC{=}CH$	$p = 0.5$	d
10	$\bullet C_C\text{–}C_2H + H \rightarrow HC{=}CH$	$p = 0.5$	d
11	$\bullet C{=}C\text{–}C_2H + C_2H_2 \rightarrow HC/{=}\backslash C\bullet$	$\dfrac{k_{a'} k_d}{k_{-a'} + k_{b'} + k_d}$	e
12	$HC/{=}\backslash C\bullet \rightarrow \bullet C{=}C\text{–}C_2H + C_2H_2$	$\dfrac{k_{-a'} k_{-d}}{k_{-a'} + k_{b'} + k_d}$	e
13	$HC_2\text{–}C{=}C\text{–}C_2H + H \rightarrow \bullet C/{=}\backslash CH$	$\dfrac{k_{-b'} k_d}{k_{-a'} + k_{b'} + k_d}$	e
a	$_C\bullet + C_2H_2 \rightarrow _C\text{–}CH{=}CH\bullet$	$4.6 \times 10^6\ T^{1.97}\ e^{-30.5/RT}$	c
a'	$^{-}C\bullet + C_2H_2 \rightarrow {}^{-}C\text{–}CH{=}CH\bullet$	$1.1 \times 10^7\ T^{1.71}\ e^{-16.3/RT}$	c
$-a$	$_C\text{–}CH{=}CH\bullet \rightarrow _C\bullet + C_2H_2$	$1.5 \times 10^{15}\ e^{-171.6/RT}$	c
$-a'$	$^{-}C\text{–}CH{=}CH\bullet \rightarrow {}^{-}C\bullet + C_2H_2$	$1.3 \times 10^{14}\ e^{-174.8/RT}$	c
b	$_C\text{–}CH{=}CH\bullet \rightarrow _C\text{–}C_2H + H$	$1.2 \times 10^{14}\ e^{-161.2/RT}$	c
b'	$^{-}C\text{–}CH{=}CH\bullet \rightarrow {}^{-}C\text{–}C_2H + H$	$4.8 \times 10^{12}\ e^{-140.3/RT}$	c
$-b$	$_C\text{–}C_2H + H \rightarrow _C\text{–}CH{=}CH\bullet$	$6.7 \times 10^7\ T^{1.67}\ e^{-3.8/RT}$	c
$-b'$	$^{-}C\text{–}C_2H + H \rightarrow {}^{-}C\text{–}CH{=}CH\bullet$	$1.5 \times 10^{10}\ T^{0.85}\ e^{-5.0/RT}$	c
c	$HC_C\text{–}CH{=}CH\bullet \rightarrow HC{=}CH + H$	$2.6 \times 10^9\ T^{0.64}\ e^{-63.6/RT}$	c
d	$HC_2\text{–}C{=}C\text{–}CH{=}CH\bullet \rightarrow \bullet C/{=}\backslash CH$	$2.5 \times 10^{12}\ T^{-0.13}\ e^{-65.7/RT}$	c

[a]The nomenclature of the surface sites is as follows: C_s denotes a surface carbon atom, C_C the boat site and _C one of its carbon atoms, C=C the chair site and ⁻C one of its carbon atoms when it is not part of the neighboring boat site, and C/=\C the top carbon atoms of a lone aromatic ring (see Fig. 1).

[b]In the units of mol/cm³, s, K, kJ/mol.

[c]Based on the high-pressure limit of the analogous reactions of one-, two-, and three-ring aromatics [19,20].

[d]An assumed reaction probability.

[e]Assuming the steady state for the short-lived intermediate.

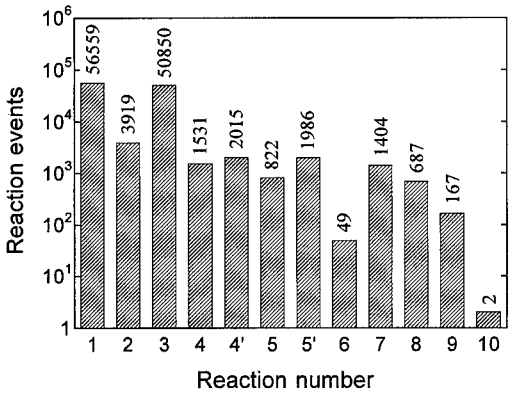

FIG. 3. Reaction events computed for surface growth at $T = 2000$ K, $P = 1$ atm, $x_{C_2H_2} = 0.1$, $x_{H_2} = 0.1$, and $x_H = 0.01$.

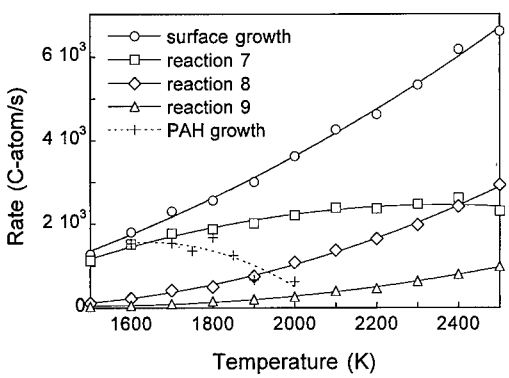

FIG. 4. Comparison of per-site rates computed for the surface (open symbols and solid lines) and PAH (the + symbols and dotted line) at $P = 1$ atm, $x_{C_2H_2} = 0.1$, $x_{H_2} = 0.1$, and $x_H = 0.01$. The symbols represent the results of actual calculations, and the lines are least-squares fits to them.

in identical runs but with different random seed numbers, was typically between 1 and 10%.

Results and Discussion

Surface Growth

A representative diagram of the numerical results is shown in Fig. 3. Reactions 1 and 3 are the fastest and the balance of their rates (or, equivalently, the ratio of their rate coefficients) in essence determines the fraction of dehydrogenated surface sites, that is, the number density of surface radicals. Deactivation of these surface radicals by molecular hydrogen, reaction 2—the reverse of reaction 1—is a relatively slow process (and in fact can be neglected). This can be contrasted with the growth of the first few aromatic rings whose rate is controlled at high temperatures (and low pressures) by the balance of reactions 1 and 2 [22]. This gas-phase regime of control by reactions 1 and 2 is switching to the solid-growth regime of control by reactions 1 and 3 with the increase in the PAH size (and pressure), that is, with the value of k_3 approaching its high-pressure limit.

The growth of the substrate surface (i.e., formation of the next-layer aromatic rings) is initiated by chemisorption of arriving acetylene molecules at surface radical sites. The fastest among them are reactions 4, 4′, and 7 (Fig. 3). Reactions 4 and 4′ do not lead directly to cyclization but produce a chemisorbed C_2H group. This adspecies may cyclize to an aromatic ring in subsequent reactions—6, 8, 10, and 11—or "desorb" by the reverse of 4 and 4′ (i.e., by reactions 5 and 5′). The "desorption" dominates under all conditions tested. In fact, reactions 4 and 5, as well as 4′ and 5′, nearly balance each other. This is not unexpected, however, because high reversibility of reactions $A_i\bullet + C_2H_2 \rightleftarrows A_iC_2H + H$, where A_i denotes an i-ring aromatic, was identified to be a distinctive feature of PAH growth kinetics from the very beginning [16]. As a sensitivity test, a run with $k_{-a} = 0$ resulted in about threefold increase in the computed surface growth rate.

Among the aromatic cyclization steps, reactions 6–11 and 13, only channels 7 and 8 contribute in a meaningful way. Adsorption of acetylene at double radical sites, reaction 9, is significant but does not contribute more than 15% to the surface growth at even the highest temperature tested, 2500 K. Reaction 7 dominates the growth at lower temperatures. However, its rate begins to level off at about 2000 K, while reaction 8 keeps accelerating and eventually catches up with reaction 7 (Fig. 4). As a result of the increasing rate of reaction 8, the net surface growth rate *increases* with temperature, as shown in Fig. 4. This is significant: It means that reversibility of the HACA mechanism cannot explain the decay in surface reactivity of soot particles, as was suggested by Mauss et al. [8,9] and Colket and Hall [7]. Indeed, reaction 7 decelerates with temperature because of the reaction-net reversibility; however, the contribution of reaction 8, predicted by the sterically resolved KMC calculations, more than compensates for this deceleration.

Figure 5 presents the results of calculations testing the effect of hydrogen atom concentration on the computed surface growth rate. The numerical results indicate (as perhaps expected from the previous discussion on the competition between reactions 2 and 3) that at low concentrations of hydrogen atoms, the rate of surface growth is proportional to H but becomes independent of H with the increase in the H concentration. The decline of the growth rate with the decrease in H concentration concurs with the previous analysis [5], identifying the decreasing H

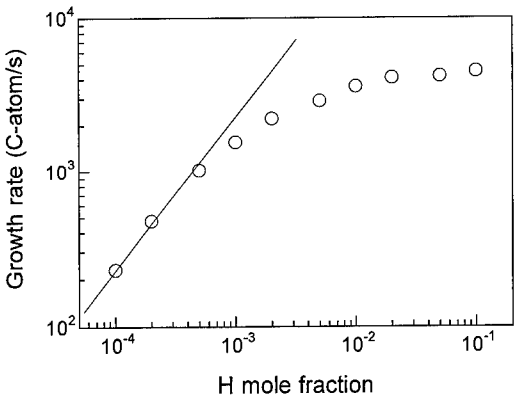

FIG. 5. Surface growth rate versus H atom mole fraction computed at $T = 2000$ K, $P = 1$ atm, $x_{C_2H_2} = 0.1$, and $x_{H_2} = 0.1$. The symbols represent the results of calculations; the solid line demonstrates the first-order kinetics in hydrogen-atom concentration.

concentration as one of the primary causes for the decay in the surface reactivity of soot particles. Also tested was the effect of C_2H_2 concentration on the surface growth rate, which produced an expected result [5], first-order concentration dependence.

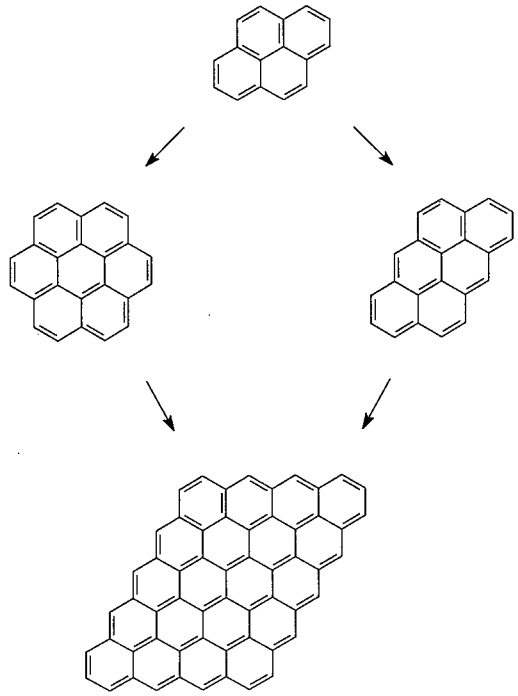

FIG. 6. Dominant reaction pathways of PAH growth.

PAH Growth

Using the same reaction mechanism, gas-phase composition, and KMC method, a series of calculations was performed with a gaseous PAH, a pyrene molecule, as the initial substrate. The computed rates of growth are shown in Fig. 4, and typical species through which the growth propagates are depicted in Fig. 6. Analysis of the computational results indicated that the growth is controlled by the formation of aromatic rings at the corners of PAH structures via reactions 11–13, followed by a rapid sequence of boat site cyclizations, reaction 7. Because of the high reversibility of reactions 11–13, the growth rate decays with temperature (Fig. 4). The zipper-type filling of the boat sites, created following the formation of a corner aromatic ring, results in zigzag PAH edges, as illustrated in Fig. 6.

Five-Member Ring Growth

The zigzag edges produced in the KMC simulated growth of PAH and the armchair boundary assumed for the growth of soot particle surface are inconsistent with one another. Indeed, within the present nucleation model [5,23], a solid particle emerges from coalescence of gaseous PAHs, and if the PAH edges are zigzag so should then be the particle edges, in conflict with the armchair substrate assumed for the particle surface growth.

One possibility of addressing this inconsistency may be provided by the nucleation model advocated recently by D'Alessio and co-workers [24] and Dobbins and Subramaniasivam [25]—nucleation through formation of aromatic-aliphatic-linked hydrocarbons (AALH) that graphitize afterwards.

Another possibility is the formation of a five-member ring, in a reaction between a zigzag surface radical site and an acetylene molecule. Once formed, such a five-member ring serves as a nucleus for the next layer growth initiated via

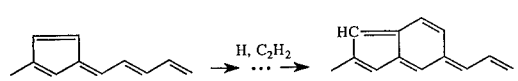

The subsequent growth of the zigzag row continues through the same zipper mechanism as discussed for the armchair surface. In support of this proposal, quantum-chemical calculations at the AM1 level [26] showed that the energetics calculated for the elementary reactions of the shown sequence are comparable to (and even slightly more favorable than) those reported for similar reactions of six-member–ring compounds [19], such as reactions *a* and *c* in Fig. 2; hence, the rates of these two reaction systems should be close to each other. This implies that the overall growth rates of zigzag surfaces should be similar to those of armchair substrates considered in the present study.

The mechanism suggested here has additional

mechanistic consequences. The formation of five-member rings should produce a curvature of the top aromatic layers of soot particles, as was indeed hypothesized recently [27]. Also, some of the cyclopenta CH sites, those formed at the surface edges (and marked so on the right-hand structure of the preceding reaction), are sufficiently stable but cannot propagate growth. Accumulation of such sites should lead to a decline in the surface reactivity.

Finally, it is pertinent to mention that the two nucleation models, AALH graphitization and PAH condensation, are not inconsistent with one another. On the contrary, they probably represent two possible extremes. For example, it was found in applying a HACA-based reaction model to a set of astrophysical environments [28] that the model predicts formation of only small-size "compact" aromatics while the same model at another set of astrophysical conditions [29] points to a large-size AALH growth.

Conclusions

Sterically resolved kinetic Monte Carlo simulations indicate that the HACA-based reaction model predicts for the growth rate of soot particle surface to *increase* and not decrease with temperature, even when the reaction reversibility is fully accounted for. This implies that the decreasing thermal stability of surface intermediates is unlikely to be responsible for the decline in surface reactivity of soot particles. In contrast, the growth of gaseous PAHs by the HACA mechanism is impeded by the reversibility of cyclization reactions and is shown to result in zigzag edges, inconsistent with the armchair substrate assumed for the particle surface growth. This inconsistency is resolved by invoking the formation of five-member rings that serve as surface nuclei for the subsequent HACA growth.

The computational results also show that the surface growth rate is proportional to the C_2H_2 concentration and independent of H at high H concentrations but declines with the decrease in the abundance of hydrogen atoms. This concurs with the previous analysis [5] identifying the decreasing H concentration as one of the primary causes for the decay in the surface reactivity of soot particles.

Acknowledgments

The work was supported by the Air Force Office of Scientific Research, Air Force Systems Command, USAF, under grant No. F49620-94-1-0226, and the Technology Development of the Engine Division of Caterpillar Inc. The U.S. government is authorized to reproduce and distribute reprints for governmental purposes notwithstanding any copyright notation thereon. The views and conclusions contained in this document are those of the authors and should not be interpreted as necessarily representing the official policies or endorsements, either express or implied, of the Air Force Office of Scientific Research or the U.S. Government.

REFERENCES

1. Bockhorn, H., Ed., *Soot Formation in Combustion: Mechanisms and Models*, Springer Verlag, Berlin, 1994.
2. Haynes, B. S. and Wagner, H. G., *Z. Phys. Chem. N. F.* 133:201–213 (1982).
3. Harris, S. J. and Weiner, A. M., *Annu. Rev. Phys. Chem.* 36:31–52 (1985).
4. Santoro, R. J., *Fall Technical Meeting of the Eastern States Section of the Combustion Institute*, 1995, pp. 37–44.
5. Frenklach, M. and Wang, H., *Twenty-Third Symposium (International) on Combustion*, The Combustion Institute, Pittsburgh, 1991, pp. 1559–1566.
6. Kazakov, A., Wang, H., and Frenklach, M., *Combust. Flame* 100:111–120 (1995).
7. Colket, M. B. and Hall, R. J., in *Soot Formation in Combustion: Mechanisms and Models*, (Bockhorn, H., Ed.), Springer Verlag, Berlin, 1994, pp. 442–468.
8. Mauss, F., Schäfer, T., and Bockhorn, H., *Combust. Flame* 99:697–705 (1994).
9. Mauss, F. and Bockhorn, H., *Z. Phys. Chem.* 188:45–60 (1995).
10. Frenklach, M., in *Carbon in the Galaxy: Studies from Earth and Space* (Tarter, J. C., Chang, S., and DeFrees, D. J., Eds.), NASA Conference Publication 3061, 1990, pp. 259–273.
11. Walker, P. L., Jr., *Carbon* 28:261–279 (1989).
12. Ehrburger, P., Louys, F., and Lahaye, J., *Carbon* 27:389–393 (1989).
13. Nagle, J. and Strickland-Constable, R. F., *Proceedings of the Fifth Conference on Carbon*, Pergamon, London, 1962, pp. 154–164.
14. Harris, S. J., *Combust. Sci. Technol.* 72:67 (1990).
15. Woods, I. T. and Haynes, B. S., *Combust. Flame* 85:523–525 (1991).
16. Frenklach, M., Clary, D. W., Gardiner, W. C., Jr., and Stein, S. E., *Twentieth Symposium (International) on Combustion*, The Combustion Institute, Pittsburgh, 1985, pp. 887–901.
17. Gillespie, D. T., *J. Comp. Phys.* 22:403–434 (1976); *J. Phys. Chem.* 81:2340–2361 (1977).
18. Kinoshita, K., *Carbon: Electrochemical and Physical Properties*, Wiley, New York, 1988.
19. Wang, H. and Frenklach, M., *J. Phys. Chem.* 97:3867–3874 (1993); 98:11465–11489 (1994).
20. Kiefer, J. H., Mizerka, L. J., Patel, M. R., and Wei, H. C., *J. Phys. Chem.* 89:2013–2019 (1985).
21. Frenklach, M. and Wang, H., *Phys. Rev. B* 43:1520–1545 (1991).
22. Frenklach, M., *Twenty-Second Symposium (International) on Combustion*, The Combustion Institute, Pittsburgh, 1989, pp. 1075–1082.

23. Frenklach, M. and Wang, H., in *Soot Formation in Combustion: Mechanisms and Models,* (Bockhorn, H., Ed.), Springer Verlag, Berlin, 1994, pp. 162–190.
24. D'Anna, A., D'Alessio, A., and Minutolo, P., in *Soot Formation in Combustion: Mechanisms and Models,* (Bockhorn, H., Ed.), Springer Verlag, Berlin, 1994, pp. 83–101.
25. Dobbins, R. A. and Subramaniasivam, H., in *Soot Formation in Combustion: Mechanisms and Models,* (Bockhorn, H., Ed.), Springer Verlag, Berlin, 1994, pp. 290–299.
26. Kazakov, A. and Frenklach, M., unpublished results.
27. Donnet, J.-B., *Carbon* 32:1305–1310 (1994).
28. Frenklach, M. and Feigelson, E. D., *Astrophys. J.* 341:372–384 (1989).
29. Morgan, W. A., Feigelson, E. D., Wang, H., and Frenklach, M., *Science* 252:109–112 (1991).

COMMENTS

D. G. Vlachos, Universtiy of Massachusetts, USA. The sticking coefficients of gaseous species for surface growth may depend on cell temperature, soot particle size, and gaseous precursor adsorbed on the particle. How do you take into account this possible dynamic change of sticking coefficients during growth of particles as a function at time?

Author's Reply. The present model is formulated not in terms of over all sticking coefficients but in terms of elementary reaction probabilities. The latter are derived from elementary reaction rate coefficients and thus carry their temperature dependence and, being defined for individual combinations of gas-phase species and surface sites, are surface site specific.

•

Prof. Antonio D'Alessio, Università di Napoli, Italy. Your model assumes that the bonding between carbon atoms is sp^2; i.e., aromatic structures prevail. Experimentally it has been found that soot particles, like other carbonaceous structures, are mixtures of sp^2 and sp^3 bondings. Would you comment about it?

Author's Reply. Analysis of reaction chemistry and associated thermochemical data and kinetic results points to predominantly aromatic character of soot for high-temperature growth environments. At lower temperatures (and fuel-rich mixtures) our model suggests a possibility of sp^3 links between aromatic structures [1]. One of the advantages of the kinetic Monte Carlo technique introduced in the present study is the ability to examine this type of question, and we plan to do so in the future.

REFERENCE

1. Morgan, W. A., Feigelson, E. D., Wang, H., and Frenklach, M., *Science* 252:109–112 (1991).

•

J. B. Howard, MIT, USA. Your focus on acetylene as the only reactant in soot growth is probably too limited, and your not taking five-membered rings into account in the Monte Carlo treatment of the kinetics limits the extent to which the results represent actual soot-growth species. Besides acetylene, other compounds deserving consideration are small aliphatic radicals and PAH including those with five-membered rings, such as methylene and ethylene bridges which are prevalent in flame-generated PAH, and probably also in surface structures of growing soot. The polycyclic edge structures mentioned in your paper would be expected to be more reactive with radicals of PAH and small aliphatics than with acetylene, and these other reactants are too abundant in sooting flames to be neglected. Is there a technical basis for focusing only on acetylene as reactant, and for not including five-membered ring structures in the Monte Carlo analysis?

Author's Reply. While the present work focuses on surface reactions of acetylene, our view of surface growth is not limited to acetylene only. For instance, we were the first to introduce PAHs as surface deposition species in detailed kinetic modeling of soot formation [1]. Our approach to "choosing" surface growth species is founded, as stated in the paper, on systematic and consistent application of the principal of chemical similarity. Detailed numerical simulations performed on this basis by us and others for a series of laminar premixed flames identified acetylene as the dominant contributor to the surface growth. It is certainly possible that in combustion environments other than laboratory laminar premixed flames, to which the attention has been drawn thus far, species other than acetylene will contribute to surface growth, similar to the case argued by us for the growth of PAHs [2].

As for the five-membered rings, there has been no prior information on their importance in surface growth. One of the key results of the present numerical study is the sug-

gested necessity for the five-membered ring surface structures. This finding is a consequence of the sterically-resolved kinetic Monte-Carlo approach to surface growth introduced in the present study. We certainly plan to extend this approach to include other growth species and different surface structures.

REFERENCES

1. Frenklach, M. and Wang, H., *Twenty-Third Symposium (International) on Combustion,* The Combustion Institute, Pittsburgh, 1991, pp. 1559–1566.
2. Frenklach, M., Clary, D. W., Gardiner, W. C., Jr., and Stein, S. E., *Twenty-First Symposium (International) on Combustion,* The Combustion Institute, Pittsburgh, 1988, pp. 1067–1076.

Twenty-Sixth Symposium (International) on Combustion/The Combustion Institute, 1996/pp. 2295–2302

SOOT SURFACE GROWTH BY POLYCYCLIC AROMATIC HYDROCARBON AND ACETYLENE ADDITION

SCOTT MACADAM, JÁNOS M. BEÉR AND ADEL F. SAROFIM
Department of Chemical Engineering
Massachusetts Institute of Technology
Cambridge, Massachusetts 02139, USA

ARNE B. HOFFMANN
Engler-Bunte Institute
Universität Karlsruhe
Karlsruhe, Germany

The two principal soot surface growth agents are believed to be acetylene (C_2H_2) and polycyclic aromatic hydrocarbons (PAH). However, their relative contributions to soot growth under various conditions is not well understood. To address this issue, soot was produced in a jet-stirred plugflow reactor (JS/PFR) under acetylene-lean and acetylene-rich conditions. The JS/PFR is a premixed ethylene-fired combustor consisting of a well-stirred reactor (JSR) in series with a plugflow reactor (PFR). Acetylene-lean conditions were attained by injecting benzene into the PFR while operating the JSR at a fuel equivalence ratio (ϕ) of 1.3. Acetylene-rich conditions were met by operating the JSR at a ϕ of 2.1 without any secondary injection. The PFR temperature was set to 1580 K and two benzene injection rates were chosen. In the acetylene-lean cases, the dominant soot growth agent was found to be PAH. Collision efficiencies between soot particles and PAH molecules were calculated using gas collision theory. With the assumption that all the observed soot growth occurred by PAH addition, collision efficiencies were found to lie between 0.11 and 0.03 for the two acetylene-lean cases and between 0.51 and 0.27 for the acetylene-rich case. The high values of the latter case suggest that the observed soot growth cannot be accounted for by PAH addition alone. This indicates that, under our acetylene-rich conditions ($\phi = 2.1$), acetylene appears to dominate soot growth. Calculated soot-acetylene collision efficiencies lay between 5.4×10^{-4} and 3.1×10^{-4}. The observed decrease in collision efficiencies with residence time was related to a decreasing H/H_2 ratio with time.

Introduction

To improve our ability to model and ultimately predict the formation of soot in both premixed and diffusion flames, a clear understanding of the pathways controlling postnucleation soot surface growth is required. This step of the overall soot formation process is of particular importance since it is where the bulk of soot mass growth takes place [1]. From an experimental point of view, it is advantageous to study the formation of soot under homogeneous conditions because this allows one to neglect mixing phenomena. For that reason, numerous investigations have been carried out using premixed laminar flat flames [2–6] rather than diffusion flames. These studies have revealed that the onset of sooting is associated with the presence of polycyclic aromatic hydrocarbons (PAHs). Under the conditions of these experiments, soot was found to appear near the peak PAH concentration and continued to grow at a rate that decreased with time.

The soot nucleation process is believed to be controlled by the reactive coagulation of large PAH molecules as opposed to molecular weight growth of PAH by acetylene addition [7]. A popular model of postnucleation soot growth postulates that this process is governed by the addition of acetylene via hydrogen abstraction [8]. Since acetylene occurs in such abundance in the postflame zones of fuel-rich premixed flames, it has been identified as the controlling soot growth agent [9]. Although acetylene concentrations are usually relatively constant with residence time, surface growth rates decrease at higher residence times. This phenomenon, which is most evident at higher temperatures, has been attributed to a decreasing soot surface reactivity with time. PAH molecules are not consumed completely in the nucleation process and their formation continues well into the soot surface growth zone. With this in mind, it has been proposed that they may participate in the soot surface growth process along with acetylene [10,11]. The implication of this is that

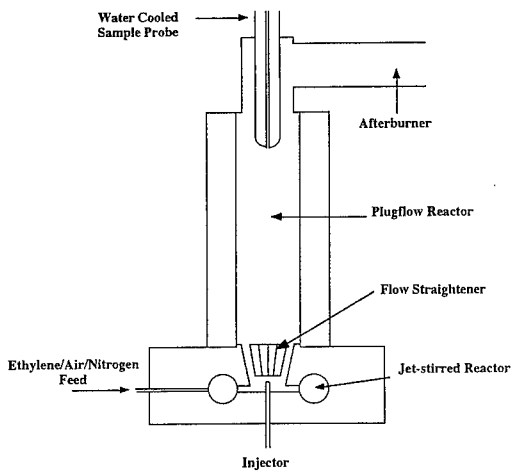

FIG. 1. Schematic of jet-stirred plugflow reactor (JS/PFR).

a comprehensive soot-formation model should include an accurate PAH formation mechanism in its surface growth stage to account for their participation in the soot mass growth process.

Although there is little doubt that both PAH and acetylene are important soot surface growth agents, their relative contributions to soot surface growth under various conditions have not yet been ascertained by experimental means. This paper presents the results of a study in which the roles of these two species were determined for the cases of premixed ethylene/air flames with and without benzene injection.

Experimental Apparatus

Experiments were carried out in the jet-stirred plugflow reactor (JS/PFR) [12]. This reactor is an enclosed premixed flame combustor fired with ethylene (C_2H_4) and run at atmospheric pressure. A schematic of the apparatus appears in Fig. 1. The jet-stirred reactor (JSR) is a toroidal-shaped chamber cast out of alumina ceramic. Ethylene, which is used as the primary fuel, is premixed with air and diluent nitrogen before being fed to the JSR through 32 jets located around the periphery of the chamber. These jets are oriented at an angle so as to promote a swirling, well-mixed flow field inside the reactor. Under normal conditions, the JSR residence time is 6 ms. Upon leaving the JSR, the combustion gases pass through a flow straightener and enter a cylindrical alumina plugflow reactor (PFR). The reactor configuration allows for the injection of an additive into the system at a point upstream of the flow straightener. With a sufficiently fuel-rich JSR feed (fuel equivalence ratio >1.8) or with the addition of an aromatic additive, significant PAH and soot formation takes place in the PFR, where the residence time is 30 ms. Samples drawn from various axial positions along the PFR centerline, all of which correspond to specific residence times, allow us to monitor the growth of both PAH and soot with time. The inherent advantages of the PFR lie in its near-isothermal and plugflowlike characteristics. The span of operating conditions includes a temperature range of 1400–1700 K and a fuel equivalence ratio range of 0.5–2.6. Samples are withdrawn from the PFR through a water-cooled stainless steel probe and analyzed for soot, PAH, and light hydrocarbons. Soot concentrations are determined by collecting soot on filters (Pallflex T60A20) and measuring the weights of the deposited material. Before weighing, the soots are rinsed with dichloromethane (CH_2Cl_2) to extract PAHs since, for our purposes, soot is defined as all dichloromethane-insoluable material. PAHs are collected by passing the sample gas through dichloromethane traps. The individual PAH concentrations are quantified by analyzing the concentrated extracts by GC-FID or HPLC. Compounds that can be identified range from naphthalene ($C_{10}H_8$) to coronene ($C_{24}H_{12}$). Light hydrocarbons, which include the C1 to C4 compounds, are analyzed by GC-FID.

The experimental strategy involved generating soot under two distinctly different conditions. These two conditions were chosen to ensure that the two PAH:C_2H_2 ratios differed significantly from each other. Acetylene concentrations in the PFR are strongly dependent on the JSR fuel equivalence ratio (ϕ) and increase significantly with increasing ϕ. In the acetylene-rich case, the JSR was operated at a relatively high ϕ of 2.1 without any secondary injection. In the acetylene-lean cases, the JSR was run at a relatively low ϕ of 1.3, but benzene was injected to promote PAH and soot formation without introducing large quantities of acetylene. Several benzene injection rates were chosen. In the acetylene-lean experiments, the PAH:C_2H_2 ratios were expected to be relatively high, thus ensuring that the PAH addition mechanism played a dominant role in soot surface growth. The JSR temperature was chosen to be 1600 K, which led to a PFR temperature of 1580 K. The relevant experimental parameters appear in Table 1. A comparison of the data obtained from the acetylene-rich experiment (case 1) and an appropriate acetylene-lean experiment (case 2) allowed us to ascertain the roles of PAH and acetylene addition in the two experiments.

Results and Discussion

To verify that the PFR acetylene levels in cases 1 and 2 of Table 1 did indeed differ significantly from each other, acetylene concentrations were measured along the PFR axis for these experiments. The data,

TABLE 1
Jet-stirred plugflow reactor experimental parameters

Case	Fuel Equivalence Ratio[a]	PFR Temperature	Benzene Injection Rate
1	2.1	1580 K	0
2	1.3	1580 K	4.2 g/min (15% of C)[b]
3	1.3	1580 K	6.4 g/min (21% of C)[b]
4	1.6	1580 K	4.2 g/min (13% of C)[b]

[a]Fuel equivalence ratio in the jet-stirred reactor (before secondary injection). The JSR feed was an ethylene/air/nitrogen premixed stream.

[b]Benzene injection rate expressed as the percentage of carbon fed to the reactor originating from benzene.

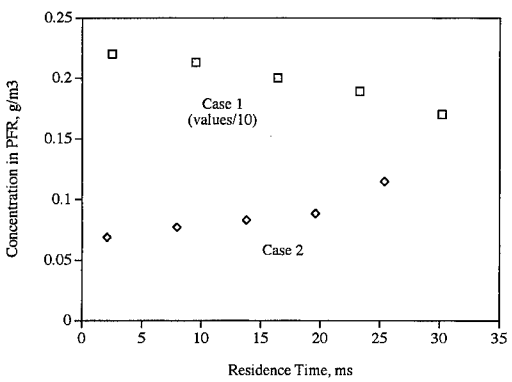

FIG. 2. Acetylene concentrations in PFR for case 1 (ϕ = 2.1) and case 2 (ϕ = 1.3, benzene = 4.2 g/min).

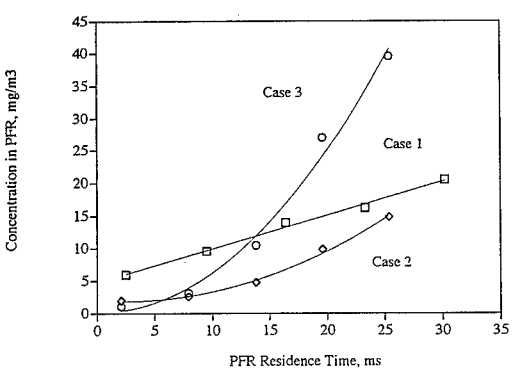

FIG. 3. Soot concentrations in PFR for case 1 (ϕ = 2.1), case 2 (ϕ = 1.3, benzene = 4.2 g/min), and case 3 (ϕ = 1.3, benzene = 6.4 g/min). Lines are smooth fits through data.

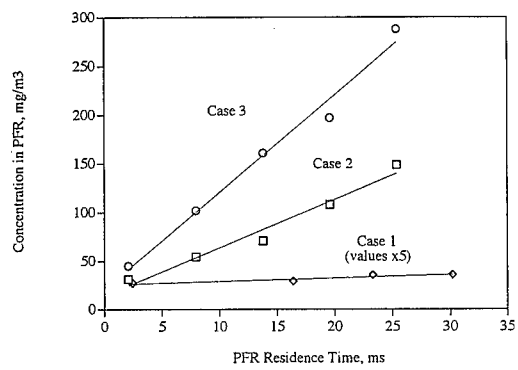

FIG. 4. Total PAH concentrations in PFR for case 1 (ϕ = 2.1), case 2 (ϕ = 1.3, benzene = 4.2 g/min), and case 3 (ϕ = 1.3, benzene = 6.4 g/min). Total PAH includes all detectable polycyclic aromatic compounds from naphthalene through cyclopenta[c,d]pyrene. Lines are smooth fits through data.

which appear in Fig. 2, indicate that the acetylene concentrations of case 1 exceed those of case 2 by a factor of between 15 and 30. This large difference supports the idea that, in case 2, acetylene must have played a minor role in the observed soot growth. If this were not true and acetylene had played an important role in this case, the observed soot growth rate would have been significantly lower than that of case 1. Figure 3, which contains the soot concentration data pertaining to cases 1, 2, and 3, indicates that the average soot growth rates were roughly equal for cases 1 and 2. The concentrations of total PAH, which includes PAH compounds from naphthalene through cyclopenta[c,d]pyrene, appear in Fig. 4. Table 2 contains concentrations of all the identifiable PAH for the three cases. From the Fig. 4 values, it is evident that significantly more PAH was formed in case 2 than in case 1. Since the average soot-growth rates of cases 1 and 2 are roughly equal and since it was concluded that in case 2, PAH must have dominated soot growth, the relatively low

TABLE 2
Concentrations (in mg/m^3) of identifiable PAH at a PFR residence time of 20 ms for cases 1, 2, and 3

Compound	Case 1	Case 2	Case 3
Phenyl-1,3-Butadyene	0.05	2.03	3.53
Naphthalene	2.27	22.9	33.5
2-Ethynylnaphthalene	0.16	2.01	4.85
Acenaphthylene	3.96	30.3	50.4
Fluorene	0.06	0.30	0.99
Ethynylacenaphthylene	b.d.l.‡	1.30	2.29
Phenanthrene	0.18	2.35	6.54
Anthracene	0.02	0.37	0.82
Phenylnaphthalene	0.05	0.64	2.31
4H-Cyclopenta[def]phenanthrene	0.13	0.91	0.14
Fluoranthene	0.20	3.26	7.23
Acephenanthrylene	0.6	1.11	2.74
Pyrene	0.37	1.16	1.47
Phenylacenaphthylene	b.d.l.‡	1.38	6.07
Cyclopenta[cd]fluoranthene	0.26	1.36	2.07
Benzo[ghi]fluoranthene	0.07	2.88	8.16
Cyclopentaacephenanthrylene (CPAP)	0.41	3.09	5.99
Cyclopenta[cd]pyrene	1.20	7.77	13.76
Chrysene	0.02	0.56	3.03

‡below detection limit

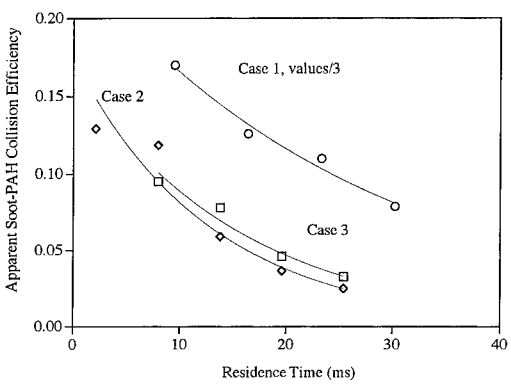

FIG. 5. Apparent soot–PAH collision efficiencies for case 1 (ϕ = 2.1), case 2 (ϕ = 1.3, benzene = 4.2 g/min), and case 3 (ϕ = 1.3, benzene = 6.4 g/min). Lines are smooth fits through data.

PAH levels in case 1 imply that a major portion of the soot mass growth in that case must have come from species other than PAH. Since this is our acetylene-rich experiment, the most abundant soot growth agent other than PAH is acetylene. Therefore, in case 1 (ϕ = 2.1 with no injection), the most dominant soot-growth agent appears to be acetylene.

To more accurately determine the relative contributions of acetylene and PAH to soot growth in case 1, collision rates between the soot particles and the various hydrocarbon molecules need to be calculated. Equating the observed soot growth rate to the product of a collision frequency and a collision efficiency allowed us to back calculate collision efficiencies as a function of PFR residence time. The process was assumed to be governed by a version of the general gas collision equation, Eq. (1). According to this particular equation, all observed soot growth is assumed to occur by PAH addition alone, and oxidation is neglected.

$$\frac{d[\text{soot}]}{dt} = \gamma_{\text{soot,PAH}} \frac{\sigma_{\text{soot}^2}}{4} \left(\frac{8\pi RT}{M}\right)^{0.5} N_{\text{soot}} [\text{PAH}] \tag{1}$$

where $\gamma_{\text{soot,PAH}}$ is the soot–PAH collision efficiency, σ_{soot} is the soot–PAH collision diameter, M is the average PAH molecular weight, and N_{soot} is the soot number density [13]. Since the expected number of collisions between soot particles during the PFR residence time is only 5% of the final number of particles, soot agglomeration was ignored. This allowed us to assume a constant soot-number density with residence time. The soot-number density was based on soot particle–size measurements by transmission electron microscopy (TEM). Particle diameters

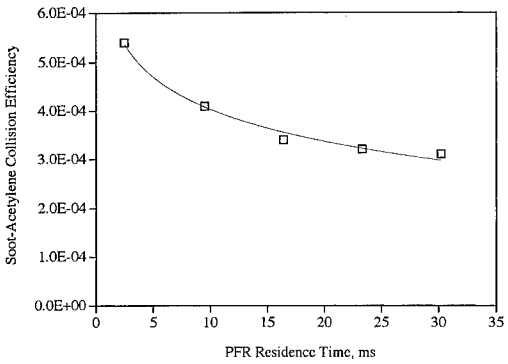

FIG. 6. Soot-acetylene collision efficiencies for case 1 (ϕ = 2.1). Line is smooth fit through data.

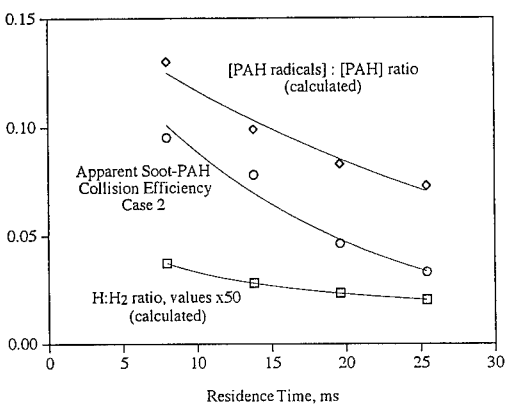

FIG. 7. Soot–PAH collision efficiencies and calculated values of the $H:H_2$ and [PAH radicals]:[PAH] ratios for case 2 (ϕ = 1.3, benzene = 4.2 g/min). Lines indicate trends.

were averaged by weighting the cross-sectional areas ($0.25\ \pi\sigma^2$) with collision velocity. By applying Eq. (1) to the experimental data, the apparent soot–PAH collision efficiencies were calculated at various PFR residence times for the different experimental cases. From Fig. 5, which contains the results pertaining to cases 1, 2, and 3, it is evident that the apparent collision efficiencies for cases 2 and 3 (where benzene was injected) are substantially lower than those of case 1. Since it was concluded that PAH dominate soot growth in the benzene injection experiments, the apparent collision efficiencies calculated for these cases probably do not differ significantly from the true PAH–soot collision efficiencies. The values for case 1, on the other hand, are higher than those of cases 2 and 3 by a factor of 5–7. These relatively high values indicate that Eq. (1) cannot account for the soot growth in case 1 since it assumes that all growth is due to PAH addition. To match the PAH–soot collision efficiencies of case 1 with those of case 2, it would be necessary to presume that approximately 20% of the soot growth in case 1 occurred by PAH addition and the remaining 80% by acetylene addition. This is further evidence that acetylene dominated the soot surface growth that occurred under the ϕ = 2.1 conditions of case 1. The effect of increasing the benzene injection rate from 4.2 g/min (case 2) to 6.4 g/min (case 3) was to increase soot and PAH concentrations by factors of 4 and 2, respectively (as indicated by Figs. 3 and 4). However, the collision efficiencies differ from each other by only 20–25%. This suggests that, in the case of benzene injection, the mechanism by which available PAH molecules add to available soot particles is not strongly dependent on the absolute PAH and soot concentrations.

Since it is apparent that acetylene dominated soot growth in case 1, the soot-acetylene collision efficiencies were calculated for that case by applying Eq. (1) to soot-acetylene interactions and assuming that 80% of the observed soot growth occurred by acetylene addition. The results of this calculation appear in Fig. 6. Like the soot–PAH collision efficiencies, these values showed a decline with increasing PFR residence time, a trend seen in other sooting flames [9]. In the case of soot–PAH collisions, the probability of a PAH adding to the soot particle is significantly higher if the PAH is a radical rather than a parent molecule. If it is assumed that the collision efficiency between a PAH radical and a soot particle is unity, the measured soot–PAH collision efficiencies may be correlated with the fraction of PAH species present as radicals. Since we lack the capability of measuring radicals directly in the PFR, we have to resort to estimating radical species by assuming partial equilibrium. The abstraction process is represented by reaction 1.

$$\mathrm{PAH} + \mathrm{H}\cdot \Leftrightarrow \mathrm{PAH}\cdot + \mathrm{H}_2 \quad \text{(reaction 1)}$$

PAH and H_2 concentrations are available for each experimental case. H concentrations were estimated using a Chemkin package [14]. The equilibrium constant for the reaction involving each significant PAH was estimated using a Therm package [15]. Equilibrium constants were calculated for primary aryl, secondary aryl, and vinyl radicals [16]. H/H_2 ratios and total PAH radical concentrations (the latter expressed as fractions of the total PAH concentrations) are plotted in Fig. 7, along with the case 2 soot–PAH collision efficiencies. The PAH radical fractions appear to approximate the soot–PAH collision efficiency values and display the same downward trend with increasing residence time.

In the case of soot-acetylene interactions, which are particularly relevant to case 1, the probability of a collision resulting in a reaction is strongly dependent on the soot surface properties. The property of most interest is the density of active sites on the soot surface [17]. These active sites may be considered

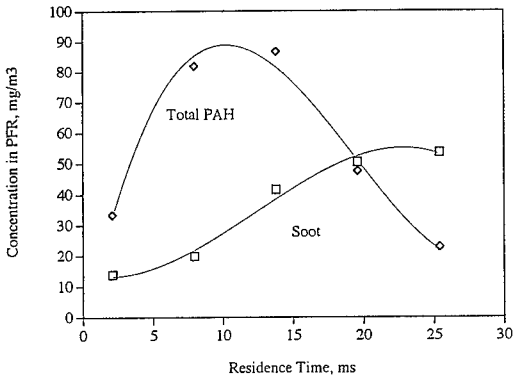

FIG. 8. Soot and PAH concentrations for case 4 (ϕ = 1.6, benzene = 4.2 g/min). Lines are smooth fits through data.

TABLE 3
Contributions of PAH and acetylene to soot growth for case 4

PFR Residence Time	Contribution from PAH	Contribution from C_2H_2
7.9 ms	79%	21%
13.8 ms	78%	22%
19.6 ms	18%	82%

to be in equilibrium with H and H_2 in much the same way as PAH radicals are. With this in mind, any observed change in soot surface reactivity may be attributed to the depletion of gaseous radicals [18], although other factors such as annealing of the surface may also be responsible [9]. The soot-acetylene collision efficiencies calculated for case 1 were observed to decrease by a factor of approximately 2 along the PFR. The H/H_2 ratio plotted in Fig. 7 also decreased by a factor of approximately 2. Therefore, changes in the concentrations of gaseous species surrounding the growing soot particles can, in case 1, account for the observed change in surface reactivity. This does not rule out the possibility of annealing playing some role. Under our experimental conditions, annealing does not appear to play a major role but may become more significant at higher temperatures.

In case 4, the experimental parameters were chosen to allow the contributions of both soot growth mechanisms to be significant. The feed to the JSR was set at a moderately high but nonsooting fuel equivalence ratio of 1.6. This supplied the PFR with relatively large quantities of acetylene while benzene was injected into the PFR to promote PAH formation. The soot and PAH concentrations measured in case 4 appear in Fig. 8. From this plot, it is evident that substantially more soot was formed than in case 2, where the benzene injection rate was equal. The concentration of PAH, unlike case 2, increased initially, peaked, and then decreased at higher residence times. This was attributed to the increased role of soot as a PAH sink because of the higher soot levels. To estimate the relative contributions of acetylene and PAH to soot growth in case 4, collision efficiency information is required for either the soot-acetylene or soot–PAH interactions. Since this is unavailable for case 4, soot-acetylene collision efficiency values calculated for case 1 were used. Eq. (1) was then used to calculate the portion of the observed soot growth originating from acetylene addition. Table 3 contains the results of this analysis.

These results illustrate how the role of PAH in soot surface growth decreases in importance once PAH concentrations decline. Since acetylene levels are more constant with residence time, acetylene becomes more dominant at later stages of the growth process. This idea of PAH controlling soot growth in the early stages and acetylene controlling growth in the later stages has been proposed by others [19].

Conclusions

In the cases of benzene injection with a baseline ϕ of 1.3, the dominant soot surface growth pathway was found to be the PAH addition route. Soot–PAH collision efficiencies were calculated to lie between 0.11 and 0.03, depending on PFR residence time. These values did not vary significantly with benzene injection rate. With a JSR ϕ of 2.1, where no benzene was injected, soot surface growth route appeared to be dominated by acetylene addition. The soot-acetylene collision efficiencies lay between 5.4×10^{-4} and 3.1×10^{-4}. The trend of decreasing soot–PAH collision efficiency values with residence time was related to changes in radical PAH concentrations with time. PAH radical concentrations were calculated using thermodynamic data, assuming that radical PAHs were formed by the abstraction of H atoms from parent PAH molecules and that partial equilibrium existed. It was found that these values are sensitive to the H/H_2 ratio, which was determined to decline with residence time. The observed drop in soot-acetylene collision efficiency with time was also attributed to the decreasing H/H_2 ratio. This was ascribed to the fact that, in the case of soot surface growth by acetylene addition, the process is dependent on the density of active sites on the soot surface and that these active sites are formed by hydrogen abstraction. For the case of benzene injection into a moderately fuel-rich (ϕ = 1.6) baseline, PAH was found to contribute approximately 80% of the soot growth at lower residence times (<15 ms)

but only 20% at higher times (>15 ms). This was attributed to declining PAH concentrations after 15 ms.

Acknowledgments

The authors are grateful to Dr. Christopher J. Pope and David Kronholm for their help with the modeling effort; to Cord Manegold for his participation in the experimental setup; to Elaine Plummer and John Larusso for their analytical expertise; to Lenore Rainey for her microscopy expertise; and to the Environmental Protection Agency Center on Airborne Organics and Electric Power Research Institute for their financial support.

REFERENCES

1. Bockhorn, H., Fetting, F., Wannemacher, G., and Heddrich, A., *Ber. Bunsenges. Phys. Chem.* 91:819 (1987).
2. Bonne, U., Homann, K. H., and Wagner, H. G., *Tenth Symposium (International) on Combustion,* The Combustion Institute, Pittsburgh, 1965, p. 503.
3. Tompkins, E. E. and Long, R., *Twelfth Symposium (International) on Combustion,* The Combustion Institute, Pittsburgh, 1969, p. 625.
4. D'Alessio, A., Di Lorenzo, A., Sarofim, A. F., Beretta, F., Masi, S., and Venitozzi, C., *Fifteenth Symposium (International) on Combustion,* The Combustion Institute, Pittsburgh, 1975, p. 1427.
5. Lam, F. W., Howard, J. B., and Longwell, J. P., *Twenty-Second Symposium (International) on Combustion,* The Combustion Institute, Pittsburgh, 1988, p. 323.
6. Lam, F. W., Longwell, J. P., and Howard, J. B., *Twenty-Third Symposium (International) on Combustion,* The Combustion Institute, Pittsburgh, 1990, p. 1477.
7. McKinnon, J. T. and Howard, J. B., *Twenty-Fourth Symposium (International) on Combustion,* The Combustion Institute, Pittsburgh, 1992, p. 965.
8. Frenklach, M. and Wang, H., *Twenty-Third Symposium (International) on Combustion,* The Combustion Institute, Pittsburgh, 1990, p. 1559.
9. Harris, S. J. and Weiner, A. M., *Combust. Sci. Technol.* 32:267 (1983).
10. Marr, J. A., "PAH Chemistry in a Jet-Stirred Plugflow Reactor System," Ph.D. Thesis, Massachusetts Institute of Technology, 1993.
11. Marr, J. A., Giovane, L. M., Longwell, J. P., Howard, J. B., and Lafleur, A. L., *Combust. Sci. Technol.* 101:301 (1994).
12. Nenniger, J. E., "Polycyclic Aromatic Hydrocarbon Production in a Jet Stirred Combustor," Ph.D. Thesis, Massachusetts Institute of Technology, 1983.
13. Miller, J. H., *Twenty-Third Symposium (International) on Combustion,* The Combustion Institute, Pittsburgh, 1990, p. 91.
14. Kee, R. J., Rupley, F. M., and Miller, J. A., "CHEMKIN II: A Fortran Chemical Kinetics Package for the Analysis of Gas Phase Chemical Kinetics," Sandia Report SAND89-8009, 1989.
15. Ritter, E. R. and Bozzelli, J. W., *Int. J. Chem. Kinet.* 23 (9):767–778 (1991).
16. Howard, J. B., *Twenty-Third Symposium (International) on Combustion,* The Combustion Institute, Pittsburgh, 1990, p. 1107.
17. Woods, I. T. and Haynes, B. S., *Combust. Flame* 85:523–525 (1991).
18. Mauß, F., Schäfer, T., and Bockhorn, H., *Combust. Flame* 99:697 (1994).
19. Harris, S. J. and Weiner, A. M., *Twenty-Second Symposium (International) on Combustion,* The Combustion Institute, Pittsburgh, 1988, p. 333.

COMMENTS

Antonio D' Alessio, Universita di Napoli, Italy. What is the percentage of PAHs in the total material extracted from the sampled particulates?

Author's Reply. Our HPLC analyses indicate that approximately 50% of our dichloromethane soluble material (also known as "total tar") consists of PAH.

•

P. R. Westmoreland, University of Massachusetts, USA. Does your "total PAH" concentration include PAH species containing five-membered rings?

Author's Reply. Our total PAH concentrations comprise all PAH species detectable by GC-FID and HPLC, which includes compounds containing five-membered rings.

•

M. Frenklach, University of California at Berkeley, USA. How do you differentiate the contribution of PAH and C_2H_2 to particle surface growth from that to particle *nucleation?* I may argue, based on our analysis of laminar premixed flames [1], that the increase in PAH concentration increases particle nucleation, and hence increases the initial surface area, which in turn increases the surface growth rate you observe in your experiments.

REFERENCE

1. Kazakov, A., Wang, H., and Frenklach, M., *Combust. Flame* 100:111–120 (1995).

Author's Reply. The fact that our PFR residence time (30 ms) exceeds the typical time required for soot nucleation leads us to believe that nucleation occurred in the JSR and in the low residence time zone of the PFR. Also, TEM analyses show that the bulk of our soot particles lie in the 20–30 nm size range. Since soot nuclei diameters are less than 10 nm, this indicates that most of their mass growth was due to post-nucleation surface growth.

•

M. Toqan, ABB, USA. What will happen at higher temperatures? Would the same conclusions apply at 1800–1900 K? Don't you think that acetylene might dominate the process at the SE temperatures!

Author's Reply. Since PAH radicals are more stable at higher temperatures, we would expect soot-PAH collision efficiencies to be higher at 1800–1900 K. This would imply that the role of PAH in soot surface growth increases with temperature.

Twenty-Sixth Symposium (International) on Combustion/The Combustion Institute, 1996/pp. 2303–2310

SOOT FORMATION IN THE PYROLYSIS OF BENZENE/ACETYLENE AND ACETYLENE/HYDROGEN MIXTURES AT HIGH CARBON CONCENTRATIONS

V. G. KNORRE,[1] D. TANKE,[2] TH. THIENEL[2] AND H. Gg. WAGNER[2]

[1]*Moscow State Technical University*
Leningrad Prospect 64, 125829 Moscow

[2]*Georg-August-Universität Göttingen*
Institut für Physikalische Chemie
Tammannstraße 6
37077 Göttingen, Germany

The soot formation in the pyrolysis of benzene/acetylene mixtures and acetylene/hydrogen mixtures diluted in argon was measured behind reflected shock waves using a light absorption technique. For this process, the induction period τ, the soot growth rate constant k_f, and the soot yield SY were determined. The experiments were performed in the temperature range between 1560 and 2580 K at pressures of 6 and 60 bar, for different carbon concentrations ($1–16 \times 10^{-6}$ mol/cm^3) and different ratios of the components.

For the benzene/acetylene mixtures, the induction times did not show a significant effect related to pressure or mixture ratio and were placed between the induction times for the pure substances. Increasing the benzene/acetylene ratio considerably increases the soot growth rate constant k_f at high temperatures. The previously observed bell shape of the soot yield curves as a function of temperature could be confirmed for all mixtures, with maximum soot yields at a temperature of about 1800 K. The soot yield data obtained for benzene/acetylene mixtures show a remarkable synergistic effect. Increasing the pressure or the benzene/acetylene ratio in benzene-rich mixtures decreases the soot yield. In the case of acetylene/hydrogen mixtures, a considerable suppressive influence of the hydrogen additive on the soot yield was observed.

Soot particle diameters were determined by transmission electron microscopy and can be described by a narrow, log-normal size distribution function. The average particle diameters are in the range of 20 $\pm$ 5 nm for all conditions of temperature and pressure employed in this study and they show a tendency to increase with increasing carbon concentration. Assuming spherical particles, final particle number densities in the range of 10^{11}–10^{13}/cm^3 were obtained.

Introduction

The process of soot formation has been investigated for quite some time [1–4]. There are, however, some phenomenological aspects that still need further consideration. Here, results obtained from shock tube pyrolysis experiments are of particular interest. For many hydrocarbons except benzene, the rate of soot formation passes through a maximum around 2000 K [5,6]. In order to obtain further information about the soot formation kinetics in pyrolysis processes at higher temperatures, experiments in binary mixtures have been performed.

There are several papers on soot formation in binary mixtures [7–12]. It was found in shock tube experiments that the addition of acetylene to 1,3-butadiene and to allene increases both the soot yield and the amount of soot [12]. When acetylene is added to benzene, the opposite effects were found. The amount of soot formed increased but the soot yield decreased. These experiments were performed at pressures between 1 and 3 bar. In Ref. 10 it was concluded that in a flow reactor at near atmospheric pressure and a temperature of 1473 K during pyrolysis of benzene/acetylene mixtures, the soot particle nuclei were formed only from acetylene. A nucleation of soot particles from benzene is assumed to be completely inhibited and its molecules are consumed only by the growth of particles formed from acetylene.

It was shown recently that many features of the soot formation processes change considerably toward higher pressures, especially for pressures above 10 bar [6,13,14]. In order to cover a large range of conditions, the work reported here was devoted to soot formation in shock tube pyrolysis of benzene/acetylene and acetylene/hydrogen mixtures behind reflected shock waves. Experiments were conducted in the temperature interval between 1560 and 2580 K, and for two different pressures, namely, 6 and 60

TABLE 1
Experimental conditions

Series	T (K)	P (MPa)	C_6H_6:C_2H_2	[C] (mol/cm^3/10^6)
1	1670–2150	6.2	1:3	1.2
2	1670–2210	6.2	1:3	5
3	1860–1980	6.1	1:2.5	8.4
4	1560–2580	6.3	1:1	5
5	1850	6.1	1:1	16
6	1650–2250	5.8	2.5:1	12
7	1680–2500	6.0	10:1	9
8	1700–2400	0.64	1:2.5	6
9	1570–2400	0.64	1:1	5
10	1460–2170	0.66	2.5:1	9
11	1600–2400	0.5–11	1:0	0.4–4
12	1600–2400	2.5–5.5	0:1	1–4
Series	T (K)	P (MPa)	C_2H_2:H_2	[C] (mol/cm^3/10^6)
13	1630–2360	6.0	1:1	2
14	1680–2420	6.0	1:1	4

bar. Carbon concentrations were varied from 1 to 16 $\times 10^{-6}$ mol/cm^3. The main goal of this investigation was to obtain data about mutual influence of the mixture ratios in benzene/acetylene and acetylene/hydrogen mixtures at high carbon concentrations, and various pressures and temperatures. Investigated were the induction time of soot formation τ, the formal soot growth rate constant k_f, the soot yield SY, and the final particle diameter d.

Experimental

The experimental set-up has been described elsewhere [6,15], therefore, only the main details are given. The experiments were conducted behind reflected shock waves in a 70 mm i.d. steel shock tube with a 4.5 m-long driven section, a 3.5 m-long driver section, and a 28 mm-thick tube wall. Shock speed and the pressure time profile were measured with Kistler piezo-electric pressure transducers. Shock parameters were computed following the standard procedure [16,17] using the measured incident shock speed. The difference between the calculated and the measured pressure was less than 2%, and the estimated accuracy of the temperature calculation is ± 30 K.

The conversion of hydrocarbon to soot was measured via the attenuation of the light beam from a 15 mW He-Ne laser operated at $\lambda = 632.8$ nm, and a 50 mW In-Ga-As laser operated at $\lambda = 1064$ nm. The optical observation plane was positioned 28 mm from the end-plate of the shock tube. The light extinction profiles $I(t)$ were converted into soot yield profiles $SY(t)$ using Beer's law (see, e.g., Ref. 18), a refractive index of $m = 1.57 - 0.56i$, a soot density of 1.86 g/cm^3, and the molar mass of carbon M_C.

The test gas mixtures were prepared manometrically and mixed by convection in stainless steel cylinders at least 48 h before use. The gases acetylene (> 99.6% Linde), hydrogen (> 99.9% Messer-Griesheim), and argon (> 99.998% Messer-Griesheim) were used without further purification. Benzene (> 99.9% Riedel-De *Haën*) was purified by distillation.

Soot particles were collected on carbon-film-coated copper grids (mesh size 400) and their diameters were determined by transmission electron microscopy (TEM). For several experiments, especially with a high soot volume fraction, the soot formed was collected to determine the specific soot surface area and the final soot yield by the gravimetric method.

Experimental Results

Fourteen series of experiments with various carbon concentrations, acetylene/hydrogen ratios, benzene/acetylene ratios, and two different pressures were performed. The conditions of the experiments are summarized in Table 1.

Time History of Soot Formation

In Fig. 1, one can see time histories of soot formation for a (1:3) benzene/acetylene mixture at 60 bar and a constant carbon concentration of 1.2×10^{-6} mol/cm^3. The soot yield profiles were obtained by extinction measurements at a wavelength of 1064 nm. All profiles have a typical induction period and S-shape form. The induction period decreases with temperature. The temperature dependence of the maximum slope of the profiles and

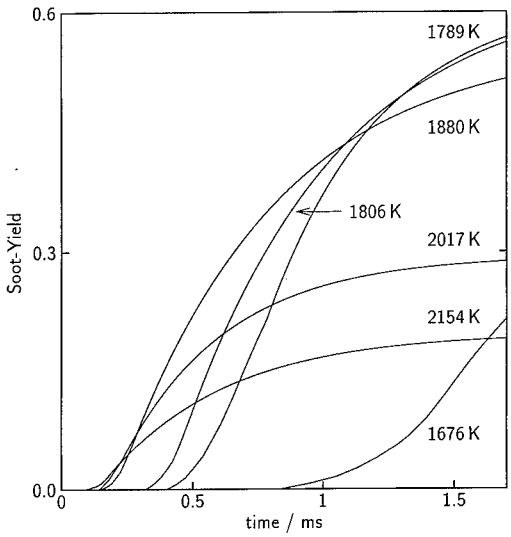

FIG. 1. Six time histories of soot formation measured at a pressure of 60 bar for a (3:1) benzene/acetylene mixture, $[C] = 1.2 \times 10^{-6}$ mol/cm^3 and for $\lambda = 1064$ nm. The related temperature is indicated at each curve.

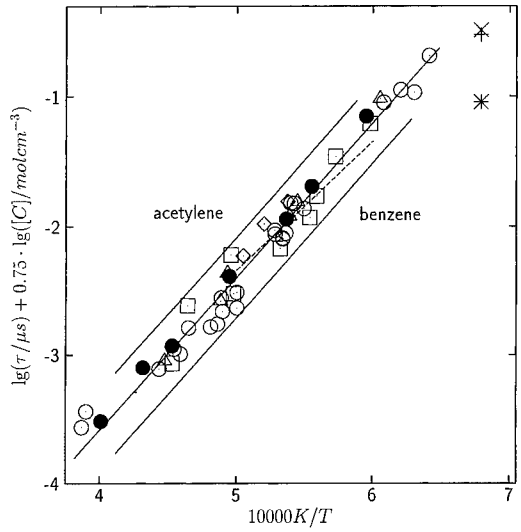

FIG. 2. Arrhenius type plot of the normalized induction time ($\tau \cdot [C]^{0.75}$) for mixtures with various benzene/acetylene ratios (B:A) and carbon concentrations for 60 bar; ⊡, (B:A) = (1:3), [C] = 1.2–5 $\times 10^{-6}$ mol/cm^3; ◇, (B:A) = (1:2.5), $[C] = 8.4 \times 10^{-6}$ mol/cm^3; ⊙, (B:A) = (1:1), $[C] = 5$–16×10^{-6} mol/cm^3; △, (B:A) = (2.5:1), $[C] = 12 \times 10^{-6}$ mol/cm^3; ●, (B:A) = (10:1), $[C] = 9 \times 10^{-6}$ mol/cm^3; solid lines, best fits for acetylene (upper), benzene/acetylene (middle) and benzene (lower); +, benzene, $[C] = 3.9 \times 10^{-6}$ mol/cm^3 [10]; ×, acetylene, $[C] = 1.3 \times 10^{-6}$ mol/cm^3 [10]; °, benzene/acetylene, $[C] = 5.2 \times 10^{-6}$ mol/cm^3 [10]; dashed line, acetylene, $[C] = 2 \times 10^{-6}$ mol/cm^3 [24].

the final soot yields pass through a maximum. In comparison to extinction measurements performed at 633 nm, the induction periods measured were always longer, but the maximum slopes and soot yields after the inflection point did not change with the wavelength.

Induction Time

In the present work, the induction time is defined using the intersection of the tangent at the inflection point of the soot yield curve with the time axis [6,19]. The value of the induction time depends, as mentioned, somewhat on the experimental technique used. However, the order of magnitude and the dependence on parameters such as pressure, temperature, and carbon concentration are similar for different experimental techniques. To fit the induction times, the following expression is used:

$$\tau = A_{\mathrm{Ind}} \cdot \exp(E_{\mathrm{Ind}}/RT)/[C]^n \qquad (1)$$

Figure 2 shows the normalized induction times for benzene, acetylene, and their mixtures at 60 bar in an Arrhenius plot. According to Fig. 2, the following parameters are obtained for all mixtures at $\lambda = 633$ nm: $A_{\mathrm{Ind}}^{633} = 4.36 \times 10^{-15}$ sec (mol/cm^3)$^{0.75}$, $E_{\mathrm{Ind}} = 228$ kJ/mol, and $n = 0.75$. The activation energy for the mixtures coincides with that for pure benzene and acetylene [19]. The logarithm of the preexponential factors $\lg(A_{\mathrm{Ind}}^{633})$ are in the middle between those for the pure hydrocarbons. Induction times of the mixtures at 6 bar are close to that for pure acetylene, and therefore, these data are not indicated separately in Fig. 2. Using different wavelengths, the induction time is usually longer in the case of the longer wavelength. For $\lambda = 1064$ nm, we obtained a slightly higher preexponential factor ($A_{\mathrm{Ind}}^{1064}/A_{\mathrm{Ind}}^{633} \approx 1.3$) and practically the same apparent activation energy.

For a (1:1) acetylene/hydrogen mixture at 60 bar and a carbon concentration of 4×10^{-6} mol/cm^3, the induction times coincide with those of ethylene [6], containing the same carbon and hydrogen concentration, and are 25% longer than for pure acetylene.

Soot Growth Rate

The soot volume fraction profiles after the inflection point are approximated by an empirically obtained first order rate law, where k_f is the soot growth rate and f_v is the soot volume fraction

$$\frac{df_v}{dt} = k_f \cdot (f_{v\infty} - f_v) \qquad (2)$$

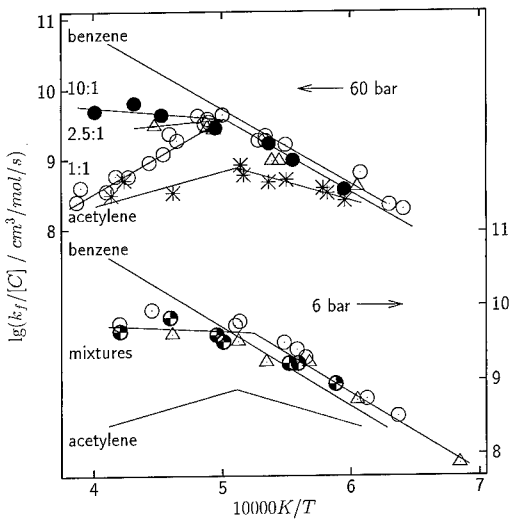

FIG. 3. Temperature dependence of the normalized first order rate constant ($k_f/[C]$) for benzene, acetylene, benzene/acetylene, and acetylene/hydrogen mixtures at 6 bar (lower part) and 60 bar (upper part). For 60 bar: ⊙, (B:A) = (1:1), [C] = 5 × 10^{-6} mol/cm³; △, (B:A) = (2.5:1), [C] = 12 × 10^{-6} mol/cm³; ●, (B:A) = (10:1), [C] = 9 × 10^{-6} mol/cm³; *, (C_2H_2:H_2) = (1:1), [C] = 2–4 × 10^{-6} mol/cm³; solid lines, best fits, benzene (upper), acetylene and acetylene/hydrogen (lower) [22]. For 6 bar: ◐, (B:A) = (1:2.5), [C] = 6 × 10^{-6} mol/cm³; ⊙, (B:A) = (1:1), [C] = 5 × 10^{-6} mol/cm³; △, (B:A) = (2.5:1), [C] = 9 × 10^{-6} mol/cm³; solid lines, best fits, benzene (upper) and acetylene (lower).

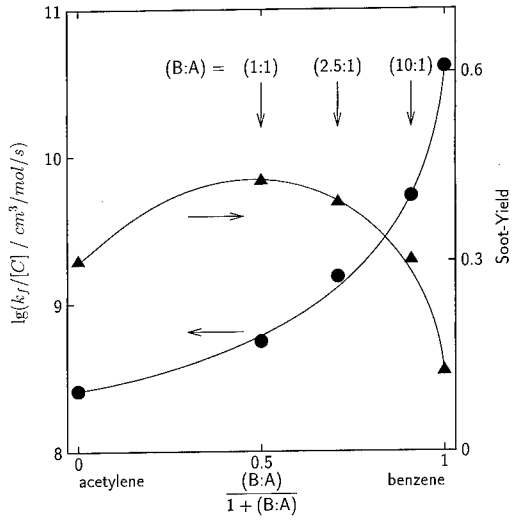

FIG. 4. The benzene mixture fraction dependence of the normalized first order rate constant ($k_f/[C]$) (●) and the final soot yield (SY_∞) (▲) for benzene, acetylene, and their mixtures at 60 bar and 2400 K. The related mixture composition is indicated at each point.

$$SY_\infty = \frac{f_{v\infty}}{[C]_{total}} \cdot \frac{\rho_{soot}}{M_C} \quad (3)$$

Equations 2 and 3 give a convenient way to calculate k_f and the final soot yield SY_∞. For near atmospheric pressure flames, k_f has been interpreted as an effective measure of the "active lifetime" of soot particles, assuming that they are loosing their reactivity [5,13,14,20,21].

Figure 3 shows the temperature dependence of the normalized rate constant ($k_f/[C]$) for several benzene/acetylene mixtures at 6 and 60 bar, acetylene/hydrogen mixtures at 60 bar, and for different carbon concentrations in an Arrhenius diagram. In the upper part of Fig. 3, rate constants at 60 bar for three benzene/acetylene mixtures, namely, (B:A) = (1:1), (2.5:1), (10:1), two (1:1) acetylene/hydrogen mixtures, pure acetylene, and pure benzene are shown. Carbon concentrations are given in Table 1 (series 4, 6, 7, 11–14). For temperatures below 1950 K, all curves, except those for the pure acetylene and acetylene/hydrogen mixture, have an apparent activation energy of 205 kJ/mol and a preexponential factor of about 1.2 × 10^{15} cm³/mol/s. The soot growth rate constants in the pyrolysis of acetylene and acetylene/hydrogen mixtures coincide [22], and their apparent activation energy is lower than for other hydrocarbons within the temperature range used.

While decreasing the benzene/acetylene ratio, the apparent activation energy on the high-temperature side decreases toward a negative value. This effect is shown more explicitly in Fig. 4 at 2400 K. Here, the normalized rate constants are given for five benzene mixture fractions (B:A)/[(B:A) + 1]. Increasing the benzene mixture fraction from zero to one increases the rate constant more than two orders of magnitude. A small addition of acetylene to benzene leads to a strong decrease of k_f.

In the lower part of Fig. 3, rate constants determined at 6 bar for five benzene/acetylene mixtures, namely (B:A) = (1:2.5), (1:1), (2.5:1), pure acetylene, and pure benzene (series 8, 9, 10, 11, and 12) are shown. Again, the apparent rate constant for temperatures below 1950 K is similar to that for benzene, and for higher temperatures it depends on the fuel composition. All rate constants for the mixtures seem to be slightly higher than for 60 bar. The differences in k_f for the mixtures investigated are smaller than the scattering of the data.

Soot Yield

The final soot yield is defined as carbon finally present as soot referred to the total carbon content of the mixture. The soot yield curves show the bell

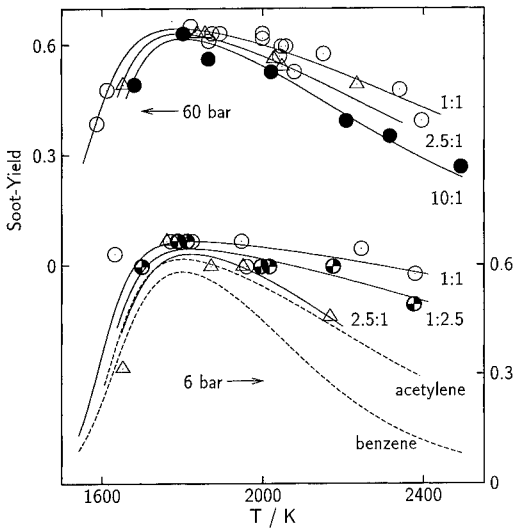

FIG. 5. Temperature dependence of the soot yield in the pyrolysis of benzene, acetylene, and their mixtures at pressures of 6 bar (lower part) and 60 bar (upper part). For 60 bar: ⊙, (B:A) = (1:1), $[C] = 5 \times 10^{-6}$ mol/cm^3; △, (B:A) = (2.5:1), $[C] = 12 \times 10^{-6}$ mol/cm^3; ●, (B:A) = (10:1), $[C] = 9 \times 10^{-6}$ mol/cm^3; for 6 bar: ◐, (B:A) = (1:2.5), $[C] = 6 \times 10^{-6}$ mol/cm^3; ⊙, (B:A) = (1:1), $[C] = 5 \times 10^{-6}$ mol/cm^3; △, (B:A) = (2.5:1), $[C] = 9 \times 10^{-6}$ mol/cm^3; dashed lines, best fits for acetylene and benzene, $[C] = 4 \times 10^{-6}$ mol/cm^3 [19].

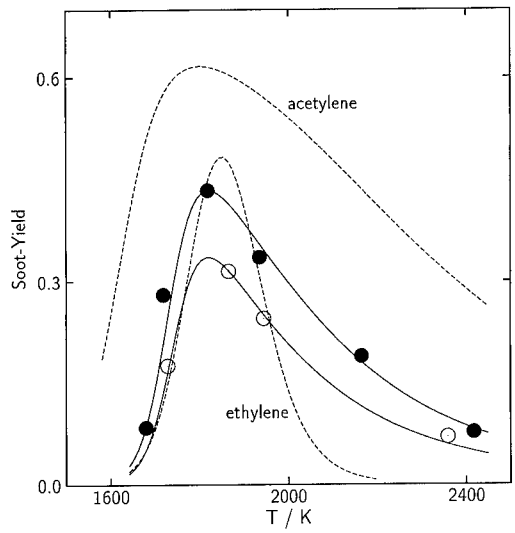

FIG. 6. Temperature dependence of the soot yield in the pyrolysis of acetylene/hydrogen mixtures at a pressure of 60 bar for two different carbon concentrations and an acetylene/hydrogen ratio equal unity. ●, $[C] = 4 \times 10^{-6}$ mol/cm^3; ⊙, $[C] = 2 \times 10^{-6}$ mol/cm^3; solid lines, best fits; dashed lines, best fits for ethylene (lower) and for acetylene (upper), $[C] = 4 \times 10^{-6}$ mol/cm^3 [19].

shape observed in previous papers for near atmospheric pressure [18,23] and for higher pressures [15]. Soot yields for benzene/acetylene mixtures from the same sets of experiments that were used to describe k_f are shown in Fig. 5 for pressures of 6 and 60 bar. All soot yield curves shown there exhibit a pronounced maximum at about 1800 K (see also Fig. 1). For comparison, data for pure acetylene and pure benzene [19] are included ($[C] = 4 \times 10^{-6}$ mol/cm^3). The soot yields for the (1:1) mixture are higher than for the pure hydrocarbons. For a temperature of $T = 2400$ K, the soot yield increases two to four times compared with that for benzene. The highest soot yields determined here are related to the smallest investigated benzene/acetylene ratio (1:1) and the lowest carbon concentration (5×10^{-6} mol/cm^3). This effect is shown more explicitly in Fig. 4 for five benzene mixture fractions (B:A)/[(B:A) + 1]. Practically all soot yields at high temperature are higher than for the pure compounds at equal carbon concentration.

Figure 6 presents the results for the soot yield from two (1:1) acetylene/hydrogen mixtures with different carbon concentrations of 2 and 4×10^{-6} mol/cm^3, respectively. Soot yield data for ethylene (with the same C:H ratio as the mixtures) and for acetylene are shown for comparison ($[C] = 4 \times 10^{-6}$ mol/cm^3) [19]. Again, the soot yield maxima are near 1800 K. The addition of hydrogen reduces the soot yield from acetylene approximately to the data for ethylene with the same C and H atom concentration. The slope of the soot yield curve for the acetylene/hydrogen mixture is, however, distinctly different from that for ethylene, showing much higher soot yields at high temperatures. A reduction of the carbon concentration for the acetylene/hydrogen mixture by a factor of 2 reduces the soot yield by a factor of approximately 0.7.

Particle Size

Soot particles were deposited on grids under all conditions given in Table 1. The samples were examined by means of TEM. The visual impression of all micrographs obtained from different experiments is very similar. The micrographs show spherical primary particles which are mainly agglomerated in long chains. The diameters of the primary spherical particles can be described by a log-normal size distribution function with a geometric standard deviation of $\sigma_g = 0.15 \pm 0.05$. The average soot particle diameters are in the range of 15–25 nm for all experimental conditions employed and they show a tendency to increase with increasing carbon concentration. Furthermore, the specific surface was determined by the method of nitrogen adsorption at the temperature of liquid nitrogen. Therefore, 20–200

mg soot (depending on the final amount of soot) was sampled mechanically, corresponding to 90% of the optically determined soot yield. A specific surface of 120 $m^2/g \pm 10\%$ was found, independent of the experimental conditions employed. This holds for a typical final soot volume fraction of 5×10^{-5} in a final soot particle surface of 110 cm^2 in 1 cm^3 gas volume. The specific surfaces obtained may be influenced by the physical and chemical properties of the soot particle surface and may not depend only on the geometric surface of the particles.

Discussion

Soot formation experiments in the pyrolysis of benzene/acetylene and acetylene/hydrogen mixtures behind reflected shock waves were performed in order to check the influence of the ratio of the mixture components on the soot formation process.

The induction times in the benzene/acetylene pyrolysis are between those for the pure hydrocarbons at 60 bar. It should be noted, however, that a small carbon fraction coming from acetylene leads to a strong increase of the induction period. In the case of 3.3% "acetylene-carbon" of the total carbon concentration, two times longer induction times than for pure benzene under otherwise equal conditions were measured (see the filled circles in Fig. 2). Therefore, an acetylene addition to benzene definitely increases the delay for the start of the soot formation.

In the work of Tesner et al. [10], induction times at 1473 K were measured in a flow reactor with high concentrations of pure benzene, acetylene, and a (1:1) benzene/acetylene mixture. The normalized induction times for both pure fuels were placed on the extrapolated benzene fit in Fig. 2. The normalized induction time for their mixture is three times shorter. This is different from the results reported here and may be due to the different technique applied. Induction times were obtained from Fussey et al. [24] using the shock tube technique for 2% acetylene in argon at 10 bar ($[C] = 2 \times 10^{-6}$ mol/cm^3). Normalizing this data using equation 1 shows that their data are in the same range as our data but with a somewhat lower apparent energy of activation.

The preexponential factor of k_f depends somewhat on the fuel structure and pressure. Decreasing the pressure from 60 to 6 bar increases the preexponential factor for the mixtures slightly. The temperature dependence of the formal rate constant k_f is similar for several hydrocarbons at temperatures below 1950 K. Toward higher temperatures, k_f for many hydrocarbons passes through a maximum at a temperature of (1950 ± 50) K and decreases with further increasing temperature [5,6,19]. One exception is benzene, where the k_f grows continuously toward higher temperatures [6,19]. The benzene/acetylene mixtures studied show the same temperature dependence on k_f as aliphatic and aromatic hydrocarbons below the maximum temperature at 60 bar. For higher temperatures and with increasing acetylene content in the mixture, the slope of the k_f curve changes from that for pure benzene toward zero, and finally to negative values, as for acetylene. The rate constants of the (1:1) benzene/acetylene mixture are similar to those of aromatic hydrocarbons with one short side chain such as phenylacetylene, toluene, and styrene at 60 bar [19,22]. This effect is clearly demonstrated for 2400 K in Fig. 4 and has to be seen in connection with the induction periods and especially with the soot yields.

Below 1800 K, the influence of the mixing ratio on the soot yield is relatively small. Above 2000 K, the influence of the mixture composition becomes quite strong, and high soot yields are reached (see Figs. 4 and 5). In fact, the soot yields for all benzene/acetylene mixtures investigated in that temperature range are higher than those for the pure fuels. Obviously, a marked synergistic effect takes place for benzene/acetylene mixtures. Frenklach et al. [12] performed shock tube pyrolysis experiments at 2–3 bar and carbon concentrations between 0.5 and 1×10^{-6} mol/cm^3. They reported that addition of allene and 1,3-butadiene to acetylene increases soot yields. Decreasing soot yields were found for benzene/acetylene mixtures. This differs from the results reported here for high carbon concentrations and pressures.

For the acetylene/hydrogen mixtures investigated, a strong soot suppression effect was observed. Induction times are longer and soot yields are lower than for pure acetylene. Decreasing the carbon concentration by a factor of two in the mixture decreases the soot yield less than a factor 2. This is similar to the behavior of pure acetylene [19]. Soot yield reduction by the addition of hydrogen to acetylene was also reported in Ref. 12 at the conditions mentioned above. Their soot yield maximum at a temperature of 2150 K was reduced from 3% to 1%. No soot was found at 1800 K, where the soot yield maximum appears for the conditions applied here. That difference is probably due to the different experimental conditions and especially the different carbon concentrations used. High carbon concentrations broaden the soot yield curves toward higher temperatures, shown in Fig. 6. These experiments with acetylene/hydrogen mixtures show clearly that the beginning of the pyrolysis process has a pronounced influence on the formation of soot precursors.

The particle number densities have not been measured by optical methods in these experiments. From the TEM pictures and the known soot yields, one may, however, estimate the number density of soot particles. For an experiment at 60 bar and a carbon concentration of 10^{-5} mol/cm^3, a final soot volume fraction of $f_{v\infty} \approx 5 \times 10^{-5}$ was found. The

average final particle diameter was determined by TEM to be 20 nm. This leads to a mean particle volume of $\bar{v}_\infty$ 4×10^{-18} cm^3. The number density is described by $N = f_v/\bar{v}$. This results in a final number density of approximately 10^{13}/cm^3. For the other experiments, similar results can be calculated. These high particle number densities indicate that the coagulation must come to an end quite early in the soot formation process. From the Smoluchowski equation for coagulation

$$\frac{dN}{dt} = -k_{\text{coag}} \cdot N^2 \tag{4}$$

one can estimate a characteristic half time of coagulation $\tau_{\text{coag}} = (k_{\text{coag}} \cdot N)^{-1}$. For the shocked gas, a Knudsen number in the order of 1 was calculated. This value is usually ascribed to the so-called transition regime from the slip flow to continuum regime [25]. For an approximate calculation, this value can be used in the case of the free-molecular regime [26]. A calculation on the basis of the theoretical expression gives characteristic times for coagulation under the conditions applied in the range of 10–100 μs. Therefore, especially for high temperatures, the coagulation of particles must play its essential role at the beginning of the soot formation process. The particles loose their ability to stick together very early, otherwise N_∞ would be much lower.

The formation of high soot yields in the mixtures of benzene/acetylene at high temperatures comes together with a drop of the formal rate constant k_f, which is a measure for the active life time ($\tau_f = k_f^{-1}$) for soot formation. Its value may be influenced by properties of the particles as well as by properties of the reacting gas mixture. This decrease of τ_f could explain the right part of the soot yield curve in Fig. 4. Apparently, it does not hold for acetylene itself. That might be taken as a hint for the influence of the gas-phase composition during soot formation. After long times, the gas-phase composition will be nearly the same for both pure fuels in Fig. 4. A quantitative description of the effects reported here requires fairly detailed information, especially about the behavior of the particles, and is too lengthy to be given here.

For rich, premixed ethylene/air flames burning at 70 bar and a surplus carbon concentration of $[C]_{\text{surplus}} = 10^{-5}$ mol/cm^3, a particle diameter of 20 nm, a number density of 10^{13}/cm^3, and a final soot particle surface of 100 cm^2/cm^3 were found [27,28]. These three important parameters for the soot formation process coincide with our pyrolysis data. This indicates that the different chemical environment in high-pressure flames, especially the oxygen-containing species, seem to have little influence on the later part of the soot formation process.

Conclusion

The shock tube pyrolysis experiments with benzene/acetylene and acetylene/hydrogen mixtures at high carbon concentrations (1–16 $\times$ 10^{-6} mol/cm^3) and pressures showed the following:

- Mean TEM particle diameters are obtained in the range of 20 nm. They can be described by a narrow log-normal size distribution function. The average specific surface of the soot particles is 120 m^2/g. At the high carbon concentrations applied, the particle coagulation stops early, and high final particle number densities could be calculated.
- In the case of benzene/acetylene mixtures, the induction times are placed between those for pure benzene and acetylene.
- For temperatures below 1800 K, the soot growth rate constants are nearly the same for the pure fuels and the mixtures applied. For temperatures above 2000 K, the soot growth rate constant for the mixtures drop from the values for pure benzene to pure acetylene (at 2400 K for two orders of magnitude).
- For temperatures higher than 2000 K, soot yields are definitely higher for the (1:1) benzene/acetylene mixture than for the pure fuels.
- In the case of acetylene/hydrogen mixtures, a considerable suppression influence of hydrogen regarding induction time and soot yield was found.

Acknowledgments

This work was sponsored by the Commission of the European Community within the frame of the JOULE program within the contract JOU2-CT92-0055.

REFERENCES

1. Wagner, H. Gg., *Seventeenth Symposium (International) on Combustion,* The Combustion Institute, Pittsburgh, 1978, p. 3.
2. Haynes, B. S. and Wagner, H. Gg., *Prog. Energy Combust. Sci.* 7:229 (1981).
3. Lahaye, J. and Prado, G., *Soot in Combustion Systems and Its Toxic Properties,* Plenum Press, New York and London, 1983.
4. Glassman, I., *Twenty-Second Symposium (International) on Combustion,* The Combustion Institute, Pittsburgh, 1988, p. 295.
5. Geck, C. C., Diplom Thesis, Universität Göttingen, Göttingen, 1975.
6. Bauerle, St., Karasevich, Y., Slavov, St., Tanke, D., Tappe, M., Thienel, T., and Wagner, H. Gg., *Twenty-*

Fifth Symposium (International) on Combustion, The Combustion Institute, Pittsburgh, 1994, p. 627.
7. Haynes, B. S., Jander, H., Mätzing, H., and Wagner, H. Gg., *Nineteenth Symposium (International) on Combustion*, The Combustion Institute, Pittsburgh, 1982, p. 379.
8. Harris, S. J. and Weiner, A. M., *Twentieth Symposium (International) on Combustion*, The Combustion Institute, Pittsburgh, 1984, p. 969.
9. Kent, J. H. and Wagner, H. Gg., *Twentieth Symposium (International) on Combustion*, The Combustion Institute, Pittsburgh, 1984, p. 1007.
10. Tesner, P. A. and Shurupov, S. V., *Combustion Sci. Technol.* 92:61 (1993).
11. Tesner, P. A. and Shurupov, S. V., *Combustion Sci. Technol.* 105:147 (1995).
12. Frenklach, M., Yuan, T., and Ramachandra, M. K., *J. Energy Fuels* 2:462 (1988).
13. Böhm, H., Hesse, D., Jander, H., Lüers, B., Pietscher, J., Wagner, H. Gg., and Weiss, M., *Twenty-Second Symposium (International) on Combustion*, The Combustion Institute, Pittsburgh, 1988, p. 403.
14. Bönig, M., Feldermann, Chr., Jander, H., Lüers, B., Rudolph, G., and Wagner, H. Gg., *Twenty-Third Symposium (International) on Combustion*, The Combustion Institute, Pittsburgh, 1990, p. 1581.
15. Hwang, S. M., Vlasov, P., Wagner, H. Gg., and Wolff, Th., *Z. Phys. Chem. Neue Folge* 137:129 (1991).
16. Greene, E. F. and Toennies, J. P., *Chemische Reaktionen in Stoßwellen* (Translated by H. Gg. Wagner), Dr. Dietrich Steinkopff Verlag, Darmstadt, 1959.
17. Gardiner, W. C. Jr., Walker, B. F., and Wakefield, C. B., *Shock Waves in Chemistry* (A. Lifshitz, Ed.), Marcel Dekker, 1981.
18. Graham, S. C., Homer, J. B., and Rosenfeld, J. L., *Proc. R. Soc. Lond. A* 344:259 (1975).
19. Tanke, D., Ph.D. Thesis, Universität Göttingen, Göttingen, (1995).
20. Haynes, B. S. and Wagner, H. Gg., *Z. Phys. Chem. Neue Folge* 133:201 (1983).
21. Mätzing, H. and Wagner, H. Gg., *Twenty-First Symposium (International) on Combustion*, The Combustion Institute, Pittsburgh, 1986, p. 1047.
22. Thienel, Th., Ph.D. Thesis, Universität Göttingen, Göttingen, (1996).
23. Frenklach, M., Taki, S., and Matula, R. A., *Combust. Flame* 49:275 (1983).
24. Fussey, D. E., Gosling, A. J., and Lampard, O.: *Combust. Flame* 32:181 (1978).
25. Hidy, G. M. and Brock, J. R., *The Dynamics of Aerocolloidal Systems*, Pergamon Press, New York, 1979.
26. *Physical Enciclopedia*, Moscow, 1994, Vol. III.
27. Heidermann, Th., Ph.D. Thesis, Universität Göttingen, Göttingen, (1995).
28. Heidermann, Th., Jander, H., and Wagner, H. Gg., to be published.

COMMENTS

Pavel A. Tesner, VNIIGAS, Russia. What is your opinion about your experimental result that the induction time for acetylene-benzene mixture falls between that of acetylene and benzene?

Author's Reply. The behavior of the induction periods for the benzene/acetylene mixtures compare well with the behavior of benzene or acetylene with other hydrocarbons like n-hexane, ethylene etc.

•

R. D. Kern, University of New Orleans, USA. Shock tube experiments on benzene pyrolysis show considerable decomposition at 2400 K [1]. The products of the decomposition are mostly C_2H_2, C_4H_2 and H_2. The decomposition of benzene is strongly endothermic ($\approx$ 136 kcal/mol), while the formation of soot particles is exothermic. What are the magnitudes of the temperature fluctuations in the reflected shock zone for the benzene mixture due to decomposition and soot formation at 2400 K? Is comparison of the soot yields of pure benzene and pure acetylene at the reaction temperature of 2400 K valid? Your result is that the soot yields of C_6H_6 and C_2H_2 are approximately equal at 2400 K. However, pure C_6H_6 at 2400 K is mostly a mixture of its products. Is this the reason that the soot yields of C_6H_6 and C_2H_2 are approximately the same value at 2400 K?

REFERENCE

1. Kiefer et al., *J. Phys. Chem.* 89:2013–2019 (1985).

Author's Reply. The reaction enthalpies of the benzene and acetylene pyrolysis do indeed influence the temperature behind the shock wave. This was one of the reasons, why we performed the experiments at high carrier gas densities. Under the conditions in the paper the temperature variation due to the pyrolysis reaction was, based on the analysis of the products in the pyrolysed gases, generally below 50 K. The soot yields at 2400 K are given in the paper (for acetylene about 30% and for benzene about 13%). The remaining carbon is mostly present as acetylene.

Twenty-Sixth Symposium (International) on Combustion/The Combustion Institute, 1996/pp. 2311–2317

A SIMPLIFIED PHENOMENOLOGICAL MODEL FOR SOOT GROWTH BASED ON PLUG FLOW REACTOR EXPERIMENTS

BERND BARTENBACH AND WOLFGANG LEUCKEL
Engler-Bunte-Institut
der Universität Karlsruhe (T.H.)
Lehrstuhl und Bereich Feuerungstechnik
76128 Karlsruhe, Germany

The advantages of well-defined experimental conditions as provided by a plug flow reactor (PFR) are used to make an approach toward a phenomenological and quantitative description of soot mass growth in flames and combustion systems. On the basis of gravimetrically determined residence time–resolved soot concentration profiles, a quantitative correlation is proposed including the effects of temperature, stoichiometry, and residence time as the main parameters of influence. Gaseous hydrocarbon fuels, such as methane, propane, and acetylene, have been investigated concerning their differences and parallels in soot formation. It was shown that a simple autocatalytical approach and an assumed superposed deactivation process of the soot surface is sufficient to interpret experimental results in a wide range of temperature, fuel, residence time, and stoichiometry conditions. Under approximately isothermal conditions, as realized in the PFR, soot growth rate increases with time up to a maximum value after a certain reaction time that is dependent exclusively on temperature. With increasing residence times beyond that maximum, soot growth decreases and finally ceases. The influence of temperature on these profiles, in particular the reaction time at which the maximum growth rate appears, is given in terms of an Arrhenius expression, independent of fuel specification. The activation energy was evaluated at 192 kJ/mol. Stoichiometry was found relevant for the final soot concentration after long residence times. An expression using the C/O ratio as a correlating parameter is proposed in accordance with recent literature. The remaining influence of temperature on the "final" soot concentration is discussed more qualitatively, with respect to an additional influence of a subdivided stoichiometry as realizable in the plug flow reactor, to try to distinguish premixed and turbulent diffusive combustion. A final soot yield decrease was observed when increasing the temperature from about 1200 to 1650°C.

Introduction

The prediction of soot concentration fields in technical combustion systems (e.g., boilers, furnaces, and gas turbine combustors) is still a field of intensive research. A reliable and industrially applicable soot formation chemistry scheme—without experimental approval in any particular case—is not yet available. Only a few results are reported where flames of a laboratory type are being well described by a detailed soot chemistry [1,2]. The motivation for the attempts toward a reliable soot formation model for hydrocarbon flames, with sufficient technical accuracy is related to the importance of radiative heat transfer prediction for those systems. Heat transfer rates and therefore efficiency of the related processes are enhanced by the presence of soot. On the other hand, emission of soot into the atmosphere must be prevented. These contrary aspects have to be kept in mind when dealing with the problem of controlling soot formation and destruction.

This work presents a model correlation capable of calculating soot concentrations or soot mass growth rates. The growth rate correlation can be incorporated into more extensive numerical flame modeling, which, in combination with related transport phenomena, will provide the soot concentration. The implementation of a similar but even more simplified growth rate correlation into a flame code for turbulent diffusion flames was presented as a first attempt in a previous publication [3].

Since this work is focused on predictions under conditions of close-to-application turbulent diffusion flames in which detailed data of stable and, especially, unstable intermediates such as PAH or small radicals are difficult to predict, this study seeks to develop a model correlation that is formulated in terms of temperature, residence time, and stoichiometric ratio as the independent field variables. These parameters are readily accessible in both laboratory-scale and technical flames. Similar efforts on simplified, global soot growth kinetics are reported in recent literature [4,5]. Taking into account that the bulk of soot mass is being formed during the process of soot surface growth, it is assumed for

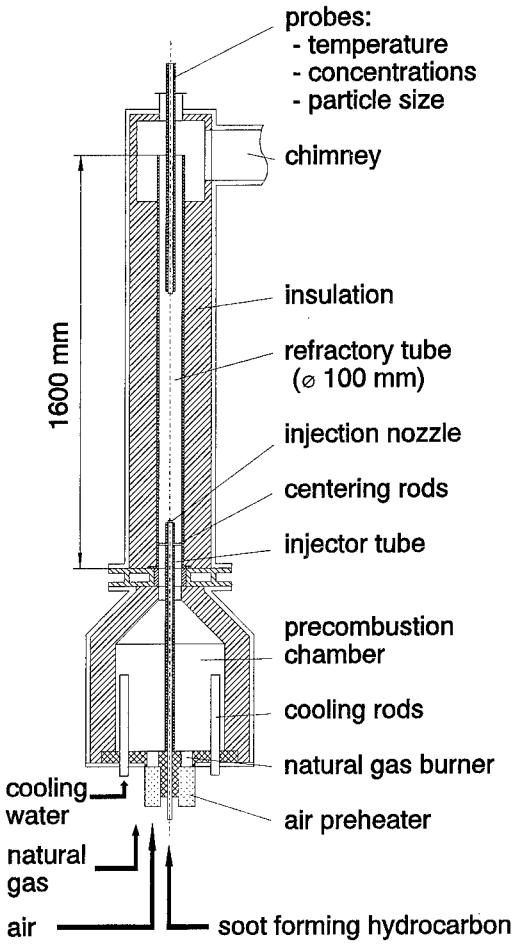

FIG. 1. Plug flow reactor.

simplicity that it is justifiable to neglect the nucleation step in the model calculation.

The model presented is calibrated empirically by reliable sets of data from a plug flow reactor. The experiments in this reactor were carried out under well-defined conditions of temperature, stoichiometry, and residence time, and therefore are a reliable basis for the model formulation in terms of these parameters.

The fuels investigated here are the gaseous hydrocarbons methane, propane, and acetylene. They are relevant to the commonly used technical fuels natural gas (→methane) and LPG (→propane) and to the suspected most important soot growth species, acetylene.

Experimental

A plug flow reactor system (Fig. 1) was used for experimental investigations on soot growth under well-defined but variable conditions. Hot flue gas produced from natural gas in a precombustion chamber enters the actual reactor tube at temperatures between 1100 and 1600°C. The precombustor flue gas temperature is controlled by air preheaters and cooling rods and therefore, can, be varied independently of the chosen combustion stoichiometry in a certain range. The primary burner is able to operate in an air equivalence ratio (λ_I) range between 2 and 0.5. Through a multihole injection nozzle (15 holes, 0.7-mm diameter) placed in the lower part of the actual reactor tube, soot-forming hydrocarbons were injected perpendicularly into the main flow. Injector lance and nozzle are water cooled to prevent fuel cracking before the injection. The initial molar fraction of the injected hydrocarbons in the reactor tube was varied up to 6% for methane, 3% for propane, and 4% for acetylene. The corresponding overall stoichiometry after injection covered a range of air equivalence ratios from 0.4 to 0.9. Temperatures in the range of 1000–1700°C could be generated and maintained fairly constantly along the reactor tube.

The mixing zone downstream of the injection nozzle, with a residence time less than 10 ms, is followed by the starting soot mass growth combined with characteristic gas-phase reactions. Using various suction probes at different distances downstream of the injection nozzle, residence time–resolved measurements of soot and gas species concentrations, soot particle size distributions (as described previously [6,7]), and gas temperatures have been performed. The probes are water cooled, thus quenching any reaction in the sample flow at their tips, but insulated at their surfaces to minimize heat losses from the reactor. The range of residence time in the reactor tube covered by those measurements was 10–50 ms. Soot mass concentrations were calculated by weighing the soot deposit on a sintered bronze filter mounted directly inside the tip of the suction probe as shown in Fig. 2. The soot mass capacity of the bronze filter could be extended by adding a glass fiber filter. Thus, an early abandonment of soot sampling due to a blockage of the bronze filter was avoided. The soot concentration measurements could be reproduced with an accuracy of ±5%, including, for example, the uncertainty in the weighed soot mass in a range of ±0.05% to ±0.5%.

Gas temperature was determined by suction pyrometry, with an estimated accuracy of about ±5 K. Gas species concentrations were measured either continuously (CO_2, CO, H_2, O_2) or discontinuously (light hydrocarbons, especially CH_4, C_2H_2, and C_2H_4) by conventional techniques.

Results

The results from the plug flow reactor suggest that temperature dominates the observable shape of soot

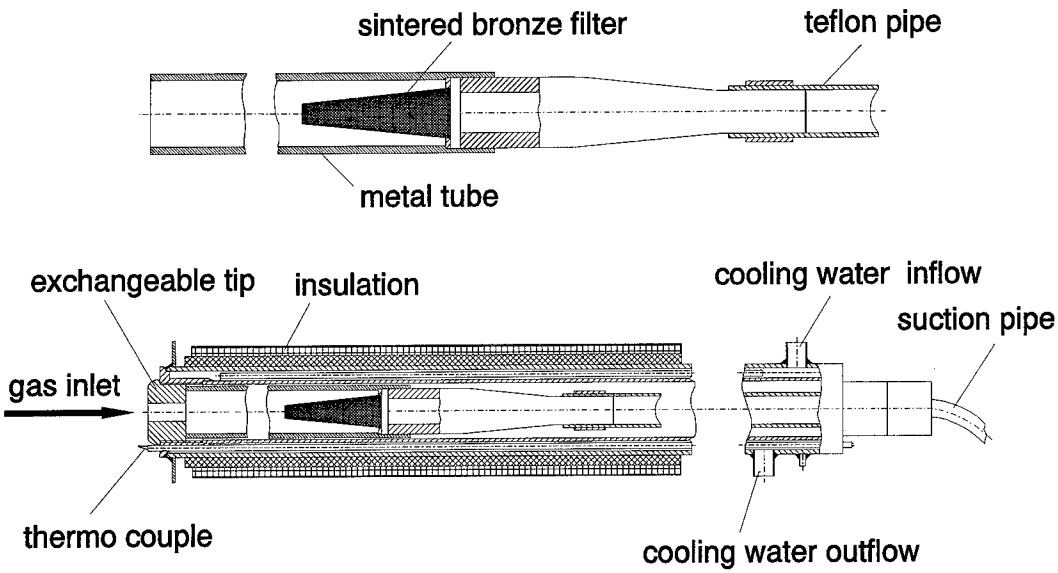

FIG. 2. Suction probe for gravimetrical soot sampling.

concentration/residence time curves. Based on time intervals of 10–50 ms, the soot growth rates show an increasing, constant, or decreasing tendency with time, depending on the applied reaction temperature. The temperature was controlled to be approximately constant during this range of time, that is, along the reactor tube (maximum variation ≤30 K). Soot concentration profiles show a steadily increasing growth rate with time at low temperatures (up to 1350°C), a fairly constant growth rate at moderate temperature (close to 1350°C), and a strong decline or even zero growth rate at temperatures higher than 1350°C. This observation was made independent of the investigated fuel. A few examples for this behavior chosen from a large number of experimental data are given in Figs. 3–5.

The effect of decreasing soot growth at high temperatures and residence times was also investigated and reported by other authors [8–11] and correlated by a first-order law for soot growth [11]. Their results were taken from premixed laminar flat flames, where isothermal conditions did not exist at all during the observed decay of soot growth. There could be four reasons for this decrease of soot growth: (a) lack of growth species after they are consumed by either soot surface growth or gas-phase oxidation reactions, (b) decline of temperature in the postreaction zone, (c) time-progressive deactivation of the soot surface, or (d) changes in the gas-phase composition excluding the growth species concentration (e.g., H-atom decay) [1,2]. Because the plug flow reactor provides the advantage of approximately isothermal conditions, reason b can be eliminated. The detailed soot formation chemistry given by Mauss et al. [2] identifies reasons a and especially b, related to d, as the predominating effects for the decay of soot growth in the postreaction zone of premixed laminar flames. They stated that no additional deactivation effect, as mentioned by Woods et al. [12], has to be taken into account, because it—to some extent—was already included in the structure of their reaction scheme.

The deviation from constant growth rates for low residence times and temperatures has not been reported clearly in the literature. In global descriptions and models of soot formation in the past [11], the initial soot growth was mostly characterized by an induction period for soot inception and a subsequent constant finite growth rate up to high residence times, before the onset of decay. The results of the present work suggest that induction time and constant growth rate should be replaced by a continuously increasing growth rate from zero or a small finite value up to a temporarily constant maximum rate before the decay. A comparatively small induction period might exist, but from the present results, this seems to be negligible over a wide range of temperature and stoichiometry. A schematic diagram that illustrates the suggested three phases of soot growth is shown in Fig. 6. Soot concentration, normalized by the constant value ($c_{s\infty}$), which is reached asymptotically after long residence times, is plotted versus residence time normalized by a characteristic value of time (t_{IP}), chosen to be the one where growth rate passes its maximum, equal to the point of inflection of the related concentration curve.

A quantitative formulation of the observed effect of temperature on the phenomenological behavior of soot growth in a given span of time can be

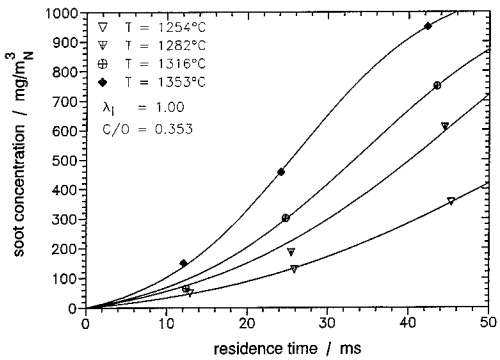

FIG. 3. Soot concentration versus residence time—example for methane (solid lines are correlations).

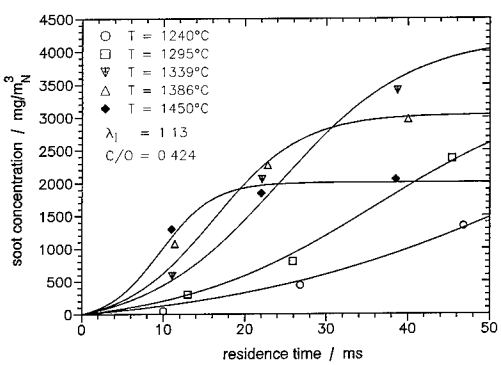

FIG. 4. Soot concentration versus residence time—example for propane (solid lines are correlations).

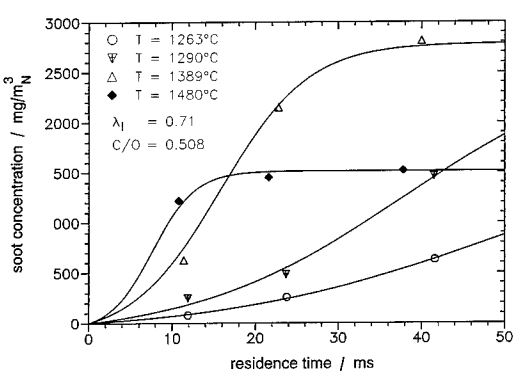

FIG. 5. Soot concentration versus residence time—example for acetylene (solid lines are correlations).

proposed: The temporal position of the maximum growth rate, that is, the point of inflection of the measured curves, shifts toward smaller values of residence time with increasing temperature. To develop an adequate correlation for this effect, a simple approach for the apparent soot growth rate, comparable to the one from Haynes and Wagner but closer to the experimental data from this work, was performed. Soot mass growth was assumed to be a kind of autocatalytic reaction:

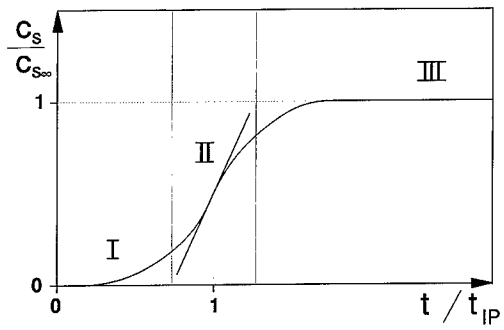

FIG. 6. Schematic diagram for temporal soot growth profiles; t_{IP} is the characteristic time at the point of inflection.

$$A(+S) \rightarrow S \tag{1}$$

Hence, the soot growth rate depends on the concentration of growth species (c_A), convertible to soot, and the concentration of reactive sites on the soot surface—that is, indirectly on the concentration of soot (c_S). When deactivation and agglomeration are first neglected for this simplified approach and a rate constant k only depending on temperature is used, then the following is obtained:

$$\frac{dc_S}{dt} = k \cdot c_A \cdot c_S \tag{2}$$

Because an integration of Eq. (2) leads to an expression for the increase of soot concentration, Eq. (3), that in principle provides a fair description of the three phases of soot growth discussed previously, Eq. (3) was taken as a basis for correlating the measured profiles of soot concentration and evaluating the dependences of the interesting parameters. The subscript *0* represents initial values ($t = 0$); ∞ represents $t \rightarrow \infty$.

$$\frac{c_S - c_{S0}}{c_{A0}} = \frac{e^{gt} - 1}{e^{gt} + q} \approx \frac{c_S}{c_{S\infty}}$$

$$\text{for } c_{S0} \ll c_S; \text{ with } g = k \cdot c_{S\infty} \text{ and } q = \frac{c_{A0}}{c_{S0}} \tag{3}$$

c_{S0} can be interpreted as the comparatively small amount of initial soot nuclei and related active sites on the surface. The initial concentration of growth species c_{A0} is assumed to be converted into soot ($c_{S\infty}$) eventually. Therefore, c_{A0} and $c_{S\infty}$ are equivalent. The parameter g in the exponent parts should be a function of temperature, because of the included rate constant k, and a function of stoichiometry. Calibrating this equation by the measured growth profiles, it turns to an expression in which a

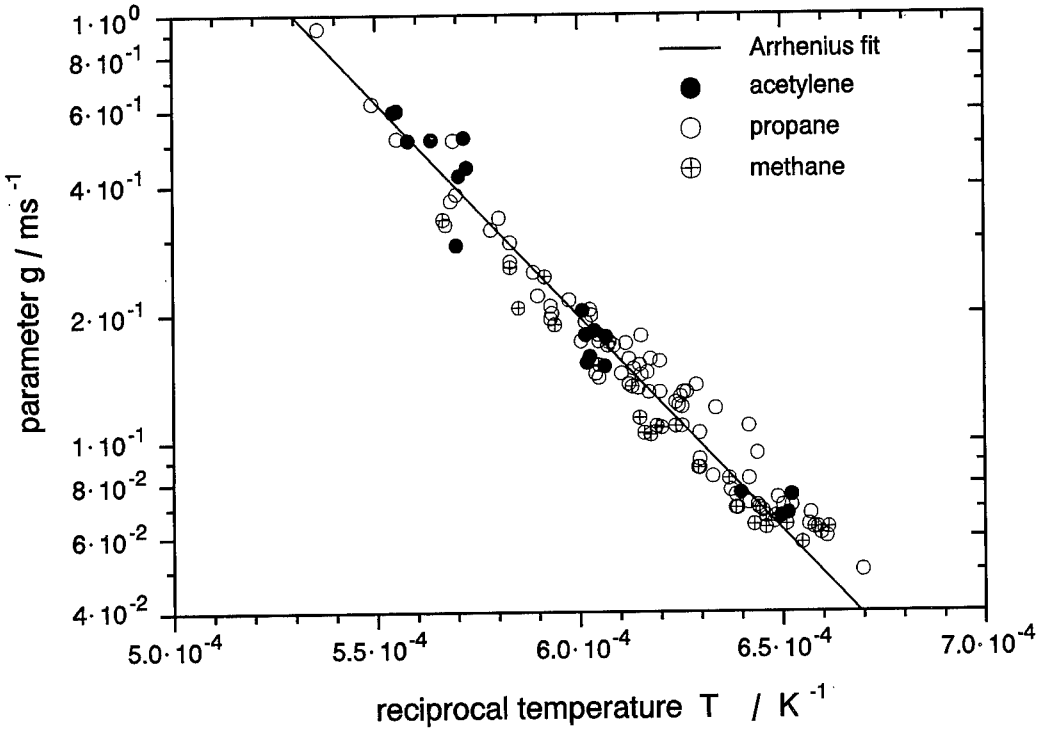

FIG. 7. Arrhenius plot for the parameter g—different fuels and stoichiometries.

preexponential factor represents the final soot concentration c_{S_∞} that depends on the stoichiometry due to the pure autocatalytic aspect (i.e., the lack of growth species after some time) and on temperature due to the deactivation processes. Deactivation could be essential, referring to some plug flow reactor results that show zero growth rates at high temperatures although acetylene, as a major growth species, remained in finite concentrations. With respect to the autocatalytic approach, the parameter q of Eq. (3) should refer to the initial ratio of growth species concentration to the concentration of active sites on soot nuclei. The value of this relation can be suggested to be relatively high ($\gg 1$). In reality, q was found to be about 20 and fit the experimental data best. If the results for parameter g from fitting this correlation to the experiments, with q kept constant at 20, are plotted versus the reciprocal absolute temperature such as an Arrhenius plot (Fig. 7), it can be seen that an Arrhenius-like correlation (Eq. [4]) seems to be adequate to express the temperature dependence:

$$g = f \cdot \exp\left(-\frac{E}{R \cdot T}\right) \tag{4}$$

A surprising effect is that neither stoichiometry nor fuel specification influences the value of the parameter g. Thus, the preceding statement, that temperature is the only essential parameter for the shape of soot growth profiles, is being verified. Now it is possible to calculate the dependence on residence time for three different fuels by the same apparent activation energy $E = 192$ kJ/mol and frequency factor $f = 2.041 \times 10^5$ ms^{-1}.

Focusing on the influence of stoichiometry on the final soot concentration, the attempt was made to fit this by an expression (Eq. [5]) proposed in several previous publications (e.g., Boehm et al. [14] and Huth et al. [7,15]), wherein C/O represents the overall C/O ratio, not distinguishing between primary and secondary fuel for the staged stoichiometry in the plug flow reactor. $C/O_{\text{crit.}}$ is its critical value for the start of soot formation.

$$c_{S_\infty} \sim (C/O - C/O_{\text{crit.}})^n \tag{5}$$

To do so, experimental soot concentration/time curves, smooth fitted by the correlation of Eq. (3) and shown as solid lines in Figs. 3–5, were composed in isothermal data sets by interpolation. Plotting the final soot concentrations versus an adequate parameter of stoichiometry (i.e., the C/O ratio corresponding to references mentioned [7,14,15]) at constant temperature, characteristic profiles can be obtained that could be fitted by correlation (5) (e.g., Fig. 8, fuel: propane). The exponent n in Eq. (5) was reported to be dependent mainly on the fuel. A minor

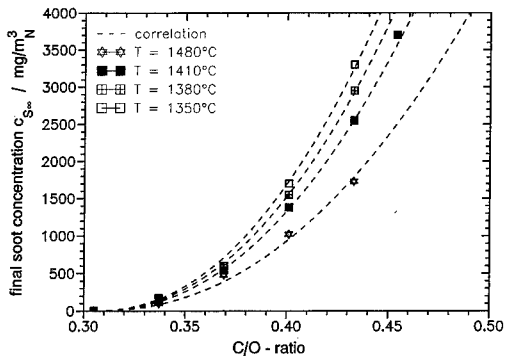

FIG. 8. "Final" soot concentration versus C/O ratio—example for propane.

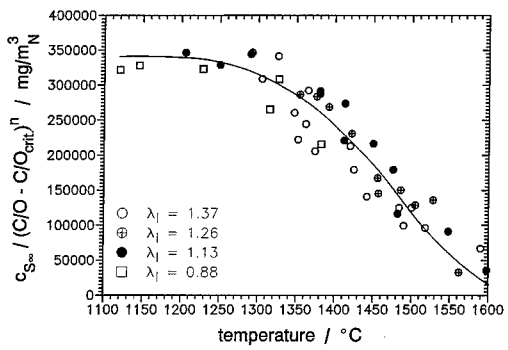

FIG. 9. "Final" soot concentration modified by the C/O ratio correlation, Eq. (5) versus temperature.

influence of temperature has been discussed elsewhere [7] but has not been specified definitely. In this work, the values of n are quite close to those from premixed flame measurements. A very small variation with temperature might also exist.

The definite values for parameters n and $C/O_{crit.}$ of Eq. (5) could be determined for the fuels propane ($n = 2.2 \pm 0.2$, $C/O_{crit.} = 0.305 \pm 0.02$) and acetylene ($n = 2.4 \pm 0.2$, $C/O_{crit.} = 0.325 \pm 0.02$). Values for methane are of the same order but are not cited here since they are not as accurate because soot formation from methane was somewhat poor, depending on the particular conditions.

The critical C/O ratio for the soot formation has been determined to be far lower in plug flow reactor experiments than in premixed flames [8]. This might be due to the less important role of competitive oxidation reactions in case of the plug flow reactor, where oxidation occurs mainly in the precombustion stage and, therefore, partially or fully separated from the soot-forming reactions. Thus, a suppression of soot formation at comparatively low C/O ratios due to early oxidation of soot and precursors by oxygen or oxygen-related radicals, as in premixed flames, is avoided. From that perspective, results from the plug flow reactor have more significance for conditions in wide fuel-rich ranges of turbulent diffusion flames, where soot formation occurs partially separated from the oxidation reactions as well—that is, at low concentrations of oxygen and oxygen-related radicals. In this context, it must be taken in consideration that there is a tendency toward enhanced soot formation at moderately elevated oxygen concentrations, as will be reported elsewhere [13].

To complete the correlation for the soot growth proposed previously, the coefficients of proportionality of Eq. (5) have to be formulated in terms of temperature and, probably, of the primary stage stoichiometry. If the influence of primary stoichiometry is neglected for simplification, a diagram such as Fig. 9 (for propane) can be plotted. It shows the influence of temperature on the finally formed soot concentration from propane. Soot concentration values have been reduced by dividing them through the expression accounting for the influence of the overall C/O ratio as provided in Eq. (5). The result shows that there is a certain scattering of the data, some of which may be due to the neglected influence of primary stoichiometry.

It can be stated that there is a clear tendency of increasing soot yields with decreasing temperature. At temperatures of about 1650°C, soot formation is nearly ceasing. On the left-hand side of the graph, a stagnating soot yield in the range of the lowest temperatures of 1100–1300°C is observable. The occurrence of a maximum for the final soot concentration in a certain range of temperature, as discussed by Boehm et al. [14] and more quantitatively by Huth [7,15], could not be confirmed. There might be a maximum at temperatures exceeding the resolvable range to lower values (<1200°C). It must be taken into account that the final soot concentrations resulting from the low temperature runs are extrapolated values from the residence time correlation in Eq. (3) and therefore not as accurate.

Conclusions

- Soot growth phenomenology can be described satisfactorily by means of a correlation based on the strongly simplifying assumption of an autocatalytic reaction superposed by a deactivation process that is dominated by the reaction temperature. Similar expressions can be used for the fuels methane, propane, and acetylene, which have been investigated.
- Under approximately isothermal conditions, as realized in the plug flow reactor experiments, soot growth rates increase with residence time, reach a maximum value, and decrease to zero for higher residence times. For increasing temperature, the

maximum is shifting toward shorter residence time.

- The influence of temperature on the residence time–resolved soot concentration profiles can be formulated in terms of an Arrhenius expression. The activation energy was determined to be 192 kJ/mol independent of the type of soot-forming fuel (methane, propane, acetylene).
- Stoichiometry exclusively influences the amount of soot that may be formed theoretically when residence time approaches infinity. A quantitative expression can be achieved in terms of the C/O ratio, its critical value at the soot formation limit, and an additional parameter, weakly influenced by fuel specification.
- The plug flow reactor provided the possibility to shift from nearly premixed flame conditions to conditions of turbulent diffusive combustion by staging the fuel/oxygen stoichiometry. The oxygen distribution variations show only minor effects on the value of final soot concentration but, in comparison with results from premixed flames, a stronger influence on the critical C/O ratio.
- Deactivation of the soot surface is expressed by a decreasing of the "final" soot concentration with temperature increasing from about 1200 to 1650°C for propane. A maximum of this soot yield at a certain temperature, as reported in previous publications, could not be observed within the investigated parameter variations of the present work.

Acknowledgments

The authors gratefully acknowledge financial support within the joint research program of the Sonderforschungsbereich 167 by the Deutsche Forschungsgemeinschaft.

REFERENCES

1. Frenklach, M. and Wang, H., *Twenty-Third Symposium (International) on Combustion,* The Combustion Institute, Pittsburgh, 1990, pp. 1559–1566.
2. Mauss, F., Schäfer, T., and Bockhorn, H., *Combust. Flame* 99:697–705 (1994).
3. Bartenbach, B., Hirsch, C., Huth, M., and Leuckel, W., *Chem. Eng. Process.* 33:401–408 (1994).
4. Gore, J. P. and Faeth, G. M., *Twenty-First Symposium (International) on Combustion,* The Combustion Institute, Pittsburgh, 1986, pp. 1115–1124.
5. Stewart, C. D., Syed, K. J., and Moss, J. B., *Combust. Sci. Technol.* 75:211–226 (1991).
6. Huth, M. and Leuckel, W., *Twenty-Third Symposium (International) on Combustion,* The Combustion Institute, Pittsburgh, 1990, pp. 1493–1499.
7. Huth, M., "Untersuchung der Rußbildung bei partieller Brennstoffoxidation und Pyrolyse," Dissertation, Engler-Bunte-Institut, University of Karlsruhe, 1992.
8. Bockhorn, H., Fetting, F., Heddrich, A., and Wannenmacher, G., *Twentieth Symposium (International) on Combustion,* The Combustion Institute, Pittsburgh, 1984, pp. 979–988.
9. Baumgärtner, L., Hesse, D., Jander, H., and Wagner, H. G., *Twentieth Symposium (International) on Combustion,* The Combustion Institute, Pittsburgh, 1984, pp. 959–987.
10. Harris, S. J. and Weiner, A. M., *Combust. Sci. Technol.* 38:75–87 (1983).
11. Haynes, B. S. and Wagner, H. G., *Z. Phys. Chem.* 133:201–213 (1982).
12. Woods, I. T. and Haynes, B. S., in *Soot Formation in Combustion—Mechanisms and Models* (Bockhorn, H., Ed.), Springer Verlag, Heidelberg, 1994, pp. 275–289.
13. Bartenbach, B., Dissertation, Engler-Bunte-Institut, University of Karlsruhe, in preparation.
14. Böhm, H., Hesse, D., Jander, H., Lüers, B., Pietscher, J., Wagner, H. G., and Weiss, M., *Twenty-Second Symposium (International) on Combustion,* The Combustion Institute, Pittsburgh, 1988, pp. 403–411.
15. Huth, M. and Leuckel, W., in *Soot Formation in Combustion—Mechanisms and Models* (Bockhorn, H., Ed.), Springer Verlag, Heidelberg, 1994, pp. 371–381.

Twenty-Sixth Symposium (International) on Combustion/The Combustion Institute, 1996/pp. 2319–2326

C_2H_2 AND PAH AS SOOT GROWTH REACTANTS IN PREMIXED C_2H_4-AIR FLAMES

TIMOTHY G. BENISH, ARTHUR L. LAFEUR, KOLI TAGHIZADEH AND JACK B. HOWARD
Department of Chemical Engineering and Center for Environmental Health Sciences
Massachusetts Institute of Technology, Cambridge, MA 02139

The assumption that all of the soot mass growth in flames occurs by C_2H_2 reaction with the soot particles is widely used in soot modeling, thereby taking no explicit account of published evidence that polycyclic aromatic hydrocarbons (PAHs) are important contributors to soot growth. In one of the most influential flame studies leading to the simple C_2H_2-soot mechanism, PAH concentrations were not measured but were assumed to be too low for these species to be significant in soot growth. The original basis for the C_2H_2-soot mechanism has been reassessed in the present study by measuring PAH concentrations in premixed C_2H_4-air flat flames used in the original study and by using the data to evaluate the contributions of both PAH-soot and C_2H_2-soot reactions in these flames. Polycyclic aromatic hydrocarbons were found in sufficient concentrations for their contribution to soot growth to be important. The observed mass growth rates of the total PAHs and soot are consistent with a simple mechanism in which both C_2H_2 and PAHs react with soot and C_2H_2 reacts with PAHs. The PAH-soot reaction occurs with a collision efficiency of order 5000 times larger than that of the C_2H_2-soot reaction and contributes 95% or more of the soot mass growth. With fundamentally reasonable rate coefficients, this mechanism gives a faster route for conveying carbon from C_2H_2 to soot than could be achieved with a direct C_2H_2-soot reaction. The relatively high PAH-soot reactivity presumably reflects the radical character of the reaction. PAHs with five-member rings in their periphery, which are expected to contribute to the high reactivity, constitute an estimated 70% by mass of the identified PAHs.

Introduction

Soot formation in combustion continues to be of practical and scientific interest. The formation includes an inception and nucleation stage thought to involve reactions of heavy polycyclic aromatic hydrocarbon (PAH) molecules leading to particulate species [1]. The next stage involves growth by coagulation of the particles along with mass addition from molecular reactants, whose identity is an open question and the main focus of this paper.

Though PAHs have been widely accepted as the soot inception reactants, they are neglected in many growth models in response to the belief that acetylene alone dominates mass growth (e.g., see many of the papers and discussions of a recent workshop [2]). Soot growth by C_2H_2 was promoted by Harris and Weiner [3] after studying several C_2H_4-air flat flames. They concluded that only acetylene satisfies the requirements for a soot growth reactant and proposed a simple model in which soot mass growth rate is proportional to soot surface area and C_2H_2 concentration. PAHs were not measured and were believed to be in insufficiently high concentrations to be counted as possible soot growth reactants.

In contrast to the simple C_2H_2 model described, PAHs have been found to be important soot growth reactants in ethylene combustion in a plug flow reactor [4,5], in the same system with naphthalene injection [6,7], and in C_6H_6/O_2 flames [1]. Smedley et al. [8] reached a similar conclusion based on measurements in two ethylene-air flames studied by Harris and Weiner [9]. Furthermore, rate coefficients deduced by fitting the simple C_2H_2-soot mechanism to data [10] are larger than would be expected for C_2H_2 addition chemistry, consistent with the possibility of a significant contribution of PAHs within the C_2H_2 rate coefficient [11]. In view of these observations, reassessment of the original basis for the simple C_2H_2-soot growth mechanism is warranted. To that end, the present study was designed to measure PAH concentrations in the particular flames [3] from which Harris and Weiner first formulated their acetylene model and to evaluate the contributions of both PAHs and C_2H_2 to soot mass growth in these flames.

Experimental

Premixed C_2H_4-air flat flames at 1 atm, shielded by an annular N_2 stream, were stabilized on a 5-cm-diameter porous plug burner. A water-cooled plate ~35 mm above the burner surface helped stabilize the flame and protect the sampling apparatus. Feed rate to the burner was 8.65 L/min standard

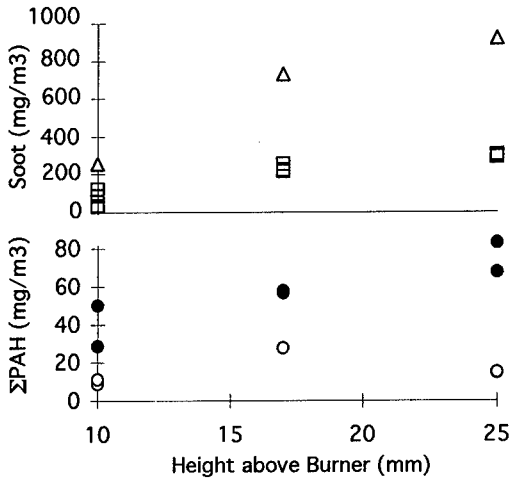

FIG. 1. Soot and ΣPAH concentrations at different positions in flame. C/O = 0.79 (□,△,●); 0.70 (○). Data source: present study (□,●,○); Harris and Weiner [3] (△).

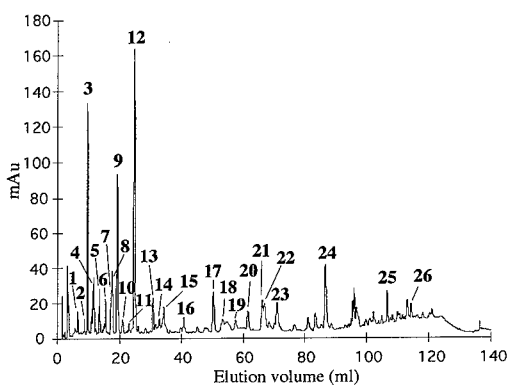

FIG. 2. HPLC chromatogram of soot extract at 368 nm wavelength (C/O = 0.70, 10 mm).

temperature and pressure (STP) with C/O = 0.70 and 0.79 (ϕ = 2.1 and 2.4). The flame conditions were the same as those used by Harris and Weiner [3], though the burner diameter was 1 cm smaller.

The flames were sampled isokinetically at a rate of ~0.60 L/min STP by a water-cooled quartz probe with a 1 mm orifice diameter. Flame products at 10, 17, and 25 mm above the burner were collected on cartridge filters (Balston DFU 9933-05), which have been shown to collect the majority of soot and PAHs [12]. After sampling for 45 min, the filter, probe interior, and connecting lines were washed with dichloromethane (DCM) and the resulting solutions were filtered though a 0.2 mm syringe filter to remove insolubles. The mass of material extracted from the soot and soluble in DCM, denoted ΣPAH, was measured by weighing a portion of each solution and allowing the DCM to evaporate.

To verify that the extractable material was composed primarily of PAHs, each sample was concentrated under nitrogen, exchanged into DMSO, and injected into an HPLC-DAD with a C18 Reverse Phase Vydac Column. Peak areas were converted to concentrations for select PAHs by calibration with a 16-PAH standard. By observing species that had similar UV spectra, the calibrations were extended to approximate concentrations of most of the remaining identified PAHs.

Soot samples were collected from the flames using the same sampling apparatus, but with the massive cartridge filter replaced by a lighter 0.22 mm flat Teflon filter to permit accurate weighing of the collected soot. The filter, probe, and connecting lines were washed with DCM to remove all soot, and each solution was filtered through a second 0.22 mm filter. The material on the filter was dried in a dessicator and weighed, and the result was used to calculate the soot concentration in the flame. Soot particle sizes were measured with a TUPCON 002B high-resolution electron microscope, operated at 200 keV. Soot from the filter was dispersed in toluene using intense ultrasonic agitation, and a drop of the suspension was evaporated on holey carbon film supported on a 200-mesh copper grid.

Results

Soot concentration profiles for the C/O = 0.79 flame are compared in Fig. 1 to the previous results [3], which were obtained by light absorption measurements and found to be three times higher than the present measurements throughout the postflame region. Choi et al. [13] recently reported optically measured soot concentrations that exceeded gravimetric measurements by a factor of 2. However, the present results are in excellent agreement with interpolated values from optical measurements of Feitelberg [14] in similar C_2H_4 flames at C/O = 0.77 and 0.80 and therefore are employed in this study. The amount of soot retrieved from the C/O = 0.70 flames was insufficient to make accurate weighings, so the previous soot concentration measurements [3], reduced by a factor of 3 as for the C/O = 0.79 case, are used here.

Twenty-six PAHs were identified individually by HPLC from the extracted solutions (Fig. 2) and are shown in Table 1. These species account for 49% of the ΣPAH mass. Whether the discrepancy is due solely to high-molecular-weight PAHs not seen by HPLC or in part to inaccuracies in the calibration assumptions is not known. Fourteen of the identified PAHs, accounting for an estimated 70% by mass of the identified species, contain in their periphery five-member rings, of special interest here because of their relatively high reactivity.

TABLE 1
Identified flame compounds and their estimated mass fractions of total PAHs

	Structure	Formula	Mass	Name	Mass % of ΣPAH
1		$C_{13}H_8O$	180	Phenalenone	NA
2		$C_{10}H_8$	128	Naphthalene	2.9
3		$C_{12}H_8$	152	Acenaphthylene	12.5
4		$C_{14}H_8$	176	Ethynyl-acenaphthylene	4.0[a]
5		$C_{14}H_{10}$	178	Phenanthrene	1.2
6		$C_{15}H_{10}$	190	Cyclopenta[def] phenanthrene	0.5[b]
7	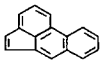	$C_{16}H_{10}$	202	Acephen-anthrylene	0.5[c]
8	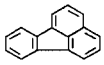	$C_{16}H_{10}$	202	Fluoranthene	2.8
9		$C_{16}H_{10}$	202	Pyrene	4.1
10	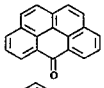	$C_{19}H_{10}O$	254	6H-Benzo[cd] pyren-6-one	NA
11	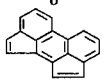	$C_{18}H_{10}$	226	Cyclopentaace-phenanthrylene	0.4[d]
12	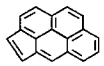	$C_{18}H_{10}$	226	Cyclopenta[cd] pyrene	9.4[c]
13	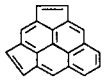	$C_{20}H_{10}$	250	Dicyclopenta [cd,mn]pyrene	1.1[c]
14	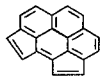	$C_{20}H_{10}$	250	Dicyclopenta [cd,fg]pyrene	0.4[c]
15	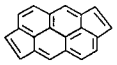	$C_{20}H_{10}$	250	Dicyclopenta [cd,jk]pyrene	1.1[c]
16	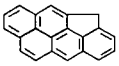	$C_{21}H_{12}$	264	Benzo[a]pyrene w/CH2 bridge	0.6[e]
17	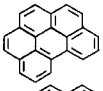	$C_{22}H_{12}$	276	Benzo[ghi] perylene	1.3
18	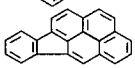	$C_{22}H_{12}$	276	Indeno[1,2,3-cd]pyrene	0.4
19	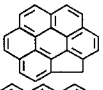	$C_{23}H_{12}$	288	Benzo[ghi] perylene w/CH2 bridge	0.2[f]
20	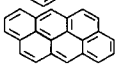	$C_{22}H_{12}$	276	Anthanthrene	0.6[g]
21	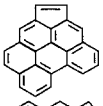	$C_{24}H_{12}$	300	Cyclopenta[fg] benzo[ghi] perylene	1.2[f]
22	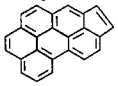	$C_{24}H_{12}$	300	Cyclopenta[cd] benzo[ghi] perylene	0.8[g]
23	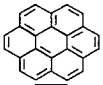	$C_{24}H_{12}$	300	Coronene	0.8[h]
24	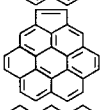	$C_{26}H_{12}$	324	Cyclopenta-coronene	1.8[h]
25		$C_{30}H_{14}$	374	Naphtho[8,1,2-acb]coronene	0.6[f]
26		$C_{32}H_{14}$	398	Ovalene	0.05[h]

Quantitation done using calibration for
[a]Acenaphthylene
[b]Phenanthrene
[c]Fluoranthene
[d]Pyrene
[e]Benzo[a]pyrene
[f]Benzo[ghi]perylene
[g]Indeno[1,2,3-cd]pyrene
[h]Dibenzo[ah]anthracene
NA = identified but not quantified.

Additional measurements and properties obtained from other studies are given in Table 2. Flame temperatures and C_2H_2 concentrations for the C/O = 0.79 flame were obtained by interpolation of Feitelberg's measurements in similar C/O = 0.77 and 0.80 flames [14]. An average temperature and C_2H_2 concentration for the C/O = 0.70 flame were obtained from data of Bönig et al. [15]. In both flames, the total number of moles in the region studied was assumed to be 50% larger than the feed value.

ΣPAH was taken to have an average molecular weight of 200 g/mol, on the basis of the molecular

TABLE 2
Additional measurements and calculated values

	10 mm	17 mm	25 mm
C/O = 0.79			
Temperature (K)	1750	1700	1660
Soot particle diameter (nm)	9.2	13	25
Soot number density (cm^{-3})	1×10^{11}	1×10^{11}	2×10^{10}
C_2H_2 mole fraction	0.032	0.028	0.026
C/O = 0.70			
Temperature (K)	1700	1700	1700
Soot particle diameter (nm)	4.8	7.4	14
Soot number density (cm^{-3})	1×10^{11}	1×10^{11}	2×10^{10}
C_2H_2 mole fraction	0.013	0.013	0.013

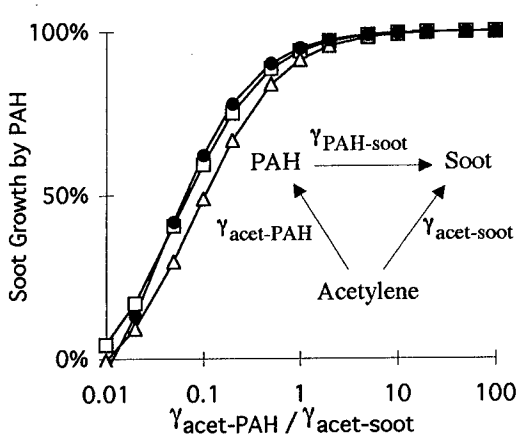

FIG. 3. Effect of the relative reactivity of soot and ΣPAH. C/O = 0.79. (□) 10 mm, (△) 17 mm, (●) 25 mm.

weights and mass fractions of the identified compounds, and an average collision diameter of 0.74 nm [16]. Soot particles were approximated as spheres of density 1.8 g/cm³. Soot number densities for the C/O = 0.79 flame were calculated from the total mass collected and the average diameter of soot particles from electron micrographs (Table 2). The same number densities were assumed to apply also to the C/O = 0.70 flame in accordance with the observed invariance of number density with C/O ratio [17].

For each measured point in the postflame region, soot and ΣPAH concentrations were plotted (Fig. 1) and the mass growth rates were found by approximating derivatives at each point. Soot and ΣPAH balances were then calculated as follows, assuming (see reaction mechanism in Fig. 3) PAH growth is the net of C_2H_2 addition to PAHs and PAH addition to soot, and soot growth results from addition of C_2H_2 and PAHs, ignoring oxidation in view of the fuel-rich postflame conditions:

$$R_{soot} = Z_{acet\text{-}soot}\gamma_{acet\text{-}soot}m_{acet} + Z_{PAH\text{-}soot}\gamma_{PAH\text{-}soot}m_{PAH} \quad (1)$$

$$R_{\Sigma PAH} = Z_{acet\text{-}PAH}\gamma_{acet\text{-}PAH}m_{acet} - Z_{PAH\text{-}soot}\gamma_{PAH\text{-}soot}m_{PAH} \quad (2)$$

where R = mass growth rate (g cm^{-3} s^{-1}), Z = collision rate calculated from kinetic theory, γ = collision efficiency, and m = molecular mass. Eqs. (1) and (2) permit two of the three collision efficiencies to be computed from the data and known properties. Solving for $\gamma_{PAH\text{-}soot}$ and $\gamma_{acet\text{-}soot}$ in terms of $\beta = \gamma_{acet\text{-}PAH}/\gamma_{acet\text{-}soot}$, and then computing the fraction of the soot mass growth contributed by PAH addition, in other words, $(R_{soot})_{PAH}/R_{soot}$ gives

$$\gamma_{PAH\text{-}soot} = r_1(\beta - r_2r_3)/(\beta + r_3) \quad (3)$$

$$\gamma_{acet\text{-}soot} = r_4(1 + r_2)/(\beta + r_3) \quad (4)$$

$$(R_{soot})_{PAH}/R_{soot} = (\beta - r_2r_3)/(\beta + r_3) \quad (5)$$

where $r_1 = R_{soot}/Z_{PAH\text{-}soot}$, $r_2 = R_{\Sigma PAH}/R_{soot}$, $r_3 = Z_{acet\text{-}soot}/Z_{acet\text{-}PAH}$, and $r_4 = R_{soot}/Z_{acet\text{-}PAH}$.

Although $\gamma_{acet\text{-}PAH}$ and $\gamma_{acet\text{-}soot}$ are not well-known, their ratio can be approximated closely enough, as follows, to permit solution of the preceding equations. On the basis of observed reaction rates and the various C—H bond energies involved, the reactions involve radicals and the predominant radical centers or active sites are edge carbons of PAH gaseous molecules or condensed layers [11]. The collision efficiency is approximately proportional to the fraction of radical carbons within PAHs or soot. For a given temperature and gas composition, this fraction depends on the H/C ratio, in other words, the fraction of carbons that can become active by loss of an H atom, and the types of C—H

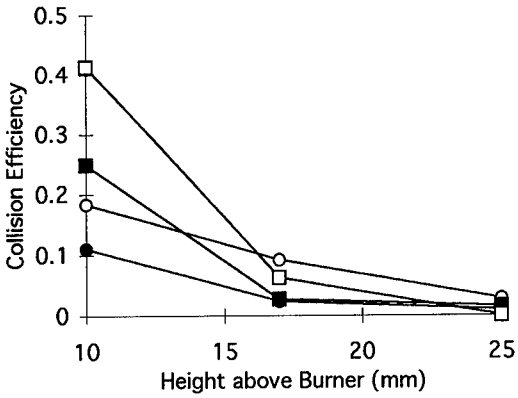

FIG. 4. Collision efficiencies at different distances from burner. $\gamma_{acetylene\text{-}soot} \times 10^4$. (□) C/O = 0.70, (○) C/O = 0.79. $\gamma_{PAH\text{-}soot}$: (■) C/O = 0.70, (●) C/O = 0.79.

bonds present. The H/C ratio decreases from near unity for the smallest PAHs to 0.4 for the largest PAHs identified here (Table 1), and from ca. 0.3 to 0.5 for young soot to ca. 0.1 for older soot having undergone annealing accompanied by dehydrogenation during longer residence times in the flame. Also, the distribution of C—H bond types, which include those of carbon atoms in five- and six-member rings, tends toward smaller fractions of the more reactive types as the H/C ratio decreases. Therefore, the progression to larger PAHs and to soot of increasing particle size and age in the flame is accompanied by a decreasing reactivity for carbon addition to the material.

The decrease in reactivity is well-known in the case of soot growth [3,18–20]. The trend for soot meets the trend for PAHs at the transition from soot precursors to nascent soot particles, the material at the transition being incipient soot. An overall decrease in reactivity during the transition can be expected to result initially from radical recombination and addition and, then, in the incipient soot, from intramolecular condensation involving dehydrogenation, cross-linking, and ring formation. Accordingly, the reactivity of the soot precursors presumably exceeds that of the nascent soot particles. Furthermore, $\gamma_{acet\text{-}PAH}$ exceeds the value for soot precursors because the former represents all PAHs, among which the soot precursors make up the least reactive fraction. Also, once soot growth is under way, $\gamma_{acet\text{-}soot}$ is always smaller than the value for nascent soot particles. Therefore, the overall reactivities represented by $\gamma_{acet\text{-}PAH}$ and $\gamma_{acet\text{-}soot}$ will differ more than those of the soot precursors and the nascent soot particles. Thus, $\gamma_{acet\text{-}PAH}/\gamma_{acet\text{-}soot}$ can be assumed to be considerably larger than unity during soot growth, and from Fig. 3, we conclude that most of the soot growth occurs by PAH addition.

To calculate representative collision efficiencies $\gamma_{acet\text{-}PAH}/\gamma_{acet\text{-}soot}$ was set to 1, which is an underestimation given the previous discussion. The collision efficiencies obtained, shown in Fig. 4, are within the range of values found previously [1,4,7,11] when the contributions of both C_2H_2 and PAHs are taken into account ($\gamma_{acet\text{-}soot} = 1 \times 10^{-5}$ to 7×10^{-4}; $\gamma_{PAH\text{-}soot} = 0.1\text{–}0.5$). The collision efficiency for PAHs with soot is of the order of 5000 times that for acetylene with soot, presumably reflecting the radical character of many PAHs under flame conditions. Noteworthy in this regard is the prevalence of species (Table 1) containing, in their periphery, five-member rings and, hence, relatively easily removed H atoms. The relatively high reactivity, as well as the substantial concentration of PAHs in the present flames, is reflected by the ~95% or higher contribution of ΣPAH to soot growth in both flames. If the soot concentrations reported by Harris and Weiner [3] for the C/O = 0.70 flame were used without the factor of 3 reduction described earlier, both collision efficiencies for this case would roughly double and the soot growth contribution by PAHs would decrease ~5%.

Both $\gamma_{acet\text{-}soot}$ and $\gamma_{PAH\text{-}soot}$ drop ~90% through the region studied. This is not inconsistent with the hypothesis that reactivity is controlled by the number of radical sites on PAHs and soot, which is expected to decrease significantly as temperature, concentrations of H-abstracting radicals such as H atoms, and H/C ratio of the soot all decrease in the postflame region [11,21]. Current experimental work is focusing on this issue.

Discussion

The present results support the earlier plug flow reactor findings [4–7] regarding the important role of PAHs in soot growth and, at the same time, extend the range of conditions under which this behavior has been observed. The following evidence indicates the behavior may also be important under other, quite different, flame conditions.

Extensive recent studies of soot formation in premixed C_2H_2-air flat flames at pressure up to 100 bar [22] exhibit features that combined with the present results are consistent with an even stronger dominance of PAHs over C_2H_2 as a sootgrowth reactant than is seen at atmospheric pressure. Data shown in Fig. 5 reveal that, as pointed out by Böhm et al. [22], the fraction of the carbon fed that is found as C_2H_2 in the flame decreases with increasing pressure, whereas the fraction found as ΣPAH changes relatively little. The $\Sigma PAH/C_2H_2$ mass ratio is 100 times larger at 70 bar than at 1 bar where, according to the present study, ΣPAH is already dominant over C_2H_2 as the soot growth reactant. Therefore, essentially all of the soot growth at the higher pressures would be expected to occur by PAH addition.

Soot mass growth in diffusion flames has recently been modeled along with the gas-phase chemistry, assuming the growth reaction to be first order in acetylene concentration (C_2H_2) [23]. Several

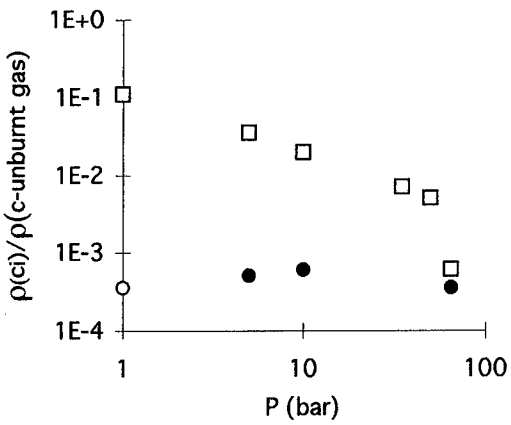

FIG. 5. Carbon densities of (□) acetylene and (●,○) ΣPAH for premixed C_2H_4-air flat flames at different pressures. Data: (○) present study, distance from burner = 10 mm, C/O = 0.70, $v_{unburnt\,gass}$ = 7 cm/s, T ~ 1700 K; (●,□) Böhm et al. [22], C/O = 0.68, $v_{unburnt\,gas}$ = 6 cm/s, 1600 ≤ 1750.

different assumptions about the dependence of growth rate on soot surface area were tested by comparing model predictions against experimental data. The best fit was obtained when the growth rate r_s was assumed to be independent of soot surface area [23], consistent with other observations from premixed flames [24] and diffusion flames [25], and proportional to the soot particle number concentration n_s. The growth rate coefficient, defined as $k = r_s/n_s(C_2H_2)$, was found to be 10^{-12} m^3 s^{-1} $\exp(-12{,}100/(T/K))$.

From simple kinetic theory, k can be shown to correspond to a collision efficiency of $\gamma_{\text{acet-soot}} = k(2\mu/\pi RT)^{1/2}/\sigma^2$, where σ and μ are the collision diameter and reduced mass for C_2H_2-soot collisions. At 1700 K, this $\gamma_{\text{acet-soot}}$ decreases from 2 to 10^{-3} as the effective soot particle diameter increases from 1 nm, for the smallest particle included in the model fitting [23], to 20 nm, typical of the end of growth. The collision efficiency in principle cannot exceed unity and should be some factors of 10 less than unity for C_2H_2 addition to a radical site in the possible structures of a 1-nm soot particle. Therefore, the assumed growth of soot by C_2H_2 alone is clearly an empirical representation of a growth process whose true rate exceeds the fundamental limit of the assumed mechanism. If C_2H_2 is the carbon source for soot growth, a mechanism is required that gives a faster rate of removal of carbon from C_2H_2 than can be achieved with C_2H_2-soot collisions. Such a mechanism is C_2H_2 addition to PAHs, followed by PAH addition to soot (Fig. 4). Agreement of this mechanism with the data represented by the previously mentioned k can also be seen from the strong increase in $\gamma_{\text{acet-soot}}$ with decreasing particle size, consistent with the reasoning that $\gamma_{\text{acet-PAH}}$ exceeds $\gamma_{\text{acet-soot}}$ and, hence, from Fig. 3, consistent with most of the soot mass growth actually coming from PAH addition.

Conclusions

PAHs have been measured in the ethylene-air flames studied by Harris and Weiner [2] when they concluded that acetylene is the only significant reactant in soot growth. PAHs were found in sufficiently high concentrations that their contribution to soot growth appears to be important. Therefore, PAHs should be considered reactants in soot growth models.

The observed mass growth rates of the total PAHs and soot are consistent with a simple mechanism in which both C_2H_2 and PAHs react with soot and C_2H_2 reacts with PAHs. The PAH-soot reaction occurs with a collision efficiency of order 5000 times larger than that of the C_2H_2-soot reaction and contributes 95% or more of the soot mass growth.

The relatively high PAH-soot reactivity presumably reflects the radical character of the reaction. PAHs with five-member rings in their periphery, which are expected to contribute to the high reactivity, constitute an estimated 70% by mass of the identified PAHs.

Acknowledgments

This investigation was supported in part by the National Institute of Environmental Health Sciences Center Grant NIH-5P30-ES02109; the Health Effects of Fossil Fuels Utilization Program Grant NIH-5P01-ESO1640, and the Division of Chemical Sciences, Office of Basic Energy Sciences, Office of Energy Research, U.S. Department of Energy Grant DE-GF02-84ER13282. We thank K. Das Chowdkury and Lenore Rainey for electron microscopy.

REFERENCES

1. McKinnon, J. M., and Howard, J. B., *Twenty-Fourth Symposium (International) on Combustion,* The Combustion Institute, Pittsburgh, 1992, pp. 965–971.
2. Bockhorn, H. *Soot Formation in Combustion* (Bockhorn, H, Ed.), Springer Verlag, New York, 1994, p. 596.
3. Harris, S. J. and Weiner, A. M., *Combust. Sci. Technol.* 31:155–167 (1983).
4. Lam, F. W., Longwell, J. P., and Howard, J. B., *Twenty-Second Symposium (International) on Combustion,* The Combustion Institute, Pittsburgh, 1989, pp. 323–332.
5. Lam, F. W., Longwell, J. P., and Howard, J. B., *Twenty-Third Symposium (International) on Combustion,* The Combustion Institute, Pittsburgh, 1991, pp. 1477–1484.

6. Marr, J. A., Allison, D. M., Giovane, L. M., Yerkey, L. A., Monchamp, P., Longwell, J. P., and Howard, J. B., *Combust. Sci. Technol.* 85:65–76 (1992).
7. Marr, J. A., Giovane, Longwell, J. P., Howard, J. B., and Lafleur, A. L., *Combust. Sci. Technol.* 101:301–309 (1994).
8. Smedley, J. M., Williams, A., and Bartle, K. D., *Combust. Flame* 91:71–82 (1992).
9. Harris, S. J. and Weiner, A. M., *Twenty-Second Symposium (International) on Combustion,* The Combustion Institute, Pittsburgh, 1989, pp. 333–339.
10. Harris, S. J. and Weiner, A. M., *Combust. Sci. Technol.* 32:267 (1983).
11. Howard, J. B., *Twenty-Third Symposium (International) on Combustion,* The Combustion Institute, Pittsburgh, 1990, pp. 1107–1127.
12. Marr, J. A., "PAH Chemistry in a Jet Stirred/Plug Flow Reactor System," Ph.D. Thesis, Massachusetts Institute of Technology, 1993.
13. Choi, M. Y., Mullholland, G. W., Hamins, A., and Kashiwagi, T., *Combust. Flame* 102:161–169 (1995).
14. Feitelberg, A. S., "The Efforts of Metal Additives on Soot Formation," Ph.D. Thesis, Massachusetts Institute of Technology, 1993.
15. Bönig, M., Feldermann, C., Jander, H., Lüers, B., Rudolph, G., and Wagner, H. G., *Twenty-Third Symposium (International) on Combustion,* The Combustion Institute, Pittsburgh, 1990, pp. 1581–1587.
16. Pope, C. J., "Fluxes and Net Rates of High Molecular Weight Material in a Near-Sooting Benzene-Oxygen Flame," M.S. Thesis, Massachusetts Institute of Technology, 1988.
17. Haynes, B. S., Jander, H., and Wagner, H. G., *Ber. Bunsenges, Phys. Chem.* 84:585–592 (1980).
18. Haynes, B. S. and Wagner, H. G., *Z. Phys. Chem.* 133:201 (1982).
19. Bockhorn, H. and Schäfer, T., *Soot Formation in Combustion* (Bockhorn, H., Ed.), Springer Verlag, New York, 1994, pp. 253–273.
20. Woods, I. T. and Haynes, B. S., *Soot Formation in Combustion* (Bockhorn, H., Ed.), Springer Verlag, New York, 1994, pp. 275–288.
21. Mauss, F., Schafer, T., and Bockhorn, F., *Combust. Flame* 99:697–705 (1994).
22. Böhm, H., Feldermann, C., Heidermann, T., Jander, H., Lüers, B., and Wagner, H. G., *Twenty-Fourth Symposium (International) on Combustion,* The Combustion Institute, Pittsburgh, 1992, pp. 991–998.
23. Lindstedt, P. R., *Soot Formation in Combustion* (Bockhorn, H., Ed.), Springer Verlag, New York, 1994, pp. 417–441.
24. Wieschnowsky, U., Bockhorn, H., and Fetting, F., *Twenty-Second Symposium (International) on Combustion,* The Combustion Institute, Pittsburgh, 1988, pp. 343–350.
25. Delichatsios, M. A., *Combust. Sci. Technol.* 100:283–298 (1994).

COMMENTS

M. Frenklach, University of California—Berkeley, USA. The presented experimental results do *not* contradict the model of soot formation based on acetylene as the dominant surface growth species. The opposite conclusion reached in your study originates [1] from the assumption of equality for the collision efficiencies of acetylene with PAH and of acetylene with soot, whereas the former should be much smaller than the latter due to the stronger reaction reversibility [2].

REFERENCES

1. Kazakov, A. and Frenklach, M., "On the Relative Contribution of Acetylene and Aromatics to Soot Particle Growth," submitted to *Combust. Flame.*
2. Frenklach, M., "On Surface Growth Mechanism of Soot Particles," *Twenty-Sixth (International) Symposium on Combustion,* The Combustion Institute, Pittsburgh, 1996, in press.

Author's Reply. Consideration of reversibility without taking PAH structure into account can be misleading. It is true that the net forward rate of acetylene addition to a given type of radical site in the periphery of a PAH increases with increasing molecular weight of the PAH, according to chemical activation calculations assuming all vibrational modes in the PAH contribute to the stabilization of the adduct and hence to the decrease of the reverse reaction rate [12]. However, these calculations show that reversibility slows the net acetylene addition by less than a factor of 3 for even the smallest PAH considered here, which alone would not dismiss the importance of PAH in soot growth (Fig. 3). In addition, the smaller PAH are less pericondensed, have higher H/C ratios, and have a larger fraction of peripheral carbon atoms in more reactive five-membered rings. These properties tend to offset the effect of decreased adduct stabilization and reversibility.

•

Antonio D'Alessio, Università di Napoli, Italy. PAH considered as soot growth reactants are not easily analyzable. You considered a molecular weight of about 200 n for them. Why this law value for not chomatographable species?

Author's Reply. This value was used for the average molecular weight of ΣPAH because we have no additional in-

formation on the PAH inventory other than the species identified by chromatography, and we can not speculate on the composition of the remaining dichloromethane-soluble material. The results from the kinetic model are not highly sensitive to the molecular weight of ΣPAH nor to the replacement of ΣPAH with the set of identified species. Methods for identifying larger PAH are currently under investigation.

•

M. Frenklach, University of California—Berkeley, USA. In response to the comment made by Professor D'Alessio, I would like to mention that we were the first to introduce PAH as surface growth species in detailed modeling of soot in flames [1]. Thus, the issue is not whether we believe or not in PAH being a possible surface growth species but is that the results reported in the present work do not provide indisputable evidence [2] for PAH being the dominant growth species in the Harris and Weiner flame [3].

REFERENCES

1. Frenklach, M. and Wang, H., *Twenty-Third (International) Symposium on Combustion,* The Combustion Institute, Pittsburgh, p. 1559.
2. Kazakov, A. and Frenklach, M., *Combust. Flame,* submitted.
3. Harris and Weiner, A. M., *Annu. Rev. Phys. Chem.* 36:31–52 (1985).

Twenty-Sixth Symposium (International) on Combustion/The Combustion Institute, 1996/pp. 2327–2333

THE EFFECT OF TEMPERATURE ON SOOT INCEPTION IN PREMIXED ETHYLENE FLAMES

A. CIAJOLO, A. D'ANNA, R. BARBELLA, A. TREGROSSI AND A. VIOLI
Istituto Ricerche Combustione, CNR
Napoli, Italy

The temperature dependence of soot and related hydrocarbon formation was studied in fuel-rich, premixed C_2H_4/O_2 flames by changing the flame temperature but keeping a constant C/O ratio. Three flames with temperature levels between the low- and high-temperature soot threshold of the bell-shaped domain of soot formation were analyzed.

In addition to the formation of pyrolytic species such as acetylene, benzene, polycyclic aromatic compounds (PAHs), and soot, the large formation of a tarlike material was revealed in the soot preinception region of the flames. The chemical analysis and spectroscopic characterization of these species showed that tar is made up of high-molecular-weight compounds in which aliphatic and aromatic functionalities coexist. The decrease in the concentration and the aromatic character of tar was found to correspond with soot inception, indicating that it could be responsible for soot nucleation. PAH molecules indirectly participate in soot inception, providing the building blocks of tar and/or participating in further soot surface growth.

The influence of temperature on soot formation was found to be different at the extremes of the bell-shaped domain of soot. In the flame near the low-temperature soot threshold, benzene, PAHs and pyrolytic species are formed in larger amounts, but low temperatures hinder the reactive coagulation of PAH molecules and aliphatic radicals into tarlike material, hindering, in turn, soot production. The buildup of tarlike material and the process of aromatization occur too slowly to allow the massive soot inception if the flame temperature is not high enough. At higher temperatures, oxidation is very active in the secondary oxidation zone of the flame, thus destroying PAHs that are not then available for formation of tarlike species. Consequently, soot inception is reduced. In the intermediate-temperature flame, where maximum soot formation was found, the temperature level is ideal for the formation of both PAHs and tar and their transformation to soot particles.

Introduction

The influence of mixture composition (C/O ratio) and temperature on soot formation in rich combustion has usually been studied by following the compositional changes of the burned gases related to C/O and temperature changes in laminar, premixed flames. Generally, it has been found that an increase in the C/O ratio causes an increase in the soot volume fraction, whereas at a constant C/O ratio, a temperature exists characteristic for the C/O ratio where soot volume fraction exhibits a maximum value. At higher and lower temperatures, soot volume fraction strongly decreases and a low- and high-temperature threshold for soot formation can be identified [1].

In previous work [2], the influence of C/O on the distribution of light hydrocarbons, soot, polycyclic aromatic hydrocarbons (PAHs), and high-molecular-weight species condensed along rich, premixed C_2H_4/O_2 flames has been studied. The results indicate that by increasing the C/O ratio, the larger depletion of total aromatic carbon, which corresponded with soot formation, had to be attributed more to the participation of these species to soot inception than to their oxidation.

In this work, the effect of flame temperature on the formation of soot and aromatic species is analyzed by following the distribution of carbon and hydrocarbon species along rich, premixed C_2H_4/O_2 flames at a constant mixture composition (C/O = 0.8) and different cold-gas flow velocities, namely, different flame temperatures. An evaluation of the spectroscopic characteristics of the species condensed along the flame and their dependence on flame temperature is also reported as an alternate diagnostic tool to follow the compositional changes of high-mass aromatic species not otherwise analyzable by chromatographic techniques.

Experimental

Soot and condensable species (CS) and gaseous combustion products were sampled by means of a stainless steel, water-cooled probe (i.d. = 2 mm) in atmospheric-pressure, rich, premixed C_2H_4/O_2

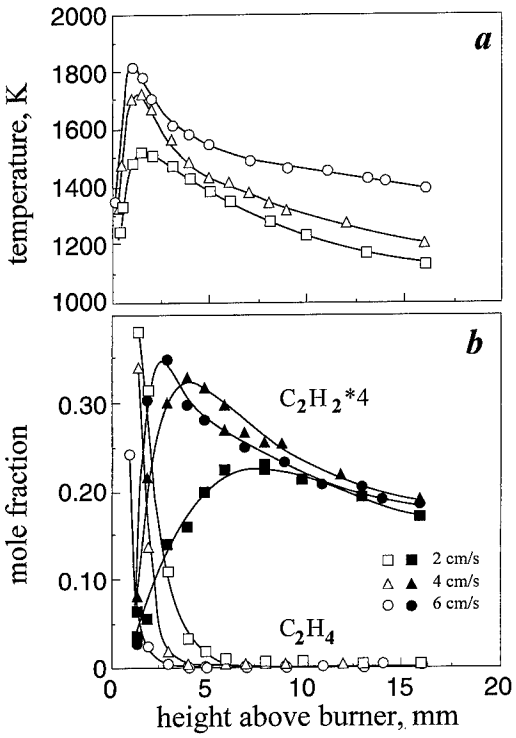

FIG. 1. (a) Temperature, and (b) ethylene and acetylene concentration profiles in flames with different cold-gas flow velocities (v = 2, 4, and 6 cm/s).

flames. Three flames were produced at a constant mixture composition (C/O = 0.8) and different cold-gas flow velocities (2, 4, and 6 cm/s). The flames were stabilized on a water-cooled, sintered-bronze burner (d = 60 mm) surrounded by a shroud of nitrogen.

Temperatures were measured by a fast-response, silica-coated, 25-μm Pt/Pt-13%Rh thermocouple with a bead size of ca. 50 μm. A fast insertion procedure was used to prevent massive soot deposition on the thermocouple bead. Temperature data were corrected for radiation losses.

On-line gas chromatography with thermal conductivity and flame ionization detectors was used for the analysis of light hydrocarbons. Soot and condensable species were collected on a teflon filter and in a cold trap placed before the filter and extracted by dichloromethane (DCM) to separate the condensed species that are soluble in DCM from the insoluble carbonaceous material, defined as soot. The amounts of CS and soot were determined gravimetrically. Polycyclic aromatic hydrocarbons in the condensed species with molecular masses up to 300 u were analyzed by gas chromatography–mass spectrometry (GC-MS) on an HP5890 gas chromatograph coupled with an HP5970 mass spectrometer.

Mass spectrometry of the CS in the range of 200–1000 u was done by direct injection of the samples into a mass spectrometer through a particle beam HP 59980B generator used as an interface between the pumping system of the liquid chromatograph HP1050 and the mass spectrometric system HP 5989A. Methanol was used as a mobile phase, and the pumping system was connected to the particle beam (PB) generator through a Rheodyne loop valve. The PB generator nebulizes and vaporizes the flow, separating the volatile mobile phase from the sample particles, which are introduced into the mass spectrometer source. In the vaporization phase, the more volatile components of the sample are lost together with the mobile phase, hindering the detection of components with molecular mass below 200 u. This technique was tested with a mixture of standard PAHs and the response of PAHs was almost similar for PAHs up to 400 u.

Ultraviolet-visible absorption of the condensed species dissolved in DCM was measured on an HP 8452A spectrophotometer using standard 1-cm path-length quartz cells. The specific absorptivity of standard PAHs was measured to evaluate the contribution of identified PAHs to CS absorptivity. Fourier transform-infrared (FT-IR) spectra of the samples dissolved in DCM and dried onto KBr disks were obtained using a Perkin–Elmer 1600 FT-IR spectrometer.

Results

The axial profiles of the flame temperature measured in rich, premixed ethylene/oxygen flames at 2, 4, and 6 cm/s of cold-gas flow velocity are reported in Fig. 1a, where the rise of the maximum flame temperature, from 1520 to 1820 K, with increasing cold-gas flow velocity can be observed. The maximum temperature is located around the flame front. Thereafter, the temperature decreases in all the flames and more rapidly in the flame with the intermediate temperature level. The rise in flame temperature, in turn, increases the burning velocity, which shortens the main reaction zone. This is demonstrated by the more rapid fuel consumption at higher flame temperatures as shown in Fig. 1b where the axial profiles of C_2H_4 concentration are reported for the three cold-gas flow velocities.

The concentration profiles of acetylene (C_2H_2), the most abundant hydrocarbon species produced in the rich combustion of C_2H_4, are also reported in Fig. 1b. Acetylene is already present at the beginning of the flame and reaches peak concentration at the end of the main oxidation zone, where the fuel concentration attains its minimum value. Beyond the main oxidation zone, C_2H_2 slightly decreases, leveling off to an almost constant value that does not depend on the flame temperature.

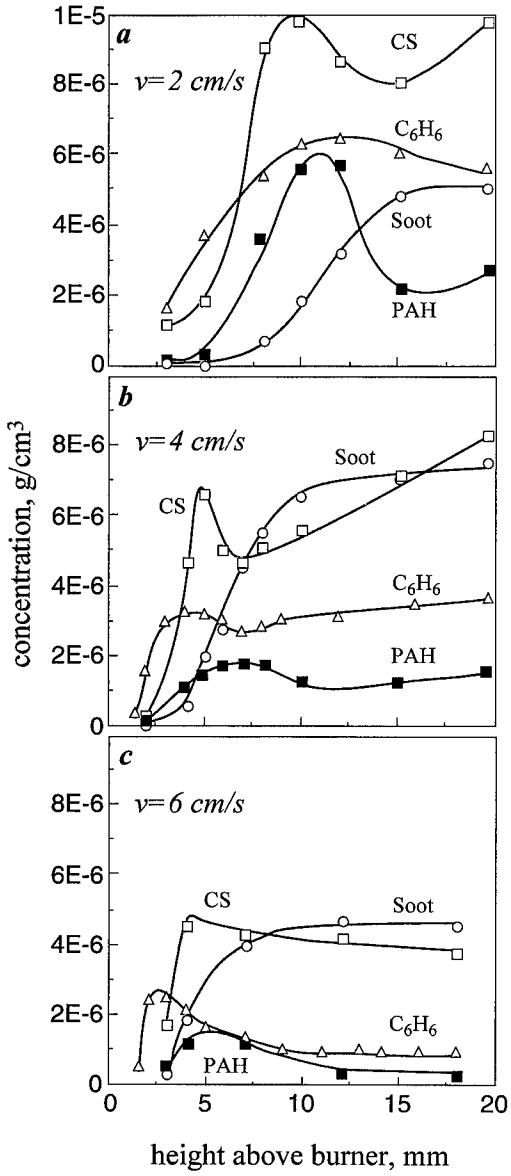

FIG. 2. Concentration profiles of soot, benzene, polycyclic aromatic hydrocarbons (PAHs), and condensed species (CS) in flames with different cold-gas flow velocities: (a) 2 cm/s, (b) 4 cm/s, and (c) 6 cm/s.

Benzene, soot, PAHs, and CS concentrations are about one order of magnitude lower than acetylene concentration as shown in Fig. 2, where their concentration profiles are reported for the three examined flames. Benzene is formed in the main oxidation zone and reaches peak concentration at the beginning of the postoxidation region in all the flames. Formation of C_6H_6 is greater in the lower temperature flame (Fig. 2a), where its concentration after the maximum value slowly decreases, rapidly attaining an almost constant value. In the hotter flame (Fig. 2c), benzene concentration is very low and rapidly decreases downstream from its maximum. In the flame at intermediate temperature (Fig. 2b), benzene concentration shows the same rise-decay profile exhibited by the hotter flame but is observed to increase again downstream from the reaction zone. This behavior is usually observed in sooting flames of aliphatic fuels [2–6].

In as much as benzene is the most abundant aromatic species produced at the beginning of the flame, soot and CS are the most abundant high-molecular-weight products at the end of the flame, at least in the hotter flames. Soot formation occurs just at the end of the main oxidation region and steeply rises, attaining an almost constant value in the post-oxidation zone of the flame. The higher the flame temperature, the earlier soot inception occurs (Fig. 2c), but the maximum soot concentration is found in the intermediate-temperature flame (Fig. 2b).

Polycyclic aromatic hydrocarbons from naphthalene (128 u) to coronene (300 u), usually found in sooting flames [2–6], were quantified by GC-MS in the condensed species. Polycyclic aromatic hydrocarbons with molecular weight within the range 300–400 u were detected by PB-MS, but their contribution to the total PAHs is almost negligible. The profiles of the sum of their concentrations show that PAHs are formed in larger amounts in the low-temperature flame (Fig. 2a) than in the higher-temperature one (Fig. 2c), and their maximum concentrations occur in all the flames slightly after the maximum in benzene concentration. Polycyclic aromatic hydrocarbons follow a trend similar to that of C_6H_6 in the higher-temperature flames: a rise-decay profile at the end of the main reaction zone with the complete destruction of the species in the hotter flame. A secondary increase in PAHs is seen only in the intermediate-temperature conditions (Figs. 2b and 2c). In the cooler flame (Fig. 2a), PAH concentration follows the initial increasing trend exhibited by benzene, but, downstream of the flame, PAH concentration sharply decreases whereas benzene remains almost constant.

The sum of PAHs partially contributes to the species condensed along the flames, as can be seen by comparing PAH concentration with the concentration of CS (Fig. 2). Condensed species are detected early within the main oxidation zone, and their concentration rapidly increases, reaching a maximum downstream of the flame front where soot begins to appear. Thereafter, CS concentration diminishes as the soot concentration increases. Similarly to the behavior of benzene and PAHs, CS concentration decreases in the post oxidation zone of the hotter flame (Fig. 2c), whereas in the cooler flames, it decreases and then increases again (Figs. 2a and b).

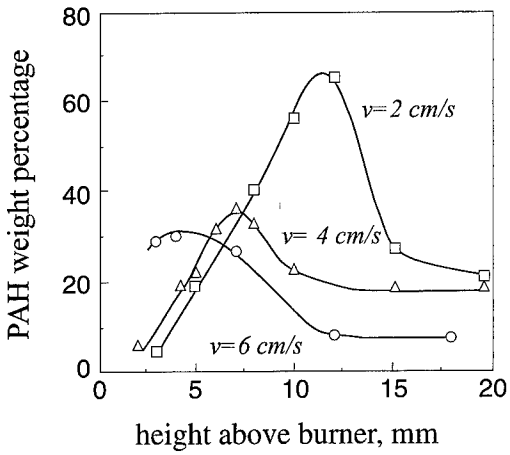

FIG. 3. Weight percentage of PAHs in the CS in flames with different cold-gas flow velocities.

The weight percentage of PAHs in the CS, reported in Fig. 3, shows that the PAH contribution is higher as the flame temperature is lowered and that in all the flames, it increases, reaching a maximum value at or just after the maximum of CS concentration (Figs. 2 and 3). Thereafter, PAH contribution decreases, becoming very low, particularly in the hotter flame.

It is evident that a significant part of the CS is not analyzable by conventional gas and liquid chromatographic techniques, but its chemical nature can be inferred by means of ultraviolet-visible absorption measurements. Condensable species showed broad absorption spectra, mainly peaking in the ultraviolet region and extending into the visible region. Evaluating the molar extinction coefficient of CS from the absorption measurements is impossible because their composition is unknown. Consequently, the absorptivity $E(\lambda)_{CS}$ of the CS has been expressed, referring to a weight unity $E(\lambda)_{CS} = A(\lambda)/cb$ ($cm^{-1}/g\ l^{-1}$), where $A(\lambda)$ is the measured absorbance at a fixed wavelength, c is the concentration of the CS expressed in grams per liter of solution, and b is the path length expressed in centimeters (1 cm).

The contribution of PAH absorptivity $E(\lambda)_{PAH}$ to CS absorptivity was calculated by multiplying the specific absorptivity of each of the identified PAHs ε_i^{PAH} (these quantities were measured experimentally) by their respective contribution to the CS (y_i^{PAH} = PAH_i weight/CS weight).

The absorptivities of CS (E_{CS}) and PAHs (E_{PAH}) at λ = 300 nm are reported in Fig. 4 for the three flames. In the cooler flames (Figs. 4a and 4b), the absorptivity of CS is very low at the flame front, increases to a maximum value, and then decreases in the post oxidation zone of the flame. In the hotter flame (Fig. 4c), the absorptivity profile does not show a peak but decreases monotonically along the whole flame. The maximum absorptivity value is roughly the same for the three examined flames and occurs near the onset of soot inception, whereas the final value of absorptivity is higher as the flame temperature is lowered.

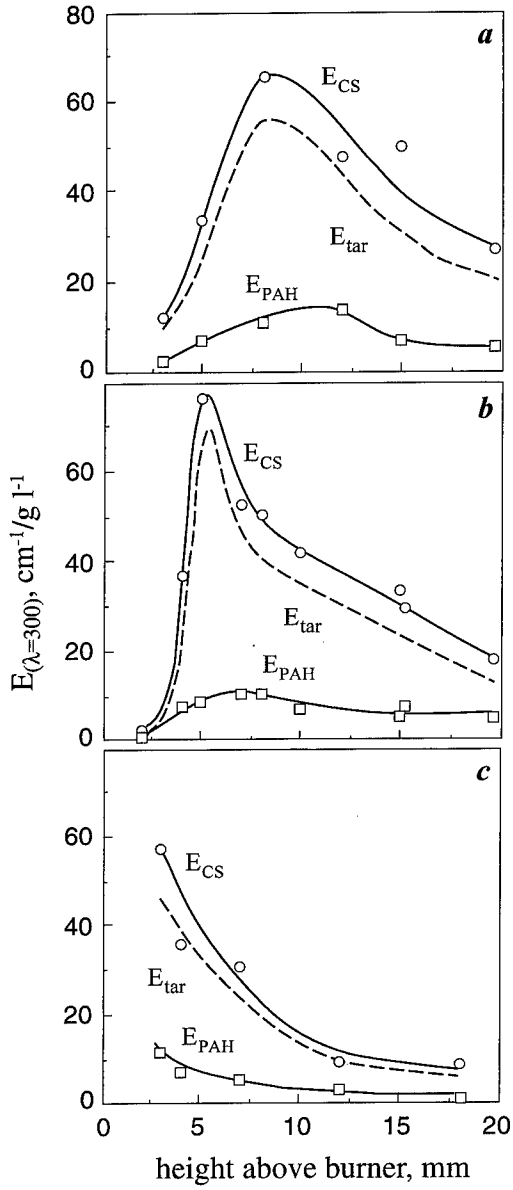

FIG. 4. Absorptivity profiles of CS, PAHs, and tarlike species at λ = 300 nm in flames with different cold-gas flow velocities: (a) v = 2 cm/s, (b) v = 4 cm/s and (c) v = 6 cm/s.

Polycyclic aromatic hydrocarbon absorptivity profiles follow the CS profiles, but as already found for

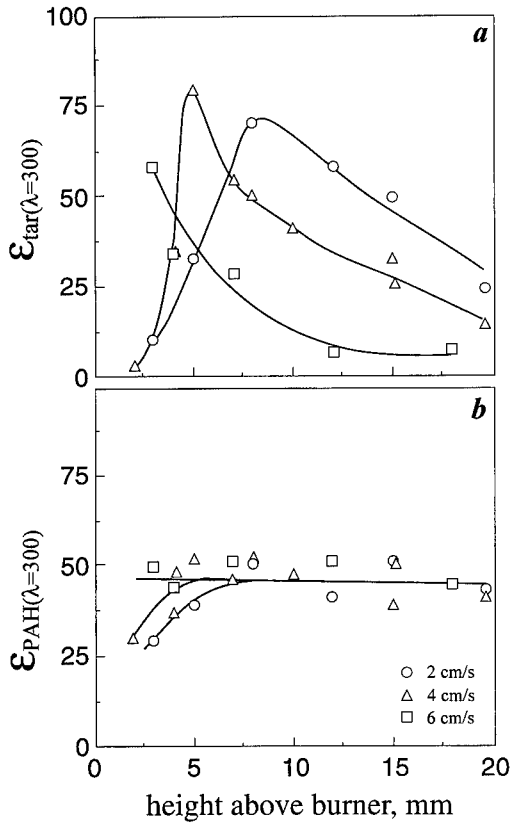

FIG. 5. Axial profiles of specific absorptivity of (a) tarlike species ε_{tar} and (b) PAHs ε_{PAH} in flames with different cold-gas flow velocities.

the gravimetric balance, PAH presence does not explain the CS absorptivity. Other unidentified species with a large absorptivity must contribute to CS absorptivity.

The absorptivity of the unidentified species, named tarlike species, was calculated by subtracting the total PAH absorptivity E_{PAH} from the CS absorptivity E_{CS}, and is denoted in Fig. 4 by a dashed line. The specific absorptivity of tar can be obtained by dividing its absorptivity by the weight contribution to the CS (y_{tar} = weight tar/weight CS):

$$\frac{E_{CS} - E_{PAH}}{y_{tar}} = \varepsilon_{tar}$$

The axial profile of ε_{tar}, reported in Fig. 5a, follows the same trend as that of CS absorptivity, showing a peak value at the same point as that of soot inception (Fig. 2). Downstream from the peak value, the specific absorptivity decreases toward a value that increases as the flame temperature decreases. The specific absorptivity of the PAH mixture ($\varepsilon_{PAH} = E_{PAH}/y_{PAH}$) immediately rises at the beginning of the flame (Fig. 5b) to a value that remains constant along the flame axis, and does not significantly change by varying the flame temperature.

Discussion

The existence of a temperature domain in which soot concentration shows a bell-shaped profile has been demonstrated in both premixed flames and shock tube pyrolysis experiments [1,7,8]. In this work, the flame temperature of premixed C_2H_4/O_2 flames was influenced by changing the cold-gas flow velocity covering the maximum temperature range between 1520 and 1820 K. In this range, soot concentration passes through a maximum at 1720 K, which is in agreement with the results obtained by Wagner et al. [1] in premixed flames and by Graham [7] and Frenklach et al. [8] in shock tube experiments. Conversely, PAH formation is favored at the lower flame temperature (1520 K) and steeply decreases in the temperature range investigated.

The ultimate C_2H_2 loading is not dependent on the flame temperature even though some differences exist in the shape of the profiles along the flame axis of the three flames. These differences can also be observed in the concentration profiles of other species (benzene, soot, and PAHs) and are due mainly to the strong effect of flame temperature on the burning velocity and, in turn, on the flame structure. In particular, in the higher-flame-temperature regime, the most important compositional changes occur near the burner. Here, pyrolytic and oxidative regions overlap, favoring C_2H_4 pyrolysis, which leads to a large production of C_2H_2 within the primary oxidation zone of the flame (Fig. 1b). Conversely, the formation of benzene, PAHs, and condensed species is depressed in high-temperature conditions: benzene and PAHs disappear almost completely downstream in the flame (Fig. 2c).

At the intermediate flame temperature level, the yield of C_2H_2 in the primary oxidation zone is slightly lower (Fig. 1b), whereas benzene and PAH formation is enhanced (Fig. 2b) with respect to the hotter flame (Fig. 2c). Their further oxidation seems to be less active than in the higher temperature conditions, as shown by the slower decrease of concentrations of C_2H_2, benzene, and PAHs at the end of the primary oxidation zone (Figs. 1b and 2b). Later, benzene and PAH concentrations show a second increase, as usually observed in aliphatic fuel flames [2–6].

In the lower-flame-temperature conditions, C_2H_4 dehydrogenation leading to C_2H_2 formation is depressed, whereas the net production of benzene and PAHs is increased. Acetylene and benzene concentrations attain an almost constant value downstream of the flame front because the temperature is too

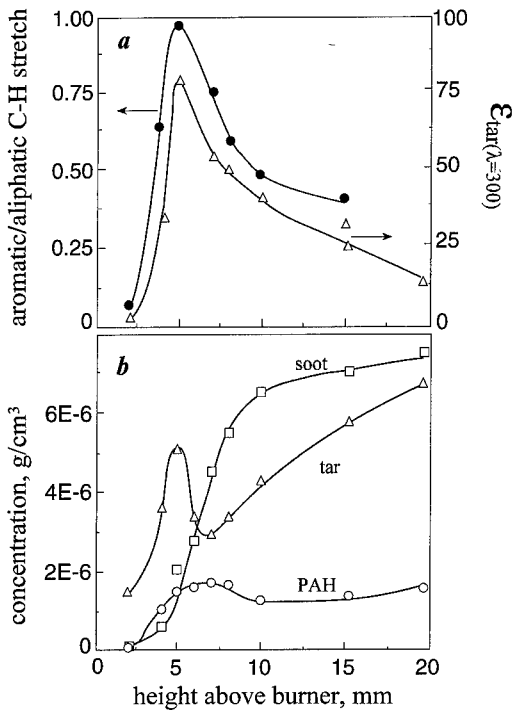

FIG. 6. (a) Infrared aromatic to aliphatic C—H stretch and ultraviolet absorptivity and (b) soot, PAHs, and tar concentration profiles for the flame at $v = 4$ cm/s.

low to favor their further oxidation. In spite of the lower oxidative effectiveness, PAH and CS profiles exhibit a significant decrease downstream in the flame, which cannot be attributed merely to oxidation.

As already discussed, the maximum formation of PAHs occurs at a lower temperature than with the maximum formation of soot, even though the temperature range covered in this work was not extended enough to embrace the bell-shaped profile for PAHs. This indicates that a relationship exists between PAH formation and soot formation, but the same behavior can be observed in the trends of more abundant species such as benzene and CS (Fig. 2). Moreover, it is worth emphasizing that as previously reported [2,9], PAHs constitute only a fraction of the condensable species formed in rich combustion (Figs. 2 and 3), the remainder being species of aromatic character but of unknown chemical composition [2,10]. The presence of these tarlike species has also been revealed by Howard and co-workers [11–13] in the postoxidation zone of aliphatic and aromatic hydrocarbon flames and by Dobbins and coworkers [14,15] in the fuel-rich side of diffusion flames.

Because tarlike material is soluble in DCM, its molecular weight should be lower than that of soot particles but higher than 300 u because it is not analyzable by GC and liquid chromatography (LC) techniques, whose mass limits are ca. 300 u. The mass spectrometric analysis of these species directly injected by a particle beam generator into the mass spectrometer has shown the presence of condensed PAHs with molecular mass between 300 and 500 u, but these species constitute only a negligible portion of the tarlike material.

Evaluation of the spectroscopic characteristics of CS in the ultraviolet region has shown that the chemical nature of the tar species changes along the flame, as shown by the change of the ultraviolet-visible absorption (Fig. 4). Conversely, the class of identified PAHs shows an almost constant absorptivity along the flame because PAH distribution inside the CS was almost the same in every flame condition.

The specific absorptivity of tar is lower than that of PAHs within the main oxidation zone of the flame (Fig. 5), showing that these compounds at the beginning of the flame are structures in which aromatic and aliphatic functionalities coexist. By increasing the residence time, the specific absorptivity of tar increases, exceeding that of PAHs (Fig. 5). This may be due to the cleavage of alkyl radicals and the loss of aliphatic character or to a dehydrogenation process, with the consequent increase of the aromatic character of tar up to a maximum in correspondence to soot inception.

This can be seen more clearly in Fig. 6, where the spectroscopic characteristics (ultraviolet absorptivity and the ratio of infrared aromatic to aliphatic C—H stretch signals) of the tarlike species are reported for the intermediate temperature flame, along with the concentrations of soot, PAHs, and tar. Both the specific absorptivity and the infrared aromaticity of tar increase up to a maximum value that corresponds to the peak value of tar concentration. Thereafter, the concentration of tar and its aromatic character drop, occurring at the same time as soot nucleation. This indicates that the more-aromatic fraction of the tar participates in soot inception. The residual part of the tar has a low-aromatic character (low absorptivity and infrared aromatic to aliphatic C—H ratio) for further inception of soot nuclei. The tarlike species are newly formed at the end of the flame but with a rate lower than before because of the lower temperature, which also does not allow tar to undergo the aromatization process as shown by the low absorptivity and infrared aromaticity measured in the postinception region of the flame.

Polycyclic aromatic hydrocarbon molecules contribute indirectly to the soot-inception process, being the building blocks of tar species and participating with C_2H_2 to the following surface growth process. It is worth noting that the second increase in PAH concentration occurs only when soot particles are no longer active for surface growth and, hence, when soot concentration reaches its final

value, whereas the second increase in the tarlike species is always observed to occur just after the soot nucleation zone.

Conclusions

The effect of flame temperature on the soot inception process in a range in which soot concentration exhibits the bell-shaped curve has been followed by measuring the concentration and spectroscopic characterization of PAHs and tar species. At a high flame temperature, oxidation is very active in the secondary zone of the flame, thus consuming PAHs, which in turn are not able to form the tarlike species postulated to be soot precursors on the basis of their concentration profiles and spectroscopic characteristics. As a consequence, soot inception and growth are reduced. The concentration of PAHs and tarlike species cannot increase again in the postoxidation zone of the flame because of the high temperature conditions.

In the lower-temperature flames, the secondary oxidation process is less effective and the net production of PAHs is larger compared to those of the intermediate-temperature flames. Nevertheless, the temperature is too low to favor PAH coagulation into tar and the subsequent transformation of tar into soot nuclei. In the intermediate-temperature flame, where maximum soot formation was found, the temperature level is ideal for the formation of both PAHs and tar and their transformation to soot particles.

REFERENCES

1. Bohm, H., Hesse, D., Jander, H., Luers, B., Pietscher, J., Wagner, H. G., and Weiss, M., *Twenty-Second Symposium (International) on Combustion,* The Combustion Institute, Pittsburgh, 1988, pp. 403–411.
2. Ciajolo, A., D'Anna, A., Barbella, R., and Tregrossi, A., *Twenty-Fifth Symposium (International) on Combustion,* The Combustion Institute, Pittsburgh, 1994, pp. 679–685.
3. Homann, K. H., *Twentieth Symposium (International) on Combustion,* The Combustion Institute, Pittsburgh, 1985, pp. 857–870.
4. Bockhorn, H., Fetting F., and Wenz H. W., *Ber. Bunsenges. Phys. Chem.* 87:1067 (1983).
5. Bockhorn, H., Fetting F., Heddrich, A., and Wannemacher G., *Twentieth Symposium (International) on Combustion,* The Combustion Institute, Pittsburgh, 1984, pp. 979–988.
6. Haynes, B. S., in *Fossil Fuel Combustion* (Bartok, W. and Sarofim, A. F., Eds.), Wiley, New York 1991, pp. 261–326.
7. Graham, S. C., *Proc. R. London, Ser. Soc. A* 377:119 (1981).
8. Frenklach, M., Clary, D. W., Gardiner, W. C., and Stein, S. E., *Twenty-First Symposium (International) on Combustion,* The Combustion Institute, Pittsburgh, 1988, pp. 1067–1076.
9. D'Alessio, A., D'Anna, A., D'Orsi, A., Minutolo, P., Barbella, R., and Ciajolo, A., *Twenty-Fourth Symposium (International) on Combustion,* The Combustion Institute, Pittsburgh, 1992, p. 973.
10. Ciajolo, A., D'Anna, A., and Barbella, R., *Combust. Sci. Technol.,* 100:271 (1994).
11. Lam, F. W., Howard J. B., and Longwell, J. P., *Twenty-Second Symposium (International) on Combustion,* The Combustion Institute, Pittsburgh, 1988, pp. 323–332.
12. Lam, F. W., Longwell, J. P., and Howard J. B., *Twenty-Third Symposium (International) on Combustion,* The Combustion Institute, Pittsburgh, 1990, pp. 1477–1484.
13. McKinnon, J. T. and Howard, J. B., *Twenty-Fourth Symposium (International) on Combustion,* The Combustion Institute, Pittsburgh, 1992, pp. 965–971.
14. Dobbins, R. A. and Subramaniasivam, H., in *Mechanisms and Models of Soot Formation* (Bockhorn, Ed.), Springer-Verlag, Heidelberg, 1994, pp. 290–301.
15. Dobbins, R. A. and Fletcher, R. A., *Combust. Flame* 100:301 (1995).

Twenty-Sixth Symposium (International) on Combustion/The Combustion Institute, 1996/pp. 2335–2341

POLYCYCLIC AROMATIC HYDROCARBON AND SOOT FORMATION IN PREMIXED FLAMES OF CH_3Cl/CH_4 AND CH_4

JIAWEI HUANG AND SELIM M. SENKAN
Department of Chemical Engineering
University of California
Los Angeles, California 90024, USA

The microstructures of atmospheric-pressure, laminar, premixed flames of CH_3Cl/CH_4 and CH_4 have been studied under similar fuel-rich ($\phi = 2.5$) and carbon density (1.9×10^{-5} mole/cm^3) conditions using both heated microprobe and cold-trap sampling, followed by analysis by gas chromatography/mass spectrometry (GC/MS). The mole fraction profiles of a large number of species, including aromatic and polycyclic aromatic hydrocarbons (PAHs) have been determined. In addition, the temperature and relative soot profiles were obtained using thermocouples and He-Ne laser light extinction measurements, respectively. These experiments indicated that although the CH_3Cl/CH_4 flame was more sooting, the levels of all the aromatics and PAHs were significantly lower, some by as much as a factor of 10, than the CH_4 flame in the postflame zones. This is a surprising result that contradicts the generally held belief that increased soot formation is associated with higher PAH levels. These measurements also provide new information on flame chemistry and suggest that the major effect of chlorine is the rapid incorporation of PAHs into soot.

Introduction

Polycyclic aromatic hydrocarbons (PAHs), which are formed at trace levels in combustion and incineration processes, are of considerable practical interest because of the potential toxicities of some PAH isomers [1,2]. In addition, PAHs are believed to play a major role in soot formation and growth [1,3–5]. The effects of chlorine on PAHs and soot formation in flames is also of practical importance because chlorinated hydrocarbons (CHCs) are major components of many industrial wastes that are treated by combustion/incineration for their ultimate disposal.

It is well known that chlorine or chlorinated hydrocarbons promote soot formation in flames [6]. Since PAHs are believed to be soot precursors, the promotion of soot by chlorine has been attributed to increased PAH formation [7].

Previously, the oxidation and pyrolysis of CH_3Cl was studied in premixed laminar flames in the presence of CH_4 by Karra and Senkan [8], and more recently by Wang et al. [9], where the emphasis was on the formation of CO, CO_2, and C_2 products. Related studies in flow reactors were also conducted [10–14]. Probably the most relevant prior work is the jet-stirred tank/plug flow reactor study of Marr et al. [15], where the effects of postflame additions of CH_3Cl on PAH formation in ethylene combustion was studied. These investigators used a water-cooled probe to withdraw samples from the plug-flow section of the reactor, and determined the amounts of PAHs formed by analyzing the solvent extracts. The levels of most PAHs formed in the presence of CH_3Cl were generally higher within the conditions investigated, with the exception of cyclopenta[*cd*]pyrene whose mole fractions were lower.

In this paper, we compare the microstructures of atmospheric-pressure, laminar, premixed, flat flames of CH_3Cl/CH_4 and CH_4 under similar, fuel-rich conditions, with particular emphasis on aromatics and PAHs.

Experimental

The atmospheric-pressure, premixed, laminar, flat flames studied were stabilized over a 50-mm-diameter porous bronze burner with an argon shroud [16]. Gases were introduced using high-accuracy mass flow meters (MKS, Burlington, MA). Flame sampling was accomplished using an air-heated microprobe that had a 0.150-mm orifice at its tapered tip [16]. A quartz wool filter was also used to remove soot particles. The sampling system, which includes the probe, the soot filter, transfer lines, and GC valves, was maintained at about 300°C and at subambient pressures to minimize the condensation and/or adsorption of PAHs on surfaces.

The samples withdrawn from within the flame were then directly analyzed using a gas chromatograph/mass spectrometer (Hewlett-Packard 5890/5972A, GC/MS) without preconcentration [16].

Identification of species was accomplished by matching the GC retention times to pure components as well as the mass spectral fragmentation pat-

TABLE 1
Precombustion conditions of the flames studied

Parameters flame	CH_3Cl/CH_4	CH_4
Equivalence ratio	2.5	2.5
C/O ratio	0.71	0.63
Cold gas velocity (cm/s)	4.46	5.17
Carbon density (mole/cm^3 at 298 K)	1.9×10^{-5}	1.9×10^{-5}
Ar(%)	19	14.7
CH_3Cl(%)	23.8	–
CH_4(%)	23.8	47.4
O_2(%)	33.4	37.9

terns to MS libraries. Species mole fractions were then determined using multilevel calibration mixtures with an estimated accuracy of about ±15% for major species and ±20% for the remaining ones. For species for which calibration standards were not available, the relative ionization cross section method was used [17]. This method has been shown to be accurate to within a factor of 2 in our prior experiments [16]. Species profiles were generated by moving the burner relative to the stationary quartz probe with the aid of a vertical translator having a precision of about 0.01 mm.

Temperature profiles were measured by using a 0.075-mm Pt-Pt/13%-Rh thermocouple with a bead diameter of about 0.15 mm. It was freshly coated with silica and vitrified to minimize catalysis, and was kept in the flame for as short time as possible to minimize soot accumulation. The clean thermocouple was inserted into the flame at a predetermined location and the temperature reading was recorded promptly. Following the temperature measurement, the thermocouple was withdrawn and the accumulated soot was burned off using a small propane torch. The cleaned thermocouple was then reinserted into the flame for the measurement of the temperature at another position. The temperature profiles reported here were also corrected for radiation losses by assuming an emissivity of 0.2 for the bare and 0.5 for the soot-coated thermocouple [18]. Thermocouple measurements were used to ascertain the absence of radial variations in flame properties.

Early in the experiments, we discovered that some of the two- and four-ring PAH species had been subject to surface-catalyzed chlorinations at sampling line temperatures of around 300°C. This problem was addressed by developing and using additional sampling procedures that minimize surface reactions and by modifying the results from the direct, on-line sampling procedure described above. In the first procedure, the temperature of the entire sampling system was reduced to about 120°C. Although these experiments did not allow for the direct determination of PAHs, as they readily adsorb on surfaces at 120°C, we were able to confirm that the concentrations of major species and one-ring aromatics were not affected by surface reactions at 300°C sampling temperatures.

In the second procedure, a cold-trap system was developed to determine the levels of heavier PAHs. In this case, the microprobe was cooled by circulating room-temperature air through it (about 25°C). The probe was also connected to a 600 cm^3 steel tank. Flame sampling was accomplished by evacuating the tank to about 10^{-3} torr using a mechanical vacuum pump, and by filling it with samples withdrawn from within the flame through the probe until the pressure in the tank reached 80 torr. This ensured the acquisition of the same amount of sample each time. The sampling time varied between 12 and 15 s, depending on the flame and the distance above the burner. After the experiment, the probe and quartz wool filter (where most of the high molecular weight PAHs were retained) were washed with methylene chloride. The liquid extracts were then concentrated to 2.5 cm^3, and 5-μl samples were injected to the GC/MS for analysis. This process was repeated both for the CH_3Cl/CH_4 and CH_4 flames. Since there are no complicating surface reactions in sampling CH_4 flames [16], PAHs determined by direct gas analysis of this flame were used to calibrate the results of the cold-trap experiments.

A helium-neon gas laser (Model 1508-O, Uniphase) was used to determine the relative soot volume fraction profiles in the flames. For this, the laser beam was passed through the center of the flame parallel to the burner surface, and the intensity was monitored by a power meter to determine the transmitted light. The burner was then moved up and down to generate light transmission profiles, which are related to soot volume fraction profiles [4,19].

Results and Discussion

The precombustion compositions and other parameters of the $CH_3Cl/CH_4/O_2/Ar$ and the $CH_4/O_2/Ar$ flames studied are listed in Table 1. As can be seen from this table, the two flames had the same equivalence ratio (2.5 by considering H_2O, CO_2, and HCl as the preferred combustion products) and carbon density (1.9×10^{-5} mole/cm^3 at 1 atm and 298 K). We also tested these flames at the same equivalence ratio and argon dilutions, leading to closer peak temperatures and burning velocities, with similar results and conclusions described later.

In each flame, we were able to quantify over 50 species, including CO, CO_2, H_2O, H_2, HCl, and C_1–C_{18} hydrocarbons and their chlorinated analogs, including a large number of aromatics and PAHs. These measurements covered a mole fraction range

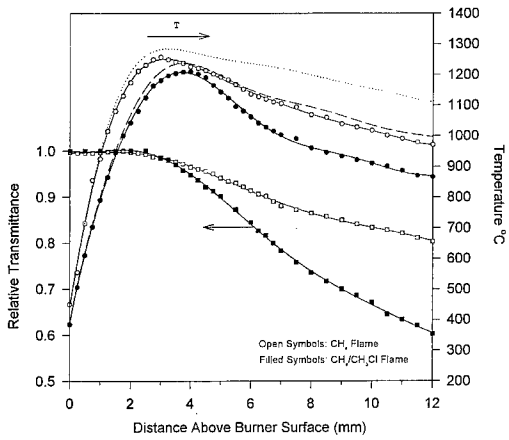

FIG. 1. Relative transmittance and temperature profiles along the flames. Dashed lines are temperature profiles corrected for radiation.

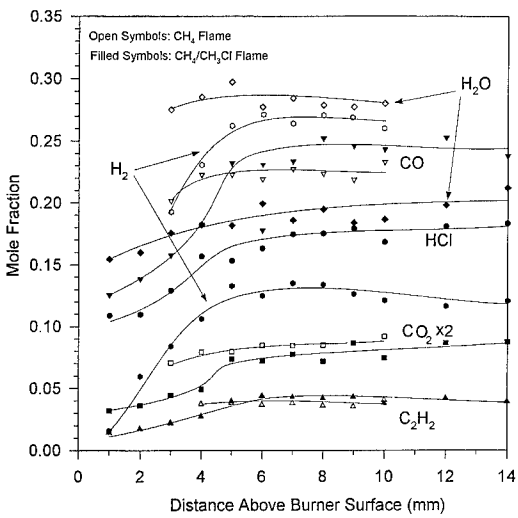

FIG. 2. Comparison of mole fraction profiles for major products.

of 0.25–1 $\times$ 10^{-7}. Space limitations prevent us from presenting all the measurements, thus we will emphasize comparisons of major and trace aromatic and polyaromatic species. However, it is significant to note that regular (i.e., nonchlorinated) polycyclic aromatic hydrocarbons dominated the PAH abundance in the CH_3Cl/CH_4 flame. Although some chlorinated hydrocarbon byproducts were formed, the levels of these CHCs were below 500 ppm [20]. Species mole fraction profiles not reported here due to length restrictions can be obtained upon request from the authors.

A number of practical difficulties exist in the acquisition of accurate flame structure data from atmospheric-pressure, premixed flames. These difficulties include probe-induced distortions in the concentration profiles due to flame attachment and spatial averaging, especially in regions of steep concentration gradients, and the possible continuation of reactions in the sampling probe and transfer lines. We have expended considerable time and effort in the past to develop optimal flame sampling techniques, and these are discussed in our earlier publications [16,20].

In Fig. 1, the temperature and laser beam transmission profiles for the two flames are presented. Although we did not quantify the actual soot volume fractions, it is very clear from these data that the CH_3Cl/CH_4 flame was more sooting than the CH_4 flame, and that soot formation began at about 4 mm from the burner surface. In addition, the CH_4 flame was hotter than the CH_3Cl/CH_4 flame and peaked slightly earlier. Lower temperatures in the CH_3Cl/CH_4 flame can be attributed to more soot formation in this mixture.

In Fig. 2, the mole fraction profiles for the major products, which include CO, CO_2, HCl, H_2, H_2O, and C_2H_2 for the CH_3Cl/CH_4 flame (filled symbols), are compared to the CH_4 flame (open symbols). In this and subsequent figures, lines have been drawn through the data points to indicate trends. It should be noted that data points within 1–2 mm from the burner should be considered unreliable because of probe-burner interactions. The growth rate of soot has been suggested to be directly proportional to C_2H_2 concentration and surface area [21]. As can be seen from Fig. 2, the levels of C_2H_2 were only slightly higher in the CH_3Cl/CH_4 postflame zone. The fact that these two flames had similar C_2H_2 concentrations, yet different soot levels, raises questions regarding the role acetylene plays in soot and PAH formation.

It is also evident from Fig. 2 that the levels of H_2 and H_2O were substantially higher in the CH_4 flame than the CH_3Cl/CH_4 flame. This, however, is not surprising, as the formation of HCl (ca. 18% in the postflame zone) ties up substantial amounts of hydrogen because it is the preferred combustion product for chlorine.

In Figs. 3 and 4, the mole fraction profiles are presented for C_3–C_6 hydrocarbon intermediates which include C_3H_4(CH_2CCH_2 and CH_3CCH), C_4H_2, C_4H_4, C_4H_6(CH_3CCCH), C_5H_6(cyclopentadiene), C_6H_2(CHCCCCCH), and C_6H_4(3-hexen-1,5-diene). As can be seen from these figures, the concentrations of species with C/H ratios less than 1 (C_3H_4, C_4H_6, and C_5H_6) were higher in the CH_4 flame, and concentrations of all the species with a C/H ratio larger than or equal to 1(C_4H_2, C_4H_4, C_6H_2, and C_6H_4) were higher in the CH_3Cl/CH_4 flame. These results are consistent with the availability of more hydrogen atoms in the CH_4 flame. C_4H_2 and C_3H_4 were the most abundant species in this group for both flames. As seen in Fig. 4, C_4H_4 mole fractions

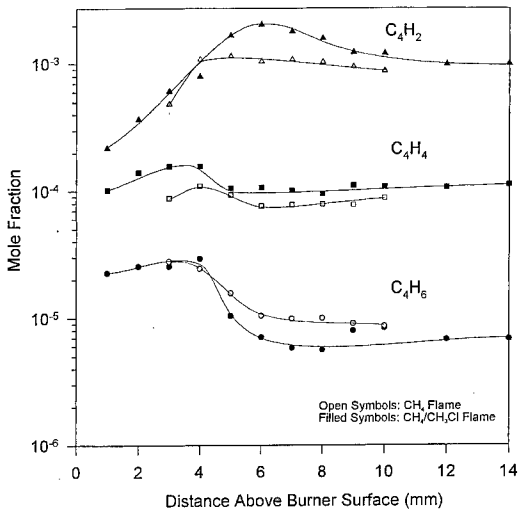

FIG. 3. Comparison of mole fraction profiles for C_4 aliphatic species.

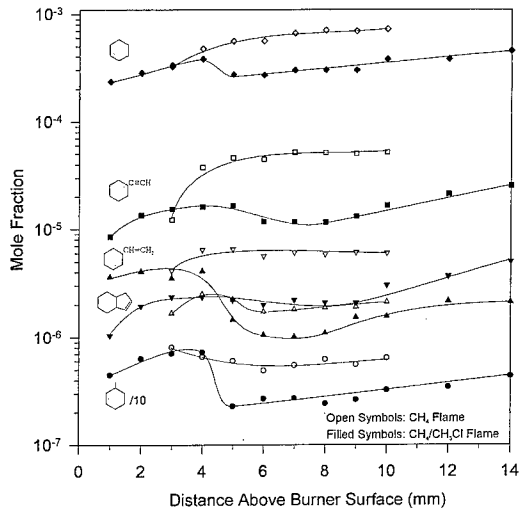

FIG. 5. Comparison of mole fraction profiles for 1-ring aromatic species.

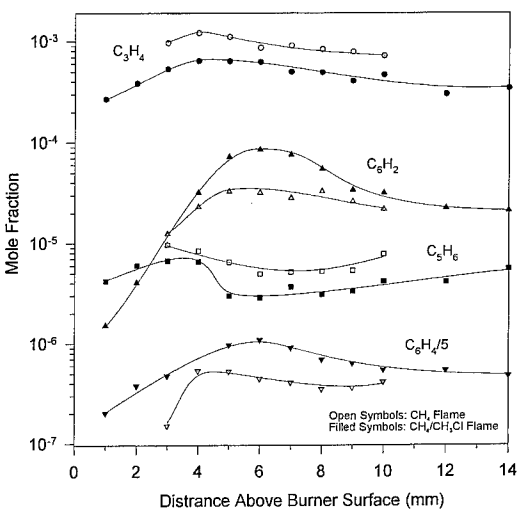

FIG. 4. Comparison of mole fraction profiles for C_3, C_5 and C_6 aliphatic species.

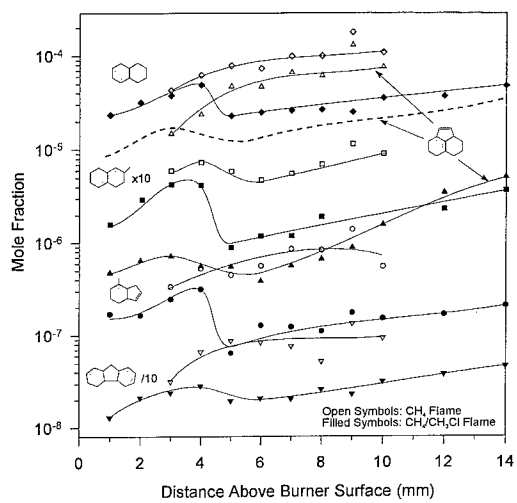

FIG. 6. Comparison of mole fraction profiles for two-ring aromatic species. Dashed line is the acenaphtylene profile determined by the cold-trap sampling procedure.

were a factor of 10 lower than those of C_4H_2, and those for C_4H_6 were lower by another factor of about 6.

In Fig. 5, the mole fraction profiles of one-ring aromatic hydrocarbons formed are presented. Benzene was the most abundant in this group reaching levels as high as 200–800 ppm, followed by phenylacetylene (20–50 ppm), toluene (3–8 ppm), and styrene (1–5 ppm). The most significant aspect of the results presented in Fig. 5 is that above 4 mm from the burner surface, where soot formation also sets in (Fig. 1), the concentrations of all of these aromatics in the CH_3Cl/CH_4 flame were significantly lower than those in the CH_4 flame, by at least a factor of 2. This is a surprising result because higher levels of aromatics are generally associated with more sooting flames [1,3,4].

The mole fraction profiles of PAHs also exhibited trends similar to the one-ring aromatics described above, and the PAH levels in the CH_3Cl/CH_4 flame were substantially lower than the CH_4 flame. In Fig. 6, the concentration profiles of two-ring PAHs are

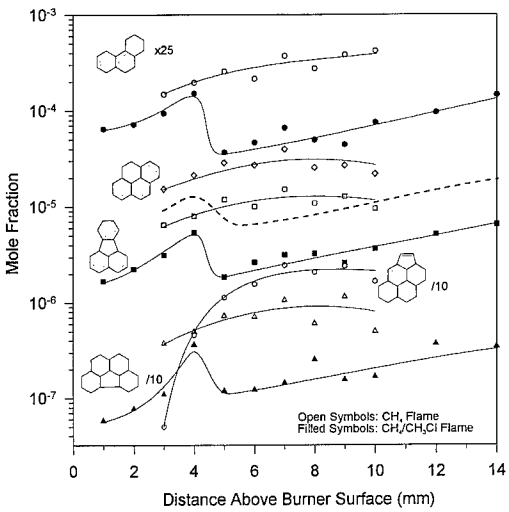

FIG. 7. Comparison of mole fraction profiles for two-ring aromatic species. Dashed line is the pyrene profile determined by the cold-trap sampling procedure.

presented. Naphthalene ($C_{10}H_8$) was the most abundant species in this group with mole fractions in the CH_4 flame being nearly a factor of 4 higher than in the CH_3Cl/CH_4 flame. Naphthalene is followed by acenaphthylene ($C_{12}H_8$), methyl naphthalene ($C_{11}H_{10}$), methyl indene ($C_{10}H_{10}$), and fluorene ($C_{13}H_{10}$), with similar postflame ratios between the two flames. It should be noted that for the case of acenaphthylene, its mole fraction profile in the CH_3Cl/CH_4 flame was determined both by direct sampling and analysis (filled triangles) and by the cold-trap sampling and solvent extraction procedure (dashed lines). The latter was necessitated by the chlorination of acenaphthylene in the heated sampling probe and transfer lines.

In Fig. 7, the mole fraction profiles of three- and four-ring PAHs are presented. These PAHs include phenanthrene ($C_{14}H_{10}$), pyrene ($C_{16}H_{10}$), fluoranthene ($C_{16}H_{10}$), cyclopenta[*cd*]pyrene ($C_{18}H_{10}$), and benzo[*ghi*]fluoranthene ($C_{18}H_{10}$). As evident from this figure, concentration profiles of these PAHs also followed the same pattern, with mole fractions in the CH_3Cl/CH_4 flame being significantly lower than in the CH_4 flame. In fact, the differences in mole fractions between the two flames were as high as a factor of 10 for the case of phenanthrene. When CH_3Cl flame samples were first directly analyzed, neither pyrene nor cyclopenta[*cd*]pyrene were detected. Instead, fluoranthene was the only $C_{16}H_{10}$ isomer observed. In addition, significant levels of chlorinated pyrenes were also noted in samples analyzed directly [20]. The analysis of cold-trap samples, however, indicated the presence of significantly higher levels of pyrene than fluoranthene, with fluoranthene levels virtually identical to those determined using the heated sampling probe. These results indicate that the heated sampling probe and/or transfer lines must have selectively chlorinated pyrene, but not fluoranthene. The reasons for these intriguing results are not clear and are being investigated. The mole fraction profile of pyrene determined by the cold-trap technique is indicated by the dashed line in Fig. 7. Chlorine also suppressed the formation of cyclopenta[*cd*]pyrene to undetectable levels, a result which is consistent with previous studies [15].

Although we are not in a position to predict quantitatively the surprising result that chlorine reduces PAH levels while promoting soot formation, several explanations can be offered. The first and most likely scenario is that chlorine accelerates PAH conversion to soot. Second, chlorine may inhibit PAH formation in the first place and promote soot formation via reactions that do not involve PAHs.

In the first case, it is has been recognized that H radicals play a crucial role in activating PAHs and soot [3–5] in flames. The basic reactions can be represented by

$$\mathrm{PAH} + \mathrm{H} = \mathrm{PAH}^{\circ} + \mathrm{H}_2 \tag{1}$$

$$\mathrm{soot} + \mathrm{H} = \mathrm{soot}^{\circ} + \mathrm{H}_2 \tag{2}$$

where $^{\circ}$ indicates an activated, (i.e., radical) entity. In flames containing chlorine, additional reactions involving Cl radicals must also be considered as described by

$$\mathrm{PAH} + \mathrm{Cl} = \mathrm{PAH}^{\circ} + \mathrm{HCl} \tag{3}$$

$$\mathrm{soot} + \mathrm{Cl} = \mathrm{soot}^{\circ} + \mathrm{HCl} \tag{4}$$

The reactions 1–4 have equilibrium constants (K_p) in the range 1–10 at flame temperatures, thus the partial pressures of H_2 (P_{H2}) and HCl (P_{HCl}) would have a considerable effect on the fraction of PAH and soot that will be activated. Heterogeneous reactions 2 and 4 require special attention; in addition to reaction thermochemistry and kinetics, the rates of diffusion of species to soot surfaces, both external and internal [5], and sticking probabilities [22] must be considered in assessing their importance. Reaction 2 should remain dominant even in the CH_3Cl/CH_4 flame because of the higher diffusivities of H and H_2 relative to Cl and HCl. On the other hand, Cl and HCl would be favored species based on sticking potentials.

Once PAH$^{\circ}$ and soot$^{\circ}$ are generated, PAHs can be converted to soot via reactions such as

$$\mathrm{PAH}^{\circ} + \mathrm{soot}_i = \mathrm{soot}^{\circ}_{i+\mathrm{PAH}} \tag{6}$$

$$\mathrm{PAH} + \mathrm{soot}^{\circ}_i = \mathrm{soot}^{\circ}_{i+\mathrm{PAH}} \tag{7}$$

$$\mathrm{PAH}^{\circ} + \mathrm{soot}^{\circ}_i = \mathrm{soot}_{i+\mathrm{PAH}} \tag{8}$$

As can be seen in Fig. 2, postflame P_{H_2} in the CH_3Cl/CH_4 and CH_4 flames were 0.28 and 0.12 atm, respectively. Consequently, reactions 1 and 2

should proceed to the right more in the CH_3Cl/CH_4 flame than in the CH_4 flame. In this regard, it is important to note that chlorine only minimally alters the levels of H radicals in the postflame zone, because the following thermoneutral reaction

$$Cl + H_2 = HCl + H \quad (9)$$

whose $K_p = 1$, is rapidly equilibrated. In addition, reactions 3 and 4 would also be major contributors to PAH and soot activation in the CH_3Cl/CH_4 flame [7].

Chlorinated hydrocarbons also decompose at temperatures lower than the analogous hydrocarbons because of the relatively weak C–Cl bond [6]. Consequently, they can form a larger number of soot nuclei early in the flame, leading to higher surface area soot aerosols which can more efficiently scavenge the PAHs. All of these considerations suggest that PAHs are rapidly incorporated into soot in the CH_3Cl/CH_4 flame.

In the second case, CHCs may also suppress PAH formation because they are excellent H radical scavengers [6,23]. For example, the reaction

$$CH_3Cl + H = CH_3 + HCl \quad (10)$$

can effectively compete with reaction 1 or PAH precursors in the cooler (i.e., earlier) parts of the flame, thereby decreasing the rate of formation of PAHs. However, if this mechanism is true, then soot growth must occur via reactions that do not involve PAH. The direct addition of smaller hydrocarbons, such as C_2H_2, has been proposed to be such a soot growth species [3–5]. However, as noted before (see Fig. 2), C_2H_2 levels in the CH_3Cl/CH_4 flame were nearly the same in the postflame zone. Finally, oxidation cannot account for the lower PAH levels observed in the CH_3Cl/CH_4 flame because of the well-known flame inhibition characteristics of CHCs [23].

In summary, the microstructures of fuel-rich CH_3Cl/CH_4 and CH_4 flames, determined under similar equivalence ratio, carbon density, and argon dilution, indicate the formation of significantly lower concentrations of PAHs in the CH_3Cl/CH_4 flame than in the CH_4 flame, although the former was more sooting. These results are both surprising and significant because they invalidate the generally held belief that increased soot formation is associated with higher PAH levels. The measurements provide valuable new data for the development and verification of detailed reaction mechanisms, and suggest that the major effect of chlorine is the rapid incorporation of PAHs into soot.

Acknowledgments

This research was supported, in part, by the National Science Foundation CTS-9311848, the U.S. Environmental Protection Agency Grant No. R819178-01, and the UCLA Center for Clean Technology. We also thank I. Gargurevich for useful comments.

REFERENCES

1. Longwell, J. P., *Nineteenth Symposium (International) on Combustion,* The Combustion Institute, Pittsburgh, 1982, p. 1339.
2. Klaassen, C. D., Amdur, M. O., and Doull, J., *Casaret and Doull's Toxicology,* 2nd ed., Macmillan, New York, 1986.
3. Frenklach, M., Clary, D., Gardiner, Jr., W. C., and Stein, S. E., *Twentieth Symposium (International) on Combustion,* The Combustion Institute, Pittsburgh, 1984 p. 887, Frenklach, M. and Warnatz, J., *Combust. Sci. Technol.* 51:265 (1987); Kazakov, A., Wang, H., and Frenklach, M., *Combust. Flame* 100:111 (1995).
4. Bockhorn, H., (Ed.), *Soot Formation in Combustion: Mechanisms and Models,* Springer Verlag, Berlin, 1994.
5. Mauss, F., Schafer, T., and Bockhorn, H., *Combust. Flame* 99:697 (1994).
6. Senkan, S. M., Robinson, J. M., and Gupta, A. K., *Combust. Flame* 49:305 (1983).
7. Mckinnon, J. T. and Howard, J. B., *Combust. Sci. Technol.* 74:175 (1990); Frenklach, M., *Combust. Sci. Technol.* 74:283 (1990).
8. Karra, S. B., Gutman, D., and Senkan, S. M., *Combust. Sci. Technol.* 54:333 (1987).
9. Wang, L., Jalvy, P., and Barat, R. B., *Combust. Sci. Technol.* 97:13 (1994).
10. Mitchell, T. J., Benson, S. W., and Karra, S. B., *Combust. Sci. Technol.* 107:223 (1995); Weissman, M. and Benson, S. W., *Prog. Energy Combust. Sci.* 15:273 (1989); Weissman, M. and Benson, S. W., *Int. J. Chem. Kinetics* 16:307 (1984).
11. Granada, A., Karra, S. B., and Senkan, S. M., *Ind. Eng. Chem. Res.* 26:1901 (1987).
12. Fisher, E. M. and Koshland, C. P., *Combust. Flame* 90:185 (1992).
13. Ho, W. P., Yu, Q. R., and Bozzelli, J. W., *Combustion Sci. Technol.* 85:23 (1992).
14. Hung, S. and L. D., Pfefferle, *Combust. Sci. Technol.* 87:91 (1993).
15. Marr, J. A., Allison, D. M., Giovane, L. M., Yerkey, L. A., Monchamp, P., Longwell, J. P., and Howard, J. B., *Combust. Sci. Technol.* 85:65 (1992).
16. Castaldi, M. J., Vincitore, A., and Senkan, S. M., *Combust. Sci. Technol.* 107:1 (1995).
17. Fitch, W. L. and Sauter, A. D., *Anal. Chem.* 55:832 (1983).
18. Bradley, D., and Matthews, K. J., *J. Mech. Eng. Sci.* 10:299 (1968).
19. Prado, G. J. Jagoda, K. Neoh, and J. Lahaye, *Eighteenth Symposium (International) on Combustion,* The Combustion Institute, Pittsburgh, 1981, p. 1127.

20. Huang, J. W. and Senkan, S. M., *Environ. Sci. Technol.*, submitted.
21. Harris, S. J. and Weiner, A., *Combust. Sci. Technol.* 72:67 (1990).
22. Boudart, M. and Djega-Maridossou, G., *Kinetics of Heterogeneous Catalytic Reactions,* Princeton University Press, Princeton, NJ, 1984.
23. Valeiras, H., Gupta, A. K., and Senkan, S. M., *Combust. Sci. Technol.* 36:123 (1984).

COMMENTS

Kermit C. Smyth, NIST, USA. We have recently made measurements in propane and ethylene diffusion flames which also suggest that higher soot levels do not necessarily lead to higher PAH concentrations [1]. For both steady and flickering conditions, the peak soot concentrations in the ethylene flames are twice as high as in the propane flames, yet the PAH fluorescence is approximately twice as stronger for the propane flames.

REFERENCE

1. Smyth, K. C., Shaddix, C. R., and Everest, D. A., submitted to *Combust. Flame.*

Author's Reply. We are pleased to learn that our findings are corroborated by the measurements made in diffusion flames of propane and ethylene as well. We should point out that the lack of correlation between soot formation and PAH was first noted in our laboratories when comparing the chemical structures of fuel-rich (sooting) premixed flames of methane, ethane, and propane at the similar equivalence ratio of 2.5 and argon dilution [1]. This study led to the determination that, although the methane flame produced less soot than the ethane flame, the levels of PAH in the methane flame were higher than the ethane flame. On the other hand, the propane flame produced more soot than the ethane flame and slightly higher PAH levels than the methane flame.

REFERENCE

1. Senkan, S. M. and Castaldi, M. J., *Combust. Flame,* in press (1996).

Twenty-Sixth Symposium (International) on Combustion/The Combustion Institute, 1996/pp. 2343–2350

RE-INITIATION OF SOOT SURFACE GROWTH IN PREMIXED COUNTER-FLOW FLAMES

M. MARQUARDT AND F. MAUß
Fachbereich Chemie, Universität Kaiserslautern
Erwin Schrödinger Straße 54, 67663 Kaiserslautern
Federal Republic of Germany

B. JUNGFLEISCH, R. SUNTZ AND H. BOCKHORN
Institut für Chemische Technik, Universität Karlsruhe
Kaiserstraße 12, 76128 Karlsruhe
Federal Republic of Germany

In order to contribute to the discussion of the active-site approach for surface growth reactions versus recovery of radicalic surface sites by reactions with species from the gas phase, experiments in counterflow, premixed flames have been performed. Soot particles are generated in premixed, fuel-rich ethyne/argon/oxygen flames counterflowing against nonsooting flames of the same components or lean carbon monoxide/argon/oxygen flames. The nonsooting flames produce a high level of hydrogen atoms combined with a variation of the concentration of other gaseous species so that surface growth by H abstraction from C—H sites at the surface of soot particles may be reinitiated in the stagnation region of the sooting flame. These flames are compared with single, premixed, sooting flat flames in which the soot volume fraction attains a final plateau f_v^∞ due to the decay of surface growth. The experimental results clearly demonstrate that depending on the flow conditions in the counterflow flames, a second onset of soot formation is detected. This second onset of soot formation can be traced back to surface growth. The experimental findings are discussed by referring to results from modeling of these flames using the hydrogen-abstraction–hydrocarbon-addition (HACA) mechanism for surface growth. From this, a shift of the competing effects of surface growth and oxidation is identified to be responsible for the reinitiation of surface growth.

Introduction

Knowledge of soot formation in hydrocarbon flames has been considerably improved during recent years. The progress that has been achieved is documented in a number of experimental investigations of laboratory flames, experiments in shock tubes, and numerical modeling of sooting flames. Several reviews (e.g., [1–7]) provide a comprehensive view of the subject. Particularly, the growth of soot particles in laminar, premixed flames has been studied extensively [8–14].

It is well accepted that in premixed flames, the main processes of soot formation are particle inception, surface growth, and coagulation of soot particles. Particle inception and surface growth determine the total mass of soot, whereas particle coagulation only affects the size and the number density of the soot particles. It has been shown [9,11,12] that particle inception contributes only to a small fraction of the final soot mass, whereas the larger part of soot is formed by surface growth of the soot particles in later stages of soot formation. Therefore, numerous investigations and modeling have addressed surface growth of soot particles.

Surface growth of soot particles in premixed hydrocarbon flames is dominated by reactions of ethyne with the surface of soot particles. Other processes such as depiction of polycyclic aromatic hydrocarbons (PAHs) from the gas phase contribute comparably little to surface growth. One approach toward the understanding of surface growth of soot particles on the basis of a detailed reaction mechanism has been introduced in Refs. [15 and 16]. The basic principle of the mechanism, which has been adopted and extended by a number of authors [17–19], is the extension of the planar growth of PAHs according to a radicalic HACA sequence to surface growth of soot particles.

The sequence of reactions extended by the oxidation of soot particles with OH and O_2, reactions (5) and (4a and b) [20], is given in Table 1. Radicalic sites at the soot particle surface are formed by abstraction of H atoms from arylic C—H bonds by H and to a minor extent by OH radicals from the surrounding gas phase according to reactions (1a) and (1b) (see Table 1). The generated soot radicals are supposed to grow by the addition of ethyne. This is followed by a cyclization step and the cleavage of a

TABLE 1
HACA mechanism for surface growth of soot[a]

	reaction	k_0	E_A
1a	$C_{soot,i}H + H \overset{k_{1a}}{\leftrightarrow} C^{\bullet}_{soot,i} + H_2$	$1.2 \cdot 10^{14}$	21.8
1b	$C_{soot,i}H + OH \overset{k_{1b}}{\leftrightarrow} C^{\bullet}_{soot,i} + H_2O$	$1 \cdot 10^{12}$	54.2
2	$C^{\bullet}_{soot,i} + H \overset{k_2}{\rightarrow} C_{soot,i}H$	$1 \cdot 10^{13}$	
3a	$C^{\bullet}_{soot,i} + C_2H_2 \overset{k_{3a}}{\leftrightarrow} C^{\bullet}_{soot,i}\,C_2H_2$	$1 \cdot 10^{13}$	
3b	$C^{\bullet}_{soot,i}C_2H_2 \overset{k_{3b}}{\leftrightarrow} C_{soot,i+1}H + H$	$1 \cdot 10^{10}$	
4a	$C^{\bullet}_{soot,i} + O_2 \overset{k_{4a}}{\leftrightarrow} C^{\bullet}_{soot,i-1} + 2\,CO$	$2.5 \cdot 10^{12}$	
4b	$C^{\bullet}_{soot,i}C_2H_2 + O_2 \overset{k_{4b}}{\leftrightarrow} C^{\bullet}_{soot,i} + 2\,CHO$	$2.5 \cdot 10^{12}$	
5	$C_{soot,i}H + OH \overset{k_5}{\rightarrow} C^{\bullet}_{soot,i-1} + CH + CHO$	$7 \cdot 10^{13}$	

[a]See refs. 15–17.
Rate coefficients are given for forward reactions.
Units for k_0: cm^3, mol, s; Units for E_A: kJ mol^{-1}

C—H bond at the surface of the growing soot particle. The soot radicals either can add ethyne (reaction 3a) or are deactivated by the reverse reactions (−1a) or (−1b) by molecular hydrogen and water molecules, thereby being prevented from growing. Depending on the structure of the intermediate, ethynyl–soot radical, a further addition of ethyne may follow. The reaction route (3b) provides cyclization of the intermediate adducts to aromatic rings containing six carbon atoms that are stabilized by the cleavage of a C—H bond and incorporated into the growing soot particles. Similar reasoning may be applied to the formation of five-member rings or other cyclic structures.

Thermal cleavage of aryl C—H bonds according to the reverse reaction (−2) contributes negligibly to the formation of soot radicals, whereas the reverse reaction (2), namely, the deactivation of soot radicals by recombination with H atoms, may be important under certain conditions. Surface growth of soot by reactions with PAHs, compare Ref. 14, can be added easily to the reaction scheme.

Another approach to surface growth of soot particles employs the concept of active sites at the surface of the soot particles; compare, for example, Refs. 8–10. According to this, surface growth is dominated by the number of active sites accessible for heterogeneous decomposition of gaseous growths species (compare ethyne) that cover the surface and are not supposed to be affected by coagulation and surface growth of the soot particles. The loss of reactivity against surface growth is explained by a "tempering process" of the soot particles decreasing the number of active sites. In Ref. 21, experiments on sooting ethylene/air flames are reported where no correlations have been found between local conditions, especially concentrations of hydrogen atoms or the local temperature, and the number of active sites for surface growth. Other experiments [22,23] in premixed co-flowing acetylene/oxygen and hydrogen/oxygen flames under sooting and nonsooting conditions reveal that hydrogen atoms when diffusing into the soot-forming region may inhibit the surface growth.

To contribute to the discussion of the active site approach for surface growth reactions versus recovery of radicalic surface sites by reactions with species from the gas phase, experiments in counterflow, premixed twin flames are reported in the following. Soot particles are generated in a premixed, fuel-rich ethyne/argon/oxygen flame counterflowing against nonsooting flames of the same components or carbon monoxide/argon/oxygen flame. The nonsooting flames produce a high level of hydrogen atoms so that surface growth, according to reaction (1a), may be reinitiated in the stagnation region.

Experimental

A premixed, sooting ethyne/argon/oxygen flame, stabilized on a flat-flame burner, is counterflowing against a premixed, nonsooting flame of the same fuel or a carbon monoxide/argon/oxygen flame, stabilized on a second burner (compare Fig. 1). The experimental conditions of the flames are given in Table 2. Each of the two burners consists of a water-cooled brass plate with ca. 800 holes of 1-mm diameter uniformly distributed over a circular area of 80-mm diameter at the center of each burner. The

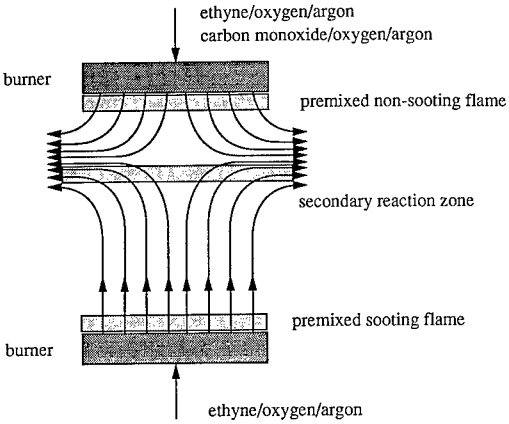

FIG. 1. Schematic of the counterflow, premixed flames.

distance between the opposite burners is 40 mm. For more details of the experimental setup, see Ref. 24.

The flames are investigated at low pressure (12 kPa) to obtain a better spatial resolution of the soot-formation zone. The burner system is equipped with all facilities for optical access. The measurements reported in this paper comprise soot volume fractions, mean particle radii, and number densities.

Extinction and Scattering Measurements

For extinction measurements, an argon-ion laser operating at a wavelength of 488 nm with a maximum power of 1.3 W was used as a light source. The optical path through the investigated flames was determined by shielding tubes purged with nitrogen.

Two-dimensional planar scattering measurements were performed with a vertically polarized laser light sheet, obtained by expanding the laser beam using two cylindrical lenses. The light scattered at 90° was analyzed with an intensified CCD camera (384 × 576 Pixel, 14-bit) with respect to its intensity, polarization, and wavelength. The scattering area of 40 mm in the radial direction and 27 mm in the axial direction was defined by a zoom objective in front of the camera. The scattering data are corrected with respect to thermal radiation of the flames. The experimental setup was calibrated with pure argon.

The extinction coefficients k_{ext} are evaluated with Lambert–Beer's law according to Eq. (1), where I_0 and I are the intensities of the incident and attenuated light, respectively, and d is the length of the optical path:

$$\ln \frac{I}{I_0} = -k_{ext} d \tag{1}$$

The soot volume fraction fv can be derived from Eq. (2), where m is the complex refractive index of the soot particles, λ the wavelength, and $f(r)$ the particle size distribution:

$$fv = \frac{-k_{ext}}{\frac{6\pi}{\lambda} Im\left(\frac{m^2 - 1}{m^2 + 2}\right)} = \frac{4}{3}\pi N_T \int_0^\infty r^3 f(r)\, dr \tag{2}$$

TABLE 2
Experimental conditions of the investigated flames

Sooting flame						
Flame no.[a]	Symbol	Ar[b]	O_2	C_2H_2	CO ratio	
1	□	200.0	59.2	74.1	1.25	
Counterflow flame fuel C_2H_2						
Flame no.	Symbol	Ar	O_2	C_2H_2	CO ratio	Stagnation plane[c]
a	+	200.6	95.2	38.1	0.40	h = 20 mm
b	○	120.0	57.1	22.9	0.40	h = 25 mm
Counterflow flame fuel CO						
Flame no.	Symbol	Ar	O_2	CO	CO ratio	Stagnation plane[c]
c	Δ	120.0	34.3	45.7	0.40	h = 25 mm

[a]Flames are referenced in the text by numbers; for example, flame 1 means sooting flame No. 1 without counterflow flame; flame 1c means sooting flame No. 1 with counterflow flame c (carbon monoxide), etc.

[b]Flow rates are given in l_N/h, pressure 12 kPa.

[c]The position of the stagnation plane is given relative to the lower burner.

Scattering from a laser light sheet gives a two-dimensional picture of the scattering coefficient Q_{vv}, which depends on local number density N_T and particle size according to Eq. (3), of the soot particles in the counterflow, premixed twin flames:

$$Q_{vv} = \frac{16\pi^4}{\lambda^4} \left|\frac{m^2 - 1}{m^2 + 2}\right|^2 N_T \int_O^\infty r^6 f(r)\, dr \qquad (3)$$

The scattering and extinction data are evaluated with respect to the median particle radius and the number density by the combination of Eqs. (2) and (3), assuming a complex refractive index of the soot particles of $m = 1.57 - 0.59i$ [25], a spherical shape of the soot particles, and a logarithmic normal-size distribution with a standard deviation of 0.34 [11]. The systematic errors arising from the assumptions are discussed in Ref. 11.

Modeling

Modeling of the investigated flames was performed by solving the one-dimensional convective-diffusive flame equations for flat flames or the convective-diffusive flame equations for counterflow flames as given in Ref. 17. All transport properties are calculated according to Ref. 26.

The gas-phase kinetics up to the formation of the first aromatic ring consisting of ca. 250 elementary reactions among 52 chemical species is taken from Ref. 27. The first aromatic ring (compare benzene) is supposed to be formed via the reaction $C_3H_3 + C_3H_3 \rightleftharpoons c - C_6H_6$. The further growth of benzene to small PAHs follows the mechanism suggested by Frenklach [15,16], assuming the growth of the PAHs being a fast polymerization process where quasi-stationarity can be applied to the single components.

The model encompasses two pathways to soot from PAHs (compare particle inception and deposition of PAHs at the surface of the soot particles). Both pathways are formulated by the coagulation equations with coagulation coefficients calculated using the free molecular regime approximations. The equations are also used to simulate coagulation of soot particles.

Heterogeneous surface growth and oxidation of soot particles follow the mechanism given in Table 1, which contains the following modifications, compared with the mechanism in Refs. 15 and 16. The reverse of reaction (1b) accounts for the radical site consuming influence of H_2O. The growth step consists of two reactions—carbon addition and ring closure—and the reverse of reactions (3a) accounts for the limitation of surface growth at high temperatures. More details of the model are given in Refs. 17 and 19.

The modeling leads to a finite number of differential equations for the mass fractions of each chemical species and an infinite number of differential equations for the number density of soot particles of each size class. The latter system of equations is reduced to a limited number by using the method of moments [16]. The energy equation is solved, including radiative heat losses, in the limit of the thin-gas approximation.

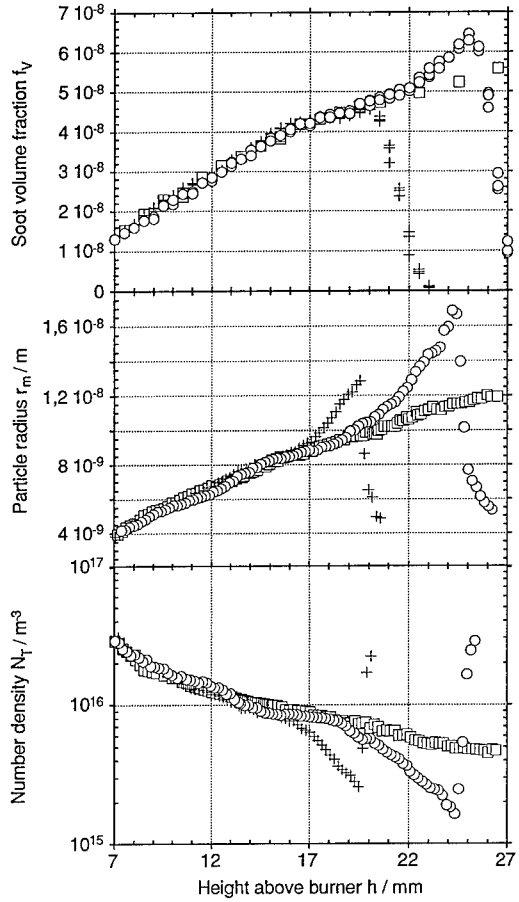

FIG. 2. Measured soot volume fractions f_V, mean particle radii r_m, and particle number densities N_T along the centerline of flames 1 (□), 1a (+), and 1b (○).

Results and Discussion

Profiles of soot volume fractions, mean particle radii of soot particles, and particle number densities along the centerline of flames 1, 1a, and 1b as evaluated from extinction and two-dimensional scattering are given in Fig. 2. Soot volume fractions increase continuously in flame 1 (without counterflow flame) and attain a final value f_v^∞ of about $6 \cdot 10^{-8}$ in the burned gas region of the flame. Particle number densities decrease according to coagulation of soot

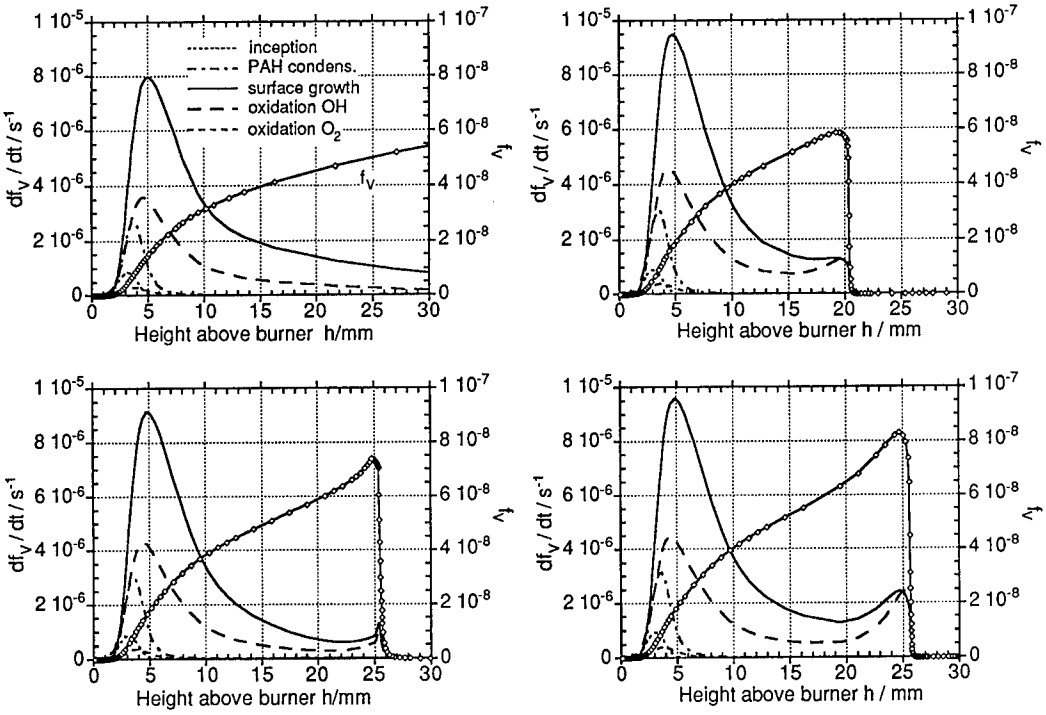

FIG. 3. Calculated soot volume fractions and contributions of particle inception, PAH condensation, surface growth, oxidation by OH, and oxidation by O_2 to the appearance rates of soot for flames 1 (upper left), 1a (upper right), 1b (lower left), and 1c (lower right).

particles, and consequently, the mean particle radii increase mainly because of coagulation.

In flame 1a (with counterflow flame), soot volume fractions increase similarly to those of flame 1 in the soot-forming region. Toward the stagnation plane of the counterflowing flame, the soot volume fractions decrease sharply due to oxidation of soot. In the region of the stagnation plane, particle number densities decrease faster, compared to flame 1. This is due to the beginning of oxidation of soot by which smallest particles are consumed completely. Consequently, the mean particle radii increase faster, compared to flame 1. Near the stagnation plane of the flames, particle number densities strongly increase and the mean radii strongly decrease. The increase of particle number density correlates with the burnout of the soot particles. This result agrees well with that of Neoh et al. [28] and may be explained with the internal burning of soot particles that leads to a breakup of the porous soot particles into smaller units.

Figure 3 (upper part) displays the calculated soot volume fractions at the centerline of flames 1 and 1a as well as the contributions of particle inception, surface growth, PAH condensation, and oxidation by OH and O_2 to the appearance rate of soot (oxidation by OH and O_2 are negative contributions). On the basis of the employed model, the major part of soot is formed by surface growth of soot particles. Figure 3 reveals that oxidation of soot by OH via reaction (5) from Table 1 competes with particle inception and surface growth as well at low heights above the burner. Other processes such as condensation of PAHs contribute little to the appearance rates under the prevailing experimental conditions.

At low heights above the burner, the profiles of the different contributions to the appearance rate are similar for both flames. However, near the stagnation plane of flame 1a, the oxidation rate via reaction (5) increases again so that the soot is consumed by oxidation. The oxidation by molecular oxygen in that region is negligible. Surface growth rates in flame 1a remain at relatively low values in the stagnation plane region because for the applied flow velocities and C/O ratios, the concentration profiles of OH and H level in such a way that initiation of surface growth via reaction (1a) and (1b) is overruled by oxidation by OH. It should be noted that the differences between surface growth rates and oxidation rates in the stagnation region are small when plotted versus the height above the burner. Because of the low flow velocities, reaction times are, however, very large. The calculated and measured soot volume fractions agree reasonably.

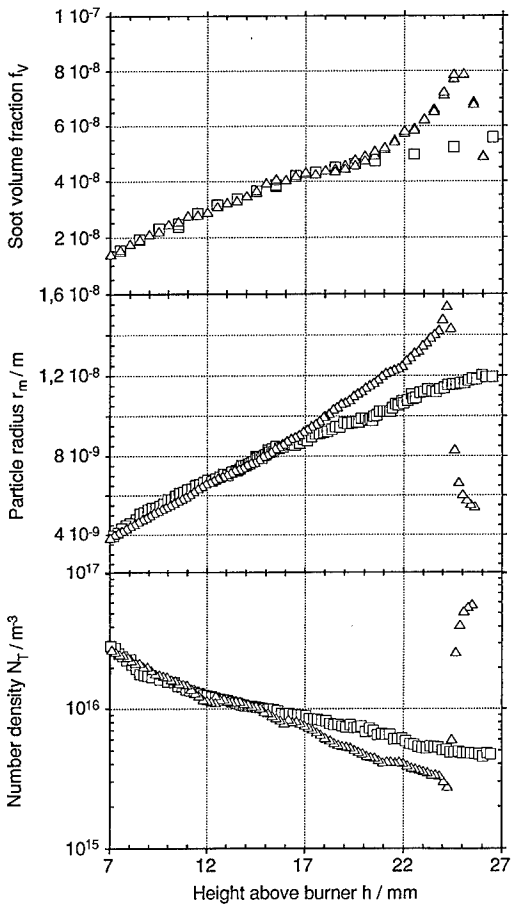

FIG. 4. Measured soot volume fractions f_V, mean particle radii r_m, and particle number densities N_T along the centerline of flames 1 (□) and 1c (△).

To distort the balance between oxidation via the reaction

$$C_{soot,i}H + OH \xrightarrow{k_5} C^*_{soot,i-1} + CH + CHO$$

and initiation of surface growth via the reactions

$$C_{soot,i}H + H \underset{k_{1b}}{\overset{k_{1a}}{\leftrightarrow}} C^*_{soot,i} + H_2$$

$$C_{soot,i}H + OH \leftrightarrow C^*_{soot,i} + H_2O$$

in the stagnation plane region of the counterflowing flames on account of oxidation, the flow velocities of the flames are changed so that the stagnation plane moves toward the upper burner (flame 1b).

Figure 2 contains, as well, the profiles of soot volume fractions, mean particle radii of soot particles, and particle number densities along the centerline of flame 1b. Soot volume fractions increase much stronger shortly below the stagnation region of flame 1b than in the same region of flame 1a. In flame 1a, soot volume fractions are scarcely affected by the counterflow in the region shortly below the stagnation plane, whereas the counterflow in flame 1b causes a considerable increase in the soot volume fraction. The increase is clearly due to an increase of the surface growth both because particle number densities decrease sharply in the region of the second onset of soot formation and because mean particle sizes increase. This can also be seen from Fig. 3 (lower left part) where the calculated soot volume fractions and the different contributions to the appearance rate of soot are given for flame 1b. The increase in soot volume fraction in the vicinity of the stagnation plane for flame 1b, which is somewhat overestimated by the model, is caused by surface growth of soot, whereas particle inception as modeled contributes negligibly to the second onset of soot formation. The net production of soot can be traced back to a relative shift of surface growth and oxidation rates because of oxidation effecting larger net production of soot by surface growth near the stagnation region.

Another means to increase the level of H atoms in the stagnation region of the counterflowing flames is to generate them by chemical reactions. One appropriate reaction for the chemical generation of H atoms is the reaction $CO + OH \rightarrow CO_2 + H$, which consumes OH radicals and generates H atoms. To achieve this, the fuel of the upper flame of the counterflow flames has been changed to carbon monoxide so that the reaction occurs at the oxygen-rich side of the stagnation plane (flame 1c).

Figure 4 gives profiles of soot volume fractions, mean particle radii of soot particles, and particle number densities along the centerline of flames 1 and 1c. The figure clearly exhibits that the second onset of soot formation leads to higher soot volume fractions in flame 1c than in flame 1b (see Fig. 2). Again, this effect is due to the reinitiation of surface growth because number densities decrease and mean particle sizes increase in the region of the second onset of soot formation before soot is oxidized. Another source for the decrease of number densities in the region of the second onset of soot formation could be the influence of the restarting surface reactions on the coagulation efficiencies of the soot particles. In Ref. 13, coagulation has been observed to cease in the absence of species reacting in surface growth reactions.

Figure 3 (lower right part) contains the calculated soot volume fractions and the calculated contributions of the different soot-generating and soot-consuming processes to the appearance rate of soot for flame 1c. In flame 1c, the differences between surface growth rates and oxidation rates remain larger so that more soot is accumulated before it is consumed by oxidation. It should be noted that only a small relative shift of the profiles of surface growth rates and oxidation rates generates the second onset of soot formation in flames 1b and 1c.

The complete interaction of surface growth with the different gas-phase species becomes obvious when deriving a rate expression for the appearance rate of soot from the mechanism in Table 1. If the number density per unit surface area of the "soot radicals" is replaced by the assumption of quasistationarity, the appearance rate can be written as

$$\frac{df_V}{dt} = \left\{\left(k_{3a}[C_2H_2]\frac{k_{3b}}{k_{3b} + k_{-3a} + k_{4b}[O_2]} - k_{4a}[O_2]\right)\cdot\chi(C^{\circ}_{soot,i}) - \left(k_{-3b}[H]\left(1 - \frac{k_{3b}}{k_{3b} + k_{-3a} + k_{4b}[O_2]}\right) - k_5\,[OH]\right)\cdot\chi(C_{soot,i})\right\}\cdot S \quad (4)$$

where χ means the surface number density and S the surface area. If the ring closure via reaction 3b is fast compared to the fragmentation and oxidation reactions, then the factor $a = k_{3b}/(k_{3b} + k_{-3a} + k_{4b}[O_2]) \approx 1$ and there is mainly a competition between surface growth via reactions (3a) and (3b) and oxidation via reaction (5). If the fragmentation and oxidation reactions are fast, then $a \approx 0$ and H atoms contribute also to the destruction of soot. This may also be the case for $k_{3a}[C_2H_2]$ being small compared to the other term in the preceding equation. This could be the prevailing condition in the flames from Refs. 22 and 23 where H atoms (and hydrogen molecules) as well as OH diffuse into the formation zone of soot. For other flame conditions, both terms may vary in the same way by changing the flame conditions so that there is scarcely a net effect on the appearance rates [21]. In the counterflow flames investigated in this work, the situation changes very quickly from one limit to the other when crossing the stagnation region and the reinitiation of soot formation via surface growth is very sensitive to small changes of the local conditions. The changes in local conditions include changes in the species concentration gradients, the local chemistry induced by different fuels, and the temperatures.

Conclusions

Experiments in counterflow, premixed twin flames were conducted. Soot particles were generated in a premixed, fuel-rich ethyne/oxygen flame counterflowing against a nonsooting flame of the same components or of carbon monoxide.

The experimental results clearly demonstrate that depending on the flow conditions in the counterflow flames, a second onset of soot formation is detected. This second onset of soot formation can be traced back to surface growth because number densities decrease and mean particle radii increase.

The nonsooting flames produce hydrogen atoms combined with a variation of the concentration of other gaseous species, so that surface growth by H abstraction from C–H sites at the surface of soot particles is reinitiated in the burned-gas region of the sooting flame before soot particles are oxidized in the stagnation region of the counterflowing flames.

The experimental findings are interpreted by comparing with results from modeling of these flames using the HACA mechanism for surface growth. On that basis, a shift of the competing effects of surface growth and oxidation is identified to be responsible for the reinitiation of surface growth. Some apparently conflicting results from other experiments under different conditions can be explained by this approach.

Acknowledgments

This research was partially supported by the Commission of the European Communities, the Swedish National Board for Technical Development (STU), and the Joint Research Committee of European car manufacturers (Fiat, Peugeot SA, Renault, Volkswagen, and Volvo) within the IDEA and IDEA-EFFECT programs.

REFERENCES

1. Haynes, B. S., and Wagner, H. G., *Prog. Energy Combust. Sci.* 7:229 (1981).
2. Glassman, I., *Twenty-Second Symposium (International) on Combustion,* The Combustion Institute, Pittsburgh, 1988, p. 295.
3. Howard, J. B., *Twenty-Third Symposium (International) on Combustion,* The Combustion Institute, Pittsburgh, 1990, p. 1107.
4. Homann, K. H., *Twentieth Symposium (International) on Combustion,* The Combustion Institute, Pittsburgh, 1984, p. 857.
5. Siegla, D. C. and Smith, G. W., Eds., *Particulate Carbon: Formation during Combustion,* Plenum Press, New York, 1981.
6. Lahaye, J. and Prado, G., Eds., *Soot in Combustion Systems and Its Toxic Properties,* Plenum Press, New York, 1983.
7. Bockhorn, H. Ed., *Soot Formation in Combustion—Mechanisms and Models,* Springer Verlag, Berlin and Heidelberg, 1994.
8. Harris, S. J. and Weiner, A., *Twenty-Second Symposium (International) on Combustion,* The Combustion Institute, Pittsburgh, 1988, p. 333.
9. Harris, S. J., *Combust. Sci. Technol.* 72:67 (1990).
10. Woods, I. T. and Haynes, B. S., *Combust. Flame* 85:523 (1991).
11. Bockorn, H., Fetting, F., Heddrich, A., and Wannemacher, G., *Twentieth Symposium (International) on Combustion,* The Combustion Institute, Pittsburgh, 1984, p. 979.

12. Haynes, B. S. and Wagner, H. G., *Z. Phys. Chem.* 133:201 (1982).
13. Böhm, H., Feldermann, C., Heidermann, T., Jander, H., Luers, B., and Wagner, H. G., *Twenty-Fourth Symposium (International) on Combustion,* The Combustion Institute, Pittsburgh, 1992, p. 991.
14. McKinnon, J. T. and Howard, J. B., *Twenty-Fourth Symposium (International) on Combustion,* The Combustion Institute, Pittsburgh, 1992, p. 965.
15. Frenklach, M. and Wang, H., *Twenty-Third Symposium (International) on Combustion,* The Combustion Institute, Pittsburgh, 1990, p. 1559.
16. Frenklach, M. and Wang, H., in *Soot Formation in Combustion—Mechanisms and Models* (Bockhorn, H., Ed.), Springer Verlag, Berlin and Heidelberg, 1994, p. 162.
17. Mauß, F., Trilken, B., Breitbach, H., and Peters, N., in *Soot Formation in Combustion—Mechanisms and Models* (Bockhorn, H., Ed.), Springer Verlag, Berlin–Heidelberg, 1994, p. 325.
18. Colket, M. B. and Hall, R. J., in *Soot Formation in Combustion—Mechanisms and Models* (Bockhorn, H., Ed.), Springer Verlag, Berlin and Heidelberg, 1994, p. 437.
19. Mauß, F., Schäfer, T., and Bockhorn, H., *Combust. Flame* 99:697 (1994).
20. Mauß, F., Schäfer, T., Bockhorn, H., and Fetting, F., *Z. Naturforsch.* 50a:11 (1995).
21. Woods, I. T. and Haynes, B. S., in *Soot Formation in Combustion—Mechanisms and Models* (Bockhorn, H., Ed.), Springer Verlag, Berlin and Heidelberg, 1994, p. 275.
22. Bachmann, M., Wiese, W., and Homann, K. H., *Twenty-Fifth Symposium (International) on Combustion,* The Combustion Institute, Pittsburgh, 1994, p. 635.
23. Wiese, W. and Homann, K. H., *VDI-Berichte* 1193:227 (1995).
24. Schäfer, T., Dissertation, TH Darmstadt, 1994.
25. Dalzell, W. H. and Sarofim, A. F., *J. Heat Transfer* 91:100 (1969).
26. Kee, R. J., Dixon-Lewis, G., Warnatz, J., Coltrin, M. E., and Miller, J. A., "A FORTRAN Computer Code Package for the Evaluation of Gas-Phase Multicomponent Transport Properties," Sandia National Laboratories, Report SAND86–8246, 1992.
27. Warnatz, J. and Chevalier, C., in *Combustion Chemistry* (Gardiner, W. C. Jr., Ed.), Springer Verlag, in press.
28. Neoh, K. G., Howard, J. B., and Sarofim, A. F., *Twentieth Symposium (International) on Combustion,* The Combustion Institute, Pittsburgh, 1984, p. 951.

COMMENTS

Peter Lindstedt, Imperial College, UK. In your presentation the topic of internal burning of soot particles was discussed, thus is the "surface area" a relevant parameter to consider?

Author's Reply. Indeed, the "surface area" of the soot particles is a relevant parameter to consider in soot surface growth as well as in soot particle oxidation.

The controversy that has been discussed frequently is how "surface area" has to be counted, see e.g. [1–4]: Is it the inner surface of a porous soot particle rather than the outer surface of a complex structured soot particle? The present results indicate that oxidation occurs more likely at the inner surface of porous soot particles.

REFERENCES

1. Bockhorn, H., Soot Formation during Combustion: Recent Developments in Mechanisms and Models, Joint Meeting of the British and German Sections of the Combustion Institute, S.1, The British Section of the Combustion Institute, Cambridge 1993.
2. Bockhorn, H. (Editor), *Soot Formation in Combustion—Mechanisms and Models,* Springer Verlag, Berlin, Heidelberg, 1994.
3. Bockhorn, H. and Schäfer, Th., "Growth of Soot Particles in Premixed Flames by Surface Reactions," in H. Bockhorn (IIrsg), *Soot Formation in Combustion—Mechanisms and Models,* S. 253, Springer Verlag, Berlin, Heidelberg, 1994.
4. Mauss, F., Schäfer, Th., Bockhorn, H., *Combust. Flame* 99:697 (1994).

Twenty-Sixth Symposium (International) on Combustion/The Combustion Institute, 1996/pp. 2351–2358

INFLUENCE OF HYDROGEN ADDITION TO FUEL ON TEMPERATURE FIELD AND SOOT FORMATION IN DIFFUSION FLAMES

Ö. L. GÜLDER, D. R. SNELLING AND R. A. SAWCHUK
National Research Council of Canada
Combustion Research Lab., M-9, Montreal Road
Ottawa, Ontario K1A 0R6, Canada

Overventilated, coflowing axisymmetric laminar diffusion flames of ethylene, propane, and butane were used to study the influence on soot of hydrogen addition to the fuel. The flame temperatures were measured by CARS along the flame axis as well as at off-axis radial locations. CARS spectra taken in heavily sooting regions exhibited poor fits due to C_2 absorbtion of part of the fundamental band of the nitrogen spectrum. It was found that C_2 absorbtion was confined to frequencies greater than 2313 cm^{-1}. We, therefore, implemented a strategy that fitted only the CARS spectra in the frequency range smaller than 2313 cm^{-1}. Measured soot concentrations and the flame temperature data with and without hydrogen and helium dilution were evaluated and the relative influences of dilution and direct chemical interaction on soot formation, as a result of hydrogen addition, are presented. It is shown that when hydrogen or helium is added to the fuel as a diluent in moderate quantities, the changes in the temperature field of the coflow diffusion flames are negligible. When allowance is made for the influence of dilution, addition of hydrogen to the fuel side of an ethylene diffusion flame reduces the soot formation. For propane and butane flames, hydrogen addition does not show any influence on soot formation apart from the dilution effect.

Introduction

The influence of H atom concentration on soot formation in flames was noted by Arthur [1]. He observed that suppression of H atom concentration in flames is accompanied by suppression of flame luminosity (due to carbon) [1]. Frenklach argued that the addition of hydrogen to the fuel side of a diffusion flame may promote soot formation in the flame due to increased chain branching, leading to higher concentrations of H atom [2].

Gaseous fuel mixtures such as petroleum gas and coke-oven (coker) gas contain some amount of hydrogen in addition to methane, ethane, propane, ethylene, and other low carbon number gaseous hydrocarbons. For this reason, the effect of hydrogen addition to fuel on soot formation in diffusion flames has some practical implications.

Very few studies exist in the literature on the influence of hydrogen addition on soot formation. In premixed flames of benzene and kerosene, addition of hydrogen caused a slight increase in yellow luminosity [3]. Addition of hydrogen to premixed ethylene flames reduced the critical C/O ratio; but the actual soot yield was not significantly affected by addition of up to 3% hydrogen to the unburned gases [4].

During the thermal decomposition of natural gas, dilution by hydrogen slowed down the formation of carbon black particles [5]. Johnson and Anderson found that addition of hydrogen drastically reduced the carbon formation in the pyrolysis of acetylene [6]. In coflow methane-air diffusion flames, addition of hydrogen to the fuel increased soot number density, although soot yield decreased with increasing hydrogen fraction in methane [7]. Deardon and Long [8] observed some reduction in sooting rates when hydrogen was added to ethylene and propane diffusion flames on a Wolfhard-Parker burner. Reductions in sooting rates were almost the same as those achieved by adding equal molar volumes of nitrogen. Jones and Rosenfield [9] showed that a mixture of ethylene and hydrogen, to give a C/H ratio equivalent to that of propane, yielded the same amount of soot as propane in a coflow laminar diffusion flame. In a similar study, Schug et al. [10] added hydrogen to acetylene diffusion flames to study the influence of C/H ratio on sooting tendency of fuels. They demonstrated that an equal molar mixture of acetylene and hydrogen did not have the same sooting characteristics as ethylene. Du et al. [11] observed a substantial decrease in the soot inception limit (i.e., a decrease in the soot particle inception rate) with hydrogen addition to the fuel in a counterflow propane-air diffusion flame. It was argued that [11], while the observed influence of hydrogen could be due to chemistry, it could also be explained on purely physical grounds.

It seems that work done to date does not provide a clear picture on the influence of hydrogen on soot formation in diffusion flames. The only consensus is

that adding hydrogen to the fuel in diffusion flames has an overall effect of reducing soot.

In the present work, the influence of hydrogen addition to the fuel on the temperature field of the flame and soot formation in overventilated, coflow laminar diffusion flames of ethylene, propane, and butane was investigated. The flame temperatures were measured by CARS along the flame axis as well as at off-axis radial locations. The line-of-sight average soot volume fractions as a function of axial location along the centerlines of diffusion flames were measured by laser light extinction. Experimental data with and without hydrogen and helium dilution were evaluated using the techniques employed previously [12,13], and the relative influences of dilution and direct chemical interaction on soot formation, as a result of hydrogen addition, are presented.

Methodology

When a gaseous diluent or additive is added to the fuel side of a diffusion flame, one can expect the influence of three potential effects on soot formation [13,14]: (1) a dilution effect resulting from the change in the amount of carbon per unit mass of the fuel gas mixture, (2) a thermal effect due to a change in flame temperature field upon diluent addition, and (3) a direct chemical interaction (excluding the changes in chemical reaction rates as a result of a change in temperature) due to changes in the species concentrations.

In the present study, hydrogen was added (up to 30%) to the fuel in ethylene, propane, and butane diffusion flames. The same experiments were repeated by replacing the hydrogen with helium, which has similar molecular diffusion characteristics but is an inert diluent. The effect of adding 30% of hydrogen (or helium) is to increase (or decrease) the adiabatic flame temperature by less than 4 K, and it is expected that the temperature field of the flame would not be altered significantly by hydrogen or helium addition. We carried out extensive CARS temperature measurements in these flames to test this conjecture.

Burner and Soot Measurements

In ethylene flames, the ethylene flow rate was set to 194 ml/min (at room temperature and atmospheric pressure) which gives a flame burning near to its smoke point height, i.e., no soot escapes from the visible tip of the flame. Propane and butane flow rates were set to 119 and 81 ml/min, respectively, to have visible flame heights similar to ethylene. Propane and butane flames, at these flow rates, burn well below their respective smoke point heights.

The fuel nozzle of the burner is a stainless-steel pipe of 12.7-mm inner diameter. Air is supplied from a concentric converging nozzle of 100-mm inner diameter. The fuel and the diluent flow rates were monitored by calibrated rotameters. The air, before exiting from the converging nozzle, passed through a bed of glass beads and a set of wire-mesh screens to prevent flame instabilities. A flame enclosure made of flexible steel mesh with appropriate holes protected the flame from air movements in the room while providing optical access. The burner assembly sits on a positioning platform with accurate vertical and horizontal movement capability.

The line-of-sight average soot volume fractions along the centerline of the flames were measured by the transmission of an Ar-ion (514.5 nm) laser beam. The visible flame diameter was measured by a reading telescope with an eyepiece. Typical flame diameters over the lower half of the flames were around 8–12 mm. Each division of the scale on the eyepiece corresponds to 0.125 mm. The repeatability and the reproducibility of the flame diameter measurements were within ± 1 scale division. The soot volume fraction F can then be calculated assuming Rayleigh extinction [12]. The complex refractive index of the soot particles was taken as $m = 1.89 - 0.48i$ [15] to be consistent with our previous soot work. A schematic of the experimental rig was reported previously [16].

The line-of-sight average light extinction and the flame diameter were measured, as a function of the axial position, along the centerlines of ethylene, propane, and butane diffusion flames with and without hydrogen or helium dilution.

CARS Temperature Measurements

The basic CARS system has been described previously [17]; for the present temperature measurements the pump and Stokes lasers used were a single mode Nd:YAG and a modeless dye laser [18], respectively. In a CARS experiment, two laser beams of frequency w_p and w_s are brought to a common focus, and if the frequency difference $w_p - w_s$ corresponds to a Raman active transition, then a third laser beam (CARS beam) at frequency $w = 2w_p - w_s$ is produced. Temperature measurements in air-fed combustion are most commonly performed using the shapes of CARS spectra of nitrogen, which is present in large concentrations.

The CARS beam is generated through the third-order nonlinear susceptibility which consists of a resonant and a nonresonant part. The nonresonant component is real and typically arises from spectrally distant electronic or vibrational transitions of the various constituents present. For most contributing species, the nonresonant component is effectively constant over the typical spectral range of interest. In premixed combustion, nitrogen is everywhere the dominant species, and the total nonresonant susceptibility varies little from reactants to products. How-

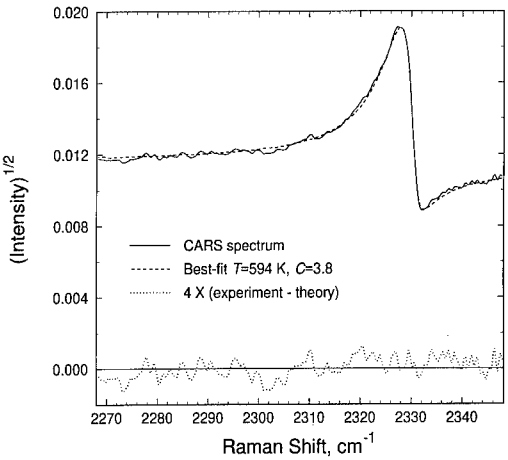

FIG. 1. CARS spectrum in a 40% ethylene + 60% CO_2 flame showing large nonresonant background.

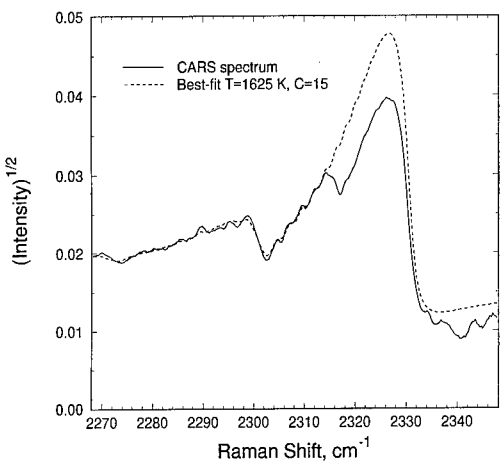

FIG. 2. CARS spectrum in the sooting region of an ethylene flame showing the C_2 absorption. Fit region is confined to 2268–2313 cm^{-1}.

ever, in diffusion flames, both the nitrogen mole fraction and the total nonresonant susceptibility vary greatly.

It thus proved necessary to fit an additional parameter, C, as well as the temperature, frequency shift, and scaling parameter when fitting the experimental CARS spectra to a library of theoretical CARS spectra. C is the ratio of the nitrogen mole fraction to the total third-order nonlinear susceptibility, and the CARS spectra can be stored in a form that allows spectra of varying C to be recovered [19].

Fitting C accounted for the effect of varying composition on the CARS spectra of nitrogen, but in the most heavily sooting region of the flame, an additional problem was encountered. CARS spectra taken in these heavily sooting regions exhibited poor fits, and the temperatures were anomalously high when the spectra were fitted over a Raman shift frequency range of 2268 to 2348 cm^{-1}. This problem, which has been encountered by others [20,21] who have performed similar CARS temperature measurements in heavily sooting flames, is attributed to C_2 absorbtion of part of the fundamental band of the nitrogen CARS spectrum. The C_2 radicals are probably formed by laser heating of the soot. We found the C_2 absorbtion to be confined to frequencies greater than 2313 cm^{-1}, as observed by Bengston et al. [21]. We therefore implemented a strategy that fitted only the CARS spectra in the range $w < 2313$ cm^{-1}.

A best fit to an experimental CARS spectrum taken in a fuel rich region of an ethylene diffusion flame diluted by CO_2 is shown in Fig. 1. The effect of the large nonresonant background is evident and a reliable fit to experiment can be obtained when the additional parameter C is varied.

The results of fitting a CARS spectrum taken in a sooting region of the laminar diffusion flame is shown in Fig. 2. A strong C_2 absorbtion band between 2313 and 2348 cm^{-1} is clearly evident. For this spectrum, the fitting range was confined to a Raman shift frequency range of 2268 to 2313 cm^{-1}. Neglecting the C_2 absorbtion and fitting the full CARS spectrum results in a temperature that is 470 K higher than the reduced range fit temperature. In nonsooting flames, where there is no C_2 absorbtion, partial range fits produced almost identical temperatures to those obtained from the full spectrum fits, although the precision was somewhat lower.

Results and Discussion

Temperature Field

The results of CARS temperature measurements in propane flames with and without hydrogen or helium dilution are shown in Figs. 3 and 4. The radial temperature profiles of pure propane, 84% propane/16% hydrogen, and 84% propane/16% helium flames are almost identical at both axial heights of 10 and 20 mm (Fig. 3). The local temperatures that are most relevant to soot formation and growth for these three fueling conditions are within the experimental error margins for CARS temperature measurements. The peak temperature reached is about 225 K lower than the adiabatic flame temperature.

The temperature profiles measured along the centerline of the flames are shown in Fig. 4. The effect of added hydrogen and helium on centerline temperatures is negligible. Also shown in Fig. 4 is the profiles of the flame shapes that did not change with hydrogen or helium addition to the fuel side.

Temperature profiles measured by CARS in eth-

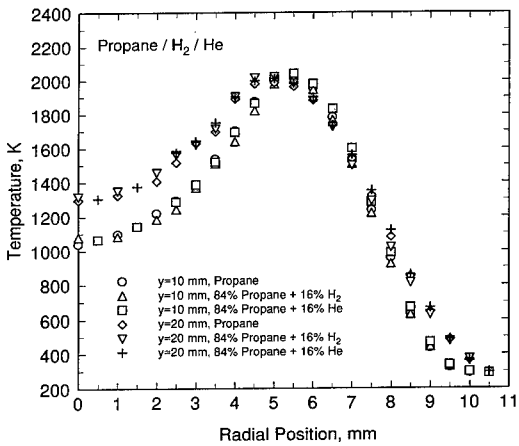

FIG. 3. Measured temperature profiles as a function of radial position at two axial heights in propane flames with and without hydrogen or helium dilution. Propane flow rate is constant at 119 ml/min.

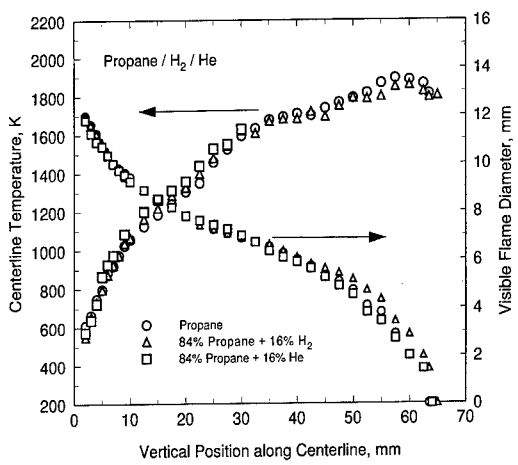

FIG. 4. Measured centerline temperature profiles as a function of axial position along the flame centerline in propane flames with and without hydrogen or helium dilution. Also shown are the visible flame diameter profiles.

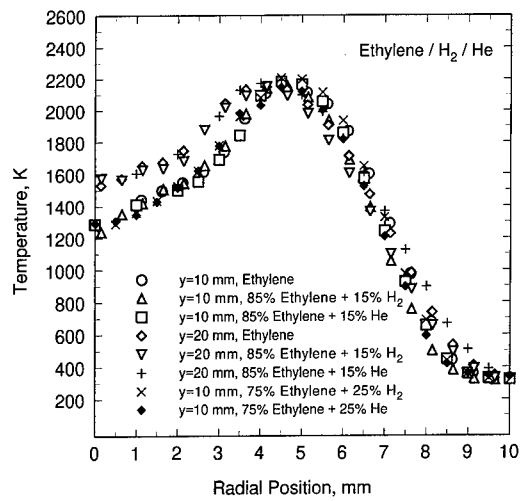

FIG. 5. Measured temperature profiles as a function of radial position at two axial heights in ethylene flames with and without hydrogen or helium dilution. Ethylene flow rate is constant at 194 ml/min.

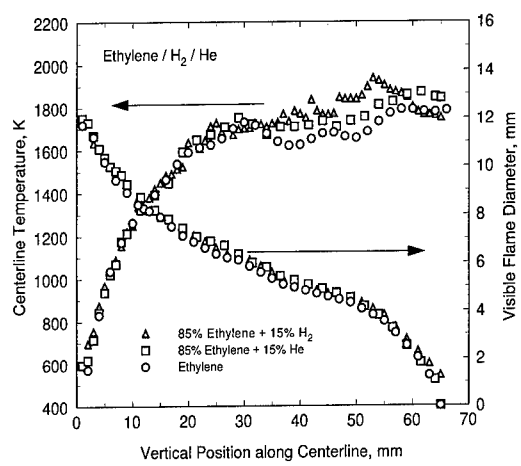

FIG. 6. Measured centerline temperature profiles as a function of axial position along the flame centerline in ethylene flames with and without hydrogen or helium dilution. Also shown are the visible flame diameter profiles.

ylene and hydrogen- or helium-diluted ethylene flames are plotted in Fig. 5. The effect of hydrogen or helium dilution on temperature is not large enough to be measured. The centerline temperature profiles in these flames are again in agreement for the lower part of the flame where soot inception and growth take place (Fig. 6). At the higher axial locations, there are differences in temperatures. These differences are due mainly to higher soot concentrations in this region. In the upper portion of the ethylene flames, the CARS spectra showed significant C_2 absorption which made the prediction of the gas temperatures less accurate. It should be remembered that the soot concentrations in ethylene flames are several times higher than those in propane flames [22,23]. Although the differences in soot concentrations of diluted and undiluted flames are small (see Figs. 7 and 8), increased radiative heat loss from the flames due to higher soot concentrations is expected to reduce the gas temperatures. In spite of the noisy data, the general trend of the temperature

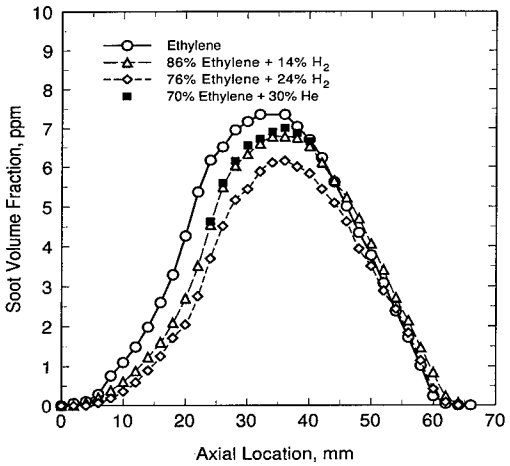

FIG. 7. The line-of-sight soot volume fraction profiles along the centerline of ethylene, ethylene/hydrogen and ethylene/helium flames. Data points represent averages of several repeat measurements, and the typical standard deviation is about 0.1 ppm.

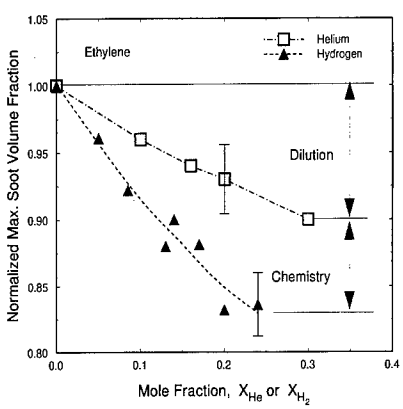

FIG. 8. The variation of the influence of dilution and direct chemical interaction on soot formation in ethylene flames with hydrogen concentration in the fuel gas mixture. The data are normalized with respect to maximum soot volume fraction obtained without any dilution. The magnitude of the error bars correspond to twice the sample standard deviation obtained from multiple measurements.

profiles in the upper portion of the ethylene and diluted ethylene flames agree with this prediction.

Temperature measurements (uncorrected) by fine wire thermocouples in coflow pure ethylene and ethylene/helium flames found that helium dilution reduces the maximum flame temperature (i.e., maximum temperatures in Figs. 3 and 5) and results in a broader flame shape, but the centerline temperature profile remains unaffected [10]. Our temperature results in helium-diluted flames of ethylene and propane disagree with the former two conclusions of Schug et al. [10]. The differences between our measured maximum flame temperatures were within the precision of the CARS technique. Further, in Ref. 10, ethylene and helium were in equal molar amounts, whereas in Fig. 5 the dilution is limited to 25% helium. It should be noted that the thermocouple measurements introduce a disturbance to the measurement location and its vicinity, and require radiation correction. For these reasons, Schug et al. [10] classify their measurements as approximate.

Du et al. [11,24] observed a considerable increase in maximum flame temperature (measured by thermocouples) with the addition of hydrogen in counterflow diffusion flames of propane and ethylene. As a consequence of this observation, they concluded that hydrogen addition to propane suppresses soot significantly, because in spite of measured increase in temperature, soot inception rates were lower with hydrogen addition. Since the flames studied by Du et al. [24] were highly strained, the preferential diffusion of the hydrogen was responsible for the increased flame temperature and the high mobility of hydrogen played an important role in the observed suppression of soot formation. The laminar coflow flames were not subject to similar strain rates, and the moderate quantities of dilution by either hydrogen or helium did not change the temperature field of the flames.

To assess the relative influences of the thermal, concentration, and chemical effects of gaseous diluents on soot formation, the following parameters in the diluted and the undiluted flames should be taken into consideration: the characteristic flame temperatures, residence times, the flame diameters, and fuel and oxidant mole fractions. Since the temperatures are not significantly affected by either hydrogen or helium addition, the observed effects, if any, will be due to dilution, direct chemical interaction, and the residence time.

Soot Measurements

The visible flame heights and the flame diameter profiles did not change noticeably by hydrogen or helium addition to the fuel (Figs. 4 and 6). It seems that the flame residence time and visible flame structure are not influenced by the hydrogen or helium addition. Thus, any changes in sooting characteristics when hydrogen or helium is added to the fuel can be attributed to dilution and direct chemical interaction effects.

The line-of-sight average soot volume fraction profiles, as a function of axial position, of hydrogen and helium diluted ethylene flames are shown in Fig. 7. For clarity, 14 and 24% hydrogen in ethylene, and 30% helium in ethylene are plotted. Even for the highest fraction of hydrogen in ethylene, the ob-

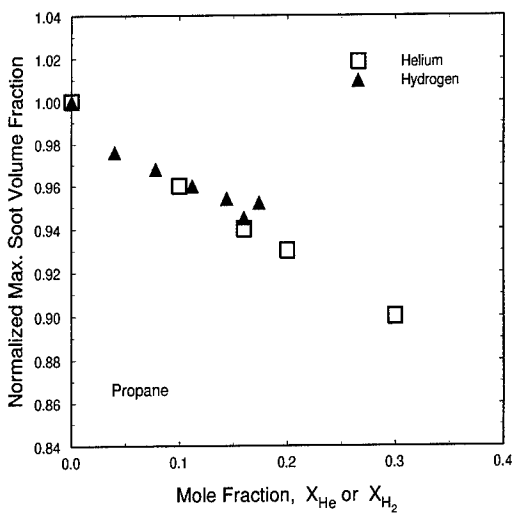

FIG. 9. The influence of adding hydrogen and helium on soot formation in propane flames. The data are normalized with respect to maximum soot volume fraction obtained without any dilution.

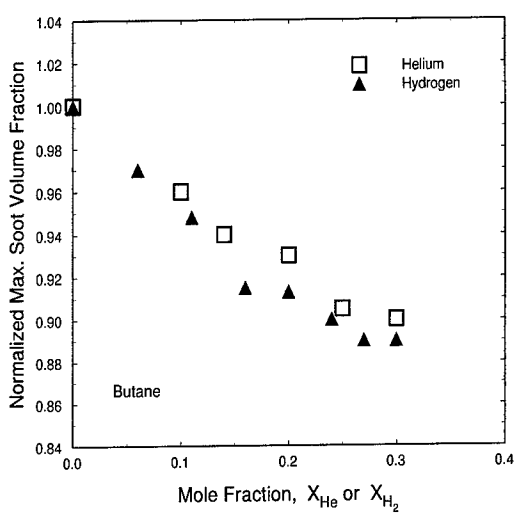

FIG. 10. The influence of adding hydrogen and helium on soot formation in butane flames. The data are normalized with respect to maximum soot volume fraction obtained without any dilution.

served reduction in soot volume fraction is not substantial. The effect of helium is weaker: 30% helium and 14% hydrogen have almost the same overall suppressive effects. Data points in Fig. 7 represent averages of several repeat measurements, and the typical standard deviation is about 0.1 ppm.

Axelbaum et al. [25], Axelbaum and Law [26], and our previous work [12,13] showed that soot formation rate in diffusion flames is first order in fuel mole fraction in the fuel gas mixture when the remainder of the fuel gas is an inert diluent like nitrogen that has comparable diffusion coefficient to that of the fuel gas and the oxidant. For diluents like helium and hydrogen, which have significantly higher diffusion coefficients than the fuel and the oxidant, the dependence on fuel mole fraction can be different than first order. It was demonstrated [12,13] that maximum soot volume fraction in coflow diffusion flames scales as follows:

$$F_m \sim [X_{F,O}]^{\alpha} \cdot \tau \cdot \exp(-E_a/RT_a) \qquad (1)$$

where $X_{F,O}$ is the mole fraction of fuel in the fuel gas mixture, α is the order of dependence of soot formation rate on fuel mole fraction, τ is the characteristic residence time, E_a is the activation energy, and T_a is the adiabatic flame temperature. The activation energy inferred from the experimental data was 200 kJ/mole [12,13]. For equivalent residence times (i.e., flames with same visible height), equation 1 can be expressed as

$$dF/dt \sim [X_{F,O}]^{\alpha} \exp(-E_a/RT_a) \qquad (2)$$

For flames with equivalent temperature fields, soot formation rate is proportional to the initial fuel concentration raised to the power α.

When hydrogen is added to the fuels used in this study, there is a dilution effect due to the reduced concentration of carbon per unit volume of fuel gas mixture. When this dilution effect is subtracted, the remainder of the change observed in soot would be due to the direct chemical interaction induced by the hydrogen added.

The change in the maximum soot volume fraction with hydrogen and helium content in ethylene is shown in Fig. 8. The magnitude of the error bars corresponds to twice the sample standard deviation obtained from multiple measurements. If hydrogen did not have any chemical influence on soot, then the data points for hydrogen and helium dilution would coincide, as per equation 1. The difference between the measured values with hydrogen and with helium dilution is due to the overall chemical suppressive effect of hydrogen when added to ethylene.

The results for propane and butane are shown in Figs. 9 and 10, respectively. For both fuels, hydrogen and helium addition result in comparable reductions. Hydrogen addition to propane and butane does not influence soot formation apart from a dilution effect identical to helium. This suggests that the influence of hydrogen on soot formation may not be the same in diffusion flames of alkenes and alkanes. This is possibly due to the amount of molecular hydrogen, $[H_2]$, and hydrogen atom, [H], produced upon pyrolysis of ethylene and propane (or butane). In the former, the added hydrogen could

influence the ratio $[H]/[H_2]$, which was proposed as the controlling parameter in PAH growth (leading to the first soot nuclei) [27]. In propane and butane, on the other hand, there might be an abundance of $[H_2]$ and [H] as a result of pyrolysis, and the effect of added hydrogen becomes negligible.

The data in Figs. 8–10 suggest that, for helium dilution, the value of exponent α in equation 1 is about 0.3. This value of α is different than $\alpha \sim 1$ in flames where nitrogen or similar inerts are used as diluents. It seems that the transport effects must be considered to assess the nature of low molecular mass diluents. Schug et al. [10] proposed that the high thermal diffusivity of helium makes it less effective at suppressing soot than argon. Axelbaum et al. [28] suggested that the high molecular diffusivity of helium is responsible for this behavior.

Concluding Remarks

In this work, the influence of hydrogen addition to the fuel on soot formation in overventilated, axisymmetric laminar diffusion flames of ethylene, propane, and butane was investigated. The flame temperatures were measured by CARS along the flame axis as well as at off-axis radial locations. The line-of-sight average soot volume fractions as a function of axial location along the centerlines of diffusion flames were measured by laser light extinction. Experimental data with and without hydrogen and helium dilution were evaluated using the techniques employed previously, and the relative influences of dilution and direct chemical interaction on soot formation as a result of hydrogen addition were presented.

It was shown that when hydrogen or helium is added to the fuel as a diluent in moderate quantities, the changes in the temperature field of the coflow diffusion flames are negligible.

When allowance is made for the influence of dilution, addition of hydrogen to the fuel side of an ethylene diffusion flame reduces the soot formation. For propane and butane flames, hydrogen addition does not show any influence on soot formation apart from the dilution effect.

Acknowledgments

The authors thank two anonymous reviewers (of an earlier version of this article) who suggested that helium should be used as diluent to evaluate the dilution effect of hydrogen. We thank Mr. M. F. Baksh for his capable assistance with the experimental work. Assistance of Dr. T. Parameswaran and Mr. R. Matz with the CARS data analysis is gratefully acknowledged. The work described herein has been supported by National Research Council's internal funds (Subproject MCR 03) and by the Canadian Government's PERD program (Project No. 15113).

REFERENCES

1. Arthur, J. R., *Nature* 165:557–558 (1950).
2. Frenklach, M. in *Soot Formation in Combustion. An International Round Table Discussion* (H. Jander and H. Gg. Wagner, Eds.), Vandenhoeck & Ruprecht, Göttingen, 1990, pp. 36–37.
3. Street, J. C. and Thomas, A., *Fuel* 34:4–36 (1955).
4. Haynes, B. S., Jander, H., Mätzing, H., and Wagner, H. Gg., *Nineteenth Symposium (International) on Combustion,* The Combustion Institute, Pittsburgh, 1983, pp. 1379–1385.
5. Tesner, P. A., *Seventh Symposium (International) on Combustion,* The Combustion Institute, Butterworth, London, 1958, pp. 546–553.
6. Johnson, G. L. and Anderson, R. C., *Proceedings of 5th Conference on Carbon,* Vol. 1, Pergamon, New York, 1962, pp. 395–405.
7. Tesner, P. A., Rabinovitch, H. J., and Realkes, I. S., *Eighth Symposium (International) on Combustion,* The Combustion Institute William and Wilkens, Baltimore, 1960, pp. 801–806.
8. Deardon, P. and Long, R., *J. Appl. Chem.* 18:243–251 (1968).
9. Jones, J. M. and Rosenfield, J. L. J., *Combust. Flame* 19:427–434 (1972).
10. Schug, K. P., Manheimer-Timnat, Y., Yaccarino, P., and Glassman, I., *Combust. Sci. Technol.* 22:235–250 (1980).
11. Du, D. -X., Axelbaum, R. L., and Law, C. K., in *Chemical and Physical Processes in Combustion* (1988 Fall Technical Meeting Eastern States Section of the Combustion Institute), Clearwater, FL, 1988, pp. 46.1–46.4.
12. Gülder, Ö. L. and Snelling, D. R., *Combust. Flame* 92:115–124 (1993).
13. Gülder, Ö. L., *Combust. Flame* 92:410–418 (1993).
14. Du, D. X., Axelbaum, R. L., and Law, C. K., *Twenty-Third Symposium (International) on Combustion,* The Combustion Institute, Pittsburgh, 1991, pp. 1501–1507.
15. Lee, S. C. and Tien, C. L., *Eighteenth Symposium (International) on Combustion,* The Combustion Institute, Pittsburgh, 1981, pp. 1159–1166.
16. Gülder, Ö. L., *Combust. Flame* 101:107–114 (1995).
17. Snelling, D. R., Sawchuk, R. A., Smallwood, G. J., and Parameswaran, T., *Rev. Sci. Instrum.* 63:5556–5564 (1993).
18. Snelling, D. R., Sawchuk, R. A., and Parameswaran, T., *Appl. Opt.* 33:8295–8301 (1994).
19. Hall, R. J. and Boedeker, L. R., *Appl. Opt.* 23:1340–1346 (1984).
20. Eckbreth, A. C., Anderson, T. J., and Dobbs, G. M., *Twenty-First Symposium (International) on Combustion,* The Combustion Institute, Pittsburgh, 1987, pp. 1747–1754.
21. Bengston, P.-E., Aldén, M., Kroll, S., and Nilsson, D., *Combust. Flame* 82:199–210 (1990).

22. Gülder, Ö. L. and Snelling, D. R., *Twenty-Third Symposium (International) on Combustion,* The Combustion Institute, Pittsburgh, 1991, pp. 1509–1515.
23. Gülder, Ö. L., *Combust. Flame* 88:74–82 (1992).
24. Du, D. X., Axelbaum, R. L., and Law, C. K., *Combust. Flame* 102:11–20 (1995).
25. Axelbaum, R. L., Flower, W. L., and Law, C. K., *Combust. Sci. Technol.* 61:51–73 (1988).
26. Axelbaum, R. L. and Law, C. K., *Twenty-Third Symposium (International) on Combustion,* The Combustion Institute, Pittsburgh, 1991, pp. 1517–1523.
27. Frenklach, M., *Twenty-Second Symposium International on Combustion,* The Combustion Institute, Pittsburgh, 1989, pp. 1075–1082.
28. Axelbaum, R. L., Law, C. K., and Flower, W. L., *Twenty-Second Symposium (International) on Combustion,* The Combustion Institute, Pittsburgh, 1989, pp. 379–386.

COMMENTS

M. A. Delichatsios, RMRC, USA. It is not *purely* the fuel dilution that affects soot formation: more precisely it is the stoichiometric ratio. This value is different for helium and hydrogen for the same degree of fuel dilution because hydrogen needs oxygen for consumption but helium does not. Thus, the location of maximum reaction rate would change. This phenomenon, however, may compensate for the difference in molecular diffusivity between hydrogen and helium so that the visible flame envelope does not change as the experiments suggest.

Author's Reply. Contrary to Delichatsios' expectations, our CARS measurements did not show any significant changes in the location of the maximum temperature contours of the flames upon addition of hydrogen or helium. It should be noted that 30% hydrogen by volume in butane corresponds to a hydrogen mass fraction of about 1.5%.

Twenty-Sixth Symposium (International) on Combustion/The Combustion Institute, 1996/pp. 2359–2368

EXPERIMENTS AND NUMERICAL SIMULATION ON SOOT FORMATION IN OPPOSED-JET ETHYLENE DIFFUSION FLAMES

H. WANG, D. X. DU,* C. J. SUNG AND C. K. LAW
Department of Mechanical and Aerospace Engineering
Princeton University
Princeton, NJ 08544, USA

An experimental and computational study is presented for soot formation in counterflow diffusion flames of ethylene and air. Experimentally, the soot extinction and scattering profiles are determined for four well-controlled flames subjected to different straining rates. Computationally, the experimental situations are simulated by combining the numerical formulation of the counterflow flame with a model of soot particle inception, coagulation, and growth, with the moment description of particle size distribution function. Numerical simulation yields satisfactory results when compared to the experimentally determined soot profiles. It is shown that the surface addition of acetylene is the dominant process of soot mass growth for the present counterflow diffusion flames, and that in order to predict the experimental soot growth, the soot surface radical sites must be conserved upon its reaction with acetylene. While the comparison between numerical calculation and experimental data is satisfactory, we have also identified uncertainties on which further work is needed within the framework of the soot model, particularly surface radical dynamics.

Introduction

With the significant advance in the understanding of soot formation, it is now possible to describe soot formation in laminar premixed flames from fundamental chemical reaction mechanisms and detailed soot particle dynamics [1]. Predictions using detailed soot models yield fairly satisfactory results [2–5]. Although these models differ in the detailed treatment of the soot formation and growth processes, their underlying concept is the same. That is, the soot formation process is described by particle inception via the coalescence of aromatic soot precursors, namely the polycyclic aromatic hydrocarbons (PAHs), followed by coagulation of the particles and surface growth through PAH condensation and acetylene surface reaction [2,6–8].

For diffusion flames, while detailed simulations of soot formation in the counterflow have been reported [5,9,10], none has been extensively verified against experimental data. This, in part, is due to the lack of detailed soot measurements in diffusion flames which are suitable for rigorous comparison with numerical simulation, such as those in the counterflow configuration. The need for such data is even more crucial in light of the recent modeling study by Hall et al. [10], who suggested that the surface reaction model of Refs. 2 and 3 cannot account for soot growth in counterflow methane-air diffusion flames. In their study, the computed soot profiles were qualitatively compared to the measured data of Zhang et al. [11]. To further examine the predictability of the soot surface growth model for diffusion flame situations, it is important to compare the numerical results with experimental data on a quantitative basis, so the aspects of the soot growth model that may require modification can be identified.

In response, we have conducted a series of systematic experimental and numerical simulation studies on nonsooting ethylene-air and acetylene-air counterflow diffusion flames, which has been previously reported [12], and on sooting counterflow ethylene-air flames, which is the subject of this paper. The specific purposes of the present study are (1) to obtain experimental velocity and soot extinction and scattering profiles for ethylene-air counterflow diffusion flames under various strain rates, and (2) to simulate soot formation using a detailed model of soot inception and growth. The detailed sooting structure is then discussed, and the need for further work identified.

Experimental Methodology

The experimental methodology is similar to that reported previously [13,14]. The visual structure of the counterflow diffusion flame is schematically shown in Fig. 1. The flame is established at 1 atm by opposing jets of ethylene and air from two identical aerodynamically shaped high-contraction-ratio

*Permanent Address: Department of Energy Engineering, Zhejiang University, Harqzhou, China.

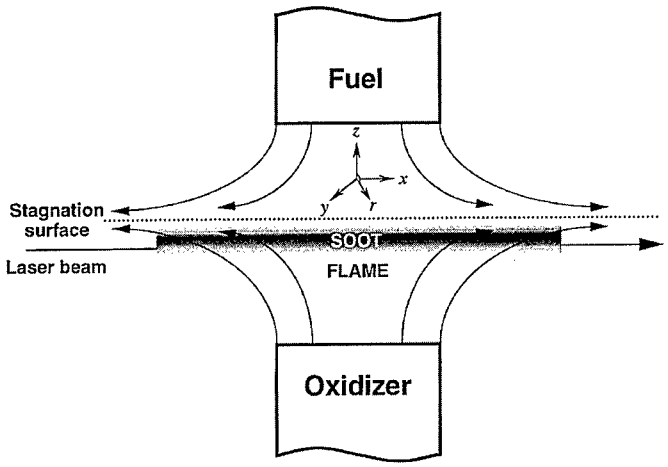

FIG. 1. Schematic diagram of flame and sooting structure of the present counterflow diffusion flames burning ethylene (fuel) and air (oxidizer).

nozzles with a 1-cm exit diameter. The nozzle separation distance is also 1 cm. Outer shroud nitrogen flow is used to isolate and stabilize the flame such that entrainment and flame flickering are minimized. For all flames examined in this study, the blue diffusion flame is seen on the oxidizer side of the stagnation plane, with the yellow soot layer situated between the stagnation plane and the blue flame.

Soot scattering and extinction measurements are made simultaneously with an argon-ion laser operating at 514.5 nm. The laser beam is modulated by a mechanical chopper and then focused with a 26.4-mm focal length lens. The detection of the scattered light is accomplished with a photomultiplier whose output is processed by a lock-in amplifier interfaced to a microcomputer.

The line-of-sight transmittance, I/I_0, is measured in a two-dimensional space defined by the y and z axes in Fig. 1. A measurement at a radial distance y from the centerline yields the integrated value of the extinction coefficient along the optical path [15],

$$-\ln[I(y)/I_0] = 2\int_y^\infty k_{ext}(r)\frac{r}{\sqrt{r^2 - y^2}}dr \quad (1)$$

where $(r/\sqrt{r^2 - y^2})dr = d\sqrt{r^2 - y^2}$ is the optical length. The local extinction coefficient, $k_{ext}(r)$, is obtained with two deconvolution techniques, namely, a discrete "onion-peeling" technique and the inversion of the Abel integral [9], which yield essentially the same results. The soot volume fraction, F_v, is then obtained from [16],

$$k_{ext} = \frac{6\pi}{\lambda}\,\mathrm{Im}\left\{\frac{m^2 - 1}{m^2 + 2}\right\}F_v \quad (2)$$

where λ is the wavelength of the incident laser beam, and $m = 1.58 - 0.57i$ [17], the complex refractive index. To avoid ambiguous assumptions regarding the particle size distribution function, no further derivation of the particle diameter and number density is made. The numerical simulation is directly compared to the soot volume fraction and scattering coefficient, Q_{vv}. The velocity profile along the forward stagnation streamline was determined using standard single-component, laser-Doppler velocimetry (LDV) with aluminum-oxide seed particles of nominal 0.3-μm diameter.

Computational Methodology

Soot formation in counterflow diffusion flames is simulated by combining the numerical formulation of the counterflow problem [18,19] with a soot model. The general formulation of the soot model is the same as that in Ref. 3. The rth moment of the particle size distribution function is defined as $M_r = \Sigma_i i^r N_i$, where N_i is the number density of particles, and i denotes the number of C atoms in a soot particle. As noted in Ref. 5, a total of 3 moments, including the zeroth moment, is sufficient for reliable soot calculations.

Soot particle transport via diffusion, thermophoresis, and convection is considered. In the large Knudsen number limit, the governing equation of the rth moment is

$$\frac{d}{dz}\left[D_{i_0}\frac{dM_{(r-2/3)}}{dz} - v_T M_r\right] - \rho v\frac{d(M_r/\rho)}{dz} + \dot{M}_r = 0,\ r = 0, \ldots, \infty \quad (3)$$

where D_{i_0} is the diffusion coefficient of the smallest soot particle i_0, ρ the mass density of the gas mixture, v the axial gas velocity, and v_T the thermophoretic velocity,

$$v_T = -\frac{3}{4}\left(1 + \frac{\pi\alpha_T}{8}\right)^{-1}\frac{\mu}{\rho}\frac{1}{T}\frac{dT}{dz} \quad (4)$$

In the above equation, μ is the gas viscosity, T the temperature, and α_T the thermal accommodation

coefficient ($\alpha_T = 1$) [20]. The soot source term, $\dot{M}_r$, includes contributions from inception, coagulation, PAH surface condensation, and surface reactions. Assuming that the soot cloud is optically thin, soot radiation is taken into account by including an additional term in the energy conservation equation, as given by

$$q_r = 2hc^2 \sum_{l}^{\infty} \kappa_l (\pi c_2)^l \left(\frac{k_B T}{hc}\right)^{l+2} M_{l/3}(l+1)! \cdot \sum_{i=1} i^{-(l+2)}, \text{ for } l = 3, 5, 6, 7, \text{ and } 8 \quad (5)$$

where h is the Planck's constant, c the speed of light, k_B the Boltzmann constant, and κ_l are functions of the complex refractive index of soot material [21].

The gas-phase reaction chemistry is taken primarily from an updated reaction mechanism of acetylene and ethylene oxidation and PAH formation in flames [22]. Details of the reaction mechanism can be found in Refs. 12 and 22 and are available upon request. In this mechanism, benzene is produced through the reactions of $C_4H_x + C_2H_2$ [23–25] and the recombination of C_3H_3 ($k = 2 \times 10^{13}$ $cm^3mol^{-1}s^{-1}$) [26]. The aromatics growth follows mainly the H-abstraction—C_2H_2-addition mechanism [23]. It is noted that the reaction kinetics of PAH formation is still quite uncertain. During the course of this study, it was found that reactions of the aromatic radicals with ethylene and ring-ring condensation reactions (e.g., phenyl + benzene → biphenyl + H) are also important and must be included in order to produce PAHs in quantities significant enough for soot inception.

It is assumed that particle inception is initiated by the coalescence of two pyrene molecules. The specific gas-surface reactions include (1) surface activation and deactivation via S_i–H + H = $S_i\cdot$ + H_2 (R1), S_i–H + OH = $S_i\cdot$ + H_2O (R2), and $S_i\cdot$ + H → S_i–H (R3), (2) oxidation via $S_i\cdot$ + O_2 → $S_{i-1}\cdot$ + products (R4), S_i–H + OH → S_{i-1}–H + products (R5), and S_i–H + O → S_{i-1}–H + products (R6), and (3) surface growth via two alternate reactions, $S_i\cdot$ + C_2H_2 → S_{i+2}–H + products (R7a) or $S_i\cdot$ + C_2H_2 → $S_{i+2}\cdot$ + products (R7b). The last two reactions differ in the assumption whether the radical site on the soot surface is preserved after the reaction. Reaction model R7a has been used in predicting soot growth in premixed flames [2,3]. The rate coefficients of the surface reactions (R1–4 and R7) are assumed to be equal to those of the analogous reactions of benzene and phenyl [3]. The reaction probabilities for OH (R5) and O (R6) are 0.13 and 0.5 [27], respectively.

The fraction of soot surface sites available for reaction [2] is assigned with a value of 1. This is reasonable considering that soot growth occurs predominantly at temperatures below 1500 K in the present diffusion flame situation, and that α was found to approach unity at about the same temperature [28]. Lastly, gaseous species production and consumption due to soot surface reactions are rigorously accounted for in the species conservation equations.

Calculations were performed in the axisymmetric configuration with 1 atm pressure and 300 K upstream temperature. To reconcile the difference in the potential flow adopted in the calculation and the mixed flow in the actual flames, the mass fluxes at nozzle exits were chosen such that the calculated velocity profile just ahead of the thermal mixing layer visually align well with the measured ones in both the absolute value and gradient. Such an alignment then yields the relevant local strain rate and temperature profile. It is noted that such a procedure is reliable, as a previous study [29] demonstrated that calculations performed in this manner yielded temperature profiles in excellent agreement with experiment. We further note that the computed velocity and temperature profiles within the thermal mixing layer is independent of the assumption of the boundary conditions chosen in the calculation [30].

Results

Table 1 summarizes the conditions of the four counterflow ethylene-air diffusion flames examined in the present study. The four flames differ in the volumetric flow rates of the reactant streams, and thus the strain rate, K, defined as the negative of the measured velocity profile ahead of the thermal mixing layer on the oxidizer side of the stagnation surface. The experimental strain rates vary from 117 s^{-1} for flame 1 to 58 s^{-1} for flame 4. As shown in Table 1, the computed strain rate for each flame is larger than the corresponding experimental result because of the specific potential flow boundary condition employed in the calculation. This discrepancy is unimportant, since the computation reproduces the entire velocity profile within the thermal mixing layer, which forms the best basis for comparison between experiment and numerical simulation.

Figures 2 and 3 present the velocity, soot volume fraction, and scattering coefficient profiles for flames 1 and 3, respectively. Also shown in the upper panels of these figures are the computed temperature profiles. It is seen that in the thermal mixing layer the calculated velocity profiles (dotted lines) deviate from the LDV measurements. This is a reasonable outcome because the LDV seed particles experience the thermophoretic force within the thermal mixing layer. The measured velocity therefore deviates from the actual gas velocity. To verify this result, we have calculated the LDV seed particle velocity using the computed temperature profile by following the procedure of Refs. 31 and 32. The results shown by the solid lines in Figs. 2a and 3a agree reasonably well with the experimental measurements.

TABLE 1
Flame conditions

Flame no.	Flow rate (cm³/s)		Strain rates[a] (s^{-1})		T_{max}[b] (K)	$F_{v,max} \times 10^7$		$Q_{vv,max} \times 10^5$ (cm^{-2} $ster^{-1}$)	
	C_2H_4	Air	Expt	Calc		Expt	Calc[c]	Expt	Calc[c]
1	40.6	35.2	117	159	2068	1.7	1.4	0.2	0.4
2	33.1	28.5	95	147	2073	2.4	1.6	0.7	0.6
3	25.1	25.2	79	126	2081	2.8	2.0	1.4	1.2
4	21.8	18.5	58	99	2094	3.3	2.9	2.9	3.6

[a]Determined from the velocity profile ahead of the thermal mixing layer on the oxidizer side of the stagnation surface.
[b]T_{max} is obtained from numerical simulation.
[c]Computed with the reaction model R7b (see text).

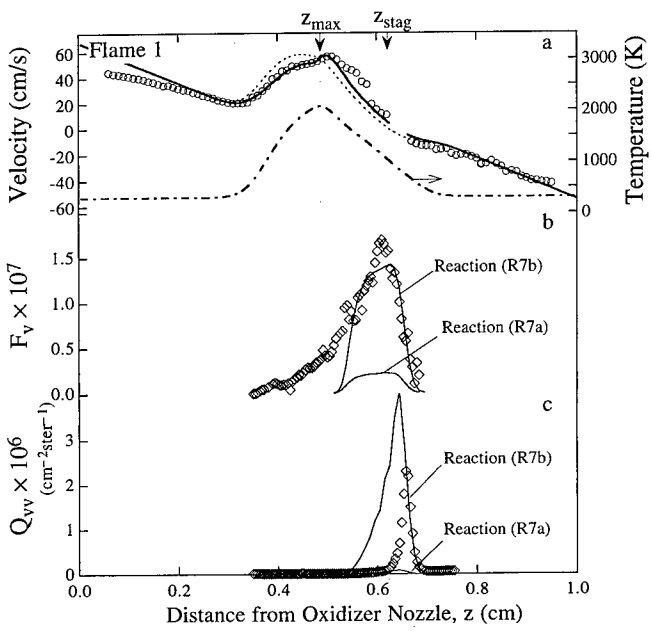

FIG. 2. Experimental (symbols) and computed (lines) (a) velocity and temperature profiles, (b) soot volume fraction, and (c) scattering coefficient in flame 1. The solid and dotted lines in panel (a) are, respectively, obtained with and without considering the effect of thermophoresis on LDV measurements.

As expected, the measured maximum F_v and Q_{vv} increase with decreasing strain rate (Table 1). For the flames studied herein, soot formation and growth are roughly confined to the region between the two vertical, dotted lines shown in Figs. 2 and 3. One side of the soot window is located at the flame sheet ($z = z_{max}$) where PAH growth and particle inception occurs, while the other side corresponds to the stagnation surface. The $F_{v,max}$ is attained near, but across the stagnation surface on the fuel side, where soot growth persists and the particle diameter continues to increase. Because Q_{vv} is proportional to $\langle d^6 \rangle$, and hence is more sensitive to large particles, the maximum Q_{vv} signal is always observed on the fuel side of the stagnation surface.

Comparisons of the experimental soot profiles with the numerical results are presented in Figs. 2 and 3 for flames 1 and 3, respectively. The comparison between experimental data and numerical results is comparable for flames 2 and 4. It is seen that (1) the qualitative sooting structure of the flames is well predicted, and (2) the experimental soot profiles and the magnitude of increase in $F_{v,max}$ and $Q_{vv,max}$ due to reduced straining are well reproduced by the growth model based on reaction R7b (Table 1). Soot predictions with reaction R7a are less satisfactory than with reaction R7b, as the computed results are lower than the experimental data by about an order of magnitude in $F_{v,max}$ and two orders of magnitude in $Q_{vv,max}$. It is important to note, however, that even

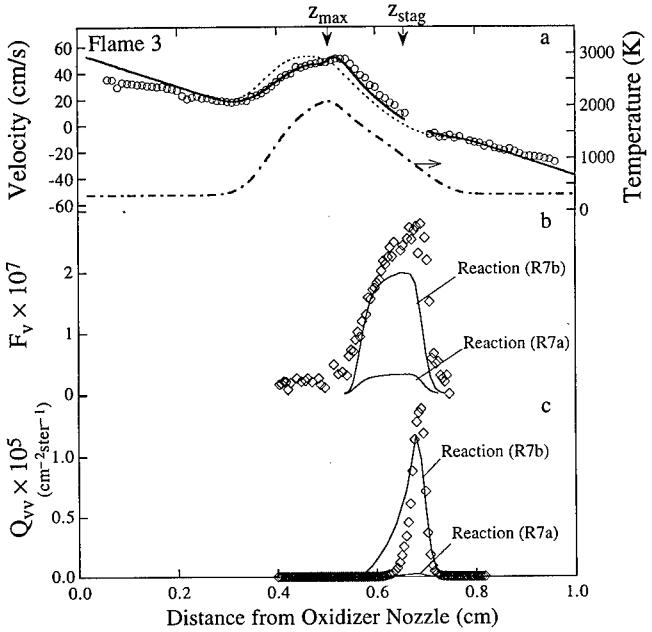

FIG. 3. Experimental (symbols) and computed (lines) (a) velocity and temperature profiles, (b) soot volume fraction, and (c) scattering coefficient in flame 3. The solid and dotted lines in panel (a) are, respectively, obtained with and without considering the effect of thermophoresis on LDV measurements.

this level of agreement is encouraging, considering that many detailed processes involved in PAH formation and growth, and soot formation in such flames still remain uncertain [1].

It is seen in Figs. 2 and 3, that while the rise in the computed F_v profiles occurs downstream from the location of the maximum flame temperature, the experimental profiles rise earlier, with the F_v value typically on the order of 5×10^{-8}. For the flame size employed in the present study, this F_v value would correspond to an attenuation of the incident laser beam by 0.7% or $I/I_o \sim 0.997$, which is well below the signal-to-noise ratio for accurate measurement. Therefore, the disagreement is most likely caused by the difficulty in obtaining reliable experimental data under this specific condition.

Discussion

Sooting Structure

The present simulation results reveal the sooting structure consistent with previous understanding of soot formation in counterflow diffusion flames [10,11,13,14]. Detailed flame and sooting structures computed for flame 3 are presented in Fig. 4. Unless otherwise indicated, the results shown in Fig. 4 are obtained with reaction R7b. It is seen that z_{max} coincides with the location where molecular oxygen vanishes (Fig. 4a). Toward the fuel side of the axial location from z_{max}, soot nucleation starts. As seen in Fig. 4a,b, C_2H_2 and aromatics concentrations begin to increase beyond z_{max}, followed by the onset of soot inception as seen in Fig. 4c. Particles then grow in size toward the stagnation surface, with the C_2H_2 surface reaction being the dominant mass growth process. Soot oxidation is dominated by reactions with OH. It is seen in Fig. 4d that the oxidation rates are significantly lower than the surface growth rates.

The dynamics of soot particles are governed by contributions from convection, thermophoresis, and soot production and destruction, as depicted in Fig. 4e for the particle number density, M_0. It is seen that the production rate, $\dot{M}_0$, due to particle inception peaks around $z = 0.55$ cm, which is balanced by convection and thermophoresis acting in the same direction and carrying the particles toward the stagnation surface. Further downstream near the stagnation surface, the particle production rate becomes negative due to coagulation. To balance the negative particle production rate, the convection and thermophoresis terms change sign. Such a balance extends to the stagnation surface. As coagulation persists ($\dot{M}_0 < 0$), thermophoresis brings in particles to sustain the process, which also causes the "spill" of soot particles across the stagnation surface. Into the fuel side of the stagnation surface, convection and thermophoresis balance each other. Thermophoresis pushes particles toward the fuel nozzle, but convection brings them back. Because of the high strain rates employed in our study, the effect of soot radiation is small in all four flames, causing less than 1 K decrease in temperature throughout the flame.

Surface Growth Model

As stated above, the reaction model R7a does not provide sufficient surface growth rate. It is seen in

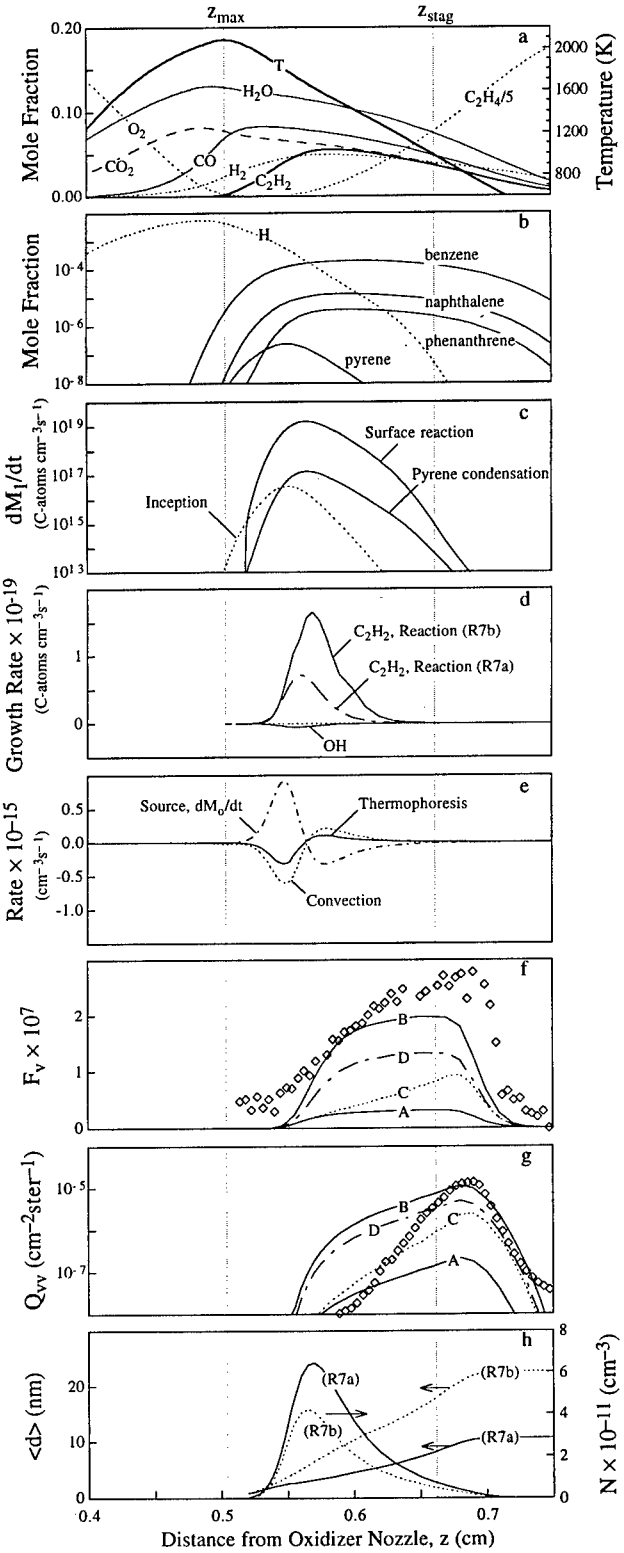

FIG. 4. Detailed flame and soot structure of flame 3: (a and b) computed major species and aromatics mole fraction, and temperature profiles, (c) soot mass growth rate, (d) soot surface growth/oxidation rates, (e) contribution of particle transport and production on soot dynamics, (f and g) comparisons of model predictions with experimental soot volume fraction and scattering coefficients (curve A, C_2H_2 reaction model R7a; curve B, reaction R7b; curve C, reaction R7a, including aromatics surface condensation with a sticking coefficient of 1, but without corresponding aromatics consumption; and curve D, reaction R7b, with aromatics surface condensation and corresponding consumption), and (h) average soot particle diameter and number density.

Fig. 4f that the F_v profile (curve A) computed with reaction R7a is substantially lower than the experimental profile. More importantly, the computed profile is flat, contrary to the experimental result which shows a persistent soot mass growth toward and across the stagnation surface. As seen in Fig. 4d, the rate of surface growth computed with reaction R7a shuts off at the axial location ($z \approx 0.60$ cm), far from the stagnation surface ($z_{stag} \approx 0.66$ cm). The reason is that both temperature and H atom concentration decrease significantly away from z_{max}. Since the reaction model R7a assumes that each C_2H_2 reaction destroys a radical site, and such a radical site cannot be easily regenerated because of the declining temperature and diminishing H atom concentration, the surface growth process stops.

Artificial increases in the inception rate or the rate coefficient of reaction R7 elevates the computed F_v and Q_{vv} values, but they do not change the flatness of the F_v profile, and hence cannot explain why soot mass growth is retarded. Including C_2H_4 as a growth species shows minimal effect on the computed soot profiles. An additional test with reaction R7a was made by allowing all aromatics species to condense onto soot with a unity sticking probability, and neglecting their consumption. As shown by curves C in Fig. 4f,g, the resulting F_v and Q_{vv} values are still substantially lower than the corresponding experimental data.

The above results then point to the inadequacy of reaction R7a in describing the surface growth process in the present diffusion flame situation, although the same reaction was shown to be adequate for the prediction of soot formation in laminar premixed flames [2,3]. The success for premixed flames can be attributed to the fact that such flames have high temperature and high H atom concentration in the soot-forming zone, and thus the surface radicals can be readily regenerated through the H-abstraction reaction by the H atoms. The counterflow diffusion flame lacks such characteristics. For example, the H atom mole fraction at the stagnation surface is computed for flame 3 to be 10^{-7} (Fig. 4b), while the temperature is around 1000 K (Fig. 4a). Such conditions are extremely unfavorable for surface radical regeneration.

Unlike reaction model R7a, reaction R7b assumes that the surface radical sites are preserved after reaction with C_2H_2. With this assumption, the surface growth is sustained to locations of lower temperatures and closer to the stagnation surface (Fig. 4d). Consequently, the maximum F_v and Q_{vv} are in closer agreement with the experimental data. The enhanced surface growth rate increases the particle diameter by a factor of 2, as shown in Fig. 4h. However, it is seen in Fig. 4g that the Q_{vv} signal calculated with reaction R7b is substantially larger than the experimental counterpart at locations immediately after particle inception (cf., curve B and experimental data at $z = 0.6$ cm), and hence calculations with reaction R7b overpredict the growth rate in the corresponding high temperature region. On the other hand, reaction R7a predicts better the Q_{vv} signal at the same axial locations. It appears, then, that while reaction R7a is more adequate at the high-temperature, high H atom concentration region of the soot window, reaction R7b is needed in order to sustain surface growth toward the low-temperature, near stagnation-surface locations.

The above findings are in fact consistent with the dynamics of gas-phase chemically activated reactions. At low temperatures, the dominant product of acetylene reaction with a large gaseous aromatic radical is most likely to be an adduct (a radical) [25]. At high temperatures, however, the process of C_2H_2 addition followed by H elimination becomes dominant with the resulting aromatic product being a nonradical species. Obviously, while the former mechanism is consistent with the surface reaction R7b, the latter corresponds to R7a. The two reaction models actually represent the two limiting cases.

We note that the dynamics of surface radical sites has been a much-debated subject. It has been suggested [33] that surface growth does not show correlation with the reaction environment, e.g., H atom concentration and temperature, and the number of the surface active sites is determined by the number present on the soot particles as they are first formed. This is contrary to the suggestions that surface radical sites are always produced and regenerated through reaction with the gaseous H atoms [2,7]. The results obtained in the present study suggest that the two surface growth concepts can be reconciled in that, while at high temperatures reaction R7a prevails, and hence, the further growth process can be sustained only if the surface radicals are regenerated through the surface H-abstraction reaction; at relatively low temperatures the surface radical is conserved upon the addition of acetylene, such that further surface growth rate is independent of the H atom concentration, and shows only weak dependence on temperature.

Comparing the prediction using reaction R7b with the experimental F_v profile (Fig. 4f), it is seen that the top of the computed profile is still flatter than the experimental counterpart, suggesting that additional processes may be present for the growth process. A likely candidate for such processes is PAH-surface condensation. Since the temperature near the stagnation surface is quite low, aromatic species such as benzene and naphthalene may condense readily onto the soot surface. As previously discussed, curves C in Fig. 4f,g are computed with reaction R7a and with aromatics condensation. It is seen that, although the magnitudes of F_v and Q_{vv} are low, shapes of the profiles are in good agreement with experiment. This result provides evidence that PAH condensation may indeed be important. How-

ever, including PAH condensation with a temperature-independent sticking probability of unity and the corresponding PAH consumption in the calculation with reaction R7b shows adverse effects. As shown in Fig. 4f,g, curve D represents the result of such a computation, and the computed $f_{v,\max}$ and $Q_{vv,\max}$ are now significantly lower than the base case (curves D). The reason is that the consumption of PAHs effectively reduces the inception rate, and hence, the soot surface area. Consequently, the surface growth rate is reduced. On the other hand, if a temperature-dependent PAH sticking probability is introduced, such that sticking is inefficient in the high-temperature inception zone but favored in the low temperature growth region, further improvements of the model can be made. However, no further attempt is justified at this time because such a temperature dependence is not yet well understood.

Concluding Remarks

There are two major contributions from the present study. First, we have experimentally determined the soot profiles in a series of counterflow ethylene diffusion flames with different extents of straining. Second, through numerical simulation using a fundamental model of soot formation, we show that the current understanding on the detailed physical and chemical processes of soot formation can well account for the experimentally observed soot production rate. It is shown through experiment that soot growth persists into the low-temperature region near and at the stagnation surface. It is also demonstrated that the surface addition of acetylene is the dominant process of soot mass growth, and that in order to predict the experimentally determined soot volume fraction and scattering coefficient, soot surface radical sites must be conserved upon its reaction with acetylene toward the low-temperature region of the soot growth window. Further work is required to better understand the dynamics of surface radical sites and the sticking probabilities of PAH with soot particles.

Acknowledgment

This work was supported by the Office of Naval Research under the technical monitoring of Dr. Gabriel Roy. The authors would like to thank Professors R. L. Axelbaum of Washington University at St. Louis and M. Y. Choi of the University of Illinois at Chicago for their helpful discussions on soot measurement.

REFERENCES

1. Bockhorn, H., (Ed.), *Soot Formation in Combustion—Mechanisms and Models,* Springer-Verlag, Berlin, 1994.
2. Frenklach, M. and Wang, H., *Twenty-Third Symposium (International) on Combustion,* The Combustion Institute, Pittsburgh, 1991, p. 1559.
3. Frenklach, M. and Wang, H., in *Soot Formation in Combustion—Mechanisms and Models,* (Bockhorn, H., Ed.), Springer-Verlag, Berlin, 1994, p. 165.
4. Colket, M. B. and Hall, R. J., in *Soot Formation in Combustion—Mechanisms and Models,* (Bockhorn, H., Ed.), Springer-Verlag, Berlin, 1994, p. 442.
5. Mauss, F., Trilken, B., Breitbach, H., and Peters, N., in *Soot Formation in Combustion—Mechanisms and Models,* (Bockhorn, H., Ed.), Springer-Verlag, Berlin, 1994, p. 326.
6. Haynes, B. S. and Wagner, H. Gg., *Prog. Energy Combust. Sci.* 7:229–273 (1981).
7. Howard, J. B., *Twenty-Third Symposium (International) on Combustion,* The Combustion Institute, Pittsburgh, 1990, p. 107.
8. Harris, S. J. and Weiner, A. M., *Combust. Sci. Technol.* 31:155–167 (1983).
9. Breitbach, H., Goettgens, J., Mauss, F., Pitsch, H., and Peters, N., *Twenty-Fifth Symposium (International) on Combustion,* The Combustion Institute, Pittsburgh, 1994, p. 1357.
10. Hall, R. J., Smooke, M. D., and Colket, M B., *Physical and Chemical Aspects of Combustion: A Tribute to Irvin Glassman,* Gordon and Breach, New York, in press.
11. Zhang, C., Atreya, A., and Lee, K., *Twenty-Fourth Symposium (International) on Combustion,* The Combustion Institute, Pittsburgh, 1992, p. 1049.
12. Sun, C. J., Sung, C. J., Wang, H., and Law, C. K., *Combust. Flame,* 1996, in press.
13. Du, D. X., Axelbaum, R. L., and Law, C. K., *Twenty-Third Symposium (International) on Combustion,* The Combustion Institute, Pittsburgh, 1990, p. 1501.
14. Du, D. X., Axelbaum, R. L., and Law, C. K., *Twenty-Second Symposium (International) on Combustion,* The Combustion Institute, Pittsburgh, 1988, p. 387.
15. van de Hulst, H. C., *Light Scattering by Small Particles,* Dover, New York, 1981.
16. D'Allesio, A., in *Particulate Carbon: Formation During Combustion,* (D. C. Siegla and G. W. Smith, Eds.), Plenum, New York, 1981, p. 207.
17. Dalzell, W. H. and Sarofim, A. F., *J. Heat Transfer* 91:100–104 (1969).
18. Smooke, M. D., Puri, I. K., and Seshadri, K., *Twenty-First Symposium (International) on Combustion,* The Combustion Institute, Pittsburgh, 1986, pp. 1783–1792.
19. Puri, I. K., Seshadri, K., Smooke, M. D., and Keyes, D. E., *Combust. Sci. Technol.* 56:1–22 (1987).
20. Gomez, A. and Rosner, D., *Combust. Sci. Technol.* 89:335–362 (1993).
21. Penndorf, R. B., *J. Opt. Soc. Am.* 52:896–904 (1962).
22. Wang, H. and Frenklach, M., *Combust. Flame,* in press.
23. Frenklack, M. and Warnatz, J., *Combust. Sci. Technol.* 51:265–283 (1987).

24. Westmoreland, P. R., Dean, A. M., Howard, J. B., and Longwell, J. P., *J. Phys. Chem.* 93:8171–8180 (1989).
25. Wang, H. and Frenklach, M., *J. Phys. Chem.* 98:11465–11489 (1994).
26. Miller, J. A. and Melius, C. F., *Combust. Flame* 91:21–39 (1992).
27. Neoh, K. G., Howard, J. B., and Sarofim, A. F., in *Particulate Carbon: Formation During Combustion,* (D. C. Siegla and G. W. Smith, Eds.), Plenum, New York, 1981, p. 261.
28. Kazakov, A., Wang, H., and Frenklach, M., *Combust. Flame* 100:111–120 (1995).
29. Law, C. K., Sung, C. J., Yu, G., and Axelbaum, R. L., *Combust. Flame* 98:139–154 (1994).
30. Sung, C. J., Liu, J. B., and Law, C. K., *Combust. Flame* 102:481–492 (1995).
31. Sung, C. J., Law, C. K., and Axelbaum, R. L., *Combust. Sci. Technol.* 99:119–132 (1994).
32. Sung, C. J., Kistler, J. S., Law, C. K., and Nishioka, M., *Combust. Flame* 105:189–201 (1996).
33. Woods, I. T. and Haynes, B. S., in *Soot Formation in Combustion—Mechanisms and Models,* (Bockhorn, H., Ed.), Springer-Verlag, Berlin, 1994, p. 275.

COMMENTS

Peter Lindstedt, Imperial College, UK. In the experiments of Tsuji and co-workers (e.g., [1]) it was noted that flames turn blue at high rates of strain. Furthermore, it has been shown [2] that benzene formation in diffusion flames is strongly sensitive to the rate of strain. This issue is important as it reflects on the dynamics of soot/PAH formation in diffusion flames. Did you investigate this effect experimentally or computationally?

REFERENCES

1. Tsuji, H., *Prog. Energy Combust. Sci.* 8:93 (1982).
2. Leung, K. M. and Lindstedt, R. P., *Combust. Flame* 102:129 (1995).

Author's Reply. The effects of strain rates on PAH and soot formation and flame extinction have been examined experimentally by our group previously [1,2]. Specifically, the critical strain rates of flame extinction, K_E, PAH fluorescence, K_F, and soot-particle light-scattering, K_P, were systematically determined for counterflow diffusion flames burning methane, ethane, propane and butane [1]. It was shown that for every fuel the critical strain rates follow the order of $K_E > K_F > K_P$. Indeed this experimental finding is important as it reflects the effect of hydrodynamic time on reaction processes in the flame. A computational study is being performed which will further delineate the processes governing the observed responses of PAH and soot formation on strain rates.

REFERENCES

1. Du, D. X., Axelbaum, R. L., and Law, C. K., *Twenty-Second Symposium (International) on Combustion,* The Combustion Institute, Pittsburgh, 1988, p. 387.
2. Du, D. X., Axelbaum, R. L., and Law, C. K., *Twenty-Third Symposium (International) on Combustion,* The Combustion Institute, Pittsburgh, 1990, p. 1501.

•

J. B. Howard, MIT, USA. Could you please indicate the accuracy with which your calculations predicted the concentration profiles of acetylene, pyrene, and other PAH?

Author's Reply. The accuracy of the acetylene concentrations was indirectly verified in our previous study [1] of near sooting ethylene and acetylene counterflow diffusion flames. We did not measure the concentration profiles of PAH species in the present study due to difficulties in obtaining such data reliably in these flames. There are, therefore, uncertainties in the inception rate as predicted by the model. We note, however, that the major conclusion of the present study regarding soot particle growth, and particularly the important issue of preserved surface radical sites in the low-temperature region of the flame, is unaffected by the particle inception rate and hence the accuracy of the PAH concentration prediction.

REFERENCES

1. Sun, C. J., Sung, C. J., Wang, H., and Law, C. K., "On the Structure of Nonsooting Counterflow Ethylene and Acetylene Diffusion Flames," *Combust. Flame,* in press.

•

Dr. Arvind Atreya, University of Michigan, USA. I have two questions:

1. In our previous work [1] we found that the velocity profile calculated by using the measured temperature profile and multi-component mixture transport properties (also a function of temperature) is very sensitive to the temperature profile. This is particularly true for the location of the gas stagnation plane. We expect the reverse to be also true. Since temperature is an important parameter, I am curious to find out what are the errors in your velocity profile measurements and consequently what are the errors in your predicted temperature.
2. Our measured C_2H_2 concentrations [2] in counterflow diffusion flames are significantly lower that those pre-

dicted by GRI-Mech 2.1.1. What mechanism are you using to test your predicted C_2H_2 concentrations?

REFERENCES

1. Reference 11 of your paper.
2. Atreya, A., Zhang, C., Kim, H. K., Shamim, T., and Suh, J., "The Effect of Changes in the Flame Structure on the Formation and Destruction of Soot and NO_x in Radiating Diffusion Flames," *Twenty-Sixth Symposium (International) on Combustion,* The Combustion Institute, Pittsburgh, 1996.

Author's Reply. For nonsooting and near-sooting flames, our previous studies [1–4] have demonstrated that if velocity (temperature) profiles can be accurately measured and hence used as a reference of computational alignment, the corresponding flame structure including temperature (velocity) as well as species profiles can be simulated quite well with detailed chemistry and transport properties. Such a procedure is also expected to be reliable for the studies of sooting flames. When using velocity profile as a reference, it is noted that significant error associated with LDV measurement in flame can result from thermophoretic effects on the seeding particles. Furthermore, it is seen from Figs. 2a and 3a that the computed particle velocity profiles (considering the thermophoretic force) within the thermal mixing layer agree well with the LDV measurements. This indicates that the computed temperature profile is reasonably reliable since thermophoretic force is highly sensitive to the temperature profile. More importantly, we have found that the minor temperature uncertainty does not affect the major conclusion of the paper regarding the predictability of the soot model comparing reaction models R7a and R7b.

The gas-phase reaction mechanism employed in this study was based on GRI-Mech 1.2 for small species pyrolysis and oxidation, modified to predict the laminar flame speeds of acetylene and ethylene [1]. For large species formation and growth, the reaction set was based on a detailed reaction mechanism of PAH formation and growth developed for laminar premixed ethylene and acetylene flames [6]. In our previous study [1], it is shown that the reaction mechanism employed in this study predicts very well the acetylene concentration profiles measured in a number of nonsooting and near-sooting counterflow ethylene and acetylene diffusion flames, hence providing a partial verification of the mechanism with regard to acetylene concentration predictions.

REFERENCES

1. Sun, C. J., Sung, C. J., Wang, H., and Law, C. K., "On the Structure of Nonsooting Counterflow Ethylene and Acetylene Diffusion Flames," *Combust. Flame,* in press.
2. Law, C. K., Sung, C. J., Yu, G., and Axelbaum, R. L., *Combust. Flame* 98:139–154 (1994).
3. Sung, C. J., Liu, J. B., and Law, C. K., *Combust. Flame,* 102:481–492 (1995).
4. Sung, C. J., Law, C. K., and Axelbaum, R. L., *Combust. Sci. Technol.* 99:119–132 (1995).
5. Sung, C. J., Kistler, J. S., Law, C. K., and Nishioka, M., *Combust. Flame* 105:189–201 (1996).
6. Wang, H. and Frenklach, M., "A Detailed Kinetic Modeling Study of Aromatics Formation in Laminar Premixed Acetylene and Ethylene Flames," *Combust. Flame,* submitted.

Twenty-Sixth Symposium (International) on Combustion/The Combustion Institute, 1996/pp. 2369–2377

FLAMELET MODELING OF SOOT FORMATION IN LAMINAR ETHYNE/AIR-DIFFUSION FLAMES

M. BALTHASAR,[1] A. HEYL,[2] F. MAUß,[1] F. SCHMITT[1] AND H. BOCKHORN[2]

[1]*Fachbereich Chemie, Universität Kaiserslautern, Erwin Schrödinger Straße 54, 67663 Kaiserslautern Federal Republic of Germany*

[2]*Institut für Chemische Technik, Universität Karlsruhe Kaiserstraße 12, 76128 Karlsruhe Federal Republic of Germany*

Formation, surface growth, and oxidation of soot in an axisymmetric laminar diffusion flame have been calculated using a detailed chemical model for soot formation and oxidation. The laminar flamelet concept has been employed to couple chemical reactions in the gas phase with the flow field. The flow field of the flame is calculated by solving the Navier–Stokes equations in axisymmetric formulation using the SIMPLER algorithm for pressure correction. In addition to the momentum conservation equations, a conservation equation for the mixture fraction and a transport equation for the soot volume fraction are solved in the CFD code. The required source terms for the transport equation for the soot volume fraction are calculated in the mixture fraction/scalar dissipation rate space for laminar flamelets and tabulated in a library. Surface growth and oxidation rates are weighted with the locally calculated soot volume fractions, whereas the source term for particle inception is taken directly from the flamelet calculations.

Radiative heat losses from the gas-phase products have been taken into account in the limit of optically thin gases. The soot formation rates are influenced by the heat losses at low scalar dissipation rates.

The calculated soot volume fractions agree well with the experimental data from Gomez et al. The sensitivity of the calculated soot volume fractions with respect to the different contributions to the appearance rates has been analyzed.

Introduction

Under ideal conditions, the combustion of hydrocarbons leads to carbon dioxide and water; also, the combustible mixture may be specified by stoichiometric composition. Then a maximum of heat is released and a maximum of chemical energy is available for mechanical work.

The local conditions in practical combustion devices such as industrial furnaces, gas turbines, or internal combustion engines deviate far from ideal conditions. If the local concentration of oxygen is not sufficient to convert the fuel into water and carbon dioxide, other products of incomplete combustion and pollutants appear. The "chemical time" for the formation and destruction of these products and the time available for mixing the fuel-rich fluid parcels and oxidizer determine the amount of pollutants in the exhaust of the combustion device.

One class of pollutants is particulates and soot. Large progress has been achieved in recent years in understanding and modeling soot formation during incomplete combustion of hydrocarbons [1–3,23].

One type of model for soot formation is based on detailed reaction mechanisms for the gas-phase chemistry and the formation, growth, and oxidation of soot particles. Particularly, Frenklach has introduced a surface growth mechanism similar to the planar growth of PAH [4–6]. This approach has been adopted and modified by several groups [7–10]. The result for modeling sooting flames is a large system of equations containing the respective conservation equations for the mass fractions of the gas-phase chemical species, the enthalpy, and a limited number of transport equations for some moments of the soot particle size distribution.

This large set of differential equations presently can be solved within acceptable computer time for one-dimensional systems only. To overcome this deficiency, different approaches to model soot formation have been developed, describing the gas-phase chemistry by reduced mechanisms [11,12] or relating the soot formation to a quasi fuel [13–15] or quasi-intermediate species [16]. The latter models have to be calibrated for specific fuels. Predicting of soot formation in turbulent flames using these models leads to some closure problems.

Other approaches to calculate the formation of soot in diffusion flames are based on the laminar flamelet concept. In laminar diffusion flamelets, scalar quantities (e.g., species mass fractions, temperature, and density) are related to mixture fraction and

scalar dissipation rate. The species mass fractions, temperature, and so forth are unique functions in the mixture fraction/scalar dissipation rate space that can be gathered in flamelet libraries. In contrast to this, soot mass fractions are not uniquely correlated with mixture fraction/scalar dissipation rate [13,17]. Therefore, the flamelet concept cannot be adopted to sooting flames without modifications. It could be shown that the rates of soot formation can be correlated with local conditions (i.e., mixture fraction/scalar dissipation rates) in diffusion flames [13,17] or in partially premixed counterflow twin flames [18]. This finding can be used to modify the flamelet concept in modeling sooting diffusion flames by expanding the flamelet libraries with correlations of soot formation (and oxidation) rates versus mixture fraction/scalar dissipation rates.

Modeling of sooting diffusion flames then is performed by solving the transport equations for the flow field and the mixture fraction and calculating the scalar dissipation rates. The chemistry is coupled to the flow field via correlations of the mass fractions and temperature versus mixture fraction/scalar dissipation rates from flamelet libraries. An additional transport equation has to be solved for the mass fraction of soot. The appearance rates of soot (rate of particle inception, surface growth, and oxidation) that enter into the source term of that transport equation are gathered from laminar flamelets as well. With this concept, the closure problem for the turbulent reaction rates can be handled much more easily.

The necessary appearance rates can be calculated from calibrated models [13,14]. They are also predictable on the basis of a detailed chemical soot model [19]. The aim of the present paper is to demonstrate modeling of sooting diffusion flames on a flamelet approach as mentioned previously. This is exemplified for a laminar ethyne/air diffusion flame that has been investigated in Ref. 20. The validation of the concept for laminar flames is the first step in the application of this concept to turbulent diffusion flames.

It should be emphasized that detailed models of the kind used in this study essentially depend on the quality of kinetic parameters and the knowledge of the reaction channels of the species involved. These models only reproduce phenomena observed in the formation of the bulk of soot. The formation of high molecular tarry structures in an early stage of soot formation or the fine structure of soot are not covered by these models.

Modeling

Reference Flame

The experimental data are taken from investigations of soot formation in laminar ethyne/air diffusion flames performed by Gomez et al. [20]. The soot volume fraction was measured on the centerline of axisymmetric ethyne/air diffusion flames by laser light scattering/extinction at several levels of dilution with nitrogen. The fuel stream of the chosen flame consists of 68.25 mol % N_2 and 31.75 mol % ethyne; the oxidizer is air. The experiments were conducted with a burner consisting of two concentric tubes at atmospheric pressure. Fuel was emitted through the inner tube (i.d. 10 mm), the oxidizer through the outer one (i.d. 10 cm).

Flow Field

The numerical simulation of the laminar flow field includes the solution of the overall continuity equation, the Navier–Stokes equations in low Mach number formulation, and a transport equation for the mixture fraction Z, representing the normalized element mass fraction. The generalized conservation equation in cylindrical coordinates for a dependent variable ϕ for stationary axisymmetric problems can be written as

$$\frac{\partial(\rho u\phi)}{\partial x} + \frac{1}{r}\frac{\partial}{\partial r}(r\rho v\phi) = \frac{\partial}{\partial x}\left[\Gamma_\phi \frac{\partial\phi}{\partial x}\right] + \frac{1}{r}\frac{\partial}{\partial r}\left[\Gamma_\phi r \frac{\partial\phi}{\partial r}\right] + S_\phi \quad (1)$$

The source term S_ϕ contains all parts of the conservation equation, which cannot be included in the convection or diffusion terms. For the flame under consideration, the system of equations is set up by the following:

Continuity: $\phi = 1$; $S_\phi = \Gamma_\phi = 0$

Axial momentum: $\phi = u$; $\Gamma_\phi = \eta$

$$S_u = -\frac{\partial p}{\partial x} + \frac{\partial}{\partial x}\left(\eta\frac{\partial u}{\partial x}\right) + \frac{1}{r}\frac{\partial}{\partial r}\left(r\eta\frac{\partial u}{\partial x}\right) - \frac{2}{3}\frac{\partial}{\partial x}\left[\eta\left(\frac{\partial u}{\partial x} + \frac{1}{r}\frac{\partial(rv)}{\partial r}\right)\right] + \rho g$$

In the preceding equation, ρg represents buoyancy effects.

Radial momentum: $\phi = v$; $\Gamma_\phi = \eta$;

$$S_v = -\frac{\partial p}{\partial r} + \frac{\partial}{\partial x}\left(\eta\frac{\partial u}{\partial r}\right) + \frac{1}{r}\frac{\partial}{\partial r}\left(r\eta\frac{\partial v}{\partial r}\right) - \frac{2}{3}\frac{\partial}{\partial r}\left[\eta\left(\frac{\partial u}{\partial x} + \frac{1}{r}\frac{\partial(rv)}{\partial r}\right)\right]$$

Mixture fraction: $\phi = Z$; $\Gamma_z = \eta/\sigma_\phi$; $\sigma_\phi = 0.7$; $S_\phi = 0$

The resulting equations are solved with a two-dimensional solver for elliptic flow problems employ-

ing the method of finite volumes. To suppress numerical diffusion, the higher-order discretization scheme QUICK [21] is used. The system of nonlinear equations with a block-pentadiagonal system matrix has been solved after resolving the block structure with an ADI method combined with the Thomas algorithm. The pressure correction has been obtained by the SIMPLER algorithm [22].

Coupling of Flow Field and Chemical Reactions

In the flamelet regime of combustion, the composition of the flame gases can be gathered from flamelets. In laminar flamelets, all scalars are unique functions in the mixture fraction/scalar dissipation rate space [24]. Consequently, their balance equations are transformed into this space:

$$\rho \frac{\chi}{2} \frac{\partial^2 T}{\partial Z^2} - \sum_{i=1}^{n} \frac{h_i}{c_p} \dot{w}_i - \dot{q}_R = 0 \tag{2}$$

$$\rho \frac{\chi}{2} \frac{\partial^2 Y_i}{\partial Z^2} + \dot{w}_i = 0 \tag{3}$$

where the scalar dissipation rate χ is defined by

$$\chi = 2D \left[\left(\frac{\partial Z}{\partial x} \right)^2 + \left(\frac{\partial Z}{\partial r} \right)^2 \right] \tag{4}$$

Here Y_i are the species mass fractions, T is the temperature, and Z is the mixture fraction. $\dot{q}_R$ refers to radiative heat losses of gas-phase compounds, which are taken into account in this work in the limit of optically thin gases. $\dot{w}_i$ is the chemical production rate of species i, h_i the species enthalpy, c_p the constant pressure specific heat capacity, and ρ the mass density.

For the investigated ethyne/air flame, a library of flamelets has been calculated. To achieve greater precision in the calculations, a flamelet code with an adaptive grid was used. The chemical model consisted of 581 chemical reactions and 71 chemical species for the ethyne/oxygen/nitrogen flames. The rate coefficients where taken from Refs. 25 and 26. The stationary solutions were stored in a library containing profiles of temperature, mass density, and mass fractions of all chemical species in dependence on mixture fraction and scalar dissipation rate. The coupling of chemistry and flow field was performed via the mixture fraction and the scalar dissipation rate, which were provided by the flow field calculations. For every grid point of the flow field, the mass fractions of the gaseous species and temperature and the mass density are interpolated from the flamelet libraries.

Modeling of Soot Formation

The mass fraction of soot Y_S is postprocessed, solving its transport equation for the flow field in consideration. Diffusion and thermophoresis are taken into account.

$$\begin{aligned} \frac{\partial(\rho u Y_s)}{\partial x} + \frac{1}{r}\frac{\partial}{\partial r}(r\rho v Y_s) &= \frac{\partial}{\partial x}\left[\rho D \frac{\partial Y_s}{\partial x}\right] \\ &+ \frac{1}{r}\frac{\partial}{\partial r}\left[\rho D r \frac{\partial Y_s}{\partial r}\right] \\ &+ \frac{\partial}{\partial x}\left[0.54\eta \frac{1}{T}\frac{\partial T}{\partial x} Y_s\right] \\ &+ \frac{1}{r}\frac{\partial}{\partial r}\left[0.54\eta r \frac{1}{T}\frac{\partial T}{\partial r} Y_s\right] \\ &+ \left[\frac{d}{dt}(\rho s f v)\right] \end{aligned} \tag{5}$$

Here, η is the dynamic viscosity, $\rho s = 1860\ \mathrm{kgm}^{-3}$ the density of soot, and f_v the soot volume fraction proportional to the first moment of the soot particle size distribution [29].

The source terms in Eq. (5), that is, the different contributions to the soot appearance rates, are stored as well in the flamelet libraries. The different contributions are calculated with the detailed chemistry soot model, the basic concept of which is given in Ref. 4. Modifications concerning the treatment of the different classes of PAH are described extensively in Ref. 7. The mechanism and rate coefficients are taken from Ref. 4. Changes of the rate coefficients are documented in Ref. 30. The main features of this model are as follows:

The chemical reactions in the gas phase up to small PAH are taken from a detailed kinetic mechanism provided by Chevalier et al. [25], expanded and revised by new kinetic rate data from Baulch et al. [26]. The formation of soot precursors up to benzene and the further growth of small PAH follows a compilation, which is basically taken from Frenklach et al. [4] and Miller et al. [27]. The same mechanism as for flamelet calculation of the gas-phase reactions has been used.

The further growth of PAH is assumed to be a fast polymerization process, which leads to steady-state assumptions for the PAH concentrations. This results in a system of algebraic equations for the mass fraction of each PAH.

The formation and further growth of soot particles includes all possible coagulation processes of particles and PAH, which are assumed to follow Smoluchowski's equations in the free molecular regime. Also, the heterogeneous surface reactions are taken into consideration. Particle inception is considered as a coalescence of two PAH species to a three-dimensional particle. Surface growth of soot particles is described by a mechanism [8,28,30] that is based on the HACA mechanism introduced by Frenklach [4]. Oxidation of soot particles is assumed to occur via the attack of OH radicals and oxygen. Details of the mechanism are given in Ref. 30.

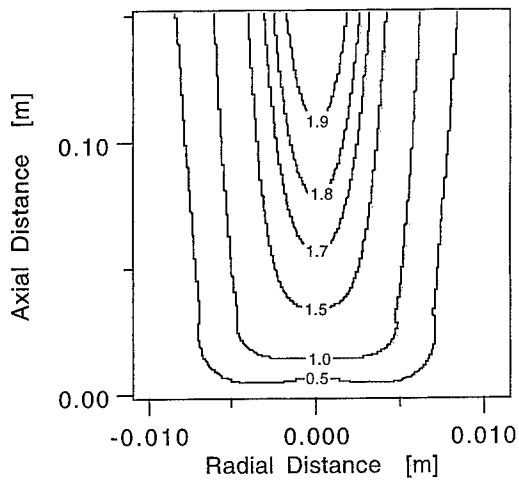

FIG. 1. Two-dimensional profiles of the axial velocity u [m/s].

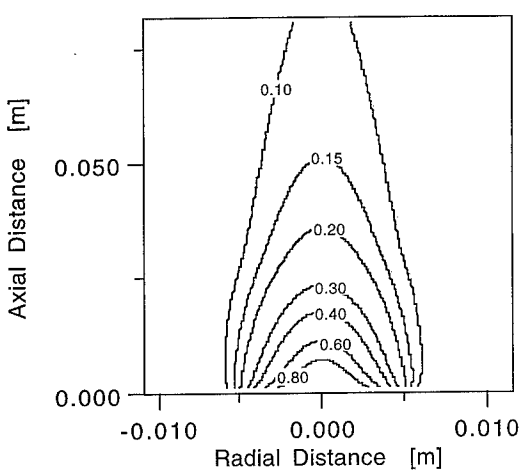

FIG. 2. Two-dimensional profiles of the mixture fraction Z. The isoline of Z_{st} describes the contour of the flame (Z_{st} = 0.2).

Because the source term in Eq. (5) for the first moment of the particle size distribution contains some other (broken) moments [29], two equations for two moments are solved in the flamelet space. The broken moments are derived by interpolation. Relating the Lewis numbers of the different size classes Le_j to the Lewis number of the smallest particle Le_1 by

$$Le_j = j^{2/3} Le_1 \tag{6}$$

the following equation for the moment M_r in terms of the mixture fraction is used:

$$\frac{1}{4}\frac{\partial \rho\chi}{\partial Z}\left[\frac{\partial M_r/\rho}{\partial Z} - \frac{1}{Le_1}\frac{\partial M_{(r-2/3)}/\rho}{\partial Z}\right] - \rho\frac{\chi}{2Le_1}\frac{\partial^2 M_{(r-2/3)}/\rho}{\partial Z^2} - \dot{M}_r = 0\text{b} \tag{7}$$

The first moment ($r = 1$) is directly proportional to the soot volume fraction [29]. The source term $\dot{M}_r$ contains the previously mentioned processes for soot formation.

Profiles of the source terms for particle inception $(\partial f_v/\partial t)_{pi}$ and heterogeneous surface reactions $1/f_v(\partial f_v/\partial t)_{sg,ox}$ related to the local soot volume fraction are obtained by solving the transport equation, Eq. (6), simultaneously with the flamelet equations for the scalar quantities. Because experimental investigations show that the soot appearance rate is proportional to the soot volume fraction [23], the source terms for surface growth and soot oxidation are normalized with the soot volume fraction. The different contributions to the appearance rate of soot are stored in the flamelet libraries as a function of mixture fraction and scalar dissipation rate. The coupling of the flow field and the rates of soot formation is performed in the same way as for the composition and temperature of the gas phase via the mixture fraction and the scalar dissipation rate that are provided by the flow field calculations. The soot volume fraction and the different parts of its appearance rate are interpolated from the libraries at every grid point of the two-dimensional flow field.

Results and Discussion

Soot formation in a nitrogen-diluted axisymmetric ethyne/air-diffusion flame experimentally investigated by Gomez et al. [20] has been calculated. The two-dimensional profiles of axial velocities and mixture fraction predicted with the CFD calculations are given in Figs. 1 and 2. The acceleration of axial velocity is caused by the increase of temperature by a factor of 7 and the corresponding buoyancy effects. The diameter of the inlet tube is 10 mm. The fuel volumetric flow rate is 1.79 cm^3/s. For the current dilution of the fuel, the stoichiometric mixture fraction is calculated to be Z = 0.2. This value of Z, which is also shown in Fig. 2, represents the contour of the flame. The calculated flame height of h = 38 mm corresponds reasonably well with the measured one of h = 42.2 mm.

Figure 3 shows the isotherms resulting from the chemical reactions in the gas phase that are coupled to the flow field via flamelet libraries. The peak value of the calculated temperature is 2180 K. The adiabatic flame temperature has not been attained because radiation heat losses are taken into account in the flamelet calculations.

The different contributions to the source term of

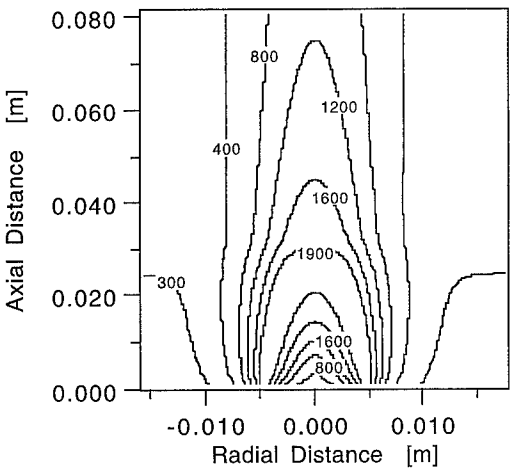

FIG. 3. Two-dimensional profiles of the temperature [K].

soot volume fraction for a scalar dissipation rate of $\chi = 10s^{-1}$ related to the mixture fraction are plotted in Figs. 4A–4C. This scalar dissipation rate refers to a height of 7 mm above the burner, as can be seen from Fig. 4D. Soot is formed mainly by heterogeneous surface growth reactions occurring at values of Z between 0.6 and 0.23. The maximum surface growth rate is found close to the stoichiometric mixture fraction at Z = 0.267, where the concentration of H radicals is high and the temperature is about 1800 K. For lower values of Z, the temperature increases and the reverse reactions of the carbon addition prevent a further surface growth so that surface growth becomes slightly negative. The contribution of particle inception to the source term of the soot volume fraction equation is minor. The soot is oxidized in the fuel-lean area of the flamelet between Z = 0.1 and 0.2.

The profiles of rates of the different soot-forming processes have been calculated for several scalar dissipation rates, exemplified by the normalized surface growth rate in Fig. 5. At high scalar dissipation rates and large mixture fractions (small heights above the burner), the maximum surface growth rates decrease with decreasing dissipation rate. This is caused by the increasing temperature, resulting in higher rates

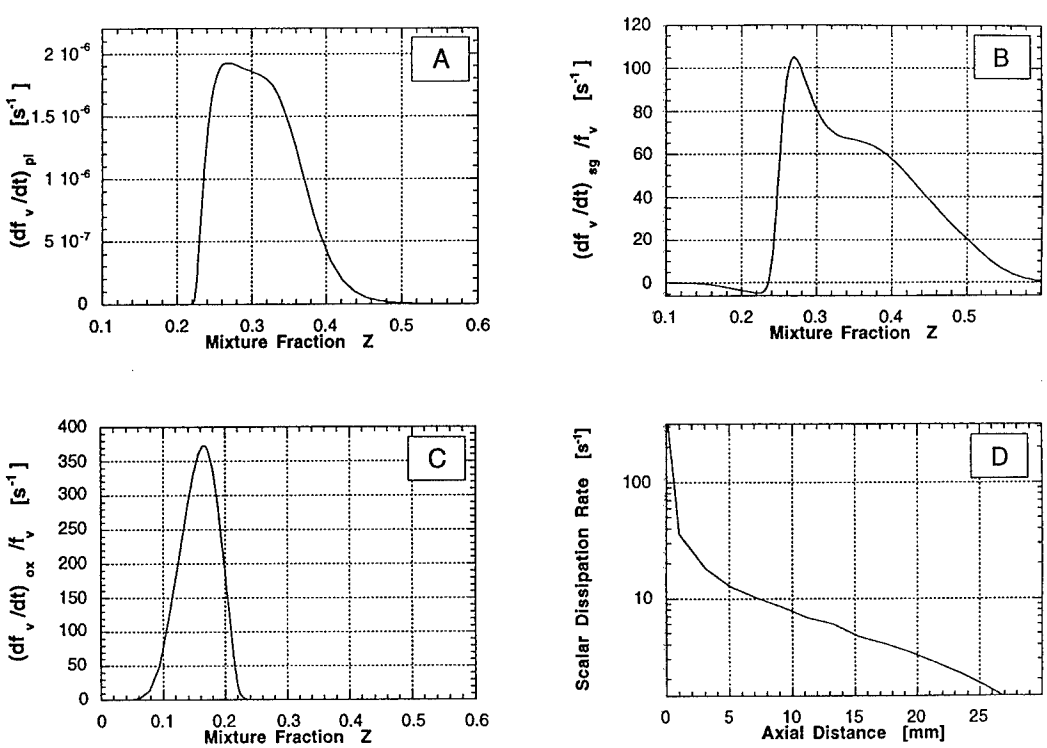

FIG. 4. Flamelet profiles of particle inception rates (A), normalized surface growth rates (B), and oxidation rates (C) at $\chi = 10[s^{-1}]$ in dependence of Z. Centerline profiles of scalar dissipation rate χ in dependence of the height above the burner (D).

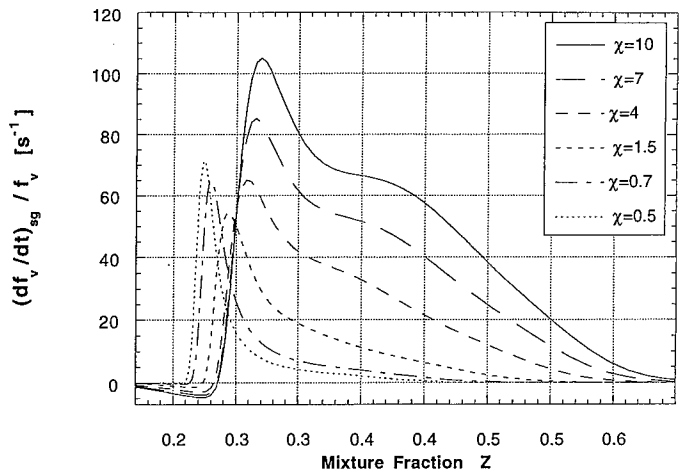

FIG. 5. Flamelet profiles of surface growth for different scalar dissipation rates.

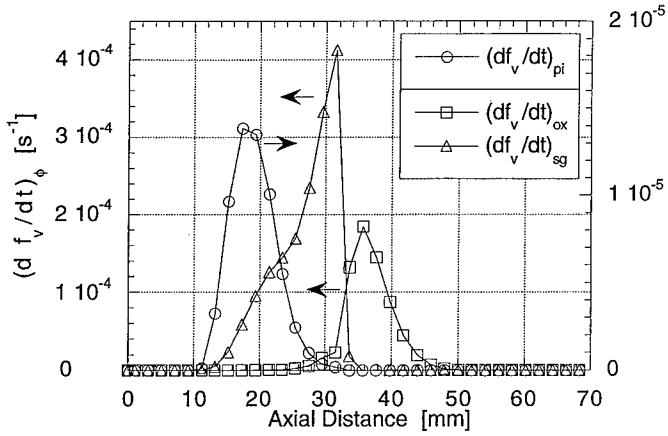

FIG. 6. Centerline profiles of particle inception, surface growth, and oxidation rates.

of the reverse reactions of carbon addition. At $\chi = 1.5\ s^{-1}$ and small mixture fractions (increasing height above the burner), the maximum surface growth rates increase again with decreasing dissipation rate since the maximum temperature of the flamelet decreases because of radiative heat losses.

The resulting profiles of particle inception rate and nonnormalized surface growth rate and oxidation rate at the centerline of the investigated flame are shown in Fig. 6. Particle inception starts at 10 mm and has a maximum value of $1.4 \times 10^{-5}\ s^{-1}$ at 18 mm height. Surface growth appears after the first particles are formed. The slope of surface growth rate profile first increases up to a height of 20 mm, then decreases again between 20 and 25 mm. At 25 mm, the scalar dissipation rate reaches the value of $1.5\ s^{-1}$ (compare Fig. 5 with 4D). Below this axial position, the slope of surface growth rate profile increases again up to its maximum of 32 mm. At this height, the local mixture fraction is higher than 0.22 (see Fig. 2) and surface growth reactions suddenly stop. Beyond this distance, soot is oxidized by fast heterogeneous reactions mainly with OH.

The calculated soot volume fraction on the centerline is compared with the experimental data from Ref. 20 in Fig. 7. The agreement between calculations and experiment are reasonable considering the scatter in the experimental results. However, it is found that an increase of surface growth rates by 20% leads to an increase by a factor of 2 in the calculated soot volume fractions. The sensitivity of the soot volume fraction with respect to particle inception rates is low. An increase of the oxidation rates does not influence the maximum amount of soot formed but results in a steeper decrease of soot volume fractions between 30 and 40 mm.

The high sensitivity of the predicted soot volume fractions with respect to the surface growth rates demands a further evaluation of the influence of different flamelet boundary conditions (e.g., heat losses, different initial temperatures) on the calculated soot volume fractions. Therefore, the previ-

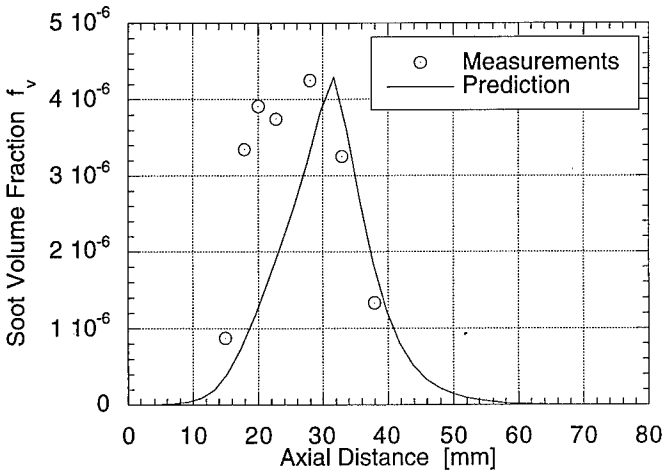

FIG. 7. Comparison of numerical calculations and measurements by Gomez et al. for centerline profile of soot volume fraction.

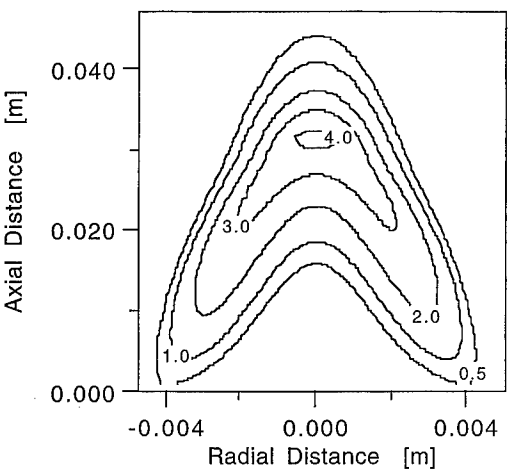

FIG. 8. Two-dimensional profiles of soot volume fraction $f_v \times 10^6$.

ously presented concept of flamelet modeling of soot formation is limited to flames in which formation of soot has only little effect on the flame structure as shown in Refs. 6 and 9. This is the case for slightly sooting flames such as the one investigated.

A two-dimensional contour plot of the soot volume fraction is shown in Fig. 8. Soot appears first at a radial distance of 4 mm, and the maximum soot volume fraction is found on the centerline.

Conclusions

Numerical modeling of soot formation in an axisymmetric laminar diffusion flame has been performed using a detailed chemical soot model. The flow field was coupled with the gas phase by the laminar flamelet concept providing two-dimensional profiles of all scalar quantities involved.

An additional transport equation for the soot volume fraction was solved. The source term of these equations containing the rates for particle inception, surface growth, and oxidation were obtained from the flamelets and tabulated in libraries. Because of the dependence of surface growth and oxidation on the local soot volume fraction, these terms have been normalized with soot volume fractions.

This approach is limited to flames in which soot formation has only little effect on flame structure. As shown previously, this assumption is valid for the majority of slightly sooting flames [6,9].

Radiative heat losses have been taken into account in the limit of thin gases. An influence of the radiative heat losses on the rates of surface growth at low scalar dissipation rates was found.

The calculated soot volume fractions on the centerline agree well with the experimental measurements. The sensitivity of soot volume fraction with respect to the different soot-forming processes was investigated. Changes of surface growth rate affect the calculated soot volume fraction essentially, whereas variations in particle inception rate show no remarkable effect on soot volume fractions.

Acknowledgments

This research was partially supported by the commission of the European Communities, the Swedish National Board for Technical Development (STU), and the Joint Research Committee of European car manufacturers (Fiat, Peugeot SA, Renault, Volkswagen, and Volvo) within the IDEA and IDEA-EFFECT programs.

REFERENCES

1. Lahaye, J. and Prado, G., (Eds.), *Soot in Combustion*

Systems and Its Toxic Properties, Plenum Press, New York, 1983.
2. Jander, H. and Wagner, H. G., *Soot Formation in Combustion—An International Round Table Discussion,* Vandenhoeck & Ruprecht, Göttingen, 1990.
3. Bockhorn, H., (Ed.), *Soot Formation in Combustion—Mechanisms and Models,* Springer Verlag, Berlin and Heidelberg, 1994.
4. Frenklach, M. and Warnatz, J., *Combust. Sci. Technol.* 51:265 (1987).
5. Frenklach, M. and Wang, H., *Twenty-Third Symposium (International) on Combustion,* The Combustion Institute, Pittsburgh, 1990, p. 1559.
6. Frenklach, M. and Wang, H., in *Soot Formation in Combustion—Mechanisms and Models* (Bockhorn, H., Ed.), Springer Verlag, Berlin and Heidelberg, 1994, p. 162.
7. Mauß, F., Trilken, B., Breitbach, H., and Peters, N., in *Soot Formation in Combustion—Mechanisms and Models* (Bockhorn, H., Ed.), Springer Verlag, Berlin and Heidelberg, 1994, p. 325.
8. Colket, M. B. and Hall, R. J., in *Soot Formation in Combustion—Mechanisms and Models* (Bockhorn, H., Ed.), Springer Verlag, Berlin and Heidelberg, 1994, p. 437.
9. Hall, R. J., Smooke, M., and Colket, M. B., in *Physical and Chemical Aspects of Combustion: A Tribute to Irvin Glassman* (Sawyer, R. F. and Dryer, F. L., Eds.), in press.
10. Mauß, F., Schäfer, T., and Bockhorn, H., *Combust. Flame* 99:697 (1994).
11. Fairweather, M., Jones, W. P., Ledin, H. S., and Lindstedt, R. P., *Twenty-Fourth Symposium (International) on Combustion,* The Combustion Institute, Pittsburgh, 1992, p. 1067.
12. Lindstedt, P. P., in *Soot Formation in Combustion—Mechanisms and Models* (Bockhorn, H., Ed.), Springer Verlag, Berlin and Heidelberg, 1994, p. 417.
13. Stewart, C. D., Syed, K. J., and Moss, J. B., *Combust. Sci. Technol.* 75:211 (1991).
14. Moss, J. B., in *Soot Formation in Combustion—Mechanisms and Models* (Bockhorn, H., Ed.), Springer Verlag, Berlin and Heidelberg, 1994, p. 544.
15. Magnusson, B. F., Hjertager, B. H., Olsen, J. G., and Bhaduri, D., *Seventeenth Symposium (International) on Combustion,* The Combustion Institute, Pittsburgh, 1978, p. 1383.
16. Said, R., Garo, A., and Borghi, R., submitted to *Combust. Flame.*
17. Kent, J. H. and Honnery, D. R., in *Soot Formation in Combustion—Mechanisms and Models* (Bockhorn, H., Ed.), Springer Verlag, Berlin and Heidelberg, 1994, p. 199.
18. Schäfer, T., Mauß, F., Bockhorn, H., and Fetting, F., *Z. Naturforsch.* 50a:11 (1995).
19. Mauß, F., Schäfer, T., and Bockhorn, H., VDI-Berichte Nr. 1193, VDI-Verlag, Düsseldorf, 1995, p. 235.
20. Gomez, A., Littman, M. G., Glassman, I., *Combust. Flame* 70:225 (1987).
21. Leonard, B. P., *Comp. Meth. Appl. Mech. Eng.* 19:S.59–98 (1979).
22. Patankar, S. V., *Num. Heat. Transf.* 4:S.409–425 (1981).
23. Haynes, B. S. and Wagner, H. G., *Prog. Energy Combust. Sci.* 7:229 (1981).
24. Peters, N., *Prog. Energy Combust. Sci.* 10:319 (1984).
25. Chevalier, C., Louessard, P., Müller, U. C., and Warnatz, J., *Int. Symp. on Diagnostics and Modelling of Combustion in Internal Engines COMODIA* 90, Kyoto, The Japan Society of Mechanical Engineers, 1990.
26. Baulch, D. L., Cobos, C. J., Cox, R. A., Frank, P., Hayman, G., Just, T., Kerr, J. A., Murrells, T., Pilling, M. J., Troe, J., Walker, R. W., and Warnatz, J., *J. Phys. Chem. Ref. Data* 21:411–429 (1992).
27. Miller, J. A. and Melius, C. F., *Combust. Flame* 70:21–39 (1992).
28. Mauß, F. and Bockhorn, H., *Z. Phys. Chem.* 188:45–60 (1995).
29. Frenklach, M. and Harris, S. J., *J. Coll. Interf. Sci.* 118 (1) (1987).
30. Marquardt, M., Mauß, F., Jungfleisch, B., Suntz, R., and Bockhorn, H., "Re-Initiation of Soot Surface Growth in Premixed Counter-Flow Flames" *Twenty-Sixth Symposium (International) on Combustion,* The Combustion Institute, Pittsburgh, 1996, pp. 00–00.

COMMENTS

M. A. Delichatsios, FMRC, USA. Your paper shows that the *global* soot formation rate (df_v/dt) depends on mixture fraction (i.e. only on gaseous phase) but not on surface area of soot particles. We think that this result is consistent with our model [1] for soot formation. This global model does not contradict the importance of soot forming by growth on particle surface. It seems, however, that one of your coauthors (F. Mauß) thinks that your global model shows that $1/f_v\ df_v/dt$ is a function of mixture fraction, and not df_v/dt. Please, you should clarify. If F. Mauß's claim is correct, then one can easily argue [1] that such a model (i.e. $1/f_v\ df_v/dt$ = function of mixture fraction) is inconsistent with laminal flame diffusion smoke-point data.

REFERENCE

1. Delichatsios, M. A., "Phenomenological Model for Soot Formation," *CST,* 1994.

Author's Reply. Our statement was that soot formation rate is indeed dependent on "surface area." However, the

inner surface of a porous soot particle rather than the outer surface of a complex structured soot particle is the relevant quantity. This could be demonstrated by experiments where the outer surface area has been changed by suppressing coagulation of soot particles leaving the other burning conditions unchanged [1]. In the present approach, all quantities determining the soot formation rates—including the "surface area"—can be expressed by means of the mixture fraction. The soot surface growth rates have been stored in the flamelet libraries for numerical reason in the form $1/f_v\ df_r/dt$.

REFERENCE

1. Bockhorn H. and Schäfer, Th., "Growth of Soot Particles in Premixed Flames by Surface Reactions," in (H. Bockhorn, Ed.), *Soot Formation in Combustion—Mechanisms and Models*, Springer Verlag, Berlin, Heidelberg, 1994, p. 253.

Twenty-Sixth Symposium (International) on Combustion/The Combustion Institute, 1996/pp. 2379–2386

CFD PREDICTION OF COUPLED RADIATION HEAT TRANSFER AND SOOT PRODUCTION IN TURBULENT FLAMES

N. W. BRESSLOFF, J. B. MOSS AND P. A. RUBINI
School of Mechanical Engineering
Cranfield University, Cranfield
Bedfordshire, MK43 OAL, England

A novel coupled strategy is presented for predicting soot and gas species concentrations, and radiative exchange in turbulent combustion. The relatively slow processes governing soot formation are described by a model that accounts for radiative loss. In contrast to past studies, it is coupled here to the discrete transfer radiation model (DTRM), incorporating a weighted sum of gray gases (WSGG) solution to the radiative transfer equation, in an elliptic computational simulation. Incorporation of the WSGG solution in the DTRM provides a better representation of the nongray radiative properties of combustion media than that offered by other more straightforward strategies, and without excessive computational expense. Combustion is modelled by an eddy breakup concept and the k-ε turbulence model, with temperature evaluated from the solved enthalpy field. This complete strategy—the first reported of its kind—is applied to a confined, turbulent, jet diffusion flame burning methane in air. Confinement of the flame demands that account should be taken of the conjugate heat transfer at the boundaries. Numerical results are compared to experimental measurements of mixture fraction, temperature, and soot volume fraction, and generally good agreement is achieved. Additionally, the computation of radiative exchange is considered in detail.

Introduction

Progress in the representation of increasingly complex combustion chemistry in CFD predictions of turbulent burning in engines, stationary powerplants, and building fires has exposed significant shortcomings in the accompanying models of sooting processes and radiative heat transfer. While laboratory-scale flames burning hydrocarbon fuels with high H/C ratios at atmospheric pressure are weakly sooting and optically thin, most nonpremixed burning in practical systems does not exhibit these characteristics. Uncertainties in computed gas temperatures of > 100 K associated with radiative exchange may then undermine much of the investment in extended reaction schemes, for example, for improved emissions prediction. The three-dimensional nature of most practical combustion geometries may impose additional constraints on the modeling approaches that may be usefully implemented in relation to the attainable resolution consistent with computational economy. The present study, therefore, develops a methodology that combines a laminar flamelet–based description of soot formation, an eddy breakup combustion model, and radiative energy exchange by the discrete transfer method within the CFD framework of an elliptic flow-field calculation. The methodology is evaluated through detailed comparisons between CFD prediction and experimental measurement in a confined, methane jet flame.

While coupled radiation and soot kinetics computations of laminar flames have been reported recently [1,2], mean closure problems have led most turbulent flame calculations to focus more narrowly on one aspect or the other. Perturbed state relationships, incorporated in fast chemistry/conserved scalar combustion models, have supplanted radiative heat loss in some predictions [3,4], for example, while in others, approximate descriptions of radiative flux in the optically thin limit, in the absence of detailed soot prediction, have been introduced into balance equations for mean mixture enthalpy [5,6].

The comparatively slow chemistry of soot formation requires that additional balance equations be solved for soot properties, while their strong temperature dependence insists that the influence of turbulent fluctuations also be accommodated in their averaged forms. The processes of soot formation and associated radiative heat loss are therefore closely coupled. A multiple flamelet approach in which families of soot source terms, expressed as functions of mixture fraction, are distinguished by the degree of radiative loss experienced and averaged over the mixture fraction pdf [7], is here linked to an eddy breakup model of combustion heat release [8]. Thermal radiation is modeled using the discrete transfer radiation model [9] incorporating a weighted sum of gray gases solution to the radiative transfer equation [10]. This entails separate equations for each gray gas component, with coefficients

derived for mixtures of soot, CO_2, and H_2O [11]. Additionally, the formulation includes treatment of gray boundaries [12].

The complete strategy is evaluated by detailed comparison with measurements of mean mixture fraction, soot volume fraction, and temperature in a confined, turbulent, methane jet flame. While the present paper focuses on the integration of the several distinctive but interacting model elements that make up the fully coupled calculation, a comparatively simple flame configuration has been adopted in order to provide a comprehensive data set for evaluation purposes.

Experimental Measurement

Detailed scalar measurements are reported by Brookes [13] for a coflowing, turbulent, methane jet flame confined within a cylindrical liner. This confined flame configuration has also been employed in earlier sooting studies of prevaporized kerosine flames [14], to which reference should be made for general detail.

In the present application, methane issues from a cylindrical tube, 4.07 mm in diameter, at a flow rate of 10.3 g/min. The jet flame is rim stabilized by an annular premixed pilot flame. A coflowing air stream occupies the remainder of the inlet contained within a pyrex cylindrical liner of 155 mm internal diameter. The overall equivalence ratio is 0.25.

Radial profiles of time-averaged mixture fraction, measured by microprobe sampling and mass spectrometric analysis, temperature by exposed bead, fine-wire thermocouple, and soot volume fraction by integrated laser absorption and tomographic inversion are reported at discrete flame heights of 150, 300, 350, and 425 mm.

Numerical Simulation

Computational simulation is performed using a finite volume, general curvilinear CFD code called SOFIE (Simulation of Fires In Enclosures) currently being developed at Cranfield. A SIMPLEC pressure correction algorithm [15] for colocated velocities and pressure is used to evaluate the flow field [16]. Momentum interpolation [17] and a second-order TVD discretization scheme [18] are employed to ensure a numerically stable solution without nonphysical oscillations and false diffusion. The discretized equations are solved using a line-by-line, tridiagonal matrix algorithm. Further details of these techniques are available in the literature cited.

An important demand of numerical accuracy concerns the extent to which a converged solution is independent of the underlying grid. In the present study, 3600 internal flowing nodes are used in a prismatic sector of the axisymmetric geometry with mirror symmetry boundary conditions imposed on the two longitudinal faces thus produced. Finer resolutions yielded less than a 1% change in velocities and temperatures across radii at five distinct heights.

In common with previous studies of axisymmetric jet flames, a top-hat inlet profile is assumed with velocities of 20.16 and 0.61 m s^{-1} for methane and air, respectively. Although the flame is confined within a pyrex casing, which is itself contained inside a pressure vessel, only the inner flow field is modeled. However, the internal face of the pyrex casing is treated as a conjugate heat transfer boundary condition. Additionally, the pyrex is assumed to be emitting as a gray surface ($\varepsilon = 0.8$), but no account is taken of the transmission properties of the material. Flowing boundaries are assumed to radiate as blackbodies at the temperature of the adjacent gas.

Combustion Model

Combustion is modeled by an eddy breakup concept such that fuel consumption is governed by the rate of mixing. Fast chemistry is assumed along with unity Lewis number and equal diffusivities of heat and mass. Chemical reaction occurs by a one-step mechanism in which fuel and oxidant react to generate a mixture of simple products. Separate balance equations are solved for mixture fraction and mass fraction of fuel. The mixing rate is predicted by a high Reynolds number k-ε turbulence model [19] with modifications to the constants as recommended for confined, round turbulent jets [20].

Mass fractions of oxidant, diluent, and products are determined directly from their respective state relationships. Combustion is coupled to all transported properties via the effect of heat release on temperature, and hence on radiative loss and density.

Energy conservation is represented by a balance equation for total enthalpy, which, in Cartesian coordinates using tensor notation, is

$$\frac{\partial}{\partial x_j}(\bar{\rho}\tilde{u}_j\tilde{H}) = \frac{\partial}{\partial x_j}\left(\frac{\mu_{\text{eff}}}{\sigma_t}\frac{\partial \tilde{H}}{\partial x_j}\right) + \overline{S_R} \tag{1}$$

Total enthalpy is defined by

$$\tilde{H} = \sum \tilde{Y}_i(h^0_{f,i} + \tilde{\Delta h}_i) \tag{2}$$

where $h^0_{f,i}$, $\tilde{\Delta h}_i$, and $\tilde{Y}_i$ are the enthalpy of formation, the sensible enthalpy, and the mass fraction of species i. Mean specific heat, c_p, is calculated from

$$c_p(\bar{T}) = \sum (\tilde{Y}_i c_{p_i}(\bar{T}))\Big/\sum \tilde{Y}_i/W_i \tag{3}$$

where the individual molecular specific heats for CH_4, CO_2, H_2O, O_2, and N_2 are expressed as temperature polynomials [21]. The mean temperature, $\bar{T}$, is given by

$$\bar{T} = \left[\tilde{H} - \sum \tilde{Y}_i (h^0_{f,i} - \bar{T}_0 c^*_{p_i}(\bar{T}_0))\right]/c \quad (4)$$

where $Tc^*_{p_i}(T)$ represents the integrated polynomials. Calculation of the radiative sink/source term, S_R, is described below. Radiative loss is manifested as a sink of energy, and thus reduces the energy available to increase sensible enthalpy (and temperature). This intimately linked equation set is closed by the calculation of density, which, for ideal gases is

$$\rho = P/R_0 T \sum \tilde{Y}_i / W_i \quad (5)$$

Soot Prediction

As described in the introduction, an important feature of this work is the elliptic representation of radiation, and the coupling between radiative exchange and the concentrations of combustion products, especially soot. The kinetic processes governing soot formation (nucleation, surface growth, and coagulation) are strongly dependent on temperature and density. Consequently, the prediction of soot volume fraction is very sensitive to radiative loss. The soot model is based upon solution of balance equations for soot number density, n, and soot mass concentration, f_v [22,23]. To facilitate the representation of these quantities in Favre-averaged balance equations, n and f_v are replaced by $\phi_n = n/(\rho N_0)$ and $\phi_f = (\rho_s/\rho) f_v$, respectively; N_0 denotes Avogadro's number (6×10^{26}) and ρ_s signifies soot density (assumed to be 1800 kg m^{-3}). The equations are of the same form as equation 1, with total enthalpy replaced by either of ϕ_n or ϕ_f, and source terms given by [13]

$$S_n = \bar{\alpha} - \bar{\rho}^2 \bar{\beta} \tilde{\phi}_n^{7/3} \tilde{\phi}_f^{-1/3} \quad (6)$$

and

$$S_f = \bar{\delta} + \bar{\rho} \bar{\gamma} \tilde{\phi}_n^{1/3} \tilde{\phi}_f^{2/3} \quad (7)$$

Here, α and δ represent the influence of nucleation on the number density and soot volume fraction, while β and γ characterize the processes of coagulation and surface growth, respectively. These soot formation parameters, described in Ref. 23, are modeled in terms of properties describable by state relationships. Consequently, mean values of the respective source terms are evaluated by integration over the local pdf of mixture fraction. Acetylene is used as the soot precursor, and the state relationship for the mass fraction of acetylene is considered invariant with radiative loss.

A scheme has now been established to couple these source terms to the level of radiative loss [7]. The methodology is an extension of the laminar flamelet concept, which in its standard form is unable to adequately represent finite rate chemistry by unique state relationships [6]. Thus, a library of flamelets for enthalpy, temperature, and density, are generated, with each flamelet accounting for a different level of radiative loss. Then, by comparing the total enthalpy derived from solution of its balance equation with the statistically integrated values obtained from the flamelet library, it is possible to determine which temperature and density flamelets are required to evaluate the parameters in the soot model. Statistical integration is performed with a β-function pdf determined from the Favre-averaged values of mixture fraction and its variance. Soot oxidation has not been included in the present work since uncertainties still attach to the representation of the mean source term in circumstances where the soot and oxidizing species concentrations are highly correlated [7].

Radiation Model

Thermal radiation is modeled using the discrete transfer radiation model (DTRM). The DTRM employs a ray tracing procedure whereby the radiative transfer equation (RTE) is solved along paths representative of the angular discretization of boundary cell faces. Consequently, radiative loss (or gain) of an individual control volume is evaluated as a balance between emission and absorption for all rays traversing that control volume. Summation of the final intensity at the end of a line of sight in all directions then yields the incident flux. For gray boundaries, the radiosity is represented by a combination of the emitted intensity and the reflected component of the incident intensity [9].

In typical engineering problems, the DTRM is weakened by the "ray effect" resulting from the finite angular discretization of the solid angle hemisphere. The "ray effect" is exacerbated in axisymmetric geometries due to the failure of most rays to traverse regions close to the centerline. Unfortunately, a severe computational penalty is incurred by using a very large number of rays in an attempt to overcome this. Alternative methods of discretization are available that produce a more even distribution of rays [24]. In the present case, it is necessary to communicate information to and from the centerline of the axisymmetric geometry without dramatically increasing the number of rays; thus, the original method of discretization is modified so that a ray is always launched perpendicular to boundary faces. We used 129 rays in a compromise between accuracy and computational storage and speed.

One of the key attractions of the DTRM is the physically tractable representation of solution to the RTE. This feature of the method has been investigated elsewhere [12,25], and good performance has been demonstrated for a weighted sum of gray gases solution to the RTE using coefficients to represent the radiative properties of CO_2-H_2O-soot mixtures. In this approach, the coefficients $a_{m,n,n'}(T)$, k_n, and $k_{n'}$ [11], normally employed to evaluate the total emissivity,

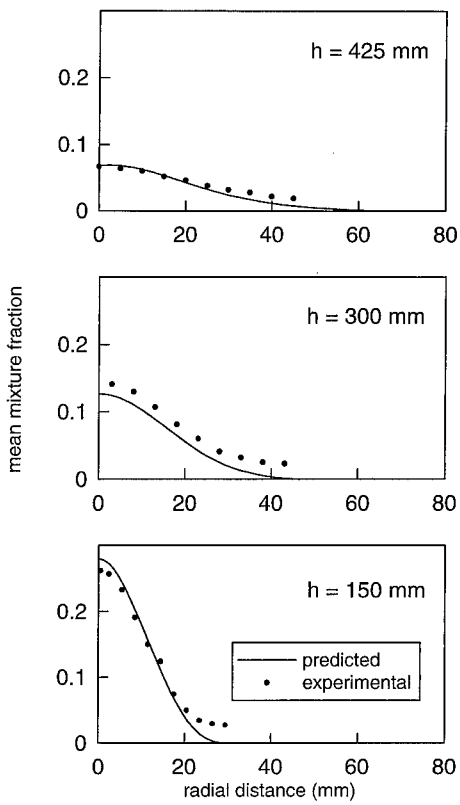

FIG. 1. Radial variation of mean mixture fraction at heights of 150, 300, and 425 mm above the inlet.

$$\varepsilon = \sum_{n,n'} a_{m,n,n'}(T)\{1 - \exp[-k_n[p_h + p_c] - k_{n'}\rho_s f_v]L\} \quad (8)$$

are used to solve a separate transfer equation for each gray gas. Here, p_h and p_c denote the partial pressures of H_2O and CO_2, respectively. The subscripts n and n' signify individual soot and gaseous components such that equation 8 reduces to the soot-free and soot-dominant limits. In the present paper, each pair of these values is represented by a single value, j, and the subscript m, denoting a mixture of soot and gas, is dropped. Solution of the RTE yields the intensity

$$i_j = i_{0j} \prod_{r=1}^{N} \tau_{j,r} + \sum_{r=1}^{N} \left[a_j i_{b,j,r} \varepsilon_{j,r} \prod_{r'=r+1}^{N} \tau_{j,r'} \right] \quad (9)$$

for the jth gas having traversed N elemental path lengths. Transmissivities, $\tau_{j,r}$, emissivities, $\varepsilon_{j,r}$, and the blackbody intensity, $i_{b,j,r}$, are evaluated using mean properties across individual paths, assumed constant for each control volume. For black boundaries, the emitted radiation, $i_{0,j}$, is given by the blackbody intensity multiplied by the a_j coefficient, both evaluated at the boundary temperature [10]. When boundaries are gray, the inclusion of reflection demands a more detailed analysis. Separate expressions are required for the incident radiation of each gray gas, so that the reflected radiation in the individual transfer equations results solely from irradiation due to the same component. Therefore, at every boundary surface, for each gray gas, the incident intensity must be summed across all rays [12]. So, for gray boundaries, the initial intensity (denoted by subscript 0) of the jth gray gas is

$$i_{0j} = \frac{1}{\pi}\left[a_j(T_0)\varepsilon_0 \sigma T_0^4 + [1 - \varepsilon_0] \sum_{m=1}^{M} w_m i_{m,j} \right] \quad (10)$$

where σ signifies the Stefan-Boltzman constant. The summation represents the total incident flux due to M rays for the jth gas, with weightings, w, determined by the method of discretizing the solid angle hemisphere [24]. This strategy is in contrast to the approach that solves a single RTE using total emissivities evaluated from equation 8 [26]. When gaseous radiation is significant, as in the case of methane, it is expected that the simpler approach underestimates absorption, due to averaging of strong absorption in certain wavebands across the whole spectrum.

Results and Discussion

Predicted radial variations of mixture fraction and temperature are compared against experiment at heights of 150, 300, and 425 mm in Figs. 1 and 2, respectively. The agreement for mixture fraction is generally good (cf. Fig. 1). There is some uncertainty relating to mixture fraction measurements by probe sampling in leaner regions at the edges of sooting flames due to carbon retained in the sampling lines. Nonetheless, mixing is comparatively poorly modeled there, and this is reflected in both the computed mixture fraction profiles and in the slower spreading of the temperature predictions shown in Fig. 2. Again, at heights of 150 and 300 mm, temperature is well predicted, particularly in terms of the negative gradient. Differences of less than 10% are observed along the axis, and the maxima are captured with similar accuracy. Close agreement also prevails near to the centerline at a height of 425 mm, but spreading of the flame is less well represented, with temperature predictions falling significantly below the measured values. Weaknesses in the k-ε turbulence model and neglect of turbulent fluctuations are believed to be largely responsible for this poor performance.

Due to the weakly sooting nature of methane-air flames at atmospheric pressure, combined with the difficulty of accurately recording low levels of soot concentration, measurements of soot volume fraction were performed only at heights of 300, 350, and

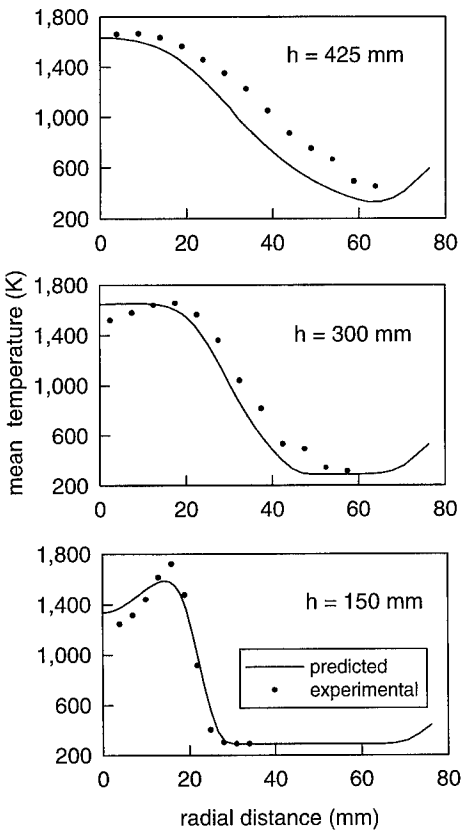

FIG. 2. Radial variation of mean temperature at heights of 150, 300, and 425 mm above the inlet.

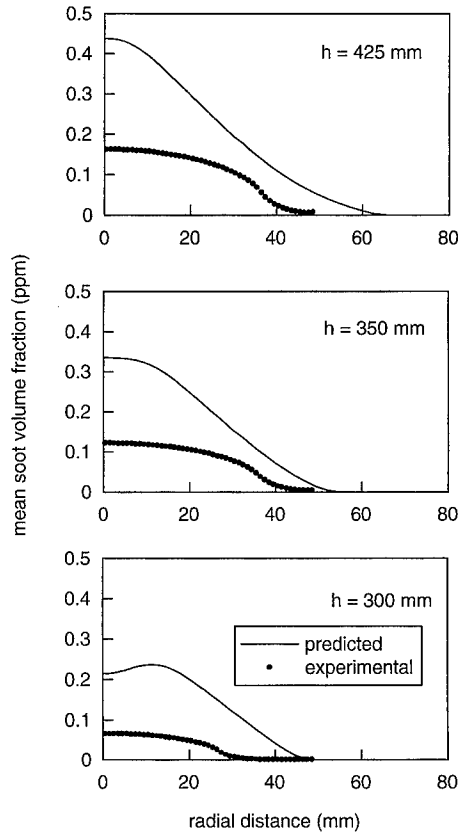

FIG. 3. Radial variation of mean soot volume fraction at heights of 300, 350, and 425 mm above the inlet.

425 mm above the inlet. Radial variations at these heights are compared in Fig. 3. The numerical predictions are expected to be somewhat greater than the measured values due to the exclusion of oxidation from the soot model. Nonetheless, the key trends in the evolution with downstream distance are captured by the computed profiles. Even in the absence of oxidation, the rate of increase of centerline soot concentration is reduced as the mixture fraction (and fuel concentration) falls.

The coupling between radiation and soot formation in the present configuration can be expected to demonstrate discernible interaction only close to the centerline in regions where there are significant levels of soot. Even there, the presence of relatively high concentrations of CO_2 and H_2O will tend to dominate the radiative effects of the gas-soot mixture [25]. These characteristics are clearly represented in Fig. 4 which shows the radiative exchange at heights of 150 and 300 mm. A comparison is made between the output from the predicted gas-soot mixture, and the output when soot is neglected. In both cases, maximum radiative loss occurs at a height of

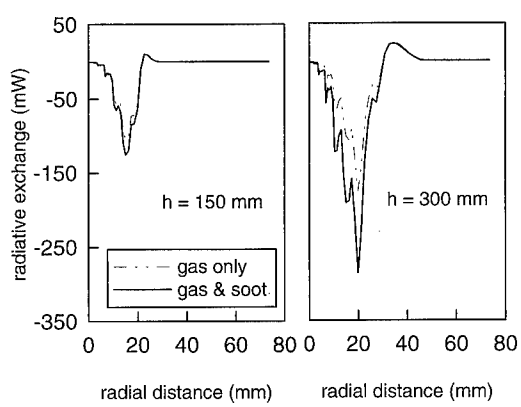

FIG. 4. Comparison between radiative exchange due to soot-CO_2-H_2O and CO_2-H_2O mixtures at heights of 150 and 300 mm.

approximately 300 mm and at a radius of almost 20 mm. Although it is physically unrealistic to view net radiative exchange as a linear combination of that due to individual components, the adjustment for overlap is relatively small. Consequently, it is reasonable to describe the loss from the mixture at 150 mm as being only slightly greater than for gases alone. By 300 mm, the soot contribution has become more significant as concentrations approach 0.1 ppm. The molar fractions of CO_2 and H_2O at this height are approximately 0.08 and 0.16, respectively.

Paradoxically, both soot and gas species concentrations, and temperature are maximized further downstream than the 300-mm height. It must be emphasized, however, that radiative exchange is a balance between emission and absorption. Although higher concentrations and temperature may produce greater emission at one location rather than another, increased absorption in neighboring regions can result in lower net radiative loss.

The oscillating nature of radiative exchange present in Fig. 4 is a feature of the "ray effect." Within the constraints imposed by computational memory and speed, these oscillations are damped to an acceptable level by using 129 rays per boundary face. It is also to be noted that the balance between radiative loss and the total radiative flux at boundaries for this number of rays differed by approximately 10%. When 65 rays were used in the same calculation, an almost identical balance was obtained. However, unacceptably large oscillations were produced in the radiative source term distribution.

With respect to the overall energy balance, an error of less than 3% exists on this 3600-node grid using 129 rays. Within the computational domain, over a third of the available chemical energy is radiated to the boundaries. The radiative loss from methane-air flames is normally about 20% [27], but this factor is augmented in the present case due to higher temperatures accompanying confinement of the flame.

Finally, an important feature affecting convergence rates concerns the frequency at which the radiation algorithm is called relative to the main CFD routine. Early in the calculation, a low frequency is acceptable, but eventually this has a deleterious effect on convergence as a large perturbation is inflicted on the enthalpy equation. It is not necessary, however, to recalculate the radiative field with every CFD iteration; indeed, such an approach is exhaustive. A compromise adopted in this analysis is to call the radiation algorithm after 20 CFD iterations. On a DEC Alpha 200 4/100 workstation, the CFD and radiation algorithms require 3.3 and 103.2 seconds of cpu time per iteration, respectively.

Conclusions

A general strategy has been described for the prediction of turbulent, nonpremixed hydrocarbon combustion that combines modeling of finite rate soot formation, sensitive to the influence of turbulent scalar fluctuations, with a simplified representation of combustion heat release and detailed solution of the accompanying coupled equation of radiative exchange.

The effect of radiative loss on the temperature-dependent chemistry of soot nucleation and surface growth is accommodated through an extended flamelet approach. Radiative exchange is computed using the discrete transfer radiation model with properties established from the local mean concentrations of CO_2, H_2O, and soot. A weighted sum of gray gases solution to the radiative transfer equation is employed, including interaction with gray boundaries. The coupled solution for radiative exchange, even for this comparatively weakly sooting fuel, reveals the importance of both absorption and emission within the turbulent flame zone.

Radiation properties, emissivities, and intensities have been computed from local mean values of state variables. The influence of turbulent fluctuations on these properties (turbulence/radiation interaction) is not included in the computation of radiative exchange. Their implications in confined flames burning more heavily sooting fuels remains to be established.

Detailed comparisons between prediction and experiment in a confined, methane jet flame for the critical properties mixture fraction, soot volume fraction, and temperature demonstrate the effectiveness of the approach within an elliptic flow-field calculation. Therefore, extension to more complex geometries of the finite volume CFD approach and the accompanying submodels as described herein, is now envisaged. With the aid of embedded grids, it will be possible to accurately resolve the characteristics of a combustion source, without demanding unfeasible computer resources, as would be required if the same grid resolution were employed throughout the computational domain.

Acknowledgments

The authors are pleased to acknowledge the contribution of Steven Brookes, in particular, in making available his property measurements in the methane jet flame, and of EPSRC through the award of the research grant under which this study was undertaken.

REFERENCES

1. Kaplan, C. R., Baek, S. W., Oran, E. S., and Ellzey, J. L., *Combust. Flame* 96:1–21 (1994).
2. Sivathanu, Y. R. and Gore, J. P., *Combust. Flame* 97:161–172 (1994).
3. Crauford, N. L., Liew, S. K., and Moss, J. B., *Combust. Flame* 61:63–77 (1985).

4. Fairweather, M., Jones, W. P., Ledin, H. S., and Lindstedt, R. P., *Twenty-Fourth Symposium (International) on Combustion,* The Combustion Institute, Pittsburgh, 1992, pp. 1067–1074.
5. Faeth, G. M., Jeng, S.-M., and Gore, J. P., *Heat Transfer in Fire and Combustion Systems,* ASME, New York, 1985, HTD 45, p. 137–151.
6. Kent, J. H. and Honnery, D., *Combust. Sci. Technol.* 54:383–397 (1987).
7. Young, K. J. and Moss, J. B., *Combust. Sci. Technol.* 105:33–53 (1995).
8. Magnussen, B. F. and Hjertager, B. H., *Sixteenth Symposium (International) on Combustion,* The Combustion Institute, Pittsburgh, 1976, pp. 719–729.
9. Lockwood, F. C. and Shah, N. G., *Eighteenth Symposium (International) on Combustion,* The Combustion Institute, Pittsburgh, 1981, pp. 1405–1414.
10. Modest, M. F., *J. Heat Transfer* 113:650–656 (1991).
11. Truelove, J. S., *HTFS DR33,* AERE, Harwell, Oxon, England, 1975.
12. Bressloff, N. W., Moss, J. B., and Rubini, P. A., "Assessment of a Differential Total Absorptivity Solution to the Radiative Transfer Equation as Applied in the Discrete Transfer Radiation Model," *Num. Heat Transfer* 29(3):381–397 (1996).
13. Brookes, S. J., "Soot Production and Thermal Radiation from Turbulent Jet Diffusion Flames," Ph.D. Thesis, Cranfield University, Cranfield, England, 1996.
14. Young, K. J., Stewart, C. D., and Moss, J. B., *Twenty-Fifth Symposium (International) on Combustion,* The Combustion Institute, Pittsburgh, 1994, pp. 609–617.
15. Patankar, S. V., *Numerical Heat Transfer and Fluid Flow,* Hemisphere Publishing, New York, 1980.
16. Melaaen, M. C., *Num. Heat Transfer B* 21:1–19 (1992).
17. Majumdar, S., *Num. Heat Transfer* 13:125–132 (1988).
18. van Leer, B., *J. Comput. Phys.* 14:361–370 (1974).
19. Launder, B. E., and Spalding, D. B., *Mathematical Models of Turbulence,* Academic Press, London, 1972.
20. Rodi, W., Ph.D. Thesis, University of London, London, 1972.
21. McBride, B. J., Gordon, S., and Martin, A. R., NASA TM4513, 1993.
22. Moss, J. B., Stewart, C. D., and Syed, K. J., *Twenty-Second Symposium (International) on Combustion,* The Combustion Institute, Pittsburgh, 1988, pp. 413–423.
23. Syed, K. J., Stewart, C. D., and Moss, J. B., *Twenty-Third Symposium (International) on Combustion,* The Combustion Institute, Pittsburgh, 1990, pp. 1533–1541.
24. Bressloff, N. W., Moss, J. B., and Rubini, P. A., *Proc. Third European Conf. on Industrial Furnaces and Boilers,* INFUB, Rio Tinto, Portugal, 1995, pp. 208–215.
25. Bressloff, N. W., Moss, J. B., and Rubini, P. A., "The Differential Total Absorptivity Solution to the Radiative Transfer Equation for Mixtures of Gases and Soot," *Num. Heat Transfer,* accepted for publication, 1996.
26. Abbas, A. S. and Lockwood, F. C., *Twenty-First Symposium (International) on Combustion,* The Combustion Institute, Pittsburgh, 1986, pp. 285–292.
27. Jeng, S.-M. and Faeth, G. M., *J. Heat Transfer* 106:886–893 (1984).

COMMENTS

Werner Krebs, Siemens KWU, Germany. In your presentation you use the weighted sum of gray gases (WSGG) model for representing the radiant properties of soot and gases. Have you compared your predictions with detailed spectral calculations?

Author's Reply. With respect to WSGG solution comparison to detailed spectral calculations: comparisons have been performed in Ref. [1] which show that the WSGG solution agrees very closely with a narrow band solution in predictions of line of sight intensities and volumetric flux across typical diffusion flame profiles of temperature, gaseous species concentrations and soot volume fraction.

REFERENCE

1. Bressloff, N. W., Moss, J. B., and Rubini, "The Differential Total Absorptivity Solution to the Radiative Transfer Equation for Mixtures of Gases and Soot," *Numerical Heat Trans.* (1996), accepted.

•

Ahmed F. Ghoniem, Massachusetts Institute of Technology, USA. Did you perform the simulations without the radiation model and compare its results with those obtained with the radiation model? This would be very instructive in determining the impact of radiation on these flows, when it should be included, and how much is the accuracy compromised by leaving it out.

Author's Reply. A number of issues are important here. First, the inclusion of radiative loss is necessary even for the relatively lightly sooting flame analyzed above. If the flame is assumed adiabatic, temperature over-prediction of a few hundred Kelvin yields over an order of magnitude higher soot concentration. Second, earlier simplifications of the complete model have attempted to include the effect of radiation by assuming a fixed level of loss and perturbing the associated flamelets [1]. Moreover, such an approach produces a poor representation of soot distribution since

losses are significantly under-predicted in some regions and over-predicted in others. A better compromise between accuracy and computational cost is facilitated by employing only one of the bracketing flamelets in the evaluation of soot source terms, instead of applying a full interpolation procedure from the accompanying enthalpy flamelets and shared enthalpy field. The final point concerns the degree of accuracy employed in the calculation of radiative loss. Since the weighted sum of gray gases solution described above provides some representation of the non-gray character of thermal radiation, it is to be preferred to more approximate methods which do not, and which fail to capture the path length variation of radiative intensity. However, these differences tend to decrease as the soot loading increases [2].

REFERENCES

1. Syed, K. J., Stewart, C. D., and Moss, J. B., *Twenty-Third Symposium (International) on Combustion,* The Combustion Institute, Pittsburgh, 1990, pp. 1533–1541.
2. Bressloff, N. W., Ph.D. Thesis, CFD Prediction of Coupled Radiation Heat Transfer and Soot Production in Turbulent Flames, Cranfield University, England, 1996.

Twenty-Sixth Symposium (International) on Combustion/The Combustion Institute, 1996/pp. 2387–2395

ASSESSMENT OF SOOT VOLUME FRACTIONS FROM LASER-INDUCED INCANDESCENCE BY COMPARISON WITH EXTINCTION MEASUREMENTS IN LAMINAR, PREMIXED, FLAT FLAMES

J. APPEL,[1] B. JUNGFLEISCH,[2] M. MARQUARDT,[1] R. SUNTZ[2] AND H. BOCKHORN[2]

[1]*Fachbereich Chemie*
Universität Kaiserslautern
Erwin Schrödinger Straße 54, 67663 Kaiserslautern, Germany

[2]*Institut für Chemische Technik*
Universität Karlsruhe
Kaiserstraße 12, 76128 Karlsruhe, Germany

For the validation of detailed chemical models for soot formation, and for their application to turbulent flames, 2-D measuring techniques are necessary to derive locally resolved soot volume fractions, particle sizes, and number densities. In one-dimensional laminar flames, these particle properties are derived from Rayleigh-scattering/extinction techniques. The extinction technique, as a line-of-sight method, is not appropriate for investigation of three-dimensional, nonstationary, turbulent systems. Therefore, for turbulent flames, other measuring techniques have to be developed that can be employed in combination with, for example, Rayleigh scattering.

One technique that has been applied to obtain soot volume fractions in laminar flames is Laser-Induced Incandescence (LII) [1]. The major task in applying this technique is to clarify in which way the relative LII signals should be calibrated to yield absolute soot volume fractions. In this work, the LII technique is investigated systematically in laminar, premixed, ethyne/argon/oxygen flames using a pulsed, high-power Nd:YAG laser. Therefore, the LII signals are compared with soot volume fractions obtained using extinction.

The systematic investigation of the LII technique under different detection conditions (camera gate width and gate delay times) shows that there are inconsistencies between calibrated LII signals and soot volume fractions from extinction. The aim of this work is to explain these inconsistencies by a numerical simulation of the LII signal, based on mass and energy balance equations of the heated soot particles for different flame conditions. Additionally, a sensitivity analysis with respect to different parameters of the balance equation is performed. The results indicate that geometric irregularities of the soot particles probably have to be taken into account for correct prediction of soot volume fractions using LII.

Introduction

The formation of soot, that is, the conversion of a hydrocarbon fuel molecule containing a few carbon atoms into a carbonaceous agglomerate of some millions of carbon atoms is an extremely complicated process. To control the emission of soot from real (turbulent) combustion systems, the understanding of the formation and oxidation of soot is necessary. On the basis of this understanding, detailed models may be developed that can be used to predict and control soot formation. For the development and validation of models for soot formation and oxidation soot volume fractions, particle number densities and particle sizes must be known. To measure these quantities in turbulent systems, a locally resolving 2-D measuring technique is necessary. From extinction, only line-of-sight averaged soot volume fractions can be obtained. One possibility for measuring soot volume fractions, particle sizes, and number densities locally resolved in turbulent systems is the simultaneous application of LII and Rayleigh scattering.

Numerous works on the LII technique have demonstrated its applicability for obtaining spatially resolved soot volume fractions [1–4]. In this technique, the soot particles are exposed to high laser fluxes. As a consequence, they partially evaporate and emit thermal radiation. The soot volume fractions in laminar flames are obtained by calibrating the LII signals against the soot volume fractions obtained by other methods, for example, extinction. Published experimental results also show that with LII, the soot volume fractions are sometimes underestimated compared with soot volume fractions obtained using extinction.

The aim of this work was to investigate the influence of particle properties on the LII signals. There-

TABLE 1
Flow rates of the flames

Flame	Ar	O_2	C_2H_2	C/O
1	200	60.6	72.7	1.2
2	200	59.2	74.1	1.25
3	200	57.9	75.4	1.3

fore, the experimental LII signals from laminar, premixed, sooting flames for different detection conditions such as gate width and gate delay time of the intensified CCD camera were compared with theoretical calculations.

Experimental Setup

Three laminar, premixed, moderately sooting, flat, ethyne/argon/oxygen flames were investigated. In order to increase the spatial resolution of the flame zones, the flames burned at a pressure of 12 kPa. The flames were stabilized on a flat flame burner with a diameter of 80 mm. The flames data is listed in Table 1 (flow rates are given in L_N/h).

The absolute soot volume fractions of these flames were obtained by extinction measurements with a continuous wave Ar^+ laser at 488 nm. A photomultiplier was used for the determination of the extinction. Absorption by molecular absorbers contributes very little at that wavelength and under these experimental conditions. Soot volume fractions are obtained from extinction using

$$\ln \frac{I}{I_0} = -k_{ext} \cdot d \tag{1}$$

where I_0 and I are the intensities of the incident and attenuated light, respectively, and d is the length of the optical path. For small particles ($r \ll \lambda$), the soot volume fraction f_V can be derived from equation 2. Herein, m is the complex refractive index of the soot particles, λ the wavelength, N_T the particle number density, and $P(r)$ the particle size distribution [5] as given by

$$f_V = \frac{-k_{ext}}{\frac{6\pi}{\lambda} \cdot \boldsymbol{Im}\left(\frac{m^2 - 1}{m^2 + 2}\right)} = \frac{4}{3}\pi \cdot N_T \cdot \int_0^\infty r^3 \cdot P(r) \cdot dr \tag{2}$$

In addition to extinction, Rayleigh-scattering also was measured to obtain mean particle radii necessary for the calculation of the spectral response function. The technique used and the evaluation of the scattering measurements are described in detail in Ref. 14.

For the LII measurements, a pulsed, frequency-doubled Nd:YAG laser (λ_{exc} = 532 nm, FWHM = 10 ns) was used. The laser beam diameter is limited by an aperture of 1.5 mm, and the laser flux is varied by changing the amplifier capacitor voltage and/or inserting a meshed grid. The laser intensity normally used was $5 \cdot 10^7$ W/cm^2, where the LII signal is very insensitive to fluctuations in the laser power [1]. The incandescence signal was collected at 90° to the direction of the laser beam and imaged onto the entrance slit of a spectrograph. The resulting spectrum was detected by an image-intensified CCD camera. The camera was used in a one-dimensional mode by binning all sensor elements of the chip perpendicular to the wavelength axis. Different gate delays with respect to the laser pulse and gate widths can be adjusted at the camera. By setting a delay of approximately 90 ns, interferences from PAH fluorescence and laser-induced fluorescence of C_2 and Rayleigh scattering are avoided, because of the long lifetime of LII in comparison with the other laser-induced signals. For each height above the burner, 300 single spectra were obtained and averaged. The averaged spectra of the flame luminosity were obtained in the same way without illuminating the flame with the laser beam. The raw LII spectra were corrected with the spectra from thermal radiation.

Theoretical Basis of Laser-Induced Incandescence

When soot particles are exposed to high laser fluxes ($\approx 10^7$ W/cm^2), their temperatures rise rapidly as a consequence of absorbed laser energy. A first mathematical description of this process, based on energy and mass balances has been provided by Eckbreth [6]. Melton [7] has summarized the results of this theory for a single particle such that

$$\left(K_{abs}(r)q - \frac{8k_a(T - T_0)}{G\lambda} - \frac{4\Delta H_v}{W_v}\rho_v U_v - q_{rad} - \frac{4}{3}\rho_s C_{p,s} r \frac{dT}{dt}\right)\pi r^2 = 0 \tag{3}$$

The individual terms of the equation are the absorbed laser power, the energy loss by heat transfer to the medium, the energy consumed by vaporization of soot, the energy emitted by thermal radiation, and the internal temperature rise. The meaning of each symbol is described in the Nomenclature section.

As proposed by Tien et al. [13], the complex refractive index $m = 1.9 - 0.55i$ is appropriate for the emitted wavelength of the frequency-doubled Nd:YAG laser. For small particles, K_{abs} can be calculated from $K_{abs} = C_{abs}/\pi r^2 \approx C_{ext}/\pi r^2 = -8\pi/\lambda_{exc} r \cdot \mathbf{Im}\{(m^2 - 1)/(m^2 + 2)\}$. To obtain $T(t)$, equation 3 is numerically integrated using a Runge-Kutta

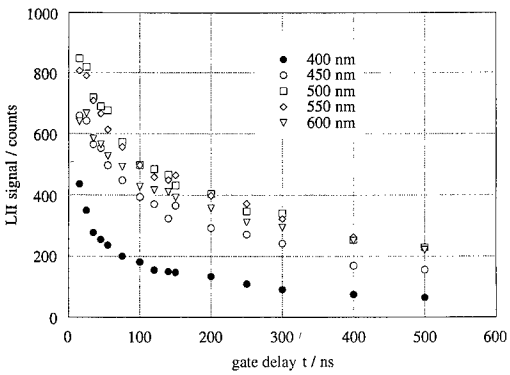

FIG. 1. LII signals from soot particles in a premixed, acetylene/argon/oxygen flames (C/O ratio 1.25) at 11 mm above the burner, as a function of gate delay (gate width, 40 ns).

method for a particular choice of the excitation wavelength λ_{exc},q and T_0.

Similarly to Melton [7], for small particles ($K_{abs} \approx K_{ext}$) a spectral response function $R(r, t, q, T, T_0, T_a, \lambda_{em})$ is derived with the help of the Planck-radiation formula with an emission wavelength λ_{em} and the ambient temperature $\overline{a}$. Considering a log-normal particle size distribution of the soot particles [14], $P(r)$, with a mean particle radius r_m and a standard deviation $\sigma = 0.34$, the temporal evolution of the spectral response function for a particle size distribution is given by

$$J(t, q, \lambda_{em}) = \int_0^\infty N_T \cdot P(r) \cdot R(r, t, q, T, T_0, T_a, \lambda_{em}) \cdot dr \quad (4)$$

$$(\lambda_{em}, t) = \frac{N_T \cdot (2 \cdot \pi^3)^{0.5} \cdot c^2 \cdot h}{\lambda_{em}^5 \cdot \sigma} \times \int_0^\infty K_{abs}(\lambda_{em}, r) \cdot r \times \exp\left(-\frac{[\ln r - \ln \bar{r}_m]^2}{2 \cdot \sigma^2}\right) dr \times \left[\left[\exp\left(\frac{h \cdot c}{\lambda_{em} \cdot k \cdot T(t)}\right) - 1\right]^{-1} - \left[\exp\left(\frac{h \cdot c}{\lambda_{em} \cdot k \cdot T_a}\right) - 1\right]^{-1}\right] \quad (5)$$

In the calculation, a change in the particle radius during the exposure to the laser pulse is not considered because the effected changes are small. Finally, the detected LII signal I_{LII} is obtained by

$$I_{LII} = \int_{t_1}^{t_2} J(t, q, \lambda_{em}) dt \quad (6)$$

where t_1 is the gate delay of the camera with respect to the laser pulse, and $t_2 - t_1$ is the gate width of the camera.

Results and Discussion

Temporal Shape of the LII Signal

In Fig. 1, the LII signal for flame 2 at 11 mm above the burner is plotted as a function of the gate delay for different detection wavelengths (λ_{em} = 400, 450, 500, 550, and 600 nm). The gate width of the camera was 40 ns. The delay was varied in steps of 10, 20, and 50 ns, respectively, up to 500 ns. An approximately exponential decay of the LII signal with increasing gate delay can be observed, which is typical for the cooling of soot particles.

LII Spectra for Different Detection Gates

LII spectra of flame 1 for different heights above the burner are shown in Fig. 2 and Fig. 3, respectively, for two different gate widths: 80 and 500 ns. In both cases, a gate delay of 110 ns was chosen. The decrease of the LII signal at larger wavelengths ($\lambda_{em} > 570$ nm) is an artifact caused by the decreasing spectral sensitivity of the detection system. For a gate width of 80 ns, Swan band emissions of C_2 radicals at 472 and 516 nm [15] are detected for nearly all heights above the burner. With increasing gate width, the signals from the Swan band emissions, in comparison to the LII signal, are weaker, and at a gate width of 500 ns the signals from the emission of the radicals nearly vanish, according to the shorter lifetime of C_2 radicals in comparison to the LII signal. The profiles of the spectrally resolved LII signals are similar for all heights above the burner, although the mean particle radii increase from about 1.9 nm at 5 mm above the burner to about 15.9 nm at 60 mm above the burner.

LII Signals as a Function of Height above the Burner

In Fig. 4, the soot volume fractions of flames 1, 2, and 3 are given as a function of the height above the burner for different detection wavelengths. The LII signals were detected with a gate delay of 90 ns and a gate width of 250 ns. The LII signals for each flame differing in the C/O ratio are converted to absolute soot volume fractions by single-point calibration, with the soot volume fractions obtained from extinction measurements at 11 mm above the burner.

For flame 1, agreement between soot volume fractions obtained from calibrated LII and extinction measurements can be found accidentally, whereas for flame 2, the soot volume fractions are underestimated using calibrated LII measurements at greater heights above the burner. In flame 3, the LII

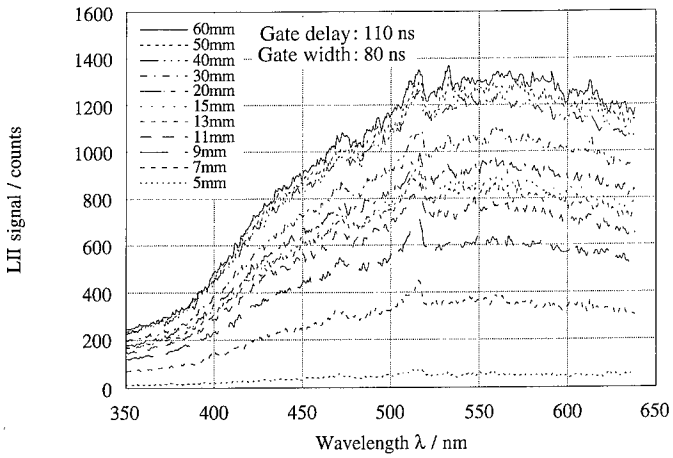

FIG. 2. LII spectrum of flame 1 at different heights above the burner, gate delay 110 ns, gate width 80 ns.

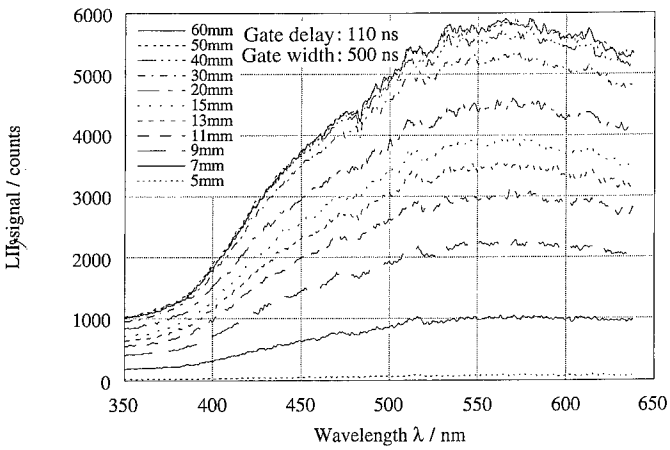

FIG. 3. LII spectrum of flame 1 at different heights above the burner, gate delay 110 ns, gate width 500 ns.

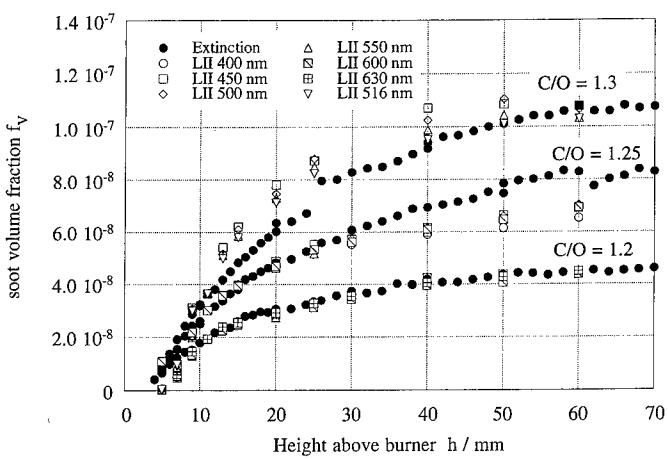

FIG. 4. Soot volume fractions from extinction and LII signals for different C/O ratios (1.2, 1.25, 1.3), gate width 250 ns, gate delay 90 ns, calibration point 11 mm above the burner.

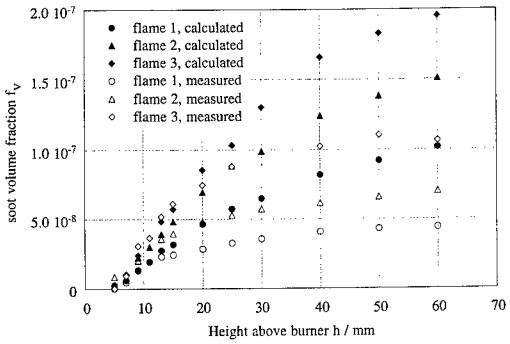

FIG. 5. Comparison of soot volume fractions obtained from measured and calculated LII signals for flames 1, 2, and 3 at 500 nm detection wavelength.

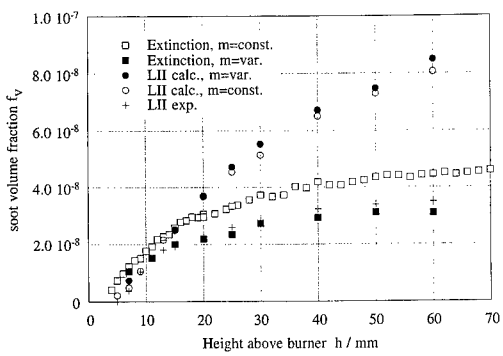

FIG. 6. Soot volume fractions from extinction, measured, and calculated LII signals, evaluated with constant and variable refractive index for the flame 1 at 500 nm detection wavelength.

measurements lead to even larger soot volume fractions between 15 and 40 mm above the burner, compared with the extinction measurements. For other gate delays and/or gate widths, similar discrepancies between the LII-estimated soot volume fractions and those obtained by extinction measurements also occur for flame 1. Because the extinction of the laser light is only a few percent, these discrepancies cannot be explained by absorption of the LII signal in the sooting flame.

Clearly, different detection wavelengths do not significantly influence the profiles of the LII signal's dependence on height above the burner. Even an evaluation of the soot volume fraction from the LII spectra at $\lambda_{em} = 516$ nm (including C_2 fluorescence emission) does not change the profiles. The determination of soot volume fractions from calibrated LII signals detected with other gate delays and gate widths does not produce a better agreement between both techniques. Calibration of the LII signals with soot volume fractions derived using extinction at other heights would shift the soot volume fractions in their relative position, however, would not eliminate the systematic discrepancies. The calibration point was chosen because the soot particles in the investigated flame at this height meet the assumptions inherent in the calculations of the LII signal reasonably, as described later.

Comparison between Calculated and Experimental LII Signals

In order to compare theoretical with experimental LII signals, equation 6 has to be integrated using the chosen detection conditions and particle properties. In Fig. 5, a comparison between soot volume fractions obtained from measured and calculated LII signals at $\lambda_{em} = 500$ nm is given. The measured (open symbols) and the calculated (filled symbols) values are calibrated with the corresponding soot volume fractions obtained from extinction measurements at 11 mm above the burner. The final soot volume fractions obtained from the calculations are approximately a factor of 2 larger than the values obtained from experiments. Even the slopes of the calculated and measured profiles are different.

Influence of a Variable Refractive Index on the Calculated LII Profile

The differences between calculated and measured LII signals could possibly be attributed to a change in the refractive index m with increasing particle size (increasing "age" of the particles) [13,14,16]. Consequently, equations 3 and 5 have been solved for flame 1 considering a variable refractive index. Mean radii of $\bar{r}_m = 3.0$ nm and $\bar{r}_m = 15.9$ nm were determined by Rayleigh scattering experiments in the investigated flame at 7 mm and 60 mm above the burner, respectively. The refractive index m for the different particle diameters has been assumed to vary from $m = 1.37 - 0.41i$ to $m = 1.79 - 0.74i$. The extinction measurements were also evaluated using a variable refractive index.

In Fig. 6, soot volume fractions obtained using extinction, from calculated LII signals at $\lambda_{em} = 500$ nm and from LII measurements (gate delay, 110 ns; gate width, 250 ns) at $\lambda_{em} = 500$ nm are shown. The profiles of the soot volume fraction from the calculated LII signals is not significantly affected when using a constant (○) index of refraction or a variable (●) one. Changing the refractive index influences the absorption efficiency K_{abs}, the mean particle radius $\bar{r}_m$, and the number density N_T in a way that the effects were approximately compensated for in equations 3–5.

Influence of Nonspherical Particles on the Calculated LII Profile

In order to evaluate the influence of nonspherical particles on the LII signal profile, a change in the

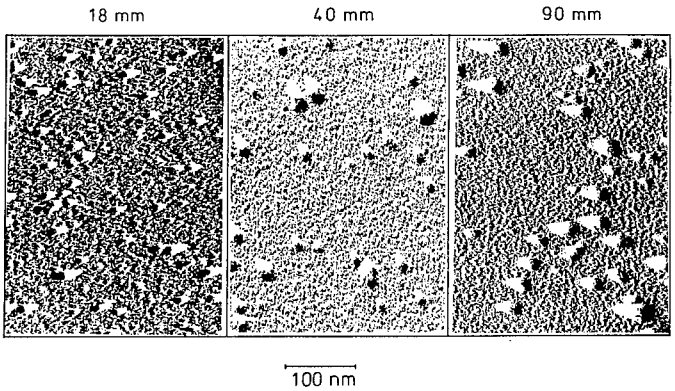

FIG. 7. TEM images of soot particles from flame 1 at different heights above the burner.

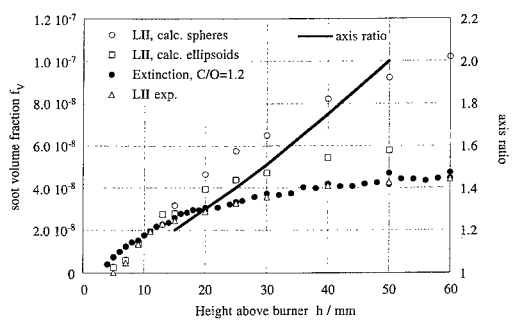

FIG. 8. Comparison of soot volume fractions obtained using extinction, measured, and calculated LII signals with emphasis on spheres and ellipsoids for flame 1 at 500 nm detection wavelength.

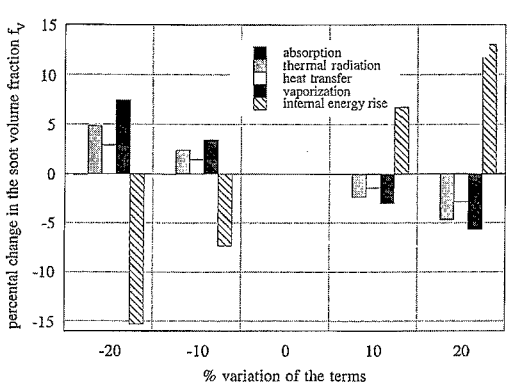

FIG. 9. Resulting changes in the soot volume fraction f_V when varying the terms of equation 3 for flame 1 at 11 mm above the burner and 500 nm detection wavelength.

structure of the soot particles from spheres to ellipsoids with increasing height above the burner was taken into account [17] when solving the equations 3–5. From transmission electron microscopy (TEM) images, it is clear that coagulation and surface growth reactions of soot particles may lead to a change in particle shape from spheres to ellipsoids [14]. Fig. 7 shows TEM images of soot particles from flame 1 at different heights above the burner, where this change of the particle shape (dark area) is clear.

In Fig. 8, the soot volume fractions obtained from extinction, measured and calculated LII signals are shown. The calculation of the LII signals are carried out for spheres and ellipsoides with an increasing axis ratio, which is deduced from the TEM images..

The axis ratio affects all terms in equation 3, for example, the aspect ratio for absorption, the absorption efficiency as given by the Mie theory, and the heat transfer and the heat accumulation term; the latter term depends on the volume of the particle and, therefore, to a higher power on the aspect ratio (see later). The change in the axis ratio in Fig. 8 is indicated by the solid line. A variation in the shape of the particle has a strong influence on the temperature $T(t)$ and the spectral response function $J(t)$. Therefore, the LII signal and the soot volume fraction profile are seriously affected. The calculated LII profiles for ellipsoids with varying axis ratios are in better agreement with the LII measurements than the profiles for spheres. All parameters entering equations 3–5 are estimated on the basis of the best available data, that is, the composition of the gas phase, flame temperature, and experimental results for the particle properties in the investigated flames.

For the ellipsoides, the corresponding K_{abs} has been calculated in the following way: on condition that the volume of a spherical particle is identical with that of the rotational ellipsoid, the projection area of the ellipsoid is calculated for a statistical orientation of the nonspherical particle with respect to the propagation of the laser beam [17]. By this, a projection averaged radius for a spherical particle equivalent to the ellipsoid can then be calculated.

Simulation of Changes in the Particle Properties

During the heating of the particles by the laser pulse, partial evaporation and subsequent cooling may alter the particle properties, for example, the refractive index and density. To simulate changes in these properties affecting the energy and mass balance of the heated particles, the individual terms of equation 3 (thermal radiation, vaporization, heat transfer, and internal temperature rise) were decreased and increased by 20 and 10%, respectively. Figure 9 indicates the relative change of the soot volume fraction at 11 mm above the burner for flame 1, when reducing or increasing each term of equation 3. The maximum relative change is caused by varying the term of enthalpy accumulation (internal temperature rise). All terms in the heat balance equation 3 except the internal temperature rise include the surface area of the particle. These terms are affected by the aspect ratio of statistically oriented, nonregular particles (ellipsoids). The internal temperature rise term depends on the volume of the particle. When dividing the heat balance equation by the surface area, only the internal temperature rise term remains dependent on particle size or parameters that describe the particle shape. Therefore, a change in the internal temperature rise term gives the largest relative change in the soot volume fractions when varying particle shape. A small variation in the particle shape as observed in the investigated flames may result in large deviations between the calculated and measured LII signals.

Conclusions

Laser-induced incandescence of soot particles in premixed, flat, laminar, ethyne/oxygen/argon flames has been investigated systematically by varying the detection conditions of the optical system. The LII signals were converted to soot volume fraction by single-point calibration using the data from extinction measurements.

The results exhibit some discrepancies between the profiles of soot volume fractions obtained by LII and those from extinction measurements. To understand these discrepancies, the LII signals were calculated based on mass and energy balances of the heated soot particles.

The final soot volume fraction profiles obtained from the calculated LII signals are about a factor of 2 larger than those obtained from extinction measurements. Changing the refractive index or the radiative properties for calculating the LII signals gives only small variations in the calculated LII signal. Taking a change of the particle shape from spheres to ellipsoids into account, a much better agreement between the profiles of the soot volume fractions from calculated LII signals and measured LII signals is achieved.

A sensitivity analysis of the heat balance of the particles shows that the internal enthalpy accumulation is the most important term in the heat balance. This is most sensitive to changes in the particle shape.

Nomenclature

K_{abs}	Mie absorption efficiency
r	soot particle radius
q	laser intensity
k_a	thermal conductivity [8]
T	particle temperature
T_0	ambient flame temperature
λ	mean free path
G	geometry-dependent heat transfer factor [9]
ΔH_v	vaporization heat of carbon [10]
W_v	molecular weight of carbon vapor
ρ_v	density of carbon vapor [11]
U_v	vapor velocity
q_{rad}	thermal radiation intensity
ρ_s	density of solid carbon [12]
$C_{p,s}$	specific heat of carbon [10]

Acknowledgment

This research was partially supported by the commission of the European Communities, the Swedish National Board for Technical Development (STU), and the Joint Research Committee of European Car Manufacturers (Fiat, Peugeot SA, Renault, Volkswagen, and Volvo) within the IDEA programs.

REFERENCES

1. Bengtsson, P.-E. and Aldén, M., *Appl. Phys. B* 60:51–59 (1995).
2. Tait, N. P. and Greenhalgh, D. A., *Ber. Bunsengs. Phys. Chem.* 97:1619–1625 (1993).
3. Quay, B., Lee T.-W., Ni, T., and Santoro, R. J., *Combust. Flame* 97:384–392 (1994).
4. Shaddix, R. C., Harrington J. E., and Smyth, K. C., *Combust. Flame* 99:723–732 (1994).
5. van de Hulst, H. C., *Light Scattering by Small Particles*, Wiley and Sons, New York, 1957.
6. Eckbreth, A. C., *J. Appl. Phys.* 48:4473–4479 (1977).
7. Melton, L. A., *Appl. Opt.* 23:2201–2208 (1984).
8. Oran, E. S. and Boris, J. P., *Prog. Energy Combust. Sci.* 7:1–72 (1981).
9. Chapman, S. and Cowlings, T. G., *Mathematical Theory of Non-Uniform Gases*, Cambridge U.P., London, 1970.
10. Barin, I., *Thermochemical Data of Pure Substances*, VCH, Weinheim, 1993.
11. Leider, H. R., Kuckovian, O. H., and Young, D. A., *Carbon* 11:555, 1973.

12. E. Bartholomé, E. Biekert, H. Hellmann, H. Ley, W. M. Weigert, and E. Weise (Eds.), *Ullmanns Enzyklopädie der Technischen Chemie,* VCH, Weinheim, New York, 1977, Vol. 14, p. 634.
13. Tien, C. L. and Lee, S. C., *Eighteenth Symposium (International) on Combustion,* The Combustion Institute, Pittsburgh, 1988, p. 1159.
14. Bockhorn, H., Fetting, F., Wannemacher, G., and Heddrich, A., *Ber. Bunsengs. Phys. Chem.* 91:819–825 (1987).
15. Bengtsson, P.-E. and Aldén, M., *Combust. Flame* 80:322–328 (1990).
16. Charalampopoulos, T. T. and Felske, J. D., *Combust. Flame* 68:283–294 (1987).
17. Asano, S. and Yamamoto, G., *Appl. Opt.* 14:29–49 (1975).

COMMENTS

Kermit C. Smyth, NIST, USA. I have questions in three areas: First, the model calculations are confusing, in that you conclude that the internal enthalpy accumulation term is sensitive to particle shape. However, the internal temperature rise is due to volume absorption. In the small-particle Rayleigh limit, the particle shape is irrelevant.

Second, the data presented in Fig. 4 were obtained with a detector delay of 90 ns, which strongly biases the measurements in favor of larger particles [1]. However, the differences between the extinction results and the LII measurements do not follow a consistent trend with increasing C/O ratio (and presumably increasing primary particle size). Can your analysis explain these results? A single calibration between the LII and extinction data would give a more meaningful comparison between the measurements and would better establish relative trends.

Finally, for your calibration point at H = 11 mm, the soot volume fraction is relatively low (2–4 $\times$ 10^{-8}) for the three flames under investigation. Have you accounted for the contribution of molecular absorbers when using 488 nm radiation for the extinction measurements? Many investigators have observed PAH fluorescence in sooting premixed flames at this excitation wavelength [2]. Did you carry out measurements to verify that the profile of the soot volume is flat at all heights in your low-pressure flames?

REFERENCES

1. Ni, T., Pinson, J. A., Gupta, S., and Santoro, R. J., *Appl. Opt.* 34:7083–7091 (1995).
2. Haynes, B. S., Jander, H., and Wagner, H. Gg., *Ber. Bunsenges. Phys. Chem.,* 84:585–592 (1980); Prado, G., Jagoda, J., Neoh, K., and Laharye, J., *Eighteenth Symposium (International) on Combustion,* The Combustion Institute, Pittsburgh, 1981, pp. 1127–1136.

Author's Reply. Considering Eq. (3), all terms except the accumulation term, which depends on particle volume, depend on the surface or aspect ratio of the particle, respectively. Variations of the surface to volume ratio, e.g. caused by changes in the particle shape, affect the accumulation term most.

The main result of the study is that the present theoretical interpretation of the measured LII-signals has some drawbacks that have to be eliminated in future applications of the LII technique. From that, one single calibration of the LII measurements would have elucidated the general trends better than a calibration within each flame at 11 mm high above the burner. The best calibration point in the single flames would be a similar "chemical" state of the soot particles in the different flames that depends on the burning conditions.

We measured depolarisation of the scattered light at 488 nm and possible fluorescence at other wavelengths. Polarisation was about 99.5% and fluorescence was negligible under the prevailing conditions. From that we can conclude, that the concentration of PAH (most of the PAH show fluorescence) is in a range that the measurements are biased negligibly by absorption under the prevailing conditions. The profiles of soot volume fractions are flat in the investigated flames as could be demonstrated by two-dimensional scattering measurements.

•

David A. Everest, NIST, USA. The detection scheme used, long delay and wide gate, yields a signal that is highly dependent on the effective primary particle radius (volume/area) and will selectively detect particles with larger effective radii. What is the particle size that you are most efficiently detecting? Is there a detection scheme that would be independent of the particle radius?

Figure 7 indicates possible changes in soot shapes for flame 1; however, the experimental data is in excellent agreement with your extinction measurements. Is it possible that the effective primary particle radius (volume/area) in flame 1 does not change much from the radius at the calibration height? What is the variation in particle size in each of the three flames?

In flames 2 and 3, the calibration is made earlier in the particle development than in flame 1, which will result to larger changes of the primary particle size from the calibration point. Detection with a delayed gain gives an LII signal dependence upon particle diameter greater than cubic, thus overestimating the soot volume fraction at higher heights. Does this explain the results of flame 3? How would the modeling analysis for non-spherical particles affect the comparisons for flames 2 and 3?

Author's Reply. Soot particles in premixed flames exhibit a particle size distribution which can be approximated best

by a log-normal size distribution. In calculating the LII-signals we used this kind of size distribution. It is right, that smaller particles are detected better with smaller delays. However, the principal deviations between measured and calculated LII-signals have been present for all the different detection conditions we applied.

The particle radii at 5 mm height above the burner amount to approximately 2 nm. They increase to about 20 nm at a large height above the burner. Conditions in the different flames differ not so much that the history of the primary particles would be such different.

It is right that the best calibration point in the single flames would be a similar "chemical" state of the soot particles in the different flames. Soot volume fraction profiles from extinction and LII clearly show that the two techniques give different slopes of the profiles at small heights above the burner and large heights, respectively. Thus agreement of the profiles can be forced by shifting the point of calibration. The main result of the study is, however, that the measured LII-signals cannot be interpreted with the present approach for the heat balance of the particles unless a change in the structure of the particles is accounted for. This affects the particles in all of the investigated flames.

Twenty-Sixth Symposium (International) on Combustion/The Combustion Institute, 1996/pp. 2397–2404

INVESTIGATION OF SOOTING IN NORMAL-GRAVITY DROPLET COMBUSTION USING LIGHT EXTINCTION AND GRAVIMETRIC TECHNIQUES

KYEONG-OOK LEE, KIRK A. JENSEN AND MUN YOUNG CHOI
Department of Mechanical Engineering
University of Illinois at Chicago
Chicago, IL 60607, USA

Normal-gravity soot volume fraction (f_v) measurements performed for combustion of single toluene droplets under atmospheric and reduced pressures are presented. Because of the transient nature of the flame and the sooting region, a full-field light extinction/tomographic inversion technique was used. The reduction in sooting as a function of pressure was assessed by using the maximum soot volume fraction at various axial positions above the droplet. The maximum soot volume fraction was reduced by 70% when the pressure was reduced from 1 to 0.4 atm. The observed variation in sooting cannot be attributed solely to the changes in the adiabatic flame temperature (caused by reductions in pressure). The variations in residence time in the changing flow configurations caused by reductions in the system Grashof number also contribute to the reduction in sooting.

The gravimetrically measured soot yield was also compared to the optical measurements of f_v to determine the existence of a correlation between the two techniques. The total soot yield was proportional to the maximum f_v and displayed the same linear variation when the pressure was reduced. Therefore, the nonintrusive light extinction measurements can be calibrated (with the gravimetric measurements) to not only provide f_v within the flame (which is important for radiation characterization and soot/flame structure analysis) but to simultaneously measure the total particulate emission through the open-tipped flames (which is important in assessing the environmental impact of hazardous droplet combustion).

Introduction

In many normal-gravity droplet combustion studies, significant soot formation and emission have been encountered [1–9]. The degree of sooting was found to be influenced strongly by the fuel chemical structure [2,7,10]. Practical combustors that use sooty fuels require increased hardware maintenance and innovative strategies to reduce pollutant emission to the environment. Many of the important characteristics of droplets burning under normal-gravity conditions are also sensitive to the soot concentrations within the flame [2,7,10,11]. Therefore, to understand the process of soot formation and destruction in droplet combustion, it is necessary to obtain accurate soot concentration measurements within the flame [7].

The most common diagnostic technique for soot measurement in normal gravity is direct bulk sampling in which soot is collected on fiber filters and then weighed to determine the mass. Using this technique, Kadota and co-workers [1] demonstrated that the mass of the emitted soot increases as a function of pressure (for experiments performed from 0.1 to 1 MPa) for various hydrocarbon fuel droplets. Similarly, Nakanishi and co-workers [2] demonstrated that there was a limiting level of forced convection (which was a function of the initial fuel structure and ambient air temperature) that produced nearly soot-free burning conditions. Although direct sampling has proven to be a useful diagnostic tool, it becomes cumbersome to perform and requires repeated experiments to produce enough mass for detection using conventional scales. Furthermore, droplet flames exhibit dynamic behavior (due to the changes in the droplet and flame dimensions as burning progresses), resulting in transient influences by the soot within the flame on the burning characteristics. These transient behaviors cannot be captured by a bulk measurement technique such as direct sampling. Therefore, alternate methods that can provide temporal and spatial resolution of the soot structure bear consideration [7,12–14].

Kadota and Hiroyasu [3] first measured soot concentrations in droplet flames using nonintrusive optical techniques under normal-gravity conditions. In their study, light scattering/extinction measurements were performed using porous spheres and suspended droplets. They assumed that the soot particles exhibited constant optical and physical properties and that therefore the resulting scattered light measurements were equated to the concentration of soot. However, it is likely that, depending on the time–temperature histories experienced by the soot

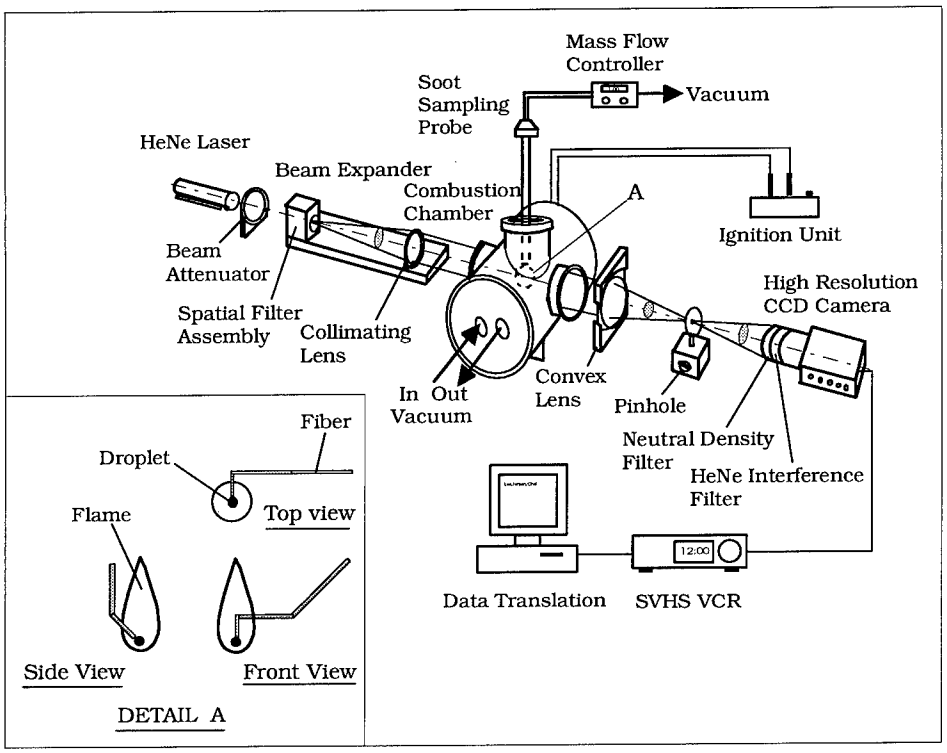

FIG. 1. Schematic of the full-field light extinction and gravimetric sampling apparatus. Displays the orientation of the suspending quartz filament.

particles, differences in the physical and optical properties of the soot particles may occur as a function of time and location within the flame. This can significantly compromise their assumptions. In addition, light extinction measurements were performed at a fixed location below the droplet and the radial variation was deduced by assuming that the regressing flame maintained constant spherical structure. This approach will produce unrealistic results in the region above the droplet (where most of the soot is present) where it displays both spatial and temporal variations.

The transient nature of droplet flames requires diagnostic techniques that can instantaneously survey the entire soot field for analysis. Recently, Vander Wal and co-workers [12,13] and Gupta and co-workers [14] performed two-dimensional laser-induced incandescence (LII) measurements to obtain temporally and spatially resolved soot volume fractions, f_v, for isolated droplet flames. The advantage of using this technique is that soot concentration is proportional to the intensity of the incandescence that results from the rapid heating of soot by a high-power, short-duration laser. However, obtaining quantitative values requires accurate calibration using an independent technique such as gravimetric methods [15].

The motivation for the present work is to apply a nonintrusive full-field light extinction technique to measure the f_v distributions for single droplets that can provide insights regarding the structure of the transient sooting region [16]. (Greenberg, Griffin, and Ku first used this technique to measure soot concentrations in laminar gas-jet diffusion flames in microgravity [17–19].) Experiments were performed under normal and reduced pressure conditions to measure accurately the reductions that can be caused by modification of the flame structure and adiabatic flame temperature. Another aspect of this work is to combine the previously mentioned optical technique with the gravimetric sampling of the soot mass to determine the correlation between the soot volume fraction and soot yield measurements. Such a correlation can improve the usefulness of the light extinction technique for not only providing detailed information regarding the sooting region (within the flame) but also for simultaneously measuring the soot yield nonintrusively.

Experimental Description

Figure 1 displays the schematic of the experimental apparatus. The 12 l combustion chamber is made

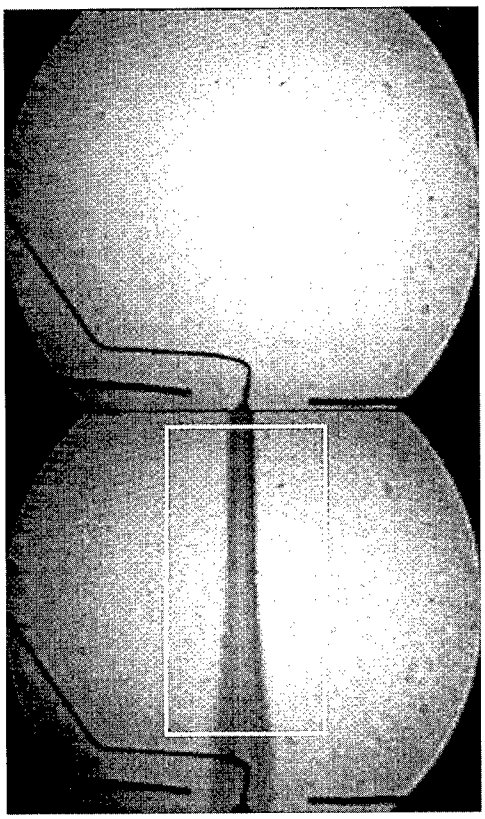

FIG. 2. Photograph of a background and sooting image of toluene burning in 0.5-atm air.

of stainless steel and provides three ports for optical access. Light from a 10-mW HeNe laser, operating at 632.8 nm, is first passed through a variable neutral density filter (to maximize the laser intensity without causing saturation) and expanded using a Newport LC-V expander/collimator to produce a 50-mm-diameter beam. The beam is directed through opposing optical ports (each fitted with 51-mm-diameter quartz windows) of the chamber. The transmitted beam is then imaged through a second spatial filter using a high-resolution CCD camera. Image quality interference filter and a neutral density filter (o.d. 3.0) are placed directly in front of the camera to discriminate against flame and stray emissions. The video output from the camera is saved directly onto an S-VHS recorder at 30 frames/s.

For each experiment, 5.0 μL of fuel was deposited on a bead that was formed at the end of the suspending quartz fiber (fiber diameter is approximately 150 μm) using a hypodermic needle. The unique orientation of the fiber as shown in inset A in Fig. 1 was designed to minimize interactions with the flame. The droplet was ignited using two opposing stationary electrodes that were positioned sufficiently far from the droplet to prevent interactions with the flame.

The recorded image was then digitized frame by frame using a high-resolution (512 × 480 pixels) data acquisition board. Figure 2a displays the image of the expanded laser beam acquired by the camera before ignition. The two horizontal lines (at the bottom) are the ignition wires, and the diagonally oriented object is the quartz fiber. At each pixel location shown in Fig. 2a, the gray level was converted to intensity (the output of the detection system was calibrated by using various neutral density filters). The use of a single background image (to obtain the incident laser intensity distribution) was sufficient for the entire duration of the experiment since the laser/detection system was very stable with an rms fluctuation of the measured light intensity less than 0.5% of the total magnitude of the intensity.

The gravimetric experiments were performed by sampling the soot emitted from the open-tip flame. The sampling probe consisted of a 25.4-cm-long, 13-mm-i.d. stainless steel tube fitted to a stainless steel 47-mm Gelman filter assembly. Teflon filters with a collection efficiency greater than 99% for particles larger than 0.1 μm were used [20]. The flow through the filter assembly was regulated and held constant with a mass flow controller. Detailed descriptions of this technique can be found in Ref. 15.

Light Extinction Soot Volume Fraction Measurements

Figure 2b displays the photograph of a burning toluene droplet in reduced-pressure air at 0.5 atm at $t = 1.0$ s. The dark region showing axisymmetric characteristics corresponds to locations where soot particles are present. Figure 3a depicts the intensity ratio distribution (calculated by dividing the intensity at each pixel location in the region bounded with the white box in Fig. 2b by the intensities along the corresponding region in Fig. 2a). The background and soot-containing images were first filtered using a 3 × 3 pixel mean filter and then averaged using a moving 5-pt operator along the radial direction at each axial height. A third-order curve-fitting procedure was used to determine the center at each vertical position, and the intensity ratios calculated on either side of the center were then averaged [16]. The intensity ratio distribution (which corresponds to the line of sight transmittance) shown in Fig. 3a was used to determine the soot volume fraction along each vertical location by applying a 3-pt Abel inversion [16,21]. The soot extinction constant used in this study was determined from a light extinction/gravimetric calibration technique [22]. A full-field deconvolution algorithm that can analyze the two-dimensional images (spatial resolution up to 480 × 512 pixels) was used to calculate the entire f_v distribution simultaneously.

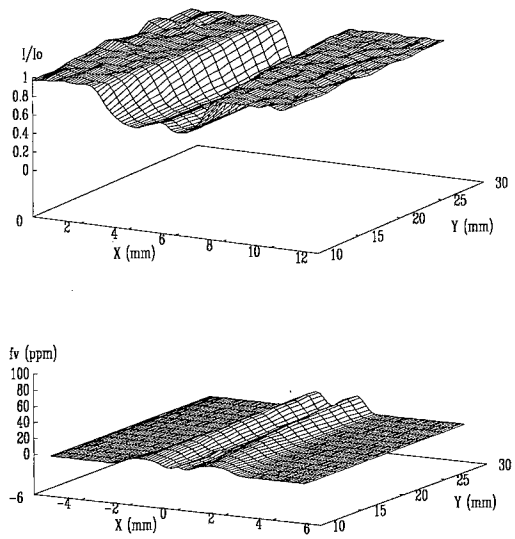

FIG. 3. (a) Two-dimensional intensity ratio distribution for toluene droplet burning in 0.5-atm air (1 s after ignition). (b) Two-dimensional soot volume fraction distribution for toluene droplet burning in 0.5-atm air (1 s after ignition).

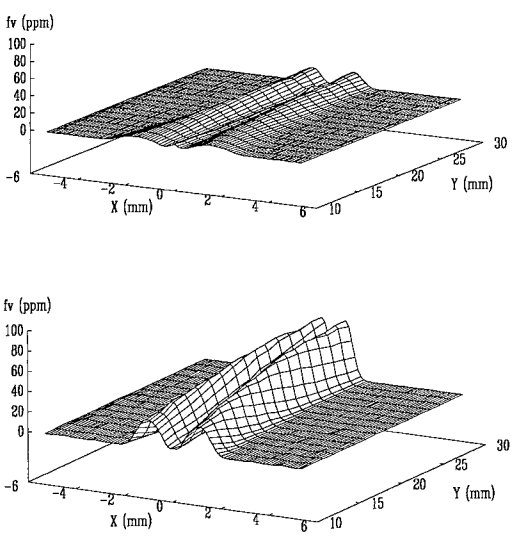

FIG. 4. Two-dimensional soot volume fraction distributions for toluene droplet burning in 0.4- and 1.0-atm air (1 s after ignition).

Figure 3a displays the intensity ratio plot for a toluene droplet burning in air at a reduced pressure of 0.5 atm at 1.0 s after ignition. The deconvolved f_v distributions using the previously mentioned technique are shown in Fig. 3b. The soot volume fractions at each axial location increase as a function of radial position (away from the centerline) until they reach a maximum value at the annular regions (corresponding to the location of maximum f_v), which are just inside the luminous boundaries of the flame [14]. Along the annular region, f_v also increases continuously as a function of axial position. Because of the limited field of view (approximately 26 mm in our experiment), the extent of the sooting region was beyond the measurement volume (as shown in Fig. 2a, significant concentrations of soot were emitted through the open-tipped flame). The region containing the bulk of the soot concentrations (annular region) within the region of analysis is, however, very narrow, which agrees with previous measurements of the structure of the sooting regions for both gaseous and liquid buoyancy-dominated flames under normal gravity [12–14,23]. Similar distributions measured at various times during the burning process indicate that the maximum soot volume fraction, $f_{v,\max}$, increases slightly as a function of time until quasi–steady-state conditions are attained and then rapidly decreases because of the reductions in the droplet size with attendant decrease in the flame size.

Pressure Reduction Effects

The control of soot formation and emission during droplet combustion is important for many practical applications related to hardware maintenance and environmental concerns. The variation of the ambient pressure as an effective parameter to reduce sooting in diffusion flames was first reported by Parker and Wolfhard [24]. Milberg [25] observed a linear dependence of the sooting rate as a function of pressure for acetylene/air diffusion flames. Using pressures of 1.0–2.5 atm, Flower and Bowman [26] reported that the soot yield increased approximately linearly as a function of pressure for laminar axisymmetric ethylene diffusion flames. Previous droplet combustion studies have also used pressure reduction as an effective technique for producing quasi-spherical droplet flames and for controlling soot formation [7,10,27]. Randolph and Law [7] and Choi and co-workers [10] used the spatial extent of the luminous flame or the luminosity as an indication of the presence of soot to observe that the degree of sooting in droplet combustion was affected strongly by pressure reductions below 1 atm. However, the flame luminosity is most sensitive to the soot concentrations and temperatures just within the envelope flame and therefore does not provide information regarding the structure of the entire sooting region. For these reasons, full-field light extinction experiments were performed to determine accurately the effects of pressure reduction on sooting in droplet combustion.

Figures 4a and 4b display the f_v distributions

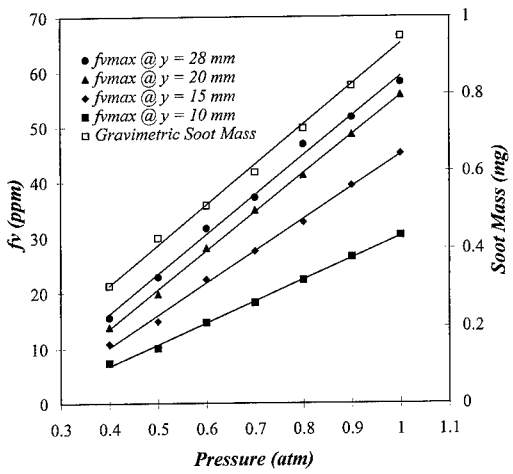

FIG. 5. Maximum soot volume fraction measured at specific axial positions at various pressures. The gravimetrically determined mass of soot per droplet is also plotted.

measured for toluene droplets burning under various ambient pressures of 1 and 0.4 atm. Using the transient measurements of soot volume fraction distributions, the image producing the maximum soot volume fraction at a height of 28 mm above the droplet was chosen at each pressure and analyzed for comparison. As the ambient pressure is reduced, several changes in the soothing behavior become obvious. The pressure variation from 1 to 0.4 atm produced a 70% reduction in the maximum soot volume fraction. It was also evident that the widths of the annular region and the luminous region of the flame (which were simultaneously measured using the second CCD camera) at each height were enlarged while the lengths of the luminous regions were reduced. This variation in the flame structure is caused by reductions in the system Grashof number (ratio of buoyant to molecular transport) at the lower pressure [27].

Figure 5 shows the $f_{v,\max}$ at various vertical locations above the droplet plotted as a function of the ambient pressure from 0.4 to 1.0 atm in 0.1-atm increments. The maximum soot volume fraction at each axial location decreases linearly with reductions in the ambient pressure. It is generally regarded that the variations in the sooting propensity caused by reduced pressure for diffusion flames are associated with the lower flame temperatures that lead to a slower rate of fuel pyrolysis in the fuel-rich region [28]. However, as suggested by the work of Flowers and Bowman [26], the variations in flame temperature cannot completely account for the observed changes in the soot yield. In the present droplet study, the $f_{v,\max}$ is reduced nearly 70% between 1.0 and 0.4 atm. However, the difference in the adiabatic flame temperature is calculated to be only on the order of 30 K [29]. Recent work by Gülder and Snelling [30] using laminar diffusion flames predict only a 10–15% reduction in the soot volume fractions for a 30 K change in the adiabatic flame temperature. Therefore, the effect of temperature variation only partially contributes to the reduction in the soot concentrations that are observed in this study.

The reduction in ambient pressure can also modify the flow configuration with the attendant changes in the residence time. The residence time of the fuel molecules in the region bounded by the droplet surface and the flame is proportional to $(l\rho/\Delta\rho g)^{0.5}$, where l is the characteristic length, ρ is the density of the gas, and g is gravitational acceleration [31]. Since the ratio of the density divided by the density change is governed primarily by changes in the temperature (which is not significantly affected by pressure variations), the residence time formulation can be simplified to $(l/g)^{0.5}$. As the pressure is reduced, the resulting smaller characteristic length, l (which is estimated in this case to be the luminous height of the flame) and increased importance of diffusion (caused by pressure reduction) can shorten the residence time of the fuel molecules within the high-temperature region during which pyrolysis and soot formation can occur.

The total particulate mass measurements during burning of droplets are important for assessing the degree of environmental hazards. Using the f_v distributions shown in Figs. 4a through 4d, it is possible to calculate the mass of soot within the measurement volume [14,15]. For sooty fuels such as toluene, benzene, and chlorinated hydrocarbons, the extent of the sooting region is much larger than the optical measurement volumes conventionally used [12,13,15], as shown in Fig. 2b. Therefore, it is not possible to measure the entire extent of the sooting region and the corresponding soot contained within the measurement volume by using full-field light extinction technique. Although the direct sampling technique is a viable option for measuring soot yield, it may not be suitable for situations in which the droplets are burning either in high-temperature and/or corrosive environments (due to degradation of the collecting filters) or in space-limited applications (such as in microgravity droplet combustion experiments). Therefore, alternate methods that can be used for soot yield measurements are needed.

Gravimetric Sampling Measurements

Previously, Randolph and Law [7] observed an important correlation between the soot index (measured using a sampling probe) and the luminous region of the flame for moderately sooting droplet flames producing mild soot emission. However, for the flames in the present study, large concentrations

of soot beyond the open-tip flame (which does not emit visible radiation) were apparent. The motivation for this phase of the work is to perform gravimetric sampling experiments for comparisons with the simultaneous optical measurements to determine whether a correlation exists between the two measurements. Gravimetric sampling has been used extensively for the calibration of various optical techniques. Choi and co-workers [22,32] determined the dimensionless extinction constants for calibration of the light extinction technique for various premixed and diffusion flames, while Vander Wal and co-workers [15] calibrated the emission intensity of laser-induced incandescence to obtain quantitative soot volume fraction information.

The simultaneous gravimetric sampling and light extinction comparison experiments were performed using the experimental apparatus shown in Fig. 1 for toluene droplets burning under various reduced pressures. The entrance of the gravimetric sampling probe was placed approximately 50 mm above the droplet to eliminate interferences with the burning process. Before the experiment, three teflon filters were weighed using an electronic scale with 0.01-mg accuracy. One of the filters was placed inside the sampling assembly, and the other two filters were used to scrape the soot collected on the inner walls of the probe using a glass plunger (therefore, all of the soot emitted from the flame was used for the soot yield calculations). Since the mass of soot collected per droplet can be a small value (at 0.4 atm, the collected mass per droplet was only 0.3 mg), the soot produced from 20 droplets at each reduced pressure was collected. All three filters were then placed in a dessicator for approximately 8 h to remove water and other volatile contents before weighing.

Figure 5 also displays the gravimetrically sampled soot mass per droplet at various reduced pressures for comparisons with the $f_{v,\max}$ measurements (the solid lines are shown only to denote the trends). The collected soot emitted through the open-tip flame displays a linear relationship with the ambient pressure and follows the trends observed for $f_{v,\max}$ measurements at each axial position. The correlation may be due to the fact that during quasi-steady conditions that encompass a significant portion of the overall burning time, the maximum soot volume fraction measured at each time step (separated by 1/30 s) varied by only approximately 10% at each pressure. Furthermore, the instantaneous mass of soot contained within the measurement volume (which was calculated by integrating the soot distribution at each height along the radius and multiplying by the density of soot) remained relatively constant during the quasi-steady burning phase. This relationship suggests that for a given fuel, the soot mass can be estimated by calibrating the light extinction measurement of $f_{v,\max}$ with the gravimetric soot mass measurements. For example, with the ratio of the soot mass and $f_{v,\max}$ measurements at 1 atm as the calibration factor, the soot yield at reduced pressures can be predicted using $f_{v,\max}$ measurements with an average deviation of less than 10%. It is now possible to simultaneously measure both the detailed soot concentration distribution within the flame and the total emitted mass of soot using light extinction measurements.

Conclusions

A full-field light extinction/tomographic inversion technique was used to assess the degree of sooting in normal-gravity droplet combustion at various ambient pressures. These measurements provided temporally and spatially resolved structure of the sooting region within the flame. The maximum soot volume fractions above the droplet displayed a linear variation when pressure was reduced. However, these variations cannot be attributed solely to the changes in the adiabatic flame temperatures (caused by pressure reductions). The reductions are more likely caused by the changing flow configuration and shorter residence times for fuel pyrolysis and reactions leading to soot formation.

Experiments performed using simultaneous gravimetric sampling and full-field light extinction indicate a direct relationship between soot volume fraction and the total soot yield. Soot yield measurements performed under reduced pressure also displayed linear variation as the optically measured soot volume fractions. The calibrated optical technique can be used for simultaneously measuring the detailed structure of the sooting region within the flame and for measuring the total soot emitted to the environment nonintrusively.

Acknowledgments

The authors gratefully acknowledge helpful advice regarding the implementation of full-field technique provided by P. Greenberg, D. Griffin, B. Whiteside, and D. Urban of NASA-LeRC. We would also like to thank R. Vander Wal, P. Ferkul, and D. Schultz for helpful discussions regarding this work. This work was supported by NASA-LeRC through grant #NAG3-1631. K. A. J. would like to acknowledge support from the AMOCO Foundation Fellowship.

REFERENCES

1. Kadota, T., Hiroyasu, H., and Farazandehmer, A., *Combust. Flame* 29:67 (1977).
2. Nakanishi, K., Kadota, T., and Hiroyasu, H., *Combust. Flame* 40:247 (1981).
3. Kadota, T. and Hiroyasu, H., *Combust. Flame* 55:195 (1984).

4. Vranos, A. and Liscinsky, D. S., *Combust. Sci. Technol.* 38:145 (1984).
5. Sangiovanni, J. J. and Liscinsky, D. S., *Twentieth Symposium (International) on Combustion,* The Combustion Institute, Pittsburgh, 1984, p. 1963.
6. Green, G. J., Dryer, F. L., and Sangiovanni, J. J., "Soot Agglomeration in Isolated, Free Droplet Combustion," Eastern States Meeting of the Combustion Institute, Gaithersburg, MD, 1984.
7. Randolph, A. L. and Law, C. K., *Combust. Flame* 64:267 (1986).
8. Kitano, M., Kobayashi, H., and Sugimoto, T., *Combust. Sci. Technol.* 78:19 (1991).
9. Choi, M. Y., Dryer, F. L., Green, G. J., and Sangiovanni, J. J., AIAA Paper No. 93-0823, 1993.
10. Choi, M. Y., Dryer, F. L., Haggard, J. B. Jr., and Borowski, B., "Observations of the Burning Behavior of Hydrocarbon Droplets in Reduced Pressure Environments," Eastern States Meeting of the Combustion Institute, Orlando, FL, 1990.
11. Jackson, G. S. and Avedisian, C. T., *Proc. R. Soc. London, Ser. A* 446:255 (1994).
12. Vander Wal, R. L., Dietrich, D. L., and Choi, M. Y., "Relative Soot Volume Fractions in Droplet Combustion via Laser-Induced Incandescense," Eastern States Meeting of the Combustion Institute, Clearwater Beach, FL, 1994.
13. Vander Wal, R. L. and Dietrich, D. L., *Appl. Opt.* 34:1103 (1995).
14. Gupta, S. B., Ni, T., and Santoro, R. J., "Spatial and Time Resolved Soot Volume Fraction Measurements in Methanol/Benzene Droplet Flames," Eastern States Meeting of the Combustion Institute, Clearwater Beach, FL, 1994.
15. Vander Wal, R. L., Zhou, Z., and Choi, M. Y., "Spatially-Resolved Spectral and Temporal Characterizations and Gravimetric Sampling Calibration of Laser-Induced-Incandescence," *Combust. Flame* 105:462 (1996).
16. Lee, K. O., Jensen, K., and Choi, M. Y., "Measurement of the Soot Volume Fraction of Single Droplets Using Light Extinction Technique," Central States/Western States/Mexican National Meeting of the Combustion Institute, San Antonio, TX, 1995.
17. Griffin, D. W. and Greenberg, P. S., "Selected Microgravity Combustion Diagnostics Techniques," 2nd International Microgravity Combustion Workshop, Cleveland, OH, 1992.
18. Greenberg, P. S., "Laser Doppler Velocimetry and Full-Field Soot Volume Fraction Measurements in Microgravity," 3rd International Microgravity Combustion Workshop, Cleveland, OH, 1995.
19. Greenberg, P. S. and Ku, J. C., "Soot Volume Fraction Imaging," *Appl. Opt.* (1995), submitted.
20. Liu, B. Y. H., Pui, D. Y. H., and Bubow, K. L., *Characteristics of Air Sampling Filter Media,* Vol. 3, (Marple, V. A. and Liu, B. Y. H., Eds.), Ann Arbor Science, Ann Arbor, MI, 1983 Chapter 70, p. 989.
21. Dasch, C. J., *Appl. Opt.* 31:146 (1992).
22. Choi, M. Y., Mulholland, G. W., Hamins, A., and Kashiwagi, T., *Combust. Flame* 102:161 (1995).
23. Santoro, R. J., Yeh, T. T., Horvath, J. J., and Semerjian, H. G., *Combust. Sci. Technol.* 41:203 (1987).
24. Parker, W. G. and Wolfhard, H. G., *J. Chem. Soc.* 3:2038 (1950).
25. Milberg, M. E., *J. Phys. Chem.* 63:578 (1959).
26. Flower, W. L. and Bowman, C. T., *Twenty-First Symposium (International) on Combustion,* The Combustion Institute, Pittsburgh, 1986, p. 1115.
27. Miyasaka, K. and Law, C. K., *Eighteenth Symposium (International) on Combustion,* The Combustion Institute, Pittsburgh, 1981, p. 283.
28. Glassman, I., *Combustion,* Academic Press, Orlando, FL, 1987.
29. Gordon, S. and McBride, B. J., NASA SP-273, 1989.
30. Gülder, Ö. L. and Snelling, D. R., *Combust. Flame* 92:115 (1993).
31. Ostrach, S., *Adv. Heat Trans.* 9:161 (1972).
32. Zhou, Z. and Choi, M. Y., "Measurement of Dimensionless Extinction Constant of Soot Generated Using Various Fuels," Central/Western/Mexican National Meeting of the Combustion Institute, San Antonio, TX, 1995.

COMMENTS

Norbert Peters, RWTH Aachen, Germany. Have you or do you intend to compare your experiments with kinetic calculations?

Author's Reply. Currently, there is a lack of accurate descriptions of the effects of sooting and radiation on spherically-symmetric droplet burning behavior. Comparisons with numerical models (which exclude the sooting and radiation effects) indicate that the measured burning rate and flame location are significantly smaller than the predictions [1].

We intend to use our experimental measurements to calibrate a new droplet combustion model [2] based on the work of Marchese and Dryer [3] which considered gas-phase radiation. In the new model, soot formation, growth and accumulation effects will be incorporated by using empirical formulations.

REFERENCES

1. Choi, M. Y., Dryer, F. L., Green, G. J., and Sangiovanni, J. J., "Soot Agglomeration in Isolated, Free Droplet Combustion," AIAA Paper #93-0823 (1993).
2. Dryer, F. L., Personal Communication, 1996.
3. Marchese, A. J. and Dryer, F. L., "The Effects of Non-Luminous Thermal Radiation in Microgravity Droplet Combustion," *Combust. Sci. Technol.* (1996), in press.

Twenty-Sixth Symposium (International) on Combustion/The Combustion Institute, 1996/pp. 2405–2411

THE REACTION OF PHENOXY RADICALS WITH MONO-CHLOROBENZENE AND ITS MEANING FOR GAS-PHASE DIOXIN FORMATION IN INCINERATION

HORST-HENNING GROTHEER AND ROBERT LOUW
Center for Chemistry and the Environment
Gorlaeus Laboratories, Leiden University
P.O. Box 9502, 2300 RA Leiden, The Netherlands

The reaction of (chlorinated) phenoxy radicals with chlorophenols recently has been discussed as a source of gas-phase dioxin formation in incineration. As a surrogate for this reaction, we studied the analogous reaction (1) of phenoxy (ΦO) with chlorobenzene (ΦCl) in a well-stirred reactor between 728 and 984 K. The slow combustion of phenol served as a continuous ΦO source, and chlorobenzene was used as co-fuel. Stable end products and reactants were analyzed by gas chromatography (GC), in particular ΦCl, dibenzofuran (DF), and diphenylether (ΦOΦ), the direct product of reaction 1. This made it possible to measure k_1 in competition with ΦO recombination, reaction (2) for which an overall rate coefficient had earlier been established in our laboratory. The Arrhenius parameters for reaction (1) are

$$A_1 = 4.8 \times 10^8 \text{ L/mol s}, E_{a1} = 24.5 \text{ kcal/mol}$$

When these parameters are adopted for the reaction of chlorinated phenoxy radicals with chlorophenol, an agreement with an earlier kinetic analysis of Shaub and Tsang is achieved that has a meaning for dioxin formation. The given parameters render this reaction at temperatures below 1000 K too slow to contribute significantly as a gas-phase dioxin source. However, since gas-phase dioxin formation recently has been detected in a flow reactor during trichlorophenol combustion with maximum yields of dioxin around 900 K, another dioxin source must be found consequently, we suggest the gas-phase recombination of chlorinated phenoxy radicals.

Introduction

Dioxins and related compounds, that is, polychlorinated dibenzodioxins, dibenzofurans, and biphenyls, are currently assumed to be formed mainly through heterogeneous reactions on fly ashes via two major pathways. Through de novo synthesis, as proposed by Stieglitz and coworkers [1], dioxins may be built up from their elements in a sequence of steps and under the catalytic effect of metals. The second pathway is formation from precursors [2,3], that is, compounds structurally similar to dioxins, so that only a few reaction steps are required for dioxin formation. The most likely precursor molecules are chlorinated phenols.

The question of the relative importance of these two major mechanisms has not yet been answered clearly, although a study by Lenoir and co-workers [4] indicates that precursor formation is dominant for many conditions of incinerator operation. However, this view is not generally accepted [5].

Gas-phase formation from precursors had been considered in a kinetic analysis by Shaub and Tsang [6] (ST) in 1983. In their model, which consists of only 13 steps, the key reaction for formation is

$$P + P^{\bullet} \rightarrow PD + Cl \qquad (a)$$

Here, the notation of ST is used in which the chlorinated and nonchlorinated forms of a compound are denoted cumulatively by a single letter. *P* stands for chlorinated phenols and $P^{\bullet}$ for chlorinated phenoxy radicals. *PD* is an ether with a phenolic hydroxyl group; *PD* is assumed to yield dioxins (DD) in a fast reaction with OH radicals. A high activation energy of 26 kcal/mol was attributed to reaction (a) so that only at higher temperatures significant *PD* and hence dioxin yields may be expected. In this temperature regime, however, thermal breakdown of phenoxy radicals becomes increasingly important. (For a very useful discussion, see Dransfeld [7].) As a consequence, the proposed gas-phase mechanism yields very little dioxin production and only at relatively high temperatures.

Contrary to this prediction, significant gas-phase dioxin formation recently has been detected by Dellinger and co-workers [8] in flow reactor experiments. They studied the slow combustion of 2,4,6-trichloro and 2,4,6-tribromophenols under conditions of an insignificant contribution of surface reactions. Maximum dioxin yields were obtained around only 600°C.

To achieve a match between their experimental data and the ST prediction, Dellinger et al. adjusted

the rate coefficient of reaction (a) by using an activation energy of 19.5 kcal/mol for chlorinated phenols and 8.8 kcal/mol for the corresponding brominated case. The frequency factor was left at its ST value of $A_a = 10^9$ L/mol s. At 600°C, the temperature at which Dellinger et al. found maximum dioxin yields, the following rate coefficients are obtained:

$$k_{a(\mathrm{ST})} = 293 \text{ L/mol s, contrary to}$$

$$k_{a(\mathrm{Dellinger,\ Cl})} = 12.6 \times 10^3 \text{ L/mol s and}$$

$$k_{a(\mathrm{Dellinger,\ Br})} = 6.15 \times 10^6 \text{ L/mol s}$$

The ST model as modified by Dellinger et al. was later combined with a surface-mediated model [9] to simulate the high dioxin yields that have been found in a heterogeneous spouted bed combustor at short residence times of about 0.1 s and at temperatures between 580 and 680°C (i.e., under conditions characteristic for the boiler region of an incinerator [9]).

In an attempt to verify the approach of Dellinger et al., the present study focuses on reaction (a). Although phenoxy radicals may be prepared cleanly in a fast flow reactor [10], such an instrument is unsuitable for this study, since reaction (a) is far too slow even when considering the high Dellinger values. At 600°C and at the low pressures in a fast flow reactor, even when using undiluted phenol, one can at best expect first-order rate coefficients around 1–10 s^{-1} in comparison to wall loss coefficients for phenoxy radicals of up to 800 s^{-1} [10].

Consequently, we decided to use the slow combustion of phenol in an atmospheric pressure, well-stirred reactor (tank reactor) as a continuous source of phenoxy radicals. As a co-fuel, we used chlorobenzene (ΦCl) rather than chlorophenol. This means we measured the surrogate reaction

$$\Phi\mathrm{O} + \Phi\mathrm{Cl} \rightarrow \Phi\mathrm{O}\Phi + \mathrm{Cl} \qquad (1)$$

This replacement will have only a small influence on the reaction rate because the attack of phenoxy radicals occurs at the Cl substituted site and should be little affected by the presence or absence of the phenolic OH. Using chlorobenzene as a surrogate compound for chlorophenol provides the following advantage: The direct reaction product is diphenyl ether (ΦOΦ) rather than the phenolic PD compound. Since the ether is more stable, it can be more easily recovered from the complex reaction mixture. A second advantage of this approach is that dioxin-related products arising from reaction (1) can be distinguished easily from those of phenoxy recombination. The former show up as ethers, whereas the latter are dioxins and/or furans, depending on chlorination. In the present case, with nonchlorinated phenoxy radicals, the product is only dibenzofuran, DF, reaction (2) [11].

$$2\Phi\mathrm{O} \rightarrow (\text{-H, -HO}) \rightarrow \text{dibenzofuran (DF)} \qquad (2)$$

Experimental

For the formation of diphenylether and neglecting other sources and sinks, one may write

$$d[\Phi\mathrm{O}\Phi]/dt = k_1[\Phi\mathrm{O}][\Phi\mathrm{Cl}]$$

Under the conditions of a well-stirred reactor, with all concentrations being independent of space and time, the integration yields

$$\Delta[\Phi\mathrm{O}\Phi] = k_1[\Phi\mathrm{O}][\Phi\mathrm{Cl}]\tau = [\Phi\mathrm{O}\Phi]_{\mathrm{out}} \qquad \text{(i)}$$

since no ΦOΦ is fed into the system. τ is the residence time. $[\Phi\mathrm{O}\Phi]_{\mathrm{out}}$ and $[\Phi\mathrm{Cl}]_{\mathrm{out}}$ can be measured directly. The concentration of phenoxy radicals is related to the dibenzofuran yields. It was shown in this laboratory [11,12] that the self-reaction of phenoxy radicals leads, in a series of steps, nearly exclusively to DF. The overall rate coefficient, k_2, for DF formation from ΦO recombination is weakly temperature dependent and may be expressed, at least in the lower portion of the temperature range of this study [11] by

$$k_2 = 1.6 \times 10^{11} \exp(-11.08 \text{ kcal/mol}/RT) \text{ L/mol s}$$

For the well-stirred reactor, and neglecting other DF sources or sinks, it may be written

$$\Delta[\mathrm{DF}] = k_2[\Phi\mathrm{O}]^2\tau = [\mathrm{DF}]_{\mathrm{out}} \qquad \text{(ii)}$$

When combined with Eq. (1), this yields

$$k_1 = \{k_2/[\mathrm{DF}]_{\mathrm{out}}\tau\}^{1/2}[\Phi\mathrm{O}\Phi]_{\mathrm{out}}/[\Phi\mathrm{Cl}]_{\mathrm{out}} \qquad \text{(iii)}$$

This means that in the present approach, k_1 is measured in competition with reaction (2). If partial flow rates (in mmol/h and denoted by parentheses) are used, and if the residence time is expressed in terms of the total flow, f, and T, then Eq. (iii) for our geometry becomes

$$k_1 = 0.753 \times 10^{-4}T \times f\{k_2/(\mathrm{DF})_{\mathrm{out}}\}^{1/2}(\Phi\mathrm{O}\Phi)_{\mathrm{out}}/(\Phi\mathrm{Cl})_{\mathrm{out}} \qquad \text{(iiia)}$$

Here, the rate coefficients are in L/mol s. We are unable to find other DF or ether sources in our system. The issue of their sinks will be addressed later.

Experiments were carried out at atmospheric pressure in a cylindrical quartz reactor of 300 mL volume and 6.0 cm internal diameter. The reactor was immersed in a controlled laboratory furnace that provided uniform temperatures up to about 1000°C.

N_2 and O_2 flows were measured with calibrated capillary flow meters. These gases (in a ratio around 3:1) amounted in most cases to >95% of the total flow that was typically around 400 mmol/h, resulting in residence times of about 40 s. Under these conditions, the approximation of a well-stirred reactor holds as was previously shown [11] by using suitable test reactions.

Liquid reactants were introduced and calibrated by means of motorized syringes and vaporized be-

TABLE 1

Concentrations of the reactants and of some products of the 885-K experiments. Residence time is 39.5 s. The DF and $\Phi O\Phi$ seeds are added in a separate run for the determination of their consumption (see text).

Inflows (mmol/h): ΦOH (4.29); ΦCl (11.8); O_2 (86.3); N_2 (285)
Output: ΦOH (0.47); ΦCl (8.4); HCl (2.9)
key PICs: DF (0.13); $\Phi O\Phi$ (0.0017)
seed concentrations: DF (0.26); $\Phi O\Phi$ (0.024)
gaseous products: CH_4(1.1); CO (40.8); CO_2 (6.2); C_2H_2 (0.47)

fore entering the reactor. These entrance and exit tubes from the reactor were heated to about 200°C to prevent condensation at the walls. Phenol was typically used in flows of 5 mmol/h, dissolved in 5 mmol/h H_2O. In some cases, phenol was dissolved in benzene. Chlorobenzene concentrations were comparable to phenol concentrations.

Condensable gaseous products were collected in two serial cooled traps filled with water/toluene to which an internal standard (o-dichlorobenzene) was added. Noncondensable product gases were analyzed by taking 0.5-mL samples from gas bulbs. The latter samples were analyzed for C_1 and C_2 compounds using a Hewlett Packard 428 GC with a flame ionization detector and equipped with a Carboplot 007 column and a methanizer. Calibration was achieved through standard gas mixtures. Aromatic compounds were quantified using a Hewlett Packard 5890A GC-FID equipped with a CP-SIL5-CB column. Portions of 1 μL of the liquid samples were injected at a split ratio of 1:15. Absolute concentrations were deduced from the peak areas. The calibration was determined independently by injecting standard mixtures (see also, Ref. 13). In addition, product signals were identified by using a Hewlett Packard 5890 GC-MS.

N_2 and O_2, both 99.99%, were supplied by Hoekloos in standard cylinders. Phenol, Merck 99.5%; chlorobenzene, Baker 99%. Other reagents were generally of analysis grade, 99% or better.

Results

Characterization of the Reaction System and Its Products

Incomplete slow combustion gives rise to substantial amounts of the usual (end) products such as CO and recovered reactants. In this case, the products of incomplete combustion (PIC), target compounds DF and $\Phi O\Phi$, and—not surprisingly—a number of other aromatic compounds could be identified by GC and GCMS. As an example, the profile of our 885-K experiment, residence time 39.5 s, is outlined in Table 1 (the seed concentrations will be explained later).

By GCMS analysis of the liquid condensate, the presence of both o- and p-chlorophenol was determined to be near the level of DF. These products are common in the slow combustion of phenol in the presence of HCl. They can be explained by the reaction of ΦO with chlorine atoms [13,14]. The oxidation (hydroxylation) of ΦCl can lead to all three isomers of ClΦOH; this happens (see later), but the m- and p-isomers had the same GC retention time. Note that formation of chlorophenol also implies the presence of ClΦO radicals and ΦO. Interestingly, GCMS revealed the presence of all four isomers of mono-Cl-DF. The sum of their concentrations was about one-fifth of the level of DF. This suggests that all three ClΦO radicals undergo a combination reaction with (excess) ΦO. Chlorine-free dibenzodioxin (DD) was present in trace amounts (~1% of DF) along with biphenyl. A number of other (ultra)trace products could also be identified, including styrene, monobenzofuran, its chlorinated congener, and methylphenols. Such products, as well as methane and acetylene, result from oxidative breakdown of benzene rings; however, a discussion of these processes is beyond the scope of this paper. Finally, the chlorine balance is quite good: HCl accounts for 85% of the decomposed ΦCl and the chlorophenols constitute the majority of the remaining 15%.

Check of the Kinetic Approach

To demonstrate the validity of Eq. (iii) and its equivalent form, Eq. (iiia), measurements were carried out at 888 K for a wide range of stoichiometries of phenol and the co-fuel chlorobenzene (i.e., the intake flow of the latter was varied between 5.9 and 118 mmol/h for otherwise unchanged conditions). The use of even lower ΦCl flows was unreasonable since the $\Phi O\Phi$ yields became too small. The maximum ΦCl flow was limited by the need to keep this flow small in comparison to the total flow.

The results are shown in Fig. 1. The measured DF yields and $\Phi O\Phi$ yields ($\Phi O\Phi \times 10$) are plotted against the measured $(\Phi Cl)_{out}$ abundances. Note the log scale for $(\Phi Cl)_{out}$: As the ΦCl concentration increases, the DF yields also increase. This is due to the formation of Cl atoms during ΦCl consumption. The Cl atoms then go on to generate more ΦO radicals. The $\Phi O\Phi$ yields increase much more than those of DF. Consequently, k_1 values as calculated from corresponding triples of $\Phi O\Phi$, DF, and ΦCl by using Eq. (iii) (or Eq. (iiia)) are essentially constant. The scatter of less than 15% in either direction is caused mainly by the uncertainty in the $\Phi O\Phi$ measurement that is due to the fairly small concentrations. In addition, artifacts from previous

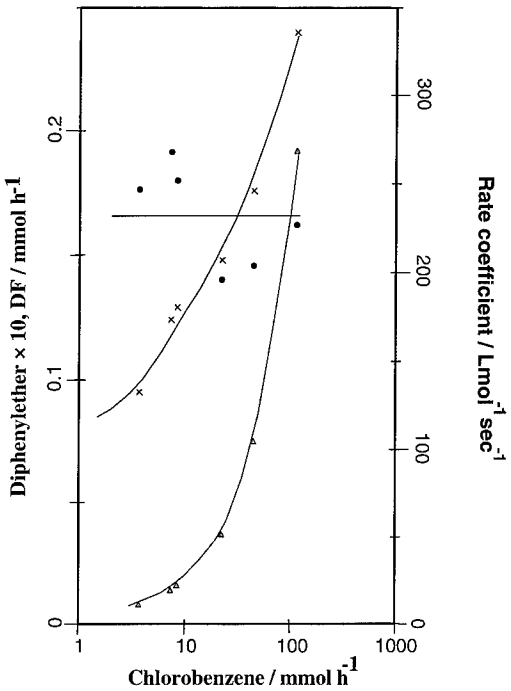

FIG. 1. DF yields (crosses) and $\Phi O\Phi$ yields (10-fold increased, triangles) as a function of $(\Phi Cl)_{out}$ at 888 K. Note the log scale of the abscissa. Also shown are the resulting raw values for k_1 (circles) from Eq. (iiia). Residence times are about 40 s throughout.

experiments can occur if the traps are not cleaned very carefully between runs.

Obviously, in Fig. 1, no systematic dependency of k_1 on ΦCl is observed. This supports the validity of Eq. (iii) for the present case. A vastly different situation is encountered when ΦCl is replaced by ΦBr, as will be published elsewhere [15]. Because of kinetic complications, the apparent rate coefficient for $\Phi O + \Phi Br$ is strongly dependent on the ΦBr concentration and drops from 606 L/mol s for $(\Phi Br)_{out}$ = 2.7 mmol/h to 239 L/mol s for $(\Phi Br)_{out}$ = 18.0 mmol/h. To verify that $\Phi O\Phi$ stems from chlorobenzene, a control run was conducted at 879 K in which ΦCl was replaced by benzene. Results in terms of conversion and yield of DF were comparable, but the formation of $\Phi O\Phi$, already small in the case of ΦCl, was decreased by more than one order of magnitude. As mentioned previously, Cl atoms are consumed mainly by the excess of phenol and chlorobenzene. This ensures that the reverse of reaction (1) cannot play a significant role.

Temperature Dependence of k_1 and Consumption of DF and $\Phi O\Phi$

Measurements were carried out in a temperature range of 728–984 K. At temperatures below this range, ΦOH conversions were too small to give accurately measurable DF and $\Phi O\Phi$ signals. At higher temperatures, our system was close to complete combustion. Again, the DF and $\Phi O\Phi$ signals were too small for accuracy. Maximum yields of products of incomplete combustion, some of them as carbonacious material, were observed around 900 K.

Data relevant for our measurements are shown in Table 2. The k_1 values as derived from Eq. (iii) or (iiia) are actually raw data and have to be corrected for subsequent consumption of DF and $\Phi O\Phi$ mainly because of OH radicals. Obviously, a useful approach would be to simulate these losses. Because the currently available kinetic model is not sufficiently reliable, an experimental approach was used to account for these effects. To this end, ΦOH/ΦCl mixtures were seeded with known amounts of DF/$\Phi O\Phi$ under otherwise unchanged conditions. The seed concentrations were chosen so that the respective signals were large enough to be discerned easily

TABLE 2
Data relevant for the deduction of k_1 values from Eq. (iii) or (iiia). Raw data are corrected for subsequent consumption of DF and $\Phi O\Phi$ (see text); f is the total flow

	Material flows/mmol/h				Rate coefficients/L mol s		
T/K	f	$\Phi O\Phi$	ΦCl	DF	k_2	$k_{1,raw}$	$k_{1,corr}$
728	393.3	0.00034	11.80	0.1290	7.34 E7	14.8	18.1
775	393.3	0.00100	10.90	0.1690	1.17 E8	55.4	73.1
787	396.4	0.00099	11.43	0.1172	1.31 E8	68.0	95.9
837	396.4	0.00132	9.73	0.1564	2.00 E8	121.1	174.4
885	396.4	0.00165	8.37	0.1291	2.87 E8	245.6	376.0
933	396.4	0.00129	5.98	0.0746	3.98 E8	438.5	702.0
929	393.3	0.00242	6.29	0.0634	3.87 E8	826.8	1323
984	393.3	0.00056	3.19	0.0214	5.42 E8	814.5	1368

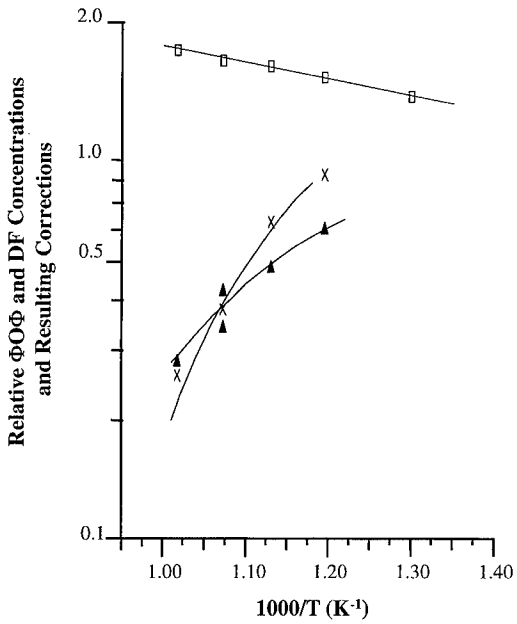

FIG. 2. DF (crosses) and $\Phi O\Phi$ (triangles) depletion during the slow combustion of our $\Phi OH/\Phi Cl$ mixtures. The resulting combined corrections to our k_1 raw data are given by the (accidentally) straight line and vary in our temperature range between 30% and 70%.

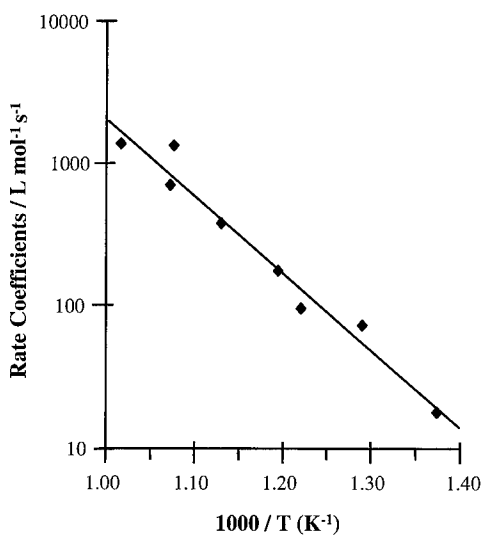

FIG. 3. Arrhenius plot for the reaction of ΦO with chlorobenzene between 728 and 984 K resulting in $A_1 = 4.8 \times 10^8$ L/mol s, $E_{a1} = 24.5$ kcal/mol. It is assumed that these Arrhenius parameters are also valid for the reaction of phenoxy radicals (ΦO) with chlorophenol.

from the corresponding product signals. On the other hand, the extra DF/$\Phi O\Phi$ amounts had to be sufficiently small so as to leave the reactive system unchanged. As an example, the DF/$\Phi O\Phi$ seed concentrations used in the 885-K experiment are given in Table 1.

From the recovered DF/$\Phi O\Phi$ yields, the respective fraction surviving our reactive system could be determined (see Fig. 2). It can be seen that at our highest temperature, only 23% of the DF and 29% of the $\Phi O\Phi$ survive. Since these effects at least partly cancel, the resulting correction factor that must be applied to k_1 is 1.7 for this temperature. For our lowest temperature, we get a correction factor of 1.3.

With the correction factors as outlined, one arrives at the corrected values for k_1 as shown in Table 2 and Fig. 3. The straight line in Fig. 3 is the result of a least-squares treatment. The corresponding parameters are

$$A_1 = 4.8 \times 10^8 \text{ L/mol s}$$

$$E_{a1} = 24.5 \text{ kcal/mol}$$

with a correlation coefficient of $r = -0.984$.

Discussion

Dibenzofuran is the main organic product from the slow combustion of phenol. In slow partial combustion and under pyrolysis conditions, DF is clearly formed by the combination of two phenoxy radicals [16]. Under the present conditions, at 873 K, with $k_2 \approx 3 \times 10^8$ L/mol s, the concentration of phenoxy is about 2×10^{-8} mol/L. This is nearly 10^{-3} of the phenol concentration or 10^{-4} of the chlorobenzene concentration. The small but significant production of $\Phi O\Phi$ in the presence of ΦCl—which nearly vanishes completely if ΦCl is replaced by benzene—substantiates reaction (1) and therefore also displacement of Cl by chlorinated ΦO as in reaction (a) of the ST model.

The Arrhenius parameters found in the current study are surprisingly close to those assumed by ST. In fact, our k_1 value at 600°C is 345 L/mol s rather than ≈300 from ST parameters for reaction (a). From known thermochemical data [17], the overall reaction $\Phi O + \Phi Cl \rightarrow \Phi O\Phi + Cl$ is endothermic by 17 kcal/mol. The energy diagram of Fig. 4 shows the levels of the starting compounds, the intermediary adduct radical, and the products. Whether TS1, TS2, or something in between represents the overall barrier of 25 kcal in the forward direction is not yet known.

In principle, formation of $\Phi O\Phi + Cl$ in reaction (1) is but one exit channel of the addition reaction of ΦO radicals to ΦCl. Given its low activation energy, other exit channels seem improbable to us. Because of its instability, there cannot be a significant

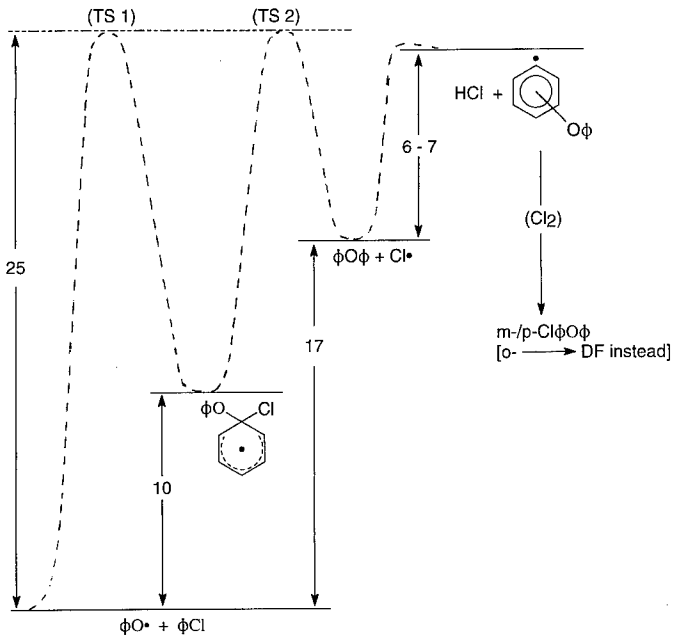

FIG. 4. Energy diagram for the reaction $\Phi O + \Phi Cl$; units: kcal/mol.

buildup of the ΦO-chloro-cylohexadienyl adduct. For these reasons, our rate coefficient k_1 will be very close to the overall reaction rate coefficient for the addition of ΦO to chlorobenzene.

The high rates for the conversion of 2,4,6-trichlorophenol to the corresponding dioxins observed by Dellinger [8] were interpreted with k_a a factor of 40 larger than the ST value to maintain compatibility with the ST mechanism. This was accommodated by reducing the activation energy from 26 to 19.5 kcal/mol. When going from ΦCl to (ortho)chlorinated phenols, there will be no significant change in the endothermicity (17 kcal) of the displacement of Cl by phenoxy. The lower activation energy of Dellinger is less than 3 kcal beyond the product level (see Fig. 4), which is unrealistic. The gas-phase free radical chlorination of $\Phi O\Phi$ to Cl$\Phi O\Phi$ has been described [18]. The key step is the abstraction of a H atom [19] that is endothermal by at least 6 kcal/mol [20]. Splitting of the ether by Cl to ΦCl was not mentioned and therefore is at best a minor reaction. The right-hand side of Fig. 4 represents this chlorination pathway and underscores that the overall barrier for reaction (1) must be well above 20 kcal/mol. Dioxin formation under Dellinger's conditions is therefore not due to a ST-type reaction (a) but can best be rationalized via a faster combination of two (tri)chlorophenoxy radicals, analogous to reaction (2), in a way outlined earlier for o-Cl-phenol [10].

To assess which of the two pathways (radical/radical or radical/chlorophenol) predominates under real combustion conditions of municipal solid waste, for example, the ratio of the concentrations of (chlorinated) phenol (hereafter denoted POH) and phenoxy (PO) is crucial. At temperatures near 1000°C, k_a will be about 2×10^3 L/mol s. The effective rate constant for the self-reaction of two PO radicals will be at least 2×10^8 L/mol s. Thus, the step PO + POH of the ST mechanism will dominate only if [POH]/[PO] is substantially larger than 10^5.

We infer that in real combustion, for example, of municipal solid waste (when phenols are at best only very minor constituents of the feed and thus have to be formed in situ) and with T around 900–1000°C, the [POH]/[PO] ratio is at best 10^3. Such values are also measured in the combustion of benzene [21]. In these situations, the key step of the ST mechanism cannot compete effectively with the self-reaction of phenoxy radicals.

This can change, however, at relatively low temperatures and when phenols form part of the feed and, more generally, in pyrolytic rather than combustion reactions. At very high temperatures, the [POH]/[PO] ratio may increase because of the rapid decomposition of phenoxy radicals to yield CO [22,23]—but then combustion nears completion, dioxin production and survival fading out as well.

In summary, these gas-phase pathways do not contribute much to the polychlorinated dibenzofurans and dioxins—at least in MSW processing incinerators; here, surface-catalyzed condensations and/or (oxy)chlorinations in the air-pollution control devices play a role [1–3]. It is still unresolved to which extent so-called de novo formation via (graphitic) coal particles or precursor reactions participate [4,5]. In the latter case, (chloro)phenols are commonly

accepted as key intermediates, but other predioxins can be involved such as lower chlorinated dibenzofurans, dioxins, and related structures as part of the PICs of the primary combustion process. Effectively reducing dioxin formation by minimizing the yields of precursors obviously requires a more detailed understanding of the steps governing the formation/destruction of these species. Consequently, in an extension of the present work, we plan to study model reactions under relevant conditions.

Meanwhile, experiments as described in this paper (with bromobenzene rather than chlorobenzene) are under investigation in our laboratory. Initial results suggest that formation of $\Phi O \Phi$ is only about as fast as with ΦCl [15]. This means that the reaction $\Phi O + \Phi Br$ cannot be used to explain the high dioxin formation rates with tribromophenol, which were observed by Dellinger et al. [8] to be a factor of 500 higher than in the chlorinated case. This again substantiates our interpretation that the phenoxy + phenoxy pathway is followed.

Acknowledgments

H. H. G. gratefully acknowledges the technical help of and many discussions with Dr. M. Jacqueline Kanters and Ing. Wibo van Scheppingen. Support of the State of Baden-Württemberg through the project PWAB under P 42895 is also acknowledged.

REFERENCES

1. Stieglitz, L., Zwick, G., Beck, J., Roth, W., and Vogg, H., *Chemosphere* 18:1219 (1989).
2. Dickson, L. C. and Karasek, F. W., *J. Chromatography* 389:127 (1987).
3. Ballschmiter, K., Braunmiller, I., Niemczyk, R., and Swerev, M., *Chemosphere* 17:995 (1988).
4. Dickson, L. C., Lenoir, D., and Hutzinger, O., *Environ. Sci. Technol.* 26:1822 (1992).
5. Huang, H. and Buekens, A., *Chemosphere* 31:4099 (1995).
6. Shaub, W. M. and Tsang, W., *Environ. Sci. Technol.* 17:721 (1983).
7. Dransfeld, P., Verein Deutscher Ingenieure Bildungswerk, BW 778, Germany, 1991.
8. Sidhu, S. S., Maqsud, L., Dellinger, B., and Mascolo, G., *Combust. Flame* 100:11 (1995).
9. Ghorishi, S. B. and Altwicker, E. R., *Hazard. Waste Hazard. Mater.* (1996), accepted.
10. Buth, R., Hoyermann, K., and Seeba, J., *Twenty-fifth Symposium (International) on Combustion,* The Combustion Institute, Pittsburgh, 1994, p. 841.
11. Born, J. G. P., Ph.D. Thesis, Leiden University, 1992.
12. Born, J. G. P., Louw, R., and Mulder, P., *Chemosphere* 19:401 (1989).
13. Kanters, M. J., Ph.D. Thesis, Leiden University, 1996.
14. Kanters, M. J. and Louw, R., *Chemosphere* 32:89 (1996).
15. Grotheer, H. H., Kanters, M. J., and Louw, R., Fourteenth International Symposium on Gas Kinetics, Leeds, 1996.
16. Arends, I. W. C. E., Louw, R., and Mulder, P., *J. Phys. Chem.* 97:7914 (1993).
17. Stein, S. E.., Rukkers, J. M., and Brown, R. L., NIST Structures and Properties Database, version 2.0, NIST Standard Reference Data, National Institute of Standards and Technology, Gaithersburg, MD, 1994.
18. Engelsma, J. W. and Kooyman, E. C., *Recl. Trav. Chim. Pays-Bas* 80:526 (1961).
19. Dorrepaal, W. and Louw, R., *Int. J. Chem. Kinet.* 10:249 (1978).
20. Davico, G. E., Bierbaum, V. M., DePuy, C. H., Ellison, G. B., and Squires, R. R., *J. Am. Chem. Soc.* 117:2590 (1995).
21. Zhang, H.-Y. and McKinnon, J. T., *Combust. Sci. Technol.* 107:261 (1995).
22. Lin, C. Y. and Lin, M. C., *J. Phys. Chem.* 90:425 (1986).
23. Olivella, S., Solé, A., and Garcia-Raso, A., *J. Phys. Chem.* 99:10549 (1995).

Twenty-Sixth Symposium (International) on Combustion/The Combustion Institute, 1996/pp. 2413–2420

EFFECTS OF AMBIENT WATER IN THE COMBUSTION ENHANCEMENT OF HEAVILY CHLORINATED HYDROCARBONS: STUDIES ON DROPLET BURNING

H. WANG, D. L. ZHU, Y. SASO* AND C. K. LAW
Department of Mechanical and Aerospace Engineering
Princeton University
Princeton, NJ 08544, USA

An experimental and computational investigation has been conducted on the oxidation and combustion of chlorinated hydrocarbon droplets in a hot, oxidizing environment, with emphasis on the effects of ambient water on the droplet burning intensity. The experimental results demonstrate that the presence of a small amount of water in the environment, say 5–10% by volume, can substantially increase the droplet burning rate and reduce the droplet ignition and extinction temperatures of heavily chlorinated hydrocarbons (HCHCs) and their mixtures whose chlorine-to-hydrogen ratio is close to unity. The computational simulation with detailed chemistry and transport yields good qualitative and quantitative agreement with the experimental results and identifies that this beneficial effect of water arises from its reaction with the Cl atoms, producing the active hydroxyl radicals that subsequently promote the CO to CO_2 conversion and generate the H atoms needed to initiate radical-chain branching. From the practical viewpoint, it is suggested that while the presence of water in combustion environments can potentially enhance the destruction efficiency and combustion stability in halogenated-waste incinerators, it can, however, diminish the effectiveness of halogen-based fire-retarding or fire-suppressing agents.

Introduction

Many hazardous, halogen-containing organic wastes are incineration resistant [1,2]. The presence of halogens not only lowers the heat of combustion as compared to the nonhalogenated hydrocarbons but they also tend to lock the available hydrogen in the form of hydrogen halide. For heavily chlorinated hydrocarbons (HCHCs) in which the chlorine-to-hydrogen ratio is either close to or exceeds unity, the reaction system then lacks the necessary hydrogen atoms to initiate radical chain branching. As such, HCHCs usually do not burn under normal conditions. Even if they do, the burning process is frequently retarded, exhibiting low burning rates and strong tendency of flameout.

A viable approach toward enhancing the destruction efficiency of hazardous waste incinerators is to blend nonhalogenated hydrocarbon fuels with the incineration-resistant halogenated hydrocarbon wastes so that the resulting mixture can be rendered to burn well [3]. Indeed, Sorbo et al. [4] and Sorbo and Chang [5] demonstrated that droplets of HCHCs, such as 1,1,2,2-tetrachloroethane (TECA) and tetrachloroethene (PERC), can be rendered to burn vigorously by adding a small quantity (20–25% by volume) of an alkane. Furthermore, Li and Law [6] showed that by blending HCHC wastes with lightly chlorinated hydrocarbons (LCHCs) as substitutes for the nonchlorinated hydrocarbons, both hazardous wastes can be destroyed without any cost expenditure for the hydrocarbon fuel stocks. The controlling parameter for such a blending strategy appears to be the chlorine-to-hydrogen ratio (Cl/H) of the fuel–waste blend in that, through its influence on the flame temperature, vigorous burning is observed for Cl/H < 1, while the burning intensity rapidly decreases as Cl/H exceeds unity.

While the positive results of Refs. 4–6 offer encouraging possibilities in formulating rational blending strategies for efficient and economical waste incineration, we are still confronted with the difficulty of incinerating wastes or waste blends whose Cl/H is close to or exceeds unity. In this regard, we note a recent modeling study [7] for the experimental data of Ref. 6 on the droplet burning of mixtures of equally volatile TECA and nonane, using detailed transport and semidetailed reaction kinetics. An interesting observation of this study is that the addition of a small quantity of water vapor in the ambient air, say 5–10% by volume, enhances the burning intensity of the HCHC-alkane and HCHC–LCHC fuel blends. The effect appears to be particularly pronounced when the fuel Cl/H ratio is close to unity

*Permanent Address: National Research Institute of Fire and Disaster, Fire and Disaster Management Agency, Ministry of Home Affairs, 14-1 Nakahara 3-chome, Mitaka, Tokyo 181, Japan.

and was attributed to the role of water in providing an additional source of hydroxyl radicals through its reaction with the chlorine atoms.

This preliminary observation of the potential beneficial effect of water addition on chlorinated waste incineration is of interest for several reasons. Practically, the possibility of extending the performance capability of incinerators through water injection is attractive because it requires minimal change in the incinerator design and basically no operational cost expenditure. Furthermore, since halogenated hydrocarbon combustion is also of interest to fire research, we recognize the possibility that the presence of excessive moisture in a fire situation, due to either high humidity or water spraying, could actually diminish the effectiveness of halogen-based fire-retarding or fire-suppressing agents, especially for the fact that these agents are usually heavily halogenated. Fundamentally, the role of water in the chemistry of chlorinated or halogenated hydrocarbon combustion has not been systematically studied and adequately understood, at least in flame environments. Finally, if water were found to be an important chemical component in chlorinated hydrocarbon combustion, then future experimental and modeling studies, both at the laboratory and incinerator/field scales, may need to take this factor into consideration.

In view of the above considerations, we have conducted a fairly extensive study on the effects of ambient water on the ignition, extinction, and steady burning of blends of chlorinated hydrocarbons. We shall again adopt droplet burning as the model problem because it is conveniently suited for the study of liquid fuels. It is also to be recognized that understanding gained from such a study is expected to be largely applicable to other combustion configurations or situations, at least those involving diffusional burning. The study involves experimental substantiation and quantification of the beneficial effects of ambient water and further computational simulation aiming to identify the controlling chemical kinetic structure and mechanism of the various combustion situations. We shall demonstrate that droplet burning is indeed enhanced in a water-containing environment and that the numerical model developed in Ref. 7 predicts well the gasification/burning rates at different levels of water addition. As such, models of this nature can be used as a partial guidance for exploring optimal waste incineration conditions.

The experimental specification and a brief description of the computational methodology are given in the next section, which is then followed by presentation and discussion of results on the burning rate enhancement and the reduction of the extinction and ignition temperatures.

Experimental and Computational Methodologies

A schematic of the experimental apparatus can be found in Ref. 4. The experiment basically involves generating a stream of monodisperse droplets with controlled size and spacing by using the ink-jet printing technique. The initial droplet diameters ranged from 230 to 270 μm. The droplets are injected downward into the postcombustion flow of a flat-flame burner and subsequently gasified with or without ignition and steady burning depending on the ambient temperature and constituent (O_2, N_2, H_2O, and CO_2) concentrations. The data taken include the instantaneous droplet size recorded by stroboscopically back-lighted microphotography.

The variations of the ambient temperature and H_2O concentration are well controlled, achieved by manipulating the flow rates of predried methane, carbon monoxide, oxygen, and nitrogen supplied to the flat-flame burner such that the postcombustion flow always contains 20 $\pm$ 0.5 mol % oxygen in equilibrium concentration. Active droplet gasification and burning are confined to the chamber segment within which the gas temperature variation is within $\pm$20 K. Typical thermocouple-measured temperature profiles, corrected for radiation, are shown in the inset of Fig. 1. For reference, the maximum temperature over the droplet lifetime will be quoted in data comparison.

Experiments were conducted for binary mixtures of TECA with *n*-nonane and with 1-chloroheptane. The normal boiling points of these fuels are about equal, and preferential gasification of the individual constituents has been shown to be insignificant [6]. The purities of the reagents used are 99%, 98+%, and 99% for nonane, TECA, and chloroheptane, respectively.

The numerical simulation was performed by employing a quasisteady, spherical diffusion flame model of simultaneous fuel vaporization, pyrolysis, and combustion with imposed liquid-fuel composition, ambient temperature, and ambient constituents and their concentrations. While details of the numerical model are given in Ref. 7, several points need to be mentioned here. The d^2-law [8] burning rate constant is obtained from the mass flux obtained by solving the eigenvalue of the boundary value problem of species and energy conservation equations. The fuel liquid is an ideal miscible mixture, obeying Raoult's law [8]. The Sandia Chemkin programs [9] and premixed flame code [10] were used, with boundary conditions modified for the latter in accordance with the problem defined above. The reaction mechanism employed in the numerical simulation consists of 190 reactions and 90 chemical species. It is detailed for TECA decomposition and small species ($C_1H_xCl_y$–$C_3H_xCl_y$) oxidation but semidetailed for the nonane reactions, which include

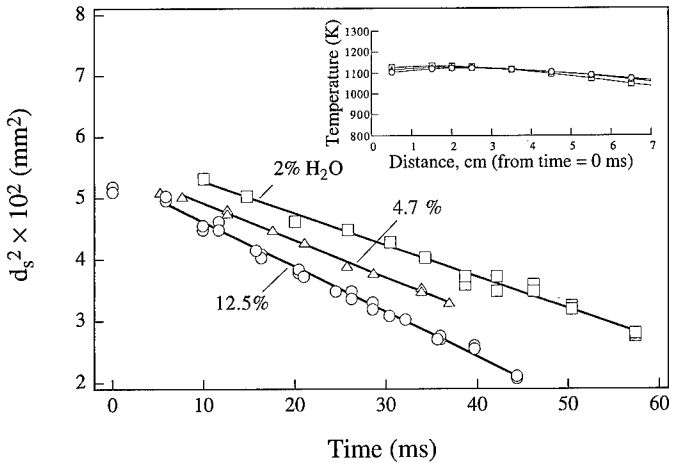

FIG. 1. The d^2-law plot for droplet of 90% TECA–10% nonane gasifying at 2, 4.7, and 12.5% ambient water levels; inset: the corresponding temperature profiles within the active chamber segment. The d^2-law gasification rate constant is equal to the slope of the d_s^2-time relationship. For clarity of presentation, the data for 2% water is shifted by +10 ms.

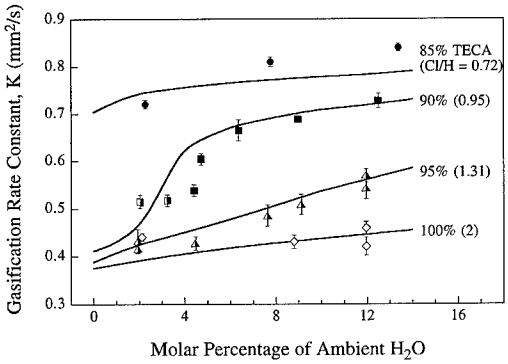

FIG. 2. Variation of the d^2-law rate constant as a function of molar percentage of ambient water. Symbols are experimental data obtained at the maximum ambient temperature of 1130 K (open symbols: no luminosity observed; half-filled symbols: bluish-green luminous streak; filled symbols: bright yellow streak followed by a blue tail). Lines are numerical predictions under the conditions similar to the experiment.

the nonyl radical formation through H abstraction by H, O, OH, and Cl, followed by its decomposition to C_3H_6, C_2H_4, and CH_3 fragments in one global step. The reaction kinetics is compiled based on the work of Refs. 11–19.

Results and Discussions

Visual Observations

We first describe the visual appearance of the droplet gasification process with and without a flame streak as a result of the variation of ambient water concentration. The droplet burning 90% TECA–10% nonane in 2% water and at 1130 K ambient temperature is characterized by a very faint bluish-green luminous streak that is only visible in a darkened room. Such a faint luminosity is similar to previously observed gasification of pure TECA [6], whose gasification rate is the same in either oxidizing and nonoxidizing environments [4]. This faint luminosity therefore indicates only mild oxidation without significant temperature rise from the ambience, instead of active oxidative heat release associated with a vigorous burning process. At 4.7% water, a bright but short, yellow luminous streak can be observed, which is followed by a long, faint, bluish glow. Such a bright yellow luminous streak indicates enhanced burning intensity. When the water concentration is increased to 12.5%, the yellow luminous streak is brighter and lasts over a longer period of the droplet lifetime. Summarizing the visual observations, we see that while the droplet clearly undergoes intense burning in the 12.5% water environment, it basically does not burn at the 2% water level.

d^2-Law Burning Rate Constant

Based on the classical d^2 law of droplet combustion, Fig. 1 presents the temporal variation of the square of the droplet diameter, d_s, with a maximum environment temperature around 1130 K. As demonstrated in previous studies [4–6], the nearly linear variation clearly shows that the d^2 law holds quite well. The slope of the d^2-t relationship plotted in Fig. 1 then yields the gasification rate constant, defined as $K = -d(d_s^2)/dt$.

Figure 2 shows K as a function of the ambient water level for a number of TECA–nonane mixtures. Here, the filled symbols represent runs in which bright yellow luminosity was clearly seen, while the half-filled and open symbols respectively indicate that a faint, bluish-green glow and no luminosity was observed. The values in the parentheses indicate the

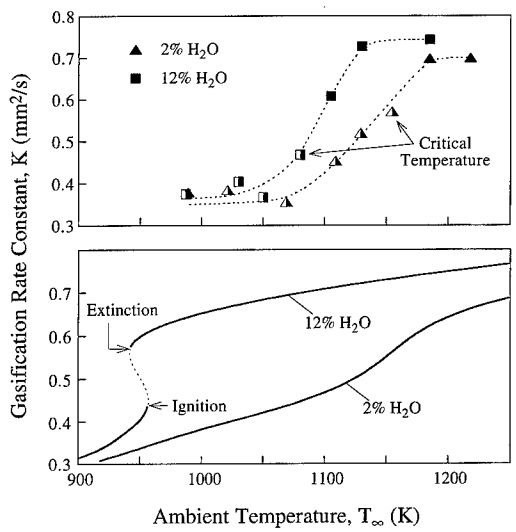

FIG. 3. Variation of the d^2-law rate constant as a function of the ambient temperature for droplets of 90% TECA–10% nonane at two different ambient water levels. Top panel: experimental data (half-filled symbols: bluish-green luminous streak; filled symbols: bright yellow streak; lines: fit to data); bottom panel: numerical predictions.

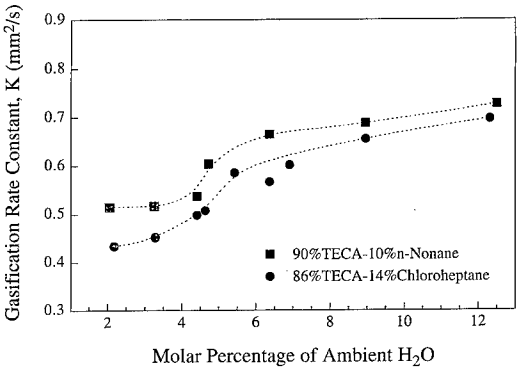

FIG. 4. Comparison of the experimental d^2-law rate constant as a function of molar percentage of ambient water for droplets of 86% TECA–14% chloroheptane and 90% TECA–10% nonane mixtures at the maximum ambient temperature of 1130 K.

Cl/H ratio of the given fuel mixture. The error bar is based on one standard deviation from the linear regression procedure. The results show that while the effect of water on burning rate enhancement is mild for either the 85% TECA–nonane mixture or pure TECA, it is intensified for the 90% and 95% TECA–nonane mixtures. For the 90% TECA case, the fairly abrupt transition from the lower burning rates (~0.5 mm^2/s) to the higher burning rates (~0.7 mm^2/s) is associated with the transition from a faint, bluish-green glow to intense yellow, as seen in the visual observations just discussed.

Also shown in Fig. 2 are the numerical calculations, which are seen to compare well with the experimental data in terms of the predicted gasification rate constant and the transition from no burning to vigorous burning with water addition. The above observational, experimental, and computational results therefore conclusively demonstrate the beneficial effect of water addition in enhancing the droplet burning rate of HCHCs.

The dependence of the burning rate on the ambient temperature has also been studied. The upper and lower panels of Fig. 3 respectively plot the experimental and computed K as a function of the maximum ambient temperature for 90% TECA–10% nonane droplets burning in environments containing 2% and 12% water. The computed results clearly show the potential occurrence of distinct ignition and extinction events, as characterized by the nonmonotonic, folded S-curve, as the ambient water content increases from 2% to 12%. While such distinct transition events are not captured by the experiment, possibly due the gentle nature of the S-curve folding, the experimental data do show that the critical temperature at which the yellow luminous streak is first observed decreases by 50–70 K as the water content increases from 2% to 12%. Such a temperature variation, although on the same order as that in the ambient gas flow within the active chamber segment, certainly indicates the qualitative effect of water on the ignition and extinction characteristics. The experimental results further show that, for a given temperature, the gasification rate is substantially increased with increasing water content. Finally, recognizing the variation of the ambient temperature inside the chamber over the droplet lifetime and that the numerical simulation is performed for a fixed ambient temperature, the agreement between experiment and simulation can be considered to be quite satisfactory.

To demonstrate that the identified effect of water is independent of the fuel type, and to further substantiate the previous results that the burning characteristics of HCHC–LCHC and HCHC–nonchlorinated hydrocarbon mixtures can be roughly correlated by the mixture Cl/H ratio [6], we plot in Fig. 4 the variation of the burning rate constant as a function of the ambient water level for the 86% TECA–14% chloroheptane mixture and compare it with the 90% TECA–10% nonane mixture with the equal Cl/H ratio of 0.95. As expected, the dependence on the ambient water concentration is basically identical for the two fuel mixtures, and the TECA–chloroheptane droplet exhibits the same burning rate enhancement with water addition.

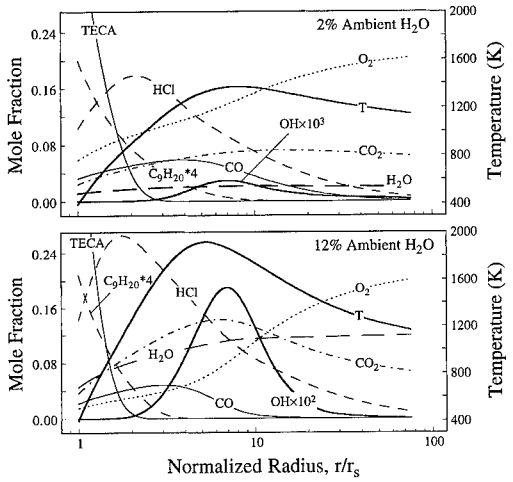

FIG. 5. Computed major species, OH, and temperature profiles for droplet of 90% TECA–10% nonane at the ambient temperature of 1100 K, where r_s is the droplet radius.

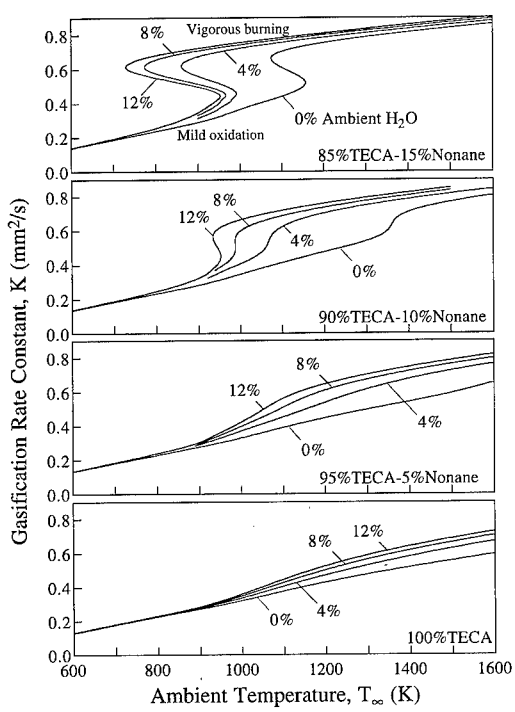

FIG. 6. Computed dependence of d^2-law rate constant on ambient temperature and ambient water vapor levels.

Numerical Simulation

In order to identify the kinetic cause for the observed behavior, we have performed a full range of detailed numerical simulation for the reaction system. Selected numerical results are shown in Figs. 5–7. We first recognize that since the postflame water concentration of the downward flat flame cannot be manipulated without changing the carbon dioxide concentration, the effect of ambient CO_2 on the burning rates needs to be assessed. Thus, computation was performed by varying the ambient CO_2 concentration (by replacing N_2) from 0% up to the highest possible level of 24%, while maintaining the same level of water vapor. The computed gasification rate constants for the 90% TECA–10% nonane mixture, with the 2 and 12% ambient water concentration, show practically no dependence on the ambient CO_2 concentration, at least to the extent detectable in the experiment.

To substantiate the difference in the detailed reaction zone structure for situations without and with the burning characteristics, we plot in Fig. 5 the major species concentration and temperature profiles for 90% TECA–10% nonane mixture at 1100 K ambient temperature and 2 and 12% ambient water levels, respectively. It is seen that in the 2% water case, the rise in temperature from that of the environment is small, with the maximum temperature only about 300 K higher than the ambience. Such a low flame temperature is unfavorable for soot formation [20], which explains why the gasification process does not exhibit yellow luminosity. Furthermore, a significant amount of oxygen penetrates through the reaction zone and reaches the droplet surface. In addition, the oxidation of CO to CO_2 is sluggish, as the CO concentration is persistently high even at a distance of 50 times the size of the droplet. Nonetheless, the computational results suggest that mild oxidation does occur, which explains the faint, bluish-green luminosity observed in our experiment.

In the vigorous burning, 12% H_2O case shown in the lower panel of Fig. 5, the extent of oxygen leakage through the flame is less pronounced, and the CO burnout is also more prompt. Furthermore, the temperature rise is significant, with the maximum flame temperature reaching ~1900 K. This specific vigorous burning, diffusion flame condition favors the formation of soot, hence explaining the bright yellow luminosity observed in our experiment of similar conditions.

To further explore the system response in terms of the ignition and extinction characteristics, we have plotted in Fig. 6 the calculated gasification rate constant as a function of temperature for the four fuel mixtures of Fig. 2, while in Fig. 7, the maximum OH concentration and maximum temperature are plotted as functions of ambient temperature for the mixture of 90% TECA–10% nonane. The results clearly

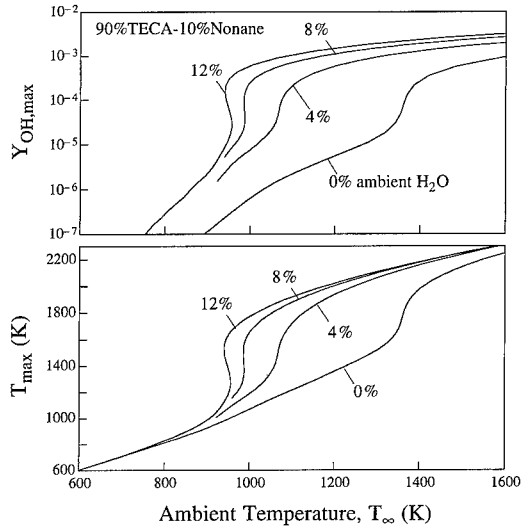

FIG. 7. Computed variation of (top) maximum OH mass fraction, $Y_{OH,max}$, and (bottom) maximum flame temperature, T_{max}, on ambient temperature for droplet of 90% TECA–10% nonane.

show that distinct ignition and extinction events, as characterized by the folded *S*-curves, are favored with decreasing Cl/H ratio and increasing ambient water content. The attainment of ignition and higher gasification rates is particularly sensitive to water addition for the heavily chlorinated case of 90% TECA–10% nonane. In general, the results show that the gasification rates, with and without vigorous diffusional burning, can be substantially enhanced with the addition of a small amount of ambient water. It is also seen in Fig. 6 that, at a constant ambient temperature of 1100 K, the increase in the ambient water concentration does not cause jumps from the lower branch to the upper branch of the *S*-curves. This justifies the continuous and smooth curves plotted in Fig. 2 for the variation of computated gasification rate constant as a function of ambient water concentration.

To examine the specific effects of ambient water on the chemical reaction system, we examined the reaction pathways based on the semidetailed reaction mechanism of Ref. 7. We found that the key reactions include

$$Cl + H_2O \rightarrow HCl + OH \qquad (R1)$$

$$OH + CO \rightarrow CO_2 + H \qquad (R2)$$

$$H + O_2 \rightarrow O + OH \qquad (R3)$$

The Cl atoms are readily available from the thermal decomposition of TECA, due to the low C–Cl bond strength [13,14]; from the decomposition of the intermediate species CClO via $CClO \rightarrow CO + Cl$ (R4), and from the H and Cl shuttling reactions, e.g., $C_2Cl_2 + H \rightarrow CHCCl + Cl$ (R5), where C_2Cl_2 is the major decomposition product of TECA. Its subsequent reaction with O atoms, $C_2Cl_2 + O \rightarrow CCl_2 + CO$ (R6), and the reactions $CCl_2 + O_2 \rightarrow COCl_2 + O$ (R7), $COCl_2 + Cl \rightarrow CClO + Cl_2$ (R8), $Cl_2 + H \rightarrow HCl + Cl$ (R9), and $HCl + H \rightarrow H_2 + Cl$ (R10) complete the reaction cycle. This reaction sequence must necessarily start from reaction (R1). Thus, whether such a cycle can initiate depends largely on the availability of H_2O.

We note that the shift between the reactant and product balance in reaction (R1) by the addition of a small quantity of high-temperature H_2O has been reported through a sensitivity test in the modeling study of Ho et al. [17]. Such a shift was seen to perturb the OH concentration and, hence, affect the CO-to-CO_2 conversion. The present results shown in the upper panel of Fig. 7 further demonstrated that an increase in the H_2O concentration indeed increases significantly the maximum mass fraction of the OH radicals. The increased water concentration then promotes the conversion of CO to CO_2, which is normally inhibited by chlorine during HCHC combustion [21]. Furthermore, the perturbation from the ambient H_2O is so significant under the experimental condition of the present study that it dictates the ignition and extinction characteristics for a given fuel mixture.

While the success of droplet burning enhancement by water vapor is clearly demonstrated in our study, it is important to recognize that the effect is most pronounced for fuel mixtures of Cl/H ratios around unity, as demonstrated for the 90 and 95% TECA–nonane mixtures with the Cl/H ratios corresponding to 0.95 and 1.31. This is not surprising considering that while there are sufficient H atoms in mixtures with $Cl/H \ll 1$ to initiate the chain branching process, for heavily chlorinated hydrocarbon mixtures with the Cl/H ratio $\gg 1$, the hydrogen supplied by water through reactions (R1) and (R2) is insufficient to initiate chain branching (R3) because the H atoms are now effectively scavenged by reactions (R5), (R9), and (R10) due to increased chlorine content in the reaction system.

Concluding Remarks

In the present study, we have demonstrated the viability of water vapor in enhancing chlorinated hydrocarbon waste incineration. We found that with the presence of a small quantity of water vapor in the combustor, say 5–10% by volume, the destruction rate of heavily chlorinated hydrocarbon wastes can be significantly enhanced. Furthermore, the presence of water vapor reduces the temperature of droplet ignition/flame extinction and, hence, increases the stability of the overall incineration pro-

cess. As such, the destruction efficiency is expected to be enhanced and the production of the undesirable intermediate toxic products reduced. The results also suggest that for the same family of chemical compounds, the effectiveness of ambient water vapor in burning rate enhancement is similar as long as the fuel mixture contains the same chlorine-to-hydrogen ratio and thus further substantiate the conclusion of Ref. 6 that the droplet burning characteristics of the chlorinated hydrocarbon mixtures can be correlated with the mixture Cl/H ratio.

It is also shown that the numerical model developed in Ref. 7 successfully predicted and explained the effects of water addition. Through such a simulation study, we identify that the beneficial role of ambient water arises mainly from its reaction with the chlorine atoms, which are readily available through the thermal decomposition of chlorinated hydrocarbons initiated by the weak C–Cl bonds. This reaction yields the hydroxyl radical, which undergoes further reaction with CO, generating the H atoms. The further reaction of the H atoms with O_2 produces the chaining branching effect necessary for the burning process to start and sustain.

It is of interest to examine if the presence of water may have the additional beneficial effect of reducing by-product emission from chlorinated hydrocarbon waste combustion. It is expected that the enhanced burning intensity and the OH concentrations can reduce the emission of these by-products. Furthermore, the potential influence of water in diminishing the effectiveness of halogenated fire-retarding and fire-suppressing agents also merits study.

Acknowledgments

This work was supported by the Thermal Systems Program of the U.S. National Science Foundation under the technical monitoring of Dr. Milton Linevsky. Y. Saso is supported by the Overseas Research Program of the Science and Technology Agency, Japan.

REFERENCES

1. Dempsey, C. R. and Oppelt, E. T., *Air and Waste* 43:25–73 (1993).
2. Kramlich, J. C., Heap, M. P., Seeker, W. R., and Samuelsen, G. S., *Twentieth Symposium (International) on Combustion,* The Combustion Institute, Pittsburgh, 1985, pp. 1991–1999.
3. Law, C. K., *Combust. Sci. Technol.* 74:1–15 (1990).
4. Sorbo, N. W., Law, C. K., Chang, D. Y. P., and Steeper, R. R., *Twenty-Second Symposium (International) on Combustion,* The Combustion Institute, Pittsburgh, 1989, pp. 2019–2025.
5. Sorbo, N. W. and Chang, D. P. Y., *Combust. Sci. Technol.* 85:419–435 (1992).
6. Li, T. X. and Law, C. K., *Twenty-Fifth Symposium (International) on Combustion,* The Combustion Institute, Pittsburgh, 1994, pp. 291–297.
7. Wang, H., Sung, C. J., and Law, C. K., "On the Mild and Vigorous Oxidation of Mixtures of Chlorinated Hydrocarbons in Droplet Burning", MAE Report No. 2058. Princeton University, 1996; *Combust. Flame,* in press.
8. Law, C. K., *Prog. Energy Combust. Sci.* 8:169–199 (1982).
9. Kee, R. J., Rupley, F. M., and Miller, J. A., *Chemkin-II: A Fortran Chemical Kinetics Package for the Analysis of Gas Phase Chemical Kinetics,* Sandia Report SAND 89-8009B, Sandia National Laboratories, Albuquerque, NM, 1989.
10. Kee, R. J., Grcar, J. F., Smooke, M. D., and Miller, J. A., *A Fortran Program for Modeling Steady Laminar One-Dimensional Premixed Flames,* Sandia Report SAND 85-8240, Sandia National Laboratories, Albuquerque, NM, 1985.
11. Kerr, J. A. and Moss, S. J., *Handbook of Bimolecular and Termolecular Gas Reaction,* CRC Press, Boca Raton, FL, 1981, Vols. I, II.
12. Tsang, W. and Hampson, R. F., *J. Phys. Chem. Ref. Data* 15:1087–1279 (1986).
13. Chang, W. D., Karra, S. B., and Senkan, S. M., *Combust. Sci. Technol.,* 49:107–121 (1986).
14. Tsang, W., *Combust. Sci. Technol.* 74:99–116 (1990).
15. Tsang, W., *J. Phys. Chem. Ref. Data* 20:221–273 (1991).
16. Won, Y. S. and Bozzelli, J. W., *Combust. Sci. Technol.* 85:345–373 (1992).
17. Ho, W. P., Yu, Q.-R., and Bozzelli, J. W., *Combust. Sci. Technol.* 85:23–63 (1992). Ho, W. P., Barat, R. B., and Bozzelli, J. W., *Combust. Flame* 88:265–295 (1992).
18. Frenklach, M., Wang, H., Bowman, C. T., Hanson, R. K., Smith, G. P., Golden, D. M., Gardiner, W. C., and Lissianski, V., "An Optimized Kinetic Model for Natural Gas Combustion," *Twenty-Fifth International Symposium on Combustion,* Irvine, CA, 1994, Work-In-Progress Poster Session 3, Number 26.
19. Wang, H., Hahn, T. O., Sung, C. J., and Law, C. K., *Combust. Flame* 105:291–307 (1996).
20. Glassman, I., *Twenty-Second Symposium (International) on Combustion,* The Combustion Institute, Pittsburgh, 1988, pp. 295–311.
21. Bose, D. and Senkan, S. M., *Combust. Sci. Technol.* 35:187–202 (1983).

COMMENTS

Philip H. Taylor, University of Dayton, USA. Which TECA isomer did you study and do you expect a change in your results for the two possible isomeric configurations?

Author's Reply. 1,1,2,2-tetrachloroethane was used in the present study. We do not expect that the results would be different if we used the isomer 1,1,1,2-tetrachloroethane, because the physical properties of the two isomers, including boiling points, adiabatic flame temperatures, and transport properties, are nearly identical. Furthermore, the fuel mixtures were found to undergo significant decomposition before reaching the oxidizing zone, leading to scrambling of the elements in the fuel mixture. Hence, it is most likely that the intermediate species as a result of decomposition are also similar for the two isomers. We further note that, as was found in both the present and previous [1] studies, the fuel characteristics which affect significantly the droplet burning intensity is not the fuel structure, but the Cl-to-H ratio in the fuel mixture.

REFERENCE

1. Li, T. X. and Law, C. K., *Twenty-Fifth Symposium (International) on Combustion,* The Combustion Institute, Pittsburgh, 1994, pp. 291–297.

•

Yiannis A. Levendis, Northeastern University, USA. Very interesting work. Do you expect any penalties of the high concentrations of water on the combustion efficiency (lower adiabatic flame temperature, heat loss for vaporizing the water, etc.)? Also, do you expect enhanced HCl emissions that may condense more readily in the exhaust ducts at the presence of high concentrations of water and cause corrosion?

Author's Reply. Indeed excessive water addition may have an adverse effect on the burning intensity through flame temperature reduction, etc. On the other hand, the global reaction of HCHC with water, yielding mainly CO_2, CO, H_2, CH_4 and HCl, is exothermic. Hence, the flame temperature reduction and heat loss due to water evaporation can be potentially compensated by the chemical heat release of the reaction between HCHC and water. Clearly, a sensible incineration strategy will rely on process optimization with respect to the factors discussed above.

In response to the second question, we expect that it is easier to deal with HCl than with other undesirable toxic combustion byproducts, such as Cl_2 and phosgene. A large concentration of water may indeed increase the total amount of HCl in the flue gas, but it may also reduce the molar concentration of HCl in the condensed-water solution, and hence may even reduce corrosion.

Twenty-Sixth Symposium (International) on Combustion/The Combustion Institute, 1996/pp. 2421–2430

THE EFFECT OF THE BULK EQUIVALENCE RATIO ON THE PAH EMISSIONS FROM THE COMBUSTION OF PVC, POLY(STYRENE), AND POLY(ETHYLENE)

THOMAI PANAGIOTOU AND YIANNIS A. LEVENDIS
Department of Mechanical Industrial and Manufacturing Engineering Northeastern University
Boston, MA 02115, USA

JOEL CARLSON AND PAUL VOUROS
Department of Chemistry Northeastern University
Boston, MA 02115, USA

This is an investigation on the effects of the bulk equivalence ratio on the polynuclear aromatic hydrocarbon (PAH) emissions from the combustion of poly(vinyl-chloride) (PVC), poly(ethylene) (PE), and poly(styrene) (PS) particles. Steady-flow dispersions (clouds) of the above types of polymer particles, 150–212 μm in diameter, were burned in a drop-tube, electrically heated furnace at different bulk equivalence ratios (ϕ_{bulk} = 0.1–7.3) or were pyrolyzed in N_2. The gas temperature and residence time in the furnace were 1100°C and 1 s, respectively. (a) The total (specific) amounts of condensed and gaseous-phase PAH emissions increased with the equivalence ratio. In the present experiments, the recorded maxima in the total amounts of PAHs were obtained under pyrolysis in N_2 and accounted for 0.7, 4, and 4% of the input masses of PVC, PE, and PS, respectively. (b) PVC particles were found to oxidize effectively in air, since only minimal amounts of PAHs were produced at $\phi_{bulk} \leq 1$. Chlorinated organics were found at high ϕ_{bulk} or in N_2. Combustion of PE and PS particles produced substantial amounts of PAHs at, or near, stoichiometric conditions. PE particles were prone to flash pyrolysis and readily formed group flames ("puffs"), even at mildly fuel-rich or near-stoichiometric conditions. (c) PAH emissions from pyrolysis of PE and PS were sensitive to the particle mass loading (mass of polymer per mass of N_2) in the furnace. This was not the case for PVC. (d) For all polymers, the percentage of naphthalene in the total amount of PAHs was influenced by the combustion conditions and experienced a minimum close to stoichiometry. (e) Finally, the experimentally measured molar fractions of pairs of selected PAH isomers were compared with those obtained from chemical equilibrium calculations. For all polymers, the pairs fluoranthene (F)–acephenanthrylene (AP) and cyclopenta[cd]pyrene (CP[cd]P)–benzo[ghi]fluoranthene (B[ghi]F) were at equilibrium, while the pairs fluoranthene (F)–pyrene (P) and benzo[k]fluoranthene (B[k]F)–benzo[a]pyrene (B[a]P) were not at equilibrium. PS produced much higher soot emissions than PE or PVC.

Introduction

An investigation was conducted on the polynuclear aromatic hydrocarbon (PAH) emissions from the combustion/pyrolysis of waste plastics. Millions of tons of plastics are discarded every year [1]. Although, recently there has been an effort to recycle selected plastics, such as poly(ethylene-terephthalate) and high-density poly(ethylene) (PE), most waste plastics are not recycled and end up in landfills. Considering the large specific volume of plastics [2,3] and the scarcity of landfill space [3], landfilling may not be optimum. Therefore, since the heating value of plastics is comparable to that of petroleum, waste to energy conversion is a viable option for the destruction of plastics, if emissions of toxic combustion by-products are prevented.

In past research, pyrolysis by-products were identified and decomposition mechanisms were proposed for plastics at gas temperatures up to 800°C [4–15]. Different decomposition mechanisms were postulated for various polymers [4,5,13,14], and the pyrolyzates were found to include methane, hydrogen, the monomer itself, and other oligomers. Previous work also addressed the combustion of polymers at various conditions [15–17,24–27] and identified resulting PAH emissions [18–23,28–29]. Most previous work, however, involved either oxidation/pyrolysis of polymers at temperatures below those of interest to waste combustion or identification/quantitation of only a small number of PAHs.

The combustion characteristics of single-spherical, 30–350 μm, polymer particles were studied previously at Northeastern University, at T_{gas} of 800–1200°C [24–27]. Flame temperatures, flame sizes, and burn times were measured. Combustion rates

of poly(styrene) (PS) and PE particles were found to be governed by gaseous diffusion and pyrolysis rates, respectively. The ignition of poly(vinyl-chloride) (PVC) particles was suppressed initially, presumably by HCl in the pyrolyzates. Upon ignition, a rather thick flame formed around each PVC particle, which was argued to be quasi-premixed [24,26].

Exploratory investigations on the semivolatile organic by-products from combustion of polymers were also performed at this laboratory, where the effects of temperature, residence time, and transient combustion were studied [28,29]. Increasing the gas temperature from 800 to 1200°C or the gas residence time in the furnace from 1 to 2 s, the amount of PAHs decreased drastically[1]. PE and PS produced comparable amounts of PAHs, while PVC produced lesser amounts. For PVC, there was evidence that the specific amounts of PAHs decreased with the sample size. To the contrary, reducing the size of PE did not decrease the specific amounts of PAHs. The behavior of PS was between those of PE and PVC.

This study is part of an ongoing investigation on the effects of the combustion parameters on the PAH emissions from waste plastics. Particularly, the effect of the bulk equivalence ratio, defined as $\phi_{bulk} = (m_{fuel}/m_{air})_{actual}/(m_{fuel}/m_{air})_{stoichiometric}$, on the PAH emissions produced by pyrolysis/combustion of PVC, PE, and PS was examined.

Experimental Apparatus and Procedure

Plastic Particles Burned

Medium molecular weight spheroidal PVC particles and PE flakes were obtained from Aldrich Chemical, while 8% cross-linked spherical PS particles were obtained from Duke Scientific. Sieving provided batches in the range of 150–212-μm particles.

Vertical Furnace—Particle Fluidizing System

The vertical (drop-tube) laminar flow furnace used in these experiments has been described elsewhere [28,29]. The combustion zone of the furnace was an alumina tube, 3.5 cm in diameter and 25-cm long. A particle fluidizing system [28,29] was used to supply a steady stream of particles to the top of the furnace, through a water-cooled injector.

Combustion Experiments

As the particles fell into the furnace cavity, they gasified/burned in 20–100 ms [24–27]. The gas flow rate and temperature were set to 3 lpm and 1100°C, respectively; the resulting gas residence time was 1 s. The mass flow rate of the particles was varied in the range of 0.001–5 g/min, in order to achieve the desired bulk equivalence ratios, $0.1 \leq \phi_{bulk} \leq 7.3$.

Unlike previous research [29], where both steady-state and transient flows of particles ("puffs") were burned, herein all experiments involved steady-state flows of particles, to achieve a uniform equivalence ratio during combustion. The term *thick clouds* was used in this text to describe situations where interactive particle combustion was expected. In such cases, $\dot{m}_{gas}/\dot{m}_{polymer}$ was lower than 15; therefore, the ratio of the interparticle distance, l, to the particle diameter, a, can be calculated to be $l/a \ll 75$, see Ref. 30. The term *dilute clouds* was used to describe situations where $\dot{m}_{gas}/\dot{m}_{polymer} \geq 100$; therefore, $l/a \gg 75$, and thus, no particle interactions were expected [30]. Note that stoichiometric air-to-polymer mass ratios are as follows: 14.7 for PE, 13.1 for PS, and 5.2 for PVC, assuming that the combustion products contained only CO_2, H_2O, N_2, and HCl for PVC.

Sampling and Extraction of PAHs

The sampling stage was placed directly at the bottom of the furnace [28] so that the total amount of the furnace effluent, cooled to 70°C, passed through. It encompassed a glass-fiber filter for capturing the soot and, thus, the condensed-phase PAHs and a bed of XAD-4 resin for adsorbing the gaseous-phase PAHs. Occasionally, some fine soot leaked around the edges of the filter and was deposited on the XAD-4 resin. Thus, the results reported for the gaseous-phase PAHs include traces of condensed-phase amounts. The glass-fiber filter and the XAD-4 resin were extracted with methylene chloride, spiked with 100 μg of d_8-naphthalene, in a precleaned *Sohxlet* apparatus [28,29]. After extraction, the methylene chloride solutions were concentrated under low vacuum to 1 mL.

GC-MS Analysis

The samples were spiked with a 100-μg aliquot of d_{10}-anthracene. A comparison of the peak areas for the d_8-naphthalene and d_{10}-anthracene in the total ion chromatogram (TIC) provided a measure for the extraction/condensation efficiency and was used as a basis for the semiquantitative data provided herein. Identification was mainly limited to species belonging to the Title III of the 1990 Clean Air Act Amendments [31]. The GC/MS system consisted of a Hewlett-Packard (HP) Model 5890, Series II GC and an HP Model 5971 mass selective detector. The GC/MS conditions and data reduction techniques were described previously [29]. No PAHs were detected in laboratory blanks (plain XAD-4 extracts) or combustion blanks.

All experiments were conducted once, since re-

[1]In this text the "amount of PAHs" is expressed per unit mass of polymer burned, i.e., signifies specific quantities.

TABLE 1
PVC. Compounds, MWs, and respective amounts in μg/(g of PVC) from combustion/pyrolysis. Blanks represent concentrations <1 μg/g.

Phase of PAHs	Gas.	Gas.	Gas.	Gas.
Gas-to-polymer mass ratio	5.2	2.7	0.7	9.4
Equivalence ratio (ϕ)	1	2	7.3	N2
Benzoic acid 122	158			
Naphthalene 128	83	598	952	3196
Biphenyl 154			96	112
Acenaphthylene 152	50	366	928	1084
Dibenzofuran 168			8	
Fluorene 166			36	53
Phenanthrene 178	19	293	622	451
Anthracene 178				86
4H-Cyclopenta[def]phenanthrene 190			32	42
Fluoranthene 202	82	589	337	562
Acephenanthrylene 202	12	84	26	119
Phenanthro[4,5-bcd]thiophene 208	10			6
Pyrene, 202	59	465	192	309
Benzo[ghi]fluoranthene 226		39	21	75
Benzo[c]fluoranthene 226			18	36
4H-Cyclopental[cd]pyrene 228			6	91
Benz[a]anthracene 228			21	34
Chrysene/Triphenylene 228			12	10
Benzo[b, j and k]fluoranthene 252			64	163
Benzo[a]fluoranthene 252			5	17
Benzo[e]pyrene 252			23	33
Benzo[a]pyrene 252			36	73
Perylene 252			9	21
Indeno[7,1,2,3-cdef]chrysene 276				32
Indeno[1,2,3-cd]pyrene 276				82
Benzo[ghi]perylene 276				51
Anthanthrene 276				22
Total PAHs (μg/g of PVC)	315	2434	3444	6760
Total PAHS > C11 (μg/g of PVC)	232	1836	2492	3564
% of Naphthalene in total PAHs of the sample (gas. + cond.)	26%	25%	28%	47%

production of exactly the same ϕ was difficult. Typical errors arise in the capture, extraction, and quantitation of PAHs in the GS-MS spectra, the latter experiencing a standard deviation of 10%. The experimental procedure was kept consistent in all tests.

Results

The species, their molecular weights (MWs), and their respective (specific) amounts that were identified in the combustion/pyrolysis effluent of PVC, PE, and PS are shown in Tables 1, 2, and 3, respectively; for brevity, only selected experiments are listed in these tables. With the exception of PS, little soot was captured on the filter, and analysis showed that it contained smaller amounts of PAHs than the XAD-4. Only those filters that contained substantial amounts of condensed PAHs are listed. (The exact fractions of the PAHs in the solid (soot) and gaseous phases were reported elsewhere [32] to depend on the temperature of the sampling stage. That was not the case for the *total* PAHs.) Also, only one entry for benzo[b, j and k]fluoranthene was recorded, because these isomers eluted almost simultaneously; hence their accurate quantitation was not possible.

Emissions from PVC

Only a few PAHs, in small amounts, were found in the effluent of fuel-lean combustion. The major compounds captured at $\phi_{bulk} \leq 1$ were organic acids, including benzoic and small amounts of hexadecanoic and octadecanoic acids, which disappeared in the fuel-rich runs. Benzoic acid was also reported

TABLE 2
PE. Compounds, MWs, and respective amounts in $\mu g/(g$ of PE) from combustion/pyrolysis. Blanks represent concentrations <1 $\mu g/g$.

Phase of PAHs	Gas.	Gas.	Gas.	Gas.	Gas.
Gas-to-polymer mass ratio	11.3	7.2	4	12.8	5.5
Equivalence ratio (ϕ)	1.3	2	3.7	N_2	N_2
Naphthalene 122	1,525	4,276	10,060	7,738	12,224
Benzothiophene 134				36	80
2-Methylnaphthalene 142			140	66	149
1-Methylnaphthalene 142			154	58	115
Biphenyl 154		40	354	188	496
Acenaphthylene 152	1,371	3,092	5,888	5,645	8,973
Acenaphthene 154					69
Dibenzofuran 168					55
Fluorene 166	85	126	426	310	560
Phenanthrene 178	792	1,710	1,656	2,024	4,698
Anthracene 178	89	265	84	221	356
4H-Cyclopenta[def]phenanthrene 190	165	305	158	322	539
Fluoranthene 202	860	1,982	606	1,494	2,768
Acephenanthrylene 202	248	534	210	483	814
Phenanthro[4,5-bcd]thiophene 208	30	47		88	
Pyrene 202	1,092	2,442	526	1,705	3,556
Benzo[a]fluorene 216			42	47	93
Benzo[b]fluorene 216			76	34	64
1-Methylpyrene 216			50	89	157
Benzo[ghi]fluoranthene 226	250	434	128	350	563
Benzo[c]phenanthrene 228	83	181	13	112	93
4H-Cyclopental[cd]pyrene 226	1,149	1,438	370	1,494	1,800
Benz[a]anthracene 228	58		40	29	186
Chrysene/Triphenylene 228			12	22	45
Benzo[b, j and k]fluoranthene 252	201	135	160	275	431
Benzo[a]fluoranthene 252			60	50	106
Benzo[e]pyrene 252	104		60	114	185
Benzo[a]pyrene 252	224		114	270	360
Perylene 252	53		24	55	89
Indeno[7,1,2,3-cdef]chrysene 276	51			53	67
Indeno[1,2,3-cd]pyrene 276	131			116	156
Benzo[ghi]perylene 276	289			153	174
Anthanthrene 276	145			86	107
Total PAHs ($\mu g/g$ of PE)	8,995	17,007	21,411	23,727	40,128
Total PAHs > C11 ($\mu g/g$ of PE)	7,470	12,731	11,351	15,989	27,904
% of Naphthalene in total PAHs of the sample (gas. + cond)	17%	25%	47%	32%	31%

elsewhere in fuel-lean combustion of *o*-dichlorobenzene [23] and toluene [33]. The amounts, as well as the number of PAHs detected herein, increased progressively in fuel-rich combustion, and maxima were recorded during pyrolysis in N_2 (see Table 1), where 0.7 wt % of PVC was converted to PAHs.

The total amounts of PAHs heavier than naphthalene ($>C_{11}$) are plotted in Fig. 1i as a function of ϕ_{bulk}, at T_{gas} = 1100°C. Superimposed are the PAH amounts obtained from pyrolysis in N_2 of thick and dilute clouds of PVC particles. The total amounts of PAHs ($>C_{11}$) from pyrolysis in N_2 of thick and dilute particle clouds were comparable, even when T_{gas} was lowered to 1000°C. Therefore, the amount of PAHs from pyrolysis in N_2 did not depend on the thickness of the particle cloud, i.e., the concentration of the pyrolyzates. The amount of PAHs did not depend on the gas temperature either, in the range of 1000–1100°C. However, most of the PAHs from the pyrolysis of thick clouds were fused, while those from

TABLE 3
PS. Compounds, MWs, and respective amounts in $\mu g/(g$ of PS) from combustion/pyrolysis. Blanks represent concentrations <1 $\mu g/g$.

Phase of PAHs	Gas.	Gas.	Gas.	Cond.	Gas.	Cond.	Gas.
Gas-to-polymer mass ratio	17.4	13.1	8.7	8.7	3.9	3.9	10.6
Equivalence ratio (ϕ)	0.8	1	1.5	1.5	3.4	3.4	N_2
Naphthalene 122	114	869	2,168	87	3,274	420	8,780
Benzothiophene 134							23
2-Methylnaphthalene 142							66
1-Methylnaphthalene 142							55
Biphenyl 154	29	422	542	467	883	280	2,502
Acenaphthylene 152	56	1,156	2,050	505	2,409	1,338	7,644
Fluorene 166		89	21	22	97	34	566
Phenanthrene 178	76	959	2,108	836	2,485	2,561	7,436
Anthracene 178		129	302		248	303	456
4H-Cyclopenta[def]phenanthrene 190		121	129	73	142	175	397
Fluoranthene 202	32	658	1,644	769	1,850	2,551	3,372
Acephenanthrylene 202	15	220	422	222	431	613	968
Phenanthro[4,5-bcd]thiophene 208		26	41	21	37	32	144
Pyrene 202	33	425	1,059	481	1,013	1,398	1,549
Benzo[a]fluorene 216							104
Benzo[b]fluorene 216							92
Benzo[ghi]fluoranthene 226	23	151	297	141	227	398	517
Benzo[c]phenanthrene 228		59	158	75	126	201	162
4H-Cyclopental[cd]pyrene 228		382	655	292	779	1,150	1,506
Benz[a]anthracene 228		40	175	63	28	256	281
Chrysene/Triphenylene 228		21					
Benzo[b, j and k]fluoranthene 252		69	94		132	268	684
Benzo[a]fluoranthene 252							145
Benzo[e]pyrene 252					32		185
Benzo[a]pyrene 252							257
Perylene 252							87
Indeno[7,1,2,3-cdef]chrysene 276							90
Indeno[1,2,3-cd]pyrene 276							167
Benzo[ghi]perylene 276							88
Anthanthrene 276							35
Total PAHS ($\mu g/g$ of PS)	378	5,796	11,865	4,054	14,193	11,978	38,358
Total PAHs > C11 ($\mu g/g$ of PS)	264	4,927	9,697	3,967	10,919	11,558	29,578
% of Naphthalene in total PAHs of the sample (gas. + cond.)	30%	15%	18%		23%		23%

pyrolysis of dilute clouds were substituted [29]. A possible explanation is presented in a later section. The (specific) amount of PAHs ($>C_{11}$) increased by an order of magnitude, as ϕ_{bulk} increased from 1 to 2 and it stayed rather constant thereafter (see Fig. 1i).

The following chlorinated compounds were identified in pyrolytic conditions: dichloro-ethyl benzene, tetrachloro benzene, chloro-ethyl benzoic acid, chloro-phenanthrene, and dichloro-biphenyl. At $\phi = 7.3$, dichloro-biphenyl and dichloro-acenaphthylene were present. No chlorinated species were identified under other conditions.

Emissions from PE

Only traces of PAHs were detected in the combustion products of PE particles at $\phi_{bulk} \leq 0.5$. At $\phi_{bulk} > 1$, the amount of PAHs increased abruptly, reached a maximum at $\phi = 2$, and then plateaued at higher ϕ_{bulk}, reaching asymptotically the pyrolytic emissions of thick clouds at $m_{N_2}/m_{pol.} = 12.8$. Although the total amount of PAHs at $\phi_{bulk} = 2$ was higher than that at $\phi_{bulk} = 1.3$, fewer species were identified in the former case. Specifically, most of the high MW PAHs (such as benzo[a and e]pyrene, perylene, and anthanthrene) were not detected at $\phi_{bulk} = 2$. Furthermore, while in thick cloud

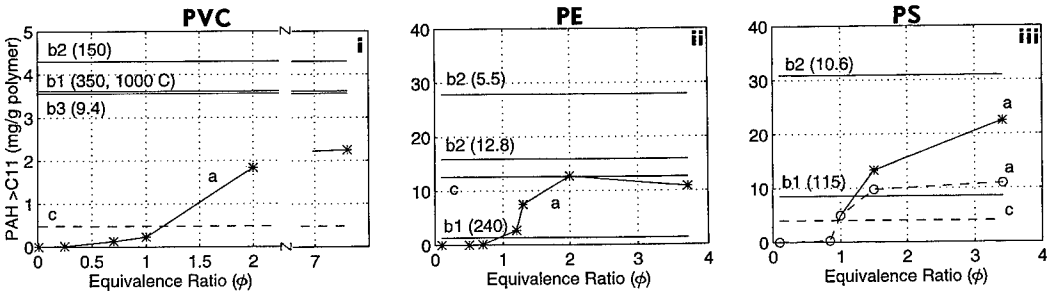

FIG. 1. Total specific amounts of PAHs ($>C_{11}$) as a function of ϕ_{bulk} denoted as line *a*. Superimposed are the amounts of PAHs ($>C_{11}$) from pyrolysis of particle clouds at different N_2 to polymer mass ratios (numbers in parenthesis) denoted as lines *b1*, *b2*, and *b3*, and transient "puff" combustion, described in Ref. 29, and denoted as line *c*. Solid lines depict both gaseous and condensed PAHs, while dash lines depict only gaseous PAHs. Unless otherwise denoted, all experiments were performed at T_{gas} = 1100°C. Stoichiometric fuel loading values, $m_{air}/m_{pol.}$, were 5.2 for PVC, 14.7 for PE, and 13.1 for PS. Plots are as follows: (i) PVC, (ii) PE, and (iii) PS.

pyrolysis experiments, all the major PAHs were present (see Table 2), and in dilute cloud pyrolysis, some of the heavy MW PAHs were missing [29]. It is evident that both the particle loading and the existence of a flame (combustion) influences the number of species and their amounts, but their respective role is unclear. The percentage of mass of PE converted to PAHs increased with ϕ_{bulk} and the maximum recorded amount was 4 wt % during pyrolysis of the thickest particle cloud, $m_{N_2}/m_{pol.}$ = 5.5. In Fig. 1ii, the total amount of PAHs heavier than naphthalene is plotted with ϕ_{bulk} at T_{gas} of 1100°C. Superimposed are the respective PAH emissions in pyrolytic atmospheres at three particle loadings. Comparing the three runs in N_2 with $m_{N_2}/m_{pol.}$ = 5.5, 12.8, and 240, it is evident that as the particle loading (i.e., the concentration of the pyrolyzates) increased, the amount of PAHs emitted also increased.

Emissions from PS

While the total PAH emissions from combustion of PS particles at $\phi_{bulk} \leq 0.8$ were low (see Table 3), they increased almost 15 times as ϕ_{bulk} increased from 0.8 to 1.0. A milder increase in the PAH amounts was noticed as ϕ_{bulk} further rose from 1.0 to 3.4. The highest values of PAHs were recorded during the pyrolysis of a thick particle cloud in N_2, with $m_{N_2}/m_{pol.}$ = 10.6. Generally, PS produced much more soot than PE and PVC. Fuel-lean mixtures produced little soot, and most PAHs were found in the gaseous phase. Thereafter, the amounts of soot, along with the condensed PAHs, increased with ϕ_{bulk} at a higher rate than the PAH emissions in the gaseous phase. At a ϕ_{bulk} = 3.4, the condensed and gaseous amounts of PAHs were similar. However, only small amounts of soot (and condensed PAHs) were observed in the pyrolytic runs in N_2. The percentage of mass converted to PAHs increased with ϕ_{bulk}, and the highest recorded value amounted to 4 wt %, during pyrolysis of a thick particle cloud in N_2. In Fig. 1iii, the total amount of PAHs heavier than naphthalene is plotted with ϕ_{bulk} at T_{gas} of 1100°C. Superimposed are respective PAH emissions in N_2 at two particle loadings. For PS, as was the case for PE, pyrolysis of dilute particle clouds resulted in lesser amounts of PAHs ($>C_{11}$) than the pyrolysis of thick clouds. However, the amount of PAHs from PE was found to increase roughly proportionally to the particle loading, while that from PS increased by a smaller factor.

Isomerization of PAHs

The mutagenicity of PAHs has been reported to differ greatly between components of isomer pairs [34]. For instance, fluoranthene is mutagenic, while its isomer pyrene is not. Howard et al. [34] measured concentrations of selected PAH isomer pairs in the effluent of ethylene combustion (ϕ = 1.2–2.2, T_g = 1240–1425°C) doped with naphthalene. In addition, they calculated the equilibrium concentrations of the following isomer pairs:

1. fluoranthene (F)–pyrene (P),
2. fluoranthene (F)–acephenanthrylene (AP),
3. cyclopenta[cd]pyrene (CP[cd]P)–benzo[ghi]-fluoranthene (B[ghi]F), and
4. benzo[k]fluoranthene (B[k]F)–benzo[a]pyrene (B[a]P).

For each of these isomers, seven sets of thermodynamic data are given in Ref. 34, estimated in different ways. Using these data, the ranges for the equilibrium concentration ratios for isomer pairs were calculated herein, at T_g = 1100°C, and were compared with experimental results from fuel-rich combustion and pyrolysis of PVC, PE, and PS (see Table 4). As in Ref. 34, the isomer pairs 2 and 3 were found to be close to equilibrium, while pairs 1 and 4 were

TABLE 4
Calculated equilibrium molar ratios and experimental molar ratios of selected PAH isomers

Molar Ratios at 1100°C	Equilibrium Calculations	PVC Experim.	PE Experim.	PS Experim.
F/P	$(1.2–41) \times 10^{-3}$	1.3–1.8	0.8–0.9	1.5–2.2
F/AP	2.9–13.2	4.8–7.0	3.0–3.7	3.4–4.3
CP[cd]P/B[ghi]F	3.6–37.3	1.2	3.2–4.6	2.2–3.4
B[k]F/B[a]P	$(0.1–29) \times 10^{-3}$	2.2	>0.9	>2.7

Experimental conditions: fuel-rich combustion or pyrolysis in N_2 with $m_{N_2}/m_{pol.} \leq 11.4$, $T_{gas} = 1100°C$.

not in equilibrium. Note that the experimental results for pairs 1 and 4 cannot be explained considering the calculated equilibrium concentrations either at temperatures approaching 1550°C (close to flame temperatures) or at the sampling temperatures, ≈70°C. Therefore, the measured molar ratios for isomer pairs 1 and 4 appear to result from kinetic limitations. Especially for pair 1, the experimental molar ratios from the combustion of PVC and PE were found to depend more on the polymer itself than on the combustion or pyrolysis conditions. For these cases, the ratio F/P stayed rather constant in the range of 0.8–0.9 for PE and in the range of 1.3–1.8, for PVC. For PS, F/P increased from 1.0 at $\phi_{bulk} = 0.8$ to 1.8 at $\phi_{bulk} = 3.4$, and it was 2.2 in N_2. To the contrary, Ref. 34 reported that F/P decreased from 1.4 to 0.4, as ϕ_{bulk} increased from 1.2 to 2.2.

Overall Discussion

The ratio of the mass of polymer to the mass of gas ($\propto \phi_{bulk}$, in the presence of air) introduced in a furnace was found to be a very important parameter on the emissions of PAHs. The PAH compounds and amounts from combustion/pyrolysis of PVC, PE, and PS exhibited both similarities and differences as ϕ_{bulk} changed.

PVC

PAH emissions from PVC were hardly detectable at fuel-lean conditions, $\phi_{bulk} \leq 1$, which is indicative of effective oxidation. Even at fuel-rich conditions, the PAH emissions from PVC were 10 times lower than those from the other polymers. The effective destruction of PAHs may be explained based on earlier observations [27,29] on the combustion of PVC particle clouds. Individual particles burned as separate entities, at most ϕ_{bulk} examined, surrounded by envelope flames. While such flames were spheroidal and very luminous, indicating strong soot radiation, no soot was detected (by shadow photography) to escape the flames or remain in the furnace after extinction [26]. Presumably, the PAHs and their precursors were consumed in the flames. To verify that, indeed, PVC particles burn effectively even at severely fuel-rich conditions, a ϕ_{bulk} as high as 7.3 was explored. The total PAH emissions remained rather constant in the range of $\phi_{bulk} = 2–7.3$, at values quite lower than those detected during pyrolysis. Many particles still burned with individual flames even at very high ϕ_{bulk}.

The pyrolysis experiments of PVC in N_2 indicated that the particle loading (i.e., the concentration of pyrolyzates) did not affect significantly the amount of PAHs produced. This observation suggests the importance of intramolecular reactions on the formation of PAHs during combustion of PVC. To the contrary, the formation of such species in nonpolymeric, nonaromatic, chlorinated hydrocarbons has been identified by detailed chemical kinetics modeling to incorporate intermolecular reactions [35]. It is plausible that after the evolution of HCl from PVC, the remaining poly(olenes) fold and condense further to produce PAHs. This argument may be supported by (a) the fact that PAHs were observed elsewhere [7] during pyrolysis of PVC in a TGA at temperatures as low as 400–500°C, lower than the temperatures for PAH formation from acetylene and (b) the fact that substituted PAHs were only observed in the combustion/pyrolysis products of PVC, which suggests that the mechanism of formation of PAHs for PVC may be different than those for PE and PS.

Pyrolysis of thick and dilute clouds of PVC particles resulted in mostly fused and mostly substituted PAHs, respectively. This may be related to the dependence of the pyrolysis mechanisms on the sample size, reported elsewhere [8].

PE

PAH emissions from PE were sensitive to $\phi_{bulk} \leq 2$ and resulted in high amounts, even at intermediate ϕ_{bulk}. An explanation may be offered, based on visual observations on the combustion behavior. PE particles entering the furnace in thick clouds readily exhibited flash pyrolysis due to heat transfer from the flames of already burning particles [27,29]. In such cases, a large group flame enclosing all particles and

their pyrolyzates was formed, displacing air. Thus, even in the case of overall fuel-lean conditions, locally fuel-rich combustion may have occurred inside the resulting large flame. Such a situation could have impeded the oxidation of PAHs and, thus, produced high emissions. Flash pyrolysis and group combustion occurred readily above $\phi_{bulk} = 1$ or even below when mixing was disturbed. Upon occurrence of a group flame, further increase in ϕ_{bulk} did not appear to matter, and PAH emissions plateaued, reaching asymptotically the pyrolytic emissions. Actually, this was the only polymer where a random momentary upset condition, "puff," denoted by lines c in Fig. 1, produced maximum PAH emissions under oxidizing conditions.

The increase in the amount of PAHs produced from pyrolysis of PE with the particle loading (i.e., the pyrolyzate concentration) suggests that the main pathway, for the formation of PAHs from PE, may be through interactions among the straight chain pyrolyzates [9].

PS

While at rigorously fuel-lean conditions the combustion of PS was fairly effective, the appearance of substantial amounts of PAHs commenced prior to the stoichiometric point and rapidly increased thereafter with ϕ_{bulk}. Enhanced emissions of soot and associated condensed PAHs were recorded under fuel-rich conditions. Cinematographic observations on the combustion of PS particles revealed that they burned with flames forming long wakes, from which strings of soot escaped and took a long time to oxidize [25]. In group combustion, the tendency of PS particles for flash pyrolysis was lower than that of PE but higher than that of PVC particles.

The sensitivity of PAH emissions to the particle loading varied for each polymer. The order from the least sensitive to the most sensitive was PVC, PS, and PE. This may be explained with an argument that the intramolecular cyclization of PVC pyrolyzates, upon evolution of HCl, is more prompt than the intermolecular condensation reactions of the aromatic rings of PS that, in turn, are more prompt than the aliphatic fragmentation reactions for PAH formation from PE.

The percentage of naphthalene in the PAH emissions of all polymers varied significantly with the combustion/pyrolysis conditions. For all polymers, it experienced minima in the neighborhood of stoichiometry (see Tables 1 through 3).

Recommendations for Waste-to-Energy Applications

From this work, the following recommendations may be drawn: PS should be burned with considerable amounts of excess air ($\phi_{bulk} < 0.8$) to minimize the emissions of PAHs and soot. Maximum emissions occur at pyrolytic or severely fuel-rich conditions. PVC is less sensitive to ϕ_{bulk}, and small amounts of excess air suffice for its complete combustion. Even at high ϕ, PVC appears to utilize oxygen effectively, and its PAH emissions are lower than those in purely pyrolytic atmospheres. PE is the most sensitive of the polymers to ϕ_{bulk} for $\phi_{bulk} \leq 2$. Even if burned in finely shredded particles, at moderately lean ϕ_{bulk}, flash pyrolysis may occur, and the resulting large diffusion flames impede the oxidation of PAHs. Substantial amounts of excess air are recommended, but prevention of puffs is difficult, and thus, complete destruction of PAHs may require very fuel-lean conditions, $\phi < 0.5$, as explored in Ref. 26, or an afterburner. PS has a strong tendency to soot at all conditions, but especially at high ϕs; most soot, however, is highly agglomerated and can be easily captured. PE emitted small amounts of fine soot, only at high ϕs. The emissions of soot from PVC were minimal.

Conclusions

The effect of the equivalence ratio on the PAHs from combustion/pyrolysis of PVC, PE, and PS particles (150–212 μm) in diameter was studied. Combustion/pyrolysis took place in a drop-tube, electrically heated furnace at 1100°C, in air, or N_2.

1. For all polymers, the total amounts (specific) of PAHs increased with ϕ_{bulk}; the highest amounts of PAHs (accounting for 0.7, 4, and 4 wt % for PVC, PE, and PS, respectively) were emitted under pyrolytic conditions, and in N_2 at varying particle loadings.
2. While minimal amounts of PAHs were emitted from PVC at $\phi_{bulk} \leq 1$, substantial amounts were emitted from PE and, especially, PS at similar conditions. This was related to their combustion behavior in thick clouds. The emissions of PVC were lower by an order of magnitude than those of PE and PS at fuel-rich conditions. Chlorinated organics were identified in the effluent of PVC burning in $\phi_{bulk} = 7.3$ and pyrolysis in N_2.
3. The (specific) amounts of PAHs from pyrolysis of PE and PS in N_2 were found to increase with the particle loading in the furnace. There was no such indication for PVC. This difference may indicate the importance of intramolecular cyclization in the formation of PAHs from PVC, and intermolecular reactions for PS and PE.
4. The percentage of naphthalene in the PAHs varied with combustion/pyrolysis conditions. For all polymers, it reached minima at ϕ_{bulk} around stoichiometry.
5. For all polymers, the isomer pairs: fluoranthene–acephenanthrylene and cyclopenta[cd]pyrene–benzo[ghi]fluoranthene were found to be in equilibrium. For all polymers, the pairs fluoranthene–pyrene and benzo[k]fluoranthene–benzo[a]pyrene were not found to be in equilibrium.

6. PS emitted large amounts of soot at a broad range of ϕ, while PVC and PE emitted low amounts of soot only at high ϕ. Soot emissions of all polymers under pyrolytic conditions, in N_2, were low. Future work will quantify emissions of soot.

Acknowledgments

This research was supported by EPA Grant #R-819245-01-0. The authors would like to acknowledge the U.S. Army Research Lab in Natick, MA, for the GC-MS and Mr. Yuri Dunayevskiy for reducing the GC/MS data.

REFERENCES

1. Ehrig, R. J. (Ed.), *Plastics Recycling. Products and Processes,* Hanser Publishers, Munich, 1992, p. 1.
2. Leaversuch, R. D., *Mod. Plastics* 45:44–47 (1987).
3. Plastics Recycling Action Plan for Massachusetts, Commonwealth of Massachusetts, Department of Environmental Engineering, D. S. Greenbaum, Commissioner, 1987, p. 17.
4. Cullis, C. F. and Hirschler, M. M., *The Combustion of Organic Polymers,* Clarendon Press, Oxford, 1981, pp. 125–288.
5. Scott, D. S., Czernik, S. R., and Radlein, D. St. A. G., *Energy Fuels* 4:407–411 (1990).
6. Kelen, T., *Polymer Degradation,* Van Nostrand Reinhold Company, New York, 1990, p. 77.
7. Knümann, R. and Bockhorn, H., *Combust. Sci. Technol.* 101:285–299 (1994).
8. Bockhorn, H., Hornung, A., Hornung, U., Teepe, S., and Weichmann, J., Investigation of the Kinetics of Thermal Degradation of Commodity Plastics. Presented at the Fourth International Congress on Toxic Combustion Byproducts, Berkeley, CA, June 5–7, 1995.
9. Beyler, G., in *Handbook of Fire Protection Engineering,* Society of Fire Protection Engineers (National Fire Protection Association, Eds.), Quincy, MA, 1988, pp. 1, 165–178.
10. Darivakis, G. S., Howard, J. B., and Peters, W. A., *Combust. Sci. Technol.* 19:267–282 (1990).
11. Chang, E. P. and Salovey, R., *J. Pol. Sci.* 12:2927–2941 (1974).
12. Winslow, F. H. and Matreyek, *J. Pol. Sci.,* XXII:315–324 (1954).
13. Danforth, J. D., Spiegel, J., and Bloom, J., *J. Macromol. Sci.-Chem.,* A17(7):1107–1127 (1982).
14. Billmeyer, F. W., *Textbook of Polymer Science,* Wiley, New York, 1984, p. 143.
15. Chung, S.-L. and Tsang, S.-M., *J. Air Waste Manage. Assoc.* 41:821–826 (1991).
16. Chung, S.-L. and Lai, N.-L., *J. Air Waste Manage. Assoc.* 42(8):1082–1088 (1992).
17. Wu, C.-H., Chang, C.-Y., Hor, J.-L., Shih, S.-M., Chen, L. W., and Chang, F. W., *Waste Manage.* 13:221–235 (1993).
18. Elomaa, M. and Saharinen, E., *J. Appl. Pol. Sci.* 42:2819–2824 (1991).
19. Hawley-Fedder, R. A., Parsons, M. L., and Karasek, F. W., *J. Chromatogr.,* 314:263–273 (1984).
20. Hawley-Fedder, R. A., Parsons, M. L., and Karasek, F. W., *J. Chromatogr.* 315:201–210 (1984).
21. Hawley-Fedder, R. A., Parsons, M. L., and Karasek, F. W., *J. Chromatogr.* 315:211–221 (1984).
22. Linak, W. P., Kilgroe, G. D., McSorley, J. A., Wendt, J. O. L., and Dunn, J. E., *JAPCA* 37(1):54–65 (1987).
23. Van Dell, R. D., Mahle, N. H., and Hixson, E. M., *Combust. Sci. Technol.* 101:261–283 (1994).
24. Panagiotou, T. and Levendis, Y. A., *Combust. Flame* 99:53–74 (1994).
25. Panagiotou, T., Levendis, Y. A., and Delichatsios, M. A., *Combust. Sci. Technol.* 103:63–84 (1994).
26. Panagiotou, T. and Levendis, Y. A., *Combust. Sci. Technol.,* 112:117–140 (1996).
27. Panagiotou, T., Ph.D. Thesis, Northeastern University, Boston, MA, 1995.
28. Wheatley, L., Levendis, Y. A., and Vouros, P., *Environ. Sci. Technol.* 27(13):2885–2895 (1993).
29. Panagiotou, T., Levendis, Y. A., Carlson, J., Dunayevskiy, Y. M., and Vouros, P., *Combust. Sci. Technol.* 116–117:91–130 (1996).
30. Annamalai, K. and Ryan, W., *Progr. Energy Combust. Sci.* 18:221–295 (1992).
31. Miller, C. A., Srivastava, R. K., and Ryan, J. V., *Environ. Sci. Technol.* 28:1150–1158 (1994).
32. Williams, P. T., *J. Inst. Energy* 65:46–54 (1992).
33. Longwell, J. P., *Nineteenth Symposium (International) on Combustion,* The Combustion Institute, Pittsburgh, 1982, pp. 1339–1350.
34. Howard, J. B., Longwell, J. P., Marr, J. A., Bushy, W. F. Jr., Lafleur, A. L., and Taghizadeh, K., *Combust. Flame* 101:262–270 (1995).
35. Frenklach, M., *Combust. Sci. Technol.* 74:283–296 (1990).

COMMENTS

George W. Mulholland, NIST, USA. How was the equivalence ratio controlled during the drop tube measurements and the muffle furnace measurements? What was the effect of the equivalence ratio on the smoke production for the three plastics?

Author's Reply. The bulk equivalence ratio in the drop-tube furnace was controlled by changing the mass flowrate of the polymer particles, while the flowrate of the air was held constant. The bulk equivalence in the muffle furnace was not controlled and, thus, was not defined.

As the equivalence ratio increased, the soot emissions from each polymer increased. It was found that the soot yield from PS was much more sensitive to the equivalence ratio than either that of PE or PVC. Large amounts of soot were collected from PS at $\phi > 1.5$, meanwhile only small amounts of soot were collected from PE and PVC even at the highest ϕ's explored herein; 3.7 and 7.3 respectively.

•

T. Kashiwagi, NIST, USA. In one of your results, there are no differences in PAH amount when PVC (or PE?) was pyrolyzed in N_2 and also burning in air. Could you elaborate why?

A large amount of plasticizers are generally added for PVC (rarely used as 100% PVC for end product due to its brittle nature). Then, the degradation of PVC might be modified by that of the plasticizers. Do you expect that your conclusion on PVC might still be applicable?

Author's Reply. The results showed that the magnitude of PAH emissions from clouds of PVC particles in pyrolytic environments (N_2) were rather independent of particle mass loading and gas temperature. Combustion in air produced different amounts of PAHs depending on the bulk equivalence ratio, see Fig. 1, and temperature, see Refs. [28] and [29]. This independence of the pyrolytic emissions (in N_2) of the particle loading may suggest the importance of intramolecular reactions on the formation of PAHs from PVC, as opposed to intermolecular reactions, which do depend on the concentration of the pyrolyzates and, thus, on the particle loading. Also for PVC, the total amounts of PAHs $> C_{11}$ from combustion in air at fuel-rich equivalence ratios ($2 \geq \phi \geq 7.3$) remained practically constant with ϕ and were lower than the amounts from pyrolysis in N_2. This is another indication of the importance of intramolecular reactions on the formation of PAHs from PVC. Neither PE nor PS exhibited such behavior.

The combustion behavior of PVC may be affected by the type and amount of plasticizer additives. Rigid PVC which contains only small amounts of plasticizers [14] is typically used for pipes and the results herein may describe its combustion/pyrolysis behavior. However, the combustion behavior of PVC containing as much as 30 wt.% plasticizers [14] (such as dioctyl phthalate, trioctyl phosphate or poly(propylene glycol) esters) may differ from that of pure PVC, observed herein.

Twenty-Sixth Symposium (International) on Combustion/The Combustion Institute, 1996/pp. 2431–2437

INFLUENCE OF TURBULENT MIXING ON THE PYROLYSIS OF CHLOROFORM USING DETAILED CHEMICAL KINETICS

MARKUS KRAFT AND ELMAR STÖCKELMANN
Fachbereich Chemie, Universität Kaiserslautern
Erwin Schrödinger Straße 54, 67663 Kaiserslautern
Germany

HENNING BOCKHORN
Institut für Chemische Technik, Universität Karlsruhe
Kaiserstraße 12, 76128 Karlsruhe, Germany

The influence of turbulent mixing on the pyrolysis of chloroform is systematically investigated. This analysis is performed by means of the probability density function (PDF) transport equation for a turbulent flow reactor. The feed of the model reactor consists of a stream of hot argon and a cold chloroform stream diluted with argon. The turbulence considered is homogeneous and isotropic, which leads to reduction of spatial dimensions and enables the implementation of all 32 species of the detailed mechanism. From the PDF of the species, the time evolution of all statistical moments can be revealed. Additionally, the PDF of reaction rates and integrated reaction rates (molar amounts of species through a specific reaction) is calculated. From this, a detailed analysis of the influence of the turbulent mixing on the reaction paths is performed. The turbulent mixing is modeled by a standard particle interaction model and by the binomial Langevin model extended to several scalars. The differences of these models are analyzed and discussed. The time evolution of the lower statistical moments are qualitatively the same; however, the shape of the PDF, i.e., the higher statistical moments, differs significantly. Both mixing models lead to the conclusion that the decay of chloroform can be slightly accelerated for a certain range of turbulent mixing and slowed down outside this range. For presented initial conditions, this range is stated. Additionally, it can be shown that the time evolution of intermediates is strongly dependent on the mixing.

Introduction

The incineration of hazardous waste offers an effective disposal methodology. However, the production and emission of products of incomplete combustion (PICs) may cause severe environmental problems. Therefore, knowledge about the degradation of the hazardous chemicals as well as their formation during the combustion process is sought. Particularly in the case of chlorocarbon combustion, this is an important issue. Recently, significant progress has been made in understanding the chemical kinetics of chlorinated hydrocarbon combustion [1,2]. There is experimental evidence that, besides chemical kinetics, the degradation of chlorinated hydrocarbons is strongly influenced by molecular mixing [3]. Incineration involves oxidative and pyrolytic processes. These pyrolytic processes occur, for example, in the feed process where mixing is not complete and in pockets of nonmixed fuel gas that travel through the incinerator. Generally, incineration occurs under turbulent flow conditions.

The first objective of the present study is to present a tool for investigating the influence of turbulence on a complex chemical system. This tool is based on the probability density function (PDF) transport equation [4,5]. This PDF is of very high dimension in the case of a multicomponent system. Therefore, the simple case of isotropic homogeneous turbulence is considered, which reduces the spatial dimension [6]. This approach is similar to the work of Chen [7] and Correa and Braaten [8] and is an alternative to Kerstein's model in Refs. 3 and 9. The molecular diffusion term in the PDF equation is modeled with a particle interaction model as in Refs. 7 and 8 but also with a modification of the random walk model by Valiño [10,11], which is superior to the particle interaction models in its asymptotic behavior. Besides the joint composition PDF, the time evolution of the PDF for the reaction rates and the integrated reaction rates (molar amounts of species through a specific reaction) is presented. This makes a thorough discussion of the influence of turbulence on reaction paths feasible.

The second objective of this paper is to apply this tool to the pyrolysis of chloroform under turbulent flow conditions. The sensitivity of reaction paths to

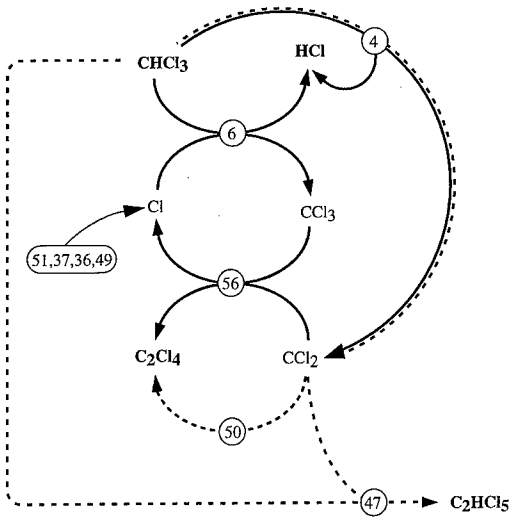

FIG. 1. Reaction paths with reaction numbers as in Ref. 2. Start phase (dashed lines), transition phase, and end (solid lines) phase are displayed.

mixing and to different models for turbulent diffusion is discussed.

The Pyrolysis of Chloroform

The detailed mechanism for the pyrolysis of chloroform, as introduced in Ref. 2, contains 32 species and 67 elementary reactions. There, the pyrolysis of chloroform takes place in a tubular plug-flow reactor that can be described by the time evolution of the concentrations of chemical species in a homogeneous gas phase moving along the tubular reactor. This is equivalent to a perfectly-stirred reactor (PSR) with no inflow or outflow. At the start, only $CHCl_3$ diluted with argon at atmospheric pressure is present. Main products are C_2Cl_4 and HCl. The species CCl_4, and C_2HCl_3 are by-products and important intermediate species are C_2HCl_5, CCl_2, Cl, and CCl_3. The pyrolysis starts at 750 K, and the half-life time of $CHCl_3$, which can be identified as characteristic time, is exponentially dependent on temperature and independent on the concentration of $CHCl_3$. As a consequence of the time evolution of the reaction rates, the chloroform pyrolysis in a PSR without feed can be subdivided into different phases: a very short start phase, a transition phase, and an end phase. Here, only the reactions with high conversion rates are presented. The reaction numbers refer to the mechanism published in Ref. 2.

Start Phase

The initial step of the pyrolysis is the dehydrochlorination of $CHCl_3$, resulting in dichlorocarbene and hydrogen chloride.

$$CHCl_3 \rightleftharpoons CCl_2 + HCl \qquad (4)$$

The carbene reacts with chloroform in an insertion reaction to pentachloroethane (see Fig. 1).

$$CCl_2 + CHCl_3 \rightleftharpoons C_2HCl_5 \qquad (47)$$

Besides these two reactions, Cl abstracts H from chloroform in reaction (6). Since at this early stage of the pyrolysis the concentration of atomic chlorine is not very high, reaction (6) is not very important. Reaction (4) (70%) and reaction (47) (20%) dominate the degradation of chloroform. During this early stage, the dichlorocarbene dimerizes to tetrachloroethylene in reaction (50).

$$2CCl_2 \rightleftharpoons C_2Cl_4 \qquad (50)$$

Dichlorocarbene is consumed in reactions (47) and (50) at equal parts. Furthermore, atomic chlorine is formed in reactions (51), (37), (36), and (49). Figure 1 shows the main reaction paths of the start phase indicated with a dashed line.

Transition Phase

The very short start phase is followed by a transition phase. The increasing number of chlorine radicals leads to a higher rate of the H abstraction in reaction (6)

$$CHCl_3 + Cl \rightleftharpoons CCl_3 + HCl \qquad (6)$$

The CCl_3 radical is formed almost exclusively in this reaction. Reaction (56) produces, in combining the radicals CCl_3 and CCl_2 to C_2Cl_4 + Cl, the necessary Cl radicals and the main product tetrachloroethylene.

$$CCl_2 + CCl_3 \rightleftharpoons C_2Cl_4 + Cl \qquad (56)$$

As indicated in Fig. 1, reactions (6) and (56) (solid line) establish a circle in which chloroform and the dichlorocarbene is consumed and the main products tetrachloroethylene and hydrogen chloride are formed. The transition phase is finished when the rates of reaction (6) and (4) attain their maximum.

End Phase

Subsequently, the reaction paths do not change any more. The degradation of chloroform is to the same parts due to reaction (6) and (4). The dimerization of dichlorocarbene is not much involved in the formation of the product C_2Cl_4. The intermediate product C_2HCl_5 is completely decomposed to either products or intermediate species. The system is in equilibrium after chloroform is totally decomposed. Besides the main products C_2Cl_4 and HCl, the by-products tetrachloromethane CCl_4 and C_2HCl_3 are formed.

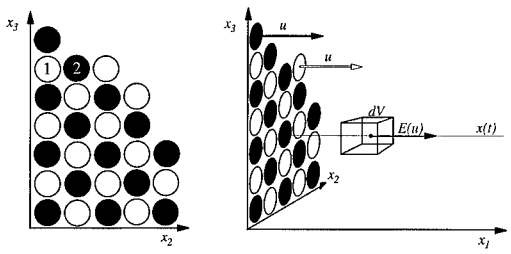

FIG. 2. Configuration of the WSR. Two composition streams $\phi^{(1)}$ and $\phi^{(2)}$ are injected into the WSR. The time evolution of the joint composition PDF of the volume element dV moving downstream is calculated using the PDF transport equation.

Turbulence Modeling

To study the influence of turbulent flow conditions on the pyrolysis of chloroform, including all 32 involved species, it is necessary to consider a simple flow in favor of lower computational cost.

Figure 2 shows the well-stirred reactor (WSR) configuration. It is assumed that two streams, given by the composition vectors $\phi^{(1)}$ and $\phi^{(2)}$, are injected with the same velocity into the WSR. The feed is constant in time. At the inlet of the reactor, homogeneous isotropic turbulence is created and the turbulent fluctuations decrease along the reactor axis [8,7]. The decay time of the velocity fluctuations $\tau = k/\varepsilon$ is set constant. Here, k is the turbulent kinetic energy and ε is the dissipation rate. The decay time of the scalar fluctuations is assumed to be proportional to the decay time of the scalar fluctuations $\tau = C_\phi \tau_\phi$. It is assumed that the reactor is adiabatic and that the pressure in the reactor is constant. There are two limiting cases for the turbulent time τ. For $\tau \to \infty$, the two streams do not mix at all, and for $\tau = 0$, the mixing takes place instantaneously. This last case is equivalent to the time evolution of the concentrations of species in a homogeneous gas phase in a PSR without feed.

The turbulent flow in the reactor can be described in terms of the time evolution of the one-point joint composition mass density function (MDF) [7,8] with the initial conditions $\mathcal{F}(\psi; 0) = \mathcal{F}_0(\psi) = 1/2\rho(\psi)[(\delta(\psi - \phi^{(1)}) + \delta(\psi - \phi^{(2)})]$. The time evolution of the joint composition MDF can be calculated from its transition PDF $f_t(\psi; t)$ using $\mathcal{F}(\psi; t) = \int f_t(\psi; t)\mathcal{F}_0(\varphi; t_0)d\varphi$. The equation for the time evolution of the transition probability density is given in Ref. 4. For a single scalar it is

$$\underbrace{\frac{\partial}{\partial t} f_t}_{\text{change in time}} = \underbrace{-\frac{\partial}{\partial \psi}\left[E\left(\frac{D}{\rho}\nabla^2\phi \mid s_t, s_0\right) f_t\right]}_{\text{molecular diffusivity}} - \underbrace{\frac{\partial}{\partial \psi}(Sf_t)}_{\text{chemical source}} \quad (1)$$

In the following, f_t is denoted as f. The second term in Eq. (1) on the right-hand side is the chemical source term, which describes the transport of the transition PDF in the scalar space due to chemical reactions. The molecular diffusion term $E(D/\rho\, \nabla^2\phi \mid s_t, s_0)$ is conditional upon the transition of event $s_0 = \{\phi = \psi\}$ with $\mathcal{F}(\psi, t_0)$ to the event $s_t = \{\phi = \psi\}$ with $\mathcal{F}(\psi, t)$. The conditional expectation in (1) is not known and needs to be modeled. In the following, two mixing models are used and compared in their performance.

Particle Interaction Model (Janicka, Kolbe, Kollmann (JK) [12,13])

The decay of the turbulent fluctuations is modeled by the interaction of stochastic particles. The uniformly distributed random variable α determines the mixing of the particles.

$$-\frac{\partial}{\partial \psi}\left[E\left(\frac{D}{\rho}\nabla^2\phi|s_t, s_0\right)f\right] = \frac{2\beta C_\phi}{\tau}\left[\int\int K(\psi, \psi_a, \psi_b) f(\psi_a) f(\psi_b)\, d\psi_a d\psi_b - f(\psi)\right]$$

with

$$K = \int A(\alpha)\delta\left(\psi - (1-\alpha)\psi_a - \frac{1}{2}\alpha(\psi_a + \psi_b)\right) d\alpha\Big)$$

$$A(\alpha) = \begin{cases} 1 : 0 \le \alpha \le 1 \\ 0 : \text{else} \end{cases}$$

$$\beta = 1.5$$

Diffusion Model (Binomial Langevin (BL) [10])

The decay of the fluctuations is modeled by a deterministic drift that contracts the PDF to its mean and a noise that blurs the PDF to have a Gaussian asymptotic behavior. The operator $\partial_b^2/\partial_b\psi^2$ is the generator of a binomial stochastic process that tends to a diffusion process for decaying fluctuations.

$$-\frac{\partial}{\partial \psi}\left[E\left(\frac{D}{\rho}\nabla^2\phi|s_t, s_0\right)f\right] = -\frac{\partial}{\partial \psi}[A(\psi, t)f] + \frac{\partial_b^2}{\partial_b\psi^2}[B(\psi, t)f] \quad (2)$$

with

$$A(\psi, t) = -\frac{1}{2}\left\{1 + k\left[1 - \frac{D(\phi)}{\psi^2}\right]\right\} \frac{C_\phi}{\tau}[\psi - E(\phi)] \quad (3)$$

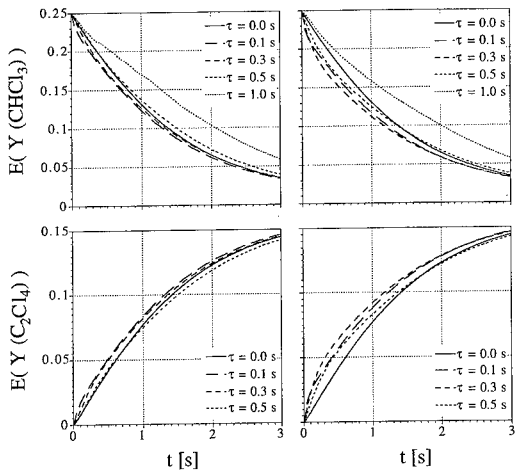

FIG. 3. Time evolution of the mean mass fractions of chloroform and tetrachloroethylene in PSR and WSR for varying τ [left: particle interaction model (JK); right: binomial Langevin model (BL)].

$$B(\psi, t) = k\left\{1 - \frac{[\psi - E(\phi)]^2}{\psi_\circ^2}\right\}\frac{C_\phi}{\tau}D(\phi) \quad (4)$$

$$\psi_\circ = \begin{cases}[\psi_{\max} - E(\phi)] : [\psi - E(\phi)] \geq 0 \\ [\psi_{\min} - E(\phi)] : [\psi - E(\phi)] < 0\end{cases} \quad (5)$$

and the empirical constant $k = 0.1$.

Various particle interaction models have been used by several authors to model molecular diffusion over the past 15 years. They are efficient to use in Monte Carlo codes, and they satisfy linearity and independence principles as well as boundedness. They do not describe a decaying composition field in isotropic homogeneous turbulence correctly, according to DNS results. The binomial Langevin model overcomes this deficiency. The extension to several scalars and boundedness is guaranteed by a projection technique. The solution procedure for the PDF transport equation is described in Refs. 4 and 5. The initial PDF is represented by 1000 stochastic particles or point measures. The PDF transport equation is then solved using an operator-splitting technique that introduces a first-order approximation error. The mixing term is calculated via a random walk according to the mixing model for each particle. The stiff system of ordinary differential equation (ODE) for the chemical reaction source term of each particle has been calculated using the Sandia code SENKIN [14].

Statistical Analysis of the Chemical Source Term

The chemical source term is a function of the composition vector $\phi = (Y_1, \ldots, Y_K, h)$ and is described by I elementary reactions. The reaction rate of reaction i is given as $q_i = q_i(Y_k, T)$. The temperature T is a function of enthalpy and composition variables $T = T(h, Y_k)$. The integrated reaction rates over the time interval $[0, t]$ s are given as $Q_i = \int_0^t q_i\, dt$. These two variables are statistically described by their probability densities $f_q(q_1, q_2, q_3, \ldots, q_I; t)$ and $f_Q(Q_1, Q_2, Q_3, \ldots, Q_I; t)$. These densities are calculated when evaluating the chemical source terms of the representative stochastic particles using the CHEMKIN library [14,15]. From the densities, the mean conversion $E(Q_i)(t) = \int Q_i f_{Q_i}(Q_i, t)\, dQ_i$ and mean reaction rates of the reaction i at time t $E(q_i)(t) = \int q_i f_{q_i}(q_i, t)\, dq_i$ can be calculated.

The Chloroform Pyrolysis in the WSR

For the adiabatic and constant pressure configuration presented above, the following initial conditions are chosen. The two streams are a hot (1035 K) inert argon stream and a cold (700 K) mixture consisting of chloroform diluted with argon [$Y(CHCl_3) = 0.5$, $Y(Ar) = 0.5$]. The pyrolysis of chloroform is studied for varying turbulent times $\tau \in [0,1]$ s in the time interval [0,3] s. After 3 s, the mixture is homogeneous for the turbulent times considered. The results of the WSR simulation for $\tau = 0$ correspond to the PSR situation with the following initial conditions:

$$Y(CHCl_3) = 0.25 \quad Y(Ar) = 0.75$$
$$T = 850\ \text{K} \quad p = 1\ \text{atm} \quad (6)$$

In this case, the two streams are perfectly mixed instantaneously. For these initial conditions, the half-life time of chloroform is approximately 1 s. The mixing of the streams with different heat capacity leads to a decrease in the mean temperature because argon has a lower heat capacity than chloroform. This decrease in temperature is compensated by the heat production of the pyrolysis of chloroform. The two mixing models show good agreement in the mean values. Figure 3 shows that the decay of chloroform is influenced by the time of mixing. For $0\ \text{s} < \tau < 0.5$ s, the degradation of chloroform is slightly faster and for increasing τ, $\tau > 0.5$ s, the pyrolysis is slower than in the PSR case because mixing of the hot argon stream and the colder chloroform stream is so slow that more of the chloroform experiences even lower temperatures. As consequence of this, the progress of the pyrolysis is exclusively determined by the mixing rate for $\tau > 0.5$ s.

In the following, only the case for $\tau < 0.5$ s is considered. The acceleration of the decay of chloroform leads to a slight increase of the products (see Fig. 3). The two mixing models show qualitatively the same behavior, but the deviations from the PSR situation is higher when the BL model is used. In Fig. 4, the time evolution of the intermediate product C_2HCl_5 is displayed. The production of C_2HCl_5 is very strongly influenced by the mixing model. The

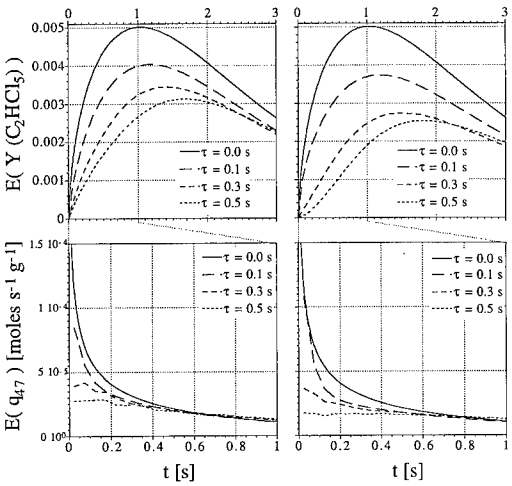

FIG. 4. Time evolution of the mean mass fractions of the intermediate species C_2HCl_5 and the mean reaction rate of reaction 47 for varying τ [left: particle interaction model (JK); right: binomial Langevin model (BL)].

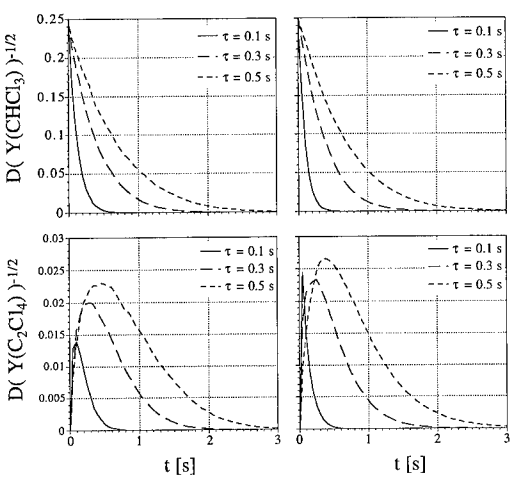

FIG. 5. Time evolution of the standard deviation of chloroform and C_2Cl_4 for varying τ [left: particle interaction model (JK); right: binomial Langevin model (BL)].

time for the maximum mass fraction of C_2HCl_5 as well as the maximum itself changes for varying τ. This is due to the inhomogeneous flow condition that slows down the mean reaction rates. The production of the by-products C_2HCl_3 and CCl_4 is also strongly influenced by the turbulent flow. The higher τ, i.e., the larger the inhomogeneity of the flow, the more by-products are formed (no figure). Figure 5 shows the time evolution of the standard deviation of chloroform and the product C_2Cl_4. The decay of the chloroform variance is the same for both mixing models. The smaller the turbulent time, the faster

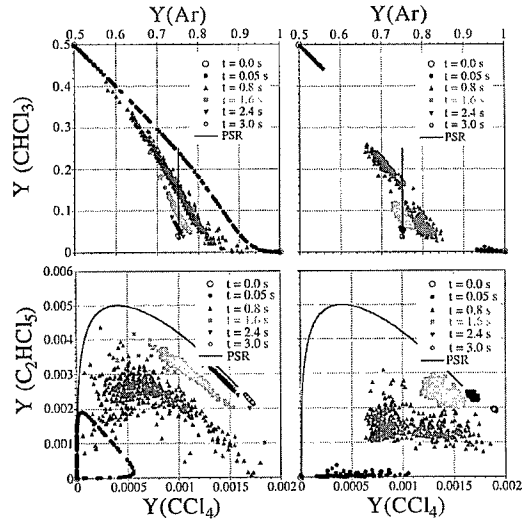

FIG. 6. Two-dimensional PDF of $CHCl_3$, Ar, and CCl_4, C_2HCl_5 for fixed $\tau = 0.5$ s [left: particle interaction model (JK); right: binomial Langevin model (BL)].

the decay to the homogeneous situation. After 3 s, the flow can be considered homogeneous even for $\tau = 0.5$ s.

The standard deviation of the products is first increasing due to reactions driven by the pyrolysis and then decaying because of the mixing. The position and value of the maximum standard deviation is strongly dependent on the mixing model. The reason for this dependence is revealed by the time evolution of the PDF.

In Fig. 6, the discrete joint PDF of argon and chloroform $f(Y(Ar), Y(CHCl_3))$ and the joint PDF of the by-product CCl_4 and the intermediate species C_2HCl_5, $f(Y(CCl_4), Y(C_2HCl_5))$, is displayed at different times for fixed $\tau = 0.5$ s. The solid line represents the trajectory of the PSR in the composition space. The left-hand side of the figure shows the time evolution, according to the JK model, and the right-hand side, according to the BL model. The discrete PDF is composed out of a number of stochastic representations (particles) in the composition space. The trajectory of these particles is determined by the chemical reaction, and the mixing, according to the used model. Both models reproduce the decay of the variance in the same way. In the case of JK, the whole range of states between the initial states is already adopted by the particles after the first time step (see Fig. 6 for $t = 0.05$ s). This is due to the different rates of mixing implied by the uniformly distributed random number α. Only in particles with high temperature and high mass fraction of chloroform does pyrolysis take place. This effect changes the virtual line between the two initial states from a straight line to a bent curve. The BL model does not produce all intermediate states instantaneously.

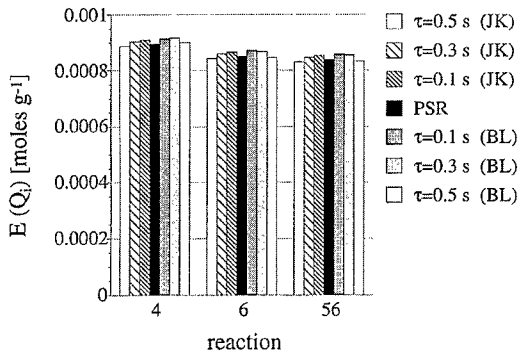

FIG. 7. Mean conversion of main reactions for varying τ.

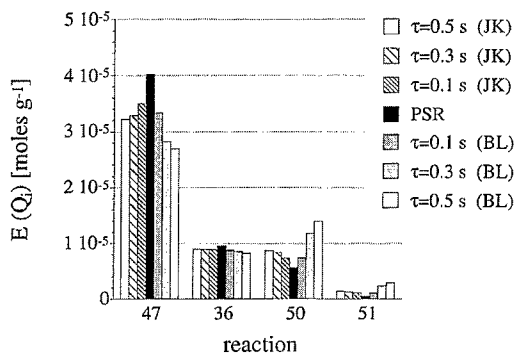

FIG. 8. Mean conversion of side reactions for varying τ.

There are two effects that superimpose. A linear drift that moves all particles toward each other and a white noise that blurs the delta distribution from the start. This leads to more hot particles with chloroform than in the case of JK mixing and explains the differences in the time evolution of means of the products.

The differences between the mixing models are even more obvious in the case of the PDF of CCl_4 and C_2HCl_5. The JK model moves the particles that represent $f(Y(CCl_4), Y(C_2HCl_5))$ closer to the trajectory of the PSR, and the variance is higher than in the case of the BL model. If the turbulent time is varied to smaller τ, the particle trajectories move closer to the PSR trajectory. Furthermore, it must be noted that, in the case of the WSR, it is not possible to distinguish the start, transition, and end phase because at a certain time, all phases superimpose. This superposition is controlled by the mixing model.

In Figs. 7 and 8, the means of the integrated reaction rates of important reactions are displayed. The integrated time interval, [0,3] s, is equal to the time that the two streams need to be mixed completely. The statistical moments of the integrated means are estimated by integrating the discrete PDF of the reaction rates. Figure 7 shows the mean conversions of reactions (4), (6), and (56). These reactions exhibit the same qualitative behavior for different turbulent times τ. Reactions (4) and (6) decompose chloroform, and reaction (56) forms one of the main products, C_2Cl_4. These main reaction channels of the pyrolysis are shifted slightly toward higher values for turbulent times $0 \text{ s} < \tau < 0.5 \text{ s}$ compared to the integrated reaction rate for the PSR. For $\tau > 0.5$ s, the mean is less than the PSR conversion. Figure 8 displays the mean integrated reaction rates of reactions (47), (36), (50), and (51). The mean conversion of reaction (47), which forms the intermediate species C_2HCl_5, decreases significantly for higher values of τ. Reaction (50) forms in a less turbulent environment much more C_2Cl_4 than in the homogeneous case. This explains the observation in Fig. 3. The mean reaction rates of the atomic chlorine producing reactions (36) and (51) behave differently with respect to turbulent mixing. Reaction (36) is the only reaction where the models give a different qualitative behavior. The BL model exhibits a slight decrease of the mean integrated reaction rate, whereas the JK model slightly increases the mean integrated reaction rate. In reaction (51), more chlorine radicals are formed in the less turbulent case.

Conclusions

1. The WSR configuration described with the PDF transport equation including a detailed chemical reaction analysis represents a suitable tool to investigate the influence of turbulent mixing, as described by the model on the reaction paths of a complex chemical system.
2. The particle interaction mixing model produces qualitatively the same results for means and variances of the involved chemical species as the binomial Langevin model extended to several scalars. But there are quantitative differences in means and variances, and the shape of the PDF differs significantly.
3. The decay of chloroform can be slightly accelerated in a certain range of turbulent times and slowed down outside this range. The time evolution of the intermediate C_2HCl_5 and the byproducts CCl_4 and C_2HCl_3 are strongly dependent on turbulent mixing.
4. The analysis of the statistical moments of reaction paths shows large differences between the sensitivity of reaction paths with respect to turbulent mixing. For the discussed initial conditions with different temperature in the two streams, one can find reactions that are accelerated, e.g., reaction (50), reactions that are slowed down, e.g.,

reaction (47), and reactions that are almost not influenced by turbulent mixing, e.g., reaction (56).

5. In future work, this method of analyzing the effect of turbulence on reaction paths shall be applied to oxidative systems also. Furthermore, comparison to experimental data is under way [16].

Acknowledgment

The financial support of this work by the Max-Buchner-Forschungsstiftung of the DECHEMA, Grant No. MBFST 1821, is gratefully acknowledged.

REFERENCES

1. Barat, R. B., Sarofim, A. F., Longwell, J. P., and Bozelli, J. W., *Combust. Sci. Technol.* 74:361–378 (1990).
2. Won, Y. S. and Bozelli, J. W., *Combust. Sci. Technol.* 85:345–373 (1992).
3. Brouwer, J., Sacchi, G., Longwell, J. P., and Sarofim, A. F., *Combust. Sci. Technol.* 101:361–382 (1994).
4. Pope, S. B., *Prog. Energy Combust. Sci.* 11:119–192 (1985).
5. Kraft, M., Klos, T., and Bockhorn, H., *Prog. Indust. Math.* ECMI94 (Neunzert, H., Ed.), Wiley, New York, 1996, pp. 184–191.
6. Kraft, M., Schneider, K., Schmitt, F., and Bockhorn, H., *Chem. Ing. Technik* 9:1131–1132 (1995).
7. Chen, J. Y., *Combust. Sci. Technol.* submitted.
8. Correa, S. M. and Braaten, M. E., *Combust. Flame* 94:469–486 (1993).
9. Menon, S., Calhoon, W. H., Goldin, G., and Kerstein, A. R., *Twenty-Fifth Symposium (International) on Combustion,* The Combustion Institute, Pittsburgh, 1994, pp. 1125–1131.
10. Valino, L. and Dopazo, C., *Phys. Fluids A* 3(12):3034–3037 (1991).
11. Hulek, T. and Lindstedt, R. P., Technical Report TF/94/24, MED, Imperial College, London, 1994.
12. Janicka, J., Kolbe, W., and Kollmann, W., *J. Nonequil. Thermodyn.* 4:47–56 (1979).
13. Pope, S. B., *Combust. Sci. Technol.* 28:131–135 (1982).
14. Kee, R. J., Rupley, F. M., and Miller, J. A., Sandia Report SAND89-8009B UC-706, 1993.
15. Lutz, A. E., Kee, R. J., and Miller, J. A., Sandia Report SAND87-8248 UC-4, 1992.
16. Procaccini, C., Macadam, S., Longwell, J. P., Sarofim, A. F., Kraft, M., and Bockhorn, H., *Twenty-Sixth Symposium (International) on Combustion,* The Combustion Institute, Pittsburgh, 1996.

Twenty-Sixth Symposium (International) on Combustion/The Combustion Institute, 1996/pp. 2439–2445

ADSORPTION OF METALLIC MERCURY ON ACTIVATED CARBON

DESPINA KARATZA,[1] AMEDEO LANCIA,[2] DINO MUSMARRA[1] AND FRANCESCO PEPE[3]

[1]*Istituto di Ricerche sulla Combustione, CNR*
P.le Tecchio 80, 80125 Napoli, Italy

[2]*Dipartimento di Ingegneria Chimica, Università di Napoli "Federico II"*
P.le Tecchio 80, 80125 Napoli, Italy

[3]*Facoltà di Scienze Ambientali, Seconda Università di Napoli*
Via Arena 22, 81100 Caserta, Italy

Gaseous emissions of mercury compounds from anthropic activities can cause severe harm to the ecosystem. The main sources of anthropic mercury emissions to the atmosphere are exhaust gases from coal combustion and municipal solid waste incineration. In this work, attention was focused on the adsorption of metallic mercury on commercially available activated carbon (Darco G60). The study was performed in an apparatus at laboratory scale in which a gas stream at a given temperature, Hg^0 concentration, and mass flow rate was contacted with a fixed bed of adsorbent material. Breakthrough curves and adsorption isotherms were obtained for bed temperatures of 90°, 120°, and 150°C and for Hg^0 concentrations in the gas in the range of 0.9–6.0 mg/m^3. The experiments showed that the adsorption process is a favorable one, and the gas–solid equilibrium data were used to evaluate the Langmuir parameters. Furthermore, it appeared that the higher the temperature, the lower the adsorption capacity, with a heat of adsorption of about −22 kJ/mol. The differential equations modeling the adsorption phenomenon were integrated, leading to the evaluation of a kinetic parameter describing the experimentally determined breakthrough curves.

Introduction

Mercury is present in traces in coal and in municipal solid waste (MSW) with concentrations varying from 0.1 to 1.0 g/t for coal and from 0.5 to 9.0 g/t for MSW [1], so that both coal combustion and MSW incineration result in atmospheric emissions of this pollutant. Because of the reducing properties of SO_2, about 80% of mercury from coal-fired power plants is emitted as Hg^0, with a flue gas concentration of 1–4 μg/m^3 [1–3]. On the other hand, related to mercury emissions from MSW incinerators, the situation is reversed: in that case, because of a relatively high concentration of HCl, mercury is emitted mainly as $HgCl_2$ [4,5] and only about 25% mercury is emitted as Hg^0, with a flue gas concentration of 25–250 μg/m^3 [2].

The need for the development of technologies capable of achieving high removal efficiencies for mercury emissions control led many researchers to focus on evaluating the adsorption capacity shown by different solids. Adsorption of oxidized mercury was studied by Schager [3], who measured experimentally the capture of elemental and oxidized mercury by different sorbents, finding that oxidized mercury is more easily adsorbed than elemental mercury. Specifically, he dealt with the adsorption capacity with regard to oxidized mercury exhibited by different materials, such as activated carbon, fly ash, and calcium compounds (CaO, $CaSO_4$), and found that activated carbon has the highest adsorption capacity, while calcium compounds have the lowest. Later, Lancia et al. [5] and Karatza et al. [6–8] dealt with adsorption of mercuric chloride on different solids. Lancia et al. [5] studied the influence of temperature on the adsorption of mercuric chloride by calcium hydroxide. They found that the lower the temperature, the higher the adsorption capacity. Karatza et al. [6] evaluated the mercuric chloride adsorption capacity showed by fly ash collected in a full-scale MSW incinerator. They showed that fly ash is a suitable sorbent for mercuric chloride removal and that the adsorption capacity decreases when temperature increases. Karatza et al. [7,8] studied the adsorption of mercuric chloride on activated carbon and on the same carbon impregnated with Na_2S, again considering the dependence on temperature. They found that impregnation of the carbon with Na_2S strongly enhances the adsorption capacity and that the adsorption process is exothermic both for "raw" carbon and for Na_2S impregnated carbon.

The study of adsorption of mercury in the elemental form was performed by Otani et al. [9,10], Henning et al. [11], Gullett and Jozewicz [12], and Krishnan et al. [13]. Otani et al. [9,10] studied the behavior of elemental mercury in the gas phase and

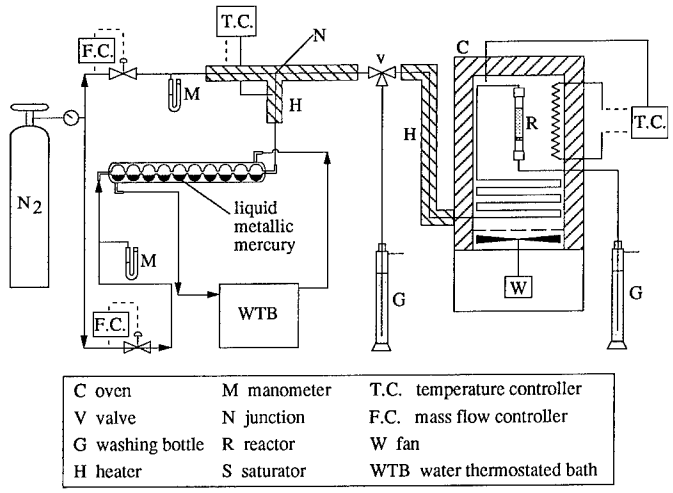

FIG. 1. Sketch of the experimental apparatus.

its adsorption on different porous solids, namely activated carbon, sulfur impregnated activated carbon, zeolites, and fly ash. They pointed to the links existing between adsorption capacity and superficial properties of the solid, including the concentration of the impregnating species, and showed that impregnating porous solids with sulfur enhances the adsorption capacity. These results were confirmed by Henning et al. [11], who used activated carbon impregnated with sulfur or KI.

Gullett and Jozewicz [12] tested six carbons with different physical characteristics. They found that the adsorption capacity spans over a wide range and, in general, that the lower the temperature, the higher the adsorption capacity. They found that the adsorption capacity is related exponentially to surface area and, possibly, a mixed, physical-chemical adsorption mechanism is involved in elemental Hg uptake by activated carbon.

Krishnan et al. [13] studied the effect of temperature on the adsorption of elemental mercury on two kinds of thermally activated carbons and on one kind of sulfur impregnated carbon. They found that the surface area has a strong effect on the adsorption capacity of all the sorbents tested and that while both thermally activated carbons exhibit an almost double adsorption capacity at 23°C with respect to that at 140°C, sulfur impregnated carbon is almost temperature insensitive. They also used desorption tests to reach a deeper insight of the physics of the process and suggested that, while physical adsorption is the prevailing mechanism for capture by thermally activated carbon at low temperatures, chemisorption is the prevailing one in other cases.

The scope of the present work is a systematic study of metallic mercury adsorption on a commercially available activated carbon, with the aim of obtaining thermodynamic data for the sorbent–sorbate interaction. The dependence of the adsorption capacity and of the removal rate on temperature will be discussed, and the results will be compared with those relative to the adsorption of mercuric chloride on the same adsorbent [7,8]. Experiments were performed in an apparatus at laboratory scale in which an N_2 gas stream containing Hg^0 vapors was contacted with a fixed bed of adsorbent material. Adsorption isotherms and breakthrough curves were obtained varying the temperature in the range of 90–150°C and the Hg^0 concentration in the gas stream in the range of 0.9–6.0 mg/m^3. The Langmuir parameters for the adsorption isotherms were determined, and a model based on the assumption of kinetic control was used to evaluate the kinetic parameters of the process.

Experimental

The apparatus used for the experiments of mercury adsorption is sketched in Fig. 1. In this apparatus, a gas stream, at required temperature and Hg^0 concentration, was produced, and mercury adsorption on a fixed bed was carried out. The gas stream was obtained by evaporating liquid mercury contained in a thermostat-regulated glass saturator into a stream of pure nitrogen. The saturator was made of a horizontally placed string of 10 empty glass spheres 30 mm ID, connected by short and narrow glass tubes (about 1 mm ID, 5 mm long), into which about 350 g liquid mercury (reagent grade Hg^0 from BDH) were deposited. This design allowed both a relatively large gas–liquid contact area (in the spheres) and a good mixing of the gas (in the tubes). The mass flow rate of nitrogen into the saturator was kept constant by a hot-wire flow rate controller, and the Hg^0 concentration in the gas stream fed to the reactor was controlled by varying the temperature of the saturator and by diluting in the junction *N* the

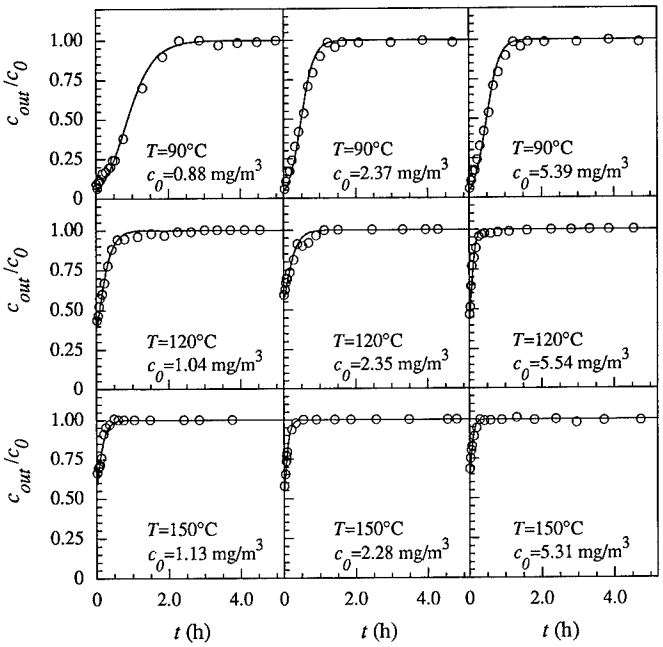

FIG. 2. Breakthrough curves for bed temperatures of 90°, 120°, and 150°C and for different Hg^0 concentrations in the gas fed to the reactor. ○ experimental measurements; — model results.

saturated stream with a stream of pure nitrogen, the flow rate of which was controlled by another hot-wire flow rate controller.

The diluted stream was fed to a glass reactor containing the sorbent. The reactor was 35 mm ID and 60 mm high and was kept in a thermostat-regulated oven equipped with a PID temperature controller. The adsorbing bed was made of about 0.61 g adsorbing particles mixed with 3.0 g 100-μm glass beads as inert, and its length (L) was 4 mm. This arrangement was chosen with the aim of avoiding channeling while keeping a small reactive surface. Furthermore, to avoid losses of powder in the gas stream, a downward flow was used in the reactor. Commercially available activated carbon (Darco G60 from BDH) was used as sorbent. The bulk density of the carbon is 450 kg/m^3, the average diameter of the solid particles is 3.5 μm, and the BET surface area is 230 m^2/g.

The experiments were conducted varying the temperature (T) of the adsorbing bed and the Hg^0 concentration in the inlet stream to the bed (c_0), whereas the gas–solid relative velocity was fixed in all runs. In particular, c_0 ranged from 0.9 to 6.0 mg/m^3 and T from 90 to 150°C, while the gas flow rate was kept at about 7.22×10^{-5} m^3/s, which corresponds to a gas superficial velocity of 7.52×10^{-2} m/s. The Hg^0 concentration in the outlet gas stream from the reactor was determined, as a function of time, by absorbing the gas by means of gas washing bottles for about 1 min. A $KMnO_4$ aqueous solution acidified by H_2SO_4 [14] was used, and the samples were analyzed by means of cold vapor atomic absorption (CVAA), using $NaBH_4$ as reducing agent. Such procedure was considered accurate, since no mercury was found in the gas exiting the washing bottle when another bottle was placed in series to the first. Besides, the quantity of mercury adsorbed on the bed was measured by leaching after each run the bed material with aqua regia (HNO_3 + 3HCl) and then analyzing the solution by means of CVAA; a difference not larger than 8% was found in the mercury material balance.

Results

For each experiment, the breakthrough curve was obtained by measuring the Hg^0 concentration in the outlet stream from the reactor at different times; it was assumed that thermodynamic equilibrium had been reached when the outlet concentration became equal to the inlet concentration. In Fig. 2, some breakthrough curves are reported as a ratio of the outlet to the inlet concentration (c_{out}/c_0) versus time for the three temperatures considered: 90, 120, and 150°C. In particular, for each temperature, the breakthrough curves for three different concentrations of Hg^0 in the inlet gas to the reactor are reported. The time necessary for saturation is on the order of several hours, depending on the experimental conditions. The experimental results show that the higher the temperature, the lower the saturation time; furthermore, it appears that when the Hg^0 concentration in the gas phase increases, the time necessary to reach the saturation becomes shorter.

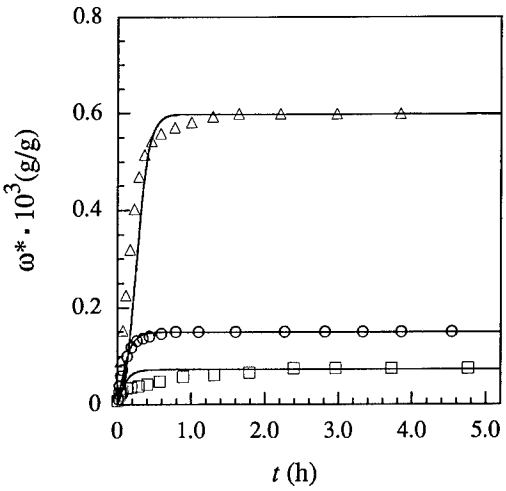

FIG. 3. Total adsorbate loading curves versus time. △ T = 90°C, c_0 = 5.39 mg/m³; ○ T = 120°C, c_0 = 5.54 mg/m³; □ T = 150°C, c_0 = 5.31 mg/m³, — model results.

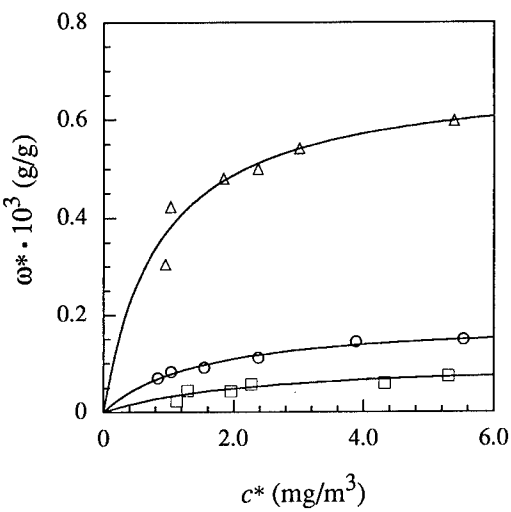

FIG. 4. Adsorption isotherms for Hg^0 on Darco G60 carbon. △ T = 90°C; ○ T = 120°C; □ T = 150°C;—Langmuir equation.

Figure 3 shows the total adsorbate loading ω_{tot}, expressed as a ratio between mass of adsorbed Hg^0 and mass of sorbent in the bed, as a function of time. The total adsorbate loading, which is calculated on the basis of the breakthrough curves, starts from zero and increases with time to reach a constant value, a condition in which the solid is saturated and is in thermodynamic equilibrium with the gas. Figure 3 shows that the lower the temperature, the higher the adsorption capacity and, similar to the results reported in the previous figure, the lower the temperature, the higher the saturation time.

The amount of mercury found on the solid at saturation (ω^*) represents the adsorbate loading in thermodynamic equilibrium with the gas phase at concentration c^*. Values of ω^* obtained for different concentrations of the gas stream give the adsorption isotherms reported in Fig. 4 for the three temperatures of 90, 120, and 150°C. The isotherms are of the favorable kind, and they show that the higher the temperature, the lower the adsorption capacity, confirming the exothermic nature of the adsorption process under consideration.

Discussion

The experimental results clearly show that the adsorbate loading at equilibrium depends on the gas-phase concentration, and therefore the phenomenon under consideration is an adsorption process rather than a gas–solid reaction. The maximum adsorbate loading found is 6×10^{-4} g/g, which, assuming hexagonal close packing of a monolayer of Hg^0, results in a surface coverage of less than 0.2 m²/g. Since the available surface area is three orders of magnitude higher than this, it is clear that a large fraction of the carbon surface is unused. This suggests that the adsorption capacity is linked to the interaction between gaseous Hg^0 and specific surface active sites σ, according to the following pseudoreaction:

$$Hg^0 + \sigma \underset{k_2}{\overset{k_1}{=}} (Hg^0 - \sigma) \qquad (1)$$

Using the Langmuir isotherm to describe the sorbent–sorbate interaction, the rate of the process can be expressed as the difference between the adsorption rate and the desorption rate. The former is proportional to the Hg^0 concentration in the gas phase and to the difference between the number of sites available for adsorption and the number of occupied sites, whereas the latter is simply proportional to the number of occupied active sites; hence, the overall rate is expressed by the following equation:

$$r = k_1(\omega_{max} - \omega)c - k_2\omega \qquad (2)$$

where c is the Hg^0 concentration in the gas phase, ω is its concentration as adsorbate on the solid, ω_{max} is the asymptotic adsorbate concentration, and k_1 and k_2 are the kinetic constants of the adsorption and desorption reactions, respectively. At equilibrium ($r = 0$), such a rate equation leads to the well-known Langmuir isotherm

$$\omega^* = \omega_{max}\frac{Kc^*}{1 + Kc^*} \qquad (3)$$

where K is the equilibrium constant related to the kinetic parameters by the equation

TABLE 1
Langmuir and kinetic parameters for Darco G60 activated carbon

T(°C)	K (m³/g)	ω_{max} (g/g)	k_1 (m³/gs)	k_2 (s⁻¹)
90	1.20×10^3	6.92×10^{-4}	0.415	3.45×10^{-4}
120	668	1.91×10^{-4}	0.505	7.56×10^{-4}
150	420	1.07×10^{-4}	0.630	1.50×10^{-3}

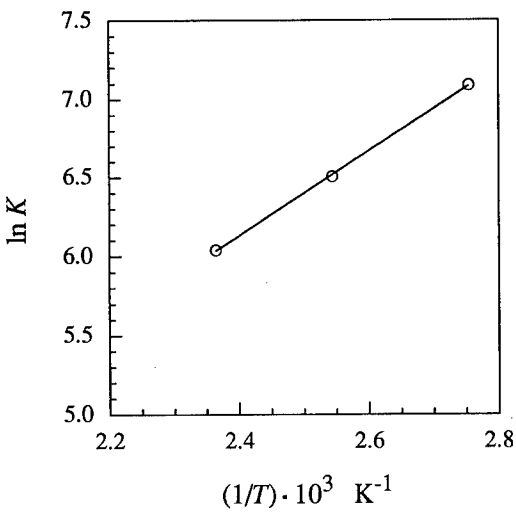

FIG. 5. Arrhenius plot for the equilibrium constant K.

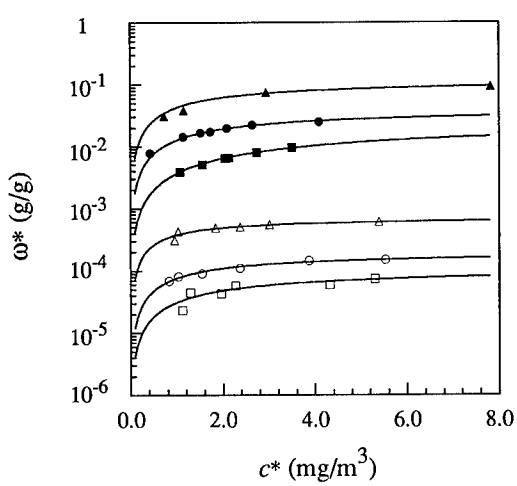

FIG. 6. Comparison between adsorption isotherms on Darco G60 carbon for Hg^0 (present work) and $HgCl_2$ (Ref. 8). Hg^0: △ T = 90°C, ○ T = 120°C, □ T = 150°C; $HgCl_2$: ▲ T = 120°C, ● T = 150°C, ■ T = 200°C;—Langmuir equation.

$$K = k_1/k_2 \tag{4}$$

The equilibrium data of Fig. 4 were used to evaluate the Langmuir parameters for the different temperatures under investigation. Using a nonlinear regression technique, such parameters were calculated and are reported in Table 1. The Langmuir isotherms obtained on the basis of the values of Table 1 are also included in Fig. 4 (continuous lines). The values reported in Table 1 show that both K and ω_{max} decrease when temperature increases. In particular, in agreement with the physical meaning of the equilibrium constant K, it is possible to hypothesize a dependence on the temperature of the Arrhenius type, according to the following equation [15]:

$$K = K_0 \exp\left(-\frac{\Delta H_{ads}}{RT}\right) \tag{5}$$

where K_0 is the preexponential factor and ΔH_{ads} is the heat of adsorption. A nonlinear regression gave, for K_0, the value of 0.72 m³/g and for ΔH_{ads}, the value of −22 kJ/mol, which is in the same order of magnitude of the heat of condensation for Hg^0. The values of K, together with the continuous line obtained using Eq. (5) with K_0 = 0.72 m³/g and ΔH_{ads} = −22 kJ/mol, are reported in Fig. 5 in the form of an Arrhenius plot.

The comparison between the experimental results presented in Fig. 4 and those reported in the other papers devoted to Hg^0 adsorption [9–13] is difficult because those papers do not report equilibrium data readily comparable with the adsorption isotherms of Fig. 4. Therefore, in Fig. 6, the results relative to Hg^0 adsorption on Darco G60 carbon presented here are compared to the results relative to $HgCl_2$ adsorption on the same carbon reported in Ref. 8. In that work, it was shown that $HgCl_2$ adsorption is also an exothermic process, and similar values were found for K_0 and ΔH_{ads} (0.33 m³/g and −25 kJ/mol, respectively). However, mercuric chloride is much more easily captured by Darco G60 than metallic mercury, and this circumstance is reflected in the fact that the asymptotic adsorbate concentrations for $HgCl_2$ are about 500 times those for Hg^0.

The values of the kinetic constants k_1 and k_2 used in Eq. (2) can be evaluated from the experimental breakthrough data, considering a balance of Hg^0 adsorbed in the bed. Indicating the axial coordinate in the bed with x and the time with t, it is

$$V\frac{\partial c}{\partial x} + \varepsilon\frac{\partial c}{\partial t} + \rho_b\frac{\partial \omega}{\partial t} = 0 \tag{6}$$

where V is the superficial velocity of the gas, ε is the external void fraction of the bed, and ρ_b is the bulk density of the adsorbent particles. Such a balance equation has to be associated with a constitutive equation for the rate of accumulation on the solid: neglecting the diffusional resistances and consider-

ing Eq. (2), the constitutive equation can be expressed as follows:

$$\frac{\partial \omega}{\partial t} = k_1(\omega_{max} - \omega)c - k_2\omega \quad (7)$$

Eqs. (6) and (7) have to be integrated subject to the following boundary conditions:

$$\begin{cases} t = 0;\ 0 \le x \le L;\ c = 0;\ \omega = 0 \\ t \ge 0;\ x = 0;\ c = c_0 \end{cases} \quad (8)$$

The system of Eqs. (6) and (7) with the boundary conditions (8) was solved using the analytical method proposed by Rhee et al. [16]. Using the values of K and ω_{max} experimentally determined for the different temperatures, the Hg^0 concentration profiles in both the gas and solid phase could be obtained as a function of time. A comparison between model and experimental results was possible in terms of c_{out} and ω_{tot}, which can be obtained easily from the solution of Eqs. (6) and (7). The only parameter in such equations is k_1, which was estimated by fitting model calculations to experimental breakthrough curves. Values of k_1, together with values of k_2 obtained by Eq. (4), are reported in Table 1. Furthermore, breakthrough and adsorbate loading curves calculated using the values reported in Tables 1 are reported in Figs. 2 and 3 (continuous lines). As expected, the values of k_1 and k_2 depend significantly on bed temperature but are independent of the Hg^0 inlet concentration to the adsorbing bed: such observation is in good agreement with the physical meaning of these parameters, the value of which is not expected to be affected by the Hg^0 concentration in the gas phase.

Conclusions

A fundamental study of Hg^0 adsorption on activated carbon was carried out to describe the effect of the main operating variables on the gas–solid interactions. Experiments carried out varying the Hg^0 concentration in the gas phase between 0.9 and 6.0 mg/m^3 and the adsorption temperature between 90 and 150°C showed that the adsorption process is favorable and exothermic.

The adsorption isotherms are of the Langmuir kind, and it was possible to evaluate the characteristic constants for such isotherms (the equilibrium constant K and the asymptotic adsorbate concentration ω_{max}), together with the heat of adsorption (ΔH_{ads}). The analysis of the data suggested that the mercury–carbon interaction takes place mainly on specific active sites disseminated on the carbon surface. Furthermore, it was shown that the heat of adsorption is in the same order of the heat of condensation for metallic mercury.

To evaluate the kinetic parameters of the process, a model was used that assumes that the kinetic resistance to adsorption on the solid surface is the limiting step for gas–solid transport. The comparison between the experimental breakthrough data and those predicted by the model was satisfactory and indicated a good agreement with the hypothesis made.

Nomenclature

c	Hg^0 concentration (g/m^3)
k_1	kinetic constant of the adsorption reaction (m^3/g s)
k_2	kinetic constant of the desorption reaction (s^{-1})
K	equilibrium constant (m^3/g)
K_0	preexponential factor (m^3/g)
L	length of the adsorbing bed (m)
r	adsorption rate (s^{-1})
R	gas constant (J/mol K)
t	time (s)
T	temperature (K)
V	superficial velocity (m/s)
x	axial coordinate in the bed (m)

Greek symbols

ΔH_{ads}	heat of adsorption (J/mol)
ε	external void fraction (−)
ρ_b	bulk density (g/m^3)
ω	adsorbate loading ($g_{Hg^0}/g_{sorbent}$)
ω_{max}	asymptotic adsorbate concentration ($g_{Hg^0}/g_{sorbent}$)

Superscripts

*	equilibrium

Subscripts

0	*inlet*
out	*outlet*
tot	*total*

Acknowledgments

The authors wish to express their gratitude to Mr. Fabio Salierno for his help in carrying out the experimental work.

REFERENCES

1. Pacyna, J. M. and Munch, J., *Water Air Soil Poll.* 56:51 (1991).
2. Hall, B., Schager, P., and Lindqvist, O., *Water Air Soil Poll.* 56:3 (1991).
3. Schager, P., Ph.D. Dissertation, University of Göteborg, Göteborg, Sweden, 1990.
4. Hall, B., Lindqvist, O., and Ljungström, E., *Env. Sci. Technol.* 24:108 (1990).

5. Lancia, A., Musmarra, D., Pepe, F., and Volpicelli, G., *Combust. Sci. Technol.* 93:277 (1993).
6. Karatza, D., Lancia, A., Musmarra, D., Pepe, F., and Volpicelli, G., *J. Chem. Eng. Jap.* 29(6) (1996).
7. Karatza, D., Lancia, A., Musmarra, D., Pepe, F., and Volpicelli, G. *Combust. Sci. Technol.* 112:163 (1996).
8. Karatza, D., Lancia, A., Musmarra, D., Pepe, F., and Volpicelli, G., *Haz. Waste Haz. Mat.* 13:95 (1996).
9. Otani, Y., Kanaoka, C., Usui, C., Matsui, S., and Emi, H., *Env. Sci. Technol.* 20:735 (1986).
10. Otani, Y., Emi, H., Kanaoka, C., Uchijima, I., and Nishino, H., *Env. Sci. Technol.* 22:708 (1988).
11. Henning, K., Keldenich, K., Knoblauch, K., and Degel, J., *Gas Sep. Pur* 2:20 (1988).
12. Gullett, B. K. and Jozevicz, W., International Conference on Municipal Waste Combustion, Williamsburg, VA (USA), 1993.
13. Krishnan, S. V., Gullett, B. K., and Jozevicz, W., *Env. Sci. Technol.* 28:1506 (1994).
14. Wilshire, N., Knoll, J. E., and Ward, T. E., *J. Air Waste Manage. Assoc.* 43:117 (1993).
15. Carrà S. and Morbidelli, M., *Chimica Fisica Applicata* Hoepli, Milan, Italy, 1983.
16. Rhee, H. -K., Aris, R., and Amundson N. R. *First Order Partial Differential Equations,* Vol. 1, Prentice Hall, Englewood Cliffs, NJ (USA), 1986, p. 166.

Twenty-Sixth Symposium (International) on Combustion/The Combustion Institute, 1996/pp. 2447–2453

MECHANISMS GOVERNING TRACE SODIUM CAPTURE BY KAOLINITE IN A DOWNFLOW COMBUSTOR

PHILIP O. MWABE AND JOST O. L. WENDT
Department of Chemical and Environmental Engineering
The University of Arizona, Tucson, AZ 85721, USA

A 17-kW, 6-m-long gas-fired laboratory combustor was used to investigate the postflame reactive capture of trace sodium species by kaolinite. Emphasis was on alkali/sorbent interactions occurring in flue gas at temperatures above the alkali dewpoint and on the formation of water-insoluble reaction products. Reaction time–temperature profiles replicated those in typical boilers and were varied by injecting kaolinite at different axial points along the combustor. The effects of chlorine and sulfur on alkali capture were investigated by doping the flame with Cl_2 and SO_2. Variations in sorbent particle sizes allowed the separate effects of reaction kinetics and transport within the particles to be isolated.

The actual capture reaction is proposed to be between alkali hydroxide and activated kaolinite and remains so in the presence of chlorine and sulfur. Hence, chlorine reduces sodium capture significantly because it lowers the gas-phase concentration of the sodium hydroxide. The primary effect of sulfur, on the other hand, is to elevate the sodium species dewpoint and, by thus lessening the time for reaction between gaseous sodium and substrate, to diminish the overall capture. A simple first-order kinetic model is proposed for sodium (hydroxide) capture by metakaolinite and is best fitted by the (global) volumetric rate constant:

$$k_v = 4.5 \pm 0.5 \times 10^7 \exp(-2{,}657 \pm 75/T) \text{ cm}^3 \text{ gas/(cm}^3 \text{ porous solid s)}$$

Chemical kinetics control for small particles under 2 μm, whereas intraphase pore diffusion controls for larger sorbent particles. A maximum sorbent utilization of 50% was realized, and an optimum sorbent injection window of 1200–1400 K was identified.

Introduction

The fate of trace sodium during combustion is important for two reasons. First, sodium released during pulverized coal combustion has been associated with hard bonded deposits on convection heat transfer surfaces in boilers. Second, the presence of sodium vapor in hot flue gases from coal combustion or coal gasification systems constitutes a major impediment to the development of combined cycle systems. Sodium is not easily removed at high temperatures and tends to condense on cooler turbine blades downstream.

One possible solution is to inject into the combustor suitable additives that can react with the gas-phase alkali species before the onset of condensation. Previous investigators have used both bench scale reactor studies [1–3] and combustor studies [4–8] to investigate both the reactive and physical captures of sodium by clay-based sorbents. However, the reaction kinetics (k_v, given as $1.92 \times 10^{10} \exp(-16{,}104/T)$ cm^3 gas/cm^3 solid s) extracted by Uberoi et al. [3] from their thermogravimetric reactor studies, in which reactions occur on large, individual, captive sorbent flakes between 773 and 1173 K over time scales of minutes, are in sharp contrast to the higher-temperature drop tube studies of Wibberly and Wall [9]. In those studies, reactions forming sodium silicates in flue gases containing sodium, sulfur, chlorine, water vapor, and silica particles occurred over time scales of seconds. Pilot scale experiments on a 330 kW furnace [5] showed that injected clay materials reduced superheater deposit strength. Fundamental drop tube tests [6], in which a synthetic coal was mixed with sorbents in known quantities, showed that (a) capture reactions proceeded within short coal combustion time scales; (b) capture of sodium from NaCl was less than that from Na acetate; (c) sulfur also depressed capture; and (d) kaolin was a more effective sorbent than either alumina or silica alone. It was the purpose of the research reported here to complement and build on these studies and to focus on kinetics and kinetic mechanisms of sodium/kaolinite interactions, under practical combustor conditions, with and without sulfur or chlorine present.

Theoretical Considerations

When kaolinite particles are injected into a hot environment (above 723 K), the kaolinite

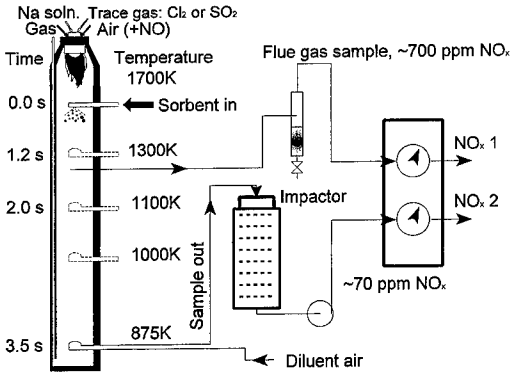

FIG. 1. Downflow laboratory combustor, showing typical time/temperature history, and particle sampling system.

($Al_2O_32SiO_2H_2O$) is activated to form metakaolinite ($Al_2O_3SiO_2$), which is hypothesized [10] to react with NaOH to form nephelite ($2Na_2OAl_2O_32SiO_2$), which is water insoluble [11]. Metakaolinite is deactivated above 1223 K [12] and ultimately forms mullite ($3Al_2O_32SiO_2$) and silica (SiO_2), which also can react with NaOH to form water-soluble silicates (Na_2OnSiO_2). In the binary nephalite/sodium metasilicate system there is a eutectic at 1173 K at a weight fraction of 0.5 [13], indicating the power of sodium to form sticky liquids from refractory compounds at relatively low temperatures. In this research, emphasis is on reactive capture of sodium to form water-insoluble products rather than physical capture such as condensation (and coagulation). Hence, high-temperature deactivation of metakaolinite should be avoided. Chemical reaction products can be distinguished from physical condensates by simple water-solubility tests, and this facet forms the basis for analytical work described here.

Multicomponent equilibrium calculations predict [14] that in the absence of sorbent, chlorine, or sulfur, the primary gaseous sodium species at temperatures above 1100 K is NaOH [15,16]. At the dewpoint, the condensate is Na_2CO_3. In the presence of excess chlorine, the dominant gaseous sodium species is NaCl(g), the dewpoint is lowered (by 200 K), and the condensate is NaCl(s). Sulfur, on the other hand, increases the dewpoint for sulfur compounds (with condensate Na_2SO_4) by about 250 K. In the presence of kaolinite, sodium alumino-silicate ($2Na_2OAl_2O_32SiO_2$[s]) is thermodynamically favored at temperatures higher than 1300 K except at very high chlorine concentrations.

If gas-phase reactions are sufficiently rapid, one would expect thermodynamically predicted gas-phase sodium speciation to be approximated. In that case, the presence of chlorine lowers the gas-phase concentration of NaOH, which Gallagher [10] hypothesized to be the sodium species that reacts with metakaolinite. Hence, one would expect chlorine to diminish the (finite) rate of sodium capture, assuming that reactive capture is controlled by rates rather than equilibria. Sulfur, on the other hand, has little effect on the equilibrium gas-phase speciation of sulfur, which is still primarily NaOH. Sulfur, therefore, is hypothesized not to change the (finite) sodium capture rate. However, by greatly increasing the dewpoint (at which point Na_2SO_4[s] is formed and the reactant, NaOH[g], removed), the presence of sulfur diminishes the time available for reaction (assuming a declining temperature in a plug flow reactor). We shall use these gas-phase equilibrium-based arguments as a working hypothesis to interpret experimental results presented in this paper. Ultimately, the results themselves will demonstrate the validity of this hypothesis.

Laboratory Combustor

The center piece for the experimental research was a 0.15-m I.D., 6 m long, insulated, 17-kW downflow combustor, which has been described in detail in the literature [17,18]. For this research, it used an overall fuel-lean gas flame through which 20 cc/min, 0.2 M, sodium acetate solution was injected. There was evidence that portions of the spray impacted on the refractory quarl, which made it impossible to achieve closure in the overall Na mass balance, as detailed later. However, this is not a serious problem for the results presented here for two reasons: (1) overall sodium recovery was constant (at 40%) because the combustion changes investigated occurred downstream in the far postflame and so had negligible influence on spray behavior and (2) data interpretation centered on analyses of the samples collected rather than on precise a priori knowledge of input flows. Sorbent could be injected and sample could be withdrawn through any one of 14 sample ports, as shown on Fig. 1. Sorbent was fed at regulated rates that ranged from 0.5 g/min to 4 g/min (corresponding to a particle/flue gas mass loading of under 1% and a number density under 10^6 particles/cm^3) by a variable screw feeder and transported pneumatically with 28 slpm air. The sample passed through a water-cooled, isokinetic (10/1) dilution quenched probe to a 28.3 alpm Anderson impactor (Fig. 1) with eight stages and an after filter (AF). The particle size, taken as the upper cutoff d_{50}, representing the particle size entering each stage from the stage above, is shown on the abscissa of Fig. 2. The lower cutoff d_{50} for each stage represents the particle size leaving a stage. Gas analyses were accomplished using standard continuous emission monitors, and NO was used to measure sample dilution precisely (Fig. 1).

This type of laboratory combustor is appropriate for this research for several reasons: (a) both its com-

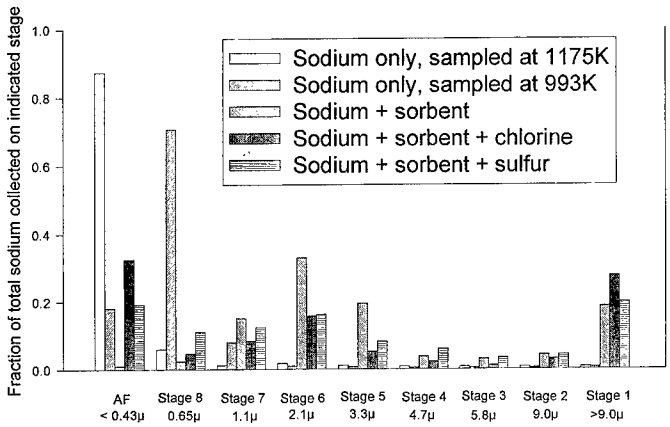

FIG. 2. Screening experiments: distribution of sodium among impactor stages for five different cases.

bustion environment (gaseous and particulate) and its temperature/time scales are representative of full-scale boilers (Fig. 1); (b) its aerodynamics have been shown to be approximately one-dimensional with respect to temperature and gas-phase concentrations [10,14], thus allowing the extraction of rates and mechanisms; and (c) a sufficiently large particulate sample could be extracted for analysis without that process itself affecting the combustion environment. Consequently, this research focused on mechanisms of sodium/kaolinite interactions as these apply to practical boiler environments.

Approach

First, qualitative insight into pertinent mechanisms was obtained through screening studies in which the separate effects of sorbent injection, chlorine, sulfur, and sorbent particle size were examined. Next, for each of three different systems (Na/kaolinite, Na/chlorine/kaolinite, and Na/sulfur/kaolinite), a multivariable regression analysis was performed to quantify effects of sodium/sorbent equivalence ratio and sorbent injection temperature on reactively captured, water-insoluble sodium. Then, portions of the integral data were taken from one of the three response functions and used to estimate an initial global reaction rate coefficient for the reaction between sodium and kaolinite. This rate coefficient was then tested for consistency with sorbent particle size data obtained during the screening tests. Finally, the same rate coefficient was used in a plug flow reactor model to predict experimental results for all conditions examined in both the Na/S/kaolinite and Na/kaolinite systems.

Experimental Results

Temperature Profile

For all experiments reported here, the temperature gradient in the combustor was set by the gas flame and could be given as a function of residence time by

$$\frac{dT}{dt} = -3.42 \times 10^{-4}T^2 + 0.22T = 1/\Psi(T) \quad \text{K/s} \tag{1}$$

defining $\Psi(T)$, which is used in data analysis later.

Screening Experiments

Figure 2 shows size-segregated data from five runs. The ordinate denotes the fraction of total sodium (on all stages) that was collected on a given stage (average of two replicates, with reproducibility within 8% for Na). The abscissa shows the stage number (Stage 1 includes the separator cup above it) and the corresponding value of the upper particle d_{50}, based on a particle SG = 1. The two bars at the left of each data group show the particle size distribution (psd) for a (nominal) 140 ppmv sodium without sorbent or any additives in flue gases. The far left-hand bar denotes samples withdrawn at 1173 K, which is above the dewpoint of 1073 K. A very fine submicron fume, collected on the after filter, is formed in the probe, and measurable coagulation in the probe (to form larger particles collectible on Stage 8) is not observed because of the dilution. The neighboring bar denotes samples withdrawn below the dewpoint at 993 K and shows effects of coagulation within the furnace. However, unscavenged sodium can be found predominantly on the after filter and Stage 8. The % Na recovery, based on the feed, was always between 39% and 43% and was independent of sampling position, suggesting that the problem upstream lay with the spray at the burner. The % Na recovery lay within the prior range for all experiments subsequently conducted and was the same for other trace metals (e.g., potassium) when they were present [14].

Comparison between the center and left of center

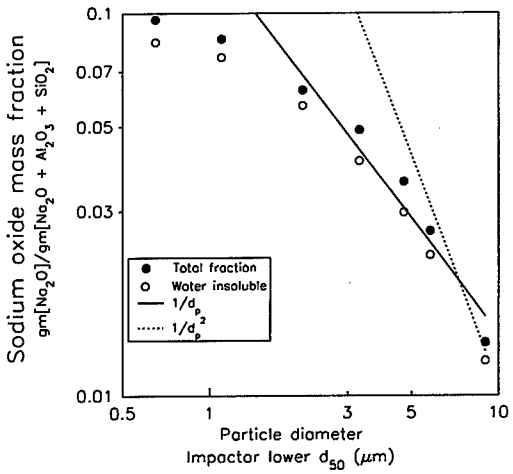

FIG. 3. Effect of sodium enrichment as a function of collected particle size. Sorbent was coarse kaolinite.

bars in each group in Fig. 2 shows that sorbent injection at 1473 K (Port 3) increased the sodium-rich particle size (sampled after 2.8 s at 993 K at Port 12) from ~0.65 μm to ~2.1 μm. The sodium psd now tracked the raw kaolinite psd. With sorbents, 95% of the sodium is found in Stages 1–7, whereas, without sorbents, 95% of the sodium is on the after filter and Stage 8. Reactively captured, water-insoluble sodium accounted for 78% of the total sodium in the sample denoted on the center bars. Only 22% of the sodium was water soluble. The total sodium-to-sorbent equivalence ratio, ϕ, was 0.33, equivalent to 0.09 g Na_2O per g sorbent, if it were all insoluble. When sorbent flow rates were decreased to create excess Na conditions ($\phi \geq 1$, based on sample analyses), only 50% of the theoretical capture capacity of 0.27 g insoluble Na_2O/g sorbent was ever realized [14].

The two right-hand bars in each group on Fig. 2 show the size segregation of sodium in the presence of chlorine (molar Cl/Na = 5) and sulfur (molar S/Na = 5). Clearly, Cl diminishes the fraction of Na captured, as is evident from the amount collected on the after filter compared to the sodium/sorbent-only case. Here, only 75% of the total sodium is found in Stages 1–7 and only 52% of the total is water insoluble, compared to 78% without Cl. Sulfur also diminishes sodium capture, with 55% of the sampled sodium being water insoluble. These results are consistent with the different gas-phase equilibria–based effects of chlorine and sulfur discussed previously.

Figure 3 shows the effects of sorbent particle size, here noted as the lower d_{50} cutoff. Here, a coarse kaolinite sorbent powder with only 40% of the mass having particle diameters less than 10 μm was injected at 1473 K. Impactor samples were withdrawn at 923 K at Port 11 after 2.8 s. Total Na_2O fraction and the water-insoluble fraction are shown in the same plot. Clearly, reactive capture forming insoluble Na_2O dominates throughout. There is only weak enrichment on smaller particles between 0.65 μm and 3 μm, suggesting transition between pore diffusion and chemical reaction control. Between 3 and 9 μm, the size dependence follows $1/d_p$, suggesting pore diffusion–controlled reaction, while for even larger particles one might argue for a $1/d_p^2$ dependence, suggesting gas-film diffusion control. In Fig. 3, the maximum sorbent utilization based on nephalite for the submicron particles is 30%, whereas for the largest size class shown (9 μm it was under 5%.

In general, the screening studies suggested that for a given sodium vapor concentration and with sorbent particles less than 3 μm in diameter, the most important variables that determine the amount reactively captured are the sorbent injection temperature and the sodium/sorbent equivalence ratio, ϕ.

Multiple-Regression Studies

Separate response functions for integral, insoluble sodium capture $g^*(T_{inj}, \phi)$ [g insoluble Na_2O/g sorbent] were obtained for (a) Na/sorbent only, (b) Na/sorbent/Cl, and (c) Na/sorbent/S as functions of sorbent injection temperature T_{inj} (determined from sorbent injection location) and sodium sorbent equivalence ratio, ϕ (determined from ratio [total mol Na] [mols Al] in the sample. Temperature profiles were unchanged.

Sodium (250 ppm), Only

Statistical analysis, using the SPSS statistical computational package on 28 data points in which T_{inj}—the sorbent injection temperature—and ϕ—the sodium/kaolinite equivalence ratio—were varied over the ranges 1098 K $< T_{inj} <$ 1557 K and $0.08 < \phi < 1.98$, yielded the following response surface:

$$g^* = (-0.145 \pm 0.054)\phi^2 + (0.088 \pm 0.064)T^*\phi + (0.168 \pm 0.088)\phi$$

$$T^* = \frac{T_{inj}(\mathrm{K})}{1273} \qquad (2)$$

with a coefficient of determination or model $R^2 = 0.95$ and an F-test statistic, $F^* = 218$, which is much larger than the appropriate $F(0.95, 2, 25)$ value of 3.39. Hence, a strong correlation has been established. From Eq. (2), it is concluded that sodium capture by kaolinite is a weak function of higher-order terms of injection temperature but a strong function of alkali-to-sorbent-loading ratio and cross terms of injection temperature and equivalence ratio.

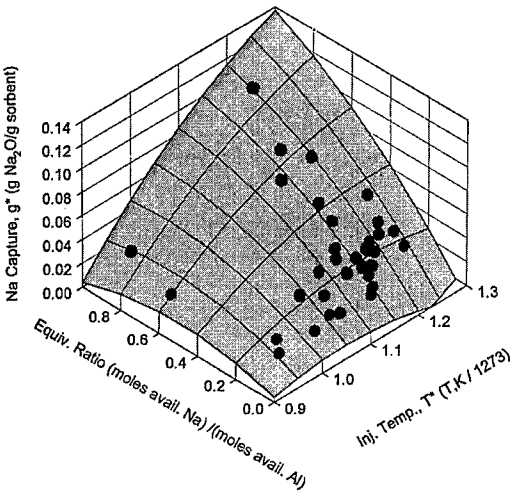

FIG. 4. Response surface for sodium capture in an excess SO_2 environment, as generated by least-square regression, resulting in Eq. (4). Experimental data are posted on the surface.

Sodium (250 ppm) with Cl (700 ppm Added Cl_2)

Thirty-five samples were considered, and sorbent injection temperature T_{inj} and ϕ were varied over the ranges 1123 K $< T_{inj} <$ 1622 K and $0.08 < \phi < 1.50$. Statistical analysis gave the best fit for sodium capture in the presence of chlorine as

$$g^* = (0.107 \pm 0.026)T^*\phi - (0.055 \pm 0.028)\,\phi^2 + (0.016 \pm 0.006)$$

$$T^* = \frac{T_{inj}(\mathrm{K})}{1273} \tag{3}$$

Here, $R^2 = 0.87$, and $F^* = 99.5$, compared to $F(0.975, 2, 32) = 2.7$. Subsequent to performing this analysis, six additional (replicate) runs were completed, and they also fitted the correlation well. The shape of the surface described by Eq. (3) is similar in shape to that of Eq. (2) but with a greater temperature dependence at the higher equivalence ratio values.

Sodium (250 ppm) and SO_2 (700 ppm)

Twenty-nine samples were considered, and sorbent injection temperature T_{inj} and ϕ were varied over the ranges 1138 K $< T_{inj} <$ 1509 K and $0.12 < \phi < 0.9$. Statistical analysis gave the best fit ($R^2 = 0.92$, $F^* = 55.5$; $F(0.975, 5, 23) = 3.21$) for sodium capture in the presence of excess sulfur as

$$g^* = -0.360\,T^{*2} + 0.754\,T^* + 0.372\,T^*\phi - 0.061\,\phi^2 - 0.274\,\phi - 0.383$$

$$T^* = \frac{T_{inj}(\mathrm{K})}{1273} \tag{4}$$

which describes the surface shown in Fig. 4. The shape of this surface shows a much greater dependence on T_{inj} at high values of ϕ than did the preceding two surfaces. According to our gas-phase equilibrium–based hypothesis, SO_2 elevates the dewpoint to around 1123 K, shortening the time available for reaction. Variation of sorbent injection temperature, accomplished by changing injection locations, changes both reaction temperature (a weak variable, according to Eq. [2]) and the reaction time (the dominant variable here). The shape of the response surface clearly shows insignificant sodium capture at temperatures below $T^* = 0.88$ (or $T_{inj} =$ 1123 K) for all the sorbent flow rates.

Discussion

Estimation of a Rate Coefficient from Partial Data

We restrict attention to that experimental domain in which the integral capture is completed with little change in the concentration of gas-phase sodium up to the point where reaction ceases. According to our working hypothesis, sulfur terminates the capture reaction after short times. We further limit attention to data in which Na was far in excess, that is, at $\phi \approx 1$, since the data show that because of melting, 50% sorbent utilization is the maximum achievable. Hence, the experimental domain under consideration is that portion described by the Na/SO_2/sorbent response surface shown on Fig. 4 and given by Eq. (4), with $\phi = 1$.

The integral capture g^* [g insoluble Na_2O/g sorbent] can be formulated with respect to sorbent injection temperature T_{inj} as

$$g^*(T_{inj}, p^0_{Na}) = \int_{T_{inj}}^{T_{dwpt}} R_g(p_{Na}, T)\,\Psi(T)dT \tag{5}$$

where $R_g(p_{Na}, T)$ is the local rate of reaction [g Na_2O/g sorbent s] and the time variable has been converted to local temperature using $\Psi(T)$ from Eq. (1). Note also that T_{inj} and T are independent.

Setting $R_g(p_{Na}, T) = R_g(p^0_{Na}, T)$ and $g^*(T_{inj}, p^0_{Na}) = g^*(T_{inj}, [\phi = 1])$, it follows, using Leibnitz's Rule, that

$$R_g(T_{inj}, [\phi = 1]) = \left(\frac{1}{\Psi(T_{inj})}\right)\frac{\partial g^*}{\partial T_{inj}}\bigg|_{\phi=1} \tag{6}$$

Now, replacing T_{inj} with T,

$$R_g(T) = k_v(T)\left(\frac{p^0_{Na}}{RT}\right)31\left(\frac{\varepsilon}{(1-\varepsilon)\rho_p}\right)\frac{g\ Na_2O}{g\ \text{sorbent, s}} \tag{7}$$

where ε, ρ_p, and R are porosity, particle density, and gas constant, respectively. Hence, the global rate coefficient

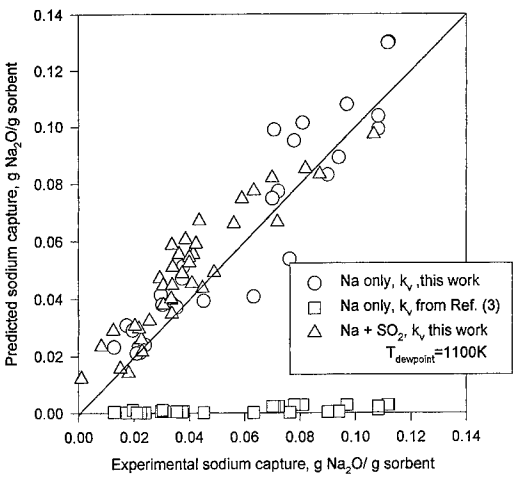

FIG. 5. Comparison between plug flow reactor predictions and experimental data for Na/kaolinite/S and Na/kaolinite systems. Also shown are predictions using kinetics from Ref. 3.

$$k_v(T) = \frac{\rho_p RT}{31 p_{io} \Psi(T)} \frac{(1-\varepsilon)}{\varepsilon} \cdot \left.\frac{\partial g^*(T)}{\partial T}\right|_{\varphi=1} \frac{\text{cm}^3\text{ (gas)}}{\text{cm}^3\text{ (porous solid) s}} \quad (8)$$

and using the values of $\rho_p = 2.64$ g/cm^3, $\varepsilon = 0.58$ [12,19], and $p^0_{\text{Na}} = 100$ ppm (corresponding to an alkali recovery of 40%, based on sodium input), together with the partial derivative of g^* with respect to T (from Eq. [4] with $T = T_{\text{inj}}$ and $\phi = 1$), the rate parameter $k_v(T)$ is given as

$$k_v(T) = \sum_{k=1}^{k=3} a_k T^{k+1};\ a_1 = -9.83,$$
$$a_2 = 2.02 \times 10^{-2},\quad a_3 = -7.68 \times 10^{-6} \quad (9)$$

which can be fitted into Arrhenius format to yield

$$k_v = 4.5 \pm 0.5 \times 10^7 \exp(-2{,}675 \pm 75/T) \frac{\text{cm}^3\text{ (gas)}}{\text{cm}^3\text{ (porous solid) s}} \quad (10)$$

Consistency with Particle Size Effect Data

At 1500 K, the effective diffusivity for the porous particle is calculated to be [14]: $D_e = 0.052$ cm^2/s. The value of the Thiele Modulus,

$$\varphi = \frac{d_p}{6}\sqrt{\left(\frac{k_v(1-\varepsilon)}{D_e}\right)}$$

at which reaction rates and diffusion rates are equal, is 0.3 [20], and from Fig. 3, this should occur at a particle size $d_p = 2\ \mu$m. From this, a value for $k_v = 10.0 \times 10^6$ cm^3 gas (cm^3 solid s) is inferred, which compares well to the value calculated from the response surface of $k_v = 8.0 \times 10^6$ cm^3 gas (cm^3 solid s).

Comparison between Predictions and Data

A simple model of a plug flow reactor without axial diffusion but with a known axial temperature profile was developed [14] to use the rate coefficient derived previously to predict axial gas-phase sodium-concentration profiles. After numerical integration, this allowed the amount of sodium reactively scavenged to either the dewpoint or the sample point to be calculated and compared to experimental values. Figure 5 shows comparisons between predictions and a model for sodium/sorbent/SO_2 runs and sodium/sorbent runs. Agreement between theory and experiment is good. This supports our working hypothesis that although it diminishes reaction times, sulfur does not affect kinetic rates. Also shown are predictions using the (NaCl-based) kinetic rate constant from Ref. 3; these do not seem to apply to our system at all, probably because of the effect of chlorine.

Effect of Chlorine

It is possible to adjust the (low) rate coefficient from Ref. 3 to account for a gas-phase equilibrium between NaCl, NaOH, H_2O, and HCl and the assumption that only NaOH reacts with the substrate. Then, (modified) predictions, using the adjusted Ref. 3 coefficient, fall into the same domain as our data but the scatter is now so large that this comparison is not shown. Possibly the prior equilibrium assumption is not valid. Hence, without better estimates for gaseous NaOH concentrations, our sodium/sorbent/chlorine capture values, which were about 30% lower than those of sodium alone, cannot be well predicted at this time.

Conclusion

Kaolinite is effective in capturing alkali species in an in situ application through chemical reaction between alkali hydroxide and metakaolinite. The rate of sodium capture, in a practical furnace environment, is given by

$$\frac{d[\text{Na}_2\text{O}]}{dt} = 31\, k_v \cdot V_s \cdot C_{\text{Na}} \frac{\text{g Na}_2\text{O}}{\text{g sorbent s}} \quad (11)$$

where V_s = sorbent pore volume in cm^3/g sorbent, C_{Na} = gaseous sodium concentration in gmol Na/cm^3 gas, and k_v is given by Eq. (10). The optimum sorbent injection window was found to be in the

range of 1173–1373 K. This optimum is linked to the onset of condensation on one hand and to the transformations of metakaolinite at high temperatures to form stable mullite structures with the subsequent release of silicon species on the other hand.

Sulfur reduces sorbent effectiveness through the raised dewpoint of the sulfate condensate with the consequent reduction in the gas-phase residence time scale available for gas–solid reactions. Chlorine in the flue gas reduces sorbent effectiveness by approximately 30%, most probably by decreasing the concentration of the reactive sodium species.

Acknowledgments

Partial funding from the U.S. Agency for International Development and the U.S. Department of Energy, University Coal Research Program, under Contract # DE-FG22-90PC90285, is gratefully acknowledged.

REFERENCES

1. Luthra, L. K. and LeBlanc, H. O., "Reducing High Alkali Vapor Activities in Coal-Fired Combined-Cycle Systems by Adsorption." Paper presented at The Electrochemical Society Conference on Corrosion in Fossil Fuel Systems, Detroit, 1982 p. 101–110.
2. Punjak, W. A., "High Temperature Interactions of Alkali Vapours with Solids During Coal Combustion and Gasification." Ph.D. Dissertation, University of Arizona, Tucson, 1988.
3. Uberoi, M., Punjak, W. A., and Shadman, F., *Prog. Energy Combust. Sci.* 16:205–211 (1990).
4. Klinzing, G. E., Blanchere, J. R., Weintraub, M., Martello, D., and Shannon, S., "Use of Solid Collectors for Control of Emissions in Advanced Coal Conversion Processes." Final Report for Contract DE-AC21-84MC21387, U.S. DOE, Morgantown Energy Technology Center, Morgantown, WV, 1986.
5. Lindner, E. R., Kosminski, A., and Williams, R. G., "Effects of Additives on Fouling Behavior Characteristics of South Australian Brown Coals." In *Mineral Matter and Ash Deposition from Coal* (R. W. Bryers and K. S. Vorres, eds.), Engineering Foundation Conferences, United Engineering Trustees, 1990, pp. 331–345.
6. Wall, T. F. and Lindner, R. L., *Twenty-Third Symposium (International) on Combustion,* The Combustion Institute, Pittsburgh, 1990, pp. 1313–1321.
7. Spiro, C. L., Chen, C. C., Kimura, G. S., Lavigne, R. G., and Schields, P. W., *Prog. Energy Combust. Sci.* 16:213–220 (1990).
8. Logan, R. G. and Richards, G. R., *Prog. Energy Combust. Sci.* 16:221–233 (1990).
9. Wibberley, L. J. and Wall, T. F., *Fuel* 61:87–92 (1982).
10. Gallagher, N. B., "Alkali Metal Partitioning in a Pulverized Coal Combustion Environment." Ph.D. Dissertation, University of Arizona, Tucson, 1992.
11. Wilhelm, E., *The Physical Chemistry of Silicates.* University of Chicago Press, Chicago, 1954.
12. Tsuzuki, Y. and Nagasawa, K., *Clay Sci.* 3(5):87–102 (1969).
13. Levin, E. M., Robbins, C. R., and McMurdie, H. F., *Phase Diagrams for Ceramists,* American Ceramic Society, Columbus, OH, 1964.
14. Mwabe P. O., "Mechanisms Governing Alkali Metal Capture by Kaolinite in a Downflow Combustor." Ph.D. Dissertation, University of Arizona, Tucson, 1993.
15. Durie, R. A., Milne, J. W., and Smith, M. Y., *Combust. Flame* 30(3):221–230 (1977).
16. Steinberg, M. and Schofield, K., *Prog. Energy Combust. Sci.* 16:311–317 (1990).
17. Scotto, M., Peterson, T. W., and Wendt, J. O. L., *Twenty-Fourth Symposium (International) on Combustion,* The Combustion Institute, Pittsburgh, 1992, pp. 1109–1117.
18. Bool, L. E., Peterson, T. W., and Wendt, J. O. L., *Combust Flame* 100(1/2):262–270 (1995).
19. Uberoi, M. and Shadman, F., *Ind. Eng. Chem. Res.* 30(4):624–631 (1991).
20. Smith, J. M., *Chemical Engineering Kinetics,* McGraw-Hill, New York, 1981.

COMMENTS

Majed Toqan, ABB, USA. How did you make sure that the capture was taking place in the reactor and not in the sampling system? Did you do an experiment in which the impactor would have the large particles and sodium vapor is passed over it to see if the particles you generate are the same as what was collected in the reported experiments? Sodium condensation on the particles might have an impact on the arrived conclusions.

Author's Reply. Reactive capture taking place in the sampling probe was minimized by diluting the sample stream with ambient air at the probe at a dilution ratio of 10:1 or higher. This resulted in high quenching rates on the sample stream which served to freeze any further reactions from taking place. Condensation on the probe or on the sampling system e.g. the impactor, on the other hand, would form water soluble sodium salts which were considered as uncaptured sodium in the analysis even if such sodium were found on the particles.

Captured sodium was defined as the *water insoluble* sodium in the kaolinite particles. Any condensed sodium or sodium that had reacted with free silica to form silicates ($Na_2O \cdot nSiO_2$) were considered as uncaptured in the results presented.

Twenty-Sixth Symposium (International) on Combustion/The Combustion Institute, 1996/pp. 2455–2462

A REAL-TIME MONITOR FOR TOXIC METAL EMISSIONS FROM COMBUSTION SYSTEMS

STEVEN G. BUCKLEY,[1] CATHERINE P. KOSHLAND,[2] ROBERT F. SAWYER[1] AND DONALD LUCAS[3]

[1]*Department of Mechanical Engineering*
University of California
Berkeley, CA 94720, USA

[2]*School of Public Health*
University of California
Berkeley, CA 94720, USA

[3]*Lawrence Berkeley National Laboratory*
University of California
Berkeley, CA 94720, USA

Excimer laser fragmentation-fluorescence spectroscopy (ELFFS) simultaneously detects many airborne toxic metal species in real time and in situ. With ELFFS, sub-ppm single-shot detection limits are achieved for Ba, Cr, Mn, Ni, Pb, and Tl in postcombustion gases of methane-air flames. Spectra of metals both singly and in mixtures illustrate the response of ELFFS to metals injected into a flame. Background interference from combustion products is negligible.

We investigate aspects of the technique relevant to application in real-world devices. The detection signal changes linearly with concentration for each metal injected in the postflame gases. The signal also changes with the aerosol size, which is a strong function of temperature. We find that the ELFFS signal depends on the aerosol surface area, suggesting that the signal evolves from surface ablation. In the cooled gases, where the temperature and aerosol size are constant, the signal is constant, and similar signal levels are observed for four different Pb species injected into the flame. These characteristics are discussed along with the detection limits, and we conclude that ELFFS is a technique capable of functioning as a real-time emissions monitor for the toxic metals listed above.

Introduction

Current and proposed regulations limit the stack concentrations of many toxic and carcinogenic metals to levels on the order of 10–100 ppb [1]. Current continuous and semicontinuous monitors are generally not sensitive enough to meet the requirements imposed by regulations. Instead, samples must be analyzed using time-intensive procedures that limit the ability of operators to connect process variables to emissions and virtually eliminate the chance for real-time process control and intervention. Common practice for incineration is to complete detailed source testing with a series of trial burns during the permitting process. Following trial burns, indicators of process performance such as temperature, oxygen, and CO concentration are monitored to ensure that operation remains within the regime deemed "safe" during the trial burns.

There are several difficulties with this procedure. Indicators of combustion performance mentioned above are useful for assessing the destruction of organic waste and fuels, but not for assessing air emissions of metal species that are not destroyed in the flame. Combustion parameters, such as the cooling rate of the stack gases, affect each metal species differently. In addition, coal-fired power plants, waste incinerators, and other processes have continuously variable feedstocks. For example, an EPA study found that in typical urban refuse, the ranges of concentrations for some trace metals were barium, 35–100 ppm; chromium, 10–175 ppm; lead, 110–1300 ppm; and manganese, 50–480 ppm [2]. The variability of trace metals in coal reported in the same study was even greater. Given a changing input stream, it is clear that metal emissions from many industrial combustion devices cannot be controlled by monitoring bulk parameters alone and that there is a need for continuous monitoring methods for metals.

In this paper, we discuss the use of excimer laser fragmentation-fluorescence spectroscopy (ELFFS) as a method for real-time, in situ monitoring of many toxic metals. Metals are typically present in exhausts from high-temperature processes in the form of oxides, chlorides, or other simple molecules. Most of

these molecules are not readily detectable using fluorescence techniques. The ELFFS process is based on photofragmentation of these molecules using UV light to produce atoms in excited electronic states, which fluoresce as they relax to the ground state [3]. This technique requires only one laser and, unlike methods such as laser-induced fluorescence or resonance-enhanced multiphoton ionization, does not require tuning to wavelengths that correspond to specific molecular or metal transitions. ELFFS takes advantage of the fact that most compounds of interest have significant absorption of 193 nm light [4]. As a consequence, many metals can be detected simultaneously, using well-characterized atomic fluorescence lines throughout the UV and visible spectrum.

ELFFS is an in situ technique that works at atmospheric pressure. Laser focusing and fluorescence detection is accomplished using ordinary UV grade lenses. Because no sampling probe is necessary, problems associated with nonisokinetic sampling, probe reactions, and fouling are avoided. These attributes plus the broadband nature of ELFFS detection make it attractive for monitoring purposes.

Photofragmentation fluorescence has long been used to study kinetics and reacting systems [5–7]. Recently, the application of this technique to monitoring air emissions of sodium and potassium from coal combustors has been reported [8–10]. In our laboratory, we use ELFFS to detect CHCs, ammonia, and metals [11–16].

ELFFS should be differentiated from laser spark spectroscopy [17–19], an in situ technique that is also used to determine the metal content of particles and gasses in hot process streams. Spark spectroscopy uses a higher laser intensity to generate an optically dense plasma with temperatures on the order of 10,000 K, resulting in thermal excitation of nearly every atomic line, as well as a large broadband background signal. The major challenge in spark spectroscopy is interpretation of the signal. Quantification requires the nontrivial calculation of plasma temperatures, which may vary across the interrogation region. Interference can exist between species, as many more atomic lines are generated than are observed using ELFFS. Detection limits reported for metals are as low as 5 ppb for Hg [19] but are typically in the 100 ppb to 10 ppm range. A commercial instrument based on this technique is under development at Sandia National Laboratories [20].

The ELFFS Technique

A generalized mechanism for the ELFFS process is

$$MXY + (n)h\nu_{\text{laser}} \Rightarrow MX + Y$$

$$MX + 2h\nu_{\text{laser}} \Rightarrow M^{*} + X$$

$$M^{*} \Rightarrow M + h\nu_{\text{atom}}$$

where M is the metal atom, M^{*} is an electronically excited metal atom, MX is a diatomic fragment, and Y represents any other atoms in the original species. $h\nu_{\text{laser}}$ is the laser photon energy, and $h\nu_{\text{atom}}$ is the energy of an emitted photon from the excited atom.

The metal atom M does not absorb the laser photons directly, as atomic transitions do not match the excimer wavelength for any of the metals studied. We use an ArF excimer laser, which produces photons at a wavelength of 193 nm (51,680 cm^{-1}). This energy can be compared with the bond strength of most metal oxides and chlorides, which is in the range of 25,000–35,000 cm^{-1} [21], and the energy of observed atomic transitions, which is in the same range. While only a single 193-nm photon is required to photofragment the diatomic molecules, for all of the metals studied it takes a second photon to produce atomic fragments that can be detected by fluorescence. The multiphoton dependence of the technique suggests that ELFFS might be highly sensitive to laser intensity, but we found that all metals tested have a linear dependence on the laser pulse energy. As discussed elsewhere [14,15], the linear dependence is due either to saturation or changes in the focal region as the laser is focused.

The major competition for fluorescence is quenching, which for typical metals is roughly two orders of magnitude faster than fluorescence. However, we have shown that changes in quenching rates due to species variation in a typical combustion system should have only a minor effect on the fluorescence yield [14,15].

Experimental

A schematic of our experiment is shown in Fig. 1. The experiments are performed in the postflame region of a premixed methane-air flat flame and in the exhaust of a methane-air flow reactor. For the flat flame, we use a 3-cm-diameter Meker burner, upon which we can stabilize premixed flames over a wide range of equivalence ratios. The reactor, a 1.2-m-long, 3.25-cm-diameter stainless steel tube with a movable flame holder, allows us to vary the exit temperature by moving the flame. Flows are metered using rotometers, combined in a gas manifold, and arrive at the burner and reactor premixed.

Metals are introduced using a TSI model 9032 nebulizer, which atomizes a solution of the metal chloride(s) to be injected (0.0005–0.05 M, Aldrich, 98%+ purity). The bulk flow of the atomizer was calibrated using two methods: capture of aerosol in an impinger train followed by UV absorption measurements of the resulting ion concentration using a Hewlett Packard 8452A absorption spectrometer

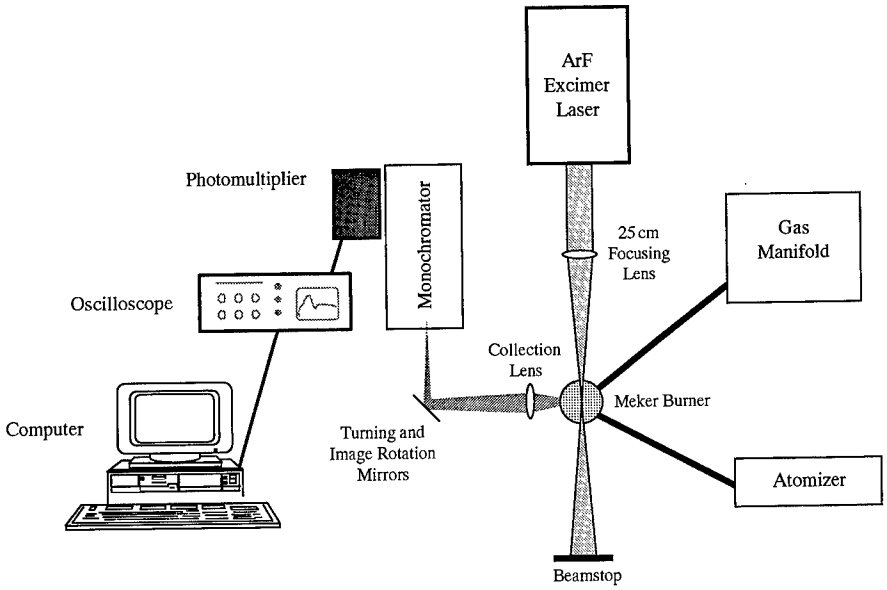

FIG. 1. Experimental apparatus.

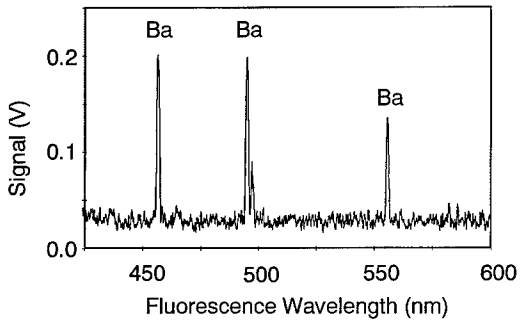

FIG. 2. Postflame single-laser ELFFS of 10-ppm $BaCl_2$ injected into the standard flat flame.

and the Mohr method for determination of chloride in solution [23]. Concentration is varied at the point of injection by changing the solution concentration of the metal salt solution.

The Lambda Physik EMG102 MSC excimer laser develops 120-mJ pulses of 193-nm light, which are focused using a 25-cm UV-grade plano-convex fused silica lens. This creates a minimum laser cross section of 2×0.5 mm and a peak intensity of 1.2×10^5 J/m^2, which, given the 20-ns pulse width of the laser, is roughly an order of magnitude less than the peak intensity needed for optical breakdown in a typical combustion device [22]. Because the photofragmentation laser is only mildly focused, the creation of a plasma is avoided, and thermal effects are negligible. Calculations based on measured laser absorption show that the maximum temperature rise in the detection region is less than 100 K.

Fluorescence is collected at right angles and imaged using a single plano-convex lens onto the entrance slit of a 0.3-m McPherson scanning monochromator. The 0.4-mm slit width used corresponds to a bandpass of 1.1 nm. A 280-nm high-pass Schott glass filter (WG-280, CVI Laser Corp.) is mounted at the monochromator entrance to help reject scattered 193-nm light from the photofragmentation laser. The light passed by the monochromator enters a Hamamatsu R928 photomultiplier tube (PMT); the generated signal is digitized using a LeCroy 9410 digital oscilloscope and sent to an IBM-compatible PC for storage and processing. For fluorescence spectra, the maximum signal from the PMT is recorded as the wavelength is varied. Because these experiments occur at atmospheric pressure, where quenching is fast, the fluorescence pulse is coincident with the laser pulse, and the maximum PMT signal corresponds well with the integrated fluorescence signal.

Results

Typically, each metal species is injected alone into the flat flame, to avoid common-ion interactions in solution. Figure 2 shows an ELFFS spectrum of barium chloride injected into a 0.8 equivalence ratio methane/air flat flame stabilized on a Meker burner (concentration of barium in postflame gases is approximately 10 ppmv). This is a single-shot spectrum

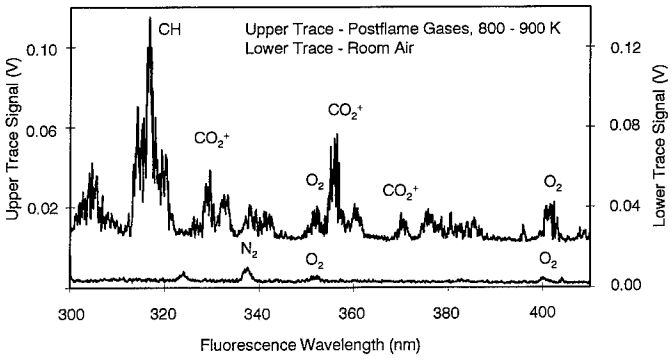

FIG. 3. Single-laser ELFFS background spectra.

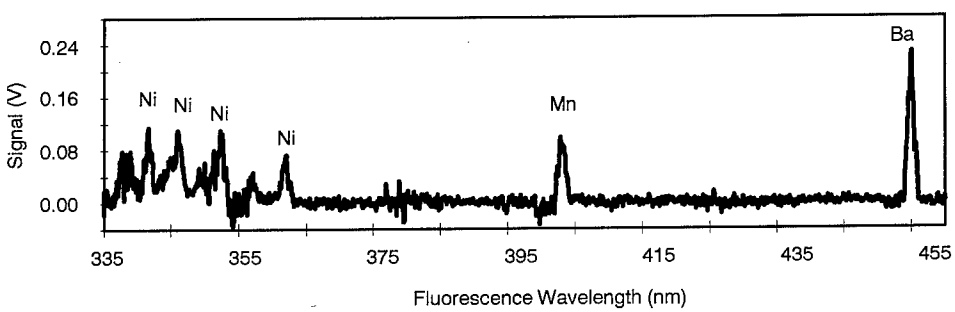

FIG. 4. Postflame single-laser ELFFS of mixture of $BaCl_2$, $NiCl_2$, and $MnCl_2$ injected at 3 ppm each into the standard flat flame.

with a resolution of 24 shots/nm, averaged over five points to reduce the noise. This corresponds to an average over 0.21 nm, smaller than the 1.1 nm bandpass of the monochromator. The measurement point is approximately 5 cm above the flame, where a type K thermocouple uncorrected for radiation indicates a temperature of 400–500 K. Strong peaks due to barium fluorescence are observed at 455.4 nm ($6p^1\ ^2P_{3/2} - 6s^1\ ^2S_{1/2}$), 493.4 nm ($6p^1\ ^2P_{1/2} - 6s^1\ ^2S_{1/2}$), and 553.6 nm ($6p^1\ ^1P_1 - 6s^2\ ^1S_0$).

No fluorescence from background species is observed at the detector gain needed to observe the peaks in Fig. 2. At higher magnification, the ELFFS signal from room air shows peaks from N_2 and O_2, while the ELFFS signal from hot postcombustion gases without metals injection reveals peaks due to CH and other combustion products and intermediates. These background features are evident in Fig. 3, which shows both an ELFFS spectrum of room air and a spectrum of hot combustion gases at approximately 16 times more magnification than the spectrum in Fig. 2. The combustion background was produced in the same flame as in Fig. 2, with deionized water injected into the flame instead of metal salt solution. Assignments of some of the peaks are shown in the figure. The O_2 peaks increase in intensity between the room air spectra and the combustion background spectrum despite the decrease in O_2 concentration, as they are due to hot-band excitation of O_2. In general, ELFFS fluorescence from background species is not a problem for metals detection.

Figure 4 shows a spectrum of a mixture of 3 ppm each of Ba, Mn, and Ni, with the combustion background subtracted. Chlorides of each metal were injected together. Several prominent peaks due to Ni are observed between 335 and 365 nm, a Mn peak is observed at 403.0 nm, as well as the Ba peak at 455.4 nm. The Ba peaks at 493.4 and 553.6 were also observed but are not shown in the figure. As with all ELFFS transitions observed in this work, the emission lines observed in Fig. 4 are allowed transitions to the ground state from low-lying excited states of the metal atoms.

Figure 5 illustrates the relationship between metal concentration and signal detected at the 357.8-nm line of chromium. The symbols in the figure represent the average signal collected over 1000 laser shots with the laser running at 20 Hz, while the line is a least-squares fit of the data. The metal concentration was varied by changing the concentration of metal in the solution injected into the flame. All of the metals tested exhibited a linear signal response to concentration over the range 100 ppb–10 ppm.

At flame temperatures, most metal species should be completely volatilized at concentrations at or be-

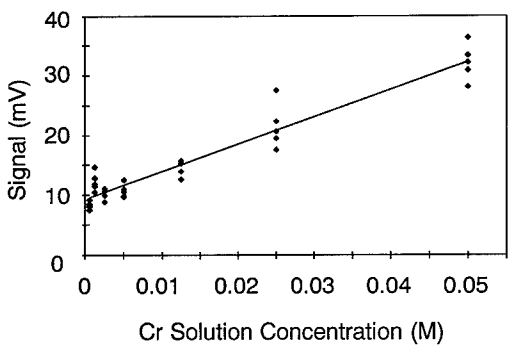

FIG. 5. Change in Cr single-laser ELFFS signal at 357.8 nm with $CrCl_3$ solution concentration.

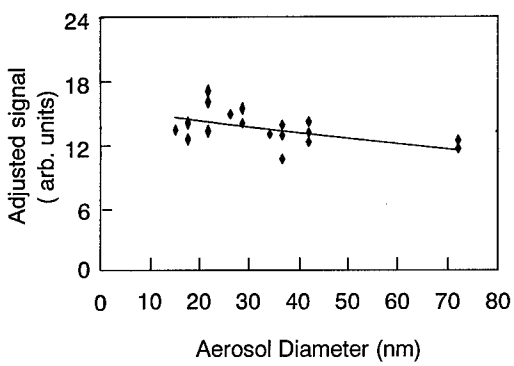

FIG. 6. Dependence of single-laser ELFFS signal on total particle surface area.

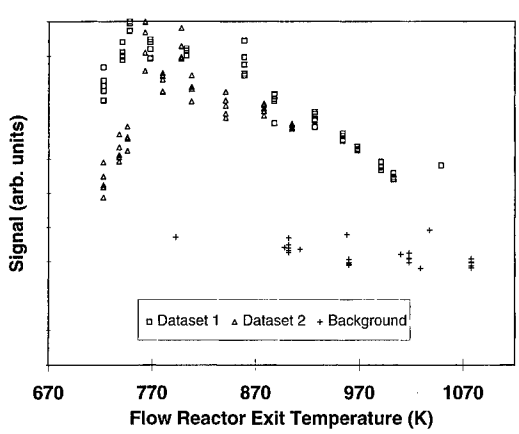

FIG. 7. Variation in the lead signal at 405.8 nm with flow reactor exit temperature.

low 1–10 ppm [24], while at room temperature, nearly every metal-containing species (with the exception of atomic mercury) is present in the solid phase. The ELFFS signal persists from flame temperatures to room temperature, indicating that the signal is obtained from a combination of gas-phase species and metal-containing aerosol. Hence, a changing aerosol size distribution might affect the ELFFS signal.

To determine the effect of aerosol size on the ELFFS signal, nonflame experiments were performed in which the concentration of the metal salt solution was varied. Changing the solution concentration of the metal salt changes the diameter of the particles produced by the nebulizer following the evaporation of water but does not change the number concentration of the particles. The quantity of metal injected is known from the solution concentration, and a characteristic diameter can be calculated for the final aerosol. The size distribution is not known, however. Figure 6 shows emission on the $^3P_1^0$–$^3P_2^0$ lead transition at 405.8 nm following lead nitrate injection, with the signal divided by the relative total surface area based on the diameter of the particles in the plume. Each data point is the average of 500 laser shots. The nearly horizontal regression line shown in the figure indicates that the ELFFS signal has a strong dependence on the aggregate surface area of particles in the plume, while normalizing the signal to the particle volume (or metal concentration) produces a dependence with a strongly negative slope. This means that at the intensity we use, the ArF laser is not vaporizing entire particles, but rather it is vaporizing some of the molecules from the surface. This contrasts with spark spectroscopy studies, which have found that particles up to 10 μm in diameter can be completely vaporized in a breakdown plasma [25]. Hence, the ELFFS signal is expected to be a function of the particle size distribution in the postflame gases.

Figure 7 shows the ELFFS signal for Pb as a function of temperature from 720 to 1080 K, obtained by monitoring emission on the $^3P_1^0$–$^3P_2^0$ transition at 405.8 nm in the postflame gases of the flow reactor. Lead nitrate was injected into the flow reactor at a concentration of 3.0 ppm, with the equivalence ratio of the methane/air flame at 0.87. Each data point is a 200-shot average obtained with the laser at 20 Hz. The data were taken in random order with respect to temperature to eliminate any systematic error. Datasets obtained on two different days show that at the highest temperatures, the signal increases as temperature decreases, peaks at approximately 750–780 K, and then decreases as the gases cool further. The lower dataset shows the ELFFS signal monitored at the same wavelength for the same flame with deionized water injected instead of metal solution.

Both datasets in Fig. 7 show an increase in the Pb

TABLE 1
Single-shot and 100-shot average detection limits for detectable metals using single-laser ELFFS

Metal	Species and Concentration	Best Line (nm)	Signal (mV)	Noise (mV)	S/N	Single-Shot Detection Limit (ppb)	100-Shot Avg. Detection Limit (ppb)
Barium	$BaCl_2$ 10 ppm	455.4	200	3	100	100	10
Chromium	$CrCl_3$ 10 ppm	357.8	30	3	10	1000	100
Lead	$PbCl_2$ 1 ppm	403.0	60	3	20	50	5
Manganese	$MnCl_2$ 10 ppm	405.8	44	3	14.7	700	70
Nickel	$NiCl_2$ 10 ppm	300.3	80	4	20	500	50
Thallium	$TiCl_3$ 4 ppm	377.5	2600	2	867	5	0.5

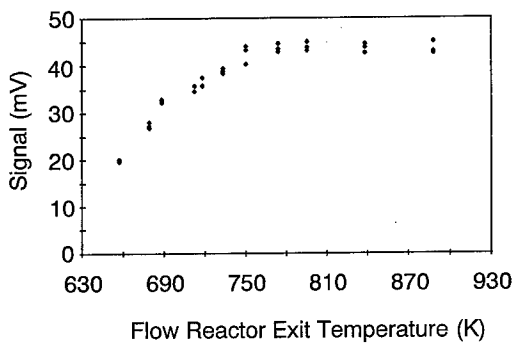

FIG. 8. Variation in the manganese signal at 403.0 nm with flow reactor exit temperature.

signal as exit temperature decreases from 1080 to 770 K. The major products for this flame at these temperatures are expected to be PbO and Pb [26,27]. The variation of vapor pressure with temperature for both of these species is very similar. Pb has a vapor pressure of 3 ppm at 962 K, while PbO has a vapor pressure of 3 ppm at 968 K [24]. The increasing signal is primarily attributed to nucleation; lower temperatures near the walls could cause some nucleation before the centerline temperature indicates sufficient supersaturation. Nucleation typically produces a high number concentration of nanometer-sized particles, with a high surface-to-volume ratio [28]. At temperatures below 770 K, the ELFFS signal begins to fall rapidly, as the aerosols mature and increase in size and the surface-to-volume ratio drops.

Each metal has a different set of properties that lead to unique aerosol characteristics, and hence, each metal is expected to have a different ELFFS dependence on temperature. These differences are illustrated by the data of Fig. 8, which shows the single-laser ELFFS signal monitored at 403.3 nm for 3.5 ppm of Mn under similar conditions as the Pb data in Fig. 7. The temperature 770 K corresponds to the saturation vapor pressure of $MnCl_2$ under these conditions; unfortunately, no data could be found for MnO. However, despite the changes in signal as the gases cool, consistent spectra were obtained for each metal tested in the cool (approximately 400 K) postflame gases where the particle size distribution is relatively constant.

A simple approach to quantifying detection limits demonstrates the sensitivity that can be achieved with this apparatus. The detection limit is defined as the concentration at which the signal-to-noise ratio equals 1. The signal at the metal peaks is compared to the estimated noise level in the surrounding spectral region to calculate a single-shot detection limit, shown in Table 1. Assuming the noise is random (e.g., shot noise), Poisson statistics apply, and averaging over N shots reduces the noise by $\sqrt{N}$. The maximum repetition rate of our lasers is 100 Hz; a 1-s averaged detection limit is also shown in Table 1.

With the exception of the thallium measurement, each detection limit measurement was made with the PMT voltage set to 700 V. The PMT voltage was set to 500 V for the thallium measurement to avoid saturation, and the signal was scaled using measured PMT amplification factors to yield a representative signal.

Because the single-laser ELFFS process has been used only in a laboratory setting, without optimization of the experiment, the detection limits in Table 1 are an upper-limit estimation. Factors such as impaction of aerosol in the burner and entrainment of room air in the plume from the burner make the metal concentration in the sample volume lower than the injected value; these losses have not been quantified. Similarly, the substitution of bandpass filters for the monochromator could substantially improve the throughput of the detection system, as could improved collection optics.

Conclusions

The experiments described in this paper show that single-laser ELFFS is a viable detection method for

many toxic metal species in postcombustion gases. Detection limits below 1 ppm have been obtained in the laboratory for Ba, Cr, Mn, Ni, Pb, and Tl without optimization of the experimental apparatus, suggesting that single-laser ELFFS could be used as an environmental monitor for these species. Spectral interferences between metal species are insignificant; various species in mixtures of metals can easily be distinguished from each other and from the combustion background. Species that cannot be detected with this method can be probed using two-laser ELFFS [15].

In some cases, the experimental parameters have a significant effect upon the fluorescence signal. Under the conditions of these experiments, the single-laser ELFFS signal for Pb is proportional to the surface area of the aerosol; hence, the signal is a function of metal concentration divided by the particle diameter. This variation makes the single-laser ELFFS signal a strong function of temperature in the region of the postflame zone where condensation and nucleation are important. Each species has different aerosol properties and is expected to exhibit a unique dependence on temperature. Spectra taken in cool postflame gases (approximately 400 K) are consistent for each metal observed.

At a given temperature, the single-laser ELFFS signal varies linearly with metal concentration. Furthermore, the technique has similar sensitivity to several Pb species. These factors make the single-laser ELFFS signal easy to interpret, and the simple optics needed ease implementation. In summary, the single-laser ELFFS technique is a promising method for monitoring many airborne toxic metals from combustion processes.

Acknowledgment

This research is supported by the National Institute of Environmental Health Sciences Superfund Basic Research Program (Grant Number P42 ESO 47050-01).

REFERENCES

1. Linak, W. P. and Wendt, J. O. L., *Prog. Energy Combust. Sci.* 19:145–185 (1993).
2. Edwards, L. O., Muela, C. A., Sawyer, R. E., Thompson, C. M., Williams, D. H., and Delleney, R. D., *Trace Metals in Combustion Systems,* U.S. EPA, 1981.
3. Rensberger Weiland, K. J., Wise, M. L., and Smith, G. P., *Appl. Opt.* 32:4066–4073 (1993).
4. Okabe, H., *Photochemistry of Small Molecules,* Wiley, New York, 1978.
5. Zare, R. N. and Herschback, D. R., *Appl. Opt. Suppl.* 2:193–200 (1965).
6. Karney, Z., Naaman, R., and Zare, R. N., *Chem. Phys. Lett.* 59:33–37 (1978).
7. Oldenborg, R. C. and Baughcum, S. L., *Anal. Chem.* 58:1430–1436 (1986).
8. Hartinger, K. T., Monkhouse, P. B., Wolfrum, J., Baumann, H., and Bonn, B., *Twenty-Fifth Symposium (International) on Combustion,* The Combustion Institute, Pittsburgh, 1994, pp. 193–199.
9. Helble, J. J., Srinivasachar, S., Boni, A. A., Charon, O., and Modestino, A., *Combust. Sci. Technol.* 81:193–205 (1992).
10. Chadwick, B. L., Domazetis, G., and Morrison, R. J. S., *Anal. Chem.* 67:710–716 (1995).
11. Lucas, D., Koshland, C. P., McEnally, C. S., and Sawyer, R. F., *Combust. Sci. Technol.* 85:271–281 (1992).
12. McEnally, C. S., Sawyer, R. F., Koshland, C. P., and Lucas, D., *Appl. Opt.* 33:3977–3984 (1994).
13. McEnally, C. S., Sawyer, R. F., Koshland, C. P., and Lucas, D., *Twenty-Fifth Symposium (International) on Combustion,* The Combustion Institute, Pittsburgh, 1994, pp. 325–331.
14. Buckley, S. G., McEnally, C. S., Sawyer, R. F., Koshland, C. P., and Lucas, D., *Combust. Sci. Technol.* 118:171 (1996).
15. Buckley, S. G., "Laser Detection of Toxic Metals in Combustion Systems," Ph.D. Thesis, University of California, Berkeley, 1995.
16. Vitovec, W. M., personal communication.
17. Radzlemski, L. J., Loree, T. R., Cremers, D. A., and Hoffman, N. M., *Anal. Chem.* 55:1246–1252 (1983).
18. Ottesen, D. K., Baxter, L. L., Radziemski, L. J., and Burrows, J. F., *Energy and Fuels* 5:304 (1991).
19. Lazzari, C., deRosa, M., Rastelli, S., and Ciucci, A., *Laser Part. Beams* 12:525–530 (1994).
20. Flower, W. L., Peng, L. W., Bonin, M. P., and French, N. B., *Fuel Proc. Technol.* 39:277–284 (1994).
21. Huber, K. P. and Herzberg, G., *Constants of Diatomic Molecules,* Van Nostrand, New York, 1979.
22. Eckbreth, A. C., *Laser Diagnostics for Combustion Temperature and Species,* Abacus, Cambridge, MA, 1988.
23. Fischer, R. B., *Quantitative Chemical Analysis,* W. B. Saunders, Philadelphia, 1961.
24. *Smithells Metals Reference Book,* Butterworth-Heinemann, Oxford, 1992.
25. Yalcin, S., Crosley, D. R., Smith, G. P., and Faris, G. W., in *The Fourth International Congress on Toxic Combustion Byproducts* (C. P. Koshland, Ed.), Gordon and Breach, Berkeley, CA, 1995.
26. Lin, W. Y., Sethi, V., and Biswas, P., *Aerosol Sci. Technol.* 17:119–133 (1992).
27. Eddings, E. G. and Lighty, J. S., *Combust. Sci. Technol.* 85:375–390 (1992).
28. Friedlander, S. K., *Smoke, Dust, and Haze,* Wiley, New York, 1977.

Twenty-Sixth Symposium (International) on Combustion/The Combustion Institute, 1996/pp. 2463–2470

EFFECTS OF EXTERNAL ACOUSTIC EXCITATION ON ENHANCED TRANSPORT IN A RESONANT INCINERATOR

G. PONT, J. W. WILLIS, A. R. KARAGOZIAN AND O. I. SMITH
Department of Mechanical and Aerospace Engineering
University of California
Los Angeles, CA 90095-1597, USA

The research described here focuses on the enhancement of energy transport and waste surrogate destruction in an acoustically resonant dump combustor. While prior studies focused on flow field interrogation and the nature of waste destruction under conditions of natural acoustic excitation, the present study focuses on the device's behavior under externally forced acoustical conditions. External forcing was accomplished here using a loudspeaker situated in the plenum section of the device, allowing strong excitation of acoustic resonances. The effect of this external forcing on waste destruction in the device was found to be significant. Results show that, for specific forcing frequencies (coincident with the system natural modes), marked improvement in destruction and removal efficiencies (DREs) of the waste surrogate SF_6, by four orders of magnitude and perhaps higher, could be achieved. When the device was forced at frequencies other than natural modes, little improvement over the nonforced combustor performance was achieved. External forcing at very high frequency natural modes yielded some improvement in waste destruction, but to a lesser extent than at lower frequency natural modes. OH^* chemiluminescence images indicated that the enhancement of waste destruction at certain natural modes coincided with flame shortening and broadening, likely arising due to vortex shedding during the acoustical excitation. This alteration in flame structure during excitation of specific natural modes appeared to materially enhance energy transport to the regions in which waste was injected, as evidenced by reduced flame liftoff under such conditions. These observations suggest that acoustically resonant combustor conditions can render this device extremely efficient as well as highly controllable.

Introduction

The dump combustor is a device that has been studied extensively over the past half century because of its ability to burn fuel and contain heat in a relatively compact configuration. Acoustically driven combustion instabilities are known to occur in such devices when pressure oscillations and periodic heat release associated with the combustion are in phase [1]. Transverse acoustic modes are associated with periodic, transversely alternating vortices shed coincident with flame structures, the so-called screech phenomenon [2]. Longitudinal acoustic modes are also associated with vortex shedding in such combustors; a number of research groups over the years have sought to control such combustion instabilities through the use of externally applied acoustical forcing [3–6]. Acoustically excited combustion processes have also been studied in pulse combustor systems [7–10]. Local extinction by flame stretch is observed to delay ignition; later relaxation of strain allows thermal ignition to take place in a volumetric fashion, significantly increasing heat and mass transfer rates. Numerical simulations of acoustically resonant combustion systems [10–12] have indicated the importance of periodic vortex shedding in sustaining the acoustical excitation [1,13].

Over the past few years, our research has focused on the development and investigation of a small-scale, two-dimensional dump combustor (or "resonant incinerator") which has been found to be capable of destroying hazardous waste surrogates to a high degree [14–19]. The acoustic character of the incinerator is found to be correlated with classical combustion instabilities according to the Rayleigh criterion [1,13] in which energy input occurs nearly in phase with pressure oscillations to sustain the acoustic resonance. The degree of waste surrogate destruction in the device has been found to correlate somewhat with naturally occurring acoustic conditions [15,17,19]. Destruction and removal efficiencies (DREs) for the gaseous waste surrogate sulfur hexafluoride (SF_6) are observed to be as high as 99.999999% ("8 nines") under quiet conditions and occasionally under acoustically resonant conditions [19]. This is four orders of magnitude above the EPA requirement of 99.99% DRE for hazardous waste incinerators [20]. Liquid waste surrogate (acetonitrile) destruction in the device, in contrast, is not only found to be less dependent on the acoustic character of the device, but is actually found to

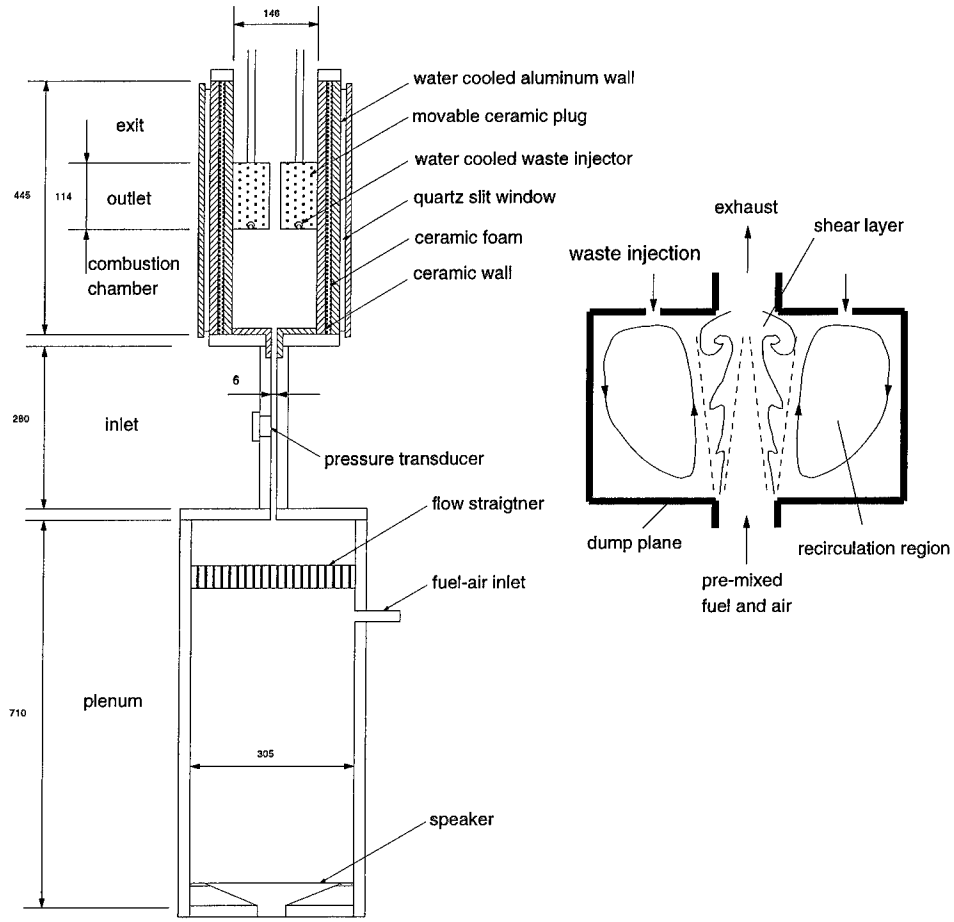

FIG. 1. Schematic of the dump combustor, including features of the combustion chamber cavity. Dimensions are given in millimeters.

dampen preexisting natural acoustic modes due to the heat removal process associated with vaporization [19]. Nevertheless, DREs for acetonitrile can be quite high (greater than 6 nines, the detection limit of the diagnostic equipment) if sufficient excess oxygen is available for combustion of the waste surrogate.

The present experiments focus on the ability of the resonant incinerator to destroy waste surrogates under externally forced (not naturally occurring) acoustical conditions. Based on prior results, it may be desirable to excite acoustical modes in the device in order to improve waste destruction without having to alter the equivalence ratio, cavity length, flow velocity, or other parameters necessary to excite natural modes. The present work also seeks to understand the advantages of exciting certain acoustic modes over others with respect to waste destruction and energy transport, using chemiluminescence imaging of the reaction zone. This study opens the possibility of active rather than passive control of the resonant incinerator, that is, actively forcing the combustor at a frequency that optimizes waste destruction.

Experimental Apparatus and Procedure

The two-dimensional dump combustor used in the present experiments is shown schematically in Fig. 1, with an expanded view of flow/reaction processes in the combustion cavity. The combustor's basic features have been described previously, and will only be summarized here. The reader is referred to Refs. 17 and 19 for additional details.

Propane and air at room temperature were introduced into the plenum section of the combustor, then were mixed and accelerated through an inlet

section before entering the combustion cavity at a sudden expansion or "dump plane." Premixed flames could be stabilized due to the formation of high temperature recirculation regions downstream of the dump plane [21], but as noted above, vortex shedding coincident with the flames could occur under conditions of natural acoustic excitation [14–19]. The spanwise depth of the inlet, combustion cavity, outlet, and exit sections (30.5 cm) were usually sufficient to produce a visually two-dimensional flame over the entire span, although under certain experimental conditions the flow in the cavity became turbulent and the flame/flow structures became three-dimensional. The inlet width in the present configuration was the same as that in Ref. 19 (0.6 cm), as compared with 2.0 cm in the device described in Ref. 17. This narrowing of the inlet allowed high-frequency acoustic modes to be naturally excited with greater ease. Quartz windows bounded each end of the system in the spanwise direction, allowing appropriate optical access; additional quartz window slits were installed in the side walls to allow the introduction of a sheet of laser light for optical diagnostics [16].

A set of movable ceramic plugs defined the outlet section of this combustor. Waste surrogate was introduced through injectors embedded in these plugs as indicated in Fig. 1. Injection into the recirculation zones allowed wastes to be trapped for relatively long residence times under high-temperature conditions so that they could be destroyed more efficiently. Water-cooled stainless steel injectors were used to introduce gaseous waste surrogates into the cavity [15,17]; there were forty 0.3-mm-diameter holes in the spanwise direction along each injector.

Acoustic data were taken using pressure transducers located in the plenum and inlet. In recent studies of the present combustor [19], a low-frequency "chugging" mode (at approximately 50 Hz) typically occurred at low equivalence ratios and longer combustion cavity lengths; this acoustic mode tended to create large vortex structures at the dump plane which expanded periodically to disturb the recirculation zones, hence waste destruction under these conditions was poor [17,19]. Other low-frequency oscillations ($\approx$150 Hz) tended to be excited under rich-burning and long cavity conditions. High frequency natural modes ($\approx$500–600 Hz) dominated at shorter cavity lengths and equivalence ratios close to unity; these conditions could yield excellent waste destruction [19]. Another characteristic acoustic mode, near 290 Hz (close to the 250-Hz hydrodynamic instability mode under these conditions), appeared to be sensitive to plenum conditions only. These high-frequency modes all depended on the presence of a standing wave in the system and were observed from shadowgraph images to correspond to flame wrinkling and small-scale periodic vortex shedding from the dump plane. An acoustically "quiet" mode in which flames and recirculation cells were stabilized and no significant acoustic output was detected occurred for a variety of cavity lengths and equivalence ratios, and also was found to produce excellent conditions for waste destruction [15,17,19].

To continue to evaluate the performance of this dump combustor as an incinerator, the waste surrogate SF_6 was injected in the present study in the gaseous phase with additional nitrogen. SF_6 is an extremely refractory compound, which shows no degradation at temperatures below 1000°C [22]. It has been ranked as one of the twenty RCRA Appendix VIII compounds that are most difficult to destroy. Thus, SF_6 is a good surrogate for studying waste destruction processes that may be susceptible to thermal bypassing. Detection of waste destruction in the present device was made using a gas chromatograph equipped with an electron capture detector for SF_6 measurements sensitive to $\leq$1 ppb, yielding a detection limit for SF_6 of nearly 8 nines.

External acoustical forcing was accomplished in the present experiment using a loudspeaker situated at the bottom of the plenum section of the device. Using a signal generator, it was possible to produce a sine wave of varying frequency, then to amplify the signal and pass it to the speaker. This enabled a sweep through a range of input forcing frequencies from 0 to 1000 Hz to be performed, with forcing amplitude variation up to 150 dB, although frequencies below 200 Hz were difficult to attain consistently with the present speaker. Thus, it became possible to force the loudspeaker at frequencies corresponding to the natural modes of the device as well as other frequences, and to determine the effects of this forcing on DREs.

It was of interest to determine differences in flame characteristics within the combustor under different acoustical forcing conditions. The technique of OH^* chemiluminescence was used here in order to image the reaction zone in a time-dependent manner. OH^* chemiluminescence is thought [23] to result from the radiative decay of electronically excited radicals produced within the reaction zone by the reaction

$$CH + O_2 \rightarrow CO + OH^*$$

The chemiluminescence image thus depicts the heart of the reaction zone, the only region with significant concentrations of CH. Persistence of species is not a problem here (as compared with OH planar laser-induced fluorescence imaging) because CH is destroyed by rapid bimolecular reactions, not the much slower termolecular processes that dominate OH removal in the postflame region. Therefore, one may expect to obtain a well-defined image of the flame zone, both spatially and temporally. For most conditions explored here, the two-dimensional nature of the flow structures rendered OH^*

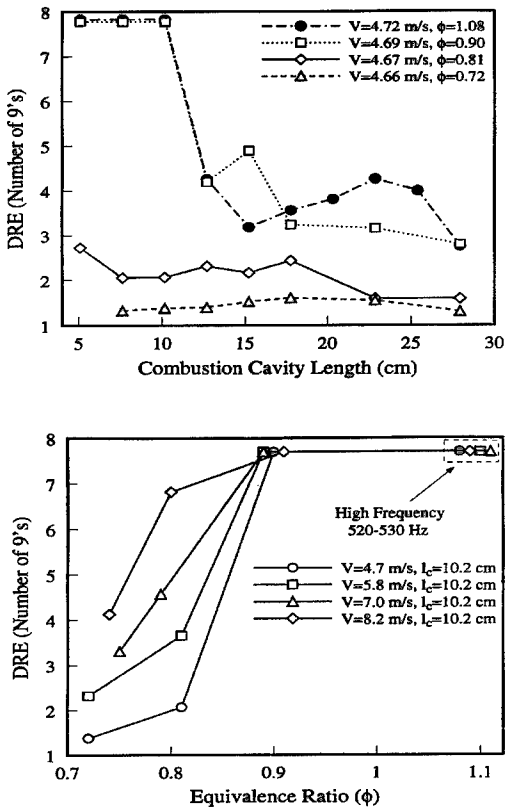

FIG. 2. (a) Destruction and removal efficiencies (DREs) of SF_6 in the resonant incinerator as a function of combustor cavity length for inlet velocities $V \approx 4.7$ m/s and for various equivalence ratios. Acoustic resonance occurs only at the highest equivalence ratio ($\phi = 1.08$) for cavity lengths below 11 cm. (b) Destruction and removal efficiencies (DREs) of SF_6 in the resonant incinerator as a function of equivalence ratio for a cavity length $l_c = 10.2$ cm and various inlet velocities. Acoustic resonances occur at the equivalence ratios above 1.

chemiluminescence images reasonably clear depictions of 2-D flame oscillations.

The OH* chemiluminescence measurements were made with a subset of the equipment used for PLIF imaging, described in Refs. 16 and 19. An intensified CCD camera was synchronized to the pressure oscillations detected in the inlet to be able to capture variations in OH* chemiluminescence within the combustion cavity over a period of oscillation. The integration time of the image intensifier was 250 μs, long enough to provide adequate signal-to-noise, but short with respect to the period of even the highest frequency modes observed. A bandpass filter centered around 312 nm was used in an attempt to isolate fluorescence from the $X^2\,\Pi(v = 0) \leftarrow A^2\Sigma(v = 0)$ states of OH.

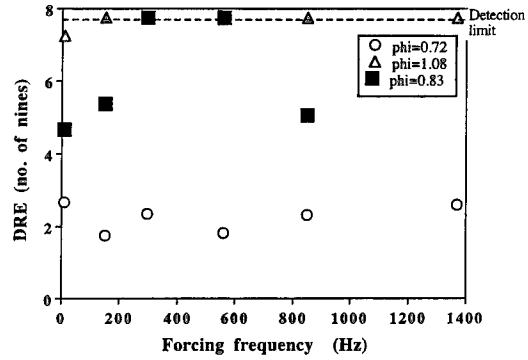

FIG. 3. Destruction and removal efficiencies (DREs) of SF_6 in the resonant incinerator during externally forced acoustical excitation for equivalence ratios of 0.72 (circles), 0.83 (filled squares), and 1.08 (triangles). For no external forcing (zero frequency), the only naturally resonant condition is for $\phi = 1.08$.

Results and Discussion

Recent results for the destruction of SF_6 in the resonant incinerator *without* external forcing are shown in Fig. 2a,b. DREs, given in numbers of nines, varied with the length of the combustion cavity (Fig. 2a) and with the equivalence ratio ϕ of the core flow (Fig. 2b). SF_6 destruction or pyrolysis, and hence the stability and local temperature of the recirculation regions, became quite high, increasing by four or more orders of magnitude, as the length of the combustor cavity was reduced or the equivalence ratio was increased. It is important to note that in Fig. 2a the combustor was not operating in an acoustically excited mode except when $\phi = 1.08$ at short cavity lengths, while in Fig. 2b the combustor operated in an acoustically resonant high frequency mode when ϕ was near unity. As seen before [19], very high DREs, nearly to 8 nines (the detection limit of the GC), were attained under quiet or certain acoustically resonant conditions that were made to occur naturally.

External acoustical forcing was applied via the loudspeaker in the plenum to produce oscillations at natural as well as other frequencies. Figure 3 shows the effects of forcing at various frequencies on DREs for the combustor, for several different operating conditions. For lower equivalence ratio conditions which produced poor DREs when the combustor was naturally quiet ($\phi = 0.72$, the circles), external forcing did little to significantly increase DREs. Under certain naturally resonant conditions that produced high DREs without external forcing ($\phi = 1.08$, the triangles), forcing from the loudspeaker did relatively little to improve the destruction, although the DREs measured (exceeding 8 nines) were at the detection limit of the GC and actually could be much higher than shown with external forcing. When

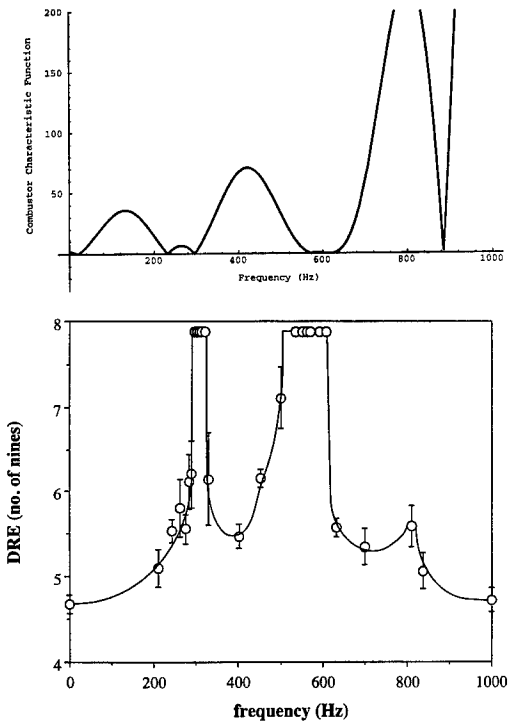

FIG. 4. The lower plot shows destruction and removal efficiencies (DREs) of SF_6 in the resonant incinerator during externally forced acoustical excitation for the case where equivalence ratio $\phi = 0.83$. Comparison is made with characteristic function of the system (shown in the upper plot), computed from the 1-D model described in Refs. 14, 18; system zeroes correspond to natural modes.

external forcing was applied under conditions associated with an intermediate ϕ and no natural excitation ($\phi = 0.83$, the filled squares), it was seen that certain forcing frequencies significantly increased DREs, by four orders of magnitude or more, compared with conditions without external forcing. DREs were also found to increase monotonically with forcing amplitude at these optimal frequencies. It is of interest to understand precisely *why* such a profound increase in waste destruction can occur at these specific frequencies, that is, to understand what material changes occur in the reaction processes to cause such an augmentation.

This question was answered in part by examining in greater detail the changes in DREs with frequency for the $\phi = 0.83$ case; this is shown in the lower part of Fig. 4. Clearly, at specific frequencies (roughly $\Omega \approx 300$ Hz, 500–600 Hz, 800 Hz), significant augmentation in incinerator performance could be achieved, while between these modes, performance returned nearly to the unforced behavior. The forcing frequencies that caused this augmentation were close to the natural acoustic modes that, theoretically, could occur under the given operating conditions. This is demonstrated in the upper portion of Fig. 4 in the plot of the characteristic function of the system as a function of frequency, computed from a one-dimensional acoustic model as described in Refs. 14 and 18. The model represents the various elements of the incinerator (plenum, inlet, cavity, etc.) as separate components of an acoustical system, and represents the oscillatory heat release initiated by vortex shedding in the combustion cavity as a sinusoidal volume source. The zeroes of the acoustical system's characteristic function in general correspond to system resonant modes or eigenvalues. It is clear from this comparison, however, that certain natural modes ($\Omega \approx 295$ Hz, 560 Hz) were superior to others ($\Omega \approx 830$ Hz) in terms of their effect on combustor performance. It is interesting to note that there were actually two natural modes that occurred between 500 and 600 Hz; these apparently caused the very broad peak in the DREs in this frequency range. If the detection limit of our GC were higher than 8 nines, it is likely that two peaks in DREs would be observed in this range.

OH^* chemiluminescence images, which indicate the oscillatory behavior of the flame/reaction zone, supplied further information with respect to the advantages of forcing at specific frequencies. Fig. 5 shows the differences in OH^* chemiluminescence in the combustion cavity for a number of different cases explored, with consistently normalized chemiluminescence intensities. Figure 5a shows a temporally averaged OH^* chemiluminescence image for the case without external forcing, while Fig. 5b–e shows instantaneous chemiluminescence images for the cases with external forcing at increasing frequencies for similar positions within the acoustic cycle. The flame structure in the absence of acoustical excitation (Fig. 5a) appeared elongated and was stabilized fairly closely to the dump plane, yet it appeared much more diffuse and in fact more three-dimensional (visually) than the acoustically resonant flames. External forcing at the natural frequencies producing high DREs ($\Omega = 295$ Hz and 560 Hz) showed flame structures that were significantly more compact and visibly more two-dimensional (Fig. 5b and d, respectively), with some degree of lifting at the dump plane. These flames appeared to be more coherent compared with those in the unforced case; some flame broadening was observed, likely due to the deformation of the flames by small-scale vortices, as evidenced in OH PLIF images [16]. External forcing at a nonnatural frequency ($\Omega = 430$ Hz, Fig. 5c) produced flame structures that appeared thinner than those forced at natural modes; these in fact were visually more similar to the unforced case (Fig. 5a), although the flame was much more lifted in the OH^* images and periodically jumped to very high positions within the cavity. Excitation at a high-frequency natural mode ($\Omega = 830$ Hz, Fig. 5e)

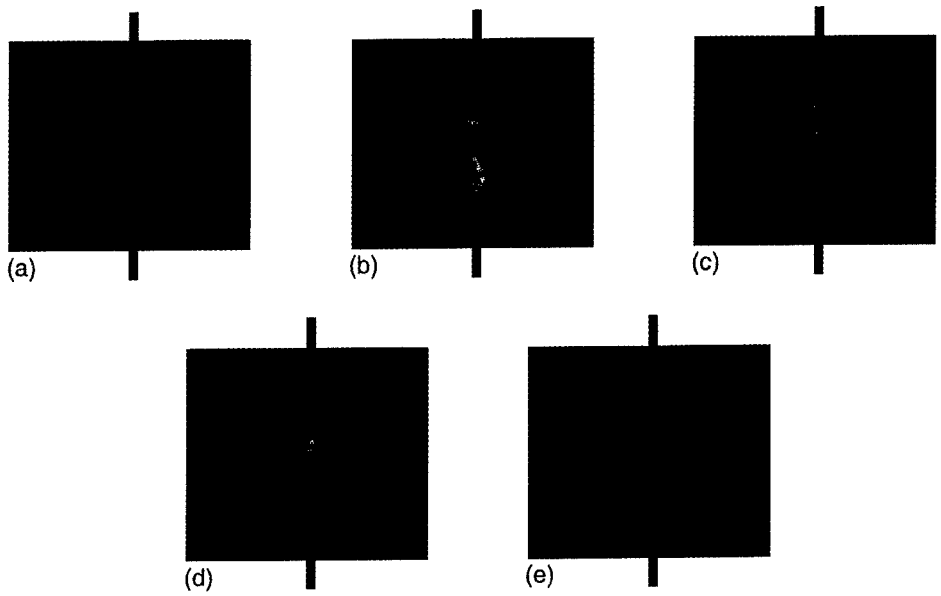

FIG. 5. OH* chemiluminescence images of the combustion cavity for an equivalence ratio $\phi = 0.83$. Highest chemiluminescence intensity is indicated by red; lowest by blue. Cases shown are for conditions of (a) no external forcing, (b) external forcing at 295 Hz (a natural mode), (c) external forcing at 430 Hz, (d) external forcing at 560 Hz (a natural mode), and (e) external forcing at 830 Hz (a natural mode).

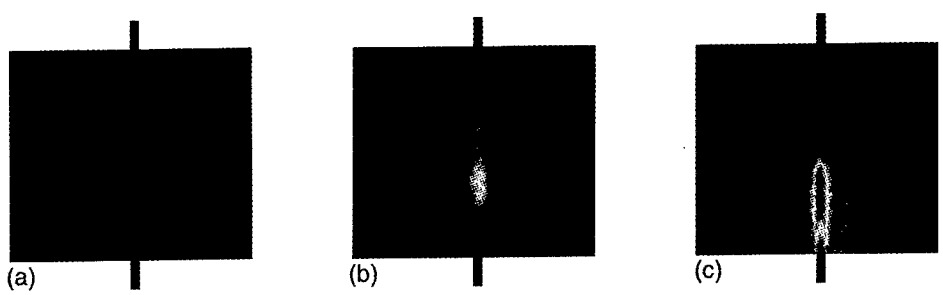

FIG. 6. OH* chemiluminescence images of the combustion cavity for external forcing at 295 Hz. Highest chemiluminescence intensity is indicated by red; lowest by blue. Cases shown are for equivalence ratios (a) $\phi = 0.72$, (b) $\phi = 0.92$, and (c) $\phi = 1.08$.

similarly produced a thinner and much more highly lifted flame structure than seen in Fig. 5b or d.

It was first recognized by Marble and Adamson [24] that the flame liftoff distance from a bluff-body flameholder increases with decreasing recirculation zone temperature. The present observations of liftoff suggest that the temperatures within the recirculation zones for the cases in Fig. 5c,e could be much lower than in Fig. 5b,d. These temperature differences could explain the enhancement of SF_6 destruction in the latter two cases where high temperatures are required for acceptable waste destruction rates. The increased recirculation zone temperatures under optimal acoustic excitation were also suggested by recent temperature field measurements in the resonant incinerator [26]. The lessened broadening of the flame in Fig. 5e as compared with the other natural modes (Fig. 5b,d) also indicated that the flame had trouble keeping up with oscillations that occur at such a high frequency, as suggested by Egolfopoulos [25].

If there was not sufficient chemical energy input to the system during the reaction process, acoustic excitation, even at naturally resonant frequencies, did not materially affect combustor performance, as indicated by the $\phi = 0.72$ case in Fig. 3. These differences in global energy input were borne out inthe OH* chemiluminescence images shown in

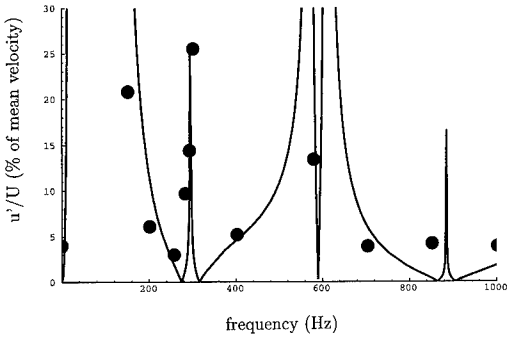

FIG. 7. The symbols represent hot-wire measurements of velocity fluctuations at the dump plane for cold flow conditions as a function of forcing frequency; comparison is made with 1-D model predictions of velocity perturbations at the dump plane [14,18] under cold conditions.

Fig. 6a–c, for fixed external forcing at 295 Hz (at or near a natural resonance) with increasing values of ϕ. As equivalence ratio was successively increased in Fig. 6a–c (see also Figure 5b, the case where $\phi = 0.83$), the flame became less and less lifted. The case where $\phi = 1.08$ (Fig. 6c) appeared to have the most coherent 2-D flame structure, the highest relative concentration of OH^* in the flame zone, and likely had the most efficient energy transport to the recirculation zones, although the detection limit of the GC restricted the extent to which this transport could be completely quantified. The moderate equivalence ratio cases, however ($\phi = 0.83$ and $\phi = 0.92$ in Figs. 5b and 6b, respectively), appeared to have enough enhancement of energy transport from the flame zone due to acoustic excitation to produce the same high DREs. From the point of view of combustor performance, then, acoustic excitation could perform a similar function to increasing equivalence ratio by providing a greater rate of energy transport to optimal locations.

The nature of flame liftoff may be studied further by measuring velocity fluctuations at the dump plane using a hot-wire anemometer under different acoustic forcing conditions for cold flow conditions. The experimental results are shown as the symbols in Fig. 7. Calculations of the velocity perturbation at the dump plane are also shown in the figure; these were made using a one-dimensional model with volumetric forcing downstream of the dump plane to represent energy addition via forcing [18]. Scaling between experimental and theoretical results was achieved by matching the velocity fluctuations at a single frequency (295 Hz). The experimental peaks in velocity fluctuations at the dump plane occurred at the natural frequencies that produced the peaks in DREs; forcing off-resonance or at a very high frequency mode (≈830 Hz) yielded relatively small velocity perturbations. The model showed similar behavior, consistent with the presence of a standing wave in the system under resonant conditions. These observations suggest that high-amplitude velocity fluctuations were associated with the flame instability that broadens the flame zone while enhancing energy transport to and temperatures within the recirculating regions.

Concluding Remarks

This study demonstrates that externally forced as well as naturally occurring acoustical oscillations can have a dramatic effect on the present combustor when operating as an incinerator. DREs for a temperature-sensitive waste surrogate (SF_6) were found to increase by four orders of magnitude (perhaps more) when acoustical forcing was imposed at system characteristic frequencies, as long as there was enough global energy available in the chemical reaction, that is, a high enough equivalence ratio for the reaction. With external forcing at natural modes of the system, flame structures were made more compact and broadened, likely due to vortex shedding which materially enhanced the transport of energy to the recirculation zones where waste destruction occurred. Flame liftoff characteristics as evidenced by OH^* chemiluminescence images were consistent with higher recirculation zone temperatures during external forcing at desirable natural modes. Forcing at natural modes appeared also to significantly increase velocity fluctuations at the dump plane for the geometry studied.

While the present studies reinforce the desirability of acoustically resonant combustion for enhanced energy transport [8,9], there is new evidence here for the desirability of *specific* natural acoustic mode excitation over other modes. Acoustic excitation at specific natural modes can be viewed as performing a similar function to increasing equivalence ratio by providing a greater rate of energy transport to optimal locations into which waste is injected. This can have important implications for practical use of this device in that one can achieve excellent incinerator performance even with reduced flow rates of auxiliary (core) fuel, as long as appropriate acoustic excitation is maintained.

The study also suggests the possibility of actively controlling the behavior of a resonant combustor for incineration applications; this could be particularly useful in ensuring recovery from incinerator upset conditions, for example, that could occur due to sudden changes in waste characteristics. It is hoped that future studies in this device will explore in more detail the ability of the external forcing to actively control waste destruction.

Acknowledgments

This work has been sponsored by the National Science Foundation under Grant CTS 90-21021 and by the Office

of Naval Research under Grant N00014-93-1-1383, with Dr. Klaus Schadow of the Naval Air Warfare Center (China Lake) as grant monitor.

REFERENCES

1. Rayleigh, Lord, The Theory of Sound, Vol II, Dover Publications, New York, 1945, p. 227.
2. Rogers, D. E. and Marble, F. E., *Jet Propulsion* 26:456–462 (1956).
3. Yu, K., Trouve, A. and Candel, S., AIAA Paper No. 91-0367, 1991.
4. Schadow, K., Gutmark, E., and Wilson, K. J., AIAA Paper No. 90-2447, 1990.
5. McManus, K. R., Vandsburger, U., and Bowman, C. T., *Combust. Flame* 82:75–92 (1990).
6. McManus, K. R., Poinsot, T., and Candel, S. M., *Prog. Energy Combust. Sci.* 19:1–12 (1993).
7. Stewart, C. R., Lemieux, P. M., and Zinn, B. T., *Combust. Sci. Technol.* 94:427–446 (1993).
8. Bai, T., Cheng, X. C., Daniel, B. R., Jagoda, J. I., and Zinn, B. T., *Combust. Sci. Technol.* 94:245–258 (1993).
9. Keller, J. O., Barr, P. K., and Gemmen, R. S., *Combust. Flame* 99:29–42 (1994).
10. Barr, P. K. and Keller, J. O., *Combust. Flame* 99:43–52 (1994).
11. Kailasanath, K., Gardner, J., Boris, J., and Oran, E., AIAA Paper No. 87-1065 (1987).
12. Najm, H. N. and Ghoniem, A. F., *Combust. Sci. Technol.* 94:259–278 (1993).
13. Putnam, A. A., *Combustion-Driven Oscillations in Industry,* American Elsevier, New York, 1971.
14. Logan, P., Lee, J. W., Lee, L. M., Karagozian, A. R., and Smith, O. I., *Combust. Flame* 84:93–109 (1991).
15. Smith, O. I., Marchant, R., Willis, J., Lee, L. M., Logan, P., and Karagozian, A. R., *Combust. Sci. Technol.* 74:199–210 (1990).
16. Cadou, C., Logan, P., Karagozian, A., Marchant, R., and Smith, O., *Environ. Sensing Combust. Diagn. SPIE Proc. Ser.* 1434:67–77 (1991).
17. Marchant, R., Hepler, W., Smith, O. I., Willis, J., Cadou, C., Logan, P., and Karagozian, A. R., *Combust. Sci. Technol.* 82:1–12 (1992).
18. Willis, J. W., Lee, L. -M., Karagozian, A. R., and Smith, O. I., *Combust. Sci. Technol.* 94:469–481 (1993).
19. Willis, J. W., Cadou, C., Mitchell, M., Karagozian, A. R., and Smith, O. I., *Combust. Flame* 99:280–287 (1994).
20. Oppelt, T., *J. Air Pollut. Control Assoc.* 37:558 (1987).
21. Zukoski, E. E. and Marble, F. E., *Proceedings of the Gas Dynamics Symposium on Aerothermochemistry,* Northwestern University Press, Evanston, IL, 1956, pp. 205–210.
22. Proctor, C. L., Berger, M. C., Fournier, J. R., and Roychoudhury, S., *Sulfur Hexafluoride as a Tracer for the Verification of Waste Destruction Levels in an Incinerator,* Report ESL-TR-86-47, Air Force Engineering and Services Laboratory, Tyndall AFB, 1987.
23. Gaydon, A. G., *The Spectroscopy of Flames,* 2nd Ed., John Wiley & Sons, New York, 1974, p. 287.
24. Marble, F. E. and Adamson, T. C., *Jet Propulsion* 24:85 (1954).
25. Egolfopoulos, F. N., *Twenty-Fifth Symposium (International) on Combustion,* The Combustion Institute, Pittsburgh, 1994, pp. 1381–1402.
26. Cadou, C. P., Karagozian, A. R., and Smith, O. I., *Bull. Am. Phys. Soc.* 40:2002 (1995).

COMMENTS

Bo Leckner, Chalmers University of Technology, Sweden. You have presented results from a research reactor of small size. Can you scale up your results to a unit of larger size?

Author's Reply. We have pointed out previously [14–19] that the most logical application of the technology described here is for incineration on the site of small waste generators. We actually have investigated reactors of two sizes. The results reported here were obtained in a device four times larger than that used in our original investigations [14–15]. Although the firing rates reported here are all around 30 kW due to the capacity of the laboratory compressed air supply, experiments with the smaller device suggest that firing rates in excess of 80 kW should be achievable. For a typical organic waste with high heating value (e.g., benzene), this corresponds to a feed rate of approximately 2 gal/hr. Thus, in terms of firing rate, a large degree of scale-up may not be necessary for some applications.

The principal difficulty with simply enlarging the device geometrically is that it becomes increasingly difficult to prevent bifurcation of the recirculation cell within the cavity, especially at high waste injection rates. Where difficult-to-destroy, low heating value wastes are concerned (SF_6 being an extreme example), it is highly desirable to maximize the residence time by stabilizing a single, large recirculation cell. At the present scale, this limits the cavity aspect ratio to no more than two and the waste mass flowrate to less than 10% of the core mass flowrate. Here our present two-dimensional device would best be scaled up by increasing the spanwise dimension, e.g. the depth.

In other applications involving readily burnable wastes, adequate mixing between the fuel-lean core flow and the rich recirculation region is more important than residence time distribution. Here the DRE is optimized at aspect ratios above two, where the interfacial area between the two regions is larger, and we find that the capacity at fixed DRE can be increased simply by increasing the aspect ratio.

Twenty-Sixth Symposium (International) on Combustion/The Combustion Institute, 1996/pp. 2471–2477

COMPACT INCINERATOR AFTERBURNER CONCEPT BASED ON VORTEX COMBUSTION

T. P. PARR, E. GUTMARK, K. WILSON, D. M. HANSON-PARR, K. YU, R. A. SMITH AND K. C. SCHADOW
Research and Technology Department, Code 474320D
Naval Air Warfare Center Weapons Division
China Lake, CA 93555-6001, USA

A design concept for a compact incinerator afterburner based on actively controlled vortex combustion was developed and tested at ~5 kW and ~50 kW. Acoustic control of fluid dynamics was used to enhance mixing and increase the DRE (destruction and removal efficiency) for a waste surrogate. A detail study of the concept of utilizing vortex combustion for incineration was undertaken in a small-scale flame using advanced laser diagnostics to elucidate and optimize the fluid dynamic mechanisms. The system was then scaled up by ~10, optimized, and evaluated for performance.

The open loop active control methodology is based on the concept of combustion in periodic axisymmetric vortices. Acoustic excitation was used both to stabilize coherent vortices in the central jet air flow and to control circumferential gaseous fuel and waste injection into the shear layer at the right time during vortex formation.

The gaseous-fueled actively controlled 4.5 kW incinerator was able to surpass 99.997% DRE even when the gaseous benzene waste surrogate constituted 66% of the total combustible content and the combustible to total air ratio (Φ) was 0.974; lowering Φ below this increased the DRE to beyond our detection limit. The DRE for gaseous benzene exceeded 99.999% in the 50-kW system when combustible to air ratios were kept below 0.78. Parameters found critical to maintenance of high DRE at both energy scales were the fraction of circumferentially entrained air, the entrainment geometry, the forcing levels, and the phase angle of fuel injection with respect to the vortex roll-up.

The 50-kW combustor was also evaluated for stack emissions and combustion efficiency. The controller improved combustion efficiency and lowered emissions: CO dropped from 2900 ppm to as low as 2 ppm. Unburned hydrocarbons were also reduced. Under some conditions the controller also reduced NO_x levels down to as low as 12 ppm.

Introduction

The interaction between turbulent mixing and combustion is important in many applications such as airbreathing propulsion systems, energy conversion, incinerators, and other chemical reactors and industrial processes. Studies of turbulent mixing established the role of organized, coherent, large-scale vortical structures in the mass and momentum transfer across shear layers between two fluids in motion [1–3]. Manipulating these structures alters the mixing process. Active control methods have enhanced the spreading rate of the shear layer by mechanical or acoustic excitation of the initial shear layer, and thus accelerated the mixing between the two streams [4,5].

The understanding of the mechanisms governing turbulent mixing and their control was extended to turbulent combustion. New, laser-based diagnostic techniques [6] with high temporal and spatial resolution, which yield species-specific two- and three-dimensional maps of the combustion region, accelerated the process; the important role of controlling the large- and small-scale mixing on the combustion process was determined [7]. Numerous studies on the application of active control to suppress combustion instabilities were reviewed recently by Candel [8] and McManus et al. [9]. Active control by shear layer excitation was applied to enhance energy release [10–13] and to mitigate the production of pollutants [14]. Fluid dynamic control has also been applied to hazardous waste incineration [15,16].

At the Naval Air Warfare Center the work on active combustion control included open and closed loop control of small-scale (~10 kW) and large-scale (~1 MW) combustors to enhance their performance by increasing energy release, extending flammability limits, and stabilizing combustion [17]. The focus shifted recently to the development of compact waste incinerators for use aboard Navy ships. The common underlying concept of the combustion processes discussed in the present paper is vortex combustion. In practical combustors, the combustion process occurs at different locations within the combustion chamber depending on the air/fuel mixture and the fluid dynamic and thermodynamic

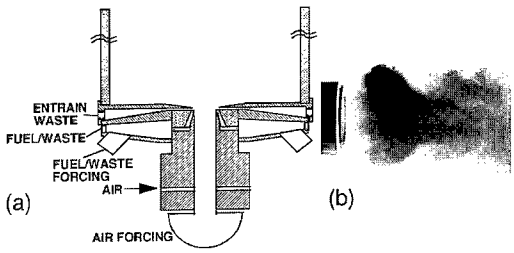

FIG. 1. (a) Schematic diagram of the laboratory incinerator. The fuel/waste injection angle is 15° to the central air flow as shown. The waste could be introduced via the central air, the fuel, or the entrainment flows. (b) Mie scattering image of the coherent vortex produced in the larger-scale dump combustor incinerator via acoustic forcing; flow is left to right.

conditions. Even if the average conditions are proper, local conditions are often not right for efficient combustion. The vortex combustion technique ensures that the combustion is confined to vortices within the combustor where optimal local conditions can be maintained. The vortex provides intense mixing and the long residence time necessary for complete combustion. The fuel injection system can be designed to place it in regions that provide the best conditions for combustion. The purpose of the present paper is to study the method of synchronized fuel injection into air vortices, and its use in the design of incinerator afterburners for gaseous pyrolysis products. The application is compact afterburners for shipboard general waste incinerator primary chambers. The methodology may also have landside applications such as compact, on-site medical waste incinerators.

Experimental

Laboratory Incinerator

A 4.75-kW ducted laboratory annular diffusion flame (Fig. 1a) was used for the small-scale tests. The central air was issued through a 22-mm circular nozzle at about 3.3 m/s (Re = 3500). The jet was acoustically forced at a level of up to a 30% rms (root mean square) velocity to produce steady, coherent vortices. Ethylene was injected circumferentially into the air jet through 24 1.6-mm holes and modulated acoustically at a level of nearly 100% rms velocity. Additional air was injected circumferentially into the flame through a 3.7-mm wide gap at a 36-mm maximum diameter. This is called the "entrainment flow" because in free jet experiments it was found, using PIV (particle imaging velocimetry), that the vortex shedding strongly (and periodically) entrains external air in a thin annulus near the dump plane. In ducted tests, the controller would not work without this extra entrainment air supplied by the plate shown in Fig. 1a. In all cases, the fuel-to-air ratio quoted includes both the central and entrainment air flows. The combustion took place downstream of the sudden expansion in a water-cooled duct 120 mm in diameter by 622 mm. The destruction of the waste surrogate was probed at 420 mm from the sudden expansion.

An open loop active control system was used to force the air vortices and to inject the fuel at selected phase angles relative to the vortex formation. The central air flow was driven acoustically at 100 Hz, the preferred mode of the jet under the present operating conditions. The fuel was forced at either 100 or 200 Hz, that is, either once or twice per air vortex. The entrainment air was not directly forced. The phase angle of fuel injection was controlled using a commercial delay. All DRE (destruction and removal efficiency) results reported here for the laboratory burner are for 100/200-Hz forcing. PLIF imaging of the mixing and combustion processes were done at both 100/100 and 100/200 Hz. The fluid dynamic mechanisms for 100/100 Hz are very similar to 100/200, yet simpler, so those results will be shown below. The marginal enhancement of operation at 100/200 Hz probably relates more to the higher efficiency of the acoustic drivers at 200 Hz rather than a fundamental change in fluid dynamic mechanism. The power delivered to the acoustic drivers is very modest: DREs beyond 99.999% can be obtained with only 3.2 W of electrical power.

The waste surrogate chosen was benzene, third on the U.S. Environmental Protection Agency (EPA) list of thermally stable, difficult to destroy, hazardous compounds [18]. Gaseous benzene was introduced into the laboratory incinerator either with the fuel, the main air, or the entrained air. When introduced into the main or entrained air, the system is partially premixed with respect to the waste. It is always entirely a diffusion flame with respect to the ethylene fuel.

The remaining benzene in the exhaust was monitored with an on-line mass spectrometer at m/e = 78. The DRE was calculated from the benzene concentration remaining in the exhaust: DRE(%) = 100 × [1 − (benzene out/benzene in)]. DREs are also often quoted as "nines," where 99.99% DRE corresponds to 4 nines and DRE(nines) = $-\log_{10}(1 - \mathrm{DRE}(\%)/100)$). The sensitivity limit of the on-line mass spectrometer corresponds to DREs of 4 to 5 nines (2-min average), depending on the amount of waste loading. A mass scan from 50 to 200 amu showed nothing but benzene. The sampling probe had multiple ports to average over the radial profile.

Advanced laser diagnostics such as planar laser-induced fluorescence (PLIF) and particle imaging velocimetry (PIV) were employed to clarify the mixing and combustion processes. For PLIF, the beam

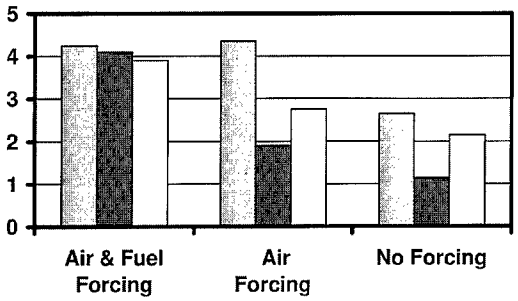

FIG. 2. Destruction and removal efficiency (DRE), in "nines," for the laboratory-scale dump combustor burning benzene as a surrogate waste (30% of the combustible content). The bars in each group of three are, from left to right, waste introduction via the entrainment, fuel, and air, respectively. Four "nines" DRE corresponds to 99.99% destruction of the input benzene.

from a tunable Nd:YAG pumped dye laser was formed into a sheet and passed through the centerline of the flame just downstream of the sudden expansion plane. Fluorescence was imaged at right angles using a gated image intensified 752 × 240 charge-coupled device (CCD) camera. Various excitation emission wavelength combinations allowed imaging of various scalars. Although we have done simultaneous imaging of two scalars at once, for this paper we made use of phase-locked imaging to compare different scalars. The central air, entrainment air, or fuel could be tagged with acetone. Acetone fluoresces when excited near 280 nm [19] and imaged near 400 nm. If the laser is set to 282.45 nm, it will also excite OH radicals in the flame, which can be imaged with another camera at 315 nm. The laser pulse will also heat soot particles in the flame, and the laser induced incandescence (LII) can be imaged using a camera gated with a slight time delay (to discriminate against either acetone or OH fluorescence, which decays within nanoseconds). Finally, polycyclic aromatic hydrocarbons (PAHs) formed in the flame can be imaged with PLIF. Here, the PAH fluorescence was excited at 280 nm and imaged broadband at wavelengths beyond 335 nm; this probably monitors a mixture of many relatively small and medium PAH molecules produced in the flame. Undelayed, the camera records both PAH and soot LII, and with a slight delay it records only soot LII. Thus, we could image essentially six scalars: central air, entrainment air, fuel, OH, PAH, and soot. However, because we used only a single laser and single camera, all correlations are based on phase averaging. Although extensive PLIF and LII imaging of air, fuel, entrainment air, PAH, and soot were done, because of space limitations only the vortex cycle of central air, fuel, and OH will be shown. Results from the other images will be discussed briefly.

The PIV measurements were done very simply. The light source was a fiber optic microscope illuminator formed into a sheet using a cylindrical lens. The flow was seeded with sieved powdered milk, and light scattering was imaged with the intensified CCD gated in phase with the vortex roll-up process with a dot-dash pattern so that flow reversal could be determined. The images were reduced manually using internally generated point and click software.

Larger-Scale Incinerator

The larger scale incinerator, a direct scaleup of the laboratory unit, was gaseous fueled and generated 47–70 kW of heat release. The inlet diameter was 38.4 mm and the dump 178 mm. The velocity of the inlet jet was 10.3–15.3 m/s for a Reynolds number of 26,000–39,000, based on the jet diameter. The inlet flow was forced using a high-speed acoustic valve (Ling Electronics) and, despite the order of magnitude increase in flow rate over the laboratory combustor and nearly an order of magnitude increase in Reynolds number, it was easy to generate coherent vortices using less than 5 W, as shown by Mie scattering flow visualization in Fig. 1b.

The fuel was introduced circumferentially through 38 holes of 2.3-mm diameter fed from an acoustically forced plenum as in the smaller-scale incinerator. The gaseous benzene was introduced with the fuel jets (gas burner or GB) or with the entrainment flow (afterburner or AB). In the AB configuration, the entrainment region had a mixture of nitrogen, ethylene, and benzene to simulate the output of a primary pyrolysis chamber. In this configuration, what were the "fuel" jets in the GB configuration were supplied with secondary air instead, and no "extra" fuel was used. In all the larger-scale incinerator tests reported here, the benzene constituted about 10–17% of the combustible content. Emissions were measured with a stack gas analyzer, Coso model 6000. A multiholed, water-cooled probe averaged across the stack radial profile. The sensitivity of this device, as listed by the manufacturer, was 1 ppm for CO and NO_x, and 0.01% for unburned hydrocarbons (UHC).

Results and Discussion

Laboratory Incinerator

The actively controlled laboratory incinerator allowed DRE of benzene beyond 5 nines. The highest DRE was obtained for a combined forcing of the air and fuel, with a phase that ensures homogeneous mixing of the waste inside the air vortices (Fig. 2). With the controller off, the flame is tall, yellowish-orange, and *extremely* sooty. The walls of the quartz combustor become nearly opaque with soot in a

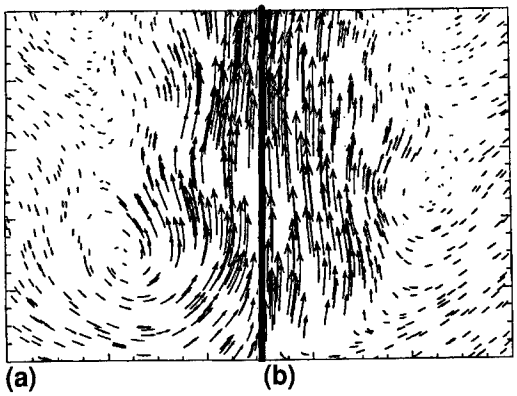

FIG. 3. PIV images of velocity fields for the laboratory system operated as a free jet. The left plot (a) shows the strong vorticity and base entrainment when the controller is operated at the proper phase angle between the central air vortex shedding and the fuel jet forcing, while the right plot (b) shows the loss of vortex coherency and lower entrainment rate when the improper phase angle is used. Only flow to one side of the centerline (bold vertical line) is shown.

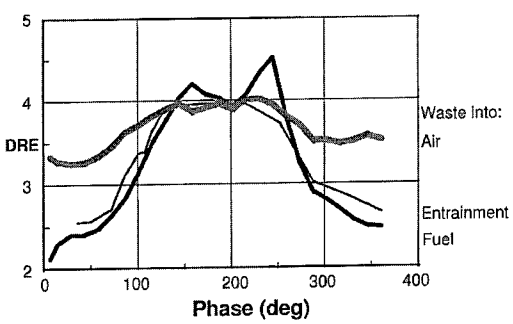

FIG. 4. The effect of the relative phase angle between air vortex shedding and fuel injection on the DRE of benzene in the controlled lab incinerator for introduction into the fuel (medium line), entrainment (thin line), or air (thick line). The Φ for the fuel introduction case was 1.08, and the benzene constituted 21% of the combustible content.

matter of seconds, and quite a lot of soot went up the stack into the scrubber system. The DRE in this case is as low as 92% when the benzene is introduced with the fuel. When the controller is turned on and optimized, the flame becomes entirely blue with no soot production whatsoever, even at equivalence ratios of unity. The DRE under these conditions is above 99.99%, independent of where the benzene is introduced (central air, fuel, or entrained air). Clearly, when the waste is introduced into the central air flow, it is premixed (although the extra ethylene fuel is not premixed and the flame is still partially diffusional). Even when the waste is premixed, the controller enhances the destruction efficiency by nearly two orders of magnitude.

Note from Fig. 2, that when the benzene is introduced with the fuel, creation of coherent air vortices is not enough to insure high DRE; the fuel/waste must be modulated at the proper phase angle to introduce the waste into the proper regions of the vortex roll-up. When this is done, the emissions decrease by over two orders of magnitude. There appears to be no effect when the benzene is introduced into the entrainment region, but this is because the air vortex generation naturally modulates the entrainment flow, as shown by PIV and PLIF imaging. Figure 3a shows PIV results for a free jet without the entrainment flow or plate but with the controller on. There is clear evidence of the strong vorticity, but it is also clear that this vorticity leads to strong entrainment of surrounding air near the exit plane. Images at other phase angles showed that the entrainment rate is periodic. When the controller is operated at the improper phase angle between fuel and air (which leads to sooty combustion), the vortices are much less coherent and the entrainment lower and not localized at the exit plane (Fig. 3b). It was the discovery of this high base entrainment rate that lead us to design the ducted incinerator with circumferential entrainment flow via the entrainment plate.

The forcing level required for optimal DRE was only 10% of the mean velocity. The total electrical power level into the speakers for optimal DRE was only 3.2 W which compares to the 4750 W the flame generates. Increasing the forcing level beyond this modest level did not improve the DRE. The highest DRE was obtained at an overall equivalence ratio slightly below stoichiometric. The DRE dropped drastically for average overall system equivalence ratio beyond unity (due to lack of oxidizer) and for low equivalence ratio (<0.7) due to destabilization of the flame, which can lead to waste escape paths. The entrainment of at least 25% secondary air was critical to obtain high DRE. DREs beyond 4 nines could be maintained even when the benzene constituted 66% of the combustible content.

Figure 4 shows that the phase angle between air vortex shedding and fuel injection is important to maintaining high waste DRE independent of where the waste was injected. The effect was strongest with the benzene introduced via the fuel or entrainment ports: the proper phase angle has over 2 nines better DRE. The data of Fig. 5 was taken at an equivalence ratio of 1.08, slightly higher than normal, so that the entire cycle of phase angles could be mapped without the DRE extending beyond our detection limit.

Figure 5 shows the mixing and fluid dynamic processes leading to this phase sensitivity. Composite PLIF phase-locked images of the mixing between the main air and fuel, and the combustion zone (obtained by imaging OH) are shown (the entrained air

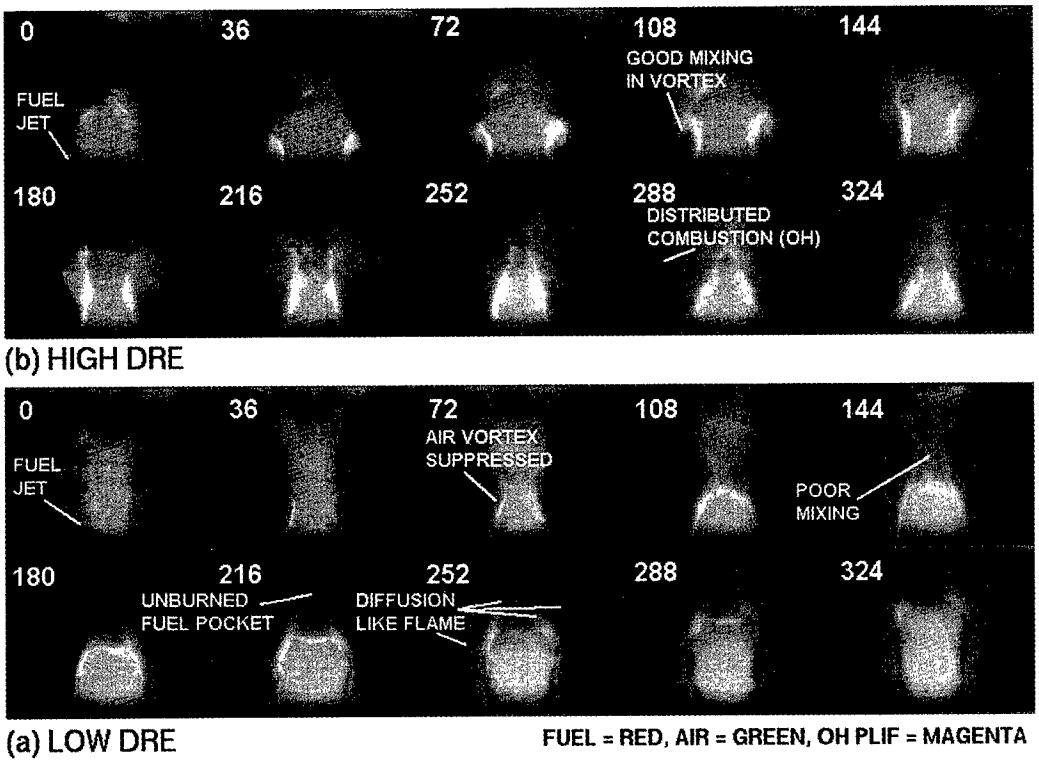

FIG. 5. (a) PLIF image sequence for fuel (red), central air (green), and OH (blue) for laboratory incinerator operating under the controller conditions that lead to low DRE and high soot formation. Each frame is a different phase angle in the roll-up cycle of the central air vortex (i.e., 10 ms). (b) The same for the high-DRE, low-soot condition of the controller.

flow visualization is not shown, for clarity: overlapping regions of three primary colors can lead to any color, so it is not possible to show more than three scalars). In each of these frames, the flow is vertical and the field of view is about 50 mm. The time evolution is presented as ten phase angles in the air vortex roll-up cycle. Without the aid of PLIF movie playback, the images are hard to follow, so we will briefly summarize the fluid dynamic mechanisms determined from the PLIF measurements.

The images were taken for single fuel pulsing during a single cycle of air vortex roll-up; PLIF movies of the dual pulse injection are even more complex, but the underlying fluid dynamic mechanisms are nearly the same. When the proper fuel phasing angle is used (Fig. 5b), the fuel/waste injection mixes well with both the central air incipient vortex as well as with the entrained air flow. Note the overlap of the red (fuel) and air (green) to make yellow, showing good mixing of air and fuel. The flame is lifted but stabilized near the dump on the first vortex rollup. The OH PLIF shows good combustion distributed widely throughout the region around and above the first vortex.

When the improper phase angle is used (Fig. 5a), the fuel/waste jet pulse appears to come at just the wrong time and enters the region between air vortices leading to localized high equivalence ratios and partially slicing off the incipient air vortex, decreasing the coherency. Notice fuel regions (red) leaving the top of the field of view without being mixed with air. The OH profile has a typical diffusion flame–like double edge in the shear layer as regions of poorly mixed fuel/waste combust via diffusion. In this case, PLIF and LII images not shown here indicate that PAHs are formed close to the flame holder in the fuel-rich annulus (about one-fifth to one-half of the way from the bottom of each frame) and that soot particles begin to become apparent downstream (about the top one-fourth of each frame).

Large-Scale Incinerator, Gas Burner Configuration

The lessons learned using the small, laboratory-scale incinerator were applied to the larger-scale incinerator with over an order of magnitude scale-up of flow rate and energy release. The larger-scale incineration tests in the GB configuration also showed DRE > 5 nines. The flame is far downstream of the dump plane and extremely sooty (yellow) without

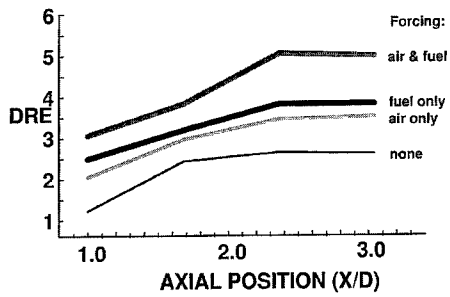

FIG. 6. Benzene DRE (in nines) as a function of axial position x/D (where x is the axial distance downstream from the dump and D is the dump diameter) for various conditions of the controller. The top curve is the entire controller optimized; the next down is for forcing of the fuel jets only; the next for air forcing only; and the bottom for no forcing at all.

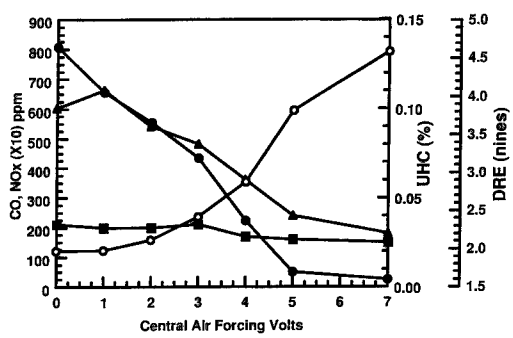

FIG. 7. Benzene DRE (in nines, right axis, ○), unburned hydrocarbons (UHC axis on right, ▲), CO ppm (●), and NO_x ppm times 10 (■) for the afterburner configuration of the 47-kW incinerator shown as a function of forcing level on the controller. As control authority is exercised, the benzene DRE goes up and the CO, UHC, and, to some extent, the NO_x go down.

control, and is intensely blue, shorter, and moves upstream to a location just beyond the dump plane with control.

Figure 6 shows the DRE for benzene waste surrogate measured at various conditions of the controller and at various axial positions (overall Φ = 0.78). For air and fuel forcing, the DRE extends beyond the EPA requirement of 4 nines for axial distances beyond x/D = 1.7 (D is the dump diameter). This corresponds to a power density of 6500 kW/m^3. The DRE is much larger when the air is forced and the fuel pulsed at the proper phase angle, and is at a minimum when the phase is 180° from the optimum. This indicates that the same mechanisms seen in the 4.5-kW laboratory incinerator are important in the 47-kW incinerator. The power requirements for forcing are minimal: the highest DRE was obtained at a Ling power of 5 W. In the larger-scale incinerator tests shown here, the fuel was pulsed at the *same* frequency as the air vortex shedding, i.e., 120 Hz for a Strouhal number of 0.41 given the air flow of 10.3 m/s.

The gas burner DRE optimized at Φ = 0.75. Subsequent tests with a flue-gas analyzer showed poor combustion efficiency at the station where 4 nines DRE was obtained: the CO was >10,000 ppm and unburned hydrocarbons (UHC) were also quite high. Dropping the Φ to 0.55 maintained high DREs and control authority while dropping CO to below 2 ppm, UHC to below the detection limit of 0.01%, and NO_x to 20 ppm (all at x/D = 3.1). The unforced flame under these conditions produced 2900 ppm CO, 0.19% UHC, and 65 ppm NO_x, showing that the controller improves the combustion efficiency and NO_x as well as DRE. Changing the relative phase angle between vortex shedding and fuel/waste modulation created the same sine-like curves in CO and UHC as for benzene DRE, showing that the mechanisms that improve DRE decrease CO and UHC. These experiments were done at an increased central air flow of 15.3 m/s (to get the measured preferred mode of the jet up to a 190-Hz acoustic resonance in the inlet) so the heat release rate stayed about the same (49 kW). The optimum fraction air in the entrainment flow was about 18% of the total air in these tests.

Large-Scale Incinerator, Afterburner Configuration

The controller was able to exercise control over the combustion in the afterburner configuration as well, although the optimum DREs were somewhat less than for the GB configuration (4.5 vs. >5.5 nines, at x/D = 3). The same effect of relative phase between secondary air and central air forcing was seen with the optimum phase giving 4.4 nines and nonoptimum only 3.2 nines. The CO and UHC were minimized at the phase angles that maximized DRE. The NO_x was not strongly affected and remained below 20 ppm. As the forcing was increased, the DRE rose and the CO and UHC decreased (Fig. 7). The NO_x decreased slightly for increasing forcing levels. Thus, the controlling mechanisms seen in the GB configuration follow-over to the AB configuration, even though the combustible content is not directly forced. The acoustic levels in the AB configuration, however, were significantly less than in the GB mode, and the flame longer. Without direct 100% modulation of the combustibles, there is less of a periodic heat release in the chamber and perhaps less coherent vortices leading to lower DREs. Future work is being directed at enhancing the indirect modulation of the pyrolysis simulant.

Conclusions

Active combustion control has been used to enhance mixing in incinerator afterburner experiments

and increase DRE. A detailed study of the concept of utilizing vortex combustion for incineration in a 4.7-kW laboratory dump combustor burning gaseous fuel was extrapolated to a more practical system with 47-kW heat release in gaseous burner and afterburner configurations.

The active control is based on combustion in periodic axisymmetric vortices. Acoustic excitation was used to create vortices and to introduce fuel into the vortex at the right time. The 4.7-kW incinerator was able to surpass 99.997% DRE for gaseous benzene. Critical parameters were the fraction of circumferentially entrained air and the phasing angle of fuel injection with respect to the air vortex roll-up.

Advanced laser diagnostics were used to elucidate the fluid dynamic mechanisms involved in this control methodology. The acoustic excitation of the flow generated coherent vortices, and properly phased injection of fuel and waste into these vortices, along with circumferential entrainment of excess air, lead to excellent mixing and efficient combustion within the vortices. The formation of pockets of high and low equivalence ratio were minimized.

The control methodologies studied using gaseous fuel and waste were extended to a dump combustor afterburner/incinerator of 47- to 70-kW energy release. The DRE for gaseous benzene exceeded 99.999% in this system when combustible to air ratios were kept below 0.78. Again, the use of synchronous fuel injection into coherent air vortices was found to be critical to maintaining high DREs.

REFERENCES

1. Crow, S. C. and Champagne, F. H., *J. Fluid Mech.* 48:545–591 (1971).
2. Brown, G. L. and Roshko, A., *J. Fluid Mech.* 64:775–816 (1974).
3. Ho, C. M. and Huerre, P., *Annu. Rev. Fluid Mech.* 16:365–424 (1984).
4. Oster, D. and Wygnanski, I. J., *J. Fluid Mech.* 123:91–130 (1982).
5. Ho, C. M. and Huang, L. S., *J. Fluid Mech.* 119:443–473 (1982).
6. Hanson, R. K., *Twenty-First Symposium (International) on Combustion,* The Combustion Institute, Pittsburgh, 1986, pp. 1677–1691.
7. Gutmark, E. J., Parr, T. P., Hanson-Parr, D. M., and Schadow, K. C., *Combust. Sci. Technol.* 66:107–126 (1989).
8. Candel, S., *Twenty-Fourth Symposium (International) on Combustion,* The Combustion Institute, Pittsburgh, 1992.
9. McManus, K. R., Poinsot, T., and Candel, S., *Prog. Energy Combust. Sci.* 19:1–29 (1993).
10. McManus, K. R., Vandsburger, U., and Bowman, C. T., *Combust. Flame* 82:75–92 (1990).
11. Yu, K., Trouve, A., and Candel, S., AIAA Paper no. 91-0367, 1991.
12. Gutmark, E. J., Wilson, K. J., Schadow, K. C., Parker, B. E., Barron, R. L., and Smith, G. C., Thirty-First AIAA Aerospace Sciences Meeting, Reno, NV, AIAA Paper no. 93-0117, 1993.
13. Padmanabhan, K. T., Bowman, C. T., Powell, J. D., *Combust. Flame* 100:101–110 (1995).
14. Chen, L., McDonell, V. G., and Samuelson, G. S., WSS/CI Fall Meeting, Paper no. 92-75, 1992.
15. Smith, O. I. et al., *Combust. Sci. Technol.* 74:199–210 (1990).
16. Marchant, R. et al., *Combust. Sci. Technol.* 82:1–12 (1992).
17. Schadow, K. C., Hendricks, E. W., and Hansen, R. J., *Proceedings of the 18th ICAS Congress,* Beijing, China, 1992, p. 942.
18. Lee, C. C., Huffman, G. L., and Sasseville, S. M., *Hazard Waste Hazard Mater.* 7:385 (1990).
19. Lozano, A., Yip, B., and Hanson, R. K., *Exp. Fluids* 13:369–376 (1992).

Twenty-Sixth Symposium (International) on Combustion/The Combustion Institute, 1996/pp. 2479–2485

COMBUSTION STUDIES ON CONCENTRATED DISTILLERY EFFLUENTS

N. M. PATEL, P. J. PAUL, H. S. MUKUNDA AND S. DASAPPA
Department of Aerospace Engineering
Indian Institute of Science
Bangalore—560 012, India

Studies on ignition and combustion of distillery effluent containing solids consisting of 38 ± 2% inorganics and 62 ± 2% of organics (cane sugar derivatives) have been carried out in order to investigate the role of droplet size and ambient temperature in the process of combustion. Experiments were conducted on (1) liquid droplets of effluent having solids concentration 65% and (2) spheres of dried (100% solids) effluent of diameters ranging from 0.5 to 25 mm. These spheres were introduced into a furnace where air temperature ranged from 500 to 1000 °C, and they burned with two distinct regimes of combustion—flaming and glowing. The ignition delay of the 65% concentration effluent increases with diameter as in the case of nonvolatile droplets, while that of dried spheres appears to be independent of size. The ignition delay shows Arrhenius dependence on temperature. The flaming combustion involves a weight loss of 50–80%, depending on ambient temperature, and the flaming time is given by $t_f \sim d_0^2$, as in the case of liquid fuel droplets and wood spheres. Char glowing involves weight loss of an additional 10–20%, with glowing time behaving as $t_c \sim d_0^2$ as in the case of wood char, even though the inert content of effluent char is as large as 50% compared to 2–3% in wood char. Char combustion has been modeled, and the results of this model compare well with the experimental results.

Introduction

All distilleries produce an effluent commonly known as "vinasse," an amount equal to 10–15 times that of the volume of alcohol. Dry vinasse or effluent contains about 38–40% inorganic salts of potassium, sodium, magnesium, and calcium in the form of chlorides, sulfates, and phosphates, and about 60–62% organic compounds, in particular, sugar (cane sugar, $C_{12}H_{22}O_{11}$). Besides a strong pungent smell and intense dark color, effluent has a large biological oxygen demand (BOD) and chemical oxygen demand (COD) in the range of 45 and 100 g/L, respectively, and hence, the effluent is included in the list of highly polluting chemicals. Among the methods of effluent disposal, biomethanation and incineration of concentrated effluent are the options. In the biomethanation route, biogas digesters convert the organic matter into methane and carbon dioxide. However, the discharged effluent from the biogas plant still has unacceptable levels of BOD to allow discharge into land or river. Other routes, such as biocomposting, are contemplated in order to dispose the effluent safely. Yet, there have been considerable difficulties in meeting the rigorous pollution standards. Considering the incineration route, all the organic matter can be treated, and the inorganic matter, amounting to 6–7% of the effluent, needs to be disposed. This material can be used as a fertilizer. Another route along incineration process is the gasification of concentrated effluent. This process can be described as substoichiometric combustion, in which oxidation reactions between the organic matter and oxygen in the oxidant (air), and reduction reactions between the products of combustion and unconverted carbon, lead to the generation of a combustible gas called producer gas containing CO, H_2, CH_4, CO_2, and N_2. This can be used as a fuel in an internal combustion engine or gas turbine in single fuel or dual-fuel mode to generate electricity. Hence, this method provides power while having zero effluent discharge. This process has been addressed inadequately and the limited field experience available on this technique at present has been negative. One of the issues is that the fundamental process associated with incineration and gasification aspects of effluent has not been understood. One phase of combustion, namely, the flaming combustion during which the volatile matter is oxidized in air, is common to both combustion and gasification. During the second phase, carbon reacts with oxygen in case of combustion and with CO_2 and H_2O in the case of gasification. This paper deals with the combustion aspects of the effluent.

It is known that recovery boilers in paper industries utilize black liquor that is concentrated to better than 65% to ensure good combustion. The effluent from the distillery having 10–11% solids can be treated similarly if it is concentrated to better than 65%. This provides the motivation to study the combustion characteristics of concentrated effluents. If gasification is to be pursued or incineration of lower

concentration effluents is to be handled, it may be imperative to deal with one zone of combustion with higher concentration effluents supporting the combustion of lower concentration effluents. It is for this reason that it is useful to understand the behavior of dried effluents. Two limiting conditions are considered for study in this work. The first is the simpler case of dried solid sphere combustion. This is similar to wood sphere combustion, the difference being the presence of a large amount of inorganic material (~38%), which is a significant heat sink in these quantities; it could also be catalytic. Wood has lignin, which is more difficult to pyrolize compared with sugar. The second part is the study of tiny drops of concentrated effluent to assist in understanding better combustion of sprayed effluent material.

Experimental Procedure

The basic material used for the dry sphere experiments was effluent concentrated to 70%, having the appearance of thick, heavy oil or grease. Since it is difficult to make spheres with this substance, the effluent was further concentrated to 85% by slow convective heating at temperatures between 50 and 110 °C. Loss of sphericity was corrected, and finally, the material was dried in a vacuum desiccator containing silica gel and phosphorus pentoxide. Remaining moisture was gradually removed in a hot air oven at a slow rate. Finally, the spheres were heated at 110 °C for 24 h, before being stored in cooled conditions in a vacuum desiccator. Prior to each experiment, the samples were characterized for weight, and the average diameter was calculated from measurement across three orthogonal axes. The density of the samples varied from 650 to 800 kg/m^3.

The samples were mounted on three adjustable nichrome prongs and then inserted into the furnace, which was maintained at a fixed temperature. The combustion process was timed from the moment the sample was introduced into the furnace. Series of experiments were conducted separately, and the variation of surface temperature with time was recorded. Here, the sample was held taut between nichrome prongs held in a horizontal position along with a thermocouple junction (Pt–Pt13%Rh, 50 μm coated with cerium oxide of 0.2 μm in thickness) touching the surface under small tension so as to be firmly in position. In the case of droplets of 65% concentration, the droplets of 0.5–3 mm in diameter were suspended around the 50-μm thermocouple bead and introduced into the furnace. Apart from the transient temperature data, the combustion process was captured on a video camera for subsequent analysis. The initial droplet diameter was measured using a traveling microscope, and further changes in diameter due to the hot ambience was measured using video recording of the event where the drop size was compared with the predetermined length of a wire fixed on a holder located in the same plane as the suspended droplet.

Experimental Observations

It was found that a minimum ambient gas temperature was required to achieve ignition (flaming of volatiles in gas phase). This feature depends on the dry effluent sphere diameter; large spheres ignite at as low as 530 °C. At temperatures below this, there would be smoldering combustion, with no visible flame. Most of the experiments were performed at 700 °C for which ignition occurred for all dry effluent spheres with diameter in excess of 2 mm. The combustion process was observed to be consisting of two phases. In the first phase, a gaseous flame envelopes the sphere as in the case of liquid droplet combustion. The source of fuel for the flame comes from the gases due to pyrolysis of the solid material. During the flaming process, a lot of fumes were observed to be issuing from the burning zone. This stopped at or a little after the end of flaming. It is suggested that the fumes seen must be the inorganics being carried away by the volatiles. The change in diameter is negligible at the end of this flaming phase. The second phase has no gaseous flame, and the char burns by heterogeneous oxidation with gradual growth of ash layer from the outer surface. The material maintained sphericity throughout the combustion. In some cases of large diameter spheres, flaming and char glowing overlapped for a small duration due to possible incomplete devolatilization in some regions. Some of the observations are qualitatively similar to those made by Mukunda et al. [1] for wood spheres and those made by Kuwata et al. [2] for cellulose spheres.

Combustion of 65% effluent droplets also exhibits the two phases of combustion. However, the minimum ignition temperature was observed to be more than 900 °C for a drop of diameter 2.5 mm. For these cases, water expulsion is accompanied by an increase in diameter of about 40–45%. In this process, the escaping volatiles create a large number of very small pores.

One question that became important was to determine if the condensed-phase pyrolysis or phase transformation was exothermic, as in the case of wood. To explore this hypothesis, thermogravimetric analysis was carried out on the samples of effluent char. These showed clear exortherms at 450 and 560 °C, indicating exothermicity of the decomposition process much like wood.

The Mathematical Model

The primary assumption made in the model is that the conversion process is one-dimensional. Taking

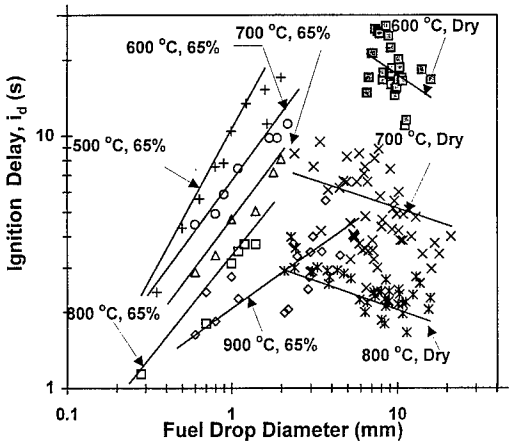

FIG. 1. Variation of ignition time with the liquid drop diameter (65% concentration) and dried spheres of effluent material at 500, 600, 700, 800, and 900 °C.

this assumption, the processes taking place during flaming are the combustion of volatiles, as for wood spheres—diffusion-limited gas-phase combustion, modeled by the Burke–Schumann theory with appropriate initial and boundary conditions [1]. As has been discussed above, the mathematical framework developed in Ref. 1 can be directly utilized in the treatment of the flaming process and, therefore, will not be addressed here.

The processes taking place during combustion of porous char spheres are similar to those treated in Ref. 3 involving the diffusion and convection of the species and energy in the porous medium and the heterogeneous reaction between the gaseous species and the char. These are modeled in the present analysis using the unsteady spherically symmetric, one-dimensional conservation equations.

The primary difference between wood spheres and dry effluent spheres is the amount of inorganics—about 1% for wood and 39% for the effluent spheres.

Choice of Parameters

The choices of physical, thermodynamic, and transport properties of dry effluent material and char based on measured and literature information are as follows: For the dry effluent,

$$\rho_c = 730 \text{ kg/m}^3 \; c_p = 1.40 \text{ kJ/kg K}$$

$$k_c = 2.1 \text{ W/m K} \; k_g = 0.063 \text{ W/m K}$$

for the char,

$$\rho_c = 1650 \text{ kg/m}^3 \; r_p(t = 0) = 50 \; \mu\text{m}$$

$$c_p = 1.25 \text{ kJ/kg K}$$

$$H_c = 32.60 \text{ MJ/kg} \; k_c = 1.85 \text{ W/m K}$$

$$k_g = 0.071 \text{ W/m K}$$

and rate parameters for the C + O_2 reaction are

$$A_c = 1/150 \; E_1/R = 1700 \text{ K} \; E_2/R = 20{,}000 \text{ K}$$

$$A_f = 0.0875 \text{ mol/m}^2 \text{ s}$$

where k_c is the conductivity of the solid phase at temperatures of 1000–1200 K. The presence of a large amount of inorganic material affects the conductivity of the porous carbon-inorganic matrix. It must be emphasized that the char is composed of nearly equal amounts of carbon and inorganic matter—oxides, chlorides, sulfides, and sulfates of potassium, sodium, magnesium, and calcium. The thermal conductivity data of several inorganics and char were examined from standard literature. These indicate to values anywhere between 0.5 and 2 W/m K. The conductivity of porous carbon is also within the same range at high temperature. In light of this and the known significant influence of thermal conductivity [3], it was decided to choose a value to match the burn time at one point. This value is 1.25 W/m K. The initial radius of the pore is obtained from Ref. 4, where wood char was used for measurements. The parameters in the kinetic expression used presently were not altered from those of wood char [5]. The rate of the backward reaction k_2 is obtained from the appropriate equilibrium constants. The emissivity of the sphere surface, used for radiant heat loss calculation, is taken as 0.95.

Results and Discussion

Figure 1 shows the dependence of ignition delay (i_d) on the diameter of the spherical particle. Results for both the concentrated liquid and the dried spheres are shown in the figure. In the case of liquids, there is increase in delay with drop diameter much like nonvolatile droplets [6]. The ignition delay decreases with increase in ambient temperature, as can be expected. In the case of dry spheres, even though there is scatter of data, it appears reasonable to conclude that the delay time is nearly independent of the size or that there is a slight decrease in the delay with increase in size. Earlier experimental data on highly volatile fuels and nonvolatile fuels, as well as their blends [6,7], suggest that the decreasing trend of ignition delay with size is due to fuels that are more volatile. The dry effluent appears similar to volatile fuels with regard to ignition delay. Similar results are also reported by Ragland and Weiss [8] and Boukara et al. [9] for bituminous coal.

Figure 2 shows the dependence of ignition features on a diameter vs. ambient temperature plot. A clear boundary between the flaming and nonflaming zone is noticeable. Again, this feature has been

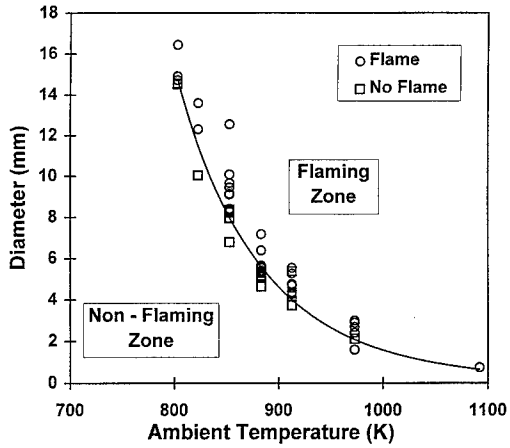

FIG. 2. Boundary between ignition and no ignition on temperature vs. sphere diameter plot for dried effluent.

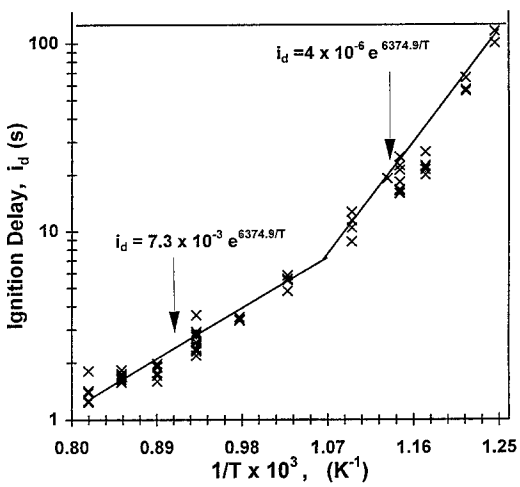

FIG. 3. Ignition delay vs. temperature for different diameter spheres of dried effluent.

observed earlier by Takei et al. [6] and explained to be due to a competition between chemical heat release rate and diffusion of reactants in space. For the case of dry effluent spheres, ignition delay correlates well with temperature following the Arrhenius law, as can be noted from Fig. 3.

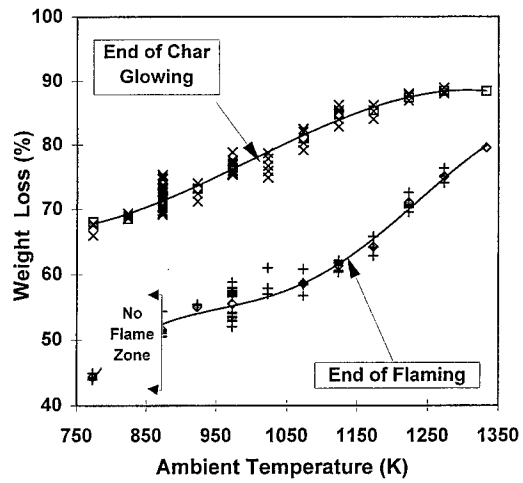

FIG. 4. Plot of weight lost by dried affluent spheres of various diameters at different ambient temperatures at the end of flaming and char glowing.

Figure 4 shows the weight loss at the end of flaming as well as glowing. The data are constructed from a large number of tests for flaming and glowing separately. The portion marked "no flame zone" shows the domain below which only smoldering combustion takes place. Typical weight loss at the end of flaming increases from 50% to as high as 80% at 1330 K. Since an analysis of the dry samples indicated an organic content of 60–65%, the observation on weight loss noted above implies loss of a fair amount of inorganics along with organics during the flaming process. This is supported by the physical observation of fumes exuding from the burning sphere. In order to understand this behavior, the samples from the original effluent, as well as the char and the ash from experiments at various

TABLE 1
Analysis of the initial sample, char, and ash for experiments at different temperatures

Nature of Material	Temperature (K)	Initial Sample (g)	Char (g)	Ash (g)	Loss during Flaming (%)	Loss during Glowing (%)
Organics	773	60.3	27.9	0.6	53.6	97.7
Inorganics	773	39.7	26.6	30.2	33.1	−13.6
Organics	873	60.3	24.9	0.6	59.7	97.8
Inorganics	873	39.7	23.1	26.4	41.9	−14.3
Organics	973	60.3	22.7	0.5	62.2	97.9
Inorganics	973	39.7	21.6	22.8	45.5	−5.5

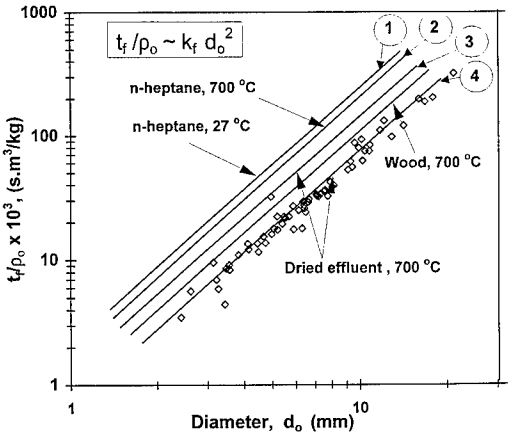

FIG. 5. Flaming time vs. diameter for dried effluent material at different temperatures. Results for n-heptane and dried wood sample are also shown.

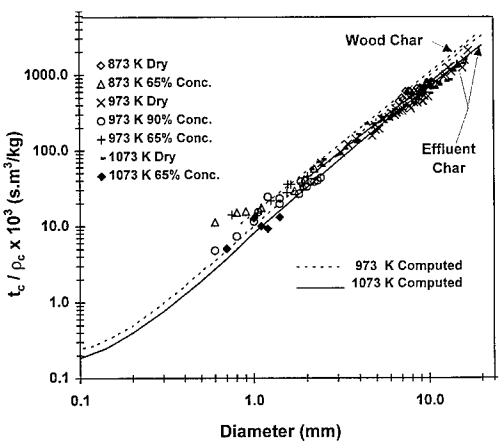

FIG. 6. Glowing time vs. diameter for concentrated liquid droplets and dried effluent at various temperatures. Also shown are the results for wood char. Comparison with model prediction included in the figure.

temperatures, were subjected to chemical analysis. The results of the analysis of original material, char, and ash are shown in Table 1.

The material lost during flaming increases from 53.6 to 62.2% for an ambient temperature rise from 500 to 700 °C. This increase will be far more at higher temperatures, as indicated in Fig. 4. One of the curious aspects of the results is that the amount of inorganics found in ash is more than in char. More careful examination showed that the sulfate content in the char is much less than that either in the ash or in the original effluent. A chemical analysis showed sulfides in the char, which were absent both in the original effluent and in the ash. Hence, it is inferred that part of the metal sulfates present in the original effluent were reduced to sulfides in the high-temperature–reducing atmosphere in the presence of carbon during flaming combustion [10] and converted back to sulfates during glowing combustion. Other salts also might behave similarly, causing a net increase in the amount of inorganics during the char glowing phase.

The weight loss during char combustion is about 17–20% of the original weight of the sample for temperatures up to 1150 K, and decreases to 7% at 1330 K. It is therefore reasonable to assume that the weight loss during char combustion is constant below about 1150 K.

The data of flaming time, normalized by initial density with diameter (dried sample), are presented in Fig. 5 along with similar data for wood spheres [1] and n-heptane [7] for comparison purposes at an ambient temperature of 700 °C on a log–log plot. The flaming time normalization with density is to account for variations in density that occurs in the process of making dry effluent spheres, and the expectation that the combustion time varies linearly with density. Curves 1 and 2 are for n-heptane burned at ambient temperatures 27 and 700 °C, respectively. Curve 2 for 700 °C is presented to exhibit a comparison with dried effluent combustion and is obtained using standard liquid droplet combustion calculations, taking into account burning constant dependence on thermodynamic and transport properties. Curves 3 and 4 are for effluent burned at 700 °C. Curve 3 is obtained by normalizing burn time with density that is equivalent to 60% fuel mass, which devolatilized during the flaming process, and curve 4 is normalized with initial density of the dried effluent. A curve fit to this data is of the form $t_f \sim d_0^2$, indicating diffusion-dominated combustion. As can be seen, flaming time in the case of n-heptane is larger since it gets completely consumed with zero diameter and zero weight, unlike that for effluent and wood. These data can be interpreted in another way. If one constructs a nondimensional burn time, τ, defined by

$$\tau = t_f \frac{k_w}{\rho_w c_{pw}} \frac{1}{d_0^2} \tag{1}$$

where the quantities subscripted by w refer to solid phase, the quantity τ works out to be 0.117 for effluent and 0.105 for wood. For n-heptane, it is about 0.1. Thus, this quantity seems to give a value that is fairly constant for all these substances.

Figure 6 presents the experimental data of char glowing time normalized with char density of the dried effluent, effluent with 65% concentration of solids and wood char, and with diameter d_0 for combustion in air under ambient temperatures of 700, 800, and 900 °C. Computations of char combustion in air with the data indicated earlier are shown in

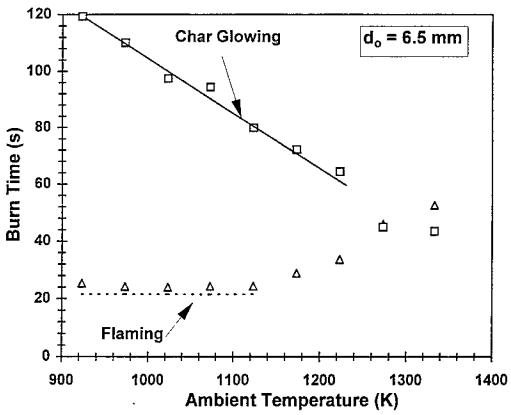

FIG. 7. Flaming and char glowing time as a function of ambient temperature for dried effluent.

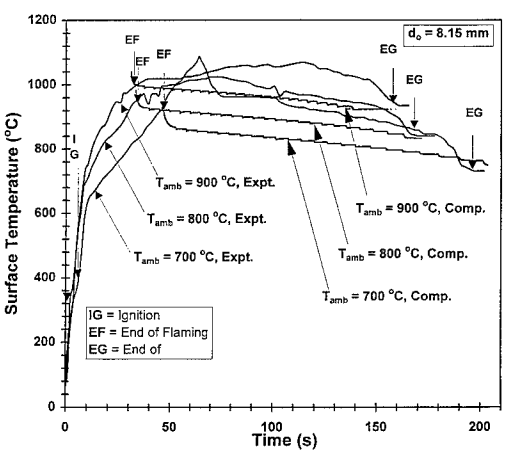

FIG. 8. Surface temperature variation with time.

the same figure by lines. The slope of the line gives the exponent in $t_c/\rho_c \sim d_0^m$ as $m = 2$. The line remains straight up to a lower end diameter of 1 mm. Below this, the line becomes curved, the slope decreasing with decrease in diameter, indicating increasing reaction control at lower diameters.

Figure 7 shows the burn time (both flaming and glowing) of a 6.5-mm-diameter sphere as a function of temperature. The computed flaming and glowing times are also shown in the figure. As discussed earlier, there is a small increase in the mass loss during the flaming period as temperature increases, which is compensated by increase in heat flux, and as a result, the flaming time remains nearly independent of ambient temperature up to 1150 K. Beyond this temperature, the percentage weight loss increases rapidly with ambient temperature (Fig. 4), causing increase in flaming time. Char glowing time decreases with ambient temperature because of the increase in reaction rate and to a certain extent due to increase in the transport properties. Even though the oxygen–carbon reaction is essentially diffusion controlled and consequently insensitive to changes in the rate constants, the increase in the rate of the reduction reaction between CO_2 and carbon causes a decrease in the overall char glowing time with increasing ambient temperature. It is observed from the computational results that as the temperature increases, the CO_2 fraction decreases, and CO fraction increases at the center of the sphere, indicating increasing C–CO_2 reaction rate.

The result of the thermal probing is presented in Fig. 8, which contains the surface temperature variation with time during combustion for a sample of 8.15 mm in diameter at 700, 800, and 900 °C. After ignition, there is a sharp temperature rise followed by a slow rise in temperature until the peak. The peak in temperature is observed during active char glowing since the reaction front is shifted to the surface where ambient oxygen diffuses into the porous char, resulting in char combustion. This is followed by a gradual fall in surface temperature until the end of char glowing. Predictions of the temperature profile during char combustion, extracted from the model calculations, are also presented in Fig. 8. The difference in the two results is about 100 K in all three cases. The possible reason for this is that the inorganic compounds in the ash catalyze the exothermic reactions in the gas phase (oxidation of CO), causing higher temperatures in the ash layer.

Concluding Remarks

This paper has presented results of the combustion behavior of concentrated and dried distillery effluent spheres. The ignition time increases linearly with diameter for concentrated effluent and is nearly independent of size for dried effluent. The flaming behavior is similar to that for liquid droplets (*n*-heptane) but with a faster burn rate; the burn rate compares with a wood sphere when suitably nondimensionalized. Char burn rate is again diffusion controlled down to very small diameter spheres. The behavior is modeled using one-dimensional, spherically symmetric conservation equations, and the model predicts most of the features of char combustion satisfactorily.

REFERENCES

1. Mukunda, H. S., Paul, P. J., Shrinivasa, U., and Rajan, N. K. S., *Twentieth Symposium (International) on Combustion,* The Combustion Institute, Pittsburgh, 1984, pp. 1619–1628.
2. Kuwata, M., Stumbar, E., and Essenhigh, R. H., *Twelfth Symposium (International) on Combustion,*

The Combustion Institute, Pittsburgh, 1969, pp. 663–674.
3. Dasappa, S., Paul, P. J., Mukunda, H. S., and Shrinivasa, U., *Chem. Eng. Sci.* 49:223–232 (1994).
4. Groeneveld, M. J., "The co-current moving bed gasifier," Ph.D. Thesis, Twente University of Technology, Netherlands, 1980.
5. Blackwood, J. D. and Ingeme, A. J., *Aust. J. Chem.* 13:194–209 (1960).
6. Takei, M., Tsukamoto, T., and Nioka, T., *Combust. Flame* 93:149–156 (1971).
7. Kumagai, S., Sakai, T., and Okajima, S., *Thirteenth Symposium (International) on Combustion,* The Combustion Institute, Pittsburgh, 1971, pp. 779–785.
8. Ragland, K. W. and Yang, J., *Combust. Flame* 60:285–297 (1985).
9. Boukara, R., Gadiou, R., Gilot, P., Delfosse, L., and Prado, G., *Twenty-Fourth Symposium (International) on Combustion,* The Combustion Institute, Pittsburgh, 1992, pp. 1127–1133.
10. Brown, G. H. and Sallee, E. M., *Quantitative Chemistry,* Prentice-Hall, Englewood Cliffs, NJ, 1963.

Twenty-Sixth Symposium (International) on Combustion/The Combustion Institute, 1996/pp. 2487–2493

THE ENERGY AND ENVIRONMENTAL IMPLICATIONS OF USING SEWAGE SLUDGE AS A CO-FIRED FUEL APPLIED TO BOILERS

T. ABBAS,[1] P. COSTEN,[1] G. De SOETE,[2] K. GLASER,[3] S. HASSAN[1] AND F. C. LOCKWOOD[1]

[1]*Thermofluids Section, Department of Mechanical Engineering*
Imperial College of Science, Technology and Medicine
London SW7 2BX, UK

[2]*Institute Francais Du Petrole*
1 et 4, avenue de Bois Preau
BP 311-92506 Rueil-Malmaison, France

[3]*Universität Stuttgart, Institut fur Verfahrenstechnik und Dampfkesselwesen*
Pfaffenwaldring 23. 70550 Stuttgart 80, Germany

An assessment has been made of the technical feasibility of co-firing pulverized sewage sludge in a utility boiler with regard to the change in envisaged combustion performance and the possible additional impact on the environment from toxic metals and NO_x emissions. Data have been reported for three PF flames—bituminous coal, sewage sludge, and an equal blend, by mass, of the two fuels in a 0.5-mW down-fired furnace.

The experimental results, supported by complementary predictions of the fuel particle trajectories, show that the flame stability performance of the blended fuel is slightly improved as compared with the single-fuel flames. The overall combustion characteristics of the sewage sludge flame were found to be similar to those previously observed for low-rank coals (e.g., lignite). The nitric oxide emissions were higher for the sewage and the blended flame—an observation that is not solely reflected in the nitrogen content of the fuels but also in subtle changes in initial ignition behavior. A comparative analysis of the concentrations of selected metals (Zn, Cu, Cr, Mn, Ni, Cd, Pb) in various solid particle fractions collected near the furnace exit for the three flames shows that the metal enrichment on submicron ash particles was lowest for the sewage sludge flame and increased with the proportion of coal (fuel rank). The formation of a higher submicron fraction of ash particles from lignite coal reported in the literature, however, was not observed for the sewage sludge flame. These observations showed that the vapor pressure alone does not provide a sufficient explanation for metal partitioning in the presence of large quantities of minerals. Other processes such as fragmentation, mineral/metal interactions, and metal oxidation/chlorination become increasingly important.

From an operational view-point, the co-firing of dried, pulverized, sewage sludge (DPSS) slightly enhanced flame performance, while the metal emission values in the flue gas, as well as the metal leachability values, remained lower than recommended EU legislative limits. The 25% increase in NO_x observed could in part be ameliorated through available NO_x reduction techniques.

Introduction

The disposal of waste materials, whether from industrial, agricultural, or biological activity, is becoming a major concern due to a combination of the increasing amounts being produced, the reduction in available economic landfill sites, and environmental pressure restricting previous disposal routes, such as sea dumping. Many of these wastes, however, have sufficient energy value to either complement or supplement existing fossil fuels in conventional furnaces or be burned in an energy-from-waste facility. This burning of the waste again generates significant public opposition based upon perceived risks associated with air-borne metal emissions and the release of toxic gases. Even after burning, the quality of any solid residue also causes disquiet, particularly in regard to the level of unburned combustibles and the leachability of residual metal compounds.

The selection of an appropriate combustion method is largely based on the characteristics of the waste material to be burned and the prevailing regulations. The broad range of material to be disposed of is matched by the diverse incineration practices used. A wealth of published literature focuses on the combustion and pollution aspects under the conditions that prevail in these waste combustors [1–4]. The aim of the present investigation, however, has been to concentrate on one topical waste, sewage sludge, and to assess the technical and environmen-

tal feasibility of suspension co-firing it with pulverized coal in a utility boiler. This work, which complements the authors' continuing research on "waste-to-energy concepts," was undertaken in a large-scale laboratory furnace.

Comparative detailed combustion data for three flames established in the furnace are presented, namely, a base-case coal flame (Hem Heath, UK) (flame A), a sewage sludge flame (flame C), and an equal blend by mass (26% by thermal input of sewage) of the two (flame B). The comprehensive data archive collected includes flame stability performance, major gas species, gas temperature, stable fuel-derived nitrogen compounds (NO, HCN, NH_3) and major and trace toxic metals (Zn, Pb, Cu, Cr, Mn, Ni, and Cd). The rationale for the selection of these particular metals was (a) their high concentrations in the fuels studied and (b) their toxicity and wide range of volatility. Leaching tests are also reported for selected toxic metals in order to assess the "long-term" commercial usage of the bottom ash.

The Furnace and Experimental Techniques

The vertically oriented and down-fired (0.5 mW) furnace at Imperial College has an internal diameter of 0.6 m and a height of 3.0 m. The PF burner with a refractory quarl, situated in the roof, is of double concentric design incorporating a moveable-block swirler. A comprehensive description of the furnace, gas sampling probes, and instrumentation can be found elsewhere[5].

All relevant major gas species concentrations of CO, CO_2, NO, and O_2 were recorded using NDIR, chemiluminescence, and paramagnetic-type instruments, respectively. Due to space limitations, CO and CO_2 are not included here. Concentrations of stable HCN and NH_3 were measured according to a previously established absorption technique [6]. Gas temperatures were recorded using bare-wire 40-μm Pt/Pt-13% Rh thermocouples.

A new protocol for the quantification of toxic metal emissions data from the solid fuels used was established. For the collection of solid particles for subsequent toxic metal detection, an additional on-line nitrogen-quench particle sampling train [7] was installed. An Andersen, Inc., eight-stage atmospheric cascade impactor was used for the separation of the captured solid particles into nine particle size ranges (0–0.4, 0.4–0.7, 0.7–1.1, 1.1–2.1, 2.1–3.3, 3.3–4.7, 4.7–5.8, 5.8–9.0, and 9.0 $\geq \mu$m). For subsequent analysis using an atomic absorption spectrometer (AAS), the samples from the cascade impactor were dissolved in 10 mL of an acid cocktail [HF (49%), HNO_3 (70%), HCl (39%), deionized water, by volume 100, 100, 300, 500 mL, respectively]. The development and optimization details of the sampling and analytical procedures are reported elsewhere [7].

For the leachability test, an EU waste compliance procedure [8] was followed wherein a weighed sample of bottom ash was dissolved in a distilled water bath, followed by several days of constant, controlled agitation. The liquid sample was subsequently analyzed for any leachate composition.

The specifications of the coal, sewage sludge, and blend used in the investigation, including the particle-size distribution and elemental analysis of major, minor, and trace metal contents, is given in Table 1. The furnace operating conditions, for example, swirl number, momentum ratio, and heat input, remained constant throughout.

Experimental Results

Flame Stability

For a particular burner, fuel feed rate, and fuel type and composition, the stability performance of the flame produced is controlled by the level of swirl in the combustor air stream as well as its primary and secondary jet velocities. The flame stability criteria adopted herein defines a stable flame as one that is both lit-back and anchored to the burner quarl. Such a flame exhibits a lower NO formation at its root and higher combustion efficiency.

Figure 1 shows the comparative stability limits for the three flames. The relatively broad limits of the stability curve for the Hem Heath coal (flame A) are typical of those previously observed for other bituminous coals in this laboratory. The stability curve of the sewage sludge (flame C), however, is, as expected, restricted to similar narrow limits seen for low-rank fuels, such as lignite coals [9], with calorific values below 20 mJ/kg. More importantly, the coal–sewage sludge blend flame (flame B) shows a slight improvement in stability performance over that of the base-case coal flame. The relatively smaller fraction of the higher volatile content sludge particles continue to provide an ignition source at higher momentum ratios, which assists in initiating the devolatilization of the coal particles, thereby slightly extending the stability performance toward the higher momentum ratios.

The difference in the stability limits for the three flames stems from the particles' trajectories and their residence time in the internal recirculation zone (IRZ). The position and character of the IRZ itself relative to the burner quarl is also a crucial factor affecting flame stability. In order to gain a better understanding of the size and position of the burner IRZ, computational simulations were performed using the 2D CINAR code, which has been recently extended to account for multimode combustion of various grade fuels [10]. The predicted

TABLE 1
Specifications of fuel and metal concentrations

Proximate analysis (wt % as received)	Flame A Coal	Flame B Blend	Flame C Sludge		Flame A Coal (mg/kg)	Flame B Blend (mg/kg)	Flame C Sludge (mg/kg)
Moisture	1.7	2.4	3.0	Fe	2,335	8,741	13,141
Volatile matter	34.0	40.3	46.6	Al	146	5,423	10,700
Fixed carbon	59.3	32.8	6.2	Zn	28	470	1,002
Ash	5.0	24.6	44.2	Cu	14	191	463
Ultimate analysis				Pb	16	184	381
(wt% dry)				Mn	19	170	272
Carbon	77.9	53.0	28.1	Cr	4	119	209
Hydrogen	4.6	4.2	3.7	Ni	6	32	47
Nitrogen	1.8	2.4	3.0	V	7	12	17
Sulfur	0.9	0.9	0.8	As	5	13	20
Chlorine	0.7	0.5	0.2	Mo	<2	3	5
Oxygen (by difference)	7.4	12.0	17.0	Hg	<2	<2	<2
Bulk density	603.3	606.2	609.0	Co	<2	4	6
(kg/m^3)				Cd	5	8	10
Heating value, (MJ/kg)	31.7	21.5	11.2				

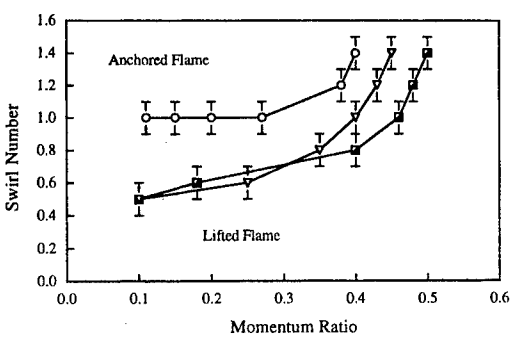

FIG. 1. Flame stability limits: (∇) flame A (coal); (◪) flame B (coal sludge), and (○): flame C (sewage sludge).

gas flow patterns and particle trajectories in the NBR for the three flames, with the same inlet locations and four representative particle sizes (10, 22, 45, and 90 mm), are shown in Fig. 2. From this information, it appears that for the blend flame, the observed slight increase in the particles' penetration depths into the IRZ results in a greater particle residence time, with the early devolatilization of sewage sludge particles intensifying the combustion reactions by producing a hotter IRZ. For the sewage sludge flame (flame C), however, the largest particles leave the IRZ with reduced residence times prior to completing their devolatilization. This restricts the flame stability limits to higher swirl numbers and lower momentum ratios necessary to maintain an adequate particle residence time in the IRZ for devolatilization to be initiated.

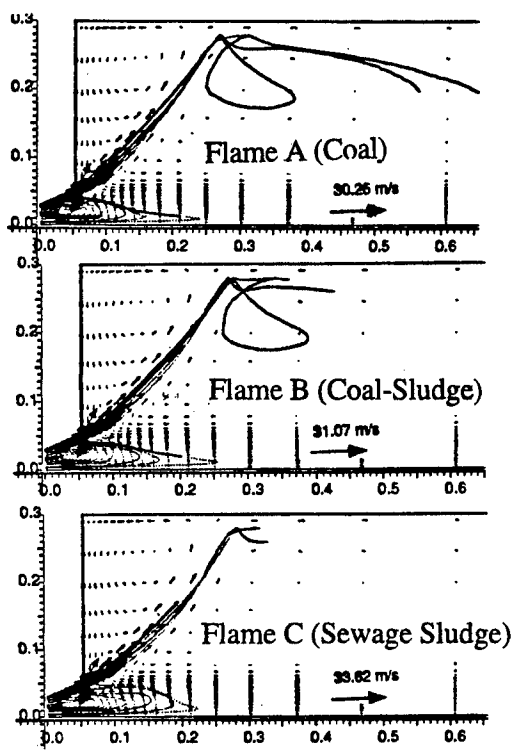

FIG. 2. Predicted gas flow and particle trajectories.

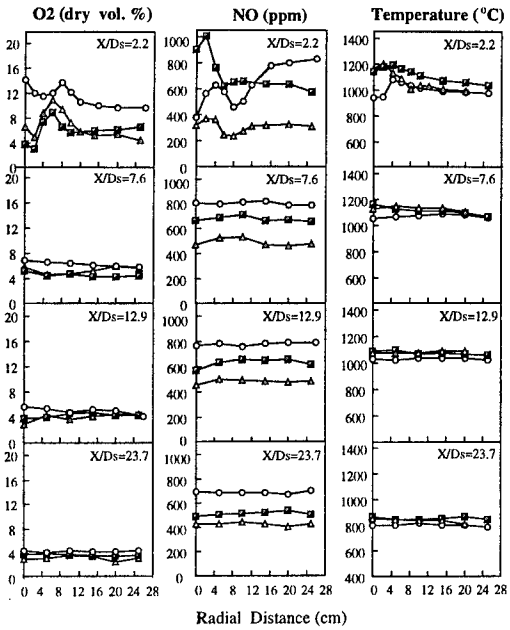

FIG. 3. Gas species profiles: (△) flame A (coal); (◪) flame B (coal sludge), and (○): flame C (sewage sludge).

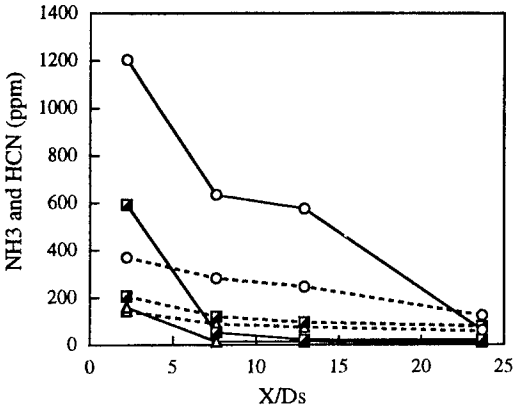

FIG. 4. NH_3 (——) and HCN (- - -) concentration profiles: (△) flame A (coal); (◪) flame B (coal sludge), and (○) flame C (sewage sludge).

In-Flame Combustion Data

Radial profiles of gas species concentrations are presented in Fig. 3 for four axial locations, expressed in terms of the distance from the burner throat divided by its diameter (56 mm), *X/Ds*. The concentrations of HCN and NH_3 along the combustor axis are presented in Fig. 4. At the nearest location to the burner, *X/Ds* = 2.2, the reactions for flame B (blend) are more intense in the radial direction up to $R \leq 20$ mm and are accompanied by a sharp increase in NO formation.

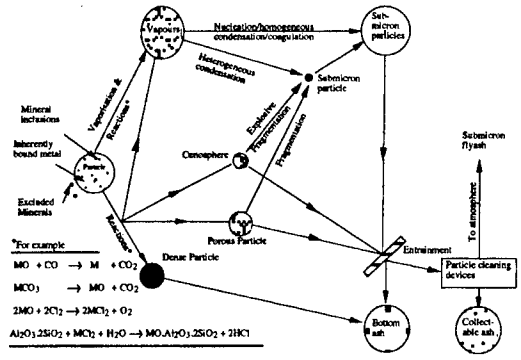

FIG. 5. Metal partitioning mechanism.

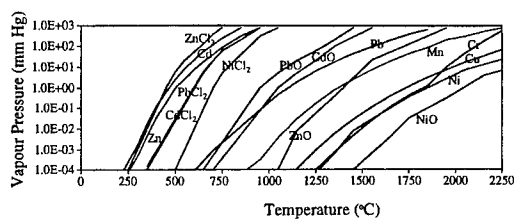

FIG. 6. Vapor pressure curves.

The influence of the secondary air stream for the three flames is seen in the region 40 mm $\leq R \geq$ 80 mm through a steep rise in O_2 along with a corresponding decrease in NO, as well as gas temperature. Further away from the axis, $R \geq 160$ mm, the relatively flat profile delineates the extent of the external recirculation zone (ERZ), which returns combustion products from downstream. The peak values of HCN and NH_3 (Fig. 4) also occur at this axial location. Further downstream at *X/Ds* = 7.6, the O_2 and NO profiles are relatively flat, indicating the completion of mixing.

As expected, NO emissions increased in both the sewage sludge and its blend flames (B and C). The higher nitric oxide formation rate for the sewage sludge flame is seen to be more pronounced in the early stages of combustion, where its slower volatile release rate and the lower temperatures of the IRZ extend the nitrogen liberation region toward the oxygen-rich secondary air. Compared with the coal flame (A), the nitric oxide emissions increased by 25% and 75% for the blend (B) and the sewage sludge flame (C), respectively.

The comparatively similar particle burnout of 98.2% and 97.8% for the coal and the sewage sludge–coal blend flames, respectively, indicates very similar overall combustion efficiencies, whereas the particle burnout of the sewage sludge flame

TABLE 2
Formation of total submicron particles for flames A, B, and C

Flame	Gram submicron particles per gram fuel burned	Fraction of ash as submicron particles	Submicron particulate matter in flue gas mg/m^3 1 atm, 0°C, 11% O_2
A	0.0012	0.0239	73
B	0.0015	0.0061	130
C	0.0020	0.0046	309

TABLE 3
Metal enrichment factors in submicron ash

Flame	Zn	Pb	Cu	Cr	Mn	Ni	Cd
A	8.2	11.6	11.9	7.3	2.9	10.3	22.3
B	6.1	8.04	3.7	6.1	1.7	8.5	21.7
C	5.5	2.5	2.0	1.3	0.9	4.5	18.9

TABLE 4
Concentration of elements in treated flue gas, mg/m^3 @1 atm, 0°C, 11%O O_2

Flame	Zn	Pb	Cu	Cr	Mn	Ni	Cd
A	0.023	0.019	0.018	0.0033	0.0057	0.0063	0.0112
B	0.106	0.055	0.026	0.027	0.011	0.0098	0.0064
C	0.268	0.047	0.046	0.013	0.013	0.011	0.0091

(91.2%) was significantly lower. Some operational problems (e.g., slag build-up) were also encountered when firing sludge alone due to the high mineral content of the fuel. Such practical difficulties were not observed for the blend, entertaining the possibility of efficient co-firing of the pulverized sewage sludge up to 26% by heating value and 50% by weight without any major fouling.

Toxic Metal Emissions

A possible mechanism for the formation of submicron particles enriched in metal species for typical utility combustion conditions, as has been suggested by several researchers [3,11], is shown in Fig. 5. This figure is useful in explaining the data, particularly the enrichment of metals on small particles as a result of either the self-nucleation or the adsorption of volatile metal species due to their high surface areas. An additional influence is the vapor pressure behavior of selected metal species, which is shown in Fig. 6 over the temperature range of 250–2250°C. Under the combustion temperature conditions of the flames studied, this figure reveals that the vapor pressure of a few elements (cadmium, lead, and zinc) is such that they would be expected to completely volatilize within the flame zone, while other metals (copper, chromium, and nickel) with lower vapor pressures would only partially vaporize at the observed temperatures.

The amount of submicron particles collected for the three flames as grams per gram of fuel burned, the fraction of their respective ash content, and the total particulate matter in the untreated flue gases are given in Table 2. The submicron particle fraction decreases from flames A to C, which may be attributed to the reduction in the comparative chlorine content and the depletion of submicron particles due to comparatively higher metal–mineral interaction in flames B and C. Generally, low-rank, high-volatile coals produce more submicron particles as compared with high-rank coals [12]. However, it appears that ranking alone is not the sole criterion for the ash volatilization behavior during PF combustion. Rather, it is the composition, ash content, and distribution of its mineral matter in the fuel that dictates the depletion of submicron particles.

Toxic metal enrichment factors for the metals studied are given in Table 3. These were calculated as the ratio of the concentration of an element in the submicron particles to that in the total ash collected, including all particle sizes. Generally, the element enrichment factors are higher for the coal and blend flames. Elements that are significantly enriched in the submicron particles of all the flames include Zn, Pb, Cu, Cr, and Ni, while Cd is a highly enriched element in both the submicron particles and the submicron fumes of all three. The metal enrichment trend in submicron particles for the sewage sludge flame is relatively low, as compared with the other flames. Table 4 summarizes the concentration of elements in the flue gas after cleaning, assuming a typical electrostatic precipitator (ESP), submicron particle capture efficiency (93%). The particulate matter emissions and concentration of toxic metals in the flames satisfy the limits prescribed by the EU for incinerators [13].

The presence of chlorine, the excess of mineral matter, and the mode of the occurrence of toxic

TABLE 5
Metal enrichment factors in submicron ash

Flame	Cd	Zn	Pb	Ni
D	7.20	5.34	3.52	1.95
E	7.10	6.90	3.99	0.11
F	9.95	8.96	4.24	2.32

metals in the fuel may have a significant effect on the formation and metal enrichment of submicron particles, depending on the combustion conditions. To address these effects on metal partitioning (Fig. 5), an experimental regime is being undertaken in which metal oxides, chlorides, carbonates, sulfides, and organometallics of Cd, Zn, Pb, and Ni are being extraneously added to the dried, pulverized sewage sludge (DPSS). As part of this work, results already have been obtained for the metal enrichment on submicron particles for the DPSS (flame D), DPSS with metal oxides (flame E), and chlorides (flame F) by injecting these fuels through the center of an asymmetric natural gas/air flame in a high heating rate (10^5 K/s), flat-flame turbulent jet (FFTJ) apparatus. The results are given in Table 5.

The mass fraction of submicron particles in the sewage sludge flame was increased from 0.004 for the DPSS to 0.008 and 0.05, respectively, when metal oxides and chlorides were added to the DPSS. The results suggested that the extraneous metal chlorides are partitioned more to submicron particles as compared with the conditions where metal oxides were added. The effect of chlorides addition to cadmium and zinc was more pronounced with a higher cadmium and zinc enrichment on submicron particles. Little or no enrichment of Ni was anticipated in both flames (D and E) due to the low vapor pressures of nickel and its oxide (Fig. 6). However, the slight enrichment of Ni in the pure sewage sludge flame is in agreement with other reported results in coal and sewage sludge flames [14,15]. This enrichment was attributed to the partial vaporization of Ni metal or the conversion of some of it to more volatile compounds (i.e., $NiCl_2$) and/or through particle fragmentation [16].

From these observations, it would appear that the hypothesis that metal partitioning is primarily controlled by its vapor pressure is inadequate in the presence of large quantities of minerals and other processes, such as fragmentation and mineral–metal interactions, become increasingly important.

Finally, leachability values of the high ash sewage sludge (flame C), attributed to the formation of insoluble metal compounds during combustion, were carried out to assess the viability of using the bottom ash commercially. The results for Cu, Zn, Cr, Ni, Pb, and Cd were found to be below the allowable EU standard.

Concluding Remarks

The technical feasibility of using DPSS as a supplementary fuel for coal-fired utility boilers has been assessed in a laboratory furnace. No deterioration in burner stability performance or combustion efficiency was observed for a 26% by heat input blend of sewage and coal. The nitric oxide emissions, however, increased by 25% and 75% for the blend and sewage sludge flames, respectively, as compared with the coal flame.

The overall combustion characteristics of the sewage sludge flame are similar to those previously observed for lignite coals. The formation of a higher submicron fraction of coal particles reported in the literature, however, was not recorded in the sewage sludge flame. Metal enrichment on submicron particles was lowest for the sewage sludge flame, and this tendency increased with the metal chlorides and fuel rank (coal/sewage sludge blend to coal flames).

The toxic metal emissions and leachability values for the three flames were well below the EU recommended values. Although slagging problems were encountered with the sewage sludge flame, there was no problematic build up with the blended flame. The primary disadvantage of co-firing sludge to be addressed is the 25% increase in NO emissions due in part to the higher nitrogen content of the fuel, which could be ameliorated through NO_x reduction technology.

From the results of our investigation, it would appear that the concept of co-firing of sewage sludge with pulverized coal in a power station boiler is technically feasible. In order to provide further information for owner/operators, work is now continuing on the effect of co-firing on elements other than the flame, such as slagging and fouling.

Acknowledgments

The authors are particularly indebted to the European Union for its financial support of this work under the APAS programme. An appreciation must also be accorded to J. Charoensuk for his assistance with the flow field calculations. We are also grateful to Dr. W. Linak and R. Srivastava (EPA, USA) for their technical help and guidance for the quantification of toxic metals.

REFERENCES

1. Lighty, J. S., Eddings, E. G., Lindtren, E. R., Xiao-Xue, D., Pershing, D. W., Einter, R. M., and McClennen, W. H., *Combust. Sci. Technol.* 74:31 (1990).
2. Marchant, R., Hepler, W., Smith, O. I., Willis, J.,

Cadou, C., Logan, P., and Karagozian, A. R., *Combust. Sci. Technol.* 82:1 (1992).
3. Linak, W. P., Srivastava, R. K., and Wendt, J. O. L., *Third International Conference and Seminar on Municipal Waste Combustion,* March 30–April 2, Williamsburg, VA, 1993.
4. Linak, W. P., Srivastava, R. K., and Wendt, J. O. L., *Twenty-fifth Symposium (International) on Combustion,* The Combustion Institute, Pittsburgh, 1994.
5. Costa, M., Costen, P., and Lockwood, F. C., *J. Inst. Energy* 64:64 (1991).
6. Abbas, T., Costen, P., and Lockwood, F. C., *Combust. Flame* 91:346 (1992).
7. Abbas, T., Costen, P., Glaser, K., Hassan, S., and Lockwood, F. C., *On Sewage Sludge/Coal Flames in a Down-Fired Laboratory Furnace,* Internal Report No. TF/95/20, Thermofluids Section, Mechanical Engineering Department, Imperial College, London, 1995.
8. CEN (1994). CEN/TC 292/WG2 DOC 25, Revision 10 (CEN/TC 292/WG2 Doc 38).
9. Costa, M., Costen, P., and Lockwood, F. C., *Fuel* 69:403–406 (1990).
10. Abbas, T., Costen, P., Kandamby, N. H., Lockwood, F. C., and Ou, J. J., *Twenty-fifth Symposium (International) on Combustion,* The Combustion Institute, University of California, Irvine, 1994.
11. Barton, R. G., Clark, W. D., and Seeker, W. R., *Combust. Sci. Technol.* 74:327 (1990).
12. Quann, R. J., Neville, M., and Sarofim, A. F., *Combust. Sci. Technol.* 74:245 (1990).
13. EU/89/429, Metal Air Emissions for Incinerators.
14. Smith, R. D., Campbell, J. A., and Nielson, K. K., *Fuel* 59:661–665 (1980).
15. Bennet, R. L. and Knapp, K. T., *Environ. Sci. Technol.* 16:831–836 (1982).
16. Mullholand, J. A. and Sarofim, A. F., *Environ. Sci. Technol.* 25:268–274 (1991).

COMMENTS

S. Dasappa, Indian Institute of Science, India. In your presentation you have not indicated the a/f ratio for carrying out the combustion. What was the criterion used for setting the a/f ratio for the sludge?

Author's Reply. The air-fuel ratio was decreased for sewage sludge and its blend while maintaining both the excess air and thermal inputs the same for all three flames. Under combustion conditions, the excess air is the controlling parameter than the ratio of air to fuel for example concerning flame stability and NO_x formation.

•

Luigi Pistone, SNAM Progetti, Italy. I would imagine a strong influence of the burner size and power input on the observed phenomenology. Please comment.

Author's Reply. We agree with this comment. For this reason, base case sewage sludge flames were taken in both large-scale laboratory furnace as well as in the small-scale turbulent jet apparatus (FFTJ). The sewage sludge flames studied in the FFTJ apparatus where metals were added in various forms are therefore only compared with the sewage sludge flame of FFTJ.

Twenty-Sixth Symposium (International) on Combustion/The Combustion Institute, 1996/pp. 2495–2502

TRANSFORMATIONS OF SLUDGE WASTE DURING COMBUSTION IN A LOW-HIGH-LOW TEMPERATURE REACTOR

JANUSZ A. KOZIŃSKI, RAAFAT SAADE AND GUOHUI ZHENG
McGill University
McGill Metals Processing Centre
Department of Metallurgical Engineering
3450 University St., FDA 119
Montreal, QC, Canada H3A 2A7

A new method of multizone combustion of a pulp/paper sludge in a low-high-low (LHL) temperature reactor is investigated. Experiments are conducted in a TGA-FTIR (thermogravimetric furnace coupled with Fourier transform infrared spectrometer) facility simulating realistic particle-metal and particle-gas interactions. The influence of time–temperature profiles on morphology, heavy (Cr, Cd), and light (Ca, Si) metal distributions inside ash particles formed during sludge combustion is determined. Sludge samples (70 g) are heated to 1770 K at an average rate of 75 K/min, kept at 1770 K for four different residence times (R_0 = 0 s, R_1 = 60 s, R_2 = 300 s, and R_3 = 900 s), and then suddenly quenched (15 K/s) to simulate LHL temperature regions. In order to obtain time-resolved data on the structural and compositional transformations of the sludge, samples are subjected to a variety of analytical techniques: wavelength-dispersive X-ray spectrometry, scanning electron microscopy, X-ray diffractometry, and atomic force microscopy. Sludge undergoes dramatic morphological transformations from a mixture of complex fibers, skeleton-like structures (45–110 μm), highly porous particles, to dense compact spheres (5–30 μm). Structural changes influence the distribution of metals in the solid residue. Toxic metals (Cr, Cd) are concentrated at the particle core and are successively surrounded by nonporous dense layers rich in Ca, K, Al, Na, and Si. It appears that the multilayered ash particle microstructure can be attributed to internal transformations caused by the LHL combustion. It is found that the residence time of 300 s at 1770 K is optimal to encapsulate Cd inside the particle core. A model of a final ash particle formed at the optimal residence time is designed and a mechanism of the heavy metal microencapsulation is proposed. Calculations show that metal diffusion does not seem to be the dominant process responsible for Cd migration inside the ash particle.

Introduction

The ever-increasing quantities of solid wastes (projected growths of 1% annually from 279 MMT in 1995 being expected [1]) are the source of the growing need for proper waste disposal methods. One proven technology is waste combustion. However, products of waste burning include ash particles that contain hazardous heavy metals (e.g., Cr and Cd). It is evident that minimization of metal release from a host substrate is critical in limiting the emissions of toxic heavy metals. Therefore, our research is aimed at two goals: first, the development of a practical method for encapsulation of hazardous metals during the high-temperature treatment of sludge wastes, and second, a better understanding of the fate of metals during waste combustion.

In this paper, two things are done: (1) It is shown that combustion of contaminated sludge can yield ash particles with toxic metals safely encapsulated. Further, a structural evolution and ash particle model are interpreted. (2) Conventional waste combustion is modified by applying low-high-low (LHL) temperature regions in a thermal reactor such that heating and cooling rates are relatively fast in the "low" regions, and temperature is constant in the "high" temperature zone. A simple mathematical model is also developed for the diffusion of heat and metal (Cd) inside an ash particle. A practical, unambiguous, and presumably consistent method may therefore be available for the efficient and clean utilization of waste sludges.

Experimental Approach

Our approach is shown in Fig. 1 (column A). It illustrates an idea of applying the multizone temperature method to dispose of contaminated sludges. This idea originated from interesting preliminary results obtained by one of the authors (JAK) and his colleagues during pilot-scale research in a fluidized bed combustor [2,3], which left some unanswered questions regarding solid and metal

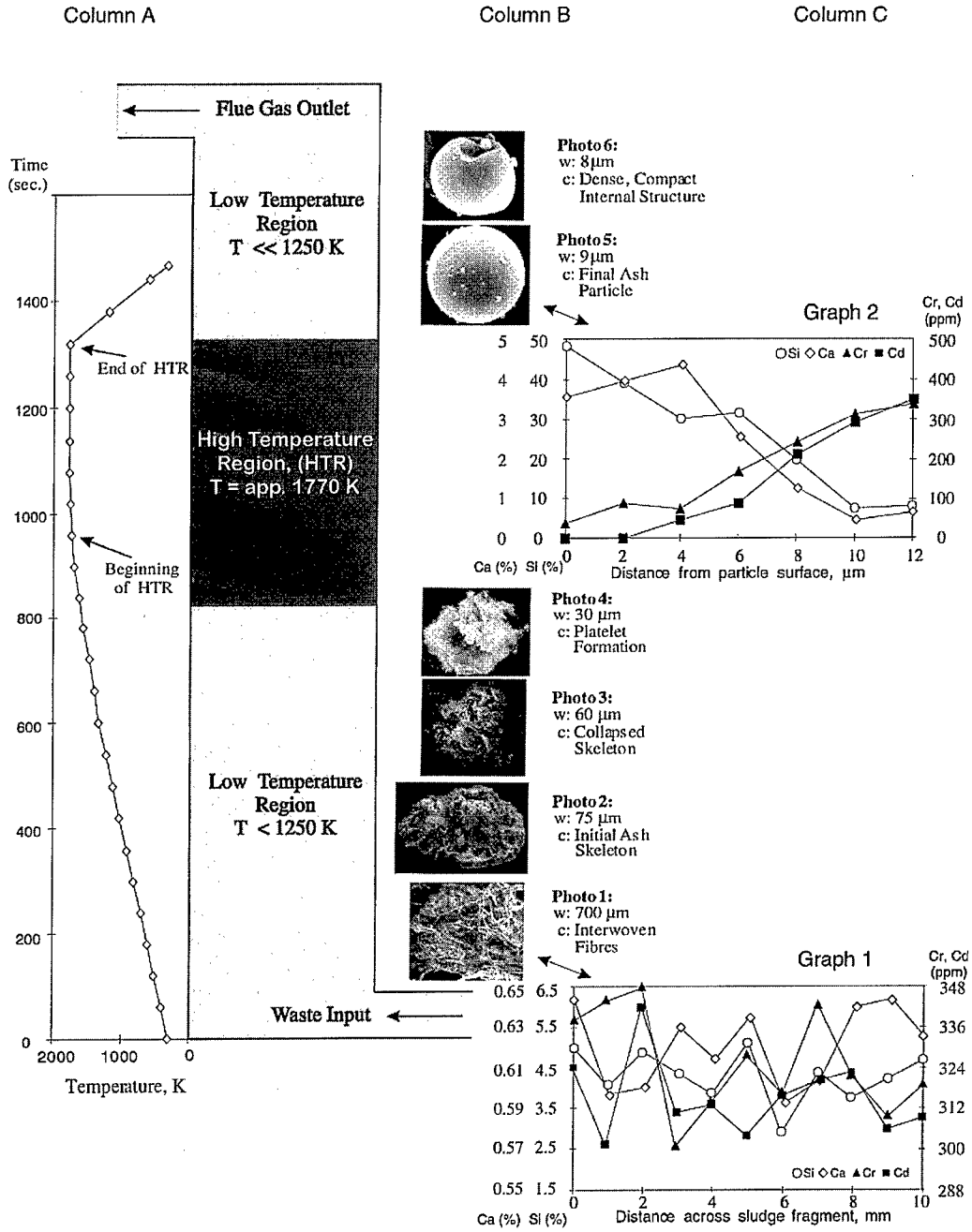

FIG. 1. Illustration of a multizone combustion method applied to the disposal of contaminated sludges. *Column A* explains the idea of the LHL temperature reactor. The waste is initially fed into the low-temperature region (<1250 K), then subjected to the high-temperature treatment (1770 K), which is followed by another low-temperature zone (≪1250 K). An experimental temperature–time profile obtained at a residence time of 300 s in the HTR is also shown. *Column B* presents a sequence of microphotographs taken with a scanning electron microscope showing morphological changes in the sludge waste during combustion. The following symbols are used to describe each photo: *w* (maximum width) and *c* (basic characteristics of the photo). *Column C* contains two graphs displaying metal occurrence in solid material. Graph 1 presents random distribution of Ca, Si, Cr, and Cd in the feed sludge. A length of a sludge fragment is 10 mm. Graph 2 shows radial profiles of Cr, Cd, Ca, and Si concentrations inside the cross section of the dense, compact ash particle with equivalent diameter of 24 μm. Such particles were final structures formed during sludge combustion experiments in the LHL temperature reactor.

transformations. In the current research, the multizone concept was tested in a furnace separated into three zones where a high-temperature region (HTR; 1770 K) was imposed in the middle of two low-temperature regions (<1250 K). This type of reactor was called a LHL temperature furnace. The experiments were conducted in a computer-controlled facility consisting of a high-temperature Cahn TGA-171 thermogravimetric furnace (TGA) coupled with Mattson FTIR Galaxy 5020 Fourier transform infrared (FTIR) spectrometer. This TGA-FTIR system can simulate the residence time, temperature histories, and chemical environment of commercial waste remediation units, allowing for a variety of particle-metal and particle-gas interactions. Changes in the sample weight, temperature, as well as gas composition inside the furnace are measured continuously. The temperature and pressure limits are 1970 K and 1.0 atm, respectively. The length of the heated zone is 300 mm with a homogeneous zone of 100 mm. There are access ports for the collection of solid and gas samples during waste combustion. However, due to the molten ash phase, we were not able to extract ash samples from the furnace during the combustion at the highest temperature (1770 K).

Methodology

Sludge waste from a pulp and paper mill was chosen because of the increasingly higher amounts of this material generated by the industry (e.g., 2200 tones/day of dry sludge in Canada alone). Its disposal in landfills is becoming a serious concern, due to its large volume and contamination with heavy metals (e.g., Cd, Cr), thus creating a residue management problem. Irregular fragments of the sludge (see Fig. 1, column B, photo 1) were made of complex fibers (30–60-μm wide; 100–600-μm long) mixed with the aluminosilicate matrix. There were holes at the center of most of the fibers. They were probably intrinsic features of the vegetal used to produce the fiber. The sludge was predried and sieved to fragments smaller than 20.0 mm in diameter. It contained 10.00% moisture, 40.10% carbon, and 26.72% oxygen, while the heating value was 15,800 kJ/kg. Ash concentration was 20.37%. Ash elemental analyses showed a dominance of SiO_2, Al_2O_3, and CaO (56.46%, 29.43%, and 4.47%, respectively) with high levels of alkalis ($Na_2O + K_2O = 2.01\%$). The sludge was doped and well mixed with chromium and cadmium, and the concentration aimed for each metal was 350 ppm. Aqueous solutions of $Cr(NO_3)_3 \cdot 9H_2O$ and $Cd(NO_3)_2 \cdot 4H_2O$ were used.

The influence of time–temperature profiles on the heavy (Cr, Cd) and light (Ca, Si) metal distributions in ash particles was determined. A sample of sludge waste (70 g) was heated to 1770 K at an average rate of 75 K/min. It was then kept at 1770 K for four different residence times: $R_0 = 0$ s, $R_1 = 60$ s, $R_2 = 300$ s, and $R_3 = 900$ s. After being heated, samples were suddenly quenched with nitrogen in a water-cooled chamber in order to simulate LHL temperature regions. The cooling rate was at least 15 K/s. A typical temperature profile at $R_2 = 300$ s is shown in Fig. 1 (column A).

In this paper, we present results obtained for the solid ash particles. The results represent averages for about 3000 individual particles. Particle morphology and size were determined by secondary electron imaging on a JEOL 840 scanning electron microscope operating at 15 keV. The internal ash structure and metal concentrations were obtained with JEOL 8900 SuperProbe electron probe microanalyzer equipped with five wavelength-dispersive spectrometers. Measurements were conducted at 100-s counting times, 20-keV accelerating voltage, and 100-nA beam current. The electron beam width was less than 0.5 μm, and the penetration was less than 1.0 μm. Different phases of the particle internal microstructure were determined by a Rigaku X-ray diffractometer with an 18-kW high-intensity rotating anode (40 kV, 20 mA, Cu$K\alpha$ radiation). Particle surface data were obtained from an atomic force microscope (AFM) Digital Nanoscope III.

Results and Discussion

During combustion, the sludge waste underwent dramatic morphological transformations, which are presented in Fig. 1 (column B, photos 1–6). At low temperatures, up to 450 K, the solid residue looked similar to the initial sludge (photo 1). When most of the volatile fraction of the sludge (primarily CO_2, H_2O, CO, and hydrocarbons) was released before the temperature reached 750 K, the morphology changed into skeleton-like (photo 2). Between 800 and 1200 K, there was an intensive burning accompanied by a collapse of the skeleton-like structure (photo 3) and formation of initial platelets on the particle surface (photo 4). It was observed that the combustion process was enhanced around the holes located at the center of the primary sludge fibers, resulting in fibers breaking into individual smaller fragments. It was not determined, however, whether fibers and matrix both transformed into the same type of ash. Further burning at the highest temperature (1770 K) and subsequent fast cooling (10 K/s) significantly changed ash morphology. No fibers or platelets were seen. There were spherical ash particles (5–30 μm in diameter) with submicron fragments bound to the external surface (photo 5). The particles were completely filled with dense, compact material and had relatively smooth surfaces (photo 6). The surfaces observed on high-resolution AFM revealed a mixture of individual dendrites 20 nm in width. Such dendritic structure most likely came

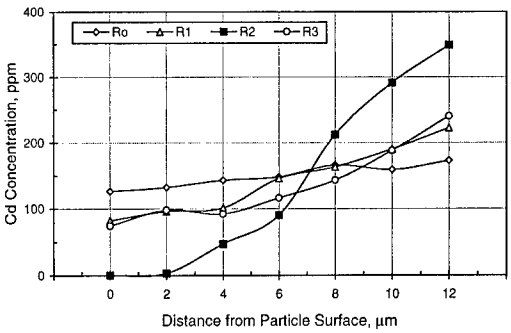

FIG. 2. Radial concentration profiles of Cd in the cross section of the final ash particle with equivalent diameter of 24 μm. Variations in Cd concentration are shown at four different residence times in the HTR: $R_0 = 0$ s, $R_1 = 60$ s, $R_2 = 300$ s, and $R_3 = 900$ s. Cadmium is mostly partitioned in the particle center at R_2. When the residence time is shorter or longer, Cd tends to be rather uniformly distributed inside the particle.

from the sudden solidification of the ash material after its melting in the high-temperature region.

Morphological changes influenced the distribution of metals in the solid residue. The distribution profiles of Si, Ca (representing light metals) and Cr, Cd (representing heavy toxic metals) in the feed sludge after it was doped with heavy metals and prior to combustion are shown in Fig. 1 (column C, graph 1). No associations between light- and heavy-metal elements in the sludge particles were observed. All of the metals were found to be randomly dispersed inside the sludge. Thus, no initial elemental segregation was observed for both the heavy and the light metals inside the feed waste.

Radial profiles of metal concentrations inside the final ash particles that went through the entire LHL temperature cycle are shown in Fig. 1 (column C, graph 2). Data reported were collected when the residence time was 300 s at 1770 K. It is seen that Si dominated on the external surface. Its concentration decreased steadily from 48.4% at the surface to 7.4% and 8.1% in the particle center. Maximum concentration of Ca (4.4%) was located 4.0 μm below the Si-rich region. The amount of Ca in the center was significantly smaller (0.6%). Thus, in the final ash material, Si and Ca were mostly located in the external surface and subsurface layers. Heavy metals (Cr, Cd) were primarily found near the particle core (8.0–12.0 μm from the surface). Cr concentrations rose from 37 ppm at the external surface to 337 ppm in the particle center. No Cd was found in the first 2.0 μm of the surface layer. Its amount grew from 47 ppm at 4.0 μm distance from the surface to 349 ppm in the core. It is evident that the final ash particle was built of a heavy-metal core surrounded by a light-metal external shell. However, particle internal microstructure strongly depended on the ash residence time in the high-temperature region (1770 K). This is shown in Fig. 2, where variations in Cd concentration inside the ash particle are plotted for four residence times. At the residence time $R_0 = 0$ s (which meant that the solid material was continuously heated to 1770 K and immediately quenched), Cd distribution was almost uniform over the entire cross section of the final ash particle. This sharply contrasted with the profile obtained at 300-s residence time ($R_2 = 300$ s), where Cd was partitioned in the particle core and was not detected in the surface layers. Cd concentration profiles at $R_1 = 60$ s and $R_3 = 900$ s residence times revealed the presence of Cd both on the particle surface and in the center. Data presented in Fig. 2 suggest that the residence time influences heavy-metal distribution inside the ash particles. The residence time of 300 s was optimal to concentrate Cd in the particle core. Residence times of 0 and 60 s were too short, and 900 s was too long for the establishment of an entirely layered microstructure (i.e., the light-metal shell and the heavy-metal core). In those cases, a tendency to rather uniform Cd distribution was observed. Since at 1770 K ash was molten, the results indicate that migration of metallic fragments inside the molten particle interior may affect an internal microstructure of the ash.

Additional elemental mapping inside the final ash particles formed with a residence time $R_2 = 300$ s at $T = 1770$ K indicated that their outer surface is composed of layers dominated by light metals: Si was mostly present on the external surface, then Na, Al, K, and Ca revealed their highest concentrations. Thus, the surface was considerably enriched in light-metal elements compared to the particle interior. The increase in surface concentration of the light metals was accompanied by an increase in the surface concentration of oxygen (X-ray diffraction tests), suggesting that the metals were present in oxidized forms (SiO_2, Na_2O, Al_2O_3, K_2O, and CaO). Heavy metals (Cr, Cd, Sb, Pb, Ni, Zn, and Cu) were primarily located in the regions near the particle core (6.0–12.0 μm from the surface). It appears that the multilayered ash particle microstructure can be attributed to internal transformations caused by the LHL temperature treatment.

A model of a final ash particle heated at the optimal residence time (300 s) is proposed in Fig. 3. The particle is dominantly composed of a dense, compact matrix with an exterior aluminosilicate shell (4–6 μm). It contains light-metal oxides, with dominance of Si and Al compounds, creating external surface layers. Low-melting compounds of Na and K are also contained in those regions. A characteristic layer of Ca is located in the subsurface region, 4.0 μm below the surface. The interior of the particle is mostly filled with the network of trace heavy metals (Cr, Cd, Sb, Pb, Ni, Zn, and Cu) concentrated within the

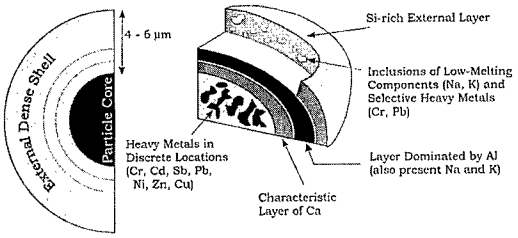

FIG. 3. Model of the final ash particle, illustrating the presence of the external light-metal shell (Si, Al, Na, K, Ca) and a particle core where heavy metals (e.g., Cr, Cd) are discretely located.

particle center. They are essentially encapsulated inside the light-metal shell. Thus, the ash particles generated in the LHL temperature reactor are capable, during their structure evolution, of preventing a significant portion of toxic metals (81.7%) from escaping into the flue gas stream. Indeed, the interaction of Cr and Cd oxides with SiO_2 and/or Al_2O_3 to form silicates and/or aluminosilicates may prevent full vaporization of Cr and Cd from the sludge material. Conversion of Cd and Cr oxides to aluminosilicates occurs between 1200 and 1400 K, and interactions of Cr metal with SiO_2 to form chromium silicates are also likely [e.g., 4–6]—especially since Si is so abundant in the ash.

The evolution of the heavy-metal microencapsulation is illustrated in Fig. 4. As the waste material is subjected to successive temperature ranges, it undergoes a number of transformations numbered from I to VII. In stage I [combustion/volatile organic compounds (VOC) release], the waste undergoes heating, drying, and then combustion of the VOC fraction of the sludge. By the time the resulting solids have reached a temperature of 700 K, the residual mineral matter is essentially an irregular framework of individual fragments, resembling randomly organized porous skeletons ranging from 45 to 110 μm in diameter. The high porosity of this material presents numerous pathways for oxygen to enter the interior of such agglomerates. As the temperature to which the solid structures are subjected continues to increase, the skeletons collapse and break up into porous particles. Thus, in stage II (fragmentation), the weakening of the skeletal structure due to combustion of the organics and the breaking of the links forming the aggregates favor the formation of porous ash containing grains and granules of different shapes. In stage III (surface melting and

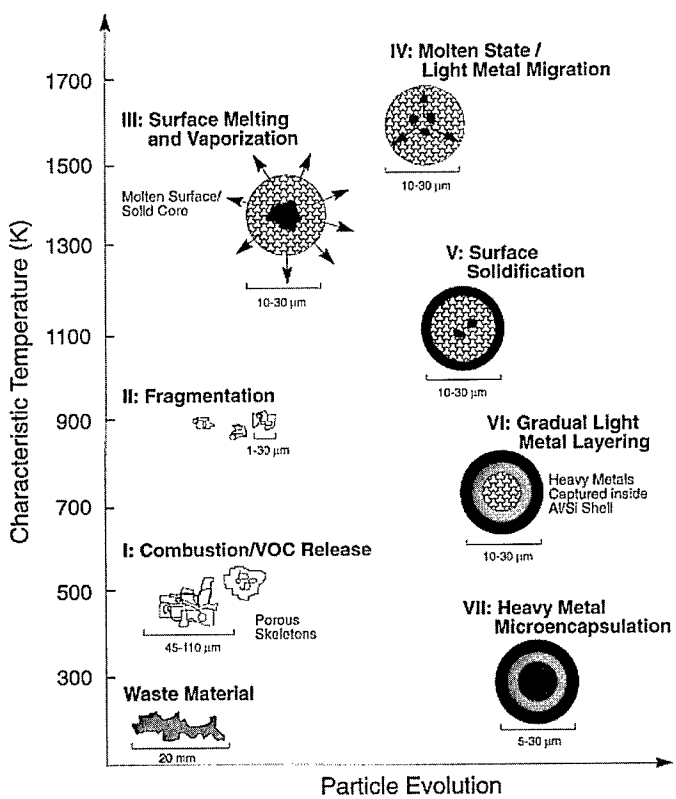

FIG. 4. Mechanism of heavy-metal microencapsulation.

vaporization), the porous ash particles are subjected to temperatures exceeding the softening point of the ash (~1300 K). As the temperature increases toward 1600 K, the surface of the ash particles softens and melts. Low melting point alkali eutectics, forming from the Na, K, and Ca present in the ash, encourage the fusion process. This surface transformation permits the vaporization of volatile species from the outer liquid layer of the particles. When the particles attain the peak temperature in the range of 1700–1770 K, they enter stage IV (molten state/light-metal migration) of the transformation process and are nearly completely molten. Because of their very high fusion temperature, the aluminosilicates may remain as discrete mushy pockets, whose surface will still be able to interact with both light and heavy metals, potentially forming easily melting eutectics or new compounds that adsorb heavy metals, thereby trapping them at the core [7]. At the high temperatures attained in stage IV, conditions permitting the migration of light metals to the particle surface develop. Individual light-metal fragments can migrate over distances greater than 3–7 μm before particle structure compacting [8]. The attraction of light elements to the surface from inside the particle can be explained in terms of the Gibbs adsorption isotherm, which states that the surface free energies decrease when solutes form surface excesses. Therefore, they migrate to the surface from within the molten particle to decrease surface free energy by an increase in chemical potential of solute. During melting, surface free energy is minimized as a result of surface tension forces acting on the melt. Silicate material can be expelled, due to surface tension, to the surface of the molten ash particle. Thus, it can be concentrated on the particle surfaces. Light elements are transported to locations left by other species vaporized from the surface. Upon entering stage V (surface solidification), the molten ash particles begin to cool down abruptly, and a solid skin forms, precluding any more surface losses. The pores on the particle surface are enclosed very rapidly during the particle structure solidification, and the structure itself becomes dense. Heavy-metal fragments are significantly less mobile than light metals; therefore, they do not have enough time to be transported to the surface. They are trapped (encapsulated) inside the particle. Those processes lead to a concentration gradient across the diameter of the particle with heavier species enriched close to the core regions. However, melting of heavy-metal compounds at the particle surface and their subsequent diffusion through the fused product layer may also be important. Diffusion within the aluminosilicate phase could occur via solid-state diffusion, as described by others [7,9]. When the voids in the particle surface are occupied by migrating species and are subsequently closed off, vaporization of volatile species will cease. Since the core of the particle is still molten, light metals may still continue to migrate inside the particle. The heavier components will segregate at the core, and metals such as Cr and Pb may react with the aluminosilicates present and thus be immobilized. In stage VI (gradual light-metal layering), the particle structure is nearly completely solid, only the very core remains fluid but viscous. As the perimeter gradually solidifies, light-metal–rich layers begin to take shape. Once the particle has been completely cooled to stage VII (heavy-metal microencapsulation), the microencapsulation is complete, yielding the layered particle structure presented in Fig. 3. The ash has attained a compact structure. The heavy metals are concentrated at the core of the particle and are successively surrounded by nonporous dense layers rich in Ca and then Al, K, Na, and Si. The heavy metals are effectively isolated from the particle surface and encapsulated in the core of the final ash particle.

Modeling/Calculations

A simple mathematical model of Cd diffusion inside an ash particle was developed. The diffusion process was assumed to occur predominately in the HTR (see Fig. 1, column A) where the particle is molten. It was accepted that at the entrance to the HTR, temperature gradient travels from the particle surface toward the center, while at the exit of the HTR, the higher temperature is located around the core, and the surface of the particle is subjected to decreasing temperature. Both the conduction of temperature and diffusion of metal (Cd) through the ash particle were simulated. They were described by the governing heat and mass diffusion equations [10]. The diffusion region was assumed to be homogeneous and isotropic. A sink term was included in the mass conservation equation to account for the mass loss [7,10]. The governing equations in a one-dimensional isotropic medium were solved using a simple explicit one-step method with Dirichlet boundary conditions at surfaces. The initial conditions included a constant temperature profile across the particle diameter. The initial temperature was equal to the value found at the beginning of the HTR (1770 K) and then changed as a function of time at the particle surface. Numerical computations began where the ash particle entered the HTR. Simulations were carried out to determine the time required to attain the experimental Cd concentration profiles shown in Fig. 2. Cd migration was considered as a function of metal diffusion only, without any influence of vaporization or condensation. Data presented in Fig. 5 illustrate the measured and computed values of the residence time required to achieve the Cd concentration profiles at four residence times: R_0 = 0 s, R_1 = 60 s, R_2 = 300 s, and R_3 = 900 s. The numerical computations are

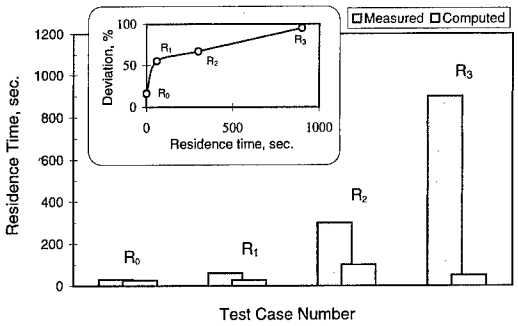

FIG. 5. Comparison of the measured and calculated time necessary to attain Cd concentration profiles shown in Fig. 2. Calculations are performed for different residence times of the ash particle in the HTR. Top curve represents percentage deviation between experimental and numerical modeling values of Cd concentrations at residence times $R_0 = 0$ s, $R_1 = 60$ s, $R_2 = 300$ s, and $R_3 = 900$ s.

unacceptable for residence times R_3, R_2 and R_1 and compare well with experimental data for residence time R_0. A deviation, defined as a percentage difference between experimental and computed values of time, increases with increasing residence time. It rises from 16.7% at R_0; 55.0% and 66.7% at R_1 and R_2, respectively; and reaches 94.4% at R_3. Such change in the deviation could be attributed to the nonlinearity of the problem at hand. It also implies that processes other than metal diffusion play an important role in Cd migration inside the ash particle, especially at long residence times.

The present simulations reveal that the process cannot be modeled as a lumped system and unveils the process to be highly nonlinear and dynamic. In addition, diffusion does not seem to be the dominant phenomenon accounting for the transport of Cd. The influence of vaporization and condensation needs to be quantified.

Conclusions and Implications

We have proposed a novel approach to the thermal treatment of metal-contaminated sludge wastes. Instead of a furnace with a uniform temperature distribution, the suggested reactor is separated into three zones, where a high-temperature region is imposed in the middle of two low-temperature regions. It has been shown that it is possible to produce a compact and dense ash from pulp and paper sludge by applying LHL temperature treatment. Furthermore, by carefully controlling the residence time, as well as heating and cooling rates of the ash produced by the combustion of the sludge, the heavy metals, originally present randomly throughout the noncombusted material, are now preferentially concentrated in the core of the final ash particles. An important objective has thus been attained by LHL temperature processing. The heavy-metal components of the sludge have been effectively segregated within the ash particles and encapsulated by a nonporous compact shell of light metals.

We anticipate, however, some practical problems. For example, a fraction of volatile elements such as Cd and Pb may recondense onto the fine submicron particles and be released from the furnace; also, sludge feeding into the LHL temperature reactor may be complicated due to its irregular morphology. Certainly, we realize the potential pitfalls on the pathway from our experimental observation to a large-scale application. Clearly, further engineering improvements will be needed.

The environmental implications of the LHL sludge treatment are several fold. The microencapsulation of the heavy metals may have important consequences on their leachability once the ash is landfilled. The condensed light-metal layers surrounding the heavy-metal–rich cores of the ash particles may prevent the metals from leaching under acidic conditions. The safety of the landfill will therefore be increased. Finally, if the heavy metals are indeed immobile (as an on-going study will ascertain), the ash may be classified as nontoxic and could be considered for recycling as a component of a construction material, thereby reducing environmental impacts considerably.

Acknowledgments

It is a pleasure to acknowledge J. Broomberg, I. Makarow, and J. Krawiec for their technical contributions during the course of this research and the Natural Sciences and Engineering Research Council of Canada for its support of this program (Grants OGP-0170464 and EQP-0173628).

REFERENCES

1. Niessen, W. R., *Combustion and Incineration Processes: Applications in Environmental Engineering,* Marcel Dekker, New York, 1995, pp. 1–4, 112–171.
2. Kozinski, J. A., Rink, K. K., and Lighty, J. S., *13th International Conference on Fluidized Bed Combustion,* ASME, New York, 1995, Vol. 1, pp. 139–147.
3. Rink, K. K., Kozinski, J. A., and Lighty, J. S., *Combust. Flame* 100:121–130 (1995).
4. Wendt, J. O. L., *Twenty-Fifth Symposium (International) on Combustion,* The Combustion Institute, Pittsburgh, 1994, pp. 277–289.
5. Linak, W. P., Srivastava, R., and Wendt, J. O. L., *Combust. Flame* 100:241–250 (1995).
6. Eddings, E. G., Lighty, J. S., and Kozinski, J. A., *Environ. Sci. Technol.* 28:1791–1800 (1994).

7. Guthrie, R. I. L., *Engineering in Process Metallurgy*, Oxford University Press, New York, 1993, pp. 20–22, 46–66, 238–270.
8. Hulett, L. D. and Weinberger, A. J., *Environ. Sci. Technol.* 14:965–970 (1980).
9. Atkins, P. W., *Physical Chemistry*, W. H. Freeman & Co., New York, 1990, pp. 197–200.
10. Yovanovich, M., Teertstra, P., and Culham, R. J., *J. Thermophys. Heat Trans.* 9:385–390 (1995).

COMMENTS

Johan E. Hustad, SINTEF Energy, Norway. In your presentation you mentioned the heating rates and the importance of the temperature and residence times. What was the initial particle size and sample size in your T6A-measurement and do you think the particle size is of importance to the results?

You claim that the ash is non-hazardous by looking at the dense character of ash particle and the enclosure of the heavy metals in the center of the particles. Did you perform any leachability tests to prove that?

Author's Reply. The weight of the sludge waste sample was 70 g. It was a mixture of randomly shaped fragments with sizes smaller than 20.0 mm in diameter. The size of the majority of individual ash particles was between 5 μm and 30 μm in diameter. We have observed similar ash particles even if the sludge sample size was changed. At the present state of analysis it seems that the ash particle size is not critical for the heavy metals encapsulation. However, due to the limitations in an electron beam width (0.5 μm) and its penetration (1.0 μm) we were unable to analyze quantitatively submicron particles.

We have performed short-term Toxicity Characteristic Leaching Procedure (TCLP) tests in order to identify the presence of leachable heavy metals. The tests showed no presence of Cr and Cd at detectable concentrations (>0.1 mg/L). Verification of the heavy metals immobilization inside the ash particles is a focus of an on-going long-term leachability study. In this study we simulate the leaching process which the ash would undergo if disposed of in a sanitary landfill.

•

Ashwani K. Gupta, University of Maryland, USA. The composition of waste varies both temporally and spatially. Can you please comment on the uniformity of light and heavy metals in the waste sample just prior to the experimental study. What is the accuracy and precision of the reported data?

Author's Reply. Distribution of light (Ca, Si) and heavy metals (Cr, Cd) across a 10 mm long sludge fragment has been shown in the paper in Fig. 1 (column C, graph 1). As you can see from the metal concentration profiles, they were randomly scattered inside the sludge prior to burning. In order to determine local concentrations of metals in the sludge particles we applied electron probe microanalysis coupled with wavelength-dispersive X-ray spectrometry. An inaccuracy of metal analyses in supermicron structures was below 5%, since each metal concentration was significantly higher that its detection limit [1]. The precision of particle size measurements was typically within 93–95% range if at least 2,000 particles per sample were analyzed [2,3]. Our results represent averages for about 3,000 individual particles.

REFERENCES

1. Scott, V. D., Love, G., and Reed, S. J. B., *Quantitative Electron Probe Microanalysis*, Hemel Hempstead, New York, 1995, pp. 73–211.
2. Srinivasachar, S., Senior, C. L., Helble, J. J., and Moore, J. W., *Twenty-Fourth Symposium (International) on Combustion*, The Combustion Institute, Pittsburgh, 1992, pp. 1179–1187.
3. Benson, S. A., Jones, M. L., and Harb, J. N., in *Fundamentals of Coal Combustion for Clean and Efficient Use* (L. D. Smoot, Ed.), Elsevier, Amsterdam, 1993, pp. 299–327.

•

A. E. Jacob Akanctuk, Stanford University, USA. This is an interesting paper with respect to potential control strategies for heavy metals release. The critical question is whether the observed changes in radial profiles of heavy elements are due to: (1) inward diffusion of the heavy metals or (2) vaporization of heavy elements at the particle periphery. Any ideas?

Author's Reply. The final partition of heavy metals in the ash particle core and light metals in the external shell is due to both metal diffusion and vaporization. It seems, however, that heavy metals vaporization may not be significant because we were able to retain 81.7% of the initial amount of heavy metals present in the sludge. It is probably due to the fact that the encapsulated heavy metals like Cr and Cd may react with ash aluminosilicates which may prevent their vaporization. In the paper, we suggested that the light metal migration/diffusion appears to be more important than that of the heavy metals.

Twenty-Sixth Symposium (International) on Combustion/The Combustion Institute, 1996/pp. 2503–2515

INVITED TOPICAL REVIEW

MODERN TOOLS FOR DIESEL ENGINE COMBUSTION INVESTIGATION

WERNER HENTSCHEL
Volkswagen AG
Research and Development
D-38436 Wolfsburg, Germany

This paper describes the operating principle and the current development status of high-speed direct-injection diesel engines used in passenger cars. This type of engine has an advantage in efficiency of the order of 30% compared with current gasoline engines with three-way catalyst and has a high potential for further improvement, such as reduction of NO and soot emissions. The present state of knowledge of diesel engine combustion has benefited from optical diagnostic techniques that permit deeper insights into the in-cylinder processes such as flow generation, fuel injection and spray formation, atomization and mixing, autoignition and combustion, and the formation and reduction of pollutants. Part of the work described was carried out within the European (diesel) engine research programs IDEA and IDEA EFFECT. Finally, a summary is given of future trends in combustion diagnostics and engine developments, with emphasis on the significance of the DI diesel engine as a power plant for passenger cars both inside and outside of Europe.

Introduction

It is well-known that the direct-injection (DI) diesel engine is the most effective way of converting fossil fuels for vehicle propulsion. Because its low fuel consumption results in low CO_2 emission, the DI diesel engine contributes minimally to the greenhouse effect. The connection between global CO_2 emissions and the greenhouse effect is well-known and need not be discussed here. Because of their excellent thermodynamic efficiency diesel engines with direct injection are widely used as power plants for trucks, heavy machines, and ships. Optimized for a single operating point, thermal efficiencies of 50% are achieved. The superior fuel economy of DI diesel engines compared to gasoline and indirect-injection (IDI) diesel engines of similar capacity is the driving force behind the strong interest in Europe in the use of small, high-speed DI diesel engines in passenger cars. Even today, 48% of the new passenger cars in France are equipped with a diesel engine (DI and IDI); the percentage is expected to exceed 30% in the entire European market within the next few years.

Key challenges for future and worldwide acceptance of diesel engines in passenger cars are a further significant reduction of the emissions, mainly of NO_x and particulates, to meet the increasingly stringent environmental regulations; see Fig. 1 for the step-by-step reduction of the emission limits in Europe. The exhaust gas consists primarily of the components N_2, O_2, CO_2, and H_2O. Only a minor part is restricted by exhaust emission standards (CO, HC, NO_x, and particulates). It is important to note that the absolute amount of these components in the exhaust gas is limited, but their concentrations are not. The usual method for determing car exhaust emissions is to run the vehicle on a dynamometer test bed in a well-defined test cycle (speed-versus-time profile) and calculate emissions in grams per unit of distance (g/km or g/mile) from the measured concentrations; see Haahtela et al. [1] for details. Besides the efficiency of the engine, one should keep in mind that the fuel consumption of a car, and therefore the CO_2 emission, depends strongly on its weight and on the driving style. It is assumed that the so-called 3-liter car (a car with an average fuel consumption of about 3 L/100 km) will have an empty weight of about 650–700 kg and will be equipped with a small DI diesel engine.

In Europe, major car manufacturers within the European Council for Automotive Research and Development (EUCAR) and within the former Joint Research Committee (JRC) have initiated and supported joint research activities to improve our fundamental understanding of the complex processes that take place throughout diesel combustion. Because this research is expensive, fundamental, and of common interest, it has been subsidized since 1990 mainly by the European Community and, to a smaller extent, by the Swedish National Board for Industrial and Technical Development and the Austrian Research Promotion Fund.

In the IDEA program (Integrated Diesel European Action, 1990–1993), the main objectives were as follows:

- The investigation of the fuel spray behavior, autoignition, flame propagation, and pollutant for-

mation in real or simulated diesel engine conditions.
- The preparation of a database for model development and validation.
- The development of a documented and validated code for the computation of the complete three-dimensional diesel combustion process.

For more details, see Schindler [2,3] and Hentschel et al. [4] and numerous technical papers dealing with specific topics from this field.

The research work was continued in the IDEA EFFECT research program (Integrated Development on Engine Assessment with Environment Friendly Fuel Efficient Combustion Technology, 1993–1996). This program also includes the combustion in a gasoline engine (continuation of the former JRC program on homogeneous combustion) and endeavors to better understand the fundamentals of the processes of internal combustion and to model them. The main effort is directed at basic experimental research and at modeling the fundamental physics and kinetics with appropriate submodels. The final goals are the improvement of the three-dimensional time-dependent code through incorporation of the obtained submodels and the validation of the code for gasoline and diesel engines with real combustion chamber design.

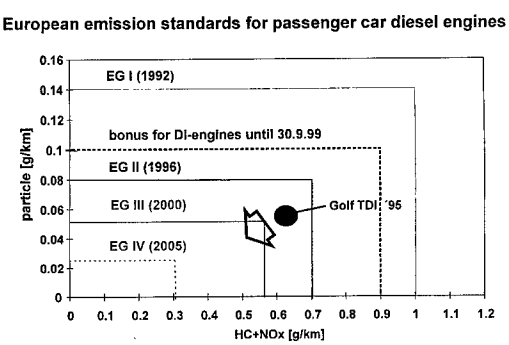

FIG. 1. Development of European emission standards for passenger car diesel engines (EG IV standards in discussion).

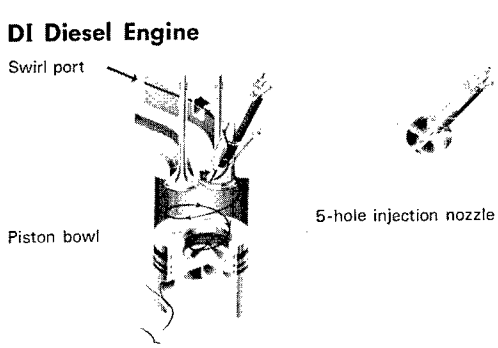

FIG. 2. Characteristic features of the direct-injection diesel engine.

In Germany, additional research activities have been concentrated in Aachen in the special research field of internal combustion (Sonderforschungsbereich Motorische Verbrennung) under the chairmanship of F. Pischinger, funded by the German Science Foundation.

It is the purpose of this paper to show how the in-cylinder processes, such as swirl-flow development, fuel injection, atomization and vaporization, mixing, autoignition, combustion,and pollutant formation, can be analyzed by means of advanced optical techniques. Therefore, the paper starts with a description of the operating principle and the present status of high-speed DI diesel engines. The techniques for the investigation of the different in-cylinder processes, such as laser light sheet, laser doppler velocimetry, laser shadowgraphy, high-speed photography, Mie scattering, and various spectroscopic techniques, are not explained in great detail, but emphasis is on the description of typical results achieved by them. Where possible, discussion is restricted to techniques that have been or can be applied to small, high-speed DI diesel engines with a bowl diameter of about 40 mm. Alternately, measurements on larger DI diesel engines or in pressure chambers under engine-like conditions are discussed. In the literature review, emphasis is on recent publications on selected topics in the field of diesel combustion research. Finally, the outlook is examined with regard to future trends in diagnostics and the potential for further engine improvements.

DI Diesel Engine

Combustion in a modern, high-speed DI diesel engine for passenger cars is a nonstationary, partly diffusion-controlled process in a turbulent flow field. Characteristic features of the DI diesel engine, sketched in Fig. 2, are the swirl intake port in the cylinder head, the out-of-axis bowl-shaped combustion chamber in the piston, and the multi-hole injection nozzle that is located nearly centrally with respect to the piston bowl.

The intake air enters the cylinder through the helical port and generates a swirl flow in the cylinder. At the end of the compression stroke, the flow in the piston bowl is a combination of an accelerated swirl flow and a superimposed squish flow that produces the required turbulence. The diesel fuel is injected at high pressure (20–80 MPa) through the tiny orifices (184 μm) of the five-hole injection nozzle into the hot compressed air (about 5 MPa and 800 K). It forms clouds of fine droplets (1–20 μm) that propagate throughout the bowl and mostly hit the bowl

wall. Droplet decay and coalescence occur during this process. A part of the fuel vaporizes, mixes with the hot air, and creates an ignitable mixture. Initial autoignitions take place in zones with relative air/fuel ratios of around 0.7 [5], mostly on the lee side of the sprays. Thus, combustion starts as a partly premixed flame, and the evaporation process of the remaining droplets is supported by the combustion heat. The second phase of the combustion is characterized by a lack of oxygen in the burning areas and thus the local air/fuel ratio decreases, which is followed by an increased soot formation. If the fuel is still being injected, the burning is similar to a diffusion flame. Soot and NO formation depend on the local air/fuel ratio and on the local flame temperature. Therefore, an effective mixing is essential for good combustion and can be achieved by a sophisticated tuning of gas flow (including turbulence) and fuel injection.

When designing and optimizing the DI diesel engine, the engineers have to balance the contradictory requirements and goals:

- Optimum efficiency (low fuel consumption).
- Low noise and vibration (slow pressure rise).
- Low NO_x emission.
- Low soot emission.

The laws of thermodynamics state that the efficiency of a combustion engine is high if the temperature difference between the two levels is large, meaning that the combustion gas reaches a high end temperature. This can be achieved by an early and compact injection of the fuel and maximum heat release soon after the top dead center (TDC) position of the piston. Unfortunately, this type of combustion has severe disadvantages with respect to engine noise and emissions. In general, the fuel efficiency of DI diesel engines is about 15% higher than that of IDI diesel engines (e.g., of swirl chamber type). Because higher air charging is possible, a higher specific power output (kW/L) and a better soot characteristic is realized. The advantage in efficiency compared with a standard gasoline engine equipped with a three-way catalyst, as used widely throughout the world, is 30% or more.

Engine noise and vibration are generated by a steep rise of the cylinder pressure by a sudden combustion of premixed fuel. This high pressure gradient ($dp/d\alpha$) can be smoothed by spreading the injection over a time longer than the ignition delay. In addition, the measures discussed later will also influence the engine behavior positively. NO and soot formation are closely connected with the combustion process itself. NO is formed when a high temperature acts on nitrogen in the presence of oxygen for a sufficient time. Because nitrogen is always present in the air and oxygen is present because of the lean combustion in a diesel engine (integral view) and is formed by thermal dissociation of CO_2 and H_2O in the flame, the only way to reduce NO formation is to reduce the flame temperature. This can be done by late fuel injection with the start of injection close to or even after TDC (which leads to a retarded combustion in the expansion stroke) or by exhaust gas recirculation (EGR), which is described later in this article. Both measures are in use on modern DI diesel engines.

It is well-known from flame studies that the soot volume fraction depends on the fuel concentration and the flame temperature. It reaches high values for relative air/fuel ratios below 0.6 at temperatures between 1450 and about 2000 K [6 to 8]. To prevent high sooting conditions, a good mixture preparation is essential. It can be achieved by an extended high-pressure injection in a swirl flow with sufficient turbulence. In addition, intake air charging leads to more oxygen in the cylinder, thereby forcing the oxidation of the formed soot. The slight reduction in fuel efficiency resulting from all these measures is a small price to pay in relation to the overwhelming efficiency advantage of the DI working principle.

Exhaust gas recirculation is discussed here in greater detail; see also Heywood [9], Arcoumanis et al. [10,11], Mitchell et al. [12], and Dürnholz et al. [13]. EGR returns a part of the exhaust gas to the combustion chamber by mixing it with fresh air in the intake manifold; it thus increases the intake gas temperature, increases the concentration of CO_2 and H_2O, and decreases the concentration of O_2 in the intake air. It leads to a richer mixture in line with the reduced O_2 concentration and also recirculates minor components such as CO, NO_x, and radicals that may influence autoignition. The autoignition time may be increased, flame temperature and thus flame luminosity is reduced by the larger amount of inert gases, and noise is reduced by the slower combustion speed.

With the EGR rate defined as the percentage of intake air replaced by exhaust gas, the influence of EGR on NO_x and soot is shown in Fig. 3, measured on a research version of the Volkswagen TDI diesel engine operating without turbo charging at 2000 rpm and part load. The NO_x concentration decreases dramatically by about a factor of 10, whereas the soot concentration (given in soot numbers according to Bosch) increases. This contrary tendency limits the application of EGR to moderate values of 30–50%, depending on the engine operating conditions. Two facts should be mentioned: First, the recirculated exhaust gas still contains oxygen because the diesel combustion is rather lean and second, the exhaust emission of NO (in g/km) is even lower because only part of the engine exhaust gas leaves the tailpipe.

Operating an engine with EGR, the percentage of O_2 in the intake air decreases whereas CO_2 and H_2O (vapor) are increased simultaneously. To separate the influences, dilution of the intake air and synthetic intake air mixtures were used in systematic studies. Mitchell et al. [12] only diluted the intake

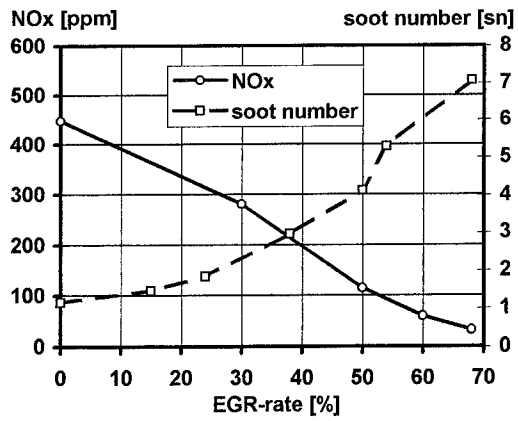

FIG. 3. Influence of exhaust gas recirculation (EGR) on NO_x and soot.

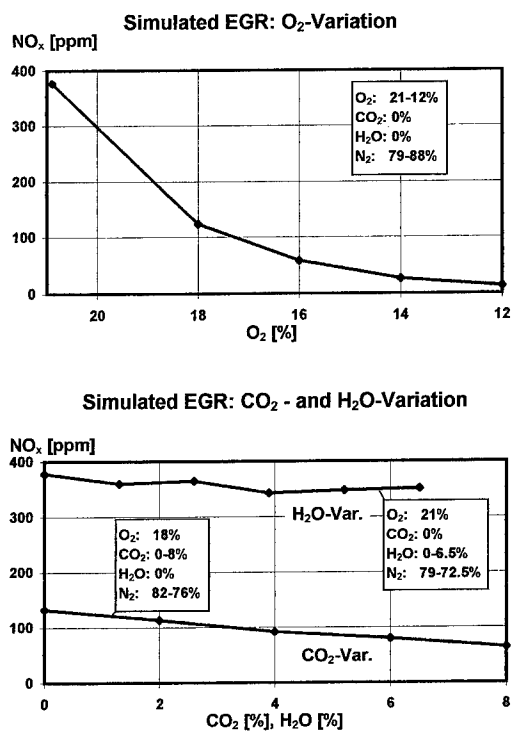

FIG. 4. Influence of O_2 (top) and CO_2 and H_2O concentration (bottom) in the intake gas of exhaust NO as a simulation for EGR.

air with N_2 or CO_2 (thereby reducing the O_2 content) and found out that both dilutions were effective in reducing NO. Röpke et al. [14] used completely synthetic intake gas mixtures that allowed them to vary the concentrations of O_2, CO_2, and H_2O independently by substituting a part of the N_2 or O_2. The results are summarized in Fig. 4; for experimental details, see Refs. 14 and 15. The effects on combustion are examined by measuring the NO concentration in the exhaust gas. It is clearly seen that the variation of the H_2O content has almost no effect and the variation of CO_2 leads to only a slight decrease in the NO concentration, which can be explained by the increase of the molar heat capacity and subsequently by a slightly cooler flame. Reducing the O_2 content leads to drastically lower NO concentrations and thus was found to be the dominant influence on flame temperature.

All the measures described are realized in state-of-the-art, high -speed DI diesel engines for passenger cars such as Volkswagen's 1.9-L TDI diesel engine. The engine employs major innovations and advances such as, direct injection with a two-stage fuel injection system with a five-hole injector; turbocharging with charge air cooling; exhaust gas recirculation; and a distributor pump with an electronic control system to manage fuel injection timing and quantity; turbocharging boost pressure; the amount of exhaust gas recirculation, and glow plug times. Additional emission control is provided by the use of a diesel catalytic converter for the reduction of NO_x, CO, and HCs. More details about the engine can be found in Hentschel et al. [16] and Arcoumanis et al. [10].

Diagnostics of Diesel Combustion Processes

The investigation of diesel combustion processes is explained along the chain from the injector up to pollutant formation. The phenomena of diesel spray combustion are summarized in Fig. 5. Most of the experiments were carried out directly inside the combustion chamber of a DI diesel engine (with a bowl diameter of about 40 mm where possible) or under diesel engine conditions in pressure chambers. Keep in mind that basic questions can often be answered by using basic tools and do not always require sophisticated techniques.

Transparent Engine

Direct optical access to the combustion chamber is a prerequisite for the application of optical measurement techniques to internal combustion engines. An example is the transparent version of the 1.9-L DI diesel engine described previously. Figure 6 shows a partly sectionalized view of the engine design with elongated pistons in an intermediate housing between the cylinder head and the crank case, with quartz glass windows in the bottom of the bowl, in the upper part of the liner, and with quartz glass plates in the upper bowl area; for details see Refs. 4 and 17. Similar designs—mostly as single-cylinder engines—are in use in many research labs

Phenomena in Diesel Spray Combustion

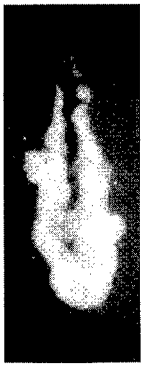

photo: LAT, RWTH Aachen

Process	Phenomena	Measurements
nozzle flow	cavitation	nozzle flow / exit velocity
spray propagation	spray breakup coagulation atomization	fuel distribution spray length and angle droiet size distribution droplet velocity
vaporization mixing	interaction gas - spray	gas velocity and turbulence vapour concentration local air-fuel ratio
pre-reactions auto-ignition	radical formation ignition spots premixed flame	local temperature ignition delay and location
combustion	diffusion flame	flame propagation flame temperature in-cylinder pressure
	combustion noise	noise spectrum
pollutant formation	soot formation NOx formation	soot concentration NO concentration
post-reactions	soot oxidation	soot concentration particle size spectrum

FIG. 5. Phenomena in diesel spray combustion.

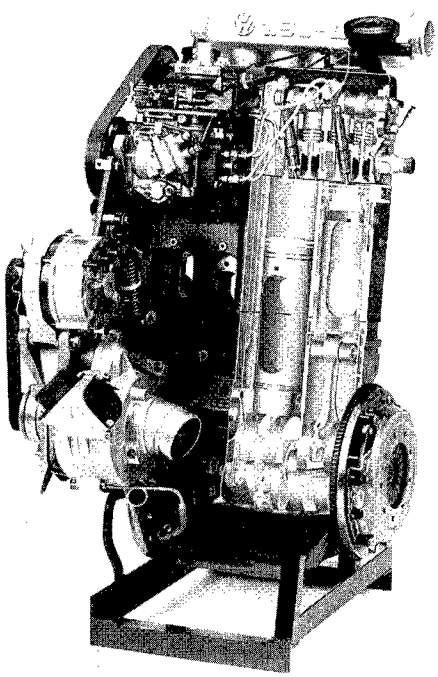

FIG. 6. The Volkswagen transparent 1.9-L DI diesel engine with multiple optical access to the combustion chamber.

all around the world such as Imperial College London [10,18], Pennsylvania State University [12,19], Sandia National Laboratories Livermore [20], Tokyo Institute of Technology [21,22], and AVL Graz [23]. Investigations of fundamental phenomena can be studied advantageously in pressure chamber experiments such as the Aachen pressure chambers, which provide large-scale optical access and continuous operation at up to 5 MPa and 800 K [5,24,25].

Nozzle Flow

The processes inside the injector have been investigated by Chaves et al. [26] with regard to flow and cavitation phenomena inside the nozzle hole by use of a special glass nozzle with a hole diameter of 200 μm and a high-speed video recording technique. For injection pressures greater than 20 MPa, cavitation occurs inside the nozzle hole when the chamber pressure is in the order of 4 MPa; thus, a mixture of fuel and vapor always leaves the nozzle. The flow velocity inside the nozzle that is equal to the exit velocity was measured by a light barrier technique to be about 180 m/s for injection pressures typical for engine part load operation.

Recent studies of Schaller et al. [27] by a holographic method show the appearance of a compact liquid core during the very early acceleration phase of the spray (first few microseconds). The fuel remaining in the nozzle hole is shifted out when the needle starts to open. It takes some 10 μs until the final exit velocity is reached.

Different types of laser light sheet techniques have been applied to observe the flow field, spray formation, and distribution of gaseous components by Rayleigh scattering and laser-induced fluorescence.

In-Cylinder Flow

For flow investigations, the movement of tracer particles is recorded with a high-speed camera [1,4] or by laser doppler velocimetry (LDV) measurements [28]. The development of the in-cylinder and in-bowl flow in a plane 5 mm below the cylinder head during intake and compression stroke is visualized in the sketches of Fig. 7. The sketches give a

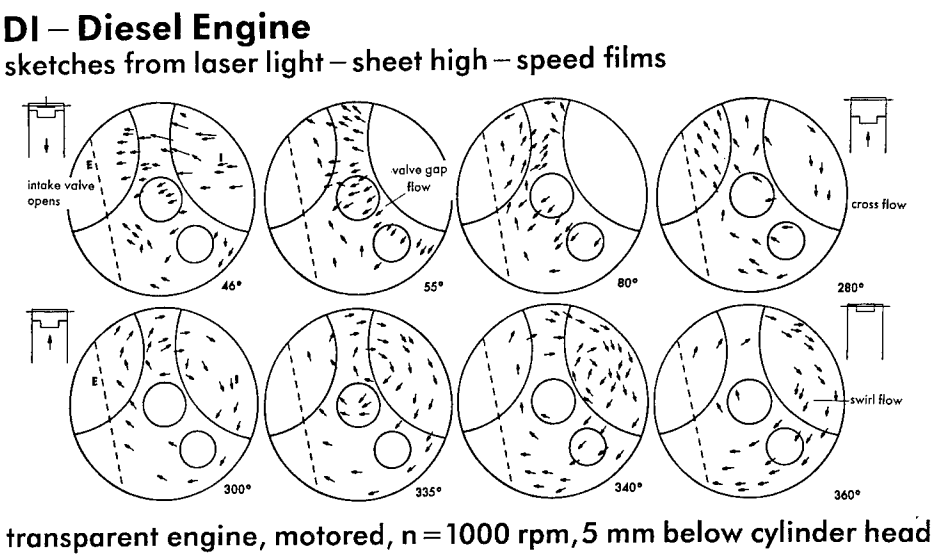

FIG. 7. Sketches of the in-cylinder flow development during intake and compression stroke.

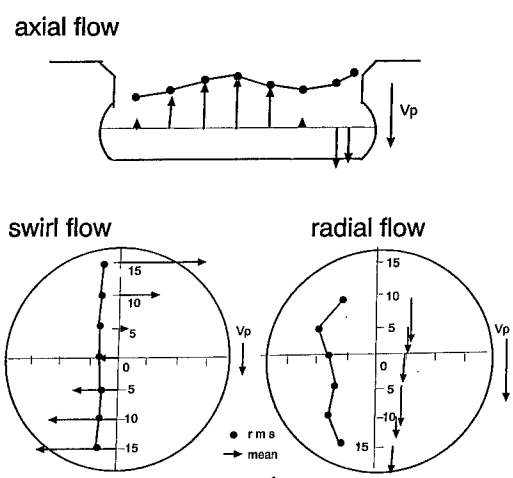

FIG. 8. LDV flow measurements in the piston bowl at TDC, engine motored at 1000 rpm (courtesy of Arcoumanis).

clearer impression of the flow development than single, high-speed film frames. Characteristic features are the valve gap flow during intake phase and the development of the swirl flow at the end of the compression stroke. A two-dimensional quantitative and cycle-averaged flow field is achieved using frame-by-frame particle tracking and subsequent interpolation, thus leading to the data sets required for further calculations [4]. This procedure is very time-consuming and of limited accuracy (i.e., because of the large size of the tracers) and will probably be replaced in the near future by fully video/digital particle image velocimetry techniques.

Accurate flow velocity measurements including turbulence are only achieved by LDV. Acroumanis and co-workers' [28] results from crank-angle resolved but cycle-averaged analysis 11 mm below the cylinder head at TDC inside the piston bowl are presented in Fig. 8. Mean and rms velocities are given in terms of the mean piston speed v_p. The swirl flow with high tangential velocity values of up to $3\,v_p$ close to the bowl wall is superimposed by a turbulent tumble flow that is initiated by the move from the large toward the small squish area because of the out-of-axis location of the bowl in the piston (see Fig. 2). Although swirl is the dominating flow structure in the piston bowl, tumble and turbulence are essential for perfect mixing, a prerequisite for high-power output at a low soot level. At present, a combination of simple light sheet flow visualization and accurate LDV measurements at some selected locations is an efficient strategy for achieving a maximum of information on the time-dependent in-cylinder flow field.

Spray Propagation

Most of the research work on spray propagation was performed with free sprays or in pressure chambers, but these conditions are often far removed from the situation inside a high-speed diesel engine. For example, the droplet velocity achieved by using the five-hole nozzle and part load injection quantities was about 200 m/s when sprayed in the free atmosphere and only about 26 m/s inside the engine [18]. In addition, the length of the liquid spray was 20–30 mm in a high-pressure environment, but in

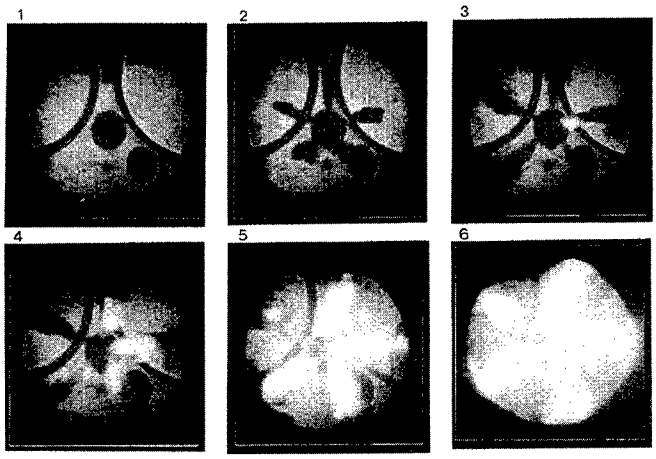

FIG. 9. Spray development, autoignition, and combustion in the piston bowl recorded by laser shadowgraphy and high-speed filming; engine 2000 rpm, part load.

the typical bowl-shaped combustion chamber of the small DI diesel engine, the maximum spray penetration length is about 18 mm before the spray hits the wall. Thus, most of the experimental data from the literature, such as from truck engines or rapid compression machines [20,21,23–25,29–32] are not directly usable to describe the in-cylinder situation of the type of engine selected.

Observation of the spray was effected using numerous techniques. They can be classified by the type (continuous or pulsed), the direction of illumination with respect to the observation (back, side, or top illumination), and the type of observation (short-time video or high-speed film). Spray tip penetration and spray angle can be derived from the pictures.

A typical spray propagation sequence is shown in Fig. 9, taken in a quasi–back illumination technique (reflecting cylinder head) on color-reversal film with a high-speed film camera [1,4]. The laser illuminates the scene inside the combustion chamber from below through the piston window and is performed with light pulses about 7 μs in length cut from a continuous argon ion laser by an acousto-optic modulator. There are slight differences in the shape of the sprays and in the penetration depth. The droplets move straight from the nozzle hole to the bowl wall. At high framing rates, pictures are taken every 1–2 °CA at moderate engine speeds, which is usually fast enough for a time-resolved analysis of spray formation and propagation. The use of a camera-synchronized copper vapor laser that delivers shorter and more powerful light pulses simplifies the experimental setup and increases the performance of the system. On the other hand, even simple experimental arrangements such as the combination of a pulsed bright light–emitting diode and a gatable CCD camera allow statistical analysis of the spray tip penetration; see Chaves et al. [33]. Because of the limited data transfer rate from most types of (also intensified) CCD cameras to the connected computer, only one picture can be taken per cycle.

The evaluation of the spray tip penetration from videos or films is independent of the measurement technique to the greatest possible extent, but the spray angle depends on the technique. Laser schlieren and shadowgraphy high-speed film measurements result in significantly larger values for the spray angle than those yielded by registration of the light scattered by the small droplets [34]. These facts have to be considered when experiments are compared with simulations. In the matter of spray penetration, it is important to distinguish between the liquid and the gaseous portions of the spray length. Depending on the experimental boundary conditions, the length of the liquid core is limited to about 20 to 30 mm, whereas the vapor phase may exceed 50 mm. Thus, pure fuel vapor will only exist if the bowl diameter is large enough.

A combined study of the temporal and one-dimensional spatial development of spray and flame propagation can be done by an electronic high-speed line-scan technique developed at AVL Graz [23,35]. Periodic scanning of the line camera at 15-μs intervals provides high-speed sequential recording of the projected spray shadow and flame radiation.

Droplet Velocity

The droplets of the spray are characterized by their velocity and size distribution. The droplet velocity, measured by LDV, depends to a large extent on the injected fuel quantity and covers a range of approximately 25 m/s [18] to more than 100 m/s [35] at a distance of more than 10 mm downstream from the nozzle hole. It requires a certain amount of time to generate an air flow by the fuel droplets in the direction of the wall, which subsequently reduces the drag of the following droplets. Figure 10 presents the radial droplet velocities 10 mm downstream

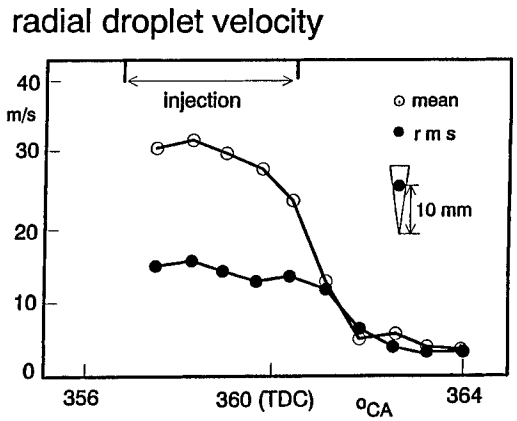

FIG. 10. LDV measurements of the radial droplet velocities 10 mm downstream of the nozzle in the piston bowl (courtesy of Arcoumanis).

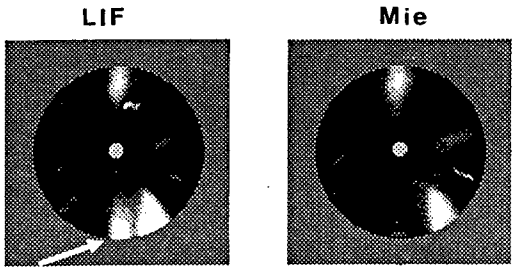

FIG. 11. Visualization of the liquid/vapor phase (left, LIF) and the liquid phase (right, Mie scattering) during fuel injection; the arrow indicates the vaporized fuel plume (courtesy of Sick).

of the nozzle at low load conditions [18]. It agrees closely with the evaluated spray tip velocities [4]. Measurements closer to the nozzle are unlikely to be possible because of the high droplet density.

Droplet Size

Droplet size measurements in diesel sprays are mostly carried out by PDA. A prerequisite is the existence of spherical droplets of moderate density. Until now, no droplet size distributions have been achieved from inside small-sized DI diesel engines. From single-cylinder research engines [35] and pressure chamber experiments, we learn that most of the droplets are less than 10 μm in diameter and very few are larger than 20 μm.

Fuel Vaporization

The tiny fuel droplets vaporize rapidly because of their high individual velocity and the high temperature in the compressed gas (800–1000 K), and an ignitable mixture is formed assisted by the strong turbulence in the piston bowl. The application of planar laser techniques for the visualization and measurement of the fuel vapor distribution and thereby the calculation of the relative air/fuel ratio is highly desirable. Unfortunately, the simultaneous presence of liquid and vapor makes it difficult to apply spectroscopic techniques such as Rayleigh scattering and laser-induced fluorescence. It was shown by Sick et al. in a feasibility study on our engine that laser-induced fluorescence in combination with Mie scattering can be used to distinguish between the liquid and gaseous phases [36]. At the bottom of the left-hand image of Fig. 11, the vaporized diesel fuel can be seen as an additional signal (arrow) compared to the Mie scattering image on the right. Both images were averaged over 32 cycles.

Planar Rayleigh scattering for two-dimensional measurements of the vapor phase of fuel distribution in the main combustion zone of a large-scale DI diesel engine has been demonstrated by Espey et al. [31]. The field of view was 27 mm downstream from the nozzle and carefully checked to ensure it was absolutely free of droplets. Because of the high in-cylinder pressure and the large scattering cross section of the long diesel fuel molecules, the received Rayleigh vapor signal was relatively strong and quantitative evaluation of the equivalence ratio near the leading edge of the vapor jet was performed.

Spray-Wall Interaction

In our small engine, the sprays are shifted slightly near the wall of the bowl because in that area the swirl flow is high and the droplets have slowed down. The droplets hit the bowl wall and splash into a cloud of very tiny droplets that are moved around by the swirl flow. The formation of a liquid film on the bowl wall cannot be observed because of the nature of the setup.

Autoignition

Autoignition is observed on the films by the bright light emission of soot particles because soot has been formed at the very beginning of the diesel combustion. The first self-luminescence is observed about 0.5–1 °CA before the detected heat release calculated from the in-cylinder pressure trace. The spatial distributions of the autoignition locations averaged over many cycles are shown in Fig. 12. They depend significantly on the engine load. The fuel vapor is shifted by the swirl flow out of the sprays and ignites on the lee side of the sprays. Under low load conditions, the autoignition starts near the center of the piston bowl close to the nozzle; for part load, the locations are orientated along the spray axis from the nozzle to the bowl wall; and for full load, most of the

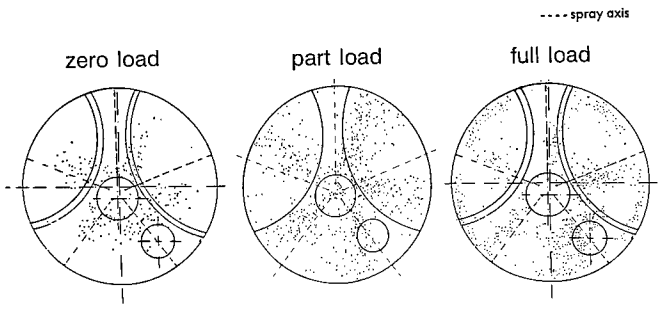

FIG. 12. Spatial distribution of the autoignition locations in the piston bowl for different engine loads.

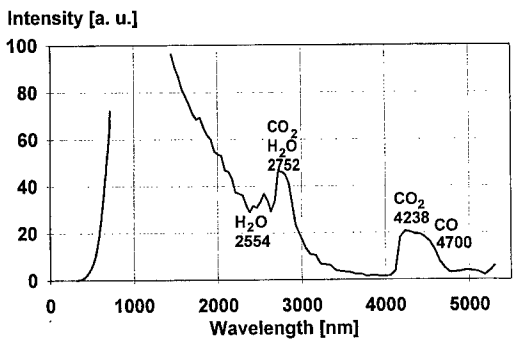

FIG. 13. Spectral distribution of the diesel engine light emission in the visible and infrared; engine 2000 rpm, part load.

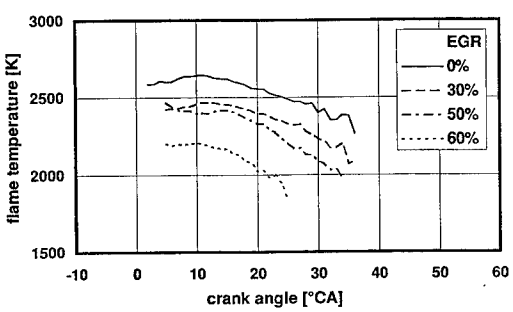

FIG. 14. In-cylinder flame temperature depending on the EGR rate, measured by a five-color multispectral pyrometry; engine 2000 rpm, part load.

autoignition locations are close to the wall downstream of the swirl flow. The autoignition areas converge and finally the sprays burn completely along the shifted spray axis (see Fig. 9). In the later stage of combustion, the compact flame areas disperse into several small, hot areas. Basic studies on the self-ignition behavior of model diesel fuels have been conducted in a high-pressure shock tube. They allow precise measurements of the ignition-delay times depending on temperature and pressure (see Pfahl et al. [37]).

Flame Temperature

An easy way to get information about combustion behavior is to probe the light emitted by the combustion. Even with small optical probes, mounted, for example, in the glow plug bore, a variety of information can be obtained, including onset and duration of the combustion. Spectral analysis of the combustion light has long been used to calculate the flame temperature in diesel engines. The emission spectrum of Fig. 13, measured from 400 nm to 5.2 μm with a gap between 800 nm and 1.4 μm, is similar to Planck's radiation curve at a temperature above 2000 K. Band radiation of CH (431 nm) or C_2 (516 nm) is difficult to distinguish from the continuous radiation in the visible [38,39], but in the infrared (IR), the band radiation of H_2O (2.75 μm) and of CO_2 (4.2 μm) is clearly visible [40,41].

Most authors use the spectral intensity at two wavelengths in the visible (rising edge of Planck's curve) and calculate the time-dependent temperature under certain assumptions for the wavelength-dependent emissivity of the soot; see Kamimoto et al. [42,43] and Hötger et al. [44,45]. Taking into account the spectral intensity at five wavelengths, extrapolation to the highest temperatures in the flames is possible, as outlined by Pittermann [46]. The dependence of the flame temperature on the chosen EGR rate is shown in Fig. 14, measured on the Volkswagen DI diesel engine by Pittermann's five-color method. As expected, the temperature decreases with increasing EGR rate. Of course, flame temperatures can also be calculated from the IR emission outside of the bands at the falling flank of the spectral curve [40].

The technique was extended to a two-dimensional application by using two CCD cameras with appropriate filters to display the two-dimensional temperature distribution in the transparent engine at one selected crank angle per cycle. Measurements by Arcoumanis et al. [10,11] have demonstrated the high-temperature locations along the shifted spray axes and verified the idea about EGR and in-cylinder combustion processes.

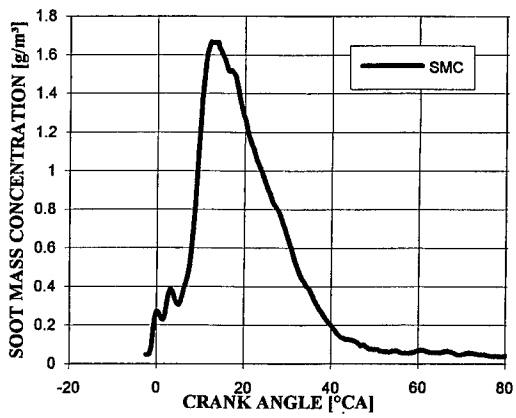

FIG. 15. Formation and oxidation of soot during the combustion cycle measured by a light extinction technique.

NO Distribution

NO is formed in the high-temperature regions of the combustion and thus correlating the local temperature with the local NO concentration is of interest. The two-dimensional quantitative measurement of the NO concentration in gasoline engines by laser-induced fluorescence (LIF) with laser light in the deep UV (193 or 226 nm) has been successful in recent years, but the situation is much more difficult in diesel engines. During combustion, the in-cylinder gas becomes clouded by intermediate soot and, in addition, it is more or less opaque probably because of the presence of cracked hydrocarbons. First results of two-dimensional NO measurements shortly after the end of the combustion were reported by Sick et al. [36] and Alatas et al. [19]. The fast gas sampling valve technique provides accurate cycle-averaged concentration figures but at a reduced level of spatial resolution; see Lepperhoff et al. [47]. To avoid the formation of high NO concentration, the flame temperature should be as low as possible. Some NO_x reduction strategies for DI diesel engines are discussed by Herzog et al. [48].

Soot Distribution

Different techniques can be applied on a DI diesel engine to measure the soot mass concentration: analysis of the self-luminescence of the soot during combustion [43–45], laser-induced incandescence (LII) and scattering [19,30,49], light extinction technique [12,16,24,50], and in-cylinder gas analysis with a fast gas sampling valve [47].

Luminescence analysis is easiest to apply to an engine and may assist in engine development as demonstrated by Hötger [45], but the technique is restricted to the period in which light is irradiated by the soot particles. Thus, no information can be gained about the soot oxidation process late in the combustion stroke. Laser-induced incandescence (LII), frequently used in combination with planar scattering, is well suited for getting information of the two-dimensional soot distribution and good progress is being made with quantification of the images obtained. As a prerequisite for LII, two large optical windows are required and only one image per cycle is achieved. Thus, LII will become more important for fundamental studies but has only limited applications on near-production engines. Combining a two-wavelength radiation measurement with light scattering measurements, information about particle size, number density, and volume fraction have been achieved within a single-cylinder truck engine by Tree et al. [49]; however, the location of measurement was restricted to a small spot near the piston bowl wall. Typical soot particle sizes are between 30 and 50 nm [51]. Using a fast sampling valve for the soot mass concentration measurement, crank angle (or time) resolution is restricted because a minimum opening time of the valve of about 1 ms is required to probe the combustion chamber. Thus, very rapid soot formation processes cannot be detected.

The light extinction technique is, in principle, easy to apply even on standard production engines with only small modifications to the engine for optical access. Just two small windows are required on opposite sides of the liner. It has been used successfully for the investigation of transient soot formation processes in a pressure chamber [50] and shock tubes and is able to deliver data throughout the complete combustion cycle. The rapid formation of soot in the early combustion stage is followed by an oxidation process within the succeeding 30–40 °CA (see Fig. 15). The rates of soot formation and oxidation and the maximum soot mass concentration during the main combustion stage depend largely on the in-cylinder gas temperature and pressure, the timing of the injection, and the type of fuel. Typical maximum soot mass concentrations are 3–4 g/m^3 [51] or 1–2 g/m^3 [16], corresponding to about 10% of the total fuel mass injected. It is important to note that most of the soot is oxidized in the same cycle and will not contribute to the exhaust. In pressure-chamber experiments, nearly all of the soot formed is oxidized because the high-temperature environment remains [24] and comparison between different fuels can be performed more easily [52]. To promote soot oxidation, the temperature must be kept high enough for a sufficient time.

It is assumed that the presence of the hydroxyl radical OH plays an important role in the soot kinetics. The OH concentration is an excellent marker of the diffusion flame zone (Dec et al. [53]). It has recently been shown that OH and soot exist separately from each other in the leading portion of a spray flame and that OH is formed earlier than the soot (Kamimoto et al. [54]). Basic soot research has been performed by Bockhorn et al. [55–57], D'Anna

et al. [58–60] and Jander et al. [7,61] and optical techniques have often been used for these studies.

Future Trends and Discussion

It is important to obtain a detailed knowledge of all aspects of the physics and kinetics of multicomponent fuels under high-pressure (up to 15 MPa) and high-temperature (up to 2700 K) conditions.

Diagnostics

Currently, the development status of many spectroscopic techniques is on the threshold from a qualitative to a quantitative state. Some techniques, such as temperature measurement during the compression stroke (see Sick et al. [62]), have been applied successfully on the engine, whereas others have to be improved or modified to provide data from a small engine's combustion chamber. The situation regarding spark-ignition engines and pressure chambers, in which the conditions are somewhat easier, shows the potential for future work. Fuel droplet velocities and sizes, mixture fields, combustion temperatures, and locally resolved concentration of reactants and combustion products are expected to be obtainable from engines that are similar to production engines with respect to their combustion chamber geometry and operated at standard operating conditions.

Modeling and Simulation

The point of many experiments is to obtain data for the formulation of models of the physical and chemical processes. Precise models are essential for the design of computer codes for the complete calculation of mixture preparation and combustion and cover the span from the spray description [25,63,64] to the kinetics of soot [65–67].

Research Needs

There are still many unresolved questions in the process chain of diesel engine combustion. For a better understanding of the basic phenomena and a more precise prediction and modeling, we need to know about the following: spray breakup and atomization; the influence of fuel decomposition during vaporization on the formation of an ignitable mixture; the spray/wall interaction even of very tiny droplets; the interaction of the turbulent gas field with the evaporating fuel; the dependence of autoignition and combustion on the local mixture composition under the influence of temperature and pressure; and the soot formation and oxidation processes such as local soot concentration and soot sizes in the nonhomogeneous combustion field.

Engine Improvements

To improve the worldwide acceptance of diesel engines we have to deal with two essential tasks: the reduction of both NO_x and soot emission. The method is well-known in principle. The NO_x concentration can be reduced by a reduction of the flame temperature, which can be effected for example by a lower oxygen content or an increased content of inert gas of the intake air (as with EGR) or by better premixing to achieve a partly homogeneous lean mixture before the start of combustion. Reduction of the soot concentration in the exhaust gas can be achieved by decreasing soot formation or increasing soot oxidation. More thorough mixing will prevent rich-flames with local relative air/fuel ratios below 0.6. Oxidation can be improved by a high-temperature level for sufficient duration in the presence of oxygen. Unfortunately, this is counterproductive with respect to the NO problem.

The measures that can be implemented are various and can only be outlined here:

- Improved in-cylinder gas flow such as controlled swirl and turbulence through a variable intake geometry, multivalve cylinder head, and optimized bowl shape.
- Improved injection system with a vertical nozzle, injection rate shaping such as pre-injection and split injection or a shorter deactivation period, and finer sprays achieved by high-pressure injection with injection pressures up to 200 MPa (e.g., by unit-injector or common-rail systems).
- Improved and controlled combustion procedure through a reduced flame temperature (higher EGR level, cooled EGR, better premixing), avoidance of over-rich zones, and faster start of oxidation.
- Improved fuel quality (reformulated fuels) with lower sulphur and aromatic content and increased cetane number.

Advanced tools—diagnostics and models—are required to better understand the combustion process of DI diesel engines, and will increasingly used to further optimize the engines with respect to a reduced emission of NO_x and soot, together with a low fuel consumption level for maximum environmental protection.

Acknowledgments

I would like to thank my colleagues in the scientific community who have contributed to this work with new results, recent papers, and discussions. Some aspects of the work have been done within the European research programs IDEA and IDEA EFFECT in the past six years. The intensive and fruitful cooperation between universities, research institutes, and industry has provided an excellent basis for improving our knowledge of diesel combustion processes in engines.

This work has been partly funded by the European Commission within the framework of the JOULE and the JOULE II programs, the Swedish National Board for Industrial and Technical Development (NUTEK), the Austrian Research Promotion Fund (FFF), and the European Council for Automotive Research and Development (EUCAR: Fiat, Peugeot, Renault, Rover, Volkswagen, and Volvo) within the IDEA and the IDEA EFFECT programs.

REFERENCES

1. Haahtela, O., Hentschel, W., and Schindler, K.-P., in *Unsteady Combustion* (Culick, F., Heitor, M. V., and Whitelaw, J. H., Eds.), Nato ASI, Series E, Applied Science, Vol. 306, Kluwer Academic Publ., Dordrecht, 1996, pp. 267–282.
2. Schindler, K.-P., SAE Paper No. 92-0591, 1992.
3. Schindler, K.-P., "Integrated Diesel European Action (IDEA)." Final Report, Wolfsburg 1994 (restricted distribution).
4. Hentschel, W., Schindler, K.-P., and Haahtela, O., SAE Paper No. 94-1954, 1994.
5. Knoche, K. F. and Heinze, T., Proceedings of the Colloquium SFB 224 Motorische Verbrennung, Aachen, 1988, in German.
6. Schindler, K.-P. and Bockhorn, H., in *Arbeitsprobess des Verbrennungsmotors,* Graz, 1991, in German.
7. Bönig, M., Feldermann, C., Jander, H., Lüers, B., Rudolph, G., and Wagner, H. G., *Twenty-Third Symposium (International) on Combustion,* The Combustion Institute, 1990, pp. 1581–1587.
8. Pischinger, F., Schulte, H., and Jansen, J., *VDI-Berichte* 714: 61–93 (1988), in German.
9. Heywood, J. B., *Internal Combustion Engine Fundamentals,* McGraw Hill, New York, 1988.
10. Arcoumanis, C., Bae, C., Nagwaney, A., and Whitelaw, J. H., SAE Paper No. 95-0850, 1995.
11. Arcoumanis, C., Nagwaney, A., Hentschel, W., and Röpke, S., SAE Paper No. 95-2356, 1995.
12. Mitchell, D. L., Pinson, J. A., and Litzinger, T. A., SAE Paper No. 93-2798, 1993.
13. Dürnholz, M., Eifler, G., and Endres, H., SAE Paper No. 92-0725, 1992.
14. Röpke, S., Schweimer, G. W., and Strauss, T. S., SAE Paper No. 95-0213, 1995.
15. Röpke, S., Ph.D. Thesis, Wolfsburg/Magedburg, 1996, in German.
16. Hentschel, W. and Richter, J.-U., SAE Paper No. 95-2517, 1995.
17. Hentschel, W., in *Application of Metrological Laser Methods in Machines and Systems,* (Frankowski, G. et al., Eds.), Physical Research, Vol. 15, Akademie-Verlag, Berlin, 1991, pp. 113–133.
18. Arcoumanis, C., Hu, Z., and Whitelaw, J. W., *Int. Symp. COMODIA 94,* 1994, pp. 205–211.
19. Alatas, B., Pinson, J. A., Ltzinger, T. A., and Santavicca, D. A., SAE Paper No. 93-0973, 1993.
20. Dec, J. E. and Espey, C., SAE Paper No. 95-0456, 1995.
21. Kosaka, H., Nishigaki, T., Kamimoto, T., and Harada, S., SAE Paper No. 95-2451, 1995.
22. Matsui, Y., Kamimoto, T., and Matsuoka, S., SAE Paper No. 79-0491, 1979.
23. Winkelhofer, E., Fuchs, H., and Philipp, H., SAE Paper No. 93-0862, 1993.
24. Wiartalla, A., Bäcker, H., and Dürnholz, M., SAE Paper No. 95-0233, 1995.
25. Hohmann, S., Klingsporn, M., and Renz, U., SAE Paper No. 96-0630, 1996.
26. Chaves, H., Knapp, M., Kubitzek, A., Obermeier, F., and Schneider, R., SAE Paper No.95-0290, 1995.
27. Schaller, J. K., Bilstein, W., and Stojanoff, C. G., "PARTEC 95," Proc. ILASS, Nümberg, 1995, pp. 51–62.
28. Arcoumanis, C., Whitelaw, J. H., Hentschel, W., and Schindler, K.-P., *Proc. Inst. Mech. Engrs.* 208:191–205 (1993).
29. Baritaud, T., Heinze, T. A., and LeCoz, J. F., SAE Paper No. 94-0681, 1994 .
30. Dec, J. E., SAE Paper No. 92-0115, 1992.
31. Espey, C., Dec, J. E., Litzinger, T. A., and Santavicca, D. A., SAE Paper No. 94-0682, 1994.
32. Espey, C. and Dec, J. E., SAE Paper No. 95-2456, 1995.
33. Chaves, H., Hentschel, W., Obermeier, F., and Stasicki, B., SAE Paper No. 96-1206, 1996.
34. Münch, K.-U. and Leipertz, A., SAE Paper No. 92:2204, 1992.
35. Fuchs, H., Pitcher, G., Wiesler, B., Wigley, G., and Winkelhofer, E., *MTZ Motortechnische Zeitschrift* 54 (2):3–10 (1993), in German.
36. Arnold, A., Dinkelacker, F., Heitzmann, T., Monkhouse, P., Schäfer, M., Sick, V., Wolfrum, J., Hentschel, W., and Schindler, K.-P.: *Twenty-Fourth Symposium (International) on Combustion,* The Combustion Institute, 1992, pp. 1605–1612.
37. Phahl, U., Fieweger, K., and Adomeit, G., *Twenty-Sixth Symposium (International) on Combustion,* The Combustion Institute, 1996.
38. Funatsu, K. and Nagase, K., SAE Paper No. 95-0610, 1995.
39. Möser, P. and Hentschel, W., SAE Paper No. 96-1199, 1996.
40. Ohmstede, G. and Hentschel, W., SAE Paper No. 95-2516, 1995.
41. Classen, E., Campbell, S., and Rhee, K. T., SAE Paper No. 95-0605, 1995.
42. Matsui, Y., Kamimoto, T., and Matsuoka, S., SAE Paper No. 79-0491, 1979.
43. Matsui, Y., Kamimoto, T., and Matsuoka, S., SAE Paper No. 80-0970, 1980.
44. Mayr, B., Hötger, M., and Puschmann, H., *MTZ Motortechnische Zeitschrift* 53(1):3–8 (1992), in German.
45. Hötger, M., *MTZ Motortechnische Zeitschrift* 56 (5):278–280 (1995), in German.
46. Pittermann, R., *MTZ Motortechnische Zeitschrift* 56(2):78–84 (1995), in German.

47. Wölfle, M., Strömberg, S., Lepperhoff, G., and Houben, M., SIA Paper No. 93-088, 1993.
48. Herzog, P. L., Bürgler, L., Winkelhofer, E., Zelenka, P., and Cartellieri, W.: SAE Paper No. 92-0470, 1992.
49. Pinson, J. A., Mitchell, D. L., Santoro, R. J., and Litzinger, T. A., SAE Paper No. 93-2650, 1993.
50. Bäcker, H. and Wiratalla, A., *Int. Symp. COMODIA 94,* 1994, pp. 565–570.
51. Tree, D. R. and Foster, D. E., SAE Paper No. 94-0270, 1994.
52. Bäcker, H., Wiartalla, A., and Dümholz, M., Proc. CIMAC Congress, Interlaken, May, 1995.
53. Dec, J. E. and Coy, E. B., SAE Paper No. 96-0831, 1996.
54. Kosaka, H., Nishigaki, T., Kamimoto, T., Sano, T., Matsutami, A., and Harada, S., SAE Paper No. 96-0834, 1996.
55. Bockhorn, H., Ed., *Soot Formation in Combustion,* Springer Verlag, Berlin, 1994.
56. Bockhorn, H., Fetting, F., Heddrich, A., Meyer, U., and Wannemacher, G., *J. Aerosol Sci.* 19(5):591–602 (1988).
57. Wieschnowsky, U., Bockhorn, H., and Fettig, F., *Twenty-Second Symposium (International) on Combustion,* The Combustion Institute, 1988, pp. 343–352.
58. D'Alessio, A., Minutolo, P., Gambi, G., and D'Anna, A., *Ber. Bunsenges. Phys. Chem.* 97:1574–1582 (1993).
59. Cijajolo, A., D'Anna, A., Barbella, R., and Bertoli, C., *Combust. Sci. Technol.* 87(1–6):127–137 (1992).
60. Cavaliere, A., Barbella, R., Cijajolo, A., D'Anna, A., and Ragucci, R., *Twenty-Fifth Symposium (International) on Combustion,* The Combustion Institute, 1994, pp. 167–174.
61. Hanisch, S., Jander, H., Pape, T., and Wagner, H. G., *Twenty-Fifth Symposium (International) on Combustion,* The Combustion Institute, 1994, pp. 577–584.
62. Roller, A., Arnold, A., Decker, M., Sick, V., Wolfrum, J., Hentschel, W., and Schindler, K.-P., SAE Paper No. 95-2461, 1995.
63. Chaves, H. and Obermeier, F., SAE Paper No. 96-1126, 1996.
64. Curtis, E. W., Uludogan, A., and Reitz, R. D., SAE Paper No. 95-2431, 1995.
65. Peters, N., Müller, U. C., Pitsch, H., and Wan, Y. P., 5th Symp. Der Arbeitsprozeß des Verbrennungsmotors, Graz, September, 1995.
66. Pitsch, H., Wan, Y. P., and Peters, N., SAE Paper No. 95-2357, 1995.
67. Li, X. and Wallace, J. S., SAE Paper No. 95-2428, 1995.

COMMENTS

A. Kowalewicz, Radom Technical University, Poland. For the case of the VW research "3-liter" engine it appears that fuel burns in the presence of very high excess air and thus a lot of heat is rejected with exhaust gases.

What is your opinion about throttling the air in order to more closely approach an overall about-stoichiometric air-fuel ratio (for each cycle), as was applied in Mercedes Benz diesel engines in the past?

Author's Reply. The diesel engine takes advantage of the fact that it operates very lean, especially at part load. This is a prerequisite to achieve the required low emissions. Throttling the engine destroys this advantage and, in addition, would reduce the efficiency of the engine due to the throttling losses.

Twenty-Sixth Symposium (International) on Combustion/The Combustion Institute, 1996/pp. 2517–2524

APPLICATION OF A REDUCED KINETIC MODEL FOR SOOT FORMATION AND BURNOUT IN THREE-DIMENSIONAL DIESEL COMBUSTION COMPUTATIONS

P. BELARDINI,[1] C. BERTOLI,[1] C. BEATRICE,[1] A. D'ANNA[2] AND N. DEL GIACOMO[1]

[1]*Istituto Motori C.N.R.*
Napoli, Italy

[2]*Istituto Ricerche Combustione C.N.R.*
Napoli, Italy

Using a modified version of the Kiva-2 code, three-dimensional computations of combustion and soot formation were performed, burning tetradecane and *n*-heptane in a direct injection, naturally aspirated diesel engine. A coupled soot formation and combustion model is proposed. Assuming acetylene as the crucial pyrolitic species, the model takes into account the fuel-to-acetylene pyrolysis, acetylene oxidation, soot nucleation, and surface growth and soot oxidation. The numerical predictions are compared with the experimental data of heat-release patterns and with the in-cylinder measurements of acetylene concentration and soot volume fraction. C_2H_2 data were collected using a fast-acting valve, while soot loading was measured with the two-color technique. The improved code is able to predict correctly the combustion and heat-release patterns of the two fuels without any retuning of the model constants. The computational results demonstrate that the reduced kinetic soot model is capable of predicting, with satisfactory accuracy, the local amount of soot and pyrolytic products in the combustion chamber, keeping the main features of the diesel combustion.

Introduction

In recent years, engine manufacturers have significantly improved diesel engine performance to meet more and more stringent limits in emissions regulations. However, the next regulatory step for diesel-exhaust emission limits, planned for the end of the century in European countries and the United States, has issued a further challenge to engine designers in producing engines at ultralow emission levels without reducing of the thermal efficiency. This goal requires a better understanding of the in-cylinder, soot formation and oxidation processes, which can be obtained both from experiments and numerical simulations.

In the past, there have been some attempts to model pollutant formation in diesel engines. Hiroyasu et al. [1] set up and tested a model based on a two-step formulation, one for the soot formation and another for soot oxidation, in a simple Arrhenius form. The computed results were compared with experimental data measured at the engine exhaust. The same model was also used by Belardini et al. [2], who compared the numerical results with the in-cylinder species measurements, obtained with a high-speed sampling technique. Patterson et al. [3] performed extensive calculations of a quiescent-chamber engine to evaluate the NO_X particulate trade-off, adopting the Hiroyasu expression for soot formation and the Nagle et al. [4] mechanism for soot oxidation. The numerical predictions correlate well with the insoluble fraction measurements. Zellat et al. [5], modeling a swirl-chamber engine, used a soot-formation model derived from Tessner et al. [6] and a soot-oxidation model based on the Magnussen et al. hypothesis [7]. The computed data show qualitative agreement with the experimental results. The Tessner model coupled with the Farmer model [9] was also used by Nagakita et al. [8]. In the latter model, the soot-oxidation phenomenon was described using Nagle and Magnussen theories. The computational results, compared with in-cylinder measurements obtained by back-illumination photography, show good qualitative agreement.

More recently, attempts have been made to use multistep models. In particular, Yoshihara et al. [10] studied a natural gas–fueled diesel engine, using 70, 6, and 12 reactions to model methane and benzene combustion and the PAH growth, respectively. The nucleation is described as PAH coalescence from pyrene, while the surface growth is described by the HACA reaction sequence as reported by Frenklach and Wang [11]. The model was able to compute the correct amount of soot at the engine exhaust but was prohibitive in terms of computational time for a three-dimensional, CFD calculation. Fusco and Forster [12] applied an eight-step formulation to model the inception, surface growth, coagulation,

and oxidation processes of soot by using global rate expressions, with acetylene assumed as the growth species. No direct comparison with experimental data was performed. Gorokhovski and Borghi [13] used a linked ignition/combustion/soot-formation kinetic model, with two equations to predict the soot volume fraction and the global intermediate species. For the soot-oxidation rate, the Lee et al. formula was used [14]. The computational results seemed to be reasonable, but no comparison with experimental data was reported. Pitsch et al. [15] studied an *n*-heptane spray into a high-temperature, high-pressure chamber, using the flamelet concept and a detailed, kinetically based soot model. The comparison with the experimental data was quite good, but the computational cost of this very new approach was not quantified.

A compromise between a comprehensive description of the in-cylinder soot loading process and the computational cost of full three-dimensional diesel combustion calculations can be obtained using reduced kinetic schemes that with few steps, are able to retain the main global features of the diesel combustion process. A model, first proposed by Leung et al. [16] and Fairweather et al. [17], was very attractive for this purpose because of the few steps involved. In the model, acetylene was assumed as the crucial pyrolitic species for nucleation and surface growth processes [18–20]. Three steps were used to describe nucleation, surface growth, and carbon oxidation processes, respectively. Belardini et al. [21–22] implemented, in the standard kinetic routine of Kiva-2 code, a slightly modified version of this model, simulating fuels of different quality. As a preliminary step, a fuel-pyrolysis reaction was added to the soot model itself. The preexponential factor of this reaction is dependent on the fuel used. This fact, in addition to the very high and probably unrealistic activation temperature of the reaction (about 70,000 K), were a limit to the proposed mechanism.

In the present paper, a new version of the soot model was implemented and tested to overcome the problems outlined previously. A coupled soot-formation and combustion model is proposed assuming acetylene as the crucial pyrolitic specie. The model takes into account the fuel-to-acetylene pyrolysis, acetylene oxidation, soot nucleation and surface growth, and soot oxidation. The numerical predictions are compared with the experimental data of heat-release patterns and with the in-cylinder measurements of acetylene concentration and soot volume fraction.

Combustion and Soot Models

In this work, simulations of combustion in diesel engines were performed using a modified version of the Kiva-2 code [23]. This modified version of the code contains a spray–wall interaction model in a form first described by Naber et al. [24] and Amato et al. [25]. In addition, some improvements in the atomization process were introduced. Atomization is treated in the Kiva-2 code with the TAB model [26]; however, Liu et al. [27] found that in comparison with experiments, this model gives worse results than the Wave model developed by Reitz [28]. Both the TAB and the Wave models start with the injection of a spray with the same diameter as the nozzle hole and develop the atomization process. The models include a set of characteristic constants whose values influence both the Sauter mean diameter of the drops and the tip penetration. These constants must be adjusted to correlate with the numerical results to the experimental data, but both models, as shown by Belardini et al. [29], are mainly sensitive to the numerical value of the breakup time constant. The TAB model underestimates the tip penetration, because of its tendency to break up the jet too quickly into very small droplets. On the other hand, the Wave model is better behaved in the first phase of the atomization process. Thus, in Ref. 29, a hybrid model was used in which the Wave model is used to start the process, leading to large-diameter injected drops. After the initial phase of injection, the TAB model is used when the drop diameter is less than 95% of the maximum diameter of the injected drops. The optimum values of model constants are chosen to obtain the best of the experimental, tip penetration data. This hybrid approach is used in the numerical analysis of present paper.

The soot model is characterized by full coupling with the combustion mechanism. The model is characterized by the following steps: the liquid fuel is injected; the fuel vaporization and dispersion is computed by the Kiva-2 code; fuel vapor forms acetylene by a single-step reaction:

$$C_mH_n \Rightarrow \frac{m}{2}\,C_2H_2 + \frac{(n-m)}{2}H_2 \qquad \text{(R1)}$$

acetylene formation from fuel vapors; the acetylene produced is oxidized at high temperatures by a single-step stoichiometric reaction:

$$C_2H_2 + 5O_2 \Leftrightarrow 4CO_2 + 2H_2O \qquad \text{(R2)}$$

acetylene oxidation. The corresponding reaction rate has been expressed [21,22] as

$$\omega = \min(\omega_{\text{premix}}, \omega_{\text{diff}})$$

where

$$\omega_{\text{premix}} = A_2\, e^{E_2/T}\,[C_2H_2]^m[O_2]^n$$

$$\omega_{\text{diff}} = B\frac{\varepsilon}{\kappa}\,\min\left([C_2H_2], \frac{[O_2]}{s}\right)$$

The terms in brackets are molar concentration in

TABLE 1
The engine characteristics.

Compression ratio	17
Bore	10.0 cm
Stroke	9.5 cm
Conn. rod length	17.8 cm
Comb. chamber	Toroidal
E.A.R. shape fact.	4.6
Injection	4 holes $f = 0.28$
Spray cone angle	160

mol/cm^3; κ and ε are the turbulent kinetic energy and its dissipation rate; s is the stoichiometric ratio. The values of A_2 and E_2 are determined along with the other constants, and represent the preexponential factor and the activation temperature for the premixed combustion, respectively; B has a value of 5, and represents the proportionality factor for diffusive combustion. This model, derived from Magnussen, is the most commonly used in multidimensional diesel combustion computations [1,2,5].

Simultaneous with acetylene combustion, the three-step soot formation and oxidation model of Leung et al. is used to evaluate soot loading for each computational cell using the following mechanism:

$$C_2H_2 \Rightarrow 2C + H_2 \text{ nucleation} \quad \text{(R3)}$$

$$C_2H_2 + nC \Rightarrow (n + 2)$$
$$C + H_2 \text{ surface growth} \quad \text{(R4)}$$

$$C + 0.5O_2 \Rightarrow CO \text{ carbon oxidation} \quad \text{(R5)}$$

Moreover, the carbon particle concentration resulting from the nucleation equation must consider the agglomeration process:

$$nC \Rightarrow C_n \text{ agglomeration} \quad \text{(R6)}$$

The balance equations for acetylene and carbon are given by

$$\frac{d[C_2H_2]}{dt} = \omega_1 - \omega_2 - \omega_3 - \omega_4$$

$$\frac{d[C]}{dt} = \omega_3 + \omega_4 - \omega_5$$

where ω_i is the ith equation reaction rate.

In Eqs. (R1) to (R6), these rates may be expressed in the following form:

$$\omega_1 = A_1\, e^{-E_1/T}\, [C_mH_n]$$
$$A_1 = 2.4\ 10^{14}\ E_1 = 25{,}000$$

$$\omega_2 = A_2\, e^{-E_2/T}\, [C_2H_2]^{0.5}\, [O_2]^{1.25}$$
$$A_2 = 0.55\ 10^{12}\ E_2 = 14{,}000$$

$$\omega_3 = A_3\, e^{-E_3/T}\, [C_2H_2]$$
$$A_3 = 0.95\ 10^{6}\ E_3 = 21{,}100$$

$$\omega_4 = A_4\, e^{-E_4/T}\, (\rho N)^{1/6}\, [C]^{1/3}\, [C_2H_2]$$
$$A_4 = 2.4\ 10^{5}\ E_4 = 12{,}100$$

$$\omega_5 = A_5\, e^{-E_5/T}\, T^{1/2}\, (\rho N)^{1/3}\, [C]^{2/3}\, [O_2]$$
$$A_5 = 1.6\ 10^{7}\ E_5 = 14{,}000$$

$$\omega_6 = A_6\, T^{1/2}\, (\rho N)^{11/6}\, [C]^{1/6}$$
$$A_6 = 2.09.0((6MW_c)/\pi\rho_c)^{1/6}\, \sqrt{6K/\rho_c}$$

Here, ρN is the particle number density [particles/cm^3], T is the cell temperature [K], MW_c is the carbon molecular weight, $\rho_c = 2$[g/cm^3] is the soot density, and K is the Boltzmann constant.

To model the ignition-delay phenomenon, oxidation of acetylene at high temperatures starts in each computational cell when the following condition is reached:

$$\int_0^{t_{ig}} \frac{1}{\tau_d} d\tau = 1$$

For the ignition-delay time τ_d, the empirical correlation by Hardenberg and Hase [30] was use,

$$\tau_d = \frac{n}{6} * (0.36 + 0.22S_p) * \exp\left(E_A^*\left(\frac{1}{RT} - \frac{1}{17{,}190}\right) + \left(\frac{21.2}{p - 12.4}\right)^{0.63}\right)$$

where 0 is the time at which injection starts, n is the engine speed [rpm], T is the cell temperature [K], p is the cell pressure [bar] and S_p is the mean piston speed [cm/s]. This ignition-delay mechanism is sensitive to the fuel cetane number via the energy activation term

$$E_A = \frac{618{,}840}{CN + 8}[\text{J/mol}]$$

This term has been slightly modified from the original formulation by Belardini et al. [22] to obtain a better fit to the experimental data for a number of test cases. Finally, the in-cylinder NO_X concentration is computed using the standard Zeldovich modified, three-step mechanism with the constant rate of Bowman [31].

The Experimental Apparatus

A single-cylinder diesel engine was used for the experiments. Its features are reported in Table 1. It is equipped with a cylinder pressure transducer, line pressure transducer, and needle lift transducer. The fluid dynamic characteristics of this engine were observed previously by laser Doppler velocimetry measurements [32]. Two quartz windows were mounted on the head of the engine to obtain pictures of the

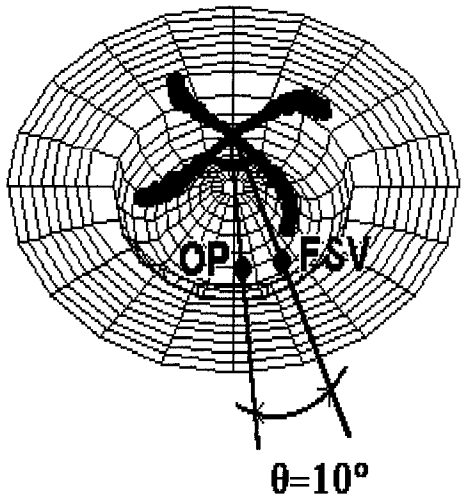

FIG. 1. In-cylinder measuring locations (filled circles) with respect to the fuel jet position: fiber-optical probe (OP) and fast sampling valve (FSV).

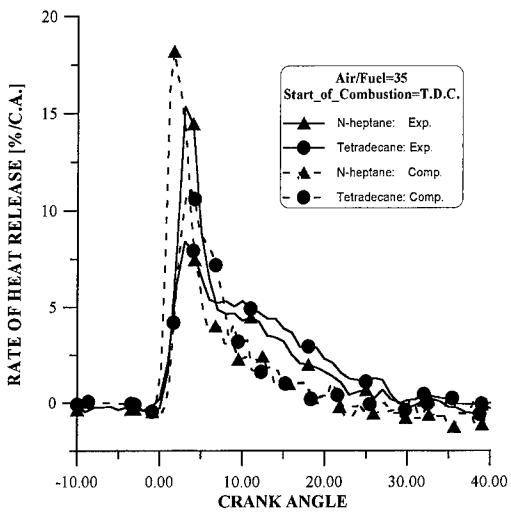

FIG. 2. Rate of heat release for tetradecane and *n*-heptane combustion. Full lines, experimental values; dotted lines, computed values; engine speed, 1250 rpm; air/fuel ratio, 35.

injection and combustion processes by high-speed cinematography and to apply the two-color technique for soot temperature and loading measurements, as outlined in Ref. 33. In this work, the uncertainty in temperature and soot volume fraction measurements was ±56 K and ±28%, respectively.

The engine was equipped with a second head in which a fast-acting valve allowed direct sampling of the combustion products. The fast-acting valve is located in the combustion chamber at about the same radial position as one of the optical access ports and allows the correlation of the soot optical measurements and the sampled species measurements. The relative position of the two control volumes, respectively denoted as OP and FSV, is sketched in Fig. 1; the optical access for the radiance signal measurement is located on the engine cylinder head and directed into the chamber 24° downstream from one of the sprays. The fast sampling valve is positioned at about 14° from the jet axis and at 20 mm from the nozzle outlet. The electronic control system for the sampling valve is able to open the needle for about 5–7° CA for each engine combustion cycle at 1250 rpm. The sample value timing can be controlled to allow the determination of an ensemble averaged, crank-angle resolved concentration profile of the different combustion products during the engine cycle. The sampling procedure is repeated for as many as 100,000 combustion cycles to collect a meaningful volume of products. Water cooling of the valve and gas expansion through the valve lead to a high quench rate. The sample volume for each cycle is about 5 cm^3 at standard conditions. The gaseous products are collected in a small Teflon bag and processed by IR analyzers for CO and CO_2 and by a chemiluminescence analyzer for NO_X. Light hydrocarbons (low C6) are analyzed by a gas chromatograph equipped with a flame ionization detector. The overall coefficient of variation, evaluated on four sets of experiments, is 10% for NO_X and O_2 measurements and 15% for C_2H_2 measurements.

Results and Discussion

The numerical and experimental tests were carried out at a fixed engine speed of 1250 rpm. The injection timing was set to obtain combustion start at top dead center (TDC) and a fixed fuel injected mass of 0.02 g/cycle, which corresponds to a global air/fuel ratio of 35. The fuels used were tetradecane and *n*-heptane. In a previous work [33], it was observed that the relative influence of the fuel aromatics content on soot loading decreases as the fuel cetane number increases. In the near future, reformulated diesel fuels will be characterized by high cetane numbers and low aromatics content. Thus the fuels chosen for this work represent the lower and the upper limits of the future diesel fuel formulations.

To obtain the same combustion-start angle using two fuels that are characterized by different values of cetane number (56 for *n*-heptane and 93 for tetradecane), the injection timing was set at 3.5° CA before top dead center (BTDC) for tetradecane and at 4.5° B.T.D.C for *n*-heptane. In both cases, the injection duration was about 7° CA.

In Fig. 2, the experimental rate-of-heat-release

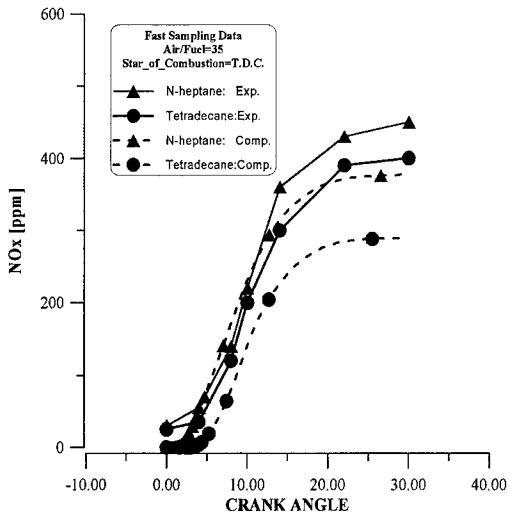

FIG. 3. NO_X concentration for tetradecane and n-heptane combustion. Full lines, experimental values; dotted lines, computed values; engine speed, 1250 rpm; air/fuel ratio, 35.

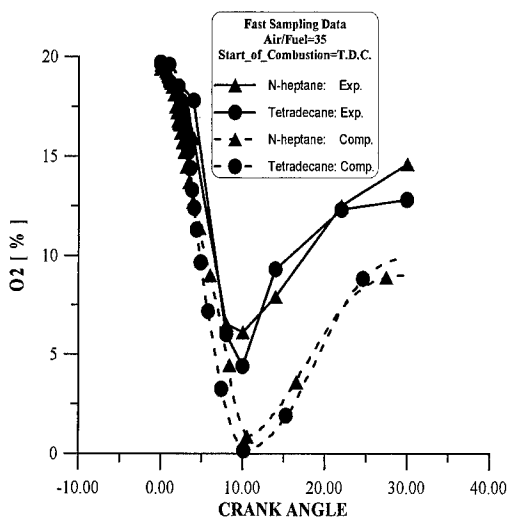

FIG. 4. O_2 concentration for tetradecane and n-heptane combustion. Full lines, experimental values; dotted lines, computed values; engine speed, 1250 rpm; air/fuel ratio, 35.

patterns are compared with the numerical computations for both fuels. Due to different cetane numbers, the heat-release curves have different shapes. However, their main characteristics are reproduced properly by the simulations. The accuracy of the combustion calculation is quite good. The numerical heat-release data plotted are based on the computed

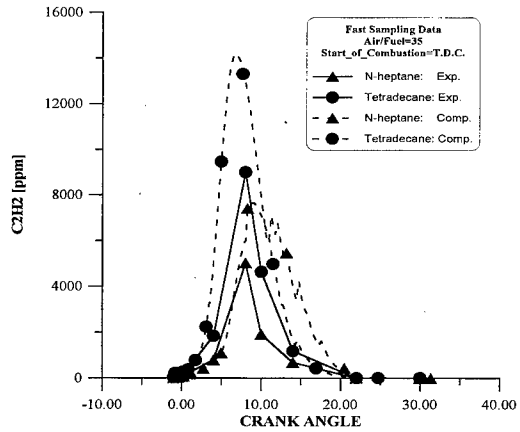

FIG. 5. Acetylene concentration for tetradecane and n-heptane combustion. Full lines, experimental values; dotted lines, computed values; engine speed, 1250 rpm; air/fuel ratio, 35.

time step, without any smoothing, the small time steps result in numerical curves that are not very smooth. The computed, in-cylinder species are specified with the same criterion used in the experiments. (Data are referred to the same control volume used in the experiments, that is, approximately a frustum of solid cone, of about 32° angle for the case of optical measurement and a disk-shaped volume with the sampling valve diameter for the case of fast sampling data.) The numerical results are reported at each computed time step, but the data in Figs. 3–5 are averaged over 5° CA to correspond with the sampling technique. The species measurements are referred to different volumes depending on whether, sampled with the fast valve or measured with the optical technique. The events occurring in the optical control volume are relative to the combustion-product pockets that departed from the first control volume some crank angle degrees before, depending on the swirl velocity. The swirl ratio during the early expansion stroke is about 4 (as determined by three-dimensional computations performed with the Kiva-2 code). Therefore, the time shift between the two measurements is 2.5° CA. However, as previously discussed, the fast-sampling technique uses a sampling window of about 5° CA for each combustion cycle. Therefore, choosing an appropriate crank position and using ensemble average data processing, the sampling measurements for the sampling window correlate properly with the products present in the two-color-measurements control volume. So the results obtained with the two different techniques may be compared locally in the combustion chamber without significant error.

In Fig. 3 the computed and measured NO_X evolution is shown. The model underestimates the

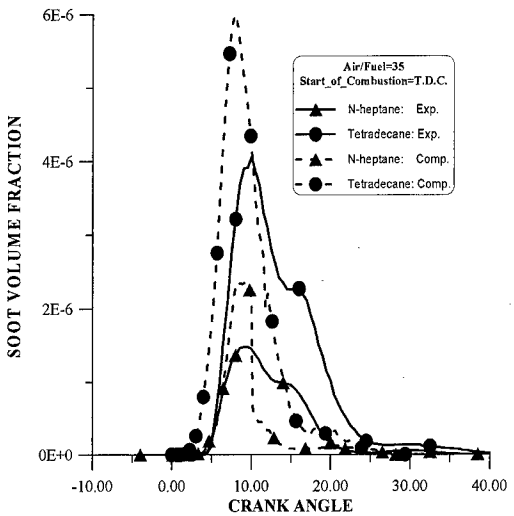

FIG. 6. Soot volume fraction for tetradecane and n-heptane combustion. Full lines, experimental values; dotted lines, computed values; engine speed, 1250 rpm; air/fuel ratio, 35.

experimental results in the late expansion stroke in a manner similar to the underestimate of heat release in the same zone. The molecular oxygen evolution in fast-sampling control volume is shown in Fig. 4. It may be observed that there is no significant difference between n-heptane and tetradecane: this implies the same mixing levels in both cases. Therefore, the differences detected in the soot formation process may be ascribed mainly to the kinetic effects. The computed and measured curve shapes are similar, but the computations overestimate the oxygen consumption in the numerical sample volume. This implies that the size of the numerical sample volume is smaller than the experimental sample volume. Considering the medium resolution grid sizing, it is easy to overestimate or underestimate the control volume, especially after 10° CA when the cell size is increasing. The computed acetylene concentration is compared with the experimental measurement in Fig. 5. The computed acetylene patterns are scaled properly with the measured data, reproducing the decrease of the acetylene concentration peak illustrated by the n-heptane combustion with respect to the tetradecane combustion.

The crank angle phasing of the curves is flattened by the data processing, because the collected data are averaged over 5° CA. This method is not applied to the soot measurements, inferred by the two-color method. In this case, the phase shifting of the curves is properly reproduced, as shown in Fig. 6, where measured and computed results of soot volume fraction are reported for both fuels tested. Within the measurement accuracy, the agreement between computed and measured data may be considered satisfactory. The peak of the soot values for the different fuels is scaled with the peak of acetylene concentration. It is well correlated to the shape of the heat-release curve showing a decrease of soot loading when the premixed phase of combustion increases in n-heptane combustion. The second soot peak in the experimental curves may be due to the combustion products of the second jet that enters the measuring volume. In any case, it must be noted that in the experimental as well as in the numerical analysis, these results represent a small volume inside the combustion chamber. This is an important point, because in our opinion, a three-dimensional code should be able to follow the details of the combustion process. Comparing numerical and experimental data, however, the measurement volume must be carefully evaluated; when the control volume is positioned differently, different results are obtained. This is an additional problem in accuracy that is very difficult from the experimental and the numerical point of view. Within these limitations, the model seems able to simulate the main features of the diesel combustion process, confirming the experimental trends and reproducing the soot-loading characteristics of tetradecane and n-heptane combustion using the same model constants.

Conclusions

The coupled combustion and soot-formation model, characterized by fuel-to-acetylene pyrolysis, acetylene oxidation, soot nucleation and surface growth, and soot oxidation, seems able to predict the combustion and the heat-release patterns of two reference fuels without adjusting the model constants. Despite the strong simplifications that were introduced, the computational results demonstrate that the reduced, kinetic soot model may reproduce, with satisfactory accuracy, the concentrations of soot and pyrolytic products locally in the combustion chamber, keeping the main features of the diesel combustion.

The absolute accuracy of the predictions is not fully satisfactory. The model overpredicts both acetylene and soot volume fraction. However, it should be noted that better results can be obtained with a careful optimization of the model constants. This process is quite difficult because of the full coupling between the combustion and the soot-formation model. Therefore, further work is required to evaluate the best choice of the model constants, considering, in addition, a wider range of engine operating conditions.

REFERENCES

1. Nishida, K. and Hiroyasu, H., SAE Paper No. 89-0269, 1989.

2. Belardini, P., Bertoli, C., Ciajolo, A., D'Anna, A., and Del Giacomo, N., SAE Paper No. 92-2225, 1992.
3. Patterson, M. H., Kong, S. C., Hampson, J. H., and Reitz, R. D., SAE Paper No. 94-0523, 1994.
4. Nagle, J. and Strickland-Constable, R. F., *5th Conference on Carbon,* Pergamon Press, London, 1982, pp. 154–164.
5. Zellat, M., Rolland, T. H., and Poblow, F., SAE Paper No. 90-0254, 1990.
6. Tessner, P. A., Snegriova, T. D., and Knorre, V. G., *Combust. Flame* 17:253–260 (1971).
7. Magnussen, B., Hjertagen, B., Olsen, J. G., and Bhaduri, D., *Seventeenth Symposium (International) on Combustion,* The Combustion Institute, Pittsburgh, 1978, pp. 1383–1393.
8. Nagakita, D., Nagaoka, M., Fujikawa, T. K., Ohsawa, T., and Yamaguchi, S., SAE Paper No. 90-2081, 1981.
9. Farmer, R., Edelman, R., and Wang, E., *Particulate Carbon,* Plenum Press, New York, 1981, pp. 299–320.
10. Yoshihara, Y., Kazakov, A. H., Wang, A., and Frenklach, M., *Twenty-Fifth Symposium (International) on Combustion,* The Combustion Institute, Pittsburgh, 1994, pp. 941–948.
11. Frenklach, M. and Wang, A., *Twenty-Third Symposium (International) on Combustion,* The Combustion Institute, Pittsburgh, 1990, pp. 1559–1566.
12. Fusco, A., Knox-Kelecy, A. L., and Foster, D. E., *COMODIA* (Japanese) 94:571–576 (1994).
13. Gorokhovski, M. and Borghi, R., SAE Paper No. 93-0075, 1993.
14. Lee, K. O., Thring, M. W., and Beér, J. M., *Combust. Flame* 6:137–145 (1962).
15. Pitsch, H., Wan, Y. P., and Peters, N., SAE Paper No. 95-2357, 1995.
16. Leung, K. M., Lindsedt, R. P., Jones, W. P., *Combust. Flame* 87:289–305 (1991).
17. Fairweather, M., Jones, W. P., Ledin, H. S., and Lindstedt, R. P., *Twenty-Fourth Symposium (International) on Combustion,* The Combustion Institute, Pittsburgh, 1992, pp. 1067–1074.
18. Smith, O. I., *Prog. Energy Combust. Sci.* 7:275–291 (1981).
19. Glassman, I., *Twenty-Second Symposium (International) on Combustion,* The Combustion Institute, Pittsburgh, 1988, pp. 295–311.
20. Wagner, H. G. G. and Weiss, M., *Twenty-Second Symposium (International) on Combustion,* The Combustion Institute, Pittsburgh, 1988, pp. 259–311.
21. Belardini, P., Bertoli, C., Del Giacomo, N., and Iorio, B., SAE Paper No. 93-2650, 1993.
22. Belardini, P., Bertoli, C., Cameretti, M. C., and Del Giacomo, N., *COMODIA* (Japanese) 94:315–323 (1994).
23. Amsden, A. A., O'Rourke, P. J., and Butler, T. D., Los Alamos National Laboratory Report No. LA-11560-MS, 1989.
24. Naber, J. D., Enright, B., and Farrel, P., SAE Paper No. 88-1316, 1988.
25. Amato, U., Belardini, P., Bertoli, C., and Del Giacomo, N., *IMEchE C* 430–445 (1991).
26. O'Rourke, P. J. and Amsden, A. A., SAE Paper No. 87-2089, 1987.
27. Liu, A. B., Mather, D., and Reitz, R. D., SAE Paper No. 93-0072, 1993.
28. Reitz, R. D., *Atomisation Sprays Tech.* 3:309–337 (1987).
29. Beatrice, C., Belardini, P., Bertoli, C., and Cameretti, M. C., SAE Paper No. 95-0086, 1995.
30. Hardenberg, H. O. and Hase, F. W., SAE Paper No. 79-0493, 1979.
31. Bowman, C. T., "Kinetics of Pollutants Formation and Destruction in Combustion," *Prog. Energy Combust. Sci.* 1:33–45 (1975).
32. Belardini, P., Bertoli, C., Corcione, F. E., and Valentino, G., SAE Paper No. 92-0155, 1992.
33. Bertoli, C., Beatrice, C., di Stasio, S., and Del Giacomo, N., SAE Paper No. 96-0832, 1996.

COMMENTS

Neil Bressloff, Cranfield University, UK. How have you accounted for the coupling between radiative loss and soot formation?

Author's Reply. The coupling between radiative loss and soot formation was not considered in the model.

•

P. Cadman, University of Wales, UK. Your model incorrectly predicts the soot burnout rate. If you use recent determinations of soot burnout with oxygen [1,2], NO [3] and with hydroxyl [4] which are faster, particularly above 1500 K than older work, would this improve the predictions of net soot concentrations of your engine?

REFERENCES

1. Cadman, P. and Denning, R. J., in *Seventeenth International Symposium on Shockwaves,* Y. Kim (Editor), AIP Press, 1990, p. 751.
2. Cadman, P. and Denning, R. J., *J. Chem. Soc. (Faraday),* in press (1996).
3. Cadman, P. and Denning, R. J., in *Combustion Technologies for a Clean Environment,* M. da Carvalho, (Editor), 1995, p. 765.
4. Cadman, P., Denning, R. J., and Morris, I. L., this Symposium, Poster 2-040.

Author's Reply. Soot oxidation is a crucial point and we should look into it. We will try to use the soot burnout rate

that you suggested in the future in order to improve the prediction of net soot concentration in our engine.

•

Micheal G. Norris, Engelhard Corp., USA. Would an OH-based oxidation not do a better job of oxidizing soot within flame where O_2 levels are low?

Author's Reply. Soot oxidation by OH was not considered in our calculation. However OH radicals are expected to play an important role only for soot contained in the fuel-rich eddies. The amount of O_2 in every computational cell is high with respect to the OH concentration determined by equilibrium considerations. As a consequence, the oxidation by O_2 prevails over the whole examined range of crank angles.

Twenty-Sixth Symposium (International) on Combustion/The Combustion Institute, 1996/pp. 2525–2531

ANALYSIS OF PYROLYSIS PROCESS IN DIESEL-LIKE COMBUSTION BY MEANS OF LASER-INDUCED FLUORESCENCE

R. RAGUCCI
Istituto di Ricerche sulla Combustione
C.N.R. Napoli, Italy

M. DE JOANNON AND A. CAVALIERE
Dipartimento di Ingegneria Chimica
Università Federico II
Napoli, Italy

Inelastic light scattering, excited at $\lambda = 266$ nm, has been measured from 300 to 600 nm in a tetradecane pulsed spray injected into a high-temperature (900 K), high-pressure (4 MPa), nearly quiescent environment.

In each detection, spectra along the radial direction of the spray cross section have been simultaneously detected by means of a gated, intensified CCD camera. The inelastic light scattering has been attributed to laser-induced fluorescence (LIF) based on its spectral behavior and dependence on the laser intensity.

Maxima of the fluorescence signal in the UV range occur in the central part of the test section, just after the ignition time, both in the averaged and individual measurements. These are related to formation of light, pyrolytic species and to early presence of reactive zones inside the spray core.

LIF in the visible spectral region appears later and attains its maximum between 0.5 and 1 ms after the ignition, and just before the maximum of elastic scattering signal due to soot particles. The visible fluorescence is almost uniformly distributed along the spray diameter and undergoes a very peculiar nonlinear dependence on the laser fluence. This feature can be used to distinguish between LIF, laser-induced incandescence, and fluorescence from photofragmented species. LIF in the visible region is also attributed to pyrolytic species, which several papers specify to be polycyclic aromatic hydrocarbons (PAH) with several rings. Extension of this LIF signal throughout the spray cross section and its early detection indicate the need for particular care in improving the diesel combustion process, even in the very early stage after spray ignition, before massive soot formation, if organic pollutants such as PAH have to be minimized.

Introduction

Soot diagnostic techniques are based either on laser light scattering (LLS) effects or on laser-induced incandescence (LII). LLS techniques rely on the discriminative criteria based on the polarization ratio [1,2], which can discriminate between liquid phase and submicronic particulates. Techniques based on LII rely on thermal emission from soot particles heated by means of an intense laser pulse [3,4]. In this case, a compressed dynamic range of detectable signals is obtained relative to those of elastic scattering [5]. Applications capable of detecting spatial distributions of soot in a single pattern have been exploited successfully in diesel combustion diagnostics [5–8]. The combination of LII and LLS results in more quantitative assessment of size and number concentration of soot-particle clouds [8].

The evolution of pyrolytic processes has been inferred from the spatial distribution of soot determined using LLS and/or LII techniques [1,5,10]. In addition, characteristic length scales of the whole spray combustion process [1], and of the soot oxidation process [10] have been hypothesized.

The few papers devoted to identification of pyrolytic species, as opposed to soot particles in diesel-like conditions, are based mainly on sampling and chemical analysis techniques [1,10–12]. They have shown that low molecular weight pyrolysis products are present before ignition [12] whereas high molecular weight species and PAH are formed mainly after ignition [1,10,11].

Optical techniques have demonstrated their potential in characterizing pyrolytic processes both in atmospheric pressure flames [13–15] and in a diesel spray bomb [16] with temporal and spatial resolution much higher than that typical of sampling-based techniques. In these experiments, formation of PAH compounds and their temporal and spatial evolution have been observed by means of fluorescence techniques.

The work presented in this paper uses the same

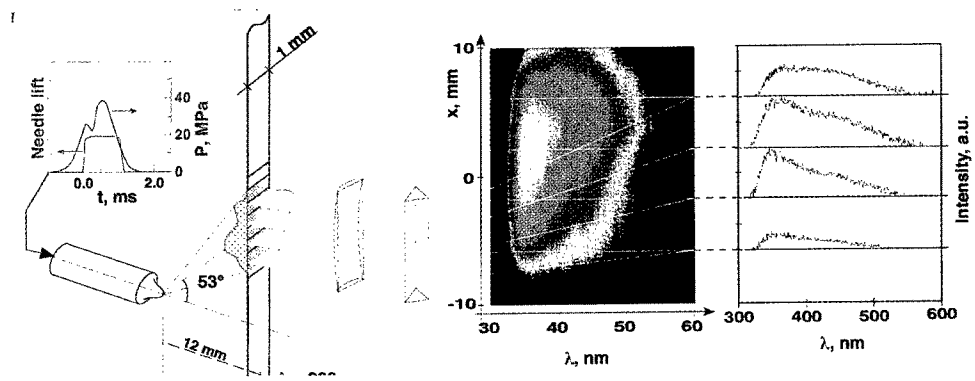

FIG. 1. Schematic drawing of the experimental setup and measurement procedure.

approach for the characterization of pyrolytic species, as opposed to soot, in a diesel spray combustion process, which was previously characterized [1,10] in terms of condensed phases by means of elastic light scattering. Gaseous and condensable species were characterized by means of sampling techniques. The combination of elastic and inelastic scattering measurements is now used to observe the presence of pyrolytic species, distributed throughout the spray core during the combustion process but formed before the detection of massive amounts of soot. However, it is not possible to give clear insight on the relationships between these compounds and soot.

Experimental Setup

The characteristics of the experimental apparatus have been described in previous work [1,2,10]. Therefore, only a brief description is given in this section with specifications of some details relevant to the current results.

A five-hole injector, typical of those used in light duty engines, injects 6 mg/stroke/hole of tetradecane into a high-pressure (4 MPa), high-temperature (900 K), nearly quiescent air environment. The injection lasts 1.2 ms, as is shown in Fig. 1. One of the five spray plumes, tilted 53° on the horizontal plane to minimize the attenuation of the scattered light, is crossed by a Nd:YAG laser sheet (0.3 × 3 mm cross section). Either the second (λ_0 = 532 nm) or the fourth harmonic (λ_0 = 266 nm) of the laser could be used.

The scattered light is collected by means of a condensing lens and a flat field holographic spectrograph, schematically represented in Fig. 1 as a prism. The pattern obtained at the exit plane of the collection system is a rectangular field in which any horizontal line represents the spectrum at a given spatial position in the imaged field (right-hand side of Fig. 1). This pattern is recorded by means of an intensified CCD camera, gated (20 ns) on the laser pulse (10 ns), and then digitized by means of an 8 bit A/D converter.

In the current work, each pixel corresponds to light at fixed wavelength and spatial position collected from a control volume 1 mm wide (fixed by the chosen entrance slit), 200 μm tall, and 300 μm thick (because of the laser sheet thickness). Spectral calibration has been performed using standard lamps. Response linearity and spectral resolution of the apparatus have been verified by measuring radical emission (e.g., C_2, OH) and soot incandescence from a gaseous diffusion flame. Moreover, the sensitivity of the various elements of the CCD array has been taken into account by dividing each image by a calibration image, representative of both spatial and spectral nonuniformity of the detection system. Unfortunately, it was not possible to collect the calibration image of a signal of well-known intensity under the same conditions used during the experiments to make absolute calibrations.

One hundred measurements were run for each selected time step. Most of the measurements shown in this paper refer to ensemble averages. All time values reported in the following are measured as time difference (Δt) between the actual measurement time and the average ignition time that occurs 0.95 ms after the needle lift.

Results

A temporal sequence of average spatial–spectral patterns, whose light intensities are reported in a linearly spaced, false color scale is shown in Fig. 2. Only half of the measured pattern is reported because of the radial symmetry of the spray. No signal could be detected during the first 100 μs after the spray ignition (i.e., Δt < 0.1 ms). At Δt = 0.15 ms, light could be detected between 300 and 400 nm,

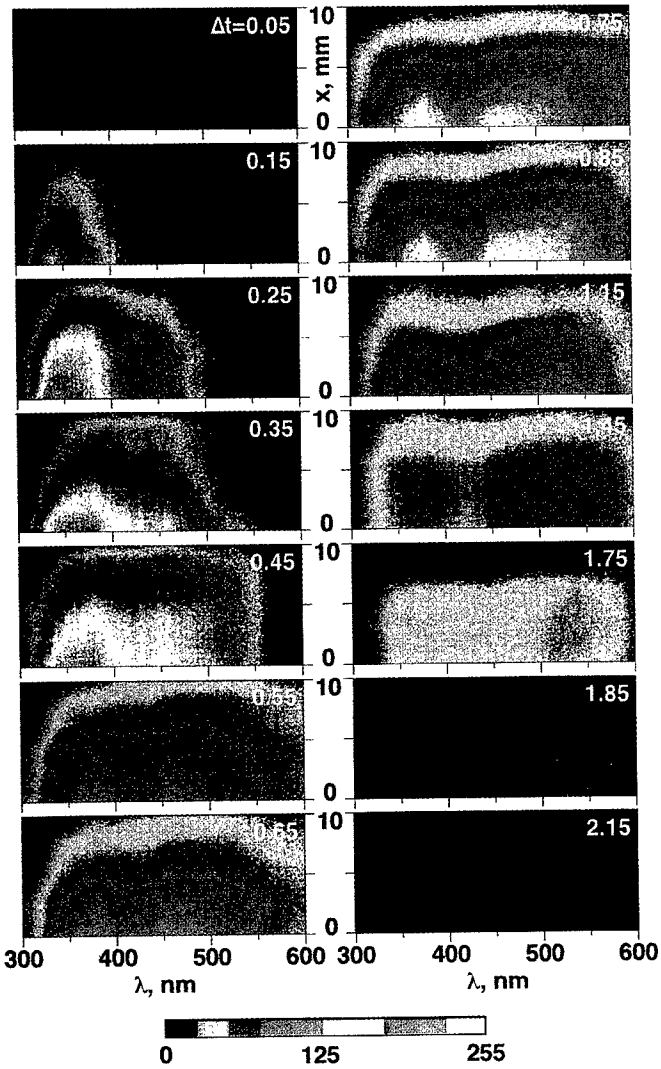

FIG. 2. Average spatial–spectral patterns collected at different times (Δt) after spray ignition.

but only for a limited portion of the spray. The pattern extends along the spatial coordinate (i.e., along the vertical direction) for less than 0.1 ms. In fact, at $\Delta t = 0.25$ ms, the patterns cover the whole spatial domain observed (20 mm). The maximum intensity at $\lambda = 350$ nm is located in the central part (the red color) of the pattern and decreases continuously toward the periphery. This characteristic is observed in all the patterns of the sequence. A green or blue area is always present between 300 and 450 nm, and it is always limited along the spatial coordinate by an azure area, that is, a relatively low level of light intensity. Only after 1.5 ms does this area become nearly uniform with relatively low light intensity. The spatial extent of this region does not change significantly in the whole sequence.

The second main feature of the pattern sequence is the extension of the spectra toward longer wavelength starting from 0.25 ms. This is shown by the displacement of the green–azure region toward the right-hand side of each individual pattern between 0.15 and 0.65 ms. This region is still present after 0.75 ms but becomes weaker after 1.25 ms. Eventually, it disappears as is observed in the last two frames at 1.85 and 2.15 ms.

The average light intensity at $\lambda = 350$ nm (collected at $\Delta t = 0.35$ ms after ignition time) versus the distance from the spray center is reported with a black line in Fig. 3. The spatial distribution of the averaged inelastic scattering exhibits a nearly symmetric shape with respect to the spray centerline with a pronounced maximum in the center. The gray line in the same figure is the spatial profile of the light intensity recorded for a single event. It is an

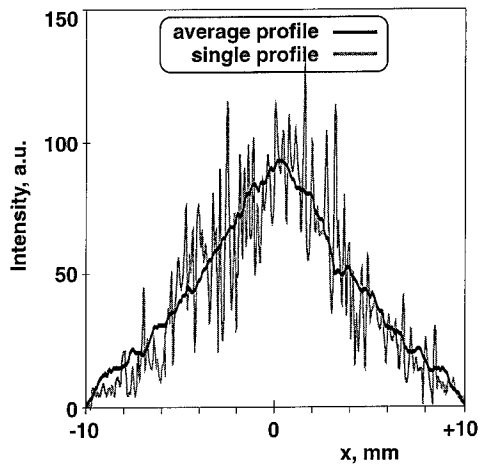

FIG. 3. Single and average spatial profiles at $\lambda = 350$ nm collected at $\Delta t = 0.35$ ms.

oscillating function of the space coordinate and is widely dispersed around the average value. This implies that nonuniformity of species, which leads to the inelastic scattering, extends to the central part of the spray and is related to spatial length scales much smaller than the full spray diameter.

The temporal behavior of the inelastic light scattering can be evaluated in Fig. 4. The curves identified by empty symbols are related to the temporal evolution of the light intensity collected from the full spray diameter (the integral of the signal along the space coordinate of Fig. 2) at fixed wavelength starting from ignition time ($\Delta t = 0$). The profile at $\lambda = 350$ nm increases before all the other. It shows maxima at 0.25 and 0.85 ms. The curve at $\lambda = 450$ nm has a shift of 0.1 ms with respect to that at 350 nm at the beginning and reaches its maximum at 0.45 ms. Subsequently, it proceeds similarly to that at $\lambda = 350$ nm passing through a relative maximum followed by a continuous decrease to $\Delta t = 2.5$ ms. The curve at $\lambda = 550$ nm begins to increase after $\Delta t = 0.35$ ms and reaches its maximum at 0.85 ms, when all the profiles corresponding to shorter wavelengths pass through a relative maximum; it then decreases similar to the trends of the other curves. All the profiles at different wavelengths between 350 and 550 nm follow a behavior that can be considered an interpolation of the three described profiles. Examples of this intermediate behavior are curves at $\lambda = 400$ nm and $\lambda = 500$ nm that are placed, respectively, between 350 nm/450 nm and 450 nm/550 nm.

The temporal profiles of the elastic scattering signals integrated along the spray diameter (the vertically polarized scattered light and the polarization ratio [10]) are represented in Fig. 4 with full symbols. They behave quite differently from the inelastic profiles. In fact, the curve of vertically polarized light intensity is very high at ignition time ($\Delta t = 0$ ms), then decreases to the minimum at $\Delta t = 0.65$ ms. After $\Delta t = 0.65$ ms, the curve increases again until it attains a well-identified maximum at about $\Delta t = 1.35$ ms. It then decreases similar to the inelastic scattering profiles. This is the only temporal range in which the elastic and inelastic signals show similar trends. The polarization ratio is relatively high and constant before $\Delta t = 0.7$ ms. After this time, it drops abruptly, maintaining very low values (around 10^{-2}) until $\Delta t = 2.5$ ms.

The results presented up to this point are all in the category of optical measurements having a linear response to the incident laser power. This is not a trivial statement because the consistency of the results and their repeatability has been achieved only when the linear response of the inelastic signals was tested in the whole temporal range.

Figure 5 shows this type of test by plotting the inelastic signals versus the laser fluence. The curves with empty symbols refer to inelastic light scattering intensity collected at $\Delta t = 0.35$ ms after ignition time at $\lambda = 350$ and 400 nm. It has been normalized to unity for signals collected at a laser fluence of 3.3×10^8 W cm^{-2}. The linear trend is evident for both the reported wavelengths.

On the other hand, the curves pertaining to

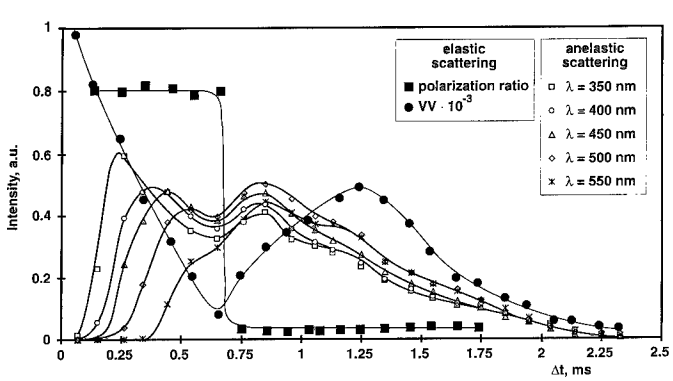

FIG. 4. Temporal profiles of spatially averaged (on the spray diameter) elastic and inelastic scattering signals. The VV scattering intensity (●) divided by 10^3 and the polarization ratio (■) are relative to an incident wavelength $\delta_0 = 532$ nm. The inelastic signals (empty simbols) are relative to $\delta_0 = 266$ nm.

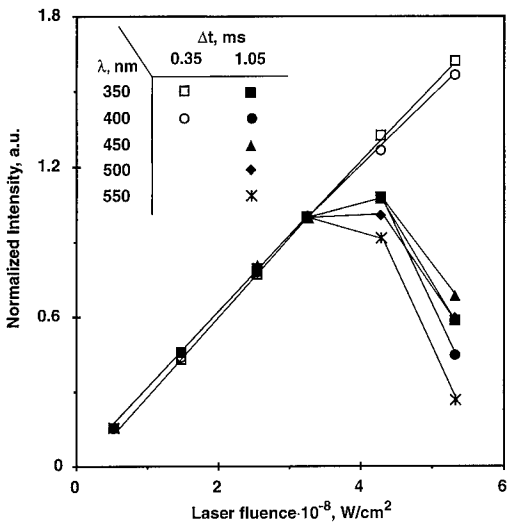

FIG. 5. Light intensity collected at different wavelength versus the incident laser fluence. Empty symbols are relative to Δt = 0.35 ms; full simbols are relative to Δt = 1.05 ms.

measurements at Δt = 1.05 ms show a linear behavior only for laser fluence up to 3.2×10^8 W cm^{-2}, whereas they change the trend between 3.2×10^8 W cm^{-2} and 5×10^8 W cm^{-2}, and decrease for higher values of the laser intensity. It is worth noting that this trend is followed by all curves (i.e., for signals detected in the whole spectral range from 350 to 600 nm) and that this type of behavior is common to all the measurements after Δt = 0.7 ms.

Discussion

It has been shown [10,17] that diesel spray combustion under the present experimental conditions and after ignition evolves in quiescent conditions with a temporal evolution that does not depend on the distance from the nozzle outlet. This implies that the analysis, within a fixed spray cross section, can be considered representative of the whole process and that an increase or decrease in integrated signal, either on the whole cross section or along a diameter, should be attributed to species that are generated or consumed inside the control volume. For instance, the decrease of the elastic scattering signal reported in Fig. 4 is attributed to the liquid fuel consumption by vaporization. This is easily supported by the expected spray evolution that has been analyzed previously [1,10]. This implies that signals have to be attributed to liquid fuel, as confirmed by the fact that the polarization ratio is around 0.8 before Δt = 0.7 ms according to experimental and theoretical considerations described in the literature [2,10].

The values of polarization ratio after Δt = 0.75 ms is lower than 2×10^{-2} (see Fig. 4). Consequently, the corresponding elastic scattering signal can be attributed to submicronic scatterers [2,10]. Furthermore, these scattering signals were determined to be much higher than those caused by low molecular weight gaseous species, so that it can be due only to condensed phase species or to large macromolecules with a very high molecular weight. Chemical analysis of sampled material, as discussed in a previous paper [10], and visible emission detected in this temporal range support the assumption that the elastic scattering signal is due to soot particles.

A more difficult task is attributing the inelastic scattering signal to possible optical effects such as Raman, fluorescence, incandescence, or emission/fluorescence from species formed by single- or multiphoton dissociation. Raman can be disregarded easily because its cross section is very low [18], whereas the inelastic signals reported here imply a much higher cross section [19]. The part of inelastic spectrum for wavelengths shorter than 400 nm and for $\Delta t < 0.5$ ms cannot be attributed to laser-induced incandescence (LII) because, even for the highest hypothesized temperature of soot skin (on order of 5000 K), the LII spectrum does not present the same spectral distribution [20,21]. Also, the visible part of the spectra behaves differently from that of LII spectra, which are reported in the literature to be quite uniform for $\lambda > 500$ nm [20,21]. In fact, the measured spectra show (see Fig. 2) a well-defined decrease in light intensity, which occurs in the most red-shifted condition between λ = 500 and 600 nm.

Moreover, the LII contribution to inelastic scattering has to be disregarded, since no delayed signals could be detected for 100 ns after the laser pulse. This is also confirmed by the dependence of the inelastic light scattering on the laser fluence as shown in Fig. 5 for Δt = 1.05 ms and taking into account that the same trends have been verified in the time interval between Δt = 0.7 ms and Δt = 2.5 ms. The curves show a decrease of the inelastic signals for a fluence higher than 4×10^8 W cm^{-2}. It is reported in the literature that LII undergoes an increase or, at most, saturation [3,20,22] for a laser intensity between 10^7 and 10^9 W cm^{-2}. A decrease of LII signals with increasing laser fluence has only been observed with a rectangular-shaped laser beam and/or for longer detection gate [23,24] (i.e., in conditions different from those used in the present work). Therefore, LII cannot explain the decrease of inelastic light scattering.

The same argument can be used for neglecting LIF or emission from photolyzed species. Furthermore, the signal should be an increasing or constant function of the laser fluence, since both the concentration of photofragmented species and their elec-

tronic excitation can only rise with increasing laser intensity or can be, at most, saturated as has been demonstrated in a study on the fluorescence from C_2 by laser-vaporized soot [21].

In conclusion, we attribute the inelastic signal, after $\Delta t = 0.7$ ms, to LIF of species that are photofragmented at a laser fluence higher than 3.5×10^8 W/cm^2. A more specific attribution either to single species or a category of species can be made on the basis of the available information in similar combustion processes. In fact, broadband spectra with two fluorescence maxima in the UV and in the green region have been reported for rich premixed gaseous flames [14], for *n*-heptane diffusion flames [15], and for other diffusion flames [25]. For all of these conditions, the fluorescence spectra have been related to PAH species that extend their emission spectra toward the red region according to the number of aromatic rings, as is well-known [26]. This conclusion is supported by sampling measurements performed under the same experimental conditions of the present work using a different fuel (tetradecane/α-methylnaphthalene 60/40 vol. %) [1]. In that work, the maximum of PAH species was attained soon after the ignition time as occurred for LIF signal maxima in the present case. Unfortunately, the poor time resolution of sampling techniques does not permit a direct correlation of early presence of LIF signals with early formation of PAH compounds.

In any case, it seems clear that the detected LIF signals are due to species that are formed after the ignition time. The same measurements in high-temperature, high-pressure N_2 environment did not yield appreciable LIF. The spatial distribution of the average- and single-shot LIF at $\lambda = 350$ nm reported in Fig. 3 is an example of how to exploit UV LIF. This is direct evidence both of the presence of fluorescent species formed at a temperature higher than that of the environment well inside the spray core and of early occurrence of pyrolytic oxidative processes inside the plume. This had been only hypothesized in the past by the late presence of soot clouds in the middle of the spray cross section and on very small length scales [1,10].

The LIF shown in Fig. 4 is high between 0.5 and 1 ms for all wavelengths from 350 to 550 nm. The presence of inelastic light scattering at $\lambda > 400$ nm is related to LIF from PAH having a large number of condensed aromatic rings as discussed earlier. It is of interest to emphasize that the assertion that inelastic scattering is due to LIF does not seem questionable. Also, if a fraction of the signal should be attributed to LII, the information content does not change. In fact, in both cases (LIF and LII), the inelastic scattering is due to early formation of heavy pyrolytic products (large PAH or soot). Furthermore, visible LIF extends over the cross section with a uniform increase toward the core as is shown in Fig. 2. Such spatial distribution supports the assertion that the LIF is due to pyrolytic species, because the oxygen depletion is more likely to occur in the spray core. It is also of interest to mention that the LIF maxima precede LLS maximum, which is attributed to soot. This statement is not a claim that these fluorescent species are precursors of soot particles, but it indicates the occurrences of pyrolysis and the need to prevent the reacting plume from quenching (e.g., by wall impingement) even before the soot formation.

The LIF after $\Delta t = 1$ ms is a decreasing function of time according to the temporal trends in Fig. 4. This indicates a uniform decrease of fluorescent-species concentration, under the hypothesis of constant fluorescence quenching and negligible convective transport (as has been demonstrated thoroughly in a previous paper [10]). The only acceptable explanation of this evolution is that oxidation of fluorescent species proceeds in a similar way to that occurring for soot [10].

Finally, two points should be stressed explicitly. The first is that the lack of LII signal that is well identified and exploited in diesel engine environment by several authors [5,7,8] can be due to low soot concentration related to the experimental conditions reported here. In fact, it has been shown [1] that less than 3% of carbon conversion to soot is obtained in this condition. Such a low level of carbon-to-soot conversion is not mandatory for the feasibility of LIF measurements. However, a verification of the relative importance of LII and LIF signals has to be performed to validate the significance of experimental data.

The second point is that UV fluorescence spectra has been measured for *n*-heptane injection, before ignition time [16]. The different behavior outlined here may be due to a much longer ignition delay reported for the injection of *n*-heptane. This, perhaps, allows enough time for the formation of fluorescent, low molecular weight, aromatic compounds before the ignition.

Conclusions

Diagnostics Aspects

UV fluorescence excited by the fourth harmonic of Nd:YAG laser is a direct signature of the early combustion process in diesel-like conditions. This is of interest for observation of very rich zones in which OH detection [27] or other reaction markers cannot be used.

Visible fluorescence can be distinguished, under the conditions reported in this paper, by laser-induced incandescence using its intensity dependence on laser fluence. "Photolyzable" species are responsible for such behavior. This is a further qualifying feature that can be used fruitfully in simpler

experiments relating to shock tubes and stationary gaseous flames.

Combustion Aspects

Reactive zones are shown to be present very early in the spray core by means of direct signature of species formed after ignition. In the past, this effect could be only hypothesized on the basis of spatial nonuniformity of soot clouds, which has been well proven [1,8,10] for diesel combustion.

LIF in the green region of the spectral range appears between the maxima of UV-LIF and elastic light scattering. Being caused by either LIF or LII implies, in both cases, that heavy pyrolytic products are formed and distributed across the whole spray at a short distance from the nozzle outlet.

Acknowledgment

This work was partly funded by the Commission of the European Communities within the frame of the JOULE Program contracts JOU2-CT94-0367 and JOU2-CT94-0055.

REFERENCES

1. Ragucci, R., Cavaliere, A., Ciajolo, A., D'Anna, A., and D'Alessio, A., *Twenty-Fourth Symposium (International) on Combustion,* The Combustion Institute, Pittsburgh, 1992, pp. 1565–1571.
2. Ragucci, R., Cavaliere, A., and D'Alessio, A., COMODIA 90:371–376 (1990).
3. Melton, L. A., *Appl. Opt.* 23:2201–2208 (1984).
4. Eckbreth, A., *J. Appl. Phys.* 48(11):4473–4479 (1977).
5. Dec, J. E., zur Loye, A. O., and Siebers D. L., SAE Paper No. 91-0224, 1991.
6. Espy, C. and Dec J.; SAE Paper No. 93-0971, 1993.
7. zur Loye, A. O., Siebers, D. L., and Dec, J. E., COMODIA 90:523–528 (1990).
8. Pinson, J. A., Mitchell, D. L., Santoro, R. J., and Litzinger, T. A., SAE Paper No. 93-2650, 1993.
9. Won, Y., Kamimoto, T., and Kosaka, H., SAE Paper No. 92-0114, 1992.
10. Cavaliere, A., Barbella, R., Ciajolo, A., and Ragucci, R., *Twenty-Fifth Symposium (International) on Combustion,* The Combustion Institute, Pittsburgh, 1995, pp. 167–174.
11. Barbella, R., Ciajolo, A., D'Anna, A., and Bertoli, C., *Twenty-Third Symposium (International) on Combustion,* The Combustion Institute, Pittsburgh, 1990, pp. 1079–1085.
12. Ikegami, M., Li, X., Nakayama, Y., and Miwa, K., SAE Paper No. 83-1290, 1983.
13. Beretta, F., D'Alessio, A., D'Orsi, A., and Minutolo, P., *Combust. Sci. Technol.* 85:455–470 (1992).
14. D'Alessio, A., D'Anna, A., D'Orsi, A., Minutolo, P., Barbella, R., and Ciajolo, A., *Twenty-Fourth Symposium (International) on Combustion,* The Combustion Institute, Pittsburgh, 1992, pp. 973–980.
15. Petarca, L. and Marconi, F., *Combust. Flame* 78:308–325 (1989).
16. Eisele, G., "Diagnostics of Diesel Engine Combustion by Laser Induced Fluorescence," Ph.D. Thesis, LTT-RWTH, Aachen, Germany, 1994.
17. de Joannon, M., Cavaliere, A., and Ragucci R., Joint Meeting of the Combustion Institute (Italian and Portuguese Sections), VII-7, 1994.
18. Greenhalgh, D. A., in *Optical Diagnostics for Flow Processes* (Lading, L., Wigley, G., and Buchhave, P., Eds.), Plenum Press, New York, 1994, p. 357.
19. Kerker, M., *The Scattering of Light,* Academic Press, New York, 1969.
20. Bengtsson, P. E. and Aldén, M., *Appl. Phys. B* 60:50–59 (1995).
21. Quay, B., Lee, T. W., Ni, T., and Santoro, R. J., *Combust. Flame* 97:384–392 (1994).
22. Dash, C. J., *Appl. Opt.* 23:2209–2215 (1984).
23. Ni, T., Pinson, J. A., Gupta, S., and Santoro, R. J.; *Appl. Opt.* 34:7083–7091 (1995).
24. Vander Wal, R. L. and Weiland, K. J., *Appl. Phys. B* 59:445–452 (1994).
25. Prado, G., Garo, A., Ko, A., and Sarofim, A., *Twentieth Symposium (International) on Combustion,* The Combustion Institute, Pittsburgh, 1984, pp. 989–996.
26. Berlman, I. B., *Handbook of Fluorescence Spectra of Aromatic Molecules,* Academic Press, New York, 1971.
27. Arnold, A., Dinkelacker, F., Heitzmann, T., Monkhouse, P., Schäfer, M., Sick, V., Wolfrum, J., Hentschl, W., and Schindler, K. P., *Twenty-Fourth Symposium (International) on Combustion,* The Combustion Institute, Pittsburgh, 1992, pp. 1605–1612.

COMMENTS

Allan P. Smith, AEA Technology, UK. How can you be certain that the maximum PAH LIF intensity corresponds to the maximum PAH Concentration given the uncertainties in quenching of PAH LIF?

Authors' Reply. We agree that radial distribution of PAH concentration can not be inferred on the grounds of the presented results. In fact, in the paper it is only stated that LIF signals present bell-shaped radial profiles and, due to the lack of information on quenching and absorption effects inside the spray plume, no conclusions are advanced about PAH concentration profiles.

Anyway, the comment does not affect the main conclusion of the paper, i.e. reactive zones, in which heavy pyrolytic compounds are formed, are present very early and are distributed over the whole spray section.

Twenty-Sixth Symposium (International) on Combustion/The Combustion Institute, 1996/pp. 2533–2540

SPECTRAL EXTINCTION MEASUREMENTS OF SPRAY COMBUSTION IN A DIVIDED-CHAMBER DIESEL ENGINE SYSTEM

FELICE E. CORCIONE, GIUSEPPE MAZZIOTTI AND BIANCA MARIA VAGLIECO
Fluid-Dynamics and Combustion Division
Istituto Motori, CNR, Naples, Italy

Spectral flame extinction measurements from UV to visible with high temporal and spatial resolution were performed in an optically accessible divided-chamber diesel system. This system was developed ad hoc by modifying a real engine to realize a soot-forming premixed spray combustion at high pressure, high temperature, and high swirl. The large optical accesses of the divided chamber allowed us to follow the progress of fuel injection, vaporization, autoignition, and combustion by direct high-speed photography (8000 frames/s). Light extinction measurements were carried out in 153 different spatial locations for 250 consecutive combustion cycles from the start of injection to the end of combustion. The photographic sequences have shown that the spray is strongly distorted and mixed downstream of the high-swirling flow, resulting in a well premixed region in which the combustion starts. Then, the combustion proceeds rapidly, involving the entire chamber volume. Consequently, the flame luminosity increases, denoting fast soot formation–oxidation processes in the region close to the tangential duct in which the mixing is higher. The analysis of the extinction spectra in the UV and visible range has allowed us to follow spatially and temporally the soot formation process and to identify the nature of the particulate matter and the agglomeration degree of soot particles, as well as the time history of the soot volume fraction.

Introduction

Diesel combustion is a two-phase, turbulent, mixing-controlled process that includes short timescale phenomena such as turbulence production and dissipation, spray breakup and evaporation, and pollutant formation. For this reason, it can be appropriately investigated by using in situ diagnostic techniques with high temporal and spatial resolution.

Recently, combined optical techniques were used in transparent engines, which allowed us to find valuable information on instantaneous structure of flow field [1], fuel spray distribution and evaporation [2,3], mixture preparation [4,5], self-ignition [6], spatial distribution of key transient species such as OH radicals [7,8], and, finally, soot temperature and volume fraction [9–11]. Moreover, considerable progress was made concerning the physical and chemical characterization of particulate matter by multiwavelength light scattering and extinction methods [12,13]. These polychromatic techniques are particularly promising because carbonaceous material and large aromatic molecules exhibit absorption bands between 200 and 350 nm [14,15]. More recently, the application of these techniques to the exhaust of a diesel engine made it possible to evaluate the average particle size and number density of the particulate matter, its agglomeration state, and its optical properties [16]. However, no systematic studies of the wavelength dependence of light extinction in UV and visible in-cylinder soot forming in diesel engines have yet been carried out, since the early measurements were limited to the visible range [17].

The present paper deals with the spectral measurements of the extinction coefficients in both the visible and near UV inside an optically accessible divided-chamber diesel system developed specifically for the experiment by modifying a real engine to realize a soot-forming premixed spray combustion at high pressure, high temperature, and high swirl. The main objective is to identify temporally and spatially the zones in which the soot is formed with respect to the distribution of the injected fuel and to characterize the physical and chemical nature of soot particles.

The large optical accesses of the divided chamber have allowed us to follow the progress of fuel injection, vaporization, autoignition, and combustion by direct high-speed photography and to make flame emissivity and light extinction measurements in different spatial locations with high temporal resolution from the start of injection to the end of combustion.

By combining the complementary information coming from the photographic sequences and the

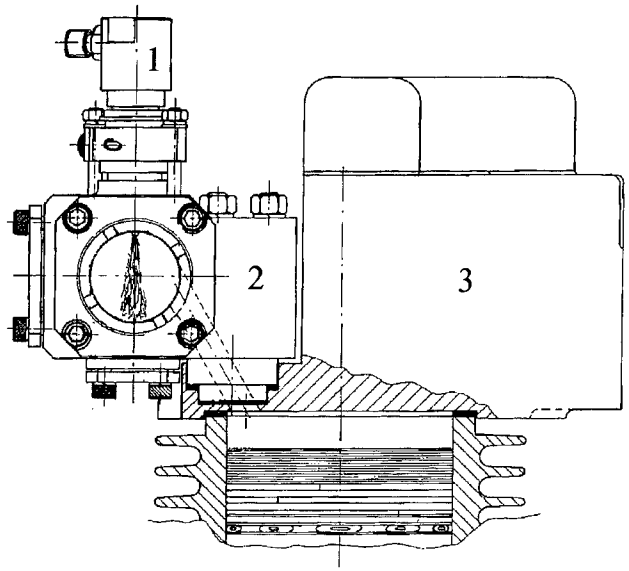

1. Injector
2. Divided combustion chamber
3. Piston engine

FIG. 1. Layout of the modified engine.

extinction measurements, different aspects of the combustion and soot formation processes have been analyzed and discussed.

Experimental Description

Divided-Chamber Diesel System

A four-stroke, water-cooled, single-cylinder D.I. diesel engine (10-cm bore and 9.5-cm stroke), representative of heavy-duty engines, with displacement of 750 cm^3 and volumetric compression ratio of 21.3:1, was used. The engine was modified to gain large optical accesses of the external high-swirl, divided combustion chamber as shown in Fig. 1. Three major modifications were made:

1. The standard piston with a toroidal bowl was replaced with a flat one.
2. An external divided chamber with the same piston-bowl volume of the real engine (21.3 cm^3) with three optical accesses, two in the longitudinal direction and one in that orthogonal, was set up on the top of the engine. It was connected with the engine cylinder by a tangential duct that realized a strong counterclockwise swirl estimated to be more than 50 times the angular engine speed.
3. The injection nozzle with a single hole of 0.027 cm was located centrally on the top of the divided chamber. It was electronically controlled to operate a fixed number of combustion processes.

Measurements of diesel combustion were performed at an engine speed of 2000 rpm. Injecting 8.3 mg European commercial diesel fuel per stroke, a high air-fuel ratio was realized, allowing operation of the engine for many minutes without obscuring the optical windows. Details of the specifications of the test engine are reported in Refs. 8 and 18.

Optical Apparatus

Polychromatic emissivity and extinction measurements were carried out by the experimental setup shown in Fig. 2. A high-pressure Xenon flash lamp with its broadband emission spectrum was used because of the high emission intensity reached in the 200–350 nm range. The light pulses had a short rise time of 5 μs and a duration of 1.2 ms. The silica lens L1 (f = 50 mm) focused the light beam on the control volume inside the combustion chamber. The flame emissivity and extinct light by the flame were collected and focused with a fused silica lens L2 (f = 150 mm) on the entrance slit of a 32-cm focal length luminous spectrograph, blazed at λ = 300 nm. The spectral image formed on the polychromator exit plane was detected on a gated image intensifier coupled with a CCD camera with a resolution of 512 × 384 pixels.

The high spatial resolution of the CCD camera allowed detection of nine items about each location simultaneously. Thus, the total measuring points in the combustion chamber were 153 at 17 locations. In the present paper, measurements relative to the

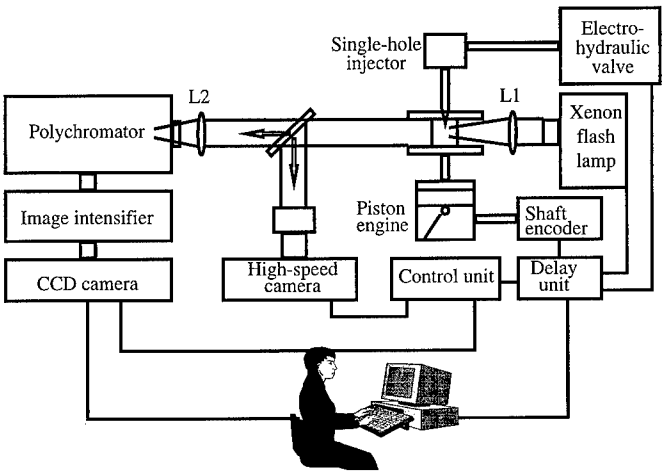

FIG. 2. Optical setup.

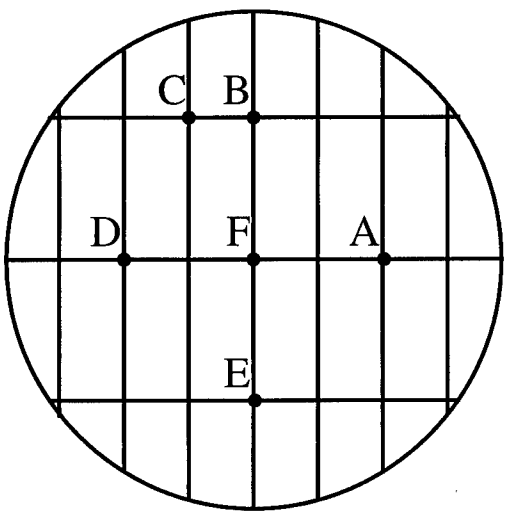

FIG. 3. Location of optical measurement points.

locations *A, B, C, D, E,* and *F* shown in Fig. 3 are reported. Location *A* is close to the air entrance, *B* and *C* are just on the spray close to the nozzle exit, *D* is also on the spray but close to the chamber wall, and, finally, E and F are on the first appearance of the flame. To minimize the statistical uncertainty of the results, the measurements were ensemble averaged on 250 consecutive combustion cycles. The synchronization trigger of the fuel injection, image intensifier, and CCD camera was driven by the needle lift signal through a unit delay. Spectral and absolute calibration of the flame emissivity was achieved by detecting the emissivity from a calibrated Tungsten lamp, with color temperature of 2600 K, operating under the same conditions as those described previously. The extinction coefficients were obtained by measuring the spectrum of the emission of the flame S_λ^f, the light of the lamp directed to the polychromator without the flame A_λ^1, and the light coming from the attenuated lamp and the emission with the flame A_λ^{1+f} in the optical path L:

$$K_{\text{ext}} = L^{-1} \ln \left[\frac{A_\lambda^1}{(A_\lambda^{1+f} - S_\lambda^f)} \right] \tag{1}$$

Theory of Light Extinction

The extinction is the attenuation of electromagnetic wave by scattering and absorption as it transverses a cloud of particles in a gas or liquid and is defined as

$$K_{\text{ext}} = NC_{\text{ext}}(D_{\text{eq}}, n, k, \lambda) = NQ_{\text{ext}}(D_{\text{eq}}, n, k, \lambda)\, \pi \frac{D_{\text{eq}}^2}{4} \tag{2}$$

where N is the number density of the particles in the cloud, C_{ext} is the total cross section for extinction, n and k are the real and imaginary part of the complex index of refraction, $m = n - ik$, D_{eq} is the equivalent (mean) diameter of soot particles, and λ is the wavelength of the incident light. Note that the extinction cross section is the sum of absorption and scattering cross sections:

$$C_{\text{ext},\lambda} = C_{\text{abs},\lambda} + C_{\text{sca},\lambda} \tag{3}$$

For small homogeneous spheres (as compared to wavelength of radiation), the Lorenz–Mie solution converges to Rayleigh approximation, where extinction can be approximated considering a monodisperse size distribution as

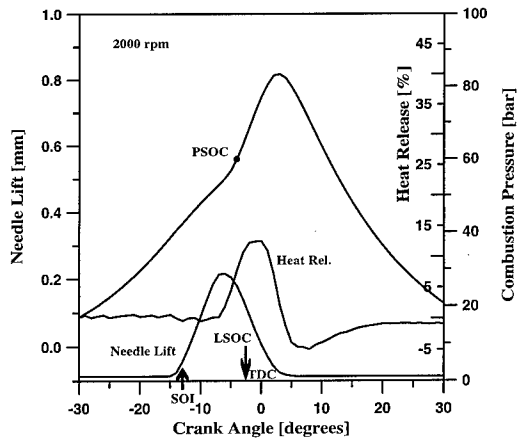

FIG. 4. History of combustion pressure, needle lift, and rate of heat release.

$$Q_{\text{ext}} = -\frac{\pi D_{\text{eq}}}{\lambda}\left[Im\left(\frac{m^2 - 1}{m^2 + 2}\right)\right] \tag{4}$$

The soot volume fraction can be calculated from Eqs. (2) and (4) considering the complex index of refraction $m = 1.9 - i0.55$ at $\lambda = 488$ nm [19]:

$$f_v = \frac{K_{\text{ext}}^{\lambda} \cdot \lambda}{\left[6\pi\left(Im\left(\frac{m^2 - 1}{m^2 + 2}\right)\right)\right]} \tag{5}$$

Results and Discussion

During the intake process, airflow through the swirl-generating inlet port and inlet valve into the cylinder acquires a strong rotational movement. Then, during the compression stroke, the piston rises and the airflow is compressed through the tangential inlet duct into the combustion chamber where a strong counterclockwise swirling motion is induced. Measurements of the tangential component of the flow, carried out by a laser Doppler velocimeter in the last 40° of the compression stroke [20], show that the swirl reaches its maximum values just a few degrees before top dead center. The fuel is then injected around this crank angle at high transient pressure by a real injection system into the swirling flow. After the ignition-delay time, the onset of combustion causes a pressure increase above the compression curve that is converted into mechanical work.

Figure 4 reports the history of the combustion pressure, needle lift, and rate of heat release. The injection starts 13° crank angle before top dead center (CAD-BTDC) with a duration of 16° about TDC. After an ignition delay of 9°, the combustion pressure increases rapidly, resulting in a fast combustion of the accumulated injected fuel. The crank angle is called pressure start of combustion (PSOC) and is shorter than the luminous start of combustion (LSOC) that is the time from the start of injection (SOI) to the first appearance of the luminous flame determined from the photographic sequence. In the present experiments, PSOC is 2° shorter than LSOC. The duration of the luminous visible combustion in the divided chamber is 15°. The rate of heat release shows only one peak because 90% of the total fuel is injected during the ignition-delay time, meaning that the combustion process is a sort of premixed and mixing controlled combustion instead of a diffusive combustion.

Combustion Visualization

To examine the temporal and spatial evolution of the combustion process, films were taken with a 16-mm HYCAM-II high-speed camera at a film speed of 8000 frames/s. The camera generated light spots on the edge of the film corresponding to defined crank angles. The photographic system operated synchronously with a digital data acquisition system to acquire the injection and combustion parameters. Since the transient injection system takes time to reach its behavior stability, 16 consecutive combustion phenomena were detected on the film. It was observed that the stability was reached after the seventh combustion cycle.

Figure 5 shows the direct photographic sequence of the flame, starting from the first appearance of the combustion and proceeding until the flame moves in the main chamber. It is interesting to note that the strong counterclockwise swirling flow distorts the spray and contributes to entrained air in it. The combustion starts downstream from the spray where it is most atomized and the mixture is most premixed. Then, the combustion proceeds rapidly, involving the entire chamber volume. Consequently, the flame luminosity increases, denoting fast soot formation–oxidation processes in the region close to the tangential duct where the mixing is greater.

Spectral Extinction Measurements

Figure 6 shows the history of soot volumetric fraction determined in the six locations, equally distributed in the chamber volume, *A, B, C, D, E,* and *F.* This distribution was determined by the procedure shown in the previous section. The soot formation starts simultaneously in the locations *A, E,* and *F* in which the autoignition occurs. Soot forms also in the rich, unburned fuel–containing core of the fuel spray (location *D*), close to the flame region, where the fuel vapor is heated by mixing with hot, burned gases. In locations *B* and *C*, positioned about the

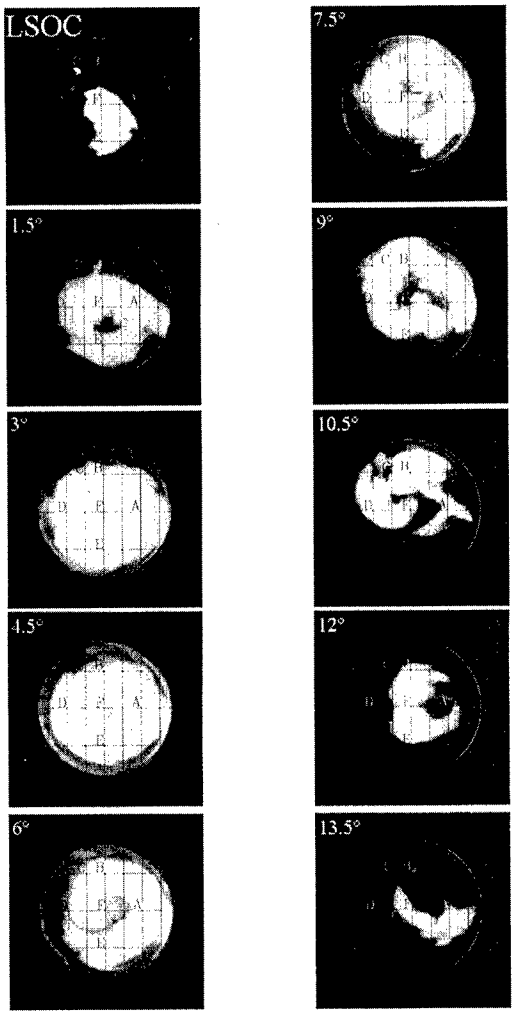

FIG. 5. Direct photographic sequence of spray combustion at 8000 frames/s. Location of optical measurement points.

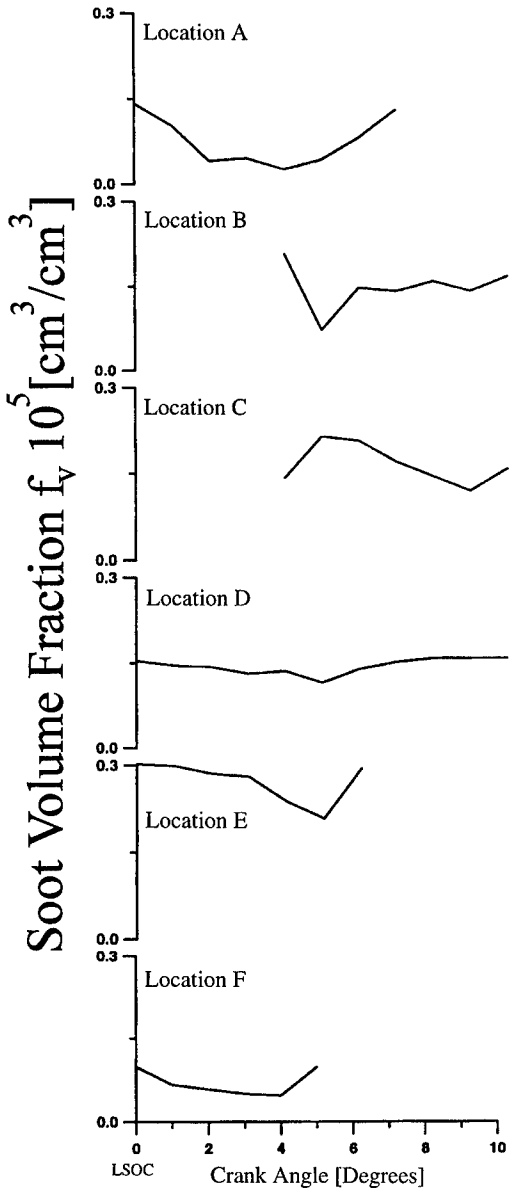

FIG. 6. History of soot volume fraction in six locations.

liquid core of the spray just at the exit of the nozzle, soot appears 4° after LSOC because of the late arrival of the flame. Moreover, in all locations, soot oxidizes when it contacts unburned oxygen supplied by the strong swirling flow. After a few crank angle degrees, depending on the location, soot forms again for two reasons. The first is related to the lack of oxygen caused by the exit of the gases from the chamber induced by the piston motion during the expansion stroke (locations *A*, *D*, *E*, and *F*). The second relates to the final stage of the injection that releases fuel at low pressure and, consequently, does not have time to burn completely (locations *B* and *C*). From a quantitative point of view, locations *B* and *C* form more soot because they are situated in the zone richer in fuel. Location *E* forms more soot as well because the swirling flow moves the burning zones from the inlet duct toward the center of the chamber by the strong rotational motion.

To give information about the physical and chemical composition of the flame, the extinction spectra in the UV and visible, relative to more representative locations *A*, *C*, and *D*, were selected. Location *A* represents the most mixed zone because it is strongly influenced by the inlet air coming from the engine

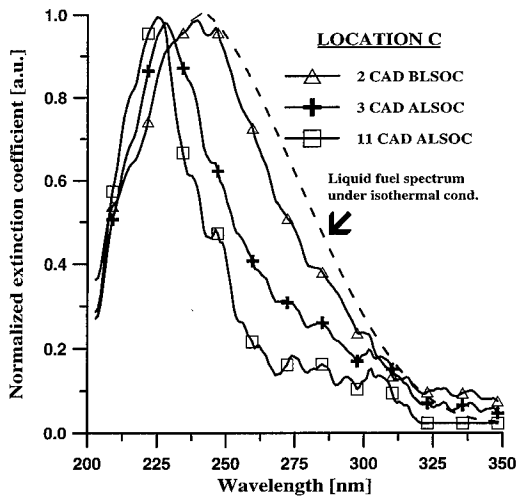

FIG. 7. Normalized extinction spectra in the UV range for location *C*.

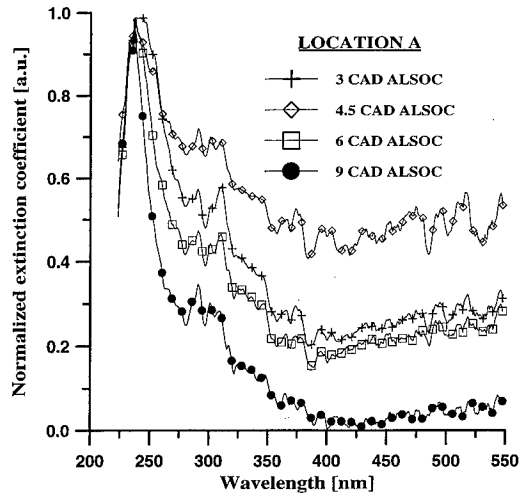

FIG. 9. Normalized extinction spectra from UV to visible for location *A* at 3°, 4.5°, 6°, and 9° after luminous start of combustion.

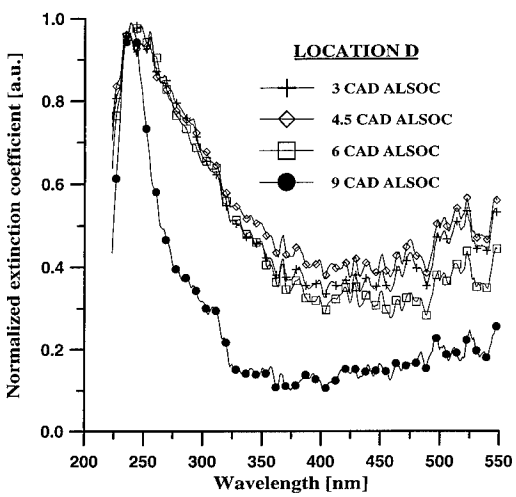

FIG. 8. Normalized extinction spectra from UV to visible for location *D* at 3°, 4.5°, 6°, and 9° after luminous start of combustion.

cylinder; location *C* is just on the spray, and *D* is positioned close to the chamber wall. Figures 7–9 show the normalized extinction spectra at different CAD after the start of injection and combustion. Figure 7 shows the spectra in the UV range at 2° before LSOC and 3° and 11° after LSOC for the location *C*. It shows that 2° before LSOC, the maximum peak is around 250 nm, denoting the presence of liquid fuel. This behavior is confirmed when comparing the extinction spectrum with that obtained using a spectrophotometer analysis of the same fuel under isothermal conditions. At 3° and 11° after LSOC, the peak moves toward 225 nm, suggesting that the nature of the particulate can be associated to that of carbonaceous material as confirmed by the absorption bands reported in Ref. 15.

Figure 8 shows the normalized extinction spectra determined in location *D* from UV to visible at different degrees after LSOC. The curves relative to 3°, 4.5°, and 6° after LSOC exhibit the maximum peak around 235 nm, and their shape is broader than the curve at 9° after LSOC. This last result is very interesting because it defines the nature of the particulate matter and indicates that the average size of soot particles is influenced by the temporal evolution of the combustion phenomenon [13]. Spectral extinction measurements, carried out in the engine exhaust by the present authors [16], confirm this result and indicate also that the particulate matter formed in the combustion chamber and that obtained in the exhaust have the same nature. The particulate appears as a disordered structure with very little graphitic nature. The broader shape of the spectra is due to the agglomeration process of the soot particles induced by the quenching effect of the chamber wall, which lowers the temperature of the flame [8].

Figure 9 shows the normalized extinction spectra in location *A*. The UV peak remains remarkably constant, denoting the stability of soot composition at different degrees after LSOC. However, there are differences in the falloff of the curves in the visible range that can be due to the different soot particle agglomeration state [16]. The interpretation of the results in this location is more difficult because of the fluid-dynamic effect of the swirling flow that moves the hot gases toward the main chamber during the engine expansion stroke. Nonetheless, it can

be noted that the strong movement of the gases reduces the temperature stimulating the agglomeration process of the particles.

Conclusions

Spectral flame extinction measurements from UV to visible with high temporal and spatial resolution were performed in an optically accessible divided-chamber diesel system. This system was developed for our specific purposes by modifying a real engine to realize a soot-forming, premixed spray combustion at high pressure, high temperature, and high swirl. The progress of fuel injection, vaporization, autoignition, and combustion were followed by direct high-speed photography (8000 frames/s). Polychromatic extinction measurements were carried out in 153 different spatial locations for 250 consecutive combustion cycles from the start of injection to the end of combustion.

The high-speed photographic sequences of the combustion show that the strong counterclockwise swirling flow, induced by the tangential inlet duct, distorts the spray and contributes to entrained air in it. The combustion starts downstream from the spray where it is most atomized and the mixture is most premixed. Then, the combustion proceeds rapidly to involve the entire chamber volume. Consequently, the flame luminosity increases, suggesting fast soot formation–oxidation processes in the region close to the tangential duct where the mixing is higher.

Spectral flame extinction measurements show that the soot formation starts simultaneously in the locations in which the autoignition occurs, as well as in the rich, unburned fuel–containing core of the spray, close to the flame region, where the fuel vapor is heated by mixing with hot, burned gases. Then, in all locations, soot oxidizes when it contacts unburned oxygen supplied by the strong swirling flow.

Looking at the shape of the extinction spectra, the particulate matter formed in the combustion chamber and that obtained in the exhaust have the same nature. It appears as a disordered structure far from graphitic nature. Finally, the average size of soot particles is influenced by the temporal evolution of the combustion phenomenon.

Nomenclature

λ	wavelength of the incident light [nm]
A_λ^l	spectral signal of lamp
A_λ^{l+f}	spectral signal of lamp attenuated by flame
C_{ext}	cross section for extinction
D_{eq}	equivalent (mean) diameter of soot particles [cm]
eq	equivalent
f_v	soot volume fraction [cm^3/cm^3]
Im	imaginary
K_{ext}	extinction coefficient [cm^{-1}]
k	imaginary part of the complex index of refraction
L	optical path [cm]
$m = n - ik$	complex index of refraction
n	real part of the complex index of refraction
N	number density of the particles in the cloud [cm^{-3}]
Q_{ext}	extinction efficiency
$C_{abs,\lambda}$	absorption cross section [cm^2]
$C_{sca,\lambda}$	scattering cross section [cm^2]
abs	absorption
ext	extinction
f	flame
l	lamp
sca	scattering
S_λ^f	flame emissivity signal
v	volume [cm^3]

REFERENCES

1. Corcione, F. E. and Valentino, G., *Combust. Flame* 99:387–394 (1994).
2. Suzuki, M., Nishida, K., and Hiroyasu, H., SAE Paper No. 93-0863, 1993.
3. Yeh, C., Kosaka, H., Kobori, S., and Kamimoto, T., SAE Paper No. 94-1953, 1994.
4. Browne, K. R., Partridge, I. M., and Greeves, G., SAE Paper No. 86-0223, 1986.
5. Baritaud, T. A., Heinze, T. A., and Le Coz, J. F., SAE Paper No. 94-0681, 1994.
6. Edwards, C. F., Siebers, D. L., and Hoskin, D. H., SAE Paper No. 92-0108, 1992.
7. Arnold, A., Dinkelacker, F., Heitzmann, T., Monkhouse, P., Schafer, M., Sick, V., Wolfrum, J., Hentschel, W., and Schindler, K. P., *Twenty-Fourth Symposium (International) on Combustion,* The Combustion Institute, Pittsburgh, 1992, pp. 1605–1612.
8. Corcione, F. E., Mazziotti, G., and Vaglieco, B. M., SAE Paper No. 96-0838, 1996.
9. Samy, M. I. and Borman, G. L., SAE Paper No. 91-0728, 1991.
10. Dec, J. E., SAE Paper No. 92-0115, 1992.
11. Espey, C. and Dec, J. E., SAE Paper No. 93-0971, 1993.
12. Menna, P. and D'Alessio, A., *Nineteenth Symposium (International) on Combustion,* The Combustion Institute, Pittsburgh, 1982, pp. 1421–1428.
13. Vaglieco, B. M., Beretta, F., and D'Alessio, A., *Combust. Flame* 79:259–271 (1990).
14. Clar, E., *Polycyclic Hydrocarbons,* Vol 1 and 2, Academic Press, London, 1974.

15. Gilbert, L. A., *Fuel* 41:351–357 (1962).
16. Corcione, F. E., Vaglieco, B. M., Monda, O., and Menguç, P. M., *Combust. Sci. Technol.* 102:283–299 (1994).
17. Backer, H. and Wiartalla, A., *Int. Symposium COMODIA,* 1994, pp. 565–570.
18. Corcione, F. E., Fusco, A., Mazziotti, G., Vaglieco, B. M., and Papetti, F., SAE Paper No. 95-2427, 1995.
19. Lee, S. C. and Tien, C. L., *Eighteenth Symposium (International) on Combustion,* The Combustion Institute, Pittsburgh, 1981, pp. 1159–1166.
20. Auriemma, M., Macchioni, R., and Valentino, G., private communications, 1995.

Twenty-Sixth Symposium (International) on Combustion/The Combustion Institute, 1996/pp. 2541–2547

AN EXPERIMENTAL DATABASE FOR DIESEL SPRAY COMBUSTION

E. WINKLHOFER
AVL List GmbH.
Kleiststrasse 48
A-8020 Graz, Austria

An experimental study has been made in an optically accessed research diesel engine to measure the influence of fuel injection pressure and nozzle hole diameter on spray penetration, spray cone angle, and flame liftoff distance. The experiments are documented with data for the fuel injection pressure, the rate of injection, rate of heat release, and cylinder pressure. The optical in-cylinder investigations comprise measurements of spray propagation, spray tip velocity near the nozzle (spray discharge velocity), and flame liftoff position.

The experiments provide a set of data describing the influence of fuel injection pressure, nozzle hole diameter, and nozzle type on spray discharge velocities, spray propagation, and flame liftoff distance. In addition to the measurement of axial spray and flame parameters, a phenomenological study of lateral spray distribution gives demonstrative examples for the stability and possible fluctuations of spray direction, as well as spray width variations between the start and end of injection.

The data demonstrate the governing influence of fuel injection pressure and spray hole diameter on the temporal and spatial distribution of the spray and consequently on the location of autoignition and flame distribution. The study also includes an analysis of the influence of the internal nozzle geometry—that is, the inflow conditions into the nozzle holes—on spray tip propagation.

Introduction

In engine engineering, the modeling of diesel spray combustion is slowly and cautiously being accepted for conceptual studies of diesel combustion systems [1–3]. The reason for this caution is seen in the sheer complexity of the task. Today's primary interest for the engineering application of spray combustion modeling, the shaping of temporal combustion rates, involves the high-pressure hydrodynamics of the fuel injection process, two-phase fluid dynamics, and multicomponent fuel evaporation for the mixture formation process and high-pressure combustion chemistry of a heterogeneous and inhomogeneous fuel-air mixture.

This complex field implies the use of simplified models [1], and the interpretation of numerical results requires knowledge about the models' correctness and limitations. This creates the need for well-described experimental data capable of serving as a database for model verification.

On the other hand, there is considerable interest in the practicalities of matching fuel injection systems to the space available in engine combustion chambers. In particular, the development of small, high-speed direct injection (DI) diesel engines requires the careful optimization of the fuel injection process in view of the temporal rates of fuel injected and its spatial distribution in the combustion chamber. Together with the air motion present at the time of injection, the fuel injection process is the major engineering element in governing spray combustion.

Therefore, both the spray and combustion modeling, as well as engine engineering, require quantitative spray data such as spray penetration length and velocity, spray angle, the time and location of ignition, and the spatial distribution of the flame under the influence of the fuel injection operating conditions.

The aim of the present study is to provide such quantitative experimental data describing fuel injection and spray propagation and their influence on flame position in view of the operating parameters of the fuel injection system in a quiescent diesel engine combustion chamber.

Experimental

The investigations of the diesel spray injection and combustion have been made in an optically accessed research engine. The engine is constructed from a two-stroke, loop-scavenged single-cylinder production engine and is equipped with a cylinder head containing a cylindrical combustion chamber. Optical access to this combustion chamber is provided by flat quartz windows that allow observation of sprays and flames over a length of about 25 mm. Peak compression pressure and temperature are 53 bar and 850 K, respectively.

For the present study, diesel fuel was injected with

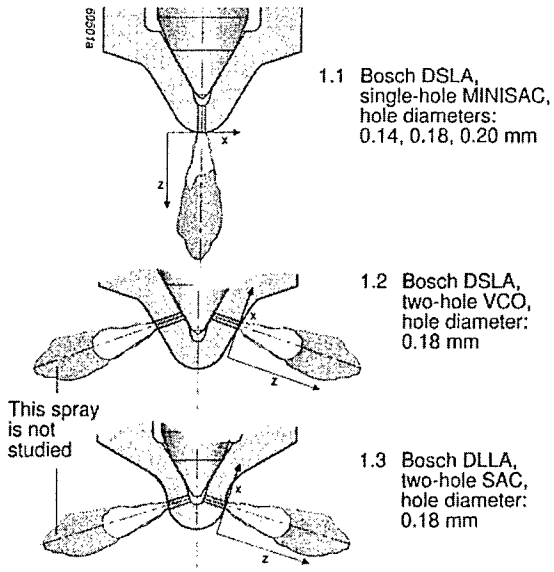

FIG. 1. Geometry of the nozzles used in this study.

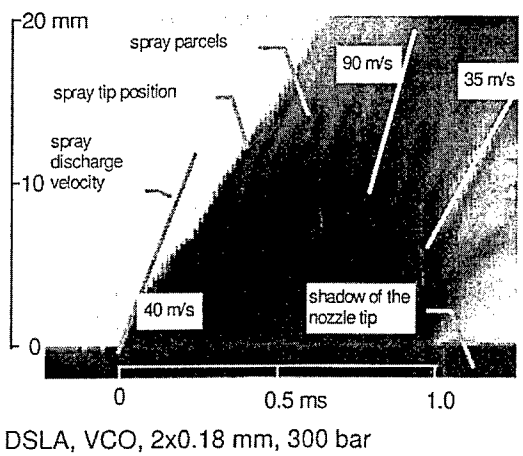

FIG. 2. Axial propagation of the spray tip and of spray parcels. Velocities are derived from length–time gradients.

injector nozzles mounted on top of the cylinder head. Single-hole nozzles were used to study the influence of different nozzle hole diameters. The single-hole nozzles were of the Bosch DSLA type with the hole drilled into the front end (the MINISAC) of the nozzle body. This axial single-hole arrangement is shown in Fig. 1.1. It ensures highly symmetric fluid flow conditions inside the MINISAC volume toward the entrance of the hole; thus, inlet flow conditions into the holes should be similar for the three different hole diameters investigated.

Injectors for production engine applications usually are equipped with nozzle holes drilled into the side of the nozzle tip. These situations were studied with nozzles shown in Figs. 1.2 and 1.3. A DSLA-type nozzle was equipped with a pair of holes located in the needle seat area (valve-covered orifice [VCO] holes). The pair of holes in the DLLA-type nozzle was drilled into the nozzle tip (the SAC) volume. Inlet flow conditions into these holes are thus governed by the nozzle hole orientation and, especially in the VCO nozzle, by the vicinity of the needle at the start and end of the fuel injection period.

Fuel injection pressure was drawn from a pressure-accumulator system; start and end of injection were governed by solenoid valves. With this pressure-accumulator system, injection pressure was regulated between 200 and 1500 bar. Pressure levels were constant throughout each fuel injection period.

The single-cylinder engine was run at a speed of 500 rpm, and the start of injection (SOI) was at 0.6° CA BTDC. Laser Doppler measurements of the air motion in the combustion chamber showed relatively small velocities of around +/− 5 m/s just before injection.

Spray propagation and spray width variations were measured with a high-speed linescan camera [4]. The spray was illuminated with an external light source, and its shadow was imaged onto the camera's linear diode array. The temporal resolution was defined by the linescan period of 15.3 μs. The spatial resolution was given by the linear array of 128 active pixels that were used to observe an object length of 5–8 mm for the spray width measurement and about 25 mm for the spray penetration measurement, respectively.

This recording of the spray shadow documents the presence of the high-density spray regimes. Even if there is no information on quantitative density levels, the method allows one to follow the temporal variation of spray contours. Thus, following the spray tip shadow yields quantitative data about spray tip propagation and consequently about spray tip velocities. In particular, the spray discharge velocity in the vicinity of the nozzle is determined from the initial gradient of the spray penetration slope as shown in Fig. 2.

With the dilution and disruption of the spray, the propagation of spray parcels can be followed during the ongoing fuel injection process and their velocity may be extracted from the length–time gradient also shown in Fig. 2. This information about the propagation of the high-density spray regime is essential in linking fuel injection properties with the processes of spray atomization and combustion in the downstream, low-density spray regimes.

Flame position and the temporal variation of the flame are recorded with the same linescan camera arrangement as used for the spray shadow measurements. However, instead of illuminating the combustion chamber with an external light source, the

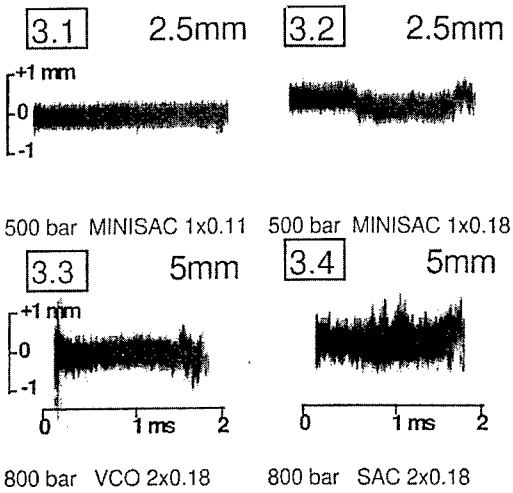

FIG. 3. Temporal variation of spray position and width in cross sections 2.5 and 5 mm downstream of the nozzle hole. MINISAC-, VCO-, and SAC-type nozzles.

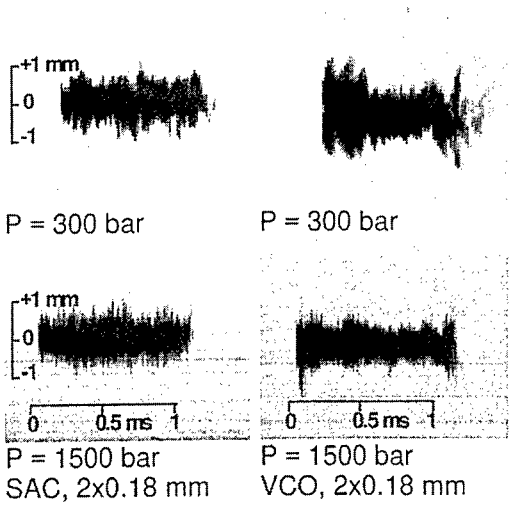

FIG. 4. Temporal spray width variation at the axial cross section $z = 5$ mm; SAC and VCO nozzles yield different spray patterns.

flame luminosity itself is now recorded with the high-speed camera system.

Fuel injection conditions such as injection pressure and start and end of injection are monitored together with the combustion chamber pressure for each engine cycle. The cylinder pressure measurements were also used to determine the instantaneous rates of heat release by means of a thermodynamic cycle analysis. The injected fuel quantity and the rate of fuel injection (ROI) were measured on a fuel flow rig [5].

Results

Lateral Distribution

The study of temporal spray width variations near the nozzle orifice documents the direction and diameter of the spray throughout the fuel injection period. They are usually constant, as seen for the 1 × 0.11-mm nozzle in Fig. 3.1, but even under the nominally constant pressure conditions of the accumulator fuel injection system and with the axial single-hole nozzles, spray orientation and spray diameter may fluctuate between the start and end of injection. The fluctuations seen with the 1 × 0.18-mm nozzle in Fig. 3.2 were found to be highly repetitive and are presumably caused by hydraulic instabilities inside the nozzle.

Significant influence on spray width variations is found in VCO-type nozzles during the opening and closing phase of the injector needle. This is documented in Fig. 3.3 with spray width measurements taken at the spray cross section 5 mm downstream of the nozzle hole. The initial spray width is about 2–3 times larger than the width throughout the ongoing injection and rises again at the end of injection. The very short (<70 μs) duration of this widened spray period corresponds with the influence of the needle seat on the inflow conditions to the hole of the VCO nozzle. This broad initial spray distribution was not found in the SAC-type nozzle shown in Fig. 3.4.

Examples of a systematic comparison of sprays injected with VCO- and SAC-type nozzles at pressure levels between 200 and 1500 bar are given in Fig. 4. The spray width patterns confirm the influence of the needle opening and closing phase in the VCO nozzle; however, this influence is less pronounced with increasing fuel injection pressure. In contrast to the VCO nozzle, the sprays injected with the SAC-type nozzle holes are narrow at the start and end of injection but broader during the main injection period.

Lateral Flame Distribution

Studies of spray ignition processes [6–8] suggest that the location of spray ignition is determined by the transport of those fuel portions that enter the combustion chamber in the early phase of injection and by the evaporation and mixing of these fuel portions with air surrounding the spray. Consequently, the different initial spray patterns of the VCO and the SAC hole nozzles should result in ignition flame patterns governed by the different behavior of the initial spray portions. The time-resolved records of flame distribution in the cross section 10 mm downstream of the nozzle tip as shown in Fig. 5, however, did not demonstrate any noticeable influence of the initial spray patterns of VCO or SAC hole nozzles.

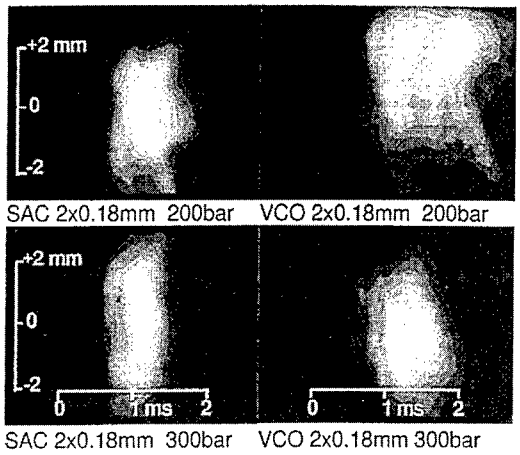

FIG. 5. Temporal flame width variation of SAC and VCO sprays at $z = 10$ mm, $P = 200$, and 300 bar. Data averaged for groups of five sprays.

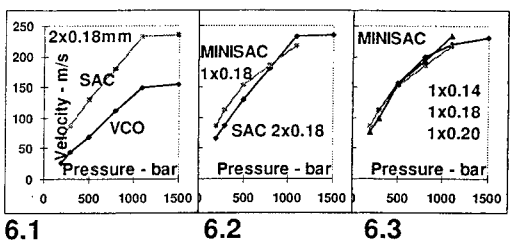

FIG. 6. Spray discharge velocities for various nozzle types and injection pressure levels. Data averaged for groups of five sprays.

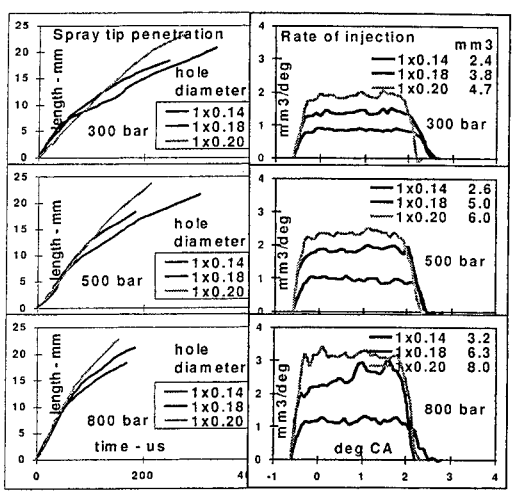

FIG. 7. Spray tip penetration and rate of injection for single-hole MINISAC nozzles. Data averaged for groups of five sprays.

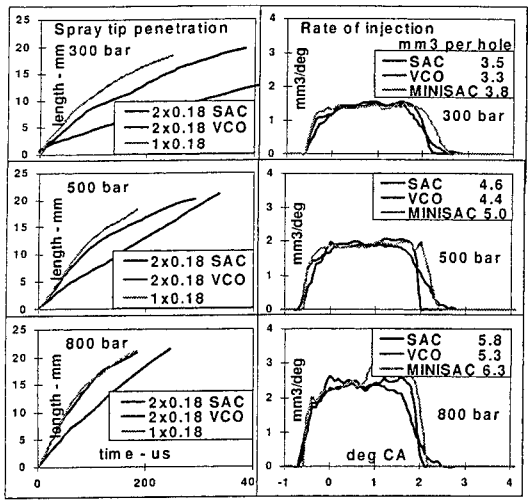

FIG. 8. Spray tip penetration and rate of injection for 0.18-mm SAC, VCO, and MINISAC nozzles. Data averaged for groups of five sprays.

Under the present engine conditions, in particular with the ignition delay of 890 μs, the turbulent mixing during the ignition-delay interval may be too effective and does not allow preservation of the influence of the initial spray distribution on the later ignition and flame distribution.

Axial Spray Distribution

Spray discharge velocities, extracted from the spray propagation measurements by the procedure given in Fig. 2, are summarized in Fig. 6. The comparison of VCO and SAC hole sprays in Fig. 6.1 shows the systematic lag of initial penetration rates of the VCO sprays, which again corresponds with the influence of the needle seat throttling at the start of injection.

Further comparison of spray discharge velocities is given in Figs. 6.2 and 6.3. As expected, the primary influence of fuel injection pressure is well established. For nozzles of the MINISAC single-hole type, however, spray discharge velocities and hence the initial rate of spray propagation are independent of the nozzle hole diameter, as shown in Fig. 6.3 for hole diameters of 0.14, 0.18, and 0.20 mm. Furthermore, the SAC and MINISAC sprays have similar discharge velocities.

This comparison of discharge velocities suggests the predominant influence of fluid flow conditions inside the nozzle [9]. In the SAC and MINISAC nozzles, the fuel first fills the nozzle tip volume and then discharges through the nozzle hole. However, in the VCO nozzle, the inflow into the nozzle hole is throttled initially by the rising gap between injector needle and needle seat.

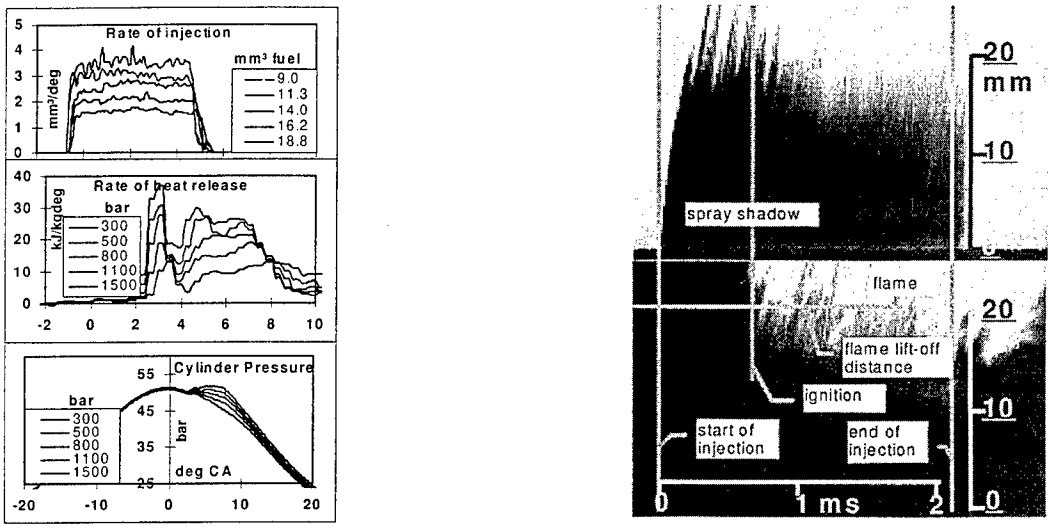

FIG. 9. A set of data describing fuel injection and combustion with conventional rate and pressure measurements and a specific diagram for axial spray propagation and flame distribution at $P = 800$ bar. MINISAC nozzle 1×0.18 mm.

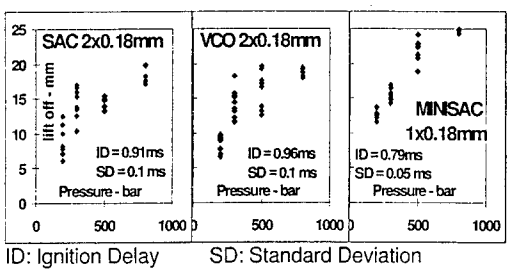

FIG. 10. Flame liftoff distances for various nozzle types and injection pressure levels. Data are given for individual sprays.

Spray Tip Penetration

The spray discharge velocities measured within a time interval of about 50 μs after the start of injection and along a distance of some 5 mm downstream of the nozzle were found to be independent of nozzle hole diameters and, consequently, independent of the mass and momentum of fuel entering the combustion chamber. The further propagation of the spray, however, is affected by the transfer of momentum into the surrounding gas via drag forces and by evaporation. This momentum transfer decelerates the spray, and now spray tip propagation downstream of the nozzle is expected to depend not only on fuel injection pressure but also on the mass of fuel injected and hence on nozzle hole diameter.

Data for the three MINISAC holes, together with the respective rates of fuel injection, are given in Fig. 7. They confirm the influence of the nozzle hole diameter and demonstrate the dependence on fuel injection pressure. Similar investigations have been published in Ref. 7 for hole diameters between 0.11 and 0.27 mm, but there the limited flexibility of the fuel injection pump did not allow this systematic investigation of fuel injection pressure levels.

Sprays injected with holes of the same diameter but with the MINISAC, SAC, and VCO nozzle type are compared in Fig. 8, again together with data for the rate of fuel injection. The results further emphasize the predominant influence of the fluid flow conditions inside the nozzle already noted in the discharge velocity analysis.

Axial Flame Distribution

The recording of the axial flame distribution and its temporal variation along with the study of the spray propagation, is shown in Fig. 9. It demonstrates the axial position of the flame relative to the spray throughout the injection and combustion process. The optical data are complemented with a set of conventional rate and pressure measurements to describe the injection and combustion process. Such measurements provide precise data for the mass of fuel injected, ignition delay intervals, location of ignition, flame liftoff distance, and rate of heat release. The data reduction procedure is sketched in Fig. 9. The ignition-delay interval is determined by the identification of the start of injection and the start of flame radiation. The flame liftoff distance is identified by the local rise of flame radiation intensity. Because both parameters are extracted from uncalibrated light intensity measurements, they are influenced by camera sensitivity, camera aperture, and window transparency. Therefore, to allow the

relative comparison of the sprays, these experimental parameters have been kept constant throughout the investigations.

The accuracy of ignition-delay intervals measured by this procedure for each individual spray is within $+/-50$ μs, because both the start of injection and the start of luminous combustion are easily identified by the large signal gradients in the linescan records. The accuracy of determining the flame liftoff distance, however, is poor and since the liftoff distance itself is governed by stochastic processes of turbulent fuel-air mixing in the periphery of a turbulent spray, the extracted liftoff parameters are used primarily for the relative comparison of the individual sprays.

The summary of flame liftoff data is given in Fig. 10 for sprays injected with holes of 0.18-mm diameter at injection pressure levels between 200 and 800 bar. At higher injection pressure levels, the faster propagation of the spray gives rise to larger liftoff distances. Liftoff distances are similar for the sprays injected with the two-hole SAC and VCO nozzles but significantly larger for the axial single-hole MINISAC nozzle, even if its ignition-delay time is smaller.

Discussion and Summary

The data obtained in this study demonstrate and quantify the predominant influence of fuel injection pressure and of nozzle hole diameters on the temporal and spatial distribution of the spray. Moreover, the effect of nozzle hole types on spray propagation was measured, and the results could be ascribed to the influence of fluid flow inside the nozzle tip.

Emphasis was put on the analysis of the early spray propagation phase because it governs the further distribution of fuel and the formation of a combustible fuel-air mixture. The data obtained for the ignition and combustion phases reflect the overall trends of spray propagation. The distance between the nozzle hole orifice and the location of ignition and flame position is enlarged considerably with the faster and further propagation of the spray.

The particular structure of the fuel sprays found to be characteristic for the nozzle hole types (especially during the needle opening and closing phase) was not found in the analysis of ignition and flame distribution. This is reflected by the time intervals relevant for the temporal sequence of spray propagation, local mixture distribution, and combustion. The influence of the needle opening phase was found to be on the order of 70 μs, followed by the spray tip propagation phase of about 400 μs at 300 bar and 150 μs at 800 bar fuel injection pressure. Ignition occurred about 0.9 ms after the start of injection. Thus, it is evident that the spray structure formed within the needle opening phase of 70 μs is unlikely to be preserved throughout the ignition-delay interval of about 0.9 ms.

In view of today's spray and combustion modeling efforts, the results derived from the optical analysis together with corresponding data for the rates of fuel injection and of heat release as given in Fig. 9 serve as reference for model verification [10].

REFERENCES

1. Takenaka, Y., Kudo, Y., Kakegawa, T., Shiozaki, T., and Aoyagi, Y., "The Spray Models and Their Influence on Ignition," SAE Paper No. 95-0279, 1995.
2. Ahmadi-Befrui, B., Wiesler, B., and Winklhofer, E., "The Propagation of Fuel Sprays in a Research Diesel Engine—A Joint Numerical and Experimental Analysis," SAE Paper No. 91-0181, 1991.
3. Kong, S. C., Han, Z., and Reitz, R. D., "The Development and Application of a Diesel Ignition and Combustion Model for Multidimensional Engine Simulation," SAE Paper No. 95-0278, 1995.
4. Winklhofer, E., "High Speed Optical Diagnostics of Combusting Diesel Sprays," in *Combusting Flow Diagnostics,* (Durao, D. F. G. et al, Eds.), Kluwer, Dordrecht, The Netherlands, 1992, pp. 455–468.
5. Bosch, W., "The Fuel Rate Indicator: New Measuring Instrument for Display of the Characteristics of Individual Injection," SAE Paper No. 96-0749, 1996.
6. Edwards, C. F., Siebers, D. L., and Hoskin, D. H., "A Study of the Autoignition Process of a Diesel Spray via High Speed Visualization," SAE Paper No. 92-108, 1992.
7. Winklhofer, E., Ahmadi-Befrui, B., Wiesler, B., and Cresnoverh, G., "The Influence of Injection Rate Shaping on Diesel Fuel Sprays—An Experimental Study," I. Mech. E. Paper 206:173–183, (1992).
8. Winklhofer, E., Fuchs, H., and Philipp, H., "Diesel Spray Combustion—An Optical Imaging Analysis," SAE Paper No. 93-0862, 1993.
9. Bruni, G., Fiore, A., Laforgia, D., and Fiorentino, L., "3-D Analysis of the Flow through a Multihole VCO Nozzle for DI Diesel Engine," SAE Paper No. 95-0085, 1995.
10. Winklhofer, E., AVL Internal Report, 1996.

COMMENTS

W. Hentschel, Volkswagen Ab, Germany. In what way would a swirl flow and the presence of a bowl wall influence the early spray formation?

Author's Reply. The interaction of spray and flow field is governed by the drag forces between the gas surrounding the spray and the spray droplets or spray fragments. Here the velocity difference and the density ratio between liquid and gas phase are the main factors of influence.

In swirling flow fields, we see distinctive stages of spray propagation:

Spray core regime: Fuel sprays are injected into the flow field at discharge velocities of 40 up to 200 m/s and at spray cone angles of about 20 deg. as shown in this paper. Hence, near the nozzle there is a high concentration of fuel propagating at high velocities and the flow field just has minor influence on the bulk of the spray motion.

Spray dispersion: Further along its propagation the spray is dispersed and its decreasing concentration allows for an efficient transfer of momentum between the droplets and the gas phase. In swirl type flow fields the circulation of droplets along with the gas motion is observed [1].

Spray vapor regime: With the evaporation of fuel, the spray concentration is further decreased. Fuel vapor flow is governed by the turbulent mixing with the surrounding in-cylinder air and by the large scale convective air motion and consequently is carried along with the swirl flow.

The spatial extent of these regimes is governed by fuel injection parameters as given in this paper and by the in-cylinder gas density and gas motion. Rate shaping injectors with initial injection throttling can considerably reduce spray discharge velocities and consequently the initial propagation phase and thus allow the flow field to interact with the spray closer to the nozzle.

Combustion chamber walls take influence as they

- govern the peripheral gas motion,
- redirect the fuel vapor jet, and
- give rise to complex droplet–wall interaction.

Twenty-Sixth Symposium (International) on Combustion/The Combustion Institute, 1996/pp. 2549–2556

NEAR-FIELD ENTRAINMENT IN UNSTEADY GAS JETS AND DIESEL SPRAYS: A COMPARATIVE STUDY

R. ANDRIANI AND A. COGHE
Dipartimento di Energetica, Politecnico di Milano,
P.le Leonardo da Vinci,
32-20133 Milano Italy

G. E. COSSALI
Facoltà di Ingegneria, Università di Bergamo
Via Marconi, 6-Dalmine (BG) Italy

Entrainment of surrounding gas into diesel sprays and impulsively started, axisymmetric round jets was investigated experimentally to identify the main characteristics of the gas/fuel mixing process. Diesel sprays and gaseous jets were injected into quiescent air under different ambient temperature and density. The entrainment was evaluated by measuring the air velocity normal to a cylindrical control surface surrounding the jet/spray cone. The comparison was performed over two periods: (a) the initial transient period, characterized by a strong variation of the entrainment velocity, due to the passage of the jet-head vortex; (b) the quasi-steady period, after the passage of the jet head, where the entrained gas velocity undertakes only smooth variations because of the varying injection conditions. A strong similarity between gas jets and diesel sprays was observed in the transient period when appropriate dimensionless variables were introduced, whereas differences were observed during the quasi-steady period, which may be related to the different momentum transfer mechanism acting during that period. A simple qualitative model, based on an analogy with the movement of a growing solid sphere, is also provided to interpret the experimental results about the leading vortex of diesel sprays and impulsively started gas jet.

Introduction

Single- or multiphase fluid jets have the characteristic of entraining the surrounding fluid. For axisymmetric steady gaseous jets, the mass flow rate through a section normal to the jet axis is equal to

$$m(z) = 2\pi \int_0^\infty \rho U(r, z)\, r dr \qquad (1)$$

where ρ is the gas density, $U(r, z)$ is the axial velocity, z, r the axial and radial coordinates. If m_o is the injected mass flow rate and the jet is steady, $m_e = m - m_o$ is the entrained mass flow rate. The entrainment in axisymmetric steady gas jets has received considerable attention both theoretically and experimentally. Ricou and Spalding [1] investigated the fully developed region from $z/D = 50$ to 200 (D = nozzle diameter) by using injected and surrounding gases of equal or different density. They directly measured the entrained mass flow supplied through a porous wall surrounding the jet and showed that its rate increased linearly with the distance from the nozzle exit (in the far field, $m_e \cong m$), for jet Reynolds number higher than 25,000. They also measured the entrainment coefficient defined as

$$K_e' = \frac{dm_e}{dz}\left(\frac{D}{m_o}\right)\left(\frac{\rho_o}{\rho_e}\right)^{1/2} \qquad (2)$$

where ρ_o and ρ_e are the densities of the injected and surrounding fluid. The entrainment coefficient was found to be constant ($=0.32$). Hill [2] applied a similar technique to both the near and far field and found that $K_e' = 0.32$ for $x/D > 13.6$ and $Re > 30{,}000$.

Although measurements in the near-field region have shown discordance, the entrainment coefficient has generally been found to be lower than that in the fully developed region. The air entrainment can be determined by direct measurement of the axial velocity profile and numerical integration of Eq. (1). Uncertainties can arise because of the lack of axial symmetry and higher relative errors near the jet edge, which can be amplified by the integration. As reported by Hill [2], early works based on this method show quantitative differences in the near-field zone and the common indication that the entrained mass flow rate does not increase linearly with z. More recently, the entrained mass flow rate determined by a constant-temperature thermoanemometer [3] and a laser Doppler anemometer [4] was found to increase linearly; the entrainment coefficient is thus constant ($=0.183$ and 0.24, respectively). Hill [2] by using an adaptation of the porous wall method, found that the entrainment coefficient

increased with nozzle distance in the near-field region ($x/D < 13.6$) from about 0.12 to the far-field constant value (0.32); the behavior was independent of Reynolds number in the range covered by the experiments, $6 \times 10^4 - 29 \times 10^4$.

Impulsively started gas jets have received less attention, although lately the possible application of gaseous fuel injection in the automotive field is motivating the search for more detailed information. A theoretical analysis of the transient behavior of a laminar jet was given by Abramovich and Solan [5]; based on it and on the early work of Turner [6], a theoretical analysis of an impulsively started gas jet was given by Witze [7], who also reported detailed flow velocity and tip penetration measurements. He claimed that the suddenly started jet quickly reaches the steady state condition after the transit of the leading vortex.

Even though air entrainment in steady and unsteady full cone sprays is important in many applications (such as internal combustion engines), this phenomenon has received comparatively little attention and the similarity between gas and spray jets has often been claimed. The entrainment of hot air into diesel sprays under engine conditions controls evaporation rates, mixing rates, and liquid penetration length [8]. A common finding of recent work was the nonlinear dependence of the entrained-mass flow rate on the nozzle distance [9–11] also in the so-called far field (hundreds of diameters downstream from the nozzle). The numerical value of the entrainment coefficient K_e' (also called nondimensional entrainment rate) was found to vary over several orders of magnitude and usually to be lower than the corresponding value for steady gas jets.

Indeed, the mass flow rate through a jet cross section is expected to have a linear dependence on the nozzle distance whenever the momentum flow rate through any section is independent on axial distance and self-similarity of the velocity gas profiles exists; both conditions are fulfilled in steady turbulent gas jets as long as z/D is sufficiently high ($z/D > 14$) [2]. However, no reliable information about the validity of those hypotheses is available for unsteady jets and steady and unsteady full cone sprays. The previously mentioned nonlinear dependence on the nozzle distance of the entrained mass flow rate in sprays seems to support the expectation that gas momentum flow rate does change with axial distance because the momentum exchange between the injected liquid and gas phase is not as efficient as in gas jets. Thus, it takes place over a longer distance from the nozzle, likely up to $z/D > 200$ [12].

The purpose of the present work was to compare the entrainment process originated by impulsively started gas jets and diesel sprays operated under a variety of experimental conditions; the study has been limited to the near-field region, extending up to 60 mm from the nozzle, because it presents the major interest for engine applications.

Experimental Setup

Gas or liquid fuel was injected in a closed cylindrical chamber (206 mm inner diameter) equipped with four quartz windows and designed to withstand variable air temperatures and pressures. Both the gas and diesel injectors were aligned with the chamber axis and positioned with the tip protruding less than 1 mm from the top flat wall. More details about the experimental setup can be found elsewhere [13].

The gas nozzle (3-mm diameter) was connected to a stagnation chamber through an electronically controlled solenoid valve; the back pressure was monitored and remained almost constant during the measurement period (50 ms). The nozzle discharge coefficient was measured under stationary conditions and then used to evaluate the injected mass flow rate from the injection pressure during unsteady injections; the injected air density was evaluated assuming an adiabatic irreversible gas flow through the nozzle.

A single-hole Bosch injector (0.25-mm nozzle diameter) was used for the spray experiments; ordinary diesel oil ($\rho = 820$ kg/m^3) was supplied by a Bosch high-pressure injection pump driven by a variable-speed electric motor and operated in single injection mode. The nozzle opening pressure was fixed at 21.4 MPa, and the injection pressure history was measured at the injector inlet by a pressure transducer and found very repeatable (within $\pm 0.5\%$, based on the rms value). The injected mass flow rate was calculated from the pressure trace, accounting for the average nozzle discharge coefficient measured by collecting and weighing the injected fuel over many injections and by measuring the injection duration (3.3 ms) by laser beam obscuration.

Entrained air velocity was measured by a dual-beam LDV system (DANTEC), comprising a 5-W Ar^+ laser and a 40-MHz Bragg cell for frequency shifting and directional sensitivity. The backscatter configuration was used with a geometrical measurement volume 1 mm in length and 0.1 mm in diameter. The data processor (Dantec PDA) allowed 1-μs time resolution in data acquisition. For the jet experiments, the ambient air was seeded with aerosol micrometric particles, whereas droplets left behind from previous injections (arithmetic mean diameter $\approx 5\mu$m, measured by PDA) were used as tracer particles for the spray experiments. The needle lift opening at 21.4 MPa (spray experiments) or the TTL signal activating the solenoid valve (jet experiments) was used to trigger data acquisition.

Measurement Technique

The method adopted in the present work to measure the entrainment was the same as that used in

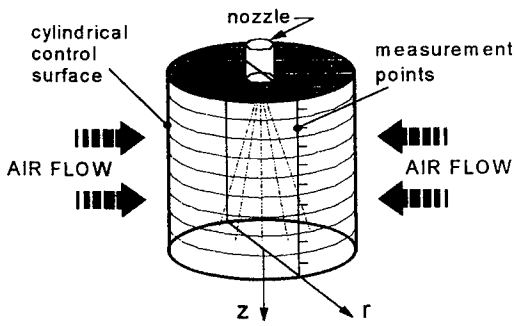

FIG. 1. Schematic of the cylindrical control surface that defines the measurement locations.

previous investigations [10,14] and consisted of measuring the air velocity normal to a cylindrical control surface enclosing the jet. The cylinder can be subdivided into many rings (Fig. 1), and the air mass flow rate entering through any ring (partial entrained mass flow rate) can be estimated from the measured normal velocity:

$$m_{p,e} = \int_{\text{Ring}-p} \rho_e V(z, t)\, d\Omega \qquad (3)$$

The total entrained air mass flow rate crossing any section of the cylinder normal to its axis is then evaluated by summing all the partial entrained mass flow rates from the top plate ($z = 0$) to the actual z position. The major advantage of this method is that it can be applied easily to unsteady jets. The actual measurements of the radial velocity component were performed along two opposite straight lines parallel to the jet axis (from $z = 2.5$ to 57.5 mm, 5-mm step), and each measurement was considered representative of the air velocity relative to a half ring (Fig. 1). The choice of the radius of the cylinder was critical. In fact, a small radius is expected to reduce the relative error in the measured velocity because the entrainment velocity increases going toward the axis; on the other hand, near the jet/spray edge, the measurement of the radial velocity becomes less accurate because of interference with the jet turbulent boundaries and the existence of a non-negligible axial velocity component. Tests were carried out to optimize the choice [10], and a cylinder radius of 10 mm for the spray and 20 mm for the gas jet was chosen as the best compromise.

Results and Discussion

Table 1 summarizes the conditions under which the experiments on diesel spray and gas jet were performed. Gas density was calculated from the measured air temperature and pressure using the perfect gas law; for the spray experiment, the effect of suspended particles in the air on the average density of the entrained flow was estimated to be lower than 0.1% for the worst condition [13]. Data were collected over many consecutive injections and ensemble averaged over time windows of 0.1 ms for the spray and 0.3 ms for the gas jet; the estimated statistical error of the mean velocity, $U(z, t)$, was lower than 4% for the quasi-steady period.

Observation of the measured velocity (both for diesel spray and gas jets) reveals two distinct time periods: (a) the *initial transient period*, character-

TABLE 1
Operating conditions.

Experiments	Ambient pressure (MPa)	Temperature (K)	Ambient density (kg/m^3)	Density ratio $\frac{\rho_e}{\rho_j}$	Injection pressure (MPa)	V_v (m/s)
Spray—A	0.1	298	1.17	0.00142	70[a]	83.1
Spray—B	0.6	298	7.02	0.00853	70[a]	55.2
Spray—C	0.1	373	0.93	0.00114	70[a]	89
Spray—D	0.6	373	5.60	0.00682	70[a]	58
Spray—E	0.57	393	5.04	0.00685	70[a]	55.8
Spray—F	0.1	413	0.84	0.00103	70[a]	96.4
Spray—G	0.6	413	5.06	0.00616	70[a]	64.2
Spray—H	0.69	473	5.07	0.00685	70[a]	65
Spray—I	0.1	298	1.17	0.00142	140[a]	94.3
Jet—A (Air)	0.1	298	1.17	0.954	0.144	20.6
Jet—B (Air)	0.1	298	1.17	0.84	0.22	22.4
Jet—C (CO_2)	0.1	298	1.17	0.63	0.14	18.7
Jet—D (CO_2)	0.1	298	1.17	0.585	0.25	21.0

[a]peak pressure

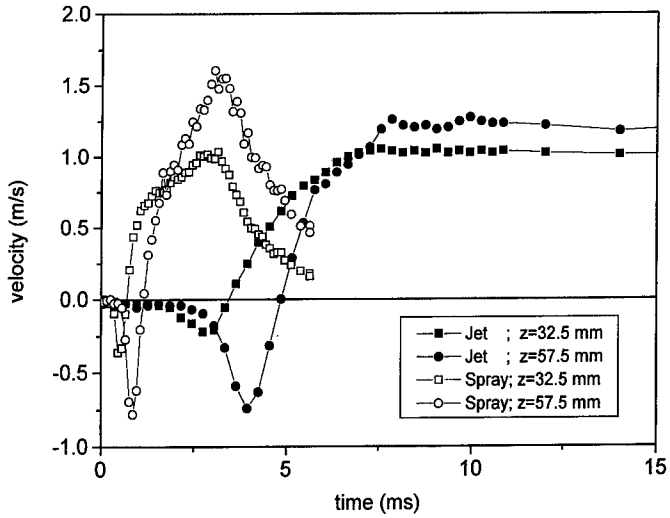

FIG. 2. Entrainment velocity versus time as measured by LDV for both gas jet A and diesel spray B.

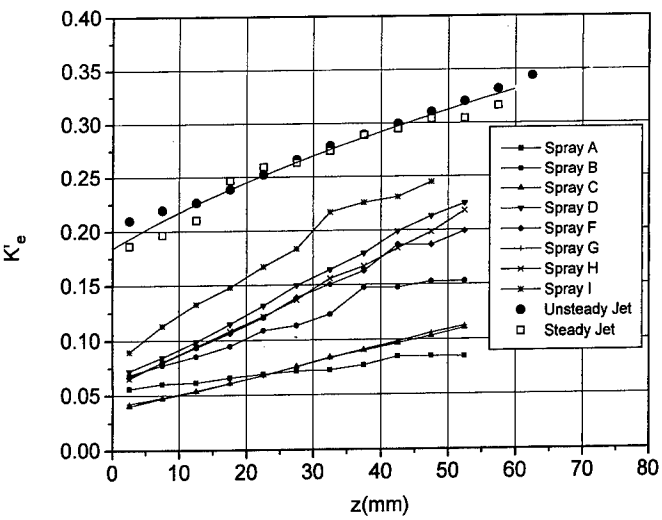

FIG. 3. Entrainment coefficient in steady and unsteady gas jets and diesel sprays.

ized by a wide oscillation of the radial velocity (Fig. 2), with a characteristic interval during which it is negative (i.e., directed outward) implying the passage of the jet head vortex; (b) the *quasi-steady period* after the passage of the head vortex, when the radial velocity is positive (i.e., directed inward) and undertakes only smooth variations because of the varying injection conditions. The characteristics of those periods are so different that it proves useful and necessary to separate the analysis of the results.

Quasi-Steady Jet Period

Entrainment during this period can be evaluated through the nondimensional entrainment rate, K'_e, for both gas jets and diesel sprays. Figure 3 shows the measured values of K'_e for the impulsively started gas jet, as well as the results obtained on steady gas jets injected through the same nozzle, with *Re* ranging between 5200 and 53,000. The comparison indicates that the quasi-steady approximation is adequate, at least for entrainment data, and confirms that quasi steadiness is quickly reached after the passage of the head vortex, as already pointed out by Witze [7]. Moreover, K'_e is not constant in the near field, confirming the results of Hill [2], although the far-field value, 0.32, is reached only for $z/D \cong 20$ rather than $z/D \cong 14$; this discrepancy may be due to the different nozzle design, which may also influence the potential core length [7].

For the unsteady diesel spray, K'_e depends on z over the whole investigated region up to $z/D \approx 200$, with a strong dependence on gas temperature and

density. Figure 3 shows the main differences between entrainment into gas jets and diesel sprays; which can be explained by considering that the momentum exchange in gas jets is due mainly to turbulent mass transfer from the injected fluid to the ambient gas. In liquid sprays, on the other hand, momentum is transferred mainly by viscous drag acting on the liquid droplets, although the component associated with mass transfer may play a more relevant role in evaporating sprays.

A tentative correlation of the spray results was given by Cossali et al. [13]:

$$K_e' = 0.044\left(\frac{z}{D} + 13\right)^{0.50}\left(\frac{\rho_e}{\rho_o}\right)^{0.31}\left(\frac{T_e}{273}\right)^{1.0} \quad (\text{for } z/D < 200), \tag{4}$$

where ρ_e and T_e are the entrained gas density and temperature and ρ_o is the injected fuel density. The unsteady gas jet results of Fig. 3 were fitted best by the following correlation:

$$K_e' = 0.0718\left(\frac{z}{D} + 7.77\right)^{0.460} \quad (\text{for } z/D < 18) \tag{5}$$

From Eqs. (4) and (5) it appears that the magnitude of K_e' at comparable z/D may be much lower in diesel sprays than in gas jets, because of the less-efficient, momentum-transfer mechanism. However, to obtain similar penetration for gas jets and diesel sprays in a swirling, in-cylinder flow and a comparable amount of injected fluid in the same time interval, the following conditions should be fulfilled:

$$\frac{m_{o,s}}{m_{o,j}} \cong 1; \frac{J_{o,s}}{J_{o,j}} \cong 1 \tag{6}$$

where s and j stand for *spray* and *gas jets*, m_o is the injected mass flow rate, and J_o is the injected momentum flux. By assuming uniform distribution of the velocity at the nozzle exits, U_o, Eq. (6) requires that $U_{o,j} \cong U_{o,s}$; this implies $D_j/D_s \cong (\rho_{o,s}/\rho_{o,j})^{0.5}$. At downstream location z, the nondimensional distances that appear in Eqs. (4) and (5) are related by

$$\zeta_j = \frac{z}{D_j} = \frac{z}{D_s}\left(\frac{\rho_{o,j}}{\rho_{o,s}}\right)^{1/2} = \zeta_s\left(\frac{\rho_{o,j}}{\rho_{o,s}}\right)^{1/2}$$

On substituting in Eqs. (4) and (5) and integrating Eq. (2) for $K_{e,s}'$ and $K_{e,j}'$, we obtain the ratio between the entrained mass flow rate for gas jets and diesel sprays at the same nozzle distance z, under the conditions imposed by Eq. (6)

$$\frac{m_{e,j}(z)}{m_{e,s}(z)} \cong 1.63\left(\frac{\rho_{o,s}}{\rho_{o,j}}\right)^{1/2}\left(\frac{\left[\zeta_s\left(\frac{\rho_{o,j}}{\rho_{o,s}}\right)^{1/2} + 7.77\right]^{3/2} - 7.77^{3/2}}{[\zeta_s + 13]^{3/2} - 13^{3/2}}\right)\left(\frac{\rho_{o,s}}{\rho_e}\right)^{0.31}\left(\frac{273}{T_e}\right) \tag{7}$$

where the exponent of $(z/D + 7.77)$ in Eq. (5) was taken equal to 1/2. Under enginelike conditions, $z = 30$ mm, $D_s = 0.25$ mm, $\rho_{oj}/\rho_{o,s} = 0.023$, $T = 960$ K, and $\rho_e = 22$ kg/m^3, Eq. (7) gives $m_{e,j}/m_{e,s} \approx 0.70$, showing that diesel sprays may entrain more air than gas jets.

Initial Transient Period

The initial transient period is characterized by a wide oscillation of the radial air velocity outside the jet cone that can be attributed to the passage of the jet head vortex. It was possible to evaluate the average velocity, V_v, at which this structure is convected downstream, by measuring the time at which the velocity curve crosses the zero line (Fig. 2) at consecutive z locations and interpreting it as the time at which the center of the head vortex passes across the measurement location. A common feature of all the experiments is that this velocity does not change significantly with z in the investigated range ($0 < \zeta_j < 20$; $0 < \zeta_s < 210$); for a diesel spray, V_v is about 30% lower than the tip velocity, as measured by a high-speed image acquisition system.

The head velocity depends on the entrained and injected density ratio, for both the diesel spray and the gas jet (Fig. 4), but it is almost independent of the injection velocity. This is implied by the observation that the spray head velocities for high- (140 MPa) and low-pressure (70 MPa) cases are only slightly different. This is also true for the gas jet experiments (Jet *A-B* and Jet *C-D*).

The entrained velocity time history of gas jets and diesel sprays shows a qualitative resemblance to that caused by the passage of a solid sphere moving at constant velocity along the jet centerline. A solid sphere would produce a symmetric oscillation of the velocity, with minimum and maximum values of the same magnitude. In the present case (Fig. 2), $V_{min}/V_{max} < 1$ as shown in Fig. 5 where this ratio is plotted versus $z^* = z/b$ (b is the distance of the measurement location from the jet axis) for both sprays and jets. A sphere of increasing radius would produce a similar velocity oscillation with a ratio $V_{min}/V_{max} < 1$. The lines in Fig. 5 represent the values of V_{min}/V_{max} calculated for a sphere moving at constant velocity, but with an increasing radius given by $r^* = k\tau^n$ (where $r^* = r/b$ and $\tau = tV_v/b$). Calculations were performed by assuming quasi steadiness of the

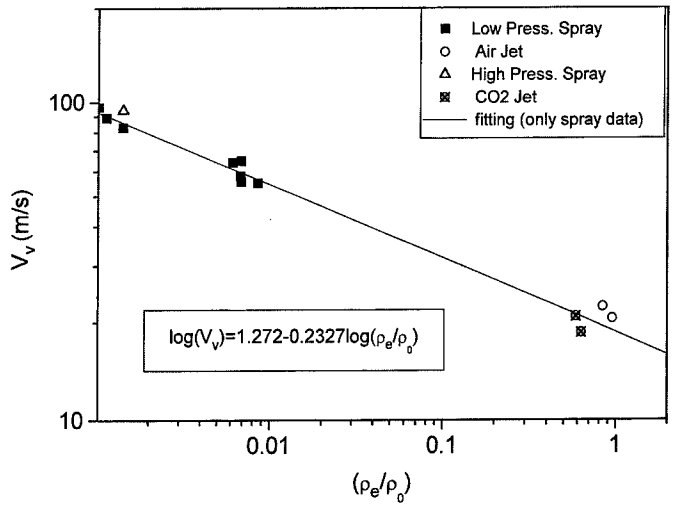

FIG. 4. Velocity of the head vortex versus ambient gas/fuel density ratio; V_V appears to be proportional to $(\rho_e/\rho_o)^{-0.23}$.

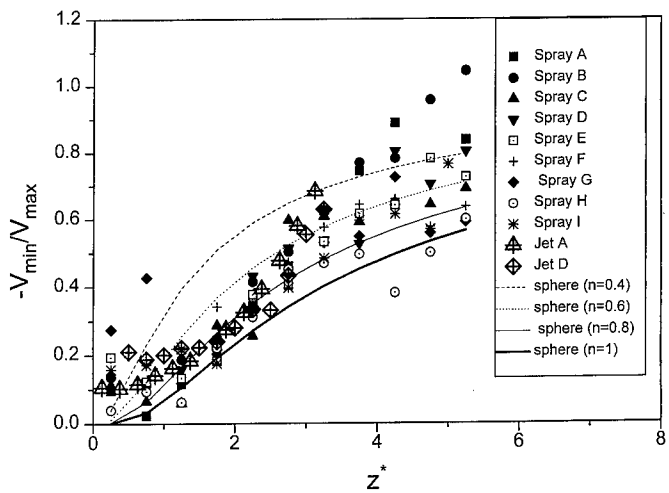

FIG. 5. V_{min}/V_{max} ratio versus z^* for gas jets and diesel sprays and comparison with the solid sphere model.

flow around the sphere, which is equivalent to neglecting the acceleration term in the Euler equation—a simplification that was estimated quantitatively to be acceptable for the present dynamic conditions.

The model of a growing sphere for the jet head evolution, proposed by Witze [7], implies that the jet/spray head does not entrain gas during its movement and its size increases only because of the quasi-steady jet that feeds it. To support this hypothesis, the axial velocity along the spray axis was measured before and during the passage of the head; comparison with the expected values of the axial velocity for the case of a solid sphere moving at the velocity of the spray-head vortex showed strong but inconclusive analogies.

The similarity of the unsteady behavior of sprays and jets is emphasized when nondimensional variables are used. In terms of $\tau = tV_e/b$, the duration of the velocity oscillation $\Delta\tau$ (Fig. 6) becomes comparable at the same nondimensional distance $z^* = z/b$; however, for a growing sphere, $\Delta\tau$ would reach the asymptotic (i.e., $z^* \to \infty$) value of 0.5 that is much lower than the values obtained for sprays and jets. The observed similarity of gas jets and sprays, despite the large difference in injection conditions and flow characteristics (one- and two-phase flows), suggests that the head structure is determined mainly by the gas entrainment into the quasi-steady jet/spray rather than the type and characteristics of the injected fluid.

Figure 7 compares the time history of $v^* = V/V_{max}$ at different z^*, for both the diesel spray and the gas jet. The similarity of the velocity histories in nondimensional form suggests the existence of a common underlying mechanism and confirms the

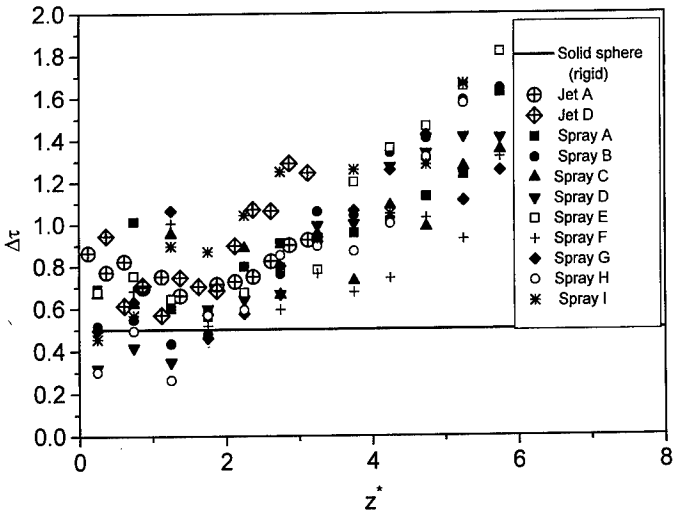

FIG. 6. Duration of the velocity oscillation for gas jets, diesel sprays, and the solid sphere model versus z^*. $\Delta\tau$ is defined as the nondimensional time interval between the minimum and zero crossing in the velocity time history.

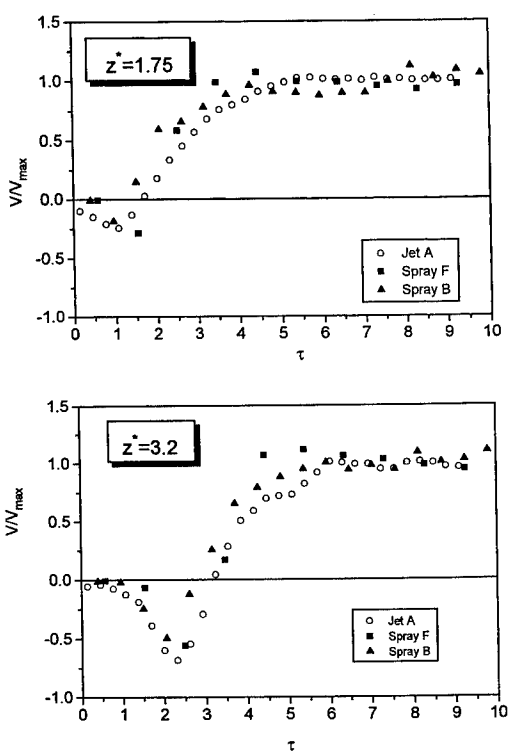

FIG. 7. Entrainment velocity versus τ for gas jet A and diesel sprays B and F in nondimensional form at two nondimensional nozzle distances. V_{max} is the entrainment velocity after the passage of the head vortex.

similarity between gas jet and diesel spray when observed on a proper nondimensional basis. It should be pointed out that entrainment of surrounding gas into the jet begins only after the passage of the head vortex; thus, it is the head vortex penetration and not the tip penetration that controls the length of the region in which gas is entrained.

Conclusions

From the experiments performed on gas jets and diesel sprays, two important temporal characteristics were identified:

a. A transient period: caused by the passage of the jet head vortex and characterized by a strong similarity between jets and sprays when appropriate dimensionless variables were introduced. The jet head vortex was found to move at almost constant velocity that appears to depend strongly on the entrained–to–injected density ratio ($V_v \sim (\rho_e/\rho_o)^{-0.23}$) and slightly on the injection velocity. The motion of the surrounding gas revealed a considerable analogy with the motion of the gas around a solid sphere moving at velocity V_v, and after proper nondimensionalization, jet and spray entrainment velocities compared well.
b. A quasi-steady period: this was reached quickly after the passage of the head vortex, when the gas entrainment begins and the nondimensional entrainment rate depends on the nozzle distance, for both jets and diesel sprays. Tentative correlation of the available data shows a similar dependence of K_e' on z, while the magnitude of K_e' at comparable z/D may be much lower in diesel sprays than in gas jets. However, diesel sprays and gas jets entrain a comparable quantity of surrounding gas in the near field ($z/D < 20$ for gas

jets and $z/D < 200$ for diesel spray) under comparable conditions in terms of injected mass, penetration capability (Eq. [6]), and distance from the nozzle.

The comparison of computer simulations with measured entrainment data could provide valuable information about the capability of the model to predict correctly the large-scale phenomena such as liquid/gas momentum transfer; it should be more meaningful than the usual comparison with tip penetration data, which are often technique dependent.

Acknowledgments

The experiments were performed at CNPM—CNR Laboratory in Milan. The authors would like to thank Mr. G. Brunello for his cooperation and help during the experiments.

REFERENCES

1. Ricou, F. P. and Spalding, D. B., *J. Fluid Mech.* 11(1):21–32 (1961).
2. Hill, B. J., *J. Fluid Mech.* 51(4):773–779 (1972).
3. Bogulawski, L. and Popiel, O. C., *J. Fluid. Mech.* 90(3):531–539 (1979).
4. Lightman, A. J., Andrews, R. J., Magill, P. D., Bradley, R. P., Reeves, C. M., Stutrud, J. S., and Roquemore, W. M., Symposium on Turbulence, 1984.
5. Abramovich, S. and Solan, A., *J. Fluid Mech.* 59(4):791–801 (1973).
6. Turner, J. S., *J. Fluid Mech.* 13:356–368 (1962).
7. Witze, P. O., Sandia Report SAND 80-8617, 1980.
8. Espey, C. and Dec, J., SAE Paper No. 95-2456, 1995.
9. Ruff, G. A., Sagar, A. D., and Faeth, G. M., AIAA 26th Aerospace Sciences Meeting, Nevada, 1988.
10. Coghe, A., Cossali, G. E., and Brunello, G., SAE Paper No. 91-0178, 1991.
11. Hosoya, H. and Obokata, T., *Sixth International Symposium on Applications of Laser Techniques to Fluid Mechanics*, July 20–23, Lisbon, Portugal, 1992, p. 37-5.
12. Wu, K. J., Santavicca, D. A., Bracco, F. V., and Coghe, A., *AIAA J.* 22(9):1263–1270 (1984).
13. Cossali, G. E., Coghe, A., Gerla, A., and Brunello, G., SAE Paper No. 96-0862, 1996.
14. Cossali, G. E., Coghe, A., and Brunello, G., SAE Paper No. 93-0920, 1993.

COMMENTS

Thierry Baritaud, IFP, France. What do you think will be the effect of modern injection systems with high pressure and smaller droplets on the air entrainment?

Author's Reply. The exchange of momentum between the injected liquid phase and the ambient gas phase strongly depends on aerodynamic drag. The momentum transfer rate is higher for smaller droplets. The injection of smaller droplets is expected to bring closer to the nozzle the region where the entrainment coefficient should be independent of nozzle distance (drops-gas equilibrium region) and where the spray would behave like a particle-laden jet.

•

N. Peters, RWTH Aachen, Germany. How did the entrainment coefficient for Diesel sprays in your measurements depend on the density ratio?

Author's Reply. The definition of entrainment coefficient (Eq. 2) contains the factor $(\rho_e/\rho_o)^{1/2}$ which renders the entrainment coefficient (Ke) in gaseous jets independent of the density ratio. The constancy of Ke in steady gaseous jets can be derived theoretically assuming self-similarity of the gas axial velocity profiles and constancy of the momentum flux through any jet cross section. For Diesel sprays such a derivation is no longer valid, and in fact, the measured entrainment coefficient depends on the density ratio as $(\rho_e/\rho_o)^{0.31}$ (Eq. 4).

Twenty-Sixth Symposium (International) on Combustion/The Combustion Institute, 1996/pp. 2557–2564

FLAME LIFTOFF IN DIESEL SPRAYS

JERZY CHOMIAK
Chalmers University of Technology
5-412 96 Göteborg, Sweden

ANDERS KARLSSON
AB Volvo, Technological Development
Göteborg, Sweden

Flame liftoff and stabilization in nonstationary n-heptane sprays is studied for diesel engine–like conditions using a numerical simulation involving complex chemistry and a novel subgrid stirred reactor model of turbulence-chemistry interaction. By following ignition and flame formation processes, it is shown that the flame stabilizes at a certain point due to the upstream propagation of a triple flame where the leading edge is at the stoichiometric surface and the combustion occurs both on the lean and on the rich side. Due to the evaporative cooling, large injection velocities, and the strong flame stretch, the stabilization distance is very large. This allows a considerable amount of air to enter the central part of the flame to feed the internal rich flame, and a large amount of fuel to escape combustion in the stoichiometric flame and support the external lean flame. Both soot and NO_x emissions reduction are expected to follow for large liftoff distances (i.e., high pressure and small orifice injection). The flame stabilization mechanism is a result of complex physical and chemical interactions and cannot be described by a simplified theory but to the leading order is determined by the chemical reaction time at the leading edge, the turbulent diffusivity, and the flow velocity so that there exists a balance between the local convection velocity and the triple flame propagation speed. The unburned/burned gas density ratio determining the shape of the leading edge of the flame is important in this process. Due to fast evaporation, the spray properties have little effect on flame stabilization except for the heat of evaporation affecting the temperature at the stoichiometric surface and the combustion kinetics of the fuel. Liftoff trends are studied, and available data on liftoff distances are compared with the predictions. The accuracy achieved is good.

Introduction

Recently, there has been a renewed interest in flame liftoff, mainly in conjunction with flame stabilization in diffusion flame–based combustion equipment [1–7]. Since liftoff is close to blowoff, operation in the lifted flame mode is considered to be abnormal and no aspects of liftoff other than the critical conditions were studied in the literature. In diesel sprays, due to strong evaporative cooling of the leading edge of the flame, high injection velocities, and small sizes of the injection orifices, highly lifted flame operation is typical and other aspects become important, particularly, the effects of liftoff on emissions. Since the liftoff causes substantial premixing and, thus, strongly changes the combustion conditions, the effects can be important.

The paper focuses on the mechanism of diesel flame stabilization, analyzes trends in liftoff behavior, and makes comparisons with some current theories of flame stabilization and the available data on liftoff distances. The pollutant formation consequences of the liftoff operation are also discussed. Because we are interested in the basic physics of the processes, simple axi-symmetric spray geometry is studied with no wall interaction and no cross flow which well reproduces the basic features of contemporary, direct injection diesel engines with quiescent combustion systems and a single-component model fuel. We selected n-heptane for that purpose because it has a cetane number close to 50, typical for diesel fuels, and also because the detailed reaction mechanism for it is well known [8–10]. However the physical properties of n-heptane differ substantially from typical diesel fuels.

The Model and Numerical Method

A detailed discussion of the model and numerical method can be found in Ref. 11. Here, we have to restrict ourselves to a simplified description focusing on features of the model that are different from those in standard approaches: the chemical kinetics and turbulence-chemistry interaction. Some details of the approach can also be found in Refs. 12 and 13.

TABLE 1
Rate coefficients for the generic reaction mechanism, A $[mol/m^3]$, β and E_a $[kJ]$ are the Arrhenius coefficients in $k = AT^{\beta}\exp(-E_a/RT)$ and $[RH]$ is evaluated as $[H_2C_{7/8}]$

	Reaction	A	β	E_a
1	$RH + O_2 \rightarrow \dot{R} + HO\dot{O}$	$1.11\ 10^7$	0.04	201.19
2	$RH + \dot{O}H \rightarrow \dot{R} + H_2O$	$1.01\ 10^3$	1.25	3.42
3	$\dot{R} + O_2 \rightarrow RO\dot{O}$	$2.00\ 10^6$	0.00	0.00
4	$RO\dot{O} \rightarrow \dot{R} + O_2$	$2.00\ 10^{15}$	0.00	117.23
5	$RO\dot{O} \rightarrow \dot{R}OOH$	$5.44\ 10^9$	0.59	44.97
6	$\dot{R}OOH \rightarrow RO\dot{O}$	$6.01\ 10^{10}$	0.59	44.97
7	$\dot{R}OOH + O_2 \rightarrow HOORO\dot{O}$	$2.00\ 10^6$	0.00	0.00
8	$HOORO\dot{O} \rightarrow \dot{R}OOH + O_2$	$2.00\ 10^{15}$	0.00	117.23
9	$HOORO\dot{O} \rightarrow HOO\dot{R}OOH$	$1.92\ 10^9$	0.71	44.48
10	$HOO\dot{R}OOH \rightarrow \frac{1}{16}O_2 - RH + \frac{7}{8}CO + \dot{O}H + ROOH$	$1.00\ 10^9$	0.00	31.40
11	$ROOH \rightarrow -\frac{15}{16}O_2 + \frac{7}{8}CO + \dot{O}H + HO\dot{O}$	$8.40\ 10^{14}$	0.00	180.03
12	$\dot{R} + O_2 \rightarrow -\frac{7}{16}O_2 + \frac{7}{8}CO + HO\dot{O}$	$2.00\ 10^6$	0.00	25.10
13	$RH + HO\dot{O} \rightarrow \dot{R} + HOOH$	$4.11\ 10^5$	0.26	70.77
14	$RH + \dot{O} \rightarrow \dot{R} + \dot{O}H$	$2.15\ 10^6$	0.31	21.13

A Lagrangian-Eulerian formulation is used to analyze the droplet motion and flow field. Turbulent dispersion of the droplets is modeled by random walk and droplet collisions, including bouncing collisions, permanent coalescence and coalescence and separation, as well as droplet break-up are accounted for. Forced convection is considered in the droplet heating and evaporation model. When the critical conditions are reached, the droplet is instantaneously transferred to the gas phase and uniformly distributed within a computational cell. The analysis of the gas phase involves solving equations for mass, momentum, and energy. The variable density k-ε model for turbulence is also included. The spray model consists of separate algorithms of the individual processes which are then coupled together by a method of fractional steps or time-step splitting. The above framework may now be considered standard and closely follows the approach of Amsden et al. [14]. Only a modified droplet break-up model is introduced, assuming the continuous reduction of the droplet size of large droplets due to stripping and a sudden destruction after a characteristic deformation time as a result of bag break-up. Both processes form droplets that are stable in local flow conditions. A prediction of gas-phase penetration for evaporating n-heptane sprays in very close agreement with experiments was obtained by using the spray model, with a fairly good prediction of the liquid-phase penetration [13].

Chemical Kinetics

The detailed diesel spray combustion models known from the literature [15], with the exception of Ref. 16 and the more recent ones [17,18] use very crude reaction models (either single-step chemistry or eddy break-up or both with a switching criterion) and, thus, are unable to reproduce the very complex ignition or, extinction and combustion behavior of higher hydrocarbons as a function of temperature and pressure. In the advanced diesel spray combustion models, the "Shell" mechanism [19,20] is most often used. Since the mechanism does not provide reactions for the postignition combustion, phase switching to an irreversible global reaction after ignition is applied. This switch does not provide a good basis for flame propagation, and stabilization studies in which ignition and extinction phenomena are important. Thus, a more complex, reduced n-heptane reaction model has been developed for our study based on the Refs. 8 and 9. It contains a fairly extensive treatment of the primary propagation reactions based on simple, lumped fuel reactants and a detailed treatment of the CO-H_2-O_2 system. The primary reactions involving the fuel are shown in Table 1. The remaining reactions are well established and are omitted here. The full system of 59 reactions used can be found in Refs. 11–13. Very good accuracy in predicting the experimental shock tube ignition delays [21] was achieved using the system over a wide range of temperatures and pressures [11–13].

Turbulence-Chemistry Interaction

Modeling the diesel combustion process requires a turbulence-chemistry interaction model that can cover the full range of chemical and turbulence time scales, from distributed, slow chemical reactions to turbulent, mixing controlled fast chemical reactions. Furthermore, the model must be able to deal with both premixed and diffusion-controlled combustion and the very difficult in-between case of partially premixed combustion. The above requirements

practically exclude the possibility of using flamelet modeling to treat the complex chemistry, due to the large dimensionality of the flamelet libraries, computer power limitations for on-line flamelet calculations, and problems in treating ignition and extinction processes. Flamelet-like subgrid turbulence-chemistry interaction is, however, possible if the molecular diffusion terms of the flamelet treatment are simplified. An obvious solution is to use a local stirred reactor model for the turbulence-chemistry interaction, thus omitting the molecular fluxes calculation but accounting for them by including the Kolmogorov scale mixing in the interaction and random turbulent motion of the reacting regions. Such an approach is proposed here. It is based on the pioneering works of Magnussen summarized in Refs. 22 and 23, and Gonzales and Borghi [24]. In the model, we assume that each cell is composed of reacting and nonreacting locally uniform elements. The interaction of all elements occurs by "exchange with the mean." For the mean value we have

$$Y_i = (1 - \kappa)\, Y_i^{\mathrm{N}} + \kappa Y_i^{\mathrm{R}} \tag{1}$$

where κ is the molecularly mixed fraction of the cell volume available for chemical processes, and the superscripts R and N indicate properties in the reacting and the nonreacting volume, respectively. The rates of change of mean species concentration can, thus, be calculated as

$$\overline{\dot{\omega}_i} = \kappa \dot{\omega}_i \tag{2}$$

In this way, complex chemistry, large-scale segregation, and micromixing effects are included in the simulation, and only the internal nonuniformities of the molecularly mixed reacting regions are disregarded.

The problem now arises how to estimate the reacting volume fraction (κ). It seems to be quite clear that it is to be proportional to the ratio of the chemical reaction time (τ_{ch}) to the total conversion time in the reactor, i.e., the sum of micromixing (eddy break-up) time (τ_{m}) and reaction time (τ_{ch}), as given by

$$\kappa = \frac{\tau_{\mathrm{ch}}}{\tau_{\mathrm{m}} + \tau_{\mathrm{ch}}} \tag{3}$$

The estimation of both times is a problem, however.

Let us first discuss the mixing time problem. Normally, only the large-scale eddy break-up times are considered. This method was tried by the authors with good results in the ignition delay prediction for the sprays, but with poor results in the energy release rate predictions. The time appeared to be much too long. Magnussen [22,23] assumed that the reactions occur in the fine structure part of the flow only, and proposed certain geometry and kinematics of the fine structures as well as a certain mechanism of heat and mass exchange with the surroundings to obtain the proper time scales. Basically, the characteristic dimension of the fine structures is assumed to be close to the Kolmogorov scales and their interaction with the surroundings based on Kolmogorov times. Gonzales and Borghi [24] propose to consider the whole spectrum of time scales. However, multiple time scales are difficult to account for in case of complex reactions. A compromise is to consider only the two most important time scales: the eddy break-up time leading from large-scale nonuniformities to Kolmogorov-scale nonuniformities, and the Kolmogorov time scale determining the local molecular interaction for the reactions. To account for both times in the simplest way, we used a geometrical mean of the two, as given by

$$\tau_{\mathrm{m}} = \sqrt{\frac{k}{\varepsilon}\left(\frac{\nu}{\varepsilon}\right)^{1/2}} = \left(\frac{1}{Re_{\mathrm{T}}}\right)^{1/4} \frac{k}{\varepsilon} \tag{4}$$

Since there are as many times as reactions, a synthetic quantity, which best represents the changes in the reacting system, must also be selected for the global chemical time, τ_{ch}. The global conversion rate of the fuel and oxygen is to be used for that purpose. Accounting for the limiting species leads to

$$\frac{1}{\tau_{\mathrm{ch}}} = \max\left\{\frac{-\dot{\omega}_{\mathrm{RH}}}{Y_{\mathrm{RH}}}, \frac{-\omega_{\mathrm{O_2}}}{Y_{\mathrm{O_2}}}\right\} \tag{5}$$

Within a cell, the concentration, Y_i^{R}, of species i in the reactor volume fraction follows the equation

$$\frac{\partial}{\partial t}(Y_i^{\mathrm{R}}) + \frac{\partial}{\partial x}((U + u')\, Y_i^{\mathrm{R}}) + \frac{1}{r}\frac{\partial}{\partial r}(r(V + v')Y_i^{\mathrm{R}}) = \frac{1}{\rho} S_{Y_i,d} + \frac{Y_i - Y_i^{\mathrm{R}}}{\tau_{\mathrm{m}}} + \dot{\omega}_i \tag{6}$$

and the reactor enthalpy, h^{R}, is given by

$$\frac{\partial}{\partial t}(h^{\mathrm{R}}) + \frac{\partial}{\partial x}((U + u')\, h^{\mathrm{R}}) + \frac{1}{r}\frac{\partial}{\partial r}(r(V + v')h^{\mathrm{R}}) = \frac{1}{\rho}\left(\frac{\partial p}{\partial t} + S_{h,d}\right) + \frac{h - h^{\mathrm{R}}}{\tau_{\mathrm{m}}} \tag{7}$$

where $S_{\phi,d}$ are the phase interaction terms. In these equations, the turbulent diffusion of reacting elements has been replaced by a random-walk process similar to the model used for particle dispersion. A randomly chosen fluctuating component (u', v') is added to the mean velocity and acts during the minimum of the eddy lifetime or residence time of the reactor in the computational cell.

Some Numerical Details

The gas-phase equations are solved by using the finite volume technique on a cylindrical mesh, and by using a staggered-grid arrangement for the velocities. The convective and diffusive fluxes are represented by the hybrid of central and upwind differ-

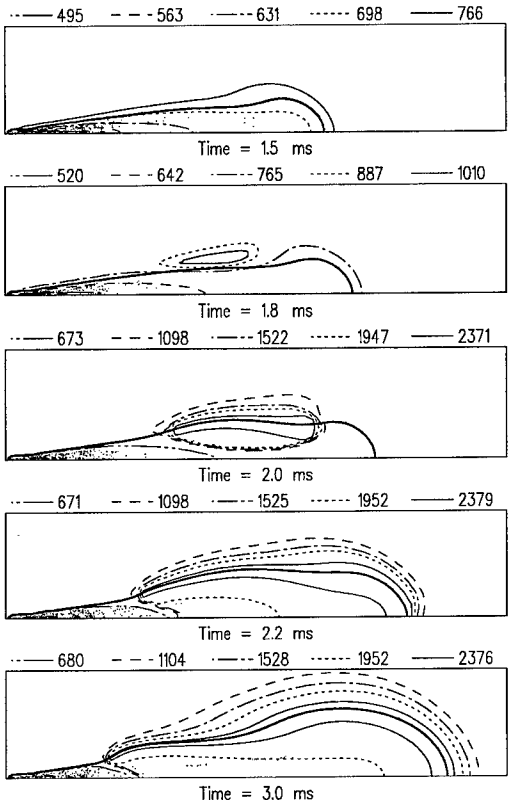

FIG. 1. Reactor temperature field (K) at different times after injection start. Constant injection speed 223 m/s during the whole calculation period; injection nozzle diameter 0.2 mm; air temperature 800 K; pressure 50 bar. Large chamber. Thick line shows the stoichiometric surface. Maximum spray penetration ~75 mm.

encing schemes and are evaluated in a fully implicit fashion. All source terms are, if possible, treated as fully implicit, at least by means of suitable linearization. A special treatment is developed for the spray and chemical source terms, as discussed later. Starting from specified initial field conditions, the evolution of the spray is obtained using a time-marching procedure. The time-advanced solution for the nonlinear coupled system of equations is found through a sequence of guess-and-correct operations in the so-called SIMPLE-C algorithm. An alternating direction implicit (ADI) scheme, using the Thomas algorithm in the different sweeps, together with the method of underrelaxation are used in order to increase the convergence rate. When walls are present, standard wall functions are used, zero normal gradients are assumed otherwise.

The species equations are split into a convection/diffusion part and a chemical source part. For the convection/diffusion part, the same procedure as for other scalar properties is applied, and for the chemical source part a fully implicit (backward) Euler integration method with a local adaptive time step is used. The latter is implemented as a postprocedure after each global time step, strongly reducing the computational effort, but with minor or no numerical errors introduced as long as the global time step is kept small (typically 1–10 μs) as compared with the time scales of the convection/diffusion processes. This result will, in fact, always be the case if the recommended restriction on the global time step (not allowing droplets to pass more than one computational cell in one time step) is considered.

According to the Lagrangian formulation of the droplet phase, all droplet equations are expressed as ordinary differential equations. The integration of these is done by using an explicit (forward) Euler method for droplet position, a semi-implicit Euler method (described later) for droplet mass and enthalpy, and a fully implicit (backward) Euler method for droplet momentum.

The fully implicit integration of droplet momentum is possible if the relative velocity is calculated from "old" time-level velocities. To likewise find a fully coupled procedure for droplet mass and energy and gas-phase energy will be very difficult, and if such a procedure can be found, it will be very costly owing to the complex nonlinear linkages between the evaporation and the heat-up processes. An alternative is to integrate the droplet mass and energy equations using a drop-adaptive time step, and to simultaneously solve simplified equations for the gas-phase density, fuel mass concentration, and energy. The latter enhances the accuracy and eliminates temperature overshoots and unrealistically high evaporation rates. This approach also has the advantage of allowing the two processes to be treated in sequence at every "intermediate" time level, but with minor or no numerical errors introduced, thus greatly reducing computational requirements. The procedure was adopted in the present work.

Results

Flame Development and Structure

Simulations were first conducted for constant injection speed. Figure 1 illustrates the processes of ignition and flame formation, Fig. 2 the fully developed flame structure. As can be seen, ignition occurs locally in a small, lean premixed region at the side of the vapor jet, moves quickly toward the stoichiometric surface as a nonadiabatic, auto-ignition wave, and propagates both downstream and upstream along the stoichiometric surface with very different velocities. The downstream propagation due to the addition of the convection velocity and flame

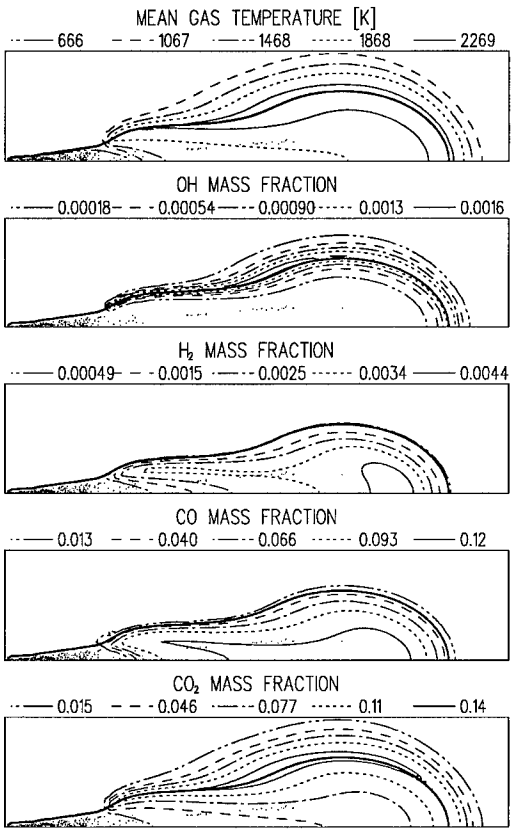

FIG. 2. Fully developed flame structure at 3 ms after injection start. Conditions as in Fig. 1. Thick line shows the stoichiometric surface.

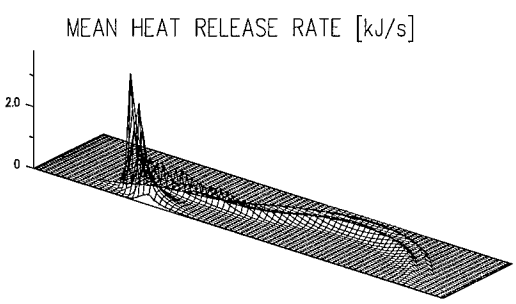

FIG. 3. Energy release rate structure of the flame at 3 ms after injection start. Conditions as in Figs. 1 and 2.

propagation is fast leading to a rapid energy release (the diesel knock), whereas the upstream propagation against the convection velocity is slow. Both the upstream and downstream propagating flames are typical triple flames for which the leading edge is at the stoichiometric surface and in which the combustion occurs both on the lean and the rich side.

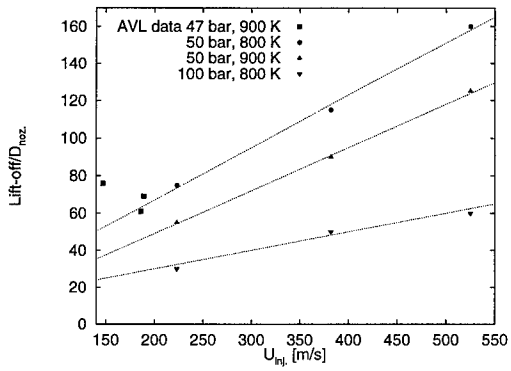

FIG. 4. Normalized liftoff distance as a function of injection velocity for different air temperatures and pressures.

The upstream flame finally stabilizes at a considerable distance from the nozzle which allows a large amount of air to enter the central part of the spray and a large amount of fuel to omit the combustion in the stoichiometric flame with obvious consequences for soot and NO_x emissions. The fully developed flame structure is shown in Fig. 2. Comparing Figs. 1 and 2, one can note the very substantial difference between the reactor (reacting subgrid fraction) and mean temperatures. A very interesting feature is the high temperature in the core of the spray generated by the reactions in the rich branch of the leading triple flame, and high concentrations of the radicals and partially reacted fuel ($CO + H_2$) in the central part of the jet. The overall flame structure differs considerably from the classical Burke-Schumann structure, resulting from continuous flame sheet models. This is further illustrated in Fig. 3, showing the heat release rate structure of the Figs. 1 and 2 flame for the time of 3 ms after start of injection. A very high energy release peak can be seen at the flame stabilization point, rapidly decreasing further downstream due to decreasing mixing (turbulence) intensity. The mixing intensity and, consequently, energy release rate are minimal at the leading point where laminar-like conditions occur. A double-layer flame appears close to the leading point. The double flame is a transient and short-time event caused by diffusion of the fuel injected during ignition delay from the bulk of the flow back toward the flame and burning in the high temperature region. The fuel does not react far from the flame due to dilution (over-leaning).

Lift-off Distances and Core Equivalence Ratios

Figure 4 shows the lift-off distances as a function of injection velocities, nozzle diameters, ($D_{noz.}$) air temperatures, and pressures. A very interesting feature of the results is the linear dependence of the liftoff height normalized by the nozzle diameter on

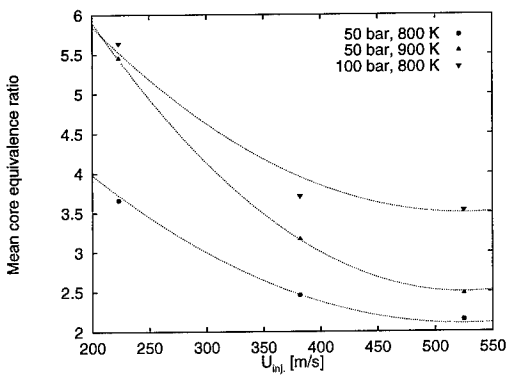

FIG. 5. Core equivalence ratio as a function of injection velocity for different air temperatures and pressures.

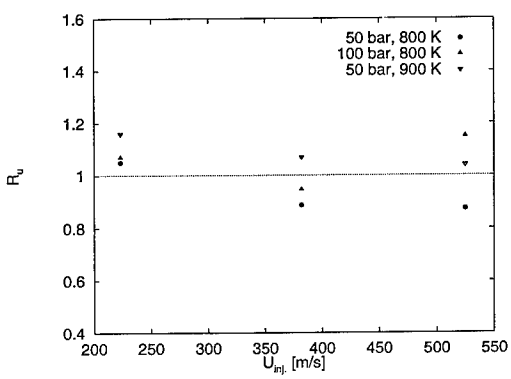

FIG. 6. Ratio of the axial convection speed to the turbulent triple flame speed (R_u) at the flame stabilization point.

injection velocity observed previously in many gas jet experiments [4,25,26]. Experimental data obtained by Winklhofer et al. [27,28] for $T = 900$ K and typical diesel fuel are also shown in the figure. It can be seen that the predicted liftoff distances are close to the measured ones. The most remarkable for diesel sprays however, is that the liftoff distances are orders of magnitude larger than what is observed for gas jets at normal temperatures. This difference is caused by very high flow velocity and small nozzle diameters, both leading to very large flame stretch and cooling by the evaporating fuel. On the other hand, flame stabilization is made possible due to the high temperatures and pressures in the combustion chamber. Figure 5 shows the overall core equivalence ratio in front of the rich branch of the triple flame as a function of fuel injection velocity, air temperature, and pressure. The level of dilution is remarkably high. Parallel to air entrainment into the spray core, an equivalent amount of fuel bypasses the stoichiometric surface and diffuses away from the flame region to be burned in a lean flame. The core dilution by air leads to reduced soot formation, whereas the lean burning decreases NO_x production but also leads to bulk quenching and increased HC emissions. Thus, in general, calculations not accounting for the liftoff cannot lead to correct emission predictions, and this phenomenon becomes very important indeed. The simultaneous reduction of particulate and NO_x emissions with increasing injection pressure was demonstrated experimentally for a quiescent combustion system similar to that in our calculations [29].

The very strong effect of combustion chamber pressure on the liftoff distances and core equivalence ratios is of particular interest since contemporary, highly super-charged diesels with intercoolers operate at very high pressures and reduced temperatures. The sensitivity to pressure indicates that the flame stabilization phenomenon is linked to low-temperature chemical reactions, that is, it is related to auto-ignition. This relationship in turn means that the upstream propagating flame is actually a nonadiabatic (flame supported) auto-ignition wave. The reduction of the liftoff and core dilution at high pressures explains why high-pressure diesels have both higher soot and NO_x emission indexes.

Test of Flame Stabilization Theory

The computations have shown that the numerical model predicts the flame liftoff in accordance with available experimental data. Now, we would like to compare our results with existing theories of flame lift. The theories were reviewed recently by Pitts [7] and Sanders and Lamers [2], so we will avoid a more extensive discussion. First of all, we shall note that due to large liftoff distances in the flames under consideration, premixed conditions prevail in the flame stabilization zone and, thus, the most appropriate theory appears to be the premixedness theory of Vauquickenborne and van Tiggelen [30]. The theory assumes that the fuel and air along the stoichiometric contour of the lifted flames are completely premixed and that flame stabilization occurs at the position where the local turbulent flame propagation velocity is equal to the local time-averaged axial velocity. For the turbulent flame speed in this reaction-time-limited case invoking the KPP theorem [31] and considering the strong streamline curvature of the triple flame [32], we shall use

$$u_T = 2\sqrt{\frac{\rho_1}{\rho_2}}\sqrt{\frac{D_T}{\tau_c}} \tag{8}$$

where D_T is the local turbulent diffusivity and τ_c the local reaction time composed of the mixing and chemical times

$$\tau_c = \tau_m + \tau_{ch} \tag{9}$$

Figure 6 shows that the ratio of the convection speed

to u_T as a function of injection speed for different temperatures and pressures is close to unity, which proves the theory. However, the problem is that no simple expression can be provided for τ_c.

Flame liftoff is a steady-state concept that may be considered unappropriate for the inherently unsteady diesel-type flames. However, for fully developed flames, the flame stabilization occurs on a short time scale (typically 0.2 ms), thus the problem may be treated as quasistationary. In our calculations, only constant injection speeds are considered.

Summary

Diesel spray flame stabilization has been studied using time-dependent, multidimensional, reactive flow simulations based on Navier-Stokes equations and Lagrangian droplet treatment, accounting for droplet collisions, evaporation, and interaction with turbulence. Complex reaction chemistry and a novel turbulence-chemistry interaction model based on subgrid stirred reactor approximation were used in the simulations. Although the computations are based on axi-symmetric geometry and single component fuel, they are able to capture the basic fluid mechanical interactions that are important for flame formation and liftoff. The liftoff heights are in reasonable agreement with the few known experiments, and the predicted liftoff height increases linearly with nozzle exit velocity, which is a very well known feature of lifted turbulent diffusion flames. The computations are compared with the premixedness flame stabilization theory and are in agreement with the theory in that flame stabilization is shown to occur on the stoichiometric surface at a height where the local axial velocity is approximately equal to the turbulent triple flame propagation velocity. In the region upstream of the flame stabilization point, strain rates exceed the chemical times and there is no appreciable chemical reaction even though a stoichiometric surface and high temperatures exist there. The very large liftoff distances for diesel flames result in a large amount of air being able to enter the fuel core and a large amount of fuel to avoid burning in the stoichiometric flame. Both soot and NO_x emission reduction can follow for high-pressure, small orifice injection. Future work will focus on detailed simulations of the emissions.

Acknowledgment

This work was supported by a grant from the Swedish Board of Technological Development, NUTEK.

REFERENCES

1. Scheffer, R. W., Namazian, M., and Kelly, J., *Combust. Flame* 99:75–86 (1994).
2. Sanders, J. P. H. and Lamers, A. P. G. G., *Combust. Flame* 96:22–33 (1994).
3. Kaplan, C. R., Oran, E. S., and Baek, S. W., *Twenty-Fifth Symposium (International) on Combustion,* The Combustion Institute, Pittsburgh, 1994, pp. 1183–1189.
4. Lee, B. J., Kim, J. S., and Chung, S. H., *Twenty-Fifth Symposium (International) on Combustion,* The Combustion Institute, Pittsburgh, 1994, pp. 1175–1181.
5. Scheffer, R. W., Namazian, M., Filtopoulos, E. E. J., and Kelly, J., *Twenty-Fifth Symposium (International) on Combustion,* The Combustion Institute, Pittsburgh, 1994, pp. 1223–1231.
6. Bradley, D., Gaskell, P. H., and Lau, A. K. C., *Twenty-Third Symposium (International) on Combustion,* The Combustion Institute, Pittsburgh, 1990, pp. 685–692.
7. Pitts, W. M., *Twenty-Second Symposium (International) on Combustion,* The Combustion Institute, Pittsburgh, 1988, pp. 809–816.
8. Ranzi, E., Gaffuri, P., Faravelli, T., and Dagaut, P., *Combust. Flame* 103:91–106 (1995).
9. Chevalier, C., Pitz, W. J., Warnatz, J., Westbrook, C. K., and Melenk, H., *Twenty-Forth Symposium (International) on Combustion,* The Combustion Institute, Pittsburgh, 1992, pp. 93–101.
10. Müller, U. C., Peters, N., and Liñán, A., *Twenty-Fourth Symposium on Combustion,* The Combustion Institute, Pittsburgh, 1992, pp. 777–789.
11. Karlsson, J. A. J., "Modeling Auto-Ignition, Flame Propagation and Combustion in Non-Stationary Turbulent Sprays," Ph.D. Thesis, Chalmers University of Technology, Göteborg, Sweden, 1995.
12. Karlsson, J. A. J., Berglind, T., and Chomiak, J., *The Third International Symposium on Diagnostics and Modeling of Combustion in Internal Combustion Engines,* The Japan Society of Mechanical Engineers, Tokyo, 1994, pp. 275–280.
13. Karlsson, J. A. J., and Chomiak, J., 21st International Congress on Combustion Engines (CIMAC 95), The Institution of Mechanical Engineers, London, 1995, Paper D01.
14. Amsden, A. A., O'Rourke, P. J., and Butler, T. D., *KIVA-II: A Computer Program for Chemically Reactive Flows with Sprays,* Los Alamos National Laboratory Report No. LA-11560-MS, Los Alamos, NM, 1989.
15. Reitz, R. D. and Rutland, C. J., *Prog. Energy Combust. Sci.* 21:173–196 (1995).
16. Theobald, M. A., "A Numerical Simulation of Diesel Auto-Ignition," Ph.D. Thesis, Massachusetts Institute of Technology, Cambridge, MA, 1986.
17. Gorokhovski, M. and Borghi, R., SAE Paper 930075 (1993).
18. Kong, S. -C. and Reitz, R. D., *Trans. ASME, J. Eng. Gas Turbines Power* 115:781–789 (1993).
19. Cox, R. A. and Cole, J. A., *Combust. Flame* 60:109 (1985).
20. Hu, H. and Keck, J. C., SAE Paper 872110 (1987).
21. Ciezki, H. and Adomeit, G., *Combust. Flame* 93:421–433 (1993).

22. Byggstøyl, S. and Magnussen, B. F., *Turbulent Shear Flows 4,* Springer Verlag, Berlin, 1985, pp. 381–395.
23. Gran, I. R., "Mathematical Modeling and Numerical Simulation of Chemical Kinetics in Turbulent Combustion," Ph.D. Thesis, The Norwegian Institute of Technology, Trondheim, 1994.
24. Gonzales, M. and Borghi, R., *Turbulent Shear Flows 7,* Springer Verlag, Berlin, 1991, pp. 293–311.
25. Kalghatgi, G. T., *Combust. Sci. Technol.* 41:17–29 (1984).
26. Brondwell, J. E., Dahm, W. J. A., and Mungal, G., *Twentieth Symposium (International) on Combustion,* The Combustion Institute, Pittsburgh, 1984, pp. 303–310.
27. Winklhofer, E., Ahmadi-Befrui, B., Wiesler, B., and Cresnoverh, G., *Proc. Inst. Mech. Eng.* 206:173–183 (1992).
28. Herzog, P. L., Bürgler, L., Winklhofer, E., Zelenka, P., and Cartellieri, W., SAE Paper 920470 (1992).
29. Zelenka, P., Kriegler, W., Herzog, P. L., and Cartellieri, W., SAE Paper 900602 (1990).
30. Vauquickenborne, L., and van Tiggelen, A., *Combust. Flame* 10:59–69 (1966).
31. Hakberg, B. and Gosman, A. D., *Twentieth Symposium (International) on Combustion,* The Combustion Institute, Pittsburgh, 1984, pp. 225–232.
32. Veynante, D., Vervisch, L., Poinsot, T., Liñán, A., and Ruetsch, G., *Proceedings of the 1994 Summer Program,* Center for Turbulence Research, NASA Ames/Stanford Univ. pp. 55–73.

Twenty-Sixth Symposium (International) on Combustion/The Combustion Institute, 1996/pp. 2565–2572

A SIMPLE MODEL OF IGNITION MODES OF DENSE DROPLET CLOUDS

D. THIBAUT* AND S. CANDEL
EM2C Laboratory, CNRS, École Centrale Paris
F-92295 Châtenay-Malabry, France

Multiphase combustion is of practical importance in many applications and has received growing interest in the last few decades. However, all the details of the mechanisms involved in this field of research are far from being fully understood. The aim of this work is to bring a new insight to the coupling between vaporization and ignition of a dense cloud of droplets. Therefore, a system of one-dimensional equations including source terms for the vaporization is solved numerically for a spherical cloud of fuel droplets in a hot, oxidizing atmosphere. The different cases investigated show two main ignition modes: internal homogeneous or external diffusion ignition. The analysis of the results proceeds in two steps: first, analytical expressions are derived for the temporal evolution of the cloud before ignition; second, the characteristic time of homogeneous and diffusion ignition is estimated continuously during the vaporization process. This decomposition provides useful information about the dynamics of the phenomenon. The coupling between cooling and chemical reaction is explained on the basis of this decomposition. A classification of the ignition modes follows from this analysis, and an ignition diagram is proposed.

Introduction

In all liquid-fueled combustors, it is well known that injection characteristics govern the flame structure and the overall efficiency of the device. A detailed understanding of the mechanisms related to multiphase combustion is more and more a key to the development of nonpolluting and high-performance devices. The mode and delay of ignition are important questions in designing diesel, aircraft, or rocket engines.

Although single-droplet ignition and combustion have been studied extensively, the case of droplet clouds is not as well documented. Controlled experiments are less easy to design, and modeling is less advanced. Basic understanding is achievable by suitably combining theoretical considerations and numerical simulations. Mawid and Aggarwal [1] are studying numerically the ignition of a fuel cloud in contact with a high-temperature wall in a one-dimensional domain. Their model takes into account isolated droplet burning as well as gaseous reaction. The liquid phase is represented by droplet groups followed in a Lagrangian way (point-source method). The addition of a volatile component to the liquid phase is shown to have a great influence on the ignition delays. In a recent review, Annamalai and Ryan [2] prefer a space-averaged formulation for the liquid phase based on a droplet-number-density description (group method). The results obtained with their technique are compared with Labowsky's [4] more fundamental studies of droplet arrays relying on the method of images. The two approaches are in good agreement, demonstrating the validity of the group method in the case of dense clusters of droplets [3,4]. The group method is used by Correa and Sichel [5] in an asymptotic study of vaporization and ignition of spherical clouds. The chemical reaction is supposed to develop in the external gas phase. The results highlight the propagation of a vaporization wave toward the saturated core. Rangel and Continillo [6] are investigating theoretically the ignition of droplet clusters in the field of a vortex. The initial temperature distribution leads to a thermal runaway in the premixed vortex center in their analysis. Bellan and co-workers [7,8] have conducted detailed studies on the ignition and combustion of clusters of droplets. Equations are solved for the droplet and for the continuous gas phase. Each particle is assumed to be surrounded by a sphere of influence and interacts with the ambiance through it, (see, for example, [7,8]). The combustion mode (isolated droplet combustion, flames inside or outside the cloud) is determined on the basis of several criteria [9]. Convective effects associated with the relative motion of the droplets and the gas can also be taken into account in the model. An ignition Damköhler number is calculated and compared to a critical value to determine the onset of reaction [10].

The present study is motivated by questions arising in the design of premixed, prevaporized gas-turbine combustors (Fig. 1a). In these devices, ignition in the premixing tube is to be avoided. In most

*Also with Snecma, Centre de Villaroche, F-77550 Moissy-Cramayel, France.

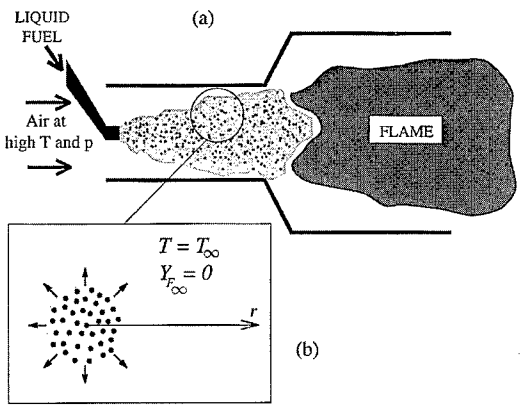

FIG. 1. (a) Schematic representation of a lean, premixed combustor. (b) Simplified problem investigated in this work: a droplet cloud in a hot, oxidizing atmosphere.

cases, the residence time in this tube is shorter than the complete evaporation time of the droplets. The particles are wrapped around in clusters by vortical structures developing in sheared and swirled zones downstream of the injector. It is therefore relevant to study the temporal evolution of a droplet cloud in a convective system of coordinates. This approach is followed in the work of Bellan and Harstad [7], as mentioned earlier. In the same way, Thévenin and Candel [11] are investigating the ignition of gaseous diffusion flames rolled up in vortices. These authors distinguish two modes: a premixed mode of ignition in the viscous core of the structures and a diffusion mode outside the vortex when the center is too cold. The present work follows this line of thought. Its objective is not to describe the practical problem in its full complexity but to provide a comprehensive model of auto-ignition modes of droplet clouds. To analyze this point, one may examine the simplified situation of a spherically symmetrical droplet cloud placed in a hot, oxidizing atmosphere (Fig. 1b). We will thus describe the ignition of small droplets that rapidly adjust their velocity to the surrounding motion.

In all the cases presented here, the group combustion number G [12] is of the order of 10^5. The interdroplet length-to-diameter ratios l/d are less than 10. In these conditions, individual droplet flames cannot exist. The model proposed in this article reproduces the competition between the vaporization process and the heat release due to combustion by solving the unsteady, reactive equations inside and outside the cloud. The model describes the structure of external cluster flames or the auto-ignition of the internal mixture in formation. A prediction method of the ignition mode and a way to estimate the delay are then devised.

Model Formulation

The physical system of interest in this work is schematized in Fig. 1b. A monodisperse spray of droplets is placed in a hot, oxidizing atmosphere at a given pressure. No fuel is present in the cloud interior at the beginning of the simulation. Initial temperature within the cloud is uniform. It can be set either equal to or different from the ambient value. The liquid particles stay inert in the gas, and their distribution is characterized by a constant density n. Using the group-averaging method, the liquid phase is represented by a continuous mass source and heat sink. The vaporization is modeled by a d^2 law for each droplet in the cloud with the local temperature as the driving temperature. Temperature within the liquid phase is supposed to be uniform and equal to the saturation temperature. Isolated droplet burning is not taken into account. Density is given by the perfect gas law.

In the ignition process, the initial temperature increment is small. Specific heat and thermal conductivity are thus assumed constant in the domain, with Lewis number equal to unity. The values of physical parameters used in this study refer to heptane and can be found in the Nomenclature. In order to study the interplay between kinetics, vaporization, and diffusion, we have chosen to use a single-step Arrhenius reaction between fuel (F) and oxidizer (O):

$$\nu_F F + \nu_O O \rightarrow \nu_P P$$

The chemical source term will be written as follows:

$$\dot{\omega} = B\left(\frac{\rho Y_O}{W_O}\right)\left(\frac{\rho Y_F}{W_F}\right)\exp\left(-\frac{T_a}{T}\right)$$

This formulation yields an ignition delay and has the advantage of simplifying the analysis. In order to keep the proper characteristic times, the pre-exponential factor B has been adjusted to reproduce experimental ignition delays of homogeneous heptane-air mixtures. Flame structures presented in this work suffer from these limitations and are qualitative. In a specific application, detailed kinetics, transport algorithms, and thermodynamic properties could be used.

The conservation equations for the gas phase [13] are listed below:

$$\frac{\partial \rho}{\partial t} + \frac{1}{r^2}\frac{\partial}{\partial r}(r^2 \rho v) = n\dot{m}$$

$$\rho\frac{\partial Y_F}{\partial t} + \rho v\frac{\partial Y_F}{\partial r} - \frac{1}{r^2}\frac{\partial}{\partial r}\left(r^2 \rho \mathcal{D}\frac{\partial Y_F}{\partial r}\right) = n\dot{m}(1 - Y_F) - \nu_F W_F \dot{\omega}$$

$$\rho\frac{\partial Y_O}{\partial t} + \rho v\frac{\partial Y_O}{\partial r} - \frac{1}{r^2}\frac{\partial}{\partial r}\left(r^2 \rho \mathcal{D}\frac{\partial Y_O}{\partial r}\right) = -n\dot{m}Y_O - \nu_O W_O \dot{\omega}$$

TABLE 1
Values of the main parameters for the simulations

Case	p (bar)	T_∞ (K)	T_{c0} (K)	d_0 (μm)	l (μm)	τ_V (ms)	Ign. delay (ms)	Mode
1	30	900	900	40	100	9.72	4.94	external
2	30	1100	1100	20	100	1.81	0.79	internal
3	30	1100	900	40	100	9.72	4.13	external

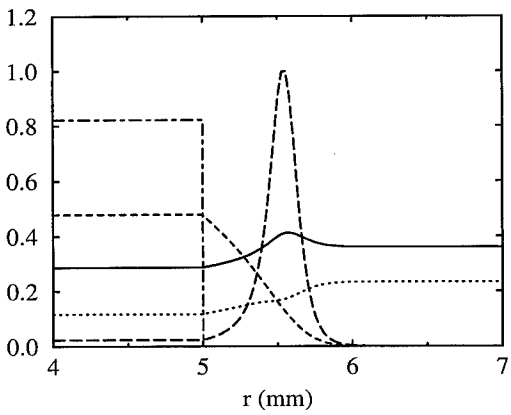

FIG. 2. Case 1, t = 4.5 ms. External ignition regime. ——: $T/2500$ K; ····: Y_O; – – –: Y_F; — —: $\dot{\omega}$; ·–·–: d/d_0. The initial cloud radius is 5 mm.

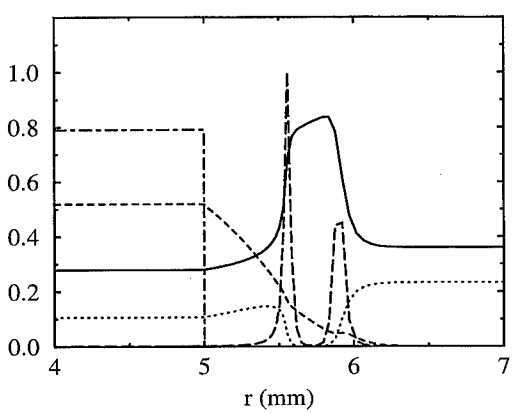

FIG. 3. Case 1, t = 5.5 ms. Double flame structure. ——: $T/2500$ K; ····: Y_O; – – –: Y_F; — —: $\dot{\omega}$; ·–·–: d/d_0.

$$\rho c_p \frac{\partial T}{\partial t} + \rho v c_p \frac{\partial T}{\partial r} - \frac{1}{r^2}\frac{\partial}{\partial r}\left(r^2 \lambda \frac{\partial T}{\partial r}\right) = n\dot{m}c_p\,(-L/c_p + T_S - T) + \nu_F W_F Q \dot{\omega}$$

The vaporization rate of a droplet in the cloud is related to the diameter evolution $\partial d^2/\partial t = 8(\lambda/\rho_l c_p)\ln[1 + c_p(T - T_S)/L]$. As boundary conditions, zero gradient at the origin and prescribed temperature and composition at $r = \infty$ close the problem.

Typical Ignition Sequences

At the beginning of each computation, no fuel is present in the interior of the cloud. The droplets vaporize, the temperature diminishes, and vapor diffuses toward the hot surroundings. Different ignition scenarios are possible depending on the relative velocities of vaporization and chemical reaction. Two cases illustrating the different ignition modes are discussed hereafter. The values of the parameters used in the computations are listed in Table 1.

External Ignition (Case 1)

When the cooling due to vaporization is important, the chemical reaction is quenched in the cloud. Combustion begins in the surrounding gaseous phase where some fuel has diffused in the high-temperature ambiance (Fig. 2). This case will be denoted as external ignition. It is not purely a diffusion-flame ignition because the flame develops between the internal, premixed region and the external, oxidizing atmosphere. After ignition, the reaction zone splits into two parts (Fig. 3). A rich, premixed flame travels inward to the cloud. A classic diffusion flame burns the excess of fuel downstream of the first premixed front.

Internal Ignition (Case 2)

In the case of lower fuel loadings, the temperature remains high enough in the cloud and may lead to thermal runaway (Fig. 4). When oxidizer is consumed in the cluster, the homogeneous reaction vanishes, and the vaporization supplies fuel to an external diffusion flame (Fig. 5).

Comparison between the heat release levels reached at ignition in the two modes shows that the homogeneous mechanism is an order of magnitude more powerful than the diffusion mode. This point is particularly relevant to the design of rocket engines, for example, where it is well known that violent, premixed ignition can have disastrous

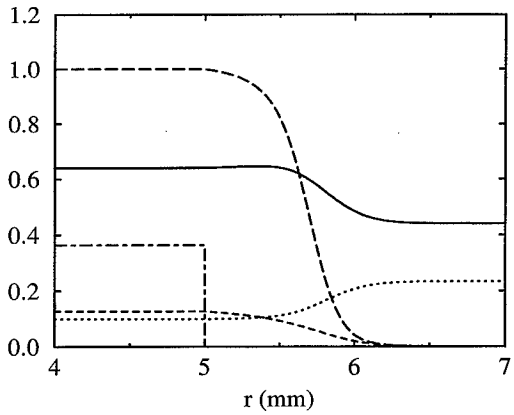

FIG. 4. Case 2, $t = 0.8$ ms. Internal ignition regime. ——: $T/2500$ K; ····: Y_O; – – –: Y_F; — —: $\dot{\omega}$; ·–·–: d/d_0. The initial cloud radius is 5 mm.

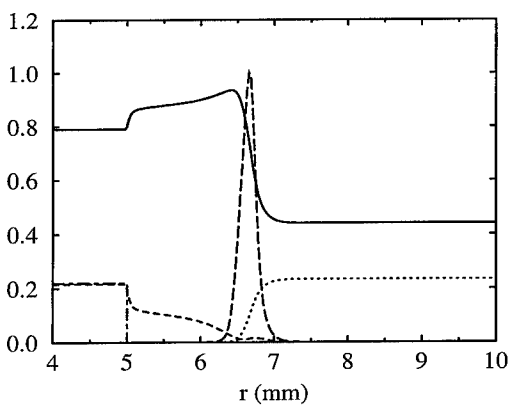

FIG. 5. Case 2, $t = 1.2$ ms. External diffusion flame combustion. ——: $T/2500$ K; - - -: Y_O; – – –: Y_F; — —: $\dot{\omega}$; ·–·–: d/d_0. Note that the radial scale in this plot differs from that used in Fig. 4.

consequences for the combustion chamber. A reliable method for predicting the ignition mode is, in general, of great interest.

Ignition Analysis

The latter discussion suggests that the time evolution of cloud temperature (T_c) and cloud composition (Y_{Fc}, Y_{Oc}) is of prime importance in the analysis of the ignition phenomenon. Approximate analytical expressions for T_c, Y_{Fc}, and Y_{Oc} can be derived from the conservation equations by setting spatial gradients to zero. Constant density and constant Spalding number $B_T = c_p(T_{c0} - T_S)/L$ are used in this approximation analysis. Chemical reaction is supposed to be negligible before ignition. Integration yields

$$\begin{cases} Y_{Fc} = 1 - (1 - Y_{Fc,0}) \exp[g(t)] \\ Y_{Oc} = Y_{Oc,0} \exp[g(t)] \\ T_c = T_S - L/c_p + (T_{c,0} - T_S + L/c_p) \exp[g(t)] \end{cases} \tag{1}$$

where

$$g(t) = Y_F^{\lim}\left[\left(1 - \frac{t}{\tau_V}\right)^{3/2} - 1\right] \text{ and}$$

$$Y_F^{\lim} = \frac{4}{3}\pi\left(\frac{d_0}{2}\right)^3 \frac{\rho_l}{\rho} n$$

The droplet characteristic vaporization time is given by

$$\tau_V = \frac{d_0^2 \rho_l c_p}{8\lambda \ln\left(1 + c_p \dfrac{T_{c,0} - T_S}{L}\right)}$$

These relations describe the state of the cloud at any time t during vaporization. An appropriate description of the ignition modes is then needed. The external ignition mechanism concerns a reactive interface between hot air and the mixture characterized by Y_{Fc}, Y_{Oc}, and T_c. By analogy with a diffusion-controlled situation, one may use Liñan's analysis to estimate the characteristic ignition time [14]:

$$\tau_{\text{diff}} = f(\beta_1) t_1$$

where

$$\beta_1 = \frac{T_a(T_\infty - T_c)}{T_\infty^2} \text{ and}$$

$$t_1 = \frac{W_O c_p T_\infty^2}{B\rho Y_{Oc} Y_{Fc} Q T_a} \exp\left(\frac{T_a}{T_\infty}\right)$$

In a parallel way, an asymptotic expression can be easily derived for the ignition delay of a homogeneous, premixed mixture that characterizes the internal mode:

$$\tau_{\text{hom}} = \frac{W_O c_p T_c^2}{B\rho Y_{Oc} Y_{Fc} Q T_a} \exp\left(\frac{T_a}{T_c}\right)$$

The ignition of the cloud can be decomposed in two successive steps: a first, cooling phase during which internal temperature drops and mass fractions evolve according to the relations (1) and a second, reactive phase characterized by the delay τ_{diff} or τ_{hom}. The effective duration of the ignition process can be written as the sum of these two times. It is convenient to introduce the following notations:

$$\theta_{\text{diff}}(t) = t + \tau_{\text{diff}}[Y_{Fc}(t), Y_{Oc}(t), T_c(t)]$$

$$\theta_{\text{hom}}(t) = t + \tau_{\text{hom}}[Y_{Fc}(t), Y_{Oc}(t), T_c(t)]$$

Figure 6 compares θ_{diff} and θ_{hom} for the internal ignition case presented in this study (case 2). The

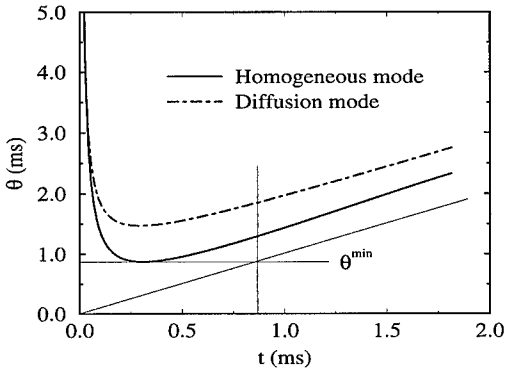

FIG. 6. Case 2, internal ignition regime. Comparison of θ_{diff} and θ_{hom}.

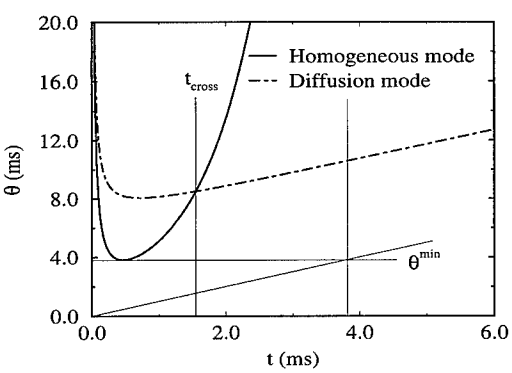

FIG. 7. Case 1, external ignition regime. Comparison of θ_{diff} and θ_{hom}.

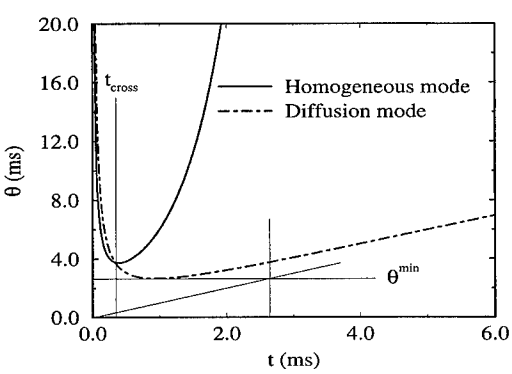

FIG. 8. Case 3, external ignition regime. Comparison of θ_{diff} and θ_{hom}.

two curves show a minimum: At the beginning of vaporization, ignition is impossible because the fuel mass fraction is too low. Inversely, after a long time, the cloud is cold, and chemical reaction is slower. For this case, the homogeneous ignition time θ_{hom} is shorter than for the diffusive time θ_{diff} during all the vaporization, and this explains the internal ignition observed in the computation. The minimum value $\theta^{\min}$ corresponds to the ignition time actually calculated with a good precision.

The same representation for case 1 is shown in Fig. 7. The minimum value $\theta^{\min}$ equals 3.81 ms and is reached for the homogeneous regime. But at t = 3.81 ms, the diffusion mode is predominant because of the shorter ignition time. The homogeneous mode prevails only for a short time, and external ignition is finally observed. The critical time t_{cross} where the two curves θ_{hom} and θ_{diff} intersect (see Fig. 7) thus appears to be an important parameter in the analysis.

Figure 8 shows a third case where the diffusive time is always shorter than the homogeneous time. This situation has been obtained by imposing a cold initial temperature inside the cloud.

As far as the internal ignition mode is concerned, the delay corresponds to the value $\theta_{\text{hom}}^{\min}$ predicted by the characteristic time approach. The external ignition delay cannot be estimated with such good accuracy. This last remark is probably due to the external interface not being purely diffusive, as mentioned earlier.

One may wonder if the same reasoning will apply to homogeneous mixtures. In that case, the first contribution to θ_{hom} will be zero, and ignition will be, as expected, determined by τ_{hom}.

Ignition Diagram

Three characteristic times are relevant to the description of the coupling between vaporization, cooling, and ignition of a cloud of droplets:

- $\theta_{\text{hom}}^{\min}$ is the minimal ignition time achievable in the internal homogeneous regime.
- $\theta_{\text{diff}}^{\min}$ is the minimal ignition time in the external diffusive regime.
- t_{cross} is the instant after which diffusive ignition becomes faster than premixed ignition.

It is convenient to characterize an ignition case by the two ratios $\theta_{\text{hom}}^{\min}/\theta_{\text{diff}}^{\min}$ and $t_{\text{cross}}/\theta_{\text{diff}}^{\min}$. The plane may then be subdivided into four regions (Fig. 9):

- Region I is characterized by $\theta_{\text{hom}}^{\min} < \theta_{\text{diff}}^{\min}$ and $\theta_{\text{hom}}^{\min} < t_{\text{cross}}$. The homogeneous mixture will ignite faster than the external diffusion flame. The second inequality ensures that the chemical reaction in the homogeneous mixture has enough time to develop before the change to diffusive mode at $t = t_{\text{cross}}$.

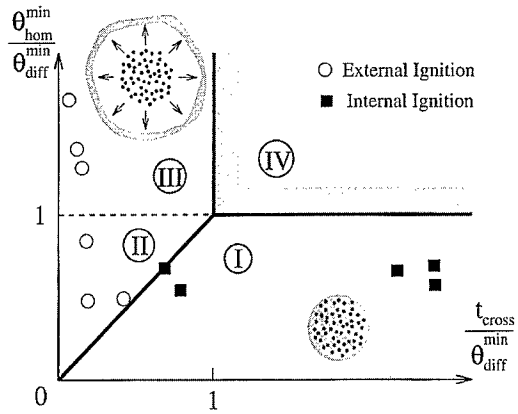

FIG. 9. Classification of the ignition modes as a function of the ratios $\theta_{hom}^{min}/\theta_{diff}^{min}$ and $t_{cross}/\theta_{diff}^{min}$. Open symbols: external ignition. Filled symbols: internal ignition.

- In region II, the relations between the characteristic times are now $\theta_{hom}^{min} < \theta_{diff}^{min}$ and $\theta_{hom}^{min} > t_{cross}$. The minimum ignition time is obtained in the homogeneous regime. However, the corresponding delay is longer than the period dedicated to the homogeneous mode because of intensive cooling. Ignition will finally occur outside the cloud in the external diffusive mode.
- In region III, the inequality $\theta_{hom}^{min} > \theta_{diff}^{min}$ leads to external ignition.
- Region IV is not of physical interest. An explanation is given in the Appendix of this article.

A simple method for predicting the ignition mode can be derived from this analysis as follows:

1. Plot θ_{hom} and θ_{diff} as a function of t conformably to the relations (1).
2. Determine the minima θ_{hom}^{min} and θ_{diff}^{min}, as well as the critical crossover time t_{cross}, where the two curves intersect each other.
3. Report the ratios $\theta_{hom}^{min}/\theta_{diff}^{min}$ and $t_{cross}/\theta_{diff}^{min}$ in the ignition diagram of Fig. 9. The regions discussed above indicate the ignition mode. In the internal regime, θ_{hom}^{min} provides a good estimate of the ignition delay.

Extensive calculations are in excellent agreement with the classification proposed in this article, as shown in Fig. 9, where open and filled symbols correspond, respectively, to external and internal ignition.

Conclusion

A simple model of the autoignition of dense clouds of droplets in a hot, oxidizing atmosphere has been investigated by one-dimensional numerical computations. Two main ignition modes have been identified depending on the relative intensity of the combustion heat release and the heat sink due to vaporization. If the cooling is fast compared to the characteristic ignition time of the homogeneous mixture in the center of the cloud, combustion begins outside in the hot ambiance. The reaction evolves in a double flame after ignition: A rich, premixed front propagates inward through the vaporizing cloud, and a diffusion flame establishes itself farther out in the surrounding atmosphere. If vaporization is less intense, temperature remains high in the cloud, and homogeneous ignition can occur. After ignition, combustion is sustained by an external diffusion flame when all the oxidizer is consumed in the cloud.

A characteristic time approach has been developed in order to classify the different cases as a function of the initial conditions. First, analytical expressions have been derived for the temporal evolution of the temperature and the composition of the cloud. At each instant, characteristic ignition times in internal, homogeneous mode and external, diffusion mode are then estimated asymptotically. In most cases, results show that the system follows two successive phases. At first, when vaporization has just begun, the interior of the cloud is still hot, and internal, premixed ignition prevails. After a certain critical time, cooling has suppressed the homogeneous reaction mode, and ignition is more probable outside the cluster. Comparison between the minimum ignition times in both homogeneous and diffusive modes, and with the critical crossover time after which premixed ignition is no longer possible, yields a reliable description of the ignition mechanisms.

A diagram is proposed on the basis of the relative magnitude of these characteristic times. The prediction method that arises from this classification is easy to use and can be of interest in practical applications where a violent, premixed ignition is often harmful to the combustion device and has to be avoided.

Appendix

In this appendix, we wish to show that region IV in the ignition diagram (Fig. 9) has no physical meaning. This region is such that $t_{cross} > \theta_{diff}^{min}$ and, simultaneously, $\theta_{hom}^{min} > \theta_{diff}^{min}$. We will now show that these two inequalities are incompatible. For this analysis, it is convenient to refer to the t-θ diagram (Figs. 6–8). The two curves $\theta_{diff}(t)$ and $\theta_{hom}(t)$ feature the following asymptotic behavior: For $t \to \infty$, the cloud temperature is low and diffusive ignition prevails ($\theta_{hom} > \theta_{diff}$ for $t \to \infty$). Inversely, at the beginning of vaporization, the mixture in formation is hot, and only small amounts of fuel have diffused outside the cloud. The homogeneous ignition is then faster for $t \to 0$ ($\theta_{hom} < \theta_{diff}$ for $t \to 0$). Given that

θ_{diff} and θ_{hom} have only one minimum and considering the inequality $\theta_{\text{hom}}^{\text{min}} > \theta_{\text{diff}}^{\text{min}}$, the asymptotic behavior of the two curves implies that $\theta_{\text{diff}}^{\text{min}}$ is reached at a time t_d^m, which is greater than the crossover time t_{cross}: $t_d^m > t_{\text{cross}}$.

Now, one has by definition $\theta_{\text{diff}}^{\text{min}} = t_d^m + \tau_{\text{diff}}(t_d^m)$. Consequently, $\theta_{\text{diff}}^{\text{min}}$ is greater than t_{cross}, which is in disagreement with the first condition defining region IV. This clearly shows that region IV should not be considered.

Nomenclature

B	pre-exponential factor 3.3×10^5 mol^{-1} m^3 s^{-1}
c_p	specific heat 1950 J kg^{-1} K^{-1}
d	droplet diameter m
$\mathcal{D}$	mass diffusion coefficient m^2 s^{-1}
$l = n^{-1/3}$	interdroplet distance m
L	latent heat of vaporization 295×10^3 J kg^{-1}
$\dot{m}$	droplet vaporization rate kg s^{-1}
n	droplet number density m^{-3}
Q	heat of combustion per unit mass of fuel 42×10^6 J kg^{-1}
r	radial coordinate m
t	time s
T	temperature K
T_a	activation temperature 12,870 K
T_S	droplet temperature K
v	radial velocity m s^{-1}
W_F	fuel molecular weight 0.1 kg mol^{-1}
W_O	oxidizer molecular weight 0.032 kg mol^{-1}
Y_F	fuel mass fraction —
Y_O	oxidizer mass fraction —
λ	thermal conductivity 0.00215 W m^{-1} K^{-1}
ν_F	fuel stoichiometric coefficient 1
ν_O	oxidizer stoichiometric coefficient 11
$\dot{\omega}$	reaction rate mol m^{-3} s^{-1}
ρ	gas-phase density kg m^{-3}
ρ_l	liquid-phase density 582 kg m^{-3}
τ	characteristic chemical time s
θ	ignition time s

Subscript

c	cloud interior
diff	diffusive mode
hom	homogeneous, premixed mode
0	initial condition

Acknowledgments

This work is supported by SNECMA. Computational time was provided by IDRIS.

REFERENCES

1. Mawid, M. and Aggarwal, S. K., *Combust. Flame* 81:59–72 (1990).
2. Annamalai, K. and Ryan, W., *Prog. Energy Combust. Sci.* 18:221–295 (1992).
3. Ryan, W., Annamalai, K., and Caton, J., *Combust. Flame* 80:313–321 (1990).
4. Labowsky, M., *Combust. Sci. Technol.* 22:217–226 (1980).
5. Correa, S. M. and Sichel, M., *Nineteenth Symposium (International) on Combustion,* The Combustion Institute, Pittsburgh, 1982, pp. 981–991.
6. Rangel, R. H. and Continillo, G., *Twenty-Fourth Symposium (International) on Combustion,* The Combustion Institute, Pittsburgh, 1992, pp. 1493–1501.
7. Bellan, J. and Harstad, K., *Combust. Flame* 79:272–286 (1990).
8. Fichot, F., Harstad, K., and Bellan, J., *Combust. Flame* 98:5–19 (1994).
9. Bellan, J. and Harstad, K., *Combust. Sci. Technol.* 53:75–87 (1987).
10. Law, C. K. and Chung, S. H., *Combust. Sci. Technol.* 22:17–26 (1982).
11. Thévenin, D. and Candel, S., *Phys. Fluids* 7(2):434–445 (1995).
12. Chiu, H. H. and Liu, T. M., *Combust. Sci. Technol.* 17:127–142 (1977).
13. Williams, F. A., *Combustion Theory,* The Benjamin/Cummings Publishing Company, 1985.
14. Liñan, A. and Crespo, A., *Combust. Sci. Technol.* 14:95–117 (1976).

COMMENTS

Dr. Josette Bellan, Jet Propulsion Laboratory, USA. We have published about 3 years ago in Combustion and Flame (authors: Fichot, Bellan and Harstad) a paper where we calculate ignition for a configuration almost identical to yours except that: (a) we calculate the evaporation rate from first principles taking drop interactions into account, (b) we calculate the two-way dynamic interaction between flow and drops, and (c) we can have an arbitrarily large number of drops. Our results show that ignition depends upon the initial slip velocity in a complex way. Have you compared your simplified calculations with our more realistic predictions? Are your results realistic?

You mentioned that there is drop interaction in the cloud. The use of the classical D^2 law precludes accounting for this interaction. Since the initial slip velocity is null, how

is the drop interaction impacting the model through the thermodynamics?

Author's Reply. We do not take convective effects into account in our study. We are aware of this limitation and that we may miss some aspects of the complicated process of spray ignition. However, we believe that our model is well suited to the injection of small particles as is the case in a LPP combustor. In this situation, the droplets are rapidly in dynamic equilibrium with the gas, and one may neglect the slip velocity as a first approximation.

We mentioned that our model deals with dense clouds where isolated drop ignition is not possible. We did not intend to take drop interaction into account in the evaporation process.

•

Friedrerich Dinkelacker, University of Erlangen, Germany. Are you aware of experimental evidence of the two ignition types you proposed?

Author's Reply. Our model has not been compared to experimental results. Let us mention that Chiu and Lin presented the same type of transient behavior in studies of premixed clusters combustion (Anomalous Group Combustion of Premixed Clusters, H. H. Chiu and C. L. Lin, this Symposium), p. 000.

•

A. Kowalewicz, Radom Technical University, Poland. Did you determine the evaporation constant K for the following: (a) a cloud of droplets, and if you did, how does it depend on the configuration of droplets? (b) a single droplet in the cloud, and if you did, what is the probability density function for the K value?

Author's Reply. The evaporation constant (noted B_T in our text) is related to a single droplet in the cloud. We assume that the droplets are distributed uniformly and that there are no changes in the value of B_T due to heterogeneities in the spatial distribution of the particles. Thus we use implicitly a delta function for the B_T probability density function.

•

Y. Neumeir, Gerogia Tech, USA. How practical is the assumption of a spherical cloud for gas turbine injection when there is a continuous, flowing cloud of droplets?

Author's Reply. Our model has been built to follow the ignition of small droplets convected in groups in the premixing section of a LPP device. A spherical cloud can be seen as a convective element of the entire spray. It can be used to represent the multidimensional problem of the continuous cloud by the temporal study of a simplified local system.

Twenty-Sixth Symposium (International) on Combustion/The Combustion Institute, 1996/pp. 2573–2579

SELF-IGNITION OF HYBRID (H_2 + ATOMIZED LIQUID HYDROCARBON FUEL + GASEOUS OXIDIZER) MIXTURES AT ENGINE RELEVANT CONDITIONS

B. E. GELFAND, A. M. BARTENEV, S. V. KHOMIK, S. P. MEDVEDEV AND A. N. POLENOV
N. N. Semenov Institute of Chemical Physics, RAS
117977, Moscow, V-334, ul. Kosigina, 4, Russia

The self-ignition of several nondiluted hybrid mixtures of gaseous hydrogen + atomized liquid hydrocarbon fuel + gaseous oxygen was studied at high pressure. Decane has been used as a representative hydrocarbon liquid fuel. Hydrogen mass fraction range was (3–35%) in compound fuel.

Experiments have been performed using the reflected shock wave technique. Recordings of pressure and light emission were analyzed. The hybrid mixtures exhibited only strong self-ignition modes. It was demonstrated that hydrogen is a very weak promoter of self-ignition phenomena for the mixtures of atomized decane + gaseous oxygen. Additional experimental data on the self-ignition features of hydrogen + oxygen mixtures at high pressure were obtained.

Introduction

The addition of hydrogen to hydrocarbon fuels is considered as a prospective way to increase process efficiency, both in internal combustion engines and in liquid propellant rocket engines. The addition of hydrogen to hydrocarbons leads to the improvement of emission characteristics, changes in the dynamics and feedback response of fuel consumption, and an increase in the heat of combustion. Three-component compositions (for example, hydrogen + kerosene + oxygen/air) are rather attractive as prospective fuels for utilization in the next generation of liquid propellant rockets or airbreathing engines.

The key phenomena are self-ignition, burning, and detonation in three-component combustible systems. There is a lack of experimental information about the features of the above steps in nondiluted combustible mixtures at a pressure level of $P > 10$ bar, which is typical for engines. And it is rather surprising that the problem of hybrid mixtures self-ignition has never been discussed in the literature. There exist only scattered contradictory data on the self-ignition of homogeneous multicomponent gaseous mixtures: $CH_4 + H_2 + O_2 + Ar$. Only a limited amount of experimental data is available concerning the effect of hydrogen on $CH_4 + O_2 + Ar$ self-ignition [2]. Experiments [2] were performed for hydrogen mass fraction in compound fuel where $\eta_{H_2} = m_{H_2}/(m_{H_2} + m_{CH_4}) = 0.3\%$, and $\eta_{H_2} = 2\%$.

It was pointed out by Rafael and Sher [3] that the data [2] give no basis for definite conclusions about variations of self-ignition time delays for multifuel homogenous mixtures at high temperature, 1600 K $< T <$ 1800 K, and moderate pressure, $P < 10$ bar. It was shown [3] that the interpretation of certain of the results [2] does not correspond to the data obtained. Some of the conclusions from Ref. 3 were based on kinetics calculations whose validity was not confirmed by experiments [5]. Only qualitative predictions were made [1,3] about the possibility of the similarity of ignition delays of hydrogen and some hydrocarbons at moderately high temperature and high pressure. A very weak influence of hydrogen addition on some gaseous hydrocarbon self-ignition at $P = 1$ bar, 1200 K $< T <$ 1400 K, and $\eta_{H_2} \ll 1\%$ was pointed out in Ref. 1.

Cheng and Oppenheim [4] investigated the self-ignition characteristics of compound fuel $H_2 + CH_4$ in O_2 + Ar atmosphere at temperatures 1200 K $< T <$ 2000 K, pressure $P < 3$ bar, and hydrogen mass fractions of 5–20%. Additional reduction in time delays (τ_{itr}) was found for multifuel compositions in the range $\tau_{iH2}(T) < \tau_{itr}(T) < \tau_{iCH4}(T)$. However $\tau_{iH2} \ll \tau_{iCH4}$ in this range of parameters and the case of mixtures $H_2 + CH_4$ considered in Ref. 4 is not typical for a full set of hydrogen + hydrocarbon compound fuels. Moreover, the dependencies $\tau(T, \eta_{H2}, \ldots)$ in Ref. 4 are not suitable for the applications at high pressure and nondiluted mixtures. As a result, the existing database is not sufficient for reliable recommendations about the possible modifications of combustion processes using three-component combustible mixtures.

The phenomenology of combustion processes in three-component hybrid mixtures may be elucidated only on the basis of proper experimental investigations. According to the state of the art, it is important to investigate the explosion phenomena in two-component (gaseous fuel + gaseous oxidizer, atomized fuel + gaseous oxidizer) and in three-component systems with the help of a similar experimental

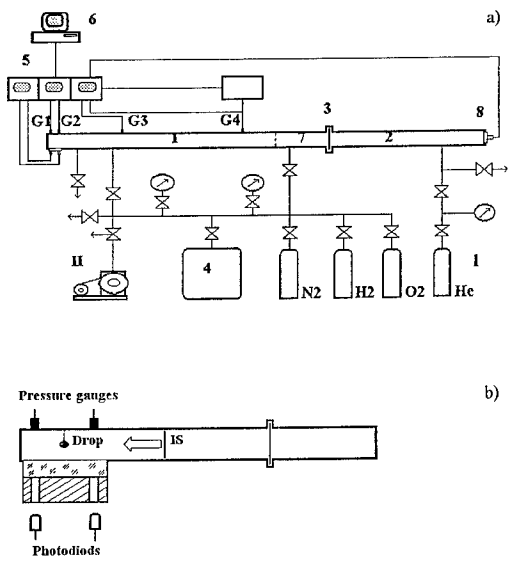

FIG. 1. Experimental apparatus.

technique. It is assumed that representative measurements may be produced in shock tubes. The shock tube is the only experimental facility with short compression and heating times. The shock tube possesses have definite advantages concerning cleanliness and complete coverage of pressure and temperature without the necessity of changing the measurement technique for different gaseous or atomized liquid fuels.

Experimental Apparatus and Procedure

The main feature of the shock-tube technique is the ability to cover easily the range of pressure (1 bar $< P <$ 200 bar) and temperature (800 K $< T <$ 2500 K). There is no problem in a shock tube with setting the exact composition of oxidizing gaseous medium. The simplicity of the dispersion of liquid (or pulverized) materials by gas flow behind the shock waves permits a comparison of self-ignition characteristics for gaseous atomized liquid and pulverized solid fuels under similar conditions of pressure, temperature, and composition of oxidizing continuous medium. In the shock tubes, the pressure and temperature behind the incident (P_1, T_1) and reflected (P_2, T_2) shock waves are functions of the Mach numbers M. Due to the changing initial pressure in a low-pressure chamber (LPC), one can carry out the experiments at M = const. and T = const. at different pressures behind shock waves.

For measuring ignition delay of hybrid mixtures, the available laboratory shock tube [6,9] was modified to meet the above-mentioned requirements (Fig. 1a). LPC, 1, is a rectangular 34-by 50-mm cross section, 1000 mm long with carefully polished walls and no grease. The LPC was divided from the high pressure section (HPC), 2, by means of a bursting membrane, 3. The HPC is a circular stainless steel tube 50 mm in diameter with variable length ($0.4 < L < 0.7$ m). Variation of HPC length enables control of the pressure profile in the incident shock wave (ISW). The HPC and LPC are filled with a gas using a gas-feed system, I, and evacuation system, II.

For measuring shock wave velocity and pressure profiles, pressure gauges, G1–G4, are flash mounted along the waveguide. Gauge G4 is also used for triggering a measuring system. G1 and G2 are mounted at the side wall in the vicinity of the LPC endwall. The use of these gauges permits measurements of the velocity of explosion processes behind a reflected shock (RS). The end of the LPC is equipped with a window. It permitted use of a specially designed photodiode (PD) measuring system near the endwall of the LPC. A test mixture was prepared in a mixing vessel, 4, with an electric fan. Technically pure gaseous ingredients, H_2, O_2, and N_2, were taken from industrial containers. For recording, signals from the pressure transducers, G1–G4, and the photodiode, digital oscilloscopes, 5, and a PC-based data processing system, 6, were used.

The pressure around the self-igniting drops was also monitored using two pressure gauges installed on the side wall. The light emission during self-ignition was registered with the help of a detector system made from a photodiode placed opposite the pressure gauges. The fuel drop hangs at the center of the test section of the shock tube at the tip of a thin metallic wire (see model in Fig. 1b).

The experimental technique with a single hanging drop [6] has advantages over the techniques that use a line of drops or a spray [7]. These require a special feeder for the drops at the top wall, and a receiver of the liquid at the bottom wall. The presence of the attached volumes influence the self-ignition phenomena. The injection of the fuel into the low-pressure chamber creates conditions for liquid film formation on the bottom wall [7]. It is very difficult to recognize in this case the true source of the tiny mist involved in the self-ignition phenomena. Additionally, the heating of the thin liquid layer produced soot formation on the tube walls. In the technique using a single hanging drop, the presence of liquid film before the arrival of the shock wave is excluded and the pollution of the wall is minor.

The liquid hydrocarbon fuel was n-decane. The main parameters of n-decane are: surface tension, $\sigma = 239 \cdot 10^{-3}$ N/m; density, $\rho_f = 730$ kg/m^3; viscosity $\mu = 1.27 \cdot 10^{-3}$ Ns/m^2.

A complete picture of the main wave interactions in the shock tube is presented in Fig. 2a. Figure 2a was obtained with the help of a special computing program [8]. Line IS on the distance (x) – time (t) diagram shows the incident shock. Line RS denotes

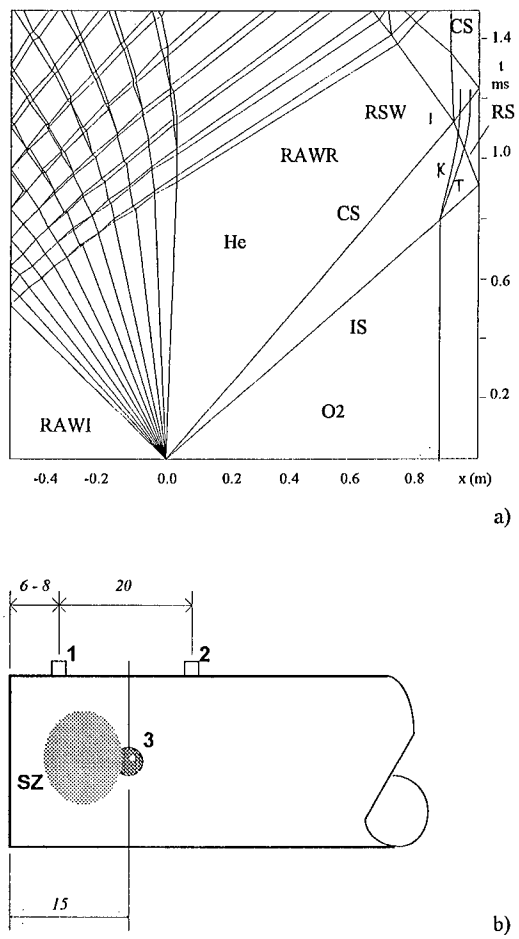

FIG. 2. Distance-time wave diagram with spray formation apparatus.

the reflected shock. Line CS presents the trajectory of contact surface between a driver gas (He) and a driven oxidizing gas (air, oxygen, etc.). A set of lines presents the fan of incident rarefaction waves (RAWI) and the fan of reflected rarefaction waves (RAWR). Intersection of RS and CS near point I produces refracted shock wave (RSW) in the driver gas and refracted wave in driven gas preliminary compressed by IS and RS. The trajectory of a drop hanging at a distance of 15 mm from the endwall is represented by the vertical line (at $x = 0.85$ m).

The trajectory of drops, after interaction with IS and RS, splits into two parts. These parts are back (K) and head (T) boundaries of atomized liquid fuel. The compression of a spray behind RS is followed by decompression in RAWR. Different variants are possible when a spray experiences additional pressurization by a pressure wave refracted from the contact surface. If the drop is hanging at a larger distance from the endwall, then the complete picture of wave interactions will be the same, but the trajectory of the drop movement will be somewhat different.

The location of secondary spray back and head boundaries in relation to the endwall was determined in preliminary runs. Fortunately, the locations of these boundaries are approximately the same as in the previously illustrated case with $\Delta l = 15$ mm. The main difference is connected with the ratio of preevaporated fuel mass (m_{pr}) to the mass of tiny drops (m_t) given at initial conditions $m_0 = m_t + m_{pr}$, where m_0 is the mass of the parent drop.

The method of preparation of the heterogeneous mixture for self-ignition behind IS is presented in Fig. 2b. The IS breaks up decane droplets (3) and creates a selfignition zone (SZ). The most distant edge of the SZ is located 15 mm from the endwall. Arrangement of the gauges 1 and 2 is clear from Fig. 2b. This arrangement enables observation of the phenomena inside the SZ (gauge 1) and outside the SZ (gauge 2).

The self-ignition zone (SZ) in shock tube experiments can be considered as the analog of the combustion zone in a combustion chamber. The temperature increase inside the SZ in shock tube experiments passes through two stages. In the first (preliminary) stage, the IS raises the temperature up to T_1 in a short period of $50 \cdot 10^{-6}$ s. In addition, the gas flow behind the IS disperses the fuel inside the SZ volume. In the second or main stage, the temperature increases up to T_2. This level corresponds to the temperature behind RS. The processes of vaporization and component mixing proceed simultaneously. The SZ response on the pressure and temperature jumps can be considered as an indicator of chemical activity and stability of the self-ignition processes in dispersed fuel. The mixture composition can be characterized by the volumetric average value. The local composition is practically unknown.

By contrast to the case with dispersed fuel, the self-ignition zone, SZ, in a homogenous hydrogen + oxygen mixture in a shock tube has a rather definite geometrical boundary. The compression of the gaseous mixture is governed by gas dynamics laws and can be described in terms of the displacement of the main surfaces (IS, RS, CS, RAWR). Eventually, the pressure gauges located as shown in Fig. 2 are immersed in a volume of combustible mixture. In this case, it is possible to investigate wave phenomena in a premixed, combustible gaseous mixture. The local mixture composition corresponds to the initial uniform mixture and is known a priori.

Thermodynamic calculations of operating conditions for a three-component system with liquid atomized hydrocarbon (HC) + gaseous H_2 + gaseous oxidizer (O_2 or air) are based on the parameter that defines the hydrogen mass fraction of compound fuel: HC + H_2. The total fuel flow rate is

$m_\Sigma = m_{H2} + m_{HC}$. Then, the hydrogen mass fraction η_{H2}, at flow rate m_{H2}, and HC (in the present case, decane) flow rate m_{HC} is defined as $\eta_{H2} = m_{H2}/(m_{H2} + m_{HC}) = (1 + \lambda)^{-1}$. The ratio of HC and H_2 flow rates is $\lambda = m_{HC}/m_{H2}$. Parameters η_{H2} and λ describe the composition of a compound in the self-ignition zone of the shock tube according to accepted experimental procedure. The fully atomized liquid decane is placed inside the volume between the plane of the droplet hanger and the endwall. Thus, the expected dimensions of the self-ignition zone occupied by compound fuel: (decane + H_2) consist of a parallelepiped with length $L = 15$ mm, cross section $S = 34 \times 50$ mm^2, and volume $V = L \times S = 25.5$ cm^3. The weight of liquid fuel dispersed in that self-ignition zone is $m_{HC} = N\,(4/3\,\pi R^3\,\rho_f)$ for N decane droplets with radius R before IS. In general, $N = 1$ or $N = 2$. The mass of hydrogen m_{H2} in the self-ignition zone after a double shock compression behind IS and RS in gaseous mixture (H_2 + O_2) is $m = \beta\rho_2 V$. The gas density behind RS is related to the initial gas density $\rho_0 = P_0/(R^* T_0)$ ahead of the IS as

$$\frac{\rho_2}{\rho_0} \approx f(M)$$

$$= \frac{(\lambda + 1)M^2[2\gamma M^2 - \gamma + 1]}{[(\gamma - 1)M^2 + 2][(\gamma - 1)(2M^2 - 1) + 2]}$$

Here, β is the hydrogen volume fraction in preliminary, prepared gaseous mixture H_2 + O_2, M is the Mach number of IS, $\gamma = c_p/c_v$ (specific heats ratio), T_0 is the initial temperature ahead of the IS (as usual, $T_0 = 293$ K), P_0 is the initial pressure in the LPC, and R^* is the universal gas constant.

The variation in the gasdynamic function $f(M)$ can be easily compensated for by an appropriate choice of mixture composition and initial pressure P_0. Thus, the method of the investigation permits measurements of the self-ignition time delays of triple hybrid mixtures, *viz.*, fine atomized decane + H_2 + O_2 over a range of hydrogen mass fraction in the compound fuel (3–35%).

Results and Discussion

The following cases may be distinguished according to the known experimental data [1–7,9] for double mixtures: (gaseous H_2) + (gaseous O_2) and (atomized decane) + (gaseous O_2):

1. Moderate temperature, $T < 1000$ K, and medium pressure, 10 bar $< P <$ 20 bar
2. Moderate temperature, $T < 1000$ K, and high pressure, $P >$ 20 bar
3. High temperature, $T > 1000$ K, and medium pressure, 10 bar $< P <$ 20 bar
4. High temperature, $T > 1000$ K, and high pressure, $P >$ 20 bar

This simplest scheme of possible cases is based on the specific regions in the pressure + temperature plane, which correspond to various self-ignition regimes [4–7,9] as follows:

1. The mild self-ignition in a gaseous mixture: (H_2 + O_2), and the strong self-ignition in a heterogeneous mixture: (atomized decane + O_2)
2. The strong self-ignition in a gaseous mixture: (H_2 + O_2), and the strong self-ignition in a heterogeneous mixture: (atomized decane + O_2)

Relying on this classification, several special cases of triple-mixture self-ignition can be analyzed. In addition, the data on the self-ignition of compound fuel (decane + H_2) + 50% O_2 + 50% N_2 are used to simulate the burnout of the initial component.

Figure 3a shows the time dependencies of pressure (lines P) and luminosity (lines L) during the self-ignition of a gaseous premixed mixture: 15% H_2 + 85% O_2 (top), heterogeneous two-phase mixture: decane + O_2 (middle), and hybrid mixture with compound fuel: 15% H_2 + 85% O_2 + decane (bottom). The column of graphs in Fig. 3a was obtained using a pressure gauge and photodiode placed 6 mm from the endwall. As mentioned [5,9], the self-ignition of mixture, H_2 + O_2 (or air), is mild without sharp, powerful pressure spikes at $T_2 = 970 \pm 10$ K and $P_2 = 27 \pm 3$ bar. At the same conditions, the heterogenous mixture, decane + O_2, ignites in a strong mode with powerful pressure disturbances. The most interesting is the self-ignition of a hybrid mixture with compound fuel, Decane + H_2, at the same pressure + temperature conditions and $\eta_{H2} = 9\%$. As seen from Fig. 3a, the injection of atomized decane into a gaseous mixture, 15% H_2 + 85% O_2, results in strong ignition escalation. The self-ignition time delay in this case is not less than that for the heterogeneous mixture, decane + O_2. Therefore, at above-mentioned pressure and temperature conditions, gaseous hydrogen is not a promoter of the self-ignition of atomized decane. Pressure disturbances do not disappear when the combustion wave propagates from a hybrid combustible mixture (zone SZ in Fig. 2a) to a gaseous mixture region at a distance of more than 15 mm from the endwall.

Also, it is possible to compare the duration of the luminosity in two-component (gaseous or heterogeneous) and hybrid combustible mixtures. This parameter characterizes indirectly the rate of the fuel conversion to combustion products. It is worth pointing out, that hydrogen addition into the mixture decane + O_2 prolongs the duration of the combustion in a heterogeneous system.

Fig. 3b illustrates the effect of pressure on self-ignition. The pressure is increased up to $P_2 = 58 \pm 4$ bar in comparison with the previous case, while the temperature remains at $T_2 = 970 \pm 10$ K. The self-ignition of the mixture decane + O_2 proceeds

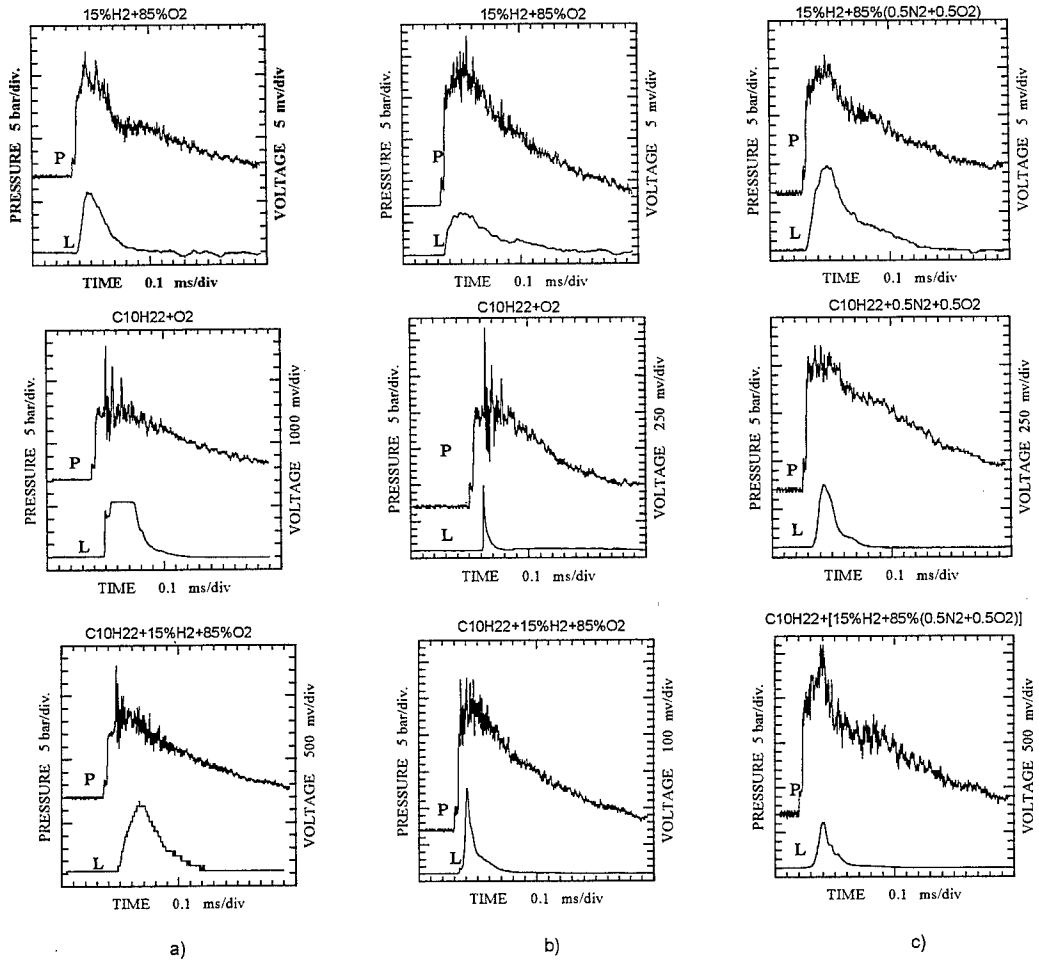

FIG. 3. Typical (pressure + light) time histories during self-ignition of two-component (gaseous hydrogen + gaseous oxygen, liquid atomized decane + gaseous oxygen) and hybrid (gaseous hydrogen + liquid atomized decane + gaseous oxidizer) mixtures.

in the strong mode with significant random pressure spikes. The self-ignition of the mixture 15% H_2 + 85% O_2 is close to the mild mode but with more noticeable pressure disturbances than at lower average pressure. The self-ignition of a hybrid mixture with hydrogen mass fraction in the compound fuel with $\eta_{H2} = 14\%$ at $P_2 = 58 \pm 4$ bar is strong and self-ignition time delay is $\tau_{iH2} < \tau_{iHyb} < \tau_{HC}$. Hydrogen admixing into the heterogeneous mixture decane + O_2 prolongs the duration of the luminosity signal because $\Delta\tau_3 > \Delta\tau_2$, but $\Delta\tau_1 > \Delta\tau_3$. Here, $\Delta\tau_1$, $\Delta\tau_2$, $\Delta\tau_3$ are durations of the luminosity during the self-ignition of the mixtures 15% H_2 + 85% O_2, decane + O_2, and 15% H_2 + 85% O_2 + decane. The difference in self-ignition time delays in hybrid and heterogeneous mixtures is negligible in spite of the significant volumetric and mass concentration of hydrogen in the hybrid mixture. It means that hydrogen remains a weak promoter of atomized decane self-ignition at moderate temperature and high pressure.

Fig. 3c illustrates the influence of the inert dilutent that simulates the generation of combustion products. The tests presented in Fig. 3c were performed at higher temperature, $T_2 = 1180 \pm 20$ K, and pressure, $P_2 = 68 \pm 4$ bar, with the gaseous oxidizer consisting of 50% N_2 + 50% O_2. Upper graphs correspond to the gaseous mixture 15% H_2 + 85% ($0.5N_2 + 0.5O_2$). Middle graphs correspond to the heterogeneous mixture atomized decane + 50% N_2 + 50% O_2. Bottom graphs correspond to the hybrid mixture atomized decane + 15% H_2 + 85%($0.5N_2 + 0.5O_2$) at hydrogen mass fraction η_{H2} = 12% in compound fuel. Similar to a pure oxygen

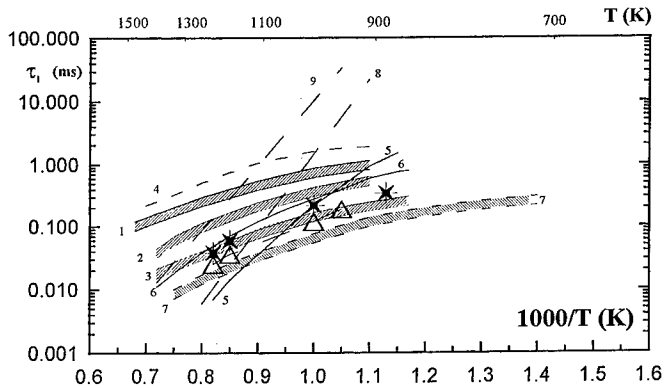

FIG. 4. Self-ignition time delays of gaseous, two-phase, and hybrid combustible mixtures. Lines: (1) decane + O_2, P = 10–15 bar; (2) ibid., P = 40–50 bar; (3) ibid., P = 65–80 bar; (4) ibid., P = 4–6 bar; (5) 7.5% H_2 + 92.5% O_2, P = 10–15 bar; (6) 7.5% H_2 + 92.5% O_2, P = 40–45 bar; (7) 15% H_2 + 85% O_2, P = 30–40 bar; (8) 7.5% H_2 + 92.5% O_2, P = 10 bar (calculated); (9) ibid., P = 40 bar (calculated). Points: hybrid mixtures, °, 7.5–15% H_2 + 92.5–85% O_2 + atomized decane, P = 25–30 bar; Δ, ibid., P = 50–60 bar.

atmosphere, the self-ignition modes of hydrogen and decane in equimolar oxygen + nitrogen oxidizer is strong, with $\tau_{iH2} < \tau_{iHC}$. The transition to the hybrid mixtures is usually accompanied by the essential increase of pressure oscillations so $\Delta P_{Hyb} > \Delta P_{HC}$. Moreover, the self-ignition time delay becomes $\tau_{iHyb} > \tau_{iHC} > \tau_{iH2}$. As was mentioned, the duration of the luminosity signal $\Delta\tau_{Hyb} > \Delta\tau_{HC}$.

Results of self-ignition time delay measurements are plotted in Fig. 4 for the set of double-component, premixed, gaseous and nonpremixed, heterogenous mixtures. Lines 1, 2, 3, and 4 correspond to heterogeneous mixtures (decane + O_2). Lines 5, 6, and 7 correspond to premixed gaseous mixtures (H_2 + O_2).

Also plotted are the results of calculations for homogeneous gaseous mixtures (hydrogen-oxygen) on lines 8 and 9. Relative positions of calculated dependencies $\tau_{iH2} = \tau_{iH2}(P, T)$ and measured values $\tau_{iHC} = \tau_{iHC}(P, T)$ partially confirm the prediction [1] about the possibility of intersection between corresponding curves so that $\tau_{iH2} < \tau_{iHC}$ at $T > T_1^\circ$, but $\tau_{iH2} > \tau_{iHC}$ at $T < T_1^\circ$ (T_1° is some reference value of temperature). The region of approaching ignition delays of heterogeneous and homogeneous mixtures is $T_1^\circ \cong$ 1000–1400 K. Especially high possibility of ignition times approaching τ_{iH2} and τ_{iHC} lies in the range $T <$ 1000 K, $P >$ 40 bar. This fact explains the independence of decane-oxygen self-ignition from hydrogen additives at moderate pressure and temperature. A definite discrepancy between τ_{iH2} and τ_{iHC} takes place at T = 1400–1500 K. In that domain, the hydrogen additive to the decane-oxygen mixture slightly reduces self-ignition time delay so that $\tau_{iH2} < \tau_{iHyb} < \tau_{iHC}$.

The present experimental data have cast some suspicion on the theoretical conclusions [3] about a strong hydrogen effect on the combustion of hydrocarbons (butane) at $P >$ 30 bar and $T <$ 1000 K. Calculation results [3] and the present experimental results come into agreement at $T >$ 1200 K. For example, it was pointed out in Ref. 3 that the time delay changes negligibly in compound mixtures (hydrogen + n-butane) at η_{H2} = 6%. Also confirmed is the conclusion [3] about the relation $\tau_{iH2} < \tau_{itr} < \tau_{iC4H10}$. The difference between τ_{iH2} and τ_{itr} is no more than twice, as shown in the experiments.

Therefore, we can expect that at high pressure and moderate temperature ($T <$ 1100 K), the addition of hydrogen to the decane-oxygen mixture at $\eta_{H2} <$ 10% does not change self-ignition delay because $\tau_{iH2} \cong \tau_{iHC}$. At high temperature conditions ($T >$ 1200 K), the addition of hydrogen to the decane-oxygen mixture slightly reduces the self-ignition delay.

The main difference between combustion processes in double-gaseous (heterogeneous) and triple-hybrid mixtures with compound fuel is a different type of pressure oscillation. As a rule, the self-ignition of triple mixtures with compound fuel is accompanied by large pressure amplitudes in the self-ignition zone. In every test considered, the injection of liquid hydrocarbon into a homogeneous gaseous mixture of hydrogen-oxygen results in a changing self-ignition regime. Usually, the mild regime transforms into a strong one.

It seems that the basic reason for the change in the pressure oscillation regime is the violation of spatial uniformity of the combustible mixture. In fact, the dispersion of liquid fuel inside the zone filled by the homogeneous, gaseous combustible mixture leads to the appearance of cavities with transient temperature and composition. The local temperature variation is conditioned by heat losses due to liquid fuel vaporization. The variation of composition is determined by different concentrations of dispersed fuel relative to the place of the initial droplet. Temperature decreases inside particular (distinct) volumes of the self-ignition zone, and the variation of the mixture composition results in prolongation of the triple mixtures combustion.

Conclusions

1. It was found on the basis of careful experimental

investigations that the admixing of hydrogen into a two-phase mixture (decane + O_2 at $T < 1100$ K, $P > 40$ bar, and hydrogen mass fraction $\eta_{H2} < 15\%$) does not change the self-ignition time delay.

2. Hydrogen is a weak promoter of atomized decane self-ignition in an oxygen atmosphere at $T > 1100$ K, $P > 40$ bar, and hydrogen mass fraction $\eta_{H2} < 15\%$.
3. The injection of atomized hydrocarbon fuel in a premixed gaseous H_2 + O_2 mixture causes a transformation from the mild self-ignition regime to a strong ignition regime.
4. The self-ignition of hybrid mixtures is accompanied by more intensive pressure disturbances than in the double-component gaseous mixtures.
5. The duration of combustion for heterogeneous mixtures (Decane + O_2) does not decrease as a result of hydrogen addition at hydrogen mass fraction $\eta_{H2} < 15\%$.
6. Existing chemical kinetics models are of limited value in describing the process of hybrid mixture combustion at pressure and temperature levels relevant to engine conditions.

Acknowledgments

The authors wish to acknowledge the partial financial support of the Rockwell International Rocketdyne division. Additional financial support was provided by the Russian Foundation of Fundamental Research.

REFERENCES

1. Hawthorn, R. D. and Nixon, A. C., *AIAA J.* 3:513–520 (1966).
2. Lifshitz, A., Scheller, K., and Burcat, A., *Combust. Flame* 16:311–321 (1971).
3. Rafael, S. and Sher. E., *Twenty-Third Symposium (International) on Combustion*, The Combustion Institute, Pittsburgh, 1990, pp. 1789–1796.
4. Cheng, R. K. and Oppenheim, A. K., *Combust. Flame* 58: 125–139 (1984).
5. Voevodsky, V. V. and Soloukhin, R. I., *Tenth Symposium (International) on Combustion*, The Combustion Institute, Pittsburgh, 1965, pp. 279–283.
6. Gelfand, B. E., Kalinin, O. N., Borisov, A. A., and Tsyganov, S. A., *Dokl. Acad. Sci. USSR* 240:627–629 (1978).
7. Wierzba, A. S., Kauffman, C. W., and Nicholls, J. A., *Combust. Sci. Technol.* 9:233–245 (1974).
8. Yu, M., Esser, B., Lenartz, M., and Gronig, H., *Shock Wave J.* 2:245–255 (1992).
9. Gelfand, B. E., Popov, O. E., Medvedev, S. P., Khomik, S. V., Kusharin, A. Yu., and Agafonov, G. L., *Dokl. RAS* 330:457–459 (1993).

Twenty-Sixth Symposium (International) on Combustion/The Combustion Institute, 1996/pp. 2581–2587

ADVANCED DIAGNOSTICS FOR MINIMIZING HYDROCARBON EMISSIONS FROM A DIRECT-INJECTION GASOLINE ENGINE

MICHAEL C. DRAKE, DONALD T. FRENCH AND TODD D. FANSLER
General Motors Research & Development Center
Warren, MI 48090-9055, USA

Minimizing unburned-hydrocarbon (HC) emissions at light load is essential for realizing the potential fuel-economy, cold-start, and transient-HC advantages of direct-injection (DI) stratified-charge engines. This paper summarizes the application of several advanced diagnostics to understand and quantify HC sources in an experimental DI two-stroke engine. Single-cycle (two-dimensional) and multicycle-averaged (two-dimensional and reconstructed three-dimensional) laser-induced-fluorescence (LIF) imaging of gasoline (1) characterizes the highly stratified fuel distribution at the time of ignition, (2) identifies cyclic variations in the fuel concentration near the spark gap as a principal cause of misfires and partial burns, (3) reveals regions of fuel-air mixture around the periphery of the fuel cloud that are too lean to burn, and (4) detects the outgassing of unburned fuel from the fuel injector nozzle-exit crevice late in the engine cycle. Cyclic variations are investigated further by collecting continuous, time-resolved data on liquid fuel distributions, combustion, and exhaust hydrocarbon emissions over many consecutive engine cycles. Specifically, high-speed (4000 frames/s) video imaging of the fuel spray and of spectrally resolved combustion luminosity is combined with simultaneous exhaust-HC sampling using a close-coupled fast-response (~2 ms) flame-ionization detector. Cylinder pressure is also digitized simultaneously, so that the imaging results can be correlated with the heat released and the exhaust HC mass for each engine cycle. The results (1) show that combustion begins as partially premixed flame propagation and ends as slower mixing-limited or diffusion burning, (2) reveal quantitatively the fate of unburned fuel in misfire and partial-burn cycles, and (3) provide strong evidence that the dominant HC sources are incomplete combustion of the injected fuel cloud and late release of fuel trapped in the injector nozzle-exit crevice (rather than fuel trapped in the piston top-ring-land crevice, which is the dominant HC source in conventional homogeneous-charge four-stroke engines).

Introduction

Both two-stroke and four-stroke direct-injection stratified-charge (DISC) spark-ignition (SI) engines have attracted interest as automotive power plants because of their potential advantages in fuel efficiency and in reduced emissions during starting and speed-load transients. However, DISC engines suffer from elevated unburned-hydrocarbon (HC) emissions at light loads, which are sometimes worsened by misfires and partial burns. Available evidence points toward bulk flame quenching as the dominant HC source [1–4]. By contrast, in conventional homogeneous-charge four-stroke SI engines, the dominant HC source is thought to be fuel-air mixture that is forced into crevices (in particular the piston top-ring-land crevice) during compression and combustion and that subsequently outgases from the crevices but fails to burn as the cylinder pressure and temperature fall [5].

Here, we first summarize new insight into DISC-engine combustion that has been obtained using two- and three-dimensional laser-induced-fluorescence (LIF) imaging of fuel and simultaneously acquired cylinder-pressure data [6,7]. These techniques, although valuable for characterizing fuel-air mixture preparation and combustion, provide little *quantitative* information about HC emissions during individual engine cycles. We have therefore integrated high-speed exhaust-HC sampling [8] with simultaneous high-speed spectrally resolved imaging and cylinder-pressure measurements. Our analysis provides engine-out HC *mass* data that we relate to imaging and heat-release data on a cycle-by-cycle basis. The results offer further insight into the fate of unburned fuel in the cylinder and the relative importance of various HC sources in a two-stroke DISC engine.

Experiment

Engine

Figure 1 shows a simplified schematic of our engine (see also Table 1). It is a single-cylinder version of an experimental V6 DI two-stroke engine, and it uses the same crankcase-compression scavenging,

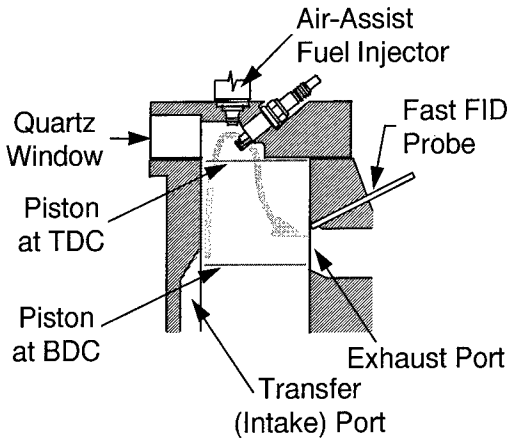

FIG. 1. Simplified schematic of optical two-stroke direct-injection stratified-charge engine. Gray curved line indicates scavenging airflow pattern. Not shown here is a conventional heated-line FID probe that is mounted further downstream from the exhaust port.

TABLE 1
Engine specifications and operating conditions

Displacement	0.5 L
Bore	86 mm
Stroke	86 mm
Connecting-rod length	191.5 mm
Compression ratio (trapped)	6.5
Exhaust Port Opens (EPO)	90°ATDC (*a*fter *t*op *d*ead *c*enter crankshaft position)
Intake Port Opening (IPO)	120°ATDC
Intake Port Closing (IPC)	240°ATDC
Exhaust Port Closing (EPC)	270°ATDC
Fuel	Amoco 91 RON gasoline
Fuel-injection pressure	540 kPa (gauge)
Coolant temperature	90°C

cylinder block, piston, rings, air-assist fuel-injection [6,7], ignition, and lubrication systems as the V6 engine. To provide optical access, the combustion chamber in the cylinder head is modified to a nearly rectangular shape, with flat quartz windows forming two orthogonal sides. A piezoelectric transducer mounted in the rear wall of the combustion chamber measures cylinder pressure as a function of engine crank angle (14-bit pressure digitization at 0.5° intervals), from which individual-cycle heat-release rates, fuel-mass burned, and so forth are evaluated.

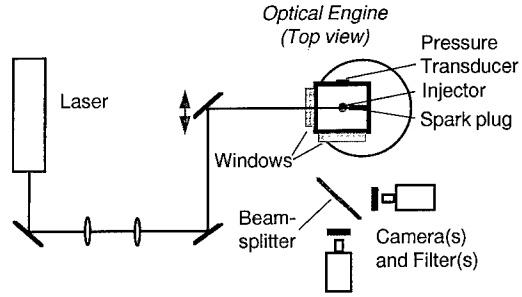

FIG. 2. Schematic diagram of laser-based imaging apparatus.

Exhaust-port pressure measurements are also used to determine exhaust mass flow rates (as described later). *Time-resolved* exhaust-HC concentrations are measured with a Cambustion HR200 fast-response flame-ionization detector (FID), whose probe is close mounted to minimize mixing and sampling response time (~2 ms here). *Time-averaged* HC concentrations are measured with a conventional heated-line FID located further downstream in the exhaust passage.

The engine is fueled with commercial gasoline and fired continuously; note that we do not alternate fired and (one or more) nonfired cycles as is sometimes done to reduce thermal and mechanical stresses. At the light and moderate loads studied here, the optical engine closely replicates the prototype engine's indicated work, fuel consumption, combustion stability, and time-averaged engine-out HC emissions [6,7]. To reduce window fouling, the engine was typically warmed up only 30–60 s before beginning optical measurements.

Optical Diagnostics

Figure 2 illustrates the imaging experiments. For fuel-LIF imaging, a thin (~0.5 mm) sheet of UV laser light (266 nm wavelength; ~10 ns pulse duration; ~40 mJ pulse energy) is formed from the output beam of a frequency-quadrupled Nd:YAG laser and is directed through the combustion chamber's side window. Fluorescence excited from components of commercial gasoline is collected through the front window, filtered to reject elastically scattered light and flame luminosity, and imaged onto a cooled, intensified slow-scan CCD camera (Princeton Instruments ICCD-576; 200-ns gate duration). The laser is fired (at most once per engine cycle) to acquire single-laser-shot or multishot averaged images at selected crank angles.

High-speed imaging experiments use a copper-vapor laser (CVL) (511 and 577 nm wavelengths; ~30 ns pulse duration; ~2 mJ pulse energy). Light from the CVL sheet that is Mie scattered by the liquid

fuel spray together with natural flame luminosity is directed by a reflective beam splitter to a pair of image-intensified Kodak EM1012 high-speed video cameras, one of which is sensitive to ultraviolet wavelengths. The CVL fires continuously at 4000 pulses/s (once per camera frame). Interference filters (~10 nm FWHM) isolate combustion luminosity from radical species, for example, OH (306 nm), CH (432 nm), and C_2 (516 nm). At 900 and 1500 rpm engine speeds, images can be recorded continuously every 1.35° and 2.25° crank angle over as many as 60 and 100 consecutive engine cycles, respectively.

Results

Fuel-Fluorescence Imaging

Figure 3a is a three-dimensional rendering of the fuel-vapor distribution in the combustion chamber 1° crank angle before firing the spark (i.e., 40°BTDC) at a 1500 rpm cruise condition. The raw LIF data were taken as a series of 11 two-dimensional tomographic images; each was a 16-shot average image recorded successively as the UV laser sheet was moved in 2.5-mm steps across the combustion chamber. Although LIF from liquid- and vapor-phase gasoline cannot be distinguished spectrally, Fig. 3a represents fuel vapor because Mie-scattering images, which respond only (and sensitively) to liquid, show that essentially no liquid fuel remains in the combustion chamber at this crank angle [6,7].

Although we were not able to determine absolute fuel concentrations or equivalence ratios of multicomponent gasoline from the measured fuel LIF intensities, we obtained approximate fuel/air equivalence ratios from the LIF data by assuming that (1) at fixed crank angle, the fluorescence intensity is proportional to the fuel concentration and (2) at spark time, the fuel-air equivalence ratio $\phi \approx 1$ near the spark gap for optimized engine operation [6]. Clearly, the fuel-air distribution exhibits steep gradients and encompasses a wide range of equivalence ratios. Figure 3b shows that, just before spark, ignitable mixture (estimated roughly as $0.6 < \phi < 1.6$) is present only within a thin shell.

Cyclic variations in engine performance, including misfires and partial burns, are a major practical problem in SI engine development. Single-shot two-dimensional fuel LIF imaging just before ignition reveals appreciable cyclic variation in the overall shape and location of the fuel cloud and significant cyclic variation in the fuel concentration near the spark gap. Figure 4 is a histogram of the fuel-LIF intensity in a small ($\approx 0.75 \times 1 \times 0.5$ mm) region just above the spark gap that was evaluated from 50 single-cycle two-dimensional images with the light sheet directed through the central plane that contains the fuel-injector and spark-plug centerlines. Relating LIF intensity to equivalence ratio as described previously shows that a few cycles were either too rich or too lean for successful ignition and rapid flame propagation, consistent with the incidence of misfires and partial burns determined from simultaneously acquired cylinder-pressure data [6].

The release of fuel trapped in the injector nozzle-exit crevice as the cylinder pressure falls has also been detected by LIF imaging, as illustrated in Fig. 5. Beginning typically about 50°ATDC, the emerging fuel forms a low-velocity plume that remains largely intact until fresh air from the transfer (intake) ports reaches the combustion chamber around 150°ATDC, by which time combustion has long since ceased (see next section). Most of the injector-crevice flow is vapor, although Mie-scattering images reveal liquid mist during part of the crevice-flow period [7]. Little of this crevice flow reacts because it is fuel-rich, it mixes very slowly with cylinder gases, and the cylinder gases are relatively cool and very dilute (residual fraction ~65% at light load).

High-Speed Spectrally Resolved Imaging

DISC-engine HC emissions typically are highest at the lightest loads when injection is delayed to increase charge stratification [1–4]. In the remainder of this paper, we discuss 900-rpm, near-idle operation with a narrower-spray injector that leads to 40% lower engine-out HCs on average (but also to more frequent misfires) than the injector used in the LIF experiments just described. Taken from a continuous 4000-frames/s video record of 60 consecutive engine cycles, Fig. 6 shows selected images of the fuel spray and spectrally resolved combustion luminosity during ignition and early flame growth for three consecutive cycles. Simultaneously acquired cylinder-pressure data and the mass-burning rate evaluated therefrom are shown in Fig. 7 together with individual-cycle exhaust-HC results.

Cycle 14 in Figs. 6 and 7 represents fairly typical combustion. Cycle 15 is a misfire: detectable flame luminosity disappears shortly after the end of the ≈1-ms spark discharge (spark fired at 30°BTDC), and only ≈2% of the injected fuel is consumed. Some of the unburned fuel remaining in the cylinder (see next section) burns during cycle 16, producing above-average combustion luminosity and heat release. The fuel sprays from the three cycles (illustrated at mid-injection) are all typical and offer no clear explanation for the flame extinction in cycle 15, but the near-absence of 520-nm radiation suggests that it is a lean misfire. (During early combustion, the 520-nm luminosity originates from both C_2-radical and continuum emission and hence indicates comparatively rich burning. CH-radical emission,

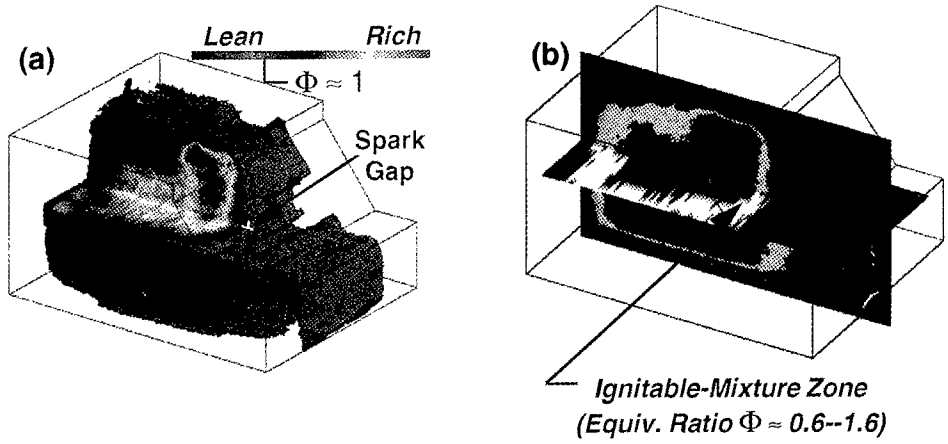

FIG. 3. Three-dimensional LIF images of average fuel distribution 1° before ignition at 1500 rpm cruise condition. (a) Isosurface rendering with top front quadrant removed to show interior. (b) Ignitable-mixture region rendered in yellow along two intersecting cutting planes that pass through the spark gap.

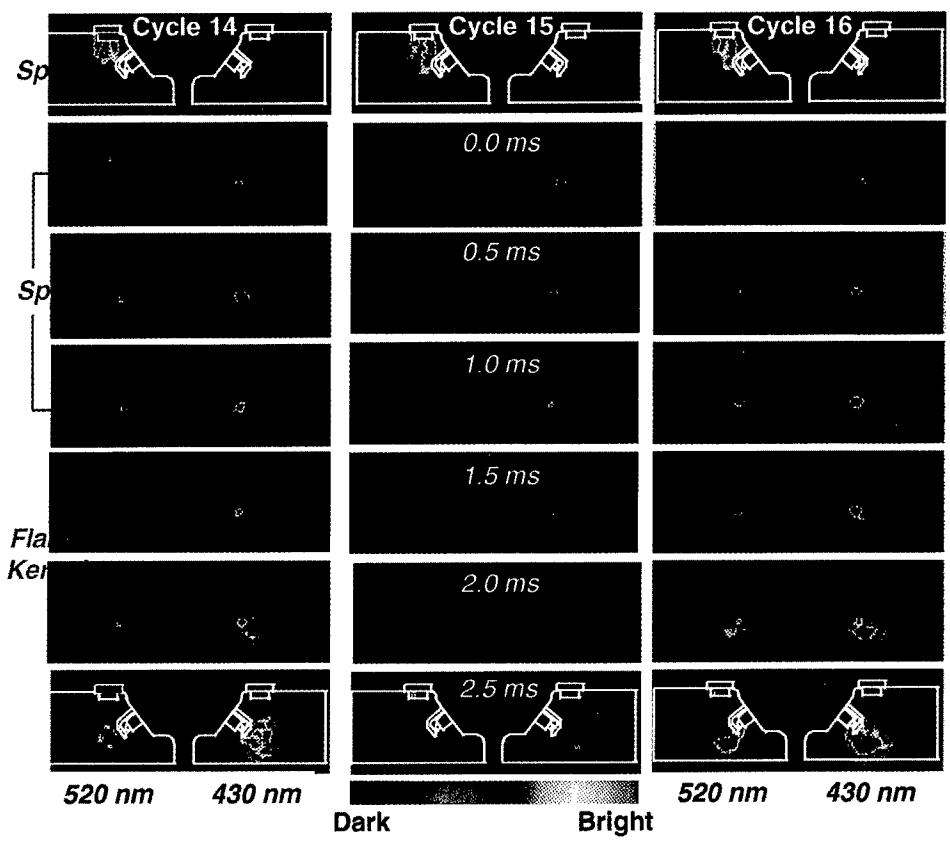

FIG. 6. Spectrally resolved dual-camera images from three consecutive engine cycles (narrow-spray injector; 900 rpm light-load test condition). The spray images at the top of each column are formed by Mie-scattered 511-nm laser light that passes through the 520-nm filter. Combustion-luminosity images begin at spark (denoted time 0.0 ms) and continue at 0.5-ms (2.7° crank-angle) intervals. Detected light intensity is depicted using the rainbow false-color scale shown at the bottom of the figure.

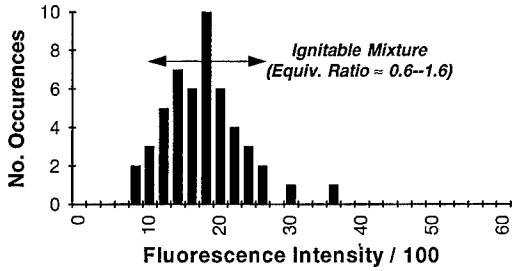

FIG. 4. Histogram of fuel LIF intensity within small region immediately above spark gap.

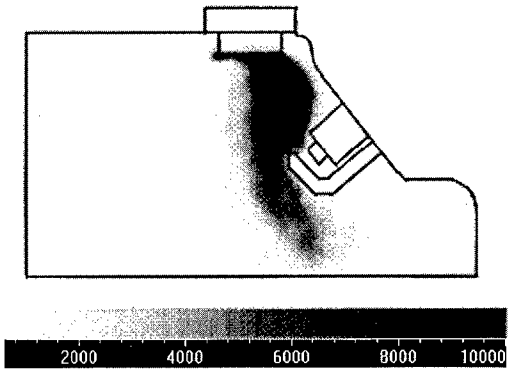

FIG. 5. LIF image of fuel emerging from injector nozzle-exit crevice at 150°ATDC.

associated primarily with $\phi \approx 1$ burning, contributes significantly to the 430-nm luminosity recorded.)

The mass-burning-rate curves in Fig. 7 for cycles 14 and 16 display an initial rapid partially premixed combustion phase during which ≈40% of the fuel is consumed, a transition phase (≈40–60% mass burned), and finally a slow mixing-limited or diffusion-burning phase during which the burning rate decreases approximately linearly with the amount of unburned fuel remaining in the cylinder [4,6,7]. Detectable heat release lasts until just before the piston uncovers the top of the exhaust port (see Fig. 1) at 90°ATDC.

Individual-Cycle HC Emissions Measurements

To interpret the fast-FID data for HC concentration or mole fraction [HC(θ)] versus crank angle θ (e.g., Fig. 7) and to quantify the HC mass emitted each cycle, we have evaluated the exhaust mass flow rate $dM_{exh}(\theta)/dt$ *for each cycle* from the measured cylinder and exhaust pressures $P_{cyl}(\theta)$ and $P_{exh}(\theta)$ by approximating the process as spatially uniform, quasi-steady flow through an orifice—the exhaust port—whose effective flow area $A_{eff}(\theta)$ was determined in separate steady-flow measurements. The individual-cycle HC concentration and $dM_{exh}(\theta)/dt$ are then converted to HC mass flow rate $dM_{HC}(\theta)/dt$ (Fig. 7) using effective molecular weights of the fuel and exhaust gas (the latter evaluated from

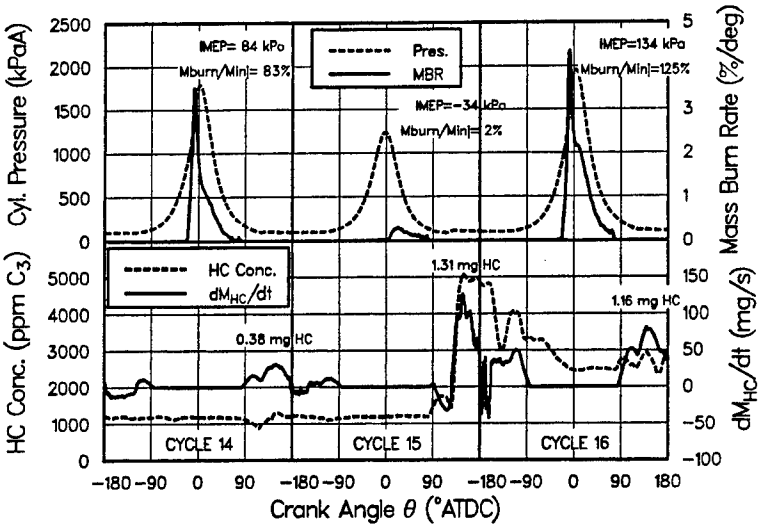

FIG. 7. Heat-release and fast-HC-sampling results for the same three engine cycles as in Fig. 6. (*Upper*) Cylinder pressure (dashed line) and mass burning rate (solid line). (*Lower*) HC concentration (dashed line) and HC exhaust mass flow rate dM_{HC}/dt (solid line). Note that the HC concentration data have been shifted in crank angle to account for the fast-FID sampling delay. Also labeled for each engine cycle are the indicated work produced (expressed as indicated mean effective pressure [IMEP]), the total mass of fuel burned relative to the average mass of fuel injected, and the total HC mass that leaves the cylinder during the exhaust event.

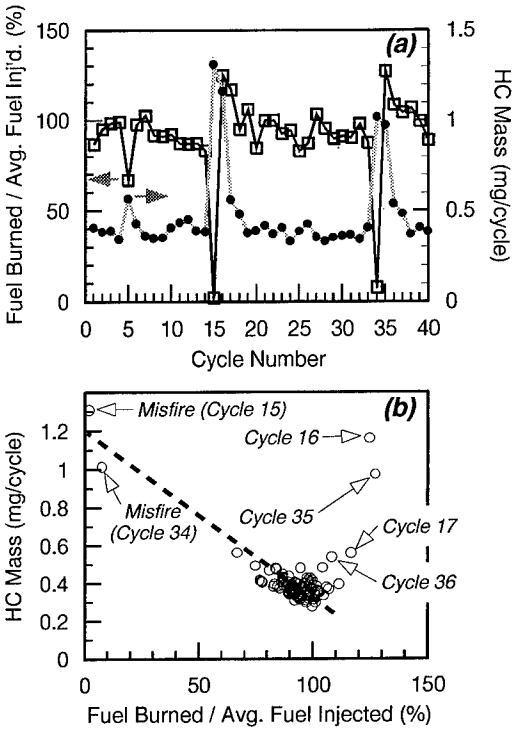

FIG. 8. Correlation between individual-cycle heat-release and exhaust-HC-mass data (900 RPM). For clarity, the upper graph includes data from only the first 40 of the 100 engine cycles shown in the lower graph.

emissions data). Integrating $dM_{HC}(\theta)/dt$ from exhaust-port opening (90°ATDC) to exhaust-port closing (90°BTDC, i.e., −90°ATDC in the next cycle) yields the total exhaust-HC mass for each cycle (labeled in Fig. 7). Ensemble-averaged, mass-flow-weighted HC emissions evaluated thus from the fast-FID data agree well with simultaneously acquired time-averaged HC data from the conventional FID over a wide range of HC levels and operating conditions (0–30% misfires).

For normal cycles (e.g., cycle 14 in Fig. 7), the HC mass flow rate $dM_{HC}(\theta)/dt$ exhibits four important features: (1) the cylinder blowdown peak as the piston uncovers the top of the exhaust port (90°ATDC); (2) a second, higher peak as the transfer (intake) ports are uncovered (120°ATDC) and fresh air flows into the cylinder; (3) backflow from the exhaust into the cylinder around BDC; and (4) a final outflow peak as the rising piston covers first the transfer ports and finally the exhaust port (120°–90°BTDC of the following cycle). Misfire cycles (e.g., cycle 15) exhibit not only elevated HC concentration and net HC mass outflow but also initial backflow instead of a normal cylinder blowdown. When the exhaust port closes after a misfire, the fast-FID HC concentration declines slowly because of mixing within the exhaust system.

Figure 8a shows that the engine's high residual fraction (~65% at light load) leads to a strong coupling between cycles: a misfire increases HCs for about three cycles. Most of the unburned fuel remains in the cylinder, where some burns during the next cycle (cycles 16 and 35 in Fig. 8 consume ~25% more fuel than the average quantity injected). Much of the fuel retained after a misfire escapes combustion, however, as implied by the fact that the cycle just after a misfire has HCs comparable to the misfire cycle itself. Note that, provided outliers associated with such cycles (e.g., cycles 16, 17, 35, and 36) are excluded, the HC mass falls off linearly with the fuel mass burned (Fig. 8b).

Discussion and Conclusions

Coupling in-cylinder optical diagnostics (two- and three-dimensional fuel LIF imaging; 4000-frames/s video imaging of the liquid fuel spray, and spectrally resolved combustion luminosity) with high-speed probe measurements (individual-cycle cylinder-pressure and fast-FID exhaust-HC sampling) has provided the most direct and quantitative characterization available of the processes that lead to exhaust-HC emissions from a stratified-charge SI engine. The results imply that the major HC sources (and approaches to minimizing HC emissions must therefore) differ significantly between two-stroke stratified-charge and conventional premixed-charge four-stroke SI engines.

Misfires and partial burns, associated with cyclic variation in local equivalence ratio at ignition, contribute significantly to HC emissions, but only ~25% of the injected fuel appears in the exhaust immediately after a misfire because of the reduced exhaust mass flow combined with the two-stroke engine's high residual fraction. The top-ring-land crevice is not a significant light-load HC source in this DISC engine because charge stratification ensures that gases trapped in the crevice contain relatively little fuel. The fast-FID data support this because the first gas to leave the cylinder (e.g., 85°–120°ATDC in cycle 14 of Fig. 7b) comes from near the top-ring-land crevice and typically has lower HC concentration than that observed during the main scavenging phase (120°ATDC–120°BTDC).

Most of the cylinder contents and 60–70% of the total HC mass are exhausted during the main scavenging phase when the exhaust mass flow and HC concentration are both high. These HC emissions result primarily from four sources of incomplete combustion: (1) misfires and partial burns, as discussed previously; (2) injected fuel that overmixes, forming regions of mixture that are too lean to burn (e.g., outside the ignitable-mixture zone in Fig. 3b);

(3) fuel that outgases from injector crevices (Fig. 5); and (4) fuel-rich pockets that mix and react too slowly to burn completely [6,7]. The relative importance of these four sources has not been quantified individually and is expected to vary with specific engine design and operating conditions.

REFERENCES

1. Wood, C. D., SAE Paper No. 780341, 1978.
2. Lancaster, D. R., I. Mech. E. Paper C397-80, 1980.
3. Giovanetti, A. J., Ekchian, J. A., Heywood, J. B., and Fort, E. F., SAE Paper No. 830587, 1983.
4. Frank R. M. and Heywood, J. B., SAE Paper No. 892058, 1989.
5. Cheng, W. K., Hamrin, D., Heywood, J. B., Hochgreb, S., Min, K., and Norris, M., SAE Paper No. 932708, 1993.
6. Fansler, T. D., French, D. T., and Drake, M. C., SAE Paper No. 950110, 1995.
7. Drake, M. C., Fansler, T. D., and French, D. T., SAE Paper No. 952454, 1995.
8. Collings, N., SAE Paper No. 880517, 1988.

COMMENTS

Norman Chigier, Carnegie Mellon University, USA. On the basis of your measurements, can you prescribe the ideal spray characteristics in terms of drop size, velocity, number density and spray angle for different operating conditions?

Author's Reply. The detailed in-cylinder measurements for this engine as described in this and previous papers [6,7] illustrate the importance of precise control of the fuel distribution, particularly at the time of spark for light and medium load conditions. For stable ignition, the equivalence ratio at the spark gap must be between roughly 0.6 and 1.6. However, to minimize HC emissions, fuel in regions where the equivalence ratio is <0.6 must be minimized because it is too lean to burn, and fuel in regions where the equivalence ratio is >1.6 must mix with air fast enough to burn before the cylinder pressure drops too much and reactions are quenched. Also, the injector must work over a wide range of engine speed and load conditions, including heavy load where one wants homogeneous stoichiometric operation for maximum power. What are the ideal spray characteristics which fit these criteria? Although the answer will always depend in significant part on design-specific details (e.g., combustion-chamber shape, location of the spark plug, etc.), four desirable characteristics emerge: (1) high repeatability, (2) good atomization even for fuel injected into elevated cylinder pressure close to TDC, (3) a compact spray cone angle with steep gradients at the periphery of the spray cloud for stratified operation, and (4) small drop sizes to enhance vaporization and mixing. Advanced injection systems, e.g., air-assist injection, have led to new development efforts in two-stroke DI engines for automotive, marine, and motorcycle applications, and several companies are also pursuing four-stroke DI engine development.

•

A. Kowalewicz, Radom Technical University, Poland. What was fuel/air ratio, especially for stratified charge operation of the engine? What was the source of fuel which was supplied to the engine for cycles that apparently burned more than 100% of the fuel injected, as shown in the top graph of Figure 8?

Author's Reply. During light and moderate load operation, the engine runs at a very lean overall equivalence ratio. Two conditions were described in the paper: a light-load/near-idle condition at 900 rpm, where the average trapped equivalence ratio is 0.44 and a moderate-load/cruise condition at 1500 rpm, where the trapped equivalence ratio is 0.69. More details regarding the engine operating conditions can be found in reference 7.

Under the conditions described in our paper, this engine operates at a very high residual fraction of ~ 0.65 (i.e., nearly two thirds of the cylinder contents are left over from the previous cycle). Thus, following a misfire (i.e., cycles 15 and 34 in the example shown in Figure 8), subsequent cycles contain a lot of unburned fuel from the residual contents in addition to the fuel injected during the cycle. A significant fraction of the unburned fuel in the residual is burned in the 3 cycles following any misfire, so the total fuel burned during these cycles can be higher than the fuel injected.

Twenty-Sixth Symposium (International) on Combustion/The Combustion Institute, 1996/pp. 2589–2596

POLARIZATION SEPARATED SPATIALLY RESOLVED SINGLE LASER SHOT MULTISPECIES ANALYSIS IN THE COMBUSTION CHAMBER OF A REALISTIC SI ENGINE WITH A TUNABLE KrF EXCIMER LASER

MICHAEL KNAPP, ANDREAS LUCZAK AND VOLKER BEUSHAUSEN
Laser Laboratorium Göttingen
Hans-Adolf-Krebs Weg 1
37077 Göttingen, Germany

WERNER HENTSCHEL AND PETER MANZ
VOLKSWAGEN AG
38436 Wolfsburg, Germany

PETER ANDRESEN
University of Bielefeld
Universitätsstraße 25
33615 Bielefeld, Germany

For precise spontaneous Raman scattering measurements of species densities in hydrocarbon fueled combustion, it is vital to separate the Raman scattered light from interfering (broadband) fluorescence light. This paper describes the application of a detection scheme for separated and simultaneous acquisition of both polarization components of the laser-induced emissions (i.e., perpendicular and parallel to the polarization of the incident laser light). Using highly polarized incident laser light, the Raman scattered light maintains almost this polarization, whereas broadband fluorescence and most laser-induced predissociation fluorescence (LIPF) emissions are strongly depolarized. Therefore, it is possible to extract the Raman signal by subtracting the signals separately obtained for the two polarization directions (i.e., vertical polarized light consists of fluorescence and parallel polarized light consists of fluorescence and Raman scattering). This detection scheme is used to acquire high-precision single laser shot multispecies, polarization separated, and crank angle–resolved spectra in the combustion chamber of a firing spark-ignition (SI) engine.

In addition, a combinative approach for cycle-resolved mixture composition and exhaust gas analysis is demonstrated. In this approach, the air-fuel ratio before ignition and the NO LIF intensity in the burned gas are measured within the same engine cycle using the different polarization properties of Raman scattered and fluorescence light.

The measurements are carried out in a standard production, four-cylinder SI engine that is modified only slightly to allow optical access. The engine data have not been changed by these modifications (e.g., the compression ratio is maintained at 10).

Introduction

Spontaneous Raman scattering is a major spatially precise laser diagnostic technique for species and temperature measurements in fluid dynamic and combustion processes [1]. The advent of powerful lasers operating in the ultraviolet spectral region allows one to take advantage of the scaling of the scattering cross section with the fourth power of the frequency and of additional resonant enhancement because of the vicinity of molecular absorption bands [2,3]. For measurements in hydrocarbon-fueled combustion, it is vital to distinguish the desired Raman signals from interfering laser-induced (broadband) fluorescence. Signal separation using the different polarization properties of LIF and Raman scattered light has been suggested previously by other authors [4,5,6].

The application of polarization analysis for the determination of interfering (broadband) fluorescence from combustion intermediates in the combustion chamber of a firing spark-ignition engine and in the spray flame of an oil-burning furnace has been demonstrated by Grünefeld et al. [7]. They recorded two subsequent images. One image was taken with the electric vector of the incident laser beam perpen-

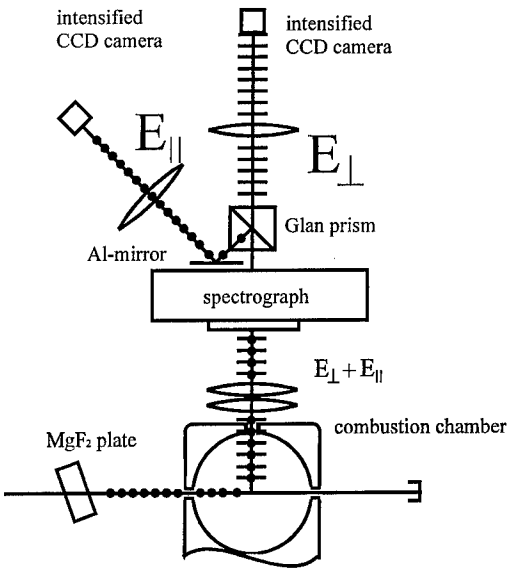

FIG. 1. Top view of the optical setup. The Glan prism is positioned in the focal plane of the imaging spectrograph. Two intensified CCD cameras acquire the light with different polarization direction. The electric field vector is sketched as a dot or as a line, dependent on its orientation.

dicular to the observation axis. In this case, they obtained maximum Raman signal and the unpolarized broadband fluorescence background signal. Then a second image was taken with the electric vector of the laser light rotated by 90°, that is, with the electric vector parallel to the observation axis. For this alignment, the unpolarized fluorescence background and the depolarized portion of the Raman signal were acquired. Both images had to be taken one after the other in subsequent engine cycles. Consequently, the technique is not suited to single shot measurements. Nevertheless, for measurements in stationary flames, this technique has offered high measurement precision for averaged measurements as described by Luczak et al. [8]. An approach for simultaneous detection of both polarization directions is described by Brockhinke et al. [9]. They used an experimental setup involving two optical-multichannel analyzer detection units. The detection axis of both units were placed at right angles to each other and in a plane perpendicular to the incident laser beam. Unfortunately, this configuration is not suited for engine applications with limited optical access. Barat et al. [10] described flame thermometry via Rayleigh scattering excited by highly polarized light at 532 nm. They used a simple polarizing beam splitter to separate both polarization directions, one composed of the desired Rayleigh scattering, background glare, and black body radiation and the other the sum of background glare and black body radiation. Both composite signals were detected by photomultipliers and subtracted from each other to extract the pure Rayleigh signal.

For the measurements described in this paper, the different polarization directions are separated in the focal plane of a spectrograph, thus making possible single laser shot and multispecies measurements in a combustion device with limited optical access. This detection scheme will be described in detail in the section Optical Setup. Each polarization component is imaged separately onto two intensified CCD cameras. For pure polarization analysis, the detection is possible with only one camera, but we record two independent spectra in one single engine cycle. For example, measurements are carried out in which the laser is fired twice. In this case, the tunable KrF excimer laser is tuned to an NO transition within the $A^2\Sigma^+ \leftarrow X^2\Pi$, (0, 2) γ-band system. The Raman scattered light with the polarization direction parallel to the electric vector of the incident laser light from the first laser shot before ignition is used to characterize the charge (i.e., to determine the air-fuel ratio and residual water content). The second laser shot is triggered within the combustion stroke of the same cycle and excites NO fluorescence, which is detected with the second camera system recording light polarized perpendicular to the polarization direction of the incident laser light.

Experimental

Test Engine

The investigations reported here are carried out in one cylinder of a standard production, four-stroke, four-cylinder, in-line SI-engine supplied by VOLKSWAGEN AG. The engine is modified to facilitate optical access by placing a spacer plate between cylinder head gasket and crank case. The spacer plate has three cylinder-like orifices, as outlined in Fig. 1. They are the housings of quartz windows with a diameter of 10 mm. The pistons are extended to maintain the compression ratio at 10. In our case, we attached great importance to keeping the engine design is as close as possible to a production line engine. There is no piston window, and we accepted the blocking of the windows in the spacer plate by the piston near top dead center (TDC). The measuring cylinder is also equipped with a pressure transducer. The engine is mounted to a motor/dynamometer combination that allows flexible operation at different speed and load settings. *Iso*-octane (C_8H_{18}) is used as fuel because it does not absorb the ultraviolet radiation of the KrF excimer laser, the Raman scattered light, or LIF.

Optical Setup

Figure 1 shows the principal optical setup. The light source is a tunable excimer laser (EMG 160

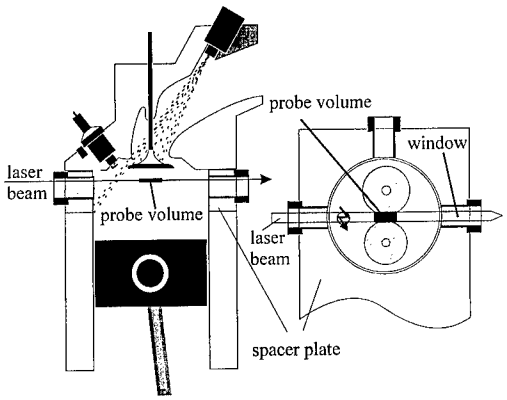

FIG. 2. Schematic of the combustion chamber geometry and optical configuration. The location of the probe volume with respect to the combustion chamber geometry and the laser beam orientation are shown.

MSC, Lambda Physik) operated with a KrF gas filling. Its optical configuration is altered according to the description by Grünefeld [7]. The laser light is formed with a single lens (f = 2000 mm) and directed through the combustion chamber. The cross section of the laser beam forming the measuring volume is approximately 4 mm × 1 mm. The location of the measuring volume with respect to the combustion chamber geometry is sketched in Fig. 2. The orientation of the electric field vector of the laser light crossing the combustion chamber can be rotated by tilting a birefringent MgF_2 plate in the beam path using a stepper motor. The detection axis is perpendicular to the laser beam. A section of the laser beam 15 mm in length is imaged onto the entrance slit of a low-resolution flat field spectrograph by a combination of two spherical lenses providing 1:1 imaging.

The spectrometer (f# 3.8, 275 mm focal length, Czerny–Turner type with in-line optical path) has high output and good imaging qualities. In the spectral plane of the spectrograph, a Glan prism (aperture 20 mm) is mounted to separate both polarization components. A detailed description of the polarization separation will be given in the following section. One beam leaves the prism without deflection, whereas the other is totally reflected internally and leaves the prism at the side. An aluminum mirror is used to reflect the latter in the direction of the detection optics. Two spherical lenses, one for each polarization component, collect the polarization separated and spectrally dispersed light and refocus it onto two separate Peltier-cooled intensified CCD cameras. The CCD cameras have a dynamic range of 12 bit and a chip size of 384 × 286 pixel. The image data and simultaneously acquired analog data (pressure traces) are transferred to a multiplexer that is linked to a single PC. Laser trigger and camera actions are all synchronized with the engine crankshaft, making possible the acquisition of spectra at defined crank angles.

Choice of the Polarization Separating Component

Because of limited optical access, and to minimize the instrumentation, we separate the polarization components in the focal plane of the spectrograph. In this case, there are some special requirements for the polarization separating device. First, high output in the spectral range of interest for both polarization directions is a must. This means the analyzer must have high transmission, low reflection, and low scattering and must not vignette the beams in the range of 248 nm (Rayleigh) to 273 nm (H_2O Raman). In principle, prism polarizers made of calcite with an air spacing and large aperture are useful analyzers for this application. On the one hand, the absorption coefficient for calcite rises for wavelengths smaller than 300 nm. The transmission of unpolarized light through a Glan prism such as ours at 300 nm is about 45%, whereas it drops to about 30% at 248 nm. This suggests the use of other materials such as crystalline quartz or magnesium fluoride, which can transmit wavelengths as short as 160 nm and 120 nm, respectively [11].

On the other hand, the birefringence of calcite is one order of magnitude larger than for those materials at 250 nm. A small birefringence makes the design of the polarizing prism difficult, since the angle of incidence for which the polarization directions are still separated is determined by the value of the birefringence. The prisms are generally made in two parts. One ray (usually the extraordinary ray) passes through the entire prism while the other ray is totally reflected at the air spacer because of the difference in the refractive index. Thus, the greater the birefringence, the greater the usable angular polarized field.

A large angle of acceptance is vital for our application, as illustrated by the following calculation. With a nominal reciprocal linear dispersion of 3 nm/mm of our spectrograph, a spectral interval of 25 nm spreads over a distance of Δx = 8 mm in the focal plane. Since to $\Delta x \approx f_{\text{spectrograph}} \times \Delta\theta$, the angular spread of the system ($\Delta\theta$) can be calculated. With $f_{\text{spectrograph}}$ = 275 mm and Δx = 8 mm, the angular spread is $\Delta\theta$ = 1.6°, which can be covered by a Glan (air-spaced Glan-Thompson prism) made of calcite. Additionally, the f# of the spectrometer has to be taken into account since it determines the angle of aperture at each wavelength. For an f# 3.8, this angle is 15°. In principle, this angle cannot be covered by the Glan prism, which offers a usable angular polarized field symmetrical about the prism axis of about 12° (at 215 nm). However, it turned out that because of the confocal parameter of our imaging system, it is possible to place the Glan prism directly in the focal plane of the spectrograph without loss of po-

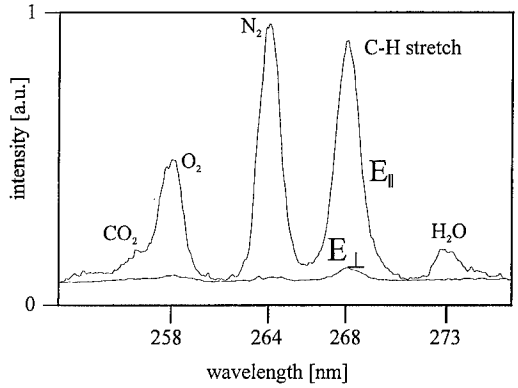

FIG. 3. Spectra taken at 690°KW in the combustion chamber of a firing SI engine. Both spectra are recorded simultaneously and are averaged over 10 engine cycles. One spectrum shows the desired Raman scattering with the electric vector parallel to the polarization direction of the incident laser light. The other spectrum shows the depolarized portion of the Raman emissions.

larization separation quality. If the prism is cemented together (glycerine or mineral oil are used in the ultraviolet), the field of view could be increased to 30° [12]. In this case, additional losses caused by stronger absorption by glycerine or mineral oil need to be taken into account.

Calibration and Data Analysis

For calibration of the different overall sensitivities of both optical paths (different cameras, polarization-dependent reflectance of the grating), unpolarized light of a mercury pen lamp is used. The lamp is placed in the combustion chamber orientated parallel to the spectrometer entrance slit and is operated to obtain high output at the 253.4 nm line. All spectra shown in the following are corrected for the different overall sensitivity of the corresponding optical path.

Absolute calibration of the frequency-dependent transmission of the detection system is not necessary since the quantities of interest, including the equivalence air-fuel ratio and the residual water content, can be determined from the ratio of two Raman signals as described later. To characterize the in-cylinder mixture, the laser is fired before ignition. Figure 3 shows two spectra averaged over 10 cycles acquired in the compression stroke at 690° crank angle (CA), that is, 30°CA before combustion TDC. The engine was operated at low speed and part load (1500 rpm, manifold pressure 53 kPa [40 Nm load], stoichiometric air-fuel ratio). One spectrum gives the desired polarized Raman signals and the broadband contribution, whereas the other shows the depolarized portion of the Raman signals and the broadband portion. Subtracting the latter from the first, the broadband portion can be removed. However, the background fluorescence shows no pronounced curvature; therefore, it is possible to extract the Raman signals in principle by interpolating the background emission from both sides of the Raman lines. In this spectroscopically clean precombustion environment, our technique is more suited for temperature measurements via Rayleigh scattering since polarization analysis can be used to monitor contributions of Mie and surface scattered light, while simultaneously acquired multispecies Raman spectra can be used to account for variations in mixture fractions. In our case, Mie and surface scattered light at the laser wavelength do not interfere with the spontaneous Raman scattering that appears at a different wavelength.

Five different Raman lines can be identified in Fig. 3. These lines correspond to the five important species that occur in the charge before ignition: CO_2, O_2, N_2, fuel (here C_8H_{18}), and H_2O. The intensity $I(i)$ of each line is proportional to the density ρ_i of the corresponding species (i = CO_2, O_2, N_2, fuel, H_2O) and also to the single-shot laser energy E, to the Raman scattering cross section σ_i of species i, and to the overall detection efficiency C: $I(i) = \rho_i E \sigma_i C$. Laser pulse energy and detection efficiency vary from cycle to cycle because of shot-to-shot laser power fluctuations and decreasing transparency of the combustion chamber windows. However, the quantities of interest, such as the equivalence air-fuel ratio or residual water content, can be calculated as ratios of two densities, as described by Grünefeld [7]. The air-fuel ratio is proportional to the ratio of I (O_2) and I (fuel), and the water content is proportional to the ratio of I (H_2O) and I (N_2). In this case, variations of E and C play no role and measurement precision is determined essentially by the photon statistical noise (shot noise) [1]. The single-shot measuring precisions at 690°KW for these conditions, according to photon statistical noise, are N_2 and fuel 2%, O_2 3%, and H_2O 10%.

It should be noted that because of accumulation of deposits of oil and partially burned hydrocarbons on the windows, their frequency-dependent transmission may fluctuate from cycle to cycle. Therefore, transmission spectra of the windows were recorded. The ratio of the window transmission at 258 nm (spectral position of O_2 Raman scattering) to the transmission at 278 nm (spectral position of fuel Raman scattering) drops by about 1% during 15 min engine operation at part load. This introduces an additional error of the same magnitude.

Furthermore, the quartz windows could be susceptible to stress-induced birefringence. However, it seems that this effect plays no role in our case since

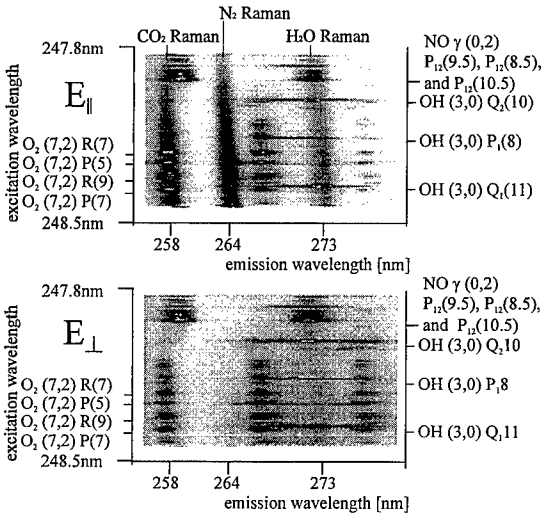

FIG. 4. Simultaneously acquired excitation emission spectra. The spectra were acquired at 60° crank angle after combustion TDC. (a) Emissions with the electric vector parallel to the polarization direction of the incident laser light: Raman scattered light of the majority species (CO_2, N_2, H_2O) in the burned gas and laser-induced fluorescence of O_2, OH, and NO. (b) Emissions with the electric vector perpendicular to the direction of polarization of the incident laser light: laser-induced fluorescence of O_2, OH, and NO.

we didn't observe pressure- and temperature-dependent changes in the known polarization ratio of N_2.

The absolute calibration of the relative ratios is accomplished by measurements at certain engine operating conditions. For example, measurements while an engine is motored allow calibration of the water content since the mole fraction of water in ambient air is known; measurements before ignition in the fired case allow calibration of the cycle-averaged ratio of oxygen and fuel according to the cycle-averaged equivalence air-fuel ratio measured by a λ probe or determined from exhaust gas analysis.

To characterize the combustion environment, we started by recording excitation-emission spectra. The principal acquisition strategy is described elsewhere [13]. Figures 4a and 4b show excitation-emission spectra recorded simultaneously in the combustion stroke 60° CA after TDC. The engine is operated at 1500 rpm with a stoichiometric air-fuel mixture and a manifold pressure of 53 kPa (part load 40 Nm). The laser frequency (y axis) is scanned from 247.8 nm to 248.5 nm. Scattered and fluorescence light, with the electric vector parallel to the electric vector of the polarized incident laser light, are shown in Fig. 4a. Ideal combustion of a stoichiometric *iso*-octane–air mixture results in an exhaust gas composition of 13% CO_2, 14% H_2O, and 73% N_2. The Raman scattering of these majority species and fluorescence light of O_2, OH, and NO can be observed. Some absorption lines of the vibrational transition (3, 0) in the $A^2\Sigma^+ \leftarrow X^2\Pi$ band of OH, absorption lines of the O_2 Schumann–Runge bands $B^3\Sigma^- \leftarrow X^3\Sigma^-$, and rovibronic transitions in the NO ($A^2\Sigma^+ \leftarrow X^2\Pi$) γ (0, 2) band are accessible with the KrF excimer laser.

The line assignments of some prominent lines are given in Figs. 4a and 4b. At 264 nm (excitation with 248.5-nm light), the N_2 Raman line shows up as a nearly vertical line in Fig. 4a. The intensity of the Raman scattering is fading when the excitation frequency approaches the high end of the tuning range. By readjusting the expansion prisms and the grating of the excitation laser, we obtain a pulse energy of about 150 mJ at the absorption wavelength of the P branch bandhead of the NO_γ (0, 2) band at 247.94 nm (40,332 cm^{-1}), which is 70% of the maximum available pulse energy in the center of the tuning range.

Figure 4b shows the spectra acquired simultaneously with the second camera system, which captures the light with the electric vector perpendicular to the polarization direction of the incident laser light. In this case, no Raman lines are visible because of their small depolarization; however, the strongly depolarized fluorescence signals of O_2, OH, and NO are recorded.

The feasibility of NO LIF measurements with the unshifted wavelength of a KrF excimer laser for a qualitative analysis of NO formation in the combustion chamber of an SI engine has been described in a previous paper [18]. It offers several advantages compared to detection schemes of NO at 193 nm or 226 nm. Radiation at 248 nm is less absorbed in hydrocarbon combustion environment than radiation at 193 nm or 226 nm. To avoid line interferences by O_2 and OH fluorescence, we excite NO at 247.94 nm (40,322 cm^{-1}). At this frequency, the rotational transitions P_{12} (8.5), P_{12} (9.5), and P_{12} (10.5) of the violet-shaded P branch bandhead of the NO_γ (0, 2) band are excited simultaneously.

These two spectra demonstrate the potential of the technique. First, it is possible to record both polarization components separately and to analyze spontaneous Raman scattering and (broadband) fluorescence. Especially in hydrocarbon-fueled combustion environments with the well-known strongly interfering broadband fluorescence, this is a great advantage. Second, using two cameras, the two polarization separated spectra can be recorded time resolved, for example, within one engine stroke.

It should be mentioned that the separation of Raman scattering and LIF holds only for broadband fluorescence. For example, Doherty and Crosley [14] reported on a significant degree of polarization in LIF in OH ($A^2\Sigma^+ \leftarrow X^2\Pi$ system) in the burned gases of a flame at atmospheric pressure. A more

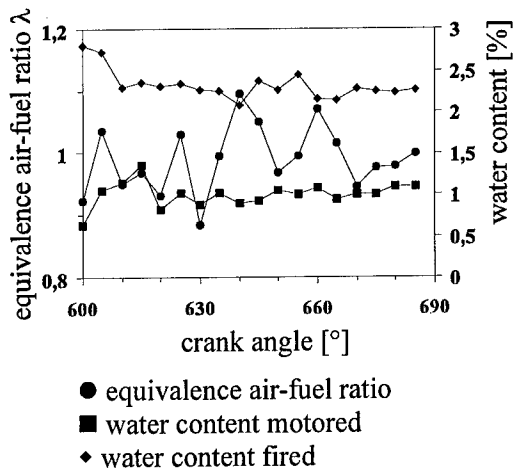

FIG. 5. Equivalence air-fuel ratio and water content (for motored and fired engine operation) as a function of crank angle. Each data point is extracted from an average of 10 laser shots accumulated on chip.

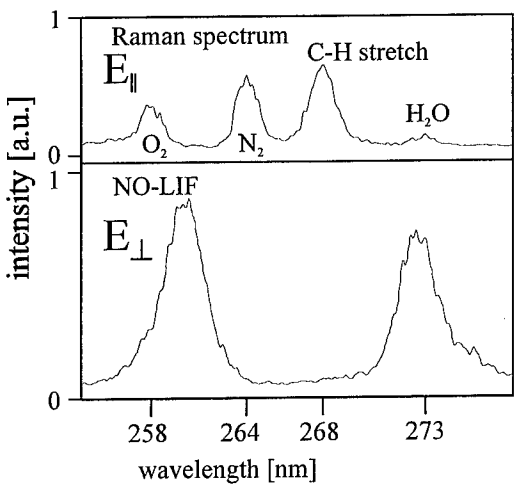

FIG. 6. Single laser shot spectra before ignition and 85° crank angle after ignition in the burned gases of the same cycle. The first spectrum is acquired when the laser is fired at 690° crank angle and contains the Raman scattering with the electric vector parallel to the polarization direction of the laser light. The second spectrum is acquired 10 ms (120° crank angle) later (i.e., in the combustion stroke) and shows NO LIF emissions.

general treatment of the theory of polarization of the radiation of diatomic molecules is given by Feofilov [15]. The polarization properties of NO, OH, and O_2 fluorescence excited with a tunable KrF excimer laser in different atmospheric flames have been studied by Frodermann [16].

Engine Results

As an example for mixture composition analysis, Fig. 5 presents the cycle-averaged equivalence air-fuel ratio and water content (for fired and motored engine operation) as a function of crank angle during compression stroke. Every data point is calculated as described previously from spectra acquired by integrating on chip over 10 subsequent laser shots at each crank angle. This acquisition strategy introduces an additional error because the signals are averaged before calculating their ratio [17]. In addition, it is not possible to make a statement on the fluctuations of the quantity of interest. However, Fig. 5 illustrates that no charge stratification is visible within the measuring volume. Before ignition (ignition takes place at 695°CA), the averaged equivalence air-fuel ratio (λ) reaches its desired value of $\lambda = 1.00$.

In addition, measurements are carried out where the laser is fired twice in a single engine cycle. First, it is fired before ignition at 690°CA to record the Raman scattering for mixture composition analysis. Second, it is fired during the combustion stroke of the same cycle at 90°CA after combustion TDC to excite NO fluorescence. Because of the flow in the cylinder, the measurement of NO as combustion product does not correspond to the initial charge at this point.

For this combinative approach, we chose an engine operating condition with higher speed and load (2000 rpm, manifold pressure 88 kPa [80 Nm load], $\lambda = 1.00$). For this engine speed, the laser has to be capable of firing at 100 Hz (120°CA equals 10 ms) with constant pulse energy. Figure 6 shows a pair of single-shot spectra taken at 690°CA and 90°CA within one engine cycle with the laser tuned to the NO resonances at 247.94 nm (40,332 cm^{-1}). One spectrum with the electric vector parallel to the polarization direction of the incident laser light contains the Raman signals desired for mixture composition analysis, that is, CO_2, O_2, N_2, C—H, and H_2O at 690°CA, and the other shows the depolarized emission spectrum of NO excited 120°CA later. Pairs of polarization separated single–laser-shot spectra of this type are acquired in 150 subsequent engine cycles. Figure 7 shows the NO LIF signal as a function of equivalence air-fuel ratio that was detected in the same cycle before ignition using Raman scattering. According to Fig. 7, the average air-fuel ratio is $\lambda = 1.00 \pm 0.09$.

The measured data points do not correspond to the well-known variations of exhaust NO concentration with air-fuel ratio. This is understandable because the in-cylinder gas flow transports the mixture portion analyzed with the first laser shot away from the measuring volume, and the burned gas analyzed with the second pulse is not fixed in space either.

The observation of any correlations would be

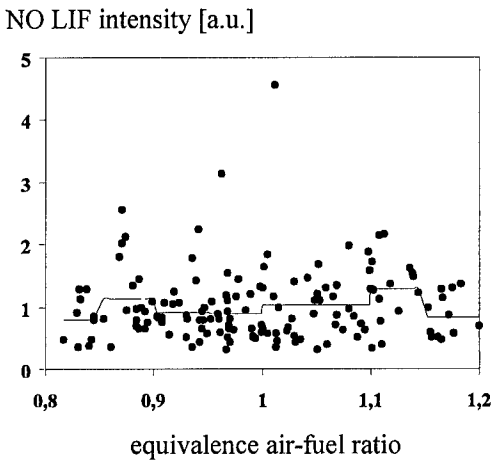

FIG. 7. NO LIF intensity as a function of equivalence air-fuel ratio. The data points correspond to the simultaneously measured air-fuel ratio and NO LIF in 150 subsequent engine cycles. Also shown is the averaged NO LIF intensity as a function of equivalence air-fuel ratio.

more likely if the measuring volume was a greater fraction of the combustion chamber volume. For the results presented here, the measuring volume is 15 mm × 4 mm × 1 mm = 60 mm^3. This corresponds to a fraction of approximately 0.1% of the combustion chamber volume at 690°CA. Figure 7 also shows the averaged NO LIF intensity as a function of air-fuel ratio, for example, the first section of the line gives the averaged NO LIF intensity in the interval from $0.8 < \lambda < 0.85$.

Summary and Conclusions

A technique is presented for polarization separated, spatially resolved, single–laser-shot multispecies analysis. A tunable KrF excimer laser is used for Raman measurements during compression and combustion stroke of a realistic SI engine. The Raman scattered and fluorescence light is separated according to the different polarization properties in the focal plane of a spectrometer using an air-spaced Glan prism made of calcite. This approach offers the opportunity to detect simultaneously the desired Raman signal and the interfering (broadband) LIF to obtain high single-shot measuring precision.

In addition, a combinative approach for cycle-resolved mixture composition and exhaust gas analysis is demonstrated. The air-fuel ratio before ignition and NO LIF intensity in the burned gas are measured within the same engine cycle using the different polarization properties of Raman scattered and fluorescence light.

Future work will be aimed at temperature measurements using polarization separated Rayleigh scattering. The polarization technique will be used to account for interfering Mie scattering and surface scattered light.

This technique is also suited for planar imaging; therefore, double-pulse measurements of two-dimensionally resolved Rayleigh scattering is possible. The study of in-cylinder flow dynamics using a double laser pulse for two-dimensionally resolved and polarization separated tracer visualization is another very promising application.

In conclusion, an imaging system for combinative measurement approaches is presented. Some initial results from an SI engine are described and prove the feasibility of the technique. To illustrate the potential, examples for possible future work are given.

Acknowledgments

This work has been funded by the Bundesministerium für Bildung, Wissenschaft, Forschung und Technologie, and VOLKSWAGEN AG Wolfsburg. We thank Mr. D. Holdorf, VOLKSWAGEN AG, for designing the spacer plate.

REFERENCES

1. Eckbreth, A. C., *Laser Diagnostics for Combustion Temperature and Species,* Abacus Press, Cambridge, 1988, pp. 163–219.
2. Kobayashi, T., Konishi, M., Ohtaka, M., Taki, S., Ueda, M., Kagawa, K., Inaba, H., in *Laser Diagnostics and Modeling of Combustion* (Linuma, K., Asanuma, T., Oshawa, T., and Doi, J., Eds.), Springer Verlag, Berlin, 1987, pp. 133–140.
3. Bischel, W. K. and Black, G., *AIP Conference Proc.* No. 100, American Institute of Physics, New York, 1983, pp. 181–187.
4. Arguello, C. A., Mendes, G. F., Leite, R. C. C., *Appl. Opt.* 13:1731 (1974).
5. Bailly, R., Pealat, M., and Taran, J. P. E., *Opt. Commun.* 18:68 (1976).
6. Kelly, P. B. and Hudson, B. S., *Chem. Phys. Letters* 114:451–455 (1985).
7. Grünefeld, G., *Laser Diagnostics Applied to Practical Combustion and Flow Systems,* Cuvillier Verlag, Göttingen, 1994.
8. Luczak, A., Beushausen, V., Eisenberg, S., Knapp, M., Schlüter, H., Andresen, P., Malaobabic, M., and Schmidt, A., *Combust. Sci. Technol.* accepted for publication (1996).
9. Brockhinke, A., Kohse-Höinghaus, K., and Andresen, P., submitted to *Opt. Lett.* (1995).
10. Barat, R. B., Longwell, J. P., Sarofim, A. F., Smith, S. P., and Bar-Ziv, E., *Appl. Opt.* 30(21):3003 (1991).
11. Bennett, J. M. and Glassman, A. T., in *Handbook of Laser Science and Technology* Vol. 4 (Weber, M. J.,

Ed.), CRC Press, Boca Raton, FL, 1986, pp. 221–250.
12. Hecht, E., *Optics*, Addison-Wesley, Reading, MA, 1987, pp. 290–291.
13. Reckers, W., Hüwel, L., Grünefeld, G., and Andresen, P., *Appl. Opt.* 32(6):907 (1993).
14. Doherty, P. M. and Crosley, D. R., *Appl. Opt.* 23(5):713 (1984).
15. Feofilov, P. P., *The Physical Basis of Polarized Emission*, Consultants Bureau, New York, 1961, pp. 99–117.
16. Frodermann, M., University of Bielefeld, private communication, 1995.
17. Eckbreth, A. C., *Combust. Flame* 31:231–237 (1978).
18. Knapp, M., Luczak, A., Schlüter, H., Beushausen, V., Hentschel, W., and Andresen, P., *Appl. Opt.* (1995). In press.

COMMENTS

E. Winklhofer, AVL-List, Austria. You have shown data for NO-LIF at a rather late time of combustion at 90° CA ATDC. Ignoring mechanical restraints, how close to TDC can you measure NO? What are the limits set forth by pressure, gas composition or other factors of influence?

Author's Reply. In the presented study, rotational-vibrational transitions of NO are excited via the $A^2\Sigma^+ \leftarrow X^2\Pi$ (0,2) band system around 248 nm and detection was carried out at wavelengths greater than the excitation wavelength. The excitation wavelength chosen for NO LIF allows us to avoid laser beam attenuation by the combustion gases, i.e., radiation at 248 nm is less absorbed than at 226 nm or at 193 nm and allows NO LIF excitation at all crank angles [18]. Interference free detection was possible because a polarization separating detection scheme was employed. However, in a recent study [18] single laser shot planar NO distributions were obtained using the same excitation scheme but observing the fluorescence at shorter wavelength than the excitation wavelength, i.e., at 226 nm and 237 nm. It should be emphasized that the absorption problem is also present for the fluorescence light, i.e., NO fluorescence at 226 nm will be as strongly absorbed by the combustion gases as the 226 nm laser wavelength. This problem can be avoided for example by spectrally excluding this emission from detection. It was possible to acquire planar NO-LIF distributions with good signal-to-noise ratio at all crank angles in an optically accessible engine and to locate areas of NO formation during combustion. This detection scheme allows us to selectively detect NO LIF even under high pressure conditions since no interfering emissions show up at wavelengths shorter than the excitation wavelength. If quantification of the data is desired broadening of the absorption lines and effects like quenching, RET, and VET are ultimately accounted for by performing in-situ calibration. This can be done by seeding known amounts of NO.

•

Tobias Plessing, RWTH-Aachen, Germany. The Raman cross sections are strongly dependent on temperature. Did you take this effect into account for your calibration?

Author's Reply. The Raman scattering cross-sections exhibit only small changes in the relevant temperature interval which ranges from 300K gas temperature in the early intake stroke to about 700K in the late compression stroke. Furthermore, temperature fluctuations at a fixed crank angle are relatively small and therefore hardly affect the corresponding ratios of Raman scattering cross-sections. Nevertheless, calibration measurements in the relevant range of temperature were done. The ratios of H_2O to N_2 and of O_2 to N_2 were calibrated in-situ during motored engine operation. In this case, the mole fractions of these species are known, and they are homogeneously mixed. This calibration can also be performed for the C-H Raman signal if the vaporized isooctane is homogeneously delivered into the cylinder. A premixed air-isooctane mixture was prepared by sucking a certain fraction of the intake air through a big reservoir filled with isooctane during motored engine operation. The results of the calibration measurements will be presented elsewhere [1].

REFERENCE

1. Knapp, M., Beushausen, V., Hentschel, W., Manz, P., Grünefeld, G., and Andresen, P., "In-Cylinder Mixture Formation Analysis with Spontaneous Raman Scattering Applied to a Production SI Engine," submitted to 1997 SAE International Congress, February 24–27, Detroit, Michigan.

Twenty-Sixth Symposium (International) on Combustion/The Combustion Institute, 1996/pp. 2597–2604

QUANTITATIVE 2D SINGLE-SHOT IMAGING OF NO CONCENTRATIONS AND TEMPERATURES IN A TRANSPARENT SI ENGINE

C. SCHULZ, V. SICK AND J. WOLFRUM
Physikalisch-Chemisches Institut, Ruprecht-Karls-Universität Heidelberg
Im Neuenheimer Feld 253
69120 Heidelberg, Germany

V. DREWES, M. ZAHN AND R. MALY
Daimler-Benz AG, Aero- and Thermodynamics Department
Stuttgart, Germany

The formation of nitric oxide in a transparent spark-ignition (SI) engine was studied experimentally using a combination of planar laser-induced fluorescence and Rayleigh scattering. Simultaneous images were obtained after excitation with a single pulse from a tunable KrF excimer laser. Tuning the laser to 247.9 nm allows excitation of the NO A-X (0,2) band, and subsequent fluorescence emission is spectrally well separated to image Rayleigh scattering from the same laser pulse. The advantages of using the (0,2) band for excitation of NO under engine conditions are demonstrated, and quantitative distributions of NO concentrations are shown along with temperature fields calculated from the Rayleigh images. We investigated various engine operation conditions with propane and *iso*-octane as fuels. Cycle-resolved measurements show strong cycle-to-cycle variations of the NO formation with peaks in the spatial NO distribution, whereas the temperature field is nearly homogeneous, leading to the conclusion that small variations in the temperature distributions lead to peak NO concentrations via the Zeldovich mechanism.

Introduction

Nitric oxide, one of the major pollutants in combustion, is of particular interest in improving the environmental acceptance of internal combustion engines. A substantial amount of NO released by combustion processes is formed in spark-ignition (SI) and compression-ignition (CI) engines used in cars and trucks. To meet the future legislative regulations, much effort is put into the development of new and improved engines. To optimize the combustion process, a detailed understanding of the elementary physical and chemical steps involved, as well as their coupling, is necessary. This allows a mathematical description of the combustion process with the ability of predicting optimal combustion chamber geometries and operating conditions. The full treatment of chemical and physical processes with direct numerical simulation methods (DNS) far exceeds today's computing power. Other models with reduced computing demands are therefore used to simulate the processes in internal combustion (IC) engines. Each of these approaches needs input and feedback, preferably from quantitative experiments.

Laser-induced fluorescence (LIF) has been used in the past for the detection of a large variety of combustion-relevant species [1] in engines, pointwise, and two-dimensional arrangements [2]. Most of these studies, however, are qualitative in their results. Nitric oxide has been detected in a SI engine [3] as well as in diesel engines [4,5]. These investigations applied two-dimensional laser-induced fluorescence using a tunable ArF excimer laser operating at 193 nm. Rotational transitions in the NO D-X (0, 1) band were excited. Despite the high sensitivity of this excitation scheme, there are several limitations for quantitative application in engines. Spectral separation of LIF from O_2 is difficult [6,7]. Another limitation of this method is absorption of the exciting laser beam, especially higher pressures in early stages of combustion, shortly after top dead center (TDC). This is due mainly to intermediates formed during combustion, such as unsaturated hydrocarbons, partially oxidized hydrocarbons, and PAH molecules. In an investigation of the NO formation in a transparent SI engine fueled with propane, Bräumer et al. [8] used excitation at 225 nm with a Raman-shifted tunable KrF excimer laser in the A-X (0, 0) band. However, when using *iso*-octane, gasoline, or diesel fuel, the absorption by intermediates, as discussed previously, occurs again. Also, at concentration levels found in engines, NO can cause significant absorption of the laser beam as well. Schulz et al. [9] describe the use of exciting NO in the A-X (0, 2) band to minimize absorption at the shorter UV

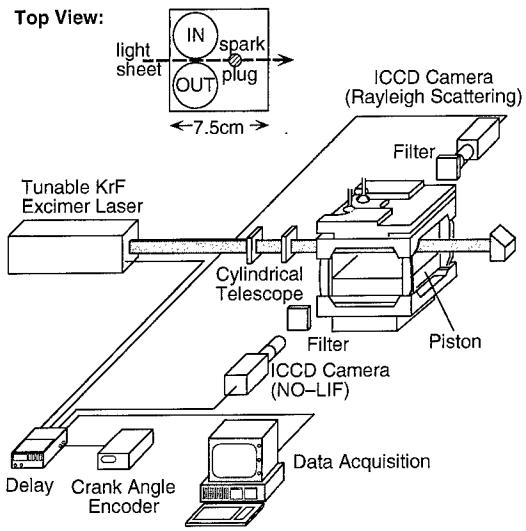

FIG. 1. Experimental setup for the simultaneous single-shot measurement of NO concentration and temperature fields in a transparent SI engine. The insert shows a top view to illustrate the position of the laser light sheet.

TABLE 1
Technical data of the transparent SI engine

Cross section	7.5 × 7.5 cm
Stroke	6.7 cm
Clearance volume	37.7 cm^3
Compression ratio ε	10:1
Maximum speed	2000 rpm
Actual speed	1000 rpm
Resolution of crank angle encoder	1 °CA, i.e. 167 μs @ 1000 rpm
Ignition timing	340 °CA
Fuel	propane or *iso*-octane
λ (Air/fuel ratio)	1.0

wavelengths. We use this scheme for quantitative measurements of NO distributions in a transparent, square-piston SI engine fueled with propane or *iso*-octane. Since the formation of NO is strongly dependent on temperature, simultaneous information on the temperature distribution is desirable. As shown by Orth et al. [10], temperature fields can be measured by Rayleigh scattering in the transparent engine.

Experimental

Optical access in the single-cylinder engine was possible for the entire combustion chamber. This was achieved by building the combustion chamber walls from polished quartz plates, mounted on a small Hatz single-cylinder engine (see Fig. 1). The piston is not lubricated, thus allowing extended measurements without obscuring layers on the windows. An electrical motor and brake permits the engine to run at different speeds and loads. The engine could be operated with gaseous or liquid fuels. Flow controllers (Brooks) were used to carefully control the flow rates of all gases. For liquid fuels, an L-Jetronic injection system (Bosch) was used. With an optical encoder, the crank angle positions (CA) were measured. These data, together with the measured actual cylinder pressure were stored with the images taken with the laser-imaging system. Additionally, the encoder signals were used to trigger the laser system and the image intensifiers of the cameras (Princeton Instruments ICCD-576 GIRB). Table 1 summarizes technical data of the engine design and operating conditions.

The beam from a tunable, narrow band ($\Delta\nu = 1$ cm^{-1}) KrF excimer laser at 248 nm (Lambda Physik, LPX 150) was formed into a vertical light sheet (65 mJ/pulse in a 12 × 0.5 mm cross section) using cylindrical lenses, and aligned through the cylinder in a plane directly below the spark plug between the intake and outlet valve. This is depicted in the insert of Fig. 1. The pulse energies were measured on a single shot basis behind the engine. Perpendicular to the light sheet plane, the slow scan cameras were mounted on opposite sides of the engine. The image intensifiers were triggered for exposure times of 250 ns to exclude detection of the self-luminosity of the flames. A combination of four mirrors with narrow spectral-reflection characteristics centered around 230 nm and a 0° mirror centered at 248 with a half-width at half maximum (HWHM) of 10 nm were used to isolate the NO fluorescence from any other fluorescence, mainly from O_2 and the Rayleigh signals caused by the 248 nm light [9,11]. Rayleigh signals were filtered similarly with a filter set centered at 248 nm. Signals from the two intensified, slow-scan cameras were digitized, stored, and later processed using the software package Khoros [1,12]. The pressure curve was measured for each engine cycle with a crank angle resolution of 1° and stored with the corresponding images.

Analysis of Data and Results

The head of the O_{12} branch of the NO A-X (0, 2) band is accessible with a tunable KrF excimer laser at 247.95 nm, which provides enough energy to obtain good signal strengths for imaging purposes. The lower state population varies around an average population by ±5%/100 K over the temperature range of our measurements. Calculations [13] and experiments in high–pressure flames [11] show that with excitation at 247.95 nm, the interference with O_2

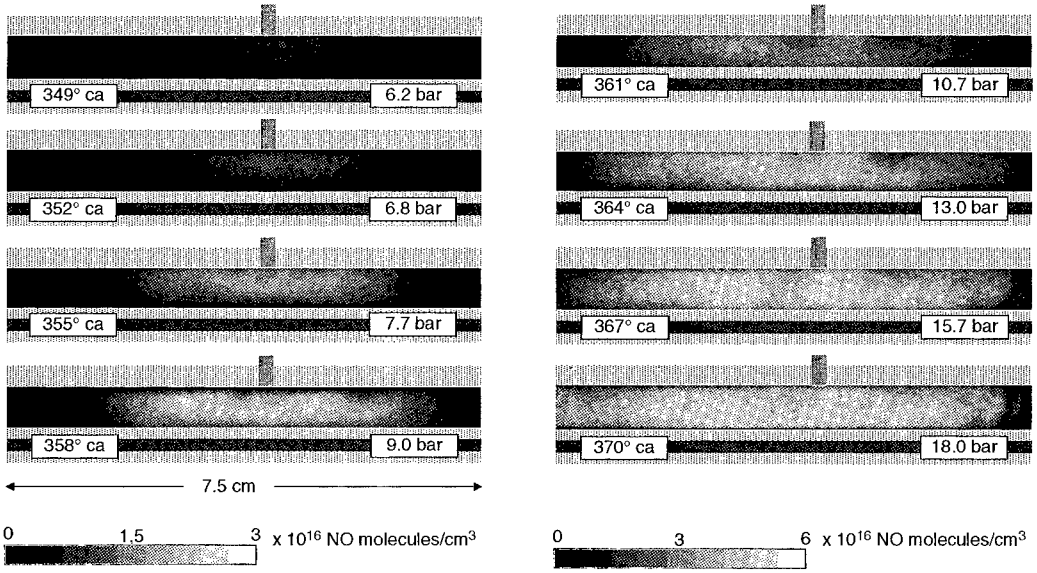

FIG. 2. Absolute NO concentration fields in the transparent engine fueled with propane/air at $\lambda = 1.0$ as a function of the crank angle. Ignition timing was at 340 °CA; the engine speed was 1000 rpm. The grey bar indicates the spark plug position. The figure shows averages over 25–30 frames. Note the different color codings for the two columns. The images at 367 and 370 °CA are corrected for absorption effects (see text).

Schumann–Runge transitions is minimized using a detection bandpass centered at 230 nm ± 8 nm). The effect of oxygen fluorescence and some minor anti-Stokes–Raman signals from nitrogen and water on the measured NO concentration add up to less than 5% of the NO LIF signals. This was determined experimentally in a lean (air/fuel ratio $\lambda = 1.1$. based on oxygen/fuel), high-pressure methane/air flame, operated at 10 bar in the presence of 1000 ppm NO [11]. The images shown here were measured under stoichiometric conditions. Additionally, emissions caused by PAH molecules, OH radicals, and so forth will be at longer wavelengths and can thus be suppressed efficiently.

Quenching must be taken into account for quantitative LIF concentration measurements. Published data for quenching cross sections for a variety of colliders with NO [14–16] were used to compute the total quenching rate in a premixed methane/air flame. The concentrations of all major species and of radicals such as OH, O, H, and CH were included in the calculation. The calculations show constant quenching rates within ±5% in areas where NO is formed in the engine [8], that is, mainly in the exhaust gas zone. This means that it is not necessary to correct the fluorescence images for quenching effects on a pixel by pixel basis. The absolute magnitude of the quenching rate in the burned gas depends on the kind of fuel used, since this determines the amounts of carbon dioxide and water (the major quenching species) present in the burned gas.

NO absorption lines are strongly broadened with increasing pressure [17,18], also, the center wavelengths of the lines are shifted [18]. Dependent on pressure, the overlap of the laser line and the absorption line is varying. For the analysis of the engine measurements, the spectral profile of the laser was calculated as a Gaussian profile with a measured FWHM of 1 cm^{-1}. The overlap of this line with the absorption spectrum of NO as a function of pressure was included in the data reduction. Taking the laser characteristics and the absorption spectrum into account, we calculate, using the simple two-level model, that the intensities used in the experiments were less than the saturation intensity.

The engine was first operated with propane/air mixtures. The data discussed here were all obtained for stoichiometric mixtures. Ignition timing was at 340 °CA and the engine was running at a speed of 1000 rpm. All engine measurements were taken as single-shot images to allow the correction of each image for pressure effects as described. Also, variations in laser pulse energy were taken into account. Averaged concentration distributions were then calculated from the corrected single-shot images. Figure 2 shows a series of averaged (25–30 single images) NO concentration images for different times after ignition, taken around top dead center. Only images from cycles with maximum pressures higher than 18 bar were included in the analysis. The area where NO is formed expands rapidly into the combustion chamber. In addition to the spatial growth,

the absolute concentration of NO rises very rapidly. (Note that the color coding for the right-hand column of Fig. 2 is different from that on the left.) At 367° and 370 °CA, some absorption of the laser beam was measured. These images were corrected for by analyzing the images according to Beer's law. While keeping the left side of the images unchanged, the intensities were increased from left to right, according to the measured absorption. Absolute concentrations were determined by comparing LIF signals measured at 352 °CA for the case where the engine was running with propane/air only, to runs where different amounts of known quantities of NO were added to the fuel. Pressure and temperature effects on the LIF signals were included in the calibration procedure as described earlier.

For a crank angle position, where high concentrations of NO were measured, a comparison of the excitation at 225 nm (0, 0 band) to that at 248 nm (0, 2) is given in Fig. 3. The averaged images were taken in the same engine, fueled with propane/air, at the same crank angle positions (364°). In the right image, measured with excitation at 248 nm, the absorption is negligible. The left image, measured with excitation at 225 nm, shows significant absorption along the laser beam path. In addition to the absorption by NO, other intermediates could contribute to the overall absorption at this stage of the engine cycle. The calculated absorption by NO alone for this condition is 30% for 225 nm and 0.2% for 248 nm for 7.5 cm (i.e., the cylinder diameter).

Having demonstrated that it is possible to measure quantitative NO concentration distributions in an engine, we measured single-shot image pairs showing LIF of NO on one image and Rayleigh scattering on the other. The Rayleigh signals were then converted into temperature images using the procedure as described by Orth et al. [10]. Image processing allowed us to distinguish automatically between burned and unburned gases. The corresponding areas were analyzed with the appropriate Rayleigh scattering cross sections, 232×10^{-28} cm^2 for unburned and 171×10^{-28} cm^2 for burned gases, leading to a total uncertainty of 15% for the temperature measurements. The simultaneously measured image pairs, obtained with a single laser shot, directly show the correlation between temperature and NO concentration. The images of Fig. 4, taken at 352 °CA have been selected from engine runs, where the peak pressures were 20 ± 0.5 bar, with the actual pressure at the time of the measurements being 6.9 ± 0.1 bar. Strong variations from cycle to cycle were found in the magnitude and the spatial distribution of temperature and NO concentrations. Profiles along the lines, as indicated in the lower image pair of Fig. 4, show that the temperature distribution is rather homogeneous, compared to variations of a factor of 2 in the NO concentrations (Fig. 5).

Finally, the engine was fueled with stoichiometric *iso*-octane/air mixtures. The image series of Fig. 6 shows the increase of the NO concentration in the engine as a function of increasing crank angles. Compared to the images shown in Fig. 2, two major differences can be seen. Although the ignition timing (340 °CA) is identical for both operating conditions, the flame propagates more slowly for the *iso*-octane/air mixtures. The first significant NO formation is visible at 349 °CA for the propane case in contrast to 352 °CA for *iso*-octane. Again, as in the case for propane/air mixtures, images at late crank angles were corrected for absorption effects as described previously for Fig. 2. The peak NO concentrations measured for *iso*-octane are lower than for propane. When burning *iso*-octane, the flame develops much slower in our engine and measured peak pressures are lower compared to the propane fueled engine. This indicates lower peak temperatures and in turn lower NO concentrations.

Conclusions

The successful use of a tunable KrF excimer laser for quantitative imaging of nitric oxide concentration distributions in a SI engine was demonstrated. Laser-induced fluorescence signals can be converted into quantitative concentration data if the actual pressure at the time of the measurement is known. For the temperature range found in our experiments, the influence of temperature on the fluorescence signal due to variations in the lower state population (±5%) can be neglected without introducing large systematic errors. The absolute concentration was determined by adding known amounts of nitric oxide into the intake. The uncertainty of the absolute nitric oxide concentrations using the excitation in the A-X (0, 2) band are similar to uncertainties when using the A-X (0, 0) band (i.e., 30%) [8]. Contributions to the uncertainty are mainly given by the calibration procedure that includes the calculation of the quenching cross sections and the overlap integral of laser and absorption line. The excitation at 248 nm prevents problems with laser beam attenuation along the beam path compared to excitation at 225 or 193 nm, even when the engine is fueled with *iso*-octane. At 193 nm, the laser beam is absorbed within a few millimeters, and absorption as high as 90% at 225 nm is observed in the transparent engine. For excitation at 248 nm, the absorption is less than 20%.

The spatial and temporal evolution of nitric oxide formation in a SI engine were studied for stoichiometric propane/air and *iso*-octane/air mixtures. For both conditions, the initial formation of NO shortly after ignition is slow; later in the engine cycle, when temperatures are high, it accelerates. While averaged NO distributions are reproducible between engine runs, strong cycle-to-cycle fluctuations are found for every engine operating condition. Spatial

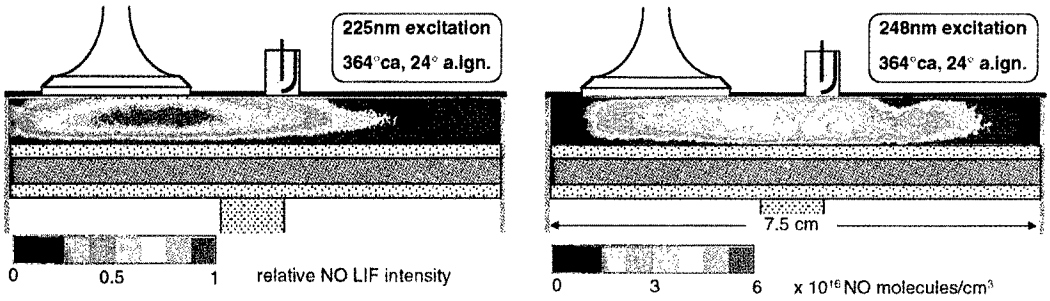

FIG. 3. Comparison of the NO LIF signal using two different detection schemes. The upper image was taken after excitation of the NO A-X (0, 0) band at 225.25 nm. In this case, strong absorption of the incoming laser beam can be seen. In the lower image, obtained after excitation of the NO A-X (0, 2) band at 247.95 nm, absorption of the excitation beam is negligible. The left image shows LIF signals in relative units, whereas the data in the right image show absolute concentrations.

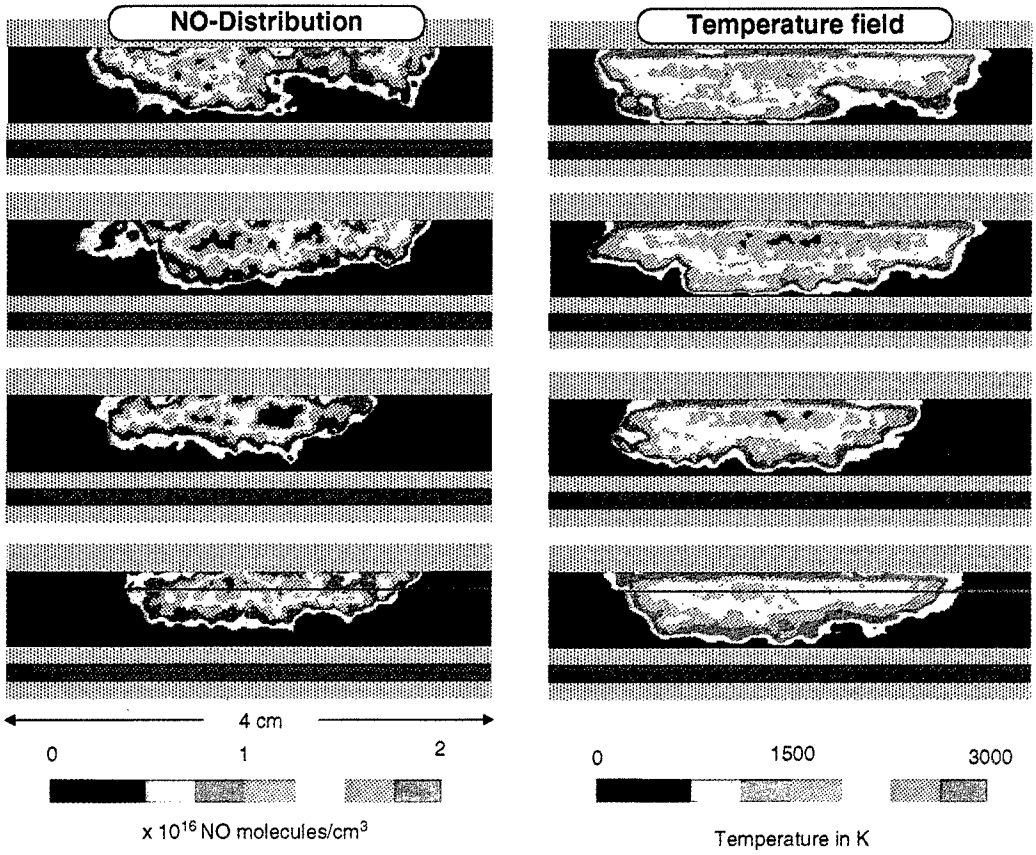

FIG. 4. Simultaneous single-shot absolute NO concentration and temperature fields in the transparent engine fueled with propane/air at $\lambda = 1.0$. Ignition at 340 °CA; detection at 352 °CA, 1000 rpm. The horizontal line in the lowest picture indicates the position of the profiles shown in Fig. 5.

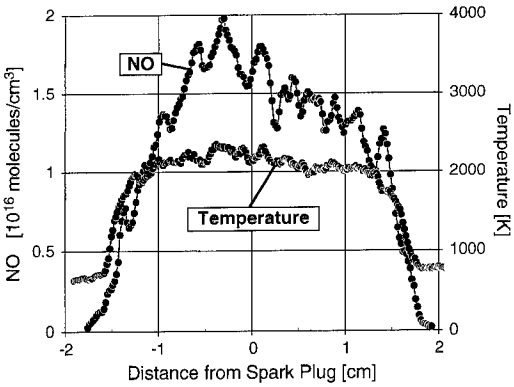

FIG. 5. Instantaneous absolute NO concentration and temperature profiles as indicated in Fig. 4.

distributions of NO and high-temperature regions are well correlated. Combining single-shot planar Rayleigh temperature measurements with the NO images, more information about the NO formation can be revealed. Simultaneously measured NO and temperature distributions using only a single laser pulse show that the spatial temperature variation is relatively small in the burned gases. However, NO concentrations show strong variations, demonstrating that even small differences in temperatures strongly affect NO formation. This indicates in agreement with the strong temperature dependence of the rate coefficient for NO formation via the Zeldovich mechanism that this mechanism is the dominant NO formation path in the engine. The reasons for these temperature inhomogeneities have to be addressed in future work.

Acknowledgments

This work has been funded by the Bundesministerium für Bildung und Forschung under contract No. 13N6283. Contributions to the calibration of the NO concentrations from A. Bräumer and the assistance of T. Tempel during the data reduction are acknowledged.

REFERENCES

1. Eckbreth, A. C., *Laser Diagnostics for Combustion Temperature and Species,* Abacus Press, Turnbridge Wells, UK, 1988.
2. "Symposium on Laser Diagnostics for Industrial Processes," *Ber. Bunsenges. Phys. Chem.* 97 (1993).
3. Andresen, P., Meijer, G., Schlüter, H., Voges, H., Koch, A., Hentschel, W., Oppermann, W., and Rothe, E. W., *Appl. Opt.* 29:2392–2404 (1990).
4. Arnold, A., Dinkelacker, F., Heitzmann, T., Monkhouse, P., Schäfer, M., Sick, V., Wolfrum, J., Hentschel, W., and Schindler, K. P., *Twenty-Fourth Symposium (International) on Combustion,* The Combustion Institute, Pittsburgh, 1992, pp. 1605–1612.
5. Brugman, T. M., Klein-Douwel, R., Huigen, G., van

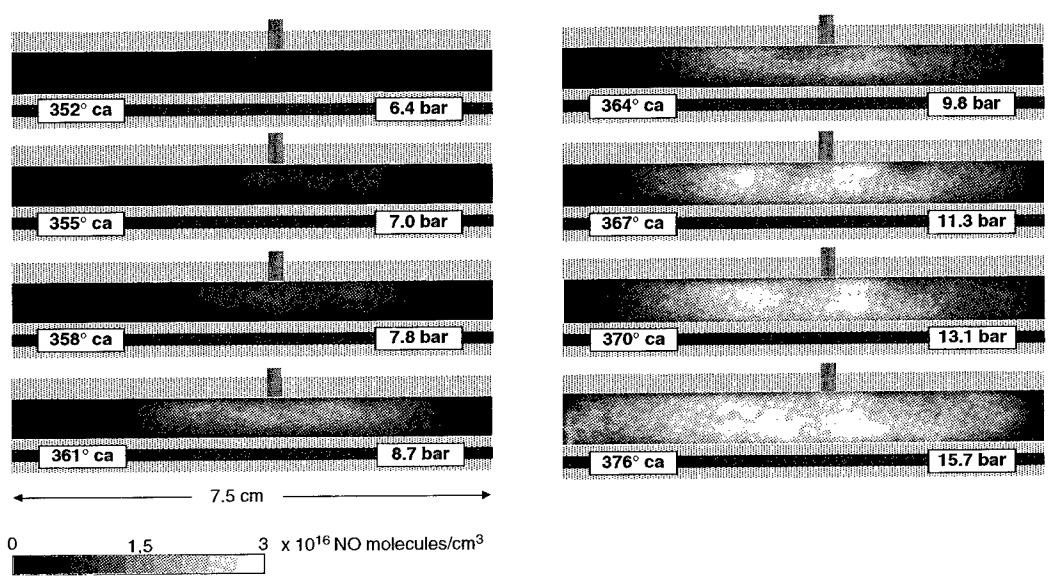

FIG. 6. Absolute NO concentration fields in the transparent engine fueled with *iso*-octane/air at $\lambda = 1.0$ as a function of the crank angle. Ignition at 340 °CA, 1000 rpm. The grey bar indicates the spark plug position. The figure shows averages over 25–30 frames. Because of the lower flame speed compared to propane/air flames, the NO formation develops more slowly compared to Fig. 2. The images at 370 and 376 °CA are corrected for absorption effects (see text).

Walwijk, E., and ter Meulen, J., *J. Appl. Phys. B* 57:405–410 (1993).
6. Wodtke, A. M., Huwel, L., Schlüter, H., Meijer, G., Andresen, P., and Voges, H., *Opt. Lett.* 13:910–912 (1988).
7. Sick, V. and Wolfrum, J., *Joint Meeting of the British/German Sections of the Combustion Institute,* Cambridge, 1993, pp. 299–302.
8. Bräumer, A., Sick, V., Wolfrum, J., Drewes, V., Maly, R. R., and Zahn, M., SAE Paper No. 95-2462, 1995.
9. Schulz, C., Yip, B., Sick, V., and Wolfrum, J., *Chem. Phys. Lett.* 242:259–264 (1995).
10. Orth, A., Sick, V., Wolfrum, J., Maly, R. R., and Zahn, M., *Twenty-Fifth Symposium (International) on Combustion,* The Combustion Institute, Pittsburgh, 1994, pp. 143–150.
11. Schulz, C., Sick, V., Heinze, J., and Stricker, W., in "Laser Application to Chemical and Environmental Analysis." OSA Technical Digest Series 3:133–135 (1996).
12. The software package 'Khoros' is freeware from the University of New Mexico, available on several Internet servers.
13. Sick, V. and Szabadi, M., *J. Quant. Spectrosc. Radiat. Transfer* 54:891–898 (1995).
14. Paul, P. H., Gray, J. A., Durant, J. L. Jr., and Thoman, J. W. Jr., *Appl. Phys. B* 57:249–259 (1993).
15. Paul, P. H., Gray, J. A., Durant, J. L. Jr., and Thoman, J. W. Jr., *AIAA J.* 32:1670–1675 (1994).
16. Furlanetto, M. R., Thoman, J. W. Jr., Gray, J. A., Paul, P. H., and Durant, J. L. Jr., *J. Chem. Phys.* 101:10452–10457 (1994).
17. Dodge, L. D., Colket, M. B. III, Zabielski, M. F., and Seery, D. J., DOT-FAA Report No. FAA-EE-80-28, UTRC, East Hartford, CT, 1979.
18. DiRosa, M. D. and Hanson, R. K., *J. Quant. Spectrosc. Radiat. Transfer* 52:515–529 (1994).

COMMENTS

Yung-cheng Chen, Tsing Hua University, ROC. Using KrF Excimer laser at 248 nm, it is possible to have C-atom fluorescence interfere with the Rayleigh signals for temperature determination. This effect could be very severe for higher hydrocarbon combustion in engine conditions. How do you quantify this interference?

Author's Reply. Strong C-atom fluorescence is reported [1] to appear at 247.8 nm after exciting flames at 193 nm with near air-break-down laser intensities ($3 \cdot 10^{10}$W/cm^2). This is due to photodissociation of CO_2 forming CO with a subsequent dissociation via a two-photon process and a resonant excitation of the produced C atom.

Our measurements are carried out at 247.95 nm, a frequency not resonant with the C 2^1D–3^1P^0 transition. However spectroscopic measurements [2] show no increase of the Rayleigh signal at 247.8 nm which would be due to the low natural abundance of C atoms under engine combustion conditions.

REFERENCES

1. Laufer, G., et al., *Opt. Lett.* 13:99–101 (1988).
2. Schulz, C., et al., *Appl. Opt.,* submitted.

•

W. Hentschel, Volkswagen R&D, Germany. What will happen with your NO-LIF-Signals if you run the engine with standard gasoline fuel instead of *iso*-octane?

Author's Reply. Using standard gasoline fuel with a high concentration of aromatic compounds will probably cause an attenuation of the incident laser beam in the unburnt gas region outside the flame front. The extent of this effect has not been investigated yet. We don't expect a strong influence of the fuel composition on the spectroscopic properties of the burnt gas region which is where we expect to measure NO.

•

Thierry Baritaud, IFP, France. How do you explain your NO concentration is not maximum at $\lambda = 1.1$ (as compared to 0.8 or 1) while pressure levels are quite similar?

What is the time evolution of your NO for the different cases as measured with LIF?

Did you capture post-combustion integrated NO levels with exhaust measurements?

Author's Reply. Our measurements show NO number densities along cross sections through the middle of the combustion chamber. For comparison of the overall production of NO at different air–fuel ratios, consideration of actual pressures and flame-diameters is necessary. We performed measurements at $\lambda = 0.8$, 1.0, and 1.1. The flame speed is maximal in the rich flame and minimal at $\lambda = 1.1$. Since the NO formation via the Zeldovich mechanism is very slow, the speed of growth of the burnt gas region where NO is formed has an important impact on the NO number densities shown in the measurements.

Whereas in the rich flame the NO number density increases very slowly with time and the NO distribution behind the flame front is rather homogeneous, the measurements under stoichiometric and lean ($\lambda = 1.1$) conditions show a steep temporal rise in NO concentration and there is a strong maximum in the middle of the burnt gas region indicating the very efficient NO formation by the thermal mechanism. Since the amount of NO is quite similar at λ

= 1.0 and 1.1, the maximum of NO formation may be in between.

The measurements were performed in the skip-fired engine. Since no cycle-resolved NO measurement in the exhaust gases was available, a comparison of the measurement to post-combustion NO levels was not possible.

•

Hans ter Meulen, University of Nijmegen, The Netherlands. You showed a nice agreement between experimental and calculated pressure broadened absorption spectrum of NO. Aside of the line broadening, an intensity decrease will be induced at high pressures. This intensity decrease will probably be linearly proportional to the density of those particles which are most efficient in the quenching, but may not be linearly proportional to the total density or the density of NO. Consequently this loss of signal may not be compensated for by the increase of intensity due to a larger density. Shouldn't you take this into account in your analysis of the NO density distributions?

Author's Reply. The pressure dependence of NO LIF signal intensity is due to changes in the number density, the excitation efficiency that depends on line broadening effects and collisional quenching. In the burnt gas region NO is most efficiently quenched by H_2O and CO_2. There are only minor changes in the concentration of these species behind the flame front, resulting in an overall quenching cross section that is constant within 10% [8]. Hence, quenching scales linearly with the total pressure.

Twenty-Sixth Symposium (International) on Combustion/The Combustion Institute, 1996/pp. 2605–2611

AN EXPERIMENTAL STUDY ON QUENCHING CREVICE WIDTHS IN THE COMBUSTION CHAMBER OF A SPARK-IGNITION ENGINE

SHIZUO ISHIZAWA
Department of Mechanical Engineering
Gunma College of Technology
Maebashi, Japan

Hydrocarbon (HC) emissions from spark-ignition engines are now a major environmental problem in many cities of the world. It is difficult to reduce HC emissions during engine warm-up because the catalysts do not work well at low temperatures. The sources of unburned HCs from spark-ignition engines seem to be crevices in the combustion chamber, oil layer, deposits, and quench layer on the cylinder wall surfaces. Single-surface and two-surface flame quenching (crevice) play a large role in generating unburned HCs. Two-surface flame quenching distances (quenching crevice width) in the combustion chamber of a spark-ignition engine were investigated using an ion probe capable of detecting flame arrival at a narrow width. The crevice width could be controlled precisely. Because engine combustion has cycle-by-cycle fluctuations, quenching crevice widths were estimated by the statistical analysis. It was defined as the width when the ion detector could detect flame arrival in 50 of 100 cycles. The effects of the mixture equivalence ratio, exhaust gas recycle (EGR) rate, ignition timing, charging efficiency, and combustion chamber wall temperature on the quenching crevice width were investigated. HC emissions in the exhaust port, cycle-by-cycle combustion fluctuation, and temperature of a quenching plate of the ion probe in the combustion chamber were also estimated in the experiments. The quenching crevice width was relatively uniform at the surface of the combustion chamber except in the area close to the ignition spark plug and end gas. The quenching crevice width increased with leaner mixture ratio, larger EGR rate, lower charging efficiency, greater ignition timing, and lower wall temperature.

Introduction

Since unburned hydrocarbons (HCs) exhausted from spark-ignition engines are recognized as one of the main causes of photochemical air pollution, a great deal of experimental and theoretical research has been done.

The quenching distance in the combustion chamber of a spark-ignition engine was first estimated in photographic studies done by Daniel [1]. Subsequently, HCs from small crevices in the combustion chamber, especially the piston top land crevice, have been investigated extensively [2–5]. Later, it was found in constant-volume combustion chamber experiments that the lubricant layer on the combustion chamber surface contributed significantly to the amount of unburned HCs [6–7]. Several studies examined the interaction between the mixture and the oil layer in the combustion chamber and the cylinder of the engine [8–10]. Recently, the main sources of HCs are thought to be quenching crevices and the oil layer on the combustion chamber walls under normal steady-state operating conditions [11]. However, single-surface flame quenching effects on unburned HCs will be larger with an increase of EGR gas or a decrease of equivalence ratio.

Quenching distances have been measured with various experimental methods. Recently, the effect of wall temperature on single-surface quenching distance was investigated intensively [12]. In most cases, however, the quenching distances have been estimated in the experiments involving a burner flame, a constant-volume combustion chamber, and a CFR engine [13–14].

In this study, two-surface flame quenching distance (the quenching crevice width) in the cylinder of a spark-ignition engine that had a conventional hemispherical combustion chamber was measured with an ion current detector that was fitted to the top of a specially designed probe. It was assumed that the singe-surface quenching distance is proportional to that of two-surface distance. The effect of engine operating parameters on the quenching crevice and the relationship between the quenching crevice width and HCs were investigated. An experimental equation for quenching crevice width was formulated as a function of the maximum cylinder pressure and wall temperature.

Experimental Method and Apparatus

Experimental Engine and Operating Conditions

A single-cylinder four-stroke spark-ignition engine was used in the experiments. The engine specifications are given in Table 1. The combustion

TABLE 1
Engine specifications

No. of cylinders		1
Valve train		OHV
Bore and stroke		85 × 78 mm
Combustion chamber configuration		Hemispherical
Compression ratio		8.5
Valve timing	Intake valve	12° BTDC—48° ATDC
	Exhaust valve	60° BBDC—10° ATDC

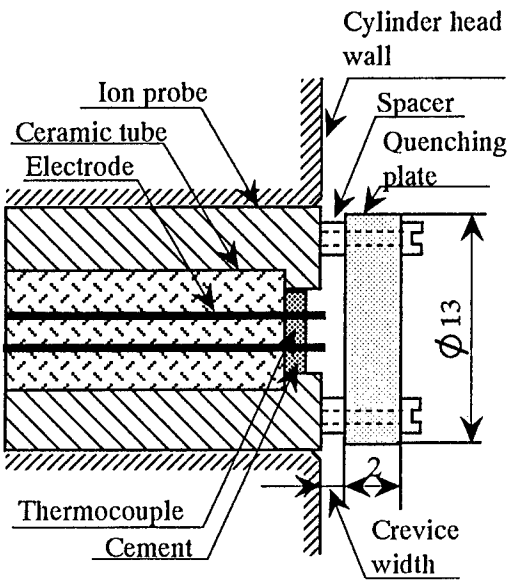

FIG. 1. Schematic of ion detector.

chamber had a hemispherical shape and fuel was supplied to the engine with a magnetic-electronic–controlled fuel injector installed in the intake pipe. Since emissions from vehicles are a major source of urban air pollution, the engine was operated under conditions equivalent to the load of city driving, that is, a vehicle speed of 40 km/h (approximately 1400 rpm) and engine load of 0.31 MPa indicated mean effective pressure. To study the influence of the mixture equivalence ratio, EGR rate, ignition timing, charging efficiency, and combustion chamber wall temperature on the quenching crevice width, these engine operating parameters were varied in the experiments. Gasoline obtainable in the Japanese domestic market was used as the fuel.

Measurement of Quenching Crevice Width, HC Concentration, and Cylinder Pressure

A schematic of flame ion detector and quenching crevice width measurement technique is shown in Fig. 1. It has a narrow crevice between the quenching plate and ion probe tip of the ion detector. In the preliminary experiment using a Bunsen burner, the function of the ion probe to detect ion current was verified. The crevice width was controlled precisely by a spacer made of aluminum foil. Measurements were made at increments of 0.1 mm. The electrodes were supplied with a voltage of 50 V to detect the ion current. If the flame was extinguished before reaching the electrodes, no ion current was detected. The surface temperature of the quenching plate was measured with a thermocouple (constantan). Although the temperature of the other plate projecting into the combustion chamber was not measured, both wall temperatures were assumed to be equivalent. Quenching crevice width was defined as the width at which the ion detector could detect flame arrival in 50 of 100 cycles (50%). Quenching crevice width depends on the definition of flame quenching criteria. If the criteria of 50% flame arrival is made larger, the quenching crevice width will also increase. However, the dependence on the engine operating parameters of the measured quenching widths was expected to be equivalent. The ion current was observed with an oscilloscope and photographed with a camera. Piezoelectric pressure sensor and a charge amplifier were used to measure the cylinder pressure. Cycle-by-cycle combustion fluctuations were estimated by analyzing the cylinder pressure data of 400 continuous cycles. Since the exhaust gas was sampled at the exit of the exhaust port 20 mm from the exhaust valve, there was little influence of oxidation of HC in the exhaust pipe on HC-emission measurement. The ion detector was replaced with a blind plug when the exhaust gas was sampled, so that the effect of the detector's quenching crevice on the exhaust HC concentration was removed. The HC-emission concentration was analyzed by a flame ionization detector (FID).

Results and Discussion

Output of Ion Detector

An example of the ion current detected by the ion probe and the cylinder pressure is shown in Fig. 2. Maximum ion current was detected just after the maximum cylinder pressure occurred. It is expected that the flame reaches the ion probe at the end of the combustion process. Ion current outputs for more than 70 continuous cycles are shown in Figs. 3 and 4. In Fig. 3, because the mixture ratio supplied to the cylinder was stoichiometric, the flame was

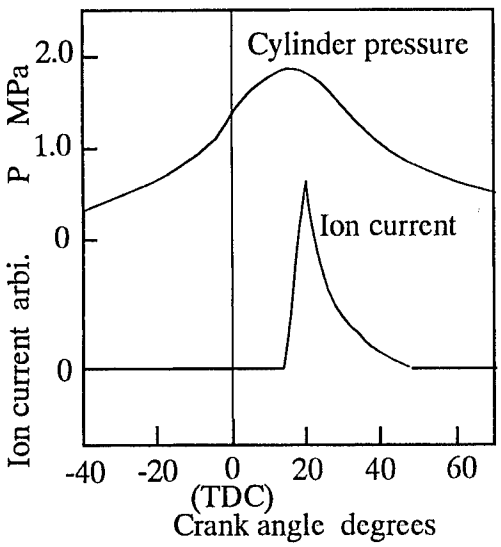

FIG. 2. Cylinder pressure and ion current. Engine conditions: 1400 rpm, ϕ = 1.0, MBT ignition timing, IMEP = 0.31 MPa central ignition and ion detector location of *D*.

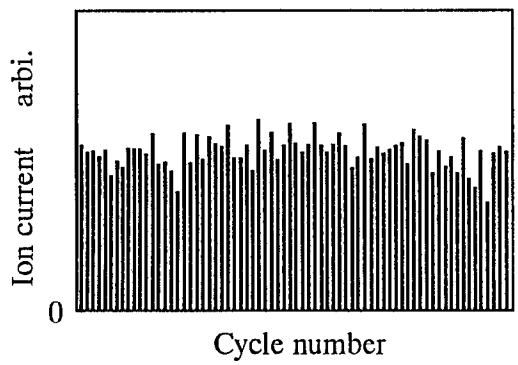

FIG. 3. Ion current. Engine conditions: 1400 rpm, ϕ = 1.0, MBT ignition timing, IMEP = 0.31 MPa central ignition and ion detector location of *D*.

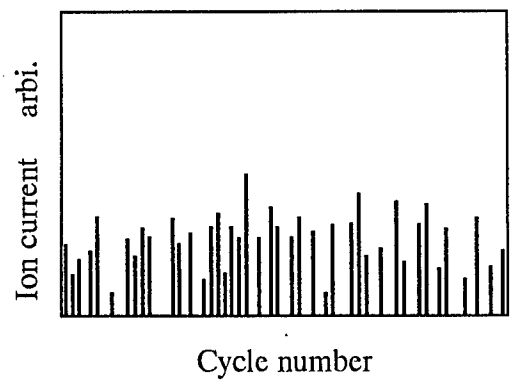

FIG. 4. Ion current. Engine conditions: 1400 rpm, ϕ = 0.87, MBT ignition timing, IMEP = 0.31 MPa central ignition and ion detector location of *D*.

able to enter the crevice and an ion current was detected by the ion probe in every cycle. The flame reached the electrodes in the crevice of the detector, but each cycle had a different ion current and showed cycle-by-cycle fluctuation.

The results in Fig. 4 indicate that cycle-by-cycle fluctuations became larger and some cycles lacked an ion current when a leaner mixture was supplied to the cylinder. Because engine combustion has cycle-by-cycle fluctuations, quenching crevice widths should be estimated by statistical analysis.

Effect of Location of Spark Plug and Ion Detector on Quenching Crevice Width

The dependence of the quenching crevice width (*Wc*) on the location of the spark plug and the ion detector in the cylinder head is shown in Fig. 5. Two locations were examined. In one case, the spark plug was located in the center of the combustion chamber (central ignition) and, in the other case, in the neighborhood of the cylinder bore far from the center of the cylinder (side ignition). For central ignition, *Wc* was measured at four different locations. Widths of about 0.4 mm were measured at three points, but that at the point near the spark plug was 0.28 mm. Because of the flame propagation in the combustion chamber, the flame arrival time depends on the location of the spark plug and the ion detector. The flame reaches the ion probe at the end of the combustion process. The cylinder pressure reaches a maximum and begins to decrease before the end of combustion. Since the unburned gas temperature in the crevice of the ion detector near the spark plug was higher than those of other locations, the flame could enter the crevice more easily.

The lower portion of Fig. 5 shows the *Wc* results for side ignition. Two points showed about the same *Wc* results as the values obtained with central ignition, but *Wc* at the point far from the spark plug was about 1.45 mm. This width was much larger than the other measurements and may have been caused by delayed flame arrival and lower unburned gas and flame temperatures. The measured widths were relatively uniform at the surface of the combustion chamber, excluding the points near the spark plug and far from it. The spark plug was located in the center of the combustion chamber and the ion probe at point *D* to obtain average quenching crevice width characteristics in the combustion chamber in the following experiment.

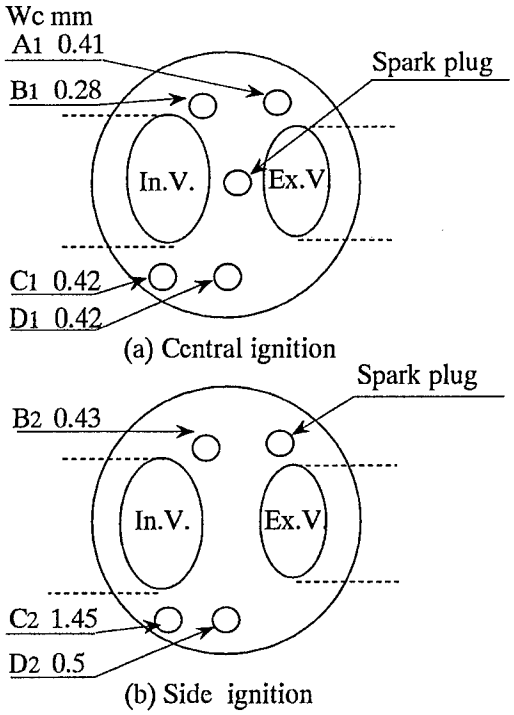

FIG. 5. Effect of location of spark plug and ion detector on quenching crevice width (a) central ignition, (b) side ignition. Engine conditions: 1400 rpm, ϕ = 1.0, MBT ignition timing, IMEP = 0.31 MPa.

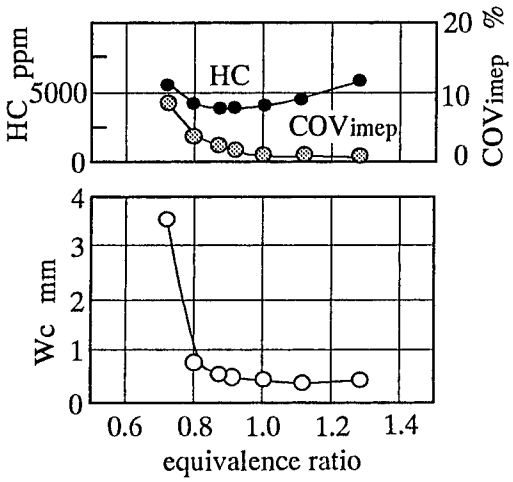

FIG. 6. Effect of equivalence ratio on quenching crevice width. Engine conditions: 1400 rpm, MBT ignition timing, IMEP = 0.31 MPa.

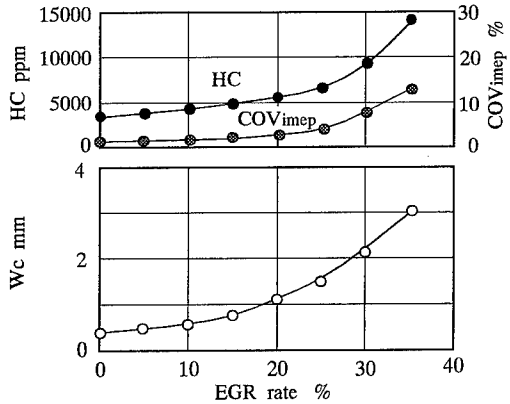

FIG. 7. Effect of EGR rate on quenching crevice width. Engine conditions: 1400 rpm, ϕ = 1.0, MBT ignition timing, IMEP = 0.31 MPa.

Characteristics of Quenching Crevice Width

The dependence of Wc on the mixture equivalence ratio is shown in Fig. 6 for maximum brake torque (MBT) ignition timing along with the HC concentration to examine the relation between the flame quenching distance and exhaust HCs. The coefficient of variations in indicated mean effective pressure (COV_{imep}) was also shown in Fig. 6 to indicate the cycle-by-cycle combustion fluctuations. The smallest *Wc* was obtained at an equivalence ratio of 1.13. When the engine was operated on a leaner mixture, *Wc* increased; when the mixture equivalence ratio was below about 0.8, *Wc* began to increase sharply. Cycle-by-cycle combustion fluctuation and the number of cycles in which slow burning occurred increased. In this case, there may have been some cycles in which the flame was quenched in the crevice before it reached the electrodes and other cycles in which the flame was extinguished before it reached the detector. It is difficult to distinguish the cycles in which flame quenching occurred in the crevice of the detector from those in which slow and partial burning occurred because of the quenching crevice measuring technique. *Wc* was affected by slow and partial burn when the engine was operated on a lean mixture. In the case of rich mixture operation, HC emissions increased because of incomplete combustion caused by lack of oxygen. The HC emission concentration was lowest when the engine was operated on a mixture equivalence ratio between 0.8 and 0.9. When a leaner mixture was supplied, HC emissions also increased. In these conditions, the quenching layer is expected to contribute significantly to HC emission.

Figure 7 shows the characteristics of *Wc*, HC-emission concentration, and COV_{imep} under engine operation with EGR. The quenching crevice width became larger with an increasing EGR because of a

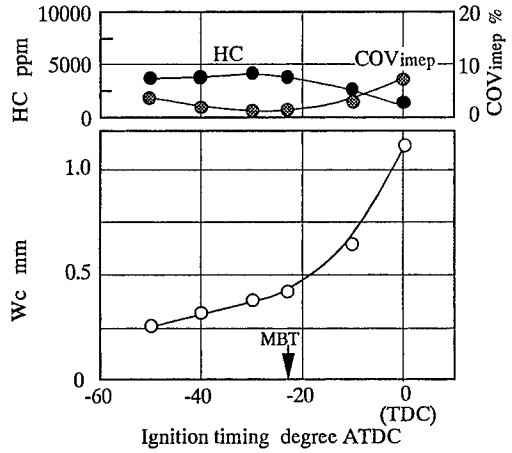

FIG. 8. Effect of ignition timing on quenching crevice width. Engine conditions: 1400 rpm, ϕ = 1.0, IMEP = 0.31 MPa.

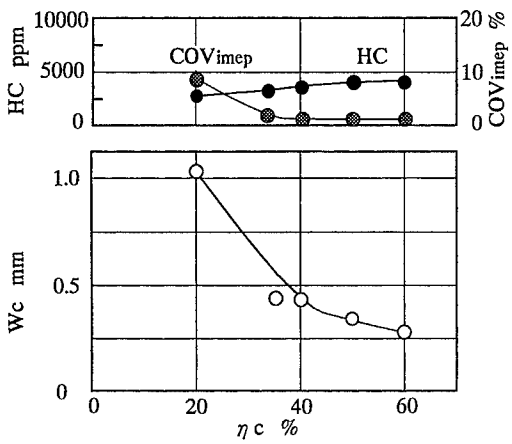

FIG. 9. Effect of charging efficiency on quenching crevice width. Engine conditions: 1400 rpm, MBT ignition timing.

lower flame temperature. As the EGR rate became larger, cycle-by-cycle fluctuations increased and the number of cycles in which the flame propagated slowly and combustion duration was lengthened also increased. In these cycles, because of lower flame and unburned gas temperatures, the flame was extinguished in the crevices or before entering them. In the partial burning cycles, there was not enough time to complete combustion before the exhaust valve opened and the flame could not reach the detector [15]. The HC concentration and *Wc* showed good correlation as EGR increased. Since HCs released from sources in the combustion chamber except from the quenching layers have little dependence on EGR rate, the quenching layers are expected to contribute significantly to total HC emissions. At EGR levels greater than about 30%, *Wc* was affected by the slow and partial burning, as well as those in the lean mixture experiments.

Figure 8 shows the *Wc* results, HC-emission concentration, and COV_{imep} when the ignition timing was chosen as the operating parameter. *Wc* was reduced as the ignition timing was advanced. When the ignition timing was retarded from MBT ignition timing, *Wc* and COV_{imep} increased, whereas the HC-emission concentration decreased. Compared with MBT ignition timing operation, the combustion duration was longer and the gas temperature in the cylinder higher during the late expansion and early exhaust strokes. Since *Wc* and the HC concentration show a poor correlation, it is believed that mixing and the gas temperature play an important role in the oxidation of HCs released from the quenching layer after flame propagation in the cylinder during the expansion and exhaust strokes [16–18]. *Wc* measured at TDC ignition timing would be affected by the slow burning because of the increase of cycle-by-cycle fluctuations.

Figure 9 shows the *Wc* results, HC-emission concentration, and COV_{imep} as a function of charging efficiency. As the charging efficiency increased, *Wc* decreased while the HC-emission concentration increased. The decrease in *Wc* is due to the increased cylinder pressure when the flame reached the quenching crevice. HC emissions arising from surface quenching would be expected to decrease similarly, implying this mechanism is not dominant under these conditions. HC emissions from the piston top crevice would be expected to be independent of the charging efficiency, since the fraction of the fuel that is trapped is unchanged. The cause of the observed increase in HC-emission concentration with charging efficiency remains unknown.

To investigate the dependence of the quenching width on the quenching wall temperature, *Wc* was estimated at different coolant temperatures. Experiments were performed with two air-fuel mixtures, one stoichiometric and the other a lean mixture. The *Wc* results and HC-emission concentration are shown in Fig. 10. It is seen that *Wc* decreased with a rising wall temperature. Since the flammability limit was extended because of reduced heat loss from the flame to the combustion chamber walls, the flame was able to enter the crevices more easily. The HC-emission concentration also showed dependence on the wall temperature and decreased as the wall temperature rose. It was reported recently that the single-surface quenching distance varied approximately linearly with low wall temperature in the steady flame experiments [12].

Dependence of Quenching Crevice Width on Cylinder Pressure and Temperature

Friedman and Johnston [13] proposed an equation describing the dependence of quenching distance on pressure and temperature of the form:

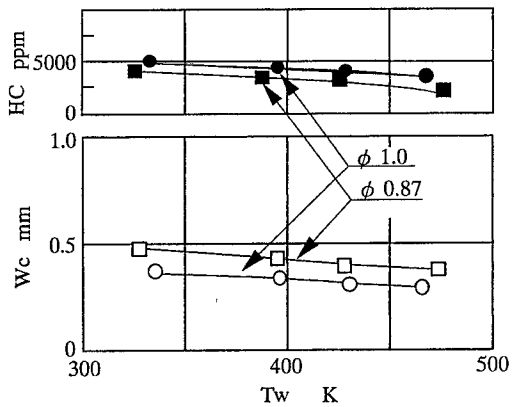

FIG. 10. Effect of cylinder wall temperature on quenching crevice width. Engine conditions: 1400 rpm, MBT ignition timing.

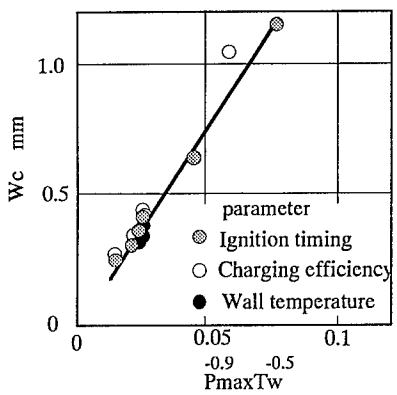

FIG. 11. Experimental dependence of quenching width on cylinder pressure and cylinder wall temperature. Engine conditions: 1400 rpm, $\phi = 1.0$.

$$Wc = K_1 P_{max}^{-0.9} T_w^{-0.5} \quad (1)$$

where K_1 is a constant, P_{max} is the absolute maximum cylinder pressure (MPa), and T_w is the quenching wall temperature (K). The parameters in the equation will depend on stoichiometry and dilution; thus, for proper comparison with literature results, we present data in this form only without EGR and at a single engine speed of 1400 rpm. Figure 11 shows a good correlation with $K_1 = 14.8$. Friedman and Johnston [13] found $K_1 = 4.2$ for their measurements of critical flashback slit width with propane as the fuel. Goolsby and Haskell obtained $K_1 = 7.0$ from measurements of quenching crevice widths in a CFR engine with *iso*-octane fuel [14]. The differences are probably due mainly to differences in the fuel, although other design and operating parameters could play a part.

Conclusion

Two-surface flame quenching distances (the quenching crevice width) under various engine operating conditions were investigated with a specially equipped ion probe that could control a width precisely and detect the flame arrival at a narrow width.

The quenching crevice width was relatively uniform at the surface of the combustion chamber and did not depend sensitively on the location in the combustion chamber, excluding the area close to the spark plug and the end gas area. It was narrower near the spark plug than in other locations and widest in the end gas region.

The quenching crevice width increased with a leaner mixture ratio, larger EGR rate, lower charging efficiency, greater ignition timing retard, and lower wall temperature. When the mixture equivalence ratio was below about 0.8 and EGR rate exceeded about 30%, it began to increase sharply. This may be due to the increase of cycle-by-cycle fluctuation in addition to a lower flame temperature. As the unburned mixture becomes lean or diluted with EGR, the flame quenching layers contribute significantly to total HC emissions.

An experimental equation for the quenching crevice width that was effective for a near-stoichiometric mixture, without EGR and identical engine speed, was deduced as a function of the quenching plate temperature and maximum cylinder pressure.

Acknowledgments

The author wishes to thank Mr. M. Hashimoto and Mr. Y. Hashizume in the Nissan Research Center of Nissan Motor Co. for their invaluable assistance in conducting the experiments.

REFERENCES

1. Daniel, W. A., *Sixth Symposium (International) on Combustion,* The Combustion Institute, Pittsburgh, 1957, pp. 886–894.
2. Wentworth, J. T., *SAE Transactions* 77:403–416 (1968).
3. Wentworth, J. T., *Combust. Sci. Technol.* 4:97–100 (1971).
4. Adamczyk, A. A., Kaiser, E. W., and Lavoie, G. A., *Combust. Sci. Technol.* 33:261–277 (1983).
5. Namazian, M. and Heywood, J. B., SAE Paper No. 82-0088, 1982.
6. Kaiser, E. W., Adamczyk, A. A., and Lavoie, G. A., *Eighteenth Symposium (International) on Combustion,* The Combustion Institute, Pittsburgh, 1981, pp. 1881–1890.
7. Adamczyk, A. A., Rothschild, W. G., and Kaiser, E. W., *Combust. Sci. Technol.* 44:113–124 (1985).
8. LoRusso, J. A., Kaiser, E. W., and Lavoie, G. A., *Combust. Sci. Technol.* 25:121–125 (1981).

9. Dent, J. C. and Lakshminarayanan, P. A., SAE Paper No. 83-0652, 1983.
10. Ishizawa, S. and Takagi, Y., *JSME Int. J.* 30:310–317 (1987).
11. Heywood, J. B., *Internal Combustion Engine Fundamentals,* McGraw Hill, New York, 1988, pp. 596–619.
12. Cleary, D. J. and Farrel, P. V., SAE Paper No. 94-0683, 1994.
13. Friedman, R. and Johnston, W. C., *J. Appl. Phys.* 22:791–797 (1950).
14. Gooisby, A. D. and Haskell, W. W., *Combust. Flame* 26:105–114 (1976).
15. Kuroda, H., Nakajima, Y., Sugihara, K., Takagi, Y., and Muranaka, S., SAE Paper No. 78-0006, 1978.
16. Drobot, F. H., Cheng, W. K., Trinker, F. H., Kaiser, E. W., Siegl, W. O., Cotton, D. F., and Underwood, J., *Combust. Flame* 99:422–430 (1994).
17. Min, K., Cheng, W. K., and Heywood, J. B., SAE Paper No. 94-0306, 1994.
18. Hellstrom, T. and Chomiak, J., SAE Paper No. 95-2539, 1995.

Twenty-Sixth Symposium (International) on Combustion/The Combustion Institute, 1996/pp. 2613–2618

A FIBER-OPTIC PROBE TO MEASURE PRECOMBUSTION IN-CYLINDER FUEL-AIR RATIO FLUCTUATIONS IN PRODUCTION ENGINES

MATTHEW J. HALL AND MICHAEL KOENIG
Department of Mechanical Engineering
The University of Texas at Austin
Austin, TX 78712-1063, USA

An infrared fiber-optic spark plug probe has been developed that will measure the instantaneous fuel-air ratio of the unburned fuel-air mixture near the spark plug in the cylinder of a production automobile engine. The heart of the device is a probe that is placed into the spark plug hole of an engine. It can house both a spark electrode and a pair of optical fibers. Radiation from an infrared source is supplied to one fiber, while the other fiber carries the absorption signal from the probe to a detector and data acquisition equipment. The probe measures variations in the light transmitted through a region surrounding the spark gap due to fluctuations in the fuel concentration in this region. It can record variations in the air-fuel ratio in an engine cylinder at high enough rates to show how engine operating conditions affect the mixing inside the engine cylinder.

The probe was tested in a CFR engine motored at 600 rpm using propane as the fuel. The probe measured the fuel/air ratio spatially averaged over a distance of 8 mm from the tip of the spark plug. The temporal resolution of the measurements was 2.6° crank angle. Four air/fuel equivalence ratios were examined for each of two conditions: one in which the fuel was introduced far upstream of the intake, allowing homogeneous mixing, and one in which the fuel was introduced at the intake port. In the cases where the fuel was introduced at the port, strong inhomogeneities were measured during the intake stroke. The mixture in the vicinity of the spark plug became relatively homogeneous by the middle of the compression stroke.

Introduction

An infrared, fiber-optic spark plug has been developed that will measure the instantaneous air-fuel ratio of the unburned gas mixture near the spark plug in the cylinder of a production automobile engine. The probe fits into the spark plug hole in the cylinder head of a spark-ignition (SI) engine. It can house both a spark electrode and a pair of optical fibers. Radiation from an infrared source is supplied to one fiber, while the other fiber carries the return radiation from the probe to a detector; the signal is then recorded by data acquisition equipment. The fiber-optic probe can record variations in the air-fuel ratio in an engine cylinder at rates high enough to show how engine operating conditions affect the mixing inside the engine cylinder.

The motivation for the development of this device is for use as a diagnostic tool for engine development and analysis. Proper mixing of the fuel and air in a spark-ignition engine is very important for both performance and emissions. Poor mixing resulting in inhomogeneities in the cylinder can lead to poor driveability, but more importantly to excessive emissions. This is a crucial issue as the auto companies struggle to meet the stringent emissions standards set by the 1990 amendments to the Clean Air Act that will require them to significantly reduce emissions in the near future.

In recent years, auto makers have almost universally switched to port fuel injection for their engines to provide the most accurate metering of fuel to each cylinder of the engine. An undesirable consequence of this is that fuel-air mixing problems within the cylinder have intensified. Carburetor and throttle body fuel injection systems introduce the fuel far upstream of the engine intake port; this provides additional time for mixing to occur before the fuel-air mixture reaches the cylinder. Port fuel injectors provide better control of the amount of fuel supplied to each cylinder, but because of their close proximity to the cylinder, there is less time for mixing with the air to occur. This may result in mixture inhomogeneities. The conditions of the mixture in the spark gap near the time of ignition strongly influence ignition and subsequent flame propagation. Studies have shown that the time for the flame kernel to grow to a size of the order of 1 cm correlates strongly with burn duration and peak cylinder pressure [1,2].

Another potentially important application is for direct injection spark-ignition engines in which the fuel is injected directly into the engine cylinder rather than into the intake manifold at the entrance to the cylinder. Rapid mixing is especially important

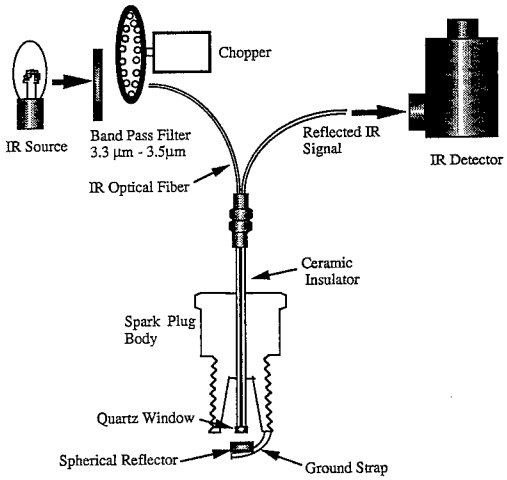

FIG. 1. Schematic of experimental setup.

for these engines since the fuel is often injected relatively late in the cycle resulting in even less time for the fuel to mix with the air. These engines often purposely make use of a stratified fuel-air mixture in which mixing inhomogeneities are desired to, for example, present a richer mixture near the spark plug during ignition. A probe is being developed to quantify these inhomogeneities. It is likely, however, that in firing engines, inhomogeneities associated with the mixing of the fresh charge with the residual are more significant than those of the intake flow.

In-cylinder mixing of the fuel and air has been examined previously by several researchers. Lee et al. [3] used Rayleigh scattering to measure air-fuel mixture fluctuations in the vicinity of the spark plug. Reboux et al. [4] used planar laser-induced fluorescence to image fuel-air ratio fluctuations in an optical engine. Espey et al. [5] and Zhao et al. [6] used planar Rayleigh scattering to image fuel vapor concentrations in optical engines. Sleightholme [7] used a fast-response flame ionization detector to measure in-cylinder mixture inhomogeneities in a SI engine. Morishima and Asai [8] determined mixture strength in an SI engine by measuring the absorption of ultraviolet light by gasoline vapors. Their configuration was similar to that used here. They passed the UV light through a quartz rod mounted in a sensor that fit into the spark plug hole. A mirror mounted on the sensor, 5 mm from the end of the rod, reflected the light, which was transmitted through a second quartz rod. Sohma et al. [9] and Ohyama et al. [10] measured air-fuel ratio fluctuations in SI engines by detecting the UV and visible emissions from CH and C_2 radicals, respectively, in the burned gases.

Several researchers have used optical fibers to make in-cylinder measurements of engine flow and combustion processes. Witze et al. [11] developed a spark plug with optical fibers that detected the luminous emission from the flame kernel. These researchers were able to quantify the rate of early flame growth and its movement [12]. Spicher et al. [13] developed an engine that used large arrays of optical fibers to detect in-cylinder flame location by detecting flame luminosity. More recently, Philipp et al. [14] developed a tomographic technique to locate the flame position in the engine cylinder using a fiber-optic instrumented head gasket. Shoji et al. [15] used optical fibers to gather spectroscopic measurements of radical behavior in an engine under knocking conditions.

To the authors' knowledge, this research presents the first use of infrared grade optical fibers for engine measurements and specifically, for infrared absorption spectroscopy to make in situ measurements of gaseous species within an engine cylinder. The use of these fibers for remote spectroscopic sensing has been examined extensively by researchers at the Technical University of Vienna [16], and Mongia et al. [17] have used them for IR absorption measurements of methane concentration fluctuations in a non-premixed burner.

Methodology

Experimental Setup and Principle of Operation

The recent availability of infrared transparent optical fibers made the development of the probe possible. Typical telecommunications optical fibers do not transmit radiation beyond approximately 1.5 μm. This necessitated the use of IR grade chalcogenide fibers (from Amorphous Materials, Inc.), which are transparent (losses between 0.5 and 4 dB m^{-1}) from approximately 2.5 to 12.5 μm. The fibers had a core diameter of 500 μm and were glass clad and plastic coated. A schematic of the device is shown in Fig. 1. The probe is housed within a conventional spark plug body. A pair of optical fibers was located along the axis of the plug body, inserted into a 4.8-mm-diameter ceramic rod with four 0.8-mm-diameter holes. One fiber was placed in each of two holes. A tungsten wire spark electrode can be situated in one of the two remaining holes but was not used for the work presented here since only motored measurements were gathered (the fourth hole was not used). The ends of the fiber were flush with the in-cylinder end of the ceramic rod and spark plug housing. The radiation from the IR light source (a 50-W quartz tungsten-halogen bulb) was collimated using a 25-mm focal length (fl) concave mirror and passed through a 3.3–3.5-μm IR band-pass filter to a second 25-mm fl concave mirror that focused the radiation, coupling it into one of the fibers. The IR band-pass filter allowed the transmission of the radiation corresponding to the C—H stretch vibrational band,

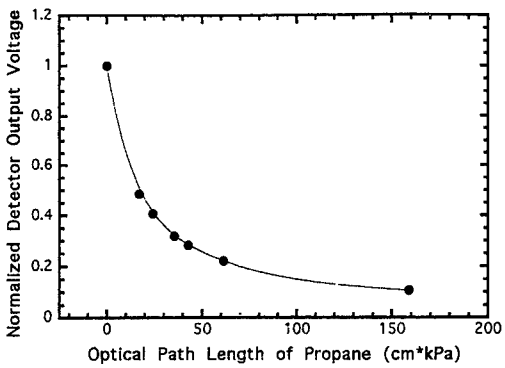

FIG. 2. Normalized detector output voltage (V/V_O) versus optical path length (partial pressure x path length) for propane measured in a combustion bomb at a temperature of 25°C and total pressure of 100 kPa.

the strongest absorption feature that is common to all hydrocarbon fuels. Before entering the fiber, the radiation passed through a chopper wheel that produced a square wave signal of 1.3 kHz.

The radiation exited the fiber in the engine cylinder, passed through a 1-mm-thick quartz window, and was reflected back by a 4.5-mm fl concave copper mirror brazed to the ground electrode of the spark plug body. This mirror can be replaced to change the focal length to alter the spatial resolution and the sensitivity of the measurements. The reflected IR radiation entered the second fiber after some of it had been absorbed by the fuel vapor in the spark gap. The radiation traversed a distance inside the engine equal to twice the distance between the edge of the quartz window and the mirror before entering the second fiber. This resulted in a path length of 1.6 cm and, hence, a spatial resolution of 0.8 cm. It should be noted that this is considerably larger than a typical spark plug gap. The reflected signal received by the transmitting fiber was detected by an InSb liquid N_2 cooled IR detector after being focused by another pair of concave mirrors. The output was read by the A/D converter of a PC at a sample rate of 25 kHz. The PC simultaneously recorded the time, radiation intensity, and engine cylinder pressure. Since the mirror is larger than a typical spark plug electrode, it will cause some disturbance of the flow; it is doubtful, however, that it will seriously affect large-scale inhomogeneities. The signal-to-noise ratio of the measurements ranged from about 40 to more than 100, allowing us to resolve fuel concentration fluctuations of about +/−2–3% or less.

The radiation intensity at a given wavelength can be related to the average concentration of fuel vapor in the spark gap through Beer's law:

$$\ln \frac{I_o}{I} = \sigma_{\text{fuel}} C_{\text{fuel}} L \qquad (1)$$

where I is the measured intensity of the radiation detected in the 3.3–3.5-μm band, I_0 is the intensity of radiation detected with no fuel present, σ_{fuel} is the absorption cross section of the fuel, C_{fuel} is the average fuel concentration, and L is the optical path length (twice the distance from the ends of the fibers to the mirror).

Signal Strength

An important question at the onset of the research was what absorption path length would be required to obtain a sufficient amount of absorption for the measurements. Very little information on hydrocarbon absorption intensities exists in the literature, so required path lengths were estimated based on the work of Fuss et al. [18], as well as, their unpublished work on propane.

The variation in the signal from crank angle to crank angle indicates the variation in the integrated concentration of fuel vapor in the spark gap that may be due to compression and/or fluctuations in mixture homogeneity. The absorption increases during the compression stroke as the mixture density increases. The fluctuations can be separated from the systematic change because of the compression by subtraction during data analysis. The signal then yields the cycle-to-cycle variation in mixture strength at each crank angle. The measurements of instantaneous mixture strength can be made quantitative through a calibration procedure using a well premixed fuel/air mixture of known equivalence ratio in the engine for comparison.

In the case of liquid fuels, droplets are usually not present just before ignition, having vaporized earlier; however, the presence of droplets along the optical path or wetting of the mirror may also be detectable since this may cause a sudden dropout of the signal. This aspect has yet to be investigated, however.

Results and Discussion

Testing and Evaluation

Initial testing of the probe and detector system was conducted in a high-pressure combustion vessel. The vessel was pressurized with propane/air mixtures to pressures similar to those in an engine just before ignition (about 13 atm). Figure 2 shows the transmittance signal as a function of the optical density of propane (product of the concentration and path length). The intensity was found to monotonically decrease as the optical density of the propane increased. The response was not the simple exponential function predicted by Beer's law at a given wavelength. This deviation from Beer's law was to be expected because the measurements were integrated over the 3.3–3.5-μm band in which the

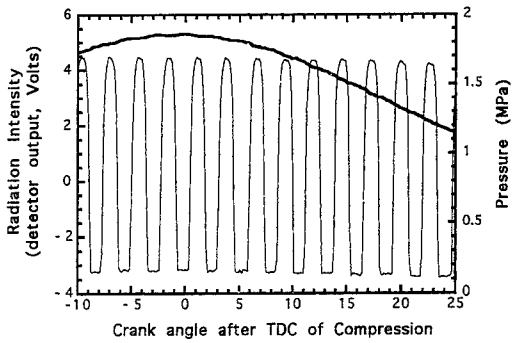

FIG. 3. Chopped signal of the radiation intensity reaching the detector for a narrow band of crank angle around TDC of compression. The cylinder pressure is shown as well.

adsorption cross section of propane varies with wavelength; it is thus an integration of many different exponential functions. These tests also ensured that the probe could withstand elevated pressures.

Engine Experiments

The probe was tested in a high-speed CFR engine motored at 600 rpm using propane as the fuel. The airflow rate was measured using a bellows-type flow meter. The engine was operated unthrottled and the volumetric efficiency was 79%. A surge tank was located 0.4 m upstream of the intake port. The propane was introduced as a continuous flow and metered by a calibrated rotometer. The compression ratio was 8.4.

Four air/fuel equivalence ratios were examined for each of two conditions: one in which the fuel was introduced 3 m upstream of the surge tank, allowing homogeneous mixing, and one in which the fuel was introduced 10 cm upstream of the intake port. The four equivalence ratios (ϕ) were 0.0, 0.78, 1.14, and 1.46. The probe measured the fuel/air ratio spatially averaged over the 8-mm distance between the edge of the window and the mirror.

Figure 3 shows the detector signal and cylinder pressure as a function of crank angle degrees from TDC for a $\phi = 0.0$ case. The baseline voltage of the signal was found to rise and fall slightly along with the cylinder pressure (difficult to resolve in Fig. 3). This may have been due to surface emissions from the mirror or ceramic as the in-cylinder temperatures changed through the cycle. The peak height of the modulated signal did not change significantly since there was no fuel present. The temporal resolution of the measurements was 2.6° crank angle, equal to the separation between the peaks in the chopped signal. The 2.6° crank angle resolution of the measurements was arbitrary and determined by the speed of our chopper motor. There were about

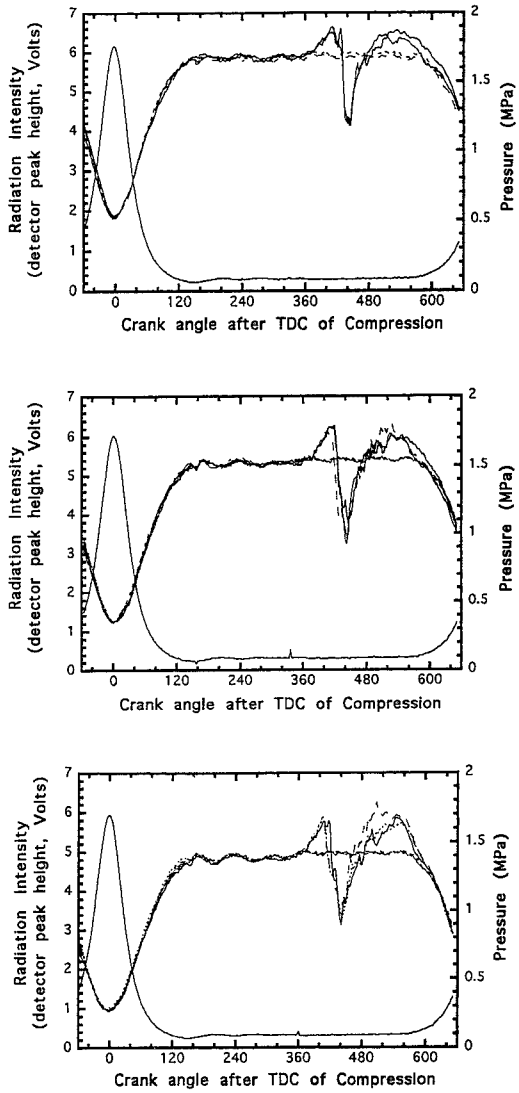

FIG. 4. (a) Radiation intensity versus crank angle for $\phi = 0.78$. Two upstream and two port injected cycles are shown along with the cylinder pressure. (b) Radiation intensity versus crank angle for $\phi = 1.14$. Two upstream and three port injected cycles are shown along with the cylinder pressure. (c) Radiation intensity versus crank angle for $\phi = 1.14$. Two upstream and three port injected cycles are shown along with the cylinder pressure.

22 measurements between chops. The rms fluctuation of the preaveraged data was less than 1% of signal amplitude for the raw data shown in Fig. 3. The radiation signals were analyzed using a data reduction code that found each individual peak height as the difference between the highest average of the five points at a peak minus the average of the lowest

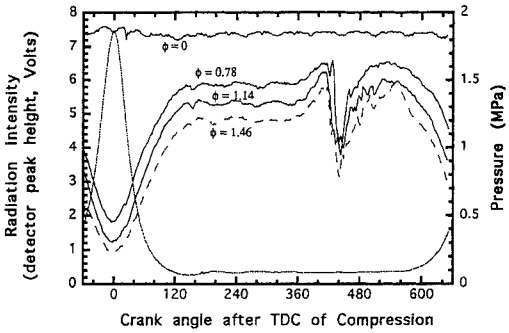

FIG. 5. Radiation intensity versus crank angle for the four equivalence ratios. One port injected cycle is shown for each.

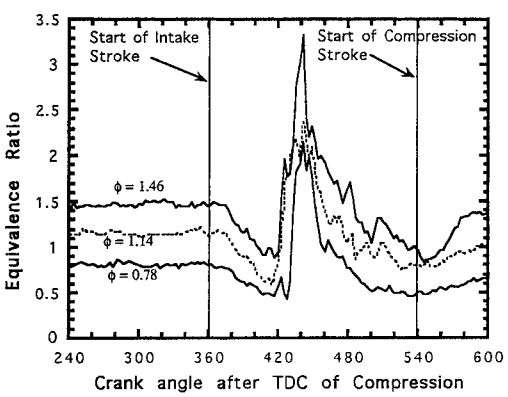

FIG. 6. Equivalence ratio in the region of the spark gap versus crank angle for three individual port injected cycles each having a different nominal equivalence ratio.

average of five points in the troughs on either side. This corrected for changes in baseline height.

Figure 4 shows the peak heights over the complete engine cycle for the three nonzero equivalence ratio cases and compares runs in which the fuel was added far upstream with the runs using port injection. Each part of the figure shows two or three cycles taken with upstream injection and two or three cycles with port injection. The engine cylinder pressure is also shown. The peak heights shown represent the intensity of radiation reaching the detector during each crank angle interval and is an indication of the instantaneous equivalence ratio in the vicinity of the spark plug.

For each of the three equivalence ratios, the same characteristics are noted. The fuel and air are well mixed by the middle of the compression stroke and through the exhaust stroke. Within the accuracy of the measurements, no cycle-to-cycle or crank-angle-by-crank-angle fluctuations are seen through the exhaust stroke. Some oscillations in the signal that are repeatable from cycle to cycle can be seen during the exhaust stroke; however, these are related to pressure fluctuations rather than to fluctuations in the local equivalence ratio. A dramatic difference between the upstream and port injection cases can be seen beginning with the start of the intake stroke. As the mixture enters the cylinder, the signal rises, indicating that the mixture is initially fuel lean; this represents the composition of the charge that entered the cylinder toward the end of the previous cycle. The signal then drops rapidly, indicating a very rich mixture; this is due to the slug of rich mixture that accumulated near the fuel injection point between intake events. The signal then rises again as the fuel-lean mixture is inducted toward the end of intake. As the charge mixes during the end of the intake stroke and the beginning of the compression stroke, the mixture becomes homogeneous, at least over length scales equal to and greater than the spatial resolution of 8 mm. While the homogeneity of the mixture in the surge tank was not verified, the extremely good reproducibility of the upstream injection measurements is a good indication of the homogeneity on the scale of the spatial resolution; in addition, the symmetry of the signal about TDC indicates that the mixture was homogeneous.

Figure 5 shows peak height data from one cycle for each of the four equivalence ratios for the port injection case. The figure provides a quantitative calibration that can be used to determine the instantaneous equivalence ratio. It can be seen, for example, that for the $\phi = 1.46$ case, the mixture in the spark gap is at one point as lean as approximately $\phi = 0.8$ during the intake stroke and for the $\phi = 0.78$ cycle, the mixture in the spark gap became richer than $\phi = 1.5$.

The data taken from the homogeneous charge cases were used to convert the intensity signal from the IR detector into equivalence ratio (or equivalently fuel concentration) data. This was done at each crank angle interval in the engine cycle to account for the effects caused by variations in density and temperature. A least-squares fit to a rational function of the form

$$\phi = \frac{\left(a - \frac{I}{I_o}\right)}{\left(b + c\frac{I}{I_o}\right)} \tag{2}$$

was used, where ϕ is the equivalence ratio, a, b, and c are the coefficients that are fit to the homogeneous charge data, I is the signal intensity taken from the probe, and I_O is the signal intensity taken from the probe during the no fuel case. I_O and I were evaluated at each crank angle interval in the engine cycle to correct for variations in the background light intensity. This calibration was done using an algorithm that performs a parabolic expansion of χ^2 to create

a least-squares fit of the data to an arbitrary function [19].

Some of the results from this analysis are presented in Fig. 6, which shows the equivalence ratio at each 2.6° crank angle interval through most of the engine cycle for three individual port injected cycles, each having a different nominal equivalence ratio. The behavior reflects the data shown in Fig. 5. The accuracy of the derived equivalence ratios that are richer than $\phi = 1.46$ will be somewhat less than the leaner equivalence ratios because those data were extrapolated rather than interpolated from the homogeneous case data.

Summary and Conclusions

An infrared fiber-optic spark plug probe has been developed that will measure the instantaneous fuel-air ratio of the unburned fuel-air mixture near the spark plug in the cylinder of a production automobile engine. The probe was tested in a CFR engine motored at 600 rpm using propane as the fuel. The probe measured the fuel/air ratio spatially averaged over a distance of 0.8 cm from the spark plug. The temporal resolution of the measurements was 2.6° crank angle.

The probe was found to be very sensitive to changes in the density of the propane in the cylinder; these are the result of either changes in the total pressure or the local equivalence ratio. By calibrating the probe using homogeneous mixtures of known equivalence ratio, it is possible to obtain quantitative cycle-resolved measurements of the local equivalence ratio near the spark plug.

For cases in which the fuel was introduced near the intake port, strong mixture inhomogeneities were measured during the intake stroke. The mixture in the vicinity of the spark plug became relatively homogeneous by the middle of the compression stroke.

Acknowledgments

The support and help of Dr. Richard Anderson, Mr. William Clemens, and the Ford Motor Company made this research possible. The assistance of Mr. Tim Timko of Champion Spark Plugs is gratefully acknowledged.

REFERENCES

1. Hall, M. J., Transactions of the Society of Automotive Engineers, Paper No. 890991, 1989.
2. Young, M. B., Transactions of the Society of Automotive Engineers, Paper No. 810020, 1981.
3. Lee, K.-H. and Foster, D. E., SAE Paper No. 95-0814, 1995.
4. Reboux, J., Puechberty, D., and Dionnet, F., SAE Paper No. 94-1988, 1994.
5. Espey, C., Dec, J. E., Litzinger, T. A., and Santavicca, D. A., SAE Paper No. 94-0682, 1994.
6. Zhao, F.-Q., Taketomi, M., Nishida, K., and Hiroyasu, H., SAE Paper No. 93-2641, 1993.
7. Sleightholme, G. R., SAE Paper No. 90-0484, 1990.
8. Morishima, R. and Asai, K., SAE Paper No. 92-0235, 1992.
9. Sohma, K., Yukitake, T., Azuhata, S., and Takaku, Y., SAE Paper No. 91-0499, 1991.
10. Ohyama, Y., Ohsuga, M., and Kuroiwa, H., SAE Paper No. 90-1712, 1990.
11. Witze, P. O., Hall, M. J., and Wallace, J. S., Transactions of the Society of Automotive Engineers, Paper No. 88-1638, 1988.
12. Witze, P. O., Hall, M. J., and Bennett, M. J., Transactions of the Society of Automotive Engineers, Paper No. 90-0023, 1990.
13. Spicher, U., Schmitz, G., and Kollmeier, H.-P., SAE Paper No. 88-1637, 1988.
14. Philipp, H., Plimon, A., Fernitz, G., Hirsch, A., Fraidl, G., and Winklhofer, E., SAE Paper No. 95-0681, 1995.
15. Shoji, H., Shimizu, T., Yoshida, K., and Saima, A., SAE Paper No. 95-2407, 1995.
16. Mizaikoff, B., Taga, K., and Kellner, R., *Vibrational Spectrosc.* 8:103–108 (1995).
17. Mongia, R., Tomita, E., Hsu, F., Talbot, L., and Dibble, R., AIAA Paper No. 96-0174, 1996.
18. Fuss, S. P., Ezekoye, O. A., and Hall, M. J., 1995 ASME International Mechanical Engineering Congress and Exposition, San Francisco, Paper 95-WA/HT-32, November, 1995.
19. Bevington, P. R., *Data Reduction and Error Analysis for the Physical Sciences*, McGraw Hill, New York, 1969.

Twenty-Sixth Symposium (International) on Combustion/The Combustion Institute, 1996/pp. 2619–2626

TIME-RESOLVED INVESTIGATION OF HOT SPOTS IN THE END GAS OF AN S. I. ENGINE BY MEANS OF 2-D DOUBLE-PULSE LIF OF FORMALDEHYDE

B. BÄUERLE AND J. WARNATZ
Universität Stuttgart
Institut für Technische Verbrennung (ITV)
Pfaffenwaldring 12, D-70569 Stuttgart, Germany

F. BEHRENDT
Universität Heidelberg
Interdisziplinäres Zentrum für Wissenschaftliches Rechnen (IWR)
Im Neuenheimer Feld 368, D-69120 Heidelberg, Germany

Within the last few years, the understanding of the origins of engine knock has advanced considerably. Numerical experiments have shown that inhomogeneities in temperature distribution of premixed gases of only 10 K, or even less, can lead to the onset of autoignition. This is called ignition by exothermic centres (ETCs) or, more colloquially, by "hot spot". Still, there is no experimental technique available to detect such small temperature fluctuations directly. In an earlier paper, the existence of hot spots was verified by application of two-dimensional laser-induced fluorescence (2D-LIF) using formaldehyde as tracer. In the two-stage ignition of hydrocarbons, formaldehyde is formed early and then is decomposed very rapidly after ignition.

The core of the experimental set-up consists of a modified, single-cylinder, two-stroke engine with full optical access to the combustion chamber from above. The engine is run with primary reference fuel (PRF), a mixture of *n*-heptane and *iso*-octane. Two excimer lasers, coupled into one dye laser, make the double-pulse excitation of formaldehyde possible. The fluorescence signals are detected with two intensified, charge-coupled device (ICCD) cameras, amplified, and stored in a PC.

Under different knocking conditions, pairs of two-dimensional LIF pictures, separated by 50 μs and less, and corresponding pressure traces have been recorded. These pairs of frames show both the evolution of hot spots in the end-gas region as well as the evolution of the regular flame front at the border between unburned end gas and burned exhaust gas. Hot spot expansion speeds between 30 and 750 ms^{-1} have been detected, as well as flame front reverse speeds between 10 and 180 ms^{-1}.

Introduction

Both increasing pollutant emission originating from still-growing individual traffic and consumer demands for more fuel economy are major reasons to increase the efficiency of combustion engines. This can be done by simply increasing the engine compression ratio. However, as it increases, a limiting value is reached above which engine knock sets on, giving an upper limit of fuel economy by impairing the engine power output and deteriorating its torque. In addition, heavy or prolonged knocking may seriously damage engine parts such as pistons and the cylinder head. The knocking sound originates from both vibratory movements of the charge [1] and steep pressure pulses exciting the engine block. Hence, knocking combustion is an undesirable mode of combustion that has been of scientific interest right from the beginning of motorization. A first paper by Mallard and Le Chatelier dates back to 1883 [2], followed by a paper from Nernst in 1905 [3], and one by Clerk in 1926 [4]. From then on, scientific reports on knocking combustion have been published regularly.

In knocking combustion, thermochemical and gas-dynamic effects are involved as well as the stochastic nature of hot-spot occurrence. This undesired mode of combustion is initiated by exothermic centers (ETCs), so-called hot spots, occurring at one or more sites in the end gas due to inhomogeneities in its temperature [1,5]. In numerical experiments, differences in temperature of 10 K [6], or even less [1], were found to initiate spontaneous autoignition. The evolution of a hot spot is characterized by three stages: induction, ignition, and expansion appearing as flame front propagation. In an internal-combustion (i.c.) engine, the remaining end gas (unburned) is enclosed by the combustion-chamber walls, and the regular flame front and is compressed by both the piston and the hot burned gases behind the

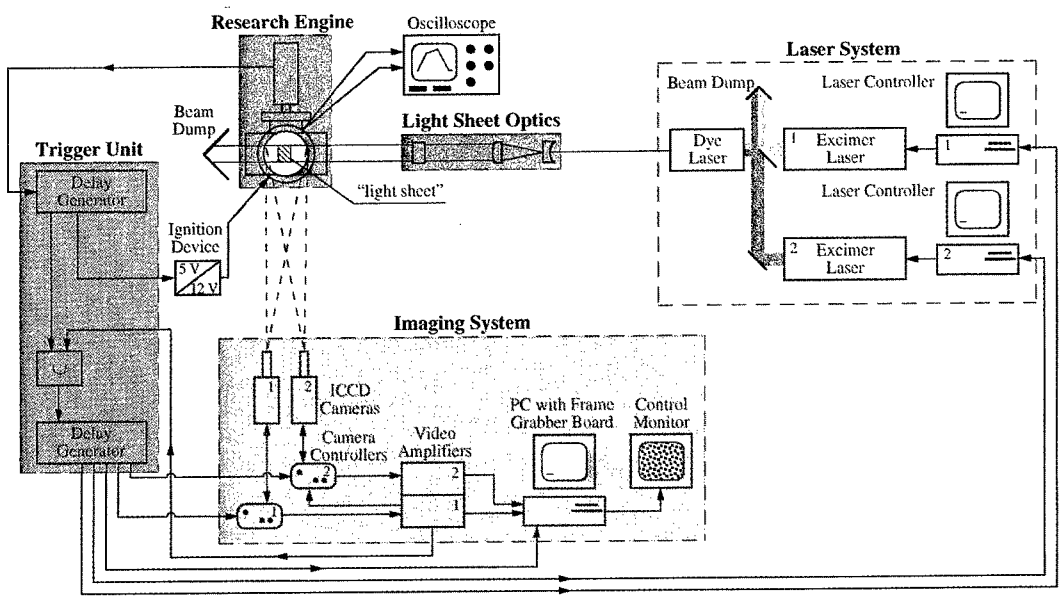

FIG. 1. Schematic of the experimental set-up.

regular flame front. At temperature and pressure levels sufficiently high, the end gas will autoignite, starting at the hot spots, before the regular flame front can consume the remaining charge.

In some cases, when the rate of energy release inside the hot spot(s) is high enough, shock waves will develop. These can also initiate a detonation wave if the chemical reaction front accelerates sufficiently that it eventually travels with one of the shock waves. This self-sustaining process is possible due to the large temperature rise as a result of both chemical energy release and compression by the shock waves. Local stresses attained from the combined load by the heat release from detonation and pressure levels due to the shock wave can significantly exceed the material tensile strengths in the surface layers of piston and cylinder (to a depth of 15 μm) [7] and, hence, cause the damage mentioned above.

As yet, it is not possible to directly detect temperature fluctuations as small as 10 K (or less) at temperature levels of ≈700 K and higher. However, the thermochemical aspect of hot spots will give some information enabling their detection spectroscopically within the end-gas region. Autoignition in hydrocarbon combustion begins with a two-stage ignition, the detailed chemical processes of which are fairly well understood. During the induction time, in cool flames—where low-temperature chemistry governs chemical reaction processes—a lot of partially oxidized species (e.g., peroxides) are formed. Later in the ignition process, these will internally rearrange to form aldehydes (e.g., formaldehyde). This is a relatively slow process. Finally, after autoignition has taken place and high-temperature chemistry governs the chemical reaction processes, these intermediates will be oxidized very quickly to form carbon dioxide. Experimentally, formaldehyde was detected in knocking spark-ignition (s.i.) engine cycles as early as 1933 by Rassweiler and Withrow [9]. As an intermediate species, occurring under cool-flame conditions and producing fairly high concentrations, it has been detected in a jet-stirred reactor [10,11].

Because of this "slow" formation in the low-temperature chemistry regime and directly following "fast" consumption under high-temperature conditions, formaldehyde is a good natural tracer for hot spots and burned gases, respectively. Its abundance in the end gas—concentrations of up to 12,000 ppm (averaged) and 35,000 ppm (single shot) have been measured [12]—together with its simple excitation makes it an ideal tracer for studying the evolution of hot spots by means of a two-dimensional double-pulse laser-induced fluorescence (2-D double-pulse LIF) technique.

Experimental

The experimental set-up used here is an extended and slightly modified version of that described in earlier papers [13,14]. The set-up (Fig. 1) comprises five main units: the laser system, the light-sheet optics, the research engine with oscilloscope (pressure traces), the imaging system, and a trigger unit.

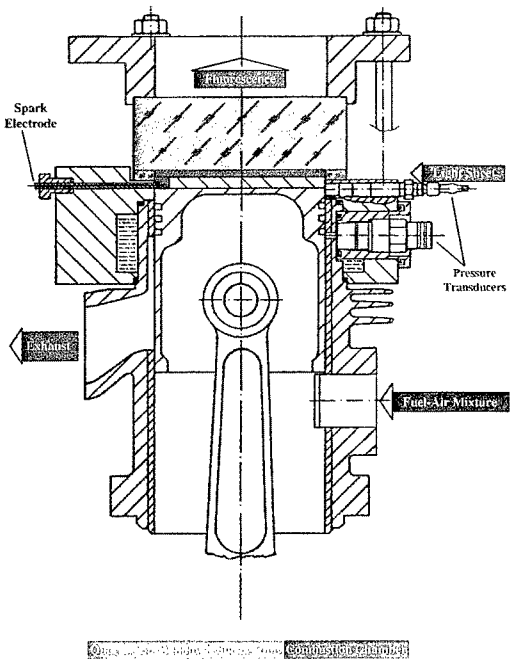

FIG. 2. Cross section of the research engine.

In order to obtain the temporal evolution of hot spots, ultra-high-speed detection with frame intervals down to 10 μs is needed. This is equivalent to a frame rate of 100 kHz and exceeds available excimer-laser repetition rates by several orders of magnitude. Therefore, two excimer lasers (both Lambda Physik LPX 205i) are used, where excimer 1 and the dye laser (Lambda Physik FL 3002) are aligned for maximum energy output ($\approx$2.6 mJ). Afterward, the beam of excimer 2 is steered into the dye laser by means of two mirrors. One of the two mirrors reflects only half of the beam into the dye laser, the other half is directed into a beam dump. The rear of this mirror also cuts off half of the beam of excimer 1, which is also directed to the beam dump. With this laser set-up, a second, but weaker, dye laser beam ($\approx$1.3 mJ) is obtained. Its lack of beam power, in comparison to the power of beam 1, is confirmed by the fact that beam 2 can be aligned only by using two external mirrors. Any change of the alignment inside the dye laser deteriorates the power of both beams, or the dye-lasing obtained by one of them vanishes.

The dye-laser beams of both input beams travel along the same light path. They are shaped into a two-dimensional laser light sheet by means of three quartz cylinder lenses. The first two of them form a Galileian telescope, expanding and collimating the beam in its horizontal plane. The third lens is turned 90° and focuses the light in the horizontal plane into a sheet of less than 60 μm thickness in its line of focus.

The above-mentioned tracer species, formaldehyde, is excited at 353.2 nm, the 4_0^1 transition in the $\tilde{A}^1A_2 \leftarrow \tilde{X}^1\ A_1$ band. The fluorescence can be detected in the visible blue between 400 and 450 nm.

The research engine is a modified, industrial, single-cylinder, two-stroke engine (ILO L 372) with a displacement of 372 cm^3 and a bore of 80 mm. Figure 2 shows a cross section of the engine cylinder with the piston at top dead center (TDC). Both the piston and the cylinder have undergone major modifications, and the cylinder head has been replaced by a full-sized quartz window. Except for a pocket for the spark electrode, which is introduced through the top end of the cylinder wall, the combustion chamber is disc shaped with a clearance height of only 4 mm. This ensures that flame propagation can be looked upon as essentially two-dimensional, which has been verified in former investigations. A quartz ring at the upper end of the cylinder enables the excitation-laser light sheet to traverse the combustion chamber in a plane parallel to the piston crown. The fluorescence signal obtained is detected perpendicularly to that plane through the full-sized top window.

In the experiments, the engine is run under full load and kept at constant speed of 1000 rpm by an electric dynamometer coupled to the crank shaft. Speed fluctuations are minimized by means of a large flywheel. The fuel, a PRF of 90 ON, is supplied by the original carburettor. The in-cylinder pressure is measured by a relative pressure transducer (Kistler 6001, upper, see Fig. 2) and an absolute pressure transducer (Kistler 4045-A20, lower, see Fig. 2) and stored using a digitizing oscilloscope (Tektronix 11201).

The frames are taken by two intensified, charge-coupled device (ICCD) cameras (Proxitronic Nanocam). Lens equipment and stray-light filters are described in Refs. 13 and 14. The overall weaker signals require the use of video amplifiers, which in addition offer output connector sockets for the video synchronization signal. This signal has to be fed into the logical AND gate in the trigger unit in order to always achieve chip readout at the same moment. This also ensures a constant quality of the frames. The PC and the frame-grabber board are both described in more detail in Refs. 13 and 14.

The trigger unit comprises two four-channel, digital, pulse/delay generators (Stanford Research SRI 250) and an AND gate. The first delay generator receives a master trigger from the shaft encoder of the engine and produces one trigger signal to drive the ignition device and a second one to be fed into the AND gate. If this trigger and the video-synchronization signal are present at the same time, the second delay generator will receive a master trigger in

order to start the lasers, the cameras, and the PC (in that order).

Results and Discussion

Two pairs of images of laser-induced fluorescence of formaldehyde and their corresponding pressure traces of the respective engine cycles, chosen from a wide number of pairs of frames, are presented here. Each pair is taken from an individual knocking cycle. Ignition timing was set to 16° crank angle before top dead center (CA BTDC). Skip firing ensures good cylinder filling [13,14]. The use of two excimer lasers and two cameras makes it feasible to attain a short-time temporal resolution of the rise and evolution of hot spots in a knocking engine cycle. Figures 3, 4 and 6, 7 show four frames taken by double-pulse excitation of formaldehyde, looking into the combustion chamber from above via the full-size top window. The camera gates (exposure times) have been set to 50 ns, to fully enclose the laser pulses of 28 ns duration (nominally). The original grey values produced by the frame-grabber board are transformed, applying a false-color code in which 0 (no intensity) is denoted by white and 255 (maximum intensity) by red.

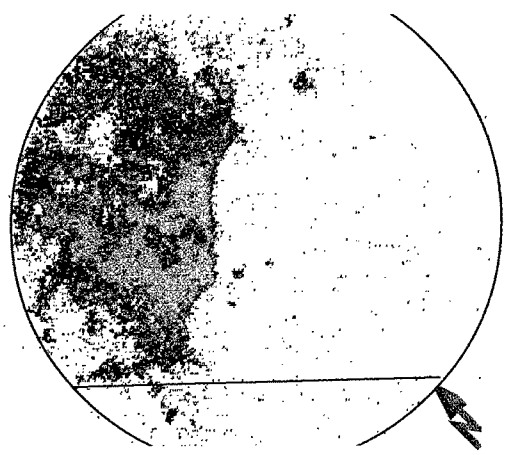

FIG. 3. First frame of 2-D double-pulse LIF of formaldehyde (9.6° CA ATDC).

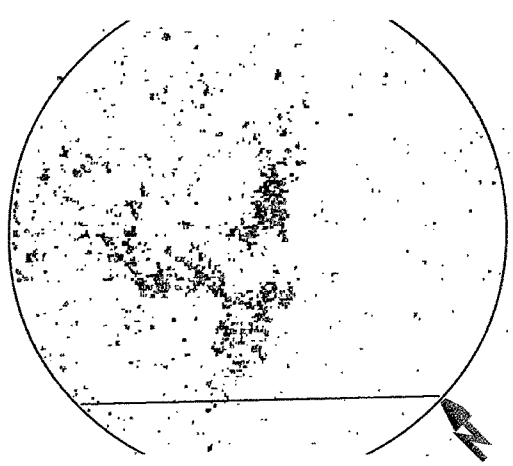

FIG. 4. Second frame of 2-D double-pulse LIF of formaldehyde (+0.3° CA).

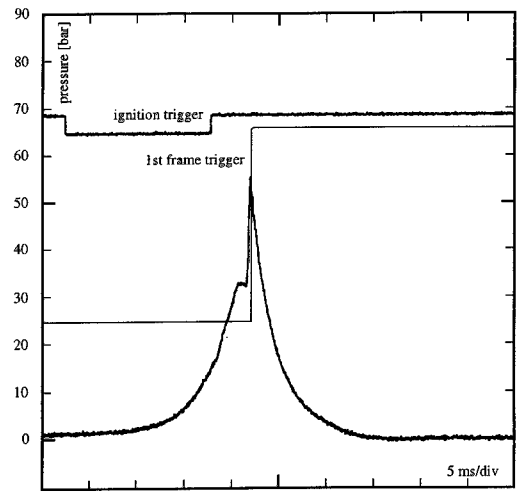

FIG. 5. Corresponding pressure trace for Figs. 3 and 4.

In the LIF-frames, the solid circular lines represent the cylinder walls. The dashed line in the lower half of an image represents the left border of the laser light sheet, which travels from right to left; its right-hand border is outside of the image. The red arrow on the lower right indicates the position of the spark electrode. It is noticeable that the corresponding second frame of each pair (Figs. 4 and 7) exhibits much weaker fluorescence due to the weaker second laser beam. Above the dashed lines within the range of the light sheet, the end-gas region on the left-hand side (colored areas) with enclosed hot spots (white), and the burned gases on the right-hand side (white) can be seen. The border between end gas and burned gas shows the contour of the regular flame front originating from the spark electrode. The corresponding pressure traces are plotted versus time and show the ignition trigger marks as well as the trigger marks of the first frame. Due to the very short delay between the two frames, in these plots, the trigger mark of the second frame coincides with the one of the first. Both frame and ignition triggers are fixed with respect to the crank shaft angle. Hence, the pressure traces after ignition can move relative to the trigger marks due to cycle-to-cycle variations.

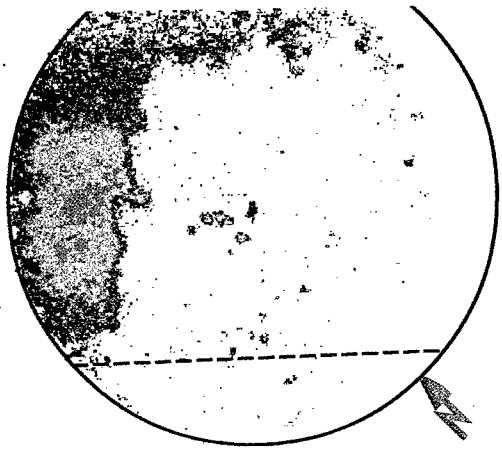

FIG. 6. First frame of 2-D double-pulse LIF of formaldehyde (6.6° CA ATDC).

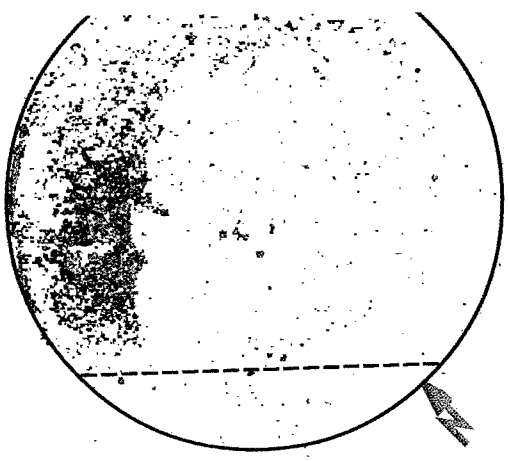

FIG. 7. Second frame of 2-D double-pulse LIF of formaldehyde (+0.06° CA).

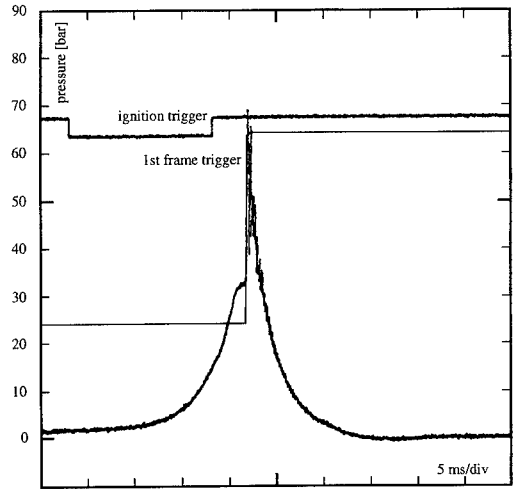

FIG. 8. Corresponding pressure trace for Figs. 6 and 7.

Figure 3 shows the first frame of a double-pulse pair taken at 9.6° crank angle after top dead center (CA ATDC), 4.27 ms after ignition. It shows various hot spots of different sizes within the end-gas region. Near the center of the light sheet, some regions of higher fluorescence intensity can be seen due to higher power in the center of the laser beam. At the right-hand border of the end-gas region, the regular flame front shows an unwrinkled contour. This phenomenon has been observed in quite a number of frames, but has yet not been associated to an effect relevant to knocking combustion, such as pressure gradient, hot-spot expansion speed, etc. The same effect has been detected with an ultra-high-speed Schlieren technique (up to some 700,000 frames per second) by König et al. [15] and Bradley et al. [16] during a joint project using the same engine type. The pressure trace (Fig. 5) shows a "moderately" knocking cycle with a peak pressure of 55 bar and a pressure gradient of 55.7 bar/ms between the first local minimum pressure and the peak pressure. The trigger location for the first frame is immediately after the pressure peak. This can also be seen from the relatively large sizes of the hot spots in Fig. 3. This late timing causes the second frame (Fig. 4), taken 0.3° CA (50 μs, respectively) later, to show a very weak fluorescence intensity. In addition to the usually weaker excitation, this is due to the advanced state of reaction. Nevertheless, it can be calculated from these two frames that hot-spot expansion speeds of 170–180 ms^{-1} are attained. Furthermore, it can be seen that the regular flame front is driven back, contrary to its original direction of propagation. Reverse speeds of 90–100 ms^{-1} are found.

The second pair of frames (Figs. 6, 7) is taken during a very "violently" knocking cycle, as can be seen from the pressure trace in Fig. 8. The cycle exhibits a very steep gradient of 75.8 bar/ms, arising directly from the first local maximum pressure of 32.3 bar. The peak pressure reaches a very high value of 68.4 bar and declines with strong oscillations that still attain local maxima of 65.2 bar and 50.0 bar. The latter clearly exceeds the peak pressure of most of the "moderately" knocking cycles. The first frame shows the situation at the onset of autoignition (see trigger mark in Fig. 8). Several small hot spots along the cylinder wall, as well as some end-gas-enclosed ones, can be seen. The original size of the enclosed hot spots in the first frame (Fig. 6) is approximately 0.5–1.0 mm, and it is difficult to recognize them as hot spots (no intensity = white) due to insufficient printer resolution. One of these hot spots is situated in the region of highest intensity (red) and is

enclosed by weaker (blue) fluorescence intensity. This structure can clearly be seen in the second frame, taken 0.06° CA (10 μs) later. This hot spot and a second one, situated at the wall just above the horizontal line of symmetry, have been used to evaluate hot-spot expansion speeds in this cycle. Even at this early stage, they attain speeds of 350–500 ms^{-1} (at the wall) and up to 750 ms^{-1} for the enclosed hot spot. In comparison to this, reverse speeds of the regular flame front are rather moderate. Because of the early state of autoignition, velocities of 30–180 ms^{-1} are found. It is possible that this changes a few microseconds later, as, at the time given, most of the end gas has not yet reacted.

Conclusions

To avoid the undesired mode of knocking combustion, one has to understand the underlying processes. Numerical simulations of end-gas autoignition show local fluctuations in temperature of 10 K [6] and even less [1] being sufficient to initiate autoignition in the end-gas region. This has been validated in several experimental investigations [13–15].

Up to now, detection of hot spots by spectroscopic means has been performed only in single-shot mode, delivering only a single image per cycle. Ultra-high-speed Schlieren frames can temporally resolve the evolution of hot spots, but, due to the fact that this technique is based on density gradients, the effects made visible might result from either temperature or pressure gradients.

In order to combine the temporal resolution of the ultra-high-speed Schlieren technique and the unambiguous character of the spectroscopic method, the 2-D double-pulse LIF experiment was set up. The results presented here are taken from a wide number of frame pairs recorded with their corresponding pressure traces. The first pair presented has been taken in a "moderately" knocking cycle with a pressure gradient of 55.7 bar/ms and a peak pressure of 55 bar. The trigger for the first frame is slightly after peak pressure. This can be seen from the relatively large sizes of the hot spots detected and from the fact that in the second frame there is hardly any visible fluorescence. Here, hot-spot expansion speeds between 170 and 180 ms^{-1} and reverse speeds of the regular flame front between 90 and 100 ms^{-1} are detected. The second pair has been taken in a very "violently" knocking cycle with a pressure gradient of 75.8 bar/ms, a peak pressure of 68.4 bar, and very strong oscillations on the downward slope of the pressure trace. The trigger of the first frame is early with respect to the pressure trace. It is situated in the pressure rise leading to peak pressure. This early state is underlined by the small sizes of the hot spots. In this case, they are situated at the wall as well as isolated within the end-gas region. Expansion speeds of 350–500 ms^{-1} (at the wall) and up to 750 ms^{-1} (enclosed hot spots) are calculated, whereas the flame-front reverse speeds only attain values of 30–180 ms^{-1}.

The results presented here clearly verify the concept of hot spots as a starting point for processes leading to engine knock. A possible and desirable extension of this work is the application of multiple laser shots separated by a few microseconds to get a better impression of the evolution of hot spots. Additionally, a numerical study of two interacting flame fronts, one originating from the electrode, the other from a hot spot, should allow an interpretation of the flame-front reversal reported here.

Acknowledgments

The authors would like to thank the "Physikalisch-Chemisches Institut" of "Universität Heidelberg" for supplying parts of the imaging software and leaving the video amplifiers and optical equipment with us.

The authors would also like to thank Dr. R. R. Maly and Dr. G. König, Daimler-Benz, for their support during the early phase of the experiments.

Finally, the authors would like to thank F. Hoffmann for his support during the preliminary experiments, and E. Kull for his great assistance.

REFERENCES

1. Oppenheim, A. K., *The Knock Syndrome—Its Cures and Its Victims,* SAE Paper 841339, 1984.
2. Mallard, E. and Le Chatelier, H., *Ann. Mines* 8:274–568 (1883).
3. Nernst, W., *Z. Deutscher Ing.* 49:1426–1436 (1905).
4. Clerk, D., *Trans. Faraday Soc.* 22:338–375 (1926).
5. König, G., Maly, R. R., Bradley, D., Lau, A. K. C., and Sheppard, C. G. W., *Role of Exothermic Centers on Knock Initiation and Knock Damage,* SAE Paper 902136, 1990.
6. Goyal, G., Maas, U., and Warnatz, J., *Simulation of the Transition from Deflagration to Detonation,* SAE Paper 900026, 1990.
7. Klein, R., *Twenty-Fifth Symposium (International) on Combustion,* The Combustion Institute, Pittsburgh, 1994, pp. 553–579.
8. Pollard, R. T., in *Hydrocarbons,* (C. H. Bamford and C. F. H. Tipper, Eds.), Elsevier, Amsterdam, 1977, Chap. 2.
9. Rassweiler, G. M. and Withrow, L., *Ind. Eng. Chem.* 25:1359–1366 (1933).
10. Dagaut, P., Reuillion, M., and Cathonnet, M., *Combust. Sci. Technol.* 95:233–260 (1994).
11. Dagaut, P., Reuillion, M., and Cathonnet, M., *Combust. Flame* 101:132–140 (1995).
12. Kull, E., "Laserinduzierte Fluoreszenz bei instationärer Hochdruckverbrennung von Kohlenwasserstof-

fen," Diploma Thesis, Inst. f. Techn. Verbrennung, Universität Sttutgart, 1994.
13. Hoffmann, F., Bäuerle, B., Behrendt, F., Warnatz, J., *Third International Symposium on Diagnostics and Modeling of Combustion in Internal Combustion Engines, COMODIA 94,* Yokohama, Japan, 1994, pp. 517–522.
14. Bäuerle, B., Hoffmann, F., Behrendt, F., Warnatz, J., *Twenty-Fifth Symposium (International) on Combustion,* The Combustion Institute, Pittsburgh, 1994, pp. 135–141.
15. König, G., Maly, R. R., Schöffel, S., Blessing, G.: *Gas/Surface Interactions and Damaging Mechanisms in Knocking Combustion: Effects of Engine Conditions,* Sixth Periodic Report, CEC-Research Contract: JOUE-0028-D-(MB), 1991.
16. Bradley, D., Pan, J., Sheppard, C. G. W.: *Gas/Surface Interactions and Damaging Mechanisms in Knocking Combustion—Turbulence and Flow Field Effects,* Sixth Periodic Report, CEC-Research Contract: JOUE-0028-D-(MB) (1991).

COMMENTS

Andrew G. Astill, AEA Technology plc., UK. Your paper described the use of LIF of formaldehyde to monitor regions of high temperature in the unburnt gas. I have two questions.

1. Have you investigated the temperature dependence of the fluorescence quenching of formaldehyde LIF and have you accounted for the variation in local composition leading to local variation in fluorescence quenching cross sections?
2. What is your S/N for each image? It appeared to me that the 2nd image, for each pair, had a number of pixels in the burnt zone with the same color code as the majority of the formaldehyde LIF. If this is noise then most of the LIF was also noise. If not, how is the formaldehyde re-appearing in the burnt gas zone in the 2nd image of each pair?

Author's Reply. We have investigated the temperature dependance of the fluorescence quenching of formaldehyde in synthetic air and nitrogen. For the temperature region the images are taken in, there is only a slight, negligible dependence due to nearly equal population of the two levels involved in the excitation process. Besides, we know from literature that quenching by oxygen is negligible, and that fuel molecules exhibit an even weaker quenching cross section. Therefore we do not expect a significant influence of variation in local mixture composition.

The average noise level is 20 grey values with a peak signal level of 256. The "noise pixels" you noticed in the unburnt of the second images have maximum values of 25 whereas the "signal pixels" exhibit levels of at least 50 to 60. Some of the brighter "noise pixels" are related to particles on either the piston top or the top window and can be seen on the same position on subsequent pairs of images.

•

John Griffiths, University of Leeds, UK. As you have described, the formation and destruction of formaldehyde is related to changes from "low temperature" to "high temperature" mechanisms. Have you been able to use your quantitative kinetic understanding and some knowledge of sensitivity of the detection system to infer a maximum temperature of the end gas that has not been consumed in autoignition centers?

Author's Reply. We have performed simulations of knocking cycles (former single shot experiments) with detailed reaction mechanisms and found good agreement with both the respective pressure traces and the measured (one-dimensional) peak concentrations of formaldehyde. These computations gave us temperatures of 770 K of the unconsumed end gas.

•

John B. Heywood, M.I.T., USA. Two questions about the smooth flame fronts you observed when autoignition occurred: Did you observe such smooth flames when knock did not occur? Do you have any explanation for the cause of this flame front smoothing?

Author's Reply. In preliminary experiments for our earlier single-shot experiments we have also taken images in non-knocking cycles. None of these images showed any flame front smoothing, no matter at which point of time during the cycle they were taken. As for the second question, so far, we have no explanation for this effect, nor can we specify any correlations between the occurrence of the flame smoothing and the measured data.

•

W. Hentschel, Volkswagen R&D, Germany. You have visualized the unburned gas region by LIF of formaldehyde. Why do you expect to achieve the same type of images when performing simple LIF of the unburned fuel (e.g., standard gasoline or tracers in a model fuel)?

Author's Reply. There are several reasons why we used formaldehyde as a tracer:

a. It is a natural tracer which does not have to be added to the fuel (important for simulations using detailed reaction mechanisms),

b. its abundance in the end gas region (In experiments under same conditions with one-dimensional excitation of formaldehyde we measured peak concentrations of 12,000 ppm, averaged, and 35,000 ppm, single shot.), and

c. the simple excitation which produces ample signal under engine conditions using primary reference fuel.

Basically, the same type of images can be expected, but one also must expect a weaker signal. This occurs due to the fact that a considerable amount of the mixture and hence the fuel, is already in a state of reaction (intermediate species) at the considered instant. These intermediates might not be excited and hence give no signal, although the fuel has not yet completely reacted to final products and can be looked upon as burnt (exhaust).

Twenty-Sixth Symposium (International) on Combustion/The Combustion Institute, 1996/pp. 2627–2635

MODELING TURBULENT COMBUSTION AND POLLUTANT FORMATION IN STRATIFIED CHARGE SI ENGINES

T. A. BARITAUD, J. M. DUCLOS AND A. FUSCO
Centre de Recherche sur la Combustion Turbulente
Institut Français du Pétrole
BP 311, 92506 Rueil-Malmaison, France

A conditional averaging approach is used to model combustion and pollutant formation in stratified charge spark-ignition (SI) engines. A set of diagnostic equations follows the local composition and temperature of the unburned gases during combustion. The coherent flame model is chosen to simulate combustion and extended to rich or diluted conditions. NO and CO reaction rates are computed conditionally based on the burned gas temperature with two contributions: a source-term function of the flamelet density and unburned gas composition and temperature, and another source term including equilibrium and kinetic mechanisms in the burned gas. The coupled combustion and pollutant models are implemented in the Kiva-2 code and tested on a simple engine geometry for a set of operating conditions including variation of equivalence ratio, dilution by residual gases, and fuel stratification. The ability of the model to reproduce observed trends for combustion rate is demonstrated. The influence of the local laminar flame on the burn rate is pointed out.

A much larger production rate of NO and CO during combustion, resulting in higher computed NO levels for most of the operating conditions and similar final CO levels after combustion completion, is observed for the conditional averaging as compared to the usual ensemble averaging procedures. The predicted levels of emissions are comparable to measured engine values.

Introduction

The design of new, efficient and environmentally friendly engines is becoming extremely complex because of the number of options that must be tested to find the best trade-off. Three-dimensional modeling of the internal flow can provide a significant reduction of the industrial development phases. However, computational fluid dynamics is not yet used to predict combustion and emissions reliably. The complex nature of reacting flows in engines involving multiphase, turbulence, heat and species transfer, combustion, and chemical kinetics makes it extremely difficult to model.

In spark-ignited engines, combustion occurs in three phases: ignition, propagation, and flame-wall interaction. This takes place in a transient flow formed by the intake process and subsequent mixing. The mixture is made up of newly admitted air, gaseous fuel originally gaseous or liquid, and burned gases from the previous cycle and/or exhaust-gas recirculation. Heat transfer to the wall occurs continuously. At ignition time, the mixture is not homogeneous in concentration or temperature. Experiments [1–3] have shown that combustion occurs in engines in the flamelet regime. This has stimulated the development of flamelet models to simulate the combustion process.

Pollutants are essentially HC, NO_x, and CO. NO and CO are controlled by the local equivalence ratio and temperature and formed at the flame front and in the burned gases. HC comes essentially from trapping of the charge in the crevices and in the wall oil film.

NO production is mainly thermal in SI engines. The equivalence ratio is never much larger than 1, making prompt NO unlikely, as confirmed by the measurements of Bräumer et al. [4]. Moreover, the volume occupied by the flamelets, where prompt NO could be produced, is negligible as compared to the volume occupied by the burned gases. The production of NO_2 is negligible since it is decomposed almost instantaneously because of the high temperature of burned gas. CO production in the flame front is a function of the local equivalence ratio. In most practical CFD calculations, CO kinetics is computed from simple CO-CO_2 equilibrium laws.

In CFD codes such as the Kiva code [5], 1989, reaction rates are usually computed based on ensemble-averaged values of concentrations and temperature. Because of their high nonlinearity, the actual reaction rates of pollutants formed essentially in the burned gases may differ greatly from those computed with averaged cell values. This difference is expected to be greatest in the flamelet regime of combustion, which is characterized by a thin reacting zone (flamelet) separating the burned and unburned phases of the mixture. Pollutant calculations

based on conditional averaging such as those used by Gosman et al. [6] for knock calculations should bring significantly improved modeling predictivity.

The first goal of this study is to develop new models to extend the range of application of the CFM to stratified charge such as that found in actual engines by using a conditional averaging technique. The second goal is to use this conditional approach to compute NO and CO formation. The models developed are implemented in the Kiva-2 code, tested for a range of operating conditions, and compared to engine measurements.

Extension of the CFM to Stratified Charges

Application of the Coherent Flame Model to SI Engines

The coherent flame model for combustion was developed on an empirical basis. The reaction rate is computed as the product of a flame surface density and a laminar flame velocity. A recent development (CFM2a) corrected the stretch term, α, with the intermittent turbulent net flame stretch (ITNFS) model according to Meneveau and Poinsot [7]. It has been applied successfully in SI engines by Boudier et al. [8], Zhao et al. [9], and Torres and Henriot [10].

Extensions of the CFM to actual situations found in SI engines are required. The laminar-ignition, LI-CFM initiation model of Boudier et al. [8] and the flame interacting with surface and turbulence (FIST) wall-flame model of Poinsot et al. [11] have been proposed. The important issue of partial premixing is still to be addressed. The incomplete mixing ahead of the flame front implies that composition and temperature are changing locally and temporally during flame propagation. This causes changes of the local laminar flamelet velocity and burned gas temperature and composition that must be accounted for.

Most engine CFD codes solve Favre-averaged equations for species and temperature. The mass and momentum exchange is computed with a turbulence model (most often the k-ε model) providing turbulent diffusion coefficients and with a law of the wall for momentum and heat transfer. The quantities obtained are essentially mean scalars and velocity and turbulent kinetic energy and its dissipation.

When combustion begins, new terms are computed: source terms and flamelet area density with the CFM, for instance. For flamelet models involving the assumption of burned and unburned phases in the combusting cells, the original set of computed mean variables is not sufficient to describe the separate properties of the two phases without adding variables. In this work, only the two-phase scalar variables will be computed separately, with turbulence and velocity terms being determined unconditionally. The unburned gas properties are determined by implementing equations that are not coupled directly with the unconditioned mean values, as proposed by Veynante et al. [12]. The added set of diagnostic equations follows the unburned gas properties only to modify the local laminar flame speed, S_L, and thickness, δ_L, and to evaluate some of the CFM terms and compute pollutant kinetics.

Formulation of the CFM2a for Lean Combustion

The original Favre-averaged set of equations solved for fuel, oxygen, temperature, and combustion used in Boudier et al. [8] for lean combustion was

$$\frac{\partial \bar{\rho} Y_F}{\partial t} + \frac{\partial \bar{\rho} u_k Y_F}{\partial x_k} = \frac{\partial}{\partial x_k}\left(\frac{\mu_t}{\sigma_F}\frac{\partial Y_F}{\partial x_k}\right) - \overline{\dot{\omega}_F} \tag{1}$$

$$\frac{\partial \bar{\rho} Y_O}{\partial t} + \frac{\partial \bar{\rho} u_k Y_O}{\partial x_k} = \frac{\partial}{\partial x_k}\left(\frac{\mu_t}{\sigma_F}\frac{\partial Y_O}{\partial x_k}\right) - s\,\overline{\dot{\omega}_F} \tag{2}$$

$$\frac{\partial \bar{\rho} e}{\partial t} + \frac{\partial \bar{\rho} u_k e}{\partial x_k} = -P\frac{\partial u_k}{\partial x_k} + \frac{\partial}{\partial x_k}\left(\kappa\frac{\partial T}{\partial x_k}\right) + \frac{\partial}{\partial x_k}\left[\frac{\mu_t}{\sigma}\sum_{i=1}^{N} h_i \frac{\partial Y_i}{\partial x_k}\right] - \bar{\rho}\varepsilon + \dot{Q}_c + \dot{Q}_w \tag{3}$$

$$\overline{\dot{\omega}_F} = \rho_u Y_F^0 S_L \Sigma \tag{4}$$

$$\frac{\partial \Sigma}{\partial t} + \frac{\partial u_k \Sigma}{\partial x_k} = \frac{\partial}{\partial x_k}\left(\frac{\nu_t}{\sigma_\Sigma}\frac{\partial \Sigma}{\partial x_k}\right) + S - D, \tag{5}$$

with $D = \beta\,\rho_u Y_F^0 S_L/\bar{\rho} Y \Sigma^2$ and $S = \alpha\,\varepsilon/k\,f\,(u'/S_L, L/\delta_L)\,\Sigma$ with the ITNFS stretch. The expression for D was slightly different than expressed here, but it gives the same results with the usual turbulence and flame conditions in SI engines. This set was completed by the usual equations for mass, momentum, and a k-ε model for turbulence.

This set of equations was solved using mean properties in the cells, except for the evaluation of S_L, which was estimated from the unburned gas properties for a uniform equivalence ratio mixture and an unburned gas temperature obtained assuming isentropic compression after ignition, and neglecting heat transfer to the walls during combustion. Moreover, it was assumed that no residuals were trapped in the charge.

Extension to Rich and Diluted Mixtures and Diagnostic Equations for the Unburned Phase

Favre-averaged diagnostics equations that are not directly coupled to Eqs. (1) through (5) are added to follow the evolution of the unburned gases ahead of the flamelets. $Y_{F,u}$ and $Y_{O,u}$ are, respectively, the mass of fuel and oxygen in the unburned gases divided by the total mass. Y_F^u and Y_O^u are, respectively,

the mass of fuel and oxygen in the unburned gas divided by the mass of unburned gas. h_u and T_u are the enthalpy and temperature in the unburned gases:

$$\frac{\partial \bar{\rho} Y_{F,u}}{\partial t} + \frac{\partial \bar{\rho} u_k Y_{F,u}}{\partial x_k} = \frac{\partial}{\partial x_k}\left(\frac{\mu_t}{\sigma_F}\frac{\partial Y_{F,u}}{\partial x_k}\right) - \overline{\omega \mathrm{F,u}} \quad (6)$$

$$\frac{\partial \bar{\rho} Y_{O,u}}{\partial t} + \frac{\partial \bar{\rho} u_k Y_{O,u}}{\partial x_k} = \frac{\partial}{\partial x_k}\left(\frac{\mu_t}{\sigma_F}\frac{\partial Y_{O,u}}{\partial x_k}\right) - \frac{s}{\Phi}\overline{\omega_{F,u}} \quad (7)$$

$$\overline{\omega_{F,u}} = \rho_u Y_F^u S_L \Sigma \quad (8)$$

$$\frac{\partial \bar{\rho} h_u}{\partial t} + \frac{\partial \bar{\rho} u_k h_u}{\partial x_k} = \frac{\partial}{\partial x_k}\left(\frac{\mu_t}{P_r}\frac{\partial h_u}{\partial x_k}\right) - \bar{\rho}\varepsilon + \frac{\bar{p}}{\bar{\rho_u}}\frac{\partial p}{\partial t} + \dot{Q}_{w,u}. \quad (9)$$

The flame surface density destruction term of Eq. (5) becomes $D = \beta \rho_u Y_O^u S_L / \bar{\rho} Y_O \Sigma^2$ when the equivalence ration is greater than 1. S_L and δ_L are then deduced from the computed, unburned equivalence ratio and temperature.

This formulation for D can lead to trouble since D becomes large when the limiting reactant disappears, which is expected for oxygen in the rich case. However, engine calculations always include post-flame gas kinetics (such as CO-CO_2, for instance) that produce O_2, which should not be considered in D. Thus, a better formulation is $D = \beta \rho_u Y_O^u S_L / \bar{\rho} Y_{O,\mathrm{u}} \Sigma^2$, which is not influenced by the burned gas composition. Y_F^u and Y_O^u can be evaluated from $Y_{F,u}$ and $Y_{O,u}$ if the ratio of nitrogen to oxygen is constant in the unburned gases.

In the set of equations, Eqs. (6) through (9), it is assumed that gas-phase exchange occurs independently in the burned and unburned regions, except through the reaction rate at the interface, which is fully consistent with the flamelet regime. Recent direct numerical simulation of flame–wall interaction by Bruneaux et al. [13], with locally low reaction rates, has shown that the flamelet concept was still valid and that there was no inert mixing across the flamelets. Another assumption underlying these equations is that exchange fluxes are statistically occurring through the whole external area of the cell.

Eq. (9), describing the evolution of the enthalpy, is retained instead of an energy equation because it provides an easier way to integrate the contribution of combustion heat release through the total pressure variation as formulated in the third term on the right-hand side. It also supposes a Lewis number of 1, which is the case in Kiva-2. The last term, $\dot{Q}_{w,u}$, representing heat transfer of the unburned gases with the walls, is taken as the heat transfer computed with the model of Diwakar [14] such as implemented by Gilaber and Pinchon [15] but taking into account the unburned gas temperature. The unburned gas temperature is deduced directly from the enthalpy.

The laminar flame speed, S_L, is a function of the equivalence ratio and temperature in the unburned gases, as well as its thickness, δ_L. It also depends on the burned gas temperature that can be estimated from the state of the computed cell. Finally, there is also a dependence on the pressure and on the amount of residual gases in the unburned region. δ_L is computed according to Blint's work [16] and S_L from the correlation of Metghalchi and Keck [17], which accounts for residuals.

NO and CO Formation

NO and CO are formed and evolve both in the flame front and in the burned gases. Typical of SI engines, the volume of the laminar flamelets is small as compared to the volume of the hot burned gases (which are hot for a long time). Hence, it is expected that most of the pollutant kinetics is controlled by the phenomena in the bulk of the burned gases. However, the possibility of creation of pollutants directly in the flamelet that acting as a local and temporal source term must be considered.

Complex chemical schemes are very dependent on temperature, composition, and pressure, while the accuracy of these computed quantities in CFD codes is presently limited. Hence, schemes with a limited number of steps and species, which allow a reasonable predictivity-versus-computing-time trade-off are preferred. Although flamelets are thin, CFD codes predict average statistical variable values in each cell of the domain. This produces a large combustion zone with a weak temperature gradient including intermediate temperatures that do not exist in individual engine cycles, while the quantity of interest for computing pollutants is the temperature of the burned gases.

Determination of the Burned Gas Temperature

The procedure previously described to extend the CFM to stratified charge involves the computation of the unburned gas temperature, T_u, and composition, $Y_{j,u}$, along with the averaged values in the domain. The burned fraction of each cell can be obtained from the ratio $b = Y/Y_F^u$. Hence, it is possible to compute the enthalpy in the burned gases by

$$h_b = \frac{h - bh_u}{1 - b} \quad (10)$$

from which T_b can be computed.

For very small burned fraction, Eq. (10) can be ill-determined. Thus, if $c < 0.01$, the burned-gas temperature of the cell is evaluated as if it has

completely burned adiabatically with the correction for chemical equilibrium described in the next section. The influence of this approximation on pollutant calculations is marginal.

Pollutant Kinetics

A new approach is developed to compute NO and CO for both rich and lean combustion. First, a source term of species created at the flamelets is determined. From the composition of the unburned gases and the thermodynamic state of the cell, it is assumed that the flamelets produce species from which atom production corresponds to the burn rate in the cell as computed by $\overline{\omega_{C_j,u}} = \rho_u Y^u_{C_j} S_L \Sigma$ from the CFM model. These species are distributed in product molecules and radicals, corresponding to the equilibrium mechanism (11) proposed by Meintjes and Morgan [18] at the burned-gas temperature:

$$\begin{aligned} 2N &\leftrightarrow N_2 \\ 2H &\leftrightarrow H_2 \\ 2O &\leftrightarrow O_2 \\ H_2 + O_2 &\leftrightarrow 2OH \\ 2OH + O_2 &\leftrightarrow H_2O \\ CO + O_2 &\leftrightarrow CO_2. \end{aligned} \tag{11}$$

The assumption of equilibrium may appear too simple. However, SI engine flamelets are very thin, and if the equilibrium is reached at a distance of a few flame widths, it can still be considered as a flamelet source term.

In the burned gases, the same equilibrium mechanism is used, but without the CO-CO_2 contribution. It is coupled to a kinetic mechanism for slower reactions using a numerical-implicit procedure proposed by Ramshaw and Chang [19]. The kinetic reactions are for thermal NO (extended Zeldovich) and CO and CO_2. The purpose of kinetic CO-CO_2 is to deal with lower temperatures (close to walls, for instance). The constants are from Seshadri and Williams [20] and Heywood [21]

$$\begin{aligned} CO + OH &\leftrightarrow CO_2 + H \\ N + O_2 &\leftrightarrow NO + N_2 \\ N_2 + O &\leftrightarrow NO + N_2 \\ N + OH &\leftrightarrow NO + H \end{aligned} \tag{12}$$

and the chemistry is supposed frozen below 1300 K. Chemistry is computed conditionally on the burned gas fraction in each cell based on the amount of each species, the estimated burned-gas temperature, and the pressure.

Engine Simulations

The conditionally averaged combustion and pollutant models have been implemented using KMB, an extended version of Kiva-2 [22] and applied in a two-dimensional mesh representative of the cylindrical engine geometry of Baritaud [23]. This engine has a bore and stroke of 86 × 82 mm and a compression ratio of 6.2. The clearance height at top dead center (TDG) is 15.4 mm. A swirl flow of intensity 3.8 and nearly solid body rotation was observed at bottom dead center (BDC). The volumetric efficiency for all simulated cases is 0.5. The spark plug is located on the cylinder axis, 7.5 mm below the head, and the spark energy was 20 mJ (2 ms × 10 w). The fuel is propane. The computed axisymmetric domain is a plane delimited by the cylinder axis and liner and the piston and head surfaces. The turbulence level at the time of ignition and 1200 rpm was determined to be about 2 m/s. The computational mesh is fine near the wall, and the ignition point, located on the chamber axis, was 40 cells in the radial direction and 42 in the axial direction. The work of Boudier et al. [8] had shown that this was sufficient to have a grid-independent combustion simulation; the LI-CFM model of the authors was used. The FIST flame–wall model is implemented to provide correct behavior of the combustion rate close to the walls.

The runs are conducted starting at compression BDC. k, ε, and a transverse swirl-velocity profile representative of the measured values are imposed. The concentration fields are also imposed at BDC, according to realistic values measured by Deschamps et al. [24] and in the validity range of the S_L correlation.

Stratified Charge Combustion

Numerical tests were conducted to assess the validity of the equations and coding. The equation system (6) through (8) with the new formulation of the destruction term D was compared, in the case of homogeneous rich and lean combustion, to the original equation set (1) through (5). Inactivating the conditional unburned enthalpy equation (keeping the approximation of an unburned temperature corresponding to an isentropic compression starting at ignition) gave consistent results. The final amount of the excess species (fuel Y_F or oxygen Y_O) also gave the consistent results. The conditional enthalpy equation was tested by comparing the evolution of the predicted unburned temperature with the adiabatic compression temperature during combustion. This was done for an adiabatic, homogeneous-mixture combustion with $O_{w,u} = 0$. The two values of unburned temperature stayed within 1 K. Finally, the simple correction of S_L with residual gases showed no application problems.

TABLE 1
Computed operating conditions for stratified charges

HFHT	Homogeneous mixture, $\Phi = 0.9$
VFHT	Vertial fuel stratification, $\Phi = 1.0$ at spark/cylinder axis and 0.8 at liner side wall at -25 CAD
HOFHT	Horizontal fuel stratification, $\Phi = 1.1$ at top wall and 0.7 at lower wall at -25 CAD
HFIT HFCT	Homogeneous mixture, $\Phi = 0.9$, isentropic unconditioned and conditioned T
VFIT VFCT	Vertical fuel stratification, $\Phi = 1.0$ at spark/cylinder axis and 0.8 at liner wall at -25 CAD, isentropic unconditioned and conditioned T

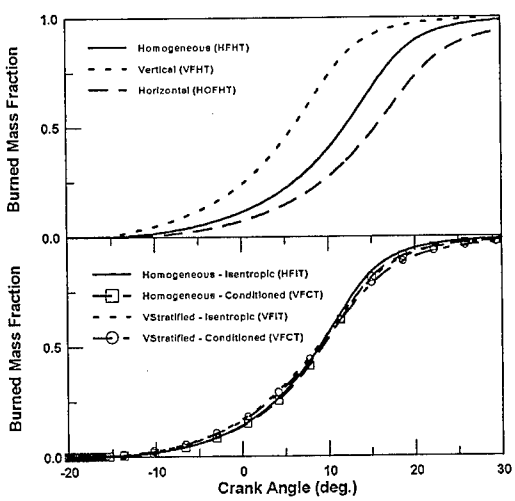

FIG. 1. Fuel burned mass fraction in the combustion chamber. *Effect of fuel stratification:* homogeneous HFHT, vertically stratified VFHT, and horizontally stratified HOFHT. *Effect of isentropic unconditioned/conditioned temperature:* homogeneous HFIT, HFCT, and vertically stratified VFIT, VFCT.

Calculations of stratified charge combustion are now presented. They involve variation of the stratification of fuel and residuals and the heat transfer effects described in Table 1. At this stage, pollutant chemistry in the burned gases is not considered in order to provide a clearer understanding. The wall temperature is 400 K.

The effect of a stratification of the fuel charge is shown in Fig. 1 by comparing burned mass fractions for cases HFHT (homogeneous), VFHT (vertical fuel stratification), and HOFHT (horizontal fuel stratification). Stratification patterns imposed at TDC result in the stratification amplitude at TDC given in Table 1. The ability of the model to reproduce the expected trends in a stratified charge is clear. As found experimentally by Deschamps et al. [24] igniting a stratified mixture on the richer side favors the global combustion speed as compared to the homogeneous case. A horizontal stratification gives a lower heat-release rate. The fields of S, S_L, and $\bar{\omega}_F$, when the flame is in the middle of the chamber for the horizontal stratification case HOFHT, are plotted in Fig. 2. With a higher equivalence ratio, S_L is larger at the top of the chamber than at the bottom. In the leaner and lower part of the chamber, the flame surface density, Σ, is larger. The resulting combustion rate is larger in the region of larger S_L, showing the importance of the laminar flame speed even in the very turbulent environment of engine chambers. This emphasizes the essentiality of an accurate determination of S_L to predict the combustion rate accurately; the conditional averaging procedure proposed in this work is necessary.

The effect of using a conditional temperature to determine S_L is now discussed. This time, Y_F^u and Y_O^u are solved directly as tracers without source terms. A new, three-dimensional version of the LI-CFM ignition model, equivalent to the two-dimensional LI-CFM for the present calculation, is activated. The effect of conditioning the unburned temperature, instead of using an isentropic evolution to compute the laminar flame speed, has an effect mostly in the second half of the combustion process (Fig. 1). The reason is that heat exchange with the walls is the unique source of temperature inhomogeneity in the test cases and more strongly affects the gases close to the walls. In actual engines, there would be more temperature variation across the chamber due to mixing with residuals and more complicated chamber shapes. The time evolution observed in a cell 1 mm from a wall in Fig. 3 shows that 20–30 K differences between isentropic and conditioned temperature are obtained and lead locally to 10–20% differences in laminar flame speed.

Pollutant Formation

To compute the pollutants conditionally, the same numerical configuration is retained. The chemical equilibrium and kinetics schemes already presented are coupled with this system to observe the evolution of NO and CO.

Runs are made for homogeneous charge with Φ

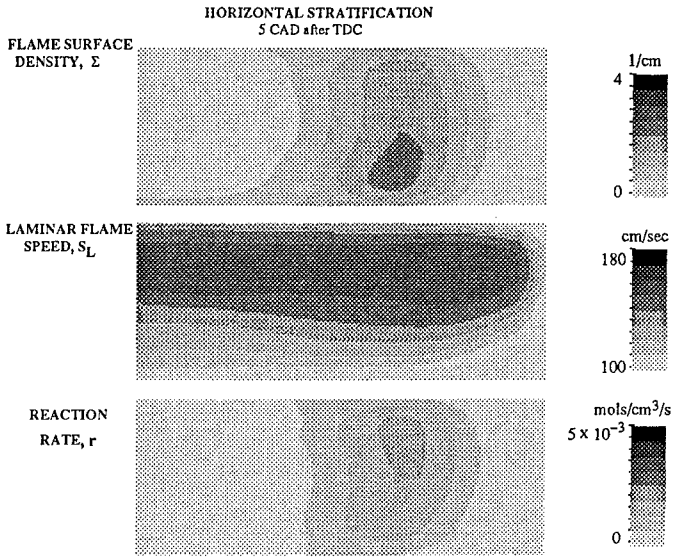

FIG. 2. Spatial distribution of flame surface density Σ, laminar flame speed S_L, and reaction rate $\dot{\omega}_F$ for case HOFHT with horizontal fuel stratification. 5°CA after TDC. Average equivalence ratio $\Phi = 0.9$.

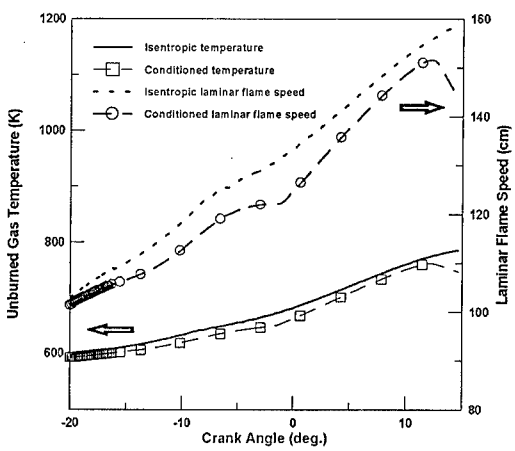

FIG. 3. Evolution of isentropic and conditioned unburned temperature T_u and resulting S_L in a cell 1 mm from a 400-K wall for the fuel stratified case VFCT.

ranging from 0.85 to 1.1, engine speeds of 1200 and 2400 rpm, and vertically and horizontally stratified charges with mean Φ of 0.85 and 1.0. Comparisons between unconditioned and conditioned pollutant calculations are made. For the nontemperature-conditioned cases, the coupled kinetic systems are used based on the averaged cell temperature, while the source terms at the flamelets were only CO_2 and H_2O.

Detailed engine measurements not being available, the pollutant predictions of the simple two-dimensional engine case will be compared to typical exhaust levels measured at IFP and reported in Table 2 for a 4-valve commercial engine. In this engine, it is possible to stratify the charge as shown by Deschamps et al. [24]. The numbers are indicative of trends when varying parameters, but care should be taken when doing comparison with the present calculations (e.g., different geometry, turbulence, stratification, spark location and timing).

During combustion, the new conditioned kinetic scheme and procedure predict a larger rate of production of CO (Fig. 4). However, because of the long residence time of the chemical species in the fully burned gases, the values given by the old and new procedure become almost equal after a certain delay following combustion completion. The end values are close to the equilibrium values for all the lean cases. The variation of equivalence ratio predicts evolution and levels close to the measured values in Table 2, the absolute levels being lower in the modeled chamber with $0.85 < \Phi < 1.1$, since the contribution of the unburned HC chemistry present in the experiment is not considered. For the same reason, the calculations do not predict CO for lean combustion. The model shows its ability to reproduce the CO elevation for a rich case and a horizontally stratified charge case, with an equivalence ratio ranging between 1.1 and 0.9 at ignition time. The production rate for a lean, vertically stratified case with average Φ of 0.85 and ignition on the rich side also produces more CO than the homogeneous case. Finally, adding 20% residual gases while keeping the same volumetric efficiency produces an expected decrease of CO because of diluted and leaner combustion.

The difference in the evolution of NO between the conditioned and unconditioned runs shown in Fig. 5, depends on the operating conditions. With a homogeneous equivalence ratio of 0.99, NO is not

TABLE 2
Measured exhaust emissions in 4-valve SI engine: 1200 rpm, 441 cm^3, compression ratio 8.7, volumetric efficiency 0.6, optimized ignition timing for each point, fuel *iso*-octane. In the three right columns are corresponding configurations of Table 2 and computed values from Figs. 4 and 5 with the modeled flat head engine.

Measured and computed cases and values 4-valve engine configurations	NO ppm	CO %	Ign. timing	"Equivalent" computed case	NO ppm	CO %
Homogeneous charge, medium turbulence, side ignition, $\Phi = 1$	3128	0.43	−11	HFCT, $\Phi = 0.99$	3660	0.23
Homogeneous charge, high turbulence, side ignition, $\Phi = 1$	3458	0.24	−6.5	HFCT, $\Phi = 0.99$	3660	0.23
Stratified charge, medium turbulence, side ignition on rich side, $\Phi = 0.9$	3000	0.64	−16	VFCT, $\Phi = 0.85$	4400	0.05
Stratified charge, medium turbulence, side ignition on rich side, $\Phi = 0.8$	5700	0.2	−17	VFCT, $\Phi = 0.85$	4400	0.05
Stratified charge, medium turbulence, side ignition on rich side, $\Phi = 0.8$, 15% EGR	293	0.21	−25	VFCT, $\Phi = 0.85$, 20% residuals	160	0.03

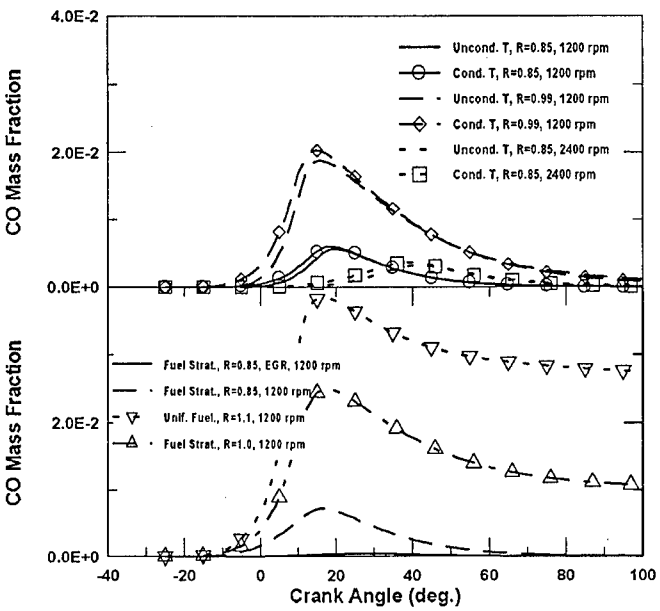

FIG. 4. CO integrated relative mass in the combustion chamber.

significantly influenced by the conditioning. However, for the leaner homogeneous cases at $\Phi = 0.85$, where NO is expected to peak, the NO formation rate is much higher. This is because with the conditioning procedure, the production of NO begins in a cell as soon as some hot burned gas exists. The resulting levels after the completion of combustion can differ by as much as 20% with the tested conditions. The predominance of the NO thermal kinetics is reflected in the lower NO level at higher engine speed where there is less time available for the same crank angle period. The rich homogeneous case also behaves well, with a marked reduction of NO. In all cases, the obtained levels are very close to those measured, and, more importantly, the influence of the varied parameters is similar. Lower values for the lower compression ratio, flat-head engine is expected, but it is probable that the weaker wall heat transfer in the computations is partially compensating. Both the computed fuel-stratified cases produce less NO, with a larger difference for the leaner case, although there was no attempt to optimize ignition timing. Adding 20% residuals produces a dramatic decrease of NO because of both diluted charge and delayed combustion causing very low burned-gas temperatures.

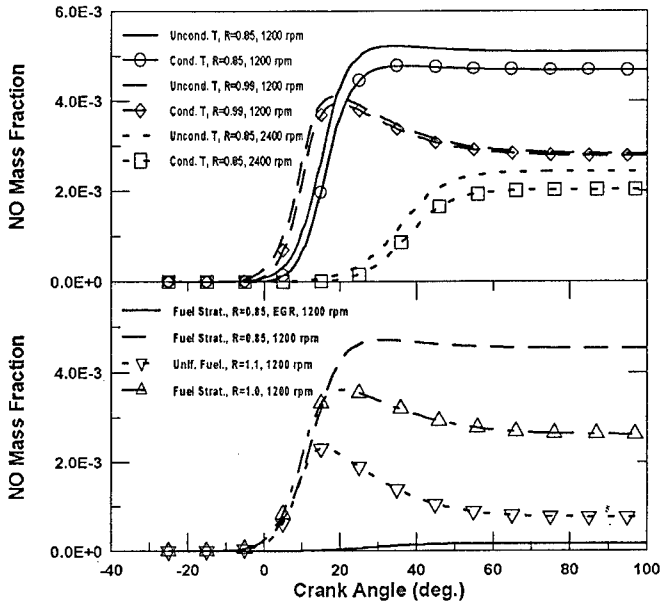

FIG. 5. NO integrated relative mass in the combustion chamber.

Conclusion

The conditional approach developed to compute the scalar properties (equivalence ratio, temperature, dilution) of the unburned gases in the flamelet regime coupled to the coherent flame model has been shown to allow CFD codes to simulate the combustion of stratified charge such as that found in SI engines. It is valid in the flamelet combustion regime, and for all equivalence ratios, if combustion stays in the premixed mode. The observed behavior is very similar to the experimental observations, although there are no relevant data available to quantify in detail the accuracy of the predictions. It will be necessary to design specific experiments in which flow and stratification are well controlled to validate stratified charge combustion models. Improvements can be sought, including the use of a more accurate laminar flame speed versus gas composition, pressure, and temperature or handling of close-to-extinction combustion.

The calculation of NO and CO using a chemical approach coupling equilibrium and kinetic schemes with source terms at the flamelet, and with bulk reactions conditioned by the actual temperature of the burned gases in the combusting cells, leads to more realistic results than conventional, simple ensemble-averaged procedures. Computations of a set of typical SI engine conditions for charge stratification have shown the ability of the new conditioned combustion and pollutant approach to reproduce the pollutant production behavior and levels usually measured in engines. There is a lack of local measurements of pollutants inside the combustion chamber that precludes a direct validation of the models. Improvements of chemical schemes easily could be included in the presented approach.

Despite the lack of detailed validation by relevant experiments, the present approach is a significant step toward modeling of combustion and pollutants in engines. The major features of engine combustion and NO and CO formation in actual SI engines have been taken into account, and the simulation system obtained allows for an estimation of the impact of engine design on performances and emissions.

Nomenclature

S_L	laminar flame speed
δ_L	laminar flame thickness
Σ	flame surface density divided by the mass in the cell
$\dot{\omega}_F$	reaction rate of the fuel
S	production/stretch term of flame surface
D	destruction/curvature term of flame surface
s	stoichiometric ratio
$\dot{Q}_w$	heat transfer to the wall
$\dot{Q}_c$	chemical heat release
Φ	equivalence ratio
$Y_{F,u}$	mass of unburned fuel divided by the mass in the cell
Y_F^u	mass of unburned fuel divided by the mass of the unburned gases in the cell
e_u	energy of the unburned gases divided by the mass in the cell
k	kinetic energy of the turbulence
ε	dissipation rate of the kinetic energy
μ_t	turbulent viscosity
P_r	turbulent Prantdl number

σ_F turbulent Schmidt number for the fuel
u subscript or superscript for the unburned gas-phase properties
b subscript or superscript for the burned gas-phase properties

No subscript or superscript for averaged quantities in the cells. In the equations, the variables are essentially Favre averages and the usual tilde symbol is omitted.

REFERENCES

1. Baritaud, T. A. and Green, R. M., SAE Paper No. 86-0025, 1986.
2. zur Loye, A. O. and Bracco, F. V., SAE Paper No. 87-0454, 1987.
3. Wirth, M. and Peters, N., *Twenty-Fourth Symposium (International) on Combustion,* The Combustion Institute, Pittsburgh, 1992, pp. 493–501.
4. Bräumer, A., Sick, V., Wolfrum, J., Drewes, V., Zahn, M., and Maly, R., SAE Paper No. 95-2462, 1995.
5. Amsden, A. A., O'Rourke, P. J., and Butler, T. D., Report LA-11560-MS, Los Alamos National Laboratories, 1989.
6. Gosman, A. D., Marooney, C. J., and Weller, H. G., *COMODIA* 90:59–64 (1990).
7. Meneveau, C. and Poinsot, T., *Combust. Flame* 86:311–332 (1991).
8. Boudier, P., Henriot, S., Poinsot, T., and Baritaud, T., *Twenty-Fourth Symposium (International) on Combustion,* The Combustion Institute, Pittsburgh, 1992, pp. 503–510.
9. Zhao, X., Matthews, R., and Ellzey, J., *COMODIA* 94:157–162 (1994).
10. Torres, A. and Henriot, S., *COMODIA* 94:151–156 (1994).
11. Poinsot, T., Haworth, D., and Bruneaux, G., *Combust. Flame* 95:118–133 (1993).
12. Veynante, D., Lacas, F., Maistret, E., and Candel, S. M., *7th Turbulent Shear Flows,* Springer Verlag, Berlin, 1991, pp. 367–378.
13. Bruneaux, G., Poinsot, T. J., and Ferziger, J., *Combust. Flame* 107:27–44 (1996).
14. Diwakar, R., SAE Paper No. 84-0230, 1984.
15. Gilaber, P. and Pinchon, P., SAE Paper No. 88-0516, 1988.
16. Blint, R. J., *Combust. Sci. Technol.* 49:79 (1986).
17. Metghachi, M. and Keck, J. C., *Combust. Flame* 48:191–210 (1982).
18. Meintjes, K. and Morgan, A. P., General Motors Research Publications GMR-5827, 1987.
19. Ramshaw, J. D. and Chang, C. H., *J. Comput. Phys.* 116:359–364 (1995).
20. Seshadri, K. and Williams, F. A., in *Turbulent Reacting Flows* (Libby and Williams, Ed.), Academic Press, London, 1994.
21. Heywood, J. B., in *Internal Combustion Engine Fundamentals,* McGraw Hill, New York, 1988.
22. Habchi, C. and Torres, A., *First European CFD Conference Symposium,* 1992, pp. 502–512.
23. Baritaud, T. A., SAE Paper No. 89-2098, 1989.
24. Deschamps, B., Snyder, R., and Baritaud, T. A., SAE Paper No. 94-1993, 1994.

COMMENTS

Micheal Drake, General Motors, USA. Your paper shows models of large scale stratification of A/F in engines. How will your model work for smaller spatial scale of stratification?

Author's Reply. The effect of small scale fluctuations of gas composition at a scale smaller than the computing cell size of the order of 1 mm is not taken into account. There is actually not even an equation to compute these fluctuations in the presented model. Their effect could be important if they are large and lead locally to flame extinction for instance. However, most LIF measurements in engines shows that local values of A/F fluctuations rarely exceed 10 to 20%.

•

L. A. Rahn, Sandia National Laboratories, USA. How important is radiation in the modeling of pollutant production in an engine?

Author's Reply. Radiation effects on bulk gas temperature are supposed to be very limited in SI engines since the medium is transparent (no soot). It is generally neglected in the energy balance. When computing NO which is sensitive to small temperature differences, some effects could possibly be observed, but such effects should certainly be lower than present uncertainties in the calculations.

•

George Lavoie, Ford Motor Co., USA. Does your model take into account the effect of wall layer on NO_x formation? Since much of the combustion takes place near the wall due to expansion, do you think that this effect is important?

Author's Reply. There is no specific treatment for NO in the wall layer. However, the fact that the unburned and burned gas temperatures are conditionally computed and that a law of the wall for heat transfer is applied separately for these two phases allows for a good determination of thermal NO levels. Moreover, the mesh density is increased close to the walls. Finally, even if a large fraction of combustion occurs close to the wall, it is not located in the boundary layer, and very little specific wall effects are expected.

Twenty-Sixth Symposium (International) on Combustion/The Combustion Institute, 1996/pp. 2637–2644

RELATION BETWEEN FLAME PROPAGATION CHARACTERISTICS AND HYDROCARBON EMISSIONS UNDER LEAN OPERATING CONDITIONS IN SPARK-IGNITION ENGINES

NICOLAS HADJICONSTANTINOU, KYOUNGDOUG MIN AND JOHN B. HEYWOOD
Sloan Automotive Laboratory
Massachusetts Institute of Technology
Cambridge, MA 02139, USA

The objective of this work was the investigation of the hydrocarbon emissions of a spark-ignition (SI) engine under very lean operating conditions. A series of experiments has been conducted in which cycles exhibiting high hydrocarbon (HC) emissions were analyzed using the fast response flame ionization detector (FID) in conjunction with a recently developed diagnostic, the head gasket ionization probe. It was found that for relative air/fuel ratios (λ) close to 1.4, single-cycle emissions correlate with single-cycle maximum pressure and indicated mean effective pressure (IMEP), which suggests that around that point postflame oxidation starts becoming less important. For relative air/fuel ratios greater than 1.4, cycles with very high emissions appear. We have divided these partial burns into two types depending on their HC-emission signature profiles and flame propagation characteristics. The first type is a global, slow-burning cycle that does not finish the oxidation of the charge by the time the exhaust valve opens. The second type is a normal burning cycle that exhibits a localized quench phenomenon: although the flame has propagated to the extremities of the cylinder, it has left a region of the charge unburned. The two types of cycles have different IMEP and flame speeds for the same mass fraction of the charge burned, as well as different HC emissions because of the different spatial and temporal location of the partial burn and the varying degrees of postflame oxidation the HC are subjected to.

Introduction

In recent years, much attention has been focused on the concept of lean-burning spark-ignition (SI) engines as a means of improving the engine efficiency. Lean air/fuel ratio excursions can also occur during transient periods of operation. However, as the air/fuel ratio is increased above the stoichiometric value, the speed and repeatability of combustion deteriorates. Poor combustion is one source of engine-out hydrocarbon (HC) emissions. It is well-known that as the air/fuel ratio of an engine is increased above a certain value, the engine HC emissions increase rapidly. This is attributed to decreasing flame speeds that result in lower peak cycle pressures and temperatures and, eventually, flame quenching [1].

Slow flame propagation may also result in the charge continuing to burn after the exhaust valve opens, which in turn means that more of the charge escapes combustion. Two reasons for this are the adverse conditions (low pressure and temperature) for burning encountered during the exhaust process and high flame stretch rates. Even if the preceding effects do not cause flame quenching, they result in a further reduced burning rate and, thus, in an incomplete burn. However, retarded burning also means that less work is extracted from the mixture and so the exhaust gas tends to be hotter. This hotter exhaust would tend to increase HC oxidation in the cylinder and exhaust port. The HC emissions of a cycle are influenced by the balance of these two opposite trends. We were interested in what happens to this balance when the engine is run well lean of stoichiometric and whether any new HC-emission effects become important in this operating regime.

The objective of this work was to combine the fast response FID hydrocarbon analyzer with the newly developed head gasket ionization probe diagnostic [2] to gain insight into the relationship between HC emissions and flame propagation characteristics, especially near the operating limit when combustion quality is poor.

Experimental Apparatus

The engine used for this study was a Ricardo Hydra Mark III single-cylinder research engine with a bore and stroke of 85.7 and 86 mm and a compression ratio of 8.3:1. The engine has two valves and two overhead camshafts, each driving a single valve. The combustion chamber shape is hemispherical, with a radius of curvature of 51 mm. The spark plug lies between the two valves but is offset from the center by 17 mm. A similar hole, symmetrically

placed with respect to the center of the combustion chamber, accommodates the water-cooled pressure transducer.

A laminar airflow element was used to measure the airflow rate into the engine. The air/fuel ratio was measured by an NTK exhaust gas air/fuel ratio analyzer. The head gasket ionization probe used in our experiments was manufactured at MIT using standard printed circuit board techniques [3]. The probe has eight electrodes equally spaced around the circumference of the cylinder bore. The cooling water flow rate was set to its maximum to keep the head gasket as cool as possible. The cooling water temperature was 50°C. Although this value is approximately 40° lower than the usual operating temperature, the conclusions of this work will not be affected by the difference, primarily because the focus is in flame propagation before the flame reaches the wall.

Because of the hemispherical combustion chamber shape and the cross-flow valve arrangement, the flow field was characterized as a weak tumbling flow (at 45.7 cm of H_2O pressure drop and 11.4 mm valve lift the tumble frequency was 48 Hz with negligible swirl). The experiments were performed using MBT spark timing. Gaseous propane (the fuel) was introduced continuously through an orifice 5 cm away from the inlet valve seat and was metered using a manually operated valve.

Data Analysis

Obtaining the Flame Contours from Flame Arrival Times

A model was developed [4] to convert flame arrival times at the eight head-gasket electrode locations into approximate flame contours at any given time. The model is based on the assumption that the flame evolution curve for any engine can be expressed in the form

$$\frac{r}{r_0} = f\left(\frac{t}{t_0}\right) \tag{1}$$

that is, the distance traveled by the flame in any direction normalized by a known distance r_0 is given by a function of the time to travel there t normalized by the time t_0 taken to travel to r_0. The function f is obtained from analysis of flame propagation in other S.I. engines that is scaled to account for the different geometry of this combustion chamber. We also assume that the flame evolution obeys this relation in every direction. Hence, given eight arrival times and the distances of the ionization probes from the point of ignition, by setting r_0 to 25 mm, for example, we can solve for the eight t_0 values (i.e., the time it took for the flame to reach a radius of 25 mm in the eight different directions). Then, for a given time t, we calculate the distance traveled in the eight probe directions and join these flame locations smoothly using a spline fit to produce the flame contour at time t. Although the flame contour is two dimensional, it was shown in Ref. 4 that estimating the inflamed volume by assuming that the contour extends spherically in the third dimension, with a radius equal to the radius of a best-fit circle to the two-dimensional contour, gives a good approximation of the mass fraction burned.

Calculation of Mass-Averaged HC Emissions per Cycle

The fast response flame ionization detector (FID), because of its high-frequency response, allows the HC-emission signature of a single cycle to be recorded for its entire duration. The exhaust gas was sampled from two locations. For most of the study, it was sampled 15 cm from the exhaust valve seat. This was the shortest distance at which the HC concentration was relatively uniform across the exhaust pipe and hence could be used to calculate the mass-weighted average emissions per cycle. The output signal from the fast response FID gives the instantaneous HC concentration at the sample location. To obtain a proper average of the HC emissions of a single cycle, the emissions signature must be mass averaged using the instantaneous exhaust gas mass flow rate. This is calculated using an energy balance on the time-varying contents of the cylinder during the blowdown process and exhaust stroke [5]. The instantaneous mass flow is given by

$$\frac{\dot{m}}{m} = \frac{1}{\gamma}\frac{\dot{p}}{p} + \frac{\dot{V}}{V} - \frac{\gamma - 1}{\gamma}\frac{\dot{Q}}{pV} \tag{2}$$

where $\dot{m}$ is the mass flow rate, m is the total mass in the cylinder, p is in-cylinder pressure, V is cylinder volume, and γ is the ratio of specific heats. After leaving the cylinder, the exhaust gas has to travel for 15 cm before it reaches the probe. The time taken for this (the delay introduced) is calculated by integrating the velocity of the exhaust gas by dividing it into thin gas layers that do not mix. It is also assumed that there is no heat loss to the exhaust port wall. The fast response FID internal delay is calculated using SATFLAP [6], a program developed for that purpose. The time-varying HC concentration is corrected for all the delays discussed previously before being integrated. The mass-averaged single-cycle HC emissions are then

$$[\overline{HC}] = \int_{EVO}^{IVO} [HC]\,\dot{m}dt \Big/ \int_{EVO}^{IVO} \dot{m}dt \tag{3}$$

Later in the study, the sampling point was moved much closer to the valve (1 cm) so that the emission profile characteristics could be attributed to the physical processes taking place during the exhaust stroke such as the blowdown process that occurs after exhaust valve opens and the piston scraping the quench layer off the cylinder liner during the exhaust stroke. The details of the operation, calculation

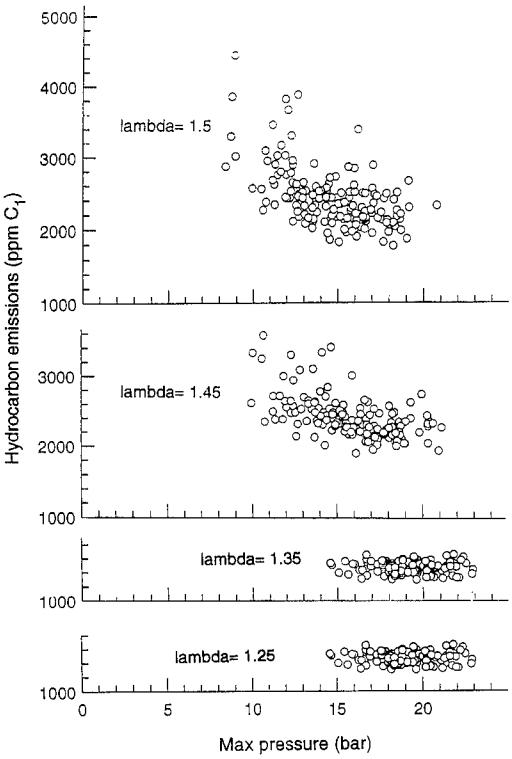

FIG. 1. Mass-averaged hydrocarbon emissions plotted against maximum pressure for 120 cycles (inlet pressure = 0.5 bar, MBT spark timing, 1600 rpm).

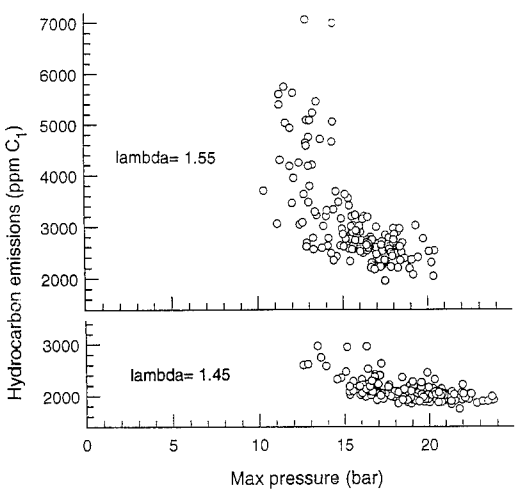

FIG. 2. Mass-averaged hydrocarbon emissions plotted against maximum pressure for 120 cycles (inlet pressure = 0.5 bar, MBT spark timing, 2500 rpm).

of delay times, and general setup of the FID are covered in Ref. 5.

Calculation of Fuel Mass Fraction Burned for Individual Cycles

The mass fraction of the fuel charge burned by the individual cycles was obtained by an analysis performed on the pressure trace of each cycle. The analysis is a one-zone burn-rate analysis with submodels for the effects of residual fraction, heat transfer, and crevices [7]. Burn durations were obtained from these mass-fraction burned profiles.

Experimental Results and Discussion

As explained previously, the HC concentration profile through each exhaust process, 15 cm downstream of the exhaust valve, was used to obtain single-cycle mass-averaged HC emissions. At the same time, the flame arrival times were recorded, and, hence, the flame contours for all the cycles were available. Experiments were conducted at 1600 and 2500 rpm in the relative air/fuel ratio ranges 1.25–1.5 and 1.25–1.55, respectively. The spark timing was always chosen to give the maximum brake torque. At the lean end of the range studied, the percentage of misfiring cycles was substantial (approaching 10%).

We first observe (Figs. 1 and 2) that the mean HC-emission level increases when the relative air/fuel ratio increases. Cycle simulation calculations for this engine showed that increasing the relative air/fuel ratio from 1.0 to 1.45 resulted in a decrease in exhaust gas temperature of 150 K at the exhaust valve opening, large enough to cause a change in the HC-emission behavior of the two operating conditions. HC oxidation mechanisms are very complicated but are often approximated by one-step reactions with fitted coefficients. The Arrhenius-type dependence of these rates on the temperature is responsible for the fast transition or switching behavior of these reactions. Fitted results of a kinetics calculation based on the mechanism by Dagaut et al. [8] suggests that

$$\frac{d[C_3H_8]}{dt} \propto \exp\left(\frac{-25{,}000}{T}\right)$$

A temperature change of 1100–1250 K results in a 20-fold increase in the reaction rate. The average (over 300 cycles, excluding the partial burns) mass fraction burned decreases from $\lambda = 1.25$ to 1.45 but only by 0.5% (95% versus 94.5%), which not only cannot account for the twofold increase in hydrocarbons but suggests that fewer unburned HCs left the cylinder in the leaner case. The preceding indicates that a decrease in the amount oxidized is the major reason for the increase in HCs observed.

Figure 1 also shows that for λ up to about 1.35,

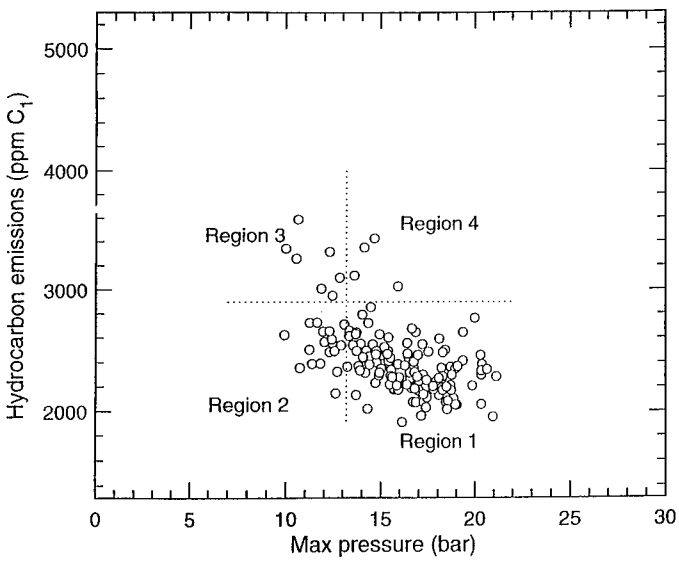

FIG. 3. Characterization of single cycle behavior of data in Fig. 1 at $\lambda = 1.45$ into four different regimes.

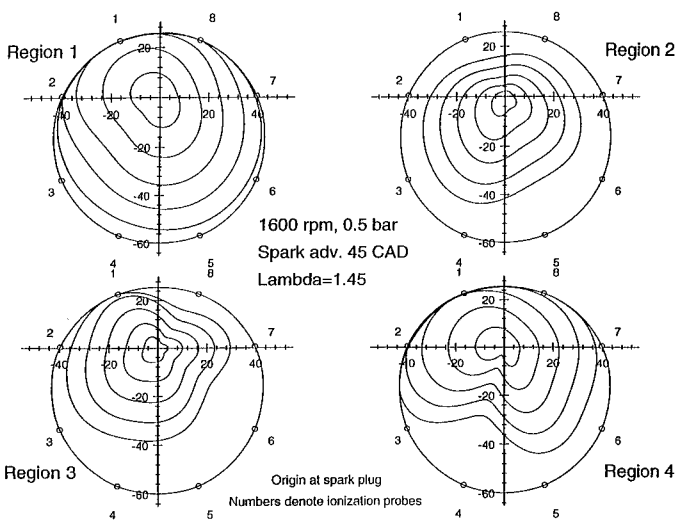

FIG. 4. Representative flame evolution contours for the four regions identified in Fig. 3.

the individual-cycle HC emissions are independent of the value of the maximum pressure that is a measure of the burn rate (a faster burning cycle gives a higher maximum pressure). The individual-cycle HC emissions show similar behavior when plotted against the area of the flame contours of those cycles, determined at the same time after spark discharge, which is another measure of the speed of combustion. For λ below about 1.35, any tendency for the HC emissions to increase because of late burning is apparently offset by the additional oxidation caused by increased temperatures during most of the expansion and exhaust strokes. However, when λ increases to 1.45, we see that the HC emissions of slow-burning cycles are higher than those of fast-burning cycles. A plausible explanation for the behavior is that for these very lean operating conditions, the expansion and exhaust stroke gases are becoming too cool for significant postflame oxidation to occur. Hence, while more hydrocarbons escape normal combustion by the mechanisms explained previously, the portion that is oxidized is smaller.

In addition to these phenomena, for relative air/fuel ratios greater than 1.4, single cycles with very high HC-emission values start to appear, which cannot be attributed to reduced oxidation alone. To study these cycles more systematically, we divided individual cycles into four separate groups or regions (Fig. 3) according to their behavior. Figure 4 shows the flame contours from representative cycles in

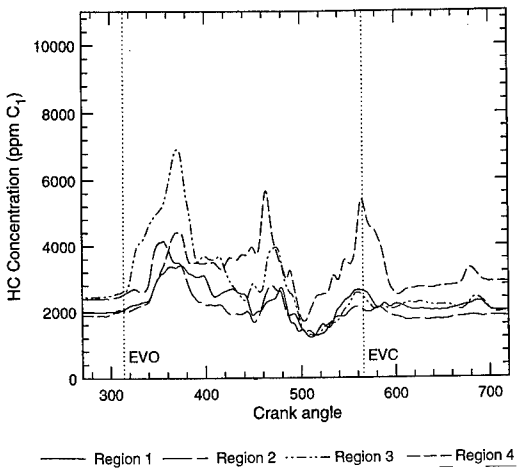

FIG. 5. Representative single-cycle hydrocarbon-emissions profiles measured 15 cm from exhaust valve seat for the regions identified in Fig. 3 (λ = 1.45, 1600 rpm).

TABLE 1
Summary of results for two different sampling locations.

Mass fraction Burned (region)	IMEP (bar)	HC emission peak at	2–20% burn duration
Case 1: Sampling 15 cm from valve			
85% (3)	2.831	B1[a]	61
85% (3)	3.153	B1 & Ex str[a]	53
86% (3)	3.166	Bl[a]	60
87% (4)	3.318	End Ex str[a]	46
87% (3)	3.209	B1 & Ex str[a]	53
87% (3)	3.013	Bl[a]	53
89% (4)	3.519	Ex str[a]	47
Case 2: Sampling 1 cm from valve			
74% (3)	2.071	Bl & Ex str[a]	74
79% (4)	2.586	End Ex str[a]	58
85% (3)	3.13	Bl & Ex str[a]	50
86% (3)	2.525	Bl[a]	65
89% (4)	3.282	End Ex str[a]	50
89% (3)	3.065	Bl & Ex str[a]	56
91% (4)	3.44	End Ex str[a]	44

[a]agreement with proposed explanation

each region where the respective contours for all cycles were plotted at the same time after spark onset. In region 1, the cycles are described as normal. Some are slower burning and some faster, but none are excessively so. In region 2, we have the cycles that are substantially slower burning, which have higher HC emissions (for λ greater than about 1.4, as discussed). Cycles in region 3, however, have significantly higher HC emissions but about the same slower burn rates as in region 2. Cycles from region 3 are globally slow burning (the flame contours are closely spaced and do not fill the cylinder cross section in the same time as do cycles from region 1); cycles from region 4 are on average faster burning but exhibit a slow burning region of charge. In cycles from region 3, slow burning probably continues after the exhaust valve opens, and, hence, these cycles tend to have HC emissions at the level of cycles from region 4 although they normally burn less fuel before the exhaust valve opens (average mass fraction burned, based on a pressure trace analysis, is 87% compared to that for cycles from region 4, which is 90%). Their IMEP values, however, which reflect how usefully the mixture was burned, are lower than those of cycles from region 4 (the comparison was made for cycles with the same maximum mass fraction burned). Although maximum pressure was used as a sorting parameter for the various types of cycles, when plotted against the cycle IMEP, the HC emissions exhibit the same behavior as in the maximum pressure plots and the same regions can still be identified containing the same cycles (as previously).

Cycles from region 3 undergo slow burning in all flame propagation directions. The resulting low pressures and temperatures favor incomplete charge burning during the main combustion period. Flame propagation stops where the effective air/fuel ratio will be even higher because of mixture inhomogeneties or residual gas fraction dilution. Cycles from region 4 also undergo incomplete combustion. The relatively high IMEP and maximum pressure values of these cycles suggest an initially fast flame propagation and relatively small amounts of unburned fuel. The small amount of unburned fuel points to a localized flame extinction. This extinction is more likely to occur in the middle part of the expansion stroke because of the more adverse conditions for flame propagation. An example of a phenomenon that would lead to region 4 behavior would be flame extinction by stretching when the piston moves down the cylinder. Cycles from region 4 are also rarer than those from region 3.

Hence, cycles from region 3 that are expected to have unburned HC distributed in the bulk of the exhaust gas and the extremities of the cylinder would tend to have high HC-emission signatures (Fig. 5) extending all the way from blowdown (the early part of the exhaust process where the bulk of the exhaust gas exits the cylinder) to the last part of the exhaust stroke, on the other hand, cycles from region 4 with less mixture left unburned exhibit a peak at a specific point in the exhaust stroke (depending on where the localized unburned region is). Note that because of the much higher mass flow rate of exhaust gases, blowdown contributes more to the overall HC emissions [5].

Table 1 (case 1: 1600 rpm, λ = 1.45, spark timing = 45 BTC) summarizes the results of a set of 300

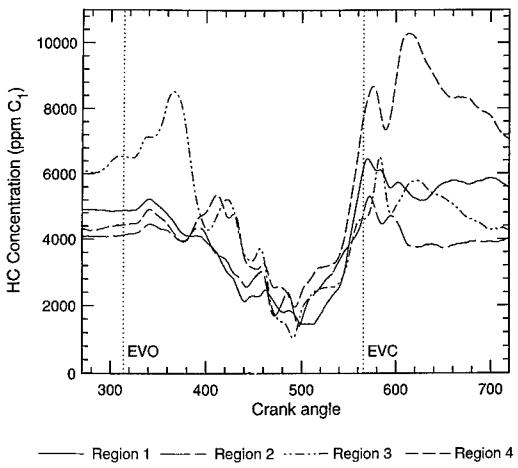

FIG. 6. Representative single-cycle hydrocarbon-emissions profiles measured 1 cm from exhaust valve seat (λ = 1.45, 1600 rpm).

cycles. The first column gives the mass fraction of the fuel burned (obtained from pressure trace analysis) and the region in which the cycle lies based on its flame contour behavior. The second column gives the IMEP of the cycle. A region 3 cycle should have a lower IMEP than a region 4 cycle that has the same mass fraction burned. The third column gives a description of the HC-emission profile of the cycle. The fourth column gives the 2–20% mass burn angle in CAD. This burn angle was chosen because region 4 cycles start to slow down after 25% (to about 40%) of the charge was burned, which corresponds to approximately 15 CAD ATC. Agreement is seen between the expected and obtained HC profiles, even though there was an occasional excursion of HC emissions halfway along the exhaust stroke for cycles belonging to region 4, as can be seen in Fig. 5.

Changing the Sampling Location

It is expected that mixing and oxidation will occur in the exhaust port. Hence, to be able to relate the HC emissions in a Lagrangian manner to their source, the FID sampling probe was moved close to the exhaust valve seat. This enabled us to obtain HC-emission signatures that could be related directly to the physical processes taking place during the blowdown period and the exhaust stroke. The disadvantage of this method is that the emission signature depends on the radial position of the probe. Therefore, the emission profile cannot be mass averaged because a major assumption in the mass averaging process is that the HC concentration is uniform across the exhaust pipe section. However, we have seen that the mass-averaged HC emissions agree with the rest of our observations.

The sampling location was thus moved to two new locations (case 2): 1 cm from the valve seat in the center of the tube and 1 cm from the valve seat close to the exhaust port wall. Typical emission profiles for these two locations were averaged and compared to verify that the HC concentration varies across the exhaust port. The two locations give HC profiles that are radically different compared to the ones sampled 15 cm from the valve seat [5].

The existence of cycles falling into one of the four categories defined previously is still evident from the flame contours, which are in no way affected by the change in sampling location. The HC-emission profiles follow the expected pattern qualitatively (see Table 1, case 2). Now cycles from region 3 have a peak in the beginning that usually extends to the end of the exhaust stroke. Cycles from region 4 have a peak at the end of the exhaust stroke. The change in shape of the emission profiles depending on the sampling location is attributed to nonuniform flow out of the cylinder, mixing, and varying extent of oxidation of the exhaust gases in the exhaust port [9]. Additionally, the signals are shifted to the right, relative to Fig. 5, because no correction for the delay introduced by the 1-cm travel distance from the exhaust valve was applied. The flow near the valve is highly nonuniform with high-velocity jets issuing into stationary gas, so no meaningful bulk velocity could be defined. Figure 6 shows HC profiles—examples of signatures having a peak at the beginning (blowdown) and the end of the exhaust stroke (hence belonging to region 3) or later on in the exhaust stroke (belonging to region 4), and signatures of normal (regions 1 and 2) cycles. Of course, the behavior of single cycles has a continuous spectrum and the division between the two trends is not absolute; some cases lie close to the boundary between these trends.

The data in Table 1 are representative of a series of experiments performed at various relative air/fuel ratios at the two engine speeds of 1600 and 2500 rpm. All the data are consistent with those presented.

Conclusions

The series of experiments described and interpreted here has shown the following: first, that mean engine HC-emission levels increase when the relative air-to-fuel ratio increases from stoichiometry because of decreasing HC oxidation and, second, that when close to stoichiometry, there is no correlation between individual cycle burn rate and HC emissions, because changes in the two factors (flame speed and exhaust gas temperature) governing the emissions balance each other out. However, a correlation appears when the engine is running substantially lean. In the initial stages, this is manifested

as a gradual increase in the HC emissions as the burn rate and the maximum pressure of individual cycles decrease. When the relative air/fuel ratio increases further, partial burns, that is, cycles that have abnormally high HC emissions that are a result of low flame speeds, start to appear.

These partial-burn cycles can be the result of either a globally (and at all times) slow-burning flame that has not completed combustion by the time the exhaust valve opens or a locally slow-burning or quenched region that usually develops toward the end of the combustion process. They can be distinguished from normally burning cycles by their flame propagation characteristics, a heat-release analysis, or the HC-emission signature.

Nomenclature

Bl blowdown
BTC before top center
CAD crank angle degrees
Ex exhaust
EVO exhaust valve opens
FID flame ionization detector
HC hydrocarbon
IMEP indicated mean effective pressure
IVO inlet valve opens
MBT maximum brake torque
rpm revolutions per minute
ST spark timing
str stroke

Greek symbols

λ relative air/fuel ratio

Acknowledgments

We would like to thank Brian Corkum for his helpful suggestions. The project has been funded by an Industrial Consortium for Engine Research, the members of which are Chrysler Corporation, Ford Motor Company, General Motors Corporation, Renault S. A., Peugeot S. A., and Volvo Car Corporation.

REFERENCES

1. Heywood, J. B., *Internal Combustion Engine Fundamentals,* McGraw Hill, New York, 1988, Chapter 11.
2. Witze, P. O., "Cycle Resolved Multipoint Ionization Probe Measurements in a Spark Ignition Engine." SAE Paper No. 892099, 1989.
3. Cheng, A. S., "The Head Gasket Ionization Probe as a Combustion Diagnostic for Spark Ignition Engines." S.M. Thesis, Department of Mechanical Engineering, Massachusetts Institute of Technology, 1994.
4. Hadjiconstantinou, N. and Heywood, J. B., "A Model for Converting SI Engine Flame Arrival Signals into Flame Contours." SAE Paper No. 950109, 1995.
5. Min, K., "The Effects of Crevices on the Engine-Out Hydrocarbon Emissions in a Spark Ignition Engine," Ph.D. Thesis, Department of Mechanical Engineering, Massachusetts Institute of Technology, 1994.
6. Cambustion Ltd., "HFR 400 High Frequency Response Flame Ionization Detector User Manual," 1992.
7. Cheng, H. M. and Heywood, J. B., "Evaluation of a One-Zone Burn-Rate Analysis Procedure Using Production S.I. Engine Pressure Data." SAE Paper No. 932749, 1993.
8. Dagaut, P., Cathonnet, M., and Boettner, J. C., *Combust. Sci. Technol.* 56:23 1987.
9. Finlay, I. C., Boam, D. J., Bingham, J. F., and Clark, T. A., "Fast Response FID Measurement of Unburned Hydrocarbons in the Exhaust Port of a Firing Gasoline Engine," SAE Paper No. 902165, 1990.

COMMENTS

A. Kowalewicz, Radom Technical University, Poland. Did you observe any correlation between HC emission and COV max pres.?

Did you measure torque (normalized vs λ), indicated efficiency vs λ, and emission of NO_x, CO, *HC* vs λ?

What is your opinion on the following problem: What is a better indicator of cycle-to-cycle variations on lean limit of engine operation: COV max pressure or COV_{imep}?

Author's Reply. Our data in Figs. 1 and 2 show that average HC emissions rise as the engine operates leaner and COV of maximum pressure increases.

The engine performance parameters you list did behave as would be expected as the engine is leaned out.

The more basic engine combustion parameter in cyclic variability is the burn rate or duration. The variation in imep and in maximum pressure depends on the variation in burn rate, but it also depends on the actual spark timing relative to the timing that gives maximum torque.

•

Dr. H. Zhao, Brunel University, UK. Have you considered the cause of local extinction?

Author's Reply. The observed local flame extinction is

most likely due to higher local flame straining combined with the decreasing pressure and unburned gas temperature as the expansion stroke develops.

•

C. Westbrook, LLNL, USA. Did you carry out any speciated emissions measurements? From my own past experience, I would expect that especially at your intermittent conditions, there would be lots of products of incomplete oxidation, especially formaldehyde.

Author's Reply. We did not speciate the hydrocarbon emissions. We agree that it is likely that slow burning cycles do produce larger quantities of incomplete oxidation products.

Twenty-Sixth Symposium (International) on Combustion/The Combustion Institute, 1996/pp. 2645–2652

OXIDATION OF HYDROCARBONS FROM LUBRICANT OIL LAYERS IN SPARK-IGNITION ENGINES

MICHAEL G. NORRIS, WOLF BAUER AND SIMONE HOCHGREB
Massachusetts Institute of Technology
Cambridge, MA 02139, USA

The postflame oxidation of hydrocarbons desorbed from the lubricant oil layer in spark-ignition engines is investigated through simulations and comparison with experimental measurements. A one-dimensional reactive-diffusive model is formulated for the process of desorption and oxidation of hydrocarbons emerging from the lubricant oil layer. Energy, mass, and species conservation equations are solved through the expansion stroke, using simplified assumptions for the turbulent diffusivity, boundary layer growth, and chemical reaction rates.

Simulation results show that under the current assumptions both reaction and diffusion rates are controlling. Chemical reaction rates peak over a narrow range of temperatures throughout the expansion stroke. This oxidation zone moves away from the wall during the expansion stroke due to heat transfer and volumetric expansion. Sensitivity analysis shows that the single most important parameter determining the oxidation of hydrocarbons from the oil layer is turbulent diffusion, which must be included for predictions to be of the same order of magnitude as experimental values. Other important parameters are chemical reactivity of the hydrocarbon and the initial boundary layer thickness.

Good agreement is obtained regarding the sensitivity of oxidation levels to dopant type and the most sensitive operating parameters: dilution and coolant temperature. This good agreement indicates that oxidation of unburned hydrocarbons in engines may well be represented by such simplified models. However, a factor of 3 discrepancy in the prediction of absolute values for the oxidation levels suggest that substantial refinement is required in the submodels.

Introduction

The search for methods to control emissions of unburned hydrocarbons (HCs) from spark-ignition engines has motivated numerous investigations into the mechanisms of production of exhaust hydrocarbon emissions [1,2]. Most of the work in this area has focused on quantifying the fraction of hydrocarbon fuel that escapes oxidation during the main combustion event [3,4]. The current conceptual model, based primarily on indirect experimental evidence, holds that this unburned fuel emerges from the various sources (crevices, oil layers, deposits) after flame passage. Approximately three-quarters is then oxidized as it mixes by diffusion and convection with the hot burned gases during the expansion and exhaust strokes before leaving the engine [1]. Predictive models for the oxidation of hydrocarbons from arbitrary sources do not yet exist. However, it is possible to gain insight into the parameters that control the process by designing simplified experiments to isolate one particular source of hydrocarbons, and by making suitable assumptions about the nature of the oxidation process in-cylinder.

This paper presents a model for the diffusive-reactive oxidation of hydrocarbons (HCs) emerging from an oil layer during the expansion stroke in a spark-ignition engine. Quantitative comparisons are made with results of recent experiments designed to directly measure the rate of oxidation of HCs emerging from the oil layer [5]. The work shows that a relatively simple, one-dimensional model can successfully predict the effects of operating parameters and the effects of the type of hydrocarbon emerging from the lubricant oil layer.

Experiments

The experiments, described in detail in Ref. 5, were carried out in a modified engine operating on a single cylinder. The lubricant oil was doped by continuously adding liquid HC upstream of the oil pump, while the engine was fired with hydrogen, thus isolating the desorbed dopant as the only source of carbon dioxide, carbon monoxide, and unburned HCs in the exhaust. The ratio of measured HC to total carbon represents the total fraction of HC not oxidized. Burned gas pressures, temperatures, radical concentrations, and the emergence rate of unburned HCs in the experiment were controlled to be typical of a gasoline-fired engine. Several dopants (toluene, isooctane, *p*-xylene, hexane, and MTBE) were used at different operating conditions, which

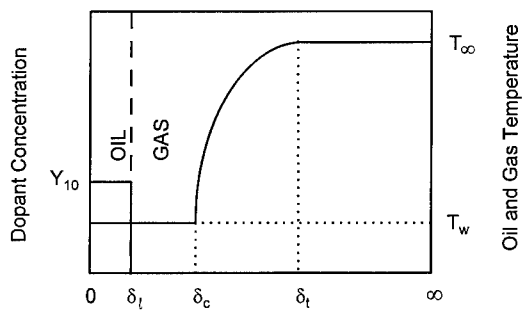

FIG. 1. Schematic of calculation variables and initial conditions. Schematic not to scale: $\delta_\ell \sim 1\ \mu$m, $\delta_c \sim 0.1$ mm, and $\delta_t \sim 1$ mm.

varied about a baseline condition: 1500 rpm, IMEP = 360 kPa, MBT spark timing, $\phi = 0.95$, 20% nitrogen dilution, and 90°C coolant temperature.

The measured ratio of HC to total carbon was corrected for the fraction of the HCs reacted during flame passage, oxidized in the port, and retained in-cylinder. The corrected measured values of the fraction of dopant oxidized in-cylinder (f) could then be compared to calculated values. It is assumed that all hydrocarbons in the gas phase are completely oxidized when the flame passes through the cylinder. This assumption is supported by the very small quench distances expected for the hydrogen flame (~0.01 mm). The fraction of HCs oxidized in the port was estimated with an empirical model based on Hamrin's work [6] with additional data from Mendillo and Heywood [7] and Drobot et al. [8], assuming that the port oxidation process in these experiments is similar to that in hydrocarbon-fired engines [7,8]. The fraction retained in the residual is estimated from a method to predict the residual mass fraction by Fox et al. [9] using additional measurements of the hydrocarbon concentration in the exhaust with a fast FID. Details of the estimates for each correction are described in Ref. 10.

Model Description

The one-dimensional model is an extension of a model developed by Min [11] to investigate the oxidation of crevice-stored HCs. A model for the desorption of dopant from the oil layer, a turbulent diffusion model, and one-step oxidation rate equations for toluene, isooctane, and MTBE were added.

Model Assumptions

The model assumes that oxidation of HCs during expansion takes place as planar, one-dimensional transport of energy, mass, HC, and oxidizer through the thermal boundary layer gas adjacent to the gas-oil interface (Fig. 1). Whereas there is clearly an axial component to the gas transport due to the piston motion, the gradients controlling oxidation during the piston downstroke (temperature and species) are in the radial direction in a thin region near the wall. The curvature of the cylinder can be neglected, as the radial domain in which reaction processes are taking place (~3 mm) is much smaller than the engine bore (86 mm). The flux of HCs from the oil layer into the gas phase is governed by the diffusion of dopant from the lubricant oil. The pressure is assumed to be uniform throughout the cylinder, and the gas temperature outside the thermal boundary layer is assumed to be the adiabatic core temperature predicted by a separate cycle simulation code [12]. The initial thickness of the thermal boundary layer and its subsequent growth are based on previous experiments [13]. The diffusion rate in the gas phase is the sum of molecular and turbulent eddy diffusivities, the latter estimated from a gradient diffusion model. The reaction term is expressed by a one-step rate function of the HC and oxygen concentrations.

Governing Equations

Gas side

The model solves the following differential equations for continuity, energy, and species (see Fig. 1 and Nomenclature for a description of the variables):

$$\frac{\partial \rho}{\partial t} + \frac{\partial(\rho u)}{\partial x} = 0$$

$$\frac{\partial Y_i}{\partial t} + u\frac{\partial Y_i}{\partial x} = \frac{\partial}{\partial x}\left(D_i \frac{\partial Y_i}{\partial x}\right) + \frac{\dot{\omega}_i}{\rho}\ (i = 1, 2)$$

$$\frac{\partial T}{\partial t} + u\frac{\partial T}{\partial x} - \frac{1}{\rho c_p}\frac{dp}{dt} = \frac{1}{\rho c_p}\frac{\partial}{\partial x}\left(k_e \frac{\partial T}{\partial x}\right) - \frac{\Delta h_r}{\rho c_p}\dot{\omega}_i \quad (1)$$

with boundary conditions

$$T(\delta_\ell, t) = T_w(z)$$

$$T(\infty, t) = T_\infty(t)$$

$$\left.\frac{\partial Y_1}{\partial x}\right|(\delta_\ell, t) = \frac{D_{1\ell}\rho_\ell}{D_{1g}\rho_g}\left.\frac{\partial Y_{1\ell}}{\partial x}\right|(\delta_\ell, t)$$

$$Y_1(\infty, t) = 0$$

$$\left.\frac{\partial Y_2}{\partial x}\right|(\delta_\ell, t) = 0$$

$$Y_2(\infty, t) = Y_{2\infty} \quad (2)$$

The initial conditions for the gas-side equations are

$$T(x, 0) = T_w \text{ for } 0 < x < \delta_c$$

$$T(x, 0) = T_\infty + \frac{T_\infty - T_w}{\kappa} \ln\left(\frac{x - \delta_c}{\delta_t - \delta_c}\right) \text{ for } \delta_c < x < \delta_t$$

$$T(x, 0) = T_\infty \text{ for } \delta_t < x < \infty$$

$$\left.\begin{aligned} Y_1(x, 0) &= 0 \\ Y_2(x, 0) &= Y_{2\infty} \end{aligned}\right\} \text{ for } \delta_\ell < x < \infty \qquad (3)$$

One-dimensional calculations for each element along the liner are started as they are exposed to the cylinder gases at the top of the piston crown. Crevice gases are assumed to initially form an isothermal layer between the oil layer and the burned gases. The initial radial variation in temperature across the thermal boundary layer ($T(x, 0)$) is a fit to measurements by Lucht et al. [14] near the cylinder head, with a constant $\kappa = 6.0$. Wall temperatures are assumed to be fixed with time, and to vary linearly along the stroke according to measured cylinder liner temperatures.

The one-dimensional continuity equation would in general overstate $\partial u/\partial x$, as the axial expansion term $\partial v/\partial x$ is neglected, effectively reducing the temperature gradient. The model addresses the issue by specifying the boundary layer thickness before each time step using the experimental correlation in equation 4. The assumed initial value and evolution of the thermal boundary layer thickness are based on schlieren measurements of the thermal boundary layer in an optical engine [13] as given by

$$\delta_t = 1.0 + 0.6(\alpha t)^{1/2} Re^{0.2} \qquad (4)$$

where δ_t is in mm, $Re = w_\infty(L_z - L_s)/\nu$ and $w_\infty = S_p(L_z - L_s)/(L - L_s)$.

The piston crevice is modeled as a simple isothermal volume at the corner of the piston and cylinder. The mass flow rate out of the crevice is determined by applying the ideal-gas law and the cylinder pressure history from the cycle simulation code.

Turbulent diffusion model

The model includes the effect of turbulence by using effective mass (D_e) and thermal (α_c) diffusivities as the sum of turbulent and molecular contributions, with the turbulent Prandtl and Lewis numbers assumed to be unity. The turbulent diffusivity is based on the gradient diffusion assumption [15] in the particular form

$$\nu_T = c_\mu(x - \delta_\ell)k^{1/2} \qquad (5)$$

where the k-ε model constant $c_\mu = 0.09$ is employed and the turbulent kinetic energy is assumed to be constant through the boundary layer. Equation 5 is appropriate for x smaller than the integral length scale of the flow, which is typically 2–6 mm at TDC [16,17] and increases as turbulence decays with time.

Turbulent decay is determined from the k-ε equations by assuming turbulence homogeneity,

$$\frac{dk}{dt} = -\varepsilon, \quad \frac{d\varepsilon}{dt} = -\frac{c_{\varepsilon 2}\varepsilon^2}{k} \qquad (6)$$

with a constant $c_{\varepsilon 2}$ equal to 1.9. These integrate immediately to

$$\frac{k}{k_0} = (1 + 0.9 \cdot t/\tau_0) - c_k \qquad (7)$$

where $\tau_0 = \lambda_0/k_0^{1/2}$ and $c_k = 1.11$. The time origin was chosen from experimental data as the point (15 CAD past the end of combustion) when the turbulence level begins to decay [18]. The initial length scale (λ_0) was chosen to be 3 mm, based on data from Ref. 17. Experimental evidence suggests that turbulent kinetic energy (k) scales with piston speed [16]. Assuming isotropic turbulence, the initial turbulent kinetic energy is calculated as

$$k_0 = \frac{(\chi \overline{S_p})^2}{2} \qquad (8)$$

where $\chi = 0.75$ for the modern pent-roof engine used in these experiments [18,19].

Oxidation model

The oxidation rate is determined from a one-step global reaction expression of the form

$$\dot{\omega}_1 = M_1 A \left(\frac{\rho_1}{M_1}\right)^a \left(\frac{\rho_2}{M_2}\right)^b \exp(-E/RT) \qquad (9)$$

where the ρ_1 and ρ_2 are the mass concentrations of HC and oxygen under fuel-lean conditions. The constants A, a, b, and E were extracted from time-dependent simulations by Wu [20] under lean to stoichiometric conditions (Table 1).

Desorption model

The desorption of HC from the lubricant oil layer is governed by one-dimensional diffusion

$$\frac{\partial Y_{1\ell}}{\partial t} = D_{1\ell} \frac{\partial^2 Y_{1\ell}}{\partial x^2} \qquad (10)$$

with the boundary conditions

$$\left.\frac{\partial Y_{1\ell}}{\partial x}\right|_{(0,t)} = 0$$

$$Y_{1\ell}(\delta_\ell, t) = \frac{p}{H^*} \frac{M_g}{M_1} Y_1(\delta_\ell, t)$$

$$\left.\frac{\partial Y_{1\ell}}{\partial x}\right|_{(\delta_\ell,t)} = \frac{D_{1g}\rho_g}{D_{1\ell}\rho_1} \left.\frac{\partial Y_1}{\partial x}\right|_{(\delta_\ell,t)} \qquad (11)$$

TABLE 1
Global reaction rate and solubility constants

Fuel	Reaction rate A $\left(\frac{cm^3}{mole\ s}\right)$	E $\left(\frac{kcal}{mole}\right)$	a	b	Solubility[b] (1/kPa) c	d
p-xylene[a]	7.78 10^{14}	40.9	0.583	1.515	9.81	−23.3
toluene	7.78 10^{14}	40.9	0.583	1.515	7.46	−17.9
iso-octane	2.49 10^{16}	49.8	0.836	1.08	7.47	−16.8
MTBE	3.56 10^{12}	50.6	0.843	0.489	4.13	−7.66

[a]Assumed same reaction rate as toluene.
[b]Solubility = $1/H^*$.

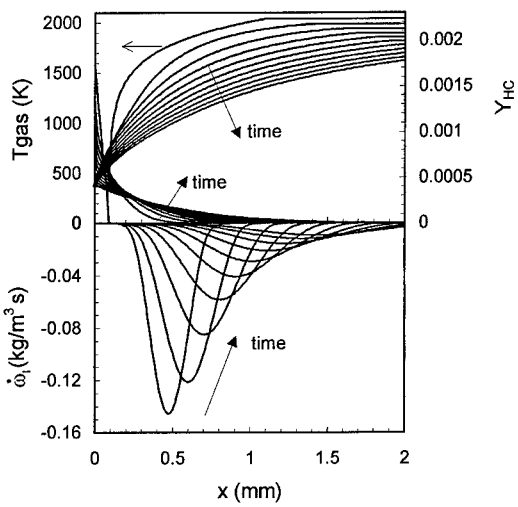

FIG. 2. Temperature, hydrocarbon mass fraction, and oxidation rate as a function of radial distance from oil layer for axial location 0.75 L_s above bottom center. Baseline conditions with toluene dopant. The lines are 4 CAD apart, with the top line corresponding to 48 CAD after TDC for temperature and mass fraction, and to 52 CAD for the oxidation rate.

The modified Henry's constant (H^*) is evaluated from an experimental correlation [21]

$$\log_{10}H^* = c \log_{10}(T) + d \qquad (12)$$

with T in kelvin and the constants c and d as listed in Table 1. The initial dopant concentration in the oil layer is an input from experimental measurements. The oil layer thickness δ_ℓ is assumed to vary with distance along the stroke as described in [22].

Solution Method

Equations 1–10 are solved numerically using the Crank-Nicholson method [23] with a node spacing of 0.01 mm within a domain of 3 mm, for a minimum time step of 2.64 μs at eight axial positions. The solution for each axial location (z) proceeds from the time it is uncovered by the piston top compression ring until the piston reaches BDC at the end of the expansion stroke. The resulting mass of dopant desorbed (dm_d/dz) and the mass of dopant surviving in the gas phase (dm_{HC}/dz) per unit axial length are integrated over the stroke length to obtain the oxidized fraction through BDC, $f = (m_d - m_{HC})/m_d$.

Results and Discussion

The model allows close examination of the details of the desorption and oxidation of dopants in the experiment. The results can then be used to interpret the effects of dopants and operating conditions observed in the experiments as well as the sensitivity of the model to various input parameters.

Desorption and Oxidation at the Cylinder Wall

The evolution of temperatures and the HC mass fractions in the gas phase are shown in Fig. 2. The temperature profile quickly evolves to a monotonic curvature, while temperatures continue to drop due to expansion and heat transfer to the wall. The imposed boundary layer thickness is noticeable as a slope discontinuity. The HC mass fraction drops off quickly away from the wall due to diffusion and oxidation.

Figures 2 and 3 show that oxidation takes place over a narrow zone, peaking at a common temperature. As reactants diffuse away from the wall, the oxidation rate increases with temperature until a maximum, then decreases at higher temperatures as reactant concentrations decrease. This oxidation zone moves away from the wall due to heat transfer and volumetric expansion. The oxidation rate decreases over time as HC concentrations in the

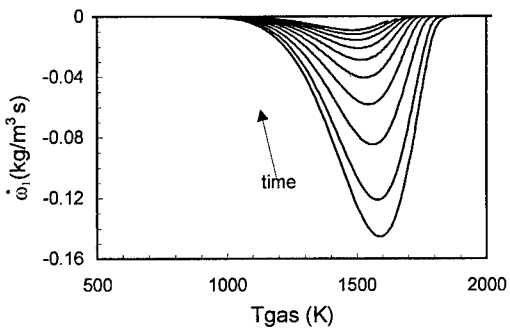

FIG. 3. Oxidation rate evolution as a function of gas temperature for the same conditions as Fig. 2. The lines are 4 CAD apart, and the first line corresponds to 52 CAD after TDC. Note that the oxidation rate is zero at 48 CAD.

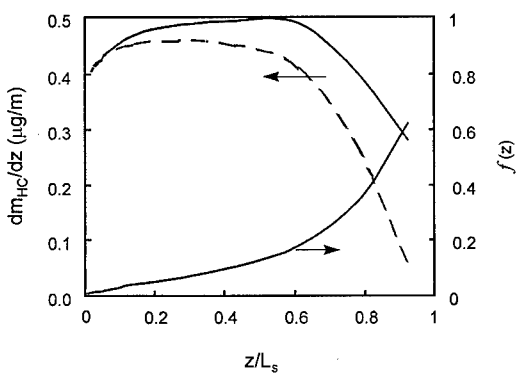

FIG. 4. Axial distribution of desorbed (solid line) and surviving (dashed) toluene dopant for baseline conditions and the fraction oxidized in-cylinder (thin line) as a function of axial location.

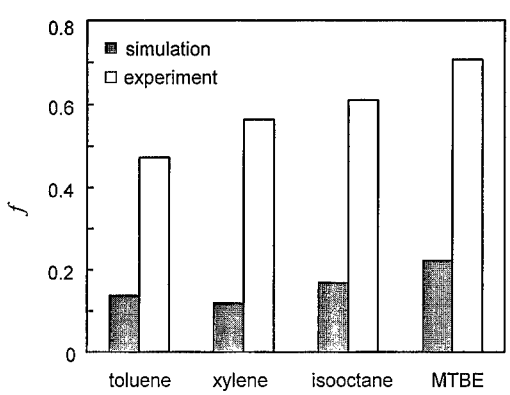

FIG. 5. Calculated and experimental values for the fraction of postflame desorbed dopant oxidized in-cylinder (f) for several hydrocarbons at baseline conditions.

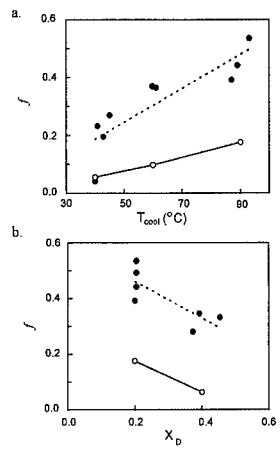

FIG. 6. Calculated (open) and experimental (closed) fraction of postflame desorbed dopant oxidized in-cylinder versus coolant temperature (a) and N_2 dilution level (b) for toluene dopant at baseline conditions.

oxidation zone decrease. The peak oxidation rate temperature depends on reaction rate parameters, core temperatures, and the transport rate of HCs from the oil.

Fraction Oxidized and Dopant Effect

The dopant species added to the oil affect the fraction of HC oxidized through their chemical reactivity and solubility in the oil, which impacts the rate of desorption from the oil layer. Figure 4 shows that HCs released early in the expansion stroke when the temperatures are highest ($z/L_s \rightarrow 1$) are oxidized at a much higher rate than those desorbed further down the cylinder axis.

The simulation predicted values of the fraction oxidized (f) of the postflame desorbed dopant (before BDC) are one-third of the experimental values for the dopants tested (Fig. 5). An underestimation is certainly expected, since the simulations are carried out only through BDC, where the one-dimensional model assumptions break down. However, simply extending the calculations through the end of the exhaust stroke should not increase the fraction oxidized by more than 20% (estimated from calculations carried out to IVO), since the reaction rates beyond BDC should be fairly low. Additional sources of uncertainties are discussed later.

Nevertheless, the calculated *change* in f as a function of dopant species is in good agreement with the experimental values, indicating that the one-dimensional model contains a reasonable balance between the reaction and transport rates in the gas phase.

Operating Condition Effect

Operating conditions affect the fraction of dopant oxidized through cylinder temperatures and

TABLE 2
Calculated parametric sensitivities

Parameter	Value	Calculated f at BDC	% Δ
	0.0	0.01	−93
Turbulence	0.75 $\bar{S}_p$	0.14	–
	1.50 $\bar{S}_p$	0.19	36
Turbulence decay	$c_k = 1.11$	0.14	–
	$c_k = 0$	0.32	128
Chemical reactivity	0.5 A	0.10	−28
	A, E	0.14	–
	2.0 A	0.18	29
Initial boundary layer (mm)	2.0	0.12	−14
	1.0	0.14	–
	0.5	0.18	39
Experiment f		0.46	

turbulence levels. The fraction oxidized in-cylinder derived from experiments shows a strong response to nitrogen dilution levels and coolant temperature. Lower coolant temperatures decrease the rate of dopant desorption by increasing the oil layer thickness, lowering liquid diffusion rates and increasing solubility. Thus, although the cylinder temperatures are essentially unchanged by coolant temperature, the fraction of hydrocarbons exposed to high cylinder temperatures is reduced and this results in a lower oxidized fraction (f). Although the correct trend in the fraction oxidized with coolant temperature is predicted, the sensitivity is lower than measurements indicate (Fig. 6a).

Increasing the amount of nitrogen dilution in the intake mixture significantly reduces the in-cylinder temperatures. These lower temperatures result in a significantly lower fraction oxidized in-cylinder. Both calculated and experimental values for f exhibit similar sensitivity to dilution at the levels shown (Fig. 6b).

Sensitivity Analysis

In spite of the good agreement in the change of the oxidation level with different parameters, there is clearly a large discrepancy between the experimental and simulation values. Some of the discrepancy can be attributed to uncertainty in the experimental value (±75%) which is due to assumptions made regarding port oxidation and residual gas fractions in determining the experimental values from the overall oxidation level; however, it is unlikely the factor of three difference is due entirely to this uncertainty. Sensitivity analysis was performed in order to identify the main parameters governing the final predicted fractions of hydrocarbons oxidized.

The most important parameters are listed in Table 2: initial turbulence levels, turbulence decay rate, the chemical activation energy, and the initial boundary layer thickness. Diffusive transport from the walls must necessarily be turbulent in order to obtain reasonable oxidation rates. Calculated values, however, are more sensitive to turbulence decay rather than the initial value of the turbulent kinetic energy. A change of a factor of 2 in the reaction rate promotes only a 30% change in the oxidized fraction, since the process is partially controlled by transport rates as well as reactivity. The initial boundary layer thickness also has a significant effect by creating an initial low-temperature zone when most of the reaction is taking place. The effect of crevice size, dopant desorption into crevice, and the assumption of a specified thermal boundary layer have small effects on the extent of oxidation relative to the other parameters.

Summary and Conclusions

A model for predicting the extent of oxidation of unburned hydrocarbons desorbing from the lubricant oil layer is proposed. The one-dimensional equations for energy, mass, and species conservation are solved for the postflame environment through the expansion stroke, with simplified assumptions for the turbulent diffusivity, boundary layer growth, and reaction rate.

Simulation results show that under the current assumptions, both reaction and diffusion rates are controlling. Chemical reactions peak over a narrow range of temperatures throughout the expansion stroke. This oxidation zone moves away from the wall during the expansion stroke due to heat transfer and volumetric expansion. Sensitivity analysis shows that turbulent diffusion must be included for predictions to be of the same order of magnitude as experimental values. Other important parameters are chemical reactivity of the hydrocarbon and the initial boundary layer thickness.

The large discrepancy in the absolute values brings into question the submodels for chemical kinetics, turbulent diffusion, and heat transfer, which deserve substantial refinement before absolute comparisons can be made. However, good agreement is obtained regarding the sensitivity of oxidation levels to dopant type, dilution, and coolant temperature. The favorable comparison of the behavior of the extent of oxidation with the variables considered indicates that the oxidation of unburned hydrocarbons in engines may well be represented by such models.

Nomenclature

a	concentration coefficient in one-step reaction expression
A	pre-exponential term in one-step reaction expression
α	thermal diffusivity
b	concentration coefficient in one-step reaction expression
BDC	bottom dead center piston position
c	coefficient for fit of Henry's constant
c_p	specific heat
c_μ	k-ε model constant
c_k	turbulent energy decay constant
d	coefficient for fit of Henry's constant
δ	thickness
D_{ij}	diffusivity of species i in phase j
E	activation energy
f	fraction of dopant oxidized in-cylinder
γ	ratio of specific heats
H^*	modified Henry's constant for the dopant in the oil
Δh_r	specific enthalpy of the reaction
k	turbulent kinetic energy
k	thermal conductivity
κ	temperature gradient fit constant
L	piston crown position relative to BDC
L_s	stroke length
L_z	axial position relative to the piston-crown BDC position
λ	turbulent integral length scale
m	mass
M	molecular weight
p	gas pressure
R	universal gas constant
Re	Reynolds number
ρ	density, mass concentration
S_p	instantaneous piston speed
$\bar{S}_p$	average piston speed
t	time
T	gas temperature
TDC	top dead center piston position
u	radial velocity
ν	kinematic viscosity
$\dot{\omega}$	reaction rate
w	axial velocity
x	radial coordinate
Y	mass fraction
χ	ratio of initial turbulence to average piston speed constant
z	axial coordinate, $z = 0$ at BDC position of piston crown

Subscripts

c	crevice
cool	coolant temperature
d	desorbed dopant
e	effective
g	gas phase
HC	desorbed dopant present at end of expansion
i	species index (1: hydrocarbon, 2: oxygen)
ℓ	liquid phase (oil)
0	initial value
t	thermal boundary layer
T	turbulent
w	wall
∞	core gas

Acknowledgments

The project has been supported by the MIT Industrial Consortium on Engine-Fuels Interactions, the members of which are Chevron Res. Co., Exxon Res. Eng. Co., Nippon Oil, and Shell Oil Co. The assistance of Profs. W. Cheng with the experimental facility and suggestions by Prof. J. Heywood are gratefully acknowledged.

REFERENCES

1. Cheng, W. K., Hamrin, D., Heywood, J. B., Hochgreb, S., Min, K. D., and Norris, M. G., Soc. Aut. Eng. Paper 932708, Warrendale, PA, 1993.
2. Lavoie, G. A. and Blumberg, P. N., *Combust. Sci. Technol.* 21:225 (1980).
3. Namazian, M. and Heywood, J. B., Soc. Aut. Eng. Paper 820088, Warrendale, PA, 1988.
4. Dent, J. C. and Lakshminarayanan, P. A., Soc. Aut. Eng. Paper 830652, Warrendale, PA, 1983.
5. Norris, M. G. and Hochgreb, S., Soc. Aut. Eng. Paper 960096, Warrendale, PA, 1996.

6. Hamrin, D. A. and Heywood, J. B., Soc. Aut. Eng. Paper 950984, Warrendale, PA, 1995.
7. Mendillo, J. D., and Heywood, J. B., Soc. Aut. Eng. Paper 810019, Warrendale, PA, 1981.
8. Drobot, K., Cheng, W. K., Trinker, F. H., Kaiser, E. W., Siegl, W. O., Cotton, D. F., and Underwood, J., *Twenty-Fifth Symposium (International) on Combustion,* The Combustion Institute, Pittsburgh, 1994.
9. Fox, J. W., Cheng, W. K., and Heywood, J. B., Soc. Aut. Eng. Paper 931025, Warrendale, PA, 1993.
10. Norris, M. G., "Oxidation of Hydrocarbons Desorbed from the Lubricant Oil in Spark Ignition Engines," Ph.D. Thesis, Department of Mechanical Engineering, MIT, 1995.
11. Min K. D. and Cheng, W. K., *The Third International Symposium on Diagnostics and Modeling of Combustion in Internal Combustion Engines,* COMODIA 94:1, 1994.
12. Poulos, S. G. and Heywood, J. B., Soc. Aut. Eng. Paper 830334, Warrendale, PA, 1983; and modifications since then.
13. Lyford-Pike, E. J. and Heywood, J. B., *Int. J. Heat Mass Transfer* 27:1873 (1984).
14. Lucht, R. P., Dunn-Rankin, D., Walter, T., Dreier, T. and Bopp, S. C., Soc. Aut. Eng. Paper 910722, 1991.
15. Launder, B. E. and Spalding, D. B., *Mathematical Models of Turbulence,* Academic Press, New York, 1972.
16. Heywood, J. B., *Internal Combustion Engine Fundamentals,* McGraw-Hill, New York, 1988.
17. Hadded, O. and Denbratt, I., Soc. Aut. Eng. Paper 910478, Warrendale, PA, 1991.
18. Hall, M. J., Bracco, F. V. and Santavicca, D. A., Soc. Aut. Eng. Paper 860320, Warrendale, PA, 1986.
19. Foster, D. E. and Witze, P. O., Soc. Aut. Eng. Paper 872105, Warrendale, PA, 1986.
20. Wu, K. C., Hochgreb, S., and Norris, M. G., *Combust. Flame* 100:193 (1995).
21. Schramm, J. and Sorenson, S. C., *J. Chromat.* 538:241 (1991).
22. Norris, M. G. and Hochgreb, S., *Proceedings of the Eighth International Symposium on Transport Phenomena,* San Francisco, CA, 1995, in press.
23. Ferziger, J. H., *Numerical Methods for Engineering Applications,* Wiley-Interscience, New York, 1981.

COMMENTS

Thierry Baritaud, IFP, France. Could you comment on the relevance of 1-step chemistry for a temperature range of 500 K to 2000 K?

Author's Reply. Recent 1D simulations of the problem involving transport and detailed chemical kinetic of propane [1] indicate that the reaction rate peaks around 1300–1500 K throughout the expansion, regardless of the initial condition of the mixture. Therefore, the approximation through 1-step chemistry reduced as in a flame mechanism may not be a bad approximation. A more rigorous test of the hypothesis is being tested in work in progress.

REFERENCE

1. Wu, K. and Hochgreb, S., "One-Dimensional Modeling of Hydrocarbon Oxidation Processes in Spark Ignition Engines," presented at the Third Workshop on Modeling of Chemical Reaction Systems, Heidelberg, July 24–27, 1996.

Dr. R. Maly, Damier-Benz AG, Germany. What type of characteristics did you use in your model for the spatial dependence of k (turbulent kinetic energy) on approaching the wall?

Author's Reply. The most simple model is to assume that turbulent kinetic energy is spatially constant in the combustion chamber. This is not true as its value decreases near walls due to blocking. Very close to the wall it is further damped by viscosity, as is the lengthscale [1]. Also, the viscosity is non-constant due to the strong temperature gradients. Detailed modeling is beyond the scope of this study. Rather, we use this model as an upper bound for the impact of turbulence on the diffusivity.

REFERENCE

1. Malan, P. and Johnston, J. P., "Heat Transfer in Shear-Free Turbulent Boundary Layers," Report No. MD-64, Thermoscience Division, Dept. of Mech. Eng., Stanford Univ., Oct. 1993.

Twenty-Sixth Symposium (International) on Combustion/The Combustion Institute, 1996/pp. 2653–2660

HEAT RELEASE RATES DUE TO AUTOIGNITION, AND THEIR RELATIONSHIP TO KNOCK INTENSITY IN SPARK IGNITION ENGINES

D. BRADLEY,[1] G. T. KALGHATGI,[2] M. GOLOMBOK[2] AND JINKU YEO[1]

[1]*Department of Mechanical Engineering*
University of Leeds
Leeds, LS2 95T, England

[2]*Shell Research Ltd.*
Thornton Research Centre
P.O. Box 1, Chester CH1 3SH, England

Net chemical heat-release rates have been estimated experimentally, throughout the combustion, from a single-cylinder gasoline engine, running on paraffinic and aromatic fuels. These rates are compared for autoigniting and nonautoigniting cycles and, by means of a differencing procedure, the heat release rate due to autoignition found. Comparison of heat release rates in the propagating flame and in autoignition show that in knocking combustion, almost half the total energy release can occur in autoignition. Pressures were measured with transducers and gas temperatures prior to autoignition by the CARS technique. The measurements enabled volumetric autoignition heat release rates to be obtained. When plotted against the reciprocal temperature of the unburned gas just prior to autoignition, an activation temperature and Arrhenius constant were obtained for each fuel in a single global expression for the autoignition heat release rate. These constants are reexpressed in terms of the actual temperature and fuel concentration to give a more accurate kinetic representation. This is used in an analysis of the conditions necessary for the pressure wave generated at autoignition to couple with the chemical kinetics sufficiently to lead to a developing detonation. At the inception of knock, for the same temperatures and pressures, the maximum autoignition heat release rates for the paraffinic fuel are two to three times those for the aromatic fuel. Because of this, the paraffinic fuel is more prone to developing detonation than is the aromatic fuel.

Introduction

Most attempts to predict knock in gasoline engines have focused on the autoignition delay time as a determining parameter. While a value for this might result in successful prediction of whether or not autoignition would occur, it gives no indication of the knock intensity. Neither, over a full range of generically different fuels, does the delay time correlate well with octane number. This is because the delay time is dependent upon cool flame reactions and registers their completion with the onset of much more rapid exothermic reactions. On the other hand, the octane rating depends upon the onset of intense pressure pulses generated by this high exothermicity. The present work attempts to gain some rudimentary understanding of the relationship of this final heat release rate to knock intensity, for a paraffinic and an aromatic fuel. Accurate, quantitative analysis of the phenomenon is doubly difficult: first, because it is difficult to measure the relevant parameters under the rapidly changing conditions, and second, the chemistry is not well understood.

The procedure adopted was to obtain the heat release rate due solely to autoignition from the difference between the overall heat release rates in knocking and nonknocking combustion. The peak heat release rate due to autoignition occurs at the onset of knock. From the total heat release due to autoignition up to this instant, it is possible to estimate the equivalent mass at various stages of autoignition reaction, and hence find at that instant the autoignition heat release rate per unit mass. An Arrhenius global expression that is first order in fuel concentration is assumed for autoignition. Provided an appropriate mean temperature can be attributed to the autoigniting gas, then, from results over a sufficiently wide range of temperature, it is possible to derive an Arrhenius "A" factor and activation temperature from Arrhenius plots. Such values are shown to provide a rough basis for assessing the propensity of different fuels to damaging knock.

Earlier attempts to derive the rate of burning from measured indicator diagrams used single zone models [1,2]. The two-zone first law analysis developed by Chun and Heywood [3,4] is used here to estimate the heat release rate; discussion about the scope and applicability of this approach to knocking combustion can be found in Ref. 5. If Q is the net thermal-energy gain (chemical heat release minus heat loss) and θ is the crank angle, then

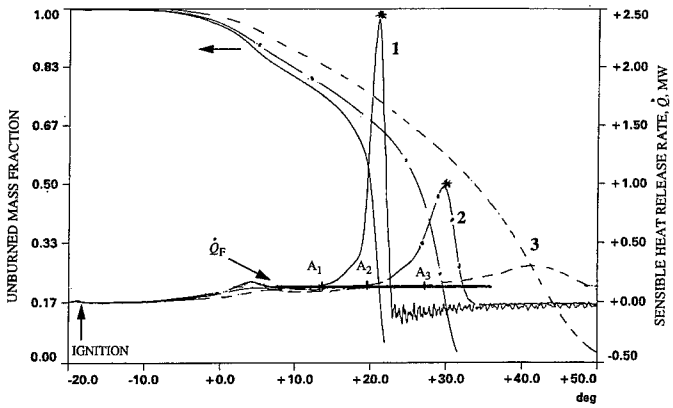

FIG. 1. Net heat release rates, $\dot{Q}$, and unburned mass fractions, at different crank positions, for knock intensities of 1490 (curve 1), 111 (curve 2), and 6.5 (curve 3) kPa. Asterisks indicate onset of knock. Fuel PRF 91.7, stoichiometric mixture.

$$\frac{dQ}{d\theta} = \frac{1}{\gamma - 1} V \frac{dP}{d\theta} + \frac{\gamma}{\gamma - 1} P \frac{dV}{d\theta} \qquad (1)$$

in which γ is the ratio of specific heats, V the cylinder volume, and P the pressure. Up to the instant of ignition, for the temperatures of the unburned gas, the values of γ were those plotted in Ref. 6. Thereafter, the values were given by the two-zone analysis [4].

During the compression stroke there is some small convective heat loss to the walls, which increases after ignition when combustion gases reach the wall. Temperature measurements in the unburned gas by the CARS (coherent anti-Stokes Raman spectroscopy) technique have yielded additional information on the heat released prior to autoignition by reactions in the cool flame regime. A measure of the extent of this is provided by the elevation of the temperature (for several fuels, but not propane) above that to be expected from the extension of the polytropic compression law observed for unburned, nonreacting gas into this regime [5,7,10]. The elevations for 90% *iso*-octane–10% *n*-heptane were in line with those computed by the five reaction, "parrot" autoignition model [7]. Kalghatgi et al. [5] applied equation 1 up to the time just prior to the development of high knock intensities and compared temporal profiles of net heat releases with those in nonknocking cycles. Inherent in equation 1 is the assumption that the pressure, P, is equalized throughout the cylinder. The equation becomes invalid when there are strong pressure pulses.

The present work attempts to separate the volumetric heat release rate of autoignition from that of the main propagating flame, and from this, to obtain approximate activation temperatures and rate constants in an empirical global expression for the autoignition volumetric heat release rate. Much evidence has accrued to suggest that paraffinic fuels have a greater propensity to intense knock than aromatic fuels [9]. The fuels used, therefore, were a primary reference fuel (PRF) mixture of *iso*-octane/*n*-heptane with motor and research octane numbers (MON and RON) of 91.7 (PRF 91.7), and a toluene/*n*-heptane mixture of the same MON, but with a RON of 102.

Experimental Method, Results, and Their Interpretation

A Ricardo E6 research engine with a compression ratio of 10.18 was employed. It ran with full throttle at 1200 rpm with a stoichiometric mixture, and propensities to knock were controlled by variations in ignition timing. These altered the compression of the end gas, the temperatures of which were measured prior to autoignition by the CARS technique. This and other aspects of the experimental work are described in more detail in Refs. 5, 7, and 10. It was found that the temperatures so measured could be related empirically to the pressure measured by a water-cooled Kistler 6001 transducer, wall-mounted close to the spark plug. Pressure data were sampled at a rate of 500 kHz and analyzed with FAMOS software. Knock intensity is defined as the maximum amplitude of the pressure signal filtered between 5 and 25 kHz. Knock intensities of up to 3 MPa were observed and knock onset was defined, arbitrarily, by the filtered pressure exceeding 10 kPa. Typical cyclic records of variations of pressure and of $d\dot{Q}/d\theta$ are given in Refs. 5 and 8.

Shown in Fig. 1 for three different values of knock intensity are the rates of change, $\dot{Q}$, of Q with respect to time, t, in megawatts, plotted against crank angle degrees from top center. The net heat release Q is obtained by integrating $\dot{Q}$ and is shown in Fig. 2 for the three cycles considered. Combustion is assumed to end when Q reaches its maximum value Q_m. The mass fraction of unburned gas at any crank angle θ is given by $\{1 - Q(\theta)/Q_m\}$ and is also shown in Fig. 1. These results are for the PRF 91.7 fuel. Later oscillations in the values of $\dot{Q}$ arise solely from oscillations in the pressure record and are indicative

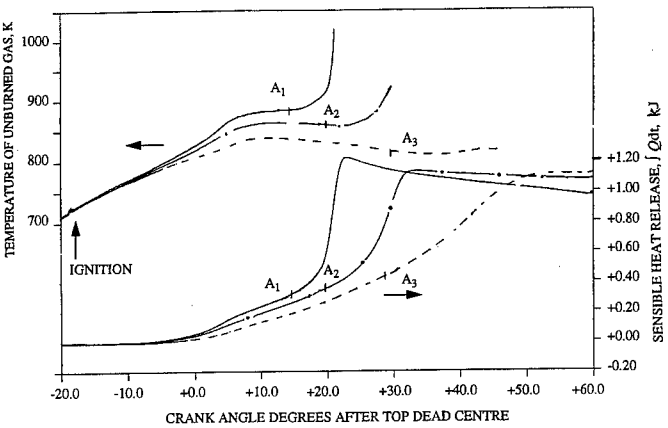

FIG. 2. Unburned gas temperatures and accumulated heat release, $\int \dot{Q} dt$, for the three cycles shown in Fig. 1. The temperature records terminate where $\dot{Q}$ is a maximum.

only of the onset of knock. Measurements of the intervals of time between the attainment of the maximum value of $\dot{Q}$, namely $\dot{Q}_m$, and the transducer indication of the onset of knock (if any), suggest the intervals correspond to the time for an acoustic wave to travel from a possible hot spot site to the transducer. Thus, in knocking cycles, the maximum heat release rate, $\dot{Q}_m$, can be regarded as a trigger for the knock. The mass fraction of unburned gas decreases at a rate that increases with the knock intensity. Clearly, knock induces a rapid "clean-up" of unburned gas. The analysis described below shows that for the highest knock intensity in the figure, about 40% of the mass of the original charge is consumed in autoignition reactions. This falls to about 10% for the lowest knock intensity.

The lower trace in Fig. 1 is the ensemble average value of $\dot{Q}$ between 5° and 35° crank angle after top center for nonknocking cycles, $\dot{Q}_F$, attributed to flame propagation minus a small heat loss. These values were cyclically repeatable with a 95 % confidence limit for <5% of the mean. An estimate of the heat release rate solely due to autoignition was obtained by subtracting $\dot{Q}_F$ from $\dot{Q}$. We shall analyze the maximum value of the heat release rate from autoignition, $\dot{Q}_{am}$ given by $\dot{Q}_{am} = \dot{Q}_m - \dot{Q}_F$. In this equation, it is assumed that at the instant of maximum heat release rate, the heat released by the propagating flame minus the heat loss in an autoigniting cycle at a given crank angle position, is the same as in an average nonautoigniting cycle.

The equivalent mass of the autoigniting gas, m_a, as a fraction of the total charge mass, m_{tot}, is given by the ratio of the total heat released by autoignition up to this instant to the total heat release as given by

$$\frac{m_a}{m_{tot}} = \frac{\int_{\theta_A}^{\theta^*} (\dot{Q} - \dot{Q}_F) d\theta}{\int_{\theta_0}^{\theta_{end}} \dot{Q}\, d\theta} \qquad (2)$$

where θ_0 and θ_{end} represent the start and end of burning, θ^* is the crank angle at which $\dot{Q}_{am}$ is attained, and θ_A is the crank angle at the start of autoignition, when $\dot{Q} = \dot{Q}_F$. The term "equivalent mass" is used to emphasize reaction is still occurring.

Shown in Fig. 2 are the temperatures of the unburned gas for the three cycles. They were found from an empirical expression that related unburned temperature to pressure, based on CARS measurements [5]. It can be inferred from Figs. 1 and 2 that both the knock intensity and $\dot{Q}_m$ increase with the pressure and temperature of the end gas. After the attainment of $\dot{Q}_m$, pressures were not equalized in knocking combustion.

Discussion

The Nature of Autoignition

The limited optical access to the engine prevented observation of the structures of both the propagating flame and the autoigniting centers. However, the general patterns of the latter can be inferred from the high-speed cine schlieren and self-luminous photographs of engine autoignition, with very good fields of view, of Sheppard, Maly, and coworkers [11–14]. In addition, valuable information is conveyed by the shadow photographs of autoignitions in shock tubes of Adomeit and coworkers [15,16]. This evidence shows autoignition seldom occurs uniformly throughout the end gas. In particular, it would appear that knock usually originates at randomly localized exothermic centers, or hot spots. Just prior to the onset of knock, the end gas is occupied by hot spots, deflagrating kernels, and unburned gas.

Hot spots can originate from imperfect mixing of the fuel and air [17,18], the mixing of residual hot gas from the previous cycle with the colder fresh charge, heat transfer at the walls, and the desorption of reactive species from wall deposits. The length

scales associated with these phenomena are probably those of turbulence, the integral length scale of which is about 1 mm in a conventional gasoline engine. In the regime of the negative temperature coefficient for the autoignition delay time [7], autoignition may be initiated in the cooler regions, close to the wall, rather than at a hot spot in the core [19].

In contrast, in the higher temperature regime, a sufficiently large hot spot is inherently unstable. Initially, the heat released is lost by conduction to the surrounding gas, but because the heat release rate increases exponentially with increasing temperature, the reaction runs away in a localized explosion. The smallest hot spot radius at which the heat release within the hot spot can be sustained in a steady state just prior to thermal explosion is the critical radius. This can be estimated from thermal explosion theory and is of the same order as an integral length scale. Hot spots with a radius greater than this critical value locally will explode. The more reactive the mixture, the smaller is the critical radius.

Following earlier suggestions of Oppenheim and coworkers [20], in Refs. 15 and 16, distinctions are made between mild and strong autoignitions: the former associated with a deflagration, the latter with, ab initio, a blast wave and developing detonation. In addition, it is not uncommon for separate deflagrating kernels to coalesce and, under increasing pressure and temperature, to initiate a detonation. Probably, Voevodsky and Soloukhin were the first to distinguish these two regimes of autoignition. In their seminal paper [21], they showed the chemical kinetic basis of the distinction for hydrogen-oxygen mixtures. Demarcation between the regimes was plotted in the pressure-temperature plane and was indicated also by gradient changes on Arrhenius plots of induction time against reciprocal temperature. In the high-temperature regime, strong ignition at a single point was sufficient to create a detonation front, whereas at low temperature, mild ignition was associated with the merging of several centers.

Autoignition Heat Release Rate Parameters

One of the aims of the present work was to estimate bounds for overall activation temperatures for the autoignition heat release rate and preexponential parameters in a global Arrhenius expression. In the three-zone model employed here, all the autoignited and autoigniting gas is grouped together into one volume of mass m_a and temperature T. The other two volumes are comprised entirely of either unburned or burned gas. The assumed global expression for the volumetric autoignition heat release rate is that employed in previous studies [9,11] and is first order in fuel concentration:

$$\dot{q} = A\,\rho m_f \Delta H \exp(-T_a/T) \qquad (3)$$

A is an Arrhenius constant, ρ is the density of the autoigniting mass m_a, m_f the mass fraction of the fuel, ΔH the heat of reaction, and T_a the activation temperature.

The numerical solutions for hot spot pressure generation of Lutz et al. [22], based on full chemical kinetics and the momentum equation, show the pressure wave to move away from the hot spot as $\dot{q}$ attains its maximum value. In the present work, the onset of knock occurs soon after $\dot{Q}_m$ is attained, some interval of time after autoignition had been initiated. The associated mean volumetric autoignition heat release rate in the autoigniting volume is given by $\dot{q}_{am} = \dot{Q}_{am}\rho/m_a$. Values of $\dot{Q}_{am}/m_a$, the rate of autoignition heat release per unit mass of the autoigniting gas, are used in an attempt to evaluate A and T_a. Equation 3 then gives

$$\ln(\dot{Q}_{am}/m_a) = \ln(Am_f\Delta H) - T_a/T \qquad (4)$$

Difficulties arise because of our inability to measure instantaneously heat release rates and the corresponding temperatures. It is, however, possible to correlate the experimental data with the initial mass fraction of fuel, m_{fu}, and the unburned gas temperature, T_u, at the instant when $\dot{Q}_m$ is attained. These values are used in equation 4 with $\ln(\dot{Q}_a/m_a)$ plotted against $1/T_u$ in Fig. 3, for the two fuels. For the paraffinic fuel, two regimes can be identified, as shown in Ref. 21 for hydrogen. The slope of the line in the higher-temperature knocking regime yields a value of activation temperature based upon these unburned properties, $T_{au} = 5{,}590 \pm 650$ K. The corresponding value of $\log(A_u/s)$, based upon the unburned mixture properties is 5.92 ± 0.05. In contrast, the data for the aromatic fuel are more scattered and there is less evidence of two clear-cut regimes. It is assumed that the value of T_{au} is unchanged, and a straight line is drawn through the points parallel to the upper line. The data on the diagram give, in addition to the same value of T_{au}, a value of $\log(A_u/s)$ of 5.51 ± 0.05. The above values are obtained with values of m_{fu} and ΔH respectively, of 0.06486 and 38.2 MJ/kg for the paraffinic, and 0.0711 and 34.9 MJ/kg for the aromatic fuel.

The next section analyzes the chemical interaction of the pressure wave as it moves from a hot spot. A more accurate kinetic description linked to actual values of temperature, T, and fuel mass fraction, m_f, of the autoigniting gas, rather than to T_u and m_{fu}, is required. The symbols A, T, and T_a refer to gas in the autoigniting zone. It is possible to relate these values to those in the unburned zone by the application of equation 4 to both sets of values. The left side of the equation is the same in both cases. Equating right side terms gives

$$\ln(\dot{Q}_a/m_a) = \ln(Am_f\Delta H) - T_a/T$$
$$= \ln(A_u m_{fu}\Delta H) - T_{au}/T_u \qquad (5)$$

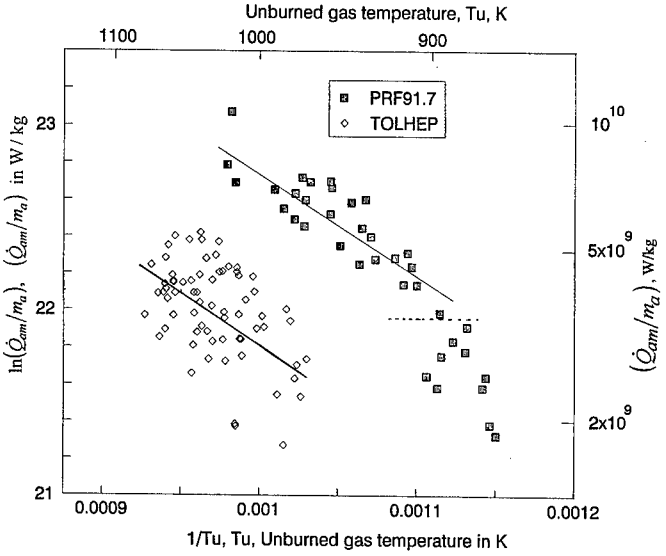

FIG. 3. Plot of $\ln(\dot{Q}_a/m_a)$ against $1/T_u$ for both fuels. Straight line fitted to high-temperature points, above horizontal broken line, to estimate T_{au} for PRF 91.7. Parallel to this is the straight line relationship for toluene/*n*-heptane.

Over the present range, it is assumed, not unreasonably, that T increases with T_u, and $T = T_u + \Delta T$. We further assume that ΔT is a constant and that m_f is related to reaction progress by

$$m_f = m_{fu}[(T_b - T)/(T_b - T_u)] \quad (6)$$

in which T_b is the computed burned gas adiabatic temperature [23] at a pressure of 4 MPa, and $T_u = 1000$ K. Values of T_b for the paraffinic and aromatic fuels employed were 2760 K and 2796 K, respectively. From these assumptions, equation 5 and its differential with respect to $1/T_u$ yield

$$T_a = \left(\frac{T_u + \Delta T}{T_u}\right)^2 \times \left(T_{au} + \frac{\Delta T T_u^2}{[T_b - (T_u + \Delta T)][T_b - T_u]}\right) \quad (7)$$

and

$$\ln A = \ln A_u - \ln\left[\frac{T_b - (T_u + \Delta T)}{T_b - T_u}\right] + T_{au}\frac{\Delta T}{T_u^2} + \frac{\Delta T(T_u + \Delta T)}{[T_b - (T_b + \Delta T)][T_b - T_u]} \quad (8)$$

Clearly, with no measurements available, the estimation of ΔT presents problems. In the early stage of autoignition the heat release rate is low. The present analysis applies to the later stage at the initiation of knock, where it is a maximum and the temperature at a hot spot is higher. If the temperature were uniform within the autoigniting volume, the heat release rate would be a maximum with a temperature rise ΔT of about 1,100 K for both the mixtures considered (see also Ref. 22). However, some of the gas in the autoigniting volume will be at a lower temperature and this will reduce the effective temperature in the reaction rate expression. Thus, $T_u < T < T_u + 1100$ K. Consideration of computed heat release rates at autoignition centers led to an assumed ΔT of 800 K. With this value of ΔT for the paraffinic fuel, T_a was evaluated as 20,290 ± 2,960 K, and log(*A*/s) as 8.66 ± 0.44. The corresponding values for the aromatic fuel were 19,360 ± 2,610 K, and log(*A*/s) as 8.01 ± 0.34. The error bands arise from those on A_u and T_{au}, as well as from the range of T_u values. If a higher value of ΔT is assumed, the values of T_a and A given by equations 7 and 8 are increased. For example, if ΔT is decreased to 700 K, with $T_u = 1{,}000$ K, T_a is decreased by 2407 K.

Modes of Autoignition

The amplitude of the pressure pulse emanating from the hot spot that initiates knock is increased if it is coupled with the exothermic reactions. Engine autoignition can occur in both the mild and strong regimes. The former includes benign autoignition with deflagration, but no knock; the latter, at higher temperature, might include developing detonation. The influence of chemical parameters on these modes is particularly important in the light of the damage caused by a developing detonation [9,11].

Study of this influence involved numerical analysis of the propagation of a pressure wave originating at a hot spot, and its chemical interactions. This requires solutions of the equations of global mass and fuel, together with those of momentum and energy. The reaction is again assumed to be of the simple, single-step, Arrhenius type, equation 3, but molecular transport processes are neglected. Fuller details

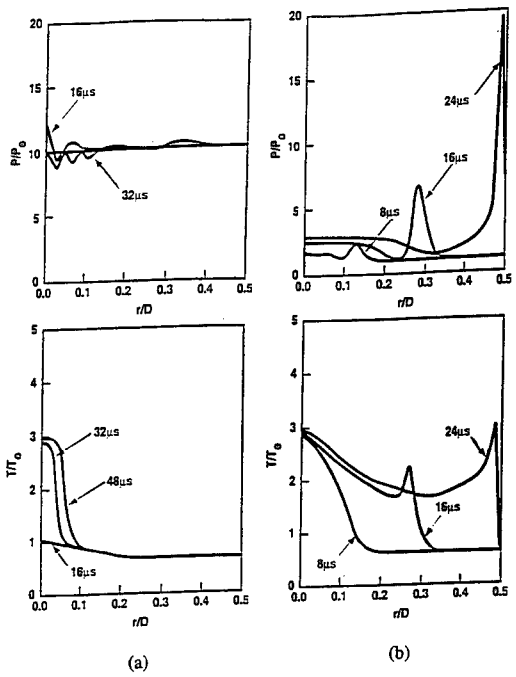

FIG. 4. Computed radial propagation of pressure and temperature waves after hot line autoignition. r/D is radius normalized by cylinder diameter. (a) T_a = 20,000 K, deflagration mode, (b) T_a = 15,000 K, developing detonation mode. See text for other parameters.

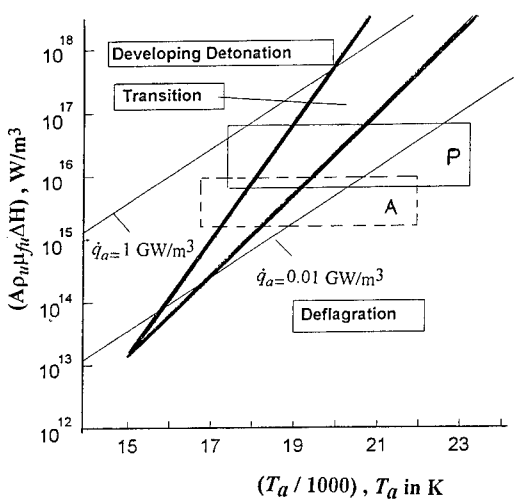

FIG. 5. Computed dependence of mode of autoignition on the kinetic parameters of equation 2. Two lines show volumetric heat release rates of 0.01 and 1.0 GWm^{-3} at 1,000 K and 4 MPa. Temperature gradient away from hot spot −23.5 K/mm. The boxed areas, A and P, show the range of values for the Arrhenius constants for aromatic and paraffinic fuels, respectively.

of this analysis are given in Ref. 11. Here, the computations are for cylindrical coordinates. The hot spot becomes a hot line, a central axis of autoignition, from which the pressure wave propagates radially outward through the reactive mixture. The motivation for the analysis is solely to understand the chemical interaction with the pressure wave. The temperature is assumed to decrease with distance from the central axis, with a constant temperature gradient.

Shown in Fig. 4 are computed, dimensionless profiles of pressure and temperature for two different activation temperatures, against radius, at three different times. Pressures are normalized by the initial pressure, P_0, of 4 MPa; temperatures, by the initial temperature, T_0, of 1,000 K at the axis; and radii by the cylinder diameter, D, of 85 mm. The initial temperature gradient, away from the hot spot, is linear and equal to −23.5 K/mm, but when the temperature falls to 600 K, it remains constant at this value. The influence of temperature gradients in the unburned gas is discussed in Ref. 11. The initial value of $\rho m_{fu}\,\Delta H$ at the center is 32 MJ/m^3, and the value of A is 3×10^6 s^{-1}. In Fig. 4a, T_a is 20,000 K. The pressure wave is weak and it attenuates as it moves outward. The temperature wave moves outward with a lower velocity, and the two waves are uncoupled. These aspects characterize the deflagration mode [11]. In Fig. 4b, for the lower activation temperature of 15,000 K, the pressure pulse strengthens as it propagates, and both waves are strongly coupled throughout the propagation. These aspects characterize the developing detonation mode. At an intermediate activation temperature, T_a of 17,000 K, the pressure pulse initially is amplified by chemical reaction, but is subsequently attenuated. This represents an initial coupling of chemical reaction and shock that is later uncoupled.

Extensive computations were made over a range of values of A and T_a. The results are summarized in the plots of $A\rho m_{fu}\Delta H$ at the same initial, normalizing conditions, against T_a, normalized by the initial temperature at the hot line, 1000 K, in Fig. 5. The thick lines delineate the modes of autoignition, and as before, $\rho m_{fu}\Delta H$ is 32 MJ/m^3. As an indication of the exothermicity, the thinner lines give the initial value, in GW m^{-3}, of $\dot{q}_a$ at the hot spot (or, more correctly, hot line) initial temperature of 1,000 K and initial pressure of 4 MPa. The developing detonation mode is entered above a threshold volumetric heat release rate of about 1 GW m^{-1} at this temperature and pressure. Below about 0.01 GW m^{-3}, the deflagration mode prevails and any knock is probably benign. In the transition regime, initially the pressure pulse is coupled to reaction and is amplified, but subsequently it becomes uncoupled and decays.

It is now possible to identify the regimes in the present study on this diagram. For the same initial, normalizing conditions, the present, experimentally

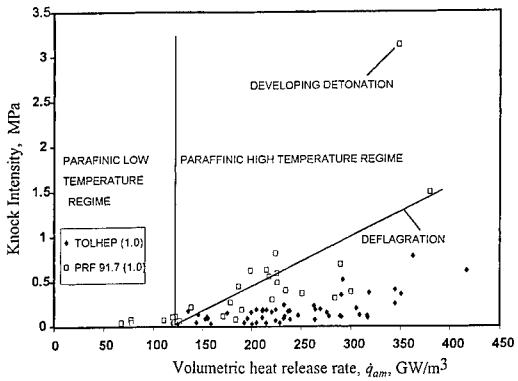

FIG. 6. Influence of mean volumetric autoignition heat release rate, $\dot{q}_{am}$ on knock intensity. Single point at high knock intensity is probably a developing detonation.

measured bounds for values of $A\ \rho_u m_{fu} \Delta H$ and $T_a/1000$ are shown for both fuels. The boxed areas, A (aromatic) and P (paraffinic), show the ranges of the preexponential constant and the activation temperature. The value of ΔT is 800 K. Despite the wide uncertainty bands, there is a clear indication that differences in the chemical characteristics at autoignition explain the greater tendency of paraffinic fuels to develop damaging detonative characteristics. The activation temperatures of both fuels appear to be similar, but the preexponential constant for the paraffinic fuel is higher than that of the aromatic fuel.

The experimentally measured influence of the mean, volumetric autoignition heat release rate, $\dot{q}_{am}$, on knock intensity is shown by the symbols in Fig. 6 for both types of fuel. Low- and high-temperature autoignition regimes have been assigned on the diagram for the paraffinic fuel. In the high-temperature regime, the knock intensity is initially proportional to the volumetric heat release rate. However, as the temperature increases still further, a nonlinearity is introduced into the relationship because of the coupling of the pressure wave with chemical reaction in a developing detonation. The single point at high knock intensity is probably associated with a developing detonation.

Conclusions

1. It has proved possible to separate the heat release rate due to engine autoignition from that due to flame propagation. In knocking combustion, nearly half the energy may be released in autoignition.
2. Because CARS temperatures can be measured only prior to autoignition and because the autoigniting volume is not accurately known, it is difficult to assign values to the Arrhenius constant and activation temperature in an overall, global kinetic expression for the volumetric heat release rate by autoignition. Nevertheless, some bounds are tentatively postulated for these values for the two fuels.
3. For similar temperatures and pressures, the maximum autoignition heat release rates for the paraffinic fuel are about two to three times those for the aromatic fuel. These heat release rates are related to knock intensity.
4. An analysis shows the bounds for the global kinetic constants that can lead to a damaging, developing detonation on the one hand, and benign autoignition on the other. The paraffinic fuel is the more likely to enter the former regime.

REFERENCES

1. Rassweiler, G. M. and Withrow, L., *SAE Trans.* 185–204 (1938).
2. Amann, C. A., SAE Paper No. 852067, 1985.
3. Krieger, R. B. and Borman, G. L., ASME Paper 66-WA/DGP-4.
4. Chun, K. M. and Heywood, J. B., *Combust. Sci. Technol.* 54:133–143 (1987).
5. Kalghatgi, G. T., Golombok, M., and Snowdon, P., *Combust. Sci. Technol.* 110/111:209 (1995).
6. Heywood, J. B., *Internal Combustion Engine Fundamentals,* McGraw Hill, New York, 1988.
7. Bradley, D., Kalghatgi, G. T., Morley, C., Snowdon, P., and Yeo, J., *Twenty-Fifth Symposium (International) on Combustion,* The Combustion Institute, Pittsburgh, 1995, pp. 125–133.
8. Golombok, M., Kalghatgi, G. T., and Tindall, A., SAE Paper No. 952405, 1995.
9. Bradley, D. and Morley, C., in *Low Temperature Combustion and Autoignition,* (M. J. Pilling, Ed.), to be published.
10. Kalghatgi, G. T., Snowdon, P., and McDonald, C. R., SAE Paper No. 950690, 1995.
11. König, G., Maly, R. R., Bradley, D., Lau, A. K. C., and Sheppard, C. G. W., *SAE Trans.* 99:840 (1990).
12. König, G. and Sheppard, C. G. W., *SAE Trans.*, 99:820 (1990).
13. Pan, J. and Sheppard, C. G. W., SAE Paper No. 942060 (1994).
14. König, G., Maly, R. R., Schöffel, S., and Blessing, G., *Effects of Engine Conditions,* Final Report, Contract: JOUE-0028-D-(MB), Commission of the European Community, 1993.
15. Blumenthal, R., Fieweger, K., Komp, K. H., and Adomeit, G., Fifteenth International Colloquium on the Dynamics of Explosions and Reactive Systems, Boulder, 1995.
16. Fieweger, K., Pfahl, U., and Adomeit, G., Twentieth International Symposium on Shock Waves, Passedena, 1995.

17. Neij, H., Johansson, B., and Aldén, M., *Combust. Flame* 99:449 (1994).
18. Berckmüller, M., Tait, N. P., Lockett, R. D., and Greenhalgh, D. A., Ishii, K., Urata, Y., Umiyama, H., and Yoshida, K., *Twenty-Fifth Symposium (International) on Combustion,* The Combustion Institute, Pittsburgh, 1995, pp. 151–156.
19. Schreiber, M., Sadat Saka, A., Poppe, C., Griffiths, J. F., Halford-Maw, P., and Rose, D. J., SAE Paper No. 932758 (1993).
20. Oppenheim, A. K., *Phil. Trans. Roy. Soc. Lond. A* 315:471–508 (1985).
21. Voevodsky, V. V. and Soloukhin, R. I., *Tenth Symposium (International) on Combustion,* The Combustion Institute, Pittsburgh, 1965, pp. 279–283.
22. Lutz, A. E., Kee, R. J., Miller, J. A., Dwyer, H. A., and Oppenheim, A. K., *Twenty-Second Symposium (International) on Combustion,* The Combustion Institute, Pittsburgh, 1989, pp. 1683–1693.
23. Morley, C., private communication.

COMMENTS

P. Monkhouse, University Heidelberg, Germany. Two synthetic mixtures were selected for this work, whereas real gasoline is a mixture of aliphatics and aromatics. It would be interesting to know more about the criteria for your selection. Also, could you use and extend these results to design an "optimized" fuel, in particular with respect to knocking?

Author's Reply. The fuels were selected to allow a study of why a fuel with a higher aromatic content knocks with lower intensity than a paraffinic fuel of the same MON. Reference 5 describes results for refinery streams used in blending real gasolines. The motivation behind this work is indeed to develop optimized fuels which would knock benignly.

•

Rudolf R. Maly, Daimler-Benz AG, Germany. In your model you collected the different exothermic centers in the end gas into a single volume. Could you please comment on whether this is admissible in view of the strong fluid dynamic interactions occurring in the end gas when the exothermic centers react separately causing mutual interactions?

Author's Reply. Inadequacies in our modeling reflect the current inadequacies in measurement techniques. The temperature distribution in the autoignited and autoigniting gas is unknown and probably the greatest limitation of the present treatment is the inability to distinguish between these two sub-zones. The volume of the autoigniting region can be significantly smaller than that of the region already autoignited. This implies that the actual volumetric heat release rate in the autoigniting region is significantly greater than the average values quoted in the paper.

•

Simone Hochgreb, Massachusetts Institute of Technology, USA. The method you described is useful in the analysis of the relative knock-related heat release from different fuels. However, the need for temperature measurements for the analysis limits somewhat the general use of the method. How different would the results be if the temperatures used were calculated without heat release (i.e. adiabatic compression)? Alternatively, how general is the correlation used to calculate the actual temperatures from CARS measurements?

Author's Reply. It is because the end gas temperature just before autoignition is elevated above that to be expected from simple adiabatic compression of a non-reacting charge that the CARS temperature measurements were necessary. The relevant elevations of temperature above the adiabatic, due to cool flame reactions, can be 200 K for both fuels [5]. Interestingly, there was no elevation for a slightly rich propane-air mixture.

Twenty-Sixth Symposium (International) on Combustion/The Combustion Institute, 1996/pp. 2661–2668

HEAT TRANSFER MODELING DURING KNOCK AND FLAME QUENCHING IN AN ENGINE CHAMBER

O. A. EZEKOYE
Department of Mechanical Engineering
University of Texas at Austin
Austin, TX 78712, USA

Heat-transfer rates present in an engine cylinder undergoing knock are known to be larger than the rates associated with normal engine operation. Further, at the time of knock, the largest heat fluxes are associated with locations on the cylinder wall where the flame is locally quenching. In this study, heat-transfer processes at the flame–wall interface during a knock event are investigated computationally and analytically. Computationally, the governing equations for a one-dimensional, flame-quenching event are solved using a reduced chemical reaction mechanism. Analytically, scaling relations for the flame heat-release rates are used in the governing equations to determine the heat-transfer rates. It is found that while pressure transients modify the wall heat flux, the absolute value of the pressure is the most significant parameter in predicting the maximum heat flux. The wall heat flux profiles are predicted for both the analytical and computational models. In the range of pressures examined, a linear relationship was found between the peak flux and pressure, both for the computational and analytical models. The linear relationship between the pressure and peak flux was found to be invalid when the flame-quenching process was disrupted by the pressure fluctuations for pressure oscillations with a characteristic time on the order of the quenching process.

Introduction

Under normal operating conditions, the cylinder walls of an internal combustion engine are subjected to extremely large heat fluxes resulting from the flame propagation and quenching processes within the chamber. For normal operating conditions, significant material wear and degradation does not occur; however, in unusual circumstances, cylinder wear from thermal stresses can take place. A specific undesirable operating condition is the knocking condition that occurs when reactant charge within a cylinder autoignites. When the timescale of the autoignition is much shorter than the characteristic acoustical time of the cylinder, an oscillatory, transient pressure wave is induced by the autoignition process. Typical cylinder pressure traces for nonknocking and knocking conditions are shown in Fig. 1 [1]. Knock is indicated in the pressure history by the appearance of an oscillatory component on the chamber pressure signal. The heat-transfer rates present in a cylinder undergoing knock have been shown to be significantly larger than the rates associated with normal engine operation [1]. In Lu et al. [1], the measured peak heat flux during knocking was shown to vary linearly with the peak-pressure amplitude for a given knocking event. While the experimental verification of the increased heat-transfer rates associated with knock was provided, the physical mechanisms controlling the enhanced rates were not given. Three possible processes interact to potentially enhance the knocking heat-transfer rates. First, there is an increased convective velocity associated with the strong expansion caused by autoignition, which may aid in increasing the heat-transfer rates. Second, the pressure transient term in the energy equation (dP/dt) is more substantial for a knocking condition than for a nonknocking condition and thus serves as an increased source term. Finally, the transient density variation, which is specified by the equation of state, affects the local heat-release rate that correlates with the peak heat flux.

While there have been many notable investigations of flame quenching [2–5], the effects of strong pressure transients typically have not been examined. Several studies have examined the role of pressure transients on heat-transfer rates in the absence of reactions [6,7]. Keck [6] examined the effects of a generalized time-dependent pressure on a gas thermal boundary layer and, using an integral method analysis, developed general expressions for the displacement thickness and the heat-transfer rate. Heperkan and Greif [7] examined the heat transfer during shock-induced ignition of an explosive gas by analytically solving the mass and energy conservation equations to derive an expression for the temperature profile in the thermal boundary layer. Yang and Martin [8] extended the type of analysis used in the previously mentioned references [6,7] by including the effects of reactions. By using

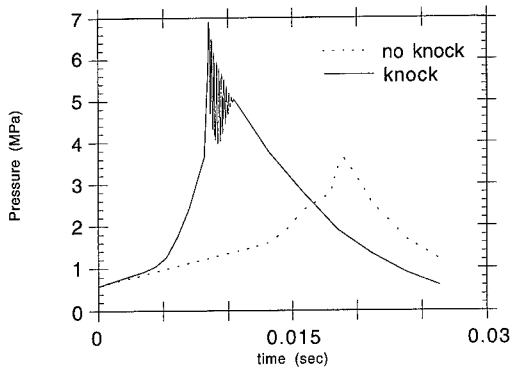

FIG. 1. Comparison of cylinder pressure traces for knocking and nonknocking conditions. Engine simulator was operated at 600 rpm with n-heptane (data from Lu et al. [1]).

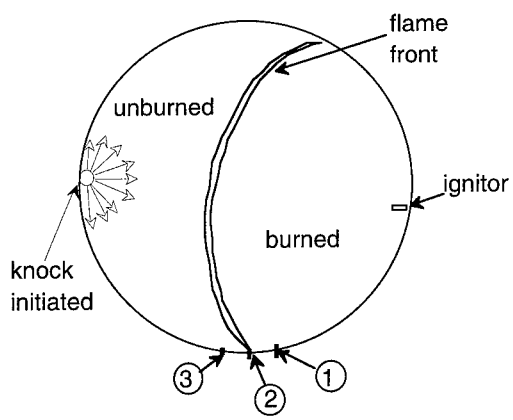

FIG. 2. Schematic diagram of cylinder at the time of knock. Locations 1, 2, and 3 represent heat flux measurement locations.

an empirical expression for the heat-release rate and also for the quench distance, they quasi-analytically model the heat transfer profile associated with the knocking pressure profile specified in Lu et al. [1]. The analytical model presented in this work differs from that of Yang and Martin, both in the specification of the reaction term and in the solution procedure. Bush et al. [9] investigated the implications of specifying appropriate heat-transfer rates to suppress knock by using a computational scheme for the flame propagation and quenching process. A computational investigation is used in this study to examine the processes that determine the knocking heat-transfer rate enhancement. Using both an actual engine pressure trace and a hypothetical oscillating pressure profile, comparisons of the analytical and computational approaches for a knock event are made; it is shown that the analytical model possesses many of the observed physical effects described by the computational study.

There are several possible conditions that may exist in the cylinder at the time of knock. As shown in Fig. 2, there are locations within the chamber (1) where the flame has long quenched at the time of knock (2) where the flame reaches at the time of knock, and (3) where the flame has not reached. Associated with these different locations are different heat-transfer responses to the knocking phenomena. The heat-transfer response to knocking for the three specified cases is investigated, and the physical process most dominant in the heat-transfer augmentation is discussed.

Theory

Experiments have shown that the wall heat flux time history during flame quenching is independent of the orientation of the flame–wall interaction [10]. Computational investigations have supported this result [11,12]. Using this finding, a relatively simple flame–wall interaction is chosen to model the knock-quenching processes. The flame is assumed to propagate perpendicularly to a wall and effectively stagnate on it. The physical process may be modeled by solving the mass-, species-, energy-, and momentum-conservation equations. The Lewis number is assumed to be unity.

$$\frac{\partial \rho}{\partial t} + \frac{\partial(\rho v)}{\partial y} = 0 \tag{1}$$

$$\rho\left(\frac{\partial Y_i}{\partial t} + v\frac{\partial Y_i}{\partial y}\right) = \frac{\partial}{\partial y}\left(\rho D\frac{\partial Y_i}{\partial y}\right) - \dot{\omega}_i \tag{2}$$

$$\rho c_p\left(\frac{\partial T}{\partial t} + v\frac{\partial T}{\partial y}\right) = \frac{\partial P}{\partial t} + \frac{\partial}{\partial y}\left(k\frac{\partial T}{\partial y}\right) - \sum_i \Delta H_i^0 \dot{\omega}_i \tag{3}$$

$$\rho\left(\frac{\partial v}{\partial t} + v\frac{\partial v}{\partial y}\right) = \frac{\partial P}{\partial y} + \frac{\partial}{\partial y}\left(\mu\frac{\partial v}{\partial y}\right) \tag{4}$$

Based on scaling analysis of the engine chamber used in Lu et al. [1], a self-consistent chamber frequency, f, of 5 kHz is found if one assumes an average gas temperature of 2000 K within the system. That is, $f = c/2L$, $c = \sqrt{\gamma RT}$, and $\gamma \equiv c_p/c_v$. The chamber characteristic length, L, is 90 mm. The knocking pressure wave behaves similarly to a traveling wave at the time of knock and induces advective effects as it slowly damps out in time. However, it is assumed in this study that near the wall (where quenching occurs), the pressure is spatially uniform and temporally varying. An estimate of the effects of the tangential velocity can be made by comparing the ratio of the quench thickness to the thickness of

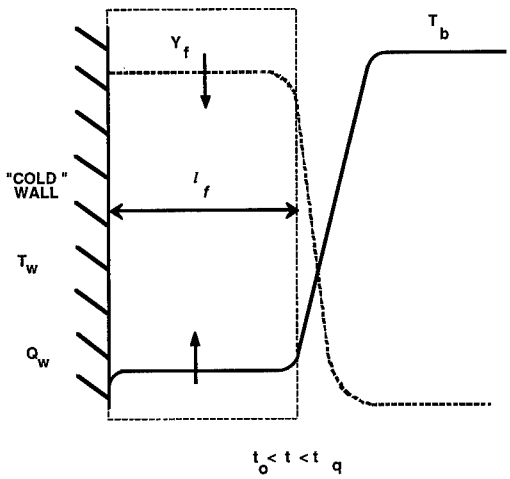

FIG. 3. Schematic diagram of flame quenching as described by the analytical model. The flame is represented by the rectangular heat-release zone that stagnates on the cold wall.

the Stokes layer (as specified by the frequency), or $L \equiv d_q/\sqrt{\nu/f}$. For the high-pressure conditions examined, d_q is of the order 10 μm and an average value of ν is 100×10^{-6} m²/s. Scaling shows that $L \ll 1$, implying that viscous effects damp the oscillating velocity.

Analytical Model

Treatment of the reaction rate terms in the analytical model parallels the development in Isshiki and Nishiwaki [13] and in Ezekoye and Greif [11]. At the quench time, flame propagation is assumed to rely weakly on the temperature profile (i.e., low activation-energy reactions), and the species equation is decoupled from the energy equation when the reactant temperature achieves a relatively low ignition temperature. Since flame propagation is thus primarily governed by reactant species evolution, scaling on the species equation provides the characteristic length and time scales for the combustion analysis—specifically, the quenching event. In this manner, the heat-transfer analysis is specified solely by the energy equation with an exothermic source term specified through scaling on the species equation. It proves useful to formulate the energy equation in a Lagrangian coordinate system, (t, ψ), by using the von Mise transformation with $\rho/\rho_o = \partial\psi/\partial y$ and $\rho v/\rho_o = -\partial\psi/\partial t$. A nondimensional time variable is defined by $P_o d\tau = P(t)dt$. The resulting energy equation is

$$\frac{\partial T}{\partial \tau} = \frac{\gamma - 1}{\gamma}\frac{T}{P}\frac{dP}{d\tau} + \alpha_o \frac{\partial^2 T}{\partial \psi^2} + \frac{P_o Q'''}{\rho P c_p} \quad (5)$$

The heat-transfer analysis begins at a time t_o when the flame is one flame thickness away from the wall. Since the reaction rate is assumed to be weakly dependent on the temperature, and the reactant temperature within one flame thickness of the wall is assumed to be at the ignition temperature, the heat-release rate is distributed over a flame-thickness length away from the wall (Fig. 3). The heat-release rate has been replaced by the quantity Q''' in the energy equation. The fundamental issue of the analytical model is the specification of Q''' temporally and spatially. For time less than t_o, where t_o refers to the flame-arrival time, the temperature distribution and, therefore, the wall heat flux are associated strictly with the transient pressure field (i.e., dP/dt). At t_o, the reaction zone moves adjacent to the wall. Over a time associated with complete consumption of the reactant species, $t_q - t_o$, the exothermic reaction proceeds. After t_q, the time at which all the reactants have been consumed, the reaction extinguishes. The wall heat flux is associated primarily with the volumetric heat-release rate adjacent to the wall and does not depend strongly on the initial temperature profile. In fact, it is strictly independent of the initial temperature profile for times less than the thermal-diffusion timescale referenced to the flame thickness. It is valid, therefore, to specify the boundary conditions on the energy equation as $T(\psi, \tau = 0) = T_o$; $T(\psi = 0, \tau) = T_o$; $\partial T/\partial y\ (\psi \to \infty, \tau) = 0$.

The scaling of the volumetric heat-release rate, Q''', is given by the expression

$$Q''' \equiv \frac{\rho S_u c_p \Delta T}{l_f}[H_s(t - t_o) - H_s(t - t_o - \Delta t_q)] \quad (6)$$

where all scalings of the parameters within the preceding expression are specified by approximate pressure and temperature dependencies and H_s is the unit step function. The flame thickness is specified in terms of the laminar flame speed, S_u, and the species mass diffusivity, $l_f = D/S_u$. Using the definition of the species diffusivity and the Lewis number, the heat-release rate is specified to be

$$Q''' \equiv \frac{(\rho S_u c_p)^2 \Delta T}{kLe}[H_s(t - t_o) - H_s(t - t_o - \Delta t_q)]$$

Next, scalings for the laminar flame speed, $S_u(T)$, thermal conductivity, $k(T)$, and density, $\rho(T, P)$ are used. The laminar flame speed is assumed to vary quadratically with the unburned gas temperature; the weak pressure variation is neglected. Using these values, the final form of the volumetric heat release is given by

$$Q''' \equiv \left(\frac{P}{P_o}\right)^2 \left(\frac{T}{T_o}\right) \frac{\rho_o S_{u,o} c_p \Delta T}{l_{f,o}} [H_s(t - t_o) - H_s(t - t_o - \Delta t_q)]$$

The scalings indicate that the volumetric heat-release rate is quadratic in pressure and linear in unburned gas temperature. The physical implication of the Q''' scaling is that the heat-release rate is equal to the enthalpy flux through a steadily propagating flame divided by the flame thickness. Reference values of the parameters used in the analytical model can be found in Table 1.

Similar to Ref. 7, pressure-transient terms are respecified in terms of a compression temperature, T_∞, which is constructed as the solution to

$$\frac{dT_\infty}{d\tau} = \frac{\gamma - 1}{\gamma} \frac{T_\infty}{P} \frac{dP}{d\tau} \tag{7}$$

The energy equation can then be written as

$$\frac{\partial T}{\partial \tau} = \frac{T}{T_\infty} \frac{dT_\infty}{d\tau} + \alpha_o \frac{\partial^2 T}{\partial \psi^2} + \frac{P_o Q'''}{P \rho c_p} \tag{8}$$

A new, dependent temperature variable, ϕ, is defined as $\phi = T/T_\infty - 1$ and satisfies the following differential equation and boundary conditions:

$$\frac{\partial \phi}{\partial \tau} = \alpha_o \frac{\partial^2 \phi}{\partial \psi^2} + \frac{P_o Q'''}{P \rho c_p} \tag{9}$$

$$\phi(\psi, \tau = 0) = 0; \ \phi(\psi = 0, \tau) = T_o/T_\infty(\tau) - 1;$$

$$\partial\phi/\partial\psi \ (\psi \to \infty, \tau) = 0$$

Within the limits considered, the wall heat flux is found by using the Laplace transformation and is given by the expression

$$q_w = -k \left.\frac{\partial T}{\partial y}\right|_{y=0} = -k_o T_o \left(\frac{P}{P_o}\right)^{2\gamma - 1/\gamma} \left.\frac{\partial \phi}{\partial \psi}\right|_{\psi=0} \tag{10}$$

where

$$\left.\frac{\partial \phi}{\partial \psi}\right|_{\psi=0} = \frac{1}{\sqrt{\alpha_o \pi}} \int_0^\tau \left(\frac{P_o}{P}\right)^{2\gamma - 1/\gamma} \times \frac{Q'''[H_s(\tau' - \tau_o') - H_s(\tau' - \tau_o')]}{\rho c_p T_o (\tau - \tau')^{1/2}} + \frac{\left(\frac{P_o}{P}\right)^{1-\gamma/\gamma} - 1}{2(\tau - \tau')^{3/2}} d\tau' \tag{11}$$

Computational Model

Similar to the analytical model, the conservation equations are transformed by use of the von Mise transform and solved in a Lagrangian coordinate system. Although a one-step reaction mechanism may be used for this investigation, a two-step mechanism for propane specified by Westbrook and Dryer [14], which has better pressure-dependent effects than a single-step mechanism, was used. The two-step mechanism is composed of an irreversible fuel oxidation step and a reversible carbon monoxide oxidation step. Details for solution of the governing equations may be seen in Ezekoye et al. [11].

Results

Pressure Histories and Flame Trajectory

A pressure profile reconstructed from Lu et al. [1] is shown in Fig. 1. A square piston engine simulator was run at 600 rpm to investigate detailed heat flux measurements during a knocking event. The fuel used for these tests was *n*-heptane, and the initial, unburned-gas temperature and wall temperature were between 50 and 65°C. For this study, a curve fit was used to interpolate the pressure history into the combustion model. From Fig. 1, it can be seen that knock begins at approximately 8.5 ms. Computational and analytical predictions of the wall heat flux will be shown at various flame-quenching times; these times correspond to different points on the pressure history. To reiterate, the model results represent flame quenching at different locations within the chamber as knock occurs (Fig. 2). While some locations will have had flame quenching long before the knocking process (e.g., location 1 in Fig. 2), others may still be surrounded by unburned gases at the time of quenching (location 3 in Fig. 2).

At each cylinder wall location, the flame is assumed to stagnate locally on the wall in a one-dimensional orientation. It is possible to describe a local flame trajectory that defines the local perpendicular distance as the flame approaches the wall. For the three hypothetical wall locations shown in Fig. 2, the associated flame trajectories as determined by the computational results are presented in Fig. 4, along with intermediate trajectories; each trajectory corresponds to a separate laminar flame computation, and these flames are referred to in the figure legend by their ignition times. Each flame quenches at a different location at different times and, thus, locally experiences different pressure effects at the time of quench. From the pressure history shown in Fig. 1, it is noted that the knocking event takes place from approximately 8.5 to 11 ms. The flame reaches location 1 at a time of approximately 8 ms and does not experience the knocking pressure until after the flame has extinguished locally. In contrast, the flame approaches location 2 and quenches during the knock process. Finally, the

TABLE 1
Parameters used in analytical model

Su_o m/s	k_o W/(mK)	c_{po} J/(gK)	T_o K	α_o m^2/s	$l_{fo} \equiv \frac{\alpha_o}{Su_o}$ m
0.4	26.3×10^{-3}	1.0	300	$22. \times 10^{-6}$	50×10^{-6}

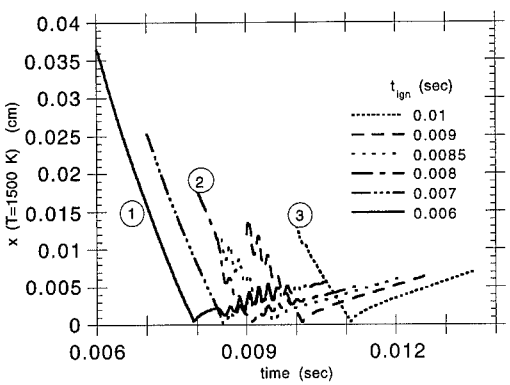

FIG. 4. Local flame trajectories as determined by the computational model. Trajectories represent the path of the 1500-K isotherm.

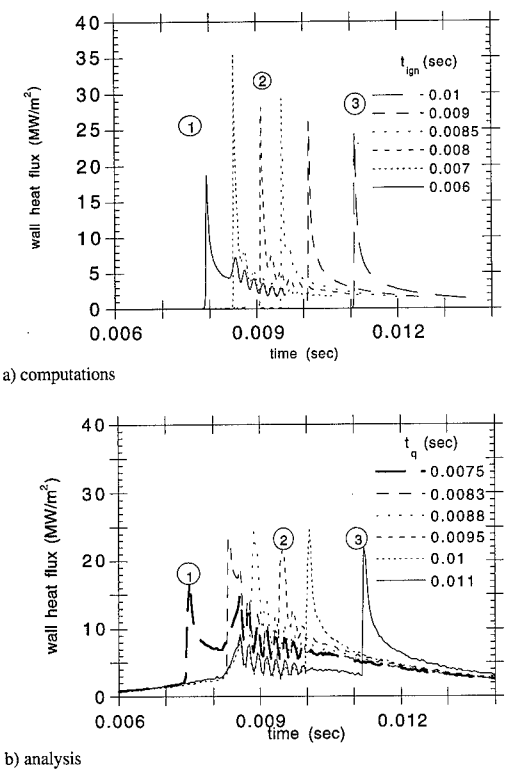

FIG. 5. Local heat flux histories at various hypothetical wall locations within a chamber experiencing a specified knock event.

flame traverses the knocking pressure history before it quenches at location 3.

The wall heat flux for six flame quench times is shown in Fig. 5. When the flame quenches at the time of knock, it can be seen that the heat flux profile shows the characteristic wave effect produced by the pressure oscillations. It is also noted that the heat flux profile has a stronger damping coefficient than the pressure oscillations. In Fig. 5b, the wall heat flux is shown for the analytical calculations. The analytical model predicts the correct trends in terms of pressure heating of the wall and the subsequent flame quenching and diffusional cooling periods. The analytical model is dependent on the choice of characteristic values specified for the heat-release rate and quench time. Representative values from the literature were chosen and maintained for all of the results that shown (see Table 1). The calculations are capable of resolving the timescales over which the heat-transfer process occurs; it takes approximately 0.03 ms for the heat flux to reach its peak value from one-half the value of the peak for both the experiments and the computations. The peak heat fluxes predicted by the numerical simulations vary over the range of 18–35 MW/m^2, while those specified by the analytical model vary between 10 and 35 MW/m^2 (results shown in Fig. 5b are a sample of the analytical data set). It will be shown and discussed in a later section that the differences between the computational and analytical results are associated primarily with the pressure at the instant the flame quenches.

Base Pressure Effect

To clarify the role of the absolute effect of the base pressure on the heat flux history, the heat flux is plotted against the pressure at the time the heat flux attains its maximum value. This result is displayed for both the computational and analytical work in Fig. 6, and comparisons are made between the two sets of results and the experimental data fit of Lu et

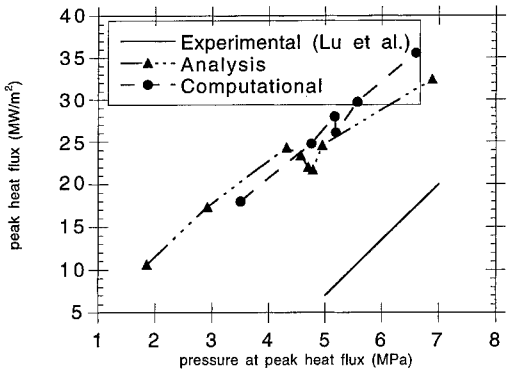

FIG. 6. Comparisons of the peak heat flux–pressure relationship for experimental, analytical, and computational data.

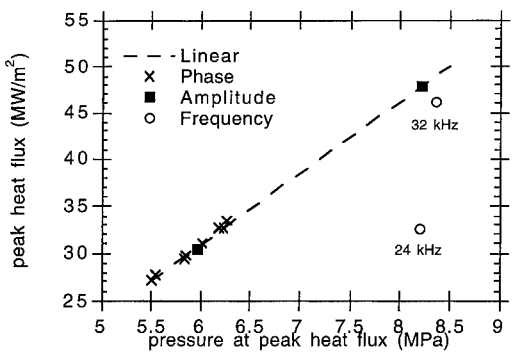

FIG. 7. The effects of phase, amplitude, and frequency on the linearity of the peak heat flux–pressure relationship are examined for the sinusoidal pressure history. High-frequency data are found to deviate from the linear relationship.

al. [1]. It can be seen that for locations where the pressure oscillations are small relative to the heat-release rate, the peak flux is proportional to the pressure. Both the computations and the analysis show a roughly linear relationship between the peak heat flux and the pressure at the time of quench. It is also shown that a nearly constant offset exists between the peak fluxes measured in the experimental study and those computed in this study. It is believed that these differences are associated with convective effects. The theoretical peak heat fluxes correspond to laminar flame conditions, while the experiments are likely to be characterized by more flame wrinkling. Not surprisingly, the peak mean heat flux for the wrinkled-flame quenching process is shown to be smaller than the corresponding laminar value. Poinsot et al. [4] show a factor of approximately one-half between the mean (area averaged) peak heat flux and peak laminar flux.

There are several ways to identify the basis of the linear dependence of the peak heat flux on pressure. The clearest approach is to recognize that the heat flux scales such as $k_o \Delta T/l_f$, where the only pressure-dependent term is the flame thickness, which scales similar to P^{-1}. For an intermediate range of pressure (4.5–6 MPa), there are deviations from the linear relationship. This range of pressures corresponds to quenching processes occurring at the time of knock, and other factors appear to alter the linear relationship. The secondary effect responsible for the deviation from linearity of the heat flux pressure relationship is associated with the pressure derivative (dP/dt) at the time of quench. Inspection of the governing equations suggests that if the pressure derivative is negative a cooling effect occurs, whereas if the pressure derivative is positive, an increased heating effect occurs. Thus, the primary effect in specifying the quenching heat-transfer rate at the time of knock is the base pressure, but a modification occurs for times in which the knocking intensity coincides with the quenching process. For the engine knock condition, the timescale of quenching (0.03 ms) is sufficiently smaller than the characteristic pressure timescale, $1/f$, that the value of the pressure derivative is nearly constant at the time of quenching and appears as either a constant source or sink term in the energy equation.

The effect of the pressure transiency during quenching was investigated in greater detail by introducing a well-characterized pressure signal of the form $P = P_o + A\cos(\omega t + \theta)$ into the calculations. For a fixed offset pressure, $P_o = 5.8$ MPa, the amplitude A, frequency f, and phase θ were varied for a quenching flame. In Fig. 7, the effects of phase, amplitude, and frequency on the relationship between peak flux and quench pressure are shown. It is found that the pressure-signal amplitude does not significantly alter the linear relationship. Changes in the phase slightly modify the linear relationship through the pressure transiency source/sink. A striking effect is noted as the frequency is changed. The frequency effect was examined at 24 and 32 kHz. At these higher frequencies, the timescale for the pressure signal becomes comparable to the timescale for flame quenching, and it is possible for the pressure wave to disrupt the quenching process. This effect is seen in Fig. 7 for the 24-kHz frequency where quenching began as a pressure expansion occurred. For this 24-kHz data point, the maximum pressure at the time of quench is significantly lower than the value that would be expected given the linear relationship. For sufficiently high frequency conditions, the quench pressure is an ambiguous parameter and defined simply as the instantaneous pressure at the time of peak heat flux.

Conclusions

A one-dimensional, flame-quenching analysis was performed to clarify the role of strong pressure

transients on heat-transfer rates during knocking conditions in a combustion chamber environment. It was shown that reasonable predictions of the trends in the wall heat flux could be made by using a simplified, laminar computational model of the knocking process in which pressure gradients associated with the knocking process are neglected. A simplified analytical model based on scaling of the volumetric heat-release term in the energy equation was also shown to qualitatively describe the heat-transfer process, pressure-transient effects. The pressure-transient effects are noted to moderately modify the heat-transfer processes in wall locations where heat-release effects are negligible and to more strongly modify the heat-transfer rates in locations in which the flame has quenched. The single most important effect responsible for the magnitude of heat flux values appears to be the absolute pressure. In the range of pressures examined, a linear relationship was found between the peak flux and pressure for both the computational and analytical models. The average slope of both curves is approximately 6 MW/(m^2 MPa), which agrees well with the results of Lu et al. [1]. A constant bias between the theoretical results and experimental results is believed to arise from the flame-wrinkling effects (fluid mechanics) present in the experiments. Overall, the linearity of the pressure–peak flux relationship was found to be invalid when the flame-quenching process was disrupted by the pressure fluctuations for pressure oscillations with characteristic time on the order of the quenching process.

REFERENCES

1. Lu, J. H., Ezekoye, O. A., Iiyama, A., Greif, R., and Sawyer, R. F., "Effect of Knock on Time-Resolved Engine Heat Transfer," SAE Paper No. 89-0158, 1989.
2. Bush, W. B., Fendell, F. E., and Fink, S. F., "Effect of Boundary Thermal Constraints on Planar Premixed-Flame/Wall Interaction," *Combust. Sci. Technol.* 24:53 (1980).
3. Vosen, S. R., Greif, R., and Westbrook, C. K., "Unsteady Heat Transfer during Laminar Flame Quenching," *Twentieth Symposium (International) on Combustion,* The Combustion Institute, Pittsburgh, 1984, 75.
4. Poinsot, T. J., Haworth, D. C., and Bruneaux, G., "Direct Simulation of Flame-Wall Interaction for Premixed Turbulent Combustion," *Combust. Flame* 95:118–132 (1993).
5. Wichman, I. S. and Bruneaux, G., "Head-On Quenching of a Premixed Flame by a Cold Wall," *Combust. Flame* 103:296–310 (1995).
6. Keck, J. C., "Thermal Boundary Layer in a Gas Subject to a Time Dependent Pressure," *Lett. Heat Mass Transfer* 8:313–319 (1981).
7. Heperkan, H. and Greif, R., "Heat Transfer during the Shock-Induced Ignition of an Explosive Gas," *Int. J. Heat Mass Transfer* 25:267–275 (1982).
8. Yang, J. and Martin, J. K., "Predictions of the Effects of High Temperature Walls, Combustion, and Knock on Heat Transfer in Engine-Type Flows," SAE Paper No. 90-0690, 1990.
9. Bush, W. B., Fendell, F. E., and Fink, S. F., "Modeling End-Gas Knock in a Rapid-Compression Machine," *AIAA J.* 23:8 (1985).
10. Lu, J. H., Ezekoye, O. A., Greif, R., and Sawyer, R. F., "Unsteady Heat Transfer during Side Wall Quenching of a Laminar Flame," *Twenty-Third Symposium (International) on Combustion,* The Combustion Institute, Pittsburgh, 1990.
11. Ezekoye, O. A., Greif, R., and Sawyer, R. F., "Increased Surface Temperature Effects on Wall Heat Transfer during Unsteady Flame Quenching," *Twenty-Fourth Symposium (International) on Combustion,* The Combustion Institute, Pittsburgh, 1992.
12. Ezekoye, O. A. and Greif, R., "A Comparison of One and Two Dimensional Flame Quenching: Heat Transfer Results," ASME NHTC, Atlanta GA, 1993.
13. Isshiki, N. and Nishiwaki, N., "Basic Study on Inside Convective Heat Transfer of Internal Combustion Engines," *Proceedings of the Fifth International Heat Transfer Conference, Vol. II,* Tokyo, 1974, p. 344.
14. Westbrook, C. K. and Dryer, F. L., "Simplified Reaction Mechanisms for the Oxidation of Hydrocarbon Fuels in Flames," *Combust. Sci. Technol.* 27:31–43 (1981).

COMMENTS

Rudolf R. Maly, Daimler-Benz AG, Germany. Could you please comment on whether your model actually captures the heat transfer associated with the passage of the thin front of the shock wave?

Author's Reply. It is assumed in the heat transfer model that the shock front is sufficiently thin (relative to the flame thickness and to the engine length scales) and also sufficiently fast (much faster than the flame speed) that as it sweeps through the chamber it does not spatially distort the quenching process. After each passage of the thin shock, it is assumed that the pressure is spatially uniform in the vicinity of the quenching location. Thus, each shock passage serves only to modify the temporal local pressure environment.

Michael Golombok, Shell Research, UK. You have shown wall heat flux (Mw/m^2) and mentioned heat release rates (Mw/m^3). From this data you can calculate the ratio of power loss at wall divided by power (i.e. sensible heat release per unit time).

What is the extent of variation of this as a function of time? Does it rise sharply with knock intensity?

Author's Reply. It is important to note that the heat flux that we calculate is a local phenomena. Throughout the engine chamber there are a multitude of local heat flux profiles. Each differs from the others according to the time at which the flame front locally quenches at its location. If we were to incorporate our model into a global model which tracked a flame sheet in some general engine chamber, then we would be able to spatially integrate the heat fluxes (MW/m^2) and specify the total heat loss (W) through the chamber walls. Similarly, the pressure transience, dp/dt, (MW/m^3) associated with knock is a local quantity. The volume integrated quantity is related to the total power released by the autoignition process. For a global model (i.e., using our local results in a larger scale system) it would be possible to determine the ratio of heat loss to autoignition power. Just using our local model, however, it is impossible to calculate this ratio without specifying the overall extent of the combustion chamber since heat flux (MW/m^2) and pressure transience (MW/m^3) are dimensionally dissimilar. A worthwhile next step to this research would be to consider global effects of the type that you propose.

Twenty-Sixth Symposium (International) on Combustion/The Combustion Institute, 1996/pp. 2669–2677

AUTOIGNITION CHEMISTRY IN A MOTORED ENGINE: AN EXPERIMENTAL AND KINETIC MODELING STUDY

HENRY J. CURRAN, PAOLO GAFFURI, WILLIAM J. PITZ AND CHARLES K. WESTBROOK
Lawrence Livermore National Laboratory
Livermore, CA 94550, USA

WILLIAM R. LEPPARD
General Motors Research Laboratories
Warren, MI 47090, USA

Autoignition of isomers of pentane, hexane, and primary reference fuel mixtures of *n*-heptane and *iso*-octane has been studied experimentally under motored engine conditions and computationally using a detailed chemical kinetic reaction mechanism. Computed and experimental results are compared and used to help understand the chemical factors leading to engine knock in spark-ignited engines. The kinetic model reproduces observed variations in critical compression ratio with fuel molecular size and structure, provides intermediate product species concentrations in good agreement with observations, and gives insights into the kinetic origins of fuel octane sensitivity. Sequential computed engine cycles were found to lead to stable, nonigniting behavior for conditions below a critical compression ratio; to unstable, oscillating, but nonigniting behavior in a transition region; and eventually to ignition as the compression ratio is steadily increased. This transition is related to conditions where a negative temperature coefficient of reaction exists, which has a significant influence on octane number and fuel octane sensitivity. Improvements in the detailed kinetic reaction mechanism include better treatments of dihydroperoxide radical species and more accurate thermochemical quantities, which lead to better reverse reaction rate expressions.

Introduction

Engine knock provides a practical limit to the efficiency of spark-ignition engines. Fuel molecular size and structure play significant roles in determining knock tendency and octane rating [1]. Recent studies [2–13] have examined chemical factors influencing engine knock, indicating that distinctions between different carbon-hydrogen bonds and variations in ring strain energy affecting rates of alkylperoxy radical isomerization reactions are particularly important.

Isomers of pentane, hexane, heptane, and octane represent an interesting family of fuels for study of knock chemistry. In particular, *n*-heptane and *iso*-octane (2,2,4-trimethyl pentane) are primary reference fuels (PRF) determining octane rating of automotive fuels. The research octane number (RON) of the fuels studied here range from RON = 0 for *n*-heptane to RON = 104 for 2,3-dimethyl butane and are summarized in Table 1. Variability in octane number and knock tendency is clearly due to the molecular size and structure of these isomers.

Hexane isomers, one pentane isomer, and a number of PRF mixtures were studied experimentally, employing motored engine techniques. Kinetic modeling was applied to interpret the experimental results. The model was also used to predict conditions for autoignition of the other isomers of pentane and PRF mixtures.

Previous studies developed a picture of paraffinic hydrocarbon kinetics under engine conditions. This approach showed [10] how proknock and antiknock additives including tetra-ethyl lead (TEL) and methyl-tert-butyl ether (MTBE) alter fuel autoignition chemistry and change knock tendencies of hydrocarbon fuels. However, these studies used only octane numbers, integrated quantities that cannot provide detailed tests of the reaction mechanisms. Recent work [11] studied autoignition of hexane isomers under motored conditions, providing the first species-specific concentration comparisons between model calculations and engine measurements.

Experimental studies

A Waukesha Cooperative Fuels Research (CFR) engine was operated under motored conditions with stoichiometric fuel-air mixtures, an engine speed of 600 rpm, intake temperature of 403 K, and intake manifold absolute pressure of 80 kPa. A limited

TABLE 1
Summary of fuels included in this study

Fuel	RON[a]	Experimental critical CR[b]	Predicted critical CR[c]
0 PRF	0	6.3	(6.0)[d]
n-hexane	25	6.4	(6.0)
25 PRF	25	6.8	(6.0)
50 PRF	50	7.3	8.75
60 PRF	60	n/a	10.0
n-pentane	62	n/a	(6.0)
70 PRF	70	n/a	11.25
2-methyl pentane	73	8.1	8.7
3-methyl pentane	75	8.4	8.7
75 PRF	75	9.1	11.75
2,2-dimethyl propane	85	n/a	9.0
2-methyl butane	92	12.0	17.7
85 PRF	85	10.5	12.25
90 PRF	90	12.0	14.75
2,2-dimethyl butane	92	11.5	10.5
95 PRF	95	13.7	16.25
100 PRF	100	16.7	17.3
2,3-dimethyl butane	104	19.0	19.5

[a]Research octane number (RON).

[b]Experimentally measured critical compression ratio. Pentane isomers not measured experimentally.

[c]Critical compression ratio predicted by the computational model.

[d]Values indicated by (6.0) ignited at CR = 6.0 but are expected to have a critical CR only slightly lower than 6.0.

number of experiments were carried out for *iso*-octane and other fuels at 500 and 900 rpm. Extent of reaction was controlled by varying the compression ratio (CR), holding intake manifold temperature and pressure constant. The engine CR was increased to a critical value where autoignition was observed. This value was found to vary from one fuel to another and depended strongly on fuel size and structure. Chemical species concentrations were measured in the cool exhaust stream under steady operation.

Intake fuel/air composition was monitored with a modified Beckman Model 109A flame ionization detector (FID) in the intake system just upstream from the intake valve. These measurements were periodically confirmed by firing the engine, determining the equivalence ratio with standard exhaust-gas analysis.

A typical motored engine run involved stabilizing the intake temperature and pressure while motoring the engine on air at the desired speed and a very low CR. After stabilization, ignition was turned on and fuel admitted. The fuel rate was adjusted to achieve a stoichiometric equivalence ratio, measured simultaneously by the intake charge FID and exhaust gas analyzers. The engine was fired for approximately ten minutes to assure stable fuel delivery and burn accumulated lubricating oil from the combustion chamber. The ignition was then turned off and compression ratio adjusted to the desired setting. After stable operation was achieved, carbon monoxide and oxygen exhaust concentrations were recorded and exhaust gas samples acquired. The sampling location was a few centimeters into the exhaust duct; at exhaust temperatures of these experiments, little additional reaction is expected between the time the charge leaves the combustion chamber and the time the gas enters the sampling system.

Analytical Equipment

Carbon monoxide was measured continuously using a Horiba Model AIA-23 infrared analyzer. Exhaust oxygen concentration was continuously measured using a Horiba Model MPA-21 oxygen analyzer. Both instruments were calibrated prior to each measurement with certified gaseous calibration standards. Exhaust sampling and analyses of other stable intermediate species were performed as described previously [14–16] using gas chromatography and the DNPH derivatization technique of Lipari and Swarin [17] for aldehydes and ketones.

Exhaust gas samples for GC analysis were obtained either with heated, gas-tight syringes or with the gas sampling system described in Ref. 14. Samples were analyzed using a two-dimensional gas chromatographic technique [14,18]. Unknown intermediate species were identified by a combination of gas chromatographic–mass spectrometry (GC-MS) and gas chromatography–Fourier transform infrared spectroscopy (GC-FTIR). Samples for the GC-MS and GC-FTIR analyses were liquid and were obtained by pulling a fraction of the exhaust through a condensation trap immersed in a dry ice–isopropanol bath. Liquid samples were used in preference to gaseous ones as the concentrations of the unknowns were higher, providing better responses to both analytical techniques.

Experimental Results

Measured exhaust concentrations of CO are shown for hexane isomers in Fig. 1, and experimental PRF mixtures in Fig. 2. Below some CR, there is virtually no reaction; as the CR increases, CO concentration and extent of reaction increase until, at some critical value, autoignition is observed, all without spark ignition in the combustion chamber. For each case, autoignition was observed at a CR slightly greater than the highest value for which a CO concentration is shown in Figs. 1 and 2. Experimental variation in critical CR is correlated with RON in Table 1. Note however, that this correlation is not especially precise; the two fuels with RON = 25 were measured to have critical CR values of 6.4 and

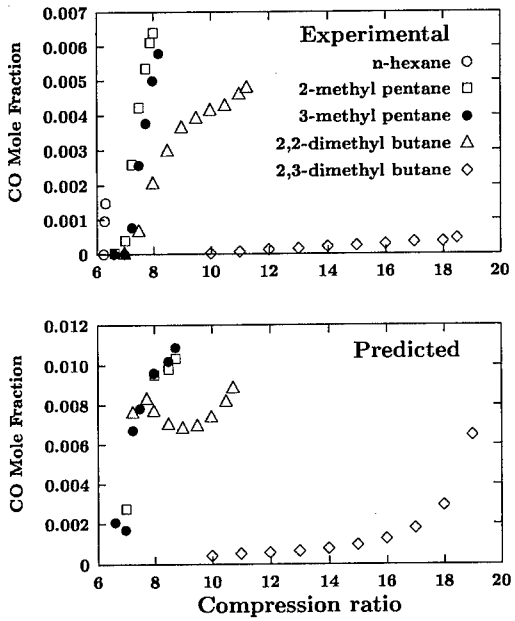

FIG. 1. CO exhaust concentrations as functions of compression ratio for the five isomeric hexanes. For compression ratios slightly greater than the last point plotted for each fuel, autoignition was observed. The upper curves show computed model results, the lower curves show experimental results.

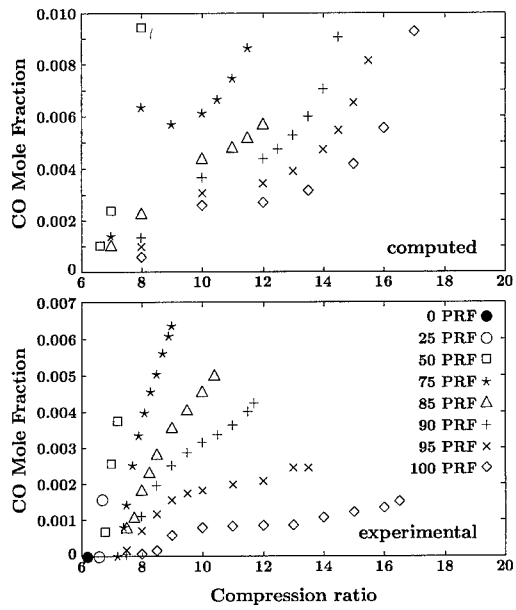

FIG. 2. CO exhaust concentrations as functions of compression ratio for selected PRF mixtures. For compression ratios slightly greater than the last point plotted for each fuel, autoignition was observed. The upper curves show computed model results, the lower curves show experimental results.

6.8, while the two fuels with RON = 75 had critical CR values of 8.4 and 9.1. This variability reflects the fact that although these measurements were carried out in a real engine at the same engine speed as that used to determine RON, the operating conditions (i.e., motored here vs. fired in RON tests) are still not entirely the same. Differences in critical CR in Table 1 show how sensitive RON and critical CR measurements can be to operating conditions. Measured values for critical CR are shown as filled symbols in Fig. 3, illustrating how critical CR is insensitive to RON for values less than about 60, but more sensitive for higher RON values.

Chemical species concentrations were measured in exhaust gases at each CR. Of particular interest are results measured at the highest compression ratio that did not produce autoignition. Selected results are shown for 2-methyl pentane at 600 rpm in Table 2. Comparable results for the other hexane isomers can be found in Ref. 11, while results for the PRF mixtures are qualitatively similar to those in Table 2. Major products are CO, formaldehyde, and ethene for all fuels. Also, each fuel produces a wide variety of larger olefins and oxygenated hydrocarbon species whose identities and concentrations depend on the fuel being studied.

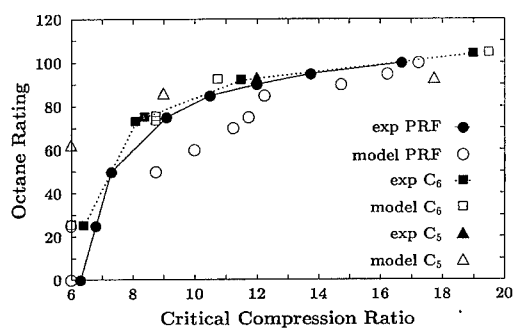

FIG. 3. Correlations between research octane number (RON) and critical compression ratio. The lines connect experimentally determined values, with the solid line describing the PRF mixtures and the dashed line describing the hexane isomers. The filled symbols indicate experimental critical compression ratios, the open symbols indicate computed values.

Computational Model

Modeling computations were carried out using the HCT code [19] used in past studies of engine knock and autoignition [10–13]. The engine is treated as a homogeneous reactor, ignoring spatial variations in temperature and species concentrations. Experience

has indicated that these model limitations do not have a serious impact on the simulations, except for near-limit phenomena discussed later.

Effects of piston motion, heat losses to the engine chamber walls, blowby, fuel trapping in crevice volumes, and other processes were included by specifying the combustion chamber volume history using a slider-crank formula described by Heywood [20], and by calibrating the distributed heat loss submodel by reproducing measured pressure-time histories in nonreactive experiments. By treating heat loss as a homogeneous phenomenon, this model does not distinguish between a hotter core and a cooler boundary layer, but for low engine speeds and motored conditions, this is not expected to be a serious source of error.

It was essential to include effects of residual gas composition on successive engine cycles. Unlike fired cycles where residual gases are CO_2, H_2O, and N_2, under motored conditions the residual gas fraction has a complex composition. Partially reacted species influence the overall gas mixture reactivity, as discussed by Green et al. [21]. At each CR, experimental engine data provide initial gas temperature, residual gas fraction, and initial pressure for the simulation. As reaction time increases, the slider-crank formula and heat transfer rate account for all relevant processes except chemical reaction, which is computed explicitly by the model.

TABLE 2
Experimentally measured and computed exhaust species concentrations for combustion of 2-methyl pentane under motored conditions at 600 rpm close to autoignition[a]

Species	Experimental concentration (ppm)	Model concentration (ppm)
Carbon monoxide	6,390	9,760
Formaldehyde	2,107	4,800
Ethene	579	2,300
Acetaldehyde	1,457	686
Propionaldehyde	479	744
Acetone	138	2,400
Acrolein	159	169
Isobutene	534	453
2-methyl pentane	12,505	8,860
2-methyl-1-pentene	356	827
2-methyl-2-pentene	215	872
2,2,4-trimethyloxetane	243	244
2,2-dimethyltetrahydrofuran	323	498
2,4-dimethyltetrahydrofuran	248	414

[a]Experiments are at CR = 8.0, model results at CR = 8.75.

Reaction Mechanism

The detailed chemical kinetic reaction mechanism was based on previous knock modeling studies [10–13]. Details of the reaction mechanisms are described in Ref. 11, and only a brief summary of the most important features is presented here. A major recent improvement has been a thorough update of the thermochemical variables for many species in the model, using bond additivity rules of Benson [22] as implemented by Ritter and Bozzelli, with updated H/C/O and bond dissociation groups [23,24].

Effectively, all fuel consumption occurs by H atom abstraction reactions with OH, HO_2, H, O, and CH_3 radical species. Distinctions are made between the abstraction of H atoms from primary, secondary, and tertiary sites in the fuel molecule [10,12]. Although β-scission of alkyl radicals R is included in the mechanism, under the present conditions most alkyl radicals react via addition of O_2 to produce RO_2. Internal H atom transfer within the RO_2 species produces QOOH compounds [10–13]. Rates of these reactions depend on the type of C–H bond being broken and the size of the intermediate transition state ring involved.

These QOOH species can follow any of four different reaction paths in addition to reverse isomerization back to RO_2. These reactions include (1) addition of another O_2 species to produce O_2QOOH; (2) O–O bond scission followed by formation of cyclic ether products, and two reaction paths that are possible only for certain types of QOOH radicals. Except for addition of the second O_2 to QOOH, all of these reaction sequences produce a single OH or HO_2 radical and are effectively chain propagation paths.

In previous models, decomposition of O_2QOOH species was treated in an approximate fashion. Now we have improved treatment of these reactions [25–31], assuming that an O–O bond is broken, producing OH radicals and a stable ketohydroperoxide species. Subsequent decomposition of ketohydroperoxide produces additional radical species, providing chain branching. Since production of ketohydroperoxide provides only one OH radical, chain branching is delayed until the ketohydroperoxide decomposes, resulting in an induction time, a phenomenon not available in previous mechanisms which has been found to be important in some simulations [11]. While uncertainties in the kinetic mechanism remain, the mechanism has been thoroughly tested and represents the best currently available.

Computed Results

Engine simulations were carried out for each stoichiometric fuel/air mixture, beginning at intake valve closing at 151.8 degrees before TDC. For the first cycle, the fuel/air mixture consisted entirely of un-

TABLE 3
Computed mole fractions of fuel and formaldehyde during successive model engine cycles[a]

Engine cycle	95 PRF CR = 12.0		*n*-hexane CR = 5.75		75 PRF CR = 7.0	
	i C_8H_{18}	CH_2O	nC_6H_{14}	CH_2O	i C_8H_{18}	CH_2O
1	1.56e-2	1.76e-5	2.16e-2	1.36e-11	1.25e-2	4.35e-8
2	6.95e-3	3.12e-3	2.16e-2	2.37e-10	1.26e-2	6.16e-6
3	8.83e-3	2.49e-3	2.16e-2	3.34e-9	5.08e-3	4.51e-3
4	8.60e-3	2.57e-3	2.16e-2	5.26e-8	1.12e-2	8.77e-4
5	8.64e-3	2.55e-3	2.15e-2	1.23e-6	5.02e-3	4.71e-3
6	8.64e-3	2.55e-3	1.78e-2	1.72e-4	1.12e-2	9.15e-4
7			autoignition		5.02e-3	4.71e-3
8					1.12e-2	9.15e-4

[a]The first series (95 PRF, CR = 12.0) describes results for CR less than the critical value, the second series (*n*-hexane, CR = 5.75) shows ignition on the seventh engine cycle, the third series (75 PRF, CR = 7.0) shows oscillatory behavior.

reacted fuel and air; on subsequent cycles, the starting mixture combined unreacted fuel/air and a fraction of residual products, including stable and radical species, from the previous cycle. Each cycle begins at the same temperature. Enough cycles were computed until products of a given cycle were essentially identical to those of the previous cycle, with occasional exceptions as noted later. For example, concentrations of *iso*-octane and formaldehyde, a characteristic intermediate species, at the end of each of six motored cycles at a CR of 12.0 using 95 PRF are shown in Table 3. When the species concentrations converged as illustrated here, the series of cycles was terminated. Eventually, a critical CR was reached where autoignition was observed. Usually, this autoignition was predicted to occur not on the first cycle but after several cycles, during which concentrations of intermediate species increased steadily from one cycle to the next. This behavior is illustrated in Table 3 for *n*-hexane at a CR of 5.75.

At still higher CR values, autoignition continued to be observed in computed results, defining a critical value for the CR. Predicted critical compression ratios are compared with experimental results in Table 1. General trends are reproduced well by the model; ranking of the different fuels is correctly predicted, and specific numerical values for each fuel are close to observe values.

Computed values of critical CR are summarized in Fig. 3. Overall computed results follow the experimental curve quite closely. Recall that no experiments were run with two of the three pentane isomers, so the model calculations represent predictions; agreement for these fuels is also good. Computed critical CR values for PRF mixtures between PRF50 and PRF75 show the most significant difference from the curve representing the measured results, although computed results for higher and lower PRF mixtures agree well with the measurements. Closer examination of the computed results for these PRF mixtures show that negative temperature coefficient (NTC) phenomena play a significant role in oxidation of these mixtures. This point will be discussed in detail in the next section, but it appears that these discrepancies are due to the interaction between the NTC kinetic behavior and the model assumption that the engine can be approximated as a spatially homogeneous reactor.

Fuel Octane Sensitivity

Computed results show features not observed in the experiments. For 2-methyl pentane, 3-methyl pentane, 2,2-dimethyl butane, and all of the PRF mixtures with RON greater than 50, at compression ratios substantially lower than the critical value, sequential nonigniting cycles demonstrated an oscillatory behavior, with high values on one cycle and low values on the next cycle as illustrated for the 75 PRF mixture in Table 3. Although only *iso*-octane and formaldehyde are shown, virtually all radical and molecular species in the mechanism displayed the same oscillatory behavior.

For some of these fuels exhibiting oscillatory behavior, as CR was increased further, autoignition was predicted, generally at a CR of about 7.5, much lower than the experimentally observed critical CR. However, as the CR was increased even further, autoignition ceased and did not recur until the critical value indicated in Table 1. For example, autoignition was predicted for 2-methyl-pentane at compression ratios of 7.25, 7.5, and 7.75, while at CR of 8.0 through 8.75 no autoignition was predicted. Similarly, in the case of 3-methyl-pentane, autoignition was predicted at a CR of 7.75, while no ignition was predicted at lower compression ratios or at higher values until the critical value of 8.75 was exceeded.

For these oscillatory cases, CO results reported in Figs. 1 and 2 are the averages of the two values.

Closer examination of the kinetic behavior in these models shows that fuel/air mixtures are passing through a region of negative temperature coefficient (NTC). At compression ratios close to the 7.25–7.75 range, these reactive mixtures reach temperatures where overall rate of reaction reaches a temporary maximum, resulting in autoignition. Then, as CR increases further, temperatures near TDC pass into this NTC region, and the rate of reaction decreases, resulting in nonigniting behavior. Finally, at higher compression ratios the overall rate of reaction reaches the same level as that computed at a CR of 7.75, and ignition is again predicted.

The present experiments did not observe this intermediate ignition region. However, for 2-methyl pentane, sporadic ignition was observed experimentally at a CR of 8.0, indicating that not every cycle ignited. Recently, Li et al. [32] used a slightly different motored technique including a PRF mixture with RON = 87. Li et al. held the inlet pressure fixed at 108.2 kPa, increasing inlet temperature until autoignition began to occur at inlet temperatures of 377 K. As temperature was increased further, autoignition continued until the temperature reached 480 K where autoignition ceased. Autoignition did not reoccur as the inlet temperature was increased further. Due to facility limitations, Li et al. were unable to increase inlet temperature enough to achieve renewed autoignition, but their observations were very similar to those noted here.

Additional evidence of NTC behavior is provided by earlier motored engine experiments by Leppard [14–16]. Leppard examined fuel octane sensitivity, which concerns differences in chemical reactivity under research and motored conditions. Alkane fuels have low octane sensitivity, with research and motored octane numbers nearly equal, while other fuels show significantly different motor and research octane numbers. Leppard's work indicated that higher temperatures, lower pressures, and shorter residence times encountered under the motor octane test procedures accentuate NTC behavior of alkane fuels, leading to "super-rated motor octane quality" for paraffin fuels. As a result, under motored octane test procedures, ignition is delayed until higher compression ratios. The corresponding ignition of aromatic and olefinic fuels is not retarded by NTC behavior, leading to apparently poorer octane quality under motor conditions. As pointed out by Leppard, it is more appropriate to regard aromatic and olefin fuels as representing "normal" behavior, with paraffins representing unusual trends due to the influence of the NTC for these fuels. The present study demonstrates that NTC behavior is observed for these paraffinic fuels under research octane conditions as well.

NTC features predicted by the model were not seen in the experiments. There are many reasons why this could be expected. Species measurements were averaged over hundreds of cycles so that most oscillatory, cycle-to-cycle behavior would be smoothed out. Also, model assumptions of homogeneous reaction in the engine chamber, combined with a distributed heat loss rate, is only approximately valid. Spatial temperature variations exist in the experiments due to heat transfer to the engine walls. These variations do not have much influence on the overall system behavior, but under conditions close to the NTC region, areas in the chamber with different temperatures will demonstrate differing responses to temperature increases.

Differences between experimental and computed results for fuels with significant NTC behavior such as the PRF50–PRF75 mixtures in Fig. 3 can best be understood by realizing that the computations represent an idealized description of the combustion chamber. Under NTC conditions, the overall rate of reaction declines and the fuel/air mixture becomes more resistant to ignition than at lower compression ratios and gas temperatures and requires a larger CR to achieve autoignition. In the real engine, because of heat transfer and other nonideal phenomena, not all reactive mixture in the combustion chamber follows this same reaction path and is therefore more reactive than the majority of the reactive mixture. Since ignition in the engine requires only a small portion of the reactive mixture to ignite, the most reactive portion that initiates ignition will not be that portion that is being described by the kinetic model. The observed engine performance will therefore require a significantly lower compression ratio to achieve autoignition than is predicted by the idealized kinetic model. These trends produce the results in Fig. 3 in which the model predictions for the PRF50–PRF75 mixtures indicate more ignition resistance than observed experimentally. This type of behavior represents a limit to the applicability of kinetic models to describe practical engine combustion.

Chemical Species Concentrations

For comparisons, species concentrations were evaluated at the highest compression ratio for which autoignition was not observed, where the greatest fuel consumption would be expected. This comparison is provided for selected species in Table 2. Agreement between computed and experimental species concentrations is good, especially when it is considered that these are time-integrated quantities that cover production and consumption over wide ranges of temperature and time. Total fractions of large olefins, cyclic ethers, and oxygenated species including aldehydes and ketones all show excellent agreement with observations, and relative distribu-

tions of different isomeric forms of these intermediates are also well reproduced by the model.

Dominant chemical species observed in the exhaust are those species common to virtually all hydrocarbon partial oxidation, including CO, formaldehyde, ethene, and isobutene. Oxygenated species include those common to all hydrocarbons such as formaldehyde, acetone, acetaldehyde, and acrolein. Cyclic ethers and larger olefins are very particular to the composition of the primary fuel, as illustrated for 2-methyl pentane in Table 2.

In particular, when 2-methyl pentane is the fuel, the dominant cyclic ethers produced are the 5- and 4-membered ring structures that are products of isomerization of the hexylperoxy radicals. The same is true for *iso*-octane, but the specific structures are particular to *iso*-octane evolution. The production of tetrahydrofurans can be related kinetically to details in the decomposition paths of QOOH radicals [10]. Similar behavior is seen in Table 2 for the larger olefins; when 2-methyl pentane is the fuel, C_5 olefins are produced, while C_7 and C_8 olefins are produced in *iso*-octane combustion.

Finally, good agreement between computed final concentrations and measured concentrations in the exhaust indicates that the kinetic model is reliably reproducing the kinetic evolution in the motored engine. Continuing mechanism refinements are needed to improve the agreement, but these and related recent studies [11] represent the first direct comparison of species-specific engine results with kinetic modeling predictions, and agreement between measured and computed concentrations within factors of 2 or better at this point is exceptional.

Summary

Autoignition of a variety of hydrocarbon fuels and fuel mixtures was studied experimentally using motored engine techniques and computationally using a detailed chemical kinetics model. Relative ordering of the critical compression ratios for autoignition of these fuels and the major intermediate chemical species produced are well reproduced by the model. Negative temperature coefficient phenomena were observed for several of the fuels and fuel mixtures, and this behavior was related to the more general problem of fuel octane sensitivity. The ability of the kinetic model to provide accurate intermediate chemical species concentrations, even for complex species such as the cyclic ethers and other oxygenates, provides a demanding test of the chemical model not possible in the past, lending confidence in the validity of the model description of the autoignition chemistry of these hydrocarbon fuels under conditions relevant to engine processes.

Acknowledgments

The authors are pleased to acknowledge the contributions of Professor Joseph Bozzelli and Dr. Nick Marinov for their insights and suggestions in this work. This work was supported in part by the U.S. Department of Energy, Office of Transportation Technologies, and the Office of Basic Energy Sciences, Chemical Sciences Branch, and carried out under the auspices of the U.S. Department of Energy by the Lawrence Livermore National Laboratory under contract W-7405-ENG-48.

REFERENCES

1. Lovell, W. G., *Ind. Eng. Chem.* 40:2388–2438 (1948).
2. Vermeersch, M. L., Held, T. J., Stein, Y. S., and Dryer, F. L., *SAE Trans.* 100:645–657 (1991).
3. Cernansky, N. P., Green, R. M., Pitz, W. J., and Westbrook, C. K., *Combust. Sci. Technol.* 50:3–25 (1986).
4. Lignola, P. G., DiMaio, F. P., Marzocchella, A., Mercogliano, R., and Reverchon, E., *Twenty-Second Symposium (International) on Combustion,* The Combustion Institute, Pittsburgh, 1989, pp. 1625–1633.
5. Chakir, A., Bellimam, M., Boettner, J. C., and Cathonnet, M., *Int. J. Chem. Kinet.* 24:385–410 (1992).
6. Cavaliere, A., Ciajolo, A., D'Anna, A., Mercogliano, R., and Ragucci, R., *Combust. Flame* 93:279–286 (1993).
7. Dagaut, P., Reullon, M., and Cathonnet, M., *Combust. Sci. Technol.* 95:233–260 (1994).
8. Minetti, R., Carlier, M. Rivaucour, M. Therssen, E., and Sochet, L. R., *Combust. Flame* 102:298–309 (1995).
9. Griffiths, J. F., Hughes, K. J., Schreiber, M., and Poppe, C., *Combust. Flame* 99:533–540 (1994).
10. Westbrook, C. K., Pitz, W. J., and Leppard, W. R., SAE paper SAE-912314, Society of Automotive Engineers, Warrendale, PA, 1991.
11. Curran, H. J., Gaffuri, P., Pitz, W. J., Westbrook, C. K., and Leppard, W. R., SAE Paper SAE-952406, Society of Automotive Engineers, Warrendale, PA, 1995.
12. Westbrook, C. K., Warnatz, J., and Pitz, W. J., *Twenty-Second Symposium (International) on Combustion,* The Combustion Institute, Pittsburgh, 1988, pp. 893–901.
13. Chevalier, C., Pitz, W. J., Warnatz, J., Westbrook, C. K., and Melenk, H., *Twenty-Fourth Symposium (International) on Combustion,* The Combustion Institute, Pittsburgh, 1992, pp. 93–101.
14. Leppard, W. R., SAE paper SAE-892081, Society of Automotive Engineers, Warrendale, PA, 1989.
15. Leppard, W. R., SAE paper SAE-902137, Society of Automotive Engineers, Warrendale, PA, 1990.
16. Leppard, W. R., SAE paper SAE-922325, Society of Automotive Engineers, Warrendale, PA, 1992.
17. Lipari, F. and Swarin, S. J., *J. Chromatog.* 247:297–306 (1982).
18. Perry, K. L., *J. Chromatog. Sci.* 28:624–627 (1990).
19. Lund, C. M., *HCT-A General Computer Program for Calculating Time-Dependent Phenomena Involving One-Dimensional Hydrodynamics, Transport, and Detailed Chemical Kinetics,* Lawrence Livermore Na-

tional Laboratory report UCRL-52504, Lawrence Livermore National Laboratory, Livermore, CA, 1978.
20. Heywood, J. B., *Internal Combustion Engine Fundamentals,* McGraw-Hill, New York, 1988.
21. Green, R. M., Cernansky, N. P., Pitz, W. J., and Westbrook, C. K., SAE paper SAE-872108, Society of Automotive Engineers, Warrendale, PA, 1987.
22. Benson, S. W., *Thermochemical Kinetics,* Wiley, New York, 1976.
23. Lay, T. and Bozzelli, J. W., Eastern States Meeting of the Combustion Institute, Paper no. 100 (1993).
24. Ritter, E. R. and Bozzelli, J. W., *Int. J. Chem. Kinet.* 23:767–778 (1991).
25. Ranzi, E., Gaffuri, P., Faravelli, T., and Dagaut, P., *Combust. Flame,* 103:91–106 (1995).
26. Curran, H. J., Gaffuri, P., Pitz, W. J., and Westbrook, C. K., in preparation, 1997.
27. Curran, H. J., Pitz, W. J., Westbrook, C. K., Hisham, K., and Walker, R. W., "An Intermediate Temperature Modelling Study of the Combustion of Neopentane," *Twenty-Sixth Symposium (International) on Combustion,* The Combustion Institute, Pittsburgh, 1996.
28. Cox, R. A. and Cole, J. A., *Combust. Flame* 60:109–123 (1985).
29. Hu, H., and Keck, J. C., SAE Paper 872110, Society of Automotive Engineers, Warrendale, PA, 1987.
30. Morley, C., Combust. Sci. Technol. 55, 115–123 (1987).
31. Sahetchian, K. A., Rigny, R., and Circan, S., *Combust. Flame* 85:511–514 (1991).
32. Li, H., Prabhu, S. K., Miller, D. L., and Cernansky, N. P., SAE Paper SAE-942062, Society of Automotive Engineers, Warrendale, PA, 1994.

COMMENTS

Rudolf R. Maly, Mercedez-Benz Research Institut, Germany. Your model is obviously capable of predicting autoignition chemistry for a *pure fuel* component of a *given molecular structure.* Is the model also capable of predicting the correct autoignition chemistry for a *mixture* composed of pure components with *different molecular structures* and a *suitable additive* which, experimentally, has the same autoignition behavior as a pure component?

Author's Reply. Many of the fuels analysed in this paper are primary reference fuel (PRF) mixtures and as such are the types of mixtures you refer to in your question. Our model is also capable of modeling whether there is a difference between a pure component fuel of a given structure, and a mixture of a pure component fuel and an additive such as methyl tert-butyl ether (MTBE) [Reference 10 of the present paper]. There is no reason why our model would not apply to multi (more than two) component mixtures but we have not, as yet, tried to perform such an analysis. However, the current state of the art in modeling aromatics is not sufficient to include their oxidation in such a multi-component mixture.

•

P. Dagaut, CNRS-LCSR, France. For a variety of conditions ON ~ 50 to 80 the model has difficulties to follow the data relative to the maximum compression ratio. Could this discrepancy come from the fact that the model used here has not yet been validated for these fuel mixtures (n-heptane—iso-octane) or is it due to simplifications in the physical model?

Author's Reply. It is unclear whether these discrepancies mean that refinements are needed in the physical model or in the chemical kinetic mechanism. We were able to use the same approach to model critical compression ratios for pure-component hexane isomers and obtained good agreement with experimental results. These results lead us to believe that the physical model is adequate. We have validated the n-heptane mechanism over a wide range of temperature and pressure, modeling experimental results obtained in a shock tube, rapid compression machine, plug flow reactor and in your jet stirred reactor. The iso-octane mechanism has not been validated over this broad range of conditions. We intend to carry out this work in order to solve the problem of these discrepancies. It may also be necessary to carry out similar validation studies for PRF mixtures.

•

John B. Heywood, MIT, USA. Correcting for the effects of heat transfer and crevice flows for compression ratios from 6 to 19 is a challenging task. There are two basic approaches: (1) to cool all the gas uniformly; (2) to cool primarily a boundary layer and consider the case to be adiabatically compressed and expanded. The latter gives higher gas temperatures. Why did you choose the former assumption of cooling the gas uniformly?

Author's Reply. In modeling fuel oxidation in internal combustion engines one would ideally need to use a multidimensional CFD modeling approach with detailed chemistry. However, this approach would be extremely expensive and time consuming. We have considered two approaches: (a) cooling the gas uniformly or (b) assuming the gas is adiabatically compressed. The adiabatic core

treatment tends to predict the onset of autoignition correctly since spontaneous ignition is controlled by the hottest portion of gas in the cylinder. However, in using the core assumption one tends to over estimate the concentrations of intermediates species produced at compression ratios prior to autoignition. To predict the intermediate products formed prior to autoignition, the uniform cooling assumption gives better agreement with experimental measurements. The average intermediate concentrations measured at the exhaust port more closely follow the average temperature rather than the adiabatic core assumption. We have not attempted to model the engine assuming a boundary layer with an adiabatic core.

Twenty-Sixth Symposium (International) on Combustion/The Combustion Institute, 1996/pp. 2679–2684

DEFLAGRATION-TO-DETONATION TRANSITION IN END GASES

C. K. CHAN AND W. A. DEWIT
AECL Research
Pinawa, Manitoba, Canada

Flame acceleration and deflagration-to-detonation transition (DDT) experiments were performed in a 28-cm-diameter, 6.4-m-long combustion duct filled with obstacles. The run-up distances (the distance between the ignition point and the location of onset of detonation) for DDT and the flame speeds just before onset of detonation were measured for detonable H_2-airsteam mixtures. For less-sensitive mixtures, flame acceleration also occurred and choked velocities were reached within the length of the duct, but DDT events were not observed. Because of reflection of the precursor shock off the end plate, the gas mixture in the end gas region was further pressurized. Transition to detonation occurred in the end gas region for some of these less-sensitive mixtures. As a result of higher initial pressures, DDT in the end gas region produced very high overpressures at the end plate. Because of the high pressure and temperature created by the reflection of the precursor shock, the end gas region provides the most favorable conditions for DDT. If DDT did not occur in the end gas region, the resulting overpressures were found to be much lower. The pressure traces measured at the end gas region clearly indicated the limiting mixture composition for transition from deflagration to detonation. The limiting mixture composition, therefore, can be used to represent the transition limits for choked flames. However, being limited by the size of the end gas region, the present study does not reveal the effects of scale, particularly related to turbulence in the transition process. Thus, it is not certain whether the limiting mixture composition will be the same in situations in which turbulence also plays a key role in the transition process.

Introduction

The overpressure generated during a deflagration-to-detonation transition (DDT) is usually much higher than the normal Chapman–Jouguet (CJ) detonation pressure. This is attributed to the onset of detonation that occurs in the precompressed region ahead of the accelerated flame. For flames that have achieved choked velocities (velocity of the flame equals the sonic velocity of the burned gas), the pressure between the precursor shock and the reaction zone is three times the initial pressure of the mixture [1]. However, if the precursor shock is allowed to collide and reflect off the end plate, the pressure in this end gas region can be much higher. If a transition to detonation occurs in the end gas region, the peak pressure is extremely high. In laboratory experiments with relatively sensitive mixtures, unusually high pressures resulting from a DDT in the end gas were observed [2–4]. It has been also observed that the pressure generated in pipelines during some accidents could be extremely high, capable of causing damage to the pipeline [5]. In these accidents, DDT often occurred in the end gas region of the pipeline.

Onset of detonation (the initial step of a DDT) depends on the chemical induction time and the energy-release rate in the gas mixture. Therefore, the chemical kinetic properties of the mixture are the key parameters that control the transition process. It has been observed that the precursor shock can be strengthened locally by multiple reflection off obstacles causing a local explosion in the mixture. Such a shock-focusing effect is found to be the most likely mechanism leading to onset of detonation [6] for flame propagation in tubes filled with obstacles. Compression of a gas mixture caused by reflection of the precursor shock at the end plate further sensitizes the gas mixture by increasing its pressure and temperature. End gases, therefore, provide a more favorable condition for a DDT to occur than bulk gas. Furthermore, the chemical kinetic properties for insensitive mixtures vary significantly with only a small change in mixture composition. DDT in the end gas region, therefore, is very sensitive to the mixture composition. This paper describes results of a recent study on DDT in end gases for H_2-airsteam mixtures in an attempt to expand our current understanding on transition limit.

Experimental Apparatus

Experiments were performed in a 28-cm-diameter, 6.4-m-long combustion tube with H_2-airsteam mixtures at 100 kPa initial pressure to examine the run-up distance and the pressure generated by a DDT in a closed tube filled with obstacles. The run-up distance is defined as the distance between the

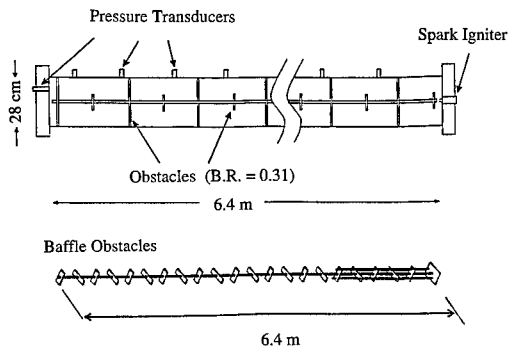

FIG. 1. Schematics of the experimental apparatus and the obstacle configuration.

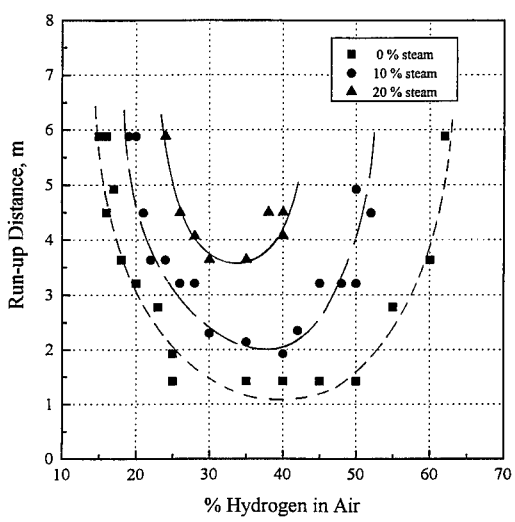

FIG. 2. The run-up distances for various hydrogen-air-steam mixtures in a 28-cm-diameter duct-filled with obstacles (B.R. = 0.31).

ignition point and the location of onset of detonation. Rectangular baffle-type obstacles having a blockage ratio of 0.31 and a spacing of 28 cm were mounted inside the tube to induce flame acceleration. Schematics of the apparatus and the obstacle configuration are shown in Fig. 1. The test mixture was prepared by the addition of gases to an initially evacuated tube by the sum of partial pressures. The gases were further mixed by circulating the mixture via an external pump. The gas mixtures were ignited at one end of the tube by an electrical spark (~1 mJ). Piezoelectric pressure transducers were mounted at various locations along the tube and at the end plate to monitor the flame speed and the pressure development inside the tube. Although pressure transducers cannot sense the arrival of a slow flame front, they can detect the precursor shock front associated with an accelerated flame (with a flame speed >300 m/s). For supersonic deflagration, the precursor shock and the reaction zone propagate at roughly the same speed [7].

Results and Discussion

Upon ignition, it was observed that a flame could accelerate very rapidly in the duct. After a flame had accelerated beyond a certain critical speed, a sudden jump in the flame speed to detonation velocity was observed. Assuming the final velocity of the detonation corresponds to the CJ detonation velocity of the mixture, the run-up distances were estimated to an accuracy equivalent of half the distance between consecutive pressure transducers (~0.5 m). For insensitive mixtures, transition to detonation was not observed before the flame reached the end of the duct even though flame acceleration to choked velocities was achieved. Figure 2 shows the run-up distances for various H_2-airsteam mixtures. It should be mentioned that this run-up distance is not an intrinsic property of the mixture. The run-up distances depend on the size of the duct and the obstacle configuration. Since all experiments were performed under the same boundary conditions, the run-up distance provides a comparison of the sensitivity of the mixture in terms of flame acceleration and DDT. For example, the run-up distances increase by a factor of 2 for every 5 vol. % decrease in H_2 concentration in lean mixtures (<30% H_2 in H_2-air) or a 5 vol. % increase in rich mixtures. However, the effects of steam on lean and rich mixtures are very different. A 10 vol. % increase in steam will have the same effect on the run-up distance as a 5 vol. % decrease in H_2 concentration for lean mixtures. For rich mixtures, a 10 vol. % increase in steam will have the same effect as a 10 vol. % increase in H_2 concentration.

Figure 2 shows that for dry, 10%, and 20% steam mixtures, the run-up distances can be represented by a family of U-shaped curves. These results suggest that the run-up distance is inversely proportional to the sensitivity of the mixture represented by parameters such as the detonation cell width or the laminar burning velocity of the corresponding mixture. Since the run-up distance is an indirect measure of the rate-of-flame acceleration, it is reasonable to expect that the run-up distance is related to deflagration parameters rather than detonation parameters. In Fig. 3, the run-up distances are plotted against the laminar burning velocities of the mixtures. Results show that the correlations are very different for lean and rich mixtures. The run-up distances are inversely proportional to the laminar burning velocities of the mixtures for both groups. However, for mixtures having the same laminar burning velocity, lean mixtures have shorter run-up

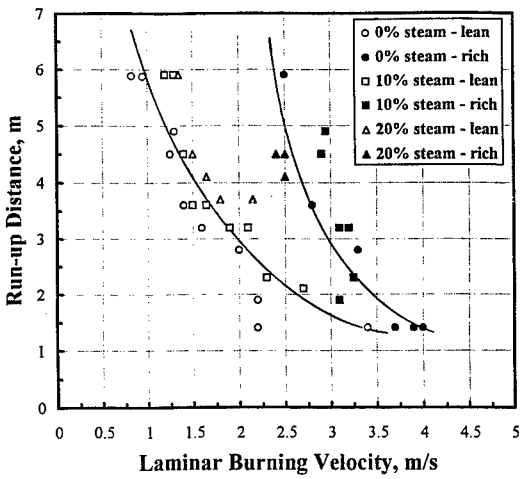

FIG. 3. The run-up distances versus the laminar burning velocities of the mixtures.

distances. This result is somewhat unexpected. Since lean mixtures have lower expansion ratios across their flames, they should accelerate at a lower rate and have longer run-up distances. Therefore, laminar burning velocity alone cannot fully quantify the run-up distance. It should be pointed out that the sonic velocities for lean and rich mixtures are very different for H_2-airsteam mixtures. For example, the sonic velocities for 10% and 70% H_2 in dry H_2-air mixtures are 364 m/s and 587 m/s, respectively. Since the temperature in the precompressed region ahead of the flame depends on the Mach number of the precursor shock, the sonic velocity of the mixture can strongly influence the kinetics and the probability of an onset of detonation in this precompressed region. These results suggest that because of the high sonic velocities of the rich mixtures, the flames have to accelerate to higher flame speeds (thus longer run-up distances) before a DDT can occur. Therefore, a single critical flame speed cannot be used as a criterion for DDT in accelerated flames.

For dry H_2-air mixtures, the run-up distances as defined previously were not observed in mixtures containing less than 15% or more than 62% of hydrogen by volume. Based on the run-up distance measured in this series of experiments, the limiting mixtures for DDT are 15% and 62% H_2 by volume for dry mixtures, 19% and 52% H_2 in H_2-air for mixtures containing 10% steam, and 24% and 40% H_2 in H_2-air for mixtures containing 20% steam. In this series of experiments, no DDT was observed for mixtures consisting of 30% or more steam by volume. In terms of the concentration by volume in the mixtures, the last two sets of numbers become 17.1% and 46.8% and 19.2% and 32.0%. It should be mentioned that the limiting mixtures determined in these experiments may be different from the limiting mixtures determined using a different apparatus. Furthermore, the run-up distances for the limiting mixtures approach the length of the combustion duct. Therefore, based on the run-up distances alone, it is not certain that these limiting mixtures represent the true DDT limits.

The peak overpressures measured at the end plate are shown in Fig. 4 for dry H_2-air mixtures. For those experiments in which DDT occurred before the flame had reached the end plate, the peak pressures measured along the tube were about 1–1.5 MPa. As a result of nonlinear amplification of the detonation waves as they collided and reflected off

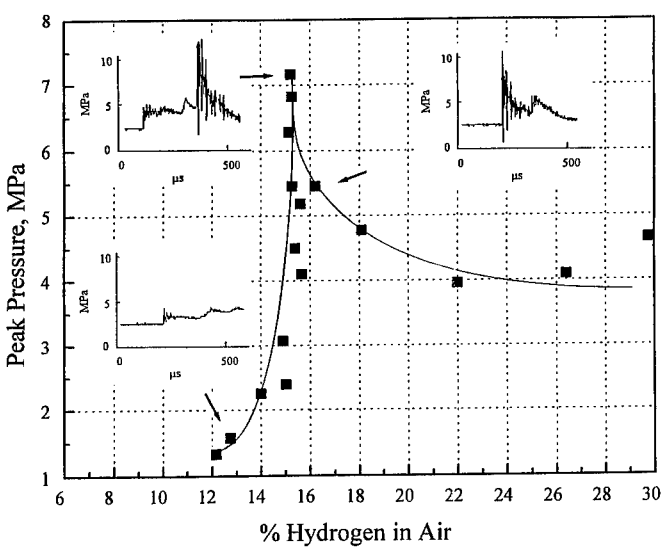

FIG. 4. Peak overpressure measured at the end plate for dry hydrogen-air mixtures.

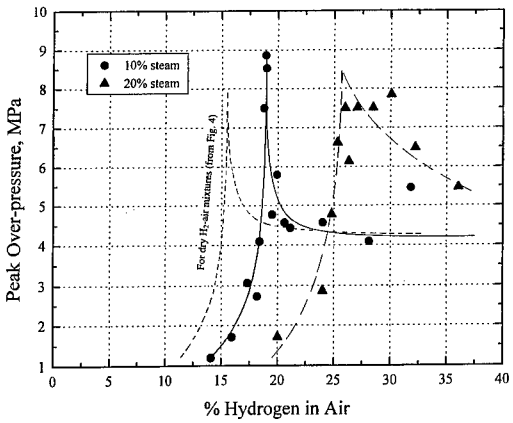

FIG. 5. Peak overpressures measured at the end plate for various hydrogen-air mixtures with 10% and 20% steam.

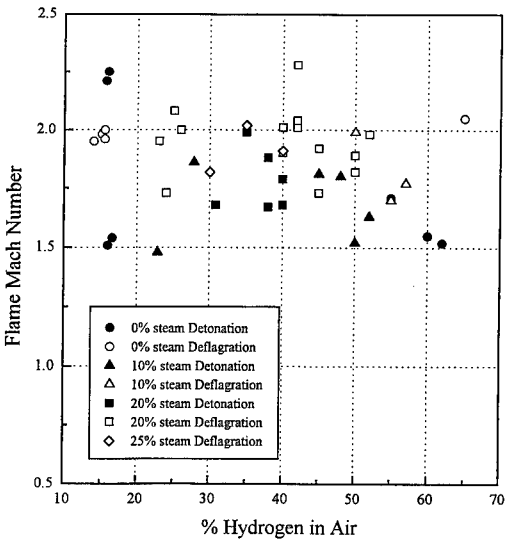

FIG. 6. The critical flame Mach numbers for DDT resulting from flame acceleration in H_2-air-steam mixtures.

the end plate, much higher peak pressures were measured at the plate. For those more sensitive mixtures ($H_2 > 18\%$), the peak overpressures were found to be about 4–5 MPa with a duration of about 50 μs. This represents the pressure load generated by a detonation wave. For mixtures containing about 15% H_2, the observed peak pressures varied greatly. Some of the pressures were found to be higher than 7 MPa. As shown in Fig. 2, transition to detonation for this mixture occurred near or at the end of the duct. Pressure traces in Fig. 4 show that depending on whether DDT occur before or after the precursor shock have collided and reflected off the end plate, the peak pressures can be very different. The very high pressures were caused by DDT in the precompressed region after the precursor shock had collided and reflected off the end plate. The pressure traces show that the pre-DDT pressure in the end gas was about 2 MPa (20 times the initial pressure of the mixture). Assuming isentropic compression, the temperature in the end gas was about 700 K, which is very close to the autoignition temperature of the mixture (T_{ig} = 730 K). Autoignition can occur readily in this sensitized mixture if other perturbations are present. The time between the detonation peak and the arrival of the precursor shock suggested that the onset of detonation was likely triggered by the interaction of the reflected shock with the reaction zone. For the cases in which the sufficient conditions for DDT were not present (<15% H_2), the peak pressures were much lower. However, the burning rate in the gas could still be very high and was capable of generating blast waves of moderate magnitude. For 12% to 14% H_2 mixtures, the pressures ranged from 1.5 MPa to 2.5 MPa. These pressures are higher than the corresponding detonation pressures of the mixtures.

The peak overpressure at the end plate for H_2-airsteam mixtures with 10% and 20% steam are shown in Fig. 5. The peak overpressure data show similar trends to those for the dry mixtures with the maximum peak overpressure ranging from 8–9 MPa. The maximum values occur at 19% and 25% hydrogen for 10% and 20% steam mixtures, respectively. Results in Figs. 4 and 5 agree with the limiting concentration in the run-up distance data shown in Fig. 2. Because of the reflection of the precursor shock off the end plate, the end gas region is the most susceptible location for a DDT to occur. These results demonstrate conclusively that transition to detonation in the end gas can be used as a means to establish a transition criterion (in terms of the limiting composition). For example, 15% H_2 for dry mixtures, 19% H_2 for mixtures with 10% steam, and 25% H_2 for mixtures with 20% steam can be considered the limiting mixture for DDT.

The flame speeds just before DDT (referred to as the critical flame speed) were also determined in this series of experiments. These data, expressed as the flame Mach numbers (flame speed normalized by the sonic velocity in the uncompressed mixture), are shown in Fig. 6 (solid symbols). Most of the critical flame Mach numbers are within the range of 1.5–2.0. Results also show that the higher the steam content, the higher the critical flame Mach number. This implies that it is more difficult to trigger a DDT in mixtures containing high steam content. This confirms the idea that kinetic properties play a dominant role in controlling the transition process. These results also agree with a previous observation that as a result of the higher sonic velocities of rich mixtures, it is more difficult (requires higher flame speeds) to

trigger a DDT. For those cases in which DDT was not observed, the maximum flame speeds (the average speed between the last two pressure transducers) are also shown in Fig. 6 (open symbols). These Mach numbers (no DDT) are mostly higher than the critical flame Mach numbers for DDT. This implies that these mixtures have been shock heated to higher temperatures than those more sensitive mixtures. It should be pointed out that the Mach number of choked flames are about 2 [1]. These results confirm that the apparatus in this study is sufficiently long to allow flame acceleration to choked velocities (maximum flame speed and hence maximum precompression achievable in the end gas) to be attained. Data also show that for sensitive mixtures, DDT is probable if its flame Mach number exceeds about 1.5. For less-sensitive mixtures, DDT is not possible even though the flames have already accelerated to much higher flame Mach numbers and shock heated to higher temperatures. Therefore, the critical flame Mach number of 1.5 can be interpreted as a criterion (a necessary condition) for DDT in accelerated flames.

The existence of a critical flame Mach number implies that the dominant mechanism for DDT in H_2-airsteam mixtures is related to the strength of its precursor shock. These results agree with the finding from an earlier study [6] that compound reflection and deflection of the precursor shock by collisions with obstacles along its path cause local strengthening of the shock wave (commonly referred to as shock focusing). Such shock-focusing effects can create local hot spots capable of causing direct initiation of detonation. It was also demonstrated in the previous study that if the local hot spot is bigger than a certain critical size, the phenomenon is not apparatus dependent. This implies that the critical conditions remain the same regardless of the scale of the experiment. For onset of detonation, it is reasonable to expect that this critical size is of the order of the detonation cell width of the mixture. The detonation cell width for a dry H_2-air mixture containing 15% H_2 at 100 kPa is about 30 cm [8]. Since the cell width is inversely proportional to the pressure of the mixture, the cell width in the end gas region (20 times the initial pressure) is expected to be much smaller. Presently, the detonation cell width for the mixture in the end gas was not measured. Nevertheless, it is likely that the end gas region is large enough for a detonation to establish itself if a DDT is possible. It should be pointed out that because of the size of the apparatus, the turbulence in the end gas region is expected to consist of mainly small-scale structures. Compression in the end gas region further reduces the scale of the turbulent structure. As a result, this series of experiments cannot fully reveal the effects of turbulence in facilitating the onset of detonation. It has been observed in large-scale experiments [9] that DDT is possible in H_2-air mixtures containing 12.5% H_2. This result clearly demonstrated that under certain situations, turbulence can play an important role in DDT. Nevertheless, the present results suggest that for accelerated H_2-airsteam flames in tubes, turbulence is not the dominant mechanism for DDT. If turbulence were the dominant mechanism, the critical flame Mach numbers would be below 1 because the maximum turbulent fluctuation velocity is limited to the sonic velocity. That no DDT was observed for flames with flame Mach numbers lower than 1.5 indicates that the initiation of detonation by shock focusing created by the reflection of the leading shock off obstacles is the dominant mechanism for DDT in accelerated flames. Therefore, the limiting conditions determined in this study only represent cases when shock-induced local explosion is the dominant mechanism for the transition process.

Conclusion

Flame acceleration and transition to detonation experiments were performed in a 28-cm-diameter, 6.4-m-long combustion duct filled with obstacles. For mixtures whose run-up distances for DDT approach the length of the duct, the overpressures at the end of the duct were found to be much higher than the normal CJ detonation pressure. This is attributed to the fact that DDT occurred in the precompressed region created by the reflection of the precursor shock wave off the end plate. It was observed that the resulting overpressures can vary significantly depending on whether a DDT occurred in this region. For insensitive mixtures, the chemical kinetics of the mixture can change significantly for a small change in composition. As a result, a small change in mixture composition can prevent the onset of detonation even in the precompressed end gas region. Since a local explosion caused by local strengthening of the precursor shock due to multiple reflections off obstacles is the dominant mechanism for onset of detonation in accelerated flames, the critical conditions for onset of detonation in the end gases can therefore be used to represent a DDT limit of the mixture. Results showed that the apparatus is sufficiently long to allow flame acceleration to choked velocities (maximum flame speed) to be attained and sufficiently large for a detonation wave to establish itself in the end gas. However, being limited by the size of the apparatus and thickness of the end gas region, this study does not reveal the effects of turbulence on the transition process. It has been demonstrated that under certain situations, turbulence can play a key role in the transition process. As a result, the limiting conditions (as indicated by the boundary between DDT and no DDT in the end gas) are likely still apparatus dependent.

Acknowledgments

This work was funded jointly by Atomic Energy of Canada Limited, Ontario Hydro, Hydro Quebec and the New Brunswick Electric Power Commission under the COG agreement.

REFERENCES

1. Lee, J. H. S., Knystautas, R., and Chan, C. K., "Turbulent Flame Propagation in Obstacle Filled Tubes," *Twentieth Symposium (International) on Combustion,* The Combustion Institute, Pittsburgh, 1984, p. 1663–1671.
2. Kogarko, S. M., "Investigation of the Pressure at the End of a Tube in Connection with Rapid Non-Stationary Combustion," *Sov. Phys. Tech. Phys.* 2(9):1875 (1958).
3. Behrens, U., Langer, G., Stock, M., and Wirkner-Bott, I., "Deflagration-Detonation Transition in Hydrogen-Air-Steam Mixtures—Relevance of the Experimental Results for Real Accident Situations," *Nuclear Engineering Design* 30:43–50 (1991).
4. Zhang, F. and Thibault, P. A., "Transition from Deflagration to Detonation with a Dense Aluminum-Dust Slug in a Combustible Gas," accepted for publication in *Shock Waves.*
5. Craven, A. D. and Greig, T. R., "The Development of Detonation Over-Pressure in Pipelines," *Chem. E. Symp.* No. 25, 1968, pp. 41–50.
6. Chan, C. K., "Collision of a Shock Wave with Obstacles in a Combustible Mixture," *Combust. Flame* 100(1/2):341 (1995).
7. Chan, C. K. and Greig, D., "The Structure of Fast Deflagration and Quasi-Detonation," *Twenty-Second Symposium (International) on Combustion,* The Combustion Institute, Pittsburgh, 1988, pp. 1733–1739.
8. Berman, M., "Hydrogen Behavior and Nuclear Reactor Safety," Chapter 2, *Recent Development in Hydrogen Technology Vol. 2* (K. D. Williamson and F. J. Edeskuty, eds.), CRC Press Inc., Boca Raton, FL, 1986.
9. Dorofeev, S. B., Sidorov, V. P., Dvoinishnikov, A. E., and Breitung, W., "Deflagration to Detonation Transition in Large Confined Volume of Lean Hydrogen-Air Mixtures," *Combust. Flame* 104:95–110 (1996).

Twenty-Sixth Symposium (International) on Combustion/The Combustion Institute, 1996/pp. 2685–2692

EXTENTS OF ALKANE COMBUSTION DURING RAPID COMPRESSION LEADING TO SINGLE- AND TWO-STAGE IGNITION

A. COX, J. F. GRIFFITHS AND C. MOHAMED
School of Chemistry, The University
Leeds LS2 9JT, UK

H. J. CURRAN, W. J. PITZ AND C. K. WESTBROOK
Lawrence Livermore National Laboratory
Livermore, CA 94350, USA

Extents of reactant consumption have been measured during the course of spontaneous ignition following rapid compression of *n*-pentane and *n*-heptane and also of PRF 60 (*n*-heptane + *i*-octane, 2,2,4-trimethylpentane) in stoichiometric mixtures with air. Compressed gas temperatures of 720–750 K and 845–875 K were studied at reactant densities of 131 mol m^{-3}. At the lower gas temperature, there was no evidence of reactant consumption during the course of the compression stroke. Two-stage ignition occurred at these temperatures, but only modest proportions of *n*-pentane were consumed during the first stage (<15%), whereas about 40% of *n*-heptane reacted under the same conditions. At the higher compressed gas temperature, the oxidation of *n*-pentane began only after the piston had stopped, whereas more than 30% of the *n*-heptane had already been consumed in the final stage of the compression stroke. The first stage of a two-stage ignition was evident during the compression of the *n*-heptane mixture under these conditions. The behavior of the PRF 60 mixture differed somewhat from that of *n*-pentane despite the similarity of the research octane numbers. Although there was a preferential oxidation of *n*-heptane at T_c = 850 K, which persisted throughout the early development of spontaneous ignition during the post-compression period, oxidation of both components of the PRF 60 mixture began before the piston had stopped. Numerical simulations of the spontaneous ignition under conditions resembling those of the rapid compression experiments show that the predicted reactivity from detailed kinetics is consistent with the observed features. The modeling results also substantiate the characterization of single and two-stage ignition in compression machines.

Introduction

The spontaneous ignition (or autoignition) characteristics of hydrocarbons have been of interest to chemists and engineers for many decades. The current interest relates predominantly to combustion in reciprocating engines and the occurrence of knock in spark-ignition (SI) engines in particular. For the temperatures that are reached during compression in engines or rapid compression machines (RCM), spontaneous ignition often occurs in two stages. At sufficiently high compression temperatures, the ignition occurs in a single stage. However, for highly reactive fuels, the two-stage character may persist in the higher temperature regime because the first stage chemistry can occur during the course of the compression stroke. The extent to which this takes place is governed by the reactivity of the fuel and the pressure and temperature to which the reactant charge is finally compressed. This chemistry is ignored completely in experimental or numerical studies that are not begun until the conditions correspond to those of the postcompression period. For example, the extent of reaction and its effect on autoignition cannot be measured in shock tubes or when reactants are admitted very rapidly to preheated vessels. It has been taken into account in some numerical simulations of combustion in engines [1].

In previous studies in an RCM, it was shown from the pressure–time records that during the combustion of *n*-C_7H_{16} and *n*-C_6H_{14} at compressed gas temperatures above 750 K, a sufficiently rapid exothermic reaction occurred in the final stages of piston motion that there was an enhancement of the gas temperature beyond that reached by adiabatic compression alone [2]. This arose because the first (or cool flame) stage of a two-stage ignition coincided with the end of the compression stroke. The corollary is that spontaneous ignition that is observed as a single-stage ignition in a shock tube at gas temperatures above 850 K may continue to evolve in two stages in a compression machine (engine or RCM), so the measured ignition delays would not be the

same. It was also shown in the earlier studies [2] that little or no oxidation occurred during the compression stroke when a less-reactive fuel, such as n-C_4H_{10}, was involved. In such circumstances, the ignition delays for gas temperatures above 750 K in a shock tube or RCM are likely to be in reasonable agreement [3]. In RCM studies, the ignition delay (t_i), measured from the pressure records, is defined as the time from the end of compression to the maximum rate of pressure rise in ignition [2–6].

In the present work, we report direct experimental measurement of the extents of reactant consumption during the development of spontaneous ignition of alkanes in an RCM, with particular emphasis on reactivity during the compression stroke. Three fuels have been studied in stoichiometric mixtures in air, namely n-C_5H_{10}, n-C_7H_{16}, and the PRF 60 mixture 0.4 n-C_7H_{16} + 0.6 i-C_8H_{18} (2,2,4-trimethylpentane). PRF 60 was chosen because its research octane number is close to that of n-C_5H_{12} (RON = 62.5).

Over the last decade, there has been considerable development of numerical approaches to the prediction of spontaneous ignition phenomena by modeling the detailed chemistry and its associated heat release [1,7]. Ignition delays have been a primary focus of attention [7], with additional validation of the models against experimental studies of the formation of intermediate and final molecular products [1,5,6,8,9]. Thus, it is both timely and opportune to apply numerical modeling to the experimental results reported here for reactant consumption.

The purpose of the computation here is not to test the present state of numerical modeling; the goal is to substantiate the characterization of single and two-stage ignition and the conditions in which the first stage reaction is subsumed into the compression so that ignition appears as a single stage in the postcompression period. The initial, numerical studies of the binary PRF 60 proved to be less satisfactory than those for the modeling of n-C_5H_{10} and n-C_7H_{16} oxidation, possibly through difficulties associated with the i-octane oxidation model. A spatial uniformity of temperature and concentration of species is assumed in the kinetic analysis to restrict the numerical integration to that of ordinary differential equations, as is normally the case. However, spatial inhomogeneities of temperature and concentration are known to exist to varying extents throughout the course of piston motion of rapid compression machines and throughout the postcompression interval in which spontaneous ignition develops fully [10–12].

Experimental and Numerical Methods

Experimental Studies

Full details of the apparatus and experimental procedures have been described previously [2,13–16]. In summary, fuel vapor was premixed with air consisting of 21% oxygen and a 79% composite of nonreactive components comprising argon or nitrogen. The proportions of the inerts were varied to alter the overall heat capacity of each mixture and hence the ratio C_p/C_v ($= \gamma$). Thus, a range of compressed gas temperatures could be covered at a fixed compression ratio of the machine (CR = 11.00 ± 0.15:1). Experiments were performed at the compressed gas temperatures of 720–750 K and 845–875 K. Mixtures, stored in a Pyrex glass vacuum line, were transferred at an initial pressure of 33.3 kPa to the combustion chamber and then compressed into a cylindrical combustion chamber by a piston that was driven by compressed air and that stopped at top dead center (TDC), the stroke taking 22 ms. The cylinder and combustion chamber temperature (T_i) were maintained at 323–348 (±1) K. The compressed gas density was 131.0 ± 1.5 mol m^{-3} in all experiments.

Pressure–time data during the compression and throughout the postcompression period were measured by Kistler transducer and recorded digitally on a PC at a sampling rate of 200 μs per point via an A/D converter, 200 ms in total. Chemiluminescent emission accompanying reaction was measured by photomultiplier in selected experiments (Thorn EMI 9924B). In general, the ignition delays, measured in three to six experiments at each reactant composition and compressed gas temperature, were reproducible to ±2.0 ms at long durations and ±1.0 ms at short durations. The compressed gas temperature, T_c, was derived from the measured pressures at the start and end of compression, p_i and p_c, and taking into account the temperature dependence of γ, using the relationship

$$\int_{T_i}^{T_c} \frac{\gamma}{\gamma - 1}\, d\ln T = \ln\left(\frac{p_c}{p_i}\right)$$

To analyze the reactant and product compositions at intermediate stages, the reaction was quenched by the bursting of a diaphragm (99% Al, 0.1 mm thickness) in the end wall of the combustion chamber, which formed the cylinder head. This was followed by the expansion of the reactant mixture into a hemispherical dump tank (1.5 dm^3), as described previously [13]. The time at which the diaphragm burst was controlled by a time-delayed signal generated at a threshold pressure during the compression stroke that was used to actuate an electromagnetically driven needle. The condensable components were then pumped to a cold trap coupled to the vacuum line. To obtain time-dependent profiles for the reactant consumption, many experiments were performed under the same compression conditions but with quenching after different intervals. The results for each set of experimental conditions were obtained from a number of separate

$$\begin{array}{ccccccccccc} & & & & & & & & \text{cyclic ether} + \text{OH} & & \\ & & & & & & & & \text{or } \beta \text{ scission} + \text{HO}_2 & & \\ \text{RH} & \xrightarrow[\text{X}]{\text{O}_2} & \text{R} & \underset{\downarrow \text{O}_2}{\overset{\text{O}_2}{\rightleftharpoons}} & \text{RO}_2 & \rightleftharpoons & \text{QO}_2\text{H} & \overset{\text{O}_2}{\rightleftharpoons} & \text{O}_2\text{QO}_2\text{H} & \rightleftharpoons & \text{OQ}'\text{O}_2\text{H} + \text{OH} \rightarrow \text{branching} \\ & & & & & & \downarrow & & & & \\ \text{alkene} + \text{HO}_2 & & & & & & & & \text{alkene} + \text{HO}_2 & & \end{array}$$

mixtures made up to the same composition. To standardize the extents of reaction in a series of experiments, the sealed cold trap was allowed to warm to laboratory temperature and a standard volume of n-C_4H_{10} was injected into the trap via a septum cap. After complete mixing, a gaseous sample was withdrawn from the trap via a microsyringe and injected into the analytical system. A separation of the mixture was performed by gas chromatography (Carlo Erbe) on a fused silica, Poraplot Q-coated, capillary column (25 m × 0.32 mm), and a quantitative analysis was obtained from the integrated peak areas of the eluting compounds. The proportions of the fuel remaining in each experiment were obtained from a determination of the peak area of the primary fuel peak relative to that of n-butane. This result was then normalized to a constant peak area that represented the n-butane signal.

The extents of reaction were measured relative to the amount of reactant measured following compression under nonreactive conditions. Product compositions were not analyzed in the present work.

Numerical Analysis and Kinetic Model

The numerical modeling calculations were carried out using the HCT program [17], which solves the coupled nonlinear differential equations for conservation of mass, momentum, energy, and each chemical species in finite-difference form. The compression stroke was simulated ab initio from the initial conditions and reactant compositions for the experimental results, adiabatic conditions being assumed. The reaction mechanism included more than 2000 elementary chemical reactions with their reverse steps. This reaction mechanism includes submechanisms for oxidation of C_1–C_8 hydrocarbon species, validated against a variety of experimental data for ignition and combustion environments [1]. These mechanisms include reactions governed by formation and consumption of alkylperoxy radical species that are appropriate to low temperatures.

Distinctions were made between the rates of abstraction of H atoms from primary, secondary, and tertiary sites in each alkane and between equilibrium constants for addition of molecular oxygen to different types of alkyl radicals. The most significant, subsequent reactions of the alkylperoxy radicals ($C_nH_{2n+1}OO$) so formed are their isomerizations via internal H-atom abstraction, at rates that depend primarily on the type of C—H bond being broken and the ring strain energy of the intermediate transition state [8]. The many distinct $C_nH_{2n}OOH$ radicals can decompose thermally, producing hydroxyl radicals and cyclic ethers. Depending on their specific structure, some alkylperoxy radicals can also decompose to produce stable alkene or oxygenated species and HO_2 or OH radicals. All of these reactions lead to chain propagation. The only reactions of alkylperoxy radicals that lead to vigorous chain branching involve addition of a second oxygen molecule producing ketohydroperoxide intermediates that then decompose to produce radicals. Rates and equilibrium constants for these reaction paths have been developed in recent studies [1,8,9]. The kinetic structure to represent alkane oxidation at low temperatures may be summarised in the equation above [9,18,19].

Results

Combustion at T_c = 720–750 K

Measured pressure change and the measured and computed proportions of reactants consumed during the spontaneous ignition of n-C_5H_{12} and n-C_7H_{16} at $\phi = 1$ are shown in Figs. 1 and 2. The records begin at 2 ms before the end of piston motion and continue throughout the development of ignition. The pressure record shown in Fig. 1 also includes the sharp fall that occurred when the quenching diaphragm was punctured. This illustrates the rate of expansion of the products into the dump tank. In this case, the pressure did not reach the maximum that was normally attained at ignition (>3.0 MPa).

Both n-C_5H_{12} and n-C_7H_{16} exhibited a two-stage ignition after the end of compression, which was evident both in the pressure record and in the accompanying chemiluminescent emission from the reaction (Figs. 1 and 2). The first stage of two-stage ignition is interpreted as the development from the end of compression to the point of inflexion in the pressure rise [4–6]. There was very little or negligible consumption of either reactant before the piston had stopped. Whereas nearly 40% of the n-C_7H_{16} had reacted by the end of the first stage (Fig. 2), less than 15% of the n-C_5H_{12} had been consumed (Fig. 1). There was a particularly sharp acceleration in the rate of consumption of n-C_5H_{12} during the development of the second stage, and 80% of it had been

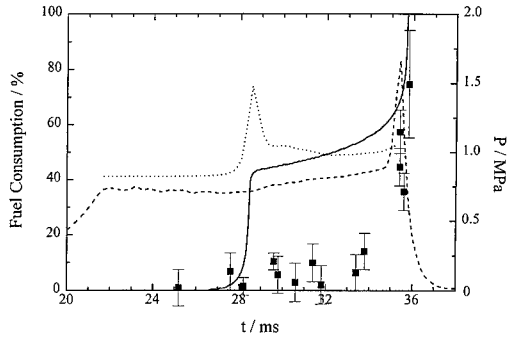

FIG. 1. Fractional extent of consumption (%) of n-C_5H_{12} at $\phi = 1$ during ignition following rapid compression to $T_c = 750 \pm 5$ K. The error bars represent variations in results from multiple analyses of each sample collected in the cold trap. Piston motion stops at 22 ms, as shown in the pressure–time record (broken line). The pressure fall associated with a typical quenching of reaction is shown at the end of the pressure record. The peak in the light emission (uncalibrated) accompanying the first stage of ignition is also shown (dotted line). Computations of the extent of reactant consumption are given as a solid line.

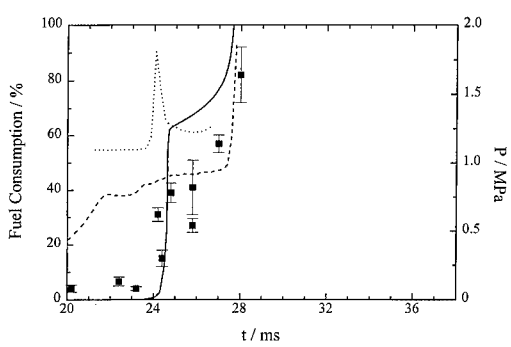

FIG. 2. Fractional extent of consumption (%) of n-C_7H_{16} at $\phi = 1$ during ignition following rapid compression to $T_c = 750 \pm 5$ K. The combustion chamber pressure, light output, and computed extent of reaction (%) are shown as in Fig. 1.

consumed at the highest quenching pressure (1.9 MPa). The discrepancies of experimental results in Fig. 1, which imply that there is a lower extent of conversion at a later time during the development of the hot stage of ignition, arise from the small variations in ignition delay from one experiment to another. Similar features occur in subsequent figures.

The numerical evidence for the occurrence of two-stage ignition during n-C_5H_{12} and n-C_7H_{16} combustion at the same compressed gas temperatures as in the experiments is unequivocal, and the computed first-stage and overall ignition delays are in excellent agreement with the experimental results. In each case, the predicted extents of reaction at the end of the first stage exceed those in the experiments, with 40% and 60% for n-C_5H_{12} and n-C_7H_{16}, respectively, being consumed. The model results show a negligible extent of reaction at the end of compression.

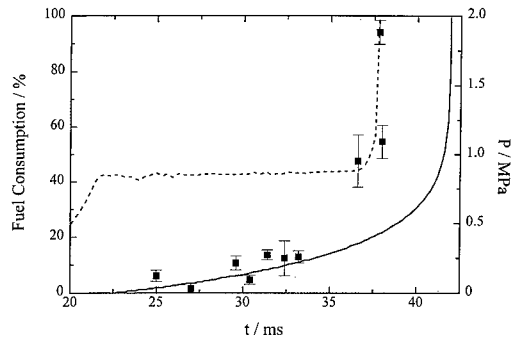

FIG. 3. Fractional extent of consumption of n-C_5H_{12} at $\phi = 1$ during ignition following rapid compression to $T_c = 853 \pm 4$ K. No light output is given because there was no significant emission before the final stage of combustion. The combustion chamber pressure and computed extent of reaction (%) are shown as in Fig. 1.

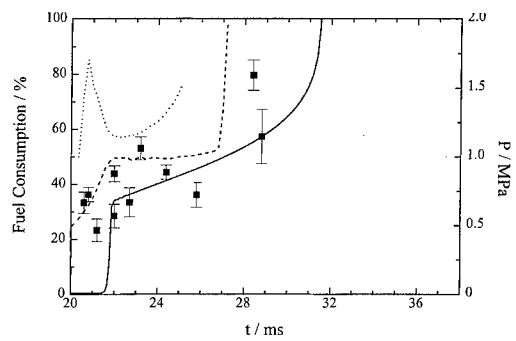

FIG. 4. Fractional extent of consumption of n-C_7H_{16} at $\phi = 1$ during ignition following rapid compression to $T_c = 870 \pm 5$ K. A significant amount of n-C_7H_{16} has reacted before the piston stops (22 ms), and there is accompanying cool flame light emission (dotted line). The combustion chamber pressure and computed extent of reaction (%) are shown as in Fig. 1.

Combustion at T_c = 845–875 K

The experimental and numerical reactant consumption profiles and the experimental pressure–time records for the combustion of n-C_5H_{12} and n-C_7H_{16} are shown in Figs. 3 and 4. The spontaneous ignition of n-C_5H_{12} at a compressed gas temperature of 853 ± 4 K developed in a single stage (Fig. 3). There was no measurable reactant consumption

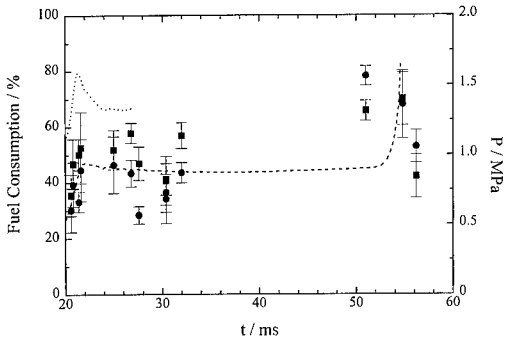

FIG. 5. Fractional extent of consumption (%) of n-C_7H_{16} (■) and i-C_8H_{18} (●) in a PRF 60 mixture at $\phi = 1$ during ignition following rapid compression to $T_c = 864 \pm 4$ K. A significant proportion of n-C_7H_{16} and i-C_8H_{18} has reacted before the piston stops (22 ms), and there is accompanying cool flame light emission (dotted line). The combustion chamber pressure is shown as a broken line.

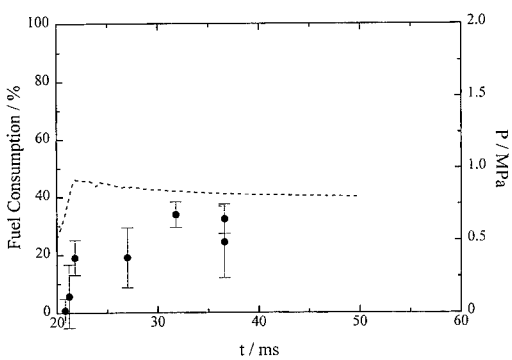

FIG. 6. Fractional extent of consumption (%) of i-C_8H_{18} (●) at $\phi = 0.6$ following rapid compression to $T_c = 860 \pm 5$ K. Piston motion stops at 22 ms, as shown in the pressure record (broken line). Ignition did not occur, and there was little light emission accompanying the early stage of reaction.

before the piston motion stopped, and the extent of fuel consumption increased smoothly (but slowly at first) throughout the postcompression interval.

The pressure record for the combustion of n-C_7H_{16} at $T_c > 850$ K also appeared to be a single-stage ignition. However, the profile for reactant consumption was quite different from that measured for n-C_5H_{12} (Fig. 4). Reactant consumption began more than 1 ms before the piston had stopped and 40 ± 5% of the n-C_7H_{16} had been consumed by TDC. As was shown by the light output record, this reaction was associated with the first-stage (or cool flame) chemistry.

The interpretation of events from numerical studies of each fuel compressed to $T > 850$ K is in categorical qualitative support of the experimental observations. The consumption of n-C_5H_{12} became significant only about 2 ms after the end of compression and reached ~10% about halfway through the ignition delay (Fig. 3). For n-C_7H_{16}, 33% of the fuel was predicted to have reacted before the piston had stopped, even though the simulated start of reaction was slightly later than in the experiments (Fig. 4). In each case, throughout most of the postcompression period, the relative extent of reactant consumption that was predicted to occur was in good agreement with the experimental results. Significant departures of the simulated profiles from the experimental results became evident only at predicted gas temperatures in excess of 920 K, and the final stages of the simulated ignition were slower in completion.

The experimental results obtained from ignition of the binary mixture 0.6 i-C_8H_{18} + 0.4 n-C_7H_{16} (PRF 60) at a compressed gas temperature of 864 ± 4 K are shown in Fig. 5. The interpretation from the pressure record in the postcompression period is of a single-stage ignition ($t_i = 32 \pm 2$ ms). However, the consumption of both reactants began while the piston was still moving and there was a weak cool flame emission before the end of compression (Fig. 5). More n-C_7H_{16} than i-C_8H_{18} had reacted (45 ± 5% versus 37 ± 5%) by the time the piston stopped. Very little of either fuel was further consumed during the early part of the postcompression period, but there was an acceleration in the rate of consumption in the final stage of ignition during which there was no appreciable distinction between the behavior of n-C_7H_{16} and i-C_8H_{18}.

Supplementary experimental measurements have also been made of the proportion of i-C_8H_{18} consumed in a reactive mixture containing only the i-C_8H_{18} component (that is, i-C_8H_{18} at $\phi = 0.6$) but of similar heat capacity to that of the PRF 60 mixture. Ignition of this composition did not occur follow ing compression to 130 mol m^{-3} and $T_c = 860 \pm 5$ K, but nevertheless approximately 20% of the reactant had been consumed before the end of compression and there was a gradual increase to 30% during a 10-ms interval of the postcompression period (Fig. 6).

Discussion

Adiabaticity, Heat Loss, and Spatial Temperature Variations

Compression at the piston speeds used in the Leeds machine has been shown previously to be virtually adiabatic [2]. Thus, assumptions of adiabaticity of the system and spatial uniformity of temperature and concentration in the numerical modeling during the compression stroke is very satisfactory. However, spatial temperature variations develop within the

combustion chamber during the postcompression period as a result of heat transport to the combustion chamber walls. The heat-loss rates are highest just after compression ceases because the residual gas motion is greatest at this stage [11]. Thereafter, the rate of heat loss decreases as the gas motion decays. In the present calculations, adiabaticity was assumed also throughout the postcompression period. The simulation of ignition delay thus implies that the behavior is dominated by conditions in the adiabatic core [21], but there are complexities of the interaction between the kinetics and a nonhomogeneous temperature field in a temperature range where a negative temperature dependence of reaction rate exists [11,12].

The calculated extent of reaction at any time after the end of compression, with adiabatic conditions assumed, may be expected to be an overestimate relative to an experimental measurement that is obtained from the amount of reactant remaining within a nonuniform temperature regime comprising cooler regions surrounding an adiabatic core. The heat-loss rate throughout the postcompression period may be characterized by a Newtonian heat-transfer coefficient in a zero-dimensional numerical model [22]. However, its application can adversely affect the predicted reactivity because there is a highly nonlinear response of the chemical kinetics to reactant temperature. Rates and extents of reaction cannot be averaged in a simple way throughout a combustion chamber in which spatial variations in temperature exist, and so the correction has not been attempted in this work.

Extents of Reaction in Single- and Two-Stage Ignition and during Compression

The greater reactivity of n-C_7H_{16} over that of n-C_5H_{12} at $T_c \sim 750$ K is not only reflected in the shorter ignition delay but also is manifest directly in the extents of reaction measured in the first stage of two-stage ignition (Fig. 1 and 2). In previous rapid compression studies, Fish et al. [23] measured approximately 25% consumption of 2-methylpentane during the first stage of two-stage ignition at T_c = 808 K. For n-C_4H_{10}, Minetti et al. [5] showed that there was only 10–15% reactant consumption during the first stage of two-stage ignition at T_c = 708 K, whereas approximately 25% consumption of n-C_7H_{16} occurred during the first stage of its two-stage ignition at T_c = 667 K [6].

The activity of the alkanes at the reactant temperatures associated with the first stage may be attributed to the generalized sequence shown in the numerical background. Each alkane is capable of generating a number of different isomeric forms of the alkyl (R), alkylperoxy (RO_2), hydroalkylperoxy (QO_2H), or other species. The slow development of the first stage may be attributed to the chain-thermal interaction in which the thermal feedback is required to accelerate the degenerate branching route [19]. Its rate is controlled largely by the activation energies associated with the RO_2/QO_2H isomerizations, but the properties of each of the other steps play a part in the quantitative behavior. The more vigorous acceleration in rate of n-C_7H_{16} consumption in the first stage of two-stage ignition, which was found both experimentally and numerically, testifies to its much more facile chain-branching route than that of n-C_5H_{12}. The limit on chain branching is set by the displacement of the R/RO_2 equilibrium toward dissociation as the reactant temperature increases beyond 800 K. This is the primary kinetic origin of the negative temperature dependence of reaction rate since the main (nonbranching) propagation is taken up with relatively low exothermicity by HO_2 radicals [19].

There are both chemical and thermal consequences of oxidation in the final stages of compression. The thermal contribution is an augmentation of the gas temperature beyond that which would be reached by rapid compression alone, and the effect can be seen in the difference between the pressures attained under reactive and nonreactive conditions [2]. The temperature increase predicted in the numerical simulations for n-C_7H_{16} combustion is 30 K.

The difference in reactivity shown by n-C_7H_{16} and n-C_5H_{12} also accounts for the ability of n-C_7H_{16} to react during the compression stroke when compression occurs beyond T_c = 800 K (Figs. 3 and 4). Although thermal feedback has some effect on gas temperature, the reactant temperature is forced through the most reactive temperature regime (750–800 K) at a rate determined by the compression stroke. At a piston speed of 12 m s^{-1} in the Leeds rapid compression machine, there is sufficient time for n-C_7H_{16} to react. Although this is not the case for n-C_5H_{12} under the present conditions, it could be so for n-C_5H_{12} or other fuels of similar reactivity at higher reactant densities.

Schlieren imaging of spontaneous ignition in the rapid compression machine shows that the hot stage often begins at a single center, and the bulk of the reactants are consumed in a propagating combustion wave before many (and sometimes any) other centers are initiated [24]. Consequently, a reaction quenched on the rising pressure profile of the final stage of ignition gives rise to a product composition drawn from segregated burned gas and partially oxidized reactants. Thus, the extents of reaction in the late stage of reaction that are predicted numerically from a zero-dimensional model cannot be expected to match quantitatively the experimental behavior. Differences in the duration of the overall ignition delay, which in the present numerical analyses tend to be slightly longer than the experimental measurements, may be attributed to the same marked

departures in the experiments from the idealization in the final stages of combustion.

Combustion of a PRF 60 Mixture

Although there were significant quantitative differences in the form of the predicted profiles for the PRF 60 mixture that still have to be addressed, the predicted ratio of extents of reaction throughout the ignition delay at temperatures below 900 K, $d[n\text{-}C_7H_{16}]/d[i\text{-}C_8H_{18}]$ was 1.24. This is in excellent agreement with the experimental measurements at the end of compression (1.2 ± 0.1). It follows that the relative concentration of alkyl radicals, $d[n\text{-}C_7H_{15}]/d[i\text{-}C_8H_{17}]$, generated in the PRF 60 mixture in this environment is $(40/60) \times 1.2 = 0.83 \pm 0.02$. This ratio is consistent with an almost exclusive role of H-atom abstraction by OH radicals, as can be derived from the ratio for $k(n\text{-}C_7H_{16} + OH)/k(i\text{-}C_8H_{18} + OH)$ in the range 800–900 K, taking into account the numbers of primary, secondary, or tertiary C—H bonds in $n\text{-}C_7H_{16}$ and $i\text{-}C_8H_{18}$ and the respective Arrhenius parameters [25]. The relatively weak selectivity in favor of C_8H_{17} radical formation in the mixture 0.4 $n\text{-}C_7H_{16}$ + 0.6 $i\text{-}C_8H_{18}$ would shift very substantially toward C_8H_{17} radical formation in PRF mixtures containing higher proportions of $i\text{-}C_8H_{18}$.

Oxidation of $n\text{-}C_7H_{16}$ generates a rate of chain branching that is much more intense than that of $i\text{-}C_8H_{18}$, since the structure of the C_7H_{15} radicals leads to higher rates of peroxy radical isomerization [1], ultimately causing chain branching from keto-hydroperoxide decomposition. Increasing fractions of $i\text{-}C_8H_{18}$ in PRF mixtures would therefore reduce the overall rate of combustion because the rate of chain branching would decrease. This is apparent in a qualitative way in a comparison between the reactivity at high compressed gas temperatures between $n\text{-}C_7H_{16}$ and PRF 60 (Figs. 4 and 5) and between PRF 60 and $i\text{-}C_8H_{18}$ at $\phi = 0.6$ (Figs. 5 and 6). The "net branching factor" cannot be quantified from these global measurements in the rapid compression machine. However, the proportion of alkyl radicals from each reactant that eventually contributes to the low-temperature chain-branching channels can be derived from numerical simulations [26], although at present it appears that the branching characteristics included in the model for $i\text{-}C_8H_{18}$ oxidation are not yet as vigorous as is observed in practice.

The Effect on Ignition Delay of Reactant Consumption in the Compression Stroke

It must be expected that reaction in the compression stroke has a significant effect on the subsequent development of ignition. Although not amenable to experimental test in an RCM, this can be assessed quantitatively by a numerical analysis in which a comparison is made between the computation in a fully reactive compression simulation and when the chemical calculation is started only at the temperature and pressure attained at the end of compression.

Such calculations for $n\text{-}C_7H_{16}$ combustion at $T_c >$ 850 K show that when 33% or more of the fuel has already been consumed in the compression stroke and has conditioned the system accordingly, the ignition delay is about half of that predicted from a nonreacted compressed gas state [26]. The model calculations also show clearly that, even in conditions in which no identifiable fuel consumption has been observed at the end of the compression stroke, a significant extent of chemical activity may have already developed. For example, in the high-temperature compression of $n\text{-}C_5H_{12}$, at the time compression is complete, although no $n\text{-}C_5H_{12}$ consumption is calculated (<0.1%) or observed, C_5 radicals, such as RO_2 and QOOH, as well as C_5 alkenes and cyclic ethers, are all present in excess of ppm concentrations. In this respect, the fuel + air mixture is preconditioned at the end of the compression stroke and the subsequent ignition delay is 10% shorter than would be predicted if a truly unreacted mixture were assumed.

Conclusions

In both the experimental results and the supplementary modeling analysis, it has been shown that considerable fuel consumption can take place before completion of the compression stroke when sufficiently high compressed gas temperatures are reached. By implication, this will occur in other machines with comparable or slower compression rates. When knock occurs in a spark-ignition engine (at <2000 rpm^{-1}, say, at an average piston speed of 4–6 m s^{-1} with a stroke of 6–10 cm), there is a similar time interval during which spontaneous oxidation of the fuel + air mixture to develop appreciably, especially at high gas densities.

Acknowledgments

The authors thank EPSRC for financial support.

REFERENCES

1. Westbrook, C. K., Pitz, W. J., and Leppard, W. R., SAE Paper No. 91-2314, 1991.
2. Griffiths, J. F., Halford-Maw, P. A., and Rose, D. J., *Combust. Flame* 95:291 (1993).
3. Ohta, Y., Hayashi, A. K., Fujiwara, T., and Takahashi, H., *Prog. Astro. Aeronaut.* 113:225 (1988).
4. Halstead, M. P., Kirsch, L. J., Prothero, A., and Quinn, C. P., *Proc. R. Soc. London, Ser. A* 346:515 (1975).
5. Minetti, R., Ribaucour, M., Carlier, M., Fittschen, C., and Sochet, L. R., *Combust. Flame* 96:201 (1994).

6. Minetti, R., Carlier, M., Ribaucour, M., Therssen, E., and Sochet, L. R., *Combust. Flame* 102:298 (1995).
7. Chevalier, C., Pitz, W. J., Warnatz, J., Westbrook, C. K., and Melenk, H., *Twenty-Fourth Symposium (International) on Combustion,* The Combustion Institute, Pittsburgh, 1992, p. 1293.
8. Curran, H. J., Pitz, W. J., Westbrook, C. K., Hisham, H. W. M., and Walker, R. W., submitted for publication (1996).
9. Curran, H. J., Gaffuri, P., Pitz, W. J., Westbrook, C. K., and Leppard, W. R., SAE Paper No. 95-2406, 1995.
10. Park, P. and Keck, J. C., SAE Paper No. 90-0027, 1990.
11. Griffiths, J. F., Jiao, Q., Schreiber, M., Meyer, J., and Knoche, K. F., *Twenty-Fourth Symposium (International) on Combustion,* The Combustion Institute, Pittsburgh, 1992, p. 1809.
12. Schreiber, M., Poppe, C., Sadat Sakak, A., Griffiths, J. F., Rose, D. J., and Halford-Maw, P. A., SAE Paper No. 93-2758, 1993.
13. Beeley, P., Gray, P., and Griffiths, J. F., *Combust. Flame* 39:269 (1980).
14. Griffiths, J. F. and Hasko, S. M., *Proc. R. Soc. London, Ser. A* 393:371 (1984).
15. Griffiths, J. F. and Perche, A., *Eighteenth Symposium (International) on Combustion,* The Combustion Institute, Pittsburgh, 1981, p. 893.
16. Griffiths, J. F., Jiao, Q., Schreiber, M., Meyer, J., and Knoche, K. F., *Combust. Flame* 91:209 (1992).
17. Lund, C. M., Lawrence Livermore National Laboratory report UCRL-52504, 1978.
18. Morley, C., *Combust. Sci. Technol.* 55:115 (1987).
19. Griffiths, J. F., *Prog. Energy Combust. Sci.* 21:25 (1995).
20. Cartlidge, J. and Tipper, C. F. H., *Combust. Flame* 5:187 (1961).
21. Hu, H. and Keck, J. C., *Twenty-First Symposium (International) on Combustion,* The Combustion Institute, Pittsburgh, 1986, p. 521.
22. Griffiths, J. F., Hughes, K. J., Schreiber, M., and Poppe, C., *Combust. Flame* 99:533 (1994).
23. Fish, A., Haskell, W. W., and Read, I. A., *Proc. R. Soc. London, Ser. A* 313:261 (1969).
24. Mohamed, C. and Pan, J., 1996, unpublished results.
25. Kwok, E. S. C. and Atkinson, R., *Atmospheric Environ.* 29:1685 (1995).
26. Curran, H. J., Pitz, W. J., and Westbrook, C. K., to be published.

Twenty-Sixth Symposium (International) on Combustion/The Combustion Institute, 1996/pp. 2693–2700

HETEROGENEOUS/HOMOGENEOUS REACTION AND TRANSPORT COUPLING DURING FLAME-WALL INTERACTION

P. POPP AND M. SMOOKE
Yale University, Department of Mechanical Engineering

M. BAUM
NEC Europe Ltd.

The effect of surface chemistry and transport modeling on the head-on quenching process of laminar propane/air and methane/air flames is investigated numerically. The fully compressible, one-dimensional Navier–Stokes equations with detailed mechanisms for diffusion and chemical kinetics (gas-phase and surface) are solved using a sixth-order finite-difference scheme in space and a third-order Runge–Kutta scheme in time. Important applications are in the modeling of flame-wall interaction processes in piston engines, their related experimental measurements, and general surface chemistry modeling. The latter is due to the interaction being unsteady in contrast to typical boundary layer or stagnation point flow studies over reactive surfaces. Also the surface response takes place in the high coverage zone. It is found that in order to simulate quenching at higher wall temperatures accurately, the process of diffusion, adsorbtion, and surface recombination especially for the free radical H and OH have to be described. This results in an increasing wall heat flux with wall temperature in excellent agreement with existing experimental data. If the participation of the surface in the reaction channels of the near-wall gas-phase species is excluded (either because of the physical surface properties or because of the boundary treatment in the simulations), the quenching structure is completely changed with strongly exothermic radical recombination reactions dominating the interaction. The developed detailed surface mechanism contains 10 reactions, involving four surface species, and seven gas-phase species. It takes into account the breakdown of the Langmuir adsorption concept for high surface coverages and includes a precursor-state model for the adsorption of H_2, H, and OH.

Introduction

Whereas former engine codes did not use any specific corrections for flame-wall interaction, modern engine codes emphasize the importance of quenching models. Those are based on the concept of a quenching layer and assume that transport and surface effects are negligible. Recent research [1,2] indicates that (1) those assumptions might not be valid for high wall temperatures as encountered under operating conditions or even in insulated engines and (2) the experimental value of the wall heat flux during flame-wall interaction, which is the only parameter that is easily accessible and can be used to baseline numerical against experimental data, might depend on the surface material of the thin-film gauge used (which is, in general, platinum). To investigate this situation, we have studied, numerically the quenching situation as can be found in constant-volume combustion chambers [3–5] for an inert and a platinum surface over a range of wall temperatures between 300 and 600 K. A laminar flame approaches head-on the chamber wall and is quenched at atmospheric pressure. Special attention is given to the homogeneous/heterogeneous reaction behavior and transport coupling at 600 K. We consider stoichiometric methane- and propane-air flames.

Problem Setup

Solution Method

The complete set of Navier–Stokes equations is solved on a one-dimensional domain. The numerical scheme is sixth-order in space and third-order in time [1]. Chemistry is described by detailed reaction and diffusion mechanisms (TRANSPORT [6], CHEMKIN [7]). Cross-diffusional effects are taken into account [8]. Surface reaction data are calculated via SURFACE CHEMKIN [9]. For further details see Ref. 2.

Gas-Phase Chemistry

The gas-phase reaction scheme for the methane-flame calculations [10] consists of 52 elementary reactions and 17 species considering only the C_1 path.

TABLE 1

The detailed, kinetic surface-reaction mechanism. When rate coefficients are given, the rate expression is in Arrhenius form: $k = A \exp(-E_a/RT)$. Note that in the limit of high coverage, reactions 1, 3, and 6 are coverage independent.

	Reaction	A or γ	E_a (kJ/mol)	Comment
	Non dissociative radical adsorption			
R_1	$H + Pt(s) \rightleftharpoons H(s)$	1.0		sticking coeff.
R_2	$O + Pt(s) \rightleftharpoons O(s)$	1.0		sticking coeff.
R_3	$OH + Pt(s) \rightleftharpoons OH(s)$	1.0		sticking coeff.
	Dissociative radical adsorption			
R_4	$HO_2 + 2Pt(s) \rightarrow OH(s) + O(s)$	1.0		sticking coeff.
R_5	$H_2O_2 + 2Pt(s) \rightarrow OH(s) + OH(s)$	1.0		sticking coeff.
	Dissociative H_2/O_2 adsorption			
R_6	$H2 + 2Pt(s) \rightarrow H(s) + H(s)$	0.023		sticking coeff.
R_7	$O_2 + 2Pt(s) \rightarrow O(s) + O(s)$	0.046		sticking coeff.
	Surface recombination reactions			
R_8	$H(s) + O(s) \rightleftharpoons OH(s) + Pt(s)$	1.0 E +21	11.5	rate coeff.
R_9	$H(s) + OH(s) \rightarrow H_2O + Pt(s)$	1.0 E +21	17.4	rate coeff.
R_{10}	$OH(s) + OH(s) \rightarrow H_2O + O(s)$	1.0 E +21	48.2	rate coeff.

The C_2 path, i.e., the conversion of CH_4 to higher hydrocarbons is neglected because recent research [1] demonstrated a negligible influence on flame-quenching characteristics. The gas-phase reaction scheme for the propane-flame calculations [11] consists of 87 reactions and 31 species.

Surface Chemistry

Based on recent work [12–15], a detailed, kinetic surface-reaction mechanism (Langmuir–Hinshelwood type) for flame quenching on platinum surfaces has been developed (Table 1). It consists of 10 reactions involving four surface and seven gas-phase species. It considers nondissociative adsorption of H, O, and OH, dissociative adsorption of HO_2 and H_2O_2, and dissociative adsorption of H_2 and O_2. It accounts for subsequent surface reactions between adsorbed species, and desorption of adsorbed products and intermediate species into the gas phase. The pre-exponential factors of the surface reactions are estimated by transition-state theory to be of the order of 10^{21}. Activation energies are taken from Ref. 12. Reverse reactions are determined from thermochemistry [15]. Sticking coefficients are given for initially clean surfaces. The variation of all adsorption reactions with coverage but those involving H_2, H, and OH is assumed to follow the Langmuir adsorption isotherm:

$$RR_i^{ads} = [X_i]\Theta^m(\mathrm{Pt})fi(\gamma)\sqrt{\frac{RT}{2\pi W_i}} \qquad (1)$$

RR_i^{ads} is the adsorption rate of the ith gas-phase species, $[X_i]$ is its gas-phase concentration adjacent to the wall, W_i is its molecular weight, $\Theta(\mathrm{Pt})$ is the free-surface site fractions, and m is the order of the adsorption reaction (0 for the coverage-independent adsorption of H_2, H, and OH, 1 for nondissociative adsorption, and 2 for dissociative adsorption). For small values of the sticking coefficient γ, $f(\gamma) = \gamma$, and for high values, $f(\gamma) = \gamma/(1 - \gamma/2)$ because the near-wall velocity distribution becomes non-Maxwellian [16]. The square root term in Eq. (1) denotes the collision frequency of the ith gas-phase species with the surface.

Initial Conditions

An undisturbed flame as calculated by PREMIX [17] is placed about five flame thicknesses away from the wall. For more details on the inert wall initial conditions, see Ref. 2. Initial conditions for the surface site fractions H(s), O(s), OH(s), and Pt(s) are determined by solving the full system of equations on a coarse grid without a flame. Initializing with other than the steady-state solution can lead to erroneous physical results, such as fuel depletion adjacent to the wall or large perturbations in the flow field adjacent to the wall due to extremely high Stefan velocities.

Boundary Conditions

The wall temperature boundary condition is T_W = constant during one simulation in agreement with experimental evidence [5,18,19]. All other surface

boundary conditions depend on the reactivity of the surface and the (numerical) treatment of the gas-phase diffusion processes.

Inert wall/no cross diffusion

This boundary condition is the standard boundary condition in quenching simulations, whether in engine code or theoretical studies of this phenomena [3–5,20,21]. The corresponding velocity boundary condition is simply $u_W = 0$, and the species boundary condition is $\partial Y_i/\partial x = 0$, $i = 1,2, \ldots, N_g$, where N_g is the total number of gas-phase species and Y_i the mass fractions. This boundary condition is only valid for wall temperatures between 300 and 400 K [2].

Inert wall/cross diffusion

Again $u_W = 0$; however, the driving force of species diffusion is no longer only the concentration gradient but also the temperature gradient that leads to the specification of species diffusion velocities. Those are defined as $V_i = 1/(X_i\bar{W}) \sum_{j \neq i}^{N_g} W_i D_{ij} \nabla X_j - (D_i^T \nabla T)/(\rho Y_i T)$, $i = 1, \ldots, N_g$. X_i are the gas-phase mol fractions, W is the mean molecular weight, D_{ij} is the ordinary multicomponent diffusion coefficient matrix, and D_i^T is the thermal diffusion coefficients. For a nonreacting wall, the diffusion velocity has to be zero normal to the surface; i.e.,

$$V_{W_i} = 0 \tag{2}$$

Reacting wall

For heterogenous reactions, the gas-phase mass flux of each species to the surface is balanced by the creation or depletion rate $\dot{s}_i$ of that species by surface reactions; i.e., $\rho Y_i(V_i + u) = \dot{s}_i W_i$, $(i = 1, \ldots, N_g)$. This leads to an induced velocity, the so-called Stefan velocity, which occurs when there is a net mass flux between the gas and the surface:

$$u_W = \frac{1}{\rho} \sum_{i=1}^{N_g} \dot{s}_i W_i \tag{3}$$

Once the Stefan velocity is known, the diffusion velocity can be readily evaluated:

$$V_{W_i} = \frac{\dot{s}_i W_i}{\rho Y_i} - u_W \tag{4}$$

Diagnostics

Special attention is focused on the wall heat flux and the flame structure during quenching. The wall heat flux as measured by a thin-film gauge [22] for a reactive surface is given by $q_W = \lambda_W \, \partial T/\partial x|_W - \sum_{i=1}^{N_g} \dot{s}_i W_i h_i$, with h_i the specific enthalpy of the ith species. For an inert wall, this reduces to $q_W = \lambda_W = \lambda_W \, \partial T/\partial x|_W$. Radiative heat transfer is neglected based on previous research [5,18,23]; q_w is normalized using the laminar flame power to yield the nondimensional wall heat flux: $\Phi = q_w/(\rho \, c_p \, S_l \, \Delta T)$, where ρ denotes the unburned gas density, c_p its specific heat at constant pressure, S_l the laminar flame speed, and ΔT the temperature difference between the burned and the unburned gases. The maximum wall heat flux that occurs during flame-wall interaction will be denoted by Φ_Q. The flame position is tracked as the location of the maximum heat release in the flame $x(\dot{w}_{\max})$. The corresponding distance between the flame and the wall is normalized to yield a Peclet number: $Pe = x(\dot{w}_{\max})/\delta_f$. The laminar flame thickness is defined as $\delta_f = (dT/dx|_{\max})/\Delta T$ as in Ref. 24. All times are normalized by the laminar flame time, which is given by $t_f = S_l/\delta_f$. Thus, $\tau = t/t_f$ and τ_Q denotes the time when the maximum wall heat flux Φ_Q is obtained and is referred to as the moment of quenching.

Flame-Wall Interaction

Gas-Phase Chemical Kinetic Results

The influence of either an inert wall with cross-diffusion in the gas phase [Eq. (2)] or a reactive wall [Eq. (4)] on gas-phase chemistry in the near-wall region is demonstrated. Mass fraction and net heat-release profiles per species at the moment of quenching are presented. The distance from the wall is nondimensionalized by the laminar flame thickness. The wall temperature is 600 K. For more information on the inert wall calculations as well as the low wall temperature domain, see Ref. 1.

Figure 1 compares species profiles for both boundary conditions. For Peclet numbers larger than 1.0, the influence of the boundary condition on the species mass fractions is negligible as it is for their net heat-release rates (Fig. 3). However, there are large differences adjacent to the wall. The reactive surface results in (1) much larger mass fractions of fuel and oxygen (same spatial extension but higher peak values with differences in the peak value of methane of a factor of 2) but much lower radical wall concentrations (this is the opposite situation as can be found, for example, in boundary layer or stagnation point flow situations over reactive surfaces where the near-wall region is depleted of fuel but the radical concentrations are increased) and (2) higher near-wall concentrations of carbon monoxide but smaller concentrations of carbon dioxide and water. The behavior of the propane flame is the same as that of the methane flame in terms of the major product and radical profiles. However, the surface mechanism considered does not affect the intermediate hydrocarbons resulting in a peak of their mass fractions directly at the wall as well as a near-wall concentration that is of the same order as the

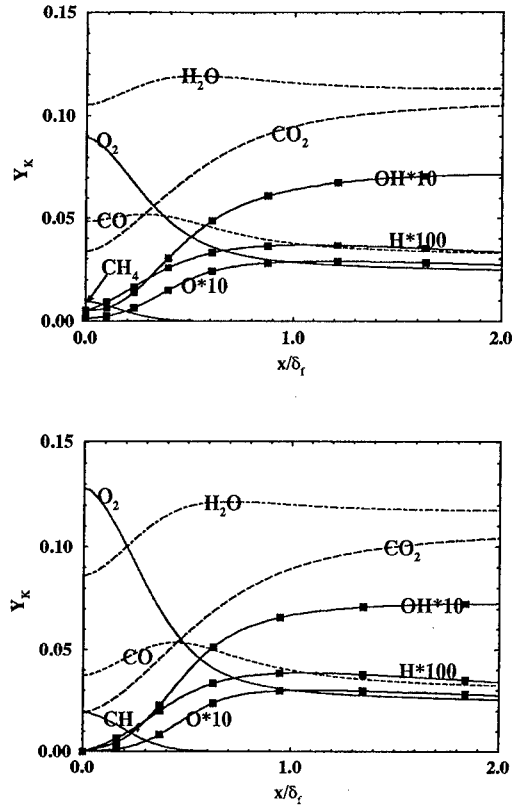

FIG. 1. Species mass fractions for a CH_4/air flame at the moment of quenching. Upper graph: inert wall [Eq. (2)]. Lower graph: reactive wall [Eq. (4)].

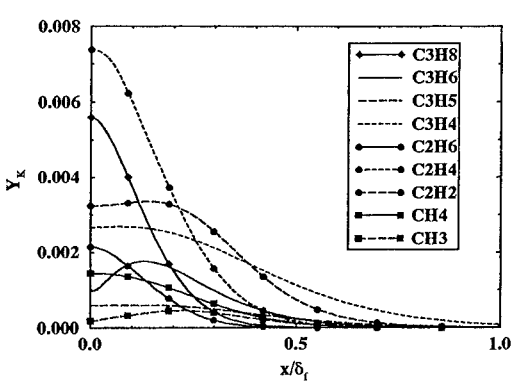

FIG. 2. Intermediate hydrocarbon mass fractions for a C_3H_8/air flame at the moment of quenching (reactive wall).

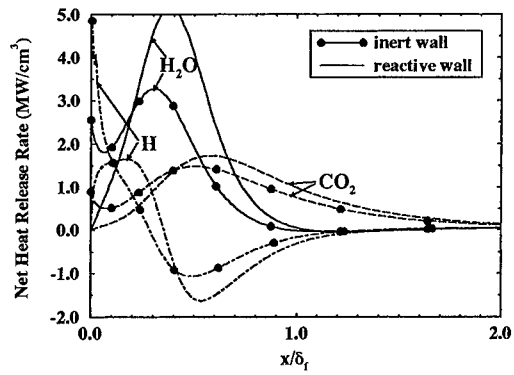

FIG. 3. Species net heat-release rates for a CH_4/air flame at the moment of quenching (comparison: inert–reactive wall).

fuel (Fig. 2). Of particular importance is the large amount of acetylene, which is known as a major soot precursor. Large concentrations of intermediate hydrocarbons with peak values at the wall were also reported by Kiehne et al. [25].

Free radicals and most intermediates are trapped between the decaying induction zone of the flame and the wall because their concentration gradients during quenching are directed toward the wall. The only remaining reaction paths are low-activation energy recombination reactions or surface adsorption reactions. If the participation of the surface in the reaction channels of the gas-phase species is excluded (either because of surface properties or because of the boundary condition in the numerical simulations), reactions proceed through the highly exothermic recombination reactions. This results in large heat-release rates adjacent to the surface (Fig. 3) that are primarily due to the water formation via the radical recombination reaction $H + OH \rightarrow H_2O$, the carbon dioxide formation via $CO + OH \rightarrow CO_2 + H$, and the recombination reaction of the methyl radical with the H radical to form methane. Those reactions are only possible because of the accumulation of especially the free and highly reactive radicals H and OH in this region. Other but less exothermic recombination reactions involve O, HO_2, and H_2O_2. If the surface (at least a Pt surface) participates in the radical reaction channels, then radical adsorption reactions dominate radical recombination reactions, leading to a negligible near-wall concentration of free radicals and much smaller heat-release rates. This also explains why the reactive surface results in lower CO_2 and higher CO concentrations adjacent to the wall. From Fig. 3 it becomes obvious that the boundary condition chosen not only influences the amount of heat released directly at the wall but also influences the shape, peaks, and distance from the wall of the heat-release

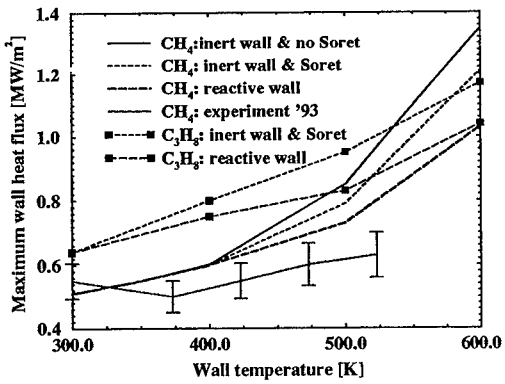

FIG. 4. Variation of the dimensional maximum wall heat flux with wall temperature for a stoichiometric methane/air and propane/air flame.

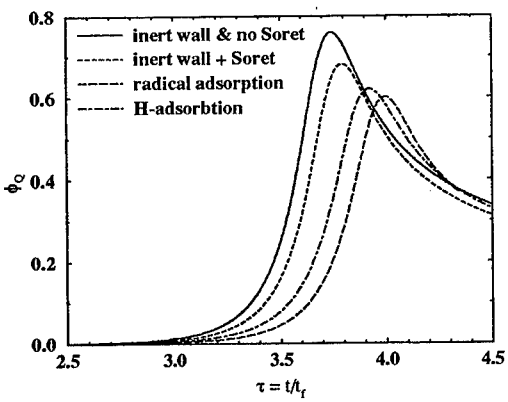

FIG. 5. Variation of the dimensionless maximum wall heat flux with wall temperature for a stoichiometric methane/air flame.

profiles. The inert wall assumption results in profiles that are closer to the wall but with smaller peak values due to the more intense burning because of the high exothermic recombination reactions. Still, although the surface chemistry reduces significantly the near-wall heat-release rates (and a Pt surface yields certainly a maximum effect in comparison to other surface materials), a quenching layer does not exist under the conditions investigated in this study. This is of particular importance for the modeling in internal combustion engines where this concept, that is, the assumption of the existence of a thin layer adjacent to the wall where no major chemical reaction and heat release takes place, is commonly used. Our results reveal that in contrast to the low wall-temperature region [1], such an assumption is never valid for higher wall temperatures. All heat-release rates peak within a distance close to the wall that is less than half a flame thickness. Peak values are decreased only between 30 and 40% with respect to free flame values.

Wall Heat Flux Variations

Figure 4 shows the variation of the dimensional maximum wall heat flux with wall temperature and its dependency on gas-phase modeling assumptions and surface conditions. The methane-flame simulations indicate the existence of two temperature domains: a low- (300–400 K) and a high-temperature domain (>400 K). In the low-temperature region, all numerical results overlap and are within the experimental uncertainty of the experiment (which used a Pt thin-film gauge [4]). This demonstrates that surface and cross-diffusional effects play only a minor role and thus, the species boundary condition can be modeled by a zero-concentration gradient condition. On the contrary, there is a large spread in the curves in the high wall-temperature region. The simulations neglecting cross-diffusion and surface chemistry predict the highest value of the peak wall heat flux and show the largest discrepancies with the experimental values. Accounting for cross-diffusional effects but keeping the inert wall condition reduces the wall heat flux over the whole high wall-temperature domain but still yields values that are much outside the experimental uncertainty. The reduction in the maximum wall heat flux at the high end of the wall temperatures investigated (600 K) by taking cross-diffusion into account is 12%. The largest decrease in the numerical values is reached by considering surface chemistry. This contribution produces a larger decrease the higher the wall temperature, and this relationship results in an excellent agreement between the simulations and the experiment. The reduction in the maximum wall heat flux at 600 K is 18% in comparison to the calculations accounting for cross-diffusion, and 31% in comparison to the simulations without surface chemistry and cross-diffusion. The behavior of the propane-flame–wall interaction is, in principle, the same as for the methane flame with values for the maximum wall heat flux of the same order. However, the influence of surface chemistry is already felt earlier. This pattern is not surprising considering the fact that a propane flame ignites at much lower temperatures than a methane flame over a Pt surface.

The evolution of the maximum nondimensional wall heat flux during the quenching of a methane flame is presented in Fig. 5. The wall heat flux for all modeling conditions increases rapidly up to a maximum value and decays slowly after quenching. Despite this similarity, there are some important differences. The neglect of cross-diffusional effects and surface reactions yields higher peak wall heat fluxes and heat losses through the wall. This effect is clearly visible before quenching occurs and even afterward. In addition, it leads to a faster burning during the

interaction. Surface chemistry and cross-diffusion delay quenching. This effect was already observed in the heat-release profiles. Φ_Q of the CH_4 flame is almost constant (0.54) in the range of wall temperatures between 300 and 500 K and increases up to 0.60 at 600 K. Φ_Q of the C_3H_8 flame is somewhat lower with a value around 0.52 in the low wall-temperature region, which decreases slightly to 0.49 at 600 K.

Transport Effects

Taking cross-diffusional effects (Soret and Dufour) as well as surface chemistry into account complicates strongly gas-phase modeling and the treatment of the wall boundary conditions. Especially with regard to engine codes, it is thus desirable to reduce the complexity of the physical problem to a level that is easier to handle. It turns out that the dominant effect is the Soret effect, even in the presence of a reactive wall. This effect accounts for a species flux that is inversely proportional to the molecular weight of the species and directly proportional to the temperature gradient in the flow field and is directed toward the hot gases. Because the maximum temperature gradient in the flow field is a factor of about 4 higher than in a free flame [2] during quenching, especially H radicals are removed from the near-wall region. This results in lower heat-release rates of the exothermic radical recombination reactions adjacent to the wall even when surface chemistry is accounted for and, subsequently, in a lower wall heat flux. The Dufour effect is also important for lighter-weight species. In contrast to the Soret effect, it accounts for an energy flux that is due to concentration gradients. Because those concentration gradients are decreased, its influence is even smaller during quenching than it is for a freely propagating flame. The Stefan velocity was found to have very small values. Thus, in a next step, we imposed numerically a zero Stefan velocity (but kept the surface reactions), i.e., $U_W = 0$. This did neither affect the wall heat flux nor the flame structure during quenching. We conclude that the influence of the Stefan velocity on flame-wall interaction is negligible.

Surface Chemistry

Figure 6 illustrates the time-dependent surface response to the quenching of the methane flame at a wall temperature of 600 K as predicted by our surface mechanism Table 1. Prior to flame-wall interaction, the surface is dominated by adsorbed atomic oxygen [$\Theta(O) = 0.99$] and consists of only a few free surface sites [$\Theta(P) = 10^{-2}$]. The high oxygen coverage results from the very rapid O_2 dissociation reaction. Due to its relatively low adsorption energy, the hydrogen coverage is very low [$\Theta(H) = 10^{-10}$]. So is the hydroxyl coverage [$\Theta(OH) = 10^{-4}$].[1] Surface reactions proceed very slowly, and the stationary state is controlled by the diffusion of gas-phase species to the surface. The surface starts to feel the approaching flame at about $\tau_Q - 0.2$ via an increase in the H adsorption rates. H radicals diffuse farther in front of the flame due to their low weight. During the interaction, the hydroxyl and the atomic hydrogen coverage increase continuously and reach their maximum value shortly after τ_Q [$\Theta(OH) = 10^{-2}$, $\Theta(H) = 10^{-7}$]. The number of free surface sites decreases slightly up to the moment of quenching and increases continuously afterward. Oxygen coverage is seen to decrease throughout the interaction. During quenching, the interaction becomes controlled by radical adsorption kinetics. H radicals are quickly adsorbed on the surface and react readily with adsorbed oxygen atoms to form adsorbed hydroxyl radicals. The maximum of the O(*s*) consumption and the maximum of the OH(*s*) production both occur at τ_Q, whereas the maxima of the adsorption reactions occur shortly afterward. During the interaction, both water formation reactions compete effectively for OH(*s*) with the hydroxyl recombination reaction dominating at the moment of quenching. The maximum water formation occurs at $\tau_Q + 0.2$. At this time, the gas phase is almost completely depleted of radicals, and surface production rates are decaying. The surface thus delays the exothermic water formation via the radical recombination of H and OH to times larger than τ_Q. This indicates that a simplified global recombination step would probably overpredict the wall heat flux since such a model predicts the maximum in the water production at τ_Q and not afterward.

If a Langmuir adsorption concept is assumed for all adsorption reactions, the surface mechanism is not capable any longer to remove sufficiently free radicals from the gas phase. This results in large radical recombination reactions (H, OH) adjacent to the wall and a wall heat flux, Φ_Q, of 0.64 (instead of 0.60). The breakdown of this concept is not surprising since it is, strictly speaking, only valid in the low coverage domain. In the case of high surface coverage, adsorption reactions for hydrogen (as well as CO) on Pt surfaces are known to be coverage independent [12]. Their adsorption proceeds through a mobile precursor rather than an inmobile surface state. Due to the high mobility of H and OH, it

[1]The associative desorption of H_2 and O_2 was originally included in the surface mechanism. Because it does not influence our obtained results but requires a much smaller time step in the calculations, they were omitted in Table 1. The same is true for H_2O adsorption. CO adsorption was not considered since its rates are very small at 600 K and its further dissociation becomes only relevant for temperatures larger than 800 K.

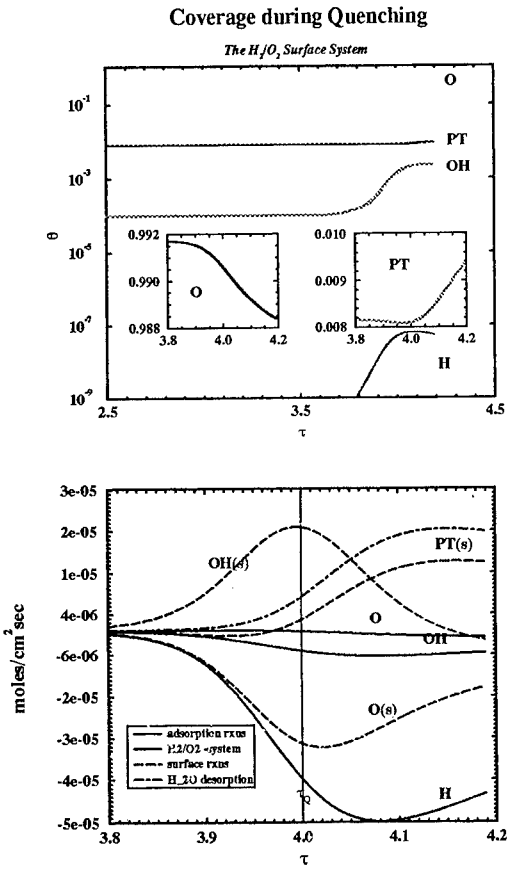

FIG. 6. Upper graph: surface coverage for the surface radical mechanism. Lower graph: surface reaction rates.

seems reasonable to assume that these radicals are adsorbed as well via a precursor state in which they can diffuse rapidly over large distances to find a free site. However, this is not true for O, HO_2, and H_2O_2. Although the oxygen atom is quite mobile, it faces an increasing energy barrier for adsorption due to repulsive forces by already adsorbed O atoms. HO_2 and H_2O_2 are not only much less mobile but they require as well the availability of two free neighboring adsorption sites, which is not likely for high surface coverages.

Finally, we considered a reduction of the surface mechanism from Table 1: First, the hydrogen/oxygen adsorption reactions were neglected. This affected neither the wall heat flux nor gas-phase species distributions during the interaction but shifted the surface from high to low surface coverage [Θ(Pt) = 0.51]. Second, additional neglect of the adsorption of HO_2 and H_2O_2 did not further change the surface coverage and left as well the wall heat flux unaffected. However, their concentrations and net production rates adjacent to the wall become much higher than in the free flame. This suggests that for the conditions under which the simulations were performed, their influence on the quenching process is negligible, but a possible influence at higher pressures can not be excluded. Third, considering only H adsorption reduces significantly the wall heat flux in comparison to the inert wall calculations but results in a higher value as well as in a phase error in comparison with the complete surface mechanism (Fig. 6).

Conclusions

We presented the results of numerical simulations in combination with detailed reaction mechanisms for the head-on quenching of stoichometric methane- and propane-air flames at atmospheric pressure for 300 K $< T_W <$ 600 K with a focus on the high–wall-temperature domain. It is found that in this domain, transport and surface chemistry effects have a considerable influence on the near-wall flame structure and, in particular, decrease the peak wall heat fluxes. Hence, wall heat flux measurements using thin-film gauges have to be evaluated extremely carefully when the film material does not match the normal wall material, as is typically the case. Numerical simulations have to describe correctly the process of diffusion, adsorption, and surface recombination of especially the free radicals H and OH. Since the interaction takes place in the high–surface-coverage region, the Langmuir adsorption concept breaks down. A precursor state model for at least H and OH has to be considered. The situation might be more complicated for higher hydrocarbons as indicated by the peaks of the intermediate hydrocarbons adjacent to the wall for the propane-flame wall ineraction.

Acknowledgment

Patrick Popp is grateful to the Commission of the European Communities (Science Foundation) who, by granting him an individual fellowship, made partly possible this work.

REFERENCES

1. Popp, P. and Baum, M., *Combust. Flame,* to appear, 1996.
2. Popp, P. and Baum, M., SAE F&L Meeting 1995; Toronto, 1995.
3. Connelly, L., Greif, R., Sawyer, R. F., and Lee, D., *Fall Meeting,* The Combustion Institute/Western States Section, Berkeley, CA, 1992, Vol. WSCI 92-109.
4. Connelly, L., Ogasawara, T., Lee, D., Greif, R., and Sawyer, R. F., *Fall Meeting,* The Combustion Institute/Western States Section, Stanford, CA, 1993, Vol. WSCI 93-077.

5. Ezekoye, O. A., Greif, R., and Lee, D., *Twenty-Fourth Symposium (International) on Combustion,* The Combustion Institute, Pittsburgh, 1992, p. 1465.
6. Kee, R. J., Warnatz, J., and Miller, J. A., Sandia National Laboratories (SAND83-8209), 1983.
7. Kee, R. J., Rupley, F. M., and Miller, J. A., Sandia National Laboratories (SAND89-8009B), 1989.
8. Popp, P., Hilka, M., Baum, M., and Poinsot, T., *Using Direct Numerical Simulation to Study Turbulent Combustion,* Centre de Recherche sur la Combustion Turbulente, 1995, pp. 67–95.
9. Kee, R. J., Rupley, F. M., and Coltrin, M., Surface chemkin 4.0: A fortran package for analyzing heterogeneous chemical kinetics at a solid-surface–gas-phase interface. Technical Report SAND90-8003C, UC-706, Sandia National Laboratories, August, 1994.
10. Warnatz, J., *Ber. Bunsenges. Phys. Chem.* 87:1008–1022 (1983).
11. Peters, N. and Rogg, B., in *Lecture Notes in Physics* (S. Verlag, ed.), Springer-Verlag, Heidelberg, 1993.
12. Fridell, E., Rosen, A., and Kasemo, B., *Langmuir* 10:699–708 (1994).
13. Hellsing, B., Kasemo, B., and Zhdanov, V., *J. Catalysis* 132:210–228 (1991).
14. Ljungstrom, S., Kasemo, B., Rosen, A., Wahnstrom, T., and Fridell, E., *Surf. Sci.* 1(216):63–92 (1989).
15. Warnatz, J., Allendorf, M., Kee, R., and Coltrin, M., *Combust. Flame* 96 (1994).
16. Motz, H. and Wise, H., *J. Chem. Phys.* 32:1893–1894 (1960).
17. Kee, R. J., Grcar, J. F., Smooke, M., and Miller, J. A., PREMIX: A Fortran program for modeling steady laminar one-dimensional flames. Technical Report SAND85-8240, Sandia National Laboratories, 1985.
18. Huang, W. M., Vosen, S. R., and Greif, R., *Twenty-First Symposium (International) on Combustion,* The Combustion Institute, Pittsburgh, 1986, pp. 1853–1860.
19. Yang, J. and Martin, J., *SAE* 900690:1551–1561 (1990).
20. Jennings, M., Int. Congress and Exposition, SAE Paper 920589, Detroit, 1992.
21. Jennings, M. J. and Morel, T., SAE (910459), 1990.
22. Lu, J. H., Ezekoye, O., Greif, R., and Sawyer, F., *Twenty-Third Symposium (International) on Combustion,* The Combustion Institute, Pittsburgh, 1990, pp. 441–446.
23. Poinsot, T., Haworth, D., and Bruneaux, G., *Combust. Flame* 95(1/2):118–133 (1993).
24. Blint, R. J., *Combust. Sci. Technol.* 49:79–92 (1986).
25. Kiehne, T. M., Matthews, R. D., and Wilson, D. E., *Twenty-First Symposium (International) on Combustion,* The Combustion Institute, Pittsburgh, 1986, pp. 1583–1589.

COMMENTS

Dr. R. Maly, Daimler-Benz AG, Germany. It appears to me that the modeling is systematically overpredicting the wall heat flux if compared to the experimental data for temperatures above 500 K, do you have an explanation for possible reasons?

Author's Reply. Please, note that (1) the numerical results are in general higher than the experimental results due to the absence of heat losses. (2) Since there are no experimental data for $T_w > 523$ K no conclusion can be drawn regarding the tendency of the experimental wall heat flux for higher wall temperatures. In addition, since the influence of surface chemistry was unknown to the experimentalist the experimental uncertainty at high T_w should be actually higher than the quoted 11%.

•

Ofodike A. Ezekoye, University of Texas–Austin, USA. Our most recent computational work on flame quenching shows that in the low wall temperature range ($T_w <$ 373 K, P = 1 ATM) water film condensation has a notable effect (i.e., approximately 10%) on the magnitude of the wall heat flux. For complex chemistry simulations, I anticipate that the depletion of vapor H_2O will also affect the overall quenching dynamics. Do you include water phase change in your present computations and what effect do you think it would have on your predicted quenching results?

Author's Reply. Water phase changes were included in the complex chemistry calculations.

•

C. Morley, Shell Research and Technology, UK. Your mechanism does not appear to include CH_3O_2 which could become an important radical at the low temperatures (<800 K) near the wall. The rate of radical removal in this region by radical-radical reactions could be affected by its inclusion.

Author's Reply. We looked at the effects of various radicals which become important at low temperatures. Those included not only CH_3O_2 but also HO_2 or H_2O_2. Although their reaction rates are much larger adjacent to the wall during quenching than they are for a free flame, they are not the dominant radicals.

For a more detailed discussion of how some species influence the quenching process one may wish to consult: P. Popp and M. Baum, "An Analysis of Heat Transfer, Reaction, and Pollutant Formation Mechanisms during Flame Wall Interaction," *Combust. Flame,* 1996.

Twenty-Sixth Symposium (International) on Combustion/The Combustion Institute, 1996/pp. 2701–2708

1-D SIMULATION OF A SPARK DISCHARGE IN AIR

M. SCHÄFER, R. SCHMIDT AND J. KÖHLER
Institut für Physikalische Elektronik
Universität Stuttgart
Pfaffenwaldring 47, D-70569 Stuttgart, Germany

The development and radial expansion of a spark is simulated using a finite element method. The calculations start from a weakly conducting channel as left by the passage of a streamer. Plasma heating during breakdown is provided by an L-C combination resembling the equivalent circuit of the spark plug. Once the effective current provided by this circuit drops below a certain level, a current source with a linearly decreasing current with time was used to model the subsequent arc or glow phases. The simulations cover a time range from nanoseconds up to 10 μs, when the axial symmetry of the channel is broken by 2-D effects such as reverse gas flow along the electrodes.

It is shown that equivalent plasma kernels can be produced by assuming initial conditions where the breakdown energy is deposited within a very small cylindrical volume of ambient mass density. This also causes the emission of a strong shock which is indispensable for the achievement of the same shape of the kernel.

Calculations for ambient pressure and temperature as well as for 5 bar/550 K were conducted. The influence of the breakdown energy, the radiation, and the current delivered by the current source on the fully evolved spark channel is discussed. It is suggested how to use the calculated thermodynamic properties of the plasma kernel as initial conditions for flame-kernel calculations using a chemical reaction scheme.

The fluid-mechanical Euler equations, including thermal conductivity, radiation losses, and Joule heating, are implemented using a Taylor-Galerkin formalism. The electric field is calculated using a time-independent potential formulation. This is implemented in the frame of the finite element program Flux Expert (Flux Expert is a registered trademark of DT2i).

Introduction

The generation of technical sparks for the ignition of combustible mixtures in internal combustion engines is still a subject of current research and development. The aim is to develop systems of high reliability in a wide range of engine conditions with respect to lean combustion, enhanced electrical efficiency, and operating time of the spark plug. As the requirements for each of these points are mutually exclusive in some respect, a high level of understanding of the governing physical mechanisms is necessary for system optimization.

Extensive experimental work was done to reveal basic relationships between the energy input during the traditionally defined spark phases (breakdown, arc, and glow phase), the efficiency of energy transfer to the plasma, and their influence on flame-kernel development. A summary of this work can be found in Refs. 1 and 2. The major experimental tool was a space-resolved analysis of ion spectra yielding electron densities and electron and gas temperatures. From these data, radial mass density and pressure profiles were inferred. While this method works well for temperatures $T > 15{,}000$ K [3], lower temperatures $T < 10{,}000$ K can be detected using molecular spectra with much lower radiation densities. These spectra cannot be evaluated in the vicinity of intense ion radiation, and therefore, radial data of the plasma channel including the formation of a shock front at its perimeter are not available. The radius of the plasma channel and the position of the shock front were detected by Schlieren photography and interferometric techniques. The pressure within the plasma region was then estimated using the Rankine-Hugoniot relations for shock waves [3] and, more accurately, relations derived from the self-similar propagation of strong shocks [4,5].

A diagnostic hole exists between 100 ns and 1–5 μs where intermediate temperatures are predominant. This time range, however, is often used for setting initial conditions for calculations including energy release by exothermal chemical reactions leading to flame-kernel development and propagation [6–9].

The calculations presented in this paper provide a complete overview of the temporal and spatial evolution of a plasma channel created by a spark discharge and successive plasma heating (arc or glow phase). The time range covered starts after streamers have created a weakly conducting area prior to gas breakdown. The one-dimensional description of

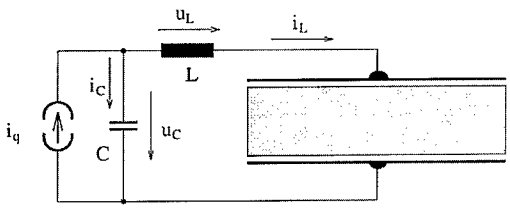

FIG. 1. Equivalent circuit of a spark plug. The stray capacitance and inductance of the spark plug are lumped into C and L. The current source provides plasma heating during the quasi-stationary discharge phase. The shaded area represents the plasma region.

the spark is valid up to 10–15 μs when heat conduction into the electrodes becomes important and the recirculation phase [10] starts to conduct cold gas along the electrodes into the plasma. At the same time, exothermal energy release by chemical reactions contributes significantly to the total energy dissipated within the plasma region, and the observed plasma radii in air and combustible mixtures begin to diverge [11].

Based on these calculations, four fluid-dynamical phases for the formation of a plasma channel will be defined. These phases characterize the evolution of the plasma column during the creation of a spark and its transition into a quasi-stationary discharge that is characteristic for technical ignition sparks.

A simplified method for creating initial conditions is presented. It allows the omission of an external circuitry for driving the gas breakdown. However, the emission of a strong shock from the initial channel is indispensable for the creation of an equivalent flow field and an equivalent distribution of the state variables.

Models

Streamer and Breakdown

After a threshold of local electrical field strength is reached, charge carrier multiplication by the Townsend mechanism and the subsequent formation of streamer heads take place. The result of the passage of a streamer is a weakly conducting channel that sets initial conditions for the simulation of the spark. The simulation of the streamer itself is computationally expensive because kinetic models [12–14] have to be used. The transferred charge and energy during this first 3–5 ns of a spark is negligible compared to the total charge and energy stored in the electrode capacitance. The maximum electron density is taken from experiments [15] and simulations [12] to be $n_e = 2 \times 10^{20}$ m^{-3}, and the radial distribution is approximated by a Gaussian profile with $\sigma = 20\,\mu$m. Together with an electron mobility $b = 0.06$ m^2/Vs, the radial electric conductivity is $\kappa = bn_eq$.

Joule heating is assumed to be the dominant mode of energy transfer between electrons and gas. This assumption is valid if the electron temperature corresponds to the gas temperature. Because of the high pressure and the high degree of ionization within the channel, thermalization occurs within the first 10 ns after spark onset [3].

External Circuit

The electric energy deposited into the gas during breakdown is originally stored in the stray capacitance of the electrodes that is part of the lumped equivalent circuit of a spark plug (Fig. 1). The channel resistance drops to 1–10 Ω/mm during breakdown. Later, plasma heating is driven by the induction coil with a typical secondary main inductance L_s of 40 H. The coil drives a current i_L which depends only on its stored magnetic energy $i_L = (2E_I/L_s)^{1/2}$. The current during the quasi-stationary discharge can therefore be approximated by a time-dependent current source with a linearly decreasing current. Cable and coil capacities that could provide a current contribution of an intermediate time scale are usually minimized or avoided by mounting the coil directly on the spark connector, and are therefore not considered.

Fluid Mechanics

The cylinder symmetric flow during breakdown is described by the inviscid fluid-mechanical Euler equations. Heat conductivity in the radial direction is also implemented and was seen to have an effect on the axial temperature after about 1 μs. Heat source terms are provided by Joule heating depending on the local electrical field strength and conductivity $q_j = \kappa|\boldsymbol{E}|^2$. Radiation loss q_{rad} from the optically thin channel was implemented using Kramer's semiclassical approximation [16] for continuum-radiated power by free-free and free-bound transitions.

Thermodynamic and Transport Data

In the temperature range below 25,000 K, polynomial fits of thermodynamic properties by Weilmuenster [17] and tabulated transport data (thermal and electric conductivity) by Yos [16] were used.

To cover an extended temperature range $\hat{T} \approx$ 50,000 K and pressure range $\hat{p} \approx 300$ bar, our calculations were performed under the assumption of a mixture of perfect gases (N_2, O_2, NO, e^-, N, O, N^+, O^+, NO^+, N^{2+}, O^{2+}, N^{3+}, O^{3+}) in thermodynamic equilibrium. The thermodynamic data is derived from the knowledge of the plasma composition

and the thermodynamic properties of its constituents [18].

The calculation of the electric conductivity is based on Spitzer's theory of fully ionized gases [19] using the above determined plasma composition. The results were fitted for smooth continuation to the low-temperature values. The coefficient of thermal conductivity is calculated from the coefficient of electrical conductivity using the generalized Wiedemann-Franz law [20].

Model Equations

Fluid Mechanics

For the description of a traveling pressure wave, the use of the inviscid Euler equations is sufficient. However, the hot plasma channel that is left behind after the emission of the shock wave requires the inclusion of a heat diffusion term due to the steep temperature gradients encountered.

The general time-dependent differential equation [21] at time n is

$$\left[\frac{\partial \mathbf{U}}{\partial t}\right]^n = -\,[\mathrm{div}\,\underline{\mathbf{F}} + \mathrm{div}\,\underline{\mathbf{G}} + \boldsymbol{Q}]^n \qquad (1)$$

where $\boldsymbol{U} = \{\rho, m, \iota_t\}^t$. The vector of the main variable is constituted of the conservation variables mass density, momentum, and total internal energy density. $\boldsymbol{F} = \{\rho u, mu, (\iota_t + p)u\}^t$ stands for convective, and $\boldsymbol{G} = \{0, 0, -\lambda\,\mathbf{grad}\,T\}^t$ for diffusive flux quantities, u being the velocity and λ the thermal conductivity. Source terms are designated $\boldsymbol{Q} = \{0, \mathbf{grad}\,p, -q_j + q_{\mathrm{rad}}\}^t$. The expansion of $\boldsymbol{U}$ by a Taylor series in time, retaining terms of second order gives

$$\boldsymbol{U}^{n+1} = \boldsymbol{U}^n + \Delta t \left.\frac{\partial \boldsymbol{U}}{\partial t}\right|^n + \frac{\Delta t^2}{2}\left.\frac{\partial^2 \boldsymbol{U}}{\partial t^2}\right|^{n+\alpha} + o(\Delta t^3) \qquad (2)$$

where $\alpha \in [0,1]$. As a formal approximation in time, we have the freedom of splitting the second-order time derivative into two parts and then treating one part implicit in time and the remaining part explicitly.

Having already discretized in time, only partial derivatives in respect to space are permitted further on. Therefore, the terms $\partial \boldsymbol{U}/\partial t$ are recursively replaced using equation 1. Second-order accuracy is needed only for convective terms $\underline{\boldsymbol{F}}$; therefore, $\underline{\boldsymbol{G}}$ is omitted from second-order terms and evaluated at $n + \alpha$ using the same arguments as above. The final equation is

$$\boldsymbol{U}^{n+1} = \boldsymbol{U}^n - \Delta t\{[\mathrm{div}\,\underline{\mathbf{F}} + \boldsymbol{Q}]^n + [\mathrm{div}\,\underline{\mathbf{G}}]^{n+\alpha}\} + (\Delta t^2/2)\,\{\mathrm{div}\,[(\mathrm{div}\,\underline{\mathbf{F}} + \underline{\mathbf{Q}})\,\underline{\mathbf{A}}] + \underline{\mathbf{S}}(\mathrm{div}\,\underline{\mathbf{F}} + \boldsymbol{Q})\}^{n+\alpha} \qquad (3)$$

with

$$\underline{\mathbf{A}} = \partial\underline{\mathbf{F}}/\partial \boldsymbol{U} \text{ and } \underline{\mathbf{S}} = \partial \boldsymbol{Q}/\partial \boldsymbol{U}$$

Artificial Diffusion

Artificial diffusion is added for each dependent variable to suppress spurious oscillations. The diffusion must only have an effect in the vicinity of the shock front and vanishes in smooth regions [21]. The artificial diffusion is a balancing diffusion as it balances the negative diffusion inherent to the Galerkin treatment [22].

The driving force of dominating convective transport is the pressure gradient. Because of this, we implemented the method of MacCormack and Baldwin [23] which uses the second derivative of the pressure variable. The artificial diffusivity is

$$\tilde{k} = C_a h^3 \left|\frac{\partial^2 p}{\partial x^2}\right| \qquad (4)$$

where h is the typical element dimension in the direction of the derivative and C_a a coefficient of appropriate dimensionality. It is highly localized near the shockfront.

Electric Field

Assuming a symmetrical arrangement of the electrode, the considered fluid region is in the plane of symmetry. The only nonzero components of the electric field vector $\boldsymbol{E}$ are in the axial direction. The fluid region can then be considered to be placed between two equipotential planes.

This simplified method requires the knowledge of the potential difference $\Delta\varphi$ between the electrodes. By integrating $\kappa(r)$ along the radius, the resistance R_{pl} of the plasma is known. $\Delta\varphi$ is obtained from simulating the equivalent circuit (Fig. 1) simultaneously, using the calculated R_{pl} from the last solution of the fluid-mechanical problem. For later times, when the current source plays the major role, the LC circuit is omitted because its time constant is now short compared to the permissible time steps of the fluid-mechanical problem. The current is now driven by setting up a control loop with PI characteristics.

The voltage drop across the anode and cathode sheaths is of minor interest because during breakdown the voltage drop is small compared to the breakdown voltage. During the quasi-stationary discharge, the fall region can be considered as a voltage source (with zero resistance) inserted between the equipotential planes and the current source. It consumes electrical power that can be thought of as being directly transferred to the electrodes [24] and does not influence the plasma column.

Results

The most important parameters in these calculations are the energy deposited during breakdown

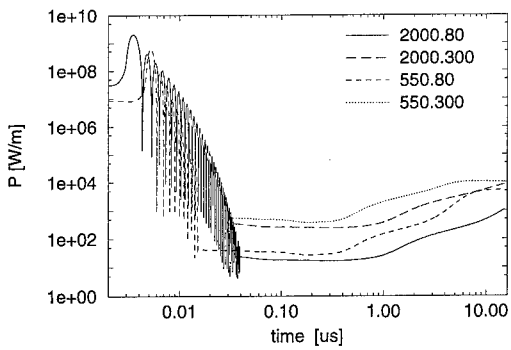

FIG. 2. Dissipated electric power in the spark channel for different breakdown energies and heating currents.

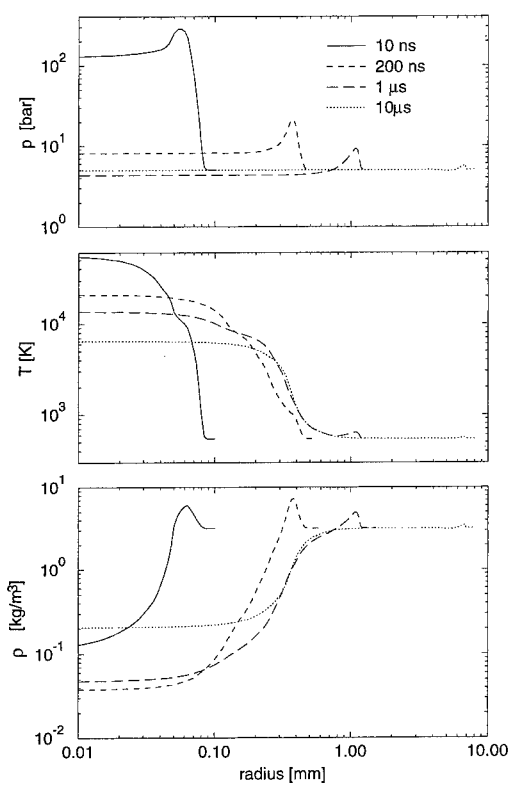

FIG. 3. Thermodynamic properties, ρ, p, and T for a breakdown energy of 2 J/m at 5 bar/550 K. The points in time correspond to the beginning of self-similar propagation phase II (10 ns), the beginning of the emission of the shock wave (200 ns), the maximum under pressure (1 μs) both phase III and to phase IV with an independent traveling pressure wave (10 μs). For the definition of the phases, refer to Fig. 7.

and the subsequent current for plasma heating. Two ambient conditions were considered: 1 bar/273 K and 5 bar/550 K. We use the following convention to denote the different numerical experiments: the first number is the energy deposited during breakdown in millijoules per meter, the second is the maximum current of the current source in milliamps. (Energy and power are given in units per length, taking into account the cylinder symmetry of the plasma.) The breakdown energies 275 mJ/m and 550 mJ/m are deposited at 1 bar using a capacitance of 5 pF and 10 pF, respectively, at 10,490 V breakdown voltage and a spark gap of 1 mm. Energy of 1 J/m and 2 J/m was deposited at 5 bar using a breakdown voltage of 20,000 V with the same 5 pF and 10 pF, respectively. The current source used in these simulations was 80 mA, ending at 1 ms to model a transistorized ignition system (TCI) with its quasi-stationary glow phase, and 300 mA decreasing within 250 μs to zero which provides the extended arc phase of a capacitor discharge ignition system (CDI). Additionally, the letter K might be appended indicating that the energy was not deposited during a breakdown process, but that as initial condition of the calculations, an isothermal channel of ambient mass density existed where the breakdown energy was deposited homogeneously.

In Fig. 2, the dissipated electrical power during the plasma heating is shown. Fig. 3 shows the temporal evolution of the important fluid mechanical variables, ρ, p, and T. The points in time were chosen to demonstrate the transition between different spark phases, as will be defined in the discussion section.

In the context of combustion, the behavior of the plasma channel itself is important. We defined the plasma channel to be a cylindrical volume limited by an isothermal surface. The isotherm was chosen to be 1,000 K. This value is somewhat arbitrary, but it is supposed that cracking processes of hydrocarbon fuels in combustible mixtures will start at that temperature. Mass trapped within the hot cylinder will contribute its stored chemical potential energy to the formation of a flame kernel at later times. It is pointed out that a change of the isotherm does not principally change the behavior of the channel.

The radial expansion of the plasma channel is shown in Fig. 4. The straight line in this log/log plot gives the slope of the time law for self similar expansion of a cylindrical shock: $r \sim t^{1/2}$. The expansion rates for all considered breakdown energies finally deviate from this slope when a pressure wave begins to separate from the channel. While the radius of the plasma channel stays almost constant, the mass of the channel decreases drastically (Fig. 5).

An important point in discussions was always the efficiency of different phases of a spark discharge [1]. For this purpose, the increase in thermal energy of the mass contained within the channel, its kinetic

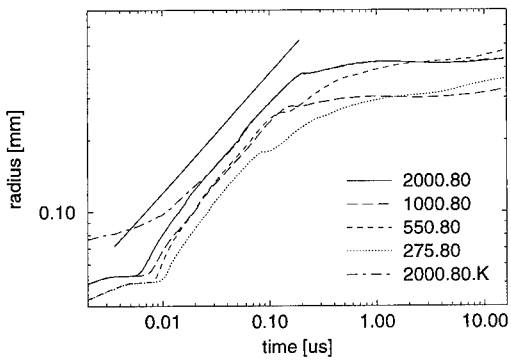

FIG. 4. Time-dependent radii of the spark channel. The channels of the weaker discharges grow faster after the beginning separation of the shock front because of a weaker reverse flow. The slope of the straight line is parallel to the expansion law for self-similar propagation.

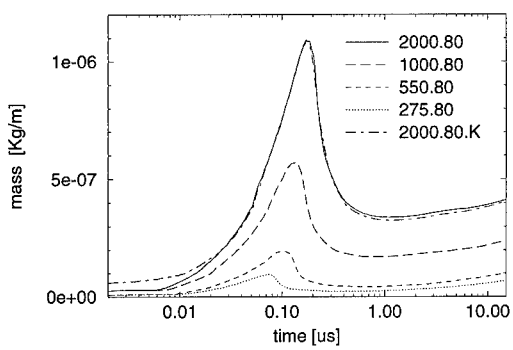

FIG. 5. Temporal development of the mass confined within the spark channel.

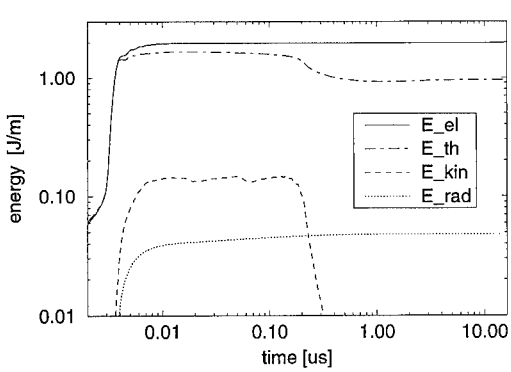

FIG. 6. Partition of the electrical energy input E_{el} into thermal energy E_{th} and kinetic energy E_{kin} within a plasma channel for a breakdown energy of 2 J/m at 5 bar/550 K. The total energy radiated is E_{rad}.

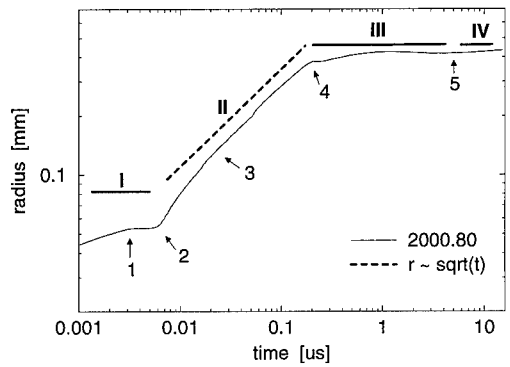

FIG. 7. Phases of spark channel development demonstrated for the radial expansion of an isothermal surface of 1000 K. The roman numbers indicate the phases: I, breakdown; II, expansion; III, shock emission; and IV, diffusion. The arabic numbers indicate changes of the dominant flow characteristics and are referred to in the text.

energy, and the total radiated energy are presented in Fig. 6. The kinetic energy disappears from within the channel once the shock wave has separated. It is now carried away by a weak shock transforming into an acoustic wave. The increase in entropy within this kind of pressure waves is small [25] and, therefore, the kinetic energy is carried far away into the surrounding medium.

Discussion

Spark Phases

With the knowledge of all fluid-mechanical variables in space and time, it is possible to define four distinct phases of spark channel formation and evolution. These phases are determined by the type of flow and are relevant for the deposition of thermal energy into the plasma. The change of flow type is best demonstrated by a log/log plot of the radial expansion of the plasma channel as already defined.

During phase I, the breakdown of the gas takes place. Up to point 1 in Fig. 7, heating occurs within the wide conductive channel produced by the hot electrons of the streamer. With rising gas temperatures, thermal electrons are produced that increase the conductivity. Because of the Gaussian profile of the initial conductivity distribution, this will occur first on the axis. The dissipated power P_{el} is proportional to the conductivity κ for $E(r)$ = const. Therefore, the plasma core is heated faster than the outer regions; the current contracts on the axis. The radial expansion of the isotherm 1000 K is stagnating while peak temperatures in excess of 50,000 K and pressures higher than 1000 bar occur. During this stage between points 1 and 2, which lasts 3–4 ns, about

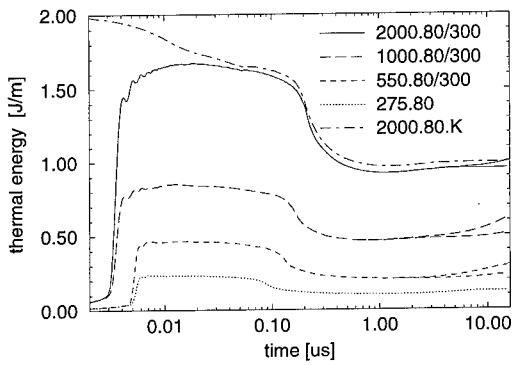

FIG. 8. Temporal development of the thermal energy contained within the plasma channel. The upper part of the split curves starting at 5 μs belong to the 300-mA current heating (instead of 80 mA).

95% of the breakdown energy is deposited within the channel.

During expansion phase II, a shock front is created and, starting after 10–15 ns at point 3, self-similar shock propagation is observed. In the case of cylinder symmetry, theory [4] predicts an increase in radius $r \sim t^{1/2}$. This law of motion is valid for strong shocks, that is, the ambient pressure is negligible in the Rankine-Hugoniot relations. The channel resistivity reaches a minimum that is lower at higher breakdown energies. The resistivity reached during this phase will influence the heating rate in conjunction with the current source until late into phase IV (Fig. 2).

With the departure from self-similar propagation, the shock front separates from the channel (point 4). During phase III, an independently travelling pressure wave is formed. About 2/3 of the total mass (Fig. 5) and almost one-half of the channel's thermal energy (Fig. 8) is carried away by the wave. In its wake, the axial pressure decreases to about 15% below ambient. At 1 μs, a reverse flow starts that compensates the axial underpressure. Convective transport still dominates heat diffusion, so that the expansion speed of channel radius stagnates or is even reversed.

Phase IV is diffusion dominated. The pressure within the channel has reached ambient pressure again. The temperature profile flattens out due to thermal conduction. Heat is generated in the central filament with a radius of about 150 μm. This phase starts at 4–5 μs.

Influence of Initial Conditions

The simulation of the breakdown phase is computationally expensive because small time steps ($\Delta t \approx 2 \times 10^{-12}$s) are required. Alternative initial conditions were set by a homogeneous energy distribution within a finite radius and, importantly, of ambient mass density. The radius was chosen to be the luminous radius at 20 ns, when most of the breakdown energy is already deposited. The luminous radius is about half the shock radius observed at that time. Typical radii are 40–60 μm. If the radius is set too large, the shock front will not propagate in a self-similar mode. The depletion wave that is reflected at the axis will not be able to catch up with the shock front, and secondary fronts are observed. While the total energy content of the channels (Fig. 8) and the total masses (Fig. 5) are equivalent after 30 ns, the axial pressures coincide after 200 ns, and the temperature profiles become comparable after the final part of phase III.

Influence of Radiation

Energy loss due to radiation is generally very small: 0.4–.8% of the breakdown energy is lost for the 1 bar calculations, 1.2–2.4% for the 5 bar calculations with higher breakdown energies. In general, higher breakdown energies will cause higher radiation losses. Radiation is roughly proportional to p^2 for temperatures higher than 25,000 K.

Efficiency

The efficiency η of the energy deposition into the gas might be defined as the additional thermal energy carried by the mass within a cylinder defined by an isothermal surface relative to the energy stored in the capacitor prior to breakdown. Because of the influence of the emitted shock wave, η has to be determined at the end of phase III, that is, roughly after 4 μs. Efficiencies in the range of 40–55% were found, depending on the ambient pressure and the isothermal temperature of the cylinder surface chosen. Only a weak dependence on the breakdown energy itself is observed. Efficiencies measured by calorimetric methodes [26] are higher, ranging from 60 to 72%.

During phase IV, Joule heating (Fig. 8) exceeding 5000 W/m is necessary to balance energy loss from the channel due to heat diffusion. Larger currents cause the plasma core to cool down slower so that the channel resistance stays lower. Because less Joule heating takes place under constant current conditions, the difference in heating rates is less than expected from the quotient of the applied currents (Fig. 2). This is important when considering the system efficiency where the energy loss to the electrodes is proportional to the current.

Conclusions

Four basic phases of the spark channel development can be identified: breakdown, shock-deter-

mined expansion, emission of a shock wave, and, after roughly 4–5 μs, the diffusion-dominated phase. Energy transfer takes place primarily during the breakdown phase and later again with the beginning of the diffusion phase, when the axial temperatures and therefore the conductivity is sufficiently low.

Because the formation of the final temperature profile does not strongly depend on the time function of energy deposition into the plasma, a cylindrical channel with homogeneous energy distribution at ambient mass density might be chosen as the initial condition. The pressure within this cylinder must be sufficiently high (300 bar) to create a strong shock and provide a phase of self-similar propagation.

The increase of thermal energy in the plasma channel is 40–55% of the electrical energy provided during breakdown. The influence of radiation loss rises with the breakdown energy deposited. For these calculations with a maximum breakdown energy of 2 J/m, the radiation loss was $\eta_{rad} = 2.4\%$. Radiation losses reduce the total efficiency by approximately $\eta_{rad}/2$.

Acknowledgments

This work was partially supported by the Commission of the European Community, contract JOU 2-CT 92-0081.

REFERENCES

1. Maly, R., in *Road Vehicles Powered by Spark Ignition Engines,* (J. C. Hillard and G. S. Springer, Eds.), Plenum Press, New York, 1984.
2. Maly, R., Saggau, B., Vogel, M., and Ziegler, G., *Optimierte Zündung und Entflammung,* BMFT Abschlußbericht 522-7291 TV 7652 6, Inst. f. Physikalische Elektronik, Universität Stuttgart, 1980.
3. Albrecht, H., Bloss W. H., Herden, W., Maly, R., Saggau, B., and Wagner, E., Society of Automotive Engineers, Warrendale, SAE 770853, 1977.
4. Drabkina, S. I. *Abhandlungen aus der sowjetischen Physik,* III:295–309 (1953).
5. Sedoy, L. L. *Similarity and Dimensional Methods in Mechanics.* Academic Press, New York, 1959.
6. Sher, E., Ben-Ya'ish, J., and Kravchik, T., *Combust. Flame* 89:186–194 (1992).
7. Bradley, D. and Lung, F. K., *Combust. Flame* 69:71–93 (1987).
8. Ishii, K., Tsukamoto, T., Ujiie, Y., and Kono, M., *Combust. Flame* 91:153–64 (1992).
9. Sloane, T. M., *Combust. Sci. Technol.* 86:121–133 (1992).
10. Borghese, A., D'Alessio, A., Diana, M., and Venitozzi, C., *Twenty-Second Symposium (International) on Combustion,* The Combustion Institute, Pittsburgh, 1988, p. 1651.
11. Herden, W. and Maly, R., *Combust. Flame* 30:207–210 (1977).
12. Wu, C. and Kunhardt, E. E., *Phys. Rev. A* 37(11):4396–4406 (1988).
13. Geary, J. M. and Penney, G. W., *Phys. Rev.* 17:1483–89 (1978).
14. Rodriguez, A. E., Morgan, W. L., Touryan, K. J., Moeney, W. M., and Martin, T. H., *J. Appl. Phys.* 70(4):2015–22 (1991).
15. Volk, G., "Zeitaufgelöste Bestimmung von Plasmaparametern der stillen Entladung in Stickstoff," Ph.D. Thesis, Universität Stuttgart, Stuttgart, 1992.
16. Yos, J. M., *Transport properties of nitrogen, hydrogen, oxygen, and air,* Tech. Memorandum RAD TM-63-7, AVCO Corp., Wilmington, MA, 1963.
17. Tannehill, J. C., Srinivasan, S., and Weilmuenster, K. J., *Simplified Curve Fits for the Thermodynamic Properties of Equilibrium Air.* NASA reference publication 1181, NASA, 1987.
18. Gurvich, L. V., Veyts, I. V., and Alcock, C. B., *Thermodynamic Properties of Individual Substances.* Hemisphere, New York, 1989.
19. Spitzer, L., and Härm, R., *Phys. Rev.* 89:977 (1953).
20. Hochstim, A. R., *Kinetic Processes in Gases and Plasmas.* Academic Press, New York, 1969.
21. Zienkiewicz, O. C. and Taylor, R. L., *The Finite Element Method,* Vol. 2. McGraw-Hill, London, 1991.
22. Brooks, A. N. and Hughes, T. J. R.., *Comp. Methods Appl. Mech. Eng.* 32:199–259 (1982).
23. MacCormac, R. W. and Baldwin, B. S., AIAA paper, 75-1:1–8, American Institute of Aeronautics and Astronautics, New York, 1975.
24. Ziegler, G. F. W., Wagner, E. P., and Maly, R. R., *Symposium (International) on Combustion.* The Combustion Institute, Pittsburgh, 1984.
25. Truckenbrodt, E., *Fluidmechanik,* Vol. 1, Springer, Berlin, 1992.
26. Ziegler, G. F. W., "Entflammung magerer Methan/Luft-Gemische duch kurzzeitige Bogenund Glimmentladungen," Ph.D. Thesis, Universität Stuttgart, Stuttgart, 1991.

COMMENTS

E. Sher, Ben-Gurion University of the Negev, Israel. This paper addresses one of the most important processes in spark ignition engines, namely, spark ignition and flame initiation. Cycle-by-cycle variations and HC emissions are strongly related to the evolution of the early stages of combustion. The authors present a beautiful model by which they can study the effect of various operational parameters, such as the energy deposition law, on the ignition success.

Their simplified model which is based on 1D analysis, while ignoring initial flow field at the spark gap and fuel burning chemistry, yields a simple and practical model. However the effect of these assumptions on their conclusions should carefully be evaluated. For example:

1. At t = 0.1 μs, the radius of the spark channel is in the order of 0.3 mm (Fig. 4). For an electrode gap of 1 mm, the distance between the spark center and the electrode is 0.5 mm. It is therefore expected that heat losses to the electrodes at this time are not less important than heat losses due to thermal conductivity to the surrounding.
2. Rigorous calculations (using Chapman and Cowling, and Spitzer and Harm models) [1,2] showed that during breakdown the channel resistance is in the order of 0.1 Ω/mm (Fig. 4 in [1]) while the authors used a value of 1-10 Ω/mm. If a lower value is used, a higher current is resulted and energy dissipation at the electrodes surfaces becomes very significant. Theoretical analysis (Fig. 19 in [1]) with a 2D model showed that these losses become comparable (if not higher) to the amount of the introduced energy.
3. Could the authors estimate which part of the energy difference between E_{input} and $E_{thermal}$ (Fig. 6) is lost to the electrodes, conducted to the surrounding and convected away by the expansion (shock) wave.
4. How would the conclusions, as concerned with the energy deposition law, be affected if the heat release by fuel burning is not neglected?
5. It could be very beneficial if the authors would evaluate the relative importance of the energy deposition law to the cyclic variability, as compared to the effect of the arbitrary velocity vector (due to turbulence effects) at the spark gap during spark onset.

REFERENCES

1. Kravchik, T., Sher, E., and Heywood, J. B., "From Spark Ignition to Flame Initiation," *Combust. Sci., Technol.* 108:1–30 (1995).
2. Kravchik, T. and Sher, E., "Numerical Modeling of Spark Ignition and Flame Initiation in a Quiescent Methane-Air Mixture," *Combust. Flames* 99:635–643 (1994).

Author's Reply. Questions 1, 3, and 5 essentially pertain to the question about the validity of the 1D approach concerning ambient flow fields and axial heat conduction:

- The radial expansion of the channel is due only to convection. Gas velocities at .1 μs are still in access of 500 m/s. Radial thermal conduction as well as initial ambient flow fields play a negligible role until mid-phase III. For later times ambient flow fields can be accounted for only by using full 3D calculations.
- After 50-100 ns the electrode sheaths for a typical glow discharge will be fully established [1]. The energy dissipated within the sheath and presheath region is required to produce the charge carriers to sustain the discharge and also keep up the temperature gradient between the electrodes and the plasma. The plasma column is therefore thermally decoupled from the electrodes.
- The experimentally determined energy loss to the electrodes is 5% for the breakdown and up to 70% for the glow discharge (Ref. 1 in paper). The efficiencies given here are based only on the power dissipated within the plasma. Electrode effects are not included in the 1D calculation.

The channel resistance of 0.1 Ω/mm referred to in question 2 is lower than reported in this paper because of the initial conditions chosen. In the cited papers the initial radius of the conducting cross section is 120 μm at T = 35000 K. The maximum extension of the 10000 K isotherm (to have comparable situations) that occurred during our calculations was 60 μm at peak temperatures of 20000 K.

Chemical heat release (question 4) at the periphery of the channel will reduce axial heat flux. Higher axial temperatures with a lower channel resistance and hence a lower Joule heating rate results.

REFERENCES

1. Craggs, J. D., "Spark channels," in Meek, J. M. and Craggs, J. D., (Editors), *Electrical Breakdown of Gases*, Wiley & Sons, Chichester, 1978.

•

Rudolf R. Maly, Daimler-Benz AG, Germany. Did you compare your results to experimental data and what were the results?

Author's Reply. We compare the calculations to measurements done by Maly et al. (Ref. 1 in paper). This was a discharge with a breakdown energy of .275 I/m and a gap of 2.3 mm between pointed (Rogowsky-shaped) electrodes.

The agreement of the measured and calculated shock-diameter is excellent, the time of the beginning separation of the shock from the plasma channel is well reproduced. The agreement for the further development of the plasma radius is good up to 7 μs. Then there is a deviation from the measurements. This is mainly due to the unusual electrode shape and gap length. Beginning 2D flow in the axial direction along the electrodes break the 1D assumptions made.

Twenty-Sixth Symposium (International) on Combustion/The Combustion Institute, 1996/pp. 2709–2716

ANALYTICAL STUDY ON FLAME STABILIZATION IN RECIPROCATING COMBUSTION IN POROUS MEDIA WITH HIGH THERMAL CONDUCTIVITY

J. G. HOFFMANN*
ABB Power Generation Ltd.
Gas Turbine and Combined Cycle Power Plant Development
CH-5401 Baden, Switzerland

J. G. HOFFMANN, R. ECHIGO, S. TADA AND H. YOSHIDA
Department of Mechanical Engineering and Science
Tokyo Institute of Technology
Meguro-ku, Tokyo 152, Japan

A unique feature of reciprocating combustion in porous media is the system's capability to sustain combustion of extremely dilute fuel gases and to maintain steep temperature gradients in the inlet and outlet area of the porous media. However, for porous media with a high thermal conductivity, which are considered for application in thermoelectric conversion, the temperature gradients decrease; without a steep temperature gradient, reaction occurs in a wide region of the porous medium and it becomes difficult to establish a stable flame position. To counter this problem, a new arrangement of the porous media with a center space is proposed that stabilizes flame position for a wide operating range. Additionally, the new system largely extends the flammable range and reduces the specific energy input needed to sustain combustion. Overall, the effectiveness to generate a temperature difference in porous media with high thermal conductivity could be improved by the new system.

Besides flame stabilization, an additional interesting feature of introducing a center space is the possibility of fuel injection into it, which leads to increased maximum temperatures (i.e., to a heat release at a higher energy level). This presents a great advantage over conventional reciprocating combustion in porous media where the maximum temperature is limited by the temperature of self-ignition for the premixed combustible gases.

Introduction

Based on practical experience, a sophisticated superadiabatic combustion system was recently introduced by Swedish engineers using reciprocating flow in porous media [1]. Reciprocating combustion in porous media (hereafter referred to as RCPM) works by introducing premixed combustible gas alternately from both sides of a porous medium with a periodic change of flow direction. As a result, typically trapezoidal temperature profiles with maximum temperatures high enough to sustain combustion are formed inside the porous medium, while the entrance gas is kept at ambient conditions. Early studies concentrated on the theoretical understanding and description of RCPM and on the flammable limit for extremely dilute fuel gases, which is a favorable feature, for example, to mitigate pollutant emissions into the atmosphere [2–4].

As a new application of RCPM, beyond mere combustion of waste gases to reduce their negative impact on the environment, the combination of RCPM with direct thermoelectric power generation was suggested. For high-efficiency thermoelectric conversion, high-temperature differences and gradients have to be generated with a minimum heat input. This can be realized for porous media consisting of thermoelectric materials [5–7]. To provide the driving temperature differences for the thermoelectric conversion, the previously mentioned temperature distribution with steep temperature gradients in the inlet and outlet region, demonstrated in the original RCPM, is essential. However, presently available porous thermoelectric materials, especially metallic porous materials that are feasible for this system, have several orders higher thermal conductivity than the materials considered in previous studies on RCPM [2–4], and thus little knowledge on possible temperature profiles is available. Even so, high-conductivity materials are favorable to increase the power density; they not only cause adverse effects on the temperature profiles, eventually leading to less than

*Formerly at Department of Mechanical Engineering and Science, Tokyo Institute of Technology, Meguro-ku, Tokyo 152, Japan.

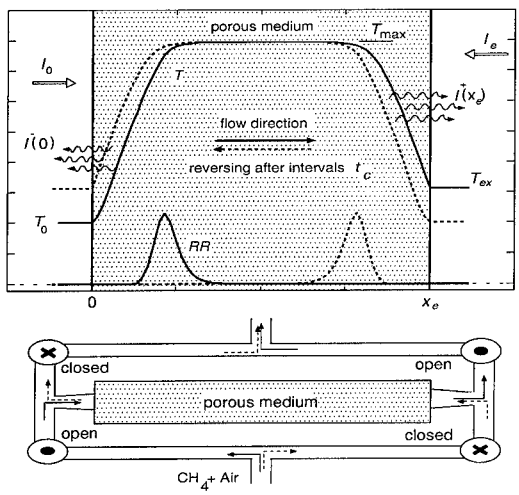

FIG. 1. Schematic model of the reciprocating combustion system and the profiles of temperature T and reaction rate RR.

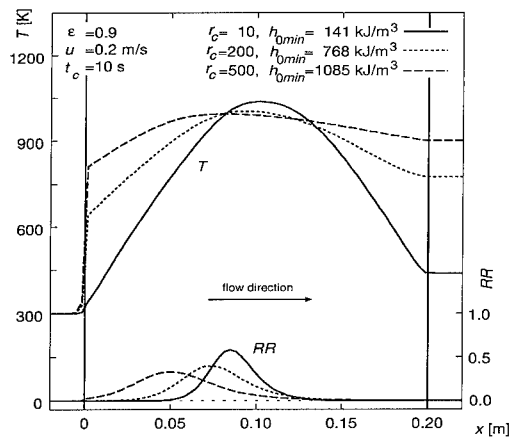

FIG. 2. Profiles of the gas temperature T and reaction rate RR for thermal conductivity ratios r_c = 10, 100, and 500 with minimum heat input $h_{0\min}$ to sustain combustion in the conventional system and with ε = 0.9, u = 0.2 m/s, and t_c = 10 s.

adiabatic temperatures, but also problems in flame stabilization.

In this study, attention is focused on a new approach to stabilize the flame and form the desirable temperature distribution irrespective of the thermal conductivity of the porous medium. Further, in this system, the positions where maximum and minimum temperatures occur are fixed for a wide range of parameters, thus enabling the optimized arrangement of thermoelectric pairs in the porous medium.

Analytical Model

Figure 1 shows a schematic view of the conventional superadiabatic reciprocating combustion system and physical model assuming one-dimensional flow and heat transfer. To counter the previously mentioned problems observed for porous media with high thermal conductivity (Fig. 2), the extended new model, whose structure can be seen in Fig. 3, is introduced. By opening a center space and introducing an additional porous medium in it, an arrangement of three porous media PML, PMC, and PMR with two gaps GL and GR is obtained.

The aim of this new arrangement is to keep the temperature of the porous medium at the inlet and outlet side below reaction temperature, while allowing the temperature to increase in the center space for fast and complete combustion, thus stabilizing the flame in the center space. To ensure reignition after a change of the flow direction, the central porous medium PMC, simply called *reigniter*, is introduced (the term *center space* denotes the region GL + reigniter + GR). Since each of the three porous bodies is treated individually and analogously, the

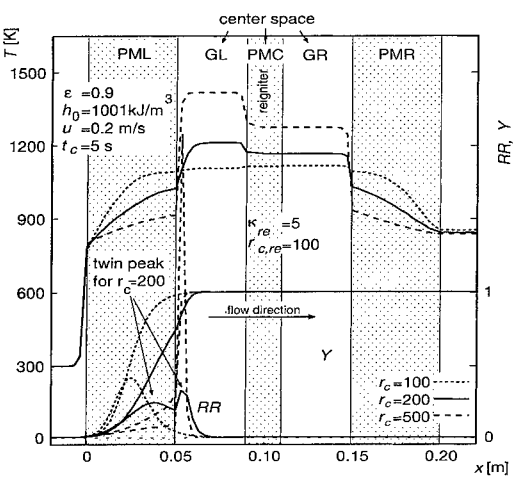

FIG. 3. Thermal structure and influence of the thermal conductivity ratio r_c for combustion in porous media with a central gap and with ε = 0.9, h_0 = 1001 kJ/m³, u = 0.2 m/s, t_c = 5 s, and $r_{c,re}$ = 100.

treatment of the single porous body, as used to discuss the problems encountered in high thermal conductivity porous media (Fig. 2), is explained in detail here.

In this combustion system, the convective heat exchange between working gas and porous medium is crucial, but the radiative heat transfer intensified by the porous medium is also essential, because it leads to a favorable energy recirculation in the combustion zone as well as adverse heat losses to the upstream and downstream sides. Here, we assume that the

homogeneous porous medium with geometrical and optical lengths x_e and $\tau_e = \kappa x_e$, respectively, emits and absorbs thermal radiation and that scattering can be neglected. Fresh premixed combustible gas (CH_4 + air) is introduced alternately from both sides of the porous medium with a constant velocity u. For practical applications, the flow velocity is in the order of 1 m/s where pressure drops in highly porous media can be neglected. The flow direction is reversed at regular intervals t_c, which represents the half cycle of the system. The flame location, indicated by the reaction rate RR, is not specified beforehand but is determined by the temperature profile and yield of combustion products; therefore, it changes with the cycle time t_c. The entrance gas temperature at $x = 0$ or $x = x_e$ is $T_0 = 298$ K. Radiation of the working gas is insignificant, and both ends of the porous medium are exposed to black surfaces at the ambient temperature T_0, providing incident radiative intensities I_0 and $I_e = \sigma T_0^4$. Complementary assumptions for heat transfer and the reaction are as follows: The physical properties are constant; the Lewis number is unity; the porous medium is noncatalytic; and combustion is a one-step Arrhenius-type reaction.

Basic Equations

With the preceding assumptions, the energy equations for both gas and solid phases as well as the conservation equation of combustion products can be formulated. The conservation equation for combustion yields

$$\rho \frac{\partial Y}{\partial t} + \rho u/\varepsilon \frac{\partial Y}{\partial x} = D\rho \frac{\partial^2 Y}{\partial x^2} + W \tag{1}$$

where the porosity ε is set to unity when applied for the free space. The reaction rate W is formulated by Arrhenius-type reaction kinetics

$$W = A\rho(1 - Y)\exp(-E/RT) \tag{2}$$

The energy equations
(gas phase in free space)

$$\rho c_p \frac{\partial T}{\partial t} + \rho c_p u \frac{\partial T}{\partial x} = \lambda \frac{\partial^2 T}{\partial x^2} + h_0 W \tag{3}$$

(gas phase in porous medium)

$$\varepsilon \rho c_p \frac{\partial T}{\partial t} + \rho c_p u \frac{\partial T}{\partial x} = \varepsilon \lambda \frac{\partial^2 T}{\partial x^2} + \varepsilon h_0 W - \alpha_p n_p A_p (T - T_s) \tag{4}$$

(porous medium)

$$(1 - \varepsilon)\rho_s c_s \frac{\partial T_s}{\partial t} = (1 - \varepsilon)\lambda_s \frac{\partial^2 T_s}{\partial x^2} - \frac{\partial q^r}{\partial x} + \alpha_p n_p A_p (T - T_s) \tag{5}$$

where the heat release by combustion is denoted by $h_0 W$. With the radiative flux

$$q^r(\tau) = -2\pi\left\{\left[I_0 E_3(\tau) + \int_0^{\tau} I_b(\tau')E_2(\tau - \tau')d\tau'\right] - \left[I_e E_3(\tau_e - \tau) + \int_{\tau}^{\tau_e} I_b(\tau')E_2(\tau' - \tau)d\tau'\right]\right\} \tag{6}$$

where $\tau = \kappa x$, the radiative term on the right-hand side in Eq. (5) is obtained as

$$\frac{\partial q^r(\tau)}{\partial x} = -2\pi\kappa\left\{I_0 E_2(\tau) + I_e E_2(\tau_e - \tau) - 2I_b(\tau) + \int_0^{\tau} I_b(\tau')E_1(\tau - \tau')d\tau' + \int_{\tau}^{\tau_e} I_b(\tau')E_1(\tau' - \tau)d\tau'\right\} \tag{7}$$

where $I_b(\tau)$ and $E_n(\tau)$ are the black body radiation intensity and exponential integral function of the nth order, respectively. They are in the form:

$$I_b(\tau) = \sigma T_s^4(\tau)/\pi, \quad E_n(\tau) = \int_0^1 \mu^{n-2}\exp(-\tau/\mu)d\mu \tag{8}$$

The boundary conditions are assumed as follows for positive flow direction:

$$T = T_0,\ Y = 0 \text{ at } x = x_{00} \tag{9}$$
$$\frac{\partial^2 T}{\partial x^2} = 0,\ \frac{\partial^2 Y}{\partial x^2} = 0 \text{ at } x = x_{ee}$$

and for negative flow direction:

$$T = T_0,\ Y = 0 \text{ at } x = x_{ee} \tag{10}$$
$$\frac{\partial^2 T}{\partial x^2} = 0,\ \frac{\partial^2 Y}{\partial x^2} = 0 \text{ at } x = x_{00}$$

where x_{00} and x_{ee} are equidistant from the porous body.

Numerical Simulation

Numerical simulations are performed by solving the system of time-dependent simultaneous partial differential equations, Eqs. (1) through (5), with appropriate boundary and initial conditions, using the control volume method with fully implicit time integration SOR [7]. The porous medium considered as standard consists of fine solid particles 20 μm in diameter and has a porosity $\varepsilon = 0.9$. The thickness of the conventional arrangement is $x_e = 0.2$ m. The heat-transfer coefficient α_p was estimated from asymptotic values of $Nu = 2$ around spherical particles forming the porous medium and the value of the specific surface area of the porous medium $A_p n_p = 10{,}000\ m^{-1}$. The absorption coefficient of the porous medium is determined mainly by the geometrical configuration of the material. Independent of the porosity, a typical absorption coefficient $\kappa = 500$

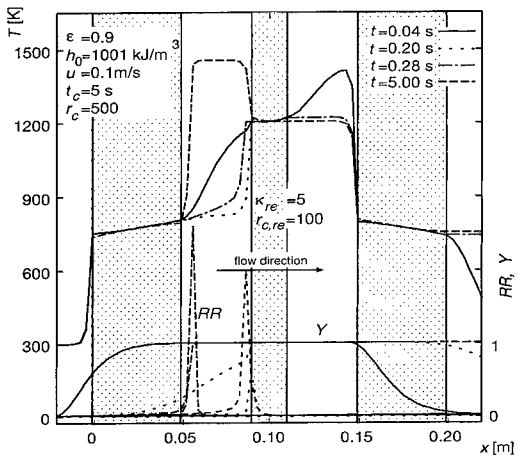

FIG. 4. Profiles of the gas temperature T, reaction rate RR, and yield of combustion products Y during reignition after a change in the flow direction and with $\varepsilon = 0.9$, $h_0 = 1001$ kJ/m^3, $u = 0.1$ m/s, $t_c = 5$ s, $r_c = 500$, and $r_{c,re} = 100$.

m^{-1} is used. The effective heat capacity ratio is $\Gamma = (1 - \varepsilon)\rho_s c_b/\rho c_p = 1000$. For the new arrangement with a center space, the length of the inlet and outlet porous plates are kept at $x_1 = 0.05$ m and the length of the reigniter at $x_{re} = 0.02$ m. Except when noted otherwise, the thermal conductivity ratio of the reigniter is kept at $r_{c,re} = 1$, the porosity at $\varepsilon_{re} = 0.9$, and the absorption coefficient at $\kappa_{re} = 5$ m^{-1}, for which only a negligible effect on the overall process has been observed. The values of the frequency factor and the activation energy in Eq. (2) were estimated from the burning velocity measured at equivalence ratio of $\phi = 0.53$ and 1.0, resulting in $A = 2.6 \times 10^8$ s^{-1} and $E = 130$ kJ/mol [8].

Results and Discussion

Influence of the Thermal Conductivity in Conventional Reciprocating Combustion in Porous Media

Figure 2 shows the influence of the ratio of the porous medium's thermal conductivity to the fluid's thermal conductivity $r_c = (1 - \varepsilon)\lambda_s/\lambda$ in the conventional system. The profiles of temperature T and the reaction rate RR at the end of one-half cycle are shown. The heating values $h_{0\min}$ used here are the minimum values necessary to sustain combustion at the corresponding thermal conductivity ratio. With increasing conductivity ratio r_c, the temperatures at the inlet and outlet end of the porous medium increase, while the maximum temperature in the center of the porous medium does not change considerably. Consequently, the temperature gradients at the inlet and outlet side decrease; this effect is especially pronounced at the downstream side. The small temperature gradients lead to a wide reaction zone; this again causes a heat release over a wide area, rather than at a fixed position, which is also adverse to the formation of a steep temperature gradient. Higher temperatures at the outlet result in high convective heat losses, and increasing temperatures at both ends of the porous medium cause increased radiative heat losses, thus leading to an increase in $h_{0\min}$.

Thermal Structure in Reciprocating Combustion with a Center Space

The temperature profiles and flame positions for moderate and high thermal conductivity porous material in a reciprocating system with a center space are shown in Fig. 3. For a moderate thermal conductivity ratio $r_c = 100$, the flame locates in the upstream porous body (PML) and the thermal structure is hardly affected by the center space. Thus, the typical trapezoidal temperature profile, known for reciprocating combustion in porous media, is established.

For higher conductivity ratios, here $r_c = 500$, the flame moves downstream and is stabilized at the upstream end of the gap (GL). In this case, the temperature of the premixed gases leaving the PML is kept low enough to prevent fast reaction inside the porous medium, while the gases are preheated to a temperature level where combustion in the center space occurs. Once combustion occurs, the gas temperature increases rapidly. Before leaving the porous body, the burned gases are cooled down and part of their heat is recovered by the downstream porous medium PMR.

Reignition after a Change in the Flow Direction

As mentioned previously, the premixed combustible gases enter the center space with a temperature at which reaction takes place at a very low rate. Depending on the flow parameters, this low temperature prohibits self-ignition after reversing the flow direction. The effect of the reigniter is shown in Fig. 4. Just after a reversal of the flow direction, the burned gases that remained inside the PML first have to be replaced by fresh premixed gases at the "new" upstream side. By the time fresh premixed gases reach the GL, the gas temperature has dropped to a level where no self-ignition occurs. Consequently, the premixed gases flow into the GL without reaction. Once they reach the reigniter, the premixed gases are heated to a temperature level sufficient to start reaction, which can be seen after about 0.28 s for the parameters chosen in Fig. 4. After initiation of reaction, the flame moves

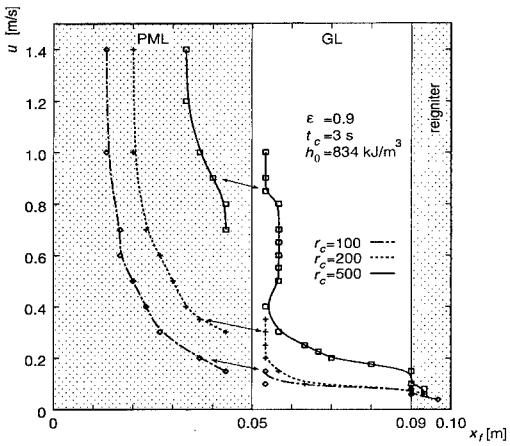

FIG. 5. Dependence of the flame position x_f on the flow velocity u for thermal conductivity ratios r_c = 100, 200, and 500 and with ε = 0.9, h_0 = 834 kJ/m^3, and t_c = 3 s.

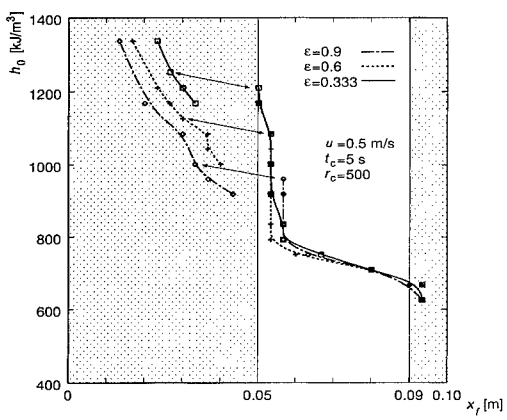

FIG. 6. Extended range of stable flame position with decreasing porosity ε for porosities ε = 0.9, 0.6, and 0.333 and with u = 0.5 m/s, t_c = 5 s, and r_c = 500.

upstream and is stabilized by the upstream porous medium PML.

Flame Stabilization in the Center Space

In Fig. 5, the dependence of the flame position x_f on the flow velocity is shown for the inlet half of the porous body (PML + GL), where x_f is defined as the location of the maximum reaction rate *RR*. With increasing flow velocity, the flame moves upstream but is stabilized at the upstream end of the GL. With increasing conductivity ratio r_c, the velocity range for which the flame is stabilized at the upstream end of the GL is widening; it increases from u = 0.15–0.2 m/s for r_c = 100 to u = 0.4–0.8 m/s for r_c = 500. For a limited range of u, maxima of the reaction rate inside the gap and inside the porous medium (i.e., two peaks for *RR*, as can be seen for r_c = 200 in Fig. 3) can occur. In a high-conductivity porous medium, the reaction rate *RR* is relatively low even if the local maximum exists. Hence, a considerable fraction of unburned gas reaches the center space; unlike in the porous medium, temperature and reaction rate increase rapidly, leading to the second maximum. The flow velocity, where the flame moves from the GL into the porous medium and vice versa, that is, for which both maxima have the same size, is indicated by arrows.

In the case of moderate thermal conductivity (r_c = 100), an increase in the flow velocity that is equivalent to an increase of the heat input quickly leads to an increase of the maximum temperature in the porous medium. Once the porous medium is heated sufficiently, reaction can start inside it. In contrast, even though combustion can start in the gap for relatively low temperatures, a higher heat input is needed to heat high-conductivity porous media to the temperature level where the flame can move upstream into the porous medium; thus, the flame is stabilized at GL up to relatively high flow velocities for r_c = 500.

With decreasing flow velocities, the temperature in the gap decreases, which eventually causes the flame to move downstream. The flame is stopped by the reigniter before it is finally extinguished. The flame stabilized by the reigniter is not the object of this study and therefore not further discussed here. For the same reasons, a similar behavior was observed for the dependence of the flame position on the heating value of the premixed gases.

Since the flow velocity inside the porous medium is inversely proportional to the porosity, the residence time of the gases inside the porous medium decreases with decreasing porosity, thus leading to a further increase in the range of a stable flame position in the center space with decreasing porosity (Fig. 6).

Combustible Limit and Minimum Heat Input

Figure 7 shows the combustible limits for both conventional and new systems as a function of the thermal conductivity ratio r_c. The minimum heating value $h_{0\min}$ increases with increasing thermal conductivity ratio but can be reduced considerably by introduction of a center space for a wide range of parameters. For u = 0.1 m/s, the center space leads to lower $h_{0\min}$ for the whole range of investigated conductivity ratios and to a maximum reduction of 33% for r_c = 1000. With increasing flow velocities, the region in which the center space leads to an extended combustible range is reduced to high conductivity ratios, which are the aim of this study. Consequently, the minimum heat input per inflow/

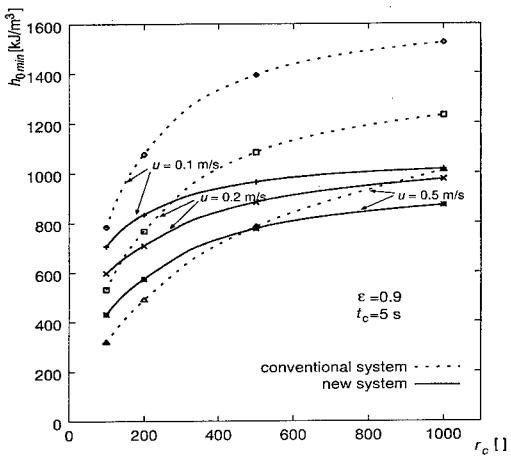

FIG. 7. Dependence of the minimum required heating value $h_{0\min}$ on the thermal conductivity ratio r_c for flow velocities u of 0.1, 0.2, and 0.5 m/s and with $\varepsilon = 0.9$ and $t_c = 5$ s.

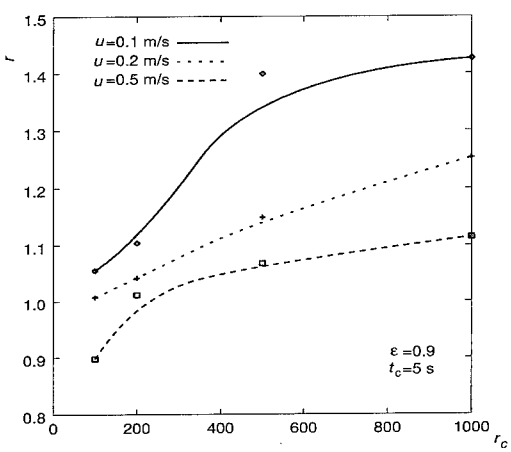

FIG. 8. Ratio r of temperature difference generation between new and old system at the combustible limit and with $\varepsilon = 0.9$ and $t_c = 5$ s.

outflow area $q_{\min} = uh_{0\min}$ is also reduced for these conditions.

Effective Generation of Temperature Differences

Since the thermoelectric power output is proportional to the temperature difference sustained in the elements, it is desirable to achieve maximum temperature differences with minimum heat input for good efficiencies. Therefore, as one index to compare the two systems of RCPM in respect to future applications for thermoelectrics, the ratios of achieved temperature differences in the porous medium to the minimum heat input of both systems

$$r = \frac{([T(x_1) - T(0) + T(x_e - x_1) - T(x_e)]/q_{\min})_{\text{new}}}{([T(x_1) - T(0) + T(x_e - x_1) - T(x_e)]/q_{\min})_{\text{conv}}} \tag{11}$$

is shown in Fig. 8.

This ratio increases with the thermal conductivity ratio r_c and with decreasing flow velocities, leading to an improvement of up to 40% for a flow velocity of 0.1 m/s and a thermal conductivity ratio of 1000. For the low flow velocity of 0.1 m/s, a steep increase is observed between $r_c = 200$ and 500. This increase is due to a drastic decrease in the conventional system's performance in this range, which is caused by an increase of the inlet temperature of the porous medium to the level where reaction starts. As can be seen in Fig. 1, no temperature gradient is generated downstream of the flame position. Therefore, once reaction starts from the inlet of the porous medium, the released heat is not effectively used to generate temperature differences.

For the high flow velocity of 0.5 m/s, a decrease in the ratio r is observed for moderate r_c. For moderate r_c and high flow velocities, a steep temperature gradient is realized in the conventional system. With a center space, this temperature gradient is cut off before sufficiently high temperatures are reached, leading to a drop in the system performance.

Fuel Injection into the Center Space

The new system provides the possibility of using fuel injection into the center space instead of combustion of premixed gases. With fuel injection at sufficiently high temperatures, the flame position is determined by the position of injection rather than by the temperature of self-ignition. Here fuel injection and perfect mixing at the upstream end of the center space are assumed, and reaction occurs immediately when the fuel is injected into the preheated air (Fig. 9). Because the fuel gas flow is less than 1% of the total flow, the influence of the gas injection on the flow is neglected. As shown here, for porous media with low thermal conductivity ($r_c = 1$), the maximum temperature increases with the thickness of the porous sides x_1. With an increase in x_1, the temperature gradient can be sustained for a longer distance, leading to a higher maximum temperature and therefore to heat release at a higher temperature level. In other words, higher temperature differences, which can act as a driving force for thermoelectric conversion, can be achieved with the same heat input simply by changing the injection point. Because the radiant heat flux increases with higher temperature levels, the temperature gradient decreases with the temperature. Since high temperature levels are regarded here, no reigniter has to be introduced into the center space.

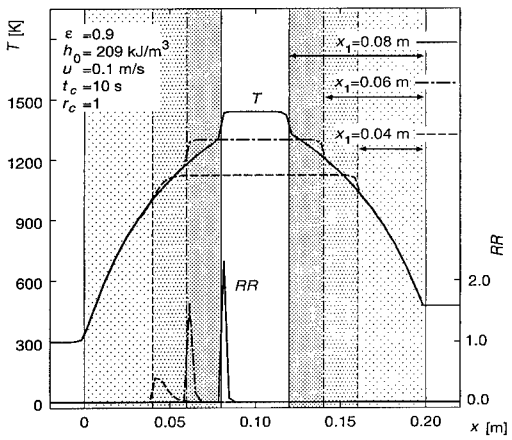

FIG. 9. Dependence of the temperature profile and maximum temperature on the thickness of the porous sides x_1 for fuel injection in the center gap and with $\varepsilon = 0.9$, $h_0 = 209$ kJ/m^3, $u = 0.1$ m/s, $t_c = 10$ s, and $r_c = 1$.

Conclusions

A numerical analysis of reciprocating combustion in porous media, along with a center space, has been carried out. The drawbacks of reciprocating combustions in porous media of high thermal conductivity, for example, high minimum heat input to sustain combustion and an unstable flame position, were discussed. To ensure a defined flame position for a wide range of working parameters and to reduce the minimum required heat input, the introduction of a center space to the original system has been suggested. The effective stabilization of the flame position and a reduction of the minimum heating value of up to 33% for a thermal conductivity ratio of 1000 at a flow velocity of 0.1 m/s has been achieved. Further, an enhanced stabilizing effect of low porosities in combination with a center space has been demonstrated. However, there is still room for improvements by variations of the flow system.

To counter the limitations on the maximum temperature imposed by the self-ignition of premixed gases, fuel injection in the center space is suggested. It has been shown to be an effective means to increase the maximum temperature, thus leading to heat release at high exergy levels.

Nomenclature

A frequency factor for reaction kinetics, s^{-1}
A_p surface area of an equivalent particle (πd_p^2), m^2
c_p specific heat of gas phase at constant pressure, kJ/(kg K)
c_s specific heat of porous medium, kJ/(kg K)
D diffusivity, m^2/s
d_p diameter of spherical particles forming the porous media, m
E activation energy, kJ/mol
E_n exponential integral functions of nth order
h_0 heating value for uniform heating, kJ/m^3
I^+, I^- radiative intensities to upstream and downstream direction, W/m^2
I_b black body radiation intensity, W/m^2
I_e, I_0 incident radiation intensity, W/m^2
Nu Nusselt number ($= \alpha_p d_p/\lambda$)
n_p number density of porous particles, m^{-3}
$q_{\min}$ minimum heat input per unit area, kW/m^2
q^r radiation flux, W/m^2
R universal gas constant, kJ/(kmol K)
r ratio of temperature differences to heat input of new to conventional system
r_c thermal conductivity ratio ($= [1 - \varepsilon]\lambda_s/\lambda$)
RR dimensionless reaction rate
T temperature, K
T_{ex} temperature of the exhaust gases, K
$T_{\max}$ maximum process temperature, K
t time, s
t_c half cycle, s
u gas velocity, m/s
W reaction rate, m^3/(m^{3}s)
x coordinate, m
x_e length of porous medium, m
x_{re} length of the reigniter, m
x_1 length of porous medium left and right of central space, m
Y product mole fraction

Greek Symbols

α_p heat-transfer coefficient around a particle, W/(m^2 K)
Γ heat capacity ratio between two phases
ε porosity
κ absorption coefficient, m^{-1}
λ (effective) thermal conductivity, W/(m K)
μ integration variable of the exponential integral function
ρ density of gas, kg/m^3
ρ_s bulk density of porous medium, kg/m^3
σ_b Stefan–Boltzmann constant, W/(m^2 K^4)
τ optical length ($= \kappa x$)
τ_e optical thickness of the porous medium ($= \kappa x_e$)
ϕ equivalence ratio

Subscripts

0 initial state
00, *ee* boundaries of calculation domain
new new system with center space
conv conventional system
re properties of reigniter in center space
s porous medium

REFERENCES

1. "A New Method of Destroying Organic Pollutants in Exhaust Air," ADTEC Co., Ltd., commercial report, Sweden, 1990.
2. Echigo, R., *3rd ASME/JSME Thermal Engineer. Joint Conf.*, vol. 4, Reno, 1991, pp. xxi–xxxii.
3. Hanamura, K., Echigo, R., and Zhdanok, S. A., *Intl. J. Heat Mass Transfer* 36(13):3201–3209 (1993).
4. Hoffmann, J., Echigo, R., Tada, S., and Yoshida, H., 8th International Symposium on Transport Phenomena in Combustion, San Francisco, 1995, 7-C-5.
5. Echigo, R., Yoshida, H., Tawata, K., and Tada, S., 12th Intl. Conf. on Thermoelectrics, Yokohama, 1993, VI-5.
6. Echigo, R., Yoshida, H., Tawata, K., Koda, M., and Hanamura, K., *10th Intl. Heat Transfer Conf.*, vol. 3, Brighton, 1994, pp. 173–178.
7. Echigo, R., Yoshida, H., Tawata, K., and Tada, S., *4th ASME/JSME Thermal Engineer. Joint Conf.*, vol. 4, Lahaina, 1995, pp. 389–396.
8. Yoshizawa, Y., Sasaki, K., and Echigo, R., *Intl. J. Heat Mass Transfer* 31(2):311–319 (1988).

Twenty-Sixth Symposium (International) on Combustion/The Combustion Institute, 1996/pp. 2717–2723

INTERPRETATION OF k-ε COMPUTED TURBULENCE LENGTH-SCALE PREDICTIONS FOR ENGINE FLOWS

Z. HAN AND R. D. REITZ
Engine Research Center
University of Wisconsin-Madison
Madison, WI 53706, USA

F. E. CORCIONE AND G. VALENTINO
Fluid Dynamics and Combustion Division
Istituto Motori
CNR—Naples, Italy

Three-dimensional computations of motored-diesel engine flows were made and compared with measured turbulence parameters. The tangential component of velocity, turbulence intensity, and integral length scale were measured in an engine featuring a re-entrant bowl combustion chamber (0.435 L, 21:1 compression ratio) using a laser doppler velocimetry (LDV) system. A two-probe–volume system was used to measure directly the lateral integral length scales of the tangential (swirl) velocity component. The measurements were made in a horizontal plane 5 mm below the engine head from 100° before top dead center (TDC) in the compression stroke to 60° after TDC in the expansion stroke. The engine was motored at 600, 1000, and 1500 rev/min. An ensemble-averaging technique was used, and the lateral integral length scales were obtained from the correlation coefficients of the velocity fluctuations at two separated spatial points. The computations considered two turbulence models, namely, a standard k-ε and a modified RNG k-ε model. The results show that for nonequilibrium, rapidly distorted engine turbulence, the macro length scale ($k^{3/2}/\varepsilon$) from two-equation turbulence models is not directly proportional to the integral length scale, as is the case in equilibrium turbulence. Instead, a new interpretation of the turbulence model length scale is given for rapidly distorting engine flows and is shown to be proportional to the product of the integral length scale and the turbulent Reynolds number.

Introduction

In internal combustion engines (ICEs), the fuel evaporation and mixing processes are strongly influenced by the turbulent nature of the in-cylinder flows [1,2]. The velocity gradients in the mean flow are one of the major sources of energy for the turbulence. The air jets created by flows during the intake process interact with the cylinder wall and moving piston to generate large-scale rotating flows, both in the vertical and the horizontal planes. Breakdown of the former flow structures occurs during compression and produces turbulence. This process is also influenced significantly by squish-generated flows in engines that feature piston bowls or domed heads. The behavior of the in-cylinder turbulent flow can be characterized by monitoring the kinetic energy and the integral length-scale variation of the turbulent eddies that contribute to the turbulence production during the intake and compression processes [3,4]. Thus, the determination of turbulence length scales is important in the study of in-cylinder flow processes.

Direct length-scale measurements have been made in engines. Wakuri et al. [5] used a hot wire anemometer (HWA) to investigate variations of mean velocities, turbulence intensities, timescales, and spatial scales of the fluctuation velocity during the compression stroke. Longitudinal spatial length scales were derived from cross-correlation coefficients of the fluctuations velocity. Wakuri et al. showed, for the first time, that spatial length scales decrease monotonically in the last 60° of the compression stroke. Collings et al. [6,7] measured integral and micro–length scales in a motored ICE using "flying" LDA. Also, Ikegami et al. [8] measured the lateral integral length scale in an engine using a laser homodyne velocimetry (LHV) technique. The elongated-volume laser doppler velocimetry (LDV) technique was used by Fraser and Bracco [9] to measure the lateral fluctuation integral length scales for 64 crank-angle degrees about top dead center (TDC). They showed that the length scale reached a minimum 5°–10° before TDC.

Direct measurements of the integral length scales made by previous investigators were made in

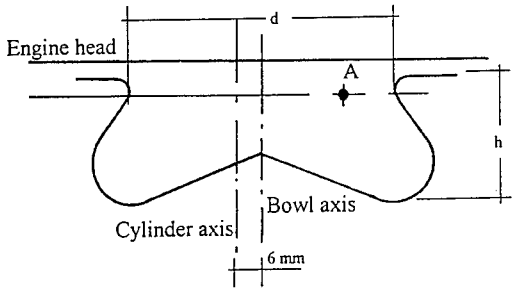

FIG. 1. Section of the re-entrant combustion chamber showing the location of measurement point A (20 mm from the cylinder axis). Chamber diameter d = 32 mm, maximum chamber depth h = 16 mm.

engines with relatively simple combustion chamber geometries (e.g., flat piston, cylindrical bowl, etc.). More recently, Corcione and Valentino measured the integral length scale in a medium-duty diesel engine equipped with a conventional toroidal combustion chamber [10] using a two-probe–volume LDV technique. They made measurements during the last 30° of the compression stroke and showed a monatonic decrease of the lateral integral scales until TDC.

Efforts have been made to model in-cylinder turbulence using k-ε turbulence models [11]. In this case, the turbulence energy k is used to calculate the turbulence intensity, and the macro–length scale is assumed to be proportional to $k^{3/2}/\varepsilon$ (ε is the dissipation rate of k). The present paper addresses the validity of this length-scale assumption, which is valid for equilibrium turbulence. Engine turbulence undergoes rapid distortion (compression/expansion) due to the piston movement, and it is likely to be nonequilibrium in nature. To test the influence of nonequilibrium effects, the measured turbulence quantities and, particularly, the integral length scale were compared with model predictions. A new length-scale analysis is presented for rapidly distorted turbulence, and a correlation is proposed that relates $k^{3/2}/\varepsilon$ to the integral length scale and to the turbulence Reynolds number. This new interpretation of computed turbulence length scales for engine flows is found to give excellent agreement with the experimental results.

Experiments

An optically accessible engine capable of running at high speed without lubricating oil was used for the measurements. The engine is representative of modern, light-duty diesel engines for passenger cars and was manufactured by modifying a commercial single-cylinder Lombardini diesel engine (86-mm bore, 75-mm stroke, volumetric compression ratio 21:1). The engine featured sealed crank shaft and connecting rod bearings, and autolubricating, bronze-Teflon piston rings. These devices greatly reduced the problem of window fouling and allowed the engine to run up to 30 min at 600 rev/min (5 min at 3000 rev/min). In addition, the LDV system used molybdenum disulfide (MoS_2) self-lubricating particles (~1 μm in diameter) instead of conventional titanium dioxide (TiO_2) particles that can be very abrasive for pistons and cylinders.

The LDV system comprised a 4-W argon-ion laser that utilizes two strong lines at 488 and 514.5 nm, standard optics by Dantec working in the backscatter mode, two photomultipliers, and two burst spectrum analyzers (BSA). The signal quality of the individual components was improved by introducing an optical fiber between the laser beam output and the optics. The system can extract Doppler frequencies from bursts with a very poor signal-to-noise ratio and provides a high data rate at high engine speeds with more than 80% of the data validated. An optical shaft encoder, with a resolution of 0.1°–0.6° of crank angle, was connected directly to the engine crank shaft to drive a trigger device for the two BSAs. Data were sent to a PC computer via an IEEE488 parallel interface and analyzed off-line.

The laser beams entered the cylinder through a 30-mm-diameter quartz window in the head. The instantaneous tangential component of the velocity was measured at 600, 1000, and 1500 rev/min from 100° before to 60° after TDC. Figure 1 shows the location of the measurement point and the geometry of the combustion chamber used. The chamber has a volume of 15.6 cm^3 with a diameter d of 32 mm and a maximum depth h of 16 mm. The clearance height at TDC is 1 mm. The measurement point (A) was located on the horizontal plane 5 mm below the engine head, 14 mm from the bowl axis (20 mm from the cylinder axis). The mean velocity and the turbulence intensity were computed by ensemble averaging the experimental data collected on about 1000 consecutive engine cycles.

Two approaches have been used for computing the mean velocity and turbulence in ICEs ensemble and cycle-resolved analyses [3]. Each technique emphasizes different aspects of the turbulence. In particular, the cycle-resolved technique gives information about flow fluctuations about some arbitrarily chosen, low-frequency, time-varying "mean" flow in each engine cycle. The ensemble-averaging technique does not require the use of an assumed cutoff frequency, but it does include fluctuation due to mean flow variations from cycle to cycle [12]. However, for the present deep bowl-in-piston–type engine with its very high squish-flow component, cyclic variability effects would be expected to be much less important than in flat-piston engines.

The LDV system consists of four beams that form two-probe volumes with two separated, adjacent

mirrors. One probe volume was fixed, and one was moved from 0 to 15 mm, allowing the simultaneous measurements of the same velocity component at different adjacent spatial locations. The scattered light is collected with the two photomultipliers and analyzed by the burst spectrum analyzers. Simultaneous velocity pairs were checked by off-line software based on the encoder resolution. The acceptance window width-of-coincidence data were varied from 0.1 crank-angle degree to 0.3 crank-angle degree with no significant difference in the results.

Three types of turbulence-length scale are relevant in engine flows [13,14]. The integral scale, L_I, represents the extent of coherent motions and is a measure of the large eddies. It is determined by the area under the velocity fluctuation correlation curve formed at two adjacent points. The Taylor microscale, λ, is determined from the osculating parabola to the same correlation curve. It is believed to be a rough measure of the spacing of the very thin shear layers in which viscous dissipation occurs. The Kolmogorov microscale is determined from the energy dissipation rate and the kinematic viscosity, and it is a measure of the size of the smallest turbulence structures.

For homogeneous, isotropic turbulence, two correlation curves can be defined: the longitudinal and the lateral obtained from the parallel and the perpendicular velocity fluctuations, respectively [15]. In homogeneous, isotropic turbulence, the longitudinal integral length scale is two times the lateral integral length scale, and the turbulence scales can be determined from the timescale of the turbulence velocity using Taylor's hypothesis.

For nonstationary, nonhomogeneous, engine in-cylinder flows, in which the Taylor's hypothesis is not valid, direct measurement of the lateral integral length scale is required. The lateral integral length scale was estimated using the two-probe–volume LDV system, computing the spatial correlation coefficient for different adjacent positions, x, of the two probe volumes. The distance between the two probe volumes, δx, was increased until no spatial correlation was noted between the two fluctuation velocity components. Then, the lateral integral length scale, $L_g(\theta)$, was estimated at each crank angle, θ, computing the integral of the correlation coefficient curve, $R(\theta, \delta x)$, by $L_g(\theta) = \int_0^{x^*} R(\theta, \delta x)\, dx$, where x^* is the first point in which the spatial correlation coefficient curve becomes zero. To estimate the lateral integral length scale from the correlation coefficient versus separation, an exponential decay function was used to fit the experiment data: $R(\theta) = Ae^{-bx}$ where the coefficient A and b were computed by a least-squares method. More details of the experimental techniques are given in Ref. 3.

Model

The three-dimensional transport equations of mass, momentum, energy, and turbulence were solved with a modified version of the KIVA-II computer code [16]. The computations were performed using the engine geometry of Fig. 1 with a mesh resolution of 26, 38, and 30 grid nodes in the axial, radial, and azimuthal direction, respectively. This grid resolution was found to give adequate, grid-independent results [17]. Two turbulence models were tested. The standard k-ε model was used with an added term to account for nonzero velocity dilatation (compressibility) [16]. In addition, a modified RNG k-ε model [17] was applied that has the general form

$$\frac{\partial \rho k}{\partial t} + \nabla\cdot(\rho u k) = -\frac{2}{3}\rho k \nabla\cdot u + \tau\colon \nabla u + \nabla\cdot(\alpha_k \mu \nabla k) - \rho\varepsilon, \quad (1)$$

$$\frac{\partial \rho \varepsilon}{\partial t} + \nabla\cdot(\rho u \varepsilon) = -\left[\frac{2}{3}C_1 - C_3 + \frac{2}{3}C_\mu C_\eta \frac{k}{\varepsilon}\nabla\cdot u\right]\rho\varepsilon\nabla\cdot u + \nabla\cdot(\alpha_\varepsilon \mu \nabla \varepsilon) + \frac{\varepsilon}{k}[(C_1 - C_\eta)\tau\colon \nabla u - \mathbf{C_2}\rho\varepsilon], \quad (2)$$

and $\mu_t = \rho C_\mu k^2/\varepsilon$, where ρ, u, τ, μ_t, and μ are density, velocity, stress tensor, turbulent viscosity, and effective viscosity, respectively.

In the ε equation, terms involving the quantity C_η are equivalent to the R term in the original RNG k-ε model [18], where $C_\eta = \eta(1 - \eta/\eta_0)/(1 + \beta\eta^3)$, $\eta = S(k/\varepsilon)$ is the ratio of the turbulent-to-mean strain timescale, and S is the magnitude of the mean strain. To take into account compressibility, a velocity dilatation term with coefficient C_3 appears in the ε equation, where [17]

$$C_3 = \frac{-4 + 2C_1 + 3(v_0\nabla\cdot u)^{-1}(dv_0/dt) + (-1)^\delta\sqrt{6}\, C_\mu C_\eta \eta}{3}. \quad (3)$$

Here, v_0 is molecular viscosity, and $\delta = 1$ if $\nabla\cdot u < 0$; $\delta = 0$ if $\nabla\cdot u > 0$. Other model constants of the present implementation of the RNG model are $C_\mu = 0.0845$, $C_1 = 1.42$, $C_2 = 1.68$, $\alpha_k = \alpha_\varepsilon = 1.39$, $\eta_0 = 4.38$, and $\beta = 0.012$ [19]. In the standard k-ε model, $C_\mu = 0.09$, $C_1 = 1.44$, $C_2 = 1.92$, $C_3 = -1.0$, $\alpha_k = 1.0$, and $\alpha_\varepsilon = 0.769$ [16].

A recently formulated wall function model [20], which accounts for gas-density variation

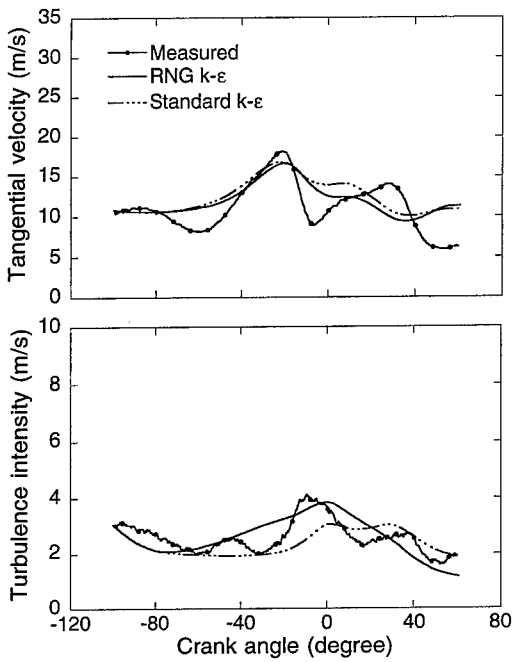

FIG. 2. Tangential velocity (top) and turbulence intensity (bottom). Engine speed = 1500 rev/min.

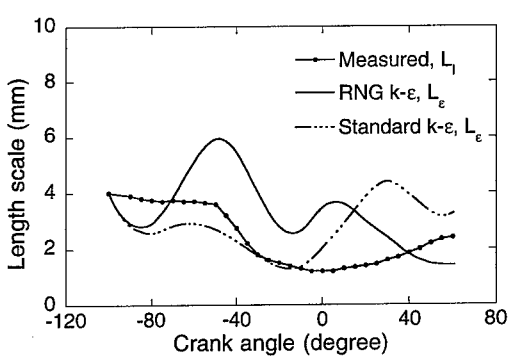

FIG. 3. Comparison of the measured integral length scale and the computed length scale ($k^{3/2}/\varepsilon$). Engine speed = 1500 rev/min.

(compressibility), was adopted for the wall boundary calculations. The computations were started at 100° before TDC after intake valve closure. To initialize the computations, the mean axial velocity was assumed to scale linearly from the piston speed at the piston surface to zero at the cylinder head surface. An empirical swirl profile [16] was used such that the tangential velocity at the measuring position was equal to the measured data. The turbulence intensity and length scale were initialized uniformly throughout the cylinder using the measured data.

Results and Discussion

The measured and computed tangential velocity and turbulence intensity at 1500 rpm engine speed are given in Fig. 2. As can be seen, the RNG model and the standard k-ε model predict almost the same tangential velocity, and they agree with the measurement at location A in Fig. 1 reasonably well throughout the compression and expansion strokes. However, the detailed flow oscillations of the measurements are not followed precisely. The prediction of the turbulence intensity is also seen to be fairly good using both models. However, the standard k-ε model predicts somewhat lower levels of turbulence intensity during compression. This behavior has also been found in a different engine geometry [17].

Two-equation, k-ε turbulence models give for the turbulence macro–length scale [16,17], $L_\varepsilon = C_\mu^{3/4}k^{3/2}/\kappa\varepsilon$, where κ is the von Karman constant. Some studies have been carried out to compare the measured integral length scale, L_I, with the predicted length scale, L_ε [8,9], and to justify the use of these models for engine flows [21], on the assumption that the L_ε is proportional (or equal) to the L_I. The present measured lateral integral length scale L_I is compared with the predicted length scale L_ε in Fig. 3. It is seen that the standard k-ε model appears to work better in the compression stroke than does the RNG model, and the RNG model prediction does not agree with the measured trend because it predicts that the length scale increases during the compression stroke and then decreases during the expansion stroke, opposite to the measured trend.

However, is it correct to assume that the L_ε is directly proportional to the integral length scale L_I in engine flows? And if not, how are the length scales related?

It has been shown by Tennekes and Lumley [13] that the integral length scale is directly proportional to $k^{3/2}/\varepsilon$ for equilibrium turbulence in a steady, homogeneous, mean shear flow. In this case, the transport equation of turbulent kinetic energy reduces to

$$-\overline{u_i u_j}S_{ij} = 2\nu_0\overline{s_{ij}s_{ij}} \tag{4}$$

where u_i is the fluctuating velocity, S_{ij} and s_{ij} are the mean and fluctuating rate of strain, respectively, and an overbar represents a Reynolds average. Equation (4) states that in this flow, the rate of production of turbulent energy by mean flow gradients equals the rate of viscous dissipation. If $S_{ij} \sim k^{1/2}/L_I$ and $-\overline{u_i u_j} \sim u'^2$ (u' is turbulence intensity) are assumed and $\varepsilon = 2\nu_0\overline{s_{ij}s_{ij}}$ is defined, then it follows that L_I is directly proportional to L_ε under the equilibrium turbulence condition.

However, in an engine, the flow undergoes rapid compression and expansion due to the piston movement, and engine turbulence is likely to be nonequilibrium in nature. Figure 4 illustrates the volume-averaged ratio of the turbulent-to-mean–strain

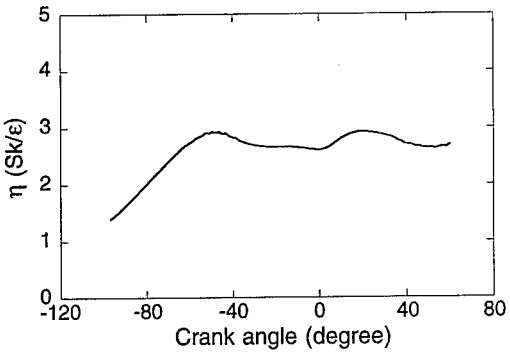

FIG. 4. Variation of the ratio of turbulent to mean-strain timescale (volume averaged).

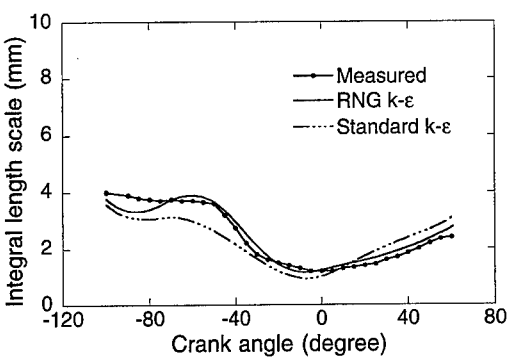

FIG. 5. Comparison of the measured and predicted integral length scales using Eq. (6). Engine speed = 1500 rev/min.

timescale at 1500 rev/min. This ratio ranges mostly from 2 to 3, which indicates the present engine flow is indeed evolving under rapid distortion conditions [22]. Since engine turbulence is nonequilibrium, the assumption that $L_I \sim L_\varepsilon$ for engine turbulence is quite questionable, and it may not be justified to directly compare the measured integral length scale with the predicted length scale.

Wu et al. [22] performed DNS computations of flows under rapid compression conditions. They found that the Taylor length scale λ and the integral length scale L_I remain proportional to each other during a rapid compression. A similar finding was made experimentally by Dinsdale et al. [7] in engine measurements. The result is also consistent with that obtained from a rapid distortion analysis of isotropic compressed turbulence given by Reynolds [23] and Wu et al. [22]. Accordingly, $L_I \sim \lambda$, and if it is assumed that the Taylor relation [13] $\varepsilon = 10\nu_0 k/\lambda^2$ holds also for isotropic compressed turbulence (which is reasonable because it follows from the definition of the Taylor length scale [13]), we have

$$\varepsilon \sim \frac{k^{3/2}}{L_\varepsilon} \sim \frac{\nu_0 k}{\lambda^2} \tag{5}$$

therefore,

$$L_\varepsilon \sim L_I Re_t \quad \text{or} \quad L_\varepsilon = C L_I Re_t \tag{6}$$

where Re_t is the turbulent Reynolds number, which is defined as $u' L_I/\nu_0$, and C is a constant, which can be shown to be

$$C = \left.\frac{L_\varepsilon}{L_I Re_t}\right|_{t=0} = \left(\frac{3}{2}\right)^{1/2} \frac{C_\mu^{3/4}}{\kappa} \left[\frac{\nu_0}{L_I^2}\frac{k}{\varepsilon}\right]_{t=0} \tag{7}$$

where the reference time $t = 0$ is at the beginning of the computation.

The significance of Eq. (6) is that it relates the integral length scale (L_I, which can be measured) and the model length scale (L_ε, which can be computed) for flows under rapid compression/expansion conditions. It shows that in a rapidly distorted isotropic turbulence, L_ε (or $k^{3/2}/\varepsilon$) is no longer directly proportional to L_I as it is in equilibrium turbulence. Instead, it is proportional to the product of L_I and the turbulent Reynolds number.

Figure 5 compares the measured integral length scale with the computed length scale, which is deduced by using Eq. (6) for the same case shown in Fig. 3. The value of the proportionality constant, C, in Eq. (6) cannot be determined by using Eq. (7) here, because ε at $t = 0$ is not known. $C = 0.005$ was chosen so that the measurement and computation could be compared in magnitude. As can be seen in Fig. 5, the computed length scale using the standard and the RNG turbulence models now agrees with the measured one very well in trend.

The same comparison is made in Fig. 6 for 1000- and 600-rev/min engine speed cases. In these two cases, the initial swirl ratio and the turbulence length scale were set to be the same as those used in the 1500-rev/min case (consistent with the measurements [3]), and the initial turbulence intensity was scaled linearly with the engine speed based on the value used in the 1500-rev/min case. The proportionality constant, C, was thus set to be 0.0075 and 0.0125 for the 1000- and 600-rev/min cases, respectively, based on Eq. (7). Again, very good agreement between measurements and the computed length-scale trends can be seen.

From Figs. 5 and 6, it can be concluded that Eq. (6) provides a more reasonable physical interpretation of the length scale L_ε for engine flows. Although the turbulence scaling arguments that led to Eq. (6) cannot give the value of the proportionality constant, C, it is shown in Eq. (7) that the value of this constant depends on the engine design (L_I), initial gas temperature (ν_0), and initial turbulence conditions (k/ε). C is proportional to the initial turbulence timescale and, hence, to the reciprocal of the engine speed.

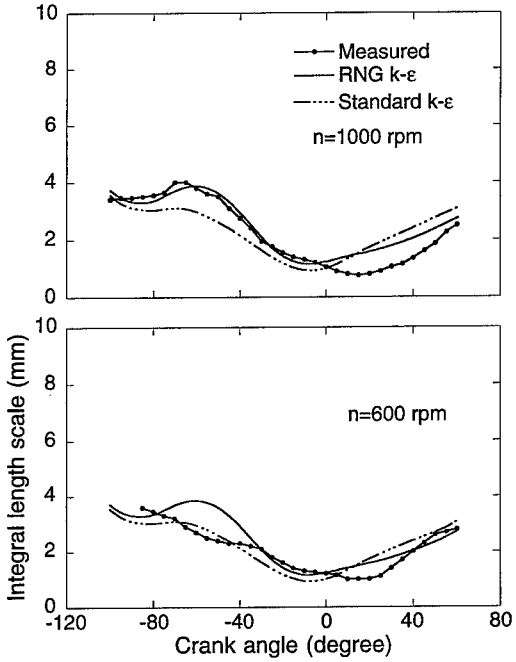

FIG. 6. Comparison of the measured and predicted integral length scales using Eq. (6).

It is also interesting to see that the obtained integral length scales at TDC seem insensitive to engine speed (i.e., about 1 mm for all the cases considered). This result confirms those previously reported by Ikegami et al. [8]. It can be explained that because the spatial scale can be related to the mean velocity and a timescale, the mean motion scales with engine speed while the timescale decreases, resulting in a spatial scale that is about constant.

The physical interpretation of L_ε given by Eq. (6) for rapidly compressed turbulence can also be used to assess previously suggested physical constraints on macro–length scales in engine flows. Morel and Mansour [21] argued that L_ε should decrease during compression and increase during expansion, scaling with the instantaneous cylinder dimension. This postulate is based on their assumption that L_ε is to be the size of the large eddies. For an isotropic compressed engine turbulence, Morel and Mansour [21] assumed that ρL_ε^3 = const. As indicated by Eq. (6), this only holds if the turbulent Reynolds number remains constant during compression, which seems physically unlikely in an engine flow. Hence, this scaling postulate is questionable.

However, it is physically reasonable to expect that the size of large eddies should scale in some way with the cylinder dimension. The problem with Morel and Mansour's postulate is that it is assumed that L_ε is proportional to L_I, representing the size of the large eddies. In fact, Coleman and Mansour [24] have recently shown that the constraint satisfied during a rapid compression is, instead, $\rho\lambda^3$ = const. Since $L_I \sim \lambda$, this can be recast as ρL_I^3 = const. Hence, for a rapidly compressed turbulence, the physical scaling postulate and its mathematical representation become consistent with each other and, as seen in Figs. 5 and 6, the size of large eddies, represented by L_I, decreases during the compression process and increases during the expansion process.

Summary and Conclusions

Computations were made of the in-cylinder flow in a practical diesel engine geometry under motoring conditions, and the results were compared with LDV measurements. The standard k-ε model [16] and a modified RNG k-ε model [17] were tested. It is shown that both models can reproduce the measured tangential velocity and turbulence intensity variation during the compression and expansion strokes reasonably well.

The present comparisons with turbulence length-scale measurements show that in rapidly distorted engine turbulence, L_ε (or $k^{3/2}/\varepsilon$) is no longer directly proportional to the integral length scale, L_I; as is the case in equilibrium turbulence. Instead, when results from rapid distortion analyses are introduced, the k-ε model macro–length scale is shown to be proportional to the product of L_I and the turbulent Reynolds number. With this relation, computed integral length-scale trends agree very well with the measured, lateral integral length scale at three engine-speed conditions. The present study also suggests that the appropriate constraint for rapidly distorted (compressed/expanded) turbulence is ρL_I^3 = const. rather than ρL_ε^3 = const. This is a more reasonable postulate for engine turbulence and is supported by the measurements and computations of the present study.

Acknowledgments

Support for the computational work was provided by the Army Research Office under Grant DAAH04-94-G-0328. Both ZH and RDR would like to acknowledge additional support from Ford Motor Co., Caterpillar Engine Co., and DOE/NASA-Lewis. The helpful comments of Profs. Chris Rutland and Gary Borman are appreciated. Thanks also to Drs. M. Auriemma and R. Macchioni for carrying out part of the experimental work.

REFERENCES

1. Tabaczynski, R. J., *Prog. Energy Combust. Sci.* 2:143–165 (1976).

2. Heywood, J. B., *Internal Combustion Engine Fundamentals,* McGraw-Hill, 1988.
3. Corcione, F. E. and Valentino, G., *Combust. Flame* 99:387–394 (1994).
4. Auriemma, M., Corcione, F. E., Macchioni, R., and Valentino, G., SAE Paper 952385, 1995.
5. Wakuri, Y., Kido, H., Murase, E., and Wang, Z., *Memories of the Faculty of Engineering, Kyushu Univ.* 43:179–191 (1983).
6. Collings, N., Roughton, A. W., and Ma, T., SAE Paper 871692, 1987.
7. Dinsdale, S., Roughton, A., and Collings, N., SAE Paper 880380, 1988.
8. Ikegami, M., Shioji, M., and Nishimoto, K., SAE Paper 870372, 1987.
9. Fraser, R. A. and Bracco, F. V., SAE Paper 880381, 1988.
10. Corcione, F. E. and Valentino, G., SAE Paper 902080, 1990.
11. El Tahry, S. H. and Haworth, D. C., *J. Propulsion Power* 8:1040–1048 (1992).
12. Rask, R. B., in *Fluid Mechanics of Combustion Systems* (T. Morel, R. P. Lohmann, and J. M. Rackley, Eds.), American Society of Mechanical Engineers, Fairfield, NJ, 1981, pp. 11–20.
13. Tennekes, H. and Lumely, J. L., *A First Course in Turbulence,* MIT Press, Cambridge, MA, 1972.
14. Reynolds, W. C., in *Combustion Modeling in Reciprocating Engines* (J. N. Mattavi and C. A. Amman, Eds.), Plenum Press, New York, 1980, pp. 41–68.
15. Hinze, J. O., *Turbulence,* 2nd ed., McGraw-Hill, New York, 1975.
16. Amsden, A. A., O'Rourke, P. J., and Butler, T. D., LA-11560-MS, Los Alamos National Labs., 1989.
17. Han, Z. and Reitz, R. D., *Combust. Sci. Technol.* 106:267–295 (1995).
18. Yakhot, V. and Orszag, S. A., *J. Sci. Comput.* 1:3–51 (1986).
19. Yakhot, V., Orszag, S. A., Thangam, S., Gatski, T. B., and Speziale, C. G., *Phys. Fluid A* 4:1510–1520 (1992).
20. Han, Z. and Reitz, R. D., *Int. J. Heat Mass Trans.* (1996). In press.
21. Morel, T. and Mansour, N. N., SAE Paper 820040, 1982.
22. Wu, C. -T., Ferziger, J. H., and Chapman, D. R., Department of Mechanical Engineering Technical Report No. TF-21, Stanford University, Stanford, CA, 1985.
23. Reynolds, W. C., in *Turbulence Models and Their Applications,* Vol. 2, EYROLLES, Paris, 1984.
24. Coleman, G. N. and Mansour, N. N., *Phys. Fluids A* 3:2255–2259 (1991).

COMMENTS

Jim O' Connor, Varity Perkins, England. Which turbulence model should be used for in-cylinder calculations (e.g. diesel combustion)?

Author's Reply. We have found that the RNG k-ε model predicts better combustion results for diesel engines than the conventional k-ε model in comparisons with experiment data. The RNG model predicts relatively lower viscosity and therefore gives better resolution of large-scale flame structures. The effects of turbulence models on diesel combustion modeling were discussed in [17] of the paper.

Twenty-Sixth Symposium (International) on Combustion/The Combustion Institute, 1996/pp. 2725–2732

EFFECT OF HARDWARE ALIGNMENT ON FUEL DISTRIBUTION AND COMBUSTION PERFORMANCE FOR A PRODUCTION ENGINE FUEL-INJECTION ASSEMBLY

V. G. MCDONELL, L. ARELLANO, S. W. LEE AND G. S. SAMUELSEN
UCI Combustion Laboratory
University of California,
Irvine, CA 92697-3550, USA

The hardware in a production combustor cannot be constrained within strict tolerances due to (1) manufacturing variations and (2) provisions for thermal expansion that often preclude exact alignment of all parts over the operating cycle. The demand for higher performance is directing attention to the relationship of hardware alignment to combustor performance. The present article reports on a systematic characterization of hardware alignment on both the spray structure (nonreacting) and associated combustion performance for a practical fuel-injection/swirler assembly. Planar, liquid laser-induced fluorescence (PLLIF) and phase Doppler interferometry (PDI) are utilized for the nonreacting assessment, whereas emissions and temperatures are used to characterize the reacting case. It is found that misalignment of 2.54 mm has a significant effect on the fuel distribution while having only a modest effect on the gas-phase aerodynamics and overall droplet sizes. Quantification of the fuel distribution using unmixedness indices allows for correlations between the fuel distribution and combustion performance to be established and assessed. It is found that the effect of alignment on the fuel distribution under nonreacting conditions directly translates into an impact on combustion performance in terms of mean pollutant levels and stability as well as the spatial distribution of the patterns of the pollutants at the exit plane. The study also demonstrates that PLLIF has a potential for screening designs relative to PDI due to its efficient application. However, the complex phenomena occurring in liquid-fired combustion systems suggests that PLLIF images are not sufficient in general, since changes in droplet size and aerodynamic structures can affect directly the combustion performance as well as the fuel distribution.

Introduction

Efforts to reduce emissions from present day aircraft engines have focused upon the combustor. Geometric and operational features of combustors are, as a result, receiving especially close scrutiny. Currently, trial and error is utilized to optimize the performance of existing designs. Little attempt has been made to develop a mechanistic understanding of the processes occurring within the combustor due to the time and effort required to obtain the necessary detailed measurements. For one particular geometry, illustrated in Fig. 1, some basic understanding of the processes occurring is being provided from detailed studies conducted with state-of-the-art diagnostics such as phase Doppler interferometry (PDI) and CARS [e.g., 1–3]. However, these diagnostic tools are time consuming to apply and, as a result, tend to preclude extensive characterization of many geometries and conditions. This shortcoming tends to make the trial-and-error approach appealing in meeting short-term requirements.

Once trial and error is applied, improved performance is generally realized. However, a successful design must demonstrate robustness to manufacturing tolerances and other practical considerations. It has been demonstrated previously that performance of the device shown in Fig. 1 is sensitive to the geometry of the various components [4] as are other injector/swirler configurations [e.g., 5–8].

The present study evaluates sensitivity of performance using an injection assembly in which the degree of misalignment can be controlled. The range of the misalignment considered is consistent with that found in practice as the engine cycles through different power settings ("0.1 in." or 2.54 mm). Figure 1 depicts the nature of the misalignment—the nozzle and primary swirler shift relative to the venturi, secondary swirler, and flare.

Phase Doppler interferometry is a natural choice for this study since it can measure gas velocity as well as size, velocity, and local volume flux of droplets. However, it is evident that *more efficient* diagnostic tools are required for (1) problem solving in research and (2) screening production hardware. In addition, such tools must address the critical aspects of the problem. For example, the role of fuel/air unmixedness in combustion performance has been demonstrated for liquid-fueled direct and prevapor-

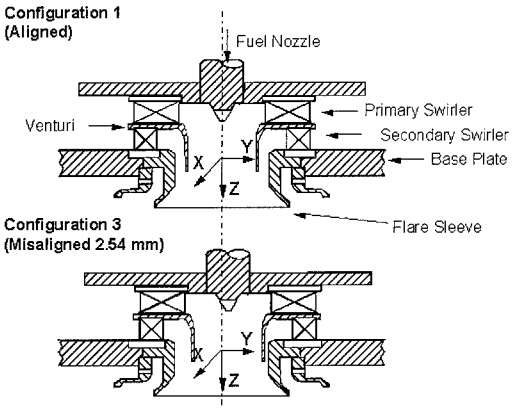

FIG. 1. Cross-section schematic of the practical fuel-injection assembly.

ized systems as well as for gaseous-fueled premixed systems [e.g., 9–11].

Of these studies, only Fric [10] explicitly studied the fuel distribution prior to combustion, and the system considered was premixed and gas fueled. Studying the fuel distribution in a liquid-fired combustor is more challenging, especially for a direct-injection system. As a result, efforts have been recently directed at development of planar, liquid laser-induced fluorescence (PLLIF) to measure more efficiently the fuel distribution produced by liquid-based systems [12]. PLLIF is applied in the present study to (1) efficiently assess the role of hardware alignment on fuel distribution and (2) develop correlations between fuel distribution and combustor performance.

The objectives of the present study are to evaluate the role of hardware misalignment on fuel distribution and combustor performance and to assess the utility of PLLIF as a diagnostic and screening tool. The approach taken is (1) apply PLIFF and PDI in the nonreacting environment to characterize the effect of hardware misalignment, (2) characterize the effect of the misalignment on combustion performance, and (3) apply and correlate indices of mixing to the combustion results.

Experiment

Facility

The facility utilized for the nonreacting studies features a 450- × 450-mm square duct oriented vertically. The swirl cup is fed by a 150-mm-diameter plenum located centrally within the duct and injects the spray downward. Additional details are described elsewhere [13]. A separate facility is utilized for the reacting flow emissions measurements and features an upfired arrangement. For the reacting studies, an 80-mm-i.d. quartz tube serves as the combustor liner. In this case, the liner is 5D (D = 80 mm) in length and features an area contraction of 50% at the exit to mimic backpressure.

Diagnostics

PLLIF is utilized to characterize the planar distribution of the fuel. In this technique, a laser is spread into a sheet that is passed through the spray. The energy in the laser induces fluorescence from molecules in the liquid. In the present case, a small amount of fluorescein is doped into methanol and is stimulated with an argon-ion laser operating at the 0.4880-μm wavelength. As a planar imaging technique, PLLIF is relatively quick to apply. Despite the attractiveness of PLLIF, the complexity of liquid-fueled combustion systems, especially those that are swirl stabilized, precludes "simple" characterization relative to the combustion performance. For example, droplet size and velocity play a critical role in the combustion process and, in the absence of some knowledge of these quantities, any observed role of fuel distribution may be fortuitous. Similarly, the nature of the aerodynamics plays a role. For example, the size and extent of the recirculation zone can result in various residence times that may play as much a role as fuel distribution in combustion performance. As a result, characterization of behavior other than fuel distribution is required in general. Hence, tools (such as PDI) that offer proven information regarding details of the gas and droplet behavior remain necessary in spite of their inherently time-consuming operating process. PDI (Aerometrics 3100-S) is utilized in the nonreacting case to measure the gas-phase velocities and droplet characteristics.

For the reacting cases, a set of standard-source, monitoring equipment was utilized (HORIBA, Ltd.). Unburned hydrocarbons, oxygen, carbon monoxide, carbon dioxide, and oxides of nitrogen were measured at the exit plane of the combustor at Cartesian coordinates in 8-mm increments. A 6.5-mm-diameter water-cooled stainless steel extractive probe was used in conjunction with a heated sample line to convey the sample to the emissions analyzers. The measurements obtained are reported on a "dry basis."

Temperatures were measured in the same grid locations using a thermocouple (type K). The temperature measurements reported are not corrected for catalytic effects or radiation losses.

Conditions

The main circuit of the production, duplex fuel injector for this swirl cup was utilized for these studies. Methanol was employed to allow the fluorescein

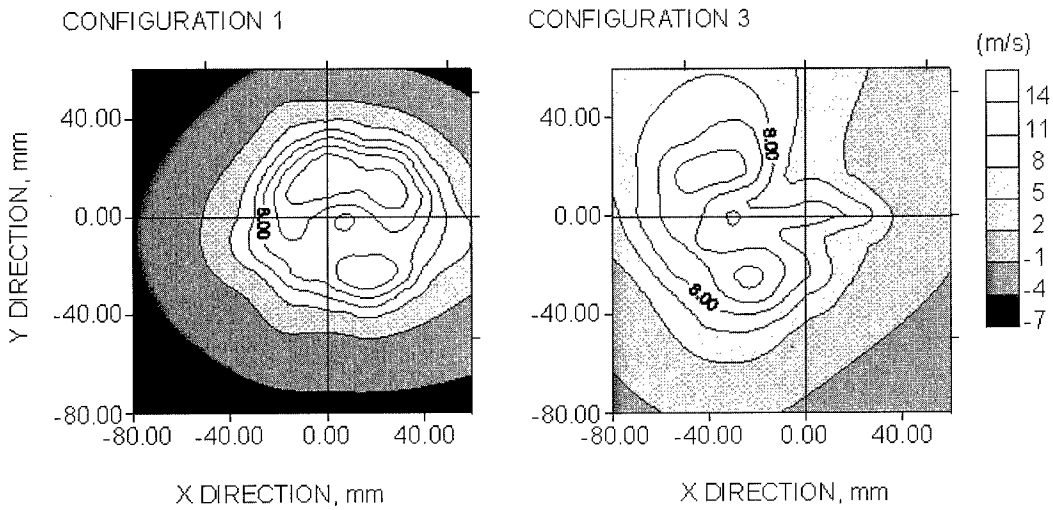

FIG. 2. Comparison of gas-phase mean axial velocity (m/s) at Z = 50 mm.

dye to be utilized with the argon-ion laser-based PLLIF system, as discussed above. In each case, 4% pressure drop relative to the ambient pressure (101 kPa) was utilized. Air preheat of 400 K was utilized in the reacting case (60 K above the methanol boiling point). A methanol flow rate of 9 kg/h was utilized, and an overall equivalence ratio of 0.82 was maintained.

Results

Although results were obtained for three configurations (misalignment of 0, 1.27, and 2.54 mm), configurations 1 (0 mm) and 3 (2.54 mm) are emphasized. Due to the inherent asymmetry of configuration 3, single radial profiles obtained via PDI do not capture the essential features of the flow. Rather, data acquired in planes have the greatest utility in determining the effect of the misalignment. Hence, the majority of the data presented are from a plane 50 mm downstream of the exit of the flare. PDI measurements were acquired at locations in a grid arrangement in 4-mm increments. To obtain the information presented for each case, 241 point measurements, requiring days to obtain, were required. In contrast, the PLLIF images were acquired in a matter of minutes.

The nonreacting cases are presented first, followed by the emissions characteristics. Following the measurements, discussion regarding the correlation between the results is provided.

Nonreacting Characterization

Aerodynamics

Measurements of the effective area revealed differences of less than 2% for the three configurations. In addition, since the same swirler was used for each case, it was expected that the size and extent of the recirculation zone would be similar. To confirm this, PDI was applied to determine the effect of the misalignment on the gas velocity. The results for the mean axial velocity are presented in Fig. 2 for the two extreme cases. Recall that the nozzle assembly is shifted in the $+Y$ direction for configuration 3. The general structure for configuration 1 is relatively symmetric, and the variation is typical for similar "axisymmetric" practical hardware [1,2,4,6–8]. In configuration 3, the high-velocity region moves in the $+Y$, $-X$ direction relative to configuration 1. However, by 50 mm, the recirculation zone has closed for both cases, and the general magnitude of the velocities is similar, confirming that the similar effective areas result in similar general aerodynamic structure.

Droplet size

The effect of the misalignment on the droplet sizes determined by PDI is shown in Fig. 3. Configuration 1 again reflects a relatively symmetric pattern compared to configuration 3. While a region of locally smaller drops in the $-X$ region of the spray is observed, the difference in the general droplet sizes is small, suggesting that the basic atomization mechanism is not altered by the misalignment.

Fuel distribution

Figure 4 presents a comparison of the spatial distribution of the fuel. In this case, data from PDI and PLLIF are presented. The PDI results are shown in Figs. 4a and 4b for configurations 1 and 3, respectively. These results indicate trends similar to the size and velocity shown previously. However, the

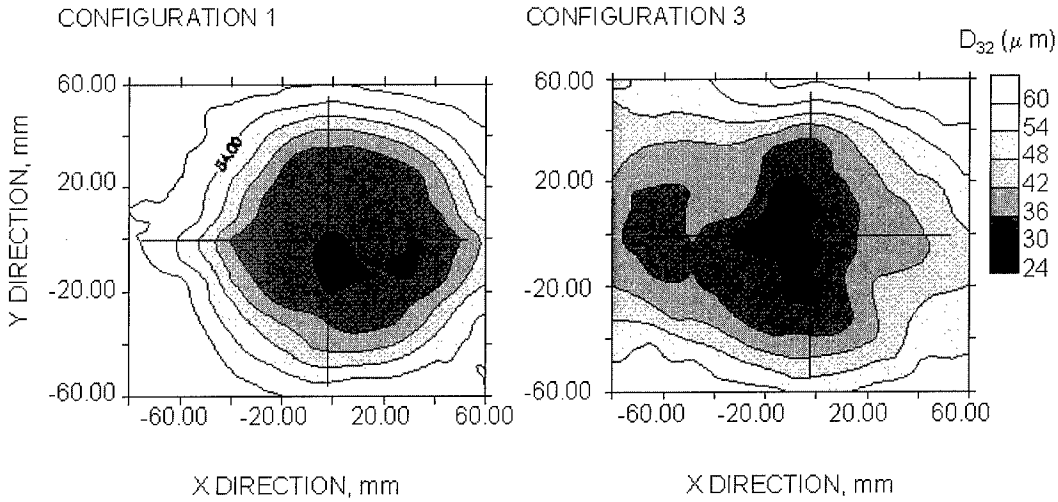

FIG. 3. Comparison of droplet distribution D_{32} (μm) at Z = 50 mm.

peak in fuel distribution becomes more pronounced for configuration 3 in a manner consistent with observations for another injector assembly [7]. A peak in the fuel distribution occurs in the $+X$, $+Y$ quadrant in contrast to the peak in gas-phase velocity and minimum in drop size that occur along the $-X$ direction. The impact of the misalignment on the fuel distribution is far more substantial than on the drop size or aerodynamics.

Figure 4 also presents the fuel distribution results as measured by PLLIF. These results are shown in Figs. 4c and 4d for configurations 1 and 3, respectively. These results are based on the average of 32 frames from the CCD camera which requires significantly less time to obtain than collecting the 200+ points via PDI. The images reveal identical structure in the fuel mass distribution.

Reacting Characterization

For the reacting characterization, measurements of the exit plane emissions are presented. It is expected that the general behavior of the aerodynamics, droplet velocities, and temperatures for configuration 1 are similar to that found elsewhere [3]. Figures 5–7 present contours of [CO], [HC], and [NO_x]. The [CO] emissions are presented in Fig. 5 and reveal a systematic increase in asymmetry with increased misalignment. Note that the scale on the contours changes for each configuration. Figure 6 presents the contours of the unburned hydrocarbons. This time, configurations 2 and 3 reveal a region of locally high emissions relative to configuration 1. Finally, Fig. 7 presents contours of the [NO_x] levels at the exit. Like the CO, the NO_x levels reveal systematically degraded symmetry with increased misalignment.

Correlations

To quantify the differences observed, the degree of nonuniformity described by "unmixedness," U, determined using the expression in Eq. (1) [14], is applied:

$$U = \frac{c_{\text{var}}}{c_{\text{avg}}(1 - c_{\text{avg}})} \tag{1}$$

where

c_{var} = variance in field c

c_{avg} = average of c.

Equation (1) can be applied to arbitrary distributions and is applicable for either space ("spatial unmixedness," U_s) or time ("temporal unmixedness," U_t). U ranges in value from 0 to 1, and lower values of U reflect more uniform fields. Since fuel distribution is affected significantly by the misalignment and is known to be a critical factor in combustion performance, Eq. (1) is applied to this quantity. In this case, the PLLIF results are considered with an area of interest shown in Fig. 4 to determine the spatial unmixedness of the fuel.

Figure 8 compares the spatial unmixedness, U_s, based on the PLLIF images and the lean blow-off limit. The results reveal that U_s increases systematically with an increase in the misalignment and that the stability improves in a corresponding fashion.

Figure 9 presents the correlation between the mean concentrations (right axis) and the unmixedness (left axis) of the emissions results presented in Figs. 5–7 and U_s based on the PLLIF images. The slight dependence of the mean NO_x level on U_s based on the nonreacting fuel distribution observed is within experimental error and is not strong enough to draw a conclusion. Recalling that this case is op-

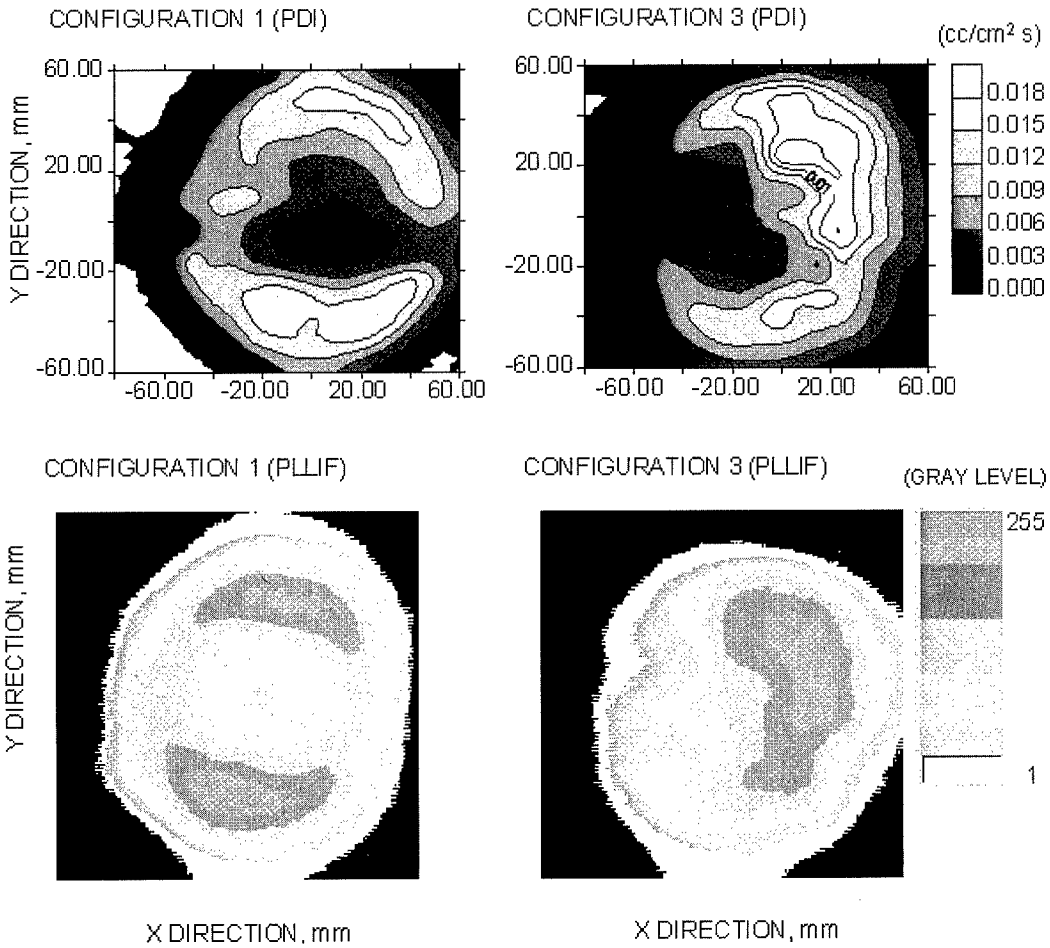

FIG. 4. Comparison of volume flux (cc/cm^2 s) from PDI and PLLIF intensity (proportional to liquid volume) for configurations 1 and 3 at axial distance Z = 50 mm from flare exit.

erating at an overall equivalence ratio of 0.82, the expected NO_x dependency is not obvious. Previous work [11] suggested that NO_x levels should decrease with higher U_s values when the overall equivalence ratio exceeds 0.7. However, the mean levels of CO and UHC exhibit increases corresponding to increases in U_s. The left axis in Fig. 9 is used to assess U_s (i.e., the patterns) based on the measured emissions quantities at the exit plane, with U_s based on the nonreacting fuel distribution. U_s, based on CO and UHC correlates well with U_s based on the nonreacting fuel distribution. Finally, a weak anticorrelation is observed between U_s based on NO_x and U_s based on the nonreacting fuel distribution.

Summary and Conclusions

A systematic study of the effect of hardware misalignment on the nonreacting spray structure and combustion performance for a practical fuel-injection/swirler assembly has been conducted for a single condition. PLLIF and PDI were utilized for the nonreacting assessment, whereas emissions and temperatures were used to characterize the reacting case. The following conclusions are drawn from the work:

- The effect of misalignment typically encountered by production hardware during operation on the nonreacting flow field is significant. The fuel distribution is dramatically impacted, whereas the gas-phase structure remains similar with the exception of a shift in the flow direction; the overall droplet sizes remain similar.
- A nearly linear relationship between the spatial unmixedness of the fuel ascertained via PLLIF in the nonreacting spray and lean blow off was found, which is consistent with previous studies.
- Significant correlation was found between the lev-

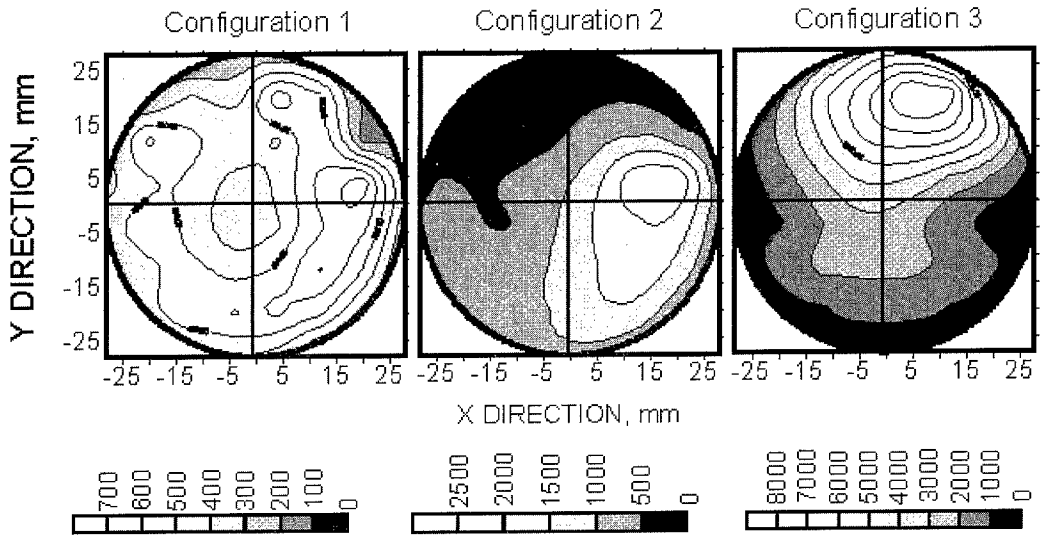

FIG. 5. CO concentration contours at exit plane (ppm).

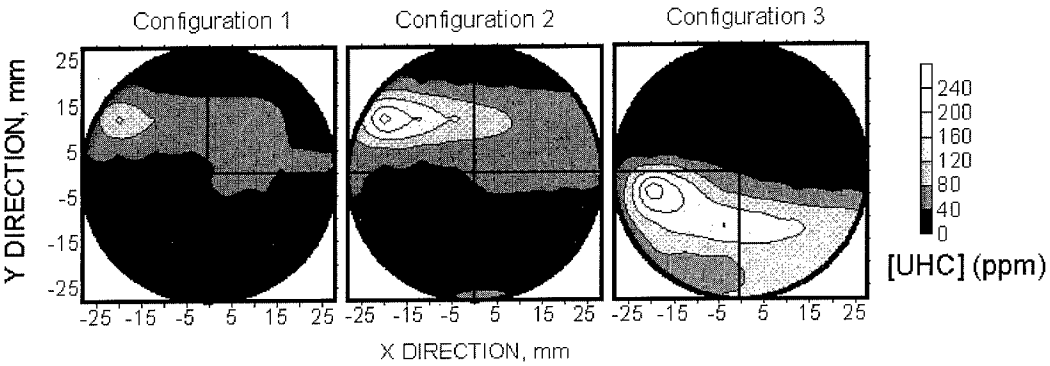

FIG. 6. UHC concentration contours at exit plane.

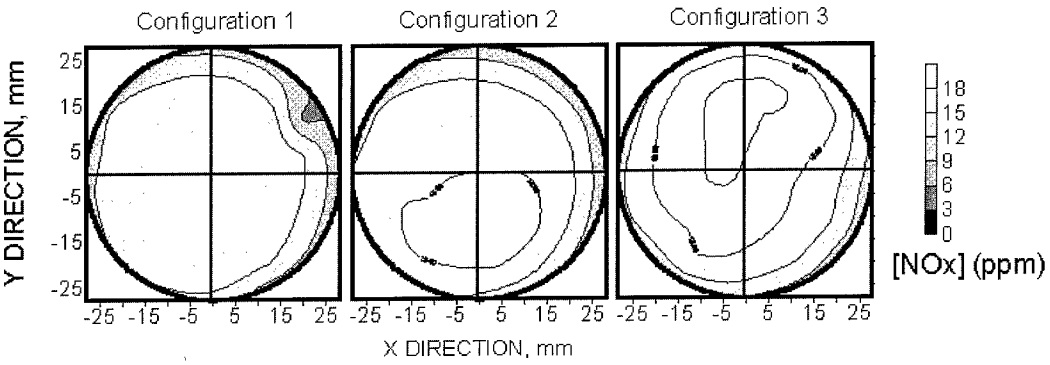

FIG. 7. NO_x concentration contours at exit plane.

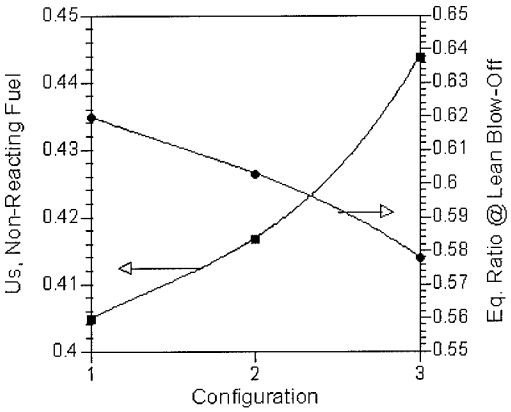

FIG. 8. Relation between configuration spatial unmixedness from PLIFF images and lean blow-off limit.

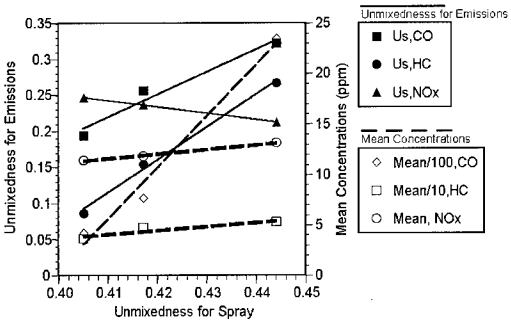

FIG. 9. Relationship between unmixedness for spray, unmixedness for emissions, and mean concentrations of emissions.

els of CO and hydrocarbons produced and the spatial unmixedness based on nonreacting fuel distributions characterized by PLLIF.

- Significant correlation was also found between the spatial unmixedness of CO and hydrocarbons at the exit plane and the spatial unmixedness of the fuel based on PLIFF images.
- The efficiency of PLLIF makes it an attractive tool for screening fuel distributions produced by practical devices.
- The results suggest that improving the robustness in the concentricity of the design can help meet increasingly stringent emissions regulations.

Acknowledgments

GE Aircraft Engines is gratefully acknowledged for supplying the hardware utilized and support for swirl cup studies and diagnostics development. The assistance of Jason Campbell in the computations associated with the images is appreciated.

REFERENCES

1. Wang, H. Y., McDonell, V. G., and Samuelsen, G. S., *J. Propulsion Power* 10:441–445 (1994).
2. Wang, H. Y., McDonell, V. G., and Samuelsen, G. S., *J. Propulsion Power* 10:445–451 (1994).
3. Takahasi, F., Schmoll, J., Switzer, G. L., and Shouse, D. T., *Twenty-Fifth Symposium (International) on Combustion,* The Combustion Institute, Pittsburgh, 1994, pp. 183–191.
4. Wang, H. Y., McDonell, V. G., and Samuelsen, G. S., *ASME J. Eng. Gas Turb. Power* 117:282–289 (1995).
5. McDonell, V. G. and Samuelsen, G. S., *ASME J. Eng. Gas Turb. Power* 112:44–51 (1990).
6. Rosfjord, T. J. and Eckerle, W. A., *J. Prop. Power* 7:849–856 (1991).
7. Cohen, J. M. and Rosfjord, T. J., *J. Prop. Power* 9:16–27 (1993).
8. Rosfjord, T. J. and Russell, S., *J. Prop. Power* 5:144–150 (1989).
9. Pompei, F. and Heywood, J. B., *Combust. Flame* 19:407–418 (1972).
10. Fric, T., *J. Prop. Power* 9:708–713 (1993).
11. Lyons, V. J., *AIAA J.* 20:660–665 (1982).
12. Igushi, T., McDonell, V. G., and Samuelsen, G. S., An Imaging System for Characterization of Liquid Volume Distributions in Sprays, *Proceedings, 6th Annual ILASS-Americas Conference,* 1993, submitted to *Atomization and Sprays.*
13. McDonell, V. G. and Samuelsen, G. S., *AIAA J. Prop. Power* 7:684–691 (1991).
14. Dankwertz, P. V., *Appl. Sci. Res., Sec. A* 3:279–296 (1952).

COMMENTS

Prof. Sigmar Wittig, University of Karlsruhe, Germany. I was surprised to see relatively small effects of alignment deviations on the droplet size distribution. Do you have an explanation?

Author's Reply. In this device, the breakup of the liquid film deposited upon the venturi is the primary mechanism of atomization. As a result, it is expected that the droplet size will not be strongly affected if the filming mechanism is not strongly affected. In the present case, the misalignment does not change the location of the simplex nozzle relative to the venturi and, as a result, has little impact on filming mechanism and the subsequent droplet sizes.

•

Prof. M. M. ElKotb, Cairo University, Egypt. As we know swirling flow creates hollow conical spays, what is the effect of the surrounding cup on the stabilization and penetration of the spray?

Author's Reply. The general characteristics of the spray fields produced by dome hardware similar to that used in the present study have been documented [1–3]. The larger droplets appear in the "hollow" cone portion of the spray, and penetrate "ballistically" into the chamber. A fraction of the mass from the simplex atomizer is transported directly into the core of the spray. Also in the core, a significant population of fine droplets are backmixed to the cup, and are likely to be a key to stabilization. In addition to providing swirl, the location of the cup relative to the atomizer serves to enhance the mixing of the fuel and air prior to exiting the flare.

REFERENCES

1. Wang, H. Y., McDonell, V. G., and Samuelsen, G. S., *Twenty-Fourth Symposium (International) on Combustion,* The Combustion Institute, Pittsburgh, 1992, pp. 1457–1463.
2. Wang, H. Y., McDonell, V. G., Sowa, W. A., and Samuelsen, G. S., *AIAA J. Propulsion Power* 10:441–445, (1994).
3. Wang, H. Y., McDonell, V. G., Sowa, W. A., and Samuelsen, G. S., *AIAA J. Propulsion Power* 10:446–451 (1994).

•

Arvind K. Jasuja, Cranfield University, UK. Could you comment on the extent of attenuation encountered by the laser light sheet in your spray experiments and any corrections made for its compensation? In the context of dense, practical sprays at high pressures, severe attenuation can be encountered, thus potentially undermining the utility of the PLIF technique.

Author's Reply. In the present spray, the attenuation through the spray is less than 10%, thus the impact of "dense spray effects" are small. For "dense" (i.e., optically thick) sprays, efforts are currently underway to account for such effects and are described in detail [1,2].

REFERENCES

1. Talley, D. G., Thamban, A. T. S., McDonell, V. G., and Samuelsen, G. S., in *Recent Advances in Spray Combustion: Spray Combustion Measurements and Model Simulation,* K. K. Kuo, ed., Vol. 171, *Progress in Astronautics and Aeronautics,* AIAA, pp. 113–142, 1996.
2. Talley, D. G., Verdieck, J. F., Lee, S. W., McDonell, V. G., and Samuelsen, G. S., Paper 96-0469, Accounting For Laser Sheet Extinction In Applying PLLIF To Sprays, presented at 34th AIAA Aerospace Sciences Meeting, Reno, NV, January, 1996, submitted to *J. Propulsion Power.*

Twenty-Sixth Symposium (International) on Combustion/The Combustion Institute, 1996/pp. 2733–2739

THE EFFECTS OF FUEL–AIR MIXING ON NO_X FORMATION IN NON-PREMIXED SWIRL BURNERS

TAKASHI TERASAKI
Research Laboratory, Noritz Corporation, Tokyo, Japan

SHIGERU HAYASHI
Thermofluid Dynamics Division, National Aerospace Laboratory, Tokyo, Japan

This paper describes the low NO_x emissions achieved by a non-premixed, direct fuel-injection burner, equipped with a unique double swirler for gas turbine combustors. The burner has circular and annular air channels to which swirlers are fitted. The inner channel converges into a throat, and gaseous fuel is injected into the air flow by a multihole fuel nozzle. The NO_x emissions and combustion efficiency of the double-swirler burner with natural gas fueling were compared with those of conventional swirl burners of different hub diameters. The measurements of gaseous species concentration in the combustion region at the flame tube exit were made at atmospheric pressure; at inlet air temperatures of 650, 950, and 1100 K; and at equivalence ratios down to the lean flame stability limit. Among the burners tested, the double-swirler burner achieved the lowest NO_x emissions level: at 1800 K gas temperature and 15 m/s reference air velocity, the emissions indices for NO_x with the double-swirler burner, and the conventional small-hub swirler and large-hub swirler burners were 0.5, 1.1, and 2.2 g/kg fuel, respectively. The reasons that the double-swirler burner achieved the lowest NO_x emissions are discussed on the basis of the profiles of gaseous species concentration and gas temperature as well as on the data of fuel–air mixing in the combustion region.

Introduction

The operating temperatures of gas turbines and air-breathing engines go up continuously for better thermal efficiency. Combustor inlet air temperatures of the 900–1000 K level are targeted in research programs of propulsion systems for the next generation supersonic transport [1] and large high-bypass ratio engines of pressure ratios as high as 40. The operation at higher combustion temperatures leads to significantly increased NO_x emissions, provided that the available NO_x control strategy remains the same. The regulations for pollutant emissions from gas turbines and aircraft, especially for NO_x, will be more stringent in the near future. Therefore, the development of low-NO_x combustion technology that is effective at high-temperature operating conditions is required.

It is generally recognized that premixed combustion of lean, homogeneous mixtures has a potential for achieving very low levels of NO_x emissions, even at high inlet air temperatures [2]. At very high inlet air temperatures, however, mixture preparation upstream of the combustion region would lead to autoignition of the injected fuel, which is favored at increased pressures. Unexpected combustion in the mixture preparation zone would damage the combustor hardware and endanger the engine safety.

Some researchers [3–5] have reported the capability of low-NO_x emissions for non-premixed burners, which are completely free from problems such as autoignition and flashback. The experimental results obtained at atmospheric pressure and moderate inlet air temperatures showed that low-NO_x emissions were achieved not only for gaseous fuel [3,4] but also for kerosene sprays [5], while maintaining high combustion efficiency even near flame stability limits. A feature common to these burners is enhanced mixing of fuel and excessive combustion air just downstream of the burner exit by means of strong swirling flows or interacting impinging jets. NO_x emissions depend significantly on the homogeneity of unburned mixtures [6,7] and on the characteristic lifetime of burned gas pockets in the combustion region. Rapid mixing increases mixture homogeneity and shortens the characteristic time for NO_x formation. Later, Tacina [8] categorized these non-premixed, low-NO_x burners into "direct fuel injection."

In the present study, the potential for low-NO_x emissions of the double-swirler burner, developed by Hayashi [9], is investigated at inlet air temperatures up to 1100 K using natural gas. The fuel is widely used for advanced high-temperature stationary gas turbines for power generation and is supposed to be used for future hypersonic propulsion

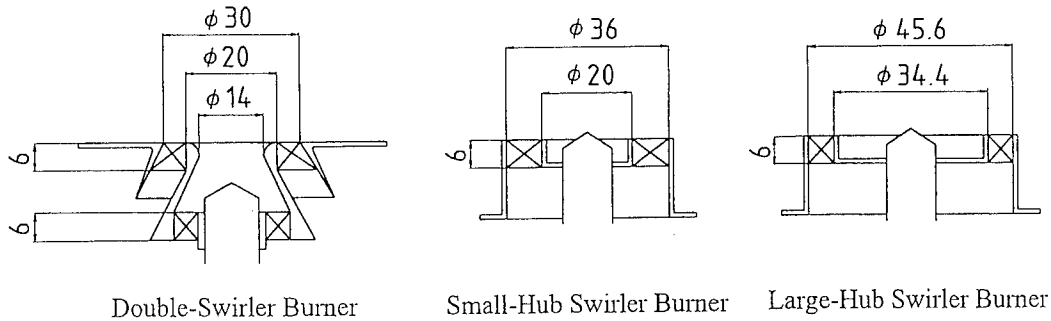

FIG. 1. Schematic drawing of double-swirler and conventional swirl burners used.

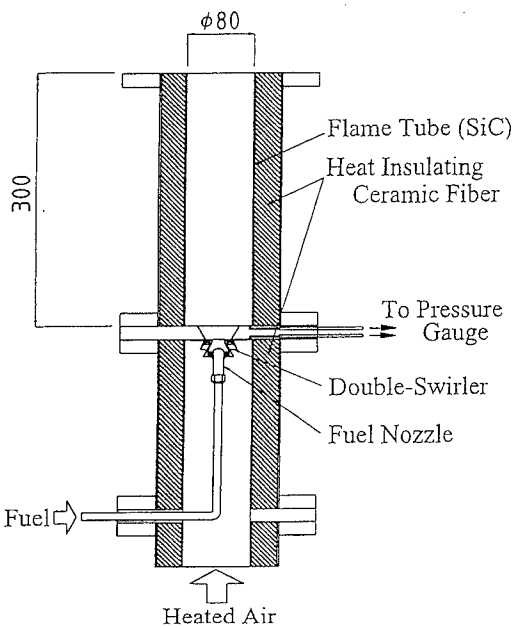

FIG. 2. Schematic drawing of experimental combustor fitted with double-swirler burner.

engines [1]. The NO_x emission levels for the double-swirler burner are compared with those for two conventional burners fitted with large-hub and small-hub swirlers. The reasons for the difference in the levels of NO_x emissions measured for the three burners are discussed on the basis of the measured profiles of gas temperature, local equivalence ratio, and gaseous species including CO, CO_2, HC, O_2, NO, and NO_x in the combustion region. The data of fuel–air mixing, measured under nonburning conditions, are also used for the discussion.

Experimental

Burner Modules

The burner modules used in the present study are schematically shown in Fig. 1. The double swirler is composed of coaxial and corotational swirlers with 16 curved vanes of an angle of 45° and a multihole fuel nozzle. Combustion air is split between inner circular and outer annular passages with a ratio of about 1:2. The large-hub and small-hub swirlers, composed of 16 curved vanes of an angle of 45°, have the same annular passage area. The nominal swirl numbers of the small-hub and large-hub swirlers are 0.8 and 0.88, respectively. According to the criterion in Ref. 10, both produce a "strong" swirl, which provides a central recirculation behind the hub.

There is a significant difference between the flow structures downstream of the double swirler and conventional swirlers. The conventional swirler provides a recirculation zone formed behind the hub, through which fuel is injected to the annular air jet. The double swirler, on the other hand, provides a recirculation zone, with its apex close to the throat. A high-velocity jet issuing from the center orifice prevents flash back, and the resulting short residence time excludes the possibility of autoignition in the passage.

The conventional swirl burners are mounted flush to the end wall of the flame tube while the double-swirler burner is mounted on back of the end wall flange of 16 mm in thickness, as shown in Fig. 2. The flange has a diverging conical passage connecting the swirler and the flame tube. The flame tube is a silicone nitride tube, 300 mm in length, 80 mm in diameter, and 10 mm in wall thickness, blanketed with ceramic fiber for minimizing heat losses.

Combustion air is electrically heated, and its flow rate is measured by an orifice flowmeter, and fuel flow rate is measured by a mass flowmeter.

Procedures

Emissions characteristics were investigated for fuel-lean mixtures at inlet air temperatures of 650, 950, and 1100 K and at reference air velocities of 10 and 15 m/s, averaged over the cross-sectional area of the flame tube.

Representative gas sampling was made at 300 mm from the end of the wall by using an X-shaped, area-

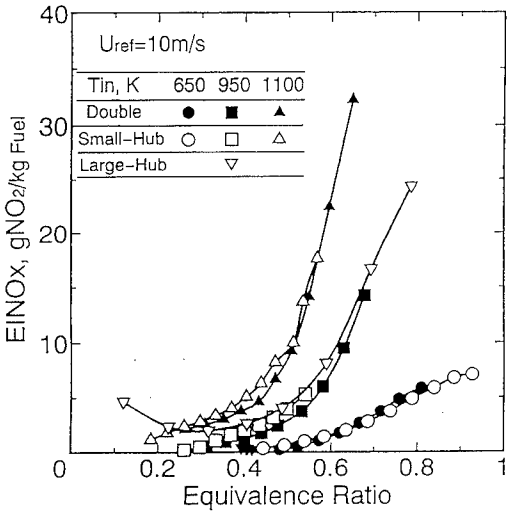

FIG. 3. Effects of inlet air temperature on NO_x emissions from double-swirler and conventional swirl burners.

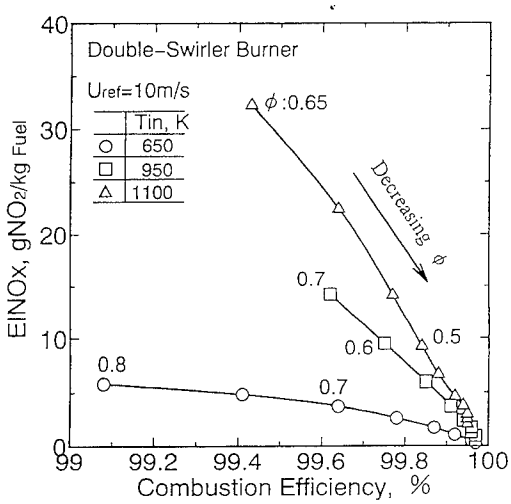

FIG. 4. Correlation of NO_x emissions and combustion efficiency for double-swirler burner.

averaged gas sampling probe with 36 holes in total. To prevent condensation of water vapor in the sampling probe and lines, the feed rate of cooling water to the probe was controlled, and the sampling line was electrically heated to a temperature of about 430 K. Burned gas samples were diluted with pure nitrogen using a capillary flow mixer before entering the gas analyzer. The concentrations of O_2, CO, CO_2, HC (as CH_4), NO, and NO_x were measured by the standard gas analysis procedures: chemiluminescence for NO, nondispersive infrared absorption for CO and CO_2, flame ionization for HC, and paramagnetic analysis for O_2. The NO_2–NO converter with stainless steel catalyst was calibrated using standard NO_2 gas to confirm conversion efficiencies greater than 96%. Combustion efficiencies were calculated from the measured gas compositions, assuming that the final combustion products at complete combustion were water vapor and carbon dioxide. Equivalence ratios were calculated not only from the measured air and fuel flow rates but also from the gas compositions measured for the area-averaged gas samples. The equivalence ratios calculated based on the area-averaged gas analysis data at the flame tube exit agreed with those from the measured fuel and air flow rates to accuracies better than 5% for all experimental conditions.

The local species concentrations in the combustion region were measured for the three burners by using a single-hole gas sampling probe at 650 K inlet air temperature, 10 m/s reference air velocity, and 0.5 overall equivalence ratio. The sampling probe was traversed along the diameter at each measurement cross section, and sampled gas was analyzed by the procedure described above.

The mixing of injected fuel and air in the combustion region was investigated under nonburning conditions. A mixture of 1% methane and air, instead of fuel, was injected from the fuel nozzle, and local fuel concentrations in the flame tube were measured using a minute single-hole probe and a flame ionization detector.

Results and Discussion

NO_x Emissions

Six multihole fuel nozzles of different configurations were preliminary tested for the double-swirler and conventional swirl burners. The results revealed that the effects of number, size, and position of holes and fuel-jet angle of the fuel nozzle on the NO_x emission levels were very small, suggesting that mixing of fuel and air was mainly controlled by the swirling air flow. Therefore, a multihole fuel nozzle with 16 jet holes was used for the later experiments. The total cone angle of fuel jets is 60° for the double-swirler burner and 120° for the conventional swirl burners.

The $EINO_x$ for the three burners is shown in Fig. 3. The effect of inlet air temperature is significant, and $EINO_x$ increases more steeply with equivalence ratio at higher inlet air temperatures. The NO_x emissions for the double-swirler burner are lower than those for the conventional swirl burners at lower equivalence ratios (<0.7). It is generally difficult for conventional swirl burners to attain very low NO_x emissions without deteriorating combustion efficiency [11].

The $EINO_x$-combustion efficiency correlations for the double-swirler burner are shown in Fig. 4 for

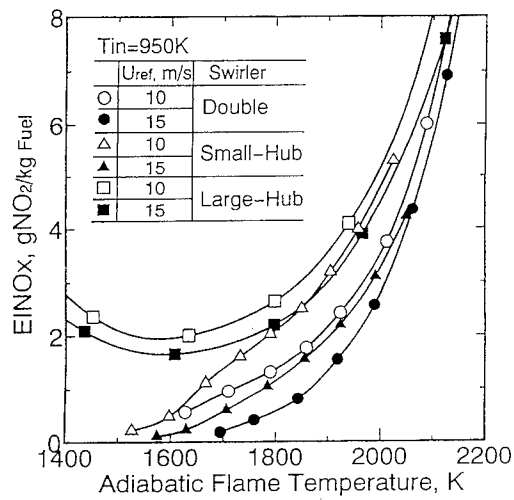

FIG. 5. Comparison of NO_x emissions from double-swirler and conventional swirl burners.

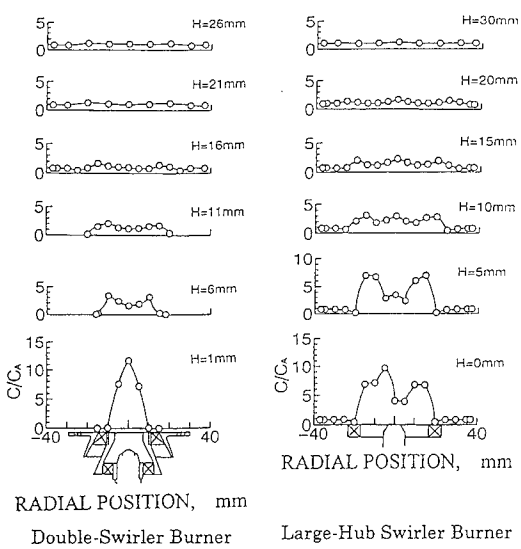

FIG. 6. Normalized fuel concentrations in combustion region for double-swirler and large-hub swirler burners under nonburning condition.

different inlet air temperatures. The numerical values attached to some data points represent equivalence ratios at which the emissions data were measured. With decreasing equivalence ratio along each line, the $EINO_x$ decreases while combustion efficiency increases. Thus, both very low NO_x emissions and very high combustion efficiency (>99.9%) are achieved simultaneously, even at fairly lean conditions. This trend is quite different from that of the conventional swirl burners, for which combustion efficiency deteriorates at very lean conditions. The measured concentrations of HC were less than a few parts per million. The trend of measured CO concentration with overall equivalence ratio was consistent with that of the prediction by adiabatic equilibrium calculations, though the measured CO concentration was lower than the predicted at greater equivalence ratios.

The NO_x emissions levels measured at 950 K inlet air temperature and at 10- and 15-m/s reference air velocities are plotted against adiabatic flame temperature in Fig. 5. For the sake of clarification, only the data measured at flame temperatures up to about 2100 K are included in the figure. The $EINO_x$ for the double-swirler burner is always the smallest, and an increase of reference air velocity results in lower NO_x emissions levels. At 1800 K adiabatic flame temperature and 15-m/s reference air velocity, the $EINO_x$ for the double-swirler burner is about half of that for the small-hub swirler burner and about one-fourth of that for the large-hub swirler burner. The $EINO_x$ for the double-swirler and the small-hub swirler burners decreases monotonically with decreasing adiabatic flame temperature. The $EINO_x$ for the large-hub swirler burner, which sustained flame until the fuel flow was cut off, reaches a minimum at an adiabatic flame temperature of around 1600 K.

Fuel–Air Mixing under Nonburning Conditions

Enhanced mixing of fuel and air in the combustion region is very effective in suppressing NO_x formation. Fuel–air mixing in the double-swirler and the large-hub swirler burners was investigated under nonburning conditions at an inlet air temperature of 350 K and a reference air velocity of 5 m/s.

The profiles of nondimensional fuel concentration C/C_A, where C and C_A are the local and overall fuel concentrations, are shown in Fig. 6. In this figure, H represents the distance from the swirler exit to the measurement cross section. The profiles of C/C_A show the radial spread of fuel jets and progress of fuel–air mixing. In the double-swirler burner, at $H = 1$ mm, the profile is a cone with its apex on the axis, suggesting that the mixing of air and fuel in the inner channel is far from complete. The profile comes to have two peaks ($C/C_A = 3.5$) at $H = 6$ mm, but is almost flat at $H = 16$ mm. More uniform profiles of C/C_A are observed further downstream (i.e., $H = 21$ and 26 mm). The measured flame temperature profiles show that the flame started at $H = 10$ mm. Thus, it is expected that mixtures of high uniformity are formed in a very short distance from the double-swirler exit. The M-shaped C/C_A profiles just downstream of the fuel nozzle of the large-hub swirler burner reflect penetration of the fuel jets. With increasing axial distance, the two peaks are diminished and uniform fuel distributions result at $H = 30$ mm.

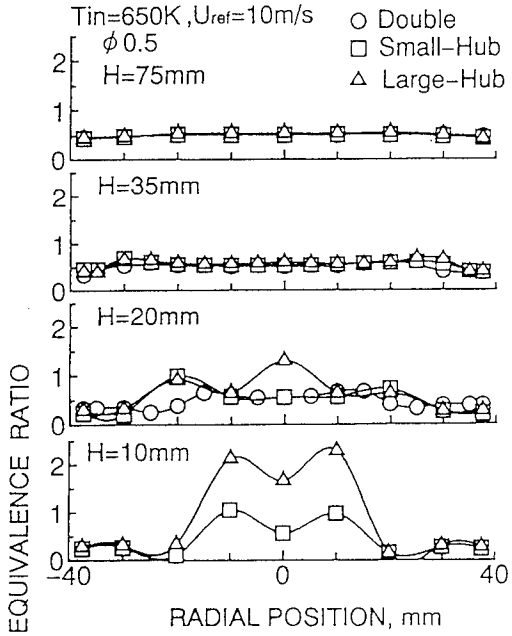

FIG. 7. Profiles of equivalence ratio in combustion region for double-swirler and conventional swirl burners.

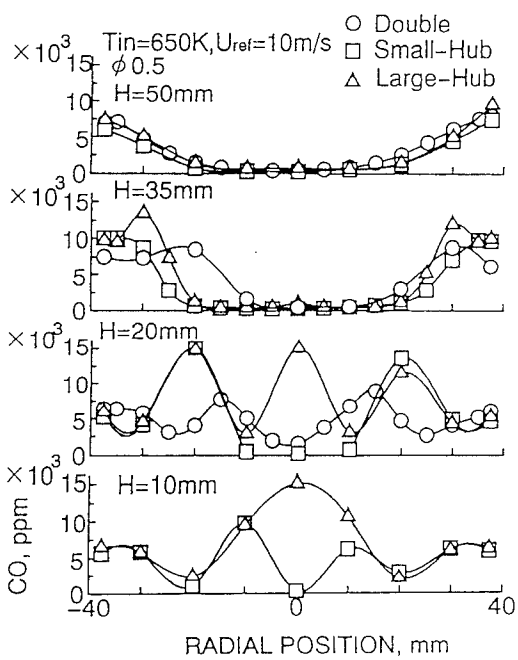

FIG. 8. CO concentrations in combustion region for double-swirler and conventional swirl burners.

Uniform profiles of fuel–air ratio are obtained in a shorter distance in the double-swirler burner than in the conventional swirl burner. A comparison of the fuel concentration profiles shows that the fuel-rich region is smaller in the double-swirler burner than in the large-hub swirler burner. That rapid fuel–air mixing in the double-swirler burner is the reason for the lower NO_x emissions of the double-swirler burner.

Profiles of Equivalence Ratio and Gaseous Species Concentrations

Measurements of species concentrations and gas temperatures were made at different axial positions in the flame tube at 650 K inlet air temperature, 10-m/s reference air velocity, and 0.5 overall equivalence ratio.

Local Equivalence Ratio

The profiles of local equivalence ratio in the three burners are compared in Fig. 7. At $H = 10$ mm, the profiles for the conventional swirl burners are M-shaped and the mixtures are rich in the central region of the large-hub swirler burner. The profiles are increasingly uniform with axial distance. They almost agree with each other at $H = 35$ mm, and very uniform profiles result at $H = 75$ mm for all the burners.

A comparison of the development of profiles for the burners shows that fuel–air mixing is the slowest in the large-hub swirler burner. The fuel-rich zone in the large-hub swirler burner is the reason for high NO_x emissions of the burner.

Carbon Monoxide and Unburned Hydrocarbons

The CO profiles for the three burners are compared in Fig. 8. The variation of the CO profile with axial distance is generally consistent with that of HC profile, which is not included in the paper because the allowable length of a paper is limited. It is shown that the hub size has a significant effect on the CO and HC profiles at $H = 10$ and 20 mm. The CO concentration is highest on the axis for the large-hub swirler burner while minimum for the small-hub swirler burner. Except for the central region, the CO and HC profiles are the same for the conventional swirl burners. At $H = 50$ mm, the profile of CO concentration became high near the flame tube wall, and HC concentration became very low over the cross section. The oxidation of CO in the region near the wall is slow because of lower gas temperatures, though the profiles of CO become nearly uniform for both burners at $H = 100$ mm.

Oxides of Nitrogen

Figure 9 shows the profiles of NO_x emissions in the flame tube for the three burners. It is shown that

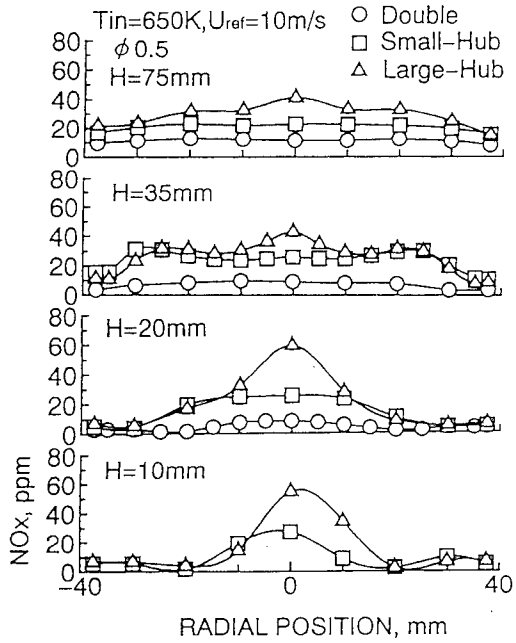

FIG. 9. NO_x concentrations in combustion region for double-swirler and conventional swirl burners.

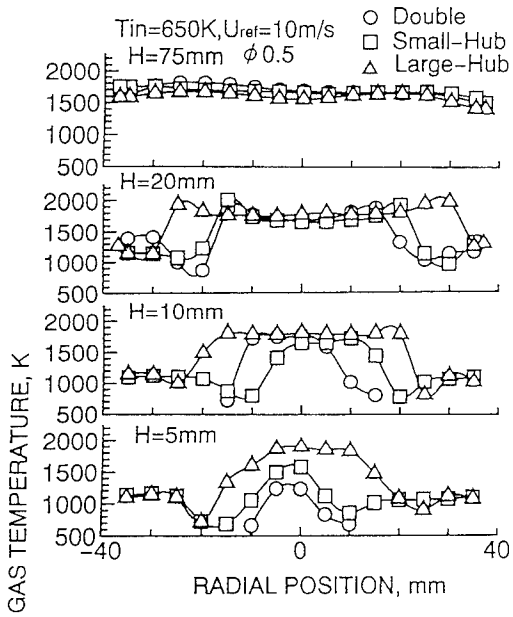

FIG. 10. Profiles of gas temperature in combustion region for double-swirler and conventional swirl burners.

at $H = 20$ mm, the *peak* NO_x concentration for the double-swirler burner is about one-third of that for the small-hub swirler burner and about one-sixth of that for the large-hub swirler burner. With increasing axial distance, the NO_x concentration decreases in the central region, and uniform profiles result. The reduction of NO_x concentration in the central region for the large-hub swirler burner is remarkable. The profiles are nearly uniform at $H = 75$ mm not only for the double-swirler burner but also for the small-hub swirler burner. A comparison of the NO_x concentrations measured at $H = 75$ mm for both burners shows that the NO_x concentration (about 10 ppm) for the double-swirler burner is about half of that for the small-hub swirler burner. The NO_x profile for the large-hub swirler burner is not uniform even at $H = 75$ mm and has a region of high NO_x concentrations (about 50 ppm) on the axis. It is noted that the NO_x concentration increases remarkably in the upstream region of the flame tube and increases little in the downstream region of $H = 75$ mm. The order of the three burners in respect to NO_x emissions concentrations at $H = 75$ mm does not change until the flame tube exit, as shown in Fig. 5. The profiles of equivalence ratio for the double-swirler burner, as shown in Fig. 7, are more uniform than those of conventional swirl burners. Moreover, the regions of high gas temperature in the upstream region of the flame tube is smaller in the double-swirler burner than in the conventional swirl burners, as shown in Fig. 10. The results confirm that the NO_x concentration, especially in the upstream region of the flame tube, for the double-swirler burner is lower than that for the conventional burners.

Conclusions

In this study, a non-premixed, direct fuel injection burner with a unique double swirler was developed for low-NO_x and low-CO emissions gas turbine combustors. The emissions characteristics of the burner are compared with those for the swirl burners of conventional configurations. The reasons for the low emissions of the double-swirler burner are discussed on the basis of the measured profiles of equivalence ratio and gaseous species concentrations, as well as of the data on fuel–air mixing in the combustion region.

Major conclusions are as follows:

1. The compatibility between low-NO_x emissions and high combustion efficiency was demonstrated using the double-swirler burner, which directly injected natural gas into the combustion region. The NO_x emissions levels for the burner were significantly lower than those for conventional swirl burners. The NO_x emission levels for

the large-hub swirler burner were much higher than those for the small-hub swirler burner.

2. NO_x was formed rapidly in the upstream region of the flame tube.
3. The profile of equivalence ratio in the upstream region of the flame tube for the double-swirler burner was more uniform than that for conventional swirl burners. The mixing of fuel and air was more rapid in the double-swirler burner than in the conventional swirl burners, which resulted in uniform equivalence ratio profiles in the combustion region. The improved mixing of directly injected fuel and air in the double-swirler burner is the reason for the lower NO_x emissions of the burner.

REFERENCES

1. Shaw, R. J., Gilkey, Samuel, and Hines, Richard, Engine Technology Challenges for A 21st Century High-speed Civil Transport, *ISAAC 93-7064*, 1993.
2. Hayashi, S., Effects of Heterogeneity of Mixtures on Gaseous Emissions in Premixed/Prevaporized Combustion, 1983 Tokyo International Gas Turbine Congress, pp. 245–251, 1983.
3. Hussain, U. S., Andrews, G. E., Cheung, W. G., and Shahabadi, A. R., Low NO_x Primary Zones Using Jet Mixing Shear Layer Combustion, *ASME 88-GT-308*, 1988.
4. Alkabie, H. S., Andrews, G. E., and Ahmad, N. T., Lean Low NO_x Primary Zones Using Radial Swirlers, *ASME 88-GT-245*, 1988.
5. Hayashi, S., Compatibility between Low-NO_x Emissions and High-combustion Efficiency by Lean Direct Injection Combustion, *ASME 95-GT-276*, 1995.
6. Lyons, V. J., Fuel/Air Nonuniformity—Effect on Nitric Oxide Emissions, *AIAA J.* 20(5):660–665 (1982).
7. Fric, T. F., Effect of Fuel-Air Unmixedness on NO_x Emissions, *AIAA 92-3345*, 1992.
8. Tacina, R. R., Low NO_x Potential of Gas Turbine Engines, *AIAA-90-0550*, 1990.
9. Hayashi, S., *Technical Memorandum*, TM470, National Aerospace Laboratory, 1982.
10. Beer, J. M., and Chigier, N. A., *Combustion Aero-Dynamics*, Appl. Sci. London, 1972.
11. Koff, B. L., Aircraft Gas Turbine Emissions Challenge, *ASME 95-GT-422*, 1993.

COMMENTS

Prof. C. Bruno, University of Rome, Italy. The results presented are extremely interesting in that very high combustion temperatures correspond to very low levels of NO_x. At very low equivalence ratio and low combustion temperatures, there is recent evidence that N_2O may form, compensating for the NO reduction. Will the authors look into this issue in the future?

Author's Reply. Thank you very much for your interest in our study and for your suggestion. We are very sorry to say that the N_2O concentration has not been measured. We are now preparing to measure N_2O.

•

Christian Eigenbrod, ZARM Institute, Germany. How high is the pressure drop of your swirler compared with the conventional type?

Are the spin directions of the two swirlers parallel or counterwise?

Author's Reply. We did not measures the pressure drop of the conventional swirler. The pressure drop of the double-swirler was about 7% at 650 K inlet air temperature, 10 m/s reference air velocity, and 0.5 equivalence ratio.

The double-swirler is a co-rotational swirler.

Twenty-Sixth Symposium (International) on Combustion/The Combustion Institute, 1996/pp. 2741–2748

A NUMERICAL AND EXPERIMENTAL STUDY OF FUEL EVAPORATION AND MIXING FOR LEAN PREMIXED COMBUSTION AT HIGH PRESSURE

M. RACHNER, M. BRANDT, H. EICKHOFF AND C. HASSA
DLR, Institute for Propulsion Technology
Köln, Germany

A. BRÄUMER, H. KRÄMER, M. RIDDER AND V. SICK
Physikalisch-Chemisches Institut, Universität Heidelberg
Heidelberg, Germany

A prevaporizer-premix duct with complete optical access operating at pressures up to 15 bar and at temperatures up to 850 K has been built to investigate in detail the coupled processes of atomization, evaporation, and mixing of kerosene at conditions relevant to aeroengines and stationary gas turbines. Phase-Doppler anemometry (PDA) was used to measure liquid-phase properties and laser-induced fluorescence for the liquid and gaseous fuel. The evaporation and dispersion properties of the prevaporizer were simulated with a Lagrangian particle tracking computer program. For the flat prefilming atomizer used, complete evaporation was obtained within 100 mm without autoignition. Dynamic pressure, important for a sufficiently fine atomization, was about 3% of total pressure. Comparing parametric variations of the experiments with the computations, it was found that air temperature had the largest influence on evaporation, whereas pressure only had an indirect effect through atomization quality. In the same way, the initial spray temperature was shown to be an important parameter for evaporation, and it should be measured. The spray acceleration and evaporation history was reproduced sufficiently well for engineering purposes both with and without taking into account spray feedback on the gas phase. The dispersion was not sufficient for practical use in premix ducts. Turbulence generators are needed to promote spray dispersion and vapor mixing.

Introduction

Lean, premixed combustion of gaseous fuels has been applied in stationary gas turbines as a low-emission combustion concept with considerable success. For liquid fuel-based stationary engines and aeroengines, the realization of lean, premixed, prevaporized (LPP) combustion is hindered by the hazards of autoignition and flashback at high combustor inlet temperatures and pressures. For aeroengines, space and weight constraints aggravate the design problems. However, in light of increasing pressure ratios of subsonic engines and high inlet temperatures of supersonic engines, both promoting increased NO_x formation, the potential of an almost 10-fold reduction of NO_x compared to conventional diffusion flame combustors justifies a long-term, multistep research effort, such as one undertaken in a program of the European Commission uniting engine manufacturers, research organizations, and universities [1].

The aim of the experiments reported in this contribution was to investigate the processes of atomization, evaporation, and mixing in detail at conditions relevant to aeroengines and high-performance stationary gas turbines in a prevaporizer model with complete optical access. Comparison of the experimental results with numerical predictions can improve the understanding of the underlying physics considerably, and with computer codes validated at the relevant conditions, designers can take full advantage of gains to be achieved with geometrical variations at dramatically reduced costs. The results of such a comparison are given in this paper.

Experiment

To achieve complete evaporation fast enough, the lowest possible initial drop-size diameter has to be produced. Hence, an atomization study [2] was undertaken to identify atomizers suitable for prevaporization configurations prior to the evaporation experiment. A flat prefilming airblast atomizer gave the lowest drop-size diameters at the relevant engine conditions. Consequently, such an atomizer, Fig. 1, was used in the present study. The liquid is spread over the surface of the atomizer through a slit, forming a thin film, and is atomized by the high-momentum air stream. The spray is then accelerated from

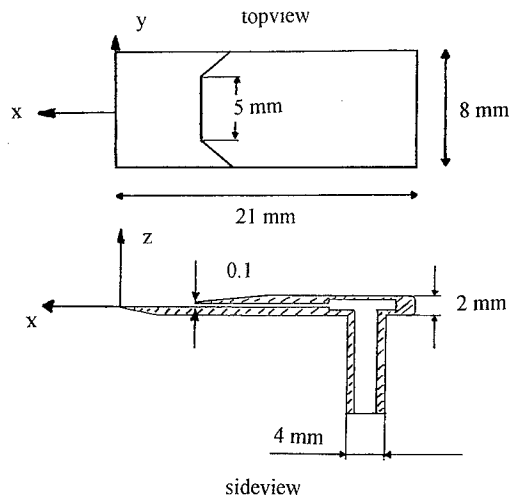

FIG. 1. Flat, prefilming airblast atomizer.

the small film velocity to the velocity of the surrounding gas. The fuel-flow-per-atomizer width was chosen in accordance with prevaporizer air-to-fuel ratios.

The atomization quality of airblast atomizers exhibits a dependence on ambient pressure. The evaporation rate is influenced by the acceleration history, which, in turn, is governed by the particle Stokes number, depending on the gas-to-droplet density ratio and particle diameter. The Stokes number also influences the turbulent dispersion of the droplets. It is therefore not possible to decouple evaporation and mixing from atomization, nor can the influence of a variation of the thermodynamic parameters be isolated in the experiment. Thus, it had to be carried out at actual engine conditions with practical fuels, i.e., kerosene Jet A. The pressure was varied from 3 to 15 bars and the temperature between 550 and 850 K, covering the cruise conditions of many aeroengines and full load of stationary turbines. It was assumed that the largest part of the allowable combustor pressure loss can be used to generate the prevaporizer pressure head, so the bulk air velocity in the prevaporizer was only varied between 80 and 120 m/s, with most of the measurements made at 120 m/s. The autoignition correlation of Ref. 3 for kerosene gives ignition delays of only a few milliseconds for these conditions. Therefore, it was decided to limit the prevaporizer length to 150 mm.

Experimental Apparatus

The test cell is shown in Fig. 2. The outer pressure housing has three-way optical access and is isolated from the heat of the hot, inner quartz duct by the cooling air flow surrounding the inner duct. The prevaporizer duct had a rectangular inner cross section of 25 by 40 mm. The air was heated by a 520 kW electrical heater. The facility and the measurement techniques are described in detail in Ref. 4 and the experimental results in Ref. 5.

Droplet sizes and velocities and liquid volume fluxes were measured by a two-component Phase-Doppler anemometer (PDA) [6]. As Phase-Doppler anemometry is restricted to a single particle in the measurement volume, the liquid volume fluxes were corrected by a particle rejection probability based on Poisson statistics [15]. However, accurate measurements close to the atomizer lip ($x < 30$ mm) were not possible due to very high particle concentrations. The postprocessing of the liquid volume flux

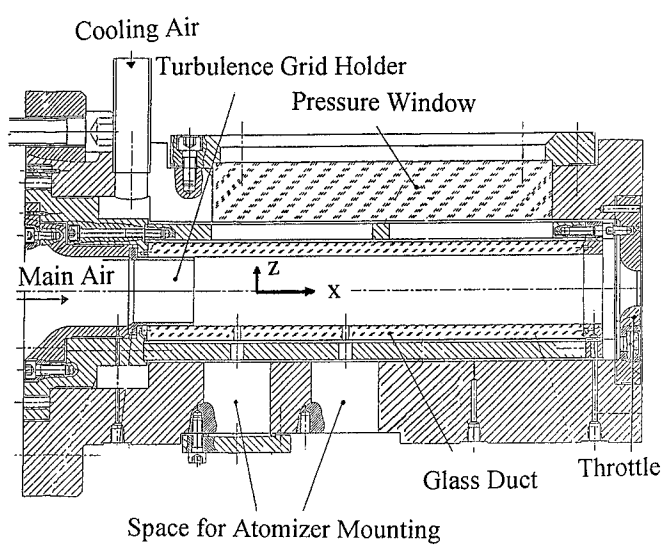

FIG. 2. Test cell.

accounted for the shape of the measurement volume, limited by the slit in the receiving optics and its orientation relative to the mean flow direction [4]. Test measurements on a nonevaporating kerosene spray at comparable conditions, but at ambient temperature, showed that the resulting error was within 15% of the nominal flux, if the particle concentrations were not too high. This error margin does not include drop-sizing errors caused by refractive index changes of the heated droplets. Drop sizes were measured in first-order refraction under a scattering angle of 52°. Neglecting refractive index gradients inside the droplets, the decrease of the refractive index of kerosene when heated up from ambient temperature to its wet-bulb temperature, as reported by Ref. 16, results in a maximum drop-sizing error of 4%. At each axial position, 50–80 point measurements with 20,000 particles were made over the cross section of the duct. However, measurements at streamwise positions, with more than 99% mass evaporated, are based on a minimum of 4000 particles. Relative liquid volume fluxes were obtained by integration of all measurement points, normalized by the inlet flux. Representative spray diameters were computed by averaging over all single-point values, weighted with the local liquid volume fluxes.

A detailed description of the optical setup for the laser-induced fluorescence (LIF) measurements is given in Ref. 7. A XeCl excimer laser (17 ns pulses) and two intensified charge coupled device (CCD) camera systems allow simultaneous monitoring of Mie scattering and LIF signals of kerosene. Like other commercial fuels [8], kerosene Jet A can be excited directly at 308 nm to give strong fluorescence signals at longer wavelengths. A cylindrical lens was used to form the laser beam to a 0.2-mm-thick laser sheet, which was focused in the middle of the test duct parallel to the air flow.

Numerical Spray Model

Numerical predictions of the evaporating spray were performed by Lagrangian particle tracking. For each computational particle, representing a number of droplets, the equations for momentum, internal energy, and mass together with three equations for the particle location, i.e., eight ordinary differential equations, were solved by an Adams scheme.

A dilute spray with spherical droplets is considered. In the momentum equations only the drag term (employing Putnam's c_D formula [10]) is taken into account because the density ratio of liquid fuel to air is large. A standard evaporation model (quasi-steady, spherically symmetric Stefan flow around the droplet with Ranz–Marshall convection corrections of Nusselt and Sherwood numbers; variable Lewis number; properties of the boundary layer taken at 1/3 reference state; phase equilibrium at the droplet surface) is used (for example, [9,10]). Real gas effects are not accounted for because the present case is well below the critical pressure. No local temperature gradients are presumed inside the droplet. The multicomponent kerosene fuel Jet A is represented by a single-component fuel, the properties of which were compiled from the literature. Particle turbulent dispersion was modeled by a modified version of a spectral dispersion model [11,12]. It accounts for the exponential temporal and spatial declining of the autocorrelation of the gas velocity fluctuations at particle location along its trajectory. Neither in the evaporation model nor in the dispersion model were any constants tuned.

With this spray code, a parametric study parallel to the LPP experiments was performed. For reasons of computational economy, a homogeneous gas field with no influence of the spray on the gas flow was assumed. Typically requiring 3 h on a SCI INDICO 2 workstation, 160,800 computational particles were tracked. Taking into account full coupling between spray and gas flow in the duct (starting with a block profile for the mean gas streamwise velocity at $x = -10$ mm and neglecting atomizer wake) gave only a negligible influence on spray volume flux, representative diameters, and droplet temperature and dispersion. Hence, the spray feedback was neglected. The baseline case considered was an air pressure of 9 bars, a duct inlet temperature of 750 K, and an air velocity of 125 m/s, the turbulence intensity typically being 5%. As the dense spray region just behind the atomizer is not accessible to PDA measurements, lacking information about spray initial conditions had to be completed by assumptions. From experiments under pressure but at ambient temperature [2], an initial Rosin–Rammler droplet size distribution was extrapolated at $x = 0$. There, the given liquid volume flux of 1 g/s was distributed in z range from -0.5 to $+0.5$ mm, decreasing linearly from its maximum value at the symmetry plane $z = 0$. As in prefilming airblast atomizers, the air accelerates the droplets from the low film velocity, the mean initial particle streamwise velocity component was chosen to be small (10 m/s), and mean transverse droplet velocities were neglected. In contrast, for the droplet initial rms-velocity components, a nonzero value had to be assumed (see comment on Fig. 9) because the LIF measurements showed a strong fluctuation of the liquid in the z direction. A Gaussian distribution of the droplets' initial velocity was assumed. The droplets' initial temperature had to be guessed. A value of 343 K turned out to be reasonable (see comment on Fig. 7). All calculated, averaged quantities are defined in the same way as done in the measurements.

Results

The results of measurements and predictions to be presented refer to the baseline case (9 bar, 750 K, 125 m/s), unless stated otherwise.

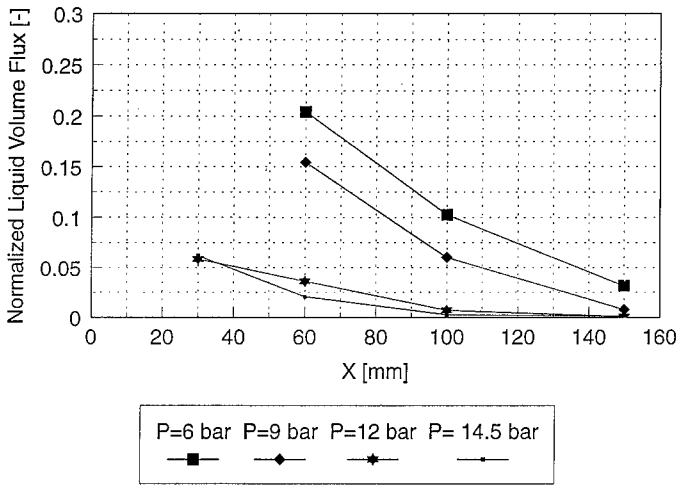

FIG. 3. Measured influence of air pressure on streamwise development of liquid volume flux.

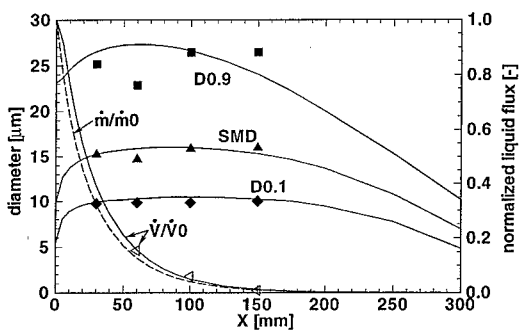

FIG. 4. Streamwise development of representative spray diameters and liquid volume and mass flux—comparison of predictions with measurements (lines = prediction; symbols = measurement).

Evaporation Characteristics

The streamwise decrease of the total liquid mass flux characterizes the progress of evaporation. Respective PDA measurements of the liquid volume flux, Fig. 3, were limited to a downstream region, where the main body of the spray has already been evaporated. This restriction is caused by the dense spray limitation of the PDA measurement technique.

Raising the pressure results in a significant enhancement of evaporation. Because of the pressure dependence of airblast atomization, the influence of pressure on the droplet behavior was studied isolated from atomization by performing numerical calculations at $p = 6$ and 14.5 bar. Hereby, all other parameters were left unchanged. The results show only a small decrease of the evaporation when raising the pressure: the normalized liquid volume flux at $x = 60$ mm was 14.6% and 17.4% for $p = 6$ and 14.5 bar, respectively. The influence of pressure on the representative diameters was similarly small. So it can be concluded that the measured pressure dependence of evaporation is mainly caused by atomization producing a finer spray at higher pressure.

That pressure insensitivity of evaporation is the result of a balance of interacting effects: higher pressure lowers the vapor mass fraction at the droplet surface for a given droplet temperature, leading to a faster temperature rise of the droplets and a higher wet-bulb temperature. In our case, we got 500 and 542 K at 6 and 14.5 bar, respectively. Moreover, raising pressure increases particle Reynolds number. This, in turn, raises Nusselt and Sherwood numbers but also causes a higher acceleration of the droplets, shortening their residence time. Finally, as pressure changes heating up and wet-bulb temperatures, the temperature dependence of thermophysical properties plays a role.

Evaporation alters the droplet size distribution, which can be characterized by representative droplet diameters. Figure 4 shows the measured and predicted streamwise development of the Sauter mean diameter (SMD), the volume undersize diameters $D_{0.9}$ and $D_{0.1}$, together with the normalized liquid volume and mass flux for the baseline case.

The computation reveals that the nearly constant diameters observed by the measurements (the dip at $x = 60$ mm might be a measurement error) in the range $x = 30$–150 mm are preceeded by a rise upstream, which turns into a decrease downstream. Reasons for that are discussed below (Fig. 6). During heating of the droplets from the presumed starting temperature of 343 K to the wet-bulb temperature of 518 K, the density of the liquid decreases by 20%. In this case, the varying liquid density causes differences between mass and volume flux of up to 10% of the starting flux, Fig. 4. Time for a starting

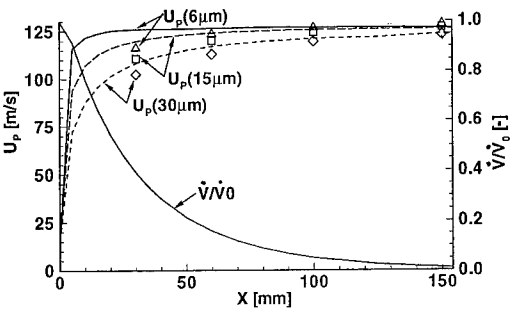

FIG. 5. Streamwise development of the averaged streamwise particle velocity component for three diameter classes ($6\,\mu m \pm 20\%$, $15\,\mu m \pm 10\%$, $30\,\mu m \pm 5\%$)—comparison of predictions with measurements (lines = prediction; symbols = measurement).

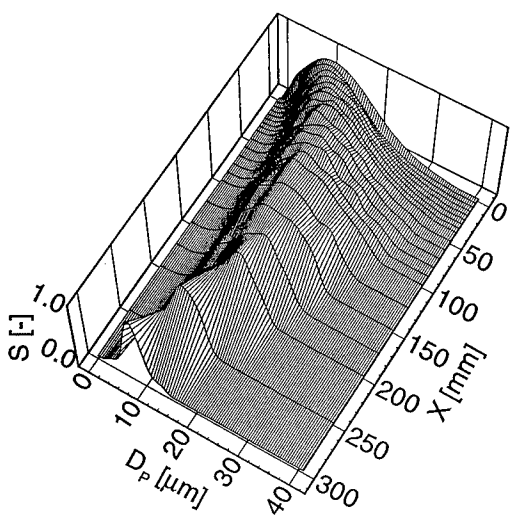

FIG. 6. Predicted streamwise development of the volumetric drop-size distribution S (each distribution normalized by its maximum value and taken at flux density maximum of streamwise position x).

6-μm droplet was 0.04 ms to reach a temperature 10 K below the wet-bulb temperature, whereas a 30-μm droplet took 0.69 ms.

Immediately after atomization, the droplets experience a rapid acceleration by the high-velocity air stream. Figure 5 shows the measured and predicted streamwise development of the averaged streamwise particle velocity component for three droplet-size classes. As already mentioned, the neglection of the spray feedback had very little effect on the computed droplet evaporation characteristics. The measured droplet velocities were overestimated up to 7% (Fig. 5, x = 30 mm), due to the momentum loss of the gas to the droplets in the dense spray region, which lowers the gas velocity locally. Indeed, better agreement was obtained when considering the spray feedback on the gas field.

Droplet dynamics is important for evaporation because relative velocity influences evaporation rate. In addition, the droplet velocity determines its residence time. These effects promote the rapid evaporation of the spray observed in the upstream region. For the present case, relative velocity effects caused by turbulent fluctuations had only a negligible effect on evaporation, as was revealed by computations with and without turbulent dispersion.

Insight into the evaporation can be gained by examining the streamwise development of the predicted volumetric drop-size distributions, Fig. 6. Three phases in the development of the size distribution can be discerned:

1. $x < 60$ mm: The initial size distribution at $x = 0$ exhibits a shift to larger diameters, whereby its shape is only slightly affected. As the small droplets heat faster, enhancing evaporation at the small-diameter end of the size distribution, the distribution shifts and the representative diameters rise, Fig. 4. The end of this phase, where still 16% of the liquid volume flux exists, approximates the end of heating.
2. x = 60–200 mm: The size distribution stops shifting, the diameter (17 μm) of its peak and its lower diameter branch change but little. However, the distribution's large-diameter branch begins to narrow. In this second phase, the dynamics of the mass transfer to smaller diameters is such that, in each bin, there is a dynamic equilibrium between source and sink, except at the large-diameter end, which loses its source. That is why the SMD and the $D_{0.1}$ remain constant, whereas the $D_{0.9}$ already decreases.
3. $x > 200$ mm: The final phase begins, where the evaporation ends: only 0.23% of the initial liquid volume flux is left. In that phase, the size distribution moves toward small diameters accompanied by a rapid narrowing toward a monodisperse spray.

From this reasoning, it can be concluded that a longer heating phase of the spray tends to make the streamwise representative diameters reach a higher maximum value and shift it further downstream. The predictions in Fig. 7, where the spray initial temperature was varied, corroborate that. Two extreme values were chosen here: the fuel supply temperature (288 K) and the wet-bulb temperature (518 K), i.e., maximum possible heating and no heating of the droplets during evaporation.

Figure 7 reveals the strong influence of the spray initial temperature on the evaporation. At x = 60 mm, the normalized liquid volume flux has decreased to 22.4 | 15.7 | 1.4% for a chosen droplet initial temperature of 288 | 343 | 518 K, respectively.

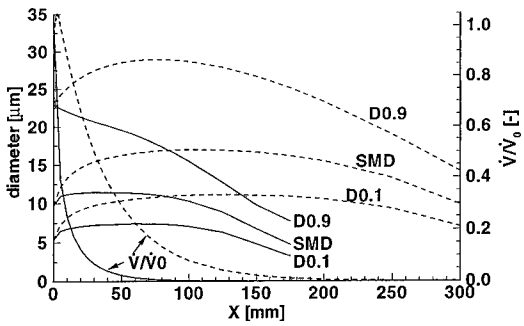

FIG. 7. Predicted influence of initial spray temperature T_P on streamwise development of representative diameters $D_{0.9}$, $D_{0.1}$, SMD, and liquid volume flux (solid lines = T_p = 518 K; dotted lines = T_p = 288 K).

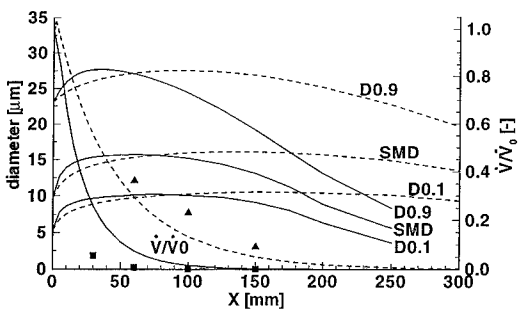

FIG. 8. Influence of air temperature T_A on streamwise development of liquid volume flux—comparison of predictions with measurements (symbols = measurement; solid lines = prediction for T_A = 850 K; dotted lines = prediction for T_A = 650 K).

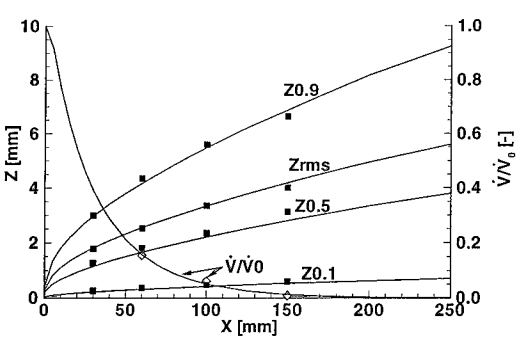

FIG. 9. Streamwise development of droplet cloud's transverse dispersion—comparison of predictions with measurements (lines = prediction; symbols = measurement; note the different scales for z and x).

The initial temperature of 343 K chosen for the baseline case seems to be justified by Fig. 4 together with Fig. 7, because then not only the liquid volume flux but also the representative diameters of the measurement were met.

The influence of the air temperature on the evaporation was studied as well by changing the air temperature of the baseline case (Fig. 8).

The measurements reveal the strong influence of the air temperature on evaporation. In the predictions shown, the same spray initial conditions as in the baseline case were used, resulting in an underestimation of the measured influence of air temperature. This was due to a finer atomization and an elevated initial spray temperature at higher air temperature.

Dispersion Characteristics

The spreading of the droplet cloud is characterized by its standard deviation $z_{\mathrm{RMS}}(x)$ and by measures like $z_{0.9}(x)$, which defines 90% of the liquid volume flux at a given streamwise position x to be located inside a z range of half width $z_{0.9}$ around the symmetry plane $z = 0$. Figure 9 shows the measured and computed streamwise development of the dispersion for the baseline case.

Extrapolation of the measurements to $x = 0$ indicates a quicker dispersion near the atomizer than downstream. An initial condition for the transverse standard deviation of particle velocity set to 17.5 m/s reproduced this behavior in the numerical results. The quicker dispersion in the atomizer near field can be attributed to liquid film oscillations (see Fig. 10), which were also seen for an atomizer of the same design at atmospheric pressure [13], in the same way as documented in [14], and to the turbulence generated by the atomizer wake. Further downstream, these disturbances are damped out, and the dispersion rate acquires an asymptotic value. There, experimental and numerical results both show a Gaussian profile of the volume flux density distribution. For the computations, a triangular initial distribution had been used (see above). The turbulent macro–length scale set to 20% of the smaller duct width reproduced the far-field dispersion behavior observed by the measurements. The sensitivity of dispersion and evaporation to the macroscale was tested by equating the macroscale and the smaller duct width (25 mm). The spray angle increased by 65%, only negligibly affecting evaporation.

The LIF shots at two uncorrelated incidents (Fig. 10) show the kerosene fluorescence of both liquid and vapor. It can be seen that the streamwise distribution is not homogeneous, which points at the time-dependant atomization behavior explained in Ref. 14. At the downstream end of the pictures, the kerosene layer is seen to turn up and down. This

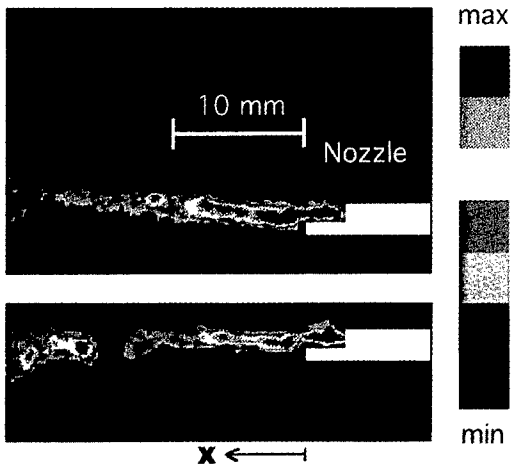

FIG. 10. Two uncorrelated instantaneous LIF shots of kerosene (vapor and liquid) fluorescence (plane $y = 0$, in range near $x = 0$).

bulk movement could be responsible for the higher initial mean dispersion rate, which then would give a less homogeneous distribution in time than the dispersion produced by the duct turbulence in the far field. For the investigated particle size distributions, the liquid dispersion was observed to progress at almost the same rate as the kerosene vapor.

Conclusions

Complete evaporation was achieved for the atomizer used in this study within 100 mm without autoignition. Dynamic pressure, being important for a sufficiently fine atomization, was about 3% of total pressure. For the small drop-size distribution of this experiment, the most rapid evaporation coincides with the acceleration phase, and prevaporization could be terminated after that at the end of the heating phase at 60 mm with only a small loss in evaporization efficiency. Air temperature had the largest influence on evaporation, whereas pressure only had an indirect effect through atomization quality. Comparison of experimental results and calculations varying the initial spray temperature showed this temperature to be an important parameter for evaporation, and it should be measured. If a significant part of fuel heating could be achieved in the atomizer fuel path without coking, considerable reductions could be made in the prevaporizer length, as apparent in Fig. 7. The spray acceleration and evaporation history was reproduced sufficiently well for engineering purposes both with and without considering spray feedback on the gas phase. It can be concluded that dispersion is not sufficient for practical use in premix ducts, where a homogeneous air–vapor mixing is strived for. Turbulence generators are needed to promote spray dispersion and vapor mixing. Respective work is in progress.

REFERENCES

1. Joos, F., Pellischek, G., in *Advances in Engine Technology* (R. Dunker, ed.), Wiley, Chichester, 1995, p. 105.
2. Brandt, M., Hassa, C., Kallergis, K., and Eickhoff, H., *Sixth (International) Conference on Liquid Atomization and Spray Systems,* Begell House, New York, 1994, pp. 750–757.
3. Spadaccini, L. J., and TeVelde, J. A., *Combust. Flame* 46:283–300 (1982).
4. Brandt, M., *Eleventh (European) Conference on Atomization and Sprays,* Nürnberg Messe GmbH, Nürnberg, 1995, pp. 33–42.
5. Brandt, M., Gugel, K. O., and Hassa, C., "Experimental investigation of the liquid fuel evaporation in a premix duct for lean premixed and prevaporized combustion," ASME 96-GT-383, *ASME Gas Turbine Conference,* Birmingham, UK, June 10–13, 1996.
6. DANTEC, *PDA User's Manual,* Dantec, Skovlunde, Denmark, 1992.
7. Arnold, A., Bräumer, A., Buschmann, A., Decker, M., et al., *Ber. Bunsenges. Phys. Chem.* 97:1650–1661 (1993).
8. Grossmann, F., Ridder, M., Monkhouse, P., Sick, V., and Wolfrum, J., *Appl. Phys. B* 62:249–253 (1996).
9. Berlemont, A., Grancher, M.-S., and Gouesbet, G., *Int. J. Heat Mass Transfer* 34:2805–2812 (1991).
10. Lefebvre, A. H., *Atomization and Sprays,* Hemisphere Publ. Corp., New York, 1989, Chap. 7 and 8.
11. Blümcke, E., Turbulente Partikeldispersion in eingeschlossenen Drallströmungen, Dissertation Ruhr-Universität Bochum, *DLR Forschungsbericht DLR-FB 92-32,* 1992.
12. Blümcke, E., Brandt, M., Eickhoff, H., and Hassa, C., *Particle & Particle Systems Characterization* 10:182–190 (1993).
13. Hassa, C., Biscos, Y., and Lavergne, G., *Sixth (International) Conference on Liquid Atomization and Spray Systems,* Begell House, New York, 1994, Poster 5.
14. Mansour, A. and Chigier, N., *Phys. Fluids A* 3:2971–2980 (1991).
15. Edwards, C. F. and Marx, K .D., *ICLASS-91,* pp. 653–660, Gaithersburg, MD, USA, July 1991.
16. Fitzky, G. and Bohn, D., Messung der komplexen Brechungsindizes von Heizöl EL und Kerosin in Abhängigkeit von Druck und Temperatur, *IDG-Bericht,* RWTH Aachen, Okt. 1995.

COMMENTS

Dr. Giancarlo Benelli, ENEL spa, Thermal Research Centre, Italy. An interesting paper on a crucial point for liquid fuel utilization in a gas turbine was presented, and also, an important conclusion was drawn: "dispersion is not sufficient for practical use in premixed ducts." Are the authors considering other vaporizing methods as alternatives to the turbulence generators proposed in their conclusions?

Author's Reply. The cited conclusion is only applicable to the atomizer used. We are considering alternative atomizers. In Ref. 2, an investigation on the suitability of atomizing concepts for LPP-ducts is presented. Also, instead of turbulence generators, swirl can be used for homogenization. That method could not be applied in our present measuring section; however, we will modify the duct to have a quadratic cross section to facilitate the investigation of swirl as a means of premixing.

•

Dr. Stefan Hoffmann, Siemens AG, KWU, Germany. Could you please comment on how your atomizer can be incorporated into a gas turbine combustor taking into account the risk of autoignition and flashback?

Author's Reply. With respect to autoignition, the atomizer has to be incorporated into a gas turbine combustor such that the fuel line has no recirculating wake. Given that, no autoignition occurred for the investigated thermodynamic conditions and a residence time of 1.25 msec. Since for pressures of 12 bars and above and temperatures above 750 K almost complete evaporation was achieved after 0.5 msec, a good autoignition safety margin is possible, provided that the same air velocity as in our experiment can be used.

With respect to flashback, the atomizer cannot be separated from the prevaporizer. Since we investigated a generic configuration without combustion, the answer cannot be given without consideration of a practical geometry, i.e., wall interactions, flame holders.

•

Dr. Josette Bellan, Jet Propulsion Laboratory, USA. You said that you treated kerosene as a single component fuel. Can you state what were the fuel properties determined? Were they functions of the temperature? Can you explain the physical mechanisms occurring in your experiment that are responsible for keeping the SMD approximately constant?

Author's Reply. Fuel properties of kerosene Jet A were drawn from a critical compilation of different sources in the literature. The temperature dependance of all fuel properties was taken into account. Jet A is a multicomponent fuel, whose actual composition is varying with the fuel supplier. Moreover, measurement error margins for kerosene property data are usually not given in the literature. So, where explicitly given, "typical" values [1] were used, and extreme literature data values were discarded. Vapor pressure for a liquid mixture is defined by both liquid composition and temperature. In our case, the kerosene was treated as a single component fuel, i.e., a unique vapor-pressure relation $p(T)$ was employed, mainly basing on values like "true vapor pressure" for kerosene (see [1,2]). There is a real need for experimental data of phase equilibrium for Jet A in the full pressure range of gas turbine use.

The diameter of each individual droplet of the spray continuously decreases by evaporation at rates of the droplet's volume (dD_p^3/dx) different for small and big droplets. Depending on the relative numbers of small and big droplets in the dropsize distribution, i.e., of its width and shape, the different evaporation behavior of small and big droplets can make the characteristic diameters of the spray be constant or even rise. For example, small droplets heat up faster than big ones, resulting in an earlier onset of evaporation at the low diameter end of the dropsize distribution. This tends to raise the characteristic diameters.

In our case, the observed constancy of the SMD during most of the spray lifetime is caused by a compensation of the decrease in droplets diameters by the inhomogeneity of the evaporation rate across the size distribution. Additional information is given in the text body to Fig. 6.

REFERENCES

1. Coordinating Research Council, Inc., Handbook of Aviation Fuel Properties, CRC Report No. 530, 1983, Atlanta, Georgia, pp. 41–48.
2. Rose, J. W. and Cooper, J. R. (Eds.), *Technical Data on Fuel,* 7th ed., London, UK, ISBN 0707301297, 1977, pp. 273–277.

Twenty-Sixth Symposium (International) on Combustion/The Combustion Institute, 1996/pp. 2749–2755

USE OF AN OPTICAL PROBE FOR TIME-RESOLVED *IN SITU* MEASUREMENT OF LOCAL AIR-TO-FUEL RATIO AND EXTENT OF FUEL MIXING WITH APPLICATIONS TO LOW NO_x EMISSIONS IN PREMIXED GAS TURBINES

RAJIV K. MONGIA, EIJI TOMITA, FRANK K. HSU, LAWRENCE TALBOT AND ROBERT W. DIBBLE
Combustion Analysis Laboratory
Department of Mechanical Engineering, University of California—Berkeley
50-B Hesse Hall, Berkeley, CA 94720-1740, USA

The lower temperatures associated with lean premixed combustion generally lead to lower NO_x emissions; however, the benefit of lean premixed combustion may be lost if the fuel and air are poorly mixed. In this paper, we describe the development of an inexpensive fiber optic probe capable of measuring the extent of mixing. The fuel concentration is determined by laser light absorption at 3.39 μm over a short path length created by using infrared transmitting fiber optics.

A hydrogen-piloted, CH_4-in-air turbulent flame with a variable fuel injection location is used to vary the degree of mixedness at the burner exit. We use the optical probe to measure the level of mixedness (nonreacting) at the burner exit. The level of mixing and the mean concentration profiles are also measured by using planar laser–initiated Rayleigh scattering. NO_x measurements are reported for several mixing distances. We show that at lean conditions ($\bar{\phi} = 0.6$), incomplete mixing causes a dramatic increase in NO_x production because of the exponential temperature dependence of NO_x formation about $\bar{\phi} = 0.6$.

We also numerically investigate how the extent of mixing affects NO_x production at various equivalence ratios and pressures. Modeling the effect of incomplete mixing on NO_x formation is done with a distribution of ϕ convolved with numerical results from a perfectly stirred reactor in series with a plug flow reactor. The model does an excellent job of predicting the NO_x increase caused by incomplete mixing at lean conditions. Model predictions at higher pressures that are typical of gas turbine conditions show good agreement with available data. In particular, for lean premixed combustion, NO_x is *not* a function of pressure if the air and fuel are well mixed.

Introduction

Lean premixed combustion is emerging as a method of meeting increasingly stringent air-quality regulations for nitrogen oxides ($NO + NO_2 = NO_x$) emissions [1]. Since NO_x formation is a strong nonlinear function of the flame temperature, lean combustion yielding a lower flame temperature will lead to reduced NO_x emissions.

Extent of Fuel Mixing in Premixed Combustion

In poorly premixed combustion, the stream approaching the flame zone contains localized pockets that are richer or leaner than the mean of the mixture. Lyons [2] showed that in premixed flames with an overall equivalence ratio less than $\phi = 0.7$, variations in the mean concentration profile cause an increase in NO_x emissions. Using point LIF on NO_2-seeded flows, Gulati and Warren [3] measured temporal concentration fluctuations in a turbulent jet. Fric [4] used the NO_2 LIF technique to show that for *lean* premixed combustion, NO_x emissions are increased when temporal nonuniformities of the fuel-air mixture are present. Graham [5] and Hase et al. [6] have observed an opposite effect for burners operating at near stoichiometric conditions; the NO_x emissions increase as the mixing improves.

The extent of mixing is quantified by the *unmixedness* U [7],

$$U \equiv \frac{c'^{\,2}_{\mathrm{rms}}}{\bar{c}\cdot(1-\bar{c})} = \left(\frac{c'_{\mathrm{rms}}}{\bar{c}}\right)^2 \left(\frac{\bar{c}}{1-\bar{c}}\right) \qquad (1)$$

where $\bar{c}$ is the mean fuel concentration and c'_{rms} is the rms fluctuation of the fuel concentration. For a perfectly mixed stream, $U = 0$; for a perfectly unmixed stream, $U = 1$. The term $[\bar{c}(1-\bar{c})]^{1/2}$ is the maximum rms possible of a signal that is bounded by 0 and 1. More generally, the maximum rms of a signal is $[(\bar{c} - c_{\min})(c_{\max} - \bar{c})]^{1/2}$ [8].

The NO_x formation rate is strongly dependent on the local equivalence ratio ϕ. To show this, we model the NO_x production for CH_4-in-air premixed flames by using a 2-ms residence time perfectly stirred reactor (PSR) in series with a 4-ms residence time plug flow reactor (PFR), as was done by Steele et al. [9].

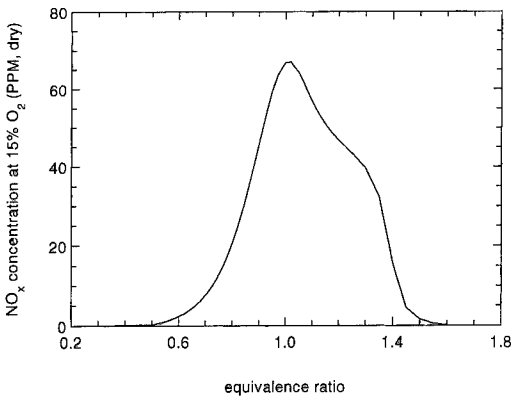

FIG. 1. NO_x at 15% O_2 versus equivalence ratio as calculated by the PSR/PFR model. The PSR has a residence time of 2 ms, and the PFR has a residence time of 4 ms. The inlet reactants are at 300 K and 1 atm.

GRI-Mech V2.11 [10], which includes nitrogen chemistry, is used for the calculations. As depicted in Fig. 1, the model predicts that the NO_x formation rate peaks at near-stoichiometric conditions.

For *lean* premixed combustion, the aforementioned LIF by Fric [4] shows that an increase in unmixedness will increase NO_x formation. Fluctuations around the mean produce regions that burn slightly richer and leaner than the overall mean equivalence ratio. The leaner regions have lower NO_x production rates than the mean equivalence ratio; however, the increase in NO_x production in the richer pockets outweighs the reduction in the leaner pockets. The net increase in NO_x emissions results from the nonlinear equivalence ratio dependence of NO_x production.

Interestingly, perfect mixing is *undesirable* when the mean stoichiometry is near $\phi = 1$, such as occurs in utility burners [5,6]. At near-stoichiometric conditions, fluctuations about the mean concentration will produce regions that are lean and rich. These lean and rich pockets will produce lower NO_x, as shown in Fig. 1. The focus of this work is to provide more detailed information on the unmixedness effect on NO_x emissions and to develop a tool to accurately measure the unmixedness.

Laser Absorption of Hydrocarbons

The use of laser absorption in combustion systems has been demonstrated by several authors including Schoenung and Hanson [11] and Nguyen et al. [12] for the measurement of CO and temperature. Several authors have studied the absorption by methane of the infrared He-Ne laser transition at 3.39 μm [13,14,15]. Emmerman et al. [16] applied absorption tomography to a methane jet into air and obtained two-dimensional maps of methane concentration. Tsuboi et al. [17] showed that ethane, propane, *n*-octane, and several other hydrocarbons also strongly absorb the 3.39-μm He-Ne laser. More recently, Drallmeier [18] used the infrared He-Ne laser in conjunction with a visible He-Ne laser to measure the fuel vapor concentration of a fuel spray. The visible laser was used to account for absorption caused by droplets in the optical path.

The Beer–Lambert law relates the transmitted intensity I to the original intensity I_o by

$$\frac{I}{I_o} = \exp(-\alpha \cdot L \cdot P \cdot x_i) \tag{2}$$

where L is the path length, α is the absorption coefficient, P is the pressure, and x_i is the mole fraction of the hydrocarbon. Because the absorption coefficient is on the order of 10 atm^{-1} cm^{-1} for most hydrocarbons [17], measurable absorption for combustible mixtures occurs with a path length of only 5 mm. The short path length defines the spatial distribution. More important, because the gas is not drawn through a sampling line, determination of the temporal characteristics is limited only by the detector and data acquisition speed. This allows measurement of the extent of mixing. Greater detail on the spectroscopy of methane in this wavelength regime can be found in the work of Cline and Varghese [19] and Perrin and Hartmann [20].

Experimental Setup

Lean Premixed Combustion System

The burner tube with annular pilot used by Karlovitz (described in the book by Lewis and von Elbe [21]) and later by Dibble and Hollenbach [22], shown in Fig. 2, has several important characteristics. The annular pilot stabilizes the flame at the same location at various equivalence ratios and levels of mixedness. Second, the combustor allows optical access for the planar Rayleigh scattering that is described in a later section. We have modified the Karlovitz burner by injecting the fuel closer to the burner exit. By changing the mixing distance l, the rms of fuel concentration (i.e., the extent of mixing) can be changed without changing the radial mean concentration profile.

As shown in Fig. 2, the burner has a methane injection tube with $d = 3$ mm, an air tube with $D = 27$ mm, and a hydrogen pilot with annular thickness of $\delta = 3$ mm. The upstream mixing distance l is varied between 33 and 63.5 cm. A fully premixed flame was produced by mixing the methane with the air well upstream and not using the methane injection tube. The methane tube bulk velocity is 25 m/s, and the air tube bulk velocity is 5.3 m/s. These flows yield a mean equivalence ratio of $\bar{\phi} = 0.6$, which is

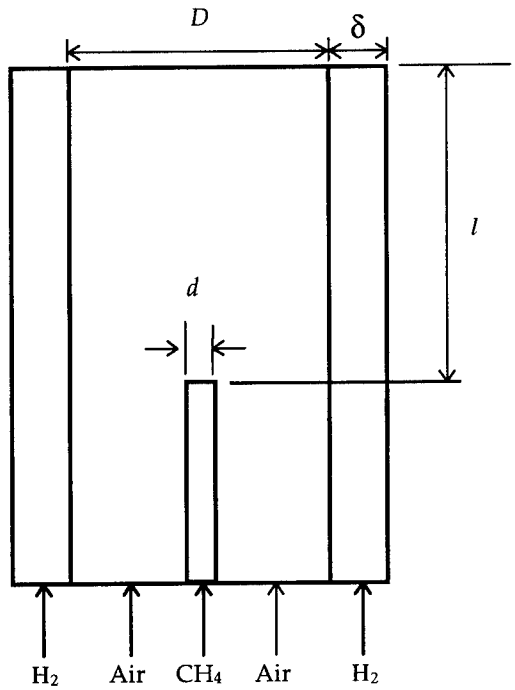

FIG. 2. Schematic of hydrogen-piloted, lean premixed burner. The mixing distance l is varied to change the unmixedness at the burner exit without changing the mean spatial distribution of fuel concentration.

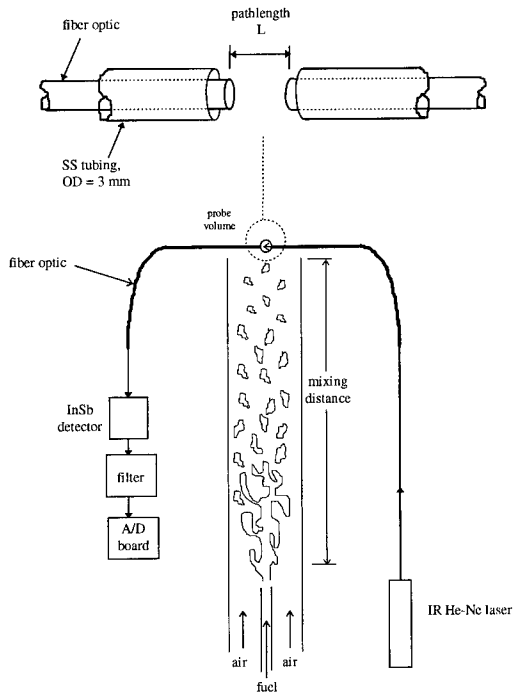

FIG. 3. Schematic of optical probe. A small probe volume is created by the gap between the infrared transmitting fiber optics. Light from a 3.39-μm He-Ne laser is focused into one of the fiber optics.

used consistently for all the test runs.

The radial profile of NO_x with only the hydrogen pilot burning, with co-flow air but no methane flow, confirms that NO_x produced by the hydrogen pilot does not penetrate to the centerline. At a distance of 17.8 cm above the burner exit, the NO_x concentration at the centerline is less than 0.5 ppm. Hermanson and Dimotakis [23] show that increasing the heat release reduces the entrainment of a jet; therefore, the expansion caused by the heat release in the premixed flame would further decrease the entrainment of pilot flame products. Accordingly, we conclude that any NO_x measured at the centerline is produced by the central premixed flame and not by the pilot flame.

Infrared Fiber Optic Probe

A schematic of the optical probe is shown in Fig. 3. Light from a 3.39-μm He-Ne laser is focused into an infrared transmitting fiber optic that guides the laser light to the probe volume. The laser light passes through the probe volume and a portion intersects another infrared transmitting fiber, which guides the light to a liquid nitrogen–cooled indium-antimonide (InSb) detector. The gap width of the probe is L = 5 mm. A low-pass filter with a cutoff frequency of 2 kHz is used before the sampling of the computer data acquisition system that converts the transmission, I/I_o, into a methane concentration. The A/D board samples at 4 kHz, sufficient to resolve fluctuations on the order of 2 kHz (Nyquist criterion). The optical probe sample volume is placed 25 mm above the burner exit along the burner centerline during the nonreacting unmixedness measurements. The probe location is where most of the combustion occurs when ignited.

Planar Laser–Initiated Rayleigh Scattering

Laser-initiated Rayleigh scattering is used to measure the two-dimensional concentration field for the nonreacting flow as described in Ref. 24. A Candela LFDL-20 pulsed dye laser tuned to 590 nm with a pulse duration of 3 μs and pulse energy of approximately 1–2 J is used as the light source. The laser beam, typically 8 mm in diameter, is focused by a cylindrical lens with a focal length of 1000 mm to form a sheet at the measurement location. The center of this laser sheet is located 25 mm above the burner exit. The imaging area is approximately 0.5 mm × 10 mm × 60 mm. The images are taken at a repetition rate of 0.5 Hz.

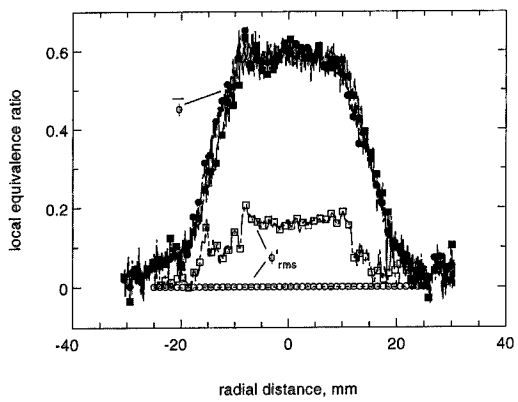

FIG. 4. Mean (solid symbols) and rms (open symbols) of equivalence ratio as a function of radius at an axial distance of 2.54 cm above the burner exit. The circles (both open and solid) are for the perfectly mixed conditions, and the squares (both open and solid) are for the l = 33-cm mixing distance (the most unmixed case studied).

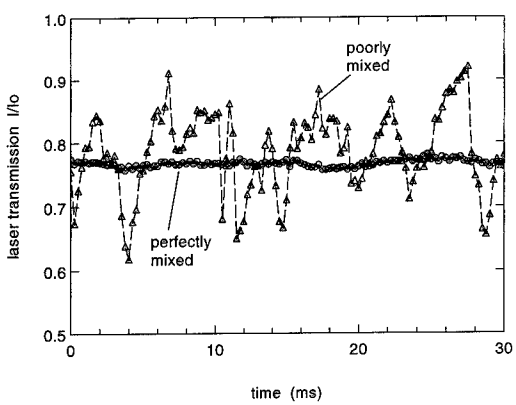

FIG. 5. Laser transmission as a function of time for two extreme mixing conditions. The circles are for the perfectly mixed condition, and the triangles are for the most unmixed condition (mixing distance l = 33 cm). The low values of laser transmission correspond to richer concentrations than the mean, and the high values of laser transmission correspond to leaner concentrations than the mean.

NO_x and O_2 Measurements in Flames

Species measurements are made at an axial location of 17.8 cm above the burner by using a quartz suction probe with a heated sample line as described in a previous work [24]. Horiba analyzers are used for all species measurements. Nitrogen oxides are measured by a chemiluminescent analyzer, CO and CO_2 by NDIR analyzers, and O_2 by a paramagnetic analyzer. Water is removed from the sample upstream of the analyzers by using an ice bath and water trap for the CO, CO_2, and O_2 measurements. The water is removed from the sample entering the NO_x analyzer by using a porous dryer, thus avoiding the problem of NO_2 absorption into water.

Model Description

The effect of unmixedness on NO_x production in the experimental combustion system is modeled numerically using a distribution of equivalence ratios in conjunction with numerical results of a 2-ms PSR in series with a 4-ms PFR. The residence times were chosen for their physical significance (for an exit velocity of 5.5 m/s, a sampling distance of 17.8 cm, and an average temperature of 1600 K; the residence time is approximately 6 ms) and then adjusted to agree with the one experiment. The PSR/PFR code is used to obtain a relationship between NO_x emissions and equivalence ratio assuming the air and fuel are perfectly mixed (i.e., the PSR/PFR code is run several times at different equivalence ratios). The average NO_x emissions of the unmixed combustion system are then computed by

$$NO_{x,avg} = \int NO_x(\phi) \cdot P(\phi) \cdot d\phi \qquad (3)$$

where $NO_x(\phi)$ is the NO_x emissions as a function of equivalence ratio as predicted by the PSR/PFR and $P(\phi)$ is the distribution of equivalence ratios for the combustion system of interest. Consistent with the experiment, $P(\phi)$ has an assumed Gaussian shape with an appropriate mean and unmixedness (or, equivalently, standard deviation).

Results and Discussion

Concentration Measurement in Nonreacting Flows

The mixing distance l was varied between 33.0 cm and 63.5 cm while maintaining a mean equivalence ratio of ϕ = 0.6. A fully premixed experiment was performed as well. The Rayleigh measurements shown in Fig. 4 confirm that the mean equivalence ratio has a uniform profile at the exit of the burner for the mixing distances studied. Figure 4 also shows that as the mixing distance decreases, the rms of the equivalence ratio increases dramatically.

Figure 5 compares the optical probe laser transmission of the fully premixed case ($l = \infty$) to that of the shortest mixing distance (l = 33 cm). Clearly, the large fluctuations in laser transmission for the 33-cm mixing distance indicates large fluctuations in methane concentration. Low levels of laser transmission correspond to high levels of methane concentration (i.e., regions that are richer than the mean). The unmixedness is better quantified by Fig. 6, which shows the distribution of methane concentration for three flow conditions: fully premixed, 57-

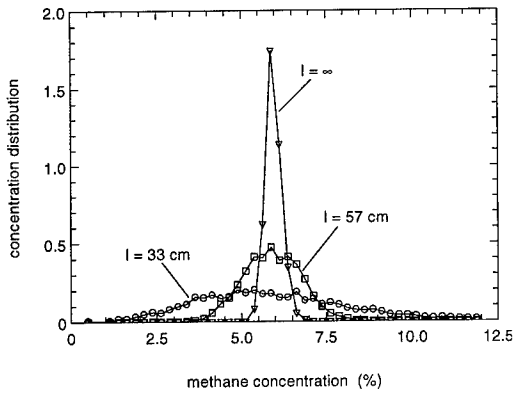

FIG. 6. Distribution of concentration as measured by the optical probe for three mixing conditions. The circles are for the most unmixed case (l = 33 cm); the squares for an intermediate mixing distance (l = 57 cm); and the triangles for the perfectly mixed condition ($l = \infty$). The width of the concentration distribution for the perfectly mixed condition corresponds to the instrument resolution.

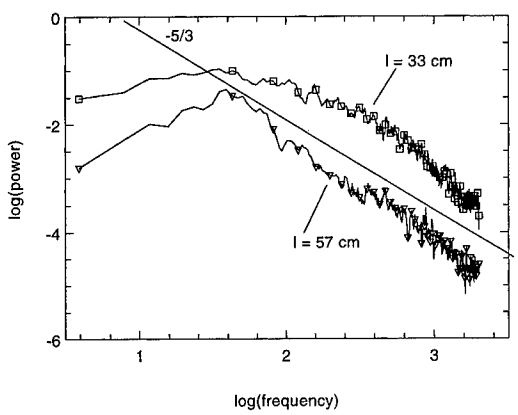

FIG. 7. Scalar power spectrum of concentration for two mixing distances. The squares are for a mixing distance of l = 33 cm, and the triangles are for a mixing distance of l = 57 cm. Both spectra exhibit the expected −5/3 slope cascade; however, the end of the cascade is not observed because the signal was filtered at 2 kHz.

cm mixing distance, and 33-cm mixing distance. The wide distribution of methane concentration for the 33-cm mixing distance includes regions that have near-stoichiometric conditions. Because of the noise in the laser and data acquisition system, the fully premixed flow condition has a measured standard deviation of approximately 0.24% concentration of methane. Therefore, in its current form, the optical probe can measure fluctuations as small as 4% in methane mole fraction (i.e., if $\bar{c}$ = 0.05, then $c_{\mathrm{rms,min}}$ = 0.002). Improvements to the data acquisition system can be readily implemented.

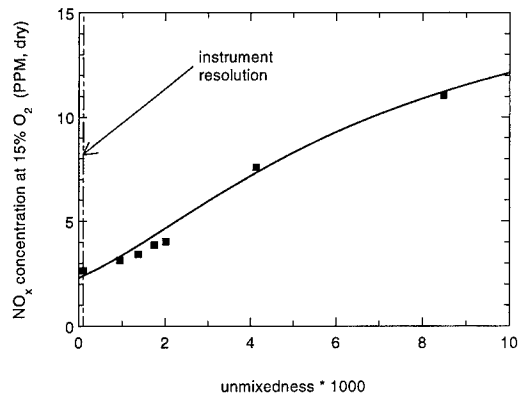

FIG. 8. NO_x emissions (dry) at 15% O_2 versus unmixedness. The symbols correspond to measured NO_x and measured unmixedness (optical probe results). The solid line corresponds to model prediction using a 2-ms PSR in series with a 4-ms PFR in conjunction with a Gaussian equivalence ratio distribution.

The scalar power spectrum of two flow conditions is shown in Fig. 7 as the logarithm of power versus the logarithm of frequency. The cascade of the scalar power spectrum occurs with the expected slope of −5/3 [25]. The end of the cascade associated with a decrease in the slope (more negative) is not observed here because of the present frequency limit of 2 kHz.

Nitrogen Oxide Emissions at Reacting Conditions

The NO_x emissions (dry) corrected to 15% O_2 are shown in Fig. 8 as a function of unmixedness as measured by the optical probe for a mean equivalence ratio of $\bar{\phi}$ = 0.6. Also included in Fig. 8 are the modeling predictions of the effect of unmixedness on NO_x formation. As noted previously, for the modeling results, a 2-ms PSR in series with a 4-ms PFR is used to generate the relationship between NO_x and equivalence ratio if the air and fuel are perfectly mixed. At an unmixedness U = 0.001, the NO_x emissions are increased by 15% with respect to the NO_x emissions from a fully premixed flame (U = 0). At an unmixedness U = 0.0085, the NO_x emissions are increased by a factor of 4. The model does an excellent job of predicting the NO_x emissions of the experimental burner, including the slight change of slope that appears at high values of unmixedness. Also shown in Fig. 8 is the resolution of the current optical probe. As depicted by the modeling predictions and the experimental results, the unmixedness resolution $U_{\min}$ = 0.0001 is sufficient for measuring whether the air and fuel are mixed well enough for low NO_x emissions.

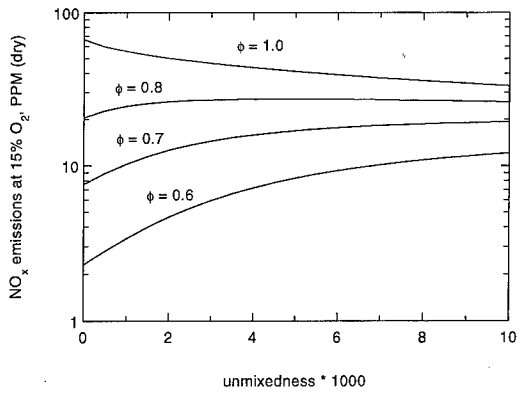

FIG. 9. Effect of unmixedness on average NO_x emissions at different mean equivalence ratios. At lean conditions, the NO_x goes up significantly with increasing unmixedness; however, at a mean equivalence ratio of $\bar{\phi} = 1.0$, increasing unmixedness decreases NO_x emissions.

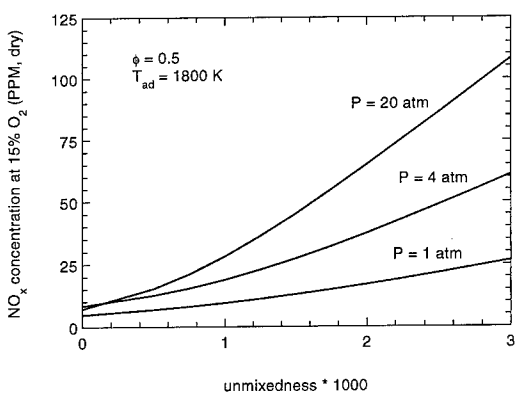

FIG. 10. Effect of unmixedness on average NO_x emissions at different pressures. The NO_x versus equivalence ratio relationship is obtained by using preheated reactants of 700 K and a 2-ms PSR in series with an 18-ms PFR. A mean equivalence ratio of $\bar{\phi} = 0.5$ is used so that the adiabatic flame temperature is 1800 K (typical gas turbine conditions).

Modeling the Effect of Unmixedness on NO_x Emissions

Eq. (3) was used to study the role that the mean equivalence ratio $\bar{\phi}$ plays on the relationship between unmixedness and overall NO_x formation. Graham and McKindley [5] showed experimentally that at *stoichiometric conditions,* the NO_x for poorly premixed combustion was *lower* than the perfectly mixed case; however, at *lean* conditions, the poorly premixed combustion had *higher* NO_x emissions. Figure 9 shows how the unmixedness affects NO_x formation at several equivalence ratios. As shown experimentally by Graham and McKindley [5] and numerically by Fig. 9, the unmixedness effect on NO_x production is significantly different depending on the mean equivalence ratio $\bar{\phi}$.

Modeling the Effect of Unmixedness at Gas Turbine Conditions

Eq. (3) was also extended to gas turbine conditions by using the PSR/PFR code with a 700 K preheat (typical of compressor outlet) to generate the NO_x versus equivalence ratio relationship. The residence time in the PSR was 2 ms, and the residence time in the PFR was 18 ms. Figure 10 shows the effect of unmixedness on NO_x generation at $P = 1$, 4, and 20 atm for a mean equivalence ratio $\bar{\phi} = 0.5$.

The mean equivalence ratio $\bar{\phi} = 0.5$ results in an adiabatic flame temperature of 1800 K. As shown, the unmixedness has a larger influence on NO_x formation at the higher pressures because the peak NO_x levels are larger at the higher pressures. Surprisingly, at low values of unmixedness ($U < 0.0008$), the pressure does not make a large difference in overall NO_x formation. This has some interesting consequences. It has been reported by Leonard and Stegmaier [26] that at sufficiently lean conditions (flame temperature <1900 K), the NO_x from a lean premixed combustor is only a function of flame temperature regardless of the pressure, amount of preheat, or residence time. Figure 10 corroborates the results of Leonard and Stegmaier [26] as long as the unmixedness U is small. For a perfectly mixed combustor ($U = 0$), the model predicts that the NO_x emissions are independent of pressure (proportional to P^0); however, the relationship evolves to being dependent on $P^{1/2}$ as the unmixedness increases.

Conclusions

Lean premixed combustion is an established method of conforming to increasingly restrictive air-quality regulations, especially for NO_x formation. The lower temperatures associated with lean premixed combustion generally lead to lower NO_x emissions; however, the benefit of lean premixed combustion may be lost if the fuel and air are poorly mixed.

A hydrogen-piloted, methane-in-air turbulent flame with a variable premixing distance is used to vary the unmixedness without changing the mean concentration profile. A novel optical probe using absorption of light from an inexpensive 3.39-μm He-Ne laser is used to measure the effectiveness of a premixer. In its current form, the optical probe is capable of measuring unmixedness as low as $U = 0.0001$.

At an overall equivalence ratio of $\phi = 0.6$, unmixedness has a dramatic effect on NO_x emissions.

For an unmixedness of $U = 0.001$, the NO_x emissions are increased by 15% compared to the NO_x emissions of the fully premixed condition ($U = 0$). At an unmixedness of $U = 0.0085$, the NO_x emissions are increased by a factor of 4. The optical probe is capable of resolving the small unmixedness levels that affect NO_x production.

A numerical model of the effect of unmixedness U on NO_x production showed good agreement with experiments. At higher pressures, the model predicts the trend observed by Leonard and Stegmaier [26]. The model shows that at very low levels of unmixedness U, the NO_x emissions are independent of pressure (for an adiabatic flame temperature of 1800 K); however, as the unmixedness increases, pressure plays an increasingly important role in the overall NO_x generated by a lean premixed combustor.

Acknowledgments

This material is based on work supported through a National Science Foundation graduate fellowship and National Science Foundation research grant CTS-9415686.

REFERENCES

1. Bowman, C. T., *Twenty-Fourth Symposium (International) on Combustion,* The Combustion Institute, Pittsburgh, 1993, pp. 859–878.
2. Lyons, V. J., *AIAA J.* 20:660–665 (1982).
3. Gulati, A. and Warren, R. E. Jr., *J. Propulsion Power* 10:54–61 (1994).
4. Fric, T. F., *J. Propulsion Power* 9:708–713 (1993).
5. Graham, D. P. and McKindley, K., 2nd European Conference on Industrial Furnaces and Burners, Algarve, Portugal, April 2–5, 1991.
6. Hase, K., Kori, Y., and Ohgl, K., 1st International Conference on Combustion Technologies for a Clean Environment, Portugal, 1991.
7. Danckwerts, P. V., *Appl. Sci. Res.* 3:279–296 (1952).
8. Dimotakis, P. E. and Miller, P. L., *Phys. Fluids A* 2:1919–1920 (1990).
9. Steele, R. C., Malte, P. C., Nicol, D. G., and Kramlich, J. C., *Combust. Flame* 100:440–449 (1995).
10. Frenklach, M., Goldenberg, M., Bowman, C. T., Hanson, R. K., Smith, G. P., Golden, D. M., Gardiner, W. C., and Lissianski, V., GRI-Mech 2.11, http://www.me.berkeley.edu/gri_mech/, 1995.
11. Schoenung, S. M. and Hanson, R. K., *Combust. Sci. Technol.* 24:227–237 (1981).
12. Nguyen, Q. V., Edgar, B. L., Dibble, R. W., and Gulati, A., *Combust. Flame* 100:395–406 (1995).
13. Emrich, R. J. and Soloukhin, R. I., *Astronautica Acta* 17:639 (1972).
14. McMahon, J., Troup, G. J., and Hubbert, G., *J. Quant. Spectrosc. Radiat. Transfer* 12:797–805 (1972).
15. Mallard, W. G. and Gardiner, W. C. Jr., *J. Quant. Spectrosc. Radiat. Transfer* 20:135–149 (1978).
16. Emmerman, P. J., Goulard, R., Santoro, R. J., and Semerjian, H. G., *J. Energy* 4:70–77 (1980).
17. Tsuboi, T., Arimitsu, N., Ping, D., and Hartmann, J.-M., *Jpn. J. Appl. Phys.* 24:8–13 (1985).
18. Drallmeier, J. A., *J. Appl. Opt.* 33:7781–7788 (1994).
19. Cline, D. S. and Varghese, P. L., *Twenty-Third Symposium (International) on Combustion,* The Combustion Institute, Pittsburgh, 1990, pp. 1861–1868.
20. Perrin, M. Y. and Hartmann, J. M., *J. Quant. Spectrosc. Radiat. Transfer* 42:459–464 (1989).
21. Lewis, B. and von Elbe, G., *Combustion, Flames, and Explosions of Gases,* Academic Press, New York, 1961.
22. Dibble, R. W. and Hollenbach, R. E., *Eighteenth Symposium (International) on Combustion,* The Combustion Institute, Pittsburgh, 1981, pp. 1489–1499.
23. Hermanson, J. C. and Dimotakis, P. E., *J. Fluid Mech.* 199:333–375 (1989).
24. Mongia, R. K., Tomita, E., Hsu, F., and Dibble, R. W., AIAA Paper 96-0174, 34th Aerospace Sciences Meeting, Reno, Nevada, 1996.
25. Dowling, D. R., "Mixing in Gas Phase Turbulent Jets," Ph.D. Thesis, California Institute of Technology, 1988.
26. Leonard, G. and Stegmaier, J., "International Gas Turbine and Aeroengine Congress and Exposition," ASME Paper 93-GT-288, Cincinnati, OH, 1993.

COMMENTS

Giancarlo Benelli, ENEL spa-Thermal Research Centre, Italy. A diagnostic technique that seems interesting for studying a lean premixed combustion system was presented. Did the author estimate the effects of probe design on the monitored mixing process?

Author's Reply. In this paper, we explore the application of the probe to lean premixed combustion. However, we anticipate widespread applications including nonpremixed combustion and piston engines.

The effect of the probe on the mixing process (disturbance of the flow) remains to be quantified. We expect the disturbance is comparable to that associated with the widely used hot wire anemometer.

Twenty-Sixth Symposium (International) on Combustion/The Combustion Institute, 1996/pp. 2757–2762

INFLUENCE OF AIR AND FUEL FLOWS ON GAS TURBINE SPRAYS AT HIGH PRESSURES

Q. P. ZHENG,* A. K. JASUJA AND A. H. LEFEBVRE
School of Mechanical Engineering
Cranfield University, Cranfield
Bedford MK43 0AL, England

A single-component phase-Doppler particle analyzer (PDPA) is used to measure local variations in drop-size distributions and drop velocities in the near-nozzle region of a practical, contraswirling, prefilming airblast atomizer. The technique of laser sheet imaging is used to obtain global patterns of the spray. Measurements are taken using air pressure drops across the atomizer of 5% and 10% and ambient air pressures of 1, 6, and 12 bar. The liquid employed is aviation kerosine at flow rates of up to 75 g/s. The results show that the previously observed effect of an increase in ambient air pressure in widening the spray cone angle is not a pressure effect per se but is due to the increase in fuel flow rate that accompanies an increase in air pressure at constant air–fuel ratio (AFR). For any given air pressure, it is found that spray cone angle increases gradually and continuously with increase in fuel flow rate. If the fuel flow rate is allowed to remain constant, the effect of an increase in air pressure is to reduce slightly the spray cone angle. In general, spray volume increases with fuel flow rate and/or reductions in air pressure. Variations in air pressure at a constant AFR, which corresponds to the normal practical situation, have little effect on either spray volume or the distribution of drop sizes in the spray.

Introduction

Much of our present knowledge of airblast fuel injectors was gained during the 1960s and 1970s on atomizers in which the atomizing air was essentially coflowing and nonswirling. In recent years, the considerable advances made in the development of laser diagnostic techniques for spray characterization have generated a number of experimental studies on the basic phenomena occurring within complex practical systems of the types currently in service on advanced turbojet engines. An important design feature of all these atomizers is that the bulk fuel is first spread into a thin, continuous sheet, a process called "prefilming," and then exposed to high-velocity, swirling air streams on both sides of the sheet. Wang et al. [1,2], McDonell et al. [3], and Hebrard et al. [4] used two-component phase-Doppler interferometry systems to make detailed measurements of drop sizes and velocities in the flows downstream of engine airblast atomizers. Jasuja and co-authors [5,6] used various nonintrusive techniques, including phase-Doppler interferometry, high-intensity spark photography, high-speed cinephotography, and video imaging to capture the dynamic and unsteady spray characteristics produced in prefilming airblast atomization. More recently, Zheng et al. [7] focused on the effects of variations in ambient air pressure on the drop sizes and velocities produced downstream of a practical, contraswirling, prefilming airblast atomizer. The objective of the present work is to extend these previous studies to include the effects of pressure on drop-size distributions, spray cone angle, and spray dimensions. The influence of atomizer pressure drop on spray properties is also examined because the use of higher liner pressure drops represents a practical means of reducing smoke and nitric oxide emissions.

Experimental

The test facility for this study has been fully described elsewhere [5,7]. High pressure air at near-ambient temperature is used to pressurize a large cylindrical vessel and is delivered to the fuel injector that is located at one end of the vessel and is arranged to spray horizontally along its major axis.

Atomizer

A cross-sectional view of the fuel injector employed is shown in Fig. 1. It is a prefilming airblast atomizer that is typical of those used in modern gas turbine engines. It features a pair of concentric air inlets that generate two separate swirling air flows in opposite directions. The design objective is to create a thin, annular sheet of fuel that is then sandwiched between the two swirling air streams. This

*Present address: Aero & Industrial Technology Ltd, P.O. Box 46, Burnley BB11 4BX, England.

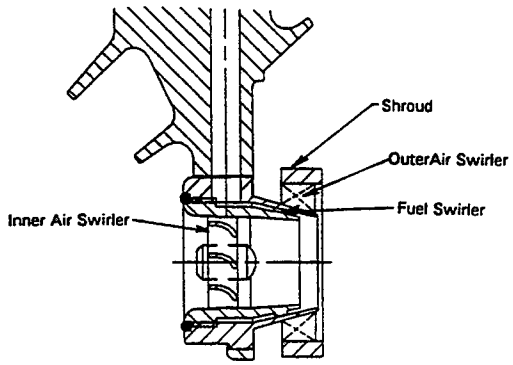

FIG. 1. Schematic diagram of airblast atomizer (courtesy of the Parker Hannifin Corporation, Gas Turbine Fuel Systems Division).

configuration generates a high shearing action between the fuel and the atomizing air that promotes atomization and helps to match the resulting spray with the combustor air flow pattern.

Optical Diagnostics

Optical access into the pressure vessel is provided by four optical-quality quartz windows. Each of these large windows has a multipoint purge feed of high-velocity air to prevent fuel deposition. Droplet sizes and velocities were measured using a single-component phase-Doppler particle analyzer (PDPA) manufactured by Aerometrics, Inc. The instrument was operated in the forward-scattering mode, with its velocity component arranged to coincide with the main axis of the conical spray. PDPA data were normally taken at a downstream distance from the atomizer exit plane of 45 mm along radii perpendicular to the spray axis. The technique of laser sheet imaging was used to obtain global images of the spray. With this technique, a pulsed Nd:YAG laser beam is converted into the form of a 0.4-mm-thick sheet that illuminates the spray flow field under investigation. The system provides a power density of 27 MW/cm^2 in the laser sheet probing volume. The elastic-scattering signals at a wavelength of 532 nm were recorded on black and white film, of ISO 400 speed, positioned perpendicular to the laser sheet. The laser pulse duration of 15 ns is generally considered short enough to freeze the particle motion. A primary magnification factor of 0.5 was selected to provide a field of view that is typical of current combustor primary-zone lengths.

Test Conditions

The test conditions were selected to correspond to those encountered in gas-turbine combustors. Most of the measurements were taken with a pressure drop across the atomizer, $\Delta P/P_A$ of 0.05, i.e., 5%, but a small number of measurements were also carried out at a higher $\Delta P/P_A$ of 0.10 in order to examine the effects of atomizing air velocity on spray structure and mean drop size. Atomizer air–fuel ratios (AFRs) ranged from 1.1 to 58. The ambient air pressures employed were 1, 6, and 12 bar at an air temperature of about 320 K. At the 12 bar condition, the maximum air and fuel mass flow rates were 0.29 kg/s and 75 g/s, respectively. Aviation kerosine (μ = 0.0013 kg/ms, σ = 0.0277 kg/s^2, and ρ = 784 kg/m^3—all at 288 K) was used throughout the test program.

Results

One phase of the test program was devoted to photographic studies using pulsed laser sheet lighting to illuminate the spray. The main objective was to examine the extent to which the overall size and shape of the spray is affected by changes in air pressure, air velocity, and fuel flow rate. Such information helps to provide a better understanding of the effects of these parameters on various aspects of combustion performance.

Spray Structure

Figure 2 shows how the physical structure of the spray is affected by an increase in ambient air pressure P_A from 1 to 12 bar while maintaining the fuel flow rate m_F constant at 35 g/s. The corresponding measurements of spray diameter at different axial locations, z, downstream of the nozzle are shown plotted in Fig. 3. All values of spray diameter shown in this and subsequent figures were obtained from high-speed photographs as an average of eight individual, instantaneous diameters measured up to the outermost visible boundaries of the spray profile. Figures 2 and 3 indicate a rapid expansion of the spray as it emerges from the nozzle which is caused by the swirling motion that is imparted to the two atomizing air streams as they flow through the contrarotating swirl vanes. From visual inspection of Fig. 2, it is clear that the effect of an increase in ambient air pressure is to reduce the spray volume. This effect is shown quantitatively in Fig. 3, which indicates a reduction in spray diameter from 80 mm to about 50 mm for an increase in air pressure from 1 to 12 bar. These measurements were carried out at a downstream distance from the atomizer of 27 mm. Measurements taken further downstream tend to be less reliable due to fluctuations of the spray boundaries, as determined from high-speed photographs, which are attributed partly to the eddies generated by the shearing action of the two contrarotating swirling air flows and also to the formation of coherent structures at the interface between the

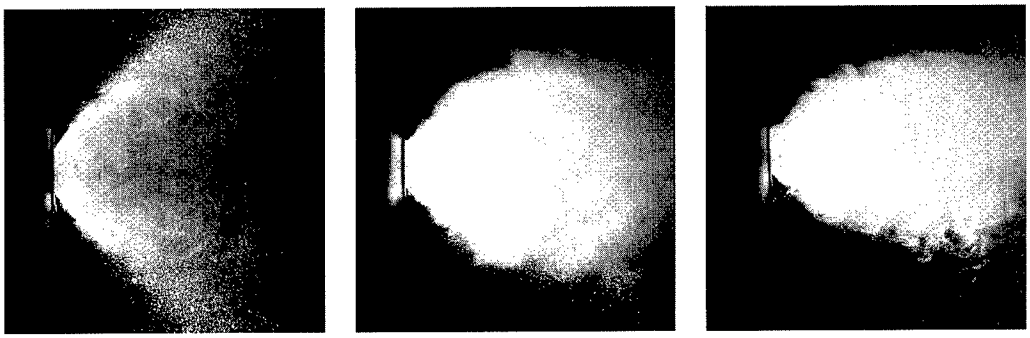

1 bar 6 bar 12 bar

FIG. 2. Influence of air pressure on spray structure for a constant fuel flow rate of 35 g/s and $\Delta P/P_A$ of 0.05.

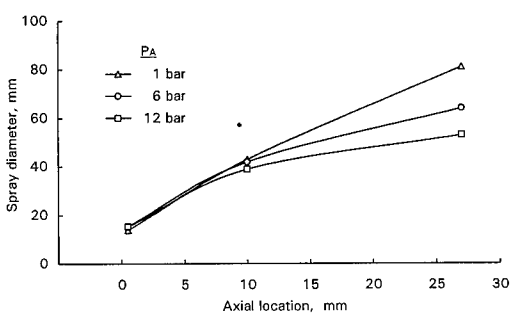

FIG. 3. Influence of air pressure on spray diameter for a constant fuel flow rate of 35 g/s and $\Delta P/P_A$ of 0.05.

high-velocity spray boundary and the surrounding quiescent air. Moreover, the trailing edges of the spray in Fig. 2 reveal less structural details than the leading edges due to attenuation encountered by the laser light sheet along its pathway through the dense spray flow field. This gives an apparent impression of spray asymmetry when in fact none is known to be present.

The observed reduction in spray diameter with increase in air pressure is not due to any change in air flow pattern, because Reynolds numbers are always high ($\gg 10^6$), but rather to the reduction in the fuel–air momentum ratio, which accompanies an increase in air pressure at constant fuel flow. As in most practical prefilming airblast atomizers, the "natural" cone angle of the spray, i.e., the angle of the spray in the absence of any atomizing air, is much wider than the angle imparted to the air by the air swirlers incorporated within the atomizer. When the atomizing air first encounters the conical fuel sheet formed at the downstream edge of the prefilmer, it tends to reduce the ensuing spray diameter by an amount that depends on the ratio of air to fuel momentum, as illustrated in Figs. 2 and 3.

In the course of the test program, a considerable body of evidence was accumulated, all of which tended to confirm the overriding importance of the fuel–air momentum ratio to spray diameter and spray volume. For example, Figs. 4 and 5 show the effects on spray dimensions of an increase in fuel flow rate from 5 to 75 g/s (corresponding to a reduction in AFR from 58 to 3.9) while maintaining the air pressure constant at 12 bar. These figures show clearly that increases in fuel–air momentum ratio, produced in this case by increases in fuel flow rate at constant air pressure, result in larger spray diameters. This influence of fuel–air momentum ratio on spray dimensions has important practical implications, one obvious example being the risk of fuel impingement on the liner walls at high fuel flow rates. In general, this influence of fuel–air momentum ratio on spray structure is beneficial to combustion performance. For example, a reduction in fuel flow rate at constant pressure causes the fuel to be associated with a smaller volume of air, thereby extending the lean blowout limit to a higher value of AFR. By the same token, an increase in fuel flow rate at constant pressure is accompanied by an increase in the amount of air participating in combustion. The effect of this additional air is generally to reduce the local fuel–air ratio and flame temperature, thereby alleviating problems of exhaust smoke and nitric oxide emissions at high combustion pressures.

Measurements carried out on the effects of atomizer pressure drop on spray size and structure yielded results that are generally consistent with the views expressed above. Thus, an increase in $\Delta P/P_A$ from 0.05 to 0.10, corresponding to a doubling of atomizing air–fuel momentum ratio, would be expected to reduce the spray diameter, and this is confirmed by the data presented in Fig. 6.

Gas turbines normally operate under conditions when an increase in combustion pressure is accompanied by an increase in fuel flow rate. Thus, the

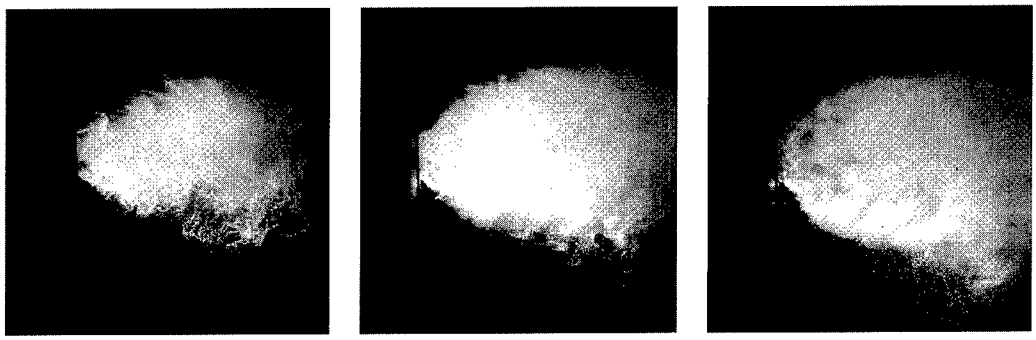

5 g/s 35 g/s 75 g/s

FIG. 4. Influence of fuel flow rate on spray structure for a constant air pressure of 12 bar and $\Delta P/P_A$ of 0.05.

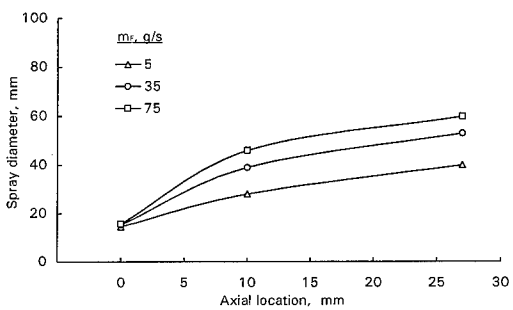

FIG. 5. Influence of fuel flow rate on spray diameter for a constant air pressure of 12 bar and $\Delta P/P_A$ of 0.05.

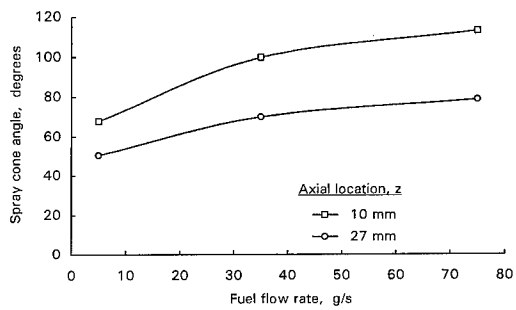

FIG. 7. Influence of fuel flow rate on spray cone angle for a constant air pressure of 12 bar and $\Delta P/P_A$ of 0.05.

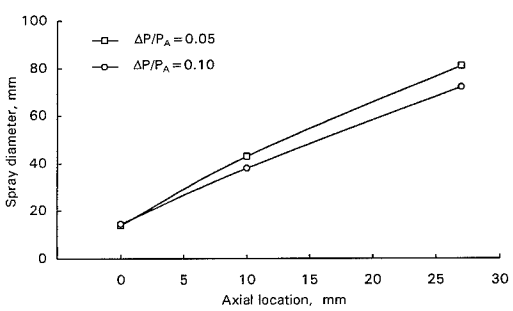

FIG. 6. Influence of $\Delta P/P_A$ on spray diameter for a constant air pressure of 1 bar and fuel flow rate of 35 g/s.

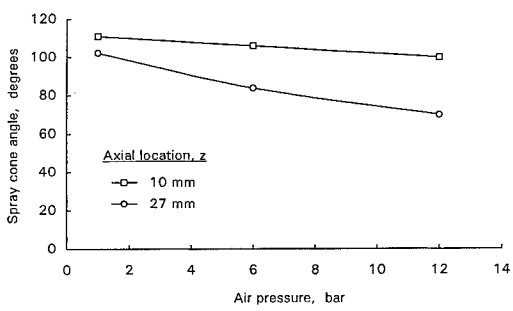

FIG. 8. Influence of air pressure on spray cone angle for a constant fuel flow rate of 35 g/s and $\Delta P/P_A$ of 0.05.

effect of an increase in pressure in reducing spray volume is opposed by the attendant increase in fuel flow rate that tends to increase the spray volume. The net result is that changes in air pressure at constant AFR have relatively little effect on spray diameter, except in the near-nozzle region ($z \approx 10$ mm).

Figures 2 and 4 show that as the droplets move downstream, the spray boundaries, which initially are in the form of a straight cone, start to become curved due to momentum exchange with the surrounding air. These curved boundaries create difficulties in the definition and measurement of cone angle. A further complication is caused by the fact that the initial diameter of the spray as it emerges from the nozzle is not only different from that of the prefilming edge but can also vary with changes in atomizer operating conditions.

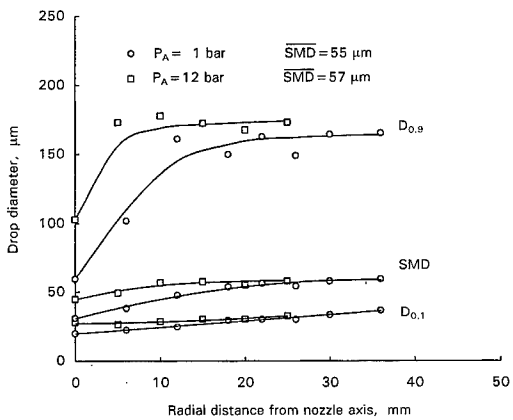

FIG. 9. Influence of air pressure on drop size distributions for a constant AFR of 3.9, $\Delta P/P_A$ of 0.05, and z = 45 mm.

The cone angles obtained by drawing straight lines from the spray diameter at the nozzle exit to the mean spray diameter (obtained as the average of several measured spray profiles), at certain specified distances downstream of the nozzle, are presented in Figs. 7 and 8. Figure 7 illustrates the influence of fuel flow rate on spray cone angle for an ambient air pressure of 12 bar. The influence of air pressure on cone angle is shown more directly in Fig. 8 over a range of air pressures from 1 to 12 bar. All the results contained in these figures are fully consistent with the notions expressed above in regard to the overriding importance of fuel–air momentum ratio to the size and shape of the spray. Essentially, the swirling and recirculating air flow patterns created by the air swirlers are independent of combustor operating conditions, and thus, the overall dimensions of the aerodynamic recirculation zone also tend to remain fairly constant. However, the spray boundaries and the radial distribution of fuel flux within the spray boundaries are both modified appreciably by changes in combustor operating conditions, mainly in so far as these changes influence the fuel–air momentum ratio of the nozzle efflux. Thus, the widening of spray cone angle with increase in fuel flow rate, as shown in Fig. 7, can be attributed directly to the concomitant increase in fuel–air momentum ratio. If a change in atomizer operating conditions should cause this ratio to decline, then the spray cone angle must also decline, as illustrated in Fig. 8. This figure shows the effect on cone angle of increasing the air pressure while maintaining the fuel flow rate constant. As expected, the reduction in fuel–air momentum ratio associated with an increase in pressure at constant fuel flow causes the cone angle to go down. However, for the more practical case in which an increase in pressure at constant AFR produces an increase in fuel–air momentum ratio, the spray cone angle actually increases in the near-nozzle region [7].

These same arguments would suggest that an increase in nozzle pressure drop at constant fuel flow rate should reduce the spray cone angle. This was confirmed by spray photographs, which showed the effect of doubling the nozzle pressure drop from 5% to 10% of the inlet pressure while keeping the fuel flow rate constant. The effect of increasing $\Delta P/P_A$ was to reduce the spray cone angle, in this case, by about 10°.

Drop Size Distributions

In two recent experimental studies on the droplet velocities and drop-size distributions obtained from practical prefilming airblast atomizers [5,7], it was shown that an increase in ambient air pressure at constant AFR could result in either a small increase or a small decrease in integrated Sauter mean diameter ($\overline{SMD}$), depending on the initial rate of interaction between the fuel and the atomizing air. In these previous studies, attention was focused mainly on the factors influencing local values of SMD within the spray volume and on $\overline{SMD}$. In this test program, an attempt was made to shed some light on the apparent insensitivity of $\overline{SMD}$ values to variations in air pressure by examining two representative diameters in addition to SMD.

The effects of increasing the air pressure from 1 to 12 bar on the radial distribution of $D_{0.1}$ (the drop diameter such that 10% of the fuel is in drops of diameter smaller than $D_{0.1}$), SMD, and $D_{0.9}$ (the drop diameter such that 90% of the fuel is in drops of diameter smaller than $D_{0.9}$) are demonstrated in Fig. 9 in which local measured values of $D_{0.1}$, SMD, and $D_{0.9}$ are shown plotted against radial distance from the centerline of the spray. For all measurements, the fuel flow rate was adjusted to maintain a constant AFR of 3.9. Figure 9 shows very little difference in local values of $D_{0.1}$, SMD, and $D_{0.9}$ at the two different levels of pressure. Although the local values of $D_{0.9}$ for small radial distances are clearly lower at the 1 bar pressure, this has little effect on $\overline{SMD}$ because most of the fuel is contained in the outer regions of the spray.

The $\overline{SMD}$ values were obtained as the mean of all the local measured values of SMD after each local value had been corrected using appropriate area and velocity weighting factors to account for the higher flow areas in the outer regions of the spray and the nonuniformity of the radial velocity distribution. Application of this procedure to the local SMD data contained in Fig. 9 revealed only a small difference in $\overline{SMD}$ between measurements carried out at 1 and 12 bar, being 55 μm in one case and 57 μm in the other. In all tests, the influence of air pressure on $\overline{SMD}$ was found to be quite small in comparison to

the effect of AFR [7]. It may be concluded therefore that not only is $\overline{SMD}$ largely independent of pressure, but so also is the distribution of drop sizes within the spray. Tests on the influence of nozzle pressure drop on mean drop size showed, as expected, that an increase in $\Delta P/P_A$ resulted in a reduction in $\overline{SMD}$. For example, measurements carried out at a distance of 27 mm downstream of the atomizer at normal atmospheric pressure showed that increasing $\Delta P/P_A$ from 0.05 to 0.10 reduced the $\overline{SMD}$ from 68 to 55 μm.

Conclusions

A series of measurements of mean and representative drop diameters, spray dimensions, and spray cone angles has been carried out on a practical, prefilming airblast atomizer of the type widely used in modern gas turbines. From tests using kerosine fuel and atomizing air at pressures up to 12 bar, the following conclusions are drawn:

1. The effect of an increase in ambient air pressure in widening the spray cone angle is not a pressure effect per se but is due to the increase in fuel flow rate that accompanies an increase in air pressure at constant AFR. For any given air pressure, the spray cone angle increases gradually and continuously with increase in fuel flow rate. If the fuel flow rate is allowed to remain constant, the effect of an increase in air pressure is to reduce slightly the spray cone angle. In general, spray volume increases with fuel flow rate and/or reductions in air pressure. Variations in air pressure at a constant air/fuel ratio, which corresponds to the normal practical situation, have little effect on spray volume. It is concluded that the main factor governing the spray cone angle and overall dimensions of the spray is the fuel–air momentum ratio. Increases in this parameter result in wider cone angles, larger spray diameters, and a displacement of the fuel flux profile toward the outer regions of the spray.
2. For the practical type of airblast atomizer employed in this investigation, variations in ambient air pressure from 1 to 12 bar have little effect on drop size distributions in the spray.
3. Increasing the air pressure drop across the atomizer reduces not only the mean drop size but also the spray cone angle.

Acknowledgments

The authors gratefully acknowledge the award of a EPSRC-Rolls Royce plc cofunded research grant GR/H82372 entitled "Laser Diagnostics for Characterization of Gas Turbine Sprays under High Air Pressure Conditions." Special thanks are due to Mr. D. Whittington for his painstaking efforts in regard to the experimental rig organization and running. Parker Hannifin Corporation of Cleveland, OH, USA, is also acknowledged for supplying the fuel injector used in this study.

REFERENCES

1. Wang, H. Y., McDonell, V. G., and Samuelsen, G. S., *Twenty-Fourth Symposium (International) on Combustion*, The Combustion Institute, Pittsburgh, 1992, pp. 1457–1463.
2. Wang, H. Y., McDonell, V. G., Sowa, W. A., and Samuelsen, G. S., *ASME J. Eng. Gas Turbines Power* 115:453–460 (1992).
3. McDonell, V. G., Seay, J. E., and Samuelsen, G. S., *ASME Paper No. 94-GT-263*, 1994.
4. Hebrard, P., Lavergne, G., Beard, P., Donnadille, P., and Trichet, P., *AGARD Conference Proceedings 536*, pp. 36/1–12, 1993.
5. Jasuja, A. K. and Lefebvre, A. H., *Twenty-Fifth Symposium (International) on Combustion*, The Combustion Institute, Pittsburgh, 1994, pp. 345–352.
6. Wynne, A. and Jasuja, A. K., *AIAA paper 91-2199*, 1991.
7. Zheng, Q. P., Jasuja, A. K., and Lefebvre, A. H., ASME Paper No. 96-GT-131, 1996. To be published in ASME Transactions.

Twenty-Sixth Symposium (International) on Combustion/The Combustion Institute, 1996/pp. 2763–2770

EFFECT OF TEMPERATURE AND CONCENTRATION FLUCTUATIONS ON RADIATIVE HEAT TRANSFER IN TURBULENT FLAMES

W. KREBS,* R. KOCH, B. GANZ, L. EIGENMANN AND S. WITTIG
Institut für Thermische Strömungsmaschinen
Universität Karlsruhe, Germany

Radiative heat transfer in turbulent flames is significantly affected by fluctuations of temperature and concentration. In an effort to better understand this complex nonlinear phenomenon, an extensive experimental investigation of a model combustor supported by a numerical analysis is presented. The combustor is fired by propane. The flame is of the diffusion type, highly turbulent, and nonluminous. The experimental techniques include detailed examination of the temperature probability density distribution by CARS N_2 thermometry, as well as time and spectrally resolved IR spectroscopy.

It was found from the CARS measurements that the temperature probability density distribution is relatively broad in the reaction zone of the model combustor, whereas in the mixing zone it is of Gaussian shape with a relatively small variance.

To gain insight into the turbulence/radiation interaction, the radiation spectra recorded at the wall of the combustor are compared to the spectra predicted by a radiation model. The radiation model takes into account the turbulent fluctuations of temperature and species concentrations and contains different methods for representing the scalar fluctuations. If both temperature and concentration fluctuations are considered in the radiation model, good agreement between predicted and experimentally recorded radiation spectra is obtained. The radiation model revealed that as a consequence of the strong temperature fluctuations, turbulence/radiation interaction is significant in the reaction zone. The effect is particularly pronounced for the 2.7 μm CO_2/H_2O radiation band and the H_2O radiation bands at lower wavelength. In the mixing zone, radiation is only slightly affected by the scalar fluctuations caused by the weak temperature fluctuations.

The present work demonstrates that turbulence/radiation interaction has a significant impact on the heat transfer to the combustor walls in the vicinity of the reaction zone and that advanced radiation models are capable of predicting this effect correctly.

Introduction

A considerable part of the wall heat load of gas turbine combustors stems from radiation caused by high flame temperatures and high pressures encountered in this type of combustor [1]. Therefore, detailed knowledge of the radiative heat load is required to determine the amount of cooling air and to predict wall temperatures.

Until now, numerous elaborate models for predicting radiative heat transfer in combustion systems have been developed. They are reviewed comprehensively in Viskanta and Mengüc [2]. Usually, the methods do not account for fluctuations in turbulent flames. However, as pointed out by several authors [3–4], the radiative heat load may be enhanced significantly by scalar fluctuations caused by the nonlinear relation between temperature, concentration, and radiative heat load. The basic effects were analyzed by us recently [5] by applying the Reynolds averaging technique to the radiative transfer equation. It could be shown that the enhancement of radiant emission caused by scalar fluctuations is more pronounced at lower wavelengths, typically less than 3 μm. Moreover, the study [5] revealed that concentration fluctuations may render the medium more transparent. This means that if the optical dimension of the turbulent eddies ($k_\lambda C l_t$) exceeds a value of 0.3, the time-averaged transmissivity will be lower than the transmissivity calculated from the time-averaged values of the absorption coefficient and the concentrations. Although this simplified analysis is suitable for evaluating the significance of the phenomenon, many questions about the physics remain open.

In continuation of our theoretical study, an experimental and numerical analysis of radiative heat transfer in a turbulent propane/air diffusion flame inside a model combustor has been performed. Special emphasis was put on the following topics:

1. Accurate representations of the temperature fluctuations are obtained from CARS measurements. Therefore, the theoretical analysis can be based on detailed experimental information of the probability density distributions of temperature.

*Current address: Siemens KWU, Mülheim, Germany.

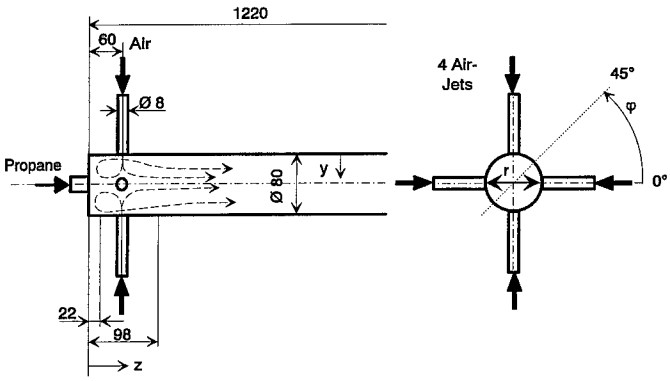

FIG. 1. Geometry and flow-pattern of the model combustor.

2. Fluctuations of radiative heat transfer have been recorded by time and spectrally resolved IR spectroscopy.
3. To prevent effects arising from a turbulent transmission function that is difficult to describe mathematically, a test case has been selected in which the optical density of the turbulent eddies is less than 0.3.

The significance of the turbulence/radiation interaction on heat transfer and on flame diagnostics will be discussed by comparing the measured IR spectra to calculated spectra. The experimental setup and the different measurement techniques will be described in the next section.

Experimental Setup

An extensive description of the model combustor and its flame characteristics is given in Bauer et al. [8]. Therefore, the description will be kept brief here. The geometry of the model combustor and the flow pattern are illustrated in Fig. 1. The diffusion flame is stabilized by four radially injecting jets that induce an upper recirculation zone. Propane is injected through an orifice at the front plate. The mass flow of propane is 1 kg/h and the mass flow of air is 33.5 kg/h, resulting in a low overall equivalence ratio of $\Phi = 0.44$. The highly turbulent reacting flow was analyzed extensively both by experimental techniques, such as Laser Doppler anemometry [8,9], Phase Doppler anemometry, and IR spectroscopy [10], and by numerical simulations. Laser Doppler anemometry revealed turbulent fluctuations of the velocity that are of the same magnitude as the time-averaged value [9]. Subsequently, the measurement techniques for investigating the turbulence/radiation interaction will be discussed. Particular emphasis is put on the measurement techniques for temperature and its fluctuations, IR radiation and its fluctuations, and species concentration.

Temperature Measurements

For investigating the turbulence/radiation interaction, detailed knowledge of the temperature fluctuations is required. Because there are steep scalar gradients and the reacting flow field is enclosed by cold walls, a nonintrusive measurement technique that does not suffer from radiative heat loss is required. Therefore, the CARS (coherent Anti–Stokes Raman scattering) measurement technique has been selected. The mobile CARS system of the DLR Stuttgart has been applied for single-pulse N_2 thermometry [11–13]. The laser beams are overlapped in the USED CARS–phase matching configuration and are focused by an achromatic lens with a focal length of 500 mm. Since the diameter of the laser beam at the focusing lens was different for the two measurement locations, the spatial resolution (the length of the probe volume in beam direction in which 95% of the CARS signal is generated) was $L_{95\%} = 2.7$ mm for $z = 22$ mm and $L_{95\%} = 1.6$ mm for $z = 98$ mm with a diameter of approximately 200 μm. The spatial resolution of $L_{95\%} = 2.7$ mm at $z = 22$ mm gave an acceptable signal-to-noise ratio. Each single-pulse CARS spectrum was analyzed by fitting theoretical spectra to the experimental data to determine the corresponding temperature. The nonresonant background was weak at most locations. Signals containing high-resonant background caused by droplets or unburned hydrocarbons were discarded during data processing. For the present experiments, the accuracy of the mean temperature is in the range of $\pm 4 - 7\%$ because of the low signal intensity at some locations. The pulse duration was 10 ns, which is far below the smallest turbulent time scales. At each location, 1200 single-pulse spectra were recorded.

IR Spectroscopy

The emission spectroscopy technique was applied to investigate radiative heat transfer to the combustor walls. As shown in Fig. 2, the experimental setup

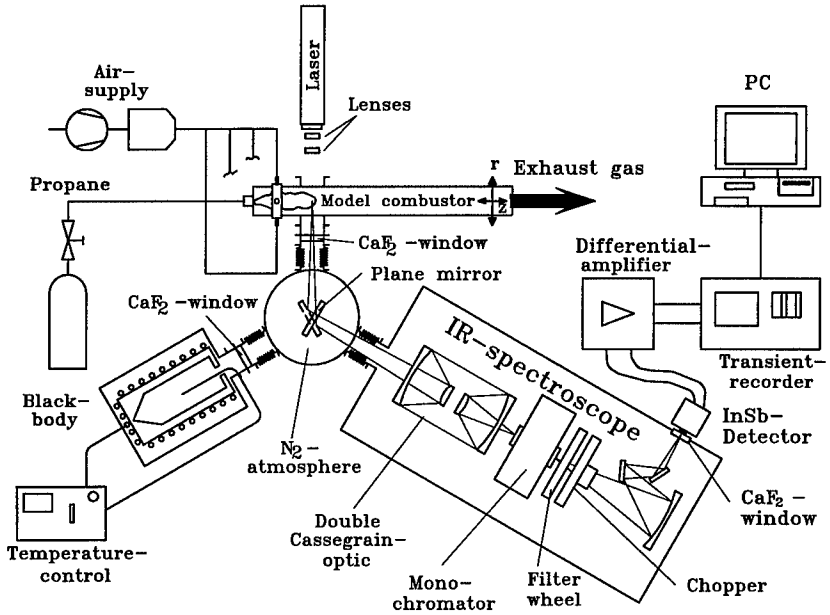

FIG. 2. Experimental set up for IR-spectroscopy.

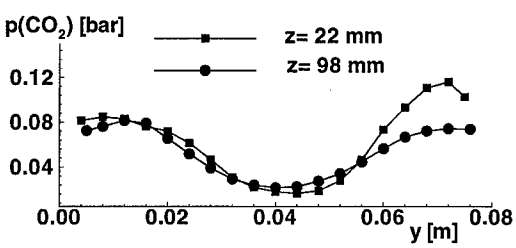

FIG. 3. Measured profiles of the time averaged partial pressure of CO_2.

consists of three main components: the model combustor, the IR spectroscope, and the black body source. The black body serves as a reference source for calibration. The IR spectroscope is configured to detect the spectral radiative intensity $I_{\lambda,n}$ in the normal direction toward the wall. The radiation is focused by gold-coated mirrors to preserve a wavelength independent optical projection. Spectral dispersion is achieved by a grating monochromator with a spectral resolution of 25 nm for $\lambda < 2.8\ \mu$m and 35 nm for $\lambda > 2.8\ \mu$m. The radiation is finally focused onto an InSb detector, which enables time-resolved measurements at a sampling rate of 1000 1/s and a high signal noise ratio of 1000. To avoid reabsorption of incident radiation caused by CO_2 and H_2O, the whole optical arrangement including the black body source is purged by N_2. This "clean" environment is separated from combustion gases by a CaF_2 window.

Gas Concentration Measurements

CO_2 concentration profiles were determined by isokinetic gas sampling using a cooled cranked probe [8]. This is necessary to reduce the local disturbance of the flow field. Because of the suction probe design, only time-averaged values can be obtained. The radial profiles of the CO_2 concentration are shown in Fig. 3 for two axial locations. The first position $z = 22$ mm corresponds to the main reaction zone. The second location $z = 98$ mm is downstream of the air injection. It represents the mixing zone where the chemical reactions are almost finished. The highest levels of CO_2 concentration are found in the reaction zones close to the wall. At $z = 98$ mm, the CO_2 concentrations are diminished because of the additional mixing with fresh air supplied by the air jets.

Experimental Results

Time-Averaged Temperatures

The profiles of the time-averaged temperatures from the CARS measurements are depicted in Fig. 4 for the reaction zone ($z = 22$ mm) and the mixing zone ($z = 98$ mm). For comparison, temperature data obtained from PtRh/Pt thermocouple measurements [8] are included, too. According to the flow field induced by the four air jets (Fig. 1), combustion takes place in the vicinity of the wall. Therefore, the highest temperatures of up to 1880 K are observed

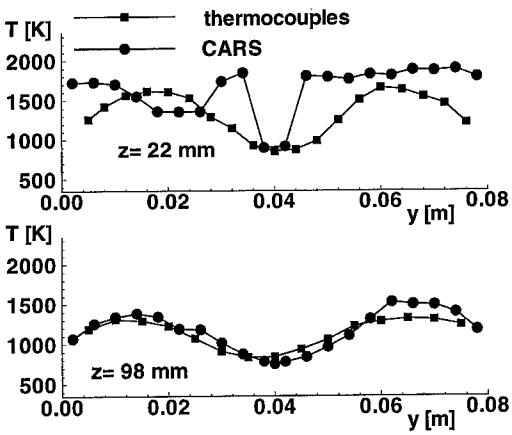

FIG. 4. Measured profiles of the time-averaged temperature.

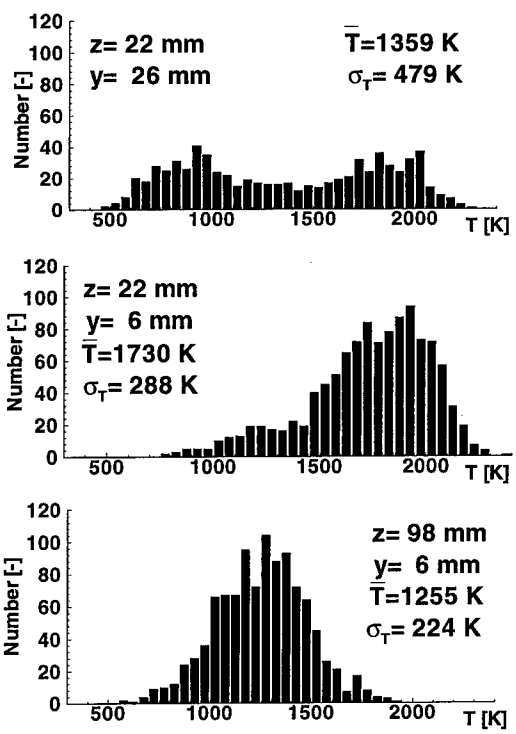

FIG. 5. Histograms of the instantaneous temperature measured with CARS.

close to the wall ($y < 20$ mm and $y > 60$ mm). Particularly in this region, major deviations between the thermocouple and the CARS N_2-thermometry data of up to 600 K are observed. These deviations can be explained by the large radiative heat loss of the thermocouples to the cold combustor walls. In the central region (30 mm $< y <$ 50 mm), the presence of fresh air from the four radial jets and unburned propane causes relatively low temperatures. The increased propane concentration at these positions is confirmed by the lower resonant-to-nonresonant ratio observed in the CARS spectra.

As expected, the temperatures in the mixing zone (z = 98 mm) are lower than in the reaction zone. Because of the relatively low temperature levels, the discrepancies between CARS and thermocouple data are smaller. However, it is obvious that the temperature profile as measured by the thermocouple is smoother than that of the CARS-N_2 thermometry because of heat transfer processes that have a significant impact on the thermocouple measurements.

Fluctuations of Temperature

Comprehensive information on turbulent flames is obtained from probability density distributions of the temperature. The probability density histograms derived from the CARS measurements are presented in Fig. 5 for three selected positions representing different regions of the reacting flow field. For comparison, temperature histograms recorded in premixed laminar flames showed a standard deviation of 4%. The first histogram taken at z = 22 mm and y = 26 mm corresponds to the reacting shear layer. At this location, the intermittence between eddies containing either hot reaction products or cold educts causes a bimodal distribution. It should be pointed out that temperatures range from 500–2250 K at this location. The width of the temperature distribution is reduced significantly in the hotter regions close to the wall, as indicated by the histogram for the position z = 22 mm and y = 6 mm. Further reduction of the width is observed downstream at z = 98 mm and y = 6 mm. Here, the histogram almost takes the form of a Gaussian distribution, indicating that the reaction processes are almost finished. Considering the different shapes of the probability density distribution, it is obvious that the temperature fluctuations cannot be represented accurately by a Gaussian distribution. Therefore, temperature fluctuations have been taken into account in the calculational model by the corresponding temperature histograms.

Time-Averaged Radiative Intensity

The measured spectra of the time-averaged radiative intensity $\overline{I_{\lambda,n}}$ normal to the wall are shown in Figs. 6 and 7 for the axial locations z = 22 mm and z = 98 mm, respectively. In both spectra, emission is restricted to the well-known radiation bands of water vapor and carbon dioxide. Furthermore, in the reaction zone, the 3.4 μm band of unburned hydrocarbons is visible, indicating that the chemical reactions are not finished at this location. No soot

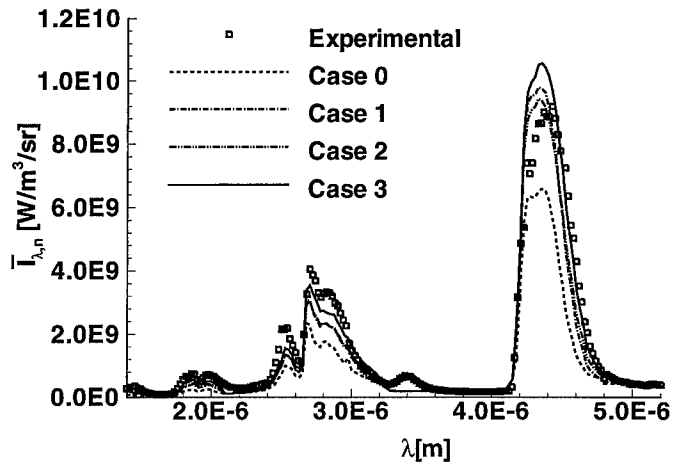

FIG. 6. Spectra of the time averaged radiative intensity, reaction zone $z = 22$ mm.

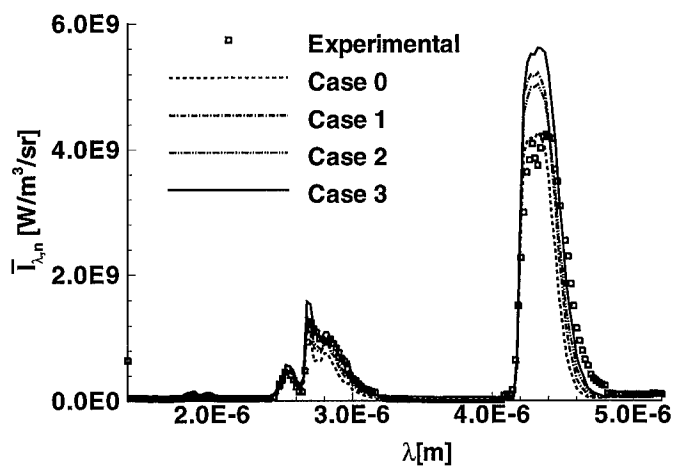

FIG. 7. Spectra of the time averaged radiative intensity, mixing zone $z = 98$ mm.

radiation was detected because of the lean combustion conditions. The very low radiative background that is visible between the radiation bands is caused by radiative emission from the opposite wall. The tem-peratures on the opposite wall were measured to be 623 K at $z = 22$ mm and 423 K at $z = 98$ mm. As expected from the temperature measurements, the radiative intensity decreases further downstream of the reaction zone.

Fluctuations of the Radiative Intensity

To illustrate the fluctuations of the radiative intensity caused by the fluctuations of temperature and concentration, the probability density distribution of the spectral normal radiative intensity for $\lambda = 4.38$ μm measured at $z = 22$ mm is shown in Fig. 8. Although the corresponding shape of the temperature PDFs deviates from a Gaussian distribution, the PDF of the radiative intensity closely resembles a Gaussian PDF. Similar Gaussian-type PDFs have been obtained for other wavelengths. This indicates that the radiative intensity at the wall is the result of a complicated integration process that will be discussed in detail in the next section.

Radiation Model

In this section, we will derive the calculational model for radiative transfer that accounts for temperature and concentration fluctuations represented by their probability density distribution. The radiation, emitted instantaneously by an absorbing, nonscattering medium within a spectral interval $[\lambda, \lambda + d\lambda]$ and in direction $\mathbf{s}$ is given by the radiative transfer equation (RTE):

$$\frac{dI_\lambda(\mathbf{s}, t)}{d\mathbf{s}} = -k_\lambda(\mathbf{s}, t)\, C(\mathbf{s}, t) I_\lambda(\mathbf{s}, t) + k_\lambda(\mathbf{s}, t)\, C(\mathbf{s}, t) I_{b,\lambda}(\mathbf{s}, t) \qquad (1)$$

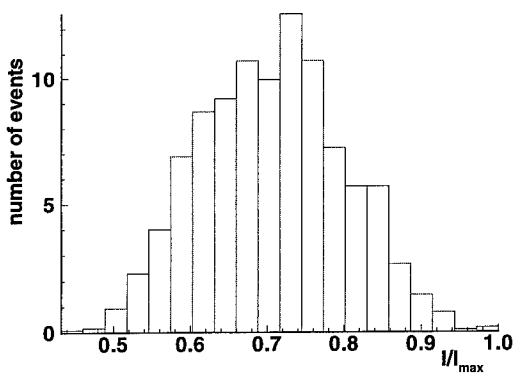

FIG. 8. Probability density distribution of the radiative intensity for $\lambda = 4.38\ \mu m$.

For clarity, the subsequent analysis is simplified by considering a single radiating species. However, the extension to several species is straightforward. Integrating Eq. (1) along the line of sight yields the integral form of the monochromatic, instantaneous radiant transport equation:

$$I_\lambda(s,t) = I_{\lambda,0}(s = 0)\exp\left[-\int_0^s k_\lambda(T(s_a,t))C(s_a,t)ds_a\right] + \int_0^s I_{b,\lambda}(T(s_a,t))k_\lambda(T(s_a,t))C(s_a,t) \exp\left[-\int_{s_a}^s k_\lambda(T(s_b,t))C(s_b,t)ds_b\right]ds_a \quad (2)$$

The first term on the right-hand side of Eq. (2) stems from the nonfluctuating radiation emitted by the combustor wall, located at $s = 0$. The second term on the right-hand side represents the contribution of the radiative emission of the medium. In both terms, the attenuation caused by absorption is taken into account by the exponential terms.

To determine the radiative heat load at the opposite wall, Eq. (2) must be time averaged. The evaluation of the attenuation causes problems, because a detailed knowledge of two-point correlations of the temperature and concentration fluctuations is required [5,6]. These two-point correlations, however, are generally not available. Therefore, in a first approximation, Eq. (2) is simplified by replacing the instantaneous terms in the exponential expressions by their time-averaged values as shown in Eq. (3).

$$I_\lambda(s,t) \approx I_{\lambda,0}(s = 0)\exp\left[-\int_0^s \overline{k_\lambda(T(s_a,t))}\,\overline{C(s_a,t)}\,ds_a\right] + \int_0^s I_{b,\lambda}(T(s_a,t))k_\lambda(T(s_a,t))\,C(s_a,t) \exp\left[-\int_{s_a}^s \overline{k_\lambda(T(s_b,t))}\,\overline{C(s_b,t)}\,ds_b\right]ds_a \quad (3)$$

This simplification is valid if the optical dimension of the turbulent eddies ($k_\lambda Cl_t$) is less than 0.3 [5]. This means that effects resulting from a fluctuating transmissivity can be neglected. The turbulent medium is then characterized by small turbulent length scales. Time averaging of Eq. (3) finally yields the following:

$$\overline{I_\lambda(s)} = I_{\lambda,0}(s = 0)\exp\left[-\int_0^s \overline{k_\lambda(T(s_a,t))}\,\overline{C(s_a,t)}\,ds_a\right] + \int_0^s \int_{T_{low}}^{T_{high}} \int_{C_{low}}^{C_{high}} I_{b,\lambda}(T(s_a))k_\lambda(T(s_a))C(s_a) \cdot p[T(s_a), C(s_a)]dCdT \exp\left[-\int_{s_a}^s \overline{k_\lambda(T(s_b,t))}\,\overline{C(s_b,t)}\,ds_b\right]ds_a \quad (4)$$

The effect of temperature and concentration fluctuations on the emission rate ($k_\lambda CI_{b,}\lambda$) is taken into account in the second term on the right-hand side of Eq. (4) by the joint probability distribution $p[T(s_a),C(s_a)]$ of temperature and species concentration.

To manage the calculations in an acceptable time, the spectral properties (k_λ) of the combustion gases CO_2 and H_2O were calculated from Narrow-Band models [7]. The monochromatic transport equation, Eq. (4), was finally integrated over small wavelength intervals covered by the Narrow-Band model. Subsequently, the results of the radiation model will be compared to the experimental data to analyze the effects of the scalar fluctuations.

Comparison between Calculated and Predicted IR Spectra

Since the optical dimension of the turbulent eddies ($k_\lambda Cl_t$) of the present combustor is smaller than 0.15, the effect of a fluctuating transmissivity can be neglected and Eq. (4) can be applied. This means that the fluctuations of the radiative intensity are caused only by the fluctuation of the emission rate ($k_\lambda CI_{b,\lambda}$) and thus depend on the local temperature and concentration fluctuations. To separate the effects, four different calculations have been performed as listed in Table 1. The cases are distinguished according to the treatment of the instantaneous temperature $T(s_a, t)$ and the instantaneous species concentration $C(s_a, t)$. Since the species concentration of H_2O was not measured, it is derived from the overall stoichiometry condition for propane combustion:

$$\overline{C(s_a, H_2O)} = 4/3\ \overline{C(s_a, CO_2)} \quad (5)$$

Concentration fluctuations that were not measured are taken into account in case 3 only. In this

TABLE 1
Definition of the four different cases

Name	Treatment of Temperature	Treatment of Species Concentration
Case 0:	$T(s_a, t) = \bar{T}(s_a)$ taken from thermocouple measurements	$C(s_a, t) = \bar{C}(s_a)$
Case 1:	$T(s_a, t) = \bar{T}(s_a)$ taken from CARS data	$C(s_a, t) = \bar{C}(s_a)$
Case 2:	$T(s_a, t)$ taken from histograms of the CARS measurements	$C(s_a, t) = \bar{C}(s_a)$
Case 3:	$T(s_a, t)$ taken from histograms of the CARS measurements	PDF for concentration is constructed using two Dirac impulses such that $C(s_a, t) = \overline{C(s_a)} + \Delta c$ *for* $T > \bar{T}$ $C(s_a, t) = \overline{C(s_a)} - \Delta c$ *for* $T < \bar{T}$ *with* $\Delta c = 0.5°\overline{C(s_a)}$ *for* $z = 22$ mm *with* $\Delta c = 0.4°\overline{C(s_a)}$ *for* $z = 98$ mm

case, it is assumed that the concentration fluctuations are strongly correlated to the temperature fluctuations. This hypothesis is based on the fact that eddies with high temperatures are enriched with reaction products, whereas eddies with low temperatures contain a low amount of reaction products.

A comparison of measured and calculated spectra for the reaction zone ($z = 22$ mm) is shown in Fig. 6. Since the nonlinearity between temperature and the black body function is more pronounced in the lower wavelength range, the effect of scalar fluctuations is more significant for the 1.8 μm H_2O and the 2.7 μm H_2O/CO_2 radiation bands. The shape of these two radiation bands is best predicted in case 3 when both concentration and temperature fluctuations are taken into account. The deviation in the central region of the 4.3-μm band stems from reabsorption effects caused by cold CO_2 in the short path between the model combustor and CaF_2 window. Therefore, this portion of the band is meaningless for comparison. Better suited for the evaluation of the predictions is the right side wing of the band. It is well understood from quantum mechanics [10] that the right wing is particularly sensitive to temperature and that it will be shifted toward higher wavelengths by temperature fluctuations. As Fig. 6 reveals, best agreement with the experimental data is obtained for the right wing of the 4.3 μm band when both temperature and concentration fluctuations are accounted for in the predictions (case 3).

As discussed previously, the combustion reactions are almost finished in the mixing zone ($z = 98$ mm). The temperature and concentration fluctuations are caused mainly by mixing processes and are therefore rather moderate. As a consequence, the width of the temperature distribution is much smaller (Fig. 5) and the effect of turbulent fluctuations on radiative heat transfer is significantly reduced. Figure 7 shows that, similar to results for the reaction zone, best agreement between the experimental and predicted spectra of the 1.8-μm H_2O, the 2.7-μm H_2O/CO_2, and the right wing of the 4.3-μm radiation bands is achieved when the temperature and concentration fluctuations are taken into account (case 3).

Conclusion

Radiative heat transfer in turbulent flames is affected significantly by the fluctuations of temperature and concentration. In an effort to better understand this nonlinear phenomenon, an extensive experimental investigation and numerical analysis of a highly turbulent reacting flow inside a model combustor have been performed. The experimental techniques include detailed examination of the temperature probability density distribution by CARS N_2 thermometry, as well as time and spectrally resolved IR spectroscopy.

From comparison of measured and calculated spectra, the following conclusions can be drawn:

1. Predictions of radiative transfer are strongly sensitive to temperature distributions. Errors in the determination of time-averaged temperatures result in significantly wrong predictions of the radiative heat load.
2. Accurate predictions of radiative heat transfer from the reaction zone, which is characterized by strong scalar fluctuations, requires accounting for both temperature and concentration fluctuations.
3. The turbulence/radiation interaction is more pronounced for the 1.8-μm H_2O and the 2.7-μm CO_2/H_2O radiation bands in comparison to the 4.3-μm band. The effect is caused by the nonlinearity between temperature and black body intensity, which is higher at lower wavelengths. This result is important with respect to gas turbine combustors featuring much higher optical densities and higher temperatures than the model combustor. The contribution of these

radiation bands to the total radiative wall heat load will be much higher under these conditions. Moreover, as radiation from soot is emitted in the lower wavelength range, too, it can be concluded that soot radiation is significantly affected by scalar fluctuations.

4. The position of the right side of the 4.3-μm CO_2 radiation band is shifted toward higher wavelengths by scalar fluctuations. This result is important for flame diagnostics based on the analysis of the shape of radiation bands.

Nomenclature

C	species concentration [bar]
I_λ	monochromatic radiative intensity [$W/m^3/sr$]
$I_{b,\lambda}$	monochromatic radiative intensity of black body [$W/m^3/sr$]
k_λ	spectral absorption coefficient [$\text{bar}^{-1}m^{-1}$]
l_t	turbulent length scale [m]
T	temperature [K]
t	time [s]

Acknowledgments

The study presented was supported by a grant from TECFLAM (Arbeitsgemeinschaft Technischer Flammen), which is gratefully acknowledged. The authors would like to thank Dr. R. Lückerath and Dr. V. Bergmann from the Institut für Physikalische Chemie der Verbrennung, DLR Stuttgart, who performed the temperature measurements with the mobile CARS system.

REFERENCES

1. Lefebvre, A. H., *Int. J. Heat Mass Transfer* 27(9):1493–1510 (1984).
2. Viskanta, R., and Mengüc, M. P., *Progr. Energy Combust. Sci.* 13:97–160 (1987).
3. Song, T. H., and Viskanta, R., *J. Thermophysics Heat Transfer* 1:56–62 (1987).
4. Gore, J. P., Jeng, S. M., and Faeth, G. M., *J. Heat Transfer* 109:165–171 (1987).
5. Krebs, W., Koch, R., Bauer, H.-J., Kneer, R., and Wittig, S., *Eurotherm Seminar No. 47, Heat Transfer in Radiating and Combusting Systems 2,* Saluggia, Italy, 1994, pp. 349–363.
6. Tan, E., and Foster, P. J., *Heat Transfer 1978,* 3:403–408, Hemisphere Publishing, Canada (1978).
7. Goody, R. M., *Atmospheric Radiation,* part 1, Clarendon Press, Oxford, 1964.
8. Bauer, H. J., Eigenmann, L., Scherrer, B., and Wittig, S., ASME Gas Turbine Conference, Paper No. 95-GT-71, 1995.
9. Jeckel, R., Noll, B., and Wittig, S., 6th *International Symposium on the Application of Laser Techniques to Fluid Mechanics,* Lissabon, 1992, p. 22.1.1.
10. Koch, R., Krebs, W., Jeckel, R., Ganz, B., and Wittig, S., ASME Gas Turbine Conference, Paper No. 94-GT-403, 1994.
11. Lückerath, R., Woyde, M., Meier, W., Stricker, W., Schnell, U., Magel, H. C., Görres, J., Spliethoff, H., and Maier, H., *Appl. Opt.* 34:3303 (1995).
12. Meier, W., Plath, I., and Stricker, W., *Appl. Phys.* B 53:339 (1991).
13. Stricker, W. and Meier, W., *Trends Appl. Spectros.* 1:231 (1993).

COMMENTS

Flemming M. B. Andersen, University of Denmark, Denmark. Did you assume that properties in neighboring cells or eddies are statistically independent?

Author's Reply. Generally, to model the effect of fluctuations of temperature and concentration on radiative transfer, 2pt correlations have to be taken into account. In this paper, the effect of 2pt correlations is neglected, which is justified by the fact that the optical density of the turbulent eddies is small enough. Therefore, Eq. (4) can be applied and information about 2pt correlations need not be provided. Concerning the numerical solution of the integrals, the discretization should guarantee a good resolution of the temperature and concentration profiles.

Twenty-Sixth Symposium (International) on Combustion/The Combustion Institute, 1996/pp. 2771–2778

STABILITY AND EMISSIONS CHARACTERISTICS OF A LEAN PREMIXED GAS TURBINE COMBUSTOR

WANG-PING SHIH, JONG GUEN LEE AND DOMENIC A. SANTAVICCA

Propulsion Engineering Research Center
Department of Mechanical Engineering
The Pennsylvania State University
University Park, PA 16802, USA

The effect of incomplete fuel-air mixing on NO_x emissions and combustion stability has been studied in an atmospheric pressure, optically accessible, laboratory-scale, premixed dump combustor. The degree of fuel-air mixing was varied systematically where the fuel distribution at the combustor inlet was quantified using two-dimensional acetone fluorescence. Combustion stability was characterized both in terms of the level of combustion-generated noise during combustion oscillations and the lean blowout limit. The structure of the flame zone was characterized using two-dimensional OH fluorescence measurements that were phase locked with the combustion-generated pressure oscillations.

As has been observed previously, it was shown that incomplete fuel-air mixing results in increased NO_x emissions at overall fuel-lean conditions. The results, however, indicate that "reaction zone" NO mechanisms, enhanced by superequilibrium O-atom concentrations, are in part responsible for more than 50% of the increased NO production.

It was also shown that incomplete fuel-air mixing in a premixed combustor can significantly reduce the stable operating range of the combustor both in terms of increasing the tendency for combustion oscillation and raising the lean blowout limit. Lastly, it was observed that during unstable combustion, the flame moves in a well-defined periodic manner; however, the details of the flame behavior and instability mechanism can vary significantly depending on the overall equivalence ratio and the degree of fuel-air mixing.

Introduction

One of the more promising ultralow NO_x gas turbine combustor concepts is the lean, premixed combustor that has demonstrated the potential for significant reductions in NO_x emissions over what can be achieved by current designs [1,2]. Since it is difficult to obtain complete fuel-air mixing in actual gas turbine combustors, because of a number of constraints such as avoiding flashback and autoignition, it is important to understand the effect of incomplete fuel-air mixing on the combustor's performance. For example, studies have shown that incomplete fuel-air mixing can have a significant effect on NO_x emissions [3,4]. In addition, since premixed combustors are more susceptible to combustion instabilities [5,6], it is also important to understand the effect of incomplete fuel-air mixing on combustion stability.

The primary objective of the research reported in this paper is to characterize the effects of incomplete fuel-air mixing on both NO_x emissions and flame stability, that is, lean blowout and combustion oscillations, in lean premixed combustors. Such information is critical for the successful development of ultralow NO_x combustors. In addition, the evolution of the flame structure during unstable combustion is characterized, providing an understanding of the underlying phenomena that may lead to insights pertinent to the development of passive and active control strategies for preventing combustion instabilities.

Experimental Approach

The optically accessible dump combustor used in this study is illustrated schematically in Fig. 1. The atmospheric pressure combustor consists of a 13.7-mm-diameter by 76-cm-long mixing section, followed by a 42-mm-diameter by 38-cm-long quartz combustion section. The flame is stabilized at the step between the mixing and combustion sections, where to increase the stable operating range of the combustor a cross-hair type flame holder made of 0.89-mm-diameter stainless steel wire is located immediately downstream of the mixing section. Although actual gas turbine combustors operate at elevated pressures, a number of studies [7–9] suggest that the effect of pressure on NO_x formation is relatively weak under fuel-lean conditions, whereas near stoichiometric condition, NO_x formation has an approximately square-root pressure dependence. With this in mind, atmospheric pressure tests can

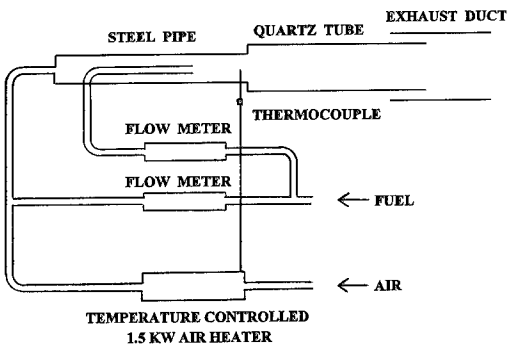

FIG. 1. Schematic drawing of dump combustor.

provide useful information regarding the behavior of lean premixed combustors.

Fuel (commercial-grade methane) is injected into the mixing section at two locations; one is 76 cm (55 mixing tube diameters) upstream of the mixing section exit, and the other is 8.2 cm (6 mixing tube diameters) upstream of the mixing section exit where the fuel is injected through a 3.4-mm-diameter co-axial fuel tube. The inlet mixture temperature is controlled at 680 ± 5 K, and the bulk velocity in the mixing section is 8.9 m/s (Reynolds number = 660). The airflow rate is 1.2 SCFM.

The degree of fuel-air mixing at the entrance to the combustion section can be varied by changing the fuel split, σ, which is defined as one minus the ratio of the mass flow rate of fuel introduced through the downstream fuel tube to the total fuel mass flow rate introduced into the combustor multiplied by 100%. It is important to note that even in the σ = 0% case, there is significant fuel-air mixing before the combustor inlet such that none of the fuel burns in a diffusion flame mode. The overall equivalence ratio ($\Phi_{overall}$) is varied from 0.4 to 1.1, and 100%, 50%, 17%, and 0% fuel splits are investigated.

Two-dimensional acetone laser-induced fluorescence (LIF) is used to quantify the fuel distribution at the combustor inlet. A conventional gas sampling system and a chemiluminescence analyzer is used to measure the radial and axial, NO and NO_x concentration profiles in the combustor. Combustion stability is evaluated both in terms of the lean blowout limit and the occurrence of combustion oscillations, which are characterized by the intensity of the combustion-generated noise as measured using a microphone located at the combustor exit. The evolution of the flame structure during unstable combustion is characterized using two-dimensional OH LIF measurements that are synchronized with the combustion-generated pressure oscillation. Since a relatively temperature-insensitive absorption line (Q_2[8] and Q_1[9] transitions in the [1,0] vibration band of the $A^2\Sigma^+ - X^2\Pi$ system) is excited, the OH fluorescence intensity can be assumed to provide a semiquantitative indication of the OH concentration. Additional information can be found in Shih's thesis [10].

Results and Discussion

Fuel Distribution for Different Degrees of Fuel-Air Mixing

Figure 2 shows the mean and normalized standard deviation of the local equivalence ratio for two incompletely mixed cases (i.e., σ = 0% and 50%) at an overall equivalence ratio of 0.6. These results are averages from 100 individual acetone fluorescence images. The field of view is 3.5 mm by 14 mm and is located immediately downstream of the mixing section exit. At the completely mixed condition (σ = 100%), not shown in Fig. 2, the local equivalence ratio distribution is uniform and steady with a value of 0.6. For the σ = 50% case, the local mean equivalence ratio ranges from 0.4 to 0.8 with a standard deviation of up to 20%, whereas in the σ = 0% case, the local mean equivalence ratio ranges from 0.2 to 1.0 with a standard deviation of up to 40%. The fuel distribution in the incompletely mixed cases can be quantified in terms of an unmixedness parameter [11], which is defined as C'/C (1 − C) where C' is the fluctuation in the fuel concentration and C is the mean value of the fuel concentration. The average value of the unmixedness parameter over the mixing section exit area is 2.0×10^{-3} for the 0% fuel split case and 2.7×10^{-4} for the 50% fuel split case.

The Effect of Incomplete Fuel-Air Mixing on NO and NO_x Emissions

Figure 3 shows the area-weighted NO and NO_x concentrations (in ppm) as a function of the distance from the step for three different fuel-air mixing conditions at overall equivalence ratios of 0.6 and 0.92. The area-weighted concentration is the area-weighted average of the radial concentration measurements, where it is assumed that the flow field is axisymmetric. At the fuel-lean condition, for all three mixing conditions, the NO and NO_x concentrations are observed to increase with distance, which is evidence of postflame NO production. At $\Phi_{overall}$ = 0.6, it is also observed that incomplete fuel-air mixing results in increased NO production, which is consistent with previous studies [3,4]. The generally accepted explanation for increased NO production at fuel-lean, incompletely mixed conditions is in terms of thermal NO production [3,4]. However, the results shown in Fig. 3 suggest that reaction-zone NO mechanisms may contribute significantly to the total NO production.

An estimate of the reaction-zone NO can be obtained by extrapolating the NO concentrations in

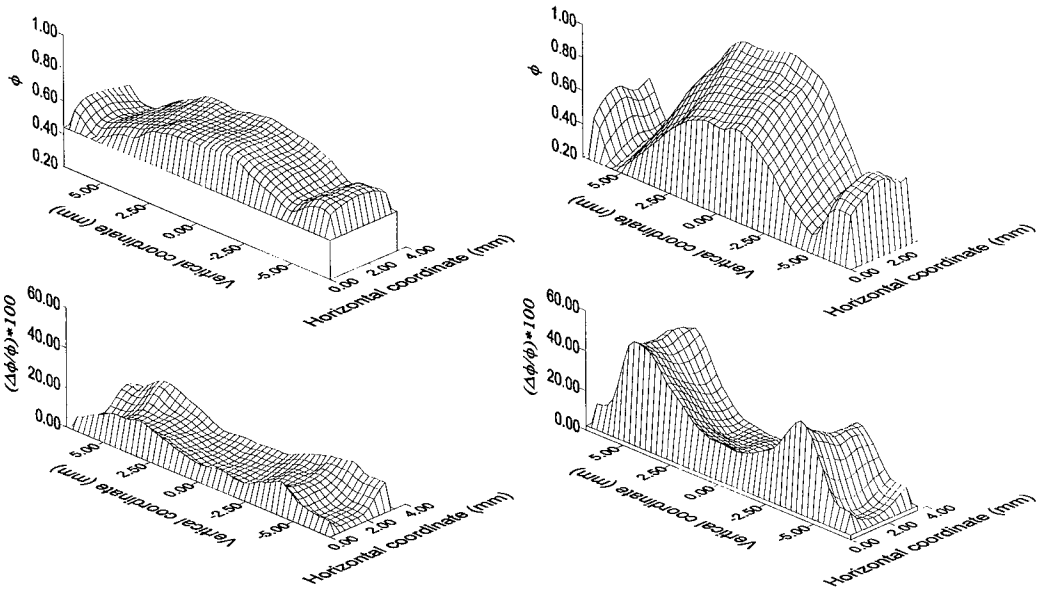

(a) σ=50% (b) σ=0%

FIG. 2. Equivalence ratio distributions for different fuel splits at an overall equivalence ratio of 0.6. Vertical and horizontal coordinates correspond to radial and axial coordinates of the combustor, respectively.

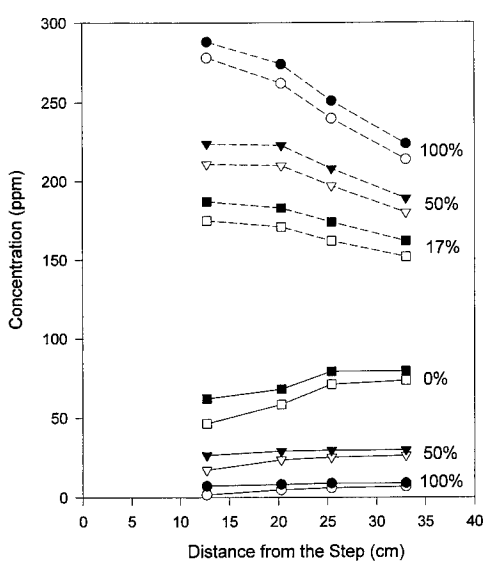

FIG. 3. Area-weighted NO and NO_x concentrations as a function of distance from step; open symbols, NO; closed symbols, NO_x; solid lines, $\Phi_{overall} = 0.6$; dashed lines, $\Phi_{overall} = 0.92$; fuel split is shown beside each curve.

Fig. 3 to the "center of gravity" of the reaction zone. The results indicate that under fuel-lean, incompletely mixed conditions, a significant amount of the NO is produced in the reaction zone (approximately 50% of the total NO in the $\sigma = 50\%$ and 0% cases), while less than 8% of the NO is produced in the reaction zone under fuel-lean, completely mixed conditions ($\sigma = 100\%$). These results indicate that the increased NO production at lean, incompletely mixed conditions cannot be explained solely in terms of the thermal NO mechanism. A possible explanation for this behavior is given later.

Model calculations have shown that in a premixed flame front, NO is formed by (1) the Zeldovich mechanism, (2) the N_2O intermediate reaction, and (3) the Fenimore mechanism, where both the Zeldovich and the N_2O intermediate mechanisms can be enhanced by superequilibrium O-atom concentrations [12]. An indication of the relative O-atom concentration can be obtained from the OH LIF measurements since one would expect partial equilibrium between OH and O [13], that is, $[O]/[O]_{equil.} = ([OH]/[OH]_{equil.})^2$.

By assuming an axisymmetric flame, a parameter, Q, can be defined as

$$Q = \frac{1}{N}\sum_{1}^{N}\int_0^r \int_0^x 2\pi\, r\, I_m^2\,(x, r)\, dx\, dr, \text{ for } I_m \geq n$$

where N is the number of the images, x and r are axial and radial coordinates, $I_m\,(x, r)$ is the OH

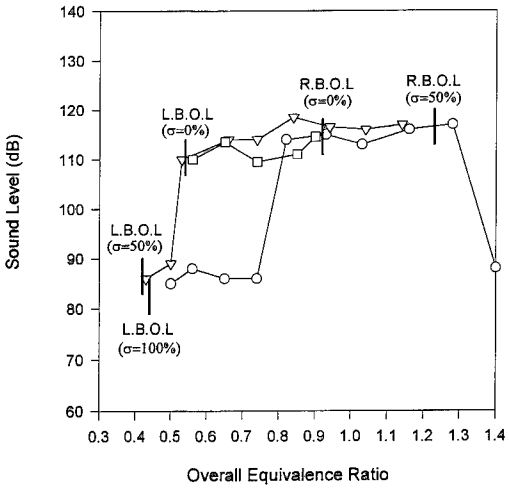

FIG. 4. Overall equivalence ratio and fuel-air mixing effects on flame stability. ○, σ = 100%; ▽, σ = 50%; □, σ = 0%.

intensity at (x, r) obtained from the two-dimensional OH LIF image and n is a selected OH fluorescence intensity threshold determined from the intensity probability distribution function. Mathematically, Q is the integration of the square of the OH fluorescence intensity over the combustion volume. It is used here as an indication of the O-atom concentration in the reaction zone. For an OH fluorescence intensity threshold of 50 (the results are relatively insensitive to the threshold value), the normalized values of Q for σ = 100%, 50%, and 0% are $Q_{100\%}/Q_{100\%} = 1.0$, $Q_{50\%}/Q_{100\%} = 2.37$, and $Q_{0\%}/Q_{100\%} = 4.08$. The increase in Q with incomplete mixing can be the result of an increased reaction zone volume and increased OH and therefore O-atom concentration, both situations leading to increased NO production. This result suggests that incomplete fuel-air mixing leads to increased superequilibrium O-atom concentration and therefore increased reaction-zone NO production in the flame zone.

Figure 3 also shows the area-weighted NO concentration as a function of distance from the step for three different fuel-air mixing conditions at an overall equivalence ratio of 0.92. It shows that, at near stoichiometric conditions, incomplete fuel-air mixing results in less NO production, which is consistent with what has been reported previously [5,6]. In the near stoichiometric case, the NO concentration decreases in the postflame region as the residence time increases. This is believed to be due to the reburning of the fuel in the postflame region [14,15], which is supported by the fact that HCN, more than 25 ppm for the σ = 100% case and 20 ppm for the σ = 50% and σ = 17% cases, was detected at the combustor exit.

The Effect of Incomplete Fuel-Air Mixing on Combustion Stability

Combustion instabilities can result in both lean blowout and combustion oscillations. The effect of incomplete fuel-air mixing on the stability characteristics of this lean premixed combustor is illustrated in Fig. 4, which is a plot of combustion-generated noise versus overall equivalence ratio for the σ = 0%, 50%, and 100% cases. In this study, when the magnitude of the combustion-generated noise was more than 20 dB above the background noise level, the combustion was considered unstable. In all cases of unstable combustion, the instability was a longitudinal instability with a single dominant frequency of ~400 Hz, which can be related to the quarter-wave natural frequency of the combustor. Also shown are the lean blowout limits for the three cases. These results show clearly that incomplete mixing results in less-stable combustion, both in terms of broadening the range over which combustion-generated oscillations occur and raising the lean blowout limit. For the completely mixed case (σ = 100%), unstable combustion occurs over the range of equivalence ratios from ~0.82 to ~1.35. In this case, the highest flame temperature occurs near the stoichiometric condition, which results in a large temperature gradient between the flame zone and the combustor wall. This large temperature gradient could induce the combustion instability in the premixed case. When Φ_{overall} is outside of this range, combustion is stable and quiet until the equivalence ratio reaches the blowout limits. That combustion becomes stable under lean and rich conditions can be attributed to the fact that the reduced heat release is not sufficient to overcome the damping in the combustor. For the σ = 50% case, unstable combustion occurs at all equivalence ratios within the blowout limits, except over a narrow range from the lean blowout limit ($\Phi_{\text{overall}} \approx 0.43$) to $\Phi_{\text{overall}} \approx 0.5$, where stable combustion is possible. For the σ = 0% case, combustion is unstable over the entire operating range of the combustor. These results indicate that the fluctuating fuel distribution under incompletely mixed conditions can contribute significantly to the heat-release fluctuations that drive unstable combustion.

The lean blowout limit is also found to be affected by incomplete fuel-air mixing. Although no significant change in the lean blowout limit was observed between the completely mixed (σ = 100%) and the σ = 50% cases, a distinct shift (from ~0.43 to ~0.55) was observed in going to the most poorly mixed case (σ = 0%).

These results on the effect of incomplete mixing on combustion stability, however, should be interpreted with care because one would expect the nature of this effect to depend on the actual shape of the fuel distribution. For example, it is possible that

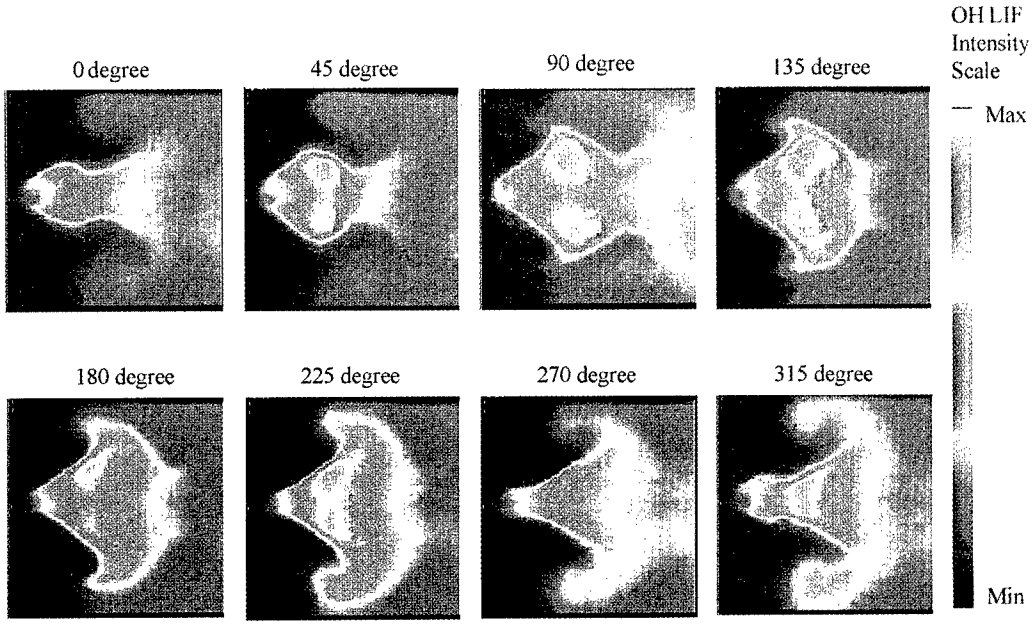

FIG. 5. Flame structure evolution for overall equivalence ratio = 0.6, σ = 50% case.

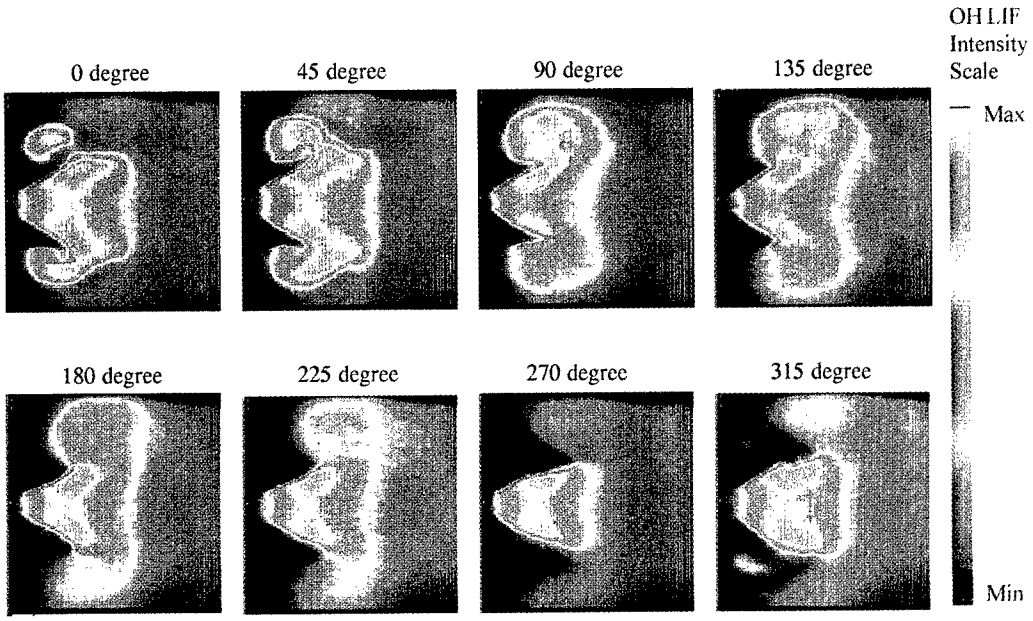

FIG. 6. Flame structure evolution for overall equivalence ratio = 0.92, σ = 100% case.

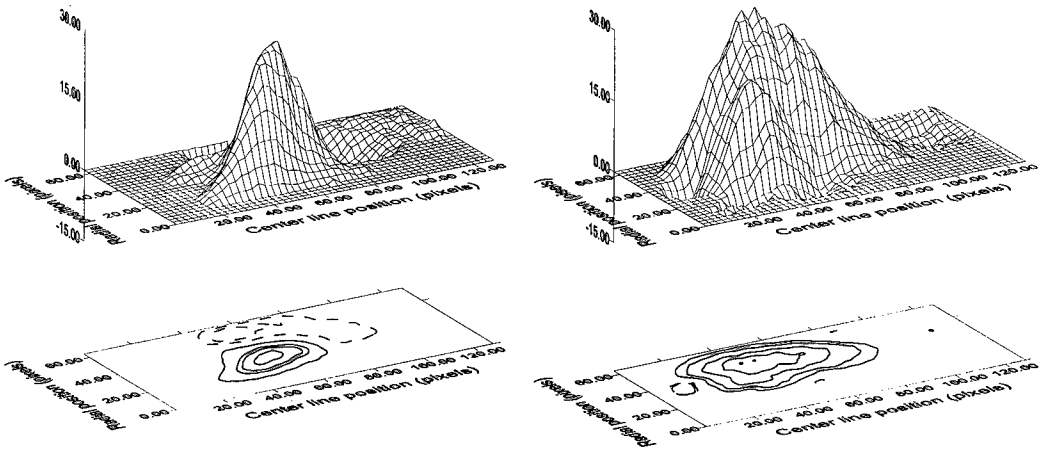

(a) $\Phi_{overall}$=0.6, σ=50% case

(b) $\Phi_{overall}$=0.92, σ=100% case

FIG. 7. Local Rayleigh index distributions for different operating conditions. Solid lines, positive region; dashed lines, negative region.

certain fuel distributions could actually improve the stability characteristics of a given combustor.

Flame Structure Evolution during Combustion Oscillations

Characterization of the evolution of the flame structure during combustion oscillations can lead to useful insights regarding the phenomenology of the instability, which in turn may suggest ways to prevent its occurrence. The flame structure evolution can be reconstructed from the phase-averaged two-dimensional OH LIF measurements. Figure 5 shows the flame structure evolution during one cycle of unstable combustion at $\Phi_{overall} = 0.6$ and $\sigma = 50\%$. The field of view of each image is 35 × 35 mm and the phase angle is referenced to the sinusoidal fluctuation of the combustion-generated pressure oscillation. Note that the phase of the pressure measurement has been shifted (by ~45°) to account for the acoustic wave propagation time between the pressure measurement location and the reaction zone. At a phase angle of 0°, there is a flame pocket immediately downstream of the flame holder. The flame pocket grows and propagates downstream as the phase angle increases. At a phase angle of 90°, which corresponds to the maximum pressure, the reaction zone begins to move into the recirculation zone and continues to do so until it reaches 225°. At a phase angle of 270°, which corresponds to the minimum pressure, the reaction zone appears to be moving out of the recirculation zone and back into the flame pocket downstream of the flame holder, until the flame resumes its original shape at 0°. In this case, the instability appears to originate in the main reaction zone immediately downstream of the flame holder, which is consistent with the notion that fluctuations in the equivalence ratio at the combustor inlet are helping to drive the instability.

For the $\Phi_{overall} = 0.92$ and $\sigma = 100\%$ case, the flame structure evolution illustrated in Fig. 6 is observed to be quite different from that discussed earlier. At a phase angle of 270°, there is a main reaction zone downstream of the flame holder (similar to the $\Phi_{overall} = 0.6$, $\sigma = 50\%$ case at a phase angle of 0°). At a phase angle of 315°, small pockets of flame are observed in the recirculation zone. These flame pockets then propagate and connect with the main reaction zone at 45°. At a phase angle of 90°, winglike structures that gradually decrease in size as the phase angle increases appear beside the main reaction zone. In this case, the instability appears to originate in the wall region and recirculation zone, while the main reaction zone, that is, immediately downstream of the flame holder, remains relatively unchanged.

Another way to analyze these measurements is in terms of the Rayleigh criterion [16], which states that when the unsteady heat release $q'(\xi, t)$ is in phase with the pressure fluctuation $p'(\xi, t)$, the pressure wave oscillation can be sustained. This criterion can be expressed in terms of the Rayleigh index, R, as follows:

$$R = \frac{1}{V}\frac{1}{T}\int_V \int_T p'(\xi, t)\, q'(\xi, t)\, dt d\xi > 0$$

where ξ is a spatial coordinate, t is time, T is the

instability period, and V is the volume of the flame. Using the fluctuating OH fluorescence intensity as an indicator of heat-release fluctuation along with the measured combustion-generated pressure fluctuation, the local and global Rayleigh indices can be calculated from the two-dimensional in-phase OH LIF images. In calculating the local and global Rayleigh indices, the pressure is assumed constant in phase and amplitude throughout the entire flame-zone, which is reasonable since the flame is concentrated near the flame holder and is small compared to the acoustic wavelength.

Figure 7 shows the local Rayleigh index over the upper half of the combustion section for the two unstable cases discussed previously, indicating that even when the overall combustion process is unstable, regions where the instability is driven ($R > 0$) and regions where it is damped ($R < 0$) exist. For the $\Phi_{\text{overall}} = 0.6$, $\sigma = 50\%$ case, the Rayleigh index is positive in the central flame pocket region where the heat release caused by the pulsating flame is in phase with the pressure oscillation. Damping of the instability happens near the wall region where the heat release in the recirculation zone is out of phase with the pressure oscillation. In the $\Phi_{\text{overall}} = 0.92$, $\sigma = 100\%$ case, as shown in Fig. 7b, the instability is driven near the wall region because the heat release from the winglike structures is in phase with the pressure oscillation. In this case, there is only a small region in the recirculation zone where damping occurs.

Global Rayleigh indices for the instability-driving regions and for the damping regions are obtained by integrating the local Rayleigh index over the respective regions. The global Rayleigh indices for the driving and damping regions, respectively, are $+0.63$ and -0.37 for the $\Phi_{\text{overall}} = 0.6$, $\sigma = 50\%$ case and $+0.92$ and -0.08 for the $\Phi_{\text{overall}} = 0.92$, $\sigma = 100\%$ case. For the $\Phi_{\text{overall}} = 0.92$, $\sigma = 100\%$ case, the instability is driven over a significant portion of the flame zone.

Recently, the use of active control to prevent combustion oscillations has been demonstrated in afterburners and dump combustors [17–19], where modulated secondary fuel injection strategies have been employed to effectively cancel out the heat-release fluctuations. Information such as that shown in Fig. 7 would be valuable in defining the optimum location for secondary fuel injection in an active control system.

Conclusion

A study of the effect of incomplete fuel-air mixing on NO_x emissions and flame stability in a laboratory scale premixed combustor is presented. As has been observed previously, it was shown that incomplete fuel-air mixing results in increased NO_x emissions at overall fuel-lean conditions. The results, however, indicate that reaction-zone NO mechanisms, enhanced by superequilibrium O-atom concentrations, are in part responsible for more than 50% of the increased NO production.

It was also shown that incomplete fuel-air mixing in a premixed combustor can significantly reduce the stable operating range of the combustor both in terms of increasing the tendency for combustion oscillation and raising the lean blowout limit. Finally, it was observed that during unstable combustion, the flame moves in a well-defined periodic manner; however, the details of the flame behavior and the instability mechanism can vary significantly depending on the overall equivalence ratio and the degree of fuel-air mixing.

Acknowledgments

Support for this research was provided by General Electric Power Generation and Westinghouse Electric PGBU.

REFERENCES

1. Anderson, D., NASA TMX-71592, 1975.
2. Semerjian, H. and Vranos, V., *Sixteenth Symposium (International) on Combustion,* The Combustion Institute, Pittsburgh, 1976, pp. 169–179.
3. Appleton, J. P. and Heywood, J. B., *Fourteenth Symposium (International) on Combustion,* The Combustion Institute, Pittsburgh, 1973, pp. 777–786.
4. Lyons, V. J., *AIAA J.* 20(5):660–665 (1981).
5. Correa, S. M., *Combust. Sci. Technol.* 87:329–362 (1992).
6. Lovett, J. A. and Abuaf, N., ASME Paper, 92-GT-120, 1992.
7. Altemark, D. and Knauber, R., *VDI Berichte* 645:299–311 (1987).
8. Leonard, G. and Correa, S., Second ASME Fossil Fuel Combustion Symposium, *ASME/PD* 30:69–74 (1990).
9. Nicol, D. G., Steele, R. C., Marinov, N. M., and Malte, P. C., *J. Engineer. Gas Turbines Power* 117:100–111 (1995).
10. Shih, W.-P., Ph.D. Thesis, Mechanical Engineering Department, Pennsylvania State University, 1995.
11. Fric, T. F., AIAA 92-3345, 1992.
12. Drake, M. C., Ratcliffe, J. W., Blint, R. J., Carter, C. D., and Laurendeau, N. M., *Twenty-Third Symposium (International) on Combustion,* The Combustion Institute, Pittsburgh, 1990, pp. 387–395.
13. Wolfrum, J., *Chem. Ing. Tech.* 44:656 (1972).
14. Chen, S. L., McCarthy, J. M., Clark, W. D., Heap, M. P., Seeker, W. R., and Pershing, D. W., *Twenty-First Symposium (International) on Combustion,* The Combustion Institute, Pittsburgh, 1986, pp. 1159–1169.
15. Nishika, M., Nakagawa, S., Ishikawa, Y., and Takeno, T., *Combust. Flame* 98:127–138 (1994).
16. Rayleigh, J., *The Theory of Sound,* Vol. 2, Dover, New York, 1945, p. 226.

17. Langhorne, P. J., Doroling, A. P., and Hooper, N., *J. Propulsion* 16(3):324–333 (1990).
18. Schadow, K. C., Gutmark, E., and Wilson, K. J., *Combust. Sci. Technol.* 181:285–300 (1992).
19. Jones, C. M., Stone, F., Shih, W.-P., and Santavicca, D. A., Eastern States Section, Paper No. 83, The Combustion Institute, 1995.

Twenty-Sixth Symposium (International) on Combustion/The Combustion Institute, 1996/pp. 2779–2786

FLUORESCENCE IMAGING OF NO AND O_2 IN A SPRAY FLAME COMBUSTOR AT ELEVATED PRESSURES

BERNARD L. UPSCHULTE, MARK G. ALLEN AND KEITH R. MCMANUS
Physical Sciences Inc.
20 New England Business Center
Andover, MA 01810, USA

Planar laser-induced fluorescence images of the distributions of nascent NO and high-temperature O_2 have been obtained in the injector near field of a spray flame combustor at pressures up to 0.8 MPa. The model combustor consists of a pressure-atomizing spray nozzle injecting liquid ethanol into a high-pressure oxygen and dilute nitrogen flow at room temperature. This flow is used to assess quantitatively fluorescence strategies in preparation for application to more practical combustor geometries. Fluorescence is excited near 226 nm using a low-power, excimer-pumped dye laser and imaged with an intensified CCD array camera. The camera is spectrally filtered to reject the strong elastic laser scatter from fuel droplets and soot particles. The NO and O_2 mole fractions in the flow field are known and controlled at several discrete chamber pressures between 0.1 and 0.8 MPa. Detailed models of linear fluorescence using the available spectroscopic database are shown to be sufficient to predict the pressure scaling of the fluorescence signal for the known values of the NO and O_2 mole fraction. This result suggests that atmospheric pressure calibrations may be extended to higher-pressure combustors without additional detailed measurements of specific temperature and major species composition fields. As with high-pressure OH imaging measurements using 283-nm excitation, hydrocarbon interferences are found to be a ubiquitous and major contributor to the fluorescence signal for the simple flow field studied to date. This contribution must be subtracted properly for quantitative measurements.

Introduction

The continued development of advanced aeropropulsion gas turbine combustors requires improved instrumentation for in situ measurements of important combustion species and gasdynamic parameters in combustors operating on liquid fuels and at pressures up to about 5 MPa. Although planar laser-induced fluorescence (PLIF) techniques for species concentrations measurements have been developed extensively for atmospheric pressure flames, much less effort has been made to explore applications to high-pressure, non-premixed combustion environments. In recent publications [1], we have demonstrated PLIF imaging of OH and PAH at pressures between 0.1 and 1.0 MPa in spray flames burning heptane, methanol, and ethanol fuels in air. Detailed models of linear fluorescence quantified the pressure scaling of the fluorescence signal in terms of a unit mole fraction of absorber. This paper extends these results to include imaging of nascent NO and O_2 in ethanol-oxygen-nitrogen flames at pressures between 0.1 and 0.8 MPa.

Fluorescence techniques appropriate for gas turbine combustors have received considerable attention recently, in the context of a number of flame environments, and can be grouped into three basic categories. In the first category, saturated single-point LIF measurements have been investigated in the postcombustion gases of laminar, premixed flat-flame burners in an attempt to explore absolutely quantitative measurements without recourse to quenching corrections [2,3], although in the case of NO LIF, saturation did not improve the quantitativeness of the result [4]. Whatever its advantages may be in single-point measurements, saturation is not achievable in imaging configurations using the relatively modest laser powers available from frequency-doubled pulsed dye lasers. The second category, which includes the present work, applies linear LIF excitation and detection strategies to high-pressure flame environments and uses modeling of the often well-understood collisional energy transfer and broadening to quantify the result. This includes demonstrations in the postcombustion gases of laminar, premixed flat-flame burners [5,6] and non-premixed spray flames [1]. This work has demonstrated reasonable and useful quantification of OH images in both high-pressure premixed [7] and non-premixed environments [1]. Quantitative NO imaging has been demonstrated in high-pressure, lean, premixed flames, with proper attention to interferences from O_2 [7].

The third category consists of approaches based on high pulse energy, tunable excimer laser excitation at 193, 248, or 308 nm [8,9] and has been dem-

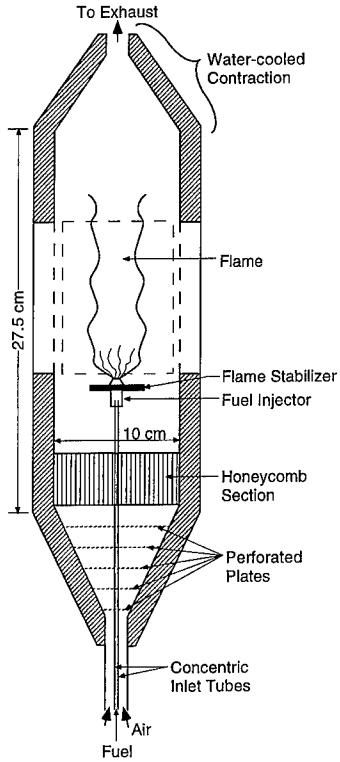

FIG. 1. Schematic diagram of high-pressure combustor test section.

onstrated in high-pressure, internal combustion engines. This approach accesses weak, predissociative transitions of OH and O_2, or the (D-X) system of NO near 193 nm, as well as broad features from hydrocarbon fragments. Fluorescence signals from the predissociative transitions increase with pressure because of the reduced effect of collisional quenching of the excited state, thereby improving the signal-to-noise levels with increasing pressure. However, the incomplete spectroscopic database associated with these transitions and unresolved issues related to the high laser pump rates employed can be barriers to quantitative interpretation of the fluorescence signal.

In earlier publications [1,10], we developed the detailed methodology describing the pressure, temperature, and composition dependencies of NO and O_2 PLIF measurements using low-power, frequency-doubled pulsed dye laser excitation. Quasi–two-level models were shown to include all of the necessary physical processes required to extend atmospheric pressure calibrations to higher pressure environments, including the effect of collisional broadening on the laser excitation efficiency, collisional energy transfer and quenching in the laser-excited states, and compositional dependence of these collisional processes. The present work provides experimental validation of these models for NO and O_2 in a simple combustor geometry in which the NO and O_2 concentration may be controlled separately.

Experimental Arrangement

The flow facility for this study consists of a high-pressure liquid-fueled combustor, described in more detail in earlier publications [1,10]. A schematic of the test section is shown in Fig. 1, consisting of an uncooled stainless steel vertical duct 27.5 cm in length with a square internal cross section (10 × 10 cm). A pressure atomizing liquid-fuel injector provides a finely atomized spray (Sauter mean diameter ~50 μm at 1 atm) with a 60° cone angle. A 4-cm-diameter, axisymmetric bluff-body stabilizer surrounds the fuel nozzle, providing a weak recirculation flame stabilization zone downstream of the injection point. Oxygen and nitrogen are supplied separately from a pressurized reservoir.

Using nearly pure oxygen atmospheres results in a substantial increase in peak flame temperatures compared to air aspirated flames and is required in this combustor to reduce soot formation. Small flow rates of N_2 (<10% by volume of total oxygen flow) allow regulation of the NO formation and an unambiguous means of determining potential interference fluorescence signals.

The test section pressure is adjusted by choking the exhaust stream using a valve/orifice combination. This flow metering strategy fixes the reactant inlet mass flows while varying the test section static pressure. Typical total oxidizer mass flow rate is adjustable between approximately 10 and 40 g/s, corresponding to area-averaged test section inlet velocities of 8 and 33 cm/s, respectively, at 1.0 MPa. The nominal fuel flowrate is 0.27 g/s, corresponding to overall fuel/air equivalence ratios near 0.2.

The test section is fitted with fused silica windows on all sides to allow optical access. Two large fused silica windows (7.6 × 12.7 × 2.5 cm) for imaging are located on opposite sides of the test section and permit viewing the first 12.7 cm of the flow field from the spray nozzle tip. Laser sheet access windows (2.5 × 12.7 × 1.25 cm) are provided on the remaining sides perpendicular to the imaging windows.

Fluorescence is excited with a frequency-doubled, excimer-pumped dye laser (Lambda-Physik) producing 2–5 mJ/pulse in the vicinity of 226 nm. A combination of spherical and cylindrical optics is used to produce the laser sheet at typically 5 cm × 0.5 mm. Images are obtained by collecting fluorescence at right angles to the laser sheet through 3 mm of UG-5 glass and a wide-band interference filter centered at 252 nm with an 85-nm bandpass us-

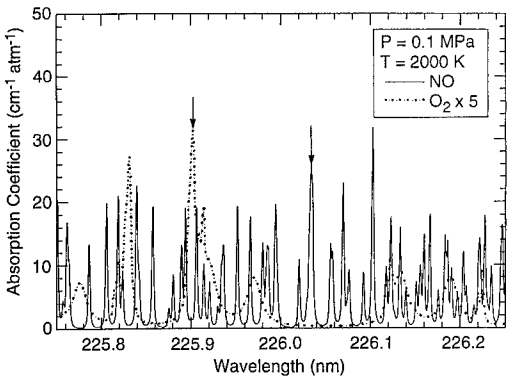

FIG. 2. Calculated absorption spectra of NO and O_2 at 0.1 MPa and 2000 K.

ing a 105 mm, *f*/4.5 Nikon UV telephoto lens attached to an intensified and cooled CCD camera. The camera consists of 576 × 384 pixels, although the images reported here are obtained with 2 × 2 binning. The resulting measurement volume is typically 0.26 mm (H) × 0.26 mm (V) × 0.5 mm (depth). The intensifier is triggered synchronously with the laser pulse and opened with a 100-ns gate.

NO and O_2 Fluorescence in High Pressure, Non-Premixed Flames

A detailed analysis of the models used to reduce NO and O_2 fluorescence images to mole fraction or concentration images has been presented earlier [10] and will not be repeated here. This analysis includes the effects of species- and temperature-dependent collisional broadening, excitation from unresolved transitions, and species- and temperature-dependent quenching. The model draws from the extensive and growing database of spectral properties and energy transfer rates for the targeted transitions of NO and O_2 [11–17]. The modeling efforts have been confirmed in the context of OH fluorescence and demonstrate that the fluorescence signal viewed by each pixel on the detector array is given by

$$S_F = [B\int I(\omega)g(\omega)d\omega](F_y)(fN_tV_c)(K\tau_l) \quad (1)$$

where the first parenthetical term is the integral overlap between the laser spectral fluence $I(\omega)$ and the molecular absorption line-shape function $g(\omega)$, multiplied by the Einstein B coefficient for absorption; the second term is the fluorescence yield; and the third term is the population in the laser-excited state, given by the product of the Boltzmann population fraction f, the total number density of absorbing species N_t, and the volume defined by the intersection of the laser-sheet thickness and the projection of the CCD pixel into the object plane. The final term is an experimental constant describing the collection efficiency of the imaging optics and the laser-pulse duration, τ. For quenching-dominated fluorescence (as is the case with NO, OH, and most other PLIF techniques), the pressure dependence of the fluorescence yield and absorber number density cancel one another so that the fluorescence signal may be approximated by

$$S_F \sim C_1\int I(\omega)g(\omega)d\omega \cdot \chi_t \quad (2)$$

where C_1 is a lumped parameter describing experimental constants, the weak temperature dependence of the Boltzmann population fraction, and the nominally constant quenching terms.

For O_2 fluorescence, the laser-excited level includes a rapid, collisionless, predissociation decay path that complicates the comparatively simple quenching-dominated fluorescence processes. Over the range of pressures reported here, the upper electronic states undergo transition from a fully predissociative decay at 1 atm to partially quenched decay at 10 atm. Thus, the pressure dependence of the fluorescence yield and absorber number density does not cancel and the fluorescence signal is related to the O_2 mole fraction using Eq. (3):

$$S_F \sim C_2\int T(\omega)F(\omega)d\omega \cdot E \cdot \chi_{O_2} \cdot P_t \quad (3)$$

where C_2 is an experimental constant; $T(\omega)$ is the filter transmission function; $F(\omega)$ is the fluorescence yield for laser excitation at frequency ω, as defined in Ref. 17, and includes the absorption overlap integral; E is the total laser fluence; χ_{O_2} is the oxygen mole fraction; and P_t is the total pressure at the measurement point. The function $F(\omega)$ contains an implicit pressure dependence that is negligible at low pressures but eventually cancels the pressure term in Eq. (3) as the fluorescence process transitions into fully quenching dominated. More details of this function are available in Refs. 7, 10, and 17.

NO Imaging Results

Figure 2 is a calculated absorption spectra near 226 nm at 0.1 MPa and 2000 K, showing portions of the NO (0, 0) band of the (A-X) system and transitions from several bands of the O_2 Schumann–Runge system. Following the strategy developed by Battles and Hanson [6], NO is excited at 226.034, coupling into the overlapped $P_{21} + Q_1$ (14), $R_{12} + Q_2$ (21), and P_1 (23) transitions of the (0, 0) band of the (A-X) system. At 1.0 MPa, collisional broadening blends neighboring NO absorption transitions so that no feature is completely resolved. Modeling of the fluorescence excitation efficiency includes an explicit integration of the known laser spectral fluence with the full absorption spectrum, thereby including the total influence of all lines.

Our approach in the present NO fluorescence

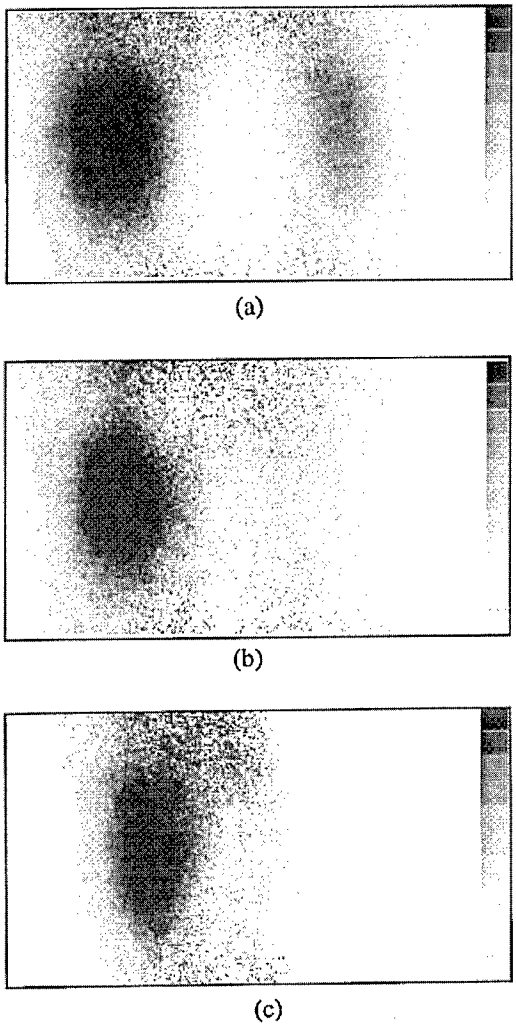

FIG. 3. Sequence of PLIF images obtained at (a) 0.3 MPa, (b) 0.5 MPa, and (c) 0.7 MPa with the laser tuned to NO resonance transitions and N_2 added to the O_2 flow. The relative signal intensity is encoded according to the gray scale shown at the right. The field of view is 2.66 cm (V) × 4.75 cm (H).

work is to add a known, small amount of N_2 to the flow field and allow the equilibrium Zeldovich chemistry to generate a known and controllable amount of NO. Images of the total laser-generated signal with the laser tuned to the NO resonance and 5% N_2 added to the O_2 flow are shown in Fig. 3 at 0.3, 0.5, and 0.7 MPa pressure. The camera field of view is 4.75 cm horizontal by 2.66 cm vertical and is centered ~5 cm above the nozzle tip. This position is approximately the same height as the maximum spray penetration at 0.1 MPa. Fifty successive laser shots have been accumulated on the CCD array to improve the signal-to-noise ratio. The images have been corrected for integrated flame luminosity and fixed camera dark noise and normalized to the vertical laser sheet intensity profile, as imaged by Rayleigh scattering from the image plane before a burner firing. The fluorescence is approximately constant in the vertical dimension and occurs just outside the flame boundary indicated by the flame luminosity obtained with the laser off. Each image has been normalized to fill the gray-scale display, and the sequence shows the gradual radial contraction of the flame as the pressure increases. The laser beam propagates from left to right across the field of view, and a pressure-dependent asymmetry reveals the presence of significant laser attenuation.

Each image represents a quantity approaching a time-averaged distribution of NO. Averaging in the highly turbulent regions near the axis of the fuel spray would yield an ambiguous distribution reflecting the effect of flow intermittency. In the relatively less turbulent regions surrounding the spray, however, single-shot and multipulse averages revealed similar broad regions of NO so that the multipulse averaging does not substantially distort the recorded flow pattern and allows correction for interferences arising from other species, as described later. These interferences are uniquely determined by turning off the trace N_2 flow and imaging the laser-induced fluorescence through the same filter as with the NO fluorescence. The resultant interference signal cannot arise from NO and is presumed to underlie the NO images shown in Fig. 3. A single-parameter, average fluorescence signal strength can be obtained by selecting a common region in each image (at the same height and encompassing the radial extent of the signal on the left side of the image) and averaging the pixel values within this region. This 0.5-cm (V) × 1.0-cm (H) region of the flame is presumed to be unaffected by laser attenuation or fluorescence trapping. Applying this procedure with the N_2 flow on and off revealed an interference signal that increased with pressure as a fraction of the NO fluorescence from 6% at atmospheric pressure to 30% at 0.8 MPa and appeared to originate from essentially the same high-temperature regions as the NO fluorescence. The corrected fluorescence signal strength decays by 20% over this pressure range.

The measured interference signal is too strong to attribute to wing absorption by O_2. Furthermore, spectrally resolved fluorescence detection using an optical multichannel analyzer failed to reveal any structure in the fluorescence. The equilibrium NO concentration for this flame condition is approximately 9000 ppm. This value is considerably higher than expected for typical gas turbine combustors, but is near the minimum we can accurately control with our present N_2 flow regulators. Calculations of the spectral absorption coefficient for this concentration yield a value of 0.05 cm^{-1}, essentially the

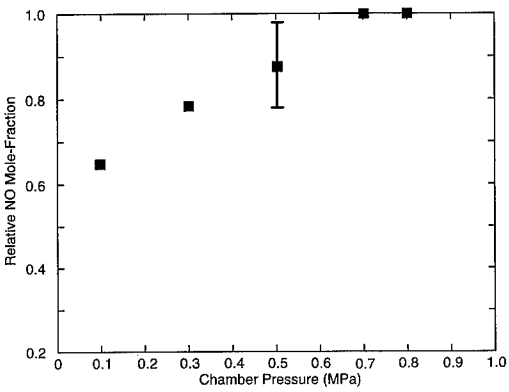

FIG. 4. Pressure scaling of the NO mole fraction at a fixed height above the spray nozzle as determined from the PLIF data.

same as that inferred from the asymmetric attenuation in the image shown in Fig. 3(a). The spectral absorption coefficient for this mole fraction of NO should increase to about 0.12 cm^{-1} at 0.7 MPa (accounting for the collisional broadening of the absorption transition). In Fig. 3c, we observe a path-averaged absorption coefficient of about 0.8 cm^{-1}. Hence, we conclude that the absorber interference increases in mole fraction with pressure and eventually dominates the laser attenuation at this wavelength. This same general behavior was observed previously for OH excitation at 283 nm and is associated with pressure-dependent soot chemistry [1].

Using the detailed fluorescence models described earlier, we can analyze the average fluorescence signal to obtain the relative NO mole fraction variations with pressure. The excitation overlap integral is calculated using the detailed collisional broadening parameters developed in Ref. 10 at a fixed laser frequency from the overlap of the 0.4-cm^{-1} laser bandwidth with the cumulative line absorption profiles for each pressure, including collisional shifting. The results of the inferred NO mole fraction scaling are shown in Fig. 4, indicating a slight *increase* in mole fraction with pressure.

The behavior of the NO mole fraction is explained by examining the typical equilibration times associated with this burner. For the estimated flame conditions of 2500 K and the measured N_2 and O_2 flow rates, the equilibrium NO mole fraction is approximately 0.9% and independent of pressure. The flow residence time required to reach the imaged region rises from about 20 ms at 0.1 MPa to about 140 ms at 0.7 MPa. The characteristic equilibration time falls from 160 ms to about 20 ms [18,19]. Therefore, above about 0.5 MPa, the NO mole fraction should be essentially constant, as the PLIF data show, to within the measurement uncertainty.

This result shows that with a model of the fluorescence process and attention to interference corrections, quantitative NO mole fraction measurements may be extended from atmospheric pressure calibrations. If a known amount of NO is added to the flow or can be calculated from equilibrium to create a radiometric calibration, then the signal level from another flow condition can be used to estimate the NO mole fraction based on this calibration and known pressure and temperature scaling. As shown in earlier modeling efforts [10], this calibration constant is only weakly dependent on typical variations in temperature and species composition expected in high-temperature flames (typical variability $< \pm 10\%$). The signal-to-noise ratio at 0.7 MPa suggests that the detection limit for the present configuration is on the order of a few hundred parts per million at this pressure. This could be reduced to below 100 ppm, however, with faster collection optics and modest increases in laser pulse energy. The noise on the interference contribution will certainly raise the detection limits compared to this signal shot-noise analysis so it is not precisely clear at present that these results can be extended to practical combustor geometries where the hydrocarbon interferences will be different.

O_2 Imaging Results

PLIF imaging of O_2 is accomplished by accessing absorbing states residing in relatively high vibrational levels ($v'' = 4, 5$) [6,20]. This results in a strong temperature dependence of the fluorescence signal, with order of magnitude increases in absorption strengths between 1500 and 2500 K. Strong vibrational and rotational dependence in the predissociation rate must also be considered to quantitatively interpret the fluorescence signal. Following the strategy pursued by Battles and Hanson [7], in the present work, the laser was tuned to 225.9 nm to excite an O_2 absorption feature comprised of three lines: $P^{5,5}(33)$—$P^{2,4}(23)$—$R^{4,5}(17)$. This transition is near the NO excitation wavelength and conveniently isolated from additional NO absorption features.

For the PLIF imaging experiments, the filters and camera parameters are identical with those for NO imaging. We assume that the small laser frequency change from NO to O_2 excitation does not change the magnitude of the interference signal since it presumably arises from broadly absorbing hydrocarbon fragments. Figure 5 presents images of the total fluorescence at 0.1, 0.5, and 0.75 MPa. Although each image is normalized to span the entire gray-scale range, the fluorescence signal increases with pressure by a factor of 5 over the range shown, as indicated by the improved signal-to-noise level. The images reflect the contraction of the flame and the increasing attenuation observed in the NO images.

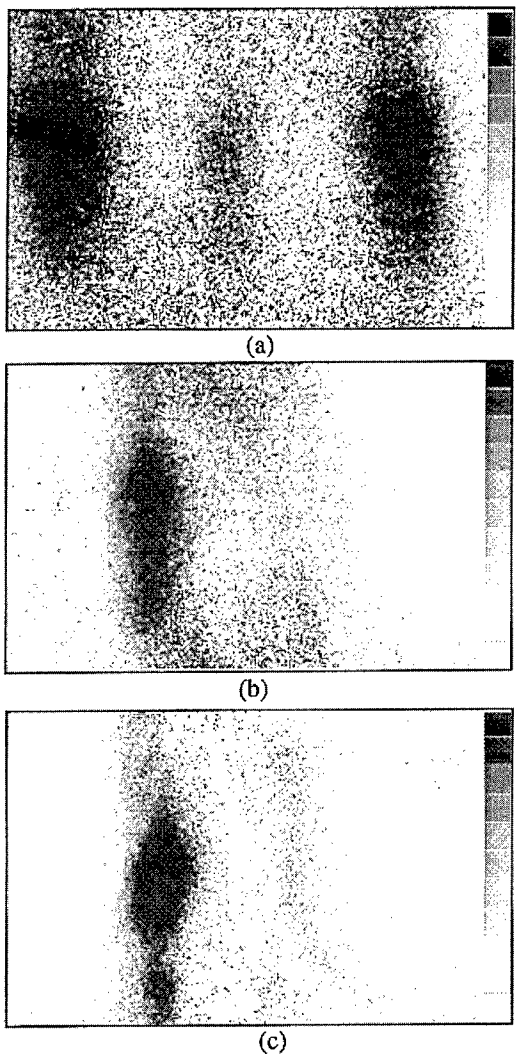

FIG. 5. Sequence of PLIF images obtained at (a) 0.1 MPa, (b) 0.5 MPa, and (c) 0.75 MPa with the laser tuned to O_2 resonance transitions. The relative signal intensity is encoded according to the gray scale shown at the right. The field of view is 3.17 cm (V) × 4.75 cm (H).

Because the O_2 fluorescence originates from a strongly temperature-dependent absorption, it is not possible to quantify absolutely the fluorescence signal in terms of the O_2 mole fraction without a separate measurement of temperature. Assuming that the nominal flame temperature is approximately independent of pressure and selecting the peak fluorescence signal in each image, however, we can use detailed fluorescence models with a constant temperature to reduce the average fluorescence signals on the left side of the image to relative mole fractions as a function of pressure. The average fluorescence signal is corrected for the interferences observed in the NO fluorescence signals. The result of this procedure is shown in Fig. 6, where we plot the relative O_2 mole fraction as a function of pressure. To within the uncertainty of the fluorescence data, the O_2 mole fraction is independent of pressure, as expected. Separate calculations of the path-average absorption coefficient are also consistent with a fixed mole fraction of molecular oxygen.

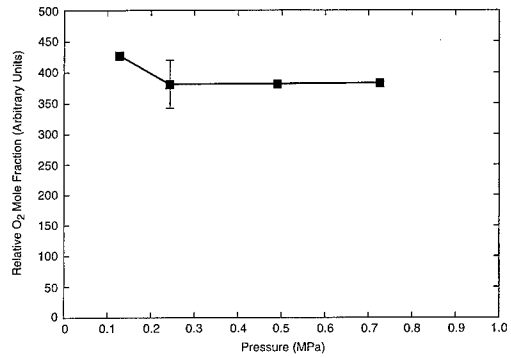

FIG. 6. Pressure scaling of the O_2 mole fraction at a fixed height above the spray nozzle as determined from the PLIF data.

As with the NO imaging results, this scaling behavior suggests that linear fluorescence models may be used to transfer quantitatively O_2 fluorescence calibrations to higher-pressure environments. Even in the present qualitative approach, imaging of regions of the flow field containing high-temperature O_2 prove useful in understanding mixing behavior in advanced, low-emission combustors by delineating areas in which the air has not mixed with fuel.

Conclusions

Fluorescence interference associated with soot chemistry and previously observed in connection with PLIF imaging of OH in spray flames [1] was also observed for the 226-nm excitation used for NO and O_2 imaging. The interference in the NO PLIF signals does not appear to arise from molecular oxygen, as has been observed in some premixed flat-flame burner studies. For NO excitation, the optical depth of the flame with respect to the laser wavelength is dominated by the interference species above about 0.5 MPa and equivalent to $\sim 1\ cm^{-1}$ at 1.0 MPa. For O_2 excitation, the optical depth of the flame with respect to the laser wavelength is dominated by the O_2 absorption and is the same order as with NO.

Detailed models of linear fluorescence using the available spectroscopic database are sufficient to predict the pressure scaling of the fluorescence sig-

nal with a constant mole fraction absorber. This suggests that a calibration measurement at a known pressure and temperature can be extended to high-pressure flame environments with minimal detailed knowledge of the overall temperature and species composition. For these non-premixed flames, interferences caused by soot precursor chemistry appear ubiquitous and must be accounted for in the data reduction. Since this implies that off-resonance images must be subtracted from on-resonance images, quantitative single-shot imaging appears problematic with a single laser/single camera system. Because we experienced similar attenuation with 283-nm excitation for OH, recently suggested schemes for NO (0, 2) excitation [21] are not expected to reduce substantially the interference observed for (0, 0) excitation, although they will reduce the effect of NO absorption. Using a relatively standard PLIF system, NO detection limits appear to be on the order of a few hundred parts per million in the absence of strong interferences, even with multipulse averaging. This detection limit might be reduced by a factor of 10 using a higher-power Nd:YAG-pumped laser system and faster collection optics, but NO PLIF measurements below 10 ppm would appear to be unfeasible, particularly in the presence of the interference levels observed in the present flame.

Challenges to quantitative imaging in high-pressure combustion systems are highly configuration specific. In the present spray flame burner, low air velocities and lack of preheating create a more poorly mixed and sooting flame than expected in production combustors at representative air mass flows and temperatures. Future work will apply these techniques in an optically accessible combustor with a high-mixing injector, preheated air, and conventional fuels. These conditions are expected to reduce the soot precursor interferences dominating the behavior of the present results and may permit extension to the higher-pressure regimes of 3.0–6.0 MPa associated with advanced combustors.

Acknowledgments

This work is supported by the U.S. Air Force Wright Laboratory under contract number F33615-93-C-2353, Dr. James R. Gord, monitor.

REFERENCES

1. Allen, M. G., McManus, K. R., Sonnenfroh, D. M., and Paul, P. H., *Appl. Opt.* 34:6287–6300 (1995).
2. Carter, C. D., King, G. B., and Laurendeau, N. M., *Appl. Opt.* 31:1511–1522 (1992).
3. Reisel, J. R., Carter, C. D., Laurendeau, N. M., and Drake, M. C., *Combust. Sci. Technol.* 91:271–295 (1993).
4. Reisel, J. R., Carter, C. D., and Laurendeau, N. M., *Combust. Flame* 95:485–489 (1993).
5. Kohse-Hoinghaus, K., Meier, U., and Attal-Tretout, B., *Appl. Opt.* 29:1560–1569 (1990).
6. Vyrodov, A. O., Heinze, J., Dillmann, M., Meier, U. E., and Stricker, W., *Appl. Phys. B* 61:409–414 (1995).
7. Battles, B. E. and Hanson, R. K., *J. Quant. Spectrosc. Radiat. Transfer* 54:521–537 (1995).
8. Andresen, P., Meijer, G., Schluter, H., Voges, H., Koch, A., Hentschel, W., Oppermann, W., and Rother, E., *Appl. Opt.* 29:2392–2404 (1990).
9. Koch, A., Voges, H., Andresen, P., Schluter, H., Wolf, D., Hentschel, W., Opperman, W., and Rother, E., *Appl. Phys. B* 56:177–184 (1993).
10. Allen, M. G., McManus, K. R., and Sonnenfroh, D. M., Paper No. 95-0172, AIAA 33rd Aerospace Sciences Meeting, January, 1995.
11. Piper, L. G. and Cowles, L. M., *J. Chem. Phys.* 85:2419–2422 (1986).
12. Chang, A. Y., DiRosa, M. D., and Hanson, R. K., *J. Quant. Spectrosc. Radiat. Transfer* 47:375–390 (1992).
13. Paul, P. H., Gray, J. A., Durant, J. L., and Thoman, J. W., *Appl. Phys. B* 55:249–259 (1993).
14. Paul, P. H., Gray, J. A., Durant, J. L., and Thoman, J. W., *AIAA J.* 32:1670–1675 (1994).
15. DiRosa, M. D. and Hanson, R. K., *J. Mol. Spec.* 164:97–117 (1994).
16. DiRosa, M. D. and Hanson, R. K., *J. Quant. Spectrosc. Radiat. Transfer* 52:515–529 (1994).
17. Lee, M. P. and Hanson, R. K., *J. Quant. Spectrosc. Radiat. Transfer* 36:425–440 (1986).
18. Gardiner, W. C. Jr., Ed., *Combustion Chemistry*, Springer Verlag, New York, 1984, pp. 361–421.
19. Baulch, D. L., Drysdale, D. D., and Horne, D. G., *Evaluated Kinetic Data for High Temperature Reactions*, Vol. 2, Butterworths, London, 1973.
20. Goldsmith, J. E. M. and Anderson, R. J. M., *Opt. Lett.* 11(2):67–70 (1986).
21. Schulz, C., Yip, B., Sick, V., and Wolfrum, J., *Chem. Phys. Lett.* 242:259–264 (1995).

COMMENTS

Alan Eckbreth, United Technologies Research Center, USA. A comment and a question. The comment: In 266um spontaneous Raman scattering experiments in the exhaust of a gas turbine burning Jet A, significant laser and signal attenuation was inferred, consistent with the laser attenuation reported in your PLIF experiments [1]. In your talk, you didn't comment on the assumption made regarding the fluorescence yield spatial variation in the combustor. Were they significant and how did you treat them?

REFERENCE

1. Eckbreth et al., *Ber. Bunsenger, Phys. Chem.* 97:1597–1608 (1993).

Author's Reply. Spatial variations in the fluorescence yield have been explicitly examined in a previous publication [1]. Using the species-and temperature-dependent quenching cross-sections in references 13 and 14 in the present paper, we examined the effect of compositional and thermal perturbations from the nominal condition of complete, adiabatic combustion from stoichiometric heptane/air flames. Because hydrocarbon species are inefficient quenchers of NO, the largest effect on the fluorescence yield originates from very fuel-rich conditions. For example, forcing 50% of the heptane to be unburned and lowering the adiabatic temperature proportionally increases the effective calibration constant by about 25%. This was the largest effect examined and is an unlikely scenario in which we would expect to observe any measurable NO fluorescence. More typical variations in temperature and CO/CO_2 concentration ratios tended to have 5–15% effects. In reference 14, Paul explicitly examines the variation in the quenching cross-section across a modelled C_2H_4-air flame and shows a negligible effect over most of the flame. For the present purposes, we have assumed that the fluorescence yield is nominally constant across the limited regions where we observe NO and that it scales simply with pressure according to the total number density.

REFERENCE

1. Allen, M. G., McManus, K. R., and Sonnenfroh, D. M., "PLIF Imaging in Spray Flame Combustors at Elevated Pressure," Paper No. 95-0172, AIAA 33rd Aerospace Sciences Meeting, 1995.

Twenty-Sixth Symposium (International) on Combustion/The Combustion Institute, 1996/pp. 2787–2793

VISUALIZATION OF FUEL DISTRIBUTIONS IN PREMIXED DUCTS IN A LOW-EMISSION GAS TURBINE COMBUSTOR USING LASER TECHNIQUES

CHRISTER LÖFSTRÖM,[1] HANS KAALING[2] AND MARCUS ALDÉN[1]

[1]*Department of Combustion Physics*
Lund Institute of Technology, P.O. Box 118
S-221 00 Lund, Sweden

[2]*VOLVO Aero Corporation*
S-461 81 Trollhättan, Sweden

A two-wavelength laser technique has been developed and applied for qualitative visualization of mixing and vaporization of the fuel in an industrial gas turbine combustor. The fourth harmonic of a YAG laser, at 266 nm, was used to visualize the gas-phase distribution by laser-induced fluorescence, whereas the second harmonic at 532 nm was used to visualize the droplets by Mie scattering. Since the experiments were made using Jet-A as fuel, which is a multicomponent mixture with hydrocarbon components having different spectroscopic and thermodynamic properties, the practical measurements were preceded by laboratory experiments aimed at spectroscopic investigations of the fluorescence emission as a function of temperature and influence from oxygen quenching on the fluorescence signal. The practical measurements were made on-site at Volvo Aero Corporation using a mobile system in which double images, yielding simultaneous LIF and Mie scattering, were recorded for different operating condition of two different gas turbine ducts. The ducts were investigated in terms of different temperatures, equivalent ratios, and duct designs. The results could thus be used as a tool in the understanding of new concepts for gas turbine combustion, for example, the LPP (lean, premixed, prevaporized) concept. Preliminary attempts were also made to investigate the accuracy and precision of the technique.

Introduction

To meet high-efficiency and ultra-low emission from combustion-driven devices, special combustion concepts have been designed and tested. In the field of gas turbine combustion, one of the driving forces is to reduce the NO_x level to its minimum. New concepts to meet this requirement are RQL (rich burn, quick quench, lean burn) and LPP (lean, premixed, prevaporized) [1,2]. In the latter case, the preheated fuel/air mixture is in strong excess of air, and the liquid fuel is vaporized. To achieve optimum combustion, special care must be taken to optimize the degree of vaporization and to create a uniform fuel/air mixture in the combustion chamber. However, the residence time of the fuel/air mixture in the premixed duct must be minimized to prevent autoignition.

In the development of combustion concepts, it is of great value to introduce and apply modern tools such as advanced modeling and diagnostics. In the previously mentioned area, large eddy simulation (LES) has become applicable [3]. In the field of diagnostics, various laser-based techniques have emerged; thanks to their inherent nonintrusive nature in combination with high temporal and spatial resolution, they have become of importance in the characterization of combustion-related phenomena (see Ref. 4 and references therein for an overview of the field).

In the development of LPP gas turbine combustors, one of the most important aspects is the character of the fuel/air mixture. In a recent application, we have shown how laser-induced fluorescence can be used for investigation of mixing behavior in a gas turbine combustor using gaseous fuel [5]. More realistically, however, is the use of liquid multicomponent fuels in which the degree of vaporization is also crucial for optimum performance. In the case of laser investigation of the degree of vaporization, two-phase diagnostics have to be investigated. This area, despite its industrial importance, is not as developed as diagnostics directed toward only one phase. One approach that has been of great importance in the diagnosis of two-phase flows was developed by Melton and is based on the introduction of so-called *exciplexes* [6]. In this approach, laser-induced fluorescence occurs in different spectral regions depending on whether the exciplexes are bound to droplets or are in the gas phase. The single most severe disadvantage of this approach, however, is that the LIF from the exciplexes is very sensitive to the presence of oxygen, which is an extremely strong quencher. Consequently, the applicability of this technique for use in real practical devices when air must be used is limited.

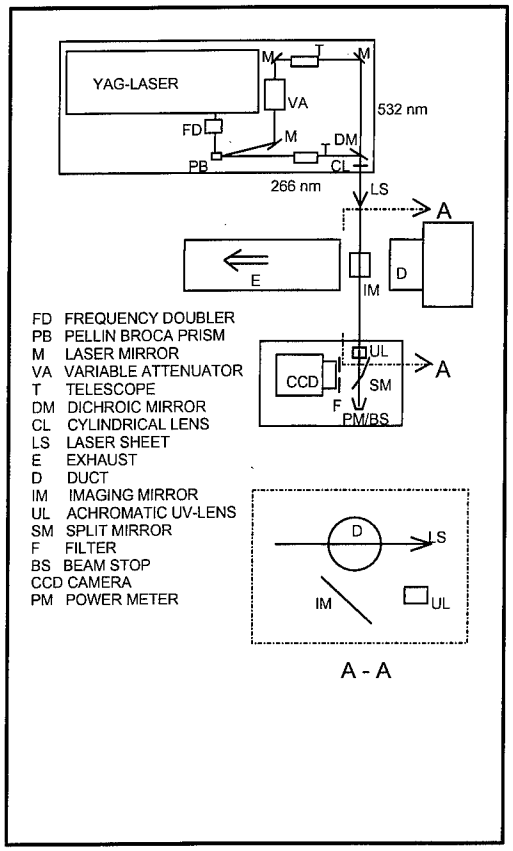

FIG. 1. Experimental setup used in the visualization experiments.

An alternative technique for two-phase visualization is to combine laser-induced fluorescence (LIF) and scattering (Mie), which, despite a lack of quantitative information, would give a valuable engineering view of the vaporization/mixing process as an aid in the design process. This technique has been applied successfully in diesel engines [7].

In the present paper, we describe the applications of a combined laser-induced fluorescence/Mie scattering technique based on multiple wavelength excitation and its use for the characterization of vaporization of Jet-A and consequent mixing with air. The study includes introductory laboratory experiments and practical application of the technique demonstrated in two premixed ducts at Volvo Aero Corporation.

Laboratory Experiments

Before the industrial application, it was necessary to perform laboratory experiments for the development of the technique and investigation of relevant spectroscopy and quenching characteristics. Based on the outcome of these investigations, adequate optical components and detectors could be chosen.

The laboratory measurements were performed mainly in a test rig that was designed for mass flow and temperature at atmospheric pressure to simulate the realistic flow conditions as closely as possible. Therefore, the air was heated by electrical heaters and the fuel was sprayed into the hot air. During the laboratory test, the air and fuel mass flows and air temperature were measured.

To visualize the degree of vaporization/mixing, a combined laser diagnostic approach using both laser-induced fluorescence (LIF) and elastic Mie scattering was used. The optical setup is shown in Fig. 1. A pulsed Nd:YAG laser (Quantel YG 781C10) was used to produce IR radiation with a pulse energy of 800 mJ in 10-ns-long pulses. By using nonlinear optical crystals, the second and fourth harmonics at 532 and 266 nm, respectively, were produced with a pulse energy of 350 and 50 mJ, respectively. The doubling crystals were positioned so that individual control of the divergences and diameters of the two beams could be achieved by using a telescope in each beam. The beams were then combined by using a dichroic mirror that transmitted 532 nm and reflected 266 nm. The beams formed a sheet with a height of about 10 mm using a cylindrical lens, f = 1000 mm. Using the individual telescopes, it was ensured that the two laser beams had their focal point at the same position. The thickness of the laser sheets was measured to be about 400 μm. The difference in thickness of the two sheets was adjusted to be less than 50 μm. The two beams were focused between the duct outlet and the exhaust inlet.

Part of the intersection area of the laser beams in the fuel/air mixture was imaged with an achromatic quartz lens, f = 100 mm, $f/2$ (B. Halle Nachfl.) onto the photocathode of an image intensifier, ϕ = 25 mm, whose output phosphor screen was imaged onto a slow scan Peltier cooled CCD camera (Wright Instrument) consisting of 385 × 578 pixel elements, each with a dimension of 22 μm × 22 μm. By using a split mirror arrangement [8], it was possible to create two images on the image intensifier. With different optical filters in the image plane, scattering from the two laser beams could be isolated spectrally, thus creating two different images.

Choosing proper optical filters required some preliminary spectroscopic investigations. The fuel, Jet-A, is a multicomponent fuel with a final boiling point of ~570 K, whose individual components are different large hydrocarbon molecules that could have dramatically different spectroscopic and thermodynamic characteristics. The purpose of this investigation was merely to measure the relative fluorescence emission when exciting the fuel at different temperatures with a laser beam at 266 nm rather than to achieve a deep spectroscopic under-

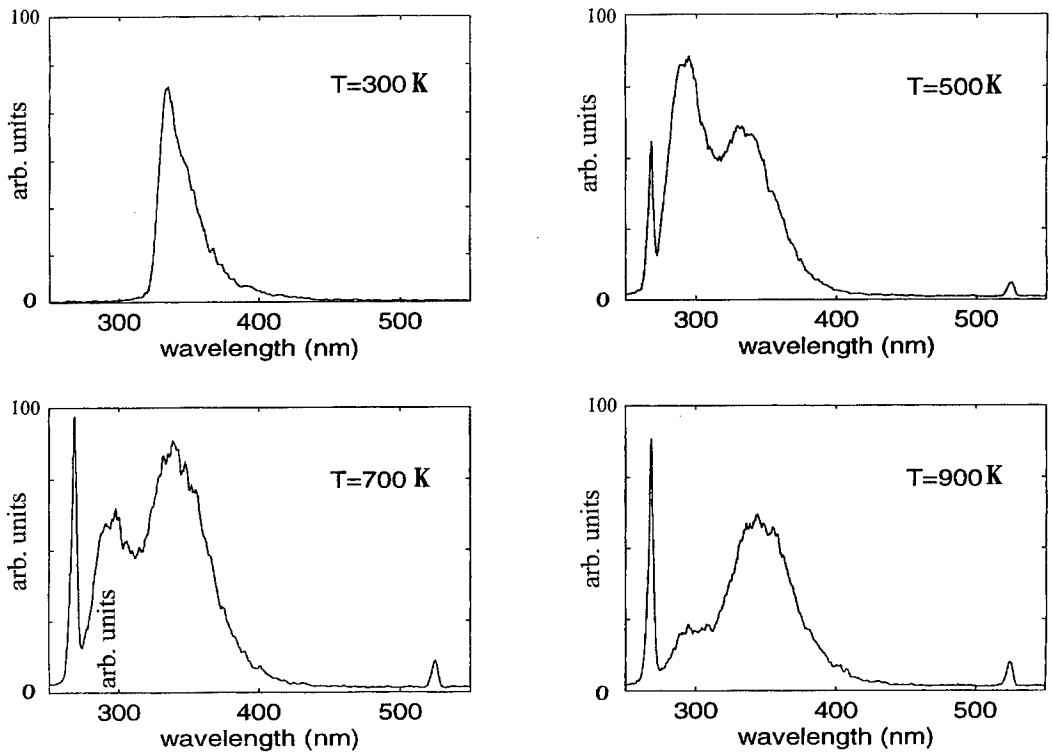

FIG. 2. Laser-induced–fluorescence spectra from Jet-A at different temperatures in air.

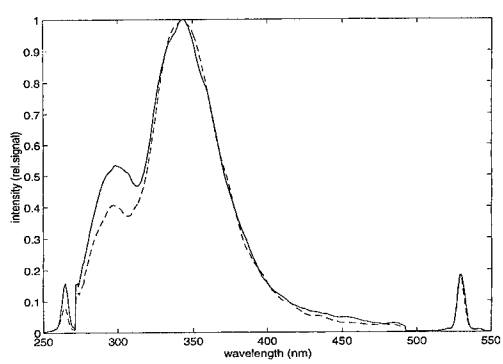

FIG. 3. Normalized laser-induced fluorescence from Jet-A at 700 K with air (solid line) and pure nitrogen (dashed line).

standing of this hydrocarbon mixture. These measurements were also made with the setup shown in Fig. 1 but with the image-intensifier/CCD detector connected to a Jarrel Ash spectrograph, *f*/3.8, with a grating of 150 rules/mm blazed at 450 nm. As a reference, the first spectrum was recorded by placing a cell containing Jet-A in liquid form at 300 K in the focal region of the UV beam. The spectrum is shown in Fig. 2 (upper left). As can be seen, this spectrum is rather unstructured and extends from 320 to 400 nm with a peak at 340 nm. Spectra were then recorded from 500 to 900 K and are also illustrated in Fig. 2, where the ordinate axis is in arbitrary units. These spectra extend from the excitation wavelength at 266 nm up to 400 nm and show double peaks in which the intensity ratio, obviously, is temperature dependent. The narrow peaks shown are due to scattering at 266 nm; the second order of this radiation appears at 532 nm. Spectra recorded using the 532-nm beam in a mixture of droplets/gas phase were to a large extent dominated by Mie scattering from the droplets. Preliminary experiments were also made with 355 nm as excitation source; however, because of the much lower fluorescence signal and the spectral interference of the fluorescence and resonance scattering, this approach was not pursued.

To get a feeling for the influence of quenching from oxygen on the signal intensity as a function of fluorescence wavelength, some preliminary experiments were also made. In this case, the fluorescence from Jet-A at 700 K diluted with air or pure nitrogen was recorded. It was seen that the signal intensity at the peak wavelength decreased by a factor of about 2 when using air compared to pure nitrogen. The normalized spectra are shown in Fig. 3. As can be seen, there is also about a 20% difference when com-

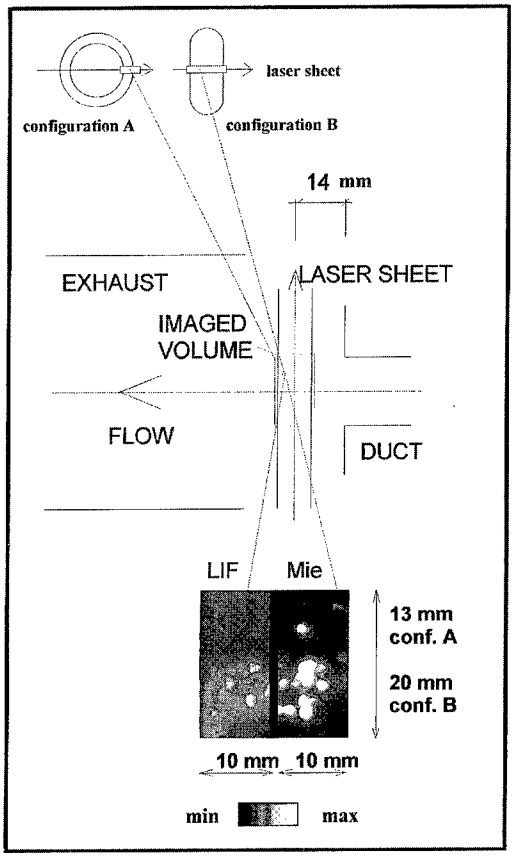

FIG. 4. Image orientation of the double image detected in the duct.

paring the intensity ratio between the two peaks in the two cases. The spectra in Figs. 2 and 3 have not been corrected for the wavelength sensitivity of the spectrograph and the detector.

From the spectral measurements, it was concluded that a Schott filter, BG3, could be used for detection of the fluorescence, whereas an interference filter at 532 nm could be used to spectrally isolate the Mie scattering. No cross talk between the two channels was thus found. With these two filters, the two-color imaging approach could be investigated. Figure 4 shows a single-shot image, at an operating condition with poor vaporization, and its orientation in the test rig. The signal intensities of images are represented by a gray scale with white for high signal and black for low signal. The laser energy in the two beams was adjusted to levels giving signal strengths within the operating range of the detector. Typical single-shot spectra thus had a signal intensity up to 10^4 counts.

From the spectral measurements and the laboratory experiments, it was seen that the UV laser beam was heavily absorbed by the liquid phase. It was thus evidenced, both from the spectral measurements and the comparison of the two single laser shots' corresponding images, that the fluorescence image to a large extent showed only gas-phase fluorescence.

To make comparisons of different duct designs under different test conditions by using images such as those in Fig. 4, it is of great importance to compensate for variations in the laser power and for normalization for the laser intensity variations across the laser sheet. The mean laser intensity was thus measured for each wavelength using a power meter, whereas the average inhomogeneities across the laser sheet were compensated for by measuring the fluorescence image from a cuvette filled with methanol containing a small amount of fluorescing dye, which was placed in the focal region before taking the measurements. Since the dye cell ideally should produce a homogeneous distribution of fluorescence, the laser inhomogeneities could be accounted for. With temperature-stabilized doubling crystals, the average beam profiles were stable within 10% for several hours, which should be compared to a measuring time of 0.5 h between each reference measurement.

Although it is not straightforward to make a complete test of the linearity of the signal as a function of number density, measurements were made in a limited range of equivalent ratios and temperatures in which the signal was seen to show a linear relationship with fuel concentration. The conclusion from the laboratory experiments was that an applicable engineering technique has been developed capable of visualizing mixing/vaporization of gas/droplet distributions in an industrial duct to a gas turbine.

Practical Experiments

Since all laboratory experiments were made with the industrial application in mind, the same experimental setup as shown in Fig. 1 was used. The laser- and beam-forming optics were built on a mobile unit that was easily transported from the laboratory to the test site. Also, the receiving optics and the detector were built on a breadboard that could be transported along with the laser system. At the test site at Volvo Aero Corporation, the only experimental difference compared to Fig. 1 was the ducts, which were designed and built for tests of a combustor for different LPP configurations.

Two different duct designs were studied, one with six Delavan pressure atomizers and rotating airflow designed by Volvo Aero Corporation, configuration A, and one with a prefilm atomizer and straight airflow designed by DRA in England, configuration B (see Fig. 5). The Volvo duct and the gas turbine combustor are described in Ref. 9. The experiments

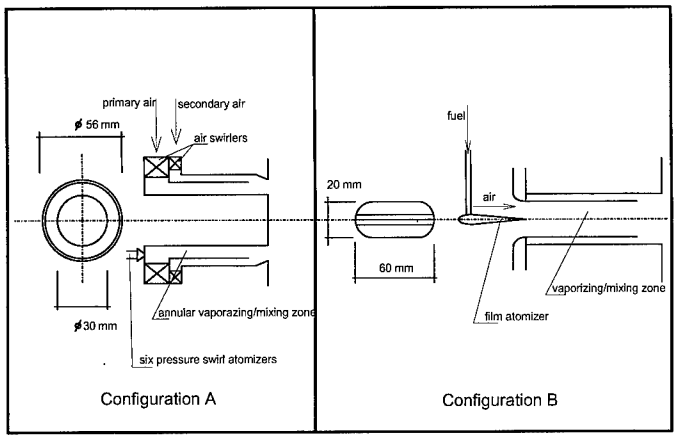

FIG. 5. Different LPP duct designs for the practical experiments.

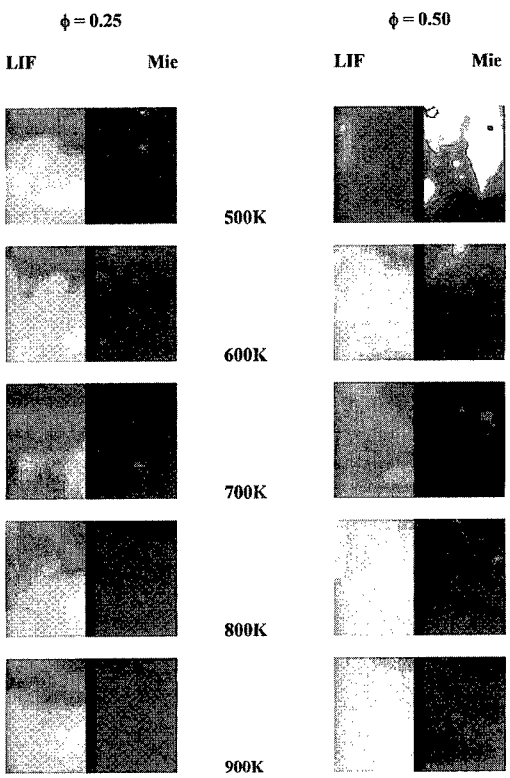

FIG. 6. Two-dimensional images of laser-induced fluorescence (LIF) and Mie scattering using duct configuration A at two equivalent ratios and different temperatures.

were carried out without the can combustor and the pilot fuel injector. The measurements were made at the outlet of the duct according to Fig. 4, thus producing a number of double images, giving indications of mixing/vaporization characteristics. After the experimental zone, the fuel-air mixture was led to an exhaust pipe and burned using propane burners.

The investigations were made at atmospheric pressure with variation of temperature, T, equivalent ratios, Φ, and duct configuration. During the measurements 20 (double-) single-shot images were recorded for each test condition. Figure 6 shows the results from the duct using configuration A at two different equivalent ratios, $\Phi = 0.25$ and 0.5, at temperatures ranging from $T = 500$ to 900 K. As can be seen, for inlet temperatures above 700 K, most of the fuel is vaporized and the distribution is concentrated in the central part of the duct. At temperatures below the final boiling point of the fuel, a large part of the fuel is still in the liquid phase. The liquid fuel is centrifuged by the swirling flow toward the outer radius of the duct from where it emerges into the combustion chamber. In Fig. 7, the results from the duct using configuration B are shown. As can be seen by using this configuration, there are strong signals in the Mie channel indicating unvaporized fuel, even at the highest temperatures. The laser beam absorption was measured for all T and air/fuel ratios and ranged up to 10% for the 532-nm beam and between 20% and 40% for the 266-nm beam using configuration A.

To use the images in Figs. 6 and 7 as an aid in understanding the design process, it is of importance to develop a quality number that can characterize the specific test condition. One approach that seemed to give the information needed was, for each double image in Figs. 6 and 7, calculate the mean fluorescence signal intensity, FS, as well as the mean Mie signal intensity, MS. These numbers, normalized with the corresponding laser intensity—I266 and I532, respectively—could then be used to form a dimensionless number, Q, defined as

$$Q = (FS/\mathrm{I266})/(MS/\mathrm{I532})$$

This number could be used for comparative studies of different duct configurations, providing the same experimental condition prevails and will give an indication of the degree of vaporization. By

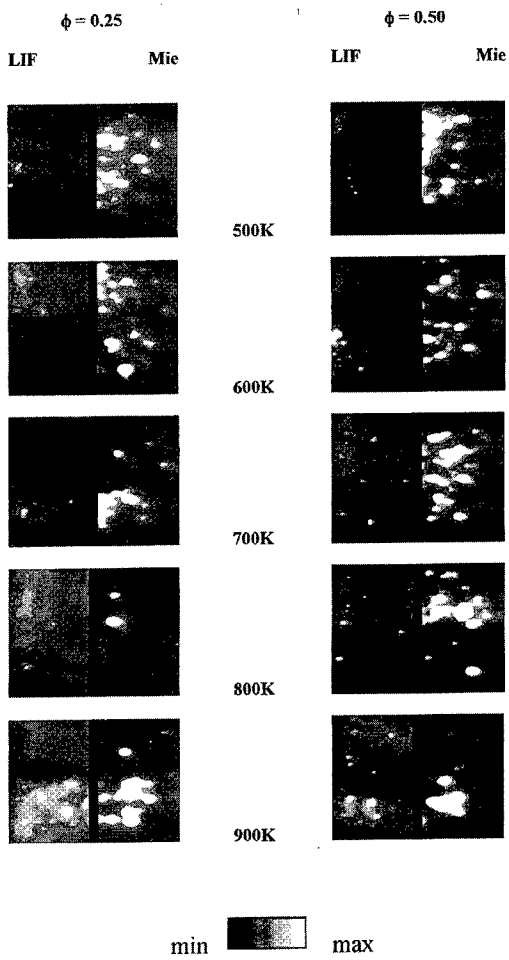

FIG. 7. Two-dimensional images of laser-induced fluorescence (LIF) and Mie scattering using duct configuration B at two equivalent ratios and different temperatures.

examining the images in Fig. 6 using configuration A, it could thus be seen that the Q number ranged from 2 at the position $T = 500$ K and $\Phi = 0.5$ to up to 50 at higher temperatures. These numbers could be compared with the values from configuration B in Fig. 7, where the numbers ranged from ~0.3 up to ~1 at higher temperatures. Thus, the result shows the applicability of the technique for comparing duct configurations.

Discussion and Conclusions

Different laser diagnostic techniques, despite the development of combustion applications over more than two decades, have been limited to a large extent to laboratory experiments, with comparatively few industrial applications with real impact on the design process. The main reasons for this are the industrial application of poorly defined, multicomponent fuels (e.g., Jet-A or diesel), often limited optical access, and the complexity of many of the techniques, especially those involving spectroscopic applications.

In the present investigation, we have faced a practical industrial problem, the mixing/vaporization of fuel and air, with great importance for optimum behavior of a potential future industrial apparatus, an LPP combustor to a gas turbine. There are considerable problems with using the existing laser technique to achieve a quantitative description of these processes. The approach with exciplexes, as stated previously, could not be used because of heavy quenching from oxygen; furthermore, it is not clear how this technique would work in a practical environment with a multicomponent fuel with strong fluorescence emission in itself.

However, to get a qualitative picture of the processes, we have developed and applied a multicolor imaging technique, based on simultaneously two-color Mie scattering and laser-induced–fluorescence emission, which have been applied to a realistic industrial device. The approach with one excitation source for both LIF and Mie [7] was not applicable in the present work because of strong self-absorption at 266 nm and weak fluorescence/strong spectral interference at 355 nm. The technique has an advantage in being comparatively simple and providing the information quickly. A disadvantage is that the Mie scattering cross section is dependent on the droplet diameter so that the Mie signal will be biased toward small droplets. Unfortunately, no droplet size information exists for both duct configurations. However, droplet size measurements from configuration A at 500 K indicated that for both equivalent ratios, the mean sizes changed less than 10% [10]. By inspection of the size distribution for these test conditions, an approximate average spread less than 20% standard deviation was also measured [10]. Another source of error is that the knowledge concerning the fluorescence signal is still comparatively vague in terms of its absolute influence from quenching and temperature variations. The laboratory experiments that were made could give an indication only that no major causes of error may be expected in this respect. These measurements revealed, however, that the potential temperature information shown in Fig. 2 may to some degree be made less accurate by a wavelength-dependent quenching, as illustrated in Fig. 3.

The precision was estimated by repeated measurements of the Q number with identical test conditions. It was thus found that a standard deviation of less than 20% was measured. Despite the problems in giving an absolute figure of the accuracy, it is clear that the technique can be used for the purpose described in the present work when a difference in the Q numbers of two orders of magni-

tude, depending on test conditions and duct design, could be seen. The experimental results have also been compared with preliminary numerical studies using large eddy simulation (LES), which showed good qualitative agreement between theory and experiments [11].

For future development, it would be of great interest to include in situ measurements of droplet sizes. This can be achieved by analyzing the state of polarization of the Mie scattered radiation [12,13]. Experimentally, this would mean that two Mie scattering images should be detected. Using two orthogonal polarizations in the two images, information about the size distribution could be achieved. The detection of several images (up to four) on the same CCD detector can be achieved by using a Cassegranian telescope with individual adjustable segments, for example. This device has previously been used successfully for simultaneously multiple-color imaging in combustion diagnostics using spontaneous emission [14].

In summary, we believe that the technique described, a combination of Mie scattering and laser-induced fluorescence and its further development, can be of great value in developing a deeper understanding of the processes involved in the design of industrial combustion devices.

Acknowledgments

This work was part of the BRITE/EURAM program, Aero CT-92-0036, "Low Emission Combustor Technology LOWNOX II." The authors are thus grateful to this organization, as well as to the Swedish Board for Technical Developments, NUTEK, for financial support.

REFERENCES

1. Simon, B., Joos, F., and Walther, R., "Possibilities and Limitations of Reducing Pollutions by Aero-Engines by Modification of the Combustor Process," Proceedings of the Second European Propulsion Forum, April 3–5, 1990.
2. Bayle-Laboure, G., "Pollutant Emissions from Aircraft Engines," Proceedings of the Second European Propulsion Forum, April 3–5, 1990.
3. Fureby, C. and Löfström, C., *Twenty-Fifth Symposium (International) on Combustion,* The Combustion Institute, Pittsburgh, 1994, pp. 1257–1264.
4. Eckbreth, A. C., *Laser Diagnostics for Combustion Temperature and Species,* Abacus Press, Cambridge, MA, 1987.
5. Löfström, C., "The Gaseous Fuel and the Combustion Air Mixing in the ABB Conical Premix EV Burner: Visualized by Planar Laser-Induced Fluorescence with Acetone as the Fuel Flow Tracer," Lund Report of Combustion Physics, LRCP-12, 1994.
6. Melton, L. A. and Verdieck, J. F., *Twentieth Symposium (International) on Combustion,* The Combustion Institute, Pittsburgh, 1984, pp. 1283–1290.
7. Arnold, A., Dinkelacker, F., Heitzmann, T., Monkhouse, P., Schäfer, M., Sick, V., and Wolfrum, J., *Twenty-Fourth Symposium (International) on Combustion,* The Combustion Institute, Pittsburgh, 1992, pp. 1605–1612.
8. Aldén, M., Edner, H., and Svanberg, S., *Appl. Phys. B* 29:93–97 (1982).
9. Johansson, P., Sjunnesson, A., and Olovsson, S., "Development of an Experimental LPP Gas turbine Combustor," ASME, The Hauge, Netherlands, 94-GT-284, 1994.
10. Bernsteen, P., Persson, R., and Henriksson, P., personal communication, Volvo Aero Corporation, 1995.
11. Kaaling, H. and Löfström, C., "Fuel/air Distribution in a Low Emission Premix Duct for a Gas Turbine," Paper presented at the Portuguese, Spanish, British, Swedish section of the Combustion Institute, Madeira, March 1–4, 1996.
12. Cavaliere, A., Ragucci, R., D'Alessio, A., and Noviello, C., *Combust. Sci. Technol.* 77:73–93 (1991).
13. Cavaliere, A., Ragucci, R., D'Alessio, A., and Noviello, C., *Twenty-Second Symposium (International) on Combustion,* The Combustion Institute, Pittsburgh, 1988, pp. 1973–1981.
14. Kauranen, P., Andersson-Engels, S., and Svanberg, S., *Appl. Phys. B* 53:260–264 (1991).

Twenty-Sixth Symposium (International) on Combustion/The Combustion Institute, 1996/pp. 2795–2801

FIBER-OPTIC SENSORS FOR LONG-WAVELENGTH PYROMETRY AND THERMOMETRY IN GAS TURBINES

ANTHONY S. BONANNO, WAYNE W. SMITH, ROSEMARY BASSILAKIS AND MICHAEL A. SERIO
Advanced Fuel Research, Inc.
87 Church Street, P.O. Box 380379
East Hartford, CT 06138-0379, USA

Radiation pyrometry and thermometry combined with fiber optics provide sensors for determining surface and gas temperatures in otherwise inaccessible locations. However, several applications require that temperature measurements be made in the long-wavelength infrared (LWIR) where widely used silica fibers are nontransmissive. This study involved the development and testing of hollow sapphire fiber-optic radiometric temperature sensors that operate in the LWIR. Hollow sapphire waveguides are suitable for use at high temperatures and transmit in the LWIR; no currently available solid-core fiber offers this combination of features. A prototype fiber-optic radiometric temperature sensor was assembled for the LWIR spectral region, and several experiments were performed to demonstrate the feasibility of developing a system that could be used in gas turbine applications. Open-tip and closed-tip hollow sapphire waveguides were used as the sensor probes and were coupled to an FT-IR spectrometer using hollow glass waveguides. Both types of sensors were tested in laboratory facilities and the closed-tip configuration was also used in a jet engine test rig. The principal findings can be summarized as follows: (1) Open-tip hollow sapphire waveguides were demonstrated to be useful sensors for remote pyrometric temperature measurements in the LWIR. Analysis of calibration data predicted an error level of less than 1% of the reading at 800°C. (2) Closed-tip hollow sapphire waveguides were demonstrated to be useful sensors for radiometric gas temperature measurements in the LWIR. (3) It was determined that interference caused by hot H_2O and CO_2 emission in the open-tip configuration could be eliminated through careful selection of the analyzed spectral region. (4) It was found that interference caused by heating of the waveguide walls in either configuration could be eliminated by limiting the throughput of the optical system.

Introduction

Radiation pyrometry and thermometry combined with fiber optics provide powerful sensors for determining surface and gas temperatures in otherwise inaccessible locations. However, several applications require that temperature measurements be made in the long-wavelength infrared (LWIR) where widely used silica fibers are nontransmissive. For example, gas turbine engine components are being fabricated from ceramic materials or are often coated with ceramic thermal barrier coatings that have low, variable emissivities at shorter wavelengths [1]. Therefore, temperature measurements would be more accurate and reproducible in the LWIR where the emissivities are typically high and stable. A second example is measurement of gas temperatures where the dynamic range must be extended to lower temperatures. In this case, shorter wavelength sensors suffer as the peak of the Planck function shifts to longer wavelengths. This study involves the development and testing of fiber-optic radiometric temperature sensors based on hollow sapphire waveguides that operate in the LWIR. Hollow sapphire waveguides are suitable for use at high temperatures and transmit in the LWIR; no currently available solid-core fiber offers this combination of features.

Hollow sapphire waveguides transmit in a wavelength band of 10–17 μm, where the refractive index of sapphire is less than that of air ($n_{air} = 1.0$). In this region, light is totally reflected at the air/sapphire interface. In the pyrometer configuration, the radiation emitted by a hot target is collected by an open-tip waveguide and propagated to the detector system. If necessary, an aperture can be used before the detector to limit the field of view of the measurement.

A similar device can be used as a gas thermometer. In this case, a hollow sapphire waveguide with an integral sapphire tip is used as the sensor. The sapphire tip is heated convectively by the gas stream and emits radiation that is transmitted to a detector via the sapphire waveguide. This is made possible by the optical properties of sapphire. The sapphire tip emits strongly at wavelengths greater than 5 μm, where the absorption index of sapphire is high, and the waveguide transmits in a wavelength band of 10–17 μm. Thus, the spectral radiance of the sensing tip is complementary to the transmission band of the waveguide. Since the sensing tip and waveguide can

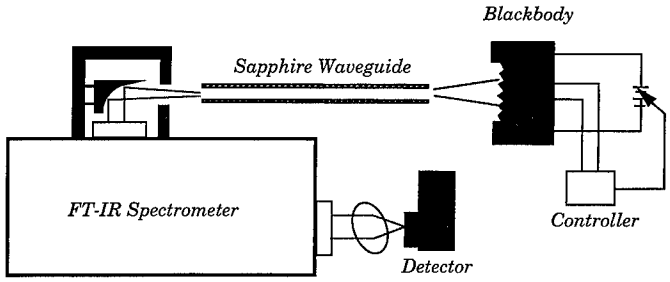

FIG. 1. Schematic of the hollow sapphire waveguide coupled to an FT-IR spectrometer.

be constructed as a small single unit, this sensor provides fast response times and excellent stability and ruggedness. Additionally, the physical properties of sapphire provide for a probe that is resistant to fouling and oxidation and is capable of operation at temperatures in excess of 1700°C.

Background

Radiation Pyrometry

Radiometric temperature measurements are based on the principle that the amount of radiation emitted by an object is related to its temperature. For an opaque, nonreflective object (black body) this phenomenon is governed by Planck's radiation law [2]:

$$U(\lambda, T) = \frac{C_1}{\lambda^5} \frac{1}{[\exp(C_2/\lambda T) - 1]} \qquad (1)$$

where $U(\lambda, T)$ is the spectral radiance, λ is the wavelength, T is the temperature in Kelvin, and C_1 and C_2 are constants. A classic instrument used for making temperature measurements on the basis of this principle is the optical pyrometer [3–5]. A pyrometer measures the radiation emitted from an object in a specified wavelength band (often in the red, where $\lambda = 0.65\ \mu$m) and uses a predefined calibration to determine the temperature. This method works well for determining temperatures of hot surfaces when the surface emissivity is well-known, but difficulties can be encountered when measuring temperatures of materials that have low emissivities or temperature-dependent emissivities, as is the case for ceramic thermal barrier coatings that are being developed for gas turbine engine components [1]. As discussed previously, these coatings can exhibit a significant change in emissivity with temperature in the visible and near infrared spectral regions.

Hollow Sapphire Waveguides

Hollow sapphire waveguides have been employed primarily for laser power delivery in medical and industrial applications [6,7]. Recently, work has also been done on applications of sapphire waveguides in remote thermometry and spectroscopy [8–10]. The high melting point of the sapphire waveguides allows them to be placed near or within flames. It is also possible to couple other types of solid core IR fibers to the hollow waveguides to exploit the flexibility of the solid fiber and the durability of the hollow waveguides.

Radiation is propagated in the air core of a hollow waveguide by total internal reflection when the refractive index of the waveguide material is less than that of the air core ($n_{air} = 1.0$). This occurs for sapphire in the spectral region of anomalous dispersion between 10 and 17 μm. The losses are high in the region of normal dispersion but are observed to be as low as 0.5 dB/m in the anomalous dispersion region. The minimum loss is dependent on the geometry of the waveguide, the launch $f/\#$, and the radius of curvature of the fiber. The configuration used for temperature sensing is depicted in Fig. 1. The sensing element consists of a hollow sapphire waveguide with an open tip, a closed tip, or a tip filled with a ceramic cement. The open-tip configuration is suitable for use as a standard pyrometer, and the closed-tip and filled-tip configurations are suitable for use as gas thermometers. The operation of the open-tip configuration is straightforward; radiation is collected into the waveguide and propagates to the detector. For the closed-tip and filled-tip configurations, the tip of the fiber reaches thermal equilibrium with the medium to be monitored, either by convective or radiative heating, and emits radiation in the spectral region where the absorption index is high. This corresponds to wavelengths >5.0 μm for sapphire and alumina cements. Next, the radiation from the tip is propagated through the waveguide to a detector. The detector signal is then used to determine the temperature from a calibration curve.

The closed-tip configuration has the advantage that the sensor can be fabricated as a single unit by melting the end of the waveguide with a CO_2 laser. This prevents problems such as incompatible thermal expansion coefficients that are encountered with the Accufiber temperature measurement [11] system, which uses a solid-core sapphire fiber coated at

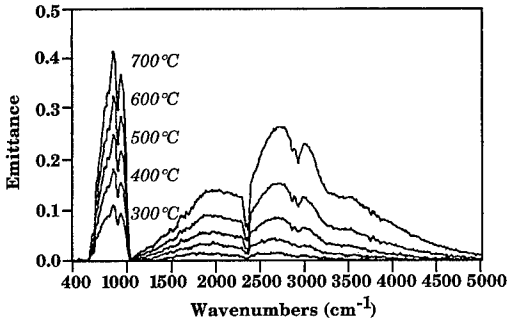

FIG. 2. Emission spectra of a black body target collected using a 790-μm i.d. open-tip hollow sapphire waveguide.

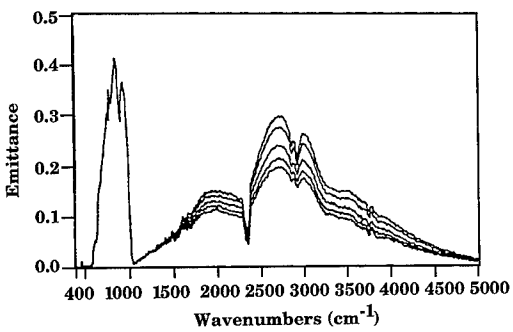

FIG. 3. Emission spectra of a 705°C black body target collected using a 790-μm i.d. open-tip hollow sapphire waveguide with the tip held at positions ranging from 0 to 2 inches from the target.

the tip with a high–melting-point metal (e.g., platinum). It is also important to note that the sensing tip acts as a black body cavity in the transmission band of the hollow waveguide since sapphire is a strong emitter in this spectral region. This eliminates the problem of a non–black body cavity encountered with the Conax Inc., (Buffalo, NY) system, in which the metal is imbedded inside the tip of a solid-core fiber. An additional advantage of using longer wavelengths is that the dynamic range of the measurement is extended to lower temperatures. Although this increased dynamic range is provided by sacrificing some sensitivity on the high temperature end of the range, significant thermal radiance is still observed at long wavelengths for high-temperature black bodies, and this signal is sufficient for determining temperature.

Experimental

It was decided that more useful data would be collected if the sensors were coupled to an infrared spectrometer instead of a simple photometer. This provided the capability to analyze the spectral properties of the data in addition to the integrated detector response for a given wavelength range. This additional information was useful for providing insight about the expected performance of sapphire waveguide-based radiometric temperature sensors. The optical system shown in Fig. 1 was used to allow evaluation of the spectral response of the waveguides. Radiation was collected from a temperature-controlled black body target or cavity through the waveguide tip and was collimated and passed through a Bomem MB series FT-IR spectrometer. Mounts for an aperture and filters were installed between the fiber and spectrometer to allow an investigation of the effects of throughput and bandwidth on the measured signal. The interferometer used in FT-IR spectrometers inherently provides modulation of the infrared radiation and therefore eliminates the need for a chopper and lock-in amplifier. A medium-band MCT detector was used for these experiments. For some experiments, the sapphire waveguides were coupled to a hollow glass waveguide that has a metallic coating on the inner wall. Extremely low coupling losses were observed since there is no loss caused by reflection at the interface. The hollow glass guides are more flexible than the sapphire guides and have good transmission properties over the entire mid-IR. However, they cannot be exposed to high temperatures.

Results and Discussion

Assessment of Capabilities and Potential Measurement Errors

The initial experiments examined the use of the open-tip hollow sapphire probe as a pyrometric temperature sensor. Figure 2 shows the measured spectral response for a large black body target held at temperatures ranging from 300 to 700°C. The energy observed at 1000–580 cm^{-1} (10–17 μm) followed the expected trend. However, energy was also observed at 5000–1000 cm^{-1} (2–10 μm). Since this wavelength range should not propagate by internal reflection in the air core of the waveguide, it is believed that some propagation occurred down the sapphire walls of the waveguides and some energy passed straight through the waveguide. It was found that coupling the sapphire guide to a glass guide eliminated most of this spurious energy. It may be necessary to use band-pass filters to ensure that this energy is eliminated completely.

To demonstrate that the sensors will give reproducible results, provided that the target fills the field of view of the waveguide tip, spectra of a 700°C black body were collected with the waveguide tip held at positions ranging from touching the target to 2 inches away. The spectra, shown in Fig. 3, clearly

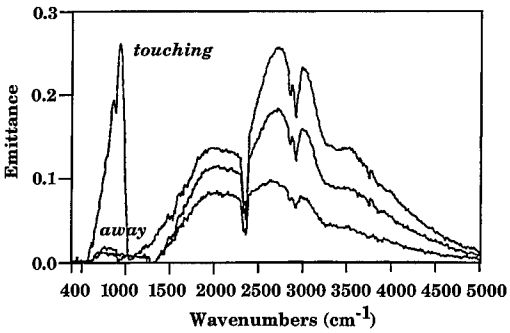

FIG. 4. Emission spectra of a 706°C black body target collected using a 790-μm i.d. closed-tip hollow sapphire waveguide with the tip held at positions ranging from 0 to 1 inches from the target.

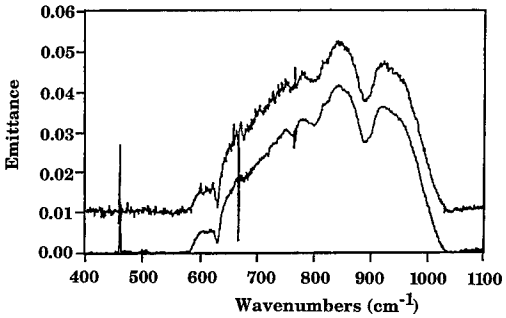

FIG. 5. Emission spectra of a 610°C black body target collected with the open-tip sensor. The upper spectrum was collected with a flame from a propane torch positioned in the field of view (the spectra are offset for clarity).

indicate reproducible results in the 1000–580 cm^{-1} region. The energy at shorter wavelengths was less well behaved. However, as discussed previously, this spectral region would be eliminated in the final design.

In contrast to the open-tip waveguides, the closed-tip waveguide behaved as a contact temperature sensor. As shown in Fig. 4, significant radiance was observed at 1000–580 cm^{-1} only when the sensor tip was in direct contact with the black body. Minimal energy was observed when the tip was not touching the black body, presumably resulting from radiative heating of the sapphire tip. This result indicates that the closed-tip sensor would not be useful for pyrometric temperature measurements but should be useful for applications in which LWIR contact temperature measurements are required, for example, gas temperatures in flames.

Several experiments were performed in the laboratory to assess the temperature-resolving capabilities and potential interferences that could be encountered. To determine the temperature-resolving capabilities, the system described earlier was set up with the open-tip sensor, and spectra of a black body target were collected while the temperature was ramped up to 800°C. The measured intensity was integrated from 700 to 900 cm^{-1} and a cubic polynomial was fit to the results. The root-mean-square error for the fit was 0.00087, which corresponds to a relative error of less than 1% at 800°C [12].

A potential source of interference for measurements made with the open-tip sensor in combustion applications involves the spectral response of hot water vapor and CO_2. At high temperatures, the high rotational levels of the low-frequency water band become populated significantly, and, therefore, water vapor radiance could potentially be observed below 1000 cm^{-1}. CO_2 bands will also be observed at 600–800 cm^{-1}. To assess this potential source of interference, high-resolution spectra of a black body target were collected using an open-tip sensor with a flame from a propane torch held between the sensor and the target. The upper and lower spectra in Fig. 5 were collected with and without the flame, respectively. Both spectra exhibit the characteristic CO_2 absorption band at 667 cm^{-1} (downward peak) that results from the presence of cold CO_2 in the beam path. In the spectrum collected with the flame, some CO_2 radiance (upward peak) is also observed near the 667 and 780 cm^{-1} bands. Some additional bands are observed between 650 and 800 cm^{-1} because of hot water vapor. Note, however, that no water bands appear between 800 and 1000 cm^{-1}; this indicates that interference should not occur in this spectral region. In the final design, it is planned to use a band-pass filter with the open-tip sensor to isolate this region and eliminate a potential source of interference. This will also serve to eliminate the spurious energy at shorter wavelengths, as discussed previously. For the closed-tip sensors, a larger spectral range could be used to provide better sensitivity since no radiance from outside the sensor tip is propagated to the detection system and, therefore, no interference from water vapor and CO_2 will be observed.

Another potential source of interference involves the environment in which the sensor is positioned. Since it is inevitable that the sensors will be used in high-temperature environments, it is important to ensure that heating of the waveguide walls will not affect the measurements. If the hot walls of the waveguide emit radiation that propagates to the detection system, then temperature measurements will be biased by the sensor environment. Initial measurements indicated that this occurs. It was also found that most of the radiation originating from the waveguide walls was propagated in the higher-order modes, that is, at a large angle of incidence with the waveguide wall. Therefore, this source of interference can be reduced greatly by eliminating the energy propagated in high-order modes. This is

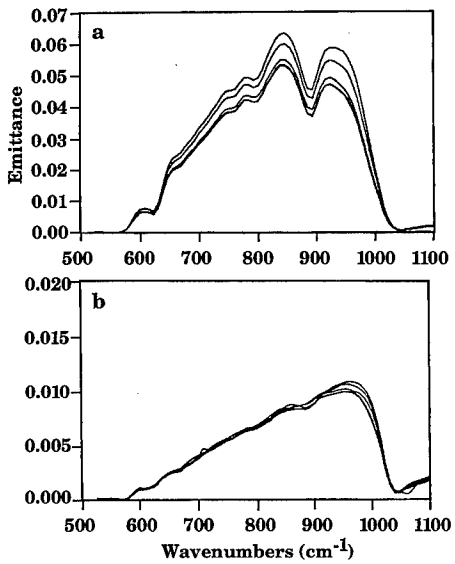

FIG. 6. Emission spectra of a 740°C black body target collected with the open-tip sensor while heating the wall of the waveguide with a torch: (a) No aperture, full field of view and (b) small aperture, limited field of view.

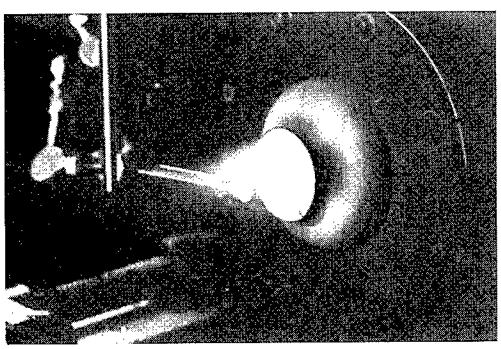

FIG. 7. Photograph of the closed-tip waveguide surrounded by a water-cooled jacket and installed in the exhaust nozzle of Pratt & Whitney's Becon Burner.

accomplished by limiting the effective throughout of the waveguide by placing an aperture between the fiber and the detection system. This also has the effect of reducing the image size that is observed by the fiber (open-tip configuration), allowing for higher spatial resolution. To demonstrate this principle, spectra of a 740°C black body were collected with the open-tip sensor while heating the waveguide wall with a torch. Temperatures of the heated waveguide were estimated by placing a thermocouple near the waveguide in the flame. Figure 6a shows the spectra obtained with no aperture as the waveguide wall was heated from ambient to above 1300°C. It is clear that the radiance at 500–1000 cm^{-1} increases as the waveguide is heated. However, when the same experiment was performed using an aperture to limit the throughput, only a slight change in radiance was observed (Fig. 6b). While this method reduces the observed signal, in this case by a factor of about 6, the improved reliability more than offsets the loss in sensitivity. A similar result was observed for the closed-tip sensor [12].

Evaluation in a Gas Turbine Test Rig

The closed-tip sensor was evaluated for measuring gas temperatures in a combustion environment during a test at Pratt & Whitney's facilities in East Hartford, Connecticut. The test facility used for this program was one of their atmospheric pressure combustor rigs (Becon Burner), which is designed to simulate the combustion processes that occur in large-scale engines. The rig was equipped with a 2-inch diameter exhaust nozzle, and gas temperatures in the exhaust plume were in the range of 1000–1200°C. A photograph of the system operating with the closed tip sensor installed is shown in Fig. 7. The spectrometer and data station were installed just outside of the combustion room, and a 2-m hollow glass extension guide was fed through the wall. The closed-tip sensor was coupled to the hollow glass guide and mounted on an *X-Y* stage to allow the sensor tip to traverse the exhaust plume in two dimensions.

In the first experiment, the closed-tip sensor was installed in a 1/8-inch outer diameter stainless steel sleeve (no water cooling), and spectra were collected at 1/4-inch axial increments and 1/2-inch longitudinal increments in the exhaust plume. The sensor was calibrated in a black body cavity before the experiment, and gas temperatures were determined online. The temperature profile of the plume determined by this experiment is plotted versus axial and longitudinal dimensions in Fig. 8. Although an aperture was used to limit the throughout, it appears that a bias was observed due to heating of the waveguide walls. The measured temperatures were about 200–300°C higher than those measured with an aspirating thermocouple probe. Furthermore, the asymmetry observed in Fig. 8 was unexpected. It appears that more of the waveguide wall was exposed to the high-temperature environment as the probe was traversed across the flame, and, therefore, the bias increased on the positive side of the axial dimension. We believe that further limiting the throughput of the optical system would have eliminated this problem, as was demonstrated earlier. However, the limitations of the optical configuration used at the test prevented further investigation.

The same experiment was repeated using the closed-tip sensor installed in a water-cooled jacket with the sensor tip exposed (see Fig. 7). The temperatures determined with this configuration were

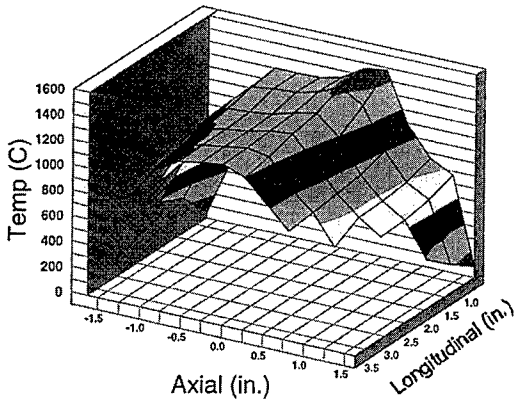

FIG. 8. Temperature profile of the Becon Burner exhaust plume determined with the uncooled closed-tip sensor. The exhaust nozzle was located at the back of the plot at 0 inches longitudinal with the center of the nozzle at 0 inches axial.

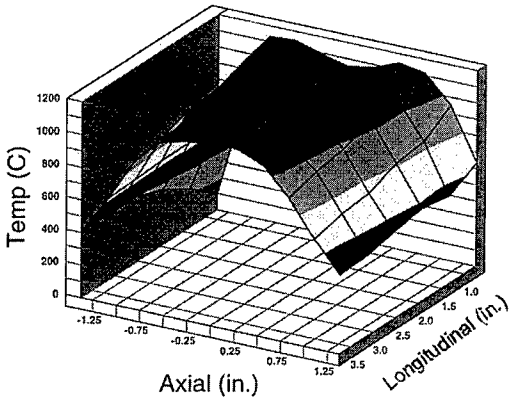

FIG. 9. Temperature profile of the Becon Burner exhaust plume determined with the water-cooled closed-tip sensor. The exhaust nozzle was located at the back of the plot at 0 inches longitudinal with the center of the nozzle at 0 inches axial.

in good agreement with those measured with the aspirating probe, and the expected symmetry in the temperature profile was also observed, as shown in Fig. 9.

Conclusions

This study demonstrated the feasibility of using hollow sapphire waveguides as temperature sensors in either the open-tip or closed-tip configurations. Both configurations were tested in laboratory facilities, and the closed-tip configuration was also used in a test rig at Pratt & Whitney, Inc. The open-tip hollow sapphire waveguides were demonstrated to be useful sensors for remote pyrometric temperature measurements in the long-wave infrared. Analysis of calibration data predicted an error level of less than 1% of the reading at 800°C. The closed-tip hollow sapphire waveguides were demonstrated to be useful sensors for radiometric gas temperature measurements in the long-wave infrared. It was found that interference caused by hot H_2O and CO_2 emission in combustion systems could be eliminated through careful selection of the analyzed spectral region. It was also found that interference due to heating of the waveguide walls could be eliminated by limiting the throughout of the optical system.

Acknowledgments

The authors gratefully acknowledge the support of this work by NASA-Lewis under Contract No. NAS3-27586. The project officer was Dr. Daniel Ng. The authors also wish to acknowledge the assistance of Mr. William Atkinson of United Technologies Pratt & Whitney (P&W) in arranging the tests at P&W and for helpful discussions of temperature measurement in gas turbine systems. Mr. Fred Fries of P&W also provided valuable assistance with the tests at P&W. Additionally, the authors would like to thank Prof. James Harrington of Rutgers University, who supplied the hollow sapphire and glass waveguides and consulted on their use as temperature-sensing devices. Finally, the authors would like to acknowledge valuable discussions on temperature measurement with Prof. Eric Suuberg of Brown University.

REFERENCES

1. Atkinson, W. H. and Cyr, M. A., "Evaluation of Sensors for Temperature Measurement of Ceramic Materials," *Proc. of the 3rd Annual HITEMP Review,* NASA Conference Publ. 10051, 1990, pp. 69.1–69.14.
2. Driscoll, W. G., Ed. *Handbook of Optics,* McGraw Hill, New York, 1978, pp. 1–13.
3. Kostkowski, H. J. and Lee, R. D., "Theory and Methods of Optical Pyrometry," *NBS Monograph* 41 (1962).
4. Dike, P. H., Gray, W. T., and Schroyer, F. K., *Optical Pyrometry,* Leeds and Northrup, Tech. Pub. A1.4000, 1966.
5. Benedict, R. P., *Fundamentals of Temperature, Pressure, and Air Flow Measurements,* Wiley New York, 1984.
6. Harrington, J. A. and Gregory, C., "Hollow Sapphire Fibers for the Delivery of CO_2 Laser Energy," *Opt. Lett.* 15:541–543 (1990).
7. Miyagi, M., Hongo, A., and Matsuura, Y., "Hollow IR Waveguides," *Proc. Soc. Photo-Opt. Instrum. Eng.* 1228:26–35 (1990).

8. Saggese, S. J., Harrington, J. A., Sigel, G. H., Jr., *SPIE Proc. on Chem., Biochem., and Env. Fiber Sensors II,* Vol. 1, 1990, p. 368.
9. Saggese, S. J., Harrington, J. A., Sigel, G. H. Jr., *Opt. Lett.* 16:27 (1991).
10. Saggese, S. J., Harrington, J. A., and Sigel, G. H., *Electron. Lett.* 27:707 (1991).
11. Berthold, J. W. III, "Industrial Applications of Fiber Optic Sensors," in *Fiber Optic Sensors,* (Udd, E., Ed.), Wiley, New York, 1991.
12. Bonanno, A. S., Smith, W. W., Bassilakis, R., and Serio, M. A., "Fiber Optic Sensors for Long Wavelength Pyrometry and Thermometry," NASA Final Report for Contract No. NAS3-27586, 1995.

Twenty-Sixth Symposium (International) on Combustion/The Combustion Institute, 1996/pp. 2803–2809

REAL-TIME ADAPTIVE FEEDBACK CONTROL OF COMBUSTION INSTABILITY

ABID KEMAL AND CRAIG T. BOWMAN
High Temperature Gasdynamics Laboratory
Department of Mechanical Engineering
Stanford University
Stanford, CA 94305-3032, USA

An active adaptive feedback control approach is utilized to minimize pressure fluctuations in a laboratory-scale dump combustor. Essential elements of the controller include sensors, actuators, and a control strategy. The actuation mechanism consists of spanwise forcing of the inlet boundary layer. This forcing is acoustically driven and has been shown to reduce the magnitude of the pressure oscillations by altering the dynamics of the flame-vortex interaction. The control strategy is based on the adaptive filtered-x least-mean-square (LMS) algorithm. Adaptive systems monitor their own performance and vary their internal structure to optimize this performance. The LMS algorithm does not require off-line gradient estimates to search for the minima on the performance surface, making it computationally efficient. A piezoelectric transducer measures the real-time pressure signal that is used as feedback as well as a measure of the error to train the adaptive algorithm. In its efforts to minimize the pressure fluctuations, the adaptive algorithm updates the weights of a digital filter, in real time. The digital filter, as well as the adaptive algorithm, resides on a digital signal processing (DSP) board. Both finite impulse response (FIR) and infinite impulse response (IIR) filter structures were investigated. It was found that the recursive direct-form filter structure is required to prevent the algorithm from driving itself toward instability.

Introduction

Combustion instabilities constitute a major design problem in many combustion devices. These instabilities result in large-scale pressure and heat release oscillations that have a detrimental effect on flame stabilization and can cause structural damage. Combustion instabilities are often vortex driven and are acoustically coupled to the combustor resonant modes. Both passive and active strategies have been used to reduce the level of pressure fluctuations. Passive control involves hardware modifications with the aim to identify and disrupt the coupling between the driving and feedback mechanisms. Reference 1 provides a good review of research in this area. Active control strategies are based on continuously perturbing a specific combustion parameter to dampen the instability limit cycle. Active methods can be classified as closed-loop or open-loop depending upon whether or not feedback from the combustor influences the perturbations. They can be further classified as being fixed-parameter or adaptive systems. Closed-loop fixed-parameter controllers have been extensively investigated and are reviewed in Ref. 2. Although these systems have shown good performance, they cannot accommodate unknown changes in the operating conditions that often occur in real combustion devices. Such changes in the operating conditions can substantially alter the system transfer function, making the application of classical control theory difficult. Consequently, interest in adaptive control of combustion instability has increased [3–8]. Closed-loop adaptive controllers monitor their own performance and vary their internal structure to optimize this performance. Their time-varying, self-learning characteristics are highly desirable for application in real combustion devices.

The overall objective of this study is to develop a real-time, active, adaptive closed-loop control scheme that minimizes the rms pressure oscillations in air-breathing combustors. Adaptive filters using the filtered-x least-mean-square (LMS) algorithm are investigated. The computational efficiency of the LMS algorithm and its ease of implementation make it highly suitable for real-time adaptive control applications. The specific research objectives include the identification of actuation strategies to minimize pressure fluctuations and the development and implementation of adaptive filter architectures that provide effective control and are stable.

Actuation and Sensing Approach

The actuation technique used to suppress the pressure fluctuations actively modifies the fluid mechanics of the combustion zone by controlling the vortex shedding from the flame stabilizer. In this

previously developed technique [9,10], a spanwise slot close to the combustor inlet introduces acoustically induced perturbations to the inlet boundary layer that alter the frequency of vortex shedding and, consequently, the frequency of the unsteady heat release. This actuation scheme was used in previous studies by introducing sinusoidal perturbations of a particular frequency [3–5]. Judicious selection of this frequency results in the partial decoupling of the unsteady heat release from the dominant combustor longitudinal acoustic mode. The rms pressure fluctuation was defined in this approach as one of the performance indices, and the forcing frequency as one of the control inputs. An adaptive optimal controller, based on the Downhill Simplex algorithm was used to find the optimum of the performance function.

The present work differs from the previous approach in that it utilizes real-time pressure signals obtained from the combustor as input to the controller. An adaptive digital filter modifies the signal by providing the correct amplitude and phase shifts at individual frequencies. This signal is then fed back into the combustor using the acoustic actuator. Hence, instead of a single frequency, the acoustic actuator imposes a frequency band. The feedback signal modifies the pressure field in the combustor and can reduce or augment the pressure fluctuations, depending on phase. Multiple instability modes, characteristic of real combustion devices, can be canceled using this technique. This work follows that of Billoud et al. [6]. The differences lie in the actuation strategies and the control algorithm that does not require a priori system identification procedures.

The sensing scheme is based on a fast-response wall-mounted piezoelectric pressure transducer placed just downstream of the inlet. The real-time pressure signal is used as feedback to the controller as well as a measure of the error, to train the adaptive algorithm. The rms of the pressure fluctuation is taken as a measure of the controller performance.

Control Strategies

Several digital filter structures were considered. The direct-form single-input finite impulse response (FIR) filter, also known as a transversal filter, was selected initially due to its ease of implementation. The input-output relationship for such a filter is given in the discrete domain by

$$y_k = \boldsymbol{W}_k^T \boldsymbol{X}_k \tag{1}$$

where

$$\boldsymbol{X}_k = [x_k\, x_{k-1} \ldots x_{k-L}]^T$$

$$\boldsymbol{W}_k = [w_{0k}\, w_{1k} \ldots w_{Lk}]^T$$

are the time-delayed input vector and the filter weight vector, respectively, and y_k is the output from the filter at the time interval k. The notation T stands for the transpose operator and the number of weights or the length of the filter is $L + 1$. The filter response is defined by its length, its weight vector, and the sampling interval. Standard digital filters have a fixed weight vector and hence their transfer function is fixed. Adaptive digital filters, on the other hand, update the coefficients of their weight vector in real time to tailor their response to a particular problem [11]. A training algorithm is utilized to adjust these weights by searching for the minima on a performance surface. This is achieved by comparing the actual filter output to a desired output to obtain an error signal. The performance of the adaptive system is defined in terms of this error (ε_k), the idea being to minimize the mean-square value, or the average power of this signal. The two basic methods of achieving this are those of steepest descent and random search. In steepest descent, adaptation starts with an arbitrary initial value $\boldsymbol{W}_0$ for the weight vector. The gradient (∇) of the mean-square-error ($\xi = E[\varepsilon_k^2]$) with respect to the weight vector ($\boldsymbol{W}$) is defined as:

$$\nabla \equiv \partial\xi/\partial\boldsymbol{W} \tag{2}$$

This gradient is measured and the weight vector is altered in accordance with the negative of the value obtained. The procedure is repeated at each sample, causing the error to be successively reduced. This method can be described by the relation

$$\boldsymbol{W}_{k+1} = \boldsymbol{W}_k + \mu(-\nabla_k) \tag{3}$$

where μ is a parameter that controls stability and the rate of convergence. Random search algorithms, on the other hand, arbitrarily change the weight vector and measure the mean-square-error before and after the change. If the change causes the error to be lowered, it is accepted, otherwise the change is rejected and a new random change is tried. The differential steepest descent (DSD) and the least-mean-square (LMS) algorithms, both based on steepest descent and the linear random search (LRS) algorithm, were considered [12]. The LMS algorithm was selected because of its highest numerical efficiency and lowest "misadjustment," which is a measure of the difference between the actual and optimal performance due to the noise in the adaptive process. To implement this algorithm, a measure of the gradient is required. In real-time applications, exact gradient information is not available due to the availability of a limited statistical sample. Conventional descent methods obtain a noisy estimate of the gradient by taking the difference between short-term averages of ε_k^2.

The least-mean-square (LMS) algorithm simplifies this problem by employing an instantaneous method of approximating the gradient. This

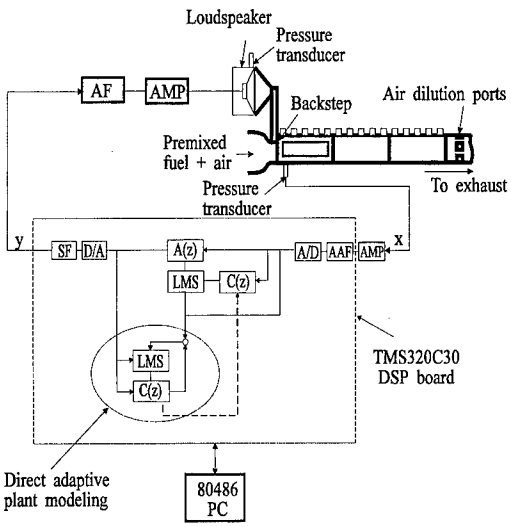

FIG. 1. Controller architecture using FIR filtered-x LMS. The part residing on the DSP board is shown in the dashed box. Here, AAF and SF stand for anti-aliasing filter and smoothening filter, respectively.

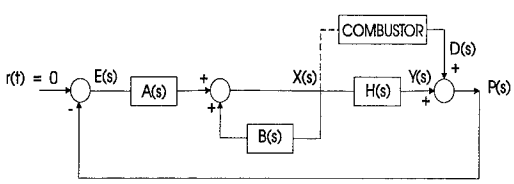

FIG. 2. Simplified recursive control architecture. Here, $P(s)$ is the Laplace transform of the pressure signal picked up by the sensor. Similarly, $D(s)$, $Y(s)$, and $X(s)$ are the transforms of the output from the combustor, the direct acoustic feedback, and the output from the recursive filter, respectively. $r(t)$ is the reference input. $E(s)$ is the error signal to the controller. $H(s)$ is the direct acoustic path from the actuator to the pressure sensor. The combination of $A(s)$ and $B(s)$ forms the recursive filter.

eliminates the need for off-line gradient estimations, making the method computationally efficient. In the LMS algorithm, instead of taking short-term averages of the square of the error signal as an estimate of ξ, the square of the instantaneous value of the error, ε_k^2, is used. With this simplification, the instantaneous gradient is

$$\nabla_k = -2\varepsilon_k \mathbf{X}_k \tag{4}$$

Thus, for the LMS algorithm, equation 3 becomes:

$$\mathbf{W}_{k+1} = \mathbf{W}_k + 2\mu\varepsilon_k \mathbf{X}_k \tag{5}$$

The computational simplicity of the LMS algorithm is apparent in equation 5. No matrix inversion or differentiation is required.

The LMS algorithm modifies the response of an adaptive filter to obtain the inverse model of the plant, which is used as the compensator. Physical systems can be classified as non-minimum-phase and minimum-phase, depending upon whether or not they have plant zeros outside the stable unit circle in the discrete z-plane. The inverse models of non-minimum-phase systems have poles outside the unit circle, making the control signal unstable. Physically, this results in the control effort increasing in magnitude until some part of the system is driven into saturation, causing loss of control. This poses a problem as it is not known a priori whether the plant is minimum phase or not. This difficulty may be overcome by allowing for the modeling delay Δ in the control architecture. Another complexity in the implementation of this strategy is that, in adaptive inverse modeling, the error signal is computed at the filter output. In actual combustion devices, however, the error signal used to modify the weight vector is the error at the plant output and not the filter output. This results in an unstable adaptive process and can find irrelevant solutions. To use ε_k directly, the input to the LMS algorithm also needs to be prefiltered by the model of the plant. The filter architecture is modified to include another adaptive process that directly models the plant ($\mathbf{C}(z)$). This model is then copied over and used to prefilter the input to the LMS algorithm. Thus, the final form of the LMS implementation is given as

$$\mathbf{W}_{k+1} = \mathbf{W}_k + 2\mu\varepsilon_k \mathbf{U}_k \tag{6}$$

where $\mathbf{U}_k$ is obtained by convolving $\mathbf{X}_k$ and $\mathbf{C}_k$. This particular implementation is known as the filtered-x LMS algorithm and is generally applied to antisound applications and to the adaptive control of noisy plants. The complete architecture of an adaptive FIR filter using the filtered-x LMS algorithm and its implementation in the combustor is shown in Fig. 1. The FIR filter itself is represented as $A(z)$.

In experiments using the FIR filtered-x LMS architecture, an instability was experienced that was due to the direct acoustic feedback from the actuator to the sensor in addition to the combustion pressure oscillations. The output from the acoustic actuator can be substantial, as is shown in Fig. 4 by the spike in the power spectrum at the forcing frequency (260 Hz). Fig. 2 shows a recursive, or infinite impulse response (IIR) filter to handle this problem [13]. Here, $H(s)$ is the transfer function of the direct acoustic path from the actuator to the pressure transducer. $X(s)$ is the output from the recursive filter. The combustion pressure oscillation is shown as $D(s)$. Using block diagram analysis,

$$X(s) = X(s)\,[\mathbf{B}(s) - \mathbf{H}(s)\,\mathbf{A}(s)] - \mathbf{D}(s)\,\mathbf{A}(s) \tag{7}$$

As we want $X(s)$ is to be a function of $\mathbf{D}(s)$ only, the filter is designed such that

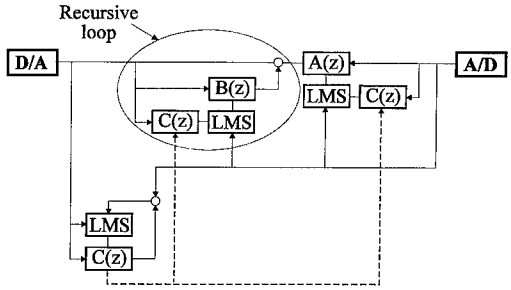

FIG. 3. Controller architecture using IIR filtered-x LMS. Only the part residing on the DSP board is shown.

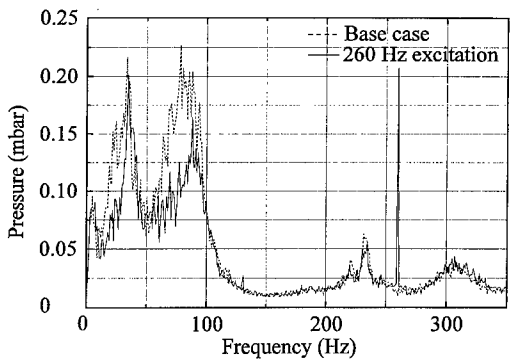

FIG. 4. FFT of pressure traces with and without acoustic excitation. Operating condition: C_2H_4-air, $\Phi = 0.6$, and inlet velocity $U_0 = 7.5$ m/s. The sharp spike at the excitation frequency is the cause of closed-loop instability due to direct acoustic feedback.

$$\boldsymbol{B}(s) = \boldsymbol{H}(s)\,\boldsymbol{A}(s) \tag{8}$$

The analysis shows that the direct feedback from the acoustic actuator can be canceled by the recursive part of the filter.

This result was used to develop another architecture based on infinite impulse response (IIR) filters to overcome the problem of closed-loop instability due to the acoustic feedback. This architecture is shown in Fig. 3. The difference between this and the architecture of Fig. 1 is the addition of the recursive loop $B(z)$. The recursive loop also adapts to the changing plant conditions utilizing the filtered-x LMS algorithm.

Experimental Setup

All experiments were performed in a laboratory-scale (≈150 kW) premixed dump combustor. The combustion facility has been described in detail in Ref. 3 and only a brief description of the apparatus is presented here. A schematic of the combustor showing the placement of the flow actuator and sensors is included in Fig. 1.

The acoustic flow actuator consists of an audio speaker mounted in a cavity. The cavity is connected to a spanwise actuation slot through a waveguide. The 0.16-cm-wide actuation slot is located 0.3175 cm upstream of the dump plane. Maximum perturbation velocities at the slot reach 20 m/s.

Two fast-response (2-μs rise time) piezoelectric pressure transducers, with frequency response of DC to 100 KHz, are used in conjunction with charge amplifiers and true rms to DC circuits. Previous axial pressure measurements have shown that the principal acoustic modes are longitudinal with the pressure anti-node near the back-step and a pressure node at the air dilution ports [10]. One of the pressure transducers is mounted just downstream of the inlet plane at the pressure anti-node to have maximum sensitivity to the combustor pressure fluctuations. The other transducer is installed in the speaker cavity to monitor the performance of the acoustic actuator.

All aspects of the combustor operation and data acquisition are controlled using a 80486-based computer. A multichannel voltmeter is used to measure the pressure signals. A data acquisition board obtains the pressure time series. The control algorithm resides on a digital signal processing (DSP) board (Spectrum Signal Processing) that utilizes a Texas Instruments TMS320C30 chip. The board has a dual-accessible memory that can be read by the main computer without interrupting the DSP chip.

Results

The performance of the acoustic actuator is shown in Fig. 4 for a representative combustor operating condition. The two power spectra represent the combustion pressure fluctuations with and without fixed-frequency spanwise excitation. The spectrum of the unforced case is characterized by large pressure oscillations at ≈40 Hz, ≈75 Hz, and ≈230 Hz. These spikes correspond to the Helmholtz (bulk) mode, quarter-wave ($\lambda/4$) longitudinal mode, and three-quarter-wave ($3\lambda/4$) longitudinal mode, respectively. In this case, a single tone (260 Hz) was used to force the flow. This forcing frequency reduced the magnitude of the bulk and quarter-wave modes by 50%.

Figure 5 shows the open-loop frequency response for the same combustor operating condition. This was obtained by exciting the acoustic actuator with a sinusoid at a fixed frequency and amplitude, measuring the rms pressure fluctuations at that frequency, and then sweeping the effective frequency range. A normalized pressure fluctuation parameter, Sp, is defined to gauge the effectiveness of the spanwise acoustic actuator. Sp is computed by

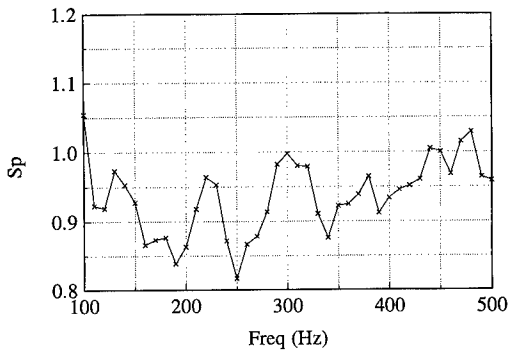

FIG. 5. Open-loop frequency response of the combustor for C_2H_4-air at $\Phi = 0.6$ and inlet velocity $U_0 = 7.5$ m/s.

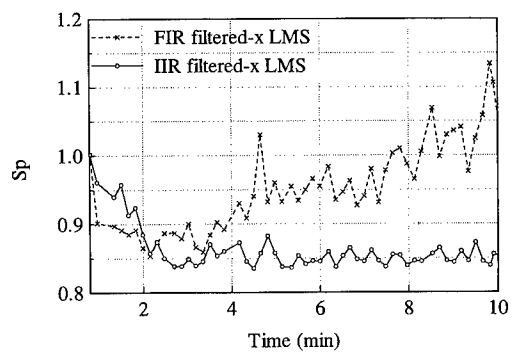

FIG. 6. Closed-loop combustion control experiments using the FIR (-×-) and the constrained-poles IIR (-o-) filtered-$\dot{x}$ LMS architectures. Operating condition: C_2H_4-air, $\Phi = 0.6$, $U_0 = 7.5$ m/s. The number of taps for the filters was 20 and the adaptation constant was 0.001. The rate of coefficient update was 1 kHz. Both architectures achieve about 15% reduction in the normalized rms pressure oscillations.

normalizing the rms pressure fluctuation level with acoustic actuation by its value in the absence of the actuator, at the same combustor operating condition. Thus, the spanwise actuator is beneficial when Sp is below unity, and detrimental when it is above. The passive coupling between the actuator cavity and the combustor acoustics, and forcing at combustor resonant frequencies, can result in values of Sp greater than unity. At the operating condition shown, forcing at 250 Hz produces the maximum reduction of 17% in the normalized rms pressure levels.

The results from a closed-loop, FIR filtered-x LMS, adaptive control experiment are shown in Fig. 6. The combustor was operated at the same conditions as in Fig. 5. The adaptation constant was kept small to reduce the adaptation noise. At the start of the adaptation process, the output of the filter is small, resulting in a value of Sp close to unity. As the

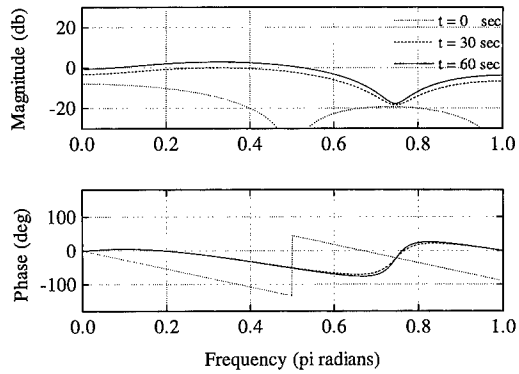

FIG. 7. Magnitude and phase response for the FIR filter structure at three different times during adaptation. The lowest curve in the magnitude plot is at $t = 0$ sec. The middle and top curves are at $t = 30$ s and $t = 60$ s, respectively. The frequency axis is normalized by the sampling frequency. π radians corresponds to the Nyquist frequency which in this case is 500 Hz. The 119-Hz external disturbance is equal to 0.238 π radians. Filter length = 4, $\mu = 0.0001$.

filter proceeds to adapt, the normalized rms pressure fluctuations decrease. The maximum reduction in the normalized rms pressure oscillations obtained during this real-time control experiment was about 15% after 2 min of adaptation. After this point in time, the filter began to systematically diverge until the controller became unstable at around the 10 min point. Multiple experiments were conducted for different values of the algorithm parameters (length and μ). This trend of initial reduction and a subsequent increase in pressure fluctuations was observed in all experiments with the FIR filter architecture.

To study this divergent behavior of the FIR filter structure, no-flow experiments were conducted. In these experiments, one of the fused silica side walls of the combustor was replaced with an audio speaker. This speaker provided a constant, single-tone external disturbance that was picked up by the pressure sensor in the combustor and fed back to the controller. The same hardware configuration was used for the signal conditioning as for combustion experiments. The acoustic actuator was used to minimize the energy of the external disturbance. The weights of the filter were recorded at different times during the adaptation process, and the magnitude and phase responses of the filter were plotted.

Figure 7 shows the magnitude and phase response at three different times during an adaptation event for the FIR filter structure. The external disturbance was a sinusoid (119 Hz, which is 0.238 π radians at the sampling frequency of 1 kHz). The lowest curves in both plots are for the filter at the beginning of adaptation. The middle curve in the magnitude plot shows the response of the filter after 30 s of

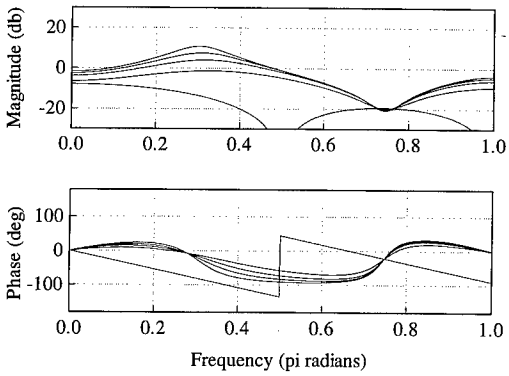

FIG. 8. Magnitude and phase response for the IIR filter structure at five different times during adaptation. Filter length used is the same as for the FIR filter. External disturbance was again 119 Hz or 0.238 π radians.

adaptation. The gain has increased so that at 0.238π radians it is almost unity. This filter weight vector corresponds to a reduction of 40% in the magnitude of the external disturbance. Further adaptation increased the gain of the filter above unity while the phase response stayed the same. This increased the direct acoustic feedback, causing the LMS algorithm to go unstable.

Results with the IIR adaptive filter are shown in Fig. 8. This figure shows the IIR filter response at five different times during an adaptation event with the gain increasing with time. The IIR filter provides more flexibility in designing the response. In this case, the gain was increased substantially above unity without the filter going unstable due to direct acoustic feedback. The reduction in the magnitude of the external disturbance after 3 min of adaptation (with the same adaptation constant) is above 75%.

Discussion

No-flow experiments have indicated that an IIR filter architecture handles direct acoustic feedback better. A set of simulations was carried out to establish that the controller instability was not associated with the LMS algorithm but was an artifact of the way that the feedback loop was closed. In the simulations, the plant was modeled as a pure delay. The same FIR filter architecture was used in the feedback loop as was used in the experiments. The difference was that instead of updating the coefficients of the weight vector using the LMS algorithm, the weights were obtained from a single-tone cancellation experiment and were kept constant during a simulation run.

It was found that the simple model of the plant as pure-delays gives a fairly accurate dynamic response for the pure tone cancellation problems. Using the weight vector obtained after 30 s (Fig. 7), a 40% cancellation was also achieved in the simulation. Using the weights obtained at the time when the controller went unstable in the no-flow experiment also resulted in an unbounded output in the simulations. No such instability was seen when the IIR filter architecture was used in the simulations.

It is confirmed that the problem of direct acoustic feedback driving the algorithm toward instability in the FIR filter structure can be overcome using an IIR structure. Adaptive recursive filters, however, are difficult to implement and have seen limited application. The reason is that during adaptation they move their poles as well as zeros and run a risk of becoming unstable if any of the poles move outside of the unit circle. Recursive adaptive filters are specially prone to this problem when used in noisy plants such as combustion systems. This difficulty occurred when the recursive adaptive filter was applied in combustion experiments. The filter would start to adapt and then suddenly stop, giving very large values for the weights. A pole-zero map of the IIR filter just prior to instability showed zeros outside the unit circle. One way to prevent this instability is to limit the coefficient placement so that no poles ever move out of the unit plane. This was implemented using Laguerre's method of finding the system poles [14]. This method offers good convergence and speed. The control algorithm was updated to keep a check on the pole placement and disallow an update of the weight vectors if the noisy adaptation process tried to place the controller poles outside the stable regime. In no-flow experiments, this strategy was successful, and controller instabilities due to direct acoustic feedback and pole placement outside of the stable regime were not observed. The technique provided similar reduction in the magnitude of the external disturbance as the IIR strategy without the constrained poles. Combustion experiments using the IIR architecture with constrained poles have shown that the technique is successful in maintaining about 15% reduction in the rms pressure oscillations without going unstable for extended periods of time, as shown in Fig. 6.

Summary and Conclusions

An active adaptive control strategy based on the filtered-x LMS algorithm was applied to reduce combustion pressure fluctuations in a laboratory-scale combustor. When configured in the FIR architecture, the controller achieved 15% reduction in the normalized pressure oscillations. The adaptive filter always drove itself toward instability after an initial period of successful adaptation due to direct acoustic feedback from the actuator. No-flow, single-tone cancellation experiments and simulations indicated that the instability lies in the FIR filter

architecture, and not in the LMS algorithm. These experiments showed that recursive filter structures are capable of handling this problem if they can be prevented from placing their poles outside of the stable regime and becoming unstable themselves. This has been implemented by developing a methodology to constrain the pole placement of the IIR filters. The technique was successful in combustion experiments where a 15% reduction in the normalized rms pressure fluctuations was maintained for extended periods of time.

Acknowledgments

The authors acknowledge the assistance of Dr. Krishnan T. Padmanabhan, Prof. Stephen M. Rock, and Frank Levy. This work was supported, in part, by the Office of Naval Research.

REFERENCES

1. Schadow, K. C. and Gutmark, E., AIAA/ASME/SAE/ASEE 25th Joint Propulsion Conference, 1989, AIAA-89-2786.
2. McManus, K. R., Poinsot, T., and Candel, S. M., *Prog. Energy Combust. Sci.* 19(1):1–29 (1993).
3. Padmanabhan, K. T., Bowman, C. T., and Powell, J. D., *Combust. Flame* 100:101–110 (1995).
4. Padmanabhan, K. T., Bowman, C. T., and Powell, J. D., *SPIE's International Symposium on Aerospace/Defense Sensing and Control and Dual-Use Photonics,* 1995, Vol. 2494, pp. 138–149.
5. Padmanabhan, K. T., Bowman, C. T., and Powell, J. D., *IEEE Trans. Control Syst. Technol.* 4:217–229 (1996).
6. Billoud, G., Galland, M. A., Huynh Huu, C., and Candel, S., *Combust. Sci. Technol.* 81:257–283 (1992).
7. Gutmark, E., Wilson, K. J., Schadow, G. C., Parker, B. E., Barron, R. L., and Smith, G. C., 31st Aerospace Sciences Meeting and Exhibit, 1993, AIAA-93-0117.
8. Neumeier, Y. and Zinn, B. T., 4th IEEE Conference on Control Applications, Paper No. 691, 1995.
9. McManus, K. R., Vandsburger, U., and Bowman C. T., *Combust. Flame* 82:75–92 (1990).
10. McManus, K. R. and Bowman, C. T., *Twenty-Third Symposium (International) on Combustion,* The Combustion Institute, Pittsburgh, 1990, pp. 1093–1099.
11. Widrow, B. and Stearns, S. D., *Adaptive Signal Processing,* Prentice-Hall, New Jersey, 1985.
12. Widrow, B. and McCool, J. M., *IEEE Trans. Antennas Propagation* AP-24(5):615–637 (1976).
13. Eriksson, L. J., Allie, M. C., and Greiner, R. A., IEEE Trans. Acoustics Speech *Signal Process* ASSP-35(4):433–437 (1987).
14. Press, W. H., Teukolsky, S. A., Vetterling, W. T., and Flannery, B. P., *Numerical Recipes,* 2nd ed., Cambridge University Press, New York, 1992, pp. 371–374.

COMMENTS

Marc Lange, Heidelberg University, Germany. Did you consider optimizing your control-force not only by minimizing the error-function but by simultaneously changing to the amount of energy which is fed into the control-mechanism? Even if you achieved a satisfactory energy-balance in the presented case, this could be important for the application of your control-scheme to other complex nonlinear systems. An unnecessarily high actuation could lead to an excitation of otherwise slaved modes, resulting in an undesirable behavior of the system.

Author's Reply. We did not optimize for the control force as in our experiment the actuator has to be given maximum power to bring the system out of an unstable regime. This is partly due to the fact that we do not have a very efficient actuator. Very strong actuation can excite stable modes. However as the system approaches stability, the power input to the actuator from the controller is reduced, thus reducing the magnitude of undesired excitation of the stable modes.

•

Thierry Poinsot, IMFT/CERFACS, France. The baseline regime which you used for control studies was a stable regime. Does your system work for unstable regimes?

Author's Reply. This work deals primarily with the development of a stable controller. The controller has been applied to a few unstable operating regimes and it does remain stable. However, the complete performance limitations of the controller have yet to be quantified.

•

Sébastien Candel, Ecole Centrale Paris, France. I was wondering why your controller took so long (about 2 min) to adapt while in our experiments [1], using the same type of methods, we could converge in about 0.1 seconds.

Author's Reply. The method used in our experiments is different from the one mentioned above. We do on-line system identification of the auxiliary path, whereas [1]did the auxiliary path system identification off-line. At this stage of our research we have focused primarily on the stability of this more complex algorithm and hence, the adaptation constant μ was kept deliberately small resulting in slower adaptation. The next set of experiments planned will test the speed of our technique by increasing the adaptation constant.

REFERENCE

1. Billoud, G., Galland, M. A., Huynh Huu, C., and Candel, S., *Combust. Sci. Technol.,* 81:257–283 (1992).

Twenty-Sixth Symposium (International) on Combustion/The Combustion Institute, 1996/pp. 2811–2818

EXPERIMENTAL DEMONSTRATION OF ACTIVE CONTROL OF COMBUSTION INSTABILITIES USING REAL-TIME MODES OBSERVATION AND SECONDARY FUEL INJECTION

Y. NEUMEIER AND BEN. T. ZINN
School of Aerospace Engineering
Georgia Institute of Technology
Atlanta, GA 30332-0150, USA

This paper describes theoretical and experimental investigations of the performance of a novel active control approach that rapidly damps detrimental combustion instabilities. Its main elements are an observer that determines the characteristics of unstable combustor modes in real time and an injector that modulates a secondary fuel injection rate at the unstable modes' frequencies. The controller is guided by Rayleigh's criterion and produces optimum damping when it generates secondary combustion process oscillations within the combustor 180° out of phase with the unstable combustor pressure oscillations. The paper describes developed open-loop approaches that determine the frequency response of the fuel injector actuator and the manner in which these results are incorporated in a closed-loop control mode to effectively and rapidly damp large amplitude rocket motor instabilities.

Introduction

Increased awareness of the potential of active control systems (ACS) to significantly improve the performance of various engineering systems (e.g., engine compressors, structures, materials) has stimulated interest in investigating ACS for controlling detrimental combustion instabilities in, for example, rockets, gas turbines, and ramjets [1–12]. An ACS generally includes sensors that measure system properties, an observer that uses the measured data to determine a full or partial state of the system, a controller that generates control signals for the actuator, and an actuator that modifies the state of the system.

An ideal ACS would "force" the combustor to follow a prescribed time dependence by appropriate modification of its dynamics. If such an ACS is applied to an unstable combustor, none of its modes would oscillate because the combustor would be overdamped at all frequencies. Such an ACS however, requires a full state observer that uses data supplied by sensors to completely describe the state of the system and actuators that can affect each of the observed states. Such an ACS also requires a model that describes the behavior of the controlled combustor including the complex interactions between the flow and combustion process oscillations.

Such full state control of combustion instabilities is presently not possible because models of controlled combustors are not available. Furthermore, since combustion instabilities are governed by partial differential equations, their state has infinite dimensions, requiring many sensors and actuators to attain full state control. (In contrast, a mechanical system that is controlled by a system of ordinary differential equations has a state of finite dimensions.) Since it is unlikely that effective model-based ACS for unstable combustors will be developed soon, this study adopted an alternate control approach. Instead of modifying the basic dynamics of the combustor, instabilities are eliminated by increasing the damping of the system at the frequencies of its unstable, resonant modes. Following Rayleigh's criterion [13], optimal damping of a given mode is attained by producing a periodic heat addition process within the combustor that is 180° out of phase with respect to the mode's pressure fluctuations.

The implementation of this control approach requires an actuator that can produce large amplitude oscillations within the combustor and survive its harsh environment. In this study, a fuel injector actuator that modulates the injection rate of a secondary fuel stream is used to produce a periodic combustion/heat addition process within the combustor. Effective application of this actuator requires knowledge of the frequency dependence of the phase lag (relative to the actuator's input signal) and the amplitude of the generated heat addition oscillations. This information is needed to ensure that at any given frequency the ACS will generate an oscillatory heat addition process of adequate magnitude and out of phase with the unstable mode pressure oscillations. Because of the complexity of the flow and combustion processes that control this secondary combustion process, no transfer function or state model capable of predicting the frequency response of the fuel injector actuator is currently available.

Attempts to resolve this problem included development of approximate descriptions of the frequency response of the actuator around the frequency at which an instability is expected [7] and the use of adaptive filters [8]. Neither can provide a satisfactory solution for multimode instabilities whose frequencies are not known apriori. This problem was resolved in this study by developing an observer that determines the frequencies, amplitudes, and phases of the unstable combustor modes in real time [14]. The effectiveness of this observer and ACS was subsequently demonstrated in numerical simulations [14].

This paper describes the implementation and performance of the investigated ACS on a small-scale gas rocket. Specifically, the paper describes the open-loop determination of the frequency response of the fuel injector actuator, which provides data needed for closed-loop control of combustion instabilities and the manner in which these results are applied by the controller in closed-loop control.

The Observer

This section outlines the operation of the utilized observer, which is a critical element of the developed ACS; for details, the reader is referred to Ref. 14. The observer analyzes the measured pressure to determine in real time the amplitudes, phases, and frequencies of the unstable combustor modes. It assumes that the measured combustor pressure $p(t)$ can be expressed as the following sum of combustor modes, which may not be harmonics of one another and have frequencies, amplitudes, and phases that may vary slowly with time:

$$p(t) = \sum_{n=1}^{n=k} S_n \sin(\omega_n t) + C_n \cos(\omega_n t) \qquad (1)$$

The observer determines the characteristics of the dominant (i.e., largest amplitude) mode by solving the integrals

$$S_n(t) = \frac{2}{T_n}\int_{t-T_n}^{t} \sin(\omega_n t)p(t)dt$$

$$C_n(t) = \frac{2}{T_n}\int_{t-T_n}^{t} \cos(\omega_n t)p(t)dt \qquad (2)$$

where the oscillation period T_n and frequency ω_n are related by $T_n = 2\pi/\omega_n$ and are not known apriori. It can be shown that the given integrals can be replaced by the following recursive formulas:

$$S_n(t + \Delta t) = S_n(t) + \frac{2}{T_n}(p(t + \Delta t) - p(t - T_n + \Delta t))\cdot\sin(\omega_n t)\cdot\Delta t \qquad (3.a)$$

$$C_n(t + \Delta t) = C_n(t) + \frac{2}{T_n}(p(t + \Delta t) - p(t - T_n + \Delta t))\cdot\cos(\omega_n t)\cdot\Delta t \qquad (3.b)$$

whose solution requires little computational effort [14].

The solution starts by assuming a value for ω_n (and, thus, T_n) and substituting T_n into Eqs. (3), which are then solved to determine the "corrected" coefficients of $S_n(t + \Delta t)$ and $C_n(t + \Delta t)$. The calculated coefficients are then substituted into the following relationship [14] that determines a corrected value of the frequency:

$$[(\omega_n)^2]^{t+\Delta t} = \left[\omega_n^2 + \frac{\omega_n\left(\frac{ds_n}{dt}\sin(\omega_n t) + \frac{dc_n}{dt}\cos(\omega_n t)\right)}{S_n\cdot\cos(\omega_n t) - C\cdot\sin(\omega_n t)}\right]^t \qquad (4)$$

where the $\omega_n s$ on the left and right sides are the corrected and previous values of the frequency, respectively. Next, a corrected value of the period T_n is substituted into Eqs. (3) to obtain corrected values of $S_n(t)$ and $C_n(t)$. This procedure is repeated and rapidly converges to the correct values of ω_n, S_n, and C_n, which can be used to determine the amplitude, phase, and frequency of the mode. This procedure can also follow slow variations of these quantities. Upon convergence, the expression describing the time dependence of the dominant mode is subtracted from the measured pressure $p(t)$ and the remaining signal is analyzed to determine the next dominant mode (within the remaining signal) using the previously given procedure. This procedure can be repeated to characterize additional modes. Our studies have also shown that the observer can identify the dominant modes of the instability even when noise is present in the measured signal.

Figures 1a–1e demonstrate the ability of the observer to identify, in real time, the hierarchy of modes in an unstable combustor. The observer was provided with the pressure signal shown in Fig. 1a, which was measured in the unstable gas rocket motor shown in Fig. 2. Figure 1a shows that the instability switches from low-to high-frequency oscillations between 0.05 and 0.064 s. This signal was analyzed by the observer and the computed frequencies and amplitudes were used to determine the time dependence of the two most dominant combustor modes (see Figs. 1b and 1c). Figure 1b shows that the frequency of the nearly sinusoidal dominant mode abruptly increases around 0.065 s to that of the second mode, while Fig. 1c shows that the second mode oscillates with a higher frequency and its amplitude decreases to practically zero around 0.065 s. Figures 1b and 1c also show that the observer can

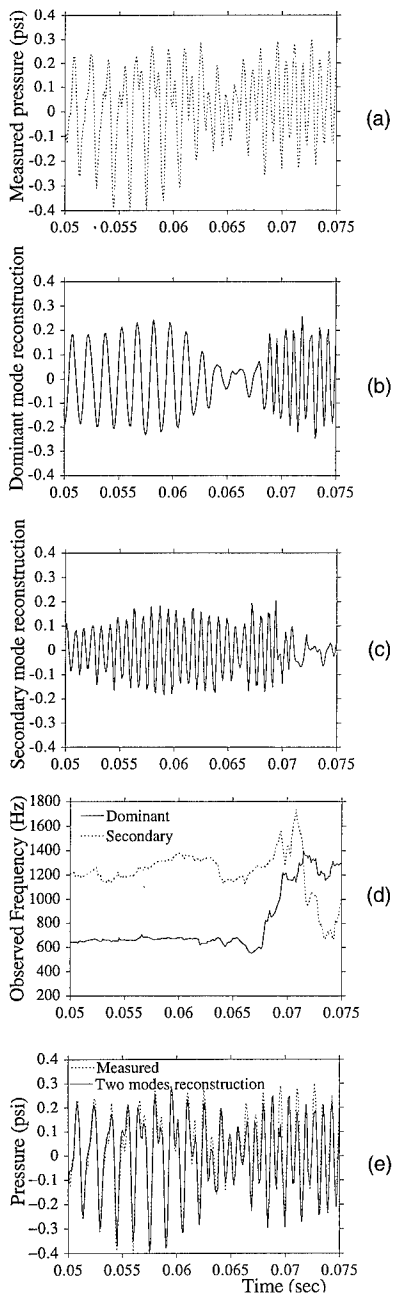

FIG. 1. (a)Time dependence of unstable pressure oscillations in the gas rocket shown in Fig. 2. (b) Time dependence of the dominant mode determined from observed mode characteristics. (c) Time dependence of the "second" mode determined from observed mode characteristics. (d) Observed frequencies of the two modes. (e) Comparison of the measured time dependence of the pressure (see Fig. 1a) with that obtained by synthesizing the two observed modes (see Figs. 1b and 1c).

simultaneously track both modes. Figure 1d presents the calculated time dependence of the frequencies of the two observed modes. It shows that the observed frequency of the dominant mode changed from 650 to 1250 Hz within only 3 ms. Finally, Fig. 1e compares the measured pressure $p(t)$ with that obtained by synthesis of the two observed modes. It clearly shows that the observer can reproduce the input pressure in real time and with high fidelity.

Open-Loop Control Studies

The open- and closed-loop performance of the ACS was studied using the gas rocket shown in Fig. 2. It consists of a reactants' feed system, a water-cooled combustor section with windows for observations and optical diagnostics, a fuel injector actuator, and computers and electronics that support the observer and controller operations. The fuel injector actuator modulates the fuel flow rate by varying the intensity of a magnetic field and, thus, the length of a magnetostrictive rod whose conical termination protrudes into the fuel line. The combustor length can be changed to permit investigation of active control of axial instabilities of different frequencies.

Before attempting closed-loop control of the developed combustor, the performance of the fuel injector actuator was investigated in open-loop tests that determined the amplitudes and phases of the heat release and pressure oscillations generated by modulating the injection rate of the secondary fuel injector over a wide range of frequencies. Since the presence of spontaneously excited instabilities within the combustor could interfere with the open-loop measurements, it was necessary to develop methods for determining the net contribution of a secondary, oscillatory fuel injection to the heat-release oscillations. Two such methods were developed. The first used a very short combustor whose natural fundamental longitudinal acoustic mode frequency was around 1800 Hz, which was significantly above the frequency range investigated in the open-loop studies. Consequently, high-frequency reaction rate and pressure oscillations driven by a combustor instability could be readily distinguished from those driven by the fuel injector actuator.

Using this combustor, the characteristics of the reaction rate and pressure oscillations generated by the fuel injector actuator were determined by a filter-photomultiplier system that measured C_2 radical's radiation from the flame and a pressure transducer, respectively. The C_2 radicals' radiation was measured through a window installed just downstream of the secondary fuel injection point. This window could not, however, view the whole combustion region, thus, preventing accurate determination of the characteristics of the global heat-release oscillations. Consequently, a linear model (described later) of the

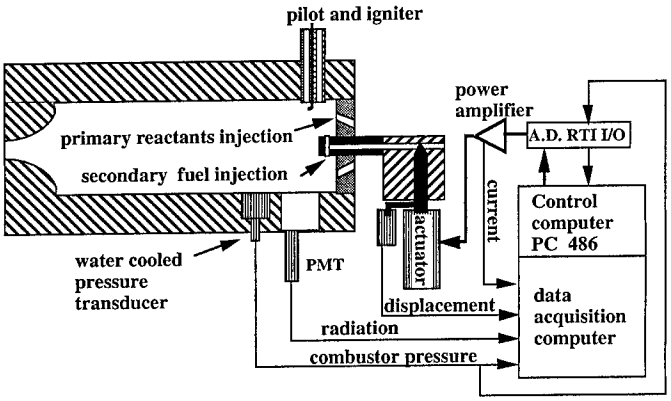

FIG. 2. A schematic of the developed, actively controlled, small-scale gas rocket.

short combustor dynamics was developed and used to determine the amplitude and phase of the generated reaction rate oscillations from the measured pressure data, while the measured C_2 radiation was used to qualitatively evaluate these quantities.

Neglecting kinetic energy terms, the energy equation for a combustor with uniform properties is

$$\frac{d}{dt}\int_V \rho e dV = \dot{q}_{\text{comb.}} + \dot{m}_a h_a + \dot{m}_f h_f - \dot{m}_e h_e \tag{5}$$

where the terms from left to right are the rate of change of the combustor internal energy, oscillatory heat release supplied by the secondary fuel injector, air and fuel enthalpy fluxes into the combustor, and the enthalpy flux exiting through the choked nozzle, respectively. Assuming a perfect gas behavior and that the flow through the nozzle is quasi-steady, the following equations can be derived:

$$\frac{d}{dt}\int_V \rho e dV = (VC_v/R)\frac{dp}{dt};\ \dot{m}_e h_e = (K_N p/\sqrt{T})C_p T \tag{6}$$

Substituting Eqs. (6) into Eq. (5), assuming that each dependent variable consists of a steady component and a small amplitude perturbation (e.g., $p = \bar{p} + p'$) and linearizing the energy equation yields

$$\frac{\dot{q}'}{\bar{\dot{m}}C_p\bar{T}} = \frac{p'}{\bar{p}} + \frac{\tau}{\bar{p}}\frac{dp}{dt} + \frac{T_e'}{2\bar{T}'} \quad \tau = \frac{VT_a\bar{p}}{\bar{T}C_a^2\bar{\dot{m}}'} \tag{7}$$

where τ is a characteristic time, C_a is the speed of sound, and the subscript a denotes the state of the incoming air. Since the temperature perturbations generated within the combustion process are expected to decay before they reach the nozzle entrance at high frequencies, the term involving T_e' is neglected in Eq. (7), yielding a relationship that can be used to determine the heat-release $\dot{q}'$ oscillations from measure pressure p' oscillations at high frequencies.

In the second open-loop investigation, the combustor section was modified to provide means for measuring the total C_2 radicals' flame radiation, thus providing means for direct determination of the global characteristics of the heat-addition oscillations generated by the fuel injector. The modified combustor however, was significantly longer than the compact combustor that was used in the first method. Consequently, the frequencies of several natural acoustic modes of the combustor were included in the investigated frequency range (e.g., the fundamental, longitudinal mode frequency was 375 Hz). Thus, the characteristics of the combustor pressure oscillation depend on the closeness of the fuel modulation frequency to that of one of the natural acoustic modes of the combustor and are affected by the amplitude and phase of the fuel modulation and acoustic properties of the combustor. Therefore, a model that relates a single acoustic pressure measurement to the characteristics of the heat-release oscillations, as was done in the first approach using Eq. (7), cannot be used.

Figure 3 describes the time dependence and spectra of pressure and C_2 radiation signals measured in the long combustor when the secondary fuel stream was modulated at 486 Hz. Figure 3a shows that the time dependence of the pressure is dominated by the 370-Hz oscillation of the unstable combustor modes. The dominance of the acoustic modes at 370 and 740 Hz is apparent in the pressure frequency spectrum (see Fig. 3b), where a smaller but clearly distinguishable contribution of the 486-Hz pressure oscillation excited by the actuator is also present. In contrast to the pressure, the time dependence and spectrum of the measured radiation are dominated by the 486-Hz frequency of the fuel injector actuator. These results show that as long as the frequency of the fuel injector is sufficiently removed from the frequencies of the natural acoustic modes of the combustor, measured flame radiation can be used to determine the characteristics of the oscillatory heat-

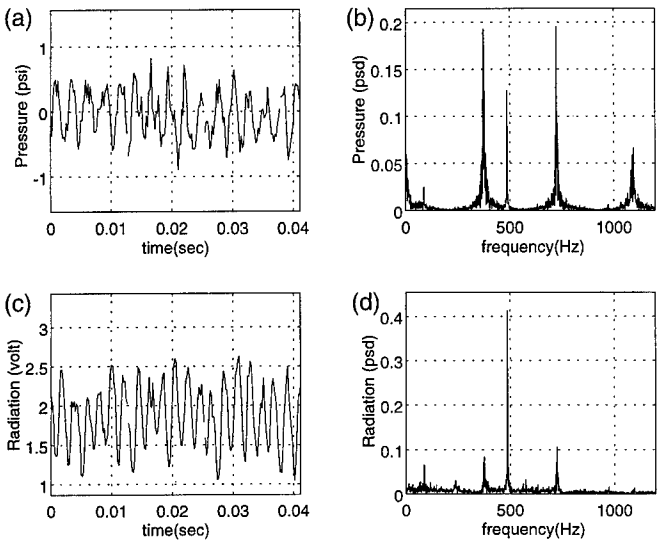

FIG. 3. Time dependence and spectra of the combustor pressure and combustion region C_2 radiation measured in an open-loop experiment.

addition process generated by the fuel injector actuator.

The frequency dependence of the magnitude and phase delay of the heat-release oscillations generated by the fuel injector actuator measured by the two methods are compared in Figs. 4a and 4b. The excellent agreement between these two sets of data that were measured using different approaches in different combustors strongly suggests that the frequency response of the heat-addition oscillations generated by the fuel injector actuator is practically independent of the acoustic field in the combustor. Furthermore, experiments in which the stoichiometry of the primary reactants' stream was changed revealed that the actuator's frequency response does not change significantly as long as the secondary fuel injection can react with available excess air. This is significant because it suggests that the frequency response of the heat-addition process produced by the fuel injector actuator will not have to be determined for each combustor that will use this actuator.

Figures 4a and 4b show that the magnitude and phase lag of the generated heat-addition oscillations monotonically decrease and increase, respectively, as the frequency increases. The monotonic increase of the phase delay with frequency suggests the presence of a pure time delay that is most likely caused by mixing processes. This time delay increases as the slope of the phase lag curve becomes steeper. When the phase lag exceeds 360°, the time delay is longer than the period of the oscillations. Figure 3b indicates that at 800 Hz, for example, the controller should account for a delay larger than one cycle.

Closed-Loop Control

Closed-loop control of the rocket shown in Fig. 2 was investigated using the developed ACS. In these tests, the observer, which was implemented on the 486 processor, identified only one mode. With one mode observation, the control signal to the actuator, y_c, is

$$y_c = G(\omega)\cdot(S\cdot\sin(\omega t + \phi(\omega)) + C\cdot\cos(\omega t + \phi(\omega))) \quad (8)$$

where S, C, and ω are the observed amplitudes and frequency of the dominant mode, while $G(\omega)$ and $\phi(\omega)$ are a gain and a phase that are determined by the controller using tabulated results obtained in the open-loop experiments. Since Fig. 4 shows that the amplitude of the heat-addition oscillations decreases with increasing frequency, the magnitude of $G(\omega)$ should increase with frequency to assure that the ACS generates heat-addition oscillations of adequate magnitude at higher frequencies.

Uncontrolled tests showed that strong instabilities occur near the lean limit. Consequently, we decided to investigate the damping of these instabilities by the ACS (see Fig. 5). These tests were conducted at an equivalence ratio of 0.74, with 20% of the fuel supplied through the fuel injector actuator. As described in Ref. 14, with one mode observation the ACS damps the largest amplitude mode, as determined by the observer, at each instant of time. However, in the example shown in Fig. 5, the ACS controlled only the mode that initially dominated the instability (i.e., 370 Hz). We chose to demonstrate the control of the initially unstable mode only, because the results provide insight into (1) the time required to attenuate large amplitude instabilities, (2) the behavior of the instability during periods in which the dominant mode is damped and the ACS is off, and (3) the manner in which noncontrolled modes are affected by the controller.

In the mode of control shown in Fig. 5, the ob-

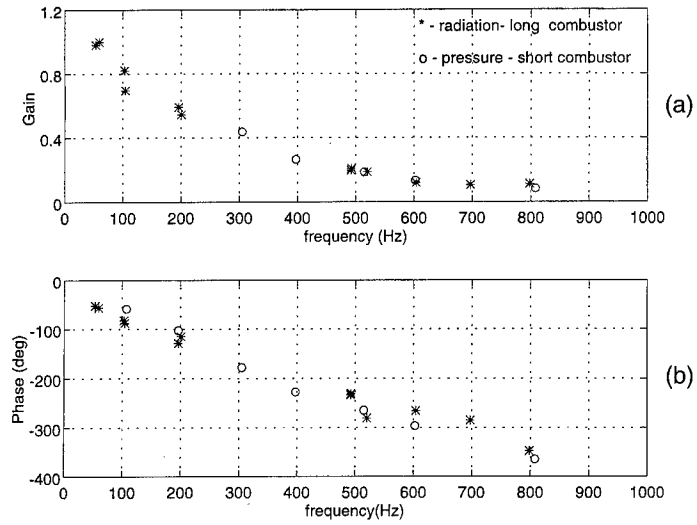

FIG. 4. Comparisons of the frequency dependence of the amplitude and phase of the heat-release oscillations produced by the fuel injector actuator obtained using Eq. (7) and pressure data measured in the short combustor and direct C_2 radiation measurements in the long combustor.

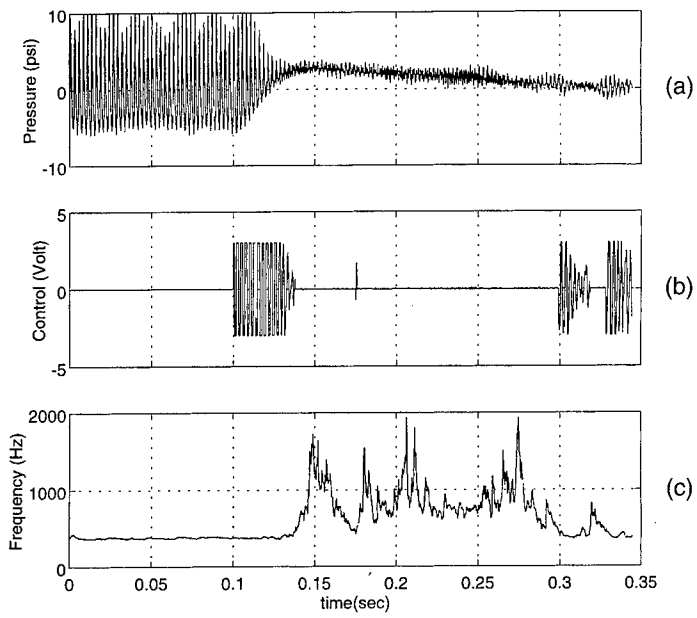

FIG. 5. Time dependence of the pressure, control signal, and observed frequency before and after the activation of a closed-loop control of the instability in a gas rocket (see Fig. 2).

server determines and memorizes the frequency of the initially dominant mode, which, in turn, determines the frequency of the secondary fuel modulation by the actuator. Once this mode is damped and the observer detects a different dominant frequency, the actuator is turned off. Without control, the initially unstable mode starts growing again and becomes dominant. Once the observer recognizes the initial frequency, the actuator is turned on again. This control process repeats itself indefinitely.

Figure 5a shows that the ACS effectively damped the instability in 40 ms, indicating that it could damp rocket instabilities before they seriously damaged the engine and/or caused mission failure. FFT analysis of the combustor pressure oscillations before and after the activation of the ACS showed that the amplitude of the dominating mode was reduced by 26 dB, which exceeds the damping provided by other ACS (see survey of results in Table 1 in Ref. 15). Figure 5b describes the control signal to the actuator, which is proportional to the magnitude of $G(\omega)$ (see Eq. [8]) and, thus, depends on the observed frequency (see Fig. 5c). Figures 5b and 5c show that the control signal goes to zero when the 370-Hz dominant mode is damped by the ACS. When this occurs, the observer identifies the 740-

Hz harmonic as the dominant mode and stops controlling the 370-Hz mode (see Fig. 5b). Consequently, the unstable 370-Hz mode starts growing again. When its amplitude reaches a threshold value, the observer identifies this mode again as the dominant mode and reactivates the actuator. As shown in Figs. 5b and 5c, this sequence of events repeats itself, resulting in effective control of the unstable 370-Hz mode, while not destabilizing other modes of the combustor. As long as the ACS was on, the combustor remained damped and exhibited behavior similar to that shown past $t = 0.15$ ms indefinitely. It is noteworthy that in this experiment and others conducted under this program, the developed ACS did not excite any stable combustor modes.

Conclusion

A novel approach for active control of instabilities has been demonstrated. The unique features of the ACS are (1) a fuel injector actuator capable of generating significant heat-release oscillations within the combustor over a 0–1000 Hz frequency range, (2) an observer that can accurately determine the frequency, amplitude, and phase of several unstable combustor modes, and (3) a control methodology that provides the actuator with a command signal, consisting of a gain and a phase, that properly accounts for the time delay caused by the nonlinear mixing and combustion processes of the secondary fuel. It is believed that once the fuel injector actuator has been scaled up to the required capacity, which needs to be determined, the developed control approach is ready for practical application in a variety of unstable combustors.

Acknowledgments

Research supported by AFOSR Contract No. F49620-93-1-0177; Dr. Mitat Birkan, Contract Monitor.

REFERENCES

1. Lee, Y. C., Gore, M. R., and Ross, C. C., *ARS J.* 23:75 (1953).
2. McManus, K. R., Poinsot, T., and Candel, S. M., *Prog. Energy Combust. Sci.* 19:1–29 (1993).
3. Bloxside, G. J., Dowling, A. P., Hooper, N., and Langhorne, P. J., *AIAA J.* 26:783 (1988).
4. Lang, W., Poinsot, T., and Candel, S., *Combust. Flame* 70:281 (1987).
5. Poinsot, T., Bourienne, F., Candel, S., Esposito, E., and Lang, W., *J. Propulsion Power* 5(1):14 (1987).
6. Poinsot, T., Veynante, D., Bourienne, F., Candel, S., Esposito, E., and Surget, J., "Initiation and Suppression of Combustion Instabilities by Active Control," Proceedings of the *Twenty-Second Symposium (International) on Combustion,* The Combustion Institute, Pittsburgh, 1988, p. 1363.
7. Langhorne, P. J., Dowling, A. P., and Hooper, N., *J. Propulsion Power* 6(3):324 (1990).
8. Billoud, G., Galland, M. A., Huynh Huu, C., and Candel, S., *Combust. Sci. Technol.* 81:257–283 (1992).
9. Gutmark, E., Parr, T. P., Parr, D. M., and Schadow, K. C., The 7th Symposium on Turbulent *Shear Flows,* Stanford University, California, Aug. 1989.
10. Gutmark, E., Wilson, K. J., Parr, T. P., and Schadow, K. C., AIAA Paper 92-0778, 30th Aerospace Sciences, Reno, January, 1992.
11. Gulati, A. and Mani, R., AIAA Paper 90-0270, 28th Aerospace Science Meeting, Reno, 1990.
12. Menon, S. AIAA Paper 90-3930, AIAA 13th Aeroacoustics Conference, Tallahassee, FL, Oct. 1990.
13. Rayleigh, L., *The Theory of Sound,* Dover Pub., New York, 1945.
14. Neumeier, Y. and Zinn, B. T., AIAA Paper 96-0758, 34th Aerospace Sciences Meeting, Reno, January 1996.
15. Sivasegaram, S., Tsai, R. F., and Whitelaw, J. H., *Combust. Sci. Technol.* 105:67–83 (1995).

COMMENTS

Prof. Claudio Bruno, University of Rome, Italy. What was the criterion for choosing the specific type of secondary fuel injection (i.e., radial jets)?

Author's Reply. The paper presented results obtained with radial jets. This configuration was chosen to maximize the effect of the secondary fuel injection, assuming that this geometry brings the injected fuel directly into the combustion zone. The authors are aware that such a configuration is unlikely in a practical combustor. Other configurations in which the secondary fuel is injected upstream the flame holder were also investigated with very good results; see our reference about open-loop tests.

•

Sebastien Candel, Ecole Centrale Paris, France. Is there a relation between your observer and the Prony algorithm of estimating a set of discrete frequencies in a signal?

Author's Reply. Indeed, both the algorithm presented in our paper and Prony's technique are concerned with iden-

tifying unknown frequencies and amplitudes of an oscillating signal (in Prony's technique exponential signal are also considered). However, the solution approaches employed by the two methods are different. Our observations are based upon spectral analysis in which time localization is obtained by adjusting the limits of the Fourier integral, whereas Prony's solution, which is not a spectral estimation technique, is based upon minimization of the following error function:

$$E = \sum_{i=1}^{N} \left(x(i) - \sum_{k=1}^{M} \alpha_k e^{\beta_k t_i} \right)^2$$

where the $x(i)$'s are measured sampled data and α_k and β_k are the parameters to be identified [1,2].

REFERENCES

1. Spyros G. Tzafesta (Ed.), *Applied Control: Current Trends and Modern Methodologies,* Marcel Dekker, Inc.
2. Marple, Jr., S. Lawrence, *Digital Spectral Analysis with Applications,* Prentice-Hall, Inc., New York, 1987.

•

Daniel Hofmann, LTT Erlangen, Germany. While I understand that you were working on a rocket combustor, did you happen to consider the possible emissions that might be perturbed by secondary fuel injection?

Author's Reply. Indeed, since the research was originally oriented to the suppression of detrimental oscillations in rocket motors, the question of NO_x production was not relevant. However, as the developed technique seemed to provide potential benefits to the suppression of pressure noise in lean burning gas turbines, the question of NO_x becomes relevant. It is, nevertheless, believed that since the controller provides injection pulses that become negligibly small once the active control system (ACS) has suppressed the oscillations, the NO_x contributed by the ACS is negligible.

Twenty-Sixth Symposium (International) on Combustion/The Combustion Institute, 1996/pp. 2819–2825

OPTIMIZATION OF GAS TURBINE COMBUSTOR PERFORMANCE THROUGHOUT THE DUTY CYCLE

N. T. DAVIS AND G. S. SAMUELSEN
UCI Combustion Laboratory
University of California
Irvine, CA 92697-3550, USA

A gas turbine combustor must operate over a range of load conditions (duty cycle) in both stationary-power and propulsion applications. With a static geometry combustor, flow splits are fixed between the dome and wall jets, and the performance optimization is either a compromise over a range of loading or possible only at one operating condition. Future designs may be required to adopt variable geometry or alternate flow modification techniques to secure peak performance throughout the duty cycle. To accommodate this variation, a feedback controller will be required. In this paper, an active control methodology is introduced in conjunction with geometric articulation to establish optimal conditions for each load setting throughout a given duty cycle. The algorithm employed is derived from the hill-climbing and downhill simplex methods. This controller successfully identifies the geometric configurations of optimal performance and rapidly selects the optimal operating configuration for all the loads investigated. This controller/combustor combination allows for rapid parametric optimization at each operating condition. In this study, both combustion efficiency and emissions of oxides of nitrogen are optimized. The combustor explored has two distinct response modes. Representative cases, one for each response mode, are illustrated. With the control algorithm used, regions of combustion instability are avoided for all the conditions explored.

Introduction

For future applications in both stationary power and propulsion, a gas turbine combustor must (a) emit a minimum of nitrogen oxides (NO_x) coincident with high combustion efficiency (i.e., low carbon monoxide and hydrocarbons) and (b) achieve this performance over the duty cycle of the engine. A particular challenge is "over the duty cycle of the engine," where optimal performance at each loading requires a different flow distribution [1].

Our study addresses this challenge by introducing and evaluating a special active control methodology in a model research combustor with a controllable flow split between the dome flow, primary jet airflow, and secondary jet airflow. The controllable flow split is achieved by geometric articulation of the effective areas of both the dome and primary jets, and a duty cycle is selected to simulate practical systems.

In commercial gas turbine engines, various methods of geometric articulation are used today. In General Electric LM 6000 engines, for example, concentric rings of premixers allow for parallel staging [2]. Solar Turbines uses a piloted premixed system ($SoLoNO_x$) in which, at low loads, the operation of the engine switches to a distinctly different mode that includes venting surplus combustor air to (a) maintain low CO emissions and (b) expand the envelope for which low NO_x operation is possible [3]. Each of these examples operates (according to public information) using an open-loop control strategy in terms of emissions feedback. An adaptive control approach (closed loop), such as that employed at single operating conditions by Brouwer et al. [4] and Padmanabhan et al. [5], will be required if combustor performance is to be optimized over the conflicting demands of a duty cycle.

Experiment

Combustor

The combustor adopted has a variable geometry design, an approach that (for some time) has been identified to mitigate pollutant emission (e.g., Henderson et al. [6] and Bahr [7]). The variable geometry metallic combustor is shown schematically in Fig. 1. This unit retains the 80-mm inner diameter (D_c) of previous static geometry experiments [8], while incorporating modularity for future studies. The total length of the combustion chamber is $3D_c$. The spacing between the quarl and the primary jets' centerline is D_c, as is the distance between the primary jets' and the secondary jets' centerline. The overall layout was selected to be representative of gas turbine combustor aerodynamics, provide relatively clean boundary conditions, be amenable to active control, and exhibit flexibility for future studies.

Control of the airflow distribution within the

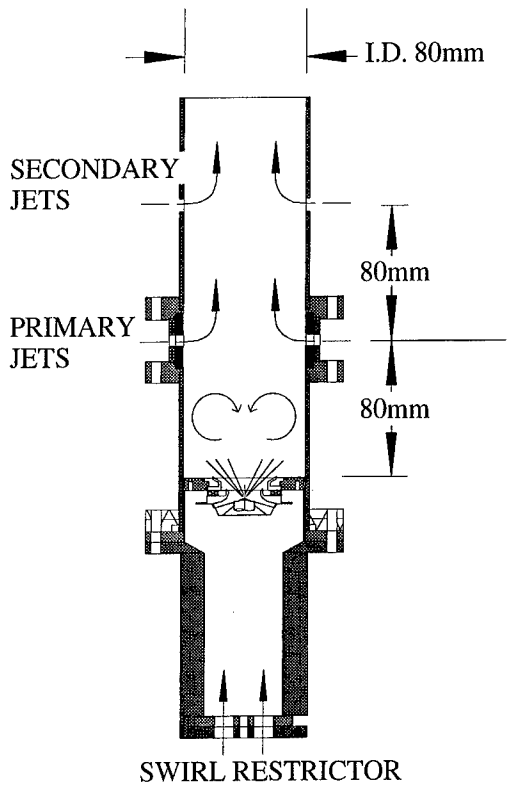

FIG. 1. Combustor, partial assumbly.

combustor allows tuning the operation of the combustor as cycle conditions vary. The unit has two articulators: a swirl flow air restrictor and b a primary airflow restrictor. The primary articulator consists of two concentric rings. By rotating the outer ring, the air distribution is apportioned by the level of overlap in the respective slots.

The swirl articulator consists of two plates drilled with matching sets of three 19-mm diameter holes. The primary jets consist of six slots nominally 8 mm tall and, when fully open, 21 mm wide. The secondary jets consist of six 10.75-mm diameter holes. Overrestriction of the swirl produces a negative effect on the combustor stability and was therefore precluded.

The current study used a production swirl cup from a GE/SNECMA CFM-56-3 gas turbine as the swirler and fuel injector. The selection of this component was predicated by a operating experience within the laboratory [9] and b the advantage of using practical hardware as an integral component of the model combustor. The atomizer component of the swirl cup was a simplex nozzle with a flow number of 1.50.

Duty Cycle

The duty cycle selected for this study is presented in Table 1. The conditions are laboratory representations of a typical operational unit. For the present experiment, pressure was maintained at 1 atm. The fuel used in this study was commercially available Jet A. It was assumed that the flow splits are distributed in relation to the effective area. Four discrete swirl flow settings and six discrete primary jet flow settings were established: The swirl had an effective area of ($\times 10^{-6}$ m^2) 98, 132, 148, and 162; the primary jets ($\times 10^{-6}$ m^2) 0, 92, 184, 367, 550, and 733; the secondary jets had a fixed effective area of ($\times 10^{-6}$ m^2) 487; and the range of airflow distributions were 7% to 28%, 0% to 56%, and 35% to 85% for the swirl, primary, and secondary airflows, respectively.

Emissions Sampling

For this series of experiments, extractive probe measurements were taken. A mixing section commingled the exhaust gas, allowing for one spatial data point to represent the entire reaction. The mixing section consisted of a 0.13-m diameter pipe 0.6 m long with four baffles to promote mixing with the sample taken 0.16 m upstream of the exit.

Four analyzers were used in the closed-loop tests conducted: O_2, CO_2, CO, and NO_x. Information

16TABLE 1
Duty cycle

Condition	Description	Equivalence Ratio φ	Inlet Temp. °C	Reference Velocity m/s	Air kg/s	Fuel kg/s $^{*}10^3$	ΔP %
1	Low Power	0.20	93	10	0.049	0.64	0.7–2.4
2 (Case I)	Med. Power I	0.25	93	12.5	0.061	0.98	1.4–6.3
3 (Case II)	Med. Power II	0.25	204	12.5	0.047	0.64	1.1–5.0
4	High Power	0.30	93	15	0.073	1.40	1.4–6.3

$^{*}U_{ref} = \dot{m}/\rho_3 A_{ref}$ where ρ_3 = density of air entering combustor and A_{ref} = cross sectional area of combustor.

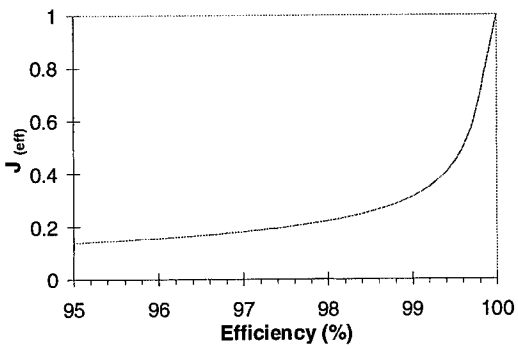

FIG. 2. Cost function for efficiency.

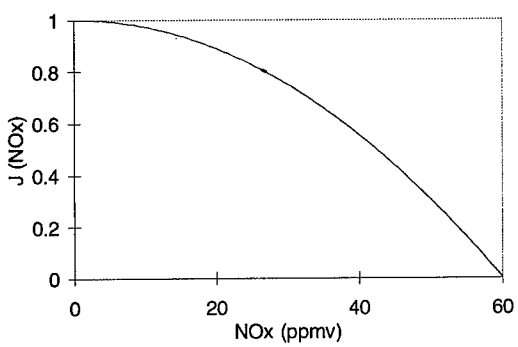

FIG. 3. Cost function for NO_x.

regarding the analyzers is detailed in Davis et al. [1]. Uniformly, the sensors have an accuracy of $\pm 1\%$ full scale, with the lowest possible range used in each case (e.g., NO_x at 100 ppm full scale gives an accuracy of ± 1 ppm).

Cost Function

Since improving combustion performance in one area (e.g., NO reduction) can degrade performance in another (e.g., combustion efficiency), a means of quantifying the trade-off is required. In optimal control, this is accomplished by establishing a mathematical representation of the system value in a cost function, J:

$$J = \omega_{\text{eff}} \circ J_{\text{eff}} + \omega_{\text{NO}_x} \circ J_{\text{NO}_x} \tag{1}$$

By convention, cost functions are normalized to the interval [0,1]. For this series of experiments, combustion efficiency and NO_x were weighted by $\omega_{\text{eff}} = 0.667$ and and $\omega_{\text{NO}_x} = 0.333$. Equal weighting of each would sacrifice efficiency disproportinately. The cost functions for effieciency, (J_{eff}) and NO_x (J_{NO_x}), are presented in Fig. 2 and 3, respectively. Maximizing J optimizes performance.

In selecting the efficiency cost function, the following criteria were satisfied: (a) significant sensitivity in the desired operating range, (b) penalization of poor efficiency, and (c) monotonically increased value as the efficiency improves. A hyperbola was found to suit the requirements. However, to increase sensitivity in poor efficiency regimes, a composite function was formed. As a result, from 99.8% to 100% combustion efficiency, the hyperbola is superseded by a linear function (Fig. 2).

For the NO_x cost function, a proportionally heavier penalty at high emissions is appropriate. At low NO_x levels, changes in the NO_x concentration should incur a small penalty and have a minor gradient. To meet these two criteria, a parabolic function was selected to represent the NO_x cost function (Fig. 3). It should also be noted that shifting the priorities of the cost function will shift the optimal region in an equivalent manner.

Control Algorithm

The algorithm described here is a hybrid that borrows from the hill-climbing and downhill simplex algorithms [10,11]. The hill-climbing technique is fairly simple: pick the steepest gradient and climb it until no more advantage is found and then turn and repeat. The downhill simplex methodology is a three-point–based algorithm that optimizes in the direction opposite of the worst point.

This hybrid algorithm is a three-point method that bases each move on the hill-climbing method, in the direction of steepest ascent, but maintains the triangular base of the simplex method. The step size is a function of cost function (e.g., the controller step size is increased if during operations the performance improves). The direction of optimization is recalculated at each iteration. (Compare this to the hill-climbing strategy, which maintains a direction for several steps.) Figure 4 highlights the operation of the controller. For further detail consult Davis [12].

Each new step results in only a single new analysis of the combustor condition. Because the calculation time is mere milliseconds, it is the number of simplex moves that determine the speed of optimization. The penalty is 45 s for each step.

The controller described herein has several advantages over the previously mentioned techniques. Due to the perspective provided by the simplex, the optimization course is altered at each step. Compare this to the hill-climbing technique in which the controller marches in one direction until no further improvement in that direction is possible. The hill-climbing algorithm is very inefficient for cases in which the controller must continually change directions. Second, the standard downhill simplex will often contract the simplex to such a small footprint that it can fixate on localized peaks. By forcing the simplex in the hybrid algorithm to maintain a

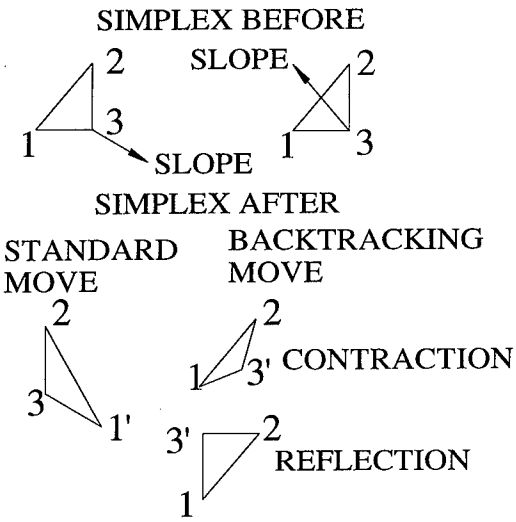

FIG. 4. Operation of the controller, initial "simplex" vs. final move.

minimum size and allowing it to redirect progress to the direction of greatest improvement, this shortcoming is avoided. Third, fewer evaluations are required compared to the downhill simplex method.

Results and Discussion

Overview

Of the conditions considered (Table 1), the results reveal (for this particular combustor and duty cycle) two general response modes: (1) low temperature (low preheat or fuel loading) and (2) high temperature (high preheat and/or high fuel loading). As a result, we direct our discussion to two of the cases. The cases selected are at the same equivalence ratio (0.25) and reference velocity (12.5 m/s). The differing characteristic is the air inlet temperature. Case I is preheated to 93°C (200°F) and Case II to 204°C (400°F). Case 1 had a response typical of the low temperature cases explored. Case II is the high temperature case considered.

The data are presented in Fig. 5. Case I is the left-hand column and Case II occupies the right-hand column. The y-axes in the three-dimensional graphs are the fraction that the primary jets are open (on an area basis). The x-axes show the fractional position of the swirler restrictor.

The first two graphs reveal the efficiency response of the system to geometric variation (*A*) and the resulting NO_x concentration, uncorrected for dilution (*B*). The third figure (*C*) is the cost function plot generated from the efficiency and NO_x profiles and represents the value of the combustor operation. The fourth figure (*D*) is a representative path that the controller takes to optimize the combustor performance.

The effects of a variable geometry approach are complex, because this is not a single input–single output system. Altering the state of either of the two control mechanisms affects several parameters including swirl intensity, pressure drop across the liner, and residence time within the primary and/or secondary regions of the combustor.

Characteristics

The low-power cases (e.g., Case I) tended to have peak operating performance where the primary jets are nearly closed. The higher-power cases (e.g., Case II) tended to have a broad optimal performance plateau with the primary and swirl articulators set to be less restricted.

No case was optimal with the primary open over 0.75. This was due to a reduction in the pressure drop, which destabilized the reaction, produced strong oscillations, and deterred acceptable burning operation (in terms of efficiency and, in some cases, NO_x).

Optimization

The optimization run for Case I was initially an operation in which the primary jets were restricted toward the fully closed position. However, a CO difference just at the sensor noise threshold (30 ppm) diverted the controller to where the swirler was overrestricted. Nevertheless, as can be seen in the figure (left bottom of Fig. 5), the controller successfully located the optimal region.

The hybrid controller, operating without the benefit of a map, established that optimal performance for Case I is associated with the primary jets closed more than originally indicated (verified by postrun analysis). Analysis reveals that the "END" point for Case I (Fig. 5D, left) is just outside of the optimal regime. This exploratory excursion reflects the continuous efforts of the hybrid controller to seek a level of higher performance. (Note: The run was arbitrarily terminated after a preset number of steps.)

The higher temperature case, Case II, experienced a markedly different optimization path. The region of optimal performance was relatively broad. Thus, the controller voyaged over a wider area, often driven by sensor noise. Eventually, the controller found the optimal operating regime where the primary and swirl restrictors were both open near their middle positions (50% open).

Comparison

The optimization for Case I was primarily an efficiency-driven operation. Only where the primary

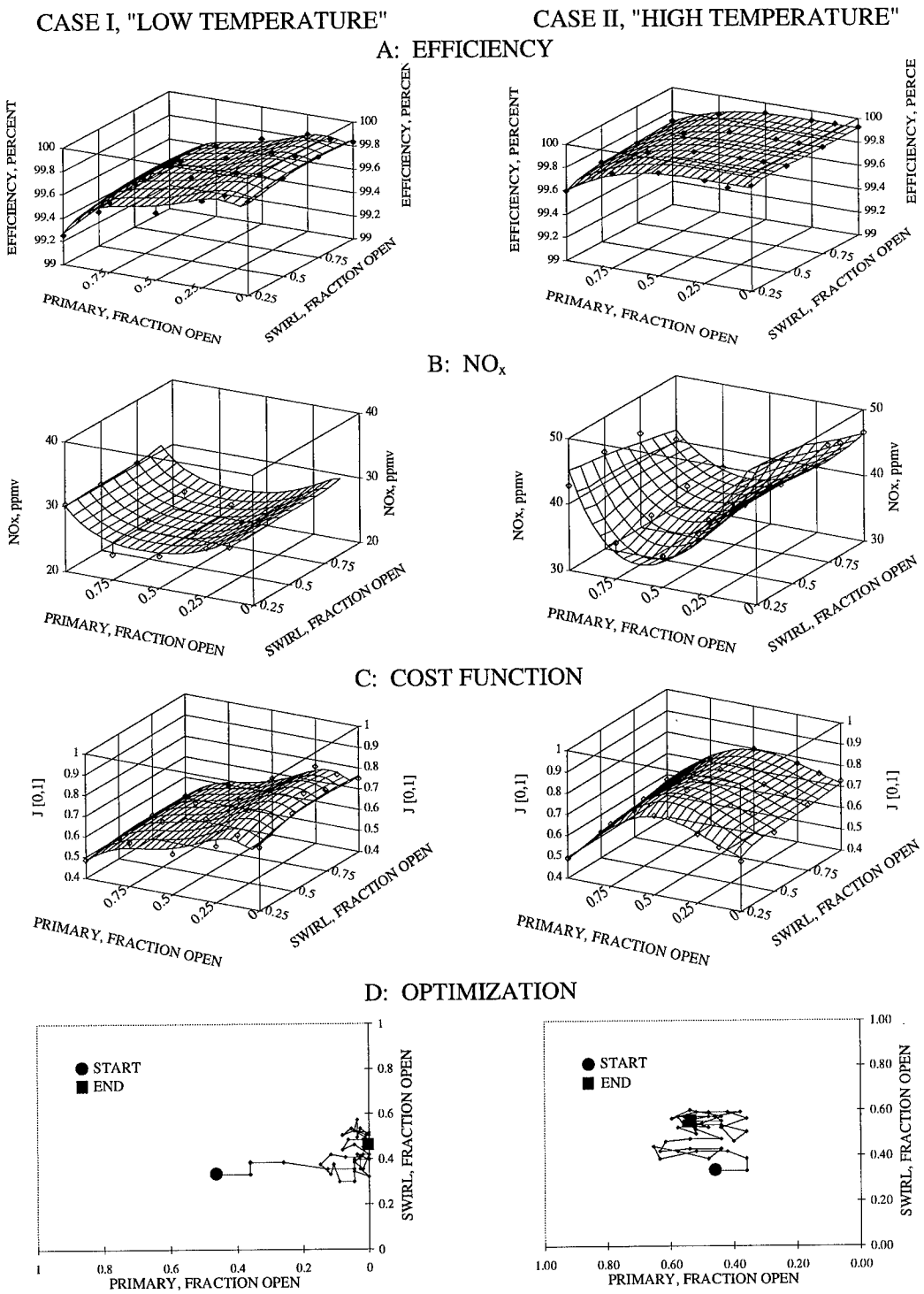

FIG. 5. Optimization results.

jets were fractionally open did the NO_x response drive the optimization. There, a barely perceptible bowing of the NO_x response drove the controller toward the swirler at half its maximum effective area.

Case II has a much broader optimal performance envelope. Within this good performance range, the controller was able to find a region of slightly better performance (3 ppm NO_x improvement). Thus, the controller was able to find improvement over best point in the original mapping. It was found that the primary jets should be slightly further open (50% versus 40%) than the screening tests suggested.

Comparison of the Present Controller to the Downhill Simplex

The difference in performance between the controller developed and presented in the present paper and the downhill simplex used in previous studies (e.g., [5]) would benefit from a test a using an identical system in which a back-to-back comparison was performed and b using a duty cycle, since the downhill simplex has been tested at single loads. This notwithstanding, several generalizations can be made:

1. The traditional downhill simplex should be less sensitive to sensor noise because of the need of the derived algorithm to calculate gradients (versus abandoning the worst point).
2. The present controller did not get "stuck" during any of the optimization runs. Thus, the present controller might prove more robust in conditions when encountering less-than-optimal hills in the response profile. Other combustion optimization studies (e.g., [5]) were forced to periodically restart the downhill simplex algorithm.
3. Overall, the present controller performed well, but less than perfectly. All runs were diverted by sensor noise and were not able to achieve the optimal geometric configuration without a detour.
4. Like the downhill simplex, the present controller employs a marching algorithm (sequential optimization). Thus, it can learn from previous steps versus a converging area search (such as that used by the Monte Carlo method), which would not be precluded from entering an unstable region (e.g., with the primary open >75%).

Summary and Conclusions

Summary

The geometric articulation scheme used in this study provided sufficient response and resolution for the optimization of a broad range of loadings. While each loading required a distinct optimal geometric configuration, the controller successfully optimized for all cases.

Higher-temperature cases possess a broader optimal operating range than the cases with reduced preheat and/or fuel loading. Lower-temperature cases, as per the cost function chosen, were primarily efficiency-driven operations with narrow peak operating regions.

Conclusions

1. The variable geometry mechanism produces a near-monotonical response that is well suited for optimization. For the geometrical manipulation employed in this study, the global peak was readily approachable. This not only simplified the optimization problem but also resulted in the algorithm exploring areas of interest in detail, since it traversed repeatedly the optimal region.
2. Gas turbine combustion is a prime candidate for successive optimal control. Due to stability limits, a random searching algorithm would not have been an acceptable choice because of the possibility of reaction extinction. However, as a result of the well-behaved response from the articulation, a successive optimization controller proved to be a quick and dependable optimization scheme.
3. Certain geometric configurations can be precluded from the control portfolio. In a practical application, it will be justified to preclude the controller from access to specific configurations that are proven to yield degraded performance. Examples in the present case include a to fully close the primary jets and b provide the option to open the primary jets greater than 75%.
4. The hybrid control algorithm proves extremely successful in optimizing the combustor over the duty cycle. The derived algorithm proved efficient in terms of cycles to reach the optimal operating region and effectiveness in reaching the optimal region. It was also able to fine-tune the location of the peak operating regime.
5. Excessive articulation can inhibit stability. Excessive constriction of the swirl airflow and full open primary jet articulation can both destabilize the reaction. In the present case, the controller successfully avoided the regions of instability because the unstable regions coincided with poor combustor operation. A sensor for instability, and the inclusion of instability in the control algorithm, would be prudent for practical applications, particularly where public safety is a factor (e.g., propulsion).

Acknowledgments

The assistance of David Beale in the collection of data is greatly appreciated. The support of the Parker Hannifin

Corporation and the UCI Combustion Laboratory Industrial Consortium is gratefully acknowledged.

REFERENCES

1. Davis, N. T., McDonell, V. G., and Samuelsen, G. S., *J. Eng. Gas Turbines Power,* in press (1996).
2. Leonard, G. and Stegmaier, J., *J. Eng. Gas Turbines Power* 116:542–546 (1994).
3. Etheridge, Colin J., ASME Paper 94-GT-255, 1994.
4. Brouwer, J., Ault, B. A., Bobrow, J. E., and Samuelsen, G. S., *Twenty-Third Symposium (International) on Combustion,* The Combustion Institute, Pittsburgh, 1990, pp. 1087–1092.
5. Padmanabhan, K. T., Bowman C. T., and Powell, J. D., *Twenty-Fifth Symposium (International) on Combustion,* The Combustion Institute, Pittsburgh, 1994.
6. Henderson, Robert E. and Blazowski, William S., AGARD-CP-125 Paper 33, 1973.
7. Bahr, Donald W., AGARD-CP-125 Paper 29, 1973.
8. Cameron, C. D., Brouwer, J., and Samuelsen G. S., *Twenty-Second Symposium (International) on Combustion,* The Combustion Institute, Pittsburgh, 1988, pp. 465–474.
9. Wang, H. Y., McDonell, V. G., Sowa, W. A., and Samuelsen, G. S., *AIAA J. Propulsion Power* 10(4):441–445 (1994).
10. Cooper, L. and Steinberg, D., *Introduction to Methods of Optimization,* W. B. Saunders Company, Philadelphia, 1970.
11. Press, H. W., Saul A. T., Vetterling, W. T., and Flannery, B. P., *Numerical Recipes in C The Art of Scientific Computing,* Cambridge University Press, Cambridge, 1992.
12. Davis, N. T., "Active Duty Cycle Optimization of Gas Turbine Combustor Performance," UCICL-ARTR-95-6, UCI Combustion Laboratory, California, 92717-3550, University of California, Irvine, 1995.

COMMENTS

Prof. Claudio Bruno, University of Rome, Italy. How dependent on the particular shape of the J function is the optimization? Can you quantify this, since J is, to all practical effect, arbitrarily (even though reasonably or plausibly) chosen?

Author's Reply. The design of the cost function (J) is an important engineering consideration. The selection of the weighting functions determine the importance of each variable whereas the component cost functions, J_{eff} and J_{NOx}, determine the shape of the optimization "surface." Altering any element of the function shifts the region of peak performance. Thus, the cost function for any given application will be system and regulation specific.

A quantitative example is to replace the two given cost functions with linear functions over the same intervals as shown Fig. 3 and Fig. 4. Further simplification is to weight both functions equally. Under this scenario, the optimal region for both operating conditions expand. The low power case experiences less aggressive optimization with lower combustion efficiency at the "optimized performance" (and a negligible change in NOx performance). For the high power case, the expansion of the optimal region precludes the controller from attaining improvement in performance from the start point. In summary, by removing engineering and regulatory insight in the specification of the cost function, emissions performance is degraded at all loadings.

•

Mark G. Allen, Physical Sciences Inc., USA. Could you please comment on the practicality and industry acceptance of air dilution jets as control actuators in aeropropulsion gas turbine engines?

Author's Reply. The strategy employed in the present application should be viewed as an air proportioning control that affects mixing for a given load. For other applications, different approaches can be implemented to affect air proportioning without the use of air dilution jets. As in the present case, some form of variable geometry is required.

Industry is receptive to variable geometry if (1) reliability is assured, and (2) the performance gains justify the complexity and associated cost. The first application is expected in stationary units. Application to propulsion units, where safety and reliability require more scrutiny, will likely follow.

Twenty-Sixth Symposium (International) on Combustion/The Combustion Institute, 1996/pp. 2827–2834

SPATIALLY SELECTIVE CHEMISTRY CONTROL IN AN OIL-BURNING FURNACE: A NEW METHOD TO REDUCE NO_x EMISSIONS DEVELOPED THROUGH COMBINED THREE-DIMENSIONAL LASER DIAGNOSTICS

ANDREAS LUCZAK, SEBASTIAN EISENBERG, MICHAEL KNAPP, HARALD SCHLÜTER AND VOLKER BEUSHAUSEN

Laser Laboratorium Göttingen
Hans-Adolf-Krebs Weg 1
37077 Göttingen, Germany

PETER ANDRESEN

University of Bielefeld
Universitätsstrasse 25
33615 Bielefeld, Germany

In contrast to many laser diagnostic activities in combustion that are dealing with more fundamental problems, the results presented here lead to a considerable improvement of combustion in a commercial oil-burning furnace (i.e., to an NO reduction of roughly 50%). New methods are combined to yield a laser diagnostic method that allows a more intelligent design of the fuel/air injection system. Planar laser-induced fluorescence (PLIF) in combination with intensified 12-bit CCD camera technology is used to find positions in the mixing device in which small portions of exhaust gas are guided directly to localized hot areas in the flame where NO formation is highly enhanced to achieve a spatially selective cooling of the flame. All PLIF measurements are carried out by averaging over several hundred laser shots using a pulsed tunable KrF^* excimer laser operating at 248 nm. These averaged data offer the possibility to interpolate between different two-dimensional images to obtain three-dimensional results of the qualitative distribution of OH, pyrolized fuel, and NO. Spatially selective NO-tracer seeding is applied in order to follow the gas flow across the flame front. By pulsing the NO gas tracer the flow velocity is determined.

Introduction

The reduction of NO in oil-burning furnaces is one of the major aims of producers of such devices because emission laws today concentrate on this compound, which is difficult to eliminate. Actually, the development of new combustion devices has reached a level where only a detailed knowledge of the combustion process (this holds, in particular, for the molecular and temperature distributions and the flow field inside the flame) allows a substantial reduction of these emissions. Especially in liquid-fueled spray flames, the combustion depends on many different parameters such as the injection geometry, which influences the efficiency of vaporization and the quality of the turbulent fuel/air mixing process. A well-known method to reduce NO_x emissions is the recirculation of exhaust gas, which reduces the temperature and therefore the NO formation. Unfortunately, the efficiency of this method is limited by the maximal possible quantity of recirculated exhaust gas, since flame instabilities and flame blowout can occur if the burner is operated with too high recirculation rates. In this study, a patented method (German patent # DE 44 16270 A1) to optimize combustion by spatially selective seeding of substances that avoids this problem was succesfully tried for the first time. This method is a new laser diagnostic approach that allows spatially selective control of chemistry in turbulent combustion based on (1) the knowledge of three-dimensional spatial distributions of different species (e.g., fuel, oxygen), which are obtained by LIF and Raman measurements, (2) the influence of injection geometry on the flow field (i.e., the knowledge of the path of the gas from the point of injection through the turbulent flow field, which is visualized using tracer LIF, and (3) local chemistry modification of the flame, by, for example, spatially well-directed injections of fuel, oxygen, or exhaust gas. Because this yields a spatially selective control of chemistry by using a tracer to monitor the flow field, the method is called *tracer-activated chemistry control* (TACC). Here, we report on the application of TACC to reduce NO_x emission in a domestic oil-burning furnace (30 kW).

Despite the experimental difficulties caused by strong interfering emissions of soot, aromatic hydrocarbons, and fuel droplets, selective detection of the

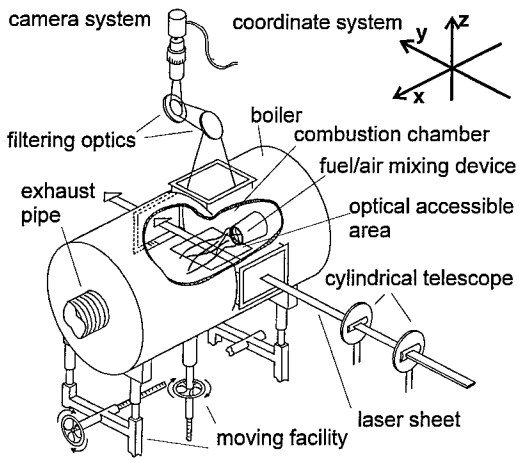

FIG. 1. Schematic diagram of the complete test rig showing the optical arrangement.

species H_2O, O_2, OH, NO, and fuel is possible even in an oil spray flame [1–3]. In this study, the transient reaction intermediate OH and highly excited O_2 ($v = 6$) are detected by laser-induced predissociative fluorescence (LIPF). NO that is formed inside the flame and that seeded as a tracer gas was detected via the $A \leftarrow X$ ($0 \leftarrow 2$)-band laser-induced fluorescence. Besides thermally excited NO ($v'' = 2$) at 248 nm, vibrationally cold NO ($v'' = 0$) was excited with 226 nm laser light. For this purpose, a Raman cell filled with hydrogen was used to convert part of the 248-nm laser light to 226 nm, as described by Dreier et al. [4]. The possibility of detecting NO via the $A \leftarrow X$ ($0 \leftarrow 2$)-band using a KrF laser was described by Frodermann et al. [5]. Examples of NO detection in a combustion engine are given in Refs. 6–8 (detection scheme: $A \leftarrow X$ [$0 \leftarrow 2$]) and 9 and 10 (detection scheme: $A \leftarrow X$ [$0 \leftarrow 0$]). Both detection methods offer the advantage that the usually strong absorption of combustion intermediates that occurs at the short wavelength of ArF* lasers (detection of NO via the D state) inside an oil spray flame [1] is avoided. Nevertheless, it is still possible to detect NO via the D state in domestic gas burners in which the laser absorption is rather low [11]. The strong temperature dependence of the NO LIF intensity with an excitation wavelength of 248 nm usually makes quantitative measurements more difficult. This disadvantage turns into an advantage if NO formation areas should be visualized. Since in boilers the NO is produced mainly by the Zeldovich mechanism [12], NO is predominantly formed in extremely hot areas and the detection of vibrationally excited NO mainly visualizes those areas. On the other hand, the temperature insensitivity of the NO detection at 226 nm proved to be advantageous for the detection of NO seeded as a tracer gas.

All resulting images are averaged over several hundred laser shots. Despite the strong turbulence in the flame, this results in highly reproducible spatial species distributions that depend strongly on the geometry of the fuel/air injection and mixing system [1,2]. The discrimination against broadband emissions from combustion intermediates is achieved by subtracting averaged images with the laser wavelength on and off the relevant molecular resonance [1]. It turned out that because of the highly asymmetric character of the flame, it is not enough to measure only in the central horizontal plane as in previous studies. Instead, three-dimensional distributions were obtained by interpolating between several different cross sections of the flame. It should be emphasized that the averaged data were not quantified, since the qualitative interpretation is sufficient, in the present case, to modify the mixing device and to reduce NO_x emission.

The Raman measurement technique proved to be very worthwhile in obtaining quantitative data in combustion systems (i.e., hydrogen flames) [13,14]. Grünefeld et al. [15] demonstrated that Raman measurements are possible even in hydrocarbon spray flame with strong interfering LIF emissions if polarization features are used appropriately. The concentrations of the majority species and the temperature obtained from Raman measurements inside the burner investigated in this study are given in Ref. 3.

Experimental

The experimental setup with boiler, optical arrangement, laser beam, and camera is shown in Fig. 1. A horizontal spray flame (about 15 cm long) is generated by a fuel/air mix operating at athmosperic pressure with a heat output 24 kW and consisting of a fuel injector nozzle and a baffle plate (ϕ 6 cm) with four radial slits. The burner is fueled with iso-octane instead of heating oil to reduce interfering fluorescence of aromatic hydrocarbons. Previous experiments [16] showed that the use of iso-octane is justified for investigations of basic behavior of the burner. More details of the burner are given in Refs. 2 and 16. The laser light was generated by a tunable pulsed KrF* excimer laser (200 mJ/pulse at 248 nm with a bandwidth of 0.2 cm^{-1} and a pulse duration of 20 ns). The laser beam was spread by cylindrical lenses to a sheet of approximately 10 cm width and 2 mm height. The fluorescence is imaged by an intensified, Peltier-cooled 12-bit CCD camera system (LaVision) equipped with a UV objective (UV Nikkor, 105 mm, f/4.5). To discriminate the laser-induced fluorescence against natural emission of the flame, the opening time of the camera is reduced to 100 ns and is synchronized with the laser pulse. To adjust the section of the flame penetrated by the laser light, the entire combustion chamber, both

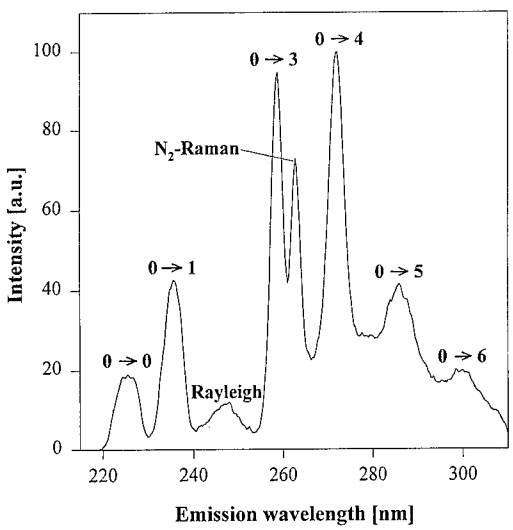

FIG. 2. NO emission spectrum obtained inside the spray flame. The $A^2\Sigma^+ \leftarrow X^2\Pi$ $(0 \leftarrow 2)$ band is excited. Rayleigh and Mie scattered light on the laser wavelength at 248 nm is suppressed using adequate filtering.

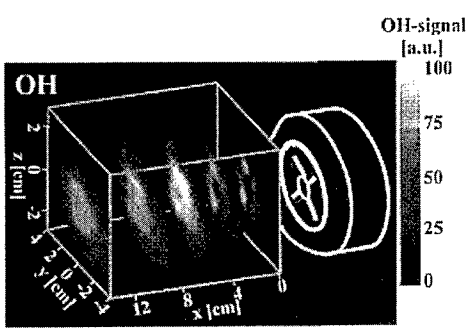

FIG. 3. OH distribution showing different two-dimensional slices in the three-dimensional space. The lowest values are not plotted.

burner and boiler, could be slid horizontally and vertically. By interpolating between the averaged data of two-dimensional images obtained at different positions, a three-dimensional data set was obtained. The data can then be visualized at any cross section through the three-dimensional volume.

The LIPF technique is applied for the detection of the OH molecule. The $A^2\Sigma^+(v' = 3) \leftarrow X^2\Pi(v'' = 0)$ transition was excited via the $P_1(8)$ excitation line. To discriminate against disturbing interfering fluorescence of pyrolized fuel, two dielectric mirrors, centered around 300 nm with a bandwidth of about 20 nm are used for the OH detection and a background substraction is performed by tuning the laser both on and off the excitation resonance of the corresponding species. The images obtained with the laser tuned off resonance yield the distribution of pyrolized fuel [1] and are analyzed here to obtain information about the spray characteristic of the injector nozzle. Experiments showed that the iso-octane itself that was used here yielded no LIF.

Since the $A^2\Sigma^+ \leftarrow X^2\Pi$ $(0 \leftarrow 2)$ band of NO can only be excited with wavelength located at the short wavelength side of the laser's tuning range, the optical components of the laser had to be adjusted very carefully. Detailed information about the excitation of this transition by a KrF^* laser is given in an earlier study [5]. Analyzing the emission spectrum obtained by exciting the $A^2\Sigma^+ \leftarrow X^2\Pi$ $(0 \leftarrow 2)$ band (Fig. 2) shows that almost no interfering emissions are obtained at short wavelength (220–240 nm) compared to long wavelength emissions, which also partly overlap with Raman branches (especially the N_2 branch) and LIPF emissions because of O_2 excited by the broadband part of the laser radiation. Consequently, only the short wavelength emissions were detected using two dielectric mirrors centered around 235 nm with a bandwidth of 20 nm. Because of other interfering light from Rayleigh and Mie scattering, an additional dielectric filter that blocks the laser wavelength was mounted in front of the camera system. While the strong temperature dependence of the $A^2\Sigma^+ \leftarrow X^2\Pi$ $(0 \leftarrow 2)$ transition is more suited to localize hot areas of thermal NO formation, the detection of NO as a tracer gas for flow field visualization is performed via the relatively temperature insensitive $A^2\Sigma^+ \leftarrow X^2\Pi$ $(0 \leftarrow 0)$ transition at 226 nm. For this purpose, the laser beam is focused into a Raman cell filled with H_2 generating several stokes and antistokes Raman emissions. The usable energy of the first antistokes Raman line at 226 nm of approximately 200 μJ proved to be sufficient for the NO detection since the vibrational ground state of NO is strongly populated and therefore the detected flourescence (e.g., $0 \rightarrow 1$, $0 \rightarrow 2$) is strong compared to the broadband emissions. The Rayleigh line was suppressed by a dielectric filter. As described previously, a background substraction was applied. According to an excitation-emission spectrum obtained using a spectrograph in front of the camera system, interfering LIF from hot O_2 could be neglected.

Results

The spatial distributions of different molecules are described by the coordinate system in Fig. 1 with the flame burning in the x-direction. All results are presented in the form of several two-dimensional images in the y-z plane with different distances x from the mixing device according to Fig. 1. The LIF intensity is given as gray values, indicated by the corresponding gray scales given in the images.

OH

The density of the transient intermediate OH is a very good measure for the local reactive activity.

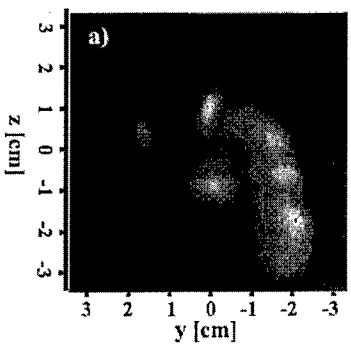

FIG. 4. Two-dimensional image of pyrolized fuel obtained directly behind the mixing device, indicating the spray characteristic of the injector nozzle.

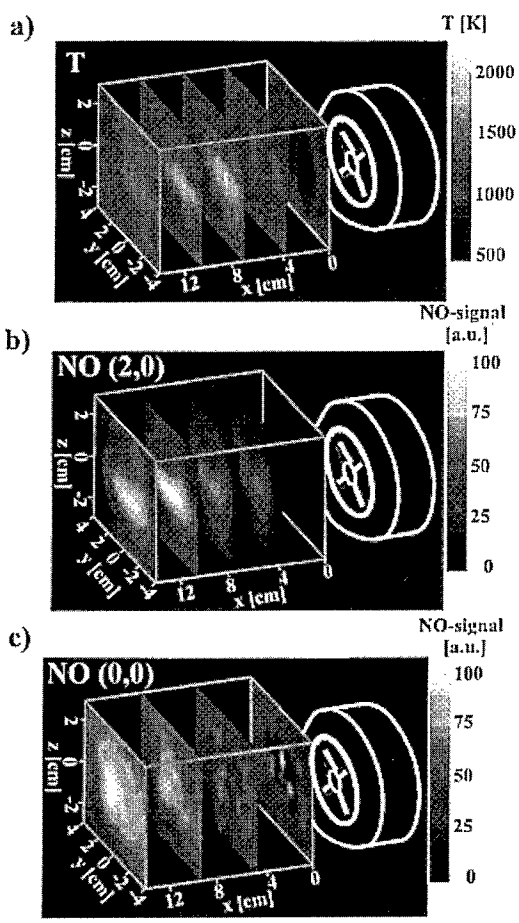

FIG. 5. Comparison of temperature distribution resulting from Raman measurements (a), NO signal resulting from the excitation of the $A^2\Sigma^+ \leftarrow X^2\Pi$ (0 ← 2) band (b), and NO signal obtained by exciting the $A^2\Sigma^+ \leftarrow X^2\Pi$ (0 ← 0) band (c).

Much activity occurs mainly where good mixing of air and fuel took place and produced an ignitable mixture. Since the quality of mixing is largely dependent on the amount of turbulence in the flow, one aim in designing new burners is to generate a reactive flow that is as turbulent as possible. Important auxiliary conditions are, in particular, the avoidance of a stoichiometric fuel-air mixture (NO_x problem) and/or overrich mixtures (soot problem). Figure 3 shows the averaged distribution of OH detected by LIPF. To visualize the area of high reactive activity, only the higher values are plotted. The influence of six mechanical guide braces inside the mixing tube is easy to recognize: The arrangement of these six braces produces a star-shaped combustion structure near the mixing tube ($x \leq 2$ cm) because of improved turbulent mixing of fuel and air. The maximum reactive activity is reached 6 cm behind the mixing tube. The center of combustion is slightly shifted to negative y-values. This can be explained by an asymmetric injection of the fuel (see results of pyrolized fuel in the following section).

Pyrolized Fuel

By tuning the laser off the OH or O_2 resonances, pyrolized fuel is visualized [1]. The resulting image obtained by a two-dimensional measurement inside the flame 2 cm behind the mixing device is shown in Fig. 4. The highly asymmetric structure is caused by the asymmetric spray characteristic of the injector nozzle due to a partial blockage in the spray channel inside the injector nozzle. It can be seen that fuel is not homogeneously distributed over the flame but is injected with the spatial characteristic of several fuel jets.

NO

As mentioned previously, the main NO formation path in oil-burning furnaces is determined by the temperature-sensitive Zeldovich mechanism [12]. This is substantiated by comparing the temperature distribution (obtained via Raman measurements [3]) in Fig. 5a with the NO signal obtained by exciting the $A^2\Sigma^+ \leftarrow X^2\Pi$ (0 ← 2) band in Fig. 5b: The area of high NO formation coincides with the area of high temperature with respect to the y and z values. Note that despite the rotational symmetry of the mixing device, this area is mainly located in the central horizontal plane. Like the OH distribution, it is shifted to negative y values. The distance of the maximal NO formation from the mixing device (x value) is slightly larger than that of the maximum of temperature because thermal NO formation depends not only on temperature but also on the residence time. Since the x direction is the mean flow direction, the residence time increases with increasing x values. At

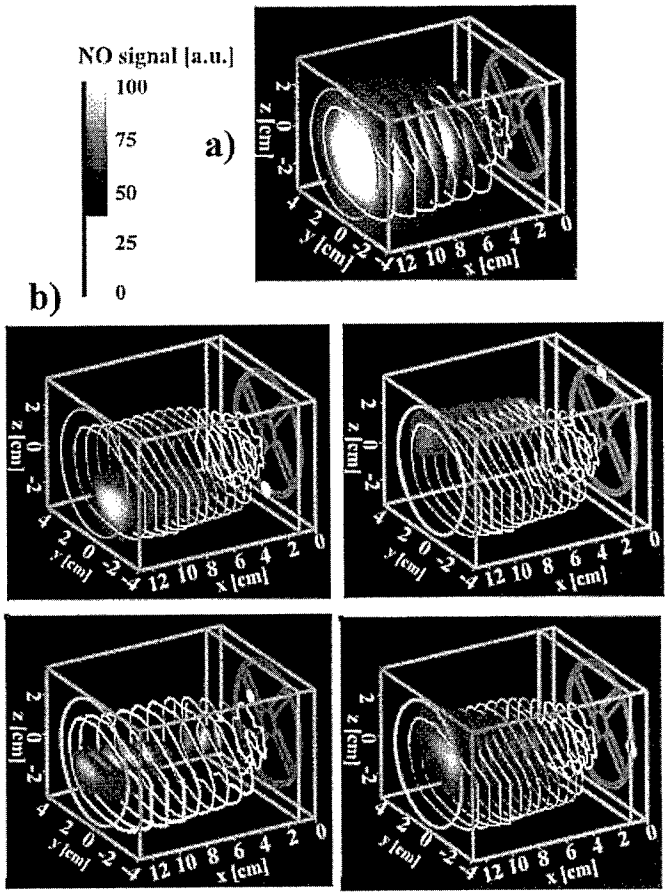

FIG. 6. Distribution of the tracer NO premixed with the combustion air (a) and seeded at different positions indicated by a white circle (b). The white rings mark the outline of high combustion intensity (OH signal).

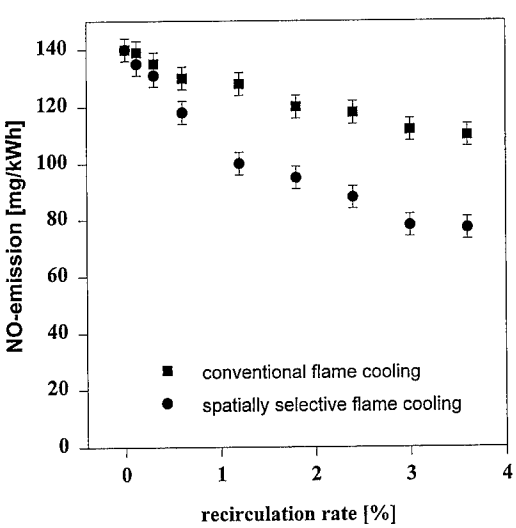

FIG. 7. Dependence of NO emission on recirculation rate. In this study, nitrogen was used instead of exhaust gas.

x values > 10 cm, the NO signal decreases again despite the still-increasing residence time. This can be explained by the detection of vibrationally excited NO ($v'' = 2$). This causes a decreasing NO signal due to decreasing temperature and therefore lower population of the higher-lying quantum states.

If the $A^2\Sigma^+ \leftarrow X^2\Pi$ $(0 \leftarrow 0)$ band of NO is excited by 226 nm laser light, the distribution given in Fig. 5c is obtained. Since the temperature dependence of this excitation is very different because ground state NO is detected, the NO signal also increases with increasing x at x values > 10 cm. In addition, NO is recognizable in the outer region at $x = 0$ cm, which is part of the relatively cool recirculated exhaust gas. The small areas of high NO concentration in the central region at $x = 0$ cm, which cannot be seen in Fig. 5b, presumably originates from the ignition flame that is located directly at the baffle plate. At this position, the NO is quickly cooled by the cold combustion air and the evaporating fuel so that it cannot be detected using the $A^2\Sigma^+ \leftarrow X^2\Pi$ $(0 \leftarrow 2)$ band.

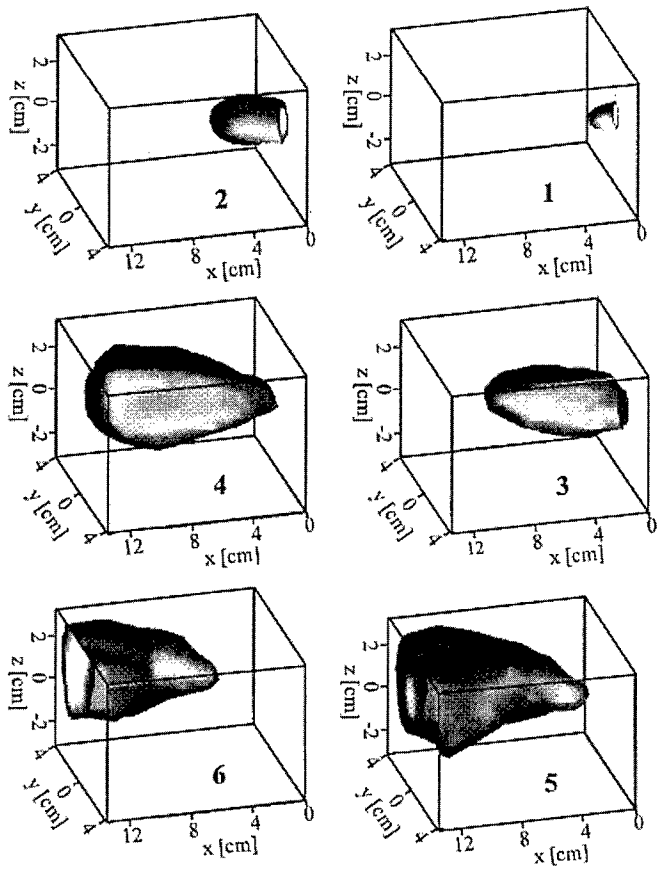

FIG. 8. Sequence of isosurfaces acquired at different time delays after the start of NO tracer gas pulse. The temporal distance between the serially numbered pictures is 3 ms.

Recirculation

Conventional Flame Cooling

A well-known method to reduce NO_x emissions is to recirculate exhaust gas to the combustion air, which reduces combustion intensity and therefore temperature and NO formation. By seeding NO as a tracer to the recirculated exhaust gas and detecting this NO by LIF subsequently in the flame, the exhaust-gas distribution over the flame can be visualized. The signal caused by thermal NO formation is small compared to the tracer NO signal and can be neglected. Figure 6a shows such a distribution of the recirculated gas within the flame when it is mixed with the combustion air without spatial selectivity. The white rings in the figure indicate the area of active combustion obtained from the OH distribution of Fig. 3. It is obvious that only a small fraction of the exhaust gas reaches the hot area of high NO formation, which implies that a large amount of exhaust gas is required to achieve a sufficient NO reduction. On the other hand, a large amount of exhaust gas leads to flame instabilities and finally to flame blow off.

Spatially Selective Flame Cooling

With NO tracer seeding by a small tube (ϕ 1.5 mm) at a well-defined spatial position, it is possible to investigate the flow of exhaust gas through the turbulent flow field. Figure 6b shows how NO is distributed over the flame for different injection positions. The injection position is indicated by a red dot in the figure. Injection of exhaust gas according to the lower right picture of Fig. 6b will mainly reach the hot area in the flame and thus allows selective cooling of the flame in this area of high thermal NO formation (for comparison see the temperature and NO distribution of Fig. 5). LIF measurements of NO at the end of the flame at $x = 12$ cm and a commercial exhaust-measuring instrument showed that NO_x can be reduced with a very low exhaust gas recirculation rate of 6% (excess air: 25 dm^3/min exhaust gas) up to 50% (conventional recirculation: 20%, Fig. 7).

Besides the method described previously, we want to present another laser diagnostic technique that could be useful in improving combustion systems: Using time-resolved tracer LIF, it is possible to trace the trajectory of a short NO tracer gas pulse through

the flame. The position of the pulse inside the flame can be visualized by contouring the NO density at the proper density level to show the surface of the pulse. A sequence of these surfaces with constant density (i.e., isosurfaces) obtained at different time delays after the beginning of the pulse (i.e., the moment of the opening of a solenoid gas valve with an opening time of approximately 5 ms) is given in Fig. 8. The mean velocity of the tracer gas pulse and therefore the flow velocity in this area of the flame was found to be roughly 16 m/s. The results of the time-resolved tracer LIF can be improved easily by using a gas valve with a shorter opening time. With this method, additional information on the characteristic of the flame can be obtained. Therefore, it is possible, for example, to investigate the influence of modifications of the mixing device on the flow velocity in different areas of the flame.

Summary and Conclusions

A patented method to actively control chemistry in turbulent combustion (in this case, to reduce NO_x emission) was successfully tested. The study showed that the method of nonintrusive laser measurement described in this paper is able to provide qualitative information on the distribution of molecular species (OH, fuel, NO) that are important to combustion. A comparison of the measured species distributions obtained by different spectroscopic techniques yields a detailed view of the flow field, combustion, and formation of pollutants (i.e., NO) inside the flame. Localizing areas of high NO formation and applying the tracer gas seeding technique yielded an NO_x reduction by a factor of two by a spatially selective cooling of the flame by exhaust gas recirculation. A simple method to determine flow velocity is used by pulsing the NO gas tracer and detecting NO LIF with temporal resolution. These results showed that laser diagnostics comprise a promising tool to optimize combustion.

REFERENCES

1. Koch, A., Chryssostomou A., Andresen, P., and Bornscheuer, W., *Appl. Phys. B* 56:165–176 (1993).
2. Schmidt, A., Thesis of Diploma, Institut für Strömungsmaschinen der Universität Hannover, 1994.
3. Luczak, A., Eisenberg, S., Schlüter, H., Beushausen, V., and Andresen, P., *Air Pollution and Visibility Measurements,* SPIE Proc. Vol. 2506, SPIE, Washington, D.C., 1995, pp. 121–131.
4. Dreier, T., Dreizler, A., and Wolfrum, J., *Appl. Phys. B* 55:381–387 (1992).
5. Frodermann, M., Doctoral dissertation, University of Bielefeld (Germany), to be published.
6. Knapp, M., Luczak, A. H., Beushausen, V., Hentschel, W., and Andresen, P., *Autotech,* Paper No. C498/15/035, 1995.
7. Knapp, M., Luczak, A., Schlüter, H., Beushausen, V., Hentschel, W., and Andresen, P., accepted for publication in *Appl. Opt.*
8. Knapp, M., Luczak, A., Beushausen, V., Hentschel, W., Manz, P., and Andresen, P., submitted for publication in *Twenty-Sixth Symposium (International) on Combustion,* The Combustion Institute, Pittsburgh, 1996.
9. Bräumer, A., Decker, M., Sick, V., and Wolfrum, J., *Berichte Energie Verfahrenstechnik* 95.2:196–205 (1995).
10. Bräumer, A., Sick, V., Wolfrum, J., Drewes, V., Zahn, M., and Maly, R., SAE Technical Paper Ser. 952462, 119, 1995.
11. Arnold, A., Bräumer, A., Busachmann, A., Decker, M., Dionkelacker, F., Heitzmann, T., Orth, A., Schäfer, M., Sick, V., and Wolfrum, J., *Ber. Bunsenges. Phys. Chem.* 97(12):1650–1661 (1993).
12. Williams, A., *Combustion of Liquid Fuel Sprays,* Butterworths, London, 1990, pp. 141–144, 159.
13. Cheng, T. S., Wehrmeyer, J. A., and Pitz, R. W., *Combust. Flame* 91:323–345 (1992).
14. Grünefeld, G., Beushausen, V., Andresen, P., and Hentschel, W., *Appl. Phys. B* 58:333–342 (1994).
15. Brockhinke, A., Andresen, P., and Kohse-Höinghaus, K., submitted to *Appl. Phys. B.*
16. Beushausen, V., Eisenberg, S., Luczak, A., Schlüter, H., Knapp, M., Andresen, P, Malobabic, M., and Schmidt, A., *Third European Conference on Industrial Furnaces and Boilers,* INFUB, Rio Tinto, Portugal, 1995, pp. 58–66.

COMMENTS

Michael Drake, General Motors R&D, USA. This approach works only if the hot spots remain in the same location over long periods of time and for all operating conditions. Experimentally, do you find this to be true in your furnace?

Author's Reply. The hot spots remained in the same location for several hours of operation of the burner which is normally operated at only one operating condition (= one load). Over longer periods of time this couldn't be checked since we installed a new burner after the experiments were finished.

•

J. Wolfrum, Universität Heidelberg, Germany. Could you determine absolute NO_x concentrations in your experiments?

Author's Reply. For our purpose to visualize areas of high thermal NO formation it was not necessary to determine absolute NO_x concentrations.

Twenty-Sixth Symposium (International) on Combustion/The Combustion Institute, 1996/pp. 2835–2841

ACTIVE INSTABILITY CONTROL WITH DIRECT-DRIVE SERVO VALVES IN LIQUID-FUELED COMBUSTION SYSTEMS

C. HANTSCHK, J. HERMANN AND D. VORTMEYER
Lehrstuhl B für Thermodynamik
Technische Universität München, Germany

Self-excited combustion instabilities originating from a feedback loop between the heat-release rate and the acoustics in the combustion chamber can cause undesirable large pressure fluctuations. One possible approach to attenuate these oscillations is the anticyclical injection of liquid fuel at the frequency of the instability.

Servo valves are possible actuators for this active instability control (AIC). They induce pressure oscillations in the fuel supply system, which lead to the desired modulation of the injected fuel flow rate. The direct-drive valve (DDV) used in this paper is applicable at frequencies of up to 450 Hz.

The pressure modulation with the DDV shows resonance frequencies at which large pressure modulations are induced. For the AIC, the modulation has to take place at the frequency of the combustion instability. Best results can be obtained if the fuel line is tuned so that one of the resonances has the same frequency as the instability to be attenuated.

With the tuned fuel supply system, the efficiency of the AIC with the DDV can be improved considerably. In a liquid-fueled turbulent spray combustor showing a self-excited combustion instability with sound pressure amplitudes reaching 153 dB at the frequency of the instability, the latter could be reduced by 30 dB. For the whole spectrum, the sound level was decreased by 9 dB.

Introduction

Self-excited combustion instabilities are caused by an interaction between the heat-release rate of the flame and the acoustics in the combustion chamber. Fluctuations in the heat release lead to fluctuations of the pressure, thus exciting the acoustics [1–4]. If the Rayleigh criterion [5] is fulfilled, a closed loop with positive feedback is established, resulting in a strong amplification of the pressure amplitudes. This often leads to intolerable high mechanical and thermal loads of the combustion chamber and secondary components [6–8]. The suppression of these oscillations is thus an important task.

Measures for the attenuation of combustion oscillations can be divided into active and passive measures [9]. The latter ones mainly consist of geometrical modifications of the combustion chamber or sound absorbing devices and Helmholtz resonators. Active methods make use of a measured signal, characterizing the pressure- or heat-release oscillation. This signal is suitably phase shifted, amplified, and then transmitted to an actuator device, which causes an anticyclical modulation of one of the relevant quantities in the self-excitation feedback loop, for example, the rate of fuel that is injected [2,9,10].

Besides piezo actuators [11,12], possible devices for modulating the flow rate of the injected fuel in liquid-fueled spray combustors are rapid action valves, for example, servo valves. The disadvantage of conventional servo valves is that, because of their limited frequency response of up to 150 Hz, they can only be applied to controlling low-band combustion instabilities [13]. As will be shown in this paper, modified valves can be applied within a considerably wider frequency range of up to 450 Hz and together with an acoustically modified fuel supply system are important actuators for the active control of self-excited combustion instabilities.

Investigation of the Pressure Modulation by the DDV

The direct-drive valve (DDV) by MOOG-Germany used for the conducted experiments is a valve that has been modified by a number of technical measures. In contrast to customary valves, for which maximum frequency usually does not exceed 150 Hz, the DDV's frequency range reaches up to 450 Hz because of these measures [14]. The spool strikes in both directions from an adjustable neutral position. At a pressure drop of 70 bar, the rated flow of the valve is 0.001 m^3/min. The actual valve fuel flow rate is a function of the spool position, that is, the free cross-sectional area in the valve.

The DDV is equipped with a linear variable differential transformer (LVDT), providing a voltage signal that is linearly proportional to the position of the spool. The measured frequency response curve

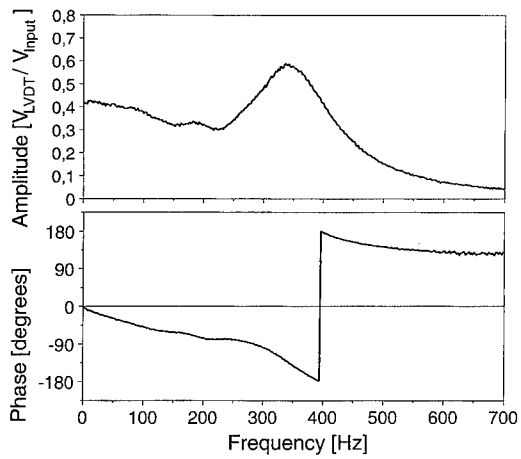

FIG. 1. Measured frequency response curve of the DDV's LVDT signal in relation to the input command signal.

of the DDV's LVDT signal in relation to the input command signal is shown in Fig. 1.

Modulation of the free cross-sectional area leads to a modulation of the fuel mass flow rate $\tilde{\dot{m}}_v(t)$ across the valve, which causes pressure fluctuations in the fuel supply line that are superimposed on the constant pressure $\bar{p}_p$ provided by the pump. These fluctuations generated in the valve excite the acoustics in the fuel line, causing an acoustic pressure field. The amplitudes in this field depend on the frequency of the excitation and are greatest when a resonance frequency in the fuel line is excited. In the static case, the mass flow rate across the injector nozzle $\tilde{\dot{m}}_N(t)$ is proportional to the pressure fluctuation in front of the nozzle $\tilde{p}_N(t)$:

$$\dot{m}_N^2 \propto p_N \text{ or } [\bar{\dot{m}}_N + \tilde{\dot{m}}_N(t)]^2 \propto \bar{p}_N + \tilde{p}_N(t) \quad (1)$$

In our case, Eq. (1) is also valid for the dynamic situation with a fair amount of accuracy, as will be shown later. Because of the importance of the resonances for the AIC, their effect is more closely investigated.

To obtain information about the frequency dependence of the pressure oscillations in front of the nozzle, or in other locations, the transfer function between the LVDT signal of the DDV and the measured pressure signal at the particular location is determined. The DDV is driven by an input voltage from a function generator with an amplitude of 2.5 V. Pressure transducers measure the pressure fluctuations $\tilde{p}_i(t)$ at a location i in the fuel line. The frequency of the input voltage $U_{in}(t)$ is modulated continuously from 0.1 Hz to 700 Hz and the LVDT signal $U_{LVDT}(t)$ and the particular pressure signal $\tilde{p}_i(t)$ at location i are recorded simultaneously. The transfer function $T_i(j\omega)$ is then obtained in dividing the calculated spectrum $\hat{\tilde{p}}_i(j\omega)$ by $\hat{U}_{LVDT}(j\omega)$:

$$T_i(j\omega) = \hat{\tilde{p}}_i(j\omega)/\hat{U}_{LVDT}(j\omega) \quad (2)$$

Averages of M measurements are taken, using the cross and auto power density spectra of the signals [15].

The apparatus used to obtain the transfer function is shown in Fig. 2. It consists of the fuel pump, a pipe L_1 (3000 mm long, inner diameter 6 mm) connecting the pump with the DDV and a second pipe L_2 (2000 mm long, inner diameter 6 mm) from the DDV to the atomizer injector nozzle (2.5 USG 60° by STEINEN). At the pump operating pressure $\bar{p}_p$ of 20 bar, an average fuel mass flow (diesel) of 11.75 kg/h is obtained. The pressure $\tilde{p}_1(t)$ in front of the DDV piston and $\tilde{p}_2(t)$ in front of the atomizer nozzle is measured (see Fig. 2).

The transfer functions $\bar{T}_1(j\omega)$ and $\bar{T}_2(j\omega)$ according to Eq. (2) are shown in Figs. 3a and 3b. (They were obtained without the inserted plenum chamber in Fig. 2.) Only the amplitudes of the transfer functions are shown; the phases are of minor importance here.

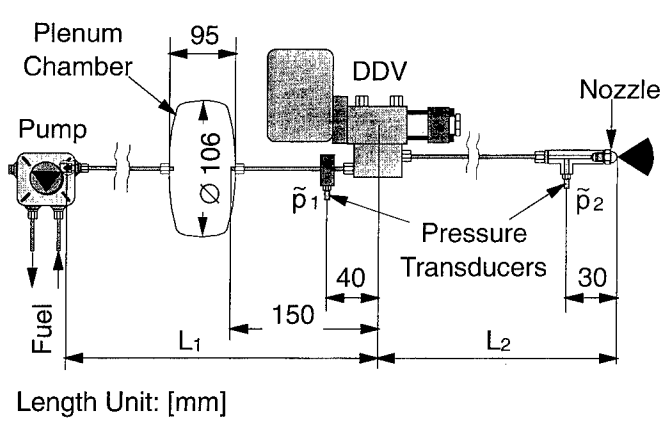

FIG. 2. Experimental setup of the fuel supply system. The inserted plenum chamber is introduced in the experiments described in the section "Acoustic Decoupling" and the following sections.

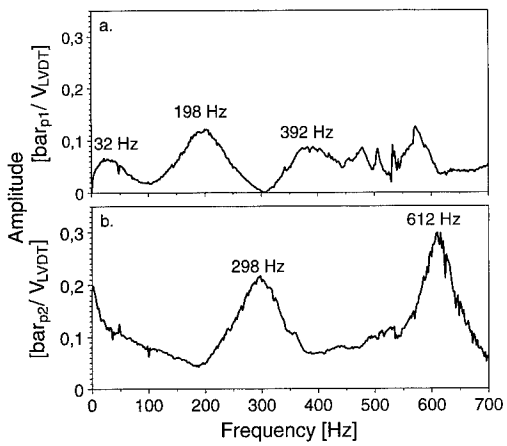

FIG. 3. a. Amplitude of the transfer function $\bar{T}_1(j\omega)$ for the pressure measured in front of the DDV. b. Amplitude of the transfer function $\bar{T}_2(j\omega)$ for the pressure measured in front of the nozzle (pipe length $L_2 = 2$ m).

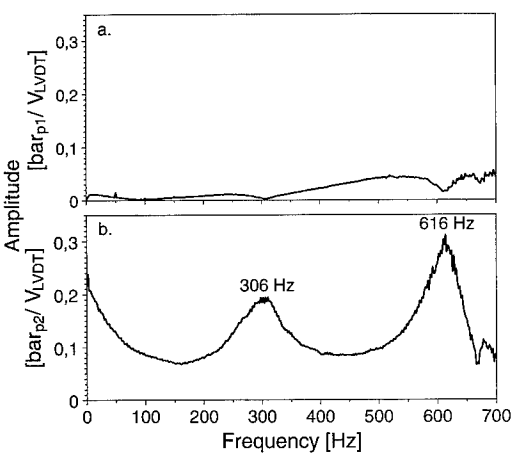

FIG. 4. a. Amplitude of the transfer function $\bar{T}_1(j\omega)$ for the pressure measured in front of the DDV with the plenum chamber inserted in the fuel line. b. Amplitude of the transfer function $\bar{T}_2(j\omega)$ for the pressure in front of the nozzle with the plenum chamber inserted in the fuel line (pipe length $L_2 = 2$ m).

The amplitude of $\bar{T}_1(j\omega)$ shows resonance peaks at 32 Hz, 198 Hz, and 392 Hz. These are the resonance frequencies of pipe L_1 corresponding to its length. $\bar{T}_1(j\omega)$ also shows several peaks between 450 Hz and 600 Hz that probably originate from acoustic influences by the pump. The shape of $\bar{T}_2(j\omega)$ shows two resonance peaks at 298 Hz and 612 Hz, but the influence of the pipe L_1 can be seen: At frequencies that are strongly excited in pipe L_1 (such as the resonance frequencies 32 Hz, 198 Hz, and 392 Hz), the amplitude transfer function $\bar{T}_2(j\omega)$ exhibits significant declines. We therefore suppose that resonances in pipe L_1 tend to decrease the pressure oscillation response to the DDV's acoustic excitation in pipe L_2.

Acoustic Decoupling

An approach to the problem is an acoustic decoupling with the aim to make the acoustics in the two pipes independent of each other. This is achieved by an abrupt widening of the cross section in pipe L_1, in front of the DDV. A cylindrical plenum chamber is inserted into the fuel supply line L_1, separating pump and valve (see Fig. 2). The overall length of pipe L_1 from fuel pump to DDV is then 3196 mm. This plenum chamber drastically reduces the influence of the acoustics in pipe L_1 on those in L_2, as shown in the following experiments. The transfer functions $\bar{T}_1(j\omega)$ and $\bar{T}_2(j\omega)$ under the given conditions are obtained as described previously. They are presented in Figs. 4a and 4b.

The shape of $\bar{T}_2(j\omega)$ in Fig. 4b shows approximately the same resonances as in Fig. 3b. The influence of L_1 on the resonance frequencies in L_2 is small. In contrast to Fig. 3a, the transfer function $\bar{T}_1(j\omega)$ in Fig. 4a reaches only small amplitudes in the considered frequency range and no longer shows the resonance peaks at 32 Hz, 198 Hz, and 392 Hz. According to this, $\bar{T}_2(j\omega)$ in Fig. 4b no longer exhibits the collapses in amplitude at 32 Hz, 198 Hz, and 392 Hz that can still be seen in Fig. 3b. In Fig. 4b, the amplitudes of $\bar{T}_2(j\omega)$ at these frequencies are increased by up to 40%. The tuning for the AIC can now be accomplished by only considering pipe L_2 and without having to take into account the negative effects of other upstream parts of the fuel line.

Tuning of the Fuel Line

To take advantage of the resonance frequencies for the AIC, the length of L_2 must be adjusted such that one of the resonance frequencies of the pipe corresponds to the frequency of the self-excited combustion instability [11,12]. Therefore, first the acoustic boundaries are determined experimentally according to Ref. 12. If the acoustic waves in the pipe are considered as plane waves, they are reflected at the boundaries of L_2 (DDV and nozzle) in a characteristic manner, which can be described by the complex reflection factor $\underline{r}$.

$$\underline{r} = r \cdot e^{j\varphi} = \hat{\underline{p}}_{\text{reflected}}/\hat{\underline{p}}_{\text{incident}} \text{ for } 0 \leq r \leq 1 \quad (3)$$

It consists of an absolute value r and a phase value φ and is defined as the ratio between the complex amplitudes of the reflected wave $\hat{p}_{\text{reflected}}$ and the incident wave $\hat{p}_{\text{incident}}$ at the boundary condition according to Eq. (3). Usually, the reflection factor is frequency dependent.

It can be shown [12] that for a pipe with the nat-

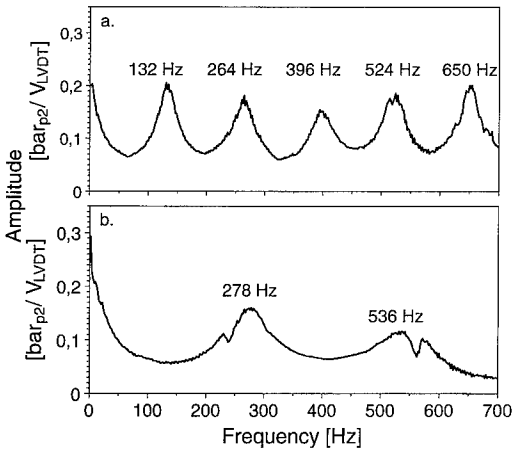

FIG. 5. a. Amplitude of the transfer function $\bar{T}_2(j\omega)$ for the pressure in front of the nozzle with the plenum chamber inserted in the fuel line and a lengthened pipe L_2 = 5 m. b. Amplitude of the transfer function $\bar{T}_2(j\omega)$ for the pressure in front of the nozzle with tuned pipe L_2 = 2.392 m.

ural frequencies $f_1, f_2, \ldots f_n$ and low flow velocities ($Ma \approx 0$), the following equation applies for the frequency-dependent phase values φ_{DDV} and φ_{Nozzle}:

$$\varphi_{DDV}(f_n) + \varphi_{\text{Nozzle}}(f_n) = (f_n \cdot 2L/c - n) \cdot 2\pi = \varphi_\Sigma(f_n) \quad (4)$$

where c stands for the speed of sound in the pipe. φ_Σ denotes the sum of the phase values $\varphi_\Sigma = \varphi_{DDV} + \varphi_{\text{Nozzle}}$.

If the resonance frequencies of a pipe with given length L are known, then for each one a corresponding φ_Σ can be calculated from Eq. (4). These φ_Σ values can be used as interpolation nodes for fitting a function $\varphi_\Sigma(f)$ to them that gives the values of φ_Σ in dependence of frequency. Then φ_Σ can be calculated for the frequency of the self-excited combustion instability and according to Eq. (5), a pipe length L_{tuned} can be calculated that will have this frequency as a resonance frequency:

$$L(f_n) = c/2f_n \cdot [\varphi_\Sigma(f_n)/2\pi + n] \quad \text{for } n = 0, 1, 2, \ldots \quad (5)$$

To determine the unknown quantity φ_Σ, pipe L_2 is lengthened to 5000 mm without altering any other part of the fuel supply system. A longer pipe is favorable because it exhibits more resonances within the considered frequency band so that more interpolation nodes $\varphi_\Sigma(f_n)$ can be calculated with Eq. (4). This improves the accuracy of the function $\varphi_\Sigma(f)$ to be obtained. The pressure transducer for pressure $\tilde{p}_2(t)$ remains in its position just in front of the nozzle. No other pressure needs to be measured.

Again, the transfer function $\bar{T}_2(j\omega)$ between the LVDT signal of the DDV—that excites the acoustics in the system in a continuous sweep from 0.1 Hz to 700 Hz—and the measured pressure signal is determined, where five resonance peaks can be distinguished: f_1 = 132 Hz, f_2 = 264 Hz, f_3 = 396 Hz, f_4 = 524 Hz, and f_5 = 650 Hz, as shown in Fig. 5a.

According to Eq. (4), out of these resonances five values for the frequency-dependent $\varphi_\Sigma(f_n)$ are calculated. To obtain the whole function $\varphi_\Sigma(f)$, a polynomial of the fourth order in f is determined with the five $\varphi_\Sigma(f_n)$ serving as interpolation nodes:

$$\varphi_\Sigma(f) = a \cdot f^4 + b \cdot f^3 + c \cdot f^2 + d \cdot f + e \quad (6)$$

with the coefficients $a = 4.14 \times 10^{-11}$ s^4, $b = -6.91 \times 10^{-8}$ s^3, $c = 3.67 \times 10^{-5}$ s^2, $d = -7.71 \times 10^{-3}$ s, and $e = 5.01 \times 10^{-1}$.

The experimental burner that we will be using to implement and test the AIC with a tuned fuel-supply system exhibits a strong self-excited combustion instability at a frequency of 275 Hz. Therefore, the fuel line—that is, the pipe L_2—will be tuned so that its first natural frequency f_1 equals 275 Hz. With the speed of sound in the fuel of c = 1325 m/s, Eqs. (5) and (6) yield for the necessary length of pipe $L_2(f_1$ = 275 Hz) = 2.392 m.

As the amplitude of $\bar{T}_2(j\omega)$, obtained for the system with the tuned fuel pipe L_2, shows in Fig. 5b, the first resonance frequency of the system at 278 Hz is very close to the desired frequency of 275 Hz.

Heat-Release Rate Modulation

For the AIC, it is important to be able to sufficiently influence the combustion with the DDV. Therefore, we tested whether in the tuned fuel supply line the induced pressure in front of the nozzle indeed causes proportional modulations of the injected fuel flow rate (as in the static case, Eq. 1) and thus a proportional fluctuation of the heat-release rate of the flame.

A liquid fuel (diesel) burner, which was also investigated in Ref. 1, is used at a stable operating point. This burner is equipped with the tuned fuel-supply system (inserted plenum chamber, tuned pipe L_2 = 2.392 m). A modified mixing system (type 1.4) from a MAN-Raketenbrenner, used as a flame holder, separates a prechamber and the actual combustion chamber. With a minimum diameter of 30.5 mm at the flame holder and an average air velocity of 52.5 m/s, a Reynolds number of $Re \approx 120{,}000$ is obtained. The turbulent combustion takes place near stoichiometric standards (ϕ = 0.95) with an average fuel mass flow of 11.75 kg/h caused by an injection pressure $\bar{p}_p$ of 20 bar. This corresponds to a thermal power of about 137 kW.

The heat-release oscillations of the combustion

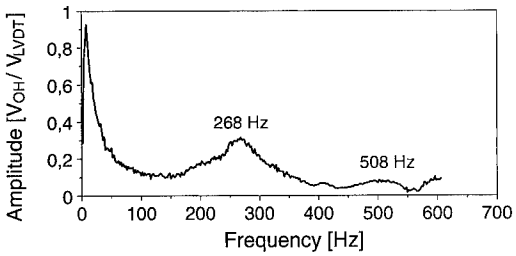

FIG. 6. Amplitude of the transfer function $\bar{T}_{OH}(j\omega)$ for the OH-emission intensity in the burner with tuned pipe $L_2 = 2.392$ m.

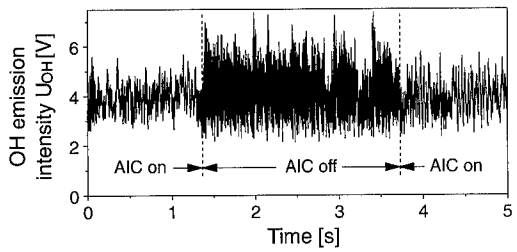

FIG. 8. Measured time signal of the OH-emission intensity in the combustion chamber with the regions marked for the AIC turned on and off.

are considered by measuring the OH-emission intensity at a wavelength of 306.7 nm with a photomultiplier. This emission is fairly proportional to the heat release. The transfer function $\bar{T}_{OH}(j\omega)$ for the OH emission is determined. The result is shown in Fig. 6.

$\bar{T}_{OH}(j\omega)$ is very similar to the transfer function of the pressure in front of the nozzle $\bar{T}_2(j\omega)$ shown in Fig. 5b. At the resonance frequencies of the fuel system, an increased modulation of the OH-emission intensity and therefore also of the heat-release rate of the flame can be obtained—which is crucial for a successful AIC.

Active Combustion Instability Control

The AIC is implemented and tested on the burner. It is identical to the one described in the previous section, but the operating point is changed to $\phi = 1.2$ from $\phi = 0.95$. Under these conditions, the burner exhibits a self-excited combustion instability at a frequency of 275 Hz with a sound pressure of up to 153 dB.

The experimental setup is shown in Fig. 7. A microphone measures the sound pressure in the combustion chamber. After removing the direct current component, this signal is used as the input signal for the controller. The controller consists of a filter, an amplifier, and an analogue phase shifter, where the phase of the signal is adequately shifted for the anticyclical fuel injection. The controller output signal serves as the input signal for the DDV. As before, the heat-release oscillations of the combustion are measured indirectly with a photomultiplier.

Figure 8 shows the measured time signal of the OH-emission intensity with the AIC turned on and

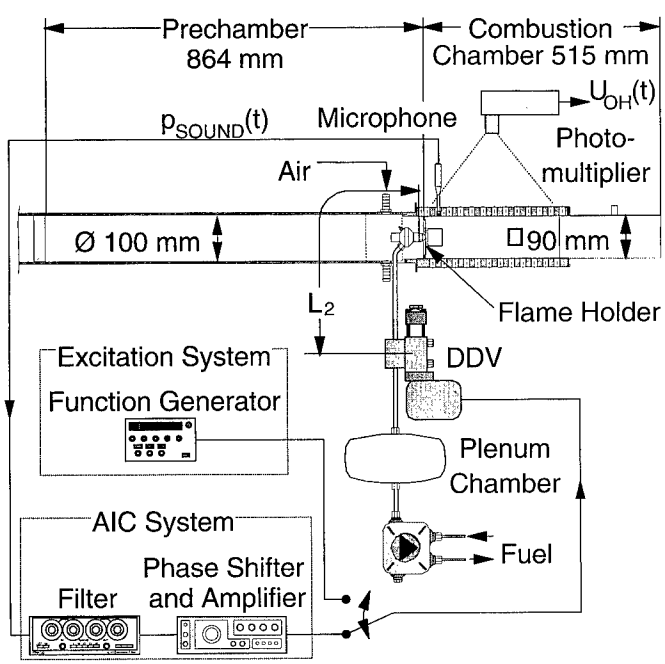

FIG. 7. Measurements on the burner equipped with the tuned fuel supply system. The figure shows the setup for measuring the OH-emission intensity with the DDV excited with the function generator. Furthermore, the configuration for the AIC experiments and related measurements (sound pressure, OH emission) is shown.

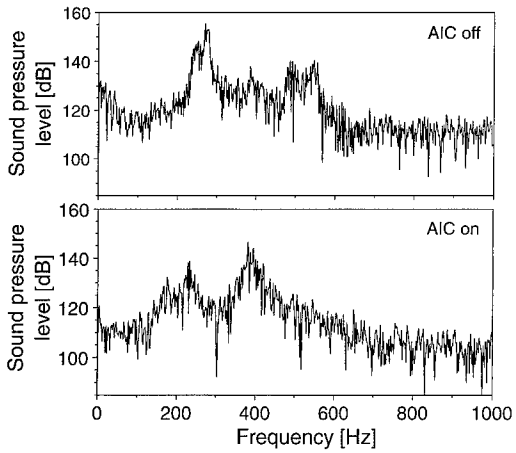

FIG. 9. Frequency analysis of the measured sound pressure: above for a period with the AIC turned off and below for a period with the AIC turned on.

off. The strong damping effect of the AIC on the oscillation of the turbulent combustion is obvious.

The frequency analysis of the measured sound pressure signal is shown in Fig. 9, with the AIC turned on and off. An attenuation of 30 dB at the frequency of 275 Hz of the self-excited combustion instability and 9 dB for the entire spectrum could be accomplished in the turbulent combustion system.

Conclusions

In liquid-fueled burners, servo valves are possible actuators for the AIC of self-excited combustion instabilities by anticyclical injection of fuel at the frequency of the combustion instability. In this paper, we use a modified valve, the DDV, which, compared to customary valves, offers a higher possible frequency range of up to 450 Hz. The modulation of the injected fuel flow rate results from pressure oscillations in the fuel supply system, induced by the DDV.

The amplitudes of this pressure modulation show specific resonance frequencies. At these resonances, the highest modulation of the pressure and thus the injected fuel flow rate can be achieved. For an efficient AIC, it is necessary to tune the fuel line to make one of its resonance frequencies equal to the frequency of the combustion instability that is to be attenuated.

The resonances are governed by the geometry of the pipes leading from the fuel pump to the DDV and from the DDV to the nozzle. They are strongly dependent on each other in their acoustic behavior, which makes the calculation of the necessary modifications for tuning difficult.

A further improvement of the performance of the AIC can be achieved when the influences the two pipes have on each other are reduced by acoustic decoupling. By inserting a plenum chamber in front of the DDV, causing a local abrupt increase in the cross-sectional area of the pipe, the disturbing effects of the upstream parts of the fuel line can be decreased. It is then easier to determine the required length of the pipe to make one of its resonance frequencies equal to the desired one. As shown, the obtainable amplitudes of the injected fuel flow rate can be increased considerably with a tuned fuel supply system.

With the improved ability to modulate the fuel injected into the combustion chamber and thus the heat-release rate in the combustion, the AIC of self-excited combustion instabilities with the DDV becomes more efficient.

REFERENCES

1. Hermann, J., Zangl, P., Gleis, S., and Vortmeyer, D., *17. Deutscher Flammentag,* Hamburg-Harburg, VDI-Bericht Nr. 1193, 1995, pp. 251–260.
2. Candel, S. M., *Twenty-Fourth Symposium (International) On Combustion,* The Combustion Institute, Sydney, 1992, pp. 1277–1296.
3. Poinsot, T. J., Trouve, A. C., Veynante, D. P., Candel, S. M., and Esposito, E. J., *J. Fluid Mech.* 177:265–292 (1987).
4. Putnam, A. A., *Combustion Driven Oscillations in Industry,* Elsevier, New York, 1971.
5. Rayleigh, Lord J. W. S., *The Theory of Sound,* Vol. 2, Dover, New York, 1945, pp. 232–234.
6. Gleis, S., Rau, W., and Vortmeyer, D., *15. Deutscher Flammentag,* Bochum, VDI-Bericht Nr. 922, 1991, pp. 337–347.
7. Preclik, D. and Spagna, P., AGARD Conference Proceedings 450, 1988, pp. 6-1–6-18.
8. Henderson, B. E. and Lewis, J. S., AGARD Conference Proceedings 450, 1988, pp. 3-1–3-8.
9. Culick, F. E. C., AGARD Conference Proceedings 450, 1988, pp. 1-1–1-73.
10. McManus, K. R., Poinsot, T., and Candel, S. M., *Prog. Energy Combust. Sci.* 19:1–29 (1993).
11. Hermann, J., Gleis, S., and Vortmeyer, D., *16. Deutscher Flammentag,* Clausthal, VDI-Bericht Nr. 1090, 1993, pp. 615–624.
12. Hermann, J., Gleis, S., and Vortmeyer, D., accepted for publication in *Combust. Sci. Technol.* 1995.
13. Patentanmelder General Electric, Erfinder Gulati A., Bigelow, E. C., *Aktive Regelung von durch Verbrennung hervorgerufenen Instabilitäten,* Offenlegungsschrift DE 40 40 745 A1, 1990.
14. Teutsch, H., *Ölhydraulik und Pneumatik,* 34, Nr. 11, pp. 754–761, 1990.
15. Bendat, J. S. and Piersol, A. G., *Engineering Applications of Correlation and Spectral Analysis,* Wiley, New York, 1976.

COMMENTS

Abid Kemal, Stanford University, USA. What is the convective time delay between the valve and the nozzle? Is it possible to reduce it, as large time delays are difficult to incorporate in control systems?

Author's Reply. With diesel oil as fuel, a mass flow rate of 11.75 kg/h and a length and inner diameter of the pipe between valve and nozzle of 2.392 m and 6 mm respectively, it takes the fuel about 17 seconds to flow from the valve to the nozzle. This is however not the time delay that is relevant for the controller. The velocity of sound in the fuel determines the time it takes for the pressure modulation at the nozzle to build up. It takes about 1.8 milliseconds for a pressure wave to travel from the valve to the nozzle. This is about half of the period of the oscillation at 275 Hz. Furthermore additional delays in the control loop, resulting from different effects in the whole system exist. One would therefore expect severe stability problems for the control. The fact that the self-excited oscillations in our burner are strictly periodical and that their frequency does not change significantly is the main reason why the simple controller that we have used works in spite of the long time delays.

Generally the pipe to the nozzle should be as short as possible especially because long pipes introduce additional damping of the pressure modulations. The ideal tuning pipe length is always zero but this is usually impossible. This was also the case with our laboratory burner where we could not reduce the pipe length any further—i.e., tune it to a lower harmonic—because of the geometry.

•

K. R. Ehrhardt, University of Karlsruhe, Germany. Is the frequency of flame oscillations a function of thermal load/fuel flow? If this is the case, is the control system also able to dampen other frequencies than being tuned for?

Author's Reply. The frequency of the oscillations is basically a function of the geometry of the burner, as the oscillations usually occur at or close to one of the natural frequencies of the burner. Changes of the thermal load or the fuel flow rate can influence the oscillation frequency if they have an impact on these natural frequencies. This can, e.g., be the case if the temperature field and with it the sound velocity in the burner changes significantly. Furthermore it must be noted, that it is strongly dependent on the equivalence ratio whether or not oscillations occur at all. These are often limited to a narrow range of possible equivalence ratios and changes in the fuel or air flow can lead to the onset or disappearance of oscillations.

The AIC system described here will show its optimum performance at the frequency it was tuned for. Usually the pressure resonance peaks in the fuel system are not very "sharp" and so small changes in the frequency will not lead to a significant loss in the performance. If more than one frequency is to be controlled the tuning has to be optimized for these frequencies as far as possible. The result will be a compromise because usually the modulations that can then be obtained for each of the frequencies will be less than for a system tuned especially for this frequency alone.

•

Neil T. Davis, University of California, Irvine, USA. Which parameters did the controller articulate (phase shift, frequency, amplitude, etc.)? Was the controller adaptive (feedback)?

Author's Reply. The controller filtered the measured sound pressure (low-pass, 0–800 Hz), phase-shifted and amplified it and added an offset. The values for amplification, offset and phase shift were determined empirically according to the best obtainable performance of the system.

The control loop is closed via the feedback of the sound pressure in the combustion chamber. However the controller is not adaptive concerning the parameters gain, offset and phase-shift. These are fixed and can only be altered manually.

Twenty-Sixth Symposium (International) on Combustion/The Combustion Institute, 1996/pp. 2843–2850

ACTIVE CONTROL OF LIQUID-FUELED COMBUSTION USING PERIODIC VORTEX-DROPLET INTERACTION

K. H. YU, T. P. PARR, K. J. WILSON, K. C. SCHADOW AND E. J. GUTMARK*

Research and Technology Division
Naval Air Warfare Center Weapons Division
China Lake, CA, 93555, USA

Pulsating liquid-fuel sprays from automotive fuel injectors were characterized and analyzed in nonreacting and reacting experiments to develop active combustion control using liquid-fuel injection. Square waves with variable duty cycle were used as an input signal for injector operation. Using ethanol pressurized to 275 kPa, pulsating injection with 100% flux modulation was achieved at frequencies as high as 1 kHz. Spray size and spatial distributions were measured from instantaneous Mie scattering images. The results showed that the pulsating sprays contained a high number of relatively large droplets that would be unfavorable for direct combustion control applications. A dump combustor experiment using these injectors showed very little dependence on phase of fuel injection. To reduce droplet size, a new injection setup was designed by combining a fuel injector with a swirl-based atomizer. In the new setup, the fuel injector functions only as a solenoid valve with high-frequency response, whereas the atomizer is used to reduce droplet size. A substantial reduction in droplet size was obtained while maintaining a similar frequency response. Using the improved injection setup, nonreacting experiments were performed in an actively controlled dump combustor to characterize spatial distribution of fuel droplets as a function of control parameters. Fuel injection was synchronized with different stages of air vortex development, and the interaction between spray droplets and large-scale flow features was investigated systematically. The results showed that the synchronized injection yielded an effective way of controlling the spatial distribution of fuel droplets in the dump combustor flow field. Finally, a reacting experiment showed that combustor controllability was significantly extended. The results open up the possibility of actively controlling liquid-fueled combustion in other practical combustors.

Introduction

Typical active control strategies for suppressing combustion instabilities are based on out-of-phase combustion-acoustic coupling [1,2] that results in reduction of acoustic energy density via the Rayleigh effect [3]. Typically, only a small amount of total fuel flow is modulated in such a way that the resulting heat-release oscillations occur out of phase with respect to the pressure oscillations. In gaseous fueled combustors, acoustic forcing can be used to control mixing between fuel and air [4]. For instance, many compression drivers such as loudspeakers have good frequency response in the frequency range of interest (100 ~ 1000 Hz) and have been used quite effectively in many active control experiments [5–7]. The acoustic compression drivers work in a gas delivery system by setting up high-amplitude velocity oscillations, but they are virtually ineffective in modulating liquid flow. The lack of proper actuators has made it difficult to extend active combustion control to a liquid-fueled system.

The present work is motivated by the desire to develop an effective active combustion control for liquid-fueled devices. Active combustion control may be run either open [8] or closed loop [9–11]. In either mode, actuator is a key element of the system architecture. Because of the coupled nature of ducted flames [12–14], an ideal actuator must control the rate of fuel supply and also affect the manner in which fuel-air mixing takes place. When considering a possible actuator for liquid-fuel injection, there were three main concerns. First, a pulsating injection of liquid fuel at fairly high frequencies was needed for practical reasons. Second, the actuator should put out enough volume flow rate to be useful in combustion applications. Finally, the droplet size needed to be sufficiently small for fast combustion response required in an in situ–type controller.

The concern on volume flow rate excluded many high-frequency injectors that have good frequency response but extremely low flow rate, such as ultrasonic injectors and other miniaturized injectors using microheating elements. Electromechanical injectors based on solenoid provided high flow rate, but their frequency response was generally low. One noticeable exception was automotive fuel injectors,

*Present address: Chairman, Mechanical Engineering Dept., LSU, Baton Rouge, LA 70803.

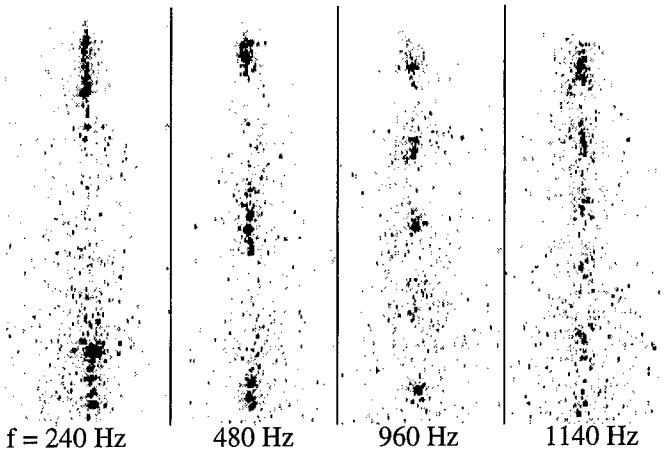

FIG. 1. Instantaneous planar Mie-scattering images of pulsating injection from an automotive fuel injector driven at various frequencies. The injection is from top to bottom. ΔP_{inj} = 275 kPa, duty cycle = 50%.

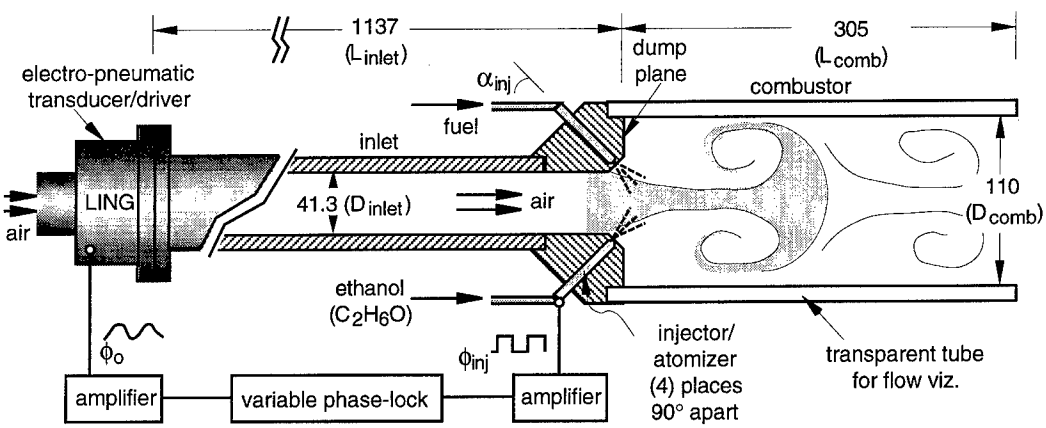

FIG. 2. Axisymmetric dump combustor using liquid-fuel injection and the schematics of controller (all dimensions in mm).

whose frequency response could be extended with a properly designed electronic control unit (ECU) [15]. A customized square wave input was used for ECU, making pulsed injection at high frequencies possible [16].

To transform pulsed fuel sprays into the corresponding oscillations in local heat release, spatial distribution of fuel droplets needs to be controlled. One possible way to control droplet spatial distribution in dump combustors is to use the interaction between droplets and vortical features in the flow. Liquid-fuel injection may be synchronized at various stages of vortex development, changing the degree of interaction with the vortex structures and thereby achieving spatial separation between groups of fuel droplets. This methodology was examined in this paper using extensive flow visualizations. For this approach to work properly, the injection must be pulsated at high enough frequencies to be synchronized with the vortex structures. Furthermore, the droplet size must be small enough for proper interaction with the flow features and also to maintain fast combustion response. While it is not difficult to achieve one or the other, satisfying both conditions required some modifications in available actuators.

Pulsating Liquid-Fuel Injection

Several automotive fuel injectors that work with electromechanically driven pintles were considered as a means to produce periodic fuel injection. A square wave with adjustable duty cycle was used for the injector ECU signal extending the frequency response. Figure 1 shows a series of pulsating ethanol injection from a fuel injector (Bosch Jetronics) that was driven at different frequencies with customized square waves. The images were obtained by illuminating the droplets with a pulsed laser sheet (20 ns pulse width) that traversed along the center axis of

FIG. 3. Natural light view of the dump-combustor flames sustained with pulsating injection using automotive fuel injectors. The dark curved lines in the flame image are actually stains on the window caused by poor combustion of fuel.

TABLE 1
Summary of operating conditions

Mean inlet velocity	12.5 m/s
Mean fuel flow rate/each injector	0.65 ~ 0.80 ml/s
Fuel injection velocity	0 ~ 20 m/s
Frequency of injection and forcing	120 ~ 360 Hz
Phase of injection wrt. vortex formation	0°, 90°, 180°, 270° deg
Combustor height (D_{comb}/D_{inlet})	2.66, ∞ (free jet)
Combustor length (L_{comb}/D_{comb})	2.4

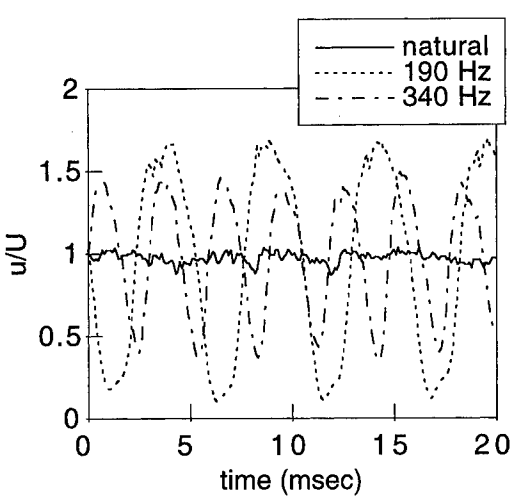

FIG. 4. Typical centerline velocity of the inlet jet at the dump plane.

the pulsating jet. They show clearly the fuel modulation at high frequencies and the extent of spatial modulation that could be obtained downstream.

Using selected automotive injectors that yielded the smallest droplet sizes, a dump combustor experiment was carried out. Figure 2 shows the experimental apparatus, which consisted of an axisymmetric dump combustor fitted with four liquid-fuel injectors that were mounted along the circumference of the inlet exit at the dump plane. The injectors were spaced 90° apart and introduced pulsating sprays into the combustor at an injection angle of 45° with respect to the airflow. An electropneumatic transducer (Ling valve 94A-M1) was mounted at the inlet upstream and imposed periodic oscillations on the inlet flow, causing a roll up of large-scale coherent vortices in the dump combustor shear layer.

Combustion experiments using pulsating ethanol injection revealed a detached flame structure that was typically unsteady under most conditions. Flames were observed to blow off quite easily, and they were seen only downstream of the recirculation zone, as shown in Fig. 3, suggesting extremely long ignition-delay time. Little or no difference was observed in flame structure as the injection phase was varied with respect to the imposed flow oscillations. The main problem appeared to be the atomization of fuel. Droplet-sized measurements, using high-speed photography [17], revealed an abundance of "huge" droplets, several hundred μm in size, that are unacceptably large for combustion control purpose.

Flow Conditions and Visualization Experiments

Table 1 shows the summary of operating conditions. Inferred from Fig. 2, the Reynolds number for the inlet jet was 3.4×10^4 and the Strouhal number ranged between 0.4 and 1.2 based on the inlet diameter. Under natural conditions, the turbulence level of the inlet jet was 3% of the mean at the dump (defined in Fig. 2). For forced conditions, the measured RMS fluctuations at the centerline ranged between 30% and 60% of the mean velocity. Figure 4 shows typical hot-wire traces of the centerline velocity for natural and forced cases.

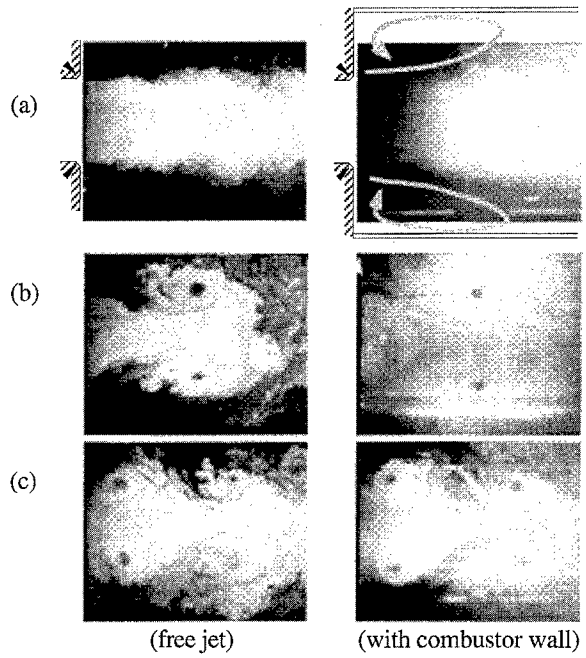

FIG. 5. Instantaneous planar Mie-scattering images of inlet jet with and without the combustor wall. $D_{comb} = 2.66\, D_{inlet}$ (a) unforced, (b) forced at 120 Hz, and (c) forced at 180 Hz.

Dump combustor flow was visualized by seeding the airflow with micron-sized smoke particles generated from a fog machine (Rosco 1500). Using a copper vapor laser (Oxford LS20-10) as the light source, planar Mie-scattering visualization was performed. First, the laser beam was shaped into a thin sheet that was aligned with two of the four injectors and along the center axis of the air jet. Then, the scattering images were taken from the normal direction using a CCD camera (Pulnix TM-7CN). Figure 5 shows the flow images without liquid-fuel injection. Forced flow images in the near field of the jet showed large-scale coherent vortices whose characteristics were quite similar between the two cases—with and without the recirculating flow created in the presence of the combustor tube. Because the image qualities were much better without the combustor window that fogged up with the injected droplets, further comparisons were made using the free-jet visualization.

The Mie-scattering technique was used in studying spatial distribution of fuel droplets. Droplets were visualized in the presence of forced and unforced airflow, which was either smoke seeded or unseeded. Both frequency and phase of the injection were systematically changed with respect to large-scale periodic flow features, and the spatial distribution of droplets was studied qualitatively from planar Mie-scattering images. Because of the periodic nature of the forced flow, it was possible to obtain phase-locked averaging of droplet distribution images, which was then compared with the underlying flow structures.

Droplet-Vortex Interaction

To supply the fuel droplets to a desired location, one can point the injector to the location and directly inject the droplets. While this is intuitively straightforward, it will work only for large droplets that are relatively unaffected by fluid motion—those droplets that are unsuitable for combustion control. The better method for combustion application is to use the fluid motion and the interaction of fuel droplets with the fluid motion to guide the droplets.

The extent of the interaction between liquid-fuel droplets and large-scale turbulent flow features such as vortices is expressed in terms of the particle Stokes number, *St*. *St* is the ratio of the characteristic timescale for particles responding to the fluid motion and that for the flow dynamics. The particle response time is estimated by assuming the drag on the particle (or fluid droplets [18]) follows Stokes's law ($Re < 1$). For particle density $\rho_p \gg \rho_{flow}$, the response time is taken to be $\tau_p = \rho_p D^2_p / 18\mu_{flow}$, which equals the time needed for the velocity difference to be reduced to e^{-1} of the original velocity difference. To assess the interaction with large vortices, the flow timescale can be defined as the large eddy turnover time or simply the period of vortex shedding (i.e., $\tau_f = 1/f$, where f is the vortex frequency. The resulting Stokes number, $St = \rho_p D^2_p f / 18\mu_{flow}$, then determines the degree of interaction between the droplets and vortices.

The droplets with very small *St* follow fluid motion very closely; their physical locations are determined entirely by fluid motion, whereas the droplets with

very large St are nearly unaffected by fluid motion and follow ballistic trajectories. Recent experiments [19–21] and computations [22–24] have suggested that only those droplets with St on the order of unity are affected by fluid motion and yet have enough momentum to be dispersed further outside the carrier fluid path. In the present experiment, the fuel droplets are distributed over a wide range of sizes, but the droplet Reynolds number for most is expected to be of the order unity or below (1-μm droplet with slip velocity $\Delta U \sim O\{10$ m/s$\}$, 10-μm droplet with $\Delta U \sim O\{1$ m/s$\}$, 100-μm droplet with $\Delta U \sim O\{0.1$ m/s$\}$, and so on), for which the Stokes analysis is valid. For slightly higher Reynolds numbers (i.e., 10-μm droplets with $\Delta U \sim O\{10$ m/s$\}$), a numerical simulation [24] using a nonlinear drag law showed no qualitative difference on droplet–vortex interaction even when the drag deviated from Stokes's value.

Because small droplets burn efficiently with short time delay, they are desirable for combustion control. For controlling spatial fuel distribution, those droplets with Stokes number close to unity would also be desirable, because they disperse even farther outside via partial interaction with the structures yet are sufficiently small for effective combustion. If droplet size distribution was such that those droplets with the latter characteristics constituted the upper end of the size distribution, more control over spatial distribution of fuel droplets could be obtained without compromising efficient combustion.

Finer Atomization

Since standard automotive fuel injectors produce a high number of relatively large droplets that burn rather slowly, they are not effective for active combustion control at relatively high frequencies. To reduce droplet size, a swirl-based atomizer with 300-μm exit diameter [25] was fitted at the fuel jet exit. In this configuration, the automotive fuel injector was used as a high-frequency solenoid valve for the fuel line. This new combination actuator improved the overall atomization characteristics while maintaining good frequency response up to 1 kHz.

Droplet size was measured from high-speed photographs of sprays. Droplet number density distributions from the new atomizing injector were nearly uniform in the frequency range investigated. Because the use of the CCD camera limited the minimal resolvable droplet size to either 75 or 300 μm, depending on the camera lens, only the size of larger droplets was quantified by this approach. The average droplet sizes are shown in Fig. 6. They were compared with the results from an automotive fuel injector at an identical downstream location. The results show about fourfold reduction in droplet size using the new atomizing injector.

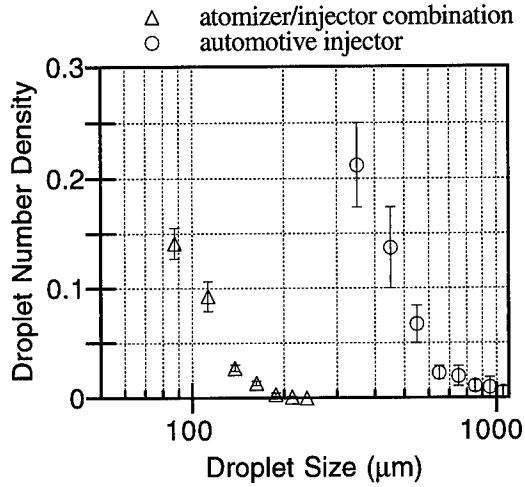

FIG. 6. Comparison of averaged droplet size distributions from two actuator systems. Ethanol spray was used for comparison at frequency range of 60–240 Hz and ΔP_{inj} of 275 kPa. An area of 2.2 cm^2 was probed where the center was 4.6 cm downstream from the injector exit.

Phase-Controlled Injection

Using the new injection configuration, the timing of injection with respect to the vortex formation process was studied. By synchronizing the injection cycle with the velocity oscillations imposed by the Ling valve, which caused large-scale vortex shedding, phase-controlled injection was performed. Phase-controlled experiment was limited to lower frequencies close to the jet-preferred mode at $fD/U = 0.2 \sim 0.6$ [26,27] because the vortical structures are best organized at those frequencies for present flow conditions. The injection frequency was always matched with the vortex frequency.

Figure 7 is a sequence of phase-lock-averaged images showing the effect of synchronized injection on fuel dispersion. For each image frame, five instantaneous images at an identical phase were averaged in an effort to filter out random features associated with instantaneous images. Each row shows four frames, each corresponding to a different phase, one quarter cycle apart. Figure 7a is the reference showing four different stages of the vortex development. Figures 7b and 7c show spatial distribution of fuel droplets, associated with pulsed injection after and before vortex shedding, respectively. In Fig. 7b, the injection occurred over the phase from $\pi/2$ to $3\pi/2$ so that the entire injection cycle trailed the vortex shedding (phase 0). Most of the droplets ended up inside the jet core. In contrast, Fig. 7c shows the injection occurring over the phase from $-\pi/2$ to $\pi/2$. The vortex shedding occurred at phase 0, while the droplets were still being injected. The resulting interaction between vortex and droplets caused

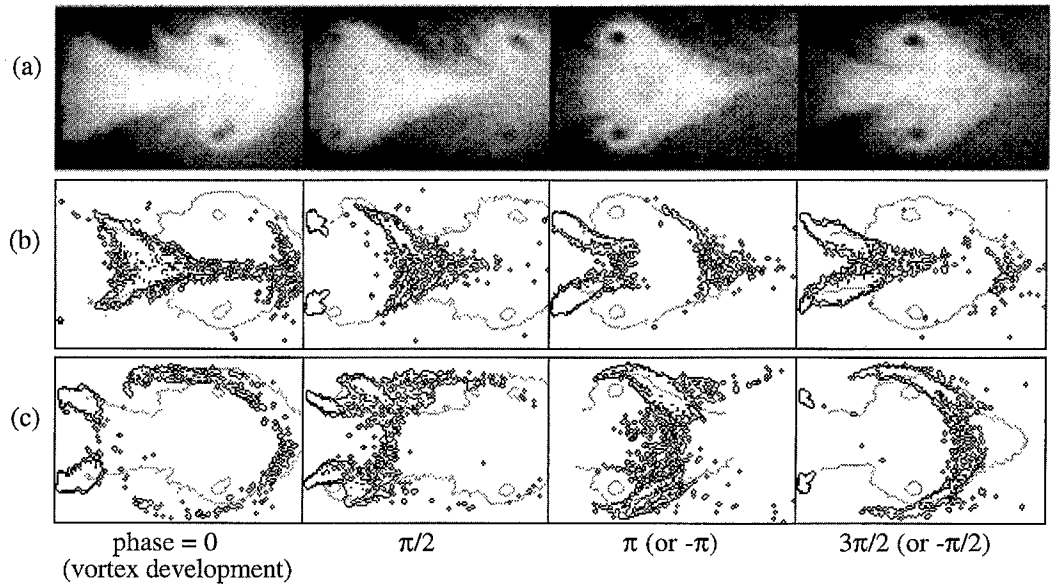

FIG. 7. Smoke visualization of flow field and contour maps of fuel-droplet spatial distribution showing the effect of injection phase on droplet dispersion at 120 Hz. (a) Air flow without fuel injection showing four different stages of vortex development. (b) Fuel injection starts at $\pi/2$ after vortex shedding and (c) at $\pi/2$ before vortex shedding. The contour lines (dark color) were obtained from phase-lock-averaged intensity of fuel-droplet Mie scattering and later were superimposed on top of the vortex contour (light color) corresponding to the same phase.

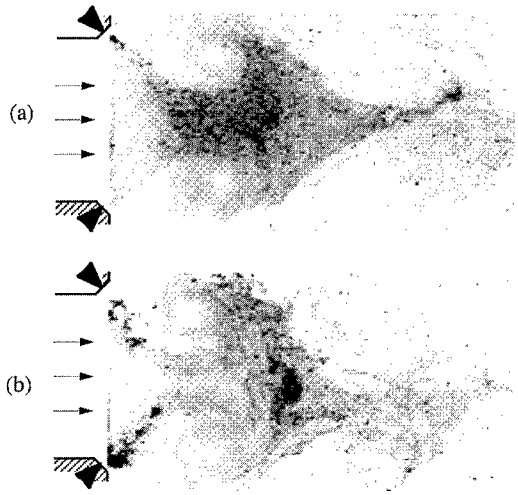

FIG. 8. Instantaneous Mie-scattering images of 180 Hz injection showing spatial distribution of ethanol droplets (black dots) in forced inlet airflow (gray). The pulsed injection started at vortex development phase (a) $\phi = 0$, and (b) $\phi = \pi$.

many droplets to be dispersed to the outer part of the vortex. Results were similar for injection occurring over the phase from $-\pi$ to 0.

Figure 8 shows instantaneous images in which both the droplets and the base flow were visualized simultaneously by injecting fuel droplets into smoke-seeded inlet flow. While it was difficult to identify small droplets from smoke particles, many larger droplets appeared as particularly intense points on the images, making distinction possible. Figure 8a represents an instant within the cycle in which the injection period covered the phase from 0 to π. Since the entire injection was taking place after the vortex shedding, the droplets were subjected to the decelerating flow field following the vortex, resulting in a poor interaction with the flow structures. Figure 8b shows a similar instant except for the injection period, which lasted from $-\pi$ to 0. For this case, the injection mostly preceded and finally coincided with the vortex shedding process. Many droplets were subjected to accelerating flow field associated with the vortex, causing a stronger interaction.

Combustion characteristics were obviously modified by droplet size and distribution control. In comparison with the previous case for which automotive injectors were used (Fig. 3), flames became more steady with reduced droplet size and were affected more readily by synchronized fuel injection. Figure 9 shows two flame photographs for similar conditions as in Fig. 3 but with the new atomizing injec-

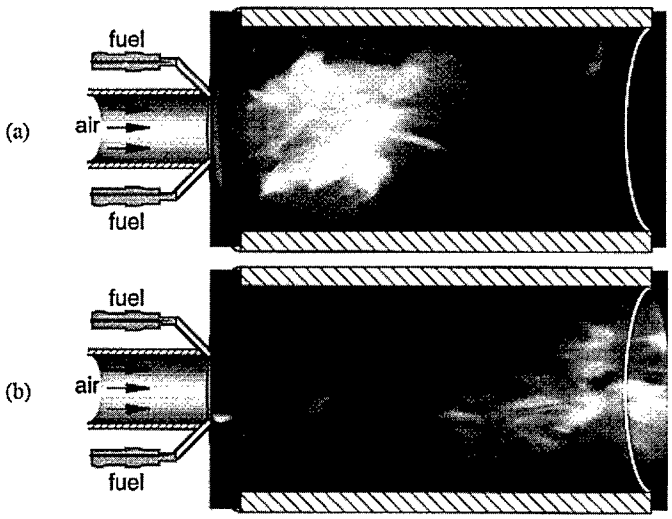

FIG. 9. Direct photographs of self-sustained flames inside the dump combustor fitted with new atomizing injectors; $f = 100$ Hz. (a) Pulsed fuel injection cycle started at vortex development phase $\phi = -\pi/2$. (b) The fuel injection cycle was not coupled with the vortex shedding process; thus, the injection phase was not synchronized with the vortex shedding.

tors. When the fuel was injected over a period covering the phase from $-\pi/2$ to $\pi/2$, which guaranteed injection during vortex shedding process, the flames became short and intense as seen in Fig. 9a. The flames were observed anchored upstream of the flow reattachment point. Figure 9b shows a flame photograph in which the periodic injection was not synchronized with the vortex shedding process. Resulting random phase injection made the flames long and detached, reminiscent of the previous case with larger fuel droplets.

Summary and Concluding Remark

Typical automotive fuel injectors were used to produce liquid fuel sprays at moderate to high frequencies. The frequency response was extended to 1 kHz using an adjustable duty-cycle square wave as the ECU control signal. The resulting sprays were characterized using planar Mie-scattering visualization with and without the presence of dump combustor airflow. Droplet size was measured and analyzed from the images. Because of the relatively high number of large droplets produced, these injectors were not suitable for direct use in combustion control applications. To reduce droplet size while maintaining high frequency response, an atomizing injector was configured by combining a pulsed injector with a fog atomizer. In the combined injector–atomizer system, the fuel injector functioned as a solenoid valve with high-frequency response while the atomizer produced finer droplets. With the new configuration, the droplet size was reduced by a factor of more than 4.

The interaction between spray droplets and large-scale flow structures was investigated in an axisymmetric dump combustor fitted with four atomizing injectors. When ethanol was injected periodically into large-scale vortices, most droplets followed the flow structures, suggesting Stokes number of order unity or lower. Spatial distribution of droplets was affected by pulsed injection synchronized with large-vortex shedding. Fuel injection that coincided with vortex shedding caused the droplets to be dispersed along the vortex perimeter, while the injection out of phase kept the droplets trapped inside the jet core. Combustion experiments using pulsed injection showed that the flame characteristics, in particular flame length and intensity, could be controlled by synchronized fuel injection. Presently, short and intense flames were observed when pulsed injection was synchronized with the vortex shedding phase. The results opened up the possibility of actively controlling practical liquid-fueled combustors.

Acknowledgments

This work was supported by the Office of Naval Research, with Dr. Gabriel Roy as the scientific officer, and by In-House Laboratory Independent Research program.

REFERENCES

1. Candel, S., *Twenty-Fourth Symposium (International) on Combustion,* The Combustion Institute, Pittsburgh, 1992.
2. Putnam, A., *Combustion Driven Oscillations in Industry,* Elsevier, New York, 1971.
3. Lord Rayleigh, *The Theory of Sound,* Dover, New York, 1945, p. 227
4. Lang, W., Poinsot, T., and Candel, S., *Combust. Flame* 70:281–289 (1987).
5. McManus, K. R., Poinsot, T., and Candel, S., *Prog. Energy Combust. Sci.* 19:1–29 (1993).

6. Gutmark, E., Parr, T. P., Hanson-Parr, D. M., and Schadow, K. C., *Twenty-Third Symposium (International) on Combustion,* The Combustion Institute, Pittsburgh, 1990.
7. Schadow, K. C., Gutmark, E., and Wilson, K. J., *Combust. Sci. Technol.* 81:285–300 (1992).
8. McManus, K. R., Vandsburger, U., and Bowman, C. T., *Combust. Flame* 82:75–92 (1990).
9. Poinsot, T., Veynante, D., Bourienne, F., Candel, S., and Esposito, E., *J. Propulsion Power* 5:14–20 (1989).
10. Gulati, A. and Mani, R., *J. Propulsion Power* 8(5):1109–1115 (1992).
11. Bloxsidge, G. J., Dowling, A. P., Hooper, N., and Langhorne, P. J., *AIAA J.* 26:783 (1988).
12. Smith, D. A. and Zukoski, E. E., Twenty-First Joint Propulsion Conference, AIAA-85-1248, 1985.
13. Poinsot, T., Trouve, A., Veynante, D., Candel, S., and Esposito, E., *J. Fluid Mech.* 177:265–292 (1987).
14. Sivasegaram, S. and Whitelaw, J. H., *J. Propulsion Power* 3:291–295 (1987).
15. Langhorne, P. J., Dowling, A. P., and Hooper, N., *J. Propulsion Power* 6:324–333 (1990).
16. Yu, K., Wilson, K., Gutmark, E., Parr, T., Smith, R., and Schadow, K. C., Thirty-Third AIAA Aerospace Science Meeting, AIAA-95-0385, 1995.
17. Lefebvre, A. H., *Atomization and Sprays,* Tayler & Francis, Bristor, PA, 1989, p. 380.
18. Batchelor, G. K., *An Introduction to Fluid Mechanics,* Cambridge Univ. Press, Cambridge, 1967, pp. 230–238.
19. Lazaro, B. J. and Lasheras, J. C., *Phys. Fluids* A1:1035–1044 (1989).
20. Longmire, E. K. and Eaton, J. K., *J. Fluid Mech.* 236:217–257 (1992).
21. Glawe, D. D. and Samimy, M., *J. Propulsion Power* 9(1):83–89 (1993).
22. Chung, J. N. and Troutt, T. R., *J. Fluid Mech.* 186:199–222 (1988).
23. Crowe, C. T., Chung, J. N., and Troutt, T. R., *Prog. Energy. Combust. Sci.* 14:171–194 (1988).
24. Chang, E. and Kaliasanath, K., Thirty-First Joint Propulsion Conference, AIAA 95-2561, 1995.
25. Parr, T. P., Gutmark, E. J., Hanson-Parr, D. M., and Yu, K., *Proceedings of Eighth ONR Propulsion Meeting,* 1995, pp. 215–224.
26. Crow, S. C. and Champagne, F. H., *J. Fluid Mech.* 48(3):547–591 (1971).
27. Gutmark, E. and Ho, C-M., *Phys. Fluids* 26(10):2932–2938 (1983).

COMMENTS

Thierry Poinsot, IMFT/CERFACS, France. In practical combustors, the effects of active control must be evaluated at constant mean operating parameters: air flow and fuel flow rates should be the same with and without control (in the mean). Automotive type actuators add an additional fuel rate which must be controlled and depends on their frequency and duty cycle. Did you measure or control these fuel rates in your system?

Author's Reply. Yes, we measured the time-averaged flow rates and they were kept constant during each test. All of the comparisons were made at identical flow rates in time-averaged sense. The average fuel-flow rate per actuator was characterized in advance as a function of frequency and duty cycle. While the flow rate varied almost linearly with duty cycle, it was only a weak function of frequency. This was true so long as the mechanical delay times, that are associated with the injector pintle opening and closing processes, were shorter than the ECU input pulsewidth (for both open and close cycles, respectively). This made the mean fuel-flow rate in a fixed duty cycle operation approximately constant up to the "effective" frequency limit. The limit frequency was highest at the midway duty cycle, typically around 50%, and decreased at duty cycles away from the midway value. Beyond the limit frequency, the flow rate was observed to decrease with frequency at low duty cycles (due to premature closing) and increase at high duty cycles (due to premature opening).

•

A. Ghoniem, MIT, USA. Droplet distribution in vortical flows is determined by when you inject the droplets as you have shown, and by the Stokes number which defines where the droplets go relative to the center of rotation. Did you look at using this concept to further optimize your design especially when the freedom in choosing the phase is limited by this stability consideration?

Author's Reply. Yes, we looked at the effect of Stokes number variation by changing the flow time scale (via vortex driving frequency variation between 120 and 360 Hz). However, the results were not conclusive since we observed a similar phase relation with frequency change. We think that was due to the fact that the imposed change in Stokes number for our case was rather small. While the droplet dispersion characteristics change with Stokes number varying over an order of magnitude, our range of Stokes number change was limited to at most a factor of three. Thus, we were probably operating at the similar Stokes number regime. Also, while the Stokes number depends more sensitively on droplet size, it is difficult to control the initial size distribution in physical experiments; the distribution is pretty much fixed by the atomizer used.

Twenty-Sixth Symposium (International) on Combustion/The Combustion Institute, 1996/pp. 2851–2858

COMBUSTION CONTROL USING A MULTIPLEXED DIODE-LASER SENSOR SYSTEM

E. R. FURLONG, D. S. BAER AND R. K. HANSON
High Temperature Gasdynamics Laboratory
Department of Mechanical Engineering
Stanford University
Stanford, CA 94305-3032, USA

A multiplexed diode-laser sensor system, comprised of two InGaAsP diode lasers and fiber-optic components, has been developed to nonintrusively measure temperature and species concentration over a single path for closed-loop process control using laser absorption spectroscopy techniques. The system was applied to measure and control the gas temperature in the postflame gases 6 mm above the surface of a Hencken burner (for multiple CH_4-air diffusion flames). The wavelengths of the lasers were independently current tuned across H_2O transitions near 1343 nm ($\nu_1 + \nu_3$ band) and 1392 nm ($2\nu_1$, $\nu_1 + \nu_3$ bands). Temperature was determined from the ratio of measured peak absorption coefficients. H_2O concentration was determined from the measured absorption coefficient of one transition set at the measured temperature. The mean temperatures recorded compared well with those measured by a thermocouple. Temperature fluctuations up to 250 Hz were measured accurately with the sensor system, demonstrating the high bandwidth of the measurement technique. A computer-controlled, closed-loop feedback circuit controlled the flame temperature in the probed region by adjusting the fuel flow in response to the difference between the measured and the desired gas temperature. The results obtained with this first-generation system demonstrate the potential of multiplexed diode lasers for rapid, continuous, nonintrusive, in situ measurements and control of combustion environments.

Introduction

Nonintrusive measurements of multiple flow field parameters have been demonstrated in a variety of flows using diode-laser absorption diagnostics [1–3]. Recently, the outputs of three independently operated diode lasers have been multiplexed into a single path using fiber-optic components to probe multiple absorption transitions of H_2O and O_2 or H_2O and CH_4 simultaneously [4,5]. These multispecies sensor systems are capable of measuring temperature, pressure, and species concentrations at kHz rates along several paths simultaneously by using appropriate fiber splitters without increasing the number of laser sources [4]. In the present investigation, a closed-loop combustion control system that combines a multiplexed diode-laser sensor with a computer-controlled feedback circuit is demonstrated to measure and control the gas temperature and H_2O mole fraction in the burned gases above a CH_4-air flame.

Theory

The theoretical basis for determining gas temperature and species concentration from measured absorption spectra recorded in combustion flows [3] and the spectroscopic parameters of the H_2O transitions (near 1343 nm [$\nu_1 + \nu_3$ band] and 1392 nm [$2\nu_1$, $\nu_1 + \nu_3$ bands]) probed [6,7] have been described previously [4,5]. In brief, the transmission of narrow line width radiation at frequency ν through a medium of length L may be described by the Beer–Lambert relation

$$T_\nu = I_\nu/I_0 = \exp(-k_\nu L) \qquad (1)$$

where T_ν is the transmittance of the medium at frequency ν, I_ν is the residual intensity at L, I_0 is the incident intensity (at ν), and k_ν is the (spectral) absorption coefficient [cm^{-1}]. The ratio of the absorption coefficients at two absorption peaks, R_{peak}, is a function of the relative populations in the participating ro-vibronic states and hence can be a strong function of temperature. Thus, in general, the gas temperature may be determined from measurements of R_{peak}. Mole fraction (or concentration) may be determined from the measured absorption at a particular wavelength using the known line strength and the measured temperature [2–5].

Experimental Method

Figure 1 shows the general arrangement of the combustion-control experiment. Details of the laser system and the operating conditions employed to control the lasers have been described previously

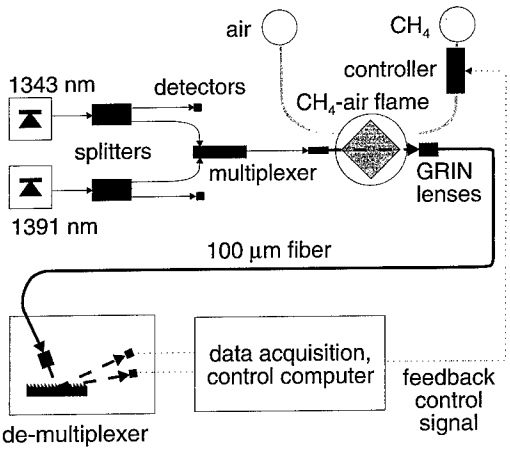

FIG. 1. Schematic diagram of the combustion-control experimental arrangement.

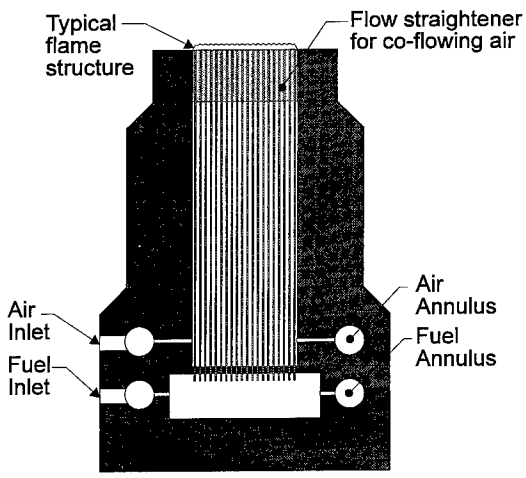

FIG. 2. Schematic diagram of the Hencken burner used to sustain a square array of non-premixed CH_4-air flamelets.

[4,5]. The system includes two, independently operated, distributed-feedback (InGaAsP) semiconductor diode lasers that (for the scanned-wavelength method) were tuned at a 1-kHz repetition rate over the desired transitions by ramp modulating the individual injection currents to yield single-sweep, spectrally resolved absorption records every millisecond. In the fixed-wavelength strategy, the laser wavelengths, monitored with a wave meter (Burleigh), were maintained (by varying the injection current) near the value that yielded maximum absorption. The individual laser outputs were combined into a single path using appropriate single-mode fiber splitters and couplers. The multiplexed, or multi-wavelength, beam was directed through the flow field using a gradient index of refraction (GRIN) lens fused to the end of the fiber. The transmitted beam was coupled into a 100-μm (core)-diameter (multimode) fiber with a 7-mm-diameter–fused GRIN lens. The larger-diameter receiving lens and optical fiber were used to maximize coupling efficiency and minimize effects of beam deflection caused by density (and thus refractive index) gradients in the probed region. The transmitted multiwavelength light was de-multiplexed (spectrally separated) into the constituent laser wavelengths by directing the beam at a nonnormal incidence angle onto a diffraction grating. The beams were diffracted at angles specific to each wavelength and subsequently monitored with InGaAs photodiodes (200-kHz bandwidth). The detector voltages were digitized by a 12-bit (Nicolet) oscilloscope and transferred via GPIB to a Pentium-based (90-MHz) personal computer.

The system was used to record H_2O absorption spectra through the product gases of a CH_4-air diffusion flame generated by a Hencken burner. The burner, shown schematically in Fig. 2, consists of a square (7-cm diagonal) array of diffusion flamelets sustained by a matrix of 0.5-mm-internal diameter, 16.7-mm-long stainless steel needle tubes that carry fuel (CH_4) from a reservoir fed by a circular annulus. At the top of the burner, the fuel exits the tubes and mixes with streams of co-flowing air to yield $\approx$460 diffusion flamelets. For the typical operating conditions (CH_4 flow rate $\approx$ 4 L/min, CH_4 velocity $\approx$ 40 cm/s in the tubes; air flow rate $\approx$ 50 L/min, air velocity in the flow straightener $\approx$ 120 cm/s), the flow was laminar ($Re_D < 100$) and the tips of the flamelets were typically less than 3 mm above the burner surface.

The flame temperature was varied by maintaining a constant air flow rate and adjusting the fuel flow rate, and thus the equivalence ratio, using a proportional, direct-acting, voltage-controlled solenoid valve. The gas temperature was measured 6 mm above the burner surface using a type-S (platinum–platinum/10% rhodium) thermocouple (130 μm or 5 mil, bare, corrected for radiation effects) as a function of the flow-controller input voltage. For the given air flow rate (50 L/min), the flow-controller voltage variation of 2.61–2.81 V yielded an essentially linear variation (to within 1%) in temperature throughout the range 1810–2200 K, demonstrating the ability to control the gas temperature by changing the CH_4 flow rate. The inverse slope of the variation of temperature with controller voltage, 0.5 mV/K, was used as the proportional gain factor (G) for the feedback control system.

Figure 3 illustrates the strategy for closed-loop control of the gas temperature in the probed region. The initial operating conditions in the burner ($T_o \approx$ 2050 K) were established by supplying a 2.74-V bias to the CH_4 flow controller, which yielded a CH_4 flow

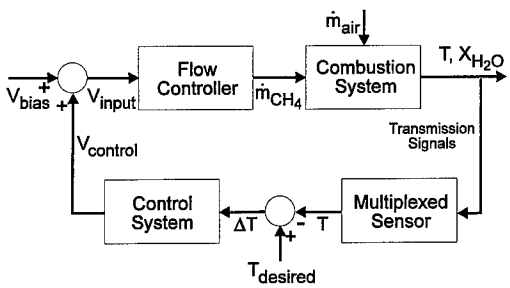

FIG. 3. Block diagram illustrating the strategy used for closed-loop control of the temperature. The system compares the measured temperature, T, with a desired value, $T_{desired}$, and introduces a control voltage, $V_{control}$, to the fuel flow controller.

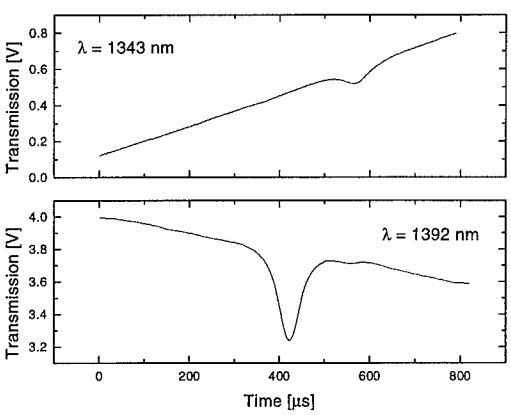

FIG. 4. Typical single-sweep (raw data) transmission signals obtained simultaneously by tuning two diode lasers at a 1-kHz rate across H_2O absorption features near 1343 nm (top frame) and 1392 nm (bottom frame) over a 7-cm-long path through the burned region above a CH_4-air flame.

rate of ca. 4 L/min while maintaining the air flow rate near 50 L/min. A flow controller voltage of 2.79 V corresponds to an equivalence ratio equal to 1. The error signal for the control algorithm was proportional to the difference between the value of temperature determined from the peak absorption ratio, averaged exponentially with previous values, and the desired set point value ($T_{desired}$). The feedback control signal $V_{control}$, the product of the temperature difference ($T - T_{desired}$) and the gain factor G, was added to the bias voltage of the flow controller to effectively adjust the gas temperature to the desired value.

Data Analysis

Figure 4 presents typical single-sweep (raw data) transmission signals obtained simultaneously by

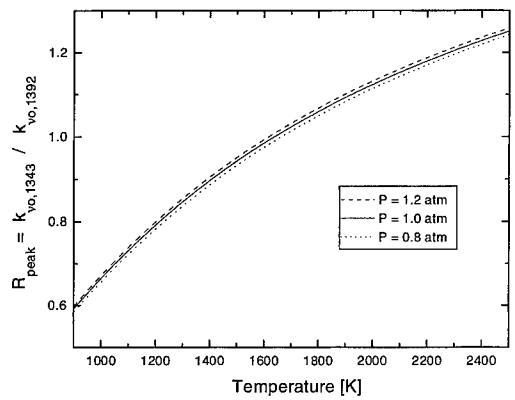

FIG. 5. The ratio of peak absorption coefficients, R_{peak}, calculated as a function of temperature for various values of total pressure for the probed H_2O transitions (for $X_{H_2O} = 0.18$).

tuning two lasers independently at a 1-kHz rate across the selected H_2O absorption features over a 7-cm-long path through the CH_4-air flame. The peak absorption coefficient for each feature was determined from (the maximum value of) the negative logarithm of the transmitted intensity normalized by the unattenuated laser intensity [3–5]. The gas temperature was determined from the ratio of the peak absorption coefficients (R_{peak}).

To illustrate the sensitivity of the measurement technique, Fig. 5 plots calculated values of R_{peak} as a function of temperature for values of total pressure (P) in the range 0.8–1.2 atm for a constant H_2O mole fraction ($X_{H_2O} = 0.18$). A 20% change in P produces a 2% change in the calculated gas temperature. Furthermore, variations in the H_2O mole fraction, which lead to a slight change in the respective absorption coefficients of the probed transitions, result in a negligible change (<0.5%) in the inferred temperature. Thus, for the present flow field conditions, a reliable determination of R_{peak} yields an accurate determination of T.

Measurements were recorded 6 mm above the flame while modulating the fuel flow rate sinusoidally at various frequencies to demonstrate the capability of the system to measure temperature fluctuations and discriminate between temperature, pressure, and H_2O mole fraction changes in the flow field. Figure 6 illustrates various power spectra, the squared Fourier transform of the time-dependent signal, obtained by applying a 2.5-Hz, 0.15-V (peak to peak) modulation to the 2.71-V bias voltage on the fuel flow controller. Figures 6a and 6b were calculated from the measured transmission intensities with the laser tuned to the peak-absorption wavelength and to a neighboring wavelength without absorption, respectively. Figures 6c and 6d were calculated from the time-dependent temperatures

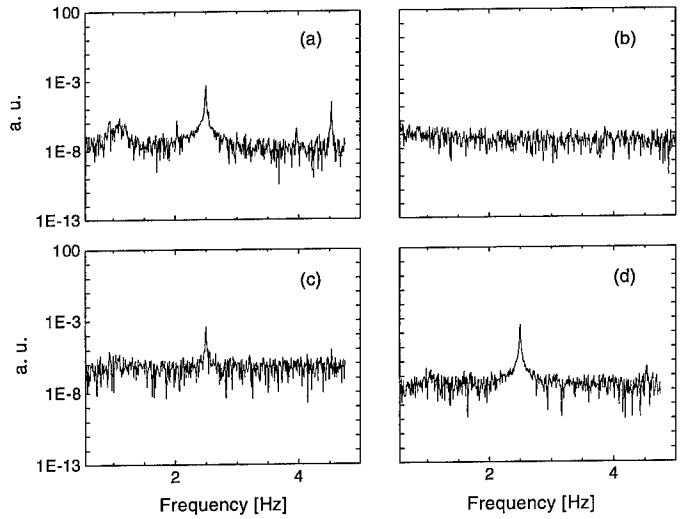

FIG. 6. Normalized power spectra for (a) transmission at peak of absorption feature (1343 nm), (b) unattenuated transmission (laser tuned off-line), (c) the measured temperature, and (d) the temperature measured with an 80-μm (3-mil) thermocouple. The spectra were recorded while sinusoidally modulating the bias voltage to the flow controller at 2.5 Hz.

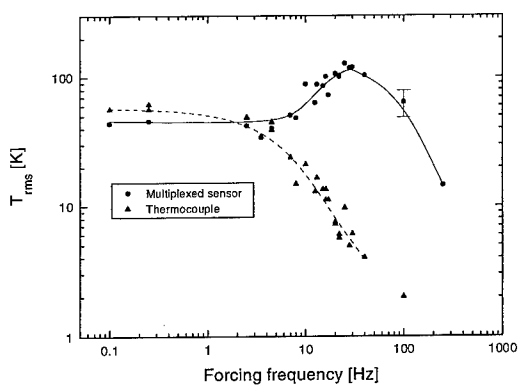

FIG. 7. Temperature (root mean square) fluctuations determined from the power spectrum at various externally induced modulation frequencies. Measurements from the multiplexed sensor (●) agree with those from an 80-μm (3-mil) thermocouple (▲) at low frequencies. As the modulation frequency increases, the thermocouple response (---) decays exponentially.

determined from R_{peak} and from a (80-μm, 3-mil) thermocouple, respectively.

Variations in the transmission intensity power spectrum that appear in Fig. 6a, but not in Fig. 6c, indicate variations in pressure or H_2O concentration (for example, the relatively strong variation near 4.6 Hz). The temperature spectra illustrated in Figs. 6c and 6d have nearly equal peak amplitudes and identical peak frequencies, as expected. The relatively smaller noise present in the trace shown in Fig. 6d is due to the significantly smaller bandwidth of the thermocouple ($\approx$4 Hz) relative to the multiplexed sensor. Not surprisingly, Fig. 6b is effectively frequency independent.

Figure 7 compares values of root mean square temperature fluctuations, T_{rms}, computed from power spectra recorded with the multiplexed sensor and the thermocouple for a range of modulation frequencies (0.1–250 Hz) applied to the fuel flow controller (with the amplitude and bias voltages described in Fig. 6). The values agree to within measurement uncertainty for modulation frequencies below 4 Hz, the approximate bandwidth (-3 dB) of the thermocouple, but differ increasingly as the excitation frequency approaches the natural buoyancy instability near 13 Hz. The increase in the difference between measured T_{rms} values with increasing flow modulation frequency is attributed to the relatively slow thermocouple response, because of the low heating rate ($Nu_{D,bead} \approx 2$) and the finite thermal mass of the bead (diameter = 160 mm). In contrast, the temporal response of the multiplexed sensor (using the fixed-wavelength technique) is effectively limited by the detection electronics (200-kHz detector bandwidth, for the present work).

As a further test of the sensor, the gas temperature above the flame was increased rapidly by supplying a voltage step (0.16 V) to the CH_4 flow controller to increase the equivalence ratio toward stoichiometric. Figure 8 illustrates the resulting temperature variation measured in the postflame gases 6 mm above the burner using the multiplexed sensor (scanned-wavelength technique) and two different thermocouples (3 mil, 5 mil) corrected for radiation effects. The measurements are in excellent agreement before the applied step (near 1825 K). After the step, the temperatures recorded by the multiplexed sensor (at a rate of one measurement every 2 ms) rise to within 37% of the final steady-state value of $\approx$2150 K in $\approx$18 ms. Note that the oscillatory

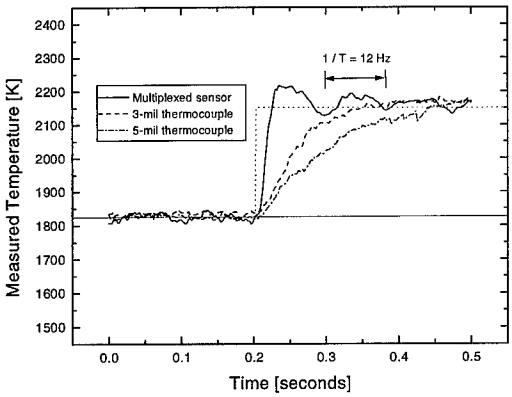

FIG. 8. Comparison of temperatures measured in the burned region above a CH_4-air flame due to an applied step change in the fuel flow rate using the multiplexed sensor and thermocouples.

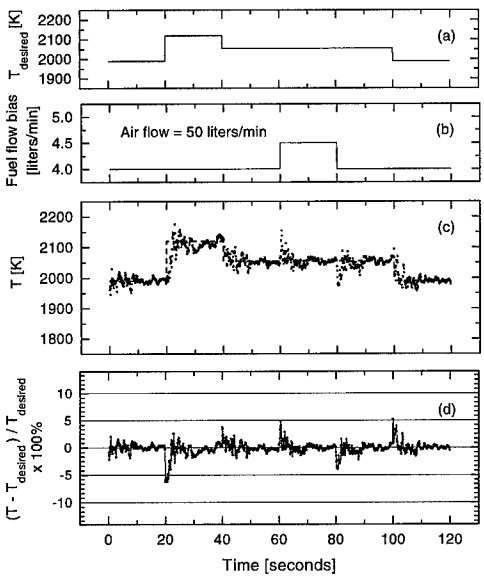

FIG. 9. Measured temperatures in the burned region above the CH_4-air flame illustrating the capability of the closed-loop control system to maintain the desired set-point temperature and compensate for perturbations in the fuel flow rate. (a) Time-dependent set-point temperature, $T_{desired}$; (b) step change in the flow controller bias voltage; (c) measured temperatures; and (d) percentage variation between the measured and the desired values.

overshoot has a significant 12-Hz component, apparently caused by a natural instability of the flame excited by the step change in the fuel flow rate. The finite response time of the burner is due predominantly to the gas residence time in the volume from the flow controller to the probed region.

Figure 9 demonstrates the capability of the system to respond to programmed changes in the desired set-point temperature, $T_{desired}$. Figure 9a illustrates a given time-dependent schedule of $T_{desired}$. Figure 9b shows a step change in the flow controller bias voltage, which results in a corresponding change in the fuel flow rate and represents an unwanted perturbation in the gas temperature that the control system is designed to minimize. Figure 9c compares the temperatures measured with the multiplexed sensor (dots) for various desired values (dashes) and includes the effects of the applied step perturbation in Fig. 9b. Figure 9d plots the percentage temperature variation $(T - T_{desired})/T_{desired} \times 100\%$. The maximum transient variation between the measured temperature and the desired value, which occurred after a step perturbation in the fuel flow rate (at t = 60 s and t = 80 s), was 6%. The standard deviation in the percentage temperature variation was less than 1% for the entire measurement interval.

The $(1/e)$ response time of the closed-loop control system, the time necessary for the mean measured gas temperature to reach a value within 37% of the normalized temperature differential $(T - T_{desired})/T_{desired}$ induced by an applied step change, was about 1 s and includes the gas flow residence time from the flow controller through the burner to the probed region (20 ms); the scan time of the lasers (1 ms); the digital transfer time through GPIB (60 ms); the computational time for data analysis and determination of feedback control signal (0.3 ms); the actuator response time (3 ms); and the time required to reset the scope trigger (40 ms). A significant reduction in the response time may be achieved by using an improved data transfer procedure to the computer, reducing the laser scan time, implementing a fixed-frequency absorption measurement strategy [3], or, most importantly, decreasing the gas volume from the flow controller to the burner surface. In addition, actuation strategies that do not rely on the gas flow rate through the supply line to or through the burner reservoir (e.g., direct acoustic modulation) may be applied to reduce the phase lag between the control signal to the actuator and the resultant gas temperature change.

Figure 10 compares values of H_2O mole fraction measured (X_{meas}) with the multiplexed sensor (dots) for the burner-operating conditions described in the top frame with estimated chemical-equilibrium values (dashes) calculated (X_{calc}) at the desired temperatures. The apparent error in the X_{meas} values ($\approx$9–10%) is due primarily to the uncertainty and fluctuations in the CH_4 flow rate through the solenoid valve (5%) and temperature fluctuations in the flow field (4–5%). Thus, measurements of species mole fraction (concentration) could also be used in a feedback system for process control.

The results of recent improvements in the closed-loop control system to suppress the effects of a step

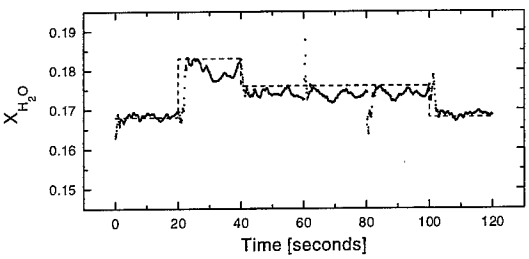

FIG. 10. Comparison of H_2O mole fractions (X_{meas}) determined (simultaneously with temperature) from peak absorption coefficient measurements (O) using the multiplexed sensor with calculated (X_{calc}) chemical-equilibrium values (---) for conditions described in Fig. 9.

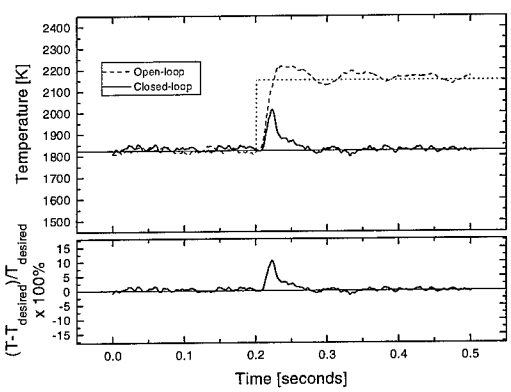

FIG. 11. Closed-loop performance using an advanced data acquisition system. The top frame includes a typical open-loop (no feedback) response for comparison. The bottom frame plots the percentage temperature variation ($T_{desired}$ = 1825 K).

change (perturbation) in the fuel flow rate are shown in Fig. 11. This system, which incorporates recent advances in computer-based, data-acquisition hardware, measures a temperature and computes an appropriate control signal every 2 ms, 50 times faster than the system demonstrated in Fig. 9. An A/D scopecard (Gage Compuscope 512), located inside the computer, replaced the GPIB-controlled oscilloscope and reduced the data transfer time from 60 to 0.7 ms. The top frame illustrates both the closed-loop performance (solid) of the control system and the open-loop response (dash) of the burner to the applied change in fuel flow rate. The bottom frame plots the percentage deviation from the desired temperature (1825 K). The maximum variation between the measured temperature and the desired value, which occurred immediately after the step change in the fuel flow rate, was 10%. The standard deviation in the percentage temperature variation was less than 1% for the total measurement interval. The $1/e$ response time of the closed-loop control system was ≈10 ms. The settling time, the time necessary for the relative temperature differential to decrease below 3% after the step, was ≈30 ms. Additional improvements in hardware that incorporate new acquisition and processing strategies should enable closed-loop control at the tuning rate of the lasers (1–10 kHz).

Application Considerations

The Hencken burner used in these experiments produces a uniform, constant-pressure flow field and thus serves as an attractive test bed for the initial development of a combustion-control system based on diode-laser absorption measurements. Current efforts are focused on reducing effects due to flow field gradients and particulates that influence the interpretation and applicability of the measurements in realistic systems. Because absorption techniques yield line-of-sight measurements, the measured parameters (gas temperature, mole fraction) represent path-averaged values over the probed region. Careful selection of the absorption transitions monitored can be used to mitigate the influence of temperature and density nonuniformities in boundary layers and nonuniform combustion regions [3]. In addition, effects due to particulates or variations in window transmission with time are minimized by tuning the laser to a nearby wavelength (with no absorption transition), periodically (at a rate faster than the scattering timescales), to determine the reference intensity I_0. Among the most difficult challenges facing implementation of the technique in large-scale industrial facilities will be the strong refractive index gradients caused along the probed path that can deflect the beam, vary the collection efficiency of laser light into the receiving fiber, and thus affect the transmitted beam intensity on the photodetector surface. In such cases, it will be necessary to modify the optical train to accommodate changes in the beam location and orientation without perturbing the intensity reaching the detector.

Conclusions

A closed-loop feedback system that incorporates a multiplexed diode-laser sensor was used to monitor and control the gas temperature along a single path in the burned gases above a CH_4-air flame. Externally induced fluctuations in the gas temperature (up to frequencies of 250 Hz) were recorded to demonstrate the rapid measurement capabilities of the sensor. The control system minimized the difference between the measured gas temperature and a desired value by actively controlling the methane flow rate to the burner using a voltage-controlled solenoid valve. The system was capable of controlling the

gas temperature in the probed region to within 1% (standard deviation) of the desired value for various set points in the range 1800–2100 K. The frequency response of the control system, limited primarily by the gas residence time in the burner, may be improved by reducing the burner reservoir volume to decrease the phase lag between the control signal and the resultant temperature change, by increasing the digital transfer rate to the computer to increase the data acquisition rate, or by using fixed-frequency absorption techniques to decrease measurement time. Multiplexed diode-laser sensing holds promise for improved monitoring and control of combustion and other high-temperature process streams, particularly for applications that require remote and nonintrusive monitoring.

Acknowledgments

This research was supported by the Strategic Environmental Research and Development Program, with K. Schadow as technical monitor, and by the U.S. Air Force Office of Scientific Research, Aerospace Sciences Directorate, with J. Tishkoff as technical monitor.

REFERENCES

1. Philippe, L. C. and Hanson, R. K., *Appl. Opt.* 32:6090–6103 (1993).
2. Arroyo, M. P., Birbeck, T. P., Baer, D. S., and Hanson, R. K., *Opt. Lett.* 19:1091–1093 (1994).
3. Baer, D. S., Nagali, V., Furlong, E. R., Hanson, R. K., and Newfield, M. E., *AIAA J.* 34:489–493 (1996).
4. Nagali, V., Furlong, E. R., Chou, S. I., Mihalcea, R. M., Baer, D. S., and Hanson, R. K., *Proceedings of the Thirty-First AIAA Joint Propulsion Conference,* AIAA-95-2684, New York, 1995.
5. Baer, D. S., Hanson, R. K., Newfield, M. E., and Gopaul, N. K., *Opt. Lett.* 19:1900–1902 (1994).
6. Toth, R. A., *Appl. Opt.* 33:4851–4867 (1994).
7. Rothman, L. S., Gamache, R. R., Tipping, R. H., Rinsland, C. P., Smith, M. A. H., Benner, D. C., Devi, V. M., Flaud, J.-M., Brown, L. R., and Toth, R. A., *J. Quant. Spectrosc. Radiat. Transfer* 48:469–507 (1992).

COMMENTS

Hans ter Meulen, University of Nijmegen, The Netherlands. What temperature are you exactly measuring and what is the experimental accuracy?

Author's Reply. The measured temperature is that which describes the relative populations in rotational quantum states in the ground vibrational state of H_2O, along a line of sight. Since the measurements were recorded at atmospheric pressure, the rotational temperature is equal to the gas (translational) temperature.

The experimental uncertainty, for this relatively uniform flame, was estimated to be about 6% and was primarily limited by uncertainties in the tabulated H_2O spectroscopic parameters at the elevated temperatures encountered (1500–2200 K) in the probed region above the flame.

•

Alan C. Eckbreth, United Technologies Res Ctr., USA. Would you describe the nature of the spatial averaging which occurs? Is the measured temperature a true linear average, or skewed to low or high temperatures along the path?

Author's Reply. Temperature is determined, in the present work, from the ratio of absorbances recorded from two rotational transitions with different lower-state quantum levels within the H_2O ground vibrational state. The total absorbance is the path integral of the product of the temperature-dependent absorption line strength, lineshape function, mole fraction of absorbing species, and total pressure over the beam path. Since the contribution to the total absorption for a particular transition at a given position is weighted by the (temperature-dependent) line strength and the partial pressure of the absorbing species, the nature of spatial averaging in the temperature measurement depends on the transitions probed and the spatial distribution of absorbing species. In the present work, the absorption strengths of the probed transitions reach their respective maxima near 600 K and 1100 K. As a result, for post-flame gases having a uniform distribution of H_2O mole fraction but slightly cooler edges, the measured temperature in the probed region would be slightly lower than the linearly averaged mean temperature value along the beam path.

•

Thierry Poinsot, IMFT/CERFACS, France. The mean temperature with control in your results is higher than without control. Is the mean equivalence ratio the same in both cases? Do you have an explanation for this change temperature?

Author's Reply. Although the mean fuel and air flow rates and thus the equivalence ratio were not changed when the fuel flow was modulated, we measured an increase of about 100 K in the mean temperature value in

the probed region (6 mm above the burner surface) after control was initiated. When temperature fluctuations were minimized, the thin flame front stabilized at a height of 3 mm above the burner surface, below the probed region, and there was a relatively small amount of CH emission in the post-flame gases. When temperature fluctuation were present (caused by speaker-induced acoustic modulation), a relatively thick flame front extended beyond the probed region and CH emission in the post-flame gases increased significantly. Thus we believe that the induced temperature fluctuations resulted in a decrease in the mean temperature value due to a decrease in the extent of reaction at the measurement location.

Twenty-Sixth Symposium (International) on Combustion/The Combustion Institute, 1996/pp. 2859–2868

ON-LINE EMISSION CONTROL OF COMBUSTION PROCESSES BY LASER-INDUCED RESONANCE-ENHANCED MULTI-PHOTON IONIZATION/MASS SPECTROMETRY

RALF ZIMMERMANN,[1,2,3] DIETER LENOIR,[2] ANTONIUS KETTRUP,[2,3] HOLGER NAGEL[1] AND ULRICH BOESL[1]

[1]*Institut für Physikalische und Theoretische Chemie*
Technische Universität München
D-85747 Garching, Germany

[2]*Lehrstuhl für Ökologische Chemie und Umweltanalytik*
Technische Universität München
D-85354 Freising, Germany

[3]*Institut für Ökologische Chemie*
GSF-Forschungszentrum für Umwelt und Gesundheit
D-85758 Oberschleißheim, Germany

Laser-induced resonance-enhanced multi-photon ionization (REMPI) represents an efficient and highly compound selective (even isomer discrimination can be achieved) ionization method and therefore is ideally adapted as an ion source for analytical time-of-flight mass spectrometry (TOFMS). The combination of mass and optical selectivity (high-resolution UV spectroscopy is involved in the REMPI-ionization process), its high sensitivity, and the high measurement speed makes the REMPI/TOFMS approach a powerful tool for on-line emission control of combustion processes. A REMPI/TOFMS–based monitor for highly time resolved analysis (sampling rate 50 Hz) of organic and inorganic compounds in the exhaust gas of internal combustion engines is already in operation; an exhaust-gas measurement is presented in the paper. However, recent investigations focus on the question of whether the REMPI/TOFMS technique combined with a supersonic Jet-inlet system (Jet-REMPI/TOFMS) is also applicable for continuous real-time monitoring of highly toxic combustion trace products. Relevant examples are polycyclic aromatic hydrocarbons (PAH, e.g., benzo[a]pyrene) and chlorinated aromatics (e.g., chlorinated dibenzo-p-dioxins/furans, PCDD/F). Such an on-line monitor is currently needed for emission control of industrial combustion processes as, for example, waste incineration (WI) facilities. In addition to some technical improvements (e.g., increase in on-line sensitivity or coupling with gas chromatography), one major prerequisite for practical applications is a thorough knowledge of the spectroscopic properties of the relevant target compounds. This contribution focuses on these spectroscopic preconditions.

In conclusion, concepts for an on-line emission monitoring of the PCDD/F-content in flue gases of WI plants by means of the Jet-REMPI/TOFMS technique are presented. They are based on either the indicator parameter relationship between, for example, chlorinated benzenes and PCDD/F in the WI-exhaust gases (real-time, on-line technique) or a fast, repetitive discontinuous trapping and enrichment before a fast gas chromatography-Jet-REMPI/TOFMS detection.

Introduction

Prerequisites for an optimal steering (e.g., active feed-back control) of technical combustion processes and for development of new emission reduction devices are reliable real-time analytical techniques. The measurement speed needed for an on-line emission control device is given by the typical regulating-time constant of the respective combustion process. In the case of an internal combustion engine, single engine-stroke resolution (~50 Hz) is desirable. For industrial incinerators (e.g., WI), acceptable measurement time intervals are much longer (min). For some compounds, such as CO, NO_x or SO_2, on-line sensors are already available. However, it is impossible to monitor traces of organic species with conventional methods. In addition to high speed and sensitivity, a high selectivity is required for on-line emission control techniques.

The two-dimensional REMPI/TOFMS analytical technique [1–8] fulfills these prerequisites. The REMPI process, using excited molecular intermediate states for ionization, involves UV spectroscopy in the ionization step (first analytical dimension).

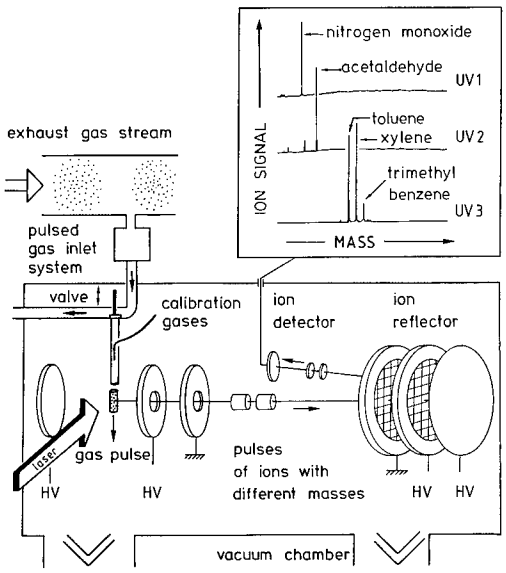

FIG. 1. Schematic representation of a REMPI/TOFMS apparatus and wavelength-selected mass spectra of automotive exhaust gas. The on-line measurements (Fig. 2) are calibrated by the use of calibration gases, which are added in defined concentrations to the exhaust gas probe pulses. The insert shows mass spectra obtained from an exhaust gas, using different laser wavelengths (UV1 = 307.6 nm for NO measurement, UV2 = 301.5 nm for detection of acetaldehyde, and UV3 = 264.1 nm to detect the monocyclic benzoid aromatics).

The second analytical dimension is a result of the mass analysis.

For selective REMPI ionization, the laser wavelength must be tuned in resonance with a specific UV-spectroscopic transition of the target compound. Only these compounds are selectively photoexcited and can absorb more photons (multi-photon absorption). If the absorbed energy exceeds the ionization potential, the target compound gets ionized (multiphoton ionization). REMPI ionization of jet-cooled molecules (Jet-REMPI) via vibronic transitions of the first excited singlet state (S_1) is highly compound selective and soft (low fragmentation rate) with efficiencies in the percentage range (e.g., up to 25% ionization yield for aniline [2]).

In WI, nonhomogeneous fuel composition leads to formation of traces of hazardous polychlorinated aromatics such as polychlorodibenzo-p-dioxins/-furans (PCDD/F) and polychlorobiphenyls (PCB) [9–11]. In many countries, the emission limits for PCDD/F, for example, have recently been tightened by new legislation. This poses an even greater challenge to on-line emission control devices. We focus our attention on chlorinated aromatics and the spectroscopic preconditions for their Jet-REMPI/TOFMS detection.

Although REMPI/TOFMS has been successfully applied to on-line trace analysis of complex exhaust gas mixtures [12–14], extensive spectroscopic studies [15] are necessary before routine analytical application on WI exhausts is feasible.

Results and Discussion

REMPI-based methods are already in use for basic combustion research purposes [16], for inorganic trace analysis [17], and for on-line analysis of automobile engine exhausts [12–14]. The latter application allows high repetition rates (full mass spectrum per laser shot, repetition rates are 10–50 Hz) in combination with sufficient sensitivity to detect ppm to sub-ppm concentrations for each single laser shot. Such high-speed gas analysis can only be performed by REMPI/TOFMS. The exhaust gas is introduced into the TOFMS ion source by a special real-time sample injection system involving an effusive molecular beam. REMPI ionization is performed directly underneath the heated (500 K), effusive beam inlet capillary. Figure 1 gives a schematic representation of a TOFMS spectrometer and shows REMPI-selected mass spectra from combustion engine exhaust gas. Although the optical selectivity is reduced in comparison to supersonic jet inlet (e.g., in mass spectrum UV3 in Fig. 1, four aromatics are REMPI ionized simultaneously), it is nonetheless demonstrated that a high-compound class selectivity is obtained. Together with the mass separation, the optical selectivity is fully sufficient for species-selected on-line engine-exhaust emission monitoring. Results of an on-line REMPI measurement of benzene, NO, and CO concentrations as a function of the engine parameters speed and throttle valve position are shown in Fig. 2.

A particularly interesting application for REMPI/TOFMS–based techniques would be the emission control of industrial incinerator effluents (e.g., at WI). The raw flue gases of WI, probed after the furnace (particularly interesting for on-line REMPI/TOFMS–emission monitoring), contain thousands of different trace chemicals in ppm to ppq concentrations [22]. To detect target compounds in the presence of the multitude of isomeric and isobaric compounds in the flue gas, the high optical selectivity of the Jet-REMPI technique is required. Different research groups already have demonstrated that for many separation problems, selective detection can also be achieved in the presence of large amounts of potential interferents [8,18–20]. Most potential interferents are not ionizable at the resonance wavelength of a target compound, because even isomers can be differentiated by their sharply structured Jet-REMPI spectra (see Fig. 3 and Refs. 5–8,18,20,23–25). However, in case of accidental ionization of an isobaric interferent (important for

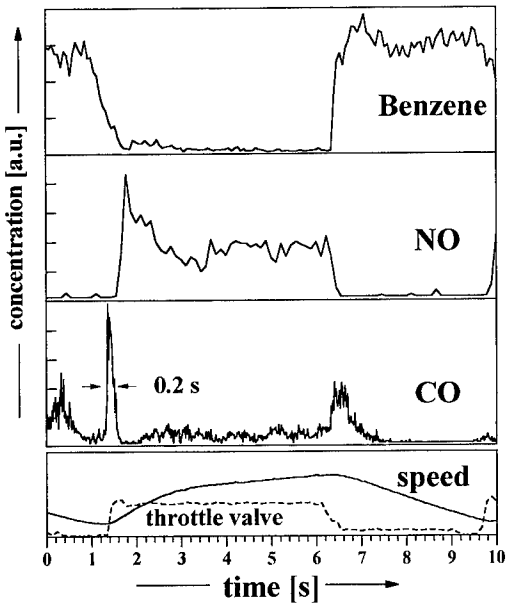

FIG. 2. Results of REMPI/TOFMS on-line emission measurements of internal-combustion engine exhaust gas (time resolution up to 50 Hz). Fast concentration changes of three species are recorded during sudden speed changes (throttle valve adjustment). High-benzene concentrations appear while the engine speed decreases (unburned fuel emission). While the throttle valve is open, the benzene level drops as a result of more ideal combustion conditions and the NO formation is increased (high temperatures). Short CO peaks appear (FWHM: 0.1–0.2 s) at the beginning and end of accelerations. Fluctuations with a period of 1–2 s are caused partly by changes in the fuel-air ratio due to the electronic emission control device (λ probe).

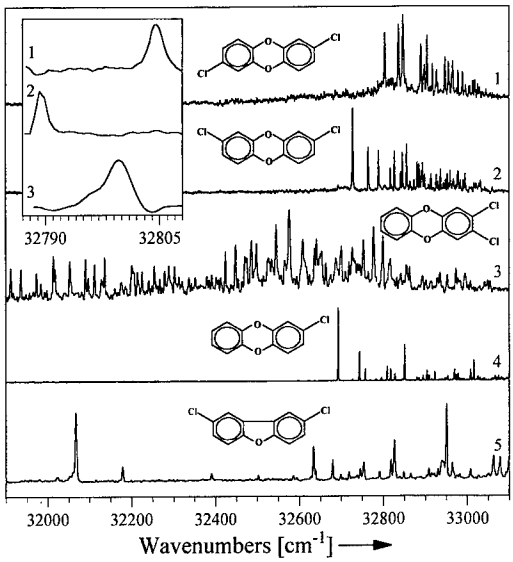

FIG. 3. REMPI spectra of some chlorinated dibenzo-p-dioxins (PCDD) and one dibenzofuran (PCDF). The samples were seeded in argon gas within the heatable jet valve before expansion in the supersonic jet. From top to bottom: one-color 1 + 1 REMPI spectra of (1) 2,7-dichlorodibenzo-p-dioxin, (2) 2,3-dichlorodibenzo-p-dioxin, (3) 2,8-dichlorodibenzo-p-dioxin, (4) 2-monochlorodibenzo-p-dioxin, and (5) two-color 1 + 1 REMPI spectrum of 2,8-dichlorodibenzofuran. Note the differences in the vibronic structure of the PCDD (dense pattern is due to floppy molecular structure) and the 2,8-dichlorodibenzofuran (distinctly spaced peaks are due to rigid molecular structure). The insert exhibits an enlarged part of the three isomeric PCDD compounds REMPI spectra (1–3), demonstrating the possibility of isomer selective ionization.

two-color ionization, see later in this paper), difference measurement techniques can be applied (comparative measurement with laser periodically tuned on and off the REMPI resonance). Recent research [18–20] indicates that principal technical preconditions for WI on-line emission monitoring are fulfilled. The required sensitivities lie in the ppb to ppt range, detection limits in the low ppb to sub-ppb range are already reached with a standard Jet-REMPI setup [18]. Recently, a decrease in detection limit by a factor of about 10 has been reached [19], using conical extraction electrodes 2 cm below the jet nozzle. However, we think that a miniaturized ion-optical arrangement with plane-parallel extraction plates that also performs increased sensitivity due to small nozzle-ionization region distance is more advantageous because of the higher ionization volume and reduced space charge effects. A configuration in which the ionization is performed directly below the jet nozzle (ions drift into a pulsed extraction field ion source by their jet velocity) is already in use for anion-ZEKE spectroscopy [21] within our group and the application for Jet-REMPI/TOFMS is in preparation.

Recent REMPI-spectroscopic reports deal either with small inorganics or aromatics (ionizable in a one-color 1 + 1 REMPI process). For most relevant compounds (e.g., higher-chlorinated molecules), no [jet-]spectroscopic data are available. Therefore, we started an extensive study of the Jet-REMPI spectroscopic properties on representatives of the PCB, PCDD, PCDF, PAH, and PCBz substance classes [23–25].

The molecular parameters to be considered are the transition energies and properties of electronically excited molecular states (e.g., absorption oscillator strength, molecular geometry changes, neutral dissociation, vibronic structure, radiative and nonradiative deactivation rates, internal vibrational redistribution rates), the ionization potential, and properties related with the REMPI-ionization pro-

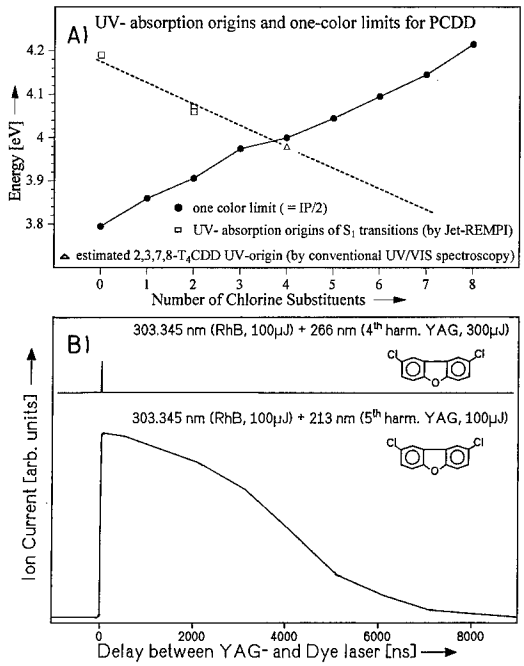

FIG. 4. (A) One-color limits (half ionization potentials [26], IP/2) and UV S_1-transitions of some PCDD (DD, 1-MCDD, 2,8-DCDD, 2,3,7-T_3CDD, 2,3,7,8-T_4CDD, 1,2,3,7,8-PCDD, 1,2,3,7,8,9-H_6CDD, 1,2,3,4,6,7,8-H_7CDD, and O_8CDD). The one-color limit is reached when the S_1-transition exhibits a lower energy than IP/2. 2,3,7,8-tetrachlorodibenzo-p-dioxin probably still can be ionized by a one-color 1 + 1 REMPI scheme via a vibronic S_1 transition. (B) 1 + 1 two-color REMPI ionization yield for 2,8-dichlorodibenzofuran as a function of the delay time between exciting and ionizing laser; 266 nm (a) and 213 nm (b) were used for ionization. Chlorinated aromatics undergo rapid S_1 deactivation by ISC into the first triplet state (T_1), reducing the REMPI-ionization efficiency drastically. By application of the short wavelength ionizing laser (213 nm, trace b) the molecules can be ionized efficiently from the T_1 state under satisfaction of the Franck-Condon propensity rule (sixfold increased ionization efficiency compared to 266 nm ionization as shown in trace a)

cess (e.g., fragmentation rates). Some of the previously mentioned spectroscopic properties are discussed subsequently for the PCDDs and two important PAHs.

Generally, the S_1 transition energy of aromatics decreases with either an increasing extent of the π system or (to a lesser extent) with an increasing number of chlorine substituents. Positional isomers (e.g., different dichlorinated dibenzo-p-dioxins, Fig. 3) show nearly identical UV-transition regions, whereas those of constitutional isomers (e.g., perylene and benzoapyrene) often exhibit larger differences. Important for optical selectivity is the vibrational fine structure of the UV transition used for REMPI (mostly S_1 state), which is determined by vibronic selection rules and by the Franck-Condon propensity rule (the abundance of totally symmetric vibrational modes with similar structural pattern as the geometry change upon excitation is enhanced). Figure 3 shows the Jet-REMPI spectra of four chlorinated dibenzo-p-dioxins (PCDD) and one chlorinated dibenzofuran (PCDF). The vibronic structure of the S_1 states of PCDD is relatively dense because of low-frequency mode progressions, which are Franck-Condon–induced by a $S_1 \leftarrow S_0$ change of the folding angle (dioxins exhibit a folded structure [26]). Nonrigid molecules often show partly congested spectra caused by high low-frequency mode activity, whereas rigid aromatics generally exhibit distinctly spaced spectra. This effect is important because it can reduce the isomeric selectivity. Figure 3 shows that the isomeric selectivity for PCDD is still fairly high, but it is not clear yet whether the spectroscopic selectivity is sufficient for total isomeric separation of the important four- to eightfold chlorinated dibenzo-p-dioxins. For the polychlorinated biphenyls (PCB), which exhibit a large dihedral-angle change upon $S_1 \leftarrow S_0$ excitation [24], the jet-spectroscopic selectivity is strongly reduced in comparison with rigid PAHs.

The ionization potential (IP) is also fundamental for REMPI. If the $S_1 \leftarrow S_0$ transition energy exceeds the IP/2 value (one-color limit), a one-color two-photon–REMPI ionization scheme is possible (only one tunable laser is needed for practical applications). Two-color or higher-order (three- or four-photon ionization) REMPI processes are necessary if this precondition is not fulfilled. Regarding the one-color limit, the polychlorodibenzo-p-dioxins represent an interesting case. Polycyclic aromatics with more than two condensed benzene rings usually exhibit an S_1-excitation energy lower than the IP/2 value and therefore need a two-color REMPI-ionization scheme. In the tricyclic dibenzo-p-dioxin molecule (DD), the central ring is not aromatic. Consequently, the S_1 transition is blueshifted by 5100 cm^{-1} in comparison with the parent aromatic (anthracene), and the DD molecule is ionizable by one-color 1 + 1 REMPI. We have predicted the IP values of higher chlorinated PCDD by a combined quantum-chemical and experimental approach [26]. Using UV-spectroscopic data ([27] and Fig. 3), we estimated the one-color limits for PCDDs (Fig. 4a). The ultratoxic 2,3,7,8-tetrachlorodibenzo-p-dioxin may remain one-color REMPI ionizable. If the S_1 lifetime is sufficiently long (phosphorescence-spectroscopic results indicate that the ISC rate is not too high for highly symmetric PCDDs [28]), an efficient detection scheme for this important compound may be possible. The other toxic PCDD congeners,

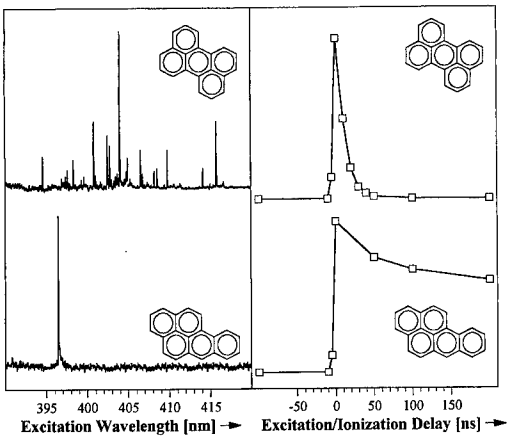

FIG. 5. Excitation wavelength and lifetime selectivity in two-color 1 + 1 REMPI spectroscopy demonstrated by the separation of benzoapyrene (BAP) and perylene (PER). (Left) Excitation wavelength selectivity. A small part of the REMPI spectra of the BAP and PER isomers. In this wavelength region (S_1 origin region of BAP) the spectral selectivity is sufficient for a complete isomeric discrimination. However, at other wavelengths co-ionization of the two isomers cannot be ruled out. In this case, the lifetime selectivity can be applied to distinguish the isomers. (Right) Lifetime selectivity: REMPI ion current curves of PER and BAP registrered as a function of the delay between the exciting (tuned to the respective S_1-origin transition) and the ionizing (quintupled Nd:YAG, 213 nm) lasers. The difference in PER and BAP excited-state lifetimes allows a perfect isomeric separation; if, for example, the delay between the exciting and ionizing laser is set to 100 ns, no PER, but 75% ion yield of the BAP molecules can be achieved.

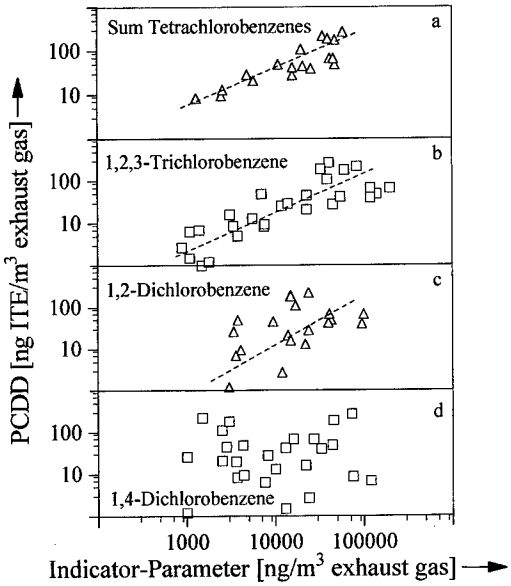

FIG. 6. Indicator parameter relationship between the polychlorodibenzodioxins (PCDD, measured in I-TEQ [11]) and polychlorobenzene (PCBz) concentration in the flue gas of a model incinerator [35]. Although the scatter of the low-chlorinated benzene measurements is very high (due to unsuitable analytical technique [35]), 1,2-DCBz exhibits a recognizable PCDD/F-indicator parameter relationship, whereas the 1,4-DCBz does not (consistent with flame chemistry studies [35]). This depicts the importance of isomer selective measurement of PCDD-indicator parameters.

which are five- to eightfold chlorinated, definitely are located in the two-color region.

In general, REMPI ionization yields may be reduced if the excited intermediate state lifetime is short in comparison with the laser pulse duration (here, 10 ns). The relevant radiationless deactivation mechanisms for aromatics are inter-system crossing (ISC) and internal conversion (IC). The IC process represents a transition from the electronically excited state into the molecular ground state (S_0), induced by large structural changes upon excitation (e.g., biphenyl derivatives). The electronic excitation energy is transformed into vibrational excitation, making a REMPI ionization impossible. Application of short pulse lasers (pulse duration in the ps range) can override this sensitivity loss, but for most compounds sufficient ionization yields still can be achieved with standard lasers (pulse duration in the 10-ns range).

The ISC process is due to a forbidden transition from an excited singlet state to the (vibrationally excited) first triplet state (T_1), favored by the presence of heavy atoms (e.g., chlorine) in the molecule due to increased spin-orbit coupling. A detection sensitivity loss can be reduced or prevented by a two-color ionization scheme. After S_1 excitation and fast ISC, the ionization must be performed from the vibrationally highly excited T_1 state. Although the ISC process is isoenergetic, the energy of the second, ionizing photon must be larger than the S_1-IP gap energy to achieve an optimal ionization efficiency by satisfying the Franck-Condon propensity rule [29] (Fig. 4). The different time behavior in the two cases is of particular interest. With 266 nm, only those molecules that remain in the short-living S_1 state are ionizable, that is, an ionization signal is obtained when the excitation/ionization lasers are exactly overlapping in time only. By application of a 213-nm laser light, the Franck-Condon propensity rule is satisfied and the molecules can be ionized efficiently from the highly vibrationally excited T_1 state. The ionization yield decreases slowly over a range of some thousand nanoseconds excitation/ionization laser delay time (triplet state lifetime). An interesting aspect is that the time profile of the two-color ioni-

zation efficiency represents an additional selectivity parameter. As an example for lifetime selectivity, the ionization yield as a function of the delay time between the excitation and ionization lasers for the isomeric PAHs perylene and benzo[a]pyrene (tracer compound for hazardous PAH in combustion exhaust or soot) is shown in Fig. 5 (right). The two-color REMPI ionization often allows an increased sensitivity in comparison to one-color REMPI, because optimal laser conditions for the excitation and ionization step can be chosen independently. Further on, lifetime selectivity can be obtained and, particularly important for the detection of chloroaromatics, sensitivity losses by fast ISC deactivation can be prevented. It should be noted, however, that the primary REMPI selectivity is reduced because of possible 1 + 1 REMPI at the color of the second (ionizing) laser via $S_2 \leftarrow S_0$ or $S_n \leftarrow S_0$ absorption either of the target compound itself or of interferents. Our results on two-color REMPI spectroscopy show that, in many cases, the unfocused second laser can be attenuated into the 10 μJ pulse energy range without appreciable ionization-signal reduction, allowing registration of PAH spectra with less than 1% $S_n \leftarrow S_0$ signal (i.e., the ionization efficiency of $S_n \leftarrow S_0$ REMPI often is reduced because of rapid, radiationless transitions). Thus, the interferences by the second laser should be manageable by difference-measurement techniques. Two-color detection efficiencies of unsubstituted PAH are good [29], enabling a REMPI/TOFMS application for PAH-emission control. In a summarized consideration of the spectroscopic results, the (aromatic) compounds relevant for WI–effluent emission control can be subdivided into three groups:

1. Aromatics ionizable in a one-color 1 + 1 REMPI process with a distinctly spaced vibrational S_1 fine structure under jet conditions (low-chlorinated benzenes [6,7,25], phenols, toluenes, and also some unchlorinated compounds: many benzene derivatives, dibenzofuran, naphthalene, fluorene).
2. Aromatics ionizable in a two-color 1 + 1 REMPI process with a distinctly spaced vibrational S_1 fine structure under jet conditions (e.g., most PAH, higher-chlorinated benzenes, and PCDF).
3. Aromatics ionizable either in a one- or two-color 1 + 1 REMPI process but with a congested or dense vibrational structure under jet conditions and/or a very fast S_1 deactivation, dissociation, or other spectroscopic problem (e.g., PCDD and PCB).

Accurate calibration techniques are very important for application of the REMPI/TOFMS approach. A calibration method for on-line measurement based on internal calibration standards already has been developed within our group [36] that allows a quantitative accuracy better than 10% for every laser shot in the low ppm region. A similar concept will be used for the measurements in WI-exhaust gas with ^{13}C-marked chlorobenzenes, for example, as calibration standards (ppb region dosage of the calibration standard[s] is managed by a dynamic gas standard technique [37]).

Conclusion

It is important to consider how the molecules of the previously defined groups can be detected in the exhaust of large-scale industrial incinerators. Two concepts for emission monitoring by REMPI/TOFMS are feasible:

1. A direct on-line approach (analogous to the combustion engine measurements, see Figs. 1 and 2) allows real-time measurements, but special techniques (e.g., ion-optics) are needed to reach the required sub-ppb sensitivity. Furthermore, the on-line signal can be summed over some hundred laser shots (20–100 Hz laser repetition rate) because time resolution in the 10 s range is sufficient for this particular application. A routine on-line application will probably be restricted to group 1 and 2 (two laser wavelengths necessary) compounds.
2. A quasi real-time approach using a rapid, repetitive sample enrichment step (e.g., with trapping tubes and subsequent sudden release by thermodesorption [30]) may be used if the sensitivity is not sufficient for an on-line detection of the desired target compound (group 2 and 3 molecules). Further on, fast gas chromatographic (GC), separation may be applied before Jet-REMPI/TOFMS detection. Recently, we presented a GC-Jet-REMPI/TOFMS coupling [20] (three-dimensional analytical system providing full optical Jet-REMPI, mass spectroscopic, and GC resolution, as well as considerably good detection limits of 200 fg for toluene, for example [20]). However, the analytical cycle time will be in the 10-min range.

The results of our spectroscopic investigation on the particularly interesting PCDD (group 3, unfavorable REMPI-spectroscopic properties) and their very low concentrations in the WI-exhaust gases (ppt, ppq, and sub-ppq concentration range) show that a reliable detection of these compounds in WI exhausts must be performed by the quasi real-time approach. Nevertheless, the aim of a real-time on-line measurement of the PCDD is reachable by application of indicator parameter relationships between the PCDD and indicator compound concentration in the flue gas of WI plants. Recent studies show that the polychlorobenzene/phenol (PCBz and PCPh) and PCB concentrations are reliable indicator parameters for PCDD/F emissions

(correlation coefficients up to $r = 0.94$ [31,32]). The reason for the correlation is the formation mechanism of PCDD/F [10], which is formed in the WI flue gas by fly-ash–based, heterogeneous catalyzed reactions at temperatures of about 550–650 K simultaneously with other chloroaromatics ("de novo" [33] and "precursor" [34] formation mechanism). The PCBz and PCPh emissions are several orders of magnitude higher than those of PCDD/F. One- or twofold chlorinated benzenes/phenols are particularly advantageous for on-line Jet-REMPI monitoring, because they are not absorbed on fly-ash particles within the relevant temperature range and exhibit favorable properties for REMPI detection (one-color 1 + 1 REMPI [8,25]). Limited literature on the occurrence of two- to sixfold chlorinated benzenes and the PCDD/F in the exhaust gas of incinerators is available. Based on data from Ref. 35, we worked out indicator parameter graphs for the two-, three-, and fourfold chlorinated benzenes versus the polychlorinated dibenzo-p-dioxins (Fig. 6). The concentrations of the three- and fourfold chlorinated benzenes in the exhaust gas of the pilot incinerator exhibit a good PCDD indicator parameter relationship. As mentioned by Fängmark et al. [35], the high scattering of the measured dichlorobenzene concentrations is mainly due to an unsuitable trapping technique (designed for low-volatility compounds). However, it is interesting that in contrast to the 1,4-dichlorobenzene, the 1,2-dichlorobenzene still exhibits a recognizable PCDD indicator relation. This difference emphasizes the necessity of isomer-selective detection. Recently, we have investigated the Jet-REMPI spectroscopy of all two-, three-, and fourfold chlorinated benzene isomers [8,25] and shown that isomer-selective REMPI detection is possible for all PCBz. Jet-REMPI/TOFMS detection limits of 600 ppt (chlorobenzene), 10 ppb (1,4-dichlorobenzene), and 30 ppb (1,2-dichlorobenzene) already have been reported by others [18]. In conclusion, PCBz (and PCPh) are highly suitable PCDD/F indicator parameters for on-line emission control by Jet-REMPI/TOFMS.

A Jet-REMPI/TOFMS apparatus, optimized for WI-exhaust on-line measurements, is under construction within our group. Also receiving attention are Jet-REMPI–spectroscopic studies on relevant pollutants, conventional indicator parameter measurements at industrial combustion facilities, and development of quasi real-time techniques (gas chromatography–Jet-REMPI/TOFMS coupling and fast enrichment techniques) for stack gas monitoring.

Acknowledgments

RZ gratefully acknowledges the receipt of a research scholarship from the DECHEMA eV, Germany and the Volkswagenstiftung eV, Germany.

On-line emission diagnosis of a waste incinerator by REMPI/TOFMS project is sponsored by the Deutsche Bundesstiftung Umwelt, Germany, and supported by the Bruker-Franzen Analytical Systems AG, Germany, and the Gesellschaft zur Entsorgung von Sondermüll in Bayern (GSB) mbH, Germany.

REFERENCES

1. Boesl, U., Neusser, H. J., and Schlag, E. W., *Zeitschrift Naturforsch* 33a:1546 (1978).
2. Antonov, V. S., Knyazev, I. N., Letokhov, V. S., Matuik, V. M., Movshev, V. G., and Potapov, V. K., *Opt. Let.* 3:37 (1978).
3. Boesl, U., *J. Chem. Phys.* 95:29 (1991).
4. Boesl, U., Weinkauf, R., and Schlag, E. W., *Int. J. Mass Spectrom. Ion Proc.* 112:121 (1992).
5. Hager, J. W. and Wallace, S., *Anal. Chem.* 60:5 (1988).
6. Tembreull, R., Sin, C. H., Li, P., Pang, H. M., and Lubman, D. M., *Anal. Chem.* 57:1186 (1985).
7. Rohlfing, E. A., *Twenty-Second Symposium (International) on Combustion,* The Combustion Institute, Pittsburgh, 1988, p. 1843.
8. Boesl, U., Zimmermann, R., Weickhardt, C., Lenoir, D., Schramm, K.-W., Kettrup, A., and Schlag, E. W., *Chemosphere* 29:1429 (1994); Zimmermann, R., Weickhardt, C., Boesl, U., Lenoir, D., Schramm, K.-W., Kettrup, A., and Schlag, E. W., *Chemosphere* 29:1877 (1994).
9. Ballschmiter, K., *Nachr. Chem. Tech. Lab.* 39:988 (1991).
10. Ballschmiter, K., Braunmiller, I., Niemczyk, R., Swerev, M., *Chemosphere* 17:995 (1988).
11. Safe, S., *Crit. Rev. Toxicol.* 22:1603 (1990).
12. Boesl, U., Weickhardt, C., Zimmermann, R., Schmidt, S., and Nagel, H., SAE-Technical Paper Series 930083-61, 1993.
13. Weickhardt, C., Boesl, U., and Schlag, E. W., *Anal. Chem.* 66:1062 (1994).
14. Nagel, H., Weickhardt, C., Boesl, U., and Frey, R., Proceedings of the 7th Resonance-Ionization-Spectroscopy Symposium, *AIP-Conference Proceedings 329,* AIP-Press, New York, 1995, p. 255.
15. Zimmermann, R., Doctoral Thesis, Technische Universität München, Germany, 1995.
16. Ahrens, J., Kovacs, R., Shafranowskii, E. A., and Homann, K. H., *Ber. Bunsenges. Phys. Chem.* 98:265 (1994).
17. Becker, J. S., Dietze, H. J., *Fres. J. Anal. Chem.* 344:69 (1992).
18. Cool, T. A. and Williams, B. A., *Combust. Sci. Technol.* 82:67 (1992); Williams, B. A., Tanada, T. N., and Cool, T. A., *Twenty-Fourth Symposium (International) on Combustion,* The Combustion Institute, Pittsburgh, 1992, p. 1587.
19. Oser, H., Thanner, R., and Grotheer, H.-H., *Europ. Symposium on Optics for Environmental and Public Safety,* SPIE Series 2504,15, München, 1995.
20. Zimmermann, R., Lerner, C., Schramm, K.-W., Ket-

trup, A., and Boesl, U., *Europ. Mass Spectrom.* 1:341 (1995); Zimmermann, R., Heger, H. J., Kettrup, A., Schramm, K.-W., Rohwer, E. R., Ortner, E. K., and Boesl, U., Proceedings of the 18th International Symposium on Capillary Chromatography, Riva del Garda, Italy, 1996, accepted.
21. Käsmaier, R., Bäßmann, C., Drechsler, G., and Boesl, U., Proceedings of the 7th Reson. Ionization Spectroscopy Symposium 1994, *AIP-Conference Proceedings* 329, AIP-Press, New York, 1995, p. 451.
22. Jay, K., and Stiglitz, L., *Chemosphere* 30:1249 (1995).
23. Weickhardt, C., Zimmermann, R., Boesl, U., and Schlag, E. W., *Rapid Communic. Mass Spectrom.* 7:183 (1993).
24. Zimmermann, R., Weickhardt, C., Boesl, U., and Schlag, E. W., *J. Mol. Struct.* 327:81 (1994).
25. Weickhardt, C., Zimmermann, R., Schramm, K.-W., Boesl, U., and Schlag, E. W., *Rapid Communic. Mass Spectrom.* 8:381 (1994).
26. Zimmermann, R., Boesl, U., Lenoir, D., Kettrup, A., Grebner, T. L., and Neusser, H. J., *Int. J. Mass Spectrom. Ion Process.* 145:97 (1995).
27. Stehl, R. H., Papenfuss, R. R., Bredeweg, R. A., and Roberts, R. W., *Adv. Chem. Ser.* 120:119 (1973).
28. Pohland, A. E., and Yang, G. C., *J. Agr. Food Chem.* 20:1093 (1972).
29. Meijer, G., de Vries, M. S., Hunziker, H. E., and Wendt, H. R., *Appl. Phys.* B51: 395 (1990).
30. Ortner, E. K., and Rohwer, E. R., *Proceedings of the Seventeenth International Symposium on Capillary Chromatography*, Riva del Garda, Italy, 1994, p. 842.
31. Öberg, T. and Bergström, J., *Chemosphere* 14:1081 (1985).
32. Kaune, A., Lenoir, D., Nikolai, U., and Kettrup, A., *Chemosphere* 29:2083 (1994).
33. Stiglitz, L., Zwick, G., Beck, J., Roth, W., and Vogg, H., *Chemosphere* 18:1219 (1989).
34. Dickson, L. C., Lenoir, D., and Hutzinger, O., *Environ. Sci. Technol.* 26:1822 (1992).
35. Fängmark, I., van Bavel, B., Marklund, S., Strömberg, B., Berge, N., and Rappe, C., *Environ. Sci. Technol.* 27:1602 (1993).
36. Boesl, U., Weickhardt, C., Schmidt, S., Nagel, H., and Schlag, E. W., *Rev. Sci. Instrum.* 64:3282 (1993).
37. Namiesnik, J., *J. Chromatog.* 300:79 (1984).

COMMENTS

J. Wolfrum, Universitat Heidelberg, Germany. You suggest the use of 1,2 dichloro-benzene as an indicator substance for toxicity equivalents of dioxins. At the required upper limit of 0.1 mg/Nm^3 in Europe this would require the detection of about 10ppt 1,2-dichloro benzene. How is your sensitivity in this case?

Author's Reply. Indicator parameter relations between chlorobenzenes and the toxicity equivalents of dioxins only have been measured in the stack gas of waste incinerators, WI (e.g. in Ref. 32 in the paper). Such indicator correlations are due to the related formation mechanisms of chloroaromatic compounds in the WI post combustion zone (300°C). Therefore one can expect the validity of the indicator parameter approach in the WI post combustion region also. In order to achieve the goal of an emission reduction by feed back control of furnace or flue gas cleaning parameter, it is necessary to get real-time on-line information from the point where the pollutants are formed. Further on, the stack gas has passed a multitude of gas cleaning facilities as e.g. wet scrubbers. The concentration of the organics in the stack gas, determined by the equilibrium between gas-phase and a huge amount of different circulating scrubbing liquids, will only fluctuate slowly around mean values. Therefore, as we have mentioned in the paper, we intend to apply the on-line Jet-REMPI-TOFMS approach to measure indicator parameters in the raw flue gas, prior to any the flue gas cleaning measures beside the electrostatic dust precipitator. The concentrations of dioxin indicators/precursors are at significant higher levels here in comparison to the stack gas. For example, polychlorobenzene concentrations (all congeners) of 9–27μg/m^3 have been registrated in the raw flue gas of a municipal-WI [1] and lower chlorinated benzenes are more prominent than the higher chlorinated ones [2,3]. From this measurements dichlorobenzene (DCB) concentrations of 200ppt up to 2ppb in the WI-raw gas can be concluded. However, during time-varying combustion conditions, indicated by carbonmonoxide-peaks, probably even much higher DCB peak-concentrations occur. Our present Jet-REMPI-TOFMS device is still not sensitive enough (we reach similar detection limits as Cool et al. (Ref. 18 in the paper) which are in the 10 ppb range for DCB's) but as shown by Oser et al., an approximately 50-fold sensitivity increase (see questions from Grotheer) can be achieved mainly by reduction of the nozzle-ionization distance. This demonstrates the large optimization potential for the REMPI-TOF technique. We are working on an sensitivity-optimized Jet-REMPI-TOFMS setup, using a free jet ion source (first results: see Ref. 3, this comment) that allows a close nozzle-ionization distance and a high ionization volume but exhibits several modifications (e.g. avoiding foci in the ion trajectory) relative to the setup from Oser et al. (Ref. 19 in the paper).

REFERENCES

1. Ide et al., *Chemosphere* 32:189 (1996).
2. Wanatabe et al., *Chemosphere* 32:177 (1996).

3. Zimmermann et al., *RIS-96 Proceedings,* AIP Press, 1996, in press.

•

Horst-Henning Grotheer, DLR Stuttgart, Germany. By using the new approach termed "DLR Jet REMPI," significant sensitivity improvements could be achieved that have been erroneously quoted in your paper to amount only a factor of about 10. The real numbers are as follows. By comparison to the literature [1] we obtained for dichlorotoluene a sensitivity increase by a factor of 200 [2], for naphtalene an increase by even a factor of 1000 [3]. For benzene the detection limit with DLR Jet REMPI is at present 1 ppt [4] with measurement times in the order of some seconds so that on-line capability is achieved.

For the reduction of dioxins from MWI's, a head-end strategy seems worthwhile which aims at the minimization of precursor emissions from the furnace by suitable techniques such as e.g. H202 injection to the post-combustion region [5]. Consequently, on-line measurements of chlorophenols (preferentially 2,4,6, trichlorophenol, see [4]) are required as input parameters for flame optimization. These measurements should be carried out close to the furnace exit. Indeed, for the boiler section a correlationship between 2,4,6 trichlorophenol and dioxin toxicity equivalents has been reported in the literature [6]. However, also in this case sensitivity is an issue and it would be interesting to get some information about your on-line sensitivities.

The success of such a reduction technique would then have to be surveyed further downstream (preferentially at the stack) by on-line measurements of suitable indicator substances such as 1,2 dichlorobenzene as suggested in the present paper.

REFERENCES

1. Tanada, T. N., Velazquez, J., Hemmi, N., and Cool, T. A., *Ber. Bunsenges. Phys. Chem.* 97:1516 (1993).
2. Oser, H., Thanner, R., and Grotheer, H. H., *Eighth International Symposium on Transport Phenomena in Combustion,* San Francisco, July 1995, proceedings in press.
3. Oser, H., Thanner, R., and Grotheer, H. H., *Fourth International Congress on Toxic Combustion Byproducts,* Berkeley, June 1995, *Combust. Sci. Technol.,* in press, 1996.
4. Oser, H., Thanner, R., and Grotheer, H. H., *1996 International Incineration Conference,* Savannah, GA, May 1996, proceedings in press.
5. Geiger, G. L., Martinez, A., Clausen, C. A., and Cooper, C. D., *I&EC Special Symposium,* ACS, Atlanta, September 1995.
6. Kaune, A., Lenoir, D., Nikolai, U., and Kettrup, A., *Chemosphere* 29:2083 (1994).

Author's Reply. A reliable comparison of different REMPI-TOF apparatus sensitivity needs a careful balancing of various parameters because the obtained detection limits (DL) are strongly dependent from e.g. laser power, the used data acquisition/analysis technique and, even more important, from the spectroscopic transition used for the REMPI-process.

The REMPI-wavelengths chosen in the DL-measurements from Oser et al. (Refs. 2–4 in the comments) differ from those used by Tanada et al. [1]. For naphthalene detection Tanada et al. (Ref. 1 in the comments) used a resonance within the weak S_1-state (301.6 nm, guarantees high selectivity), whereas in Oser et al. (Ref. 3 in the comments) the very intense S_2-state was used (278.5 nm, overlapping vibronic bands). Further on, the dichlorotoluene DL of Tanada et al. was obtained for the 2,4-isomer, whereas Oser et al. (Ref. 2 in the comments) considered the 2,5-isomer (ionization efficiencies of isomers can be very different).

Therefore the DL from Oser et al. and Tanada et al. are incomparable and the factors given in the question meaningless. The sensitivity increase by a factor of 10 due to Oser et al. given in the paper was not quoted erroneously but estimated from geometrical data (i.e. from the reduced distance x between nozzle and ionization region and $1/x^2$-dependence of the ionization yield). The new results [1] (see also Ref. 4 in the comments) quoting a DL-decrease for benzene by a factor of 90 in respect to Tanada et al. (absolute: 1ppt, S/N = 1, 100 lasershots averaged) were not available when we wrote our paper. The vibronic S_1-transition used by Oser et al. (252.87 nm) is more intense than those used by Tanada et al. (259.0 nm), leading to a DL-decrease of about a factor 50 (neglecting possible differences in laser power etc.) which is factor five better than our estimation in the paper. Nevertheless, the absolute benzene-DL of 1 ppt by Oser et al. represents a promising result, confirming the applicability of the REMPI-based concepts for on-line trace analysis. However, the main work necessary in future will be located in the field of sample acquisition, handling and calibration.

Concerning the second comment, as mentioned in the paper a careful analysis of the spectroscopic properties is necessary in order to find out the optimal ionization conditions. By using the theoretical methods described by Zimmermann et al. in Ref. 26 of the paper, we estimated the ionization potential of 2,4,6-Trichlorophenol from a quantum chemical calculation to be around 9.51 eV, leading to an one-color limit of approximately 261 nm. Regarding the location of the S_1-transition [origin: 293.89 nm, Tembreull et al. (Ref. 6 in the paper)] there is absolutely no chance to ionize 2,4,6-Trichlorophenol by one-color REMPI-ionization via this state. In principal, a one-color REMPI-detection via higher electronic states is possible, but not well suited for analytical purposes due to massive losses in spectral and mass spectrometric selectivity (many compounds show overlapping UV-bands and increased fragmentation). If it turns out that an on-line monitoring of 2,4,6-Trichlorophenol is necessary, one has to accept the more complex two-color ionization scheme (probably also other PCDD precursor/indicator-compounds with better REMPI-properties can be found). As mentioned in our pa-

per, the sensitivity losses due to rapid inter system crossing induced by chlorine substitution can be overriden by using a short-wavelength laser for the ionization step (see Figure 4b). Up to now we have not measured detection limits (DL) of compounds needing two color REMPI-steps. Our actual one-color DL (estimated from GC-REMPI-TOF measurements [20]) are in the same order of magnitude as those reported from Tanada et al. In order to increase the sensitivity a new ion source, utilizing an unskimmed, free jet (similar as in Ref. 2, below, and in Ref. 19 of the paper) is under examination. Results from first investigations of the REMPI-ionization in the vicinity of the nozzle orifice (1 to 5 mm) have been presented recently [3].

REFERENCES

1. Oser, H., Thanner, R., and Grotheer, H.-H., *Organohalogen Compounds* 27:99 (1996).
2. Weyssenhoff, H. V., Selzle, H. L., and Schlag, E. W., *Z. Naturforsch* 40a:647 (1985).
3. Zimmermann, R. et al., *RIS96-Proceedings,* AIP Press, 1996, in press.

•

Hans ter Meulen, University of Nijmegen, The Netherlands. Do you see fragmentation effects due to multiphoton processes, which might influence your analysis, especially in the case of larger aromatic molecules?

Author's Reply. For 1 + 1 two-photon REMPI ionization schemes only moderate laser powers are necessary. Therefore, fragmentation of the larger aromatics is not critical. This picture changes if REMPI processes of higher order (e.g. 1 + 2 three-photon REMPI) or nonresonant multi photon ionization (NRMPI, e.g. with intense 248 nm KrF-excimer laser or 266 nm Nd:YAG laser light) are used. Under these conditions indeed massive fragmentation can occur, making the latter REMPI-techniques less favorable for the analysis of very complex mixtures.

Twenty-Sixth Symposium (International) on Combustion/The Combustion Institute, 1996/pp. 2869–2875

INDUSTRIAL COMBUSTION CONTROL USING UV EMISSION TOMOGRAPHY

ALFRED LEIPERTZ
Lehrstuhl für Technische Thermodynamik (LTT)
Universität Erlangen-Nürnberg
Am Weichselgarten 8, D-91058 Erlangen, Germany

RALF OBERTACKE AND FRANZ WINTRICH
BFI Entsorgungstechnologie GmbH
Eggerscheidter Str. 57, D-40883 Ratingen, Germany

A new strategy for industrial combustion monitoring and control is presented which is based on UV emission spectroscopy measurements in combination with tomographic evaluation procedures. In contrast to usual closed-loop control for low pollutant combustion on the basis of flue gas composition measurements, this new strategy prevents the production of combustion NO_X by an early detection of NO_X generating flame radicals in a two-dimensional plane of the combustion system. Preliminary results for the usability of this new control strategy are presented. The tomographic sensor system for the control loop has been tested in various combustion systems. In an incineration station, a strong correlation of high temperature and high NO_X flue gas emission with the appearance of NH and CN radiative emission bands were found. Under brown coal firing conditions in a tomographic test with two single UV sensors, the radial intensity distribution was calculated. Along a line perpendicular to the connecting line of the two sensors, the determination of the temperature found by comparing the spectra with Planck's function was in good agreement with suction thermocouple measurements. Using the same burner with propane fuel, the two-dimensional CH distribution in the longitudinal cross section was detected. These measurements indicate the principal usability of the new sensor and a strategy to prevent NO_X generation in industrial combustion systems in an early stage of development.

Introduction

Effective process control in technical combustion systems for minimizing the NO_x release has become more and more difficult. When using the flue gas composition as the input value for a closed-loop control, the time scale for the control and regulation system becomes very long compared to the combustion time scales. A suitable sensor placed inside the combustor to detect the two-dimensional distribution of temperatures and concentrations of several radicals and intermediate products in a plane simultaneously will allow a faster response. If this temperature and concentration information can be correlated to the NO_X emission of the combustion system, these data can be used for setting up a new control strategy for low-pollution industrial combustion.

Ultraviolet (UV) emission spectroscopy has been used extensively for the detection of combustion radicals [1–4]. The lack of thermal equilibrium is the major drawback of this technique in flames. For real quantitative information, laser absorption methods are more appropriate (see e.g., Refs. 5 and 6). On the other hand, emission spectroscopy for flame monitoring is very easy since it requires merely a lens and a spectrometer. For most of the combustion processes in power stations, a qualitative but easy measuring method leading to a quick overview of the combustion field is advantageous over quantitative and elaborate methods with sensitive equipment [7].

Indicator Species for NO_x Production

For NO_x production in heterogeneous combustion (e.g., in fluidized-bed combustion with a temperature of approximately 1000°C), the thermal NO_X path does not play the major role [8–10]. For slightly understochiometric conditions, the "prompt" NO path is also very weak. Thus, most of the NO_X is generated from the release and oxidation of the fuel nitrogen. Following Miller and Bowman [8], the following reaction paths can be identified as the most important contributors to the NO production where NO is formed via HCN and the NCO and HNCO intermediates:

$$\text{fuel N} + \ldots\ldots \rightarrow \text{HCN} \qquad (1)$$

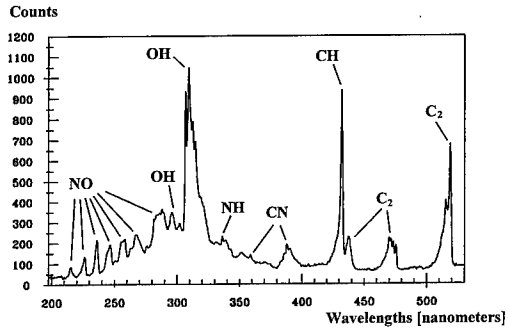

FIG. 1. Emission spectrum of an ammonia-doped butane flame.

$$HCN + O \rightarrow NCO + H \quad (2)$$

$$NCO + H \rightarrow NH + CO \quad (3)$$

$$HCN + OH \rightarrow HNCO + H \rightarrow NH_2 + CO \quad (4)$$

$$NH_2 + OH \rightarrow NH + H_2O \quad (5)$$

$$NH + H \rightarrow N + H_2 \quad (6)$$

By this path, the N radical is produced, which governs NO formation

$$N + O_2 \rightarrow NO + O. \quad (7)$$

Additionally, even when weak under these conditions, the Fenimore "prompt" NO_X path is initiated by

$$N_2 + CH_x \rightarrow HCN, CN \quad (8)$$

providing HCN for the reaction steps 2 and 4. From the reaction equations 1–8, the following molecules and radicals can be identified as possible NO precursors and indicators: NO itself, OH, (H)CN, NH, and CH.

Spectroscopy of Excited Species

Radiative flame emissions from heterogeneous industrial combustion consist of light contributions of continuum radiation from the dispersed phase following Planck's law and of band emissions from the gas-phase chemiluminescence. Diatomic molecules, and in particular all the above-mentioned species, have electronic energy transitions in the UV and visible (VIS) region [11–13], as shown in the measured spectrum in Fig. 1. The NO radical exhibits such strong contributions in a simple flame only when the flame is doped with ammonia, producing high rates of NO, which may not be typical for all the combustion processes to be investigated. Molecular nitrogen and oxygen have transitions only in vacuum UV and are not easily detectable with relatively simple spectroscopic equipment that may be considered to be applicable in hostile industrial environments. For both reasons, the detected spectral range used in our sensor system spans from 300 nm to 450 nm, as indicated in Fig. 2, providing a better spectral resolution for the gas species of most interest.

Since electronically excited states in flames are not generated by thermal excitation but by the fast release of the chemically bound energy (chemiluminescence), thermal equilibrium cannot be expected. Thus, the determination of temperature and concentration is in principle not possible. The spectral intensity of the observed transitions depends on the strength of the reaction, and the broadband intensity distribution of a transition can be considered as a more qualitative measure of the presence of a particular species [14]. Taking the spectrally resolved intensities in a plane of the flame or the combustor, the appearance of several species can be observed within the combustion field simultaneously. This information will be sufficient for the control of most combustion processes. In the presence of soot and/or dust particles, the temperature can be derived from the blackbody radiation within the same spectral region. The resulting radiative emission over the wavelength range $\lambda_0 + \Delta\lambda$ of a gas flame containing a dispersed particle phase can be calculated by [15]

$$I_\varphi(\lambda_0) = \int_{\lambda_0}^{\lambda_0+\Delta\lambda} \int_{L_\varphi} S(\lambda)\cdot[I_B(\lambda, T(x,y)) + I_G(\lambda,x,y)]\cdot \cdot \exp\{-\int_{L_\varphi} [k_B(\lambda,x',y') + k_G(\lambda,x',y')]ds'\}dsd\lambda \quad (9)$$

with the blackbody radiation

$$I_B(\lambda, T(x,y)) = \varepsilon_B \cdot c_B(x,y)\cdot A_B(x,y) \cdot \Delta\Omega/4\pi \cdot B[\lambda, T(x,y)] \quad (10)$$

and the Planck function $B(\lambda, T)$. The temperature can be determined if the components I_B and I_G can be separated in the spectrum. The separation of Planck's radiation from band emissions is shown in Fig. 2, where the Planck's functions for several temperatures have been compared to the measured spectrum. The temperature is found by subtracting the band spectrum of the gas emissions to give about 1200°C.

For a cloud of soot or dust, the emissivity ε_B depends on wavelength and may deviate from unity. This is particularly important for temperature evaluation using ratio pyrometry with the emission intensities at two different wavelengths [16,17]. Here, it is more accurate to calculate ratios for a couple of hundred pairs of wavelengths of a measured spectrum, avoiding the gas band emissions and taking the average as the temperature result. This, in a more convenient but also more time consuming way, has been done here by fitting the measured curve to the Planck's function. The accuracy was found to be

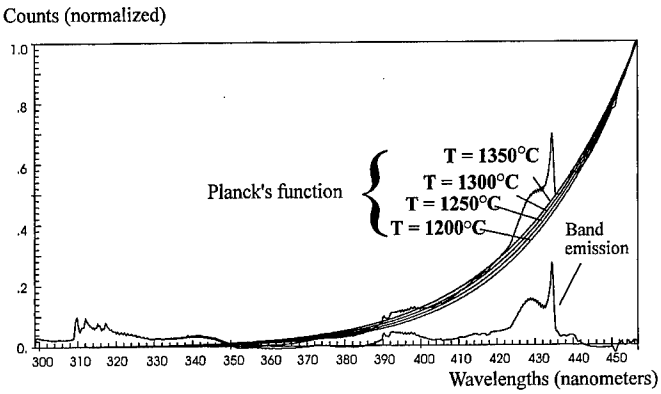

FIG. 2. Separation of blackbody radiation and band emission. Comparison with Planck's function gives a temperature of 1200°C.

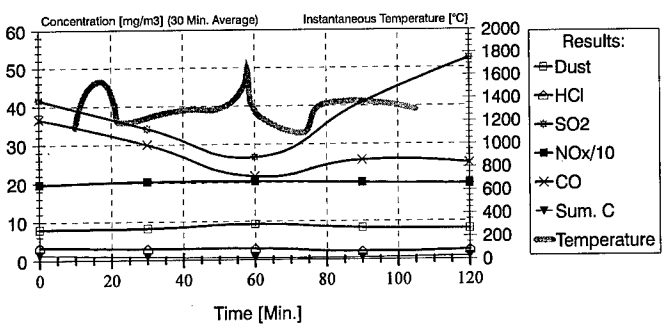

FIG. 3. Course of temperature taken from the spectra and flue gas components.

better than 20°C in simple flames and about twice this value in actual combustion systems. Any kind of distortion can be recognized by the visualization of the gas band emissions and of the blackbody radiation in the curve fit method.

For temperature evaluation, a very accurate calibration of the detection system is necessary for spectral sensitivity and detector linearity. Our system has been calibrated with a blackbody radiation source between 850 and 1350°C.

Application to Industrial Combustion Systems

The measuring principle, in a first stage without tomographic evaluation procedures, has been tested in an incineration station using a relatively simple spectroscopic configuration [18]. The temperature has been determined and compared with the values of a conventional flue gas analyser. The results are shown in Fig. 3. Due to the different time scales of the flue gas measurements and the temperatures determined from the spectra, a direct correlation between both cannot be given. An integration of the instantaneous temperature measurements, particularly taking into account the temperature peaks, may, however, show the expected indication that the strong temperature peak of nearly 1800°C correlates well with the high rates for NO_X and with the low rates for CO and SO_2 found in the flue gas data averaged over the time interval that contained the temperature peak.

Figure 4 shows the temperature in comparison with the detected band radiation of the species CH, CN, NH, and OH. Temperature and species intensities have been determined together from a single spectrum at the same time. OH and CH follow the temperature qualitatively, whereas NH and CN follow very precisely. Because of the positive correlation of high temperature and high NO_X, the appearance of CN and NH can be used as early indicators of NO_X production. A control strategy based on the CN/NH signals will yield an instantaneous response to the control system for the manipulation of the actual combustion parameters such as secondary air flow.

The Sensor and Tomography Concept

The new sensor comprises imaging optics with a detection angle of 90 degrees and a spectrometer (Fig. 5). The spatial image is projected horizontally and the spectral information vertically onto a 512 × 512 CCD array with a 12-bit A/D converter. The CCD stores the spectral information of the irradiation over an angle of 90 degrees instantaneously [18]. The CCD array has been cooled to stay at 15°C. In

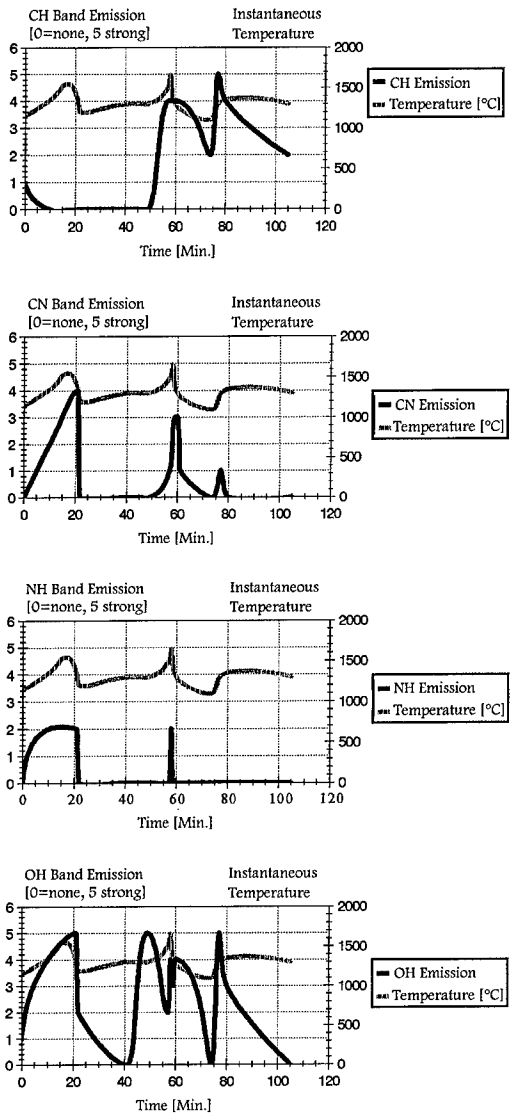

FIG. 4. Course of temperature and of CH, CN, NH, and OH taken in an incineration station.

this temperature range, the dark current counts double for each 6–7°C.

The detected signal is the radiation integrated over the optical path from the individual emitters to the detector (see equation 7), so no local information is available. Using two sensors simultaneously together with a tomographic reconstruction algorithm, local intensity values can be achieved [19–21].

Here, a tomographic algorithm was used which was developed by Setzepfandt [22] and Wübbeling [23] and which is especially adapted for fan beam tomography as proposed by Wakai et al. [24] with only two or more projections. A complete tomographic reconstruction takes less than 10 seconds for the spatial detection of six different molecular species and of the local temperature distribution.

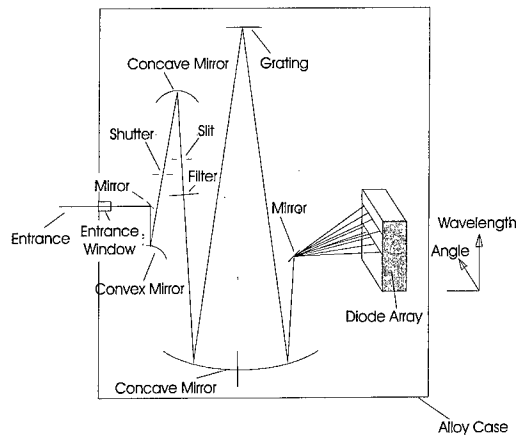

FIG. 5. Beam path inside the sensor.

Figure 6 shows the complete system in the 180-degree position as it was used for the measurements. The reliability of the tomographic algorithms has been checked by imposing sample inputs to the program. Problems came up only for signals that appeared on or close to the connecting line of the two sensors.

Measurements in a Power Station Test Facility

Tomographic measurements have been performed in a 1-MW top-fired combustor with an inner diameter of 2 m. The combustor is normally fired with brown coal and with propane for the preheating phase. The sensors were placed approximately 0.5 m below the burner outlet with a detection angle of 52 degrees. Two different measuring planes were used, the first one oriented perpendicular to the flame axis, the second one parallel to the flame axis. Figures 7–9 show results for the two different flames. Figure 7a shows the setup for the detection in a radial plane crossing a brown coal flame. Figure 7b shows the resulting intensity distribution from which local temperatures can be derived. Figure 8 presents the calculated temperature distribution perpendicular to the connecting line of the two sensors. In order to check the results, temperature measurements with suction thermocouples were taken along the same line. The comparison shows that the agreement of the two curves is quite good although the temperature detected with the sensors is about 50°C higher. The reason was the heat capacity of the combustor walls, which leads to a very slow response to changes of flame temperature. Since the tests were made starting with a high flame temperature and then changing the O_2

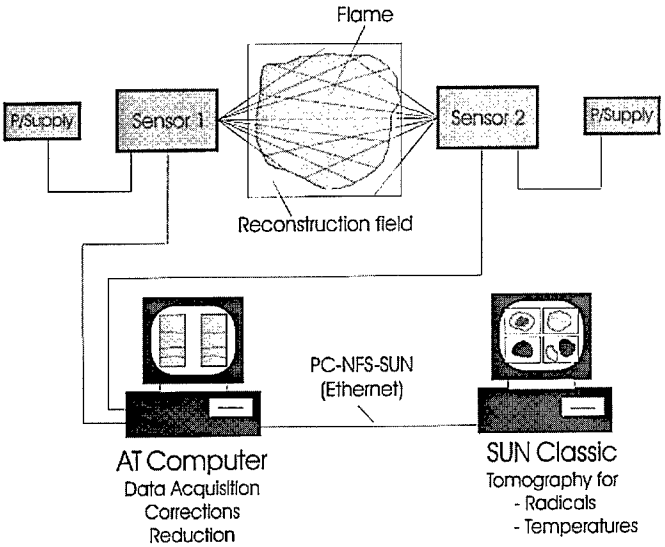

FIG. 6. Tomographic system with two sensors.

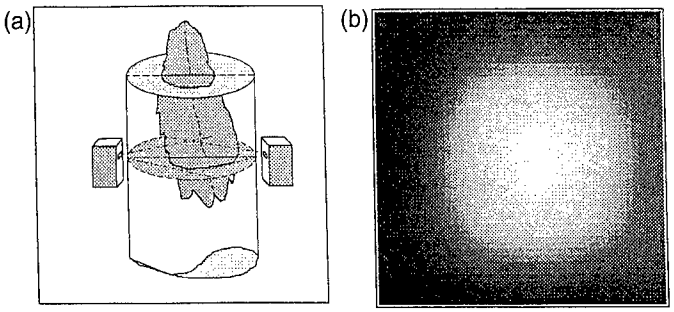

FIG. 7. (a) Position of the sensors in a brown coal fired power station test facility. (b) Tomographic result of the measurements in a plane of the combustor.

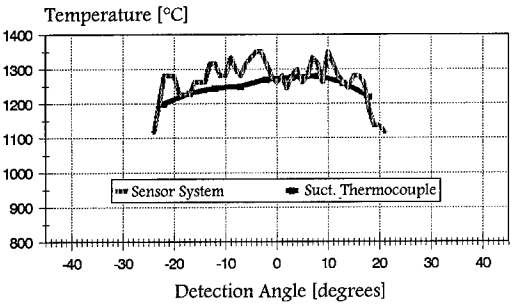

FIG. 8. Comparison of the local temperature perpendicular to the connecting line of the two sensors (Fig. 7a) taken with a suction thermocouple and calculated from the sensor spectra.

concentration in order to lower the flame temperature, the walls were still slightly hotter than the flame itself.

Figure 9a shows the position for the detection of a longitudinal plane in a propane flame. The tomographic result for the CH distribution is shown in Fig. 9b. Because of the above-mentioned ambiguity for the use of only two sensors, the reconstruction for the region near the connecting line is not very precise.

Conclusion

A new sensor system has been constructed which is based on UV emission spectroscopy and tomographic reconstruction for two-dimensional temperature and combustion radical detection. It has been tested for its applicability in industrial environments for monitoring combustion processes. Using the UV-band emission as an input value for a closed-loop control instead of the flue gas concentrations, a faster response and therefore a more effective manipulation of the combustion process will be possible. As most of the combustion processes are nonlinear, the evaluation of the spectral information given by the sensor system may be too complex for a fast control unit. For this reason, a classification strategy using neural networks [25,26] together with fuzzy tools [27] is currently being developed.

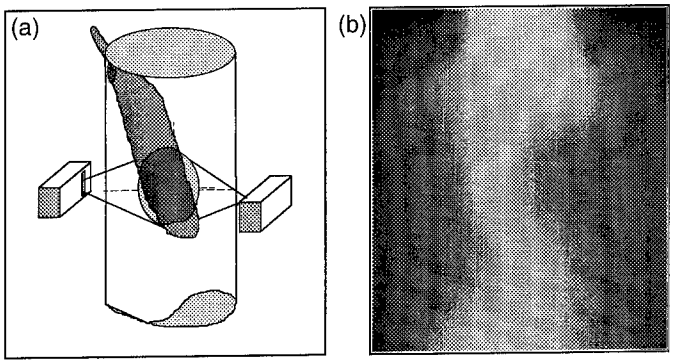

FIG. 9. (a) Position of the sensors relative to the propane flame for longitudinal detection. (b) Tomographic evaluation of the CH distribution in the propane flame.

Nomenclature

A_B	cross section of the blackbody emitters
$B(\lambda, T)$	Planck's function
c_B	particle load (concentration) at (x, y)
ds	length of the unit cell of emission from the most distant emitter (e.g., the combustor wall) to the detector, specified in coordinates (x, y)
ds'	length of the unit cell of extinction from (x, y) of the emission to the detector, specified in coordinates (x', y')
$I_\varphi(\lambda_0)$	intensity detected by the detector at an angle φ and wavelength λ_0
$I_B(\lambda, T(x, y))$	blackbody radiation at wavelength λ, position (x, y), and temperature T
$I_G(\lambda, x, y)$	molecular band emission at (x, y) of the gas phase at wavelength λ
$k_B(\lambda)$	extinction by particles at wavelength λ
$k_G(\lambda)$	molecular band extinction of the gas phase at wavelength λ
L_φ	length of line of sight at angle φ
$S(\lambda)$	spectral sensitivity
T	temperature
ε_B	emissivity of the greybody emitters
ε_G	emissivity of the gas phase
φ, φ'	detection angle
λ	wavelength
$\Delta\Omega$	angle of aperture

Subscripts

G	gas phase
B	blackbody

Acknowledgments

The present work was supported by RWE Energie AG, RWE Holding AG, and RWE Entsorgung AG and done in close cooperation with ESYTEC Energie- und Systemtechnik GmbH. The tomographic calculations in this paper were performed by Frank Wübbeling from the Universität Münster, Institut für Numerische und Instrumentelle Mathematik. The authors gratefully acknowledge fruitful discussions on the NO_x reaction pathways with Professor Henning Bockhorn from the Universität Karlsruhe (TH), Institut für Chemische Technik.

REFERENCES

1. Gaydon, A. G. and Wolfhard, H. G., *Flames, Their Structure, Radiation and Temperature,* Chapman and Hall, London, 1953.
2. Gaydon, A. G., *The Spectroscopy of Flames,* Chapman and Hall, London, 1974.
3. Uchiyama, H., Nakajima, M., and Yuta, S., *Appl. Opt.* 24:4111–4116 (1985).
4. Hertz, H. M. and Faris, G. W., *Opt. Lett.* 13:351–353 (1988).
5. Dodge, L. G., *Prog. Astronaut. Aeronaut.* 53:155–175 (1977).
6. Vanderhoff, J. A., *Combust. Flame* 84:73–92 (1991).
7. Kauranen, P., Andersson-Engels, S., and Svanberg, S., *Appl. Phys. B* 53:260–264 (1991).
8. Miller, J. A. and Bowman, C. T., *Prog. Energy Combust. Sci.* 15:287–338 (1989).
9. Williams, A., Woolley, R., and Lawes, M., *Combust. Flame* 89:157–166 (1992).
10. Aho, M. J., Hämäläinen, J. P., and Tummavuori, J. L., *Combust. Flame* 95:22–30 (1993).
11. Wallace, L., *Band-Head Wavelength of C_2, CH, CN, CO, NH, NO, O_2, OH, and Their Ions,* The Astrophysical Journal, Supplement Series, The University of Chicago Press, Chicago, 1962, pp. 165–287.
12. Herzberg, G., *Molecular Spectra and Molecular Structure: I. Spectra of Diatomic Molecules,* Van Nostrand, Princeton, 1966.
13. Huber, K. P. and Herzberg, G., *Molecular Spectra and Molecular Structure: IV. Constants of Diatomic Molecules,* Van Nostrand, New York, 1979.
14. Obertacke, R., Leipertz, A., Spiegel, H., and Wintrich,

F., *Fortschrittliche Energiewandlung und -anwendung*, VDI-Berichte 1029, Verein Deutscher Ingenieure (VDI), Düsseldorf, 1993, pp. 183–199.
15. Hall, R. J. and Bonczyk, P. A., *Appl. Opt.* 29:4590–4598 (1990).
16. Grosshandler, W. L., *Combust. Flame* 55:59–71 (1984).
17. Atal, A. and Levendis, Y. A., *Combust. Flame* 98:326–349 (1994).
18. Obertacke, R., Doctoral Thesis, Univ. Erlangen-Nürnberg, Berichte zur Energie- und Verfahrenstechnik (BEV), Heft 95.1, Esytec, Erlangen, 1995.
19. Best, P. E., Chien, P. L., Carangelo, R. M., Solomon, P. R., Danchak, M., and Ilovici, I., *Combust. Flame* 85:309–318 (1991).
20. Mewes, D. and Renz, R., *Chem. Ing. Technol.* 63:699–715 (1991).
21. Beiting, E. J., *Opt. Lett.* 16:1280–1282 (1991).
22. Setzepfandt, B., Ph.D. Thesis, Univ. Münster, Münster 1993.
23. Wübbeling, F., private communication (Ph.D. Thesis, Univ. Münster), 1994.
24. Wakai, K., Kamiya, K., Sakai, S., and Shimizu, S., "Instantaneous Measurement of 2-D Temperature and Density Distributions of Flames by a Two-Band Emission-CT-Pyrometer," SPIE's International Symposium on Optical Applied Science and Engineering, The International Symposium on Infrared Technology XVIII, San Diego, 1992. Paper No. SPIE 1762-60.
25. Gutmark, E., Parr, T. P., Hanson-Parr, D. M., and Schadow, K. C., *Twenty-Third Symposium (International) on Combustion,* The Combustion Institute, Pittsburgh, 1990, pp. 1101–1106.
26. Allen, M. G., Butler, C. T., Johnson, S. A., Lo, E. Y., and Russo, F., *Combust. Flame* 95:205–214 (1993).
27. Tao, W. and Burkhardt, H., *Vision-Guided Flame Control Using Fuzzy Logic and Neural Networks,* Information No. 5/92 SFB 238, TU Hamburg-Harburg, Hamburg, 1992.

COMMENTS

Dr. Michele Sala, Ansaldo Energia, Italy. The new sensor shows temperature values differing by about 50°C from suction pyrometer measurements. Which are the most reliable values?

Author's Reply. The suction thermocouples we used for comparative measurements probably provide the more reliable temperature values as nearly no radiation correction is necessary in this measurement situation inside the furnace. This, however, does not affect the most important messages of the paper. Besides the two-dimensional detection of flame radicals the new UV sensor offers, simultaneously, information on the two-dimensional temperature distribution within the whole furnace plane investigated. Furthermore, an inaccuracy of 30–50°C seems to be tolerable for controlling low pollutant industrial combustion systems.

Twenty-Sixth Symposium (International) on Combustion/The Combustion Institute, 1996/pp. 2877–2883

NUMERICAL SIMULATION OF A COUNTERFLOW DIFFUSION FLAME IN SUPERSONIC AIRFLOW

KENICHI TAKITA
Department of Aeronautics and Space Engineering
Faculty of Engineering, Tohoku University
Aramaki, Sendai, 980-77, Japan

TAKASHI NIIOKA
Institute of Fluid Science, Tohoku University
Katahira, Sendai, 980-77, Japan

A counterflow diffusion flame of hydrogen, developed in the forward stagnation-flow region of a porous cylinder in supersonic airflow (which can be considered as a flame of the "Tsuji-burner" in supersonic airflow), was analyzed numerically by solving the two-dimensional Navier-Stokes equations for multispecies. A counterflow diffusion flame, having a temperature distribution and concentration distributions of species in the direction of the burner surface, can be established in the very thin region behind a detached shock wave. It is shown that thermal quenching occurs when the flame approaches the surface of a porous cylindrical burner as in the case of a normal "Tsuji-burner." The decrease of static temperature or Mach number (equivalent to the flow velocity) of airflow causes flame extinction, in contrast to the case of subsonic airflow. Flame temperature approaches the stagnation temperature in the region of high static temperature and has maximum heat release at a certain static temperature. This is due to the increase of flow velocity and stretch rate based on the increase of static temperature, but appreciable flame extinction does not occur even if the stretch rate becomes much higher, because the stagnation temperature exceeds the critical temperature, which has previously been discussed for a high-temperature subsonic airflow system.

Introduction

Development of the scramjet engine has recently become a major interest for many combustion engineers and researchers. One of the interesting aspects of the scramjet engine combustor is the existence of shock waves which are established, for example, just in front of fuel jets, and produce hot air. Therefore, a counterflow diffusion flame of hydrogen obtained by using heated air has been investigated theoretically by some researchers [1–3], and attention has been paid to the fundamental aspects of combustion. Some characteristic features of such a flame are described in the reports of these researchers; for example, flame extinction never occurs at any stretch rate when the temperature of the oxidizer exceeds a critical temperature [1,2]. However, almost the same one-dimensional governing equations and the same numerical code [4] were used in these studies, and the flame stretch rate was chosen as the main parameter. The effects of the shock wave were not taken into consideration in these studies. The shock wave not only results in a hot oxidant but also changes the flow field, and the location of the shock wave fixed by the Mach number must characterize the flow pattern between the shock wave and the fuel jet surface. Therefore, the existence of a shock wave complicates the establishment of the diffusion flame.

On the other hand, two- and three-dimensional numerical simulations of a combustor of the Scramjet engine in a complicated flow field including shock waves [5] were conducted from the point of view of aeronautical engineering. Since much attention was given to the detailed structure of the flow field or to a numerical scheme, it was not possible to properly examine critical phenomena such as extinction or ignition in these simulations.

A model that can be a bridge between combustion science and aeronautical engineering is needed for a deeper understanding of combustion and the development of the Scramjet engine. Accordingly, the authors [6] analyzed a counterflow diffusion flame in supersonic airflow (which can be considered as a flame of the "Tsuji-burner" [7] in supersonic airflow) and demonstrated fundamental characteristics of this flame, using the activation energy asymptotics with a one-step overall reaction model. It was demonstrated that an extinction point appeared on the low Mach number side in the case of supersonic air-

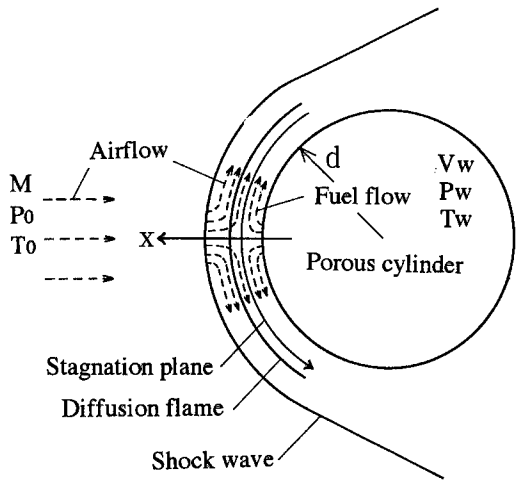

FIG. 1. Schematic of the flow configuration.

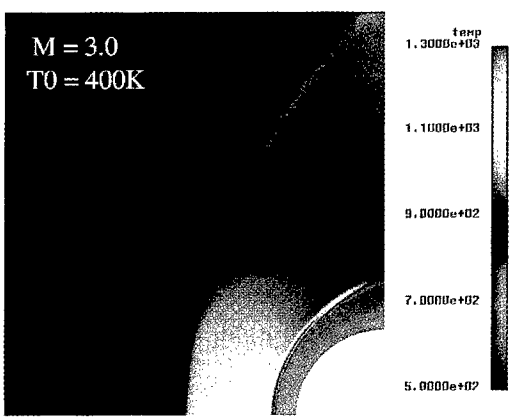

FIG. 2. Temperature contour around the burner for the case of $M = 3.0$, $T_0 = 400$ K, $V_w = 300$ m/s.

flow, in contrast with the case of subsonic airflow in which an increase of the flow velocity resulted in flame extinction. As with the authors' previous analysis, two-dimensional, compressible Navier-Stokes equations with multispecies and full chemical kinetics are calculated for a counterflow diffusion flame of hydrogen established in supersonic airflow in this study. Detailed structures and features of this counterflow diffusion flame with regard to static temperature and Mach number of airflow as main parameters are investigated.

Formulation

The configuration of the flow field is shown in Fig. 1. A fuel stream of pure hydrogen issued uniformly from a porous cylinder and a supersonic airflow form a counterflow field behind a detached shock wave. The two-dimensional, compressible Navier-Stokes equations in the generalized curvilinear coordinate for multispecies constitute the governing equations. The data of specific heats and enthalpies for each species are according to JANAF tables [8]. The transport coefficients of viscosity, thermal conductivity, and diffusion coefficients for species are obtained from the kinetic theory [9,10] based on Chapman-Enskong's theory, and Wilke's mixing rule [11] is used for mixtures. The hydrogen/oxygen combustion model by Stahl and Warnatz [12] constituted from 9 species (H_2, O_2, H_2O, H, HO_2, OH, O, H_2O_2, N_2 [inert]) and 37 elementary reactions is used in the present calculation. The validity of the model was also confirmed by Ju and Niioka's numerical simulation for ignition in the supersonic mixing layer [13,14].

The time-dependent Navier-Stokes equations are solved by the finite difference method only for the upper domain above the centerline of Fig. 1 because of the symmetry condition, and numerical results at steady state are discussed in this paper. The computational grid, which is compressed around the stagnation plane or the burner surface for high resolution, has 121 × 51 grid points. The AUSM scheme developed by Liou et al. [15] is used for the finite difference of convective terms in order to avoid a carbuncle phenomena which appears in the simulation of flow field around a blunt body in a supersonic flow. Detailed discussions of the AUSM scheme are not included in this paper, since the prevention of the carbuncle phenomena is a recent topic in the field of computational fluid dynamics and has been described in various articles. The computer code was tested [6] on the shock standoff distance of a cylinder in supersonic airflow with comparison to experimental data by Billig [16]. Good agreement between numerical results and experimental data are shown in Ref. 6.

Mach number (M), temperature (T_0), and pressure (P_0) of the upper uniform stream, and velocity (V_w), and temperature (T_w) of the fuel uniform flow are given as boundary conditions. Only the injection pressure of fuel (P_w) is determined by extrapolation from the upstream value in accordance with the theory of characteristics. Additionally, outflow boundary conditions are determined by the extrapolation from the upper-stream values. The diameter of the cylindrical porous burner is set at 0.01 m. A high fuel temperature (700 K) is given in consideration of the regenerative cooling in engines.

Results and Discussion

Structure of a Counterflow Diffusion Flame in Supersonic Flow

A typical temperature contour around a cylindrical burner in a supersonic flow is shown in Fig. 2.

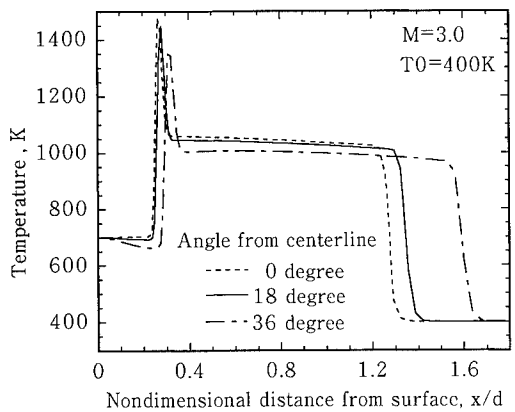

FIG. 3. Temperature distributions radial to the burner surface.

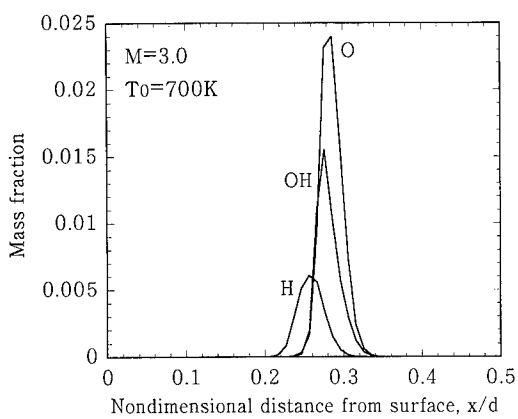

FIG. 4. Mass fractions of radicals on the centerline for $M = 3.0$, $V_w = 300$ m/s and $T_0 = 700$ K.

Boundary conditions in Fig. 2 are $M = 3.0$, $T_0 = 400$ K, $P_0 = 0.01$ MPa, $T_w = 700$ K, and $V_w = 300$ m/s (Mach number is about 0.15). The established flame seems to be independent of the detached shock wave but the shock wave determines the air temperature and the flow field. Since the supersonic airflow is the same up to the shock wave, the distance between the shock wave and the cylinder surface should determine the stretch rate in the subsonic airflow. Although dissociation of oxygen molecules occurs behind the detached shock wave, the amount of it is too small to affect the flame stability and structure in the total temperature range below 2000 K. As revealed by Fig. 2, the region where mixing and reaction occur is very narrow and so a very thin flame is formed near the stagnation plane behind the detached shock wave. The distance between the stagnation plane and the burner surface is in proportion to the momentum of fuel flow, except for very low velocity of fuel. Moreover, the curvature of the detached shock wave is much greater than that of the flame, and therefore, hydrogen is greatly accelerated along the cylindrical surface, and its temperature becomes lower than the temperature at injection.

The temperature distributions in the direction normal to the surface for three angles counted from the centerline are shown in Fig. 3. As the angle becomes larger, the flame temperature becomes lower, and then the flame is extinguished near the boundary of the computational domain in Fig. 2. This is also due to the decrease of the temperature of hydrogen in addition to the decrease of pressure. However, the main reason is the increase of the velocity gradient in the direction along the cylindrical surface, that is, an increase of flame stretch rate. The amount of H_2O as a reaction product becomes smaller in the same manner as temperature when the distance along the cylindrical surface from the stagnation point becomes larger. The maximum flame temperature and the maximum mass fraction of H_2O are given at the stagnation point, although the temperature and concentration profile can be considered almost flat in the Tsuji burner in subsonic airflow.

The mass fraction of radicals on the centerline is shown in Fig. 4 ($T_0 = 700$ K). The peak for the H radical is located on the fuel side in contrast with the O and OH radicals. If a mole fraction is chosen instead of a mass fraction, among the radicals, the H radical must have the maximum, as reported by Gutheil and Williams [1].

The Flame Stability Limit at Low Fuel Velocity

According to the early study on the counterflow diffusion flame established in the forward stagnation region of a porous cylinder [17] in subsonic airflow, the so-called Tsuji-burner, two flame-stability limits exist. One is a stretch extinction limit due to a large stagnation velocity gradient, and the other is a thermal quenching limit when fuel-ejection velocity becomes too small.

Thermal quenching by heat loss to the burner is also obtained in the present numerical simulation of a counterflow diffusion flame in supersonic airflow in the same manner as for subsonic airflow. Figure 5 shows the temperature contour around the burner under the same conditions as those of Fig. 2 except for the fuel velocity ($V_w = 50$ m/s). The shock wave and the stagnation plane approach the burner in contrast with the case in Fig. 2, and a flame zone cooled by the solid surface finally disappears. The maximum temperature is equal to the stagnation temperature, and the amount of H_2O as a product becomes almost zero. Figure 6 shows the nondimensional distance of the shock wave and the stagnation plane from the burner surface in terms of fuel velocity. Both distances become greater with fuel ve-

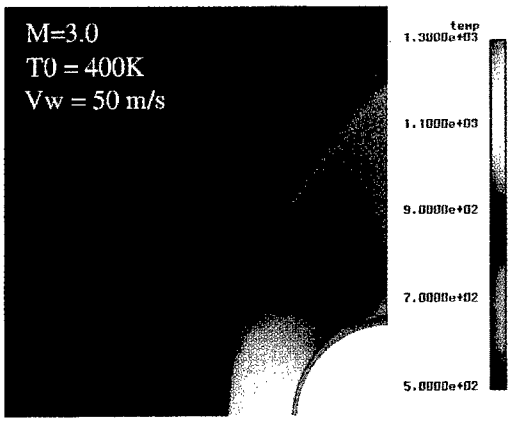

FIG. 5. Temperature contour around the burner for T_0 = 400 K, V_w = 50 m/s.

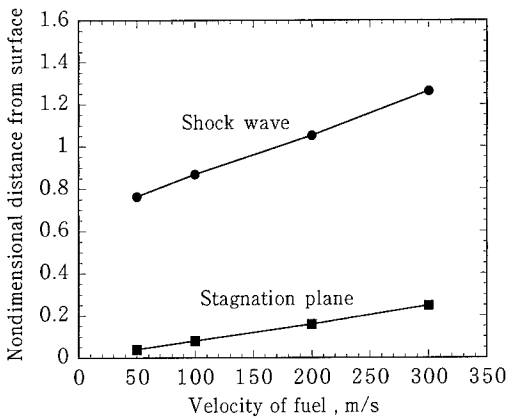

FIG. 6. The effect of fuel velocity on the nondimensional distance between the burner surface and the shock wave or the stagnation plane.

locity. The slope of the shock wave is a little larger than that of the stagnation plane, showing gas expansion due to reaction.

There is slight difference in the Mach number of the fuel flow between Fig. 2 and Fig. 5, and so the heat loss to the burner is the main reason for the extinction in Fig. 5. When the fuel velocity exceeds the critical value of fuel velocity, the maximum flame temperature and the mass fraction of H_2O do not depend much on fuel velocity. In addition, further calculation shows that the effect of fuel temperature on the flame stability or the flame structure is very small. This suggests that the conditions on the air side, where flame always exists, are extremely dominant. The other flame-stability limit caused by a large stagnation velocity gradient is discussed in the following sections.

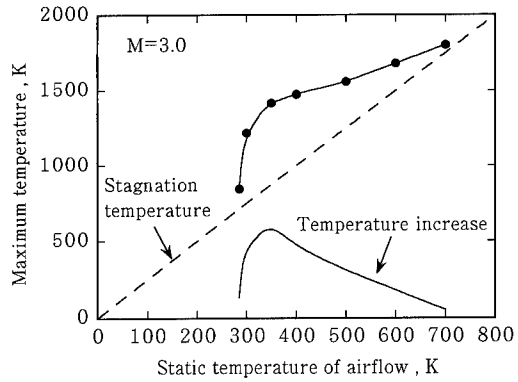

FIG. 7. Dependence of the static temperature of the upper airflow on the maximum temperature in the reaction zone, for M = 3.0 and V_w = 300 m/s.

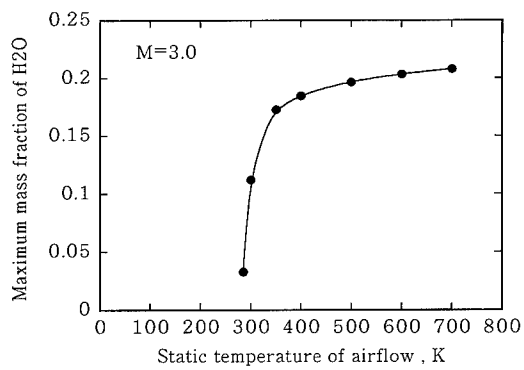

FIG. 8. Dependence of the static air temperature on the maximum mass fraction of H_2O.

Effect of Static Air Temperature

The effect of the static air temperature of the upper stream on flame stability and structure at constant Mach number is investigated in this section. Since the Mach number is the same, the pressure ratio across the detached shock wave and the distance between the stagnation plane and the burner surface are similar. The change of static temperature results in a change of total temperature due to the linear relation between these two temperatures, and so the total temperature is usually chosen as the main parameter in many supersonic combustion experiments using a supersonic wind tunnel.

The maximum flame temperature in terms of the air static temperature of the upper stream is shown in Fig. 7. The boundary conditions are M = 3.0, P_0 = 0.01 MPa, T_w = 700 K, and V_w = 300 m/s. The stagnation temperature calculated from the conservation of energy is shown in the same figure. The maximum temperatures are in the reaction zone, that is, the flame temperatures are obtained very

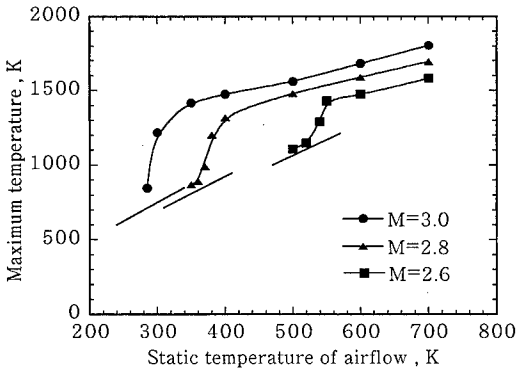

FIG. 9. The maximum temperatures for various Mach numbers.

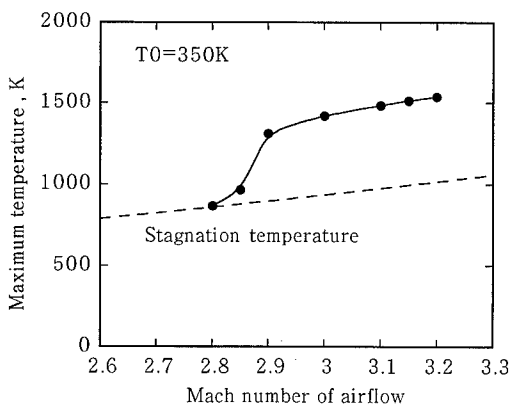

FIG. 10. Dependence of the Mach number of airflow on the maximum temperature.

close to the stagnation point. When the upper-stream temperature decreases, the flame temperature decreases rapidly and approaches the stagnation temperature around 300 K. This temperature is regarded as the extinction temperature of the upper stream. The extinction point is seen more clearly in Fig. 8, which shows the maximum mass fraction of H_2O in terms of static air temperature. When the static temperature decreases below 300 K, the mass fraction of H_2O goes to zero.

The flame temperature approaches the stagnation temperature again with an increase of the static temperature, after manifesting a maximum heat release around a static temperature of 350 K. On the other hand, the maximum mass fraction of H_2O increases monotonically with static temperature. Since the flame temperature does not become very high (1800 K at most) in this region, the effect of dissociation of products is not dominant. Therefore, the decrease of heat release in the high static temperature region is due to the increase of the stretch rate originated from the increase of flow velocity behind a detached shock wave. Actually, in spite of the large concentration of radicals at 700 K (Fig. 4), the flame temperature does not increase much in comparison with the case of 400 K.

Extinction does not occur on the high upper-stream temperature side, though the increase of static temperature may cause an increase of the flame stretch rate [$O(10^5)$]. The stagnation temperature increases with static temperature and then exceeds the so-called critical temperature [1,2] (about 1000 K). For example, when the static temperature reaches 700 K, the stagnation temperature exceeds 1600 K. Under such high temperatures, the rate of the termination reaction, $H + O_2 + M \rightarrow HO_2 + M$, is always much smaller than that of the chain-branching reaction, $H + O_2 \rightarrow OH + O$, and then appreciable extinction phenomena cannot be identified [1].

Figure 9 shows the flame temperature for different Mach numbers. The tendency of the flame temperature to approach the stagnation temperature with the increase of static temperature as well as with the decrease of static temperature can be seen for all Mach numbers. Moreover, it is shown in Fig. 9 that the total temperature at extinction becomes smaller with the Mach number of airflow. The increase of pressure may be the main reason for this phenomenon, since numerical simulations by Balakrishnan et al. [18] showed that the extinction strain rate for hydrogen flames increases rapidly with an increase of pressure.

In this study, the computation has been done in the limited range of pressure around 0.1 MPa at the stagnation point. The condition of higher pressure places severe demands on both time step and mesh size in the numerical simulations because the reaction rate becomes larger and the diffusion of the species decrease under high pressure. Careful consideration is needed as to whether a diffusion flame can be established in such an extremely thin mixing layer.

Effect of Mach Number

The flame stability limit has been examined for different Mach numbers at a constant static temperature. Figure 10 shows the maximum temperature in terms of Mach number for static air temperature of 350 K, $P_0 = 0.01$ MPa, $V_w = 300$ m/s, and $T_w = 700$ K. Stagnation pressure, distance from the stagnation plane to the burner, and location of the detached shock wave change with the Mach number of airflow.

Flame extinction occurs at a Mach number of 2.85 as seen in Fig. 10. The decrease of Mach number of the upper-stream airflow results in flame extinction in supersonic flow, in contrast with the case of subsonic flow in which flame extinction occurs when air velocity exceeds a certain critical value. This char-

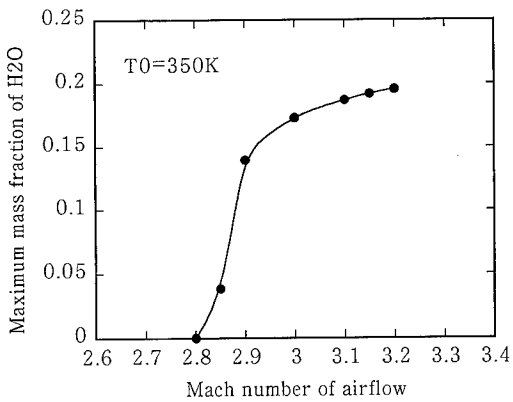

FIG. 11. Dependence of the Mach number of airflow on the maximum mass fraction of H_2O.

acteristic feature of counterflow diffusion flames in supersonic flow has been demonstrated by the use of asymptotic analysis [6]. The maximum mass fraction of H_2O under the same conditions as in Fig. 10 is shown in Fig. 11. It can be seen from this figure that the mass fraction of H_2O decreases rapidly at a Mach number of 2.85, as is the case in Fig. 7.

In Fig. 10, the flame temperature increases in parallel with the stagnation temperature, in contrast to the case in Fig. 8. At first, an increase of pressure with the Mach number was considered to be the cause. However, the pressure change is only 20% between Mach numbers 2.8 and 3.0. Calculation of the adiabatic flame temperatures at 0.1 and 0.2 MPa revealed that such a small change of pressure has only a weak effect on flame temperature, although an increase of pressure results in a greater stretch rate at extinction in the case of hydrogen fuel [18].

An increase of the Mach number of the upperstream airflow results in a higher temperature and a lower Mach number behind the detached shock wave. Airflow velocity, that is, stretch rate behind the detached shock wave, does not change much after all, because the high temperature and the low Mach number are offset. A further increase of the Mach number must cause the thermal dissociation of chemical species, and as a result, the flame temperature does not increase much and approaches the stagnation temperature again.

Concluding Remarks

The stability and the structure of a counterflow diffusion flame of hydrogen in supersonic flow was first numerically analyzed by solving the two-dimensional Navier-Stokes equations with multispecies and full chemistry. The characteristics of this flame can be summarized as follows:

1. The flame region where diffusion and reaction proceed is very narrow, and the distribution of temperature and fractions of species exists along the flame sheet. The maximum temperature and the maximum mass fraction of H_2O are obtained very close to the stagnation point. Flame extinction occurs when the Mach number of airflow decreases, as shown by the preceding asymptotic analysis.
2. Thermal quenching by heat loss to a burner occurs at very low fuel ejection velocities because the flame approaches the burner surface in the same manner as in the "Tsuji-burner."
3. The flame temperature in terms of the static temperature of airflow approaches the stagnation temperature in the high static temperature region subsequent to the maximum heat release at a certain static temperature. This is due to an increase of flow velocity and flame stretch rate in the region of high static temperature. Appreciable flame extinction does not occur at high stagnation temperatures over the critical temperature, though the stretch rate becomes very large.

Acknowledgment

The authors wish to thank Dr. Y. Ju of the Institute of Fluid Science, Tohoku University, for his valuable comments and suggestions. The first author is also grateful for the JSPS Fellowship for Japanese Junior Scientists.

REFERENCES

1. Gutheil, E., and Williams, F. A., *Twenty-Third Symposium (International) on Combustion*, The Combustion Institute, Pittsburgh, 1990, pp. 513–521.
2. Darabiha, N., and Candel, S., *Combust. Sci. Technol.* 86:67–85 (1992).
3. Kreutz, T. G., Nishioka, M., and Law, C. K., *Combust. Flame* 99:758–766 (1995).
4. Kee, R. J., Grcar, J. F., Smooke, M. D., and Miller, J. A., *A Fortran Program for Modeling Steady Laminar One-Dimensional Premixed Flames*, Sandia National Laboratories Report No.SAND85-8240, Sandia National Laboratories, 1985.
5. Hsieh, S. Y., Yang, V., Cherng, D. L., and Yang, H. T., AIAA Paper 94-3326, 1994.
6. Takita, K., and Niioka, T., *JSME Int. J. Series B* 39:440–445 (1996).
7. Tsuji, H., *Prog. Energy Combust. Sci.* 8:93–119 (1982).
8. Chase, M. W. Jr., et al., *JANAF Thermochemical Tables*, 3rd ed., *J. Phys. Chem. Ref. Data* 14(1), 1985.
9. Svehla, R. A., *Estimated Viscosities and Thermal Conductivities of Gases at High Temperatures*, NASA TR-132, 1962.

10. White, F. M., *Viscous Fluid Flow,* McGraw-Hill, New York, 1974.
11. Wilke, C. R., *J. Chem. Phys.* 18:517–519 (1950).
12. Stahl, G., and Warnatz, J., *Combust. Flame* 85:285–299 (1991).
13. Ju, Y., and Niioka, T., *Combust. Flame* 99:240–246 (1994).
14. Ju, Y., and Niioka, T., *Combust. Flame* 102:462–470 (1995).
15. Liou, M. S., and Steffen, C. J., *J. Comput. Phys.* 107:23–39 (1993).
16. Billig, F. S., *J. Spacecraft Rockets* 5:1247–1248 (1968).
17. Tsuji, H., and Yamaoka, I., *Eleventh Symposium (International) on Combustion,* The Combustion Institute, Pittsburgh, 1967, pp. 979–984.
18. Balakrishnan, G., Smooke, M. D., and Williams, F. A., *Combust. Flame* 102:329–340 (1995).

COMMENTS

H. S. Mukunda, Indian Institute of Science, India. In your plots, you use static temperature and Mach number as independent variables. For this reason, you find an anomalous behavior of maximum temperature vs Mach number i.e. at subsonic conditions temperature decreases with speed and at supersonic conditions, it increases with speed (M). If you base your plots on stagnation temperature, and the speed of flow after the shock (normal), the results will appear more rationalized.

Author's Reply. On the counterflow diffusion flame in subsonic flow, air temperature and stretch rate have been chosen as the main parameters. However, in the case of supersonic flow, strain rate depends on the location and the shape of the shock wave which can be calculated when conditions upstream of shock wave are known. Therefore, we chose Mach number and static temperature of the airflow as parameters, although the calculated results finally showed that the stagnation temperature was a strong factor for extinction and the change of strain rate with Mach number had a weak effect. Moreover, the results reveal the two-dimensionality of the flame in supersonic flow that cannot be simulated by one-dimensional calculation of a counterflow diffusion flame characterized by velocity and temperature at the boundary.

•

Jeong-Yeal Choi, Seoul National University, Korea. Your concept of a counterflow diffusion flame looks new and original, and there is possibly an application to the SCRamjet engine. However, in my experience, the original AUSM method suffers from numerical instability (not physically unstable) especially for the extension to higher (2nd or 3rd) order spatial schemes. In such cases, unphysical pressure oscillations occur after the bow shock or pressure oscillations occur in the boundary layer, though such a numerical instability can be overcome by newly developed AUSM+ or AUSM+W methods.

1. What is the spatial order of accuracy of your numerical scheme?
2. Have you ever found any numerical instability after the bow shock?
3. Have you ever tried the higher order spatially accurate numerical scheme?
4. Why don't you use the commonly used Roe's FDS-based scheme with the entropy fixing function to overcome the carbunde phenomena?
5. Have you ever found any physically unstable solution? In my opinion, the physically solution (as shown in your result) may be the result of numerical diffusion. Though AUSM is powerful in capturing the shock or other discontinuities such as a contact surface or reaction front, 1st order spatially accurate numerical schemes can smear any instabilities (which might then cause physically unstable solutions).
6. What was the integration method you used?

Author's Reply. The purpose of the work was not to investigate numerical schemes but to clarify fundamental flame characteristics of the counterflow diffusion flame in supersonic flow. For this reason, we used a first-order AUSM scheme for spatial differences of convective terms and an explicit method for time integration. At first, we chose Roe's FDS scheme (second-order), but it caused the carbuncle phenomenon at the shock wave, and so the AUSM scheme was used to avoid the carbuncle phenomenon as reported in Ref. 15. No numerical oscillation has been captured in the present calculation, but it does not necessarily deny the possibility that physical oscillations could occur.

Twenty-Sixth Symposium (International) on Combustion/The Combustion Institute, 1996/pp. 2885–2893

ON STRAINED FLAMES WITH HYPERGOLIC REACTANTS: THE $H_2/NO/F_2$ SYSTEM IN HIGH-SPEED, SUPERSONIC AND SUBSONIC MIXING-LAYER COMBUSTION

FOKION N. EGOLFOPOULOS
Department of Mechanical Engineering
University of Southern California
Los Angeles, CA 90089-1453, USA

PAUL E. DIMOTAKIS AND CHRIS BOND
Graduate Aeronautical Laboratories
California Institute of Technology
Pasadena, CA 91125, USA

We report on a numerical investigation on the dynamics and structure of strained, non-premixed and premixed, $H_2/NO/F_2$ flames. This is an important, hypergolic reacting system that has been used in high-power chemical-laser systems and, presently, relied upon in experimental studies of high-speed, supersonic and subsonic, turbulent shear-layer mixing and combustion. The study included a detailed description of the chemical kinetics and molecular transport for the $H_2/NO/F_2$ system and was conducted for a wide range of reactant concentrations and inert diluents, with flow/chemical parameters chosen to correspond to specific chemically reacting, supersonic mixing-layer experiments. Both non-premixed and premixed flames were studied using opposed-jet flow configurations. The results confirmed the experimental conclusion that, even at low reactant concentrations, the $H_2/NO/F_2$ system can sustain high Damköhler number chemical activity at high strain rates with room-temperature free streams. A comparison between the results of the present numerical simulations and the experimental chemically reacting mixing-layer studies, however, indicates that the predominant fraction of product formation in high-speed, turbulent, mixing layers must take place in a mode in which the reactants are in premixed, rather than in non-premixed, strained diffusion flames.

Introduction

Studies of reacting systems characterized by high activation energies have yielded considerable information on the details of their combustion. Hypergolic systems have not been studied to the same extent. A hypergolic mixture is comprised of stable reactants that readily react on molecular contact and can self-sustain reaction at ambient temperatures. Low activation energies of the main chain-branching/chain-propagation reactions obviate ignition sources. Furthermore, even in the presence of losses, a hypergolic system may not have distinct extinction behavior, as is the case of high-activation systems, since under any conditions, as extreme as they may be, the main reactants in contact will react chemically. Hypergolic systems may sustain arbitrarily large amounts of convective transport, as imposed by the strain-rate field, with convective fluxes overwhelming diffusive fluxes throughout the transport and reaction zones. Under such conditions, arguments [1,2] regarding the synergetic influence of strain rate and preferential diffusion ($Le \neq 1$) on the flame response may not be valid.

From a combustion point of view, there has been some interest on such systems in terms of the possible use of silane, for example, for the promotion of ignition in supersonic combustors. $H_2/NO/F_2$ hypergolic mixtures in passive diluents (e.g., N_2, Ar, He) have also found particular application as markers of molecular mixing in high-speed subsonic and supersonic mixing layers [3–5]. In this chemical system, the H_2 and NO are premixed. On contact, the NO and F_2 react spontaneously, producing F radicals that break the H_2 molecule.

In flows encountered in supersonic, turbulent mixing-layer studies, local strain rates are scaled by (outer-flow-parameter–based)

$$\sigma_\delta \equiv \frac{\Delta U}{\delta} \tag{1}$$

the ratio of the velocity difference, ΔU, across the layer, and (local) mixing-layer width, $\delta = \delta(x)$. With $\delta \approx$ 3–6 cm and $\Delta U \approx$ 400–1000 m/s, in those

experiments, characteristic strain rates, σ_δ, can be of the order of 10^4/s or higher. To the extent that incompressible turbulence scaling laws [6] are applicable to the high-speed, compressible shear layers of interest here, one can expect values of the local strain rate, σ, across molecular diffusion layers to be several orders of magnitude above σ_δ at the associated Reynolds numbers.

For incompressible turbulence, Kolmogorov [6] scaling indicates that the highest strain rates can be expected at the smallest (viscous) scales, λ_ν, of the flow, where

$$\sigma(\lambda_\nu) \sim \sigma_\delta Re^{1/2} \gtrsim 10^3\, \sigma_\delta \tag{2}$$

(see Eq. [1]), with Reynolds numbers for atmospheric pressure, compressible, mixing-layer experiments of order 10^6 or higher. While there will be regions in the flow characterized by strain rates that are lower than these values, one may safely expect that fresh reactants will first encounter each other across small-scale diffusion regions that are strained at these rates. At such high strain rates, most conventional reactants cannot sustain (stable) chemical activity. As noted, the scaling relation in Eq. (2) is taken from incompressible-turbulence theory. It should, however, provide a useful guide, at least for low-to-moderate Mach number mixing-layer flows, for which experimental data on mixing and chemical reactions are available.

The $H_2/NO/F_2$ system that has been studied experimentally and is simulated in this paper can be kinetically fast even at modest reactant concentrations and will react to produce a temperature rise that, in a background diluent gas of uniform heat capacity, can be related directly to the number of moles of chemical product in the turbulent shear layer. In this high Damköhler number limit, the rate of chemical reaction and heat release is limited by the rate of molecular mixing, which allows the latter to be measured.

Chemically reacting mixing-layer experiments indicate that the normalized temperature rise,

$$\theta \equiv \frac{T - T_\infty}{T_{\mathrm{ad}} - T_\infty} \tag{3}$$

where T_{ad} is the adiabatic flame temperature and T_∞ the temperature of the unreacted mixtures, reaches peak (mean) values in the mixing layer in the range,

$$0.45 \lesssim \langle\theta\rangle_{\max} \lesssim 0.6 \tag{4}$$

despite the fact that a fraction of the fluid is comprised of (as yet) unmixed reactant free stream fluid(s) [4]. Additionally, it was ascertained that the relatively low concentrations of the $H_2/NO/F_2$ system reactants used in these experiments (and the present simulations) resulted in mixing-limited (high-*Da*) product formation in the turbulent mixing layers [3–5]. In other words, the values in Eq. (4) reflect the efficacy and characteristics of molecular mixing, rather than finite kinetic-rate effects.

An attempt to model and assess the effect of the detailed chemical kinetics in such experiments was made by considering a simple model in which the chemical reactions were assumed to proceed in a perfectly stirred reactor (PSR) that was regarded as resulting from the homogenization of the entrained reactant species, from each of the free streams, at the entrainment ratio dictated by the shear-layer free stream parameters [7]. This approach was a definite first step but left the effects of fluid mechanics (strain rate) and molecular transport out of the picture. An effort to incorporate the effects of strain rate in terms of residence time and flame temperature in flame sheets in compressible mixing layers was reported in Ref. 8. In this study, in which the reaction between a premixed H_2/N_2 stream and a preheated air/steam stream was investigated, the turbulent-mixing environment was modeled as partitioned into PSR and strained-flame zones [9]. For the latter, values of the strain rate up to 10^5/s were considered, beyond which extinction was found to occur in the simulations.

The present investigation was undertaken to augment these previous studies by conducting a detailed numerical simulation of strained, laminar, opposed-jet reacting flows for the $H_2/NO/F_2$ system to assess some of the mechanisms affecting the details of the structure and dynamics of the resulting reaction fronts. This flow configuration provides a simple description of the behavior of local diffusion/reaction surfaces, in the turbulent shear zone, that retains the dominant features of the turbulence-chemistry interactions. The second goal is to relate the numerically determined temperatures at different strain rates and combustion modes to experimental data in high-speed subsonic and supersonic shear layers and to gain insight into the physical mechanisms of entrainment and mixing in these flows.

Numerical Approach

Numerical solutions for a counterflow configuration were obtained using well-established formulations and computer codes [10–13]. The counterflow code [11] was further modified to accommodate non-premixed and premixed reacting modes.

Non-premixed cases were simulated as an impinging F_2/inert jet onto an opposing H_2/NO/inert jet stream. Premixed combustion modes were also studied, with identical, opposing $H_2/NO/F_2$/inert jets impinging on each other or with a $H_2/NO/F_2$/inert jet impinging onto either opposing H_2/NO/inert or F_2/inert jets. The premixed mode provides an approximate description of the combustion of premixed reactants fed to the reaction zone as the result of leakage from a neighboring, high-strain-rate diffusion layer, a likely scenario in low Damköhler number, turbulent-mixing flows.

TABLE 1
Kinetic parameters of the $H_2/NO/F_2$ system.

	Reaction	A	n	E_a	Ref.
R1	$NO + F_2 \rightarrow NFO + F$	4.20×10^{11}	0.00	2285.0	[7]
R2	$NO + F + M \rightarrow NFO + M$	3.00×10^{16}	0.00	0.0	[7]
R3	$H + F_2 \rightarrow HF + F$	2.90×10^{9}	1.40	1325.0	[7]
R4	$F + H_2 \rightarrow HF + H$	2.70×10^{12}	0.50	634.0	[7]
R5	$F_2 + M \rightarrow F + F + M$	2.10×10^{13}	0.00	33700.0	[7]
R6	$HF + M \rightarrow H + F + M$	1.10×10^{19}	−1.00	134100.0	[14]
R7	$H_2 + M \rightarrow H + H + M$	8.10×10^{16}	−0.50	103240.0	[14]
R8	$H + NO + M \rightarrow HNO + M$	5.40×10^{15}	0.00	−302.0	[7]
R9	$H + HNO \rightarrow NO + H_2$	4.80×10^{12}	0.00	0.0	[7]

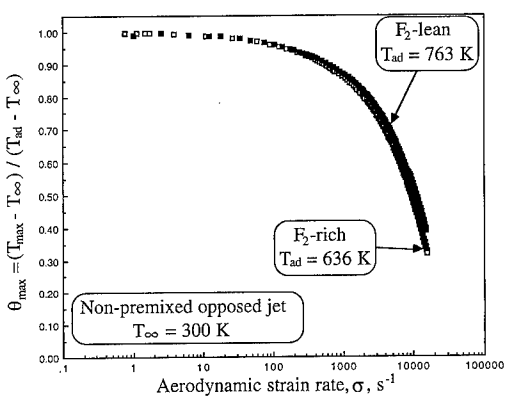

FIG. 1. Effect of aerodynamic strain-rate field on T_{max} of F_2-rich and F_2-lean, non-premixed reacting configurations.

The boundary conditions used here were similar to those described in Ref. 10. Modifications were made for the implementation of special boundary conditions for the reactant mole fractions at the nozzle exits, from which a premixed hypergolic $H_2/NO/F_2$/inert jet emerged. For this case, the premixed species were allowed to react starting at the feed nozzle exit and not within the feed nozzle itself. As a consequence, the mole fractions of the supplied reactants, at the feed nozzle exit, are modified compared to those in the upstream, unreacted mixture. To account for this effect, the boundary condition of the species mole fractions at the nozzle exit was obtained implicitly by equating the convective flux of each species in the unreacted mixture, far upstream in the burner, with the convective and diffusive fluxes at the feed nozzle exit. The kinetic scheme includes nine elementary reactions and kinetic parameters found in Table 1. The specific reaction rates are given by

$$k = AT^n e^{-E_a/RT} \tag{5}$$

where A is the preexponential factor, T the temperature, n the temperature exponent, E_a the activation energy, and R the ideal-gas constant. The units of A are expressed in mol-cm-s-K. The units of E_a are cal/mol.

Results and Discussion

Non-Premixed Mode

Velocity profiles for stagnation, non-premixed cases exhibit the usual behavior. On exiting the nozzle, the velocity develops an increasing slope that reaches a local maximum upstream of the heat-release zone. For non-premixed cases, two such locally maximum gradients can be identified, one for each of the opposing jets. In the present study, the maximum velocity gradient in the convective zone of the F_2 jet stream was prescribed as the imposed aerodynamic strain rate, σ, for reasons that will become clear later.

Numerical simulations were conducted for nine different reactant cases defined in terms of H_2, NO, and F_2 molar concentrations in their respective streams. For the first case, the inert gas was N_2. For the other eight, the inerts were He, Ar, and mixtures of the two. The molar concentrations were typical of those used in supersonic mixing-layer experimental studies [3,5].

For all cases, a solution was first established at very low strain rates. Higher strain-rate solutions were obtained by continuation, by gradually increasing the nozzle-exit velocity. As the strain rate, σ, increases, the maximum temperature, T_{max}, falls, as in high-activation systems. However, turning-point extinction does not occur in such mixtures and, while T_{max} continues to decrease with increasing σ, finite chemical activity persists at strain rates as high as tens of thousands of reciprocal seconds. This is illustrated in Fig. 1 for a F_2-rich and F_2-lean reacting configuration, in terms of the variation of the nor-

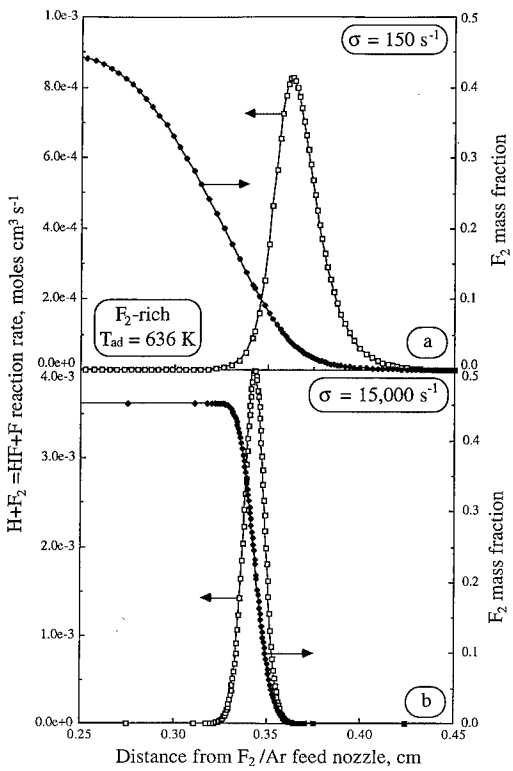

FIG. 2. Spatial variation of the mass fraction of F_2 and the reaction rate of $H + F_2 = HF + F$ for the F_2-rich case: (a) $\sigma = 150$/s and (b) $\sigma = 15{,}000$/s.

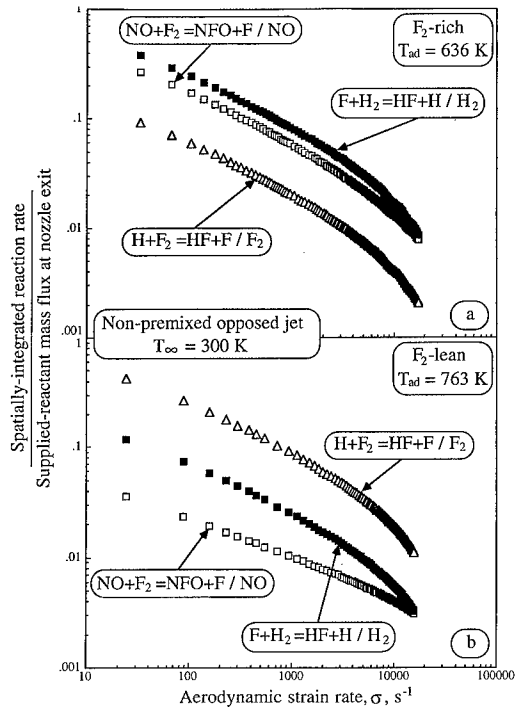

FIG. 3. Variation of the ratio of the spatially integrated reaction rate over the supplied reactant mass flux at the burner exit with the imposed aerodynamic strain rate for various species and reactions: (a) F_2-rich, (b) F_2-lean.

malized temperature rise, θ (Eq. [3]), with σ. In these simulations, T_∞ was 300 K, with T_{ad} computed from equilibrium calculations using the STANJAN program [15]. For the F_2-rich case, the molar composition was $X_{H_2} = 2\%$, $X_{NO} = 0.056\%$, and $X_{Ar} = 97.944\%$ in the H_2/NO jet stream; and $X_{F_2} = 8\%$ and $X_{Ar} = 92\%$, in the F_2 jet stream. For the F_2-lean case, the molar composition was $X_{H_2} = 10\%$, $X_{NO} = 0.5\%$, and $X_{Ar} = 89.5\%$ in the H_2/NO stream; and $X_{F_2} = 2.75\%$ and $X_{Ar} = 97.25\%$ in the F_2 stream.

The mechanisms responsible for the temperature reduction with increasing strain rate (see Fig. 1) were studied using sensitivity, species-structure, and reaction-path analyses. Reaction-path analyses confirmed that reaction (R1) is responsible for the chain initiation by releasing an F atom. This is used by reaction (R4) for H_2 consumption and the production of the final HF product and active H radicals. The H radicals then react with F_2, through reaction (R3), to produce HF and F, which is further used in reaction (R4). The chain-propagation reactions, (R3) and (R4), form a closed loop, leading to a system that can sustain itself provided fresh reactants are supplied. Reactions (R1), (R3), and (R4) support the overall system reaction rate. Any mechanism opposing their forward progress will inhibit chemical activity. Such mechanisms can be the recombination reaction of H and F radicals with themselves, as well as with other species, and reactant leakage with increasing aerodynamic strain rate.

The effect of the strain rate on the reaction-zone structure can be seen in Fig. 2, in which the (R3) reaction rate and the F_2 mass fraction are shown for low and high σ for the F_2-rich case. For low σ, F_2 is nearly consumed at the location of the maximum (R3) rate. For high σ, the thickness of the (R3) reaction zone is reduced and F_2 survives well after the (R3) rate maximum, indicating substantial reactant leakage. This is the case for all the main reactants, that is, H_2, NO, and F_2. Figure 3 depicts the ratios between the spatially integrated (R1), (R3), and (R4) reaction rates over the supplied, nozzle-exit mass fluxes (convective + diffusive) of NO, F_2, and H_2, respectively, for both F_2-rich and F_2-lean cases. As σ increases, these ratios are found to decrease, indicating increasing leakage and decreasing overall chemical activity. For the F_2-rich case, the ratio corresponding to F_2 has the lower values. F_2 is an abundant species and not expected to be fully consumed in the main reaction zone. On the other hand, the

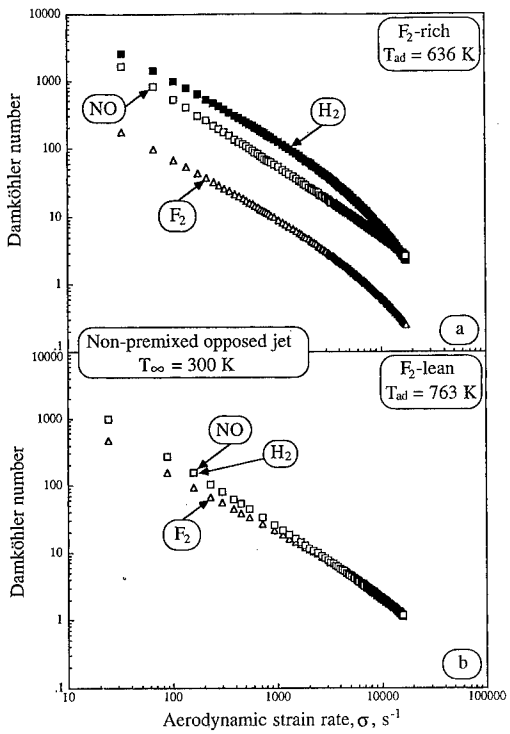

FIG. 4. Damköhler numbers, based on minimum reaction time of various species versus imposed aerodynamic strain rate: (a) F_2-rich, (b) F_2-lean.

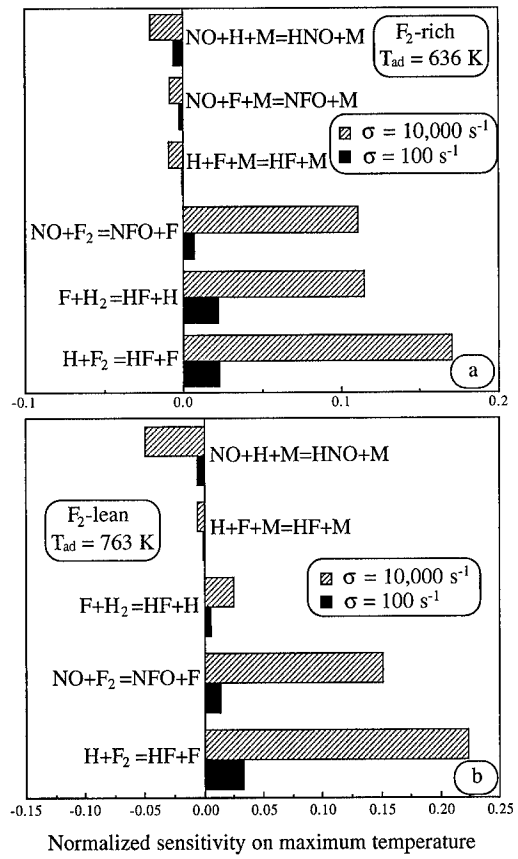

FIG. 5. Normalized sensitivity coefficients on T_{max}, at low and high strain rates: (a) F_2-rich, (b) F_2-lean.

same ratio appears to have higher values compared to the other species for the F_2-lean case, since it is the deficient species and is expected to react while transported through the main reaction zone.

The mechanism of reactant leakage is traceable to the finite timescales for the reactions. Increasing σ results in convective timescales that become comparable to chemical timescales, corresponding to reduced Damköhler numbers, *Da*. Characteristic timescales for the destruction of NO, F_2, and H_2 at the location of the maximum rate of (R1), (R3), and (R4), respectively, were determined and scaled by the strain rate, σ, to form Damköhler numbers for all three species. The results are shown in Fig. 4 for both F_2-rich and F_2-lean cases. It can be seen, that *Da* decreases with σ and attains values of order unity for high strain rates, indicating the importance of convective transport within the main reaction zone. For both F_2-rich and F_2-lean cases, the *Da* of F_2 have lower values compared to NO and H_2, whereas *Da* numbers for H_2 and NO are very close for the F_2-rich case and nearly indistinguishable for the F_2-lean case. Between 300 and 700 K, the specific (R1) reaction rate is nearly three orders of magnitude less than that of (R4). However, the (R1) reaction rate is only, roughly, one order of magnitude less than that of (R4), because F is a minor (low-concentration) species. As a consequence, the *Da* of NO is of the same order as the *Da* of H_2, given that [NO] is, roughly, an order of magnitude less than [H_2]. On the other hand, the specific reaction rate of (R3) is nearly one order of magnitude less than that of (R4) in the same temperature range, and since the F_2 and H_2 concentrations are of the same order, the chemical times corresponding to F_2 are greater than these of H_2, leading to reduced *Da* numbers for F_2. This indicates that the main leakage mechanism is that of F_2, through (R3), and this is the reason the maximum velocity gradient on the F_2 side was chosen as the scale for the aerodynamic strain rate, σ.

These observations were further supported by detailed sensitivity analysis in which the effect of individual elementary reactions on T_{max} was determined at different strain rates. Representative results are shown in Fig. 5 for the F_2-rich and F_2-lean cases. For both cases, reactions (R1), (R3), and (R4) favor T_{max}, with reaction (R3) having the highest positive sensitivity. This is anticipated. Reaction

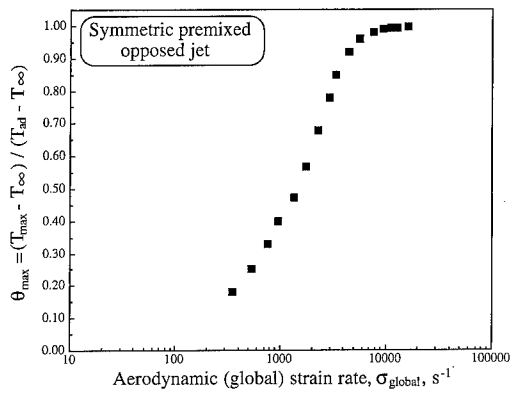

FIG. 6. Effect of aerodynamic strain rate on T_{max} for the premixed case.

(R3) has a higher activation energy compared to (R4) and its rate has a stronger sensitivity to temperature reductions resulting from reactant leakage. The other main propagation reaction, (R4), appears to be important for the F_2-rich/H_2-lean case, while it is less important for the F_2-lean/H_2-rich case; its rate increases and ceases to be a rate-limiting kinetic step. Both cases confirm that reaction (R1) is very important, initiating the reaction between the two main reactants, NO and F_2, with a relatively slow rate, thus rendering it a rate-limiting kinetic step. It is also seen that the sensitivity of reactions (R1), (R3), and (R4) on T_{max} is enhanced at high strain rates, since the reactant leakage is augmented and T_{max} depends more critically on the progress of these reactions. As expected, negative sensitivity on T_{max} is exhibited by the three-body recombination reactions (R2), (R6), and (R8), since the important H and F radicals recombine to form the less active HNO, NFO, and HF species. At high strain rates, these negative sensitivities increase in magnitude, since the system becomes more sensitive to the magnitude of the H- and F-radical pool. At high strain rates, temperatures are lower and this further enhances the importance of the three-body reactions. For the F_2-lean configuration, reaction (R2) does not have a significant negative sensitivity. F_2 is the deficient species, thus leading to a reduced F-radical pool, and NO preferentially recombines with H radicals, which are produced by the abundant H_2.

Finally, detailed reactant flux analysis revealed that the ability of such flows, that is, those with hypergolic reactants, to sustain strain rates that are considerably higher compared to high-activation flows leads to convective fluxes that are higher than diffusive fluxes throughout the flow field.

Premixed Mode

For all nine non-premixed configurations and for strain rates of the order of $\sim 10^4$/s, which are of the order encountered in supersonic mixing-layer experiments, T_{max} is reduced substantially. This indicates that chemical activity is reduced and that unreacted species will mix and react within highly strained flow structures in a premixed mode. To study this scenario, various configurations of premixed reaction in strained flow fields were investigated. For these studies, the composition of the premixed species was determined using a value of the (molar) entrainment ratio between the high-speed and low-speed stream [16] of $E_n = 1.06$. This is a representative value, as determined from the analysis of chemically reacting, supersonic mixing-layer experimental data [3,5].

Two identical premixed jets impinging against each other were studied. This configuration leads to symmetry across the stagnation plane and the solution need only be obtained over half of the domain. As a consequence of the details of this implementation, for low strain rates, losses resulting from high-temperature gradients at the nozzle exit result in T_{max} well below T_{ad}. As the strain rate increases, temperature gradients at the nozzle exit decrease, decreasing boundary losses, and T_{max} approaches T_{ad}, corresponding to homogeneously mixed reactants (see Fig. 6). In the premixed mode simulations, the convective transport was measured by a global strain rate, σ_{global}, defined as the nozzle-exit velocity divided by the half-distance between the two nozzles. The homogeneous molar composition for the calculation depicted in Fig. 6 is $X_{H_2} = 1.0291\%$, $X_{NO} = 0.0288\%$, $X_{F_2} = 3.883\%$, $X_{Ar} = 4.1\%$, and $X_{He} = 90.842\%$. For all other cases studied, the response of T_{max} to the imposed strain rate was found to be similar.

The asymptotic behavior for high strain rates (i.e., $T_{max} \rightarrow T_{ad}$) is at variance to typical, high-activation, premixed combustion, in which the combination of preferential diffusion and the strain-rate field leads to T_{max} well above or below T_{ad}. This difference is clearly attributable to the hypergolic nature of the reacting system. Detailed reactant-flux analysis revealed that the ability to establish strain rates well above values encountered in the combustion of typical fuels can result in convective fluxes that are substantially larger than diffusive fluxes everywhere. Under these conditions, traditional arguments on preferential diffusion effects cease to be valid; convection is the dominant mechanism of transport and all properties are transported at the same rate leading to a locally conserved system.

The interaction between a premixed stream with either of the original non-premixed streams was also studied. In this study, a premixed stream impinged on a non-premixed stream in which the main reactants were either the abundant or deficient reactants in the premixed fluid. In the former case, the products of the premixed stream mix and are diluted with the reactants of the non-premixed jet. In the latter

case, an additional non-premixed reaction zone is established as a result of the reaction between the reactants of the non-premixed jet with the abundant species of the premixed stream. In both cases, T_{max} was well below T_{ad} for low strain rates because of losses from the premixed stream to the nozzle boundary, as described previously. At high strain rates and similarly to the symmetric premixed configuration, T_{max} was found to approach T_{ad}.

The observations made in these simulations that, for both non-premixed and premixed systems, the convective reactant fluxes can be substantially larger than the diffusive fluxes throughout the flow field, can be corroborated through the following scaling arguments. For the non-premixed case, the convective flux, j_c, of a reactant r is given by

$$j_c = \rho u Y_{r,\infty} \tag{6}$$

where ρ is the density, u the convective velocity, and $Y_{r,\infty}$ the mass fraction of r in the free stream. The diffusive flux of r, j_d, is given by

$$j_d = \rho \mathcal{D} \frac{\partial Y_r}{\partial x} \tag{7}$$

where $\mathcal{D}$ is the mass diffusivity. By further assuming that the mass fraction of r is reduced from its free stream value, $Y_{r,\infty}$, to zero within a diffusive length l_{npm}, then

$$j_d = \rho \mathcal{D} \frac{Y_{r,\infty}}{l_{npm}} \tag{8}$$

A balance between diffusive and convective fluxes at the beginning of the diffusive zone for a non-premixed system leads to

$$l_{npm} \sim \sqrt{\frac{\mathcal{D}}{\sigma}} \tag{9}$$

where $\sigma \sim u/L$, with L the spatial extent of the strained hydrodynamic zone. Using standard scaling for these quantities, we have, for the ratio between the convective and diffusive fluxes,

$$\left(\frac{j_c}{j_d}\right)_{npm} \sim \sqrt{\frac{uL}{\mathcal{D}}} = \sqrt{Pe} \tag{10}$$

which indicates that as u and σ increase, $j_{c,npm}$ gradually dominates $j_{d,npm}$, with a ratio that scales with the square root of the convective velocity (local Peclet number).

For the case of premixed reaction, a characteristic propagation speed, S_u, that scales with the square root to the overall burning rate can be prescribed [17] so that the diffusive length is given by $l_{pm} \sim \mathcal{D}/S_u$, with a diffusive flux given by $j_{d,pm} \sim \rho Y_{r,\infty} S_u$. Thus, the ratio between the fluxes becomes

$$\left(\frac{j_c}{j_d}\right)^{pm} \sim \frac{u}{S_u} \tag{11}$$

This indicates that, for the premixed mode, the flux ratio scales (linearly) with the convective velocity, u. It may be important to note that the limiting behavior in which convective fluxes dominate, in both premixed and non-premixed systems, is not typically attainable in the case of high-activation systems (nonhypergolic reactants).

Comparison with Experimental Results

The results summarized in Fig. 1 indicate that only a negligible fraction of the normalized temperature rise, θ, can be expected to be contributed by combustion in strained diffusion-flame regions at strain rates of order 15,000/s and greater. However, such values and those substantially greater for the strain rate must be expected in the high-speed, chemically reacting shear layers (see Eqs. [1] and [2] and related discussion), for which quantitative experimental data are available. In particular, the amount of chemical product measured in these flows is not reconcilable with the predicted chemical product formation in strained-flame regions in these simulations considering the strain-rate values these flows can sustain. We are forced to conclude that the preponderant fraction of chemical-product formation in these flows occurs in the premixed mode. The conditions for this combustion mode can be expected to be created in the flow as a result of the substantial reactant leakage predicted to emanate from the high strain-rate diffusion-flame regions in the present simulations. Combustion in this mode can provide the only candidate mechanism that can contribute to the high attained values of the normalized temperature rise observed experimentally (see Eq. [4]).

Conclusions

A detailed numerical simulation was conducted for strained non-premixed and premixed hypergolic reacting flows in view of their importance as mixing markers in supersonic, turbulent reacting mixing layers. The chemical system was that of $H_2/NO/F_2$. The parameters in these simulations were derived from those used in actual experiments of supersonic, chemically reacting mixing layers. Results indicate that for such hypergolic systems in high strain-rate flows, even dilute reactant concentrations can lead to high Damköhler numbers at very high strain rates.

Our study of non-premixed flow configuration showed that as the strain rate increases, the maximum temperature, T_{max}, is reduced as a result of reactant leakage, as reported previously [8]. The mechanisms of leakage were identified through detailed sensitivity analyses as well as through analysis of the detailed structure of the reaction zone and the subsequent determination of realistic Damköhler numbers based on the various species whose leakage

affect the magnitude of T_{max}. At strain rates of the order of 10,000/s to 20,000/s and above that are typical in supersonic mixing-layer experiments, it was found that although chemical activity is present, T_{max} is reduced substantially, indicating that the reactants mix and reaction takes place in an effectively premixed mode.

The studies of premixed flow configuration were conducted by considering the impinging of two identical premixed jets and one premixed jet against a jet carrying the species of either one of the streams. In the first case, it was found that, at low strain rates, T_{max} of the premixed reaction zone is reduced as a result of losses to the upstream boundary; at high strain rates, the transport is dominated by convection and T_{max} approaches T_{ad}. In the second case, it was found that either the products of the premixed reaction zone will simply mix with the species of the opposing jet or will lead to a second non-premixed reaction zone, depending on the equivalence ratio in the premixed stream and the composition of the reactants of the non-premixed jet. In both cases, T_{max} approaches T_{ad} at high strain rates.

In view of the very high strain rates expected in these flows, a comparison of the experimentally obtained values for the normalized temperature, θ, and the fact that reactant concentrations and compositions used in the experiments and the present simulations have been shown to be in the fast-kinetic (high-*Da*) regime, we must conclude that the dominant chemical product formation occurs in a premixed mode. Strained diffusion flames formed between non-premixed reactants contribute negligibly to the overall chemical activity.

Acknowledgments

This work was supported by the Fred O'Green Assistant Professorship in Engineering at the University of Southern California and by the Air Force Office of Scientific Research, Grant No. F49620-94-1-0353, at Caltech.

REFERENCES

1. Peters, N., *Twenty-First Symposium (International) on Combustion,* The Combustion Institute, Pittsburgh, 1986, pp. 1231–1250.
2. Law, C. K., *Twenty-Second Symposium (International) on Combustion,* The Combustion Institute, Pittsburgh, 1988, pp. 1381–1402.
3. Hall, J. L., Dimotakis, P. E., and Rosemann, H., "Some Measurements of Molecular Mixing in Compressible Turbulent Mixing Layers," AIAA 22nd Fluid Dynamics, Plasma Dynamics, and Lasers Conference, Paper 91-1719 1991.
4. Dimotakis, P. E., "Turbulent Free Shear Layer Mixing and Combustion," in *High Speed Flight Propulsion Systems,* 1991, pp. 265–340.
5. Bond, C. L. and Dimotakis, P. E., "Molecular Mixing in Supersonic Shear Layers," *Bull. Am. Phys. Soc.* 38(12):2201 (1993).
6. Kolmogorov, A. N., "Local Structure of Turbulence in an Incompressible Viscous Fluid at Very High Reynolds Numbers," *Dokl. Akad. Nauk SSSR* 30:299 (1941).
7. Dimotakis, P. E. and Hall, J. L., "A Simple Model for Finite Chemical Kinetics Analysis of Supersonic Turbulent Shear Layer Combustion," AIAA/SAE/ASME/ASEE 23rd Joint Propulsion Meeting, Paper 87-1879, 1987.
8. Miller, M. F., Bowman, C. T., Miller, J. A., and Kee, R. J., "A Model for Chemical Reaction in a Compressible Mixing Layer," Western States Section/The Combustion Institute Fall Meeting, Livermore, CA, Paper 89-110, October 23–24, 1989.
9. Broadwell, J. E. and Mungal, M. G., "Molecular Mixing and Chemical Reactions in Turbulent Shear Layers," *Twenty-Second Symposium (International) on Combustion,* The Combustion Institute, Pittsburgh, 1988, pp. 579–587.
10. Kee, R. J., Miller, J. A., Evans, G. H., and Dixon-Lewis, G., *Twenty-Second Symposium (International) on Combustion,* The Combustion Institute, Pittsburgh, 1988, pp. 1479–1494.
11. Kee, R. J., private communication, 1991.
12. Kee, R. J., Rupley, F. M., and Miller J. A., "Chemkin-II: A Fortran Chemical Kinetics Package for the Analysis of Gas-Phase Chemical Kinetics," Sandia Report SAND89-8009, 1985.
13. Kee, R. J., Warnatz, J., and Miller, J. A., "A FORTRAN Computer Code Package for the Evaluation of Gas-Phase Viscosities, Conductivities, and Diffusion Coefficients," Sandia Report SAND83-8209, 1983.
14. Kontratiev, V. N., *Rate Constants of Gas-Phase Reactions,* Office of Standard Reference Data, NBS, 1972.
15. Reynolds, W. C., "The Element Potential Method for Chemical Equilibrium Analysis: Implementation in the Interactive Program STANJAN, Version 3," Mechanical Engineering, Stanford University, Palo Alto, CA, January, 1986.
16. Dimotakis, P. E., "On the Convection Velocity of Turbulent Structures in Supersonic Shear Layers," AIAA 22nd Fluid Dynamics, Plasma Dynamics, and Lasers Conference, Paper 91-1724, 1991.
17. Williams, F. A., *Combustion Theory. The Fundamental Theory of Chemically Reacting Flow Systems,* 2d ed., Addison-Wesley, Menlo Park, CA, 1988.

COMMENTS

Sébastien Candel, Ecole Centrale, Paris. You are using, in this analysis, steady-state strained flames to discuss the local structure of your flame. It is known however that reactive elements convected in a rapidly evolving strain rate field do not instantaneously adjust to the local value of the strain rate. Do you think that such effects are unimportant in your high-speed shear flow?

Author's Reply. There are many complicating effects that are important and apply to the real-flow phenomena, such as strain-rate unsteadiness, as suggested, as well as unmixedness, spatial inhomogeneities in the strain-rate and compositional field, etc. Such effects would change the estimate of the product formation and heat release in the high strain-rate shear layer flows of interest. They would not alter the important qualitative conclusion, however, that the observed, high values of product formation in these flows cannot be accounted for by assuming that a significant fraction occurs in a (steady or unsteady) strained diffusion-flame regime. The inference that product formation occurs in a premixed mode would not be altered by incorporating unsteadiness at the very high strain-rate values applicable.

Twenty-Sixth Symposium (International) on Combustion/The Combustion Institute, 1996/pp. 2895–2902

OBSERVATIONS OF H_2O FORMATION IN THE SUPERSONIC COMBUSTION OF H_2 BY HIGH-ENTHALPY AIR

M. F. MILLER, W. T. RAWLINS AND M. G. ALLEN
Physical Sciences Inc.
20 New England Business Center
Andover, MA 01810, USA

T. E. PARKER
Colorado School of Mines
Division of Engineering
Golden, CO 80401-1887, USA

We have investigated and compared the dynamics of supersonic H_2-air combustion for compression and expansion swept-ramp, three-hole injector configurations in a laboratory shock tunnel. Hydrogen fuel was injected into a Mach 3 flow of 1200 K air at 0.67 atm. The experiments used a combination of imaging and line-of-sight optical diagnostics at different locations downstream of the point of injection. Images of $OH(A^2\Sigma)$ and $OH(X^2\Pi)$ spatial distributions provide information on the near-field mixing and ignition characteristics and far-field vertical spreading of the reacting layer, while spectral measurements of $H_2O(\nu_2)$ emission provide the far-field temperatures and H_2O yields in the reacting layer. The two injector configurations display markedly different ignition characteristics but similar near-field air-fuel mixing behavior and far-field product yields. The far-field measurements at long convective flow times give final H_2O concentrations, temperatures, and OH(A) concentrations that are greatest near the bottom wall and decrease with increasing height. H_2O and OH(A) are observed only in the lower half of the duct; thus, complete mixing of the fuel with the main flow is not achieved. For both injectors, the efficiency of H_2O production compared to full equilibrium for an idealized premixed system is 30–40%. Kinetic limitations due to incomplete radical removal are relatively minor. The primary factor limiting the far-field combustion efficiency appears to be poor mixing due to the slow vertical propagation of the reacting layer, which is similar for the two injectors despite the differences in their near-field ignition behavior.

Introduction

In supersonic combustors, such as supersonic combusting ramjets or "scramjets," fuel (e.g., H_2) must be injected into a supersonic flow of high-enthalpy air, ignited, and burned to completion to achieve maximum thrust. As is well known, the efficiency of this process is limited by (1) fuel-air mixing dynamics, which affect near-field ignition, flameholding, and fuel penetration into the free stream; and (2) slow free-radical recombination rates, which limit the conversion of intermediates, OH, O, and H, to product, H_2O, during the residence time in the combustor. A number of investigations have focused on the development of fuel injection schemes that produce rapid mixing yet minimize the total losses of the system. Of particular interest is the injection of fuel parallel to the axis of the main flow direction so that the momentum of the fuel jets contributes to the total thrust of the engine. This paper reports on a comparison of the performance of two types of swept-ramp axial injectors, using line-of-sight and imaging optical diagnostics to detect H_2O and OH in a laboratory shock tunnel.

We have previously described optical observations of the combustion characteristics of transverse and axial H_2 injection into high-enthalpy (6.5 MJ/kg) Mach 3 air flows for fuel-rich overall equivalence ratios ($\Phi \approx 1.8$) [1–3]. OH planar laser-induced fluorescence (PLIF) images of the near-field ignition and fuel-air mixing region, giving insight into the mixing dynamics and turbulence scales [4]. In addition, spectrally dispersed infrared emission from the ν_2 vibrational band of H_2O gives H_2O concentration and temperature at the combustor exit [3,5]. The transverse injection exhibited prompt ignition, rapid mixing, and good penetration into the free stream flow over an axial length scale of about 20 injector diameters. The axial injection resulted in significantly slower ignition, mixing, and penetration, accompanied by lifting of the fuel jet due to vigorous combustion between the jet and the bottom wall. Despite these differences, the H_2O concentrations and temperatures observed in limited mea-

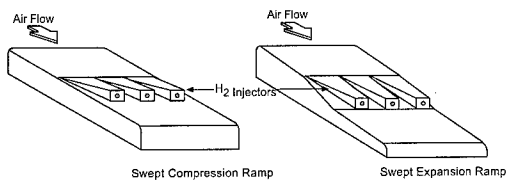

FIG. 1. Swept compression and expansion ramp injectors.

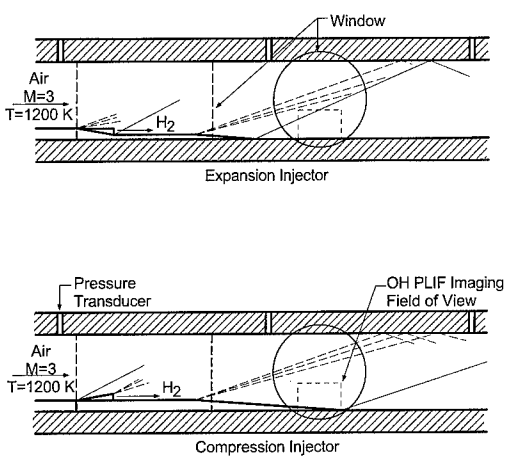

FIG. 2. Schematic of expansion and compression injectors and associated flow fields in shock tunnel. Solid lines indicate shock waves, dashed lines indicate expansion fans. Locations of pressure ports and side-viewing windows are indicated.

surements far downstream were similar for the two injector types. The H_2O concentrations measured at half the tunnel duct height indicated incomplete combustion.

In the present work, we compare the combustion characteristics of compression and expansion swept-ramp injectors, shown schematically in Fig. 1. Similar injector configurations have been studied by a number of investigators [6–8]. Swept-ramp injectors are designed to promote fuel-air mixing via streamwise vorticity generated as the higher pressure fluid on the upper surface of the ramp flows around the sides of the injector. The expansion ramp generates additional vorticity via baroclinic torque produced by interaction of a shock wave, formed at the downstream edge of the ramp, with the density gradient across the fuel-air mixing interface. Each injector was operated in a laboratory shock tunnel, injecting H_2 at an overall equivalence ratio of $\Phi = 0.3$ into a Mach 3 flow of high enthalpy ($\approx$3.8 MJ/kg) air initially at 1200 K, 0.67 atm, and 2 km/s. In addition to top-wall pressure measurements, a variety of optical measurements were conducted at three different axial locations near and far downstream of the point of injection. The optical diagnostics included observations of $H_2O(\nu_2)$ infrared emission spectra as functions of height in the duct, imaging and nonimaging measurements of $OH(A^2\Sigma)$ emission, and PLIF imaging of $OH(X^2\Pi)$ spatial distributions.

Experiment Description

The experiments were conducted in the Physical Sciences Inc. shock tunnel facility which is described in detail elsewhere [1,2]. The flow is driven by a plenum of shock-heated air in the reflected shock region of a 15.6-cm (i.d.), 17.5-m shock tube. The hot gas expands through a two-dimensional half-nozzle to a uniform Mach 3 flow in a 7.62-cm square cross section where the fuel injector assembly is mounted. Downstream (9 cm) of the fuel injection station, the flow further expands to the full duct height of 8.9 cm, propagates down the 1.8-m test section, and exits into a 1000 L dump tank. Piezoelectric transducers provide time-resolved (1 MHz) pressure measurements along the top wall of the test section at -1, 23, 46, and 120 cm downstream of the exit plane of the supersonic nozzle. Optical measurements are performed at windows 7.5, 29, and 120 cm downstream of the nozzle exit.

The fuel injectors are positioned immediately downstream of the end of the supersonic nozzle. The compression and expansion ramp injector assemblies each consist of three individual injectors (Fig. 1) with 10° ramp and sweep angles, a conical nozzle contour with a 7° half angle, and an exit plane diameter of 0.43 cm. Each injector is 1.0 cm wide at the base, 0.76 cm high, and 4.3 cm long. The injectors deliver a flow of H_2 at Mach 1.7, 190 K static temperature, 2.1 atm static pressure, and 1.8 km/s. The injected flow is initiated $\approx$1 ms prior to arrival of the air flow, and persists at a steady flow rate until well after arrival of the driver gas flow which ends the useful combustion test time. Schematics of each injector assembly installed in the test section are shown in Fig. 2 along with some of the basic flow features (e.g., shock waves, expansion fans) associated with the injector installations. The positions of the imaging locations in the near-field region of the test section are also indicated. The shock waves and expansion fans emanating from the injectors themselves are only partially drawn to emphasize that the flow over the injectors is three dimensional, therefore the waves produced by the injectors are not planar.

Optical Diagnostics

The spectrally resolved H_2O emission diagnostic is described in detail elsewhere [5]. Briefly, an infrared array spectrometer is used to observe time-resolved spectral distributions on the long-wavelength

side of the ν_2 band, 6.50–8.55 μm. The shape of the band is increasingly sensitive to temperature at the longer wavelengths, while the total intensity is sensitive to both temperature and H_2O concentration. Separate measurements of high-temperature H_2O emission for known temperatures and concentrations in a conventional shock tube determined the spectral radiant efficiency at each wavelength (W/mole sr μm) as a function of temperature [9]. Those measurements established a set of empirical calibration functions permitting determinations of temperature to 5–10% accuracies and H_2O concentration to 10–20% accuracies [5]. Corrections for self-absorption of the radiation are not required for the measurements reported here [5]. The spectrometer consists of a liquid-nitrogen-cooled 12-element HgCdTe array coupled to a N_2-purged 0.35-m monochromator, previously applied to measurements of NO infrared emission [10,11]. For H_2O, the grating is positioned so that the array elements span from 6.50 to 8.55 μm with a spectral resolution of 0.19 μm/pixel. The detector output channels are synchronously sampled at 125 kHz, giving time-resolved spectra every 8 μs. The spectrometer was positioned 120 cm downstream of the nozzle exit, and was mounted on an adjustable platform so that emission could be recorded as a function of height in the test section (one height being recorded in a single experiment). A folded gold mirror system imaged the center of the flowfield onto the entrance slit of the monochromator. Two opposing, full-height, Cleartran windows provided optical access and eliminated scattered light interferences.

OH($A^2\Sigma$) emission near 310 nm was imaged by an intensified video camera equipped with a Nikkor UV lens (f/4.5) and a UG5 filter, using a typical gate of 0.2 ms. The video fields were acquired by a framegrabber board installed in a personal computer. OH(A) emission images were acquired at 7.5, 29, and 120 cm downstream of the nozzle exit. In addition, single-point measurements of OH(A) emission were recorded at 1 MHz using a photomultiplier tube equipped with a 310-nm narrowband filter.

OH($X^2\Pi$) PLIF images [4] were recorded on an intensified CCD array camera (Princeton Instruments) equipped with a Nikkor UV lens and WG320 and UG11 filters and gated at 0.2 μs. The excitation source was a frequency-doubled, excimer-pumped dye laser, tuned to the $P_1(8)$ transition of the (1,0) band of the OH($A^2\Sigma$-$X^2\Pi$) system. The collimated laser sheet was 2.5 cm wide and approximately 0.5 mm thick. Typically, 1.2 mJ of laser energy were delivered to the test section. OH(X) PLIF images were acquired at the position 29 cm downstream of the supersonic nozzle exit. Additional single-point, 1-MHz measurements of bandpass-filtered infrared emission from NO (5.0 μm) and H_2O (6.7 μm), correlated with pressure sensor data, were used to verify the arrival and duration of the high-enthalpy flow at each optical station.

Results and Analysis

Typical top-wall pressure measurements for reacting and nonreacting (He-injected) flows gave values near 0.7 atm at the positions −1 and 23 cm downstream of the nozzle exit plane, in good agreement with the calculated static pressure at the nozzle exit. Pressures in reacting flows at 43 and 120 cm downstream were typically 1.4–1.6 atm during the test times, corresponding to steady free stream flow conditions. Comparisons between reactive and He-injected experiments indicate that most of this pressure rise is due to chemical reaction. The test times were determined from a series of fast-response (1 MHz), line-of-sight radiometric measurements consisting of NO (5.0 μm) viewed from the side at the nozzle exit, and H_2O (6.7 μm) and OH($A^2\Sigma$) (310 nm) viewed from the top looking down at each downstream station. Typical test times, following the arrival of the main air flow and prior to arrival of the driver gas, were ≈800 μs immediately downstream of the injectors and 29 cm downstream of the nozzle exit, and ≈300 μs at 120 cm.

Side-viewing OH(A) emission measurements were recorded immediately downstream of the injectors, spanning a field of view from just upstream of the injectors to approximately 10 cm downstream. No detectable OH(A) emission signal was observed in the images for either injector, signifying [OH(A)] $< 3 \times 10^5$ cm^{-3}. Using the filtered photometer at the same location, weak intermittent OH(A) emission signals were observed for the compression injector, but only marginally detectable signals were observed for the expansion injector. Thus, there is no clearly established ignition for flow times on the scale of 20 μs.

At the 29-cm station, corresponding to reactive flow times of ≈130 μs (≈30 injector step heights), both OH(A) emission and OH(X) PLIF were imaged. The OH(A) emission in this region was so strong that the camera was saturated, indicating the combustion was quite intense. The OH(A) emission image corresponding to the compression injector shows a relatively uniform region of emission along the bottom wall which extends to approximately one-third of the height of the duct. Ignition for this injector occurs upstream of the 29-cm port and out of the field of view. The image for the expansion injector is similar, except that the region of intense emission is bounded on its upstream edge by the oblique shock wave extending from the end of the bottom wall ramp (cf. Fig. 2). It appears that the heating produced by this shock wave is responsible for igniting the flow. Thus, the compression injector gives significantly more prompt ignition than the expan-

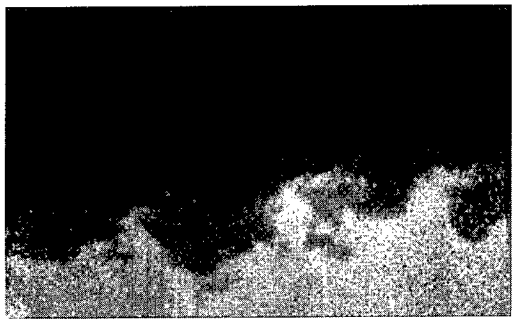

FIG. 3. PLIF image of OH($X^2\Pi$) for expansion injector, observed 29 cm downstream of the end of the supersonic nozzle. The flow direction is from left to right; the bottom wall of the test section is just below the image. The image is 6.1 cm wide and 3.8 cm high.

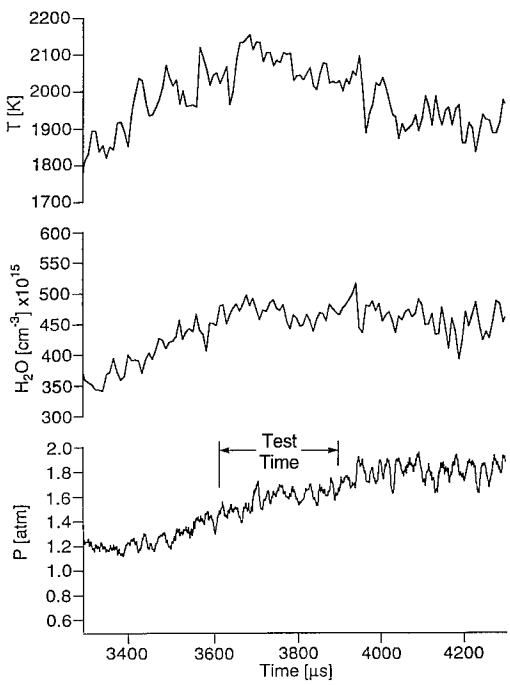

FIG. 4. Pressure, H_2O concentration, and temperature as functions of time 120 cm downstream of the nozzle exit, for the expansion injector. H_2O and temperature signals were recorded along a line of sight 1.3 cm above the bottom wall. The time base is referenced to zero at an incident shock trigger gauge in the shock tube section.

sion injector, consistent with the photometer observations of intermittent OH(A) production immediately downstream of the injectors. The saturated signal levels for both injectors correspond to $[OH(A)] > 1 \times 10^8$ cm^{-3}.

A representative OH(X) PLIF image is shown for the expansion injector in Fig. 3. Consistent with the OH(A) emission images at this location, the OH(X) PLIF images show a region of OH near the bottom wall with a turbulent mixing interface along its upper edge. A striking feature of these images is the uniformity of the OH-bearing region, i.e., the absence of any discernible fuel jet remnant. This observation suggests substantial fuel-air mixing upstream of this location. This is in marked contrast to our previous observations of incomplete mixing for larger jet diameters [3]. However, those data were obtained using a single, larger diameter injector which would be expected to generate less rapid mixing than the row of three smaller injectors used here.

Based on PLIF signal intensity and quenching analysis methods described previously [4], the maximum PLIF signal intensities for both injectors correspond to an OH(X) mole fraction of approximately 0.001. For the likely temperatures and measured pressures in this region, this OH(X) level corresponds to thermally excited OH(A) number densities that are two orders of magnitude below that observed with the OH(A) camera; this means that the OH(A) emission observed at this station is chemiluminescence. This suggests, as expected, that the combustion is still in an early state, characterized by nonequilibrium free-radical chemistry. By inference, the faint OH(A) emission observed at the injector station, where the temperatures in the igniting regions are expected to be much lower, is also probably chemiluminescence.

Measurements at the 120-cm station included OH(A) emission imaging and $H_2O(\nu_2)$ infrared emission spectroscopy. In successive identical shocks, the H_2O emission spectra were recorded at heights of 0.6, 1.3, 1.9, and 3.2 cm above the bottom wall. The observed spectral distributions were in excellent agreement with those observed in shock tube calibration experiments [9]. H_2O temperatures and concentrations were determined from the spectra as described elsewhere [3,5]. Example time traces of $[H_2O]$, T, and top-wall pressure are shown in Fig. 4. The data show that conditions are reasonably steady during the test time. Companion measurements of H_2O emission by the radiometer viewing downward from the top wall gave temporal behavior which was similar to that of the side-viewing measurements, indicating good spanwise uniformity of the flow field as expected for this distance downstream.

H_2O concentrations and temperatures are largest near the bottom wall (0.6 cm) and decrease with increasing height. This behavior is consistent with the spatial distributions observed from OH(A) emission images, as shown by the comparisons in Fig. 5. The OH(A) emission profiles were determined by averaging the 20 center columns of pixels in each image. The $[H_2O]$ and T values represent averages over the test time, with vertical error bars denoting standard deviations and horizontal error bars indi-

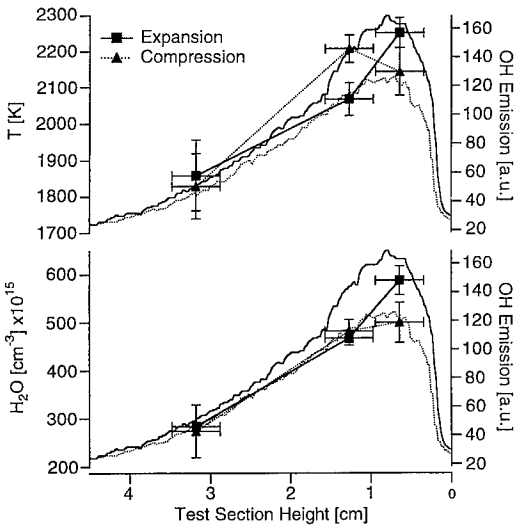

FIG. 5. H_2O concentrations, temperatures, and $OH(A^2\Sigma)$ intensities as functions of height above the bottom wall, 120 cm downstream of the nozzle exit.

cating the diameter of the spectrometer's field of view. Both injectors give similar results, with a maximum $[H_2O]$ and T of 5.8×10^{17} cm^{-3} and 2250 K for the expansion injector at 0.6 cm above the bottom wall. The standard deviations of the infrared measurements generally increase with increasing height, reflecting the decreasing signal-to-noise ratios of the radiance measurements. Consistent with the spatial distribution of the OH(A) emission, essentially all the H_2O production is occurring in the lower half of the duct, with a pronounced maximum at about 1 injector step height above the bottom wall. The peak OH(A) intensity of 160 counts, observed for the expansion injector at $\approx$1 cm above the bottom wall, corresponds to $[OH(A)] = 4 \times 10^7$ cm^{-3}.

Discussion

The ignition process in the PSI shock tunnel is initiated by the presence of excess atomic oxygen in the free stream air flow [1]. The shock-heated plenum air rapidly reaches equilibrium compositions at reflected shock temperatures of $\approx$3000 K, resulting in the formation of substantial O and NO. As this gas expands through the Mach 3 nozzle, relatively little recombination occurs, so that the expanded air flow contains super-equilibrium levels of O and NO. Kinetic modeling of the flow through the nozzle [11] for the present conditions gives O and NO mole fractions of 0.0025 and 0.035, respectively. The atomic oxygen initiates free-radical production through the following reaction with H_2:

$$O + H_2 = OH + H \qquad \text{(R1)}$$

Thus, the chemical ignition times are considerably shorter than expected for a thermal hydrogen-air system at our flow temperatures.

The ignition process in the shock tunnel results from air-fuel mixing, promoted by the flow over the injectors as described above, and the chemical reaction process. In the earliest stage of ignition, the streamwise vorticity induced by the injectors leads to the gradual ingestion of air into a fuel-rich interaction zone. As the fuel:air ratio becomes low enough, or the admixture temperature high enough, rapid free-radical generation begins and ultimately leads to sustained ignition. Ignition times computed from a kinetic model for premixed systems at 1200 K and our initial O concentrations are 5–10 μs for $0.5 \leq \Phi \leq 5$. However, the mixing of 1200-K air and 190-K hydrogen results in reduced interaction temperatures which can significantly increase the intrinsic chemical ignition time, especially for the more fuel-rich regions. As an example, for fully accommodated admixture temperatures, the computed chemical ignition times exceed 100 μs for $\Phi > 2$. By comparison, the characteristic time for mixing across the fuel jet is given by $\tau = \ell/\Delta u$, where ℓ is the jet diameter and Δu is the velocity difference between the fuel and air streams. For the jet diameters and flow conditions used here, the mixing time is on the order of 10 μs, comparable to the chemical ignition time for a 1200-K system. However, for sufficiently fuel-rich conditions, where the admixture temperature is significantly reduced by the presence of cold hydrogen, the chemical ignition times can be longer than the characteristic mixing times, leading to substantial mixing of the fuel and air prior to ignition.

Given the above considerations, it is reasonable that we observe little or no ignition on the 20-μs time scale, due to a combination of chemical and mixing limitations. As illustrated in Fig. 2, the compression injector generates an oblique shock wave upstream of the point of fuel injection; this wave heats the air by about 200 K, accelerating the ignition of the hydrogen immediately downstream. Since the flow over the injector structure is three dimensional, this temperature increase is not experienced by the entire air flow, however, the effect of this localized heating is still significant. Thus, the compression injector displays some intermittent ignition in the near field and apparently spontaneous ignition upstream of the PLIF station (29 cm). For the expansion injector, the main flow cools locally as it expands over the injector, and this cooling can inhibit the ignition of the hydrogen. The oblique shock at the base of the expansion injector (Fig. 2) should heat the hydrogen and air flows somewhat and should also promote the baroclinic torque mixing mechanism through interaction with the air-fuel interface. How-

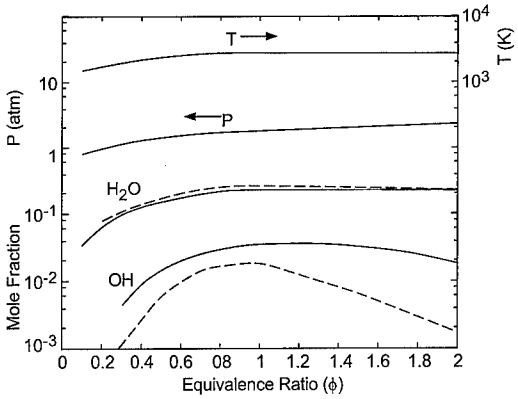

FIG. 6. Computed temperatures, pressures, and mole fractions of H_2O and OH as functions of initial equivalence ratio Φ. The solid curves denote kinetic model predictions at 120 cm computed for uniformly mixed combustion using the nozzle exit initial conditions. The dashed curves denote full equilibrium values for H_2O and OH mole fractions.

ever, the observation of minimal OH(A) emission indicates that neither of these effects is sufficient to cause significant ignition immediately downstream of the injectors. Indeed, it appears from the OH(A) emission images further downstream (29 cm) that the expansion injector flow does not fully ignite until it passes through the oblique shock at the base of the final ramp.

The OH(A) and OH(X) images at the 29-cm station (130 μs reactive flow time) show uniform distributions of combustion species within the reacting layer. This uniformity results from the mixing processes incurred upstream. For both the expansion and compression injectors, the OH(A) and OH(X) concentrations and spatial distributions are essentially the same. Thus, it appears that the compression and expansion injectors produce equivalent degrees of mixing on the 100 μs time scale. The observed OH(X) mole fraction of 0.001 is consistent with predicted OH yields for fuel-rich combustion, $\Phi \approx 5$.

The measurements at the 120-cm station sample the far-field combustion products, at flow times of 0.6–1 ms. At this point, we expect the development of fuel-lean conditions, due to continued mixing and dilution, approaching the overall equivalence ratio of 0.3. The spatially resolved data show that the reacting layer occupies at most the lower half of the duct. Thus, we expect $\Phi \geq 0.6$ in the heart of the reacting layer, and $\Phi \rightarrow 0$ at the upper edge of the layer. Straightforward kinetic modeling calculations for premixed reacting flow show that, at long reaction times well beyond the ignition and radical growth stage, the reaction system reaches a state of "partial equilibrium" [12,13] which persists for time scales much longer than the tunnel residence time. In the long-time domain, the chain-branching reactions

$$H + O_2 = OH + O \qquad (R2)$$

$$OH + H_2 = H_2O + H \qquad (R3)$$

and reaction R1 have nearly equal forward and reverse rates, and are essentially in equilibrium with each other. This results in a balance of the major species H, O, OH, H_2, O_2, and H_2O, which can be described in terms of the equilibrium constants for reactions R1–R3, the temperature, and the initial equivalence ratio Φ. As the chain-terminating and radical recombination reactions slowly convert the remaining radicals to H_2O, the partial equilibrium compositions are maintained by rapid adjustments in the forward and reverse rates of reactions R1–R3.

Computed kinetic model (120 cm) and full equilibrium compositions of H_2O and OH are compared in Fig. 6. Here, the kinetic model predictions account for pressure increases and flow deceleration due to chemical heat release, while the full equilibrium calculations do not. The species concentrations predicted by the kinetic model for these long reaction times agree within <1% with those computed from the partial equilibrium relationships. While the partial equilibrium concentrations of OH, O, and H are considerably larger than their equilibrium concentrations, the partial equilibrium concentrations of H_2O are only about 10–20% smaller than equilibrium. The calculations indicate that an H_2O mole fraction of 0.11–0.12 should be generated by a well-mixed system at $\Phi = 0.3$.

The observed H_2O mole fractions in the reacting layer range from peak values of 0.14 at the 1 cm height to 0.06 at the 3.2 cm height. These values are comparable to predicted partial equilibrium values for fuel-lean combustion, $\Phi \leq 0.6$, as shown in Fig. 6. Similarly, the relatively low observed final temperatures ($T < 2300$ K) and pressures (1.3–1.6 atm) are consistent with predicted values for $\Phi \leq 0.6$.

The overall efficiency of the combustion process can be expressed in terms of the final H_2O yield, defined as the ratio of observed and idealized H_2O fluxes at the 120-cm station. It is straightforward to show that this is given by the ratio of the vertically averaged H_2O mole fraction over the full duct height to that expected for fully mixed combustion (i.e., equilibrium at $\Phi = 0.3$). Based on the observed and equilibrium H_2O mole fractions, this analysis gives H_2O yields for both the compression and expansion injectors of 0.3. Adjusting the equilibrium value downward to allow for the effects of flow deceleration gives H_2O yields near 0.4. We conclude that the apparent combustion efficiency based on net H_2O formation is in the range 30–40%. This is considerably smaller than efficiencies deduced previously for similar injector designs based on analysis of wall pressure measurements [6].

The present results indicate similar overall combustion performance for the two injectors despite their differences in design and ignition characteristics. Since the kinetic limitation represented by the partial equilibrium phenomenon is at most a 10–20% effect as noted above, the fundamental limitation to the observed combustion performance appears to be due to the mixing processes contributing to the vertical propagation or spreading rate of the reacting layer.

Conclusions

The swept-ramp expansion and compression injector configurations display markedly different ignition characteristics. The contrasting ignition behavior may result in part from differences in local heating and cooling of the flow due to the oblique shock waves and expansion fans formed by each injector structure. The compression injector gives more prompt ignition than the expansion injector, on the approximate time scale of both the characteristic mixing time and the expected chemical ignition time for O-laden air. The near-field mixing of air into the reacting layer appears to be efficient and is equivalent for the two injectors for a flow time scale of about 100 μs.

The far-field measurements at long reactive flow times give vertical distributions of final H_2O concentrations and temperatures that indicate low combustion efficiencies of 30–40%, limited by slow vertical spreading of the reacting layer downstream of the initial mixing region. This result is consistent with previous observations of far-field combustion efficiency for a single straight axial injector with larger orifice diameter [3]. Kinetic limitations due to incomplete radical removal appear to be relatively minor. The similarity of the far-field combustion yields for the two injectors illustrates the independence of near-field ignition phenomena and overall combustion efficiency.

Acknowledgments

We are grateful for technical contributions by K. R. McManus and B. L. Upschulte, and for helpful discussions with H. H. Legner and all of PSI. This work was supported by the National Aerospace Plane Joint Program Office, Dr. Kervyn Mach, Technical Monitor.

REFERENCES

1. Parker, T. E., Allen, M. G., Foutter, R. R., Reinecke, W. G., Legner, H. H., Davis, S. J., and Rawlins, W. T., *Twenty-Fourth Symposium (International) on Combustion,* The Combustion Institute, Pittsburgh, 1992, pp. 1613–1620.
2. Parker, T. E., Allen, M. G., Reinecke, W. G., Legner, H. H., Foutter, R. R., and Rawlins, W. T., *AIAA J. Prop. Power* 9:486–492 (1993).
3. Parker, T. E., Allen, M. G., Foutter, R. R., Sonnenfroh, D. M., and Rawlins, W. T., *AIAA J. Prop. Power* 11:1154–1161 (1995).
4. Allen, M. G., Parker, T. E, Reinecke, W. G., Legner, H. H., Foutter, R. R., Rawlins, W. T., and Davis, S. J., *AIAA J.* 31:505–512 (1993).
5. Parker, T. E., Miller, M. F., McManus, K. R., Allen, M. G., and Rawlins, W. T., *AIAA J.,* 34(3):500–507 (1996).
6. Stouffer, S. D., Vansburger, U., and Northam, G. B., *Thirty-Second AIAA Aerospace Sciences Meeting,* Reno, NV, 1994, AIAA Paper 94-0587.
7. Northam, G. B., Greenburg, I., Byington, C. S., and Capriotti, D. P., *AIAA J. Prop. Power* 8:491–499 (1992).
8. Donohue, J. M., McDaniel, J. C., and Haj-Hariri, H., *AIAA J.* 32:1860–1867 (1994).
9. Rawlins, W. T., Miller, M. F., Allen, M. G., and Parker, T. E., *J. Quant. Spectrosc. Radiat. Transfer,* to be submitted, 1996.
10. Rawlins, W. T., Foutter, R. R., and Parker, T. E., *J. Quant. Spectrosc. Radiat. Transfer* 49:423–431 (1993).
11. Rawlins, W. T., Parker, T. E., Foutter, R. R., and Allen, M. G., *AIAA J.* 31:499–504 (1993).
12. Schott, G. L., *J. Chem. Phys.* 32:710–716 (1960).
13. Kaskan, W. E., *J. Chem. Phys.* 31:944–956 (1959).

COMMENTS

Dr. Günter Sweets, French-German Research Institute of Saint-Louis-France, France. If the temperature is to be deduced from the total intensity emitted by the H_2O molecules, a constant state of the gas over the optical path between the windows has to be assumed.

Do you think that the injected H_2 has been sufficiently distributed in the lateral direction and that the cooling of the gas by the side wall boundary layers can be disregarded?

Author's Reply. The temperature is deduced from the ratio of the emitted intensity at two wavelengths (e.g., 6.50 and 8.5 μm) and therefore is not sensitive to the absolute intensities. The H_2O concentration, on the other hand, is

determined from the absolute intensity at one wavelength (e.g., 6.50 μm) and the measured temperature [5].

The line-of-sight emission measurements yield path-averaged values for the temperature and H_2O concentration; thus, interpretation of the results generally requires the assumption of a uniform emitting volume. Since the water emission falls off sharply with decreasing temperature [5], regions of cold gas along the measurement path do not contribute significantly to the total emission signal; thus, the temperature measurement is relatively insensitive to the cold boundary layers along the side walls of the test section. The water concentration measurement will be more sensitive to the presence of cold gas regions, which will cause the local H_2O concentration in the emitting regions to be underestimated. Cold gas regions containing significant H_2O can also corrupt both measurements by absorbing a fraction of the emitted light, with the absorption coefficient varying with wavelength; however, by properly choosing the measurement wavelengths this effect can be minimized. For the present measurements, the flow temperature determined from various wavelength pairs yielded consistent values, indicating the boundary layers along the test section wall do not have a significant effect.

Based on the long flow development length upstream of the infrared spectrometer measurement station, approximately 120 injector heights, the hydrogen is expected to be well-distributed across the span of the test section.

Twenty-Sixth Symposium (International) on Combustion/The Combustion Institute, 1996/pp. 2903–2908

EXPERIMENTAL OBSERVATION OF UNSTEADY H_2-O_2 COMBUSTION PHENOMENA AROUND HYPERSONIC PROJECTILES USING A MULTIFRAME CAMERA

JIRO KASAHARA AND TAKAHIRO HORII
Department of Aerospace Engineering
Nagoya University

TAKUMA ENDO
Center for Integrated Research in Science and Engineering
Nagoya University

TOSHI FUJIWARA
Department of Micro System Engineering
Nagoya University Furo-cho
Chikusa-ku, Nagoya, Aichi 464-01, Japan

Projectiles were fired at hypersonic speeds into stoichiometric H_2-air mixtures. The flow fields around the projectiles were visualized using a multiframe schlieren technique. We made a comprehensive study of oscillating combustion phenomena around hypersonic projectiles with the following variable parameters: projectile nose shape, velocity, and diameter and the initial gas pressure. By studying the dependence of the oscillating combustion cycle on the projectile velocity, we could categorize the combustion cells into five modes comprised of three fundamental modes (normal cell oscillation, high-frequency cell oscillation, and envelope oscillation). An envelope oscillation superimposed on each of the normal and high-frequency modes was observed. The mode in which the envelope oscillation is combined with the high-frequency cell oscillation was observed for the first time in the present experiment. Based on the results of projectile nose-shape changes and projectile diameter changes, it was concluded that the standoff distance between the front of the projectile and the bow shock wave dominates the generation and period of the oscillating combustion, although the mechanism whereby a normal or high-frequency mode is selected was not clear. The results of the initial gas pressure changes suggest that there exists a critical initial pressure for generating oscillating combustion.

Introduction

Unsteady shock-induced combustion of a H_2-air (or H_2-O_2) mixture was investigated in the 1960s and 1970s using ballistic range projectiles [1–4]. The researchers concentrated on the unsteady, periodic motion of the exothermic reaction zone located behind the bow shock wave. McVey and Toong [3] and Alpert and Toong [4] investigated these phenomena using one-dimensional wave-interaction analysis along a stagnation stream line of the hypersonic blunt-body flow. While some phenomena could be explained by this analysis, many questions remained. Recent numerical simulations have helped to clarify the phenomena that the simple model could not explain. Matsuo, Fujii, and Fujiwara [5–9] carried out numerical analyses with a full chemical kinetics model of H_2-O_2 combustion, renewing interest in the study of unsteady combustion. However, experimental studies have not been as active. We take advantage of extensive progress in high-speed electronic cameras; high-accuracy experimental studies of oscillating combustion phenomena are not only interesting but also important for the stable operation of the new hypersonic propulsion applications, such as the ram accelerator and the oblique detonation wave engine [10].

In this paper, we show the successive, continuous-framing schlieren photographs of the oscillating combustion using a high-speed, multiframe camera. We recorded the change of oscillating combustion modes, varying four parameters: (1) projectile nose shape, (2) projectile velocity, (3) projectile diameter, and (4) initial pressure of the mixture. We report the dependence of the oscillating combustion cycle on the four parameters. In the following, we describe the experimental facility and conditions and discuss the effect of each parameter.

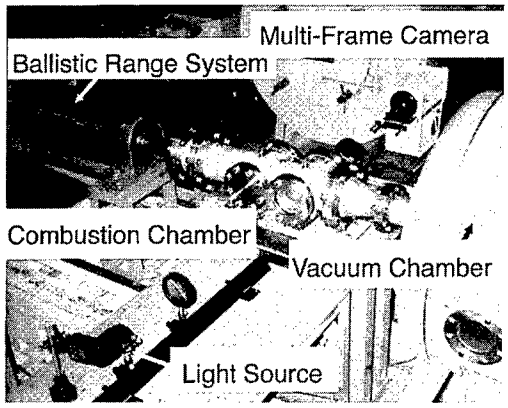

FIG. 1. Experimental facility.

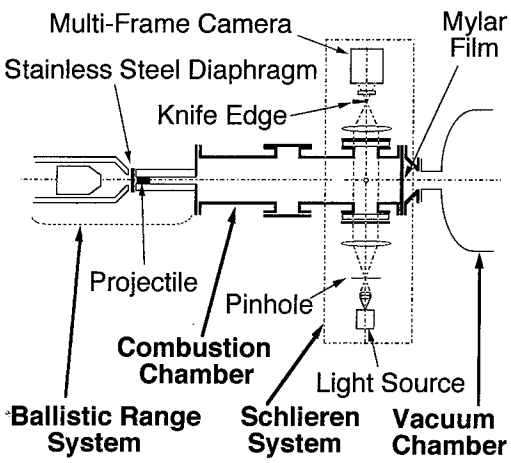

FIG. 2. Schematic diagram of the experimental arrangement (top view).

Experimental Facility and Conditions

The experimental facility is shown in Fig. 1, and a schematic diagram of the experimental arrangement (top view) is shown in Fig. 2. The experimental equipment is comprised of four elements: (1) a two-stage, light-gas gun to inject the hypersonic projectiles, (2) a combustion chamber with the gas mixture, (3) a schlieren system for observation, and (4) a vacuum chamber for the exhausted projectile and burned gas.

The two-stage, light-gas gun [11] uses high-pressure air, at 5 MPa, to drive the piston. The driver light gas is helium. The maximum projectile speed is 5 km/s. A stainless steel cylindrical tube of 140-mm internal diameter and 10-mm thickness was adopted as the combustion chamber containing the hydrogen-oxygen mixture. The combustion chamber had a 90-mm observation window on the horizontal plane, perpendicular to the centerline of the tube. The position of the bow shock wave was determined by the piezopressure gauges KISTLER 603B (Kistler Japan) attached to the wall of the combustion chamber. About 100 μs after detection, the projectile arrived at the observation window and the schlieren system recorded the flow field around the projectile. After the combustion chamber, the projectile breaks a mylar film and is recovered in a vacuum chamber. The vacuum chamber is a cylinder of 1.0 m diameter and 2.0 m^3 volume. The vacuum chamber is ready for injecting when the pressure drops to 100 Pa. As soon as the projectile breaks the diaphragm, the high-pressure burned gas is inhaled into the vacuum chamber; thus, the combustion chamber was not exposed to high pressure for long. The total time for the operation, from releasing high-pressure air in the gas gun to recovering the projectile in the vacuum chamber is about 10 ms.

The schlieren method was used for visualizing the flow field around the projectile, using a stroboscope SL540EZ (Canon) with the spark duration of 1.2 ms. The pinhole diameter was 2 mm. The objective lens was a spherical convex lens of 150 mm diameter. The knife edge was placed of either side of the optical path, depending on the experiment. Two kinds of high-speed multiframe cameras (image converter cameras) were used: an IMACON 790 (HADLAND PHOTONICS) and a FS501 ULTRANAC (NAC Inc.). The spatial resolution was approximately 0.1 mm at the objective plane. The frame camera and light source were triggered by the pressure signal from the bow shock wave. This trigger signal was delayed by a digital delay generator DG535 (Stanford Research Systems).

Experimental conditions are shown in Table 1. The molar ratio of the mixture was fixed at $2H_2 + O_2 + 3.76N_2$. The initial temperature was room temperature, which was almost constant throughout the experiment. Most of the experiments were done with a hemisphere-nose, 10-mm-diameter projectile at 0.75-atm initial gas pressure, so we consider this the standard condition.

Results and Discussion

In Fig. 3, we define some terms of oscillating combustion. The shaded area in Fig. 3 is the reaction zone, in which the exothermic reaction occurs. The reaction zone around the projectile is divided by distinct density gradients into combustion cells, each cell characterized by its diameter, D, and width, W. Generally, cells have different diameters; in some cases, they change periodically with wavelength λ. We call this periodical phenomena the envelope oscillation. To be specific, the width W or diameter D indicate maximum observable values within 30 mm of the projectile. We define *cell-oscillating period* as

TABLE 1
Experimental conditions

Fig. No.	Proj. Nose	Proj. Velocity [km/s]	Mach No.	Proj. Diam. [mm]	Initial Pres. [atm]	Initial Temp. [K]
*4a	Hemis.	1.98 ± 0.05	4.84	10.00	0.75	301.1
*4b	Hemis.	1.78 ± 0.02	4.35	10.00	0.75	300.9
*4c	Hemis.	1.92 ± 0.02	4.74	10.00	0.75	295.1
*4d	Hemis.	1.76 ± 0.02	4.30	10.00	0.75	300.9
*4e	Hemis.	1.75 ± 0.02	4.31	10.00	0.75	295.9
*5	Hemis.	1.76 ± 0.02	4.30	10.00	0.75	300.9
7a	Cone, 76°	2.38 ± 0.07	5.78	10.00	0.75	304.2
7b	Cone, 120°	2.31 ± 0.06	5.61	10.00	0.75	304.7
*7c	Hemis.	2.03 ± 0.07	4.92	10.00	0.75	305.3
*8a	Hemis.	2.03 ± 0.07	4.92	10.00	0.75	305.3
8b	Hemis.	1.93 ± 0.07	4.68	12.00	0.75	305.2
9a	Hemis.	2.00 ± 0.06	4.86	10.00	0.50	303.8
9b	Hemis.	1.99 ± 0.06	4.83	10.00	0.60	305.0
*9c	Hemis.	2.03 ± 0.07	4.92	10.00	0.75	305.3

*Standard condition: Hemisphere 10-mm diameter projectile and 0.75-atm initial gas pressure.

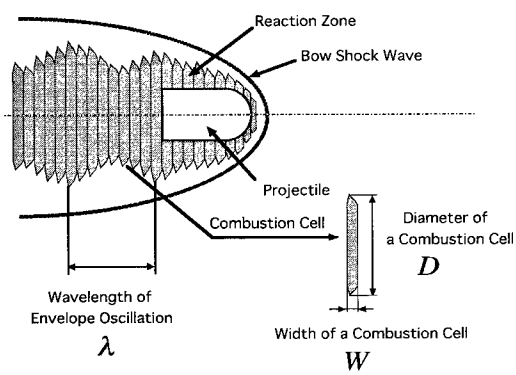

FIG. 3. Structure of oscillating combustion.

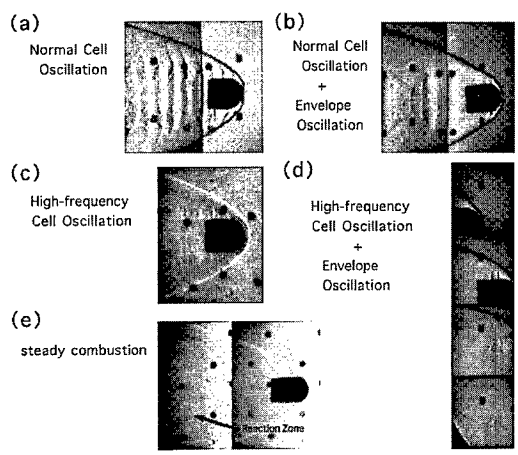

FIG. 4. Five combustion modes observed in the present experiments: (a) normal cell oscillation mode, (b) normal cell oscillation + envelope oscillation mode, (c) high-frequency oscillation mode, (d) high-frequency oscillation + envelope oscillation mode, and (e) steady combustion.

the cell width W divided by the projectile velocity relative to combustion cells, and the *envelope oscillating period* as the wavelength λ divided by the projectile velocity relative to combustion cells.

The periodic combustion observed is categorized into five modes. These modes are shown in Fig. 4. The black dots are markers for measuring the projectile velocity. Each dot is 2 mm wide and separated by 20 mm from the next dot in the same horizontal or vertical line. The markers are the same in all schlieren pictures. The normal cell oscillation (NCO) mode is shown in Fig. 4a, and the high-frequency cell oscillation (HCO) mode is shown in Fig. 4c. The high-frequency cell oscillation period is about half the normal cell oscillation period. The other mode is the envelope oscillation (EO) in which the combustion-cell envelope oscillates. The envelope oscillation can be superimposed on either the normal cell oscillation or the high-frequency cell oscillation mode. These combined modes are shown in Figs. 4b and 4d. A steady combustion mode was also observed and is shown in Fig. 4e.

In past studies [1–4], the unsteady periodic combustion around hypersonic projectile was categorized into two flow regimes. One is called the *regular regime* of high frequency and low amplitude oscillation, corresponding to Fig. 4c. The other is the

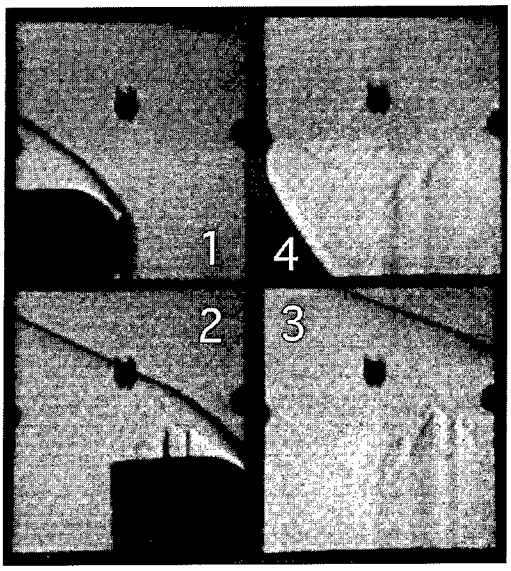

FIG. 5. High-frequency cell oscillation + envelope oscillation mode. The interframe time is 7.00 μs.

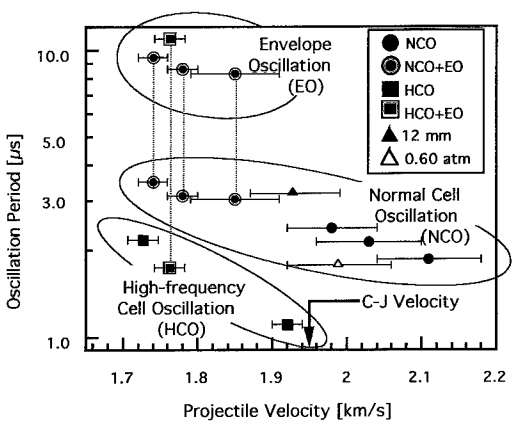

FIG. 6. The dependence of oscillation periods on the projectile velocity. Without ▲ and △, data plots on this graph are for the case of standard conditions. ▲ is a plot for 12-mm diameter and △ is a plot for 0.60-atm initial gas pressure. Error on the vertical direction is smaller than the symbol size.

large disturbance regime of lower frequency, larger amplitude, and less regular oscillation, corresponding to Figs. 4a and 4b. However, in the present study, the oscillating combustion observed is categorized into five modes, composed of three fundamental modes, namely, NCO, HCO, NCO + EO, HCO + EO, and STEADY. In particular, HCO + EO mode shown in Fig. 4d and Fig. 5 was observed for the first time in this experiment.

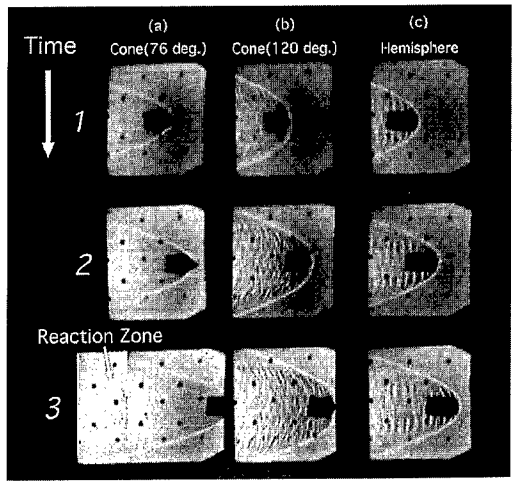

FIG. 7. Dependence of the combustion phenomena on the projectile nose shape: (a) cone, 76°; (b) cone, 120°; and (c) hemisphere. The interframe time was 5.00 μs.

Dependence on Projectile Velocity

Figure 6 shows the dependence of the combustion period mode on the projectile velocity. The steady mode was observed at projectile velocities of 1.58 and 1.75 km/s. No envelope oscillating mode was observed for velocities greater than 1.85 km/s. Higher projectile velocity had shorter oscillating periods. The envelope oscillation is observed only within 1.8 ± 0.1 km/s. It is not clear which factor determines the mode as NCO or HCO. To understand this, it is necessary to study the oscillating mechanism.

Dependence on Nose Shape

The three typical cases are shown in Fig. 7. The projectile nose shapes were as follows: 76° cone (Fig. 7a), 120° cone (Fig. 7b), and hemisphere (Fig. 7c). In nonreactive flow, the shock should be attached in the 76° cone and detached in the 120° cone. In this experiment, we observed the following: the 76° cone had an attached shock and a trailing reaction zone but no oscillating combustion. This could be due to the absence of a distance between the shock wave and the combustion zone, where the compression wave and contact discontinuity propagate and form the oscillation. In the cases of 120° cone and hemispherical nose, the shock was detached and we observed unsteady oscillating combustion.

Dependence on Diameter

The cases of projectiles with diameters of 10 and 12 mm are shown in Fig. 8. The oscillation period is 2.00 μs for the 10-mm projectile and a slightly longer

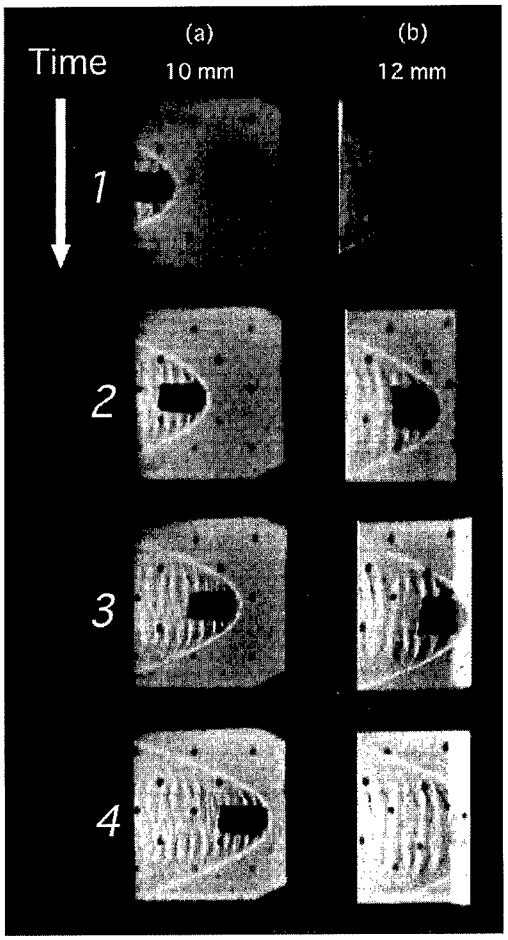

FIG. 8. Dependence of the combustion phenomena on the projectile diameter: (a) 10 mm and (b) 12 mm. The interframe time was 5.00 μs.

period of 2.78 μs for the 12-mm projectile. The difference may be explained not only by the one-dimensional wave interactions between the bow shock wave and the reaction zone but also by the three-dimensional effect of the wave propagation and interaction along the projectile surface.

Dependence on Initial Pressure of Mixture

The cases of initial pressure of mixture, 0.50, 0.60, and 0.75 atm are shown in Fig. 9. The oscillating combustion was not observed in the case of lowest pressure. The cell width and diameter in frames 1 and 2 for the 0.60 and 0.75 atm cases are almost the same, although the period of oscillation was shorter for the 0.60-atm case (see Fig. 6). Cells at 0.60 atm are not so clearly defined; this indicates a weaker density gradient. The 0.60-atm case is either the critical pressure to generate combustion cells or the observation limit of the schlieren system.

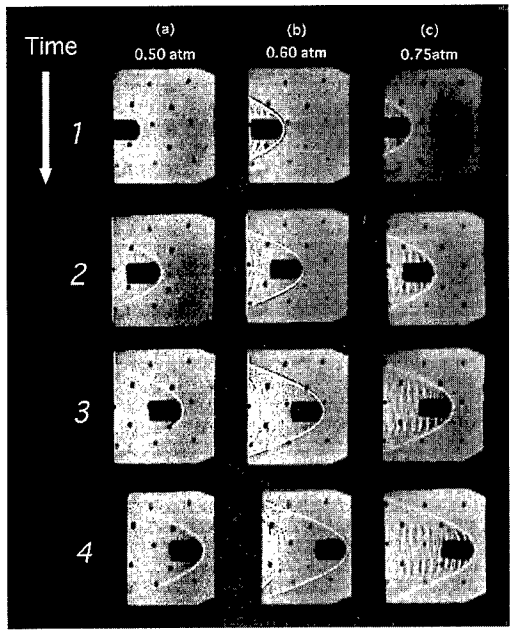

FIG. 9. Dependence of the combustion phenomena on the initial gas pressure: (a) 0.50 atm, (b) 0.60 atm, and (c) 0.75 atm. The interframe time was 5.00 μs.

Conclusions

Projectiles were fired at hypersonic speeds into stoichiometric H_2-air mixtures, and the flow fields around the projectiles were visualized using a multiframe, schlieren technique. We studied oscillating combustion phenomena with the variable parameters of the projectile nose shape, velocity and diameter and the initial gas pressure. Considering the dependence on the projectile velocity, we categorized the combustion into five modes comprised of three fundamental modes, namely, normal, high-frequency, envelope + normal, envelope + high-frequency, and steady. The mode in which the envelope oscillation is combined with the high-frequency cell oscillation was observed for the first time in the present experiment. From a comparison for the cases of the projectile nose-shape change and the projectile diameter change, it can be concluded that the distance between the front of projectile and the bow shock wave affects the generation and the period of the oscillating combustion. From a comparison of the initial gas pressure change, it may be deduced that a critical initial pressure exists for generating oscillating combustion.

Acknowledgments

The authors are grateful to Kistler Japan Co., Ltd., J. Osawa & Co., Ltd., and NAC Inc. for the provision of laboratory facilities. We thank A. Saito, T. Kamiya, T. Sato, S. Takahashi, and K. Tachibana of Nagoya University for supporting this work. The authors express their sincere thanks to Prof. N. Yoshikawa and Dr. J. E. Leblanc of Nagoya University, Dr. A. Matsuo of Keio University, and H. Sakakita of National Institute for Fusion Science.

REFERENCES

1. Ruegg, F. W. and Dorsey W. W., *J. Res. Natl. Bur. Stand. Sec. C.* 66C (1):51–58 (1962).
2. Lehr, H. F., *Astronautica Acta* 17:589–597 (1972).
3. McVey, J. B. and Toong, T. Y., *Combust. Sci. Technol.* 3:63–76 (1971).
4. Alpert, R. L. and Toong, T. Y., *Astronautica Acta* 17:539–560 (1972).
5. Matsuo, A. and Fujiwara, T., *AIAA J.* 31(10):1835–1841 (1993).
6. Matsuo, A., Fujii, K., and Fujiwara, T., AIAA Paper No. 94-0764, 1994.
7. Matsuo, A., Fujii, K., and Fujiwara, T., *AIAA J.* 33(6):1056–1063 (1995).
8. Matsuo, A. and Fujii, K., *AIAA J.* 33(10):1828–1835 (1995).
9. Matsuo, A. and Fujii, K., AIAA Paper No. 95-2565, 1995.
10. Powers, J. M., *Combustion in High-Speed Flows,* Kluwer Academic Publishers, Boston, 1994, pp. 345–371.
11. Chang, X., Hemmi, M., Sasoh, A., and Fujiwara, T., *J. Japan Soc. Aeronautical Space Sci.* 41:81–87 (1993).

Twenty-Sixth Symposium (International) on Combustion/The Combustion Institute, 1996/pp. 2909–2915

PLIF IMAGING OF HYPERSONIC REACTIVE FLOW AROUND BLUNT BODIES

M. R. KAMEL, C. I. MORRIS, I. G. STOUKLOV AND R. K. HANSON
High Temperature Gasdynamics Laboratory
Department of Mechanical Engineering
Stanford University, Stanford, CA 94305-3032, USA

Qualitative OH planar laser-induced fluorescence (PLIF) imaging experiments of supersonic reactive flows over a 40° wedge and a 19-mm-diameter blunted cylinder are reported. Hydrogen-, ethylene-, and methane-based mixtures have been used in this work. Three different free stream conditions, M_∞ = 6.7, 5.2, and 4.2, were used to study the combustion modes around the wedge and blunted cylinder. Separate schlieren imaging results were also obtained for several of the test cases, providing complementary shock wave visualization. In several cases for the wedge, shock-induced combustion was observed a finite distance behind the nonreacting oblique shock wave. For the most sensitive hydrogen mixture, an oblique detonation occurred in which the shock wave and combustion front were fully coupled. In the experiments with the blunted cylinder, two different regimes of combustion were observed. When the velocity of the flow was larger than the CJ velocity of the mixture, the mode was that of an adiabatic shock followed by a smooth combustion front. For cases of flow velocity similar to the CJ velocity or less, regular oscillations were observed on the image and in the stagnation pressure history. These observations are qualitatively consistent with previous work.

Introduction

The ongoing development of ram accelerators has sparked new interest in the flow visualization of hypersonic combustion phenomena around projectiles and blunt bodies. A new expansion tube facility has recently been built at Stanford University to enable spatially resolved, instantaneous optical measurements of high-speed reactive flow fields. This facility has been used for initial investigations of reactive flows around wedges and blunted cylinders using PLIF [1–2].

Work at Stanford is intended to complement the international development of the ram-accelerator concept first proposed by Herzberg et al. [3]. However, experimental data regarding fundamental shock-induced combustion and oblique detonation phenomena at conditions relevant to the ram-accelerator community are limited. Most experimental work performed over the past 30 years has involved firing spheres and blunted cylinders at hypersonic speeds into combustible mixtures. Schlieren photography was used to observe the different combustion modes occurring around and behind the body [4–6].

More recently, Dabora et al. [7], Viguier et al. [8], and Desbordes et al. [9] have studied oblique detonations and combustion using the "oblique shock tube" method of Dabora et al. [10]. In our approach, the projectile is fixed in the laboratory reference frame, and an expansion tube is used to generate a supersonic flow of combustible mixture around the body.

The aim of this paper is to present results and analysis of imaging experiments of supersonic reactive flows around a 40° wedge and a 19-mm-blunted cylinder. The wedge experiments are designed to study the effects of chemistry and Mach number on oblique detonations and shock-induced combustion. The cylinder experiments are designed to reproduce and further investigate the different combustion modes observed in previous works. Using the PLIF imaging technique, detailed spatially and temporally resolved information on the flame front can be obtained and is relevant to recent CFD modeling work [11].

A thorough understanding of the characteristics of the hypersonic flows generated by the expansion tube is a prerequisite to such investigations. Ongoing characterization efforts described by Morris et al. [2] allowed flow quantities to be determined using the combined information of wall pressure, pitot pressure, IR absorption, and NO PLIF measurements. This foundation in turn allowed selection of the flow conditions used in the present study. Some essentials on expansion tube and PLIF theory are presented first to provide background for the description of the facility that follows. The characteristics of the test flow and reactive gas mixtures used in the experiments are then discussed. Finally, results of the imaging experiments on combustion phenomena in supersonic reactive flows over the wedge and blunt body are presented and discussed.

Operation of Expansion Tubes

An expansion tube generally consists of three sections: a high-pressure driver, a lower-pressure driven section, and an expansion section at very low pressures. The sections are initially separated by diaphragms. When the driver/driven diaphragm is broken, the driver gas expands into the driven section, causing a shock wave to propagate ahead of it. The shock wave travels down the tube and is accelerated upon entering the expansion section, as are the gases behind it. The shocked test gas is thus accelerated via an unsteady, constant area expansion from the driven section into the lower-pressure expansion section. This is in contrast to a reflected-type shock tunnel, in which the stagnant gas near the end wall is accelerated through a steady flow, variable area expansion. Since an expansion tube can accelerate mixtures to similar high velocities (as a reflected shock tunnel) but without exposing the gases to the same high temperatures and pressures, it is well suited for use with reactive mixtures. A detailed analysis of expansion tube theory is given by Trimpi [12].

The facility at Stanford includes an additional section between the driver and driven sections, denoted as the buffer section. The buffer section is filled with an inert gas and isolates the combustible mixtures in the driven section from the hot diaphragm petals that are an issue when metallic diaphragms are used.

PLIF Description

The basis for PLIF as applied here is linear laser excitation of tracer molecules in the flow followed by broadband collection of the fluorescence from the radiative decay of these excited molecules. For each shot, the CCD array accumulated a fluorescence signal given by

$$S_f = \eta V_c n_o f_{J''} BEg\phi \qquad (1)$$

where η represents the overall efficiency of the optical setup in converting photons from fluorescence into photoelectrons incident on the detector, V_c is the collection volume, n_o is the number density of the absorbing species, $f_{J''}$ is the Boltzmann fraction of the tracer species molecules that are in the absorbing state, B is the Einstein coefficient for stimulated absorption, E is the laser energy fluence (energy per unit area), and g is the spectral convolution of the laser spectral distribution and the absorption transition. The fluorescence yield ϕ, defined as $A/(A + Q)$, where A is the Einstein coefficient for spontaneous emission from all the populated upper states and Q is the rate of electronic quenching to the lower state, represents the fraction of the molecules pumped to the upper state that decay radiatively.

At the combustion pressures obtained in this work, $Q \gg A$, hence $\phi \approx A/Q$. Since Q is proportional to the total number density n_{tot}, the fluorescence signal $S_f \sim n_o/n_{tot}$, which is the molar fraction of the tracer molecules.

OH PLIF

PLIF imaging of reactive flows relied on OH, a naturally occurring combustion radical, as the fluorescent tracer. Effective combustion visualization with OH PLIF requires that the variation in OH mole fraction in the region of interest affect the fluorescence signal more effectively than changes in other parameters in Eq. (1). The most critical issue, typically, is the temperature dependence of the Boltzmann fraction of the absorbing state. For the absorption transition considered here—the $Q_1(7)$ transition of the $A^2\Sigma^+ \leftarrow X^2\Pi$ (1,0) band of OH, located at 283.31 nm—such effects play a relatively minor role in interpreting the signal in the regions observed to contain OH, and the fluorescence intensity can be qualitatively linked to OH mole fraction.

Experimental Apparatus

Expansion Tube Facility

The Stanford expansion tube facility, accompanying lasers, and optical arrangement are described thoroughly in previous publications [1–2]. The test body is mounted 2 cm downstream of the exit of the expansion tube, inside a square viewing chamber of 27 × 27-cm cross section (Fig. 1). The viewing chamber is equipped with an opposed pair of 13 × 13-cm quartz windows for observation, and a fused silica slot for admission of the laser sheet.

Three piezo-electric pressure transducers, for shock speed and wall pressure measurements, are mounted at 30.5-cm intervals along the downstream end of the driven section. The expansion section is similarly outfitted with three transducers at 61.0-cm intervals. The driven and expansion sections are also equipped with sapphire viewing ports for optical measurements during experiments. A globar light source and IR detector are mounted on opposing sides of the expansion section port. The setup is used to detect the presence of the test gas through absorption of light by CO_2 seeded in the mixture. For flow characterization tests, the test body may be replaced with a pitot rake consisting of four pressure transducers at 19.1-mm intervals across the diameter of the tube. Data from these sensors are recorded at 1 M sample/s on a PC-based, 8-channel Gagescope CS1012 computerscope.

PLIF Setup

The laser sheet for PLIF imaging [1,13] is formed from the frequency-doubled output of a Lumonics

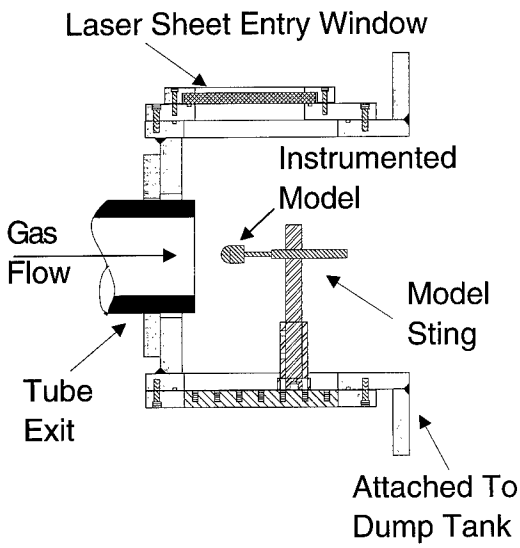

FIG. 1. Schematic of viewing section of the expansion tube facility. The laser sheet enters the section from the top entrance window. The ICCD camera is mounted at right angles to the laser sheet looking into the viewing section.

TABLE 1
Summary of Chapman-Jouget detonation parameters for reactive mixtures used in this work. Values for gases *A* and *B* based on initial conditions of $T_\infty = 350$ K, $P_\infty = 0.113$ bar. Values for gases *C*, *D*, and *E* based on initial conditions of $T_\infty = 420$ K, $T_\infty = 0.224$ bar; those for *F* are based on $T_\infty = 260$ K, $T_\infty = 0.065$ bar.

Gas	Composition	V_{CJ} (m/s)
A	10% H_2 + 5% O_2 + 85% N_2	1317
B	13.33% H_2 + 6.67% O_2 + 80% N_2	1472
C	5% C_2H_4 + 15% O_2 + 80% N_2	1693
D	7.5% C_2H_4 + 22.5% O_2 + 70% N_2	1823
E	10% C_2H_4 + 30% O_2 + 60% N_2	1915
F	16.67% CH_4 + 33.33% O_2 + 50% N_2	1957

HD-500 dye laser pumped by a Lumonics YM-1200 pulsed Nd:YAG laser. Coumarin 540A dye was used for OH PLIF transitions near 283 nm, with pulse energies of about 2.0 mJ. The sheet is roughly 0.5 mm thick × 3 cm wide at the viewing section. The fluorescence is collected onto the 578 × 384 pixel array of a Princeton Instruments intensified CCD camera. UG11 and WG305 Schott glass filters were placed in front of the camera's f/4.5, 105-mm UV objective lens in order to block elastically scattered laser light while still passing the majority of the OH fluorescence.

Exit Flow Conditions

The free stream conditions of the test gas at the exit of the expansion tube may be varied by changing the initial fill pressures at the start of the experiment. Three different conditions were used in this work to determine the effect of Mach number and pressure on the observed combustion phenomena. Background information relating to test flow characterization has been reported previously [2] and for brevity will not be repeated here.

The free stream pressure was calculated using one-dimensional normal shock theory from time-of-arrival measurements of the shock wave at three different axial locations in the expansion section. This value typically agrees with the measured wall pressure to within 5%. In a similar fashion, the velocity of the contact surface was deduced by measuring the difference in its time of arrival as measured by the IR detector and pitot rake. In our analysis, this value is assumed to be equivalent to the flow velocity immediately behind the contact surface. Note that this velocity constitutes an average value over the final 104 cm of the expansion section. The free stream Mach number was calculated from pitot pressure measurements using the standard Rayleigh formula ($\gamma = 1.35$ assumed). The value of the Mach number calculated in this fashion is typically within 10% of that predicted by isentropic theory. The flow field temperature was then calculated from the velocity and Mach number.

Mixture Selection and Properties

The primary criterion for the reactive mixture was that it not ignite anywhere inside the tube. The most severe limitation comes from the fact that the test gas is subjected to postreflected-shock conditions for a few microseconds at the driven-expansion section interface because of the finite diaphragm-opening time. Presently, Mylar diaphragms 25 μm thick are used at that interface, but other diaphragms and diaphragm opening schemes are under investigation.

Premature ignition of the test gas is characterized by one or all of the following effects. A strong reflected shock is recorded by the pressure transducer in the driven section at a location 15.2 cm upstream of the driven expansion diaphragm. The shock speeds in the expansion section and the pressure jump upon shock passage are considerably higher than in the corresponding inert case. In addition, emission from hot CO_2 combustion products is detected by the IR detector as the test gas flows by its viewing port. Finally, the PLIF images in cases of premature ignition show OH fluorescence signals in the free stream, upstream of the bow shock. Each of the mixtures shown in Table 1 could be consistently accelerated (under certain restrictions) without preignition in the driven section.

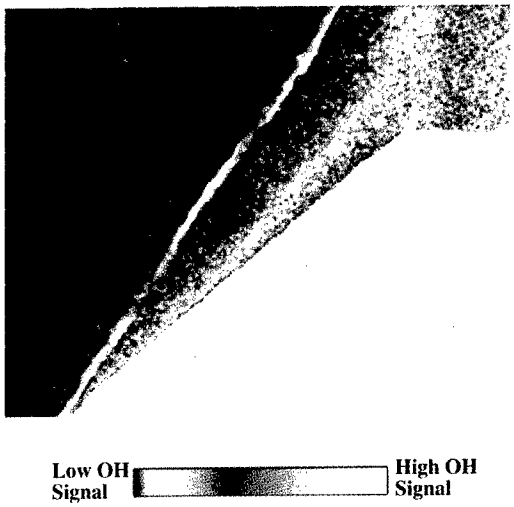

FIG. 2. Composite image of shock-induced combustion over a 40° (half-angle) wedge. The overlaid schlieren and OH PLIF results were obtained separately using the same test conditions. Gas mixture A: 10% H_2 + 5% O_2 + 85% N_2. $M_\infty = 5.2$, $T_\infty = 350$ K, $P_\infty = 0.113$ bar.

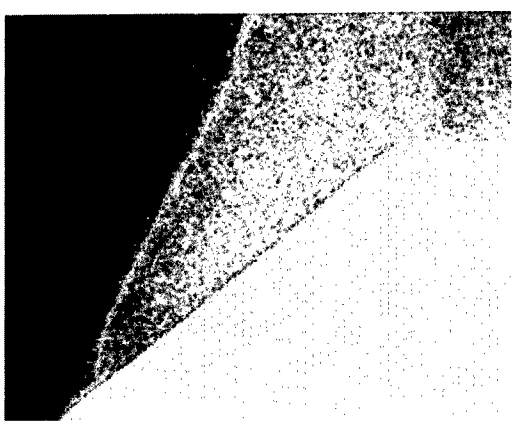

FIG. 3. Example OH PLIF image of oblique detonation wave. $V_{flow}/V_{CJ} = 1.33$. Gas mixture B: 13.3% H_2 + 6.7% O_2 + 80% N_2. $M_\infty = 5.2$, $T_\infty = 350$ K, $P_\infty = 0.113$ bar. Measured combustion wave angle is 64°, resulting in an effective $\bar{Q}_{eff} = 0.76$.

Results and Discussions

Flow over 40° Wedge

The OH PLIF technique was used in an initial investigation of combustion phenomena around the 40° half-angle, two-dimensional wedge test body. Since the OH radical is a natural product of combustion, OH PLIF is particularly well-suited for determining the reactive regions of a flow field. Both

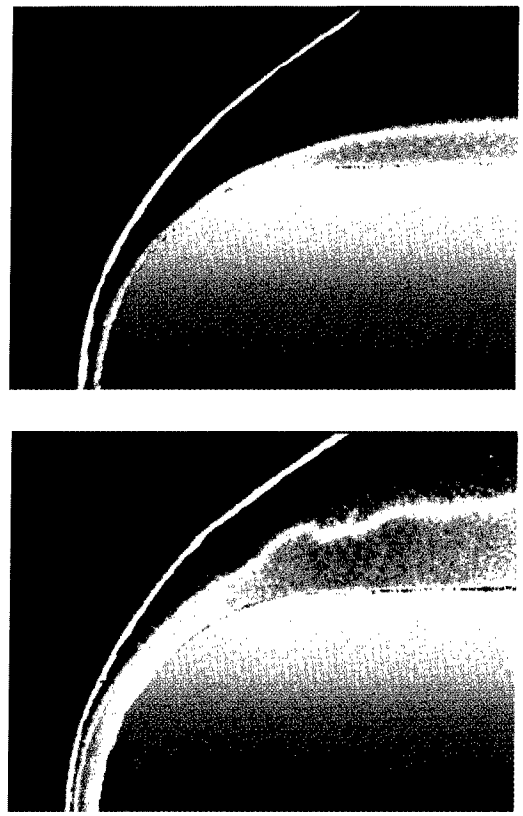

FIG. 4. Composite pictures showing an overlay of schlieren and OH PLIF images obtained separately for the same test conditions. The nominal flow conditions are $M_\infty = 6.7$, $V_\infty = 2150$ m/s, and $P_\infty = 0.065$ bar, with $V_{flow}/V_{CJ} > 1$ for both mixtures. (a) Gas mixture F: 16.7% CH_4 + 33.3% O_2 + 50.0% N_2. (b) Gas mixture C: 5% C_2H_4 + 15% O_2 + 80% N_2.

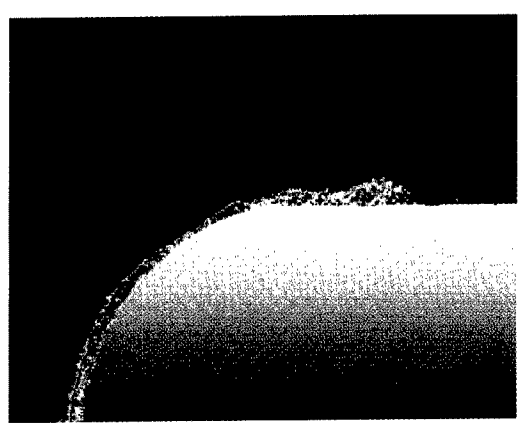

FIG. 5. OH PLIF image of $M_\infty = 4.2$ flow, $V_\infty = 1730$ m/s, and $P_\infty = 0.224$ bar around the 19 mm blunted cylinder. Gas mixture D: 10% C_2H_4 + 30% O_2 + 60% N_2. $V_{flow}/V_{CJ} = 0.90$.

hydrogen-based and ethylene-based reactive mixtures were studied using the three different free stream flow conditions. However, the ethylene-based mixture did not produce significant or reliable combustion in tests using this body. Therefore, only images representing flow fields using hydrogen-based mixtures are presented.

Shock-Induced Combustion

Several of the experiments yielded combustion around the body that was decoupled from the oblique shock wave. A composite schlieren and OH PLIF image of shock-induced combustion, using gas mixture A accelerated to the $M_\infty = 5.2$ condition, is depicted in Fig. 2. The schlieren images were obtained from different experiments and have been overlaid on the OH PLIF images to complement the latter, which does not show the location of the shock. As is evident in the figure, the combustion front initially appears to be limited to a region very close to the wedge, and then diverges at some point on the forebody. An estimate of the postshock conditions (2) along the wedge was calculated from the free stream flow information and calculated oblique shock wave angle: $T_2 = 1450$ K, $P_2 = 3.1$ bar, and a velocity parallel to the sloped wedge forebody of roughly 1.3 mm/s. As an estimate of the effective ignition-delay time, a particle path was traced from the wedge tip to the point where the combustion front began to diverge from the forebody. This method gives 8 μs, a value approximately one-half of that predicted from H_2/O_2 ignition literature [14]. The agreement is reasonable given the uncertainty in the exact postshock conditions. It is also likely that the effective delay is influenced by boundary-layer growth on the forebody.

Oblique Detonation

Additional experiments investigated a more sensitive mixture, which resulted in combustion that was coupled closely with the oblique shock. An example of this phenomena occurred when gas mixture B was accelerated to the $M_\infty = 5.2$ condition (Fig. 3). The ratio of free stream velocity to the Chapman–Jouget detonation speed is $V_\infty/V_{CJ} = 1.33$ in this case. Note that after a small induction zone near the wedge tip, the combustion front asymptotes rapidly to a steady angle away from the wedge forebody. The measured angle of this wave front, 63.7°, is significantly larger than that of the original oblique shock wave (54.4°). This leads to the conclusion that the shock/combustion wave structure is fully pressure coupled. Following the terminology of Pratt et al. [15], the wave may be classified as a weak, overdriven oblique detonation wave. Using shock polar theory, it is possible to determine the amount of energy released by the combustible mixture into the actual flow field. Using the known wedge turning angle and measured combustion wave angle, one can deduce the effective amount of heat release (Q) into the flow. In this case, $\tilde{Q}_{\text{eff}} \equiv (Q_{\text{eff}}/C_pT_\infty) = 0.76$. This value may be compared to the heat-release parameter for a normal, CJ detonation of this mixture: $\tilde{Q} = 3.13$, obtained using a (ARL) modified version of the NASA CET89 equilibrium chemistry code. Since the effective value represents only one quarter of the maximum available chemical energy, it is likely that the wave was not fully stabilized in this image.

Though not shown, a similar result occurred for mixture B when accelerated to the $M_\infty = 4.2$ condition as well. The initial induction zone (before detonation) was larger in this case, and the combustion front did not appear to have fully stabilized in front of the body.

Flow over Blunted Cylinder

When a blunt body is introduced at supersonic speed into a quiescent mixture, previous work has shown combustion structure to depend on the ratio of the body's velocity, V_b, to the mixture's CJ velocity, V_{CJ}. Three different regimes were observed. For cases in which $V_b/V_{CJ} \gg 1$, the combustion mode was that of shock-induced combustion with a smooth flame front parallel to the cylinder's body [16]. As the body velocity decreased, two other combustion modes occurred depending on the mixture sensitivity (for fixed body diameter). In the regular disturbance regime, high-frequency instabilities originating in the induction zone between the bow shock and the combustion region at the front of the body appeared. The bow shock's structure remained unaffected by the instabilities, whose frequency was proportional to the mixture's induction time. More sensitive mixtures resulted in smaller frequency oscillations of larger amplitudes that were strong enough to alter the shock's structure. In this large disturbance regime, the instabilities sometimes led to the formation of a cellular detonation wave that propagated in front of the body.

A single cylinder, 19 mm in diameter, was used in this work. A pressure transducer mounted inside the cylinder measured the front-end stagnation pressure. In the experiments presented here, the mixtures and flow conditions were changed to obtain different V_∞/V_{CJ} ratios. Since the body is fixed and the gas is accelerated around it, the velocity used here in the expression for V_∞/V_{CJ} is actually that of the test gas. Two of the three combustion regimes were reproduced with the expansion tube flows and are discussed next.

Smooth Flame Front Regime

For these experiments, mixtures C and F (Table 1) were successfully accelerated to exit velocities of 2150 m/s and a static pressure of 0.065 bar, giving V_∞/V_{CJ} values of 1.27 and 1.1 for the ethylene and

methane mixtures, respectively. Figures 4a and 4b are composite schlieren and OH PLIF images of the flow of the methane and ethylene mixtures. Both cases show evidence of shock-induced combustion close to the cylinder. The images differ considerably in the thickness of the combustion region and the standoff distance of the combustion front. That difference is consistent with the fact that the ethylene mixture has a shorter induction time than that of methane. Thus, the heat released in the stagnation region ahead of the cylinder is larger for the ethylene case. Since the bow shock standoff distance is inversely proportional to the average density in the stagnation region, the bow shock standoff distance is larger for the ethylene case, as can be seen in the images.

Another feature of the images, more evident in the methane case, is that the boundary of the OH PLIF signals around the cylinder become almost parallel to the body. This matches previous observations [16] and is explained by the bow shock's rapid weakening in the radial direction away from the body's nose, leading to an increase in induction time of the shocked gas. Eventually, the induction time approaches infinity, and the reaction front becomes coincident with the flow field streamlines around the projectile [5,17].

Regular Disturbance Regime

In an effort to observe the other combustion modes, more sensitive mixtures were used at a different flow condition. Mixtures *C*, *D*, and *E* were accelerated to 1730 m/s and a static pressure of 0.22 bar, resulting in V_∞/V_{CJ} ratios of ≤ 1. Note that these three mixtures differ mainly in their concentration of fuel/oxygen. A higher fuel/oxygen concentration causes the induction time of the mixture to decrease and the amount of chemical energy released near the nose to increase. For the mixture with the longest induction time, a small region of local combustion between the bow shock and the cylinder's nose was observed. In that case, the residence time in the stagnation region of the gas particles is less than the induction time at the postshock temperatures. As the flow expands around the cylinder, the temperature of the shocked gas decreases and the reactions are quenched. With decreasing mixture induction times, the extent of shocked gas with residence times (at the high temperatures) exceeding the induction time increases and the region of combustion spreads. With further decrease in mixture induction time, small regular oscillations in the flame front are observed (Fig. 5). The stagnation pressure traces obtained from the transducer mounted inside the cylinder also exhibited a 50-kHz regular oscillation. These oscillations are believed to be of the same nature as the ones described in previous works [5]. This observation is in agreement with the qualitative analysis of Lee [17]. In his work, Lee suggests that an increase in nose bluntness leads to an increase in energy release near the nose because of shock ignition. The increasing amount of energy release plays a role in perturbing the flow field around the projectile. In the present experiments, the amount of energy release in the nose region was increased by raising the mixture sensitivity and not by increasing the body's diameter; however, the end effect was the same.

Conclusions

An expansion tube was used to generate three different supersonic flow conditions. These conditions were used for initial imaging studies of supersonic reactive flows around a 40° wedge and a blunted cylinder test body.

The OH PLIF technique was used to investigate combustion phenomena around the wedge. The nature of this work was qualitative, though quantitative measurements of flow quantities such as rotational and vibrational temperature are realizable [18] and will be pursued in future work. In several experiments with the wedge, a shock-induced combustion mode was observed in which the deflagration front lagged considerably behind the oblique shock wave. An approximate analysis of this flow field yielded relatively good agreement with predictions from the H_2/O_2 ignition literature. In other experiments using a more sensitive gas mixture, an oblique detonation wave was observed in which the shock/combustion fronts were fully coupled. Natural emissions from the oblique detonation were significantly higher than those for shock-induced combustion.

For flows over the blunt cylinder, the features of combustion observed were in accord with the qualitative analysis and observations of previous researchers. Both the smooth flame front and the regular disturbance regimes were observed for the same body diameter by varying the mixture and flow conditions. The use of more sensitive mixtures is limited to prevent ignition of the test gas inside the expansion tube.

In the present experiments, schlieren images complemented the OH PLIF images by providing information on the shape and location of the bow shock. Simultaneous schlieren and OH PLIF imaging would represent a more reliable method of determining experimentally the induction zone length between the bow shock and the flame front.

Acknowledgments

The authors gratefully acknowledge the contributions of T. C. Island, M. D. Di Rosa, A. Ben-Yakar, and F. L. Levy to this investigation. The work was supported by the U.S. Army Research Office, with Dr. Dave Mann as technical monitor.

REFERENCES

1. Kamel, M., Morris, C. I., Thurber, M. C., Wehe, S. D., and Hanson, R. K., *New Expansion Tube Facility for the Investigation of Hypersonic Reactive Flow,* AIAA Paper No. 95-0233 presented at the 33rd. Aerospace Sciences Meeting & Exhibit, Reno, January 9–12, 1995.
2. Morris, C. I., Kamel, M., Thurber, M. C., Wehe, S. D., and Hanson, R. K., *Development of an Expansion Tube for Investigation of Combustion in Supersonic Projectile Flowfields,* AIAA Paper No. 95-2717 presented at the 31st Joint Propulsion Conference & Exhibit, San Diego, CA, July 10–12, 1995.
3. Herzberg, A., Bruckner, A. P., and Bogdanoff, D. W., *AIAA J.* 26:195–203 (1988).
4. Lehr, H. F., *Astronautica Acta* 17:589–597 (1972).
5. Alpert, R. L., and Toong, T. Y., *Astronautica Acta* 17:539–560 (1972).
6. Belanger, J., Kaneshige, M., and Shepherd, J. E., *20th International Symposium of Shock Waves (book of abstracts),* GALCIT, Pasadena, CA, July 23–28, 1995, pp. 411–412.
7. Dabora, E. K., Desbordes, D., Guerraud, C., and Wagner, H. G., *Progr. Astronaut. Aeronaut.* 133:187–201 (1991).
8. Viguier, C., Guerraud, C., and Desbordes, D., *Twenty-Fifth Symposium (International) on Combustion,* The Combustion Institute, Pittsburgh, 1994, pp. 53–59.
9. Desbordes, D., Hamada, L., and Guerraud, C., *Shock Waves* 4:339–345 (1995).
10. Dabora, E. K., Nicholls, J. A., and Morrison, R. B., *Tenth Symposium (International) on Combustion,* The Combustion Institute, Pittsburgh, 1964, pp. 817–830.
11. Matsuo, A. and Fuji, K., *Examination of the Improved Model for the Unsteady Combustion around Hypersonic Projectiles,* AIAA Paper No. 95-2565 presented at the 31st Joint Propulsion Conference & Exhibit, San Diego, CA, July 10–12, 1995.
12. Trimpi, R. L., *A Preliminary Theoretical Study of the Expansion Tube, A New Device for Producing High-Enthalpy Short-Duration Hypersonic Gas Flows,* NASA TR R-133, 1962.
13. Palmer, J. L., Houwing, A. F. P., Thurber, M. C., Wehe, S. D., and Hanson, R. K., *PLIF Imaging of Transient Shock Phenomena in Hypersonic Flows,* AIAA Paper No. 94-2642 presented at the 18th Aerospace Ground Testing Conference, Colorado Springs, CO, June 20–23, 1994.
14. Cheng, R. K. and Oppenheim, A. K., *Combust. Flame* 58:125–139 (1984).
15. Pratt, D. T., Humphrey, J. W., and Glenn, D. E., *J. Propulsion* 7:837–845 (1991).
16. Chernyi G. G., *Problems of Hydrodynamic and Continuum Mechanics,* Society for Ind. and Appl. Math., Philadelphia, 1968, pp. 145–169.
17. Lee, J. H. S., *On the Initiation of Detonation by a Hypervelocity Projectile,* presented at the Zeldovich Memorial on Combustion, Voronovo, Russia, September 12–17, 1994.
18. McMillin, B. K., Seitzman, J. M., and Hanson, R. K., *AIAA J.* 32:1945–1952 (1994).

Twenty-Sixth Symposium (International) on Combustion/The Combustion Institute, 1996/pp. 2917–2924

QUENCHING OF REACTION IN GAS-SAMPLING PROBES TO MEASURE SCRAMJET ENGINE PERFORMANCE

TOHRU MITANI

National Aerospace Laboratory, Kakuda Research Center
Kimigaya 1, Kakuda, Miyagi, 989-15, Japan

The problem of chemical quenching in gas-sampling probes was studied as a reactive, Rayleigh, and Fanno flow. The typical lengths of friction, convective heat transfer, and reactions in the probes are evaluated under the testing conditions of ramjet and scramjet engines. A reduced chemical kinetic scheme was adopted, and the reaction times were evaluated from the ignition times derived by reflected shock wave experiments. Thereby, criteria for quenching in probes were obtained analytically. The critical Damköhler number (*Da*) for quenching in an H_2-air reaction was found to be 23 (1500 K) to 10.5 (3000 K). A 2.6-fold greater *Da* was derived for CH_4-air mixtures. Because reactions in CH_4-air mixtures can be quenched even above 2200 K, combustion performance in a CH_4-fueled ramjet combustor was measured from gas analysis. However, quenching of H_2 unburned gas is more difficult than quenching of CH_4. Cooling with supersonic expansion is essential to freeze reactions in H_2-air mixtures in scramjets tested under a total temperature higher than 2000 K. A constant Mach number expansion is recommended downstream of the sampling orifice. The contour of the expansion region and the decay of total pressure were determined taking into account friction and cooling effects. Reactions with unburned H_2 can be quenched if the sampling probe works as a supersonic diffuser operating in the supercritical mode.

Introduction

An H_2-fueled scramjet engine under flight, Mach number (M) 4 to 8, and a CH_4-fueled ramjet engine for hypersonic civil transport have been tested in Japan [1,2]. In hypersonic propulsion, the gas temperature becomes extremely high. For example, the total temperature (T^0) of air supplied to the engine increases from 900 K (M4) to 2600 K (M8) and the combustion temperature exceeds 3000 K (M8).

Gas sampling is the most reliable method to evaluate combustion performance, such as combustion temperature and efficiency. This intrusive probing for flows will eventually be replaced with laser diagnostics. However, the technique is essential to calibrate the nonintrusive methods because the reliability of the laser diagnostics is still poor.

Gas is sampled on the basis of the assumption that gas composition is preserved in the sampling process. However, preservation of major species becomes difficult under such high temperatures. Oxidation of reactants in sampling probes may lead to an erroneous high combustion efficiency. Critical microprobes are presented where rapid decompression of the extracted gas is accomplished by the use of a tapered tube with a small sonic orifice inlet [3]. The problem has elements in common with chemically reactive flows in supersonic nozzles [4]. Quenching is a competition between cooling and chemical reactions. Accordingly, the relative rate between these two processes governs the phenomenon; thus, Damköhler numbers must appear.

Colket et al. examined the pressure distribution along probes having diameters of 75–2000 μm to verify that a supersonic flow is maintained in the tip region of the microprobes [5]. They described a cooling rate of 10^8 K/s in the probes and assumed quenching at a gas temperature of less than 1000 K. Kramlich et al. investigated the oxidation of NO to NO_2 and of CO to CO_2 in the probes [6,7], and Drake et al. compared four different types of probes to study the formation of NO_x [8]. Studies on the critical Damköhler number (*Da*) have not been presented yet.

Therefore, criteria for quenching in probes were investigated. The flow was treated as a reactive, Rayleigh, and Fanno flow. The one-dimensional calculations may be repeated with a full kinetic scheme using a computer [6]. However, numerical experiments are not convenient to overview the general aspects of phenomena. It is essential to start with a simplified model to identify the predominant factors determining the end-to-end accuracy of numerical calculations as well as experimental results derived from gas sampling. Employing a reduced reaction scheme made it possible to determine the critical *Da* for quenching. Combustion temperature and efficiency from gas analysis are discussed for a

CH_4 fueled ramjet. Requirements for sampling in H_2 fueled scramjets are also discussed.

One-Dimensional Flow in Gas-Sampling Probes

Quasi-one-dimensional flows, including area change, heat exchange, and wall friction, are governed by the following equation [9]:

$$\frac{dM^2}{M^2} = -\frac{2\left(1 + \frac{\gamma - 1}{2} M^2\right)}{1 - M^2}\frac{dA}{A} + \frac{(1 + \gamma M^2)\left(1 + \frac{\gamma - 1}{2} M^2\right)}{1 - M^2}\frac{dT_0}{T_0} + \frac{\gamma M^2\left(1 + \frac{\gamma - 1}{2} M^2\right)}{1 - M^2} 4c_f \frac{dx}{d} \quad (1)$$

The equation for total pressure (P^0) is

$$\frac{dP^0}{P^0} = -\frac{\gamma M^2}{2}\frac{dT^0}{T^0} - \frac{\gamma M^2}{2} 4c_f \frac{dx}{d} \quad (2)$$

For a sampling rate of 10^{-5} kg/s in a 2-mm-diameter tube, *a* typical *Re* is estimated to be 350, which means laminar flow. The friction coefficient (c_f) can be evaluated as 0.045 from the Poiseuille flow. The friction length ($x_f^* = d/4c_f$) in Eq. (1) is found as 5.5 d (=11 mm) for the tube.

The change of T^0 in probes with the wall temperature (T_w) is given by

$$\frac{dT^0}{dx} = \frac{(T_w - T^0)}{x_c^*} \quad (3)$$

where $Pr = 1$ has been assumed, so that the gas is cooled by heat transfer between T^0 and T_w. The cooling length is expressed by Nusselt number to read

$$x_c^* = \frac{c_p m}{\pi N u_d \lambda} \quad (4)$$

Nondimensionalization of Eq. (3) by x_f^* gives the solution for T^0,

$$T^0(\xi) = (T_0^0 - T_w)\exp(-L_c^*\xi) + T_w \quad (5)$$

where a cooling rate coefficient has been defined as $L_c^* = x_f^*/x_c^*$. The coefficient is estimated using the Reynolds analogy and $Pr = 1$ to be

$$L_c^* = \frac{Nu}{c_f \cdot Re \cdot Pr} = \frac{1}{2} \quad (6)$$

Thus, x_c^* is about 20 mm in a 2-mm tube and T^0 drops by $1/e$ in the distance x_c^*.

A simplified reaction model is considered that consists of a branching reaction with a strong temperature dependence and a breaking reaction [10,11]. In the model, a radical is formed by the branching reaction, $H + O_2 \rightarrow O + OH$ in H_2-air systems for instance, and transformed to a product by the breaking reaction. The reaction $OH + H + M \rightarrow H_2O + M$ was chosen as the representative breaking step among many breaking reactions. Because the reaction produces H_2O, the introduction of the reaction yields the most difficult criterion for chemical quenching in H_2-O_2 systems. Thus, the nondimensional radical-breaking rate parameter (β) is defined as a ratio between these two rates.

The concentrations of radical (X) and product (Y) are determined by

$$\frac{dX}{d\xi} = \frac{Da}{u(\xi)}\left[X \cdot \exp\left\{\frac{E}{R^0}\left(\frac{1}{T_0^0} - \frac{1}{T_s}\right)\right\} - \beta X^2\right] \quad (7)$$

$$\frac{dY}{d\xi} = \frac{Da}{u(\xi)}\beta X^2 \quad (8)$$

A reaction length (x_r^*) at $\xi = 0$ defines the Da as x_f^*/x_r^*. The reaction length is given by a product of reaction time (t_r^*) and flow speed (u). In Eqs. (7) and (8), $u(\xi)$ denotes the deviation of Da from the initial value. It is obtained solving Eqs. (1) and (2). The static properties of the gas flow (T_s and P_s) controlling reaction rate are evaluated as functions of $M(\xi)$ from T^0 and P^0.

Radical Production in Reactive Flow with Cooling

The variation of $u(\xi)$ is neglected at first. A low-speed flow suggests that friction is not important in subsonic flow. Eqs. (7) and (8) are now scaled ($\eta = \xi/Da$) with x_r^* to determine X and Y:

$$\frac{dX}{d\eta} = X \cdot \exp\left\{\theta_a\left(1 - \frac{1}{\theta}\right)\right\} - \beta X^2 \quad (9)$$

$$\frac{dY}{d\eta} = \beta X^2 \quad (10)$$

Although it is possible to solve Eq. (9) by choosing θ as the new independent variable [11], the following simplification is more appropriate to find dependencies to parameters. The variation of θ is expanded using the large expansion parameter (θ_a), where α denotes the cooling rate of sampled gas in the unit of t_r^*:

$$\theta = 1 - (\alpha/\theta_a)\eta +, \text{ and}$$

$$\alpha = \theta_a\left(1 - \frac{T_w}{T_0^0}\right)\frac{x_r^*}{x_c^*} = \theta_a\left(1 - \frac{T_w}{T_0^0}\right)\frac{L_c^*}{Da} \quad (11)$$

Substitution of Eq. (11) into Eq. (9) gives

$$\frac{dX}{d\eta} = X \cdot \exp\{-\alpha\eta\} - \beta X^2 \quad (12)$$

This nonlinear equation can be transformed with

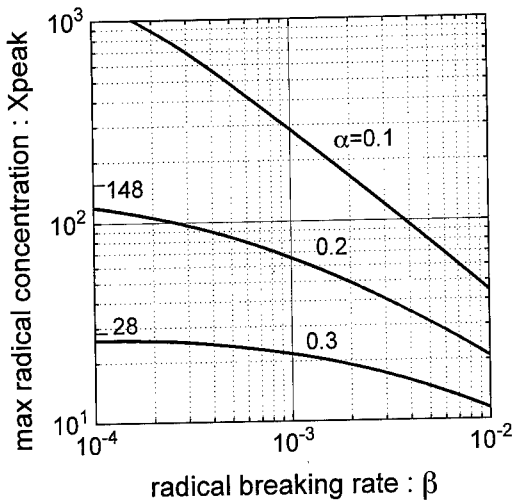

FIG. 1. Dependence of maximum radical concentration (X_{peak}) in the probes on the cooling rate parameter (α) and the radical breaking rate parameter (β).

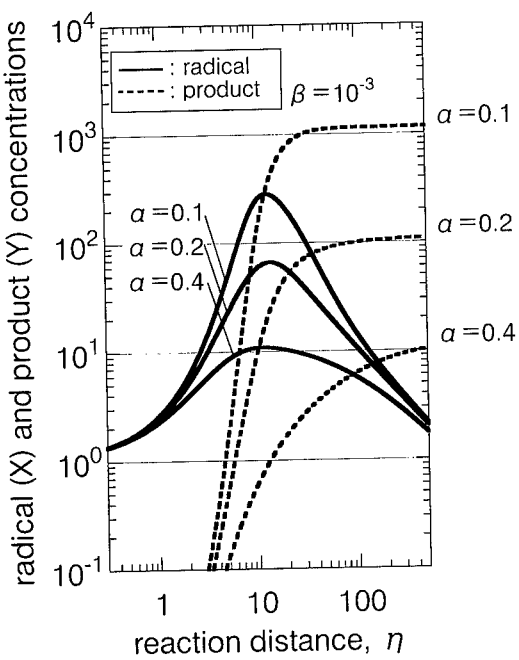

FIG. 2. Variations of radical (X) and product (Y) concentrations along the probes (numerical result for Eqs. (10) and 12 with $\beta = 10^{-3}$).

$s = \exp(-\alpha\eta)/\alpha$. The solution is expressed by an exponential integral (Ei) function:

$$\frac{1}{X} = \exp(s)\left[\exp\left(-\frac{1}{\alpha}\right) + \frac{\beta}{\alpha}\left\{-\mathrm{Ei}(-s) + \mathrm{Ei}\left(-\frac{1}{\alpha}\right)\right\}\right] \quad (13)$$

The ultimate objective of the analysis is to evaluate the change of product (Y) along the sampling probes, which is obtained by integrating Eq. (10) with Eq. (13) from $\eta = 0$ to $\eta = \infty$. An approximate treatment is possible because radical branching is dominant upstream, and the radical formed upstream will be transformed into product downstream. Eq. (9) indicates that X takes a maximum at s_{peak}, where the maximum radical concentration is given by

$$X_{peak} = \exp(-\alpha\eta_{peak})/\beta = \alpha s_{peak}/\beta \quad (14)$$

Differentiation of Eq. (13) leads to the following relation for s_{peak}:

$$\mathrm{Ei}(-s_{peak}) + \frac{\exp(-s_{peak})}{s_{peak}} = \frac{\alpha}{\beta}\left\{\mathrm{Ei}\left(-\frac{1}{\alpha}\right) + \frac{\beta}{\alpha}\mathrm{Ei}\left(-\frac{1}{\alpha}\right)\right\} \quad (15)$$

To examine dependencies of X_{peak} on α and β, an asymptotic form for $\mathrm{Ei}(-s)$ is used to obtain

$$\frac{\exp(-s_{peak})}{s_{peak}^2}\left(1 - \frac{1}{s_{peak}}\right) \cong \frac{\alpha}{\beta}\exp\left(-\frac{1}{\alpha}\right) \quad (16)$$

Specification of α and β gives X_{peak}, and the result is illustrated in Fig. 1. Representative values of β considered here lie between 10^{-2} and 10^{-4}. With a low cooling rate ($\alpha = 0.1$), X_{peak} moves from 40 to 10^3. Figure 1 also shows that X_{peak} is proportional to $1/\beta$ for small α. This is understandable because the equilibrium radical concentration becomes $1/\beta$ if α vanishes. Asymptotic values of X_{peak} with $\beta \to 0$ are also shown for 0.2 and 0.3 in Fig. 1.

Figure 1 indicates a strong α dependence of X_{peak}. This is because α is included as an argument in the exponential function in Eq. (16). Consider the case of $\beta = 10^{-3}$. The critical value to permit $X_{peak} = 300$ gives $\alpha^* = 0.1$. Rapid cooling with $\alpha^* > 0.3$ is required to lower X_{peak} to less than 20.

To confirm these conclusions, Eqs. (10) and (12) were integrated numerically with Eqs. (1) and (2). The results are given in Fig. 2, where the logarithmic scale is chosen to cover a large range of η. Figure 2 shows that radical concentrations, denoted by solid lines, increase from 1 and take a maximum, and finally decay in the streamwise distance. The product, shown by broken lines, starts from $Y = 0$ to approach asymptotic values (Y_∞). It is confirmed in Fig. 2 that Y_∞ depends strongly on the cooling rate α. For instance, Y_∞ reaches 1200 for a cooling case

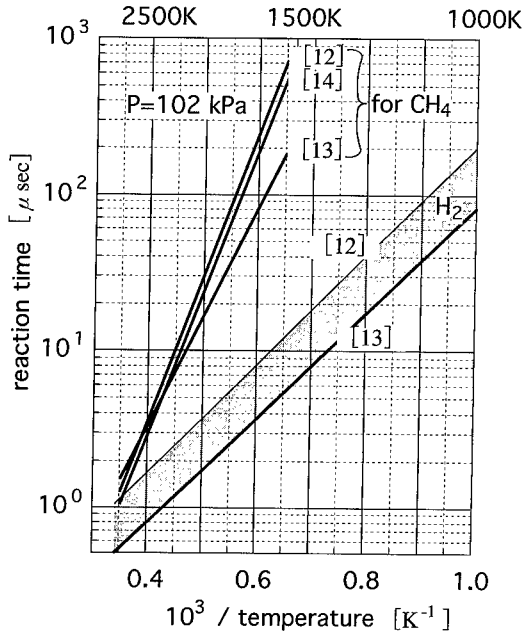

FIG. 3. Ignition time (t_{ig}) for stoichiometric CH_4-air and H_2-air mixtures cited from shock-tube experiments.

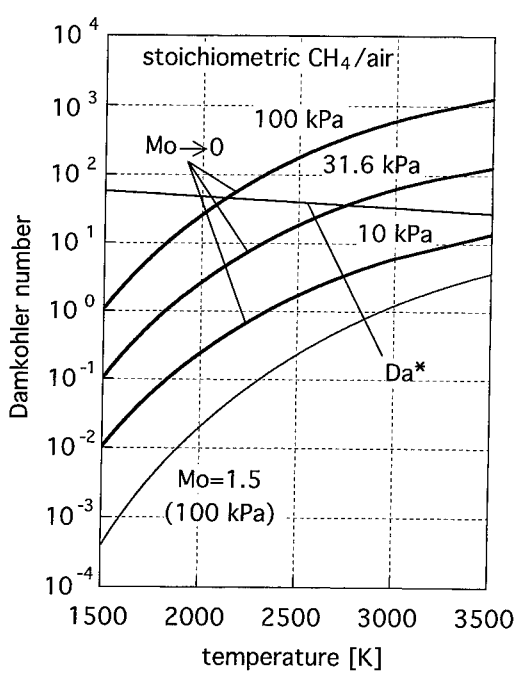

FIG. 4. Comparison of flow Damköhler number (Da) with the critical value (Da*) for reaction quenching of CH_4-air mixtures (flight Mach number ≤ 6).

(α = 0.1). It implies that the product increment is 1200 times the initial radical concentration. However, the product yield decreases to 10 if α increases to 0.4.

The radical concentration in scramjet combustors is estimated to be of the order 10 ppm under the M6 flight condition. The critical Da, to restrict the oxidation of major species within a few percentage points, is now derived as

$$Da^* = \theta_a\left(1 - \frac{T_w}{T_0^0}\right)\frac{L_c^*}{\alpha^*} = \frac{\theta_a}{0.2}\left(1 - \frac{T_w}{T_0^0}\right) \quad (17)$$

where a critical value of $\alpha^* = 0.1$ has been chosen for the flight conditions of M6 or less. A value greater than 0.3 is necessary to quench the reaction under the M8 flight condition.

Criteria for Sampling CH_4 and H_2 Combustion Gases

Reaction Times and Damköhler Number

Cheng and Oppenheim [12] and Solouhkin [13] conducted experiments using reflected shock waves to measure ignition-delay times of CH_4 air and H_2 air mixtures. Krishnan and Ravikumar correlated ignition data of CH_4 air covering 1600–2100 K and 100–600 kPa in the literature [14]. Their results are summarized in Fig. 3. The phenomenon in the tips of sampling probes inserted to supersonic flow is equivalent to an ignition problem by the reflected shock waves. Therefore, the reaction time (t_r^*) is compared with the ignition time (t_{ig}). Various definitions of ignition time and the total reaction time, required to achieve 95% of the equilibrium temperature rise, are discussed by Rogers and Schexnayder [15].

For CH_4, the reaction time in Ref. 14 falls between those found in the data in Refs. 12 and 13. Typical t_{ig} is about 20 μs at 2000 K with a value of T_a = 22,600 K. The reaction rate in the H_2 air mixture in Ref. 13 agrees with those evaluated from other experiments [16] and numerical studies [15]. In Fig. 3, the lower bound of t_{ig} for H_2 was obtained from Ref. 13 and the upper bound was cited from Ref. 12. Representative t_{ig} for H_2 mixtures ranges from 2 to 4 μs at 2000 K and is governed by T_a = 8640 K.

The value of Da was calculated for two cases, subsonic flow ($M_0 \to 0$) and supersonic flow (M_0 = 1.5). In the calculations, t_r^* has been assumed to be inversely proportional to the ambient pressure. The subsonic Da has a strong pressure dependence with P^2 rising from $t_r^*(P)$ and $u(P)$. Hence, the Da in subsonic flow is shown for different sampling pressures. Calculations for CH_4-air are shown in Fig. 4, whereas those for H_2-air mixtures are shown in Fig. 5. The shaded band in H_2 mixtures in Fig. 3 is

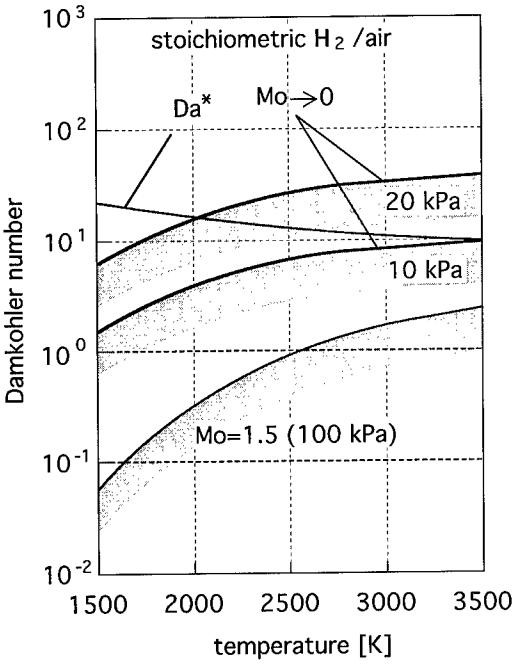

FIG. 5. Comparison of flow Damköhler number (Da) with the critical value (Da*) for reaction quenching of H_2-air mixtures (flight Mach number ≤ 6).

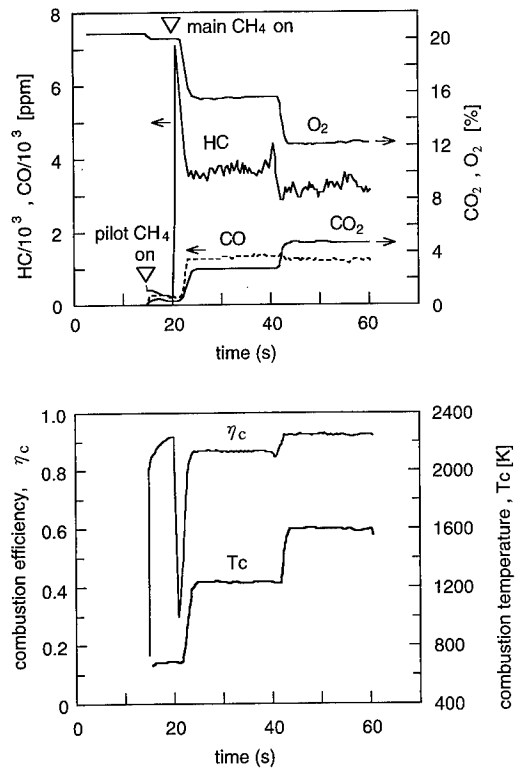

FIG. 6. Histories of gas composition measured in a CH_4-fueled ramjet experiment (a). Time histories of combustion temperature (T_c) and efficiency (η_c) evaluated from gas analysis shown in Fig. 6(a).

mapped into the evaluated *Da* bands in Fig. 5. Figs. 4 and 5 indicate that *Da* increases with increasing T_0^0 because the reaction is accelerated.

The values of *Da* in supersonic flow are found to be 1/100 of the counterparts in subsonic flow because u is about 10^3 m/s in supersonic flow. For example, the value of *Da* in M1.5 flow, indicated by the thin line in Fig. 4, ranges from 10^{-3} at 1600 K to 2.7 at 3500 K. The pressure dependence in the supersonic region becomes weak (proportional to P_s) because u is independent of the ambient pressure.

Comparison between Figs. 4 and 5 indicates that *Da* for CH_4 is 1/10 of the counterpart for the H_2 mixture if the sampling pressure is the same. This results from the slow reaction rate in CH_4 shown in Fig. 3. On the other hand, the *Da** for CH_4 is 2.6 times greater than the *Da** for H_2. This is attributed to the high activation energy in the CH_4 reaction, as found in Eq. (17). The reaction can be frozen if the flow *Da* is smaller than *Da** for each mixture. Therefore, Figs. 4 and 5 indicate that quenching is much easier in CH_4-air than in H_2-air mixtures.

CH_4-Fueled Ramjet for Hypersonic Transport

A CH_4-fueled ramjet combustor to cruise with an M5 speed is studied for an HST. The engine has dimensions of 180 mm width, 220 mm height, and 2.15 m length. The M5.6 free stream is compressed by a four-staged ramp, followed by an isentropic part, and decelerated to subsonic speeds (total compression ratio = 160). Fuel is injected from a gutter-type flame holder where the combustion pressure is 0.9 MPa and the flow velocity is ca. 100 m/s.

The tests have been successfully carried out, and thrust, T^0, and P^0 were measured. The gas was withdrawn by a water-cooled sampling rake and introduced directly to a gas analyzer stationed outside the test cell. The variations of O_2, CO, CO_2, hydrocarbons, and NO_x, together with the fuel equivalence ratio (ϕ), were monitored in real time.

Figure 6a illustrates the histories of species at the nozzle exit. For example, the small O_2 drop at t = 15 s is due to pilot CH_4 burning. The figure clearly indicates the peak of hydrocarbons due to ignition delay of the main CH_4 flow at 20 s. Thereafter, O_2 is consumed by a stepwise increase of the main CH_4 flow rate, and the concentration of CO_2 increase step by step. Residual concentrations of hydrocarbons and CO were ca. 3000 ppm and 1500 ppm, respectively.

The combustion performance is obtained by equilibrium calculations. Figure 6b shows the histories

of combustion temperature and efficiency evaluated from Fig. 6a. Because the combustion efficiency is mostly determined by unburned hydrocarbons, the ignition delay at $t = 20$ s is observed as the depression in the combustion efficiency in Fig. 6b. The combustion temperature rose from 1250 to 1600 K, and the combustion efficiency varied from 87% to 92% in Fig. 6b. The problem is whether the performance evaluated from gas sampling is reliable.

Figure 4 indicates that Da^* varies from 60.3 (1500 K) to 34 (3000 K) and that it intersects the Da curve for 100 kPa at $T^0 = 2200$ K in the subsonic limit ($M_0 \rightarrow 0$). Therefore, quenching can be achieved in the ramjet because the maximum operation temperature of the engine is 2200 K and the probes are depressurized in a subatmospheric pressure.

Combustion temperature in Fig. 6b was compared with two other measurements, namely, temperature measured by thermocouples and the characteristic exhaust velocity (C^*) evaluated from the engine pressure and mass flow rate. Good agreement was found among these three independent measurements.

Further evidence of quenching is found from the dependency of combustion efficiency on ϕ. Combustion efficiency should have increased with T^0 if quenching in the probes were insufficient. However, the experiments showed that the combustion efficiency had a maximum at $\phi = 0.6$ and decreased with increasing ϕ. These results support our conclusions that reactions in the sampling probe were suppressed in the ramjet experiments and that the combustion performance shown in Fig. 6b was reliable.

Supersonic Sampling for a H_2-Fueled Scramjet Engine

The Da^* for H_2 air mixtures is shown in Fig. 5, which ranges from 23 (1500 K) to 10.5 (3000 K). The small Da^* makes quenching difficult for H_2 mixtures. For instance, reactions with $T^0 = 2000$ K in the subsonic limit ($M_0 \rightarrow 0$) are frozen only if the sampling pressure is maintained below 20 kPa. The temperature limit may be relaxed to 2600 K if the lower bound of the shaded band shown in Fig. 5 is adopted. However, the sampling pressure cannot be lowered unconditionally because the low-pressure sampling shortens the friction-choking distance.

This difficulty is relieved if the flow remains supersonic. The solution for supersonic Fanno flow indicates that friction choking occurs at around $\xi = 1$ in water-cooled probes. Supersonic flow ultimately decelerates to subsonic by a shock wave to balance with the back pressure of the probe, as verified experimentally by Colket et al. [5]. Supersonic flow with a constant Mach number along the probes is favorable to minimize the pressure loss across the shock wave. Because the condition for a constant Mach number (M_0) in Eq. (1) is given by $dM^2 = 0$, the solutions for $A(\xi)$ and $P^0(\xi)$ are expressed as

$$A(\xi) = T^0(\xi)^{(1+\gamma M_0^2)/2} \cdot \exp\left(\frac{\gamma M_0^2}{2}\xi\right) \tag{18}$$

$$P^0(\xi) = T^0(\xi)^{-\gamma M_0^2/2} \cdot \exp\left(\frac{-\gamma M_0^2}{2}\xi\right) \tag{19}$$

Substitution of $T^0(\xi)$ given in Eq. (5) into Eqs. (18) and (19) leads to the variations of A and P^0. For instance, if the probe diameter increases by 2 ($M_0 = 1.5$) and 3 ($M_0 = 2$) at the location of $\xi = 2$, the supersonic flow maintains the initial values (M_0) along the probe. The contour, $d(x)$, was found to correspond to tapered angles of 14° ($M_0 = 1.5$) to 32° ($M_0 = 2$) recommended in Ref. 3.

From Eq. (19), the total pressure $P^0(\xi)$ for $M_0 = 2$ decays by 0.039 from the initial value. In addition, $T^0(\xi)$ lowers to $T^0(2) = 1290$ K from $T_0^0 = 3000$ K. For instance, in Fig. 5, a local Da moves from $T_0^0 = 3000$ to 1290 K along the $M_0 = 1.5$ curve and may jump to the subsonic curve for 20 kPa. In advance of the subsonic recovery, the total pressure and temperature have already decreased to suppress the reactions. Thus, supersonic expansion is crucial in sampling probes applied for H_2-air mixtures under the M8 flight condition.

This shock-free deceleration upstream of the probe orifice with supersonic flow downstream is the same as that found in a supersonic diffuser operating in the supercritical flow mode [9]. Unburned H_2 and O_2 extracted from scramjets can be preserved in the sampling probe working as a micro-ramjet with a size of a fraction of a centimeter.

Conclusions

To evaluate the performance of ramjet and scramjet engines, the criteria for quenching chemical reactions in gas sampling were investigated. The following remarks were deduced:

1. The characteristic lengths of friction, cooling, and reaction were estimated for water-cooled probes. The Damköhler number the (Da) ranges from an order of 10^{-2} in supersonic flow conditions to an order of 10^3 in subsonic flow conditions in typical probes.
2. The product yield was expressed in terms of a cooling rate parameter and a radical breaking reaction rate parameter. The critical value (Da^*) for quenching in H_2-air reaction was found to be from 23 (1500 K) to 10.5 (3000 K).
3. A 2.6-fold-greater Da^* was derived for CH_4-air mixtures. This means that reactions in CH_4-air mixtures can be quenched even at temperatures above 2200 K. Therefore, we conducted gas sampling to evaluate combustion performance of a

CH_4-fueled ramjet. Combustion temperatures from 1500 to 2100 K and combustion efficiencies from 98% to 92% with fuel rate change were evaluated by the gas analysis.

4. Cooling with supersonic expansion is essential to freeze H_2 reactions in scramjets tested under a total temperature higher than 2000 K. For this reason, the contour of the expansion region and the decay of total pressure were determined considering friction and cooling effects. Unburned H_2 and O_2 can be preserved in the sampling probes if the probes work as a supersonic diffuser operating in the supercritical mode.

Nomenclature

$A(x)$	cross-section area of sampling probes
c_f	skin friction coefficient in tube (a mean value)
c_p	specific heat of sampled gas
Da	Damköhler number of gas flow ($= x_f^*/x_r^*$) at $x = 0$
$d(x)$	diameter of sampling probe
L_c^*	cooling rate of gas ($= x_f^*/x_c^*$) defined by Eq. (6)
m	mass flow rate of sampled gas
$M(x)$	Mach number
Nu	Nusselt number of probe
$P(x)$	pressure
Pr	Prandtl number
Re	Reynolds number of probe
$T(x)$	temperature
T_a	activation temperature of reactions ($= E/R^0$)
t_{ig}	ignition delay time
t_r^*	reaction time governed by branching reaction
u	flow speed of sampled gas in probes
$X(x)$	nondimensional radical concentration, $X(0) = 1$
x	streamwise distance from the orifice inlet of probe
x_c^*	cooling length defined by Eq. (4)
x_f^*	friction length defined by $d/(4c_f)$
x_r^*	reaction length defined by $u \cdot t_r^*$
$Y(x)$	nondimensional product yield in probes, $Y(0) = 0$

Greek

α	cooling rate parameter defined by Eq. (11)
β	radical breaking rate parameter in Eq. (7)
γ	specific heat ratio ($=1.4$)
η	streamwise distance measured by x_r^* (ξ/Da)
θ	nondimensional gas temperature ($= T/T_0^0$)
θ_a	Zeldovich number defined as T_a/T_0^0; the large expansion parameter
λ	thermal conductivity of sampled gas
μ	viscosity of sampled gas
ξ	distance measured by friction length ($= x/x_f^*$)
ρ	density of gas

Superscript

0	properties at stagnation condition

Subscript

s	static properties of gas flow
0	initial properties of gas flow

Acknowledgments

The author thanks Mr. Yasuhiro Kinoshita of Kawasaki Heavy Industries and Drs. Sadatake Tomioka and Tetsuji Sunami of National Aerospace Laboratories for fruitful advice in this study.

REFERENCES

1. Kanda, T., Saito, T., Kudo, K., Komuro, T., Ono, F., and Matsui, A., AIAA paper 96-0380, 1996.
2. Tamaru, T., Shimodaira, K., Yamada, H., Kumar, S., Kinoshita, Y. and Kitajima, J., *Symposium (International) on Air Breathing Engines,* ISABE 95-7066, 1995.
3. Fristrom, R. M. and Westerberg, A. A., *Flame Structure,* McGraw Hill, New York, 1965, p. 193.
4. Williams, F. A., *Combust. Theory,* 2d ed., Benjamin/Cummings Menlo Park, CA, 1985, p. 96.
5. Colket, M. B. III, Chiappetta, L., Guile, R. N., Zabielski, M. F., and Seery, D. J., *Combust. Flame* 44:3–14 (1982).
6. Karamlich, J. C. and Malte, P. C., *Combust. Sci. Technol.* 18:91–104 (1978).
7. Malte, P. C. and Karamlich, J. C., *Combust. Sci. Technol.* 22:263–269 (1980).
8. Drake, M. C., Correa, S. M., Pitz, R. W., Shyy, W., and Fenimore, C. P., *Combust. Flame* 69:347–365 (1987).
9. Shapiro, A. H., *The Dynamics and Thermodynamics of Compressible Fluid Flow,* Wiley, New York, 1953, p. 219.
10. Linan, A. A., "Theoretical Analysis of Premixed Flame with an Isothermal Chain Reaction," Tech. Report No. 1, Instituto Nacional De Technica Aerospacial, Madrid, Spain, 1971.
11. Mitani, T., *Combust. Flame* 101:347–359 (1995).
12. Cheng, R. K. and Oppenheim, A. K., *Combust. Flame* 58:125–139 (1984).
13. Soloukhin, R. I., *Eleventh Symposium (International) on Combustion,* The Combustion Institute, Pittsburg, 1969, pp. 671–676.
14. Krishnan, K. S. and Ravikumar, R., *Combust. Sci. Technol.* 24:239–245 (1981).
15. Rogers, R. C. and Schexnayder, C. J. Jr., "Chemical Kinetic Analysis of Hydrogen-Air Ignition and Reaction Times," NASA Tech. Paper (1988).
16. Laster, W. R. and Sojka, P. E., *J. Propulsion Power* 5(4): 385–390 (1989).

COMMENTS

F. A. Williams, UCSD, USA. This is an interesting and unusual analysis of quenching in scramjet gas sampling probes. I wonder about your kinetic parameters, for example using $OH + H + M \rightarrow H_2O + M$ rather than $H + O_2 + M \rightarrow HO_2 + M$ for recombination. My paper with Balakrishnan in the *Journal of Propulsion and Power,* Vol. 10, p. 434, 1994, gives updated rate constants for hydrogen-air that could be used to test this and also for full numerical computations, which should not be difficult with so few elementary steps. Did you make such numerical calculations? Also, how did you select the value of alpha-star in your cooling-rate analysis?

Author's Reply. I chose $OH + H + M \rightarrow H_2O + M$ as a representative breaking reaction to determine the parameter, β. However, I should have used the HO_2 path as you indicated. I agree that it is a faster radical breaking step. The breaking reaction yields more favorite conditions for reaction quenching as shown in Fig. 1, because β increases by a factor of 10 or more.

I constructed a full-kinetic code with the convective cooling to identify the principal chemical steps and to compare with the conclusions I found. The calculations show that the high concentration of HO_2 initiates a radical branching reaction: $H + HO_2 \rightarrow 2OH$, though the role of radical scavenging by HO_2 is dominant over the branching. The numerical computation confirmed the conclusions derived analytically and reproduced the thermal runaway in sampling probes as discussed below.

The arbitrariness in determining the cooling rate, α^* (and then Da^*) in Eq. 17 can be eliminated by considering a small heat release in radical termination. The heating term in the energy equation, Eq. 3 for instance, yields the competition between the cooling term and produces a saddle point in the phase plane of temperature and radical concentration, (T, X). Specifying Da solutions leaves the initial condition located at (1, 1) to the upper left on the phase plane. Among them, the solutions with $Da < Da^*$ finally fall into (T_w, 0), where T_w denotes the wall temperature. However, the solutions with $Da > Da^*$ diverge to infinity. Hence the separatrix running from (1, 1) to the saddle point gives Da^* governing whether the solution (temperature and radical) vanishes (quenching) or blows up (thermal runaway). Integration of the new Eq. 3 and Eq. 7 gave Da^* as a function of the heat release rate and T_w.

Twenty-Sixth Symposium (International) on Combustion/The Combustion Institute, 1996/pp. 2925–2932

DIMENSIONAL ANALYSIS OF THE EFFECT OF FLOW CONDITIONS ON SHOCK-INDUCED COMBUSTION

JEONG-YEOL CHOI, IN-SEUCK JEUNG AND SOOGAB LEE
Department of Aerospace Engineering
Seoul National University, Seoul 151-742, Korea

A dimensional analysis is attempted to elucidate the effects of the flow conditions on the regimes of shock-induced combustion around a blunt body in stoichiometric hydrogen–oxygen mixtures. At a given Mach number, the effects of body size, inflow pressure, and inflow temperature are investigated. The analysis is based on a series of numerical simulations employing a fully implicit method and an upwind scheme. From the results of the numerical simulations with various flow conditions, different regimes of shock-induced combustion are observed ranging from decoupled shock-deflagration to overdriven detonation. From a viewpoint of nondimensionalization, the two flow-field-configuration variables (the shock standoff distance and the induction distance) and the two dimensionless parameters (the first Damköhler number and the heat release parameter) are redefined along the stagnation streamline. The configuration variables and the dimensionless parameters are evaluated from the flow-field data to analyze quantitatively the global features of a shock-induced combustion flow field. The effects of flow conditions are identified in terms of the configuration variables and the dimensionless parameters. The correlations between the configuration variables and the dimensionless parameters are also investigated to understand the effects of flow conditions within a frame of reference.

Introduction

In the late 1960s and early 1970s, there was much experimental research conducted for shock-induced combustion around a blunt body. Especially in Lehr's experiment [1], different regimes of shock-induced combustion were discovered ranging from decoupled shock-deflagration to overdriven detonation according to Mach number and mixture composition. Recently, the development of computational methods makes it possible to simulate such complex phenomena. A number of researchers [2–5] attempted to simulate Lehr's experiment and showed the validity of their computation methods. Other numerical studies [6–8] were also carried out to get physical insights for standing detonation, which is considered a possible energy conversion mechanism for very-high-speed propulsion devices, such as the ram accelerator or the detonation ramjet. In addition, the mechanism of shock-induced combustion instability has been studied and verified numerically [9–11].

Through many experimental and computational works, Mach number, mixture composition, and body size are found to have strong effects on shock-induced combustion. However, the detailed mechanism of how these parameters affect shock-induced combustion is not yet clearly understood. Furthermore, other flow variables such as inflow pressure and inflow temperature might be important parameters in shock-induced combustion, but no intensive study has been made so far. In addition, no criteria have been developed to classify the various shock-induced combustion regimes from decoupled shock-deflagration to overdriven detonation, due to the difficulty in surveying all the possible cases experimentally and the complexity of theoretical approach to analyze the shock-induced combustion flow field, which is governed by nonequilibrium chemical kinetics and highly nonlinear equations in two- or three-dimensional space where supersonic and subsonic regions coexist.

In spite of the vast amount of research conducted, there still remains a fundamental question: What are the main parameters that control the shock-induced combustion phenomena? Although some of the previous research adopted an overdrive parameter to explain the phenomena, it may not be sufficient because the overdrive parameter is only the measure of global inflow velocity such as Mach number, based on Chapman–Jouguet (C-J) detonation velocity, which is a function of C-J heat addition and the specific heat ratio of burned gas. Therefore, the overdrive parameter cannot be considered an adequate parameter for explaining the variation of the shock-induced combustion regime, which is characterized by competition between the flow velocity and the finite-rate chemistry. In addition, the effect of overdrive parameter variation can be explained by the variation of heat release if the shock standoff distance is sufficiently long to ensure the completion of combustion.

The answer to the above question might be obtained from a close examination of the governing equations. Assuming that the effects of viscosity, conductivity, and mass diffusivity are negligible, the only difference between the nonreacting and the reacting flow is the inclusion of chemistry source terms and heat of formation for each species. Therefore, in addition to Mach number, which is the only dimensionless parameter of the nonreacting flow field, the presence of these two terms leads to the definition of two dimensionless parameters that characterize the chemically reacting flow field, that is, the first Damköhler number and the heat release parameter.

Numerical Formulation of Governing Equations

This study is confined to compressible inviscid flow because the effects of viscosity, diffusivity, and conductivity are believed to be small. The Euler equations are used for the numerical simulation of supersonic reacting flow, with the global continuity equation replaced by species conservation equations. They can be expressed in Cartesian coordinate in the following conservation form containing N species:

$$\frac{\partial \mathbf{Q}}{\partial t} + \frac{\partial \mathbf{F}}{\partial x} + \frac{\partial \mathbf{G}}{\partial y} + \boldsymbol{H} = \boldsymbol{W} \tag{1}$$

where $\mathbf{Q} = (\rho_1, \cdots, \rho_N, \rho u, \rho v, e)^T$ is the conservative variable vector, $\mathbf{F}$ and $\mathbf{G}$ are the convective flux vectors, $\boldsymbol{H}$ is the axisymmetric source term, and $\boldsymbol{W} = (w_1, \cdots, w_N, 0, 0, 0)^T$ is the chemistry source term. The variables are the velocity components u and v, the total energy-per-unit volume e, and the density of the kth species ρ_k, with $\rho = \Sigma_{k=1}^{N} \rho_k$. The term w_k is the production rate of the kth species, which is determined by chemical kinetics. Pressure is evaluated by using the equation of state for a mixture of thermally perfect gases, and the temperature T is determined from the definition of total energy by the Newton–Raphson method,

$$e = \frac{\rho}{2}(u^2 + v^2) + \sum_{k=1}^{N} \rho_k \left(\int^T C_{vk} dT + h_k^o \right) \tag{2}$$

where C_{vk} is the specific heat per unit mass of the kth species at constant volume, and h_k^o is the heat of formation per unit mass of the kth species. The expressions for the specific heats as a function of temperature were obtained by using the NASA polynomials from the Appendix of Ref. 12.

The chemistry model used for the present study consists of six reacting species H, O, H_2O, OH, O_2, and H_2 with eight steps of chemical reactions. The reaction data are taken from Evans and Schexnayder [13], which have been successfully used for several shock-induced combustion calculations [2,3,5] with reasonable accuracy. This reaction mechanism is a reduced chemistry model obtained from more complete models, with the exclusion of the reactions involving H_2O_2 and HO_2, which could be important in low-temperature ignition studies.

The fully coupled Euler equations are solved using a fully implicit finite-difference method. The LU-SSOR [14] implicit factorization scheme is adopted for time integration, and Liou and Steffen's new flux-splitting method [15], named as the advection upstream splitting method (AUSM), is used for spatial discretization because of its simplicity in numerical formulation and its efficiency in computational time. Although Liou and Steffen's upwind scheme sometimes shows a nonmonotonicity problem after a strong shock, it has very good accuracy and robustness in capturing shock and reaction front in comparison with Roe's FDS-based shock-capturing methods. It is considered that the separate splitting of convection and pressure terms leads to very small numerical dissipation in comparison with other methods.

The chemistry and numerical formulation were validated by redoing numerical simulations for several shock-induced combustion cases experimentally observed by Lehr [1]. The results were compared with the experimental shadowgraph and considered to be sufficiently accurate [5].

Dimensionless Parameters

From nondimensionalization of the chemistry source term in the species conservation equations, the first Damköhler number for the kth species (Da_{I_k}), which represents the ratio of mass source from chemistry to convective transport and, accordingly, the ratio of the fluid dynamic time scale $\tau_f = R/a_o$ to the chemistry time scale $\tau_c = \rho_o/w_k$, can be defined as

$$Da_{I_k} \equiv \frac{w_k R}{a_o \rho_o} = \frac{\tau_f}{\tau_c} \tag{3}$$

where R is the radius of a blunt body, a_o is the sonic velocity of inflow, and subscript o means the value at inflow.

The distribution of the local value of Da_{Ik} shows a narrow-banded peak at the reaction zone and shows a maximum value for the production of water vapor H_2O in most cases, which is the main product of hydrogen–oxygen combustion. So, the maximum value of Da_I for the production of water vapor can be used as a representative value.

On the other hand, by isolating the heat of formation from total energy, the energy conservation equation can be written in one-dimensional form, which would be adequate for the analysis along the stagnation streamline:

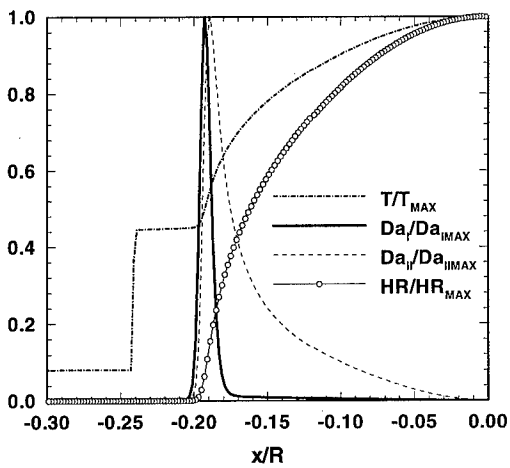

FIG. 1. Typical plot of temperature, Da_I, Da_{II}, and HR. Each curve is normalized with its maximum value. These curves are obtained from the result of the following case: $M = 5.08$, $R = 4.5$ mm ($0.6R^*$), $T_0 = 292$ K, and $p_0 = 186$ mm Hg in $2H_2 + O_2$ mixture.

$$\frac{\partial}{\partial t}\left[\rho\left(e_s + \frac{1}{2}u^2\right)\right] + \frac{\partial}{\partial x}\left[\rho u\left(h_s + \frac{1}{2}u^2\right)\right] = -\sum_{k=1}^{N} h_k^{\circ} w_k \tag{4}$$

where e_s and h_s are the sensible energy and the sensible enthalpy, respectively. The right-hand side is the heat source term representing the rate of heat release by chemical reaction.

Following the definition by Strehlow [16], the heat source term can be nondimensionalized as a ratio of chemical heat release rate to convective transport and is called the second Damköhler number (Da_{II}), defined as

$$Da_{II} \equiv \frac{-R\sum_{k=1}^{N} h_k^{\circ} w_k}{h_s a_o} \tag{5}$$

However, the effect of heat addition is not clearly identified by Da_{II} because it is coupled with reaction rate and represents just the rate of heat release. Therefore, another parameter is required to represent the effect of total heat added independent of the reaction rate.

By integrating the energy conservation Eq. (4) over two points, artificially denoted by 1 and 2, with an assumption of steady state, the effect of heat addition can be isolated from the coupling with reaction rate. Then, the energy conservation equation can be rewritten as

$$\left(h_s + \frac{1}{2}u^2\right)_2 - \left(h_s + \frac{1}{2}u^2\right)_1 = \left(\sum_{k=1}^{N} y_k h_k^{\circ}\right)_1 - \left(\sum_{k=1}^{N} y_k h_k^{\circ}\right)_2 \tag{6}$$

where y_k is the mass fraction of the kth species.

If we select point 1 as inflow, the heat addition at any point can be represented by a new dimensionless heat release (HR) parameter, defined as

$$HR \equiv \frac{-(\sum_{k=1}^{N} y_k h_k^{\circ})}{a_o^2} \tag{7}$$

where the value of $\Sigma_{k=1}^{N} y_k h_k^{\circ}$ at inflow is definitely zero. Consequently, the HR parameter represents a ratio of total heat released by chemical reaction to kinetic energy based on sonic velocity.

Figure 1 represents the typical distribution of temperature and dimensionless parameters along the stagnation line. The temperature distribution shows a stepwise variation, and the distribution of the HR parameter shows a very similar pattern of variation to the temperature distribution of the burned gas region. This similarity can be understood by the definition of HR in Eqs. (6) and (7) together with the fact that velocity is very small along the stagnation line, that is, the variation of heat addition is the same as that of sensible enthalpy. The distribution of the Da_I for H_2O production shows a very narrowbanded peak at the front edge of the second jump of the temperature distribution, which implies that an amount of heat is added at the reaction zone. Therefore, the peak point of the Da_I distribution can be considered a reaction front, and its band width can be considered a reaction zone thickness. The distribution of Da_{II} shows a maximum value at nearly the same position as that of the Da_I maximum point because it is coupled with the variation of reaction rate, which is represented as the variation of Da_I. Therefore, the effect of heat addition may not be explained from the distribution of Da_{II}, and the concept of total heat release is believed to be more useful.

Results

A series of parametric studies is conducted to investigate the effects of flow conditions on the shock-induced combustion regime. The selected flow variables are body radius R, inflow pressure p_0, and inflow temperature T_0. Calculations are performed for a hemispherical blunt body in stoichiometric H_2/O_2 mixtures at a slightly overdriven velocity of Mach number 5.08, which corresponds to the overdriven factor (flow velocity/Chapman–Jouguet detonation velocity) of 1.06 [1] at reference state. The reference values of flow variables are selected from Lehr's experiment [1]; that is, $p^* = 186$ mm Hg, $T^* = 292$ K, and $R^* = 7.5$ mm. A 100×250 uniform computational mesh was used for all cases to preserve the consistency in numerical computations. For the cases of examining the effects of pressure and temperature, a body radius of $R = 0.2R^*$ is used to clearly resolve the induction distance in the present computational domain. From the results of

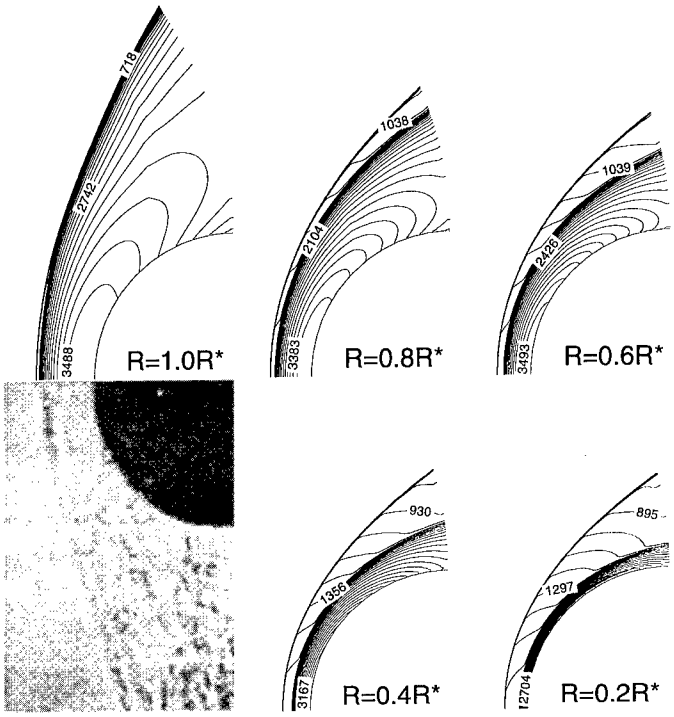

FIG. 2. Temperature contour plots of a shock-induced combustion flow field around blunt bodies of different radii: $R^* = 7.5$ mm, $T_0 = 292$ K, $p_0 = 186$ mm Hg. The lower left figure is the experimental shadowgraph for $R = 1.0R^*$ from Ref. 1.

calculations, the local Da_I for H_2O production and the local value of HR are checked along the stagnation streamline. To relate the global configuration of the shock-induced combustion flow field with dimensionless parameters, the shock standoff distance (SD) and the induction distance (ID) are obtained from the results. Here, SD is defined as the distance from the stagnation point to the shock front at which the maximum pressure gradient appears, and ID is defined along the stagnation line as the distance from shock front to reaction front at which maximum local Da_I for H_2O production occurs.

Effect of Body Size

A parametric study is carried out with respect to the body radius varying from $0.1R^*$ to $1.0R^*$ with an increment of $0.1R^*$ to investigate the effect of fluid dynamic length scale. In this case, p_0 and T_0 are fixed as the values used in Lehr's experiment. Figure 2 shows the temperature contour variation with respect to the radius of the body. The case of $R = 1.0R^*$ corresponds to Lehr's experiment and supports the reasonable accuracy of present computation. As shown in Fig. 2, the solution looks stable for all the body radii and any unsteadiness was not found. This trend is consistent with the experimental result of Lehr [1] where shock-deflagration in hydrogen–oxygen mixtures is observed to be stable.

In Fig. 2, the first gradient represents the bow shock ahead of the body, whereas the second gradient is the reaction front. It is noted that the regime of shock-induced combustion gradually changes from decoupled shock-deflagration to overdriven detonation. This is due to the induction distance decreasing relatively as the body radius increases, even though the absolute value of induction distance may not be affected by the change of body radius. Therefore, the reaction front gets closer to the shock front in the overall flow field, and the burned gas takes a larger portion of the post-shock region and expands more quickly to push the shock and the reaction front itself forward. The shock standoff distance increases as the radius of the body increases while the induction distance relatively decreases. Such explanation is characterized by the result of stagnation line analysis plotted in Figs. 3 and 4.

The shock standoff distance and the induction distance are plotted with respect to body radius in a relative (non-dimensional) length scale in Fig. 3(a) and in an absolute (dimensional) length scale in Fig. 3(b). In a relative coordinate, SD increases rapidly as the body size increases. However, ID gradually decreases while the absolute value of ID remains nearly constant. Figure 4 is the distribution of the maximum value of Da_I for H_2O production and stagnation HR. In this figure, Da_I linearly increases as the fluid dynamic time scale τ_f increases linearly with the radius, while chemistry time scale τ_c remains nearly constant. On the other hand, HR is kept

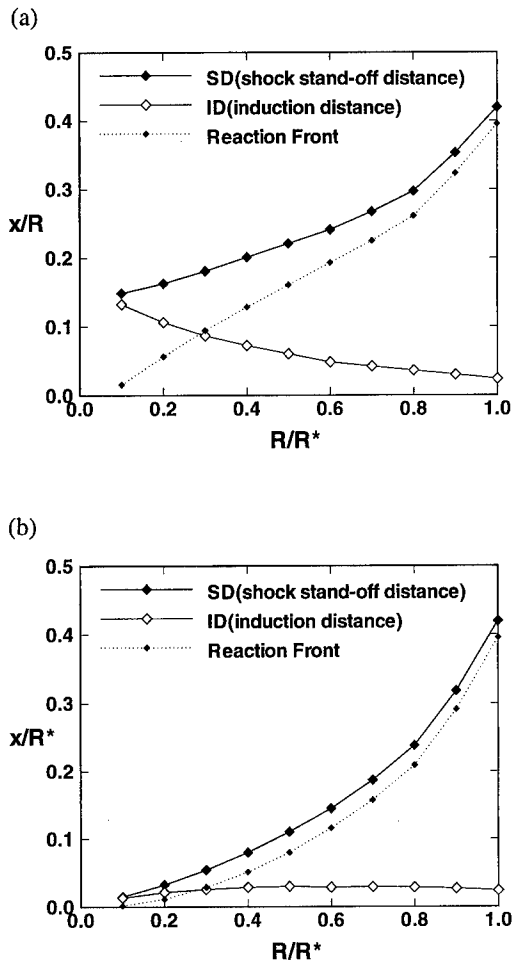

FIG. 3. Shock standoff distance and induction distance with respect to body radius: (a) relative length scale and (b) absolute length scale.

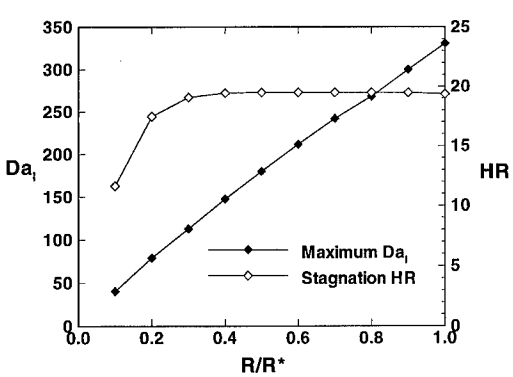

FIG. 4. Maximum Da_I for H_2O production and stagnation HR with respect to body radius.

nearly constant for all the radii, except for very small ones, because there is no variation of the heat addition across the reaction zone when the reaction is nearly completed. Thus, it is concluded that the change of the regime of shock-induced combustion with the increase of body size mainly is due to the linear increase of the Da_I.

Effect of Inflow Pressure

Calculations are performed for different inflow pressures varying from $0.5p^*$ to $3.5p^*$ to examine the effect of one of the thermodynamic state variables. Because the body radius and inflow temperatures are selected as $0.2R^*$ and 292 K, $p = 1.0p^*$ (second subfigure of Fig. 5) is identical to $R = 0.2R^*$ (last subfigure of Fig. 2) in the body-radius variation case. The temperature contours are plotted in Fig. 5. For an inflow pressure larger than $3.5p^*$, a solution cannot be obtained in the computational domain used in this study. As the inflow pressure increases, the regime of shock-induced combustion changes from decoupled shock-deflagration to overdriven detonation, which is very similar to the results for body size variation. The dimensionless parameters in Fig. 6 show a very similar trend to that of body size variation. It is worth noting that the maximum temperature increases as the inflow pressure increases, and the asymptomatically maximum value of HR shows slightly larger values than those for the body size variation. The variation of the overdrive parameter ranges from 1.07 to 1.03 with the inflow pressure variation, and the maximum deviation is limited to about 4%, which is introduced by the slight increase of heat release. Therefore, this case is also considered as Damköhler number-dominated phenomenon and is not considered a heat release parameter- or overdrive parameter-dominated phenomenon. The reason for the linear increase of Da_I is that the increase of inflow pressure causes the increase of the reaction rate, a product of the concentrations of the involved species and a reaction constant. This results in a decrease of τ_c while τ_f remains constant. Therefore, the increase of pressure means an increase of local Damköhler number. Consequently, a very similar tendency is obtained as for body radius variation. The global kinetic mechanism of shock-induced combustion may seem to be a second order reaction because the dimensionless reaction rate Da_I depends linearly on the inflow pressure.

Effect of Inflow Temperature

A series of calculations is performed for eight different inflow temperatures varying from 292 to 900 K, with a body radius of $0.2R^*$ and an inflow pressure of 186 mm Hg. $T_0 = 292$ K is identical to $R = 0.2R^*$. Computational results for selected cases are plotted in Fig. 7. This figure shows very different

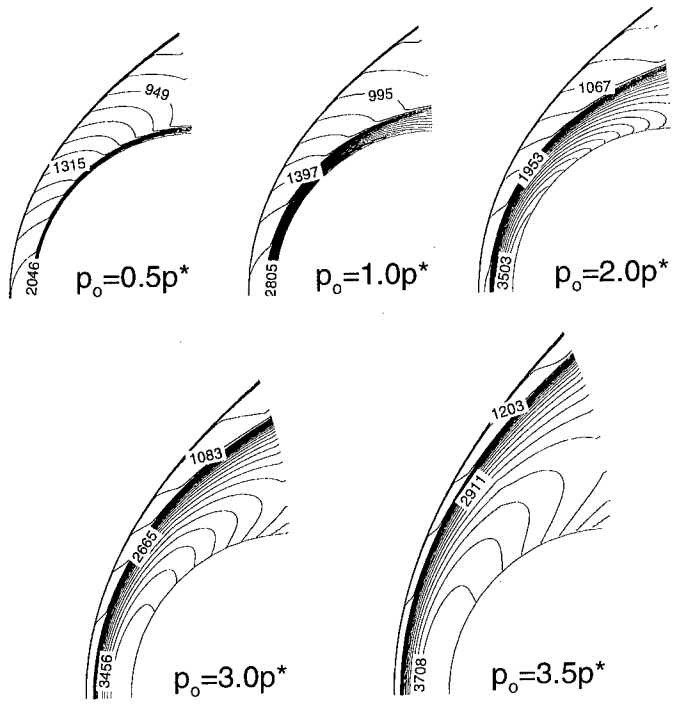

FIG. 5. Temperature contour plots of a shock-induced combustion flow field around a blunt body for different inflow pressures: $R = 0.2R^\circ$, $T_0 = 292$ K, $p^\circ = 186$ mm Hg.

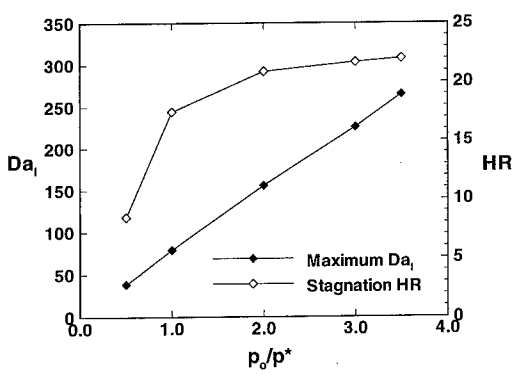

FIG. 6. Maximum Da_I for H_2O production and stagnation HR with respect to inflow pressure.

features from the results with variations of body radius and inflow pressure. Even though an increase of inflow temperatures causes the regime transition of shock-induced combustion from decoupled shock-deflagration to a coupled system, no solution is observed that can be considered overdriven detonation. The variations of Da_I and HR are summarized in Fig. 8. With an increase of inflow temperature, Da_I slowly increases but shows a maximum value of about 150, which is small in comparison to the results of the effect of body size or inflow pressure increase. The HR decreases rapidly and shows negative values for the cases of high inflow temperatures; that is, the chemical reaction is endothermic due to the dissociation of the combustion product. With a variation of inflow temperature, the overdrive parameter monotonical increases from 1.06 to 1.79, which is readily understood from the decrease of HR. As a result, the increase of inflow temperature causes the slight increase of local Damköhler number but dilutes the effect of heat addition. This is true for the whole flow field and is not restricted to the stagnation line. Therefore, the burned gas region cannot expand or push the shock front, and the reaction front is decoupled downstream.

Conclusion

From a dimensional analysis performed to investigate the effects of flow conditions on shock-induced combustion, the following features are found, and summarized in Fig. 9. The increase of body size or inflow pressure mainly leads to an increase of the shock standoff distance and a decrease of the induction distance, which means a transition from decoupled shock-deflagration to overdriven detonation. The Da_I (the dimensionless reaction rate) shows a linear dependence on body size and inflow pressure. The HR parameter maintains a nearly constant value with the variation of body size and shows an asymptotically maximum value for large inflow pressures. Therefore, the effects of these two parameters are

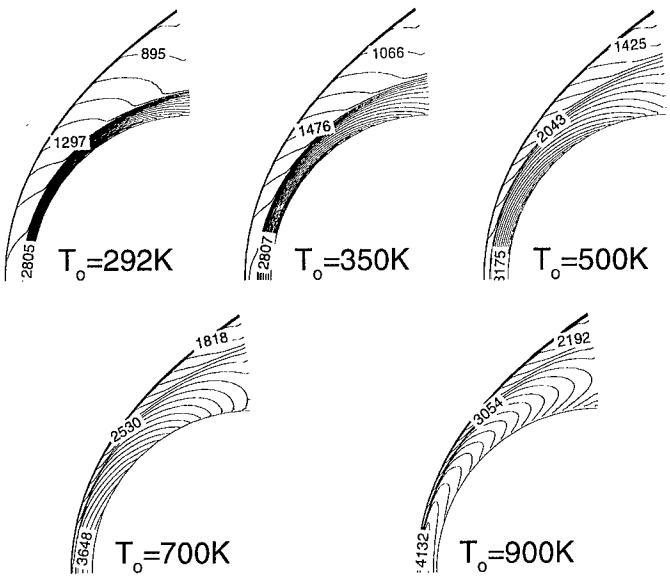

FIG. 7. Temperature contour plots of a shock-induced combustion flow field around a blunt body for different inflow temperatures: $R = 0.2R^*$, $p_0 = 186$ mm Hg.

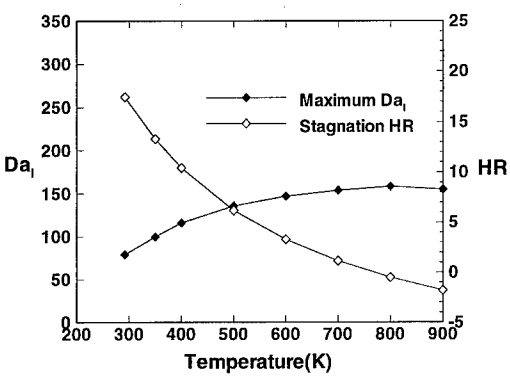

FIG. 8. Maximum Da_I for H_2O production and stagnation HR with respect to inflow temperature.

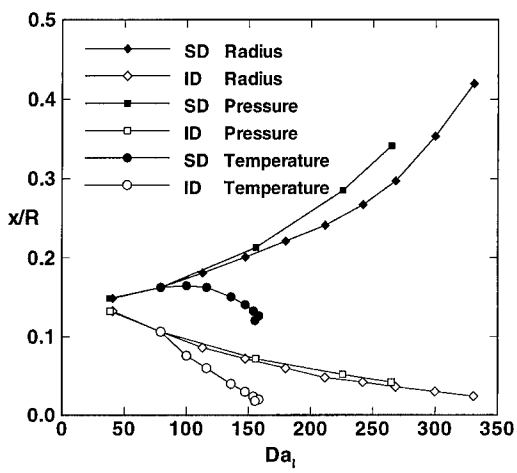

FIG. 9. Shock standoff distance and induction distance with respect to Da_I.

considered to be similar, although the increase of inflow pressure induces slightly higher values of the heat addition parameter. The higher value of HR for pressure variation may be the cause of a larger shock standoff distance for inflow pressure variation at the same Da_I. That is, the higher value of HR induces a larger shock standoff distance. The increase of inflow temperature decreases the shock standoff distance slowly and the induction distance rapidly, although the maximum value of Da_I is limited. The increase of inflow temperature mainly causes a reduction of heat release even though it may lead to a mild increase of Da_I.

From this result, it is concluded that shock-induced combustion can be explained by two dimensionless parameters, Da_I (the dimensionless reaction rate) and HR (the dimensionless heat release).

Acknowledgments

The authors gratefully acknowledge professor Kyung-Kook Cho for his encouragement and enthusiasm. This research was partly supported by the Research Fund for Young Researchers from the Korea Research Foundation awarded to the first author.

REFERENCES

1. Lehr, H. F., *Astronautica Acta* 17(4,5):589–597 (1972).
2. Lee, S. H. and Deiwert, G. S., *J. Spacecraft Rockets* 27(2):167–174 (1990).

3. Yungster, S., Eberhardt, S., and Bruckner, A. P., *AIAA J.* 29(2):187–199 (1991).
4. Wilson, G. J. and MacCormack, R. W., *AIAA J.* 30(4):1008–1015 (1992).
5. Choi, J. Y., Jeung, I. S., and Cho, K. K., *J. KSAS* 22(6):15–24 (1994).
6. Wang, Y., Fujiwara, T., Aoki, T., Arakawa, H., and Ishiguro, T., AIAA Paper 88-0478, 1988.
7. Li, C., Kailasanath, K., and Oran, E. S., AIAA Paper 92-0089, 1992.
8. Lefebvre, M. H. and Fujiwara, T., *Combust. Flame,* 100:85–93 (1995).
9. Matsuo, A. and Fujiwara, T., *AIAA J.* 31(10):1835–1841 (1993).
10. Wilson, G. J. and Sussman, M. A., *AIAA J.* 31(2):294–301 (1993).
11. Matsuo, A. and Fujii, K., *AIAA J.* 33(6):1056–1063 (1995).
12. Gardiner, W. C., Jr., *Combustion Chemistry,* Springer-Verlag, New York, 1984.
13. Evans, J. S. and Schexnayder, C. J. Jr., *AIAA J.* 18(2):188–193 (1980).
14. Shuen, J. S. and Yoon, S., *AIAA J.* 27(12):1752–1760 (1989).
15. Liou, M. S. and Steffen, C. J. Jr., *J. Comput. Phys.* 107:23–39 (1993).
16. Strehlow, R. A., *Combustion Fundamentals,* McGraw Hill, New York, 1984.

Twenty-Sixth Symposium (International) on Combustion/The Combustion Institute, 1996/pp. 2933–2939

SHOCK-WAVE-ENHANCEMENT OF THE MIXING AND THE STABILITY LIMITS OF SUPERSONIC HYDROGEN-AIR JET FLAMES

HWANIL HUH AND JAMES F. DRISCOLL

Department of Aerospace Engineering, University of Michigan, Ann Arbor, MI 48109, USA

A supersonic, non-premixed, jetlike flame was stabilized along the axis of a Mach-2.5 wind tunnel, and wedges were mounted on the sidewall in order to interact oblique shock waves with the flame. Schlieren photographs show how the interaction occurs, and measurements quantify how the flame length and the flame blowout limits are affected by the shocks. An optimum shock-interaction location was investigated by adjusting the wedge position.

It was found that shock waves enhance the fuel-air mixing such that flame lengths decreased by 20% when an optimum shock location and shock strength were chosen. Enhanced mixing resulted, in part, because the shocks turn the flow and induce radial inflows of air into the fuel jet. A Mach disk sometimes occurs, which appears to split the reaction zone into two parts and severely distorts the flame shape. Substantial improvements in the flame stability (i.e., changes in the blowout limits) were achieved by properly interacting the shock waves with the flame-holding recirculation zone. The reason for the significant improvement in flame stability is believed to be the adverse pressure gradient caused by the shock, which can elongate the recirculation zone. Excessive shock strength (or poor shock placement) caused thermal choking to occur, and the flame base moved upstream of the fuel tube exit, leading to dangerously high wall heat transfer rates. Optimization of the mixing and stability limits requires a careful matching of the shock-flame interaction location and the shock strength. The experimental results show that the best mixing and stability correspond to 10° wedges placed at an upstream position (4 d_F) such that the primary shocks create radial inflow near the flame base and interact with the recirculation zone. This upstream wedge position also allowed the second (recompression) set of shocks to provide radial inflow near the flame tip.

Introduction

Oblique shock waves that form within a scramjet combustor are often unavoidable; if the waves are sufficiently oblique to the flow, their stagnation pressure losses are not appreciable, yet they may have the positive effects of enhancing the fuel-air mixing and helping to stabilize the flame base. The purpose of the present work is to quantify and optimize certain beneficial effects of oblique shock waves on a supersonic jetlike flame.

In general, shock waves can affect a flame because they can (a) direct the airflow radially inward (toward the fuel) and thus increase the air entrainment rate, (b) create additional vorticity [1], which enhances the mixing rates, (c) create an adverse pressure gradient, which elongates recirculation zones or creates new separation zones [2], and (d) increase the static pressure, static temperature, and reaction rates. The present supersonic flame was stabilized along the axis of a Mach-2.5 wind tunnel using a thick-lipped fuel tube that acts as a bluff body. Two identical small wedges on the tunnel sidewalls create oblique shocks, and the optimum position of the shock-flame interaction and the optimum shock strength were investigated. This work is an extension of recent studies in our laboratory of supersonic jet flames with no shock waves [3,4].

Little has appeared in the archival literature concerning a shock wave interacting with a turbulent jet flame. Related studies have considered a shock wave interacting with a reacting shear layer [5,6]. Numerous studies have considered nonreacting flows that interact with shock waves; for example, the well-known work of Marble [1], Yang et al. [7], and Jacobs [8] considers a laminar, circular jet of helium that is distorted by shock-generated vorticity. Other related nonreacting flow studies involved shock waves interacting with a contoured wall injector [9,10], nonreacting vortex rings distorted by shock waves [11], and the effects of shocks on a nonreacting jet in a cross flow [12]. The mixing in nonreacting, underexpanded sonic jets having cellular shock patterns was quantified [13,14]. A useful description of the reacting supersonic jet flame itself (with no shock waves) was also provided [15,16].

One of the most pronounced effects of shock waves on fuel-air mixing has been identified by Marble [1], who showed that baroclinic torques can create shock-generated vorticity. This shock-generated vorticity has a large effect on a laminar jet [1,7–9], which has a relatively small amount of initial vorticity

and a relatively low fuel-air mixing rate. However, it is realized that shock-generated vorticity is expected to have a smaller effect on the present turbulent jet (than that reported for the laminar jet) because the high-speed turbulent jet inherently has a relatively large amount of vorticity.

Experimental Arrangement

A schematic of the experiment appears on the lower left side of Fig. 1. A jetlike flame is stabilized on the axis of a Mach-2.5 wind tunnel using a thick-lipped fuel tube, which acts as a bluff body. Air is expanded to Mach 2.5 using a nozzle that was designed using the method of characteristics; the combustor is 55 cm long and 5.7 × 4.1 cm at the fuel injection location. Two of the combustor sidewalls are parallel, whereas the other two diverge at 4° from the axis in order to prevent thermal choking. Each of the four stainless steel sidewalls has a quartz window for optical access. The facility is identical to that described in Refs. 3 and 4, except that larger windows were added and a more gradually contoured fuel tube was added that slightly changes the throat area.

Two wedges that are mounted on the diverging sidewalls are shown in Fig. 1a. Each wedge consists of a 3.2-cm-long slanted face aligned at 10° to the sidewall, followed by a 1.9-cm face that is parallel to the sidewall. The wedges span the entire 4.1-cm width of the combustor, producing a shock that is free from any observable edge effects. The leading edge of the wedge is 2.8 cm downstream of the fuel injection location in Fig. 1.

The outside diameter of the fuel tube gradually changes from 2.54 cm at the end of the tube to 1.27 cm slightly upstream of the air nozzle throat, which is 24 cm upstream. The inside diameter (d_F) is 0.70 cm. Hydrogen is injected at sonic velocity, and the fuel jet Reynolds number is typically 76,000. Although the facility has an electrical air heater capable of heating the air to 1100 K, the stagnation temperature for all of the present flames is 285 K.

Results

Figure 1 shows direct photographs and schlieren photographs of the supersonic flames. The upper flames shown in Figs. 1a through 1c and 1f represent supersonic flames that interact with shock waves generated by the two 10° wedges that are described above. The lower flames in Figs. 1d, 1e, and 1h illustrate baseline supersonic flames with no wedges present. Schlieren images of the nonreacting flow (with and without wedges) are shown in Figs. 1i and 1j. The shocks appear more distinctly with no flame because the turbulent density gradients in the flame obscure the shocks within the flame. In addition, a special case is shown in Fig. 1g in which the wedge angle is increased to 15°, resulting in thermal choking of the combustor, as described below. It can be concluded from Fig. 1 that as the fuel flow rate is increased, the supersonic flames generally become longer for cases both with and without shock waves.

The schematic of a supersonic flame with shock wave interaction is shown in Fig. 1. As seen in the schematic, the wedge produces a primary shock that reflects off the centerline and interacts with the upstream portion of the flame, near the liftoff location. Farther downstream, the additional waves that form are called the recompression shocks. The wedge corner forms expansion waves that direct the air toward the tunnel sidewalls, and the highly curved recompression shocks realign the flow in the axial direction. In Fig. 1j, a small Mach disk appears in the primary shock pattern, while Fig. 1c shows that a Mach disk can also occur in the recompression shocks within the flame. The primary shock waves extend to the centerline within the flames, shown in Figs. 1b and 1c, for example, indicating that with combustion most of the flow downstream of the recirculation zone is supersonic.

Shock waves have a dramatic effect on the shapes of the flames. A neck region (i.e., a minimum flame diameter) occurs in the flame shown in Fig. 1b due to the radial inflow caused by the shock waves. The recompression shocks tend to distort and split the flame as seen in Fig. 1c, and they create a large bulge in the flame tip as seen in Fig. 1f, probably due to shock-induced radial outflow. The recompression shocks play an important role to shorten flame lengths by enhancing the mixing and combustion of the unburned mixture in the downstream region. These enhancements are possible due to strong shocks near the centerline where the recompression shocks intersect. These strong shocks sometimes become Mach disks and can enhance mixing by generating shock-generated vorticity, and enhance combustion by increasing the local density, pressure, and temperature of the mixture, and thereby increasing local reaction rate. The location where the recompression shocks intersect the centerline appears to move upstream as the fuel mass flow rate is increased.

Figure 1g illustrates the flame observed at the onset of thermal choking. Two 15° wedges were located at $z = 2.8$ cm, as shown; the flame base is observed to move upstream and surrounds the fuel tube, leading to dangerously high heat transfer rates. The schlieren image in Fig. 1g indicates that the flow is still supersonic, as evidenced by the shock waves. Further increase in the fuel flow rate causes a strong normal shock to move upstream into the wind-tunnel nozzle, and the flow becomes subsonic in the combustor.

Figure 2 shows measured flame lengths based on Fig. 1. Flame length is defined as the distance from

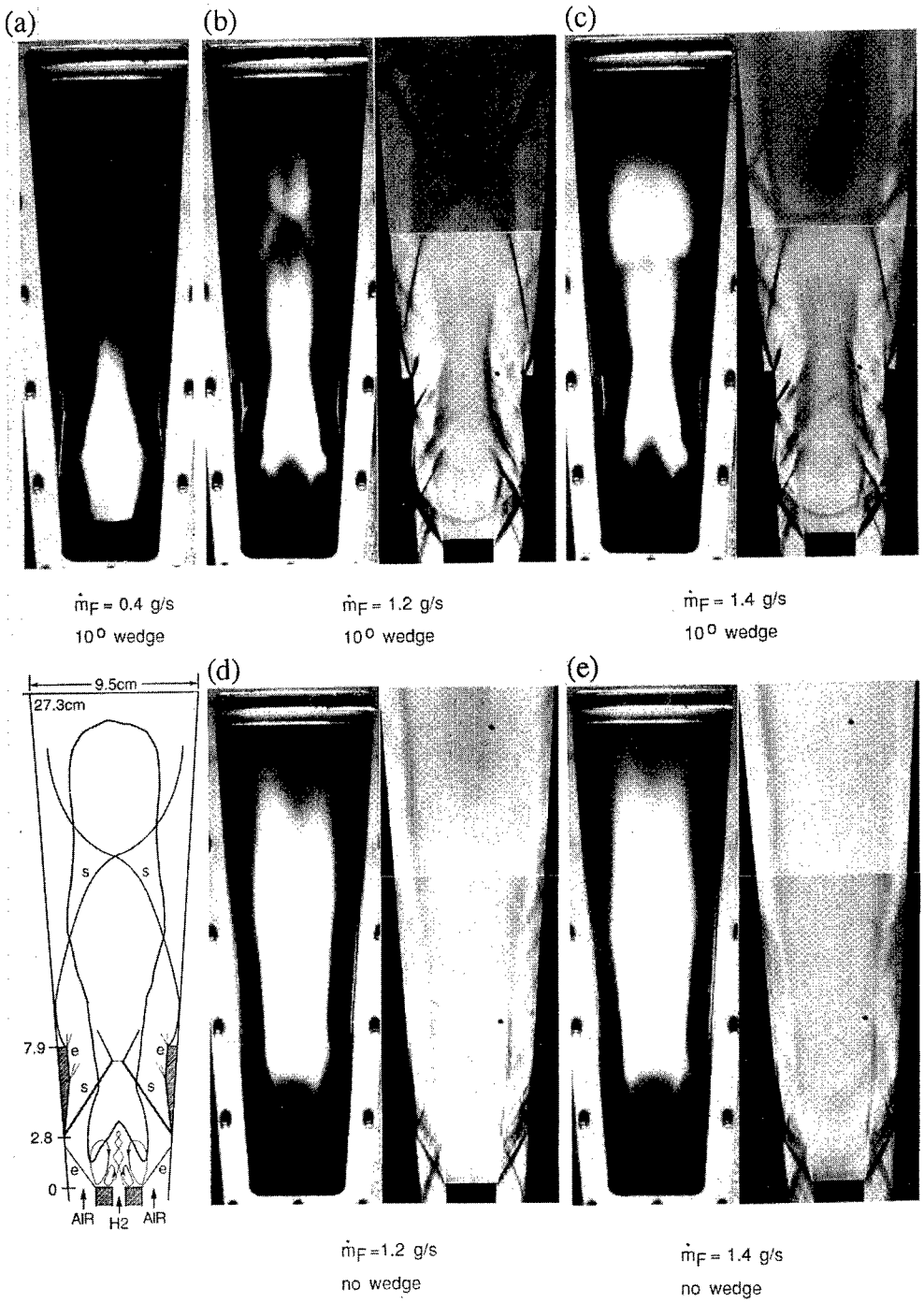

FIG. 1. (a) Direct and schlieren photographs of supersonic jetlike flames interacting with shock waves (top row) and without shock waves (bottom row). Window height = 30.5 cm (12 in.). Hydrogen fuel mass flow rate is varied from 0.4 to 1.4 g/s. For the smallest fuel flow rate of 0.4 g/s, the no-wedge case is not stable, yet with the wedge, the flame is very stable and attached. Distances in schlieren images are 20% larger than in direct photos.

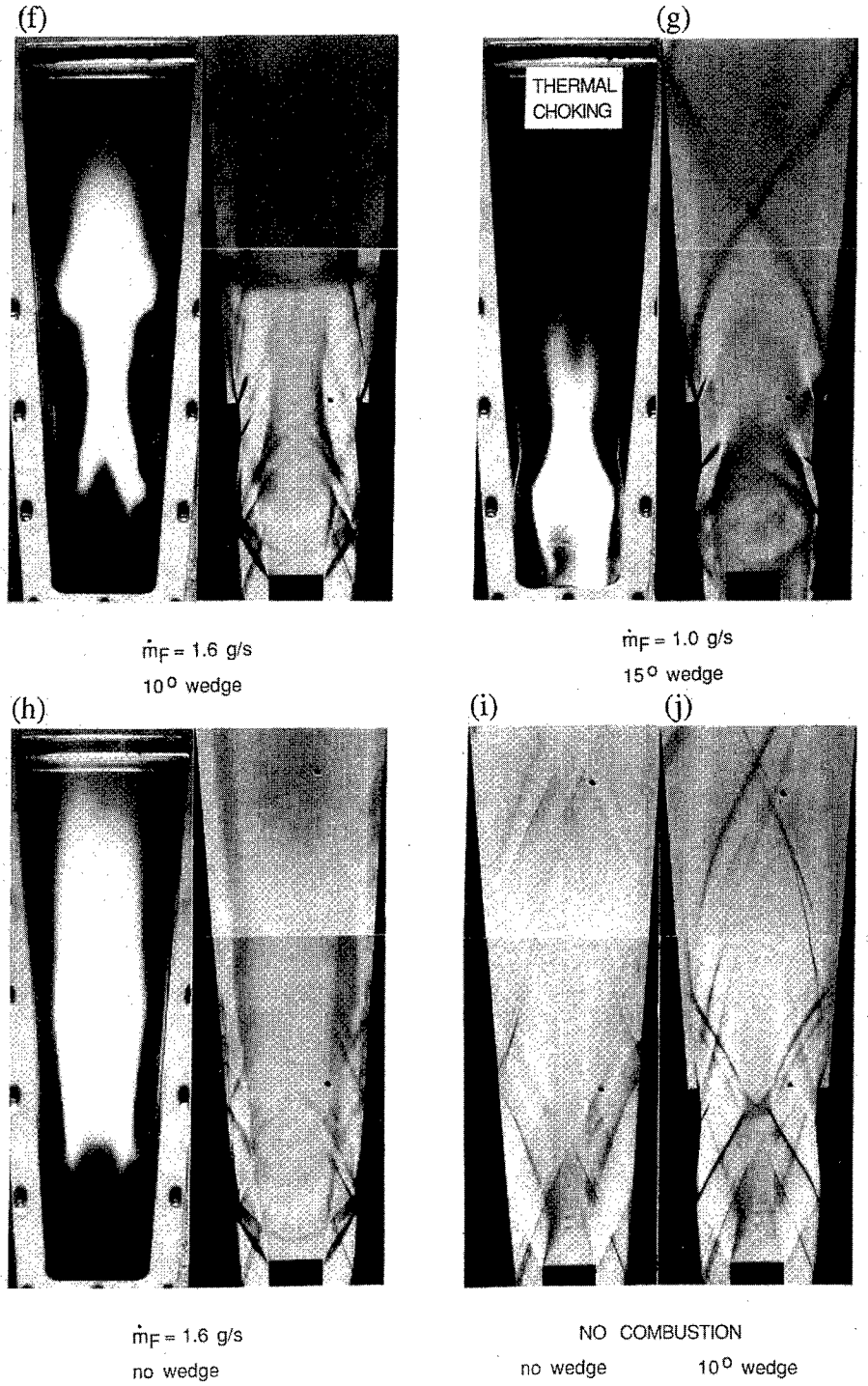

FIG. 1. (*Continued*) (f) and (h) Supersonic flames for increased fuel flow rates, with and without shock waves. (g) Onset of thermal choking caused by a 15° wedge (note that the flame moves upstream of the fuel injection plane and wraps around the fuel tube) (i) and (j) Waves present with no combustion.

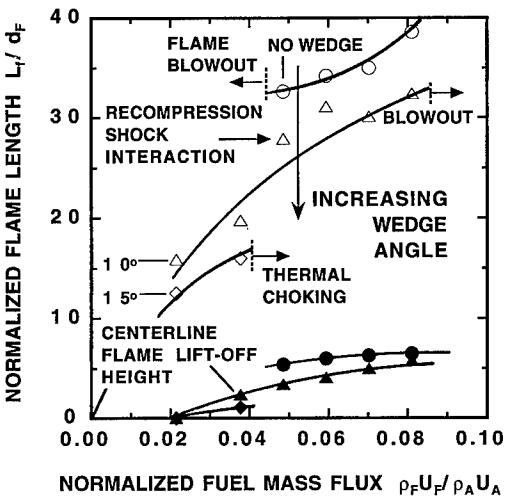

FIG. 2. Lengths of supersonic flames measured from digitized images, with and without shock waves for different wedge angles. Also shown are the flame liftoff heights on centerline. Air flow rates are constant (0.94 kg/s), fuel flow rates are varied from 0.4 to 1.6 g/s. Fuel inner diameter d_F = 0.7 cm. Wedges are located at 2.8 cm downstream of the fuel injector plane.

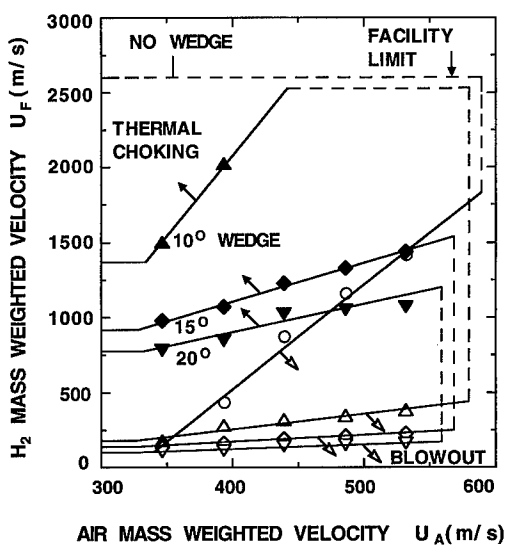

FIG. 3. Effect of shock strength on the stability limits of supersonic flames. The lines shown above define four enclosed regions within which stable flames occur. For conditions above the enclosed regions, thermal choking occurs; for conditions below the enclosed regions, blowout occurs. Increasing the wedge angle (shock strength) decreases the thermal-choking limit and the blowout limit.

the fuel injector to the farthest downstream location where the intensity of the digitized image of the flame decreases to 30% of the maximum intensity recorded in the flame. The positive slope of the curve of flame length versus fuel flow rate in Fig. 2 is similar to previous findings in our laboratory for supersonic flames with no shock waves [4]; similarly, a positive slope is reported for subsonic flames with coaxial air [17]. With coaxial air present, larger fuel flow rates generally require a longer distance to consume the fuel [17].

One major effect of interacting a shock wave with the flame is a significant reduction in the flame length, as shown by the data plotted in Fig. 2. Increasing the wedge angle (shock strength) results in a further shortening of the flames; however, thermal choking occurs for the 15° wedge (stronger shock). Figure 2 shows also the liftoff heights on centerline. The flame liftoff height tends to increase as the fuel flow rate is increased. For the lowest fuel flow rate, shown in Fig. 1a, the flame is attached to the fuel tube, but in all other cases, the flame base is lifted and stabilized within (or downstream of) the air-driven recirculation zone.

Figure 3 shows the effect of shock strength on the stability limits of supersonic flames. The hydrogen-mass–weighted velocity is defined as the hydrogen mass flow rate divided by $\rho_{F,\mathrm{ref}}(\pi/4)\, d_F^2$, where $\rho_{F,\mathrm{ref}}$ is the density of fuel at the sonic fuel injector exit for the reference condition for which the fuel stagnation pressure and temperature are 3.7 atm and 294 K, respectively. In this study, $\rho_{F,\mathrm{ref}}$ equals 0.026 kg/m^3. The air-mass–weighted velocity is the mass flow of air divided by $\rho_{A,\mathrm{ref}} A_A$, where A_A is the combustor cross section (18.9 cm^2) at the fuel injector and $\rho_{A,\mathrm{ref}}$ is 1.08 kg/m^3. Figure 3 shows four enclosed regions within which stable flames occur. Previous work in our lab [3] has shown that with no shock waves, stability limits of supersonic flames are similar in shape to those of subsonic bluff-body flames and swirl-stabilized flames [17–19], which also contain recirculation zones. Three blowout limits usually exist, corresponding to a maximum fuel flow rate, a minimum fuel flow rate, and a maximum air flow rate. Figure 3 quantifies the minimum fuel blowout limit for the no-wedge case. It was not possible to achieve a maximum fuel flow rate or a maximum air flow rate for the no-wedge case due to limited gas supplies, so the dashed lines indicate the maximum fuel and air-mass–weighted velocities at which stable flames were achieved. Increasing the shock strength (wedge angle) decreases the thermal-choking limit and the minimum fuel-blowout limit. It is concluded that shock waves significantly stabilize the flame by reducing the minimum fuel blowout limit as shown in Fig. 3. The 10° wedge shock sufficiently stabilizes the flame as shown in Fig. 1a such that it is not lifted, yet with no shock waves, the same flame blows out. The shock waves (and wedges) also reduce the max-

imum fuel flow rate, which is the upper boundary of the stable regions in Fig. 3. However, this thermal-choking limit is a facility-dependent limit rather than a general limit.

Because the present flames cannot be stabilized unless there is a sufficiently large bluff-body recirculation zone [3], it follows that the improved stability caused by the shock waves results from some type of interaction between the recirculation zone and the shocks. The strong adverse pressure gradient caused by primary shocks and wedges can create a recirculation zone in a boundary layer, for example, and shock waves can increase the size of an existing recirculation zone, as shown by Winterfeld [2]. The shocks also can raise the temperature of the recirculated gas. Vorticity created by the shock [1] also may aid in enhancing mixing and flame stabilization.

The optimum strength and location of wedges were investigated by mounting the 10°, 15°, and 20° wedges at various axial locations: $z = 1$, 4, 8.5, and 11.5 d_F. The cost paid for the total pressure loss encountered and the improvement in mixing and flame stability limits were considered together. On the basis of this criteria, the best mixing and stability corresponds to 10° wedges placed at an upstream position (4 d_F) such that the primary shocks create radial inflow near the flame base and interact with the recirculation zone. This upstream wedge position also allowed the second (recompression) set of shocks to provide radial inflow near the flame tip.

Conclusions

1. Shock waves significantly alter the shape, visible length, and blowout limits of a supersonic jet flame as shown by schlieren and direct photographs. Shock strength was varied, as well as the hydrogen flow rate and the location of the shock-flame interaction.
2. Shock waves enhance overall mixing rates because flame length decreased by approximately 30% when shocks were added. One reason for this enhancement was that the present shocks imparted a radial inflow velocity to the air at an intermediate axial location, and imparted a radial outflow velocity to the fuel and air mixture near the flame tip. Both of these effects are believed to improve mixing. The effects of other mechanisms, including the vorticity generation predicted by Marble, cannot yet be determined.
3. Shock waves greatly enhance one of the flame stability limits, namely the blowout limit associated with a minimum fuel velocity. One explanation is that the strong adverse pressure gradient caused by the shock can enlarge the subsonic recirculation zone behind the flameholder.
4. Optimization of the mixing and stability limits requires a careful matching of the shock-flame-interaction location, the shock strength, the flame length, and the geometry of the recirculation zone and wake of the flameholder. Best results occur if the primary shocks are positioned to interact with the flame base and the downstream recompression shocks, determined by the wedge placement and size, interact with the central portion of the flame. The experimental results show that the best mixing and stability corresponds to 10° wedges placed at an upstream position (4.0 d_F).

Acknowledgments

Funds for this research were made available by the Advanced Propulsion Division, Wright Patterson AFB, monitored by Dr. A. S. Nejad, AFOSR contract DOD G-F49620-95-1-0115, by Dr. J. M. Tishkoff, and by the University of Michigan.

REFERENCES

1. Marble, F. E., *Twenty-Fifth Symposium (International) on Combustion,* The Combustion Institute, Pittsburgh, pp. 1–12, 1994.
2. Winterfeld, G., *Modern Research Topics in Aerospace Propulsion,* Springer-Verlag, New York, 1991, pp. 37–47.
3. Yoon, Y., Donbar, J., and Driscoll, J. F., *Combust. Sci. Technol.* 97:137–156, 1994.
4. Driscoll, J. F., Huh, H., Yoon, Y., and Donbar, J., *Combust. Flame* 107:176–186 (1996).
5. Menon, S., AIAA Paper 89-0104, 1989.
6. Drummond, J. P., AIAA paper 91–1914, 1991.
7. Yang, J., Kubota, T., and Zukoski, E. E., *AIAA J.* 31(5):854–862 (1993).
8. Jacobs, J. W., *J. Fluid Mech,* 234:629–649, 1992.
9. Waitz, I. A., Marble, F. E., and Zukoski, E. E., AIAA paper 92-0625, 1992.
10. Eklund, D. R., Northam, G. B., and Fletcher, D. G., AIAA paper, 90-2360, 1990.
11. Cetegen, B. M., and Hermanson, J. C., *Combust. Flame* 100:232–238, (1995).
12. Heister, S. D., and Karagozian, A. R., *AIAA J.* 28 (5):819–827 (1990).
13. Cheuch, S. G., Lai, M.-C., and Faeth, G. M., *AIAA J.* 27 (5):549–559 (1989).
14. Glawe, D. D., Donbar, J. M., Nejad, A. S., Sekar, B., Chen, T.-H., Samimy, M., and Driscoll, J. F., AIAA paper 94-0711, 1994.
15. Cheng, T. S.,Wehrmeyer, J. A., Pitz, R. W., Jarrett, O. Jr., Northam, G. B., *Combust. Flame* 99:157–173 (1994).
16. Guerra, R., Waidmann, W., and Laible, C., AIAA paper 91-5102, 1991.
17. Feikema, D., Chen, R.-H., and Driscoll, J. F., *Combust. Flame* 86:347–358 (1991).
18. Chen, R. H., Driscoll, J. F., Kelly, J., Namazian, M.,

and Schefer, R. W., *Combust. Sci. Technol.* 71(4):197–217 (1990).

19. Feikema, D., Chen, R.-H., and Driscoll, J. F., *Combust. Flame* 80:183–195 (1990).

COMMENTS

Kenichi Takita, Tohoku University, Japan. Enlargement of the recirculation zone is the main factor for the flame stabilization offered in your conclusion. How about increases of static temperature and static pressure by shock interactions?

Author's Reply. The increase in the static temperature and static pressure caused by the shock wave should increase the chemical reaction rate and thus improve stability. However the location of the shock is important and for some shock locations we find that the shock does not improve stability. Therefore the increased static temperature caused by the shock does not guarantee better stability.

Twenty-Sixth Symposium (International) on Combustion/The Combustion Institute, 1996/pp. 2941–2947

NUMERICAL SIMULATION OF FLAME-STABILIZATION AND COMBUSTION PROMOTION BY PLASMA JETS IN SUPERSONIC AIR STREAMS

RYOICHI KATO AND ITSURO KIMURA

Department of Aerospace Engineering, Tokai University, Hiratsuka, Kanagawa, Japan

The mechanisms of flame stabilization and combustion promotion by plasma jets, observed in scramjet combustor experiments with transverse fuel injection, were investigated numerically, based on time-dependent, two-dimensional complete Navier–Stokes equations, with a six-species, eight-step reaction model combined with Zel'dovich chain reactions. Although most designs for scramjet combustors rely on the combination of a rearward-facing step and a plasma torch, the present study is conducted on a simple configuration without the step to make clearer the fundamental aspect of the mechanisms.

The following results were obtained:

1. A plasma jet with adequate input power and feedstock flow rate establishes a high-temperature recirculation zone with an adequate scale, which works for flame stabilization as that produced by the step. The plasma jet is also useful for the combustion promotion of the fuel jet, through the intensification of eddy diffusivity at its injection point and at the following downstream region.
2. The effectiveness of plasma jets in flame stabilization and combustion promotion increases with input electric power and feedstock flow rate, and the plasma jets with oxygen feedstock are more effective than those with air or hydrogen feedstock, as observed generally in scramjet combustor experiments.
3. A decrease of the plasma jet injection slit width, for a fixed input power and a fixed mass flow rate of feedstock, increases the effectiveness of plasma jets in some cases.
4. When the plasma jet injection slit is located downstream of the fuel injection slit, the required input power and feedstock flow rate for a desirable combustion progress are usually smaller than those when it is located upstream, in accordance with a previous supersonic–combustion experiment conducted without the step.

Introduction

Plasma jet ignition and combustion promotion in stagnant or low-speed gas such as in internal combustion engines has been studied extensively by Weinberg and co-workers [1]. The plasma jet was applied to supersonic combustion by one of the present authors and experimental results showed that it is useful not only for ignition but for flame stabilization and combustion promotion [2]. Northam et al. [3], Barbi et al. [4], and Wagner et al. [5] showed that an argon/hydrogen plasma torch is effective in supersonic combustion and that the performance of a plasma torch is sensitive to combustor geometry and/or fuel distribution. Recently, an oxygen (or air) plasma torch was developed with high performance and practical applicability, and extensive experiments were conducted for governing parameters of the plasma torches using a test combustor for scramjets [6,7].

A high-temperature jet produced by arc discharges is usually called plasma jet, or plasma torch in practical application. The combustion-reaction promotion of a plasma jet is mainly caused by radicals due to dissociation, although in the situation of high input power to plasma jets, the role of ionized species may be noticeable.

The objective of the present numerical study is to investigate the fundamental aspect of chemical and aerodynamic mechanism of flame stabilization and combustion promotion by plasma jets (torches) observed in recent scramjet combustor experiments. Although most combustor designs for supersonic combustion experiments with transverse fuel injection rely on the combination of a rearward-facing step and a plasma torch, the present numerical study is conducted on a two-dimensional configuration without the step, to make clearer the fundamental performance of plasma torches for flame stabilization and combustion promotion.

Governing Equations

The time-dependent, two-dimensional Reynolds time-averaged complete Navier–Stokes equations with species transport equations are summarized in the Cartesian coordinates as follows:

$$\frac{\partial \boldsymbol{Q}}{\partial t} + \frac{\partial \boldsymbol{F}}{\partial x} + \frac{\partial \boldsymbol{G}}{\partial y} = \boldsymbol{S} \tag{1}$$

where

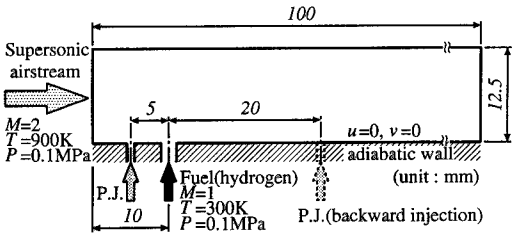

FIG. 1. Computational domain.

TABLE 1
Conditions of plasma jets (typical)

No.	feedstock	$\dot{m}_{pj}$	T_{pj}	P_{pj}	W_{pj}	ϕ
1	O_2	0.6	3300	0.053	2.9	0.189
2	O_2	0.6	5600	0.074	5.4	0.992
3	O_2	1.1	2700	0.083	3.9	0.018
4	O_2	1.1	3800	0.112	6.8	0.420
5	O_2	2.2	2700	0.166	7.8	0.013
6	O_2	2.2	3300	0.192	10.5	0.101
7	O_2	2.2	3800	0.224	13.5	0.311
8	O_2	4.5	1700	0.261	8.9	0.000
9	O_2	4.5	2700	0.332	15.5	0.009
10	O_2	4.5	3300	0.385	20.8	0.072
11*	O_2	1.1	3800	0.224	6.8	0.311
12	Air	2.5	3000	0.203	10.3	0.039
13	H_2	0.6	3800	0.224	52.3	0.342

*: width of p.j. slit is 0.5 mm

$$\boldsymbol{Q} = \begin{bmatrix} \rho \\ \rho u \\ \rho v \\ \rho e \\ \rho Y_i \end{bmatrix} \quad \boldsymbol{S} = \begin{bmatrix} 0 \\ 0 \\ 0 \\ 0 \\ \dot{w}_i \end{bmatrix}$$

$$\boldsymbol{F} = \begin{bmatrix} \rho u \\ \rho u^2 + p - \tau_{xx} \\ \rho uv - \tau_{xy} \\ (\rho e + p)\, u - u\tau_{xx} - v\tau_{xy} + q_x \\ \rho u Y_i - \rho D(\partial Y_i/\partial x) \end{bmatrix}$$

$$\boldsymbol{G} = \begin{bmatrix} \rho v \\ \rho uv - \tau_{xy} \\ \rho v^2 + p - \tau_{yy} \\ (\rho e + p)\, v - u\tau_{xy} - v\tau_{yy} + q_y \\ \rho v Y_i - \rho D(\partial Y_i/\partial y) \end{bmatrix}$$

In the preceding system, Fick's law and Fourier's law are applied for the species diffusion and heat conduction, respectively. The turbulence closure of the equations is provided by the Baldwin–Lomax algebraic model [8,9], and the Lewis number is assumed to be unity.

The hydrogen/air combustion is modeled with a finite-rate, nine-species (H_2, O_2, H_2O, OH, H, O, N_2, N, NO), eight-step reaction model with Zel'dovich chain reactions. The reaction rate constants in this system are referred to in Table 1 of Ref. 10.

Numerical Method and the Model of Flow Field

The MacCormack scheme is used for solving the two-dimensional complete Navier–Stokes equations and species transport equations in conservative form. The geometry of the computational domain is a rectangle along an adiabatic and nonslip wall as shown in Fig. 1. There is a hydrogen fuel injection slit (width: 2 mm) and a plasma jet injection slit (width: 1 mm) on the wall. The fuel injection slit is fixed at 10 mm from the left-side boundary of the computational domain, and the plasma jet injection slit is 5 mm upstream (forward injection) or 20 mm downstream (backward injection) of the fuel injection slit. The present flow field model, in which the upper boundary is not limited, is free from the problem of thermal choking.

The dimension of the grids used in the calculations are 95 × 44 for forward injections and 115 × 44 for backward injection. A grid clustering is employed at the wall in the normal direction and at the fuel and plasma jet slits in the direction of the main airstream. The minimum grid spacing at the wall in the normal direction is 0.02 mm, about one-tenth of the thickness of the boundary layer. The fuel and plasma jet injections are modeled with 10 points, or 21 points for the confirmation of calculation accuracy.

The conditions of the injected fuel (hydrogen) at the exit of the slit are 300 K, 0.1 MPa, and $M = 1$ (1317 m/s), corresponding to the mass flow rate, 2.2 g/s · cm. The inlet conditions of the main airstream are standard air (O_2 + 3.76N_2), 900 K, 0.1 MPa, and $M = 2$ (1180 m/s). The initial conditions of the airstream for calculation are the compressible boundary-layer velocity and temperature profiles for an adiabatic, nonslip wall, with fixed main airstream conditions. Plasma jets ($M = 1$ at the exit of a slit, feedstock: oxygen, air, and hydrogen) injected into the airstream are assumed to be in the state of chemical equilibrium. The conditions of typical plasma jets in the present calculation are shown in Table 1. In the table, T_{PJ}(K), P_{PJ}(MPa), and ϕ are mean temperature, pressure, and degree of dissociation (mass fraction of dissociated product) of plasma jets (p.j.) at the exit of slit, and $\dot{m}_{PJ}$(g/s · cm) and W_{PJ}(kW/cm) are feedstock mass flow rate and the input power for the unit depth (1 cm) of the slit. In the present investigation, the maximum temperature of plasma jets applied is limited to less than 6000 K, because of the reliability of available thermochemical data.

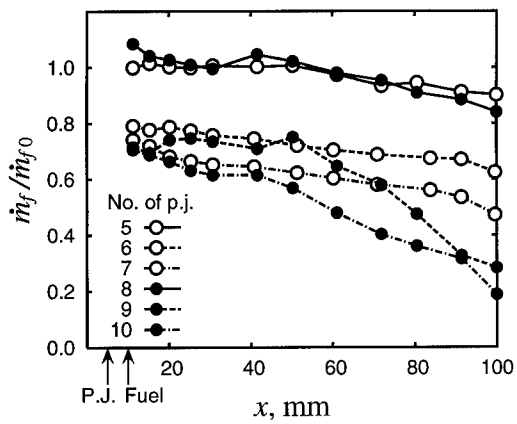

FIG. 2. The progress of combustion in the case of forward p.j. injection; the conditions of p.j. are shown in Table 1.

Calculated Results

In the present numerical study, the performance of oxygen plasma jets in flame stabilization and combustion promotion is investigated extensively, from the viewpoint that oxygen is the most effective feedstock, and the tendency of performance of plasma jets using incoming air can be estimated based on the data of oxygen plasma jets.

Under the conditions of main airstream and fuel injection, without the application of a plasma jet, the initiation of combustion is noticed in the supersonic boundary layer at the halfway point of the computational domain shown in Fig. 1, though the progress of combustion in downstream is very slow [11]. Figure 2 shows typical calculated results where plasma jets (feedstock: oxygen) are injected transversely at 5 mm upstream of the fuel (hydrogen) injection slit (forward injection), into an airstream of $M = 2$ and static temperature 900 K, taking unburned fuel (H_2) mass flow rate across a section normal to the airstream ($\dot{m}_f$, g/s · cm), normalized by the mass flow rate without p.j. application at the section ($\dot{m}_{f0}$, g/s · cm), in ordinate, and the location of the section in abscissa. In Table 1, the conditions of plasma jets related to Fig. 2 are involved. Figure 2 shows that when the plasma jet power is increased over a value, about 9 kW/cm in the case of 2.2 g/s · cm (Nos. 6,7) and about 12 kW/cm in the case of 4.5 g/s · cm (Nos. 9,10), a sudden progress of combustion occurs at the upstream of fuel injection slit, while the progress of combustion downstream is enhanced by the increase of feedstock flow rate.

The characteristics of the flow field in the case of forward injection are shown in Figs. 3 and 4. In this case (No. 7 p.j.), where a successful combustion progress is established, a high-temperature recirculation zone (clockwise) is established in the space between the fuel slit and plasma jet slit, which is taking in some part of fresh fuel injected (see Fig. 4). The power of the plasma jet is related mainly to the gas temperature in the recirculation zone and the flow rate of feedstock to the scale of recirculation zone (length and height) that depends on the strength of the shock wave formed ahead.

Figure 5 shows typical calculated results where plasma jets (feedstock: oxygen) are injected transversely at 20 mm downstream of the fuel injection slit (backward injection). In Table 1, the conditions of plasma jets related to Fig. 5 are presented. In backward injection, considerable progress of combustion occurs at the location of plasma jet injection and the degree of the sudden progress of combustion is intensified with power and feedstock flow rate of plasma jets, although a tendency of saturation is observed at a high power and large flow rate. The combustion progress in the downstream direction are enhanced by the increase of feedstock flow rate, as in the case of forward injection. It was seen in flow field maps that penetration of plasma jet in this case is better when compared to that in forward injection, as expected.

Figures 6 and 7 compare the progress of combustion in the supersonic flow field for feedstock flow rate (oxygen) in the cases of forward and backward injections, taking $\dot{m}_f(x = 100)/\dot{m}_{f0}(x = 100)$ in the ordinate and plasma jet power in the abscissa, where $\dot{m}_f(x = 100)$ is the mass flow rate of unburned hydrogen at the outlet section of computational domain; $\dot{m}_{f0}(x = 100)$ is that at the outlet section in the case without p.j. application. In the case of forward injection, the decrease of flow rate of unburned hydrogen in the region $W_{pj} > 7$ kW is expressed nearly in a single line regardless of the feedstock flow rate, although the calculated data for low feedstock flow rate are limited in relatively low input power because of the reliable limit of thermochemical data, 6000 K. In the case of backward injection, the flow rate of unburned hydrogen decreases with feedstock flow rate, but the dependency of decrease on input power becomes smaller for a large feedstock flow rate.

The impulse of a plasma jet issuing from a slit with $M = 1$ is proportional to the static pressure P at the slit exit, $\dot{m}_{pj}a = \gamma AP$, where $\dot{m}_{pj}$ and A are feedstock mass flow rate and the cross-sectional area of the slit for unit length in depth, and a, acoustic velocity. The data shown in Figs. 6 and 7 are replotted in Fig. 8, taking static pressure of plasma jets at the exit of the slit in the abscissa. In this graph, the data of backward injection for different powers and feedstock flow rates are arranged in a single curve. It is noticed here that in the present situation of two-dimensional configuration, the impulse of jet plays an important role in combustion progress, as in the case of transverse injection of a circular fuel jet into subsonic

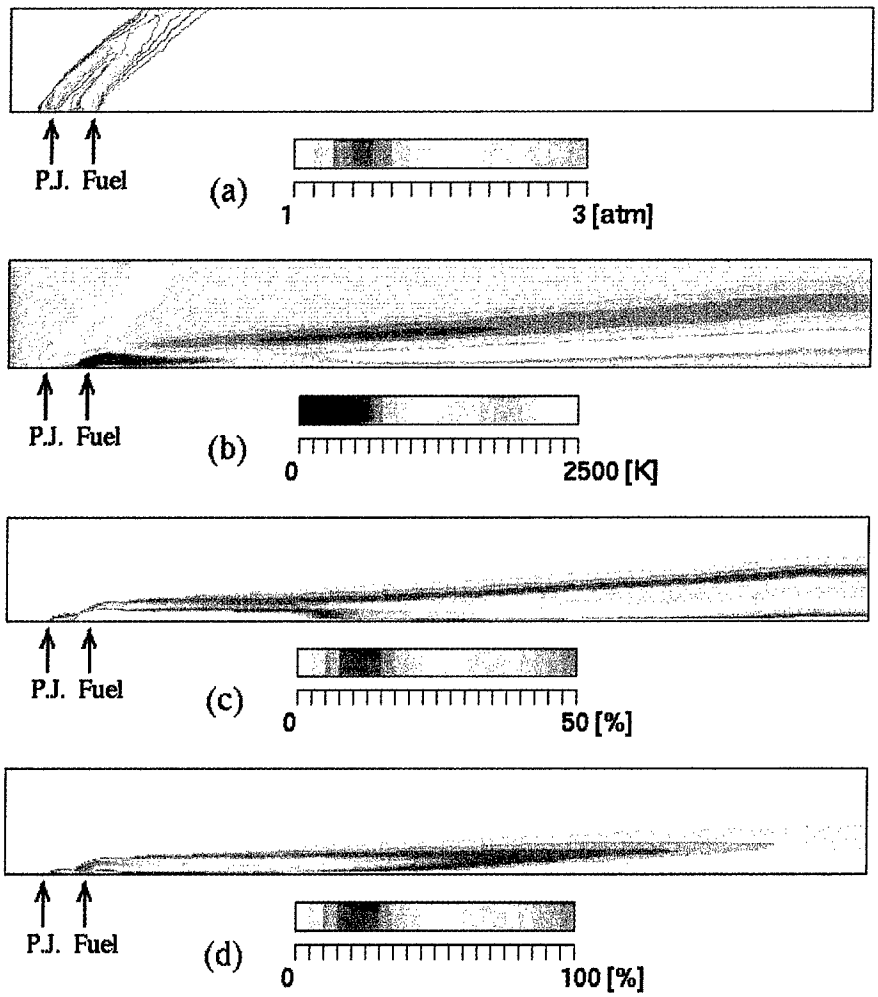

FIG. 3. The progress of combustion in the case of forward injection with No. 7 p.j., (a) static pressure (two shock waves at fuel and p.j. injection points), (b) temperature, (c) mass fraction of H_2O, (d) mass fraction of H_2.

flows, where the vortex pair and entrainment are controlled by impulse of the jet [12].

In Figs. 6 and 7, typical calculated results for a different slit width of plasma jet and for different feedstocks are also involved. The decrease of slit width from 1 mm to 0.5 mm is effective for the case of forward injection but not in the case of backward injection. It is seen in the figures that oxygen is more effective than air or hydrogen, as observed in a recent scramjet combustor [7].

Discussion

Most combustor designs for supersonic combustion experiments rely on a rearward-facing step for flame stabilization, where a recirculation zone is established [3,5–7]. The effectiveness of a plasma jet in supersonic combustion in the situation of no step had been investigated experimentally by one of the present authors [2], and the result shows that a satisfactory combustion progress is observed for the injection at backward positions, while the same plasma jet applied at forward position causes only local combustion near the fuel injection port. The present calculated results for relatively weak plasma jets agree with such experimental results qualitatively.

Northam et al. [3] and Wagner et al. [5] designed a new combustor suitable for the use of a plasma torch, in which an argon/hydrogen plasma torch is placed immediately downstream of a step, providing fuel (hydrogen) separately through a pilot injector and a primary injector located upstream and downstream of the step. Recently, Sato et al. [6] and Masuya et al. [7] designed a supersonic combustor in

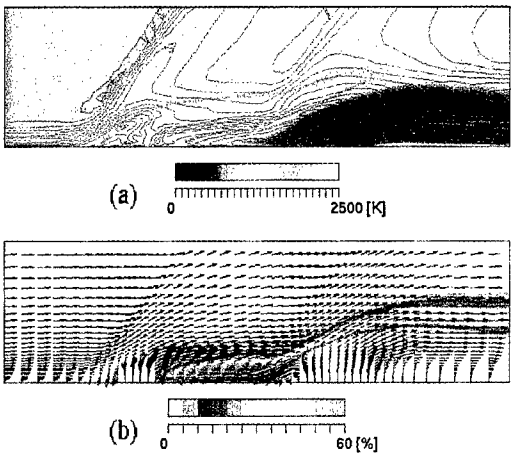

FIG. 4. The enlarged flow field of recirculation zone in the case of Fig. 3; (a) temperature and Mach number; (b) mass fraction of H_2O and velocity field.

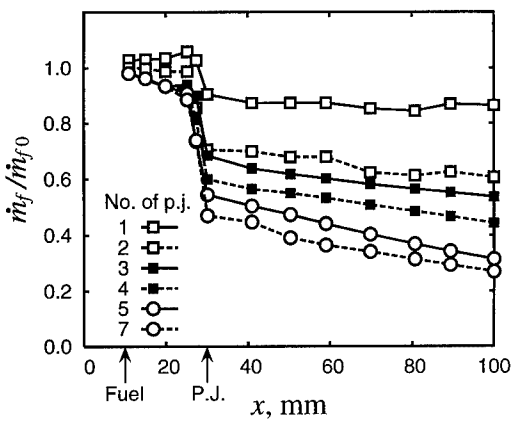

FIG. 5. The progress of combustion in the case of backward p.j. injection; the conditions of p.j. are shown in Table 1.

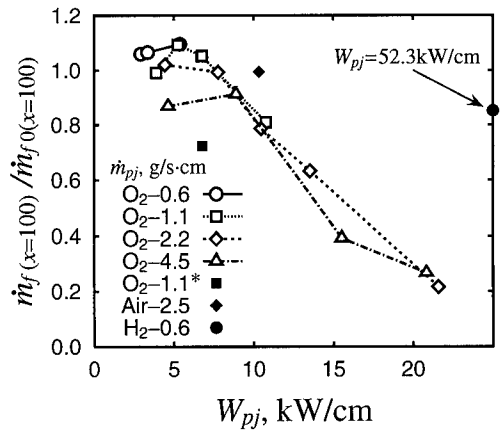

FIG. 6. The variation of mass flow rate of unburned hydrogen at the outlet section of computational domain with p.j. input power (forward p.j. injection), *: width of p.j. slit is 0.5 mm.

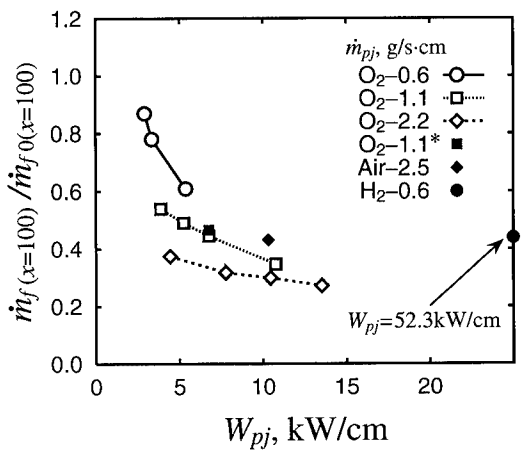

FIG. 7. The variation of mass flow rate of unburned hydrogen at the outlet section of computational domain with p.j. input power (backward p.j. injection), *: width of p.j. slit is 0.5 mm.

which a plasma torch is placed upstream of a step, while fuel (hydrogen) is provided through a port immediately downstream of the step as in the case of their supersonic combustion experiments with autoignition and compared the effectiveness of several feedstocks used in plasma torches (oxygen, air, nitrogen, and argon/hydrogen). Ref. 7 depicts the effectiveness of plasma torches, evaluated by the ignition limit of airstream total temperature, increases with input electric power and feedstock flow rate, and although the order of effectiveness of the feedstocks, air, nitrogen, and argon/hydrogen changes with operating conditions, oxygen is the most effective feedstock for all cases. For the increase of power and feedstock flow rate and for the use of oxygen as feedstock, the same tendencies as those in Ref. 7 are obtained in the present numerical simulation, although no step is considered in the calculation.

One of the important results of the present numerical simulation is that a plasma jet with sufficient power and feedstock flow rate (chemically active feedstock) can establish a recirculation zone in a supersonic airstream, which works for ignition and flame stabilization as one produced by a step. The importance of power and feedstock flow rate of plasma jets in this case may be noted as follows: Figure 8 of Ref. 2 shows that the threshold net power of p.j. (port diameter: 5 mm, feedstock: N_2, 0.22 Nl/s) necessary for ignition and flame stabilization is

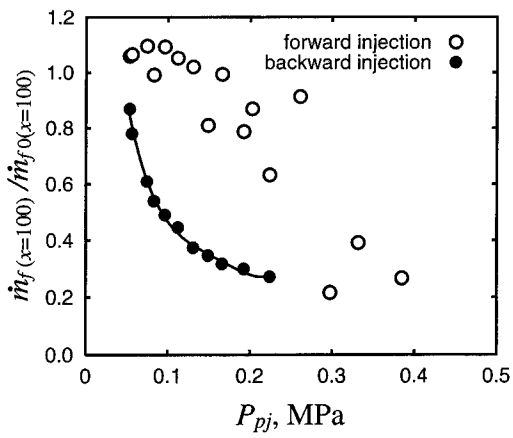

FIG. 8. The variation of mass flow rate of unburned hydrogen at the outlet section of computational domain, with static pressure of p.j. with sonic velocity at its slit exit.

1.6 kW. This suggests that the threshold net power under two dimensions is about 3.2 kW/cm and the corresponding feedstock flow rate, 0.55 g/s · cm. In the present calculation for the case of O_2 p.j. of 0.6 g/s · cm, the threshold value evaluated by extrapolation is about 3 kW/cm (Fig. 7). This is near the value deduced from experimental data, although, for the case of experiments and numerical simulations, there is some difference in velocity and temperature of the combustible mixture flowing around the recirculation zone.

It must be noted here that plasma jets work effectively for the combustion promotion of fuel jet, besides the previously mentioned flame stabilization. Plasma jets' capabilities for combustion promotion, at its injection point and at the following downstream region, is increased with input power and feedstock flow rate (see Figs. 2 and 5). The plots of eddy diffusivity in the flow fields with plasma jet injection show correspondingly (the data are not provided in this paper) that the level of eddy diffusivity in the downstream region, following the high peak at the injection point, increases with the input power and the feedstock flow rate of the applied plasma jet.

Ref. 2 shows that at the section 10 cm downstream of p.j. injection (H_2 p.j., net power: 2.3 kW), the combustion efficiency of hydrogen fuel injected (20 Nl/s) 25 mm upstream of p.j. injection into $M = 2.1$ airstream (static temperature 154 K, static pressure 1.0 atm) is 68%; similar combustion efficiency is also achieved by N_2 p.j. of net power 2.3 kW and 0.22 Nl/s. In Fig. 5, it can be evaluated by extrapolation that the rate of disappearance of hydrogen fuel at the section 10 cm downstream of O_2 p.j. of 4.6 kW/cm and 0.6 g/s · cm is about 0.4. Taking into consideration the difference in airflow velocities, turbulent diffusivities, and fuel injection rates, it is estimated that three-dimensional effect in the progress of diffusion is predominant in experimental results of Ref. 2.

Concluding Remarks

To understand fundamental mechanisms of the effects of plasma jets on flame stabilization and combustion promotion in supersonic airstreams, a numerical study was conducted for a two-dimensional configuration without a rearward-facing step. The results were compared with those of recent scramjet combustor experiments or previous supersonic combustion experiments without the step.

Although the combination of a rearward-facing step and a plasma torch is a promising method for scramjet combustors with transverse fuel injection, the present numerical simulation also suggests that flame stabilization can be made without the step using a plasma torch with adequate input power and feedstock flow rate and the possibility of combustion promotion through intensified eddy diffusivity by two or more plasma jets arranged in series downstream of fuel injection.

REFERENCES

1. Weinberg, F. J., "Electrical Discharge—Augmented Flames and Plasma Jets in Combustion," Chapter 5 in *Advanced Combustion Methods*, Academic Press, New York, 1986, pp. 277–330.
2. Kimura, I., Aoki, H., and Kato, M., "The Use of a Plasma Jet for Flame Stabilization and Promotion of Combustion in Supersonic Air Flows," *Combust. Flame* 42:297–305 (1981).
3. Northam, G. B., McClinton, C. R., and O'Brien, W. F., "Development and Evaluation of a Plasma Jet Flameholder for Scramjets," AIAA Paper 84-1408, June 1984.
4. Barbi, E., Mahan, J. R., O'Brien, W. F., and Wagner, T. C., "Operating Characteristic of a Hydrogen-Argon Plasma Torch for Supersonic Combustion Applications," *J. Propulsion Power* 5(2):129–133 (1989).
5. Wagner, T. C., O'Brien, W. F., Northam, G. B., and Eggers, J. M., "Plasma Torch Igniter for Scramjets," *J. Propulsion Power* 5(5):548–554 (1989).
6. Sato, Y., et al., Masuya, G., et al., and Kimura, I., "Effectiveness of Plasma Torches for Ignition and Flameholding in Scramjet," *J. Propulsion Power* 9(4):883–889 (1992).
7. Masuya, G., et al., Sayama, M., et al., and Kimura, I., "Some Governing Parameters of Plasma Torch Igniter/Flameholder in a Scramjet Combustor," *J. Propulsion Power* 9(2):176–181 (1993).
8. Baldwin, B. S. and Lomax, H., "Thin Layer Approximation and Algebraic Model for Separated Turbulent Flows," AIAA Paper 78-257, Huntsville, AL, 1978.
9. Uenishi, K., Rogers, R. C., and Northam, G. B.,

"Three-Dimensional Computations of Transverse Hydrogen Jet Combustion in a Supersonic Airstream," AIAA Paper 87-0089, January 1987.

10. Evans, J. S. and Schexnayder, C., Jr., "Influence of Chemical Kinetics and Unmixedness on Burning in Supersonic Hydrogen Flames," *AIAA J.* 18:188–193 (February 1980).
11. Figueira, L. F., and Deshaies, B., "The Influence of Equivalence Ratio and Sorêt Effect on the Ignition of Hydrogen-Air Mixtures in Supersonic Boundary Layers," *Proceedings of the 24th Symposium (International) on Combustion,* The Combustion Institute, Pittsburgh, 1994, pp. 29–36.
12. Karagozian, A. R. and Nguyen, T. T., "Effects of Heat Release and Flame Distortion in the Transverse Fuel Jet," *Proceedings of the 21st Symposium (International) on Combustion,* The Combustion Institute, Pittsburgh, 1986, pp. 1271–1279.

Twenty-Sixth Symposium (International) on Combustion/The Combustion Institute, 1996/pp. 2949–2956

EXPERIMENTAL INVESTIGATION OF A SCRAMJET MODEL COMBUSTOR WITH INJECTION THROUGH A SWEPT RAMP USING LASER-INDUCED FLUORESCENCE WITH TUNABLE EXCIMER LASERS

R. HÖNIG, D. THEISEN, R. FINK, R. LACHNER, G. KAPPLER AND D. RIST
Technische Universität München
Lehrstuhl für Flugantriebe
Munich, Germany

P. ANDRESEN
Universität Bielefeld
Lehrstuhl für angewandte Laserphysik
Bielefeld, Germany

Tunable excimer lasers are used to obtain two-dimensional images to study the nonreacting and reacting flow field of a hydrogen-fueled SCRAMJET model combustor with underexpanded $Ma = 1.6$ injection in the base of a swept ramp. The rectangular combustion chamber consists of an exchangeable injection module and a 3° divergent expansion duct, both with optical access from all sides at different axial locations. The inlet conditions of the vitiated $Ma = 1.9$ airflow are $T = 850$ K static temperature at a pressure of 0.96 bar. Therefore, self-ignition of the injected hydrogen mixed with air is possible but was not reached throughout the whole flow field. As an alternate solution, shock-induced ignition by an oblique shock generated by a small wedge fixed at the upper wall of the combustor has been investigated.

The spatial structure of the flow field is characterized by relative distributions of different species. Measurements of natural fluorescence of OH and laser-induced predissociative fluorescence (LIPF) of OH in axial and cross-sectional planes are presented.

The averaged fluorescence distributions turned out to be highly reproducible and illustrate clearly the gasdynamical features of the flow field, as well as the highly three-dimensional mixing process by vorticity generated by the swept ramp in flow direction. Furthermore, ignition and mixing were improved significantly by the oblique shock wave generated by the additional wedge.

Introduction

Research has been conducted for a number of years in several laboratories around the world to develop a hydrogen-fueled supersonic combustion ramjet (scramjet) for propelling an aerospace transport system at hypersonic speed [1]. To gain maximum thrust, complete fuel-air mixing and fuel-chemical energy release must be achieved during the very short residence time within the combustor and, at the same time, losses caused by injection, mixing, and combustion of the fuel must be kept to a minimum. Therefore, a considerable number of advanced injection and mixing techniques [2] have been proposed and investigated in experimental and theoretical studies. Vortex-enhanced mixing involves the use of vortices in the flow direction generated by free stream spilling around an unswept or swept ramp. The technique has been studied in several works [3,5] and significant mixing enhancement was found with greater vorticity in the flow direction and better mixing for the swept ramp injectors. However, relatively large momentum losses occur with swept ramps.

The research on scramjet combustors motivated the work on new nonintrusive measurement approaches to study the flow field inside of the combustor during operation. As pointed out by Eckbreth [6], laser-based measurement techniques offer many desirable features for the application to combustion diagnostics in supersonic flows. In several studies, the coherent anti-Stokes Raman spectroscopy (CARS) technique was used to obtain instantaneous and averaged point temperatures and to measure hydrogen and water steam mass fractions in the reacting flow field [7,8]. Furthermore, the spontaneous Raman scattering technique was used by Kasal and Algermissen [9] to find point temperatures in a supersonic hydrogen-air diffusion flame.

To overcome the problem of point measurements in turbulent flames and to prevent low Raman signal levels and the very intensive computation for CARS data reduction, two-dimensional imaging techniques based on laser-induced fluorescence excitation have

been studied extensively and developed during recent years [10,11]. Although quantification of LIF results is difficult because of quenching problems, the proposed LIF approaches have been applied successfully to a wide range of combustion systems. LIF measurements for scramjet combustor development have been performed mainly in cold flow studies, especially using iodine tracer molecules (LIIF technique) [12–16], and in the reacting flow of shock tubes [17–19]. The swept ramp injector was studied by Hartfield et al. [16] in a $Ma = 2.0$ and $Ma = 2.9$ nonreacting flow. Injection concentration measurements, conducted in cross-flow planes with the LIIF method, clearly illustrated the domination of the mixing process by vorticity generated by the swept ramp in flow direction.

In this paper, we report an investigation of the swept ramp injector concept in a reacting flow field of a hydrogen-fueled supersonic model combustion chamber at $T = 850$ K static temperature and $p = 0.96$ bar static pressure airflow inlet conditions. To visualize the structure of the flame and the distribution of OH, we used natural fluorescence (without laser excitation) and different laser-induced predissociative fluorescence (LIPF) excitation/detection schemes.

Detection Schemes

To perform these measurements with only one experimental setup, we used the UV-LFP (UV laser flash photography) approach based on tunable excimer lasers and intensified, gated cameras as discussed by Koch et al. [20]. In general (except for the natural fluorescence), the laser beam is expanded by cylindrical lenses to a light sheet that crosses the flow field in the plane of interest.

The various subsequent emissions from this area are imaged on a highly sensitive, fast-gated camera system. Spectral filtering of the emissions and state selective excitation in the case of LIF allows us to determine the structure of the flame and the spatial distributions of OH. Details of the different detection schemes are discussed elsewhere [20,21]. In the following section, we briefly summarize these approaches.

Spontaneous emission of OH molecules $A^2\Sigma^+(v' = 0, 1) \rightarrow X^2\Pi(v'' = 1, 0)$, excited by previous collisions or chemical reactions (natural fluorescence), was used to obtain the instantaneous flame structure (reaction zone and postcombustion zone) within the combustion chamber. To suppress unwanted emissions from other sources, a Schott UG-11 filter with maximum transmission wavelength around 325 nm and a bandwidth of 150 nm was mounted in front of the camera. The imaging time was 0.1 ms.

For species and quantum state selective detection with the laser-induced fluorescence approach, the pulsed excimer laser has to be tuned to resonantly excite a particular electronic transition of a molecular species present in the flow. The excited molecules may undergo subsequent processes such as stimulated emission; rotational, vibrational, and electronic energy transfer; predissociation; and a fraction of the laser-populated upper state decays by spontaneous emission of a photon from an upper to a lower energy level.

Hydroxyl-Radical

Laser-induced fluorescence of OH is performed using 248 nm KrF-excimer-laser light to excite the strongest line within the tuning range, $A^2\Sigma^+(v' = 3) \leftarrow X^2\Pi(v'' = 0), P_1(8)$ ($\upsilon = 40296.25\ \mathrm{cm}^{-1}$). The excited molecules predissociate with the rate $P \approx 10^{10}\mathrm{s}^{-1}$ [22], whereas the quench rate at atmospheric pressure is about $Q \approx 0.5 \cdot 10^9\mathrm{s}^{-1}$ [23,24]. Therefore, only 5% of the excited molecules are influenced by quenching, and the OH-LIPF signal can be considered "quench free" at atmospheric pressure. An additional advantage of the probed $v'' = 0$, $J'' = 8$ state is that its population fraction shows only a small temperature dependence within typical flame conditions. The upper-state fluorescence was detected broadband via a Schott UG-11 transmission filter. Subsequent studies showed that it is better to detect only the fluorescence via the (3–2) band to keep the systematic error low, which is caused by vibrational energy transfer in the excited state to nonpredissociative levels ($v' = 2, 1$). To record the emission of the (3–2) band, a combination of three filters has to be set up in front of the recording camera (1 × UG 11, 2 × 290/45°). Hence, a bandwidth of about 20 nm is achieved [20].

Experimental Apparatus

Model Combustion Chamber

A complete schematic of the scramjet model combustor is given in Fig. 1. The gas flows from left to right. Vitiated air ($T_t = 1375$ K, $p_t = 6.7$ bar) expands in a two-dimensional Laval nozzle and enters the combustor at a Mach number of $Ma = 1.9$, a static temperature of $T = 850$ K and a static pressure of 0.96 bar. The rectangular combustor (inlet cross section 30 × 35 mm^2) consists of an exchangeable injection module ($l = 165$ mm) and a 3° divergent expansion duct ($l = 830$ mm), both with optical access from all sides at different axial locations. The complete structure is not cooled, which limits the burning time of the combustor to about 15 s.

Details of the injection module and the swept ramp are shown in Fig. 2. The geometry of the ramp is similar to that of Ref. 3 (ramp angle: $\phi = 11°$, ramp width at the end of the injector block: $b = 10$

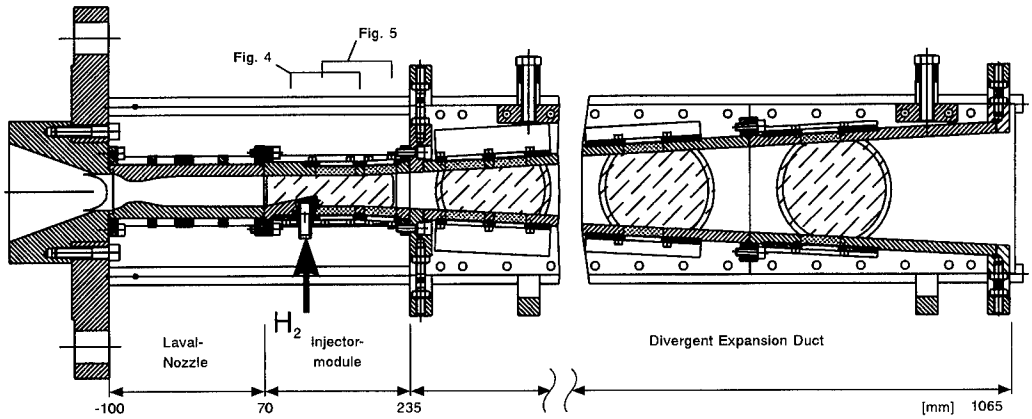

FIG. 1. Schematic of the scramjet model combustion chamber.

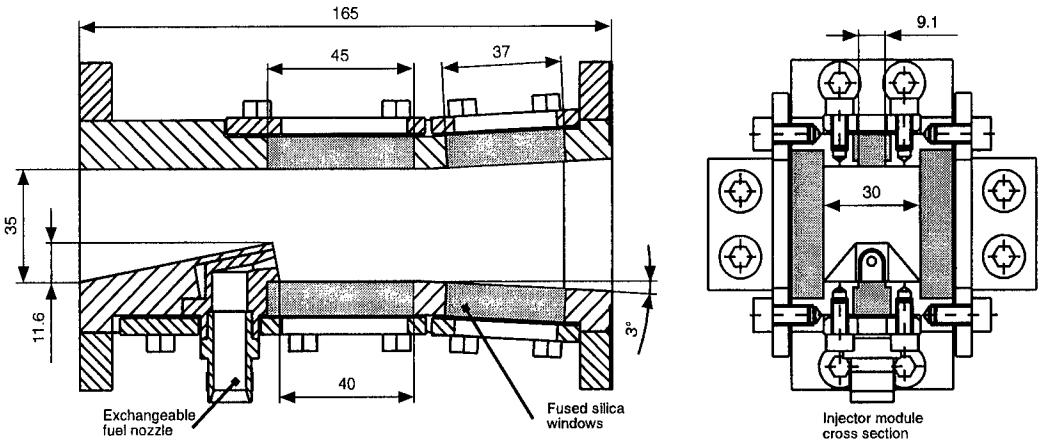

FIG. 2. Schematic of the injector module with the swept ramp and exchangeable fuel injector nozzle.

mm), but the injector nozzle, which is integrated in the ramp, can be replaced to investigate different injection Mach numbers. In all experiments reported in this paper, hydrogen was injected at a Mach number of $Ma_{H_2} = 1.6$, but the total hydrogen pressure p_{t,H_2} has been varied from $4.5 \leq p_{t,H_2} \leq 35$ bar to vary the expansion and the equivalence ratios.

LIF/LIPF Setup

Figure 3 shows a schematic of the LIF/LIPF arrangement used for two- dimensional concentration and temperature measurements. Frame-averaged concentration measurements are discussed here; for detailed information regarding temperature measurements, see Ref. 31. A tunable excimer laser (1) (Lambda Physik EMG 150 T-MSC) is used to produce a 25 × 5 mm laser beam (2) at the KrF transitions (~248 nm). The pulse duration is 20 ns, and its energy is about 250 mJ. The beam passes a calibration section (3–4), some plane mirrors (5), cylindrical lenses to form the laser sheet (6), an adjustable slit (7) 0.5 to 2 mm wide and 25 mm in length, and finally enters the test section as a sheet with the slit dimensions. The laser sheet passes through the combustion chamber (8) from bottom to top or vice versa to get additional information of laser beam absorption. The induced light emissions from the area of interest (see the shaded area in Fig. 3) leave the test section through the side windows. The light emissions to be imaged are, if necessary, filtered with a combination of dielectrically coated mirrors (9) and additional transmission filters (9) (see section on "Detection Schemes") to reduce scattered light at the laser wavelength. The two-dimensional fluorescence distributions are imaged onto a photometric digital camera (11) (LaVision Flamestar II) via a 105 mm f/4.5 Nikkor UV lens (10). The Flamestar

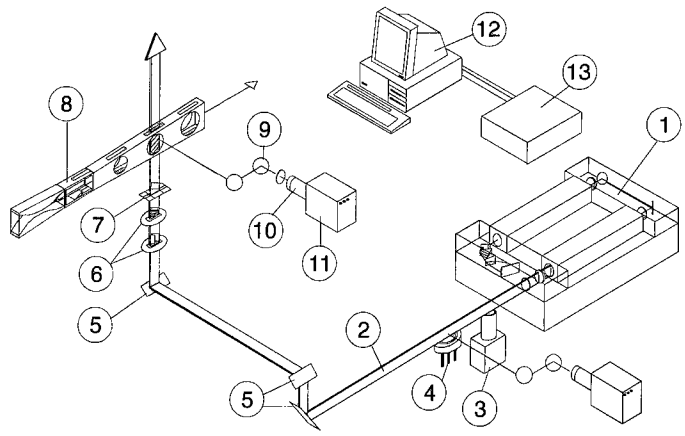

FIG. 3. Overall schematic of the LIF setup for two-dimensional imaging.

camera system consists of a UV-sensitive high–gain-image intensifier (S20 photocathode, P20 phosphor) fiber optically coupled with the CCD chip (Thomson TH7863). The intensifier is gated for 50 to 500 ns after each laser pulse to suppress unwanted natural fluorescence. The resulting grayscale pictures are digitized, stored in a computer (12), and presented in false colors on an on-line monitor. Triggering the laser and the photometric cameras and controlling the step motor to tune the laser frequency are done by a programmable input/output card of the system computer and an external camera multiplexer (13).

For measurement of spatial, state-selective density distributions of OH in the reacting flow field of the combustion chamber, fluorescence images at three different locations along the central plane and in selected cross sections of the chamber were recorded. Cross-sectional images were obtained by orienting the laser sheet perpendicular to the flow direction. The image was viewed through the same side window through which the light sheet passed. The viewing angle of the camera was set to 35° relative to the plane of the laser sheet. Distortion of the aspect ratio of the images was corrected by a horizontal spreading of the digitized images. To realize a short overall measurement time, the laser beam forming optics together with the complete detection system are mounted on a movable device, driven by a computer-controlled step motor. One set of pictures was recorded with the laser tuned to excite a specific molecule (on resonance); a corresponding set was taken with the laser tuned off resonance to quantify the noise level. The off-resonance pictures were subtracted from the on-resonance ones. In addition, a laser-beam profile correction was done for every image. Typical on/off-resonance ratios are in the order of 2.5–4.5, depending on the flame zone and the species under investigation. No attempt was made to correct the images for the Beer's absorption law of the laser beam within the combustion chamber.

Results and Discussion

All images printed in this paper are presented in color scale pictures with intensity levels according to the scale given beneath the image. The pictures are recorded with 12-bit accuracy (0 to 4095 counts), and a chosen intensity range is displayed in 64 colors. Lower and higher intensities are grouped together in one color.

Ignition and Flame Stabilization

The air supply of the test rig simulates flight Mach numbers with static temperatures at the entrance of the combustor, where self-ignition of the hydrogen-air mixture may occur but cannot be guaranteed. To investigate the ignition behavior and the flame stability we recorded the spontaneous emission of OH (without laser excitation) through a side window of the injector module with the procedure described in the previous section. A typical picture, averaged over 10 images, is given in Fig. 4.

The figure clearly illustrates that at the given flow conditions with this geometry, flame stabilization was only possible in a limited area behind the ramp close to the wall boundary layer, where residence time is long enough to heat up the gas mixture sufficiently and to allow flame stabilization. But heat release from this pilot flame seems to be too small to ignite the bulk flow. Furthermore, the high hydrogen heat capacity and its low static temperature at the exit of the fuel Laval nozzle ($T_{H_2,Ex}$ = 195 K) are detrimental to ignition.

To improve the ignition process, the hydrogen temperature could be increased (e.g., with a catalytically induced hydrogen precombustion within a prechamber of the hydrogen supply line) or the temperature of the hydrogen-air mixture could be discontinuously increased by an oblique shock [25–27]. To realize the so-called *shock-induced ignition,* a small symmetric wedge (wedge angle 14.9°) was

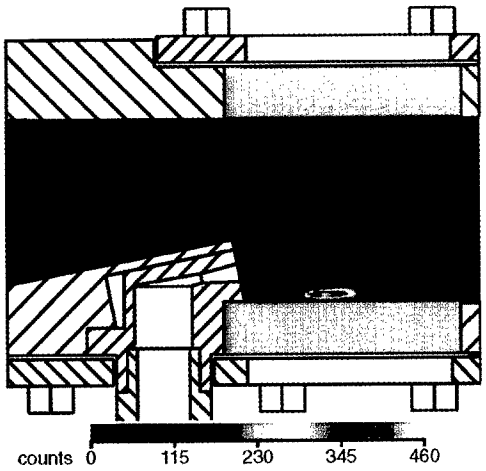

FIG. 4. Flame structure, obtained after self-ignition of the hydrogen-air mixture, as observed through the side window of the injector module (p_{0,H_2} = 30 bar, ϕ = 0.5). The picture is averaged over 10 images of the spontaneous emission of the OH molecules (without laser excitation). The emission intensities are encoded according to the color scale given beneath the image.

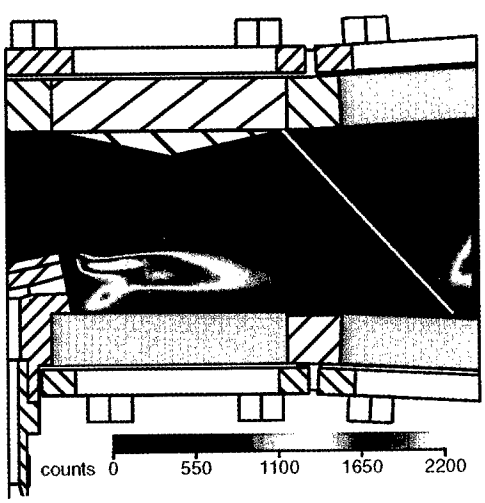

FIG. 5. Flame structure, obtained after shock-induced ignition of the hydrogen-air mixture, as observed through the side window of the injector module (p_{0,H_2} = 28 bar, ϕ = 0.45). The picture is averaged over 10 images of the spontaneous emission of the OH molecules (without laser excitation). The emission intensities are encoded according to the color scale given beneath the image. The solid line superimposed on the OH image shows the calculated oblique shock (angle of 62°) at the end of the ramp.

mounted at the top of the model combustor, as illustrated in Fig. 5.

This modification changed the character of the flow significantly and improved the ignition behavior. The subsonic flow passing the injection ramp is accelerated by the wedge, which changes the main flow cross section and acts as a convergent-divergent nozzle.

In correlation to the expansion cross-section ratio A/A_{min} of the rear end of the wedge, the flow attains a Mach number in the range of 1.58 to 1.60. At this Mach number, the edge at the wedge end generates an oblique shock with an angle of 61 to 64°. We superimposed a solid line (angle 62°) on the OH image in Fig. 5. This calculated trajectory matches the recorded picture quite well.

This simple analysis of the upper region of the flow mainly influenced by the wedge helps in understanding the flow physics concerning the observed oblique shock but does not take into account any of the following relevant facts: the three-dimensional and highly turbulent flow field caused by the swept ramp, such as the expansion at its end, the boundary layers, and the interaction of the oblique shock with the bottom wall of the combustor. Also, its reflection and the heat-release impact by the combustion process on the flow may be relevant. Complex computation would be necessary for a precise prediction of the flow field.

For these reasons, the various mechanisms improving the ignition behavior cannot yet be determined exactly. The flow speed at the ramp end is certainly lower (subsonic) compared to the combustor setup without the wedge. The oblique compression shock and its reflection raises the static temperature and improves mixing by its interaction with the boundary and shear layers. We think that both aspects are responsible for the observed ignition and stability improvement.

The diffusion flame could now be ignited and stabilized in a wide range of equivalence ratios ($0.07 \leq \Phi \leq 0.6$). The maximum equivalence ratio was restricted to limit the thermal load of the chamber. Details of the flame structure within the model combustor are given in Fig. 5. The flame root is attached behind the ramp with very high signal levels at 10–15 mm downstream of the injector. Further downstream, the flame is quenched because of the temperature decrease caused by the flow expansion behind the edge of the wedge. The high signal levels on the right side of the measurement field indicate that the oblique shock, starting at the end of the wedge, and its reflection at the bottom wall relight the flow. Figure 5 also reveals that the flame is lifted from the lower wall. This is in accordance with the predictions of Drummond et al. [4] and Riggins et al. [5], who performed CFD calculations of the reacting flow field behind the swept ramp and found a significant lift of the vortex structure.

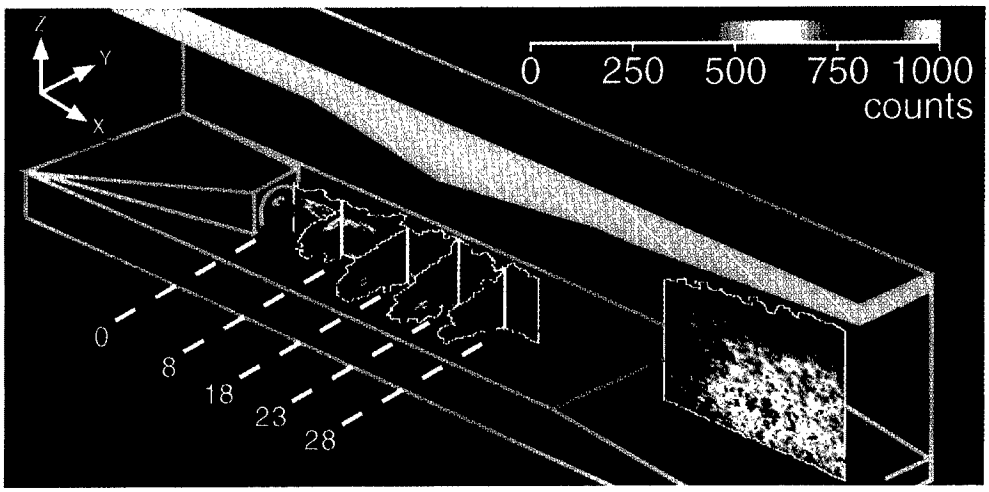

FIG. 6. Spatial flame structure within the injector module, indicated by the distribution of the OH molecules detected by LIPF (p_{0,H_2} = 29.5 bar, ϕ = 0.48). The images are averaged over 50 laser shots. The emission intensities are encoded according to the color scale given beneath the image.

Fuel-Air Mixing

To study the three-dimensional hydrogen-air mixing process of the swept ramp injector, fuel concentration profiles have to be determined in axial and in cross-sectional planes. Because two-dimensional LIF imaging of hydrogen is not practicable due to the rather high excitation energy needed for this two-photon process [28], it is more useful to perform an indirect detection (e.g., by NO doping of the fuel or air [19]). An application of this technique to the present combustor was impossible because of the strong influence of NO doping on ignition and burning characteristics of the hydrogen flame. This observation is confirmed by the results of Laster and Sojka [29], who found that an addition of 0.5 vol. % NO reduced the ignition delay time of a stoichiometric hydrogen-air mixture at a pressure of 2 bar and a temperature of 917 K by a factor of 4. On the other hand, information on the macroscopic mixing process can also be derived from the spatial flame structure. As one of the most important combustion intermediates, the OH molecule indicates the combustion zone and should therefore be detected. The OH distribution in the central axial plane of the flow, as well as in four cross-sectional planes, was recorded with LIPF. The combination of these images results in a three-dimensional map of the flame structure, shown in Fig. 6.

According to Fig. 6, the OH distribution in the central axial plane shows high signal levels in the mixing shear layer between the main stream and the flow region behind the ramp. The kernel of the fuel jet with hydrogen concentrations beyond the rich flammability limit is indicated by dark regions in the axial OH distribution. The flame quenching caused by the expansion behind the edge of the wedge starts at about 23 mm downstream of the ramp, and the flame is almost completely extinguished at about 28 mm downstream of the base of the injector ramp. Further downstream, the flame is relighted by the compression shock and the flame fills up more than 85% of the combustor height. This result is remarkable because it demonstrates that the oblique shock impinges the mixing boundary layer and enhances its spreading. Although the exact mechanism of this shock/shear-layer interaction is not clear at present, it seems to be an efficient way to improve the mixing process. Therefore, these results are in accordance with the work of Menon [30], who studied the shock/shear-layer interaction in a flow with helium injection behind a rearward-facing step and found in some cases a spreading that was more than five times the spreading observed without shock impingement.

The cross-section flame shape is characterized by the vortices as early as 8 mm downstream of the injector, and at x = 18 mm the flame zone reaches the combustion chamber side walls. At x = 23 mm, the vortex structure essentially has enclosed the flame contour, but in the upper parts, the vortex is not visible any more because of the previously explained flame-quenching process. At x = 28 mm, the influence of the vortex structure on the mixing process is essentially finished and turbulent mixing starts to become the dominant mixing process.

An overall comparison of the mixing efficiency of the injector configuration investigated in this work (swept ramp with subsequent wedge) with literature data on swept ramps [3–5,16] shows significantly better mixing. This may be caused by combustion-

and shock-generated strong pressure gradients in the flow and increased turbulence-driven mixing. On the other hand, total pressure losses associated with the large vortical-induced mixing and the oblique shocks generated by the wedge have to be considered to assess the quality of this injector design. Investigations concerning these questions still must be done.

Conclusions

The investigation of the reacting flow field of a scramjet model combustor with swept ramp injector by nonintrusive two-dimensional fluorescence measurements is summarized as follows:

1. The structure of the supersonic hydrogen-air diffusion flame, characterized by the spatial hydroxyl-radical distribution, is dominated by the vortical-induced mixing process generated by the swept ramp.
2. Mixing can be further improved by a shock/shear-layer interaction.
3. Overall mixing efficiency of the injector configuration investigated in this work (swept ramp with subsequent wedge) is significantly better than without the wedge. To completely assess the injector design, the total pressure drop must be determined.
4. At $T = 850$ K static combustor inlet temperature without the upper wedge, ignition and flame stabilization could only be achieved in a limited area behind the ramp close to the wall boundary layer.
5. With a channel step generating a recirculation zone combined with system of oblique shocks downstream of the ramp starting at the wedge end, the supersonic hydrogen-diffusion flame can be ignited and stabilized for equivalence ratios ranging from $\phi = 0.07$ to 0.6.

Acknowledgments

This research was supported by the Deutsche Forschungsgemeinschaft under responsibility of the Sonderforschungsbereich 255. The authors wish to thank Dr. M. Valk, now at ABB Baden/Switzerland, for his assistance in preparing and performing these experiments.

REFERENCES

1. Billig, F. S., *J. Propulsion Power* 9:4 (1993).
2. Bogdanoff, D. W., *J. Propulsion Power* 10:2 (1994).
3. Northam, G. B., Greenberg, J., and Byington, C. S., *AIAA/ASME/SAE/ASEE 25th Joint Propulsion Conference,* Monterey, CA, 1989, AIAA-89-2525.
4. Drummond, J. P., Carpenter, M. H., Riggins, D. W., and Adams, M. S., *AIAA/ASME/SAE/ASEE 25th Joint Propulsion Conference,* Monterey, CA, 1989, AIAA-89-2794.
5. Riggins, D. W., Mekkes, G. L., McClinton, C. R., and Drummond, J. P., *28th Aerospace Science Meeting,* Reno, 1990, AIAA-90-0203.
6. Eckbreth, A. C., in *Energy and Engineering Science Series* (Gupta, A. K. and Lilley, D. G. eds.) Abacus Press, Cambridge, MA, 1988, Vol. 7.
7. Eckbreth A. C., Anderson, T. J., and Dobbs, G. M., *Appl. Phys. B* 45 (1988).
8. Anderson, T. J. and Eckbreth, A. C., *AIAA 28th Aerospace Science Meeting,* Reno, 1990, AIAA-90-0158.
9. Kasal, P. and Algermissen, J., *Zeitschrift für Flugwissenschaften und Weltraumforschung* 13 (1989).
10. Hanson, R. K., *Twenty-First Symposium (International) on Combustion,* The Combustion Institute, Pittsburgh, 1986, p. 1677.
11. Hanson, R. K., Seitzman J. M., and Paul, Ph. H., *Appl. Phys. B* 50 (1990).
12. Fletcher, D. G., and McDaniel, J. C., *AIAA J.* 27:5 (1989).
13. Abbitt, J. D., Hartfield R. J., and McDaniel J. C., *AIAA/ASME/SAE/ASEE 25th Joint Propulsion Conference,* Monterey, CA, 1989, AIAA-89-2550.
14. Hollo, S. D., Hartfield, R. J., and McDaniel, J. C., *AIAA 21st Fluid Dynamics, Plasma Dynamics and Laser Conference,* Seattle, 1990, AIAA 90-1632.
15. Hartfield R. J., Jr., Hollo S. D., and McDaniel J. C., *28th Aerospace Science Meeting,* Reno, 1990, AIAA 90-0162.
16. Hartfield R. J., Jr., Hollo S. D., and McDaniel J. C., *AIAA 21st Fluid Dynamics, Plasma Dynamics and Laser Conference,* Seattle, 1990, AIAA 90-1518.
17. Lee, M. P., McMillin, B. K., Palmer, J. L., and Hanson, R. K., *J. Propulsion Power* 8:4 (1992).
18. Allen, M. G., Parker, T. E., Reinecke, W. G., Legner, H. H., Foutter, R. R., Rawlings, W. T., and Davis, S. J., *30th Aerospace Science Meeting,* Reno, 1992, AIAA 92-0137.
19. McMillin, B. K., Palmer, J. L., Seitzman J. M., and Hanson, R. K., *AIAA 31st Aerospace Science Meeting,* Reno, 1993, AIAA-93-0044.
20. Koch, A., Chryssostomou, A., Andresen, P., and Bornscheuer, W., *Appl. Phys. B* 56 (1993).
21. Andresen, P., Meijer, G., Schlüter, H., Voges, H., Koch, A., Hentschel, W., Oppermann, W., and Rothe, E., *Appl. Opt.* 27:2 (1990).
22. Gray, J. A., and Farrow, R. L, *J. Chem. Phys.* 95:10 (1991).
23. Schwarzwald, R., Monkhouse, P., and Wolfrum, J., *Chem. Phys. Lett.* 142:1/2 (1987)
24. Köller, M., Monkhouse, P., and Wolfrum, J., *Chem. Phys. Lett.* 168:3/4 (1990).
25. Suttrop, F., *Jahrbuch 1965 der WGLR* (1965).

26. Bellet, J. C., Donzier, H. P., Soustr, J., and Manson, N., *Fourteenth Symposium (International) on Combustion,* The Combustion Institute, Pittsburgh, 1973, p. 595.
27. Algermissen, J., *Z. Flugwissenschaf. Weltraumforsch.* 10:2, (1986).
28. Okada, T., Maeda, M., Kajiki, Y., Muraoka, K., and Akazaki, M., *Appl. Phys. B* 43 (1987).
29. Laster, W. R., and Sojka, P. E., *J. Propulsion* 5:4 (1989).
30. Menon, S., *AIAA 27th Aerospace Science Meeting,* Reno, 1989, AIAA-89-0104.
31. Hönig, R., Theisen, D., Fink, R., Kappler, G., Rist, D., and Andersen, P., accepted at *Fourth International Symposium on Special Topics in Chemical Propulsion,* Stockholm, Sweden, 1996.

Twenty-Sixth Symposium (International) on Combustion/The Combustion Institute, 1996/pp. 2957–2963

TRANSIENT SIMULATION OF SUPERDETONATIVE MODE INITIATION PROCESS IN SCRAM-ACCELERATOR

JEONG-YEOL CHOI, IN-SEUCK JEUNG AND YOUNGBIN YOON
Department of Aerospace Engineering
Seoul National University
Seoul 151–742, Korea

A numerical study is carried out to examine the detonation-initiation process of a SCRam accelerator operating in superdetonative mode by considering the injection of a high-speed conical projectile from air into a high-pressure combustible mixture. The time-accurate solutions of Reynolds-averaged Navier–Stokes equations for chemically reacting flows are obtained by using the point-implicit method and the upwind-biased third-order scheme.

As a result, two distinctive cases of detonation-initiation processes are observed: a case of unstart by the direct initiation of a detonation and a case of regular ignition to quasi-steady marching. In the former case, which is observed in a $2H_2$ + air mixture, a detonation initiates on the conical nose of the projectile when a projectile is passing through the diaphragm. The interaction between an oblique shock and a moving normal shock could be one cause of the direct initiation of the detonation. After a sufficient duration, a thermal choking condition, which is the cause of a strong drag, is attained by interactions between the shock train and the boundary layer. In the latter case, which is observed in a $2H_2 + O_2 + 5N_2$ mixture, an oblique detonation originates in the shock-impinging region where the preburned hot gas boundary layer and oblique shock interact. After ignition, the oblique detonation propagates forward and settles down on the conical nose. At this stage, the thrust is comparable to the drag, and the projectile moves with nearly constant velocity.

Introduction

For the last decade, there has been much research on the ram accelerator. The ram accelerator is a novel concept using a principle of ramjet propulsion as a propelling mechanism of a projectile in a barrel [1,2]; a combustible gas mixture is compressed by a series of shocks and then generates the thrust force by a high-speed combustion mechanism such as an oblique detonation. Even though there are several modes of ram accelerator operation, typical ones are a thermally choked mode and a superdetonative mode.

In the thermally choked mode, which is adequate for subdetonative operation, many experimental [1,3], theoretical [4,5], and numerical [6,7] studies have been done, and a number of technical advances [8,9] have been achieved in many research facilities. In the superdetonative mode ram accelerator, which is called a SCRam accelerator, the supersonic combustion is accomplished by an oblique detonation on the middle of the projectile and the thrust is obtained by the expansion of the burned gas along the conical, nozzle-shaped tail. However, only a few experimental works [10] have been done in this mode, and the combustion mechanism of the SCRam accelerator remains to be confirmed in spite of many numerical studies [11–19] on the related shock-induced combustion phenomena and the stability of the oblique detonation.

Particularly important, there has not been an intensive study on the ignition process and the resulting unstart phenomena [10] during the injection process from the launcher to the accelerator barrel, which is crucial in determining the operation limit of the SCRam accelerator. Therefore, in this study, the direct initiation of the superdetonative mode operation and its ongoing combustion process were analyzed by carrying out the unsteady Navier–Stokes numerical simulations for a $2H_2$ + air mixture and a $2H_2 + O_2 + 5N_2$ mixture.

Governing Equations

The coupled form of Reynolds-averaged Navier–Stokes equations are considered to analyze the chemically reacting supersonic viscous flow over axisymmetric geometry. The continuity equation is replaced by the species-conservation equations, and the state equation for a mixture of thermally perfect gases is used for pressure evaluation. The temperature is determined from the definition of the total energy by using the Newton–Raphson iteration method. The specific heat of each species is obtained by NASA polynomial data [20]. The mixture viscosity

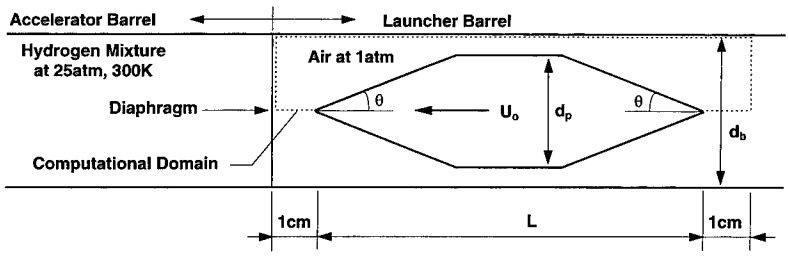

FIG. 1. SCRam accelerator configuration at starting position (U_o = 2500 m/s, L = 22 cm, d_p = 2.8 cm, d_b = 4.0 cm, and θ = 10°; the mass of the projectile is assumed to be 150 g.

and thermal conductivity, as well as the binary diffusivity of species in the gas mixture, are expressed as sums of the laminar and turbulent values. The laminar values of viscosity and thermal conductivity for each species are determined by fourth-order polynomials of temperature that are valid up to the temperature of 6000 K. The mixture viscosity and thermal conductivity are calculated using Wilke's mixing rule [21]. The binary mass diffusivity is obtained using the Chapman–Enskog theory in conjunction with Lennard–Jones intermolecular potential functions, and the diffusion velocities are found by Fick's law for convenience [21].

The hydrogen-air combustion model adopted in the present study is composed of seven species and eight reaction steps. This combustion model is a reduced reaction mechanism that has been used successfully in a number of supersonic reacting flow calculations [11,12,18,19,22]. Because the Reynolds number in the SCRam accelerator is very high, a fully turbulent flow is assumed. The turbulence model used in the present study is the Baldwin–Lomax algebraic eddy viscosity model [23]. This model is chosen for its simplicity and the lack of a sufficiently accurate model for this kind of flow. The constant turbulent Prandtl and Schmidt numbers of 0.9 are assumed to evaluate turbulent thermal conductivity and mass diffusivity. The combustion process in the SCRam accelerator is mainly accomplished by the oblique detonation, and the major viscous effects are observed at the burned gas region in which the chemical reaction is already completed. Therefore, the interactions between turbulence and chemistry are not considered in the present study since the analysis requires the direct numerical simulation or the closure of a reaction source term using the probability density function that is not yet applicable to this kind of complex flow.

Numerical Methods

The LU-SSOR fully implicit method [24] is adopted for the calculation of the steady state solution, which is used as an initial condition for the transient calculations, with the local time-stepping technique for fast convergence. For transient calculations, the governing equations are temporally integrated by the point-implicit method. In most of the cases, the time step is set to a constant value of 6.15 ns, which corresponds to the CFL number 0.5 based on the minimum grid size. The finite volume method is used for spatial discretization. The convective fluxes are formulated using Roe's FDS (flux difference splitting) method with the entropy-fixing function for the stability problem. The complete formulation of Roe's FDS method for multispecies chemically reacting flow is based on the method of Grossmann and Cinnella [25] and extended to the two-dimensional curvilinear coordinate. The MUSCL (monotone upstream method for scalar conservation law) variable extrapolation approach is used with a minmod limiter to get a high-order spatial accuracy and the TVD (total variation diminishing) property [26]. The general central difference scheme is used for viscous terms.

The numerical method used in this study was validated by performing a number of numerical simulations for the cases in which experimental data exist, such as shock-induced combustion around a blunt body and shock-boundary layer interaction problems. The comparison of the result with experimental data showed a very good agreement.

Computational Domain and Space Marching

To simulate the injection process of the SCRam accelerator projectile from air into the high-pressure mixture, the SCRam accelerator configuration, as shown in Fig. 1, is considered. It is composed of a projectile and a barrel that is divided into launcher and accelerator parts by a diaphragm. The projectile body diameter is 2.8 cm, the body length is 22 cm, and the barrel diameter is 4.0 cm. The nose and the tail of the projectile have a symmetric shape with a half angle of 10°. The launcher is filled with 1 atm air, and the accelerator is filled with a 25 atm hydrogen-oxidizer mixture maintained at 300 K. For the present simulation, two kinds of mixtures are

considered: $2H_2$ + air(O_2 + $3.76N_2$) and $2H_2$ + O_2 + $5N_2$.

The computational domain for the current simulation is extended by 1 cm before and after the projectile, and it is covered by the 400 × 60 computational grid that is uniformly distributed in axial direction and clustered to both walls in radial direction. The no-slip boundary condition is applied at the projectile surface and the barrel wall. The solid surfaces are assumed to be kept at the constant temperature of 600 K. The zero-order extrapolation is used for outflow boundary, and the symmetric condition is used at the axis of symmetry. For the transient simulation, the steady-state solution is obtained for 1 atm, 300 K air at the velocity of 2500 m/s and is used as an initial condition. The prior steady-state condition corresponds to inflow Mach number 7.19 and Reynolds number 1.49×10^8/m. The projectile velocity of 2500 m/s is regarded as a reasonable value for the superdetonative operation of the ram accelerator because it is 20% to 30% in excess of the Chapman–Jouguet (CJ) detonation velocities. The calculated CJ velocities are 2050 m/s for a $2H_2$ + air mixture and 1920 m/s for a $2H_2$ + O_2 + $5N_2$ mixture at 300 K and 25 atm.

For the transient simulation, the mixture condition is imposed at computational cells between the inflow boundary and the diaphragm. In the fixed coordinate, the diaphragm is positioned initially at the inflow boundary that is located 1 cm in front of the projectile nose. The diaphragm is artificially moved at the projectile velocity and is assumed to be broken down suddenly when it reaches the projectile nose. The projectile moves with the velocity variation until it advances a sufficient distance.

During the calculation, computational domain moves at the projectile velocity, which varies with the acceleration of the projectile. Conversely, the projectile is fixed at the computational domain. At any instance, the velocity variation Δu of the projectile is determined by Δt × acceleration and is imposed on all the computational grid points to consider the variations of axial velocity and the total energy. The force acting on the body is evaluated by integrating the pressure and the wall shear stress over the projectile surface. The acceleration of the projectile is obtained from the force divided by the projectile mass of 150 g, which is comparable to the one used in the experiment of ISL [10].

Unstart by the Direct Initiation of Detonation

For understanding the ignition process involved in the injection process from the launcher barrel to the accelerator barrel, numerical simulations are performed for the two mixtures as mentioned previously. Figure 2 shows a result for the stoichiometric $2H_2$ + air mixture, which is considered an erergetic mixture. The upper parts of the plots are the temperature distributions in degrees Kelvin and the lower parts are the pressure distributions with a unit of the atmospheric pressure, unless otherwise specified. The plots are arranged in sequence and are magnified by a factor of 2 vertically for clarity. The spatial position denoted by x_p is the projectile flight distance from the diaphragm.

At the instance of $x_p = -0.5$ cm, shown in Fig. 2a, the diaphragm is marked as a stiff pressure gradient in front of the projectile nose. Because the projectile moves only 0.5 cm from the initial state, the result is nearly the same as that of steady solution for air. A thin thermal boundary layer is formed on the body surface, and a high-temperature and high-pressure region exist at the shock-impinging point on the middle surface of the body. Just after the diaphragm breakdown, a normal shock develops and moves downstream with a following contact discontinuity and expansion waves, as shown in Fig. 2b. Although there is not any evidence of detonative ignition at this point, a bubble of detonation appears at the projectile nose after the passage of the normal shock system, which is composed of the normal shock, the contact discontinuity, and the expansion waves. Then, the bubble of detonation grows very rapidly in the radial and downstream direction. Finally, the detonation catches up with the normal shock, although it cannot expand upstream because the projectile velocity is 22% higher than that of the CJ detonation velocity. This expansion process is plotted in Figs. 2c through 2e. At this stage, the high drag force begins to act on the body because of the high-temperature and high-pressure region inside the bubble. But the drag force is limited to a small value because it acts only on the central portion of the body. The acceleration profile is plotted in Fig. 3.

As the bubble of detonation expands, a bow shock is reflected on the barrel wall and this reflection procedure is repeated on the body surface. This process is plotted in Figs. 2f through 2h. At the same time, the normal detonation propagates downstream and catches up with the nonreacting normal shock. After this shock–shock interaction, the preceding normal shock is left as a following contact surface while the normal detonation moves downstream. At this stage, a drag, which acts as a reverse thrust force, increases enormously because the high-pressure burned gas occupies all the frontal area of the body, and the projectile velocity begins to drop sharply, as shown in Fig. 3.

Thereafter, the shock reflection procedure is repeated several times until the regular pattern of the shock train is formed between the body and the wall. During this shock-train forming period, the magnitude of the acceleration is maintained at the value of about 1.5×10^4 g for a sufficient time, although the acceleration shows an oscillatory behavior because of the variation of the shock-impinging points

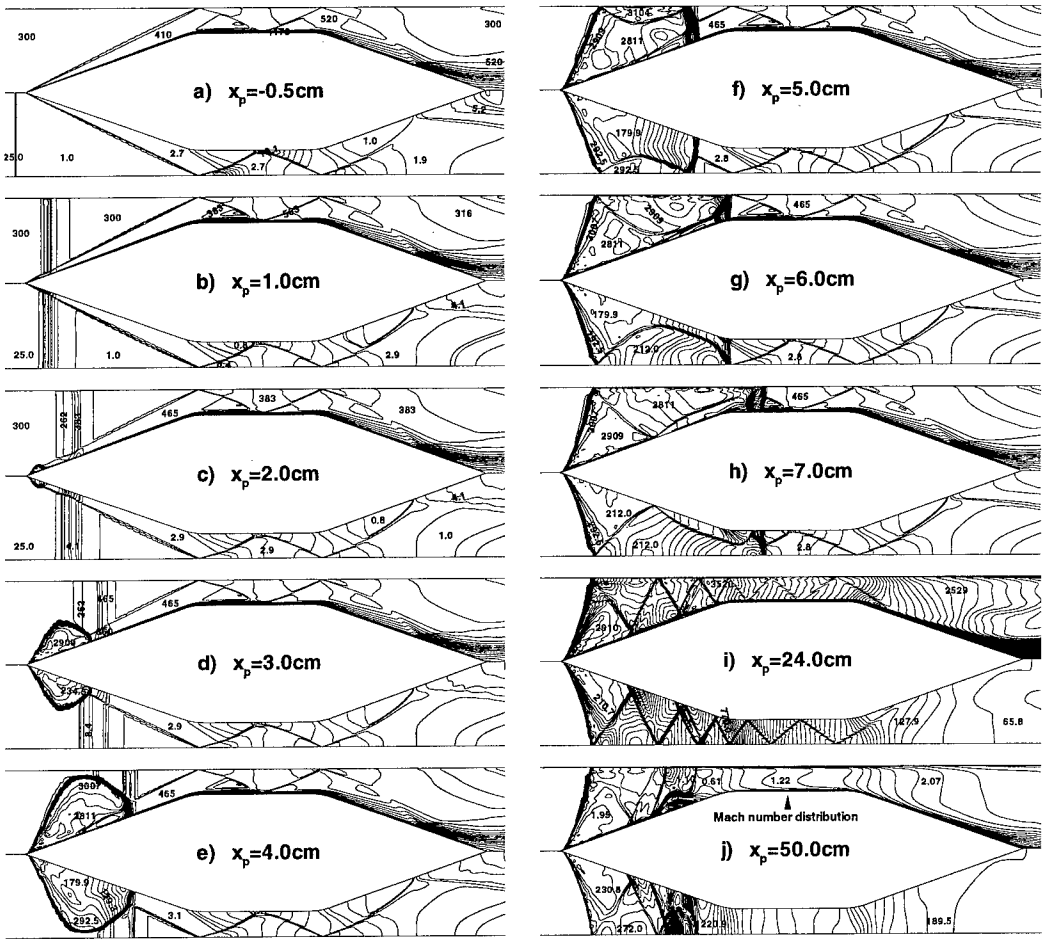

FIG. 2. Temperature distributions (upper half of each figure) and pressure distributions (lower half of each figure) in marching sequence for a $2H_2$ + air mixture. Mach number distribution is plotted for the case of x_p = 50.0 cm. The plots are magnified vertically by a factor of 2 for clarity.

on the conical nose and tail. It is noted that the numbers of the shock-impinging points as shown in Fig. 2i and the number of the bumps in the acceleration curve are approximately the same up to x_p = 24.0 cm. The sharp decrease of the projectile velocity is comparable to the experimental result of the unstart case, which is measured by Smeet et al. [10], even though the present numerical results correspond to the earlier stage of their experimental result.

It is observed that the slope of the oblique detonation attached at the nose is curved outwardly and is followed by the expansion waves. The axisymmetric effect may be the reason that such a trend could not be found from the two-dimensional simulations performed by Li et al. [17]. The slope of the oblique shock in the burned gas region is much stiffer than that in airflow, because the flow Mach number is low due to the high sonic velocity in this region, even though the magnitude of flow velocity keeps the same order of magnitude.

On the other hand, the strong shock/boundary-layer interactions (denoted as SBLI hereafter) are observed at the three shock-impinging points on the conical nose. No severe SBLI is observed after these impinging points. Significantly, the interaction is strongest at the second impinging point and is enough to generate the separation bubble and a pair of the oblique shocks around the impinging point. Such a strong SBLI is very important because the separation bubble grows in the burned gas region because of severe aerodynamic heating. The growth of the bubble leads to a large subsonic high-temperature region and separates a pair of the oblique shocks that interact. As time goes on, the severe shock–shock interactions and shock/boundary-layer interactions are repeated and form the strong

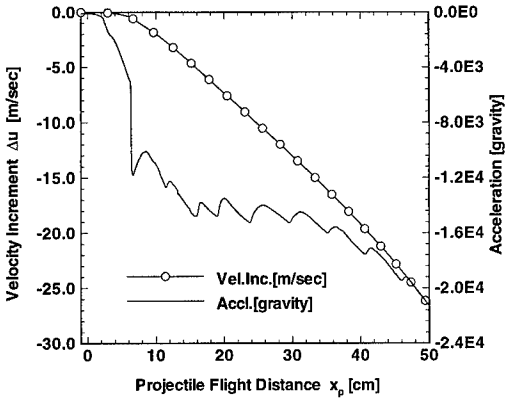

FIG. 3. Variation of velocity and acceleration along the barrel for a stoichiometric H_2 air mixture.

oblique shock ahead of the large separation bubble as shown in Fig. 2j. Finally, the thermal choking condition is provided by a strong shock in the back of the separation bubble, shown in the Mach number distribution of Fig. 2j. The thermal choking produces a severe drag force and makes the velocity of the projectile drop rapidly.

The direct ignition of detonation by the rush of a high-speed body into a reactive mixture has not been analyzed previously, even though such a phenomenon could be expected to exist and considered as a cause of SCRam accelerator unstart. The reason for the spontaneous ignition can be explained as follows. When the normal shock propagates downstream followed by contact discontinuity and expansion waves, the temperature of the region between the shock and the contact discontinuity rises up to about 60% higher than that of initial states. The temperature increases again after the interaction between the normal shock and the oblique shock attached on the conical body, even though the pressure rise is not significant. As a result, the chemical kinetic reaction rate increases, and the mixture detonates when the pressure at the nose is increased after the passage of the expansion wave for the cases of reactive mixtures such as the $2H_2$ + Air mixture used in this study.

Regular Ignition to Quasi-Steady Marching

Figure 4 shows the contour plots of a numerical simulation performed for a $2H_2 + O_2 + 5N_2$ mixture that is less energetic than a $2H_2$ + air mixture. Fig. 4a is the result when the projectile breaks through the diaphragm; at this moment, the interaction between the oblique shock and the normal shock system is shown clearly. When the projectile moves 10 cm from the diaphragm, as shown in Fig. 4b, the normal shock system passes the SBLI region and then ignition occurs in the boundary layer. After this stage, the low-pressure burned gas generated in the boundary layer expands downstream with the expansion wave while the normal shock passes through the projectile tail cone. The reflected shock from the barrel wall deflects with a larger angle when it crosses the expanding burned gas boundary. The deflection causes the forward movement of the shock impinging point. On the other hand, the mixture downstream of the impinging point burns more quickly than that in the nose boundary layer because of its compressed condition. This ignition process is shown in Figs. 4c and 4d.

The strong shock impingement forms a new oblique shock at the body surface. The oblique shock interacts with the burned gas boundary to form a normal detonation to the barrel wall, and a strong oblique shock is reflected to the body at the interaction point. At this moment, the expanding burned gas boundary acts as a strong contact discontinuity across which the temperature and density vary severely but the pressure changes negligibly. Although the reaction front downstream of the previous impinging point expands and pushes up the oblique shock, it no longer exists as a reaction front because of the development of the new detonation front. The prior process is shown in Figs. 4d and 4e. This form of interaction is maintained for a long period that is equivalent to the duration of more than a 10-cm projectile advance, until the separation bubble grows enough to make a strong oblique shock ahead of it. The growth of the separation bubble can be recognized by comparing the temperature contours at $x_p = 20.0$ cm and $x_p = 30.0$ cm. In this period, thrust is generated in a regular manner and the projectile velocity increases linearly as shown in Fig. 5. Also, the high-temperature and high-pressure burned gas expands through the conical nozzle and generates the high thrust force that corresponds to more than 5×10^3 g. The thrust coefficient (TC) varies with the acceleration of the projectile because TC is proportional to acceleration and shows a peak value of about 9 when the SCRam accelerator operates in a regular manner.

When the separation bubble is large enough to generate the oblique shock outside the burned gas boundary, the oblique shock is transformed to the oblique detonation and moves forward to the conical nose. Finally, the oblique detonation loads high-pressure force at the conical nose and results in the severe reduction of acceleration to about zero. The oblique detonation is settled down at a specific point on the conical nose after a sufficient move. This process is shown in Figs. 4g through 4i. At $x_p = 50.0$ cm, the regular pattern of the shock train is shown clearly in Fig. 4i, although there still exist strong shock/boundary-layer interactions. However, after a long period, the shock train nearly disappears and the flow field shows a chokedlike behavior as shown in Fig. 4j, even though the choking condition is not

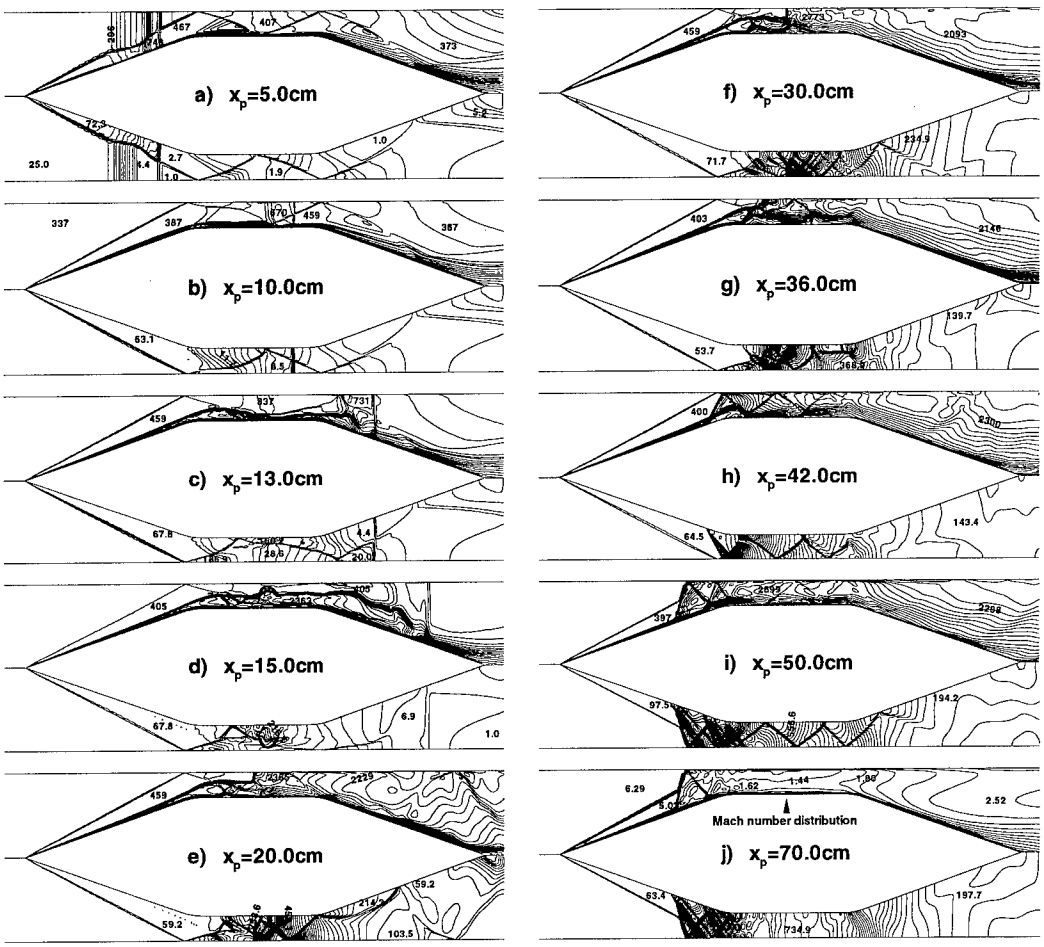

FIG. 4. Temperature distributions (upper half of each figure) and pressure distributions (lower half of each figure) in sequence for a $2H_2 + O_2 + 5N_2$ mixture. Mach number distribution is plotted for the case of $x_p = 70.0$ cm. The plots are magnified vertically by a factor of 2 for clarity.

attained. During this period, the acceleration curve in Fig. 5 shows an oscillatory behavior or a slight increase, resulting in a nearly constant velocity after the projectile advances to 50 cm; the SCRam accelerator operates in a quasi-steady manner.

Conclusion

In this study, transient simulations are performed for the initiation process of a superdetonative mode ram accelerator by considering the injection of the projectile from the launcher into the accelerator barrel. It is observed that there are two kinds of initiation processes for different mixtures: the direct initiation of oblique detonation and the regular ignition to quasi-steady movement. The understanding of the initiation processes of these cases may be important in determining the SCRam accelerator operation limit. For a $2H_2$ + air mixture at 25 atm, the direct initiation of the oblique detonation is observed at the projectile nose.

The interaction between the normal shock and the oblique shock in an energetic mixture is the possible cause of the direct initiation of the oblique detonation. At the final stage, the thermal choking is attained at the back of the separation bubble, which causes the severe deceleration of the projectile. For a $2H_2 + O_2 + 5N_2$ mixture, the regular ignition is observed, which involves complex flow field interactions. However the projectile moves at a quasi-steady manner at the final stage with a balanced force acting on the body, which is caused by the forward movement of the oblique detonation generated by the separation bubble. For the regular operation

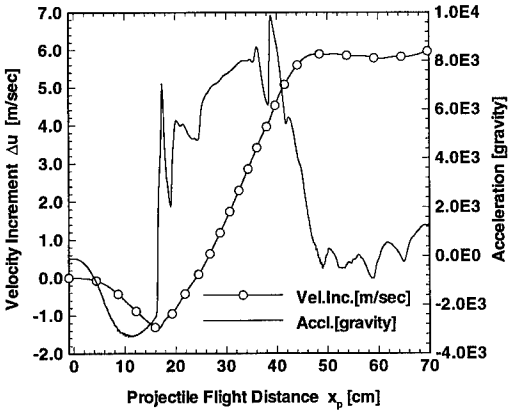

FIG. 5. Variation of velocity and acceleration along the barrel for a $2H_2 + O_2 + 5N_2$ mixture.

of the SCRam accelerator, the evolution of the separation bubble in a burned gas region should be avoided because it may lead to a thermal choking condition or generate and push forward an oblique detonation to the nose.

Acknowledgments

Authors gratefully acknowledge professor Kyung-Kook Cho for his encouragement and enthusiasm. J.-Y. Choi and I.-S. Jeung were partly supported by Turbo and Power Machinery Research Center and Korea Research Foundation.

REFERENCES

1. Hertzberg, A., Bruckner, A. P., and Bogdanoff, D. W., *AIAA J.* 26(2):195–203 (1988).
2. Bogdanoff, D. W., *J. Propulsion* 8(2):481–490 (1992).
3. Bruckner, A. P., Knowlen, C., Hertzberg, A., and Bogdanoff, D. W., *J. Propulsion* 7(5):828–836 (1991).
4. Knowlen, C., Ph.D. Thesis, University of Washington, 1991.
5. Liberatore, F., *J. Propulsion* 11(6):1366–1368 (1995).
6. Nusca, M. J., AIAA Paper 91-2490, 1991.
7. Li, C., Kailasanath, K., Oran, E. S., *AIAA J.* 12(4):807–809 (1996).
8. Bogdanoff, D. W., Knowlen, C., Murakami, D., and Stonich, I., *AIAA J.* 28(11):1942–1944 (1990).
9. Bogdanoff, D. W., *J. Propulsion* 10(4):518–521 (1994).
10. Smeets, G., Seiler, F., Patz, G., and Srulijes, J., *Twenty-Fifth International Symposium on Combustion,* Poster number: P1-56, 1994.
11. Lee, S. H. and Deiwert, G. S., *J. Spacecraft Rockets* 27(2):167–174 (1990).
12. Yungster, S., Eberhardt, S., and Bruckner, A. P., *AIAA J.* 29(2):187–199 (1991).
13. Matsuo, A. and Fujiwara, T., *AIAA J.* 31(10):1835–1841 (1993).
14. Lefebvre, M. H. and Fujiwara, T., *Combust. Flame* 100:85–93 (1995).
15. Pratt, D. T., Humphrey, J. W., and Glenn, D. E., *J. Propulsion* 7(5):837–845 (1991).
16. Power, J. M. and Stewart, D. S., *AIAA J.* 30(3):726–736 (1992).
17. Li, C., Kailasanth, K., and Oran, E. S., AIAA paper 92-0089, 1992.
18. Yungster, S., *AIAA J.* 30(10):2379–2387 (1992).
19. Yungster, S. and Bruckner, A. P., *J. Propulsion* 8(2):457–463 (1992).
20. Gardiner, W. C. Jr., *Combustion Chemistry,* Springer-Verlag, New York, 1984.
21. Bird, R. B., *Transport Phenomena,* Wiley, New York, 1960.
22. Evans, J. S. and Schexnayder, C. J., *AIAA J.* 18:188–193 (1980).
23. Baldwin, B. S. and Lomax, H., AIAA Paper 78-257, 1978.
24. Shuen, S. and Yoon, S., *AIAA J.* 27(12):1752–1760 (1989).
25. Grossman, B. and Cinnella, P., *J. Comput. Phys.* 88:131–168 (1990).
26. Hirch, C., *Numerical Computation of Internal and External Flows,* Vol. 2 Wiley, New York, 1990.

Twenty-Sixth Symposium (International) on Combustion/The Combustion Institute, 1996/pp. 2965–2972

CRITICAL CONDITIONS FOR DETONATION PROPAGATION THROUGH MIXTURE WITH DECREASING REACTION RATE

S. I. KRYUCHKOV, S. B. DOROFEEV AND A. A. EFIMENKO
Russian Research Center, Kurchatov Institute
Kurchatov Square, 123182 Moscow, Russia

A problem of detonation propagation through decreasing reaction rate gradient is examined. To estimate corresponding critical conditions, a simplified problem is considered where the width of reaction zone increases linearly with distance. The stationary solution for this self-similar problem exists only if the gradient of reactivity is below a certain critical value. The critical conditions are found analytically for a one-step Arrhenius kinetic model with large activation energy. The critical gradient is expressed through the characteristic reaction zone width, its dependence on temperature, and thermodynamic properties of the mixture. In the cases of expanding waves (cylindrical or spherical symmetry), superposition of limitations imposed by the gradient and by the wave curvature is observed. The critical gradient decreases with an increase of E_a/T_{0vN} (E_a, activation energy; T_{0vN}, von Neumann temperature for stationary detonation wave) and with the change of the wave symmetry from planar to spherical. Numerical integration of the self-similar system of flow equations for a wide range of E_a/T_{0vN} is presented. The results show that the analytical solution can be applied for moderate values of effective activation energy as well. The critical conditions are also examined by time-dependent numerical simulation. The results are in agreement with the analytical solution if E_a/T_{0vN} is less than 6–8. For higher E_a/T_{0vN}, longitudinal instability of the detonation wave becomes the most important factor.

Introduction

Propagation of explosion waves through a media with decreasing reaction rate can be observed in a variety of situations. One example is detonation propagation through a nonuniform reactive mixture where the concentration distribution is given by the initial conditions. Defining whether the detonation wave will be self-sustained in this situation is important for safety problems. Another example is spontaneous initiation of detonation through the deflagration-to-detonation transition, or turbulent jet initiation, where localized explosion occurs in a nonuniform, partially reacted and/or compressed gas [1–3]. The initial explosion wave, which consists of a leading shock and a reaction front, propagates through the region with decreasing reaction rate from an origin of localized explosion. The characteristic width of the reaction zone should grow continuously with the decrease in reaction rate. Associated energy losses can be responsible for the failure of the wave if the negative gradient in reaction rate is too strong. Corresponding critical conditions have been analyzed numerically in Refs. 4 and 5. Another important feature involved in this process is an expansion of the flow. Continuous diffraction of the wave causes additional energy losses and imposes its own limitations on the ability of explosion wave to be self-sustained. The problem of critical curvature of detonation waves has been studied in Refs. 7–11.

To estimate the critical conditions for a detonation wave transmission through a reactivity gradient, we first consider a simplified problem in which the width of the reaction zone increases linearly with distance. The problem appears to be free of any characteristic length scale. The self-similar nature of this problem makes it possible to study analytically the cases of planar ($j = 0$), cylindrical ($j = 1$), and spherical ($j = 2$) waves. We deduce here an approximate analytical solution for the critical conditions of the planar and curved detonation waves (one-step Arrhenius kinetics with high activation energy is assumed) and compare the approximate analytical solution for critical conditions with the numerical one and with that from the time-dependent numerical simulation. In practical situations, distributions of reaction rate and thermodynamic properties can be arbitrary in space. The more general situation of arbitrary distribution of mixture properties is addressed in the Discussion section.

Basic Equations

We use the Lagrangian description of the gas flow, which emphasizes the self-similarity of the problem at hand. To start, we describe the gas particle motion by the initial distances from a given point (R) and motion as a function of time $r(t)$. With the reactant mass fraction denoted by β, we assume the reaction

rate in a given particle to be described by the following relation:

$$\frac{d\beta}{dt} = -\frac{R_0}{R\tau_0}\beta \exp\left(-\frac{E_a}{T}\right)$$
$$= -\frac{R_0}{R}\frac{1}{\tau_0}\varphi(\beta, T) \tag{1}$$

Here, E_a is the Arrhenius activation energy, T is the temperature (in energy units), and R_0 and τ_0 are numerical constants. Assuming R and t for the independent variables, we obtain the following form of equations for the gas flow (see, for example, Ref. 12):

$$\left(\frac{\partial r}{\partial t}\right)_R = u$$
$$\left(\frac{\partial r}{\partial R}\right)_t = \frac{vR^j}{v_0 r^j}$$
$$\left(\frac{\partial u}{\partial t}\right)_R = -v_0\frac{r^j}{R^j}\left(\frac{\partial p}{\partial R}\right)_t$$
$$\left(\frac{\partial \varepsilon}{\partial t}\right)_R + p\left(\frac{\partial v}{\partial t}\right)_R = 0$$
$$\left(\frac{\partial \beta}{\partial t}\right)_R = -\frac{R_0}{R\tau_0}\varphi \tag{2}$$

Here, u, v (v_0), p, and ε are the radial velocity, specific volume (initial specific volume), pressure, and specific energy of the gas, respectively. We represent the specific energy of the gas in the form $\varepsilon = pv/(\gamma - 1) + \beta q$, where q is the combustion heat and $\gamma = c_p/c_v$ is the ratio of the specific heats at fixed β. The value of γ may depend on β.

Since there is no characteristic length in this problem, it is natural to search for a self-similar solution. Introducing the following dimensionless variables, $\eta = R/Dt$, $\xi = r/Dt$, $U = u/D$, $V = v/v_0$, $P = pv_0/D^2$, $E = \varepsilon/D^2$, and $Q = q/D^2$ (with D as the constant velocity of the detonation wave front and η the only independent variable), we arrive at the following system of equations that describe the gas flow behind the wave front:

$$\eta\xi' = \xi - U$$
$$\xi' = V\left(\frac{\eta}{\xi}\right)^j$$
$$\eta U' = \left(\frac{\xi}{\eta}\right)^j P'$$
$$E' + PV' = 0$$
$$\eta\beta' = B_0\frac{\varphi}{\eta} \tag{3}$$

where $B_0 = R_0/D\tau_0$ and the prime symbol, $'$, denotes differentiation with respect to η.

For the strong detonation wave, these equations have the following initial conditions at $\eta = 1$:

$$\xi(1) = 1$$
$$V(1) = \frac{\gamma - 1}{\gamma + 1}$$
$$U(1) = \frac{2}{\gamma + 1}$$
$$P(1) = \frac{2}{\gamma + 1}$$
$$\beta(1) = 1 \tag{4}$$

The problem has a self-similar solution with η as the independent variable.

When one resolves this system of equations with respect to the derivatives of the dependent variables, the well-known problem [7] of dividing by the zero-valued determinant of the system is encountered. For example, the equation for the V' value is

$$V' = \frac{V\left[\dfrac{j(\gamma - 1)(\xi - U)^2U}{\eta\xi} - \dfrac{B_0\varphi}{\eta^2}\left(Q + PV\dfrac{d(1/(\gamma - 1))}{d\beta}\right)\right]}{(C^2 - (\xi - U)^2)} \tag{5}$$

where $C = \sqrt{\gamma PV}$ is the dimensionless adiabatic sound velocity with the frozen chemical reaction.

Thus, analogous to the standard analysis of the singularity at the sonic point $\bar{\eta}$ (a point where $\bar{C} = (\bar{\xi} - \bar{U})$) [7], the physical solution (with the gas at rest near the origin of the wave) is obtained at the unique value of the parameter $Q = q/D^2$. This solution exists only if the numerator of Eq. (5) is equal to zero at the sonic point

$$\frac{j(\bar{\gamma} - 1)(\bar{\xi} - \bar{U})^2\bar{U}}{\bar{\xi}} = \frac{B_0\bar{\varphi}}{\bar{\eta}}\left(Q + \overline{PV}\frac{d(1/(\bar{\gamma} - 1))}{d\bar{\beta}}\right) \tag{6}$$

The barred terms refer to the parameters evaluated at the sonic point.

It is convenient to find the value of D for such a solution by solving the integrated form of Eq. (3). The resulting appropriate form of mass, momentum, and energy conservation equations are

$$\left[\frac{U-\xi}{V}\right]' = \frac{U-\xi}{V\eta}\left(1+\frac{jU}{\xi}\right)$$

$$\left[\frac{(U-\xi)U}{V}+P\right]' = U\frac{U-\xi}{\eta V}\left(1+\frac{jU}{\xi}\right)$$

$$\left[\frac{U-\xi}{V}\left(E+\frac{U^2}{2}\right)+PU\right]' = \frac{(U-\xi)}{V\eta}$$

$$\left[\left(E+\frac{U^2}{2}\right)+\frac{jU}{\xi}\left(E+\frac{U^2}{2}+PV\right)\right] \tag{7}$$

or in a more simple form,

$$\left[E+PV+\frac{(U-\xi)^2}{2}\right]' = \frac{(U-\xi)^2}{\eta}$$

The integrated form of these equations is correct even through the leading shock of detonation wave. Accordingly, at $\eta = 1$, we can substitute either the values before or after the shock. We prefer here the former assumption for its simplicity:

$$-1-\frac{\bar{U}-\bar{\xi}}{\bar{V}} = \int_{\bar{\eta}}^{1}\frac{U-\xi}{V\eta}\left(1+\frac{jU}{\xi}\right)d\eta$$

$$P_0-\left(\frac{(\bar{U}-\bar{\xi})\bar{U}}{\bar{V}}+\bar{P}\right) = \int_{\bar{\eta}}^{1}\frac{U(U-\xi)}{V\eta}\left(1+\frac{jU}{\xi}\right)d\eta$$

$$\left(\frac{P_0}{\gamma-1}+Q\right)-\left[\frac{\bar{U}-\bar{\xi}}{\bar{V}}\left(\frac{\overline{PV}}{\bar{\gamma}-1}+\bar{\beta}Q+\frac{\bar{U}^2}{2}\right)+\overline{PU}\right]$$

$$= \int_{\bar{\eta}}^{1}\frac{(U-\xi)}{V\eta}\left[\left(\frac{PV}{\gamma-1}+\beta Q+\frac{U^2}{2}\right)+\frac{jU}{\xi}\left(\frac{\gamma PV}{\gamma-1}+\frac{U^2}{2}\right)\right]d\eta \tag{8}$$

or in the other form,

$$\left[\frac{\gamma P_0}{\gamma-1}+Q+\frac{1}{2}\right]-\left(\frac{\bar{\gamma}\overline{PV}}{\bar{\gamma}-1}+\bar{\beta}Q+\frac{(\bar{U}-\bar{\xi})^2}{2}\right) = \int_{\bar{\eta}}^{1}\frac{(U-\xi)^2}{\eta}d\eta$$

The use of condition (6) at the sonic point leads to a particular value of Q. Integration of Eq. (8) is performed over the region with the dimensionless width $\delta = 1-\bar{\xi}$, its actual width growing with time as $l_r = Dt\delta$. The entire region can be treated as a moving body of varying mass. The body accepts mass, momentum, and energy from the incoming gas and loses the properties to the gas that leaves the region at sonic velocity. Also, as we have already seen, actual dimension of this body is growing with time. Contrary to the case of the planar CJ detonations in a homogeneous gas (where the form of the "body" is constant), the growth of the mass, momentum, and energy of the body must be considered in the total balance. This growth effectively represents losses. Thus, the physical consequences must be the same as in the problem with real losses [13,14]. Additionally, the ratio of the fuel that burns out in the engine of this body (at its back) to the total gas mass in the body is lower than in the planar case because of the wave curvature (see Refs. 8–11). Both effects are described by the integrated terms in Eq. (8). All this leads to a drop of the wave velocity in comparison with the planar CJ wave propagating through a homogeneous gas.

Analytical Model

To analytically examine Eq. (8), we use the assumption of large activation energy with respect to the von Neuman temperature and of the strong initial shock ($P_{vN} \gg P_0$). With the assumptions made, it is sufficient to solve Eq. (8) in the linear approximation with respect to δ. We can also assume that gas parameters are constant in the region between the leading shock and sonic point and that reaction stops (and $\varphi = 0$; see Eq. (12)) very close to the point where maximum heat release is observed. In the same approximation, $1-\bar{\eta} = \Delta \simeq (\gamma+1)/(\gamma-1)\,\delta$. Then Eq. (8) takes the following form:

$$1-\frac{\bar{C}}{\bar{V}} = (1+jU_{vN})\Delta = \left(1+\frac{2j}{\gamma+1}\right)\Delta = \left(1+\frac{2j}{\gamma+1}\right)\frac{\gamma+1}{\gamma-1}\delta$$

$$\frac{\bar{C}}{\bar{\gamma}\bar{V}}-\frac{\overline{CU}}{\bar{V}} = U_{vN}(1+jU_{vN})\Delta = \frac{2}{\gamma+1}\left(1+\frac{2j}{\gamma+1}\right)\Delta = \frac{2}{\gamma-1}\left(1+\frac{2j}{\gamma+1}\right)\delta$$

$$Q+\left[\frac{\bar{C}}{\bar{V}}\left(\frac{\bar{C}^2}{\bar{\gamma}(\bar{\gamma}-1)}+\bar{\beta}Q+\frac{\bar{U}^2}{2}\right)+\overline{PU}\right] = \left[\left(E_{vN}+\frac{U_{vN}^2}{2}\right)+jU_{vN}\left(E_{vN}+P_{vN}V_{vN}+\frac{U_{vN}^2}{2}\right)\right]$$

$$\Delta = \left[\frac{4}{(\gamma+1)^2}+Q+\frac{2j}{\gamma+1}\left(\frac{2}{\gamma+1}+Q\right)\right]\frac{\gamma+1}{\gamma-1}\delta \tag{9}$$

or in a more simple form,

$$Q + \frac{1}{2} - \frac{\bar{C}^2}{\bar{\gamma} - 1} - \bar{\beta}Q - \frac{\bar{C}^2}{2} = (1 - U_{vN})^2 \Delta = \left(\frac{\gamma + 1}{\gamma - 1}\right)^2 \Delta = \frac{\gamma + 1}{\gamma - 1}\delta$$

The von Neuman values are indexed by vN.

One easily finds that

$$\bar{C} = \frac{\bar{\gamma}}{\bar{\gamma} + 1}\left[1 + \left(\frac{3 - \gamma}{\gamma - 1} + \frac{4j}{\gamma^2 - 1}\right)\delta\right] \quad (10)$$

and

$$\frac{D_0^2(1 - \bar{\beta})}{D^2} \equiv 2Q\,(\bar{\gamma}^2 - 1)\,(1 - \bar{\beta}) = 1 + 2\delta \left(\frac{3 - \gamma}{\gamma - 1} + 4\frac{\bar{\gamma}^2 - 1}{\gamma^2 - 1} + \frac{4j\bar{\gamma}^2}{\gamma^2 - 1}\right) \equiv 1 + \alpha\delta \quad (11)$$

The D_0 value in this formula is the value of the CJ detonation wave velocity in the homogeneous planar case. The $\bar{\beta}$ value can be determined from condition (6). It is nonzero in the nonplanar ($j \neq 0$) case. As in the case of detonations with losses [13,14], part of the fuel does not affect formation of detonation. To evaluate this part, we note that $B_0\varphi/\eta$ is the dimensionless rate of the β value change at the end of the induction period. If we assume that the characteristic time of this change is τ_r and the induction time is τ_{ind}, then

$$\frac{B_0\,\bar{\varphi}}{\bar{\eta}} = \frac{\bar{\beta}}{\tau_r/t} = \frac{\bar{\beta}}{\tau_{\text{ind}}/t}\frac{\tau_{\text{ind}}}{\tau_r} = \frac{\bar{\beta}}{\Delta}\frac{\tau_{\text{ind}}}{\tau_r} \quad (12)$$

We deduce from condition (6) that

$$\bar{\beta} = \left(Q + \overline{PV}\frac{d(1/(\bar{\gamma} - 1))}{d\bar{\beta}}\right)^{-1} \frac{j(\bar{\gamma} - 1)\bar{C}^2\bar{U}}{\bar{\xi}}\frac{\tau_r}{\tau_{\text{ind}}}\frac{\gamma + 1}{\gamma - 1}\delta \quad (13)$$

Linear approximation for this value gives

$$\bar{\beta} = \left[2\,(\bar{\gamma}^2 - 1) + \frac{\bar{\gamma}}{(\bar{\gamma} + 1)^2}\frac{d(1/(\bar{\gamma} - 1))}{d\bar{\beta}}\right]^{-1} \frac{j(\bar{\gamma} - 1)\bar{\gamma}^2}{(\bar{\gamma} + 1)^3}\frac{\gamma + 1}{\gamma - 1}\frac{\tau_r}{\tau_{\text{ind}}}\delta \quad (14)$$

Numerical estimates show that the contribution of β to defining the ratio D_0/D is two orders of magnitude smaller than that from the term $\alpha\delta$ in Eq. (11). This is generally due to the small magnitude of τ_r/τ_{ind}. On this basis, we neglect the $\bar{\beta}$ value in further calculations and accept the relation

$$\frac{D_0^2}{D^2} = 1 + 2\delta\left(\frac{3 - \gamma}{\gamma - 1} + 4\frac{\bar{\gamma}^2 - 1}{\gamma^2 - 1} + \frac{4j\bar{\gamma}^2}{\gamma^2 - 1}\right) \equiv 1 + \alpha\delta \quad (15)$$

In the case of low activation energy, when τ_r/τ_{ind} is not so small, a larger portion of fuel can be excluded from the detonation wave formation. As a result of linear approximation, we observe here some kind of superposition principle: reactivity gradient and curvature contribute additionally to α. The j-independent part in α corresponds to a planar case. On the other hand, the j-dependent part in α does not differ from the results of Refs. 8–11 if we note that $\delta = l_r \cdot \kappa$($\kappa = 1/R$ is the curvature of the wave front). Of course, in the nonlinear approximation, an interplay between these two effects can be observed.

Critical Conditions

The actual value of δ (and, hence, that of D) can be obtained by solving the following equation:

$$\frac{\delta}{\delta_0} = \frac{D(\delta)}{D_0}\exp\left\{\frac{E_a}{T_{0vN}}\left[\left(\frac{D_0}{D(\delta)}\right)^2 - 1\right]\right\} \quad (16)$$

where δ_0 is the $l_r/Dt = \tau_{\text{ind}}(D - u)/Dt$ value, computed for the wave with $D = D_0$; T_{0vN} is the von Neuman temperature behind the planar CJ wave propagating in homogeneous gas.

The critical condition for the existence of a solution suggests equivalence between the derivatives of the left- and right-hand sides of Eq. (16) at the solution point. From this we deduce

$$\delta^{\text{cr}} = \frac{d\ln\left(\frac{D}{D_0}\right)}{d\delta}\left[1 - 2\frac{E_a}{T_{0vN}}\left(\frac{D_0}{D}\right)\right] \quad (17)$$

In the linear approximation with respect to δ Eq. (17) gives

$$\frac{1}{\delta^{\text{cr}}} = \left(\frac{E_a}{T_{0vN}} + \frac{1}{2}\right)\alpha \quad (18)$$

The corresponding critical value of δ_0 is

$$\frac{1}{\delta_0^{\text{cr}}} = e\alpha\left(\frac{E_a}{T_{0vN}} - \frac{1}{2}\right) \quad (19)$$

It should be noted that the term 1/2 was not omitted in Eqs. (18) and (19). The term is small compared to E_a/T_{0vN} within the frame of the assumptions used here. However, they do not originate from the linear approximation in δ.

The deficit of the critical detonation wave velocity is described by the following formula:

$$\frac{D^{\text{cr}}}{D_0} = 1 - \frac{1}{2}\frac{1}{\frac{E_a}{T_{0vN}} + \frac{1}{2}} \quad (20)$$

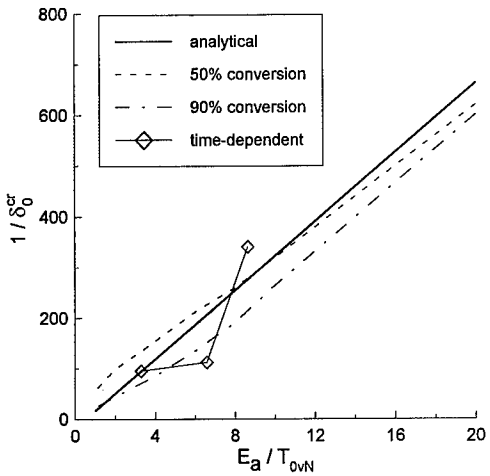

FIG. 1. Critical gradient for detonation wave transmission versus E_a/T_{0vN}. Curves, analytical and numerical solutions of self-similar problem; points, time-dependent numerical simulation.

At $E/T_{0vN} \gg 1$, this relation coincides with the formulas of detonation waves with losses [13,14] and curved detonation waves [8–11]. This universality is due to the Arrhenius character of chemical kinetics and the assumed linear relation between D/D_0 and the small, dimensionless parameter of the problem (δ in our case).

The corresponding critical gradient expressed in terms of reaction zone width of stationary CJ detonation l_r is

$$dl_r/dR = \delta_0^{cr} \tag{21}$$

Thus, a new characteristic linear scale l_r/δ_0^{cr} can be determined for a detonation wave. This linear scale is different from the reaction zone width (by a value of 10^2 for typical fuel-air mixtures) and depends on E_a/T. Using values γ and $\bar{\gamma}$ typical of gaseous detonations, one can see that the value of $1/\delta^{cr}$ is proportional to $(j + 1)$ up to the small value $(\gamma - 1)/(\gamma + 1)2\,(E_a/T_{0vN} + 1/2)$:

$$\frac{1}{\delta^{cr}} = \left(\frac{E_a}{T_{0vN}} + \frac{1}{2}\right) 2\left(4(j + 1)\frac{\bar{\gamma}^2}{\gamma^2 - 1} - \frac{\gamma - 1}{\gamma + 1}\right) \tag{22}$$

Thus, the critical conditions become more severe with the dimensionality growth.

Numerical Solutions for Critical Conditions

Expressions (18), (19), and (20) for critical conditions were obtained with the assumption of large activation energy. If we assume the one-step Arrhenius chemical reaction model, Eq. (3) can be integrated numerically for arbitrary values of the activation energy. The corresponding calculation of critical conditions was carried out using typical thermodynamic parameters for the fuel-air mixture. Specifically, a stoichiometric ethane-air mixture at 1 atm initial pressure and 273 K initial temperature was modeled. Thermodynamic parameters were given by $\gamma = 1.4$, $\bar{\gamma} = 1.24$, and $Q = 2.9$ MJ/kg.

For this mixture model, the solutions of Eq. (3) were obtained numerically for a planar case using the Runge–Kutta method. For a given B_0, the eigenvalue of D was found using a shooting method. Calculations were made for E_a/T_{0vN} ranging from 1 to 20. The solutions of the equations could be found if the gradient in the reaction rate was not too strong. The critical values of δ_0 are presented in Fig. 1. Unlike the model with high activation energy, this representation requires a definition of reaction zone width. Two characteristic widths defined by the $\beta = 0.5$ and $\beta = 0.1$ conditions were used. Figure 1 shows that the approximate analytical solution (19) for large E_a/T_{0vN} gives a good description of critical conditions for small activation energies as well.

The problem of detonation transmission through decreasing reaction rate was also examined as a time-dependent gasdynamic problem. Calculations were made using a finite-difference model for an unsteady, inviscid, compressible reacting flow based on conservation equations of mass, momentum, and energy in the Eulerian representation [6,16]. Calculations were performed for an ideal-gas equation of state (individually for products and reactants) and a one-step Arrhenius chemical kinetic model:

$$d\beta/dt = -k\beta v_0/v \cdot \exp(-E_a/T) \tag{23}$$

The thermodynamic parameters were the same as those given earlier.

The one-dimensional planar case was studied. The gradient of mixture sensitivity in space was given by variation of preexponential factor k in chemical reaction rate $1/k \sim R$. Detonation was initiated by a small, high-pressure region (5 mesh points at 50 bar) at $R = 0$. Detonation propagated first through the region with the varying k, then entered a uniform mixture with the constant k. In the uniform region, resolution of 100 mesh points per reaction width was used. Calculations were made with $E_a/T_{0vN} = 3.29$, 6.58, and 8.64. For each value of E_a/T_{0vN}, a number of calculations were performed to determine critical gradient for detonation transmission. Examples of calculations for subcritical and supercritical cases are shown in Fig. 2. As expected, detonation velocity and overpressure are smaller in comparison with stationary values when the wave propagates through reactivity gradient. In accordance with analytical solutions, this drop in parameters is small compared to stationary cases.

Critical conditions found in the time-dependent

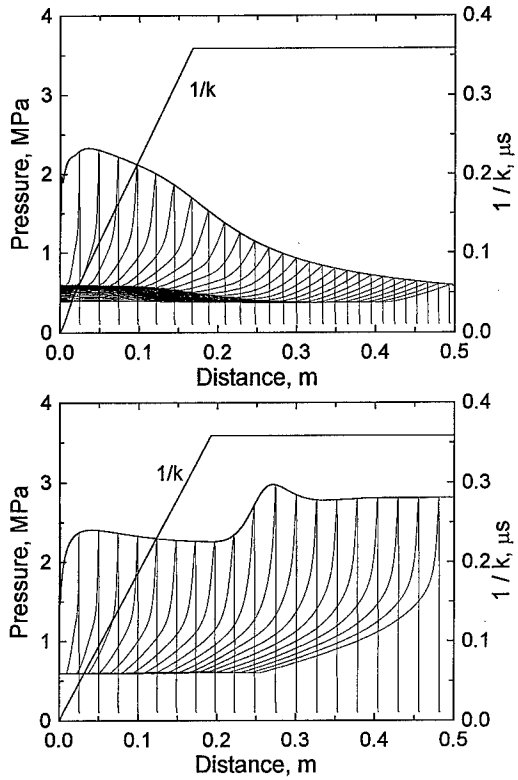

FIG. 2. Results of numerical simulation of detonation transmission through reactivity gradient for subcritical case (upper) and supercritical case (lower). Planar case, $E_a/T_{0vN} = 3.29$. Sequence of pressure profiles, maximum pressure in detonation wave versus distance, and spatial distribution of reverse reaction rate ($1/k$) are shown.

calculations are presented in Fig. 1. The values of δ_0 were determined from time-dependent calculations as dl_r/dR. Corresponding values of stationary reaction zone width l_r were calculated using the Zel'dovich–von Neuman–During model for each E_a/T_{0vN} [7]. Characteristic reaction zone width was defined by $\beta = 0.5$.

Discussion

The critical conditions found (analytically and numerically) from Eq. (3) and in time-dependent calculations show that detonation is able to propagate through a reactivity gradient only if the gradient is sufficiently small. The stronger the temperature dependence of the reaction rate, the more restrictive the condition is for the critical gradient. From the solutions of self-similar problems, the functional dependence of the critical gradient is relatively weak (approximately linear with respect to E_a/T_{0vN}), similar to the problem of detonation with losses [14]. The results of the time-dependent numerical simulation show reasonable agreement with the analytical solution for moderate values of the effective activation energies. On the other hand, an increase in E_a/T_{0vN} to 9 or more leads to a rapid increase in $1/\delta_0^{cr}$. With such large values of the effective activation energy, the detonation wave becomes unstable. It has also been shown in Refs. 15 and 19 that catastrophic instability is observed for sufficiently large values of the effective activation energy, resulting in failure of the detonation wave. In case of propagation through a reactivity gradient, this type of instability becomes even more important because of the decreased detonation speed and temperature behind the leading shock. Figure 1 shows that the numerical simulation indicates a stronger dependence of critical δ_0 on E_a/T_{0vN} as compared to the analytical solution for $E_a/T_{0vN} > 6$.

An application of the present model for critical conditions is consequently restricted by possible instabilities of the detonation wave for large values of the effective activation energy. The existence of a stationary solution for a detonation wave does not necessarily mean that such a solution should be stable. Nevertheless, the present model gives an estimate of the critical conditions for moderate values of the effective activation energy. Another restriction, which is typical for any one-dimensional analysis, is the possible effect of a multidimensional structure of the detonation wave. The present analysis shows that a reactivity gradient and wave curvature limit the ability of stationary propagation of detonation. Analogous to the problem of detonations with losses, this effect can be seen in the one-dimensional analysis. Further study is necessary to identify the effect of the multidimensional structure on the critical conditions.

We should note that the critical conditions found can be applied for the more general situation of nonlinear spatial variability of the reaction rate and thermodynamic properties. This is possible in cases of small spatial variation of gas properties in the reaction zone. In this case, an adiabatic principle similar to the approach in the theory of slightly curved detonation waves [8–11] can be applied and local linear approximation can be used to estimate the critical conditions.

In analysis of experimental data, critical conditions for initiation and propagation of gaseous detonations are usually expressed in terms of experimentally determined detonation cell size λ [1,2,7]. The detonation cell size represents an experimental measure of characteristic linear scale of the chemical reaction in a detonation wave. Therefore, an estimate of the critical reactivity gradient in terms of the cell size is useful. Using a two-dimensional simulation of the detonation wave structure [5], we can express the critical conditions found in the present work in terms of the cell width λ. For the mixture model described

earlier, a series of two-dimensional simulations has been made to determine the detonation cell sizes for each E_a/T_{0vN}. Corresponding critical gradients $dR/d\lambda$ (planar case) appeared to be equal to 10, 12.5, and 18–56 for E_a/T_{0vN} = 3.29, 6.58, and 8.64, respectively. While E_a/T_{0vN} = 3.29 and 6.58 give stable cellular structure with well-determined cell size, E_a/T_{0vN} = 8.64 gives rather irregular cellular structure. This is why the range of values is given for $dR/d\lambda$.

The characteristic length scale defined by the critical gradient is of the order of 10λ for moderate values of the effective activation energy. This means that a distance of about 10λ is required for a planar detonation wave to pass from a very sensitive part of the mixture to a region with the cell size λ. (Critical curvature for divergent waves gives a characteristic length scale of the same order of magnitude; see Eq. [15].) These estimates are in accord with typical critical conditions for detonation propagation and initiation observed experimentally [1,2,17,18].

Conclusion

We have presented approximate models for detonation propagation through decreasing reaction rate. The analytical solution for critical conditions is found for self-similar problems (linear increase of reaction width, one-step Arrhenius kinetic model with large activation energy). The critical gradient depends on mixture properties and can be expressed through characteristic reaction zone width, its dependence on temperature, and the thermodynamic properties of the mixture. Critical gradient decreases with an increase in E_a/T_{0vN} and with the dimensionality growth. In cases of expanding waves (cylindrical or spherical symmetry), superposition of limitations imposed by the gradient and wave curvature is observed.

The critical conditions obtained allow definition of a new characteristic linear scale of chemical reaction in a detonation wave. This scale (reaction zone width divided by the critical gradient l_r/δ_0) depends on reaction zone width, its behavior as a function of temperature, and the symmetry of the problem. The effect of the wave curvature on this characteristic scale appears to be similar to that analyzed in Refs. 8–11. An estimate of this characteristic scale in terms of the detonation cell size λ gives a value of the order of 10λ.

Numerical integration of the self-similar system of flow equations for arbitrary E_a/T_{0vN} shows that the analytical solution can be applied for moderate values of the effective activation energy $E_a/T_{0vN} \sim 1$ as well. The critical conditions are also in agreement with the time-dependent numerical simulation of the same problem if E_a/T_{0vN} is less than 6–8. For higher E_a/T_{0vN}, longitudinal instability of a detonation wave, which was not examined in the present study, becomes the most important factor. Further analysis is necessary to examine stability of this type of solution and to link the one-dimensional effects of reactivity gradient and curvature with the multidimensional structure of real detonations.

Nomenclature

B_0	dimensionless preexponential factor in reaction rate
C	dimensionless sound velocity
D	velocity of leading shock
E	dimensionless energy
E_a	activation energy
k	preexponential factor in reaction rate
j	dimension minus one
l_r	width of the reaction zone
$p(P)$	pressure (dimensionless)
$q(Q)$	combustion heat (dimensionless)
$r(R)$	current (initial) distance of a particle from a given point
t	time
T	temperature
$u(U)$	radial gas velocity (dimensionless)
$v(V)$	specific volume (dimensionless)

Greek

β	reactant mass fraction
γ	the ratio of specific heats at fixed β
δ	dimensionless detonation wave width
Δ	dimensionless detonation wave width referred to initial coordinates
ε	specific energy of the gas
κ	wave curvature
λ	detonation cell size
ξ	dimensionless current distance
η	dimensionless initial distance
τ_0	parameter characterizing reaction rate
$\varphi(\beta,T)$	function characterizing reaction rate

Subscripts

ind	induction
r	reaction
vN	von Neuman
0	corresponds to planar wave in homogeneous gas

Superscripts

cr	critical
–	corresponds to sonic point

REFERENCES

1. Lee, J. H. S. and Moen, I. O., *Prog. Energy Combust. Sci.* 6:359–389 (1980).

2. Shepherd, J. E. and Lee, J. H. S., Paper presented at the ICASE/NASA Combustion Workshop, Newport News, VA, 1989.
3. Utriev, P. and Oppenheim, A. K., *Proc. R. Soc. London, Ser. A* 295:13–28 (1966).
4. Dorofeev, S. B., Kochurko, A. S., and Chaivanov, B. B., *Sixteenth Symposium (International) on Loss Prevention and Safety Promotion in the Processes Industries,* Vol. 4, Oslo, 1989, pp. 22-1–22-19.
5. Dorofeev, S. B., Efimenko, A. A., and Kochurko, A. S., *15th CDERS* Boulder, CO, 1995, pp. 425–428.
6. Dorofeev, S. B., Efimenko, A. A., Kochurko, A. S., and Chaivanov, B. B., *Nuclear Engineer. Design* 148:305–316 (1994).
7. Fickett, N. and Davis, W. C., *Detonation,* University of California Press, Berkley and Los Angeles, 1979.
8. Klein, R. and Stewart, D. S., *SIAM J. Appl. Math.* 54:1401 (1993).
9. He, L. and Clavin, P., *J. Fluid Mech.* 277:227–248 (1994).
10. Klein, R., Krok, J. C., and Shepherd, J. E., *Phys. Fluids* (1995), submitted.
11. Yao, J. and Stewart, D. S., *Combust. Flame* 100:519–528 (1995).
12. Landau, L. D. and Lifshits, E. M., *Gidrodinamika (Hydrodynamics),* Nauka, Moscow, 1986, in Russian.
13. Zel'dovich, Y. B., *ZhETF* 10:542–568 (1940), in Russian; available in translation as NACA TM 1261 (1950).
14. Zel'dovich, Y. B. and Kompaneets, A. S., *Teoriya Detonatsii (Theory of Detonation),* Gostekhteorizdat, Moscow, 1955, in Russian; Academic Press, New York, 1960.
15. He, L. T. and Lee, J. H. S., *Phys. Fluids* 7:1151–1158 (1995).
16. Dorofeev, S. B., Efimenko, A. A., Kochurko, A. S., and Chugunov, A. E., "Numerical Simulation of Multidimensional Structure of Detonations," SR&DO Industrial Risk, Preprint IRIS-91/2, 1991, in Russian.
17. Alekseev, V. I., Dorofeev, S. B., Efimenko, A. A., and Kuznetsov, M. S., *15th CDERS* Boulder, CO, 1995, pp. 13–16.
18. Dorofeev, S. B., Sidorov, V. P., and Dvoinishnikov, A. E., *Combust. Flame* 104:95–110 (1996).
19. Efimenko, A. A., Dorofeev, S. B., and Shepherd, J. E., *Twenty-Fifth Symposium (International) on Combustion,* W-I-P Abstracts, UCI, v. 2, 1994, p. 251.

COMMENTS

Prof. Martin Sichel, The University of Michigan, USA. You have discussed quenching of denotation waves due to gradients in fuel concentration. How are your results related to the opposite problem of deflagration—detonation transition due to the presence of fuel concentration gradients considered, for example by Zeldovich?

Author's Reply. The studies of Ya. Zeldovich, G. Makhviladze, B. Gelfand, and colleagues in 1979, 1985, and also later studies showed that initial nonuniformities of autoignition delay time can be responsible for spontaneous onset of a detonation. The main problem addressed in these studies was the problem of formation of a strong shock-reaction complex due to interaction of spontaneous flame (reaction front) and gasdynamic of the flow. It was shown that coherence of these processes permits formation and fast amplification of pressure wave in a reactive media with spatially nonuniform autoignition delay time. The present paper addresses propagation of existing detonation complex through the region with decreasing reactivity. We do not have distributed initial autoignition delay time, and spontaneous reaction fronts. Reaction is caused by the lead shock of existing explosion wave. Generally this problem differs from that of spontaneous explosion regimes. However, both the problem of spontaneous formation of explosion wave, and that of detonation propagation through nonuniform mixtures are of importance for spontaneous onset of a detonation. Explosion wave which occurred initially due to gradient in reactivity can be quenched thereafter propagating through this gradient. Such a situation was observed in a number of computations mentioned above. The explosion wave formed in nonuniform mixture does not necessarily become a self-sustained detonation wave. It is therefore important to analyse conditions at which the wave can survive propagating through reactivity gradient. The present paper gives analytical and numerical estimates for these conditions.

Twenty-Sixth Symposium (International) on Combustion/The Combustion Institute, 1996/pp. 2973–2979

THE INFLUENCE OF INITIAL TEMPERATURE ON FLAME ACCELERATION AND DEFLAGRATION-TO-DETONATION TRANSITION

G. CICCARELLI, J. L. BOCCIO AND T. GINSBERG
Brookhaven National Laboratory
Department of Advanced Technology
Building 130, P.O. Box 5000
Upton, NY 11973-5000, USA

H. TAGAWA
Japanese Nuclear Power Engineering Corporation

The influence of initial mixture temperature on deflagration-to-detonation transition (DDT) has been investigated experimentally. The experiments were carried out in a 27-cm–inner diameter, 21.3-meter-long heated detonation tube, which was equipped with periodic orifice plates to promote flame acceleration. Hydrogen-air–steam mixtures were tested at a range of temperatures up to 650 K and at an initial pressure of 0.1 MPa. In most cases, the limiting hydrogen mole fraction that resulted in transition to detonation corresponded to the mixture whose detonation cell size, λ, was approximately equal to the inner diameter of the orifice plate, d (e.g., $d/\lambda = 1$). The only exception was in dry hydrogen-air mixtures at 650 K where the DDT limit was observed to be 11% hydrogen, corresponding to a value of d/λ equal to 5.5. For a 10.5% hydrogen mixture at 650 K, the flame accelerated to a maximum velocity of about 120 m/s and then decelerated to less than 2 m/s. This observation indicates that the $d/\lambda = 1$ DDT limit criterion provides a necessary condition but not a sufficient one for the onset of DDT in obstacle-laden ducts. In this particular case, the initial mixture condition (i.e., temperature) resulted in the inability of the mixture to sustain flame acceleration to the point at which DDT could occur. It was also observed that the distance required for the flame to accelerate to the onset of detonation was a function of both the hydrogen mole fraction and the initial mixture temperature. For example, decreasing the hydrogen mole fraction or increasing the initial mixture temperature resulted in longer transition distances.

Introduction

Under postulated severe accident scenarios in water-cooled nuclear power plants and in certain industrial chemical processes, combustible mixtures can be present at elevated temperatures. The threat of detonation initiation under such conditions has sparked interest in the effects of initial mixture temperature on flame acceleration and transition to detonation phenomena. The experimental results presented here address this issue by investigating flame acceleration and transition to detonation in a heated, obstacle-filled detonation tube.

Since the pioneering work of Laffite [1], it has been well-known that for certain mixtures a flame propagating in a long tube could accelerate to the point at which a detonation is initiated in the gas. For transition to detonation to occur, the flame must accelerate to a velocity in excess of the speed of sound in the unburned mixture. As the flame accelerates to such high velocities, compression waves are generated ahead of the flame that eventually coalesce into a leading shock wave. If this shock wave attains sufficient strength, a detonation can form in the compressed gas between the flame and the shock wave. Stroboscopic laser-schlieren movies taken of the final stages of flame acceleration leading to transition to detonation clearly show a strong leading shock wave followed by a train of compression waves originating at the accelerating turbulent flame [2]. The photographs indicate that the location of the transition to detonation, or the so-called "explosion within the explosion," always occurs within the shock-flame complex, typically in the boundary layer.

Schelkin [3] first showed that the transition distance from flame to detonation (i.e., run-up distance) could be shortened dramatically by roughening the duct walls with turbulence-generating obstacles. Obstacles generate gradients in the flow field ahead of the flame, resulting in large-scale "flame folding" [4]. Superimposed on the large-scale flame fold are small-scale shear layers produced at the obstacle edges. The increase in flame surface area caused by flame folding and the increase in turbulence intensity in the mean flow result in an enhanced burning rate. The coupling between the

burning rate and the induced flow ahead of the flame results in a feedback mechanism that promotes flame acceleration. An accelerating turbulent flame in an obstacle-laden duct generates compression waves ahead of it much like in the smooth duct. The local high temperature and pressure generated by the reflection of the leading shock wave from an obstacle face promote transition to detonation.

The exact mechanism by which a detonation is formed has yet to be identified conclusively. The shock wave amplification by coherent energy release (SWACER) mechanism has been proposed by Lee [5] to describe the process by which spatial nonuniformities in the chemical induction time in a mixture can result in the formation of a detonation. In the case of DDT resulting from flame acceleration, the nonuniformities can be due to local fluctuations in the compressed gas between the flame and the leading shock wave. The induction time gradient required for the SWACER mechanism can result from temperature gradients generated from local turbulent mixing of combustion products and fresh mixture.

A large body of experimental data exists in the literature dealing with flame acceleration and transition to detonation phenomena. A comprehensive study of flame acceleration leading to the onset of detonation in obstacle-laden tubes was undertaken at McGill University. A series of tests was performed in long tubes with inner diameters of 5, 15, and 30 cm [6,7].

In these tests, an array of orifice plates was placed inside the tubes to promote turbulence and thus flame acceleration. Typically, flame acceleration takes place in the first few meters of the tube and is followed by steady-state flame propagation to the end of the tube. The combustion front propagation during this final steady-state phase was classified into two regimes: the choking and quasi-detonation regimes [6]. In the choking regime, the flame accelerates to a final steady-state velocity that is close to the isobaric sound speed in the products, assuming a constant pressure combustion process. It is argued that the maximum steady-state flame velocity achievable is the speed of sound in the products due to choking of the flow as a result of heat addition from combustion. It has been proposed recently, based on theoretical considerations, that flame propagation in the choking regime could be described as a plane precursor shock wave driven by a Chapman–Jouget (CJ) deflagration [8]. In the quasi-detonation regime, flame acceleration leads to transition to detonation. As a result of severe momentum and heat losses from the reaction zone, the detonation wave propagates at a velocity substantially below the theoretical CJ velocity. It was established that those mixtures whose average detonation cell size, λ, was smaller than the orifice plate inner diameter, d, resulted in transition to detonation (i.e., $d/\lambda \geq 1$). This observation yields a DDT limit criterion, $d/\lambda = 1$, which defines the minimum hydrogen concentration required for transition to detonation to occur [7]. When applying the DDT limit criterion, one must keep in mind the uncertainty, in terms of cell nonuniformity, in the experimentally measured cell size. In hydrogen-airstream mixtures, this uncertainty could be as high as $\pm 25\%$ of the average cell size [9,10].

Recent experiments have been carried out to investigate the effect of initial mixture temperature on flame acceleration in an obstacle-laden tube [11]. The experiments were carried out in a 6-m-long tube with only half of the tube filled with obstacles. Experiments performed at 573 K with 32% orifice blockage resulted in very limited flame acceleration with no transition to detonation observed, whereas at 300 K, transition to detonation was readily observed with the same orifice plates. The length of the obstacle field in these experiments was likely insufficient to fully investigate the DDT phenomenon at elevated temperatures.

The objective of the present set of experiments is to characterize the effect of initial mixture temperature on flame acceleration and, most importantly, on the potential for transition to detonation. Using available cell size data for hydrogen-airsteam mixtures at elevated temperatures [10], we will determine whether the $d/\lambda = 1$ DDT limit criterion applies at elevated initial temperatures up to 650 K. Unlike previous experiments [11], the entire length of the test vessel was filled with orifice plates to maximize the distance available for the flame to achieve a steady-state velocity.

Experimental Details

The experiments were carried out in the Brookhaven National Laboratory High-Temperature Combustion Facility (HTCF), which consists of a 27-cm–inner diameter, 21.3-m-long heated detonation vessel. The vessel is made up of seven equal-length flanged sections. A detailed description of the HTCF detonation vessel, the gas handling system, and other auxiliary equipment can be found in Ref. 10. Flame acceleration is promoted by an array of obstacles placed inside the entire length of the detonation vessel. The obstacles consist of orifice plates that are 1.9-cm thick, 27-cm outer diameter and 20.6-cm inner diameter, with a 1-tube diameter (i.e., 27 cm) spacing. This spacing is maintained by fastening the orifice plates to six axially running threaded rods with nuts on either side of each plate. The threaded rods are anchored to the vessel at each vessel flange location.

The vessel is heated using ceramic bead heating pads that are strapped directly to the outside of the vessel using pipe clamps and are covered with

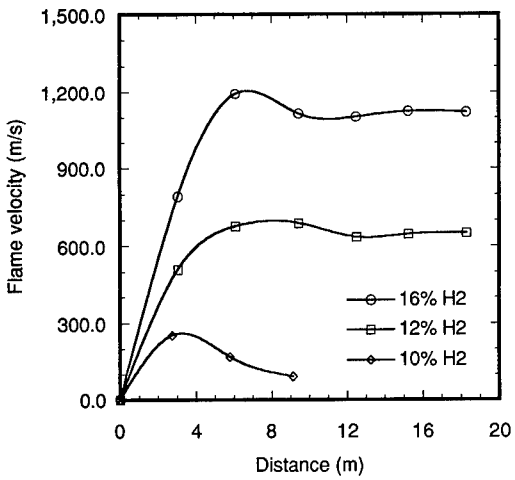

FIG. 1. Combustion front velocity versus propagation distance in three hydrogen-air mixtures at 300 K and 0.1 MPa.

roughly 5 cm of insulation. The vessel is evacuated using a large Stokes vacuum pump. The test gas is blended dynamically in a mixing chamber where the individual gas constituent flow rates are set using choked venturis. The test gas is introduced into the vessel and quickly ignited using a standard diesel engine glow plug centrally mounted on one of the vessel end plates. Three gas samples are taken just before ignition to verify the gas composition and uniformity in the vessel.

The detonation vessel is equipped with instrumentation ports located every 61 cm down the length of the tube. The combustion front velocity is derived from time-of-arrival measurements made using photodiode detectors. The photodiode spacing is large, typically 3.05 m, to filter the flame velocity measurements of local fluctuations caused by gas-dynamic effects associated with the restricted flow through the orifice plates. For slow propagating flames, the intensity of light emitted from the flame is insufficient to obtain a signal from the photodiodes, in which case the flame velocity is determined based on fast response thermocouple signals. Combustion front pressure is measured using PCB113 piezoelectric pressure transducers that are flush mounted on the tube wall. The signals from the photodiodes and pressure transducers are recorded on two digital oscilloscopes, and the thermocouple signals are recorded on a PC-based data acquisition system equipped with thermocouple conditioning software.

Experimental Results

Flame Propagation at Room Temperature

Plotted in Fig. 1 is the flame front velocity versus axial distance for three different hydrogen-air mixtures at 300 K. These three experiments characterize the spectrum of flame propagation modes observed in the current study. The various flame propagation regimes have been classified as (1) detonation, (2) choking, and (3) slow deflagrations.

In Fig. 1, the flame trajectory in the 16% hydrogen mixture is typical of steady-state flame propagation in the detonation regime. The flame acceleration takes place in the first 6 m followed by a relatively steady propagation at a velocity of 1130 m/s with a standard deviation of 22 m/s. This average velocity is roughly 27% below the theoretical CJ velocity for this mixture. There is a slight overshoot in the velocity before reaching steady state, which is typical of a DDT event. This velocity overshoot is observed, to various degrees, in all the experiments in the detonation regime. Because of the large spacing between photodiodes, the actual velocity overshoot is most likely larger. The flame trajectory shown in Fig. 1 for the 12% hydrogen mixture is typical of flame propagation in the choking regime. As in the 16% hydrogen case, the flame propagates at a relatively steady velocity after an initial acceleration phase in the first 6 m of travel. Although not particularly evident in this test, there is a velocity overshoot that typically follows the initial flame acceleration phase. The average velocity for the flame after 6 m is 644 m/s with a standard deviation of 8 m/s. This matches very closely the speed of sound in the products for this mixture. Flame propagation in the 10% hydrogen mixture is typical of flame propagation in the slow deflagration regime. The flame velocity measurements for this test were derived from four thermocouples located in the first half of the tube. For the 10% hydrogen mixture, the flame initially accelerates to a maximum velocity of about 250 m/s and then continuously decelerates to roughly 100 m/s by mid vessel. In the present study, there was no evidence of flame quenching [6], in which the flame is extinguished during flame acceleration.

Figure 2 shows a plot of the average flame velocity as a function of the mixture hydrogen mole fraction. For each test in the choking and detonation regime, the average velocity, shown as open circles, is based on measurements obtained in the last half of the vessel. Also shown is the standard deviation in the measurements used to obtain the average velocity. The theoretical curves for the mixture CJ detonation velocity and the isobaric sound speed in the combustion products are shown as solid lines. The open squares represent the *maximum* velocity measured for mixtures in the slow deflagration regime.

No abrupt change in the average propagation velocity as a function of hydrogen concentration is noted in Fig. 2 that would indicate a transition between the choking and the detonation regimes. The figure shows a continuous decrease in the average velocity from very close to the CJ detonation velocity for a 30% hydrogen mixture down to just below the

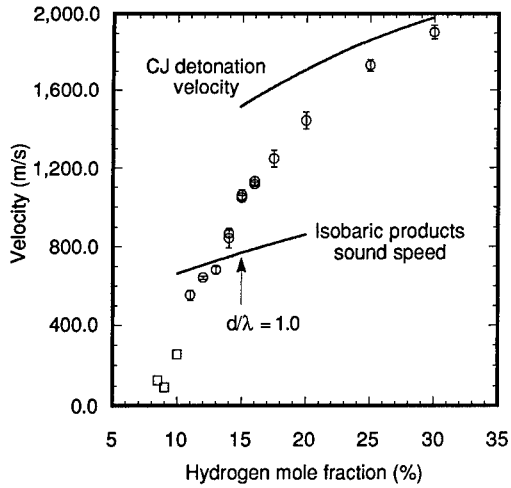

FIG. 2. Combustion front velocity versus hydrogen mole fraction for hydrogen-air mixtures at 300 K and 0.1 MPa. Open circles denote the average velocity over roughly the second half of the vessel, and bars represent the standard deviation in the measured velocities. Open squares denote the maximum flame velocity for slow deflagrations.

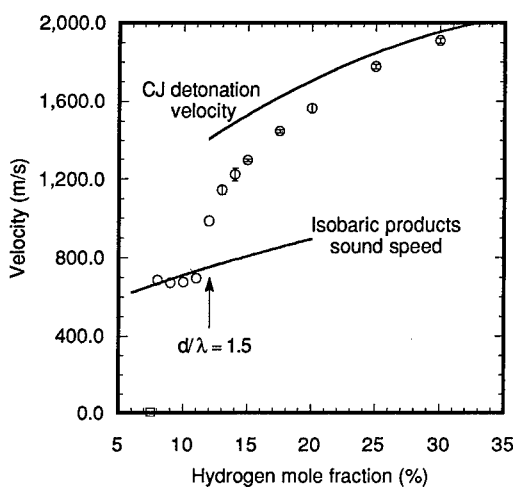

FIG. 3. Combustion front velocity versus hydrogen mole fraction for hydrogen-air mixtures at 500 K and 0.1 MPa. Open circles denote the average velocity over roughly the second half of the vessel, and bars represent the standard deviation in the measured velocities. Open squares denote the maximum flame velocity for slow deflagrations.

isobaric product sound speed for a 13% hydrogen mixture. Recall that in the detonation regime, the detonation wave propagates at a sub-CJ detonation velocity because of momentum and heat losses from the reaction zone to the tube and orifice plates. The amount of energy lost is governed by the length of the reaction zone, or detonation cell size, which increases with decreasing hydrogen concentration. The pressure measured near the end of the vessel was used to establish the lower DDT limit to be 15% hydrogen. For mixtures of 15% hydrogen and higher, the overpressure is scattered about the CJ detonation pressure and for mixtures below 15% hydrogen, the peak overpressures are below the constant volume combustion pressure [10]. The cell size for a 15% hydrogen mixture at 300 K and 0.1 MPa is about 21.8 cm [10], and the inner diameter of the rings is 20.6 cm. Therefore, the ratio d/λ equals 1.0, which is in excellent agreement with the DDT limit criterion proposed by Peraldi et al. [7].

Flame Propagation at Elevated Temperature and with Steam Dilution

The average flame velocity for hydrogen-air mixtures at 500 K is plotted versus hydrogen mole fraction in Fig. 3. Here, there is a clear demarcation of the transition from the choking to the detonation regime at 12% hydrogen. The experimental average detonation velocity data lie closer to the theoretical CJ detonation velocity compared to that observed at 300 K, in Fig. 2. For example, for a 15% hydrogen mixture, the measured velocity is 15% below the CJ detonation velocity, and at 30% hydrogen, the velocity deficit is only 2%. This can be attributable to the decrease in cell size (i.e., reaction zone length) with increased initial temperature [10] resulting in less momentum and heat losses. For mixtures between 8 and 11% hydrogen, the data follow very closely the theoretical isobaric sound speed of the product gases. The cell size for a 12% hydrogen mixture at 500 K and 0.1 MPa is about 13.5 cm [10], which yields a value of 1.5 for the ratio d/λ. Considering the uncertainty in the measured detonation cell size (e.g., up to $\pm 25\%$), as previously indicated, and the resolution of the hydrogen mole fraction between experimental points in Fig. 3, this value can be considered to be in relative agreement with the $d/\lambda = 1$ criterion for DDT transition.

Figure 4 shows the flame trajectory for several hydrogen-air mixtures at 650 K and 0.1 MPa. At this temperature, DDT occurred in 11, 12, and 17.5% hydrogen mixtures. It is clear from this figure that the detonation run-up distance increases with decreasing hydrogen concentration. For the 17.5% hydrogen mixture, DDT occurs after about 6 m of propagation, and from that distance to the end of the vessel, there is a slight decay in the detonation velocity. A similar behavior is observed in the 12% hydrogen mixture; for the 11% hydrogen mixture, DDT occurs at the end of the vessel. Decreasing the hydrogen mole fraction from 11 to 10.5% results in a benign burn. In the 10.5% hydrogen mixture, the flame accelerates to a maximum velocity of about

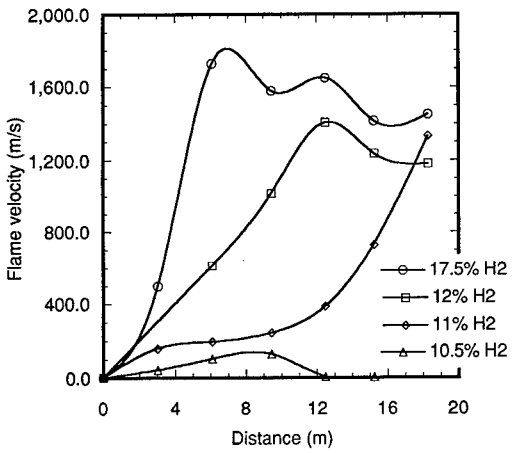

FIG. 4. Combustion front velocity versus propagation distance for hydrogen-air mixtures at 650 K and 0.1 MPa.

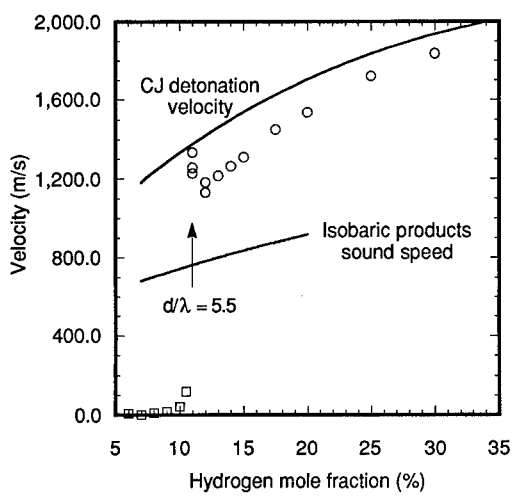

FIG. 5. Combustion front velocity versus hydrogen mole fraction for hydrogen-air mixtures at 650 K and 0.1 MPa. Open circles denote the flame velocity at the end of the vessel. Open squares denote the maximum flame velocity for slow deflagrations.

100 m/s and then decays to roughly the laminar burning velocity.

It is difficult to assign an average velocity to any of the velocity profiles shown in Fig. 4 because the detonation never achieves steady-state conditions within the length of the vessel. This is especially true for the leaner mixtures in which the run-up distances can be quite large. Therefore, in Fig. 5, the last velocity measurement taken at the end of the vessel (between 16.7 and 19.8 m) in each experiment carried out at 650 K is shown as a function of the hydrogen mole fraction. Note that these are not average velocities and thus there is no standard deviation shown. The measured detonation velocity decreases smoothly with decreasing hydrogen mole fraction just below the theoretical CJ detonation velocity. The minimum hydrogen concentration resulting in a DDT is 11% hydrogen. As indicated previously, for the 10.5% hydrogen mixture, the maximum flame velocity is only about 100 m/s. As a result, no flame propagation in the choking regime was observed. The 11 and 10.5% hydrogen tests were repeated several times to verify the observed behavior. The high detonation velocities corresponding to 11% hydrogen are the result of DDT occurring at the end of the vessel where the last velocity measurement is taken. The cell size for an 11% hydrogen mixture at 650 K and 0.1 MPa is about 3.7 cm [10]. This yields a value of 5.5 for the ratio d/λ, which means that at the DDT limit, about five detonation cells pass through the inner diameter of the orifice plate. Even if the uncertainty in the cell size measurement is taken to be a conservative $\pm 50\%$, the low end of the d/λ ratio at the limit becomes 3.7. Clearly, the observed minimum hydrogen composition of 11% for DDT at 650 K does not agree with the DDT limit criterion of $d/\lambda = 1$, which has been shown to be applicable for the data obtained at 300 K and 500 K.

As mentioned previously, due to the long detonation run-up distances at 650 K, the detonation does not achieve steady-state conditions within the length of the vessel. To reduce the run-up distance, a series of experiments was performed where the first two of the seven flanged sections (e.g., 6.1 m) were each maintained at 400 K whereas the remaining sections were heated to the test temperature of 650 K. In these experiments, transition occurred within the range of 7.6–10.1 m from the point of ignition, which is just outside the cold section, leaving sufficient distance to the end of the vessel for the detonation to achieve steady conditions. With the first 6.1 m of the vessel at 400 K, DDT occurred in hydrogen-air mixtures down to 9.5% hydrogen. Therefore, mixtures of 9.5 and 10% hydrogen, which did not transition to a detonation when the vessel was completely heated, are now observed to result in transition to detonation. The cell size for a 9.5% hydrogen in air mixture at 650 K is 4.6 cm [10]. This yields a value of 4.5 for d/λ, which is still well above the DDT criterion found to be valid for the tests at 300 K and 500 K.

The influence of steam dilution on flame acceleration and DDT phenomena was studied in hydrogen-air mixtures at initial temperatures of 400 K, 500 K, and 650 K. In these tests, the steam dilution fraction was held constant, and the ratio of the hydrogen to air was varied (i.e., hydrogen mole fraction on a dry basis). In this way, one can obtain a minimum hydrogen composition resulting in DDT for a given steam dilution and initial temperature. The results

TABLE 1
Flame acceleration limits for hydrogen-airsteam mixtures without venting

Temp (K)	Steam Dilusion (%)	Choking Limit % Hydrogen	DDT Limits % Hydrogen	DDT Limits d/λ
400	10	12	18	0.7
500	25	14	24	1.5
650	25	16	19	0.8

from these tests are summarized in Table 1, which lists the minimum hydrogen concentration that resulted in transition to detonation and the corresponding d/λ ratio. The results for all three initial temperatures are in relatively good agreement with $d/\lambda = 1$ criterion.

Discussion

The present experiments have shown that, in general, the DDT limit was found to lie in the range $0.7 \leq d/\lambda \leq 1.5$ for different initial temperatures, with and without steam. This finding is consistent with the $d/\lambda = 1$ DDT limit criterion proposed by Peraldi et al. [7]. The exception was in tests performed in dry hydrogen-air mixtures at an initial temperature of 650 K. In these tests, DDT was observed in mixtures containing 11% hydrogen or more, which corresponds to a value of $d/\lambda > 5.5$. Although this result does not violate the $d/\lambda > 1$ criterion for the possibility of DDT, it is at variance with the DDT limit of $d/\lambda = 1$, which was found to apply at all the other initial conditions.

In most cases, a plot of the average flame velocity versus hydrogen mole fraction indicates that the DDT limit represents the transition between the choking and the detonation regimes. For example, for a mixture slightly leaner in hydrogen than the hydrogen mixture at the DDT limit, the flame was observed to accelerate to a constant velocity equal to the speed of sound in the products (i.e., choking regime). Flame propagation in the choking regime is characterized by the precompression of the mixture by the leading shock wave before combustion. The DDT limit is governed by the existence of a mixture state (e.g., temperature, vorticity) behind the precursor shock wave that is favorable for detonation initiation.

There is a fundamental difference in the observed DDT limit in dry hydrogen-air mixtures at 650 K and that observed at all other conditions. The difference is that in the dry hydrogen-air experiments at 650 K, no flame propagation was observed in the choking regime. For the 10.5% hydrogen-air mixture, which is 0.5% leaner in hydrogen than the hydrogen-air mixture at the DDT limit, the flame velocity peaked at only 100 m/s. Therefore, the failure to observe transition for this composition can be attributed to the inability of the mixture to sustain flame acceleration.

It was also observed that DDT could be promoted by artificially increasing the flame acceleration rate. For example, in a 10% hydrogen mixture at 650 K, flame acceleration was severely limited and no DDT was observed. DDT was observed in the same 10% hydrogen mixtures by promoting flame acceleration by the use of the initial cold section. Note that DDT occurred near the end of the tube, far removed from the colder sections in the first 6.1 m of the tube. Therefore, the initial cold section acted only as a booster for the flame and played no direct role in the local DDT phenomenon. In the experiments reported in Ref. 11, a similar boosting of the flame acceleration was achieved by using higher blockage orifice plates in the first half of the obstacle section. This resulted in transition for mixtures that otherwise would not have resulted in DDT when the smaller blockage orifice plates were used throughout.

For hydrogen-air mixtures with 25% steam dilution at 650 K, the DDT limit was found to be 19% hydrogen, which yields a value of $d/\lambda = 1.2$. This is in close agreement with the $d/\lambda = 1$ DDT limit criterion and corresponds to the transition from the choking regime to the detonation regime. Unlike the dry hydrogen-air mixtures at an initial temperature of 650 K, the steam-diluted mixtures leaner than the DDT limit were capable of accelerating to a velocity equal to the sound speed in the burned products. Two of the important parameters that govern the rate of flame acceleration are the density ratio of the unburned to the burned gas and the mixture laminar burning velocity. Mixtures with a larger density ratio and laminar burning velocity result in higher flame acceleration rates. The density ratio across the flame and the laminar burning velocity for a 19% hydrogen in air mixture with 25% steam is 2.4 and 2.7 m/s, respectively. The density ratio and burning velocity in the dry 11% hydrogen in air mixture is 2.2 and 1.9 m/s, respectively. This indicates that the potential for flame acceleration in the steam-diluted DDT limit mixture (e.g., $d/\lambda = 1.2$) is higher than the dry

11% mixture that has a smaller cell size and thus a larger value of d/λ (e.g., 5.5).

Conclusion

Flame propagation in the heated, obstacle-laden tube used in the present experiments consists of an initial flame acceleration phase followed by a steady-state phase. The various flame propagation regimes observed are similar to those described in Ref. 6. In general, the DDT limit data could be correlated with the $d/\lambda = 1$ criterion proposed by Peraldi et al. [7]. The only exception was in the dry hydrogen-air mixtures at 650 K, where the DDT limit was observed to be 11% hydrogen, which corresponds to a value of $d/\lambda = 5.5$. This DDT limit dropped to 9.5% hydrogen ($d/\lambda = 4.2$) when the first 6.1 m of the vessel were maintained at 400 K with the rest of the vessel at 650 K. This indicates that the $d/\lambda = 1$ DDT limit criteria provides a necessary but insufficient condition for the onset of DDT in obstacle-laden ducts. In this particular case, the initial mixture condition (i.e., temperature) resulted in the inability of the mixture to sustain flame acceleration to the onset of DDT.

The detonation run-up distance, which in this geometry is governed primarily by the rate of flame acceleration, was found to be a function of the hydrogen mole fraction and the initial temperature. The detonation run-up distance was found to decrease with increasing hydrogen mole fraction, up to stoichiometric conditions, and with decreasing initial temperature.

Acknowledgments

This research is sponsored by the U.S. Nuclear Regulatory Commission and the Ministry of International Trade and Industry of Japan through the Nuclear Power Engineering Corporation of Japan. The authors would like to thank the NRC Technical Monitor, Dr. Asimios Malliakos, for his support and guidance through the course of this project and his helpful suggestions in the review of the work. The authors would also like to thank C. Finfrock for his invaluable contributions to the daily operation of the facility and running of the experiments with the aid of L. Gerlach.

REFERENCES

1. Laffite, P., *Compt. Rendu* 186:951 (1928).
2. Urtiew, P. and Oppenheim, A., *Proc. of Royal Society London Series A* 295:13–28 (1966).
3. Shchelkin, K., *Zh. Exp. Teor. Fiz. (USSR)* 10:823–827 (1940).
4. Moen, I. O., Donato, M., Knystautas, R., and Lee, J. H., *Combust. Flame* 39:21–32 (1980).
5. Lee, J. H., Knystautas, R., and Yoshikawa, N., *Acta Astronautica* 5:971 (1978).
6. Lee, J. H., Knystautas, R., and Chan, C., *Twentieth Symposium (International) on Combustion*, The Combustion Institute, Pittsburgh, 1984, pp. 1663–1672.
7. Peraldi, O., Knystautas, R., and Lee, J. H., *Twenty-First Symposium (International) on Combustion*, The Combustion Institute, Pittsburgh, 1986, pp. 1629–1637.
8. Chu, R., Clark, J., and Lee, J. H., *Proc. of the Royal Society London A* 441:607–623 (1993).
9. Tieszen, S. R. et al., *Progress Astronautics Aeronautics* 106:205 (1986).
10. Ciccarelli, G. et al., USNRC Report NUREG/CR-6391, BNL-NUREG-52482, 1996.
11. Beauvais, B., Mayinger, F., and Strube, G., ASME/JSME Nuclear Engineering Conference, Vol. 1, pp. 425–433, 1993.

Twenty-Sixth Symposium (International) on Combustion/The Combustion Institute, 1996/pp. 2981–2989

ON THE EVOLUTION OF CELLULAR DETONATION

D. SCOTT STEWART, TARIQ D. ASLAM AND JIN YAO
Theoretical and Applied Mechanics
University of Illinois
Urbana, IL 61801, USA

A detonation shock–evolution equation that predicts both pulsating and cellular detonation has been derived in the limit of near-Chapman–Jouguet detonation, weak curvature, slow temporal variation, and large activation energy with a newly applied technique of the method of successive approximation. The evolution equation describes a wave hierarchy that is consistent with the linear stability theory of the evolution equation. We define the parameter regime for which the equation applies. The transverse wave instability, as indicated from analysis, leads to cellular detonation. Triple-points tracks correspond to shock–shock intersections of the dynamic solution of smooth portions of the front. The dynamics of the cellular solution are consistent with the notion that the power of the detonation front is derived from the normal reaction zone and the triple points are generated as the interaction of the independently propagating fronts and the consequent shock–shock intersections, not as the centers of blast waves. Explicit criteria for prediction of cell widths and cell aspect ratios are given.

Introduction

Recently, Stewart and Yao [1] derived a new detonation shock–evolution equation based on the combined limits of near-Chapman–Jouguet (CJ) velocity, small shock curvature, slow temporal variation measured on the particle passage time through the reaction zone, and large dimensionless activation energy.

The compressible Euler equations, with a forward exothermic reaction measured by progress variable λ, is the basic model. The ideal specific internal energy $e(p, \rho, \lambda)$ and Arrhenius reaction rate r are

$$e = \frac{p}{\rho}\frac{1}{\gamma - 1} - Q\lambda$$
$$r(p, \rho, \lambda) = k(1 - \lambda)^{\nu} e^{-E/(p/\rho)} \qquad (1)$$

where γ is the ratio of specific heats; Q is the heat of combustion; k, ν, and E, respectively, are the premultiplying reaction rate constant, depletion factor, and activation energy.

The results build on a rational asymptotic theory that Bdzil and Stewart call Detonation Shock Dynamics [2–4] that shows that the evolution of a detonation shock can be predicted by solutions to a wholly intrinsic partial differential equation (PDE) [2]. The roots of the analysis can be traced to Wood and Kirkwood [5], whose early work showed that detonations with a sonic point within the postshock reaction zone had special character and that normal velocity of the detonation D_n of a quasi-steady, near–CJ detonation was related to the shock curvature κ.

The problem of finding the approximate evolution can be reduced essentially to solving a two-point structure problem, where the intrinsic PDE is found as a (nonlinear) eigenvalue. Simply speaking, one starts from the shock and attempts to construct an approximation to the detonation structure that satisfies pistonlike conditions at a determined (sonic) point in the reaction zone. The outcome is a nonlinear intrinsic PDE for the shock evolution that reflects the determination of the eigenvalue.

Stewart and Yao use a newly applied asymptotic technique based on the method of successive approximation (MSA), which enables the derivation of more complex shock surface evolution equations than had been obtained previously with matched asymptotic expansion methods in space and time. Specifically a $\ddot{D}_n$, $\dot{D}_n$, D_n, κ, $\dot{\kappa}$ relation was obtained for gaseous detonation with large activation energy, where $\dot{D}_n$ and $\ddot{D}_n$ are the first and second normal time derivatives of D_n, respectively, and $\dot{\kappa}$ is the normal time derivative of κ. We display the equation obtained after a brief discussion of the dimensional scales. Importantly, the intrinsic PDE presented predicts the occurrence of both self-sustained cellular and pulsating detonation, phenomena that had not been predicted before by a rationally derived asymptotic theory.

Scales

A quantity with a tilde superscript is dimensional; a quantity without is dimensionless. The dimensional length, velocity, and time scales assumed in this section are $\tilde{l}_{rz}$, $\tilde{D}_{CJ}$ and $\tilde{l}_{rz}/\tilde{D}_{CJ}$, respectively. The length, $\tilde{l}_{rz}$, is a characteristic reaction-zone (induction)

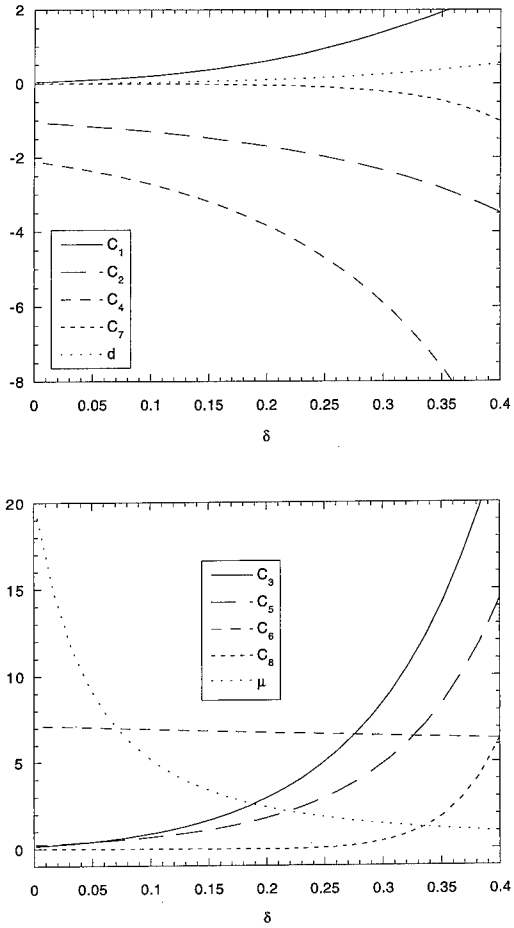

FIG. 1. (a) Constants C_1, C_2, C_4, C_7, and d versus δ for $\gamma = 1.2$. (b) Constants C_3, C_5, C_6, C_8, and μ versus δ for $\gamma = 1.2$.

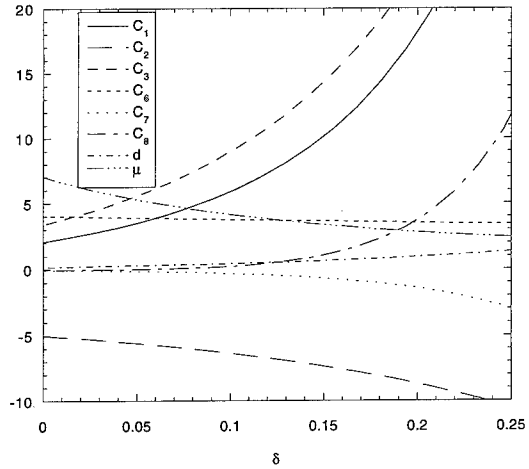

FIG. 2. Constants C_1, C_2, C_3, C_6, C_7, C_8, d, and μ versus δ for $\gamma = 1.6$.

length, given later. The density scale and pressure scale are $\tilde{\rho}_0$ and $\tilde{\rho}_0\,\tilde{D}_{\mathrm{CJ}}^2$, respectively. The dimensionless sound speed, reaction rate, and shock curvature that appear are $c = \tilde{c}/\tilde{D}_{\mathrm{CJ}}$, $r = \tilde{r}\tilde{l}_{rz}/\tilde{D}_{\mathrm{CJ}}$, and $\kappa = \tilde{\kappa}\tilde{l}_{rz}$. The scaled activation energy is $\theta = \gamma\tilde{E}/\tilde{D}_{\mathrm{CJ}}^2$. The reciprocal of the CJ-detonation Mach number squared is $\delta \equiv \tilde{c}_0^2/\tilde{D}_{\mathrm{CJ}}^2 \equiv 1/M_0^2$. The scaled heat of combustion is $q = \tilde{Q}/\tilde{D}_{\mathrm{CJ}}^2 = (1 - \delta)^2/[2(\gamma^2 - 1)]$. In the strong shock approximation $\delta \to 0$; however, in gases with highly state-sensitive reactions, δ cannot be neglected and represents a correction to the shock-state temperature. The characteristic reaction-zone length is a measure of the steady, CJ induction–zone length $\tilde{l}_{rz} = \tilde{k}^{-1}\tilde{D}_{\mathrm{CJ}}\exp[\theta/c_s^2]/\theta$, where c_s^2 represents the steady CJ shock sound speed squared (temperature). To make comparisons with published stability results, the conversions between δ, θ, and Erpenbeck's scaled activation energy [6], $E = \tilde{E}/(\tilde{P}_0/\tilde{\rho}_0)$ and heat-release $Q = \tilde{Q}/(\tilde{P}_0/\tilde{\rho}_0)$ are $E = \theta/\delta$ and $Q = \gamma(1 - \delta)^2/[2(\gamma^2 - 1)\delta]$. Later, we also use the steady half-reaction length $\tilde{l}_{1/2}$ to display results.

The Shock Evolution Equation

The intrinsic PDE for the detonation shock evolution equation derived in Ref. 1 is

$$\begin{aligned}(D_n - 1) &+ C_1\theta\ddot{D}_n e^{-2\mu\theta(D_n-1)} \\ &+ [C_2\theta + C_3 + C_4\theta(D_n - 1)]\dot{D}_n e^{-\mu\theta(D_n-1)} \\ &+ C_5(\theta\dot{D}_n)^2\, e^{-2\mu\theta(D_n-1)} + C_6\frac{\mathcal{L}_{\mathrm{CJ}}}{\theta} \\ &+ (C_7\theta + C_8)e^{-2\mu\theta(D_n-1)}\,\dot{\kappa} = 0\end{aligned} \tag{2}$$

where $\mathcal{L}_{\mathrm{CJ}}$ is

$$\mathcal{L}_{\mathrm{CJ}} = \ln|1 + d\theta\kappa e^{-\mu\theta(D_n-1)}| \tag{3}$$

The coefficients μ, d, and O_1 through C_8 are functions only of γ and δ. The expressions are derived and expressed in a sequential list in Ref. 1. Figures 1a and 1b and Fig. 2 display the relevant C_1–C_8, μ, and d versus δ for $\gamma = 1.2$ (chosen because of the large amount of past theoretical work) and 1.6 (representative of a stoichiometric mixture of H_2, O_2, diluted with 70% Ar).

To visualize the solutions predicted by Eq. (2), one imagines a smooth shock segment, with a reaction zone starting at the shock at $n = 0$ and ending at the sonic locus at n_{CJ}. The locus n_{CJ} identifies the location of the fire or thin zone of main reaction and the width of the induction zone (IZ) between the shock and fire. The leading-order formula for n_{CJ}, from Ref. 1, is

$$n_{\mathrm{CJ}} = -\frac{(\gamma - 1 + 2\delta)}{\gamma + 1}\left(\frac{c_s^4}{\alpha}\right) e^{-\mu\theta(D_n - 1)} \tag{4}$$

where $c_s^4/\alpha = \{2(\gamma - 1 + 2\delta)^2[2\gamma + \delta(\gamma - 1)]^2\}/\{(1 - \delta)[\gamma(3 - \gamma) - \delta(3\gamma - 1)](\gamma + 1)^2\}$. Thus, two fronts, one for the shock locus and one for the sonic locus, are determined by solving Eq. (2) and subsequently evaluating Eq. (4). The theory predicts the smooth and parametric variation of the states between the shock and sonic loci.

Eq. (2) has two important limits that confirm its approximate validity. In the quasi-steady limit, when only the effect of shock curvature is retained, one obtains a multivalued $D_n - \kappa$ relation that exhibits critical detonation curvature. By neglecting the time derivatives in Eq. (2), we obtain

$$D_n - 1 + C_6 \frac{\mathcal{L}_{\mathrm{CI}}}{\theta} = 0 \tag{5}$$

which is a result independently obtained by matched asymptotic methods [7,8], in contrast to the MSA technique used in Ref. 1. Neglecting the curvature terms in Eq. (2), a limiting second-order ODE in D_n is obtained:

$$\begin{aligned}(D_n - 1) &+ C_1\theta\ddot{D}_n e^{-2\mu\theta(D_n - 1)} \\ &+ [C_2\theta + C_3 + C_4\theta(D_n - 1)]\dot{D}_n e^{-\mu\theta(D_n - 1)} \\ &+ C_5(\theta\dot{D}_n)^2 e^{-2\mu\theta(D_n - 1)} = 0\end{aligned} \tag{6}$$

This ODE describes planar dynamics of near-CJ detonation.

A stability theory around $(D_n, \dot{D}_n) = (1, 0)$ can be compared with the linear stability theory of CJ detonation computed for the full reactive Euler equations, found in the work of Lee and Stewart [9]. It is shown in Ref. 1 that Eq. (6) has a stable limit cycle for parameters near those of neutral stability and correspond to the one-dimensional pulsations, similar to those first discovered by Fickett and Wood [10]. The neutral stability boundaries computed from the linearization of Eq. (6) are

$$C_2\theta + C_3 = 0 \tag{7}$$

For fixed γ, Eq. (7) can be plotted in an E–Q plane and is found to be in excellent agreement with the same stability boundary computed by Lee and Stewart [9]; hence, it provides another check of Eq. (2).

One expects the valid reduced description to be based on the solution of a well-posed initial value problem (2) that describes robust (if nonlinear) dynamics. Analysis of the linear properties of Eq. (2) indicates the limits of the description and type, however. For parameters such that the reduced description provided by Eq. (2) breaks down, we expect that additional time-dependent and higher-order curvature effects must be retained. However, we believe that Eq. (2) is adequate to qualitatively explain the evolution of systems of large regular detonation cells seen in the experiments in reduced pressure explosive gases, such as those extensively carried out by Strehlow and Lee [11,12], for example.

Review of the Derivation of Eq. (2)

The Euler equations are given by

$$\begin{aligned}&\frac{D\rho}{Dt} + \rho\bar{\nabla}\cdot\bar{u} = 0, \; \rho\frac{D\bar{u}}{Dt} + \bar{\nabla}_p = 0 \\ &\frac{De}{Dt} + p\frac{Du}{Dt} = 0, \; \frac{D\lambda}{Dt} = r\end{aligned} \tag{8}$$

The upstream state is motionless with $\bar{u} = 0$, with ambient pressure and density. In Ref. 1, the structure of the detonation is analyzed in intrinsic, shock-attached coordinates, instantaneously normal and parallel to the shock surface. The shock surface is represented in laboratory-fixed coordinates (x, y) by a function $\psi(x, y, t) = 0$. The shock surface can also be represented by a surface parameterization $\bar{x} = \bar{x}_s(\xi, t)$, where ξ measures length along the coordinate line of the surface. The outward normal (in the direction of the unreacted explosive) is given by $\hat{n} = \bar{\nabla}\psi/|\bar{\nabla}\psi|$. The total shock curvature is given by $\kappa(\xi, t) = \bar{\nabla}\cdot\hat{n}$. The intrinsic coordinates are related to the laboratory coordinates by $\bar{x} = \bar{x}_s(\xi, t) + n\hat{n}(\xi, t)$, where n, ξ are normal distance to the shock and the arclength along the shock surface. The normal shock velocity and curvature are functions of ξ and t, that is, $D_n = D_n(\xi, t)$ and $\kappa = \kappa(\xi, t)$.

The governing equations are transformed from (lab) (x, y, t) coordinates to (n, ξ, t) coordinates according to the coordinate transformation. In the limit $\kappa \to 0$, the transverse velocity u_ξ can be taken to be zero, and reduced Euler equations are derived that are accurate to $O(\kappa)$ [1,3,4,13]. With $U_n = u_n - D_n$, the reduced Euler equations can be written in a nearly conservative form obtained by placing all curvature and time-dependent terms on the right-hand side as

$$\frac{\partial(\rho U_n)}{\partial n} = -\kappa\rho(U_n + D_n) - \frac{\partial\rho}{\partial t} \tag{9}$$

$$\frac{\partial(\rho U_n^2 + p)}{\partial n} = -\kappa\rho U_n(U_n + D_n) - \frac{\partial(\rho U_n)}{\partial t} - \dot{D}_n \tag{10}$$

$$\begin{aligned}\frac{\partial}{\partial n}\left(\frac{1}{2}U_n^2 + \frac{1}{\gamma - 1}c^2 - q\lambda\right) &= -\dot{D}_n \\ &+ \frac{1}{\rho U_n}\frac{\partial p}{\partial t} - \frac{1}{U_n}\frac{\partial}{\partial t}\left(\frac{1}{2}U_n^2 + \frac{1}{\gamma - 1}c^2 - q\lambda\right)\end{aligned} \tag{11}$$

$$\frac{\partial \lambda}{\partial n} - \frac{r}{U_n} = \frac{1}{U_n}\frac{\partial \lambda}{\partial t} \tag{12}$$

The master equation,

$$(c^2 - U_n^2)\frac{\partial U_n}{\partial n} = qr(\gamma - 1) - \kappa c^2(U_n + D_n) + U_n\left(\frac{\partial U_n}{\partial t} + \dot{D}_n\right) - \frac{1}{\rho}\frac{\partial p}{\partial t} \tag{13}$$

is an alternate form of the energy equation that illustrates the special property of sonic detonation where the flow is sonic

$$\eta = c^2 - U_n^2 = 0 \tag{14}$$

and Eq. (13) is satisfied in general only if the right-hand side vanishes simultaneously, that is,

$$qr(\gamma - 1) - \kappa c^2(U_n + D_n) + U_n\left(\frac{\partial U_n}{\partial t} + \dot{D}_n\right) - \frac{1}{\rho}\frac{\partial p}{\partial t} = 0 \tag{15}$$

The pair of conditions (14) and (15) are called the *generalized CJ conditions* [5].

Eqs. (9)–(11) are integrated from the shock, at $n = 0$, to a point in the reaction zone to obtain

$$\rho U_n = -D_n - \kappa I_1 + J_1$$

$$\rho U_n^2 + p = D_n^2 + \frac{\delta}{\gamma} - \kappa I_2 + J_2$$

$$\frac{U_n^2}{2} + \frac{c^2}{\gamma - 1} - q\lambda = \frac{D_n^2}{2} + \frac{\delta}{\gamma - 1} + J_3 + J_4 \tag{16}$$

where I_1, I_2, J_1, J_2, J_3, and J_4 are integrals defined by

$$I_1 = \int_0^n \rho(U_n + D_n)d\bar{n},\ I_2 = \int_0^n \rho U_n(U_n + D_n)d\bar{n}$$

$$J_1 = -\int_0^n \frac{\partial \rho}{\partial t}\,d\bar{n}$$

$$J_2 = -\int_0^n \left[\frac{\partial(\rho U_n)}{\partial t} + \rho \dot{D}_n\right]d\bar{n}$$

$$J_3 = \int_0^n \frac{1}{\rho U_n}\frac{\partial p}{\partial t}\,d\bar{n}$$

$$J_4 = -\int_0^n \left[\dot{D}_n + \frac{1}{U_n}\frac{\partial}{\partial t}\left(\frac{1}{2}U_n^2 + \frac{1}{\gamma - 1}c^2 - q\lambda\right)\right]d\bar{n} \tag{17}$$

(The definitions of the integrals used here differ slightly from definitions used in Ref. 1, section 6.6.) If κ is set to zero and the time-dependent integrals J_1–J_4 are neglected, then Eq. (17) includes the integrals of the steady, one-dimensional Rankine–Hugoniot relations.

The rate equation (12) is used to change the independent variable in the structure from n to λ according to $dn = [U_n/(r - \lambda_{,t})]d\lambda$. Importantly, the reaction rate r appears in the denominator of the transformed integrals in λ, so in the fire r becomes exponentially large and many terms in the approximations to the integrals are exponentially small and analytic evaluation is possible. Liebnitz's rule is used to compute explicitly the integrals over $\partial\rho/\partial t$ and $\partial p/\partial t$, evaluated at the CJ point.

Thus, Eqs. (16) are modified Rankine–Hugoniot relations, which can be inverted algebraically to solve for the states ρ, U_n, and p in terms of λ and the integrals I_1, I_2, J_1, J_2, J_3, and J_4. The key is to approximate these integrals in a rational and systematic way. Once that is done, one can generate improved corrections to the states. Finally, one can insert the corrected solution into the generalized CJ conditions to deduce the value of λ_{CJ} and the eigenvalue constraints on D_n, κ and their derivatives.

The MSA technique starts with an initial approximation for the detonation structure (the one-dimensional, steady solution) and evaluates the integrals. Then the right-hand sides of Eq. (16) are considered to be known, and the system is inverted algebraically to generate a new correction to the states. This new correction is used to reevaluate the integrals for another iteration. Two iterations were carried out in Ref. 1 to generate a well-posed evolution equation that would approximate low, spatial, and temporal frequencies. The algebra required is still substantial, despite the simplification afforded by the MSA technique. However, the power of this newly applied technique is illustrated by the derivation of a substantially more complex relation than what had appeared in the older $D_n - \kappa$ theory of Bdzil and Stewart.

Wave Hierarchy

Evolution equation (2) has a wave hierarchy in the sense discussed by Whitham [14]. To illustrate this, consider the perturbation of the detonation shock from CJ, steady, plane ($D_n = 1$). Represent the shock surface as $\psi = y - t - \phi(x,t) = 0$, where ϕ is small. The definitions of the normal velocity, curvature, and surface derivatives imply $D_n - 1 \sim \phi_t$, $\dot{D}_n \sim \phi_{tt}$, $\ddot{D}_n \sim \phi_{ttt}$, $\kappa \sim -\phi_{xx}$ and $\dot{\kappa} \sim -\phi_{xxt}$. Substitutions show that Eq. (2) is a third-order PDE in time and second order in space. Our interest is in the choice of parameters γ, δ, and θ such that Eq. (2) is hyperbolic and admits transverse waves on the shock.

The highest-order wave operator comes from a pairing of $\ddot{D}_n$ and $\dot{\kappa}$, which is a time derivative of a

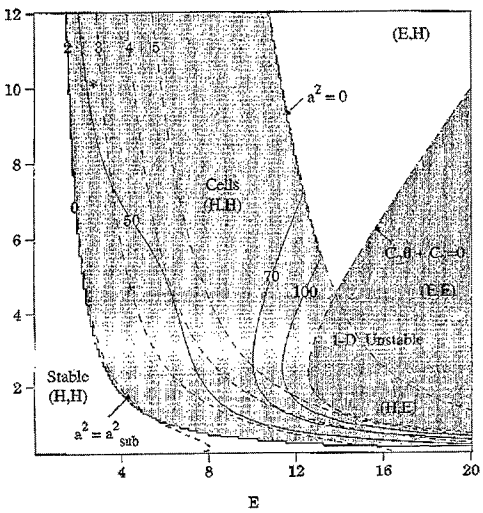

FIG. 3. Typical regions of cellular dynamics and one-dimensional unstable dynamics are shown as light and dark gray shades, respectively. Regions are labeled according to mathematical type (H, E) for hyberbolic-subelliptic, and so on. Solid numbered lines are contours of constant λ_{ns}; dashed numbered lines are contours of constant $1/a$ (cell-aspect ratio). The asterisk (*) represents the location in parameter space of a typical experiment.

second-order wave operator of the form $\partial/\partial t(\phi_{tt} - a^2\phi_{xx})$. The square of the hyperbolic wave speed is simply the ratio of the coefficient of $\dot{\kappa}$ and $\dot{D}_n$,

$$a^2 = \frac{C_7\theta + C_8}{C_1\theta} \tag{18}$$

Similarly, a subhyperbolic wave operator appears of the form $\phi_{tt} - a^2_{sub}\phi_{xx}$, from the pairing of $\dot{D}_n$ and κ, and the square of the subhyperbolic wave speed is simply the ratio of the coefficient of κ and $\dot{D}_n$,

$$a^2_{sub} = \frac{dC_6}{C_2\theta + C_3} \tag{19}$$

Finally, ϕ_t is the operator associated with $D_n - 1$ and has zero wave speed.

The conditions for Eq. (2) to be hyperbolic and subhyperbolic are, respectively,

$$C_7\theta + C_8 > 0 \text{ and } C_2\theta + C_3 > 0 \tag{20}$$

A stability criterion based on the wave speeds from Ref. 14 is

$$\begin{aligned} &0 < a^2_{sub} < a^2, \text{ stable} \\ &0 < a^2 < a^2_{sub}, \text{ unstable} \end{aligned} \tag{21}$$

Linear Instability Analysis

Eq. (2) linearized about the plane CJ detonation is

$$\phi_t + (C_1\theta)\phi_{ttt} + (C_2\theta + C_3)\phi_{tt} - (dC_6)\phi_{xx} - (C_7\theta + C_8)\,\phi_{xxt} = 0 \tag{22}$$

The dispersion relation with $\phi = e^{\omega t + ikx}$ is

$$\omega + (C_1\theta)\omega^3 + (C_2\theta + C_3)\omega^2 + (dC_6)k^2 + (C_7\theta + C_8)k^2\omega = 0 \tag{23}$$

The neutrally stable frequency, $\omega = i\omega_{Im}$, and wave number are

$$\begin{aligned} (\omega^2_{Im})_{ns} &= \frac{1}{C_1\theta}\left(\frac{a^2_{sub}}{a^2_{sub} - a^2}\right) \\ k^2_{ns} &= \frac{1}{C_1\theta}\left(\frac{1}{a^2_{sub} - a^2}\right) \end{aligned} \tag{24}$$

with the corresponding wavelength

$$\lambda_{ns} = \frac{2\pi}{k_{ns}} = 2\pi\sqrt{C_1\theta(a^2_{sub} - a^2)} \tag{25}$$

For the special one-dimensional case of $k = 0$, the neutral stability boundary is given by the condition $(C_2\theta + C_3) = 0$, which also corresponds to $a^2_{sub} = \infty$. Additionally, it can be shown that $(\omega_{Im})_{ns}/k_{ns}$ is the fastest phase speed among the unstable and neutrally stable wave numbers.

The limiting form of the complex growth rate ω, for $k \to \infty$, as calculated from the dispersion relation, is to O(1)

$$\omega = \frac{dC_6}{2C_1\theta}\left(\frac{1}{a^2} - \frac{1}{a^2_{sub}}\right) \pm ika^2 + \ldots \tag{26}$$

Consistent with this result, it can be shown for the unstable condition $a^2 < a^2_{sub}$ that there is a continuum of unstable wave numbers that in general runs from k_{ns} to $k = \infty$. Likewise, for $a^2_{sub} < a^2$, all k are stable. For the full Euler equations [15], it has been demonstrated that disturbances are stable in the limit of large wave number. Since the asymptotic theory discussed here is in reality a low wave number theory, the exact linear spectrum will possess a band of unstable wave numbers.

The valid parameter range for the application of Eq. (2) is partially indicated by its dispersion relation. For hyperbolic evolution, one must have parameters γ and δ such that $C_7\theta + C_8 > 0$. At the hyperbolic boundary where $C_7\theta + C_8 = a^2 = 0^+$, Eq. (26) shows that real growth rates for small disturbances are infinitely large. Indeed, crossing this parameter boundary corresponds to a change in type of Eq. (2) from hyperbolic to elliptic. The conclusion is, of course, that on the unphysical (elliptic) side of the boundary the asymptotic description breaks down, and additional physics in the form of dynamic and curvature corrections must be included.

The stability boundary $a^2 = a^2_{sub}$ has stable trans-

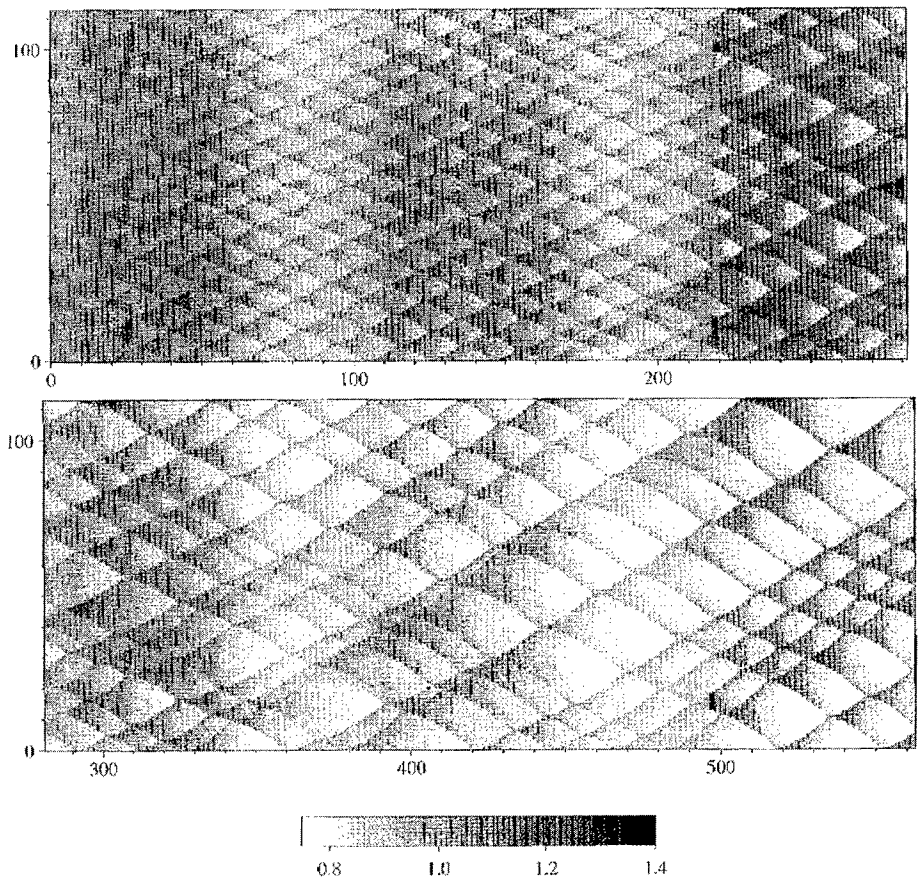

FIG. 4. Gray-scale plot of D_n versus fixed locations in space, for $Q = 10.2$, $E = 2.71$, and $\gamma = 1.6$. The spatial scale is the 1/2 reaction length, where $\bar{l}_{1/2} = 37.5\bar{l}_{rz}$.

verse disturbances on the side at which a^2 is larger than a^2_{sub}, and unstable transverse disturbances where a^2_{sub} is larger than a^2. Standard considerations of unstable wave hierarchies [14] show that on the unstable side one expects the formation of discontinuous solutions, in this case, shock–shock intersection. Indeed, this is what we find when numerical solutions of Eq. (2) are carried out (see Ref. 1 and the next section). The parameter region in which self-sustained, well-posed cellular dynamics occurs is given by the three inequalities, $C_2\theta + C_3 > 0$, $C_7\theta + C_8 > 0$, and $a^2_{\text{sub}} > a^2$. A typical region in a E–Q plane is shown in Fig. 3.

Cellular Dynamics

Here we describe a representative numerical solution to Eq. (2) that corresponds to the experiment and has parameter values in the cell region of the E–Q plane described previously. The numerical solutions were generated for a simplified version of Eq. (2), where the terms $(D_n - 1)\dot{D}_n$ and $(\theta\dot{D}_n)^2$ were dropped, whereas the nonlinearity of $\mathcal{L}_{\text{CJ}}$ was retained, so that we specifically solved

$$\begin{aligned}(D_n - 1) &+ C_1\theta\ddot{D}_n e^{-2\mu\theta(D_n-1)} \\ &+ [C_2\theta + C_3]\dot{D}_n e^{-\mu\theta(D_n-1)} \\ &+ C_6\frac{\mathcal{L}_{\text{CJ}}}{\theta} \\ &+ (C_7\theta + C_8)e^{-2\mu\theta(D_n-1)}\kappa = 0\end{aligned} \tag{27}$$

The numerical solution [16] is for the shock location $y = y_s(x, t)$, where y is the direction along the channel axis and x is the distance across the channel. Eq. (2) is further decomposed into a system of three first-order PDEs with y_s, D_n, and $\dot{D}_n$ as the dependent variables. The advective spatial derivatives that appear are treated using second-order ENO upwinding [17] and the curvature terms with central differences.

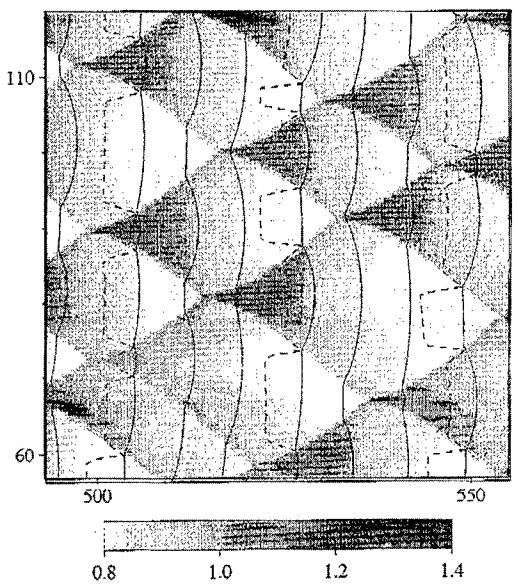

FIG. 5. Gray-scale plot of D_n with instantaneous shock fronts given as solid lines for $Q = 2.5$, $E = 5$, and $\gamma = 1.6$. The spatial scale is the 1/2 reaction length, where $\bar{t}_{1/2} = 5.49\bar{t}_{rz}$. The location of the fire for three times are given as dashed lines.

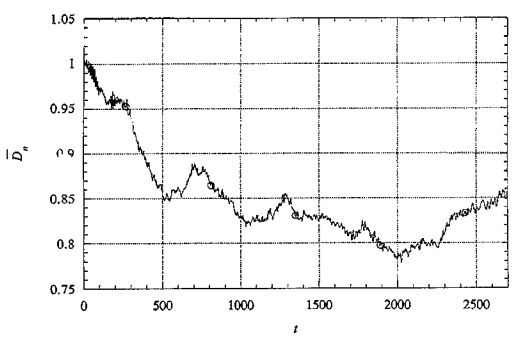

FIG. 6. Plot of spatial average of D_n, shown in Fig. 4, versus time.

Figures 4 and 5 show examples of the solution to Eq. (27) in terms of a gray-scale contour plot of the value of D_n that is attained at each fixed point in the channel when the shock crosses that point. Figure 4 is carried out for $Q = 10.2$, $E = 2.71$, and $\gamma = 1.6$ that correspond to a CJ Mach number of 4.67 as reported in Ref. 12. This contour plot effectively produces a simulated smoke foil. Two segments of the channel are shown. The shock travels from left to right, and starts from the top. At time $T = 0$, the shock is assumed to be flat, with an initial, sinusoidal velocity disturbance $D_n = 1 + 0.03\cos(\pi x/6) + 0.02\cos(2\pi x/3)$ and $\dot{D}_n = 0$, where $x = \bar{x}/\bar{t}_{rz}$. Initially, the detonation shock appears quite flat, but the strength of the small transverse waves grows. As the detonation propagates, the cells merge and grow in size and strength and appear to saturate.

Figure 5 shows similar results for $Q = 2.5$, $E = 5$, and $\gamma = 1.6$ with instantaneous contours of the shock locus (solid line) and sonic locus (broken line) displayed. In regions in which shock velocity is above CJ (overdriven), the fire is close to the shock; conversely when the shock velocity is below CJ (underdriven), the fire is relatively farther away from the shock, in accordance with observations by the experimentalists carried out with smoke foils. For both simulations, the variation in the normal detonation velocity as computed in the numerical solution is between approximately 0.7 and 1.4, which is both qualitatively and quantitatively in agreement for that reported in the experimental accounts [18,12]. Figure 6 shows a plot of the spatial averaged normal velocity of Fig. 4 as a function of time. Note that when the detonation cells are smaller, as is the case early in the channel, the speed is higher, but as the cells grow and coalesce, the average detonation speed drops below CJ.

Criterion for Cell Widths

We have found in the course of many simulations of Eq. (2) that the neutral stability wavelength, λ_{ns}, is a good predictor of the final stable cell widths observed in the simulations, if the channel walls are wide enough. Recall that λ_{ns} also corresponds to the fastest phase speed among the neutrally stable and unstable linear modes. We pose this as a criterion that

$$\lambda_{\text{cell}} = \lambda_{ns} = 2\pi/k_{ns} = 2\pi\sqrt{C_1\theta(a_{\text{sub}}^2 - a^2)}$$

Figure 3 also shows contours of constant λ_{ns} according to Eq. (25) in the E–Q parameter plane, for $\gamma = 1.2$ and $\gamma = 1.6$, that would correspond to experiments. The cell aspect ratios W/L can be predicted by the reciprocal of the transverse wave speed a, that is, $W/L = 1/a$ and are shown in Fig. 3 as numbered dashed lines.

Conclusions

Weakly curved, slowly varying asymptotics with large activation energy, derived with a newly applied technique of the method of successive approximation, has led to the derivation of a more complex class of shock surface evolution equations applicable to gases. Linear stability analysis applied to Eq. (2) indicates a wave hierarchy, pulsating and transverse wave instabilities; the latter lead to cellular instability. The triple-points tracks are found as shock–shock intersections of smooth segments of the cellular front. The cell width and the aspect ratio highly cor-

relate to the predictions of linear analysis and let us pose criteria and give explicit formulas. The theoretical predictions are consistent with the notion that the power of the detonation front is derived from the normal reaction zone and that the triple points are generated from a natural consequence of the nonlinearity of the normal front evolution and the shock–shock intersections generated by otherwise independently propagating fronts, not as the centers of blast waves. Further analysis, which may require the inclusion of more time-dependent and curvature effects and additional wave families on the shock, is needed to extend this description.

Acknowledgments

Supported by the U.S. Air Force, Wright Laboratories, Armament Directorate (F08630-94-10004) the Air Force Office of Scientific Research (F496-93-1-0532), and the Department of Energy, Los Alamos National Laboratory.

REFERENCES

1. Yao, J. and Stewart, D. S., *J. Fluid Mech* 309:225 (1996).
2. Stewart, D. S. and Bdzil, J. B., *Combust. Flame* 72:311 (1988).
3. Stewart, D. S. and Bdzil, J. B., "Mathematical Modeling in Combustion Science," *Lecture Notes* Phys. 299:17 (1988).
4. Bdzil, J. B. and Stewart, D. S., *Phys. Fluids* A, 1(7):1261 (1988).
5. Wood, W. W. and Kirkwood, J. G., *J. Chem. Phys.* 22:1920 (1954).
6. Erpenbeck, J. J., *Phys. Fluids* 7:684 (1964).
7. Yao, Jin and Stewart, D. S., *Combust. Flame* 100:519 (1995).
8. Klein, R., Kroc J. C., and Shepherd J. E., *Phys. of Fluids* (1996), submitted.
9. Lee H. I. and Stewart, D. S., *J. Fluid Mech.* 216:103 (1990).
10. Fickett, W. and Wood W. W., *Phys. Fluids* 1:528 (1966).
11. Strehlow, R. A., Llaugminas, R., Watson, R. H., and Eyman, J. R., *Eleventh Symposium (International) on Combustion,* The Combustion Institute, Pittsburgh, 1967, p. 683.
12. Lee, J. H. S., *Ann. Rev. Fluid Mech.* 16:311 (1984).
13. Klein, R. and Stewart, D. S., *SIAM J. Appl. Math.* 53(5):1401 (1993).
14. Whitham, G. B., *Linear and Nonlinear Waves*, Wiley, New York, 1974.
15. Short M., *SIAM J. Appl. Math.* accepted for publication.
16. Aslam, T. D., Ph.D. Thesis, University of Illinois, 1996.
17. Osher, S. J. and Sethian, J. A., *J. Comp. Phys.* 79:12 1988.
18. Strehlow, R., *Combustion Fundamentals*, McGraw-Hill, New York, 1984.

COMMENTS

J. M. Powers, University of Notre Dame, USA. Calculations similar to yours in two-dimensions have shown that predicted cell size can be affected by grid resolution. Have you demonstrated the sensitivity or insensitivity of your three-dimensional cell sizes to the resolution of your grid?

Author's Reply. So far, we have only developed numerical solutions for our evolution equation in two-dimensions. We have systematically refined our computational mesh by halving and obtain the same results. So we do not believe that the cell patterns shown in this paper depend on the mesh.

REFERENCE

1. Lee, H. I. and Stewart, D. S., *J. Fluid Mech.* 216:103 (1990).

J. Buckmaster University of Illinois, USA. I congratulate the authors on the innovative idea of constructing a nonlinear evolution equation to describe cellular detonations, but I have concerns about the physics implicit in your equation. My understanding is that the linear dynamics of your evolution equation defines the final cell size. The growth rate defined by the linear dispersion relation is a monotonically increasing function of wave number which vanishes at a critical non-zero wavenumber, so that all wavenumbers greater than the critical are unstable. At the same time the phase speed is monotonically decreasing. The nonlinear simulations show that a slow wave is absorbed when overtaken by a fast wave, so that ultimately only the fastest unstable waves survive. These are waves with wavenumber equal to the critical. However, the exact linear dynamics, known from numerical calculations of the eigenvalue problem, is quite different from that of your equation. There is a critical wave number, but it is the maximum wave number for instability, not the minimum. In light of this, what physical significance can be attributed to the late-time behavior of your nonlinear simulations?

Author's Reply. As we have discussed previously, we agree with your description of how the cells form as predicted solely from the evolution equation that we have derived. We do not agree that the linear dynamics of the low frequency modes of the exact Euler equation model and

our reduced evolution equation differ dramatically. They differ only in one important respect. At large wave numbers it is known that disturbances are stable. So the exact linear spectra that we are concerned with should typically have a large band of flat unstable wave numbers, bounded by stability at sufficiently small and large wavenumber. The importance of the wavenumber with maximum growth rate is then diminished and our work suggests that one might expect cell sizes to be selected in a linear sense by the fastest neutrally stable disturbance, so long as that wavenumber corresponds to the fastest phase velocity. Thus the early time dynamics of a nearly flat detonation would exhibit (smaller) cells at the maximum growth rate, but as time goes on the cells should grow towards the neutrally stable (larger) cells which have lower wavenumber and travel at faster speeds across the shock.

•

Dr. Andy C. McIntosh, University of Leeds, UK. The work is a milestone in detonation theory. It is particularly significant that cell sizes can be predicted with good qualitative agreement with experiment by using Asymptotic theory based on inverse activation energy, and inverse CJ Mach Number squared, (both regarded as small with an implication of small heat release).

I noticed that the induction zone thickness (dotted lines in Fig. 5) are remarkably one dimensional. Can the Clarke-Kapila theory be applied to these regions? In particular is the Clarke-Kapila equation (determining the progress of acoustic disturbances in a potentially explosive region) valid?

Author's Reply. Thank you for your kind comments. The calculations that lead to this theory were not explicitly based on small-heat release, although that is where the theory could be expected to apply with predictive success. In that case M_{CJ} would tend to one. A low frequency version of the Clarke-Kapila equation can be expected to apply in the induction zone.

•

F. A. Williams, UCSD, USA. While this is an attractive simulation, there is a fundamental flaw in the theory. You have a slow-evolution assumption, which ignores the existence of an infinite number of short-time instabilities in your one-step activation-energy asymptotics. Consequently, in principal you cannot accommodate the real chemistry. You must modify your chemical model to obtain a useable result.

Author's Reply. There is not a fundamental flaw in the theory. Your second statement is wrong and is based on very old, failed theories for the square wave detonation model due to researchers like Zaidel and Erpenbeck in the 60's. There is not an infinite number of short-time instabilities, nor would one expect them, unless one wanted to wait an infinite amount of time. The early treatments led to pathologies. Our work is based on large but finite activation energies.

A proper numerical treatment of the linear stability problem was carried out by H. I. Lee and myself and appeared in Ref. 1 of the paper. There we showed that for large but finite activation energy there is a finite number of (one-dimensional) instabilities and for sufficiently large frequencies, disturbances were stable. At lower values of heat release, where we expect this theory to apply, there are few number of unstable modes as predicted from exact linear theory.

Also this present work is based fundamentally on a nonlinear (not linear) description and simply assumes that the shape changes of the detonation shock are slow compared with the particle transit time through the detonation reaction zone and that the shock curvature measured on the scale of steady, one-dimensional reaction zone thickness is small. Both assumptions are confirmed by experiments and recent high-quality numerical simulations of the exact Euler equation model. These assumption are the only ingredients used. The activation-energy asymptotics for finite but large activation energy, is simply adopted as a tool to give analytical expressions for the structure of the reaction-zone and leads us to a tractable rational theory, for the dominant low frequency modes. There is no reason or principle that suggests that we can't continue to learn useful things from this simple one-step model. So far it has been, in a qualitative sense, very successful. Certainly it is important to study systems with more complex chemistry in a systematic, rational, not ad hoc way.

Twenty-Sixth Symposium (International) on Combustion/The Combustion Institute, 1996/pp. 2991–2998

DETAILED STRUCTURE AND PROPAGATION OF THREE-DIMENSIONAL DETONATIONS

DANIEL N. WILLIAMS AND LUC BAUWENS
Department of Mechanical Engineering
The University of Calgary
Calgary, Alberta, Canada T2N 1N4

ELAINE S. ORAN
Laboratory for Computational Physics and Fluid Dynamics
Naval Research Laboratory
Washington, DC, 20375 USA

Self-sustaining detonations exhibit a three-dimensional structure within the reaction zone which is much more complex than one-dimensional classical theory. While the structure of two-dimensional detonations is now fairly well understood, the details of the three-dimensional structure remain largely unknown. Numerical simulation, performed with the reactive Euler equations coupled to a single-step chemistry model, yields insight into the three-dimensional reaction zone structure. Simulations in a square channel show that, in the absence of wall losses, the three-dimensional transverse wave spacing is the same as in two dimensions. However, the transverse wave structure is much more intricate. Two perpendicular modes exist in this channel, and they are approximately one-quarter of a period out of phase. This phase shift accounts for the slapping wave phenomenon observed in experiments. The slapping wave imprints on smoke foils occur when the transverse wave collides with the wall. The curvature of the imprints is explained by the curvature of the slapping wave, which is convex toward the wall. The interaction of the two transverse waves results in a vorticity field that is much more complex than in two dimensions. In two dimensions, vorticity originates from a point singularity, which is now replaced by a line singularity that forms closed loops interconnecting the two sets of transverse waves. The interconnection changes after collisions, creating cuts and free edges on the sheet structure which otherwise remains globally interconnected. It is the vorticity in the part of the sheet initiating or ending along a free edge that rolls up into rings. The rings entrain unburned fluid behind the Mach stem, as in two dimensions. The vorticity system provides a strong coupling mechanism between the two orthogonal sets of transverse waves.

Introduction

Experimental evidence has shown that detonations have an inherently three-dimensional structure [1–4]. More recent studies indicate that the transverse wave system behind the detonation is essential in sustaining propagation [5]. Yet the details of the three-dimensional reaction zone and wave structure behind the front cannot be resolved by experiments [6] limited by diagnostics that cut along a plane of sight. For example, smoke foils show only two-dimensional slices. While some attempts have been made to perform 3D computations, the best documented attempt was made by Fujiwara and Reddy [7]. Other than this work, computations have been one- or two-dimensional [8–15]. Based upon contributions initially from experiments, followed by simulations, the two-dimensional cell structure is fairly well understood. It is only now that computers are becoming powerful enough to simulate three-dimensional detonations with adequate detail.

This paper presents results from numerical simulations of a three-dimensional overdriven detonation. Our goal was to study the transverse wave structure and to compare it with the two-dimensional structure. In addition, we are interested in slapping waves [1,2] and their imprint on smoke foils. To that effect, we have performed simulations of a detonation in a square channel that is five ZND half-reaction lengths on a side. This width corresponds to the two-dimensional transverse wave spacing determined by numerical simulations in wider channels. We chose this size based upon the expectation that, in the absence of wall effects (such as heat losses or boundary layers), which our model does not include, the spacing would be unchanged in three dimensions.

Physical and Numerical Model

The flow is described by the reactive Euler equations (equation 1). The fluid is an ideal gas with con-

stant specific heats, molecular weight, and heat of reaction. All diffusive processes (mass, thermal, viscous) are neglected, and chemistry is modeled with single-step Arrhenius kinetics.

$$\frac{\partial \rho}{\partial t} + \nabla \cdot (\rho \boldsymbol{u}) = 0 \tag{1a}$$

$$\frac{\partial (\rho \boldsymbol{u})}{\partial t} + \nabla \cdot (\rho \boldsymbol{u} \cdot \boldsymbol{u}) + \nabla \boldsymbol{p} = 0 \tag{1b}$$

$$\frac{\partial E}{\partial t} + \nabla \cdot (E\boldsymbol{u} + p\boldsymbol{u}) = 0 \tag{1c}$$

$$\frac{\partial (\rho Z)}{\partial t} + \nabla \cdot (\rho Z \boldsymbol{u}) = -K\rho Z \exp(-E^0/T) \tag{1d}$$

$$p = \rho R T \tag{1e}$$

$$E = \frac{p}{(\gamma - 1)} + \frac{1}{2}\rho \boldsymbol{u} \cdot \boldsymbol{u} + Q\rho Z \tag{1f}$$

where ρ, p, T, $\boldsymbol{u}$, E, and Z are, respectively, density, pressure, temperature, velocity, energy, and mass fraction reactant. Initial conditions are given by perturbed one- or two-dimensional ZND detonations consistent with our boundary conditions, in an inertial frame of reference, moving at the steady ZND detonation velocity. The boundary conditions consist of the unburned mixture entering the domain at the overdriven (supersonic) detonation velocity, a nonreflecting outflow, and the walls modeled as planes of symmetry (free-slip). All variables are made dimensionless with respect to the preshock (unburned) state. The parameters appearing in the problem are the ratio of specific heats, γ, the heat release, Q, the activation energy, E^0, and the overdrive parameter $f = (D/D_{CJ})^2 \geq 1$, which determines the inflow velocity, D. The Chapman-Jouguet (D_{CJ}) velocity is calculated from

$$D_{CJ} = \sqrt{1 + Q(\gamma^2 - 1)/2\gamma} + \sqrt{Q(\gamma^2 - 1)/2\gamma}$$

One additional free parameter, the reaction-rate multiplier K, sets the spatial and temporal scales.

The numerical solution uses a fractional step technique [14]. Three-dimensional solutions are constructed by direction-splitting the convective terms in the equations. The gas dynamic steps are solved using the flux-corrected transport algorithm [16], with two-step time integration [14]. FCT has previously been used to solve a wide variety of problems involving detonations [7–9,13–14].

Results

We study the case $f = 1.2$, $Q = 50$, $E^0 = 10$, and $\gamma = 1.20$, for which several numerical studies [10–13] have established the solution in one and two dimensions. Linear stability analysis shows that the ZND wave for this case is stable to longitudinal (1-D) modes [17], and only moderately unstable in the transverse directions [10–11], so that the transverse wave structure should become nearly periodic. This is an ideal case for interpreting the results because the structure remains relatively well organized. Furthermore, this parameter set roughly corresponds to low pressure H_2-O_2 mixtures, diluted with 60–80% argon or helium, for which there is a wealth of experimental cell data [1,2,18]. The H_2-O_2-Ar system creates very regular smoke foil records for a high percentage of argon dilution, which is consistent with stability analysis. For instance, for typical conditions such as 10 kPa and 300 K, the detonation Mach number would be 6.81, which corresponds to a detonation velocity of 2384 m/s. The state at the end of the reaction zone would then be 360 kPa, 4000 K, and velocity of 1584 m/s ($M = 0.689$).

An initial calculation (not shown) was started with a one-dimensional ZND wave, to which we added a symmetrical 3-D perturbation in the form of a localized explosion just behind the leading shock. We calculated one-quarter of a cell on a $170 \times 40 \times 40$ grid, corresponding to a resolution of 8 cells in the ZND half-reaction length, or approximately the highest resolution used in [7]. The results showed a very slow breakdown of the symmetry along diagonals, so reaching a periodic regime would have required many time steps.

Instead, we then used the two-dimensional periodic solution as an initial condition, onto which we added a three-dimensional perturbation that was perpendicular to the motion of the initial (2-D) transverse waves. This led to a near-periodic regime much more quickly. (This calculation used $170 \times 80 \times 80$ computational cells, or 16 cells per ZND half-reaction length, which is about twice as resolved as the highest resolution used in Ref. 7.) Figure 1 is a schematic diagram of how results are presented in Figs. 2–7, which show pressure and density gradients at six times, over one-half of a detonation cell period.

This simulation reached a periodic regime corresponding to the rectangular mode described by Strehlow [2]. Just behind the leading shock, two sets of transverse waves propagate perpendicular to one another, out of phase by approximately 90°. The longitudinal slices show the classical triple point structures, although these become somewhat obscured by the slapping wave in Figs. 3a and 4a. The front views in Figs. 2–7 are similar with frontal views obtained in experiments described in Refs. 2 and 19–20. There is good qualitative agreement between the results as far as the curvatures and the smoke foil imprints are concerned.

Discussion

The two main differences between two- [10–13] and three-dimensional results include the slapping

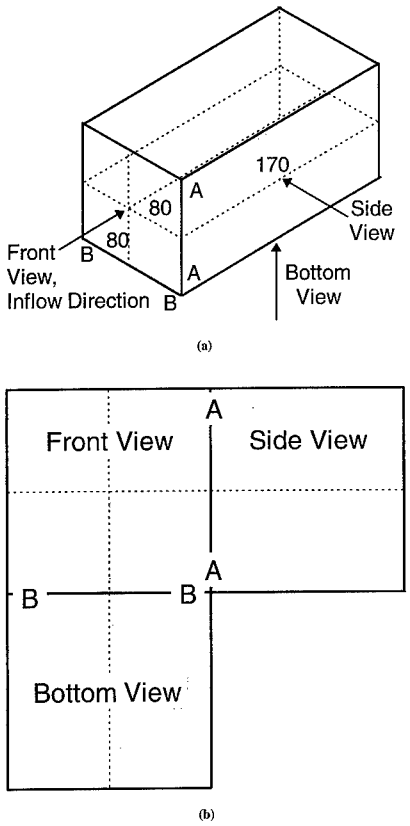

FIG. 1. A schematic diagram of how the results are displayed. (a) The shaded region is the 3-D 170 × 80 × 80 computational domain. Arrows show the viewing directions for the multiview picture in (b). (b) A view of the 3-D domain in (a) folded out, using lines AA and BB as hinge points. Each frame in Figs. 2–7 is constructed by folding out the walls of the three -dimensional domain (a) along the lines AA and BB, into a single plane (b). The upper left quadrant of each frame shows a view of the state just behind the leading shock, displayed from the perspective of an observer looking "head on" at the detonation. The upper right and lower left quadrants show longitudinal cuts along the side and bottom walls of the domain, respectively. These slices contain the structures responsible for writing smoke foil records, including triple point tracks and slapping waves. Since we are using free-slip boundary conditions, the walls represent planes of symmetry. By mirroring the images about the planes of symmetry (indicated by dashed lines), an entire cell is shown while calculating only a quarter cell (shaded area).

wave and a more intricate vorticity field. The two transverse waves are out of phase by 90°, or one-quarter of a period. These waves are responsible for the slapping wave imprints on smoke foils [1,2], which almost invariably occur partway through the cell cycle of the perpendicular transverse mode. The

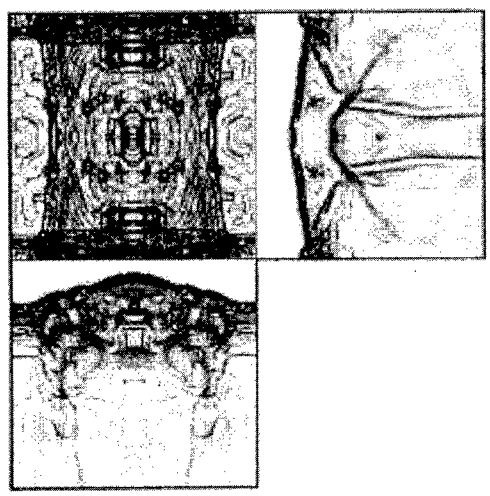

(a) Pressure gradient

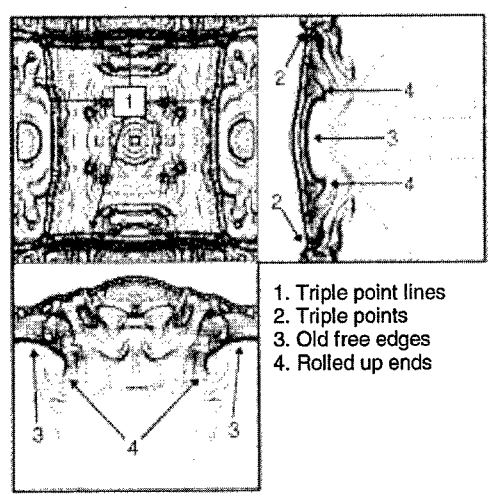

(b)Density gradient

FIG. 2. Pressure and density gradient for time step 17,650, time 65.0. This computation was performed on a 170 × 80 × 80 mesh with a minimum cell size in the longitudinal (170) direction of 16 cells per ZND half-reaction length. The gradients are displayed using a grayscale colormap which gives an effect similar to Schlieren-type images often used in experimental work. The key on each of Figs. 2–7 shows triple point lines on the front views (1), triple points on the side and bottom views (2, when visible), free edges of the vortex sheet (3), rolled-up ends of the free edges (4).

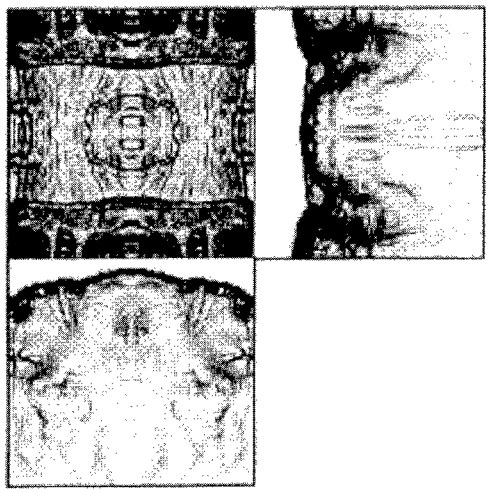

(a) Pressure gradient

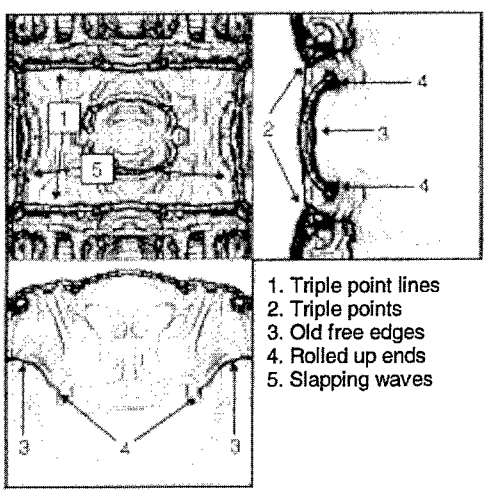

(b) Density gradient

FIG. 3. Pressure and density gradient for time step 17,875, time 65.4. Two of the triple point lines (1) on the front view have been marked as slapping waves (5), since they are in the process of colliding with the walls. The side view indicates the presence of large regions of high pressure gradients (the black regions). The high pressure gradients indicate high fluid acceleration in these regions, which would account for the slapping wave imprints on smoke foils.

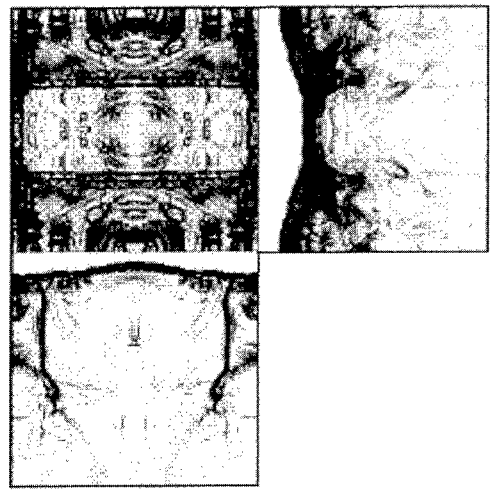

(a) Pressure gradient

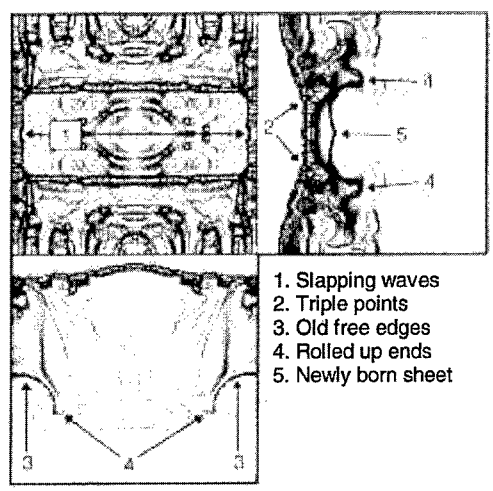

(b) Density gradient

FIG. 4. Pressure and density gradient for time step 18,160, time 65.8. While the old free edges of the vortex sheet (3,4) continue to move down stream, a new edge is visible (5) that is created in the wake of the slapping wave collision.

imprints are associated with collision with the wall of a wave moving toward the wall. Evidence for this mechanism can be seen in the front views in Figs. 3a and 4a, where the slapping wave collides with the wall. The large pressure gradients that exist behind the wave (the blackness on the side view indicates high gradients due to high local pressure spikes) indicate a large acceleration which results in soot being

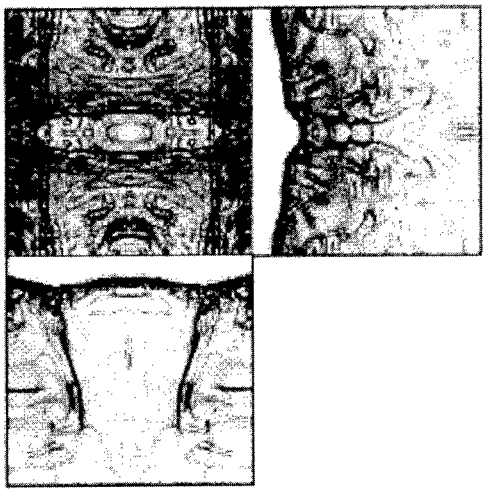

(a) Pressure gradient

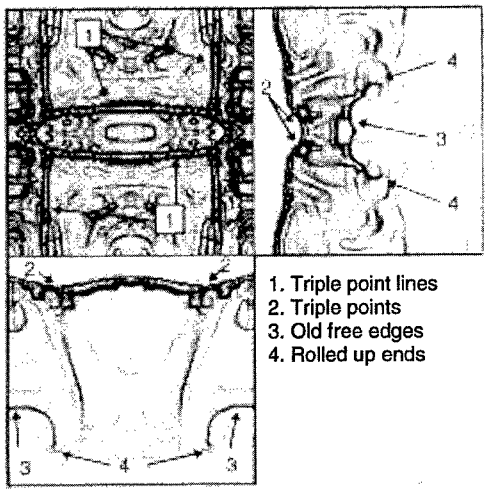

(b) Density gradient

FIG. 5. Pressure and density gradient for time step 18,380, time 66.2.

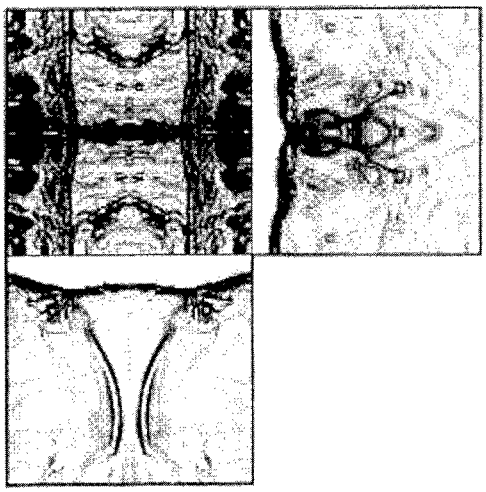

(a) Pressure gradient

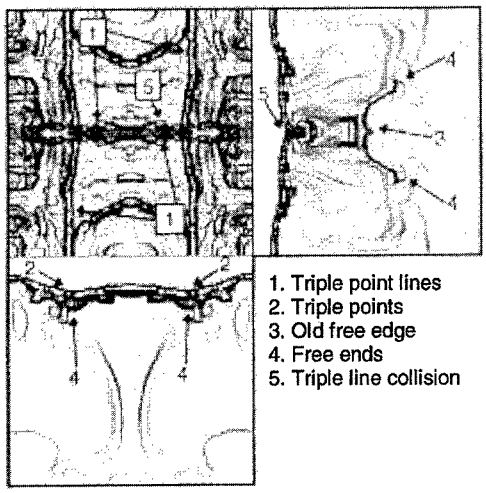

(b) Density gradient

FIG. 6. Pressure and density gradient for time step 18,650, time 66.6. In addition to the regular structures, one set of triple point lines is colliding on the front view (5). It is at this point that new free edges are created after the collision.

removed from the foil. In contrast, cell patterns are etched onto smoke foils by the vorticity generated at the triple point intersection [3].

Slapping-wave imprints form a well-defined curve which is always concave toward the direction of propagation of the detonation. Because of their curvature (see front views of Figs. 2 and 3), the vertical waves first hit the walls at the top and bottom of the duct. The impact point subsequently moves along the wall and arrives at the center last. Meanwhile the detonation also propagates, which moves the point of impact along a trajectory that is a function of both the detonation velocity and the transverse slapping wave velocity, resulting in a curve convex toward the front.

The density plots in Figs. 2–7 show a vorticity and wave structure along longitudinal slices quite different from two-dimensional results. In 2-D, vorticity generated at the triple point follows a line that rolls

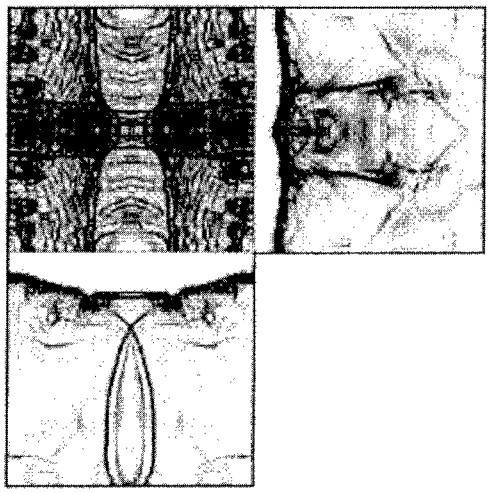

(a) Pressure gradient

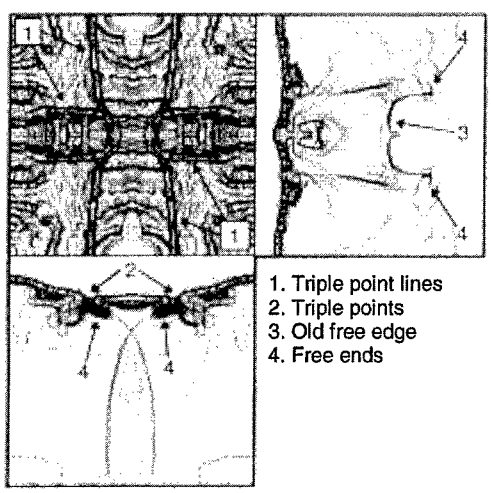

(b) Density gradient

FIG. 7. Pressure and density gradient for time step 18,895, time 66.9.

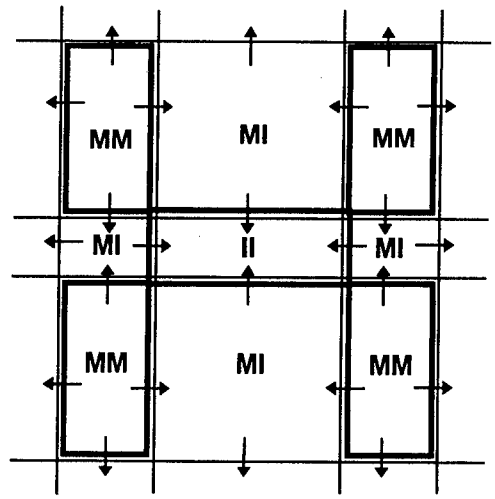

FIG. 8. A schematic diagram of the triple point structure on the leading shock front, taken from the front views of Figs. 2–7. Vortex sheets are generated along the triple point lines. They form closed loops (indicated by dark lines) and move in the direction opposite to the propagation of the triple point lines (thin lines). The front can be divided into different sections indicated by the letters MM (Mach stem–Mach stem), MI (Mach stem–incident shock), and II (incident shock–incident shock). The direction of propagation of each triple point line, indicated by small arrows, determines the type of each rectangle. Both pairs of triple point lines move away from each other around an MM region and both move toward each other around an II region; one pair closes together while the orthogonal pair moves apart around an MI region. This diagram is drawn at a time close to Fig. 5.

up into infinitely long tubes, entraining unburned fluid behind an expanding Mach stem. The three-dimensional equivalent of the triple point is now a line, best seen in the front views of Figs. 2–7, which acts as a singular line source of a vortex sheet. In 2-D, vorticity accumulates in large blobs which are cut off and shed into disconnected vortices after each collision [10–13]. In three dimensions, however, this only occurs locally but vorticity remains coupled globally, supporting Strehlow's hypothesis [2] that the two orthogonal waves are necessarily coupled.

The sequence of front views in Figs. 2–7, which clearly show the motion of the triple point lines, lead us to construct Fig. 8. The figure shows how the leading shock front can be divided into topological rectangles by the triple point lines, which have been drawn as straight lines for clarity. Considering only one set of transverse waves, the front is divided into widening Mach stem regions, which are separated by two triple point lines that move away from each other, and incident wave regions, which are shrinking. From the perspective of each set of transverse waves, each rectangle is either a Mach stem or an incident wave. Some rectangles are Mach stem regions to both sets of waves, some are in incident wave regions to both sets, and some are mixed. Thus, the front consists of Mach-Mach regions (MM), incident-incident regions (II), and mixed regions (MI). These structures are rectangles rather than squares because of the 90° phase shift. In particular, MM regions are born with finite length and zero width. Eventually, collisions occur along the narrow bound-

aries of an MM rectangle which becomes an MI rectangle, while two of the neighboring MI regions become MM regions. The other neighboring MI rectangles turn into II regions when the long boundaries collide.

As in two dimensions, slip surfaces carry vorticity, which is entrained toward the region behind the Mach stem. However, 3-D vorticity is necessarily generated either in closed rings or in rings intersecting with a wall. (For symmetrical boundary conditions, an intersection with the wall is equivalent to a ring.) The vortex sheet consists of rings generated along two *connected* families of closed loops (indicated by thick lines in Fig. 8), respectively, around MM and II rectangles, with no loop forming around the MI rectangles. The vorticity from MM rectangles is entrained toward the region behind the MM rectangle, while the vorticity from II rectangles is entrained behind the MI rectangles.

Until collisions occur, the rings form a connected set of sheets starting around MM or II rectangles, with sharp intersections at the rectangle corners. However, collisions transform MM and II regions into MI regions, and the MI rectangles into MM or II rectangles. Along the triple point lines that collide, just as in 2-D, the attached vortex sheets are cut loose, while new sheets form along the new triple point lines. This results in sudden changes in connectivity along half the rectangle boundaries where collisions occurred. Yet, the sheet structure always remains continuous, or connected, along the boundaries of the rectangles. Along the lines that collided, there are now two new free edges that correspond to the last vortex ring shed immediately before the collision, and to the first new one shed immediately after. The vorticity always appears in a closed ring but the connection has now changed. Overall, there is only one complex, fully connected vortex sheet.

Near their center, both types of free edges behave much like two-dimensional vortices. The edges of sheets behind II rectangles are cut off from the leading shock as a result of the collisions between triple point lines. Once free, these edges roll up and move rapidly downstream. Slices through a free edge, marked by arrows on the side views of Figs. 2b–4b, show the edge as it propagates downstream, also seen in Figs. 5b–7b. As the slapping wave hits the free edge, it forces it against the wall and deforms it, creating the C-shaped structure seen in Fig. 3b. A new vortex, created in the wake of the slapping wave collision, can be seen in Fig. 4b. Each new vortex takes up a position immediately behind the leading shock wave, as the near-circular patterns that appear on the front views indicate.

Conclusions

Simulation of a three-dimensional overdriven detonation shows that, in the absence of dissipative mechanisms, cell spacing in 3-D is the same as in the 2-D case. However, the resulting 3-D wave structure is much more intricate. The two interacting transverse waves are approximately one-quarter of a period out of phase, which accounts for the slapping wave patterns on smoke foils. The etchings are produced by the waves propagating in the direction normal to the wall, and their curvature is explained by the curvature of the trajectory of the impact point on the wall.

The wave structure divides the detonation front into rectangle-like figures. Vorticity is generated along approximately rectangular closed loops made up of triple point lines belonging to the two sets of transverse waves. Since only one vorticity sheet is issued from each singular line, only half of the rectangles are circled by a loop. Vorticity entrains unburned mixture behind the corresponding shock wave until a collision with another transverse wave occurs. When collisions occur, the interconnection changes on two of the four sides, and the closed loops that shed vorticity now switch to the second set of rectangles. In that process, free edges appear on the sheet where it was cut by the collision and also where a new loop started. However, on the two other sides of the rectangle where no collision occurred, the sheet remains connected. As a result, and in contrast with the two-dimensional case, a single, topologically connected vorticity sheet exists in the entire domain, and the vorticity roll-up characteristic of two-dimensional cells occurs only locally along the free edges.

Acknowledgments

Work supported by the Natural Science and Engineering Research Council of Canada. We thank Doug Phillips (The University of Calgary) and Doug Nadworny for their support.

REFERENCES

1. Strehlow, R. A., Liaugminas, R., Watson, R. H., and Eyman, J. R., *Eleventh Symposium (International) on Combustion,* The Combustion Institute, Pittsburgh, 1967, pp. 683–692.
2. Strehlow, R. A., *Combust. Flame* 12:81–101 (1968).
3. Oppenheim, A. K. and Soloukhin, R. I., *Annu. Rev. Fluid Mech.* 5:31–58 (1973).
4. Lee, J. H. S. and Moen, I. O., *Prog. Energy Combust. Sci.* 6:359–389 (1980).
5. Dupré, G., Peraldi, O., Lee, J. H., and Knystautas, R., *Prog. Aeronaut. Astronaut.* 114:248–263 (1988).
6. Lee, J. H., in *Dynamic Structure of Detonation in Gaseous and Dispersed Media* (A. A. Borissov, Ed.), Kluwer, Amsterdam, 1991, pp. 1–25.

7. Fujiwara, T. and Reddy, K. V., "Propagation Mechanism of Detonation—Three Dimensional Phenomena," in *Memoirs of the Faculty of Engineering*, Nagoya University, Vol. 41, No. 1, 1989, pp. 1–18.
8. Oran, E. S., Young, T. R., Boris, J. P., Picone, J. M., and Edwards, D. H., *Nineteenth Symposium (International) on Combustion*, The Combustion Institute, Pittsburgh, 1982, pp. 573–582.
9. Kailasanath, K., Oran, E. S., Boris, J. P., and Young, T. R., *Combust. Flame* 61:199–209 (1985).
10. Bourlioux, A. and Majda, A. J., *Combust. Flame* 90:211–229 (1992).
11. Bourlioux, A. and Majda, A. J., *Phil. Trans. R. Soc. Lond. A* 350:29–68 (1995).
12. Quirk, J. J., in *Combustion in High-Speed Flows*, (J. Buckmaster et al., Eds.), Kluwer, Amsterdam, 1994, pp. 575–596.
13. Bauwens, L. and Williams, D. N., AIAA, 1996, Paper 96-0343.
14. Oran, E. S. and Boris, J. P., *Numerical Simulation of Reactive Flow*, Elsevier, New York, 1987.
15. Williams, D. N. and Bauwens, L., *Shock Waves*, 6:93–110 (1996).
16. Boris, J. P. and Book, D. L., *Methods Comp. Phys.* 16:85–129 (1976).
17. Erpenbeck, J. J., *Phys. Fluids* 7:684–696 (1964).
18. Strehlow, R. A. and Engel, C. D., *AIAA J.* 7:492–496 (1969).
19. Takai, R., Yoneda, K., and Hikita, T., *Fifteenth Symposium (International) on Combustion*, The Combustion Institute, Pittsburgh, 1975, pp. 69–77.
20. Presles, H. N., Desbordes, D., and Bauer, P., *Combust. Flame* 70:207–213 (1987).

COMMENTS

Joseph M. Powers, University of Notre Dame, USA. Calculations similar to yours in two-dimensions have shown that predicted cell size can be affected by grid resolution. Have you demonstrated the sensitivity or insensitivity of your three-dimensional cell sizes to the resolution of your grid?

Author's Reply. We modeled a channel with fixed width. It is correct that in a large channel, one would obtain more than one cell, and that with a coarse grid, the smallest channel size for which two cells are observed instead of one depends upon resolution.

We looked at this issue in two dimensions, in the conditions (activation energy, heat release, overdrive) modeled in three dimensions. This study showed that the resolution used in three dimensions in the paper was acceptable. However, we have not attempted to repeat the sensitivity analysis in three dimensions. The problem size as presented ($80 \times 80 \times 170$) required almost the entire 512 MBytes of memory of the computer that we used.

The activation energy that we studied is relatively low, which is why the resolution that we used yields acceptable grid convergence. But it is true that for larger activation energies, more resolution would definitely be needed.

Twenty-Sixth Symposium (International) on Combustion/The Combustion Institute, 1996/pp. 2999–3005

IGNITION AND DETONATION IN N_2O-CO-H_2-He MIXTURES

ANDREI YU STARIKOVSKII
Moscow Institute of Physics and Technology
Dolgoprudny, Russia

Ignition and deflagration-to-detonation transition in the N_2O-CO-H_2 system behind the reflected shock wave in initial temperatures ranging between 1200 and 1800 K and pressures of 3–9 atm are studied. It is established that the chemical reactions are described adequately by the assumption of equilibrium between the translation-rotational and internal degrees of freedom of the molecules for shock-heated gas conditions. It is found that both the total heat release Q by the chemical reactions and the ratio of the induction period τ_{ind} of the mixture to the characteristic energy release time Θ are the parameters governing the flow pattern. Two different modes of interaction between the exothermic reaction and the gas flow are distinguished. The single-front mode, with a single discontinuity, arises when $\tau_{ind} \leq \Theta$, and two-front mode, in which a strong discontinuity formed behind the reflected shock front caused by interaction between the gasdynamic and chemical processes, arises when $\tau_{ind} \gg \Theta$.

Introduction

High-temperature kinetic processes in gases are often studied in shock tubes behind reflected shock waves [1]. Researchers [2,3,4] have attempted to model numerically the unsteady gasdynamic processes arising in shock tubes because of self-ignition of gaseous mixtures; they noticed a strong coupling between the chemical reaction and flow dynamics leading to detonation under certain conditions.

N_2O + CO + H_2 mixtures are interesting because of the peculiarities of the global N_2O + CO reaction, which, according to the data of Ref. 5, may provide superequilibrium population of the CO_2 levels due to energy release in the reactions and interactions of the vibrationally excited reaction products with reagents. For obtaining such reaction regimes, very high concentrations of the reactive gas must be used and gasdynamic phenomena must be taken into consideration.

It has been shown [6,7] that burning of N_2O-CO-H_2-He mixtures behind reflected shock waves may also produce appreciable gasdynamic perturbations, sometimes leading to detonation onset. Bearing this in mind, one should take into account the mutual influence of the chemical reaction in the system and the flow dynamic parameters when interpreting the kinetic measurements in mixtures with high energy release. The objective of this work is to study experimentally the self-ignition of N_2O-CO-H_2 mixtures within a wide range of initial conditions and to analyze the reaction kinetics, vibrationally excited products formation, and transition from deflagration to detonation.

Experimental Studies

Experiments were conducted in a shock tube 50 mm i.d. with 3.5-m-long low-pressure and 1.2-m-long high-pressure sections. A residual vacuum of $p \simeq 10^{-6}$ torr in the low-pressure section of the shock tube at a (1–2) $\times$ 10^{-4} torr/min leakage rate was provided by a vacuum system that included a steam-oil pump with a nitrogen trap. Experiments were performed after pumping the operating channel down to $p < 10^{-5}$ torr. The time interval between the end of pumping and the start of experiment was no longer than 2 min.

The velocity of the incident waves was measured between station 1 (318 mm from the end plate of the shock tube) and station 3 (13 mm from the end plate). Reflected wave velocity was measured between the end plate and station 2 (113 mm from the end plate in all runs, except those with mixture 4, 85 mm). At station 3, we monitored IR emission of N_2O at $\lambda = 3.7\ \mu$m and of CO_2 at $\lambda = 4.31\ \mu$m (see Fig. 1).

We studied ignition of five N_2O-CO-H_2-He mixtures of different compositions (see Table 1) behind reflected shock waves at temperatures and pressures ranging from 1200 to 1800 K and from 3.1 to 9.2 atm, respectively.

In the regimes corresponding to runs with mixture 1 ($T_{5_0} = 1502$ K, $p_{5_0} = 3.4$ atm, mode I) and with mixture 5 ($T_{5_0} = 1203$ K, $p_{5_0} = 9.2$ atm, mode II), the IR emission profile of N_2O, whose concentration decreases monotonically in the reaction, displays a prominent peak in both mixtures. The peak in mixture 5 is almost twice as high as the initial level of the signal.

The IR emission profile of CO_2 formed by the reaction shows a specific shape. Mixture 5 indicates a relatively slow increase in the emission intensity during the induction period, followed by a rapid acceleration to the quasi-steady level. Mixture 1 shows

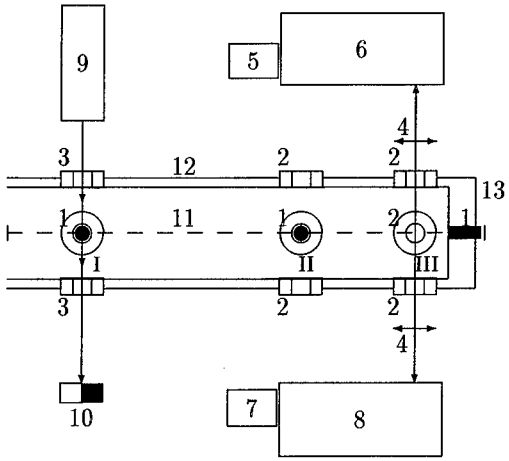

FIG. 1. Shock tube test section. 1, pressure gauges; 2, CaF_2 optical windows; 3, glass optical windows; 4, CaF_2 lenses; 5, IR-sensor Ge-Au, 77 K; 6, IR-monochromator; 7, solar-blend photomultiplier R-1657; 8, UV-monochromator; 9, He-Ne laser LG-52-3; 10, differential photodiod; 11, shock tube channel; 12, shock tube wall; and 13, shock tube end plate. I, II, III—test stations at 318, 113, and 13 mm from the shock tube end plate, respectively.

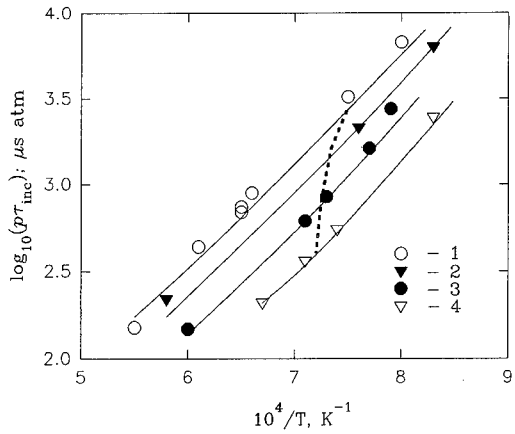

FIG. 2. The temperature dependence of the half-decay time of the N_2O IR radiation intensity at $\lambda = 3.7$ μm. Symbols, experiment; curves, numerical modeling by the detailed kinetic scheme [15]; 1, mixture 1; 2, mixture 2; 3, mixture 3; 4, mixture 5; dotted line, the threshold of transition from the single-front combustion mode to two front.

a smoother profile; no correlation was noticed between the emission intensity variation and the steep drop of the intensity of N_2O IR emission.

The pressure profiles at the end plate are somewhat similar to those of CO_2 IR emission. Whereas in mixture 5 the pressure rises steeply to the new quasi-steady level after a long plateau corresponding to the induction period, the pressure profile recorded in mixture 1 exhibits a gradual monotonic rise behind the reflected shock wave throughout the observation time.

The mixture in state 5 (state behind the reflected shock wave) ignites after the induction period is over. This produces a compression wave that propagates with a rapidly rising velocity and eventually transforms into the C-J detonation [8]. When the detonation front catches up with the reflected shock wave, a contact surface, overdriven detonation, and expansion wave arise. The contact surface keeps moving away from the end plate of the tube, the overdriven detonation propagates through state 2 (state 2 corresponds to the gas, heated by the incident shock wave only), and the expansion wave spreads toward the end plate. In mixture 1, containing no hydrogen, a rather smooth compression wave without a pronounced leading front follows the reflected shock wave.

These differences in the behavior of the flow parameters provide evidence of significant differences in the energy-release kinetics in the "dry" mixture 1 compared with mixture 5 containing 0.11% hydrogen. These differences are clearly shown in Fig. 2 by comparing the measured half-decay time of the

TABLE 1
The mixtures studied

Mixture	N_2O, %	CO, %	H_2, %	CH_4, %[a]	CO_2, %	He, %
1	9.4	20	0	0.0020	0	70.6
2	9.4	20	0.0066	0.0020	0	70.6
3	9.4	20	0.0300	0.0020	0	70.6
4	10.0	20	0.0850	0.0020	0	69.9
5	9.4	20	0.1140	0.0020	0	70.5
6	—	—	—	—	10.3	89.7

[a]Uncontrollable hydrocarbon impurities are taken into account.

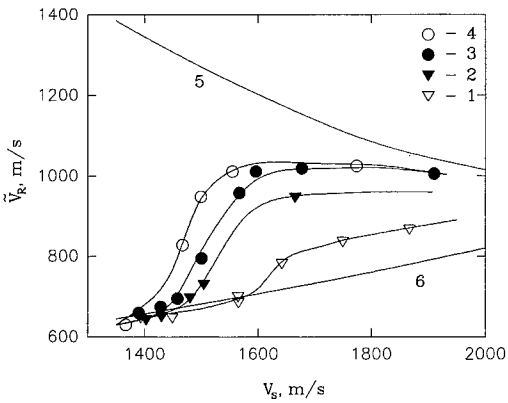

FIG. 3. The average velocity of the reflected shock wave, $\tilde{U}_R$, as a function of the incident shock wave velocity. Symbols, experiment; curves, numerical modeling by the reaction scheme [15]; 5, calculations assuming instantaneous attainment of the equilibrium composition at p_1 = 150-torr [13]; 6, calculations by the theory of ideal shock tube with frozen chemical reactions [11]; 1, mixture 1; 2, mixture 3; 3, mixture 4; 4, mixture 5.

intensity of N_2O IR emission as a function of the initial temperature T_{5_0} behind the reflected shock wave. The initial temperature T_{5_0} was calculated from the velocity of the incident shock wave assuming equilibrium of the translational, rotational, and internal degrees of freedom of the molecules and frozen chemical reactions.

It is seen that at identical pressures and temperatures, the half-decay time of the N_2O IR radiation intensity $\tau_{1/2}$ (called below the induction time) in mixture 1 is four times longer than that in mixture 5. Note that addition of only 66 ppm H_2 (mixture 2) reduces $\tau_{1/2}$ by a factor of 1.5. Comparing values of $\tau_{1/2}$ in mixture 2 with mixture 1 can be considered an additional experimental proof of a rather low level of uncontrolled impurities in the mixtures studied and demonstrates the extremely high sensitivity of the reaction kinetics in the N_2O-CO mixture to hydrogen-containing impurities.

The reflected shock wave velocity is sensitive both to the rate of the reaction and the overall exothermicity. It is well-known that the compression waves generated in the reaction zone interact with and accelerate the reflected shock wave front [9]. Obviously, the time it takes for the reflected shock wave front to travel a certain distance from the end plate depends on (1) the induction period in the mixture during which the heat release is insignificant; (2) the heat-release rate after the induction period; and (3) the overall heat-release due to the chemical reactions. If the reflected shock wave passes through the measurement base before the induction period is over, its velocity corresponds to calculations with the frozen chemical reactions.

In the other limiting case, when the induction period is very small, the time during which the reflected wave passes through the measurement base depends on the initial flow parameters and on the energy evolved during the measurement time. Figure 3 presents the results of treating the measured times during which the reflected shock wave travels between the pressure gauges at the shock tube end plate and station 2. It is seen that transition from the flow patterns, in which the heat-release effect on quantity $\tilde{U}_R = \Delta X/\Delta t$ (where ΔX is the distance between the measurement stations and Δt is the travel time; generally, $\tilde{U}_R$ is not equal to the instantaneous reflected shock wave velocity U_R) is insignificant, to those in which interaction between the chemical reaction and the gas flow is governing corresponds to various U_s (and, hence, to different T_{5_0}) values depending on the type of mixture studied. This follows, obviously, from the difference between the induction periods in various mixtures. Thus, a characteristic transition U_s value for mixture 5 is 1.45 km/s (T_{5_0} = 1320 K) and for mixture 1 is 1.6 km/s. In Fig. 2, these values are observed to occur at nearly identical induction times ($p\tau_{1/2}$ = 620 μs·atm).

The $\tilde{U}_R$ values are also different in the other end of the range, at large U_s. Whereas the data measured in the mixtures with a high hydrogen content (mixtures 4 and 5) are nearly equal to calculations performed assuming complete chemical equilibrium [10], the appropriate parameters for mixture 1 are closer to calculations with frozen chemical reactions. This is explained by changes in the composition of the reaction products in mixtures containing different amounts of hydrogen; in mixtures 4 and 5, the product composition approaches equilibrium within the measurement time, whereas in mixture 1, attainment of equilibrium requires a much longer time.

It should be noted that the measured $\tilde{U}_R$ and $\tau_{1/2}$ values depend significantly on the total pressure and the position of the measurement station with respect to the shock tube end plate, because the gas flow modes studied are essentially unsteady. The smooth dependence of these parameters on T and $\tilde{U}_S$ (Figs. 2 and 3, respectively) stems from the monotonic changes in the initial parameters (pressure, in particular) within each series of runs. To describe adequately the experimental results in numerical modeling, one should take into account explicitly the unsteady flow behavior caused by heat release in the chemical reactions and by purely gasdynamic phenomena associated with development of the dynamic boundary layers behind the incident shock wave [11].

Ignition Mode Analysis

We consider reflection of a shock wave from the tube end plate. The gas in state 5 acquires

parameters T_5 and p_5 after the wave reflection. We denote the induction time of the mixture in state 5 by τ_{ind}, defining it as a time elapsed after the shock wave reflection from the shock tube end plate until onset of intense heat release.

We analyze two conceivable versions of gas flow development that generalize the classification of the patterns of interaction between the combustion wave and reflected shock wave suggested in Refs. 8, 9, and 12:

1. Acceleration of the shock wave caused by its interaction with the compression waves generated by the combustion front without formation of strong discontinuities in state 5.
2. Transformation into the secondary shock discontinuity of the compression waves arising behind the reflected shock wave due to fast energy release by the chemical reactions.

We introduce the following assumptions:

- The gas pressure in the reaction zone varies only slightly until the secondary discontinuity is formed at instant t_{disc}, so that these changes can be neglected.
- The gas velocity in this region is small compared to the reflected shock wave velocity U_R.
- Changes in the state of the gas caused by the compression waves do not affect the heat-release rate due to the chemical reactions, at least up to $t = t_{\text{disc}}$.
- Specific heat ratio of the gas γ is constant within the same time interval.

We prescribe the heat release as a function of time τ elapsed starting with the shock wave reflection at the tube end plate as follows:

$$\frac{dQ(\tau)}{dt} = \begin{cases} 0 & \text{at } \tau < \tau_{\text{ind}} \\ A(\tau - \tau_{\text{ind}}) \exp[-(\tau - \tau_{\text{ind}})/\Theta] & \text{at } \tau > \tau_{\text{ind}} \end{cases} \tag{1}$$

These equations describe quite adequately the real-time history of the dQ/dt rate [13]. Parameters A and Θ characterize the total heat release and its rate, respectively.

Assuming the gas to be polytropic and taking into account the p = const condition yields for the expansion rate of an elementary volume δV_0,

$$\frac{d}{dt}\left\{\frac{\delta V}{\delta V_0}\right\} = \frac{1}{C_p T_0}\frac{dQ(t)}{dt} = \frac{At \exp(-t/\Theta)}{C_p T_0}$$

where C_p is the specific heat at a constant pressure and $t = \tau - \tau_{\text{ind}}$. We use the piston analogy and approximation for the velocity of the chemical reactions front U_F equal to the reflected shock wave velocity U_R. From this relation, bearing in mind the one—dimensional nature of the problem in question, we derive the expression $V = U_R t$, and using Eq. (3), arrive at

$$\frac{dV}{dt} = \frac{AU_R}{C_p T_0}\int_0^t \tau \exp(-\tau\Theta)\, d\tau = \frac{AU_R}{C_p T_0}[\Theta^2 - \Theta(\Theta + t)\exp(-t/\Theta)]$$

The rate of variation of the burning gas volume near the end plate can be interpreted in the one—dimensional formulation as a velocity, U_p, of an effective piston moving away from the shock tube end plate and compressing the gas in state 5:

$$U_p = \frac{AU_R}{C_p T_0}[\Theta^2 - \Theta(\Theta + t)\exp(-t/\Theta)]$$

The velocity of this piston is limited and, when $t \to \infty$, it tends to $U_p^\infty = AU_R/C_pT_0\,(\Theta^2)$. The instantaneous piston position is defined by the relation

$$X_p(t) = \int_0^t U_p(\tau)d\tau = U_p^\infty[t + (2\Theta + t)\exp(-t/\Theta) - 2\Theta] \tag{2}$$

As shown in Ref. 14, the position and time of discontinuity formation ahead of the piston moving in the channel are found by solving jointly two equations that define the steepening point of the compression wave front:

$$\left(\frac{\partial x}{\partial \kappa}\right)_t = 0, \left(\frac{\partial^2 x}{\partial \kappa^2}\right)_t = 0 \tag{3}$$

where x is the coordinate and κ is a parameter defining the coordinate of discontinuity formation. The $x(\kappa)$ dependence is found for a polytropic gas using the relation [14] $v = \dot{x}(\kappa)$,

$$x = X(\kappa) + (t - \kappa)\left[C_0 + \frac{\gamma + 1}{2}\dot{X}(\kappa)\right] \tag{4}$$

Here, v is the gas velocity, $X(\kappa)$ is the instantaneous piston position, C_0 is the acoustic velocity in unperturbed gas (in this case, $C_0 = C(T_{5_0})$), and the dot signifies differentiation with respect to κ.

We substitute the $X(\kappa)$ and $\dot{X}(\kappa)$ values found earlier into Eq. (4):

$$x = U_p^\infty\Theta\{(2 + \kappa/\Theta)\exp(-\kappa/\Theta) - (2 - \kappa/\Theta)\} + U_p^\infty(t - \kappa)\left\{C_0/U_p^\infty + \frac{\gamma + 1}{2}[1 - (1 + \kappa/\Theta)\exp(-\kappa/\Theta)]\right\} \tag{5}$$

Solving Eqs. (3) and (4) with due regard for the expression derived for x, we obtain for the time of discontinuity formation (the time is measured from the mixture ignition instant):

$$t_{\text{disc}} = \frac{(\gamma + 1)\kappa(3\Theta - \kappa) - 2\Theta\kappa}{(\gamma + 1)(\Theta - \kappa)} \tag{6}$$

where parameter κ is found from the following equation:

$$\left[\frac{\gamma + 1}{2}(1 + \kappa^2/\Theta^2) - 1\right]\exp(-\kappa/\Theta) = (1 - \kappa/\Theta)\left[\frac{\gamma - 1}{2} + C_0/U_p^\infty\right] \quad (7)$$

It is seen from Eqs. (5) through (7) that the time to discontinuity formation depends on the specific heat ratio of the gas, characteristic heat release time Θ, and dimensionless parameter C_0/U_p^∞, specifying the ratio of the energy released by the chemical reactions to the internal energy of the gas with frozen chemical reactions:

$$x_{\text{disc}} = U_p^\infty \Theta \Phi(C_0/U_p^\infty, \gamma), \; t_{\text{disc}} = \Theta F(C_0/U_p^\infty, \gamma)$$

where Φ and F are analytic functions. Obviously, the compression waves arising from the chemical reactions may be converted into a strong discontinuity only when

$$U_R(t_{\text{disc}} + \tau_{\text{ind}}) > x_{\text{disc}}$$

or, after the appropriate substitution, when

$$\tau_{\text{ind}} > \Theta\left\{\frac{U_p^\infty}{U_R}\Phi(C_0/U_p^\infty, \gamma) - F(C_0/U_p^\infty, \gamma)\right\} \quad (8)$$

Thus, the two-front reflection mode with formation of a secondary discontinuity that follows the shock wave reflected from the shock tube end plate, behind which heat is released intensely in the flow, arises if under the selected initial conditions and mixture composition, the induction period is long and the heat-release rate, inversely proportional to parameter Θ, is high. When the ratio between the characteristic times of induction and heat release is reversed, the compression waves have no time to produce the secondary shock wave before they overtake the primary reflected shock wave. The reflected shock wave is accelerated, but the flow behind it (state 5) remains continuous.

Figure 2 shows the boundaries between the single-front and two-front flow modes calculated using Eqs. (5) through (7) for all the mixtures studied. According to our calculations, the two-front mode is observed under the initial conditions, corresponding to the region to the right of the transition curve (for example, for regime II). At higher temperatures, the ratio τ_{ind}/Θ between the characteristic times is such that no secondary discontinuity is formed (regime I). The reflected shock wave is accelerated gradually because of its interaction with the compression waves produced by the combustion front, and, eventually, the deflagration wave is converted into an overdriven detonation wave. This behavior of the system results from a substantial decrease in the rate of heat release by the dominating chain reactions $N_2O + H \rightarrow N_2 + OH$ and $CO + OH \rightarrow CO_2 + H$ as compared to the rate of the triggering reaction of unimolecular N_2O decomposition, whose rate constant is much more sensitive to the temperature than the rate constants of chain reactions. In mixtures containing about 10% N_2O, 20% CO, and 70% He, the criterion of the two-front flow pattern formation can be approximated by relation $\tau_{\text{ind}}/\Theta \simeq 7.5$.

Numerical Modeling

As in Ref. 3, in our calculations, we employed the method of solution separation according to the physical processes. After each step in calculating the gas flow, we introduced corrections for the energy exchange between the internal and translation-rotational degrees of freedom and integrated the chemical kinetics equations involving more than 100 reactions. A total of 23 reactants were included in the kinetic scheme, N_2O, NO, NO_2, NO_3, N_2, N, H_2O, OH, HO_2, H_2, H, O_2, O, HNO, NH, CH_4, CH_3, CH_2O, CHO, CH_2, CO, CO_2, CH, and the inert components Ar and He were involved in the reactions as collision partners [15].

In this work, we used the random choice method (RCM) [16] for gasdynamics equation solution. The method described in Ref. 13 employs the exact solution of the Riemann problem at the interface between adjacent computation cells for constructing the full solution [16].

The grids used in this work comprised 200 cells, on average, along the x axis, and calculations took into account flow inhomogeneity in the gas behind the incident shock wave. Because of the large number of computational cells, we were able to calculate accurately the position of the reflected shock front (the error of its determination in the RC method equals about one step along the x axis [17]) and to resolve confidently the chemical reaction zone.

Simulation Results

The pressure profiles calculated using the previously discussed model are displayed in Figs. 4a and 4b. Profiles (a) pertain to the flow mode I profiles and (b) are the results of modeling for mode II. As mentioned earlier, this pair of experiments corresponds to the same half-decay time of IR emission of N_2O; however, in mode I, the unimolecular N_2O decomposition is fast but the major fraction of the heat is released slowly by the $CO + O + M \rightarrow CO_2 + M$ reaction. In mode II, N_2O is consumed and CO_2 builds up synchronously by the fast chain reactions $N_2O + H \rightarrow N_2 + OH$ and $CO + OH \rightarrow CO_2 + H$. The identical τ_{ind} times in these two cases are explained by appreciable differences in the temperatures: for mode I, $T_{5_0} = 1502$ K and for II, $T_{5_0} = 1203$ K; the initial rate of the unimolecular

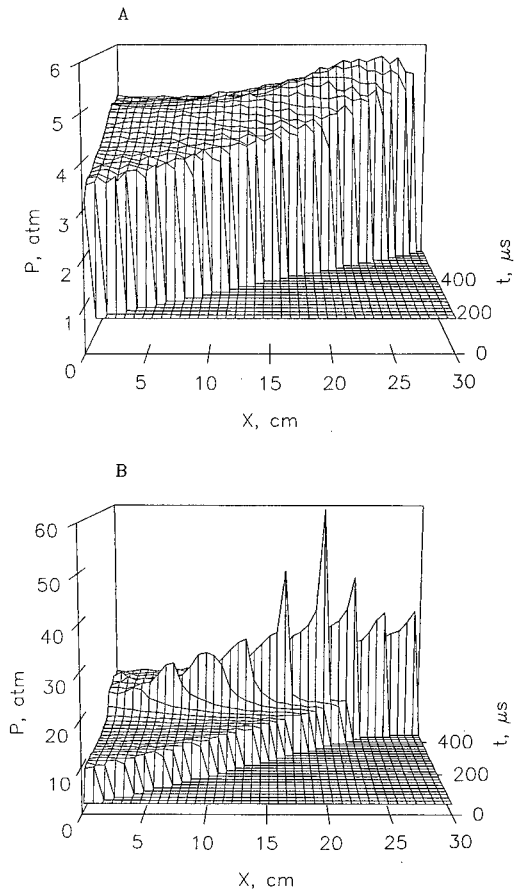

FIG. 4. The pressure profiles at various times. (a) Mixture 1, mode I; (b) mixture 5, mode II.

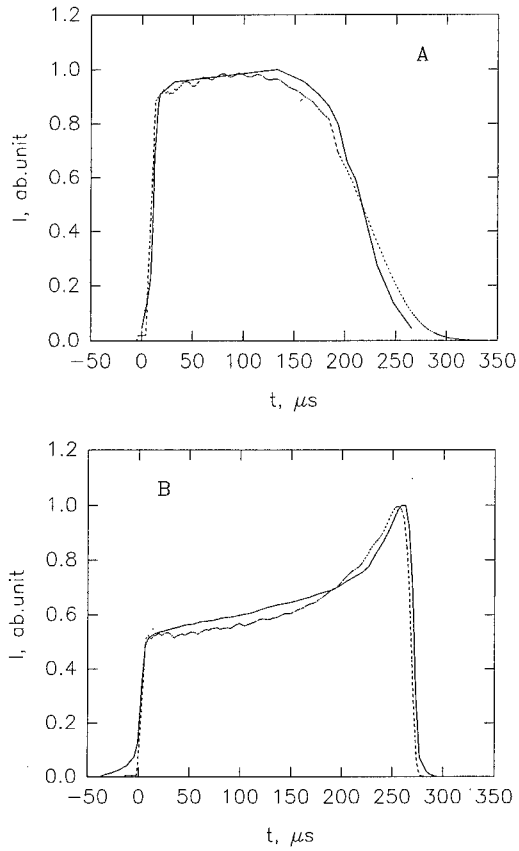

FIG. 5. IR emission profile of N_2O ($\lambda = 3.7\ \mu m$). The solid line is experiment; the dashed line represents our numerical modeling. (a) Mixture 1, mode I; (b) mixture 5, mode II.

N_2O decomposition reaction triggering the subsequent secondary reactions for mode II is 150 times as low as that for mode I.

In mode I, all the flow parameters change gradually: slow heat release in the reaction zone generates weak compression waves that catch up with the reflected shock front and accelerate it smoothly. In mode II, the reflected shock wave velocity and pressure during initial 200 μs are nearly identical, with their values calculated disregarding the chemical reactions. The thermal explosion taking place 270 μs after shock wave reflection from the end plate produces an intense compression wave that is converted into a shock discontinuity at $t \simeq 320\ \mu s$. Its further propagation through state 5 in the form of a C-J detonation wave terminates at $t = 370\ \mu s$; at this instant, the detonation front catches up with the reflected shock wave, and the merged waves give rise to an overdriven detonation wave that keeps spreading through state 2. This produces a contact surface and rarefaction wave at the site where the two waves merge. The rarefaction wave propagates toward the shock tube end plate. The gas temperature behind the primary shock wave rises steeply, and the peak pressure and density fall off.

Infrared Emission of the Gas

The IR emission profiles of N_2O and CO_2 enable us to estimate the difference between the vibrational temperature in the reaction zone and the translation-rotational temperature. The emission profiles are complicated; therefore, a systematic analysis of the measurements presents difficulties. Consequently, in this work, we compared directly the emission profiles obtained in experiment with those calculated by the equilibrium model.

The results of the comparison are displayed in Fig. 5. The results of the equilibrium calculations ($T_{tr} = T_{rot} = T_{vib}$) reproduce the experimental profiles with a high accuracy in all cases. The insignificant

deviations (not exceeding 5%) of the calculations profile from measurements of the maximum profile amplitude in all experiments can be explained by interference of a weak signal from light scattered by the polished shock tube walls.

Thus, an analysis of the IR emission profiles carried out in this section with due regard for the results of the analysis of the kinetic and gasdynamics models (see earlier) leads us to conclude that thermal explosion in N_2O-CO-H_2-He mixtures proceeds in the equilibrium regime (i.e., at $T_{tr} = T_{rot} = T_{vib}$) within a very wide range of the parameters. We failed to observe noticeable deviations from the equilibrium model at the temperature rise rates in the system up to $dT/dt = 40K/\mu s$.

Conclusions

We studied ignition and deflagration-to-detonation transition in initial temperatures ranging between 1200 and 1800 K and pressures from 3 to 9 atm. It is inferred from the measured profiles and results of numerical modeling that the chemical reactions in the N_2O-CO-H_2 system are described adequately by the mechanism suggested in Ref. 15. It is based on reactions involving free radicals and assumes equilibrium between the translation-rotational and internal degrees of freedom of the molecules within a wide range of the initial parameters of the gas flow and under different conditions in the reacting shock heated mixture.

Two different modes of interaction between the exothermic reaction and the gas flow are distinguished. The single-front mode with a single discontinuity, the reflected shock front, and two-front mode, in which the reflected shock front and a strong discontinuity formed due to interaction between the compression waves generated in the intense energy-release zone are present simultaneously in the gas flow.

From the experimental data and analytical and numerical modeling results, we infer that both the total heat release by the chemical reactions and the ratio of the induction period of the mixture to the characteristic energy-release time are the parameters governing the flow pattern. We have derived a universal quantitative criterion that relates the gas flow pattern behind the reflected shock wave to the ratio between the induction period of the system and the characteristic heat-release time, the acoustic velocity in the gas, and the overall exothermicity of the reactions.

Acknowledgment

This work was supported in part by grant 96-03-32746 from the Russian Fundamental Research Foundation.

REFERENCES

1. Fujii, N., Kakuda, T., Takeishi, N., and Miyama, H., *J. Chem. Phys.* 91:2144–2148 (1987).
2. Elchert, H., *Int. J. Hydrogen Energy* 12:171–182 (1987).
3. Takano, V., *J. Comput. Phys.* 67:173–194 (1986).
4. Oran, E. S., Young, T. R., and Boris, J. P., *Combust. Flame* 48:135–153 (1982).
5. Zaslonko, I. S. and Mukoseev, Y. K., *Kinetika Kataliz* 34:408–421 (1993).
6. Britan, A. B., Zuev, A. P., and Starikovskii, A. Y., "Fundamental Problems of Shock Wave Physics," *International School-Seminar* Chernogolovka, 1987, pp. 202–204.
7. Britan, A. B., Zuev, A. P., and Starlkovskii, A. Y., *Fiz. Goreniya Vzryva* 25:89–96 (1989).
8. Strehlow, R. A. and Dynes, H. B., *AIAA J.* 1:591–603 (1963).
9. Gilbert, R. B. and Strehlow, R. A., *AIAA J.* 4:1777–1791 (1966).
10. Starikovskii, A. Y., "Physics and Gasdynamics of Shock Waves," *International School-Seminar* The Heat and Mass Transfer Institute, Minsk, 1992, pp. 641–644.
11. Starikovskii, A. Y., *Sov. J. Chem. Phys.* 10:1234–1251 (1991).
12. Strehlow, R. A. and Cohen, A., *Phys. Fluids* 5:97 (1962).
13. Starikovskii, A. Y., *Chem. Phys. Reports* 13:1422–1474 (1995).
14. Landau, L. D. and Lifshits, E. M., *Hydrodynamics*, Nauka, Moscow, 1986.
15. Starikovskii, A. Y. *Chem. Phys. Reports* 13:151–190 (1994).
16. Chorin, A. J., *J. Comput. Phys.* 25:517–538 (1977).
17. Collela, P., *SIAM J. Stat. Comput.* 3:76–91 (1982).

Twenty-Sixth Symposium (International) on Combustion/The Combustion Institute, 1996/pp. 3007–3013

DETONATION SUPPORTED BY COMBUSTIBLE DUST DEPOSIT

BAO-CHUN FAN AND HONG-ZHI LI
Institute of Power Engineering
The Nanjing University of Science and Technology
Nanjing 210014, China

Self-sustaining detonations along a combustible dust deposit on a bottom wall have been investigated experimentally and theoretically. Experiments were conducted in a square cross-section tube. Three kinds of particles with a mean diameter of 15 μm were used: AL, RDX, and HMX. Sharp-shadow photographs were taken by means of a special optical system and shock-wave velocities were measured by pressure transducers. It has been shown that the steady-state detonation velocity is independent with initial shock wave strengths.

An analytical model has been developed to describe the two-dimensional structure of dust-film detonations. A set of equations for the two-phase turbulent-reacting boundary layer considering the particle ingestion and the interphase transfers and a general Chapman–Jouguet condition were derived. The Lees–Dorodnytzin transformation usually applied to the compressible boundary layer has been extended to fit the two-phase reacting case, and the numerical simulations have been performed by applying a Box method and an improved particle source in cell (PSIC) method, which shows that the structure of the boundary layer behind the shock front consists of an induction zone, a reaction zone, and a diffusion zone. Computed and measured results are in reasonable agreement.

Introduction

Investigations have shown that a self-sustaining detonation can propagate not only through a homogeneous media or heterogeneous suspension but also over a wall coated with a liquid fuel film [1–2] or a detonatable dust deposit [3]. Such film detonation is supported by energy releases because of combustions in a shock-induced turbulent boundary layer.

Two-dimensional models of liquid-film detonations have been developed [4–5] to predict the CJ detonation velocity and to describe its structure. A number of shock tube experiments have been conducted to research on the shock-induced dispersion of chemically inert dust deposits [6–8], which is closely related to dust-film detonations, and the theoretical models corresponding to it have also been developed based on a single continued medium model [9] a double continued medium model [10–12] or a particle-trajectory model [8,13]. But few theoretical studies have been carried out for dust-film detonations.

In the present paper, some experimental results on the dust-film detonation are presented, and a two-dimensional model, considering the dispersion, ignition, and combustion of the dust deposit behind the leading shock front and a Chapman–Jouguet condition of eigenvalue detonations are developed. Some computed results are in good agreement with the measured results.

Experimental Investigation

Experimental Technique

The setup used for the experiments is sketched in Fig. 1. A special shock tube with 2.8 m total length and 20 × 20-mm^2 cross area is mounted horizontally and consists of a driver section, a driven section, and a test section. At a high pressure produced by rapid combustion of the initiator, made of resistance wires covered with solid propellants, situated at the closed end of the driver section, the rupture of the diaphragm separating the driven section from the driver section causes a moving shock wave to interact with dust particles laden in advance on the bottom throughout the driven and the test sections. Eight pressure transducers were used for shock-velocity measurements (typical results are shown in Fig. 2) while a photodiode mounted on the same location as the eighth pressure transducer PT 8 was employed to measure the ignition delay considered to be a time difference between a pressure signal at PT 8 and a light emission signal from the ignition of particles at the photodiode as shown in Fig. 3.

The dispersion of particles from the bottom wall was observed with shadow photography at the test section windows. The optical system consisted of a spark light source, a Fresnel lens, a reflecting mirror, and a camera. The typical shadow photograph is shown in Fig. 4.

A laser extinction technique was used to show the

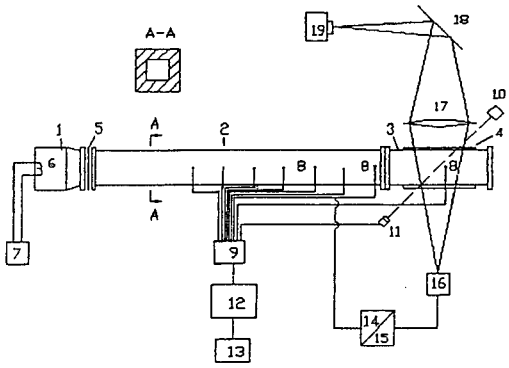

FIG. 1. Experimental apparatus: (1) driver section, (2) driven section, (3) text section, (4) test window, (5) diaphragm, (6) igniter, (7) ignition system, (8) pressure transducers, (9) amplifier, (10) He-Ne laser, (11) photo diode, (12) multichannel transient recorder, (13) computer, (14) time-delay instrument, (15) digital supply voltage meter, (16) spark light source, (17) fresnel lens, (18) reflecting mirror, and (19) camera.

formation of dust clouds. The He-Ne laser beam directed through the windows became attenuated due to the particle lifting, and the intensity was measured by a photodiode as shown in Fig. 5. The data acquisition system and the spark light source were triggered by the pressure transducer PT 7.

Experimental Results

Three kinds of particles, RDX, HMX, and AL, with a mean diameter of 15 μm were used to form combustible dust deposits with 2×10^{-4} g/cm^3 on the bottom of the tube. The variations of the shock-wave velocity in the tube for these kinds of particles measured by piezoelectric pressure transducers are shown in Fig. 6. The measured detonation velocities and properties of RDX, HMX, and AL are tabulated in Table 1.

It can be seen that the detonation velocity of an aluminum dust film is the lowest in spite of its high combustion heat, since the aluminum dust cloud induced by shock waves in air is present in lean oxygen; however for high explosive particle clouds, the equivalence ratio is approximate to unit, so that it can burn under the circumstances without oxygen. The detonation velocity of RDX film is higher than that of HMX, mainly due to the material density difference.

The strength of the initial shock wave does not affect the steady-state detonation velocity within a certain range as shown in Fig. 7 for RDX dust film. It can be seen that a steady state is reached after some propagation distances for the initial shock. Mach number M; between 2.76 and 3.4, but the initial shock wave with $M_s = 2.3$ is too weak to

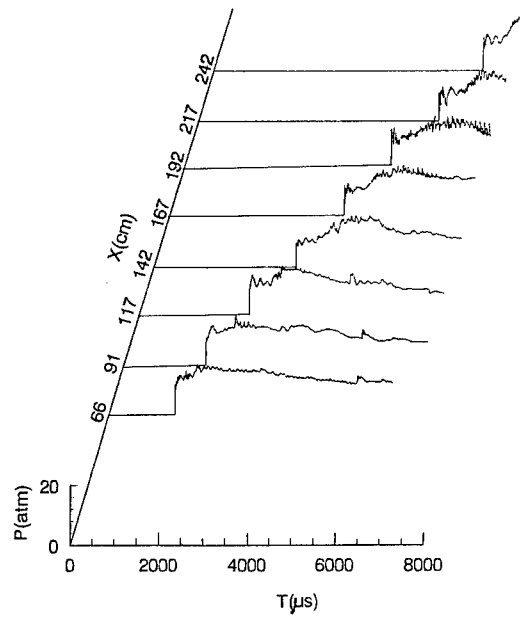

FIG. 2. Typical pressure records in a different location of the tube.

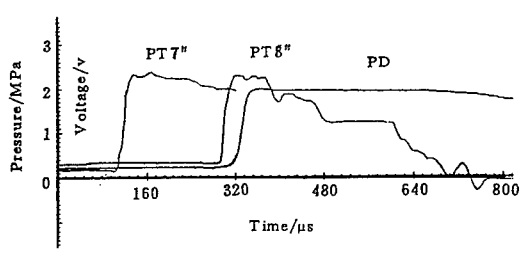

FIG. 3. Typical records of pressure profiles and dust ignition.

TABLE 1
The measured detonation velocities and properties of AL, RDX, and HMX

	Density (g/cm^3)	Combustion heat (J/Kg)	Measured detonation velocity (m/s)
AL	2.7	31000	810
RDX	1.816	9540	870
HMX	1.905	9500	830

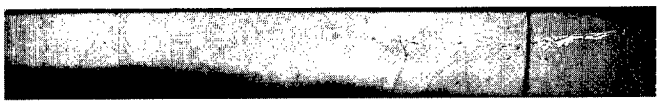

FIG. 4. Shadow photograph of dust film detonation.

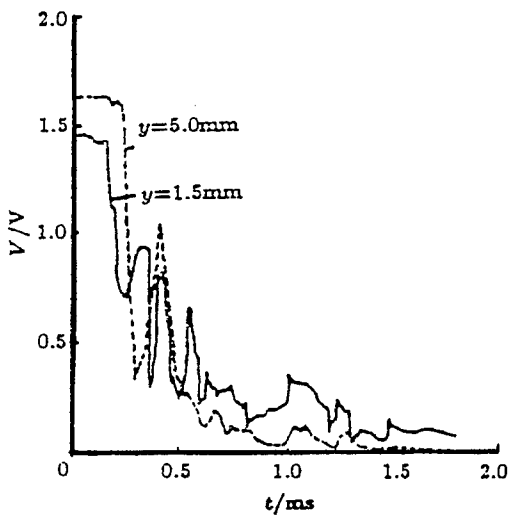

FIG. 5. Experimental results of dust concentration variations measured by laser extinction.

detonate the RDX dust. For $M_s = 4.0$, the tube is not long enough to reach the steady state.

Theoretical Investigation

Two-Dimensional Theory

Based on the following assumptions, a two-dimensional theoretical model has been developed to deal with dust-film detonations:

1. The dust-laden surface consists of an unlimited number of small particles, which are combustible, incompressible, spherical, and of uniform diameter. The volume fraction and the thermal motion of particles can be neglected.
2. Gas is treated as a perfect gas.
3. Within the viscous boundary layer, Prandtl's boundary layer concept is available.

A system of conservation equations in laboratory coordinates [14] can be reduced into a steady state in shock-fixed coordinates with a Galilean transformation.

For the gas phase,

$$\frac{\partial \rho u}{\partial x} + \frac{\partial \rho v}{\partial y} = \Gamma \tag{1}$$

$$\rho\left(u\frac{\partial Y_i}{\partial x} + v\frac{\partial Y_i}{\partial y}\right) = \frac{\partial}{\partial y}\left(\rho\left(\frac{\mu}{S_c}\right)_{\text{eff}}\frac{\partial Y_i}{\partial y}\right) + \Gamma_i \tag{2}$$

$$\rho\left(u\frac{\partial u}{\partial x} + v\frac{\partial u}{\partial y}\right) = -\frac{\partial p}{\partial x} + \frac{\partial}{\partial y}\left(\mu_{\text{eff}}\frac{\partial u}{\partial y}\right) - V_x \tag{3}$$

$$\frac{\partial p}{\partial y} = -V_y \tag{4}$$

$$\rho\left(u\frac{\partial H}{\partial x} + v\frac{\partial H}{\partial y}\right) = \frac{\partial}{\partial y}\left[\left(\frac{\mu}{P_r}\right)_{\text{eff}}\frac{\partial H}{\partial y}\right] + \frac{\partial}{\partial y}\left[\left(\mu_{\text{eff}} - \left(\frac{\mu}{P_r}\right)_{\text{eff}}\right)\frac{\partial \frac{u^2}{2}}{\partial y}\right] + S_Q \tag{5}$$

For the particle phase,

$$\frac{d\rho_p}{dt_p} = -\Gamma - \rho_p\left(\frac{\partial u_p}{\partial x} + \frac{\partial v_p}{\partial y}\right) \tag{6}$$

$$\frac{du_p}{dt_p} = \frac{1}{\rho_p}(V_x + (u_p - u)\Gamma) \tag{7}$$

$$\frac{dv_p}{dt_p} = \frac{1}{\rho_p}(V_y + (v_p - v)\Gamma) \tag{8}$$

$$\frac{dT_p}{dt_p} = \frac{1}{C\rho_p}(Q + S_{QP}) \tag{9}$$

The gas-particle reaction rate can be expressed as

$$R_s = A\exp\left(-\frac{E}{RT_p}\right)\rho_{02} \tag{10}$$

so that

$$\frac{dd_p}{dt} = -\frac{2R_s}{\bar{\rho}_p} \tag{11}$$

The momentum transfer between phases is given by

$$V_x = \rho_p f_x \tag{12}$$

$$V_y = \rho_p(f_y + f_l - g) \tag{13}$$

S_q and S_{QP} related to the energy transfer between phases have the following forms:

$$S_Q = \Gamma\left(\beta Q_c + CT_p + \frac{(u_0 - u_p)^2}{2} - C_pT - \frac{(u_0 - u)^2}{2}\right) - Q - u_pV_x - v_pV_y \tag{14}$$

$$S_{QP} = \Gamma((1 - \beta)Q_c - (u_p - u)u_p - (v_p - v)v_p) \tag{15}$$

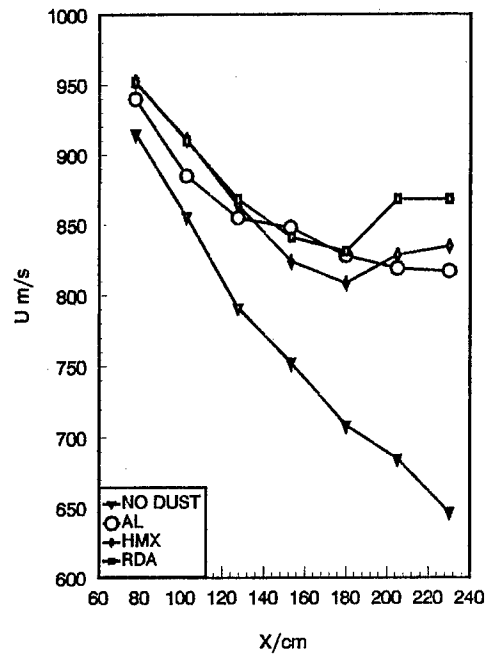

FIG. 6. Variations of experimental shock velocity with propagation distance for AL, RDX, and HMX.

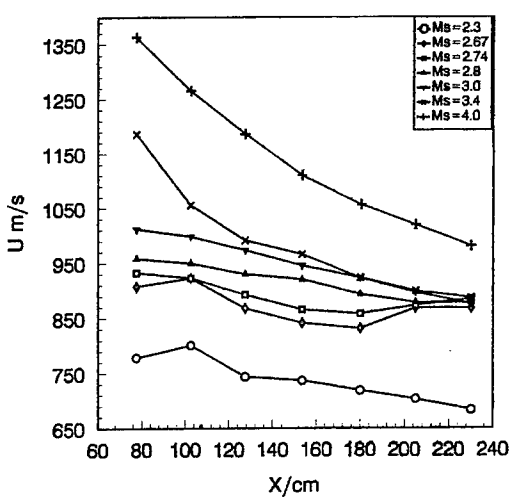

FIG. 7. Variations of experimental shock velocity of RDX dust with propagation distance for a different initial shock strength.

$$\mu_{\text{eff}} = \mu + \mu_T, \left(\frac{\mu}{P_r}\right)_{\text{eff}} = \left(\frac{\mu}{P_r}\right) - \frac{\mu_T}{P_{rT}}$$

$$\left(\frac{\mu}{S_c}\right)_{\text{eff}} = \frac{\mu}{S_c} + \frac{\mu_T}{S_{CT}}$$

the subscript T represents turbulence. Cebeci–Smith mixing length model is used to get the turbulent viscosity [15].

Chapman–Jouguet Condition

The integration of the conservation Eqs. (1) through (5) over the cross section of the tube yields the following system of ordinary differential equations:

$$\frac{d}{dx}(B_1\rho_e u_e) = \frac{A_1}{L} \tag{16}$$

$$\frac{d}{dx}(p_e + B_2\rho_e u_e^2) = \frac{A_2}{L} \tag{17}$$

$$\frac{d}{dx}\left(B_3\left(\frac{1}{2}\rho_e u_e^3 + \frac{\gamma}{\gamma - 1}p_e u_e\right)\right) = \frac{A_3}{L} \tag{18}$$

where

$$B_1 = 1 - \delta^*/L, B_2 = 1 - (\theta + \delta^*)/L$$

and

$$B_3 = 1 - (\theta_H + \delta^*)/L$$

$$\delta^* = \int_0^\delta \left(1 - \frac{\rho u}{\rho_e u_e}\right)dy$$

$$\theta = \int_0^\delta \frac{\rho u}{\rho_e u_e}\left(1 - \frac{u}{u_o}\right)dy$$

$$\theta_H = \int_0^\delta \frac{\rho u}{\rho_e u_e}\left(1 - \frac{H}{He}\right)dy$$

$$A_1 = \int_0^L \Gamma dy$$

$$A_2 = \int_0^L (u\Gamma - V_x)\,dy - \tau_w$$

$$A_3 = \int_0^L (H\Gamma + S_Q)dy - u_0\tau_w + q_w$$

The subscript e denotes free stream, δ, the thickness of the boundary layer and L, the height of the tube.

If B_i = const (i = 1, 2, 3) near the CJ plane, from Eqs. (16) through (18), it follows that

$$\frac{\gamma L}{\gamma - 1}p_e(B_4M^2 - 1)\frac{du_e}{dx} = \frac{\gamma}{\gamma - 1}u_eB_2$$

$$(G_2 - u_eG_1) - G_3 + \frac{1}{2}u_e^2G_1 \tag{19}$$

The solution will be continuous at the CJ plane only if

$$\frac{\gamma}{\gamma - 1}u_eB_2(G_2 - u_eG_1) - G_3 + \frac{1}{2}G_1u_e^2 = 0 \text{ at } M^2 = \frac{1}{B_4} \tag{20}$$

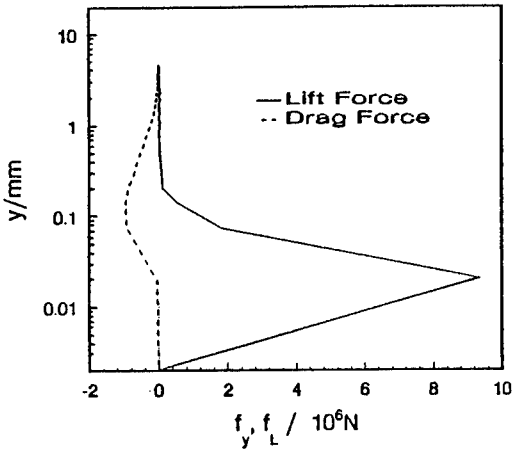

FIG. 8. Variation of lift force f_L and drag force f_y with distance from the bottom.

where $G_i = A_i/B_i$ ($i = 1, 2, 3$), and $B_4 = 1 - (\theta + \delta^*)\gamma/L$.

Three boundaries (i.e., the external edge of the boundary layer, the shock front, and the wall surface) have to be considered here. At the first boundary, parameters are obtained from Eqs. (16) through (18). To avoid singularities $\chi = \varepsilon$ a positive small quantity is taken as the second boundary, where the dust dispersion is neglected and the parameters of gas are obtained from the Blasuis solutions for $y \leq \delta(\varepsilon)$ and the *Rankin–Hugoniot relations for* $y \leq \delta(\varepsilon)$. Following Mirels [9], the condition at the wall is

$$\frac{B}{\ln(1 + B)} = 1.991 \times 10^2 \frac{M_s^2 p_\delta}{(p_\delta x)^{1/5}} \frac{\left(W + \frac{7}{3}\right)^{1/5} (W - 1)^{8/5}}{W} \quad (21)$$

where $W = \dfrac{u_0}{u_e}$, $M_s = \dfrac{u_0}{a_0}$, $B = \dfrac{(\rho_p v_\rho)_w \tau_w}{u_e(W - 1)}$

τ_w is the shearing stress at the wall.

Numerical Methods

The gas density can be split into two parts: a density production due to the solid consumption ρ_c and an intrinsical density ρ_I. Thus, Eq. (1) becomes

$$\frac{\partial}{\partial x}(\rho_I u) + \frac{\partial}{\partial y}(\rho_I v) = 0 \quad (22)$$

$$\rho_I u \frac{\partial \varphi}{\partial x} + \rho_I v \frac{\partial \varphi}{\partial y} = \Gamma \quad (23)$$

where $\varphi = \rho_c/\rho_I$, $\rho_c + \rho_I = \rho$

Introducing a stream function ψ with $\partial\psi/\partial y = \rho_I u$ and $\partial\psi/\partial x = -\rho_I v$ and independent variables $\xi = x/\lambda$ and

$$\eta = \frac{1}{\sqrt{2\xi}} \int_0^{\bar{y}} \frac{\rho}{\rho_e} d\bar{y}$$

where $\lambda = u_0\tau$, $\bar{y} = y/\lambda \sqrt{R_{e\lambda}}$, $R_{e\lambda} = \rho_e u_e \lambda/\mu e$, and $\tau = 4d_p^2\bar{\rho}_p/(3C_D Re_p \mu)$, the Less–Dorondnytzin transformation of Eqs. (2) through (5) and (22) yields a system of nondimensional differential equations that can be solved numerically by a second-order Box method. Whole particles entrained from the wall are divided into many representative samples of discrete particles described by Eqs. (6) through (9), which are integrated by the fourth-order Runge–Kutta method.

Considering a computational cell in which several representative samples of discrete particles pass through, the particle number flow rate N is constant along the particle trajectories for a steady flow and is established at the wall surface,

$$N = \frac{\rho_{pw} v_{pw}}{m_{p0}} \Delta x_p \quad (24)$$

where Δx_p is a distance between two vicinal trajectories.

The rate of solid particles **gasification** per unit volume is then given by

$$\Gamma = \frac{\pi\bar{\rho}_p}{6} \sum_{i=1}^{b} n_i((d_{pi})_{in}^3 - (d_{pi})_{out}^3))/\Delta x \Delta y, \quad (25)$$

where d_{pi} is the diameter of particles moving along the particle trajectory i; subscripts *in* and *out* denote into and out of the cell, respectively: The CJ detonation velocity u_0 is determined by Eq. (20) using an iterative method.

Numerical Results

The model described previously has been used to calculate the structure of the dust-film detonation for 15 μm RDX particles, and the results shown in Figs. 8–12 are discussed in detail next. The mechanism of the particle dispersion induced by shock waves is affected by many factors, but only the lift force and the aerodynamic drag force are considered here. The lift force accelerating particles is a dominant factor at the initial stage; the aerodynamic drag force decelerating particles becomes dominant gradually as shown in Fig. 8. The vertical particle velocity varies with the ascent of particles, as shown in Fig. 9.

The heat assignment factor β in Eq. (14) has a strong effect on the particle combustion. There is a point defined as an ignition point in Fig. 10, where curves for different heat assignments become divided considerably. The calculated and measured results for the ignition-delay time with different shock strengths are shown in Fig. 11.

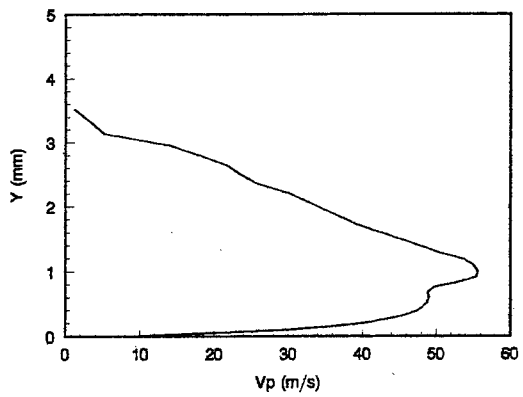

FIG. 9. Variation of vertical particle velocity with distance from the bottom.

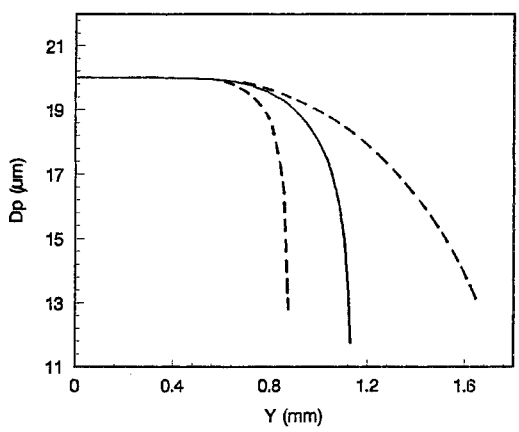

FIG. 10. Effects of heat assignment factor on particle diameter.

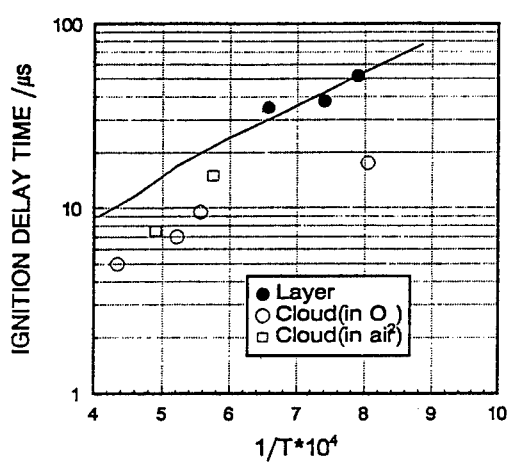

FIG. 11. Effects of shock strength on ignition delay.

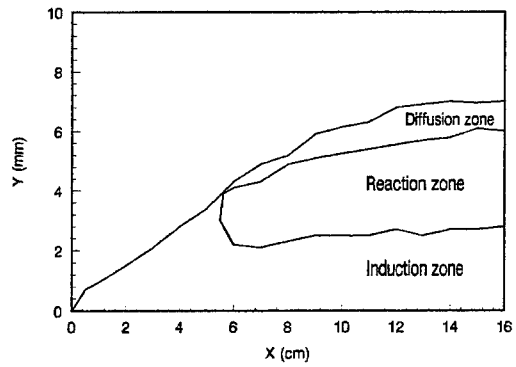

FIG. 12. Structure of dust-film detonation.

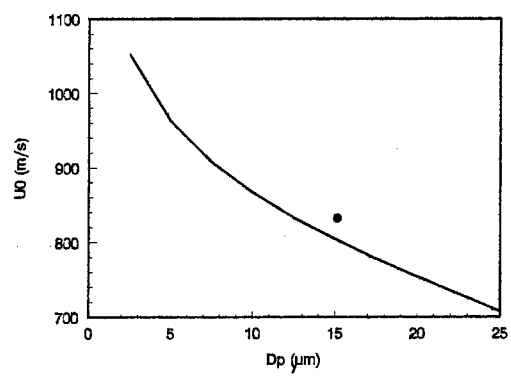

FIG. 13. Variations of dust film detonation velocity with particle diameter.

A burning dust cloud induced by shock waves consists of three distinguished zones as shown in Fig. 12—an induction zone, a reaction zone, and a diffusion zone. A particle moving in the induction zone is heated by the hot gas and begins burning as it enters the reaction zone. Finally, it is consumed completely at the upper edge of the reaction zone. The shock wave is sustained by the energy fed from the particle combustion. The variations of the detonation velocity u_0 with the initial particle diameter are shown in Fig. 13 based on the calculated and measured results.

Conclusions

A steady dust-film detonation has been observed experimentally in a square shock tube coated on the bottom with detonable dust. It has been shown that the velocity of this kind of detonation is an eigenvalue, independent of the strength of the initial shock waves. The numerical analysis based on a two-dimensional model developed here has been performed to reveal its structure and predict the CJ

detonation velocity. Computed and measured results are in reasonable agreement.

Acknowledgments

The authors of this paper are grateful for the support provided by the National Science Foundation of China under Grant No. 19232040 and the Foundation of Educational Committee of China.

Nomenclature

A	preexponential factor
C	specific heat of particle
C_p	constant-pressure specific heat of gas
d_p	particle diameter
E	activation energy
f_x	drag force on particle per unit mass in x direction
f_y	drag force on particle per unit mass in y direction
f_l	lift force
g	gravity acceleration
H	total enthalpy of gas
m_p	particle mass
p	pressure
P_r	Prandtl's number
Q	convective heat flux
Q_c	combustion heat per unit mass of particle
R	gas constant
S_c	Schmidt's number
T	temperature
u	velocity component in x direction
v	velocity component in y direction
Y_i	mass fraction of component i in gas
Γ	rate of solid consumption per unit volume
μ	viscosity
ρ	gas density
ρ_p	concentration of particle
$\bar{\rho}_p$	particle density

Subscripts

e	free stream
p	particulate phase
w	wall surface

REFERENCES

1. Bowen, J. R., Ragland, K. W., Steffes, F. J., and Loflin, T. G., *Thirteenth Symposium (International) on Combustion,* The Combustion Institute, Pittsburgh, 1970, p. 1131.
2. Sichel, M., Rao, S. C., and Nicholls, J. A., *Thirteenth Symposium (International) on Combustion,* The Combustion Institute, Pittsburgh, 1970, p. 1141.
3. Wolanski, P., Grain Dust Explosion and Control, Warsaw University of Technology, Warsaw, 1993, p. 127.
4. Fujitsuna, Y. and Tsuge, S., *Acta Astroneutica* 6:1625 (1979).
5. Rao, C. S. R., Sichel, M., and Nicholls, J. A., *Combust. Sci. Technol.* 4:209 (1972).
6. Adachi, T. and Suzuki, T. *Proceeding 15th Int. Symp. on Shock Waves and Shock Tubes,* Stanford University Press, Stanford, CA, 1986, p. 753.
7. Bolko, V. M. and Papyrin, A. N., *Combust. Explosion Shock Waves* 23(2):122 (1987).
8. Batt, R. G., Kulkarny, V. A., Behrens, H. W., and Rungaldier, H., *Proceedings of the 16th Int. Symp. on Shock Waves and Shock Tubes,* ed., H. Gronig, VCH, Weinheim, Germany, 1988, p. 209.
9. Mirels, H., *AIAA J.* 22 (8):1042 (1984).
10. Kuhl, A. L., Chien, K. Y., Ferguson, R. E., Collins, J. P., Glaz, H. M., and Callela, P., *AIP Conference Proc.* 208, ed. Kim, Y., Stanford University Press, Stanford, CA, 1990, p. 762.
11. Rayevsky, D. and Ben-Dor, G., "Shock Wave Interaction with a Low Speed of Sound Layer: Analytical and Numerical Investigation." Presented at 19th Int. Symp. on Shock Waves and Shock Tubes, Marseille, 1993.
12. Sakakita, H., Hayashi, A. K., and Ivandacv, A. I., *Proceedings of the 17th Int. Symp. on Shock Waves and Shock Tubes,* Stanford University Press, Stanford, CA, 1990, p. 563.
13. Hwang, C. C., *Int. J. Multiphase Flow* 12(4):655 (1986).
14. Soo, S. L., *Multiphase Fluid Dynamics,* Science Press, Hong Kong, 1990.
15. Cebeci, T. and Smith, A. M. O., *Analysis of Turbulent Boundary Layer,* Academic Press, New York, 1974.

Twenty-Sixth Symposium (International) on Combustion/The Combustion Institute, 1996/pp. 3015–3022

OBLIQUE DETONATION STABILIZED ON A HYPERVELOCITY PROJECTILE

MICHAEL J. KANESHIGE
Dept. Mechanical Engineering
California Institute of Technology
Pasadena, CA 91125, USA

J. E. SHEPHERD
Graduate Aeronautical Laboratory
California Institute of Technology
Pasadena, CA 91125, USA

We present new experimental results demonstrating the initiation and stabilization of an oblique detonation by a hypervelocity projectile. Projectiles 25 mm in diameter were launched at nominal velocities of 2700 m/s into stoichiometric H_2-O_2-N_2 mixtures at pressures between 0.1 and 2.5 bar. A critical threshold in initial pressure was found to be required for the establishment of detonations. Initiation events similar to DDT in propagating waves were observed after 300 mm of travel in H_2-O_2 mixtures diluted with 25% N_2. A more direct initiation process was observed in H_2-air mixtures. A stabilized but overdriven oblique detonation was observed in a stoichiometric H_2-air mixture at an initial pressure of 2.5 bar.

The pressure threshold can be explained in terms of competing reaction and flow-quenching effects along a curving streamline in supersonic flow behind a curved shock wave. This competition can be characterized by a critical Damkohler number Da^*, which is inversely proportional to the product of wave curvature κ and reaction zone thickness Δ. Only if the reaction zone is sufficiently thin in comparison with the projectile, $Da > Da^*$, is it possible to obtain stabilized detonations. Otherwise, the reactions quench and the wave splits into a nonreactive shock wave followed by flamelike contact surface. The inverse pressure dependence $\Delta \sim P_0^{-1}$ of the reaction zone length and the scaling of the wave curvature $\kappa \sim 1/a$ with the body radius a implies the standard binary scaling relationship $P_0 a$ = constant for the critical conditions of stabilization for a given mixture composition characterized by a bimolecular rate-limiting step.

Introduction

The present experiments address the issue of the critical conditions required to stabilize an oblique detonation wave on a hypervelocity projectile fired into a premixed combustible mixture. The issue of detonation initiation and *stabilization* by hypervelocity projectiles is often confused with the numerous results on shock-initiated combustion and unsteady detonation.

Most previous experiments with projectiles, notably the often-cited studies of Ruegg and Dorsey [1], Lehr [2], and Alpert and Toong [3], have been carried out under subcritical conditions and/or with projectiles traveling at less than the Chapman–Jouguet (CJ) detonation velocity. For subcritical conditions, only a limited region of shock-initiated combustion is observed behind the bow shock in the vicinity of the projectile. As the wave front recedes from the projectile, there is a distinct point at which the chemical reactions quench and the wave appears to split into a nonreactive shock and a flamelike contact surface. Much of the analysis on these flows has been directed at understanding the striking pattern of instability waves that appears on this contact surface when the projectile velocity is near the CJ value.

Unsteady detonations have been initiated [2,4–6] with a sufficiently large projectile traveling at sub-CJ velocities. In these cases, the projectile only plays a role in initiating the wave and ultimately is left far behind. The initiation threshold can be correlated by the empirical models of Lee [7] and Vasiljev [4], but no inferences about stabilization can be made since the detonations travel faster than the projectiles. Stabilized, planar, oblique detonations have been created by the diffraction of planar waves in two-layer experiments [8,9]; however, the problem of stability in those situations appears to be essentially different than in the case of projectiles because of the "aerodynamic" wedge created by the driving layer.

We conclude that despite three decades of research on this topic, there is scant experimental evidence for the existence of detonation waves

stabilized on hypervelocity (greater than CJ) projectiles. On the other hand, there has been much theoretical analysis [10,11] and speculation about this possibility. This situation has motivated us to reconsider this problem and carry out new experiments resulting in the successful demonstration of this phenomenon. The key to these new results is the careful choice of the mixture composition and projectile parameters, as discussed in the subsequent section.

Dimensional Considerations

Consider a body with characteristic dimension a entering with velocity U into a combustible mixture. The combustible mixture is characterized by a Chapman–Jouguet detonation velocity U_{CJ} and a reference reaction zone length Δ_{CJ}. In addition, the gaseous mixture will have certain reference values of the thermodynamic and kinetic parameters such as the ratio of specific heats γ, the effective activation energy E_a, the specific energy release q, and the initial sound speed c_0. Further, it is useful to consider as parameters the characteristic time scale $t_{flow} = a/w$, where w is the (normal) postshock velocity in the projectile frame and the time scale $t_{chem} = \Delta_{CJ}/w$, the time required for chemical reaction behind the bow shock (if the conditions were uniform). Finally, the lateral (transverse) extent H (actually taken to be the effective half width here) of the test section or guide tube is significant to understanding the results.

Based on these considerations, the significant nondimensional parameters are speed ratio, $\mathcal{U} = U/U_{CJ}$; Damkohler number, $Da = t_{flow}/t_{chem}$; and facility aspect ratio, $\chi = a/H$. Critical values of these parameters will be functions of the parameters characterizing the chemical reaction and gasdynamics. The significant nondimensional state parameters are Chapman–Jouguet Mach number, $M_{CJ} = U_{CJ}/c_0$; ratio of specific heats, $\gamma = C_p/C_v$; and effective activation energy, $\theta = E_a/RT_s$.

To obtain a stabilized detonation, the projectile must be fast enough and the reaction must occur quickly compared to the flow expansion time. In addition, for the detonation wave to be initiated and sustained by the projectile, the facility aspect ratio must be sufficiently small such that wave reflections from the facility boundary are not significant. The criteria for stabilizing detonation waves on projectiles apparently are that $Da > Da^*(\mathcal{U}; M_{CJ}, \theta, \gamma)$, $\mathcal{U} > 1$, and $\chi \ll 1$.

Some of these parameters are unambiguous but others require more careful consideration before they can be assigned a unique meaning. The Damkohler number in particular requires choosing a point in the flow, that is, a location on the bow shock, to evaluate the time scales. For a blunt body, a unique choice is the point directly behind the normal portion of the bow shock, leading to $Da = a/\Delta_0$ [12–14]. For a given composition characterized by a bimolecular rate-limiting step, this can be simplified [15,16] to the binary scaling relationship $Da \propto Pa$, since near the nose of the projectile, $\kappa \propto 1/a$. A more detailed analysis of the reaction zone [15,16] reveals that the local Damkohler parameter $Da = 1/\kappa\Delta$ plays the crucial role in the quenching effect, where κ is the curvature of the wave.

An alternate manner of expressing the Damkohler number would be to use a chemical length scale based on observations of detonation instability. This is the so-called cell width λ that has been used extensively in propagating detonation studies. This leads to a Damkohler-like ratio a/λ, a parameter often [17] introduced in discussing and correlating propagation detonation phenomenology such as critical diameter, initiation energy, and so forth. Detailed considerations [18] of the previous experiments reveal that the ratio a/λ must be greater than 2 to 3 for detonations to be stabilized. The present results are consistent with these considerations (see Tables 1 and 2).

These scaling ideas indicated the need for a tradeoff between projectile speed and mixture sensitivity when designing the experiment. Sensitive mixtures such as stoichiometric H_2-O_2 have small cell sizes (<1 mm at 1 bar) but require very high velocity projectiles since $U_{CJ} = 2850$ m/s. Insensitive mixtures such as typical hydrocarbon fuels in air have lower CJ velocities ~1800 m/s but much larger cell sizes of 50–70 mm at 1 bar. Our final design was a compromise, with a 25-mm-diameter projectile that could be accelerated up to 3000 m/s so that a range of H_2-N_2-O_2 mixtures could be studied with initial pressures up to 3 bar.

See Tables 1 and 2 for values of the nondimensional detonation parameters characterizing the present experiments. The reaction zone lengths given in these tables were computed using a detailed kinetic model of the chemical reaction process, realistic thermochemistry, and numerical solutions of the oblique detonation structure equations as described in Shepherd [18]. The cell widths were taken from the literature [17].

Facility and Procedures

The experiments reported here were conducted in the T5 shock tunnel laboratory of the Graduate Aeronautical Laboratories at Caltech. T5 was converted to a gas gun (see Fig. 1) by which 10 g projectiles may be launched at velocities greater than 3000 m/s.

The inside cross section of the test section was 152 mm square. The reactants in the test section were isolated from the dump tank and target assembly vacuums before each experiment by mylar

TABLE 1
Summary of T5 detonation experiments. Mixture 1: $2H_2 + O_2 + N_2$ and mixture 2: $2H_2 + O_2 + 3.76N_2$. U_{wave1} and U_{wave2} are the apparent wave speeds computed from the detonation or shock arrival times at each pair of pressure transducers

Mix	P_i (Bar)	U (m/s)	U_{wave1} (m/s)	U_{wave2} (m/s)	T5 Shot	Fig.	Δ_{CJ} μm	Δ_0 μm	Result
1	0.100	2690	2380	3200	865		667	233	shock-ind. comb.
1	0.250	2830	2580	3200	1012	3	253	70	DDT
1	0.500	2560	3460	2860	1010		120	60	detonation
1	1.000	2820	3060	3020	862		66.7	14	detonation
1	1.000	2930	3060	3110	863	4	66.7	14	detonation
2	0.100	2593	1670	2580	1021	5	1667	180	nonreactive
2	0.421	2683	2520	2710	1015	6	367	30	rn. zone decoup.
2	0.853	2880	2860	2780	1016		199	45	rn. zone decoup.
2	1.710	2720	3460	2980	1018	7	140	8.3	transition
2	2.560	2653	3510	4120	1020	8	160	7.0	detonation

TABLE 2
Nominal detonation parameters. Based on a projectile speed $U = 2700$ m/s and radius $a = 12.7$ mm. Mixture 1: $2H_2 + O_2 + N_2$ and mixture 2: $2H_2 + O_2 + 3.76N_2$. Facility aspect ratio, χ, was fixed at 0.17

Mix	P_0 (bar)	U_{CJ} (m/s)	$\mathcal{M}$	β_{CJ} (deg)	a/Δ_{CJ}	a/Δ_0	λ_{CJ} (mm)	a/λ_{CJ}
1	0.100	2300	1.17	58.4	18.7	53.6	13	0.98
1	1.000	2400	1.13	62.7	187	893	3.2	4.0
2	0.100	1920	1.41	45.2	7.5	69.4	35	0.36
2	2.560	1990	1.34	47.4	78.1	1785	5.7	2.2

diaphragms that sealed the 76 mm diameter openings. Three PCB dynamic pressure transducers were mounted in ports along one wall. Two pairs of small optical ports along the sides were equipped with diode lasers and photodiodes for measurement of projectile velocity. A pair of larger optical windows was used for photography. A third laser beam for projectile velocimetry was transmitted diagonally through the optical windows. The windows had a 165-mm-diameter clear aperture, allowing visualization of part of the top and bottom of the test section. The inside of the test section was 762 mm long. It was capable of containing detonation pressures above 100 atm.

The photographic system was adapted from the standard T5 setup. A Q-switched Nd:YAG laser pulse was expanded and sent as a collimated beam through the test section, condensed, and imaged on a film sheet. The condensed beam was filtered to reduce the effect of thermal emission. With this setup, we created shadowgraphs and differential interferograms.

Each experiment began with the firing of T5. The high enthalpy gas created at the end of the shock tube accelerated the 25-mm-diameter nylon sphere to about 2700 m/s. The projectile broke an electrical wire in the dump tank, triggering the data acquisition electronics. As the projectile passed through the test section, arrival times at the photodiode stations and the transient pressure at the transducer stations were recorded. After a delay from the break wire signal, estimated to place the projectile in the center of the window, the photograph was taken by Q-switching the Nd:YAG laser. The kinetic energy and momentum of the projectile were dissipated in a stack of aluminum plates and honeycomb in the target section. This event generated a blast wave in the test section stronger than the detonation unless the target was evacuated before the experiment.

Results

Two sets of experiments (a total of 37 tests) were performed with different reactant mixtures and with a single nominal projectile velocity. The Damkohler number was controlled by varying the initial pressure ($t_{chem} \sim P_0^{-1}$ for the present mixtures). In this

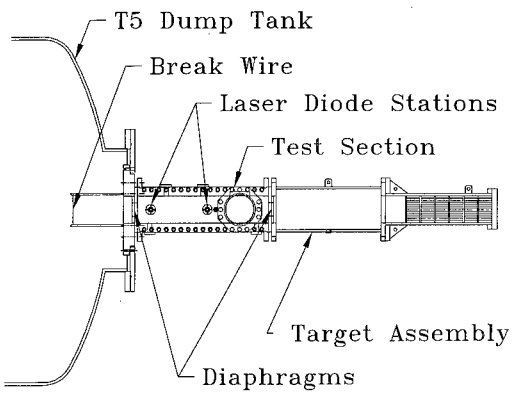

FIG. 1. Illustration of the experimental apparatus. The 3-m-long launch tube is mounted to T5 at the nozzle throat, at the upstream end of the dump tank, and extends into the dump tank.

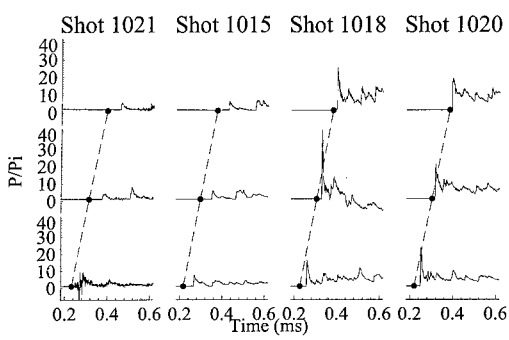

FIG. 2. Pressure plots from the $H_2 + O_2 + 3.76N_2$ experiments, with projectile trajectories computed from diode laser–photodiode data overlayed. Projectile velocity remained constant within the test section, within measurement error.

fashion, the Damkohler number was varied over an order of magnitude for both reactant mixtures. This resulted in a range of phenomena that, in order of increasing initial pressure, were:

1. No apparent reaction, bow shock resembled inert case.
2. Partial reaction near the front of the wave with quenching of the reaction that created a zone of shocked but unreacted gas.
3. A nonsteady initiation event caused by interaction of the shock wave with the confinement.
4. Prompt initiation of detonation with an oblique wave extending outward to the boundaries of the confinement.

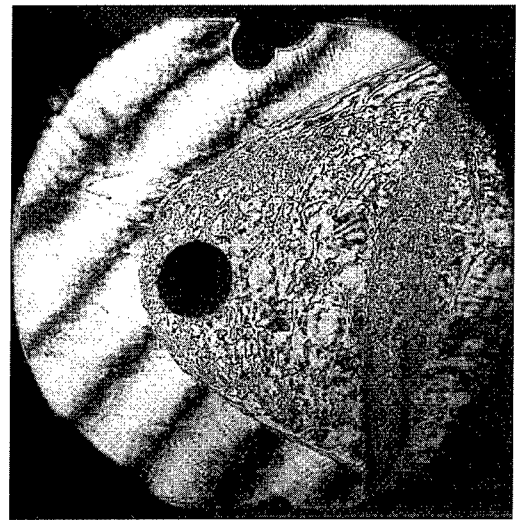

FIG. 3. T5 Shot 1012. Differential interferogram of projectile moving at 2800 m/s in $2H_2 + O_2 + N_2$ at 0.250 bar initial pressure. Bow wave shows shock-induced combustion followed by a quenching event. An explosion in the partially reacted gases appears as a second wave behind the projectile. The dark feature in the upper center is a "clamshell" fracture in one of the windows.

Although the amount of data is sparse and the variety of phenomena observed is rich, the results are reproducible. Duplicate experiments yield nearly identical results in almost all cases. In particular, the distinction between detonation (event 3 or 4) and quenching (1 or 2) is quite crisp and consistent. A summary of selected experiments and the resulting combustion events is given in Table 1.

Differential interferometry was used for visualization in the first set of experiments, using $2H_2 + O_2 + N_2$ mixtures. Shadowgraphy was employed during the second set of experiments, involving a stoichiometric mixture of H_2 and air. Uncertainty in the projectile velocity (photographic timing was accomplished with a programmable delay after the break wire signal) resulted in variation of the position of the projectile in the photographs.

In all experiments, the wall pressure was measured at three points along the test section. The arrival of the projectile was also recorded at three locations (by interruption of diode laser beams). Differences observed between the apparent wave speeds (U_{wave1} and U_{wave2}, see Table 1) and wave shapes recorded at different locations (Fig. 2) indicated unsteady behavior in the flow.

A pressure range of 0.100–1.000 bar was investigated in the first set of experiments (with a mixture $2H_2 + O_2 + N_2$). Details can be found in Bélanger et al. [19]. At the lowest pressure (0.1 bar), a small amount of reaction was observed near the nose of

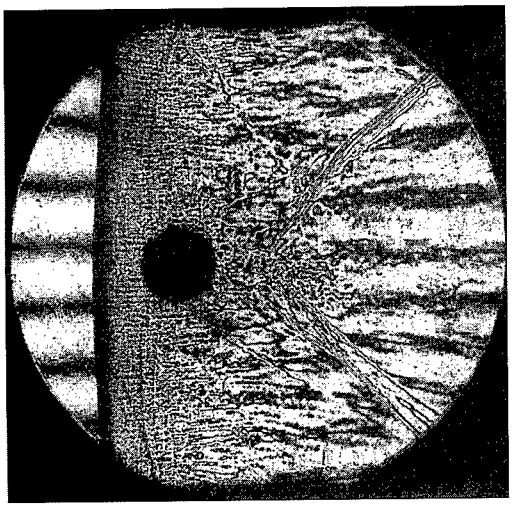

FIG. 4. T5 Shot 863. Differential interferogram of projectile moving at 2900 m/s in $2H_2 + O_2 + N_2$ at 1.000 bar. Cellular structure is visible behind the detonation. Other features are shock waves produced by boundary separation on sphere and wake recompression shocks.

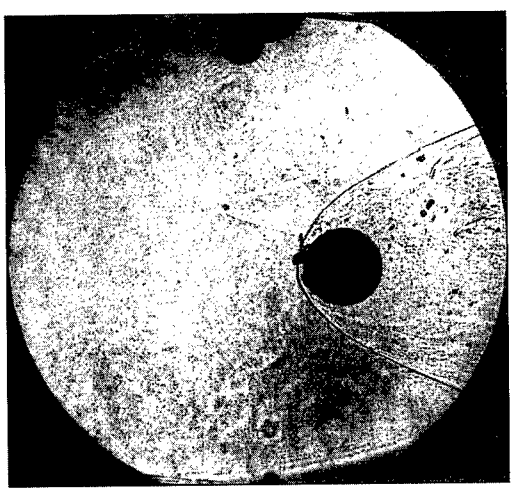

FIG. 5. T5 Shot 1021. Shadowgraph of projectile moving at 2600 m/s in $2H_2 + O_2 + 3.76N_2$ at 0.100 bar. No combustion is apparent.

the projectile. At a higher pressure of 0.250 bar, an extraordinary transient event was observed (Fig. 3). Near the projectile, the appearance of the bow wave indicated shock-induced combustion, with the reaction zone decoupling from a nonreactive shock about two diameters from the projectile. A less curved secondary wave was observed behind the projectile. This seems to indicate an explosion in the partially reacted gases behind the projectile and therefore a deflagration-to-detonation transition

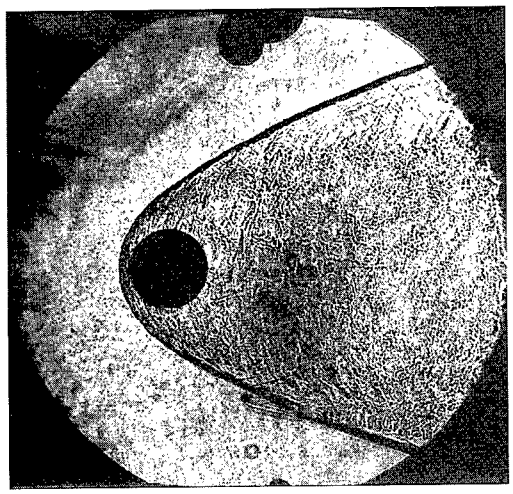

FIG. 6. T5 Shot 1015. Shadowgraph of projectile moving at 2700 m/s in $2H_2 + O_2 + 3.76N_2$ at 0.421 bar, showing shock-induced combustion that terminates in wave-splitting (quenching) event with a flamelike contact surface separating from a nonreactive shock.

(DDT) in progress. At even higher pressure (0.50 and 1.0 bar), an overdriven detonation preceded the projectile (Fig. 4). This wave was clearly a detonation, as indicated by the pressure traces and the cellular structure plainly visible behind the wave. However, the wave speed, geometry, and pressure were inconsistent with a steady process.

A larger range (0.100–2.560 bar) of pressure was examined in the second set of experiments carried out with a less-sensitive mixture $2H_2 + O_2 + 3.76N_2$. At 0.100 bar, the bow wave did not show any sign of combustion (see Fig. 5). At 0.421 bar, a clear example of shock-induced combustion with reaction failure and reaction zone detachment was observed (Fig. 6). Evidence of the lack of reaction in this region was provided by a debris particle visible in the lower half of the image. Turbulent flow and strong refraction characteristic of combustion were observed in the portion of the particle wake behind the bow shock in the region of shocked but noncombusted reactants.

An asymmetric wave shape occurred at 1.710 bar, suggesting proximity to a transition between two types of phenomena (Fig. 7). In the lower half of the picture, the bow wave was curved and the reaction zone detached, apparently at a kink in the wave. The wave was straight in the upper half of the picture, suggesting that it was self-supporting. The scale of the cellular structure in the wave shows the cell size to be comparable to the projectile radius. The bow wave at 2.560 bar initial pressure was straight over a segment between the projectile nose and a Mach reflection at the wall (Fig. 8). This wave was clearly

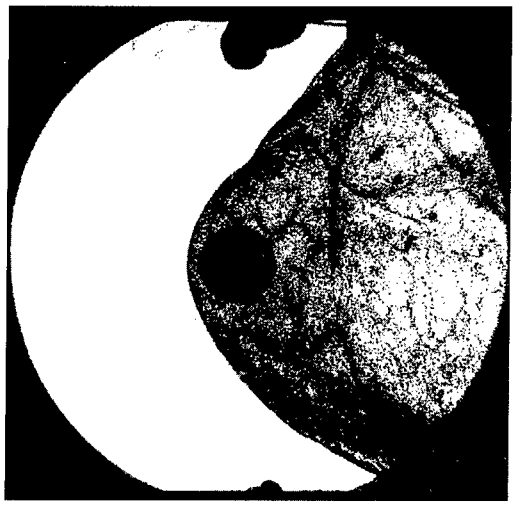

FIG. 7. T5 Shot 1018. Shadowgraph of projectile moving at 2700 m/s in $2H_2 + O_2 + 3.76N_2$ at 1.710 bar. Asymmetry of the bow wave indicates that the event is transitional. The upper half is approximately stabilized and overdriven, while quenching occurs in the lower half.

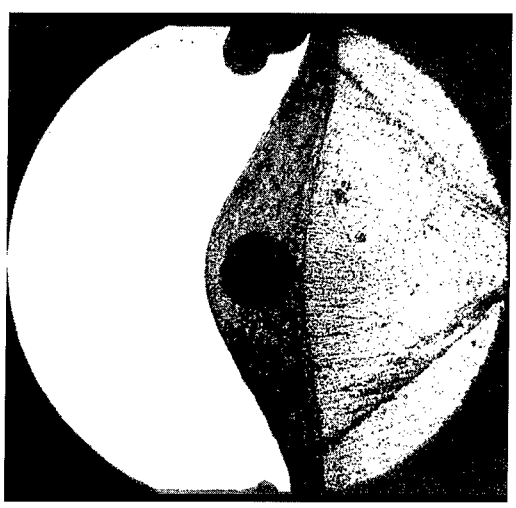

FIG. 8. T5 Shot 1020. Shadowgraph of projectile moving at 2700 m/s in $2H_2 + O_2 + 3.76N_2$ at 2.56 bar with a stabilized overdriven detonation wave and Mach reflections at the walls. The curved feature just behind the projectile is associated with the interaction of the conical wave with the square walls of the test section. Reflected waves (at 45 °) can be observed emerging from the triple points.

a stabilized oblique detonation. Relatively fine cellular structure was visible behind the wave, and the wave angle indicated that the wave was slightly overdriven but much closer to a steady configuration than in the first set of experiments.

Discussion

Notable features of the experimental results are the existence of a critical pressure threshold for initiating a detonation in both cases, the nearly planar detonation wave shape for mixture 1, and the definitive oblique detonation wave observed in mixture 2.

The two sets of experiments resulted in dramatically different detonation wave shapes. A distinct oblique wave was observed in mixture 2, whereas the detonations observed for mixture 1 were nearly normal. Both wave angles are inconsistent with steady CJ waves (see the wave angles $\beta_{CJ} = \sin^{-1}[U_{CJ}/U]$ in Table 2). However, while the straight portions of the detonations in mixture 2 were only slightly overdriven, the entire wave in mixture 1 was overdriven.

Major differences that could account for this variation are the speed ratio U/U_{CJ} and the reactivity of the mixtures. In set 1, the projectile velocity was only 12.5% higher than the detonation velocity, whereas in set 2, the projectile velocity was 40% higher than the CJ velocity (see Table 2).

Apparently, when the CJ speed is closer to the projectile speed, it takes longer for the initiation transient to die down and for the wave shape to relax to a steady-state configuration. This is related to the observations of DDT-like processes occurring in the quenched gas region. After the unsteady explosion wave observed in Fig. 3 diffracts over the projectile, an overdriven detonation will be produced. We speculate that the nearly planar wave observed in Fig. 4 is photographed immediately after such an event. We expect that this wave will decay and eventually reach a configuration similar to Fig. 8, since overdriven waves are susceptible to overtaking disturbances [20]. The effect of overdrive in Fig. 8 is much less pronounced because the CJ-wave angle is 16° lower and the initiation processes apparently occur more promptly. The full explanation requires further experimentation to resolve the initiation transient.

Quenching

One of the most striking features of the current results is the dramatic change in the wave shape and pressure histories when a critical pressure threshold is exceeded (see Fig. 2 and compare Figs. 6 and 8). We interpret this transition as the stabilization of the detonation wave on the projectile. The critical conditions for stabilization are those for which the "splitting" of the shock-reaction zone structure, observed in Fig. 6 and the lower half of Fig. 7, just occurs.

Gilinskii and Chernyi [15] were the first to consider this process in detail and identified the Damkohler parameter Pa as the controlling factor for a given composition.

Gilinskii and Chernyi determined the critical conditions by numerically solving for the flow in the vicinity of the body. An alternative procedure is to consider the local influence of the wave curvature on the processes in the reaction zone. From this perspective, the quenching process is a result of the competition of the flow expansion and chemical energy release in the region immediately behind the curved shock wave. The flow is undergoing adiabatic expansion because of the streamline curvature in a supersonic region behind a curved shock front.

This is exactly the same physical effect that causes freezing of dissociation behind curved bow shocks in hypervelocity flow over blunt bodies [16]. The structure of the reaction zone behind a straight oblique detonation [18] can be extended to the case of a weakly curved ($\kappa\Delta \ll 1$) wave using the analysis of Hornung [16], which is based on the thin-layer equations for two-dimensional (planar) hypersonic flow. A quenching criterion can be obtained by carrying out an asymptotic analysis of the temperature variation along a streamline.

The results of this analysis show that the reaction is just quenched when the wave curvature κ exceeds the critical value κ_c. This critical value is given by $\kappa_c = 1/\theta\Delta B$, where B is a function of wave angle, freestream velocity, and thermodynamic properties of the gas. This critical curvature is a strong function of shock strength and scales directly with the initial pressure P_0 for second-order reactions since $\Delta \sim P_0^{-1}$. The critical curvature increases with increasing shock strength, reaching infinity at the point on the oblique shock where the downstream flow is sonic. The minimum value of κ_c occurs near the point on the wave for which the normal velocity is close to the CJ condition.

The behavior observed in our experiments can be classified as follows: (1) subcritical, $\kappa_c < \kappa_{\text{wave}}$ for sufficiently small normal velocities, quenching occurs; (2) critical, $\kappa_c = \kappa_{\text{wave}}$ at the CJ point, this is the critical condition for oblique detonation stabilization; and (3) supercritical, $\kappa_c > \kappa_{\text{wave}}$ for all values of $U_n > U_{\text{CJ}}$, quenching never occurs, the oblique detonation is always stabilized.

Conclusions and Summary

We have presented our experimental evidence for oblique detonations stabilized on projectiles. We observe transition from quenched reaction to oblique detonation with increasing initial pressure in the reactants. We present experimental evidence of this transition and argue that the parameter $\kappa\Delta$ controls the transition.

Nonsteady processes were prominent in the present experiments. Not only does a transient take place when the projectile enters the combustible test gas, but apparently a long time must elapse to get the flow to settle into a configuration that could be described as steady state. No truly steady-state–like configurations were observed in the current experiments. We conclude that interpreting snapshots of potentially nonsteady events may be quite misleading and further experimentation is needed to clarify the initiation process.

Acknowledgments

We thank Hans Hornung for his encouragement and the use of T5, Jacques Bélanger for building the gun, and Bahram Valiferdowsi for running T5. This material is based on work supported under a National Science Foundation Graduate Research Fellowship and the Powell Fund of the California Institute of Technology.

REFERENCES

1. Ruegg, F. W., *J. Res. Nat. Bur. Stand. Sec. C.* 66C:51–58 (1962).
2. Lehr, H. F., *Astronautica Acta* 17:589–597 (1972).
3. Alpert, R. L. and T. Y. Toong, *Astronautica Acta* 17:539–560 (1972).
4. Vasiljev, A. A., *Shock Waves* 3:321–326 (1994).
5. Bendick, W. B., in *Fuel-Air Explosions* (J. H. S. Lee and C. M. Guirao, eds.), Waterloo Press, Waterloo, 1982, p. 507.
6. Higgins, A. J. and Bruckner, A. P., Fifteenth International Colloquium on the Dynamics of Explosions and Reactive Systems, Boulder, 1995; see also Higgins, A. J. and Bruckner, A. P., AIAA-96-0342, 1996.
7. Lee, J. H. S. Zeldovich Memorial Conference on Combustion, Voronovo, Russia, 1994.
8. Dabora, E. K., Desbordes, D., Guerraud, C., Wagner, H. G., *Prog. Aero. Astro.* 133:187–204 (1991).
9. Liu, J. C., Liou, J. J., Sichel, M., Kaufmann, C. W., and Nicholls, J. A., *Twenty-First Symposium (International) on Combustion*, The Combustion Institute, Pittsburg 1987, pp. 1639–1647.
10. Chernyi, G. G., in *Problems of Hydrodynamics and Continuum Mechanics*, SIAM, Philadelphia, 1969, pp. 145–169.
11. Pratt, D. T., Humphrey, J. W., and Glenn, D. E., *J. Propulsion* 7:837–845 (1991).
12. Sichel, M. and Galloway, A. J., *Astronautica Acta* 13:137–145 (1967).
13. Hornung, H. G., *J. Fluid Mech.* 53:149 (1972).
14. Wen, C. Y. and Hornung, H. G. *J. Fluid Mech.* 299:389–405 (1995).
15. Gilinskii, S. M. and Chernyi, G. G., *Fluid Dynamics* 3(1):12–19 (1968).

16. Hornung, H. G., *J. Fluid Mech.* 74:143–159 (1976).
17. Lee, J. H. S., *Ann. Rev. Fluid Mech.* 17:311–336 (1984).
18. Shepherd, J. E., in *Combustion in High-Speed Flows* (J. Buckmaster et al., eds.), Kluwer Academic Publishers, Dordrecht, the Netherlands, 1994, pp. 373–420.
19. Bélanger, J., Kaneshige, M. J., and Shepherd, J. E., in *Shock Waves, Proceedings of the 20th ISSW,* World Scientific Singapore, 1996, pp. 1119–1124.
20. Gilinskii, S. M. and Zapryanov, Z. D., *Fluid Dynamics* 2(3):90–97 (1967).

Twenty-Sixth Symposium (International) on Combustion/The Combustion Institute, 1996/pp. 3023–3031

ONSET OF OBLIQUE DETONATION WAVES: COMPARISON BETWEEN EXPERIMENTAL AND NUMERICAL RESULTS FOR HYDROGEN-AIR MIXTURES

CHRISTOPHE VIGUIER, LUÍS FERNANDO FIGUEIRA DA SILVA, DANIEL DESBORDES AND BRUNO DESHAIES

Laboratoire de Combustion et de Détonique
UPR 9028 du CNRS; ENSMA et Université de Poitiers
86960 Futuroscope Cedex, France

Stable delayed oblique detonation waves have been observed both numerically and experimentally in hydrogen-air stoichiometric mixtures for Mach numbers 6 and 7.5. The experimental results obtained using an oblique shock tube facility are compared to calculations made by solving the full conservation equations for a reactive gas. The overall flow structure obtained experimentally is compared to detailed computations of an oblique shock wave to oblique detonation-wave transition over a wedge, and resulting flow fields are analyzed on the basis of shock and detonation polars.

Introduction

Concerning the study of combustion in supersonic flow conditions, oblique shock wave (OSW) is a generic tool used to slow down the gas and to trigger and stabilize the combustion process. Standing oblique detonation waves (ODW) are advanced as an alternative to supersonic combustion in air-breathing supersonic ramjet engines, which may be used for the propulsion of hypersonic vehicles [1,2] and in the so-called ram accelerator, which consists of a high-speed projectile launched into a tube filled with a combustible mixture [3]. In this last concept, where efficiency has been demonstrated recently [4], oblique detonation or oblique shock-induced combustion initiated and stabilized around the projectile plays a key role in the superdetonative motion of the projectile. Apart from the problem of obtaining a homogeneous combustible mixture and because of the analogy that exists between the ram accelerator and the ramjet, this could be seen as proof of the validity of the detonation ramjet concept.

Classically, the existence of a standing stable ODW is made possible by the action of an obstacle that may be a wedge. Two minimum necessary conditions are nevertheless required: (1) the Mach number of the incoming flow must be larger than the Mach number of the Chapman–Jouguet wave M_{CJ} and (2) the angle of the wedge must lie within a certain range [5].

In the aforementioned geometry, a detonation occurs if the thermodynamic conditions prevailing behind the OSW can lead to the ignition of the mixture within the domain of interest. As pointed out by Zel'dovich, the duration of the shocked gas must exceed the induction delay for the onset of the detonation. This ignition delay is a very sensitive function of the local temperature and pressure of the mixture for most gases.

In the pioneer work of Liu et al. [6] and Dabora et al. [5], an oblique shock tube is used to produce OSW with different inclination angles θ at various Mach numbers. The OSW is generated by a gaseous wedge of constant angle δ that propagates at a stable velocity through the reactive mixture at rest. Previous experiments using such a facility have widely demonstrated the possibility of obtaining standing ODW in different reactive mixtures [5,7,8]. In this facility, very reproducible and stable oblique detonations are observed with varying delays depending on postshock temperature and pressure.

From the point of view of numerical calculations, the problem of ignition behind OSWs has been addressed by many authors in recent years. The transition from a nonreactive OSW to an ODW was first put into evidence by Singh et al. [9] for a mixture of $H_2/O_2/He$ with the use of a detailed chemical kinetics scheme and by Li et al. [10] using a simplified chemical kinetics of H_2 and air. The latter work gives a detailed analysis of some of the basic flow structures obtained when combustion occurs. Vlasenko and Sabel'nikov [11] further analyzed some of these basic structures and studied some cases, including composition inhomogeneities. In a numerical study of the flow around a blunt cone, Lefebvre and Fujiwara [12] investigated the influence of the Mach number and tip radius on the structures obtained when combustion occurs. Figueira da Silva and Deshaies [13] have shown that two different types of transition from the OSW to the oblique detonation may occur, depending only on the initial pressure of the mixture. In their work, a full Navier–Stokes

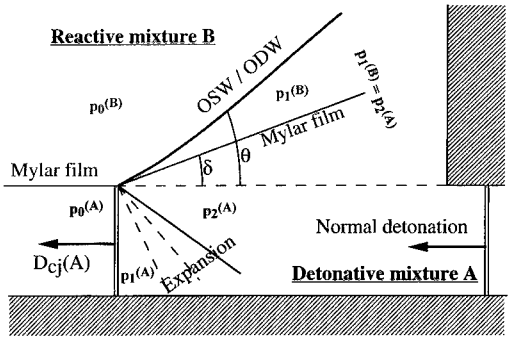

FIG. 1. Schematic representation of the experimental setup.

equation solver was used along with a detailed chemical kinetics mechanism.

In this paper, we study experimentally and numerically the detailed flow structure obtained when an OSW leads to the formation of an ODW. The experiments reported here were performed in a device analogous to the one used by Dabora et al. [5], while the computations used the techniques developed by Figueira da Silva and Deshaies [13].

Experimental Setup

Oblique Shock Tube Facility

The experimental results reported in this paper were obtained using a so-called *oblique shock tube* [7]. Such a facility is able to generate OSW and/or ODW in a quiescent reactive gas mixture. The experimental setup is divided in two parts, as shown in Fig. 1:

1. The driver section (A) contains a reactive mixture that can support a normal quasi–Chapman–Jouguet detonation wave. This mixture is chosen for its Chapman–Jouguet velocity D_{CJ}^A to be the one required for obtaining the desired Mach number M in the test section.
2. The driven test section (B) adjacent to the driver chamber is filled with test gas, a hydrogen-air stoichiometric mixture in the experiments reported here.

These two media are separated by a very thin (10-μm) Mylar film.

The lateral expansion of the detonation products of the driver mixture (A) gives birth to a (gaseous) wedge that has a constant angle δ and propagates through the test gas (B). This propagation creates an OSW in the driven mixture (B) that has an angle θ. Both the wedge and the OSW move with the Chapman–Jouguet velocity of mixture (A). Consequently, the Mach number of the wedge with respect to the test gas is $M = D_{CJ}^A/a_0^B$, where a_0^B is the speed of sound of the driven gas mixture.

The experimental results shown here concern the following mixtures:

- In the driven part (B), a stoichiometric H_2-air mixture at initial temperature $T_0^B = 293$ K and at initial pressures ranging from $0.2 < p_0^B < 0.8$ bar.
- In the driver section (A), two different mixtures at an initial temperature of $T_0^A = 293$ K were used: (1) $C_2H_2 + 2.5O_2$ at initial pressures in the range $0.4 < p_0^A < 1.6$ bar, which results in a Mach number of 6 for the test gas ($D_{CJ}^A = 2400$ m/s); (2) $C_2H_4 + 3O_2 + 8He$ at initial pressures in the range $0.4 < p_0^A < 1.6$ bar, which results in a Mach number of 7.5 for the test gas ($D_{CJ}^A = 3050$ m/s). These highly detonable mixtures exhibit very fine three-dimensional structures, so that the propagation of the detonation is practically unaffected by the lateral expansion of the gases.

Methods of Diagnosis

We use two kinds of diagnostic techniques:

1. Three pressure gauge measurements that provide the history of shock- and detonation-wave pressure and the mean inclination angle of the waves. These gauges are equidistant and positioned along the transverse direction.
2. Schlieren photographic sequences that show the detailed structure of the OSW–induced combustion.

For each shot, we also control the velocity of the driver wave, which should be very close to the Chapman–Jouguet regime, by monitoring the propagation time of the wave all along the detonation tube by means of ionization probes and pressure gauges.

Mathematical Formulation of the Problem

To obtain an explanation of the detailed flow structures found in the experiments, we perform numerical calculations of the development of supersonic reactive flow around a two-dimensional wedge.

In this work, we solve the two-dimensional, unsteady conservation equations of mass, momentum, energy, and species for a multicomponent chemically reacting gas mixture [13]. Molecular diffusion effects (heat, species, and momentum) are included—even if they are negligible in the streamwise direction, they must be considered to produce a correct description of the transverse mixing. Molecular transport coefficients and physicochemical properties are local functions of the composition and the thermal state of the gas. For the sake of simplicity, the diffusion of species is calculated using Fick's law. We consider detailed chemical kinetic

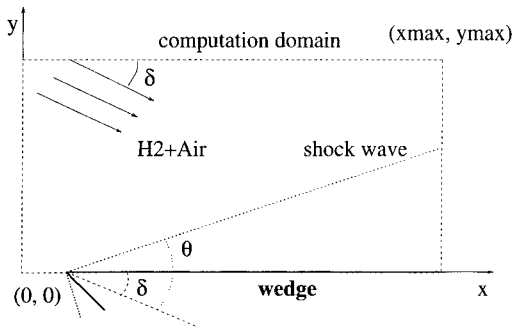

FIG. 2. Schematic representation of the computational domain.

mechanisms for hydrogen-air combustion; the rate of each elementary reaction step obeys a modified Arrhenius form.

Boundary Conditions

Computations will concern only the flow obtained experimentally on the upper side of the Mylar film, that is, in the driven mixture (B) (see Fig. 1.).

A schematic representation of the computation domain is given in Fig. 2. The Cartesian grid is aligned with the wedge surface. The premixed hydrogen-air flow with given composition, pressure, temperature, and Mach number enters the computation domain with an angle of δ, where δ is the half angle of the wedge.

The inflow conditions are fixed to the free stream values in both left ($x = 0$) and upper ($y = y_{max}$) boundaries of the domain. At the outflow boundary ($x = x_{max}$), characteristic boundary conditions are implemented. It is assumed that the boundary conditions at the contact surface between the driver and the driven gases ($y = 0$) can be represented more accurately by slip conditions ($v = \partial u/\partial y = 0$) than by no-slip conditions ($u = v = 0$) typical of solid fixed walls. Thus, in the present computations, only slip conditions will be used. The contact surface ($y = 0$) is considered adiabatic and noncatalytic ($\partial T/\partial y = \partial Y_k/\partial y = 0$, Y_k is the mass fraction of species k). The computational domain contains 190^2 points uniformly distributed over 5×2 cm^2. Such a mesh results in an overall flow structure that is grid independent but does not allow for the detailed resolution of the detonation structure.

Chemical Kinetics and Physical Properties

The chemical kinetics schemes we use involve nine species, H_2, O_2, H_2O, OH, O, H, HO_2, H_2O_2, and N_2. The chemical production rates are calculated using the CHEMKIN II package [14]. We compare the results obtained using the mechanism proposed by Miller et al. [15], which we used in our previous works [13,16], with the mechanism recently compiled by Balakrishnan and Williams [17]. These mechanisms are reproduced in Table 1. It must be noted that we have chosen to use the Arrhenius constants given by Baulch et al. [18] for reaction OH + OH $\rightarrow$ H_2O + O instead of the non-Arrhenius form proposed by Yetter et al. [19]. Indeed, as pointed out in their work, this reaction is most often in chemical equilibrium, so that the different rates proposed in the literature have a negligible effect on the results we present here.

The transport properties coefficients and thermodynamic properties are calculated using the computer packages developed by Kee et al. [20,14].

Numerical Solution Procedure

A monotone numerical method is used to accurately capture all the features present (slip lines, strong shock waves coupled with a high activation energy, strongly exothermic chemical kinetics) and to prevent nonphysical interactions between chemistry and the flow field.

Based on previous comparisons between different numerical procedures, we have chosen to use Liou's [21] Advection Upstream Splitting Method, with a second-order MUSCL extrapolation and MINMOD limiter for the primitive variables (ρ, u, v, p, Y_k) [22]. The viscous part of the fluxes are discretized using a second-order accurate central differences scheme.

The time-integration procedure used in this work is a second-order accuracy Runge–Kutta scheme. The integration of the chemical source terms is accomplished by means of an ODE package, VODE [23], after a time-step splitting procedure that preserves formal second-order accuracy [24].

The results obtained in the case of a supersonic reactive boundary layer show an excellent agreement with the calculations performed by means of a boundary-layer computer code [13].

Constant-Pressure Thermal Explosion

It can be expected that the onset of combustion behind the OSW is directly related to the induction time of the chemical kinetics. Therefore, it is interesting to recall the behavior of the chemical induction time τ_i of the zero-dimensional constant-pressure thermal explosion. This time is defined here as the one corresponding to 10% of the equilibrium H_2O mass fraction for given initial conditions.

In Fig. 3, we plot the chemical induction time τ_i for a stoichiometric H_2-air mixture as a function of the pressure for different initial temperatures, using the chemical kinetic schemes shown in Table 1. The induction time is a strongly decreasing function of the temperature and varies as $1/p$, at both the low

TABLE 1
Detailed chemical mechanisms for hydrogen-air combustion proposed by Balakrishnan and Williams and Miller et al.

Reaction	A [17]	β	E	A [15]	β	E
$H + O_2 \rightleftharpoons OH + O$	3.52E16	−0.7	17070.0	5.13E16	−0.816	16507.0
$H_2 + O \rightleftharpoons OH + H$	50.6E4	2.67	6290.0	1.80E10	1.00	8826.0
$OH + OH \rightleftharpoons H_2O + O$	1.51E9	1.14	99.0	6.00E08	1.30	0.0
$H_2 + OH \rightleftharpoons H_2O + H$	1.17E9	1.3	3626.0	1.17E09	1.30	3626.0
$H + O_2 + M \rightleftharpoons HO_2 + M$	6.76E19[a]	−1.42	0.0	2.10E18[d]	−1.00	0.0
$H + HO_2 \rightleftharpoons OH + OH$	1.70E14	0.0	874.0	2.50E14	0.00	1900.0
$H + HO_2 \rightleftharpoons H_2 + O_2$	4.28E13	0.0	1411.0	2.50E13	0.00	700.0
$OH + HO_2 \rightleftharpoons H_2O + O_2$	2.89E13	0.0	−497.0	5.00E13	0.00	1000.0
$H + H + M \rightleftharpoons H_2 + M$	1.80E18[b]	−1.0	0.0	—	—	—
$H_2 + M \rightleftharpoons H + H + M$	—	—	—	2.23E12[e]	0.50	92600.0
$H + OH + M \rightleftharpoons H_2O + M$	2.20E22[a]	−2.0	0.0	7.50E23[f]	−2.60	0.0
$HO_2 + HO_2 \rightleftharpoons H_2O_2 + O_2$	3.02E12	0.0	1390.0	2.00E12	0.00	0.0
$H_2O_2 + M \rightleftharpoons OH + OH + M$	1.20E17[c]	0.0	45500.0	1.30E17	0.00	45500.0
$H_2O_2 + OH \rightleftharpoons H_2O + HO_2$	7.08E12	0.0	1430.0	1.00E13	0.00	1800.0
$O + HO_2 \rightleftharpoons OH + O_2$	2.00E13	0.0	0.0	4.80E13	0.00	1000.0
$H + HO_2 \rightleftharpoons O + H_2O$	3.10E13	0.0	1720.0	—	—	—
$H + O + M \rightleftharpoons OH + M$	6.20E16[a]	−0.6	0.0	—	—	—
$O + O + M \rightleftharpoons O_2 + M$	6.17E15[a]	−0.5	0.0	—	—	—
$O_2 + M \rightleftharpoons O + O + M$	—	—	—	1.85E11	0.50	95560.0
$H_2O_2 + H \rightleftharpoons H_2O + OH$	1.00E13	0.0	3590.0	—	—	—
$H_2O_2 + H \rightleftharpoons HO_2 + H_2$	4.79E13	0.0	7950.0	1.60E12	0.00	3800.0
$O + OH + M \rightleftharpoons HO_2 + M$	1.00E16	0.0	0.0	—	—	—
$H_2 + O_2 \rightleftharpoons OH + OH$	1.70E13	0.0	47780.0	1.70E13	0.00	47780.0
$H + O_2 + O_2 \rightleftharpoons HO_2 + O_2$	—	—	—	6.70E19	−1.42	0.0
$H + O_2 + N_2 \rightleftharpoons HO_2 + N_2$	—	—	—	6.70E19	−1.42	0.0

Third-body efficiencies: $a, f_{H_2O} = 12, f_{H_2} = 2.5, f_{N_2} = f_{O_2} = 1.0$; $b, f_{H_2O} = 6.5, f_{H_2} = 1, f_{N_2} = f_{O_2} = 0.4$; $c, f_{H_2O} = 15, f_{H_2} = 2.5, f_{N_2} = f_{O_2} = 1.0$; $d, f_{H_2O} = 21, f_{H_2} = 3.3, f_{N_2} = f_{O_2} = 0$; $e, f_{H_2O} = 6, f_H = 2, f_{H_2} = 3$; $f, f_{H_2O} = 20$.

and high pressure ranges. In this figure, we can clearly distinguish the classical [25] nonmonotone behavior of τ_i with pressure, known as the extended second explosion limit. The steep increase in τ_i with pressure for "moderate" values of p is associated with a change of the prevailing chain branching reaction, from $H + O_2 \rightarrow OH + O$ at the low pressure range to $H + O_2 + M \rightarrow HO_2 + M$ at the high pressure range.

We also show in Fig. 3 the chemical induction time given by the empirical relationship $\tau_i = 6.9 \times 10^{-11} [O_2]^{-1} \exp(8304/T)$ proposed by Strehlow et al. [26]. The oxygen concentration $[O_2]$ is expressed in mol/l. It is clear that this formula does not allow for the presence of the second explosion limit.

Results and Discussion

In the first set of experiments, we have determined the conditions necessary to obtain transition from an OSW to an ODW. Increasing the strength of the interaction, and consequently the OSW angle and the nondimensional postshock thermodynamical parameters (p/p_0, T/T_0, . . .), we observe the onset of an ODW for values of these parameters that exceed some threshold [7].

Once a set of nondimensional values of temperatures and pressures that lead to such a transition has been obtained, we modify only the initial pressures to emphasize the effect of the chemical kinetics on the transition process. This variation is limited both by the mechanical strength and the dimension of the apparatus. For given experimental conditions, we obtain very reproducible and stable configurations of the transition so that we can measure an ignition delay from schlieren photographs easily. One example of such a transition is given in Fig. 4.

Overall Flow Structure

In this section, we compare the overall flow structure obtained in the experiments with the calculations made in the case of a rigid wedge. We choose to use the Balakrishnan and Williams chemical

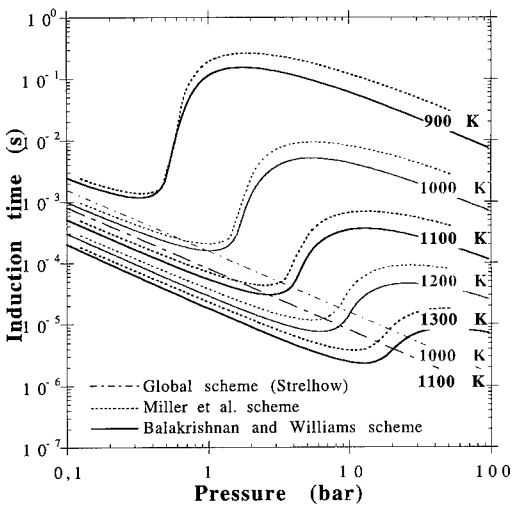

FIG. 3. Induction time of the hydrogen-air stoichiometric mixture as a function of pressure for different temperatures and chemical kinetic mechanisms.

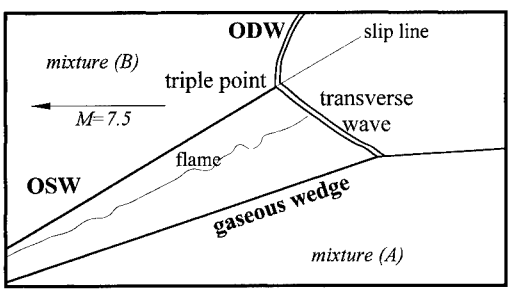

FIG. 4. Schlieren image of the flow field obtained for $T_0^A = T_0^B = 293$ K, $p_0^A = 1$ bar, $p_0^B = 0.4$ bar; (A): $C_2H_4 + 3O_2 + 8$ He; (B): H_2 + air.

kinetic mechanism. The flow conditions adopted are $M = 7.5$, $p_0^B = 0.4$ bar, $p_0^A = 1$ bar, $T_0^A = T_0^B = 293$ K, and a wedge angle of 25°, which corresponds to the expected value of the Mylar film angle obtained from the polar analysis shown later. The schlieren image of the resulting flow is shown in Fig. 4, while the calculated fields of temperature and pressure are given in Fig. 5.

The comparison of these two figures shows that, despite the presence in the experiments of a highly inclined subsonic turbulent flame that originates at the leading edge of the Mylar film, the whole structure of the flow found both in the calculation and in the experiment look alike. Indeed, the leading shock angles obtained from the experiment and the calculation, 30° and 32.5°, respectively, are in excellent agreement. The region of the flow comprised between the leading oblique shock and the flame (in the experiments) or the wedge surface (in the calculations) is essentially a region in which initiation and chain-branching reactions develop with negligible heat release. Hereafter, this region will be referred to as the induction region.

At the end of the induction region, an abrupt transition from the OSW to the ODW occurs. The crossing point between the oblique detonation and the leading shock wave defines a triple point from which a slip line emanates. This former wave reignites the flow that has passed through the leading shock wave and intersects the Mylar film, provoking a deflection of the "wedge" toward the driver gas (A).

The triple point is observed in both numerical and experimental results, but the ODW anchored to it corresponds to a different final thermodynamic state of the gases. This can be explained by the use of the shock-detonation polars shown in Fig. 6, where we have plotted the pressure-deflection and shock angle–deflection polars for the experimental and calculation conditions corresponding to Figs. 4 and 5. In Fig. 6, the final state of the burned gases obtained both in the experiments and calculations is shown. Because of the presence of a rigid wedge in the calculations, the state of the detonated gases lies vertical (constant deflection angle) from the starting point (oblique shock). On the other hand, the angle of the detonation obtained in the experiments results from the interaction between the burned gases from the driver (A) and driven (B) sections. As a consequence, the angle of the detonation obtained in the calculations is always larger than that of the experiments. The angle of the detonation wave obtained in the calculation, 49°, is in good agreement with the one predicted by the detonation polar, 45°.

We have also plotted in Fig. 6 the shock and detonation polars corresponding to the postshock gases, centered around $\delta = 25°$. Taking the value obtained for the angle of the coalesced shock from the numerical results, 67°, we can calculate a corresponding flow-deflection angle (55°) and thus a final pressure, 47 bar. This former value being much higher than the one actually calculated, 25 bar, it can be concluded that the coalesced wave we obtain does not behave as a one-dimensional shock. It must be noticed that such a wave does not correspond to a planar one-dimensional wave, since its angle is

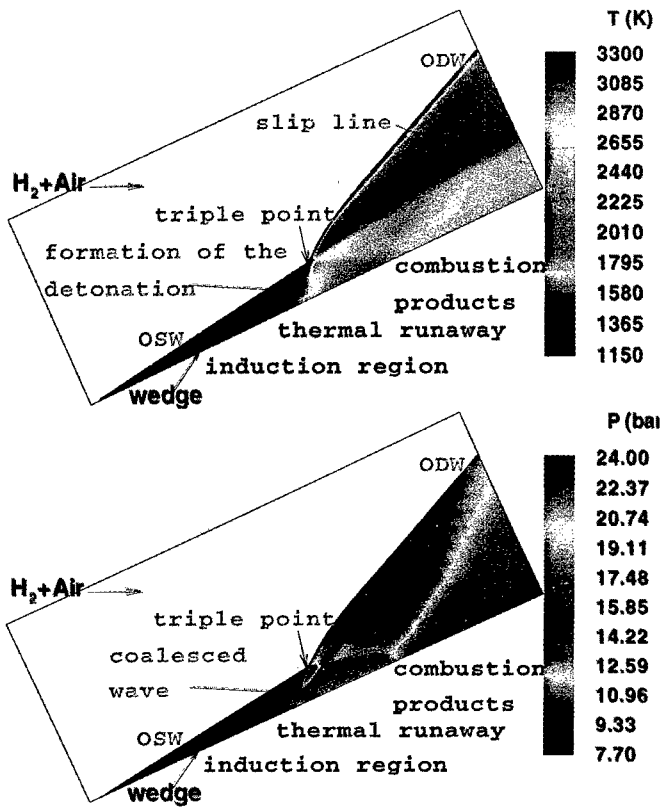

FIG. 5. Oblique detonation wave structure: temperature and pressure fields obtained in the case $T_0 = 293$ K, $M = 7.5$, $p_0 = 0.4$ bar, stoichiometric H_2-air mixture, $\delta = 25°$, 5×2 cm^2, 190^2 points.

smaller than that of the Chapman–Jouguet detonation. In the experiments, the wave that emanates from the triple point seems to be quite different.

The main difference observed between the calculation and the experimental results concerns the thermal runaway region. In the case of the calculated flow, which includes a rigid wedge, ignition occurs near the surface at a point that can be computed easily by the zero-dimensional thermal explosion problem. Indeed, the induction length we obtain, 2.0 cm, is almost equal to that calculated by the product $\tau_i u$, 1.9 cm. The pressure waves generated by the onset of combustion near the wedge surface coalesce to form a wave that is followed by a premature ignition of the shocked gases, which leads to a significant pressure rise. This coalesced wave intercepts the leading oblique shock, which has the effect of increasing its strength, thus favoring ignition of the unshocked mixture and eventually leading to the onset of an ODW. In the case of the experimental results shown in Fig. 4, such an ignition region and coalesced shock cannot be observed. In the experiments, a transverse shock wave emanates from the crossing point between the ODW and the OSW.

The Induction Process

Since the OSW-to-ODW transition is found to be controlled in the computations by the chemical induction process behind the leading shock, we attempt to verify whether such a mechanism also controls this transition in the experiments.

The detonation ignition length L of combustion behind an OSW can be expected to be a function of the chemical induction time τ_i, taken at the thermodynamic conditions prevailing behind the shock, and the local velocity of the flow, u, that is, $L \propto \tau_i u$. As already seen, the induction time of the chemical kinetics is found to be a strongly decreasing function of the temperature and a nonmonotone function of the pressure for a unity equivalence ratio.

We have deduced from the set of schlieren images, obtained as explained previously, the detonation ignition length along the wedge surface, as illustrated in Fig. 7. Departing from the triple point corresponding to OSW-to-ODW transition, we draw a characteristic wave that intercepts the wedge surface. The distance between this intersection and the crossing of the leading shock with the wedge surface

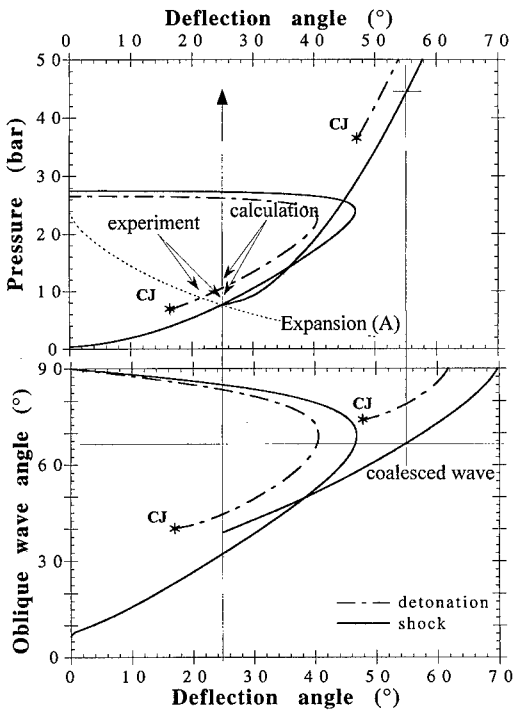

FIG. 6. Shock and detonation polars obtained for the conditions of Figs. 4 and 5.

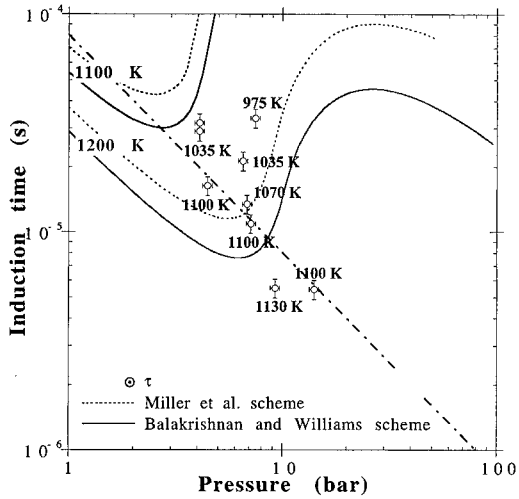

FIG. 8. Comparison between the measured τ and calculated induction times τ_i as a function of the pressure and temperature of the shocked gases.

is taken as the detonation ignition length L. The temperature, pressure, and velocity u behind the shock wave were calculated using the measured oblique shock angle and the free stream conditions. With the value of L and u obtained, one can calculate readily the ratio $\tau = L/u$. Such a procedure supposes that (1) ignition of the flow first occurs for fluid particles that have traveled longer behind the OSW and (2) once a fluid particle has ignited, the pressure waves generated by the expansion of the burned gases will modify the flow downstream of the OSW. These two hypotheses are based on the calculation results described in the following section. Another possible detonation ignition length L' could be defined using the same technique but also taking into account the position of the flame surface, as shown in Fig. 7. The results obtained show that L/L' is always of the order 2.

The resulting values of τ are plotted in Fig. 8 as a function of the pressure prevailing behind the OSW.

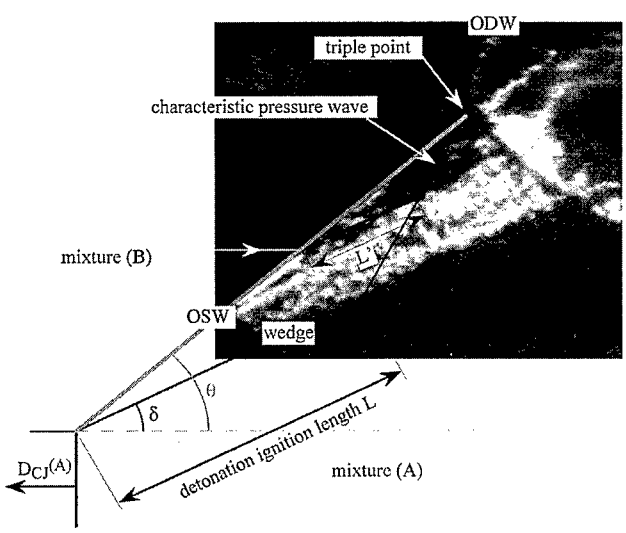

FIG. 7. Measurement procedure used to calculate the induction length from an experimental schlieren picture.

For each point, we have indicated the temperature calculated using the corresponding measured shock angle. The visual measurement technique we employ introduces an error of $\pm 1°$, which corresponds to ± 50 K on the values of temperature. In this same figure, we show the evolution of the chemical induction time τ_i with pressure for different temperatures, as calculated by solving the thermal explosion problem for the two detailed chemical kinetic mechanisms.

Figure 8 shows that the data exhibit an overall evolution that is compatible with a $1/p$ law. In the first approach, this evolution is consistent with a process controlled by a chemical induction time, where bimolecular chain-branching reactions are the limiting reactions. Unfortunately, when the values of τ are compared to those of τ_i computed using the temperature deduced from the experimental shock angle, a relatively large discrepancy is obtained. One possible origin of this discrepancy could be the aforementioned incertitude in the measure of the shock angle. Moreover, if ignition occurs in a similar way to the computation, the ignition point would take place in a region near the flame, where both temperature and composition can be modified. In the present state of our works, it remains difficult to conclude that the mechanism leading to the OSW-ODW transition in the experiments is similar to the one found in the calculations.

Summary and Conclusions

We have observed experimentally reproducible stable ODWs sustained by a wedge in hydrogen-air mixtures at an initial temperature of 293 K, pressures ranging from 0.2 to 0.8 bar and Mach numbers 6 and 7.5.

We have also performed detailed numerical calculations of the transition from an OSW to an ODW by solving the full conservation equations and using a detailed chemical kinetics mechanism. The numerical results show a good agreement, at least concerning the overall flow structure observed experimentally.

In some cases, the characteristic lengths of the OSW-ODW transition are of the same order of magnitude in both the experiments and the calculations. More detailed comparisons are required to adequately define the mechanisms that effectively control such a transition in the experiments. The first comparisons reported here seem to indicate that the position of the triple point is not as directly related to the chemical induction time of the shocked gases in the experiments as in the computations.

Acknowledgments

This work has been accomplished under contract no. 95.0019G "Combustion Supersonique PREPHA" of the Direction des Recherches et Etudes Techniques DRET/DGA of the French Ministry of Defence and the Société Européene de Propulsion.

REFERENCES

1. Libby, P. A., *IUTAM Symposium on Combustion in Supersonic Flows,* (Champion, M., and Deshaies, B., eds.), Kluwer, Dordrecht, 1995.
2. Menees, G. P., Adelman, H. G., and Cambier, J. L., [a]AGARD PEP 75th Symposium Hypersonic Combined Cycle Propulsion, Paper 26, 1990.
3. Hertzberg, A., Bruckner, A. P., and Bogdanoff, D. W., *AIAA J.* 26:195–203 (1988).
4. Smeets, G., *IUTAM Symposium on Combustion in Supersonic Flows* (Champion, M., and Deshaies, B., eds.), Kluwer, 1995.
5. Dabora, E. K., Desbordes, D., Guerraud, C., and Wagner, H. G., in *Dynamic of Explosions—Progress in Astronautics and Aeronautics,* (Leyer, J.-C., Bowen, J. R., and Soloukhin, R. I., eds.), AIAA 133:187–201 (1991).
6. Liu, J. C., Liou, J. J., Sichel, M., Kaufmann, C. W., and Nichols, J. A. *Twenty-First Symposium (International) on Combustion,* The Combustion Institute, Pittsburgh, 1987, pp. 1639–1647.
7. Viguier, C., Guerraud, C., and Desbordes, D., *Twenty-Fifth Symposium (International) on Combustion,* The Combustion Institute, Pittsburgh, 1994.
8. Desbordes, D., Hamada, L., and Guerraud, C., *Shock Waves* 4:339–345 (1995).
9. Singh, D. J., Ahuja, J. K., and Carpenter, M. K., Symposium on High-Performance Computing for Flight Vehicles, Washington, D.C., December 1992.
10. Li, C., Kailasanath, K., and Oran, E., *Phys. Fluids* 6(4):1600–1611 (1994).
11. Vlasenko, V. V. and Sabel'nikov, V. A., 30th AIAA/ASME/SAE/ASEE Joint Propulsion Conference, AIAA Paper 94-3177, 1994.
12. Lefebvre, M. H. and Fujiwara, T., *Combust Flame* 100(1/2):85–93 (1995).
13. Figueira da Silva, L. F. and Deshaies, B., 3rd Asian-Pacific Symposium on Combustion and Energy Utilisation, Hong Kong, 1995.
14. Kee, R. J., Rupley, F. M., and Miller, J. A., Technical Report SAND89-8009B/UC-706, Sandia National Laboratories, November 1991.
15. Miller, J. A., Mitchell, R. E., Smooke, M. D., and Kee, R. J., *Nineteenth Symposium (International) on Combustion,* The Combustion Institute, Pittsburgh, 1982, p. 181.
16. Figueira da Silva, L. F. and Deshaies, B., *Twenty-Fifth Symposium (International) on Combustion,* The Combustion Institute, Pittsburgh, 1994, pp. 29–36.
17. Balakrishnan, G. and Williams, F. A., *J. Propulsion Power* 10(3):434–436 (1994).
18. Baulch, D. L., Cobos, C. J., Cox, R. A., Esser, C., Frank, P., Just, T., Kerr, J. A., Pilling, M. J., Troe, J.,

Walker, R. W., and Warnatz, J., *J. Phys. Chem. Ref. Data* 21(3):411–736 (1992).
19. Yetter, R. A., Dryer, F. L., and Rabitz, H., *Combust. Sci. Technol.* 79(1–3):97–128 (1991).
20. Kee, R. J., Dixon-Lewis, G., Warnatz, J., Coltrin, M. E., and Miller, J. A., Technical Report SAND89-86246/UC-401, Sandia National Laboratories, December 1986.
21. Liou, M.-S., Technical Report TM-106524, NASA, March 1994.
22. Hirsch, C., *Numerical Computations of Internal and External Flows*, Vol. 2, Wiley, New York, 1990, pp. 493–594.
23. Byrne, G. D. and Dean, A. M., *Computers Chem.* 17(3):297–302 (1993).
24. Yee, H. C., Technical Report TM-101088, NASA, February 1989.
25. Lewis, B. and von Elbe, G., *Combustion, Flames and Explosions of Gases.* Academic Press, New York, 1961.
26. Strehlow, R. A., Maurer, R. E., and Rajan, S., *AIAA J.* 7(2):323–328 (1969).

Twenty-Sixth Symposium (International) on Combustion/The Combustion Institute, 1996/pp. 3033–3039

NUMERICAL SIMULATIONS OF THE DIFFRACTION OF PLANAR DETONATIONS IN H_2-O_2 MIXTURES

NICOLAS A. TONELLO AND MARTIN SICHEL
Department of Aerospace Engineering
University of Michigan
Ann Arbor, MI 48109-2118, USA

ELAINE S. ORAN
Laboratory for Computational Physics and Fluid Dynamics
Naval Research Laboratory, Code 6404
Washington DC 20375, USA

The results of the direct numerical simulation of the lateral diffraction of a detonation propagating in a primary layer of stoichiometric H_2-O_2 as it comes into contact with a secondary bounding layer of stoichiometric H_2-O_2 are presented. The Flux-Corrected Transport (FCT) algorithm and time step splitting were used in the simulation. The H_2-O_2 reaction was approximated using a two-step mechanism consisting of an induction period of duration τ_i followed by a heat-releasing reaction with constant reaction time τ_r. An empirical relation based on full H_2-O_2 kinetics was used for the induction time τ_i. The simulation was initiated with a plane detonation without transverse waves in the primary layer. The simulation showed that quenching as opposed to direct initiation occurs under these conditions. These results were validated by the excellent agreement with experimental framing photographs of the diffraction process when the two primary and secondary layers are separated by a collodium film thick enough to block the effect of the transverse waves. The results of the simulation were then used to describe the diffraction and quenching process in detail. Framing photographs are also shown for diffraction in the absence of a separating film. In this case, direct initiation does occur due to the propagation of transverse waves into the secondary bounding mixture. These results suggest that in the case of stoichiometric H_2-O_2 primary and secondary mixtures, transverse waves play an essential role in initiation of detonation in the secondary explosive.

Introduction

The lateral diffraction of a plane, gas-phase detonation occurs when a plane detonation propagating in a primary mixture expands laterally into a bounding secondary mixture. When the secondary mixture has a different composition from the first, refraction as well as diffraction is observed. Depending on the composition of the gaseous explosive and the geometry of the expanding channel, quenching or reignition may occur subsequent to the diffraction. Such diffractions are closely related to those that occur when detonations propagate past obstacles, and involve complex interactions between fluid dynamics and the kinetics of the governing chemical reactions. For hydrogen-oxygen (H_2-O_2) mixtures, which are of interest here, the kinetics is highly sensitive to the variations in temperature and pressure that arise during diffraction.

Experimental studies of the detonations in a tube propagating through a sudden area increase have been conducted at conditions for which either ignition or quenching may occur behind the expanding detonation [1–4]. Recently, a layered shock tube similar to that shown in Fig. 1, was used to study detonation ignition and diffraction in undiluted H_2-O_2 mixtures [5–7]. Diffraction then starts when a Chapman–Jougvet (CJ) detonation in the lower tube, the primary detonation, comes into contact with the secondary explosive mixture in the top tube. A thin separating film was used when the two mixtures were different. Various regimes of detonation transmission and propagation into the secondary mixture were observed, depending on the equivalence ratios of the primary and the secondary mixtures.

For H_2-O_2, when both mixtures in the layered tube are stoichiometric, or when the primary mixture is rich and the secondary lean, two modes of reignition of a detonation in the secondary mixture have been observed. The detonation may reignite directly behind the blast wave transmitted into the secondary mixture, before the blast wave reflects from the upper wall of the top tube. Otherwise, the secondary mixture will reignite only after the decaying transmitted shock reflects from the wall.

Examples of both types of reignition are shown in the Schlieren framing pictures from Ref. 8, shown in Fig. 2, when the primary and secondary mixtures are both stoichiometric H_2-O_2. In Fig. 2a, the mixtures are separated by a 30-nm colloid film, and direct ignition was not observed. Rather, the reaction front becomes uncoupled from the leading shock wave as the blast wave generated by the primary detonation propagates into the secondary, upper layer. The results in Fig. 2b were obtained in the absence of any separating film. Direct initiation can be observed as a disturbance from the primary wave, probably due to a transverse wave, propagates into the region between the shock and reaction front. A secondary explosion within an explosion results, and the detonation reignites before the blast reaches the upper wall of the shock tube. The film evidently was sufficiently thick to block this effect.

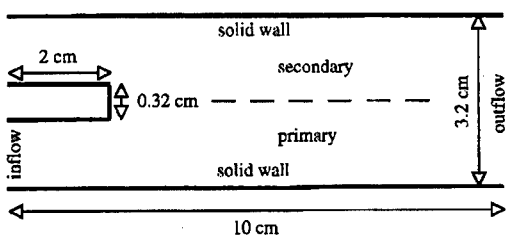

FIG. 1. Schematic diagram of the layered detonation shock tube.

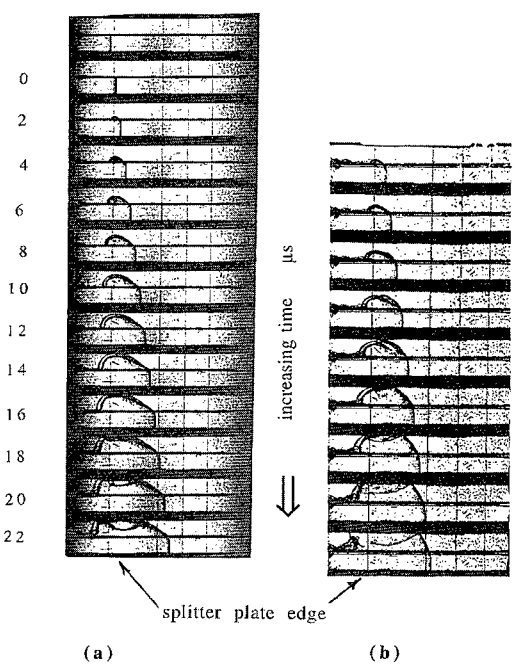

FIG. 2. (a) Diffraction of a detonation in stoichiometric H_2-O_2 when the primary and secondary mixtures are separated by a 30-nm film [5]. (b) Diffraction of a detonation in stoichiometric H_2-O_2 and direct initiation when no film is present [6].

These modes of ignition have also been observed in the detailed numerical simulations of layered detonations in H_2-O_2 mixtures heavily diluted with argon [8], which showed that direct initiation occurred only if the primary detonation was overdriven, or if physically unrealistic parameters were used in the simplified chemistry model. Recent numerical simulations by Jones et al. [9] did demonstrate direct initiation when the primary and secondary mixtures are both stoichiometric H_2-O_2-Ar if fine enough numerical resolution was used to include the transverse-wave structure. The initiation process then is similar to that shown in Fig. 2b; but, there are no experimental data for such mixtures for direct comparison with the simulations.

This paper presents the results of a detailed numerical simulation of the initial stages of the interaction in layered detonations with primary and secondary mixtures of undiluted stoichiometric H_2-O_2. These results are in reasonable agreement with the results shown in Fig. 2a in the absence of direct initiation. The high resolution used in the simulation provides a detailed diagnostic description of the detonative diffraction beyond what would be possible experimentally. An important aspect of this calculation is the incorporation of a new reduced kinetic model developed for the simulation of detonations in H_2-O_2 mixtures [7].

Physical and Numerical Model

The flow is governed by the two-dimensional Euler equations coupled to a model for chemical reactions and energy release [8]. In addition to the equations for the conservation of mass, momentum, ρv, and total energy, E, there are two additional equations for the conservation of mass of the primary and secondary mixtures. This set of coupled, nonlinear equations was solved using a fully two-dimensional version of the flux-corrected transport (FCT) algorithm as described by Boris and Book [10], which has been validated extensively for detonation calculations [11]; its formulation is not repeated here.

The full H_2-O_2 kinetics is replaced by an induction period characterized by an induction time τ_i during which radicals are formed, but the system is essentially thermo-neutral, followed by a chemical transformation period characterized by a reaction time τ_r during which product formation and heat release occur. An empirical expression for τ_i developed by Tonello [7] was used, which was validated for $T \geq 700$ K and $P \geq 1$ atm by comparison to calculations using the complete kinetics of H_2-O_2. The induction time τ_i is given by

$$\tau_i(\phi, T, P) = \frac{(\phi + 1)\left(\phi + \frac{1}{2}\right)}{\phi} \frac{\bar{R}T}{P} L_1 \exp\left\{\frac{L_2}{T} + L_3 P'' \exp\left(\frac{L_4}{T}\right)\right\} \quad (1)$$

where L_1 = 5.311 E-16(μs-mole/liter), L_2 = 8531 K, L_3 = 7.221E11 (atm^{-n}), L_4 = 21,200 K, n = 2, and $\bar{R}$ = 8314 kJ/kmol K.

The full kinetic calculations predicted that the reaction time τ_r is effectively constant at high temperatures and pressures; hence, a constant value of 2.0 μs was chosen for τ_r. Variable heat capacities during the reaction time τ_r were determined using polynomial data of Gordon-McBride [7].

The extent to which the induction period and reaction time of a fluid element are complete are characterized by induction and reaction parameters f_i and f_r defined by

$$f_i = \int_0^t \frac{dt}{\tau_i(T, P)}; f_r = \int_0^t \frac{dt}{\tau_r}$$

During induction, f_i varies from 0 to 1 while $f_r = 0$. During reaction, f_r increases from 0 to 1, when reaction is complete. f_i and f_r are convected with the fluid particles and satisfy

$$\frac{\partial(\rho f_{i,m})}{\partial t} + \nabla \cdot (\rho v f_{i,m}) = \frac{\rho}{\tau_{i,m}(T, P)} \quad (2)$$

$$\frac{\partial(\rho f_{r,m})}{\partial t} + \nabla \cdot (\rho v f_{r,m}) = \dot{\omega}_{r,m} \quad (3)$$

where $\dot{\omega}_r = 1/\tau_r$. The left sides of these equations are solved by the FCT solver, while the time-step splitting technique is used to account for the source terms on the right, as described by Oran and Boris [12]. Details of the solution procedure are given by Tonello [7].

The computational domain, which initially contains a stoichiometric H_2-O_2 mixture at 1 atm and 300 K, and the boundary conditions are shown in Fig. 1. A uniform computational grid was used with $\Delta x = \Delta y$ = 2.0E-4 cm and 500 × 160 cells, chosen on the basis that it had to accurately resolve the structure of a one-dimensional detonation. The computation is initialized by placing a one-dimensional simulation of a steady CJ solution, onto the two-dimensional grid in the primary lower section. This detonation then travels downstream through the primary mixture, and the diffraction begins as the leading shock passes the tip of the splitter plate. The initiating detonation did not include transverse waves.

Results

Overall Description

Figure 3 shows computed pressure and temperature contours at five representative times. The earliest is shortly after initiation (t = 1.72 μs), when the leading shock of the primary detonation just passes the splitter plate. The wave propagating into the secondary mixture has already reflected from the upper wall in the last contour at t = 22.35 μs. Clearly, direct initiation does not occur, and there is remarkable similarity between the simulation and the experimental framing pictures in Fig. 2a at corresponding times. The absence of transverse waves in the initiating CJ detonation appears to be equivalent to the blocking effect of the film in the experiments.

At early times, from 1.72 μs to 4.7 μs, most of the primary detonation remains plane. As the primary detonation passes the splitter plate, the detonation front and the burned gas behind it expand upward into the secondary mixture. Expansion waves move back into primary mixture. The burned primary shocked and unburned secondary mixtures are separated by a thermal contact surface that appears in the temperature contours as a dark, heavy contour behind the expanding shock.

At 1.72 μs, near this contact surface, the temperatures and pressures vary from approximately 1100 K and 10 atm (closest to the primary detonation) to 680 K and 4.5 atm (along the right edge of the splitter plate). At 4.7 μs, these decrease to 1050 K and 10.5 atm and 440 K and 2 atm. At these conditions, the induction time is too long for ignition within the time frame of these calculations. Thus, for T = 1100 K and P = 10 atm, the induction time is τ_i = 18.6 μs, and as the blast expands into the secondary mixture, these induction times increase as the temperature and pressure decrease.

At 7.8 μs, the left end of the blast wave has turned 180° around the splitter plate and connects to the top surface of the plate through a normal shock, as is also the case for the experimental frame at 8 μs. Near the splitter plate, the temperature front behind the transmitted blast rolls up around a vortex. The transmitted blast wave reaches the upper wall of the test section shortly after 12.45 μs, in agreement with experiment. By then, the primary detonation has become completely curved, and the expansion waves from the edge of the splitter plate start to reflect from the bottom wall. The thermal front and the shock continue to separate. Because of the increasing radius of curvature and the essentially vertical motion of the top part of the blast wave, the transmitted shock collides normally with the top wall. Then, the gas trapped between the top wall and the reflected shock consists of unreacted H_2-O_2. At 17.1 μs, right after reflection begins (not shown in Fig. 3), the pressure and temperature are highest right behind the reflected shock, where they reach values of 42 atm and 1060 K. Directly above and to the left of the intersection between the reflected blast and the thermal front, the pressure and temperature decrease to about 21 atm and 840 K. The large

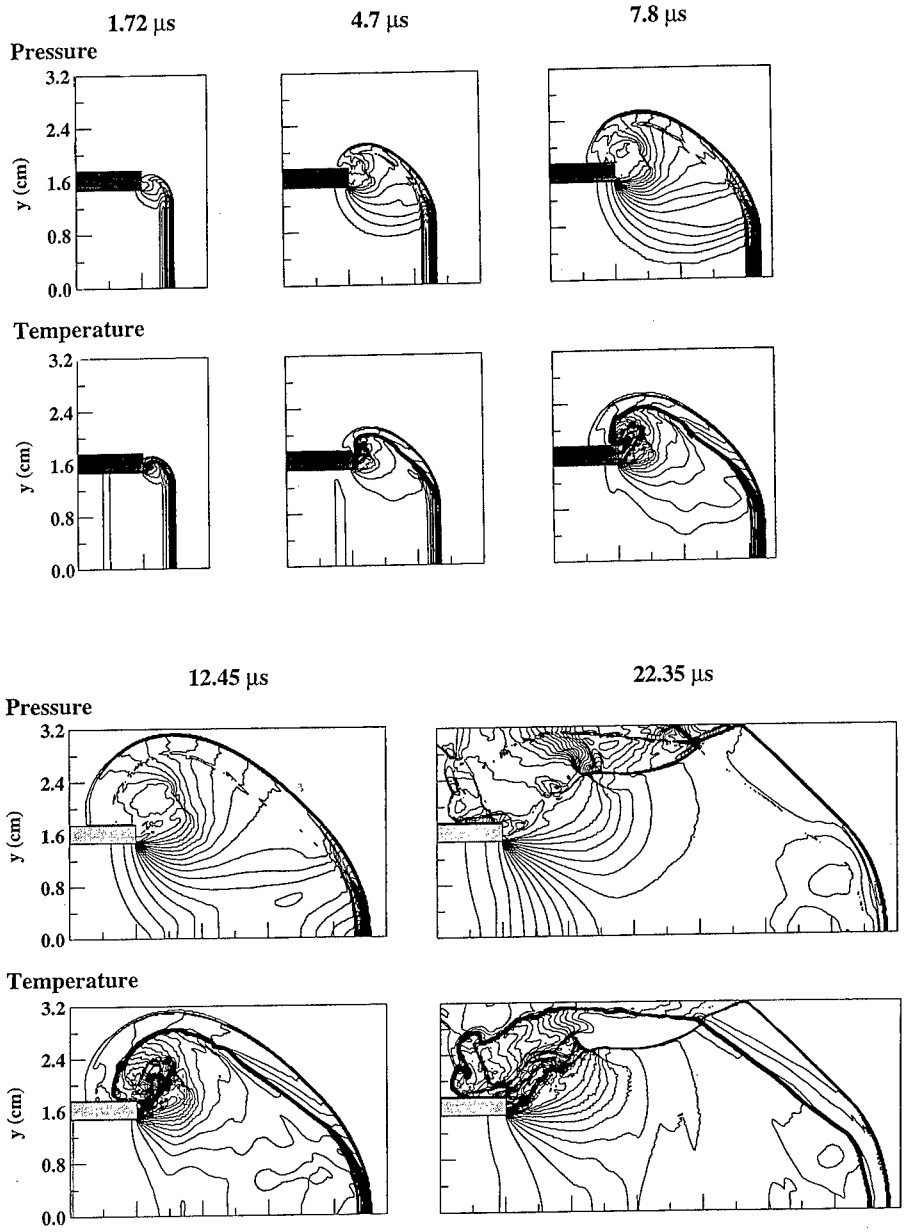

FIG. 3. Time sequence of pressure and temperature contours from the numerical simulation.

induction times corresponding to these conditions explain why reignition does not occur.

At 22.35 μs, there is no product production at any location behind the leading shock. The region between the leading shock and the temperature discontinuity behind it, in both the bottom and the top channels, appear very uniform. The pressure and the temperature in this region vary from about 11 atm and 900 K at the bottom wall, to 10.5 atm and 800 K near the top wall. Direct ignition is impossible at these low temperatures, so the primary detonation is quenched.

Diffraction around The Splitter Plate

Figure 4 provides a detailed view of the flow around the splitter plate at 9.35 μs. Pressure and temperature contours, and velocity vectors and flow

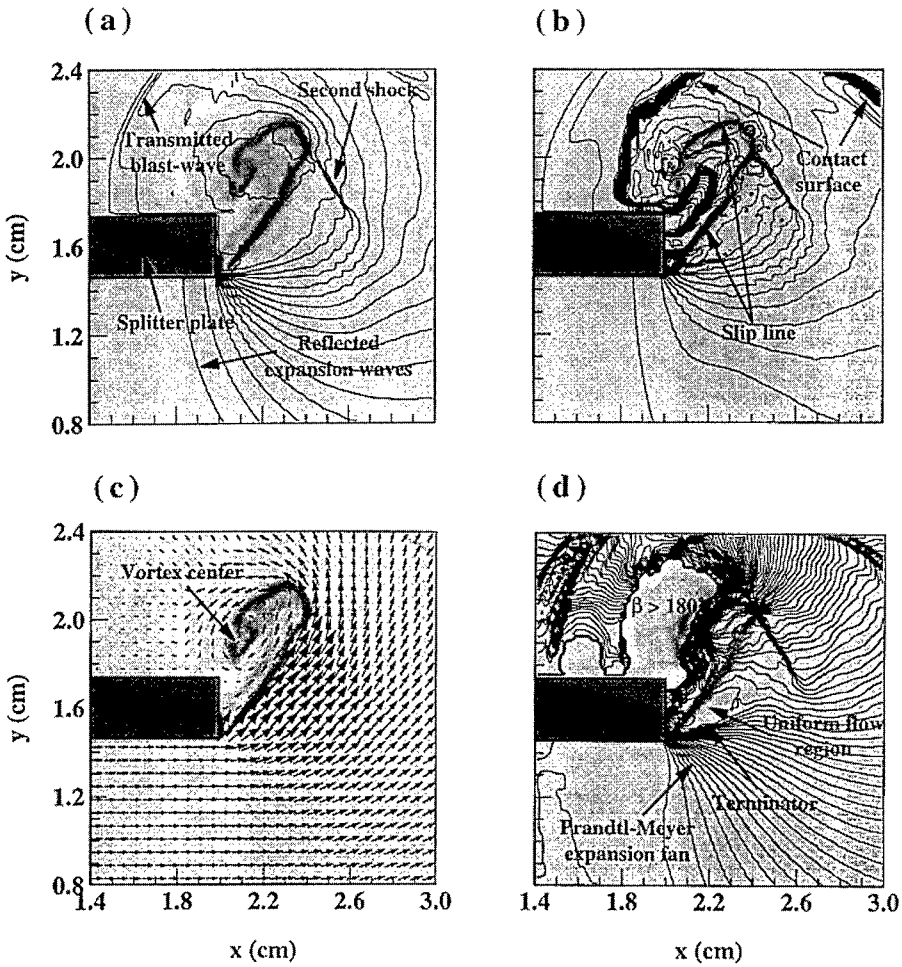

FIG. 4. Simulation of diffraction around the splitter plate at 9.35 μs. (a) Pressure contours at 0.5-atm intervals; (b) temperature contours at 100 K intervals; (c) flow velocity vectors; (d) flow angle contours. Grey-scale background proportional to counterclockwise vorticity.

angles are shown in Fig. 4 superimposed on a gray-scale image of the vorticity (counter-clockwise vorticity is darker). In Fig. 4c, the large vortex emanating from the bottom tip of the plate is shown by the heavy, dark line that moves diagonally away from the plate and then curves back around toward it.

Once the primary detonation has passed the tip of the splitter plate, the fluid underneath the plate accelerates and turns through a Prandtl-Meyer expansion fan (Fig. 4a). However, as observed experimentally [7–9], the flow separates from the edge of the splitter plate and there is a slip line across which there is a temperature and velocity discontinuity. A region of uniform flow extends from the tail of the Prandtl-Meyer expansion fan (the terminator [7]) to this slip line.

The slip line is almost straight throughout the uniform flow region (Fig. 4d), and the flow is nearly parallel to this line until it crosses the secondary shock which equilibrates the pressures in the over-expanded flow with that of the surroundings. This oblique shock extends from the slip line to the terminator and also appears in the experimental framing photographs shown in Fig. 2a as a short diagonal line just above the edge of the splitter plate. Beyond this shock, the flow continues to rotate in the counterclockwise direction driven by a vortex whose center is indicated in Fig. 4c. This vortex also bends and eventually rolls up the slip line, which ends in a coil at the vortex center.

There will be a viscous boundary layer on the splitter plate surface; but, viscous effects have not been

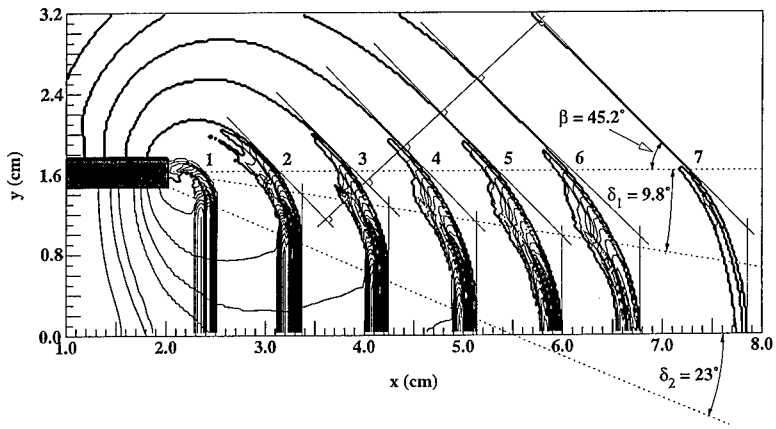

FIG. 5. Composite image of pressure contours at different times. 1, 1.7 μs; 2, 4.7 μs; 3, 7.7 μs; 4, 10.9 μs; 5, 14 μs; 6, 17.1 μs; 7, 22.36 μs.

included in the simulation. Since the flow is expanding in most of the region of interest, it is likely that the effect of the boundary layer will be minimal.

The Detonation Quenching Process

As a result of diffraction, the detonation evolves into a nonreactive shock decoupled from the reaction front behind it. This quenching mechanism is considered in more detail in Fig. 5, a composite image of pressure contours at various times. These were chosen to highlight the differences between the detonation (the straight, thick regions shown vertically along the bottom of the tube), the transmitted blast (circular regions emanating from the top of the detonation at one end, and ending at some location at the top of the plate), and the sound wave generated by the expansion (circular wave starting near where the detonation fails and connecting to the bottom of the plate).

From shock diffraction theory [5,6], the trajectory angle of the triple point, δ_2, defined by the intersection between the envelope of the sound waves and the diffracting shock, is given by

$$\delta_2 = a\tan(\sqrt{a_2^2 - (V_s^2 - u_2^2)}/V_s)$$

where V_s, a_2, and u_2 are the shock speed, the speed of sound, and the speed of the gas behind the shock. Assuming a thin reaction zone and using the CJ values at a_2 and u_2, leads to $\delta_2 = 0$. However, behind a chemically frozen shock traveling at $V_s = D_{CJ}$ (the CJ detonation velocity), a_2, = 1314 m/s, u_2 = 2332.7 m/s, and with these values, $\delta_2 = 23°$. The trajectory corresponding to this angle, shown as the dashed line, does indeed pass through the intersections of the expansion wave and the reaction front.

With increasing time, the transmitted blast wave becomes an oblique shock at an angle $\beta = 45.2°$. The intersection between the vertical line drawn at the detonation front and the oblique line of the transmitted blast (profiles 2 to 5) defines a straight line that makes an angle $\delta_1 = 9.8°$ with the horizontal. The transition from a cylindrical blast wave to an oblique shock is also evident in Fig. 2a.

In the simulation, the primary wave curvature increases with a corresponding increase in the induction time behind it so that the primary wave is quenched. This result differs from Fig. 2a which indicates that the primary detonation remains plane. This is because the film, though only 30 nm thick, shields the region between the shock and the CJ plane of the primary detonation from the expansion as the blast propagates into the secondary explosive. However, the diffraction pattern shown in Fig. 5 is very similar to that observed by Gvozdeva et al. [13] in their study of the extinction of a detonation propagating from a very small channel into an unconfined region.

Conclusions

The results of the simulation of the initial stages of the interaction in a layered detonation in stoichiometric H_2-O_2 when the transverse waves in the primary wave are neglected were in excellent agreement with experiments in which propagation of transverse waves into the secondary mixture was blocked by a thin film. The simulation reproduced the small, oblique shock wave generated by the refraction near the edge of the splitter plate separating the primary and secondary mixtures. As in the experiments, direct ignition of a detonation in the bounding mixture did not occur in the simulation.

These results provide validation for the direct numerical simulation above and for the improved chemical model for the induction time that was used.

The simulation, then, provided a powerful diagnostic tool for exploring the details of the diffraction process beyond what could be done experimentally. Thus, it was possible to follow the variation of pressure temperature, flow velocity and direction, and the variation of induction and reaction parameters in detail, and to show how and why quenching occurs. The results also indicate that an appropriate simplified model of the complex H_2-O_2 reaction plays a crucial role in developing an accurate simulation. Simulations with full chemistry still remain beyond reach for complex problems like that above.

The results also indirectly confirm that for stoichiometric H_2-O_2 primary and secondary mixtures, transverse waves play an essential role in the direct initiation of detonation in the secondary explosive, since, experimentally, direct initiation was observed in the absence of a blocking film. As already indicated above, simulations in H_2-O_2 mixtures heavily diluted with argon also showed that transverse waves play an essential role in direct initiation.

REFERENCES

1. Edwards, D. H., Thomas, G. O., and Nettleton, M. A., *J. Fluid Mech.* 95:79–96 (1979).
2. Murray, S. B. and Lee, J. H., *Combust. Flame* 52:269–286 (1983).
3. Bartlmä, F. and Schröder, K., *Combust. Flame* 66:2366 (1986).
4. Vasil'ev, A. A., *Fiz. Vzriva* 24:99–107 (1988).
5. Liou, J. J., "Analysis of Wave Interaction between a Propagating Gaseous Detonation and a Bounding Explosive Layer," Ph.D. Thesis, The University of Michigan, Ann Arbor, MI, 1986.
6. Liu, J. C., Kauffman, C. W., and Sichel, M., in *Progress in Aeronautics and Astronautics,* AIAA, New York, 1988, Vol. 114.
7. Tonello, N. A., "An Experimental and Computational Study of the Mechanisms of Detonation Transmission in Layered H_2-O_2 Mixtures," Ph.D. Thesis, The University of Michigan, Ann Arbor, MI, 1996.
8. Oran, E. S., Jones, D. A., and Sichel, M., *Proc. R. Soc. Lond.* A436:267–297 (1992).
9. Jones, D. A., Kemister, G., Sichel, M., and Oran, E. S., "The influence of Cellular Structure on Detonation Transmission" *Shock Waves,* to be published, 1996.
10. Boris, J. P. and Book, D. L., *Meth. Comp. Phys.* 16:85–129 (1976).
11. Oran, E. S., Boris, J. P., Young, T. R., Flanigan, M., Burks, T., and Picone, M., *Eighteenth Symposium (International) on Combustion,* The Combustion Institute, Pittsburgh, 1981, pp. 1641–1649.
12. Oran, E. S. and Boris, J. P., *Numerical Simulations of Reactive Flow,* Elsevier, New York, 1987.
13. Gvozdeva, L. G., Baklanov, D. I., and Sherbak, N. B., "Propagation of a Gas Detonation in Channels with a Sudden Expansion," presented at 15th International Colloquium on the Dynamics of Explosions and Reactive Systems, 1995.

Twenty-Sixth Symposium (International) on Combustion/The Combustion Institute, 1996/pp. 3041–3058

INVITED PLENARY LECTURE

SOLID FUEL UTILIZATION: FROM COAL TO BIOMASS

T. ABBAS, P. G. COSTEN AND F. C. LOCKWOOD
Department of Mechanical Engineering
Imperial College of Science, Technology, and Medicine
London SW7 2BX, UK

Biomass has always been used as a localized energy source. Its seasonal availability, low calorific value, and density make it less attractive as a fuel in a centralized power generation system mainly because of higher costs associated with its storage and transportation. Notwithstanding these constraints, biomass fuels may be used together with coal in existing combustion systems. The focus of this paper is therefore on transferring the experience that has been gained from pulverized coal combustion to that of the co-combustion of biologically derived solid fuels. The substitution of these green fuels has the potential to significantly ameliorate the environmental impact of coal utilization. This lecture comprises a few comments on equipment, and on fuel characterization, something on the relevant physical processes and experimentation, and some discussion of the mathematical modeling of the combustion of solid fuels.

Introduction

The history of the invitation to present this lecture is complex. In this respect, we should at least explain that we did not feel sufficiently versed on biomass combustion, a relative newcomer to the mainstream of the combustion world, to be able to confine the whole lecture to it. A complementary topic was required, and coal combustion was the obvious candidate with the combination conveniently masquerading under the generic heading of solid fuel use. However, the breadth of the subject material then becomes excessive rather than restricted. Ultimately, we made the decision to confine the material primarily to that of our own experience, so this is in no way a review paper. We are tempted to believe that the content may also reflect the experience of others who, having a considerable wealth of solid fuel research, and, rather than lose it with the temporary demise of coal as a primary fuel source, are transferring that experience to encompass other heterogeneous fuel types.

The motor of the industrial revolution, coal, originates from biomass that has been physically compacted and chemically carbonized over millions of years. Its compactness facilitated transport and, more importantly, the intensification of combustion. Its high carbon content facilitated coke production, which revolutionized steel making. A by-product of the associated coking process was a gaseous fuel that had all manner of convenient uses including heating, lighting, and cooking. All these functions had been provided originally by wood, but the advantages of coal gas were its higher energy and immediate availability assured once the manufacturing process and infrastructure had been established. Coal is so stable that it can be stored almost indefinitely, and, as became apparent during the course of the industrial revolution, its availability seemed virtually without limit. Indeed, it appeared to be the miracle fuel.

As time wore on and its usage increased, the inevitable downside loomed ever larger. The disadvantages had already been expounded to the public of London well before the industrial revolution (Fig. 1). Principally, it was dirty in almost every respect. Its smokiness could be cured by ensuring good mixing of the volatiles with air, but the cures were not universal because of that most major failing of coal, its variability. A variability that, because the original biomass from which it is formed was laid down under a variety of geographical, geological, and climatic conditions, is almost boundless. Mineral matter inevitably got mixed in with the biomass to create an almost equally broad range of ash characteristics and so, correspondingly, complex fouling and slagging problems within the combustion chamber and the postflame regions. Coal contains chemically bound nitrogen, sulfur, chlorine, and other polluting compounds. Even if the associated problems of all of these various unwanted materials and chemicals could be solved, an inherently more exacerbating problem remains, that is, the production of CO_2. The timescale of coal formation is tens of millions of years and the burning of it over the minuscule timescale of the industrialized world has seriously short circuited the natural carbon cycle. One of the main advantages of coal that our predecessors cherished, its high carbon content, compounds the problem. Recent research has shown that the capture and disposal of CO_2 from coal-fired utility boilers is not economically viable [1].

So one is led to ask: Why not forget coal and combust some of the biomass that is growing all around

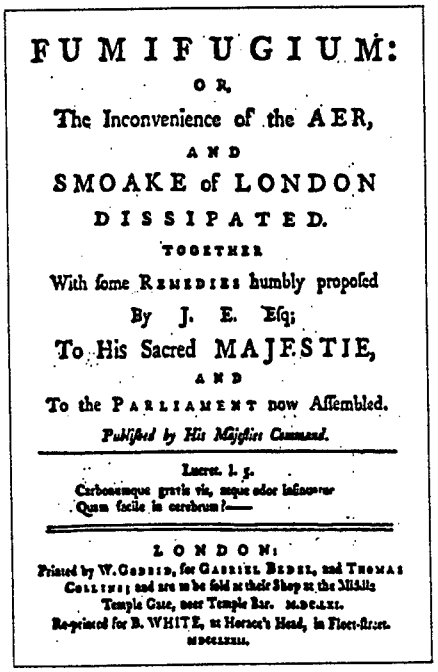

FUMIFUGIUM:
OR,
The Inconvenience of the AER,
AND
SMOAKE of LONDON
DISSIPATED.
TOGETHER
With some REMEDIES humbly proposed
By J. E. Esq;
To His Sacred MAJESTIE,
AND
To the PARLIAMENT now Assembled.
Published by His Majesties Command.

Lucret. l. 5.
Carbonemque gravis vis, atque odor infinuatur
Quam facile in cerebrum?——

LONDON:
Printed by W. GODBID, for GABRIEL BEDEL, and THOMAS COLLINS; and are to be sold at their Shop at the Middle Temple Gate, near Temple Bar. M.DC.LXI.
Re-printed for B. WHITE, at Horace's Head, in Fleet-street. MDCCLXIII.

FIG. 1. FUMIFUGIUM by John Evelyn, London, 1661.

us? Not only is it a plentiful fuel, but its use also reestablishes the natural carbon cycle. There are essentially five impediments to its wholesale adoption: (1) biomass is almost as variable as coal; (2) its calorific value is only about one-fifth (by volume) or half (by weight) of that of coal, implying huge transport costs and low energy intensities; (3) it contains many of the potentially polluting compounds that weigh against coal; (4) in most instances it is seasonal, which implies expensive storage costs if a constant supply is required; and (5) the use of agricultural land for energy crops raises a critical moral issue—either save the environment or those who are starving.

As already mentioned, because of environmental pressure, it is expected that the use of coal will decrease in the short term. In the interim, some see biomass, in the context of the renewable energies contribution, as an acceptable alternative to the nuclear option for the generation of electricity. Research and development into biomass use for energy generation has been prompted because of this shift in emphasis, leading to a release of research funds. In Europe, it has seen a ca. 30% increase during the last decade, with a projected threefold increase in its use by 2020 [2]. The recently completed European Union–funded Clean Coal Technology program [3] on cocombustion and cogasification of coal and biomass was the world's largest research and development effort, involving 31 industrial partners, research centers, and universities. Industrial contributions to this project exceeded 70% in regard to research tasks and more than 50% in the financing, thereby showing a substantial commercial interest and confidence in co-firing techniques for the future.

In light of these trends, we believe that there is a niche for these fuels in existing combustion systems. The substitution of these green fuels ameliorates the environmental impact of coal use until such time that advanced clean coal technologies can be economically competitive with conventional systems. In this paper, which concentrates on the co-firing of biomass with pulverized coal, a precis of the fundamental knowledge accrued and the tools developed through coal-related research and its relevance to biomass combustion will be presented. This includes the initial fuel characterization, flame stability performance, pollutant emissions, and other operational aspects and culminates with mathematical modeling considerations.

Coal and Biomass Fuels

The whole process of coal formation (coalification) was an unremitting geochemical evolution, starting with the decay of organic materials in swamps and followed by their metamorphosis under the influence of geological forces (depth of sinking, temperature, and tectonic shear forces). A detailed account of coalification is well beyond the scope of this review.

Biomass fuels may be defined as combustible materials resulting from silviculture, agriculture, and aquaculture, that is, fuels resulting from the growing of plants and the raising of animals. These fuels are also distinguished by the fact that biomass generally exists in a diffuse state and must be gathered up and concentrated in a single location for use, rather than being produced in a single location (i.e., a coal mine) and dispersed for use. Some specific biomass varieties being considered as useful fuels include wood and wood wastes (e.g., hogged bark and sawdust), spent pulping liquor, rice hulls, cotton gin trash, bagasse, coffee grounds, wood waste from wood structures, manure, sewage sludge, and myriad other biomass forms. We emphasize pulverized dried sewage in this paper because of its similar combustion behavior to that of lignite coals, as well as its biological origin.

Through photosynthesis, the energy stored in biomass is theoretically almost 10 times that of the world energy consumption. Currently, biomass supplies approximately 14% of humanity's total energy requirement. Much of this is inefficiently consumed by poorer people in developing countries where the practice frequently results in the long-term loss of vegetation. In the European Union (EU), "renewables" contribute to some 2% of its energy require-

ment, roughly half of which is attributed to biomass combustion. The EU plans a twofold increase by, 2005, mainly from the deployment of energy crops grown on land that is either deforested, degraded, or set aside from crop production.

There are several routes for upgrading biomass (conversion to gaseous or liquid fuels), all with disadvantages. Within the context of this paper, we should mention the producing of "biocoal" in which the biomass is coalified through low-temperature processes in which the oxygen-rich biomass precursors are transformed to cross-linked aromatic and hydrogen-rich mattes. Pressurized or confined pyrolysis allows one to follow the natural trends of organic matter maturation, to generate an artificially matured series of coals from biomass, and to observe the evolution of hydrocarbon production throughout the maturation process. This has been achieved in a bench-top cold-seal autoclave in which a few hundred grams of each maceral and raw biomass have been pyrolysed under isothermal conditions in sealed gold tubes at temperatures ranging between 150 and 500°C for more than 24 h at a constant pressure of 100 Mpa [4]. On the commercial scale, however, the process is unlikely to be energy efficient.

Some Remarks on Equipment

Several technologies have been developed for the combustion of solid fuels in the production of useful energy. These may be divided into four principal groups: moving and fixed grate type, rotary kilns, fluidized beds, and suspension fired systems. Grate firing involves the least amount of fuel preparation and permits the broadest latitude in fuel selection and combustion conditions. There are many types of proprietary grates (e.g., reciprocating, rocking) but all operate on the same principle: they agitate and move the biomass/waste derived fuels from the charging end of the grate to the discharging end, at which point the fuel should be completely burned to ashes. Often, however, combustion is uneven and the burnout less than ideal. The grate system is particularly suitable for low bulk density biomass/wastes and is generally employed in mass burn incineration plants for municipal solid waste. Rotary kiln systems are used in the cement industry and also for the incineration of high to medium bulk density biomass/wastes. The kiln is a refractory lined drum inclined at an angle to the horizontal and rotating slowly about its axis, usually with a burner located at the lower discharge end. The rotating motion of the kiln often induces a more complete mixing of solids in the bed than is achieved with grate systems. Fluidized bed combustors also promote good mixing but require some degree of fuel preparation (some degree of homogeneity and particle sizes of a few centimeters).

Solid fuels may be pulverized into fine particles (micron level) and burned in a suspension mode. These systems are the dominant technology for the combustion of coal in large-scale (ca. 500 MW) power plants. Pulverized firing also dominates the use of coal to fuel cement kilns. Additionally, suspension-fired systems find common usage in the combustion of dry, pulverized biomass materials including sander dust from furniture manufacturing and certain biomass wastes. A comparative review of these combustion technologies in relation to waste incineration has been given by Seeker [5]. In this paper, however, the main focus is placed not on incineration systems but on the co-firing of biomass with pulverized coal in large-scale suspension-fired combustors such as utility boilers and cement kilns. In these systems, all aspects of combustion and pollution performance are influenced by the time required to initiate and conclude fuel devolatilization, which is dependent on the reaction surface area per unit volume of the fuel particle. Energy is required for the diminution of a solid fuel to obtain a particle size suitable for these systems, normally less than 100 μm for coals. Different milling systems have been used for biomass, generally cutting and hammer mills, rather than the ball mills and attritors used for coal milling. It has been found during grinding tests performed for raw coals and biomass fuels that the reduction of calorific value caused by the energy input during the grind was almost double for biomass (2–3%) compared with coals (0.9–1.2%). This penalty increased significantly for biomass having a higher moisture content (>20%) and a required average particle diameter of less than 1 mm [3]. Compared with pulverized coal, biomass-derived fuels are notoriously difficult to feed using existing coal feeding systems: However discussion of this is beyond the scope of this paper.

Properties of Coal and Biomass

Coals and biomass are both complex heterogeneous solids that vary widely in their properties and in their suitability for possible applications. The well-established classification techniques for coal can be adapted successfully to accommodate other biomass-derived solid fuels. Table 1 gives the proximate and ultimate analyses of a typical bituminous coal compared with some biologically sourced fuels. From this information, we see that biomass fuels are generally low in carbon and high in volatile matter and oxygen. This last fact is the main reason for their lower calorific values that, combined with their low bulk densities, implies that larger volumes are required to supply the same heat input as for coal firing. This will dictate not only the storage requirements but also the logistics of the supply of the fuel on a regular basis. Generally, biomass fuels, with few

TABLE 1
Specifications of Fuels

Proximate analysis (Weight % as received)	Pine sawdust	Straw	Miscanthus	Peat fuel	Bituminous coal (Gottelborn)	Dried sewage sludge
Moisture	7.3	7.87	9.8	50.0	1.1	3.0
Volatile matter	76.2	77.01	69.4	30.0	35.6	46.6
Fixed carbon	13.9	17.15	16.4	16.7	52.3	6.2
Ash	2.6	5.84	4.40	3.3	9.1	44.2
Ultimate analysis (Weight %, daf)						
Carbon	52.0	42.3	51.4	57.2	80.7	53.2
Hydrogen	5.8	6.8	4.4	6.1	5.02	7.01
Nitrogen	0.12	0.4	0.48	2.7	1.43	5.69
Sulphur	0.05	0.2	0.3	0.26	1.09	1.52
Chlorine	0.03	0.4	0.2		0.04	0.39
Oxygen (by difference)	42.0	49.9	43.3	33.8	11.72	32.20
Bulk density (kg/m^3)	182	45	55	600	603.3	609
Heating Value (MJ/kg)	18.32	18.4	16.82	22.11	28.67	11.2

TABLE 2
Ash Compositions

	Acid			Base					
Fuel	SiO_2	Al_2O_3	TiO_2	Fe_2O_3	CaO	MgO	Na_2O	K_2O	Slagging factor*
Pine sawdust	18.1	2.5	0.3	2.4	55.7	6.3	1.9	8.3	0.2
Straw	75.0	1.0	0.1	0.4	3.0	1.0	13.0	1.0	0.05
Miscanthus	70.6	1.1	0.06	1.0	7.5	2.5	0.17	12.8	0.13
Peat fuel	40.3–68.6	8.9–13.3	0.4–1.0	4.6–6.6	6.2–33.2	1.6–5.8	0.8–1.1	1.2–1.8	0.12
Bituminous coal	44.0	24.8	1.47	13.4	5.01	3.12	0.4	2.61	0.38
Sewage sludge	41.3	14.3	1.2	6.8	19.8	3.2	0.7	2.0	0.87

*Slagging factor = base/acid ratio × %S.

exceptions, have lower ash contents than coals. Peat, however, is distinctly different from its biomass precursors. Physically, it has a higher moisture content, exhibiting peak values as high as 90%, and a somewhat lower volatile/fixed carbon ratio (1.8) than is normally associated with biomass. Dried sewage sludge is distinguished by its high ash and nitrogen contents compared with vegetable biomass. In addition, agricultural-based biofuels generally contain a higher percentage of nitrogen and chlorine. Note the high chlorine contents of the straw and also of the dried sewage sludge, which has implications for the corrosion of heat-transfer surfaces.

The fuel moisture content is an important parameter that deserves careful evaluation in regard to the overall combustion intensity and energy efficiency. As an example, green or "as-received" wood contains a rather high proportion of moisture. Combustion is difficult if the level exceeds 60%. To reduce this moisture content to make the fuel more suitable to co-firing in boilers implies an energy input for drying. The forced-air drying of moist wood fuel particles to 5–10% moisture requires some 1% of its gross heating value. In the case of dried, pulverized sewage sludge, the achievement of both a moisture content of 10% and a particle size appropriate to suspension firing necessitates the use of 10% of the fuel's gross calorific value.

A glance at the composition of the ash in a solid fuel, Table 2, tells something about its propensity to slag or foul a heat-transfer surface. Slagging occurs because of the presence of ash particles that are sticky because of their low melting points. In general, alkalis have low melting points and biomass fuels tend to have high concentrations of them. For example, note the high value of lime for pine wood.

Fouling occurs in the cooler regions of the combustor where alkalis such as K and Na that have high vapor pressures condense on solidified particles of alumina and silicate, forming a soft, sticky coating. The table suggests that straw will have a strong tendency to foul. The base-to-acid ratio of an ash, the fouling factor, is a fair indicator of its fouling propensity when the fuel is coal. However, for biomasses, where the concentrations depart from the usual ranges for coals, second-order chemical effects render this factor less reliable as the values shown reveal. It is worth mentioning that fluidized bed combustors tend to avoid fouling and slagging problems because of their low operating temperatures.

Characterization of Combustion Performance

Ideally, fuel characterization would be effected in full-scale plant, but this is not economically practicable. Bench-top characterization is clearly the ideal, but will the results be trustworthy? Because of this uncertainty, many reduced-scale test furnaces have been constructed. Since the various combustion processes scale in different ways, the enduring question is whether data at the reduced scale will be applicable to full-scale conditions. Recent extrapolations by means of mathematical models [6] for coal-fired low NO burners suggest that test furnace results are fairly representative of the full-scale provided that the flow is fully turbulent at the reduced scale and that the burner velocities and fractional heat losses remain constant with scale. Test furnaces almost always accommodate only a single burner so that even if, to avoid the scaling uncertainties, they are of generous proportions, doubt remains as to whether the results obtained from them will be invalidated by the interactions between the burners of the multiburner systems typical of real plans. Mathematical modeling studies have also been effected in an effort to quantify the magnitude of this worry [6] and it was concluded that, for typical engineering separation distances, the effects of mutual burner interference are unlikely to corrupt significantly test furnace results.

Though less costly than full-scale tests, test furnace operation is still not cheap, so bench-top characterization retains its appeal. In utility boilers, the pulverized fuel particles typically experience heating rates in excess of 10^5 K/s, their final temperatures can approach 1800°C, and the high-temperature dwell times can vary widely. It is important that these conditions are simulated in characterization experiments since the rates and amounts of volatiles release depend on them and these in turn affect flame stability, char burnout, and NO emissions. Conventional characterization experiments such as the proximate and thermogravimetric analyses certainly do not achieve realistic heating rates, nor do normally heated wire grids. Heating rates of 10^3 to 10^4 K/s and high final temperatures are achieved in drop tubes. However, the particle temperature, a good knowledge of which is required to calculate the devolatilization and char reactivity rate constants, is only approximately known in drop tubes because of background radiation. The weight loss, too, is subject to error, and the available residence time is usually limited.

Gibbins and co-workers [7] have developed a refined heated wire experiment capable of achieving the desired heating rates and final temperatures. Their relatively straightforward apparatus possesses many advantages. In particular, it is highly controllable in terms of heating rates, finally achieved temperatures, and hold times at these temperatures. The sample is captive so that an exact weight loss may be calculated and the sample temperatures may be measured quite precisely. The data have been shown to exhibit a high degree of repeatability. This experiment has proved to be an effective tool for fuel evaluation and selection for power stations and other equipment fired with low NO_x burners.

The flat flame turbulent jet (FF-TJ) apparatus is another recent and convenient solid fuel characterization device [8] of some merit. In this device, a particle-laden primary air stream exits a delivery tube as a turbulent jet. A flat flame burner surrounds the tube coincident with the exit plane. Some important advantages of this apparatus are the realization of adequately high particle heating rates (up to 2×10^5 K/s), the ability to achieve high final particle temperatures, turbulent as opposed to laminar flow conditions, and devolatilization and char burnout in the presence of combustion gases. In addition, the absence of significant background radiation and ease of probe access allow reliable particle temperature and gas composition information to be obtained at different stages of the devolatilization process. The comparative volatile release rates measured in this apparatus have been shown to enable the relative flame stability performances of different solid fuels when combusted in furnaces to be assessed. The relative release rates of nitrogenous species during the devolatilization of fuels may also be forecast.

Figure 2 shows some devolatilization results for various fuels obtained in the FF-TJ apparatus. For a proper comparison of the biomass fuels with coal, the former would have to be ground to the same fine particle size distribution typical of pulverized coals. This is very difficult to achieve, especially for rice husks, so the results shown are necessarily qualitative. Generally, it is apparent that the biomass fuels release a proportion of their volatile matter early and at a rapid rate followed by a slower release of the remaining content, a behavior that is roughly the reverse of that for coal. This suggests that co-firing coal with biomass fuel should strongly enhance burner flame stability, except perhaps for rice husks, which exhibit a rather slow initial volatile release. Consid-

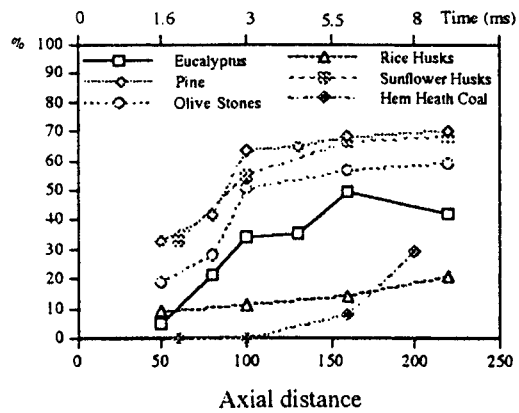

FIG. 2. Comparison of total weight loss for various fuels.

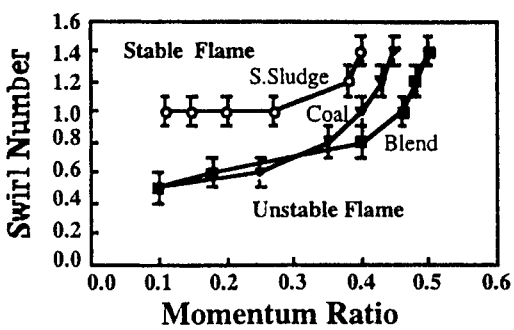

FIG. 3. Stability data of three flames.

ering pine wood, its volatile content is high, and, because much of it consists of lighter hydrocarbons and alcohols, it is released early. The implications for flame stability when co-firing are obvious. NO_x emission performance is likely to be improved as well because of the undoubted earlier ignition of this more lively volatile matter.

Flame Stability

Guaranteed flame stability is mandatory for all equipment fired with a pulverized solid fuel. In utility boilers, where, because of relatively cool walls in the proximity of the near-burner region, background radiation is rather small, flame stability is assured by aerodynamic means. A near-burner recirculation zone is created within which prolonged particle residence times are encouraged. The major part of the volatile release occurs within this zone. The volatile matter ignites there, and the recirculated products ensure rapid and mainly convective heating of the fuel particles to close the stabilization loop. This process may be contrasted with that in some cement kilns for example, where no attempt is made to create a near-burner recirculation zone. The presence of the hot clinker and refractory walls provides an intense level of background radiation sufficient to engender rapid pyrolysis and ignite the residual char. Although secure, the disadvantage of this radiant ignition process is that the flame is lifted, leading to high fuel NO emissions caused by premixing (excess oxidation of the nitrogenous content of the volatiles), in addition to the substantial thermal NO contribution caused by the locally high flame temperatures.

The energy required to close the stabilization loop is affected by the influence of the burner geometry and operating conditions on the near-field aerodynamics and by the quality of the fuel. The importance of burner aerodynamics on powdered coal flame stability has been treated extensively in the literature [9–11]. Burner injection mode, fuel character, and blending ratio are additional factors when biomass is co-fired with coal. Flame stability performance is usually well represented in terms of two parameters: the secondary air swirl number and the ratio of the primary to secondary stream momenta. Figure 3 shows stability data so plotted and obtained in the Imperial College 0.5-MW furnace for dried, powdered sewage sludge, coal, and a 50% by mass blend of these two fuels. The error bars on the figure reflect the somewhat vague experimental demarcation between the stable (lit back) flame and the unstable (lifted) flame. It can be seen that the stability limits are broadened for an appropriate blending ratio. This is due to the highly volatile content of the sewage sludge, which is rich in hydrogen, and the high calorific value of the coal combining to enhance flame stability. Similar results have been obtained when the co-fired fuel is wood sawdust [12].

An enhancement of thermal efficiency also reduces the CO_2 penalty associated with coal. Combined cycle technologies have this objective and one example studied is that in which the utility boiler is fed the vitiated air from the exhaust of a gas turbine [10]. For typical burner inlet O_2 concentrations of 16%, flame stability performance is not surprisingly restricted to narrower limits. This effect is less pronounced for a burner type in which the mixing of the fuel and the oxidant is faster (SAO) compared with a typical slower mixing design (SCO) used to produce lower NO_x emissions as shown in Fig. 4. Here, stability performance is presented as secondary air swirl number versus momentum ratio of primary jet (air + coal) to that of the secondary air.

Conversely, one can *increase* the O_2 content in the burner oxidant stream and, at the same time, dilute the secondary stream with recirculated products of combustion so as to increase the concentration of CO_2 in the exhaust gases (enrichment levels of up to 90% appear practicable), thereby possibly enabling commercially viable collection. With this combination, while maintaining the overall excess air level constant, the flame stability performance limits

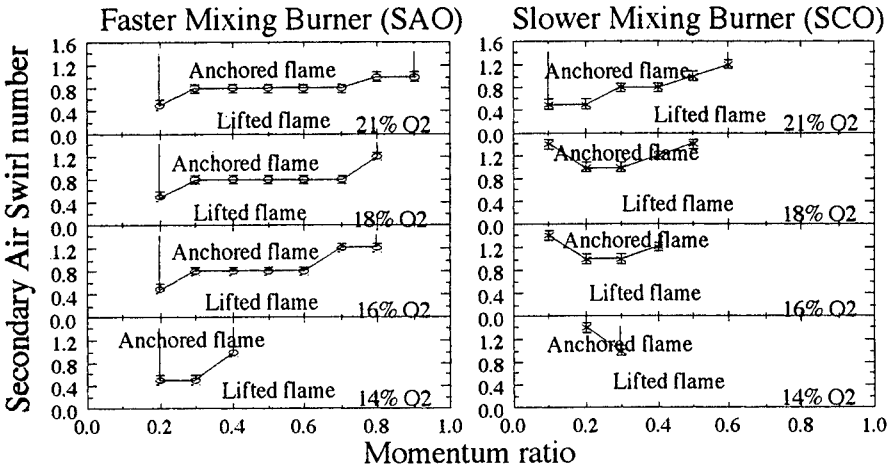

FIG. 4. Stability data for slow and fast mixing burners.

are slightly narrower than under ambient inlet air conditions. This limit can, however, be increased by injecting oxygen either in or near the coal stream, but safety restrictions are then imposed [13,14]. The introduction of biomass fuel could well ameliorate any loss in stability performance in a manner similar to that observed for ambient air conditions. In the wake of these remarks, one should note that a 500-MW power station so operated would require twice the oxygen production of Europe's largest plant.

NO Emissions and Char Burnout

The temperatures achieved in suspension-fired combustors are generally insufficient to result in the thermal NO_x making a major contribution to the overall burden, and the prompt contribution is estimated to be less than 5%. Thus, the fuel-bound nitrogen content and the near-field burner aerodynamics are key factors influencing the NO emissions emanating from suspension-fired combustors. The nitrogen content of biomass fuels is generally lower than that of most coals. In low NO burners, an attempt is made to optimize the release of this nitrogen in air-lean regions of the near-burner flow field. Much to their chagrin, burner design engineers have generally found that all measures that reduce NO_x emissions invariably reduce char burnout, so it is appropriate to treat these otherwise disparate subjects under a single heading.

The effect of the near-burner region aerodynamics on the NO formation and final char burnout in pulverized coal flames has been studied extensively during the last two decades. The NO formation in practical combustors is controlled primarily by the local availability of oxygen and the influence of the combustion aerodynamics on the injected particles. In this regard, particle size also plays an important role in establishing their trajectories in the near-burner region. As an example, for pulverized coal flames, it was found that the different burning regimes of both a larger (121 μm average) or smaller (25 μm average) particle size fraction have a significant effect on the flame shape, char burnout, and NO formation for a specific burner type compared with the standard (75% < 75 μm) grind coal with an average particle diameter of 50 μm [15]. Generally, it was found that for the smaller particles, the volatiles are released more uniformly and smoothly and that the combustion reactions occur close to the char particle, whereas, for the larger particles, the volatiles erupt as gaseous jets, engendering a more intense mixing with the surrounding oxygen, and burn more remotely from the char particles.

Biomass-derived fuels are not usually ground to the micron sizes of coal but only to a few centimeters. This is due to a combination of fuel-specific reasons, which include the higher costs associated with their grinding caused by their frequently fibrous natures and lower densities. When biomass fuels are co-fired with coal, NO formation/reduction mechanisms are complicated because of the changed combustion aerodynamics of the lower density, larger particles having different volatile release chemistries and char reactivities compared with the base fuel. As a consequence, changes occur in the manner in which oxygen diffuses into the char pores, thereby reducing the effectiveness of the heterogeneous combustion reaction, resulting in an increased level of carbon in the residual ash.

Figure 5 shows a burner configuration for biomass/coal co-firing, along with the NO emissions data. The two inner streams admit either coal or biomass fuel, with the secondary air being confined to the outer annulus. From a variety of biomass fuels co-fired with coals, it was found that effective NO

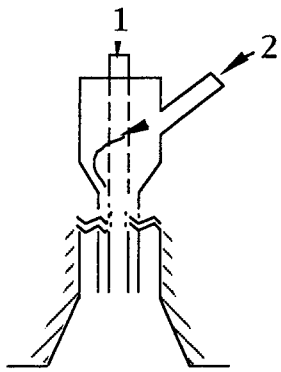

Injection Scheme	Co - Firing Thermal Ratio	NO Emissions (ppm, dry)
1	0	359
1 + Sawdust	15	365
2	0	600
2 + Sawdust	15	341
2 + Sawdust	30	250

FIG. 5. Co-firing NO emissions data for dual-fuel burner.

emissions reduction can be achieved when the fuel with the greater nitrogen content (coal or biomass) is introduced through the annular port, while the fuel of lower N content having a higher volatile content is introduced through the central port. Without the biomass fuel in the central port, this burner configuration leads to high NO emissions. When high-N fuel is introduced through the central jet, since the volatile nitrogen compounds are released in a fuel-rich zone, the flow configuration favors reduced NO emissions irrespective of the presence of low-N fuel in the annulus [12].

For a constant heat input and near-burner region aerodynamics, the substitution of a proportion of coal by biomass under co-firing conditions does, in this manner, reduce NO emissions. However, there is a limit beyond which any further reduction in NO is accompanied by a loss in carbon burnout. Nonetheless, higher NO_x reductions can be achieved when biomass is used under fuel reburning conditions downstream of primary coal flames, where, without reburning, maximum air/fuel mixing provides higher NO formation and char burnout. Reburn or fuel staging, described in more detail in the section on mathematical modeling, is now finding favor in practical combustors. The reburn fuel accounts for at most 10–20% of the total energy input. In excess of a 50% reduction in NO_x emissions over a base-case bituminous coal flame has been achieved here and elsewhere [16,17] for various reburn fuels. The ideal qualities of the reburn fuel are high reactivity with low nitrogen content, good availability, and no additional emissions burden. Therefore, several biomass fuels offer interesting possibilities within the reburn concept.

Particulate and Heavy Metal Emissions

It is imperative that any fuel introduced to supplement coal does not possess the same or more of its negative attributes. The emissions of heavy or toxic metals from biowaste fuels such as wood and sewage sludge are of special concern. All solid fuels leave a residue following burning. Most of the burned particles in coal and biomass-fired flames are collected or captured during the various stages of the process, with the exception of a small fraction of submicron particles that is entrained with the flue gases and emitted into the atmosphere unimpeded by the gas cleaning equipment. Under ideal combustion conditions, the inert residue should contain no carbon and the mineral matter should be recoverable in its original form. However, in combustion systems, good burnout is not always achieved, while volatile elements from the mineral matter vaporize and may be deposited or form small-size particles during condensation and nucleation in the lower temperature regions of the process.

The mineral matter in all fuels contains these volatile elements to a greater or lesser extent, some of which are toxic or carcinogenic (e.g., Cd, Hg, Ni, Pb). When waste-derived fuels containing toxic metals are fired in combustors/incinerators, particles in the submicron range are found to be enriched with them [18–20]. For most of the coal and biofuels considered here, the enrichment of toxic metals during combustion is generally insignificant. When considering, however, waste wood or biosolid extracts from sewage sludge as a supplementary fuel for either co-firing or reburn, toxic metal emissions become important. To assess this problem, a series of experiments was conducted in the Imperial College 0.5-MW furnace and in the FF-TJ entrained flow reactor [20]. In the first instance, furnace exit data of selected metal concentrations on various particle fractions were collected for coal, dried pulverized sewage sludge, and a blend of these fuels (50% by weight and 27% by calorific value). Further biological waste streams were simulated by adding compounds of selected elements in extraneous (oxides, chlorides, sulfides) and inherent (organometallics) forms to sewage sludge.

The metal oxides and silicate species content of the ash in three selected fuels are reported in Table 3. Interestingly, Table 4 shows that metal enrichment on submicron ash particles was lowest for the sewage sludge flame and increased with the proportion of coal (fuel rank). The formation of a higher submicron fraction of ash particles from lignite coal reported in the literature, however, was not observed for the sewage sludge flame.

TABLE 3
Metal oxides and silicate species content of ash

Fuel	SiO_2	Al_2O_3	CaO	P_2O_5	Fe_2O_3	TiO_2	MgO	Na_2O	K_2O	SO_3	Q^a	P^a	K^a
Coal	34.1	24.9	8.1	1.2	21.1	0.7	1.9	2.1	1.0	4.9	—	9.1	41.8
Blend	37.7	19.6	14.0	5.0	13.9	1.0	2.6	1.4	1.5	3.5	14.6	13.7	30.7
Sewage sludge	41.3	14.3	19.8	8.7	6.8	1.2	3.2	0.7	2.0	2.0	19.9	18.2	19.6

[a]Q = quartz, P = potassium aluminosilicate, K = kaolinite.

TABLE 4
Metal enrichment factors for three flames

Flame	Zn	Pb	Cu	Cr	Mn	Ni	Cd
Coal	8.2	11.6	11.9	7.3	2.9	10.3	22.3
Blend	6.1	8.04	3.7	6.1	1.7	8.5	21.7
Sludge	5.5	2.5	2.0	1.3	0.9	4.5	18.9

TABLE 5
Metal enrichment factors for FFTJ apparatus flames

Flame	Cd	Pb	Ni	Zn
Sewage sludge (SS)	7.2	3.52	1.95	5.34
SS + metal oxides	7.1	3.99	0.11	6.9
SS + metal chlorides	9.95	4.24	2.32	8.96
SS + metal carbonates	5.72	4.03	6.48	—
SS + metal sulphides	10.2	7.49	1.43	3.39
SS + organometallics	8.18	10.74	3.55	7.29

To address these effects on metal partitioning (Fig. 6), biological wastes containing metal oxides, chlorides, carbonates, sulfides, and organometallics of Cd, Zn, Pb, and Ni were burned in the FF-TJ reactor. Metal enrichment (defined as the ratio of the concentration of the metal on submicron ash particles divided by its concentrations on particles of all sizes) on submicron particles was lowest for the fuel-containing sulfides and this tendency increased with the metal carbonates, organometallic to metal chlorides. The results are given in Table 5. These observations indicate that vapor pressure alone does not provide a sufficient explanation for metal partitioning in the presence of large quantities of minerals. Other processes such as fragmentation, mineral/metal interactions, and metal oxidation/chlorination become increasingly important.

From an operational viewpoint, however, the combustion trials with a 100% sewage flame still produced toxic metal emissions well below the European standard. In a full-scale trial in a German utility boiler [4], although increased values of Pb, Zn, Cr, Pb Cu CO, and Ni were also seen with the implementation of sewage sludge co-firing, these values were again still within the limits of normal coal-firing operation, while the fly ash met all the requirements for its use in concrete manufacture.

The Consequences for Plant Operation

The introduction of a co-fired biomass fuel, as reviewed previously, may cause changes (some subtle, others not so) in the combustion behavior and emissions of a combustion system. The effect of noncombustible matter in pulverized coal combustion is relatively well documented [21]. In regard to the co-firing/blending of biomass, this knowledge and experience needs to be extended to account for the generally lower ash fusion temperatures and higher concentrations of alkali elements associated with some of these fuels.

As an example, raw straw has a chlorine content seven times that of coal and three times as much potassium, which imply there may be problems, especially if, as in the case of UK operation, high-chlorine coals are also used. Full-scale trials in Denmark [3] predict that if more than 10% of straw is co-fired with coal, the final ash cannot be used in cement production and if the co-firing ratio is increased to 20% it cannot be used as an additive for concrete. Furthermore, because of the higher dust burden produced, the introduction of straw co-firing would be inappropriate where certain de-NO_x and flue gas cleaning processes using gypsum are incorporated into the plant. In contrast, in the large-scale sewage sludge co-firing trials mentioned earlier, the residual ash met all the cement use requirements [22]. A further vital aspect is that of corrosion. The short-term benefits of co-firing will soon be negated if its introduction leads to a reduction in the lifetime of the heat-transfer components and flue gas conduits of the utility boiler which are expensive to replace. Again from the Danish trials, the observations suggest that the corrosion rate due to selective chlorine corrosion will be 50% higher for a 10% straw co-firing level unless better, more expensive alloys are used in the construction. Similar work by another

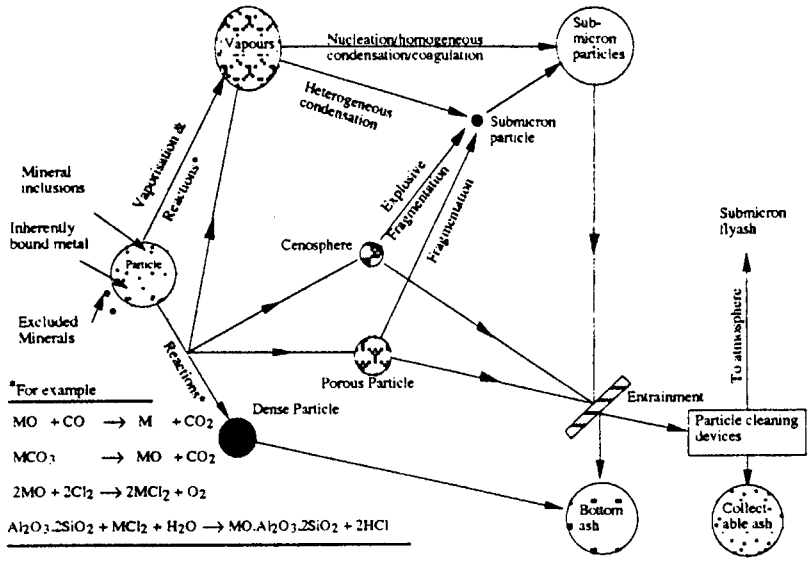

FIG. 6. Metal partitioning mechanisms during combustion.

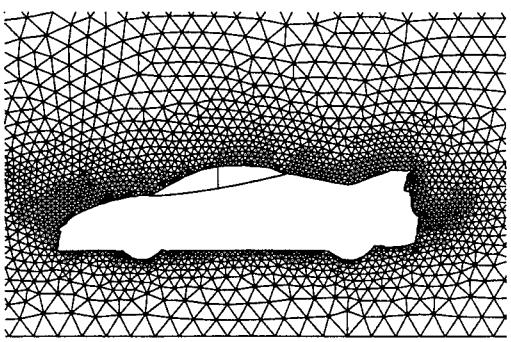

FIG. 7. Example of triangular/tetrahedral mesh.

power generator in Denmark suggests that above a certain potassium chloride concentration in the surface deposits due to the co-fired straw, the corrosion in the flue gas stream will be independent of that concentration.

Mathematical Modeling Matters

The geometry of the typical combustor exhibits two features that impede its solution by conventional finite difference treatments: the discrepancy of scale between that of the burners and that of the much larger volume of the combustion chamber and the discrepancy between the three-dimensional cylindrical geometry of the burners and the largely Cartesian geometry formed by the confining walls of the combustion chamber. Both of these difficulties would be surmounted by the existence of a numerical treatment based on a flexible unstructured grid capable of being locally refined.

This end has been partially achieved through previous work on, for example, grid embedding or zoning methods [23,24]. These involve subdividing the solution domain into fine-grid regions near the burners that are patched to coarser-grid regions elsewhere. Their principal disadvantage is that the transfer of information across the frontiers between the zones leads to severe convergence rate problems. This difficulty is circumvented by the local grid refinement (LGR) method [25] where the solution for all zones is effected simultaneously. However, the extension of this method beyond application to Cartesian forms is fraught with computational uncertainty. Body-fitted coordinate (BFC) treatments have served marvellously for the specialized geometries of gas turbine combustors [26] and in principal are applicable to those typical of furnaces. However, the previously mentioned geometric particularities of the typical furnace give rise to highly skewed control volumes that seriously impede convergence.

In view of these and other considerations, commercial software houses are adopting methods based on triangular two-dimensional/tetrahedral (three-dimensional) finite difference control volumes. Such cells enable very complex forms to be handled with ease, and local grid refinement can be effected routinely; see Fig. 7. If CFD methods founded on triangular/tetrahedral cells bring forth such major advantages, one is bound to ask why they have not previously been developed for engineering applications. Rather surprisingly, there appears to be no ready answer to this question. Although such cells

are deployed routinely in finite element methods, this class of methods has not been successful for combustion applications where the satisfaction of conservation principles is absolutely essential. Several software houses, however, now seem to be responding to this oversight and are announcing, amid considerable fanfare, new finite difference methods based on triangular/tetrahedral cells. The details of these are obscured by commercial considerations. Our own method [27,28] is based on colocated velocity and scalar control volumes. Colocated schemes give rise to interpolation difficulties, particularly in respect of pressure, which necessitate the adoption of special practices. Although we have so far found the triangular/tetrahedral methodology to be efficient and robust, it may be assured that its general application to engineering flows will require further development. This will be true particularly for solid fuels in which flexible numerical formulations are required to track the flights of particles through the unstructured meshes. Similar difficulties will arise when incorporating the typical present-day ray-tracing treatment of thermal radiation [29].

Aspects of Physical Modeling

Application to Pulverized Fuel Combustion

Gas-Phase Turbulence Modeling

Gas-phase turbulence modeling is an extensive subject area of the utmost importance to the simulation of combustion processes. However, since it is somewhat ancillary to the present theme of solid-fuel use, the treatment here will be brief. Virtually all predictions of practical combustion equipment items have been made with the conventional k-ε turbulence models. Many more elaborate models have, of course, been proposed, but they all require significantly increased amounts of computer time for very modest gains in predictive ability. Solid-fuel calculations are expensive computationally and leave no scope for modeling luxuries unless the rewards are measurable in engineering terms.

It is our experience that predictive discrepancies are all too often due to numerical inaccuracies and that the use of a finer grid and/or higher-order difference schemes is the remedy. We have explored Reynolds stress turbulence models with respect to two types of pulverized coal combustion: a nonswirling flame typical of cement kilns and a swirling flame typical of power stations [30]. Various options appear in the literature for some of the modeled terms, and it is was not clear which were preferred. We have experimented with two versions. Moreover, serious convergence difficulties were encountered not simply because of the extra equations to be solved but primarily because of the transfer of the effects of turbulence out of inherently stabilizing diffusion terms and into source terms. Rather surprisingly, when converged results were eventually procured, the Reynolds stress model did not demonstrate any consistent advantage over the simple k-ε model, at least within the constraints of the limited two-phase velocity data. The evidence suggested that the second-moment closure should be extended to the scalar equations to secure improved predictions. However, for powdered solid-fuel combustion modeling, this requires the solution of an additional 12 transport equations, which is totally impractical for engineering purposes.

Turbulence Dispersion of the Particulate Phase

Fluid turbulence confuses all aspects of combustion. The interaction between the turbulence and the particulate phase serves to perturb the particles' velocities and so disperse their spatial locations, which has implications for flame stability and the deposition of ash on heat-transfer surfaces. The vast majority of the reported mathematical models treat the particulate phase in Lagrangian fashion by tracking the flights of particles, belonging to representative, uniform-diameter-size groups released from representative entry locations, throughout the computational domain. In this hybrid procedure, influences of the particles are made known to the Eulerian solution of the gas-phase equations through source terms appended to these equations [31]. It is common practice to handle the dispersion of the particle flights stochastically by tracking successive releases of a particle in a given class and subjecting these to the random influences of the turbulence. However, to ensure statistical reliability, a sample size of 1000–10,000 is required for each class. The computer demands are impossible, with the result that such treatments are never implemented correctly and the solutions are little more than indicative.

To circumvent this problem, we have developed a method that predicts the evolution of the probability density function of the particles' velocities starting from the known distribution at entry [32]. The method is fundamentally based with the starting point in its derivation being the momentum-conservation equation for a particle. An analysis based on probability theory leads to the following equation for the rate of change of the velocity probability, $P(v_p; t)$, of a particle:

$$C(C_1 + C_2 v_p + C_3 v_p^2)\frac{\partial P(v_p; t)}{\partial v_p} + \frac{\partial P(v_p; t)}{\partial t} + C(C_2 + 2C_3 v_p)\, P(v_p; t) = 0 \quad (1)$$

where

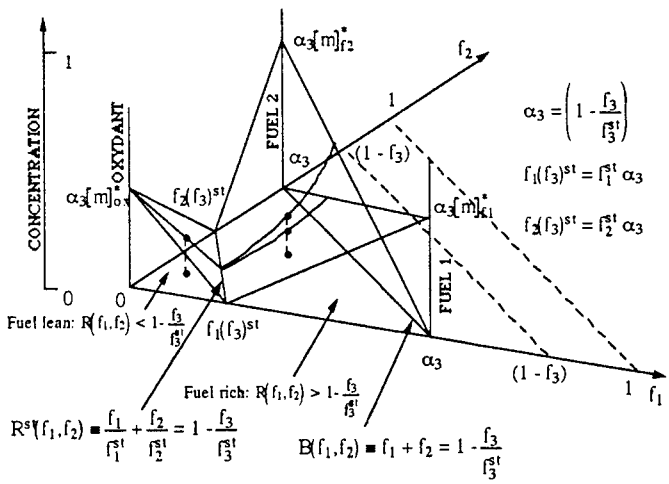

FIG. 8. Generalized mixture fraction diagram.

$$C = \frac{\rho_f A_p C_D \mathrm{SIGN}}{2m_p}$$

$$C_1 = \sigma_f^2(1 - \rho_{fp}^2) + \left(\overline{u_f} - \frac{\rho_{fp}\sigma_f}{\sigma_p}\overline{u_p}\right)^2 \quad (2)$$

$$C_2 = 2\left(\overline{u_f} - \frac{\rho_{fp}\sigma_f}{\sigma_p}\overline{u_p}\right)\left(\frac{\rho_{fp}\sigma_f}{\sigma_p} - 1\right)$$

$$C_3 = \left(\frac{\rho_{fp}\sigma_f}{\sigma_p} - 1\right)^2 \quad (3)$$

Here, C_D is the drag coefficient, SIGN is the sign of the relative velocity $(u_f - u_p)$, σ is the rms velocity, and ρ_{fp} is the gas-particle fluctuating velocity correlation coefficient.

In the solution method, the initial PDF is discretized into a sufficient number of bins and the preceding equation is solved by the method of characteristics. The procedure has proved to be orders of magnitude faster than conventional stochastic treatments [33].

Volatiles Release

This phenomenon has important consequences for flame stability and pollutant emissions. Since the volatile matter is chemically bound, its release rate is controlled by chemical kinetic parameters and temperature. For coal and biomass, this chemistry is clearly very complicated and, although simplified schemes have been proposed, it is, given the extreme variability of coal and biomass, the authors' opinion that, where possible, the release rates should be obtained for each fuel in characterization experiments for which the heating rates are high enough to be representative of combustor conditions. Empirical relations are required for the mass release as a function of the heat transfer to the particle. For other than fairly small particles (less than 20 μm, say), physical influences may be important. These are not normally modeled, but they would be accounted for in characterization experiments if these could be effected for a representative range of particle sizes.

Volatiles Combustion

In the very early stages of pyrolysis, a small quantity of light species is released. The particle softens quickly and tar vapors are evolved, entraining and ejecting molten material as they do so. Ease of ignition requires that these heavy hydrocarbons should crack, and an additional timescale is implied. However, this timescale is expected to be short in the vicinity of the flame front because of the high temperatures there and can probably be ignored. It has been customary to presume partial premixing of the volatiles with the combustion air before ignition, handled by the eddy-breakup model of Magnussen and Hjertager [34]. While some premixing may occur, the assumption of diffusion combustion is probably close to reality as confirmed by some recent calculations [35]. In any case, generalization to the multistream mixing required to treat co-firing or reburn, where the reburn fuel (e.g., biomass) differs from the main fuel, becomes hopelessly complicated unless unpremixed reaction can be presumed.

It is possible to extend the conventional mixture fraction treatment to encompass the mixing/combustion of n different fuel and oxidant streams by a generalized passive scalar formalism [35]. In regard to biomass/coal co-combustion or reburn combustion systems, the mass conservation of the evolved species during the combustion process requires the solution of three passive scalars to determine the chemical state of the mixture, and, if the fast-chemistry assumption is invoked, the instantaneous chemical state of the mixture may be obtained from a generalized mixture fraction space as shown in Fig. 8. It will be noted that since the char carbon mass

released to the gas phase from heterogeneous combustion (denoted in the diagram by f3) must represent burned products, Fig. 8 illustrates the projection of the three-mixture fraction space to a two-mixture fraction space for volatile combustion, and the conventional diagram for gas combustion is obtained for either f1 or f2 and f3 equal to zero.

Referring to Fig. 8, for fuel-lean conditions,

$$\frac{f_1}{f_1^{st}} + \frac{f_2}{f_2^{st}} < 1 - \frac{f_3}{f_3^{st}} \tag{4}$$

So, $[m]_{fi} = 0$, and $[m]_{ox}$

$$= \left\{\left(1 - \frac{f_3}{f_3^{st}}\right) - \left(\frac{f_1}{f_1^{st}} + \frac{f_2}{f_2^{st}}\right)\right\} [m]_{ox}^{*} \tag{5}$$

And for fuel rich conditions,

$$\frac{f_1}{f_1^{st}} + \frac{f_2}{f_2^{st}} > 1 \frac{f_3}{f_3^{st}} \tag{6}$$

So: $[m]_{ox} = 0$, and $[m]_{fi}$

$$= \left\{\frac{\left(\frac{f_1}{f_1^{st}} + \frac{f_2}{f_2^{st}}\right) - \left(1 - \frac{f_3}{f_3^{st}}\right)}{\left(\frac{f_1}{f_1^{st}} + \frac{f_2}{f_2^{st}}\right) - (f_1 + f_2)}\right\} f_i [m]_{fi}^{*} \tag{7}$$

$$i = 1, 2$$

In the preceding equations, the indices f and ox indicate quantities referred to fuel and oxidant streams, respectively, and the asterisk refers to the values at a physical inlet or a hypothetical inlet along the particle trajectory.

Char Combustion

Good burnout of the char is essential, partially to keep the carbon in ash low enough to ensure that ash is a viable commercial product in, for example, the building industry. It is not usually difficult to achieve good burnout of most of the char, but there will always be a least-likely-to-burn fraction characterized primarily by large particles or ash-rich particles compounded by the inevitable heterogeneity of the fuel, particularly where coal is concerned (Gibbins and co-workers [36]). The standard mathematical model allows for external diffusion near the particle surface, probably with adequate accuracy, and simulates the chemical reactivity of the fuel by presuming a first-order reaction having a single preexponential factor and a unique activation energy entirely confined to the surface of an equivalent spherical particle. Fuel variability remains the primary problem, and, again, it is preferable to attempt to determine the kinetic behavior, as characterized by the previously mentioned kinetics parameters, of each fuel in suitable characterization experiments. This is not easy, since there is now evidence that the char undergoes thermal deactivation in the high temperatures of the combustor [37]. This could reduce the preexponential factor by as much as two orders of magnitude, although the activation energy might not vary much. Modeling studies tend to confirm this, because the use of char kinetic parameters established in conventional drop tube experiments almost always leads to a serious overprediction of the char burnout.

Nitric Oxide Emissions: Biomass Reburn

Most of the NO emissions from coal- or biomass-fired combustors derives from the fuel and to a lesser extent from the prompt routes, with the notable exception of the cement kiln in which, because of the high temperatures of the process, the thermal route predominates. The full nitrogen chemistry involves some 200 elementary reactions. Considerable progress has been made in determining reduced schemes [38]. If only thermal NO_x is of concern, the Zeldovich mechanism is an extreme example. More generally, the reduced schemes are still too extensive to be embodied completely in an engineering mathematical model for solid fuels. The fuel nitrogen chemistry is inextricably linked to the main combustion reactions, so that the reduced description must encompass the C-H-O-N chemistry of the whole flame. The hope is that current advances in computing power will change this in the near future. In the meantime, one is obliged to adopt models of the fuel and prompt NO chemistry. The proposals of de Soete [39] are most often adopted to treat the fuel NO. Since the NO chemistry has negligible effect on the aerodynamics/combustion, it may be postprocessed conveniently and economically.

We choose here to consider the interesting application in which biomass is used as the reburn fuel in a coal-fired power station to reduce the nitric oxide emission. Since the reburn fuel accounts for only about 10–20% of the total fuel mass input, this represents a particularly effective use of a limited fuel source that will also reduce the CO_2 burden. The NO produced in a near-burner fuel-lean zone is consumed in a subsequent fuel-rich zone created by the addition of the reburn fuel. The reburn process is completed by the addition of overfire air in a third zone downstream to achieve the desired overall stoichiometry and ensure final burnout. The reaction model is sketched in Fig. 9. Transport equations are solved for HCN, NO, and N_2 [26,35].

Some predictions of the NO emission from the Imperial College furnace, fired on coal and with natural gas as the reburn fuel, are compared with the data for a range of reburn zone stoichiometries on the left-hand side of Fig. 10. The agreement is not bad. It should be remarked that the reburn zone stoichiometries are averaged over the reburn zone which is the reason for the apparent paradox of air-rich conditions. Fuel-rich conditions will, of course,

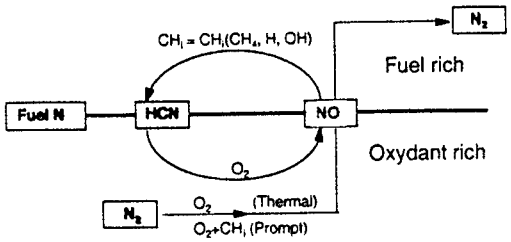

FIG. 9. Reaction model for NO formation with reburn.

exist locally within the reburn fuel supply jets. Unfortunately, we do not yet have good data for pine sawdust as the reburn fuel, so the comparison on the right-hand side of the figure between the NO emissions without reburn and with natural gas and pine sawdust as the reburn fuels are the outcomes of predictions. Given that the natural gas reburn predictions have been demonstrated to be reasonable, we may have some confidence in those for the sawdust. We conclude that reburn is a very effective NO-reduction strategy, especially because our system was not optimized, and that pine biomass, rather surprisingly, appears to be almost as good as natural gas as a reburn fuel. There is one downside that should be mentioned; because of its normally high oxygen content, large volumes of biomass are necessary to achieve the reburn stoichiometries.

Application to Gas Turbine of an ABGCC

The air-blown gasifier combined cycle (ABGCC) [26] is being developed by the Combustion Technology Centre in the UK to improve the efficiency by which electricity can be generated from coal and biomass fuels. Efficiencies of upwards of 50% are forecast. Because fluidized bed technology is employed, SO_x emissions will be low, but NO emission could still be significant since the gaseous products of the solid-fuel gasification that fuel the gas turbine component contain nitrogenous species derived from the chemically bound nitrogen of the coal. The geometry of the gas turbine is admirably suited to treatment by body-fitted coordinates. For more details, the reader is referred to Ref. 26.

Treatment of Combustion

Gasifier-generated fuels are typically characterized by low calorific values, which can result in the loss of flame stability with catastrophic consequences should the flame reestablish on the first row of turbine blades. Finite-rate chemistry models are therefore preferred when predicting the combustion of gasifier fuels. The turbulence/chemistry interaction is a formidable obstacle. The PDF transport approach represents a way forward, and both Eulerian and Lagrangian treatments are being developed. We prefer to consider the PDF calculation in a Lagrangian framework [40], largely because of its ease of application to complex grids. The species equation is written

$$\frac{dY_i}{dt} = \frac{1}{\rho}\frac{\partial}{\partial x_\alpha}\left(\rho d \frac{\partial Y_i}{\partial x_\alpha}\right) + \dot{w}(Y_1, Y_2, \ldots, T) \quad (8)$$

The first term on the right-hand side of this equation is a diffuse one, which, in a Lagrangian treatment, is very difficult to integrate. However, if the assumption of a quasi-homogeneous turbulence field can be tolerated, this difficulty can be circumvented by rewriting Eq. (8) as

$$\frac{dY_i}{dt} = \frac{\tilde{Y}_i - Y_i}{\tau_{ex}} + \dot{w}(Y_1, Y_2, \ldots, T) \quad (9)$$

where the tilde above the quantities indicates the statistical mean value in the flow field and τ_{ex} is an exchange time that is related to turbulence characteristics. The turbulent mixing of the two reactants may be depicted in an $Y_i \sim f$ plane (Fig. 11). The trajectories from A to F and B to F represent the

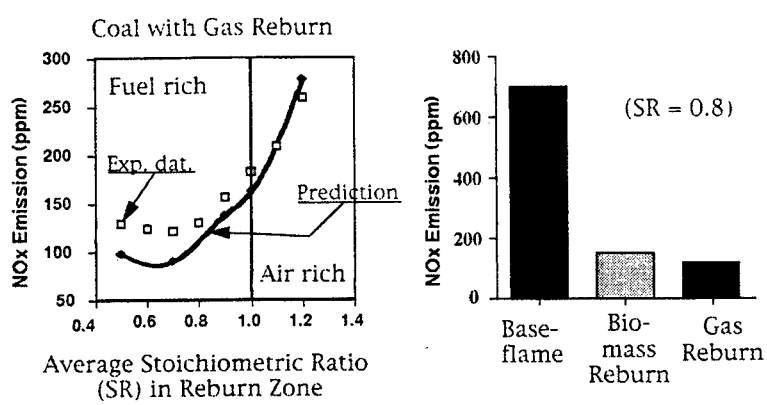

FIG. 10. Reburn data and predictions.

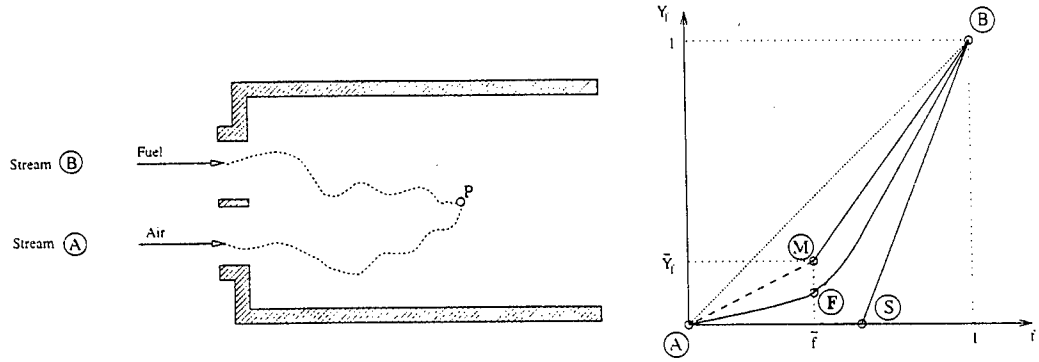

FIG. 11. Lagrangian PDF transport treatment for finite-rate chemistry.

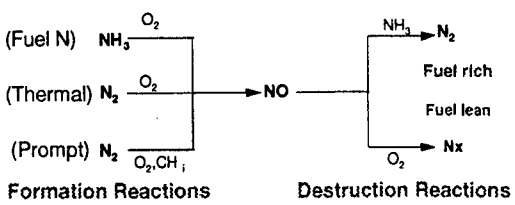

FIG. 12. NO emissions model for ABGCC gas turbine.

finite-rate reaction paths. The state S would be attained for an infinitely fast reaction. The state M is obtained when reaction occurs upstream, but not at P. The straight line A-B is obtained when the flow is inert everywhere.

The joint PDF of thermochemical quantities within $Y_i \sim f$ planes may be expressed as

$$\tilde{P}(\underline{Y}) = \tilde{P}(f) \prod_{i \neq 1} \delta(Y_i - Y_i^{\mathrm{AFB}}) \tag{10}$$

where $P(f)$ is the PDF of f, which may be presumed to be a B function. The exchange coefficient must be specified, and further validation work is required to find good values. We currently assume that it may be characterized by the inverse of the fluctuating strain rate [41], so

$$\tau_{\mathrm{ex}} = \lambda/u' = \sqrt{15\mu/\rho\varepsilon} \tag{11}$$

The mean rate of reaction is calculated from

$$\tilde{\dot{w}} = \int_0^1 \nu_i K_o (Y_{fu}^{\mathrm{AFB}})^{\nu_{fu}} (Y_{\mathrm{ox}}^{\mathrm{AFB}})^{\nu_{\mathrm{ox}}} \exp\left(-\frac{T_a}{T^{\mathrm{AFB}}}\right) \tilde{P}(f)\, df \tag{12}$$

A critical scalar dissipation rate may be envisaged beyond which the flame is quenched because of excess energy transfer. The mean reaction rate is then multiplied by a factor α that is defined by

$$\alpha = \int_0^{\chi_{\mathrm{quen}}} \tilde{P}(\chi)\, d(\chi) \tag{13}$$

where χ_{quen} is the empirically determined critical value of the scalar dissipation rate and $P(\chi)$ is the PDF of the scalar dissipation rate that we presume to have a log normal distribution. This treatment has simulated well the extinction of the flames of Masri et al. [41,42].

NO Emission

The chemistry model required here differs from that used for reburn since, in the gasification process, the fuel-bound N results in significant quantities of NH_3. The coal gas otherwise consists of CO, H_2, and N_2 as the major compounds with, in addition to the NH_3, CH_n as minor ones. Accordingly, transport equations are solved [26] for NH_3, NO, and N_2 to handle the NO chemistry. An outline of the scheme appears in Fig. 12: the kinetic parameters are those of de Soete [43].

Calculations have been performed for a General Electric Frame 6 machine running at a pressure ratio of 4 and fed with a synthesis fuel. Some predictions of the NO concentration contours are shown in Fig. 13. Close examination of the predictions reveals that the production of thermal and prompt NO is small. R1 is significant in the primary zone. Thereafter, R4 is prominent in reducing the NO to N_2 in the presence of the still-abundant NH_3. The latter occurrence is often referred to as the thermal de-NO_x reaction; it is significant, and, if not, the ABGCC technology might not be viable. Some outlet NO values have been measured, and the predictions are in remarkably good agreement with these.

Additional Important Phenomena

Fouling and Slagging

Ash deposition on the heat transfer surfaces is the bête noire of solid-fuel combustion equipment. As already mentioned, the typical mathematical model of powdered fuel combustion incorporates a Lagran-

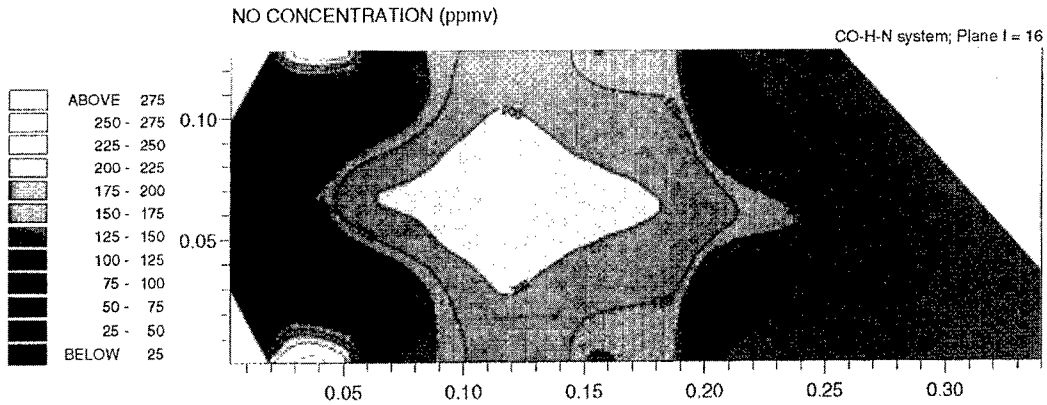

FIG. 13. NO emissions prediction for ABGCC gas turbine combustor.

gian solution of the particulate phase so the particle trajectories and velocities are known. To determine the ash deposition rate on an initially clean surface, the arrival rates and sticking efficiencies of the flyash particles must be determined. Assuming that char combustion has effectively ceased near walls and the fraction of the total particle flow actually retained on the walls is small, the ash deposition calculations can, with small error and considerable computational economy, be postprocessed [44]. Those particles with instantaneous velocities, as determined from the PEP method, sufficient to penetrate the displacement thickness of the boundary layer will reach the surface; those of smaller kinetic energy will be entrained by the boundary layer flow and either exit the combustion chamber or fall out. The sticking efficiency of a particle will be principally a function of its softness or viscosity, which in turn will depend on its temperature and chemical composition.

We have achieved reasonable predictive success using the Urbain viscosity model of Ref. 45. A critical viscosity of 10 Pa s was chosen, and eight chemical classes of particles were sampled based on the concentrations of Al_2O_2, SiO_2, CaO, and Fe_2O_3 in the fly ash of the particular coal fuel. Once a deposit begins to accumulate, the surface/particle interaction is complicated by many additional factors such as erosion by impaction, soot blowing, load cycling, and viscous flow. At the very least, modeling must be incorporated to determine the surface temperature, and so the viscosity, of the buildup with the presumption that a surface viscosity of less than the critical value will capture all arriving particles.

Toxic Metal Emissions

Little work has so far been performed on devising a mathematical model of toxic metal emission. The recent rapid growth in public awareness of this further threat to the environment assures that it will be a fruitful research area. The preparation of a complete model of the toxic metal physical/chemical processes constitutes a formidable task, and the resulting formulation would place unacceptable demands on computer resources. An obvious simplification is contained in recognition of the fact that the toxic metal processes will have negligible influence on the aerodynamics and combustion and may therefore be contained in a postprocessor. A proposed simplified modeling methodology is outlined by Fig. 6, which emphasizes the vaporization, condensation/nucleation, particle coagulation, and metal vapor chemical kinetics, including the reactions in both the gas and solid phases.

An initial char or ash particle gives rise to metal vapor and condensed metal on walls and cool particulates in the tail of the flame. The condensation process will depend on essential characteristics of the particular metal species relating to vaporization, condensation, and nucleation, which will depend on their chemical form, as a function of oxidation and chlorination, and on the local flame conditions. A first-step model would concentrate on a chemical subsystem that, it is suggested, would include metal-O_2-Cl_2 mechanisms with the phase transition of the metals or metal compounds determined by the thermodynamic equilibrium between the vapors of the metals and their chloride and oxide forms.

In this approach, however, it has been observed that the amount of metal vaporization can be overpredicted when compared with experimental data. This may result as a consequence of ignoring the chemical/physical interactions of other compounds in the vapor phase or in the ash that generally retards the evaporation process; for example, the presence of clay (montmorillonite) will reduce the Pb vapor pressure significantly. To address this issue, attempts should be made, for certain metals of major interest (e.g., Cd, Pb, Hg), to identify the conditions under which the equilibrium assumption may not be used,

and, in such instances, the quantification of their appropriate metal vaporization.

In a simple model, the metal vaporization rates can be computed for the metal compounds in the fuel in the knowledge of their thermal states and the corresponding thermodynamic data for their vapor pressures and the particle heating rates calculated from the main program for the aerodynamics and combustion. The heterogeneous condensation of metal vapor generally depends on the size of the host particles onto which the metal is condensing. By way of example, if the host particle size is much smaller than the mean free path of the gas ($\approx 0.25\ \mu$m), the growth rate of the host particle, after recourse to the kinetic theory of gases [46] may be expressed as

$$\frac{dV}{dt} = \frac{a\pi d_s^2 V_m (P - P_e)}{(2\pi M_m kT)^{1/2}}. \tag{14}$$

Here, a is an accommodation factor accounting for the fraction of molecules that collides with a surface and does not stick. Such formulas also exist for larger host particles. The reactions of metals and metal compounds with: (1) minerals or ash particles or with sorbents, both chemically or physically (adsorption) and (2) their oxidation and chlorination reactions should be considered in the computational procedure. On the former, the reactions (such as, for example, kaolinite [Al_2O_3 $2SiO_2$ H_2O]) with oxides and chlorides of lead ought to be included. The latter reactions might be restricted to include only the stable compounds at the prevailing temperature.

Conclusions

The conclusions may be very simply stated. We believe that a future exists for biomass combustion. It is far from being a mature subject. Co-firing will be high on the research agenda. We very much hope that we have shown in this lecture that there are plenty of research topics for everyone. Those with a coal combustion background will have an initial advantage, but there is plenty of scope for those from all disciplines to enter the multifaceted arena of biomass combustion.

Acknowledgments

The authors are particularly indebted to the following colleagues for their contributions to the preparation of the manuscript of this paper: J. Diedrichsen, M. Emami, J. Gibbins, S. Godoy, S. Hassan, N. H. Kandamby, F. Lee, A. Perera, C. Pikoulas, B. Shen, and S. Yousif.

REFERENCES

1. "Coal Combustion in Advanced Burners for Minimal Emissions and CO_2 Reduction Technologies," Joule Programme, EU, Final Report, JOUF-0050-C (TT), 1993.
2. European Commission, "Non-Nuclear Energy," The Framework Programme IV, V-Directorate-General XVII, 1994.
3. "Combined Combustion of Biomass/Sewage Sludge and Coals of High and Low Rank in Different Systems of Semi-Industrial and Industrial Scale," APAS Clean Coal Technology, EU, Final Report, COAL CT 92-0002, 1994.
4. Landais, P., "Assessment of Coal Potential Evolution by Experimental Simulation of Natural Coalification," *ORG. Geochem* 17:705–710 (1991).
5. Seeker, W. R., "Waste Combustion," *Twenty-Third Symposium (International) on Combustion,* The Combustion Institute, Pittsburgh, 1990, pp. 867–885.
6. Emami, M., Lazopoulos, G., Lockwood, F. C., and Pikoulas, C., "On Burner Configuration Optimisation, Prediction of the Effect of Scale Upon NO Emissions," Final Report, National Power Plc, 1994.
7. Man, C. K., Pendlebury, K. J., and Gibbins, J. R., "The Evolution of Fuel Nitrogen during Rapid Coal Devolatilization," presented at the ACS Symposium on the Impact of Environmental Constraints on Fuel Composition, ACS National Meeting, San Francisco, 1992.
8. Costa, M., Godoy, S., Lockwood, F. C., and Zhou, J., *Combust. Flame* 96:150–162 (1994).
9. Truelove, J. S. and Holocombe, D., *Twenty-Third Symposium (International) on Combustion,* The Combustion Institute, Pittsburgh, 1990, p. 963.
10. Abbas, T., Costen, P., Lockwood, F. C., and Ou, J. J., "On the Performance of Large-Scale Pulverised Coal Flames in a Simulated Combined Cycle," presented at the 7th International Conference on Coal Science, Banff, Alberta, Canada, 1993.
11. Milosavljevic, V. D., Taylor, A. M. K. P., and Whitelaw, J. H., *Twenty-Third Symposium (International) on Combustion,* The Combustion Institute, Pittsburgh, 1990, p. 957.
12. Abbas, T., Costen, P., Kandamby, N. H., Lockwood, F. C., and Ou, J. J., *Combust. Flame* 99:617 (1994).
13. Abbas, T., Costen, P., Diedrichsen, J., and Lockwood, F. C., "Characteristics of Oxygen-Enriched Pulverised Coal Flames," presented at the Third International Conference on Combustion Technologies for a Clean Environment, Lisbon, Portugal, 1995.
14. Diedrichsen, J., "The Influence of Mixing on Combustion and NO_x Formation in Pulverized Fuel Flames," Ph.D. Thesis, University of London, 1996.
15. Abbas, T., Costen, P., Lockwood, F. C., and Romo-Millares, C. A., *Combust. Flame* 93:316 (1993).
16. Abbas, T., Benos, G., Costen, P., Kandamby, N. H., Lockwood, F. C., and Perera, A., "NO_x Abatement through Fuel-Staging in Coal-Fired Furnaces," presented at the International Joint Power Generation Conference, Houston, Texas, 1996.
17. Smart, J. P. and Morgan, D. J., *Fuel* 73:1437 (1994).
18. Wendt, J. O., *Twenty-Fifth Symposium (International)*

on Combustion, The Combustion Institute, Pittsburgh, 1994, pp. 277–286.

19. Linak, W. P., Srivastava, R. K., and Wendt, J. O. L., Third International Conference and Seminar on Municipal Waste Combustion, Williamsburg, VA, 1993.
20. Abbas, T., Costen, P., De Soete, G., Glaser, K., Hassan, S., and Lockwood, F. C., "The Energy and Environmental Implications of Using Sewage Sludge as a Co-Fired Fuel Aplied to Boilers," *Twenty-Sixth Symposium (International) on Combustion,* The Combustion Institute, Pittsburgh, 1996, pp. 2487–2493.
21. Wall, T. F., *Twenty-Fourth Symposium (International) on Combustion,* The Combustion Institute, Pittsburgh, 1992, pp. 1119–1126.
22. Allen, G., IC Limited, private communication, Derby, UK, 1995.
23. Hessenius, K. A. and Rai, M. M., *Comput. Fluids* 14:43–58 (1986).
24. Thompson, M. C. and Ferziger, J. H., *J. Comput. Phys.* 82:94–121 (1989).
25. Lockwood, F. C., Pikoulos, C., and Shah, N. G., "A New Multi-Level Local Grid Refinement Technique for the Solution of the 3D Navier Stokes Equations," presented at the British Flame Day, 1992.
26. Kandamby, N. H. and Lockwood, F. C., *Twenty-Fifth Symposium (International) on Combustion,* The Combustion Institute, Pittsburgh, 251–259, 1994.
27. Lockwood, F. C. and Pikoulas, C., "Development and Validation of a Local Grid Refinement Technique for Flow Prediction Methods," Final Report, EPSRC, GR/J/14349, 1994.
28. Lockwood, F. C. and Pikoulos, C., "A New Unstructured Finite-Volume Method for the Prediction of 3D-Combustion Flows," in preparation, 1996.
29. Lockwood, F. C. and Shah, N., *Eighteenth Symposium (International) on Combustion,* The Combustion Institute, Pittsburgh, 1981, pp. 1405–1414.
30. Lockwood, F. C. and Shen, B., *Twenty-Fifth Symposium (International) on Combustion,* The Combustion Institute, Pittsburgh, 1994, pp. 503–509.
31. Migdal, D. and Agosta, V. D., *J. Appl. Mech.* 34:860–865 (1967).
32. Lockwood, F. C. and Papadopoulos, C., *Combust. Flame* 76:403–413 (1989).
33. Perera, A., "Mathematical Modelling of 2 Phase Flows for Industrial Applications," Ph.D. Thesis, Imperial College, University of London, 1996.
34. Magnussen, B. F. and Hjertager, B. H., *Sixteenth Symposium (International) on Combustion,* The Combustion Institute, Pittsburgh, 1976, pp. 719–729.
35. Kandamby, N., Lockwood, F. C., Lazopoulous, G., Perera, A., and Vigevano, L., "Mathematical Modelling of NO_x Emissions Reduction by the Use of Reburn Technologies in Utility Boilers," Presented at ASME (International Joint Power Generation Conference), Houston, Texas, October 1996.
36. Man, C. K., Pendlebury, K. J., and Gibbins, J. R., *Fuel Process. Technol.* 36:117–122 (1993).
37. Man, C. K., Gibbins, J. R., Lockwood, F. C., and Williamson, J., "Bench-Top Coal Testing for NO_x Prediction in Pulverised Coal Combustion," presented at the 4th EPRI Conference, Charleston, SC, 1994.
38. Lindstedt, R. P. and Selim, M. A., *Combust. Sci. Technol.* 99:277 (1994).
39. de Seoete, G. G., *European Symposium (International) on Combustion,* The Combustion Institute, Sheffield, 1973, pp. 439–444.
40. Conzalcz, M. and Borghi, R., *Seventh (International) Symposium Turbulent Shear Flows,* Springer Verlag, 1991, pp. 293–311.
41. Emami, M., "Prediction of Finite Rate Chemistry Turbulent Combustion," Ph.D. Thesis, Imperial College, University of London, 1996.
42. Masri, A. R., Bilger, R. W., and Dibble, R. W., *Combust. Flame* 71:245–266 (1988).
43. de Seoete, G. G., "The Role of NO and N_2O Formation/Destruction Chemistry in Coal Combustion Control Technologies," The British Coal Research Forum, Imperial College, London, April, 1993.
44. Lee, C. C. F., Ghobadian, A., and Riley, G. S., "Prediction of Ash Deposition in a Coal-Fired Axi-Symmetric Furnce," Proceedings of the 1993 Engineering Foundation Conference.
45. Srinivasachar, S., Senior, C. L., Helble, J. J., and Moore, J. W., *Twenty-Fourth Symposium (International) on Combustion,* The Combustion Institute, Pittsburgh, 1992, pp. 1179–1187.
46. Friedlander, S. K., *Smoke, Dust, and Haze.* Wiley, New York, 1977.

Twenty-Sixth Symposium (International) on Combustion/The Combustion Institute, 1996/pp. 3059–3065

A TRANSIENT TWO-DIMENSIONAL CHEMICALLY REACTIVE FLOW MODEL: FUEL PARTICLE COMBUSTION IN A NONQUIESCENT ENVIRONMENT

J. LEE, A. G. TOMBOULIDES, S. A. ORSZAG, R. A. YETTER AND F. L. DRYER
Department of Mechanical and Aerospace Engineering
Princeton University
Princeton, NJ 08544-0710, USA

A numerical model based on the spectral element method has been developed to simulate transient two-dimensional chemically reactive flows. Our numerical formulation is not only capable of including realistic transport and chemical kinetics but is also sufficiently flexible to model combustion systems in various complex geometries. In the present study, this numerical method has enabled, for the first time, the two-dimensional transient solutions of two different fuel particle combustion problems in a nonquiescent environment that includes coupled convection, detailed molecular transport, and elemental chemical kinetics. The simulations performed reveal the effects of low Reynolds number flow on the ignition and flame structure development of a spherical nonpremixed CO/air flame and on the gasification behavior of a small (200 μm in diameter) carbon particle. At a Reynolds number of unity, the steady-state non-premixed CO/air flame is spherically symmetric; however, during the ignition process, deviations from spherical symmetry are significant. As for the carbon particle simulation, the burning mode of the particle is sensitive to the Reynolds number (in the range of $0 < Re < 10$). It changes from a fast burning mode at $Re = 1$ (or less) with the presence of a reactive boundary layer surrounding the particle to a heterogeneous kinetics–controlled, slow burning mode at $Re = 10$ with nontrivial gas-phase chemistry in the wake.

Introduction

It is now possible to make realistic simulations of chemically reactive flows in one and two dimensions, and realistic three-dimensional simulations will soon be feasible. In Refs. 1–3, steady two-dimensional simulations of concentric gas-jet non-premixed methane flames using detailed kinetics are studied. In Refs. 4 and 5, transient two-dimensional simulations of the instabilities and ignition of hydrogen/oxygen premixed flames using detailed kinetics are investigated. In Refs. 6–8 octane droplet vaporization and combustion in a flow field using global kinetics are reported. Also, in Refs. 9–12, the pure vaporization of both single- and multiple-component droplets in a flow field and the effects of liquid-phase motion and heat transfer are explored.

There are many reactive flow problems that are axisymmetric; for example, fuel particle combustion (particles move relative to the ambient), laminar flow reactors, concentric co-flowing non-premixed flames, and mixtures ignited by individual hot particles. Here, we report results of a new transient numerical model that resolves the detailed couplings of convective and diffusive transport, with elemental chemical kinetics applied to simulations of axisymmetric chemically reactive flows. Our numerical model applies to one- and two-dimensional flows and, with adequate computational resources, it can also be used for full three-dimensional simulations.

Here, results will be presented for isolated fuel particle combustion problems to assess the effects of low/moderate Reynolds number flow past the fuel particle. In Refs. 13–18 we presented both experimental and numerical studies of transient combustion of droplets and carbon particles in a quiescent environment. In particular, in Refs. 14–16, 18, a one-dimensional model, which incorporated detailed transport and chemical kinetics, was used to analyze the transient combustion of hydrocarbon (methanol and heptane) droplets and carbon particles in a quiescent atmosphere.

In recent microgravity droplet (methanol or *n*-heptane) experiments [13,14,17], it was shown that even in the absence of buoyancy-induced convection, the droplet deployment technique often imparts a residual velocity on the droplet relative to the quiescent ambient ($Re \sim 1$). The computational requirements to simulate the transient two-dimensional combustion of a methanol droplet are quite demanding (because of the water dissolution phenomenon) and those for heptane are prohibitive because of the complexity of the chemical kinetics. However, a CO/air non-premixed flame generated by a porous sphere provides an effective approximation to the droplet problem, so its numerical simulation can provide a first approximation to assess the effects of slow residue motions on droplet combustion in microgravity experiments.

In previous numerical studies [16,18] on carbon particle combustion, it was found that when a small (200 μm in diameter) Spherocarb particle (a synthetic char particle, which is often used in experimental work [19,20]) is placed in a hot, quiescent environment, its combustion is characterized by finite Damköhler effects; for example, a long chemical induction time compared with transport time results in a long ignition time and consequently, particle regression can be important [16]. It is therefore expected that ignition characteristics may be sensitive to the details of convective transport.

Mathematical Formulation

The system of reduced governing equations, obtained in the low–Mach-number limit [21–23] is as follows:

$$\frac{\partial \rho}{\partial t} + v \cdot \nabla \rho = \rho \nabla \cdot v \tag{1a}$$

$$\rho \left(\frac{\partial v}{\partial t} + v \cdot \nabla v \right) = -\nabla p^1 + \frac{1}{Re} \nabla \cdot \mu \left(\underline{\underline{\nabla v}} + (\underline{\underline{\nabla v}})^T - \frac{2}{3} (\nabla \cdot v) \underline{\underline{I}} \right) \tag{1b}$$

and

$$\rho \bar{c}_p \left(\frac{\partial T}{\partial t} + v \cdot \nabla T \right) + \frac{1}{RePr} \left[\sum_i (\nabla \cdot \rho Y_i V_i H_i^s - H_i^s \nabla \cdot \rho Y_i V_i) - \nabla \cdot \lambda \nabla T \right] + \sum_i \dot{\omega}_i H_i = -\frac{\partial p^0}{\partial t} \tag{1c}$$

$$\frac{\partial \rho Y_i}{\partial t} + \nabla \cdot \rho Y_i \left(v + \frac{V_i}{ReSc} \right) = \dot{\omega}_i \tag{1d}$$

Here, ρ denotes density, v velocity, Re Reynolds number, p pressure, T temperature, μ dynamic viscosity, λ heat conductivity, Y_i mass fractions, Pr Prandtl number, Sc_i Schmidt numbers, ω_i chemical production rate, $\bar{c}_p$ average heat capacity, H_i enthalpy, and V_i diffusion velocity. The ambient conditions have been used for nondimensionalization. In this work, the term $(1/RePr\ \Sigma_i(\nabla \cdot \rho Y_i V_i H_i^s - H_i^s \nabla \cdot \rho Y_i V_i)$ in Eq. (1c), second-order transport, particle regression, and internal heat transfer are not included. At the surface of the particle, the balance of mass, energy, and species concentrations is applied. Only for the case of porous sphere burner is the surface temperature fixed. Lastly, ideal gas laws are applied.

Since the only source of compressibility for the velocity field is the energy produced by exothermic reactions, we use a numerical procedure, similar to ones derived for incompressible flow, in which the thermal divergence of the velocity field is seen as a constraint enforced by the hydrodynamic pressure. Because of the presence of chemical reaction source terms in the energy and species equations, their time integrations are performed using a high-order implicit (fifth-order) method. On the other hand, the integration of the momentum and continuity equations is performed using a newly developed high-order semi-implicit splitting procedure, which leads to minimal errors in mass conservation and a decoupled solution procedure. A pressure Poisson equation, similar to that in incompressible flow, is derived for the hydrodynamic pressure, accounting for the nonzero divergence of the velocity field [24]. Finally, the spatial discretization is based on the spectral element method [25–28].

Transport and Chemistry Models

Here, both the diffusive transport and chemical kinetics are modeled in detail using the mixture fraction formulation with correction diffusion velocities [29–31] to ensure mass conservation. As for the thermal conductivity and viscosity, mixture-averaged values are used. The gas-phase CO oxidation is modeled by a comprehensive mechanism [32].

In the Spherocarb particle problem, the gasification of carbon is governed by a finite-rate heterogeneous kinetic model [33]. Because of the high particle temperatures for the cases studied here, the production of CO_2 by heterogeneous surface kinetics is neglected. In previous studies [16,18], a constant multiplicative factor was inserted in each of the heterogeneous rate expressions to approximate the effects of Spherocarb particle porosity. The estimation of this correction factor was based on a Thiele analysis [34,35]. At ambient temperatures exceeding 1400 K, as in the cases studied here, only pores in the size range of 0.4–50 μm participate in the gasification process [35]. Thus, the correction factor was chosen to represent the additional area provided by pores in this class. We preferred this simple approach to more sophisticated heterogeneous kinetics [36–38] and porosity models [39] since they involved many uncertain model parameters. Consequently, phenomena such as changes in the pore structure and the intrinsic surface activities are not considered here.

Results

The grid used in the present work consists of 96 elements (the domain is a 20 diameter square), and fifth-order Legendre polynomials are used as interpolants. Time steps used are in the range of 5×10^{-4} to 5×10^{-5}. Descriptions of the time splitting scheme, grid structure, spectral element

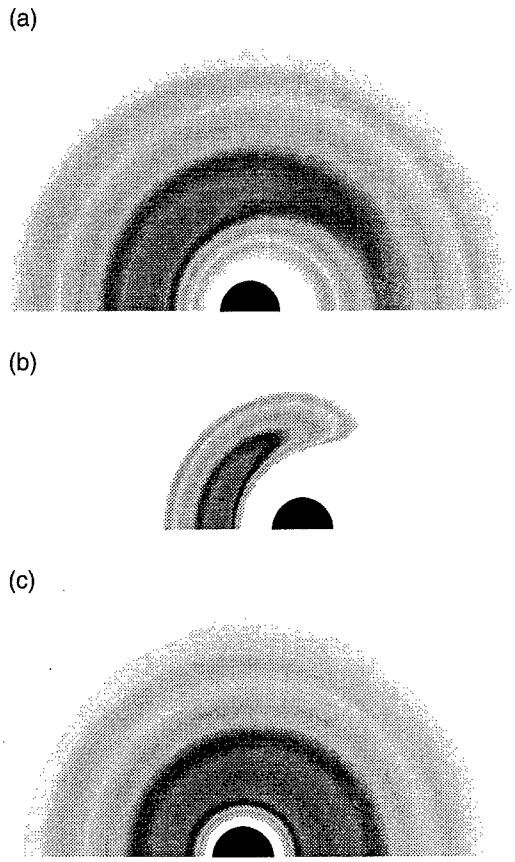

FIG. 1. (a) Isocontours of Y_{OH} for porous sphere burner at $t = 0.65$ ($0 \leq Y_{OH} \leq 2 \cdot 10^{-4}$). (b) Isocontours of temperature for porous sphere burner at $t = 0.75$ (only temperature above 1300 K is shown, 350 K [$= T_s$] $\leq T \leq$ 1380 K). (c) Isocontours of temperature for porous sphere burner at $t = 0.95$ (only temperature above 1300 K is shown, 350 K [$= T_s$] $\leq T \leq$ 1874 K).

formulations for the variable fluid properties, and convergency tests can be found in Refs. 24, 27, and 28. Calculations shown here required 1 to 4 weeks of computer time and 500 Mbytes of memory on an SGI workstation (with R8000 CPU).

Porous Sphere Burner

The ignition process of a laminar non-premixed CO/air flame generated by a porous sphere placed in a uniform "hot" ambient flow ($X_{O_2} = 0.21$, $X_{H_2O} = 0.01$, $X_{N_2} = 0.78$, $T = 1300$ K, $Re = 1$) is presented in Fig. 1. Shortly after the fuel is mixed with oxygen, local ignition occurs in the leading-edge region, which subsequently spreads and forms an envelope flame. Shown in Fig. 1a are mass fraction isocontours of radical OH(Y_{OH}) at time $t = 0.65$. The gas-phase kinetics are observed to quickly generate a radical pool in the region where the fuel and the oxidizer are mixed, although exothermic CO oxidation has not yet begun and the temperature field remains unchanged. Shortly after the induction period, the temperature begins to rise. Figure 1b shows temperature isocontours at time $t = 0.75$ (only values higher than the ambient temperature are plotted). The reaction zone is observed to spread from the leading-edge region of the sphere downstream to form an envelope flame. The temperature field at $t = 0.95$, depicted in Fig. 1c, shows a nearly spherically symmetric envelope flame.

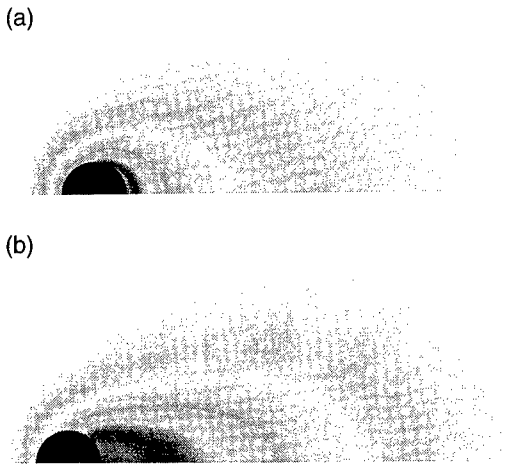

FIG. 2. (a) Isocontours of temperature for Spherocarb particle at steady state ($Re = 10$, 1400 K $\leq T \leq$ 1516 K). (b) Isocontours of Y_{CO_2} for Spherocarb particle at steady state and at $Re = 10$ ($0 \leq Y_{CO_2} \leq 2 \cdot 10^{-6}$).

Spherocarb Particle

The second simulation (Fig. 2) refers to ignition of a Spherocarb particle placed in a hot ambient stream ($X_{O_2} = 0.21$, $X_{H_2O} = 0.01$, $X_{N_2} = 0.78$, $T = 1400$ K, $Re = 10$). Shown in Fig. 2a is the steady-state temperature field. The oxygen concentration remains almost spatially uniform, which is indicative of heterogeneous kinetics–controlled gasification. The spatial distribution of CO_2, depicted in Fig. 2b, shows that the CO generated by the heterogeneous kinetics is convected downstream and further oxidized to CO_2 in the wake region. In contrast with results obtained in a quiescent environment [16,18], there is trivial gas-phase kinetics surrounding the particle. When the Reynolds number is reduced to 1, corresponding to an increase of the residence time by a factor of 10, the Spherocarb particle ignites and a chemically reactive zone forms in a boundary layer surrounding the particle. In Fig. 3a, we plot the distribution of the OH radical mass fraction during the ignition phase (at $t = 0.51$). The reaction zone is observed to spread from the trailing-edge region to

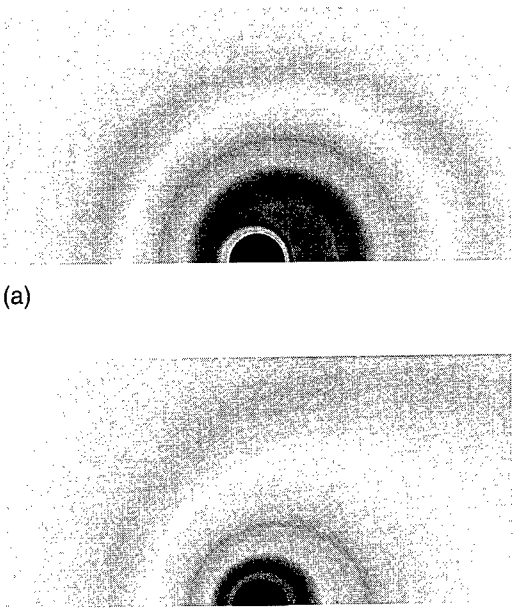

(a)

(b)

FIG. 3. (a) Isocontours of Y_{OH} for Spherocarb particle at $t = 0.51$, $Re = 1$ ($0 \leq Y_{OH} \leq 3 \cdot 10^{-7}$). (b) Isocontours of temperature for Spherocarb particle at $t = 7.6$, $Re = 1$ (1400 K $\leq T \leq$ 2403 K).

the leading-edge region and subsequently forms an envelope flame as indicated by the temperature field shown in Fig. 3b. Note that this chemically reactive zone is not a typical flame structure in that its formation is not controlled by transport and homogeneous kinetics only. In this case, the heterogeneous kinetics is coupled to the gas-phase homogeneous kinetics via transport of both enthalpy and reactive species. This solution is to be compared with that obtained in a quiescent ambient ($Re = 0$), at $t = 7.6$, which is calculated by a previously described one-dimensional model [16,18] modified to match all conditions used in the current study. The one-dimensional solution and two radial profiles of the two-dimensional solution (radial profiles along the axis of symmetry, upstream and downstream of the sphere, respectively) are plotted in Figs. 4a, 4b, and 4c. The overall gasification rates obtained are compared in Fig. 5 (with the specific density of Spherocarb taken to be 0.6). The ambient flow is seen to reduce the ignition time slightly; however, the steady-state gasification rate is not affected appreciably.

Discussion

Porous Sphere Burner

The results for the porous sphere indicate that, except during the ignition phase, a low Reynolds number ($Re = 1$) flow does not perturb the spherical symmetry appreciably. The CO/air non-premixed flame structure is quite similar to that of methanol with respect to the reaction zone thickness and the controlling heat-release mechanism. Further, the surface temperature and the flow rate of CO were chosen to approximate the surface temperature and flame standoff ratio of a methanol droplet. Thus, the slow residue droplet motion relative to the ambient in the microgravity experiments on methanol droplets is not likely to perturb the spherical symmetry. Any asymmetrical phenomena, if observed in these experiments, therefore comes from other sources such as interior droplet circulation generated by other effects [14].

Spherocarb Particle

In previous studies on the combustion of isolated carbon or, more specifically, a Spherocarb particle in a quiescent environment [16,18], it was found that in the absence of radiative heat transport, the burning behavior of an isolated carbon particle placed in a hot ambient of air is sensitive to the initial size of the particle. A 200-μm-diameter particle may undergo ignition, which is associated with the ignition of CO in the gas/phase near the particle surface, while a slightly smaller particle (140 μm) may undergo a slow and steady gasification process without any appreciable CO oxidation occurring near the particle surface. Therefore, it is expected that convection may also have strong effects on the burning behavior of a carbon particle in the same size range.

Previous spherical symmetric results [16,18] showed that in a quiescent environment, the Spherocarb particle would ignite and form a chemically reactive zone around the particle. Our results show that the particle's burning mode is sensitive to the Reynolds number. It changes from a slow gasification mode at $Re = 10$ to a fast gasification mode at $Re = 1$. The species and temperature profiles shown in Fig. 4 indicate "thick" reaction zones and significant leakage of radical species that are indicative of finite Damköhler number effects. To illustrate this, a comparison of the characteristic chemistry time and transport time was made by considering the competition for radical species among elemental reactions and diffusive loss in the gas-phase boundary surrounding the particle. The three rate-controlling elemental reactions are $H + O_2 \rightarrow OH + O$, $CO + OH \rightarrow H + CO_2$, and $O + H_2O \rightarrow OH + OH$ and their corresponding characteristic times are defined as $\tau_i \equiv 1/k_iC_i$, where k_i are the forward reaction rates and C_i are the concentrations of O_2, CO, and H_2O. Also, diffusion times $\tau_{d,i}$ are defined by the particle radius and their respective diffusivities. Using the species concentrations and temperature commensurate with the reactive boundary layer shown in Fig. 4a, these characteristic times are shown in Table 1.

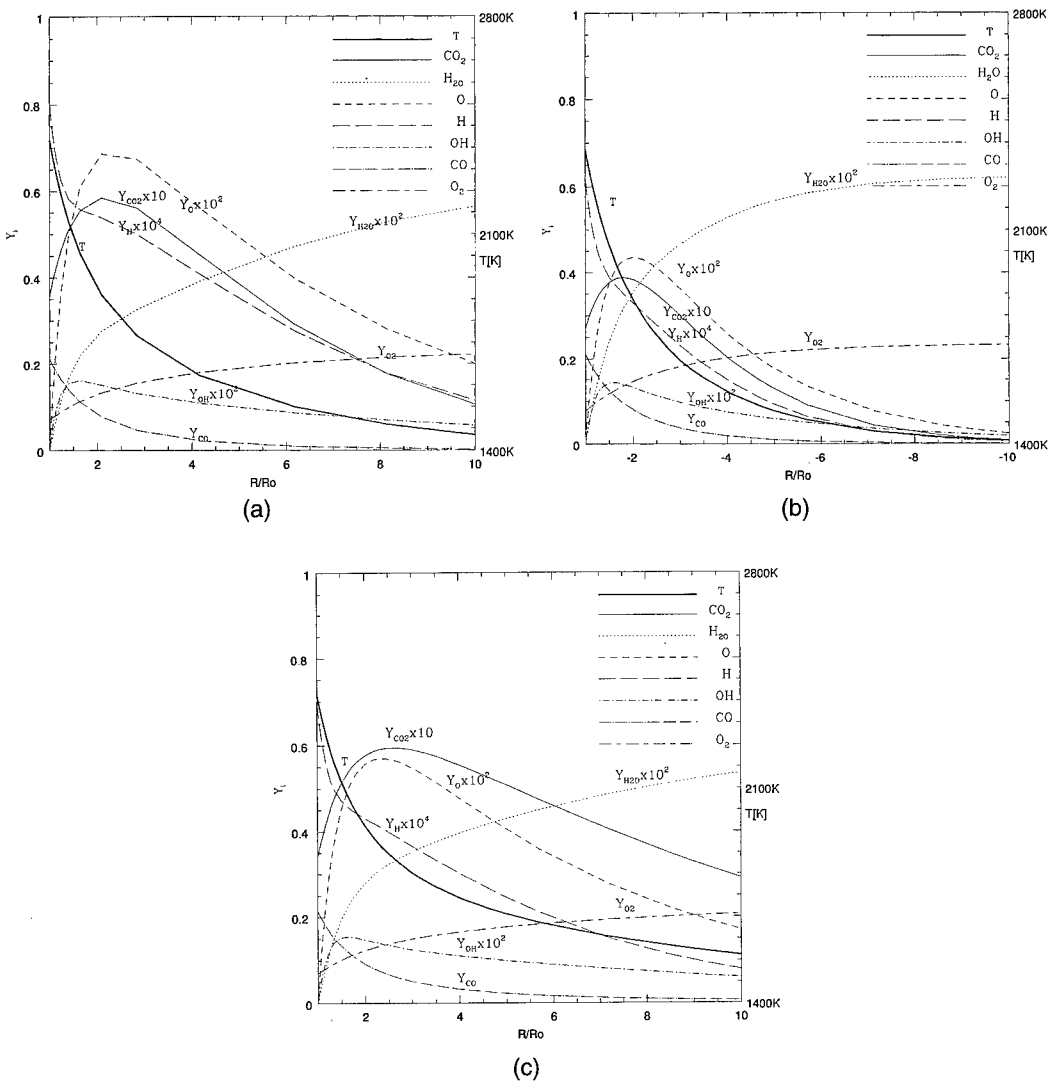

FIG. 4. (a) Radial profiles of temperature and mass fractions of selected species for Spherocarb particle at $t = 7.6$, $Re = 0$ (calculated by a one-dimensional model). (b) Radial profiles, along the axis of symmetry and starting from the front end of the particle, of temperature and mass fractions of selected species for Spherocarb particle at $t = 7.6$, $Re = 1$. (c) Radial profiles, along the axis of symmetry and starting from the rear end of the particle, of temperature and mass fractions of selected species for Spherocarb particle at $t = 7.6$, $Re = 1$.

The comparable diffusion and chemistry times (Table 1) are indicative of finite Damköhler effects, which explains the system's sensitivity to the details of transport and convection in an imposed flow field. The chemistry times shown in Table 1 are evaluated using temperatures and species concentrations found in a reactive zone; in the induction period, these chemistry times are considerably longer. Hence, when the Reynolds number is increased to 10, the transport time is reduced sufficiently to prevent ignition, and, consequently, the particle gasifies slowly with only gas-phase CO oxidation occurring in the wake region. In the fast gasification regime, such as the cases presented for $0 \leq Re \leq 1$, both the stable species O_2, CO_2, and H_2O and the radical species O and OH participate in the gasification processes. From the nontrivial concentrations of the stable species (CO_2 and O_2) at the particle surface and finite gradients of their respective concentrations, it can be inferred that neither the heterogeneous kinetics nor the molecular transport alone are controlling. On the other hand, with respect to the rad-

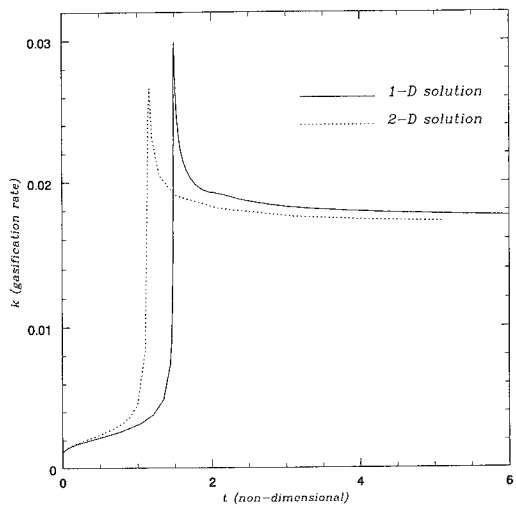

FIG. 5. Temporal variations of the gasification rates [$cm \cdot s^{-1}$] of Spherocarb particle for $Re = 0$ (one-dimensional solution) and $Re = 1$ (two-dimensional solution).

TABLE 1
Characteristic chemical reaction and diffusion times of selected elemental reactions and corresponding radical species

species	$\tau_{d,i}$	τ_i
H	$3.3 \cdot 10^{-6}$	$5.8 \cdot 10^{-7}$
OH	$1.4 \cdot 10^{-5}$	$5.0 \cdot 10^{-6}$
O	$1.3 \cdot 10^{-5}$	$4.5 \cdot 10^{-5}$

ical species, because of their high reaction rate at the particle surface, their surface reactions are diffusion controlled.

Conclusions

A new numerical model based on spectral-type methods, stiff ODE time integration, and a time splitting approach for low–Mach-number compressible flow has been developed enabling the simulation of axisymmetric chemically reactive systems using detailed transport and chemical kinetics. Simulations of a CO/air non-premixed flame generated by a porous-sphere burner show significant deviations from spherical symmetry in the low Reynolds number limit during the ignition phase in the steady state; however, spherical symmetry is minimally perturbed. Simulations of Spherocarb combustion in both a quiescent and convective environment show finite Damköhler effects that can only be captured when detailed transport and chemical kinetics are included. Consequently, the ignition of a Spherocarb particle is sensitive to the details of convection (for $0 \leq Re \leq 10$), and the particle may undergo ignition that leads to fast gasification in a mixed controlled regime or slow gasification in a surface kinetics–controlled regime, depending on the Reynolds number. This sensitivity to the details of convective transport may complicate experimental results obtained in ground-based experiments because of buoyancy-induced convection; a study of buoyancy effects will be the topic of a future study.

Acknowledgments

This work was supported in part by ARPA/ONR Contract No. N00014-92-J-1796 and NASA Lewis Research Center Contract No. NAG-1231.

REFERENCES

1. Xu, Y., Smooke, M., and Long, M., *Combust. Sci. Technol.* 90:289 (1993).
2. Ern, A., Douglas C., and Smooke, M., The Eastern States Section of the Combustion Institute, December 5–7, Clearwater Beach, FL, 1994.
3. Smooke, M., Mitchell, R., and Keyes, D., *Combust. Sci. Technol.* 67:85 (1989).
4. Patnaik G., Kailasanath, K., Oran, E., and Laskey, K., *Twenty-Second Symposium (International) on Combustion,* The Combustion Institute, Pittsburgh, 1988, p. 1517.
5. Behrendt, F., Goyal, G., Maas, U., and Warnatz, J., *Twenty-Fourth Symposium (International) on Combustion,* The Combustion Institute, Pittsburgh, 1992, p. 83.
6. Dwyer, H., *AIAA J.* 28:99 (1990).
7. Dwyer, H. and Sanders, B., *Twenty-Second Symposium (International) on Combustion,* The Combustion Institute, Pittsburgh, 1988, p. 1923.
8. Patnaik, G., Sirignano, W., Dwyer, H., and Sanders, B., The 10th International Collete on the Dynamics of Explosions and Reactive Systems, Berkeley, CA, 1985.
9. Megaridis, C. and Sirignano, W., *Combust. Sci. Technol.* 87:27 (1992).
10. Megaridis, C. and Sirignano, W., *Twenty-Third Symposium (International) on Combustion,* The Combustion Institute, Pittsburgh, 1990, p. 1413.
11. Megaridis, C., *Combust. Sci. Technol.* 92:291 (1993).
12. Megaridis, C., *Combust. Flame* 93:287 (1993).
13. Choi, M., Dryer, F. L., and Haggard, J. Jr., *Twenty-Third Symposium (International) on Combustion,* The Combustion Institute, Pittsburgh, 1990, p. 1611.
14. Marchese, A. and Dryer, F. L., accepted by *Combust. Flame* (1995).
15. Cho, S., Yetter, R., and Dryer, F., *J. Comput. Phys.* 102:160 (1992).
16. Lee, J., Yetter, R., and Dryer, F., *Combust. Flame* 101:387 (1995).

17. Williams, F. and Dryer, F., "Science Requirements Document for the Droplet Combustion Experiment," NASA Lewis Research Center Cleveland Ohio, 1995.
18. Lee, J., Yetter, R., and Dryer, F., accepted by *Combust. Flame* (1995).
19. Bar-Ziv, E., Jones, D. B., and Spjut, R. E., *Combust. Flame* 75:81–106 (1989).
20. Tognotti, L., Longwell, J. P., and Sarofim, A. F., *Twenty-Third Symposium (International) on Combustion,* The Combustion Institute, Pittsburgh, 1990, pp. 1207–1213.
21. Rehm, G. R. and Baum, H. R., *J. Res. Natl. Bur. Stand.* 83:3:297–308 (1978).
22. Chu, B.-T. and Kovasznay, L. S. G., *J. Fluid Mech.* 3:494–514 (1958).
23. Sivashinsky, G. J., *Acta Astronautica* 6:631–645 (1979).
24. Tomboulides, A. G., Lee, J., and Orszag, S. A., submitted to *J. Sci. Compt.* (1996).
25. Patera, A. T., *J. Comput. Phys.* 54:468 (1984).
26. Ronquist, E., Ph.D. Thesis, MIT, 1988.
27. Tomboulides, A. G., Ph.D. Thesis, Princeton University, 1993.
28. Lee, J. C. Y., "Simulations of Two-Dimensional Transient Chemically Reactive Flows," Ph.D. Thesis, Princeton University, 1996.
29. Kee, R., Warnatz, J., and Miller, J., Sandia National Laboratory Report SAND83-8290, 1983.
30. Coffee, T. P. and Heimerl, J. M., *Combust. Flame* 43:273 (1981).
31. Coffee, T. P. and Heimerl, J. M., *Combust. Flame* 34:31 (1983).
32. Yetter, R. A., Dryer, F. L., and Rabitz, H., *Combust. Sci. Technol.* 79:97 (1991).
33. Bradley, D., Dixon-Lewis, G., El-Dim, H., and Mushi, E., *Twentieth Symposium (International) on Combustion,* The Combustion Institute, Pittsburgh, 1984, p. 931.
34. Thiele, E. W., *Indust. Engineer. Chem.* 31:916 (1993).
35. D'Amore, M., Tognotti, L., and Sarofim, A., *Combust. Flame* 95:374 (1993).
36. Mitchell, R. R., Kee, R. J., Glarborg, P., and Coltrin, M., *Twenty-third Symposium (International) on Combustion,* The Combustion Institute, 1988, p. 69.
37. Walker, P. L. Jr., Rusinko, F. Jr., and Austin, L. G., *Advances in Catalysis and Related Subjects,* Vol. 11, Academic Press, New York, 1959.
38. Laurendeau, N. M., *Prog. Energy Combust. Sci.* 4:221 (1978).
39. Nigmatullin, R., Dissado, L., and Soutougin, N., *A Fractal Pore Model for Archies Law in Sedimentary Rocks,* IOP Publishing Ltd., Bristol, U.K., 1991.

Twenty-Sixth Symposium (International) on Combustion/The Combustion Institute, 1996/pp. 3067–3074

FLAME STRUCTURE AND COMBUSTION RATE OF BURNING GRAPHITE IN THE STAGNATION FLOW

ATSUSHI MAKINO, INAHO KATO, MASASHI SENBA, HAJIME FUJIZAKI AND NOBUYUKI ARAKI

Department of Mechanical Engineering
Faculty of Engineering
Shizuoka University
Hamamatsu 432, Japan

The combustion behavior of graphite rods in the stagnation flow of an oxidizer is studied experimentally to investigate the coupled nature caused by the interaction between the gas-phase and surface reactions. Toward this aim, not only the combustion rate but also the gas-phase temperature profile is measured as a function of the surface temperature of the burning graphite. The temperature profile over the burning graphite rod is measured with CARS thermometry. It is observed that with increasing surface temperature, the temperature profile in the gas phase shifts from that without CO flame to that with CO flame. At the ignition surface temperature, at which a CO flame is established in the forward stagnation region, it is observed that there exists a reaction zone whose temperature is nearly equal to the surface temperature. When the surface temperature is higher than the ignition surface temperature, a reaction zone whose temperature is higher than the surface temperature is observed. It is confirmed that the abrupt reduction in the combustion rate is related closely to the change of the flame structure in the gas phase caused by the establishment of the CO flame in the forward stagnation region, by which the dominant surface reaction changes from the C-O_2 reaction to the C-CO_2 reaction. Experimental results are also compared with predicted results with the gas-phase and surface kinetic parameters reported in the literature. A fair degree of agreement is demonstrated as far as the trend and approximate magnitude are concerned.

Introduction

Because of the practical importance of coal and char, a considerable amount of research has been conducted related to the combustion and/or gasification of solid fuel. The basic nature of the char combustion has been clarified and its information has been used to control the overall conversion rate of coal. Research on carbon combustion, however, is not limited to basic research on coal but can benefit aerospace applications with carbon–carbon composites (C/C composites); C/C composites have attractive mechanical properties and low density and are therefore planned for use as high-temperature, structural materials for atmospheric reentry, gas turbine blades, scram jet combustors, and so forth. A serious problem that must be clarified is their protection property for oxidation. Much of the experimental accomplishment related to the carbon combustion has been reviewed extensively by Essenhigh [1]. Nevertheless, because of the complexities involved, there remain many questions, suggesting the need for further studies. Some of them also command fundamental interest because of the simultaneous existence of the surface and gas-phase reactions that can interact with each other.

Intimate coupling between these reactions reported in theoretical works [2–7] is the momentary reduction in the combustion rate caused by the appearance of the gas-phase flame. This occurs because establishment of the flame changes the dominant surface reaction from the faster C-O_2 reaction to the slower C-CO_2 reaction. In spite of this theoretical accomplishment, there exist very few experimental results that can support theoretical works.

In the literature, emphasis has been put on the surface reactivities with gaseous oxidizers, such as O_2, CO_2, and H_2O (see Ref. 1), although surface reactivities on the same carbon are limited [8,9,10]. As for the gas-phase reactivity, it exists for a CO flame [11] that is sensitive to the water-vapor concentration. However, this combustion situation, which is called the *strong* CO oxidation, is far from that over the burning carbon, especially for that before the appearance of the CO-flame, because some of the elementary reactions are too slow to sustain the strong CO oxidation. Furthermore, experimental studies from the viewpoint that interaction exists between chemical reactions and flow have been rare and are restricted to those for obtaining combustion rate [8,9,12–14], although an experimental study observing the appearance of the CO flame over the burning graphite was made recently [15].

The present work can be considered an extension of the previous studies [6,7,15]. Emphasis in the present study is put on the measurement of the

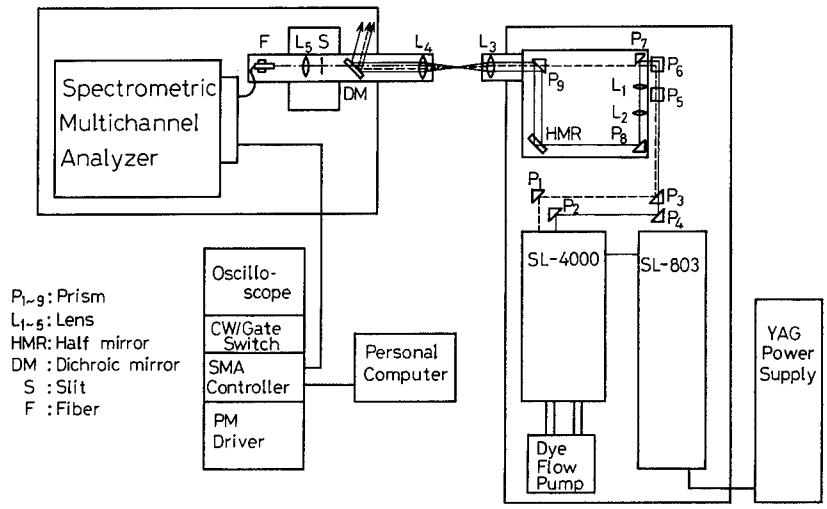

FIG. 1. Experimental configuration for the CARS instrument.

temperature profile over the burning graphite rod in the stagnation flow field. In this measurement, N_2-CARS thermometry is used to prevent undesired appearance and/or disappearance of the CO flame. Not only the influence caused by the appearance of the CO flame on the temperature profile but also that on the combustion rate is investigated. Measured results are further compared with predicted results.

Experimental

Experimental Configuration for CARS Instrument

Coherent anti-Stokes–Raman spectroscopy (CARS) offers a number of advantages over the conventional physical probing methods because it is remote and does not disturb the combustion fields. It is said that CARS is one of the best laser-based advanced combustion diagnostic techniques that can provide temporal and spatial measurements of the temperature and major species concentrations in the gas stream. Details about this laser spectroscopic technique are given in Refs. 16–19. Several recent entries [20,21] to this literature with laboratory flames and practical combustors also exist.

In the present study, measurement of temperature profiles is performed with the folded BOXCARS technique. The CARS instrument consists of a transmitter, a receiver, and a detector system (see Fig. 1). The primary pump beam with ω_1 is a 15-ns pulse of 532-nm radiation from a Q-switched Nd:YAG laser (Spectron Laser System, SL-803S). A broadband Stokes dye laser is pumped by a portion of the 532-nm green laser beam, which is directed to the dye cell to amplify the output of the oscillator (Spectron Laser System, SL-4000G) and forms the ω_2 laser. The remaining green beam is used as a pump beam. The pump and Stokes beams are manipulated to achieve the different phase matching geometry. With a lens of 250 mm focal length, the pump and Stokes beams are focused to a cylindrical interaction region (about 200 μm in diameter and about 3 mm in length), where CARS signal of ω_3 ($= 2\omega_1 - \omega_2$) is produced. Another similar lens is used to recollimate the CARS signal along with the laser beams to the receiver. The CARS signal, which is separated from the pump and Stokes beams with a dichroic mirror, is coupled to one end of the optical fiber (200 μm) mounted on a computer-controlled *X-Y-Z* translator. The other end of the fiber is coupled with a monochromator (Jobin-Yvon, U-1000), the spectral resolution of which is 1 cm^{-1}. A proximity-focused MCP (microchannel plate) image-intensified diode-array detector (IRY-512N[R]) is used to detect the CARS signal. Single-pulse spectra are acquired at the laser repetition frequency and subsequently stored in a personal computer for analysis at a later time.

Determination of Gas Temperature

In CARS thermometry, determination of temperature from CARS spectra, which is usually performed by comparing simulated results with experimental data [16–20], is quite complicated and cannot be used easily in experiments and/or practical situations. In addition, fitting procedures take time. Because of the need for taking a simpler but still accurate method in determining the temperature, a simpler method [22] has been proposed, with a representative bandwidth of the N_2-CARS spectrum. In

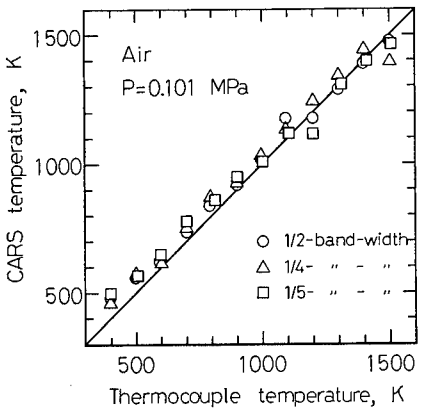

FIG. 2. The CARS temperature determined by the simple method as a function of the temperature measured by a thermocouple; the bandwidth chosen in this method is taken as a parameter.

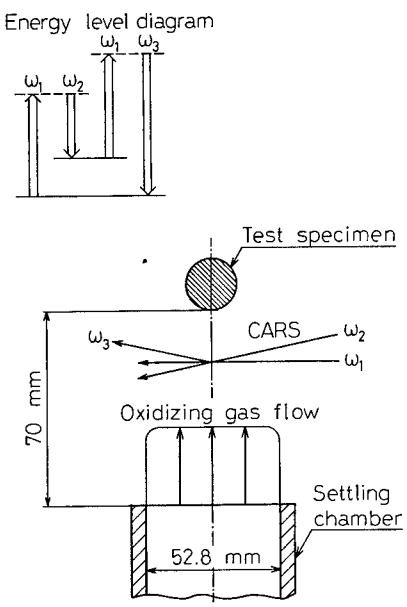

FIG. 3. Schematic drawing of the experimental setup.

this method, the bandwidth at one-fifth of the maximum height is recommended after examining dependence of the bandwidth on the temperature and pressure.

To examine this method, a preliminary experiment is made with a double-walled cylindrical high-pressure/high-temperature vessel designed to withstand up to 0.7 MPa. Thick quartz windows are installed at both ends. The gas inside is heated up to about 1500 K by an electric wire made of Kanthal (m.p. 1773 K). Measurement of gas temperature is made by a Pt/Pt-30%Rh thermocouple (0.1 mm in wire diameter) located at the center of the vessel. To avoid radiation from the heating wire, a radiation-shielding cylinder made of stainless steel is installed. The gas temperature measured by the thermocouple is maintained at a desired value within ± 5 K. It is also measured by N_2-CARS thermometry, focusing the pump and Stokes beams close to a junction of the thermocouple.

Figure 2 shows the gas temperature (air at atmospheric pressure) measured by CARS as a function of that measured by the thermocouple. The parameter is the bandwidth of the CARS spectrum at which the temperature is determined. We see that the CARS temperature is independent of the choice of bandwidth within the present experimental conditions and that the discrepancy between the CARS and thermocouple temperatures is relatively small.

Because of its simplicity in determining gas temperature and its allowable accuracy at high temperatures, this method is expected to be useful for the measurement of temperature profiles over the burning graphite rod. Since effects of pressure have not been examined in this preliminary experiment, the simple method with one-fifth bandwidth [22] is used here. In addition, to minimize experimental errors, a screening method [20] is also used with a criterion that the temperature difference between the CARS temperature deduced from one-fifth bandwidth and that from one-fourth bandwidth is within ± 50 K.

Experimental Setup and Test Specimen

Figure 3 shows the experimental setup, which is basically the same as that for previous works [6,7,15]. Air used as an oxidizer is supplied by a compressor and passes through a refrigerator-type dryer and a surge tank. The dew point from which the water-vapor concentration can be obtained is measured by a hygrometer (Panametric, Model 7000). The airflow at room temperature, after passing through a settling chamber (52.8 mm in diameter and 790 mm in length), issues into the atmosphere with a uniform velocity (up to 3 m/s), and impinges on a graphite rod to establish a two-dimensional stagnation flow. This flow field is well established and specified uniquely by the velocity gradient a ($= 4V_\infty/d$), where V_∞ is the free stream velocity and d is the diameter of the graphite rod.

The test specimen is an artificial graphite rod 20 mm in diameter, 120 mm in length, and 1.25×10^3 kg/m^3 in density. The rod is Joule heated by an alternating current (8–32 V; up to 2000 A). The surface temperature is measured by a two-color pyrometer (Chino, IR-AQ3CS). The temperature in the central part (about 30 mm in length) of the test specimen is nearly uniform.

In experiments, the test specimen is set to burn in an airflow at constant surface temperature during

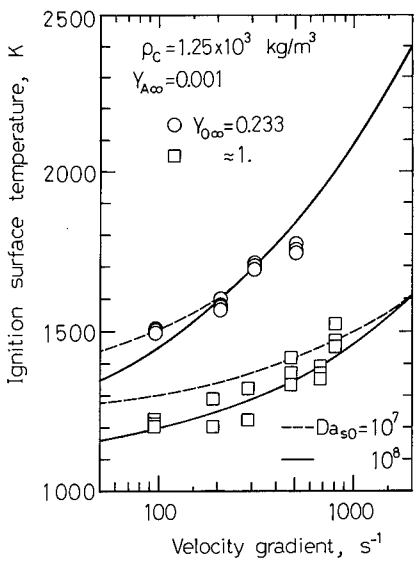

FIG. 4. The ignition surface temperature as a function of the velocity gradient, with oxygen mass fraction taken as a parameter; pressure is atmospheric and water-vapor mass fraction 0.001. Data points are experimental. Solid and dashed curves are calculated from theory [7]; the surface Damköhler number for the C-O_2 reaction is defined as $Da_{sO} = B_{sO}/\sqrt{a(\mu_\infty/\rho_\infty)}$, where a is the velocity gradient.

each experimental run. The temperature profile in the gas phase is measured by N_2-CARS thermometry. Since the surface temperature of the burning graphite rod is kept constant with external heating, quasi-steady combustion can be accomplished when we measure the temperature profile. Because of this quasi steadiness, the CARS spectrum obtained by 10 times accumulation of the 10 pulse-averaged CARS data is used to determine the gas-phase temperature. The experiment also involves recording the image of the test specimen in the forward stagnation region by a video camera and analyzing the signal displayed on a TV monitor to obtain the surface regression rate. The surface regression rate is used to determine not only the combustion rate but also the distance from the surface at which the gas temperature is measured. The combustion rate is further corrected with the density change of the test specimen in each experimental run.

Results

Ignition Surface Temperature and Combustion Rate

First, let us explain the results for the ignition surface temperature and the combustion rate, which are related to the coupled nature of the surface and gas-phase reactions. As we gradually increase the surface temperature of the graphite rod under a certain velocity gradient, combustion proceeds without CO flame up to a certain surface temperature. At that temperature, a CO flame can be established in the forward stagnation region. The surface temperature at which the CO flame first appears is called the ignition surface temperature [7]. Figure 4 shows the ignition surface temperature as a function of the velocity gradient, with oxygen mass fraction taken as a parameter. The same trend as that in Ref. 7 is observed. The ignition surface temperature increases with increasing velocity gradient and decreasing oxygen mass fraction because the CO flame can be maintained when the characteristic residence time balances with the characteristic chemical-reaction time. Solid and dashed curves are predicted ignition surface temperature obtained with the ignition criterion [7] and the global gas-phase kinetic parameters before the appearance of the CO flame [15] (see Table 1).

Figure 5a shows the combustion rate in airflow of 110 s^{-1} as a function of the surface temperature when the water-vapor mass fraction is 0.003. The same trend as that in Refs. 6 and 15 is observed. Up to the ignition surface temperature, the combustion rate increases with increasing surface temperature. The combustion in this temperature range is that with negligible CO oxidation, and hence the combustion rate in frozen mode can predict fairly well the experimental results. A further increase in the surface temperature causes a momentary reduction in the combustion rate because the appearance of the CO flame alters the dominant surface reaction from the C-O_2 to C-CO_2 reaction. Above the ignition surface temperature, the combustion is that with the strong CO oxidation. The solid curve is the predicted combustion rate with the surface kinetic parameters [15] and the global gas-phase kinetic parameters [11]; see Table 1. In numerical calculations, use has been made of the formulation [6] derived under conventional constant property assumption with unit Lewis number, constant average molecular weight, one-step overall irreversible gas-phase reaction, and first-order surface reactions. Appropriateness of the numerical calculations has already been examined in Ref. 15.

The same trend as that in Fig. 5a is observed for airflow of 200 s^{-1} (Fig. 5b). Because of the reduced boundary-layer thickness with respect to the oxidizer concentration, the combustion rate at a given surface temperature is enhanced.

Temperature Profile in the Gas Phase

Figure 6 shows the temperature profiles in the forward stagnation region. The velocity gradient of airflow is 110 s^{-1} and the water-vapor mass fraction is 0.002. The parameter is the surface temperature,

TABLE 1
List of kinetic parameters for the gas-phase and surface reactions

Reaction	i	Frequency factor B_i	Activation energy E_i	Ref.	Remarks	Reaction rate expression
(gas phase) $O + 1/2\ O_2 \rightarrow CO_2$ (global)	g	9.1×10^6	113	[15]	*weak* CO oxidation	$-d[CO]/dt = [CO][O_2]^{1/2}[H_2O]^{1/2} \times B_g \exp(-E_g/RT)$
		1.3×10^8	126	[11]	*strong* CO oxidation	
(surface) $2C + O_2 \rightarrow 2CO$	sO	4.1×10^6	179	[15]		$-d[O_2]/dt = [O_2] \times B_{sO} \exp(-E_{sO}/RT)$
(surface) $C + CO_2 \rightarrow 2CO$	sP	1.1×10^8	270	[15]		$-d[CO_2]/dt = [CO_2] \times B_{sP} \exp(-E_{sP}/RT)$

1. The subscripts g and s designate the gas-phase and the surface, respectively.
2. The subscripts O and P designate the surface C-O_2 and C-CO_2 reactions, respectively.
3. The frequency factor B_g in the gas-phase reaction is provided in (m^3/mol)/s.
4. The frequency factors B_{sO} and B_{sO} in the surface reactions are in m/s.
5. The activation energy E is in kJ/mol.
6. The brackets in the rate expressions indicate the molar concentration, mol/m^3.

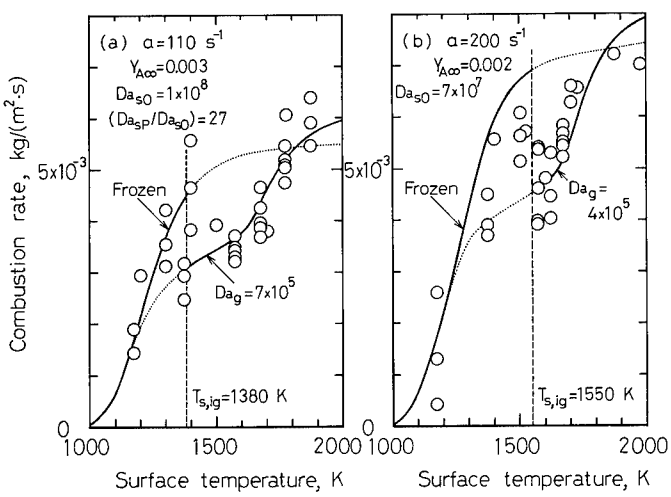

FIG. 5. The combustion rate as a function of the surface temperature; (a) for the velocity gradient of 110 s^{-1} in airflow with a water-vapor mass fraction of 0.003; (b) for the velocity gradient of 200 s^{-1} in airflow with a water-vapor mass fraction of 0.002. Data points are experimental. Curves are calculated from theory [6]; the gas-phase Damköhler number is defined as $Da_g = (B_g \rho_\infty / a) \sqrt{(\rho/\rho_\infty) Y_A / (2 W_P W_A)}$, where Y_A is the water-vapor mass fraction, W_P the molecular weight of CO_2, and W_A the molecular weight of water vapor. The ignition surface temperature $T_{s,ig}$ is calculated from theory [7].

which is controlled not to exceed ± 20 K from the given value. The ignition surface temperature observed was about 1450 K. When the surface temperature is 1400 K, the gas-phase temperature decreases monotonically, which suggests that negligible gas-phase reaction exists. When the surface temperature is 1500 K, at which a CO flame can be observed visually, a gas-phase reaction zone whose temperature is nearly equal to the surface temperature is present. Outside the reaction zone, the temperature decreases gradually to the bulk temperature. When the surface temperature is 1700 K, the gas-phase temperature first increases from the surface temperature to the maximum and then decreases to the bulk temperature. The existence of the maximum temperature suggests that a reaction zone locates away from the surface.

It may be informative to note the advantage of the CARS thermometry over the a conventional physical probing method with a thermocouple. When the thermocouple is used for the measurement of the temperature profile corresponding to the surface temperature of 1400 K (or 1500 K), it distorts the combustion field and hence makes the CO flame appear (or disappear). In this context, the present result suggests the importance of using thermometry

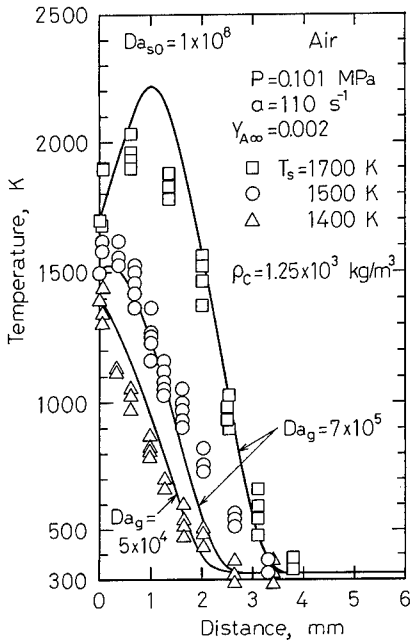

FIG. 6. Temperature profiles over the burning graphite rod in airflow (110 s^{-1} in the stagnation velocity gradient at atmospheric pressure with water-vapor mass fraction of 0.002), with the surface temperature taken as a parameter. Data points are experimental; solid curves are calculated from theory [6].

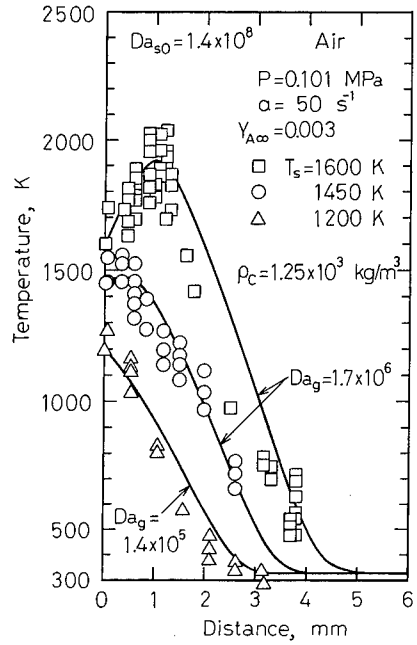

FIG. 7. Temperature profiles over the burning graphite rod in airflow (50 s^{-1} in the stagnation velocity gradient at atmospheric pressure with water-vapor mass fraction of 0.003), with the surface temperature taken as a parameter. Data points are experimental; solid curves are calculated from theory [6].

without disturbing the combustion fields, especially for the measurement at the flame ignition and/or extinction. In addition, the present results demonstrate the high spatial resolution of the CARS thermometry, so that the temperature profile within a thin boundary layer of a few millimeters can be measured.

Predicted results are also shown in Fig. 6. In numerical calculations, use has been made of the formulation [6] with conventional assumptions, mentioned in the previous section, and the kinetic parameters listed in Table 1. When a CO flame exists, the gas-phase kinetic parameters are those for the strong CO oxidation; when the CO oxidation is too weak to establish a CO flame, those for the *weak* CO oxidation are used. A fair degree of agreement between the experimental and predicted results is shown if we take into account the measurement error (± 50 K) in the present CARS thermometry.

Because it is common today to use detailed chemistry in the gas phase, our choice of the global gas-phase chemistry requires further comment. Before this investigation, we have found that the formulation with detailed chemistry [23] offers nearly the same numerical results as those with global gas-phase chemistry; thus, we have decided to use global gas-phase chemistry because of its simplicity.

Figure 7 shows the temperature profiles for the airflow of 50 s^{-1}. The ignition surface temperature observed is about 1300 K. The same trend as that in Fig. 6 is observed, although the boundary-layer thickness expands because of the reduced velocity gradient. Figure 8 shows the temperature profiles for the airflow of 200 s^{-1}. The ignition surface temperature is about 1550 K. Because of the increased velocity gradient, the boundary-layer thickness contracts compared to Figs. 6 and 7.

For Figs. 6–8, attention has been paid to controlling the surface temperature not to exceed ± 20 K from a given value. In addition, the surface temperature is intentionally set to be lower (or higher) than the ignition surface temperature by 20 K or more. If we remove these restrictions, the results are somewhat confusing. Figure 9 shows results when the surface temperature is set to 1570 K, allowing for deviation of ± 50 K. We see that gas-phase temperature away from the surface is scattered over a relatively wide range. It is not the case that this scatter is caused by CARS thermometry. It should be understood that unsteady-state combustion [24] has occurred. Since the allowable range of the surface temperature is wider than those in Figs. 6–8, and the ignition surface-temperature is within the

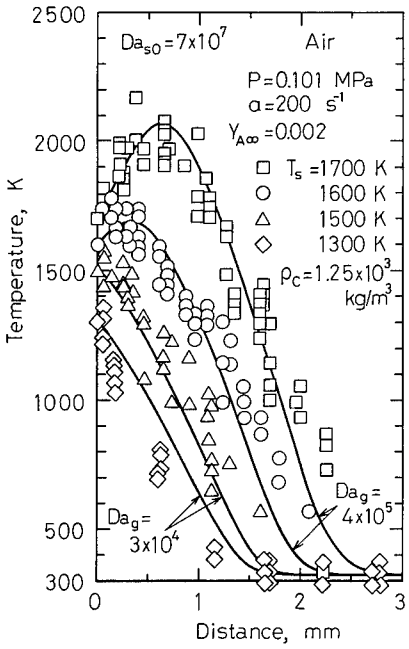

FIG. 8. Temperature profiles over the burning graphite rod in airflow (200 s^{-1} in the stagnation velocity gradient at atmospheric pressure with water-vapor mass fraction of 0.002), with the surface temperature taken as a parameter. Data points are experimental; solid curves are calculated from theory [6].

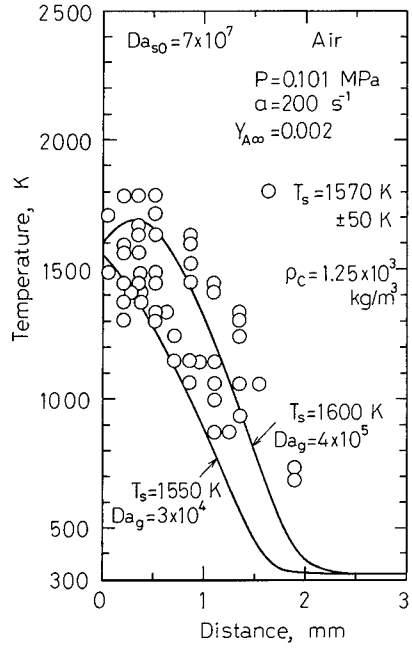

FIG. 9. Temperature profiles over the burning graphite rod in airflow (200 s^{-1} in the stagnation velocity gradient at atmospheric pressure with water-vapor mass fraction of 0.002), with the surface temperature taken as a parameter. Data points are experimental; solid curves are calculated from theory [6].

allowable temperature range for the surface temperature, we can anticipate that during this experimental run combustion proceeds without CO flame at one time while it proceeds with the CO flame at the other time. Experimental data in Fig. 9 are considered to represent the preceding combustion situations, and hence the scatter of data becomes wider than that in Fig. 8. If we make predictions of the gas-phase temperature, for surface temperatures of 1550 K and 1600 K, we see that the upper experimental data correspond to the gas-phase temperature profile for the surface temperature of 1600 K. The lower experimental data correspond to those for the surface temperature of 1550 K.

Concluding Remarks

Measurement of temperature profiles over the burning graphite rod in the stagnation field of airflow has been conducted to elucidate effects of simultaneous existence of the gas-phase and surface reactions in carbon combustion. So as not to distort the combustion field, N_2-CARS thermometry has been used for the measurement of gas-phase temperature. Besides this measurement, ignition surface temperature and combustion rate are measured.

The result is that the gas-phase flame structure changes at the ignition surface temperature at which the CO flame can be established in the gas phase. When the surface temperature is lower than the ignition surface temperature, negligible gas-phase reaction is expected because of the monotonic decrease in the gas-phase temperature. When the surface temperature is higher than the ignition surface-temperature, the temperature profile has the maximum that locates away from the surface because of the existence of the gas-phase reaction. It is confirmed that the abrupt change in the combustion rate at the ignition surface temperature is closely related to the change in the flame structure in the gas phase.

It is also confirmed that not only the ignition surface temperature and the combustion rate but also the temperature profiles can be predicted fairly well when the kinetic parameters for the surface and gas-phase reactions are known. Since the ignition surface temperature, combustion rate, and gas-phase temperature profile are closely related to the relative magnitude of the characteristic residence time and the characteristic chemical-reaction time, the present accomplishment further suggests the importance of investigating the mutual coupling of the surface

and gas-phase reactions from the viewpoint that there exists interaction between reactions and flow.

Acknowledgments

The CARS system has been built with the financial support in 1987 for preparing special equipment in Shizuoka University, Japan.

REFERENCES

1. Essenhigh, R. H., in *Chemistry of Coal Utilization* (Elliott, M. A., Ed.), Wiley, New York, 1981, pp. 1153–1312.
2. Adomeit, G., Hocks, W., and Henriksen, K., *Combust. Flame* 59:273–288 (1985).
3. Makino, A. and Law, C. K., *Twenty-First Symposium (International) on Combustion,* The Combustion Institute, Pittsburgh, 1986, pp. 183–191.
4. Matsui, K. and Tsuji, H., *Combust. Flame* 70:79–99 (1987).
5. Henriksen, K., *Twenty-Second Symposium (International) on Combustion,* The Combustion Institute, Pittsburgh, 1988, pp. 47–57.
6. Makino, A., *Combust. Flame* 81:166–187 (1990).
7. Makino, A. and Law, C. K., *Combust. Sci. Technol.* 73:589–615 (1990).
8. Khitrin, L. N. and Golovina, E. S., *High Temperature Technology,* Butterworths, London, 1964, pp. 485–496.
9. Visser, W. and Adomeit, G., *Twentieth Symposium (International) on Combustion,* The Combustion Institute, Pittsburgh, 1984, pp. 1845–1851.
10. Harris, D. J. and Smith I. W., *Twenty-Third Symposium (International) on Combustion,* The Combustion Institute, Pittsburgh, 1990, pp. 1185–1190.
11. Howard, J. B., Williams, G. C., and Fine, D. H., *Fourteenth Symposium (International) on Combustion,* The Combustion Institute, Pittsburgh, 1973, pp. 975–986.
12. Matsui, K., Kôyama, A., and Uehara, K., *Combust. Flame* 25:57–66 (1975).
13. Matsui, K., Tsuji, H., and Makino, A., *Combust. Flame* 50:107–118 (1983).
14. Matsui, K., Tsuji, H., and Makino, A., *Combust. Flame* 63:415–427 (1986).
15. Makino, A., Araki, N., and Mihara, Y., *Combust. Flame* 96:261–274 (1994).
16. Eckbreth, A. C., *Laser Diagnostics for Combustion Temperature and Species,* Abacus, Tunbridge Wells, 1988, Chapter 6.
17. Eckbreth, A. C., in *Instrumentation for Combustion and Flow in Engines* (Gurão, D. F. G., Whitelaw, J. H., and Witze, P. O., Eds.), NATO ASI Series, Series E, Vol. 154, Kluwer, Dordrecht, 1989, pp. 69–106.
18. Leipertz, A., in *Instrumentation for Combustion and Flow in Engines* (Gurão, D. F. G., Whitelaw, J. H., and Witze, P. O., Eds.), NATO ASI Series, Series E, Vol. 154, Kluwer, Dordrecht, 1989, pp. 107–122.
19. Eckbreth, A. C., in *Combustion Flow Diagnostics* (Gurão, D. F. G., Heitor, M. V., Whitelaw, J. H., and Witze, P. O., Eds.), NATO ASI Series, Series E, Vol. 207, Kluwer, Dordrecht, 1992, pp. 399–438.
20. Meier, W., Plath, I., and Stricker, W., *Appl. Phys. B* 53:339–346 (1991).
21. Singh, J. P. and Yueh, F. Y., *Combust. Flame* 89:77–94 (1992).
22. Kajiyama, K., Sajiki, K., Kataoka, H., Maeda, S., and Hirose, C., SAE Paper No. 82-1036, 1982.
23. Chelliah, H. K., Makino, A., Kato, I., Araki, N., and Law, C. K., *Combust. Flame* 104:468–480 (1996).
24. Kurylko, L. and Essenhigh, R. H., *Fourteenth Symposium (International) on Combustion,* The Combustion Institute, Pittsburgh, 1973, pp. 1375–1386.

Twenty-Sixth Symposium (International) on Combustion/The Combustion Institute, 1996/pp. 3075–3083

SINGLE-PARTICLE COMBUSTION OF TWO BIOMASS CHARS

MARY J. WORNAT
Princeton University, Department of Mechanical & Aerospace Engineering
Princeton, NJ, USA

ROBERT H. HURT
Brown University, Division of Engineering
Providence, RI, USA

KEVIN A. DAVIS
Reaction Engineering International
Salt Lake City, UT, USA

NANCY Y. C. YANG
Sandia National Laboratories, Center for Materials and Applied Mechanics
Livermore, CA, USA

In order to assess the combustion reactivities of chars produced from the pyrolysis of woody and herbaceous biomass, we have subjected particles of Southern pine and switchgrass chars to two sets of combustion experiments. In the first, a dilute stream of biomass char particles (nominal size, 75–106 μm) is burned in a laminar flow reactor at 12 mole % O_2 and a mean gas temperature of ~1600 K. In situ optical measurements reveal that at a given residence time in the early stages of char conversion, biomass char particles burn over a much wider temperature range (~450 K) than coal particles (~150 K) and that the biomass char particle temperatures span the entire range of the theoretical limits (from the slowest burning inert particles to the fastest burning diffusion-controlled particles). As biomass char conversion proceeds, however, mean particle temperatures decrease, and particle temperature distributions narrow—consequences of the preferential removal of more reactive carbon as well as a number of physical and chemical transformations of the inorganic constituents of the chars (vaporization, surface migration and coalescence, and incorporation into silicate structures). Kinetic parameters for median particles taken at the early stages of char conversion indicate that biomass chars are somewhat less reactive than low-rank lignites and subbituminous coals, somewhat more reactive than high-rank low-volatile bituminous coals, and comparable in reactivity to high-volatile bituminous coals. In the second set of combustion experiments, individual biomass char particles are suspended on an inert mesh and suddenly subjected to a hot 6 mole % O_2 environment. Video images of reflected light and near-infrared emission for a number of pine and switchgrass char particles demonstrate the heterogeneity of the biomass chars in terms of both the sequence of morphological changes and the temperature–time histories of the particles as they undergo combustion.

Introduction

The renewable nature of biomass places it among the more attractive alternatives to conventional fossil fuels. In order to evaluate the potential of biomass-derived fuels, however, it is important to have a quantitative measure of the reactivity of these fuels under conditions relevant to commercial-scale combustors. Biomass—which, in this context, includes wood, agricultural residues, and fast-growing crops—either can be burned directly as a combustor fuel [1–3] or it can first be thermally converted to solid and liquid fuels [4–9].

Our work focusses on chars produced from the pyrolysis of two biomass feedstocks—a soft wood, Southern pine, and an herbaceous material, switchgrass. The results of our biomass char studies appear in two papers. The first [5] describes the time-resolved physical and chemical transformations of the biomass chars during combustion. In that paper, the results from a variety of materials characterization techniques demonstrate that biomass char conversion is accompanied by a number of structural and compositional changes [5]: The early stages of conversion are characterized by devolatilization, which

leads to the removal of amorphous material and the release of oxygen- and hydrogen-rich gases. After devolatilization, combustion is accompanied by vaporization of some metals (particularly Na and K), surface migration and coalescence of inorganic material, and the incorporation of metals (particularly Ca) into silicate structures. Some short-range crystalline order appears in the carbon-rich portions of the chars as combustion proceeds, but the high levels of oxygen originally present in these chars foster cross-linking, which limits the extent of order ultimately attained.

Since each of the above enumerated structural and compositional transformations can affect char combustion reactivity, and since reactivity is a key factor in the evaluation of fuel behavior and combustor design, the present paper, the second in our sequence, focusses on the combustion reactivity of the biomass chars. No other study to date presents kinetic data on overall reactivity for biomass chars at the high-temperature conditions pertinent to commercial-scale pulverized fuel combustion. In this study, we subject pine and switchgrass chars to two kinds of experiments: (1) combustion of a dilute stream of char particles injected into a laminar-flow reactor and (2) combustion of stationary particles whose complete combustion histories are tracked with time. The combustion environments in both reactor setups simulate those of pulverized fuel furnaces. In the following, we report the results of *in situ* measurements taken in these biomass char experiments, discuss the factors affecting biomass char reactivity, and compare biomass char combustion behavior with that of high- and low-rank coals.

Experimental Equipment and Techniques

The biomass chars of this study are produced from pine and switchgrass particles pyrolyzed at 625°C in a vortex reactor [7] at the National Renewable Energy Laboratory in Golden, Colorado. The resulting biomass char particles are irregularly shaped [5] and produce high amounts of volatile matter, 20–25%, in the ASTM test. The ultimate analyses (on a dry basis) of the pine and switchgrass chars are 69.7% C, 3.13% H, 0.52% N, 0.05% S, 19.1% O, and 9.2% ash; and 58.8% C, 3.22% H, 0.57% N, 0.19% S, 17.0% O, and 20.9% ash, respectively. Although the biomass chars and low-rank coals [10] are not too dissimilar in organic elemental composition, the switchgrass char is singularly high in ash-forming constituents. Compared to coals, the pine and switchgrass chars contain very high levels of Si (1.93 and 5.41 mass %, respectively, on a dry basis) and K (1.03% and 2.02%, respectively).

The first set of biomass char combustion experiments is conducted in the previously described Sandia quartz-walled laminar-flow reactor [10,11]. The stoichiometry of the reactor's $H_2/CH_4/O_2/N_2$ flame is tailored to produce postflame gases simulating those in the upper furnace region of pulverized-fuel-fired boilers. A dilute stream of biomass char particles (nominal size, 75–106 μm) is injected upward through the center of the reactor, which operates at 6 or 12 mole % O_2 and a mean gas temperature of approximately 1600 K. In situ optical techniques [12,13] are employed to determine the temperatures, diameters, and velocities of individual reacting char particles at various residence times. Particle temperatures are calculated from Planck's law using optical signal intensities at 500 and 800 nm. Particle sizes are determined in two ways. The "coded aperture technique" [12] gives the particle's dimension along its axis of flow as it passes the optical window. The "area-averaging technique" gives the diameter of an equivalent spherical particle with the same total emissive intensity (with an assumed particle emissivity of 0.8 [14,15]) as the irregularly shaped particle. The two measurements are virtually coincident for equiaxed char particles.

The second set of biomass char combustion experiments is conducted in the Sandia captive particle imaging (CPI) apparatus, described in detail by Hurt and Davis [16]. Char particles of 100–200 μm are supported by an inert alumina mesh immersed in a 6 mole % O_2 hot gas stream (local gas temperature, 1250 K). An optical system consisting of a long-focal-length microscope with an internal beam splitter and two CCD cameras permits the simultaneous video recording of reflected-light and near-infrared-emission images of burning char particles. The near-infrared images are then digitized and quantitatively analyzed to determine area-averaged particle radiance temperatures.

Results and Discussion

Laminar-Flow Experiments

Plotted in Fig. 1 are the temperatures and diameters measured at a residence time of 72 ms for single particles of Southern pine char, Beulah lignite, and Pittsburgh #8 bituminous coal—all burning in a 12 mole % O_2 environment in the laminar-flow reactor. The measured particle temperatures reflect a balance between heat generated by the exothermic combustion reaction and losses from the particle by conduction and by radiation to the surroundings. The rapid burning rates of most particles cause particle temperatures to be considerably higher than the prevailing gas temperature. Readily apparent from Fig. 1 is the variation, with fuel type, in the range of burning particle temperatures. Similar to another high-volatile bituminous coal burning under the same conditions [13], the majority of the Pittsburgh #8 high-volatile bituminous coal particles

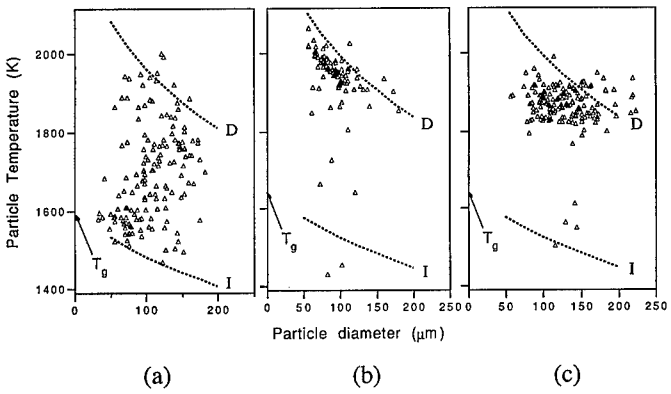

FIG. 1. Optical measurements of temperatures and sizes of single particles burning at 72 ms in 12 mole % O_2 in the laminar-flow reactor: (a) Southern pine char, (b) Beulah lignite, and (c) Pittsburgh # 8 bituminous coal. Particle diameters determined by the area-averaging technique. T_g denotes mean gas temperature. D and I correspond to diffusion and inert limits for spherical particles of equivalent diameter. Coal data from Hurt [13].

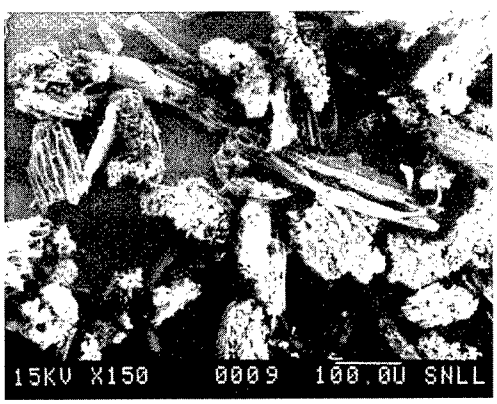

FIG. 2. Scanning electron micrograph of uncombusted Southern pine char particles.

(Fig. 1c) burn within the 150 K wide interval of 1800–1950 K—with only 2–3% of the particles burning at significantly lower temperatures. The majority of the Beulah lignite particles (Fig. 1b) also burn in a temperature interval approximately 150 K wide, from 1900 to 2050 K—but with a significantly higher percentage (~15–20%) burning at markedly lower temperatures. In contrast to the coal particles, the pine char (Fig. 1a) particle temperatures are fairly evenly distributed over a much wider (450 K) interval from 1500 to 1950 K. This huge spread in particle temperatures indicates variation from particle to particle in char properties, particle shape, and combustion reactivity. Although coals exhibit heterogeneity [17], the broader particle temperature range of the pine char particles suggests that they are even more heterogeneous.

The physical heterogeneity of the pine char particles is corroborated by the scanning electron micrograph shown in Fig. 2, which depicts uncombusted pine char particles of varying physical structure, texture, aspect ratio, and void space. (These morphological differences may result from differences in the wood components from which these particles were derived.) Similar particle-to-particle variations exist for the switchgrass char, as depicted by scanning electron microscopy [5] and by the broad range of burning temperatures of switchgrass char particles. In addition, our energy-dispersive X-ray analyses of individual biomass char particles indicate substantial particle-to-particle variation in the distribution of inorganic elements on the surfaces of the pine and switchgrass chars—suggesting compositional as well as morphological differences between particles. Variations in levels of catalytic metals such as K and Ca could account for at least some of the differences in burning temperatures from one particle to another. Espenäs [18] reports that biomass chars from another herbaceous material, straw, exhibit heterogeneity and a broad range of gasification reactivities as well.

It can be shown that the experimentally observed burning temperatures of the pine char particles do in fact span the range of the theoretical limits. At the limit of maximum particle temperature are those particles whose high reactivities cause burning rate to be controlled by the rate of diffusion of oxygen to the particle's external surface. The calculated curves in Fig. 1 marked D correspond to such diffusion-limited burning for spherical particles of equivalent diameter. Particles that burn at the diffusion limit are those whose high burning temperatures result from extremely high combustion reactivities. As the D curve calculations are based on CO as the combustion product and assumed physical properties, particle temperatures higher than the calculated D curve denote some CO_2 production or physical properties that differ from the assumed values. At the other extreme in Fig. 1 are the minimum particle temperatures, corresponding to unreactive particles. The curves marked I, the inert limits, represent the calculated temperatures of completely unreactive particles. (These particles can be lower in temperature than the surrounding gas since they lose heat by radiation to the quartz walls of the reactor.) As Fig. 1a depicts, the pine char particles span the

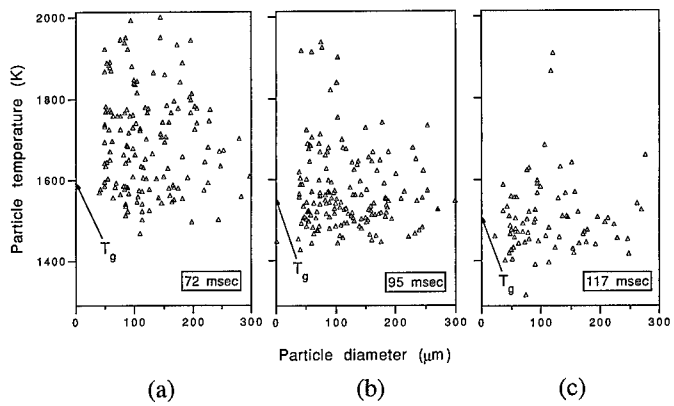

FIG. 3. Optical measurements of temperatures and sizes of single particles of Southern pine char burning in 12 mole % O_2 in the laminar flow reactor. Initial particle size, 75–106 μm. Particle residence times: (a) 72 ms, (b) 95 ms and (c) 117 ms. Particle diameters determined by the coded aperture technique. T_g denotes mean gas temperature.

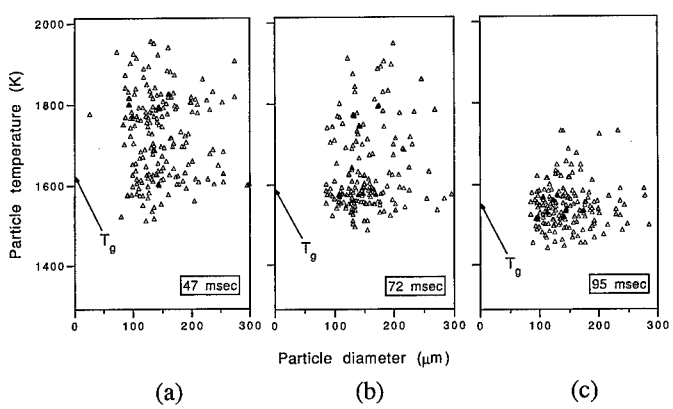

FIG. 4. Optical measurements of temperatures and sizes of single particles of switchgrass char burning in 12 mole % O_2 in the laminar flow reactor. Initial particle size, 75–106 μm. Particle residence times: (a) 47 ms, (b) 72 ms, and (c) 95 ms. Particle diameters determined by the coded aperture technique. T_g denotes mean gas temperature.

entire range of burning temperatures from inert to diffusion limited.

The heterogeneous nature of the pine char particles, compared to coal particles, is also evident in the measurements of particle diameter. Unlike particle temperature measurements (which do not depend on particle geometry since they are made by two-color pyrometry), measurements of particle size do depend on particle shape. Because the diameters plotted in Fig. 1 are area-averaged, the range of pine char particle diameters in that figure (25–175 μm) do not appear to be that broad compared to coal particles. However, if the coded-aperture-measured particle diameters are used, the appearance is very different. Plotted in Fig. 3a are the same particle temperature data as in Fig. 1a, but Fig. 3a presents particle diameters measured by the coded aperture technique. As Fig. 3a indicates, the latter diameters for pine char cover a very broad range, from 25 to 300 μm. Since particle size measured by the coded aperture technique corresponds to the particle's dimension along its axis of flow as it passes the optical window, the high aspect ratios of many of the pine char particles (evident in Fig. 2) cause the coded-aperture-measured sizes to be highly dependent on particle orientation at the time of measurement. Such orientation is not a factor in the measured diameters for coal particles, whose aspect ratios are much closer to unity. For example, coded-aperture-measured diameters for Pocahontas #3 low-volatile bituminous coal particles (burning under similar conditions) range from 110 to 190 μm [17]. Some bituminous coal particles, on the other hand, are subject to swelling during combustion, unlike lignite and biomass char particles.

Figures 3 and 4 show how the particle temperature/diameter relationships vary with residence time, from 72 to 117 and from 47 to 95 ms, for the pine and switchgrass chars, respectively. As residence time increases and conversion proceeds, two trends are apparent for the pine and switchgrass chars: the mean particle temperature decreases and the particle temperature distribution narrows. Single-particle coal data from the same reactor indicate that as coal conversion proceeds, mean particle temperatures decrease, but particle temperature distributions do not become more narrow [13,19]. We attribute the lowering of the mean particle temperatures and the narrowing of the particle temperature distribution as biomass char combustion proceeds to two causes:

the preferential depletion of more reactive carbon and the physicochemical transformations of the chars during combustion. An understanding of the effects of these two causes on overall char reactivity (and thus particle temperature) is facilitated by considering Thiele's classical theory [20] of gas–solid reactions, in the form presented by Hurt and co-workers [16,21] for coal chars. According to this theory, the overall burning rate q in zone II [22–24] scales with char properties as $q \sim (\rho_c S k_i D_{\text{eff}})^{1/2}$. Here ρ_c is the mass of carbon per unit particle volume, S is the internal surface per gram of carbon, k_i is the intrinsic reactivity of that surface, and D_{eff} is the effective diffusion coefficient in the porous particle. Values of each of these parameters can vary from particle to particle and can change as combustion proceeds. At the early stages of char conversion, a wide spread in particle temperatures indicates a char particle population whose initial reactivities (determined by the composite product $\rho_c S k_i D_{\text{eff}}$) vary greatly from particle to particle. The most reactive particles burn the fastest and at the highest temperatures; the less reactive, slower and at more moderate temperatures. As combustion proceeds, the rapid depletion of carbon from the most reactive particles leaves ash-rich particles (of lower ρ_c) whose temperatures approach the inert limit. These particles, along with those initially less reactive and still burning at moderate temperatures, dominate the char particle population at the later residence times. As a result, the mean particle temperature is lower and narrower since the highly reactive carbon responsible for the high temperatures (at lower residence times) is gone.

Parallel to this preferential loss of more reactive carbon are several physical and chemical transformations that exert a deactivating influence on these chars. As detailed in another publication [5], pine and switchgrass char samples have been extracted from the laminar-flow reactor at different residence times and subjected to a variety of analytical techniques. Elemental and X-ray diffraction analyses show that biomass char conversion is accompanied by the preferential loss of "reactivity-enhancing" oxygen and hydrogen [25–27], amorphous carbon (which is more reactive than ordered carbon [28–31]), and metals such as Na and K (which are known to catalyze char gasification [32–37]). Such losses would be accompanied by a decrease in k_i and thus in q. Scanning electron microscopy coupled with energy-dispersive X-ray analysis reveals that catalytic elements such as K and Ca, initially well dispersed within the biomass chars (and therefore more potentially effective as catalysts [36,38]), convert to less catalytically effective forms [35] by surface migration and coalescence as well as by incorporation into silicate structures. These transformations would lead to decreases in the values of k_i and perhaps D_{eff}. In addition, high-resolution transmission electron microscopy of these chars reveals that, as combustion proceeds, some short-range order appears in the carbon-rich portions of the biomass chars (as has been observed to a much greater extent in bituminous coal chars [39]), and this bit of ordering may have a slight additional deactivating effect in lowering k_i, S, and perhaps D_{eff}. Although the ordering of carbon structure has been implicated in the deactivation of bituminous coal chars with combustion and heat treatment [39,40], the transformations of the inorganic components (mentioned above) undoubtedly have a larger impact on the reactivity of our biomass chars, since alkali and alkaline-earth metal content and form have often been linked with gasification reactivity of chars from biomass [41] and low-rank coals [32–37].

Even though Figs. 3 and 4 indicate that biomass char reactivities decrease with increasing carbon conversion (and similar observations have been made for coals [16,39]), it is useful to calculate an overall burning rate for each of these chars, corresponding to a particular set of conditions, for purposes of comparison with coals. Table 1 presents average overall burning rates for the biomass chars and a suite of 10 commercially important U.S. coals of various ranks [14]—all calculated from median particle data obtained in the laminar-flow reactor and corresponding to the early stages of carbon burnout for 100 μm particles burning in a 6-mole % O_2 environment at 1500 K. The overall reactivities, calculated from global kinetic parameters [14], are expressed in terms of the rate of depletion of mass of mineral- or ash-free char per external surface area of the particle. The value of 3.66×10^{-3} gm C/cm^2 s calculated for the pine char represents an average of the two limiting cases: the first, 4.34×10^{-3} gm C/cm^2 s, corresponding to CO as the only carbon combustion product; the second, 2.98×10^{-3} gm C/cm^2 s, corresponding to the production of both CO and CO_2. In the latter case, the relative proportion of CO to CO_2 is determined by an empirical correlation derived for a wide range of coals combusted in the same reactor [14]:

$$CO/CO_2 = 3 \times 10^8 \exp(-60/RT_p)$$

In the above expression, R is the universal gas constant in kcal/mol K and T_p is the particle temperature in Kelvin. Similarly, a slightly higher overall burning rate of 4.05×10^{-3} gm C/cm^2 s, representing the average of 3.20 and 4.90×10^{-3} gm C/cm^2 s, has been calculated for the switchgrass char at the early stages of carbon burn-out. The values in Table 1 indicate that the biomass chars are somewhat less reactive than the low-rank lignite and sub-bituminous coals, somewhat more reactive than the high-rank low-volatile bituminous coals, and comparable in reactivity to the high-volatile bituminous coals. Consistent with these relative combustion reactivities are the following results from gasification studies: wood char is less reactive than lignite char but more

TABLE 1
Comparison of overall burning rates for biomass chars and various coals[a]

Fuel Name	Fuel Type	Rate[b] (gm C/cm^2 s) $\times$ 10^3
Pocahontas	low-volatile bituminous coal	1.15
Lower Kittanning	low-volatile bituminous coal	2.10
Pittsburgh #8	high-volatile bituminous coal	2.35
Illinois #6	high-volatile bituminous coal	3.30
Blue #1	high-volatile bituminous coal	4.51
Hiawatha	high-volatile bituminous coal	5.88
Dietz	sub-bituminous coal	6.06
Smith–Roland	sub-bituminous coal	6.52
Lower Wilcox	lignite	5.58
Beulah	lignite	6.52
Southern pine char	woody biomass char	3.66
Switchgrass char	herbaceous biomass char	4.05

[a]Coal data from Hurt and Mitchell [14].
[b]For 100-μm particles undergoing oxidation in 6 mole % O_2 at a gas temperature of 1500 K.

reactive than coal char in steam gasification at 1000°C [42]; coconut char is less reactive than low-rank coal chars but similar in reactivity to bituminous coal chars in CO_2 gasification at 900°C [43–45]; cottonwood and fir wood chars show comparable reactivity to lignite char in CO_2 gasification at 700–900°C [41]. In a low-temperature (450–550°C) combustion experiment, bagasse chars and brown coal chars show comparable reactivity [4].

Captive Particle Experiments

As a complement to the laminar-flow reactor, the captive particle imaging (CPI) system enables one to record the morphology and temperature histories of individual char particles throughout their combustion lifetimes—all within a reaction environment similar to the laminar-flow reactor. Figure 5 presents a sequence of video images for a Southern pine char particle (initially 100 μm in diameter), burning at 6 mole % O_2 in the CPI reactor. After ignition, the particle rotates and burns with incandescence. The incandescence disappears after about 200 ms, and the char continues to burn slowly, leaving the translucent ash residue apparent in Fig. 5d. Comparison of video histories of a number of biomass char particles reveals their heterogeneous nature: Some particles display incandescence; others do not. Some particles take much longer to burn than others. Some show evidence of bubbling molten ash on the outer surface; others do not.

The heterogeneity of the biomass char particles is more quantitatively demonstrated by Fig. 6, which portrays the temperature/time histories of several particles of switchgrass char. (Figure 6 does not include the data from extremely reactive particles whose high near-infrared emission oversaturates the detector.) Although the shapes of the temperature/time profiles are similar for all the switchgrass char particles (i.e., close to square waves), the actual temperature/time profiles and burning times vary widely. The maximum burning temperature does not vary that much from particle to particle, but the time necessary to reach the maximum temperature and the time sustained at the maximum temperature do vary significantly from particle to particle. Similar variations occur for particles of pine char (not shown), though they are somewhat less pronounced. Although caution should be exercised in extending the results of the CPI experiments to the conditions of the laminar-flow experiments, it is easy to see that variations from particle to particle in the time necessary to reach maximum temperature and the time sustained at that temperature could account for a measurable portion of the particle-to-particle temperature variation exhibited by the biomass chars in Figs. 1a, 3, and 4—since a vertical line drawn at any particular time value in Fig. 6 would intersect curves at a number of different values of particle temperature.

Conclusions

Our experiments demonstrate that the pine and switchgrass biomass chars are indeed quite reactive under conditions simulating pulverized fuel-fired boilers—their particle burning rates (at the early stages of char conversion) comparable to those of high-volatile bituminous coals. Biomass char reactivity decreases somewhat during char conversion, however, as the more reactive carbon is preferentially depleted and the inorganic constituents of the

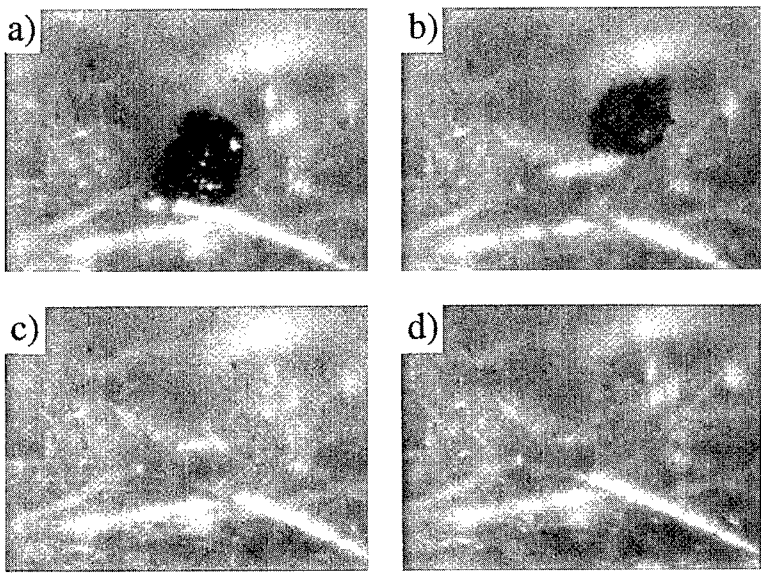

FIG. 5. Video images of a Southern pine char particle burning in the CPI reactor at 6 mole % O_2. Residence times: (a) 0 ms, (b) 83 ms, (c) 183 ms, and (d) 667 ms. Particle is read during incandescent period.

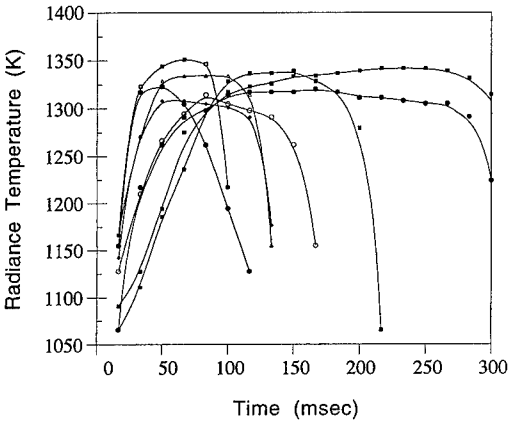

FIG. 6. Radiance temperature measured as a function of time for individual particles of switchgrass char burning in the CPI reactor at 6 mole % O_2.

chars undergo physical and chemical transformations that render them less catalytically active.

An overwhelming feature of the biomass chars is their heterogeneity, both morphological and compositional—a manifestation of which is that, under a given set of conditions, biomass chars burn at temperatures spanning the range of theoretical limits, from inert to diffusion controlled. For purposes of direct comparison with better-known fuels such as coals, we have presented surface burning rates for these biomass chars under standard combustion conditions. The irregular morphologies of the biomass chars and their wide range of burning rates would make a more rigorous and detailed kinetic analysis quite difficult. The simple median reactivities presented may be useful for engineering estimates but are, in truth, only a crude description of a very complex population behavior.

Acknowledgments

The authors gratefully acknowledge the National Renewable Energy Laboratory for financial support of this project and Donald Hardesty for management of the project. They also wish to thank James Ross, Eric Frew, and Sidney Huey for technical support.

REFERENCES

1. Tillman, D. A., *The Combustion of Solid Fuels and Wastes*, Academic Press, New York, 1991, pp. 65–119.
2. Jaasma, D. R., *Combust. Sci. Technol.* 49:213–225 (1986).
3. Miles, T. R., *Biologue* September/December:66–68 (1992).
4. Luo, M. and Stanmore, B., *Fuel* 71:1074–1076 (1992).
5. Wornat, M. J., Hurt, R. H., Yang, N. Y. C., and Headley, T. J., *Combust. Flame* 100:131–143 (1995).
6. Elliott, D. C., Beckman, D., Bridgewater, A. V., Diebold, J. P., Gevert, S. B., and Solantausta, Y., *Energy Fuels* 5:399–410 (1991).
7. Diebold, J. and Scahill, J., in *Pyrolysis Oils from Biomass: Producing, Analyzing, and Upgrading, ACS Symposium Series 376* (E. J. Soltes and T. A. Milne,

Eds.), The American Chemical Society, Washington, D.C., 1988, pp. 31–40.
8. Kinoshita, C. M. and Overend, R. P., *Biologue* September/December:68–72 (1992).
9. Wornat, M. J., Porter, B. G., and Yang, N. Y. C., *Energy Fuels* 8:1131–1142 (1994).
10. Mitchell, R. E., Hurt, R. H., Baxter, L. L., and Hardesty, D. R., Sandia National Laboratories Report No. SAND92-8208, 1992.
11. Mitchell, R. E., *Twenty-Second Symposium (International) on Combustion,* The Combustion Institute, Pittsburgh, 1988, pp. 69–78.
12. Tichenor, D. A., Mitchell, R. E., Hencken, K. R., and Niksa, S. J., *Twentieth Symposium (International) on Combustion,* The Combustion Institute, Pittsburgh, 1984, pp. 1213–1221.
13. Hurt, R. H., *Energy Fuels* 7:721–733 (1993).
14. Hurt, R. H. and Mitchell, R. E., *Twenty-Fourth Symposium (International) on Combustion,* Pittsburgh, The Combustion Institute, 1992, pp. 1243–1250.
15. Baxter, L. L., Mitchell, R. E., and Fletcher, T. H., *Energy Fuels* 2:423 (1988).
16. Hurt, R. H. and Davis, K. A., *Twenty-Fifth Symposium (International) on Combustion,* The Combustion Institute, Pittsburgh, 1994, pp. 561–568.
17. Hurt, R. H. and Mitchell, R. E., *Twenty-Fourth Symposium (International) on Combustion,* The Combustion Institute, Pittsburgh, 1992, pp. 1233–1241.
18. Espenäs, B.-G., *Advances in Thermochemical Biomass Conversion Conference,* Interlaken, Switzerland, May, 1992.
19. Davis, K. A., Hurt, R. H., Wornat, M. J., Huey, S. P., and Frew, E., Annual Meeting of the American Institute of Chemical Engineers, San Francisco, California, November, 1994.
20. Thiele, E. W., *Ind. Eng. Chem.* 31:916 (1939).
21. Hurt, R. H. and Gibbins, J. R., *Fuel* 74:471–480 (1995).
22. Smith, I. W., *Nineteenth Symposium (International) on Combustion,* The Combustion Institute, Pittsburgh, 1982, pp. 1045–1065.
23. Rossberg, M. and Wicke, E., *Chem. Ing.-Tech.* 29:181 (1956).
24. Walker, P. L., Jr., Rusinko, F., and Austin, L. G., *Adv. Catal.* 11:133 (1959).
25. Blackwood, J. D. and McTaggart, F. K., *Aust. J. Chem.* 12:533–542 (1959).
26. Jenkins, R. G., Nandi, L. P., and Walker, P. L., Jr., *Fuel* 52:288–293 (1973).
27. Snow, C. W., Wallace, D. R., Lyon, L. L., and Crocker, G. R., *Proceedings of the Fourth Conference on Carbon,* Pergamon Press, Oxford, 1960, pp. 79–85.
28. Smith, W. R. and Polley, M. H., *J. Phys. Chem.* 60:689–691 (1956).
29. Duval, X., *Ann. Chim.* 10:903–967 (1955).
30. McEnaney, B. and Willis, M. A., in *High Temperature Chemistry of Inorganic and Ceramic Materials* (F. P. Glasser and P. E. Potter, Eds.), The Chemical Society, London, 1977, p. 102.
31. Laine, N. R., Vastola, F. J., and Walker, P. L., Jr., *J. Phys. Chem.* 67:2030–2034 (1963).
32. Harker, H., *Proceedings of the Fourth Conference on Carbon,* Pergamon Press, Oxford, 1960, pp. 125–139.
33. Hirsch, R. L., Gallagher, J. E., Jr., Lessard, R. R., and Wesselhoft, R. D., *Science* 215:121–127 (1982).
34. Wigmans, T., Haringa, H., and Moulijn, J. A., *Fuel* 62:185–189 (1983).
35. Yuh, S. J. and Wolf, E. E., *Fuel* 62:252–255 (1983).
36. Radovic, L. R., Walker, P. L., Jr., and Jenkins, R. G., *Fuel* 62:209–212 (1983).
37. Lang, R. J. and Neveal, R. C., *Fuel* 61:620–626 (1982).
38. Quann, R. J. and Sarofim, A. F., *Fuel* 65:40–46 (1986).
39. Davis, K. A., Hurt, R. H., Yang, N. Y. C., and Headley, T. J., *Combust. Flame* 100:31–40 (1995).
40. Beeley, T., Crelling, J., Gibbins, J. R., Hurt, R. H., Lunden, M., Man, C., Williamson, J., and Yang, N. Y. C., *Twenty-Sixth Symposium (International) on Combustion,* 1996, pp. 3103–3110.
41. DeGroot, W. F. and Shafizadeh, F., *Fuel* 63:210–216 (1984).
42. van Heek, K. H., Strobel, B. O., and Wanzl, W., *Fuel* 73:1135–1143 (1994).
43. Reed, T. B., Solar Energy Research Institute Report No. TR-33-239, 1979.
44. Walker, P. L., Jr. and Hippo, E., *Prepr. Pap.—Am. Chem. Soc., Div. Fuel Chem.* 20(3):45 (1975).
45. Dutta, S., Wen, C. Y., and Belt, R. J., *Prepr. Pap.—Am. Chem. Soc., Div. Fuel Chem.* 20(3):163 (1975).

COMMENTS

Johan E. Hustad, Sintef Energy, Norway. You pyrolyzed the biomass samples before you introduced them in the flat flame burner in contrast what was done to the coal samples. Do you think that this affected the results?

Author's Reply. It is the case that the coal particles were not pyrolyzed before we injected them into our laminar-flow reactor, so they do release an appreciable amount of volatile matter when they are first introduced into the reactor. However, the biomass chars, though already "chars," also undergo devolatilization in the initial stages of burning since the relatively mild temperature of their preparation (625 °C) leaves them with a substantial amount of residual volatile matter (20–25% in the ASTM test). In our experiments, we are able to observationally distinguish the zone of coal devolatilization and volatiles burning from the zone of heterogeneous char combustion. All the burning rates reported in Table 1 for coals and biomass chars correspond

to the early stages of char burnout, so they are in fact on a comparable basis.

•

S. Dasappa, Indian Institute of Science, India. In your presentation you have indicated the mole fraction of oxygen as 0.12 and 0.06. But the remaining fraction which consists of products of combustion like H_2O, CO_2 are not indicated? Have you studied the effect of these on the conversion and their relative importance in comparison with O_2.

Author's Reply. Originating from a $H_2/O_2/N_2$ flame with a small amount of CH_4, the post-flame gas environment of relevance to your question contains 2.4 vol-% CO_2 and 18 vol-% water vapor. We do not have any data that directly assess the role of CO_2 or H_2O in these experiments. The classic work of Field [1], however, reports no effect of water vapor between 0% and 4% under very similar conditions, and the single-film model and supporting work of Mitchell et al. [2] consider the H_2O in the particular environment of interest here to be inert.

REFERENCES

1. Field, M. A., *Combust. Flame* 14:237–248 (1970).
2. Mitchell, R. E., Kee, R. J., Glarborg, P., and Coltrin, M. E., *Twenty-Third Symposium (International) on Combustion,* The Combustion Institute, Pittsburgh, 1990, pp. 1169–1176.

•

Thomas H. Fletcher, Brigham Young University, USA. What was the particle size variation for the "held" particle experiments? Could the *mass* variation largely account for differences in reaction times.

Please comment on the error bars in measured particle diameter and particle temperature for the biomass chars in relation to the previous coal char work.

Author's Reply. The nominal particle size ranges in the captive particle imaging experiments were 106–125 and 125–130 μm for the pine and switchgrass chars, respectively. However, because of the high aspect ratios of some particles, the actual ranges of particle dimensions could be broader than the nominal ranges as determined by sieving. Although we believe that a number of factors contribute to particle-to-particle variations in the combustion behavior of the biomass chars (as discussed in the paper), it is certainly plausible that mass differences between particles contribute at least somewhat to the differences in the radiance temperature/time profiles exhibited in Fig. 6. Consistent with this scenario is the observation, from Fig. 6, that generally the particles quickest to heat up to their maximum temperature are also the ones that spend the shortest times at that maximum temperature. It should be borne in mind, however, that a large portion of the "mass" in the biomass char particles is ash.

There is no difference in the accuracy of the *in-situ* measurements of the particle temperature for the biomass and coal chars. Temperatures measured by our two-color pyrometry technique are estimated to be accurate to within 25 K [10]. For particles that are nearly spherical, diameters are accurate to within 10 μm [10]. Particle diameter measurements, and their distinctions between the two types of chars, are fully discussed in this paper.

•

Jon Gibbins, Imperial College, UK. You have observed differences in both particle size/shape and in particle composition. Which of these do you think is more responsible for the observed distribution in reactivity?

Author's Reply. Particle morphology and composition both appear to play major roles in determining the combustion behavior of these biomass chars since the observed particle temperatures and overall reactivities are governed by both transport and chemical reaction processes. Variations in morphological factors such as particle size, shape, and pore geometry lead to particle-to-particle variations in mass transfer (and even heat transfer) processes both within and outside the particles. Variations in composition, particularly of catalytic inorganic elements, lead to particle-to-particle variations in intrinsic reactivity. Morphological and compositional factors are not always separable, however, since morphological differences among biomass char particles often denote differences in distributions of the plant components (each different compositionally) from which the chars are produced—e.g., lignitic versus cellulosic components.

Our data (Fig. 1) indicate that under the conditions of our combustion experiments, the majority of the biomass char particles burn in Zone II [22–24], in which intrinsic chemical reactivity and pore diffusion both contribute to the observed combustion rates. Because even very small differences in the amounts or chemical forms of catalytic elements can produce large differences in gasification reactivity [32–38,41], particularly for oxygen-rich chars from low rank coals or biomass, compositional differences are likely to be an important factor in yielding chars of a broad range of reactivities. As pointed out in the paper (within our discussion of Fig. 2), energy-dispersive X-ray analysis of the biomass chars shows wide variation from particle to particle in the surface concentrations of catalytic elements such as K and Ca. One might surmise that such variations also exist within the particles.

Twenty-Sixth Symposium (International) on Combustion/The Combustion Institute, 1996/pp. 3085–3094

INFLUENCE OF PRESSURE ON THE COMBUSTION RATE OF CARBON

ROBERT H. ESSENHIGH
Department of Mechanical Engineering
The Ohio State University
Columbus, OH 43210, USA

ANN M. MESCHER
Assistant Professor of Mechanical Engineering
Department of Mechanical Engineering
University of Washington
Seattle, WA 98195, USA

The influence of pressure on the combustion rates of carbon (or coal) particles is shown, by comparison of prediction with experiment, to be zero to minor in the temperature range studied. This result is contrary to the empirical (*n*th order) assumption widely adopted in much of the literature that predicts a substantial pressure dependence at all temperatures. Two models were used in the comparison, and the results were compared with three independent experimental sets of data. These experiments were measurements of burning times of single coal particles by Tidona [19] at 1, 1.5, and 2 atm; reaction rates of char particles by Monson et al. [15] at 1, 5, 10, and 15 atm; and (noncritical) ignition temperatures of coal particles in the pressure range 0.4–1.7 atm [20]. The first model was based on the fundamental Langmuir–Nusselt–Thiele suite of theoretical equations in the form of the extended resistance equation (ERE) [35]. The second model combined the Nusselt BLD analysis with the empirical *n*th order assumption that the reaction rate at all temperatures is proportional to the *n*th power of the *partial pressure* of the oxygen concentration (p_{ox}^n) [2,3]. The ERE model was able to predict the structural form of the experimental results with adequate prediction of numerical values, particularly of the reaction rates measured by Monson et al. In particular, the ERE predictions and experiments jointly showed small to no dependency of the rates on pressure, contrary to the predictions of the empirical model. We conclude that the empirical model has no experimental support for the assumptions made and that fundamentally based equations can be developed or already exist that can be used to predict carbon combustion reaction rates at elevated or reduced pressure with acceptable confidence.

Introduction

The influence of pressure on the combustion rates of carbons and coals is a significant fundamental and practical problem that has been a subject of analysis and investigation for several decades. The history of carbon reaction studies [1–3], however, shows a clear dichotomy with regard to the reaction rate equations used and, specifically, their representation of the dependence on pressure, which is the central issue in this paper. The dichotomy turns, particularly, on whether the reaction mechanism is a two-step or one-step process where the two-step model has been developed from fundamental concepts but the one-step assumption is empirical. We set these positions in context by a brief summary of the key elements of the alternate models available.

Fundamental studies originating with Rhead and Wheeler [4] and Langmuir [5] focused initially on experimentally based [4] two-step phenomenological models [5] and, specifically, an adsorption-desorption process on presumed active sites. Only the adsorption step is identified as pressure-dependent so that the pressure dependence of the overall reaction is a function of the relative magnitudes of the two steps and, thus, of temperature. In a 1981 review [1] of then-available experimental sources on effect of pressure, including combustion of coal in diesel engines, gas turbines, and shock tubes, the balance of the evidence essentially supported a marginal pressure dependence, if any, indicating on this model the dominance of the desorption step for the relevant range of experimental conditions. We show substantially the same result in this paper.

In support of the phenomenological assumptions, mechanistic (ab initio) models [6,7,8] likewise imply or use this two-step process, generally stated in terms of pressure-dependent molecular orbital analyses for the chemisorption process and pressure-independent electron binding-transfer processes for

TABLE 1
Summary (comparison) of experimental conditions and objectives

Ref. No.	Author(s)	Experimental objective	Temperature range: °C	diameter μm	pressure range: atm
[19]	Tidona	measurement of particle burning times	2200–3000	100–300	1, 1.5, 2
[15]	Monson et al.	measurement of specific reaction rates	1300–2200	70	1–15
[20]	(this work)	measurement of ignition temperatures	400–600	350–600	0.4–1.7

the desorption or film decomposition step; the last has been given particular study in connection with catalytic behavior [9]. Statistical models of the pore-tree, random pore, or fractal type [10–13] generally can use any statement of a rate expression or equation considered appropriate but do not directly address the problem at issue here.

In recent studies [2,3,14,15], however, the most commonly used approach to describe the reaction rate has been use of a single-term empirical equation, implicitly representing a one-step mechanism, although this has long been known to be at variance with experiment. Pressure is included explicitly in this equation as a power index of the oxygen partial pressure, p_{ox}^n (the nth order rate expression). As such, it predicts a primary dependence on pressure at all temperatures. The source for this expression most usually cited is Frank-Kamenetskii [16], and a recent review by Smoot [3] identifies nearly a score of flame models using the expression.

As an empirical equation, the nth order expression can only curve fit. Nevertheless, the coefficients obtained are generally represented as rate parameters, although typically such parameters have been shown to vary from one experimental condition to another [14,17] so that their value in prediction and extrapolation is well-known to be problematic. Smoot and Fletcher [18] make the point with particular emphasis, stating that the nth order expression is "coal specific, and inappropriate for extrapolative use." This clearly defines the problem at issue. Likewise, Monson et al. [15] specifically question "whether a more fundamental rate expression . . . (can) better describe the total pressure effects." This observation alone provides a prime reason for examination of the theoretical position to provide a fundamental basis in place of the acknowledged empiricism.

Thus, our objective in this paper is to examine options for theoretical prediction, based on available fundamental developments, with experimental verification from three different sources in support. Two of those sources are data published by others [15,19]; the third is data we reported in conference recently [20] and now present here in publication. These three suites of experiments, as shown in Table 1, differ markedly in method of experiment, particle size, temperature range, and experimental objective. However, as we will show, they all support the position advanced here, developed from the fundamental theory that the pressure dependence of the reaction rate can be formulated in fundamental terms. This shows a variation from independence of the absolute pressure at lower temperatures to a minor dependence for small particles at high temperature.

Experimental

Tidona Experiments

Tidona [19] measured burning times of particles as a function of diameter at three different pressures. Using the same techniques and procedures employed by Ubhayakar and Williams [21], selected particles of coal were injected into quiescent oxygen environments at room temperature and ignited with a ruby laser (consequently, they were burning in cold surroundings). Both absolute pressure and oxygen mass fractions were varied, with experimental data values reported for oxygen partial pressures of 1, 1.5, and 2 atm and oxygen mass fractions of 0.7–1. Particle sizes ranged from 100 to 300 μm. Combustion times were determined by high-speed cinemicrography and two-color optical pyrometry. The temperature records showed that after an initial temperature jump to stable combustion, the temperatures then remained substantially constant until extinction or final burnout with values in the range 2500–3300 K. The photographic records also indicated swelling of the particles by factors up to 2 at about the moment of ignition; this is consistent with other results [22].

In analysis of the data, Tidona reported that the combustion was controlled by boundary-layer diffusion (BLD) and that, as shown in Fig. 1, the burnout times varied, as expected, with the square of the initial diameter, in accordance with the standard

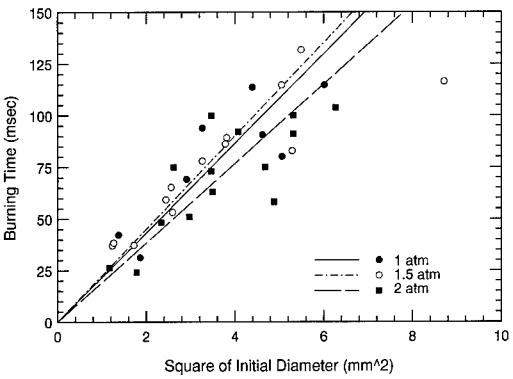

FIG. 1. Tidona Data [19]. Variation of burning time (t_b) with square of initial diameter (d_o^2), as predicted by Eq. [10] (Nusselt equation) for coal particles burning at 1, 1.5, and 2 atm; and showing independence of burning constant (slope of line, K_D) with pressure as predicted by Eq. (10). Experimental and predicted values of K_D are in agreement at 200 s/cm^2 (for values of standard deviations, see text).

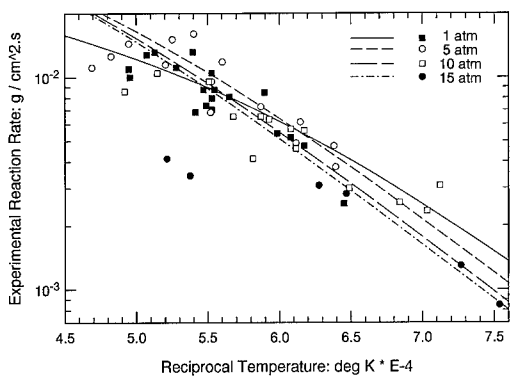

FIG. 2. Monson et al. Data [15]. Arrhenius plot of specific reaction rate (variation of log [rate] versus reciprocal temperature) for 70-μm char particles reacting at pressures of 1, 5, 10, and 15 atm compared with predictions (lines) from Eq. (10). Measurements and predictions show minor influence of pressure on reaction rate at the higher temperatures, partially modified by decreasing reaction penetration factor (ε) with increasing pressure.

Nusselt theory [23] as summarized later. Figure 1 is constructed from the reported [19] results; they show no significant influence on the burning times caused by change in pressure.

Monson et al. Experiments

Monson et al. [15] measured combustion rates of coal chars in an electrically heated drop tube reactor of generally standard design inside a pressure container. The capabilities included operation at pressures of 1–15 atm, temperatures of 700–1400°C, and particle residence times of 30–1000 ms. A modified Sandia particle imaging system [24] was used to obtain simultaneous measurements of particle velocity, temperature, and diameter. Partially reacted char residue was collected by sampling and used to determine burn off (from tracer analysis). A substantial body of results is reported in the paper; the results of relevance to our purpose here were those for data on the variation of specific reactivity (in g/cm$^2 \cdot$ s) with temperature, as shown in Fig. 2, and change in density with burn off. Figure 2 is a replot of their rate data with our independently calculated prediction lines included, using the theoretical procedure described later.

This Work

Ignition temperatures of captive coal particles in a size range similar to that of Tidona were measured by attaching the particles to thermocouples and burning them between two small electrically heated coils. Earlier work at normal pressures using this method of experiment concentrated on the study of burning times, mostly for coal particles at normal, vitiated, and elevated oxygen concentrations [25,26] and for CWF drops [27].

Unique to these experiments was the enclosure of the equipment in the pressure container and the focus on measurement of ignition temperatures by measuring the temperature variation with time (*T-t* signal) under noncritical ignition conditions and determining the ignition temperature as the point of inflection (POI) of the *T-t* curve during heat up [28,29]. The POI was obtained by differentiation of a fourth-order curve fit to the experimental *T-t* curves. The general procedure is outlined in Ref. 28 and has been most completely developed and described by Fu and Zeng [29].

The experimental system used is illustrated in Fig. 3. The heating system consists of two plane, horizontal wire resistance coils of 1 inch diameter spaced 1/2 inch apart and heated electrically. The particles are cemented to fine thermocouples and positioned between the two coils. The carrying fibers are attached to a rotor so that up to four particles can be rotated into position sequentially after successive burnout. The whole device is enclosed in a sealed container that allows a fourfold variation in pressure (from 0.4 to 1.7 atm) and is pierced by the electrical leads to heat the coils and by the TC leads for the *T-t* signal. As the particles heat up and ignite, the time-dependent TC output passes through an A/D converter and is recorded in PC (Lotus) files.

The temperature range in the experiments was determined by the range of ignition temperatures (T_{ig}) found experimentally from the POIs of the *T-t* curves, as illustrated in Fig. 4. As can be seen from this plot, there is no evident influence of pressure.

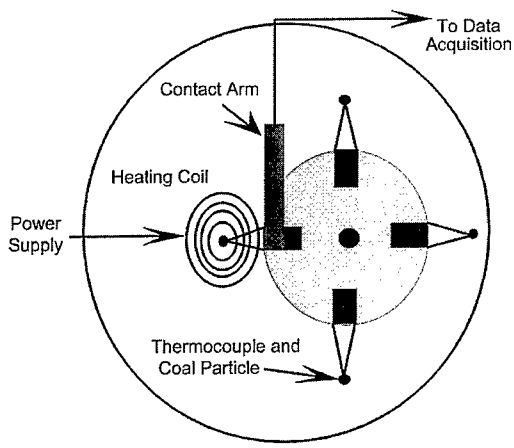

FIG. 3. This Work. Schematic (plan view) of particle-ignition device showing heating coils and hub carrying four particles on TCs and indicating connections for power supply to coils and for data acquisition (passed to A/D converter and into Lotus files).

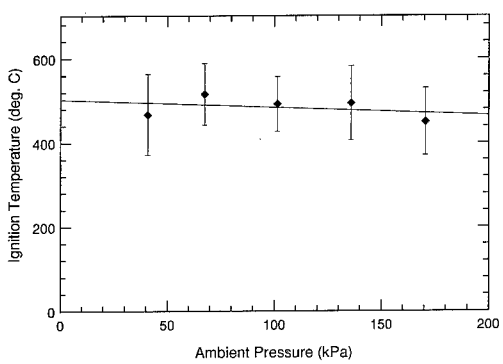

FIG. 4. This Work. Variation of (noncritical) ignition temperature (T_{ig}) with pressure showing lack of dependence of ignition temperature on pressure in agreement with Eq. (14). Bars are 1 SD on 8 measurements per point.

Theory

Choice of Model

The equations of concern for this study are those governing the combustion of a spherical particle of carbon or coal in oxygen-enriched or vitiated air with variation of absolute pressure. The standard primary description of the behavior is a two-stage physical-chemical process. *Stage 1* is the physical in-diffusion of reacting oxygen to the particle surface through any inert component and against out-diffusing reaction products (the Nusselt boundary layer or BLD diffusion process), sometimes with continuing diffusion to the interior of the particle. *Stage 2* is the chemical reaction of the oxygen at the external or internal surface of the particle; as identified in the Introduction, this can be represented as either a two-step or one-step process. Regarding the prediction of the different rate processes, there is a substantial amount of common quantitative agreement regarding the BLD process. There is also qualitative agreement that there can be joint external surface and/or internal reaction, with agreement further that the quantitative basis for determining the (physical) in-diffusion to the interior is provided by the Thiele analysis [30]. This is true even though in many boiler model programs the internal burning is stated [3,18] to be accounted for only implicitly and nonmechanistically.

BLD Equation

For the diffusion of oxygen in nitrogen through the boundary layer of a reacting carbon particle to form a mixture of CO and CO_2 at the particle surface, the standard form DE for the transport of the oxygen is [31]

$$g_{ox} = -(\rho D_{ox})\cdot(dy_{ox}/dr) + vy_{ox} \qquad (1)$$

and the solution for the oxygen supply rate to the surface of a spherical particle, $-g^s_{ox}$, is

$$\begin{aligned} -g^s_{ox} &= k^s_D(y^\infty_{ox} - y^s_{ox}) \\ &= (1 + f)\cdot C\cdot(\rho D_{ox}/a)\cdot(y^\infty_{ox} - y^s_{ox}) \end{aligned} \qquad (2)$$

Diffusion Rate Kinetics

Translation of the oxygen molar diffusion rate to the carbon surface, $(-g^s_{ox})$, into mass of carbon removed per unit area transforms Eq. (2) into the specific reaction rate, R_s [32,33]:

$$R_s = k_D\cdot(y^\infty_{ox} - y^s_{ox}) = -\sigma\cdot(da/dt) \qquad (3)$$

with

$$k_D = (1 + f)\cdot C\cdot(\rho_0\cdot D^o_{ox}/a)\cdot(T/T_0)^{0.7} \qquad (4)$$

The influence of pressure (P) on the diffusion rate depends only on the group $(\rho_0 D^o_{ox})$. Since D^o_{ox} (molar basis) is inversely proportional to pressure [31,34] and density is proportional to pressure, the product, (ρD), is then independent of total pressure over the pressure range involved in these experiments. Consequently, in BLD-controlled reactions such as Tidona's experiments, no influence of pressure is predicted.

This BLD analysis is essentially common to all approaches. The differences in viewpoint with regard to the dependence of the rate equations on pressure thus focus on the treatment of the gas–solid rate kinetics.

Gas–Solid Rate Kinetics

The alternatives for the gas–solid chemical rate kinetics differ principally in the use of: (1) a two-step reaction based on fundamental considerations, and (2) the one-step reaction adopted on an empirical basis.

1. The two-step fundamental rate expression most fully developed, and best supported experimentally, is the Langmuir [5] adsorption-desorption model (for discussion of alternatives, see Refs. 1 and 33). For nondissociative adsorption with internal reaction governed by Thiele kinetics, the modified Langmuir is obtained [33,35,36]:

$$1/R_s = (1/\varepsilon k_a \cdot y_{ox}) + (1/\varepsilon k_d) \quad (5)$$

where $\varepsilon = 1 + \alpha/3$ and α is the power index for the variation of density with diameter during reaction $(\sigma/\sigma_o) = (d/d_o)^\alpha$ [35]. It is also potentially predictable by a range of expressions depending on the zone in which the reaction takes place [36].

2. The one-step nth order reaction rate expression most consistently used by the empiricists, as cited by Monson et al. and others [2,3,14,15,17] has the form

$$R_s = k \cdot p_{ox}^n = k \cdot P^n \cdot y_{ox}^n \quad (6)$$

where k is a proportionality constant commonly identified as a (single-step) velocity constant. The power index, n, is an empirical parameter that is either specified arbitrarily or obtained from the experimental results under analysis. The effect of internal reaction is not included in this expression (see Eq. [5]); it is evidently introduced by inspection [18].

Combined Kinetics

The complete rate equations obtained after combination of diffusion and reaction have the alternate forms:

a. The extended resistance equation [35] based on the fundamental derivations

$$1/R_s = (1/k_D \cdot y_{ox}) + (1/\varepsilon \cdot k_a \cdot y_{ox}) + (1/\varepsilon \cdot k_d) \quad (7)$$

b. The empirical formulation [1,2,15,16]

$$R_s = k \cdot [p_{ox} \cdot (1 - R_s/R_{s,m})]^n \quad (8)$$

In this expression, it may be noted that the value of R_s requires solution of a $(1/n)$th-order expression. Frank-Kamenetskii [16] describes a graphical method for this. Many investigators using this expression do not appear to use a root extraction procedure.

Pressure Dependencies

The dependencies for the specified velocity constants are as follows:

1. *No dependencies.* (a) The diffusion velocity constant, k_D, given by Eq. (4), is pressure independent, as shown previously by equation development. (b) The desorption velocity constant, k_d, is pressure independent by specification.
2. *Dependency.* The adsorption velocity constant, k_a, is given by the following [33]:

$$k_a = (3/8)(\rho_o P_o/2 \cdot \pi)^{1/2} \cdot (P/P_o) \cdot (T/T_o)^{1/2} \cdot \exp(-E_a/RT) \quad (9)$$

showing a first-order dependency.
3. *Unspecified.* The pressure dependency of the empirical velocity constant, k, in Eq. (8) cannot be specified ab initio. It is arbitrarily specified, as noted, by formulation as the nth-order expression, as given in the Introduction and in Eq. (8). Numerical values of the pressure dependency (index n) have to be assumed or determined by experiment.

Results and Data Evaluation

Tidona Data

A summary evaluation of Tidona's data is provided in his original paper [19]. What we add here in summary is the equation derivation used (not given in his paper). Accepting Tidona's position that the particles were burning at the diffusion limit, the relevant rate equation is Eq. (3) with $y_{ox}^s = 0$. The solution is standard [25,32] and is most commonly written in the Nusselt square-law form [23] for the variation of time as a function of diameter, d. In the burnout limit, t_b, for an initial diameter, d_o, this gives:

$$t_b = K_D \cdot d_o^2 \quad (10)$$

where

$$K_D = \sigma_o/[8 \cdot (1 + f) \cdot C \cdot (\rho D) \cdot y_{ox}^\infty] \quad (11)$$

Figure 1 is a replot of Tidona's data according to Eq. (10). The three lines are least-squares regressions through the origin for the three pressures (respectively 1, 1.5, and 2 atm), after data check using small-number-statistics considerations [37], with corresponding K_D values 217, 226, and 192 (s/cm^2) with SDs of 16, 10, and 12. The mean K_D value is 212, which is within 1 or 2 SDs of the individual values and is within 1 SD of the (mean) value of 206 given by Tidona. It is also within 1 SD of the (approximate) value of 200 calculated from Eq. (11). For the calculation, parameter values used were $\sigma_o = 1.43$ g/cm^3, $\rho_o = 1.29 \times 10^{-3}$ g/cm^3; $D_o = 0.18$ cm^2/s; $f = 1$; $C = 1$; $y_{ox}^\infty = 0.21$; and the calculation included corrections for density reduction by volatiles loss (for VM = 39%); swelling (by a factor up to 2); temperature correction in the boundary layer to allow for cold ambient in the determination of ρD;

TABLE 2
Rate Coefficients for Figure 2

This work: Two-step (Langmuir-type) reaction: All curves: Common parameters at all pressures		Second Thiele Factor Values			
$k_a^o = 0.435$ g/cm$^2\cdot$s $k_d^o = 4.5$ g/cm$^2\cdot$s	P(atm)	1	5	10	15
$E_a = 7500$ cal/mol $E_d = 24{,}000$ cal/mol	ε	3.6	2.5	2.0	1.8

Monson et al.[15]: One-step (empirical basis) reaction:

"Rate" parameters change with pressure P(atm)	1	5	10	15
k_o (g/cm$^2\cdot$s)	1.78	0.0382	0.0227	0.0098
E(cal/mol)	14,800	3400	3800	4900

and correction for very high ambient oxygen concentration (0.7–1 mass fraction), which requires use of $-\ln(1 - y_{ox}^{\infty})$ in place of y_{ox}^{∞} [26]. The value of K_D calculated before correction was about 100 (s/cm^2) and, with the corrections, was approximately doubled in essential agreement with the experimental value. In evaluating the corrections, the density reduction by VM loss (reducing σ_o and hence K_D by approximately 2) and swelling (increasing K_D by about 4) were the two largest and accounted, overall, for a doubling (approximately) in the initially calculated value.

Therefore, what these results show is that the functional form of the diameter-squared relation is supported by experiment; the numerical value of the burning constant obtained experimentally is in agreement, within expected error, with the calculated value; and the experimental values of K_D are substantially independent of absolute pressure, in agreement with prediction.

Ignition Data (this work)

Determination of ignition temperatures under noncritical conditions depends on determining the point of inflection (POI) in the temperature–time (T-t) curve (at $[d^2T/dt^2] = 0$) rather than the (nominal) plateau (at $[dT/dt] = 0$). This is a variant of the Semenov TET analysis applied to ignition of particles as reviewed elsewhere [38]. The noncritical criterion was proposed in an earlier paper [28] and studied in detail by Fu and Zeng [29]. For a particle of mass m, specific heat c, and temperature T, the net rate of heat supply Q, to the particle as it heats up is the difference between the rate of heat released by the reaction, Q_G, and the rate of loss to the ambient, Q_L, thus

$$m \cdot c \cdot (dT/dt) = Q = Q_G - Q_L \qquad (12)$$

Solution of this equation yields a sigmoid T-t curve; and, in noncritical ignition theory, ignition occurs at the point of inflection, corresponding to the Taffanel and le Floch condition that $dQ/dT = 0$. However, the van't Hoff condition ($Q = 0$) does not hold (see Ref. 38). Using Eq. (6) as a diagnostic approximation to Eq. (5), Eq. (12), after differentiation to obtain the point of inflection, becomes, in dimensionless form [38,29],

$$d^2\theta/d\tau^2 = d\phi/d\tau$$
$$= [[\exp(-1/\theta)]/\theta_i^2 - 1/Kd]\cdot\phi = 0 \qquad (13)$$

Using the Cassel and Liebmann [39] power approximation for the Arrhenius group, $\exp(-1/\theta) = B\cdot\theta^{\beta}$; Eq. (13) becomes, after substitution and expansion,

$$\theta_i^{\beta-2} = 1/BKd = (2/Bd)\cdot(\lambda/k_o h_c y_{ox}^n) \qquad (14)$$

Eq. (14) shows dependence of ignition temperature (θ_i) on diameter and oxygen mole fraction [y_{ox}] but not on pressure; the prediction of lack of dependence on pressure is supported by the experimental results shown in Fig. 4.

Monson et al. Data

Evaluation of these data requires the use of a complete rate equation, either Eq. (7) or Eq. (8). Evaluation in terms of Eq. (8) was performed by Monson et al. with the indicative result that the fairly compact data band shown in Fig. 2 was "exploded," with a data range of more than an order of magnitude at any given temperature, and requiring markedly different values of k_o and E (listed in Table 2), for the *same* chars for curve-fitting lines at the four different pressures. This clearly shows the inadequacy of the empirical nth-order curve fit and the need for an alternate approach.

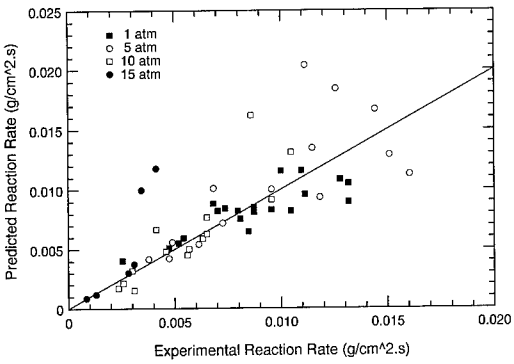

FIG. 5. Monson et al. Data [15]. Comparison of experimental (Monson data points) with calculated (this work, lines) reaction rates for the 70-μm char particles reacting at pressures of 1, 5, 10, and 15 atm.

The alternative advanced here, of the use of Eq. (7), is illustrated in the predictions shown in Fig. 2. In this figure, the same values for the reactivity parameters, k_a^o, E_a, k_d^o, and E_d, based essentially on literature values [1,33,35,40] and listed in Table 2, were used for all the curves. There is a small dependence on pressure that is due to the adsorption term (Eq. [9]), modified, as we will examine, by the reaction penetration factor ε. The values used for ε were obtained from the experimental density/diameter data reported by Monson et al. [5] for the four pressures (Table 2). The values used for the BLD parameters were in general those used in the Tidona calculations, but the BLD influence is minor to trivial in any event for the Monson experimental conditions.

The accuracy of the calculations was also checked by plotting the experimental values against the calculated values, as shown in Fig. 5. The line shown as the regression for all the data values, with omission of four outliners from the calculation based on Ref. 37, has a slope of 1.00 (exactly the theoretical value) with a SD of 0.03. The lines for the four pressure sets (1, 5, 10, and 15 atm), calculated individually, had slopes of 0.93 $\pm$ 0.04, 1.04 $\pm$ 0.08, 1.07 $\pm$ 0.06, and 1.12 $\pm$ 0.05. Adjacent lines are within 1 SD of each other, and are within 1 to 2 SDs of the theoretical value of unity. Any residual trend caused by pressure is considered marginal.

Within the noise of the measurements, Fig. 2 shows no evident trend in the *experimental* data with pressure. The *computed* lines apparently show some minor influence, but with the trends strongly influenced at a second order of magnitude by the reaction penetration factor ε, as noted previously. The three higher pressures show marginal differences that are well within the noise of the experimental data. At the lower temperatures, the lowest (1 atm) pressure line is seen to predict rates greater than at the higher pressures, with a reversal upon moving to the higher temperatures. This crossing of the lines is due to the differences in the values of ε. If the same value of ε is used, all the lines converge to a common trend line at the lowest temperatures, governed almost totally by the desorption term. As the temperature increases, the concave downward trend develops, and the lines diverge (at a second order of significance for this particle size) because of the differences in pressure. We reemphasize, however, the second-order level of any pressure influence in the experimental range of concern. With increasing temperature, extrapolation shows that the influence of pressure becomes more marked but remains substantially secondary.

Conclusions

The conclusions to be drawn from evaluation of these three suites of experiments would thus seem to be clear-cut. Where reaction is controlled by diffusion, as in Tidona's experiments, or by desorption, as in our ignition experiments, the prediction that reaction is independent of pressure is clearly supported. In the case of Monson's experiments, the situation is a little more complex but in accordance with the predictive equations and still showing relatively little influence of pressure. For those experiments, the prediction is that for a common degree of reaction penetration—value of ε—a degree of pressure sensitivity is to be expected. As seen in Fig. 2, the experimental results show little or no pressure sensitivity caused by the differences in reaction penetration, ε, as measured experimentally.

The further, more general conclusions, are that for temperatures below about 1000°C, the reaction is controlled mainly by the chemical desorption parameter and a linear fit on the Arrhenius plot is possible. However, for temperatures above 1000°C, the Arrhenius line is clearly curved as a result of the increasing importance of the adsorption term with increasing temperature; thus, the rate data on an Arrhenius plot cannot be represented adequately or accurately by a linear fit to the data, contrary to the implications of Eq. (8). Additionally, the commonality of the data as shown by Fig. 2 is partly a consequence of the differences in reaction penetration (ε) at different pressures.

These results show that the equations developed from the available fundamental theories of reaction are evidently adequate for accurate interpretation and/or prediction of carbon reaction rates. Accordingly, we see no further reason to continue the use of the empirical relations such as the nth-order expression other than for diagnostic purposes. It would appear appropriate, instead, to give proper critical attention to the fundamental theoretical developments that are already available on this point in the relevant literature.

Nomenclature

a	particle radius
d	particle diameter
D_{ox}	oxygen diffusion coefficient
E_a	adsorption activation energy
E_d	desorption activation energy
f	reaction mechanism factor ($f = 1$ for CO_2 formation; $f = 2$ for CO formation)
g_{ox}	mass rate of flux of oxygen through boundary layer
h_c	enthalpy of reaction
k_D^o	diffusion velocity constant for oxygen supply to surface
k_D	diffusion velocity constant in term of mass removal rate of carbon from surface
k_a	adsorption velocity constant: $= k_a^o, \exp(-E_a/RT)$
k_d	desorption velocity constant: $= k_d^o, \exp(-E_d/RT)$
k	empirical velocity constant: $= k_o \cdot \exp(-E/RT)$
n	empirical reaction order
p_{ox}	oxygen particle pressure
P	total pressure
Q_G	heat released by reaction in TET analysis
Q_L	heat lost from reaction system in TET analysis
r	radius
R_s	specific reaction rate at particle surface (mass removal rate of carbon per unit area)
t	time
T	temperature
T_s	surface (particle) temperature
T_g	ambient gas temperature
v	Stefan flow velocity
y_{ox}	oxygen mole fraction concentration
α	power index in density/diameter relation: $(\sigma/\sigma_o) = (d/d_o)^\alpha$
ε	reaction penetration factor: $= (1 + \alpha/3)$
σ	solid (particle) density
ρ	ambient gas density
λ	thermal conductivity

Acknowledgments

It is with great pleasure that we acknowledge provision by Dr. Monson of a disk containing complete data records reported in his paper (Ref. 15).

REFERENCES

1. Essenhigh, R. H., "Fundamentals of Coal Combustion," in *Chemistry of Coal Utilization: Second Supplementary Volume* (Ellior, M. A., Ed.) Wiley, New York, 1981, pp. 1153–1312.
2. Smith, I. W., *Nineteenth Symposium (International) on Combustion,* The Combustion Institute, Pittsburgh, 1982, pp. 1045–1065.
3. Smoot, L. D., Ed., *Fundamentals of Coal Combustion* Elsevier, New York, 1993.
4. Rhead, T. F. E. and Wheeler, R. V., *J. Chem. Soc.* 101:846–856 (1912).
5. Langmuir, I., *J. Am. Chem. Soc.* 37:1139–1366 (1915).
6. Sherman, A. and Eyring, H. J., *J. Am. Chem. Soc.* 54:2661 (1932).
7. Chen, S. G., Yang, R. T., Kapteijn, F., and Moulijn, J. A., *Ind. Eng. Chem. Res.* 32:2835–2840 (1993).
8. Moulijn, J. A. and Kapteijn, F., *Carbon* 33:1155–1165 (1995).
9. Walker, P. L., Shelef, M., and Anderson, R. T., in *Chemistry and Physics of Carbon,* Vol. 4, (Walker, P. L., Ed.), Marcel Dekker, New York, 1968, pp. 287–383.
10. Gavalas, G. R., *AIChE J.* 26:577 (1980); *Combust. Sci. Technol.* 24:197 (1981).
11. Simons, G. A. and Finson, M. L., *Combust. Sci. Technol.* 19:217–225 (1979).
12. Simons, G. A., *Combust. Sci. Technol.* 19:227–235 (1979); *Combust. Sci. Technol.* 20:107–116 (1979); *Combust. Sci. Technol.* 24:211–213 (1983); *Fuel* 59:143–144 (1980); *Carbon* 20:117–118 (1982); *Prog. Energy Combust. Sci.* 9:269–290 (1983); *Combust. Flame* 50:275–285 (1983); *Combust. Flame* 53:83–92 (1983); *Combust. Flame* 55:181–194 (1984); *Nineteenth Symposium (International) on Combustion,* The Combustion Institute, Pittsburgh, 1983, pp. 1067–1076.
13. Delfosse, L., Ponsolle, L., and Jabkhiro, el, H., *Twenty-Second Symposium (International) on Combustion* The Combustion Institute, Pittsburgh, 1989, pp. 39–45.
14. Mitchell, R. E., *Combust. Sci. Technol.* 53:165–186 (1987); *Twenty-Second Symposium (International) on Combustion,* The Combustion Institute, Pittsburgh, 1988, pp. 69–78, *Twenty-Third Symposium (International) on Combustion,* The Combustion Institute, Pittsburgh, 1990, pp. 1297–1304.
15. Monson, C. R., Germane, G. J., Blackham, A. U., and Smoot, L. D., *Combust. Flame* 100:669–683 (1995).
16. Frank-Kamenetskii, D. A., *Diffusion and Heat Exchange in Chemical Kinetics,* Princeton University Press, Princeton, NJ, 1955.
17. Hardesty, D. R., Quarterly Reports of the Sandia National Laboratories Combustion Research Facility, July 1987–June 1989; Mitchell, R. E., Hurt, R. H., Baxter, L. L., and Hardesty, D. R., "Compilation of Sandia Coal Char Combustion Data and Kinetic Analyses" Sandia Report SAND92-8208-UC-361 June, 1992.
18. Smoot, L. D. and Fletcher, T. H., *Fuel Process. Technol.* 41:363–365 (1995).
19. Tidona, R. J., *Combust. Flame* 38:335–337 (1980).
20. Mescher, A. M. and Essenhigh, R. H., "Non-Critical Ignition of Coal Particles at Elevated and Reduced Pressure," Spring Meeting of Joint Central/Western/Mexican Sections of the Combustion Institute, San Antonio, TX, April 1995.
21. Ubhayakar, S. K. and Williams, F. A., *J. Electrochem.*

Soc. 123:747–756 (1974); *Combust. Flame* 26:23–34 (1976).
22. Essenhigh, R. H. and Yorke, G. C., *Fuel* 44:177–186 (1965).
23. Nusselt, W., *V.D.I.* 68:124 (1924).
24. Tichenor, D. A., Mitchell, R. E., Henken, K. R., and Niksa, S., *Twentieth Symposium (International) on Combustion,* The Combustion Institute, Pittsburgh, 1984, pp. 1213–1221.
25. Essenhigh, R. H., *J. Engineering Power,* 85:183–188 (1965).
26. Beeston, G. and Essenhigh, R. H., *J. Phys. Chem.* 67:1349–1355 (1963).
27. Zghoul, A. M. and Essenhigh, R. H., *Proc. 2nd Annual Pittsburgh Coal Conference,* University Pittsburgh and DOE-PETC, September 1985, pp. 658–665.
28. Chen, M. R., Fan, I. S., and Essenhigh, R. H., *Twentieth Symposium (International) on Combustion,* The Combustion Institute, Pittsburgh, 1984, pp. 1925–1932.
29. Fu, W. B. and Zeng, T. F., *Combust. Flame* 88:413–424 (1992).
30. Thiele, E. W., *Ind. Eng. Chem.* 31:916–920 (1939).
31. Bird, R. W., Stewart, W. E., and Lightfoot, E. N., *Transport Phenomena,* Wiley, New York, 1960.
32. Field, M. A., Gill, D. W., Morgan, B. B., and Hawksley, P. G. W: *Combustion of Pulverised Coal,* The British Coal Utilization Research Association, Leatherhead, 1967.
33. Essenhigh, R. H., *Energy Fuels* 5:41–46 (1991).
34. Reid, R. C., Prausnitz, J. M., and Poling, B. E., *The Properties of Gases and Liquids,* McGraw Hill, New York, 1987.
35. Essenhigh, R. H., *Twenty-Second Symposium (International) on Combustion,* The Combustion Institute, Pittsburgh, 1988, pp. 89–96.
36. Essenhigh, R. H., *Combust. Flame* 99:269–279 (1994).
37. Dean, R. B. and Dixon, W. J., "Simplified Statistics for Small Numbers of Observations," *Anal. Chem.* 23(4):636–638 (1951).
38. Essenhigh, R. H., Misra, M. K., and Shaw, D. W., *Combust. Flame* 77:3–30 (1989).
39. Cassel, H. M. and Liebmann, I., *Combust. Flame* 3:167 (1959).
40. Essenhigh, R. H. and Misra, M. K., *Energy Fuels* 4:171–177 (1990).

COMMENTS

Thomas H. Fletcher, Brigham Young University, USA. You mentioned that rate coefficients were taken from the literature. How did you deal with effects of coal type? Was it only in the "second" effectiveness factor, or were the A and E values adjusted?

Author's Reply. No coal type factor was involved since the rate coefficients were only required for the Monson et al. [1] data and in that paper there was only one char. For the A and E values used in the predictions, our basis for selection was the auto-correlation plot given elsewhere [2] between ln(A) and E. This reduces the two variables, A and E, to substantively one for a given reaction. There was some adjustment of the paired values, but within the limits defined by auto-correlation plots. At this time, there would appear to be no evident coal type (rank) effect on the E (or A) values, that is to say, on the chemical components of reactivity, at least at the level of engineering measurement or use. Burn-out can be faster if the char formed is more open and there is easier access to the particle interior—determined by the Second Effectiveness factor. The apparent influence of coal rank would appear to depend less on chemical properties and more on physical conditions such as heating rate.

This is not to say that some influence of coal type may not be determined in the future but this will require in our view more complete/reliable experimental measurements (such as joint measurements of both rates and density changes, as in the Monson experiments) coupled with more complete analysis of the experimental results. This will have to be repeated for a range of coals under different char forming conditions to create a reliable data pool to determine the influence of coal type. To our knowledge, this data base does not yet exist, and the best evidence at this time is that coal rank is of minor importance.

REFERENCES

1. Monson, C. R., Germane, G. J., Blackbam, A. U., and Smoot, L. D., *Combust. Flame* 100:669–683 (1995).
2. Essenhigh, R. H. and Misra, M. K., *Energy Fuels* 4:171–177 (1990).

•

L. Douglas Smoot, Brigham Young University, USA. This analysis shows declining influence of adsorption with rising pressure with little influence of pressure dependent adsorption. Results of the previous paper in this session [1] that adsorption was the dominant suggested kinetic rate control with desorption being negligible. Is there a straightforward explanation for this observe difference?

REFERENCE

1. Croiset, E., *Twenty-Sixth Symposium (International) on Combustion,* The Combustion Institute, Pittsburgh, 1996, pp. 3095–3102.

Author's Reply. The observation that the pressure-dependent adsorption has small influence on the overall reaction rate is essentially true except at the lowest (1 atm) pressure (where the influence is between first and second order). The conditions of the previous paper [1] that the reaction was adsorption dominated suggests a conclusion that could be dependent on sufficient differences in the experimental method. One critical difference in the relative velocity between sample particle and gas stream where the particles in the Monson's [2] experiments were essentially travelling with the gas stream, but in [1] paper there was a relative velocity of 0.2 m/sec (20 cm/sec). If the boundary layer is sufficiently reduced by this then it seems to me that the conclusions of that paper must follow, if the Langmuir is, indeed, applicable. If Dr. Smoot is drawing attention to the need to start a comparative critical review of both potential rate equations and the relevant contents involved, I would totally agree and I would support such an initiative. I believe it is long overdue.

REFERENCES

1. Croiset, E., *Twenty-Sixth Symposium (International) on Combustion,* The Combustion Institute, Pittsburgh, 1996, pp. 3095–3102.
2. Monson, C. R., Germane, G. J., Blackham, A. U., and Smoot, L. D., *Combust. Flame* 100:669–683 (1995).

•

Eric Suuberg, Brown University, USA. The literature on *intrinsic* carbon oxidation kinetics shows very few examples of simple integer O_2 reaction order (e.g., Ref. 1 of this paper, or Suuberg et al. [1]). Few results support zero order. There is little doubt, as concluded in this paper, that observed orders are determined by complicated reaction sequences. It was earlier observed [1] that gasification of a char at 623 K gave an order with respect to O_2 of 2/3, whereas O_2 chemisorption (on the same char) at lower temperature was first order. Moreover, the 2/3 order observed during gasification was constant over 3 orders of magnitude O_2 pressure, apparently ruling out use of the simple Langmuir model proposed here (since it cannot predict a constant fractional order over this wide a pressure range). Thus it appears that there is still an unresolved question as to a suitable explanation for the empirical nth-order rate expression.

REFERENCE

1. Suuberg, E. M., Wojtuwicz, M., and Calo, J. W., *Twenty-Second Symposium (International) on Combustion,* The Combustion Institute, Pittsburgh, 1988, pp. 79–87.

Author's Reply. This does raise a point that needs much more experimental attention. The original literature following Langmuir does provide some data. A recent examination/test of the Langmuir is given in Ref. 33 of the paper but more tests are badly needed. Regarding Dr. Suuberg's observation [1] that he reported a $P_{ox}^{2/3}$ this also supports the need for more careful direct investigation of the Langmuir—and of the other rate expressions that are available in the literature (Temkui, etc.) In particular, the *dissociative* Langmuir could be the better description of Dr. Suuberg data, and I think this should be explored, along with the other possible candidates. My basic position is that: data I have examined *do* generally support the Langmuir, where this can be tested; the Langmuir has a theoretical basic: the nth order (power Frendlich) does not. If then the Langmuir is found the most generally supported, then we still should focus on development of an alternative equation, but based on fundamentals, rather than revert to unsound empiricism.

Twenty-Sixth Symposium (International) on Combustion/The Combustion Institute, 1996/pp. 3095–3102

THE INFLUENCE OF PRESSURE ON CHAR COMBUSTION KINETICS

ERIC CROISET, CHANTAL MALLET, JEAN-PAUL ROUAN AND JEAN-ROBERT RICHARD
CNRS—Laboratoire de Combustion et Systèmes Réactifs
1C Avenue de la Recherche Scientifique
45071 Orléans Cedex 2—France

Combustion experiments in a fixed-bed reactor were performed at 0.2, 0.6, and 1.0 MPa for temperatures between 850 and 1200 K with Westerholt bituminous coal char sized in the range 90–106 μm. The rate constants were first determined with the so-called "nth-order" overall expression of the combustion rate. Then, a simplified heterogeneous reaction mechanism including a two-stage adsorption-desorption process was proposed to understand the influence of the total pressure on the adsorption and desorption reactions. Using the technique of sudden removal of oxygen, it was found that the total pressure has no effect on the desorption rate constants. Because the combustion is controlled by the adsorption of oxygen, the adsorption rate constant appeared very similar to the overall rate constant. Increasing total pressure up to 0.6 MPa was found to decrease the rate constants if the oxygen "concentration" is expressed as the oxygen partial pressure ($r = k\,P_{O_2}^n$). If the oxygen concentration is expressed as the oxygen mole fraction ($r = k\,y_{O_2}^n$) there is only a weak effect of the total pressure on the rate constant. Another effect of a pressure increase is to decrease the transition temperature from a kinetics-controlled regime to a regime co-controlled by pore diffusion. To clarify the effect of pressure on combustion, a Langmuir adsorption isotherm was chosen and the adsorption constant was determined at 0.2, 0.6, and 1.0 MPa. It was then found that the Langmuir adsorption isotherm is particularly suitable when working at elevated pressure.

Introduction

Pressurized combustion of solid fuels for gas turbines has the potential of a high combined cycle efficiency approaching that of an oil-fired combined cycle. Although the combustion of carbon at atmospheric pressure has been studied extensively, few studies have been reported at elevated pressures. There is general agreement on the main effects of pressure. Studies at fixed gas composition [1–4] showed two trends. The first concerns diffusion-limited combustion in which no effect of pressure has been observed. This is because the higher oxygen partial pressure, due to higher total pressure, is counterbalanced by a lower oxygen diffusion coefficient. A second trend has been observed in kinetics-limited combustion. An increase in total pressure produces a rise in oxygen partial pressure, thereby accelerating the chemical rate. Monson et al. [4] and Richard et al. [5] studied the effect of total pressure, varying the gas composition to maintain the oxygen partial pressure constant. They found that an increase of pressure decreases the combustion rate. Saastamoinen et al. [6] summarized the effects of pressure for different situations as indicated in Table 1. This table shows that it is essential, for combustion under pressure, to distinguish the case of combustion at constant oxygen partial pressure from the one at constant oxygen mole fraction. The importance of this distinction has also been pointed out by Mescher and Essenhigh [7] for the formulation of the combustion rate. Indeed, they criticize the validity of the empirical nth-order equation in which the oxygen concentration is expressed as oxygen partial pressure. They prefer the more theoretical formulation of Langmuir, in which the oxygen concentration is expressed as mole fraction of oxygen. Monson et al. [4] also questioned the nth-order formulation because they found that the apparent preexponential factor and the apparent activation energy largely decrease when pressure increases.

The present work aims to clarify the influence of total pressure during char combustion. First, the trends found in the literature are confirmed by well-controlled experiments in a fixed-bed. Then the results are quantified by determining the rate constants for both an overall combustion rate and a simplified mechanism. In the latter case, the influence of pressure on the oxygen adsorption rate and on the carbon species desorption rate is considered. The combustion rate is written using the nth-order rate expression. The oxygen concentration is introduced first as a function of oxygen partial pressure and then as a function of oxygen mole fraction. This last formulation is then compared with the more theoretical Langmuir equation.

Experimental

A high devolatilized char, whose parent coal is Westerholt coal (high-volatile bituminous), was

TABLE 1
Summary of the effect of an increase in the total pressure on the combustion rate of char particle (adapted from Saastamoinen et al. [6])

Combustion regime	Combustion rate variation when total pressure increases	
	y_{O_2} constant	P_{O_2} constant
Diffusion control	weak variation	decreasing rate
Kinetic control	increasing rate	weak variation

TABLE 2
Ultimate analysis of the Westerholt char

C (%)	H (%)	N (%)	O (%)	S (%)	Ash (%)
84.9	0.76	1.6	2.34 (diff)	1.2	9.2

chosen for the experiments. The char, prepared at atmospheric pressure, was heated in a furnace at a rate of 10 K min^{-1} up to 1223 K in nitrogen. Finally, the char was crushed and sieved to the desired particle size of 90–106 μm. The ultimate analysis of this char is presented in Table 2.

The experimental setup consists mainly of a fixed-bed located in a pressurized vessel that can handle pressure up to 4.0 MPa. Since this device has been described in detail elsewhere [8], only its major features are briefly recalled. The fixed-bed is a traversed-bed type and the reactant gas stream passes through a sample bed with a space velocity of up to 0.2 m s^{-1} (stp). The temperature inside the bed is measured continuously through a type-K thermocouple. The sample mass, between 30 and 50 mg, is mixed with a mass of 150 mg quartz sand to minimize the increase of the bed temperature. In that way, the elevation of the bed temperature never exceeds 30 K. The sample is placed between two layers of quartz wool. The bottom layer is located in the lower part of the reactor, which is composed of a plate drilled with 1-mm holes, allowing the flow of gas and a passage for the thermocouple. The reactor is heated by an induction furnace (maximum temperature: 1300 K) and the temperature of the reactant gas is controlled by a thermocouple located just upstream from the bed. The burned gases are collected through a quartz probe located 2 cm above the bed and are directed to gas analyzers. The reactant gas consists of mixtures of oxygen and nitrogen.

As will be seen in the section on theory, it is essential to know the exact development of the burned gases. Yet, the pattern of formation of the gases read on the analyzers is not identical to that of the burned gas following the sample bed. Thus, a deconvolution method has been used [9,10]. It consisted of comparing the reactor and the sampling line with a succession of ideal stirred reactors.

Theory

Overall Reaction Rate

A simple expression of the global reaction rate, r, can be written in the following form:

$$r = k\, P_{O_{2s}}^{n} \quad [\mathrm{kg.m^{-2}.s^{-1}}] \text{ or } [\mathrm{s^{-1}}] \tag{1}$$

with

$$k = A \exp(-E/RT) \tag{2}$$

where k is the apparent reaction coefficient, n the apparent reaction order, A the apparent preexponential factor, E the apparent activation energy, and $P_{O_{2s}}$ the oxygen partial pressure on particle's surface. It has been established [11] that in a combustion regime controlled by kinetics (regime I), the apparent reaction order and the apparent activation energy represent, respectively, the true reaction order and the true activation energy. When pore diffusion limitation occurs (regime II), the apparent activation energy is equal to half of the true activation energy and the relationship between the apparent reaction order, n, and the true reaction order, m, is $n = (m + 1)/2$.

The overall reaction rate is determined experimentally from the gas analysis of the carbon species (in the present case, only CO and CO_2) and the change in size and density of the particles. The rate calculations are detailed in Ref. 12.

Simplified Heterogeneous Reaction Mechanism

The reaction of carbon with oxygen is a two-stage adsorption-desorption process. The mechanism used in the present work consists of three steps that represent the main reactions occurring during char combustion and is written as follows:

$$O_2 + 2(-C) \xrightarrow{k_1} 2\,(-CO) \tag{R1}$$

$$(-CO) \xrightarrow{k_2} CO + \text{free site} \tag{R2}$$

$$2\,(-CO) \xrightarrow{k_3} CO_2 + (-C) + \text{free site} \tag{R3}$$

Reaction (R1) is the reaction of dissociative adsorption of oxygen on a carbon site, whereas reactions (R2) and (R3) represent, respectively, the desorption steps leading to CO and CO_2. In this mechanism, two types of active sites were considered: the carbon sites $(-C)$ and the oxygen-covered carbon sites

$(-CO)$. The fraction of oxygen-covered carbon sites, ε, is defined in the following way:

$$\varepsilon = \frac{(-CO)}{(-C) + (-CO)} \quad (3)$$

The fraction of carbon sites is then represented by $(1 - \varepsilon)$. Finally, the reaction rates of reactions (R1), (R2), and (R3) can be written, here expressed in s^{-1},

$$r_1 = k_1 P_{O_2,}^{m_1} (1 - \varepsilon)^2 \quad (4)$$

$$r_2 = k_2 \varepsilon \quad (5)$$

$$r_3 = k_3 \varepsilon^2 \quad (6)$$

m_1 is the reaction order of the reaction (R1) and k_i is the rate constant of the reaction (Ri) and can be dependent on the fraction of oxygen-covered carbon sites, $k_i = A(\varepsilon) \exp(-E(\varepsilon)/RT)$. The three reactions of the simplified mechanism are considered as elementary reactions and thus the reaction order m_1 should be equal to 1. Yet, a method to determine m_1 experimentally will be presented (see Eqs. [14] and [15]) to verify the hypothesis of elementary reaction for reaction (R1). In the present work, only the Langmuir isotherm is considered, which assumes that the reaction rate constant is independent of the fraction of oxygen-covered carbon sites. The variation of ε is then given by the following equation:

$$\frac{d\varepsilon}{dt} = 2\, k_1 P_{O_2,}^{m_1} (1 - \varepsilon)^2 - k_2\, \varepsilon - 2\, k_3\, \varepsilon^2 \quad (7)$$

After an initial transient state ruled by Eq. (7), a steady state is reached when the adsorption and desorption rates become equal; ε then reaches a constant value, ε_e.

To determine the desorption rate coefficients, k_2 and k_3, the analysis of transient states created by sudden removal of oxygen [13] was used. After reaching steady-state combustion, the oxygen flow is suddenly removed. Because there is no more oxygen, Eq. (7) is simplified and leads to the following equation:

$$\frac{d\varepsilon}{dt} = -k_2\, \varepsilon - 2\, k_3\, \varepsilon^2 \quad (8)$$

or, as a function of the experimental rate of CO and CO_2 formation,

$$\frac{d\varepsilon}{dt} = -r_2 - 2\, r_3 \quad (9)$$

After rearrangement, integration of Eq. (8) yields

$$\Psi_1 = \frac{r_2\left[1 + 2\dfrac{(r_3)_e}{(r_2)_e}\right]}{(r_2)_e + 2\, r_2 \dfrac{(r_3)_e}{(r_2)_e} = \exp(-k_2\, t)} \quad (10)$$

where $(r_2)_e$ and $(r_3)_e$ represent the reaction rates of desorption of CO and CO_2, respectively, at the initial conditions just before the sudden removal of oxygen. The rate constant k_2 is the slope of the curve obtained by plotting $\ln(\Psi_1) = f(t)$. Since k_2 is known, it is possible to determine ε_e:

$$\varepsilon_e = (r_2)_e / k_2 \quad (11)$$

Finally, k_3 can be calculated in the following way:

$$k_3 = (r_3)_e / \varepsilon_e^2 \quad (12)$$

The rate constant for the adsorption of oxygen is determined at the steady state. At the initial conditions, corresponding to steady-state combustion, Eq. (7) becomes

$$k_1 P_{O_2,}^{m_1} = \frac{(r_2)_e + 2\,(r_3)_e}{2\,(1 - \varepsilon_e)^2} = \Psi_2 \quad (13)$$

If one considers the logarithm of Eq. (13), the latter becomes

$$\ln(k_1) + m_1 \ln(P_{O_2,}) = \ln(\Psi_2). \quad (14)$$

Ψ_2 being known, m_1 is determined by plotting $\ln(\Psi_2)$ as a function of $\ln(P_{O_2,})$. Finally k_1 is determined from Eq. (13):

$$k_1 = \Psi_2 / P_{O_2,}^{m_1} \quad (15)$$

For this simplified mechanism, it is essential to distinguish the CO_2 formed directly by the char from the CO_2 produced by oxidation of CO. The values of CO and CO_2 indicated on the analyzers are therefore corrected as proposed by Tognotti et al. [14]:

$$CO_2/CO = 0.02\, P_{O_2}^{0.2} \exp(3000/T) \quad (16)$$

Although Eq. (16) was not originally proposed for pressures above atmospheric, Monson et al. [4] have observed that the fraction of CO_2 formed is independent of the total pressure between 0.1 and 1.5 MPa.

Results and Discussion

Overall Reaction Rate

Calculations based on the mass transfer coefficient have shown that there is no limitation by oxygen diffusion from the bulk gas to the particle's surface. Thus, the partial pressure of oxygen at the particle's surface is equal to the partial pressure of oxygen in the bulk gas.

The determination of the apparent reaction order is presented in Fig. 1. The apparent reaction order was determined at a temperature of 970 K and at three different total pressures: 0.2, 0.6, and 1.0 MPa. The apparent reaction order is independent of the total pressure and has a constant value of 1. It is then concluded that, whatever the combustion in regime

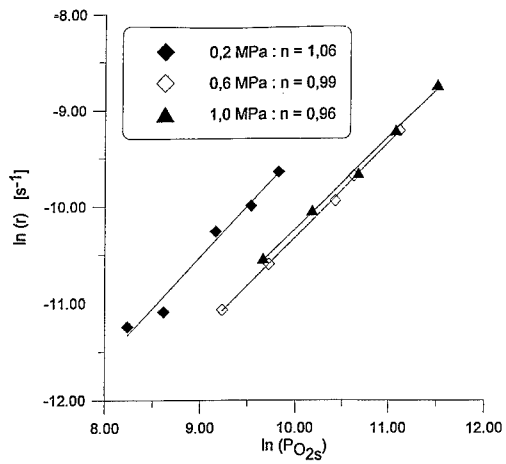

FIG. 1. Determination of the apparent reaction order at various total pressures for the overall reaction rate. The temperature is fixed at 970 K.

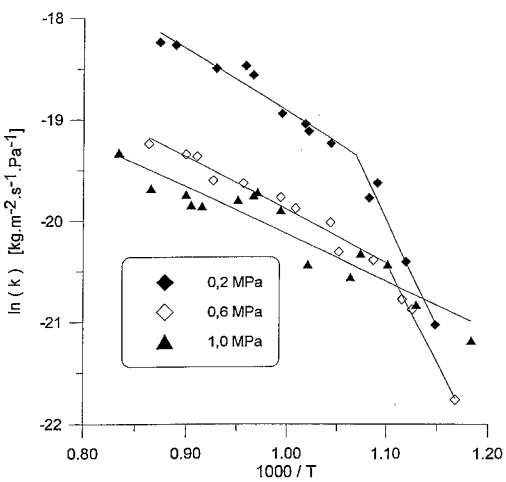

FIG. 2. Arrhenius plot for the rate constant corrected at three different total pressures: 0.2, 0.6, and 1.0 MPa.

TABLE 3

Values of A and apparent activation energies at different pressures in the case of the overall reaction rate. These values are determined from the regime II portions.

Pressure (MPa)	0.2 MPa	0.6 MPa	1.0 MPa
Apparent E (kJ mol^{-1})	51.7 ± 5.3	43.5 ± 3.3	38.8 ± 3.8
A (kg m^{-2} s^{-1} Pa^{-1})	3.0 10^{-6}	4.3 10^{-7}	1.9 10^{-7}

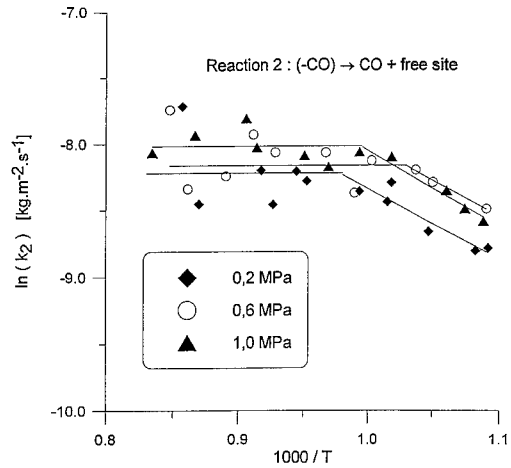

FIG. 3. Arrhenius plot for the desorption rate coefficient k_2 at three different total pressures: 0.2, 0.6, and 1.0 MPa.

I or II, the true reaction order is equal to 1, which means that the combustion is probably controlled by the adsorption of oxygen.

Figure 2 presents the Arrhenius plot of the overall rate constant. This figure shows changes in the slopes that characterize the transition from regime I to regime II. For pressures 0.2 and 0.6 MPa, the temperatures of transition from regime I to regime II are, respectively, 930 and 900 K. For 1.0 MPa, there is no change in the slope, which implies that in the temperature range of the present work, combustion is in regime II and thus the transition temperature is below 850 K. An increase in the total pressure then favors the combustion regime controlled by pore diffusion. This result confirms the conclusion of Turnbull et al. [1]. Figure 2 also shows that k decreases when the total pressure increases from 0.2 to 0.6 MPa. Above 0.6 MPa, there is a weak effect of pressure. The values of the kinetic parameters are presented in Table 3. Both the activation energy and the preexponential factor are seen to be decreasing when the pressure increases. However, the effect of pressure is more significant in the preexponential factor than in the activation energy.

Simplified Heterogeneous Reaction Mechanism

As mentioned in the theoretical section, the first step was to determine the constant of desorption of CO and CO_2 and the fraction of oxygen-covered carbon sites. The Arrhenius plot of the constant of CO desorption, k_2, is represented in Fig. 3. It was observed that the total pressure has no significant influence on k_2 and above 1000 K, the constant k_2 remains constant and equal to 3.0×10^{-4} kg m^{-2} s^{-1}. With regard to the constant rate of CO_2 desorption, it was also found that this constant does not depend on the total pressure. Above 950 K, k_3

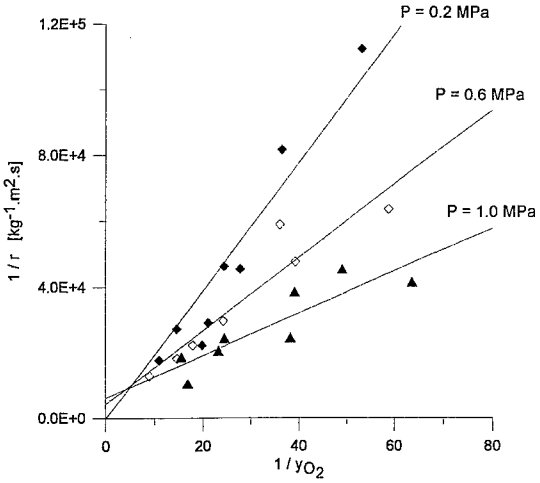

FIG. 4. Linear variation of reciprocal of reaction rate ($1/r$) with reciprocal of oxygen mole fraction ($1/y_{O_2}$) at constant temperature of 973 K.

remains constant and equal to 4.8×10^{-2} kg m^{-2} s^{-1}. The determination of the fraction of oxygen-covered carbon sites leads to the following conclusion concerning ε_e: it (1) is independent of pressure, (2) increases with temperature, and (3) is of the order of 10^{-3}. Since ε_e is much less than 1, this substantiates the proposition that the combustion is controlled by the adsorption of oxygen.

An important result is that both CO and CO_2 desorption constants are independent of the total pressure. Considering Eqs. (5) and (6), it is seen that the desorption rates do not include terms of partial pressure of any gas but only rate constant and fraction of oxygen-covered carbon sites. Hence, it is concluded that the desorption rates are independent of the total pressure.

The reaction order of reaction (R1), adsorption of oxygen, has been found to be independent of the total pressure and equal to 1. This result suggests the proposition that reaction (R1) is probably an elementary reaction. The Arrhenius plot of k_1 is actually very similar to the Arrhenius plot of the overall rate constant (Fig. 2). This result is not surprising because it has been seen that combustion is controlled by the adsorption of oxygen, which is represented by reaction (R1). However, the apparent activation energy of k_1 is not influenced by the total pressure and is equal to 42 kJ mol^{-1}. The values of the preexponential factor, expressed in kg m^{-2} s^{-1} Pa^{-1}, for the pressures 0.2, 0.6, and 1.0 MPa are, respectively, 6.1×10^{-7}, 1.9×10^{-7} and 1.5×10^{-7}. Thus, the total pressure affects only the preexponential factors, the latter decreasing when the pressure increases. Above 0.6 MPa, there is no influence of pressure.

Oxygen Partial Pressure versus Oxygen Mole Fraction

The variation of the preexponential factor of the adsorption rate coefficients as a function of the total pressure is well represented by the curve-fitting expression, $A = 4.5 \times 10^{-2}/P^{0.92}$. Then the adsorption rate, represented by Eq. (4), can be written

$$r_1 = 4.5 \times 10^{-2} \frac{1}{P^{0.92}} P_{O_{2s}} \exp(-42{,}000/RT)\,(1 - \varepsilon)^2 \quad (17)$$

or, by replacing $P_{O_{2s}}$ with the mole fraction $y_{O_{2s}}$,

$$r_1 = 4.5 \times 10^{-2}\, P^{0.08}\, y_{O_{2s}} \exp(-42{,}000/RT)\,(1 - \varepsilon)^2 \quad (18)$$

When the adsorption rate is expressed as a function of the mole fraction of oxygen, the exponent of the pressure term is very near zero compared to the case in which the adsorption rate is expressed as a function of the partial pressure of oxygen. The influence of total pressure then becomes very weak when the oxygen concentration is expressed as a mole fraction.

A formulation for the combustion rate based on the oxygen mole fraction seems to represent the effect of total pressure more satisfactorily. For the Langmuir adsorption isotherm formulation,

$$\frac{1}{r} = \frac{1}{\eta'\, k_a\, Y_{O_2}} + \frac{1}{\eta'\, k_d} \quad (19)$$

The first term on the right-hand side is an adsorption term and the second one represents desorption. The factor η' is called the second effectiveness factor by Essenhigh [15] and accounts for the internal surface participating in the reaction. The advantage of this formulation is its theoretical basis, whereas the nth-order rate expression is only empirical.

The values of $\eta' k_a$ and $\eta' k_d$ are evaluated by plotting $1/r$ versus $1/y_{O_2}$ [16]. This has been done for a constant temperature of 973 K and three total pressures, 0.2, 0.6, and 1.0 MPa, with oxygen molar fraction varying between 0.02 and 0.1 (Fig. 4). The linearity of the plots confirms the validity of the Langmuir formulation. The slopes and the intercepts yield the kinetics constants. The slope decreases when pressure increases, indicating that $\eta' k_a$ increases with pressure. The values of the intercepts $1/\eta' k_d$ are very small. This means that $\eta' k_d$ is high for all the studied pressures and confirms the adsorption control of the combustion. In fact, in this study,

$$\frac{1}{r} = \frac{1}{\eta'\, k_a\, y_{O_2}} + \frac{1}{\eta'\, k_d} \approx \frac{1}{\eta'\, k_a\, y_{O_2}} \quad (20)$$

and so, $r \approx (\eta'\, k_a)\, y_{O_2}$. This expression is similar to the formulation given in global kinetics when the

oxygen concentration is expressed as a function of the oxygen mole fraction. Figure 4 indicates a similar trend to that in Eq. (18); a pressure increase corresponds to an increase in the adsorption constant. The formulation of Eq. (18) represents, in fact, the particular case of the Langmuir approach in the case of a combustion controlled by adsorption.

Conclusion

To determine the influence of pressure on the combustion rate, experiments were performed with Westerholt bituminous coal char at 0.2, 0.6, and 1.0 MPa. The bed temperature was varied between 850 and 1200 K. In a first approach, the rate constants were calculated using the so-called nth-order overall expression. If the oxygen concentration is expressed as the oxygen partial pressure ($r = k\ P_{O_2}^n$), an increase in the total pressure up to 0.6 MPa results in a large decrease in the rate constant, followed by a quasi-constant rate constant for pressure above 0.6 MPa. If the oxygen concentration is expressed as the oxygen mole fraction ($r = k\ y_{O_2}^n$), there is only a weak effect of the total pressure on the rate constant. The transition temperature from a chemical-controlled regime to a regime co-controlled by pore diffusion decreases as pressure increases. A first-order reaction was determined experimentally to indicate that the combustion is controlled by adsorption of oxygen.

In a second approach, the technique of sudden oxygen removal was used to study the influence of pressure on the adsorption of oxygen and on the desorption of CO and CO_2. The results indicated that the total pressure has no effect on the desorption rate constants. Because the combustion is controlled by the adsorption of oxygen, the adsorption rate coefficient is very similar to the overall rate coefficient. The apparent activation energy of the adsorption rate constant is independent of the total pressure and is equal to 42 kJ mol^{-1}.

The global rate constant should vary strongly with temperature but only weakly with pressure. If the rate equation is written as the common nth-order expression, the corresponding global rate constant appears to vary strongly with pressure, which implies that the nth-order formulation does not correctly incorporate the influence of pressure. This is the reason why a Langmuir adsorption isotherm expression was chosen to account for the influence of the total pressure. A slight increase of the adsorption constant was observed when the total pressure increased. In the present experiments, because of the adsorption-controlled combustion, the Langmuir adsorption isotherm formulation is equivalent to the first-order expression as a function of the mole fraction of oxygen. The manner in which the rate expression is expressed is important in determining the effect of total pressure. An expression that includes the mole fraction of oxygen, especially by means of the Langmuir adsorption isotherm formulation, appears to be particularly suitable when working at elevated pressure.

Nomenclature

A	apparent pre-exponential factor ($kg \cdot m^{-2} \cdot Pa^{-1}$)
E	apparent activation energy ($kJ \cdot mol^{-1}$)
k	rate constant ($kg \cdot m^{-2} \cdot s^{-1} \cdot Pa^{-1}$)
k_a	adsorption constant ($kg \cdot m^{-2} \cdot s^{-1}$)
k_d	desorption constant ($kg \cdot m^{-2} \cdot s^{-1}$)
m	true reaction order
m_1	reaction order of reaction R1
n	apparent reaction order
P	total pressure (MPa)
P_{O_2}	oxygen partial pressure (MPa)
r	reaction rate ($kg \cdot m^{-2} \cdot s^{-1}$ or s^{-1})
t	time (s)
T	temperature (K)
y_j	mole fraction of the species j
(%C)	mass fraction of carbon
ε	oxygen-covered carbon site
η'	second effectiveness factor
Ψ_1, Ψ_2	definition, see Eqs. (10) and (13)

Acknowledgments

This work was supported by a grant from the European Union (JOU2-CT92-0037). The authors would like to acknowledge Gérard de Soete for his continuous interest and many helpful comments. The authors also wish to thank the anonymous reviewers for their very constructive remarks.

REFERENCES

1. Turnbull, E., Kossakowski, E. R., Davidson, J. F., Hopes, R. B., Blackshaw, H. W., and Goodyear, P. T. R., *Chem. Eng. Res. Des.* 62:223–234 (1984).
2. Mühlen, H. J. and Schulte, A., *Proceedings of the International Conferences on Coal Sciences*, Tokyo, Japan, October 23–27, 1989, pp. 269–272.
3. Horvath, A., Jakhola, A., and Hippinen, I., Finnish-Swedish Flame Days 1990, The International Flame Research Foundation, Turku, Finland, September 4–5, 1990.
4. Monson, C. R., Germane, G. J., Blackham, A. U., and Smoot, L. D., *Combust. Flame* 100:669–683 (1995).
5. Richard, J. R., Al Majthoub, M., Aho, M. J., and Pirkonen, P. M., *Fuel* 73:485–491 (1994).
6. Saastamoinen, J. J., Aho, M. J., Pirkonen, P. M., and Linna, V. L., *Energy Fuels* 10:121–133 (1996).
7. Mescher, A. M. and Essenhigh, R. H., *Central States/Western States/Mexican National Section of the*

Combustion Institute and American Flame Research Committee, San Antonio, USA, April 23–26, 1995, pp. 632–635.
8. Richard, J. R. and Rouan, J. P., *J. Analytical Appl. Pyrolysis* 15:307–317 (1989).
9. Levenspiel, O., *Chemical Reaction Engineering,* Wiley, New York, 1972.
10. Villermaux, J., *Génie de la Réaction Chimique, Conception et Fonctionnement des Réacteurs,* Tec&Doc-Lavoisier, Paris, France, 1993.
11. Smith, I. W., *Nineteenth Symposium (International) on Combustion,* The Combustion Institute, Pittsburgh, 1982, pp. 1045–1065.
12. Croiset, E., Ph.D. Thesis, University of Orléans, France, 1995.
13. De Soete, G. G., Western States Section Meeting of the Combustion Institute, Salt Lake City March 21–22, 1988.
14. Tognotti, L., Longwell, J. P., and Sarofim, A. F., *Twenty-Third Symposium (International) on Combustion,* The Combustion Institute, Pittsburgh, 1990, pp. 1207–1213.
15. Essenhigh, R. H., *Twenty-Second Symposium (International) on Combustion,* The Combustion Institute, Pittsburgh, 1988, pp. 89–96.
16. Essenhigh, R. H., *Energy Fuels* 5:41–46 (1991).

COMMENTS

Jon Gibbins, Imperial College, UK. Please give more details on your char reactivity test procedure, particularly the heating regime and conversion measurement methods.

Author's Reply. During the experiments the char is first placed in the vessel. The pressure is then raised to its desired value using pressurized nitrogen cylinders. Once the pressure has been raised and the bulk gas consists only of nitrogen, the temperature is raised to its desired value (always below to 950 °C). When the temperature is stable, the flow of nitrogen is suddenly replaced by a flow of reacting gas at desired oxygen concentration. The time at which the nitrogen is replaced by the reactant gas represents the time zero of the combustion. By assuming spherical particles, the combustion rate is

$$r = 1/6\ (\%C)\ \rho d r_m$$

where (%C) is the mass fraction of carbon in the char, ρ the apparent particle's density, d the particle diameter and r_m the specific combustion rate expressed as

$$r_m = \frac{x_{CO} + x_{CO_2}}{(1 - F_C)\int_0^\infty (x_{CO} + x_{CO_2})\,dt} \text{ with } F_C = \frac{\int_0^t (x_{CO} + x_{CO_2})\,dt}{\int_0^\infty (x_{CO} + x_{CO_2})\,dt} \text{ and } x_i \text{ mole fraction.}$$

•

Brian S. Haynes, University of Sidney, Australia. You found a desorption rate constant for surface oxide which is independent of temperature. One would expect the activation energy for this process to be at least equal to the heat of desorption. Direct measurements of surface oxide decomposition rates yield activation energies in the range 200–400 $kJ.mol^{-1}$. Do you have any explanation for why your "desorption" step has no activation energy?

Author's Reply. The CO_2 desorption constant is independent of temperature in the present work. This trend agrees with the results of de Soete [1] at atmospheric pressure. As for CO desorption it has been found that at temperature below 1000K the activation energy is about 47 $kJ.mol^{-1}$, which is much lower than the values you mentioned. It is not clear yet if it is an effect of pressure and further work is needed to clarify the combined effect of pressure and temperature on the desorption rate. To pursue this study on the particular point of CO and CO_2 desorption, it is necessary to determine the primary CO/CO_2 ratio. In our experiments the concentrations of CO and CO_2 detected on the analysers were obviously not representative of the primary CO/CO_2 ratio because of the CO oxidation in the gas phase to form CO_2. To take into account the CO oxidation the data for CO and CO_2 were corrected according to the correlation shown in Eq. (16). Unfortunately it is hard to estimate whether this correlation is adequate in our experiments. In particular, if this correlation underestimates, in our conditions, the desorption of CO at high temperatures, the consequence would be a lowering of the activation energy.

REFERENCE

1. De Soete, G. G., *Twenty-Third Symposium (International) on Combustion,* The Combustion Institute, Pittsburgh, 1990, p. 1257.

•

Leonardo Tognotti, Universitá di Pisa, Italy. In adsorption-desorption kinetic data you abstract from measurements, you consider CO and CO_2 as main products for r_1 and r_2 reactions.

Now, since part of CO is oxidized in the particle bound-

ary layer, how do you discriminate between primary CO_2 and the product of homogeneous oxidation? Sampling of gas very close to the reactor doesn't seem to me sufficient enough to ensure primary product discrimination.

In this case, how much are your results influenced by possible change of the primary CO/CO_2 ratio with temperature?

Author's Reply. We were aware of the homogeneous oxidation of CO into CO_2 in the particle boundary layers and we agree that the measurements of CO and CO_2 don't represent the primary products. Unfortunately it was impossible in our experiments to make direct measurements of the primary products. So, to discriminate these primary products we used the correlation shown in Eq. (16) to express the primary CO/CO_2 ratio. A change in this ratio with temperature would directly influence the rate constants of CO and CO_2 desorption.

•

Eric Suuberg, Brown University, USA. Much of the analysis in this paper flows from the analysis of Fig. 2, in which it is assumed that the low temperature results (at 0.2 and 0.6 MPa) are obtained in a "zone I" and go into a "zone II" condition at higher temperatures. It is stated that calculations rule out external transport limitations. Yet the change in slope (activation energy) at the transition is much greater than the factor of two they expect, based upon the simple pore diffusion transport model that they invoke. Of course different diffusion models will lead to different relationships between the true and apparent activation energies (and orders). But another possibility might exist—what if the transition involves going from zone I to *external* transport limited operation? Can this be ruled out?

Author's Reply. When passing from one combustion regime to another one the activation energy changes from 170 to 52 $kJ.mol^{-1}$ at 0.2 MPa and from 170 to 44 $kJ.mol^{-1}$ at 0.6 MPa. The factor of the change in slope at the transition regime is then on the order of three to four, and thus greater than the expected value of two. Yet on the Arrhenius plot, the external diffusion regime is characterized by an activation energy that tends toward zero at elevated temperatures. This is clearly not the case at 0.2 and 0.6 MPa and the possibility of external transport operation can be ruled out. However, at 1.0 MPa a closer look at the Fig. 2 reveals that this last possibility cannot be ruled out. Indeed, above 1000 K the slope seems to decrease toward zero, with the exception of the point at the highest temperature. This result would indicate that an increase in pressure also favors the transition from regime II to regime III.

Twenty-Sixth Symposium (International) on Combustion/The Combustion Institute, 1996/pp. 3103–3110

TRANSIENT HIGH-TEMPERATURE THERMAL DEACTIVATION OF MONOMACERAL-RICH COAL CHARS

TRUDY BEELEY,[1] JACK CRELLING,[2] JON GIBBINS,[1] ROBERT HURT,[3] MELISSA LUNDEN,[4] CHI MAN,[1] JAMES WILLIAMSON[5] AND NANCY YANG[4]

[1]*Department of Mechanical Engineering*
Imperial College
London SW7 2BX, UK

[2]*Department of Geology*
Southern Illinois University
Carbondale, IL 62901, USA

[3]*Division of Engineering*
Brown University
Providence, RI 02192, USA

[4]*Sandia National Laboratories*
Livermore, CA 94550, USA

[5]*Department of Materials*
Imperial College
London SW7 2BX, UK

Low oxidation reactivities and well-developed turbostratic crystallinity have recently been observed in residual carbon samples extracted from commercial and pilot-scale coal combustion fly ash. Thermal deactivation in high-temperature regions of the furnaces has been suggested as a likely mechanism to explain the low reactivities, but this hypothesis has never been tested directly. This paper describes the application of a new experimental technique for the direct measurement of rapid char deactivation under combustion-relevant conditions. The technique operates in inert environments to isolate the thermal deactivation mechanisms from possible oxidative mechanisms occurring in true combustion experiments.

The technique, based on an inert-gas-purged, refractory-metal, high-temperature wire mesh, is demonstrated here on monomaceral-rich fractions from four parent coals of diverse origin. The results show that char reactivity is quite sensitive to preparation conditions in the range of interest to combustion, decreasing by a factor of 30–50 between 1000°C and 1800°C in only 2 s of treatment for seven of eight samples examined. The 1800°C chars have similar reactivities to boiler fly-ash chars measured previously, lending support for the thermal deactivation hypothesis.

The results also show that thermal deactivation propensity is a function of precursor, with vitrinite-rich fractions deactivating more readily than inertinite-rich fractions. The propensity for deactivation is shown to correlate with the extent of crystalline order development as observed by high-resolution TEM fringe imaging. The paper discusses the relationship between fuel chemistry and deactivation propensity as well as the implications of the reactivity results for combustion processes.

Introduction

Recently, residual carbon samples extracted from commercial and pilot-scale coal combustion fly-ash samples have been found to have lower oxidation reactivities and more fully developed turbostratic structures than a set of laboratory-generated chars used in kinetic studies [1,2]. Thermal deactivation occurring in the high-temperature regions of the industrial furnaces has been suggested as one likely mechanism to explain the phenomenon [3]. This hypothesis, if true, would have a number of important implications for combustion systems and predictive methods for carbon burnout [3].

Most fundamental kinetic studies have been carried out on reactive chars prepared at low temperatures conveniently achievable in batch laboratory furnaces (800–1200°C), or in entrained flow reactors where char particles are exposed to lower peak temperatures and shorter residence times than are typical of industrial furnaces [3,4]. Several researchers have observed reactivity loss during low-temperature gasification [5] or during combustion in flow

reactors [6], but in these kinetic studies, reactivity may change through the simultaneous effects of gasification and thermal treatment and, as a result, it is difficult to interpret this data purely in terms of *thermal* deactivation mechanisms. An important goal of the current study is to assess the thermal deactivation hypothesis through direct measurement of reactivity loss during transient thermal treatment in high temperature *inert* environments.

The general phenomenon of carbon thermal annealing is well known [4,6–10], and has been the subject of a comprehensive review by Suuberg [11], but there is a critical need for more data on the time scales of interest to combustion [3]. Several studies have specifically addressed coal chars [4,6,8,12,13]. Charpenay et al. [13] have studied the dependence of char reactivity on pyrolysis conditions, and have correlated their measured reactivities with char hydrogen content. Annealing studies have been supported by X-ray diffraction analysis [4,6] and high-resolution transmission electron microscopy (HRTEM) which reveals the detailed underlying changes in carbon crystalline structure that accompany thermal treatment [14]. HRTEM has been used to investigate combustion-induced crystallinity development in polymer-derived carbons [15], in biomass char [16], and in coal chars [17]. Essenhigh has raised the issue of a possible connection between high-temperature annealing in furnaces and carbon burnout [18].

This paper describes the application of a new experimental technique for the direct measurement of rapid char deactivation under combustion-relevant conditions. The technique operates in inert environments to isolate the thermal deactivation mechanisms from possible oxidative mechanisms occurring in true combustion experiments. The technique is based on an inert-gas-purged, refractory-metal, high-temperature wire mesh followed by measurement of zone I reactivity by nonisothermal thermal gravimetric analysis (TGA) in a flowing oxygen/nitrogen gas stream.

The new technique is demonstrated here on monomaceral-rich fractions from four parent coals of diverse origin. Monomaceral-rich fractions were chosen for study to gain some additional insight into the potential role of inertinite-group macerals in combustion and carbon burnout. HRTEM fringe imaging is also applied to aid in the understanding of deactivation mechanisms.

Experimental

Sample Acquisition and Preparation

This study presents data on lithotypes and maceral-enriched fractions from four bituminous steam coals. One pair of lithotypes from the Herrin no. 6 (Illinois) coal seam was collected from an active surface mine in Perry County, in the southern part of Illinois, U.S.A., and another from the Ackton opencast mine, Yorkshire, U.K. The vitrain samples were hand picked from blocks of coal featuring numerous and prominent vitrain layers. The fusain samples consisted of blocks of massive fusain. The samples were ground using a rotary pulverizer and manually sieved to give a 125- to 150-μm size fraction.

Experiments were also carried out with vitrinite- and inertinite-rich samples of two South African bituminous coals, SA1 and SA2. SA1 whole coal has a volatile content of 28% and C, H, and N contents of 71.9%, 4.1%, and 1.9%, respectively, all on a dry basis. SA2 whole coal has a volatile content of 35.7% and C, H, and N contents of 69.6%, 4.4%, and 2.0%, respectively, all on a dry basis. These whole coals were ground and sieved to 125–212 μm and separated by density using a sink/float technique in cesium chloride to give maceral-enriched fractions [19]. Table 1 gives the petrographic composition of the separated fractions and their elemental and proximate analyses.

Experimental Techniques

High-temperature wire-mesh reactor (HTWM)

Samples were pyrolyzed using a high-temperature wire-mesh reactor in which a sample is held between layers of a folded piece of molybdenum mesh (106-μm aperture size) that also acts as an electrical resistance heater. A 24-V DC supply was used to deliver up to 2000 A. In all cases, the coal was heated at 10^4 K/s to the peak temperature and held there for 2 s before uncontrolled, rapid cooling. The heating program was controlled using a two-color pyrometer and a microcomputer using feedback control. Volatile products were removed by a helium gas sweep that flowed across the mesh (at atmospheric pressure). Typically, 5–10 mg of dried sample coal was used, previously ground and sieved to 125–150 μm for compatibility with the mesh material. The residual char from the HTWM runs was removed from the mesh for TGA reactivity tests (see following).

Nonisothermal thermogravimetric analysis (TGA)

Oxidation reactivities of the heat-treated char samples were measured by thermogravimetric analysis. Samples (3 mg) were heated in a thermobalance at 40 K/min to 400°C then at 15 K/min to 900°C in 7% oxygen in nitrogen at a flow rate of 25 ml/min. The sample was held at 900°C for 2–4 min to ensure total burnout. Sample weight and temperature were continuously monitored and results expressed as derivative thermograph (DTG) profiles (rate of weight loss versus sample temperature). Previous measurements indicate that residual cesium chloride from the treatment has no important catalytic effect on the reactivity of chars from the density fractions [20].

TABLE 1
Analysis of South African coal density fractions[a]

Parent coal	SA1	SA1	SA2	SA2
Density range	1.2–1.29	1.5–1.6	<1.29	1.4–1.6
Vitrinite	55.7	5.0	86.5	26.7
Pseudo-vitrinite	14.1	0	0	0
Semi-fusinite	9.8	87.0	4.8	66.3
Fusinite	0.2	3.5	0	1.7
Semi-macrinite	1.2	2.0	0	0
Macrinite	0	0	0	0
Micrinite	2.2	0	0.6	1.5
Liptinite	15.6	2.5	8.0	3.8
Resinite	1.2	0	–	–
Elemental analysis (dry basis)				
Carbon	77.7	62.1	76.6	62.0
Hydrogen	5.1	3.2	4.4	3.8
Nitrogen	2.3	1.6	2.0	1.7

[a]Maceral analysis in volume-%; point count by standard procedures: British Standards BS6127 Part 3 1981, British Standards Institution London UK. Elemental analyses in wt-%.

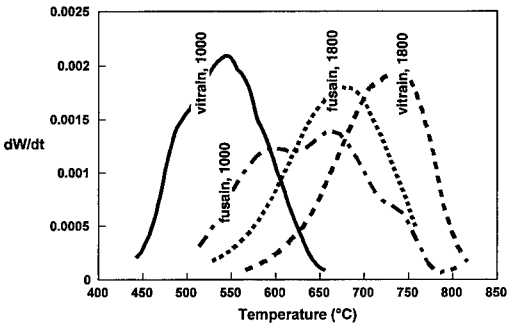

FIG. 1. Derivative thermograph (DTG) profiles for Illinois #6 lithotype chars prepared at 1000°C and 1800°C. Plotted on the ordinate is dW/dt, the instantaneous reaction rate with units of s^{-1}. W is the normalized sample weight (instantaneous sample weight divided by initial sample weight on ash-free bases). The position of the DTG peak is a measure of reactivity, with higher temperature peaks indicating lower reactivities.

High-resolution transmission electron microscopy (HRTEM)

Raw and heat-treated samples of Herrin seam lithotypes were ground, placed on a holey carbon grid, and examined in a Phillips Model CM30 TEM operating at 300 kV. Ten to 15 particles were examined in the vicinity of optically thin edges. The microstructure and porosity were first examined at relatively low magnification (89,000×), followed by examination of the carbon crystalline structure in lattice fringe imaging mode at a magnification of 2,000,000×. The fringe images were photographically enlarged to 4,000,000× for reproduction in Figs. 3 and 4.

Results

High-Temperature Thermal Deactivation

The effect of transient high-temperature heat treatment on the Herrin no. 6 lithotype chars is shown in Fig. 1. Based on the positions of the DTG peaks, the reactivity rank order in this sample set as a function of heat treatment temperature is

$$\text{(vitrain, 1000°C)} \gg \text{(fusain, 1000°C)} > \text{(fusain, 1800°C)} > \text{(vitrain, 1800°C)}$$

For the vitrain char, increasing the heat-treatment temperature from 1000°C (typical of laboratory preparation) to 1800°C (typical of flames) shifts the DTG peak to a much higher temperature, indicating a large loss of reactivity despite the short duration of the heat treatment (2 s). The fusain char, in contrast, is much less influenced by heat treatment. It is also interesting to note that the fusain char prepared at the lower heat treatment temperature exhibits a DTG peak with pronounced breadth. This broad DTG peak with multiple-peak character is believed to reflect heterogeneity within the fusain sample. The fusain lithotype is composed of a range of inertinite macerals and has been observed to yield two distinct peaks upon density fractionation [21]. The lower density peak is believed to be associated with semifusinite [21]. Heat treatment is seen to narrow the fusain DTG peak, suggesting that the reactivity

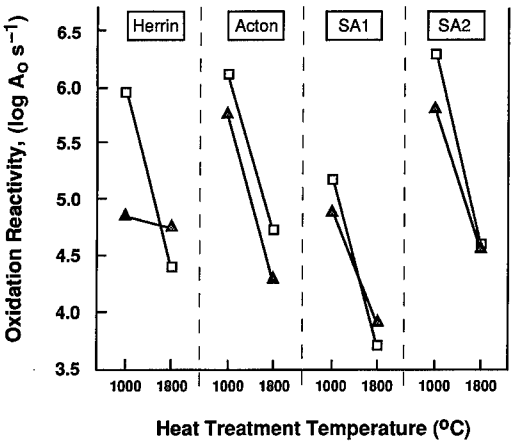

FIG. 2. Intrinsic reactivities at 50% conversion for chars from vitrain/vitrinite-rich and fusain/inertinite-rich samples prepared at 1000°C and 1800°C. Reactivities are derived from DTG profiles such as those in Fig. 1. Note the reactivity switch or convergence observed for three of the four samples as heat treatment temperature is increased to 1800°C. For comparison, the reactivity of residual carbon extracted from a fly-ash sample generated by commercial-scale combustion of Herrin seam coal is found to be log A_O = 4.53 (s^{-1}).

differences between the various components present is lessened by heat treatment.

Direct reactivity comparisons for these lithotype samples and the coal density fractions are shown in Fig. 2.* For comparison, the reactivity of residual carbon extracted from a fly-ash sample generated by commercial-scale combustion of Herrin seam coal is A_O = 4.53 (from previously published data [1]). Figure 2 clearly shows that heat treatment at 1800°C rapidly produces profound changes in char reactivity for most of the samples. The low reactivities observed after 1800°C heat treatment are similar to the reactivity of the Herrin seam residual carbon, which

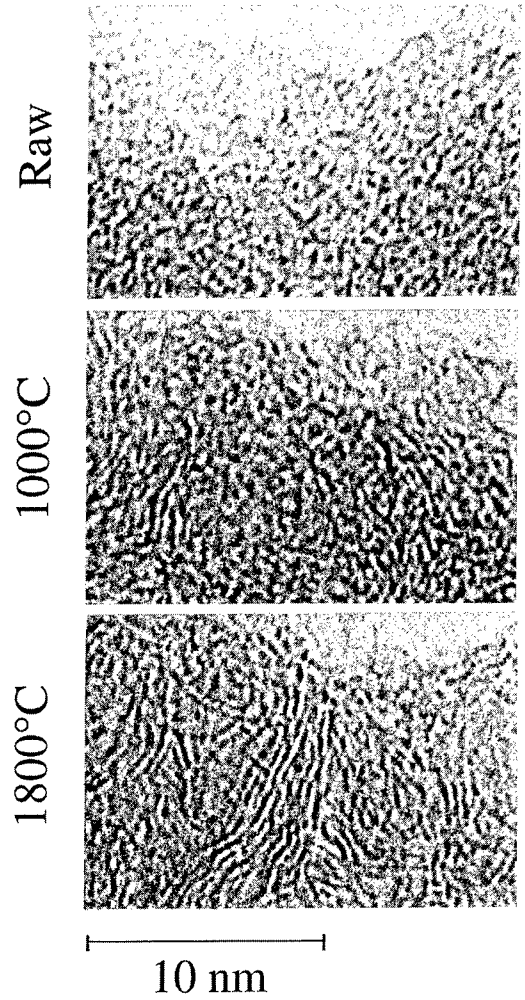

FIG. 3. Small selected regions from HRTEM lattice fringe images of raw and heat-treated vitrain samples from the Herrin seam. Magnification is 4,000,000×.

is typical of many other residual carbon materials [1]. All of the chars from the vitrain/vitrinite-rich samples examined here exhibit almost identical degrees of deactivation between 1000°C and 1800°C (factors of 30–50) despite their widely different geological origins, suggesting the existence of a broadly similar deactivation mechanism.

The inertinite-rich samples show more variability but a generally lower propensity to deactivate than the vitrinite-rich samples, the most striking example being the Herrin no. 6 lithotypes, for which the relative vitrain/fusain reactivities switch as heat treatment temperature is increased. This intriguing behavior warrants a closer look at potential deactivation mechanisms for the Herrin seam samples (see next section).

*In general, the rate of weight loss, dW/dt, and the shape of the DTG profile is determined by char reactivity, which in turn is a function of both temperature and conversion. To meaningfully compare the reactivities of two samples, one would like to match dW/dt values at a point where both conversion and temperature were equivalent. Unfortunately, this coincidence does not typically arise in DTG profiles. This study presents a quantitative comparison by extracting dW/dt values from the DTG profiles at a common conversion (50%), and using typical published activation energies for char oxidation (130 kJ/mol) to obtain preexponential factors, A_O, in the Arrhenius rate expression: $dW/dt = A_O \exp^{(-E/RT)}$. Activation energies have been shown to fall within a relatively narrow range of values for a wide variety of impure carbons [13,22].

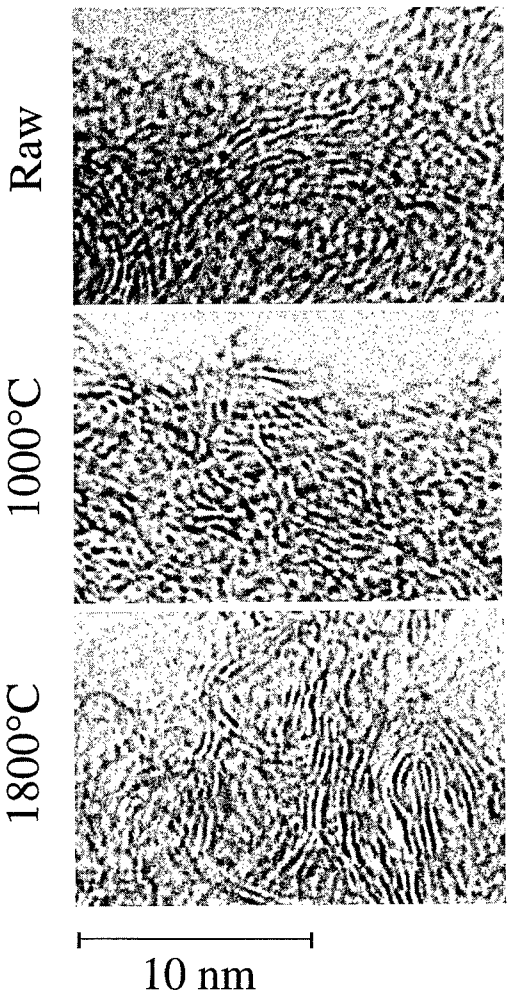

FIG. 4. Small selected regions from HRTEM lattice fringe images of raw and heat-treated fusain samples from the Herrin seam. Magnification is 4,000,000×. Note the recognizable order in the raw material.

Structural Characterization by HRTEM

Results for Herrin seam vitrain are shown in the small selected image sections in Fig. 3. (The full-field fringe images show the trends and the differences between samples more clearly, but are not practical to reproduce in their entirety.) The raw material has a homogeneous, amorphous structure with no evidence of crystalline order. The 1000°C char exhibits some recognizable crystallites with short graphene layers stacked in groups of two to five. After heat treatment to 1800°C, the char shows pronounced crystalline order. The individual graphene layers are long, continuous, and stacked in parallel groups of up to five layers.

The fusain behaves quite differently, as shown in Fig. 4. Crystalline order is already recognizable in the raw material, consisting of short graphene layers stacked in groups of up to eight. The degree of crystalline order increases slightly upon heat treatment to 1000°C. By 1800°C, both the size and linearity (degree of perfection) of the lamellar features have significantly increased.

Examination at low magnification reveals significant mesoporosity in each of the fusain samples. The tendency of inertinites to develop mesoporosity has been previously observed [23]. At 1800°C, the higher reactivity of the fusain compared to the vitrain samples may reflect better accessibility to active sites provided by the mesopore structure.

Discussion

The transient heat treatment experiments show that char reactivity is quite sensitive to preparation conditions for seven of eight samples in the range of interest to combustion, undergoing a dramatic decrease (by factors of 30–50) between 1000 and 1800°C in only 2 s of heating. While 1000°C may be a convenient preparation temperature in the laboratory, chars produced at this temperature do not have the same combustion properties as chars prepared at temperatures more typical of flames (1800°C). The similar reactivities of the 1800°C chars and the residual carbon samples [1] provides support for the theory [3] that in-furnace thermal annealing is a major contributor to the observed low reactivity of residual carbon. The documented sensitivity of char reactivity to heat treatment temperature under these conditions opens up the possibility of tailoring the flame zones of furnaces to minimize deactivation and thus maximize ultimate carbon burnout.

To illustrate the potential significance of thermal deactivation, consider a hypothetical special case in which heat treatment in an isothermal, inert, or reducing environment is followed by oxidation at the same temperature. To compare char reactivities at different temperatures in this scenario, one must account for the effect of temperature on both the oxidation and deactivation kinetics. Given a typical activation energy for oxidation of 130 kJ/mol, increasing temperature from 1000°C to 1800°C will increase intrinsic burning rates by a factor of 114 in the absence of deactivation. Adding the effect of deactivation prior to oxidation (using the data for the Herrin seam vitrain in Fig. 2), the net increase is only a factor of 3.3, corresponding to a much lower effective activation energy of 33 kJ/mol. The resulting weak dependence on temperature is not much larger than the dependence of molecular diffusion rates on temperature, which increase by a factor of 2.3 over the same temperature range based on the $T^{1.75}$ dependence of molecular diffusivity [24]).

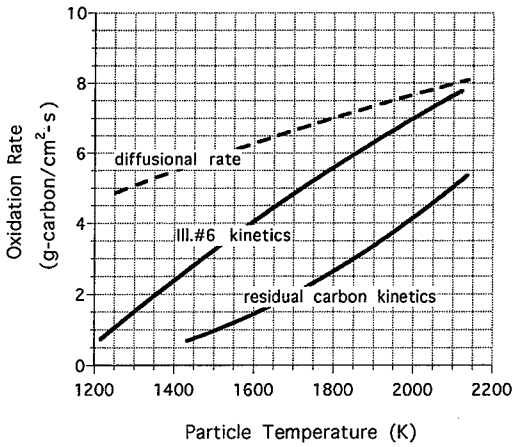

FIG. 5. Comparison of diffusion and combustion rates for char particles of varying reactivity. Predictions are for 100-μm particles burning in 7% oxygen. The entrained flow reactor char prediction is based on previously published kinetics for Illinois #6 chars [24]. The residual carbon prediction was made using the same Illinois #6 kinetics with the preexponential factor reduced by a factor of 4 based on measured burning rates for a variety of residual carbon samples [1].

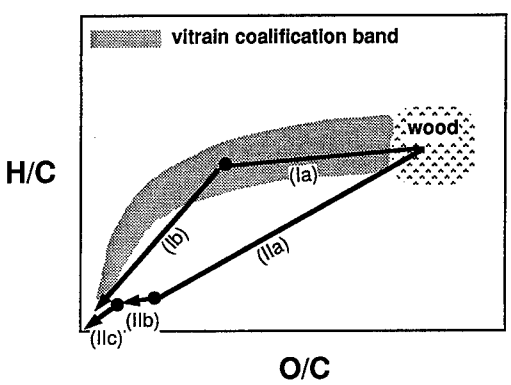

FIG. 6. Coalification diagram illustrating the pathways to high-temperature vitrinite and fusinite chars. Paths: (Ia), vitrinite coalification; (Ib), high-temperature vitrinite carbonization, involving plasticity and high carbon mobility; (IIa), fusinite formation in ancient fires; (IIb), fusinite coalification; (IIc), high-temperature fusinite carbonization.

From this calculation, we see that in cases where thermal deactivation precedes oxidation, intrinsic char burning rates may no longer be so highly sensitive to temperature. The effect on burnout may be particularly significant in the fuel-rich regions of low-NO_x firing systems, where thermal treatment and char deactivation may occur prior to significant oxidation.

In general, the low reactivities observed in fly ash carbons [1,2,20] indicate that char reactivity is more important under combustion conditions than has often been assumed. This is illustrated in Fig. 5 which compares burning rates predicted for two different char samples to the maximum, diffusion-limited rate under the same conditions. The Illinois #6 char from previous entrained flow reactor studies [25] burns well below the diffusion limit at particle temperatures below 1600 K, but approaches the limit closely as temperature approaches 2000 K. Reducing the reactivities (preexponential factors) by a factor of 4 to represent a typical residual carbon material [1], it is seen that the chars burn far from the diffusion-limited rate across the entire temperature range of interest. For this char, representative of those sampled from furnaces, reactivity will be a critical parameter determining its ultimate burnout.

The second significant result of this study is the dependence of thermal deactivation on precursor. The inertinite-rich samples as a class are generally more resistant to thermal deactivation than the vitrinite-rich samples. The differences are most pronounced for the Herrin seam lithotypes, and the degree of deactivation in these samples correlates well with the extent of crystalline structure development observed by HRTEM. The Herrin seam vitrain undergoes significant transformations during heat treatment and deactivates readily, while fusain undergoes more subtle transformations and is more resistant to deactivation. This represents another case [3,17] where crystal structure analysis by HRTEM provides valuable insight into the underlying cause of solid fuel behavior.

The propensity for structural ordering can often be related to the organic composition of the precursor. Oxygen present in organic precursors serves as a cross-linking agent that prevents rearrangement of the graphitic basic structural units during carbonization. Sulfur, being isovalent with oxygen, can also act as a cross-linking agent, especially in nonaromatic sulfur functionalities such as sulfides and thiols [26]. Hydrogen acts in the opposite sense, capping free radicals at the edges of the units and thus inhibiting cross-linking and promoting fluidity. As a function of coal rank, both fluidity and the propensity for structural ordering peaks for the low-volatile, bituminous coking coals that have the highest H/O ratios.

With this background, the behavior of vitrain and fusain can be explained by considering the two pathways in the coalification plot in Fig. 6. Path I represents coalification to vitrinite (Ia) followed by high-temperature carbonization in the laboratory (Ib). Because coalification has selectively removed oxygen, the hydrogen-rich vitrinite softens and the mobile carbon undergoes nanoscale rearrangements to approximately align layer sets. The aligned layers then coalesce readily upon heat treatment, leading

to extended layers, loss of edge sites, and loss of oxidation reactivity.

Regarding fusain, the most widely accepted theory for its origin identifies it as fossil charcoal—the product of ancient forest fires [27]. Fusain is thus charred directly from the wood precursor and follows path II, a more nearly direct path that does not follow the coalification band [28]. This charring occurs while oxygen is abundant, and the woody tissue does not soften or develop extensive crystalline order [16]. It partially carbonizes to form a weakly-ordered char-like material (inertinite) that evolves only slightly in the deposit (IIb) over geologic time [29]. When inertinite is carbonized in the laboratory (IIc), its low hydrogen content precludes fluidity, limits long-range structural rearrangement, and results in more resistance to thermal deactivation. In a sense, the relative disorder present in the initial wood has been preserved or "sealed" into place by the early and rapid carbonization.

Finally, the observed resistance of inertinite-rich chars to thermal deactivation helps to explain an apparent paradox surrounding the role of inertinite [3]—the fact that inertinite is found to yield unreactive and dense chars in laboratory studies [30–33], but that inert, unfused particles do not typically constitute a large fraction of residual carbon in commercial fly-ash samples from U.S. power stations [3,34]. The high-temperature heat treatment received in the furnace may render vitrinite-rich particles at least as unreactive as inertinite-rich particles, thus minimizing the selective enrichment of inertinite as combustion proceeds. Another factor contributing to the relative infrequency of unfused carbon particles may be the presence of inertinite fractions that are indeed fusible at high heating rates and temperatures [35].

Acknowledgments

The authors are grateful for the technical contributions of Drs. Thomas Headley and Donald Hardesty at Sandia and for the advice and sample provided by Dr. A. S. Scott of Royal Holloway, University of London. Financial support for the work at SIU and Imperial College was provided by the U.K. Department of Trade and Industry through ETSU and National Power PLC. Financial support for Sandia and Brown was provided by the Pittsburgh Energy Technology Center of the U.S. DOE and the Electric Power Research Institute.

REFERENCES

1. Hurt, R. H. and Gibbins, J. R., *Fuel* 74(4):471–480 (1995).
2. Jones, A. R., Gibb, W. H., Irons, R. M. A., Price, H. J., Stallings, J. W., and Mehta, A. K., *Proceedings of the EPRI/EPA Joint Symposium on Stationary Combustion NO_x Control,* Kansas City, The Electric Power Research Institute, Palo Alto, CA, May 1995.
3. Hurt, R. H., Davis, K. A., Yang, N. Y. C., Headley, T. R., and Mitchell, G. D., *Fuel* 74(9):1297–1306 (1995).
4. Radovic, L. R., Walker, P. L. Jr., and Jenkins, R. G., *Fuel* 62:849 (1983).
5. Sha, X. Z., Kyotani, T., Tomita, A., *Fuel* 69:1564–1567 (1990).
6. Hecker, W. C., McDonald, K. M., Reade, W., Swensen, M. R., and Cope, R. F., *Twenty-Fourth Symposium (International) on Combustion,* The Combustion Institute, Pittsburgh, 1992, p. 1225.
7. Smith, I. W. and Tyler, R. J., *Fuel* 51:312 (1972).
8. Radovic, L. R., Walker, P. L. Jr., and Jenkins, R. G., *Fuel* 62:209 (1983).
9. Solomon, P. R., Serio, M. A., and Heninger, S. G., *ACS Div. Fuel Chemistry Preprints,* 1986, p. 178.
10. Sahu, R., Levendis, Y., Flagan, R. C., and Gavalas, G. R., *Fuel* 67:275 (1988).
11. Suuberg, E. M., in *Fundamental Issues in Control of Carbon Gasification Reactivity,* Kluwer Academic Publishers, Dordrecht, 1991, pp. 269–305.
12. McCarthy, D. J., *Carbon* 19(4):297–301 (1981).
13. Charpenay, S., Serio, M. A., and Solomon, P. R., *Twenty-Fourth Symposium (International) on Combustion,* The Combustion Institute, Pittsburgh, 1992, pp. 1189–1197.
14. Millward, G. R. and Jefferson, D. A., in *Chemistry and Physics of Carbon,* (P. L. Walker and P. A. Thrower, Eds.), Marcel Dekker, New York, 1978, Vol. 14, p. 1.
15. Levendis, Y. A. and Flagan, R. C., *Carbon* 27:265 (1989).
16. Wornat, M. J., Hurt, R. H., Yang, N. Y. C., and Headley, T. J., *Combust. Flame* 100:131–143 (1995).
17. Davis, K. A., Hurt, R. H., Yang, N. Y. C., and Headley, T. H., *Combust. Flame* 100:31–40 (1995).
18. Essenhigh, R. H., in *Chemistry of Coal Utilization, Second Supplementary Volume* (M. A. Elliott, Ed.), Wiley and Sons, New York, 1981, p. 1310.
19. Crelling, J. C., *ACS Preprint, Div. of Fuel Chemistry* 39(1):13–17 (1994).
20. Beeley, T. J., Crelling, J. C., Gibbins, J. R., Hurt, R. H., Man, C. K., and Williamson, J., *Proceedings of the Eighth International Conference on Coal Science,* Elsevier Science, Amsterdam, 1995, pp. 615–618.
21. Crelling, J. C., Thomas, K. M., Marsh, H., *Fuel* 72(3):349–357 (1993).
22. Smith, I. W., *Fuel* 57:409 (1978).
23. Harris, L. R. and Yust, C. S., *Fuel* 55:233 (1976).
24. Gilliland, *Ind. Eng. Chem.* 26:681 (1934).
25. Hurt, R. H. and R. E. Mitchell, *Twenty-Fourth Symposium (International) on Combustion,* The Combustion Institute, Pittsburgh, 1992, pp. 1243–1250.
26. Derbyshire, F., *Fuel* 70:276 (1991).
27. Jones, T. P., Scott, A. C., and Mattey, D. P., *Int. J. Coal Geol.* 22:37–59 (1993).
28. Fletcher, T. H., Solum, M. S., Grant, D. M., Pugmire, R. J., *Energy Fuels* 6:643–650 (1992).

29. Teichmüller M. and Teichmüller, R. in *Textbook of Coal Petrology,* (E. Stach, Ed.), Bebrüder Borntraeger, Berlin and Stuttgart, 1975, pp. 35–54.
30. Oka, N., Marayama, T., Matsuoka, H., Yamada, S., Yamada, T., Shinozaki, S., Shibaoka, M., and Thomas, C. G., *Fuel Process. Technol.* 15:213–224 (1987).
31. Crelling, J. C., Hippo, E. J., Woerner, B. A., and West, D. P., Jr., *Fuel* 71:151 (1992).
32. Morley, C., and Jones, R. B. *Twenty-First Symposium (International) on Combustion,* The Combustion Institute, Pittsburgh, 1994, pp. 239–248.
33. Parra, J. B., Menendez, R., Alvarex, D., Lester, E., Cloke, M., *Proceedings of the Eighth International Conference on Coal Science,* Elsevier Science, Amsterdam, 1995, pp. 623–626.
34. Hower, J. C., Groppo, J. G., Rathbone, R. F., Brooks, S. M., Graham, U. M., Robl, T. L., Medina, S. S., *Proceedings of the Eleventh International Coal Testing Conference,* May 1995, pp. 49–54.
35. Thomas, C. G., Shibaoka, M., Gawronski, E., Gosnell, M. E., Brunckhorst, L. F., and Phong-anant, D., *Fuel* 72:7:907 (1993).

COMMENTS

Piero Salatino, Università di Napoli, Italy. With reference to HRTEM pictures you showed, they beautifully demonstrate the changes occurring to the turbostratic structure of coal. My concern is how far the deactivation of the chars you considered can be attributed to changes in turbostratic carbon structure rather than to modifications of mineral matter.

Author's Reply. This is a very good question to which we can only provide a partial answer. As you know, the reactivity of these natural materials (coal chars) is related in general to the combined effects of carbon active sites, catalytic active sites, and the accessibility of those sites to oxidizing gases. Heat treatment is known to destroy carbon active sites, to reduce catalytic inorganic surface area through sintering and phase transformations, and to reduce surface area. This paper does not discriminate between these three effects but focuses on the measurement of overall reactivity loss at high temperature for real coal chars.

The HRTEM micrographs give information relevant to carbon active sites and accessibility, but only limited information on potential catalytic impurities. As such HRTEM address only two of the three reactivity components. We should add, however, that the particular chars studied here were derived from traditional bituminous steam coals, whose mineral matter occurs primarily in the form of distinct mineral grains. This mineral matter may have an effect, but we do not expect it to dominate the high temperature reactivity of these coals, as is the case at low temperatures for low rank coals with high concentrations of atomically dispersed inorganics. In recent experiments at Sandia, demineralization of bituminous coals has led to net *increases* in combustion rate, suggesting that transport effects outweigh any catalytic effects under these conditions.

•

A. E. Jacob Akanetuk, Stanford University, USA. It was claimed that the increase in unburned carbon (observed with a low-NO_X burner system) is attributable to purely thermal deactivation. It was also claimed that thermal deactivation increases with increasing temperature. Why then does a low-NO_X burner system, which has lower peak temperatures, produce more unburned carbon? (Some other processes must govern the increase in unburned carbon.)

Author's Reply. We did not mean to suggest that thermal annealing is the sole cause of increased unburned carbon when conventional burners are replaced by low-NO_x burners. The major effect of low-NO_x coal burners is a delay in fuel/air mixing and we would naturally expect a corresponding increase in unburned carbon due to reduced residence time available for char particles in high-temperature, oxygen-rich zones. This is the conventional explanation and does not require an annealing mechanism. We have mentioned the possibility of an *additional* effect related to thermal annealing, which can be stated as follows. Because coal particles in low-NO_x systems spend longer times in hot, fuel-rich zones early in their lifetimes, it is possible that they become deactivated by annealing prior to significant oxidation. In this way we miss the opportunity to attack the young, reactive char with oxygen at high temperature, and must instead try to oxidize an annealed char in a lower temperature zone of the flame. This effect has not yet been proven to be important by measurements or detailed flame simulations, but is a possible implication of the annealing work presented in this paper.

Twenty-Sixth Symposium (International) on Combustion/The Combustion Institute, 1996/pp. 3111–3118

STRUCTURAL CHANGES OF CHAR PARTICLES DURING CHEMICALLY CONTROLLED OXIDATION

X. ZHANG, A. DUKHAN AND I. I. KANTOROVICH
Department of Mechanical Engineering
Ben-Gurion University of the Negev, P.O. Box 653
Beer-Sheva, Israel

E. BAR-ZIV
Nuclear Research Center-Negev, P.O. Box 9001
Beer-Sheva, Israel

A. KANDAS AND A. F. SAROFIM
Department of Chemical Engineering
Massachusetts Institute of Technology
Cambridge, MA 02139, USA

The structural changes—particle diameter, shape, porosity, fine structure—during the oxidation of highly porous synthetic char (Spherocarb) particles at kinetically controlled conditions were investigated to provide insight on the factors that govern fragmentation during combustion. More than 100 experiments were conducted in an electrodynamic chamber in the temperature range of 700–1000 K, for particles of initial diameters of 150–250 μm and densities of 0.45–1.0 g/cm^3 for carbon conversions up to 99%. Particle mass, density, size, and shape were measured continuously. Similar experiments were conducted in a thermogravimetric analyzer (TGA) to provide samples for determination of the fine structure of the chars using high-resolution transmission electron microscopy (HRTEM). For a subset of particles that were analyzed in detail, the total porosity increased from 0.60–0.76 to 0.83–0.88, when allowance is made for the observed particle shrinkage. Although the maximum porosity surpassed the value of ca. 0.7 required for percolative fragmentation in a material of uniform porosity, little fragmentation was observed. The explanation for this is that the particles have a bimodal pore size distribution and the porosity of neither the macroporous nor the microporous regions exceeded the critical porosity. The maximum final macroporosity was calculated to be 0.55–0.60. The HRTEM images showed an increased order in the microporous regions, which accounts for the densification of the chars responsible for particle shrinkage and the maintenance of particle integrity.

Introduction

The changes in particle structure during carbon oxidation are of importance because they can influence particle size and shape, which in turn influence reaction times. Moreover, the changes in structure influence particle fragmentation, which affects combustion by changing the particle size and has a major impact on the number and size of fly ash particles produced per coal particle [1,2]. There are several mechanisms of char fragmentation, including (1) percolative fragmentation where the oxidation increases the porosity until the interconnectivity of the solid matrix is interrupted, (2) fragmentation resulting from the enlargement of macropores until they interconnect and result in particle breakup, and (3) fragmentation resulting from mechanical forces acting on weakened parts of a char particle. Reports of fragmentation in the combustion literature date back to the study of Davis and Hottel [3] on the oxidation of carbon spheres and include the studies of Walker et al. [4] and Dutta et al. [5].

The focus of this paper is the changes in the particle structure during char oxidation in the chemically, kinetically controlled regime (regime I) and its impact on fragmentation. A useful reference point is percolation fragmentation, the theory of which has been developed for materials with a uniform pore size, for which various theories predict that the fragmentation occurs at porosities of ca. 0.7 (as summarized in Ref. 6). Kerstein and Niksa [6] carried out experimental measurements on large carbon particles, 52-mm-diameter and 1.5-mm-thick disks, and observed that the samples disintegrated into

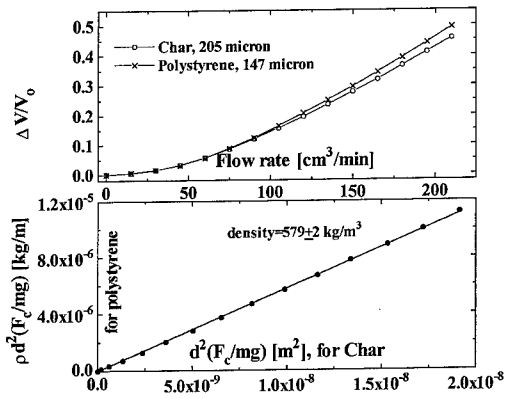

FIG. 1. Top: ratio of drag force to weight (F_c/mg = $\Delta V/V_o$) versus flow rate for polystyrene particle (x) and for Spherocarb particles (o). Bottom: (F_c/mg)ρd^2 of the polystyrene particle versus (F_c/mg)d^2 of the char particle and best fit (solid line).

very fine fragments at the predicted critical porosity. They showed that this process was reproducible. However, coal chars tend to have a wide pore-size distribution, ranging from micropores having dimensions of 2–3 nm, which account for most of the internal surface area, to macropores having dimensions in the tens of micrometers, which often account for the major fraction of the porosity. For macroporous solids, the enlargement of macropores can lead to fragmentation as particle continuity is interrupted. This was shown early for diffusion-controlled reactions and, more recently, by Weiss and Bar-Ziv [7] and Zhang et al. [8] in synthetic char particles (Spherocarb) of 200 μm reacting under chemically controlled conditions. Modeling the combustion of char, which includes aspects of pore enlargement connected to fragmentation, was carried out by Kang et al. [1], Salatino and co-workers [9–11], and Kantorovich and Bar-Ziv [12,14]. The problems in applying theory to chars are complicated by two factors. The first is the wide range of pore size distribution. The second is that the char particles shrink because of densification, a phenomenon that has a major impact on particle porosity.

The purpose of this study is to present the structural changes during oxidation to the high porosity of a synthetic char—Spherocarb. The Spherocarb particles have the advantage of being essentially ash free and spherical and yet having a high initial porosity in the range of 60–80%, distributed approximately one-third to two-thirds between microporosity and macroporosity, respectively [13]. The work was carried out in two laboratories: Ben-Gurion University, where single-particle experiments were conducted in an electrodynamic chamber, and MIT, where thermogravimetric analyzer (TGA) experiments were performed and samples were characterized by high-resolution transmission electron microscopy (HRTEM). The results of the study provide insights on how the macroporosity and microporosity evolve with increasing conversion under regime I conditions and how this evolution impacts fragmentation.

Experimental

Electrodynamic Chamber Experiments

Observation of the detailed process of fragmentation of single, highly porous char particles in regime I were carried out in an improved electrodynamic chamber (EDC). The EDC and its diagnostic systems were described in detail in recent publications [7,15–17] and will not be discussed here. In these experiments, a particle was heated vertically from the bottom by a CO_2 laser beam. The DC voltage, responsible for the levitation of the particle, is proportional to the vector sum of the gravitational, photophoretic, and free convection forces [7,15–17]. The three forces were uncoupled by periodic interruption of the laser [17]. The DC voltage was measured every second by a data acquisition system, and a CCD camera continuously recorded the shadow of the particle for size and shape measurements. Freeze-frame capabilities and shutter control facilitated the digital analysis of individual images. A Mutech Corporation frame-grabber board, model IVP, was used for image analysis. Size calibration was carried out by measurements of a 155 ± 1-μm-diameter wire, which was placed across the center of the EDC.

Particle density was measured at zero conversion by the drag force on a particle because of imposed flow, also described in Refs. 7 and 15. Figure 1 (top) presents the ratio of the drag force to weight ($\Delta V/V_o$, where ΔV is the voltage difference of flow and nonflow voltages and V_o is initial voltage without flow) of a polystyrene particle and a Spherocarb particle. The line shape depends on the flow field within the chamber (as has been shown by D'Amore et al. [18]), and the magnitude is inversely proportional to ρd^2 [7]. Because the density of the polystyrene is known, the density of the Spherocarb can be obtained from the slope of a plot of $(\Delta V/V_o)(\rho d^2)$ for polystyrene versus $(\Delta V/V_o)d^2$ for Spherocarb (as shown in the lower half of Fig. 1), which yields a density for the Spherocarb particle of 579 ± 2 kg/m^3. This method is valid for spherical particles. During char oxidation, as the particles become aspherical, the densities of particles are obtained from ratio of mass (obtained from voltage) and volume (obtained from the images of a particle from two perpendicular angles).

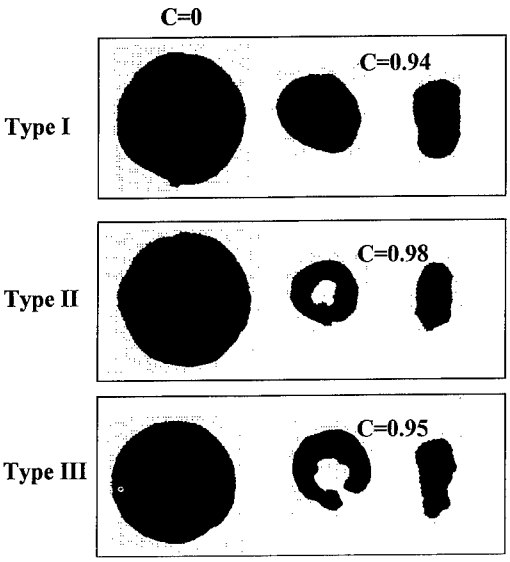

FIG. 2. Example of three types of shapes of initially spherical particles at high conversion. Type I—a disk without a hole at 94% conversion. Type II—a disk with one hole at 98% conversion. Type III—an open disk at 95% conversion. For comparison, next to each form, a print is shown of the initial particle. The prints at high conversion are from two perpendicular sides.

Thermogravimetric Analyzer and High-Resolution Transmission Electron Microscopy Measurements

Spherocarb particles at various conversions were produced by reaction in a TGA in air at a temperature of 773 K. Carbon conversions were determined by analyzing the weight versus time, starting from an initial weight of ca. 10 mg.

For HRTEM observation, the samples were ground for 5 min in a ball mill or a mortar and pestle for higher-oxidation samples in which sample size was limited. The resulting powder was then suspended ultrasonically in ethanol and deposited dropwise on lacey carbon TEM grids. An Akashi/TOPCON 002B transmission electron microscope with an LaB_6 filament operating at 200 keV was then used to record high-resolution (590-kX) images of each sample. The images were digitized, and image analysis software (SEMPER 6P, Synoptics Ltd., Cambridge, UK) developed specifically for application with high-resolution electron microscopy was used to manipulate the stored images to extract data that could characterize physically the Spherocarb.

Characterization was accomplished using a Fourier Transform of the TEM images to establish periodicities. By then applying a mask to remove unwanted noise in the image, the annulus was reverse transformed to obtain a gray, filtered image. This image was then converted to a two-color "extracted structure" by establishing an intensity threshold value for the pixel intensity. This extracted structure then became the basis for the statistical analysis of the lattice length (L_a) and d_{002} carbon spacing, as described in Ref. 19.

Results

More than 100 oxidation experiments were carried out in air and in pure oxygen, with moisture and without it, at temperatures varying from 700 to 1000 K in the EDC for conversions up to 80%. Another 22 experiments were conducted up to near complete (up to 99%) conversion. The experiments in the TGA were carried out in air at 773 K for conversions up to 97%. Note that Spherocarb oxidation in the given temperatures is intrinsic (in chemically controlled condition), as concluded by Hurt et al. [20]. The structural transformations observed are summarized next.

Particle Size and Shape

In all experiments involving the EDC, the particle underwent nonuniform shrinkage, transforming an initially spherical particle into a disk at 50–60% conversion. The particle was observed to rotate frequently up to about 40% conversion with a consequent uniform shrinkage. After that, the particle flipped occasionally and nonuniform shrinkage started, as observed previously [7,16,17]. The frequency of flips decreased noticeably when the particle evolved into a disk at about 60% conversion. At higher conversion (>85%), the particle undertook one of the following three shape types: type I—a disk without a hole; type II—a disk with one or more holes; type III—an open disk. Figure 2 shows the three types at high conversions (from two perpendicular sides) together with images of the initial particles.

In the experiments in the TGA, the particles maintained their spherical symmetry to high conversions (see Fig. 3). The differences between the shape of particles during oxidation in the EDC and the TGA are due to the nonuniform heating of particles in the EDC [17]. This nonuniform heating, induced by irradiation from below, results in a preferential reaction of the lower side of the particle, and explains the shape, the flipping of the particle as it becomes unbalanced, and the eventual formation of a hole in the center.

The results in the EDC and the TGA both show the dramatic shrinkage of the particles at high conversions. This is consistent with the previously reported densification of carbon during regime I gasification or oxidation [21,22]. The rationalization for the densification was that the oxidation or gasification reactions induced reorganization of the fine

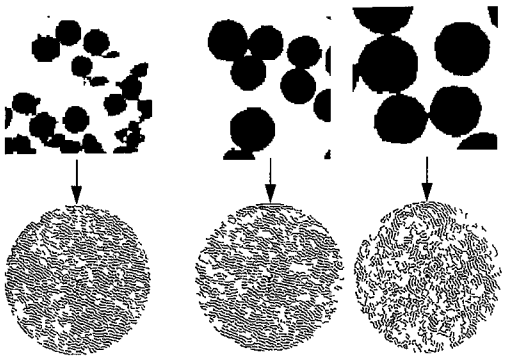

FIG. 3. Shadowgraphs of Spherocarb particles (initial diameter of 160 μm) reacted in air at 773 K and the HRTEM structures for each sample: right, 0% conversion; middle, 44% conversion; left, >97% conversion.

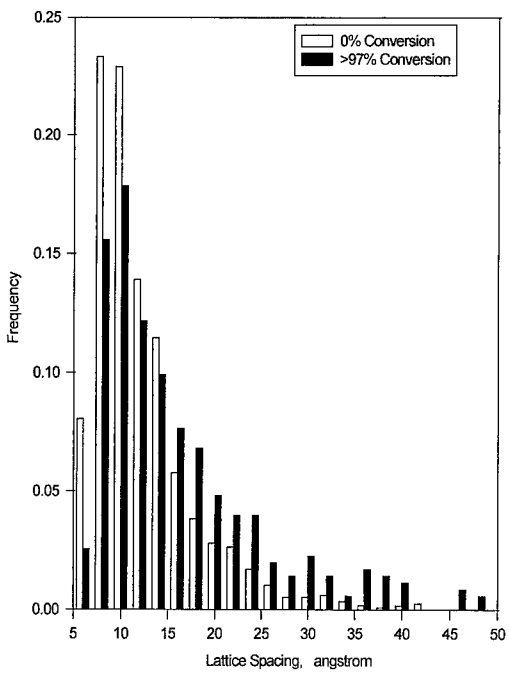

FIG. 4. Distribution of lattice lengths L_a (in Å) for Spherocarb particles at zero and >97% conversions.

structure, leading to loss of pores and contraction of the microporous regions. This hypothesis was tested in this study by the use of HRTEM to study the changes in fine structure of the char with increasing carbon conversion.

Fine Structure

The results of the images abstracted from the HRTEM using image analysis are shown together

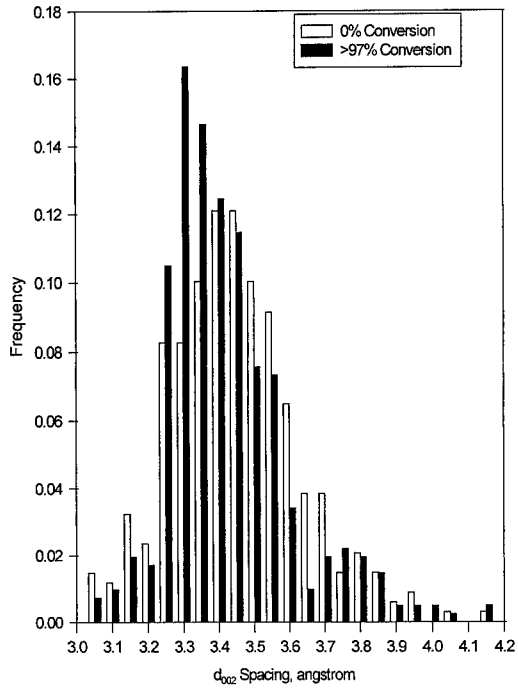

FIG. 5. Distribution of interlattice spacings d_{002} (in Å) for Spherocarb particles at zero and >97% conversions.

with the parent samples in Fig. 3. The spacing between the fringes in the picture is around 3.4 Å, slightly larger than that expected for graphites. The images showed an increasing order with conversion. A quantitative measure of the increased order is provided by the lattice length L_a of the different "graphitic planes." These are shown in Fig. 4 for the original Spherocarb and the particles at high conversion (>97%). At high conversions, there is systematic increase in the longer lattice lengths (>15 Å). The interlattice spacing also decreased slightly. The peak in the distribution function for the original Spherocarb particles was at 3.41 Å, whereas at the high conversion (>97%), the peak had shifted to about 3.3 Å (see Fig. 5). This ordering of the microporous structure has important ramifications to the fragmentation of the particles.

Fragmentation

The particles chosen for this study had a high initial porosity (61–78%). From the percolation theory for particles with a uniform pore size, the particles that started with porosities exceeding the critical value (0.7) [6] should have fragmented after very little conversion. For more than 100 experiments carried out with conversions up to 80%, no particle showed fragmentation. For 22 experiments (listed in Table 1) in which the conversion approached

TABLE 1
Summary of results of Spherocarb particles oxidized in EDC, in air at various temperatures.

Exp. no.	T[a] (K)[b]	d_o [c] (micron)[b]	ρ_o [d] (g/cm^3)[b]	ε_o [e]	Hole formed @ conversion	Fragmented @ conversion	Shape type* final burnout
e7-271	930	247	0.76	0.65	83.8	89.8	3
e7-273	880	172	0.58	0.74	86.1	none	3
e7-281	920	204	0.59	0.73	87.7	97.5	3
e7-312	900	176	0.59	0.73	none	none	1
e7-314	900	177	0.71	0.68	none	none	1
e7-315	940	200	0.78	0.64	95.9	none	2
e8-11	910	198	0.61	0.72	none	none	1
e8-12	940	189	0.45	0.80	70.9	95.1	3
e8-14	860	206	0.50	0.77	90.8	none	2
e8-21	850	212	0.58	0.74	91.0	none	1
e8-22	880	215	0.85	0.61	none	none	1
e8-23	870	187	0.78	0.65	none	none	1
e8-24	910	205	0.48	0.78	66.3	none	2
e8-31	870	219	0.68	0.69	none	none	1
e8-32	850	176	0.71	0.68	66.0	none	2
e8-33	970	187	0.63	0.71	82.8	none	2
e8-34	940	186	0.69	0.69	none	none	1
e8-41	920	185	0.51	0.77	none	none	1
e8-51	930	185	0.56	0.75	91.1	92.6	3
e8-52	900	177	0.53	0.76	none	none	1
e9	780	205			86.0	97.0	3
e10	830	205	0.579	0.74	64.7	none	3

*Type 1 is a disk without a hole; type 2 is a disk with one hole or more; type 3 is adisk that opens.
[a]T is temperature.
[b]Values in parenthesis in density column are % porosity.
[c]d_o is initial diameter.
[d]ρ_o is initial density.
[e]ε_o is initial porosity.

completion (up to 99% conversion), 5 particles experienced minor fragmentation and about half developed holes in the particle center. A particle breakup is shown in Fig. 6, which presents a typical conversion versus time curve with a sequence of shadowgraphs depicting the shape development of a Spherocarb particle of 204 μm diameter at various conversions, oxidized in air at $T = 920$ K (experiment number e7-281, in Table 1). The particle conversion was obtained from the weight loss of the particle assuming that the charge remained constant, a good assumption at this temperature [15]. The initially spherical particle turned into a disk at about 60% conversion. Spatial dimensions of the particle are included in the figure. The projected images from two perpendicular directions at 88% conversion show that the disk diameter decreased to 75% of the initial particle diameter, whereas the thickness decreased to 62% of the initial diameter and a hole appeared around the center of the disk. The hole grew with increasing conversion and, at ca. 98% conversion, evolved into an open ring. Further burning caused the particle to break into two fragments. The print at this conversion shows one-half of the broken ring. In fact, both halves were suspended in the chamber after fragmentation. These two fragments were oscillating around the center at a large distance from each other. Because only one could be suspended in the center, the field parameters (AC and DC amplitudes and AG frequency) were adjusted such that one of the fragments drifted away and the other was kept. This other fragment continued to oxidize and eventually broke into two other fragments at higher conversion.

Table 1 summarizes the results of the experiments carried out to high conversions only. From the 22 experiments, only 5 particles fragmented. One can see that fragmentation occurred only for those particles that developed opened disks—type III particles. However, not all particles that developed holes fragmented but only those particles for which the progress of the reaction produced shapes where the particle continuity was broken.

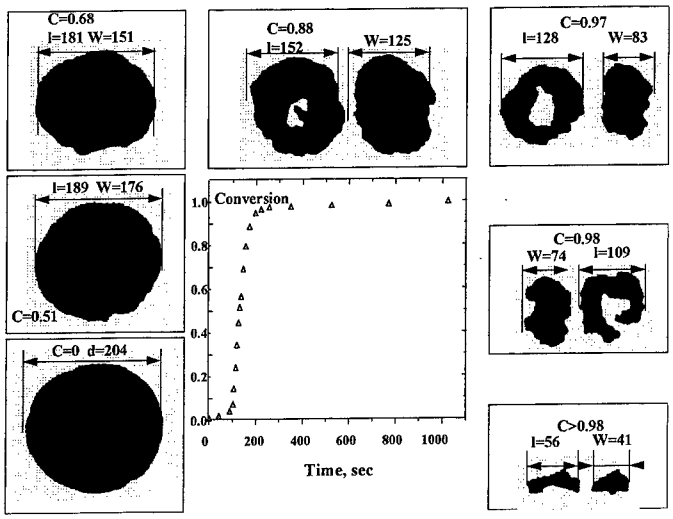

FIG. 6. Conversion versus time and a sequence of shadowgraphs presenting the development of shape of a 204-μm Spherocarb particle oxidized in air at 920 K as a function of conversion; C refers to conversion, l to length, and w to width.

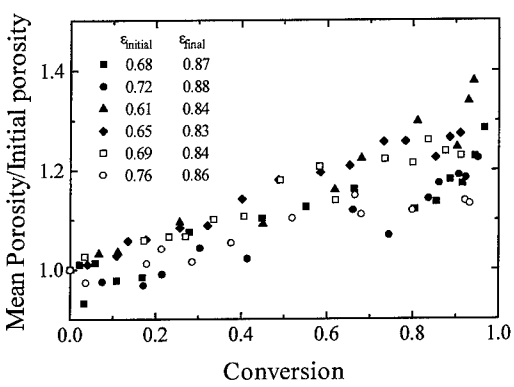

FIG. 7. Ratio of porosity to initial porosity versus conversion. Initial and final porosities are indicated.

Discussion

To understand the lack of fragmentation at high conversions in these studies, one needs to examine the separate behavior of the macroporosities and microporosities. The change in total porosity of the particles versus conversion was obtained for six experiments from the changes in particle mass and volume. The initial and final values of the porosities were obtained by assuming that the dense phase had the density of graphite (2200 kg/m^3), a reasonable assumption given the proximity of the interlattice spacings of the microstructure of the Spherocarb to that of graphite. The results in Fig. 7 demonstrate that although the porosity increase is less than would be expected in the absence of particle shrinkage, it is sufficient to provide final porosities in the range of 0.83–0.87 in excess of the percolation threshold of ca. 0.7 for a homogeneous material.

With about onethird of the porosity of Spherocarb particles being in the micropores and twothirds in the macropores [15], the initial macroporosity is in the range of 40–50%, well below the critical value, and the microporosity is half that value. Such a distribution can be considered approximately bimodal. Kantorovich and Bar-Ziv [12] showed that in the macropore scale, micromedium can be considered "quasi-solid"; therefore, the fragmentation in the macropore scale is insensitive to microporosity. Similarly, the influence of macroporosity is nonessential for processes on the micropore scale. Thus, one can consider separately fragmentation thresholds in different length scales—macro and micro. The results of Hurt et al. [22] show that the macrofeatures, including macropores, in chars shrink in proportion to the shrinkage of the entire particle, so the macroporosity will stay constant during conversion. The microporosity will increase but the values, obtained as the difference between the total porosity and the macroporosities, will always be considerably less than the threshold value of 0.7. Therefore, the lack of fragmentation of the Spherocarb particles even at high conversions can be explained by the bimodal pore distribution, where the microporous and macroporous regions maintain their integrity, because neither reaches a porosity equal to the percolation threshold.

The formation of holes around the center of the particle was a result of the uneven heating of the particle resulting in the local acceleration of the reaction rate. When the holes break through the walls of the particle, a ring is obtained and the further selective reaction can result in the fragmentation for selected particles as was observed.

The results presented in this paper on the changes in the macrostructure and microstructure of carbons

can provide guidance to the development and refinement of models [8,12,14] that can take into account the ordering that leads to shrinkage as well as the changes in the pore structure of chars with oxidation or gasification. The data obtained in the EDC showed that fragmentation is of less significance than might have been inferred from simple percolation theory. The information on the microstructure of carbons provides insights on the reordering of the carbon structure that results in the densification of the chars and the preservation of the structural integrity of particles.

Summary and Conclusions

There was no observation of fragmentation of the entire particle structure in all of the numerous (considerably more than 100) experiments carried out, including the 22 conducted to high conversions. Experimental porosity data show that the total porosity increased from an initial value of 0.6–0.76 to a final value of 0.83–0.88. For the initial polymodal pore size distribution of Spherocarb, both the macroporosity and microporosity are considerably less than the critical porosity of 0.7. Therefore, consumption of carbon inside the particle was compensated by reordering and shrinkage so that the percolation threshold is not attained for the entire particle. Evidence is provided that from the examination of the microstructure of particles at different conversions, the shrinkage is the result of the increased ordering of the graphitelike microstructures in carbons with increased carbon conversion.

It was observed that holes were formed at 65–96% conversion in 13 experiments. These holes are a consequence of nonuniform rate of reaction obtained under nonuniform laser heating. The expansion of such holes led to fragmentation in a few cases, but this mechanism of fragmentation is quite distinct from percolative fragmentation.

Acknowledgments

The authors are grateful for support received from the United States–Israel Binational Science Foundation, Grant No. 9400077/1 and the U.S. Department of Energy.

REFERENCES

1. Kang, S. G., Helble, J. J., Sarofim, A. F., and Beer, J. M., *Twenty-Second Symposium (International) on Combustion,* The Combustion Institute, Pittsburgh, 1988, pp. 231–238.
2. Helble, J. J. and Sarofim, A. F., *Combust. Flame* 76:183–196 (1989).
3. Davis, H. and Hottel, H. C., *Ind. Eng. Chem.* 26:889 (1934).
4. Walker, P. L. Jr., Rusino, F., and Austin, L. G., *Adv. Catal.* 11:133 (1957).
5. Dutta, S., Wen, C. Y., and Belt, R. J., *Ind. Eng. Chem. Proc. Des. Dev.* 16:20 (1977).
6. Kerstein, A. R. and Niksa, S., *Twentieth Symposium (International) on Combustion,* The Combustion Institute, Pittsburgh, 1984, pp. 941–949.
7. Weiss, Y. and Bar-Ziv, E., *Combust. Flame* 95:362–373 (1993).
8. Zhang, X., Dukhan, A., Kantorovich, I. I., and Bar-Ziv, E., "Bulk Fragmentation of Highly Porous Char Particles in Regime I," accepted by *Combust. Flame* 106:203–206 (1996).
9. Salatino, P. and Massimilla, L., *Powder Technol.* 66:47–52 (1991).
10. Miccio, F. and Salatino, P., *Twenty-Fourth Symposium (International) on Combustion,* The Combustion Institute, Pittsburgh, 1992, pp. 1145–1151.
11. Salatino, P., Miccio, F., and Massimilla, L., *Combust. Flame* 95:342–350 (1993).
12. Kantorovich, I. I. and Bar-Ziv, E., "Microstructural Evolution of Char under Oxidation Induced by Uneven Heating," accepted by *Combust. Flame* 105:80–91 (1996).
13. Hurt, R. H., Ph.D. Thesis, Department of Chemical Engineering, Massachusetts Institute of Technology, Cambridge, MA, 1987.
14. Kantorovich, I. I. and Bar-Ziv, E., *Combust. Flame* 97:61–78 (1994).
15. Bar-Ziv, E. and Sarofim, A. F., *Prog. Energy Combust. Sci.* 17:1–65 (1991).
16. Weiss, Y. and Bar-Ziv, E., *Combust. Flame* 101:452–460 (1995).
17. Weiss, Y., Benari, Y., Kantorovich, I. I., Bar-Ziv, E., Krammer, G., Modestino, A., and Sarofim, A. F., *Twenty-Fifth Symposium (International) on Combustion,* The Combustion Institute, Pittsburgh, 1994, pp. 519–525.
18. D'Amore, M., Donsi, G., Giordano, P., and Raso, G., "Single Particle Operations by LDA-Assisted Electrodynamic Thermogravimetry," Seventh Int. Symp. on Application of Laser Techniques to Fluid Mechanics, Lisbon, Portugal, July, 1994.
19. Palotas, A. B., Rainey, L. C., Feldermann, C. J., Sarofim, A. F., and Vander Sande, J. B., "Soot Morphology: An Application of Image Analysis in High-Resolution Transmission Electron Microscopy," accepted by *Microscopy Res. Techniques* 33:266–278 (1996).
20. Hurt, R. H., Sarofim, A. F., and Longwell, J. P., *Energy Fuels* 5:290–299 (1991).
21. Hurt, R. H., Sarofim, A. F., and Longwell, J. P., *Combust. Flame* 95:430–432 (1993).
22. Hurt, R. H., Dudek, D. R., Longwell, J. P., and Sarofim, A. F., *Carbon* 26:433–449 (1988).

COMMENTS

Thomas H. Fletcher, Brigham Young University, USA. Does Spherocarb have a shell of different porosity and reactivity, with a more porous interior?

Would the EDB keep the small particles together after fragmentation, and hence mask fragmentation events?

Author's Reply. Spherocarb particles are more or less homogeneous throughout the entire volume of the particle, both in reactivity and porosity.

When a charged particle fragments it forms smaller particles with different ratios of charge to weight. In an electrodynamic chamber (EDC) these fragments will be suspended in different positions and with different dynamic behavior. Since it is unlikely that there will be two fragments with equal mass to weight ratios, fragmentation events cannot be masked in an EDC.

•

Robert Hurt, Brown University, USA. It has been observed in captive particle imaging experiments that some pulverized char particles (typically cenospheric) become disconnected at high conversion, and that the fine fragments are not liberated, but remain attached to the primary particle, often after rearrangement to a more consolidated form, ultimately yielding a single ash particle at the end of combustion. This phenomenon may be related to Van der Waals forces between the fine fragments ($<10\ \mu m$), which are in the colloidal size range known to agglomerate spontaneously. Do you observe this in your experiments as well? It offers other mechanism to explain the lack of fragmentation and to explain shrinkage for certain particle types.

Author's Reply. We believe that Van der Waals forces (attraction) are responsible for "pulling" together the microcrystals after their edges were disconnected due to preferential reaction at edge. Therefore, the same mechanism is probably valid for both cases (one described by you and shrinkage).

•

Robert H. Essenhigh, The Ohio State University, USA. The description of the behavior of the char particles on combustion, that they developed a hole in the center, is very similar behavior to that reported by Bansall et al. [1] studying Spheron 6 though his results were generally qualitative, not quantitative to the extent reported in this paper. However, the explanation was in terms of preferential reaction at edge atoms rather than basal plane atoms on account of the Spheron 6 structure. The carbon plates were very highly organized at the particle surface, with their planes substantially parallel with the surface, but the degree of organization decreased with approach to the particle center on account of space. Consequently, reaction progressed to the center by attack on the edge atoms down the edges of the adjacent plates until the oxygen reached the center when it was possible to react-out the more randomly organized plates to produce a hole. Is this essentially the behavior being (re-)reported here? And is an explanation in terms of preferential attack on the edge atoms rather than the basal planes equivalent to what is being presented in this paper?

REFERENCE

1. Bansall, R. C., Vastola, F. J., and Walker, P. L., *J. Colloid Inter. Sci.*, 32:187–194 (1970).

Author's Reply. Spherocarb particles have random distribution of the microcrystals and therefore the effect observed cannot be attributed to the same effect as in Spheron 6. The preferential consumption at the center and consequently the local fragmentation observed is attributed to the temperature gradient imposed on the particle by non-uniform radiation. The temperature gradient forms a gradient in reaction similar to that in regime II, except that in the present case high reaction rate is at the particle center that consequently causes local percolation fragmentation at the center.

Twenty-Sixth Symposium (International) on Combustion/The Combustion Institute, 1996/pp. 3119–3125

SURFACE HETEROGENEITY IN THE FORMATION AND DECOMPOSITION OF CARBON SURFACE OXIDES

M. C. MA AND B. S. HAYNES
Department of Chemical Engineering
The University of Sydney
NSW 2006, AUSTRALIA

The formation of surface oxides on exposure of carbon (Spherocarb) to oxygen (16–6560 Pa) at temperatures at ca. 700 K has been investigated experimentally using controlled-atmosphere thermogravimetry and temperature-programmed desorption (TPD) with evolved gas analysis. Under the conditions of the study, Type B oxides are formed, with the gasification of one C atom (as CO or CO_2) for every O atom that is bound to the surface.

The broad TPD spectrum obtained for the decomposition of Type B oxides formed on an initially clean surface is invariant over a wide range of initial oxide loadings, from 45 to 990 μmol g^{-1}. It is concluded that lateral interactions between adsorbed species do not affect the kinetics of decomposition of the surface oxides and that the broad TPD spectrum results entirely from the heterogeneous nature of the carbon surface and the oxides formed on it. Activation energy distribution energies for the decomposition of Type B oxides range from ca. 225 to 475 kJ mol^{-1}.

The formation of oxides with a particular activation energy occurs purely statistically, with the fraction of new oxide, having decomposition activation energies in the range E and $E + dE$, being simply $\Psi_0(E)\,dE$, where $\Psi_0(E)$ is a characteristic of the carbon itself and independent of the oxide loading. Therefore, the rate of formation of complexes having a particular activation energy for their thermal decomposition can be expressed simply in terms of the overall rate of formation of Type B complexes and the distribution $\Psi_0(E)$, which is essentially the same as the activation energy distribution function recovered from the TPD spectra.

Introduction

The development of a turnover model of carbon oxidation requires an understanding of the kinetics of the formation and behavior of carbon surface oxides. There have been many studies of the kinetics of oxygen chemisorption on carbon and of the thermal decomposition of these complexes to yield gaseous carbon oxides [1–7]. However, it has long been apparent that no simple set of kinetic parameters can be used to describe these phenomena and more attention is now being paid to chemisorption and desorption models with variable or distributed parameters.

The success of Elovich kinetics in describing rates of oxygen chemisorption on carbons may suggest that the barrier for adsorption increases as oxides accumulate on the surface because of interactions between the chemisorbed species and unoccupied sites [1]. On the other hand, the observations are also consistent with the existence of a variety of adsorption sites on the heterogeneous carbon surface, giving rise to a distribution of activation energies for adsorption [2].

Even for desorption from a homogeneous surface, the activation energy E and the frequency factor A for the desorption process may be influenced by lateral interactions between adsorbed entities, and coverage-dependent parameters (A and E) again occur [3]. However, another source of variability in A and E may be structural heterogeneity of the surface [4–7] as has often been invoked in descriptions of the kinetics of the decomposition reactions of carbonaceous materials, such as in the pyrolysis of coal and the aging of oil shales [8–11].

An additional cause of diversity in the kinetic parameters required to describe the formation and decomposition of carbon surface oxides is that the formation of surface complexes on carbon proceeds by two stoichiometrically distinct pathways [2]. Type A occurs with the adsorption of oxygen without gasification of the substrate:

$$-C + O_2 \rightarrow -C(O_2)$$

(two Type A O atoms adsorbed)

Type B chemisorption, which is favored at higher temperatures and longer exposures to oxygen, leads to the gasification of one C atom for every O atom chemisorbed:

$$-C + O_2 \rightarrow -C(O) + CO,CO_2$$

(one Type B O atom adsorbed plus one C atom gasified).

Furthermore, when carbon surface oxides of either Type A or Type B are decomposed under inert TPD conditions, both CO and CO_2 are evolved. If the complexes are formed at low temperatures (<500 K), the mole fraction of CO_2 in the degas products may be as high as 20%, but if the complexes are formed at higher temperatures (>650 K), that fraction falls to ca. 10% or less [12].

In this paper, we address the issue of whether the heterogeneity apparent in the kinetics of decomposition of carbon surface oxides is induced by coverage-related effects such as lateral interactions, whether it is intrinsic to the carbon itself, or whether it derives from some combination of these effects. Resolution of this question then allows us to address the relationship between the formation and the decomposition of surface oxides. We employ relatively high temperature conditions ($T \approx 700$ K) so that the oxides being studied are predominantly of Type B with degas products consisting mostly (>85%) of CO.

Experimental

The experimental approach employed in this work is largely based on previously developed procedures [2,4]. In short, a sample of carbon is suspended inside a furnace from the weighing arm of a microbalance to enable weight changes associated with the formation and decomposition of surface oxides to be monitored. The experiments are conducted under a controlled flow of gas through the furnace, and the formation of gaseous carbon oxides (CO and CO_2) is determined by analysis of the gases leaving the furnace.

In the present work, a combined thermogravimetric/differential thermal analyzer (Setaram TG-DTA 92), operating at atmospheric pressure, is employed. The furnace tube in which the sample is suspended is 280 mm long with an internal diameter of 20 mm. The gas flow through the tube consists of a constant balance-head purge flow of N_2 (150 sml min^{-1}) plus an auxiliary gas flow (50 sml min^{-1}) of either N_2 or a known O_2/N_2 mixture, depending on whether inert or reactive conditions are being studied. An oxygen scrubber (Alltech Oxy-Trap) is used to remove O_2 from the high-purity N_2 streams to concentrations below 0.1 ppm to ensure their inertness; all streams are dried using molecular sieve driers. The auxiliary gas flow, controlled by mass flow controllers, is introduced at the top of the furnace tube to allow rapid, clean switching between the reaction conditions.

The sample temperature in the furnace is monitored continuously via a thermocouple in contact with the sample crucible. This thermocouple was calibrated (± 1 K) in situ using melting point standards (In, 430 K; Pb, 601 K; Zn, 693 K; Al, 993 K; Ag, 1235 K; and Au, 1338 K), with the differential thermal analysis (DTA) peak being used to identify the phase transition temperature under very slow (0.2 K min^{-1}) heating and cooling conditions. At the higher heating rates used for the temperature-programmed decomposition (TPD) of surface oxides, the actual sample temperature lags the indicated temperature—this effect was investigated using the melting point standards mixed with carbon samples, at all heating rates employed in this study (5–30 K min^{-1}). The mass of metal employed in these dynamic calibrations was $100 \pm 50\ \mu g$, which was low enough to eliminate the influence of the thermal load of the metal phase change on the dynamic lag. The dynamic temperature lag was found to range typically from 1 K at a heating rate of 5 K min^{-1} to 10 K at 30 K min^{-1}. The dynamic lag was not significantly affected by the mass of the carbon sample, even at the highest heating rates employed. The dynamic TPD temperatures reported in this work have been corrected for the lag effect and are no more than 2 K uncertain with respect to the static temperature calibration.

Gases leaving the furnace tube are analyzed continuously for CO and CO_2. The sample is split into two streams, with CO_2 being scrubbed from one stream by passage through a bed of soda lime. The two streams are then mixed with H_2 and passed across a bed of ruthenium catalyst (5%Ru on alumina, 30 mg, at 573 K), which leads to the methanation of the carbon oxides. The samples pass then to flame ionization detectors that respond to the methane, thus allowing the [CO] and the [CO] + [CO_2] concentrations to be determined from the scrubbed and unscrubbed flows, respectively. The system is calibrated at steady state with known calibration gases and dynamically by monitoring the evolution of CO and CO_2 during the TPD of calcium oxalate. This system has a sensitivity of <1 ppm, is linear to concentrations in excess of 120 ppm, and has an accuracy of $\pm 2\%$, with a time constant <10 s.

A freshly loaded sample (30 mg in an alumina cup) was outgassed initially to 1373 K under N_2 to remove any preexisting oxygen surface complexes. The sample was then cooled to the temperature desired for the exposure to oxygen. After completion of the oxygen exposure, the gas flow was switched to N_2 and the sample was cooled to near room temperature before commencement of TPD to 1373 K. Some experiments required that complexes formed at one temperature be held at another higher temperature before TPD—in these cases, the furnace temperature was adjusted rapidly (90 K min^{-1}) while

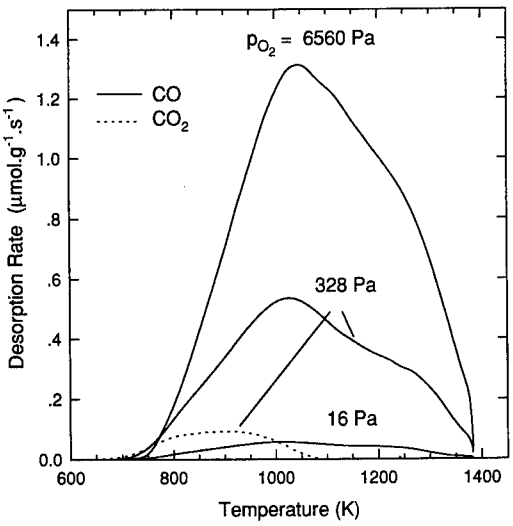

FIG. 1. Gas evolution rates during temperature-programmed desorption (TPD) at 31.6 K min^{-1} after exposure to various partial pressures of oxygen at 693 K for 60 min. The CO_2 profile is only shown for the oxygen exposure at 328 Pa.

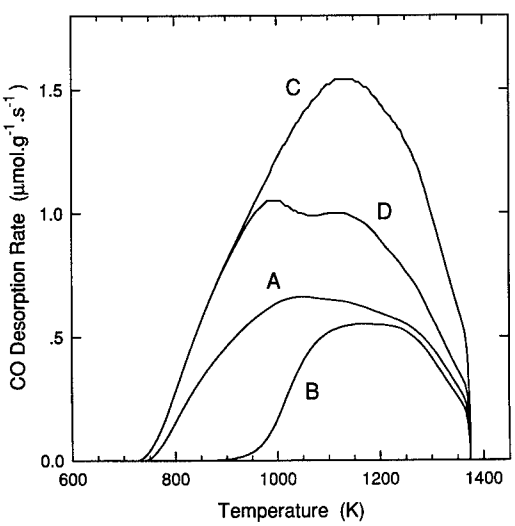

FIG. 2. CO evolution rates obtained during TPD. The sample treatment conditions before the TPD runs are identified as A, B, C, and D in the text.

ensuring that the temperature did not overshoot the soak temperature.

The carbon studied in this work is 120-μm Spherocarb, a high-purity molecular sieve carbon with a macroporous structure and a BET surface area of approximately 1000 m^2 g^{-1} [13]. There is very little change in the surface area of this carbon as burn off proceeds, at least up to ca. 50% burn off. Therefore, because each formation/decomposition cycle consumes less than 1% of the carbon, the same sample can be used for many cycles, with the reproducibility of repeat experiments being better than 5% throughout the TPD program.

Results

Figure 1 shows the results for the evolution of CO during TPD at 31.2 ± 1.2 K min^{-1} after exposure to various oxygen concentrations for 60 min at 693 K. The CO_2 evolution spectrum is shown for only one case, but the mole fraction of CO_2 in the total degas products was less than 15% in all cases. For exposures at 16, 328, and 6560 Pa, the total quantities of surface oxide were 44.6, 440, and 990 μmol g^{-1}, respectively. The fractions of the surface oxygen occurring as Type B oxide, calculated as described previously [2], were 75, 91, and 96%, respectively. Therefore, these results pertain to surface oxides predominantly of Type B, which decompose to give chiefly CO.

The influence of the presence of existing oxide on the uptake and the TPD of additional oxide was investigated in the following experiment, for which the results are shown in Fig. 2.

A. Oxides were formed initially on an outgassed carbon surface by exposure to 6560 Pa O_2 at 720 K for 30 min (598 μmol g^{-1}, 98% Type B), and the TPD spectrum for the decomposition of those oxides was determined.
B. Oxides formed in a repeat of exposure A were soaked for 60 min under N_2 at 940 K to remove the less thermally stable oxide. The TPD spectrum for the decomposition of the remaining oxide (ca. 60%) was determined.
C. The sample was subjected to exposure A, followed by exposure B, and then was exposed to O_2 (6560 Pa at 720 K for 60 min) to cause additional oxide to form. The TPD spectrum for the decomposition of the total oxide loading was determined.
D. The net TPD spectrum corresponding to decomposition of oxides formed in exposure C was calculated from the difference between the spectra obtained after exposures C and B.

Discussion

The CO-evolution spectra shown in Fig. 1 are given as normalized spectra in Fig. 3, the total area under each curve being unity. It is apparent that despite the fact very large differences are seen in the overall surface oxide loading in these three cases, the desorption spectra have very similar shapes. The spectra for the oxides formed at the lower

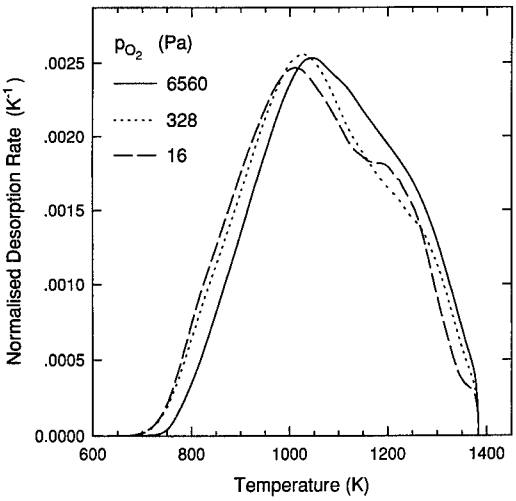

FIG. 3. Comparison of the normalized rates of CO evolution for the three cases shown in Fig. 1.

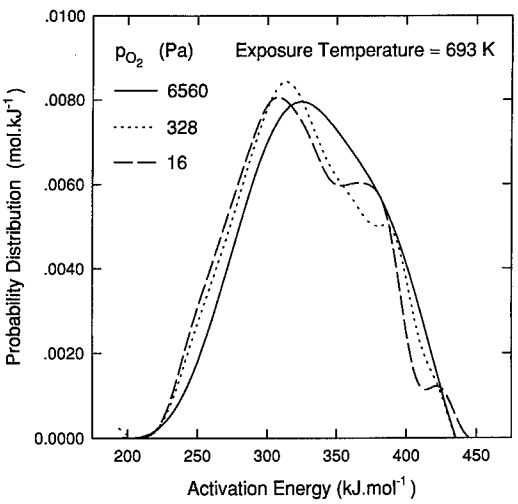

FIG. 4. Activation-energy distribution functions for the evolution of CO for the three cases shown in Fig. 1.

concentrations of oxygen, and therefore giving rise to lower oxide loadings, are shifted slightly to lower temperatures (ΔT <50 K), but this is a small effect in spectra of overall width around 600 K.

The results in Fig. 3 demonstrate that the broad temperature range over which decomposition of surface oxides occurs is an intrinsic effect, independent of loading. Certainly, coverage-dependent lateral interactions between occupied sites cannot be responsible for this observation—the initial loading after exposure at 16 Pa is similar to that remaining after 95% removal of the oxides formed in 6560 Pa, but the decomposition temperatures for these two cases are totally dissimilar (700 versus 1300 K).

The existence of a distribution of activation energies for evolution of gaseous oxides has been invoked frequently to account for the broad TPD spectrum [5–7]. In the complete absence of coverage-dependent interactions, the evolution rate for first-order kinetics is then given by Ref. 4:

$$-\frac{dn}{dT}\frac{dT}{dt} = \int_0^\infty A(E)\exp(-E/RT)\exp\left[-A(E)\int_0^t \cdot \exp(-E/RT)\,d't\right]\cdot\psi(E)\,dE \quad (1)$$

where dn/dt is the rate of decomposition of oxides during TPD and $\Psi(E)$ is the activation energy distribution function.

We have shown previously [4] that the frequency factor $A(E)$ may be recovered from a comparison of TPD spectra obtained after periods of isothermal soaking of the sample at various temperatures. The value of $A(E)$ for CO evolution is found to be effectively constant at $A = 1 \times 10^{14}\ s^{-1}$ for carbon surface oxides formed at either 693 K [14] or 520 K [4]. When A is a known constant, there is a very close correspondence between the shape of the TPD evolution spectrum and the shape of the corresponding activation energy distribution [4–7], and the TPD spectrum is essentially a probe of the site density with respect to the activation energy distribution for desorption.

Figure 4 shows the activation energy distributions recovered from Fig. 3, assuming $A = 10^{14}\ s^{-1}$. The distribution functions in Fig. 4 are all very similar. Corresponding with the lower-temperature onset of desorption after exposure to lower concentrations of oxygen, the activation-energy distribution is shifted slightly to lower energies in these cases, and a weak shoulder is seen in the distribution at $E \approx 380$ kJ mol^{-1}. Because these cases are precisely those for which there is an increasing proportion of Type A oxide (up to 23% at 16 Pa exposure), these effects may relate to Type A oxides.

The fraction of Type A oxide can also be increased by carrying out exposures at lower temperatures. Figure 5 compares the activation energy distributions obtained on exposure to 6560 Pa O_2 for 60 min at 693 and 633 K. The total oxide loadings for these cases are 990 and 572 μmol g^{-1}, with the fraction of these oxides occurring as Type B being 96% and 76%, respectively. The Type B fraction at 633 K is very similar to that obtained at 693 K and 16 Pa, and comparison of Figs. 4 and 5 reveals very similar trends in the activation energy distribution for these two cases. It should be noted that here, the low-energy (low-temperature) edge of the activation-energy distribution for desorption is affected to some extent by the oxygen exposure temperature because isothermal desorption of complexes unstable at the exposure temperature occurs during the exposure.

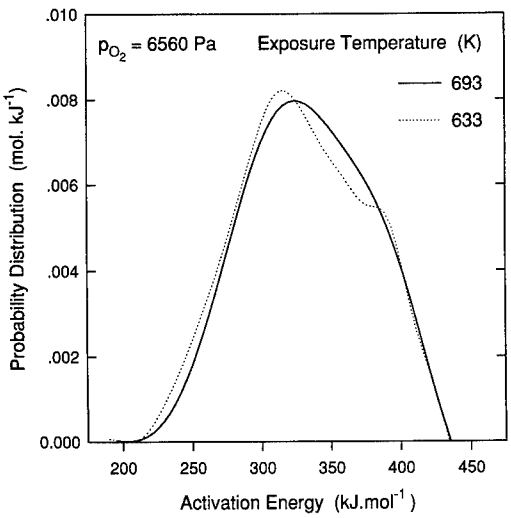

FIG. 5. Activation-energy distribution functions for the evolution of CO after exposure to 6560 Pa oxygen for 60 min at 633 and 693 K.

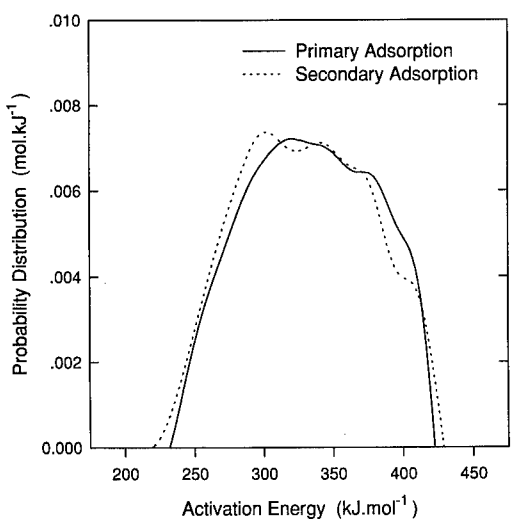

FIG. 6. Activation-energy distribution functions for the evolution of CO from a primary chemisorption of O_2 (curve A in Fig. 2) and from a second exposure after an intervening isothermal soak to remove all primary oxides with E_{des} < 300 kJ mol^{-1} (curve D in Fig. 2).

Despite this, it is clear that slight variations in the activation-energy distribution function apparent in Figs. 4 and 5 are not due to the effects of surface loading, and it may be concluded quite definitively that coverage-dependent lateral interactions are not significant.

The high values of the activation energies for surface oxide decomposition suggest that the evolution of CO is not simply the result of a single surface bond scission. The removal of substrate carbon is likely to involve multiple bonds. The breadth of the distribution corresponds to the morphological diversity of the bonding interactions on an amorphous carbon. Also, ample evidence shows that various oxide structures occur on carbon surfaces and that these would contribute also to the spread of activation energies [15,16].

There is no sign in Figs. 4 and 5 of a preferential, sequential filling of particular types of desorption sites, with the distribution of activation energies for the decomposition of these oxides remaining the same over a wide range of surface coverage. Thus, the population of the desorption sites revealed by TPD is essentially statistical despite the large changes in the adsorption conditions. This is confirmed by the comparison (in Fig. 6) of the activation-energy distributions for the oxides formed in the primary exposure in Fig. 2 (curve A) with those formed in the secondary exposure after all the less stable primary oxides (E_{des} < 300 kJ mol^{-1}) had been removed (curve D). There is no difference apparent in these activation energy distributions, even though the isothermal soaking before the secondary exposure had freed up all the low-E_{des} sites. The secondary oxide, therefore, has been distributed statistically across the entire distribution regardless of the existing site occupancies.

These results imply that the fraction of new oxide formation occurring on sites with decomposition activation energies between E and $E + dE$ is simply $\Psi_0(E)\,dE$, where $\Psi_0(E)$ is a characteristic of the carbon itself and independent of the oxide loading or the actual distribution already existing on the surface. The distributions shown in Figs. 4–6 provide a very close representation of $\Psi_0(E)$. However, it should be noted that the low-energy end of these distributions is affected by the oxygen exposure temperature and that co-formation of Type A and Type B complexes complicates the picture at lower exposure temperatures.

The maximum fraction of surface that is occupied by oxide in any of the experiments reported here is 5%. Presumably, the absence of any coverage-dependent effects in the desorption results derives from the low coverages achieved. However, given that the kinetics of adsorption are very strongly dependent on the surface oxide loading, even for loadings <1 μmol g^{-1} [2], the relationship between oxide formation and decomposition processes now needs further consideration.

We have suggested previously that there may be a distribution of activation energies for oxygen chemisorption on carbon [2], with low activation-energy sites being occupied first. If that were the case, then the adsorption sites would have to be distinct from the desorption sites, perhaps by a rearrangement or reaction or by a migration. Zhuang et al. [17] have

suggested recently that stable surface oxides can be formed, in the presence of oxygen, from oxides already adsorbed to the surface. However, it was impossible to exclude the possibility that the coverage dependence of the chemisorption kinetics could also derive from interactions between the adsorbing species and the substrate [2]. Such interactions would also give rise to coverage-dependent chemisorption kinetics without any such dependence arising in the desorption kinetics, as has been found in this work.

The present results provide an important step in the construction of a site turnover model for carbon oxidation through the Type B complexes that dominate at temperatures above ca. 700 K. The rate of formation of complexes having a particular activation energy for their thermal decomposition can be expressed simply in terms of the overall rate of formation of Type B complexes and the distribution $\Psi_0(E)$, and the kinetics of thermal decomposition of those complexes are known. It remains now to describe the overall Type B oxide formation rate and the reaction between complexes and O_2 [17] to complete the description of the oxide formation/decomposition cycle.

Conclusions

The thermal decomposition of Type B carbon surface oxides formed on Spherocarb at temperatures at ca. 700 K occurs with a broad distribution of activation energies, as revealed by TPD. The shape of the distribution function is invariant over a wide range of surface oxygen loadings, and there is no evidence of coverage-dependent effects such as lateral interactions between adsorbed species in the kinetics of decomposition of carbon surface oxides.

These results imply that the filling of the diverse sites responsible for the distributed kinetics of oxide decomposition is simply statistical, following the characteristic activation energy distribution revealed by TPD. That is, the fraction of new oxide formation occurring on sites with decomposition activation energies between E and $E + dE$ is simply $\Psi_0(E)\,dE$, where $\Psi_0(E)$ is a characteristic of the carbon itself and independent of the oxide loading. Therefore, the rate of formation of complexes having a particular activation energy for their thermal decomposition can be expressed simply in terms of the overall rate of formation of Type B complexes and the distribution $\Psi_0(E)$.

Acknowledgments

This work was funded by the Australian Research Council. M. C. Ma acknowledges the support provided by the Australian Postgraduate Award Scheme and by the Chemical Engineering Foundation of the University of Sydney.

REFERENCES

1. Bansal, R. C., Vastola, F. J., and Walker, P. L. Jr., *J. Colloid Interface Sci.* 32:187–194 (1970).
2. Brown T. C., Lear A. E., and Haynes, B. S., *Twenty-Fourth Symposium (International) on Combustion,* The Combustion Institute, Pittsburgh, 1992, pp. 1199–1206.
3. Tucker, B. G. and Mulcahy, M. F. R. *Trans. Faraday Soc.* 65:274 (1969).
4. Ma, M. C., Brown, T. C., and Haynes, B. S., *Surf. Sci.* 297:312–326 (1993).
5. Du, Z., Sarofim, A. F., and Longwell, J. P., *Energy Fuels* 4:296–302 (1990).
6. Brown, T. C., Lear A. E., Ma, M. C., and Haynes, B. S., in *Fundamental Issues in the Control of Carbon Gasification Reactivity* (Lahaye, J. and Ehrburger, P., Eds.), Kluwer Academic, Dordrecht, 1990, p. 307.
7. Calo, J. M. and Hall, P. J., in *Fundamental Issues in the Control of Carbon Gasification Reactivity* (Lahaye, J. and Ehrburger, P., Eds.), Kluwer Academic, Dordrecht, 1990, p. 329.
8. Pitt, G. J., *Fuel* 41:267–274 (1962).
9. Rennhack, R., *Brennstoff Chem.* 45:300 (1964).
10. Jüntgen, H. and van Heek, K. H., *Brennstoff Chem.* 50:172 (1969).
11. Braun, R. L. and Burnham, A. K., *Energy Fuels* 1:153–161 (1987).
12. Lear, A. E., Ph.D. Thesis, University of Sydney, 1992.
13. Floess, J. K., Longwell, J. P., and Sarofim, A. F., *Energy Fuels* 2:18–26 (1988).
14. Ma, M. C., Ph.D. Thesis, University of Sydney, 1994.
15. Zawadzki, J., in *Chemistry and Physics of Carbon,* Vol. 21 (Thrower, P. A., Ed.), Marcel Dekker, New York, 1989.
16. Zhuang, Q. L., Kyotani, T., and Tomita A., *Energy Fuels* 8:714–718 (1994).
17. Zhuang, Q. L., Kyotani, T., and Tomita A., *Energy Fuels* 9:630–634 (1995).

COMMENTS

Adel F. Sarofim, MIT, USA. This is a very elegant piece of work. The work suggests that the carbon sites formed on desorption are similar, independent of the energy of absorption. I should have expected that fresh carbon formed on desorption might be similar. It is indeed interesting that this should be independent of energy of absorption.

Author's Reply. You suggested that the preservation of the activation energy distribution function should not be surprising if carbon removed from the surface simply re-exposed fresh random surface. This might be expected for complete removal of all complexes but the fact that the same result occurs even for selective removal of low activation energy sites is quite surprising.

•

Eric Suuberg, Brown University, USA. The authors' earlier work has convincingly demonstrated that the process of chemisorption does not involve a single step, but rather, involves a complicated sequence of steps. Therefore the nature of the site at which oxygen initially adsorbs does not necessarily determine the subsequent desorption behavior. In light of this, can the observation that the distribution of activation energies is invariant with oxygen uptake be viewed as surprising? This is, incidentally, not necessarily inconsistent with the well-known distributed activation energy behavior observed to govern low-temperature oxygen uptake rates.

Author's Reply. The significance of the present work is that the "mapping" of the initial adsorption to the final desorption states is purely statistical, and therefore does not need to be known in detail. This was not the expected result but it is welcome in that it greatly simplifies the modeling of how the $C + O_2$ interaction leads to the stable surface oxide distribution revealed by TPD.

•

L. Douglas Smoot, Brigham Young University, USA. Did you or can you deduce an intrinsic CO desorption reaction rate expression (i.e. either activation energy and/or pre-exponential coefficient) from your measured rate data for CO desorption?

Author's Reply. The decomposition of surface oxides to form CO occurs with a wide distribution of activation energies. At each energy, the kinetics are first order in the site occupancy and have $A = 10^{14}\ s^{-1}$ [1]. Overall, these kinetics give rise to very complex but quite predictable behavior.

REFERENCE

1. Ma, M. C., Brown, T. C., and Haynes, B. S., *Surf. Sci.* 297:312–326 (1993).

•

Piero Salatino, Università di Napoli, Italy. In a recent paper [1] we inferred, from analysis of results of TK experiments, that a kind of "screening" effect due to build up of less reactive sites at the gas-carbon interface could take place. Do you think such a mechanism might be relevant to the surface oxide population balance addressed in your presentation?

REFERENCE

1. Salatino, P., Zimbardi, F., and Paulicelli, M., *Twenty-Fifth Symposium (International) on Combustion,* The Combustion Institute, Pittsburgh, 1994, pp. 527–535.

Author's Reply. The effect you are describing would most certainly be described by a comprehensive population balance for surface complexes distributed according to their activation energy for decomposition. In the absence of oxygen, high-E_D sites are stable and the presence of these inhibits further new complex formation.

Twenty-Sixth Symposium (International) on Combustion/The Combustion Institute, 1996/pp. 3127–3135

A NEW APPROACH TO STUDYING PORE DIFFUSIVITY DURING CHAR COMBUSTION AT FBC CONDITIONS

SHAKTI GOEL AND ADEL F. SAROFIM
Department of Chemical Engineering
Massachusetts Institute of Technology
Cambridge, MA 02139, USA

JILING LU
Department of Thermal Energy
Tsinghua University
P.R. China

A new technique of studying pore structure evolution during fluidized bed combustion (FBC) of char has been developed. Evolution of nitrogen oxides during char combustion has been found to be very sensitive toward changes in pore diffusivities. For a nonporous particle, nitric oxide is formed largely at the surface of the particle and diffuses out of the pores before it is destroyed. On the other hand, nitric oxide is formed and destroyed throughout a porous particle, resulting in lower conversions of char nitrogen to NO. The instantaneous conversion of char nitrogen to NO is very sensitive toward changes in pore structure. N_2O, which is formed by the reaction of NO with char nitrogen, can also be used as an indicator for studying changes in pore diffusivity during combustion. Since ambient NO levels and pore diffusivity determine the diffusion of NO into or out of the particle, NO concentration within the particle affects the trends in the N_2O formation with changing carbon conversion. This effect is compounded by the changes in pore diffusivity and the pore diffusion length as the char particle burns. By fitting the model to the experimental data, mesopores were found to control the pore diffusivity of the reacting species and, hence, the location of heterogeneous reactions occurring inside the pores.

Introduction

In view of an extensive literature on pore evolution, only a brief overview can be presented here. Changes in porosity of char particles affect not only the combustion efficiency but also the formation and destruction characteristics of the pollutants of combustion like nitrogen oxides. The approach of measuring total surface area to characterize carbon combustion rates has been found to be unreliable [1]. A significant amount of surface area may reside in micropores, which may not contribute to reactive processes, and mesopores may control pore diffusivity [2,3]. Previous studies have involved measuring the changes in pore volumes and pore-size distributions by burning char to different levels of conversion [4,5]. To demonstrate the phenomenon of pore structure evolution, several authors have used models that use the char carbon consumption rates as a way of understanding pore structures [6–17]. The macroscopic approach adopted by Prins and van Swaaij [6] accounts for porosity change via local carbon mass balance. The random pore model [2,7] allows for the simultaneous solution of the equation of porosity, total surface area, pore-size distribution, and the macroscopic mass conservation equations. The model, however, assumes that all the pores are accessible to the particle surface. This limitation was overcome [11] by the percolation theory [12,13], which accounts for inaccessible porosity. Percolation concepts have been used within the continuum framework [14] to describe the effect of pore system connectivity on transport and reactivity properties. Pore-size evolution has also been studied using Bethe lattice [15,16] and continuous cubic tessela-tion [17]. The models described above have relied on the rates of carbon conversion that often cannot separate the effect of chemical kinetic parameters from that of the diffusivity.

This paper proposes a new experimental and mathematical approach involving a coupling between diffusive and reactive processes during char combustion. Nitrogen oxides formed during char combustion are found to be very sensitive to changes in char porosity. Nitrogen, which is mostly bound as a heteroatom in aromatic pyridine and pyrrole rings within the coal structure [18], is released by the reaction of oxygen with these rings, resulting in an intermediate surface species, I. This intermediate then decomposes to form NO at a rate k_1 $[I]$ or reacts

with NO to form N_2O at a rate k_2 $[I][NO]$. Since these are the only two paths for the char nitrogen consumption, a fraction $k_1/(k_1 + k_2[NO])$ forms NO and a fraction $k_2[NO]/(k_1 + k_2[NO])$ forms N_2O. The nitrogen oxides, in turn, may react with char or CO on char while diffusing out of the pores and get reduced to form free molecular nitrogen. Further details on the heterogeneous mechanism can be found in Refs. 19 and 20. Equation (1) represents the diffusion and reaction of species i inside the pores of a single char particle.

$$\mathcal{D}_{pi}\left(\frac{\partial^2[i]}{\partial r^2} + \frac{2}{r}\frac{\partial[i]}{\partial r}\right) + R_i = 0 \qquad (1)$$

where $\mathcal{D}_{pi}$ is the effective pore diffusivity, $[i]$ is the concentration of species i, and R_i is the net reaction rate of formation (formation—destruction) for species i. The rate is based on the volume of the char particle. The two boundary conditions required include external mass transfer at the surface and the zero slope for species profile at the particle center, assuming the particle to be spherically symmetrical. The external mass transfer coefficient was estimated using the method proposed by Linjewile and Agarwal [21]. Equation (1) is solved for five species, namely, O_2, CO, CO_2, NO, and N_2O, using orthogonal collocation on finite elements [22]. In Eq. (1), the diffusive processes are balanced by the reaction kinetics, making the evolution of nitrogeneous species, namely, NO and N_2O, very sensitive to pore diffusion. Since N_2O is formed from the reaction of NO with char nitrogen inside the pores, the concentration of NO inside the pores is critical to the amounts of N_2O formed. A single order of magnitude analysis can be used to show the dependence of NO within the pores on different parameters. The rate of NO production is given by the product of rate of carbon consumption, r_c, for a particle, the nitrogen/carbon atomic ratio N/C, and the fraction of the char nitrogen converted to NO, $k_1/(k_1 + k_2[NO])$. The rate of NO loss from a particle is given by the rate of diffusion to the surface that is of order $4\pi R^2(\mathcal{D}_{pi}/L_p)([NO] - [NO]_s)$, where L_p is the penetration depth over which the reactions occur and R is the particle radius. This, in turn, must equal the external mass transfer rate of $4\pi R^2 k_g([NO]_s - [NO]_b)$, where k_g is the external mass transfer coefficient and the subscripts s and b represent the surface and bulk conditions, respectively.

$$[NO] = [NO]_b + \left(\frac{L_p}{\mathcal{D}_p} + \frac{1}{k_g}\right)\left(\frac{r_c(N/C)}{4\pi R^2}\frac{k_1}{k_1 + k_2[NO]}\right) \qquad (2)$$

For the case of visualization, the quadratic in [NO] was not solved here. The relationship would be further complicated if the adjustments were made for the heterogeneous NO destruction reactions. It can be seen that the NO within the pores increases as the ambient NO is increased, or the diffusion length L_p is increased, or the carbon burning rate is increased. The effect of diffusivity $\mathcal{D}_p$ is not simple as, in addition to appearing explicitly, it also influences r_c and the diffusion length. In this study, two of these parameters will be varied, the diffusion length L_p, which decreases once the particle radius decreases to values below the penetration depth, and the ambient NO concentration. The fractional conversions to NO and N_2O are strongly dependent upon the NO concentration in the pores and, therefore, provide sensitive indicators of the effective diffusivity in those pores that participate in the reaction. This paper, therefore, aims at

1. developing the technique for studying effective pore diffusivity, and
2. determining the effective pore-size class controlling the heterogeneous reactions.

If the nitrogen oxide formation from a single char particle is sensitive to pore diffusivity, then the determination of effective diffusivity by fitting the model to the experimental data should be able to provide the estimates of pore size and class. The following sections describe the experimental procedure, estimation of model parameters, and a discussion on the techniques for pore diffusivity estimation.

Experimental

The experimental setup consists of a lab-scale fluidized bed combustor (FBC) having a bed diameter of 50 mm and a static bed height of 50 mm. Single-particle experiments were carried out by burning Eastern Kentucky bituminous coal particles ranging from 2 to 10 mm in size in the FBC. For a given experiment, particles with only one size were used. The gas feed consisted of 2–8% oxygen in helium, and the bed temperature was maintained from 750°C to 850°C in the increments of 50°C. For some experiments, NO was also introduced in the feed gas such that its inlet concentration was either 500 or 2000 ppm. The flue gases were analyzed for CO, CO_2, NO, N_2O, and CH_4 as a function of combustion time using a Nicolet 520 FTIR. The raw data were converted to instantaneous conversion of char nitrogen to NO and N_2O using Eqs. (3) and (4) as a function of instantaneous particle radius. Further details on the experimental setup can be found in Ref. 23.

$$f_{NO} = \frac{[NO]}{\frac{N}{C}([CO] + [CO_2] + [CH_4])} \qquad (3)$$

TABLE 1
Arrhenius expressions for different rate constants: Rates are based on char volume

Reaction	Rate Expression	Arrhenius Expression	Units (rate constants)
$2C + O_2$	$k_{O_2}[O_2]$	$1.47 \times 10^9\, e^{-10{,}630/T}$	m^3_{gas}/m^3_{char} s
$O_2 + 2CO$	$k_{CO}[CO][O_2]^{1/2}$	$1.49 \times 10^{10}\, e^{-17{,}373/T}$	$m^{4.5}_{gas}/m^3_{char}$ $mol^{0.5}$ s
k_2/k_1 for $-I$ decomposition	see Introduction	$1.47\, e^{2433/T}$	m^3_{gas}/mol s
NO + char	$k_{NO}[NO]$	$3.32 \times 10^9\, e^{-14{,}887/T}$	m^3_{gas}/m^3_{char} s
NO + CO	$k_{NO/CO}[NO][CO]$	$7.66 \times 10^9\, e^{-15{,}626/T}$	m^6_{gas}/m^3_{char} mol s
N_2O + char	$k_{N_2O}[N_2O]$	$4.55 \times 10^9\, e^{-16{,}272/T}$	m^3_{gas}/m^3_{char} s

TABLE 2
Estimated values of effective pore diffusivities and pore radii

Bed Temperature (°C)	Initial Particle Radius (mm)	Ambient O_2 Conc. (%)	$\mathcal{D}_{pi}$(m^2/s) at $X_c = 0$	Effective Pore Radius (nm)
750	2	8	6×10^{-6}	11
800	2	8	9×10^{-6}	15
850	2	8	1×10^{-5}	17
750	1	4	2×10^{-5}	35
750	2	4	8×10^{-6}	14
750	3	4	8×10^{-6}	14
750	4	4	3×10^{-6}	5
750	5	4	3×10^{-6}	5

$$f_{N_2O} = \frac{2[N_2O]}{\frac{N}{C}([CO] + [CO_2] + [CH_4])} \quad (4)$$

where N/C is the nitrogen to carbon atomic ratio in char. The denominators denote the amount of nitrogen consumed at any given instant of time, assuming that there is no preferential consumption of organic carbon over organic nitrogen [24]. For all the experiments, the carbon balance was found to close within 5% and the carbon conversion, X_c, and instantaneous particle radius, R, were calculated using Eq. (5).

$$X_c = \frac{v\int_0^t ([CO] + [CO_2] + [CH_4])\,dt}{W_C} \text{ and}$$

$$R = R_0(1 - X_c)^{1/3} \quad (5)$$

where v is the volumetric flow rate, W_C is the initial weight of carbon in char, and R_0 is the initial particle radius.

Results and Discussion

The model parameters were estimated once the raw data for nitrogen and carbon oxides were converted to instantaneous conversion of char nitrogen to NO and N_2O. The model was fitted to the experimental data by minimizing the error between the model predictions and the experimental observations with respect to the unknown model parameters [19]. It was assumed that the reactivity of carbon and nitrogen oxidation varied in a manner such that the ratio of the two rates remained a constant as the carbon conversion increased. The model parameters estimated included the effective diffusivity and the rate constants of the following reactions: $2C + O_2 \xrightarrow{k_{O_2}} 2CO$, $-CN + O_2 \xrightarrow{(N/C)k_{O_2}} -I$, $2CO + O_2 \xrightarrow{k_{CO}} 2CO_2$, $NO + \text{char} \xrightarrow{k_{NO}} N_2$, $NO + CO \xrightarrow{k_{NO/CO}} 1/2N_2 + CO_2$, $N_2O + \text{char} \xrightarrow{k_{N_2O}} N_2$, where k_j represents the rate constant of the jth reaction and $-I$ is a nitrogenous surface intermediate. The ratio k_2/k_1 was determined for the following reactions: $-CN + O_2 \xrightarrow{(N/C)k_{O_2}} -I$, $-I \xrightarrow{k_1} NO$, $-I + NO \xrightarrow{k_2} N_2O$. Table 1 presents the rate and Arrhenius expressions for the different reactions and rate constants, respectively. Table 2 presents the effective diffusivities for different experimental conditions. Figures 1 and 2 show the model fit to the experimental data for two of the six experimental data sets (bed temperature = 750, 800, and 850°C, O_2 = 4% and 8%) for the Eastern Kentucky coal. The figures show that the model predictions assuming constant diffusivity de-

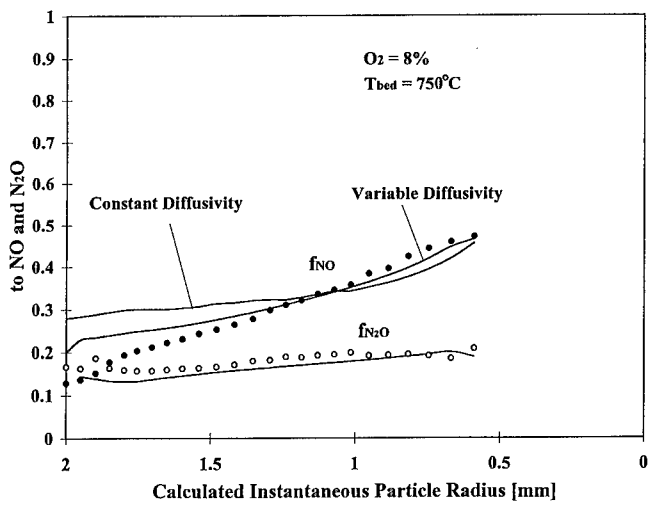

FIG. 1. Comparison of the model predictions with the experimental data; T_{bed} = 750°C.

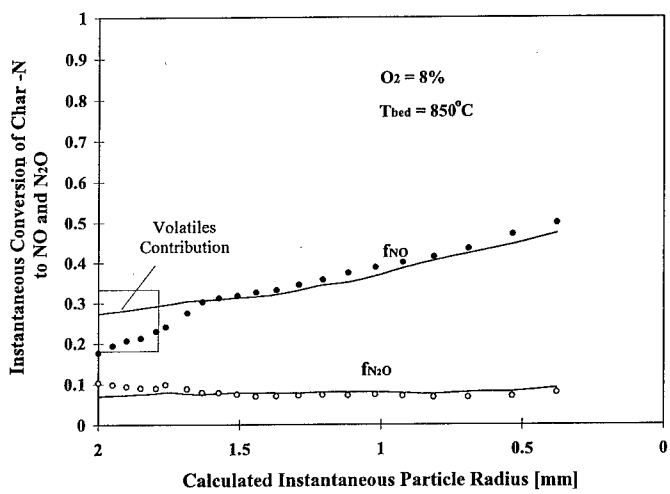

FIG. 2. Comparison of the model predictions with the experimental data; T_{bed} = 850°C.

scribe the data well when the bed temperature was 850°C. Deviations are, however, observed when the temperature was 750°C. These deviations could be due to the fact that the rate may be kinetically controlled, and Eq. (5), for the estimation of instantaneous particle radius, may no longer be valid. If the estimated particle radii are incorrect (over- or underpredicted for a given level of conversion), then the optimally fitted profile assuming constant diffusivity could be horizontally displaced. If this profile is shifted toward larger particle radii, then the error between the predicted and observed f_{NO} values increases at low conversions or large particle radii. Also, the horizontal displacement of the profiles would not explain the differences in the curvatures. On assuming that the diffusivity varied with conversion, a better match between the predictions and observations was obtained. The diffusivity was varied by a factor of 4, generally increasing with increasing conversion. The constant diffusivity approximation is expected to be valid as long as the penetration depth L_p is small relative to the particle radius. At lower temperatures, char combustion is controlled by reaction kinetics rather than pore diffusion. Oxygen is, therefore, able to penetrate deeper into the particle, react with carbon, and alter the pore-size distribution. This change in porosity will affect the nitrogen formation and destruction rates or, in other words, the instantaneous conversion of char nitrogen to NO. Hence, a variable diffusivity was required to better fit the observations. The effective pore radius r_p was calculated using Eq. (6):

$$\mathcal{D}_{pi} = \frac{2r_p}{3}\sqrt{\frac{8R_uT}{\pi M_i}} \tag{6}$$

where T is the particle temperature, R_u is the uni-

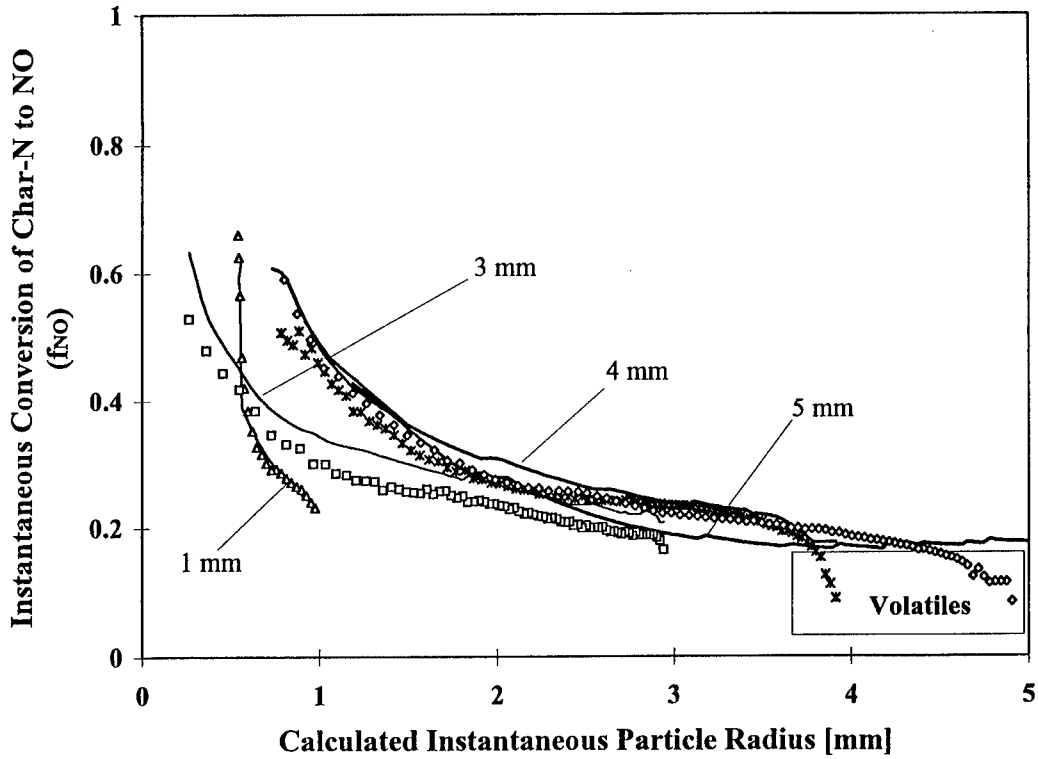

FIG. 3. Instantaneous conversion of char nitrogen to NO, f_{NO}, for different particle sizes.

versal gas constant, and M_i is the molecular weight. The results are presented in Table 2.

Besides studying the effect of temperature on f_{NO} and $\mathcal{D}_{pi}$, it would be interesting to study the f_{NO} profiles for particles with different initial sizes. If the penetration depth is small relative to the particle radius, the particle should burn as a shrinking sphere. In this limit, the results for nitrogen conversion at a given particle size, say 2 mm, will be independent of whether the initial particle radius was 5, 4, or 3 mm. The pyrolysis process for the different-sized particles may give different pore-size distribution since the particle heating rate decreases with increasing particle size.

To confirm this hypothesis, Eastern Kentucky coal particles ranging from 2 to 10 mm in diameter were burned in 4% oxygen at a bed temperature of 750°C. The resulting f_{NO} profiles are shown in Fig. 3. The figure shows that the f_{NO} profiles for the 8- and 10-mm particles overlap when the larger particle shrinks to 8 mm. The profiles, however, do not overlap when the 6- and 2-mm particles were burned. Also, the profile is steepest for the 2-mm particle. On fitting the model to the experimental observation with effective diffusivity as the only adjustable parameter, the changes in diffusivity were found to have maximum variation for the 6-mm particle. The model was able to describe the data for the 2-mm particle using constant diffusivity for the bulk of the data, with variation required only at high conversions. The effective diffusivities were estimated to lie in the range 3×10^{-6} to 2×10^{-5} m²/s, corresponding to an effective pore radius range of 5–35 nm. The experimental results presented so far have shown that the conversion of char nitrogen to NO is sensitive to effective diffusivity and any changes in it. It is, however, difficult for the reasons presented above to conduct an experiment in which the effective diffusivity can be kept constant, and one has to resort to model simulations. Figure 4 shows the results of model simulations for the cumulative or net conversion of char nitrogen to NO, F_{NO}, using Eq. (7) as a function of effective pore diffusivity for different initial particle radii and temperatures:

$$F_{NO} = \nu \frac{\int_0^t [\mathrm{NO}]\, dt}{W_N} \tag{7}$$

where W_N is the initial weight of nitrogen in char. The figure exhibits an initial increase in F_{NO} with decreasing diffusivity. The net conversion to NO then either decreases or remains unchanged with further decreases in diffusivity. In order to explain

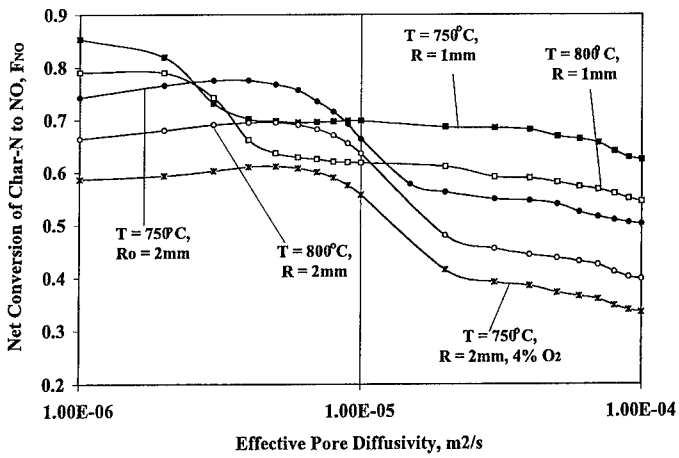

FIG. 4. Results of model simulations for cumulative conversion of char nitrogen to NO, F_{NO}, for 2% oxygen concentration as a function of effective pore diffusivity.

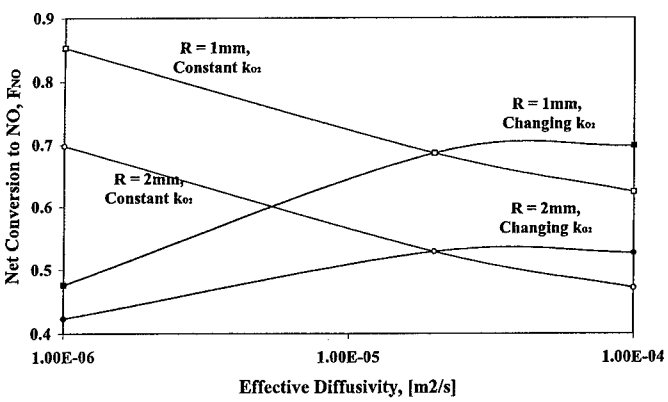

FIG. 5. Cumulative conversion of char nitrogen to NO, F_{NO}, for 2% oxygen concentration as a function of effective pore diffusivity. Char oxidation rate constant, k_{O_2}, is varied in proportion to effective diffusivity such that $k_{O_2}/\mathcal{D}_p$ is a constant.

these observations, it is important that the chemistry of NO formation be well understood. As mentioned before, the model represents a balance between the diffusive and the kinetic processes occurring inside a single char particle. The diffusivity changes affect both the rate of mass transfer of NO, governed by changes in the L_p and $\mathcal{D}_p$ terms in Eq. (2), and the rate of carbon consumption r_c, which is governed by oxygen diffusion into the particle. An increase in diffusivity increases the carbon consumption rate (which will increase the internal NO concentration) but decreases the diffusional resistance for NO (which will decrease the NO concentration). The trade-offs between these processes, plus the impact of diffusion on the NO destruction rates, lead to the complex trends in Fig. 4. Since NO kinetics are dependent on oxygen penetration depth, which, in turn, is a function of char reactivity and temperature, it would be interesting to eliminate the effects of oxidation kinetics and the oxygen penetration depth and then study the net conversion of char nitrogen to NO on changing pore diffusivity. The results of this exercise are presented in Fig. 5, where the oxidation rate constant is changed in proportion to changes in pore diffusivity such that $k_{O_2}/\mathcal{D}_p$ is a constant making F_{NO} a function only of char porosity. The figure shows that on decreasing diffusivity, the net conversion of char nitrogen to NO decreases. NO generated inside a porous particle will be able to diffuse out more easily than from a less porous one. This means that if NO generation is independent of controlling pore size, its destruction will be governed mainly by its ability to diffuse out of the pores. If NO cannot diffuse out, it will be destroyed, and the resulting F_{NO} values will be lower. In conclusion, depending on the oxygen penetration depth and the location of NO generation and destruction inside the particle, the net conversion of char nitrogen to NO may increase or decrease on decreasing pore diffusivity. This makes NO evolution very sensitive to porosity variation during char combustion, leading to the development of this technique.

Besides NO, one other product of char nitrogen oxidation is N_2O. Concentrations of N_2O diffusing out of the pores are governed by both the local NO concentration within the pores and the effective dif-

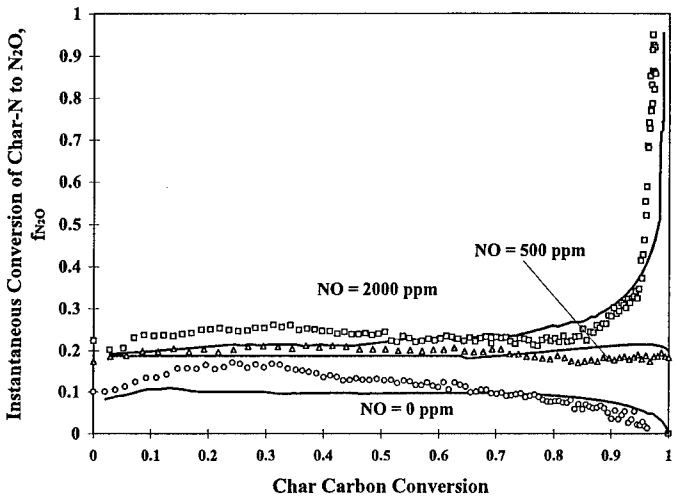

FIG. 6. Comparison of model predictions with the experimental data for the instantaneous conversion of char nitrogen to N_2O, f_{N_2O}, for different inlet NO concentrations.

fusivity. As mentioned before, it would not be possible to do an experiment in which effective diffusivity can be kept constant as a char particle burns. However, by supplying NO in the feed stream, it should be possible to alter the NO concentration within the pores. If the surrounding NO levels are higher than the pore NO levels, its flux would be directed into the pores of the particles. This will lead to surface intermediate splitting to form mainly N_2O. In order to test this hypothesis, experiments were done in which 500 or 2000 ppm NO was introduced into the fluidizing gas stream. Figure 6 shows the instantaneous conversion of char nitrogen to N_2O as a function of carbon conversion when the feed NO was 0, 500, or 2000 ppm in 2% oxygen. The figure shows that when NO concentration was 0 ppm, the instantaneous conversion of char nitrogen to N_2O exhibits a downward trend at high carbon conversions, as would be expected from the increase in the NO diffusion out of the particle at high conversion. Therefore, at conversions approaching unity, f_{N_2O} is zero. On the other hand, when 2000 ppm NO was fed into the system, then not only did the instantaneous conversion of char nitrogen to N_2O increase but the conversion profile also exhibited an upward curvature at high carbon conversions, as would be expected from an increase in NO diffusion into the particle at high conversions. On introducing 500 ppm NO, the f_{N_2O} profile is found to remain flat. These observations are consistent with the hypothesis that the local NO concentration in the pores governs the fraction of the bound nitrogen that forms N_2O. The zero slope with changing conversion suggests that when ambient NO levels are 500 ppm, the concentrations of NO inside and outside the pores are the same. This changing of the external NO concentration to produce a flat f_{N_2O} profile provides an indirect means of estimating local NO concentration inside the pores. However, N_2O is not formed at carbon conversions approaching unity when ambient NO levels are zero, leading to a drop in the f_{N_2O} profile. As is evident so far, the controlling pore-size class and, hence, the effective diffusivity will determine the NO concentrations in the pores that, in turn, will govern N_2O formation.

By fitting the model predictions to the experimental observations using the kinetic parameters estimated before, the average effective diffusivity was estimated to be 4×10^{-5} m²/s, suggesting that a 70-nm pore radius may be controlling the location of heterogeneous reactions. Variable diffusivity was required to better fit the data at high carbon conversions. Since the value of effective diffusivity estimated is close to the one determined earlier, instantaneous conversion of char nitrogen to N_2O in presence of external NO can be used as an alternative technique to determine the governing pore-size class.

Conclusions and Practical Implications

The mathematical models have shown that the conversion of char nitrogen to NO and N_2O is a function of the char oxidation kinetics, oxygen penetration depth, the fraction of char nitrogen forming NO versus N_2O, the decomposition reactions of NO and N_2O, and the transport of the reactants and products both within the pores and in the external boundary layer. The increased diffusion at high burnout is a measure of both the increased diffusivity and the shorter diffusion path as the char particle burns out. Based on the char nitrogen chemistry, two techniques have been proposed to determine the pore class controlling diffusion and any changes in the diffusivity as the particle burns. One technique requires the measurement of NO concentration as a single char particle burns, and the other one requires

the introduction of NO in the feed stream and then the measurement of the N_2O concentration in the flue gases. The conversion of char nitrogen to NO and N_2O is very sensitive to the diffusion characteristics of the char particle, namely, pore size and pore length, making the estimation and changes in effective diffusivity possible at high carbon conversions. The study shows that the effective diffusivity lies in the range of 3×10^{-6} to 4×10^{-5} m^2/s, and the effective pore radius range is 3–70 nm. This pore-size class suggests that mesopores control pore diffusion to those surfaces within a char particle that control heterogeneous kinetics. Analyses of a char particle for the different fractions of micro, meso, and macro pores at different conversions by using mercury porosimetry gives the average pore radius. This radius, however, may not be the effective pore radius, and one cannot conclude much about effective diffusivity. One hypothesis is that the micropores may be less reactive because their surfaces are dominated by basal plane rather than edge carbons of the graphite like micro domains within chars [25].

The practical ramifications of the present finding is that the pore diffusivities have an important impact on NO and N_2O formation. Some control of the NO formation from char may be achievable by controlling the rate of heating in the burner zone, which has an impact on the plastic behavior of the bituminous coals [26] and, therefore, of the diffusivities of the chars that are produced. The aim should be to suppress NO and enhance N_2O formation since N_2O is very easy to destroy thermally.

Acknowledgments

This research was funded by the U.S. Department of Energy under Contracts DE-PS22-94PC94200 and DE-PC89774-3. One of the authors (SG) wishes to thank the PEEER foundation at MIT for awarding him the Martin Environmental Fellowship and making this work possible. Another author (JL) is grateful to Tsinghua University, China, for the financial support.

REFERENCES

1. Smith, I., *Nineteenth Symposium (International) on Combustion,* The Combustion Institute, Pittsburgh, 1982, pp. 1045–1065.
2. Gavalas, G., *AIChE J.* 26:577–585 (1980).
3. D'Amore, M., Tognotti, L., and Sarofim, A., *Combust. Flame* 95:374–382 (1993).
4. Ballal, G. and Zygourakis, K., *Ind. Eng. Chem. Res.* 26:1787–1796 (1987).
5. Adams, K., Glasson, D., and Jayaweera, S., *Carbon* 27:95–101 (1989).
6. Prins, W. and van Swaaij, W., *Fuel Process. Technol.* 24:355–365 (1990).
7. Bhatia, S. and Perlmutter, D., *AIChE J.,* 26:379–386 (1980).
8. Miura, K. and Hashimoto, K., *Ind. Eng. Chem. Process Des. Dev.* 23:138–145 (1984).
9. Bhatia, S., *AIChE J.* 33:1707–1718 (1987).
10. Salatino, P., Zimbardi, F., and Masi, S., *Carbon* 31:501–508 (1993).
11. Yu, H. and Sotirchos, S., *AIChE J.* 33:382–393 (1987).
12. Stauffer, D. and Aharony, A., *Introduction to Percolation Theory,* Taylor and Francis, London, 1992.
13. Sahimi, M., *Applications of Percolation Theory,* Taylor and Francis, London, 1994.
14. Mohanty, K., Ottino, J., and Davis, H., *Chem. Eng. Sci.* 37:905–924 (1982).
15. Reyes, S. and Jensen, K., *J. Phys. Lett.* 44:13 (1986).
16. Srinivaschar, S., Toqan, M., Beer, J., and Ettouney, H., *Combust. Sci. Technol.* 57:55–70 (1988).
17. Shah, N. and Ottino, J., *Chem. Eng. Sci.* 42:63–72 (1987).
18. Hayatsu, R., Scott, R., Moore, L., and Studier, M., *Nature* 257:378–380 (1975).
19. Goel, S., Morihara, A., Tullin, C., and Sarofim, A., *Twenty-Fifth Symposium (International) on Combustion,* The Combustion Institute, Pittsburgh, 1994, pp. 1051–1059.
20. Goel, S., Zhang, B., and Sarofim, A., *Combust. Flame* 104:213–217 (1996).
21. Linjewile, T. and Agarwal, P., *Twenty-Third Symposium (International) on Combustion,* The Combustion Institute, Pittsburgh, 1990, pp. 917–925.
22. Carey, G. and Bruce, A., *Chem. Eng. Sci.* 30:587–596 (1974).
23. Tullin, C., Sarofim, A., and Beér, J., *J. Inst. Energy* 66:207–215 (1993).
24. Song, Y., Beér, J., and Sarofim, A., *Combust. Sci. Technol.* 28:177–183 (1982).
25. Rouzaud, J., Duval, B., and Leroy, J., in *Fundamental Issues in Control of Carbon Gasification Reactivity* (J. Lahaye and P. Ehrburgr, Eds.), Kluwer Academic Publishers, Dordrecht, Netherlands, 1991, pp. 257–267.
26. Gale, T., Bartholomew, C., and Fletcher, T., *Combust. Flame* 100:94–100 (1995).

COMMENTS

Jon Gibbins, Imperial College, UK. Did you see any particle-to-particle variation in your results?

Author's Reply. When the experiments were repeated using the same particle size the variation in the f_{NO} and

f_{N_2O} profiles was less than 5%. When particles of different sizes were burned we observed a significant difference in the f_{NO} and f_{N_2O} profiles which was attributed to changes in pore sizes and diffusivities (Fig. 3).

•

Doug Smoot, Brigham Young University, USA. In previous symposium, results for the pore diffusivity have been reported by different measurement methods for carbonaceous materials. Have you compared your results with these independent data?

Author's Reply. This is a very interesting question which emphasizes the need of determining the right pore diffusivity which controls the location of heterogeneous reactions within a char particle. In the 23rd symposium Valix [1] reported the experimentally determined values of pore diffusivity in the temperature range 273–500 K. Extrapolated values were then presented for higher temperatures. As an example, pore diffusivity value of 4×10^{-7} m²/s was reported at a temperature of 1073 K. At this temperature we determined $De = 2 \times 10^{-5}$ m²/s for two coals (Newlands and Eastern Kentucky bituminous coals). In general we found the diffusivity values to be one to two orders of magnitude higher than the experimentally determined ones. This suggests that experimental techniques would give an "average" diffusivity which may be significantly lower than the controlling or "effective" diffusivity. Since char contains a large fraction of micropores (which do not contribute to heterogeneous activity within the pores) the average diffusivity will be significantly influenced by micropores. In our mercury porosimetry experiments we found that the "average" pore diameter was 0.2 nm whereas using the technique presented in this paper the "effective" pore diameter was determined to be 3–70 nm. This underlines the difference between the pore size controlling surface area and pore size where reaction occurs.

REFERENCE

1. Valix et al., *Twenty-Third Symposium (International) on Combustion,* The Combustion Institute, Pittsburgh, pp. 1217–1223, 1992.

•

Yiannis A. Levendis, Northeastern University, USA. Very interesting work. What is the regime of combustion under which your fuel particles are burning in your work? Can you comment on the change of apparent kinetics vs. intrinsic kinetics with burnout? What was the value of pore diffusivity, as deduced from conventional mercury porosimetry? How does it compare with your calculated "effective" diffusivity?

Author's Reply. Thank you. There are three parts to this question. Regarding the first part, the bed temperature was varied from 750–850°C. At lower temperatures we believe the particle is burning under the kinetic controlled regime of combustion. At this temperature the changes in pore diffusivity are maximum (please refer to Fig. 1 in the paper). At higher temperatures the particle would burn as a shrinking sphere and combustion would be controlled by pore diffusion. We model the NO reduction using an intrinsic kinetic model. We have not tried to back out an apparent kinetic rate as we were interested in the reaction in the pores. Please refer to the previous question for a comparison between the pore diffusivities determined using the conventional mercury porosimetry experiments and using the approach presented in this work.

Twenty-Sixth Symposium (International) on Combustion/The Combustion Institute, 1996/pp. 3137–3144

THE IMPACT OF FRAGMENTATION ON CHAR CONVERSION DURING PULVERIZED COAL COMBUSTION

REGINALD E. MITCHELL AND A. E. JACOB AKANETUK
High Temperature Gasdynamics Laboratory
Mechanical Engineering Department
Stanford University
Stanford, CA 794305-3032, USA

Synthetic char particles with controlled macroporosity are used to study char fragmentation behavior during pulverized coal combustion. The chars are burned in an atmospheric laminar flow reactor that permits the control of gas temperature and composition. Char particles are extracted from the reactor at selected residence times and characterized for extent of mass loss and particle size distribution.

Chars of 23% and 36% porosity are subjected to environments containing 12 mol % O_2 at nominally 1500 K. Number distributions show a large increase in the numbers of small particles during devolatilization, the higher porosity char exhibiting the larger increase. Results show that char burn off increases with porosity at any given residence time, demonstrating an impact of fragmentation on char burn off. The data indicate that both particle diameter and apparent density decrease during burn off and support power-law relations between char particle mass, apparent density, and diameter.

A particle population balance model is developed and used to characterize the type of fragmentation that occurs during char oxidation and to quantify the rates of fragmentation events. The model allows for attrition-type behavior (in which only fines are produced), breakage-type behavior (in which particles break into two or three smaller particles), and percolation-type behavior (in which particles fragment into a distribution of smaller-size particles).

Calculations using the model indicate that fragmentation during burn off is percolative in nature and char burning rate parameters determined from mass loss, size, and temperature measurements are too high if account is not made for the effects of particle fragmentation. Calculations also suggest that fragmentation during devolatilization is percolative in nature and the extent of fragmentation increases with coal volatile yield. Fragmentation rates during devolatilization are estimated to be as high as five times the fragmentation rates during char oxidation.

Introduction

During pulverized coal combustion, a significant number of char particles is formed during devolatilization that have large voids within them. These macrovoids allow oxygen to penetrate the particle during char oxidation and consume the inner particle material. As a consequence, particles may fragment as interior surfaces are consumed. Char fragments burn at rates governed by their individual sizes and not at rates controlled by the sizes of their parent particles. Consequently, overall mass loss rates depend on the extent of fragmentation. This paper reports on work aimed at characterizing the impact of fragmentation on carbon conversion during pulverized coal combustion.

Three types of fragmentation behavior are considered: attrition, breakage, and percolation. During attrition fragmentation, numerous small fragments are produced while the overall sizes of parent particles diminish only slightly. During breakage fragmentation, only a few fragments are produced and these are relatively large, having sizes not much smaller than their parent particles. Percolation fragmentation refers to the transition from a connected solid network to a completely fragmented state. Whereas attrition produces fine fragments and breakage produces relatively large fragments, percolation fragmentation produces fragments ranging in size from the diameters of the parent particles to those of the small fragments.

Experimental Approach

Synthetic chars with controlled pore structures are used in the study so that complications associated with the heterogeneity of real coal chars are eliminated. The chars are produced from the polymerization of furfuryl alcohol with p-toluenesulfonic acid [1,2]. Carbon black particles added during the synthesis procedure form micropores by causing the carbonized furfuryl alcohol matrix to crack around the locations of the carbon black inclusions [3].

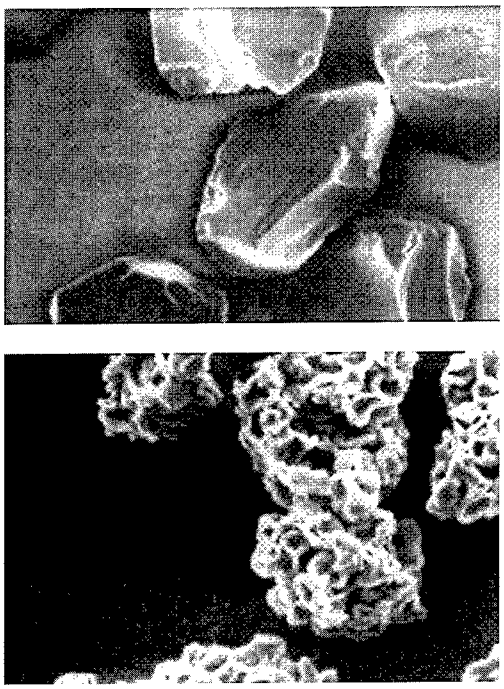

FIG. 1. Micrographs of synthetic chars having porosities of 16% (top) and 55% (bottom). Particles are in the 90–106-μm size range.

Akan-Etuk and Niksa [4] found that the addition of lycopodium plant spores produces macropores of a uniform size (~20 μm in diameter) when they vaporize during the thermal curing step of the synthesis procedure.

The chars produced are ground and size classified. True densities of the chars are determined using helium pynometry, and apparent densities are determined using mercury intrusion porosimetry combined with a tap density procedure [5] for bulk density. Figure 1 shows synthetic char particles representing a range of porosities from 16% to 55%. Mercury porosimetry indicates that the largest intraparticle pores for the 16% porosity chars are ~0.05 μm.

Chars are burned in an atmospheric, laminar flow reactor that permits the control of gas temperature and oxygen content. The reactor is similar in design to that used by Mitchell et al. [5]. Particles are injected along the reactor centerline and extracted from the reactor at selected residence times using a helium-quench solids sampling probe [5]. The reacted chars are characterized for extents of burn off (determined from the measured weights of char fed and char extracted) and particle size distributions. Size distributions are measured with a Coulter Multisizer, using 256 channels to classify approximately 20,000 particles per measurement in the 6–168 μm size range.

Theoretical Approach

The Particle Population Balance Model

A particle population balance model was developed to describe changes in the particle size distribution with time as a result of char oxidation and fragmentation. The approach taken is similar to that of Dunn-Rankin [6], who modified the model developed by Austin et al. [7] for simulating the grinding of particles using a ball mill. A number of size bins are used to describe the particle size distribution. Bin i is characterized by its upper and lower cutoffs, x_i and x_{i+1}, respectively. Bin 1 contains the largest-size particles in the distribution (diameters in the range x_1 to x_2) and bin n, the smallest-size particles (diameters in the range x_n to 0). The upper and lower cutoffs of each size interval vary by a constant factor γ, defined as

$$\gamma = \frac{x_i}{x_{i+1}} \tag{1}$$

This treatment yields uniformly spaced size intervals in the log domain and is effective in resolving size distributions in the small-size range in which particle number densities can be large.

The model is represented by a differential equation of the following form for each bin i:

$$\frac{dN_i}{dt} = -S_iN_i + \sum_{j=1}^{i} b_{ij}S_jN_j - C_iN_i + C_{i-1}N_{i-1} \tag{2}$$

where N_i represents the number of particles within bin i. S_i and C_i are the fragmentation and burning rate constants, and b_{ij} are elements of the fragmentation progeny matrix, which specify the number of fragments that enter bin i per particle that fragments in bin j.

Fragmentation rate parameters

The fragmentation rate constant gives the fraction per unit time of particles of size x_i that fragment and is expressed as

$$S_i = kx_i^{\sigma} \tag{3}$$

where the frequency of fragmentation events is given by the fragmentation rate coefficient k, and the relative tendency for a particle of size x_i to fragment is given by the fragmentation sensitivity parameter σ. Based on the investigations of Dunn-Rankin [6] and Austin et al. [7], σ is set equal to 1.0.

The distribution of fragments is specified by the elements of the fragmentation progeny matrix, b_{ij}. Particles fragmenting in bin j can produce fragments only in bin i where $i \geq j$; therefore, $b_{ij} = 0$ for $i < j$. Conservation of volume requires that

$$x_j^3 = \sum_{i=j}^{n} b_{ij} x_i^3 \tag{4}$$

where x_j is the size of the fragmenting particle and x_i are the sizes of the resultant fragments.

Attrition behavior is modeled by assuming that each particle undergoing attrition in bin j loses a small fraction f (taken as 0.1%) of its mass from its periphery during a single fragmentation event. One large fragment is produced (the parent particle) that remains in bin j (or possibly enters bin $j + 1$ if the particle had a diameter near the lower-size cutoff of bin j), and numerous small fragments are produced that fall into bins m_j to n. The subscript j on m_j indicates that the size of the largest attrited fragments depends on the size of the attriting particle. For attrition, elements of the progeny matrix are evaluated as follows:

$$b_{ij} = \begin{cases} 0 & j + 2 \le i \le m_j - 1 \\ \dfrac{f\gamma^3}{n - m_j + 1} & m_j \le i \le n \\ \dfrac{(1 - f)\gamma^3 - 1}{\gamma^3 - 1} & i = j \\ \dfrac{f\gamma^3}{\gamma^3 - 1} & i = j + 1 \\ 0 & i = n \text{ or } i < j \end{cases} \tag{5}$$

In accord with experimental observations, we assume that attrited particles can be as large as 10% of the radius of a particle.

For breakage, only a few fragments are produced, and these have sizes close to those of the fragmenting particles. For breakage in bin j, fragments may fall into bins j to $j + 1$. Presently, we assume breakage into fragments that fall into the next lower size class from the fragmenting particle. For this situation, the elements of the progeny matrix are given by

$$b_{ij} = \begin{cases} 0 & i \le j \\ \gamma^3 & i = j + 1 \\ 0 & i > j + 1 \end{cases} \tag{6}$$

Results from the percolation model of char oxidation used by Kerstein and Edwards [8] indicate that at high carbon conversions, the fragment number distribution varies linearly with mass on a log–log plot. Their results indicate that a particle ultimately yields a family of fragments such that logarithmically spaced size bins each contain an equal mass fraction of the parent particle. Employing this result, the elements of the progeny matrix for percolation are expressed as

$$b_{ij} = \begin{cases} \dfrac{\gamma^{3(i-j)}}{n - j + 1} & i \ge j \\ 0 & \text{otherwise} \end{cases} \tag{7}$$

Burning rate parameters

The burning rate constants describe the rates at which particles in bin i are reduced in diameter as a result of burning. C_i is expressed in terms of $(dD/dt)_{x_{i+1}}$, the rate of change in diameter of a burning particle of size x_{i+1}, the lower cutoff of bin i. It can be shown that

$$C_i \equiv \begin{pmatrix} \text{fraction of particles} \\ \text{in bin } i \text{ at time } t \text{ that} \\ \text{burn out of the size} \\ \text{bin per unit time} \end{pmatrix} = \frac{|dD/dt|_{x_{i+1}}}{x_i - x_{i+1}} \tag{8}$$

An expression for dD/dt in terms of the overall particle burning rate is derived from the particle's rate of mass loss, expressed as

$$\frac{dm}{dt} = -q\pi D^2 \tag{9}$$

where m is the mass of a particle of diameter D and q is the overall particle burning rate per unit external surface area. The particle mass, diameter, and apparent density are assumed to be related via the following two relations [5,12]:

$$\left(\frac{m}{m_0}\right)^{\alpha} = \frac{\rho}{\rho_0} \qquad \left(\frac{m}{m_0}\right)^{\beta} = \frac{D}{D_0} \tag{10a,b}$$

where α and β are the burning mode parameters. Justification for such power-law relations for carbon particles has been given by Essenhigh [9]. For spherical particles, α and β satisfy the relation $\alpha + 3\beta = 1$.

Differentiating Eq. (10b) with respect to time and using the result in Eq. (9) with the relation $m_0 = \pi/6\,(D_0)^3\,\rho_0$ yields

$$\frac{dD}{dt} = -\frac{6\beta q}{\rho_0}\left(\frac{D}{D_0}\right)^{(3-1/\beta)} \tag{11}$$

Employing this result in Eq. (8) yields

$$C_i = \frac{6\beta q}{\rho_0(x_i - x_{i+1})}\left(\frac{x_{i+1}}{x_i}\right)^{(3-1/\beta)} \tag{12}$$

The Char Combustion Model

The single-film model [10] of a burning carbon sphere is used to describe a burning particle. Allowance is made for CO and CO_2 formation at the particle surface, and account is made for Stefan flow. The particle burning rate per unit external surface area is given by the following implicit expression [5,11]:

$$q = k_s\left\{\frac{P}{\gamma}\left[1 - (1 - \gamma P_g/P)\exp\left(\frac{\gamma q}{k_d}\right)\right]\right\}^{1/2} \tag{13}$$

where k_s is the apparent chemical reaction rate coefficient ($k_s = A_a \exp(-E_a/RT_p)$), P_g is the oxygen partial pressure in the ambient gas, and P is the total

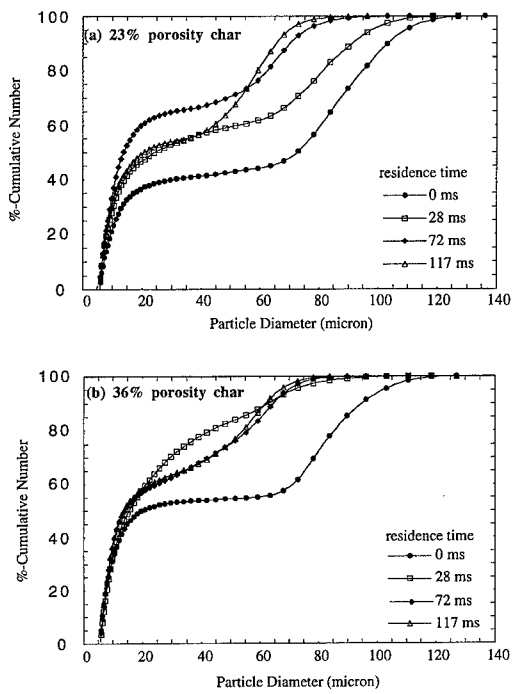

FIG. 2. Cumulative number distributions for the (a) 23% and (b) 36% porosity chars.

pressure. The volume change upon reaction per unit of oxygen present at the surface is γ and the mass transfer coefficient, k_d, is given by

$$k_d = \frac{M_C D_{ox} Sh}{DR' T_m v_o} \tag{14}$$

Here, M_c is the molecular weight of carbon; D_{ox}, the effective diffusion coefficient of oxygen in the particle's boundary layer; Sh, the Sherwood number (taken as 2); R', the gas constant; T_m, the mean temperature in the boundary layer; and v_o, the stoichiometric oxygen coefficient.

Particle temperatures during burn off are determined from an energy balance, wherein the rates of energy generation due to char oxidation are balanced by the rates of energy loss by conduction, convection, and radiation. The key adjustable parameters in the particle population balance model are the Arrhenius parameters for the apparent chemical reaction rate coefficient (A_a and E_a) and the fragmentation rate coefficient (k). These are adjusted to provide time-resolved agreement between measured and calculated extents of mass loss and particle number distributions.

Results and Discussion

The extent of fragmentation associated with the particle feeding and collection systems was assessed in cold-flow experiments. Results indicated that the feed system causes insignificant fragmentation and that the collection system causes attrition-type fragmentation with fragments as large as 10% of the radius of the attriting particles. Calculations using the population balance model with A_a set to zero (no burning) were used to determine that for chars with porosities in the range 16% to 60% passing through the sampling system, $k = 2.5\ \mu m^{-1} s^{-1} \equiv k_{probe}$.

Combustion tests were performed in 12 mol % oxygen at nominally 1500 K using chars of 23% and 36% porosity with particles in the 76–125 μm size range. Partially reacted chars were extracted from the flow reactor at residence times of 28, 72, and 117 ms. For the 23% porosity char, values for m/m_0 were determined to be 0.71, 0.21, and 0.19 at the respective residence times and for the 36% porosity char, 0.41, 0.20, and 0.21.

Figures 2a and 2b show the measured cumulative number distributions, each based on about 20,000 particles. The distributions for the 23% porosity char show increases in the number of particles having diameters less than about 20 μm up to the 72-ms residence time. Thereafter, particles with diameters in the 5–20 μm size range are being consumed faster than they are being generated.

For the 36% porosity char, the distribution at 28 ms shows a large increase in the number of particles having diameters less than about 40 μm. (A duplicate test at this residence time yielded an almost identical distribution.) Particles at this residence time were extracted just subsequent to devolatilization, as evidenced by the disappearance of luminous clouds that surround particles during volatile release. Devolatilization tests performed in a thermogravimetric analyzer indicate that the higher the weight fraction of lycopodium used in the synthesis procedure, the lower the volatile matter content of the synthetic char. Thus, the 36% porosity char has a lower volatile matter content than the 23% porosity char, as well as a more open internal structure. The data suggest that these factors (volatile matter content and void volume) enhance particle fragmentation during heat up and devolatilization.

The distributions at 72 and 117 ms indicate a reduced level of fragmentation in comparison with that during the first 28 ms in the flow reactor. Factors that govern fragmentation during heat up and devolatilization differ from those that control fragmentation during char oxidation. It is not expected that the same fragmentation rate parameters apply in the two regimes.

Figures 3 and 4 show cumulative and differential weight distributions for the 23% and 36% porosity chars. The lines are curves drawn through the data to facilitate interpretation. The distributions show a monotonic reduction of particle size with time and, hence, with mass loss. Values of D/D_0 determined using weight-averaged diameters for each size dis-

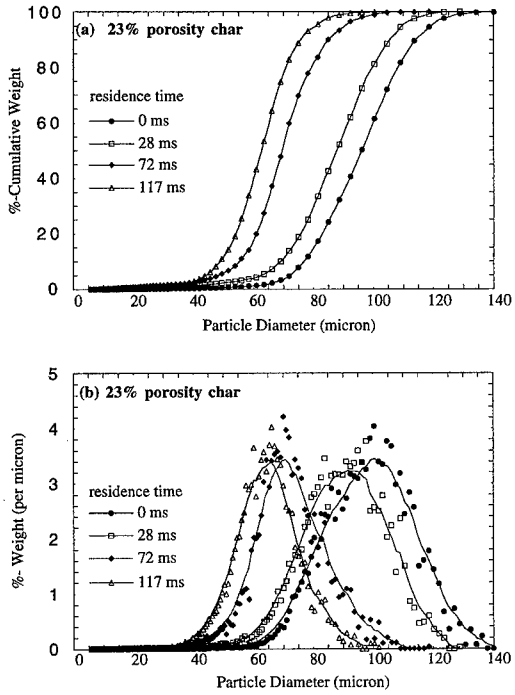

FIG. 3. (a) Cumulative and (b) differential weight distributions for the 23% porosity char.

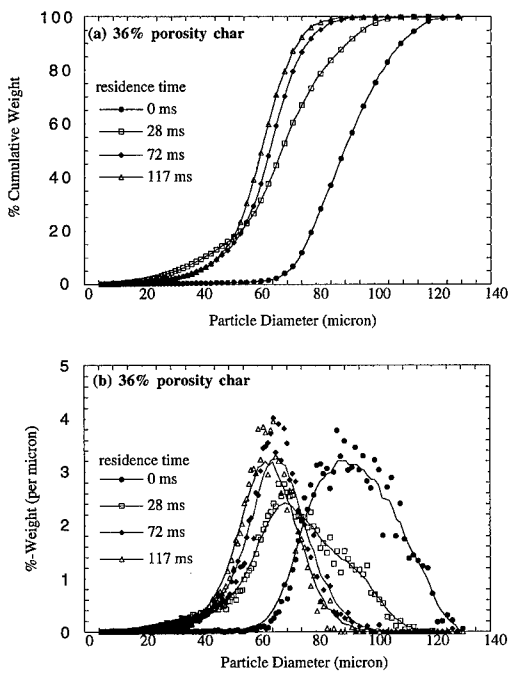

FIG. 4. (a) Cumulative and (b) differential weight distributions for the 36% porosity char.

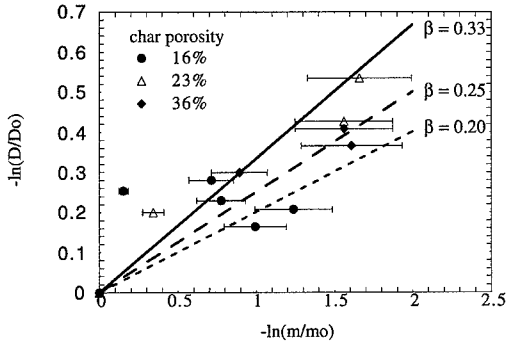

FIG. 5. Diameter and apparent density variations with burn off. The lines are calculated using Eq. (10b) and selected values of β.

tribution are plotted against the measured m/m_0 values in Fig. 5. Values obtained with a 16% porosity char are also included in the plot. The lines in the figure are calculations in accord with Eq. (10b) using selected values for the particle burning mode parameter β. For $\beta = 1/3$, particles burn at constant density; for $\beta < 1/3$, particles burn with decreases in both size and apparent density. The data support a value of β near 0.25. The corresponding value for α is 0.25, a value consistent with those determined previously [5,12].

The population balance model was used to calculate the number distributions at residence times of 72 and 117 ms using the distributions at 28 ms as starting distributions. One hundred size bins were used in the calculation with $x_i/x_{i+1} = 1.06$ and $x_n = 0.55$ μm. The set of 100 differential equations was solved using LSODE [13], an ordinary differential equation solver. Ambient conditions were specified ($T_{gas} = 1500$ K, $P_g = 0.12$ atm); char combustion model parameters were taken from the literature [5,11]. The apparent activation energy was taken as 26 kcal/mol, consistent with results of previous work [11] for chars containing 90% carbon. Adjustable parameters included A_a and k. Sampling-induced attrition-type fragmentation was accounted for by readjusting A_a to zero and k to k_{probe} at the end of the specified residence time in the reactor and integrating an additional 171 ms, the time it takes particles to pass through the sampling system.

It was not possible to determine values of A_a and k that resulted in number size distributions that reflected the measured trends when attrition- or breakage-type fragmentation was assumed. Only percolation-type fragmentation yielded calculated cumulative number distributions having the characteristic shapes of those observed.

Figure 6 shows calculated cumulative number distributions for the 23% porosity char assuming no fragmentation. To get good agreement between measured and calculated cumulative and differential

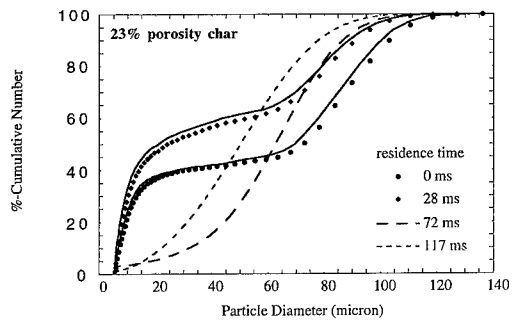

FIG. 6. Calculated cumulative number distributions (broken lines) assuming diffusion-limited burning and no fragmentation. Calculated m/m_0 values agree with the measurements at the various residence times. Solid lines through the data at 0 and 28 ms represent fits used as starting distributions in the calculations.

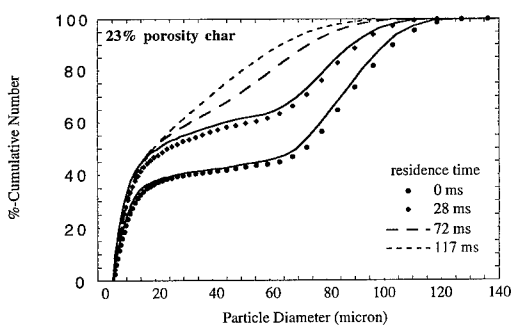

FIG. 7. Calculated cumulative number distributions (broken lines) assuming $A_a = 200$ gC/cm^2 s atm$^{0.5}$ and $k = 0.05\ \mu m^{-1}\ s^{-1}$. Calculated m/m_0 values agree with the measurements at the various residence times. Solid lines through the data at 0 and 28 ms represent fits used as starting distributions in the calculations.

weight distributions, diffusion-limited burning had to be assumed. The calculated number distributions, however, do not reflect the trends depicted in Fig. 2. With diffusion-limited burning, small particles in the feed char are completely burned before the 72-ms residence time in the reactor is reached. No increases in the numbers of small particles are predicted at the high particle burning rates needed to match the weight-loss data.

Figure 7 shows the distributions calculated assuming percolation-type fragmentation with $A_a = 200$ gC/cm^2 s atm$^{0.5}$ and $k = 0.05\ \mu m^{-1}\ s^{-1}$. With this value of A_a, particles in the 30–80-μm size range burn at rates ranging from 78% to 94% of their diffusion-limited rates in 12 mol % oxygen at 1500 K. The distributions reflect the trends observed with the data. For better agreement, it is necessary to model more accurately apparent density changes associated with fragmentation. When a particle fragments, its fragments do not have the same apparent densities as those of the smaller classes of particles into which the fragments fall. In the present particle population model, variations in apparent density for each size class of particles are determined by integrating the differential equation obtained when Eq. (10a) is differentiated with respect to time and combined with Eq. (9). Such an approach assumes that all particles in a given size class have the same apparent density, a reasonable assumption when there is no fragmentation. Only by having density classes associated with each size class can apparent density effects be modeled accurately when account is made for char fragmentation.

Using the measured size distribution at $t = 0$ ms for a starting distribution and the value determined for A_a, calculations indicate that fragmentation rates of the 23% porosity char during the first 28 ms in the flow reactor (i.e., during heat up and devolatilization) are about five times the fragmentation rates during the later stages of char oxidation. This estimate is based on the apparent density of the unburned char and assumes very rapid devolatilization rates and no swelling during devolatilization. Calculations also indicate that the frequency of fragmentation events during heat up and devolatilization is about three times higher with the 36% porosity char than with the 23% porosity char.

Conclusions

During pulverized coal combustion, particles fragment as they heat up and devolatilize and as they undergo oxidation. Results show that char burn off increases with porosity at any given residence time and that number distributions exhibit greater numbers of small particles with increases in porosity, demonstrating an impact of fragmentation on burn off rates. The fragmentation behavior can be characterized as being percolative, where fragmenting particles produce fragments of all sizes.

The data indicate that both particle diameter and apparent density decrease during char oxidation and support power-law relations between particle mass, diameter, and apparent density. Since overall particle burning rates depend on particle size, it is apparent that accurate determination of mass loss rates during the char oxidation phase of coal combustion requires that account be made for char particle fragmentation. The neglect of fragmentation can result in the determination of apparent chemical reaction rate coefficients that are too high.

A particle population model that accounts for char fragmentation and oxidation has been developed and shown to be able to predict qualitatively the evolution of the number size distribution during burn off. The adjustment of model parameters to fit data

indicates that char fragmentation is percolative in nature and that fragmentation rates increase with char porosity. The model also indicates that the rate of fragmentation during heat up and devolatilization is about five times the rate of fragmentation during char oxidation. Before the effects of fragmentation on the extent of mass loss can be predicted with greater accuracy, the model must be modified to allow for variations in density for each size class of particles considered.

Acknowledgment

This work is supported by the U.S.D.O.E. through the Pittsburgh Energy Technology Center.

REFERENCES

1. Senior, C. L., "Submicron Aerosol Formation during Combustion Of Pulverized Coal," Ph.D. Thesis, California Institute of Technology, 1984.
2. Senior, C. L. and Flagan, R. C., *Twentieth Symposium (International) on Combustion,* The Combustion Institute, Pittsburgh, 1984, pp. 921–929.
3. Levendis, Y. A. and Flagan, R. C., *Carbon* 27:265–283 (1989).
4. Akan-Etuk, A. and Niksa, S., *Energy Fuels* 5:614–615 (1991).
5. Mitchell, R. E., Hurt, R. H., Baxter, L. L., and Hardesty, D. R., "Compilation of Sandia Coal Char Combustion Data and Kinetic Analyses: Milestone Report," Sandia National Laboratories, September 1991.
6. Dunn-Rankin, D., *Combust. Sci. Technol.* 58:297–314 (1988).
7. Austin, L. G., Klimpel, R. R., and Luckie, P. T., *Process Engineering of Size Reduction: Ball Milling,* Society of Mining Engineers, New York, 1984.
8. Kerstein, A. R. and Edwards, B. F., *Chem. Engineer. Sci.* 42:1629–1634 (1987).
9. Essenhigh, R. H., *Twenty-Second Symposium (International) on Combustion,* The Combustion Institute, Pittsburgh, 1988, pp. 89–96.
10. Field, M. A., Gill, D. W., Morgan, B. B., and Hawksley, P. G. W., *Combustion of Pulverized Coal,* BCURA, Leatherhead, 1967, p. 186.
11. Hurt, R. H. and Mitchell, R. E., *Twenty-Fourth Symposium (International) on Combustion,* The Combustion Institute, Pittsburgh, 1992, pp. 1243–1250.
12. Smith, I. W., *Combust. Flame* 17:421–428 (1971).
13. Radhakrishnan, K. and Hindmarsh, A. C., "Description and Use of LSODE, the Livermore Solver for Ordinary Differential Equations," Lawrence Livermore National Laboratories, UCRL-ID-113855, 1983.

COMMENTS

Jon Gibbins, Imperial College, UK. Fragmentation by percolation certainly seems to be occurring in a real utility plant since, for situations where good burn-out is occurring, roughly 50% of the unburnt C is below 38 μm and SEM examination confirms it has come from larger, porous structures. If the particles have burnt enough to fragment, however, they will also have got hot enough for thermal deactivation so (as usual in char burn-out) there is no single mechanism that can be invoked to explain the observed results! It also appears that, when poor burnout occurs, the abundance of the larger char particles, rather than the smaller particles in the fly ash, increases, which perhaps suggests that fragmentation is not always a burnout-determining process.

Author's Reply. Yes, we agree with your conclusion that fragmentation is not the only cause of unburned carbon in ash. Indeed situations do exist where unburned carbon can be due to other factors, among them differences in reactivity of coal components, thermal annealing, and ash inhibition.

•

L. Douglas Smoot, Brigham Young University, USA. Your observation of a very large average number of fragments for each initial synthetic char particle seems to be counter to various observations for coal chars which suggest up to a few to several fragments per initial particle. Does this suggest that the synthetic particles are not representative of coal in this regard?

Author's Reply. The results of Sarofim et al. [1], Helble *et al.* [2], and Helble and Sarofim [3] support that between 3 and 5 ash particles above 10 μm in diameter and from 200 to 500 ash particles with diameters in the range 1–10 μm are produced from a single pulverized coal particle. If there were no fragmentation, one would expect only one ash particle produced per coal particle. Thus, these results suggest a much larger number of fragments generated during combustion of pulverized coal than indicated in your question. The number of fragments generated during combustion of our synthetic char are consistent with the larger numbers. Using the fragmentation rate coefficient determined for the 23% porosity char, calculations indicate that about 11 fragments per particle were generated having diameters greater than 10 μm during the 28 to 117 ms char-oxidation period in the reactor. Hundreds of smaller fragments were generated over this same time period. Thus, with regards to its fragmentation behavior, we believe that our synthetic char is representative of the char of a low-ash, low-volatile coal.

REFERENCES

1. Sarofim, A. F., Howard, J. B., and Padia, A. S., *Combust. Sci. Technol.* 16:187 (1977).
2. Helble, J. J., Neville, M., and Sarofim, A. F., *Twenty-First Symposium (International) on Combustion,* Combustion Institute, Pittsburgh, 1988, p. 411.
3. Helble, J. J. and Sarofim, A. F., *Combust. Flame* 76:183 (1989).

•

Robert Hurt, Brown University, USA. I agree with your conclusion the fine fragments can undergo "extinction", but would like to comment on the implications of the "extinction" for carbon burnout. According to our models of zone II combustion it is possible under special conditions (low gas temperature and high oxygen concentration) for fragmentation and "extinction" to result in a decrease in overall burning rate, as suggested. At the high gas temperatures and relatively low oxygen concentrations of interest to pulverized-coal-fired boilers, however, the net effect of fragmentation and "extinction" is an *increase* in overall burning rate due to increased external surface. Mathematically, as particle diameter approaches zero, the particle temperature must approach the local gas temperature (the "extinguished" state), which, in this application, however, is still high enough to produce *rapid* burnout of the fine fragment. Do your models predict the same trends—that fragmentation *favors* burnout under pulverized coal combustion conditions?

Author's Reply. In zone II, the shapes of resulting fragments play a key role in determining whether fragmentation increases or decreases burnout. If all particles and fragments are assumed to be spherical, then fragmentation enhances burnout, as predicted by our model. If all fragments were non-spherical, then fragmentation could decrease burnout owing to the impact of surface-to-volume ratio on the relative rates of heat generation and loss, which determine equilibrium particle temperatures. Because of radiative losses to the cooler combustor walls, non-spherical fragments having characteristic sizes as large as 50 μm would burn at temperatures from 50 to 100 K below the local gas temperature. Calculations using burning rate parameters determined for a lv-bituminous coal [1] indicate that a 50 μm diameter spherical particle would obtain a temperature of 1825 K in its fully-ignited state and require about 250 ms for 99% burnoff in 6% O_2 at 1800 K. A 50 μm fragment burning at a rate that limited its temperature to 1750 K could require over 650 ms to reach this extent of burnoff in 6% O_2 at 1800 K (estimated assuming a spherical particle with reduced reactivity to effect the lower temperature). Depending upon whether the fragment was generated during the early stages of char oxidation or late, sufficient time may not be available in the reactor for its complete burnout and hence, portions of this 50 μm fragment could contribute to unburned carbon in the ash.

REFERENCE

1. R. H. Hurt and R. E. Mitchell, *Twenty-Fourth Symposium (International) on Combustion,* The Combustion Institute, Pittsburgh, 1992, p. 1243.

Twenty-Sixth Symposium (International) on Combustion/The Combustion Institute, 1996/pp. 3145–3151

A GENERAL MODEL FOR DEVOLATILIZATION OF LARGE COAL PARTICLES

YUXIN ZHAO, MICHAEL A. SERIO AND PETER R. SOLOMON
Advanced Fuel Research, Inc.
87 Church Street
East Hartford, CT 06108, USA

There have been several studies on the devolatilization of large coal particles under laboratory conditions simulating large-scale fluidized or fixed-bed combustion conditions, all of which demonstrate that the process of devolatilization of large coal particles occurs over a much longer timescale than that of pulverized coals under the same conditions. This paper reports the development of a model for large coal particle devolatilization under fluidized and fixed-bed combustion conditions. The model combines a heat transfer model with a general and comprehensive coal devolatilization model, FG-DVC. It inherits the generality of FG-DVC and can be applied to coals of various types without extensive prior knowledge of the coals. This model includes a detailed treatment of coal pyrolysis reactions including the yields of individual gas species, tar yields, and tar molecular weight distributions. The changes in coal physical properties are modeled with the application of Merrick's coal physical property submodels for specific heat and thermal conductivity. Both the convective and radiative heat transfer between the gas phase and coal particles are considered and Gunn's correlation for the surface heat transfer coefficient is used. Model predictions are compared with the data of large coal particle devolatilization measured in fluidized beds and tubular reactors, for particle thermal response, total weight loss, and individual gas evolution rates. In general, the agreement with the data is very good for the particle center temperature and weight loss curves and is fair for the individual gas evolution curves.

Introduction

There have been several studies on the devolatilization of large coal particles under laboratory conditions simulating large-scale fluidized or fixed-bed combustion conditions, all of which demonstrate that the process of devolatilization of large coal particles occurs over a much longer timescale than that of pulverized coals under the same conditions. Some studies [1–3] have addressed the timescale of the devolatilization process for large particles and have established that the timescale is proportional to d^n, with n ranging from 0.32 to 2.6 and d being the diameter of the particle. The large variation of n in the reported correlations reflects the difficulty in determining the termination point of the devolatilization process. More recent studies have reported more detailed measurements of particle temperature, particle weight loss, and gas species concentrations as a function of time [4–7]. These data sets were collected under relatively well-defined conditions and can be used for model verification.

It is generally accepted that transport of heat and mass from the interior of particles to their surface controls the timescale of large coal particle devolatilization. Besides the effect on the devolatilization rates, there are speculations as to whether the volatiles undergo secondary reactions within particles as they exit. These reactions would include tar cracking, gasification reactions with char, and gas-phase reactions. However, there is no solid evidence supporting claims that these reactions are significant enough to be modeled [8]. Experiments have shown only moderate, at most, changes in yields with changing particle size. These changes may be due primarily to the indirect effects of heat transfer (i.e., that larger particles have slower thermal response). An exception is the formation of HCN and NH_3. Recent experimental results have indicated that large particle size enhances the formation of NH_3 at the expense of HCN [9]. Although mass transport seems not to cause significant secondary reactions for the major volatile gas species, there is abundant evidence that it plays an important role on the primary devolatilization reactions determining the yields of the tar. Solomon et al. [8] have given a detailed review and pointed out that longer residence times of tar could cause its precursor to be repolymerized into the char structure, leading to lower tar yields. This view is incorporated in a coal pyrolysis model, FG-DVC [8,10], which accounts for the mass transport limitations associated with tar evolution.

Models have been developed to model the devolatilization of large coal particles. Agarwal et al. [11,12] and Hajaligol et al. [13] developed large coal particle devolatilization models that combine

intraparticle heat transfer calculations with simple coal devolatilization submodels. The models by Devanathan and Saxena [14] and Bliek et al. [15] considered both heat and mass transport processes coupled with pyrolysis modeling. Bliek's model also took into consideration tar redeposition on char surfaces. Additionally, there are general models developed for pulverized coal devolatilization [8,10,16,17] that have various capabilities for predicting coal thermal decomposition under practical conditions. These models have been developed for coal particles in the micron size range, for which the intrinsic devolatilization rates dominate the timescale. Among these models, the FG-DVC model [8,10] can predict, in addition to the tar and total volatile yields, the yields of individual gas species, the tar molecular weight distribution, and the char fluidity. This model was validated for the eight Argonne Premium coals based on measurements of pyrolysis kinetics from TG-FTIR analysis, solvent extraction and solvent swelling to measure extractables and initial cross-link density, respectively, Gieseler plastometer experiments to measure fluidity, pyrolysis-FIMS to measure the tar molecular weight distribution, and ultimate analysis to determine the elemental compositions (C, H, N, S, O) [10]. A standardized approach has been established and proven successful based on the assumption that devolatilization kinetics and coal structural parameters derived at low heating rates and laboratory conditions can be extrapolated by the FG-DVC model to predict the devolatilization process at high heating rates and high-pressure conditions [8,10,18]. This model is now supported by a coal pyrolysis database so that necessary model input parameters for modeling an untested coal can be extracted from the database based on the coal elemental composition [18].

This paper reports the development of a model for large coal particle devolatilization under heating conditions relevant to fluidized and fixed-bed combustion. The model combines a heat transfer model with a general and comprehensive coal devolatilization model, FG-DVC. It inherits the generality of FG-DVC and can be applied to coals of various types without extensive prior knowledge of the coals.

Model Description

For modeling the devolatilization of large coal particles, consideration must be given to the processes of heat transfer and mass transport inside the particles. The heat transfer flux starts at the particle surface where the coal solid receives heat from surrounding gas and/or solids (bed materials) via convective and radiative transfer modes. The heat wave propagates toward the center of the particle through conduction. As a result, the coal particle devolatilizes, changing constantly its physical properties including the thermal conductivity, specific heat, and solid porosity. The volatile gases escape by going through the char pores, during which time secondary reactions may occur. The mass transport process is very complicated and is not well understood because of the complex coal pore structure. The transport of volatiles through meso and micro pores would be different and would vary from the transport through microcracks. Furthermore, modeling mass transport requires solving conservation equations for every gas species, significantly increasing the model complexity. Four possible effects of mass transport are: (1) resistance of transport through pores, leading to lower evolution rates; (2) possible secondary reactions; (3) influences on tar formation; and (4) influences on internal or external heat transfer.

Since internal mass transport would have a similar timescale as heat transfer, modeling of heat transfer should provide an adequate description of the timescale effect (effect 1 in the preceding paragraph). The secondary reactions appear to be insignificant for the major gaseous volatiles and can be ignored [8]. The secondary reactions involving formations of HCN and NH_3 will be treated separately [9]. The effect of transport limitations on tar formation has been described well by the FG-DVC model [8,10,18]. Since recent evidence suggests that volatile evolution from large particles heated under combustion conditions occurs primarily through cracks and fissures [19], the heat transfer between evolving gases and coal solids would not be very efficient. Previous considerations of the effects of volatiles evolution on the external heat transfer coefficient under similar conditions have indicated that the effect is small [8]. For these reasons, a decision was made that no further consideration would be given to mass transport.

Coal particles are considered to be spherical in the model. The particle size is assumed to remain unchanged during the devolatilization, since two counteracting processes, weight loss and swelling, lead to negligible size changes for millimeter-size coal particles in fluidized beds [4,5]. This assumption implies that the coal particle density will decrease with time because of weight loss. The devolatilization is assumed to be thermally neutral in accordance with most of the data, which indicate relatively small effects [8,20]. The key components in the model are (1) a heat transfer module; (2) a coal devolatilization module, FG-DVC; (3) a coal physical property (thermal conductivity and specific heat) module by Merrick [20]; and (4) a correlation for convective heat transfer from gas to the particle reported by Gunn [21].

Heat Transfer

The heat transfer in the particle is modeled with a standard heat conduction equation

$$\begin{cases} \rho c \dfrac{\partial T}{\partial t} = \dfrac{1}{r^2}\dfrac{\partial}{\partial r}\left(r^2 k_p \dfrac{\partial T}{\partial r}\right) + H\dfrac{\partial \rho}{\partial t} \\ -k_p \dfrac{\partial T}{\partial r}\bigg|_{r=R} = h(T|_{r=R} - T_g) + \varepsilon\sigma(T^4 - T_g^4) \\ \dfrac{\partial T}{\partial r}\bigg|_{r=0} = 0 \\ T(r,t) = T_0 \end{cases} \tag{1}$$

where T is the local particle temperature and is a function of r, the radial distance from the particle center; T_0 is the initial particle temperature; T_g is the gas temperature; R is the particle radius; ρ, c, and k_p are the particle solid density, specific heat capacity, and thermal conductivity, respectively; h is the surface heat transfer coefficient, ε is the emisivity of coal; and σ is the Stefan–Boltzman constant. $\partial\rho/\partial t$ is the local rate of devolatilization and is provided by the FG-DVC model. H is the heat of pyrolysis, which is set to zero in the current model but can be invoked if necessary.

The model divides the coal particle sphere into N shells. Coal devolatilization is modeled with FG-DVC in each shell according to the temperature given by Eq. (1). The chemical composition and density of each shell change as the devolatilization progresses, and this information is used to update the local thermal conductivity and specific heat values. The overall weight loss, gas species evolution rates, and tar evolution rates of the particle are calculated by summation over the shells.

Eq. (1) was cast into an algebraic form with a Crank–Nicholson scheme and is solved with a finite difference method. Coupling of Eq. (1) with the FG-DVC model is through the variables ρ, c, and k_p.

Coal Devolatilization

The detailed description, the experimental basis, and the applications of the FG-DVC model can be found in previous publications [8,10,18] and will not be presented here. The equation set of the model includes species rate equations for gas, tar, and char, and equations for cross-linking and bond breaking, for molecular weight distribution of tar, and for pyrite decomposition. The kinetic equations use a distributed activation energy model modified from the early model by Anthony and Howard [22].

Coal Physical Properties

The changes of the coal/char physical properties during the devolatilization are not easily quantified. The current model uses submodels proposed by Merrick [20]. Merrick's model for the specific heat of coal is based on the Einstein form of the quantum theory specific heat description of solids. The theory leads to an equation that describes the temperature and composition dependence of the specific heat of coal. The local coal/char composition from FG-DVC is used in this equation to update the specific heat. Merrick's model for coal thermal conductivity is as follows:

$$1/k_p = \left(\frac{w_C}{1.47} + \frac{w_H}{0.0118}\right)\left(\frac{273}{T}\right)^{0.5} \tag{2}$$

where w_C and w_H are the mass fractions of carbon and hydrogen, respectively. This equation assumes the contributions for each element are additive. This and any measured thermal conductivity of coal must be considered as apparent values, since coal has a porous structure and there will be extensive radiant heat transfer across the pores and cracks.

Surface Heat Transfer

The surface heat transfer from gas to particle can be convective and radiative as given in Eq. (1). One difficulty is determining the surface heat transfer coefficient, h, which is related to the particle Nusselt number, Nu, which can be correlated to the Reynolds number, Re, Prandtl number, Pr, and bed porosity, v. Several correlations have been proposed to fit the experimental data. However, reported values vary by several orders of magnitude at the same Reynolds number when Re is close to or less than 10. To resolve this discrepancy, Gunn [21] proposed the following correlation:

$$Nu = (7 - 10v + 5v^2)(1 + 0.7Re^{0.2}Pr^{1/3}) + (1.33 - 2.4v + 1.2v^2)Re^{0.7}Pr^{1/3} \tag{3}$$

This correlation is used in the model.

Comparison of the Model with Experimental Data

Two types of experimental data exist in the literature. The first type gives the devolatilization time, t_v, as a function of particle size, whereas the second type includes more detailed measurements of particle temperature, particle weight loss, and gas species concentrations as a function of time. In evaluating these data sets, it is found that the t_v data are of little use for quantitative comparisons of predictions and data; t_v is often defined as 95% or 90% devolatilization time. This value can only be determined accurately when an experiment is carried out to 100% devolatilization at a given temperature. But this condition is hardly obtainable in practice because of the asymptotic nature of coal devolatilization. Most of the pyrolysis studies were conducted at moderately high temperatures ranging from 600 to 1000°C. It is normally observed [3–5,7] that there is a long tailing in the volatiles evolution curve after

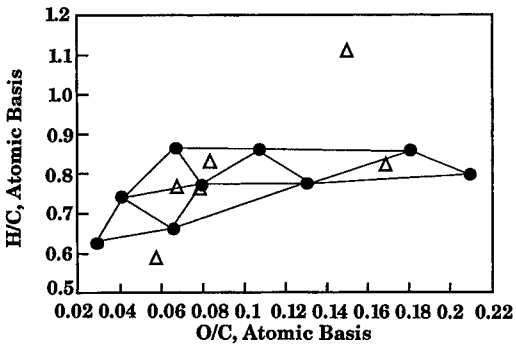

FIG. 1. Coals (triangles) used for model comparisons and the interpolation mesh used by the FG-DVC coal database. In order of increasing O/C ratio, these coals are Bulli, Pittsburgh Seam bituminous, Coal "D," Indiana bituminous, PSOC-435, Wyoming subbituminous. Since elemental composition information was not available for the Arkwright coal, it was assumed to have the same composition as the Lewiston–Stockton coal, one of the coals in the database. The mesh nodes are for the nine coals in the database that are used for interpolation[18].

the majority of the volatiles have evolved. The main components of this portion of the curve are CO and H_2, which are formed from precursor groups that are very strongly bonded in the coal matrix. Since 100% devolatilization is not attainable in practical timescales, the completion of pyrolysis has been decided arbitrarily. For a given data set recorded in a pyrolysis experiment, t_v will depend on the time the experiment is stopped.

For this reason, it was decided that only the time resolved data for large coal particle devolatilization would be used for model validation. These data were obtained from two types of experimental facilities: (1) fluidized beds and (2) tubular reactors. For the first type of experiment [4,5], coal samples of millimeter sizes were added into laboratory scale fluidized beds maintained at a given temperature. Gas samples were extracted for analysis at the outlet of the beds at a given time interval after coal sample addition. Stubington and Sumaryono [5] also measured the center temperature of coal particles with a fine thermocouple inserted into a coal particle that was inserted into a fluidized bed. Unfortunately, there is not enough information reported by Stubington and Sumaryono to allow their concentration data to be presented in a form useful for model comparison. Only the particle temperature data have been used from this paper. The tubular reactor experiments by Stubington et al. [3] and Peeler and Poynton [7] provided recordings of weight loss curves for single coal particles. Adesanya and Pham [6] measured the center particle temperature with a fine thermocouple in their tubular reactor. Both convective and radiative heat transfer from gas to particles were present for all of these experiments, except for the experiments of Adesanya and Pham [6]. In the case of fluidized beds, coal samples were added to beds with the bed materials already heated to a predetermined temperature and hence the radiation from bed materials to relatively cold coal particles would be nonnegligible. In the tubular reactors, the coal particles were heated by the surrounding gas and by radiation from the hot wall. Adesanya and Pham [6] took special measures to assure that the heat transfer was nonradiative. This experiment provides a good test for the surface heat transfer correlation used in the model.

The data used were derived from seven coal samples, five U.S. coals, one Australian coal, and one unnamed coal. The work of Stubington et al. [3] and Peeler and Poynton [7] involved a much larger number of coal samples, but only one coal was reported with weight loss data from each study.

The first step in the modeling is to assemble the FG-DVC input parameters for each coal. Traditionally, laboratory pyrolysis experiments must be performed to characterize coal samples in order to obtain the kinetics and composition data. This step has been simplified with a correlation scheme developed by Zhao et al. [18], in which FG-DVC input parameters for an untested coal can be interpolated from a coal pyrolysis database containing data from nine well-characterized coals. Coals are identified with two indices in the database: atomic ratios of O/C and H/C. The six coals whose data are used in this paper are identified as triangle symbols in a van Krevelen–style plot in Fig. 1. The triangular mesh in the plot is used for the interpolation of input parameters based on a finite element method. The solid circular dots represent the nine coals in the database [18]. For a coal that is inside one of the triangles of the mesh, the FG-DVC input parameters are calculated from the data of the coals represented by the three corners of the triangle. For coals that are not inside the range covered by the mesh, the input parameters are taken from the data of the reference coal that is closest to the corresponding triangle symbol.

In calculating the predictions, no adjustable parameters are used to fit the data. All necessary model parameters are supplied by the submodels through the procedures described previously. Pyrolysis conditions are taken from the data sources. In cases in which the superficial gas velocity was not reported in the original source, 0.2 m/s is used in the calculation.

Figure 2 shows the comparison of the particle center temperatures with model predictions for two coals. In both cases, the model predicts the temperature very well. The experimental temperature curves of the Arkwright coal (Fig. 2a) all exhibit a sudden upturn during the late stages of pyrolysis. This was explained by Adesanya and Pham [6] with

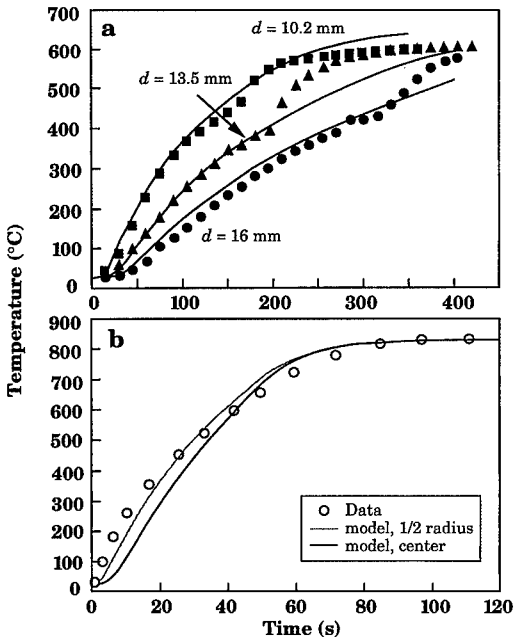

FIG. 2. Comparison of model predictions and data for particle center temperatures: (a) Arkwright coal particles heated to 650°C [6] and (b) a Bulli coal particle of 8.0 mm heated in a fluidized bed at 833°C [5].

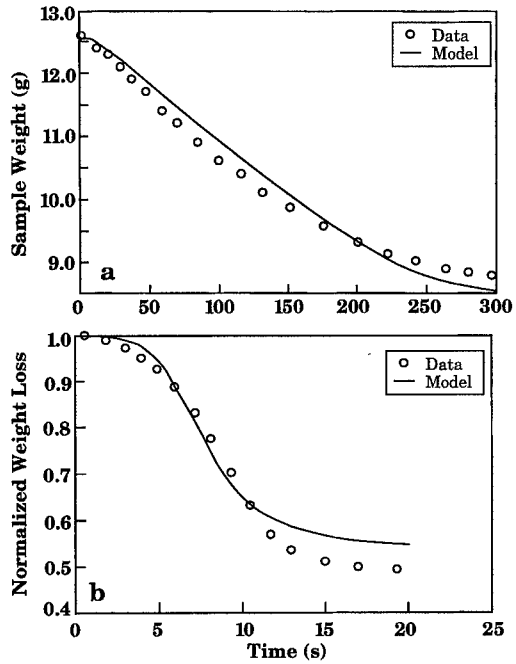

FIG. 3. Comparison of model predictions and data for coal weight loss: (a) a 29-mm coal particle at a gas temperature of 900°C [7] and (b) a 15.1-mm coal particle (PSOC-435) at a gas temperature of 850°C [3].

the observation that the particle shape changes from the starting sphere to a cylindrical shape. This change, believed to be induced by softening of the coal matrix, the drag force of gas flow, and the gravity force, reduced the effective conductive resistance to heat transfer and caused an increase in the heating rate. The data for the Bulli coal (Fig. 2b) show no signs of an initial induction period before the temperature starts to increase, as shown with the Arkwright coal. Since it is possible that the thermocouple tip might not be placed exactly at the center, a second set of predictions is also plotted for the particle temperature at half the radius, which more closely resembles the data.

The second set of comparisons is for the total weight loss curves shown in Fig. 3. Both sets of data were obtained from tubular reactors, and the particle weight was measured with either an electronic balance [7] or TGA [3]. The data in Fig. 3a are from Peeler and Poynton [7] for a coal particle with geometric mean diameter of 28.8 mm. The change of weight is very well predicted, except for a slight overprediction of the final weight loss. Figure 3b is for a PSOC-435 coal studied by Stubington et al. [3]. An underprediction of the final weight loss causes the prediction to deviate from the data in the latter stages of pyrolysis, but the overall change of the particle weight and its time scale are well predicted.

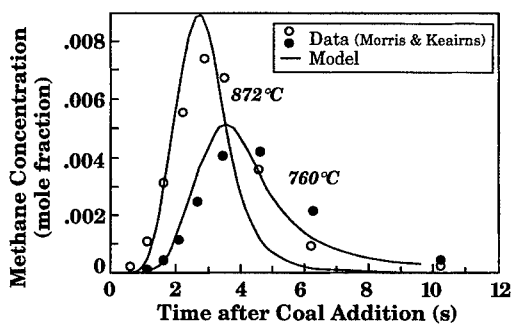

FIG. 4. Comparison of predicted in-bed CH_4 concentration with CH_4 concentration measured at the outlet of a fluidized bed for 1.55-mm coal particles from an Indiana High-Volatile C bituminous coal [4].

In the third test, the individual gas concentrations are compared with model predictions. The data are from Morris and Keairns [4] with three U.S. coals pyrolyzed in a small fluidized bed. The time-dependent gas concentrations are calculated and are compared with data in Figs. 4 and 5. Since the concentration data were measured at the outlet of the reactor, the flow dispersion will result in a time lag when these data are compared to the in-bed con-

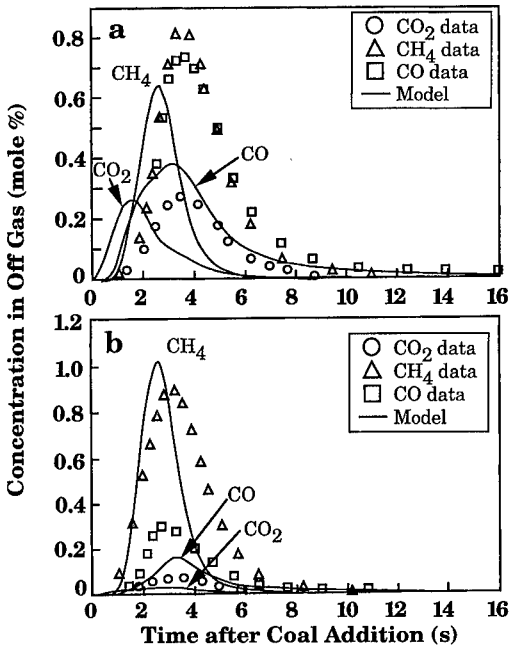

FIG. 5. Comparison of predicted in-bed gas concentrations with gas concentrations measured at the outlet of a fluidized bed for 1.55-mm coal particles at 872°C: (a) Wyoming subbituminous coal and (b) Pittsburgh Seam coal (data are from Ref. 4).

centration predictions. This lag is about 3 s according to a measurement by Morris and Keairns [4]. It can be seen in Figs. 4 and 5 that the measured gas evolution occurs over a longer time interval when compared to the predictions. Among the three gases compared, CH_4 is the best predicted, except for the Wyoming subbituminous coal. For all three coals, the model predicted yields for CO and CO_2 that are lower than the data. This may be due to (1) the fact that the model does not account for mineral sources of these gases; (2) inaccuracies in the elemental analysis used to generate the model input files; (3) weathering of the coal before use; or (4) infiltration of oxygen into the experiment. To accurately predict individual gas yields using the FG-DVC model for a nonlibrary coal, it is recommended to do at least one programmed pyrolysis experiment with gas analysis to calibrate the input files [10,18].

Conclusions

A model has been developed for devolatilization of millimeter-size coal particles under fluidized and fixed-bed combustion conditions. This model includes detailed treatment of coal pyrolysis reactions by incorporating a general coal devolatilization model, FG-DVC.

The model is supported by a coal pyrolysis database and can be used to simulate untested coals based only on elemental analysis data. The changes in coal physical properties are modeled with the application of Merrick's coal physical property submodels. Both the convective and radiative heat transfer between the gas phase and coal particles are considered, and Gunn's correlation for the surface heat transfer coefficient is used in the model. Model predictions are compared with the data of large coal particle devolatilization measured in fluidized beds and tubular reactors, for particle thermal response, total weight loss, and individual gas evolution rates. In general, the agreement with the data is very good for the particle center temperature and particle weight loss curves and fair for the individual gas evolution curves.

Acknowledgments

This work was supported by the U.S. Department of Energy Morgantown Energy Technology Center under contract No. DE-AC21-93MC30040. Dr. Norman Holcombe is the COTR. The authors wish to thank Dr. Marek Wojtowicz at AFR and Prof. Eric Suuberg of Brown University for helpful discussions.

REFERENCES

1. Howard, J. B. and Essenhigh, R. H., *Ind. Eng. Chem. Process Des. Dev.* 6:74 (1967).
2. LaNauze, R. D., *Fuel* 61:771–774 (1982).
3. Stubington, J. F., Huang, G., and Scaroni, A. W., *Fuel* 70:1105–1108 (1991).
4. Morris, J. P. and Keairns, D. L., *Fuel* 58:465–471 (1979).
5. Stubington, J. F. and Sumaryono, *Fuel* 63:1013–1019 (1984).
6. Adesanya, G. A. and Pham, H. N., *Fuel* 74:896–902 (1995).
7. Peeler, J. P. K. and Poynton, H. J., *Fuel* 71:425–430 (1992).
8. Solomon, P. R., Serio, M. A., Suuberg, E. M., *Prog. Energy Combust. Sci.* 18:133–220 (1992).
9. Wojtowicz, M. A., Zhao, Y., Serio, M. A., Bassilakis, R., Solomon, P. R., and Nelson, P. F., *Coal Science,* Elsevier, New York, 1995, pp. 771–774.
10. Solomon, P. R., Hamblen, D. G., Serio, M. A., Yu, Z.-Z., and Charpanay, S. C., *Fuel* 72:469–487 (1993).
11. Agarwal, P. K., Genetti, W. E., and Lee, Y. Y., *Fuel* 63:1748–1752 (1984).
12. Agarwal, P. K., *Fuel* 65:803–810 (1986).
13. Hajaligol, M. R., Peters, W. A., and Howard, J. B., *Energy Fuel* 2:430–437 (1988).
14. Devanathan, N. and Saxena, S. C., *Ind. Eng. Chem. Res.* 26:539–548 (1987).
15. Bliek, A., van Poelje, W. M., van Swaaij, W. P. M., and van Beckum, F. P. H., *AIChE J.* 31:1666–1681 (1985).

16. Grant, D. M., Pugmire, R. J., Fletcher, T. H., and Kerstein, A. R., *Energy Fuel* 3:175 (1989).
17. Niksa, S., *Energy Fuel* 5:673 (1991).
18. Zhao, Y., Serio, M. A., Bassilakis, R., and Solomon, P. R., *Twenty-Fifth Symposium (International) on Combustion,* The Combustion Institute, Pittsburgh, 1995, pp. 553–560.
19. Bateman, K. J., Germane, G. J., Smoot, L. D., Blackham, A. U., and Eatough, C. N., *Fuel* 74:1466–1474 (1995).
20. Merrick, D., in *Coal Science and Chemistry* (Volborth, A., Ed.), Elsevier, Amsterdam, 1987, p. 307
21. Gunn, D. J., *Int. J. Heat Mass Transf* 21:467–476 (1978).
22. Anthony, D. B. and Howard, J. B., *AIChE J.* 22:625 (1976).

Twenty-Sixth Symposium (International) on Combustion/The Combustion Institute, 1996/pp. 3153–3160

CHEMICAL STRUCTURE OF COAL TAR DURING DEVOLATILIZATION

M. WATT AND T. H. FLETCHER
Department of Chemical Engineering
Brigham Young University
Provo, UT 84602, USA

S. BAI AND M. S. SOLUM
Department of Chemistry
University of Utah
Salt Lake City, UT 84112, USA

R. J. PUGMIRE
Department of Chemical and Fuels Engineering
University of Utah
Salt Lake City, UT 84112, USA

Three coals of different rank were pyrolyzed in a drop-tube reactor at a maximum temperature of 900 K and a residence time of 160 ms. The coal and char were analyzed with solid-state ^{13}C NMR. The tar was dissolved in deuterated methylene chloride. It was found that the tar was only partially soluble in CD_2Cl_2. The nonsoluble tar portion was analyzed in the same manner as the coal and char, while the soluble tar portion was analyzed using a recently developed high-resolution ^{13}C NMR technique developed for liquid phases. The tar structure was found to be significantly different from the structure of the char and coal. The number of bridges and loops per cluster in the tar was up to 65% lower than in the char. In addition, the number of aromatic carbons per cluster in the tar was significantly lower than that found in either the coal or the char. Since the molecular weight per cluster in the tar is lower than reported average tar molecular weights, these data imply that tar is made up of a number of multiple clusters (dimers, trimers, etc.) as well as single clusters (i.e., monomers). The mass of nitrogen per cluster in the tar was found to be significantly lower in the tar than in either the coal or the char. These experimental findings suggest that changes may be necessary in current network devolatilization models to accurately describe the changes in chemical structure.

Introduction

Models of coal devolatilization have progressed from simple rate expressions based on total mass release [1,2] to empirical relationships based on the elemental composition of the parent coal [3] to models that attempt to describe the macromolecular network of the coal [4–6]. In the last several years, advancements in chemical analysis techniques have allowed quantitative investigations of the chemical structure of both coal and its pyrolysis products, including the nature of the resulting char [7,8]. A prominent research goal is to accurately predict the rates, yields, and products of devolatilization from measurements of the parent coal structure. The prediction of nitrogen species evolved during devolatilization is of current interest. These goals necessitate modeling the reaction processes on the molecular scale, with activation energies that relate to chemical bond breaking rather than to the mass of products released from the coal. Solid-state ^{13}C NMR spectroscopy has proven particularly useful in obtaining average values of chemical structure features of coal and char, while liquid-phase ^{1}H NMR spectroscopy has been used to determine some of the chemical features of coal tar [7,9–12]. Pyridine extract residues from coal and partially pyrolyzed coal chars have also been analyzed by solid-state ^{13}C NMR spectroscopy, and the extracts have been analyzed by ^{1}H NMR spectroscopy [13].

Three current devolatilization models use network approaches to describe the parent coal structure and subsequent devolatilization behavior [4–6]. Coal is modeled as an array of aromatic clusters connected by labile bridges, as illustrated in Fig. 1. Kinetic expressions are postulated for the rate of bridge scission, and statistical representations are used to determine the number of clusters liberated from the

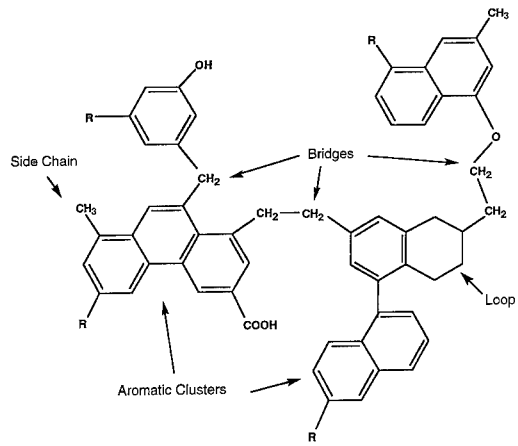

FIG. 1. Representative chemical structures identified in ^{13}C NMR analyses of coal and coal chars.

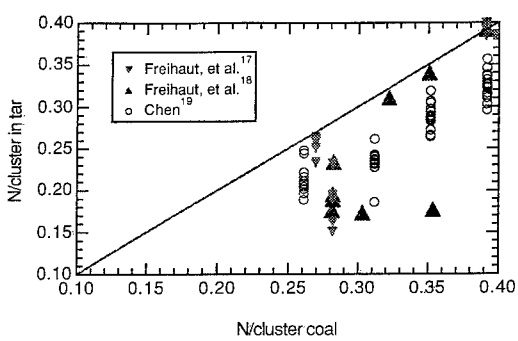

FIG. 2. Comparison of the calculated mass of nitrogen per cluster in the tar and in the parent coal.

coal lattice structure as a function of the number of bridges cleaved. The vapor pressure of liberated clusters are calculated and used to determine yields of tar versus metaplast. Cross-linking reactions eventually connect the remaining metaplast to the char matrix. Such models require knowledge of the average size of the aromatic clusters in the coal, the number of attachments (bridges and side chains) per cluster, the ratio of bridges to side chains, and the average size of the bridges or side chains. Several reviews of these models have been published [14,15]. All three of these models use the solid-state ^{13}C NMR data to some extent to guide selection of coal-dependent input parameters to describe the coal lattice structure. One model demonstrated success in using the solid-state ^{13}C NMR data directly as the only coal-dependent structural input parameters [6]. One of the common assumptions in these models is that the aromatic rings in the clusters are not broken during the pyrolysis process, and hence, the bridge-breaking rate largely controls the devolatilization rate. Therefore, the average number of aromatic carbons per cluster in the coal should be equal to that in the char and in the tar.

In a recent paper, Niksa [16] postulated that nitrogen evolution during pyrolysis could be modeled, assuming that the mass of nitrogen per aromatic cluster in the coal tar was equal to that in the parent coal. It is possible to calculate this value as follows:

$$M_{cl}^{N} = \frac{x_N}{x_C} MW_C \frac{C_{cl}}{f_{a'}} = MW_{cl} x_N \qquad (1)$$

where x_N = wt % N (daf), x_C = wt % C (daf), MW_C = molecular weight of carbon, C_{cl} = number of aromatic carbon per cluster, $f_{a'}$ = carbon aromaticity, and MW_{cl} = molecular weight per aromatic cluster. Tar data reported in the literature were used in conjunction with Eq. (1) to determine the validity of Niksa's assumption. Elemental analyses of tar samples were reported by Freihaut et al. [17,18] and by Chen [19]. It has been reported that the carbon aromaticity of the pristine tar (as estimated from ^{1}H NMR spectroscopy) is similar to that of the parent coal for both lignites and bituminous coals [10,11]. It was assumed that the number of aromatic carbons per cluster in the tar is equal to that in the coal. Results of this analysis are shown in Fig. 2. The data should fall on the 45° line if the assumption that the mass of nitrogen per cluster in the tars equals the mass of nitrogen per cluster in the parent coal is true. This analysis indicates that the mass of nitrogen per cluster in the tar does not equal that in the coal, suggesting further examination. The results in Fig. 2 are assembled from data reported in several experiments; the use of several different data sets may have caused some error in the analysis. It may also be possible that the assumptions in the analysis were in error, namely, (a) that the number of carbons per aromatic cluster in the tar is not equal to that in the coal and/or (b) that the carbon aromaticity of the tar does not equal that of the coal.

This paper describes pyrolysis experiments and chemical structural analyses of one set of coal tars and chars, thus avoiding problems associated with the above analysis. Similar sets of data have been reported [7,8] for conditions that do not minimize reincorporation of pyrolysis products into the metaplast and char. This is the first time that detailed solid-state and high-resolution ^{13}C NMR spectroscopy techniques have been applied to sets of coal tar and char samples, providing more useful chemical structural information than has been previously available from ^{1}H NMR data presented in the literature [10,11,19,20].

Experimental Apparatus

Samples of tar and char were produced at atmospheric pressure in the high-pressure controlled-

TABLE 1
Coal properties

Coal	PSOC ID	Rank	% C (daf)	% H (daf)	% N (daf)	% Ash (dry)
Pittsburgh #8 (PA)	1451D	hva bituminous	84	5.5	1.7	4.1
Illinois #6 (IL)	1493D	hvc bituminous	77	5.0	1.5	15.1
Blue #1 (NM)	1445D	sub-bituminous	77	5.7	1.3	3.6

profile (HPCP) drop-tube reactor [21], which is a laminar flow furnace with a computer-controlled wall temperature profile. The collection probe is water-cooled with gas quench jets in the probe tip. A permeable liner inside the collection probe tube allows quench gas injection radially along the length of the probe to reduce particle and tar deposition. A virtual impactor and cyclone follow the collection probe to aerodynamically separate char particles from tars and aerosols. The tars and aerosols are collected on polycarbonate filters, and tar samples are scraped from the filters rather than removed using a solvent.

The HPCP was used to pyrolyze coal samples in 100% nitrogen at a moderate gas temperature of 900 K with a residence time of 160 ms. Relatively low temperatures were used in these experiments to minimize possible secondary reactions in the evolved coal tars. Three coals of different rank were examined, with properties listed in Table 1. The 63–75-μm-size fraction was used in all of these experiments, resulting in a maximum heating rate exceeding 10^4 K/s. The "D" on the Penn State coal identification number signifies coals from a suite selected by the DOE Pittsburgh Energy Technology Center and have been well characterized [10,17–20].

^{13}C NMR Analysis

Solid-state ^{13}C NMR techniques (CP/MAS and dipolar dephasing) have been used to determine the chemical structure features of coals and coal chars [9,22]. In addition to carbon aromaticity ($f_{a'}$), the distinction between aromatic carbons with and without attachments (such as hydrogen, carbon, or oxygen) is measured. The specification of the number of aromatic carbons per cluster (C_{cl}) provides the basis for the determination of many useful chemical structural features [9]. Probably one of the most important quantities is the number of attachments per aromatic cluster, referred to as the coordination number ($\sigma + 1$), which helps determine the degree of cross-linking in the sample.

A high-resolution ^{13}C NMR technique was recently developed and applied to model compounds, mixtures, and coal-derived liquid samples [23]. This technique uses spin-lattice relaxation to differentiate protonated from nonprotonated carbons, based on relaxation differences arising from direct CH dipolar interactions. Average aromatic ring sizes and other lattice parameters are estimated using the procedures developed for solid-state ^{13}C NMR [9,22].

Tar samples were dissolved in deuterated methylene chloride (CD_2Cl_2) and then filtered. A significant amount of insoluble residue was obtained for each tar. This tar residue was subsequently analyzed using the same solid-state ^{13}C NMR technique as that used for coal char.

Results and Discussion

Tars collected at 160 ms were analyzed using the ^{13}C NMR spin-lattice relaxation technique [23]; data are presented in Tables 2 and 3. Data for the corresponding chars are also presented in Table 2. As seen in Table 3, 12–42% of the tar sample collected was insoluble in CD_2Cl_2 and was deposited on the filter as residue; this insoluble tar fraction is designated as tar residue. The average values of the chemical structure features for the composite tar were determined from combining the values for the dissolved tar and tar residue, according to the relative weight fractions of soluble tar and tar residue. These combined tar data are also presented in Tables 2 and 3. As expected, lower tar yields were observed for the lower rank Illinois #6 and Blue #1 coals than for the hva bituminous Pittsburgh #8 coal.

Comparing the NMR data for the tar, tar residue and char with that for the coal gives some interesting insight into the changing structure of coal during pyrolysis. The carbon aromaticity ($f_{a'}$) of the char is 11–32% higher than in the parent coal, which is a smaller difference between char and coal than reported previously for experiments at 1250 K [10,11,20]. The data shown here from lower temperature experiments (900 K) are at an intermediate stage of devolatilization, which is why the total volatile yields are low (see Table 3). Reported total volatile yields for all three of these coals at 1250 K were 52–54% (daf) [10,11,20]. Carbon aromaticities in the dissolved tar are similar to those of the parent coal for Blue #1 coal, but values of $f_{a'}$ in the tars from the other two coals are 8–10% higher (on a relative

TABLE 2
^{13}C NMR analysis of coals, tars, and chars[a]

Coal	Sample	f_a	f_a^C	$f_{a'}$	f_a^H	f_a^N	f_a^P	f_a^S	f_a^B	f_{al}	f_{al}^H	f_{al}^*	f_{al}^O
Pitt #8	coal	65	3	62	23	39	5	16	18	35	24	11	7
Pitt #8	char	87	5	82	27	55	6	19	30	13	7	6	3
Pitt #8	tar dis.	69	2	67	38	29	5	15	9	31	20	11	na
Pitt #8	tar res.	83	3	80	34	46	8	18	20	17	10	7	2
Pitt #8	tar com.	73	2	70	37	33	6	16	12	28	18	10	na
Illinois #6	coal	66	3	63	21	42	7	16	19	34	24	10	8
Illinois #6	char	74	4	70	23	47	7	18	22	26	17	9	4
Illinois #6	tar dis.	70	1	69	40	29	4	15	10	30	20	10	na
Illinois #6	tar res.	80	6	74	28	46	8	18	20	20	12	8	3
Illinois #6	tar com.	74	3	71	35	36	6	16	14	26	17	9	na
Blue #1	coal	60	5	55	19	36	8	13	15	40	29	11	7
Blue #1	char	71	7	64	20	44	8	14	22	29	21	8	4
Blue #1	tar dis.	63	7	56	27	29	8	16	5	37	27	10	na
Blue #1	tar res.	72	6	66	24	42	9	15	18	28	17	11	12
Blue #1	tar com.	64	7	57	27	31	8	16	7	36	26	10	na

[a]Percentage carbon (error); f_a = total sp^2-hybridized carbon (± 3); $f_{a'}$ = aromatic carbon (± 4); f_a^C = carbonyl, $\delta >$ 165 ppm (± 2); f_a^H = aromatic with proton attachment (± 3); f_a^N = nonprotonated aromatic (± 3); f_a^P = phenolic or phenolic ether, δ = 150–165 ppm (± 2); f_a^S = alkylated aromatic, δ = 135–150 ppm (± 3); f_a^B = aromatic bridgehead (± 4); f_{al} = aliphatic carbon (± 2); f_{al}^H = CH or CH_2 (± 2); f_{al}^* = CH_3 or nonprotonated (± 2); f_{al}^O = bonded to oxygen, δ = 50–90 ppm (± 2); tar dis. = tar that dissolved in CD_2Cl_2; tar res. = fraction of collected tar that did not dissolve in CD_2Cl_2; tar com. = weighted combined values of the tar res. and tar dis.; na = not available.

basis) than in the parent coal. For the Illinois #6 coal, the value of $f_{a'}$ in the dissolved tar was similar to that of the char rather than that of the coal. The $f_{a'}$ values of the tar residues of all three coals are close to the corresponding values in the chars.

The number of attachments per cluster ($\sigma + 1$) and the number of bridges and loops per cluster (BL) in the dissolved tar are significantly smaller than in the coal. In the tar residue, $\sigma + 1$ is only slightly less than in the coal, while the bridges and loops parameter (BL) is slightly higher. This indicates that cross-linking occurs in a portion of the tar that was liberated from the coal lattice. The values of BL in the chars are higher than in the parent coals, which also indicates cross-linking. The low values of side chains per cluster (SC) in the char, compared to the coal, indicate that light gas release has occurred to some extent.

The average number of aromatic carbons per cluster (C_{cl}) in the coal is 13–15, which corresponds to structures with three–four aromatic rings. The values of C_{cl} in the tar residue are similar to those found in the coal. Perhaps the most interesting data is the average cluster size of the dissolved tar, which ranges from seven to nine aromatic carbons. This is significantly lower than the values of 12–15 aromatic carbons per cluster found in the coal and tar residue (and 15–18 in the char). These values of C_{cl} in the coals and chars are in agreement with previous data [20] that showed values of C_{cl} in coals and chars ranging from 10 to 18 for coals with rank ranging from lignite to lv bituminous. The combined tar data, obtained from the weighted average parameters of the dissolved and residual tars, show that the total tar values of C_{cl} are around 8–11. As illustrated in Fig. 3, the values of C_{cl} in the combined tar are 30–50% lower than the corresponding values for the coal. These tars therefore contain a lower average number of aromatic carbons per cluster than was previously supposed.

The fact that the number of aromatic carbons per cluster in the tar residue is higher than in the dissolved tar suggests that a wide distribution of species occurs in tar. Other investigators have previously shown that large molecular weight distributions are present in tar [17,24,25]. However, the network models have taken this distribution into account by assuming a distribution of oligimers (monomers, dimers, etc.), with a fixed cluster size. The data presented here suggest a distribution of cluster sizes.

These new data on tar bring into question the assumption that the values of C_{cl} in the tar are equal to those in the parent coals, an assumption that is used extensively in the network coal pyrolysis models. According to these data, tar contains a lower average number of aromatic carbons per cluster than

TABLE 3
Derived properties of coal, tar, and char[a]

Coal	Sample	X_b	C_{cl}	$\sigma + 1$	P_o	BL	SC	MW_{cl}	MW_{att}	% V (daf)	% Tar (daf)	Tar res.
Pitt #8	coal	0.29	14	4.8	0.48	2.3	2.5	323	32	46		
Pitt #8	char	0.366	18	5.4	0.76	4.1	1.3	302	16			
Pitt #8	tar dis.	0.134	8	2.4	0.45	1.0	1.4					
Pitt #8	tar res.	0.25	12	3.9	0.73	2.8	1.1					0.25
Pitt #8	tar com.	0.163	9	2.8	0.52	1.5	1.3	178	25		28	
Illinois #6	coal	0.30	15	5.5	0.52	2.9	2.6	368	35	38		
Illinois #6	char	0.314	15	5.3	0.64	3.4	1.9	326	29			
Illinois #6	tar dis.	0.144	9	2.5	0.47	1.2	1.3					
Illinois #6	tar res.	0.27	13	4.6	0.69	3.2	1.4					0.42
Illinois #6	tar com.	0.197	11	3.4	0.56	2.0	1.3	228	30		10	
Blue #1	coal	0.27	13	5.0	0.48	2.4	2.6	371	42	23		
Blue #1	char	0.344	17	5.8	0.64	3.7	2.1	402	34			
Blue #1	tar dis.	0.09	7	3.0	0.58	1.7	1.3					
Blue #1	tar res.	0.273	13	4.7	0.54	2.5	2.2					0.12
Blue #1	tar com.	0.112	8	3.2	0.58	1.8	1.4	205	35		9	

[a] X_b = fraction of bridgehead carbons; C_{cl} = aromatic carbons per cluster; $\sigma + 1$ = total attachments per cluster; P_o = fraction of attachments that are bridges; BL = bridges and loops per cluster; SC = side chains per cluster; MW_{cl} = the average molecular weight of an aromatic cluster; MW_{att} = the average molecular weight of the cluster attachments; V = total volatile yield; tar = tar collected on filters and corrected for the tar deposited on sampling apparatus; tar dis. = tar that dissolved in CD_2CL_2; tar res. = fraction of collected tar that did not dissolved in CD_2Cl_2; tar com. = weighted combined values of the tar res. and tar dis.

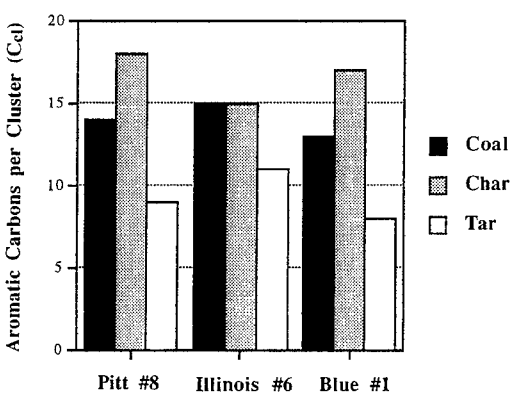

FIG. 3. Average number of aromatic carbons per cluster (C_{cl}) in the coal, char, and combined tar.

was previously supposed. A number of mechanisms are suggested to explain these findings. First, the vapor pressures of higher molecular weight structures that are freed from the coal may not be high enough to permit vaporization from the metaplast to form tar. Second, the tar molecules that are freed from the coal macromolecule may be of smaller size than expected. Third, some form of cluster rearrangement and/or ring opening may be occurring within the coal macromolecule to create smaller aromatic tar structures.

The first and second explanations may seem reasonable, but it has been shown that a distribution of tar structures with molecular weights as high as 800 daltons have been detached from the coal macromolecule and volatilize at relatively low temperatures (800 K) [25]. Several sets of data indicate that tar molecular weight distributions peak in the 250 to 400 dalton range [17,24,25]. The current experiments were performed at higher temperatures and heating rates than used by Simmleit et al. [25], and hence, large molecular weight structures would be expected to vaporize. Therefore, the first and second explanations listed above are not sufficient to explain these data.

The low values of C_{cl} in the tar (8–11) are used to predict the low values of the molecular weight per cluster (~200) shown in Table 3. The cluster molecular weight accounts for the nonaromatic portion of the cluster, such as side chains and bridges, as well as the aromatic portion [9,22]. If the average tar molecular weights are in the range of 250–400, then a significant fraction of tar molecules must contain multiple clusters (i.e., dimers and trimers). This is seen in the number of bridges and loops per cluster

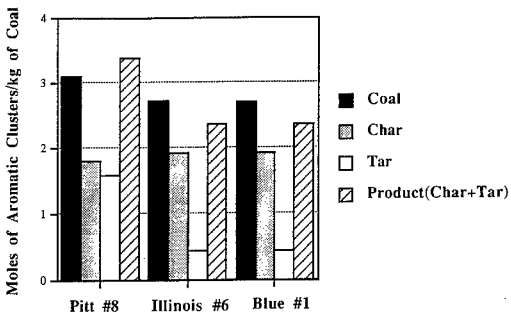

FIG. 4. Number of moles of aromatic clusters per kilogram of the parent coal for the coal, tar, and char.

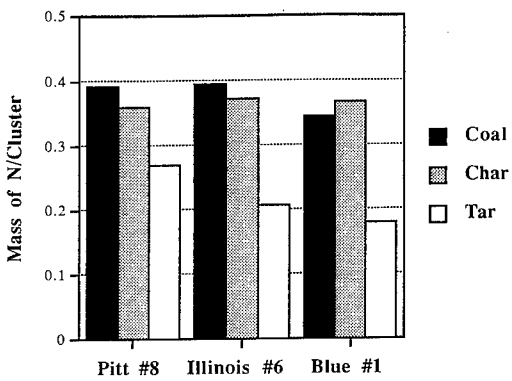

FIG. 5. Mass of nitrogen per cluster for the coal, char, and combined tar.

(BL in Table 3), which is greater than or equal to 1.0 in all of the tar and tar residue samples.

The average molecular weights of the side chains (MW_{att}) for the coal, char, and the combined tar are presented in Table 3. The MW_{att} of the coals decreases as rank increases. The values of MW_{att} in the tars are lower than in the coals by 5 to 7 daltons. The MW_{att} of the chars show a small decrease (6–8 daltons) for the Blue and Illinois chars and a large decrease (16 daltons) for the Pittsburgh char, compared with the original coal values. The Pittsburgh char value is in agreement with previous pyrolysis data at 1250 K in an inert atmosphere [10,11,20]. This agreement seems to indicate that the Pittsburgh char is much further pyrolyzed than the other two chars in this study and is consistent with the higher volatile yield for this coal. The other chars are not in agreement with the previous study, indicative of the low degree of pyrolysis for the Illinois and Blue chars.

The values of C_{cl} of the char increased from that found in the parent coal to values of 15–18. This may imply that the decrease in the value of C_{cl} in the tar is compensated by a corresponding increase in C_{cl} in the char. In previous studies, it has been shown with repeated data sets that the number of aromatic carbons per cluster in the char does not increase substantially during devolatilization [10–12,20]. In order to test the third postulated explanation for low C_{cl} in the tar, the number of moles of clusters per kilogram of parent coal (n_{cl}) was calculated in the following manner:

$$n_{cl,i} = \frac{m_i}{MW_{cl,i}} \tag{2}$$

where m_i is the mass fraction of the coal, char, or tar and $MW_{cl,i}$ is the average molecular weight of the cluster. If the assumptions are made that no aromatic clusters are included in light gases and that the number of aromatic clusters is conserved (i.e., no ring opening or condensation), then the following equation should apply:

$$n_{cl}^{\text{coal}} = n_{cl}^{\text{char}} + n_{cl}^{\text{tar}} \tag{3}$$

Results of the cluster balance (Eqs. 2 and 3) are shown in Fig. 4. The moles of aromatic clusters per kilogram in the tars from both the Illinois #6 and the Blue #1 coals are significantly lower than in their respective chars, consistent with the low tar yields observed for these coals. The values of n_{cl} in the tar and char from the Pittsburgh #8 coal are approximately equal. A comparison of the moles of clusters in the coal with the combined numbers of tar and char, according to Eq. (3), indicates that the lower rank Blue #1 and Illinois #6 coals have slightly more aromatic clusters than are accounted for in the tar and char (a difference of ~14%). The number of clusters in the Pittsburgh #8 coal is slightly lower than accounted for in the combined tar and char (a difference of ~8%). These differences are most likely within the combined experimental error of the tar yield and NMR data and seem to indicate that the degree of ring opening and/or ring condensation in these experiments is small.

Since one of the driving forces for performing this research was to help resolve the questions of nitrogen release, illustrated in Fig. 2, the data were analyzed for the mass of nitrogen per aromatic cluster (M_{cl}^{N}). Using Eq. (1) and the chemical composition and structural data obtained in this study (i.e., x_c, x_N, $f_{a'}$, and C_{cl}), the nitrogen per cluster value can be compared for the coals, chars, and tars. Figure 5 shows that the mass of nitrogen per cluster in the tar is much lower than in either the char or the parent coal (a difference of ~30–50%). The values of M_{cl}^{N} in the char are similar to that in the coals. This result raises questions regarding the appropriate method for modeling nitrogen release using advanced network devolatilization models.

Conclusions

High-resolution liquid ^{13}C NMR was used to analyze coal tar from three coals of different rank. Tar

was produced at atmospheric pressure in a drop-tube reactor at a temperature of 900 K and a residence time of 160 ms. The parent coals and chars were analyzed for comparison using solid-state ^{13}C NMR.

It was found that the tar structure is significantly different from the original coal and char. The number of bridges and loops per cluster in the tar was much lower than that found in either the coal or the char. In two of the three coals, the carbon aromaticity in the tar was greater than that in the coal. The number of aromatic carbons per cluster was in the range of 8–11 for the tars, 13–15 for the coals, and 15–18 in the chars, suggesting that the cluster size and molecular weight per cluster in the tar was significantly lower than in either the coal or the char.

The low number of aromatic carbons per cluster in the tar was somewhat surprising and contradicts common assumptions in coal pyrolysis modeling. A balance on the number of clusters in the coal versus the number in the tar and char was within 14% for all three coals. This seems to indicate minimal ring opening or ring condensation in these experiments.

The mass of nitrogen per cluster was determined from the elemental composition and the molecular weight per cluster for the coals, chars, and tars. It was shown that the nitrogens per cluster in the tar were significantly lower than in either the coal or the char and that the values for the char and coal were comparable.

The low temperatures in this set of experiments resulted in only partial devolatilization. Additional experiments are suggested at higher temperatures to further analyze coal pyrolysis products and mechanisms. The new high-resolution ^{13}C NMR technique for coal tars, in conjunction with the solid-state ^{13}C NMR technique for coals and chars, provides a significant improvement to help analyze such processes.

Acknowledgments

This work was partially sponsored by the Advanced Combustion Engineering Research Center at Brigham Young University. Funds for this center were received from the National Science Foundation, the State of Utah, 40 industrial participants, and the U.S. Department of Energy. Partial support was also received from the U.S. DOE/PETC under UCR Contract DE-FG22-95PC95215. We also thank Eric Hambly and Dominic Genetti for helping prepare, collect, and analyze samples.

REFERENCES

1. Anthony, D. B., Howard, J. B., Hottel, H. C., and Meissner, H. P., *Fifteenth Symposium (International) on Combustion,* The Combustion Institute, Pittsburgh, 1974, pp. 1303–1317.
2. Kobayashi, H., Howard, J. B., and Sarofim, A. F., *Sixteenth Symposium (International) on Combustion,* The Combustion Institute, Pittsburgh, 1976, pp. 411–425.
3. Ko, G. H., Sanchez, D. M., Peters, W. A., and Howard, J. B., *Twenty-Second Symposium (International) on Combustion,* The Combustion Institute, Pittsburgh, 1988, pp. 115–124.
4. Solomon, P. R., Hamblen, D. G., Carangelo, R. M., Serio, M. A., and Deshpande, G. V., *Energy Fuels* 2:405–422 (1988).
5. Niksa, S., *Energy Fuels* 5:673–683 (1991).
6. Fletcher, T. H., Kerstein, A. R., Pugmire, R. J., and Grant, D. M., *Energy Fuels* 6:414–431 (1992).
7. Miknis, F. P., Turner, T. F., Ennen, L. W., and Netzel, D. A., *Fuel* 67:1568–1577 (1988).
8. Vasallo, A. M., Wilson, M. A., and Edwards, J. H., *Fuel* 66:622–626 (1987).
9. Solum, M. S., Pugmire, R. J., and Grant, D. M., *Energy Fuels* 3:187–193 (1989).
10. Fletcher, T. H., Solum, M. S., Grant, D. M., Critchfield, S., and Pugmire, R. J., *Twenty-Third Symposium (International) on Combustion,* The Combustion Institute, Pittsburgh, 1990, p. 1231.
11. Pugmire, R. J., Solum, M. S., Grant, D. M., Critchfield, S., and Fletcher, T. H., *Fuel* 70:414–423 (1991).
12. Fletcher, T. H., Solum, M. S., Grant, D. M., and Pugmire, R. J., *Energy Fuels* 6:643–650 (1992).
13. Fletcher, T. H., Bai, S., Pugmire, R. J., Solum, M. S., Wood, S., and Grant, D. M., *Energy Fuels* 7:734–742 (1993).
14. Solomon, P. R. and Fletcher, T. H., *Twenty-Fifth Symposium (International) on Combustion,* The Combustion Institute, Pittsburgh, 1994, p. 463.
15. Smith, K. L., Smoot, L. D., Fletcher, T. H., and Pugmire, R. J., *The Structure and Reaction Processes of Coal,* Plenum, New York, 1994.
16. Niksa, S., *Energy Fuels* 9:467–478 (1995).
17. Freihaut, J. D., Proscia, W. M., and Seery, D. J., *Energy Fuels* 3:692–703 (1989).
18. Freihaut, J. D., Proscia, W., Knight, N., Vranos, A., Kollick, H., and Wicks, K., "Combustion Properties of Micronized Coal for High Intensity Combustion Applications," Final Report for DOE/PETC Contract DE-AC22-85PC80263 (1989).
19. Chen, J. C., "Effect of Secondary Reactions on Product Distribution and Nitrogen Evolution from Rapid Coal Pyrolysis," Stanford University, HTGL Report No. T-280 (1991).
20. Fletcher, T. H. and Hardesty, D. R., "Milestone Report for DOE's Pittsburgh Energy Technology Center," Contract FWP 0709, Sandia Report No. SAND92-8209, available NTIS (1992).
21. Watt, M., Master's Thesis, Chemical Engineering Department, Brigham Young University, 1996.
22. Orendt, A. M., Solum, M. S., Sethi, N. K., Pugmire, R. J., and Grant, D. M., in *Advances in Coal Spectroscopy* (H. L. C. Meuzelaar, Ed.), Plenum, New York, pp. 215–254, 1992.

23. Bai, S., Pugmire, R. J., Mayne, C. L., and Grant, D. M., *Anal. Chem.* 67:3433–3440 (1995).
24. Solomon, P. R., Serio, M. A., Despande, G. V., and Kroo, E., *Energy Fuels* 4:42–54 (1990).
25. Simmleit, N., Yun, Y., Muezelaar, H. L. C., and Schulten, H.-R., in *Advances in Coal Spectroscopy* (H. L. C. Meuzelaar, Ed.), Plenum, New York, pp. 295–339, 1992.

COMMENTS

Jon Gibbins, Imperial College, UK. Is the overall conclusion of your results that N will be selectively enriched in the char during primary pyrolysis?

Author's Reply. There is a lot of published data on nitrogen in coal chars that suggests that the fraction of nitrogen released as volatiles is similar to the total amount of volatiles released for many coals. The data presented here suggest that at intermediate stages of pyrolysis, the nitrogen per cluster in the tar does not mimic that in the coal or char. This may change at later stages of pyrolysis. HCN release is also another possibility. We are investigating the mechanisms for release, but cannot at this point say that nitrogen enrichment occurs in fully devolatilized chars to any great extent.

•

Eric Suuberg, Brown University, USA. Do the present results imply that correlations of tar vapor pressure, based upon molecular weight of tar alone, might be inadequate?

Author's Reply. This paper does indicate the presence of dimers and trimers in the tar, which may influence vapor pressure relations. However, it would be inappropriate to extrapolate the limited data presented here to deduce vapor pressure correlations.

•

Majed Toqan, ABB, USA. Can you estimate the influence of higher heating rates ($10^5 - 10^6$ K/s) on the distribution of nitrogen and the aromatic clusters in the char and the liquid/solid tar. It is critical to get the right split especially if one wants to use this information in the production of practical flames.

Author's Reply. Data are available from several sources on the nitrogen distribution between volatiles and char in experiments conducted at particle heating approaching 10^5 K/s, such as in flat flame burners. Drop tube reactors such as in this experiment generally operate in the 10^4 K/s range. The split in nitrogen between volatiles and char, measured by these two types of experiments, is similar. At present we do not have detailed chemical structure data on coal tars from the higher heating rate experiments since the residence time is so small.

•

Judy Wornat, Princeton University, USA. I have three comments/questions. First, I am pleased to see that you have NMR evidence of dimers and trimers in coal tar. It is consistent with the Badger mechanism we invoked in our 22nd Symposium paper [1] to explain the results we obtained by HPLC analysis of the aromatic products of pyrolysis of a high volatile bituminous coal. Our Twenty-Fourth Symposium paper [2] confirmed the occurrence of these reactions in this pyrolysis environment.

Second, it makes sense to me that you observed lower nitrogen in the tar than in the original coal since C-N bond energies within aromatic rings are less than C-C bond energies—particularly for 5-membered rings containing nitrogen (see values computed by Sanderson in Ref. 3 of the paper). Do you agree?

Finally, you may find it relevant to note that our chromatographic analyses of nitrogen-containing aromatics and our elemental analysis of soot produced from coal showed [3] that ring buildup, ring rupture, and soot formation reactions are accelerated for nitrogen-containing aromatics, relative to aromatics without ring nitrogen.

REFERENCES

1. Wornat, M. J., Sarofim, A. F., and Longwell, J. P., *Twenty-Second Symposium (International) on Combustion,* The Combustion Institute, Pittsburgh, 1998, pp. 135–143.
2. Wornat, M. J., Sarofim, A. F., and Lafleuf, A. L., *Twenty-Fourth Symposium (International) on Combustion,* The Combustion Institute, Pittsburgh, 1992, pp. 955–963.
3. Wornat, M. J., Sarofim, A. F., Longwell, J. P., and Lafleur, A. L., *Energy 6 Fuels* 2:775–782 (1988).

Author's Reply. Thank you for the references. The temperatures in the present experiments were low enough to minimize secondary reactions, and hence should be low enough to minimize the ring rupture reactions. Therefore comparative bond energies of C-N and C-C bonds would not be relevant at these temperatures.

Twenty-Sixth Symposium (International) on Combustion/The Combustion Institute, 1996/pp. 3161–3167

CONVERSION OF COAL TAR TO SOOT DURING COAL PYROLYSIS IN A POST-FLAME ENVIRONMENT

J. MA AND T. H. FLETCHER
Department of Chemical Engineering
Brigham Young University
Provo, UT 84602, USA

B. W. WEBB
Department of Mechanical Engineering
Brigham Young University
Provo, UT 84602, USA

Coal pyrolysis experiments were performed in the postflame region of a CH_4/H_2/air flat-flame burner operating under fuel-rich conditions, where the temperature and gas compositions were similar to those in the near-burner region of a large-scale coal-fired furnace. Volatiles released from the coal particles formed a cloud of soot particles at high temperatures in the absence of oxygen. The soot particles in the cloud were collected at different residence times using a water-cooled, nitrogen-quenched suction probe. Test variables included the reaction temperature and coal type. Soot yields in terms of weight percentage of dry ash-free coal were measured based on bulk soot collection experiments. The measured soot yields were related to coal rank, reaction temperature, and residence time. Size changes of soot particles due to soot agglomeration were also observed. The information obtained about coal-derived soot is useful in predictions of radiative heat transfer and pollutant formations in the near-burner region of pulverized coal-fired furnaces.

Introduction

Soot is formed naturally in hydrocarbon flames and is important to combustion systems because of radiative heat-transfer effects. Volatiles are released to the gas phase from coal particles in the initial stage of coal combustion. Secondary reactions of coal volatiles, especially coal tar, are generally thought to be the major mechanism of soot formation in coal flames [1–4]. In a coal-fired furnace, radiation from hot soot particles transfers heat from the flame zone to the surrounding walls. Soot radiation can lower the gas temperature in the flame zone by hundreds of Kelvin [5,6] and must be accurately calculated to model flame characteristics. Soot is thought to be important in coal flames for the following reasons: (1) radiation from soot is an important heat-transfer mechanism near the burner; (2) it is important to calculate correct flame temperatures in order to correctly predict or interpret NO_x formation rates and mechanisms; and (3) coal-derived soot contains nitrogen and, therefore, must be considered in NO_x formation mechanisms.

Soot formation, agglomeration, and combustion have been studied extensively in gaseous hydrocarbon flames [7]. However, relatively little research has been conducted on soot in coal flames. The most important aspects of soot are particle size and size distribution, soot volume fraction, and optical properties. The size and morphology of coal-derived soot using a thermophoretic sampling technique was reported earlier [8]. Optical properties of coal-derived soot have also been recently studied [9]. Soot volume fraction, a parameter required in radiative-transfer calculation, is related to soot yield (i.e., the percentage of parent coal being converted to soot). High-temperature coal pyrolysis experiments conducted in inert gas environments (i.e., in argon) have indicated that the soot yield is related to coal rank, reaction temperature, and residence time [3,10,11]. A trend was observed that soot yield increases with temperature and residence time, while the yield of soot plus tar remains unchanged with respect to temperature and residence time. It is thought that the data obtained in inert coal pyrolysis experiments give upper limits for soot yields. In the near-burner region of an industrial furnace, where soot is formed, the local equivalence ratios are very high (i.e., fuel rich) and oxygen concentrations are very low. However, there are still significant amounts of oxygen-containing species such as CO_2, H_2O, and OH radical, due to the recirculation of combustion products and high temperature. These oxygen-containing species may cause the decomposition of high-

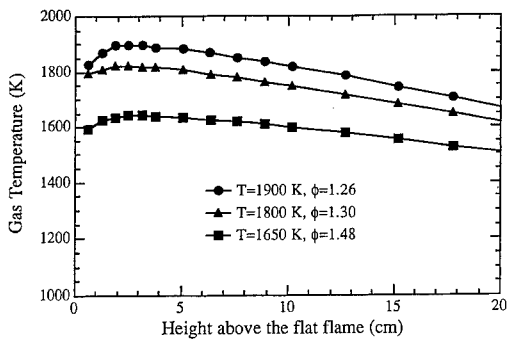

FIG. 1. Centerline gas temperature profiles in the reactor.

molecular-weight polycyclic aromatic hydrocarbons (PAH) in coal tar and, hence, decrease the soot yield. On the other hand, the gas-phase environment may also affect the transport and agglomeration of soot particles formed in the vicinity of a coal particle. Soot clouds initially formed near single coal particles in a flat-flame reactor with 8% of postflame oxygen can be converted to large rod-shaped streamers in the wakes of the coal particles [12]. In an industrial furnace, cloud behavior is more likely than single-particle combustion. A gas-phase environment representative of a pyrolysis cloud is therefore desired for coal pyrolysis experiment in order to obtain soot formation and agglomeration data applicable to practical systems. In the experiments described here, the postflame environment of a fuel-rich methane-hydrogen-air flame was used to approximate the conditions expected in a fuel-rich pyrolysis cloud in a practical furnace.

Experimental Apparatus and Procedures

Flow Reactor

The coal pyrolysis experiments were conducted in a reactor system consisting of a Hencken flat-flame burner, similar to that used by McLean et al. [12], and a 30-cm-high quartz tower used to confine the postflame gases. The cross section of the quartz tower has the same dimension as the burner outlet (5-cm by 5-cm square). Flow rates of CH_4, H_2, dilution N_2, and air were adjusted to obtain horizontally uniform, nonsooting, flat flames. Figure 1 shows corrected centerline gas temperature profiles (measured by a type B thermocouple) for three conditions, with equivalence ratio (ϕ) varying from 1.26 to 1.48 (i.e., fuel rich). The temperature values shown in the legend of Fig. 1 are approximately the maximum temperatures in the reactor. The horizontal temperature profiles were also measured and were relatively flat in the central portion of the reactor (in a cylindrical region of 3.5 cm in diameter). The average centerline gas velocity was around 3.0 m/s. Coal pyrolysis experiments were carried out in the postflame region of the CH_4/H_2/air flame. The postflame gases, mainly CO_2, H_2O, and N_2, provide a gas-phase environment similar to that in the near-burner region of industrial furnaces. Coal particles were entrained by a stream of carrier nitrogen and were fed into the center of the reactor by a syringe particle feeder, driven by a stepper motor. The feed rate of coal particles was controlled by the stepping rate of the motor and was maintained at 1.5 g/h. This low feed rate minimized the particle–particle interactions and alterations of the postflame gas temperatures due to the introduction of coal particles. When a coal particle was heated by the hot gases, the volatiles were released and expanded radially away from the coal particles. Char particles remained in a very thin stream along the centerline of the tower, while a visible volatiles cloud extended to a diameter of approximately 3 cm. The velocities of coal particles at a certain height in the reactor were measured by a high-speed video camera.

Soot Collection System

A water-cooled, nitrogen-quenched suction probe was used to collect bulk samples of soot and char at four different heights above the flat flame (or four different residence times of char particles). About 30% of quench nitrogen is introduced to 12 jets in the mouth of the sampling tube. The rest of the quench nitrogen transpires through the wall of the inside tube, made of sintered stainless steel with a pore size of 5 μm, to minimize deposition of particles on the inside wall of the probe. Water jackets enclose the transpiring tube.

A particle separation system follows the suction probe, including a virtual impactor, a cyclone, and two soot filters, as shown in Fig. 2. The virtual impactor is designed to allow small particles to pass through the side arm. All large particles travel to the cyclone, where the char particles are separated aerodynamically and collected. Both the virtual impactor and the cyclone were designed to have a cut-point diameter of 5 μm. At high temperatures and high residence times, soot agglomerates as large as 30 μm were collected by the cyclone. These soot agglomerates were separated from char particles using a sieve with openings of 38 μm. The yield of large soot agglomerates (>5 μm) in each test was determined by the difference between the weights of the cyclone-collected sample before and after sieving.

Two polycarbonate filters with a pore size of 1 μm were used to collect small soot particles. The collection efficiency of small soot particles (some of them are smaller than 1 μm) by the filters was very high; the amount of particles leaving the filters was negligible. Deposition of small soot particles on the internal surfaces of the virtual impactor and cyclone was also monitored; the final soot yield was corrected

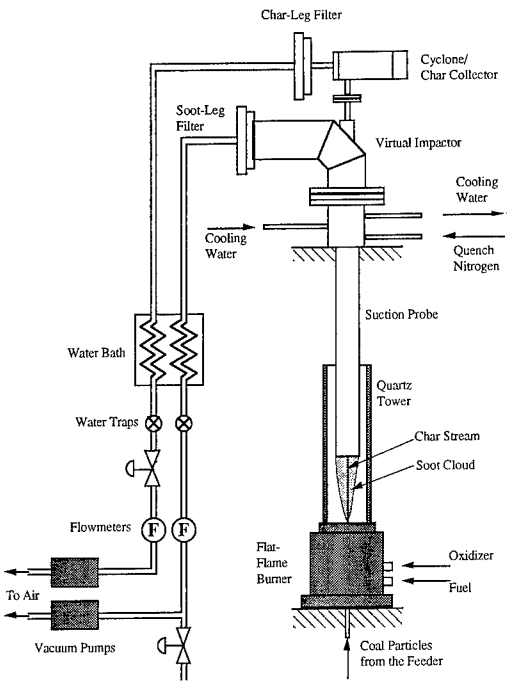

FIG. 2. Schematic of bulk collection and separation system.

by 15% for this loss due to the deposition. A more detailed description of the apparatus and experimental procedures is available [5].

Coals Tested

Six coals ranging from lignite, high-volatile bituminous coal to low-volatile bituminous coal have been tested; proximate and ultimate analyses are shown in Table 1. The "D" classification refers to a suite of coals selected for research by the DOE Pittsburgh Energy Technology Center. The 63–75-μm-diameter sieve fraction was used for all experiments presented here.

Results and Discussion

Soot Cloud

The expanding soot cloud that was observed in the fuel-rich postflame region of the flow reactor suggests that the soot escapes the vicinity of the particles. This observation contrasts the results of McLean [12] for single-particle combustion in 8% O_2, where soot streamers were observed in the vicinity of the particle and no other soot particles were observed. The soot clouds formed in the current experiment are thought to be representative of the process of soot formation in a fuel-rich volatiles cloud in the near-burner region of a practical furnace.

Large Soot Agglomerates

The bulk collection system was designed based on the assumption that the coal-derived soot agglomerates should be less than 5 μm, as assumed by other researchers [10,11]. The basis for designing this separation system was that a cut-point around 5 μm should be large enough to separate soot from char. However, the experiments performed in the flat-flame flow reactor yielded soot agglomerates as large as 30 μm. The existence of these large soot agglomerates was first noticed by the fact that the collected char samples at longer residence times were always dark black and occupied much more volume than the parent coal, while the char samples collected at the lowest residence time were usually gray and occupied less volume. Shaking a vial containing the high residence time sample caused stratification in the sample, with a low-density dark layer sitting on top of a gray layer. By ashing a sample of the top layer and a sample of the bottom layer separately, it was verified that the top layer had negligible ash content. CHN analyses on the samples of Illinois #6 also showed that the material on top had about 90 wt % carbon, much higher than the carbon content expected of devolatilized char particles (~75%).

In order to further analyze the type of particles collected in the cyclone, the samples were examined under a scanning electron microscope (SEM) (JEOL

TABLE 1
Proximate and ultimate analyses for the six coals tested

	Wt %	Wt % (dry)		Wt % (daf)				
Coal Type	Moisture	Volatiles	Ash	C	H	N	S	O
PSOC 1507D Zap lignite	19.12	41.50	15.31	69.98	5.59	1.17	2.08	21.19
PSOC 1493D Illinois #6 hva bit.	6.94	38.69	15.13	76.65	4.93	1.47	6.93	10.01
PSOC 1451D Pittsburgh #8 hva bit.	1.87	37.10	4.11	84.70	5.40	1.71	0.92	7.26
PSOC 1508D Pocahontas #3 lv bit.	0.97	15.91	11.65	90.51	4.59	1.60	0.77	2.52

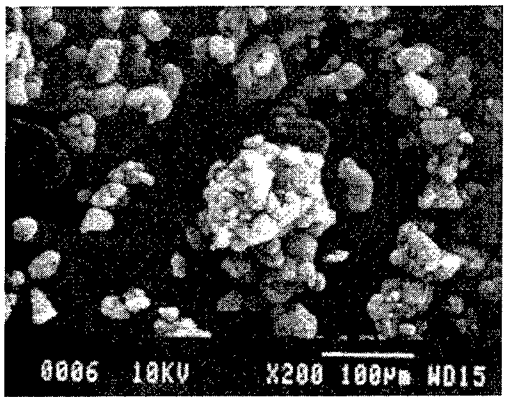

FIG. 3. SEM micrograph of soot/char mixture.

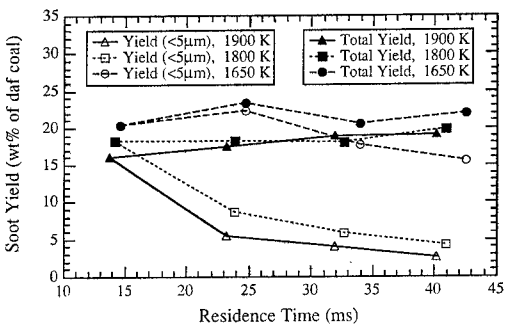

FIG. 4. Measured soot yields for Pittsburgh #8 coal.

Model 840A). An SEM micrograph of an Illinois #6 soot/char mixture collected in the cyclone at a residence time of 34 ms and temperature of 1900 K is shown in Fig. 3. The bright particles in Fig. 3 are 10–30 μm in diameter, and the gray particles are around 70 μm; the gray particles are believed to be the char particles and are similar to those reported by Gale et al. [13]. It can also be observed that the bright particles tend to fuse together to form a densely packed aggregate. The brightness of a particle in an SEM picture is related to the roughness of its surface. The surface of a gray particle at a high magnification is very smooth. In contrast, the surface of the bright particle was found to consist of a large number of tiny particles in the 50–100-nm range, similar to the soot particles deposited on the filters, collected at the same residence time and from the same coal. X-ray analysis was also performed on both gray particles and bright particles using an X-ray analyzer (Model Link ISIS) in the SEM facility. Only carbon and gold, which was used to coat the sample for better conductivity, were detected as the constitutive elements of the surfaces of the bright particles, while other metal elements were found on the surface of the gray particles. The X-ray tests eliminated the conjecture that the bright particles might be from grains of pyrite in the coal [14]. In fact, a few bright pyrite grains were found in the char sample, but their sizes were much smaller (<5 μm).

Most soot agglomerate structures reported in the literature consist of 10–100 primary particles [15], i.e., the size of an agglomerate or aggregate is limited. However, in special situations such as at microgravity [16,17], primary particles are formed in a limited region of a flame or a reactor and are not able to leave that region, resulting in soot agglomerates as large as 0.5 mm. The reason that these large agglomerates are seldom found in most simple diffusion or premixed flames at normal gravity is that free convection provides a mechanism for soot particles to disperse and leave the region in which they are generated.

Since the collection system did not cause soot particles to form large agglomerates at the lowest residence time, it is not likely that the agglomeration phenomenon was due to the collection system. However, the mechanism of formation of the large agglomerates is still unclear. One possible explanation is that the soot particles that remain in the vicinity of a coal particle grow due to thermophoretic forces or other mechanisms. In an oxygen-rich environment, a volatile flame around a coal particle exists, and large sootlike particles form in the wake of the coal particles [12]. In the oxygen-free environment of this study, the reactions between the tar and the oxygen-containing radicals may still form some type of flame even though agglomerates escape the vicinity of the coal particles.

In an effort to determine the cause for the formation of large coal-derived soot agglomerates, acetylene was injected into the flat-flame burner through the tube commonly used to inject coal particles. Soot particles were collected on the soot filters in the collection system, with no deposition in the cyclone. No large (>5 μm) soot agglomerates were formed in this system from acetylene, indicating that the agglomeration mechanism for coal-derived soot may be different than that for soot from simple hydrocarbon fuels.

In the thermophoretic sampling experiments conducted previously [8], the largest soot agglomerate collected was around 800 nm. The large agglomerates found in the bulk collection experiments are too large to be collected thermophoretically. However, the sizes of primary particles in these large agglomerates collected in this study are very comparable to the sizes of primary particles in the soot agglomerates obtained by thermophoretic sampling. The presence of large agglomerates explains why no clear trend in the soot particle size was observed as a function of either coal type or residence time in the previous thermophoretic experiments [8].

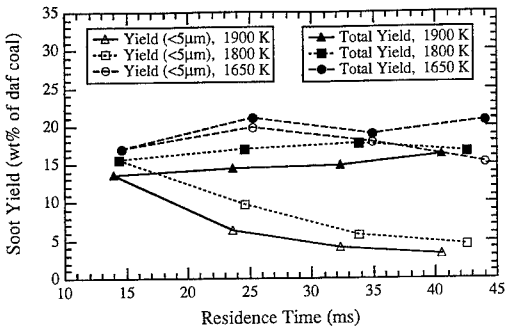

FIG. 5. Measured soot yields for Illinois #6 coal.

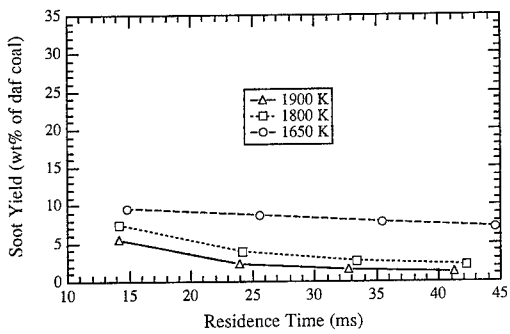

FIG. 6. Measured soot yields (<5 μm) for Pocahontas #3 coal.

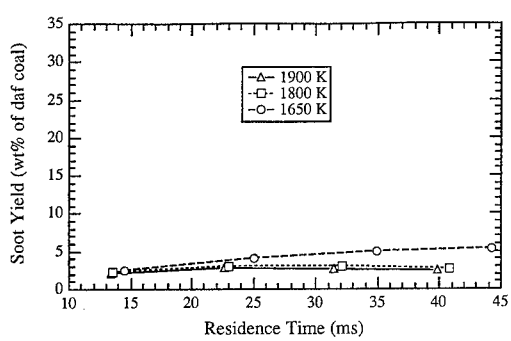

FIG. 7. Measured soot yields (<5 μm) for Zap lignite.

Soot Yield

Figures 4 through 7 show the measured soot yields versus residence time in three temperature conditions for four different coals. The soot yields for the two of the coals shown here (Pittsburgh #8, Illinois #6) were divided into two parts, one for particles less than the cut-point diameter (5 μm) and the other for those larger than 5 μm. For the Pocahontas #3 coal and Zap lignite, only the yields of small soot particles (<5 μm) were measured.

The total soot yields for Pittsburgh #8 and Illinois #6 remained almost unchanged when residence time was increased from about 15 to 42 ms. This means that the soot formation process was very fast at the temperatures examined and that oxidation or gasification of soot by oxygen-containing species (OH, H_2O, and CO_2) at long residence times was negligible. While the total mass of soot did not vary much with residence time, the size distribution of soot particles changed. The distribution of soot yields among these two size fractions is related to the soot agglomeration after primary soot particles are formed. At the lowest residence time (15 ms), all soot particles collected were smaller than 5 μm (i.e., no soot agglomerates were collected in the cyclone). The percentage of larger agglomerates increased monotonically with residence time, indicating a continuous agglomeration process.

Soot yield is related to coal rank. Comparing the soot yields at the lowest residence time for the four coals, which is related to total soot yield, the Pittsburgh #8 coal has the highest soot yields, followed by the Illinois #6, Pocahontas #3 coals, and Zap lignite. This order in soot yield is the same as the order in reported tar yield for these four coals [18,19]. Therefore, a coal with a high tar yield also has a high soot yield.

Temperature had a profound effect on soot agglomeration and a smaller effect on the total soot yield in these experiments. The lower percentages of large soot particles in the 1650 K condition at all residence times suggest that the agglomeration rate is slower at lower temperatures. In the temperature range examined, the final total soot yield for each coal decreased slightly with increases in pyrolysis temperature. This trend can be compared with the results of pyrolysis experiments conducted in inert gas environments. Figure 8 shows a plot of soot yield versus temperature for Pittsburgh high-volatile bituminous coals obtained in this study versus previously reported data. The Pittsburgh coals used by other researchers were not exactly the same as the Pittsburgh coal used in this research in terms of size cuts and seam locations but should be very close in composition. Nenniger [10] and Wornat [3] used a Pittsburgh Seam high-volatile bituminous coal (PSOC 997) with particle diameters ranging from 44 to 53 μm. Chen [11] used the same coal type as used in this study (PSOC 1451D), but used the 75–106 μm size fraction. The temperatures shown in Fig. 8 for Chen's data are actually the reactor wall temperature, which are several hundred degrees higher than the actual gas and particle temperatures. Nenniger's data show that an asymptotic value was reached at increased temperatures, while Wornat's and Chen's data show no limit. The data obtained by Nenniger, Wornat, and Chen all show that soot yield increases with temperature. While the trend shown in this study is different from the trends in inert coal

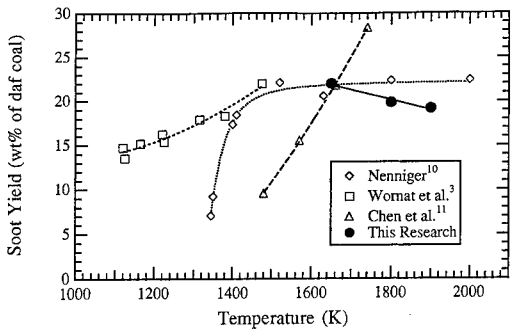

FIG. 8. Comparison of total soot yields for Pittsburgh hva bituminous coal reported in the literature versus temperature. Data reported by Nenniger [10], Wornat et al. [3], and Chen et al. [11] were obtained in an inert atmosphere (Ar). Temperatures reported by Chen were wall temperatures of the reactor; particle and gas temperatures were several hundred degrees lower.

pyrolysis experiments, it is comparable with the results obtained in the hydrocarbon flame experiments or hydrocarbon pyrolysis experiments [20]. The soot yield in simple hydrocarbon experiments always shows a bell-shaped profile when plotted against temperature; yields increase with temperature at low temperatures and decrease at high temperatures. In the current coal pyrolysis study, the soot yield data are apparently on the right side of the bell-shaped curve, which means that soot yields at 1650 K may be close to the peak yield. If the pyrolysis temperature is reduced, as in lower temperature pyrolysis experiments, the soot yield will also be reduced. Of course, if the temperature is too low (<900 K), no secondary reactions will take place, and the soot yield will be zero. Therefore, even though the soot yield versus temperature curve in this research shows a decreasing trend, the entire soot yield curve should be bell shaped if low-temperature data are considered. This can be seen by combining Wornat's soot yield profile in Fig. 8 with the profile of this research.

The decrease in soot yield with temperature can be explained by the stability of tar molecules at high temperatures and the reactions of tar by gaseous species existing in the postflame region of the flat-flame reactor. It is believed that the polymerization and cracking of PAH are competitive reactions in the soot formation processes, and the stability of the high molecular weight PAH tends to decrease with temperature. On the high-temperature side of the bell-shaped soot yield curve, increases in temperature favor the cracking reaction, which leads to a lower soot yield. Another reason for the low soot yield at high temperature might be the reactions of the oxygen-containing species, especially OH and O radicals, with tar molecules and intermediate PAH. Predicted concentrations of OH radical increased by a factor of 30 between 1600 and 1900 K [5], with little change in CO_2, H_2O, or CO. Because of the increased attack of PAH molecules by such oxygen-containing radicals, the stability of PAH is reduced further. This could also explain why the soot yields obtained in inert atmospheres were higher than the yields obtained in the postflame gas environment in this study.

Conclusions

The coal pyrolysis experiments conducted in the postflame region of the flat-flame burner, operated at fuel-rich conditions, are thought to be representative of the conditions in a pyrolysis cloud in an industrial coal-fired boiler. A soot cloud is formed that expands away from the char particle; the large soot streamers observed in previously reported experiments with 8% O_2 are not observed in the absence of O_2. Soot generated in the high-temperature postflame environment of this study is likely to undergo a fast agglomeration process. At higher residence times (>25 ms), soot agglomerates as large as 30 μm were observed. No large agglomerates (>5 μm) were observed when acetylene was injected instead of coal particles. Soot agglomeration is related to reaction temperature; high agglomeration rates were found at high temperatures. Soot formation rates were very high in the temperature range examined. High temperature tends to reduce the total soot yield slightly, probably due to the high concentration of oxygen-containing free radicals. Total soot yield is also related to the tar yield for each coal; high-volatile bituminous coals have the highest soot yields.

Acknowledgments

This work was sponsored by the Advanced Combustion Engineering Research Center at Brigham Young University. Funds for this center are received from the National Science Foundation, the State of Utah, 40 industrial participants, and the U.S. Department of Energy.

REFERENCES

1. Fletcher, T. H., Solum, M. S., Grant, D. M., Critchfield, S., and Pugmire, R. J., *Twenty-Third Symposium (International) on Combustion,* The Combustion Institute, Pittsburgh, 1990, pp. 1231–1237.
2. Pugmire, R. J., Solum, M. S., Grant, D. M., Critchfield, S., and Fletcher, T. H., *Fuel* 70:414–423 (1991).
3. Wornat, M. J., Sarofim, A. F., and Longwell, J. P., *Energy Fuels* 1:431–437 (1987).
4. Chen, J. C., Castagnoli, C., and Niksa, S., *Energy Fuels* 6:264–271 (1992).

5. Ma, J., Ph.D. Thesis, Chemical Engineering Department, Brigham Young University, 1996.
6. Mengüç, M. P. and Viskanta, R., *Combust. Sci. Technol.* 51:51–74 (1987).
7. Haynes, B. S., in *Fossil Fuel Combustion—A Source Book* (W. Bartok and A. F. Sarofim, Eds.), Wiley, New York, pp. 261–326, 1991.
8. Ma, J., Fletcher, T. H., and Webb, B. W., *Energy Fuels* 9:802–808 (1995).
9. Rigby, J., Webb, B. W., and Fletcher, T. H., "Measurement of the Optical Properties of Coal-Derived and Propane-Derived Soot in a Flat Flame Reactor," Spring Mtg. of the WSS/CI, Tempe, AZ, 1996.
10. Nenniger, R. D., Sc.D. Thesis, Department of Chemical Engineering, Massachusetts Institute of Technology, 1986.
11. Chen, J. and Niksa, S., *Twenty-fourth Symposium (International) on Combustion,* The Combustion Institute, Pittsburgh, 1992, pp. 1269–1276.
12. McLean, W. M., Hardesty, D. R., and Pohl, J. H., *Eighteenth Symposium (International) on Combustion,* The Combustion Institute, Pittsburgh, 1981, pp. 1239–1248.
13. Gale, T. K., Bartholomew, C. H., and Fletcher, T. H., *Combust. Flame* 100:94–100 (1994).
14. Baxter, L. L., "The Release of Iron During Coal Combustion," Sandia National Labs., SAND95-8234, 1995.
15. Megardis, C. M. and Dobbins, R. A., *Combust. Sci. Technol.* 66:1–16 (1989).
16. Ito, H., Fujita, O., and Ito, K., *Combust. Flame* 99:363–370 (1994).
17. Jackson, G. S., Averdisian, C. T., and Young, J. C., *Int. J. Heat Mass Transfer* 35:2017–2033 (1992).
18. Freihaut, J. D., Proscia, W. M., and Seery, D. J., *Energy Fuels* 3:692–703 (1989).
19. Fletcher, T. H. and Hardesty, D. R., "Milestone Report," Sandia Report No. SAND92-8209, available NTIS, 1992.
20. Frenklach, M., Clary, D. W., Gardiner, W. C., and Stein, S. E., *Twenty-first Symposium (International) on Combustion,* The Combustion Institute, Pittsburgh, 1986, pp. 1067–1076.

COMMENTS

Jon Gibbins, Imperial College, UK. Do you think any of the soot originates from melted coal ejected from the devolatilising particles?

Author's Reply. We have seen no evidence for ejected material; we would expect ejected material to be relatively large (>5 μm), and see very little large soot particles at early residence times.

Twenty-Sixth Symposium (International) on Combustion/The Combustion Institute, 1996/pp. 3169–3177

STATISTICAL KINETICS FOR PULVERIZED COAL COMBUSTION

ROBERT H. HURT
Division of Engineering, Brown University
Providence, RI 02912, USA

MELISSA M. LUNDEN
Combustion Research Facility, Sandia National Laboratories
Livermore, CA 94550, USA

ELLEN G. BREHOB AND DANIEL J. MALONEY
U.S. Department of Energy, Morgantown Energy Technology Center
Morgantown, WV 26507-0880, USA

Coal is a heterogeneous substance whose structure and properties are highly variable on the length scale of the particle sizes used in suspension-fired combustion systems. For certain applications the statistical variations among particles can play an important role. In this paper, three specialized, single-particle techniques are applied to quantify the variations in combustion reactivity and char particle density within pulverized char particle populations. Reactivity variations are investigated through captive particle imaging experiments and entrained flow reactor experiments employing single-particle optical diagnostics. Single-particle density variations are determined directly by a novel technique based on an electrodynamic microbalance equipped with an automated video imaging and image processing system.

From these data, a coal-general statistical kinetic model is developed and validated against a large set of single-particle temperature measurements for ten coals of various rank burning in three different combustion environments. The model incorporates a single empirical parameter describing the heterogeneity in reactivity and can adequately describe the entire database using a single coal-independent value of this parameter. The use of the model is demonstrated in a series of numerical simulations of complete burnout process for size-classified and polydisperse fuel samples. The simulations show that incorporating statistical kinetics has an important effect on burnout predictions in certain cases, the importance increasing with decreases in temperature, mean reactivity, and breadth of the particle size distribution.

Introduction

Coal is a heterogeneous substance whose structure and properties are highly variable on the length scale of particle sizes used in suspension-fired combustion systems. Most rate processes in combustion have traditionally been described by mean kinetics—formulations that do not explicitly account for these particle-to-particle variations in properties or reactivity. In some coal technologies, however, the statistical variations may play an important role, an example being in pulverized coal combustion, where residual, or unburned, carbon in fly ash typically represents less than 1-wt-% of the coal feed to a boiler. Even at the level of 1% carryover, unburned carbon can have a negative impact on ash utilization options and on overall power station economy. Aware of coal's intrinsic heterogeneity, many combustion researchers have hypothesized that the small fraction of the fuel that remains unburned originates from the least reactive, largest, and/or most dense particles in the original fuel. (Particle density increases the amount of carbon to be consumed by oxidation, thus increasing burnout time for a given reactivity). The goal of the present work is to assess this "heterogeneity hypothesis" through direct measurement of the statistical variations in reactivity and density exhibited by single pulverized char particles ($d_p \sim 100\ \mu$m).

Most combustion studies have reported mean kinetics [1–5], even in cases where the raw measurements were performed on single particles [5]. Several groups have specifically investigated fuel heterogeneity through single-particle combustion experiments [6–9], through studies on lithotypes or maceral concentrates [10,11], or through reflected light analysis of coal and combustion residues [12–17]. Overall, the existing body of work indicates that pulverized coal particles vary significantly in petrology, organic composition, pore structure, mineral

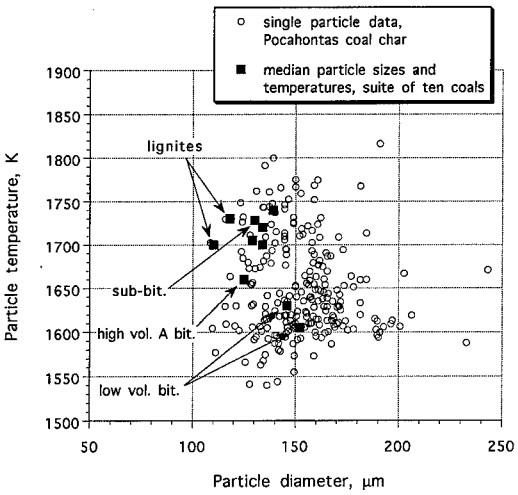

FIG. 1. Example of entrained flow reactor data in the form of measured char particle temperatures and sizes in a fixed combustion environment (local gas temperature 1645 K, 6 vol-% oxygen). Open symbols are single particle data for Pocahontas #3 coal; closed symbols are median sizes and temperatures for a set of coals of various rank.

matter [18], and particle morphology, and that these variations lead to large particle-to-particle variations in char burning rates and burnout times.

In this paper, three specialized, single-particle techniques are applied to quantify the variations in combustion reactivity and density in pulverized char particle populations. Reactivity variations are investigated through captive particle imaging experiments and entrained flow reactor experiments using single-particle optical diagnostics. Density variations are determined directly by a novel technique based on an electrodynamic microbalance equipped with an automated video imaging and image processing system [19]. From these data, a coal-general statistical kinetic model is developed and validated against data on ten U.S. coals. The model is designed to be useful for a variety of quantitative combustion calculations; it is used here as an example to numerically explore the role of heterogeneity in the carbon burnout process.

Samples and Experimental Procedures

This study focuses on a set of ten U.S. coals from the Pennsylvania State Sample Bank ranging in rank from lignite to low-volatile bituminous. This coal set has been studied previously [5] and an extensive characterization is available elsewhere [20,21]. Captive particle imaging experiments were performed on 125- to 250-μm coal particles from four of the ten parent coals (Pocahontas #3, lvb; Illinois #6, hvb; Dietz, subbit; and Beulah lignite), and single-particle densities were measured for two coal char samples (Beulah and Illinois).

Previous publications have presented descriptions of each of the three experimental apparatus: the Sandia entrained flow reactor and optical diagnostic [5,20], the captive particle imaging (CPI) apparatus [22], and the electrodynamic balance and automated video imaging system [19]. The CPI technique provides video image sequences of the complete combustion lifetimes of 100- to 200-μm particles resting on a low-density Al_2O_3-fiber gossamer suspended in a hot vitiated air stream of known temperature (1250 K) and gas composition (3–19 mole-% oxygen). The experimental procedure was the same as that described previously [21]. For each particle, the image sequences were processed to determine: (a) a swelling factor, (b) a maximum particle radiance temperature (as a measure of reactivity), and (c) the ratio of the ash particle size at the end of the sequence to the initial coal particle size, d_a/d_c.

For the determination of particle densities, particle volumes and external surface areas were first measured by recording shadow images as a function of particle rotation angle [23]. Drag coefficient to mass ratios were then determined by analyzing the response of the particles to external perturbations [24]. This data was used to determine particle mass and density by applying a drag analysis for slightly deformed spheres [19]. For this study, measurements were made on a total of 120 char particles of nominal size 106–125 μm, from raw and demineralized samples of PSOC-1493D, Illinois #6 coal, and 1507D, Beulah lignite. Prior to demineralization or analysis, the young char samples were prepared in the entrained flow reactor by sampling at 47 msec residence time, the approximate end of devolatilization.

Experimental Results

The analyses in this paper are based in part on raw data taken from the Sandia coal combustion database [20], comprising approximately 12,000 measurements of single-particle temperatures and sizes during combustion in the entrained flow reactor. The measurements were made on 50- to 150-μm diameter char particles from ten parent coals undergoing combustion in oxygen concentrations of 6 and 12 mole-%, at gas temperatures of 1500–1650 K, at particle temperatures of 1450–2000 K, and for residence times up to 120 msec. An example of this data is shown in Fig. 1, which plots mean particle diameters and temperatures for the ten chars superimposed on single particle data for one coal, Pocahontas #3. The single particle data cover a wider range of temperatures than the entire set of mean temperatures, implying that, within the Pocahontas

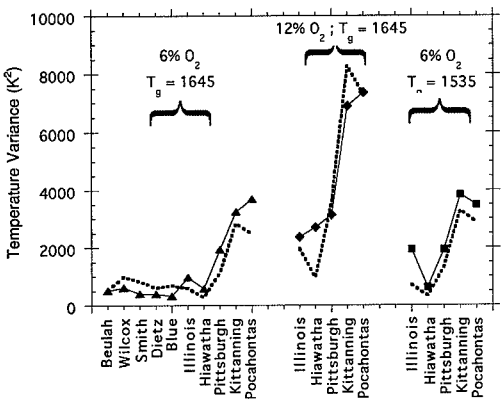

FIG. 2. Measured and predicted temperature variances for a series of coal chars burning in three different combustion environments. Symbols are measured variances; dashed lines are model predictions. All char conversions are less than 45%.

sample, there are particles with combustion behaviors typical of lignites as well as particles with combustion behaviors typical of high-rank (lvb) coals. The mean temperature and burning rate are crude descriptors of this complex behavior.

Previous analysis has shown that the temperature distributions at low conversion are caused primarily by reactivity differences inherent in the parent fuel, with variations in physical and transport properties making a much smaller contribution [25]. The distributions are stationary in the early stages of reaction (the statistical distribution properties are constant), and transient effects (departures from thermal equilibrium) have been estimated to be small [26], making these data suitable for characterizing the initial heterogeneity in the parent fuel. At high conversion, the particle temperature distributions are strongly influenced by the presence of numerous low-temperature particles identified by Mitchell [27] as highly-reacted, high-ash-content particles. This is a conversion-dependent effect that makes these distributions unsuitable for characterizing the initial heterogeneity in the parent fuel. For this analysis, therefore, we consider only that subset of the optical data for which bulk char carbon conversions are less than 45%.

At the earliest residence time (72 msec) a very small number of particles are often observed at or below the local gas temperature but are absent at the next measurement point (95 msec). These particles are believed to be in the latter stages of transient heating at the earliest residence time, but to have reached their pseudo-equilibrium temperature by 95 msec. These few particles have a negligible effect on the overall temperature variance when it is broad, but can contribute significantly when the remainder of the distribution is narrow. Therefore, the few particles at the earliest residence time that are at or below the local gas temperature were removed from the raw data for these analyses.

Figure 2 summarizes the single particle temperature statistics for the reduced data set, which forms the basis set for formulation and validation of the statistical kinetic model. The magnitude of the temperature variance plotted in Fig. 2 is a measure of the breadth of the distribution, and is seen to depend strongly on the parent fuel and combustion conditions, varying from 324 K^2 (σ = 18 K) to 8650 K^2 (σ = 93 K). To develop the statistical kinetic model, more information is needed about the origin of the reactivity distributions implied by Fig. 2, in particular about the origin of the low-reactivity tails of the distributions. Captive particle imaging experiments were therefore carried out on raw coals to allow simultaneous measurement of particle temperatures (which are indicators of particle reactivity), swelling factors (which are indicators of char particle density), and final ash particle sizes (which are indicators of ash content). No strong correlations were found in the data for any of the coals between single-particle temperatures on the one hand, and ash contents, swelling factors, or particle sizes on the other.

From these experiments it is clear that, in the early stages of combustion, single-particle reactivity varies greatly and is not closely related to ash content. Note that this conclusion relates to the early stages of the combustion process, before significant numbers of highly-reacted, ash-rich particles appear. Highly oxidized particles with very high ash contents are theoretically expected and observed to have low global reactivities [22], and indeed, are responsible for many of the low-temperature particles observed at high conversions [27]. Nor is single-particle reactivity closely related to swelling behavior. To first order, the distributions of reactivity, swelling factor, and ash content can be assumed to be mutually independent—a key result that will guide the modeling work described in the next section.

The electrodynamic balance technique was used to make a series of 120 density measurements on single char particles of Beulah lignite and Illinois #6 coal, both before and after demineralization. The single particle density data are summarized in Fig. 3. Significant variations are seen among the single particles from a single coal char, and between the mean values for the two different coal chars.

Model Formulation

In this section a statistical model is developed that describes the single-particle temperature data set summarized in Fig. 2. In the model, variations in reactivity are represented as variations in single-particle global preexponential factor, A, (g-carbon/s-

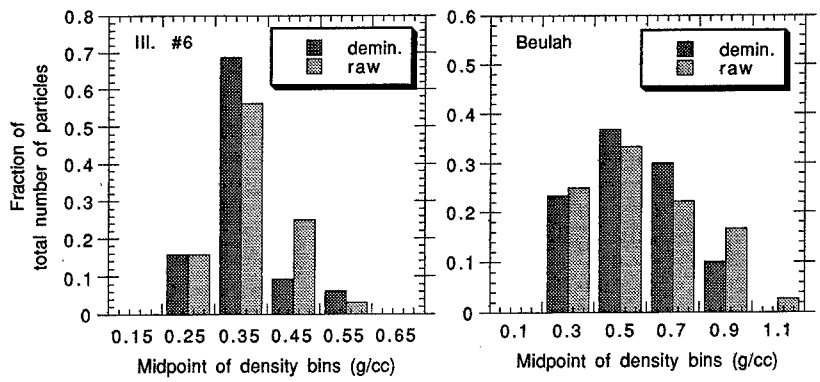

FIG. 3. Distributions of pulverized char particle density measured by the electrodynamic balance technique.

atm$^{0.5}$-cm^2-external-surface)* with global activation energy and reaction order held constant across the particle population. Single particles are allowed to vary in size, d_p, reactivity, A, and carbon density, ρ_c, defined as the mass of carbon per unit particle volume. The number fraction of particles in the incremental parameter space $dd_p\, dA\, d\rho_c$ is given by $F(d_p, A, \rho_c)\, dd_p\, dA\, d\rho_c$, where the function $F(d_p, A, \rho_c)$ fully describes the particle population. The captive particle imaging results described above further suggest that $F(d_p, A, \rho_c)$ can be expressed as the product of three independent functions,

$$F(d_p, A, \rho_c) = F_d(d_p) \cdot F_A(A) \cdot F_\rho(\rho_c) \qquad (1)$$

where F_d is the particle size distribution, F_A is the distribution of reactivities (preexponential factors), and F_ρ is the distribution of char particle carbon densities. The distributions F_d, F_A, and F_ρ can be determined in separate experiments and then superimposed to form the complete input distribution using equation 1. This paper focuses on the determination of F_A and F_ρ. The function F_d can be measured directly by conventional techniques in powder technology.

*Variations in particle reactivity arise due to variations in the intrinsic reactivity, k_i, surface areas, S, and effective diffusion coefficients, D_{eff}. The variations in intrinsic reactivity can affect the temperature dependent term (such as the activation energy, E_i, in Arrhenius kinetics) or the temperature-independent term (such as the preexponential factor, A_i, in the case of Arrhenius kinetics). Of the four parameters, S, D_{eff}, A_i, E_i, variations in three of them (S, D_{eff}, A_i) appear as variations in the global preexponential factor, A. Only variations in E_i will affect the global activation energy, E, and E_i has been shown to fall within a relatively narrow range of values for a wide variety of impure carbons [28,29]. Therefore, the model is based on an explicit description of variations in A, as a convenient approximate representation of the total heterogeneity.

The reactivity distribution function, F_A, is modeled as a gamma distribution, defined by

$$F_A(A) = \frac{e^{-\beta A}}{\Gamma(A)} A^{\alpha-1} \beta^\alpha \qquad (2)$$

where α and β are the distribution parameters and $\Gamma(A)$ is the gamma function. Unlike the Gaussian distribution, which has a lower tail extending to negative reactivities, the gamma reactivity distribution, $F_A(A)$, is defined only for $A_i > 0$. It also has the convenient property that the mean and variance are simple functions of α and β:

$$A_{mean} = \alpha/\beta \qquad (3)$$

$$\sigma_A^2 = \alpha/\beta^2 \qquad (4)$$

The complete set of reactivity distribution functions for ten coals were determined as follows. Relationships between preexponential factors and particle temperatures were first determined by solving, for each combustion condition of interest, the coupled mass and energy transport equations describing burning char particles [5]. These calculations used a single global activation energy of 20 kcal/mol and a product ratio given by $CO/CO_2 = A_c \exp^{(E_c/RT_p)}$, where T_p is the particle temperature, $A_c = 3 \cdot 10^8$, and $E_c = 60$ kcal/mol. For each coal, a mean value of the preexponential factor, A_{mean}, was determined to best match the mean particle temperatures measured optically. The distribution was then determined by choosing a value for the heterogeneity parameter, σ_A, computing α and β by equations 3 and 4, computing the distribution function by equation 2, computing the temperature distribution from the coupled mass and energy balances, and then comparing the predicted temperature variances with the measured variances in Fig. 2. A Newton-Raphson algorithm was then used to find the single value of the heterogeneity parameter, σ_A, that minimizes the sum of squared residuals between the predicted and measured variances for the entire data set.

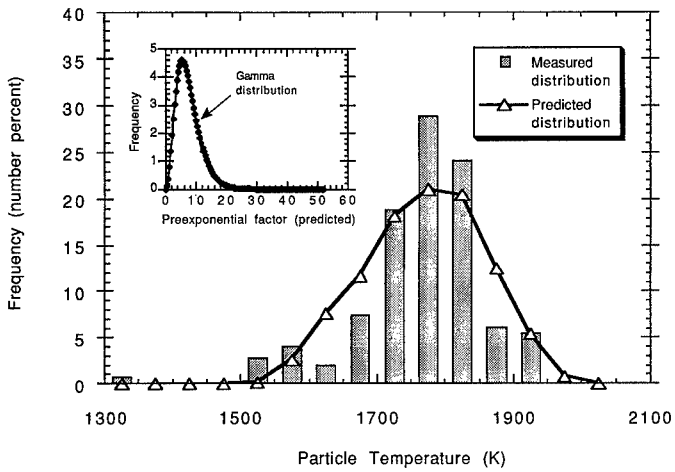

FIG. 4. Example of measured and predicted particle temperature distributions for Pocahontas #3 coal char. Combustion conditions are 12 mole-% oxygen and a gas temperature of 1645 K. Shown in the inset is the gamma distribution of preexponential factors on which the prediction is based.

The model predictions are shown as dashed lines in Fig. 2. A single, coal-independent value of the heterogeneity parameter, σ_A = 3.9 g-carbon/cm^2-s-atm$^{0.5}$, is seen to provide a good description of the entire set of single-particle temperature distributions. The success of the single parameter implies for this data set that the major effects of fuel heterogeneity on combustion can be usefully modeled without detailed coal-specific characterization. Fig. 4 gives an example comparison of measured and predicted particle temperature distributions, along with the gamma distribution of preexponential factors on which the prediction is based.

The success of this simple model indicates that the extent of fuel heterogeneity, judged by the value of σ_A, is nearly constant across this sample set, and that the wide range of temperature variances (324–8650 K^2) is due primarily to the varying combustion conditions. The largest temperature variances arise under conditions where the governing gas-particle transport relations exhibit a high sensitivity of particle temperature to reactivity. Such conditions include high oxygen concentrations and mean reaction rates far from the boundary layer diffusion limit. The success of the single value of the heterogeneity parameter, σ_A = 3.9 g-carbon/cm^2-s-atm$^{0.5}$, suggests that the statistical model can serve as a useful general engineering tool even in the absence of coal-specific data on heterogeneity. It is not yet known, however, if the single parameter can accurately describe the behavior of coals outside this sample set, in particular of coals outside North America, with very different petrologies and geologic histories.

Combustion Simulations

The statistical kinetic model is a useful tool for assessing the importance of heterogeneity under various conditions relevant to laboratory and commercial combustion processes. A computer code was written to simulate complete burnout processes for samples exhibiting particle-to-particle variations in size, reactivity, and density. The code contains a particle combustion model based on single-film theory that accounts for swelling, diameter change during oxidation, ash content, gas-to-particle heat transfer by radiation and convection, mass transfer, and global heterogeneous kinetics with a variable CO/CO_2 ratio in the primary products [20]. The burnout calculations were performed holding the reactivity, A, of each particle constant throughout conversion at its initial value. Single-particle reactivities have in fact been observed to change [25] but that change is suppressed here in order to isolate and examine the effect of heterogeneity alone.

Figure 5 shows the effect of statistical kinetics on the burnout profiles of size-classified coal particles undergoing combustion in a simulated, one-dimensional laboratory reactor under two sets of conditions. The uniform and heterogeneous samples are seen to burn at comparable rates until a carbon conversion of 60–80% is reached, after which the curves diverge, resulting in burnout times that are as much as a factor of 5 longer for the heterogeneous samples. Recent measurements in the high conversion region have indeed yielded burnout curves of this shape, attributable primarily to statistical kinetics, densities, and the effects of ash [30]. In both cases, heterogeneity is a significant effect, and it is therefore recommended, for size classified samples, that statistical kinetics be used to describe or predict combustion behavior to high burnout. Incorporating the measured density distributions was seen to have a similar, but less significant effect under these conditions.

Simulations with Particle Size Distributions

Additional burnout simulations were carried out for coal samples with broad size distributions characteristic of industrial practice. No attempt was

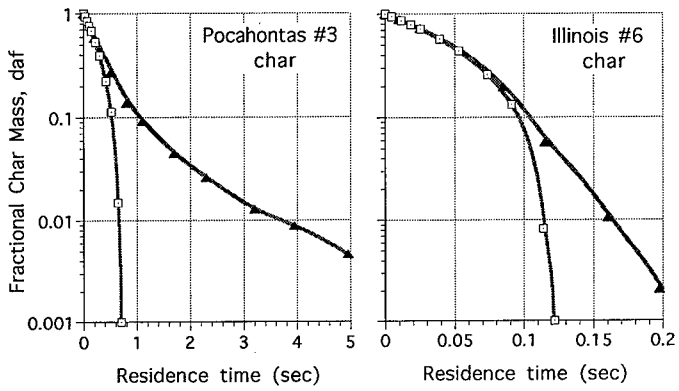

FIG. 5. Calculations showing the effect of distributed reactivity during combustion of size-classified coal particles. Initial particle diameters are 100 μm and oxygen concentration is constant at 7 mole-%. For Illinois #6 coal char, T_g = 1650 K and A_{mean} = 14.4 g-carbon/s-cm^2-atm$^{0.5}$. For the Pocahontas #3 coal char, T_g = 1450 K and A_{mean} = 8.0 g-carbon/s-cm^2-atm$^{0.5}$.

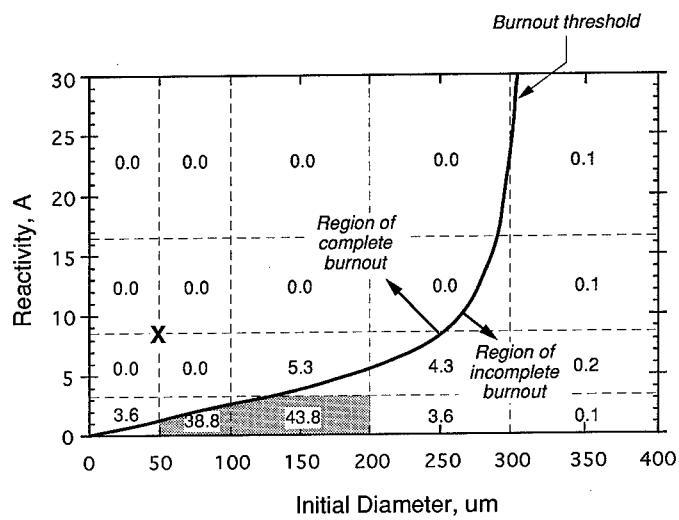

FIG. 6. The origin of unburned carbon in simulation Ib. The solid line divides the size-reactivity space into regions of complete and incomplete burnout. The cross, X, marks the position of the mean size and reactivity in the parent fuel. Sector entries are the percentages of the total unburned carbon that originate from the given size and reactivity bin in the parent fuel (sectors add to 100% of the total unburned carbon). The shaded region at low reactivity represents approximately 80% of the total unburned carbon.

TABLE 1
Conditions in the simulations with particle size distributions[a]

Label	Coal	Gas temp.	Residence time	Carbon density	Kinetic scheme	Char conversion	% Carbon in ash
Ia	Pocahontas	1450 K	2.4 s	0.63	Mean	99.96%	0.3%
Ib	Pocahontas	1450 K	2.4 s	0.63	Statistical	98.92%	8.2%
IIa	Illinois	1650 K	0.58 s	0.36	Mean	99.30%	3.2%
IIb	Illinois	1650 K	0.58 s	0.36	Statistical	99.16%	3.8%
IIc	Illinois	1650 K	0.58 s	Statistical	Mean	99.24%	3.4%

[a]All simulations employed a Rosin-Ramler size distribution (70% through 200 mesh), a fixed oxygen concentration of 7 vol-%, and coal ash content of 10%. Mean char properties taken from Mitchell et al. [20].

made to describe the complex multidimensional environment within furnaces. The goal of these one-dimensional calculations, rather, was to compare the burnout predictions of mean and statistical kinetics at relevant temperatures and oxygen concentrations, and in the presence of typical particle size distributions. Table 1 summarizes the simulation conditions and gives the results as carbon conversions and fly ash carbon contents. Under simulation I conditions (relatively low temperature and reactivity), statistical kinetics can be seen to have a large effect, increasing the unburned carbon content of ash greatly from 0.32 to 8.3% (see Fig. 6).

Fig. 6 reveals the origin of the unburned carbon fraction after 2.4 s of residence time under the conditions of simulation Ib. Note that the axis represents particle sizes and reactivities in the parent (unreacted) fuel. Approximately 80% of the unburned carbon originates from the shaded area, representing that portion of the parent fuel with reactivity in the lowest 25th percentile and with particle diameters from 50 to 200 μm. It is interesting to note that particles greater than about 200 μm will not burn out under these conditions regardless of their reactivity; even diffusion-limited burning is not fast enough to consume all the carbon in these large particles in the time available. This highlights the importance of minimizing the large particle fraction in pulverized fuel. For the size distributions used here (70% $<$ 200 mesh), however, particles larger than 200 μm are not numerous enough in the parent coal to make a large contribution to total unburned carbon. It is the particles that combine low reactivity and relatively large size that produce the bulk of the unburned carbon under the conditions in simulation Ib.

Simulations IIa,b,c employed a more reactive coal and a higher gas temperature and did not show a significant effect of statistical kinetics. Incorporating the measured density distribution for Illinois #6 in simulation IIc is also seen to have no significant effect. Based on a number of additional simulations, the different behavior in simulation sets I and II can be explained as follows. At high reactivity the burnout is quite insensitive to changes in reactivity, as boundary layer diffusion is the primary rate-limiting step. As reactivity is decreased, a threshold value is reached, below which unburned carbon increases sharply. In simulation set I the mean reactivity lies close to this threshold, and the low reactivity tail of this distribution contributes greatly to unburned carbon. In simulation II, the mean reactivity lies far from the threshold in the region where burnout is not particularly sensitive to char reactivity.

Additional simulations were also carried out to explain the density effect. Mean particle density was seen to greatly effect burnout. It was observed, however, that carbon burnout varies in a nearly linear fashion with density under these condition, so incorporation of the distributions had little effect (the low density tail increases burnout to approximately compensate for the lower burnout of the high density tail).

A general comment can be made about the simulations. The overall burnout process for these heterogeneous samples is extremely nonlinear; most of the carbon consumption occurs in the first one-sixth of the residence time available, where the concentrations of fine and reactive particles are high. The effect is even more pronounced in simulations with decreasing temperature and oxygen profiles (not discussed in detail). In general, the final stages of combustion are observed to be extremely slow due to the combined effects of low oxygen concentration, low gas temperature, low reactivity, and larger mean size in the carbon particle population. It is believed that these fuel-related effects, in addition to thermal deactivation [31], and the presence of nonuniform combustion conditions in large multiburner installations [32,33], contribute substantially to the difficulty in achieving complete conversion in many commercial pulverized coal combustion systems.

Acknowledgments

Financial support was provided to Sandia by the Pittsburgh Energy Technology Center's Advanced Research and Technology Development Program. Code development and burnout simulations were carried out at Brown University under subcontract from Sandia. The authors acknowledge the technical contributions of James Ross (TAD Technical Services), Donald Hardesty (Sandia), Reginald Mitchell (Stanford University), and useful discussions with Peter Walsh (EER), Philip Goldberg (DOE/PETC), and Arun Mehta (EPRI).

REFERENCES

1. Essenhigh, R. H., in *Chemistry of Coal Utilization,* Second Supplementary Volume, (M.A. Elliot, Ed.), John Wiley and Sons, New York, 1981, p. 1153.
2. Field, M. A., *Combust. Flame* 14:237 (1970).
3. Smith, I. W. and Tyler, R. J., *Comb. Sci. Technol.* 9:87 (1974).
4. Young, B. C. and Smith, I. W., *Combust. Flame* 76:29 (1989).
5. Hurt, R. H. and Mitchell, R. E., *Twenty-Fourth Symposium (International) on Combustion,* The Combustion Institute, Pittsburgh, 1992, pp. 1243–1250.
6. Sahu, R., Northrup, P. S., Flagan, R. C., and Gavalas, G. R., *Combust. Sci. Technol.* 60:215 (1988).
7. Wall, T. F., Tate, A. G., Bailey, J. G., Jenness, L. G., Mitchell, R. E., and Hurt, R. H., *Twenty-Fourth Symposium (International) on Combustion,* The Combustion Institute, Pittsburgh, PA, 1992, pp. 1207–1215.
8. Huang, G., Scaroni, A., *Fuel* 71:159 (1992).

9. Essenhigh, R. H., and Yorke, G. C., *Fuel* 44:177–186 (1965).
10. Thomas, C. G., Shibaoka, M., Gawronski, E., Gosnell, M. E., Brunckhorst, L. F., and Phong-anant, D., *Fuel* 72:907 (1993).
11. Crelling, J. C., Hippo, E. J., Woerner, B. A., and West, D. P., Jr., *Fuel* 71:151 (1992).
12. Bailey, J. B., Tate, A. G., Diessel, C. F. K., and Wall, T. F., *Fuel* 69:225 (1990).
13. Nandi, B. N., Brown, T. D., and Lee, G. K., *Fuel* 56:125 (1977).
14. Shibaoka, M., *Fuel* 64:263 (1985).
15. Shibaoka, M., *Fuel* 65:449 (1986).
16. Morley, C. and Jones, R. B., *Twenty-First Symposium (International) on Combustion,* The Combustion Institute, Pittsburgh, 1986, pp. 239–248.
17. Oka, N., Murayama, T., Matsuoka, H., Yamada, S., Yamada, T., Shinozaki, S., Shibaoka, M., and Thomas, C. G., *Fuel Process. Technol.* 15:213–224 (1987).
18. Barta, L. E., Horvath, F., Beer, J. M., Sarofim, A. F., *Twenty-Third Symposium (International) on Combustion,* The Combustion Institute, Pittsburgh, 1991, p. 1289.
19. Monazam, E. R. and Maloney, D. J., *Combust. Flame* 99:733–741 (1994).
20. Mitchell, R. E., Hurt, R. H., Baxter, L. L., and Hardesty, D. R., *Compilation of Sandia Coal Char Combustion Data and Kinetic Analyses: Milestone Report* Sandia Technical Report, SAND92-8208, Sandia National Laboratories, Livermore, CA, June 1992.
21. Fletcher, T. H. and Hardesty, D. R., *Compilation of Sandia Coal Devolatilization Data: Milestone Report* Sandia Technical Report, SAND92-8209, Sandia National Laboratories, Livermore, CA, May 1992.
22. Hurt, R. H. and Davis, K. A., *Twenty-Fifth Symposium (International) on Combustion,* The Combustion Institute, Pittsburgh, 1994, pp. 561–568.
23. Maloney, D. J., Lawson, L. O., Fasching, G. E., Monazam, E. R., *Aerosol Sci. Technol.* 22:60–72 (1995).
24. Maloney, D. J., Lawson, L. O., Fasching, G. E., Monazam, E. R., *Rev. Sci. Instrum.* 66:3615–3622 (1995).
25. Hurt, R. H., *Energy Fuels* 7:721–733 (1993).
26. Wall, T. F., Tate, A. G., Bailey, J. G., Jenness, L. G., Mitchell, R. E., and Hurt, R. H., *Twenty-Fourth Symposium (International) on Combustion,* The Combustion Institute, Pittsburgh, 1992, pp. 1207–1215.
27. Mitchell, R. E., *Twenty-Third Symposium (International) on Combustion,* The Combustion Institute, Pittsburgh, 1991, p. 1297.
28. Smith, I. W., *Fuel* 57:409 (1978).
29. Charpenay, S., Serio, M. A., and Solomon, P. R., *Twenty-Fourth Symposium (International) on Combustion,* The Combustion Institute, Pittsburgh, 1992, pp. 1189–1197.
30. Hurt, R. H., Lunden, M. M., and Hardesty, D. R. *The Carbon Burnout Kinetic Model,* Sandia Technical Report, in preparation, 1996.
31. Hurt, R. H., Davis, K. A., Yang, N. Y. C., Headley, T. R., and Mitchell, G. D., *Fuel* 74:1297–1306 (1995).
32. Walsh, P. M., Xie, J., Douglas, R. E., Battista, J., Zawadski, E., *Fuel* 73:1074 (1994).
33. Chen, J. Y., Mann, A. P., and Kent, J. H. *Twenty-Fourth Symposium (International) on Combustion,* The Combustion Institute, Pittsburgh, 1992, pp. 1189–1197, pp. 1381–1389.

COMMENTS

A. E. Jacob Akanetuk, Stanford University, USA. One of the proposed mechanisms for unburned carbon formation is ash occlusion. How is the extent of ash occlusion to be quantified? By comparison of results of surface analytical techniques such as energy-dispersive spectroscopy with results of bulk chemical analysis?

Author's Reply. We believe that much more work is needed to understand the observed ash inhibition in the late stages of combustion as well as carbon/mineral interactions in general. Since the physical form of the mineral matter is one key to its behavior, the tools of modern microscopy (including EDS) should play an important role.

•

Reginald Mitchell, Standford University, USA. Wide variations in the temperature of particles of the same size can be a consequence of particle-to-particle variations in ash-content. The thermal properties of the ash may lead to low-temperature particles that burn slowly, thereby contributing to unburned carbon in ash. In your analysis, was the ash-content of particles considered?

Author's Reply. We agree fully that ash can affect burning rates. In particular, very high ash content particles in the late stages of combustion react slowly and at low temperatures, and are quite conspicuous in many of the optical data sets at longer residence time [1]. The statistical kinetic model in this paper attempts to describe the *initial* distribution of reactivities in the young char sample (due to variations in particle morphology, petrology, surface area, catalytic material, ash content, etc.) that reflect heterogeneity in the parent coal. The current model does not attempt to determine the relative importance of these various factors, but simply extracts initial reactivity distributions to their combined effect. To capture the initial distribution, the model development focuses on a subset of the data taken in the early stages of combustion, before the appearance of significant numbers of these highly reacted, high-ash-content particles. Particularly for the less reactive coals, there is a range of residence times after the heat-up zone

where the conversion is very low and the measured particle temperature distributions are suitable for characterizing the intrinsic heterogeneity in the young chars.

REFERENCE

1. Mitchell, R., *Twenty-First Symposium (International) on Combustion,* The Combustion Institute, Pittsburgh, 1986, p. 1297.

•

L. Douglas Smoot, Brigham Young University, USA. Does your resulting rate reasonably account for the measured reactivities of the utility boiler effluent chars?

Typically, how important are the three effects you considered (i.e., statistical kinetics, annealing, ash inhibition) compared to carbon carryover in very large particles (>400 nm) known to exist in utility boilers?

Author's Reply. We do not, of course, know the detailed temperature/oxygen histories for the unburned carbon particles found in industrial fly ash samples, but we do believe the predictions of the CBK model (which accounts for statistical kinetics, thermal annealing, and ash inhibition) are consistent with the observed low reactivity of unburned carbon. If we consider *typical* particle temperature histories, the model predicts unburned carbon particles from utility furnaces to be significantly less reactive (factors of 2–5) than chars extracted from the Sandia laboratory entrained flow reactor, as observed [1]. The lower reactivity is due primarily to the combined effects of thermal annealing and statistical kinetics.

Particle size is a critical factor in carbon burnout. The specific practical importance of the very large particles you mention (>400 μm) depends very strongly on the number of these particles present in the pulverized fuel and thus on plant-specific grinding practices. In simulations we have performed, particles with diameters greater than 400 μm typically do not burn out and will make a large contribution to unburned carbon if they are present in large quantities initially. For many utility grind size distributions, however, the weight fraction of material in this size range is very small and the >400 μm particles are *not* the origin of the bulk of the unburned carbon. This is increasingly the case as utilities improve grinding and classification operations to minimize unburned carbon. This trend is supported out by the small number of unburned carbon particles in this size range found in many commercial fly ash samples [1].

Almost all utility grind size distributions do have large numbers of particles in the 70–200 μm size range, and our simulations suggest that much of unburned carbon often comes from these particles, with the ultimate burnout depending on a combination of particle density, size, reactivity (including the effects of statistical kinetics, annealing, and ash inhibition), and the temperature/oxygen trajectories through the boiler.

REFERENCE

1. Hurt, R. H. and Gibbins, J. R., *Fuel* 74:4 471 (1995).

Twenty-Sixth Symposium (International) on Combustion/The Combustion Institute, 1996/pp. 3179–3188

MEASUREMENTS OF COAL PARTICLE SHAPE, MASS, AND TEMPERATURE HISTORIES: IMPACT OF PARTICLE IRREGULARITY ON TEMPERATURE PREDICTIONS AND MEASUREMENTS

RAMANATHAN SAMPATH,[1] DANIEL J. MALONEY,[2] JOHN W. ZONDLO,[3] STEVEN D. WOODRUFF[2] AND YAW D. YEBOAH[1]

[1]*Department of Engineering*
Clark Atlanta University
Atlanta, GA 30314, USA

[2]*U.S. Department of Energy*
Morgantown Energy Technology Center
P. O. Box 880, Morgantown, WV 26507-0880, USA

[3]*Department of Chemical Engineering*
West Virginia University
Morgantown, WV 26505, USA

Individual coal and carbon particles were levitated in an electrodynamic balance (EDB) and characterized using high-speed diode array and video-based imaging systems to determine particle surface area, volume, drag, mass, and density. These same particles were then heated bidirectionally using a long-pulsed Nd:YAG laser to simulate combustion-level heating fluxes (heating rates on order of 10^4–10^5 K/s). Measurements of particle surface temperature, size, and laser temporal power variation were made and recorded during each heating experiment. Measured temperature histories were compared with a heat transfer analysis that accounted for variations in particle shape, mass, density, and laser heating power. Results of this study indicate that with well-characterized materials of known properties, agreement between measurement and model of within 20 K is typical throughout an entire heating and cooling profile. Large particle-to-particle variations are observed in coal particle temperature histories during rapid heating. These variations can be explained in large part by accounting for particle-to-particle property (shape, mass, and density) variations. Even when accounting for particle-to-particle shape and density variation, however, model predictions greatly underestimate observed temperature histories. It is concluded that these discrepancies are largely due to uncertainties in the thermal properties (heat capacity and thermal conductivity) typically used to model coal combustion behavior.

Introduction

Recently, Maloney et al. [1] reported results of an investigation to determine temperature histories for coal particles during the early stages of heating and devolatilization. In addition to making in situ temperature measurements, they modeled the early stages of the heating process using thermal property correlations and spherical shape assumptions that are routinely applied to coals. Their predicted temperature transients agreed well with measurements for carbon spheres during the early stages of heating. However, for coal particles, their predicted temperature transients differed significantly from measurements, with the measured temperatures being higher by a factor of 2. Significant underprediction of heating rates for coal particles have also been noted in the work of Solomon et al. [2] and Fletcher [3]. The experiments of Maloney et al. [1] were conducted in a radiative heating/convective cooling environment, whereas the studies of Fletcher [3] were conducted in a convective heating/radiative cooling environment. This fact coupled with additional analysis led Maloney et al. [1] to conclude that the difference between measured and predicted temperatures was due to uncertainties in the relevant coal thermal properties and failure to account for particle shape factors.

During rapid heating prior to devolatilization, the size and mass of coal particles remain unchanged for the first several milliseconds [1,4]. Therefore, the prediction of the temperature history prior to devolatilization requires knowledge of particle size, mass, and thermal properties. Unfortunately, coal particles are irregular in shape and have unique external surface area, volume, mass, and density [4–6]. While energy absorption and emission mechanisms depend on particle surface area (S), the temperature

response depends strongly on particle mass (ρv). So, the shape and density of individual coal particles need to be addressed carefully in any heat transfer analysis. The assumption of spherical shape can result in underestimation of particle surface area because, for example, if the shape of the particle is assumed to be a parallelepiped, cylinder, cube, or ellipsoid of equal volume, then it has a surface area larger than that of a sphere of equal volume. Also, a spherical shape assumption with the size determined from one view of the particle or with a sieve mean size can overestimate the particle volume and hence the mass, which in turn would lead to underestimation of the predicted temperature histories. Hurt and Mitchell [7] reported large particle-to-particle temperature variations in their combustion studies of single char particles. They concluded that particle-to-particle variations in physical properties are a leading cause of these large temperature differences. Thus, accounting for shape, mass, and density in the energy balance is a critical first step in modeling the temperature profiles of irregular particles. In the present work, recently developed methods were applied to measure the shape and mass of single, irregularly shaped particles prior to heating.

Sampath [4] demonstrated shape and mass measurement capabilities for single, irregular particles in an electrodynamic balance (EDB). Shape measurement involved viewing the particle at right angles using two video cameras, and measuring breadth (B), thickness (T) and length (L) of the particle. Using this BTL information, the surface area and volume of the single particles were estimated. Following the approach of Maloney et al. [8], Sampath [4] also measured the drag coefficient/mass ratio (C_d/m) for coal particles in the EDB from the trajectory of the particle that resulted from an applied stimulus. Knowing the surface area and projected area of the particle perpendicular to the motion during the trajectory, the drag coefficient was determined independently based on Stokes' Law. The mass of the particle was then separated from the C_d/m ratio. From the mass and volume, the density of the individual particles was obtained. The mean mass of a large number of single particles thus obtained using the EDB was then validated with the mean mass of several thousand coal particles obtained using an independent counting and weighing technique as described by Monazam and Maloney [6].

Maloney et al. [5] developed a more sophisticated 3-D shape measurement technique by rotating the particles about the EDB center axis using a set of tangentially directed gas jets. As the particle rotated, a video-based imaging system recorded the particle images and stored perimeter data from successive video fields. Rotation rates were measured with the aid of a second video system positioned above the balance. Surface areas and volumes were calculated by summing the surface and volume elements swept out during rotation from one video field to the next. Surface area and volume data were then used to estimate the particle drag coefficient by applying an analysis for deformed spheres derived by Brenner [9]. The particle mass was calculated based on the measured C_d/m and the calculated drag coefficient [6].

In the present paper 3-D shape, mass and density for a large number of coal particles were measured. The same particles were then radiatively heated and their temperatures measured during the subsequent heating and cooling. Particle temperatures were modeled incorporating measured particle shape and mass in the heat transfer analysis. Similar measurements were also made for carbon spheres to test the reproducibility of the temperature measurement system and to validate the numerical analysis presented in this work. The effect of shape and density on the temperature histories of coal particles is assessed by comparing model calculations using measured shape and density with that using a simple equivalent sphere method and uniform density assumptions.

Experimental Methods

The present study is unique in that detailed measurements are performed on coal particle volume, external surface area, mass, density, laser incidental area, radiant energy flux, and transient temperatures during heating and cooling.

Measurement of Particle Volume, External Surface Area, Mass, and Density

Individual coal or carbon particles were levitated in an EDB and characterized using high-speed diode array and video-based imaging systems. Fig. 1 shows the top view of the experimental system with the EDB represented by the small circle at the center of the figure. An individual particle is backlit with a red He:Ne laser at the side and with a light-emitting diode (LED) from the bottom of the balance. The magnified shadow image of the side view is split and projected onto the detector of a CCD video camera imaging system and a high-speed diode array imaging system (Fig. 1). The magnified shadow image of the bottom view is projected onto the detector of a second CCD video imaging system positioned above the balance.

The side view video imaging system was used to obtain the particle diameter for carbon spheres based on the projected image of the particle. The diode array imaging system was used to measure particle trajectory resulting from an applied stimulus. The drag coefficient/mass ratio (C_d/m) was obtained by matching the measured particle trajectory with the predictions from a simple force balance model

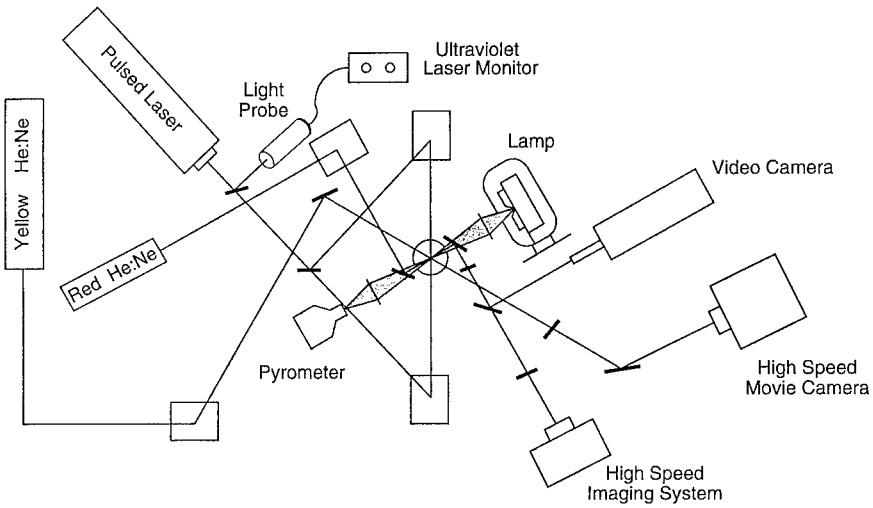

FIG. 1. Schematic diagram of measurement system.

[8] referred to as the particle dynamic model (PDM). The PDM accounts for field forces, gravitational forces, and drag forces acting on a charged particle during its motion in the EDB. For spherical particles, the equivalent diameter for predicting drag, projected area, surface area, or volume diameter are the same. From the measured size and C_d/m ratio, the mass of individual carbon spheres was calculated. Finally, from the mass and volume, the density of the carbon sphere was determined. The reader is referred to Ref. 8 for complete details.

Following the approach of Maloney et al. [5], volumes and external surface areas were obtained for individual coal particles by rotating the particles and recording image data from successive video fields as a function of rotation angle. Measured surface area and volume were used to estimate particle drag coefficient as described by Monazam et al. [6], and the particle mass was then separated from the C_d/m ratio. From the mass and volume, the particle density was determined.

Measurement of Laser Incidental Area, Temperature, and Laser Parameters

Single particles were heated bidirectionally. The actual cross-sectional area of the coal particle upon which the laser beam was incident (A_L) was also measured. This area was used to calculate the energy absorption response of the particle in the heat transfer analysis. The two opposite access ports for the heating beam were located at 60° counterclockwise and 120° clockwise to the access port for the side-view imaging system (see Fig. 1). A stable side-view cross section of the particle prior to heating was measured and was used as a reference area. The laser incidental area (A_L) was determined from the particle cross-sectional area data which was measured as a function of rotation angle. This was done by locating the reference area in the rotational data and extracting the laser incidental area by going backward 60°. The same area was confirmed by going forward 120° from the reference area.

Following the measurements of particle shape, mass, reference area, and laser incidental area, the particle was heated from opposite sides with pulsed Nd:YAG laser beams of equal intensity. Experiments were performed in a nitrogen atmosphere. The temporal power variation in the laser pulse was recorded for use in the heat transfer analysis by an ultrafast fiber optic ultraviolet light transmitter included in the beam path and coupled to a silicon photodiode (Fig. 1). Details of the laser power characterization are provided elsewhere [4,12]. Measurements of changes in particle size that accompany rapid heating were made by means of the high-speed diode array imaging system [1]. Measurements of the surface temperatures of the heated particles were performed using a single-wavelength pyrometer (see Fig. 1). Temperatures were determined based on measurements of particle size and radiant emission intensity with the application of Wein's approximation to Planck's law. The pyrometer was calibrated against a standard General Electric tungsten strip lamp to a temperature greater than 1500 K with an accuracy of ± 4 K. Signal-to-noise level for the pyrometer output exceeded 25:1 at temperatures above 800 K at the gain level employed in this work. Details of the pyrometer calibration are provided in Ref. 4. Photographic records of the particle behavior during heating were also obtained. These records provided excellent time resolution of the particle response, including rotation, swelling, volatile evolu-

tion, and the time at which the particle began to move off the imaging system array [1,4].

Measurements were made on individual particles of Spherocarb (Foxboro, Analabs, North Haven, Conn.), a spherical, nonfriable, microporous molecular sieve carbon sphere of mesh size 100/120, and PSOC-1451D, a HVA bituminous coal in the aerodynamic size range of 106–125 μm. Spherocarb and PSOC-1451D were both used in previous studies by Fletcher [3] and Maloney et al. [1] and they were used here so that the differences seen in both the present work and previous work could be examined.

Analysis

One approach to predict temperatures for irregular particles of arbitrary shape is the equivalent volume sphere approximation. Here, the temperature is calculated for a sphere with volume and mass (ρv) equal to that of the irregular particle. In addition, the energy absorption response is determined using the measured A_L. The emission response is calculated using the measured particle surface area, S_p. Heat is assumed to flow only in the radial direction of the volume equivalent sphere. The model described here is influenced by the previous model developed by Maloney et al. [1], but it has been modified to include the particle volume, density, surface area, laser incidental area, and transient laser power ($I(t)$). As a base case condition, calculations were performed using the Merrick model to assign particle heat capacities [10]. Thermal conductivities were assigned using data for coals and chars of Badzioch et al. [11]. Particles were heated with laser beams of equal intensity from two sides. It is assumed that the particle absorbs a fraction of the energy proportional to its absorptivity ($\infty = 0.85$), distributes this energy uniformly throughout its entire surface, and exchanges heat with the surrounding air. While heating, it is assumed that the particle retains its shape with no swelling, rotation, or mass loss. With the above restrictions, the temperature profile of the heating particle was obtained by solution of the Fourier equation for a sphere as

$$\rho_p C_p(T) \frac{\partial T}{\partial t} = K_p(T) \left(\frac{\partial^2 T}{\partial r^2} + \frac{2}{r} \frac{\partial T}{\partial r} \right) \quad (1)$$

The following boundary conditions were applied:
(i) The initial condition at $t = 0$:

$$T(r,0) = T_0 \quad 0 \le r \le R \quad (2)$$

(ii) The symmetry condition at the center $r = 0$:

$$\frac{\partial T(0,t)}{\partial r} = 0 \quad t \ge 0 \quad (3)$$

(iii) The energy delivered at the surface $r = R$:

$$K_p(T) \frac{\partial T(R, t)}{\partial r} = \left(\frac{2A_L \alpha I(t)}{S_p} \right) - [h(t) \{T_s - T_\infty\} + \sigma \varepsilon \{T_s^4 - T_\infty^4\}] \quad (4)$$

The left-hand side of equation 4 represents heat transfer to the particle interior by conduction from the surface, while the first term on the right-hand side accounts for heat input by radiation, and the second and third terms for cooling by convection and radiation, respectively. The measured transient laser intensity, $I(t)$, was used as the temporal laser input flux in the source term. This input flux was divided by a factor, $S_p/2A_L$, to account for the two-sided heating employed in the experimental system which gives a heating cross section of $2A_L$. The convective and radiative cooling terms were considered using the measured external particle surface area.

The transient heat transfer coefficient, $h(t)$, was determined from the transient Nusselt number, $Nu(t)$, derived by solving the partial differential equation describing the unsteady temperature in the surrounding fluid as given by [4]:

$$Nu(t)|_{r=R} = 2R \left(\frac{1}{R} + \frac{1}{[\pi k(T)t]^{1/2}} \right) \quad (5)$$

Here, $k(T)$, is temperature-dependent thermal diffusivity of the surrounding gas (N_2) that was used to rotate the particle during the measurement of its shape. A numerical solution for equations 1–5 was obtained [1] using an implicit Crank-Nicholson scheme, since it is a nonlinear unsteady-state heat conduction problem involving the temperature to the fourth power in equation 4.

Results and Discussion

Validation with Carbon Spheres

The reproducibility of the temperature measurement and the validity of the numerical analysis were first tested using carbon spheres. Temperature traces of heating and cooling for replicate experiments on one carbon sphere are presented in Fig. 2. The data for this figure were obtained by heating the particle with a laser pulse, rebalancing the particle, repeating size, C_d/m and ρ measurements, and then reheating the particle. For the data shown in Fig. 2, the same particle was rebalanced and reheated six times. The particle was heated with heating pulses of similar magnitude. The surface temperature of the particle and the transient power of the heating pulse were also measured. The data for

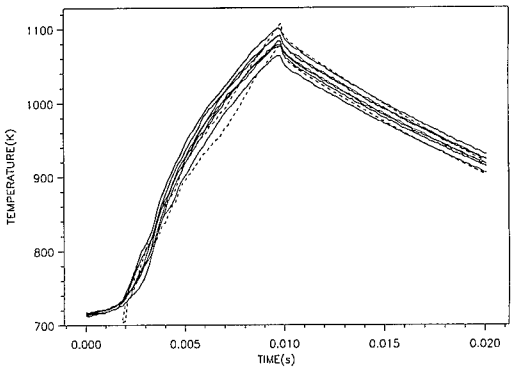

FIG. 2. Experiment reproducibility and model bound for a carbon sphere: validation of instrumentation and heat transfer analysis. Pulse intensity = 606–654 W/cm^2; duration, 10 ms. ——, Experiment (total 7 lines); ------, model (upper and lower bound).

the particle diameter, C_d/m, mass, and density showed little change from heating pulse to heating pulse and were, respectively, 135 μm, 21.5, 1.07 μgm, and 0.83 g/cm^3. It was seen that in all these experiments, the DC endcap voltage required to balance the particle remained almost the same. This suggests little change in particle mass for the carbon sphere during these experiments, since the DC endcap voltage is directly proportional to the particle mass. As illustrated, the measured temperature histories were all very similar. The heating rate employed in these experiments was $\sim 8 \times 10^4$ K/s and the heating pulse time-averaged intensities ($I(ta)$) for these experiments varied only slightly from 600 to 650 W/cm^2. The dashed lines in Fig. 2 are the model predictions for the upper and lower bound (highest and lowest heat flux cases) for the experiments shown. Based on similar experiments, Maloney et al. [1] showed good agreement between measurement and model over the first 6 ms of heating for carbon spheres, but then observed significant differences between model and measurement during the later stages of heating. The refinements made in the present work, in particular the inclusion of a time-dependent heat flux in the energy balance, enable an excellent match between model and measurement over the entire heating and cooling profile for the carbon spheres. The seven temperature profile curves presented in Fig. 2 indicate a spread of from 20 to 50 K in temperatures at any given point in time for the six replicate experiments. The dashed lines in the figure illustrate model results for the two extreme (highest and lowest) heat flux experiments. These curves define a band of temperatures with a spread from 20 to 40 K between the two curves. This comparison illustrates that most of the variation seen in Fig. 2 can be accounted for by variations in heat flux. The energy balance applied in this work can match measured temperatures to within $\pm$ 20 K over the entire range of heating and cooling. These results validate the numerical analysis presented above for carbon spheres and indicate that for spheres with well known properties we have a good handle on modeling heat transfer.

Assessment of Coal Particle Shape and Density

Experiments were conducted on single, bituminous coal particles for a range of heating rates (10^4–10^5 K/s) up to a surface temperature of about 1600 K. Four different time-averaged intensity levels (228–298, 553–707, 927–1104, and 1314–1380 W/cm^2) were employed to heat the particles. The shape information (equivalent diameters for particle surface area, volume, side projected area, and laser incidental area), the particle C_d/m, mass and density, and the time-averaged intensity of the various heating pulses are presented in Table 1. The mean surface area and volume equivalent diameters, C_d/m, mass, and density for 39 coal particles tested are in good agreement with the results obtained for 23 particles of the same coal by Monazam et al. [6]. The wide range of values seen in the surface area diameter, volume diameter, and density between coal particles suggests that when subjected to similar heating environments, the temperature response for these particles would vary significantly. This point will be illustrated more clearly in the discussion of Figs. 3–5.

Following the work of Maloney et al. [1], the volume and surface area of the particle were calculated for a 'base case' (spherical shape assumption) using the same cross-sectional area equivalent diameter measured from the side-view of the particle (provided in Table 1). The density of the coal particles was assumed to be 1.2 g/cm^3, a value taken from the literature [1,3]. Following this calculation, the actual measured surface area, volume, laser incidental area, and density were used to predict the temperatures for the second case. In both cases, Merrick's "Two-Characteristic Temperature Equation" [10] was used to calculate the instantaneous heat capacity. The thermal conductivity was estimated using an equation fitted to the temperature-dependent data for coals of Badzioch et al. [11]. Constant mass was assumed throughout.

In Fig. 3, the base case prediction for one coal particle (number 16 of Table 1: d_v = 93 μm, ρ = 1.2 g/cm^3, $S_p/2A_L$ = 2, and $I(ta)$ = 941 W/cm^2) during its heating and cooling is compared with the prediction using the actual measured shape and density (d_v = 98 μm, ρ = 1.16 g/cm^3, and $S_p/2A_L$ = 1.9). The experimental temperatures are also shown in Fig. 3 for comparison. It should be noted that the pyrometer has a lower threshold limit about 800 K, and temperatures less than 800 K are indications of pyrometer noise. As can be seen, the base case

TABLE 1
Shape, mass, density, and heat flux information for coal particles

Particle	Surface area dia, d_{sa} (μm)	Vol dia, d_v (μm)	Laser area dia, d_L (μm)	Side view dia, d_s (μm)	C_d/m (1/s)	mass m (μg)	density ρ (g/cm^3)	$I(ta)$ (W/cm^2)	$S_p/2A_L$ ratio
1	117	109	120	107	27.5	0.81	1.19	247	1.9
2	123	119	132	115	19.5	1.14	1.29	229	1.7
3	118	110	114	100	26.0	0.87	1.25	228	2.1
4	125	115	121	128	25.0	0.97	1.22	275	2.1
5	137	126	137	129	23.0	1.16	1.11	266	2.0
6	106	102	105	107	26.5	0.72	1.30	239	2.0
7[a]	121	114	110	133	25.0	0.95	1.22	298	2.4
8	118	110	109	109	25.0	0.89	1.28	584	2.3
9	110	104	99	115	28.0	0.72	1.22	583	2.5
10	115	109	104	115	28.0	0.76	1.12	553	2.4
11	106	95	103	95	36.0	0.59	1.31	584	2.1
12	88	81	85	92	47.0	0.36	1.29	577	2.1
13[b]	121	113	121	120	28.0	0.82	1.09	707	2.0
14[c]	111	102	106	103	33.0	0.65	1.18	692	2.2
15[d]	106	98	111	97	34.0	0.60	1.22	607	1.8
16	103	98	106	93	33.0	0.57	1.16	941	1.9
17	127	119	123	112	27.0	0.88	1.00	966	2.1
18	107	101	107	103	32.0	0.61	1.13	992	2.0
19	105	102	105	105	31.0	0.61	1.09	934	2.0
20	108	104	114	109	29.0	0.66	1.12	949	1.8
21	121	115	120	118	27.0	0.82	1.03	966	2.0
22	95	90	95	92	41.0	0.43	1.13	941	2.0
23	133	122	117	112	26.0	1.02	1.07	957	2.6
24	138	125	125	106	26.0	1.07	1.05	968	2.4
25	105	100	97	108	35.0	0.56	1.07	945	2.3
26	118	101	112	98	43.0	0.62	1.16	927	2.2
27	118	114	120	114	27.0	0.83	1.07	938	1.9
28	120	114	125	113	27.0	0.81	1.04	943	1.8
29	124	115	123	98	29.0	0.83	1.05	975	2.0
30[b]	109	102	111	105	35.0	0.60	1.08	1104	1.9
31[c]	123	107	125	131	32.3	0.77	1.20	1092	1.9
32[d]	130	124	132	108	23.0	1.03	1.03	1017	1.9
33[a]	124	116	115	109	26.0	0.89	1.09	940	2.3
34	109	104	97	111	28.0	0.69	1.17	1357	2.5
35	134	125	130	136	21.0	1.20	1.17	1314	2.1
36	124	116	120	102	25.0	0.93	1.14	1340	2.1
37	134	122	133	126	22.0	1.21	1.27	1344	2.0
38	111	107	108	110	28.0	0.70	1.09	1380	2.1
39[a]	129	121	116	126	22.0	1.10	1.19	1324	2.5
Avg	117	110	114	111	28.9	0.81	1.15		2.1
Std	11	10	12	11	5.8	0.21	0.09		0.2

[a]temperature data not available.

[b,c,d]2,3,5 ms pulse-width experiments. particle # 1–7 are intensity group 1, 8–15 are intensity group 2, 16–22 are intensity group 3A, 23–33 are intensity group 3B, and 34–39 are intensity group 4.

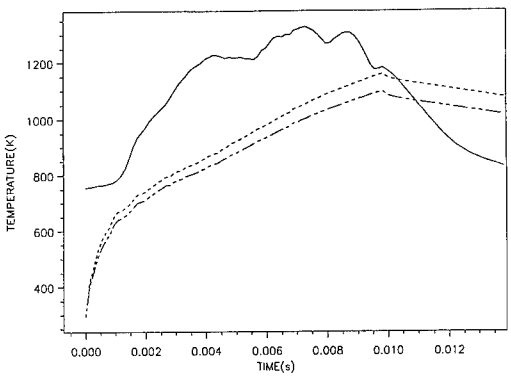

FIG. 3. Comparison of model prediction with experiment. Time-averaged heating pulse intensity = 941W/cm^2; duration, 10 ms. ——, Experiment (particle # 16); ------, model (measured shape and density); – ——, base case.

model prediction largely underestimates the experimental temperatures during the early stages of heating, thus confirming the earlier finding of Maloney et al. [1]. Figure 3 shows a plateau region in the measured temperatures at the latter stages of heating during devolatilization, and the base case assumption still largely underpredicts the measurements in this region. At the end of the 10 ms heating pulse, the measurements show a rapid cooling, whereas the base case assumption predicts a slow cooling. The temperature prediction using the measured shape and density information improved the fit somewhat during the entire particle residence time but failed to predict accurately the heating or cooling process.

Figures 4 and 5 present similar comparisons for all of the coal particles tested at two specific residence times (4 and 7 ms). These figures incorporate a broad range of heating intensities. The 4-ms (Fig. 4) heating time was chosen because at this time the particle surface temperature exceeded the pyrometer lower threshold limit (~800 K), but for most particles no significant volatile evolution was seen in the cinematographic records. The particles in the highest intensity group (particle #34–39) in Table 1 showed some slight volatile evolution by 4 ms. The particles from the lowest intensity group (particle #1–7) are not included in Figs. 4 and 5 because the temperature measurements for these particles at the 4- and 7-ms times were below the pyrometer measurement threshold. In each figure, the data have been segmented into three groups with each group being encircled to focus the reader's attention and to illustrate some important points. In addition, since the middle grouping contained numerous points with significant scatter, four experiment-model point pairs were selected in these groups and

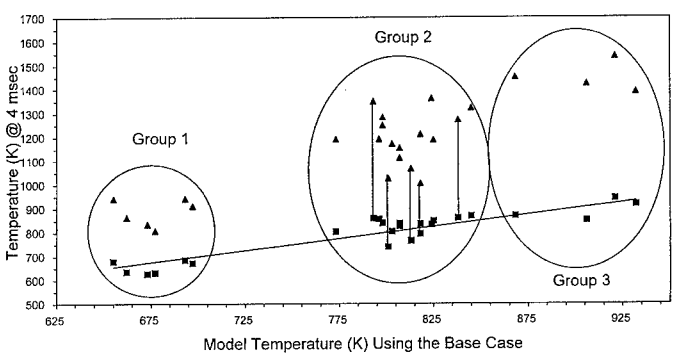

FIG. 4. Comparison of base case prediction at 4 ms with, ■, prediction using measured shape and density; and, ▲, measured temperatures. ——, Model: base case.

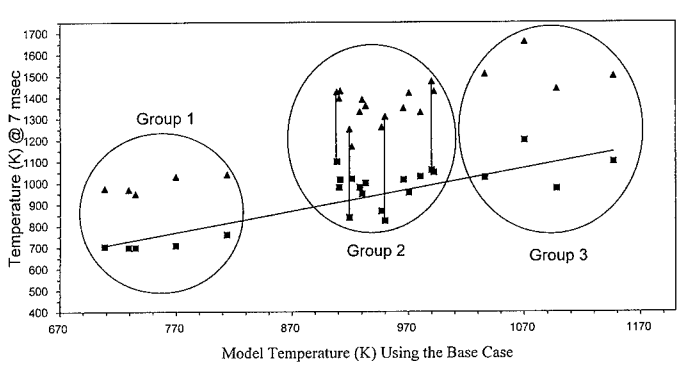

FIG. 5. Comparison of base case prediction at 7 ms with, ■, prediction using measured shape and density; and, ▲, measured temperatures. ——, Model: base case.

connected by solid lines to highlight some patterns in the data.

Important observations regarding the data in Figs. 4 and 5 include the following:

1. Model calculations using measured size and density information significantly underpredict the observed particle temperature. This observation is similar to that reported by Maloney and coworkers [1] who hypothesized that the differences between model and experiment could be due to poor understanding of coal thermodynamic and heat transfer properties and/or failure to account for particle shape considerations. The results presented in Figs. 4 and 5 indicate that even when particle shape is accounted for, significant differences arise between measurement and model. We conclude that these differences are due largely to uncertainty in the coal thermodynamic and heat transfer properties in the model.
2. Within each of the groupings, the measurements indicate a wide variation in observed temperatures even when the same nominal heat flux is applied. Within group two (the largest sample population tested) in both Figs. 4 and 5, the temperature spread for the groupings was in excess of 300 K at each of the measurement times chosen for comparison.
3. A careful examination of each groupings in Figs. 4 and 5 shows a clear pattern in which the calculated particle temperatures mirror the experimental measured temperatures. This observation is perhaps most clearly illustrated in the last grouping on the right hand side of Fig. 5, but the pattern is consistent throughout each of the groupings. This observation indicates that, although the absolute temperature predictions are in error, much of the particle-to-particle variability observed within a given group can be explained by accounting for particle shape and density variations. For example, the calculated temperatures shown in group 2 in Fig. 5 predict a spread in temperatures of 275 K due to particle shape and density variations. The corresponding measurements indicate an observed temperature spread of 305 K. Making similar comparisons for each of the groupings, between 70 and 100% of the observed temperature spread in the Fig. 5 groupings can be accounted for in the model using the shape and density measurements made in this study. In Fig. 4, between 40 and 60% of the observed temperature spread can be accounted for using the measured shape and density values. An even larger percentage of the spread can be accounted for if the model thermal properties (primarily coal heat capacity) are adjusted to improve the fit between measurement and experiment.

Conclusions

Results presented for carbon spheres support the conclusion that the measurement and analysis methods applied here offer an excellent description of the energy balance for heating of single particles in the EDB. With well-characterized materials of known properties, agreement between measurement and model of within 20 K is typical.

Large variations (several hundred degrees) are observed in coal particle temperature histories during rapid heating. These variations can be accounted for in large part due to particle-to-particle property (shape, mass, density) variations as demonstrated by the measurements and analysis presented above.

Even when accounting for particle-to-particle shape and density variations, model predictions in this study greatly underpredicted the observed temperature histories. Based on the results presented here and elsewhere [1], it is concluded that these discrepancies are due largely to uncertainty in the coal thermal properties (heat capacity and thermal conductivity) used to model coal combustion behavior. Future work in this laboratory will focus on using the measurement and analysis capabilities described here to evaluate these thermal properties under rapid heating conditions.

Nomenclature

A	particle cross-sectional area (μm^2)
C	particle heat capacity (cal g^{-1} K^{-1})
C_d/m	particle drag coefficient/mass ratio (sec^{-1})
d	particle diameter (μm)
h	heat transfer coefficient at particle surface (cal s^{-1} cm^{-1} K^{-1})
I	intensity of the laser (W cm^{-2})
K	thermal conductivity of particle (cal s^{-1} cm^{-1} K^{-1})
k	thermal diffusivity of the surrounding fluid (cm^2 s^{-1})
m	particle mass (μg)
R	particle radius (cm)
r	radial position (cm)
S	surface area (μm^2)
T	particle temperature (K)
t	Time (s)

Greek Symbols

α	particle absorptivity at 1.06 μm wavelength
ε	particle emissivity over the entire blackbody spectrum
σ	Stefan-Boltzman constant (cal s^{-1} cm^{-2} K^{-4})
ρ	particle density (g cm^{-3})

Subscripts

0	at time = 0
p	of the particle

S at particle surface
v of volume equivalent

Acknowledgments

This work was funded by Morgantown Energy Technology Center (METC), Department of Energy, under contract number DE-AP21-92MC01595. Experiments were conducted at the Single Particle Laboratory, METC.

REFERENCES

1. Maloney, D. J., Monazam, E. R., Woodruff, S. W., and Lawson, L. W., *Combust. Flame* 84:210–220 (1991).
2. Solomon, P. R., Serio, M. A., Carangelo, R. M., and Markham, J. R., *Fuel* 65:182 (1986).
3. Fletcher, T. H., *Combust. Sci. Technol.* 63:89 (1989).
4. Sampath, R., "Measurement and Prediction of Temperature Histories for Single Coal particles Prior to and During Devolatilization," Ph.D. Thesis, Department of Chemical Engineering, West Virginia University, Morgantown, WV, 1994.
5. Maloney, D. J., Lawson, L. O., Fasching, G. E., and Monazam, E. R., *Aerosol Sci. Technol.* 22:60–72 (1995).
6. Monazam, E. R. and Maloney, D. J., *Combust. Flame* 99:733–741 (1994).
7. Hurt, R. H. and Mitchell, R. E., *Twenty-Fourth Symposium (International) on Combustion,* The Combustion Institute, Pittsburgh, 1992, p. 1223.
8. Maloney, D. J., Lawson, L. O., Fasching, G. E., and Monazam, E. R., *Rev. Sci. Instrum.* 66:3615–3622 (1995).
9. Brenner, H., *Chem. Eng. Sci.* 19:519 (1964).
10. Merrick, D., *Fuel* 62:540 (1983).
11. Badzioch, S., Gregory, D. R., and Field, M. A., *Fuel* 43:267 (1964).
12. Spann, J. F., Maloney, D. J., Lawson, W. F., and Casleton, K. H., *Appl. Opt.* 32:2152 (1993).

COMMENTS

Ezra Bar-Ziv, NRCN-BGU, Israel. Perhaps part of the reason for the non-fit of the temperature measurements with model calculations is the input values for heat calculations (HC) and thermal conductivity (TC). Methods for both quantities were developed for single particles in the electrodynamic chamber (HC by Monazam et al. [1] and TC by Weiss et al. [2]).

REFERENCES

1. Monazam, E. R., Maloney, D. J., and Lawson, L. O., *Rev. Sci. Instrum.* 60:3460 (1989).
2. Weiss, Y., Ben-Ari, Y., Kantorovich, I. I., Bar-Ziv, E., Krammer, G., Modestino, A., and Sarofim, A. F., *Twenty-Fifth Symposium (International) on Combustion,* The Combustion Institute, Pittsburgh, 1994, pp. 519–525.

Author's Reply. This is phrased more as a comment than a question but we will take the opportunity to make some additional comments in this regard. We definitely believe that the problem in matching measurement to model is in the thermal property data base used in our calculations. This same data base is used in many coal combustion models. We do not believe direct measurement of C_p and K will be possible for coal particles because these properties change with temperature and chemical composition and, at the high heating rates of interest, the measurement methods do not have the speed to be effective. We do believe, however, that we can infer the particle C_p and K based on additional experiments. We have a very good handle on the particle shape and mass and by varying particle size, input laser intensity and convective load (gas thermal conductivity) we can bound the problem and learn a great deal. We hope to do such experiments at some time in the future.

•

Thomas H. Fletcher, Brigham Young University, USA. Can you explain the large temperature difference between predictions and measurement by varying the heat capacity and thermal conductivity within reported bounds?

Author's Reply. This question is addressed in part in Ref. 1 of the paper. During the first 4 ms of heating one can get reasonable fits between measurement and model by using constant room temperature values for C_p and K. However, after the first 4 ms our predictions would then greatly exceed the measurements in the region we describe as a temperature plateau. The Merrick model was developed using data from slow heating applications (coke making). The same is true for the thermal conductivity data in the literature [11]. Since these properties are not state functions it would not be surprising if they vary with large changes in heating rate. We believe that the coal behaves in a manner similar to glassy polymers, which exhibit a sharp increase in C_p at the glass transition. This increase in C_p is due to an increase in vibrational modes of freedom that occurs at the glass transition. In the coal case, at the heating rates used in this study, we hypothesize that the coal softening (glass transition) occurs at about 4 ms (as evidenced by the initiation of heavy volatiles and subsequent particle swelling) and that the sudden increase in C_p that accompanies this transition is probably the reason we see the pronounced temperature plateau. At present this is only a hypothesis but one that fits the observations. We would like

to perform additional experiments to explore this further. Sampath [4] has performed additional calculations to support this hypothesis as well as looking at the effects of heats of pyrolysis on model predictions.

•

Robert F. Chaiken, DOE/Pittsburgh, USA. Coal particle heterogeneity would include internal heterogeneities (e.g., composition, cracks, porosity). Such heterogeneities would lead to discrete jets of volatiles from the particle. Did you see these in your experimental measurements?

Author's Reply. This question is addressed in some detail by Phuoc and Maloney [1]. Occasionally, some jetting of volatiles was observed to result in particle rotation during heating, but, in general, the volatile clouds surrounding the particles were quite uniform. Based on our high speed film records, the heavy volatile evolution appeared to occur after the particles had softened and the volatile evolution process appeared physically similar to the boiling of a viscous liquid.

REFERENCE

1. Phuoc and Maloney, *Twenty-Second Symposium (International) on Combustion,* The Combustion Institute, Pittsburgh, 1988, pp. 125–134.

•

Dr. Jon Gibbins, Imperial College, UK. An excellent demonstration of coal heterogeneity! You mention differences in physical properties (e.g., shape, density) but the mineral and organic compositions will also vary. To what extent do you think these, differences also affect heating times?

Author's Reply. Differences in coal particle mineral and organic composition would manifest themselves as differences in particle density. To that extent the discussion provided in the paper should address some of your question. In addition to differences in particle mass, different maceral and mineral components might also exhibit significant differences in their respective thermal properties. For example, hydrogen rich macerals might exhibit higher heat capacities per unit mass than hydrogen poor macerals. One might expect, therefore, that variations in the mineral and organic composition could cause some of the observed differences in heating times from one particle to the next.

Twenty-Sixth Symposium (International) on Combustion/The Combustion Institute, 1996/pp. 3189–3195

LASER IGNITION AND FLAME PROPAGATION OF PULVERIZED COAL DUST CLOUDS

MASAYUKI TANIGUCHI, HIRONOBU KOBAYASHI AND SIGERU AZUHATA
Hitachi Research Laboratory
Hitachi Ltd.
Ibaraki-ken, Japan

Ignition and combustion behaviors were examined for uniformly sized, pulverized coal dust clouds that were suspended in a laminar upward flow and heated by a single-pulsed YAG laser. Effects of coal type, particle diameter, and oxygen concentration on lean limit of flame propagation and flame propagation velocity for hv and lv bituminous coals and anthracite were examined. Lean limit of flame propagation of 22–63 μm particles were examined by relation between particle concentration and flame propagation probability. The results were considered from the viewpoint of the distance between particles at which ignition of one particle from another was possible. Flame propagation velocity was examined by image processing of flame pictures. Observation with high-speed video revealed that first a few particles were heated by the laser pulse until they ignited, then the number of burning particles increased, which meant that the pulverized coal flame propagated. The maximum distance between particles for flame propagation increased with volatile content and oxygen concentration, and increased in proportion to the square root of the particle diameter. The effect of coal type on the maximum distance coincided qualitatively with the previous result obtained from millimeter-sized particles arranged in a row. However, the effect of particle diameter was larger than previously found. Flame propagation velocity was related to volatile content. Coals containing less-volatile matter had the lower maximum velocity. The effect was significant for lv bituminous coals. The flame propagation velocities of hv and lv bituminous coals were about 1.6 times the order of the oxygen concentration, which coincided with the previous result for sub-bituminous coal.

Introduction

Japan's electric power utility companies and boiler manufacturers are now concentrating on pulverized coal firing low NO_x combustion technologies. One important way to reduce the NO_x level is to insure that ignition of the coal occurs rapidly [1]. However, ignition phenomena of pulverized coals vary with coal type, particle diameter, and heating rate. Fundamental ignition data, such as ignition delay time, flammability limit and flame propagation velocity, are required for various coal types and conditions in order to design industrial coal burners.

Recently, there is increasing interest in using laser techniques to study the ignition and combustion of coal particles [2–8]. These laser ignition experiments offer the distinct advantage of easy optical access to the particle and thus permit direct observation and particle temperature measurement. For example, heterogeneous or homogeneous ignition behavior of a single coal particle suspended on a fine quartz fiber [2,3] and the oxidation rate of a single char particle in an electrodynamic balance [4,5] have been investigated. In our previous investigations, a novel experimental technique to study the ignition of pulverized coal was presented [6–8]. Pulverized coal particles were suspended in a laminar upward flow, and the particles were ignited by a single pulse from a YAG laser. Ignition behaviors of the dilute suspension of sub-bituminous and hv bituminous coals and anthracite could then be examined by using high-speed video and two-color pyrometer [6–8]. In the present investigation, this technique was extended to study cloud ignition. Lean limit of flame propagation and flame propagation velocity of hv and lv bituminous coals and anthracite were examined under a variety of particle diameters and oxygen concentrations.

A number of experiments have been carried out to examine the lean limit of flame propagation [9,10] and flame propagation velocity [11–13]. These values were shown to vary with both coal type and particle diameter. In order to examine the effects of coal type and particle diameter on these values independently, uniformly sized particles were used in the present investigation. Effects of coal type, particle diameter, and oxygen concentration on lean limit of flame propagation were also considered from the viewpoint of the average distance between particles at which one burning particle was able to ignite another.

Experimental

Figure 1 shows a schematic drawing of the laser ignition experiment. The experimental equipment

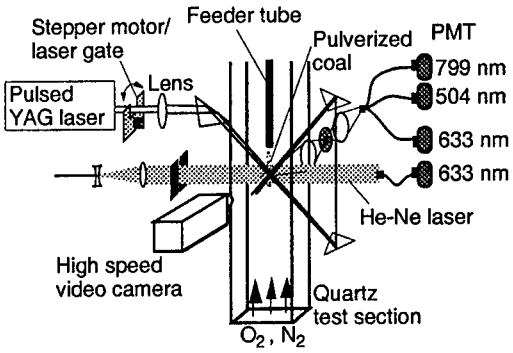

FIG. 1. Schematic drawing of the laser ignition experiment.

was almost the same as described previously [6–8], except for use of a He–Ne sheet laser to measure particle concentration. Sieve-sized particles (22 ± 2, 48 ± 4, and 63 ± 10 μm) were dropped through a tube into a laminar, upward-flow wind tunnel with a quartz test section (50 mm square cross section). The gas was not preheated, and its flow rate was set at 0.03–0.1 m/s so that the particles emerged from the feeder tube, fall slightly, and then turned and traveled upward out of the tunnel. This ensured that the particles were moving slowly downward at the ignition point, chosen to be 15 mm below the feeder tube exit.

A wire mesh was welded at the exit of the feeder tube (4 mm diameter). A jolt, provided by a solenoid valve at the feeder, caused particles to fall through the mesh and the feeder tube. The optimum-sized mesh was selected for each set of experimental conditions (particle diameter and concentration).

The YAG laser was operated at 10 Hz, and it emitted a nearly collimated beam (8 mm diameter) in the near-infrared (at a wavelength, λ = 1064 nm). The laser pulse duration was 150 μs and the energy fluctuation was less than 3%. At the ignition point, the beam diameter, normal to its propagation direction, was about 3 mm on each pass of the beam. By measuring the laser energy after each pass through the test section, we estimated that 70% and 30% of the laser energy (measured at the laser output) arrived at the ignition point of the first and second passes, respectively. Energy flux at the ignition point was 9×10^7 to 7×10^8 W/m^2. A laser "gate" (Fig. 1) permitted the passage of a single pulse to the test section. The gate was formed by cutting a wide slot in a piece of aluminum and mounting it on a controlled stepper motor. The delay time between supplying the particles and the passage of the laser pulse was controlled by synchronizing both the solenoid valve and the stepper-motor controller.

A He–Ne continuous sheet laser (wavelength 633 nm, sheet width 3 × 10 mm, laser power 5 mW) was irradiated horizontally at the ignition point, in order to observe unburned particles and to measure particle concentration. The energy flux of the He–Ne laser (2×10^{-2} W/m^2) was weak enough that the ignition and combustion phenomena were not disturbed by the laser. The particle concentrations were measured from the intensity of particle scattering by the He–Ne laser. The intensity was corrected by measuring the attenuation ratio of the He–Ne laser for each experiment.

Emissions from the igniting/burning particles and scattering particles were detected with three photomultiplier tubes (PMTs), and, concurrently, the events were recorded with a high-speed video (1000 frames/s; shutter speed, 10 μs). In all cases, the field of view was 20 × 20 mm, giving a pixel resolution of about 100-μm square. The emissions were directed into an assembly consisting of a collimating lens and a band-pass filter and were then detected by the PMTs. The center wavelength λ and bandwidth $\Delta\lambda$ of the filters were λ = 799, 633, and 504 nm and $\Delta\lambda$ = 11, 10, and 20 nm, respectively.

In the present study, the ignition and combustion behaviors of five coals were examined. Their analysis

TABLE 1
Sample analysis

Coal	Volatile Matter[a] Content	Ash[a]	C[b]	H[b]	N[b]	O[b]	S[b]
Newlands (hv bituminous)	27.8	12.2	83.1	4.6	1.9	9.9	0.5
Jellinbah East (lv bituminous)	15.7	6.8	89.3	4.7	1.3	4.2	0.5
Collinsville (lv bituminous)	13.7	23.9	88.6	3.9	1.6	5.3	0.6
Telentis (lv bituminous)	13.7	14.3	86.7	4.3	1.6	7.1	0.3
Sanxi (anthracite)	7.7	15.7	96.6	1.2	0.6	1.5	0.1

[a]Weight percent (dry basis).
[b]Weight percent (dry, ash-free basis).

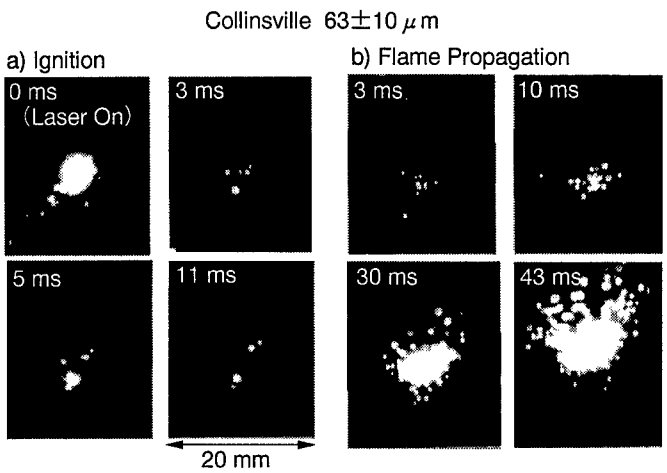

FIG. 2. Ignition and flame propagation processes of Collinsville coal in pure oxygen.

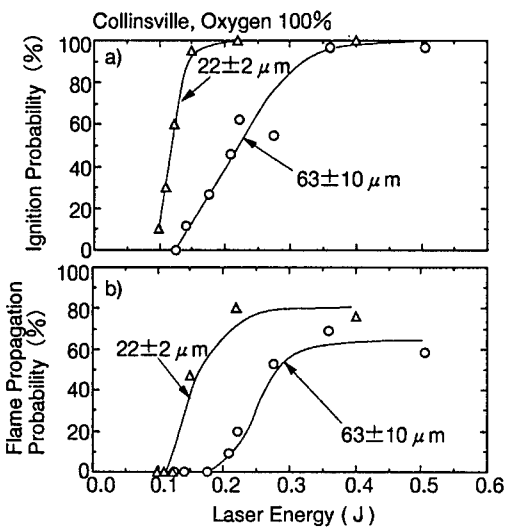

FIG. 3. Effects of laser energy on (a) ignition probability and (b) flame propagation probability. Particle concentrations were 1.0 ± 0.2 kg/m^3 for 63 ± 10 μm particles and 0.22 ± 0.04 kg/m^3 for 22 ± 2 μm particles.

results are listed in Table 1. They were sized to 22 ± 2, 48 ± 4, and 63 ± 10 μm. All samples were dried 1 h at 350 K before the experiment.

Results and Discussion

Ignition and Combustion Processes of Pulverized Coals

Figure 2 shows ignition and combustion processes of 63 ± 10 μm Collinsville coal particles in pure oxygen. Particles were heated by the laser pulse at 0 ms. Two different combustion phenomena were observed by using the high-speed video. In Fig. 2a, five particles were observed in a picture taken 3 ms after the laser pulse. We considered that these particles were ignited by direct heating of the laser. The number of burning particles did not increase during combustion, as shown in the pictures at 5 and 11 ms. We defined this phenomenon as "ignition." Another phenomenon is shown in Fig. 2b. In this case, around 10 particles were ignited by the laser pulse. However, the burning particles interacted and formed an extensive cloud, which grew rapidly in size as more particles were fed into this cloud. This phenomenon was defined as "flame propagation."

Emissions of particles floating in pure nitrogen were also examined. When a particle did not ignite, the emission from the heated particles stopped 2 ms after the laser pulse.

Lean Limit of Flame Propagation

Distributions of ignition and flame propagation probabilities of Collinsville coal particles when the laser pulse energy and coal size were varied are shown in Fig. 3. Particle concentrations were nearly constant, 0.22 ± 0.04 kg/m^3 for 22 ± 2 μm particles, and 1.0 ± 0.2 kg/m^3 for 63 ± 10 μm particles. Each point in the figure represents 20–40 ignition attempts at the stated conditions. Ignition probability was defined as ratio of the number of experiments in which "ignition" was observed to the total number of experiments. Flame propagation probability was defined as the ratio of the number of experiments in which "flame propagation" was observed to the sum of the numbers of experiments in which "ignition" and "flame propagation" were observed.

When the laser energy increased, the ignition probability increased. The ignition probabilities were 100% when the laser energy was high. Similar features are shown for flame propagation probability

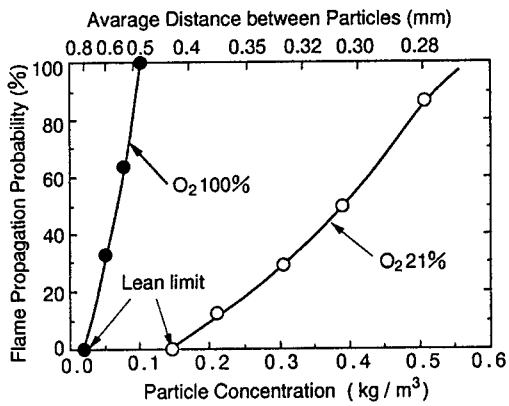

FIG. 4. Effect of oxygen concentration on lean limit of flame propagation.

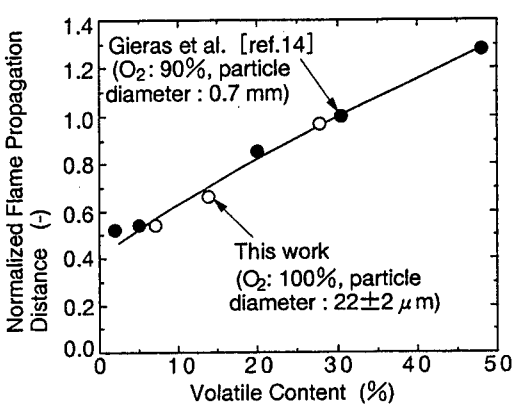

FIG. 5. Effect of coal type on flame propagation distance.

(Fig. 3b). However, when the laser energy was high enough for ignition (ignition probability was almost 100%), the flame propagation probabilities were constant, independent of laser energy. Flame propagation probability was also examined at the high laser energy condition (≥0.4 J), while particle concentration was varied. In this case, the effect of particle concentration on flame propagation probability was large.

Figure 4 shows flame propagation probability distributions for 22 ± 2 μm Newlands coal when particle concentration was varied. Laser energy was 0.4 J for each point. Ignition probability was higher than 95% at all concentrations. When oxygen concentration increased, flame propagation probability at a given concentration increased, or concentration at a given flame propagation probability decreased. For example, concentration at 50% flame propagation probability in air was about 5.7 times as much as that in pure oxygen.

No flame propagation was observed when the concentration was lower than that at 0% flame propagation probability, thus we defined the concentration of 0% flame propagation probability as the lean limit concentration of flame propagation. Lean limit of 22 ± 2 μm Newlands coal in air was around 0.15 kg/m^3.

Hertzberg et al. [9,10] have investigated lean limits of hv and lv bituminous coals. They reported lean limits of 9–40 μm Pittsburgh coal (volatile content = 33.6%) and 12–30 μm Pochahontas coal (volatile content = 16.2%) as 0.13 kg/m^3 and 0.17 kg/m^3, respectively. The value of 22 ± 2 μm Newlands coal (volatile content = 27.8%) obtained from the present investigation was higher than that of Pittsburgh coal and was lower than that of Pochahontas coal. This means that coal, which contains much volatile matter, is able to burn at lower particle concentration.

Figure 4 also shows the flame propagation probabilities as a function of average distance between particles. In this case, the distance between particles at which the ignition of one particle from another is possible was 12–20 times as long as the particle diameter burned in air and 25–40 times as long as the particle diameter burned in pure oxygen. In the present investigation, maximum distance between particles at which the flame propagation is possible was defined as "flame propagation distance (D_{max})." The flame propagation probabilities were obtained under a variety of coal types, particle diameters, and oxygen concentrations. These flame propagation probability functions were similar figures.

Figure 5 shows the effect of coal type on flame propagation distance. Coal containing less-volatile matter had the shorter flame propagation distance. For example, flame propagation distance of anthracite (Sanxi) was about half that of hv bituminous coal (Newlands).

Gieras et al. [14,15] investigated flame propagation phenomena between two particles arranged in a row under conditions of normal and zero gravity. They attached 0.5–1.2 mm coal particles to quartz needles and then examined the flame propagation distance. This provides a basic model for understanding the lean limit of flame propagation of coal cloud. In the present study, particles were distributed three-dimensionally, and particle diameters were smaller than 100 μm. The present results are compared with those of Gieras et al. [14]. The data agreed qualitatively. In Fig. 5, the flame propagation distances were shown as normalized values. The Normalization factors were determined by the following method. First, the flame propagation distance of 0.7 mm coals were normalized as that of the coal containing 30.5% volatile matter was 1.0; then, the value of 22 ± 2 μm Newlands coal was fitted with the data of 0.7 mm coals. The normalized values of other 22 ± 2 μm coals were determined from the ratios of their distance to that of 22 ± 2 μm New-

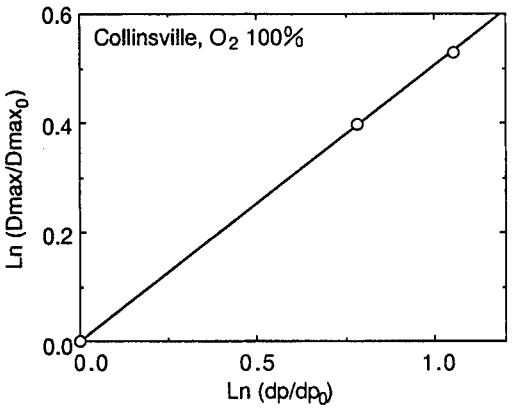

FIG. 6. Effect of particle diameter on flame propagation distance.

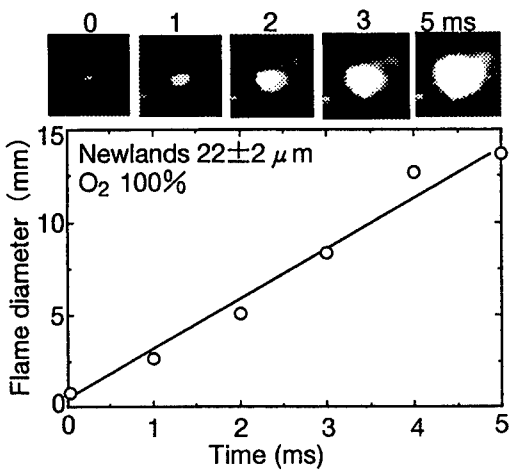

FIG. 7. Variation of flame shape.

lands coal. The absolute value of 0.7 mm coal containing 30.5% volatile matter was about 6 times as much as 22 ± 2 μm Newlands coal.

Figure 6 shows the effect of particle diameter on flame propagation distance. Gieras et al. [14] also proposed an equation to describe the effect of particle diameter on flame propagation distance:

$$(D_{max}/D_{max_0}) = (dp/dp_0)^n \quad (1)$$

where D_{max} is flame propagation distance, D_{max} is flame propagation distance at reference particle diameter, dp is particle diameter, and dp_0 is reference particle diameter.

In Fig. 6, dp_0 is 22 μm. They proposed $n = 1/3$ for 0.5–1.2 mm particles. On the other hand, the slope of the straight line in Fig. 6 gave an n for 22–63 μm particles of 0.5. When the particle diameter became smaller, or particles were distributed three-

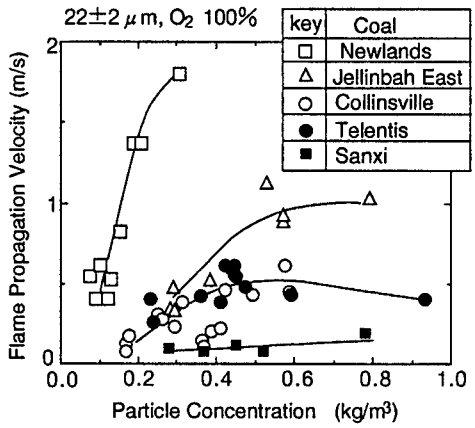

FIG. 8. Effects of coal type on flame propagation velocity.

dimensionally, the effect of particle diameter on flame propagation distance became larger.

Flame Propagation Velocity

Figure 7 shows video images of flame propagation for 22 ± 2 μm Newlands coal in pure oxygen. The particle concentration was 0.21 kg/m^3. A small cloud was formed by the laser pulse, and it spread with time. Each flame diameter in the video image was approximated as the diameter of a circle. The flame diameter tended to increase proportionally with time, and the slope of this line was assumed to be constant at an early stage of flame propagation. Flame propagation velocity was defined as the increasing rate of the flame radius and could be obtained from the flame video images.

The effects of concentration on flame propagation velocities were investigated for five coals. Figure 8 shows flame propagation velocities of 22 ± 2 μm particles in pure oxygen. Laser energy did not influence the flame propagation velocities in the range of 0.1–0.4 J. Among the five coals examined, the maximum flame propagation velocities were related to the volatile content. The effect was especially strong for lv bituminous coals. Collinsville and Telentis coals have almost the same volatile content. Their maximum flame propagation velocities and dependencies on concentration were almost the same. On the other hand, the maximum velocity of Jellinbah East coal was 1.6–2.0 times as much as that of Collinsville or Telentis coal. The difference in volatile content between Jellinbah East and Collinsville or Telentis coal is less than 15%.

Figure 9 shows effects of oxygen concentration on flame propagation velocity and particle temperatures in the flame of 22 ± 2 μm Newlands coal. There were large dependencies of oxygen concentration on flame propagation velocity and temperature. For

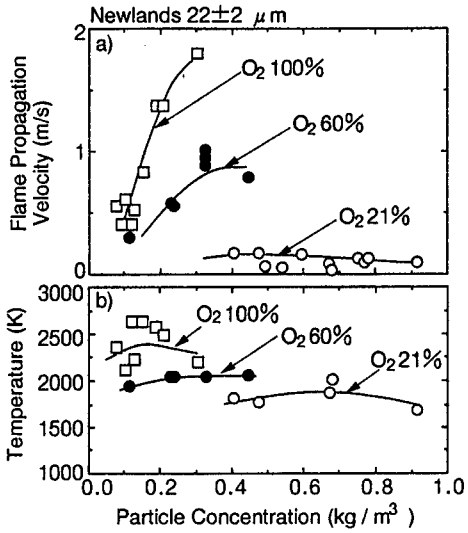

FIG. 9. Effects of oxygen concentration on (a) flame propagation velocity and (b) particle temperature of Newlands coal.

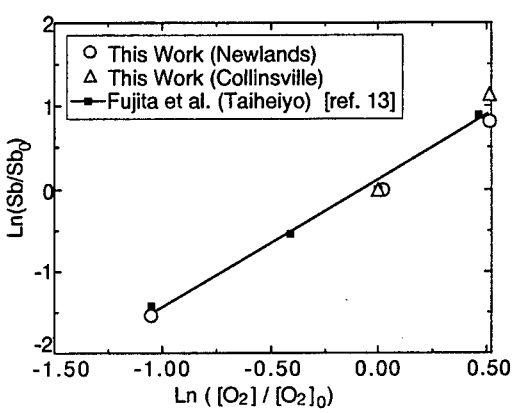

FIG. 10. Effect of maximum flame propagation velocity on oxygen concentration.

example, the velocity in pure oxygen was almost 10 times that in air. Particle temperature decreased from around 2500 to 1800 K, when oxygen concentration decreased from 100% to 21%.

Fujita et al. [13] have investigated the effect of oxygen concentration on flame propagation velocity for sub-bituminous coal (Taiheiyo coal, volatile content = 47.1%, 50% cumulative mass fraction = 47.7 μm) in microgravity. They proposed the following equation for the relation between flame propagation velocity and oxygen concentration:

$$Sb/Sb_0 = ([O_2]/[O_2]_0)^{1.6} \quad (2)$$

where Sb is flame propagation velocity, Sb_0 is flame propagation velocity at reference oxygen concentration, $[O_2]$ is oxygen concentration, and $[O_2]_0$ is reference oxygen concentration.

Figure 10 shows the effect of oxygen concentration on flame propagation velocity for various coals. In Fig. 10, $[O_2]_0$ is 60%. The straight lines obtained for all coals suggests that the effect of oxygen concentration for hv and lv bituminous coals is the same as that of sub-bituminous coal obtained previously [13].

Conclusion

Ignition and combustion phenomena of pulverized coal clouds, suspended in a laminar upward flow and heated by a pulsed YAG laser, were examined. The results in this study are as follows:

1. Two different combustion phenomena were observed. The first was that only particles ignited by direct heating of the laser beam burned. The second was that a few particles heated by the laser pulse ignited initially, followed by an increase in the number of burning particles during combustion. This phenomenon was defined as "flame propagation."
2. The lean limit of flame propagation of 22–63 μm particles was obtained from the relationship between particle concentration (or average distance between particles) and flame propagation probability. The maximum distance between particles, at which ignition of one particle from another is possible, was 12–20 times as long as particle diameter for hv bituminous coal burned in air and 25–40 times as long as particle diameter burned in pure oxygen. The effect of coal type on the maximum distance coincided qualitatively with the previous result obtained from millimeter-sized particles arranged in a row. However, the effect of particle diameter was larger than that of the earlier study.
3. The flame propagation velocity was examined using the increasing rate of flame radius. The flame propagation velocity was related to volatile content. The effect was pronounced for lv bituminous coal. The flame propagation velocities of hv and lv bituminous coals were about 1.6 times the order of the oxygen concentration, which coincided with the previous result for sub-bituminous coal.

REFERENCES

1. Azuhata, S., Narato, K., Kobayashi, H., Arashi, N., Morita, S., and Masai, T., *Twenty-First Symposium (International) on Combustion,* The Combustion Institute, Pittsburgh, 1986, pp. 1199–1206.
2. Zhang, D.-K., *Combust. Flame* 90:134–142 (1992).

3. Phuoc, T. X., Mathur, M. P., and Ekmann, J. M., *Combust. Flame* 93:19–30 (1993).
4. Bar-Ziv, E., Jones, D. B., Spjut, R. E., Dudek, D. R., Sarofim, A. F., and Longwell, J. P., *Combust. Flame* 75:81–106 (1989).
5. D'amore, M., Tognotti, L., and Sarofim, A. F., *Combust. Flame* 95:374–382 (1993).
6. Chen, J. C., Taniguchi, M., Narato, K., and Ito, K., *Combust. Flame* 97:107–117 (1994).
7. Taniguchi, M., Chen, J. C., Narato, K., Ito, K., Miyadera, H., and Kudo, K., *Kagaku Kogaku Ronbunshu* 20:834–842 (1994), in Japanese.
8. Chen, J. C., Taniguchi, M., and Ito, K., *Fuel* 74:323–330 (1995).
9. Hertzberg, M., Cashdollar, K. L., and Lazzara, C. P., *Eighteenth Symposium (International) on Combustion,* The Combustion Institute, Pittsburgh, 1981, pp. 717–729.
10. Hertzberg, M., Cashdollar, K. L., Ng, D. L., and Conti, R. S., *Nineteenth Symposium (International) on Combustion,* The Combustion Institute, Pittsburgh, 1982, pp. 1169–1180.
11. Horton, M. D., Goodson, F. P., and Smoot, L. D., *Combust. Flame* 28:187–195 (1977).
12. Smoot, L. D., Hedman, P. O., and Smith, P. J., *Prog. Energy Combust. Sci.* 10:359–441 (1984).
13. Fujita, O., Ito, K., and Sakamoto, A., *Proceeding of the Third Asian-Pacific International Symposium on Combustion and Energy Utilization,* Hong Kong, 1995, pp. 507–512.
14. Gieras, M., Klemens, R., and Wojcicki, S., *Acta Astronautica* 12:573–579 (1985).
15. Gieras, M., Klemens, R., Wolanski, P., and Wojcicki, S., *Twenty-First Symposium (International) on Combustion,* The Combustion Institute, Pittsburgh, 1986, pp. 315–323.

COMMENT

Eric Suuberg, Brown University, USA. In order to have a successful ignition of the particle cloud by the laser-ignited particles, is it necessary to have envelopment of the neighboring particles by the initial volatiles flame, or can radiation play a role in igniting neighboring particles?

Author's Reply. We think that the volatile flame touches the neighboring particles at first; then the neighboring particles ignite. The laser shot of our equipment can ignite the particles, but the energy flux of the laser beam (around 10^8 W/m^2) was about 50 times as much as the radiation of the burning particles. It is difficult to ignite the particles without convection. However, we think that the radiation can accelerate the devolatalization of the unburned particles, and shorten ignition delay time of the particles. We are planning to evaluate the effect of radiation experimentally and theoretically.

Twenty-Sixth Symposium (International) on Combustion/The Combustion Institute, 1996/pp. 3197–3204

SODIUM PARTITIONING IN A PULVERIZED COAL COMBUSTION ENVIRONMENT

NEAL B. GALLAGHER, THOMAS W. PETERSON AND JOST O. L. WENDT
Department of Chemical and Environmental Engineering
The University of Arizona
Tucson, AZ 85721, USA

Sodium transformation mechanisms during pulverized coal combustion were investigated as functions of combustion temperature and of the modes in which sodium occurred in the parent coal. The combustion experiments took place in a 17-kW laboratory downflow combustor which was designed to form a link between bench-scale reactor studies and commercial-scale combustors. Three different coals were burned under excess air conditions, and size-segregated fly-ash samples were extracted far from the combustion zone. Atomic absorption on each ash sample yielded bulk composition data. Computer-controlled scanning electron spectroscopy (CCSEM) yielded composition data of individual ash particles and allowed inference of mechanisms governing the formation of these individual particles.

It was demonstrated that partitioning of sodium in the vapor, and the subsequent fraction of sodium in the submicron fume, is greatly reduced by the presence of silicates and high temperatures. This was attributed to reaction of sodium in the vapor with solid silicates. The CCSEM analyses showed that reaction to form sodium aluminum silicates was preferred over reactions forming sodium silicates alone, although both are formed. Some physical condensation also occurs. Both included and excluded alumino-silicates are effective in reactively scavenging sodium. The maximum amount of sodium scavenged in any one particle was consistent with formation of $Na_2O \cdot Al_2O_3 \cdot 2SiO_2$. It was demonstrated that sodium from coal reacted with kaolinite additives mixed with the coal, suggesting that this is a strategy to reactively scavenge vaporized sodium. Additional bench-scale experiments and equilibrium calculations suggest that the mechanism of sodium reaction with alumino-silicates involves sodium as sodium hydroxide.

Introduction

The presence of mineral matter in coal greatly influences the energy conversion efficiency of the fuel and contributes to the emission of fly ash which can be detrimental to the environment. Alkali species in particular are known to exacerbate fouling of boiler tubes and slagging in commercial combustors [1,2] and can contribute to metals corrosion and ceramics devitrification in combustion systems [3]. Sodium and other alkalis are also known to be enriched in the small, respirable [4] particle size range of pulverized coal fly-ash emissions. Therefore, the focus of this work is to elucidate the major mechanisms that govern the partitioning of sodium into various fly-ash particle sizes, in the hope of suggesting combustion modifications that minimize or eliminate these undesirable effects attributable to alkalis.

There is evidence from both bench-scale drop tube experiments (feed rates less than 1 g coal/h) [5–8] and large-scale experiments (feed rates greater than 100 kg/h) [9], that silicates affect the fate of sodium during coal combustion. An objective of the work described here was to form a link between these bench-scale experiments and large-scale experiments. The former are typically performed using very low coal feed rates and combustion sustained by external heating. This scale allows extraction of fundamental mechanisms, but does not include gas-particle and particle-particle interactions expected on the large scale. The latter have poorly defined flows and temperatures, making extraction of a representative ash sample and interpretation of experimental results difficult.

Previous research results [10] on the laboratory scale focused on descriptions of the effect of peak temperature on vaporization of sodium during pulverized coal combustion, and on possible interactions between sodium and potassium in the coal. Using more sophisticated analysis techniques than were previously available, this work elucidates the pertinent mechanisms more precisely and determines the nature of the dominant reaction product. In this paper, sodium reaction with both included and extraneous alumino-silicates is investigated and addition of extraneous alumino-silicate is explored as a means to diminish adverse effects of sodium in coal under practical combustion conditions.

Experimental

The approach that was followed was (1) to burn mixtures of coal (plus any additive) and air under

TABLE 1
Coal analysis (as received)

	Kentucky no. 11	Beulah lignite	Loy Yang 2301
Proximate (wt %)			
Fixed Carbon	41.90	30.91	41.6
Vol. matter	33.79	29.28	44.2
Ash	20.79	9.65	1.6
Moisture	4.02	30.16	12.9
Ultimate (wt %)			
Carbon	58.06	41.30	58.6
Hydrogen	4.41	2.92	4.2
Oxygen	7.74	13.84	22.4
Nitrogen	1.18	0.82	0.4
Sulfur	4.30	1.31	0.3
Ash	20.29	9.65	1.3
Moisture	4.02	30.16	12.9
H.H.V. (MJ/kg)	23.8	16.1	22.7
[BTU/lb]	[10237]	[6942]	[9780]
Acid-soluble alkalies (ppm)			
Na	353/413	7500/7250	2900/3400
K	3623/3214	150/170	–/–
Ca	4981/4821	14125/13875	300/400
Mg	920/946	3375/3250	1100/1000
Cl (ppm)	–	95	5100

steady, self-sustained combustion conditions; (2) to extract representative, size-segregated samples of the ensuing fly ash near the exit of the combustor (always below 1200 K); and (3) to subject each size-segregated fly-ash sample to analyses, notably by computer-controlled scanning electron microscopy (CCSEM), in order to determine mechanisms through which fly-ash particles in the particulate sample were individually created. CCSEM automatically identifies an inorganic particle at random (>1000 per sample) in a polished ash sample embedded in epoxy using scanning electron microscopy and measures the area of its cross section. The electron beam is then positioned at the particle's center and its composition is approximated from its energy dispersive X-ray spectra.

"Premixed," pulverized coal-air self-sustained flames were maintained in a 17-kW down-fired laboratory combustor (i.d., 0.15 m; length, 6 m), which is described in detail elsewhere [10–13]. Experiments were performed at a stoichiometric ratio (SR) of 1.2, at coal feed rates varying from 0.5 to 5 kg/h. Flue gas analyses, using continuous emission monitors for NO_x, CO and CO_2, and O_2 (maintained at approximately 3.2% for all experiments) allowed the combustion to be monitored. Temperatures were measured at sample ports yielding a temperature profile (temperature history) for each experiment, and the temperature was varied by changing the air/coal feed rate while maintaining SR = 1.2.

Fly-ash samples were extracted through a sample port near the exit of the combustor, using an isokinetic-aspirated (by 28.3 alpm air) dilution probe [13]. Contacted by neither valves nor fittings, the diluted sample passed through a Mark II Andersen Cascade Impactor where the fly ash was size segregated onto eight stages (and trapped on ash-free Teflon filters coated with polyethylene glycol) plus an after-filter yielding 50% cutoff d_{50} values (based on specific gravity of 1.0) denoted as the abscissa of Figs. 1–3. Chemical analyses on the size-segregated samples were obtained, yielding both bulk concentrations of Al, Si, Ca, Mg, Fe, Na, and K in the ash for each size cut, using atomic absorption/emission spectroscopy (AA), and also ash compositions on a particle-by-particle basis, using CCSEM [14].

In this paper, we focus on 3 coals, out of the 8 coals studied, namely: Kentucky no. 11, Beulah lignite, and Loy Yang 2301 (an unusual coal), as shown in Table 1. These coals exhibit a range of both ash compositions and modes of sodium occurrence. Sodium occurrence can be quantified by the ratio (acid

TABLE 2
Ash compositions

	Kentucky no. 11	Beulah lignite	Loy Yang 2301
Ash (wt % as received)			
	20.79	9.65	1.7
Ash Composition (wt %)			
SiO_2	45.8	21.6	9.4
Al_2O_3	19.0	14.5	4.7
TiO_2	0.9	0.0	0.7
Fe_2O_3	20.4	12.2	16.3
CaO	4.4	17.1	3.8
MgO	0.9	4.2	14.5
Na_2O	0.3	6.1	30.7
K_2O	2.5	0.3	0.7
SO_3	5.2	21.1	19.3
P_2O_5	0.1	–	–

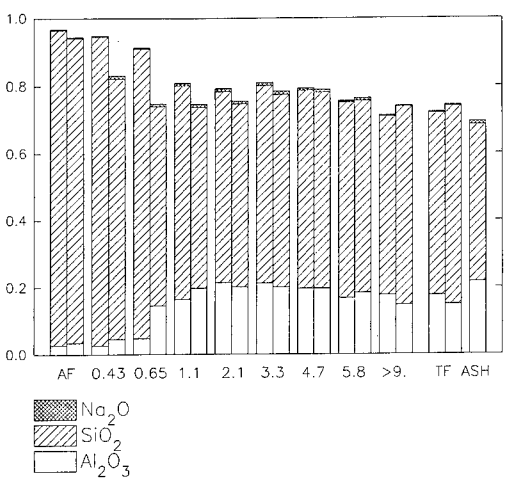

FIG. 1. Fraction oxide plot for Kentucky no. 11 as a function of the 50% impactor plate cutoff diameter. The left and right bars for each impactor plate correspond to the low and high temperature runs, respectively (peak temperatures 1380 K and 1530 K).

soluble $Na_2O)/(SiO_2 + Al_2O_3)$, calculated from coal and ash analysis results, hereafter defined, for brevity, as the Na-Si ratio. Acid soluble, in this context, is defined as soluble in ammonium acetate (2 measurements in Table 1). This ratio ranges from a low value of 0.003 for the Kentucky no. 11 bituminous coal, through a moderately high value of 0.21 for the Beulah lignite, to a very high value of 1.7 for the Loy Yang. Additionally, chlorine in the parent Beulah lignite coal was low and the sodium was presumed to be bound primarily to the organic matter, whereas in Loy Yang 2301, the chlorine and sodium were both high, in equimolar ratios, suggesting sodium chloride. The Na-Si ratio (already defined) was raised for the Kentucky coal by adding 99 g of sodium acetate trihydrate per kilogram pulverized coal, and lowered for the Loy Yang 2301 by adding 94 g kaolinite (alumino-silicate) per kilogram pulverized coal.

Results and Discussion

Effects of Temperature on Distribution of Na, Si, and Al

Figure 1 shows the size-classified (by impactor stage) weight fraction Na, Si, and Al oxide compositions for fly-ash sampled from the Kentucky no. 11 coal, burned to create measured peak temperatures of 1380 K (feed rate = 0.5kg/h) and 1530 K (feed rate = 2.1 kg/h). Silicon dominates the smallest size-cut, AF (after-filter), for both feed rates. Iron, which is not shown here, for the sake of clarity, is significant in the largest size class, $>9\,\mu m$ [12]. The stacked bar on the far right labeled ASH was calculated from the ash analysis normalized to the 7 metal oxides (Na, K, Si, Al, Ca, Fe, Mg) measured here, and the bar labeled TF is the sum of the individual impactor stages weighted by the calculated mass (from AA measurements and a known solution volume) on each stage. Thus, TF is what would be expected if a "total filter" were used in place of the impactor, and discrepancies between TF and ASH are primarily the result of loss of fly ash to the combustor walls and difficulty in sampling large particles. In situ particle size measurements [13] indicated appreciable quantities of Beulah lignite fly ash with $d_p > 30\,\mu m$. Changes in peak temperature from 1380 K to 1530 K, and therefore the subsequent time/temperature history, had little affect on the distribution of Na, Si, and Al in the fly ash for Kentucky no. 11 (Fig. 1), which has a low Na-Si ratio.

The Beulah lignite, on the other hand, shows (Fig. 2) dramatic effects of temperature on the distribution of Na, Si, and Al in the fly ash. Here, measured peak temperatures were 1400 K (feed = 1.3 kg/h) and 1560 K (feed = 2.9 kg/h). Sodium dominates the smallest two size classes at the lower temperature (left columns), but is less significant in these size classes at the higher temperature (right columns). This is consistent with observations in bench-scale drop tube studies [5] and was interpreted as an increased reaction rate of sodium with silicates at higher temperatures.

Results in Figs. 1 and 2 can be explained by the

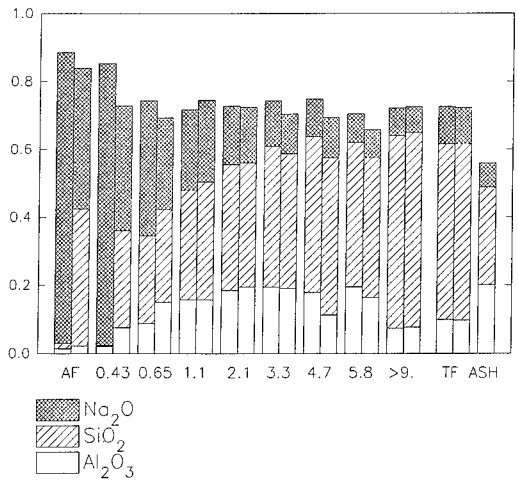

FIG. 2. Fraction oxide plot for Beulah lignite as a function of the 50% impactor plate cutoff diameter. The left and right bars for each impactor plate correspond to the low and high temperature runs, respectively (peak temperatures 1400 K and 1560 K).

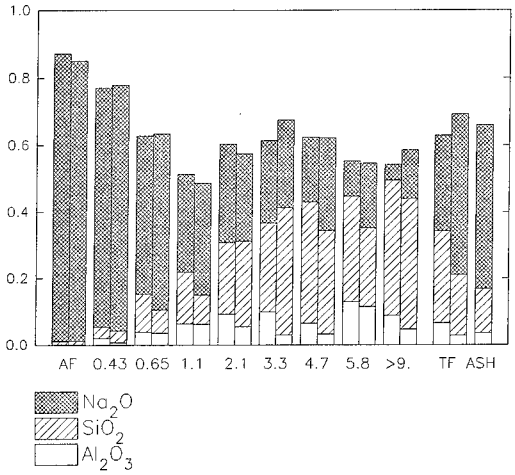

FIG. 3. Fraction oxide plot for Loy Yang 2301 as a function of the 50% impactor plate cutoff diameter. The left and right bars for each impactor plate correspond to the low and high temperature runs, respectively (peak temperatures 1530 K and 1610 K).

presence of a reaction of vaporized sodium with silicates during pulverized coal combustion. Sodium, which vaporizes during the combustion process [15–19], can nucleate and form a submicron fume, condense on existing particles, or react with fly-ash particles. This process results in enrichment of the submicron fly ash with alkali [5,6,10]. Kentucky no. 11 contains little sodium and is high in silicates. Any vaporized sodium is expected to be efficiently scavenged by silicates during combustion, resulting in little enrichment of the submicron fly ash. Figure 1 shows no measurable sodium enrichment of the submicron fly ash, suggesting that vaporized sodium has indeed been scavenged prior to condensation or nucleation. Beulah lignite has a higher Na-Si ratio, and the quantity of vaporized sodium available no longer limits reaction. In this case, temperature has a significant effect on the reaction rate. Capture of sodium at higher temperatures results in less sodium in the vapor, which can nucleate and condense in the submicron fume. Therefore, enrichment of the small particle sizes decreases as temperature increases.

At the other extreme, Loy Yang 2301 has a high Na-Si ratio and is low in silicates. Figure 3 shows fraction oxide plots for this coal burned at low (1530 K, 2.4 kg/h coal feed) and high (1610 K, 3.8 kg/h coal feed) peak temperatures. Here, temperature has little affect on the distribution of metals in the fly ash. Whereas the lack of available sodium limited reaction in Kentucky no. 11, it is the lack of available silicon that limited reaction in Loy Yang 2301. There, vaporized sodium is expected to enrich the submicron fume at all combustion temperatures, as observed in Fig. 3. Beulah lignite lies between the extremes and, hence, the result is significantly affected by temperature.

Size-Segregated CCSEM Analyses

Nature of the reaction product

Bulk analyses of sampled fly ash (Figs. 1–3) are consistent with a reaction of vaporized sodium with silicates present in the coal. However, the nature of the reacted species was unclear. CCSEM analysis results of fly ash on a particle-by-particle basis are also consistent with this interpretation and implicate alumino-silicates with a kaolinite-like composition as the major reactive silicate.

CCSEM analysis results of fly ash from high-temperature combustion (peak measured temperature of 1570 K) of Beulah lignite are shown in Fig. 4 for impactor stages 1, 3, 5, and 7. CCSEM analysis, which is performed on a particle-by-particle basis, can supply evidence for the coexistence of atomic species within individual particles. Figure 4 shows the mole fraction of sodium versus silicon in individual particles, where the height of each peak represents the number of particles with that composition. Approximately 1200 particles were examined for each impactor plate. Compositions sum to 100%, therefore the upper half of each plot represents allowable compositions. The distance of a peak (up) from a diagonal line drawn from (Na = 0; Si = 100) to (Na = 100; Si = 0) is a measure of the mole fraction of species other than sodium and silicon.

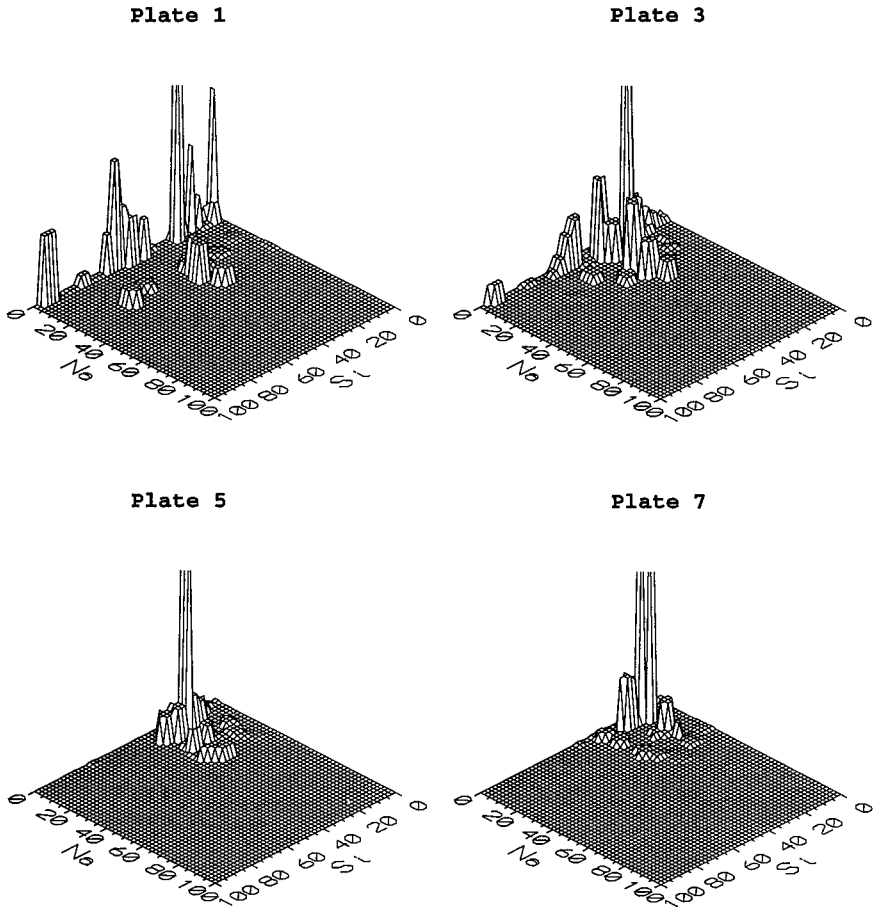

FIG. 4. CCSEM results for Beulah lignite (peak temperature 1570 K) fly ash sampled on impactor plates 1, 3, 5, and 7.

Conversely, a peak lying on this diagonal shows that it contains only the two species being plotted. On plate 1 ($d_{50} > 9\,\mu$m), there is some pure SiO_2 shown at the left-hand corner. There is also a peak on the diagonal showing particles containing only Si and Na, suggesting the formation of large particles of $Na_2O \cdot nSiO_2$, with $n = 4$. Of those particles containing both sodium and silicon, most seem to form a compound containing equimolar quantities of Si and Al (as determined from the analogous Al/Si plots not shown here). The quantity of sodium in these particles increases from a few percent to a maximum of about 33%, yielding a composition of about 33% Si, 33% Na, and 33% Al. This suggests a final reaction product of $Na_2O \cdot Al_2O_3 \cdot 2SiO_2$ (as in nephalite). This composition is evident in all measured size classes. As a result of polishing, compositions of large ash particles could be measured anywhere from near the particle surface to the true particle center. Thus, for similarly surface enriched, large particles on plate 1, the apparent compositions would indicate a range of Na concentrations up to 33%, depending on how the particles were sliced. Similar data would be obtained from a range of reaction extents. CCSEM of parent coal samples indicated that mineral matter there did not contain significant amounts of sodium prior to combustion. Therefore, although sodium reacts with large silica (SiO_2) particles (presumed to be excluded), it appears to react preferentially with a kaolinite-like mineral (presumed to be primarily included) present initially in the coal.

CCSEM results are also consistent with condensation of unreacted sodium in the smallest size classes where small composition changes have a large relative effect. There are several larger particles (plates 1 and 3) that contain Si but no Na. However, smaller particles all seem to contain some Na, possibly due to physical condensation and reaction with silicates as well. The sodium content of individual particles approached a maximum of 33% for all size classes, again suggesting a reaction product similar to $Na_2O \cdot Al_2O_3 \cdot 2SiO_2$. Note that on plate 7, very

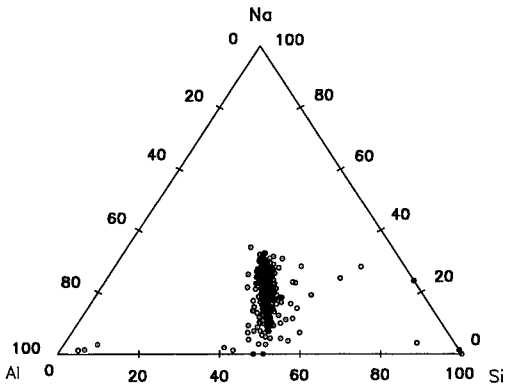

FIG. 5. CCSEM results for Loy Yang 2301 with kaolinite additive. This diagram is for particles with $d_{50} > 10\ \mu m$. The diagram for $d_{50} < 10\ \mu m$ is similar.

few small particles have only Na and Si, which is possibly due to coalescence or agglomeration of several smaller particles.

Reaction with extraneous kaolinite

To test the reaction hypothesis, kaolinite was mixed with Loy Yang 2301 as an additive and burned at a feed rate of 2.7 kg/h, resulting in a peak temperature of 1243 K. Approximately 94 g of kaolinite was added per kilogram of coal to significantly lower Na-Si. Figure 5 shows CCSEM results for particles with sizes >10 μm. Similar results were found for particle sizes <10 μm. Here, a ternary diagram is appropriate since only three species (Na, Al, and Si) dominate the fly ash, and only particles that contain greater than 80% of these three species are shown. Particle compositions lie primarily on an axis of equimolar concentrations of aluminum and silicon as is expected for kaolinite. The sodium composition varies from low values to a high point of equimolar ratios of sodium to aluminum to silicon which is consistent with the formation of $Na_2O \cdot Al_2O_3 \cdot 2SiO_2$. The observation that sodium does not exist in higher quantities in these particles is highly suggestive of reaction rather than condensation alone and is consistent with the observations for CCSEM of Beulah lignite samples. It also shows that addition of extraneous kaolinite can capture sodium and that this is a possible strategy for mitigation of detrimental effects attributable to vaporized sodium.

Effect of Chlorine

Reaction of sodium with silicates is apparent in Figs. 4 and 5; however, this mechanism is complicated by the presence of chlorine. Previous work [17,18] using a thermo-gravimetric reactor at 1273 K suggested the following reaction:

$$Al_2O_3 \cdot 2SiO_2 + 2NaCl + H_2O \rightarrow Na_2O \cdot Al_2O_3 \cdot 2SiO_2 + 2HCl \uparrow \quad (1)$$

The measured rate was very slow, with a reaction time of 0.5 h at 1273 K. Tests conducted by us [13] indicated that small NaOH pellets placed in a quartz boat vigorously reacted with the boat in a matter of seconds at 590 K. Equilibrium calculations show that with no sulfur present, sodium vapor exists primarily as NaCl and NaOH, with chlorine enhancing the amount of NaCl. Other research [20] suggests that chlorine inhibits the reaction between sodium vapor and kaolinite sorbent by decreasing the NaOH concentration available for reaction. All these results suggest that the mechanism of capture in the presence of chlorine proceeds as follows:

$$2NaCl + 2H_2O \rightleftarrows 2NaOH + 2HCl \quad (2)$$

$$Al_2O_3 \cdot 2SiO_2 + 2NaOH \rightarrow Na_2O \cdot Al_2O_3 \cdot 2SiO_2 + H_2O \quad (3)$$

This mechanism, in which NaOH is the primary sodium species that reacts with kaolinite, is equivalent to equation 1, and is consistent with work by Lindner et al. [7–9] who claimed that sodium silicate formation was significantly higher when sodium acetate was used instead of sodium chloride. Reference 20 suggests that the major effect of sulfur is to raise the sodium dewpoint by forming sodium sulfates that condense. Thus, sulfur lowers the time available for reaction between sodium vapor and kaolinite substrates, and consequently, the amount of sodium reactively scavenged.

Appreciable chlorine is present in the Loy Yang 2301 coal, and this probably exacerbated the lack of reaction with any alumino-silicates that were present. Both kaolinite and silica, but little chlorine, are present in Beulah lignite parent coal [21], and CCSEM demonstrated that sodium reacted with both, although kaolinite was preferred.

Composite Data from Eight Coals

Further evidence for sodium reaction with alumino-silicates during combustion is given in Fig. 6 where the fraction of sodium on impactor plate 8 plus the after-filter (Na_{f8A}) is plotted as a function of Na-Si, for all 8 coals studied and burned over a range of temperatures. Figure 6 shows that this ratio is a practical measure of the sodium that can vaporize and subsequently condense in the submicron fume, and that this quantity can vary over three orders of magnitude. Shaded points show additive runs in which sodium acetate or kaolinite were added as appropriate. Scatter in the plot is not surprising and can be attributed, in part, to the presence of chlorine, water vapor, or sulfur, to different experimental time/temperature histories, and to ambiguities in the

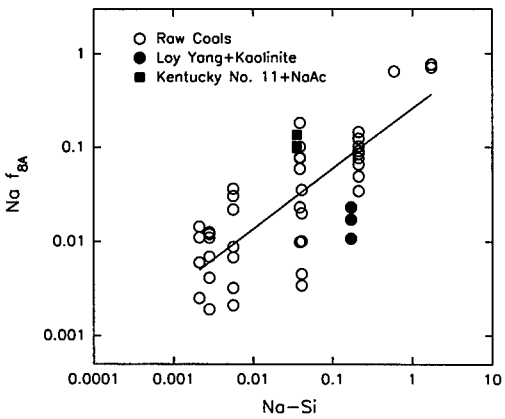

FIG. 6. Fraction of sodium on impactor plate 8 plus the after-filter (Na_{f8A}) versus the ratio Na-Si, defined as (acid soluble Na_2O)/(SiO_2 + Al_2O_3), in the parent coal.

use of ammonium acetate–extracted sodium (here designated as acid soluble sodium) in determining the mode of sodium in coal. A mechanistic model of sodium release might be necessary in order to reduce this scatter, but that is outside the scope of this work.

Conclusions

It was demonstrated under laboratory-scale combustion conditions that the fraction of sodium in the vapor, and the subsequent fraction of sodium in the submicron fume, is reduced by the presence of silicates and high temperatures. This observation was consistent with drop tube experiments and was attributed to reaction of sodium in the vapor with solid silicates such as kaolinite during the combustion process. CCSEM analyses on individual particles confirmed that sodium reacted with both included and extraneous kaolinite. Alumino-silicates (rather than silica alone) are the preferred scavengers during coal combustion. Bench-scale experiments and equilibrium calculations suggested a reaction mechanism for sodium capture that involved NaOH as the reactive sodium species.

Acknowledgments

This project was supported by PSI Technology Company, Andover, MA through the Department of Energy Contract No. DE-AC22-86PC90751. Acknowledgment is also due to Gerald Huffman's group at the University of Kentucky for performing the CCSEM.

REFERENCES

1. Raask, E., *Mineral Impurities in Coal Combustion,* Hemisphere Publ., New York, 1985.
2. Scandrett, L. A. and Clift, R., *J. Inst. Eng.* 57(433):391–397 (1990).
3. Hastie, J. W., Plante, E. R., and Bonnell, D. W., *ACS Symposium Series* 179:543-600 (1982).
4. Lodge, J. P., Jr. and Chan, T. L. (Eds.), *Cascade Impactor: Sampling and Data Analysis,* American Indus. Hygiene Assoc., Cincinnati, OH, 1986.
5. Neville, M. and Sarofim, A. F., *Fuel* 64:384–390 (1985).
6. Quann, R. J., Neville, M., and Sarofim, A. F., *Combust. Sci. Technol.* 74:245–265 (1990).
7. Lindner, E. R., Ph.D. Thesis, Dept. of Chem. and Mat. Eng., Univ. of Newcastle, Australia, 1988.
8. Lindner, E. R. and Wall, T. F., "An Experimental Study of Sodium-Ash Reaction During Combustion of Pulverized Coal," *Proceedings Mineral Matter and Ash Deposition from Coal, Fourth Engineering Foundation Conference* (Bryers, R. J. and Vorres, K. S., Eds.), Engineering Foundation, New York, 1988, pp. 321–330.
9. Lindner, E. R., Kosminski, A., Taylor, C., and Williams, R. G., "Effects of Additives on Fouling Behavior Characteristics of South Australian Brown Coals," *Proceedings Mineral Matter and Ash Deposition from Coal, Fourth Engineering Foundation Conference* (Bryers, R. W. and Vorres, K. S., Eds.), Engineering Foundation, New York, 1988, pp. 331–346.
10. Gallagher, N. B., Bool, L. E., Wendt, J. O. L., and Peterson, T. W., *Combust. Sci. Technol.* 74:211–221 (1990).
11. Scotto, M. V., Bassham, E. A., Peterson, T. W., and Wendt, J. O. L., *Twenty-Second Symposium (International) on Combustion,* The Combustion Institute, Pittsburgh, 1989, pp. 239–247.
12. Bool, L. E., Peterson, T. W., and Wendt, J. O. L., *Combust. Flame* 100:262–270 (1995).
13. Gallagher, N. B., Ph.D. Dissertation, Department of Chemical Engineering, University of Arizona, Tucson, 1992.
14. Huffman, G. P. Huggins, F. E., and Lee, R. J., *ACS Symp. Ser.* 205:235–259 (1984).
15. Wibberly, L. J. and Wall, T. F., *Fuel* 61:87–92 (1982).
16. Wibberly, L. J. and Wall, T. F., *Fuel* 61:95–99 (1982).
17. Punjak, W. A., Ph.D. Dissertation, Department of Chemical Engineering, University of Arizona, Tucson, 1988.
18. Uberoi, M., Punjak, W. A., and Shadman, F., *Prog. Energy Combust. Sci.* 16:205 (1990).
19. Srinivasachar, S., Helble, J. J., Ham, D. O., and Domazetis, G., *Prog. Energy Combust. Sci.* 16:303–309 (1990).
20. Mwabe, P. O. and Wendt, J. O. L, "Mechanisms Governing Trace Sodium Capture by Kaolinite in a Downflow Combustor," *Twenty-Sixth Symposium (International) on Combustion,* The Combustion Institute, Pittsburgh, 1996, pp. 2447–2453.
21. Helble, J. J., Srinivasachar, S., Wilemski, G., Boni, A. A., Kang, S, Sarofim, A. F., Beer, J. M., Peterson, T. W., Wendt, J. O. L., Gallagher, N. B., Bool, L., Shah, N., Huggins, F. E., and Huffman, G. P., *Transformations of Inorganic Coal Constituents in Combustion Systems,* Report #DOE/PC/90751-T12, U.S. Dept. of Energy, 1991.

COMMENTS

A. E. Jacob Akanetuk, Stanford University, USA. How would the fact that, in many cases, the sampling volume used in the EDS analysis was significantly less than the particles characterized affect the interpretation of the results?

Author's Reply. Typically energy dispersive X-ray spectroscopy yields an approximate composition from a sample volume with a about a 1 μm diameter. For larger particles this could, in part, explain some of the low sodium concentrations observed in Fig. 5. Although this would have consequences in quantifying the CCSEM results, it does not impact on our interpretation, which is consistent with sodium-aluminosilicate reaction. It is interesting to note that results for particles of size $<10\,\mu$m show a very similar distribution to that observed in Fig. 5: namely, few particles with a zero sodium concentration, and a maximum sodium concentration consistent with an equimolar Na, Al and Si particle composition.

•

P. Monkhouse, University Heidelberg, Germany. I would like to add the comment that the vapor phase part of the alkali could be measured *specifically* with the aid of recently developed methods such as the ELIF—technique [1]. In this way we have been able to measure large differences in alkali vapor release from hard coals (with high silicate silicone) content. Your results would appear to confirm the interpretation of our measurements.

REFERENCE

1. Greger, F., Hartinger, K. T., Monkhouse, P. B., Wolfrum, J., Baumann, H., and Bonn, B. *Twenty-Sixth Symposium (International) on Combustion,* The Combustion Institute, Pittsburgh, 1996, pp. 3301–3307.

Author's Reply. This is an interesting comment. Clearly, *in-situ* measurements of vapor phase sodium would be extremely useful, and we are happy that our conclusions are corroborated by your work.

Twenty-Sixth Symposium (International) on Combustion/The Combustion Institute, 1996/pp. 3205–3211

AN EXPERIMENTAL STUDY OF THE RELEASE OF NITROGEN FROM COALS PYROLYZED IN FLUIDIZED-BED REACTORS

C. -Z. LI* AND P. F. NELSON
CSIRO Division of Coal and Energy Technology
North Ryde, Australia 2113

E. B. LEDESMA AND J. C. MACKIE
School of Chemistry, University of Sydney
Australia 2006

Nitrogen release has been measured from a suite of Australian, German, and U.S. coals pyrolyzed under rapid heating conditions in two bench scale reactors. The first reactor was a single-stage fluidized bed reactor; the second was a two-stage reactor in which a fluidized bed was coupled with a tubular reactor. The two-stage reactor enabled cracking reactions of the volatiles to be studied in isolation from reactions of the char. The results show that the gas-phase N-containing species, HCN and NH_3, are formed from both brown and bituminous coals. In addition, HNCO is also observed from bituminous coals; HNCO is a plausible precursor for NH_3 formation. At high temperatures, low-volatile coals give lower yields of HCN and NH_3 than high-volatile coals. This observation, however, does not imply that tar cracking is the only source of HCN and NH_3. In fact, the results obtained in the two-stage reactor suggest that a significant proportion of the HCN is released from the char and that tar cracking is not a significant source of NH_3. A major part of the NH_3 is produced by interactions of N-containing species with the char. These results, together with previous studies of N release, demonstrate that there is no simple relationship between N functionality in coals and the composition and rate of release of the nitrogen.

Introduction

The formation of NO_x from the combustion of coal is due predominantly to oxidation of the nitrogen contained in the heterocyclic structures of the coal. During the initial pyrolytic decomposition, coal N is released as volatile N species, such as HCN and NH_3, as well as nitrogen-containing compounds in the tars, and these species are oxidized to NO or reduced to N_2. The N remaining in the char is similarly converted to NO or N_2 by processes that are still poorly understood. Improvement in our understanding of the way in which coal N is released and the role that N functionality plays in determining the composition and relative amounts of volatile and char N is necessary in attempts to improve predictive techniques for NO_x formation.

Recently, there have been some significant advances in our understanding of the chemistry of coal nitrogen during pyrolysis and combustion. Firstly, the N functionality has been extensively studied using X-ray photoelectron spectroscopy (XPS) [1–5] and X-ray absorption near edge spectroscopy (XANES) [6]. Although a consensus has not emerged from these studies as to the details of the functionality of nitrogen in coals, it is generally accepted that the nitrogen is overwhelmingly present in heterocyclic structures and that those structures of pyrrolic (5-membered) type are more common than those of pyridinic (6-member) type. Some of the problems in interpretation of the spectra arise from low signal-to-noise ratio spectra and from the dependence of the results on sample preparation [1].

Secondly, the release of nitrogen during the pyrolysis of coals has been studied over a very wide range of conditions [1,7–10]. Nitrogen is released as nitrogen containing species in tar and also as HCN and NH_3. The relative amounts of HCN and NH_3 vary and appear to depend on, inter alia, reactor temperature, type, and material. The formation of NH_3 has generated considerable debate because studies of pyrolytic decomposition of model compounds such as pyrrole and pyridine [11,12] release N as HCN and not as NH_3. Bassilakis et al.[10] measured N species from the pyrolysis of the same set of Argonne premium coal samples in a TG-FTIR reactor and in an entrained-flow reactor. The ratios of NH_3/HCN were much higher in the TG-FTIR reactor, which has much lower heating rates than the entrained flow reactor. It was postulated that HCN is the primary product and that NH_3 is formed by

*Current address: Department of Chemical Engineering, Monash University, Clayton, 3168, Australia.

TABLE 1.
Properties of coal samples used

Coal name or code	Country of origin	Ash wt%, dry	wt%, daf					
			WM[a]	C	H	N	S	O[b]
Laubag	Germany	6.5	54.4	67.4	5.0	0.7	0.9	26.0
Fortuna	Germany	12.9	43.2	67.3	5.4	0.8	0.6	26.0
Coal A	Australia	2.1	53.0	67.4	4.6	0.6	0.3	27.1
Coal B	Australia	15.6	50.8	77.9	6.3	1.2	0.7	13.9
Coal C	Australia	8.0	33.4	79.8	4.6	2.0	0.3	13.3
Prosper	Germany	8.3	34.8	79.9	6.0	1.3	1.3	11.5
Gottelborn	Germany	7.1	39.2	82.3	5.6	1.7	1.0	9.4
Ensdorf	Germany	7.6	37.9	82.4	5.7	1.8	0.8	9.3
Coal D	Australia	7.8	40.8	83.2	5.7	1.8	1.2	8.2
Coal E	Australia	19.6	22.4	86.5	4.5	1.6	1.6	5.8
Coal F	Australia	13.5	27.8	86.8	4.9	1.6	0.4	6.3
Coag G	Australia	9.0	21.4	87.8	4.5	1.8	0.4	5.5
Coal H	Australia	15.6	17.8	88.4	4.6	1.6	0.6	4.8
Pocahontas No. 3	USA	7.7	18.5	90.0	4.5	1.1	0.9	3.5

[a]volatile matter yield
[b]by difference

intraparticle transformations of the HCN. We have also recently found [13] that NH_3 can react with many types of material commonly used for the construction of bench scale reactors at elevated temperatures (>700°C), complicating the quantification of NH_3 from the pyrolysis of coal.

In spite of these advances, significant problems remain in predicting the influence of coal N on NO_x formation over the very wide range of combustion conditions employed in coal combustors. There does not appear to be any simple relationship between N functionality and NO_x production, in part because the variations in functionality do not appear to be great. A NO_x predictor index however, has recently been developed on the basis of functionality [14]. Formation of NO_x from coal combustion strongly depends on the rate of N release. In addition, the effectiveness of some control techniques such as staged air combustion depend critically on a rapid release rate of the N since this must occur in a fuel-rich region where the formation of N_2 is favored. Nitrogen incorporated in the char, in the tar, and in simple gas-phase species will likely have very different fates during subsequent combustion. Since nitrogen can be released from coal either during primary pyrolysis or during the further cracking of tars and chars, knowledge of the relative contributions of these two routes to the overall nitrogen release is very important. At present, there is no simple way to predict the composition and release rate of the N species, although significant advances have been made [15].

The purpose of the present study was to investigate the effects of pyrolysis conditions and coal characteristics on nitrogen distributions and release during coal pyrolysis. Experiments were carried out in two bench scale fluidized bed reactors. The configuration of the two-stage reactor allowed the thermal cracking of volatiles to take place in isolation from that of chars. The effects of coal rank and nitrogen functionality have been examined. Based on the experimental data, factors influencing the nitrogen distribution during coal pyrolysis—for example, nitrogen-containing aromatic ring size, substitution, and availability of donatable hydrogen—are discussed.

Experimental

Coal Samples

A suite of Australian, German, and U.S. coals was studied, ranging in rank from brown to low-volatile bituminous coals. Table 1 gives detailed analyses for these coals.

Coal Pyrolysis

The particle sizes of the coal samples used for pyrolysis experiments were between 75 and 106 μm. The coal samples were dried under vacuum at ambient temperature for at least 24 h before pyrolysis experiments. Pyrolysis experiments were carried out in two bench scale quartz fluidized bed reactors in N_2. The first reactor is similar to that described by Tyler [16]. Coal particles entrained in N_2 from a fluidized bed feeder were injected through a N_2-cooled stainless steel probe into the heated fluidized bed of zircon sand (106–150 μm) and heated at rates

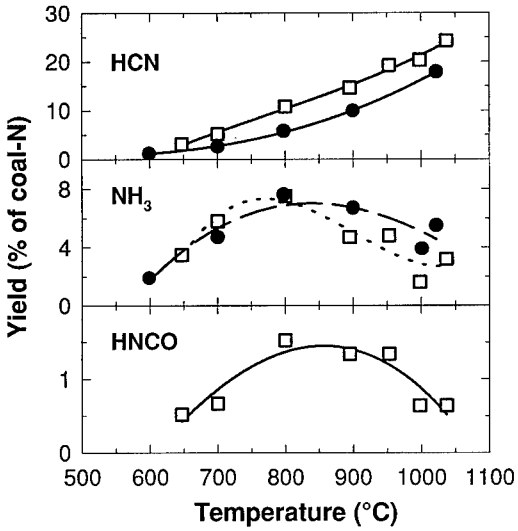

FIG. 1. HCN, NH_3 and HNCO yields from the pyrolysis of Fortuna brown coal (●) and Göttelborn bituminous coal (□) in the single-stage reactor as a function of temperature.

exceeding 10^4K s^{-1}. This reactor featured a relatively long (at least 13 cm) freeboard zone heated to similar temperature levels as the fluidized bed of zircon sand, where the nascent tars (and chars) are further thermally cracked. This reactor is denoted as the single-stage reactor in the present study. Gas residence times were 0.3–0.5 s. Particle residence times varied from as short as the gas residence time to much longer times, depending on the tendency of the coal to soften and adhere to the bed material.

The fluid bed reactor is a useful device for investigating the detailed composition of the products of the initial stages of coal pyrolysis and of the subsequent thermal cracking of the volatiles. These processes are of great importance in the ultimate combustion of the coal. However, while the heating rate is similar to that found in coal combustors, the temperatures achieved are somewhat less than those pertaining to a full-scale furnace. As a consequence, the timescale for the processes are relatively longer in the fluid bed reactor than they would be in a practical system, where conversion of the volatiles may be complete in 0.1 s.

In the second reactor, a fluidized bed reactor essentially identical to the single-stage reactor was coupled to an empty second-stage tubular reactor. The volatiles (tar plus gases) from the pyrolysis of coal in the first stage were transported to the second stage. Char particles were removed by particle settling between the two stages. The first stage was heated to 600°C to generate volatiles. The thermal cracking of volatiles at this temperature is believed to be minimal, especially for the release of nitrogen-containing species [1]. The second stage was heated separately to temperatures of 600–1000°C. The transfer line between the two stages was heated electrically to minimize the deposition of tars. Additional N_2 gas was added between the two stages to adjust the residence time of volatiles in the second stage. These residence times depended on temperature and were in the range of 0.7–1.0 s. This reactor is denoted as the two-stage reactor in the present study.

Product Characterization

During a pyrolysis experiment, tar was collected with a liquid-nitrogen–cooled trap fitted with a thimble. The tar sample was recovered by extracting the trap with dichloromethane, as described previously [1]. The tar samples thus recovered and the char samples collected in the thimbles were submitted for nitrogen analysis.

Quantification of HCN, HNCO, and NH_3 was carried out using Fourier transform infrared (FTIR) spectrometry. Gas-phase products were collected in a multipass FTIR gas cell (7.2 m total path length). Spectra were recorded and concentrations of HCN and NH_3 determined as previously described [1,8]. HNCO was identified by its absorbance in the region from about 2300 to 2200 cm^{-1} after the absorbance of $^{13}CO_2$ in the region had been subtracted [17]. Calibration of HCN and NH_3 was carried out by diluting respective standard calibration gases with N_2. The calibration of HNCO was taken from the literature [18] by assuming a linear increase in absorbance with light pass length and concentration.

Results

Figure 1 shows HCN, NH_3, and HNCO yields from the pyrolysis of a brown coal and a bituminous coal in the single-stage fluidized bed reactor. These are typical results chosen from the pyrolysis of a suite of coals. As previously reported for pyrolysis in a fluidized bed reactor [1], a maximum is observed in the NH_3 yield at a temperature of about 800°C. This decrease has been accounted for [19] by assuming that HCN is the primary N-containing product released from coals and that NH_3 is produced from the HCN by hydrogenation reactions within the coal particle. The decrease at high temperatures is a consequence of the reduced time spent by the HCN within the particle. However, we have observed recently [13] that NH_3 can be decomposed by quartz, zircon sand, and stainless steel at temperatures above 700°C.

Hydrogen cyanide yields from the coals studied (ranging from 67 to 90% C, daf basis) were observed to increase with increasing temperature, and the rate of this increase was very rapid at temperatures above 900°C.

Isocyanic acid (HNCO) yields from the pyrolysis

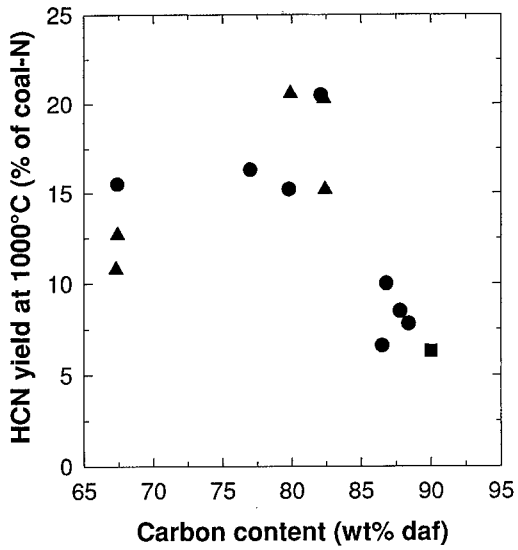

FIG. 2. HCN yields from the pyrolysis of coals at 1000°C in the one-stage reactor as a function of coal rank. (●), Australian coals; (▲), German coals; (■), U.S. coal.

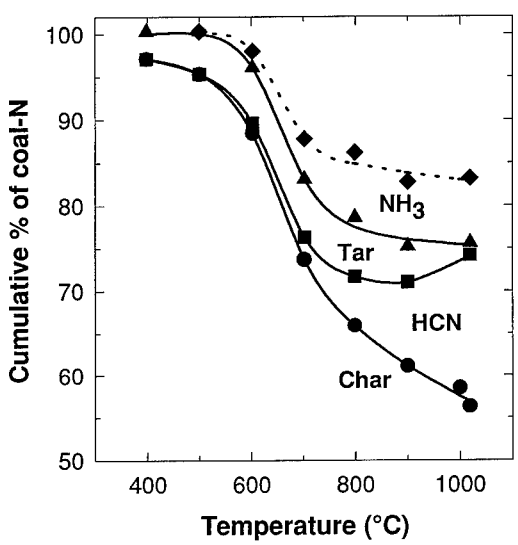

FIG. 3. Cumulative nitrogen distribution during the pyrolysis of Fortuna brown coal in the single-stage reactor as a function of temperature.

of bituminous coals were observed to maximize at about 800°C. At temperatures above 800°C, HNCO is thermally unstable and will decompose to NCO and H. No detectable HNCO yields were observed from the pyrolysis of Pocahontas No. 3, a low-volatile bituminous coal with carbon content of about 90 wt. % daf. Detection of HNCO from the pyrolysis of brown coals was more difficult because of the very

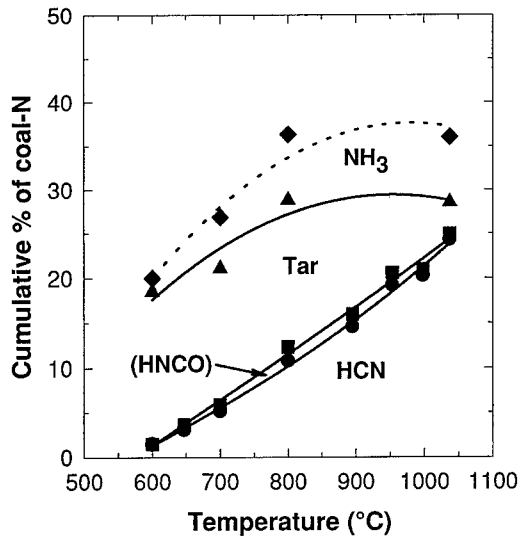

FIG. 4. Cumulative nitrogen distribution during the pyrolysis of Göttelborn bituminous coal in the single-stage reactor as a function of temperature.

large amounts of CO_2 produced during the pyrolysis of these low rank coals; however, it seems that the amounts produced were considerably less than those produced from the bituminous coals.

Data in Fig. 1 also suggest that the NH_3/HCN yield ratio at temperatures <800°C is higher from the pyrolysis of the brown coal than from the bituminous coal. Pyrolysis of other coals in the present study largely confirmed this finding. No NH_3 was detectable in the product gases from the pyrolysis of Pocahontas No. 3 coal under the same conditions.

Figure 2 summarizes the HCN yields at 1000°C as a function of coal rank (carbon content). It is clear that the nitrogen distribution during coal pyrolysis is coal rank dependent. Low-volatile coals gave much lower HCN (and NH_3) yields than the high-volatile coals.

Figure 3 shows the nitrogen distribution in char, tar, and gas phase from the pyrolysis of Fortuna brown coal. Because of the observed [13] NH_3 decomposition reactions on the reactor materials, NH_3 yields at temperatures higher than 800°C were assumed to be the same as that at 800°C. It is noted that even at 1000°C, the majority of coal nitrogen (>55%) remained in the chars. The proportion of coal nitrogen in char decreased monotonically with increasing temperature. Nitrogen in tar comprised only a small part of the coal nitrogen. There was a significant deficit in the nitrogen balance that amounted to some 17%. Possible reasons for this deficit are discussed later in this paper.

Data in Fig. 4 for the Göttelborn bituminous coal show similar trends to those in Fig. 3. The caking properties of the bituminous coals have resulted in

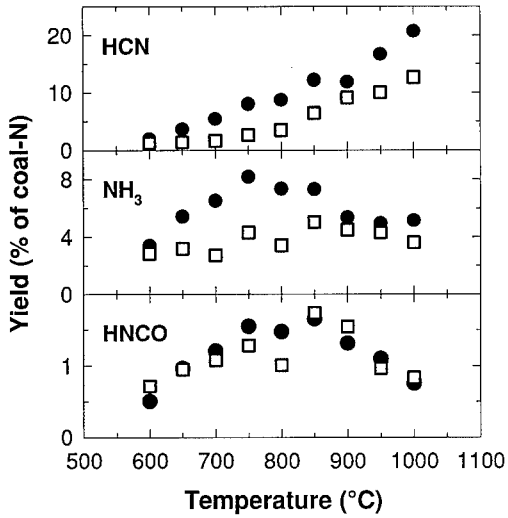

FIG. 5. Comparison of HCN, NH_3, and HNCO yields from the pyrolysis of an Australian bituminous coal (coal D) in the single-stage (●) and two-stage (□) reactors as a function of temperature.

the agglomeration of coal/char particles with the zircon sand during pyrolysis. Only a small portion of char was collected in the thimble and the majority of char was retained and heated in the bed until the termination of the experiment. The time-temperature history of this part of char was unknown. Analysis of the char collected in the thimble was therefore deemed to be unrepresentative of the whole char. Comparison of the data in Figs. 3 and 4 suggests that the proportion of coal nitrogen in tars increased considerably from the brown coal to the bituminous coal. This finding was further confirmed with other coals of similar ranks.

Data in Figs. 3 and 4 also show that the nitrogen in tars would not be enough to account for the increase in HCN and NH_3 yields at higher temperatures. Even in the case of the bituminous coals (e.g., Göttelborn in Fig. 4), the maximum amount of nitrogen in tars accounts for only about 17% of the coal nitrogen, whereas nitrogen in HCN and NH_3 at 1000°C is more than 25% of coal nitrogen. Considering that the HCN yields still tend to increase with temperature beyond 1050°C (the upper limit used in the present study), it is fair to conclude that part of HCN and NH_3 must have come from the thermal decomposition of chars. Further experiments were then carried out in the two-stage reactor to confirm and quantify experimentally the contributions of the thermal decomposition of tars and chars to the observed HCN and NH_3 yields.

Figure 5 compares the HCN, NH_3, and HNCO yields from the pyrolysis of an Australian bituminous coal (coal D) in the single-stage and two-stage reactors. The data clearly show that the thermal cracking of volatiles (mainly tars) alone in the second stage did not produce the same amount of HCN as the pyrolysis of coal in the single-stage reactor at the same temperatures. The production of HCN from the thermal decomposition of tar was negligible at temperatures lower than 750°C. The difference in HCN yield from the pyrolysis in the two reactors seems to increase with increasing temperature: about 8% more of coal nitrogen was released as HCN in the one-stage reactor than in the two-stage reactor at 1000°C. It is fair to conclude that char thermal decomposition is an important route for HCN formation.

The production of NH_3 from the thermal decomposition of tars in the second stage was observed to be not more than 2.5% of coal nitrogen. In fact, there is very little change in the NH_3 yield in the second stage over that which is produced in the first stage. Hence, it appears that the NH_3 observed during pyrolysis in the single-stage reactor derives mainly from primary coal pyrolysis and secondary decomposition of the chars.

No significant difference in the HNCO yields from the pyrolysis experiments in the two reactors was observed. This indicated that the majority of HNCO was formed from the thermal decomposition of tars.

Discussion

As discussed in the introduction, the rate and overall amounts of coal N released to the gas phase are very important in NO_x formation. The results in Fig. 2 clearly show that the yields of HCN are a function of coal rank and decrease significantly for coals of higher rank (and of low volatility). At first glance, this would seem to be related directly to the lower volatile yields from these coals, and, as a consequence, to imply that thermal cracking reactions of the tars are the source of the volatile N species. Close consideration of the data presented, however, suggests that this picture is too simplistic.

While it seems clear that tar cracking is an important source of HCN based on the results obtained with the two-stage reactor, it is also clear that it is not the only source. There is simply insufficient N present in the tars to account for the HCN produced. In fact, the data in Fig. 5 suggest that thermal cracking of tars at temperatures lower than 700°C produced negligible amounts of HCN and NH_3. The production of HCN from tar alone (Fig. 5) became significant only at temperatures higher than 800°C. This is in agreement with the data shown in Figs. 3 and 4, where nitrogen distributions in tars remained almost unchanged up to this temperature. Experiments to be reported elsewhere, however, suggested that, as the temperature was raised to 900°C,

DCM-soluble tar yields decreased to one-fourth or one-half of their maxima for Fortuna and Göttelborn, respectively. Taken together, these findings would appear to indicate that the thermal cracking reactions of tars at lower temperatures (e.g., <800°C) to gases or soot did not result in the release of tar nitrogen and that the nitrogen in tar in fact was very stable up to about 850°C. This is probably a consequence of the nature of the cracking reactions at these low temperatures, which tend to decompose the more labile aliphatic groups and do not result in decomposition of the aromatic or heterocyclic structures. Hence, primary coal pyrolysis and/or further decomposition of chars are important sources of HCN and NH_3 formation, even at relatively low temperatures (e.g., <800°C).

If the lower-volatile yield is not solely responsible for the decrease in N release as a function of increasing coal rank (Fig. 2), other factors need to be considered. It seems likely that the size (extent of condensation of rings) of the nitrogen-containing heteroaromatic ring systems is an important factor governing the nitrogen release during pyrolysis. It is generally agreed that the sizes of aromatic ring systems in coal tend to increase with increasing rank. It has been shown [20] that aromatic (also including heteroaromatic) ring system distributions ultimately govern the thermal decomposition of the coal macromolecular network. The coordination number was shown to increase as the size of the aromatic ring system increases, making the macromolecular network more difficult to decompose [20]. Moreover, the increases in the size of aromatic or heteroaromatic ring systems would tend to stabilize the ring systems.

The nitrogen in higher rank coals is more likely to be in larger heteroaromatic ring systems, making the ring systems difficult to be released from the coal and also difficult to be ruptured even at high temperatures (Fig. 2). Even though the nitrogen might be in pyrolic form, if the ring system containing the nitrogen is large, the ring system would be likely to have a high coordination number and therefore difficult to be released from the network. The large size of the ring system also implies that the ring system is stable, possibly making it more difficult to be ruptured than a smaller ring system containing pyridinic nitrogen. The HCN and NH_3 formed during pyrolysis at lower temperatures (<700°C) are thought to have their origin in the small nitrogen-containing ring systems in coal. These smaller ring systems are relatively easily ruptured compared to the corresponding larger ones.

The data in Fig. 1 showed that the HCN production covered a wide range of temperature, and it would be expected that more HCN production is likely at temperatures higher than the upper limit in the present study. Previous experimental data [2,21] have shown that HCN production continued at temperatures higher than 1200°C until the total release of coal nitrogen was observed. The observation that the production of gas-phase nitrogen-containing species (e.g., HCN) covers an extremely wide range of temperature is thought to reflect the fact that the nitrogen in coal is distributed in ring systems of a wide range of sizes.

Ammonia formation has created considerable discussion in studies of the nitrogen distribution during coal pyrolysis. Since nitrogen exists in coal as heteroaromatics, the formation of NH_3 requires the hydrogenation of nitrogen. Model compound studies [11,12] of the pyrolysis of N-containing aromatics do not result in NH_3 formation.

Various mechanisms have been proposed for the formation of ammonia. For example, Baumann and Möller [7] have suggested gas-phase HCN hydrogenation to form NH_3. Similarly, it has been suggested [10,19] that HCN may be hydrogenated on the coal/char surface to form NH_3. The observation of HNCO in the pyrolysis products is also interesting in the context of NH_3 formation from the pyrolysis of coals. Isocyanic acid readily hydrolyzes [18] on alumina surfaces to yield NH_3 and CO_2 and such surface catalyzed reactions within the coal particle are possible during coal pyrolysis. The failure to detect HNCO from brown coals is consistent with this mechanism since these coals have much higher moisture contents.

The dependence of ammonia yields on reactor types [10,19] and particle sizes [19] supports the contention that NH_3 is largely a secondary product of the decomposition of coals and arises from interactions of other N-containing precursors with the coal surface. Given the weight of the experimental evidence supporting this conclusion, it is surprising that some attempts [14] have been made to link NH_3 formation with specific functional groups in the coal and to derive a predictive NO_x formation index based on the functional forms of N in coals. Based on the results of the present study and of previous work, we would contend that nitrogen-containing species produced during coal pyrolysis are very reactive and interconversion between them is more than possible. The extent of this interconversion depends to a great extent on reactor configuration and other experimental parameters, and hence any attempts to account for the formation of particular products from the decomposition of specific functional groups is highly problematic.

The deficit in the N balance observed at high temperatures with the brown coal (Fig. 3) is possibly due to the formation of N_2 gas. Previous work [22] has shown that significant amounts of N_2 can be produced from Australian brown coals pyrolyzed in a thermobalance.

Conclusions

1. Nitrogen distributions during coal pyrolysis, especially HCN and NH_3 yields, were found to

change with coal rank, with the low-volatile coals giving lower HCN and NH_3 yields than the high-volatile coals.

2. Tar cracking and coal nitrogen functionality alone were found to be insufficient to predict the nitrogen distribution during pyrolysis.
3. Primary coal pyrolysis and/or further thermal decomposition of chars are major sources of HCN formation, even at temperatures lower than about 800°C. The importance of tar cracking reactions for the nitrogen distribution in the gas phase increases from brown coals to high-volatile bituminous coals.
4. Tar cracking does not appear to be an important source for ammonia formation. Hydrolysis of HNCO within the coal particle is a plausible source for NH_3 formation, but reactions of other N-containing precursors are probably also involved.
5. While the formation mechanisms for HNCO remain uncertain, tar cracking reactions seem mainly responsible for the observed HNCO yields.
6. Sizes of the nitrogen-containing heteroaromatic ring systems are another important factor governing the nitrogen distribution during pyrolysis. Nitrogen in coal is believed to exist in heteroaromatic ring systems of a wide range of sizes resulting in the nitrogen release from coal covering an extremely wide range of temperatures.

Acknowledgments

The award of a Rothmans Foundation Fellowship to one of us (C.-Z. Li) is gratefully acknowledged.

REFERENCES

1. Nelson, P. F., Buckley, A. N., and Kelly, M. D., *Twenty-Fourth Symposium (International) on Combustion,* The Combustion Institute, Pittsburgh, 1992, pp. 1259–1267.
2. Kambara, S., Takarada, T., Yamamoto, Y., and Kato, K., *Energy Fuels* 7:1013–1020 (1993).
3. Kelemen, S. R., Gorbaty, M. L., and Kwiatek, P. J., *Energy Fuels* 8:896–906 (1994).
4. Wójtowicz, M. A., Pels, J. R., and Moulijn, J. A. *Fuel* 74:507–516 (1995).
5. Buckley, A. N., Kelly, M. D., Nelson, P. F., and Riley, K. W., *Fuel Processing Technol.* 43:47–60 (1995).
6. Mitra-Kirthley, S. M., Mullins, O. C., van Elp, J., and Cramer, S. P., *Fuel* 72:133–135 (1993).
7. Baumann, H. and Möller, P., *Erdöl Erdgas Kohle* 44:29–33 (1991).
8. Nelson, P. F., Kelly, M. D., and Wornat, M. J. *Fuel* 70:403–407 (1991).
9. Chen, J. C. and Niksa, S., *Twenty-Fourth Symposium (International) on Combustion,* The Combustion Institute, Pittsburgh, 1992, pp. 1269–1276.
10. Bassilakis, R., Zhao, Y., Solomon, P. R., and Serio, M. A., *Energy Fuels* 7:710 (1993).
11. Mackie, J. C., Colket, M. B. III, and Nelson, P. F., *J. Phys. Chem.* 94:4099–4106 (1990).
12. Mackie, J. C., Colket, M. B. III, Nelson, P. F., and Esler, M., *Intl. J. Chem. Kinet.* 23:733–760 (1991).
13. Li, C.-Z. and Nelson, P. F., *Fuel,* in press.
14. Kambara, S., Takarada, T., Toyoshima, M., and Kato, K., *Fuel* 74:1247–1253 (1995).
15. Niksa, S., *Twenty-Fifth Symposium (International) on Combustion,* The Combustion Institute, Pittsburgh, 1994, pp. 537–544.
16. Tyler, R. J., *Fuel* 58:680–686 (1979).
17. Nelson, P. F., Li, C.-Z., and Ledesma, E., *Energy Fuels* 10:264–265 (1995).
18. Dümpelmann, R., Cant, N. W., and Trimm, D. L., *Appl. Catal. B: Environ.* 6:291–296 (1995).
19. Wójtowicz, M. A., Zhao, Y., Serio, M. A., Bassilakis, R., Solomon, P. R., and Nelson, P. F., *Proc. 8th Intl. Conf. Coal Sci.,* Vol. I, Elsevier, 1995, pp. 771–774.
20. Li, C.-Z., Wu, F., Xu, B., and Kandiyoti, R., *Fuel* 74:37–45 (1995).
21. Pohl, J. H. and Sarofim, A. F., *Sixteenth Symposium (International) on Combustion,* The Combustion Institute, Pittsburgh, 1976, pp. 491–501.
22. Phong-Anant, D., Wibberley, L. J., and Wall, T. F., *Combust. Flame* 62:21–30 (1985).

Twenty-Sixth Symposium (International) on Combustion/The Combustion Institute, 1996/pp. 3213–3221

FUNDAMENTAL STUDY ON N_2O FORMATION/DECOMPOSITION CHARACTERISTICS BY MEANS OF LOW-TEMPERATURE PULVERIZED COAL COMBUSTION

ICHIRO NARUSE, YASUYUKI YAMAMOTO, YOSHIFUMI ITOH AND KAZUTOMO OHTAKE
Department of Ecological Engineering, Toyohashi University of Technology
Tempaku-cho, Toyohashi 441, Japan

N_2O formation/decomposition characteristics and its mechanisms in pulverized coal combustion, especially at low temperature, are discussed by using a one-dimensional electrically heated laminar drop furnace for various coal types. The behavior of nitrogen compounds along the furnace axis is studied by analyzing both the sampled burning particles and combustion gas and by calculating the mass balance of nitrogen. Additionally, the effects of the combustion efficiency and the ratio of fixed carbon to volatile matter content (fuel ratio) on N_2O formation/decomposition characteristics are elucidated experimentally.

As a result, coals that evolve more HCN than NH_3 produce higher N_2O concentration. In the downstream region beyond the point where volatile matter combustion is complete, N_2O concentration increases but NO concentration decreases gradually. Increase of N_2O in this region may be caused not only by the reactions between NO and carbon in char (NO + char-C $\rightarrow$ NCO and NCO + NO $\rightarrow$ N_2O + CO) but also by the direct heterogeneous reaction between nitrogen in char and NO (char-N + NO $\rightarrow$ N_2O). For the coals with low fuel ratio, N_2O conversion decreases because of high flame temperature surrounding the coal particles caused by strong volatile matter combustion. The decomposition reaction of N_2O by H radicals produced by the oxidation reaction of CO by OH radicals also contributes near the particle surface. Thereafter, the combustion atmosphere and temperature surrounding the coal particles affects N_2O formation/decomposition characteristics. The exit N_2O concentration increases with decreasing combustion efficiency and decreasing fuel ratio. Data from testing nine different types of coal show that the exit N_2O concentration has a good correlation with the combustion efficiency and the fuel ratio.

Introduction

Recently, N_2O has been identified as one of the pollutants contributing to the global greenhouse effect and one of the trigger species for the chemical destruction of stratospheric ozone layer [1,2]. Most N_2O is considered to be formed from the agricultural activities and natural ecological cycles. The exhaust gas released from coal combustors can be seen as one of the alternate sources of N_2O production. In general, the characteristics of N_2O formation depend on the types of combustors and their operating conditions, especially the combustion temperature.

The study on N_2O formation/decomposition has been reported by using pulverized and bubbling/circulating fluidized bed coal combustors [3–15]. In summarizing the previous results, it was found that only low concentrations (<10 ppm) [13–15] of N_2O are released from the high-temperature pulverized coal combustors. In the bubbling/circulating fluidized bed coal combustion, on the other hand, relatively higher N_2O concentrations are detected (50–200 ppm) [13–15].

Our previous report [16] studied the characteristics of N_2O formation/decomposition experimentally and theoretically under high-temperature pulverized coal combustion conditions. The experimental results show that N_2O is formed mainly during the initial stage of volatile matter combustion, but that it reaches lower concentrations at the exit of the furnace. The maximum N_2O concentration for different types of coal depends on particle temperature, increasing rate of particle temperature, content of volatile matter, and flame structure formed around coal particles. It is elucidated by chemical kinetic analysis of the combustion that N_2O is produced mainly by way of the oxidation reactions of both HCN and NH_3, but that it is decomposed by H radicals that are produced by CO oxidation by OH radicals. In a later study [17] at lower combustion temperatures, the N_2O formation/decomposition characteristics have been discussed using data from a lab-scale bubbling fluidized bed coal combustor and from numerically simulating volatile matter combustion. This study finds that N_2O concentration increases when decreasing the bed temperature and increasing the excess air ratio, in agreement with other work [18,19]. N_2O seems to be formed mainly during the volatile matter combustion. HCN and NH_3, evolved as volatile-N species, contribute strongly to N_2O formation. Indeed, HCN contributes more to N_2O formation than does NH_3.

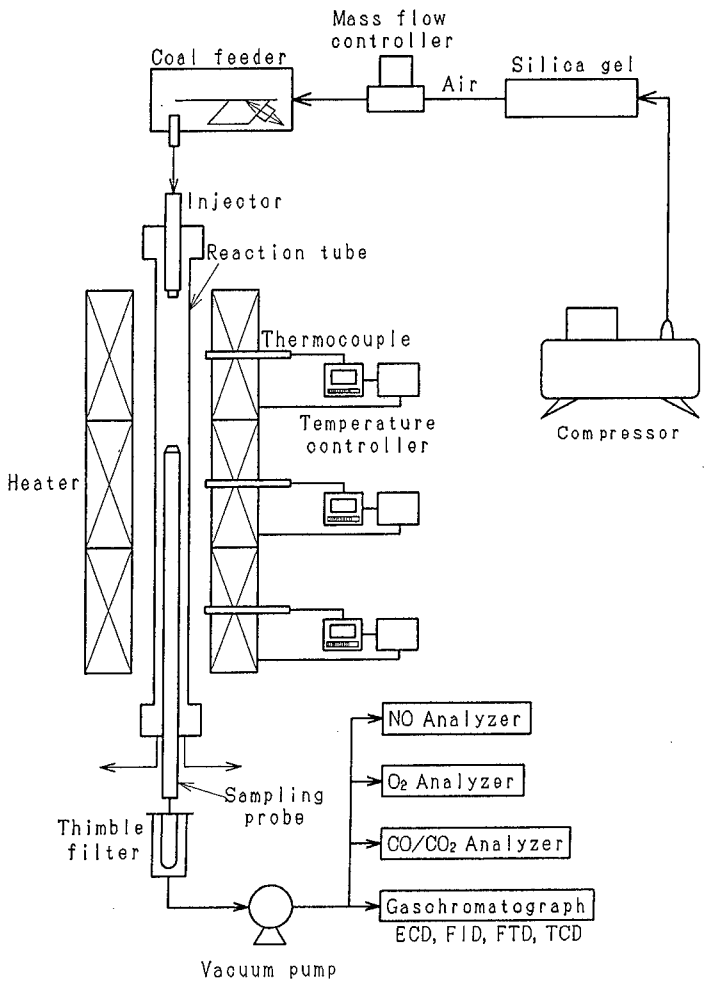

FIG. 1. Schematic diagram of electrically heated laminar flow pulverized coal furnace.

Under bubbling/circulating fluidized bed coal combustion conditions, however, there exist many kinds of particle-like fluidizing material, desulfurizer, char, ash, raw coal, and so on. Especially the desulfurizer and char among these particles are known to decompose N_2O catalytically. Therefore, it seems difficult to discuss in detail the characteristics of N_2O formation/decomposition by using bubbling/circulating fluidized bed combustors. Additionally, in the previous studies, N_2O formation/decomposition characteristics were discussed only in terms of only the change of gas species concentrations.

In the present paper, the N_2O formation/decomposition characteristics under the low-temperature pulverized coal combustion conditions are studied by using an electrically heated one-dimensional laminar drop furnace. The combustion experiments are carried out by burning nine different kinds of coal with different fuel ratios (the content ratio of fixed carbon to volatile matter) and N contents. This experimental situation can prevent the catalytic effect on N_2O decomposition since only burning coal particles exist in the furnace. From analysis of the data obtained by sampling the burning particles and the combustion gas along the furnace axis, the mass balance of nitrogen is calculated. Finally, the significant parameters to promote N_2O formation are explained by the demonstrated changes of gas species concentration and compositions of burning particles.

Experimental Apparatus and Procedures

Figure 1 shows a schematic diagram of electrically heated one-dimensional laminar drop furnace, in which the heating length is 1.3 m. The reaction tube of 41.5-mm–inner diameter made of quartz is used to prevent the catalytic decomposition reaction of

TABLE 1
Experimental conditions of combustion

Coal feed rate	0.62–0.79 $g \cdot min^{-1}$
Air flow rate	6.0×10^{-3} $m^3 \cdot min^{-1}$
Air ratio	1.1–1.2
Heat load	320 W
Furnace temp.	1073 K

N_2O by the tube wall surface. We also checked experimentally that catalytic effects of the reactor wall on N_2O formation/decomposition was minor under this temperature range. The furnace wall temperature is controlled by three sets of temperature controllers with thyristor regulators. Coal particles are fed into the tube by using a vibration microfeeder. Both combustion gas and burning particles are sampled by a water-cooled sampling probe at the tip of which an inert gas is injected to prevent the additional chemical reactions from changing the composition through the sampling tube. After that, the particles are separated by a thimble filter. The sampled gas is introduced directly into several gas analyzers. Gas species concentrations of NO, O_2, CO, and CO_2 are measured continuously by the respective chemiluminescence, paramagnetic and infrared analyzers, and HCN, NH_3, and N_2O concentrations are detected by FTD (flame thermionic detector) and ECD (electron capture detector) gas chromatographs, respectively. On the other hand, proximate and ultimate analyses of the burning particles are carried out by a thermobalance and a C-H-N analyzer, respectively. Table 1 summarizes the experimental conditions in which the furnace temperature is fixed at 1073 K. Table 2 shows the properties of tested coals. In this table, air ratio refers to the ratio of (air/fuel) to that at stoichiometric mixture. All the tested coals are sifted to select particles in the diameter range of 53–105 μm.

Experimental Results and Discussion

Formation Characteristics of Nitrogen Compounds under Low-Temperature Pulverized Coal Combustion Condition

In this section, the results for TH coal are compared with those for NL coal as an example, since the nitrogen compounds in volatile matter evolved from TH coal differ from those from NL coal as mentioned later. Figures 2 and 3 show the results of (a) the change of gas species concentration in the combustion gas, (b) the residual fraction of both volatile matter and fixed carbon contents in the burning particles, and (c) the residual fraction of carbon, hydrogen, and nitrogen contents in the char along the furnace axis for TH and NL coals, respectively.

From Fig. 2a, NH_3 concentration becomes much higher than HCN, especially just after the injector. When NH_3 concentration decreases in the ignition region, N_2O concentration increases at once. As seen from Fig. 2b, this increase correlates with a dramatic decrease in volatile matter and, hence, is thought to be caused by combustion of volatile matter. After that, N_2O concentration decreases with decreasing CO concentration since N_2O is decomposed by H radicals by way of the following reactions:

$$CO + OH \rightarrow CO_2 + H$$

$$N_2O + H \rightarrow N_2 + OH$$

In the downstream beyond about 300 mm, N_2O concentration increases again in accordance with the

TABLE 2
Properties of tested coals

Coal	Rank	Proximate analysis [mass %, dry] Volatile matter	Fixed carbon	Ash	Fuel ratio [−]	Ultimate analysis [mass %, daf] H	C	N	Higher heat value [$MJ \cdot kg^{-1}$]	Crucible swelling number
TH	Lignite	44.1	45.4	10.4	1.03	6.14	74.76	1.28	26.0	0
EN	Subbituminous	38.3	49.7	12.0	1.30	5.97	79.78	1.47	27.8	1
WB	Bituminous	32.4	58.2	9.5	1.79	5.38	80.53	1.92	28.9	1
WW	Bituminous	31.2	59.2	9.6	1.90	5.31	81.75	1.85	29.5	1
DD	Bituminous	30.5	63.0	6.5	2.06	4.69	78.29	0.95	29.7	1
NL	Bituminous	28.1	60.3	11.6	2.15	5.02	81.31	1.67	28.0	0
FD	Semianthracite	21.2	67.4	11.4	3.18	4.91	87.39	1.30	29.7	1
JE	Semianthracite	18.9	69.3	11.8	3.66	4.64	87.36	1.64	30.7	1
MT	Semianthracite	11.1	72.0	16.9	6.50	3.98	88.66	2.19	27.5	0

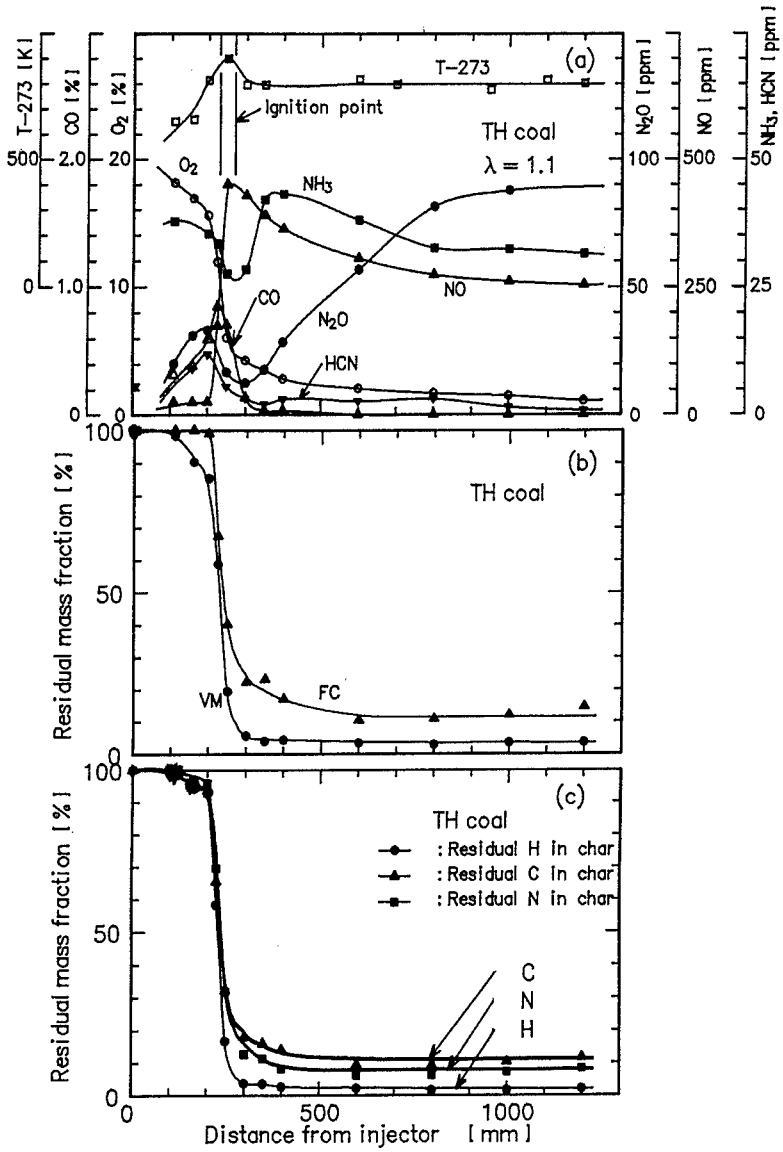

FIG. 2. Changes of (a) gas species concentration and temperature, (b) residual fraction of volatile matter and fixed carbon contents, and (c) residual fraction of C, H, and N contents along the axis of the furnace (TH coal).

decrease of NO concentration. As shown in Fig. 2c, there appears to be no change in the residual fraction of nitrogen element contained in the char particles in this region. This result suggests that the increase of N_2O concentration may be caused by the conversion reactions from NO to N_2O, as described later.

For NL coal, on the other hand, only HCN is detected as the nitrogen constituent from volatile matter, as shown in Fig. 3a. This is a major difference from what was found with the TH coal. HCN is formed rapidly in the ignition region. After that, NO and N_2O are produced at the same time as the HCN concentration plateaus. In the downstream, N_2O concentration increases with decreasing NO concentration. The tendency of NL coal there is similar to that of TH coal. As shown in Fig. 3c, the mass fraction of residual nitrogen in char particles is much higher than that of TH coal but still decreases during the course of combustion. The decreasing rate of NO concentration is also faster. This result means that the char-N contributes to the N_2O formation.

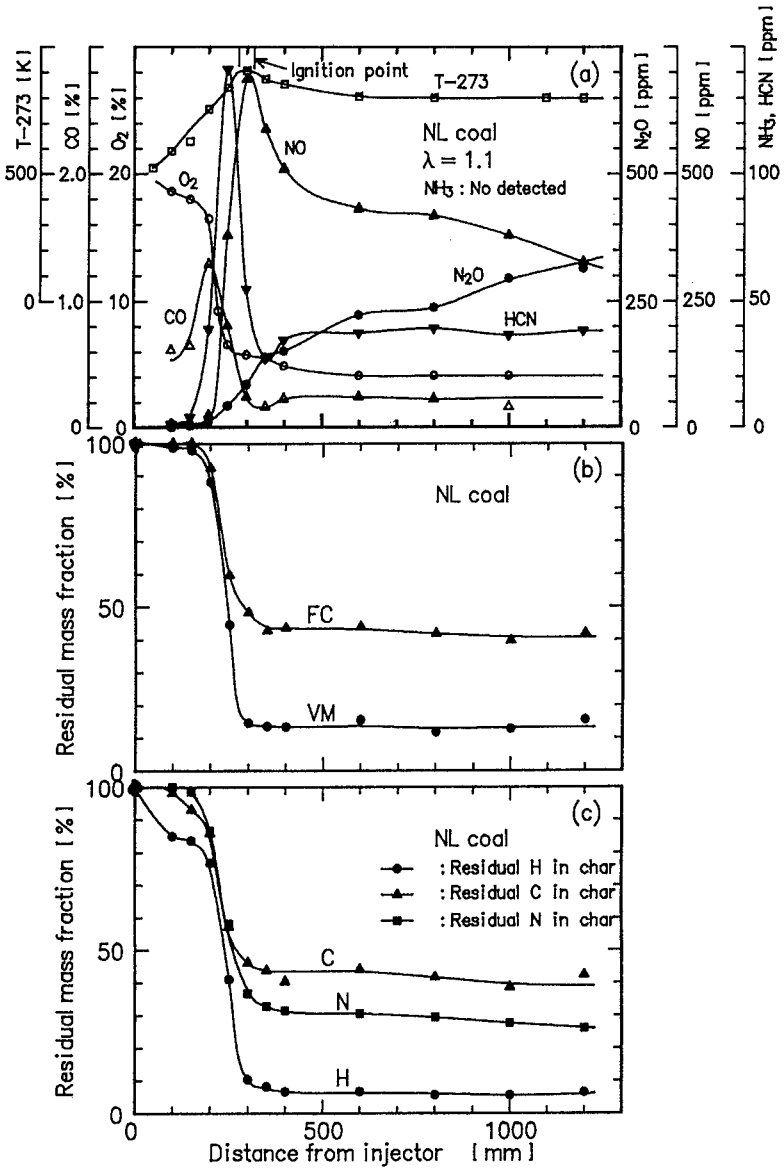

FIG. 3. Changes of (a) gas species concentration and temperature, (b) residual fraction of volatile matter and fixed carbon contents, and (c) residual fraction of C, H, and N contents along the axis of the furnace (NL coal).

N_2O concentration at the furnace exit attains 450 ppm, the value of which is about 4.5 times as much as that of TH coal. The previously mentioned result suggests that N_2O is formed easily by way of the following reactions related to HCN rather than NH_3:

$$HCN + O \rightarrow NCO + H$$

$$NCO + NO \rightarrow N_2O + CO$$

$$NH_3 + OH \rightarrow NH_2 + H_2O$$

$$NH_2 + OH \rightarrow NH + H_2O$$

$$NH + NO \rightarrow N_2O + H$$

These reaction schemes agree well with the simulated results obtained by the simulation of combustion of volatile matter under the conditions of bubbling fluidized bed coal combustion [17].

N_2O Formation Mechanisms after Volatile Matter Combustion

De Soete [20], Feng et al. [21], and Illan-Gomez et al. [22] studied the N_2O formation from char com-

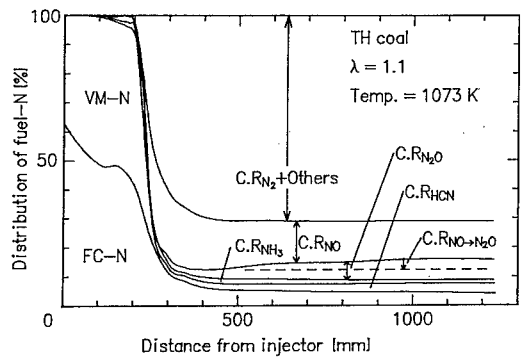

FIG. 4. Distribution of conversion of fuel-N (TH coal).

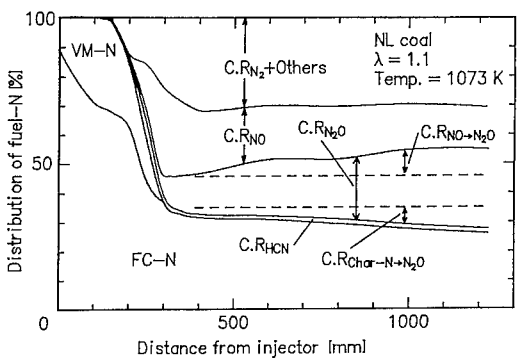

FIG. 5. Distribution of conversion of fuel-N (NL coal).

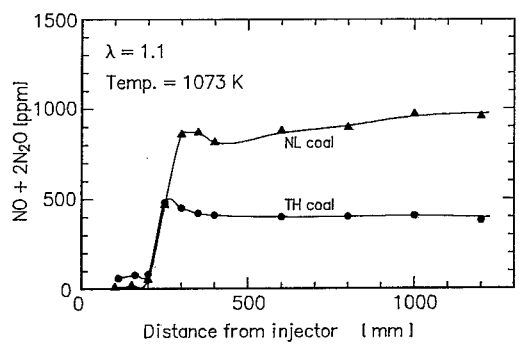

FIG. 6. Change in combined NO and twice of N_2O concentrations with reaction distance.

bustion. In their papers, a packed bed reactor of char particles was used in the experiments. Mochizuki et al. [23] and Krammer et al. [24], on the other hand, reported the resembled study as previously mentioned by using fluidized bed combustors. The data they obtained resulted in both N_2O formation and N_2O decomposition by char particles. Only the results of produced gas species concentration were discussed.

From this viewpoint, not only the gas species concentration but also the residual fraction of C, H, and N elements in the burning particles were analyzed in this study. Therefore, the nitrogen mass balance can be obtained from both gas- and solid-phase information relating to such nitrogen compounds as HCN, NH_3, NO, N_2O, and char-N. Figures 4 and 5 show the nitrogen molar fraction contained in gas and solid phases along the furnace axis, corresponding to Figs. 2 and 3, respectively. In both figures, $C.R_i$ (i: gas species) indicates the conversion ratio from fuel N to species i based on nitrogen atom, and $C.R_{NO\rightarrow N_2O}$ shows the conversion ratio from NO to N_2O. As seen in Fig. 4, $C.R_i$ for TH coal, except $C.R_{NO}$ and $C.R_{N_2O}$, becomes almost constant in the downstream region beyond 500 mm. This result suggests that the increase of N_2O is caused by the change of NO ($C.R_{NO\rightarrow N_2O}$). In Fig. 5, on the other hand, the increase of N_2O is attained by the change of NO and the oxidation reaction of char-N.

Figure 6 shows the total sum of nitrogen element in NO and N_2O along the furnace axis, based on Figs. 4 and 5. In this figure, the value of N_2O is corrected by doubling the N_2O concentration to identify both values as the nitrogen element basis. This figure indicates that the value of ($NO + 2N_2O$) becomes almost constant in the downstream beyond 400 mm for TH coal. Accordingly, it is seen that twice the increment of N_2O is equal to the decrement of NO. For NL coal, on the other hand, the value of ($NO + 2N_2O$) increases gradually in the downstream beyond 400 mm. This result suggests that both the direct conversion of NO to N_2O and the reaction of char-N to form N_2O proceed simultaneously.

Summarizing the preceding discussion, N_2O after volatile matter combustion may be formed in two ways: firstly, through heterogeneous and homogeneous reactions as

$$\text{NO} + \text{char-C} \rightarrow \text{NCO}$$

$$\text{NCO} + \text{NO} \rightarrow \text{N}_2\text{O} + \text{CO}$$

This reaction scheme is the alternate route to N_2O. Secondly, by direct heterogeneous reaction [16,17,25],

$$\text{NO} + \text{char-N} \rightarrow \text{N}_2\text{O}$$

Also noteworthy is the observation that in the riser section of a circulating fluidized bed coal combustor, the N_2O concentration increases along the furnace axis but the variation of NO concentration tends to be the reverse of that of N_2O. This result is called a "trade-off relationship" in N_2O and NO. It can be well explained by the previously proposed reaction scheme.

Influence of Coal Properties on N_2O Formation

Figure 7 shows the relation between the N_2O conversion and the combustion efficiency at the furnace

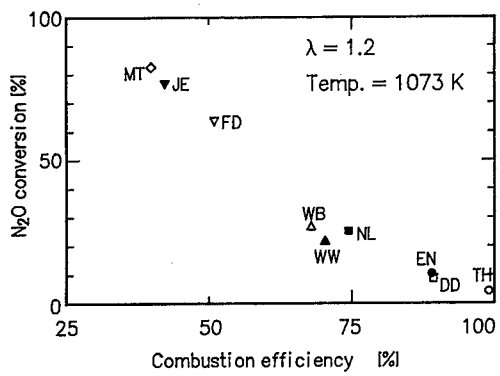

FIG. 7. Relation between combustion efficiency and N_2O conversion.

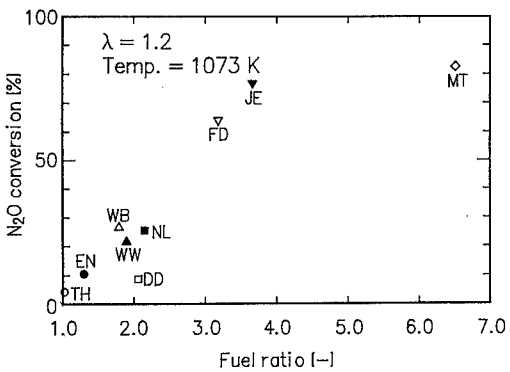

FIG. 8. Relation between fuel ratio and N_2O conversion.

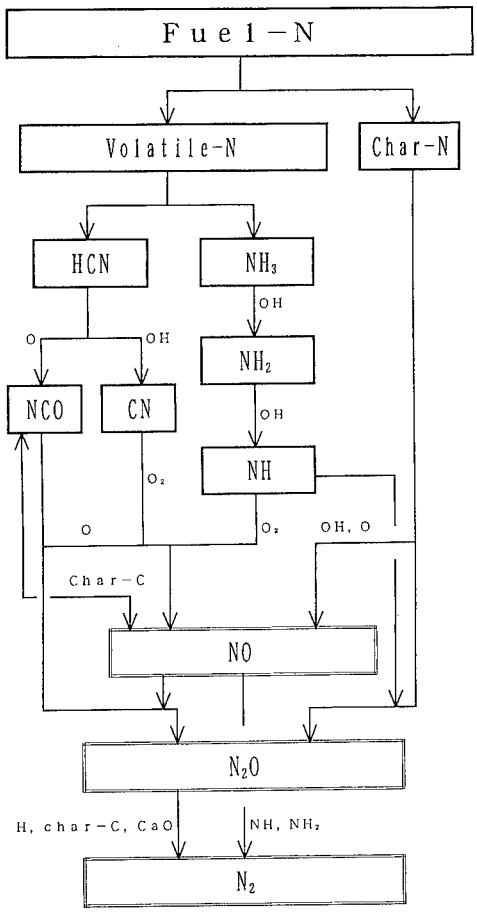

FIG. 9. Reaction schemes of N_2O formation/decomposition.

exit obtained by burning nine different types of coal. The N_2O conversion is evaluated as the total fuel nitrogen basis. This figure depicts decreasing N_2O conversion with increasing combustion efficiency. Rearranging the results of Fig. 7 as a function of fuel ratio, Fig. 8 shows that the N_2O conversion increases with increasing fuel ratio. As a general tendency, the higher combustion efficiency is attained by using coal of lower fuel ratio. These two figures show that this behavior correlates with N_2O concentration.

When coals with high combustibility such as TH coal are burned, the combustion atmosphere surrounding the coal particles exhibits high-temperature reducing conditions in which N_2O is easily decomposed. For coals of low combustibility such as MT coal, however, the atmosphere surrounding the coal particles corresponds to lower-temperature oxidizing conditions since the evolution of volatile matter is limited. Therefore, N_2O formation is favored. Behaviors of combustion and N_2O formation for MT coal are similar to those for NL coal.

Reaction Paths of N_2O Formation/Decomposition

Figure 9 summarizes the main N_2O formation/decomposition schemes in coal combustion under the low-temperature condition. The sources of N_2O are divided into volatile-N and char-N. HCN and/or NH_3 are the main constituents evolved from the nitrogen compounds in volatile matter. N_2O is formed by the oxidation reaction of HCN and NH_3 by way of NCO and NH radicals, respectively. After the volatile matter is almost consumed, N_2O is homogeneously produced subsequent to the heterogeneous reaction of NO with char-C. Further, the char-N also contributes to forming N_2O by the heterogeneous direct reaction with NO. With respect to the N_2O decomposition, on the other hand, H radicals play the important role in homogeneous decomposition of N_2O. Additionally, such particles as char and CaO also decompose N_2O catalytically as shown elsewhere [26].

Conclusions

N_2O formation/decomposition characteristics in pulverized coal combustion at low temperatures

have been studied by using a one-dimensional electrically heated laminar drop furnace for various types of coal. The behavior of nitrogen compounds has been determined by the mass balance of nitrogen included in both the sampled burning particles and combustion gas.

The experimental results are summarized as follows:

1. Coals that evolve more HCN than NH_3 produce more N_2O.
2. N_2O formation in the downstream region beyond the volatile matter combustion is caused by not only the reaction triggered by the heterogeneous reaction of NO and carbon in char (NO + char-C $\rightarrow$ NCO to lead to NCO + NO $\rightarrow$ N_2O + CO) but also the direct reaction between nitrogen in char and NO (char-N + NO $\rightarrow$ N_2O).
3. For coals with a low fuel ratio, the N_2O conversion decreases because of high flame temperature surrounding the coal particles caused by strong volatile matter combustion. Additionally, the H radicals produced by the oxidation reaction of CO also contribute to decomposing N_2O near the particle surface.
4. The exit N_2O concentration increases with the decrease of combustion efficiency; this is generally observed for burning coals with a higher fuel ratio.

REFERENCES

1. Ibusuki, T., *Nenryo Kyokai-shi* 68(3):190–199 (1989).
2. Levine, J. S., *Proc. of the 5th Intl. Workshop on Nitrous Oxide Emissions,* 1992, pp. 1–10.
3. Aho, M. and Rantanen, J. T., *Fuel* 68:586–590 (1989).
4. Amand, L. E. and Leckner B., *Combust. Flame* 84:181–190 (1991).
5. Kramlich, J. C., Cole, J. A., McCarthy, J. M., and Laniar, W. S., *Combust. Flame* 77:375–384 (1989).
6. Linak, W. P., U.S. Environmental Protection Agency, Report, EPA-600/9-89-062b, 1990.
7. Aho, M. J., Rantanen, J. T. and Linna, V. L., *Fuel* 69(8):957–961 (1990).
8. Muzio, L. J., Teague, M. E., Kramlich, J. C., Cole, J. A., McCarthy, J. M., and Lyon, R. K., *JAPCA* 39:287–293 (1989).
9. Muzio, L. J., Samuelsen, G. S., Kramlich, J. C., Lyon, R. K., and Kokkinos, A., *Twenty-Third Symposium (International) on Combustion,* The Combustion Institute, Pittsburgh, 1991, pp. 245–250.
10. Smart, J. P., Roberts, P. A., and de Soete, G. G., *J. Inst. Energy* 63:131–135 (1990).
11. Suzuki, Z. and Moritomi, H., *Nenryo Kyokai-shi* 69(12):1146–1151 (1990).
12. Shimizu, T., Fujita, D., Ishizu, K., Kobayashi, S., and Inagaki, M., *Proc. of the 12th Intl. Conf. on Fluidized Bed Combustion,* 1993, pp. 611–615.
13. Mann, M. D., Collings, M. E., and Botros, P. E., *Prog. Energy Combust. Sci.* 18:447–461 (1992).
14. Kramlich, J. C. and Linak, W. P., *Prog. Energy Combust. Sci.* 20:149–202 (1994).
15. Wojtowicz, M. A., Pels, J. R., and Moulijn, J. A., *Fuel Process. Technol.* 34:1–71 (1993).
16. Yamamoto, Y., Itoh, Y., Yuan, J.-W., Naruse, I., and Ohtake, K., *Trans. Japan Soc. Mech. Eng. B* 59(564):2560–2567 (1993).
17. Naruse, I., Imanari, M., Koizumi, K., Yuan, J.-W., and Ohtake, K., *Kagaku-Kogaku Ronbunshu* 20(2):178–185 (1994).
18. Hayhurst, A. N. and Lawrence, A. D., *Prog. Energy Combust. Sci.* 18:529–552 (1992).
19. Young, B. C., Mann, M. D., and Collings, M. E., *Processing and Utilization of High Sulfur Coals V,* Elsevier, Amsterdam, 1993, pp. 419–436.
20. de Soete, G. G., *Twenty-Third Symposium (International) on Combustion,* The Combustion Institute, Pittsburgh, 1990, pp. 1257–1264.
21. Feng, B., Liu, H., Yuan, J.-W., Lin, Z.-J., and Liu, D.-C., *Energy Fuels* 10:203–208 (1996).
22. Illan-Gomez, M. J., Linares-Salano, A., Radovic, L. R., and de Lecea, C. S.-M., *Energy Fuels* 10:158–168 (1996).
23. Mochizuki, M., Koike, J., and Horio, M., *Proc. of the 5th Intl. Workshop on Nitrous Oxide Emission,* 1993, pp. 237–244.
24. Krammer, G. F. and Sarofim, A. F., *Combust. Flame* 97:118–124 (1994).
25. Kuramoto, K., Koizumi, K., Imanari, M., Naruse, I., and Ohtake, K., *Kagaku-Kogaku Ronbunshu* 20(4):482–488 (1994).
26. Naruse, I., Yamamoto, Y., Imanari, M., Yuan, J.-W., and Ohtake, K., *Twenty-Fourth Symposium (International) on Combustion,* 1992, pp. 1415–1420.

COMMENTS

Pia Kilpinen, ABO Academi University, Finland. You made your experiments at a very low temperature, 1073 K. Did you try to analyze also other cyano or cyanid species in addition to HCN? What was the method you used for NH_3 analysis?

Author's Reply. I did not analyze other cyano or cyanid species. Both HCN and NH_3 were detected by using a gas chromatograph with a flame thermionic detector.

•

A. F. Sarofim, MIT, USA. You present an impressively complete set of gas phase concentrations. I have a concern, however, that in this system you may have radial concentration distributions which may limit the role of reaction in the latter stages. The very fast volatile combustion may be due to the consumption of the oxygen in the core. This will be followed by a slower rate of reaction as oxygen diffuses in from the annulus to the fuel-rich core. Have you investigated radial concentration profiles in your reactor?

Author's Reply. I have not analyzed radial concentration profiles in the furnace. About 90% of the combustion gas was sampled, yielding mixed concentration values. No CO or hydrocarbon were observed in the exhaust in the presence of O_2, even though NH_3 and HCN were observed.

Twenty-Sixth Symposium (International) on Combustion/The Combustion Institute, 1996/pp. 3223–3230

FUNDAMENTAL EXPERIMENT ON THE COMBUSTION OF COAL–WATER MIXTURE AND MODELING OF THE PROCESS

KEIJI TAKENO, KIMISHIRO TOKUDA AND TOSHIMITSU ICHINOSE
Nagasaki Research and Development Center
Mitsubishi Heavy Industries, Ltd.

SHOZO KANEKO
Boiler Engineering Department
Power Systems Headquarters
Mitsubishi Heavy Industries, Ltd.

A fundamental study of the combustion process of coal-water mixtures has been performed. The surface and center temperatures and the weight change of a single droplet under combustion were measured in detail, where the water content, properties of coal, initial diameter of droplet, and external heat flux were parameters. In the experiments, an infrared intensive laser was used as the external heat source to simulate the conditions around the droplets atomized in an actual furnace.

Based on the data obtained, the reaction rates in the processes of water vaporization, devolatilization, and char combustion were formulated. For the devolatilization stage, the activation energy derived by assuming a first-order reaction was almost the same as that for the mother coal, but the apparent frequency factor was much smaller than that for the mother coal by 1/140–1/50. For the stage of char combustion, also, the apparent frequency factor was much smaller. The specific surface area and the micropores in the coal particle were much reduced after undergoing processes of water vaporization and devolatilization. It's possible that the pore would be masked when the water trapped in the pore was escaping from it with the agglomeration of coal particles proceeding.

According to the data obtained and the combustion model proposed here, computer simulation codes for the combustion of a single droplet and for the combustion process in a furnace were written. The calculated results for the temperature variation and the concentrations of oxygen and unburned carbon in the exhaust gas agreed well with the experimental data obtained using a one-dimensional test furnace. This confirms the validity of the combustion model and reaction data.

Introduction

Since the oil crisis in 1978, a great deal of effort has been put into converting the energy source of power plants from petroleum to coal. In particular, the use of CWM (*c*oal-*w*ater *m*ixture) is a notable subject of research [1,2], because it has advantages in storage and transportation compared to the direct use of coal.

When a furnace is designed to maintain a high combustion efficiency, for instance, the duration during which the CWM droplets sprayed from the injector stay in the furnace should be determined appropriately. Consequently, the fundamental combustion data, such as the dependence of external heat flux, surrounding temperature, and droplet diameter on the reaction rate of a single droplet should be acquired.

Gao et al. [3] measured the variations with time of weight and temperature of a single droplet under combustion and discussed the ignition phenomena and overall combustion rates using an oven whose temperature was programmed to increase to a predetermined temperature. However, since the rate of increase was limited to several tens of degrees per second, the strength of heat flux in a commercial furnace could not be realized by this experimental technique. In the other previous studies [4–7], the heat source used was much weaker than under the actual conditions. Since the reaction rate for a coal particle is known to depend on the rate of increase and final value of the temperature [8,9], the reaction of CWM droplets under strongly radiative conditions should be investigated.

It is known that when a multiphase droplet such as an oil mixture or an oil-water slurry receives a high heat flux, the flash-boiling atomization occurs easily, and it is divided into many fragments because of the difference in the boiling points of oil and water [10,11]. However, knowledge of the flash-boiling atomization of CWM droplets when receiving the heat flux corresponding to the value for a commercial

furnace (approximately $1 \sim 2 \times 10^6$ W/m^2 adjacent to the injector) seems to be insufficient [12].

In the present study, therefore, an intensive laser was used as the external heat source, and the temperature variation, weight change, composition, and velocity of the gas spouting from the droplet surface under combustion could be measured at the same time. On the basis of these data, the combustion mechanisms of a single droplet were elucidated, and the differences in the reaction rates between a coal particle and a CWM droplet discussed.

Experimental Apparatus and Procedure

A single droplet of CWM was placed on the columnar sample holder, whose top was cut spherically to match the various diameters of droplets [2]. The droplet could maintain a spherical shape on its sample holder because of surface tension. As the external heat source a YAG laser (wavelength: 1.06 μm) with 20-W maximum power was used, and the intensity and duration could be adjusted to a predetermined level. To enhance the uniformity of distribution of radiative energy on the droplet surface, the laser beam was split into two beams that were carried through optical fibers and focused on two sides of the droplet surface from opposite directions.

To measure a minute weight change of droplet, a sensitive load cell was placed under the sample holder. The diameter change of the droplet was measured using an Ar-Ne laser (wavelength: 514.5 nm) and a high-speed video camera with a narrow-band optical filter to pass the laser ray. By using this optical method, the shape of only the droplet under combustion could be caught on photo film without being disturbed by the luminous flame [13].

The temperatures at the surface and center of the droplet were measured using a narrow-band infrared radiation thermometer and a 50-μm diameter Pt/PtRh thermocouple, respectively. To investigate the combustion process, the gas velocity spouting from the droplet surface and the concentration of H_2O in its stream were measured using laser doppler velocimetry (LDV) and coherent anti-Stokes–Raman Scattering (CARS) techniques. For the theories and detailed procedure of these laser diagnostics, refer to Refs. 1, 13, and 14. In addition, to distinguish the timing of ignition and termination of flaming, the luminous flame was detected by a photodiode.

The experimental parameters and their changing ranges were chosen to be the intensity of external radiation (0.8–2.3 $\times$ 10^6 W/m^2), initial diameter (0.5–3 mm), properties of the mother coal (four kinds), and water percentage (59.4–65.1 wt. %). The properties of CWM used are summarized in Table 1. The mother coals were bituminous and the swelling indices ranged from 0 to 2.5.

Experimental Results and Discussion

Overall Combustion Process

The sequence of the combustion phenomena observed using the Ar-Ne laser and the optical filter is shown in Fig. 1. Droplets of oil mixture or oil-water slurry are usually divided into many fragments just after receiving intensive heat flux because of the differences in boiling points of the liquid components. This phenomenon is well-known as microexplosion or flash-boiling atomization [10–12]. For a droplet of CWM, however, microexplosion was not observed regardless of the intensity of external heat flux, and the droplet behaved as a single droplet throughout the combustion process. Even when the droplet was hung from a fine wire, the phenomenon was the same. As shown in Fig. 1, it was observed that the droplet was shrinking and the numerous coal particles were adhering to, or agglomerating with, each other after water vaporization.

It was clarified from much measured data similar to Fig. 2 that the combustion process could be divided into three stages, which are water vaporization, combustion of volatile matter, and combustion of char. In the present experiment, the terminal period of the water vaporization stage overlapped somewhat with the beginning of the combustion of volatile matter; that is, a light blue flame was observed enveloping the droplet while the center temperature was still at the boiling point of water [7]. Since the overlapping period is very short compared with the whole period of water vaporization, the combustion process could be defined as consisting of three stages.

Characteristics of Three Combustion Stages

The characteristic phenomenon and the reaction rate in each combustion stage are represented as follows. The stage of water vaporization corresponds to the period from the start ($t = 0$) of heating up until the time ($t = t_1$) when the center temperature becomes higher than the boiling point of water. The weight loss at $t = t_1$ agrees with the weight of water contained within the initial droplet. Since the duration of this stage depended little on the properties of the coal but rather on the external heat flux and the water content, the rate of weight change could be expressed by the following simple equation:

$$-dW/dt = (Q_L - q_R)/L_w$$

where W, Q_L, L_w, and q_R are the weight of the droplet, the total heat input rate from the laser, the latent heat of water vaporization, and the radiation loss from the droplet surface to the ambient. The validity of this equation was confirmed by substituting the experimental data into Q_L and q_R. To estimate the term $-dW/dt$ by calculation alone, the surface

TABLE 1
Coal properties and water content of the coal-water mixtures

Analysis Items	Unit	Coal (A)	Coal (B)	Coal (C)	Coal (D)
Proximate Analysis					
Inherent Moisture	%	3.2	5.0	5.8	2.0
Fixed Carbon	%	51.3	50.9	35.1	57.9
Volatile Matter	%	31.2	34.8	43.2	25.4
Ash	%	13.8	9.3	15.9	14.7
Calorific Value	kcal/kg	6980	6910	6080	7010
(HHV)	10^3 kJ/kg	29.22	28.93	25.46	29.35
Total Sulfur	%	0.52	0.74	0.25	0.55
Ultimate Analysis (Dry Basis)					
C	%	84.2	83.8	78.2	73.8
H	%	5.6	5.9	6.3	4.3
S					
Combustible	%	0.61	0.72	0.08	—
Incombustible	%	0.02	0.14	0.23	—
O	%	7.8	8.0	14.0	5.2
N	%	1.77	1.56	1.20	1.19
Swelling Index	CSN	2.5	1.0	0	1.5
Grindability	HGI	50	57	37	94
CWM Coal Concentration	%	63.6	63.5	59.4	65.1

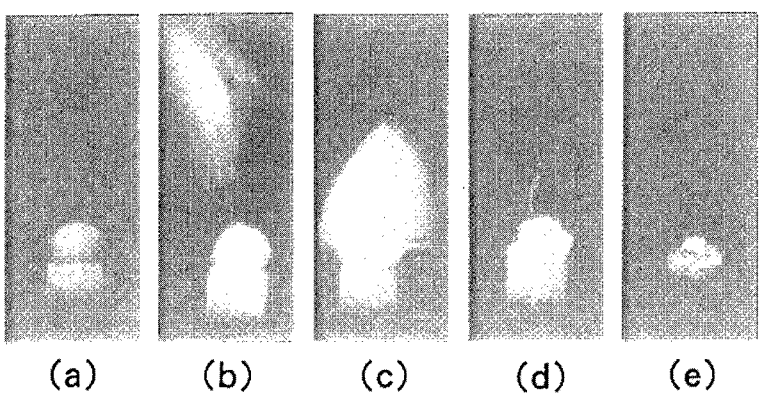

FIG. 1. Typical series of combustion processes observed through the optical filter that passed the He-Ne laser ray alone; (a) before heating, (b) water vaporization (vaporizing water is reflecting laser ray), (c) combustion of volatile matter, (d) combustion of char, (e) after combustion.

temperature of the droplet, which is indispensable in determining the value of q_R, can be obtained from the equation of thermal conduction within the droplet, assuming that the water is contained uniformly in the droplet and is vaporizing gradually from the surface toward the center, and that the droplet is divided into two regions of coal and coal-water mixture with the boundary of the two regions moving at a rate corresponding to the progress of vaporization. As seen in the next section, the rates of weight change and the duration of water vaporization calculated in this procedure agreed well with those obtained in the experiments.

The second stage of the combustion of volatile matter corresponds to the period from $t = t_1$ until $t = t_2$ when the luminous flame enveloping the droplet is extinguished. At the beginning of this stage, the nature of the reaction turns exothermic and the surface temperature increases rapidly. The time $t = t_2$ could be defined by the changes with

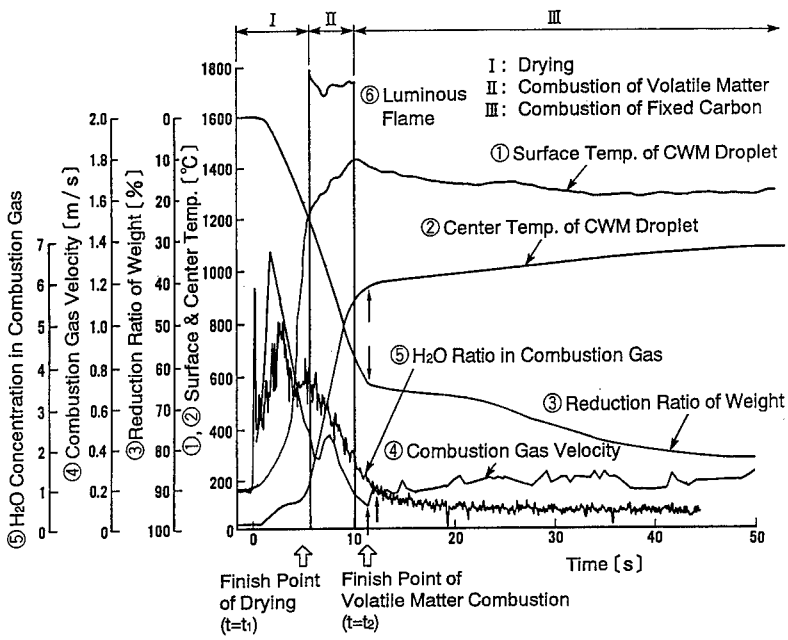

FIG. 2. Typical results of the measurements during the combustion of a single droplet of coal-water mixture (Coal: Coal (A) (d_{50} = 30 μm), water content: 36.4 wt. %, initial diameter of droplet: 2 mm, external radiation from infrared laser: 20 W).

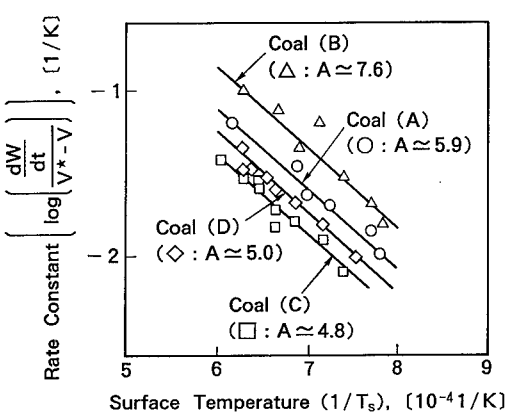

FIG. 3. Arrhenius plot assuming the first-order reaction in the stage of devolatilization.

time in the gradients of weight change, gas velocity, and H_2O concentration (Fig. 2). In the following process of the combustion of fixed carbon, there must be little measurable concentration of H_2O. The phenomenon of devolatilization must be complex, but attempts are made to correlate the devolatilization rates with the simple first-order Arrhenius expression [8],

$$-dW/dt = A_v(V^* - V)\exp(-E_v/RT_s)$$

where V, V^*, A_v, E_v, and T_s represent the mass of volatiles evolved at time t, the value of V at infinite t, the apparent frequency factor, the activation energy, and the surface temperature of the coal. It is shown in Fig. 3 that the preceding expression seems to be a fairly good approximation and that the changes of coal properties could be modeled easily by changing the values of A and V^*.

The value of E_v/R is approximately 4800–5100 K and little dependent on the kinds of coal. The value of A_v ranges from 4.8 to 7.6 s^{-1} and does not have a distinct dependence either on the weight ratio of volatile matter or on the swelling index of the mother coal. It has been reported that the values of E_v calculated in the same procedure were 4500–5600 K for lignite coal and 4000–6500 K for bituminous, that the values of A_v increased with increase of the rate of temperature rise, and that they were 300–700 s^{-1} when its rate was 10^4°C/s [15–17]. The values of E_v obtained in the present study almost agree with the previous reports, but the values of A_v differ from them by 1/140–1/50. Even considering that the rate of increase of surface temperature for the CWM droplet was smaller than that of the coal particle by one order because of the water, the values of A_v obtained experimentally are smaller than expected.

To interpret the small value of A_v, the specific surface area and the probability curve of pore sizes for a droplet that had passed through the devolatilization process were measured [18]. The surface areas

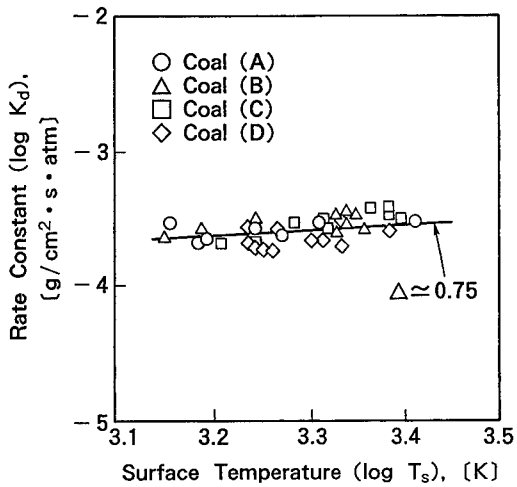

FIG. 4. Dependence of the surface temperature on the reaction rate in the stage of char combustion.

measured with the CO_2 absorption method (absorption temperature: −72°C) were 12–20 m²/g and the probability curve of pore sizes had a broad distribution between 210–630 Å without a distinct peak. These parameters depended little on the kinds of mother coal. The surface area of the char of the mother coal devolatilized in nitrogen at 1200°C is 110 ~ 150 m²/g and the probability curve of pore sizes has a peak at 30–50 Å. Thus, for the CWM droplet subject to the processes of water vaporization and devolatilization, the micropores (smaller than 200 Å) were much reduced and the relatively large pores remained, with the result a small surface area. During these processes, the coal particles in the CWM droplet were observed to swell in the early stage and shrink and adhere to or agglomerate with each other. When the water trapped in the coal particle escapes from the internal structure, the micropores in the coal particle seem to be masked with the droplet shrinking. This expectation is supported by the small value of the surface area and the reduction of micropores. It is known that for a coal with a high swelling index, the reactivity of the devolatilized coal depends largely on the heating rate and final temperature [8,9], because the porosity of char depends on the rates of devolatilization and the shrinkage of the particle after the process of swelling. For the CWM droplet, the time from the start of heat up until the end of devolatilization is longer than that for the coal particle, since the water has the same effect on swelling as devolatilization.

During the period of fixed carbon combustion, the temperature changes at the surface and center of droplet have slowed down and the concentration of H_2O adjacent to the droplet surface has been reduced to a level equivalent to the moisture in the air. In this stage, the exothermic reaction occurs at the surface of the droplet, as shown by the luminous envelope flame not being detected by the photodiode (Fig. 2). It is known that for $T_s > 1000$ K and $D > 30\ \mu$m, the Damköhler number defined at the droplet surface is very small, that is, the diffusion of oxidizing agent adjacent to the surface is the dominant factor in determining the reaction rate of carbon rather than the chemical reaction [18,19]. Since the CWM droplet was observed not to microexplode, the mean size of droplets could be expected to be more than several tens of microns during most of the combustion process. The reaction rate, therefore, can generally be shown in the following expression:

$$-dW/dt = \pi D^2 K_d = (\pi D^2) A_d T_s^n / D$$

As shown in Fig. 4, when the experimental data were rearranged according to the preceding equation, the values of A_d and n were approximately 8.4 $\times 10^{-7}$ and 0.75, and little dependent on the properties of the coal. This shows that the apparent reaction rate of fixed carbon depends less on the chemical properties of the coal than on the droplet diameter and the percentage of fixed carbon contained in the mother coal. The value of n almost agrees with that for the char, but A_d differs from the reported data for the char by 1/5–1/8 [16,17,19]. The frequency factor was much reduced because the shrinkage and agglomeration occurred after the processes of water vaporization and devolatilization. This is supported by the aforementioned measured values of the surface area and the probability curve of pore sizes.

Effects of the Droplet Size

The initial diameter of droplet used here is 5–10 times larger than that atomized from an injector, and the number of coal particles involved in a single droplet is estimated to be more than several million for the present experiment and more than several thousand for an actual injector. These numbers of coal particles, however, would be large enough to keep inhomogeneity of reaction from occurring in a single droplet.

For the large droplet, as shown in Fig. 2, the surface temperature was higher than that of the center by 300–700°C and 150–220°C in the devolatilization and char combustion stages, respectively. In this study, the reaction rates were related to the measured surface temperature, because the surface and center temperatures for the small (10–300 μm) droplets atomized from the actual injector are estimated to be almost the same. Furthermore, the reaction rate in the present experiment should be dominated by the surface temperature rather than the center temperature, since the differences between the reaction rates based on the surface and

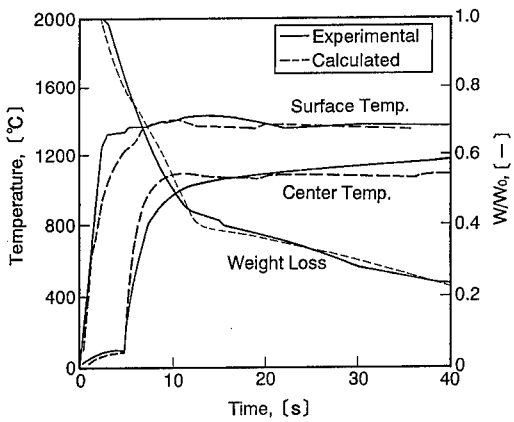

FIG. 5. Comparison of the calculated and measured temperatures (Coal: (*D*) (d_{50} = 30 μm), water content: 34.9 wt. %, initial diameter of droplet: 2 mm).

center temperatures are more than 3–15 times. During the devolatilization process, especially, the endothermic and exothermic reactions are complicated adjacent to the surface, and it is difficult to distinguish the devolatilization from the sequence of secondary polymerization [9]. With the drop tube or thermogravimetric analyzer that generally have been used in experiments on thermal decomposition, the temperature of the spot at which the reaction occurs could not be obtained, since the temperature of the gas stream or the mean temperature of the particle is usually controlled. In the present study, however, the data could be well correlated with the variations of the surface temperature measured directly, and the difficulties in the analysis could be removed.

Numerical Simulation of a Single Droplet Combustion

The energy balance in a single droplet is given in the following expression:

$$d\{C_p\rho_s(\pi d^3/6)T_s\}/dt = (Q_{RS} + Q_{ch}) - (Q_{RR} + Q_{cv} + Q_{cd} + Q_{ct})$$

where Q_{RR}, Q_{cv}, Q_{cd}, Q_{ct}, Q_{RS}, and Q_{ch} are the radiation and natural convection from the droplet surface to the ambient air, the conduction from the droplet surface toward the center of the droplet, the conductive heat loss from the surface to the sample holder and thermocouple wire, the radiative heat input from the laser beam, and the heat release of the chemical reaction, respectively. These heat fluxes are calculated according to the following assumptions. The detailed procedures of calculation are referred to in previous reports [1,2].

1. The process of combustion is divided into three stages.
2. The reaction rates at each stage are given by the experimental equations.
3. The decreased diameter of droplet after water vaporization is estimated by assuming the close-packed spheres of mother coal particles.
4. The outer shell, which is a thin section of the droplet beneath its surface, is the heat source produced by the exothermic combustion reaction.

As a typical case, the result for coal (*D*) is shown in Fig. 5, where the calculated and experimental results for the surface and center temperatures are compared. It is seen that the temperature profile and the duration time of the three combustion stages can be simulated fairly well. This confirms the validity of the combustion model proposed here and the applicability of the sequential-steps simulation. A slight overshoot in the calculated surface temperature can be explained by the fact that the water vaporization stage is assumed to change instantaneously to the next stage without overlap.

Numerical Simulation of One-Dimensional Test Furnace

The computer program to simulate the CWM combustion in a one-dimensional furnace was written by expanding the simulation of a single droplet. The CWM droplets atomized from an injector react along the gas stream, whose temperature, composition, and velocity are determined from the mass and

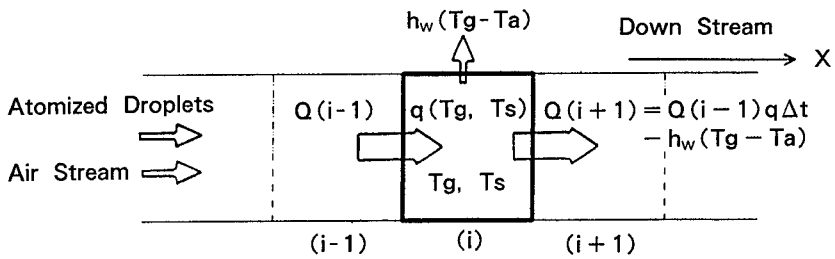

FIG. 6. Heat balance between the control volumes (calculating cells) in the numerical simulation of a one-dimensional furnace.

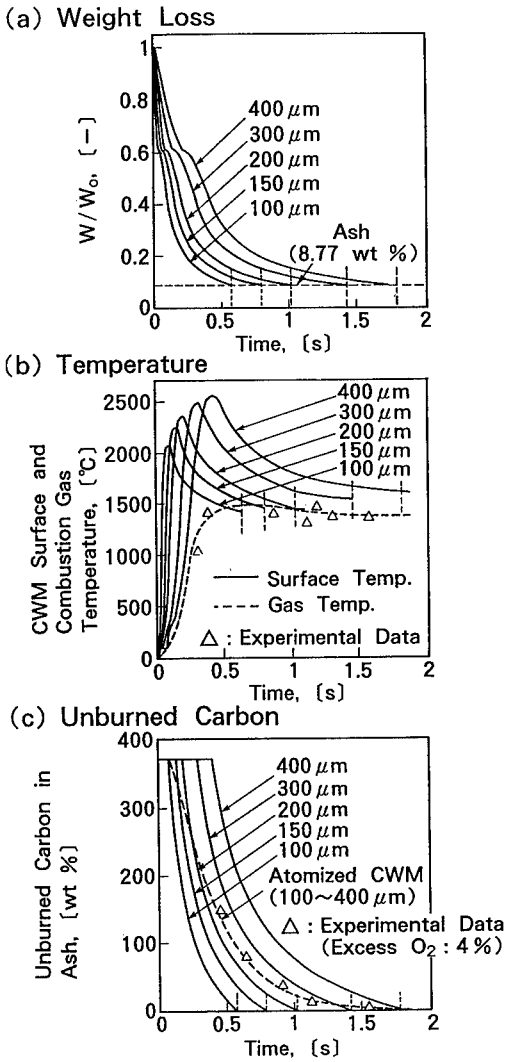

FIG. 7. Comparisons of the calculated and experimental results for (a) weight loss, (b) temperatures of droplet surface and combustion gas, (c) unburned carbon in ash.

energy balances for calculating cells arranged in the x-coordinate direction (Fig. 6). The combustion of droplet clouds whose sizes range from 100 to 400 μm in diameter were simulated. For the distribution of droplet size, the measured value for the atomizer was used. In the calculation, the terms for the heat loss to the thermocouple and sample holder were omitted from the equation of energy balance shown in the calculation model for a single droplet.

The calculated result in Fig. 7a shows that the durations of the stages of drying, combustion of volatile matter, and char combustion can be estimated as 0.14, 0.17, and 1.1 s for 300-μm diameter, and 0.03, 0.07, and 0.47 s for 100-μm diameter, respectively. These durations change drastically according to the difference in droplet size.

The temperature variations at the droplet surface in Fig. 7b show that with the decrease of droplet size, the rate of increase of temperature in the first stage increases and the maximum surface temperature decreases. These are explained by considering that with the decrease of droplet size, the temperature rises rapidly because of the small heat capacity and the radiation loss to the ambient increases because the ratio of surface area to the mass of the droplet becomes larger. In short, the small droplet has a tendency to be easily heated and cooled. The gas temperature shown in Fig. 7b agrees fairly well with the results of firing tests in a furnace of 0.6-m diameter and 4.0-m length.

In Fig. 7c, the variation of the unburned carbon in ash (W_c) with time was calculated. The rate of decrease of W_c increases as time proceeds. The dotted line in Fig. 7c is the calculated result for the cloud of droplets atomized from the injector into the furnace, and the symbols are the data obtained in the firing tests. It is seen that the calculated result agrees well with the test data and that the value of W_c depends largely on the top size of atomized CWM droplet. In the present calculation, the required time (t_d) during which the atomized CWM droplets should stay in an actual furnace could be estimated roughly as 1.5–1.7 s.

Concluding Remarks

The combustion process of a single droplet of coal-water mixture has been studied experimentally. An intensive heat flux at the level of 10^6 W/m^2 was realized by using a YAG laser as the external heat source. As a result of the present study, the following items could be obtained.

1. For the devolatilization process following water vaporization, the activation energy derived by assuming a first-order reaction of decomposition remained at the same level as that for the mother coal. On the other hand, the apparent frequency factor was much smaller than that for the mother coal by 1/140–1/50. For the stage of char combustion, the apparent frequency factor was smaller than that for the coal char by 1/4–1/8. The surface area and the micropores of the droplet subject to the processes of water vaporization and devolatilization were much reduced, compared with the values for the mother coal. It could be presumed that the small pore would be masked when the water trapped in the pore was escaping from it with the shrinkage and agglomeration of the coal particles proceeding.
2. Based on the reaction data and the combustion model proposed here, the combustion of a single droplet and the cloud of droplets injected into a

one-dimensional furnace were simulated by the numerical calculation. The calculated gas temperature, ratio of unburned carbon, and reaction time agreed well with those obtained in the experiments.

REFERENCES

1. Shirato, R., Abe, K., Takahashi, T., Kaneko, S., Funatsu, H., Shoji, K., Kawano, K., and Shinpo, I., *Eighth International Symposium on Coal Slurry Fuels Preparation and Utilization,* 1986, p. 738.
2. Kaneko, S., Suganuma, H., Kobayashi, Y., Tokuda, K., and Takeno, K., *Nineteenth Symposium on Coal Utilization and Fuel Systems,* 1994, p. 403.
3. Gao, J., Huang, Z. X., and Yao, Y. Q., *Seventh International Symposium on Coal Slurry Fuels Preparation and Utilization,* 1985, p. 463.
4. Kimoto, K., Sadamori, I., Shioda, T., Tsutimoto, N., Matsumoto, R., and Nakajima, T., *Second International Symposium on Heat Transfer,* 1988, pp. 2, 587.
5. Burgess, A. R. and Ghaffari, R., *Twenty-Second Symposium (International) on Combustion,* The Combustion Institute, Pittsburgh, 1988, pp. 2009–2017.
6. Matthews, K. J. and Street, P. J., *Proceeding of Sixth International Symposium on Coal Slurry Combustion and Technology,* Orlando, 1984, p. 109.
7. Murdoch, P. L., Pourkashanian, M., and Williams, A., *Twentieth Symposium (International) on Combustion,* The Combustion Institute, Pittsburgh, 1984, p. 1409.
8. Niksa, S., Heyd, L. E., Russel, W. B., and Saville, D. A., *Twentieth Symposium (International) on Combustion,* The Combustion Institute, Pittsburgh, 1984, p. 1445.
9. Lau, C. W. and Niksa, S., *Combust. Flame* 95:1 (1993).
10. Wang, C. H., Liu, X. Q., and Law, C. K., *Combust. Flame* 56:175 (1984).
11. Lasheras, J. C. and Fernandez-Pello, A. C., *Combust. Sci. Technol.* 21:1 (1979).
12. Daniel, J. M. and James, F. S., *Twenty-Second Symposium (International) on Combustion,* The Combustion Institute, Pittsburgh, 1988, p. 1999.
13. Noda, M., Gierulski, A., and Marowsky, G., *The Combustion Institute Joint Meeting,* 1987, p. 355.
14. Hall, R. J., *Combust. Flame* 35:47 (1979).
15. Anthony, D. B., Howard, J. B., Hottel, H. C., and Meissner, H. P., *Fifteenth Symposium (International) on Combustion,* The Combustion Institute, Pittsburgh, 1974, p. 1303.
16. Wells, W. F., Kramer, S. K., and Smoot, L. D., *Twentieth Symposium (International) on Combustion,* The Combustion Institute, Pittsburgh, 1984, p. 1539.
17. Kawaguchi, O. and Noto, T., *Twenty-Second Symposium (International) on Combustion,* The Combustion Institute, Pittsburgh, 1988, p. 97.
18. Ranz, W. E. and Marshall, W. R. Jr., *Chem. Engineering Prog.* 48(3):141 (1952).
19. Field, M. A., *Combust. Flame* 13:237 (1967).

Twenty-Sixth Symposium (International) on Combustion/The Combustion Institute, 1996/pp. 3231–3241

INVITED TOPICAL REVIEW

FLUIDIZED BED COMBUSTION: ACHIEVEMENTS AND PROBLEMS

BO LECKNER
Chalmers University of Technology
Department of Energy Conversion
S-412 96 Göteborg, Sweden

A survey is made of fluidized bed combustion with special emphasis on the behavior of the combustion chamber of an atmospheric circulating fluidized bed combustor. The following subjects are briefly touched: mixing and combustion of fuel, desulfurization, and formation of nitrogen oxides, especially N_2O. The general conclusion is that there is much work done concerning fluidized bed combustion in the form of laboratory studies, but it is uncertain how this information can be translated to the combustion chamber processes, principally because the actual processes occurring in a large-scale combustion chamber are not sufficiently known.

Introduction

The principal advantage of fluidized-bed combustion (FBC) is its ability to burn various types of solid organic fuels including wastes, achieving low emissions without flue-gas treatment. The first applications employed bubbling fluidized bed in stationary fluidized bed (SFB) boilers, but problems with erosion on in-bed cooling tubes turned the mainstream of development into circulating fluidized bed (CFB) boilers in the mid-1980s. A few pressurized fluidized bed combustors (PFBC) have also been built for combined power-cycle application.

Solid organic fuels in sizes up to around 20 mm are burned at bed temperatures of about 800–900°C. A requirement for low power consumption leads to a limitation of the amount of bed material in atmospheric FBC (typically corresponding to a 5–15 kPa pressure drop over the furnace height), whereas pressurized beds may contain more bed material. This makes atmospheric CFB combustors different from chemical process applications of CFB, such as fluidized catalytic crackers, which are narrower and operated with higher pressure drops. The air supplied for combustion serves as a fluidization medium: there is a link between fluidization and combustion that is expressed by the heat release per cross-sectional bed area, φ (MW/m^2)

$$\varphi = uH/g \approx 0.7\ uP \qquad (1)$$

Here, g(m^3/kg fuel) is the volume of combustion gas at 850°C, pressure P (bar), and 20% excess air; u(m/s) is the fluidization velocity; and H(MJ/kg fuel) is the fuel heating value.

FBC boilers are built in sizes from a few MW$_t$ (thermal power) up to several hundreds of MW$_t$. Eq. (1) shows that a high fluidization velocity (and pressure) is helpful to reduce the cross-section area. This is one reason why CFBs, having velocities up to 6 m/s, are preferred in atmospheric combustors rather than SFBs whose velocities are limited to 1–2 m/s. Applying Eq. (1) on the Gardanne plant [1], which has a fuel power of about 600 MW$_t$, gives a furnace cross-section area of 150 m^2 with φ = 4 MW/m^2. Despite the high φ, this size is considerable and there may be difficulties in the distribution of fuel and secondary air over the cross section. (In this particular boiler, the lower part, below 11 m, is divided into two legs with tapered walls to reduce the bottom area and to improve mixing of fuel and air.)

Height is not critical to the design of large CFB boilers (35–40 m is probably an upper limit), but it could be so for smaller combustors: particle separator, particle return leg, pressure seal, and heat-transfer surfaces have to be accommodated. The progress of combustion does not decide the height, unless the boiler is very small (10–20 MW$_t$) and for highly volatile fuels.

Most publications related to FBC deal either with basic knowledge obtained in small-scale equipment or with overall information on boiler behavior, such as parameter studies with measurements of external quantities. In the first case, there is an uncertainty of how to transfer the knowledge to the conditions of a combustor; in the second case, the experiences published do not reveal details of combustor processes. Because of cost of investigations and the inaccessibility of boiler furnaces, there are only a few publications describing the in-furnace processes [2–5]. Despite this lack of information, the present review discusses some selected furnace processes, principally with relation to atmospheric CFB boilers.

CFB Fluid Dynamics and Combustion

General

Primary air is introduced into the combustor through bottom nozzles. The remaining air is in-

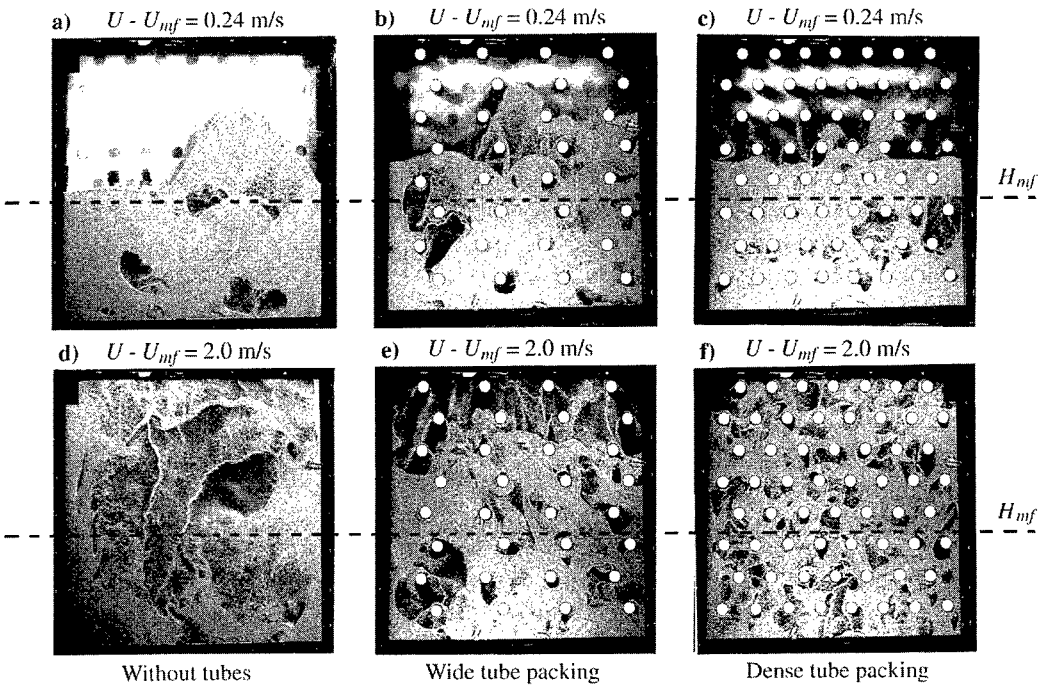

FIG. 1. Fluidization regimes in a two-dimensional (0.07 × 0.68 m) cold bed without (a, d) and with (b, c, e, f) tubes. Particle size 0.79 mm (silica sand). Fluidization velocity minus minimum fluidization velocity ($U - U_{mf}$) and bed height at minimum fluidization velocity H_{mf} are indicated. From Ref. 9.

jected as secondary air through nozzles in the walls a few meters from the bottom. For practical reasons, the fuel is fed from the sidewalls as well. Mixing between entering fuel and air flows forms the macromixing problem. There is also a local mixing problem depending on the behavior of the fluidized gas/solids medium.

Fluid Dynamics

Fluid dynamics of CFB including combustors have been reviewed [4]. Most work published on CFB, however, is directed toward other applications [6]. The bed consists of lime, sand, and ashes and extends from the bottom to the top of the CFB riser. Usually a dense (particle volume concentration according to pressure-drop measurements around 40%) bed covers the bottom. Upward from the bed, the particle concentration decays exponentially to reach less than 1 percent in the top of the riser. Typical data are particle size 100–300 μm, particle density 1600–2600 kg/m^3, bottom bed height 0.5 m, and fuel concentration 1 percent.

A characteristic feature of the bottom bed is its small height-to-width ratio. Under such circumstances, a dense bed behaves like a bubbling bed [7,8], despite a gas velocity that may exceed the single particle terminal velocity. It is difficult, of course, to know exactly what happens in a closed furnace, but Fig. 1, showing six cases from a two-dimensional cold bed, illustrates qualitatively bed behavior under different conditions. Figures 1a through 1c show a normal bubbling bed at moderate fluidization velocities—the bubbles are not seriously affected by the tubes inserted into the bed on Figs. 1b and 1c. Figures 1d through 1f show the same bed configurations at a high gas velocity. The freely bubbling bed, Fig. 1d, corresponding to the CFB bottom bed, exhibits a large, exploding bubble extending almost all the way from the bottom to the top of the bed. In beds with tubes, and, especially in the densely packed one, Fig. 1f, the picture is different: small, rapidly moving voids are formed—the bed is turbulent.

In the CFB bottom bed, tubes cannot be inserted because of erosion; the bed is freely bubbling. Gas bypassing the bed through the bubbles leaves as jets. There are no measurements from boilers to confirm this description, but it can be inferred from observations at lower velocities, which show a considerable flow of gas through the bubbles forming high-velocity jets; a mean jet gas velocity of 6 m/s at a fluidization velocity of 0.6 m/s has been registered [10]. In the CFB bottom bed, fluidization velocities are between 2 and 6 m/s, and high jet velocities could be present.

The bubbling bottom bed ejects bed material into

the splash zone, where a super-saturated particle suspension forms. This results in back-mixing of bed material falling back into the bottom bed. The exponential decay of particle concentration observed in this zone [11] is similar to that of low-velocity bubbling beds [12], which indicates a similarity in behavior of the CFB bottom bed and the conventional bubbling bed.

Particles are carried with the ascending gas stream into the upper zone where they are separated continuously at the walls into a descending particle stream forming a wall layer a few decimeters thick, with flux densities that may reach more than 100 kg/m^{2}s. Because of this separation, the density of the particle suspension decreases upward, and the net flow of particles attaining the exit is the externally recirculating flow, typically 10 kg/m^{2}s, whereas the particle separation forms an internally circulating flow. The particle concentration in the descending wall layers is three times as high as the cross-section average [13].

Solid Fuel Mixing

The fuel is fed from feed ports just above the dense bed. In a large boiler such as the Gardanne plant, there are four fuel feed points [1], one point per 20 m^2 bottom bed area. In addition, there is a fuel flux of small char particles returning with the bed material from the particle separators. The fuel particles may be carried away instantaneously if they are smaller than the single particle terminal velocity (<0.5 mm at a gas velocity of 3 m/s), but the larger particles fall down into the bed where they spread, while drying and devolatilizing, and finally burn. The fuel particles will undergo fragmentation [14], and fine char particles follow the gas stream upward.

The spread of fuel particles in the bed and optimization of the size of the fuel, considering also fragmentation, is an important issue awaiting analysis. The limited knowledge about the mixing properties of the bottom bed comes from studies on lateral dispersion coefficients D (m^2/s) [15,16] in ranges of bed size and velocity far below those of a CFB. The largest values of D given are around 0.02–0.03 m^2/s. This could be compared with a calculation [17] giving an average particle dispersion coefficient of $D = 0.01$ m^2/s for fuel injection from the bottom in a 20-m^2 bed at a fluidization velocity of 2.4 m/s. Spread of material from the top of the dense bed is probably more efficient than from the bottom, and particle downflow from the walls may also contribute to particle dispersion in the CFB case. In the absence of any other information, a value of 0.03 m^2/s will be used to calculate the average dispersion time τ_d for a horizontal distance x,

$$\tau_d = x^2/D \tag{2}$$

This time should be compared with the devolatilization time

$$\tau_v = ad^n \tag{3}$$

where d (mm) is the initial fuel particle diameter and $a = 1.6$ and $n = 1.6$ are chosen from Ref. 18.

According to Eq. (3), a 10-mm particle needs 50 s to devolatilize. During this time, the particles have spread 1.5 m according to Eq. (2). If the spread of fuel is not better than this, considerable maldistribution in the lower parts of the combustor will occur. With wet fuels, the situation is improved, since the fuel moisture delays volatile evolution [19]. For instance, the time of devolatilization measured for a 20-mm wet (40% moisture) wood particle [20] was 50% longer than that [21] of a corresponding dry (6% moisture) particle. In most designs, the lower parts of the furnace walls are inclined to reduce the bottom bed area to improve mixing and with the side effect of keeping the plume created by volatile release away from the tube walls. Regardless, considerable horizontal gas concentration differences may exist [3,5].

The char burnout time is longer, and particle mixing is not a limiting factor. Limiting factors are, instead, elutriation and burnout time of char particles carried upward in the furnace with the gas. Comprehensive reviews have been published recently concerning transfer processes of fuel particles [19] in FBC and combustor modeling [22].

Gas Mixing

The large devolatilizing particles are accommodated by the bottom bed, but the volatiles do not burn in the dense particle suspension [23,24]. In the temperature range considered, volatiles burn in large voids or above the dense bed. Devolatilization and movements of the bed result in pockets of unreacted gas moving upward. This is the picture obtained by zirconia-cell measurements of the excess oxygen at different points in a combustor during combustion of bituminous coal with different modes of air supply but under otherwise similar conditions (Fig. 2). In Fig. 2a, the probe records predominantly oxidizing conditions in the splash zone (at 0.56 m) during "no staging" when all combustion air is added as primary air. Conversely, in Fig. 2e, the conditions were reducing constantly when the primary zone stoichiometry was 0.5. During "normal staging," this stoichiometry was 0.7 and the fluctuation between oxidizing and reducing states reveals something about the flow structure. The lifetimes of the gas pockets could be several seconds at an average gas velocity of about 3 m/s (below the secondary-air nozzles). In Figs. 2b, 2d, and 2f, 7 m higher and downstream of the secondary-air supply, mixing was still not complete, not even within the time resolution of the probe (0.1 s at a gas velocity of 6 m/s; to be

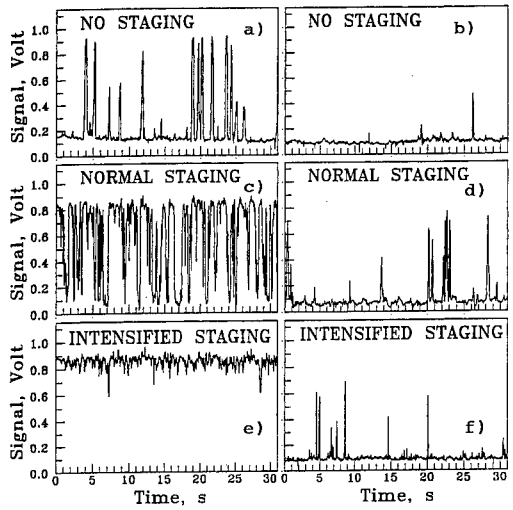

FIG. 2. Zirconia-cell measurements of oxidizing (low value) or reducing (high value) conditions, at bed temperature 850°C and excess-air ratio 1.2 in a 2.5-m^2 and 14-m-high CFB combustor burning coal. The diagrams to the left are registered on the centerline 0.56 m from the bottom and those to the right at 7.9 m from the bottom. From Ref. 25.

observable the size of the pockets should exceed 0.6 m).

The zirconia-cell measurements do not allow direct conclusions about the interaction between the bottom bed and gas combustion. However, they indicate a potential mixing problem when gaseous combustibles from char and volatiles form pockets of unburned gas moving upward. Assuming a lateral gas-mixing time in the transport zone of a CFB by analogy with Eq. (2), equal to the gas residence time z/u for dispersion over a duct with radius R (m),

$$\tau = R^2/D_{gas} = z/u$$

yields a vertical mixing length $z/R = uR/D_{gas} = 0.5\ Pe$ (z [m] axial distance, u [m/s] gas velocity, D_{gas} [m^2/s] gas dispersion coefficient). With a typical Peclet number, $Pe = 500$, from a laboratory riser [26], this relationship suggests that complete mixing is attained only at an axial distance of $z = 250\ R$. The conclusion is that, with the data used, radial mixing is not good. In the example shown in Fig. 2, the mixing was not complete after 7 m despite some assistance by the secondary-air jets. During combustion of highly volatile fuels (wood) in short (10–15 m) combustors, high cyclone temperatures are observed, a sign of insufficient mixing in the combustor, which is compensated by the cyclone. Otherwise, little is known about local mixing conditions in combustors.

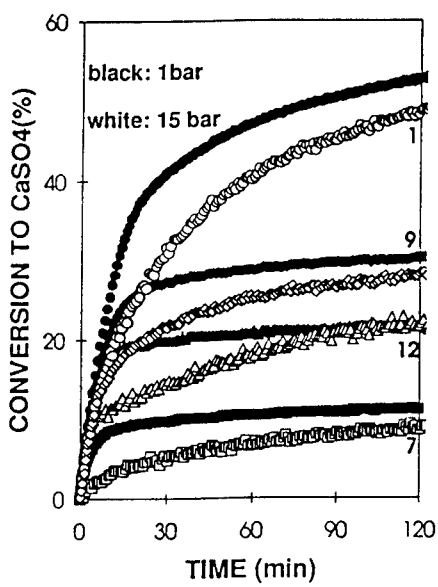

FIG. 3. Comparison of conversion to $CaSO_4$ for various limestones (numbered 1, 7, 9, and 12), measured in a thermobalance at 850°C (gas composition 0.3% SO_2, 4% O_2, 10% CO_2 [1 bar] or 20% CO_2 [15 bar], rest N_2. Size 200–400 μm). From Ref. 27.

Sulfur Capture

One of the advantages of FBC is its ability to absorb sulfur released during combustion by addition of limestone to the bed. Normally, a few times the stoichiometric amount of calcium is needed. Excess limestone or dolomite is not a problem in itself, since this material is usually cheap. However, in many countries, the cost for deposition of spent limestone is high, and there is a desire to reduce the quantity of lime. This situation and an interest in PFBC have stimulated a renewed interest for research on sulfur capture.

In an atmospheric FBC, the limestone calcines

$$CaCO_3 = CaO + CO_2 \qquad \text{(R1)}$$

and since combustors are operated with excess air, CaO is sulfated, thereby binding the sulfur released from combustion:

$$CaO + SO_2 + \tfrac{1}{2}O_2 = CaSO_4 \qquad \text{(R2)}$$

In a pressurized combustor, the CO_2 partial pressure is too high for calcination in most parts of the bed. For thermodynamic reasons, the limestone does not calcine and sulfation takes place directly:

$$CaCO_3 + SO_2 + \tfrac{1}{2}O_2 = CaSO_4 + CO_2 \qquad \text{(R3)}$$

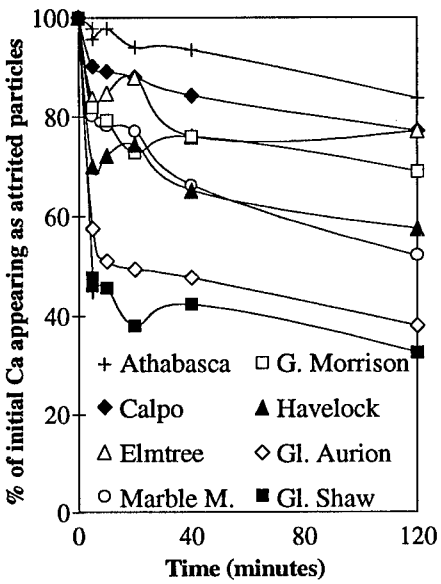

FIG. 4. Size reduction of various limestones in a laboratory circulation reactor (Temperature 850°C, 3000 ppm SO_2, 9% O_2, 9% CO_2, rest N_2. Fluidization velocity 5 m/s. Initial size 350–500 μm). From Ref. 30.

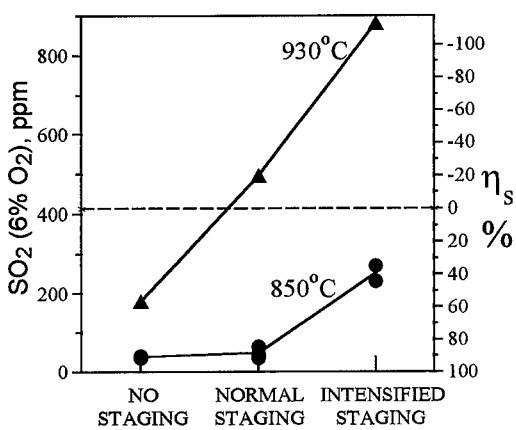

FIG. 5. SO_2 emission (or desulfurization efficiency η_s) for three cases of air supply at bed temperatures of 850 and 930°C at a given total excess-air ratio of 1.2. The measurements were made after changes from the normal staging case at 850°C. Negative desulfurization efficiency means excess sulfur emission. From Ref. 25.

For long residence times, this conversion may even be more favorable than under atmospheric conditions [27,28]. Figure 3 shows tests made in a pressurized thermobalance at atmospheric and higher pressure. Similar to Fig. 3, a large number of limestones has been investigated for sulfation under atmospheric conditions by different researchers. The conclusion is that, just like in Fig. 3, there is a great variation in conversion depending on the type of limestone. The question is, how important are these differences in sulfation properties for sulfur capture in a combustor? Two limestones tested in the laboratory, a reactive one (conversion 0.37) and a low-reactive one (conversion 0.09) were used in two (40 and 165 MW_t) atmospheric CFB boilers [29]. The conversions obtained in the boilers were 0.4–0.45 and slightly lower for the unreactive limestone. One explanation for the improved conversion in the combustor compared to the laboratory results is that the particles, originally 0.7 mm in size, break into smaller pieces but nevertheless reach long residence times. Figure 4 [30] shows that after an initial size reduction, depending on limestone type, there is a slower and similar size reduction during the final sulfation phase. In addition to conversion ability, the physical properties of the limestone and process parameters, such as particle separator efficiency (i.e., particle residence time) and fluidization conditions, play important roles. Furthermore, the combustion conditions may be decisive for sulfur capture. Next, the line from the previous section will be followed and the effects of combustion will be analyzed.

Despite overall excess air, a lime particle may be exposed to reducing conditions during a certain period of time, for instance in the particle phase of the dense bed. Subsequently, it may move into an oxidizing environment in the bubbles or in jets issuing from the dense bed, and it may be transported to the more oxidizing environment in the upper part of the combustor. One experiment made in a laboratory-scale CFB riser [31] shows how a 0.4-mm radioactive tracer particle circulated across the secondary air level 10–15 times before it was captured by the cyclone. The mean cycle residence time in each zone was about 1 s. In a larger combustor, the residence times would be larger as a consequence of the size, but, in general, little is known about the changing conditions experienced by a particle.

During reducing conditions, the sulfur captured by reaction (R2) is released

$$CaSO_4 + CO = CaO + CO_2 + SO_2 \quad \text{(R4)}$$

The influence of reducing zones in a bubbling bed was mentioned earlier [32] and further discussed in Ref. 33. A model describing sulfur capture as a competition between oxidizing (R2) and reducing (R4) conditions has been formulated [34]. An example of the effect of reducing conditions is shown in Fig. 5, from the same tests as Fig. 2 [25]. When part of the air was added as secondary air, under otherwise constant conditions, the bottom regions of the combustor became more reducing and sulfur capture deteriorated. For a few hours after a change in air supply, the sulfur emitted at a bed temperature of 930°C was even greater than the sulfur supplied by the fuel;

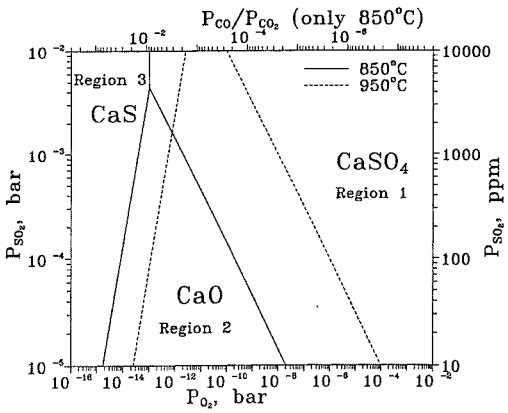

FIG. 6. Phase diagram for the system: CaO, CaS, SO_2, CO_2, and CO. From Ref. 34.

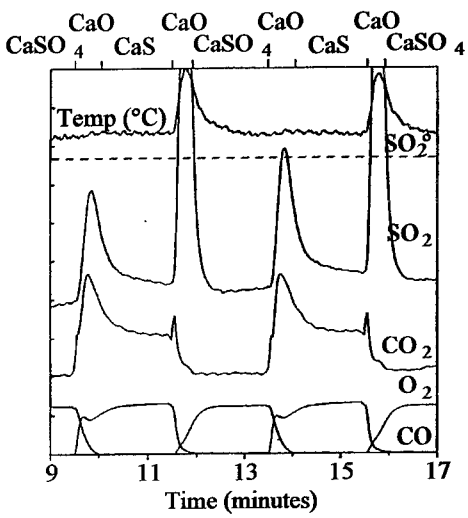

FIG. 7. Example showing temperature, SO_2, CO_2, O_2, and CO versus time under conditions alternating between oxidizing and reducing. From Ref. 41. SO_2^0 indicates inlet SO_2 concentration. Range of ordinate axis: temperature 780–880°C; SO_2 – 150 → 2000 ppm; CO_2 9 → 14%; O_2 0 → 30%; CO 0 → 35%. The products formed are indicated on top of the diagram.

the sulphur stored in $CaSO_4$ was released according to reaction (R4).

The frequencies of change between reducing and oxidizing conditions and the rates (kinetic and diffusion) of the reactions governing sulfur capture in a fluidized bed may not be known, but the thermodynamics of the system CaO, CaS, $CaSO_4$, SO_2, CO, CO_2, and O_2 can be represented in a phase diagram (Fig. 6), showing Region 1 where oxidizing conditions prevail and $CaSO_4$ is stable, Region 3, which is strongly reducing and where CaS is stable, and intermediate Region 2 where CaO is stable.

Figure 6 provides a qualitative understanding of sulfur capture. Sulfur capture takes place in Region 1. Under reducing conditions, Regions 2 and 3, $CaSO_4$ is no longer stable and may be reduced to CaS or SO_2 may be released as illustrated by Fig. 5. Sulfur can be captured as CaS, but how this takes place under interchanging conditions in an FBC is not well-known; only a few percent of the sulfur bound in the bed was CaS, even in the severe staging case of Figs. 2 and 5 [35]. Region 2 is displaced toward higher SO_2 concentrations at higher temperatures—the influence of reducing conditions becomes more important and sulfur capture is normally less efficient. This effect is even more evident at stringent sulfur capture requirements when the SO_2 concentration is low (the lower part of the diagram). For the same reason [36,37], reducing conditions have a smaller impact at high total pressures when the SO_2 partial pressure is high and fluctuations in oxygen concentration take place at a higher SO_2 pressure level. Moreover, the problems with interchanging oxidizing-reducing conditions may be less severe in a PFBC because of smaller bubbles [38] and smaller oxygen concentration fluctuations [39] compared to an atmospheric bubbling bed [40].

To better understand the processes occurring during alternating conditions, a series of experiments were carried out with a few limestone particles placed in an electrically heated quartz reactor [41]. The reactor was fed with a gas whose composition was changed cyclically to give oxidizing or reducing conditions. A typical result, with a long period (240 s) to distinguish clearly the effects, is shown in Fig. 7. At 9 min, the conditions are oxidizing and CaO reacts to form $CaSO_4$ (R2). Then conditions are changed, and the peak in SO_2 observed originates from reductive decomposition of $CaSO_4$ (R4), also indicated by the CO_2 peak. The subsequent drop in the SO_2 concentration is caused by sulfidation:

$$CaO + SO_2 + 3CO = CaS + 3CO_2 \quad (R5)$$

At 11.5 min, the system is shifted again to oxidizing conditions, and a high peak in SO_2 concentration is found as a consequence of rapid exothermal (note the temperature rise) oxidation of CaS to CaO,

$$CaS + 1.5O_2 = CaO + SO_2 \quad (R6)$$

After the SO_2 peak, sulfation takes place again. As the particles gradually become sulfated, the rate of sulfur retention decreases and after a number of cycles the peaks related to CaS (R6) disappear, except at high temperatures (950°C). This indicates that the exothermal conversion of CaS to $CaSO_4$,

$$CaS + 2O_2 = CaSO_4 \quad (R7)$$

is important, too.

It has been assumed [32] that alternating reducing-oxidizing conditions could give a better sulfur penetration into the lime particle and thus a better limestone utilization. This assumption was not confirmed by Hansen and co-workers [41], and alternating conditions do not explain the better sulfation in the CFB boiler mentioned previously [29] compared to laboratory test results.

The large-scale experiences and those in the quartz reactor emphasize the connection between combustion and desulfurization. The detailed mechanisms, such as period of changes and reaction paths, are not well-known, but the overall effects are evident: the extent of reducing conditions depends on the arrangement of fuel and air supply as well as on the mixing in the combustor. The effect on desulfurization becomes more important at atmospheric pressure, high-temperature, and stringent sulfur-removal requirements (low SO_2 partial pressure).

Desulfurization with lime in a devolatilizer and subsequent conversion of char and CaS in a combustor are deliberate separations of reducing and oxidizing conditions. It is an extreme case compared to what takes place in an FBC combustor. Applications of this type have been suggested (e.g., Topping cycle [42] and Second generation PFBC [43]), and studies of limestone conversion under related conditions have been carried out [27,44,45].

Nitrogen Oxides

The discovery that up to a few hundred ppm of N_2O are emitted from FBC gave rise to an intense research activity documented in a number of reviews [46–50]. Consideration of N_2O completed the available picture of NO formation and destruction.

The homogeneous formation mechanisms [51,52] applied to FBC [53,54] result in a predominant formation of N_2O from HCN

$$\mathrm{HCN} \xrightarrow{\mathrm{O}} \mathrm{NCO} \xrightarrow{\mathrm{NO}} \mathrm{N_2O}, \qquad \text{(R8)}$$

whereas the other principal nitrogen-containing volatile component NH_3 tends to form NO

$$\mathrm{NH_3} \xrightarrow{\mathrm{H,\ OH}} \mathrm{NH_i} \xrightarrow{\mathrm{O_2,\ OH,\ O}} \mathrm{NO}, \qquad \text{(R9)}$$

in addition to N_2.

The FBC environment may lead the path of reaction away from formation of N_2O. For instance, in reducing zones, a high hydrogen content and low heating rate pyrolysis promote formation of NH_3 [55–57]. The presence of active surfaces has similar effects: CaO [58,59] and char [59] have been found to catalyze the oxidation of HCN to NO. CaO [59] may promote formation of NH_3 from HCN in the presence of H_2, and other materials, including some ashes [50], may increase the selectivity of NO formation from NH_3. The results quoted illustrate some features of the interaction between nitrogen oxide formation chemistry and bed conditions, but the picture is not complete, and the quantitative importance of these laboratory results for an actual combustor remains to be assessed.

The nitrogen in the char is found principally in heterocyclic groups and is released as these rings are broken by oxidation. Recently, there has been a discussion on the heterogeneous formation of N_2O, which will be related briefly here.

Several routes have been proposed [60] for formation of N_2O from char. Somewhat rewritten, these are

$$\text{char-N} + \text{char-N} + \mathrm{O_2} \rightarrow \mathrm{N_2O} \qquad \text{(M1)}$$

$$\text{char-N} + \mathrm{O_2} \rightarrow (-\mathrm{NCO}) \qquad \text{(M2)}$$

$$(-\mathrm{NCO}) + \mathrm{NO} \rightarrow \mathrm{N_2O} + (-\mathrm{CO})$$

and, if the char is not completely devolatilized,

$$\text{char-N} + \text{heat} \rightarrow \text{(R8)}. \qquad \text{(M3)}$$

A complement to (M3), where reactions take place not only on the surface of the char as in (M1) and (M2) but also in the surrounding gas phase, was suggested [61]:

$$\text{char-N} + \mathrm{O_2} \rightarrow \cdots \mathrm{NCO} + \mathrm{NO} \rightarrow \mathrm{N_2O} \qquad \text{(M4)}$$

or

$$\text{char-C} + \mathrm{NO} \rightarrow \cdots \mathrm{NCO} + \mathrm{NO} \rightarrow \mathrm{N_2O}$$

Using highly devolatilized char, de Soete [62] showed that (M1) only gave a small (less than 5%) conversion to N_2O. However, if both O_2 and NO were supplied to the reactor, a higher conversion was observed [63]. This corresponds to (M2), which has been investigated further by Sarofim and co-workers [64,65]. They formulated a detailed mechanism that allows for formation of both NO and N_2O. Suzuki et al. [66] devolatilized coals at various temperatures and found that the formation of N_2O was higher for chars produced below the combustion temperature than for those produced at higher temperatures. They attributed this difference to volatiles remaining in the char after primary devolatilization—"slow" volatiles. This corresponds to a contribution to N_2O formation from (M3). They also changed the gas reaction space downstream of their fixed bed and found that a longer gas residence time yields a higher N_2O conversion. This experience was confirmed by a similar test [67] that supports the existence of (M3) or (M4). Another approach was chosen by Miettinen [68], who added ^{15}N-isotope marked NO to a fixed-bed reactor burning char and found both $^{15}N^{14}NO$ and $^{15}N^{15}NO$ in the product gas. This result either requires an extension of (M2) to accommodate two external NO molecules on the char surface or indicates the existence of (M4). To prove this, Miettinen changed the gas flow rate to the reactor and thus the

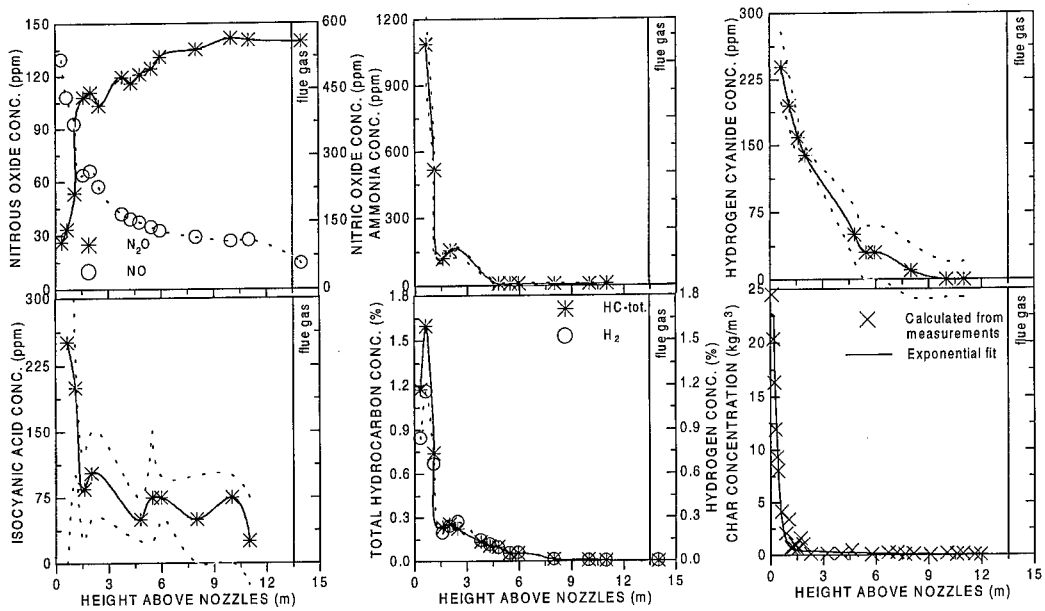

FIG. 8. Gas concentrations in a 14-m-high and 2.5-m^2 cross-section CFB combustor with a bed of silica sand and ashes burning <20 mm bituminous coal. Dotted lines indicate ranges of uncertainty in concentration. The measurements are made on the combustor centerline, and complications caused by fuel feed and secondary-air injection are not shown. Gas concentrations in ppm or % as measured [71].

gas residence time. An effect of gas residence time was found, but a simultaneous change in the oxygen concentration could have influenced the results. By adding HCN to a small silica sand FBC, Klein and Rotzoll [69] found that the conversion to N_2O was lower than in an empty reactor; for example, there was some influence of the surfaces of the bed. When they burned char in the silica sand bed, N_2O was produced; however, in a similar test with a bed of MgO, no N_2O was detected—instead the emission of NO increased. If N_2O is produced in the MgO bed, it would have to be reduced to a large extent on the surfaces of the MgO. However, MgO also has the effect (like CaO) of catalyzing the conversion of HCN to NO, which is a likely reason for the increase of NO in this case. Hence, reaction seems to have taken place in the bed and not only on the surface of the char particles; that is, (M3) or (M4) was shown to have some significance.

In response to the hypothesis of slow volatiles. Goel et al. [70] carried out a test in their small silica sand FBC, burning a bituminous coal. They did not find any influence of time of devolatilization and concluded from this result and other observations that slow volatiles do not play any role; that is, (M2) describes N_2O formation during char combustion.

The conclusion from these efforts to determine a mechanism for N_2O formation from char combustion is that all mechanisms mentioned may have some importance. In view of the different results obtained, further work is needed to determine the relative importance of the mechanisms. The homogeneous and heterogeneous destruction reactions for NO and N_2O have been treated extensively and data have been compiled and transformed for modeling [50]. One problem for quantitative modeling is that the properties of bed materials and chars differ considerably from one material to another.

If data from laboratory reactors are difficult to interpret, how understandable are those from commercial combustors? An example of the progress of combustion is given in Fig. 8 [71], showing gas and char concentrations measured by suction probe in a CFB combustor. The greatest mass of char was found in the bottom, but a considerable number of millimeter-sized char particles was found in the upper parts of the combustor, although the total mass of these particles was small. The NO concentration fell rapidly in the bottom region and then more slowly in the upper part of the combustor. The N_2O concentration, on the other hand, rose rapidly in the bottom and then continued to rise more slowly. Hydrocarbons, as well as hydrogen, represent the volatiles predominantly released and burned in the bottom part. The ammonia concentration behaved similarly to that of the volatiles, whereas HCN appeared to survive to higher levels in the combustor.

It is tempting to interpret the concentration curves of Fig. 8 using fundamental information on the behavior of the nitrogen-containing species.

However, the influence of particles on the reaction paths is not yet clear. Furthermore, interpretation of measured time-average concentrations is difficult, especially in the lower part of the bed, which is subject to large concentration and gas velocity variations; in the upper parts, there are gas pockets with different concentrations, which also complicates the interpretation. An indication of this irregularity is that conventional "slow" gas sampling measures oxygen and reducing gases simultaneously in all measurement locations. Finally, the measurements themselves are difficult in regions with high particle concentrations [72].

Despite these difficulties, certain estimates can be made. A simple plug flow model was shown [73] to represent fairly well the decomposition of N_2O injected in a CFB furnace. The kinetic data used were taken from laboratory investigations of the same chars and bed material as in the actual furnace [74]. Reduction on char was the dominant destruction mechanism in the lower part of the combustor, whereas thermal decomposition was important in the upper part and in the cyclone. Decomposition over other bed material (sand and ashes) played a minor role.

Figure 8 shows that the bottom bed is most important for NO formation and destruction, whereas N_2O is formed above the bottom bed and in the upper parts of the combustor. Therefore, the N_2O emission is not sensitive to what happens in the bottom bed [61] but is strongly dependent on the conditions in the top of the combustor [75].

Discussion and Conclusion

The CFB combustor is a complex device with a shallow, dense bed in the bottom and a transition to a more disperse particle suspension in the top. The combustor processes are influenced greatly by mixing of fuel and oxygen on different scales: the large-scale mixing of the fuel fed into the bed and secondary-air penetration, the intermediate-scale mixing of combustible gases with oxygen, and, finally, a microscale mixing giving rise to dispersion of gas and particles.

There is a lack of knowledge about the relation between fluid dynamics and combustion and about the significance of these mixing processes in combustors. Most of the work done in the field has been carried out in the laboratory on laboratory-scale equipment, and there is a need to confirm the validity of the knowledge gained for application to commercial combustors. This remark also concerns work on limestone properties for sulfur capture and the increasing fundamental knowledge on the reactions related to emissions of nitrogen oxides. In addition, there are several important tasks for FBC research that could not be covered in this brief survey—for instance, agglomeration and sintering when using biofuels, combustion of waste fuels, and related pollutant formation.

REFERENCES

1. Jaud, P., Jacquet, L., Piedfer, O., and Jestin, L., *Proc. Int. Conf. Fluid. Bed Combust.* ASME, New York, 13:721–728 (1995).
2. Åmand, L.-E., Ph.D. Thesis, Department of Energy Conversion, Chalmers University of Technology, 1994.
3. Couturier, M., Doucette, B., Stevens, D., and Poolpol, S., *Proc. Int. Conf. Fluid. Bed Combust.* ASME, New York, 11:107–114 (1991).
4. Werther, J., *Fourth International Conference on Circulating Fluidized Beds,* (Avidan, A. A., Ed.), Mobil Research and Development Corporation, Paulsboro, 1993, pp. 1–14.
5. Boemer, A., Braun, A., and Renz, A., *Proc. Int. Conf. Fluid. Bed Combust.* ASME, New York, 12:585–598 (1993).
6. Berruti, F., Chaouki, J., Godfroy, L., Pugsley, T. S., and Patience, G. S., *Can. J. Chem. Eng.* 73:579–602 (1995).
7. Svensson, A., Johnsson, F., and Leckner, B., *Powder Technol.* 86:299–312 (1996).
8. Werther, J. and Wein, J., *AIChE Symp. Series* 90:31–44 (1994).
9. Andersson, S., Johnsson, F., and Leckner, B., *Proc. Int. Conf. Fluid. Bed Combust.* ASME, New York, 10:239–247 (1989).
10. Glicksman, L. R. and Piper, G. A. III, *Powder Technol.* 53:179–186 (1987).
11. Johnsson, F. and Leckner, B., *Proc. Int. Conf. Fluid. Bed Combust.* ASME, New York, 13:671–679 (1995).
12. Kunii, D. and Levenspiel, O., *Powder Technol.* 61:193–206 (1990).
13. Zhang, W., Johnsson, F., and Leckner, B., *Fourth International Conference on Circulating Fluidized Beds,* (Avidan, A. A., Ed.), Mobil Research and Development Corporation, Paulsboro, 1993, pp. 266–273.
14. Chirone, R., Massimilla, L., and Salatino, P., *Prog. Energy Combust. Sci.* 17:297–326 (1991).
15. Borodulya, V. A. and Epanov, Y. G., *J. Engineer. Phys.* 42:528–533 (1982).
16. Shi, Y. and Fan, L. T., *Ind. Chem. Proc. Des. Dev.* 23:337–341 (1984).
17. Bellgardt, D., Schoessler, M., and Werther, J., *Proc. World Congress III of Chemical Engineering,* Vol. 4, Tokyo 1986, pp. 211–214.
18. Zhang, J. Q., Becker, H. A., and Code, R. K., *Proc. Int. Conf. Fluid. Bed Combust.* ASME, New York, 9:1203–1210 (1987).
19. Agarwal, P. K., and La Nauze, R. D., *Chem. Eng. Res. Des.* 67:457–480 (1989).
20. Borodulya, V. A., Dikalenko, V. I., Palchonok, G. I., and Stanchits, L. K., *Proc. Int. Conf. Fluid. Bed Combust.* ASME, New York, 13:935–942 (1995).

21. Winter, F., Ph.D. Thesis, University of Vienna, 1995.
22. Arena, U., Chirone, R., D'Amore, M., Miccio, M., and Salatino, P., *Powder Technol.* 82:301–316 (1995).
23. Dennis, J. S., Hayhurst, A. N., and Mackley, I. G., *Nineteenth Symposium (International) on Combustion,* The Combustion Institute, Pittsburgh, 1982, pp. 1205–1212.
24. Hayhurst, A. N., *Combust. Flame* 85:155–168 (1991).
25. Lyngfelt, A., Bergqvist, K., Johnsson, F., Åmand, L.-E., and Leckner, B., *Gas Cleaning at High Temperatures* (Clift, R. and Seville, J. P. K., Eds.), Blackie Academic & Professional, Glasgow, 1993, pp. 470–491.
26. Werther, J., Hartge, E.-U., and Kruse, M., *Powder Technol.* 70:293–301 (1992).
27. Yrjas, P., Iisa, K., and Hupa, M., *Fuel* 74:395–400 (1995).
28. Iisa, K. and Hupa, M., *Twenty-Third Symposium (International) on Combustion,* The Combustion Institute, Pittsburgh, 1990, pp. 943–948.
29. Mjörnell, M., Leckner, B., Karlsson, M., and Lyngfelt, A., *Proc. Int. Conf. Fluid. Bed Combust.* ASME, New York, 11:655–664 (1991).
30. Couturier, M. F., Karidio, I., and Steward, F. R., *Fourth International Conference on Circulating Fluidized Beds* (Avidan, A. A., Ed.), Mobil Research and Development Corporation, Paulsboro, 1993, pp. 672–678.
31. Weinell, C. E., Dam-Johansen, K., Johnsson, J. E., Gluchowski, Z., and Lade, K., *Fluidization VII,* Engineering Foundation, New York, 1992, pp. 295–304.
32. Jonke, A. A., Vogel, G. J., Carls, E. L., Ramaswami, D., Anastasia, L., Jarry, R., and Haas, M., *AIChE Symp. Ser.* 68:241–251 (1972).
33. Dennis, J. S. and Hayhurst, A. N., *Twentieth Symposium (International) on Combustion,* The Combustion Institute, Pittsburgh, 1984, pp. 1347–1355.
34. Lyngfelt, A. and Leckner, B., *Chem. Engineer. Sci.* 48:1131–1141 (1993).
35. Mattisson, T. and Lyngfelt, A., *Proc. Int. Conf. Fluid. Bed Combust.* ASME, New York, 13:819–829 (1995).
36. Sarofim, A. F., Goel, S. K., and Morihara, A., *Int. Clean Coal Technology Symposium,* Kitakyushu, NEDO/CCUJ/SCEJ, 1994, pp. 13–27.
37. Lyngfelt, A. and Leckner, B., *Proc. Int. Conf. Fluid. Bed Combust.* ASME, New York, 10:675–684 (1989).
38. Olsson, S. E., Wiman, J., and Almstedt, A. E., *Chem. Engineer. Sci.* 50:581–592 (1995).
39. Ljungström, E. and Langer, V., *J. Institute Energy* 62:34–39 (1989).
40. Ljungström, E. B., *Proc. Int. Conf. Fluid. Bed Combust.* U.S. Department of Energy, DOE/METC-85/6021, 8:853–864 (1985).
41. Hansen, P. F. B., Dam-Johansen, K., and Østergaard, K., *Chem. Engineer. Sci.* 48:1325–1341 (1993).
42. Daves, S. G., Mordecai, M., Brown, D., and Burnard, G. K., *Proc. Int. Conf. Fluid. Bed Combust.* ASME, New York, 13:1275–1282 (1995).
43. Schemenau, W. and van den Berg, C., *VDI Conference Wirbelschichtfeuerungen,* VDI-Berichte 1081, VDI-Verlag, Düsseldorf, 1993, pp. 19–44.
44. Illerup, J. B., Dam-Johansen, K., and Johnsson, J. E., in *Gas Cleaning at High Temperatures* (Clift, R. and Seville, J. P. K., Eds.), Blackie Academic & Professional, Glasgow, 1993, pp. 492–509.
45. Davies, N. H. and Laughlin, K. M., *Twenty-Fifth Symposium (International) on Combustion,* The Combustion Institute, Pittsburgh, 1994, pp. 211–218.
46. Kramlich, J. C. and Linak, W. P., *Prog. Energy Combust. Sci.* 20:149–202 (1994).
47. Wójtowicz, M. A., Pels, J. R., and Moulijn, J. A., *Fuel Process. Technol.* 34:1–71 (1993).
48. Mann, M. D., Collings, M. E., and Botros, P. E., *Prog. Energy Combust. Sci.* 18:447–461 (1992).
49. Hayhurst, A. N. and Lawrence, A. D., *Prog. Energy Combust. Sci.* 18:529–552 (1992).
50. Johnsson, J. E., *Fuel* 73:1398–1415 (1994).
51. Glarborg, P., Miller, J. A., and Kee, R. J., *Combust. Flame* 65:117–202 (1986).
52. Miller, J. A. and Bowman, C. T., *Prog. Energy Combust. Sci.* 15:287–338 (1989).
53. Kilpinen, P. and Hupa, M., *Combust. Flame* 85:94–104 (1991).
54. Hulgaard, T., Glarborg, P., and Dam-Johansen, K., *Proc. Int. Conf. Fluid. Bed Combust.* ASME, New York, 11:991–998 (1991).
55. Baumann, H. and Möller, P., *Erdgas* 44:29–33 (1991).
56. Bassilakis, R., Zhao, Y., Solomon, P. R., and Serio, M. A., *Energy Fuels* 7:710–720 (1993).
57. Leppälahti, J., *Fuel* 74:1363–1368 (1995).
58. Shimizu, T., Tachiyama, Y., Fujita, D., Kumazawa, K., Wakayama, O., Ishizu, K., Kobayashi, S., Shikada, S., and Inagaki, M., *Energy Fuels* 6:753–757 (1992).
59. Jensen, A., Johnsson, J. E., and Dam-Johansen, K., *Proc. Int. Conf. Fluid. Bed Combust.* ASME, New York, 12:447–454 (1993).
60. Kramlich, J. C., Cole, J. A., McCarthy, J. M., Lanier, W. S., and Sorley, J. A., *Combust. Flame* 77:375–384 (1989).
61. Åmand, L.-E. and Leckner, B., *Energy Fuels* 7:1097–1107 (1993).
62. de Soete, G. G., *Twenty-Third Symposium (International) on Combustion,* The Combustion Institute, Pittsburgh, 1990, pp. 1257–1264.
63. Mochizuki, M., Koike, J., and Horio, M., *Proc. of the 5th Int. Workshop on Nitrous Oxide Emissions* NIRE/IFP/EPA/SCEJ, Tsukuba, 1992, pp. 237–244.
64. Tullin, C. J., Goel, S., Morihara, A., Sarofim, A., and Beér, J., *Energy Fuels* 7:796–802 (1993).
65. Goel, S. K., Morihara, A., Tullin, C. J., and Sarofim, A., *Twenty-Fifth Symposium (International) on Combustion,* The Combustion Institute, Pittsburgh, 1994, pp. 1051–1059.
66. Suzuki, Y., Moritomi, H., Kido, N., Ikeda, M., Suzuki, K., and Torikai, K., *Proc. of the 5th Int. Workshop on Nitrous Oxide Emissions,* NIRE/IFP/EPA/SCEJ, Tsukuba, 1992, pp. 245–253.

67. Feng, B., Liu, H., Yuan, J., Lin, Z., Liu, D., and Leckner, B., *Energy Fuels* 10:203–208 (1996).
68. Miettinen, H., *Energy Fuels* 10:197–202 (1996).
69. Klein, M. R. and Rotzoll, G., *VGB Kraftwerkstechnik* 74:1072–1080 (1994).
70. Goel, S., Zhang, B., and Sarofim, A. F., *Combust. Flame* 104:213–217 (1996).
71. Åmand, L.-E. and Leckner, B., *Proc. of the Sixth International Workshop on N_2O Emissions*, ÅAU/HUT/VTT/NIRE/IFP/USEPA, Turku, 1994, pp. 95–113.
72. Kassman, H., Abul-Milh, M., and Åmand, L.-E., *Proc. Int. Conf. Fluid. Bed Combust.* 13:1447–1454 (1995).
73. Johnsson, J. E., Åmand, L.-E., Dam-Johansen, K., and Leckner, B., *Energy Fuels* 10:970–979 (1996).
74. Johnsson, J. E. and Dam-Johansen, K., *Proc. Int. Conf. Fluid. Bed Combust.* ASME, New York, 13:859–869 (1995).
75. Åmand, L.-E. and Andersson, S., *Proc. Int. Conf. Fluid. Bed Combust.* ASME, New York, 10:49–56 (1989).

COMMENTS

Ivan Milosavljevic, Air Liquide, France. When you did the 1/9 scaling, did you scale the bed particle size? According to what law was the scaling done and what are the values for non-scaled and scaled particle size and density?

Author's Reply. The scaling used in the video shown was done employing the "simplified scaling laws" described by Glicksman et al. [1]. This means that a particle size and density of 0.06 mm and 7800 kg/m^3 was used in the cold model corresponding to 0.31 mm and 2600 kg/m^3 in the hot bed of the boiler. (Actually we did not manage to fulfil completely the density criterion. The model density should have been 9725 kg/m^3.)

REFERENCE

1. Glicksman, L. R., Hyre, M. R., and Woloshun, K., *Powder Technol.* 77:177–199 (1993).

Twenty-Sixth Symposium (International) on Combustion/The Combustion Institute, 1996/pp. 3243–3251

THE FATE OF FIXED CARBON DURING THE FLUIDIZED-BED COMBUSTION OF A COAL AND TWO WASTE-DERIVED FUELS

UMBERTO ARENA,[1,2] RICCARDO CHIRONE[1] AND PIERO SALATINO[1,3]

[1]*Istituto di Ricerche sulla Combustione*
Consiglio Nazionale delle Ricerche (CNR)
Piazzale Tecchio 80, 80125 Napoli, Italy

[2]*Istituto di Energetica*
Università di Perugia
Str. S. Lucia Canetola, 06125 Perugia, Italy

[3]*Dipartimento di Ingegneria Chimica*
Università "Federico II" di Napoli
Piazzale Tecchio 80, 80125 Napoli, Italy

The fate of fixed carbon during fluidized-bed combustion of a bituminous coal and two alternative fuels, a refuse-derived fuel (RDF) and a tyre-derived fuel (TDF), was investigated. A simple model was developed based on the assumption that fixed carbon present in the bed could be lumped into a coarse particles phase and a fine carbon phase. The model is based on a network of paths representing the generation of coarse and fine char particles from the parent fuel by primary fragmentation, the fine particle production by comminution of coarse char, the combustion of the coarse and of the fine char particles, as well as the elutriation of fines.

Results of computations of carbon conversion were in good agreement with those measured in batchwise experiments with each of the three fuels. Conversion of the coal takes place mainly via fuel devolatilization to coarse char which further reacts to gaseous products. Conversion of TDF occurs via the generation, upon devolatilization, of a multitude of fines which eventually undergo combustion and elutriation. The phenomenology associated with RDF fluidized-bed combustion is intermediate between those of coal and TDF. The resulting framework for the evaluation of fixed carbon balance helps in identifying key factors in the conversion of such widely different fuels.

Introduction

Fuel flexibility is one of the reasons for the worldwide commercial success of the fluidized-bed technology, which is now available for energy production from conventional fuels as well as from wastes and alternative fuels [1]. A recent study [2] confirmed that design and operation criteria of bubbling and circulating fluidized-bed combustors can be remarkably affected by the occurrence of comminution phenomena (primary fragmentation, attrition, and char fragmentations). The existence and the relevance of these mechanisms of size reduction, extensively studied for coals over the last ten years (Ref. 3 and references therein, and Refs. 4–6), have been extended to metallurgical and petroleum cokes [7, 8], electrographite [9], refuse-derived fuel [10], ebonite, and tyre-derived fuel [11]. In particular, it has been recently pointed out that the general scenario of comminution phenomena outlined for coals and other low-volatile fuels [3] needs to be reformulated when considering waste-derived, high-volatile fuels [10,11].

The aim of the present work was the definition of a general framework able to highlight differences and similarities in the fluidized-bed combustion behaviors of low- as well as of high-volatile fuels. A simple mathematical model was developed to follow the fate of fixed carbon fed to a fluidized-bed combustor operated at steady state. The basic assumption was that carbon could be lumped into a coarse particles phase and a fine carbon phase. Experimental results obtained with three fuels [3, 10, 11] have been used as a basis to check the validity of the model. The fuels, namely a South African (SA) bituminous coal, a refuse-derived fuel (RDF), and a tyre-derived fuel (TDF), were selected because they exhibited peculiar comminution patterns that define extreme behaviors.

Experimental

Proximate and ultimate analyses of fuels tested, all available on the market, are reported in Table 1. The equivalent diameter of feed particles was always 4.1 mm. Bed inert material was silica sand, having a size range of 0.3–0.4 mm and a Sauter mean diameter of

TABLE 1
Characteristics of fuels tested

FUEL	SA COAL	RDF	TDF
Proximate analysis (%, as received)			
Moisture	2.3	1.8	1.9
Volatile Matter	23.0	75.1	63.4
Ash	14.5	13.5	4.3
Fixed carbon	60.2	9.6	30.4
Ultimate analysis (%, dry basis)			
Carbon	67.2	49.4	83.8
Hydrogen	3.7	6.9	6.9
Nitrogen	1.2	0.8	0.6
Sulphur	0.6	0.3	2.0
Chlorine	–	0.5	–
Ash	14.8	13.7	4.4
Oxygen	12.5	28.4	2.3
Low calorific value (kJ/kg)	25,400	21,100	36,800
Fuel particle density (kg/m^3)	1,420	1,230	1,070
Char particle density (kg/m^3)	1,130	1,110	1,450

TABLE 2
Experimental results of primary fragmentation tests

Fuel	S_f	N_{out}/N_{in}	x_C	d_{Sm} (mm)
SA coal	0.14	2.9	0.99	3.8
RDF	0.30	1.4	0.95	3.8
TDF	1.00	>1000	0	–

0.36 mm. Minimum fluidization velocity of the sand was 0.02 m/s at 850°C.

Experiments were carried out in two laboratory-scale, bubbling, fluidized-bed combustors, both 41 mm i.d., operated batchwise. The first, a basket-equipped combustor, was used to investigate fragmentation phenomena; fragmented and unfragmented particles could be retrieved at any time after injection by means of a basket having a mesh of 0.8 mm and characterized by chemical and sieving analyses. The second, a two-exit head combustor, was used to measure the elutriation rate of carbon fines by means of two filters periodically inserted at the combustor outlet.

Whatever the combustor used, experiments were carried out by injecting a batch of particles (with a corresponding amount of fixed carbon equal to 2 g) into a bed of 180 g of silica sand, kept at 850°C and fluidized with nitrogen or a nitrogen-oxygen mixture at a superficial gas velocity of 0.8 m/s. Details of apparatus and techniques are given elsewhere [3].

Experimental Results

The parameters that define the relevance of primary fragmentation are reported in Table 2 for the three fuels tested: the probability of particle breakage, S_f, the particle multiplication factor, N_{out}/N_{in}, the Sauter mean particle diameter of coarse fragments, d_{Sm}, evaluated on mass basis, and the mass fraction x_c of fixed carbon which is present as coarse particles just after devolatilization.

In the experiments carried out with TDF, no particles were collected by the basket ($x_c = 0$). The feed particles turned into a multitude of fines, probably as a consequence of the fast depletion of the continuous rubbery matrix. The Sauter mean diameter of the generated fragments was about 0.12 mm [11]. RDF and South African coal both underwent moderate primary fragmentation, even though coal particles presented values of S_f lower than that of RDF and produced a larger number of fragments.

Figures 1 and 2 show the carbon elutriation rates, E, evaluated at different times during batchwise experiments when the combustor was fluidized by nitrogen or by a nitrogen-oxygen mixture having an oxygen content of 1.5%, respectively. According to the standard procedure [3], char particles were fed to the combustor for tests with RDF and South African coal. Due to the above-described primary fragmentation behavior, experiments with TDF were carried out by feeding fresh fuel particles.

The TDF curve obtained under inert conditions (Fig. 1) shows the same shape and higher values for the carbon elutriation rate than those relative to oxidizing conditions (Fig. 2). These findings, coupled with the absence of coarse char after devolatilization, suggest that the key phenomenon in this case was the fast and complete degradation of the connecting matrix of tyre particles and that the extent to which generated fines were burned before escaping the

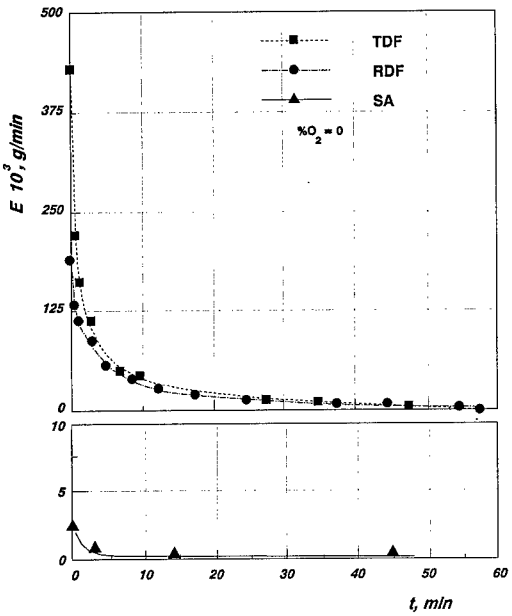

FIG. 1. Carbon elutriation rate as a function of time from batchwise experiments under inert conditions.

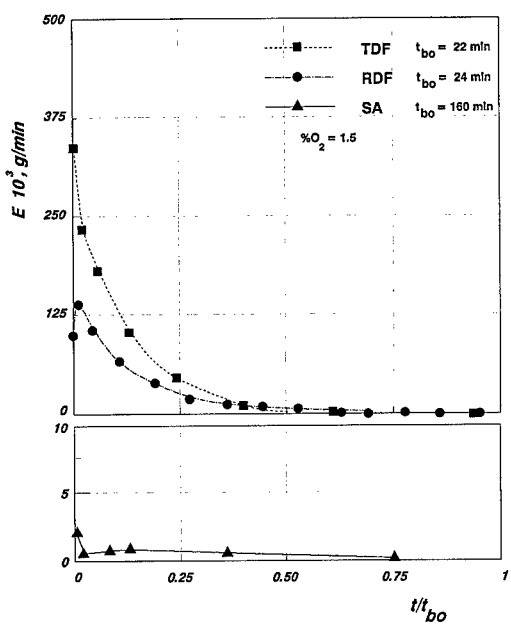

FIG. 2. Carbon elutriation rate as a function of time from batchwise experiments under oxidizing conditions.

combustor was not negligible. On the whole, the comminution behavior of TDF particles can be described by the single pattern in Fig. 3A.

For char from RDF, in spite of the limited amount of fines produced by primary fragmentation (x_c = 0.95), fine generation under inert conditions occurred at a rate more than one order of magnitude larger and over a time scale much shorter than for SA coal char. The integration of E vs. time curves over the first 80 min indicates that all the RDF fed into the combustor escaped the bed while only 3% of the SA coal char did. The experiments under oxidizing conditions showed, for RDF char particles, behavior opposite to that of SA char: carbon elutriation rates were less than those measured under inert conditions. This feature might be explained by considering that a relevant amount of carbon fines burned before leaving the combustor and that a fraction of devolatilized particles burned during the evolution of comminution, thereby leaving a reduced amount of carbon available for fines generation. On the whole, the most likely comminution patterns for RDF particles appear those sketched in Fig. 3B. Note that RDF directly generates some carbon fines upon primary fragmentation as a consequence of the incoherence of fresh material and the high content of volatile matter.

The comminution behavior of coals, summarized in Fig. 3C, is widely addressed in several studies and reviewed by Massimilla and coworkers [3].

A Systematic Approach to Fixed Carbon Balance

The fate of fixed carbon during the combustion of a fuel in a fluidized bed will be analyzed with reference to the graph of Fig. 4. Each variable indicates a mass flow rate from or to a component block. Square-shaped blocks represent the two "phases" in which the fixed carbon can be assumed to be present in the bed: coarse (block C) and fine (block F) particles. The two circle-shaped blocks represent tee nodes: the first works as a stream divider, representing primary fragmentation of fuel particles, the second works as a stream mixer, summing up gaseous products of combustion of "coarse" and "fine" fixed carbon.

The graph in Fig. 4 suggests the following balance equations on fixed carbon, present in the bed as coarse and fine "phases" under steady-state conditions:

$$F_{0C} = x_C F_0 \tag{1}$$

$$F_{0F} = (1 - x_C) F_0 \tag{2}$$

$$F_{0C} = F_{CF} + F_{CP} \tag{3}$$

$$F_{0F} + F_{CF} = F_{FP} + E \tag{4}$$

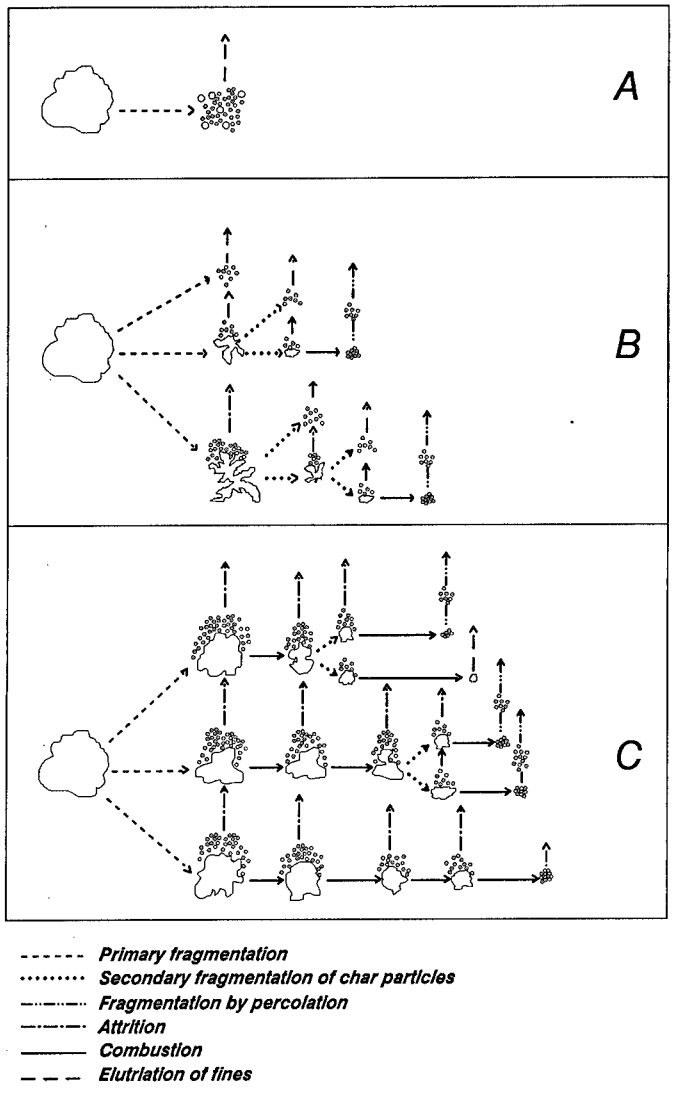

FIG. 3. Patterns of series-parallel comminution phenomena for TDF (A), RDF (B), and coals (C).

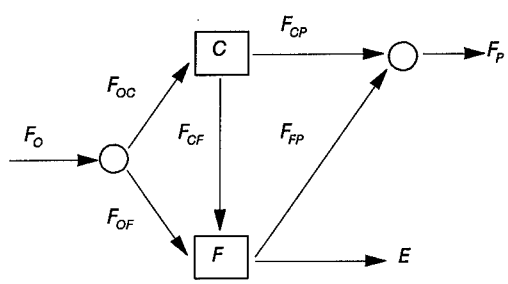

FIG. 4. The graph representing the fate of fixed carbon during fluidized-bed combustion.

$$F_0 - E = F_{CP} + F_{FP} = F_P \tag{5}$$

$$F_{CP} = \frac{6W_C M}{\rho d_C} \frac{c}{(1/k_{gC} + 6/\alpha_C k_v d_C)} \tag{6}$$

$$F_{FP} = \frac{6W_F M}{\rho d_F} \frac{c}{(1/k_{gF} + 6/\alpha_F k_v d_F)} \tag{7}$$

$$F_{CF} = k_{CF} W_C \tag{8}$$

$$E = k_{el} W_F \tag{9}$$

for which the following definitions are established:

- F represents mass flow rates from or to a phase, according to the direction indicated by the subscripts (0, feed; C, coarse particles; F, fine particles; P, gaseous products).

- W_C and W_F are the amounts of carbon in the bed as coarse and fine particles, respectively.
- The feed rate of fixed carbon, F_0, is obtained for each of the three fuels by multiplying the fuel feed rate by the fixed carbon content of the fuel, as evaluated by the devolatilization experiments in a bed fluidized with nitrogen.
- x_C is the fraction of fixed carbon in the fuel, which is present in the bed as coarse particles just after primary fragmentation. Correspondingly, $(1 - x_C)$ represents the fraction of fixed carbon that is found as fines.
- d_C and d_F are the mean diameters of the coarse and fine carbon particles.
- c is the average oxygen concentration present in the bed at steady state.
- k_{gC} and k_{gF} are the mass transfer rate coefficients of the coarse and fine particles. They are calculated from expressions for the Sherwood number.
- k_v is a combustion rate constant per unit particle volume, while α_C and α_F are the effectiveness factors of the coarse and of the fine particles [2].
- k_{CF} is a constant expressing the rate, per unit mass of coarse carbon, of fines generated by attrition and by char particle fragmentations.
- k_{el} is an elutriation constant.

Quantitative Assessment of Fixed Carbon Evolution

Evaluation of Model Parameters

Equations 1–9 can be solved once parameters expressing the rates of carbon transfer along each path outlined in Fig. 4 are known. The procedure to evaluate model parameters is separately discussed in here.

Fraction of fixed carbon as coarse phase immediately after primary fragmentation:

The fraction $x_C = F_{0C}/F_0$ of fixed carbon which is present as coarse particles after primary fragmentation was directly obtained from experimental results reported in Table 2.

Average size and density of coarse and fine carbon particles in the bed:

Following the procedure indicated in Ref. 2, the average size of coarse carbon in the bed was approximated as

$$d_C = 0.8\, d_{Sm} \left(\frac{n_2 + 1}{2}\right)^{-1/3} \tag{10}$$

where d_{Sm} is the average size of coarse fragments immediately after primary fragmentation (Table 2), and n_2 is the secondary fragmentation multiplication factor, expressing the average total number of coarse fragments generated by secondary fragmentation over a particle lifetime. As discussed in Ref. 2, 0.8 expresses the ratio between the average and the initial particle diameter according to a shrinking particle conversion model. On the basis of previous work [3,11], it was assumed that $n_2 = 1$ and $n_2 = 4$ for SA and RDF, respectively.

The average sizes of fine particles d_F were evaluated by computer-aided image analysis of carbon elutriated during batchwise combustion experiments. They were $d_F = 140$, 120, and 150 μm for SA, TDF, and RDF, respectively.

Densities of fines generated by comminution were assumed equal to those of coarse particles (Table 1).

Terminal velocities of fine particles, calculated on the basis of average particle sizes and densities for the three fuels, were close to each other and equal to about 0.2 m/s.

Parameters of the combustion kinetics of coarse and fine phases:

A value of 2 was assumed for the Sherwood number. For coarse particles, this value is smaller than that predicted by available correlations [12], but is suggested by experimental results obtained with different fuels using the same apparatus and operating conditions [8,13,14]. For fine particles, the same value was dictated by the considerations that mass transfer is dominated by molecular diffusion and that carbon fines are smaller than bed solids. The latter argument implies that the emulsion phase is not likely to represent a restriction to the diffusional flow of oxygen toward the burning, fine carbon particle. The intrinsic reaction rate constant per unit particle volume of SA char was calculated using data and the procedure indicated in the Appendix of Ref. 2. As detailed therein, a micro-macro approach was adopted to evaluate the effectiveness factor. Reaction rate constants and effective intraparticle diffusivities for the RDF and the TDF chars have been evaluated by parallel investigation [15] using a thermogravimetric technique [16]. The value of k_v was 2.1×10^3, 1.4×10^3, and 1.2×10^5 s^{-1} for SA, RDF, and TDF chars, respectively. Effective diffusivities were 3.2×10^{-5}, 3.0×10^{-5}, and 4.5×10^{-8} m^2/s in the order.

Elutriation rate:

The evaluation of the elutriation rate constant of fine particles was based on the analysis of the curve in Fig. 1 relative to TDF. Since primary fragmentation was completed before the beginning of elutriated fine collection, E could be considered as the elutriation rate after sudden injection of a batch of fine particles. The governing equation is

$$E = -\frac{dW_F}{dt} = k_{el} W_F \tag{11}$$

which, upon integration, yields

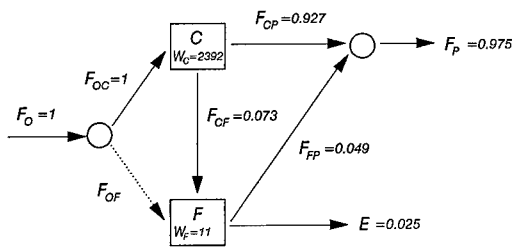

FIG. 5. Balance on fixed carbon for the South African coal.

$$W_F = W_F(t = 0) \exp[-k_{el}t] \quad (12)$$

or, equivalently,

$$E = E(t = 0) \exp[-k_{el}t] \quad (13)$$

A value of $k_{el} = 0.14$ min^{-1} was obtained by regression analysis of data points in Fig. 1.

This procedure could not be applied to char from RDF and SA coal. In these cases, rates of carbon fines at the reactor outlet resulted from the concurrence of two phenomena: the attrition of coarse particles and the subsequent elutriation of the generated fines. Model computations were carried out with reference to these fuels by assuming the same value of the elutriation constant k_{el} calculated for TDF. This assumption is reinforced by the already-noted closeness of terminal velocities of fine particles for the three fuels.

Rate of generation of carbon fines by comminution of coarse particles:

For SA coal, the value of k_{CF} in equation 8 can be estimated starting from the value of the attrition constant $k_a = 1.3 \times 10^{-7}$ proposed in Ref. 3 for the same operating conditions, taking into account that $E = k_a (U - U_{mf}) W_C/d_C = k_{CF} W_C$, where $(U - U_{mf})$ is the excess of the gas superficial velocity with respect to the minimum for fluidization.

Due to the absence of coarse particles after devolatilization, k_{CF} is meaningless in the case of fluidized-bed combustion of TDF.

The evaluation of k_{CF} for RDF is not straightforward. It was based on the time-resolved profile of carbon elutriation rates of RDF under inert conditions (Fig. 1). In the absence of combustion, the rate of carbon leaving the combustor is the result of two processes in series: comminution of coarse particles and elutriation of the generated fines. Both processes occur over comparable time scales for RDF and are linearly dependent on the coarse (W_C) and on the fine (W_F) carbon loadings, respectively (equations 8 and 9). Accordingly, the carbon elutriation rate of fines can be expressed as

$$E = k_{el} \frac{k_{CF}}{k_{el} - k_{CF}} W_C(t = 0) \cdot \{\exp[-k_{CF}t] - \exp[-k_{el}t]\} \quad (14)$$

where the value of the elutriation rate constant is fixed ($k_{el} = 0.14$ min^{-1}) and the constant k_{CF} can be evaluated by fitting equation 14 against data in Fig. 1. A value of 1.3 min^{-1} was calculated following this procedure.

Note that the value of k_{CF} evaluated for RDF according to this procedure is relative to fine generation under inert conditions. It is likely that fine generation under oxidizing conditions is affected by an enhancement due to combustion similar to that observed and widely discussed in previous studies on attrition of coals [3]. In this respect, the value of $k_{CF} = 1.3$ min^{-1} used in computations should be considered the lower bound to possible values of k_{CF}. The influence of uncertainties on the value of k_{CF} for RDF will be further addressed in discussing model results relative to this fuel.

Model Results

Input variables assumed in the computations correspond to operating conditions adopted in the combustion experiments and reported in the Experimental section. For convenience, a common arbitrary basis regarding the fixed carbon feed rate, $F_0 = 1$ g/s, was chosen in all the cases.

Model results are schematically summarized in Figs. 5–7. These represent modifications of Fig. 4 on account of calculations of carbon transfer rates along each path. In particular, the ratio F_P/F_0 is, by definition, the carbon conversion efficiency η. Calculated values of η are 0.975, 0.75, and 0.69 for SA, RDF, and TDF, respectively. They turn out to be larger than those evaluated from batchwise experiments (0.88, 0.72, and 0.55, in the order). It is likely that fine particles spent much of their lifetime in the splashing region or in the disengagement section of the freeboard, which during experiments was purposely kept at a temperature lower than 850°C [3]. It is worth noting that the comparison between values of η relative to steady-state operation of the reactor with values of η averaged over batchwise experiments is legitimate as far as the combustor can be considered differential with respect to oxygen concentration.

Figures 5–7 provide a direct indication of paths relevant to overall carbon conversion in the various cases. Discussion of results will be separately afforded for each of the three fuels.

SA coal:

Figure 5 represents the scenario most frequently encountered in combustion of coals and of other low-volatile fuels: conversion to gaseous products

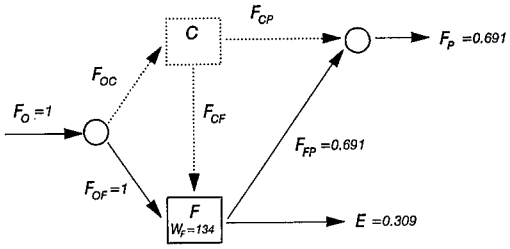

FIG. 6. Balance on fixed carbon for the Tyre-derived fuel.

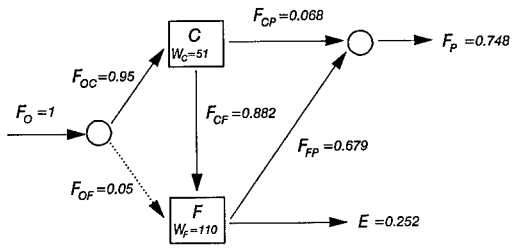

FIG. 7. Balance on fixed carbon for the refuse-derived fuel.

takes place mainly via devolatilization of the fuel to coarse char and further reaction of the latter. Bed carbon consists almost entirely of coarse particles. As a consequence, combustion kinetics are primarily controlled by mass transfer between the bulk of the emulsion phase and the particle. It must be noted that other phenomena (bubble-emulsion phase gas exchange, gas and solid flow patterns in the emulsion phase) not considered in this work may play important roles as well. Fine generation accounts for less than 10% of the overall fixed carbon balance. Though limited, this contribution can significantly affect the efficiency and the environmental impact of the operation.

TDF:

This fuel lies at the opposite limit of the broad range of fluidized-bed combustion scenarios: conversion occurs essentially through the generation of a stream of fines, followed by the parallel competitive progress of fine particle combustion and elutriation (Fig. 6). Combustion is primarily controlled by the intrinsic kinetics of char oxidation as well as by the pore space accessibility expressed by the effective intraparticle diffusivity. Elutriation is controlled by the hydrodynamics of the bed and by the interactions of the fines with the bed solids [17]. The critical influence on conversion of parameters such as the residence time of fines and the intrinsic oxidation kinetics leads to the expectation that the process be strongly sensitive to variables like bed and freeboard temperature, fluidization velocity, and bed inert size.

RDF:

The scenario exhibited by RDF appears somewhat intermediate between those observed for SA coal and TDF: though the primary product of devolatilization is coarse particles (as for SA coal) their strong propensity to comminution gives rise to huge generation of fines which (as for TDF) appear to be the primary source of gaseous products (Fig. 7). Coarse char contributes less than 10% to overall carbon conversion. It must be noted that this contribution would have been even lower if, as already discussed, a larger value of k_{CF} were assumed on account of the attrition enhancement due to combustion. On the whole, it can be stated that conversion occurs mainly through fine carbon combustion, in spite of uncertainties as to the precise value of k_{CF}. As in the case of TDF, parameters affecting the intrinsic kinetics of char oxidation, the accessibility of the pore space, and the residence time of fines are likely to be of great importance.

Conclusions

Analysis of comminution phenomena taking place during the fluidized-bed combustion of one coal and two waste-derived, high-volatile fuels was carried out by means of batchwise experiments. Results are suggestive of comminution scenarios that differ considerably from each other, depending on the physico-chemical nature of the fuel. Negligible primary fragmentation and limited fine generation by attrition were observed in the fluidized combustion of the coal. Moderate primary fragmentation of the fuel, followed by huge comminution of the char into fines, characterized the conversion of the refuse-derived fuel. Complete disintegration of fuel particles into a stream of fines upon devolatilization, followed by fine char oxidation, was observed in the combustion of the tyre-derived fuel.

A general framework for the evaluation of the fate of fixed carbon during the fluidized-bed combustion of these widely different fuels was outlined. According to the proposed approach, fixed carbon can be present in the bed as either coarse or fine elutriable particles. A network of series-parallel processes contributes to the transformation of fixed carbon through the different phases toward the final products, either gaseous products or elutriated carbon.

Quantitative assessment of fixed carbon balance was carried out with reference to each of the three fuels investigated. To this end, parameters expressing rates of carbon transfer along each path were evaluated either from independent experimentation or by working out results of batchwise experiments. Computation results help in underlining factors that

play key roles in the conversion of each of the fuels investigated. In particular, it appears that parameters that define the fate of fine carbon particles, namely their rate of generation by comminution, their residence times in the reactor, and their combustion rate, can be of utmost importance in the overall kinetics and efficiency of high-volatile fuel fluidized-bed combustion.

REFERENCES

1. Anthony, E. J., *Prog. Energy Combust. Sci.*, 21:239–268 (1995).
2. Arena, U., Chirone, R., D'Amore, M., Miccio, M., and Salatino, P., *Powder Technol.* 82:301–316 (1995).
3. Chirone, R., Massimilla, L., and Salatino, P., *Prog. Energy Combust. Sci.* 17:297–326 (1991).
4. Brown, R. C., Ahrens, J., and Christofides, N., *Combust. Flame* 89:95–102 (1992).
5. Walsh, P. M. and Li, T., *Combust. Flame* 99:749–757 (1994).
6. Miccio, F. and Salatino, P., *Twenty-Fourth Symposium (International) on Combustion,* The Combustion Institute, Pittsburgh, 1992, pp. 1145–1151.
7. Arena, U., Chirone, R., D'Amore, M., and Massimilla, L., *Combust. Flame* 57:123–125 (1984).
8. Chirone, R., D'Amore, M., and Massimilla, L., *Twentieth Symposium (International) on Combustion,* The Combustion Institute, Pittsburgh, 1984, p. 1505–1511.
9. Halder, P., Salatino, P., and Arena, U., *Can. J. Chem. Eng.* 66:163–167 (1988).
10. Arena, U., Cammarota, A., Chirone, R., and D'Anna, G., in *Proceedings of the Thirteenth International Conference on FBC,* (K. J. Heinschel, Ed.), American Society of Mechanical Engineers, Book no. H0937B, 1995, p. 943–949.
11. Arena, U., Cammarota, A., and Chirone, R., in *Fluidization VIII,* (C. Laguerie and J. F. Large, Eds.), Engineering Foundation, New York, 1996, in press.
12. La Nauze, R. D., Jung, K., and Kastl, J., *Chem. Eng. Sci.* 39:1623–1633 (1984).
13. Salatino, P. and Massimilla, L., *Chem. Eng. Sci.* 44:1091–1099 (1989).
14. Chirone, R., Salatino, P., and Massimilla, L., *Combust. Flame* 77:79–90 (1989).
15. Masi, S. and Senneca, O., private communication, 1996.
16. Masi, S., Miccio, M., Salatino, P., and Massimilla, L., *Proceedings of the Tenth International Conference on FBC,* (A. M. Manaker, Ed.), American Society of Mechanical Engineers, Book no. I0290B, 1989, p. 775–781.
17. Kitano, K., Wisecarver, K. D., Satija, S., and Fan, L. S., *Ind. Eng. Chem. Res.* 27:1259–1264 (1988).

COMMENTS

. E. Jacob Akanetuk, Stanford University, USA. The results presented support Mitchell and Akanetuk's [1] observation that fragmentation during devolatilization is the dominant mode of communication. The two studies were performed using very different carbon fuels and combustion environments, yet they yielded the same conclusion. Could you comment of how general this observation is?

REFERENCE

1. Mitchell, R. E. and Akanetuk, *Twenty-Sixth Symposium (International) on Combustion,* The Combustion Institute, Pittsburgh, 1996, pp. 3137–3144.

Author's Reply. With reference to combustion/gasification of carbon fuels in fluidized beds, the conclusion that fragmentation during devolatilization (or primary fragmentation, in the context of the present work) is *always* the dominant mode of comminution cannot be drawn a priori. Other comminution processes, like char fragmentation or attrition by abrasion, can be equally or even more relevant to the generation of elutriable fines. The three fuels considered in the present work provide extreme examples of this variety of behaviour. Only TDF undergoes significant primary fragmentation. On the contrary, generation of elutriable carbon fines during RDF and Coal combustion occurs mainly via comminution of the char. A more extensive discussion on the influence of coal properties and combustor operating conditions on the extent of primary fragmentation is provided in Ref. 3 (in paper).

•

Dr. John Stubington, University of New South Wales, Australia. Your overall model provides a nice picture and emphasizes the relative importances of the comminution processes. However, what is the effect on predicted combustion efficiencies of your assumption of oxygen concentration (1.5%), given that we know oxygen concentrations in FBC vary over a wide range, from highly-reducing conditions to as high as perhaps 18% oxygen?

Author's Reply. The overall fixed carbon combustion efficiency is determined, according to the network of Fig. 1, by the competition between parallel processes of carbon fines combustion and elutriation. Therefore, combustion efficiency will depend on variables affecting their relative rates: oxygen concentration (or excess air) but also

combustion temperature and gas superficial velocity. They are bound to influence combustion efficiency to an extent which is larger, the larger the rate of carbon fines generation by comminution. Accordingly, with reference to the three fuels considered in the present work, larger sensitivity of combustion efficiency on oxygen concentration is anticipated in the case of TDF and RDF in respect to the South African coal.

Twenty-Sixth Symposium (International) on Combustion/The Combustion Institute, 1996/pp. 3253–3259

PROGRESS OF COMBUSTION IN THE FURNACE OF A CIRCULATING FLUIDIZED BED BOILER

ANDERS LYNGFELT, LARS-ERIK ÅMAND AND BO LECKNER
Chalmers University of Technology
Göteborg, Sweden

Gas concentrations were measured in the combustion chamber of a circulating fluidized bed boiler (FBB). Sieved fractions of solid material sampled at different heights were analyzed for combustible matter. Together with the bulk density profile obtained from pressure drop measurements, these data were used to obtain the distribution of combustible matter in the combustion chamber.

High concentrations of combustible gases and low concentrations of oxygen were found in the bottom part, indicating that the bed material to a large extent is subject to reducing conditions. From the gas concentration profile, the degree of combustion/fuel conversion versus boiler height was deduced. This procedure, however, involves a major error since measured concentrations give a misrepresentation of the concentrations of the gas flow. This is explained by a through flow of gas through bubbles or voids in the bottom bed with high velocity and high concentration of oxygen.

A correction for the bypass flow was attempted, which increases the O_2 concentration in the lowest position from 2.5 to 11%. This correction compared favorably with the fuel conversion versus height, derived from the distribution of solid combustibles (char) in the combustion chamber.

The results show that the concentrations measured in the bottom part of the combustion chamber do not represent the flow and cannot, accordingly, be directly used in mass balances. This misrepresentation has consequences for the interpretation of gas measurements in the bottom part of FBBs.

Introduction

The purpose of this work is to improve understanding of combustion in circulating fluidized bed boilers (FBBs), by measuring local concentrations of gas and solid combustibles inside the combustion chamber. It is also intended to provide data that can serve for comparison with fluidized bed combustion modeling.

Most measurements of gas concentrations in fluidized bed combustors are from small units, although some data are available from larger units [1,2]. The fluidization conditions and the solids distribution in small units differ from those observed in larger units. This is reflected in measured gas concentration profiles [3], which are quite different from those obtained in the larger unit of the present study.

This work is part of a broader program involving local measurements under different operating conditions, and the present investigation treats the combustion of coal at full load and under normal air-staging conditions.

Experimental Description

The 12-MW circulating FBB used [4] is a commercial boiler, but it was built for research purposes and is equipped for various types of measurements. The square cross section of the combustion chamber is about 2.5 m^2 and the height is 13.5 m with the cyclone outlet at about 11 m above the bottom plate. The fuel was a bituminous coal with 40% volatiles and a particle size less than 20 mm ($d_{50} \sim 10$ mm). No limestone was added. The bed temperature was 850 °C, the load 8 MW, the air-to-fuel ratio 1.2, the primary-air fraction about 60%, and the dense bottom bed height about 0.5 m.

Gas concentrations were recorded by two sets of analyzers, one for flue gas sampling and the other for measurements inside the combustion chamber (CO and CO_2: infrared; O_2: paramagnetic; HC: flame ionization). The analyzers were calibrated daily and the sets could be switched to double check the accuracy. H_2 was not measured, but later measurements under similar conditions with an H_2 analyzer, and also previous measurements with a gas chromatograph [5], indicate that H_2 is well correlated to hydrocarbon concentration (HC), which allows the assumption that $H_2 = 0.9$HC (methane equivalents).

The concentrations of individual hydrocarbons were obtained from combining the results of previous measurements of individual hydrocarbons with a coal of similar type and under similar operating conditions [5], with calibration data from the HC analyzer for these hydrocarbons. Knowing the composition of hydrocarbons, the stoichiometric oxygen consumption for hydrocarbons was determined to be

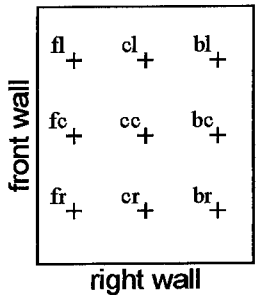

FIG. 1. Measurement positions in the horizontal cross section, 1.7 × 1.4 m.

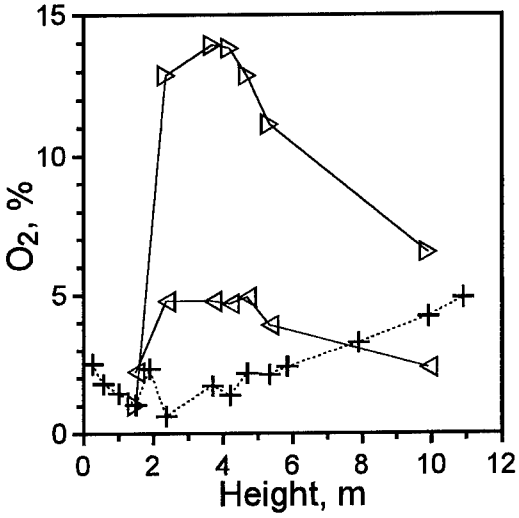

FIG. 2. Oxygen. Concentrations measured in cc (+), fc (▷), and bc (◁).

1.77% O_2 per % HC measured. (Since HC is measured in methane equivalents, that is, approximate number of carbon atoms, the constant is reasonably insensitive to changes in hydrocarbon composition.)

The suction probe for gas sampling has a shielded filter at the end of a water-cooled lance. The probe and the sampling procedure have been described previously [5]. A possible error could be the accumulation and burning of combustible material between the filter and the filter shield. Measurements were, however, made in the most difficult position of the combustion chamber with several probe types, and no significant difference was measured between them. These performance tests included a probe with a horizontal quartz filter close to the tip to prevent accumulation of solid material.

The gas concentrations were measured at various heights along the centerline of the combustion chamber (cc in Fig. 1). Due to large variations over

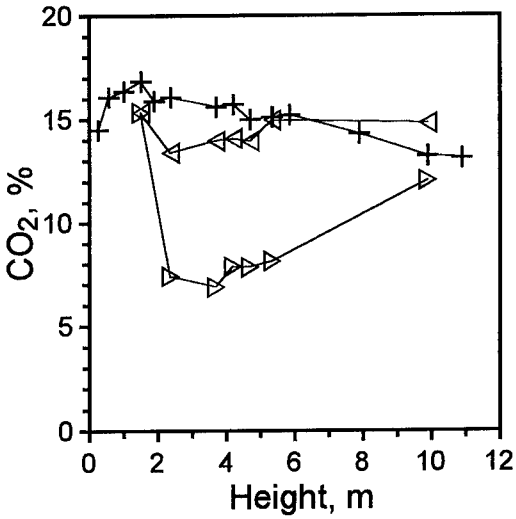

FIG. 3. Carbon dioxide. Concentrations measured in cc (+), fc (▷), and bc (◁).

the cross section, mostly caused by the secondary air, measurements were also made along two lines at the back and the front wall (bc and fc in Fig. 1) and at two heights, 3.7 and 9.9 m, in nine positions in the horizontal cross section. The nine-position measurements verified that the three-position measurements (fc, cc, and bc) gave a reasonable representation of the cross-section average and were used to improve the accuracy of the data. Thus, the cross-sectional averages were obtained from the three-position measurements, after a correction derived from the nine-position measurement data. Below the secondary air inlets, the values measured in the cc position were used as cross-section averages, since there is no significant variation in the time-average concentration over the cross section.

Results

Measured O_2, CO, CO_2, and HC concentrations are shown in Figs. 2–4 versus height above the bottom plate. An example of gas distribution over the cross section is shown in Fig. 5, showing the influence of secondary-air injection. Cross-section averages versus riser height, derived as described above, are presented in Figs. 6–8, including O_2 and CO_2 concentrations corrected for secondary air. The correction below the secondary air inlet at 2.2 m is

$$x_{corr} = x_m f_{prim} + x_{sec}(1 - f_{prim}) \qquad (1)$$

where f_{prim} is fraction of primary air, x_m is measured concentration of the gas species x, and x_{sec} is gas concentration of the secondary air. The corrected gas concentrations are needed to obtain a correct

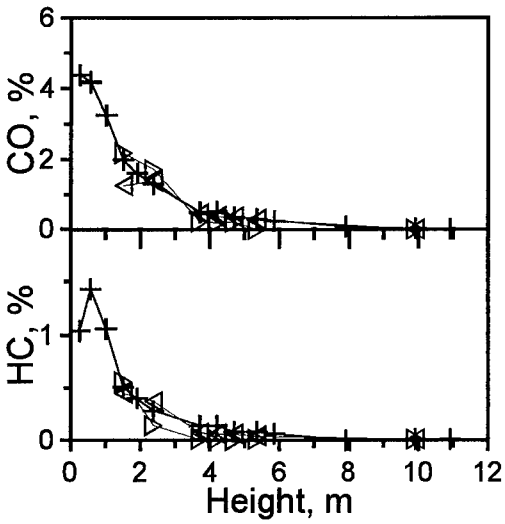

FIG. 4. Carbon monoxide and hydrocarbons. Concentrations measured in cc (+), fc (▷), and bc (◁).

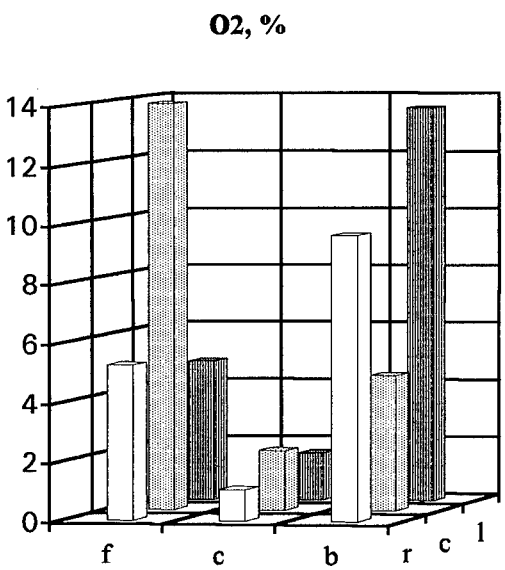

FIG. 5. O_2 concentration in the furnace cross section at 3.7-m height.

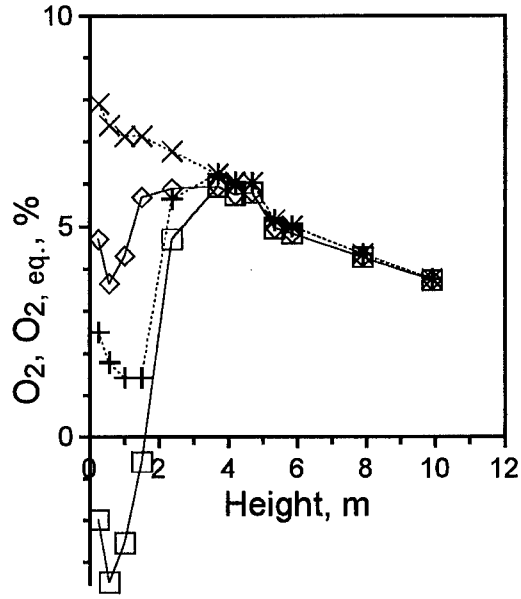

FIG. 6. Cross-section average oxygen concentration. O_2 (+), $O_{2,eq}$ (□), $O_{2,corr}$ (×), and $O_{2,eq,corr}$ (◇). Negative values represent substoichiometric conditions.

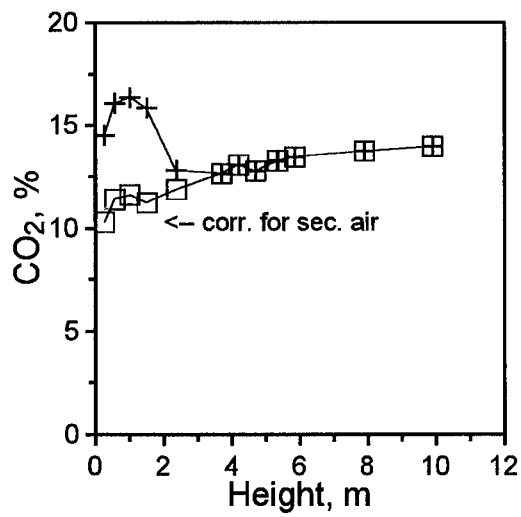

FIG. 7. Cross-section average concentration of CO_2 (×) and $CO_{2,corr}$ (□).

mass balance when used to estimate combustion versus boiler height, because concentrations measured below the secondary air inlet are compared to stack concentrations. (At 2.37 m, which is only 0.17 m above the secondary-air inlets, it is assumed that only three-fourths of the secondary air has penetrated far enough to affect the measurements.)

In Fig. 8, the combustible gases CO and HC are shown together with total combustible gas, CG, expressed as oxygen consumption:

$$CG = 0.5(H_2 + CO) + 1.77HC \quad (2)$$

The total combustible gas, CG, is subtracted from O_2 to give oxygen equivalents, $O_{2,eq}$, shown in Fig. 6:

$$O_{2,eq} = O_2 - CG \quad (3)$$

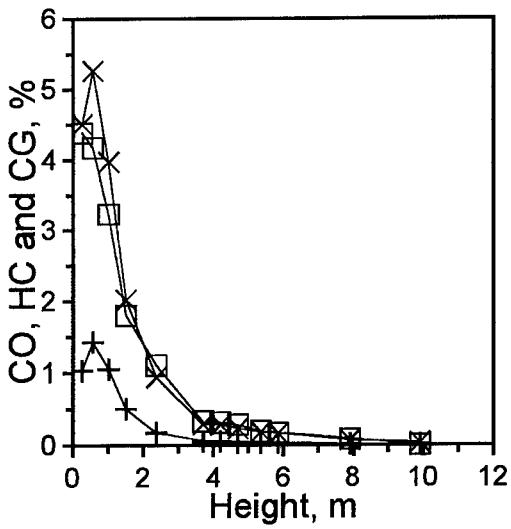

FIG. 8. Cross-section average concentrations of combustible gases: HC (+), CO (□), and CG (×).

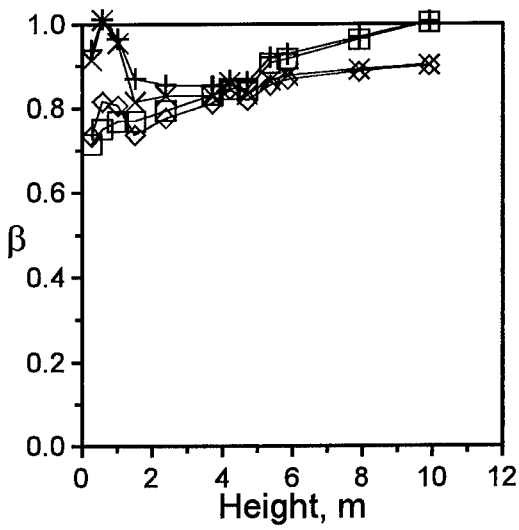

FIG. 9. Cumulative combustion/fuel conversion β versus height: β (□), β_{CO_2} (◇), β_{eq} (+), and β_{eq,CO_2} (×). Note that the values in the bottom part of the combustor are too high, due to bypass of oxygen-rich gas.

$O_{2,eq}$ is negative below the secondary-air injection level, which means that the measured gas as an average can be considered to be reducing. $O_{2,eq}$ can also be corrected for secondary air according to Eq. (1), yielding $O_{2,eq,corr}$. In the splash zone, from 0.5 to 1.5 m, where a significant reduction of $O_{2,eq,corr}$ is expected due to char combustion and volatiles release, $O_{2,eq,corr}$ instead increases (Fig. 6). This behavior, which is discussed below, is explained by a bypass of high-velocity oxygen-rich air.

From the oxygen concentration corrected for secondary air, the progress of combustion, β, versus height is derived from the fraction of oxygen consumption:

$$\beta = \frac{O_{2,in} - O_{2,corr}}{O_{2,in} - O_{2,fluegas}} \tag{4}$$

where $O_{2,in}$ is the concentration of oxygen in the gas supplied, considering that the primary air is diluted with recirculated flue gas. $O_{2,fluegas}$ is the flue gas oxygen concentration as measured in the convection path, and $O_{2,corr}$ is the measured cross-sectional average oxygen concentration, which, below the secondary-air inlet, is corrected according to Eq. (1). Similarly, a measure of the progress of combustion versus height is obtained from the CO_2 and CO measurements:

$$\beta_{CO_2} = \frac{CO_{2,corr} + \frac{1}{2} CO_{corr} - CO_{2,in}}{CO_{2,fluegas} - CO_{2,in}} \tag{5}$$

where $CO_{2,in}$ is the concentration of CO_2 in the gas supplied. Although β_{CO_2} does not include oxygen consumption from H_2O formation, the expected maximum deviation between β and β_{CO_2} is small ($\approx$1%) based on the difference between volatiles and char combustion derived below.

A measure of the progress of fuel conversion, that is, combustion and gasification, can be obtained by including the combustible gases released,

$$\beta_{eq} = \frac{O_{2,in} - O_{2,eq,corr}}{O_{2,in} - O_{2,fluegas}} \tag{6}$$

Similarly, β_{eq,CO_2} is calculated from the carbon-containing combustion gases,

$$\beta_{eq,CO_2} = \frac{CO_{2,corr} + CO_{corr} + HC_{corr} - CO_{2,in}}{CO_{2,fluegas} - CO_{2,in}} \tag{7}$$

The results are shown in Fig. 9. Here, once again, the results are not correct in the bottom part, due to bypass of oxygen-rich gas.

Another measure of the progress of combustion can be deduced from fuel distribution versus height. First, the normalized, cumulative char mass, β_{mass}, versus height, h, is obtained as

$$\beta_{mass}(h) = \frac{\int_0^h \phi_{char} \rho dh}{\int_0^{10} \phi_{char} \rho dh} \tag{8}$$

where ϕ_{char} is the mass fraction of combustibles (mainly char) obtained from analysis of solid samples taken at different heights and the local solids concentration ρ is obtained from the measured pressure

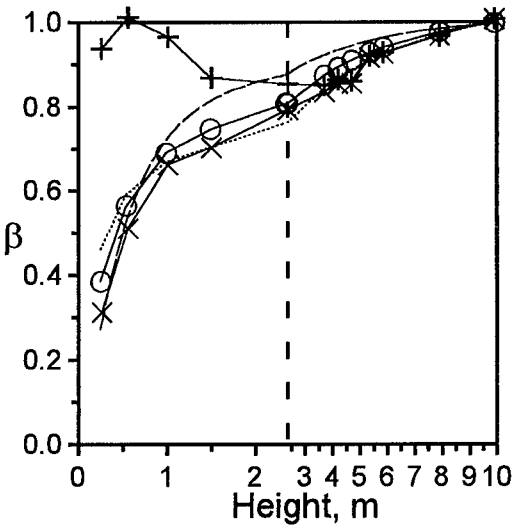

FIG. 10. β_{eq} from Fig. 9 compared to model and char data. β_{eq} (+), $\beta_{eq,mod}$ (×), β_{fuel} (○), β_{mass} (dashed curve), and $\beta_{area \cdot O_2}$ (dotted curve).

gradient. If the local char combustion is assumed to be proportional to the char surface concentration multiplied by the measured O_2 concentration, the cumulative and normalized char combustion, $\beta_{area \cdot O_2}$, is obtained:

$$\beta_{area \cdot O_2}(h) = \frac{\int_0^h \phi_{char} S_g \rho O_2 dh}{\int_0^{10} \phi_{char} S_g \rho O_2 dh} \quad (9)$$

where S_g is the outer specific area of the char derived from analysis of combustibles of sieved samples taken at different heights. To obtain a measure of where the conversion, that is, combustion and devolatilization, of the fuel takes place, the following assumptions are made:

- The measured mass distribution of the combustibles, β_{mass}, is assumed to give a representation of where the devolatilization occurs. (This is based on the assumption that the mass of the devolatilizing fuel particles has a distribution versus height that is similar to that of the char.)
- $\beta_{area \cdot O_2}$ is assumed to give a reasonable measure of where char combustion takes place.

Thus, the progress of fuel conversion, β_{fuel}, versus height is obtained by weighing

$$\beta_{fuel} = \nu\beta_{mass} + (1 - \nu)\beta_{area \cdot O_2} \quad (10)$$

where ν is the fractional volatiles content, 0.4. If β_{fuel} is compared to the results from the gas analysis, β_{eq}, a significant discrepancy in the bottom part is noted (Fig. 10). Below, a simple model illustrates how this can be explained by through flow of air at high velocity.

Correction for Bypass Flow

A simple model has been formulated to illustrate the effect of different gas velocities in the bottom part of the combustor. The purpose of the model is not to present "correct" results, but rather to highlight the lack of knowledge regarding the phenomena in this region and the need for further investigation.

It was previously shown [6] that the bottom bed of a circulating FBB operates in the "exploding bubble" regime. This causes high through flow of gas, and a modified two-phase theory can be applied to estimate the flow distribution [7]. Both theory and pressure-drop measurements indicate a dense bottom bed with a bubble volume fraction of about 0.3–0.4. The visible bubble flow is estimated to account for about 29% of the total gas flow. With a minimum fluidization velocity being 1% of the superficial velocity, this leaves a remainder of 70% as through flow or bypass flow. This through flow is assumed to be made up of bubble chains or channels creating short circuits of gas bypassing the bottom bed.

The distinction between dense phase flow, visible bubble flow and through flow is artificial, and these flows are obviously more or less mixed. The simple model assumes that a part of the flow is not mixed at all and the other part is completely mixed:

- The rapid through flow has the same concentrations as the fluidizing gas, that is, $O_{2,b}$ = 16%, and passes through a time-averaged fraction of the cross-section area, ϕ.
- The gas concentration of the visible bubble flow is equal to that of the gas in the dense phase, $O_{2,d}$.

The first assumption probably overestimates O_2 concentrations, which may be counterbalanced by an underestimate of O_2 in the second assumption.

A local measurement of the oxygen concentration spends a fraction of time (ϕ) in the rapid through flow. The measured time-averaged O_2 concentration was $O_{2,m}$ = 2.5% at 0.26 m in height, and it should relate to the concentrations of the two assumed flows according to

$$O_{2,m} = \phi O_{2,b} + (1 - \phi)O_{2,d} \quad (11)$$

By assuming values of $O_{2,d}$, we obtain various values of ϕ, according to Eq. (11) (see Table 1). From these values, the mean velocity of the gas in the rapid flow, u_b, can be obtained:

$$u_b = uf_b/\phi \quad (12)$$

where u is the superficial velocity in the bottom part (3.8 m/s) and f_b is the fraction of through flow (0.7). If the rapidly bypassing gas has not reached the bed

TABLE 1
Results from Eqs. (11)–(13)

$O_{2,d}$, %	0	0.5	1	1.5	2
ϕ	0.16	0.13	0.10	0.07	0.04
u_b, m/s	17	20	26	38	73
$O_{2,flow}$, %	11.2	11.3	11.5	11.6	11.8

temperature, the resulting velocity is lower. At 850 °C, however, the available pressure drop of 5 kPa, is theoretically sufficient to produce a maximum velocity of 180 m/s (cf. velocities in Table 1).

Due to velocity differences, the measured time-averaged oxygen concentration is biased toward slowly moving gas with low oxygen concentration. However, with the above assumptions, the average oxygen concentration of the flow can be obtained as

$$O_{2,flow} = f_b O_{2,b} + (1 - f_b) O_{2,d} \qquad (13)$$

From Table 1, it is clear that $O_{2,flow}$ is significantly higher than the oxygen concentration measured, 2.5%. Based on Table 1, we assume that $O_{2,flow}$ is 11.3% and that the fraction of flow having a high velocity and high oxygen concentration decreases exponentially with height above the dense bed. These assumptions yield $\beta_{eq,mod}$, which is compared to β_{eq} and β_{fuel} in Fig. 10. The values used in the model are assumptions, but it is believed that the general description is justified, and the model agrees reasonably well with β_{fuel}.

Discussion

The gas measurements, if not corrected for the bypass flow, indicate that 71% (β) of the combustion and 94% (β_{eq}) of the fuel conversion take place below 0.26 m. This is unlikely, considering that only 27%/24% of solid combustible mass/surface is found below this level. However, with the above assumption of a considerable bypass of air, reasonable agreement is obtained between data for the progress of fuel conversion based on measurements of solids, β_{fuel}, and gases, $\beta_{eq,mod}$.

The results illustrate the difficulties in interpreting the gas concentration measurements in the bottom zone. The measurements show that the bed material to a large extent is exposed to reducing conditions, which has previously been revealed by zirconia-cell oxygen-probe measurements [4]. However, the measured concentrations give a poor representation of the concentration of the flow due to large velocity differences. This aspect is important, not only for the understanding of the combustion process, but also for the interpretation of other measurements. The problem has previously been noted, for example, in connection with experiments in stationary fluidized beds, where the fraction of dense-phase flow is one order of magnitude greater than that of the present experiments [8]. For instance, bottom-zone measurements of high concentrations of the NO/N_2O precursors, such as NH_3, HCN, and HNCO, may lead to erroneous conclusions if the gas velocity variations are not accomodated.

For modeling, it is important to be aware of the shifts between oxidizing and reducing conditions. The measured concentrations are time averages of concentrations that vary significantly, especially in the bottom bed, where high concentrations of O_2 may occur part of the time, alternating with low concentrations of O_2 and high concentrations of reducing species during the remaining time. Apart from measurements with oxygen probes [4], at present, little is known about these variations.

The 14 secondary-air ports were carefully rinsed during a stop just before the test series. Despite this, significant variations in O_2 over the cross section occurred (see Fig. 5), indicating that an even flow distribution over the secondary-air ports was not attained. Most of the variation, however, has disappeared at the 9.9-m level. It is believed that this type of variation is not uncommon in commercial boilers.

β and β_{CO_2} differ from each other in the upper part of the combustor. Since some combustion takes place in the cyclone, β should be lower than unity. There are several possible sources of minor errors in sampling, and the fraction of combustion taking place in the cyclone cannot confidently be determined from small differences in O_2 or CO_2 concentration as measured in the top of the combustion chamber and in the flue gas channel with the sampling procedures used. (This was not the primary purpose of the investigation anyway.)

Previous measurements with other bituminous coals gave concentrations that were very similar to the present test series. Furthermore, an additional test series was conducted and evaluated, this time with limestone addition, with similar results as in the present test series. Two minor differences were noted: The β and β_{CO_2} values in the upper part did not diverge, and the CO concentration was considerably lower. The latter observation is associated with the catalytic effect of the lime.

Conclusions and Interpretation

The interpretation of gas concentrations measured by a suction probe in the lower part of the combustion chamber of a circulating FBB is difficult because of a considerable bypass flow. Some important conclusions can nevertheless be drawn:

1. High concentrations of combustibles and low concentrations of oxygen are found in the bottom part. The equivalent oxygen concentration, that is,

oxygen concentration reduced by the oxygen demand of the combustible gases, is negative in the bottom part, indicating substoichiometric conditions. This result is consistent with zirconia-cell oxygen-probe measurements [4].

2. Although the results most probably give a good representation of the time-averaged concentration in a given position, the measured gas concentrations in the bottom part cannot be used in mass balances, since they do not represent the concentrations of the gas flow. This is explained by much higher velocities of gas with high oxygen concentrations, compared with gas with low oxygen concentration and high concentration of combustible gases. The reason for this is a through flow of gas, in the form of bubbles or voids in the bottom bed. In relation to the entire gas flow in the bottom part of the combustion chamber, the measurements give too low of an oxygen concentration and too high of a concentration of combustibles. An attempted correction for the bypass flow compared favorably with data based on the distribution of solid combustibles in the combustion chamber.

3. Based on previous knowledge, and consistent with the present data, the following image of coal combustion in a circulating FBB emerges: The major part of the fuel is burned and gasified in the dense bottom bed and in the splash zone above the dense bed. Jets of gas bypassing the bottom bed decelerate above the dense bed, where they mix with a gas having a high content of combustible gas. The mixing of the gases, especially in the bottom part, is incomplete, and the measured concentrations are averages of periods with oxidizing gas, that is, high oxygen concentrations, and periods with reducing gas, that is, high concentrations of combustible gas.

Acknowledgment

The Swedish National Board for Industrial and Technical Development (NUTEK) supported this work.

REFERENCES

1. Boemer, A., Braun, A., and Renz, U., *Proc. Int. Conf. Fluid. Bed Combust.* 12:585–598 (1993).
2. Couturier, M., Doucette, B., Stevens, D., Poolpol, S., and Razbin, V., *Proc. Int. Conf. Fluid. Bed Combust.* 11:107–114 (1991).
3. Wang, X., Gibbs, B. M., and Rhodes, M., *Fuel* 73:1120–1127 (1994).
4. Lyngfelt, A., Bergqvist, K., Johnsson, F., Åmand, L.-E., and Leckner, B., in *Gas Cleaning at High Temperatures* (R. Clift and J. P. K. Seville, Eds.), Blackie Academic & Professional, Glasgow, 1993, pp. 470–491.
5. Åmand, L.-E., *Measurement of Gas Concentration Profiles in the Combustion Chamber of the 12 MW CFB at Chalmers* (in Swedish), Dept. of Energy Conversion, Chalmers University of Technology, Report A94-208, Göteborg, 1994.
6. Svensson, A., Johnsson, F., and Leckner, B., *Proc. Int. Conf. Fluid. Bed Combust.* 12:887–897 (1993).
7. Johnsson, F., Andersson, S., and Leckner, B., *Powder Technol.* 68:117–123 (1991).
8. Walsh, P., Chaung, T., Dutta, A., Beér, J., and Sarofim, A., *Nineteenth Symposium (International) on Combustion,* The Combustion Institute, Pittsburgh, 1992, pp. 1281–1289.

Twenty-Sixth Symposium (International) on Combustion/The Combustion Institute, 1996/pp. 3261–3267

COAL COMBUSTION AND GASIFICATION IN A COMPARTMENTED, FLUIDIZED-BED COAL GASIFIER

HONGMING YAN,[1] VICTOR RUDOLPH[1] AND DONG-KE ZHANG[2]

[1]*Department of Chemical Engineering*
The University of Queensland
Brisbane, QLD 4072, Australia

[2]*Department of Chemical Engineering*
The University of Adelaide
Adelaide, SA 5005, Australia

A conceptual compartmented, fluidized-bed coal gasifier (CFBCG) which separates coal combustion from gasification for synthesis gas production was investigated in a small pilot plant in two major stages: combustion-only experiments and combustion-gasification experiments. The combustion-only experiments showed that volatiles were released and burned in the compartment where coal is fed. Volatiles and char combustion were sufficient to maintain the operating temperature of the CFBCG. Solid circulation induced by two sets of v-valve/riser arrangements was crucial, and determined heat-transfer between the two beds and, thus, controlled the reaction rates. The rate of solid circulation, carbon burning rate, and carbon inventory in a bed were indirectly estimated by measuring pressure drop over a bed compartment. Since there was no ash withdrawal facility in the pilot plant, ash accumulated during prolonged operation and caused ash agglomeration at high temperatures, which further resulted in fluidization and solid circulation difficulties. Based on information and experience obtained in the combustion-only experiments, the combustion-gasification experiments were performed to study energy transfer from combustor to gasifier, and quality of the synthesis gas produced. It was found that circulation of hot solids from the combustor was sufficient to support endothermic reactions in the gasifier. High-quality synthesis gas with an H_2/CO ratio of 4 was achieved. N_2 contamination of the synthesis gas (12–22%) occurred due to air leakage from the riser and in the plenum to the gasifier. While the CFBCG concept has proved to be sound, further development is needed to improve the operatibility before practical application.

Introduction

Production of synthesis gas from coal is likely to become one of the most important processes worldwide by early next century as coal will progressively replace petroleum as feedstock for organic chemicals, in addition to its role in power generation. In synthesis gas production, two chemical reactions are involved: the desired reaction between coal and steam is endothermic, and combustion of coal matter provides heat required for the desired gasification reaction. Since this is a large-volume operation, it is preferred to use only cheap, easily obtainable feeds: air, water, and coal. In considering this operation, if coal reacts with air and steam at the same time, nitrogen is present in the product gas, which is costly to remove. If pure oxygen is used, then an expensive oxygen plant is needed.

A conceptual compartmented, fluidized-bed coal gasifier (CFBCG) has been proposed by Rudolph [1], in which the fluidized bed is divided into two compartments running the gasification and combustion reactions, respectively. The solids are freely interchanged between the two compartments by two sets of v-valve/riser arrangements. Coal particles fed into the combustion compartment burn with air to raise the solid temperature. Hot particles are then transferred into the gasification compartment and react with steam to produce high-quality synthesis gases (H_2 and CO). This paper reports our preliminary experimental investigation into the feasibility of such a compartmentalized gasifier concept in a small-scale test facility. Major results from the experiments are presented, and difficulties and problems encountered are discussed.

Experimental

Experimental Facility and Working Principles

The CFBCG is schematically shown in Fig. 1 [2]. It has a cross section of 300 × 300 mm^2, which is divided into two chambers by a vertical baffle: the smaller chamber (100 × 300 mm^2) is for gasification, and the larger one (200 × 300 mm^2) for com-

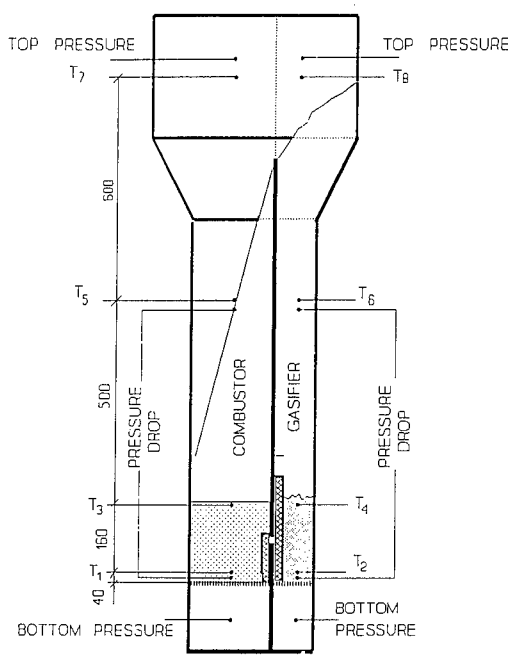

FIG. 1. Compartmented, fluidized-bed gasifier.

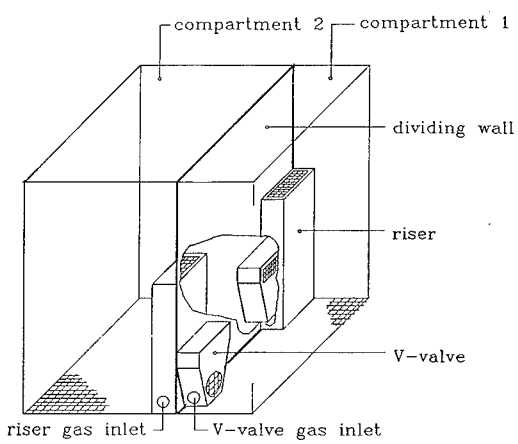

FIG. 2. An isometric view of partitioned section of v-valve and riser.

bustion. The height of the reactor is 1.6 m; the bed depth during normal operation is about 200 mm. The enlarged part at the top is to reduce gas velocity, providing an opportunity for elutriated particles to fall back to the bed. There are two exits at the top of the reactor, for flue gas discharging from the combustor and for product gas from the gasifier.

The chambers exchange solids through two v-valve/riser sets located at opposite ends of the baffle. An isometric view of a partitioned section is given in Fig. 2. During operation, one v-valve with a jet of gas pumps bed material from the larger compartment through the riser and into the smaller compartment. The other v-valve pumps material in the inverse direction, thus inducing a solid circulation between the two compartments. Details of working principles of v-valve/riser sets were given elsewhere [2,3].

Materials

An Australian bituminous coal was used in the experiments (particle size < 5.5 mm, specific energy, 21.18 MJ/kg). Proximate analyses for this coal are: fixed carbon, 0.47; volatile matter, 0.25; moisture, 0.15 on the as-received mass basis. The bed material is silica sand (a Geldart B powder, $d_p = 304\ \mu m$, $\rho_s = 2600\ kg/m^3$, $U_{mf} = 7.05$ cm/s), which acts as heat carrier in addition to its role in mixing in both beds.

Experimental Procedures

Coal particles are introduced into the combustor through an under-bed mechanical screw feeder just above the distributor. The coal and inert bed materials are rapidly mixed in the bed, and volatiles and char burn with air, rapidly heating up the solids. Some unburned volatiles and fine char particles are carried over to the combustor freeboard. Energy accumulated in the combustor is carried over to the gasifier by circulating solids. The operating temperature in the combustor is maintained below 900°C.

Once the hot burning particles and solids are carried over into the gasifier bed through the riser, they react with steam introduced into the gasifier to produce synthesis gas (H_2 and CO). The operating temperature in the gasifier bed is maintained by solid circulation rate and steam flow rate into the gasifier. This is about 20–60°C lower than that in the combustor, due to endothermic gasification reactions.

The product gas and flue gas exiting from the reactor pass through a cyclone and a water seal and are discharged to atmosphere through a stack. Analysis of the main components (H_2, CO, CH_4, and CO_2) of the gas is conducted with on-line process gas analyzers. In the experiments, gas rates to the system are set by fluidization conditions desired; and coal rate is then determined by stoichiometric considerations. All the operating parameters, flow rates of gases (air, steam, and products), operating temperatures, pressures and pressure drops, and gas analysis are logged by a PC. Details have been given elsewhere [3].

Results and Discussion

Combustion-Only Experiments

In order to understand the operability of the CFBCG system as regards coal combustion behavior

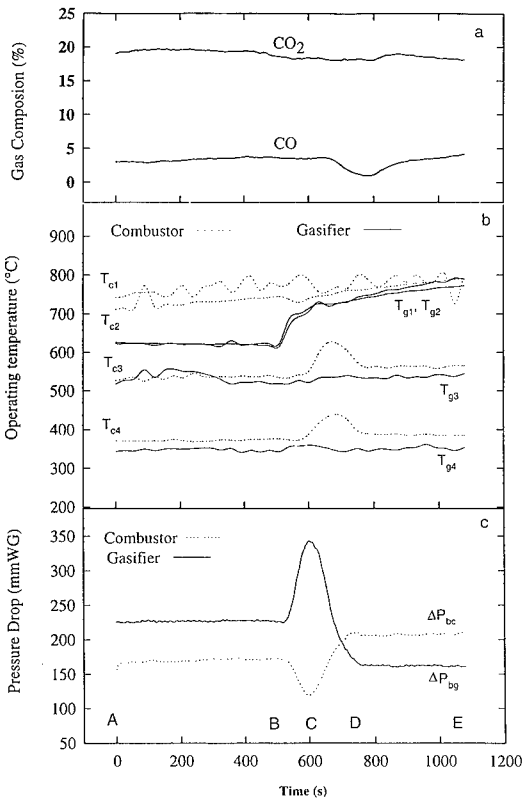

FIG. 3. A family of graphs for the initial evaluation of reactor performance.

and solid circulation at high temperatures, a series of combustion-only experiments were first trialed. In the combustion-only experiments, both beds were fluidized with air at a superficial velocity of 3 U_{mf}. Air jets (50–90 L/min) fed into the v-valve/riser were used to move particles from one compartment to the other. Coal feed rate was constant at 4.0 kg/h. The ratio of actual to stoichiometric oxygen fed to the reactor was about 0.5.

Figure 3 shows typical reactor performance under combustion-only experiments through a family of graphs depicting the history of an experiment. The relationship among solid circulation states in the reactor, changes of both gas compositions (Fig. 3a), and operating temperature (Fig. 3b) and pressure drops (representing bed depths) across the two beds (Fig. 3c) are demonstrated in the following four stages.

Stage 1, A to B

No solid circulation is introduced. Coal combustion takes place just like in a conventional fluidized-bed combustor. A slight increase of pressure drop (Fig. 3c) in the combustor compartment results due to coal accumulation in the bed. Freeboard temperatures of T_{c3} and T_{c4} (Fig. 3b) remain nearly constant although the bed temperatures T_{c1} and T_{c2} increase with time. The constant temperature profiles in both freeboards indicate that there is no volatile combustion as no oxygen is available. The gas composition profiles (Fig. 3a) show that CO concentration increases slightly, but CO_2 decreases slightly. Decreasing CO_2 formation and increasing CO formation are favored as the bed temperature increases. In the gasifier, the bed depth is nearly constant (Fig. 3c) because no coal particles are fed into it. Energy generated from combustion reaction of char within the gasifier is just enough to maintain the operating temperature (T_{g1} and T_{g2}), though somewhat lower than in the combustor.

Stage 2, B to C

At 500 s, as marked by B in Fig. 3, air flows to the v-valves and risers on the combustor side, so that solids are transferred to the gasifier. Other conditions remain unchanged. Circulation causes burning char particles and hot solids to be carried over from the combustor to the gasifier. As a result, the bed depth, as shown by pressure drop, in the combustor decreases. The relative change in the bed depth in the combustor is a half of that in the gasifier (Fig. 3c), because the cross sectional area of gasifier is a half of that of the combustor. Although mass of solids in the combustor reduces quickly, combustion conditions are essentially unchanged; the operating temperatures, as shown in Fig. 3a, continue to increase at the same rate as before.

Several changes occur on the gasifier side, however. Burning particles from the combustor are transferred to the gasifier and the bed temperatures begin to rise rapidly. The freeboard temperature, however, increases only slowly, despite the fact that additional air is available from the v-valve and riser. This is due to the fact that the gasifier freeboard contains almost no fine char particles and volatile, and therefore, no combustion takes place.

Stage 3, C to D

During this stage, the air flow to the v-valve/riser on the combustor side stops, but air flow to the gasifier side starts. In this configuration, solids and burning char particles from the gasifier are carried over to the combustor. As a result, the bed depth, as represented by pressure drop, reduces in the gasifier and increases in the combustor. A major difference, however, is that extra air to the v-valve and riser now enters the combustor freeboard in which there are unburned volatile and entrained char particles. The volatile burns rapidly along with some fine char, giving a temperature jump in the freeboard, as shown in Fig. 3b. This temperature jump provides evidence

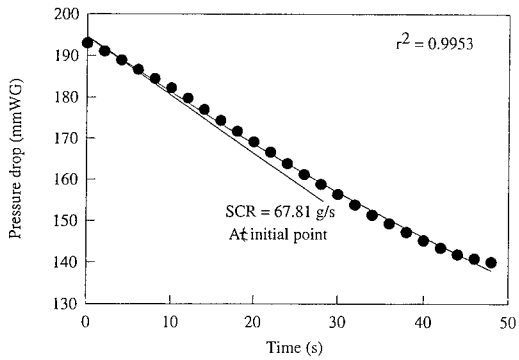

FIG. 4. Solid circulation rate measurement.

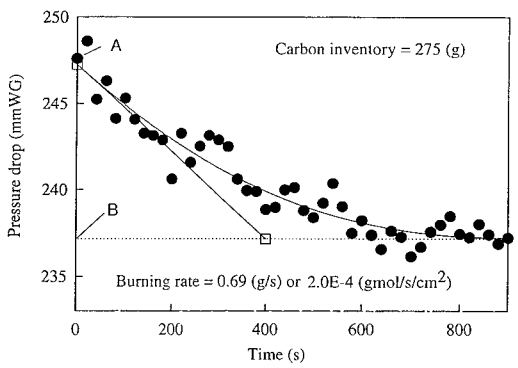

FIG. 5. Measurement of char burning rate and carbon inventory in the combustor.

of volatile combustion in the freeboard. Figure 3a also shows that CO content of the flue gas decreases; this is a result of the volatile combustion and availability of additional oxygen.

Stage 4, D to E

The operating conditions return to the same as in the first stage. Consequently, the two beds remain at a constant depth (Fig. 3c). The temperatures in the reactor increase slowly with time (Fig. 3b). The CO concentration increases and CO_2 concentration decreases due to the increasing temperature discussed before.

For a steady operation of the combustion-only experiments, fluidizing air to both compartments and air jets to the v-valve/risers for solid circulation are maintained constant, along with a constant coal feed. It is observed that CO concentration in the flue gas ranges from 3.0 to 4.0%, and CO_2 concentration ranges from 17 to 18.5%. The CO concentration does not further increase with increasing temperature because CO produced from the CO_2 reduction reaction may be reoxidized in the freeboard. The freeboard temperatures of the combustor are always 10–50°C higher than those in the gasifier freeboard, even though operating temperatures in both beds are about the same. This is because coal is fed into the combustor, allowing volatile combustion to take place in the combustor but not in the gasifier which contains only char. This provides further evidence of volatile combustion in the combustor freeboard.

Solid Circulation and Control

A key technique in the CFBCG process is the solid circulation induced by the v-valve/riser arrangements, which determined heat transfer from the combustion compartment to the gasification compartment, and thus controls reaction rates in both beds. Clearly, the rate of solid circulation depends on gas flow rates to the v-valves and risers. Determination of the solid circulation rate is difficult. In the present study, this was indirectly estimated by measuring the pressure drop [2,4] in a compartment while only one v-valve/riser set operated, transferring solids to the other compartment. Since bed pressure drop is proportional to the mass of bed material in the bubbling fluidization regime, the solid circulation rate can then be calculated from the pressure drop–time plot. As shown in Fig. 4 for stage 3 in the combustion-only experiments, the estimated solid circulation rate in this case was 67.8 g/s.

The char burning rate and carbon inventory in one compartment can also be evaluated in a similar way, that is, by stopping solid circulation and measuring pressure drop as a function of time. Figure 5 shows a typical pressure drop–time curve in the combustor corresponding to stage 2 in the combustion-only experiments. The initial slope of this curve, when solid circulation stops, gives the carbon burning rate, and that the total pressure drop difference, after a constant pressure drop is attained (all carbon is burned out), indicates the carbon inventory. In the combustion-only experiments, the burning rate in the combustor was 0.69 g/s, and the carbon inventory was 275.4 g, equivalent to 2.7–3% of total bed materials.

It was observed during experiments that solid circulation can be affected by ash accumulation and agglomeration in the beds. In the present design of the pilot plant, there is no ash discharging device. With prolonged operation, ash accumulates in the bed and ash agglomeration occurs at high temperatures (>850°C for the coal used). Ash agglomeration seriously alters fluidization conditions in the bed and can actually result in termination of solid circulation between the two compartments.

Ash agglomeration may be indicated by gradually lowered temperature readings at the bottom of a bed where no combustion occurs due to large ash agglomerates sinking to the bed bottom. A typical example of this case is shown in Fig. 6. At point A, the bed bottom temperature (T_1) is only about 350°C, while the bed top temperature (T_2) is above

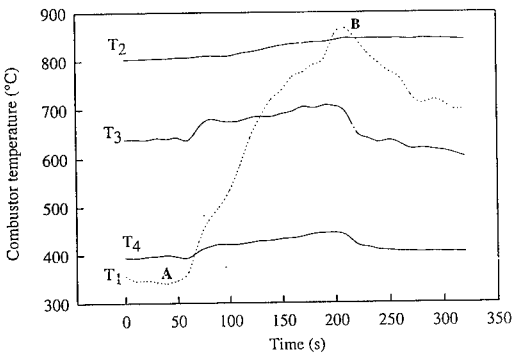

FIG. 6. Temperature profile when the ash agglomeration occurred in the bed.

TABLE 1
Air, coal, and steam feed rates[a]

	Units	Feed rate
Air to combustor	(L/min)	220–250
Air to riser	(L/min)	75–85
Air to v-valve	(L/min)	55–65
Coal feed rate	(kg/h)	5.0–6.0
Steam to gasifier	(kg/h)	4.5–5.5
Steam to riser	(kg/h)	1.8–2.3
Steam to v-valve	(kg/h)	1.65–2.25
Steam temperature	(K)	373

[a]At 298°C, 1 atm for air.

800°C, indicating that coal combustion ceased at the bottom due to ash agglomeration. This is clear when compared with Fig. 3b where both bottom and top temperatures are about the same. If agglomeration is not too severe, a sudden high air flow into the bed can break the agglomeration deposits. This does not work, however, if agglomeration is serious. Clearly, a continuous ash withdrawing device and a means to control operating temperature below 850°C are necessary. In a practical application, a cone-shaped distributor may be employed so that ash agglomerates can sink and be withdrawn from center of the cone.

Combustion-Gasification Experiments

The combustion-only experiments provided us with confidence in the operability of the system at high temperatures. Coal combustion releases sufficient energy to maintain the operating temperature. With proper control of gas flows and bed temperatures, the solid circulation system can work well. Based on this information, combined combustion-gasification experiments were performed to study the energy transfer from the combustor to the gasifier to support the endothermic reactions, and the quality of synthesis gas produced.

TABLE 2
Main gasification experimental results

Gas yield (at 298°C, 1 atm)		
Mean flue gas	420	(L/min)
Mean product gas (wet)	285	(L/min)
Mean product gas (dry)[a]	96	(L/min)
Gas composition (V%)	Flue gas	Product gas
CO	3.0–5.0	8.0–9.0
CO_2	17.0–19.	24.0–27.0
H_2	<1.0	43.0–48.0
O_2	<0.5	<0.5
N_2	77.0–80.	12.0–22.0
CH_4	<1.0	<1.0
Steam decomposition	6.5	wt%
Carbon fraction		
In combustion	4.69	wt%
In gasification	4.44	wt%
Solid mass		
In combustion	17.02	kg
In gasification	7.11	kg
Solid circulation rate	52.78	g/s
Elutriation		
From combustion	0.9	kg/h
From gasification	0.0	kg/h
Carbon conversion		
In combustion	30–45	w%
In gasification[b]	6.5	w%
Carbon content in elutriation	58–59	w%
Particle diameter		
In combustion	393	μm
In gasification	385	μm

[a]High N_2 concentration in product gas is due to air leakage that occurred in the plenum under the distributor into the gasifier.
[b]Some carbon conversion results from combustion due to the air leakage.

For the combustion-gasification experiments, the combustion operation was initially conducted in both beds until the desired operating temperature was reached. Steam was then blown into the gasifier and where it reacted with carbon to produce synthesis gas. Air, coal, and steam feed rates used in the gasification experiments are given in Table 1. Two trials of steady-state gasification over periods of hours were successful and the main gasification results are summarized in Table 2.

Figure 7 gives profiles of operating temperatures in both compartments along the height. The temperature profiles in the beds (T_1 and T_2) are found to be uniform, indicating that good mixing is achieved in both beds. It is noteworthy that the op-

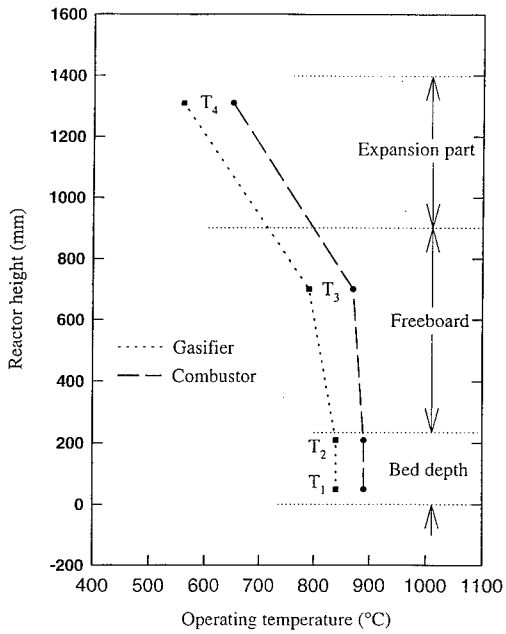

FIG. 7. Operating temperature profiles during gasification experiments.

erating temperatures in the combustor are always 40–50°C higher than those in gasifier during steady operation periods. This is because of the endothermic reactions in the gasifier.

The compositions of dry product gas under steady operation are given in Table 2. A high H_2/CO ratio is obtained because (1) the low operating temperature favors H_2 formation in the water-gas shift reaction, and (2) the large steam rate pushes the equilibrium toward hydrogen formation as well. This is in accordance with the literature [5,6]. Rudolph [5] reported that gas composition strongly depends on temperature, and H_2/CO ratio can apparently vary from about 1 to 3 as temperature drops from 900 to 750°C in gasification experiments performed in a draft tube fluidized-bed gasifier. The same conclusion was also reached by Ma [6] based on experiments with an oxygen-/steam-blowing, pilot-scale, fluidized bed coal gasifier. Ma [6] reported that a higher steam/carbon ratio and low oxygen/carbon ratio (leading to a lower operating temperature) favor a higher H_2/CO ratio in the product.

The analyses of both product and flue gases are also given in Table 2. Nitrogen in the product gas accounted for about 12–22%, due to air leakage to the gasifier from the riser and in the plenum. However, a high H_2/CO ratio of 4 is achieved. If N_2 is eliminated from the product stream, as would be the case if the seal below the plenum was not breached, the gas would have a synthesis gas quality. The CO concentration of around 3% in the flue gas indicates that incomplete combustion is not a major problem.

The relatively small fractional carbon conversion (0.065) in the gasifier shows that the rate of gasification was relatively low compared with the combustion rate, because of low gasification rates at low temperatures (~800°C) and short particle residence time (2–3 min). This finding is also in accord with the literature [7–12]. It suggests that deeper beds should be used in order to achieve a greater extent of char gasification.

Again, solid circulation is seen to be an important and significant part of the CFBCG process, which can effectively and efficiently transfer heat from the combustor to the gasifier, thus avoiding nitrogen contamination of the synthesis gas. This has considerable advantages over other means of solid-to-solid heat transfer, such as combustion in heat transfer tubes immersed in a fluidized-bed gasifier, where heat transfer is apparently less efficient and erosion of the immersed tubes is also a problem. The present study indicates that the solid circulation is easy to operate and control.

The gasification experiment data are limited due to the difficulties involved in hot experiments on this scale [2]. However, they do provide preliminary information for the evaluation of the reactor performance at elevated temperatures.

Conclusions

The concept of the compartmented, fluidized-bed coal gasifier has been experimentally assessed in a small pilot-scale plant in two major stages: the combustion-only experiments and the combustion-gasification experiments. The combustion-only experiments revealed that coal volatiles are released and burned in the combustion compartment. Volatiles and char combustion is sufficient to maintain the operating temperature. Solid circulation realised by the v-valve/riser arrangements is a crucial part of the CFBCG operation, which determines heat transfer between the two beds and thus controls reaction rates. The solid circulation rate, determined by the gas flow rates to the v-valve/riser, can be indirectly estimated by the pressure-drop measurements. Carbon inventory and carbon burning in either compartment can also be proximately evaluated by the solid circulation control and pressure-drop measurements.

The combustion-gasification experiments demonstrated that a good quality synthesis gas can be generated from the CFBCG by air blowing. The desired endothermic gasification of coal is separated from the combustion, and solid circulation carries

sufficient energy from the combustion to support the gasification reactions of coal. Contamination of the synthesis gas by N_2 is also observed, due to air leakage from the riser and in the plenum to the gasifier side. The observed carbon conversion due to gasification is low because of the low reaction temperatures and short particle residence time.

The present study illustrates that the CFBCG is sound. However, further development is needed before practical application. The major problems requiring immediate attention include air leakage to the gasifier, ash accumulation and agglomeration, and flue and synthesis gases heat recovery. Clearly, continuing improvement of the process would illuminate a cheap and efficient technology for synthesis gas production from coal.

Acknowledgment

The authors gratefully acknowledge the financial support received from the Australian National Energy Research Development and Demonstration Program (NERDDP).

REFERENCES

1. Rudolph, V., A proposal for a compartmented fluidized-bed gasifier, (National Engineering Research Development & Demonstration Program), The University of Queensland, Brisbane, 1988.
2. He, Y., Ph.D. Thesis, The University of Queensland, Australia, Brisbane, 1993.
3. Yan, H. M., Ph.D. Thesis, University of Queensland, Australia, Brisbane, 1995.
4. Yan, H. M. and Rudolph, V., *Proceedings, CHEMECA '93*, Melbourne. 1993, p. 495.
5. Rudolph, V., Ph.D. Thesis, Natal University, South Africa, 1984.
6. Ma, R. P., Felder, R. M., and Ferrell, J. K. *Fuel Process. Technol.* 19:265–290, (1988).
7. Yan, H. M. and Rudolph, V., *Proceedings, CHEMECA 95*, Adelaide. 1995, Vol. 2, p. 84.
8. Caram, H. S. and Amundson, N. R., *Ind. Eng. Chem. Process Design Dev.* 8:80–96, (1979).
9. Sundaresan, S. and Amundson, N. R., *Chem. Eng. Sci.* 34:463–467, (1979).
10. Kawabata, J. I., Yumiyama, M., Tazaki, Y., Honma, S., Takeda, S., Yamaguchi, H., Chiba, T., and Yoshida, K. *Chem. Eng. Comm.* 11:335–345, (1981).
11. Saffer, M., Ocampo, A., and Laguerie, C. *Int. Chem. Eng.* 28:46–61, (1988).
12. Eklind, H. and Svensson, O. *Ind. Eng. Chem. Process Design Dev.* 22:396–401, (1983).

Twenty-Sixth Symposium (International) on Combustion/The Combustion Institute, 1996/pp. 3269–3275

FRAGMENTATION OF SMALL COAL PARTICLES UNDER FLUIDIZED-BED COMBUSTOR CONDITIONS

B. R. STANMORE
Department of Chemical Engineering
University of Queensland 4072, Australia

A. BRILLARD
Laboratoire de Mathématiques
Université de Haute-Alsace
4 rue des Frères Lumière
68200 Mulhouse, France

P. GILOT AND L. DELFOSSE
Laboratoire Gestion des Risques et Environnement
Ecole nationale Supérieure de Chimie de Mulhouse
25 rue de Chemnitz
68200 Mulhouse, France

Particles of four coals screened to mean diameters (d_o) of 1.5 and 2.5 mm were subjected to rapid radiant heating under nitrogen and/or 5% oxygen, and the product particles were collected after some seconds. The number distributions of size for the products were compared to the original distributions. The 1.5-mm particles suffered limited breakage with some dust and a small amount of $d_o/2$ fragments produced. The amount of breakage was independent of volatile matter content, but greater with higher vitrinite materials. The behavior was consistent with the predictions of a model based on thermally induced stress. The manner of breakage of 2.5-mm particles of a very high VM coal and an anthracite were contradictory, with only some particles of the former breaking, but most of the latter. Increasing the pressure to 1.0 MPa led to less breakage with the high VM coal, suggesting that pressure from the volatiles is contributing to breakage. The degree of fragmentation under 1.0 MPa increased for the anthracite, which is consistent with the operation of the thermal stress model. The influence of oxygen on breakage in this case is determined by the volatile matter content.

Introduction

The devolatilization and burnout times of coal particles in bubbling fluidized beds have been shown to depend on particle breakage [1,2]. Most of the investigations into this effect have been concerned with larger particles, and the commonly quoted model of Chirone and coworkers [3] predicts that particle breakage should not occur in particles under about 2.5 mm in size. This results from the assumption of the model that breakage occurs when the internal pressure gradient due to the flow of volatiles exceeds the tensile strength of the coal.

The same conclusion about a 2.5-mm maximum size even for coals of high pore resistance number (PRN), was reached by Dakic et al. who examined breakage experimentally [4]. The PRN is the ratio (volatile matter content)/(equilibrium moisture content), which should give an indication of the quantity of volatiles that will be released in relation to the pore volume through which they are able to escape. Coal particles <2.5 mm with a PRN less than 10 (e.g., low-rank coals) are postulated to have sufficient flow area for the volatiles to escape without building up destructive pressures.

In the experimental work of Chirone and others [3,5,6], some breakage is still found for particles below 2.5 mm in size. Of particular interest are the results of Dacombe et al. [6] who dropped single particles of anthracite down a tube furnace. They found that the extent of breakage of particles increased with larger particle sizes and at higher temperatures. For instance, at 950°C there were about 20 daughter particles on average produced from a 1.0- to 1.7-mm feed particle, with a standard deviation of 4 or 5. For 1.7- to 2.4-mm particles, the mean increased to about 55, with a much larger spread of values.

Since much of the feed to a fluidized combustor will be less than 2.5 mm in size, it is important to gain an understanding of the processes that brings about fragmentation. No and Syred have proposed that thermal stresses will produce fragmentation in particles smaller than 1000 μm [7]. They found that radial stress is a maximum at the center and falls to zero at the surface. Tangential stress is the same as radial at the center but changes to compression at the surface. Their model predicts that there will be a 100% probability of fragmentation of 1-mm particles under cyclone firing conditions, based on failure in tension at the center of the particles.

This paper examines the possibility that thermal stresses will play an important role in the primary fragmentation in particles up to 2.5 mm in size. Fragmentation was studied experimentally and a thermal stress model developed for conditions appropriate to combustion in bubbling, fluidized beds. Since generation efficiency is favored by pressurized, fluidized beds, the effect of increased pressure was also considered.

Experimental

Four coals covering a range of types from three continents were included in the study. They ranged from an anthracite to a subbituminous coal of extremely high volatile matter (VM) content, whose properties are listed in Ref. 8. A petrographic analysis was also carried out. The samples were screened to give two size fractions with d_{50} values around 1.2 and 2.5 mm. Particle sizing of the fractions was performed by an optical technique that gave equivalent diameters based on projected area [4].

Samples of the four coals under gas at 1 atm were subjected to sudden radiant heating from an enclosure maintained at a temperature of 850°C in a reactor that has been described elsewhere [9]. Under these conditions, the heat fluxes to the particles are estimated to be equivalent to those produced if they were heated convectively with a heat transfer coefficient of the order of 150–200 W m^{-2} K^{-1}, typical of fluidized beds. In effect, the net fluxes (convective in a fluidized bed and radiative in our reactor) are estimated to vary by less than 50% initially, and less than 10% at the half-way point. The samples were maintained at the elevated temperature for prolonged periods of up to 300 s, and the size and texture changes noted at various time intervals [8]. Some tests were carried out in an atmosphere of pure nitrogen and others in nitrogen containing 5% oxygen by volume.

For our purpose, only the first result was taken, that is, at 5 s for the 1.5-mm particles and 20 s for the 2.5-mm particles. Heating was virtually complete at these times and the resulting particles can be regarded as the products of primary fragmentation. Each determination involved about 20 particles and was repeated 20 times to give a large representative sample. The product particles were collected, sized by the optical technique, and the distribution reported on a number basis.

Two of the coals were tested (2.5-mm particles) at 0.1 and 1.0 MPa pressure, both in pure nitrogen and with 5% oxygen added.

Thermal Stress Model

The thermal stress model follows that of No and Syred with differences in regard to boundary conditions. The particles were regarded as homogeneous spheres with physical properties dependent on temperature but not on residual volatile content. The temperature regime inside the particle was evaluated by a finite difference model for conductive heat transfer, with the value for thermal conductivity taken from Ref. 7. Heating of the surface was calculated for radiant flux from a blackbody at 850°C, using a view factor of unity and a coal emissivity of 0.85. The additional heating from natural convection was also included.

The thermal stresses generated are described by equations 1 and 2 [11]. In the radial direction,

$$\sigma_r = \frac{2E\alpha}{1-\nu}\left\{\frac{1}{R^3}\int_0^R Tr^2dr - \frac{1}{r^3}\int_0^r Tr^2dr\right\} \quad (1)$$

and in the tangential directions,

$$\sigma_\theta = \sigma_\phi = \frac{E\alpha}{1-\nu}\left\{\frac{1}{r^3}\int_0^r Tr^2dr + \frac{2}{R^3}\int_0^R Tr^2dr - T\right\} \quad (2)$$

The stresses can be evaluated from the calculated temperature profiles by integrating equations 1 and 2 numerically. A simpler, more illuminating approach is to fit a power law relation to the temperature profile at any time and integrate analytically. If we find a value of n from $T = T_o + (T_R - T_o)(r/R)^n$, then equations 1 and 2 give

$$\sigma_r = \frac{2E\alpha(T_R - T_o)}{(1-\nu)(n+3)}\left[1 - \left(\frac{r}{R}\right)^n\right] \quad (3)$$

$$\sigma_\theta = \sigma_\phi = \frac{2E\alpha(T_R - T_o)}{(1-\nu)(n+3)}\left[1 - \left(\frac{n+2}{2}\right)\left(\frac{r}{R}\right)^n\right] \quad (4)$$

These express the stresses simply in terms of the overall temperature range $(T_R - T_o)$ and the curvature of the temperature gradient, as denoted by n.

The stresses found were compared to those reported in the literature for failure in bituminous coals. Tensile strengths are given as 3–4 MPa [10],

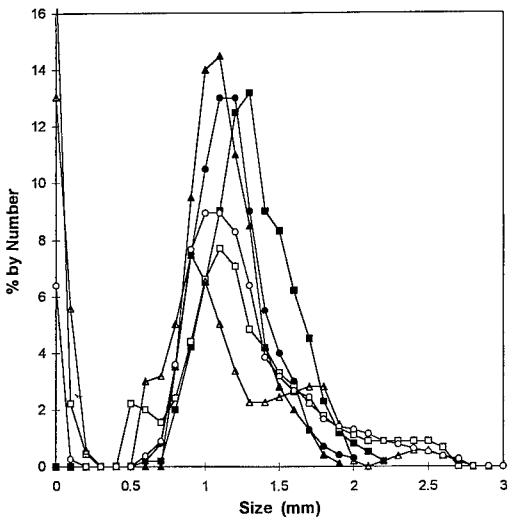

FIG. 1. Particle size distributions by number of initial and treated 1.5-mm coal samples. ■, Flambant de Provence initial; □, Flambant de Provence treated; ▲, La Mure initial; △, La Mure treated; ●, Rietspruit initial; ○, Rietspruit treated.

while compressive stress at failure is much higher, at 15 or 20 times the tensile value. Chirone reports the standard deviations for failure under tension for a number of coals as being about one-third of the applied stress at failure [11]. Brown and Hiorns [12] note that the strength of 25-mm cubes under compression is about 40 MPa for anthracites, but falls to 10 MPa for coals with 20% volatile matter. Under a triaxial stress field, great increases in axial fracture stress result, probably as fissures close.

Results and Discussion

The breakage of all coals at 1.5 mm initial size ($d_o = 1.5$) under 5% oxygen in nitrogen was slight, but similar in nature. The particle size distributions of the initial sample and the products from three of them, namely Flambant de Provence, La Mure, and Rietspruit, are shown in Fig. 1. The Ulan coal distribution, which is omitted, was similar in form to that of Flambant de Provence. In all cases, there is evidence of swelling in the form of enlarged particles (cf. Ref. 8). At the finer end of the distributions, there are many particles smaller than 0.1 mm, but virtually none between this size and 0.4 mm. Even at longer times, this particle range was not represented in the distributions. This behavior is consistent with the findings of Sundback et al. [2] who report few secondary fragments below 1 mm. A similar observation was made by Chirone et al. [13] in the case of Kentucky (K9L) coal for which no primary fragments under 1 mm were found. Even in the case of the Kentucky (K9H) coal, the amount of such particles was only around 4% on a mass basis according to the same authors, both coals differing only by their swelling indexes.

The appearance of a lower size limit to breakage is understandable because of the thermal stresses decrease in smaller particles (see later). Also, as the fragments become smaller, they will become more homogeneous in terms of both maceral and mineral content, so that there will be fewer planes of weakness. The larger value found by Sundback applies to secondary fragmentation, in which the particles will have been thermally treated and hence become stronger.

With all the coals, there is a maximum in the fractional distribution at or slightly below d_o, indicating that a significant proportion of the particles had not fragmented. From the areas under the curves in Fig. 1, it was estimated that 96% of the number of product particles for Rietspruit coal, 82% of the Ulan, and 70% of the Flambant de Provence coals were in the original size range, taken to be > 0.8 mm. With the La Mure coal, this falls to 68%. These values are tabulated in Table 1.

Except for Rietspruit, there is a second maximum or shoulder centered around the dimension $d_o/2$. When the number of particles in this region is aggregated (based on $0.4 < d < 0.8$ mm), the percent number values shown in Table 1 are found. If it is

TABLE 1
Properties and breakage behaviour of 1.5-mm particles

Coal	Rank[a] (ASTM class)	% VM d.a.f.	% Vitrinite	Est. PRN	$<d_o/10$ (%)	$d_o/2$ (%)	d_o (%)	N/N_o
Fl. de Pr.	SB	63.3	51	5	15	15	70	1.14
Rietspruit	MVB	29.5	26	20	4	0	96	1.00
Ulan	HVBA	36.1	40	20	6	12	82	1.11
La Mure	SA	9.9	84	30	16	16	68	1.15

[a]SB, Subbituminous; MVB, medium volatile bituminous; HVBA, high volatile bituminous; SA, semi-anthracite.

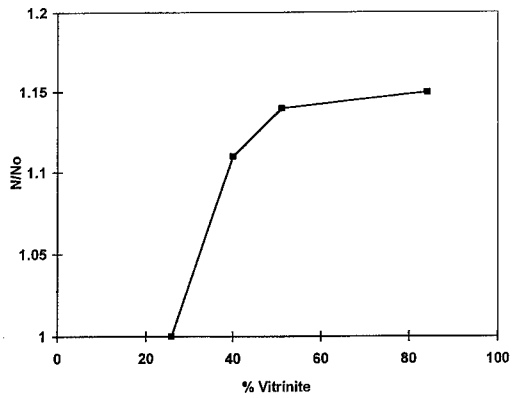

FIG. 2. Relationship between N/N_o and vitrinite content.

assumed that an average of 4 major product fragments is formed during each breakage [2], and the contribution of small fragments below 0.1 mm is neglected, the ratio of the number of major product particles to the original number, N/N_o, can be calculated. The results are included in Table 1. All the results are slightly over unity, which is typical of values reported in the literature for the breakage of small particles [11]. The appearance of a large number of smaller particles is consistent with the results of Dacombe whose counting technique could not resolve particle size.

The fragmentation behavior of the four coals differs in extent rather than form, with little difference between high- and low-volatile coals. This suggests that volatile pressure is not a major determinant. The extent of fragmentation should be explainable by some other coal property or combination of properties. There is no monotonic correlation of N/N_o with percent carbon content, nor with estimated PRN values. The latter is not surprising as the Kelvin equation predicts that the equilibrium moisture content measures porosity in pores below 0.012 μm in size [14], whereas it is claimed by Gavalas [15] that volatiles flow occurs in pores around 0.3 μm in size.

The correlation with vitrinite content is shown in Fig. 2, where it can be seen that the higher vitrinite coals tend to fragment more. Vitrinites are known to be more brittle than other macerals [16] and are disproportionately represented in the finer sizes of the broken feed in coal preparation plants [14]. The tendency for fissures to form preferentially in vitrinite macerals during the first 5 s of heating in these coals has already been noted [8]. The fissures, which appear to be the result of thermal stress, should assist in relieving internal volatile pressures in small particles.

Particle size distributions for the two coals tested at 2.5 mm under both nitrogen and 5% oxygen at one atmosphere (Flambant de Provence and La Mure) are given in Fig. 3. The tests were repeated on the same two coals at 1.0 MPa, with the results also included in Fig. 3. For both coals, the extent of breakage is much greater than for the 1.5-mm particles (Fig. 1). The smallest fragments are 0.6 mm for Flambant de Provence and 0.8 mm for La Mure.

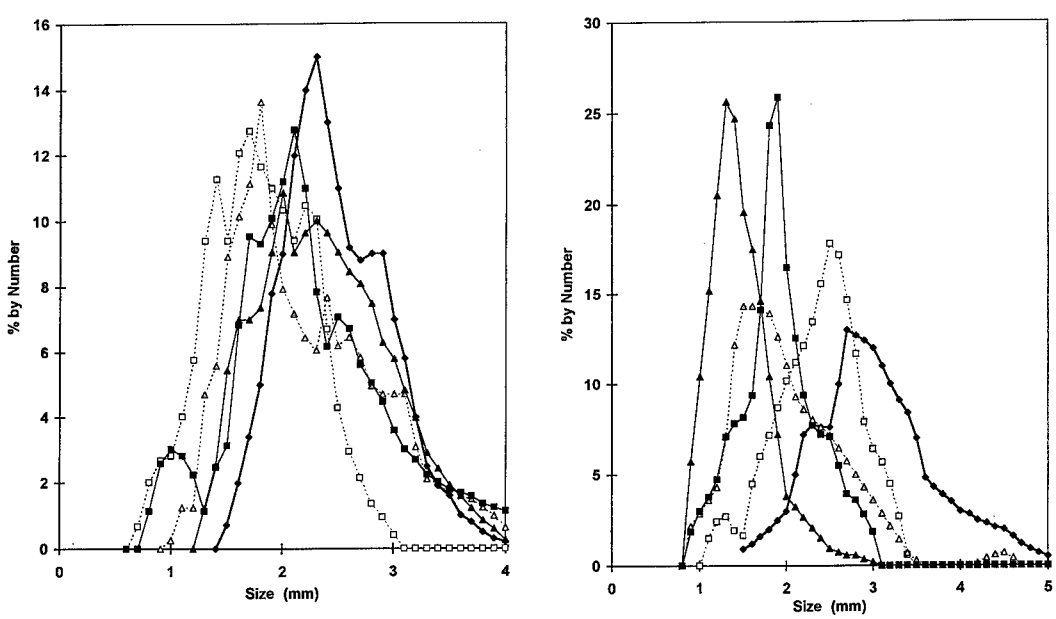

FIG. 3. Particle size distributions by number of initial and treated 2.5-mm coal samples. (a), Flambant de Provence; (b), La Mure; ◆, Initial; □, 0.1 MPa, 0% O_2; △, 0.1 MPa, 5% O_2; ■, 1.0 MPa, 0% O_2; ▲, 1.0 MPa, 5% O_2.

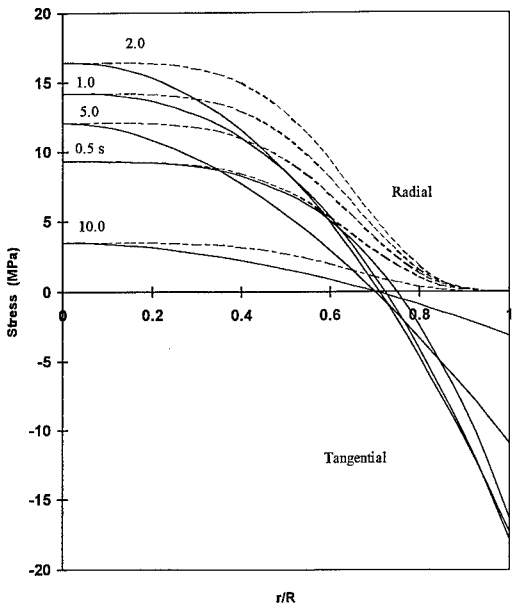

FIG. 4. Thermal stress distributions at various times in a 2.5-mm coal sphere heated by radiation at 850°C.

There is little evidence of swelling in the Flambant de Provence sample and none with La Mure, suggesting that fragmentation occurred before swelling could begin.

The fragmentation behavior of the larger sizes of the two coals is contradictory. There is a tendency for the high-volatile Flambant de Provence coal to split off fragments and retain a high proportion of particles in the original size range. On the other hand, the anthracitic, low-volatile La Mure coal undergoes extensive fragmentation, with the product size distributions tending to exhibit a self-preserving nature. That is, they resemble the form of the original distribution but move to a smaller mean size.

Only at 1 MPa and zero oxygen do the 2.5-mm Flambant de Provence particles behave in a manner similar to the 1.5-mm Flambant de Provence particles, with a small secondary peak of $d_o/2$ pieces. The maxima in the high-pressure La Mure distributions are sharp peaks in the vicinity of $d_o/2$, suggesting that under the high pressure conditions, most of the particles have broken.

One would expect a greater extent of breakage with oxygen present than without, as the rapid combustion of volatiles would result in higher surface temperatures. Both the thermal and volatile-pressure stresses will be greater at these higher temperatures. This is found to be the case at 0.1 and 1.0 MPa for the La Mure anthracite, but not for Flambant de Provence coal. The latter exhibits the opposite effect, especially at 1 atm without oxygen, where the size distribution is self-preserving and less than 25% of particles remain in the d_o range. The difference in behavior with respect to oxygen is probably related to the difference in the quantity of volatiles released by the two coals. The rapid flow of volatiles has been shown to convectively cool the outer layers of particles and prevent oxygen from reaching the surface, even when combustion is occurring [17]. This will have the effect of smoothing out the thermal stress gradients and decreasing thermally induced fragmentation.

An experimental result in support of this hypothesis has been reported previously [9]. Some of the Flambant de Provence particles, pyrolyzed in nitrogen for 60 s to remove volatiles, were reintroduced into the reactor for 30 s with 5% oxygen. The modal diameter after the pyrolysis step was 1.86 mm, but fell to 1.2 mm after the second thermal treatment (i.e., with oxygen). The modal diameter after 60 s in 5% oxygen was 1.62 mm and changed little with longer exposure time. Thus, the devolatilized material behaves similarly to low-volatile anthracite.

Under the elevated pressure, the Flambant de Provence coal particles fragment in a similar way whether oxygen is present or not. The behavior is similar to that at 0.1 MPa under oxygen, but not in the absence of oxygen. On the other hand, the La Mure coal disintegrates to a greater extent at 1.0 MPa than at 0.1 MPa. At 1.0 MPa the size distributions of product are narrow, with very few particles of size d_o remaining.

When applying the thermal stress model, the calculated temperature profiles inside the particles were readily fitted by power law distributions. The values of n were larger during initial heating and decreased with time, ranging from 3.2 to 1.9 for the 1.5-mm particles and from 3.5 to 1.8 for the 2.5-mm particles. The form and magnitude of the predicted thermal stresses was similar for both particle sizes. Those predicted inside 2.5-mm coal particles using the physical properties $E = 6 \times 10^3$ MPa^{-1}, $\alpha = 40 \times 10^{-6}$ K^{-1}, and $\nu = 0.37$ [7] are shown in Fig. 4.

The maximum (tensile) stress at the center is around 16 MPa, whereas that at the surface is a slightly higher (18 MPa) compressive stress. In the 1.5-mm particles, the maxima are lower at 13 and 15 Mpa, respectively. The compression is generated in the hotter outer layers by the restraining effect of the cooler (less expanded) interior. The transition from tensile to compressive stress occurs at about $r/R = 0.7$, consistent with the value for $n = 2$, which is $\sqrt{1/2}$. When $n = 2$, the numerical values of the stresses at the center and surface are equal, but of opposite sense.

The development of thermal stresses with time is shown in Fig. 5 for the 2.5-mm particles. The surface maximum is reached after about 1 s, while that at the center lags by a further second. The local temperatures marked on Fig. 5 indicate that, in both

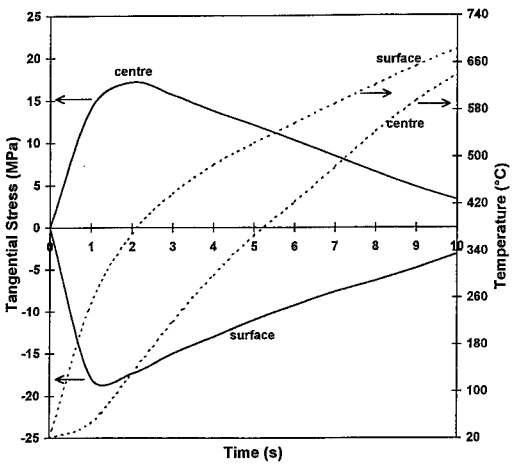

FIG. 5. Development of thermal stress (——) and temperature (- - -) with time at the center and surface of a 2.5-mm coal sphere heated by radiation at 850°C.

cases, the maxima occur below the temperatures of the plastic region (≈400°C), where devolatilization rates are highest. Thus, thermal stresses dominate at these short times and will not be relieved by plastic flow. The same conclusion can be drawn for 1.5-mm particles.

There is evidence that the tensile stresses generated cause fissuring, especially in vitrinite, thus relieving the stress at the center of the particle. Near the surface, compression is exerted in the exterior shell. In this region, there is radial tension coupled with tangential compression, which favors delamination by shearing. The magnitude predicted by the model for spheres is below the value at which breakage occurs in anthracite as measured by Brown and Hiorns [12], but is of the same order for lower-rank coals. There will be a distribution of strengths for apparently identical particles, with the probability of some failing before others.

The nature of the thermal stress fields predicted by the model therefore suggests that failure will occur by shear in brittle fracture, with pieces of the outer shell breaking away. The stress in the outer shell grows more rapidly than at the center (Fig. 5), and if outer pieces break off, the stress field at the center will relax. Real coal particles are not spherical and not isotropic, and irregular shapes will lead to stress concentrations. Thus, failure is likely to occur locally before the stress levels predicted for a sphere are reached.

According to the volatile-pressure model, an increase in external pressure should lead to less breakage. The total pressure is higher, but the pressure gradient in the pores, which generates the breakage stresses in the coal, will be less. This is because volatile transport is predominantly by Poiseuille flow, in which pressure drop is a function of velocity, viscosity, and pore size. A higher system pressure produces denser vapor products (and hence lower vapor velocities) without a corresponding increase in viscosity.

This type of behavior is found in the highly volatile Flambant de Provence coal, suggesting that volatile pressure effects are active during the 20-s period of the tests. The heat transfer calculations predict that all of the particle will be above 600°C after only 10 s. Thus, some of the breakage in the larger particles will be the result of vapor pressure effects. This is to be expected in view of its extremely high volatile matter content.

However, in the case of thermal stress, the system pressure is superimposed onto the thermal stress system, diminishing tensile but increasing compressive stresses. If the failure is by thermally induced compression, then the behavior of the La Mure coal in breaking more under pressure is consistent with the model. On this basis, thermal stresses are more important in the low-volatile La Mure anthracite than in the high-volatile Flambant de provence coal. The evidence from these tests suggests that both volatile pressure and thermal stresses operate within 2.5-mm particles heated for 20 s, in line with the conclusion of Prins et al. [18].

For the smaller 1.5-mm particles, thermal stress appears to be the major effect, with vitrinite-rich coals fragmenting more. The reasons are that all the coals behave in a similar manner; VM content is not significant and the calculated maximum thermal stress in 1.5-mm particles is only 25% less than in 2.5-mm particles. This is in agreement with Chirone et al. and the other VM-driven models which predict that fragmentation will not occur in particles below 2.5 mm. With larger particles of 2.5-mm diameter, volatile matter effects are superimposed onto thermal stress breakage. Elevated pressure leads to increased breakage in low-volatile coals, but in high-volatile coals tends to suppress the fragmentation caused by volatile matter release. The presence of oxygen increases breakage for low-volatile coal, but its effect can be negated by the flow of volatiles from high-volatile coals.

Conclusions

The manner of breakage of 1.5- to 2.5-mm-size coal particles at 850°C has been examined for different coal types, and the product size distributions are found to be influenced by a number of factors.

1. There is an influence from size. Only a few 1.5-mm particles break, probably as a result of thermal stress. In fact, both thermal stress and volatile-matter pressure should be considered. Due to the fact

that all the coals of this size behave the same regardless of their VM content and that the stress value remains important, the effect of VM could be neglected in this size range. The model of thermal stress generation suggests that external shell fragments are lost during breakage. With 2.5-mm particles, most particles fracture. The evolution of volatiles adds to breakage and may modify thermal stress fields. In general, there are no major product fragments below 0.4 mm.

2. There is an influence from maceral content, as high-vitrinite coals break more extensively.

3. There is an influence from volatile matter content. Higher system pressures favor increased fragmentation in low-volatile content coals, contrary to the volatile-pressure model, but consistent with the thermal stress model. However, the reverse applies to high-volatile content coals.

Nomenclature

E Young's modulus Pa
n power law exponent –
r radial coordinate m
R particle radius m
T temperature K
α coefficient of volumetric thermal expansion K^{-1}
ν Poisson ratio –
σ stress Pa

Subscripts

o at the center
r in the radial direction
R at the surface
θ, φ in the tangential directions

REFERENCES

1. Stubington, J. F., Linjewile, M. T., and Sergeant, G. D., *International Conference on Coal Science* (Moulijn, J. A. et al., Eds.), Elsevier, Amsterdam, 1987, p. 833.
2. Sundback, C. A., Beer, J. M., and Sarofim, A. F., *Twentieth Symposium (International) on Combustion,* The Combustion Institute, Pittsburgh, 1984, p. 1495.
3. Chirone, R. and Massimilla, L., *Twenty-Second Symposium (International) on Combustion,* The Combustion Institute, Pittsburgh, 1988, p. 267.
4. Dakic, D., Van Der Honing, G., and Valk, M., *Fuel* 68:911 (1989).
5. Chirone, R. and Massimilla, L., *Powder Technol.* 57:197 (1989).
6. Dacombe, P. J., Hampartsoumian, E., and Pourkashanian, M., *Fuel* 73:1365 (1994).
7. No, S. Y. and Syred, N., *J. Inst. Energy* 63:195 (1990).
8. Fkyerat, M., Hosseini, E., Delfosse, L., and Delebarre, A., *Twenty-Second Symposium (International) on Combustion,* The Combustion Institute, Pittsburgh, 1990, p. 1223.
9. Fkyerat, M., Gilot, P., and Delfosse, L., *Proc. 10th Int. Pittsburgh Coal Conf.* (Chiang, S. H., Ed.), Pittsburgh, 1993, p. 617.
10. Calcott, T. and Smith, G. B., in *Chemistry of Coal Utilization,* (Elliot, M. A., Ed.), John Wiley, New York, 1984, 2nd Suppl. Vol.
11. Chirone, R., Massimilla, L., and Salatino, P., *Prog. Energy Combust. Sci.* 17:297 (1991).
12. Brown, R. I. and Hiorns, F. J., in *Chemistry of Coal Utilization* (H. H. Lowry, Ed.), John Wiley, New York, 1963, First Suppl. Vol. p. 130.
13. Arena, U., Cammarota, A., and Chirone R. *Twenty-Fifth Symposium (International) on Combustion,* The Combustion Institute, Pittsburgh, 1994, p. 219.
14. Stanmore, B. R., He, Y., White, E. T., Firth, B., O'Brien, G., and O'Brien, M., *Fuel,* submitted.
15. Gavalas, G. R. and Wilks, K. A., *JAIChE* 26:201–212 (1980).
16. Hower, J. C. and Parekh, B. K., in *Coal Preparation* (J. W. Leonard and B. C. Hardinge, Eds.), 1991, Colorado, SME, p. 1.
17. Sasongko, D., Ph.D. Thesis, University of NSW, Newcastle, 1995.
18. Prins, W., Siemons, R., Radovanovic, M., and Van Swaij, in *W. P. M. International Conference on Coal Science,* (Moulijn, J. A. et al., Eds.), Elsevier Science, Amsterdam, 1987, p. 818.

Twenty-Sixth Symposium (International) on Combustion/The Combustion Institute, 1996/pp. 3277–3285

PREDICTION OF COAL-WATER SLURRY DISPERSION IN A FLUIDIZED BED COMBUSTOR

F. OKASHA
Dipartimento di Ingegneria Chimica
University of Naples "Federico II" Italy
Istituto Ricerche Combustione
National Research Council of Italy
Naples, Italy

M. MICCIO
Dipartimento di Ingegneria Industriale
Viale delle Scienze
43100 Parma PR
Italy

Coal-water slurry (CWS) injection in a fluidized bed leads to formation of three carbon phases: aggregates (A phase), tiny carbon deposits on individual bed particles (S phase), and carbon fines (F phase). The mechanism by which CWS is dispersed in a bubbling fluidized bed is analyzed by considering fundamental aspects and key stages underlying interaction of a CWS spray with hot bed solids.

A mathematical model has been developed for the formation rates of carbon phases inside the jet zone from the fixed carbon injected with CWS. The model, which takes into consideration fluid dynamics, heat, and mass transfer of the jetting region, has a predictive character and uses no adjustable parameter. A key role is played by the submodel that predicts the rate of CWS deposition on sand particles entrained by the jet. Results show that the formation rates of the three carbon phases can be controlled by adjusting injection conditions. The mathematical model may complement a code aimed at predicting and controlling combustion efficiency of CWS in actual fluidized bed boilers.

Model predictions are compared with experimental results obtained by Miccio et al. [8]. In spite of the complexity of the phenomena, the general trends of the predicted and experimental results as a function of injection conditions are the same. The agreement between the model and experimental results is not always satisfactory, but it tends to be better under injection conditions leading to generation of finer CWS droplets. Reasons for the discrepancies are discussed thoroughly.

Introduction

Coal-water slurries (CWS) are presently considered as standard fuels in Italy [1]. Since the earliest development, CWSs have been proposed [2,3] as fuels for atmospheric and pressurized fluidized bed combustors (FBC). Coal-water pastes (CWP) have been fueling PFBCs at Tidd (USA) and Vartan (S) since 1990 [4]. Recently, another water-based fossil fuel, Orimulsion, is receiving attention [5].

During an extensive study on combustion of CWSs, Massimilla and co-workers showed that carbon is allocated in the bed during steady-state CWS fluidized combustion as three phases [6,7]: an A phase, made of carbon aggregates usually larger than 1 mm that may include bed inert particles; an S phase formed by carbon deposits (<30 μm) on individual bed particles; and an F phase made of free carbon fines (<400 μm). More recently, an experimental study on interactions between a CWS spray and a sand bed [8] provided formation rates of carbon phases under typical FBC conditions without contemporary combustion.

Massimilla and co-workers used a submerged feeding technique with a horizontal, air-assisted injector. A flare-shaped jetting region is formed [9], and complex interactions occur between the CWS spray and hot surroundings. The key stage consists of drying of CWS droplets of different size while they travel inside the flare and receive heat from the surroundings. Drying of a CWS droplet inside the flare is likely to contribute to F-phase formation. The preceding stage may be interrupted by collision of the CWS droplet with a hot bed particle entrained by the jet. This case is likely to contribute to S-phase formation. This stage may also be interrupted by impingement of a CWS droplet against the boundaries and the front wall of the flare. In this case, residual

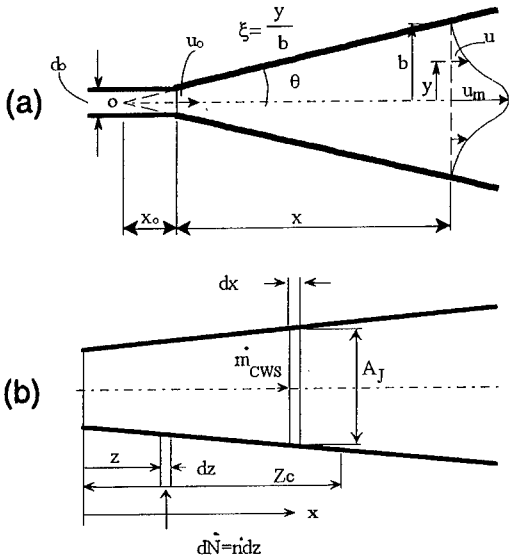

FIG. 1. Jet configuration with reference to entrainment of sand particles and settlement of CWS droplets.

water is suddenly lost in contact with hot bed particles. For large CWS droplets, it is likely that carbon aggregates are formed, whether or not including bed particles. CWS droplets of a diameter equal to or smaller than bed particle size may either form a small carbon aggregate or bind two bed particles together or spot a single bed particle with a carbon deposit. (A carbon-spotted particle is a sand particle whose surface has been partially and nonuniformly covered by carbon fines (<30 μm).

After discussing fundamental aspects underlying the mechanism of CWS interaction with the hot fluidized bed, this paper is aimed at presenting a mathematical model of CWS dispersion and formation of carbon phases. The model is intended as a tool for predicting the formation rates of carbon phases as a function of injector design and operating conditions.

Mathematical Model

The Jet Flare Flow Field

Merry's configuration is adopted for the jet (Fig. 1a) that is considered stationary. The penetration length (L_j), gas velocity (u), and gas temperature (T_f) are predicted using the following relationships:

$$\frac{L_j}{d_o} + 4.5 = 5.25\left(\frac{\rho_o u_o^2}{(1-\varepsilon)\rho_s g d_s}\right)^{0.4}\left(\frac{\rho_f}{\rho_s}\right)^{0.2}\left(\frac{d_s}{d_o}\right)^{0.2} \quad [10] \quad (1)$$

$$\frac{u}{u_m} = (1-\xi^{1.5})^2 \quad [10] \quad (2)$$

$$\frac{u}{u_o} = \frac{1}{2a_j}\frac{d_o}{(x+x_o)}(1-\xi^{1.5})^2, \quad [10] \quad (3)$$

where $a_j = 0.26 \tan\theta = 0.26\, b/(x + x_o)$

$$\ln\frac{T_{fm}-T_b}{T_{fo}-T_b} = -\frac{4h_j}{\rho_f u_o d_o C_{pg}}\left(x - \frac{d_o}{2}\right) \quad [11] \quad (4)$$

$$\frac{(T_f - T_b)}{(T_{fm} - T_b)} = 1 - \xi^{1.5} \quad [9] \quad (5)$$

Merry's correlation for L_j refers to atmospheric conditions. However, jet penetration and steadiness are known to increase with gas density and, hence, with operating pressure [9]. Eqs. (2) through (5) derive from an extension of Schlichting and Taylor similarities to a submerged jet in a fluidized bed [9] and therefore can be considered valid at pressures higher than atmospheric.

Entrainment of Gas and Solids into Jet Flare

Interstitial fluid and solid particles are entrained into the flare [10]. The gas entrainment rate is not treated explicitly because it is already embodied within Eq. (3). The following assumptions are considered for solids on the basis of investigations carried out at atmospheric pressure:

1. The solid entrainment into the jet (see Fig. 1b) takes place only in the first part of length $Z_c = 0.55L_j$ [12].
2. The solid entrainment rate per unit distance over the entrainment length is constant:

$$\frac{d\dot{N}}{dz} = \dot{n} \quad (6)$$

where $\dot{N}(z)$ is the numerical flow rate of entrained sand particles at axial position z (see Fig. 1b).

3. The overall entrainment rate of solids on a volume basis (V_E) is given by the Vostokov correlation [13]:

$$V_E = 0.2u_o(d_o/2)^2\left[\frac{\rho_o d_o}{2\rho_s d_s}\right]^{1/3} \quad (7)$$

Droplet Size Distribution

A correlation proposed by Kim and Marshall [14] for a pneumatic injector is used. The mass mean diameter ($\bar{d}_d$) and the cumulative distribution of CWS droplets (Φ_v) are given as follows:

$$\bar{d}_d = 249\left(\frac{\sigma_1^{0.41}\mu_1^{0.32}}{[(u_o - v_d(0))^2\rho_o]^{0.57}A_o^{0.36}\rho_1^{0.16}}\right) + 1260\left(\frac{\mu_1^2}{\rho_1\sigma_1}\right)^{0.17}\frac{1}{\mathrm{ASR}(u_o - v_d(0))^{0.54}} \quad (8)$$

$$\Phi_v(d_d) = \frac{1.15}{1 + 6.67 \exp\left(-2.18 \frac{d_d}{\bar{d}_d}\right)} - 0.150 \quad (9)$$

From $\Phi_v(d_d)$, the differential size distribution $\phi(d_d)$ is derived.

Drying of a CWS Droplet inside Jet Flare

According to a review of CWS droplet drying, the following general assumptions appear most reasonable:

1. CWS droplets have spherical shape with a fixed diameter (d_d) during vaporization [15,16].
2. Droplets are heated by convection in the flare and radiation from hot bed solids.
3. Vaporization rate is calculated using the difference between temperature of streaming gas (Tg_∞) and that of droplet surface (T_d) as driving potential [17].
4. A quasi-steady approximation is feasible.

Considerations derived for liquid droplets are extended to CWS without modifications [15,16], and the Spalding approach [15,18] is followed. Therefore, the droplet evaporation rate (R_{wd}) and equilibrium temperature (T_d) are, respectively,

$$R_{wd} = \frac{k_g Nu}{C_{pv} d_d} \ln\left[1 + \frac{C_{pv}(T_{g\infty} - T_d)}{L - Q_{\text{rad}}/\pi d_d^2 R_{wd}}\right] \quad (10)$$

$$T_d = T_{g\infty} - \left(\frac{L}{C_{pg}} - \frac{Q_{\text{rad}}}{\pi d_d^2 C_{pv} R_{wd}}\right) \left(\frac{1 - C_\infty}{1 - C_{ds}} - 1\right) \quad (11)$$

where the mass fraction of water vapor (C_{ds}) surrounding the droplet is calculated under the assumption that the film is saturated by vapor at the surface temperature T_d.

A modified Ranz and Marshall correlation has been used for the Nusselt number [19–21]. The moisture fraction of a CWS droplet after traveling a distance x from the nozzle is determined by the water balance

$$X_d(x, d_d) = X_d(0, d_d) - \int_0^x \frac{6}{d_d \rho_d} \frac{R_{wd}(d_d, \lambda)}{v_d(\lambda, d_d)} d\lambda \quad (12)$$

where $X_d(0, d_d)$ is the initial moisture fraction, $v_d(x, d_d)$ the droplet velocity, and λ an integrating variable.

Drying of CWS Covering Sand Particles

CWS droplets hitting an entrained sand particle are assumed to form an even shell covering the outer surface. CWS shells receive heat from the surroundings by convection and radiation, as in the case of CWS droplets, as well as extra heat stored in the hot sand particle.

For heat transfer beyond the Leidenfrost point between the hot sand surface and the CWS shell, a correlation by Berenson has been used to determine h_s [22,23]. To calculate surface temperature, the sand particle is considered a lumped body [24], being Bi $= h_s d_s / k_s = 0.0077 < 0.1$. As a result, the water evaporation rate from CWS shell (R_{wsh}) can be calculated.

Settlement of CWS Droplets on Sand Particles

CWS droplets—particularly the smallest ones—collide with entrained sand particles because of their different relative velocities. The amount of CWS settled on a sand particle (m_d) depends on the time that the particle has spent in the flare. Therefore, the entrance position, z, of every sand particle must be considered (see Fig. 1b), and, at any position $x > z$, the sand velocity $v_s(x, z)$ is also a function of z. According to Bodrov and Minaev [25] and Chernyaev et al. [26], m_d is proportional to the particle projected area through an impact efficiency η.

The mass balance on a sand particle with a growing CWS shell takes into account both further deposition of CWS droplets and moisture evaporation:

$$dm_{ss} = dm_d - R_{\text{wsh}}(x, z)\pi d_{sh}^2 dt \quad (13)$$

where $m_{ss} = m_s + m_{sh}$ and d_{sh} are the mass and the outer diameter of a CWS-covered sand particle.

Since for the sand particle, $dt = dx/v_s(x, z)$, Eq. (13) becomes

$$\frac{dm_{ss}}{dx} = \left(\overline{\frac{dm_d}{dx}}\right) - \frac{R_{\text{wsh}}(x, z)\pi d_{sh}^2}{v_s(x, z)} \quad (14)$$

where $\overline{(dm_d/dx)}$ is the variation with axial position of the CWS mass settled on the sand particle after averaging over the droplet size range [27]. At any position x (see Fig. 1b), once the settlement rate of CWS droplets ($\dot{m}_d(x)$) has been calculated [27], the CWS mass flow rate ($\dot{m}_{\text{cws}}(x)$) and the droplet size distribution ($\phi(d_d, x)$) may be recalculated by mass balances.

Motion of CWS Droplets and Sand Particles

Inside the jet, the gas velocity is significantly faster than the particle or droplet velocity and hence the drag force is several orders of magnitude larger than any other force, including gravity [26]. Considering a CWS droplet, the equation of motion is [10]

$$\frac{dv_d}{dx} = \frac{6 C_D \rho_f (u - v_d)|u - v_d|}{8 \rho_d d_d v_d} \quad (15)$$

where the drag coefficient (C_D) is given by Bird et

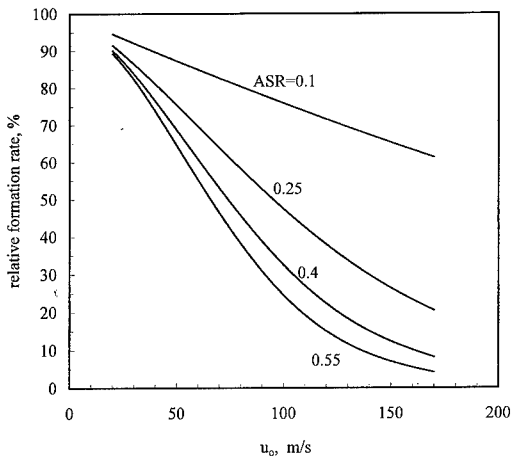

FIG. 2. Relative formation rate of A phase as a function of injection conditions (u_o and ASR).

al. [28]. The change of a sand particle velocity is determined by the momentum balance

$$\frac{d(m_{ss}v_s)}{dx} = \left(\overline{\frac{dI}{dx}}\right) + \frac{F_d}{v_s(x, z)} \tag{16}$$

where $(\overline{dI/dx})$ is the variation with axial position of the momentum of settling droplets after averaging over the droplet size range [27]. The drag force exerted by jet gases (F_d) is

$$F_d = \frac{1}{2} C_D \rho_g (u(x) - v_s(x, z)) |u(x) - v_s(x, z)| \frac{\pi d_s^2}{4} \tag{17}$$

Formation of A, S, and F Phases

The formation of the three carbon phases is considered depending on the size of CWS droplet, the occurrence of collision with a sand particle, and the ultimate moisture content of a CWS droplet reaching the end of the flare. Collisions between large CWS droplets and sand particles are neglected because large droplets are few in numbers and travel with a velocity near that of sand particles. Accordingly, the following assumptions are established:

1. CWS droplets of a size larger than a limiting diameter (d_{dl}) are assumed to form A phase. For the present work, d_{dl} was chosen equal to the average sand size (d_s).
2. All droplets that collide with sand particles are assumed to adhere to the particles if they have any residual moisture.
3. S phase carbon resulting after CWS drying and devolatilization is assumed to be a uniform shell that has covered the outer surface of a sand particle since the earliest droplet settlement.
4. Droplets smaller than d_{dl} that arrive at the end of the flare with residual moisture form S phase.
5. Droplets smaller than d_{dl} that arrive completely dry at the end of the flare form F phase.

Accordingly, the formation rates of the A, S, and F phase are

$$\dot{m}_{CA} = \int_{d_S}^{d_O} \dot{m}_{\mathrm{CWS}}(L_j)\phi(d_d, L_j) [1 - X_d(L_j, d_d)] X_{fc} dd_d \tag{18}$$

$$\dot{m}_{CS} = \int_0^{z_c} \int_z^{L_j} \int_{d_X(\lambda)}^{d_s} \frac{\frac{\pi}{4} d_s^2 \eta \dot{n}}{A_j(\lambda)} \frac{v_d(\lambda, d_d) - v_s(\lambda, z)}{v_d^2(\lambda, d_d)} \dot{m}_{\mathrm{CWS}}(\lambda)\phi(d_d, \lambda) [1 - X_d(\lambda, d_d)] X_{fc} dd_d d\lambda dz + \int_{d_X(L_j)}^{d_s} \dot{m}_{\mathrm{CWS}}(L_j)\phi(d_d, L_j)[(1 - X_d(L_j, d_d)] X_{fc} dd_d \tag{19}$$

$$\dot{m}_{CF} = \int_{d_I}^{d_X(L_j)} \dot{m}_{\mathrm{CWS}}(L_j^0)\phi(d_d, L^0_j) [(1 - X_d(L_j^0, d_d)] X_{fc} dd_d, \tag{20}$$

where d_I and d_O are the minimum and maximum diameter of CWS droplets, respectively, and d_X is the diameter of the largest CWS droplet that is completely dried at axial position x. The relative formation rates are expressed in a nondimensional form:

$$\mathrm{RFR}_i = \frac{\dot{m}_{Ci}}{\dot{m}_{CA} + \dot{m}_{CS} + \dot{m}_{CF}} \tag{21}$$

$$\text{for } i = A, S, F.$$

Results and Discussion

Model Results

The main variables influencing formation rates of carbon phases are the initial velocity of the dispersing air (u_o) and the mass ratio of the dispersing air flow rate to the CWS feed rate (ASR = $\dot{m}_o/\dot{m}_{\mathrm{CWS}}(0)$) [8,29]. The influence of those two variables was studied by the model, and results of calculations are reported in Figs. 2 to 4 in terms of relative formation rate of A, S, and F phase, respectively.

As shown in Figs. 2 and 3, an increase of u_o leads to a decrease in the formation rate of A phase and an increase in that of S phase. The main reason is that the distribution of CWS droplets is displaced toward small sizes when u_o is raised. Hence, the CWS mass mean diameter decreases, and, according

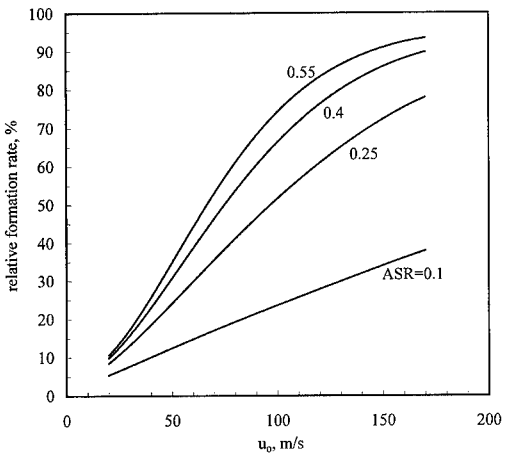

FIG. 3. Relative formation rate of S phase as a function of injection conditions (u_o and ASR).

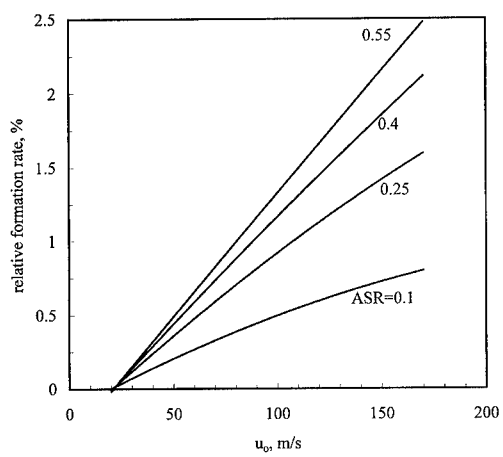

FIG. 4. Relative formation rate of F phase as a function of injection conditions (u_o and ASR).

to Kim and Marshall's [14] correlation, a larger mass ratio of small droplets is produced by the injector. Moreover, the relative velocities between small droplets and sand particles become greater as a result of increasing u_o. The last two reasons cause the quantity of CWS that settles on sand particles, and hence the formation rate of S phase, to increase at higher u_o. This is clearly demonstrated by Fig. 5, which presents the relative settling rate (RSR)

$$\mathrm{RSR} = \dot{m}_d(L_j)/\dot{m}_{\mathrm{CWS}}(0) \tag{22}$$

as a function of injection conditions. It must be recalled that $\mathrm{RFR}_S > \mathrm{RSR}$ because RFR_S includes a further contribution to formation of S phase at the end of the flare by CWS droplets with $d_d > d_X$.

The influence of ASR on the formation rates of

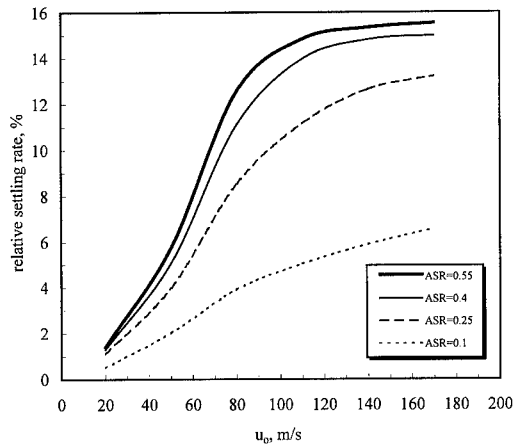

FIG. 5. Relative settling rate of CWS on entrained sand particles as a function of injection conditions.

TABLE 1
Maximum size at which dispersed CWS is dried up at the end of the flare

u_0, m/s	30	70	110	150
CWS droplet				
diameter, μm	11	23	32	35
CWS shell				
thickness, μm	1.5	2.9	2.5	1.4
diameter of equivalent sphere, μm	170	210	200	165

the three phases is also shown in Figs. 2–4. It appears that increasing ASR has the same effects as raising u_o. Thus, increasing ASR causes a decrease in RFR_A and an increase in RFR_S. Again, this result is due to the larger mass ratio of small droplets produced at higher ASR. As a consequence, the rate of CWS settlement on sand particles becomes greater (Fig. 5).

The formation rate of F phase is small, less than 3%, even under the worst conditions in the range investigated in Fig. 4. This result appears to be due to the following three reasons: First, only small droplets could be dried up before arriving at the end of the flare. Results of drying calculations are reported in Table 1 for both CWS droplets and shells. It turns out that droplets of about 20 and 30 μm are dried out at $u_o = 56$ m/s and $u_o = 98$ m/s, respectively. The second reason is the assumption that CWS droplets with very low residual moisture also adhere to a sand particle after collision. Finally, according to the Kim and Marshall correlation, the injector produces a low mass ratio of small droplets.

A sensitivity analysis has been carried out to check

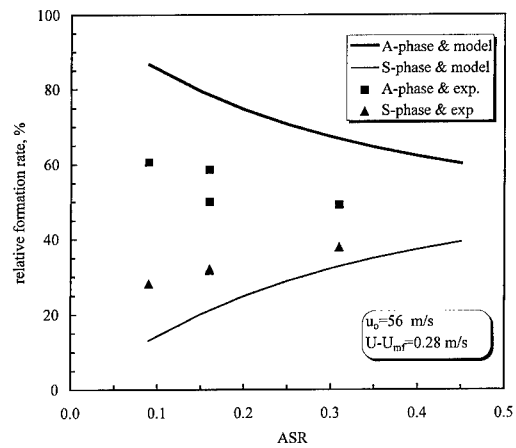

FIG. 6. A comparison between predicted and experimental results.

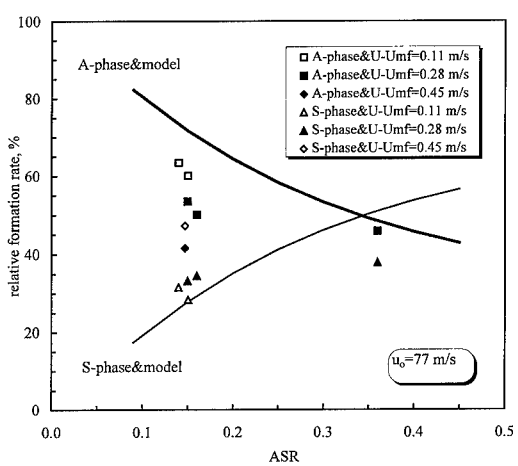

FIG. 7. A comparison between predicted and experimental results.

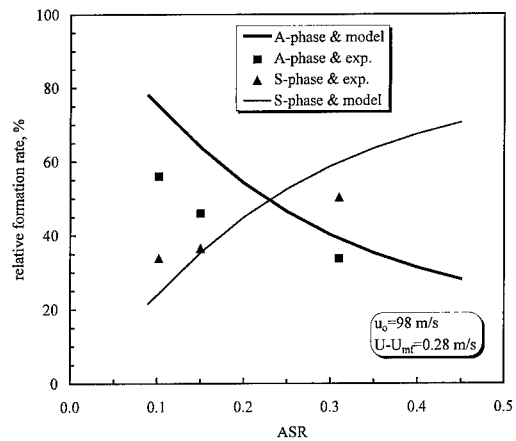

FIG. 8. A comparison between predicted and experimental results.

TABLE 2
Comparison between predicted and experimental relative formation rates.

	u_o = 56 m/s			u_o = 98 m/s		
	pred.	exp.	deviat.	pred.	exp.	deviat.
ASR			A phase, %			
0.10	85.0	60.6	24.5	75.0	56.0	19.0
0.16	76.5	58.6	17.9	62.5	45.9	16.6
0.31	66.0	49.2	16.8	37.5	33.7	3.9
			S phase, %			
0.10	15.0	27.4	−12.4	25.0	33.8	−8.8
0.16	23.0	31.7	−8.7	36.0	36.4	−0.4
0.31	33.0	37.5	−4.5	61.0	50.2	10.8
			F phase, %			
0.10	~0	12.0	−12.0	~0	10.3	−10.3
0.16	0.5	9.7	−9.2	1.5	17.7	−16.2
0.31	1.0	13.3	−12.3	1.5	16.2	−14.7

the influence that parameters or correlations subject to uncertainty have on model performance [29]. Accordingly, it was found that droplet size distribution strongly affects the model performance. Jet penetration length has a notable influence on the formation rate of F phase and therefore must be known with sufficient accuracy. All other parameters have a negligible influence.

Comparison between Predicted and Experimental Results

On the basis of an evaluation study [29], it was found that the injector used by Massimilla and coworkers generated more fine droplets than those predicted by the Kim and Marshall correlation, especially under conditions of good atomization. Despite this lack of a more reliable correlation, the comparison between model and experimental results was carried out by using the Kim and Marshall equation without any modification.

Predicted and experimental relative formation rates of A and S phase are reported over a range of ASR at u_o = 56, 77, and 98 m/s in Figs. 6, 7, and 8, respectively. Experimental results were provided by Miccio et al. [8] for a CWS made of 30% water on a mass basis. The parent fuel was an Upper Freeport bituminous coal having a swelling index of 7.5, a mass-mean diameter of about 40 μm, and a top size of about 170 μm. Experimental and predicted RFR_A and RFR_S have the same trends as a function of injection conditions.

For a first assessment of model results, Table 2 provides a quantitative evaluation of deviations between the predicted and experimental relative formation rates under exactly the same injection conditions. A discrepancy is noticed with deviations usually larger than 10%. A better assessment is obtained by plotting an orderly ensemble of results, as in Figs. 6–8. A certain deviation between predicted and experimental formation of A and S phase always exists in Fig. 6–8 and appears more evident at lower u_o (56 m/s). Moreover, Fig. 7 gives the comparison at u_o = 77 m/s with experimental results from tests carried out at different values of excess fluidization velocity ($U - U_{mf}$ = 0.11, 0.28, and 0.45 m/s). A unique curve is reported in Fig. 7 because the model equations are insensitive to ($U - U_{mf}$).

The model generally tends to overestimate the formation rate of A phase and underestimate that of S phase. The discrepancy could be ascribed to a number of reasons:

1. The model predicts the relative formation rates of carbon phases inside the jet zone. Vigorous agitation of the bed beyond the jet may act on the fate of carbon phases after their formation. In particular:
   - Carbon aggregates are subjected to fragmentation and attrition.
   - Carbon covering or spotting individual sand particles is subjected to attrition by abrasion with other bed solids.
2. The technique setup by Miccio et al. [8] that determines relative formation rates is affected by some experimental errors, as discussed.

Let us suppose attribution of discrepancy to experimental results.

At lower values of ASR and u_o, the formation rate of aggregates is predominant and their sizes are larger. Larger aggregates are more easily subject to comminution and vice versa [6,8]. Therefore, the amount of carbon lost by aggregates because of comminution is expected to decrease with ASR and u_o. Consequently, the deviation between predicted and experimental RFR_A becomes smaller with increasing ASR and u_o. The comminution of aggregates evidently reflects on the formation rate of S phase; the experimental RFR_S exceeds the predicted value at low ASR and particularly at u_o = 56 m/s.

Let us take Table 2 as a basis for discussion in spite of the limitation posed by the one-to-one comparison between data. The deviation between the experimental and predicted RFR_S is larger and negative at the lowest value of u_o (56 m/s). However, the deviation becomes smaller with increasing ASR. At u_o = 98 m/s, the deviation changes from a negative to a positive value, that is, the predicted RFR_S exceeds that from the experiment. These results might be interpreted by taking into account comminution effects. Because of comminution of carbon aggregates, some of their carbon transfers to S phase. On the other side, a part of S phase carbon transfers to fines because of attrition. Thus, there are two opposite factors: the first one causes an increase of S phase, whereas the second brings about decreasing S phase. The final result is a matter of competition between the two factors. At lower values of ASR, the formation of A phase is predominant, in particular at the lowest value of u_o. Under these conditions, the carbon transferred to S-phase because of comminution of aggregates exceeds that transferred from S phase to carbon fines. This is the case represented by Fig. 6 at the lowest value of u_o and by the far left parts of Figs. 7 and 8, that is, at lower values of ASR. On the other hand, at higher values of ASR and u_o, RFR_S is predominant and aggregate sizes are smaller. Under such conditions, the carbon transferred to S phase is less than that transferred to carbon fines because of S-phase attrition; this is the case of the far right parts of Figs. 7 and 8. A positive deviation is reported at ASR = 0.31 in Table 2.

Experimental results reported in Fig. 7 at ASR = 0.15 allow an illustration of the influence of bed dynamic forces. The agreement between predicted and experimental results is better at the lowest value of ($U - U_{mf}$), that is, 0.11 m/s. Under these conditions, dynamic forces inside the bed are lower, formation of aggregates from CWS droplets is not particularly disturbed at the jet-bed interface, and comminution outside the jetting region is lower.

The model predicts smaller values than the experiment for RFR_F (Table 2). First, the Kim and Marshall correlation provides a smaller ratio of fine droplets than that generated by the CWS injector. Second, the experimentally determined RFR_F have been affected by further generation of carbon fines outside the jetting region because of comminution of A and S phase. Because in general RFR_F are lower than both RFR_A and RFR_S, these effects are heavier as relative values.

Conclusions

Based on the study carried out, the following points are important:

1. Formation rates of carbon phases may be controlled properly by adjusting CWS injection conditions, namely the gas velocity at the outlet nozzle and the mass ratio between the flow rates of gas and CWS. Increasing u_o or ASR results in decreasing the formation rate of A phase and increasing that of S phase.
2. Model calculations have demonstrated that only small CWS droplets, with a size up to a certain

limit, dry up before reaching jet boundaries. This size becomes larger with increasing velocity of dispersing gas. Droplets smaller than 11, 23, 32, and 35 μm become completely dry at velocities of 30, 70, 110, and 150 m/s, respectively. These small droplets form carbon fines inside the bed if they do not collide with an entrained sand particle before complete drying.

3. The mathematical model of formation of carbon phases inside the jet zone has the advantages of being predictive and using no adjustable parameter. A key module is the submodel that predicts the rate of CWS deposition on sand particles entrained by the jet. However, the studied phenomena are very complex, especially those occurring at the jet-bed interfaces. Therefore, it is satisfactory that the general trends of the predicted and experimental results as a function of injection conditions are the same. The agreement tends to be better under conditions leading to generation of finer CWS droplets.
4. According to a sensitivity analysis on the influence of correlations or parameters on model results, the droplet size distribution strongly affects the model performance. Thus, great care is necessary for correlations or measurements of $\phi(d_d)$ to obtain reliable results. Jet penetration length has the greatest influence on the formation rate of F phase.
5. The mathematical model may fit with a code that is aimed at predicting and controlling combustion efficiency of CWS in actual fluidized bed boilers.

Nomenclature

a_j constant in Eq. (3)
A_j cross-sectional area of jet flare, m^2
A_O flow area of the nozzle for dispersing air, m^2
ASR mass ratio of flow rate of dispersing gas to CWS feed rate
b radius of jet region, m
Bi Biot number $h_s d_s/k_s$
C_∞ vapor concentration of surrounding gases (mass fraction)
C_D drag coefficient
C_{ds} vapor concentration at droplet surface (mass fraction)
C_{pg} constant-pressure specific heat of surrounding gas, J/kg K
C_{pv} constant-pressure specific heat of water vapor, J/kg K
d_d droplet diameter, m
$\bar{d}_d$ mass mean diameter of CWS droplets, μm
d_{dl} limiting droplet diameter, m
d_I minimum diameter of CWS droplet, m
d_O maximum diameter of CWS droplet, m
d_o nozzle diameter, m
d_s diameter of sand particle, m
d_{sh} external diameter of CWS shell, m
d_X diameter of the largest CWS droplet that is completely dried at position x, m
F_d drag force, N
g acceleration due to gravity, m/s^2
h_j heat-transfer coefficient between bed and jet flare, W/m^2 K
h_s heat-transfer coefficient by convection between sand particle and CWS shell, W/m^2 K
I momentum, kg m/s
k_g thermal conductivity of gas, W/m K
k_s thermal conductivity of sand, W/m K
L latent heat of vaporization, J/kg
L_j penetration length of jet, m
m_d settled CWS mass, kg
m_{sh} mass of CWS shell, m
m_{ss} mass of sand particle including its CWS shell, kg
$\dot{m}_{CA}$ formation rate of the A phase, kg/s
$\dot{m}_{CF}$ formation rate of the F phase, kg/s
$\dot{m}_{CS}$ formation rate of the S-phase, kg/s
$\dot{m}_{CWS}$ mass flow rate of CWS, kg/s
$\dot{m}_d$ mass rate of CWS settlement, kg/s
$\dot{m}_o$ mass flow rate of atomizing gas, kg/s
$\dot{n}$ constant in Eq. (6), 1/(sm)
$\dot{N}$ numerical flow rate of sand particles, 1/s
Nu Nusselt number hd_d/k_g
Q_{rad} heat transferred by radiation, W
RFR_A relative formation rate of the A phase
RFR_F relative formation rate of the F phase
RFR_S relative formation rate of the S phase
RSR mass ratio of all CWS settled on entrained sand particles to fed CWS
R_{wd} evaporating rate from CWS droplet, kg/m^2 s
R_{wsh} evaporation rate from CWS shell, kg/m^2 s
t time, s
T_b bed temperature, K
T_d droplet temperature, K
T_f temperature of gas inside the jet, K
T_{fm} temperature of gas on the jet axis, K
T_{fo} temperature of gas entering the bed, K
$T_{g\infty}$ temperature of surrounding gas, K
u gas velocity, m/s
U superficial fluidization velocity, m/s
u_m gas velocity on jet axis, m/s
U_{mf} minimum fluidization velocity, m/s
u_o velocity of dispersing gas at nozzle outlet at ambient conditions, m/s
v_d velocity of a CWS droplet, m/s
V_E particle entrainment rate (by volume), m^3/s
v_s velocity of sand particle, m/s
x distance from end of CWS nozzle, m
X_d mass fraction of moisture in a CWS droplet
X_{fc} mass fraction of fixed carbon in parent fuel
x_o distance from apex of cone to end of nozzle (Fig. 1), m
y radial distance from jet axis, m
z entrainment position of sand particle, m

Z_c length of entrainment of bed solids, m
ε bed voidage fraction
θ half angle of jet
ξ nondimensional radius ($= y/b$)
η target efficiency
λ traveled distance, m
μ_1 absolute viscosity of liquid, Pa s
ρ_d density of a CWS droplet, kg/m^3
ρ_f density of gas inside the jet, kg/m^3
ρ_1 liquid density, kg/m^3
ρ_o density of gas entering the bed, kg/m^3
ρ_s density of sand, kg/m^3
σ_1 surface tension, N/m
ϕ differential distribution function of CWS droplets, 1/m
Φ_V cumulative distribution function of CWS droplets

Acknowledgments

This paper is dedicated to the memory of Prof. Massimilla who inspired the genesis of the work and stimulated the authors' efforts. The authors acknowledge the JOULE Program of the European Union for financial support; the Italian Ministry of Foreign Affairs for providing Dr. Okasha a three-year scholarship; Mr. Bencivenga, Mr. Cante, and Mrs. Silvestre for their assistance in all experimental activities, and Prof. Salatino for his critical review of the whole work.

REFERENCES

1. CTI, Progetto di norma "Miscele Concentrate Combustibili Acqua-Carbone," *La Termotecnica,* October, 1995, p. 47.
2. Cen, K., Cao, K., Yoal, Z., Kang, S., Hong, J., Xie, M., Lu, D., Ni, M., and Chen, Y., *Proceedings of the 7th International Conference on Fluidized Bed Combustion,* DOE/METC-83/48, Vol. 1. 1982, pp. 253–263.
3. Roberts, A. G., Pillai, K. K., Barker, S. N., and Carpenter, L. K., *Proceedings of the 7th International Conference Bed Combustion,* DOE/METC-83/48, Vol. 1, 1982, p. 482.
4. Jansson, S. A., Proceedings of EPRI Conference on New Power Generation Technology, San Francisco, CA, October 25–27, 1995.
5. Zlatnar, M., "Orimulsion. The Revolutionary New Fuel for Power and Industry." Financial Times Management Report, FT Business Information London, 1989.
6. Massimilla, L. and Miccio, M., *Twenty-First Symposium (International) on Combustion,* The Combustion Institute, Pittsburgh, 1986, p. 357.
7. Miccio, M., Arena, U., Massimilla, L., Maresca, A., and De Michele, G., *AIChE J.* 35(12):2040–2042 (1989).
8. Miccio, F., Miccio, M., and Okasha, F., "Formation Rates of Characteristic Carbon Phases during Fuel-Water Slurry Injection in a Hot Fluidized Bed," *Powder Technol.,* (1996), accepted.
9. Massimilla, L., in *Fluidization,* 2d ed. (Davidson, J. F., Clift, R., and Harrison, D., Eds.), Academic Press, New York, 1985, pp. 133–172.
10. Merry, J. M. D., *Trans. Inst. Chem. Engineer.* 49:189–195 (1971).
11. Behie, L. A., Bergougnou, M. A., and Baker, C. G., *Can. J. Chem. Engineer.* 53:25–30 (1975).
12. Markhevka, V. I., Basov, V. A., Melik-Akhnazarov, and Orochko, D. I., *Theor. Found. Chem. Engineer.* 5:80 (1971).
13. Vostokov, A. P., "Investigation of the Granulation of Mineral Fertilizers in Fluidized Beds." Ph.D. Dissertation, Moscow Institute of Chemical Engineering, Moscow, 1980.
14. Kim, K. Y. and Marshall, W. R., *AIChE J.* 17(3):575–584 (1971).
15. Cen, K., Minghu, X., Mingjiiang, N., Xinyu, C., Zhenfu, Y., Guang, H., Chongoing, L., Deshou, L., and Chen, Y., *Proc. of 5th Int. Symp. on Coal Slurry Combustion,* Vol. II, 1983, pp. 1092–1107.
16. Ranz, W. E. and Marshall, W. R., *Chem. Engineer. Prog.* 48(3):141–146 and 173–180 (1952).
17. Robert, D. I., *Chem. Engineer. Prog.* 48(8):403–408 (1952).
18. Kenneth, K. K., *Principles of Combustion,* 1st ed., Wiley, New York, 1986.
19. El Wakil, M. M. et al., U.S. National Advisory Committee on Aeronautics. Technical Note No. 3490, 1956.
20. Rasbash, D. J., *Proc. of Interaction between Fluids and Particles,* Institute of Chemical Engineers, London, 1962, pp. 218–223.
21. Pei, D. C. T., Narasimhan, C., and Guavin, W. H., *Proc. of Interaction between Fluids and Particles,* Institute of Chemical Engineers, London, 1962, pp. 243–249.
22. Welty, J. R., Wicks, C. E., and Wilson, R. E., *Fundamental of Momentum, Heat, and Mass Transfer,* 3d ed., 1969.
23. Yang, W. G., *Proceeding of the Two-Phase Flow and Heat Transfer Symposium,* Vol. 1, Florida, 1976, pp. 51–67.
24. Holman, J. P., *Heat Transfer,* 3d ed., McGraw Hill, New York, 1972.
25. Bodrov, V. I. and Minaev, G. A., *Teor. Osn Khim. Technol.* 21(1):67–109 (1987).
26. Chernyaev, Y. I., Parfenov, A. S., and Ostrovskii, V. G., *Teor. Osn. Khim. Technol.* 23(1):75–81 (1989).
27. Miccio, M. and Okasha, F., "Modeling Droplet Deposition on Bed Particles during Fuel-Water Slurry Injection in a Fluidized Combustor," submitted for publication (1996).
28. Bird, R. B., Stewart, W. E., and Lightfoot, E. N., *Transport Phenomena,* Wiley, New York and London, 1960.
29. Okasha, F., "Meccanismo di Dispersione di Miscele Acqua-Carbone in Combustori a Letto Fluido Bollente," Ph.D. Dissertation, Naples University "Federico II," Chemical Engineering Department, 1995.

Twenty-Sixth Symposium (International) on Combustion/The Combustion Institute, 1996/pp. 3287–3294

THE EFFECTS OF PYROLYSIS TEMPERATURE AND ION-EXCHANGED METALS ON THE COMPOSITION OF BROWN COAL TARS PRODUCED IN A FLUIDIZED-BED REACTOR

BRIAN A. VERNAGLIA AND MARY J. WORNAT
Princeton University
Department of Mechanical and Aerospace Engineering
Princeton, New Jersey 08544-5263, USA

CHUN-ZHU LI AND PETER F. NELSON
Commonwealth Scientific and Industrial Research Organisation
Division of Coal and Energy Technology
North Ryde, New South Wales 2113, Australia

In order to investigate the effects of temperature and ion-exchanged metals on brown coal tar composition, we have pyrolyzed raw, acid-washed, sodium-exchanged, and calcium-exchanged Yallourn brown coal in a fluidized-bed reactor at temperatures of 600–1000°C. Tar yields adhere to the order: acid-washed > raw > Na-form > Ca-form–reflecting the cations' ability to bring about a more rigid and compact coal structure, which hinders the escape of large tar molecules evolved during coal devolatilization. Analysis of the tars by high-pressure liquid chromatography with ultraviolet-visible diode-array detection reveals that the tars are composed mainly of aliphatic species at the lowest pyrolysis temperatures. An increase in pyrolysis temperature brings about a decrease in the aliphatic components and an increase in the aromatic portion of the tar. At low temperatures, the aromatic portion of the tar is composed of a large number of mostly substituted aromatic species. The distribution of products narrows, however, as pyrolysis temperature is raised and dealkylation and decarbonylation reactions take place. Concurrently, the contribution from ring-nitrogen-containing aromatics falls, in accordance with their lower relative thermal stability. At the highest pyrolysis temperatures, tar composition is dominated by unsubstituted polycyclic aromatic hydrocarbons. Compared to temperature, sodium and calcium exhibit only modest effects on tar composition—the primary one being the suppression of the yield of aromatics containing ring nitrogen. At the lower pyrolysis temperatures, the tars from the Ca-form coal are richer in aliphatic content than the tars from the other coals, suggesting that the aliphatic products of devolatilization are less susceptible than the aromatic products to the cation-induced hindrance of tar molecule escape during coal pyrolysis. The effects of the metals become less pronounced at higher pyrolysis temperatures, however, where thermal factors govern the product distribution.

Introduction

Often associated with the carboxylic and phenolic functionalities in brown coals and lignites are metal cations, which can account for a significant portion of the inorganic constituents of low-rank coals [1–3]. These ion-exchanged metals are noted for their effects on particle ignition [4,5] and their contributions to the fouling and corrosion of burner surfaces [4,6] during combustion. Like temperature, however, they also affect the pyrolysis process at the initial stage of coal combustion-influencing the distribution of pyrolysis products among the volatile constituents, which contain a large portion of the coal's heating value [7], and the char, whose slow rate of burning is a limiting factor in combustor design [8].

A number of researchers have examined the effects of temperature or ion-exchanged metals on yields of light hydrocarbons [1,9–14], oxygen-containing gases [13–17], char [6,9,10,17], and tar [1,10,11,13,15,17,18] produced during the pyrolysis of lignites and brown coals. It is our purpose, in the work reported here, to investigate the influence of temperature and ion-exchanged metals on the composition of tars produced from an Australian brown coal, a coal for which metal cations can be reversibly removed or replaced by acid washing and ion-exchange techniques [1,19,20].

Previous studies of the effects of temperature on lignite or brown coal tar composition have involved elemental analysis [9], Fourier-transform infrared spectroscopy (FTIR) [21], and nuclear magnetic resonance spectroscopy (NMR) [22,23]. Efforts to study the effects of ion-exchanged metals on lignite

or brown coal tar composition have so far been limited to FTIR analysis [21,24]. In the present study, we analyze tar composition by two methods of high-pressure liquid chromatography (HPLC) coupled with broadband diode-array detection so that the chromatographic signals closely approximate mass concentrations [25,26]. The first HPLC technique permits us to determine tar composition by compound class. Distinctions between aromatic and aliphatic content, substituted and unsubstituted aromatics, and aromatics with and without ring nitrogen are of relevance with respect to sooting tendency [27–29], thermal stability [23,29,30], health effects [29,31], and NO_x precursor chemistry [32]. The second HPLC technique permits us to identify particular polycyclic aromatic hydrocarbons (PAH) contained in the tars.

The present work entails the fluidized-bed pyrolysis of four versions of Yallourn brown coal: raw, acid-washed, sodium-exchanged, and calcium-exchanged. In the following, we report tar composition as a function of temperature for the four Yallourn coals and interpret the results in terms of secondary pyrolytic reactions and the effects of ion-exchanged metals on coal structure.

Experimental Equipment and Techniques

The Yallourn coal of this study is a low-ash (1.1%) brown coal of the Latrobe Valley, with elemental composition 67.4% C, 4.6% H, 0.6% N, 0.3% S, and 27.1% O (by difference) on a dry, ash-free basis. It yields 53% proximate volatile matter in the Australian standard test. The metals composition of the raw coal is given by Schafer and Wornat [33]. The acid-washed coal is prepared by contact of the raw coal with a 1.3 N HCl solution over mild heat [19,34]. The sodium- and calcium-form coals are prepared from portions of the acid-washed coal by ion-exchange techniques [19,20]. The coal contains 3.25 mequiv of carboxyl groups/g daf coal [33]—of which 0, 5, 40, and 84% are in the carboxylate form for the acid-washed, raw, sodium-form, and calcium-form coals, respectively [20]. The 40% exchange limit of the Na-form coal is a consequence of the necessity to avoid extraction of organic components of the coal. However, since Na is monovalent and Ca is divalent, the number percents of Na and Ca atoms in the two cation-form coals are comparable.

To produce the tars for this study, vacuum-dried coal (of particle size 75–106 μm) is pyrolyzed in nitrogen at temperatures of 600–1000°C in a fluidized-bed reactor [9,16,21]. Heating rates are approximately 10^4 K/sec [9], and pressure is atmospheric. Particle residence times are estimated to be at least 0.3 s, adequate for full devolatilization [9]. The reactor effluent passes through a liquid-nitrogen-cooled glass trap, fitted with a Soxhlet thimble, for collection of the char and tar. The tar is recovered by Soxhlet extraction with dichloromethane (DCM). The mass of DCM-soluble tar collected is then determined from the volume of the solution and its concentration, which is measured by evaporation of two small aliquots of the solution, in a modified version of the procedure of Lafleur et al. [35].

The dichloromethane extracts are analyzed by HPLC on a Hewlett-Packard Model 1050 chromatograph, which consists of a quaternary solvent delivery system coupled to an ultraviolet-visible (UV) absorption diode-array detector. Samples are injected through a 20-μL Rheodyne injection loop, and a microswitch on the injector actuates the data system to ensure reproducible starting times. Care is taken to inject the samples at concentrations that ensure that all portions of the chromatograms are within the linear detection limits.

Two HPLC methods are employed. The first, documented elsewhere [25,36–38], employs a Jordi-Gel polydivinylbenzene column with DCM (1.5 mL/min) as the mobile phase. This method novelly separates mixtures into three groups [36]. Substituted aromatics (aromatic compounds with at least one of the following substituent groups: alkyl, aryl, hydroxyl, carbonyl, carboxyl, etheric, esteric, cyano, or nitro) elute before 16.15 min. Unsubstituted aromatics elute between 16.15 and 18.85 min. Only aromatics with ring nitrogen elute after 18.85 min, but some aromatics with nitrogen in 5-membered rings elute between 16.15 and 18.85 min. Although this HPLC method does not render species-by-species resolution of complex mixtures, it is extremely useful for the analysis of fuel-derived products, since calibration [36] of this column with an extensive set of reference compounds shows that virtually every type of fuel-derived organic species is amenable to analysis on this HPLC column. (Calibration standards include 172 different organic species spanning a broad range of molecular sizes, configurations, polarities, functional groups, ring heteroatoms, etc.) The only limitation is one of detection. Since all aromatic compounds absorb UV light, they are all detected. Purely aliphatic species, which elute with the substituted aromatics, however, are not detected unless they contain one or more UV chromophores, such as conjugated double bonds.

The second HPLC method, detailed elsewhere [39,40], utilizes a reverse-phase Vydac 201TP octadecylsilica column with time-programmed mobile phases of acetonitrile/water, acetonitrile, and DCM. This method resolves individual polycyclic aromatic compounds, which are unequivocally identified by their UV absorption spectra [40].

Both HPLC methods utilize broadband diode-array UV detection so that the chromatographic signals closely approximate mass concentrations [25,26]. As previously shown [26], the mass-based response factors for polycyclic aromatic compounds vary little

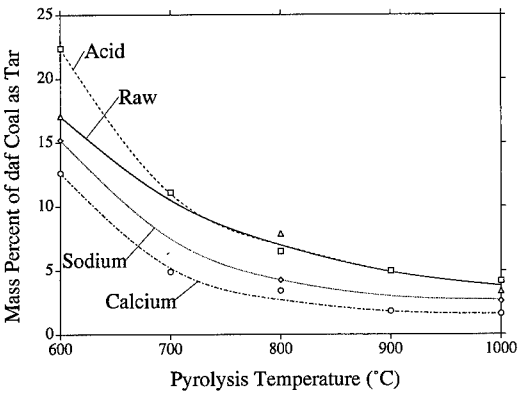

FIG. 1. Tar yields for Yallourn brown coals pyrolyzed in the fluidized-bed reactor. Raw coal, (△); acid-washed coal, (□); sodium-exchanged coal, (◇); and calcium-exchanged coal, (○).

from compound to compound as long as the UV absorbance signal is averaged over the entire wavelength range over which the compounds absorb. This condition is not fully met in our first HPLC method because the use of dichloromethane as a mobile phase precludes monitoring within the UV range that this solvent strongly absorbs. Consequently, species with significant UV absorbance below 236 nm (particularly aromatic species with fewer than three rings) will be somewhat underrepresented in the chromatograms from the first HPLC method. Although this limitation does not exist for the second HPLC method, volatile species such as benzene will still be underrepresented since they can be lost in the solvent-exchange procedure preceding the reverse-phase analysis [39].

Results and Discussion

Tar Yield

Figure 1 presents the yield of DCM-soluble tar as a function of temperature for the acid-washed, raw, sodium-exchanged, and calcium-exchanged Yallourn coals. As pyrolysis temperature increases, tar yields decrease, marking the well-documented [9,11,30,41] conversion of tar to gaseous and solid products at high temperatures. The yields for the raw coal are in good agreement with the earlier measurements of Cliff et al. [10].

Consistent with the findings of others for low rank coals [1,6,14,15,17,21,42,43], Fig. 1 shows that tar yields are reduced by the presence of ion-exchanged metals. The tar yields adhere to the order: acid-washed > raw > Na-form > Ca-form. The effects of the metals decrease, however, as temperature increases and thermal effects begin to dominate.

A number of studies investigating the effects of divalent cations [1,15,17,21,43] attribute the reduction in tar yield to the cross-linking effect of divalent cations, which link components of the coal structure by bridging together pairs of the coal's carboxyl groups. Divalent cations in fact do appear to have significant effects on the structure of Latrobe Valley brown coals. Microscopic examination of Yallourn brown coal chars recovered from our reactor reveals that the presence of ion-exchanged calcium reduces the percentage of particles going through a plastic phase during pyrolysis [43]. X-ray diffraction measurements of Brooks et al. [42] show that after pyrolysis of Yallourn coal at 400°C for 1 h, the *d*-spacings are significantly smaller in the char from the Mg-exchanged coal (3.74 Å) than in the char from the unexchanged coal (4.03 Å). Van Bodegom et al. [44] observe that solvent penetration is hindered by the presence of ion-exchanged calcium in Morwell brown coal.

In addition to the divalent metal effects, however, our results show that even the monovalent metal sodium reduces tar yield. The tar yield reducing effects of both the divalent and monovalent metals appear to be related to two structural features of these coals that are determined by proton magnetic resonance thermal analysis (PMRTA). Recent PMRTA of our acid-washed and ion-exchanged Yallourn brown coals [20] shows that under pyrolysis conditions, maximum coal fusibility increases in the order: Ca-form < Na-form < acid-washed, and that coal matrix density increases in the order: acid-washed < Na-form < Ca-form. (The raw coal could not be tested since it contains iron.) Even though sodium is monovalent, it still has the ability, perhaps by coordination with oxygen-containing functionalities, to bring about a tightening effect of the coal structure, though not to the same degree as calcium. Our results thus show that tar yield decreases with increasing rigidity (decreasing fusibility) and increasing matrix density (compactness). It is easy to see how the cation-induced compaction and rigidity of the Yallourn coal structure, as indicated by the PMRTA data [20], could account for the lower tar yields observed for the cation-form coals, since large tar molecules evolved during devolatilization would encounter greater hindrance to escape from the particles. Longer residence times within the coal structure would then cause them to be incorporated into the char, as the higher char yields and higher char H:C ratios of the cation-exchanged coals would suggest [1,43].

Aromatic Composition: Effects of Temperature

HPLC analysis of the tar samples collected at different pyrolysis temperatures enables us to trace the compositional changes that accompany the tar conversions depicted in Fig. 1. Concentrating on the

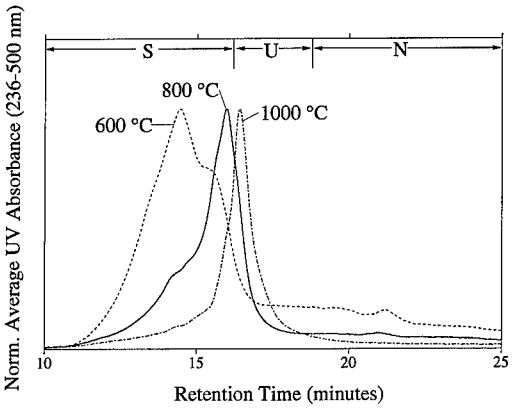

FIG. 2. Jordi column HPLC chromatograms (normalized) of tars from acid-washed Yallourn brown coal pyrolyzed at 600°C, (- - - - -); 800°C, (———); and 1000°C, (–·–·–). Regions marked "S," "U," and "N" correspond to substituted aromatics, unsubstituted aromatics, and ring-nitrogen-containing aromatics, respectively. Chromatograms of 700°C and 900°C tars omitted for clarity.

"base case" of the acid-washed coal, we first investigate the effects of pyrolysis temperature. We then examine the effects of the ion-exchanged metals.

Figure 2 presents the results of applying our first HPLC method to the tar samples from the acid-washed Yallourn coal pyrolyzed at 600, 800, and 1000°C in the fluidized-bed reactor. In order to accentuate compositional differences between samples, the three chromatograms in Fig. 2 are normalized by maximum peak height. In accordance with the elution order for this HPLC column, the "S," "U,", and "N" labels at the top of Fig. 2 denote the portions of the chromatograms representing substituted aromatic, unsubstituted aromatic, and ring-nitrogen-containing aromatic species, respectively. As Fig. 2 demonstrates, a change in pyrolysis temperature brings about a huge change in the composition of the aromatic components of the tars. At 600°C, the substituted species dominate, spanning a very broad range of elution volumes, which is indicative of a very large number of individual species. Unsubstituted aromatics and aromatics containing ring nitrogen are also present in appreciable amounts. At 800°C, the chromatogram is shifted to the right and is substantially narrower, marking the loss of many of the less thermally stable substituted aromatics and the shift to more unsubstituted aromatics. There is also a substantial depletion of aromatics containing ring nitrogen, in accordance with their lower thermal stability [29] relative to aromatics with only ring carbon. The removal of aromatics with substituent groups and ring nitrogen continues in the 800–1000°C temperature interval such that the 1000°C sample's chromatogram represents a narrow distribution of primarily unsubstituted aromatics, still with some contributions from substituted aromatics but virtually depleted of aromatics with ring nitrogen.

The temperature/composition trends exhibited in Fig. 2 are consistent with earlier results [21] obtained by Fourier-transform infrared spectroscopy (FTIR) analysis of Yallourn brown coal tars. Analysis of tars produced at 600°C shows substantial contributions from hydroxyl, etheric, carbonyl, and alkyl functional groups. As temperature is increased to 800°C and then to 1000°C, FTIR signals from all of these substituent groups fall drastically, in accordance with other studies on low-rank [12,22,23,25] and bituminous [22,23,25,30,41,45,46] coals that demonstrate dealkylation [12,23,30,41], decarbonylation [12,22,30], and de-etherization [30] of aromatic compounds subjected to high pyrolysis temperatures. Analyses of Yallourn coal tars [30] also show that FTIR signals of unsaturated functionalities such as acetylene and allene substituents rise and then fall with increasing pyrolysis temperature, similar to the yields of styrene and phenylacetylene from another Australian low-rank coal [12]. Aromatics with unsaturated substituents, therefore, may account for some of the substituted aromatics present in the Yallourn brown coal tars at the higher pyrolysis temperatures.

Aromatic Composition: Effects of Ion-Exchanged Metals

Although Fig. 1 shows that calcium and sodium have marked effects in reducing tar yield from Yallourn brown coal, Fig. 3 reveals that the ion-exchanged metals have only modest effects on aromatic composition of the tar. Plotted in Fig. 3a,b are the normalized HPLC chromatograms of raw, acid-washed, sodium-exchanged, and calcium-exchanged Yallourn brown coal tars produced at 600°C and 1000°C, respectively. At both temperatures, the chromatograms of the raw and acid-washed tar samples are virtually coincident (only 5% of the carboxyl groups in the raw coal are in the carboxylate form). One feature distinguishes the cation-form coal tar chromatograms from those of the other coals at 600°C, however. At this low temperature, the ratio of material eluting after 16.15 min to that eluting before 16.15 min is somewhat lower for the sodium-form coal tar and lower again for the calcium-form coal tar than for the tars of the raw and acid-washed coals. We suspect that the production of nitrogen-containing aromatics is suppressed in the Na-form and Ca-form Yallourn coals since the work of Durie and Schafer [3,47] indicates that some nitrogen in Latrobe Valley brown coals can be retained in the "pyrolysis residue" (i.e., char) by reaction with calcium and sodium cations in the coals. A suppression of the formation of compounds with nitrogen in 6-membered rings would reduce the chromatographic

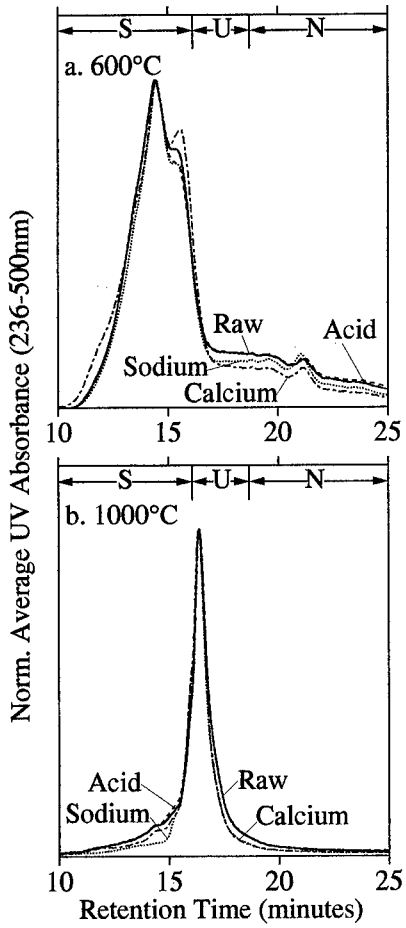

FIG. 3. Jordi column HPLC chromatograms (normalized) of tars from Yallourn brown coals pyrolyzed at (a), 600°C and (b), 1000°C. Raw coal, (———); acid-washed coal, (- - - - -); sodium-exchanged coal, (·····); and calcium-exchanged coal, (–·–·–). Regions marked "S," "U", and "N" correspond to substituted aromatics, unsubstituted aromatics, and ring-nitrogen-containing aromatics, respectively.

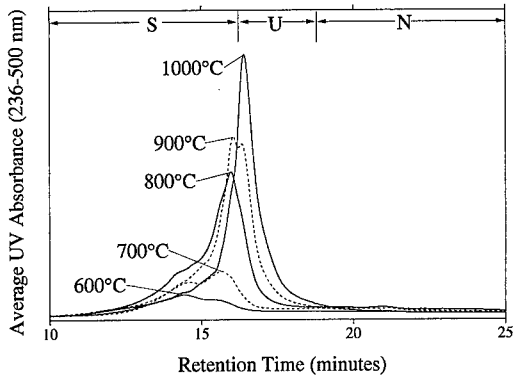

FIG. 4. Jordi column HPLC chromatograms of tars from acid-washed Yallourn brown coal pyrolyzed at indicated temperatures from 600 to 1000°C. Regions marked, "S," "U," and "N" correspond to substituted aromatics, unsubstituted aromatics, and ring-nitrogen-containing aromatics, respectively.

signal beyond 18.85 min; a suppression of ones with nitrogen in 5-membered rings could reduce the chromatographic signal anywhere past 16.15 min. That the effect is greater for calcium than sodium is consistent with calcium's divalency.

Another minor feature, the peak at ~15.5 min, distinguishes the Ca-form coal tar chromatogram from the others at 600°C. This relatively higher UV absorbance signal for the Ca-form coal tar sample in the "substituted" region of the chromatogram in Fig. 3a may be due to aliphatic species. FTIR analysis of tar samples from Yallourn brown coal [21] and a lignite [24] shows tars from Ca-exchanged coals to be substantially richer in aliphatic components than the tars from acid-washed coals. Although most aliphatic compounds do not absorb in the UV range of our detector, those containing conjugated double bonds would. (As stated earlier, aliphatic species with UV chromophores elute with the substituted aromatics on this HPLC column [36]). Alternatively, at low temperatures, the Ca-form coal may also produce a higher proportion of alkylated or partially hydrogenated aromatic species (both of which elute prior to 16.15 min) for a reason that is yet unidentified. Regardless of the causes for these minor distinctions in the Ca-form tar sample at 600°C, an increase in pyrolysis temperature lessens the effects of the metals on aromatic tar composition such that there are no longer any appreciable effects at 1000°C, as Fig. 3b portrays.

Aromatic/Aliphatic Composition: Effects of Temperature and Ion-Exchanged Metals

In order to determine the contribution of aliphatic species to the Yallourn brown coal tars, it is useful to plot the HPLC chromatograms in unnormalized form. Figure 4 presents the HPLC chromatograms of the five acid-washed Yallourn coal tars, all injected at the same total mass concentration. Because for aromatics the broadband UV absorbance signal is proportional to mass (within the limitations specified in the Experimental section), the relative areas of the five chromatograms in Fig. 4 closely approximate the relative amounts of aromatic material in the five samples. As evident in the figure, a rise in pyrolysis temperature brings about a monotonic rise in chromatographic area and thus the proportion of aromatic material in the sample. If we make the assumption (based on our own FTIR analyses of

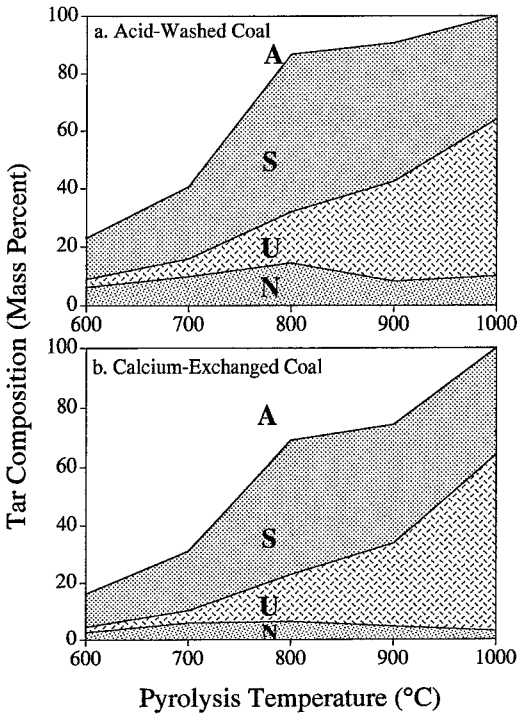

FIG. 5. Composition of Yallourn brown coal tar as a function of pyrolysis temperature. (a), Acid-washed coal; (b), Ca-exchanged coal. Areas represent mass fractions of (A) aliphatics, (S) substituted aromatics, (U) unsubstituted aromatics, and (N) ring-nitrogen-containing aromatics.

Yallourn brown coal tars [21] and on the NMR results of Collin et al. [23]) that the 1000°C tar sample contains only aromatic components (and no purely aliphatic ones), then we can estimate the aliphatic portion of each tar sample in Fig. 4 by taking the difference between the chromatographic area of that sample and the area of the 1000°C sample.

The results of that analysis appear in Fig. 5, which shows the proportion of each tar sample present as aliphatic and aromatic components, as a function of temperature, for the acid-washed and calcium-exchanged Yallourn coals. The aromatic portions are further broken down into substituted, unsubstituted, and ring-nitrogen-containing aromatics. As Fig. 5 reveals, aliphatic components compose the major portions of the tars at low temperatures but are preferentially depleted as pyrolysis temperature is raised and cracking reactions [11,12] take place. These trends, consistent with less quantitative FTIR [21] and NMR [23] results, confirm the greater thermal stability of the aromatic components, among which the unsubstituted species show the greatest thermal stability. In fact, similar to earlier results for a bituminous coal [48], our calculations show a net increase in the yield of unsubstituted aromatics from the Yallourn coal as pyrolysis temperature is increased, despite the fact that total tar yield decreases.

Also apparent from Fig. 5 is the fact that aliphatic components compose a higher proportion of the Ca-form coal's tar samples than those of the acid-washed coal (or raw or Na-form coals, for which the results are not shown). As stated earlier, this observation is consistent with our own FTIR analyses [21] as well as others' [24]. We interpret this result, along with the cation-induced tar reduction portrayed in Fig. 1, in the following way: The effect of ion-exchanged metals, as determined by PMRTA [20], in making the brown coal structure more rigid and compact apparently has a greater influence on aromatic products than aliphatic products in hindering their escape from the particle during devolatilization. The lower susceptibility of these aliphatic compounds to impedimence of motion within the coal particle may stem partly from the fact that they are mainly straight-chain as opposed to more bulky branched-chain hydrocarbons [12].

Tar Composition at High Temperature

As shown in Fig. 3b, the 1000°C tars produced from the raw, acid-washed, sodium-exchanged, and calcium-exchanged Yallourn brown coals are composed predominantly of unsubstituted aromatics. Analysis of these samples by our second HPLC method, the reverse-phase technique, reveals the identities of many of the constituent species, as illustrated in Fig. 6 for the calcium-form coal tar produced at 1000°C. Figure 6 shows that the high-temperature Yallourn brown coal tars consist of many unsubstituted PAH from two to at least six fused rings. Among the products are *cata*-annelated [49] PAH (e.g., anthracene, chrysene, and picene), *peri*-fused [49] PAH (e.g., pyrene, cyclopenta[*cd*]pyrene, benzo[*ghi*]perylene, and anthanthrene), and PAH with fused five-membered rings (e.g., acenaphthylene, acephenanthrylene, and cyclopenta[*hi*] acephenanthrylene). A detailed treatment of the results from the reverse-phase HPLC analysis of these brown coal tar samples—including the effects of temperature and ion-exchanged metals—will appear elsewhere [50].

Summary and Conclusions

Our fluidized-bed pyrolysis experiments with raw, acid-washed, sodium-exchanged, and calcium-exchanged Yallourn brown coal show, in accordance with previous findings, that carboxyl-associated cations reduce tar yields. Recent PMRTA results suggest that the cation-induced reduction in tar yield is due to the cations' ability to bring about a more rigid and compact coal structure, which then hinders the

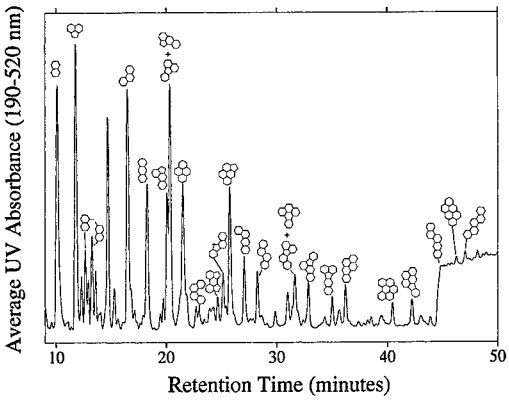

FIG. 6. Reverse-phase HPLC chromatogram of calcium-exchanged Yallourn brown coal tar produced at 1000°C. The rise in baseline at 45 min corresponds to a change in mobile phase composition to UV-absorbing dichloromethane. Structures of identified PAH are labeled above the corresponding peaks. Identified species include (from left to right): naphthalene, acenaphthylene, 1-methylnaphthalene, 2-methylnaphthalene, phenanthrene, anthracene, acephenanthrylene, fluoranthene and aceanthrylene (co-eluting), pyrene, benzo[*c*]phenanthrene, cyclopenta[*hi*]acephenanthrylene, benzo[*a*]fluorene, cyclopenta[*cd*]pyrene, benz-[*a*]anthracene, chrysene, benzo[*j*]fluoranthene and benzo-[*e*]pyrene (coeluting), benzo[*b*]fluoranthene, benzo[*k*] fluoranthene, benzo[*a*]pyrene, benzo[*ghi*]perylene, indeno[*1,2,3-cd*]pyrene, benzo[*b*]chrysene, anthanthrene, and picene.

escape of large tar molecules evolved during coal devolatilization. The effects of the metals on tar yield become less apparent at higher pyrolysis temperatures, however, where tar conversion to secondary products prevails.

Compositional analysis of the tars by HPLC indicates that they are composed mainly of aliphatic species at the lowest pyrolysis temperatures. An increase in pyrolysis temperature brings about a decrease in the aliphatic tar components, as they undergo secondary cracking reactions, and a rise in the aromatic components. At low temperatures, the aromatic portion of the tar is composed of a large number of mostly substituted aromatic species. The distribution of products narrows, however, as pyrolysis temperature is raised, and the degree of substitution in the aromatics decreases, as dealkylation and decarbonylation reactions take place. Concurrently, the contribution from ring-nitrogen-containing aromatics falls, in accordance with their lower relative thermal stability. At the highest pyrolysis temperatures, tar composition is dominated by unsubstituted PAH, including *cata*-annelated and *peri*-fused species.

Although sodium and calcium cations demonstrate a marked effect in reducing tar yield, they exhibit only modest effects on tar composition. Apparently by interacting with coal nitrogen, these cations reduce the yields of ring-nitrogen-containing aromatics produced during pyrolysis, which could influence NO_x-precursor chemistry. At the lower pyrolysis temperatures, the tars from the Ca-form coal are richer in aliphatic content than the tars from the other coals—suggesting that the aliphatic products of devolatilization are less susceptible than the aromatic products to the cation-induced hindrance of tar molecule escape during coal pyrolysis. The effects of cations on tar composition become even less pronounced at higher pyrolysis temperatures, where thermal factors govern the product distribution.

Acknowledgments

The authors thank Mr. Neil Schafer for instruction on the ion-exchange procedures, and Mr. Ken Riley for the analysis of the coals. They also wish to express their appreciation to Dr. Arthur Lafleur and Ms. Elaine Plummer, of the Massachusetts Institute of Technology, Core Laboratory in Analytical Chemistry. The award of a Rothmans Foundation Fellowship to C.-Z. Li is gratefully acknowledged.

REFERENCES

1. Tyler, R. J. and Schafer, H. N. S., *Fuel* 59:487–494 (1980).
2. Brockaway, D. J., Ottrey, A. L., and Higgins, R. S., in *The Science of Victorian Brown Coal,* (R. A. Durie, Ed.), Butterworth-Heinemann, Oxford, 1991, pp. 597–650.
3. Schafer, H. N. S., in *The Science of Victorian Brown Coal,* (R. A. Durie, Ed.), Butterworth-Heinemann, Oxford, 1991, pp. 323–357.
4. Allardice, D. J. and Newell, B. S., in *The Science of Victorian Brown Coal,* (R. A. Durie, Ed.), Butterworth-Heinemann, Oxford, 1991, pp. 651–701.
5. Durie, R. A., *Fuel* 40:407–422 (1961).
6. Morgan, B. A. and Scaroni, A. W., in *The Chemistry of Low Rank Coals, ACS Symposium Series 264,* (H. H. Schobert, Ed.), American Chemical Society, Washington, DC, 1984, pp. 255–266.
7. Jones, J. C., in *The Science of Victorian Brown Coal,* (R. A. Durie, Ed.), Butterworth-Heinemann, Oxford, 1991, pp. 465–516.
8. Smith, I. W., *Nineteenth Symposium (International) on Combustion,* The Combustion Institute, Pittsburgh, 1982, pp. 1045–1065.
9. Tyler, R. J., *Fuel* 58:680–686 (1979).
10. Cliff, D. I., Doolan, K. R., Mackie, J. C., and Tyler, R. J., *Fuel* 63:394–400 (1984).
11. Doolan, K. R., Mackie, J. C., and Tyler, R. J., *Fuel* 66:572–578 (1987).
12. Nelson, P. F. and Tyler, R. J., *Twenty-First Symposium (International) on Combustion,* The Combustion Institute, Pittsburgh, 1986, pp. 427–435.

13. Doolan, K. R., Mackie, J. C., *Twentieth Symposium (International) on Combustion,* The Combustion Institute, Pittsburgh, 1985, pp. 1463–1469.
14. Franklin, H. D., Cosway, R. G., Peters, W. A., and Howard, J. B., *Ind. Eng. Chem. Process Design Dev.* 22:39–42 (1983).
15. Solomon, P. R., Serio, M. A., Despande, G. V., and Kroo, E., *Energy Fuels* 4:42–54 (1990).
16. Wornat, M. J. and Nelson, P. F., *Twenty-Third Symposium (International) on Combustion,* The Combustion Institute, Pittsburgh, 1990, pp. 1239–1245.
17. Serio, M. A., Kroo, E., Teng, H., and Solomon, P. R., *Prepr. Pap. Am. Chem. Soc. Div. Fuel Chem.* 38(2):577–586 (1993).
18. Morgan, M. E. and Jenkins, R. G., in *The Chemistry of Low Rank Coals, ACS Symposium Series 264,* (H. H. Schobert, Ed.), American Chemical Society, Washington, DC, 1984, pp. 213–226.
19. Schafer, H. N. S., *Fuel* 49:197–213 (1970).
20. Wornat, M. J. and Sakurovs, R., *Fuel,* in press, 1996.
21. Wornat, M. J. and Nelson, P. F., *Energy Fuels* 6:136–142 (1992).
22. Collin, P. J., Tyler, R. J., and Wilson, M. A., *Fuel* 59:819–820 (1980).
23. Collin, P. J., Tyler, R. J., and Wilson, M. A., *Fuel* 59:479–486 (1980).
24. Morgan, M. E. and Jenkins, R. G., *Fuel* 65:764–768 (1986).
25. Lafleur, A. L., Sarofim, A. F., and Wornat, M. J., *Energy Fuels* 7:357–361 (1993).
26. Lafleur, A. L., Monchamp, P. A., Plummer, E. F., and Wornat, M. J., *Anal. Lett.* 20:1171–1192 (1987).
27. Davies, R. A. and Scully, D. B., *Combust. Flame* 10:165–170 (1966).
28. Glassman, I., *Combustion,* 2nd ed., Academic, Orlando, FL, 1987, Chap. 8.
29. Wornat, M. J., Sarofim, A. F., Longwell, J. P., and Lafleur, A. L., *Energy Fuels* 2:775–782 (1988).
30. Wornat, M. J., Sarofim, A. F., and Longwell, J. P., *Energy Fuels* 1:431–437 (1987).
31. Wornat, M. J., Braun, A. G., Hawiger, A., Longwell, J. P., and Sarofim, A. F., *Environ. Health Perspect.* 84:193–201 (1990).
32. Nelson, P. F., Kelly, M. D., and Wornat, M. J., *Fuel* 70:403–407 (1991).
33. Schafer, H. N. S. and Wornat, M. J., *Fuel* 69:1456–1458 (1990).
34. Schafer, H. N. S., personal communication, 1989–1990.
35. Lafleur, A. L., Monchamp, P. A., Plummer, E. F., and Kruzel, E. L., *Anal. Lett.* 19:2103–2119 (1986).
36. Wornat, M. J., Sc. D. Thesis, Department of Chemical Engineering, Massachusetts Institute of Technology, Cambridge, MA, 1988.
37. Lafleur, A. L. and Wornat, M. J., *Anal. Chem.* 60:1096–1102 (1988).
38. Lafleur, A. L. and Wornat, M. J., *Anal. Lett.* 22:493–506 (1989).
39. Wornat, M. J., Lafleur, A. L., and Sarofim, A. F., *Polycyclic Aromatic Compounds* 3:149–161 (1993).
40. Wornat, M. J., Sarofim, A. F., and Lafleur, A. L., *Twenty-Fourth Symposium (International) on Combustion,* The Combustion Institute, Pittsburgh, 1992, pp. 955–963.
41. Fletcher, T. H., Solum, M. S., Grant, D. M., Critchfield, S., and Pugmire, R. J., *Twenty-Third Symposium (International) on Combustion,* The Combustion Institute, Pittsburgh, 1990, pp. 1231–1237.
42. Brooks, J. D., Stephens, J. F., and Silberman, H., in *Proceedings of the Fifth Biennial Conference on Carbon,* Pergamon, Oxford, England, 1962, pp. 422–428.
43. Shibaoka, M., Ohtsuka, Y., Wornat, M. J., Thomas, C. G., and Bennett, A. J. R., *Fuel* 74:1648–1653 (1995).
44. van Bodegom, J. A., van Veen, R., van Kessal, G. M. M., Sinnige-Nijssen, M. W. A., and Stuiver, H. C. M., *Fuel* 63:346–354 (1984).
45. Serio, M. A., Ph.D. Thesis, Department of Chemical Engineering, Massachusetts Institute of Technology, Cambridge, MA, 1984.
46. Solomon, P. R., Hamblen, D. G., and Carangelo, R. M., in *Coal and Coal Products: Analytical Characterization Techniques, ACS Symposium Series 205,* (E. L. Fuller, Ed.), American Chemical Society, Washington, DC, 1982, Chap. 4.
47. Durie, R. A. and Schafer, H. N. S., *Fuel* 58:472–476 (1979).
48. Wornat, M. J., Sarofim, A. F., and Longwell, J. P., *Twenty-Second Symposium (International) on Combustion,* The Combustion Institute, Pittsburgh, 1988, pp. 135–143.
49. Clar, E. J., *Polycyclic Hydrocarbons,* Academic, New York, 1964.
50. Vernaglia, B. A., Wornat, M. J., Li, C.-Z., and Nelson, P. F., in preparation.

Twenty-Sixth Symposium (International) on Combustion/The Combustion Institute, 1996/pp. 3295–3300

SCATTERING OF THERMAL RADIATION IN THE FREEBOARD OF A 1 MW_t FLUIDIZED BED COMBUSTOR WITH COAL AND LIMESTONE FEEDING

M. FILLA AND A. SCALABRIN
Istituto di Chimica Industriale
Universita' di Padova
Padova, Italy

C. TONFONI
ENEL-CRT
Pisa, Italy

The effect of the scattering of thermal radiation on the emissivity of the particle holdup in the freeboard of a 1-MW_t fluidized-bed combustor in conjunction with coal, and with coal and limestone feeding is compared. The cloud absorption and scattering coefficients and the scattering phase function are those obtained by Mie theory on the basis of the physical and chemical characterization of solids samples taken at the outlet from the freeboard. The cloud emissivity has been calculated by a discrete ordinate four-flux method for cylindrical axisymmetric coordinates using Delta-Eddington approximation of the phase function to take into account both the near isotropic scattering by small particles and the pronounced anisotropic scattering by large particles with respect to thermal wavelengths.

Large particles make an essential contribution to the absorption thickness of the cloud, whereas their contribution to the effective scattering is minor compared to that of small particles, because of the increasing forward stretching of the phase function with increasing particle size parameter. The scattering of thermal radiation lowers the emissivity of the particle cloud to a larger extent in conjunction with limestone feeding by the combined effect of the increased albedo due to the low absorption index of limestone, and of the increased isotropy of scattering due to the larger proportion of small particles in the particle size distribution. The change of absorption thickness of the particle cloud at the outlet from the freeboard between the two cases is small, in spite of the near threefold increase of solids concentration measured when limestone was added to the coal feed.

Introduction

The relevance of scattering of the particle holdup of combustion products for the purpose of calculation of the rate of heat transfer to the absorbing walls has been the object of several investigations with reference to pulverized fuel firing in conventional steam generators [1–4], recently extended also to the freeboard of fluidized-bed combustors [5,6]. The contribution of the freeboard to the overall heat transfer from the 1-MW_t fluidized-bed combustor of ENEL-CRT is comparable to that of the bed, a not unusual result in the literature [7]. Radiation is the dominant mechanism, in spite of the lower temperatures with respect to conventional pulverized fuel firing, due to the high solids holdup of the combustion products. The interest in the evaluation of the importance of scattering of thermal radiation on the emissivity of the particle cloud in the freeboard in conjunction with coal feeding [6,8] is extended here to the case of coal and limestone feeding to convert atmospheric emission of sulphur dioxide from fuel sulphur to solid discharge in the form of calcium sulfate. The predictions are based on the physical and chemical characterization of solids samples at the exit from the freeboard for the purpose of determination of the radiative properties, and on a discrete ordinate flux method [6,8] for the purpose of calculation of the cloud emissivity.

Experimental

The 1-MW_t fluidized-bed combustor of the ENEL-CRT Research Establishment of Livorno, fully described by De Michele et al. [9], is sketched in Fig. 1. It consists of a 1.27-m(i.d.), 5.08-m-high cylindrical chamber, enclosed by a tube waterwall whose first 2.00 m from the distributor are refractory lined. The data relevant to this work were obtained during atmospheric operation with coal (case A), and coal and limestone (case B) feeding of a silica-sand bed of particles in the size range 0.3–1.3 mm, with average diameter $d_{p,av}$ = 0.88 mm, and minimum

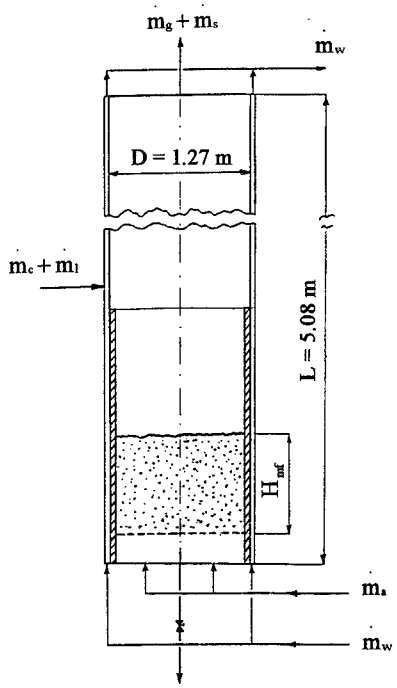

FIG. 1. Sketch of the 1-MW_t fluidized-bed combustor and main flow rates: air (m_a), coal (m_c), limestone (m_l), combustion products (m_g) and entrained solids (m_s), cooling water (m_w).

fluidization velocity U_{mf} = 0.39 m/s. The coal feed was in the size range 1–3 mm, and the limestone particle size ranged between 0.5 and 2.5 mm.

Solids samples were collected from the combustion products leaving the freeboard by two cyclones and an isokinetic probe in series. The physical and chemical characterization of the samples was carried out by Microtrac particle size laser analyzer and a scanning electron Microscope, and by thermogravimetric analysis.

The operating conditions of the combustor in the two cases considered are reported in Table 1.

Radiative Properties of the Particle Cloud

The absorption and scattering coefficients and the phase function of the particle cloud have been obtained as the following weighted averages [10] of the Mie theory single-particle efficiencies and phase function:

$$k_{a,s}(m,N,\lambda) = \int_0^\infty N(d_p)Q_{a,s}(x,m)\pi d_p^2/4d(d_p) \quad (1)$$

$$\bar{p}(\mu,m,N,\lambda) = \left\{\int_0^\infty N(d_p)Q_s(x,m)p(\mu,m,N,\lambda)\pi d_p^2/4d(d_p)\right\}\Big/k_s(m,N,\lambda) \quad (2)$$

The number probability density of the size distribution has been supplied to the equations above in the gamma function form:

$$n(d_p) = Ad_p^{-n}\exp(-bd_p^{-p}) \quad (3)$$

such that $N(d_p) = N_0 n(d_p)$, where N_0 is the number concentration of particles in the cloud. The parameters of equation 3 have been determined by nonlinear regression of the data in Table 2 to obtain the sets (A = 42.7, n = 4.21, b = 8.21, p = 2.46), (A = 6.25 × 10^3, n = 4.97, b = 9.59, p = 0.36) for case A and B, respectively.

The cumulative size distributions together with the experimental data of Table 2 are shown in Fig. 2a,b, and the corresponding number probability densities in Fig. 3. The clouds of cases A and B have been considered as consisting of two and three components with the same size distribution in the proportions determined by thermogravimetric analysis reported in Table 2. The fly-ash content includes the carryover of silica sand from comminution of the bed particles, this being a small fraction of the fly-ash production during the combustion of coal and of hardly distinguishable composition. The limestone component includes all Ca species ($CaCO_3$, CaO,

TABLE 1
Operating conditions of the 1-MW_t FBC with coal (case A) and coal and limestone (case B) feed

Bed mass	1164 kg	800 kg
Bed height at minimum fluidization	0.7 m	0.5 m
Coal feed rate (HV = 26400 kJ/kg)	111 kg/h	249 kg/h
Limestone feed rate	–	66 kg/h
Air flow rate at the distributor	1264 kg/h	2005 kg/h
Air temperature at the distributor	85°C	118°C
Bed temperature	862°C	795°C
Flue gas temperature at the freeboard exit	413°C	480°C
Mass flow rate of solids from the freeboard	17.9 kg/h	96.8 kg/h

TABLE 2
Characterization of the dust collected at the outlet of the 1-MW_t FBC freeboard

Case A													
Composition: fly ash (67%) and char (33%)													
Size Distribution from Microtrac:													
d_p (μm)	4.3	5.7	8.0	11.2	16.0	23.0	32.5	45.5	64.0	90.5	128	181	256
$\%_{vol}$	16.4	23.7	31.7	38.0	44.7	49.0	56.3	67.7	79.0	90.5	94.3	98.3	100
Case B													
Composition: limestone (71%), fly ash (19%), and char (10%)													
Size Distribution from Microtrac:													
d_p (μm)	2.4	3.4	4.9	6.9	9.7	13.6	19.2	27.1	38.2	53.7	75.7	107	176
$\%_{vol}$	3.4	5.2	8.7	16.8	22.9	31.7	41.8	53.2	66.5	74.6	87.3	94.1	100

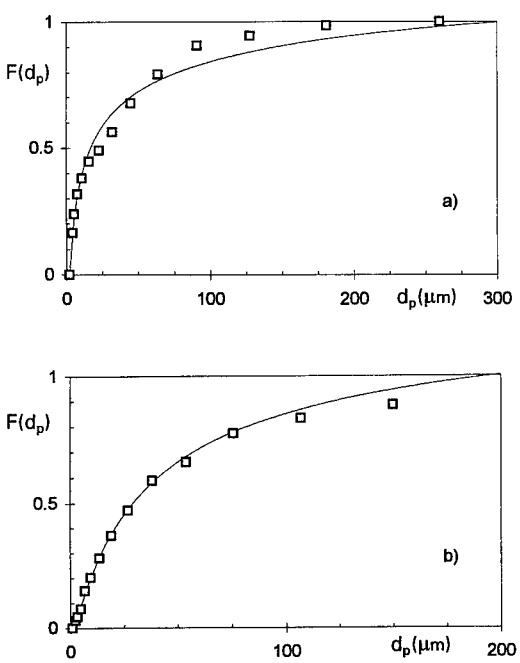

FIG. 2. Frequency size distribution by volume of the solids samples in case A (a), and case B (b); □, measured; ———, from equation 3.

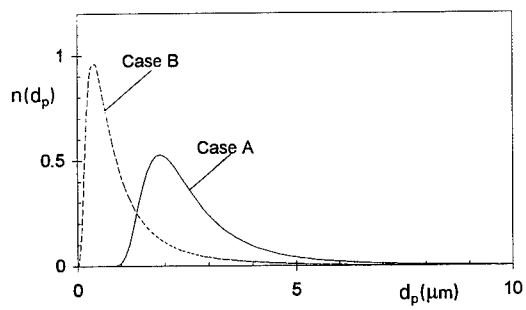

FIG. 3. Probability densities of the size distributions by number of the solid samples from equation 3.

$CaSO_4$), since both CaO and $CaSO_4$ were small fractions of the limestone content in the samples. This low C_aCO_3 conversion is an anomalous result due to the particular runs of the combustor during which the solids samples were taken, in that they were setting up runs of the feeding system.

The values of the refractive indexes used for the three components are those suggested by Mengüç and Viskanta [11] for fly ash ($m_{fa} = 1.5 - 0.02i$), Brewster and Kunitomo [12] for char ($m_c = 1.7 - 0.10i$), and that calculated in Ref. 8 by Rosseland averaging of the spectral data of Ref. 12 for limestone ($m_l = 1.55 - 0.005i$).

The cloud absorption and scattering coefficients and albedo, and the forward scattering (f_λ) and linear anisotropy ($A_{1\lambda}$) parameters of the Delta-Eddington approximation [13,14] of the phase function

$$p_\lambda(\mu) = 2f_\lambda\delta(1 - \mu) + (1 - f_\lambda)(1 + A_{1\lambda}\mu) \quad (4)$$

are reported in Table 3 in correspondence of $\lambda = 1$ μm and $\lambda = 10$ μm for the both cases A and B.

Results

The functional dependence of the spectral emissivity of the particle cloud on absorption thickness, albedo, and phase function, and on the aspect ratio of the enclosure can take the form

$$\varepsilon_\lambda = \varepsilon_\lambda(k_{a,\lambda}D, \omega'_\lambda, A_{1\lambda}, L/D) \quad (5)$$

after Delta-Eddington approximation of the phase function. The dependence on aspect ratio can be neglected in the range of practicable bed heights of this combustor.

The results of the calculation by the discrete ordinate flux method in [6,8] at 1 and 10 μm are shown in Fig. 4a,b for case A, and in Fig. 5a,b for case B, together with those for the reference cases of purely absorbing/emitting ($\omega'_\lambda = 0$) and isotropic scattering medium ($\omega'_\lambda = \omega_\lambda$). Scattering does not reduce the

TABLE 3
Radiative properties of the particle clouds

		$k_{a,\lambda}(m^{-1})$	$k_{s,\lambda}(m^{-1})$	ω_λ	f_λ	$A_{1\lambda}$
Case A						
	$\lambda = 1\,\mu m$	0.47	0.68	0.59	0.81	1
	$\lambda = 10\,\mu m$	0.20	0.53	0.73	0.47	1
Case B						
	$\lambda = 1\,\mu m$	0.51	1.65	0.76	0.38	1
	$\lambda = 10\,\mu m$	0.23	1.25	0.85	0.59	1

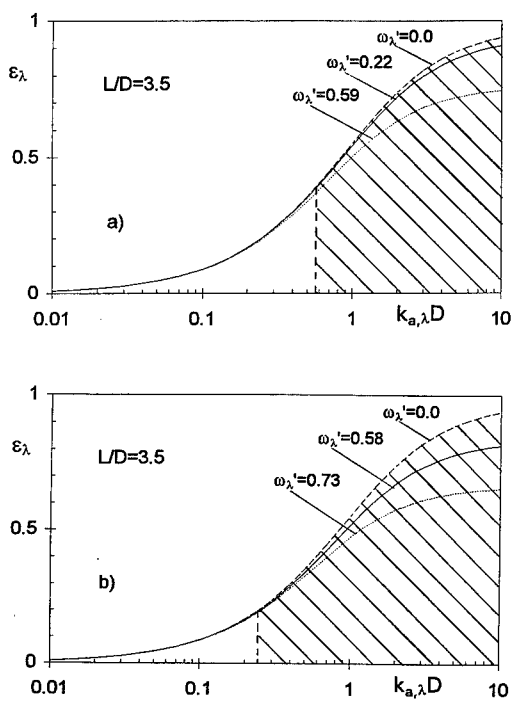

FIG. 4. Monochromatic emissivity of the particle cloud of case A as a function of absorption thickness and effective albedo at $\lambda = 1\,\mu m$ (a), and at $\lambda = 10\,\mu m$ (b), ———; of the isotropic scattering, ···; and of the purely absorbing/emitting medium, ---.

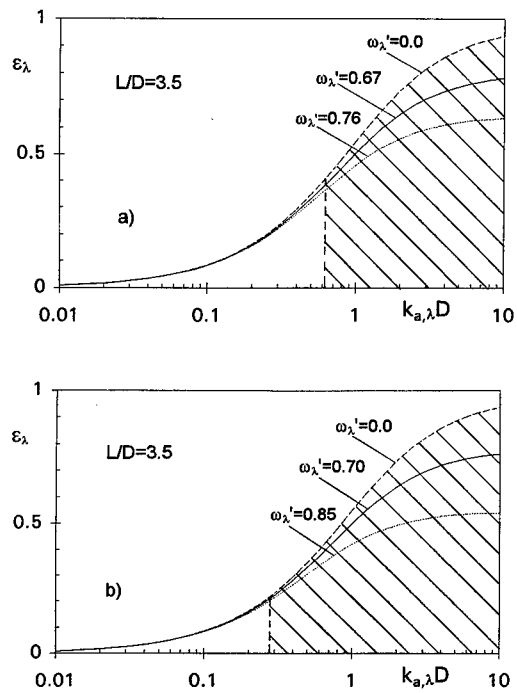

FIG. 5. Monochromatic emissivity of the particle cloud of case B as a function of absorption thickness and effective albedo at $\lambda = 1\,\mu m$ (a), and at $\lambda = 10\,\mu m$ (b), ———; of the isotropic scattering, ···; and of the purely absorbing/emitting medium, ---.

emissivity to an appreciable extent until the absorption thickness reaches the order of unity. The reduction then becomes more conspicuous in the upper end of the thermal wavelength interval in case A, as shown by the comparison of Fig. 4a and b. The key to the interpretation of this behavior is in Table 3, where the decreasing extinction of larger wavelengths by absorption predicted by Mie theory can be observed as well as that by scattering, while the albedo of the cloud increases to reach a flat maximum. This increase is further amplified in the effective albedo by the more isotropic scattering of larger wavelengths. The comparison between the two sections of Table 3 shows that the scattering coefficient and albedo of the cloud increase in case B, consistently with the low absorption index of limestone, and that the isotropy of scattering at $\lambda = 1\,\mu m$ is enhanced. As visualized in Fig. 3, limestone contributes substantially to the small particle tail of the size distribution, so that the emissivities of Fig. 5a,b exhibit the behavior of a smaller size particle cloud in case B with respect to case A.

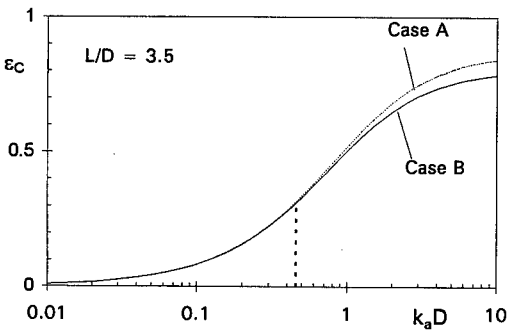

FIG. 6. Total emissivity of the particle clouds at 1000 K as a function of the absorption thickness.

The shaded areas in Figs. 4 and 5 indicate that the absorption thickness of the cloud within the freeboard increases with increasing solids concentration moving from the freeboard outlet toward the free interface of the bed. The lower bounds can be specified on the basis of the results of Table 3, since the solids samples were taken at the outlet from the freeboard. The shift of the shaded areas toward higher absorption thicknesses in case B may appear below expectation for a threefold increase of particle concentration. However, that is not the case, since it is the net result of the opposite effects of the changes of cloud composition and concentration. This may be realized by the consideration that char, the main absorbing component of the cloud, is diluted from 33% in case A to 10% in case B, where most of the solids are limestone. The contribution of the 71% limestone content of the sample to the cloud absorption coefficient is only 18.7% at 10 μm and 31.2% at 1 μm, the corresponding contributions of the 10% char content being 63.5% and 45.7%.

An estimate of the total emissivity of the particle clouds can also be obtained from

$$\varepsilon_C = \int_{\lambda_1}^{\lambda_2} \varepsilon_\lambda E_{B\lambda} d\lambda \Big/ \int_{\lambda_1}^{\lambda_2} E_{B\lambda} d\lambda \qquad (6)$$

where 96.9% of the total blackbody emissive power at 1000 K is encompassed setting $\lambda_1 = 1\ \mu$m and $\lambda_2 = 15\ \mu$m, by Planck averaging of the spectral emissivities in function of monochromatic absorption thickness and effective albedo. The measure by which the total emissivities of the particle clouds of the composition and size distribution of Table 2 differ as the solids volume fraction increases is shown in Fig. 6, where the Planck and Rosseland mean absorption thickness at 1000 K of the two clouds at the outlet from the freeboard are so close ($(k_{a,P}D)_A = 0.44$, $(k_{a,R}D)_A = 0.45$; $(k_{a,P}D)_B = 0.45$, $(k_{a,R}D)_B = 0.47$) that they can be represented in the figure by an apparently single value.

Conclusions

The addition of limestone to the coal feed in desulfurizing fluidized-bed combustion affects the radiative properties of the solids holdup in the freeboard through the change of both concentration and composition. The emissivity of the particle cloud is reduced by the combined effect of the higher albedo, due to the low absorption index of limestone, and of the increased isotropy of scattering, due to the larger weight of the small particle tail of the size distribution. The change of absorption thickness of the particle cloud at the outlet from the freeboard is small, in spite of the near threefold increase of solids concentration measured in conjunction with limestone addition to the coal feed.

Nomenclature

A_1	linear anisotropy phase function parameter
d_p	particle diameter (m)
D	freeboard diameter (m)
f	forward scattering phase function parameter
k_a	absorption coefficient (m^{-1})
k_aD	absorption thickness
k_s	scattering coefficient (m^{-1})
k_s'	effective scattering coefficient ($k_s' = k_s(1 - f)$) (m^{-1})
L	freeboard height (m)
m	complex refractive index
$N(d_p)$	number concentration probability density (m^{-3})
p	scattering phase function
Q_a	particle absorption efficiency
Q_s	particle scattering efficiency
x	particle size parameter ($x = \pi d_p/\lambda$)

Greek Symbols

δ	Dirac delta function
ε	emissivity
λ	wavelength (m)
μ	cosine of the scattering angle
ω	albedo ($\omega = k_a/(k_s + k_s)$)
ω'	effective albedo ($\omega' = k_s'/(\omega_a + k_s')$)

Other Subscripts

λ	monochromatic
P	Planck mean
R	Rosseland mean

Acknowledgments

The financial support given to this work by ENEL-CRT (Pisa) and by M.U.R.S.T. is gratefully acknowledged.

REFERENCES

1. Wall, T. F., Lowe, A., Wibberley, L. J., and Stewart, I. McC., *Prog. Energy Combust. Sci.* 5:1–29 (1979).

2. Wall, T. F., Lowe, A., Wibberley, L. J., Mai-Viet, T., and Gupta, R. P., *Combust. Sci. Technol.* 26:107–121 (1981).
3. Mengüç, M. P., and Viskanta, R., *J. Quant. Spectrosc. Radiat. Transfer* 33:533–549 (1985).
4. Filla, M. and Scalabrin, A., *Proceedings of the 6th Mediterranean Congress on Chemical Engineering,* Ingoprint, Barcelona, 1993, pp. 125–126.
5. Filla, M. and Scalabrin, A., *Proceedings of the 1st Chemical and Process Engineering Conference,* ETS, Pisa, 1994, pp. 35–47.
6. Filla, M. and Scalabrin, A., *Proceedings of the Eurotherm Seminar: Heat Transfer in Radiating and Combusting Systems 2,* ETS, Pisa, 1994, pp. 37–49.
7. Adhibatla, S. and Boggs, M., *A.I.Ch.E. Symp. Ser.* 81:55–61 (1985).
8. Scalabrin, A., "Modellistica dello scambio termico per irraggiamento nel freeboard di combustori a letto fluidizzato," *Ph.D. Thesis,* University of Padova, Padova, 1995.
9. De Michele, G., Fabbri, V., and Trebbi, G., *Riv. Combust.* 33:204–211 (1979).
10. Buckius, R. O. and Hwang, D. C., *J. Heat Transfer* 102:99–103 (1980).
11. Mengüç, M. P. and Viskanta, R., *Combust. Sci. Technol.* 44:143–159 (1985).
12. Brewster, M. Q. and Kunitomo, T., *J. Heat Transfer* 106:678–683 (1984).
13. Joseph, J. H., Wiscombe, W. J., and Weinman, J. A., *J. Atmos. Sci.* 33:2452–2459 (1976).
14. Crosbie, A. L. and Davidson, G. W., *J. Quant. Spectrosc. Radiat. Transfer* 33:391–409 (1985).

COMMENTS

L. Pistone, SNAM Progetti, Italy. Would it be possible to predict the influence of fuel (e.g. biomass) on the heat transfer to walls?

Author's Reply. Yes, if the composition and concentration of the gas and solid components of the two-phase mixture confined by the walls and the size distribution of the solids are known.

Twenty-Sixth Symposium (International) on Combustion/The Combustion Institute, 1996/pp. 3301–3307

IN SITU ALKALI CONCENTRATION MEASUREMENTS IN A PRESSURIZED, FLUIDIZED-BED COAL COMBUSTOR BY EXCIMER LASER INDUCED FRAGMENTATION FLUORESCENCE

F. GREGER, K. T. HARTINGER, P. B. MONKHOUSE AND J. WOLFRUM
Physikalisch-Chemisches Institut der Universität Heidelberg
Im Neuenheimer Feld 253, 69120 Heidelberg, Germany

H. BAUMANN AND B. BONN
Institut für Kokserzeugung und Brennstofftechnik
DMT Gesellschaft für Forschung und Prüfung mbH
Franz-Fischer-Weg 61, 45307 Essen, Germany

Absolute concentrations of total gas-phase sodium and potassium compounds were determined in the flue gas of a fluidized bed coal combustor at 10 bar using excimer laser–induced fragmentation fluorescence (ELIF). In this in situ and on-line technique, the alkali compound molecules are photodissociated by ArF-excimer laser light at 193 nm, whereby excited Na(3^2P) and K(4^2P) atoms are formed. Fluorescence from these atoms is simultaneously detected in two separate channels at 589 nm and 768 nm, respectively. The calibration system and data evaluation procedure to convert measured signals to absolute concentrations is described.

Studies on lignite and hard coal under several different combustion conditions are reported. The measured concentrations span a dynamic range of more than three orders of magnitude, with a detection limit of <0.2 ppb for Na and K. Large differences between the coals in the release of alkalis were observed. For the lignite investigated, potassium-compound concentrations up to 800 ppb and sodium-compound concentrations up to 500 ppb were determined, whereas the concentrations for the hard coal were less than 10 ppb. These large variations in alkali release reflect the very different structures of the respective coals, emphasizing the influence of mineral coal components on release and recapturing of gas-phase alkali species. It is also clear that more detailed, systematic studies are needed for a proper understanding of alkali release in PFBC.

Introduction

The release of alkali species is a factor of considerable uncertainty in evaluating advanced solid fuel conversion systems. New combined cycle schemes for electricity generation promise net efficiencies on the order of 50% for pressurized coal-fired power plants [1]. However, hot gas cleaning, that is, the removal of particulates and detrimental trace gases such as evaporated alkali compounds at suitable gas turbine inlet temperatures, is still a problem to solve if such efficiencies are to be realized. For the entrance to turbines, corrosion damage caused by alkali compounds is feared even at ppb concentrations [2], requiring a highly sensitive and fast-responding detection technique. These low tolerance limits will necessitate getter materials (e.g., bauxite) to capture alkali vapors. Indeed, some mineral components of the coals may themselves act as getters (as our present results suggest) and flue gas alkali concentrations can be strongly influenced by the fuel type and combustion conditions. To better understand and eventually to predict the release of alkali compounds from solid fuels, systematic measurements for a variety of combustion conditions, fuels, and getters are needed. Furthermore, the flue gas contains variable quantities of gaseous components, aerosols, and dust particles. Depending on temperature, chemical constituents, and dust load, a number of surface and gas-phase processes can take place that can influence the relative amounts of alkali in different physical forms.

So far, classical collective sampling techniques [3,4] have been used frequently because of their common availability but require sampling/analysis times of more than 30 min, in pressurized systems often requiring many hours. Transient behavior, for example, upon changes of combustion conditions, cannot be detected in this way, nor can different forms of alkali be clearly discriminated.

A suitable on-line method for detecting *gas-phase* alkali concentrations is excimer laser–induced fragmentation fluorescence (ELIF). The diagnostic potential of ELIF for coal combustion diagnostics was suggested by Oldenborg et al. [5]. In a previous

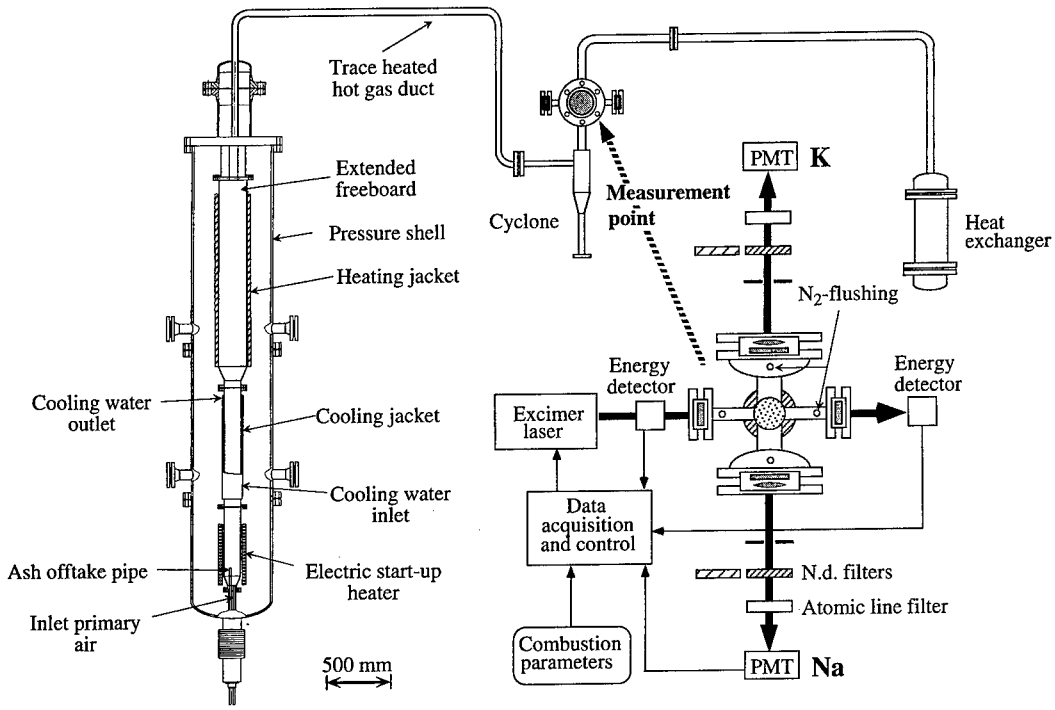

FIG. 1. Pressurized, fluidized bed reactor and the ELIF setup.

investigation [6], we demonstrated the viability of ELIF as a fast-responding, in situ, and nonintrusive diagnostic method for continuously monitoring alkali species in technical combustion devices. Absolute sodium concentrations in the flue gas of a fluidized bed reactor at DMT were determined at atmospheric pressure, and a detection limit of ~0.2 ppb was achieved. Several different coals were investigated and distinct differences in concentration history with reactor conditions and coal type could be discerned. The ELIF method was also used recently to monitor sodium concentrations in drop flow [7] and gasification systems [8], and for sodium and potassium in an entrained flow reactor [9]. In Ref. 7 only relative concentrations were measured; in the other two investigations [8,9], a calibration procedure allowed absolute concentrations to be determined. Additionally, Ref. 8 describes a method for distinguishing between NaCl and NaOH by monitoring fluorescence signals at 589 and 818 nm, since signals from the latter wavelength can energetically only be caused by NaOH.

Recently, two other on-line methods for monitoring alkali compounds were developed. In one technique, plasma-excited alkali resonance line spectroscopy (PEARLS), an N_2 plasma is used to dissociate the alkali compounds in a sample flow; the resulting atoms are detected by combined absorption and emission spectroscopy. PEARLS has been used to monitor sodium in several pressurized coal combustors [10]. Another technique is based on surface adsorption of alkali molecules and aerosols and subsequent surface ionization of the alkali atoms on a heated platinum wire [11]. In contrast to ELIF, which is sensitive only to gas-phase molecules, both of these techniques may also be sensitive to aerosols and small particles.

In most alkali measurement schemes, a gas sample is extracted from the system under investigation. Frequently, this gas sample must be filtered to remove particulates. There is uncertainty about the fate of the alkali compounds during this procedure, since reactions with the probe line material itself, deposits thereon, the filter material, or the filter cake can take place, especially if the probe line is not at process temperature. Therefore, the application of ELIF will be particularly advantageous as a truly in situ technique, observing in the process gas directly.

Experimental

The pressurized fluidized bed reactor used for our measurements has a rating of about 100 kW at 10 bar. It comprises a lower, bubbling fluidized bed combustion zone of 1.5 m bed depth and an upper, extended freeboard zone (Fig. 1). The residence time of the flue gas in the freeboard region is about

4.5 s at a fluidizing velocity of 1 m/s in the combustion section. To compensate for heat loss through the wall, the freeboard can be heated electrically. The maximum temperature at the surface of the heating jacket is 900°C.

After leaving the reactor, part of the ash is removed from the flue gas in a cyclone located immediately in front of the optical access port for the alkali measurements. To prevent condensation of alkali compounds between the reactor and the measurement point, the metallic flue gas duct and cyclone were electrically trace heated. Typical flue gas temperatures at the ELIF measurement point were ~800°C (measured at the cyclone exit). Downstream, the flue gas was cooled in a heat exchanger and the remaining dust removed in a bag filter.

To prevent wall reactions of alkali compounds, the inner surface of reactor and flue gas ducts were made entirely from steel with no refractory linings and so on. High gas velocities in the flue gas duct kept particle deposition low.

To allow operation at 10 bar, the reactor head, flue gas pipe, cyclone, and optical access were designed using heat-resistant steel. Care was taken to optimize the N_2 flushing of the windows to minimize dust deposition, to ensure that the windows withstand the foreseen operating conditions, to minimize heat loss by the flanges, to simplify detector adjustment, and to retain a compact size. This resulted in an access port with different flanges for laser beam and fluorescence detection, each equipped with high-purity quartz (Suprasil) windows encased in steel mountings.

Alkali compounds were photolyzed at 193 nm by a broadband ArF excimer laser using energy densities of several mJ/cm^2. The laser was operated at a repetition rate of 6.4 Hz; data were averaged computationally over 400 samples (corresponding to 1 min). The laser energy entering and leaving the optical access was monitored constantly and provided a measure of the effective beam transmission. Fluorescence was detected perpendicular to the laser beam by two photomultipliers coupled to boxcar integrators, using time gates of 40 and 90 ns, respectively. To suppress undesired radiation due to, for example, incandescence, atomic line filters (589 nm, FWHM = 10 nm for sodium and 768 nm, FWHM = 10 nm for potassium) were placed in front of the detectors. Exchangeable neutral density filters avoided detector saturation at high alkali concentration levels and reduced remaining background radiation. To avoid saturation caused by low but constant irradiation, the photomultiplier for potassium was gated (i.e., switched off except for one μs around the measurement time). Gating was not necessary for the sodium photomultiplier since incandescence is much weaker at 589 nm than at 768 nm.

Calibration Procedure

For calibration measurements, a quartz cell with four optical access ports was set up using the same optical conditions and geometry as for the reactor measurements. The cell was encased in a tubular oven, heatable to 1200°C. NaCl or KCl filled the attached reservoir, which was heated separately, so that the vapor pressure of the salt could be varied independently [12]. To prevent salt condensation, the oven was constructed with effective thermal insulation material and the cell was maintained at least 50°C hotter than the reservoir. Evacuated quartz tubes at the ports served both for thermal insulation and minimized absorption of the laser beam in the hot oven atmosphere.

The gas-phase alkali compounds MX were photodissociated by UV-laser light (193 nm), whereby simultaneously excited Na(3^2P) and K(4^2P) atoms M* are formed:

$$\mathrm{MX} \xrightarrow{h\nu} \mathrm{M}^* + \mathrm{X}$$

Fluorescence from M* was detected at 589 nm (sodium) and 768 nm (potassium), respectively. A calibration factor C_{det} can be determined using the alkali number densities in the calibration cell obtained from thermodynamic data and the following relation for the fluorescence signal S_{fl}:

$$S_{\mathrm{fl}} = C_{\mathrm{det}}\, E_{\mathrm{laser}}\, n_{\mathrm{MX}}\, a_{\mathrm{abs}}\, q$$

where E_{laser} is the effective laser energy in the cell, n_{MX} is the number density of the alkali salt MX, a_{abs} is its UV-absorption cross section for production of M*, and q describes the quenching effect

$$q = A/(A + Q),\ Q = \sum_i n_i v_i \sigma_i$$

with A the inverse natural lifetime of the excited alkali atom and Q the quenching rate. The value of Q was determined using measured quenching cross sections σ_i [13,14], the number densities n_i of the quenching partners i, and the relative velocities v_i of i and M*. The most important quenching partners in the flue gas were N_2, CO_2, O_2, and H_2O with typical mole fractions of 0.76, 0.14, 0.05, and 0.04, respectively.

Results and Discussion

In the measurements presented here, one lignite and one hard coal were studied. Both coals were milled to a diameter <2 mm. ELIF measurements could begin when stable reactor conditions had been reached and the two laser energy monitors E_{in} and E_{out} had been calibrated with a pyroelectric joulemeter. The ELIF signals were measured continuously for 6–7 h. At certain times, the reactor conditions (e.g., coal feed, air supply, and electrical heating powers) were varied.

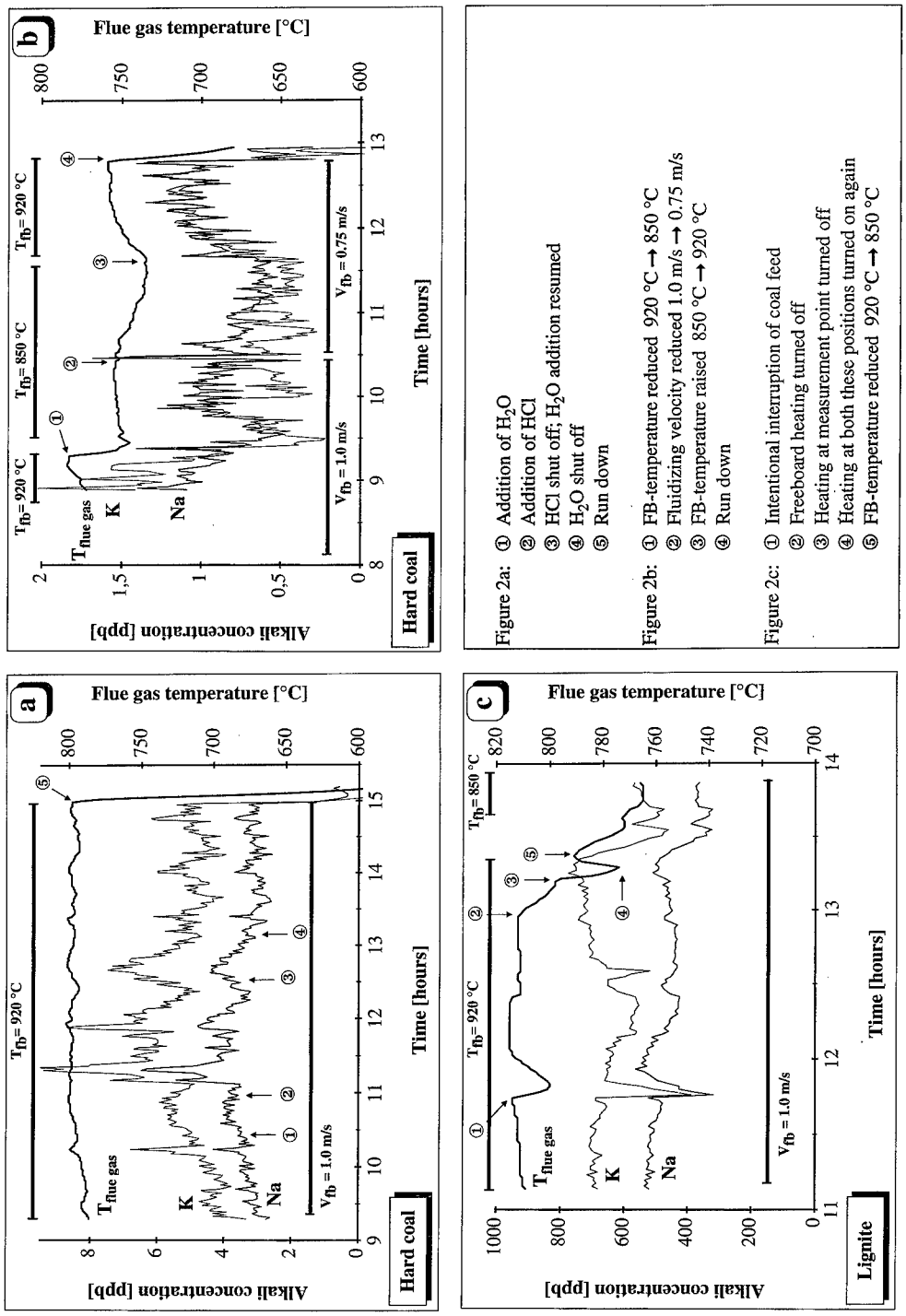

Figure 2a: ① Addition of H_2O
② Addition of HCl
③ HCl shut off; H_2O addition resumed
④ H_2O shut off
⑤ Run down

Figure 2b: ① FB-temperature reduced 920 °C → 850 °C
② Fluidizing velocity reduced 1.0 m/s → 0.75 m/s
③ FB-temperature raised 850 °C → 920 °C
④ Run down

Figure 2c: ① Intentional interruption of coal feed
② Freeboard heating turned off
③ Heating at measurement point turned off
④ Heating at both these positions turned on again
⑤ FB-temperature reduced 920 °C → 850 °C

FIG. 2. Sodium and potassium concentration histories for a hard coal and a lignite measured in the flue gas of the PFBR at 10 bar. T_{fb} = temperature of the fluidized bed; v_{fb} = fluidizing velocity.

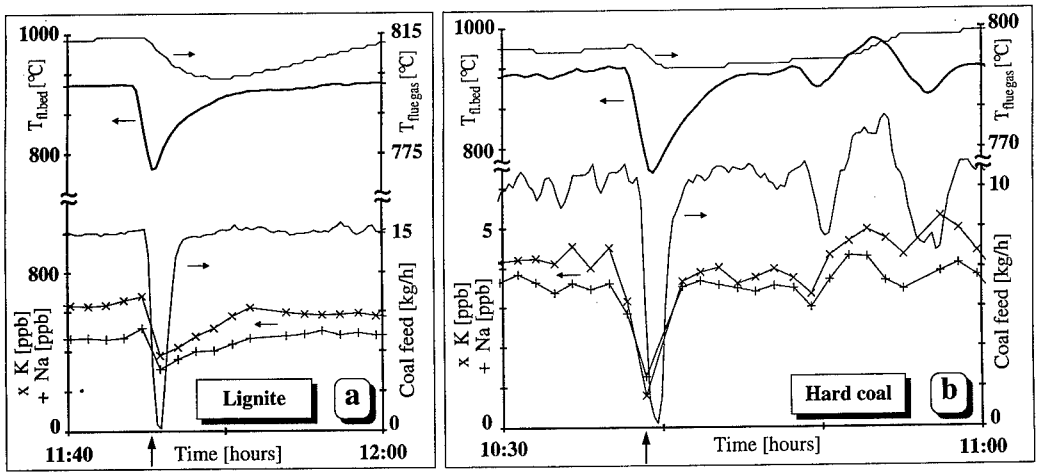

FIG. 3. Sodium and potassium concentration histories for a hard coal and a lignite with a coal feed interruption (↑).

Figures 2 and 3 show representative results for experiments under various conditions. Figures 2a and 2b show concentration profiles for the hard coal; Fig. 2c depicts that of the lignite. In each case, the temporal course of potassium and sodium concentrations is shown over the whole day, together with the corresponding history of the flue gas temperature. The general concentration level for both alkali compounds was below 10 ppb for the hard coal but in the range of 300–800 ppb for the lignite. The hard coal was used as fuel in a total of six independent measurements on different days at 10 bar pressure, the lignite in five measurements. Although day-to-day variations are seen, the alkali concentration levels were of the same order of magnitude in each measurement of the respective series. The major reasons for the large difference in measured concentrations for the present lignite and hard coal are their very different mineral compositions and the way the alkali is distributed between organic and aluminosilicate fractions. Ash analysis shows a very high proportion (~30% wt) of aluminosilicates in the hard coal, which are known to retain alkali compounds strongly [15] at the temperatures of FB combustion. In comparison, the lignite ash contains only ~3% wt aluminosilicates. In the lignite, the main part of the alkali content is present in the organic material of the coal, which is easily released at FB temperatures. The alkali content in the hard coal, in contrast, is bound chiefly in the aluminosilicates. Clearly, the quantity of alkali in the coal is not a sufficient criterium for determining the amount present in the flue gas.

During a hard coal experiment (Fig. 2a), small quantities first of H_2O (①), then HCl (②), then H_2O again (③), were introduced into the reactor to see whether extra gas-phase alkali would be released. The chlorine content of this coal is ~0.1% and was increased by 120% by adding HCl. Despite the observed fluctuations, the average level of alkali concentration is 40–50% higher during HCl addition.

In all experiments, the maximum operating bed temperature was 920°C. On reducing the FB temperature by 30–70°C (① in Fig. 2b and ⑤ in Fig. 2c) or the flow velocity from 1 m/s to 0.75 m/s (② in Fig. 2b), a decrease in alkali concentration was observed. A corresponding increase was seen for an increase in bed temperature (③ in Fig. 2b). To verify that the observed effect was not due to reactions in the freeboard or flue gas section, the freeboard heating and the heating at the measurement point were turned off successively for several minutes (②, ③ in Fig. 2c); in these cases, the alkali concentration remained constant.

Interruptions of the coal feed (Figs. 3a and 3b) lead to an immediate fall in both temperature and alkali concentrations, which returned to their previous levels on restoring the original conditions. The hard coal exhibits a large drop and a fast recovery of the (generally low) alkali concentrations. Taking into account the different temporal resolutions of ELIF (60 s) and reactor standard gas analysis (15 s), the alkali curve follows closely the coal feed (calculated from the gas analysis data and the coal's elementary analysis). The lignite, however, shows a less pronounced dip and a slower recovery of the alkali concentrations. Again, the temperature of the flue gas duct appears to have no influence. This and the effect discussed in the previous paragraph show that, for the coals investigated, the most important contribution to the measured gas-phase alkali levels is from processes in the fluidized bed.

From a survey of all experiments, the following general observations can be made:

- For constant reactor and measurement conditions,

alkali concentrations remain stable for considerable periods; for example, in Fig. 2a, the alkali concentration varies 10–15% from 13–15 h.

- Potassium and sodium concentrations followed a similar course in most experiments.
- The detection limit of 0.2 ppb for sodium and potassium can be confirmed even under pressurized conditions.
- The alkali concentrations follow most changes in operating conditions immediately.

The different response to coal feed interruption (Figs. 3a and 3b) indicates that *capture/release equilibria* of alkali in the FB are, for the hard coal of minor importance compared to release rates from newly introduced coal particles, while they may be important for the lignite. This is consistent with significant (and irreversible) recapturing of alkali compounds by hard coal minerals giving low overall alkali levels, and a weaker and reversible process for the lignite, leading to higher alkali levels.

Considering the strong influence of the mineral composition of the coal and the apparently weak influence of effects in the postcombustion zone with the same mineral matter present, *particle* temperature distributions will certainly be of major importance for the fate of alkali species. Recent results of measurements with the PEARLS technique in a pressurized entrained flow reactor at 10 bar [10] show a strong dependence on the rate of vaporization of alkali species on particle temperature, as measured by FTIR pyrometry. Thus, an important future experiment will be to perform simultaneous alkali and particle temperature measurements for PFBC conditions.

The present results cannot be compared directly with those of the previous work [6] because of differences in the coals (structure and composition) and operating conditions used. Not only our experience but also results found in the PFBC literature show that flue gas alkali concentrations can vary over orders of magnitude, depending on a whole variety of factors in a complex way that is not yet understood. A survey of PFBC/G literature shows the following trends: (a) the effect of FB temperature (also found, for example, in Ref. 4); and (b) the effect of increasing chlorine content, shown by Lee et al. [3]. Other correlations cannot yet be established clearly, since there are insufficient data under really comparable conditions (e.g., operation parameters, wall surface, particle load, coal structure). The only sure way to establish such correlations is to make measurements at the same reactor, using complementary methods simultaneously, as suggested in the Conclusions section.

Conclusions

Optical on-line diagnostics have distinct advantages for industrial combustion devices, since they are potentially in situ, nonintrusive, and give usable results in less than a minute, so that transient effects can be registered. In contrast, standard alkali sampling methods require considerably longer measurement times and bear the risk of sample changes occurring in the sampling lines.

In the course of several series of measurements, we have shown that continuous measurements of alkali concentrations with ELIF are feasible under pressurized conditions with high dust load, even over a whole day. Sodium and potassium can be detected separately and simultaneously using two detector channels. The temporal course of the alkali concentrations showed various effects that can be ascribed to operational changes or that are characteristic of the coal used. For the hard coal, concentrations were below 10 ppb, whereas for the lignite, maxima of 800 ppm potassium and 500 ppm sodium were determined. The sub-ppb detection limits for both alkalis were confirmed and a dynamic range exceeding three orders of magnitude established.

Ongoing developments and refinements of the ELIF method will allow reliable and detailed investigations of alkali release and conversion in pressurized coal combustors. Furthermore, following recent investigations [16], the extension of the ELIF method to heavy-metal compounds appears feasible. Also, a detailed comparison of ELIF with other alkali diagnostic methods such as PEARLS [10] and surface ionization [11] is in preparation. The complementary features of these methods should allow alkali species in different physical forms (gas phase, aerosols, particles) to be distinguished and thus permit insight into the fate of alkali species during and after combustion.

Acknowledgments

Support of this work by Deutsche Montan Technologie Gesellschaft für Forschung und Prüfung mbH and the Commission of the European Communities (Project No. JOU2-0037) are gratefully acknowledged. We thank U. Busch and B. Peters (DMT) and A. Schniewind (PCI) for technical assistance.

REFERENCES

1. Penner, S. S., et al., *Prog. Energy Combust. Sci.* 10:87–144 (1984); Böhm, H., *VGB Kraftwerkstechnik* 74:173–186 (1994).
2. McCarron, R. L., Belttran, A. M., Spacil, H. S., Luthra, K. L. O., *Proceedings of the 5th International Conference on FBC,* Vol. III, Development Activities, Washington, D.C., December 12–14, 1977, pp. 714–736; Lee, S. H. D., Teats, F. G., Carls, E. L., in *Chlorine in Coal* (J. Stringer and D. D. Banerjee, eds.), Elsevier Amsterdam, NL, 1991, pp. 275–296; Osborn, G. A., *Fuel* 71:131–142 (1992).

3. Lee, S. H. D. and Myles, K. M., *Proceedings of the International Conference on Fluidized-Bed Combustion,* Vol. 2, Boston, 1987, pp. 793–801; Lee, S. H. D., Teats, F. G., Swift, W. M., and Banerjee, D. D., *Combust. Sci. Technol.* 86:327–336 (1992).
4. Hippinen, I., Lee, Y., Laakainen, J., Nieminen, M., and Jahkola, A., *J. Inst. Energy* 65:154–159 (1992).
5. Oldenburg, R. C. and Baughcum, S. L., *Anal. Chem.* 58:1430–1436 (1986).
6. Hartinger, K. T., Monkhouse, P. B., Wolfrum, J., Baumann, H., Bonn, B., *Twenty-Fifth Symposium (International) on Combustion,* The Combustion Institute, Pittsburgh, 1994, pp. 193–199.
7. Helble, J. J., Srinivasachar, S., Ham, D. O., Boni, A. A., Charon, O., and Modestino, A., *Comb. Sci. Technol.* 81:193–205 (1992).
8. Chadwick, B., Domazetis, G., and Morrison, R. J. S., *Anal. Chem.* 67:710–717 (1995).
9. Greger, F., Hartinger, K. T., Hein, K. R. G., Reichelt, T., and Spliethoff, H., submitted.
10. Aho, M., Hernberg, R., Hämäläinen, J., Häyrinen, V., Paaknen, K., Rantanen, J., and Joutsenoja, T., *Liekki 2 Combustion research program project reports,* Åbo, Finland, 1996, pp. 477–482.
11. Jäglid, U., Olsson, J. G., and Pettersson, J. B. C., *J. Aerosol Sci.* 26:637–638 (1995); Jäglid, U., Olsson, J. G., and Pettersson, J. B. C., *J. Aerosol Sci.* (1996) in press.
12. Hartinger, K. T., Ph.D. Thesis, Universität Heidelberg Germany, 1994.
13. Hartinger, K. T., Monkhouse, P. B., and Nord, S., *Appl. Phys. B.,* (1996), accepted.
14. Earl, B., Herm, R., Lin, S.-M., and Mims, C. A., *J. Chem. Phys.* 56:867–882 (1972); Earl, B. and Herm, R., *J. Chem. Phys.* 60:4568–4578 (1974); Barker, J. R. and Weston, R. E., Jr., *J. Chem. Phys.* 65:1427–1442 (1976).
15. Kühn, L. and Plogmann, H., *Fuel* 62:205–208 (1983); Bachovchin, D. M., Alvin, M. A., and Day, L. M., *Proceedings of the 7th Ann. Gasification and Gas Stream Clean-Up Systems Contractors Review Meeting,* Morgantown, WV, USA, June 16, 1987, U.S. Department of Energy, Morgantown Energy Technology Center, pp. 495–504 (August 1987); Hodges, N. J. and Richards, D. G., *Fuel* 68:440–445 (1989).
16. Buckley, S. G., McEnally, C. S., Sawyer, R. F., Koshland, C. P., and Lucas, D., *Combust. Sci. Technol.* (1996) in press.

Twenty-Sixth Symposium (International) on Combustion/The Combustion Institute, 1996/pp. 3309–3315

POLLUTANT FORMATION DURING COAL COMBUSTION IN A CFB TEST FURNACE

A. REIDICK
Babcock Lentjes Kraftwerkstechnik GmbH
Duisburger Str. 375
46049 Oberhausen
Germany

H. KREMER
Lehrstuhl für Energieanlagentechnik
Ruhr-Universität Bochum
44780 Bochum
Germany

Experiments were carried out in a CFB test unit to investigate how fuel conversion and pollutant formation during coal combustion is affected by air staging. Staging of combustion air, in particular the variation of its most important parameters, the primary stoichiometric ratio and the residence time in the zone before secondary air addition were of prime importance.

An anthracite, a bituminous coal, and a lignite were used in the experiments. The exhaust concentrations and axial concentration profiles of flue gas constituents were measured. The fuel conversion and pollutant formation occur primarily in the oxygen-rich zone directly above the bottom nozzle plate. If the residence time in the air-lean operated primary zone is sufficiently long, the main combustion phase will be followed, after the consumption of oxygen, by a phase dominated by further devolatilization of the still nonconverted fuel proportion, which strongly affects formation and decomposition of pollutants in both the primary and secondary zones.

In the stoichiometric ratio range between 0.7 and 0.9, the efficiency of desulphurization is reduced because of the thermodynamic instability of the sulphur capture phases CaS and $CaSO_4$. In CFB combustion, primary stoichiometric ratio and primary residence time can be varied within a large range, in contrast to pulverized coal combustion, without significant change in the exhaust NO concentration. The reason for this is seen especially in the retardation of the H_2/O_2 mechanism and the residual char combustion, due to the low combustion temperature.

The exhaust N_2O concentration is largely determined by the homogeneous N_2O reduction through H radicals and the heterogeneous N_2O formation from NO reduction on the surface of residual char. The suppression of the heterogeneous N_2O formation in the secondary zone is an important key to the reduction of the exhaust N_2O concentration.

Introduction

Results are presented from a CFB test unit to obtain detailed understanding of the influence of air staging on pollutant formation—as exists presently for pulverized fuel firing systems. Moreover, fundamental knowledge must be established on the course of combustion and pollutant formation during coal combustion in the CFB firing system. The results submitted are extracted from a DFG (German Research Society) research project carried out at the Ruhr University, Bochum. A comprehensive description of this project can be found in Ref. 1.

Experimental

CFB Test Unit

The design of the test unit (Fig. 1) corresponds to the basic concept of the large-scale plants according to the EVT-Ahlström system [2]. The combustion

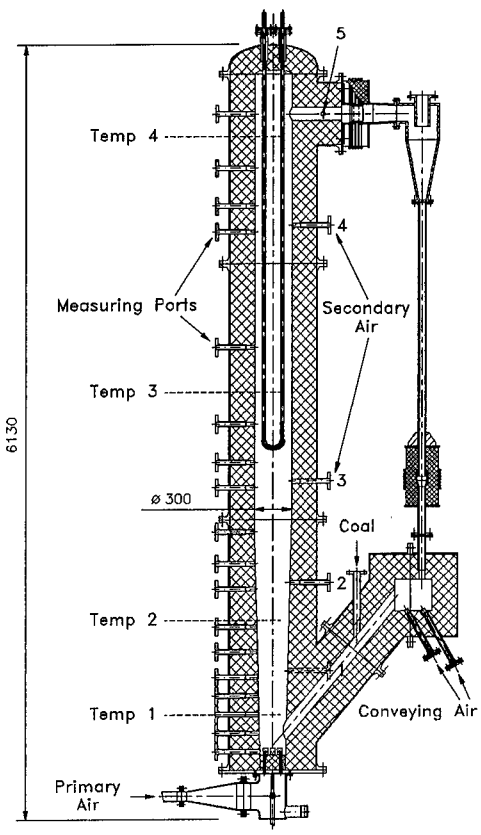

FIG. 1. CFB test unit at Ruhr University, Bochum.

chamber, particle seal, and chute are refractory lined. The cyclone and the particle return pipe are made of heat-resistant steel and provided with an external insulation. The bottom nozzle plate is equipped with six conventional bubble caps. Coal, limestone, and silica sand are supplied gravimetrically from screw feeders via a joint downcomer directly into the chute. Secondary air can be admitted to the combustion chamber on five different levels (see Fig. 1). The combustion chamber is operated autothermally. The cooling of the furnace is effected by two single U tubes, one of which is immersed in the combustion chamber and the other in the particle seal. The required furnace temperature can be set by varying the cooling load through changing the immersion depth of the U tubes.

Instrumentation

To withdraw flue gas from the combustion chamber, a total of 19 measuring ports that can be closed by ball valves are available. Their arrangement is shown in Fig. 1. In situ sampling was accomplished through a stainless steel probe cooled with compressed air. At the end of the probe, a heated miniature cyclone ensured that the gas was largely separated from the fluidized bed material, which was also withdrawn in the process. Via a heated Teflon hose, the gas sample then reached the fine dust separators and finally the gas analyzers, either in a dried (O_2, CO_2, CO, SO_2, NO, N_2O) or moist condition (C_xH_y, NH_3), depending on the monitoring principle. Sampling of the flue gas constituents was performed directly above the cyclone outlet.

For continuous monitoring of NH_3, a device was used that operated according to a relatively new principle based on microwave absorption (Siemens, MIPAN 7 KQ 2106). This gas analyzer working with moist flue gas did not show any cross sensitivities with regard to the typical constituents of flue gases derived from coal combustion. For the determination of the N_2O concentration, an IR absorption analyzer (Maihak, UNOR 6 N) was used. This method showed minor cross sensitivity to certain hydrocarbons of which the only one worth noting was CH_4 (20 vpm at 504 vpm CH_4).

Setting and Operation of the CFB Test Unit

Air staging was in operation in the combustion chamber for all the tests. One part of the combustion air, which is referred to later as primary air, was supplied via the bottom nozzle plate and the conveying air nozzles of the particle seal. The remaining combustion air, which is later referred to as secondary air, was injected via one of the five secondary air inlets shown in Fig. 1. Accordingly, the combustion chamber zone from the bottom plate up to the position of the secondary air injection is called the primary zone, whereas the combustion chamber area after the injection of secondary air is called the secondary zone. For all the tests, the proportion of the conveying air to the minimum oxygen requirement was roughly 10%.

The stoichiometric ratio in the primary zone was varied, to ensure constant fuel load and constant primary gas volume flow by replacing a certain quantity of primary air with recirculated flue gas of up to 45% of the exhaust gas. As a result, the axial temperature profile, the fluidization condition, and the residence time in the combustion chamber were similar in all tests.

An anthracite (Ruhr), a bituminous coal (Ruhr), and a lignite (Rhineland) were used in the experiments. The properties of the coals are shown in Table 1. The mass mean particle size was in the range of 2–3 mm. The nominal fuel load was 0.1 MW for the anthracite and the bituminous coal and 0.075 MW for the lignite because of its larger specific flue gas volume.

The different settings of the firing system at mean furnace temperatures of around 850°C produced superficial gas velocities of 1.8–2.6 m/s in the

TABLE 1
Coal properties

	Anthracite	Bituminous	Lignite
		wt.% (daf)	
c	91.8	82.6	68.5
h	3.8	5.3	4.8
o	1.7	8.8	25.3
n	1.8	1.9	1.1
s	0.9	1.4	0.3
VM	10.0	36.7	53.9
		wt.% (as received)	
w	5.0	7.9	54.8
a	7.6	9.0	2.0
NCV (MJ/kg)	30.68	27.11	9.70

cylindrical part of the combustion chamber. The mean gas residence time from the nozzle plate to the cyclone outlet was between 2.0 and 3.0 s, depending on the secondary air volume flow and the location of the secondary air injection.

Despite the comparably low superficial gas velocities, complete fluid-dynamic similarity to the commercial-scale plants operated in Germany was obtained by using a correspondingly fine bed material, a silica sand with a mass mean particle-size of 65 μm. The pollutant exhaust concentrations of the test unit reveal a high degree of conformity with those of commercial-scale plants in Germany. For desulphurization, a limestone powder with a mass mean particle size of 10 μm, which is normally employed for desulphurization in scrubbers, was used.

Results

Fuel Conversion

Figure 2 shows the axial concentration profiles of flue gas constituents for air-staged combustion of lignite with a primary stoichiometric ratio of 0.78 at a mean furnace temperature of 850°C. Secondary air was injected through inlet 3 (see Fig. 1). The rapid consumption of oxygen taking place within a few tenths of a second and the rapid approximation of the CO_2 concentration to the maximum value show that the major part of the fuel is converted in the most oxygen-rich zone of the combustion chamber directly above the nozzle plate. The main combustion phase (drying-devolatilization-combustion) in the air-lean operated primary zone is followed, after the consumption of combustion air oxygen, by a phase dominated by further devolatilization of the still nonconverted, partially degassed fuel. The transition between the two phases is clearly shown by the renewed rise in the concentrations of C_xH_y, CO, and NH_3.

Figure 3 shows the axial concentration profiles for the combustion of the bituminous coal. Secondary air was injected through inlet 4. As with the lignite, there is a rapid conversion of fuel directly above the nozzle plate and a transition to a devolatilization-dominated phase after the consumption of oxygen. During the combustion of the low-volatile anthracite, however, no subsequent devolatilization phase occurs (Fig. 4). Figure 5 presents the concentration profiles of the combustion process for the highly volatile bituminous coal with secondary air injected through inlet 2. With this arrangement, which corresponds to the air staging in large-scale CFB plants, the subsequent devolatilization phase is suppressed because of the short residence time in the primary zone. The addition of limestone causes a noticeable decrease of exhaust CO concentrations, something that can be attributed to the catalytic acceleration of the CO oxidation from the limestone products [3].

SO_2 Formation and Desulphurization

Figure 3 shows the SO_2 concentration profile when the bituminous coal is burned *without* addition of limestone. SO_2 is formed primarily in the main combustion zone above the bottom nozzle plate. During combustion *with* the addition of limestone, the SO_2 is captured rapidly in the oxygen- and CaO-rich main combustion zone (Fig. 5).

In principle, there are two possibilities of sulphur capture by CaO: in oxidizing atmosphere as $CaSO_4$ and in reducing atmosphere as CaS [4]. In the transition between globally oxidizing and globally reducing regimes, which obviously corresponds to a range of the stoichiometric ratio between roughly 0.7 and 0.9, neither of the two forms of sulphur capture is thermodynamically stable. Therefore, little desulphurization is to be expected, as shown in Fig. 6, for a mean furnace temperature of 870°C. Since this effect is restricted to the substoichiometric-operated primary zone, its influence on the exhaust SO_2 concentration grows with an increasing primary residence time. In large-scale CFB plants, with their relatively short primary residence times, the described effect is therefore of no real significance (see Fig. 6).

NO Formation and Decomposition

The NO concentration profiles in all figures presented demonstrate that the most important zone of NO formation is the oxygen-rich combustion regime directly above the bottom nozzle plate. Because of the low combustion temperature, fuel nitrogen is the only source of NO formation. Whether the reaction

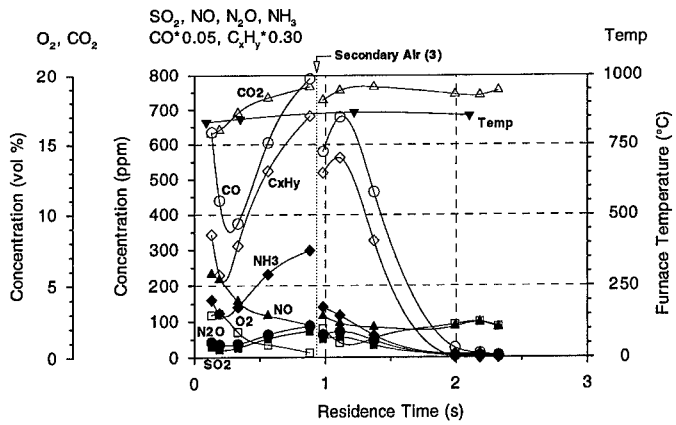

FIG. 2. Axial concentration profiles of flue gas constituents from bottom nozzle plate to cyclone outlet. Lignite: T_m = 850°C; SR_p = 0.78; SR_o = 1.1; Ca/S = 0 (inherent lime).

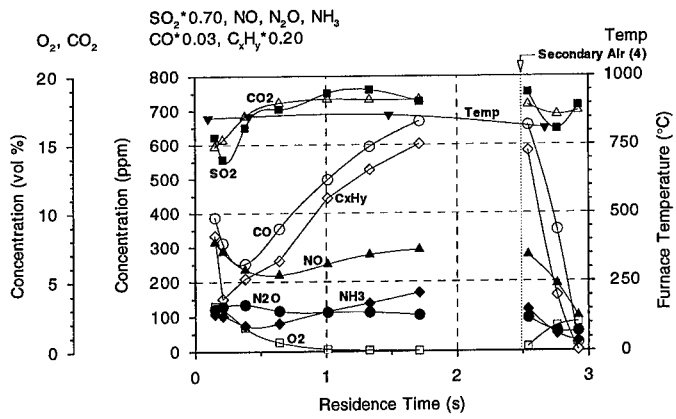

FIG. 3. Axial concentration profiles of flue gas constituents from bottom nozzle plate to cyclone outlet. Bituminous: T_m = 850°C; SR_p = 0.77; SR_o = 1.1; Ca/S = 0.

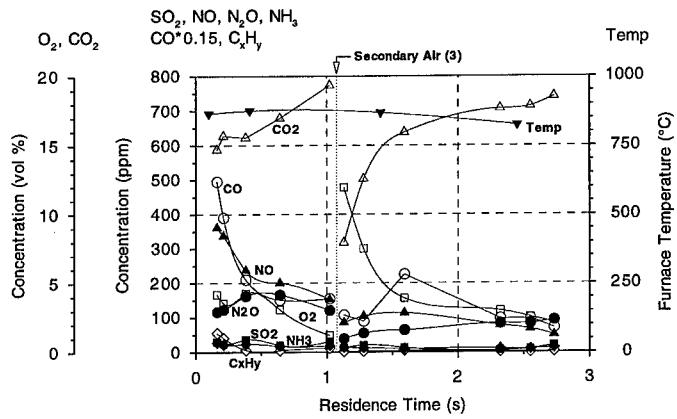

FIG. 4. Axial concentration profiles of flue gas constituents from bottom nozzle plate to cyclone outlet. Anthracite: T_m = 850°C; SR_p = 0.84; SR_o = 1.1; Ca/S = 3.6.

paths of the homogeneous reactions of the fuel nitrogen tend to form NO rather than reduce it depends on the concentration of the radicals OH and O. High concentrations of these chain propagators, which are involved in all important reactions of the overall mechanism of the homogeneous fuel nitrogen conversion, promote the formation of NO. If OH and O concentrations are low, however, the reaction paths leading to a reduction of NO and formation of N_2 are predominant. The absence of these chain propagators finally leads to inhibition of the homogeneous conversion of fuel nitrogen. The

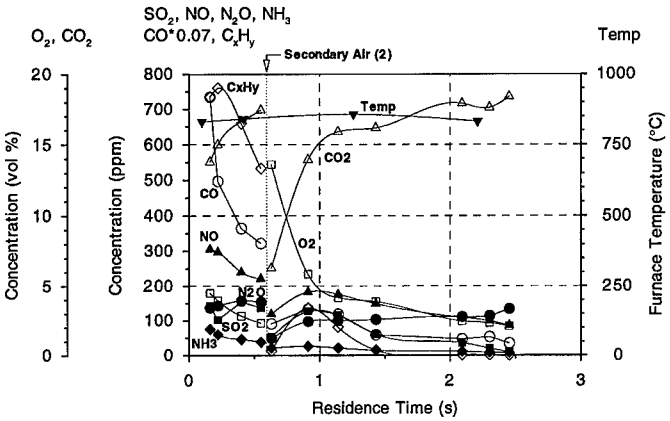

FIG. 5. Axial concentration profiles of flue gas constituents from bottom nozzle plate to cyclone outlet. Bituminous: T_m = 840°C; SR_p = 0.71; SR_o = 1.1; Ca/S = 3.

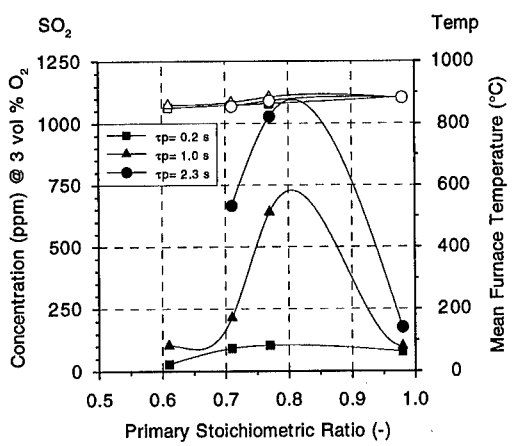

FIG. 6. Exhaust SO_2 as a function of the primary zone stoichiometric ratio at various residence times in the primary zone (τ_p). Filled symbols: exhaust SO_2; hollow symbols: mean furnace temperature. Bituminous: τ_o = 2.2–3.0 s; SR_o = 1.1; Ca/S = 3.

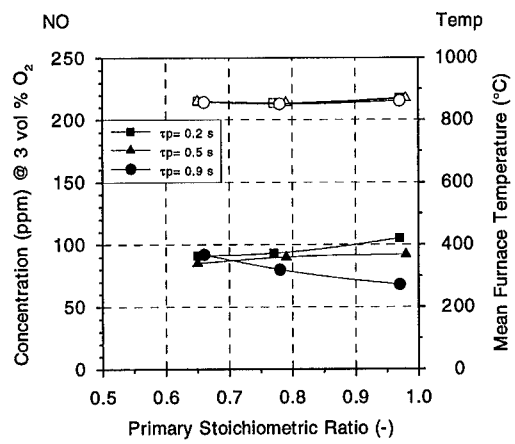

FIG. 7. Exhaust NO as a function of the primary zone stoichiometric ratio at various residence times in the primary zone (τ_p). Filled symbols: exhaust NO; hollow symbols: mean furnace temperature. Lignite: τ_o = 2.0–2.5 s; SR_o = 1.1; Ca/S = 0.

stagnation of the NO concentration in the primary zone after the consumption of the available oxygen, as seen in Fig. 3, as well as the simultaneous rise in the NH_3 concentration, indicate the inhibition of fuel nitrogen conversion inhibition. This is caused by the paucity of OH and O radicals.

The rate of formation of the chain propagators is strongly dependent on temperature. At the comparatively high combustion temperatures in pulverized coal firing systems, concentrations of OH and O radicals are high, even if only a small amount of molecular oxygen is present. At the typical CFB combustion temperature of about 850°C, however, the concentrations of these radicals are so low—even at higher O_2 concentrations—that the tendency toward homogeneous NO decomposition is clearly predominant. This is indicated in Fig. 3 by the drastic decrease of the NO concentration in the secondary zone after secondary air injection. The supply of oxygen again stimulates the formation of OH and O radicals. However, the low temperatures ensure that the rate of formation and thus concentration remain low. Consequently, on the one hand, the formation of the radicals of NH_3, HCN, and C_xH_y capable of NO reduction is rendered feasible and, on the other, their rapid oxidation is prevented.

Thus, due only to the low combustion temperature, NO reduction in CFB combustion is less dependent on oxygen concentration than in pulverized coal combustion. This leads to generally lower exhaust NO concentrations that are, in addition, hardly affected by the primary stoichiometric ratio and the primary residence time (Fig. 7), factors that are decisive in pulverized coal combustion with respect to primary NO reduction.

The stagnation of the NO concentration in the

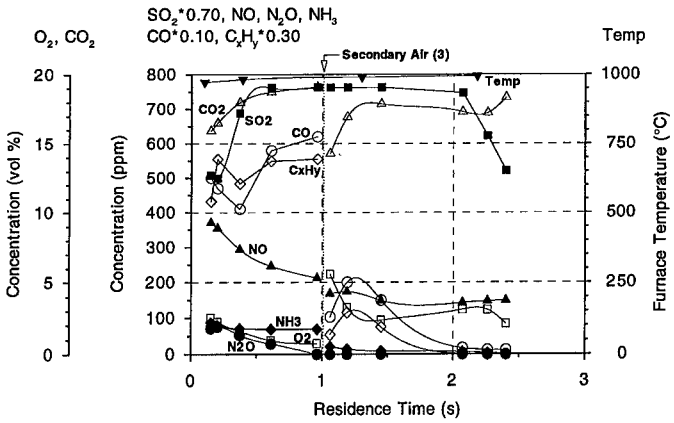

FIG. 8. Axial concentration profiles of flue gas constituents from bottom nozzle plate to cyclone outlet. Bituminous: T_m = 990°C; SR_p = 0.71; SR_o = 1.1; Ca/S = 3.

primary zone after the consumption of oxygen shown in Fig. 3 indicates that the catalytic reduction of NO on CaO, CaS, and residual char surfaces, which according to laboratory tests [3] is especially effective in the absence of oxygen, does not contribute considerably to the decomposition of NO. On the contrary, when limestone was added, an increase of the exhaust NO concentration was usually observed during the experiments.

The heterogeneous NO reduction on residual char surfaces, however, seems to be effective at least in an oxidizing atmosphere. This is shown by the decrease of the NO concentration in the secondary zone in Figs. 4 and 5. Since no gaseous reducing agents are present and the limestone products do not catalyze NO decomposition under oxidizing conditions [3], this decrease in concentration can only be correlated with the heterogeneous NO reduction on residual char surfaces.

N_2O Formation and Decomposition

The N_2O concentration profile of Fig. 3 shows that the N_2O formed in the main combustion zone, just as with the NO, is not decomposed in the following devolatilization-dominated zone. The homogeneous N_2O reduction by the reaction $N_2O + H \leftrightarrow N_2 + OH$, which seems to be the fastest homogeneous N_2O reduction reaction [5,6], is ineffective because the formation of the H radicals in the H_2/O_2 mechanism is largely inhibited by the absence of oxygen. The stagnation of the N_2O concentration shows that not only the homogeneous reduction reactions but also the thermal dissociation and the catalytic N_2O decomposition on CaO and-CaS surfaces (which has been proven to be highly efficient in laboratory-scale experiments [3]) and on residual char surfaces are of no significance under the conditions of reaction in fluidized bed combustion.

An increase of the mean combustion temperature to 990°C leads to the expected acceleration of the homogeneous reduction reactions and of thermal dissociation. Figure 8 shows that the initially formed N_2O is decomposed completely as early as in the primary zone.

Two mechanisms are of decisive importance for the formation and decomposition of N_2O in the secondary zone. The first is the previously mentioned homogeneous N_2O reduction by H radicals, which are formed in sufficient quantities during the combustion of hydrocarbons in the secondary zone if the C_xH_y concentrations in the exhaust gas of the primary zone are correspondingly high. The second one is the heterogeneous N_2O formation during the burnout of residual char that has remained unconverted in the primary zone. The effect of both mechanisms can be seen by comparing the combustion of the low-volatile anthracite and the highly volatile lignite.

The increasing N_2O concentration in the secondary zone shown in Fig. 4 is typical of the combustion of low-volatile coal. As a result of the slow char combustion coupled with the limited release of volatiles, the heterogeneous N_2O formation is predominant. This leads to high exhaust N_2O concentrations. Simultaneous NO decomposition in the absence of potential gaseous reducing agent points to the mechanism of N_2O formation from heterogeneous NO reduction on burning residual char surfaces as suggested by Tullin et al. [7].

The situation of lignite combustion is completely different (Fig. 2). The strong combustion of hydrocarbons in the secondary zone ensures a predominance of the homogeneous N_2O reduction by H radicals. This leads to an almost complete decomposition of N_2O in the secondary zone. In this context, it is crucial that the lignite char, because of its high reactivity, in contrast to hard coal char, is burned up very early in the secondary zone. Therefore, no new heterogeneous formation of N_2O can take place after completion of the hydrocarbon combustion and the corresponding depletion of H

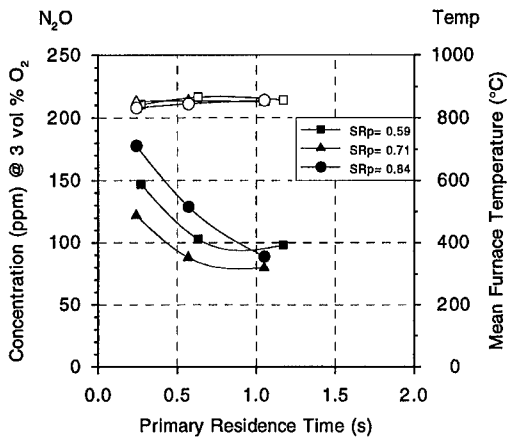

FIG. 9. Exhaust N_2O as a function of the primary zone residence time at various stoichiometric ratios in the primary zone (SR_p). Filled symbols: exhaust N_2O; hollow symbols: mean furnace temperature. Anthracite: τ_o = 2.4–2.7 s; SR_o = 1.1; Ca/S = 3.6.

radicals. For that reason, the exhaust N_2O concentration with lignite combustion is usually only a few parts per million.

Figure 5 shows that with the bituminous coal, the N_2O concentration in the secondary zone increases at the same time as NO decreases, similar to the low-volatile anthracite, if the primary residence time is short. The suppression of the devolatilization-dominated phase in the primary zone and the partial shift of the char combustion to the secondary zone, caused by the reduction of the primary residence time, lead to the predominance of heterogeneous N_2O formation in the secondary zone. The opposite happens in case of an extreme lengthening of the primary residence time (Fig. 3). The extensive devolatilization phase after the consumption of oxygen causes high C_xH_y concentrations in the exhaust gas of the primary zone. During the combustion of these hydrocarbons in the secondary zone, high concentrations of H radicals occur that, as with the lignite, cause a predominance of the homogeneous N_2O reduction. Because of the short residence time in the secondary zone, the further heterogeneous formation of N_2O is suppressed after completion of the hydrocarbon combustion. Therefore, the most efficient firing step to reduce the exhaust N_2O concentration is an increase of the primary residence time. This is shown for the anthracite in Fig. 9.

Finally, it should be pointed out that, as in the primary zone, nothing points to a considerable catalytic N_2O decomposition on CaO surfaces in the oxidizing regime of the secondary zone. The exhaust N_2O concentration is consequently not affected by the addition of limestone. The reason seems to be the overly short life of active CaO surfaces in the fluidized bed as compared to laboratory fixed bed tests.

Nomenclature

SR_o	overall stoichiometric ratio (−)
SR_p	stoichiometric ratio in the primary zone (−)
T_m	mean furnace temperature (°C)
τ_o	overall gas residence time in the furnace (s)
τ_p	gas residence time in the primary zone (s)
τ_s	gas residence time in the secondary zone (s)

REFERENCES

1. Reidick, A., "Experimentelle Untersuchung zur Schadstoffbildung bei der Kohleverbrennung in der zirkulierenden Wirbelschichtfeuerung," Dissertation, Ruhr-Universität Bochum, 1995.
2. Reidick, H., in *VDI-Berichte 601,* VDI, Düsseldorf, 1986, pp. 203–232.
3. Hansen, P. F. B. and Dam-Johansen, K., *Twelfth International Conference on Fluidized Bed Combustion,* ASME, 1993, pp. 779–787.
4. Hansen, P. F. B., Dam-Johansen, K., Bank, L. H., and Ostergaard, K., *Eleventh International Conference on Fluidized Bed Combustion,* ASME, 1991, pp. 73–82.
5. Hulgaard, T., Glarborg, P., and Dam-Johansen, K., *Eleventh International Conference on Fluidized Bed Combustion,* ASME, 1991, pp. 991–998.
6. Miller, J. A. and Bowman, C. T., *Prog. Energy Combust. Sci.* 15:287–338 (1989).
7. Tullin, C. J., Sarofim, A. F., and Beér, J. M., *Twelfth International Conference on Fluidized Bed Combustion,* ASME, 1993, pp. 599–609.

Twenty-Sixth Symposium (International) on Combustion/The Combustion Institute, 1996/pp. 3317–3324

EMISSIONS OF NITROGEN OXIDES FROM CIRCULATING FLUIDIZED-BED COMBUSTORS: MODELING RESULTS USING DETAILED CHEMISTRY

SHAKTI GOEL AND ADEL SAROFIM
Department of Chemical Engineering
Massachusetts Institute of Technology
Cambridge, MA 02139, USA

PIA KILPINEN AND MIKKO HUPA
Department of Chemical Engineering
Abo Akademi University, Turku 20520, Finland

An emissions model for a circulating fluidized-bed combustor (CFBC) has been developed. The model consists of a one-dimensional fluid dynamics model, an 8-reaction, heterogeneous mechanism, and an elaborate, 340-reversible-reactions homogeneous mechanism with 55 species accounting for the light hydrocarbons (C_1 and C_2) and the nitrogen chemistry. The mechanisms are based on independent kinetic measurements made in lab-scale studies. The rate constants have not been adjusted to better fit the circulating fluidized-bed experimental measurements. For a given set of input operation and design parameters, the model estimates the fluid dynamics parameters as a function of reactor height and calculates the species concentration profiles in the reactor. The model predictions for different species provide a satisfactory description of experimental observations available in the recent literature. The model also well describes the observation that the emissions of NO_x are either slightly higher or remain unchanged when biomass replaces coal as the fuel even though coal has ten times the bound nitrogen content of the biomass. When coal is fed to the reactor, a significant fraction of the NO formed is destroyed in situ. Destruction of NO in the CFBC is not significant for the case of biomass.

Introduction

There has been a growing need for understanding the formation and destruction mechanisms of nitrogen oxides in fluidized-bed combustors (FBCs). System modeling studies of circulating FBCs (CFBCs) have either used simplified global kinetics for the nitrogen chemistry or were aimed mainly at studying the fluid flow [1,2]. This study aims at developing an emissions model for a CFBC using a fluid dynamic model, which, while simple, describes the main features of the flow, and a detailed model for the NO_x and N_2O formation and destruction chemistry. The kinetic scheme consists of 340 reversible, homogeneous, elementary reactions involving 35 radical and 20 stable species, and 8 reactions for the heterogeneous chemistry. The rate constants of different reactions have been taken from independent work done under laboratory conditions by different research groups; no adjustments have been made in this work. The chemistry used for the CFBC model is actually similar to that used for the bubbling FBC model reported elsewhere [3]. The CFBC model, however, has completely different fluid dynamics. Furthermore, detailed measurements are available in the literature [4–6] for an industrial-scale CFBC which provides an opportunity to test the predictive ability of the model. The model predictions are compared with recent experimental studies on a 12-MWth CFBC to

1. test the trends for the concentration profiles with height of different species, viz., NO_x, N_2O, CO, CO_2, O_2, NH_3, and HCN, and
2. explain the effect of fuel variation on NO_x and N_2O emissions as coal is replaced with biomass.

The following sections provide a brief description of the chemistry of NO, NO_2, and N_2O formation and destruction, development of the emissions model, and the comparison of the model predictions with the available experimental data. This is followed by a study on the effect of variation in fuel type on emissions.

Model Development

Homogeneous Chemistry

The kinetic scheme used in the CFBC model consists of 340 reversible reactions involving 55 radical and stable species. These reactions describe the

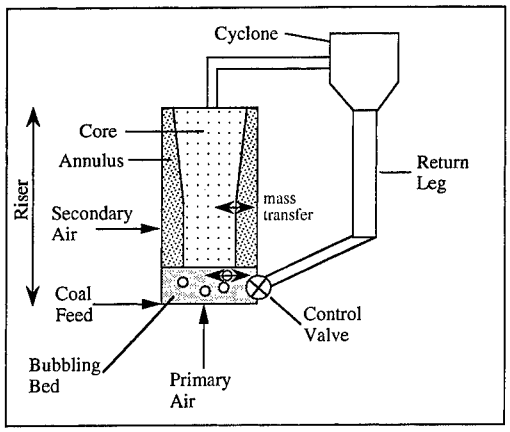

FIG. 1. Schematic of the CFBC model used in this work.

oxidation chemistry of C_1-C_2 hydrocarbons, HCN, and NH_3, and the submechanisms describing the interactions between hydrocarbons and nitrogen-containing species. The principal route to N_2O formation is via the oxidation of HCN, whereas NH_3 oxidation leads primarily to the formation of NO and NO_2 [7]. The reactions for the oxidation of HCN, NH_3, and CO were taken from Ref. 8. The kinetic schemes for the hydrocarbon oxidation and hydrocarbon-nitrogen interactions were taken from Ref. 9, and the thermodynamic data from Ref. 10.

Heterogeneous Chemistry

Nitrogen, which is bound as a heteroatom in moieties in coal containing aromatic pyridine and pyrrole rings [11], is released by the reaction of oxygen with these rings, resulting in an intermediate surface species, I, which then either splits to form NO (at a rate $k_1[\mathrm{I}]$) or reacts with NO to form N_2O (at a rate $k_2[\mathrm{I}][\mathrm{NO}]$). The fraction of the intermediate that goes to NO is $k_1/(k_1 + k_2[\mathrm{NO}])$ and that which goes to N_2O is $k_2[\mathrm{NO}]/(k_1 + k_2[\mathrm{NO}])$. The nitrogen oxides, in turn, may react with char or CO on char while diffusing out of the pores and get reduced to form N_2. This mechanism on the fate of char nitrogen has been critically tested [12] against an alternative hypothesis of slow HCN release during char combustion followed by oxidation in the gas phase to form NO and N_2O [13,14]. The experiments indicated that N_2O formation via slow devolatilization of char is negligible. Further details on the heterogeneous mechanism can be found in Refs. 15 and 16. Equation 1 represents the diffusion and reaction of species i inside the pores of a single char particle.

$$\mathcal{D}_{pi}\left(\frac{\partial^2[i]}{\partial r^2} + \frac{2}{r}\frac{\partial[i]}{\partial r}\right) + R_i = 0 \qquad (1)$$

where, $\mathcal{D}_{pi}$ is the pore diffusivity, $[i]$ is the concentration of species i and R_i is its net rate of formation (formation-destruction). The two boundary conditions required to solve equation 1 consist of a zero slope for the concentration profile at the center, and the external mass transfer condition at the particle surface. Equation 1 is solved simultaneously for O_2, CO, CO_2, NO, and N_2O using orthogonal collocation on finite elements [17]. The heterogeneous kinetic parameters were taken from Ref. 16 for Newlands bituminous coal.

Catalytic destruction of nitrous oxide on fly ash recirculated inside the CFBC loop was taken into account via the following reaction: $N_2O \rightarrow N_2 + \frac{1}{2}O_2$. Although it is known that the catalytic activity varies with ash composition, a single rate constant was used to account for the destruction reactions [18].

Since the gas chemistry considered here consists of many radical species, surface quenching of radicals was considered to be an important factor affecting the ignition of the volatiles. The quenching rate, R_{qi} for radical species i, was assumed to be controlled by external mass transfer and was calculated using $R_{qi} = k_g[i]_{\mathrm{bulk}}$, where k_g is the external mass transfer coefficient. The surface concentration of the radicals was assumed to be zero.

Fluid Dynamics Model

In order to understand the physical processes governing the emissions from FBCs, it is important to use a simple model for the fluid dynamics representing the major physical features. The CFBC loop studied in this paper consists of a riser, a cyclone, and a return leg, as shown in Fig. 1. The kinetic calculations reported in this paper are performed for the riser section of the loop. The model divides the riser into a bottom, dense bed consisting of bubbles, followed by a transient zone which merges into a dilute zone. The transient and dilute zones have a dilute core and a solid, rich annulus. The model calculates the particle velocities, void fraction, pressure drop, solid loading, diameter of the core, and gas/solid friction factors as a function of riser height. The system may experience pressure losses in the cyclone, the return leg, and the solids flow control device. The heights of the dense and dilute zones are calculated by assuming a total pressure drop of 15 kPa across the riser. Details on the fluid dynamic equations can be found in Refs. [3,19–21].

Mass Balance in the Combustion Chamber and Model Numerics

Any species entering a differential element of height dZ will either be destroyed or formed and will exit the element at a certain concentration level. The homogeneous chemistry will be active in the void fraction (ε), and the gas/solid reactions will occur in

the fractional space $(1 - \varepsilon)$. The mass balance for the i_{th} gas species over the differential element, therefore, yields

$$\frac{d[i]}{dZ} = \frac{Q}{U_{\text{b,e,c, or a}}}([i]_{\text{b or c}} - [i]_{\text{e or a}}) + \frac{\varepsilon}{U_{\text{b or c}}}\sum_{j=1}^{N_g}\alpha_{ij}R_{gj} + \frac{(1-\varepsilon)}{U_{\text{e or a}}\rho_{\text{char}}}\sum_{k=1}^{N_s}\beta_{ik}R_{si}C_{\text{char}} \quad (2)$$

where, Q is the mass transfer coefficient, C_{char} is the concentration of char, U is the velocity and subscripts b, e, c, and a represent bubble, emulsion, core, and annulus, respectively. ρ_{char} is the char density, α_{ij} is the stoichiometric coefficient for the j_{th} gas phase reaction, and β_{ik} is the stoichiometric coefficient for the k_{th} heterogeneous reaction. R_g and R_s represent the homogeneous and heterogeneous rates, respectively. A mass balance for the solid carbon phase over the differential element yields the following equation:

$$\frac{dC_{\text{char}}}{dZ} = -\frac{R_{\text{oxid}}C_{\text{char}}}{\rho_{\text{char}}U_p} \quad (3)$$

where, U_p is the particle velocity. There are 55 equations of the equation 2 type for 55 different gaseous species considered in this model, and one equation of equation 3 type for char carbon. These 56 equations are coupled, first order, nonhomogeneous, nonlinear, ordinary differential equations and are solved simultaneously for each species.

The combustion chamber is divided into N differential elements of different widths. Time splitting technique was employed and the heterogeneous and the homogeneous chemistries were integrated separately. This approach is mathematically justified since the time scales for the two chemistries and the convective flow are very different [22]. The single particle model described earlier was used to solve the five equations of equation 1 type. Surface concentrations were estimated for the five species, and the overall heterogeneous reaction rates based on the volume of the char particles were calculated [3]. Surface concentrations were required to estimate the effectiveness factor for the non-first-order reactions. A fourth-order Runge-Kutta method was used to integrate the heterogeneous chemistry. The gas-phase chemistry was integrated using the SENKIN software [23].

Model Simulations

The emissions model for a CFBC was tested by comparing its prediction of gas-phase species profiles with the measurements made in a 12-MWth CFBC [4,5], and also by showing the effect of fuel type [6] on emissions. The following simplifying assumptions were made in the model simulations:

1. Plug flow for gases and solids
2. Bubbles free of any solids
3. Instantaneous devolatilization of fuel at the reactor bottom
4. Immediate mixing of the volatiles with the feed air
5. Complete penetration and instantaneous mixing of secondary air with reactor gases
6. Volatile content of coal is 40% on an ash-free, dry basis
7. The nitrogen to carbon ratio of char and volatiles is the same as that of the parent coal

The split between the carbonaceous products of devolatilization was assumed to form 50% CH_4, 25% C_2H_4, and 25% CO. These numbers give the concentrations of hydrocarbon species measured experimentally at the bottom of the reactor. Other species formed during devolatilization were H_2, H_2O, NH_3, and HCN. As per the experimental design, the limestone feed and fly ash recycle from secondary cyclone were not considered [4,5]. The model calculations were performed for the design and operating parameters given in Table 1. The initial step of the simulations was to determine the primary air and coal feed rates on the basis that total thermal power generated from the fed coal (volatiles + char) was 9 MW.

Comparison with the Experimental Data

Figure 2 shows the model predictions for the NO_x ($NO + NO_2$), N_2O, HCN, and NH_3 axial concentration profiles. The experimental data represent the centerline concentrations and are not averaged over the bed cross section. The model predicts the trends of the experimental measurements which exhibit a rapid increase in the NO_x concentration at the bottom of the bed followed by a continuous decay, whereas N_2O shows a continuous increase. The model-predicted profiles of NO and N_2O are shifted to lower heights relative to the experiment and level off before those observed experimentally. This shift is due to the assumption that the volatiles are released instantaneously at the bottom of the bed and then mix completely with the air. This leads to the ignition of the volatiles taking place earlier than experimentally observed. Oxidation of NH_3 is found to form high levels of NO_2 initially which is subsequently reduced to form NO and N_2 via the homogeneous reactions. A significant fraction of NO is also generated by char oxidation. Subsequent reaction of NO with char leads to the formation of N_2O. Since the kinetic parameters for the char oxidation vary for different coals, a study was carried out in which the heterogeneous kinetic parameters and mass transfer coefficients were changed within the

TABLE 1
Conditions in the simulations

Riser height = 13.5 m	Riser c.s. area = 2.9 m^2
Secondary air feed point = 2.2 m	Temperature = 850°C
Operating pressure = 1 bar	Primary stoich. ratio = 0.75
Coal feed rate = 1150 kg/h	Char recycle = 850 kg/h
Excess air ratio = 1.2	Limestone feed = none
Coal (bituminous)	Biomass (wood chips)
wt.%: C = 79%, N = 1.6%	wt.%: C = 50%, N = 0.14%
$N_{vol,coal}$ = 40% of total N	$N_{vol,bio}$ = 80% of total N
NH_3, HCN = 37.5(% N_{vol}) each	NH_3 = 90(% N_{vol})
Rest N_2	Rest N_2

bounds of the literature values. The results show a better fit to the data, reflecting on the fact that the model can be fitted to reproduce the experimental observations. This, however, was not the aim of the study. Figure 3 shows the profiles of net heterogeneous rates of formation (formation-destruction) of NO and N_2O in the emulsion + annulus, and the net homogeneous rates of NO and N_2O formation in the bubbles + dilute core. In the solid-rich regions (emulsion phase and the dense annulus) of the primary zone, the net heterogeneous rates are initially positive and then become negative because the NO and and N_2O are first formed in the presence of high O_2 levels and are then destroyed via the heterogeneous reactions with char or with CO on char [24]. The NO profile in the bubbles also shows a maximum. The concentration of NO in the solid-free bubbles decreases due to its diffusion into the emulsion where it is heterogeneously destroyed. Figure 3 also shows that the net homogeneous formation rates for NO remains positive throughout the primary zone and that the destruction of NO occurs mainly via the heterogeneous reactions. One of the heterogeneous destruction reactions of NO leads to the formation of N_2O. N_2O goes through the same fate as NO in the char-rich regions. Its concentration profile in the bubble phase and the dilute core, however, exhibits a continuous increase. This increase is due to its formation from the oxidation of HCN, which continuously diffuses from the solid-rich region into the gas-rich region. The amount of N_2O generated from the homogeneous reactions compensates for the decrease in its concentration due to the diffusion into the emulsion or the annulus regions. In other words, the zone below the secondary air feed point becomes reducing for NO after a certain height but remains oxidizing for N_2O.

Figure 4 shows that the profiles of O_2, CO, and CO_2 are well described and their trends are in agreement with those of the experimental data. The model predicts earlier oxidation of CO and its profile is shifted to lower heights in the bed. Although all the volatile species ignite nearly at the same time, in practice, incomplete mixing will lead to a delay in the oxidation so that the oxidation of all volatile species may not occur completely in the primary zone. Also, if the fluidization velocity is high, the char particles may be carried over to the secondary oxidation zone (after the secondary air feed point). The primary zone, therefore, may have excess oxygen available. This observation is supported by Fig. 4 which shows that the oxygen levels do not drop to zero in the bubbles/core below the secondary air feed point. Experimental data for O_2 and CO_2 have been plotted both for the centerline and near the walls. The model predictions lie in between the two extremes. The model assumes that the secondary air mixes instantaneously with the gases from the primary zone. In practice, however, the mixing will occur over a finite height.

Since the model uses a detailed homogeneous mechanism, one can examine how the radical concentrations vary over the riser height and how they influence the formation and destruction of NO_x and N_2O. Figure 5 shows the concentration profiles of O, OH, H, and HO_2 as a function of reactor height. The concentration profiles of OH, HO_2, O, and H radicals show a peak when there is a sharp decrease in the hydrocarbon, NH_3, and HCN concentrations, signifying that the homogeneous chemistry is active here. At this location, a sharp increase in the net homogeneous rate of formation of NO and N_2O is obtained (Fig. 3). The steep decrease in the concentrations after the peak suggests the consumption of the hydrocarbons and the rapid consumption of radicals either by self-recombination in the gas phase or by quenching on the particle surface. The consumption of volatile nitrogen species leads to a peak in NO_2, NO, and N_2O profiles in both the solid-rich and gas-rich regions. The NO and N_2O concentrations in the char-rich region, however, show a rapid decrease due to their heterogeneous reactions over

char (Fig. 2). The radical concentrations were negligible in the emulsion and the annulus due to the surface quenching reactions. The model has shown a capability of showing the general trend in the vertical concentration profiles of gaseous species, with the major discrepancies being accounted for by the assumptions of instantaneous release and mixing of the volatiles at the distributor, and instantaneous mixing of the secondary air with the gases from the primary zone. The next test is on its ability to simulate results on NO_x emissions of substitution of biomass for coal as a fuel.

Changing Fuel from Coal to Biomass

Previous experimental CFBC studies have shown that NO_x emissions either remain unchanged or even increase somewhat when coal is replaced by biomass [6], which was explained qualitatively by the effect of fuel variation on the NO_x destruction rates. For the present study, the thermal input to the CFBC was kept the same irrespective of the fuel type. Other conditions for simulations are given in Table 1. Figure 6 shows the calculated and observed centerline profiles [6] of NO_x and N_2O as a function of reactor height. The data have been plotted to present the trends in the NO_x profiles. The figure exhibits that the exit levels of NO_x are higher when biomass is the fuel. Only a small fraction of NO_x formed during coal combustion exits the top of the riser. However, when biomass is burned, a significant amount of NO formed from NH_3 oxidation survives destruction and is released in an amount comparable to that from coal combustion. On the other hand, the emissions of N_2O are significantly reduced when biomass is the fuel. This is due to the near unavailability of char nitrogen and low levels of HCN formation during devolatilization.

Figure 7 presents the profiles of the net homogeneous and heterogeneous rates of formation of NO during the combustion of coal and biomass as a function of height in the riser. The heterogeneous rates remain positive during biomass combustion, suggesting that the heterogeneous destruction is not an important factor governing the emissions of nitrogen oxides. This means that NO is continuously formed when biomass is burned. The heterogeneous rates of NO formation, however, become negative as oxygen is consumed during coal combustion, meaning that NO is formed initially from char and volatile nitrogen. It is then destroyed in significant amounts by the heterogeneous reactions with char. During biomass combustion, the concentration of char itself is not high enough for the heterogeneous chemistry to be of any importance. During coal combustion, large amounts of NO and NO_2 are formed. NO_2 formed from NH_3 oxidation is either destroyed homogeneously to form N_2 or is converted to NO. NO is then destroyed by heterogeneous reactions which

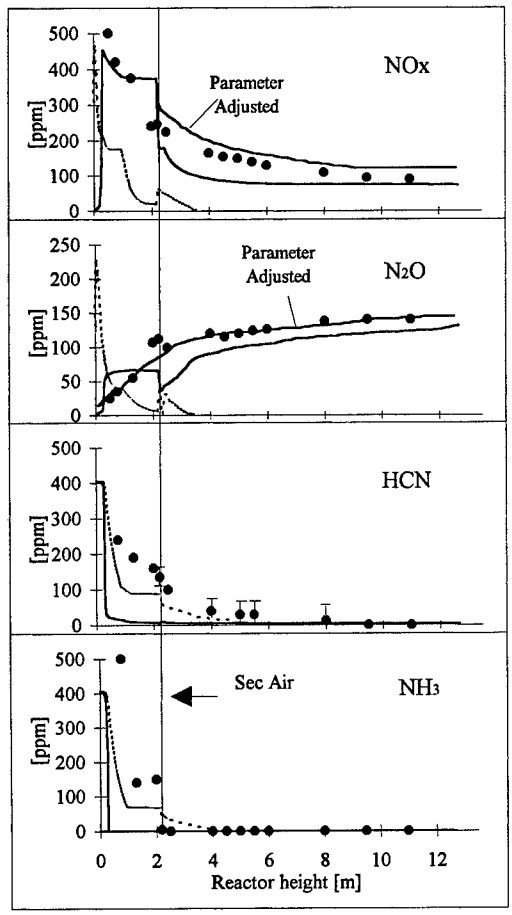

FIG. 2. Comparison of model predictions with the experimental data [5] for NO_x, N_2O, HCN, and NH_3; ——, bubble and core; – – –, emulsion and annulus; ●, NO_x, N_2O, NH_3, and HCN centerline data. Best fit concentration profiles were determined for NO_x and N_2O by adjusting the kinetic parameters of the heterogeneous mechanism and the mass transfer coefficients, showing that the model can fit the data.

dominate those of formation. It is important to note that the nitrogen content may vary with biomass type. Depending on the NH_3 levels in the volatile matter, the NO_x emissions may vary when different types of biomass are fed to the reactor. As a result, the emissions of NO_x from biomass combustion may either compare to or exceed those from coal combustion.

Conclusions

An emissions model based on a detailed kinetic scheme and fundamental and independent studies has been developed for a circulating fluidized-bed

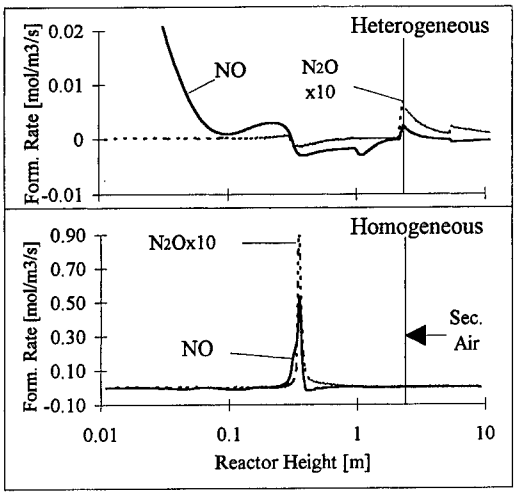

FIG. 3. Net homogeneous and heterogeneous rates of formation (formation-destruction) of NO and N_2O.

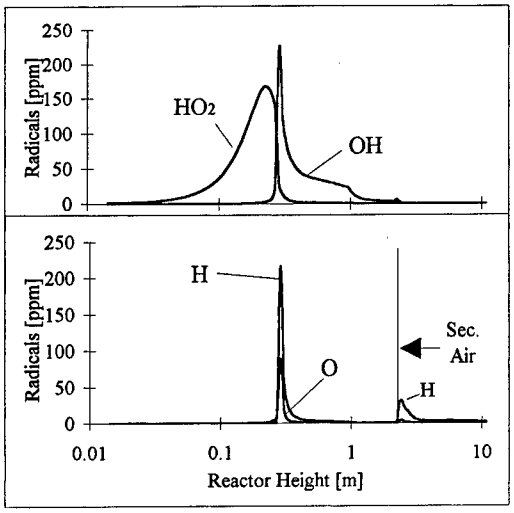

FIG. 5. Concentration profiles of O, H, OH, HO_2.

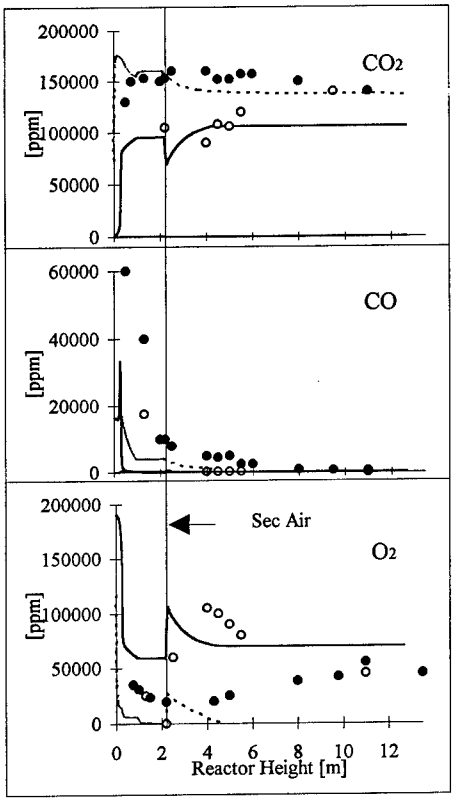

FIG. 4. Comparison of model predictions with the experimental data [4] for O_2, CO, and CO_2; ——, bubble and core; – – –, emulsion and annulus; ●, centerline data; ○, wall region data.

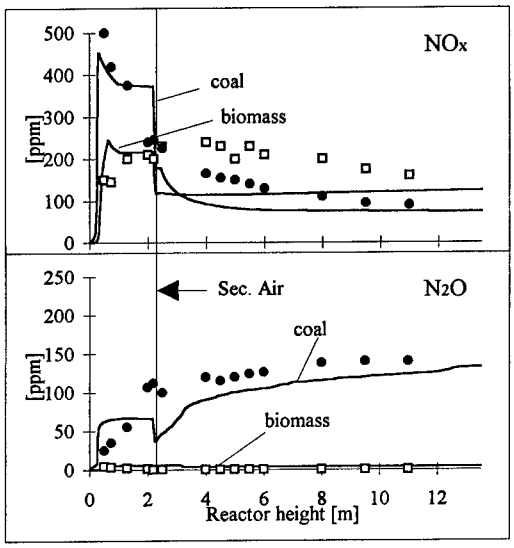

FIG. 6. Comparison of concentration profiles of NO_x and N_2O from coal combustion with those obtained from biomass combustion. The model predictions have been compared against the experimental data [6]; ●, centerline coal data for NO_x and N_2O; □, centerline biomass (wood chips) data for NO_x and N_2O.

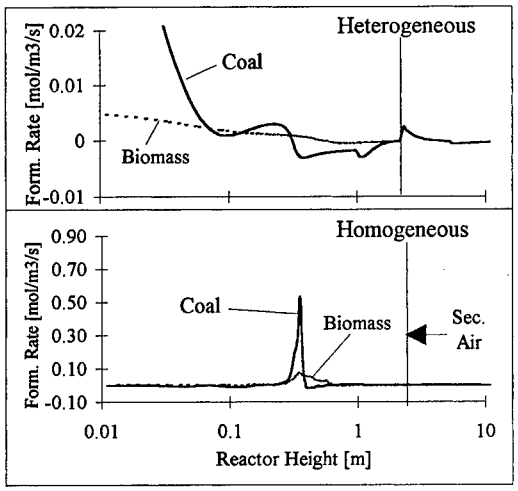

FIG. 7. Net homogeneous and heterogeneous rates of formation (formation-destruction) of NO during coal and biomass combustion.

combustor. The model was successfully tested against experimental data on both the vertical distribution of gas phase constituents in a CFBC riser and the effect on NO_x emissions of switching fuel from coal to biomass. Destruction reactions govern the emissions of nitrogen oxides when coal is the fuel. The destruction chemistry, however, is not the controlling factor when biomass is burned, and the emissions of nitrogen oxides are governed primarily by the formation reactions. The net result is that the exit levels of NO_x do not vary much when the fuel is changed from coal to biomass. Since only a small fraction of the volatile nitrogen is converted to HCN when biomass is burned and the resulting char concentration (hence, the amount of char nitrogen) is negligible, the levels of nitrous oxide released are insignificant. Conversely, when coal is burned, both the char and the volatile nitrogen contribute significantly to the N_2O emissions. The value of the model is that it provides mechanistic insights on which pathways dominate the emissions of NO_x from CFBC, insights that can be used to design optimal control strategies for NH_3 injection, hydrocarbon injection, or air staging.

Acknowledgments

The authors are grateful to Prof. L. Glicksman of MIT for his useful comments on the fluid dynamics of the model. Prof. B. Leckner and his research group at Chalmers University of Technology are acknowledged for providing the biomass data before its publication. Shakti Goel wishes to thank the PEEER group at MIT for awarding him the Martin Environmental Fellowship. The financial support by the Academy of Finland, Ahlstrom Corp., Tampella Power, Wartsila Diesel Int., Ltd. and the U.S. Department of Energy under contract DE-PS22-94PC94200 is gratefully acknowledged. The work has also been a part of the Finnish Combustion and Gasification Research Program, LIEKKI.

REFERENCES

1. Hannes, J., Renz, U., and van den Bleek, C., *Proc. 13th Intl. Conf. Fld. Bed Comb.*,ASME, 1995, pp. 287–296.
2. Tsuo, Y., Lee, Y., Rainio, A., Hyppanen, T., *Proc. 13th Intl. Conf. Fld. Bed Comb.*, ASME, 1995,pp. 1059–1069.
3. Goel, S., Beer, J., and Sarofim, A., *Proc. 13th Intl. Conf.Fld. Bed Comb.*, ASME, 1995, pp. 887–898.
4. Amand, L., Leckner, B., and Andersson, S., *Energy, Fuels* 5(6):815–823 (1991).
5. Amand, L., "Nitrous Oxide Emission from CFBC," Ph.D. Dissertation, Chalmers University of Technology, Göteborg, Sweden (1994).
6. Leckner, B., Amand, L., and Lyngfelt, A., "Combustion of Volatiles in a CFB Combustor", 2nd European Meeting of Chemical Industry and Environment, Alghero, Italy, Sept. 1996.
7. Kilpinen, P. and Hupa, M., *Combust. Flame* 85:94–104 (1991).
8. Glarborg, P., Dam-Johansen, K., and Kristenses, P., Gas Research Institute Contract No. 5091-260-2126, Denmark, Dec. 1993.
9. Glarborg, P. and Hadvig, S., *Development and Test of a Kinetic Model for Natural Gas Combustion*, Report, Nordic Gas Technology Center, Denmark, March 1991.
10. Kee, R., Rupley, F., and Miller, J., Report SAND87-8215B, Sandia National Labs, Livermore, CA, 1990.
11. Hayatsu,R., Scott, R., Moore, L., and Studier, M., *Nature* 257:378–380 (1975).
12. Goel, S., Zhang, B., and Sarofim, A., *Combust. Flame* 104:213–217 (1996).
13. Amand, L. and Leckner, B., *Energy Fuels* 7:1097–1107 (1993).
14. Moritomi, H. and Suzuki, Y., *Proc. 6th Intl. Workshop on N_2O Emissions*, Turku, Finland, 1994, pp. 263–284.
15. Tullin, C., Goel, S., Morihara, A., Beer, J., and Sarofim, A., *Energy Fuels* 7:796–802 (1993).
16. Goel, S., Morihara, A., Tullin, C., and Sarofim, A., *Twenty-Fifth Symposium (International) on Combustion*, The Combustion Institute, Pittsburgh, 1994, pp. 1051–1059.
17. Carey, G. and Bruce, A., *Chem. Eng. Sci.* 30:587–596 (1975).
18. Johnsson, J., *Fuel* 73 (9):1398–1415 (1994).
19. Yang, W., in *Circulating Fluidized-Bed Technology, II*, (P. Basu and J. F., Large, Eds.), Pergamon Press, New York, 1988, pp. 181–191.
20. Lewis, W., Gilliland, E., and Lang, P., *CEP Symp. Ser.* 58(38):65–76.

21. Glicksman, L., Yule, T., and Dyrness, A., *Chem. Eng. Sci.* 46:1561–1571 (1991).
22. Oran, E. and Boris, J., *Numerical Simulation of Reactive Flow*, Elsevier, New York, 1987.
23. Lutz, A., Kee, R., Miller, J., Report SAND87-8248 Sandia National Labs, Livermore, CA, 1987.
24. Chan, L., Sarofim, A., and Beér, J., *Combust. Flame* 52:37–45 (1983).

COMMENTS

A. N. Hayhurst, Cambridge University, UK. Could you report any more details of the sensitivity analyses, with particular respect to identifying the more important chemical reactions of fluidization processes? For instance, how important is inter-phase transport?

Author's Reply. A detailed set of sensitivity calculations will be presented at the 14th FBC conference which will be held in May 1997, in Vancouver, Canada. The aim of this paper will be to determine important pathways at different conditions. Parametric studies were carried out earlier using a "bubbling" fluidized bed model based on detailed kinetics schemes [1].

REFERENCE

1. Goel, S., Beer, J., and Sarofim, A., *J. Inst. Energy*, 1996, accepted.

Twenty-Sixth Symposium (International) on Combustion/The Combustion Institute, 1996/pp. 3325–3334

THE NO AND N_2O FORMATION MECHANISM DURING DEVOLATILIZATION AND CHAR COMBUSTION UNDER FLUIDIZED-BED CONDITIONS

FRANZ WINTER, CHRISTIAN WARTHA, GERHARD LÖFFLER AND HERMANN HOFBAUER
Vienna University of Technology
Vienna, Austria

In an exclusively electrically heated, laboratory-scale, fluidized-bed combustor (MM-FBC) made of quartz glass, the formation rates of NO, N_2O, and HCN are studied by using a high performance FT-IR spectrometer in combination with a long-path, low-volume gas cell. The emission characteristics of single, spherical fuel particles (5–15 mm in diameter) of bituminous coal, subbituminous coal, and beech wood are studied. The bed temperature is varied between 600 and 900°C. The fluidizing velocity is 0.68 m/s and the oxygen partial pressure is varied between 0.05 and 21 kPa. The bed material is silica sand with a mean diameter of 225 μm.

Besides changing combustion conditions and fuel type and diameter, an iodine addition technique is applied to study the relative importance of the homogeneous and the heterogeneous chemistry during devolatilization and char combustion. Iodine addition suppresses the radical concentrations to equilibrium levels and has proven as a very effective method for kinetic measurements.

With a semitheoretical model, the measurement results are discussed and reaction paths are evaluated.

The formation characteristics during devolatilization can be explained mainly by the homogeneous HCN oxidation and NO and N_2O formation. NO and N_2O formation during char combustion consists of two different paths. NO is mainly heterogeneously formed by char-nitrogen oxidation. But a volatile species, which has been identified as HCN, is simultaneously released in low concentrations. This species is homogeneously oxidized to NCO which further reacts with the heterogeneously produced NO to form N_2O.

Introduction

To minimize the emission of pollutants, much effort has been put into changing the fuel or the operating conditions of fluidized-bed combustors (FBCs) including bed temperature, bed material, air staging, and excess air. These results can be found in the literature (an overview is given in Ref. 1) but not once do they show controversial trends. For further progress, a deep understanding of the principal formation and destruction mechanism of the pollutants, especially NO and N_2O, is essential.

NO and N_2O emissions are dependent on the fuel and fuel characteristics, the complex homogeneous and heterogeneous formation and destruction paths, temperature and residence times, fluid dynamics, combustor geometry, heat and mass transfer, and so forth [2,3]. Because of these complex interrelations, it is necessary to study these processes separately and to analyze their relative importance. Accompanying laboratory-scale experiments are essential for the correct interpretation of data from pilot plants or industrial boilers.

This study focuses on the formation of NO and N_2O during devolatilization and char combustion of single fuel particles under FBC conditions. In single fuel particle experiments, no fuel particle–fuel particle interactions exist and the emissions can be directly related to the single fuel particle. The temperatures of the single fuel particles are measured by implanting thermocouples and do not have to be calculated. Extensive heat and mass transfer studies provide a profound basis on Nusselt and Sherwood number correlations. A flexible, laboratory-scale multimode, fluidized-bed combustor (MM-FBC) is used where combustion conditions are well defined and can be independently varied. The MM-FBC has been optimized to obtain formation rates.

In the literature, there exists some work investigating NO and N_2O formation of single coal particles under FBC conditions [4–7]. But there is no deep understanding of the fractional conversion of fuel nitrogen to NO and N_2O during devolatilization and char combustion [8]. Especially concerning char combustion, different hypotheses are discussed in literature [9] explaining NO and N_2O formation. One hypothesis claims that N_2O is strictly heterogeneously formed by the direct oxidation of the fuel nitrogen. In other hypotheses, NO is assumed to react with char-nitrogen. N_2O can also be formed homogeneously by reaction of a released volatile species (e.g., HCN) with NO.

The aim of this work is to get a deeper insight into NO and N_2O formation of different fuels during

TABLE 1
Proximate and ultimate analysis of the fuels. Parentheses indicate values after devolatilization.

	Bituminous coal as received	Subbituminous coal as received	Beech wood as received
Proximate analysis	(After devol.)	(After devol.)	(After devol.)
Heat value (MJ/kg)	32	16	17.5
Density (kg/m^3)	1524 (832)	1250 (600)	670 (150)
Volatile matter (w-%)	30	32.2	81.7
Moisture (w-%)	6.0	25.3	5.6
Ash content (w-%)	2.4	12.3	0.3
Fixed carbon (C-fix) (w-%)	61.6	30.2	12.4
Ultimate analysis	(After devol.)	Water ash free	
Carbon (w-%)	86.8 (85.65)	68.11 (73.1)	49.76 (87.31)
Hydrogen (w-%)	4.27 (0.94)	2.84 (1.05)	5.94 (1.63)
Nitrogen (w-%)	1.48 (1.76)	0.64 (0.9)	0.11 (0.24)
Sulfur (w-%)	0.5 (0.32)	1.52 (0.73)	<0.02 (<0.02)
Oxygen diff. (w-%)	6.95 (11.3)	26.88 (24.2)	44.17 (10.83)

devolatilization and char combustion under fluidized-bed combustor conditions. The transient NO and N_2O emission behavior is characterized and its dependencies on bed temperature and oxygen concentration are shown. To study the relative importance of the radical chemistry during devolatilization and char combustion, an iodine addition technique has been developed and proven as a very useful investigation tool.

Experimental

Single, spherical particles are formed from three different solid fuels: a bituminous coal, a subbituminous coal, and beech wood. The fuel particle diameters are 5, 10, and 15 mm. The proximate and the ultimate analyses are given in Table 1.

The MM-FBC is made of quartz glass to minimize the catalytic reactivity of the walls and to allow observation inside the combustor. The inner diameter of the main quartz tube is 35 mm and the height is 240 mm (Fig. 1). Ni/CrNi thermocouples are used at different positions to control the combustion temperature. It is exclusively electrically heated by two heating shells. The bed temperature is varied between 600 and 900°C. The bed material is silica sand with a mean diameter of 225 μm. The static bed height is about 40 mm. Air/nitrogen mixtures are used to vary the oxygen partial pressure of the fluidizing gas between 0.05 and 21 kPa. The superficial velocity is 0.68 m/s and controlled by two mass-flow controllers. In the case of iodine addition, solid iodine was placed in a flask which was warmed up in a water bath. Thus, the iodine sublimated and enriched the fluidizing gas which was lead through the flask (Fig. 1).

To obtain the instantaneous concentrations of various gaseous species (CO_2, CO, CH_4, other hydrocarbons, NO, N_2O, HCN, and other species) in the flue gas, a high-performance FT-IR spectrometer (BIO-RAD, FTS 60A) was used. The spectrometer

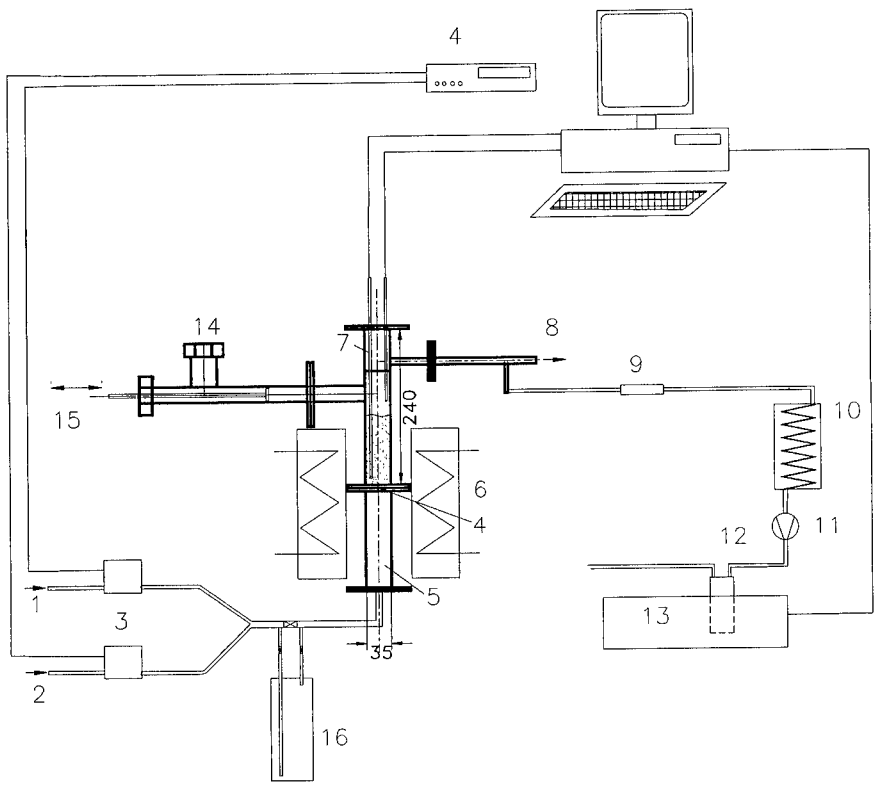

FIG. 1. The experimental set-up of the multimode, fluidized-bed combustor (MM-FBC): 1,2, inlet of the fluidizing gas (air, nitrogen); 3, mass-flow controllers; 4, display for the mass flow; 5, preheating zone; 6, heating shells; 7, thermocouple; 8, to the chimney; 9, filter; 10, cooler; 11, pump; 12 and 13, gas cell and FT-IR spectrometer; 14 and 15, fuel inlet; 16, flask for iodine addition in a water bath.

is combined with a long-path, low-volume gas cell (Foxboro LV7, cell volume = 223 cm^3, optical path length = 7.25 m). The design of the MM-FBC, the operating conditions, the sampling line, the FT-IR recording options, and the gas-cell have been optimized to obtain formation rates (i.e., short residence times, high scan rates of 1.2 scans/s at a high resolution of 0.5 cm^{-1}). NH_3 has not been detected in significant amounts by the FT-IR, possibly due to adsorption in the sampling line, its low concentration, and time dependence.

The single fuel particles were fed into the MM-FBC and their formation rates as well as the operating conditions were recorded during devolatilization and char combustion. Additionally, the ignition and the extinction of the flame of the volatile matter, the phenomenological behavior, fuel particle temperatures, and the fluid-dynamical behavior have been investigated. Mass balances of the fuel carbon lead to kinetic data of devolatilization and char combustion. These results have been reported elsewhere [10–12] and were used whenever necessary as a basis to predict the NO and N_2O formation rates.

Experimental Results

Bituminous Coal

Figure 2 shows the typical concentration histories of CO_2 and the nitrogen-containing species NO, N_2O, and HCN during devolatilization and char combustion of a single bituminous coal particle with an initial diameter of 10 mm at 800°C and an oxygen concentration of 10 kPa in the MM-FBC.

During devolatilization, the rapid increase of all species can be clearly seen. The NO concentration in the flue gas reaches its maximum of about 190 ppm ± 10 ppm after the particle has been in the combustor about 60 s (after the first third of the devolatilization period). The HCN concentration also increases rapidly but its maximum is only slightly above 20 ppm ± 2 ppm. These two peaks are followed by the increase of N_2O to a maximum of about 20 ppm ± 2 ppm. With decreasing amount of volatile matter in the fuel particle, the formation rates of all species decrease toward their corresponding char combustion levels. Integrating the formation

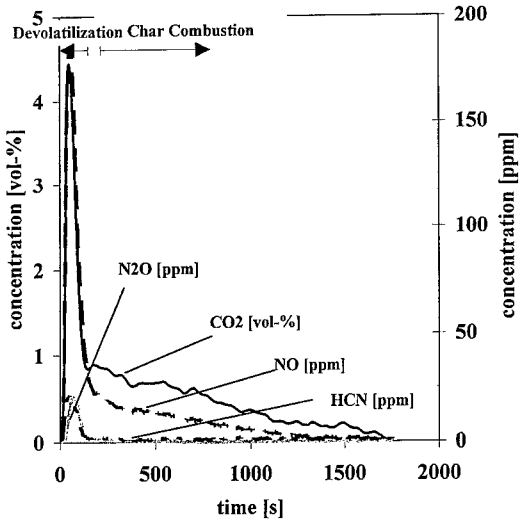

FIG. 2. Concentration histories of CO_2, NO, N_2O, and HCN during devolatilization and char combustion of a 10-mm bituminous coal particle at 800°C and 10 kPa oxygen partial pressure in the fluidizing gas in the MM-FBC.

rates over the devolatilization period leads to the percentage of conversion of the volatile nitrogen, that is, the nitrogen that is released during devolatilization (28 w-% of the fuel nitrogen), to NO (38 w-%), N_2O (8 w-%), and HCN (4 w-%) (refer to Table 2).

During char combustion, all formation rates are at low levels compared to the formation rates during devolatilization. In the first fifth of char combustion, the concentration levels are about 20 ppm ± 2 ppm NO, 2 ppm ± 0.5 ppm N_2O, and 2 ppm ± 0.5 ppm HCN and they are steadily decreasing. But the time scale of char combustion is longer than the time scale of devolatilization (about 10 times) and compensates to a certain extent the low formation rates. Integrating the formation rates over the char combustion period leads to the percentage of conversion of the char nitrogen, that is, the nitrogen that is released during char combustion (72 w-% of the fuel nitrogen), to NO (16 w-%), N_2O (1.5 w-%), and HCN (1.4 w-%) (refer to Table 2). The relative importance of devolatilization and char combustion for NO, N_2O, and HCN formation can be found by comparing the amount of fuel nitrogen converted to NO, N_2O, and HCN for devolatilization (14 w-%) and char combustion (14 w-%) (Table 2). This reveals that devolatilization and char combustion are of nearly equal importance for the formation of these species.

Varying combustion conditions, the above-mentioned percentages of conversion (listed in Table 2) will change. Increasing the bed temperature during devolatilization from 600 to 900°C increases the conversion of volatile nitrogen to NO from 6 to 49 w-% (of the volatile nitrogen), whereas HCN decreases from 20 to 2 w-%. Conversion to N_2O stays at low levels between 600 and 700°C (1–2 w-%) but reaches a maximum around 800°C (8 w-%) and slightly declines toward 7 w-% at 900°C. Increasing the oxygen partial pressure in the fluidizing air from 0.05 to 21 kPa leads, in the beginning, to an increase of the conversion to NO from 6 to 38 w-% (around 10 kPa), then it slightly decreases toward 33 w-%. N_2O slightly increases from 1 to 9 w-%, whereas HCN slightly decreases from 9 to 2 w-%.

For char combustion, a temperature increase from 600 to 900°C increases the conversion of the char nitrogen to NO from 5 to 26 w-% (of the char nitrogen), whereas the conversion to HCN decreases from 7 to 1 w-%. The conversion to N_2O stays at low levels; a maximum can be found about 800°C (1.5 w-%). Varying the oxygen partial pressure from 5 to 21 kPa, the conversion to NO decreases from 31 to 16 w-% (at 10 kPa) but, at higher oxygen levels, increases to 24 w-% (at 21 kPa) again. A slight minimum can also be found at 10 kPa in the case of char-nitrogen conversion to N_2O (1.5 w-%). The conversion to HCN continuously decreases from 4 to 1 w-% (at 21 kPa).

An iodine addition technique has been developed and proven to be a very successful tool for studying the relative importance of the radical chemistry during devolatilization and char combustion of a single fuel particle under FBC conditions. Enriching the fluidizing gas with iodine vapor (concentration levels in the MM-FBC are about 1000 ppm) leads to dramatic changes of the species concentrations but does not effect the heterogeneous carbon conversion rates; neither changes of the devolatilization time nor changes of the char burnout have been found. Contrary to the heterogeneous chemistry, the homogeneous is effected: flame ignition is inhibited and the CO levels increase whereas the CO_2 levels slightly decrease. This characteristic behavior is based on the inhibiting effect of iodine. It suppresses the radical concentrations to equilibrium levels and slows down radical reactions (e.g., the CO-OH oxidation reaction, compare with Ref. [13]).

Figure 3 shows the strong effects of iodine addition during devolatilization. The NO concentration dramatically decreases, N_2O completely vanishes, whereas the HCN level doubles.

Figure 4 shows the effects of iodine addition on NO, N_2O, and HCN during char combustion. The instantaneous conversion of the fuel nitrogen to NO, N_2O, or HCN is defined as the instantaneous ratio of the fuel nitrogen measured as NO, N_2O, or HCN to the released amount of carbon (as CO_2, CO, CH_4, and hydrocarbons). Furthermore, this ratio is normalized by division of the nitrogen to carbon ratio of the fuel (N/C, see Table 2). The carbon conversion of the fuel particle is obtained by measuring the

TABLE 2

The fuel-nitrogen-to-carbon ratio before and after devolatilization (in parentheses). The increase of this ratio after devolatilization. The splitting of the fuel nitrogen in volatile and char nitrogen. The nitrogen conversion to NO, N_2O, and HCN during devolatilization on the basis of volatile nitrogen and fuel nitrogen. The summarized fuel-nitrogen conversion to NO, N_2O, and HCN during devolatilization. The same for char combustion.

	Bituminous coal (After devol.)	Subbituminous coal (After devol.)	Beechwood spheres (After devol.)
N/C [1]	0.017 (0.021)	0.0094 (0.012)	0.0021 (0.0027)
N/C − change (%)	24	28	29
Volatile-N (w-%)	28	26	68
Char-N (w-%)	72	74	32
Devolatilization			
NO/vol-N (w-%)	38 ± 3	40 ± 5	28 ± 3
NO/fuel-N (w-%)	11 ± 1	10 ± 2	19 ± 3
N_2O/vol-N (w-%)	8 ± 1	3 ± 2	0.7 ± .2
N_2O/fuel-N (w-%)	2 ± .5	1 ± .5	0.5 ± .2
HCN/vol-N (w-%)	4 ± 1	7 ± 2	10 ± 2
HCN/fuel-N (w-%)	1 ± .5	2 ± .5	7 ± 2
N to (NO, N_2O, HCN)/fuel-N (w-%)	14 ± 2	13 ± 3	26 ± 5
Char combustion			
NO/char-N (w-%)	16 ± 2	18 ± 2	31 ± 3
NO/fuel-N (w-%)	12 ± 2	13 ± 2	10 ± 2
N_2O/char-N (w-%)	1.5 ± .5	0.5 ± .2	4 ± 2
N_2O/fuel-N (w-%)	1.0 ± .5	0.3 ± .2	1.5 ± 1
HCN/char-N (w-%)	1.4 ± .5	3.5 ± .5	13 ± 2
HCN/fuel-N (w-%)	1.0 ± .5	2.5 ± .5	4 ± 1
N to (NO, N_2O, HCN)/fuel-N (w-%)	14 ± 3	16 ± 3	15.5 ± 4

carbon-containing species in the flue gas and by integrating them over time. After devolatilization and the first stages of char combustion, iodine was added to the fluidizing gas. The instantaneous conversion to NO only slightly increases whereas the conversion to N_2O drops to zero. The conversion to HCN significantly increases.

Comparison to Other Fuels

To study the influence of the fuel type on the NO, N_2O, and HCN formation characteristics, additional measurements with spherical subbituminous and beech wood particles (10 mm in diameter) were performed at the same operating conditions in the MM-FBC. Basically, the concentration histories show qualitatively the same behavior as presented in Fig. 2.

As explained in the section on bituminous coal, the conversion of nitrogen in terms of volatile, char, and fuel nitrogen during devolatilization and char combustion are given in Table 2. Although there exist strong differences in the nitrogen content of the fuels (Table 1), many parallels can be found. The splitting of the fuel nitrogen to volatile nitrogen and char-nitrogen is the same for the two coals (Table 2). The retaining nitrogen to carbon ratio after devolatilization increases (about 27%). The nitrogen conversions during devolatilization and char combustion are very similar for the two coals. The higher conversion of nitrogen to HCN of the subbituminous coal is compensated by the lower conversion to N_2O. This is also valid for the beech wood particles during devolatilization. During char combustion, the char-nitrogen conversions to NO, N_2O, and HCN of the beech wood are substantially higher than the char-nitrogen conversions of the coals. But the summarized fuel-nitrogen conversion to NO, N_2O, and HCN is nearly the same for all three fuels (about 15 w-%) due to the different splitting of the fuel nitrogen of the beech wood.

Varying combustion conditions, the listed nitrogen conversions of the fuels will change (compare with the section on bituminous coal). But similar to the concentration histories, they show the same trends.

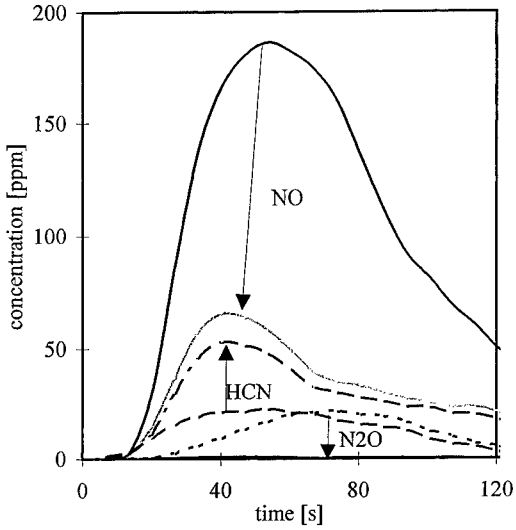

FIG. 3. Concentration histories of NO, N_2O, and HCN during devolatilization of a 10-mm bituminous coal particle at 800°C and 10 kPa oxygen partial pressure in the fluidizing gas in the MM-FBC. The arrows indicate the concentration changes when iodine is added.

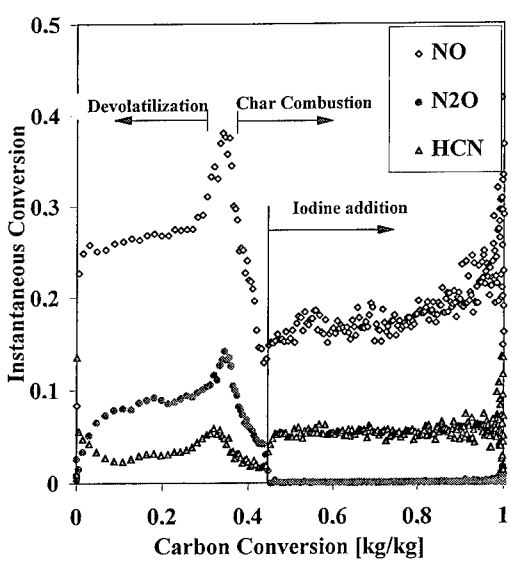

FIG. 4. Instantaneous conversion to NO, N_2O, and HCN versus carbon conversion of a 15-mm bituminous coal particle, at 750°C and 10 kPa oxygen partial pressure in the fluidizing gas in the MM-FBC. Iodine is added after about 0.45 carbon conversion during char combustion.

Modeling

The aim of the modeling work is to understand the NO and N_2O formation during devolatilization and char combustion presented in the experimental section. The subject of this semitheoretical approach is to use well-known parameters to predict and explain the measured species concentrations.

The following measured parameters have been used for input: the combustion conditions of the MM-FBC (bed temperature and temperature profiles, flame characteristics, the input oxygen partial pressure, superficial gas velocity, bed voidage, mean bed particle diameter); the concentration histories of oxygen, CO, CO_2, and hydrocarbons in the flue gas; and fuel data (fuel particle diameter, ultimate and proximate analysis before and after devolatilization, particle temperature).

For comparison of experimental and modeling results, the bituminous coal has been used. The model calculates the instantaneous concentration profiles of NO, N_2O, HCN, NH_3, and the nitrogen-containing radicals (NCO, NH_2, NH) by considering homogeneous and heterogeneous reactions inside the fluidized bed as well as the homogeneous chemistry in the freeboard (compare with Refs. 2 and 3). In Table 3, the set of the used chemical reactions is given. The measured carbon-conversion rates are taken as the basis for the calculations. The volatile nitrogen is assumed to be released proportional to the carbon release during devolatilization as HCN and NH_3. The HCN/NH_3 ratio has been varied as an input parameter from 1/1 to 1/0 to study the relative importance of these intermediates on NO and N_2O formation. Best agreements with the measurements have been found with a HCN/NH_3 ratio of 9/1. During char combustion, the char-nitrogen release is taken proportional to the carbon conversion as NO and HCN. Released from the particle's surface, they are taken as 20 and 4 w-%, respectively. The radical concentrations (OH, HO_2, O, H) are estimated by using the CO_2 and CO concentration histories (similar to Ref. 14). This enables the decoupling of the nitrogen chemistry from the carbon-oxidation chemistry. Iodine addition decreases the level of the radicals, again estimated by using the CO_2 and CO concentrations. The flame of the volatiles is considered in the instantaneous temperature profile of the combustor. A detailed description of the model will be published elsewhere.

Discussion

The NO and N_2O formation and destruction paths (Fig. 5) have been analyzed and evaluated for the bituminous coal with the model under measurement conditions. The bold arrows indicate the main reaction paths. Typical modeling results are given in Fig. 6 as a concentration versus time plot. It can be

TABLE 3
The set of chemical reactions used in the model. Arrows in one direction indicate irreversible reactions, arrows in both directions reversible reactions. M indicates a third body

Number	Used reactions	Catalyst	References
(1)	$NCO + O \rightarrow NO + CO$		15
(2)	$NCO + OH \leftrightarrow NO + CO + H$		15
(3)	$NH + O \leftrightarrow NO + H$		17
(4)	$NCO + NO \leftrightarrow N_2O + CO$		15
(5)	$NH + NO \leftrightarrow N_2O + H$		18
(6)	$NH_2 + NO \rightarrow N_2 + H_2O$		19
(7)	$N_2O + H \leftrightarrow N_2 + OH$		15
(8)	$N_2O + OH \leftrightarrow N_2 + HO_2$		15
(9)	$N_2O + O \leftrightarrow 2\ NO$		21
(10)	$N_2O + O \leftrightarrow N_2 + O_2$		21
(11)	$N_2O + M \leftrightarrow N_2 + O + M$		22
(12)	$HCN + O \leftrightarrow NCO + H$		15
(13)	$NH_3 + O \leftrightarrow NH_2 + OH$		20
(14)	$NH_2 + O \leftrightarrow NH + OH$		23
(15)	$NO + CO \rightarrow 1/2\ N_2 + CO_2$	Bedmat.	16
(16)	$NO + 2/3\ NH_3 \rightarrow 5/6\ N_2 + H_2O$	Bedmat.	16
(17)	$NH_3 + 3/4\ O_2 \rightarrow 1/2\ N_2 + 3/2\ H_2O$	Bedmat.	16
(18)	$NH_3 \rightarrow 1/2\ N_2 + 3/2\ H_2$	Bedmat.	16

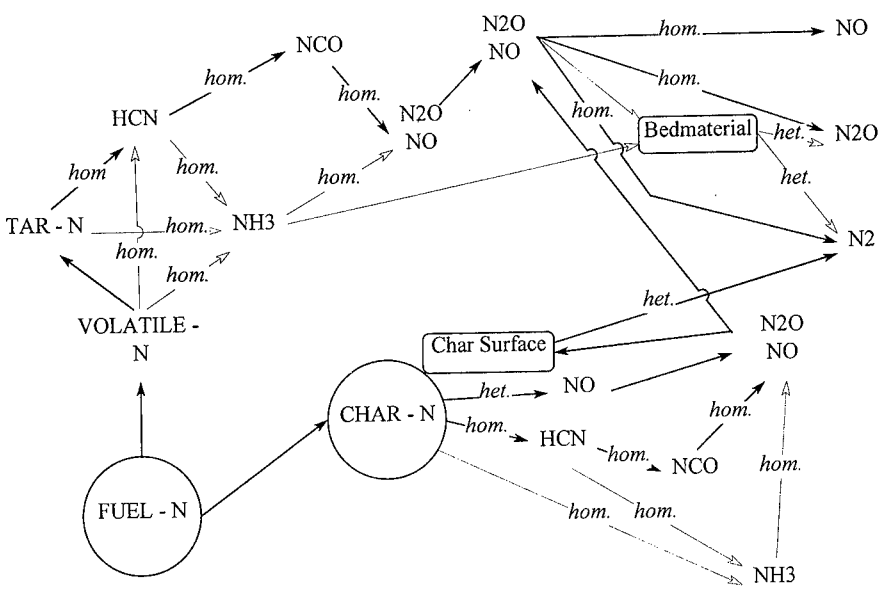

FIG. 5. The reaction paths of fuel nitrogen to NO and N_2O. Bold arrows indicate the main reaction paths evaluated from the model for bituminous coal.

seen that iodine addition causes an increase of HCN and a decrease of NO and N_2O during devolatilization. During char combustion, the NO level is nearly unaffected, HCN increases and N_2O decreases.

During devolatilization, the release rates of NO, N_2O, and HCN are very high relative to their release rates during char combustion (Fig. 2), corresponding with the carbon-conversion rates. The conversion of the fuel nitrogen is based on carbon conversion. Basically, the concentration levels of NO are higher because two nitrogen atoms are necessary to form N_2O. This implies that more reactions and

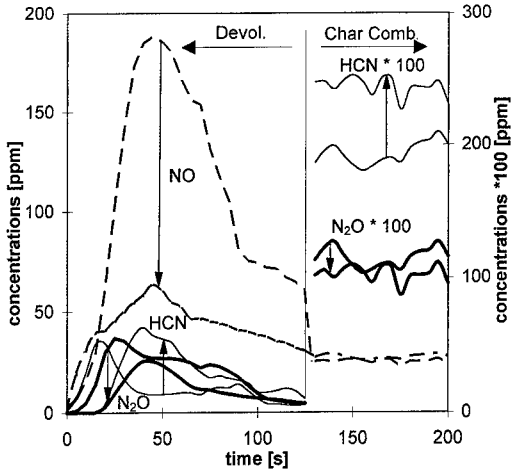

FIG. 6. Modeling results of the concentration histories of NO, HCN, and N_2O of a bituminous coal particle (10 mm in diameter, at 800°C, 10 kPa oxygen) during devolatilization and char combustion in the MM-FBC. The arrows indicate the changes when iodine is added. For better presentation, the HCN and N_2O concentrations during char combustion are multiplied by 100.

longer residence times are necessary to combine these nitrogen atoms. Due to the longer char combustion period, the lower release rates of NO, N_2O, and HCN are compensated to a certain extent, and devolatilization and char combustion are of nearly equal importance for the formation of these species. This is also somehow valid for beech wood. Although the percentage of fuel nitrogen as volatile nitrogen is much higher in comparison to the coals, the conversion rates to NO and N_2O are lower (Table 2). The two coals show nearly the same conversion rates for volatile nitrogen and char nitrogen.

NO and N_2O formation during devolatilization is based on gas-phase chemistry (compare with Ref. 2). This can be clearly seen after iodine addition. The addition of iodine suppresses the radical reactions leading to lower levels of NO and N_2O (Fig. 3). HCN is the main precursor of NO and N_2O. This can be seen in several figures (Figs. 2–4 and 6). The N_2O peak shortly follows the NO and HCN peaks (Figs. 2, 4, and 6). Iodine addition increases HCN and decreases NO and N_2O (Figs. 3 and 6), implying that the oxidation reactions of HCN to NO and N_2O are inhibited (reactions 12, 1, 2, and 4 in Table 3), leading to higher concentrations of the precursor. The dependencies of bed temperature and oxygen partial pressure in the flue gas (described in the experimental results) reveal similar trends on the formation rates. HCN is decreasing with increasing temperature and oxygen partial pressure, whereas NO and N_2O are increasing to a certain extent. The modeling results indicate that HCN is the main precursor of NO and N_2O during devolatilization. The very low levels of NO and N_2O cannot be completely explained by model calculations (Fig. 6). Increasing destruction rates due to higher CO concentration levels may be the reason. Modeling results of the bituminous coal indicate that NH_3 is of minor importance for NO and N_2O formation due to its conversion via reactions 17 and 18 (Table 3).

NO and N_2O formation during char combustion is based on a different mechanism. Again, this can be clearly seen in the iodine addition experiments (Fig. 4). The effect of iodine addition on the NO level is minor. This indicates that NO formation is based on a heterogeneous mechanism inside the pore structure or at the surface of the fuel because heterogeneous chemistry is nearly independent from radical concentrations. In contrast to NO, HCN steeply increases, whereas N_2O steeply decreases. During char combustion, a volatile species which has been identified as HCN is released in low concentrations. This species is homogeneously oxidized to NCO which further reacts with the heterogeneously produced NO to form N_2O. Inhibiting the homogeneous oxidation path of HCN (reactions 12, 1, 2, and 4 in Table 3) leads to a steep decrease of N_2O and a steep increase of HCN. The NO concentration level is nearly unaffected. It slightly increases because the NO destruction reaction with NCO (reaction 4 in Table 3) to form N_2O is inhibited. But the N_2O level is much lower than the NO level. Modeling results support this mechanism (Fig. 6). Additional evidence can be found when comparing the two coals during char combustion (Table 2). A decrease of the N_2O level is compensated with an increase of HCN and NO. And varying the bed temperature and the oxygen partial pressure (described in the experimental results) leads to a decrease of HCN but in an increase of NO and N_2O to a certain extent.

Conclusions

Devolatilization and char combustion are of nearly equal importance for NO and N_2O formation for the two coals. The higher formation rates during devolatilization are compensated by the shorter time scale. In the case of beech wood, devolatilization is more important, although the higher percentage of fuel nitrogen as volatile nitrogen is compensated to a certain extent by lower conversion rates in comparison to the coals.

The NO concentration levels are higher than the N_2O concentration levels during devolatilization and char combustion due to the formation mechanisms and residence times.

Iodine addition has proven to be a very effective method to study the relative importance of homogeneous and heterogeneous chemistry in kinetic experiments.

Iodine addition experiments confirm that NO and N_2O formation during devolatilization is based on a homogeneous mechanism. HCN is the main precursor of NO and N_2O (compare with [2]). The formation characteristics can be explained by the homogeneous HCN oxidation and NO and N_2O formation reactions (reactions 12, 1, 2, and 4 in Table 3).

NO and N_2O formation during char combustion is different. NO is primarily heterogeneously formed by char-nitrogen oxidation. But a volatile species, which has been identified as HCN, is simultaneously released in low concentrations. This species is homogeneously oxidized to NCO which further reacts with the heterogeneously produced NO to form N_2O.

Acknowledgment

The authors want to acknowledge Ben Anthony, CANMET, Ottawa who awoke their interest in iodine addition under FBC conditions.

REFERENCES

1. Winter, F., Ph.D. Thesis, Vienna University of Technology, Vienna, 1995.
2. Kilpinen, P. and Hupa, M., *Combust. Flame* 85:94–104 (1991).
3. Johnsson, J. E., *Fuel* 73:1398–1415 (1994).
4. Tullin, C. J., Sarofim, A. F., and Beer, J. M., *J. Inst. Energy* 66:207–215 (1993).
5. Tullin, C. J., Goel, S., Morihara, A., Sarofim, A. F., and Beer, J. M., *Energy Fuels* 7(6):796–802 (1993).
6. Klein, M. and Rotzoll, G., *Sixth International Workshop on Nitrous Oxide Emissions,* Åbo Akademi, Turku, Finland, 1994, pp. 239–253.
7. Miettinen, H., Paulsson, M., and Strömberg, D., *Energy Fuels* 9(1):10–19 (1995).
8. De Soete, G. G., "Relative Contribution of Homogeneous and Heterogeneous Reactions to the Emissions of NO and N_2O at Fluidized-Bed Conditions," presented at the Institute of Chemical Engineering, Fuel Technology and Environmental Technology, Vienna University of Technology, 1995.
9. Kramlich, J. C., Cole, J. A., McCarthy, J. M., Lanier, W. S., and McSorley, J. A., *Combust. Flame* 77:375–384 (1989).
10. Winter, F., Krobath, P., and Hofbauer, H., *Thirteenth International Conference on Fluidized Bed Combustion,* ASME, Orlando, FL, 1995, pp. 1477–1487.
11. Winter, F., Wartha, C., and Hofbauer, H., *Third International Conference on Combustion Technology for a Clean Environment,* Lisbon, Portugal, 1995, Sec. 15.2.
12. Winter, F., Prah, M. E., and Hofbauer, H., "Intra-Particle Temperatures under Various Fluidized-Bed Combustor Conditions: The Effect of Drying, Devolatilization, and Char Combustion", *Combust. Flame,* 1995, submitted.
13. Anthony, E. J., Bulewicz, E. M., and Preto, F., *Twelfth International Conference on Fluidized-Bed Combustion,* ASME, La Jolla, CA, 1993, pp. 41–52.
14. Bulewicz, E. M., Janicka, E., and Kandefer, S., *Tenth International Conference on Fluidized-Bed Combustion,* ASME, San Francisco, 1989, Vol. 1, pp. 163–168.
15. Miller, J. A. and Bowman, C. T., *Prog. Energy Combust. Sci.* 15:287 (1989).
16. Johnsson, J. E., *Kinetics of Heterogeneous NO_x Reactions at FBC Conditions,* CHEC Report No. 9003, Technical University of Denmark, Lyngby, 1990.
17. Mertens, J. D., Chang, A. Y., Hanson, R. K., Bowman, C. T., and Masten, D. A., "A Shock Tube Study of the Reactions of NH with NO, O_2, and O," Western States Section/The Combustion Institute Meeting, Livermore, California, 1989, Paper no. WSS/CI-89-96.
18. Glarborg, P., Miller, J. A., and Kee, R. J., *Combust. Flame* 65:177 (1986).
19. Hanson, R. K. and Saliman, S., in *Combustion Chemistry,* (W. C. Gardiner Jr., Ed.), Springer-Verlag, New York, 1984, p. 361.
20. Bätz, P., Ehbrecht, J., Hack, W., Rouyeorolles, P., and Wagner, H. G., *Twenty-First Symposium (International) on Combustion,* The Combustion Institute, Pittsburgh, 1988, p. 1107.
21. Davidson, D. F., DiRosa, M. D., Chang, A. Y., and Hanson, R. K., *Eighteenth International Symposium on Shock Waves,* Springer Verlag, 1991, Vol. 2, p. 813.
22. Glarborg, P., Johnson, J. E., and Dam-Johanson, K., *Combust. Flame* 99:523–532 (1994).
23. Glarborg, P. and Hadvig, S., *Development and Test of a Kinetic Model for Natural Gas Combustion,* Report, Nordic Gas Technology Centre, 1991, p. 83.

COMMENTS

A. N. Hayhurst, Cambridge University, UK. Your model has CO reducing NO to N_2. Did you measure the effect of iodine on the concentration of CO within the bed?

Could you give some details of the conditions in the bed; in particular were the bubbles fast and what was the cross-flow factor? Also did the burning char particle circulate around the bed (or, on the other hand, float)?

Author's Reply. One aim of the NO/N_2O model was to study different possible effects (especially destruction reactions) which might be of importance for the interpretation of the measurements. Iodine addition increases the CO level which might reduce NO.

But the fuel particle is mainly located in the upper part of the fluidized bed (ca 0 to 4 cm below the surface) and

moves frequently up to the bed's surface and back again resulting in low gas—bed material contact times decreasing the importance of the heterogeneous destruction reactions. Additionally, the catalytic reactivity of pure silica sand is rather low compared to bed materials containing char and ash.

CO was not obtained within the bed but shortly after the particle as described in the paper. The cross-flow factor has not been measured but can be estimated from Kunii and Levenspiel [1] and is in the range of 0.5 to 1 depending on operating conditions.

REFERENCE

1. Kunii, D. and Levenspiel, O., *Fluidization Engineering*, Wiley, New York, 1991.

•

Bo Leckner, Chalmers University of Technology, Sweden. It has been shown that N_2O is formed heterogeneously during char combustion. In your case the iodine added is supposed to eliminate the gas phase formation of N_2O and prevent the conversion of HCN to N_2O. This seems to take place, but heterogeneously formed N_2O seems to disappear too when iodine is added. Does it mean that there is no heterogeneous formation on N_2O or does the iodine influence the surface reaction as well?

Adel Sarofim and Shakti Goel, MIT, USA. Until seeing your results, we were reasonably convinced that the heterogeneous mechanism developed at MIT for NO and N_2O was the valid one, although there are some experiments (e.g., [1]) that provide reasonable evidence that homogeneous reactions cannot be ruled out. This paper provides interesting data which seem to further support a homogeneous pathway. There seems to be need to examine further the differences between what appears to be conflicting evidence on the relative roles of heterogeneous versus homogeneous reactions. Transient release of nitrogen oxides on oxygen interruption (e.g., [2,3]) are consistent with the role of oxide formation on the surface both for the nitrogen oxides and the CO. Have you examined such transients on cutting off oxygen, and perhaps also iodine? In your presentation you claimed that iodine atoms did not influence the surface reactions based on the lack of change of the carbon oxidation rate on iodine addition. Iodine may compete with NO for the nitrogenous surface complexes and prevent the formation of N_2O without affecting the char consumption rate. Examination of the influence of iodine on the transient emissions of oxide complexes on turning off the oxygen might provide useful insights.

REFERENCES

1. Klein and Rotzoll, *6th N_2O Workshop*, Turku Finland, 1994.
2. Krammer and Sarofim, *Combust. Flame* 97:118–124 (1994).
3. Goel, Zhang, and Sarofim, *Combust. Flame* 104:213–217 (1996).

•

Prof. Mikko Hupa, ABO Akademi University, Finland. How did you take into account the influence of the iodine on the radical levels in your model?

How can you exclude the direct influence of the added iodine on the char nitrogen release chemistry?

Author's Replies. The concentrations of the OH, H, HO_2, and hydrocarbon radicals depend on the carbon oxidation chemistry and are not significantly affected by the nitrogen chemistry and its radicals.

The concentrations of the radicals related to carbon oxidation are estimated by the measured concentrations of CO and CO_2 similar to Bulewicz et al., 10th FBC Conf., 1989. Iodine addition changes the CO and CO_2 concentration levels by suppressing the OH and H radicals. Using the CO and CO_2 measurements it allows to us estimate the radicals' concentration levels also during iodine addition.

M. Hupa's second question and the questions of A. Sarofim and S. Goel and B. Leckner are regarding possible effects of iodine with the surface chemistry especially for N_2O formation during char combustion.

It has been shown during the presentation and it is shortly listed in the paper that the addition of iodine does not change the carbon conversion rates during devolatilization nor during char combustion. Char combustion is a strictly heterogeneous process but no effects on iodine addition have been found. It is very unlikely that iodine changes only the nitrogen-containing surfaces.

A competing reaction of iodine with NO for possible nitrogenous surface complexes and a small contribution of heterogeneously formed N_2O cannot be completely excluded with these measurements.

But the homogeneous chemistry of iodine is well understood and the transient behavior of NO, N_2O and HCN formation during char combustion has been studied by significantly changing the combustion conditions (e.g. temperature, radical concentrations in the gas-phase, etc.) revealing strong evidence that N_2O is homogeneously formed.

Experiments where the oxygen and the iodine is turned off are interesting and will be considered in our future work but there exist some possible draw-backs of this method, e.g. the time-scale for gas dispersion in the reactor.

Twenty-Sixth Symposium (International) on Combustion/The Combustion Institute, 1996/pp. 3335–3342

NITROGEN CHEMISTRY IN FBC WITH LIMESTONE ADDITION

ANKER JENSEN, JAN ERIK JOHNSSON AND KIM DAM-JOHANSEN
Department of Chemical Engineering
The Technical University of Denmark
Building 229, 2800 Lyngby, Denmark

A laboratory study of NO and N_2O formation from limestone-catalyzed HCN oxidation under fluidized-bed combustion (FBC) conditions is reported. The experiments include the influence of NO and O_2 on HCN oxidation over calcined limestone, formation of $CaCN_2$ by reaction between HCN and calcined limestone, and oxidation of $CaCN_2$ and simultaneous HCN oxidation and sulfation of the limestone in the presence of NO. For oxidation of HCN over calcined limestone at O_2 concentrations of about 5000 ppmv or more, NO is formed with a selectivity of 50–60%. At a temperature of 1025 K, the selectivity for N_2O formation exhibits a maximum at an O_2 concentration of 1000–2000 ppmv. The presence of NO in the inlet gas enhances the formation of N_2O. The selectivity for NO and N_2O decreases and increases, respectively, with increasing degree of sulfation of the limestone. The results from the present work and from the literature are used to discuss how limestone addition influences the nitrogen chemistry in FBC. The results indicate that (1) the NO emission decreases for low volatile fuels such as pet coke because NO is reduced by CO over the calcined limestone; and (2) for medium- to high-volatile fuels, the NO and N_2O emission increases and decreases, respectively, because calcined limestone catalyzes the oxidation of volatile nitrogen (HCN and NH_3) to NO and the decomposition of N_2O. For large CFBCs, limestone has only a small effect on N_2O. This is partly because a major part of the N_2O emitted is formed in the upper part of the riser where the solids concentration is low and little N_2O is destroyed heterogeneously.

Introduction

The importance of coal combustion for production of electricity and district heating is increasing throughout the world. There is also a trend toward increased use of biomass combustion to reduce the net emission of CO_2. Fluidized-bed combustion (FBC) has the advantage of fuel flexibility and, in Denmark, circulating fluidized-bed (CFB) technology is considered for combustion of mixtures of coal and biomass [1]. This technology has low emissions of NO due to the low combustion temperatures of 1073–1173 K, but the emissions of N_2O from coal combustion are high in this temperature range. This is of concern because N_2O is a greenhouse gas and contributes to depletion of the ozone layer. Limestone is added to FBC for sulfur capture and has been reported to influence the emissions of NO and N_2O. The purpose of this paper is to present new results on limestone-catalyzed oxidation of HCN, an important volatile nitrogen species, and discuss the nitrogen chemistry in FBC with limestone addition.

Experimental

The oxidation of HCN was carried out in a fixed-bed quartz laboratory reactor placed in a three-zone oven described elsewhere [2,3]. The reactor was designed to minimize homogeneous reactions before and after the solid catalyst. The conversion of HCN in the empty reactor at 1123 K and 5000 ppmv O_2 was about 15% but very little NO and N_2O was formed. The gas analyzers were IR (CO, CO_2, N_2O), UV (NO, SO_2), and paramagnetic (O_2) instruments. In some experiments, HCN was measured by a gas chromatograph with a flame ionization detector.

Seven limestones of high purity (50–55 wt. % CaO) were tested, but most experiments were performed with two Danish limestones: Stevns Chalk and Faxe Bryozo. Stevns Chalk is a young, porous limestone with a high sulfur capture capacity, and Faxe Bryozo is a limestone with an intermediate sulfur capture capacity. More information about the limestones is given in Refs. 2 and 4.

Results

The conversion of HCN and the selectivities for formation of NO and N_2O were defined as

$$X_{HCN} = \frac{\text{molar flow of HCN in} - \text{molar flow of HCN out}}{\text{molar flow of HCN in}} \quad (1)$$

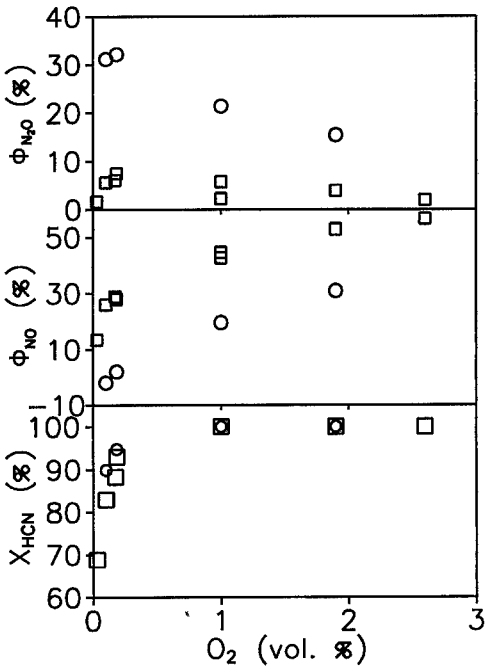

FIG. 1. Influence of O_2 and NO on oxidation of HCN over calcined limestone. Temperature, 1025 K; flow rate, ca. 1860 Nml/min; limestone, Stevns Chalk; mass of uncalcined limestone, 0.25 g; particle diameter, 0.25–0.3 mm; inlet concentration, 396–420 ppmv HCN. □, Without NO; ○, 520 ppmv NO in the inlet.

$$\phi_{NO} = \frac{\text{molar flow of NO out} - \text{molar flow of NO in}}{\text{molar flow of HCN in} - \text{molar flow of HCN out}} \quad (2)$$

$$\phi_{N_2O} = \frac{2 \cdot \text{molar flow of } N_2O \text{ out}}{\text{molar flow of HCN in} - \text{molar flow of HCN out}} \quad (3)$$

Influence of NO and O_2

Experiments were performed at 1025 K with Stevns Chalk to test the influence of O_2 and NO on HCN oxidation. Figure 1 shows the influence of O_2 with and without 520 ppmv NO in the inlet gas. Without NO, the conversion of HCN increases from about 70% at 300 ppmv O_2 to 100% for O_2 concentrations above 1 vol. %. The selectivity for NO formation increases from 15 to 56% when the O_2 concentration increases from 300 ppmv to 3 vol. %. The selectivity for N_2O formation increases from 2% at 300 ppmv O_2 to a maximum of 6–8% at 2000 ppmv O_2 and then decreases with increasing O_2 concentration. The HCN conversion with NO present is slightly higher than without NO when the O_2 concentration is below 1 vol. %. The selectivity for NO formation is negative at low O_2 concentration and lower than without NO in the inlet, indicating that NO is reduced by HCN. The N_2O selectivity in the presence of NO is higher than without NO. Experiments without NO in the inlet gas were also performed with Faxe Bryozo at 1015–1167 K and gave similar results. The formation of N_2O decreased with increasing temperature in the range 1025–1175 K, but the NO formation increased [2].

Formation and Oxidation of $CaCN_2$

In experiments with a high HCN concentration surrounding the limestone particles, a residue was sometimes deposited on the limestone. During combustion of this residue, CO, CO_2, NO, and N_2O were formed. An experiment was therefore performed in which HCN was passed through a bed of calcined limestone. A comparison of an IR spectrum of the solid product with a reference spectrum showed that the residue was $CaCN_2$.

The oxidation of $CaCN_2$ at 1023 K was investigated after reacting HCN with calcined Stevns Chalk for a given time. When HCN was removed from the inlet gas, O_2 was added and the solid product burned off. In the first period, CO and CO_2 were the only gaseous products, but during burn-off of the solid product, NO and N_2O were also formed. The integral NO and N_2O selectivities from oxidation of $CaCN_2$ are shown in Fig. 2 versus the amount of $CaCN_2$ initially formed. The selectivities were defined as mole N in NO or N_2O formed per mole N oxidized, assuming that two N atoms are oxidized for each C atom. The selectivities for NO and N_2O are 20–22% and 20–28%, respectively, independent of the amount of $CaCN_2$. The result from a single experiment with 550 ppmv NO and 1000 ppmv O_2 in the inlet gas is also shown. The N_2O selectivity increases to 40%, and the NO selectivity (not shown) is close to zero.

Sulfation Experiments

Preliminary results from simultaneous HCN oxidation and sulfation of six limestones were reported in Jensen et al. [5]. The results showed that the catalytic activity of the limestones decreased by conversion of CaO to $CaSO_4$. Simultaneously, the selectivity for NO formation decreased from 50–60% to 18–23%, and the selectivity for N_2O formation increased from almost zero but was still below 10%. The increase in the selectivity for N_2O formation may be partly due to a lower rate of decomposition of N_2O over sulfated limestone compared to

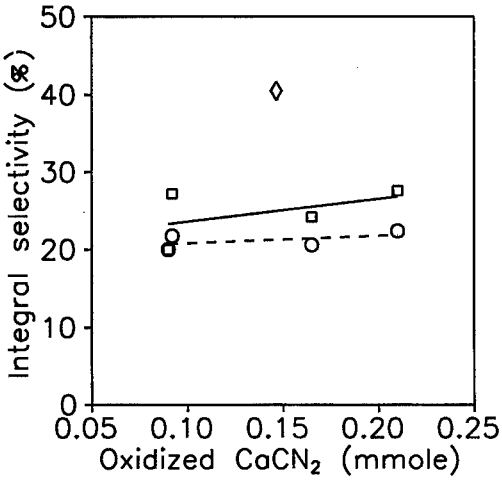

FIG. 2. Selectivities for NO and N_2O from combustion of the reaction product between HCN and calcined limestone, $CaCN_2$. Temperature, 1023 K (limestone calcined at 1123 K); flow rate, 1783 Nml/min; limestone, Stevns Chalk; mass of uncalcined limestone, 0.25 g; particle diameter, 0.25–0.3 mm; inlet concentrations, 420 ppmv HCN, 0.5–1.0 vol. % O_2 except for the case with NO in the inlet gas where the O_2 concentration was 1000 ppmv. ○, NO; □, N_2O; ◇, N_2O with 500 ppmv NO in the inlet. The lines are best fit. Dashed line, NO; full line, N_2O.

calcined limestone [6]. Results from simultaneous sulfation of Stevns Chalk and HCN oxidation with NO in the inlet gas are shown in Fig. 3. The HCN conversion decreases with increasing particle size, indicating influence of mass transfer limitations. The selectivity for NO formation decreases with increasing degree of sulfation and is lower than without NO in the inlet [2]. The N_2O selectivity increases with increasing degree of sulfation and is 25–28% at complete sulfation, about 2.5 times higher than without NO in the inlet. The NO and N_2O selectivities decrease and increase, respectively, with increasing particle size. This is probably related to the decreasing conversion of HCN with increasing particle size, and thereby higher HCN concentration in the fixed bed. In the presence of a higher HCN concentration, more NO is reduced, partly forming N_2O. If SO_2 was removed from the inlet gas, the limestone regained a large part of its catalytic activity, the NO selectivity increased, and the N_2O selectivity was almost unchanged. It was found that the catalytic activity of the sulfated limestone decreased with increasing SO_2 concentration up to about 1000 ppmv where it reached an asymptotic level. An influence of SO_2 has not been observed for NH_3 oxidation over limestone [3]. In the absence of both O_2 and SO_2, $CaSO_4$ was reductively decomposed to CaS and CaO by a fast reaction with HCN, and the formation of NO and N_2O decreased [2].

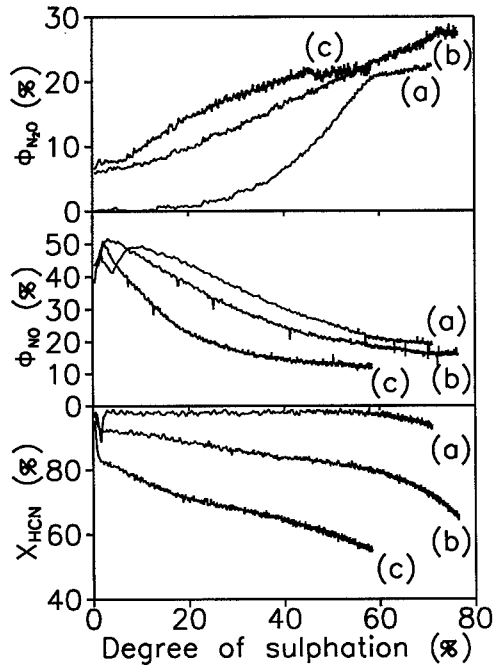

FIG. 3. Influence of particle diameter and NO on oxidation of HCN during simultaneous sulfation. Temperature, 1123 K; flow rate, 2000 Nml/min; limestone, Stevns Chalk; mass of uncalcined limestone, 0.25 g; inlet concentrations, 290 ppmv HCN, 1450 ppmv SO_2, 4800 ppmv O_2, 430 ppmv NO. (a), 0.25–0.30 mm; (b), 0.85–1.0 mm; (c), 1.7–2.0 mm.

A summary of the NO and N_2O selectivities from oxidizing HCN over seven different calcined and sulphated limestones with about 5000 ppmv O_2 is shown in Fig. 4. The NO selectivity from HCN oxidation over calcined limestone is high, 50–60%, and the N_2O selectivity is close to zero. The rate of HCN oxidation over sulfated limestone in the presence of 1450 ppmv SO_2 is lower than over calcined limestone, and the NO selectivity is 20–30%. The N_2O selectivity is higher for the sulfated limestone, 5–10%, and it increases to 22–28% in the presence of 430 ppmv NO. The rate of HCN oxidation is faster and the NO selectivity is higher over sulfated limestone in the absence of SO_2 than in the presence of 1450 ppmv SO_2, but the N_2O selectivity is not significantly influenced by the SO_2 concentration.

Discussion of the Influence of Limestone Addition on the Emissions of NO and N_2O

In this section, the influence of limestone addition on the nitrogen chemistry in FBC is discussed. Table 1 lists important effects of limestone addition on the nitrogen chemistry. Besides the effects listed in

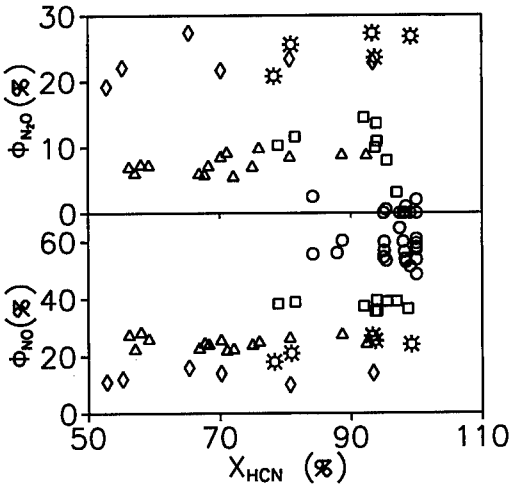

FIG. 4. Selectivities for NO and N_2O when oxidizing HCN over calcined and sulfated limestone. Results from seven different limestones are included. Temperature, 1123 K; flow rate, ≈ 1900 Nml/min; mass of uncalcined limestone, 0.25 g; particle diameter, 0.25–0.3 mm, 0.85–1.0 mm, 1.7–2.0 mm. Inlet concentrations, ≈300 ppmv HCN, ≈5000 ppmv O_2. ○, Over calcined limestone; △, over sulfated limestone in the presence of 1450 ppmv SO_2; □, over sulfated limestone without SO_2 present; ◇, over sulfated limestone in the presence of 1450 ppmv SO_2 and 430 ppmv NO; ☼, over sulfated limestone in the presence of 430 ppmv NO.

TABLE 1
Important effects of limestone addition on the nitrogen chemistry in FBC

Effect		Reference
$NH_3 + O_2 \xrightarrow{CaO} NO + N_2$	(R1)	3
$HCN + O_2 \xrightarrow{CaO} NO + N_2$	(R2)	This work, 7, 8
$HCN + O_2 \xrightarrow{CaSO_4} NO + N_2O + N_2$	(R3)	This work, 2
$HCN + H_2O \xrightarrow{CaO} NH_3 + N_2$	(R4)	9
$CO + 1/2\ O_2 \xrightarrow{CaO} CO_2$	(R5)	10
$N_2O \xrightarrow{CaO} N_2 + 1/2\ O_2$	(R6)	6
$NO + CO \xrightarrow{CaO} 1/2\ N_2 + CO_2$	(R7)	11
$NO + 5/2H_2 \xrightarrow{CaO} NH_3 + H_2O$	(R8)	5
Lower SO_2 concentration in the combustion chamber, results in higher radical concentrations		10, 12

Table 1 for which experimental evidence is available, it has been speculated that HCN can be converted to NH_3 with $CaCN_2$ as an intermediate [13,14] through the net reactions R9–11

$$CaO + 2HCN \rightarrow CaCN_2 + CO + H_2 \quad \text{(R9)}$$

$$CaCN_2 + 3H_2O \rightarrow CaO + CO_2 + 2NH_3 \quad \text{(R10)}$$

$$CaCN_2 + H_2O + 2H_2 + CO_2 \rightarrow CaO + 2NH_3 + 2CO. \quad \text{(R11)}$$

The influence of limestone addition on emissions of NO and N_2O from FBC is summarized in Table 2. The table gives information on the type of plant, the volatile content of the fuel, the NO and N_2O emissions without limestone addition, and the emissions with limestone addition relative to the values without addition. For batch addition, the reported relative values are the maximum effect observed in the transient. Table 2 supports the following general conclusion: limestone addition most often results in a higher NO emission and a lower N_2O emission. This is most pronounced in laboratory or bench-scale plants and at high ratios of Ca/S. Furthermore, the NO emission is more often influenced by limestone addition than is the N_2O emission. In principle the effect of limestone addition may be calculated using appropriate reactor and kinetic models. However, a kinetic model for the reactions in Table 1, including the effect of sulfation of the limestone, is not available. Instead, the observations in Table 2 are discussed qualitatively, based on the reactions in Table 1.

A Decrease in NO Emission

A decrease in NO emission after the addition of limestone has been observed in a bench-scale CFB [22] and a full-scale, bubbling, fluidized bed (BFB) [25]. Unfortunately, N_2O was not measured in these investigations. In both cases, the fuel was pet coke with a low volatile content of about 10 wt. % (daf). As a result, very little volatile nitrogen which could be oxidized to NO over limestone is released during devolatilization. Consequently, the net effect of limestone addition is to catalyze the reduction of NO, primarily by reaction with CO (equation R7). It has been reported that NO is not reduced by CO over calcined limestone if the molar CO/O_2 ratio is below 2 [10]. It has also been reported that reducing zones exists in FBCs [25,27]; apparently, the local CO/O_2 ratio is high enough to allow NO reduction by CO over calcined limestone to take place. In Refs. 7 and 26, an increase in the NO emission by limestone addition was observed during combustion of coals with a volatile content similar to that of pet coke in laboratory-scale BFB and CFB. Possibly,

TABLE 2
Summary of the influence of limestone addition on NO and N_2O emissions from FBC

				Effect on NO emission		Effect on N_2O emission	
Ref.	Size/type	Fuel VM (wt.% daf)	Ca/S	No limestone (ppmv 6% O_2)	Relative emission[a]	No limestone (ppmv 6% O_2)	Relative emission[a]
15	200 MW/CFBC	32.7	–	–	–	6	1.0
16	165 MW/CFBC	33.0	LS[b] I: 20, 38	30	1.5, 27	140	0.93, 075
16	165 MW/CFBC	33.0	LS[b] II: 20, 36	30	1.3, 18	140	0.96, 086
17	110 MWe/CFBC	–	5.4[c]	183	1.2	37	1.0
18	72 MW/CFBC	38.2	–	48	2.2	55	1.0
19	12 MW/CFBC	39.0	3.0	52	1.4	106	0.94
12	12 MW/CFBC	39.5	115, 2.1, 43	45	15, 2.7, 62[d]	164	090, 0.72, 052[d]
20	1 MW/CFBC	40.9	3.7	121	1.9	168	0.9
20	1 MW/CFBC	50.0	2.3	141	2.0	48	1.1
21	08 MW/CFBC	37.6	1.5	–	1.5	–	0.84
22	0.15 MW/CFBC	10.6[e]	2.5–3	270	0.25	–	–
22	015 MW/CFBC	41.2	2–3	127	1.73	–	–
23	Lab/CFBC	25.7	LS[b] bed	61	5.2	265	0.29
7	Lab/CFBC	13.9	Batch	88	1.83	150	0.81
7	Lab/CFBC	30.1	Batch	83	1.54	178	0.78
7	Lab/CFBC	50.0	Batch	67	1.91	194	0.63
24	Lab/BFBC	44.2	4, 8, LS[b] bed	–	145, 2.0, 286	–	071, 0.41, 007
25	16 MW/BFBC	10[e]	1.5	–	0.2–04	–	–
26	Lab/BFBC	14.6	Batch	347	1.76	86	0.91
26	Lab/BFBC	30.7	Batch	367	1.95	71	0.83
26	Lab/BFBC	44.6	Batch	347	1.94	57	0.75

[a]The relative emission is defined as (emission with limestone addition)/(emission without limestone addition).
[b]LS, limestone.
[c]Estimated.
[d]Steady state was not achieved.
[e]Pet coke.

more volatile nitrogen is released from the coals, despite their low volatile content, and catalytically oxidized to NO, as per equations R1 and R2 in Table 1. Another possibility is that mixing of fuel and O_2 is better in the laboratory combustors than in the larger bench- and full-scale combustors such that the local CO/O_2 ratio is low in laboratory combustors and no NO reduction takes place.

An Increase in NO Emission and a Decrease in N_2O Emission

In most investigations, an increase in the NO emission and a decrease in the N_2O emission by limestone addition has been observed during combustion of coals with a medium to high volatile content [7,12,16,21,23,24,26]. This effect has been explained by catalytic oxidation of NH_3 to NO (equation R1) and decomposition of N_2O (equation R6). This mechanism does not include an influence of limestone on the formation of N_2O. An additional mechanism was proposed in Refs. 5 and 7. Without limestone addition, a large part of the HCN is oxidized homogeneously with a low selectivity for NO formation and a high selectivity for N_2O formation [28]. When limestone is added, HCN is oxidized catalytically by equation R2, with a high selectivity for NO formation and a low selectivity for N_2O formation at O_2 concentrations above about 5000 ppmv. Another mechanism is based on catalytic conversion of HCN to NH_3, either by direct hydrolysis or through equations R9–11 [13,14]. This will result in a lower N_2O emission because NH_3 is oxidized both homogeneously [28] and catalytically by equation R1, with a low selectivity for N_2O formation [3]. However, the rate of HCN hydrolysis to NH_3 (equation R4) is much slower than the rate of HCN oxidation (equation R2), and Shimizu et al. [9] concluded that equation R4 is of minor importance. The mechanism of equations R9–11, based on formation of $CaCN_2$, is probably not important either because $CaCN_2$ is formed mainly in the absence of or at low concentrations of O_2, and despite the presence of reducing zones, the lowest local average O_2 concen-

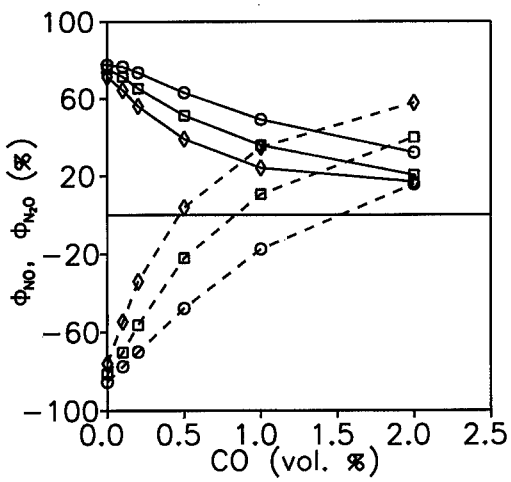

FIG. 5. NO and N_2O selectivity from homogeneous oxidation of HCN in a plug flow reactor, calculated with a chemical kinetic model [31]. Pressure, 1 bar; inlet concentrations, 4 vol. % O_2, 10 vol. % CO_2, 4 vol. % H_2O, 300 ppmv HCN, 400 ppmv NO. ○, 1073 K; □, 1123 K; ◇, 1173 K. Dashed lines, NO; full lines, N_2O.

tration is probably not below 1 vol. % [29]. If formed, $CaCN_2$ is not likely to react in equations R10 and R11, but rather to be oxidized with significant N_2O formation as the result (Fig. 2). Furthermore, the limestone particles will be partly sulfated, and in the absence of O_2, HCN will react with $CaSO_4$ instead of forming $CaCN_2$.

It has been shown [10,12] that the lower SO_2 concentration in the combustion chamber caused by limestone addition influences the radical concentrations, probably owing to less radical recombination. This may result in a higher NO emission and a slightly lower N_2O emission [12]. Finally, the catalytic oxidation of CO (equation R5) may result in a lower CO concentration in the combustion chamber although this has not been verified yet. It was suggested [10] that the lower CO concentration results in less NO reduction over char surfaces. However, the CO concentration in the pores of char particles is very high, and the lower CO concentration in the bulk gas is not expected to influence NO reduction over char significantly. An effect of a lower CO concentration is more likely caused by less reduction of NO over bed material.

The conclusion is that the most probable reactions leading to an increase in the NO emission and a decrease in the N_2O emission are R1, R2, and R6. In these three reactions, the catalyst is CaO and the amount of free CaO surfaces in the bed is determining for the effect of limestone addition on the NO and N_2O emission, as shown in Refs. 7, 12, 23, 24, and 26.

An Increase in NO Emission and No or Little Influence on N_2O Emission

This is observed mainly in large-scale CFBCs [15,17–20] burning medium- to high-volatile coals. The concentration profile of NO in CFBC without limestone addition [29] shows that the formation of NO takes place mainly in the bottom part, and NO is reduced along the riser. On the other hand, the N_2O concentration profile indicates that N_2O is formed along the riser [29]. Calculations by Johnsson et al. [30] for a 12-MW CFBC indicate that more than 50% of the N_2O emitted is formed above the secondary air inlet. The solids concentration in the dense bed in the bottom is about 1000 kg/m^3, decreasing to 10–20 kg/m^3 above the secondary air inlet. Since NO is formed mainly in the bottom region where the concentration of limestone is high, the NO formation will increase due to reactions R1 and R2 when limestone is added. For N_2O, several points should be made. In the bottom of the riser, the concentrations of combustibles, CO, H_2, and hydrocarbons are several percent [29]. The homogeneous oxidation of HCN in the presence of 300 ppmv NO and combustibles, simulated by CO, was investigated using a chemical kinetic model [31] and a plug flow code. The results in Fig. 5 show that the maximum selectivity for N_2O formation from HCN oxidation is above 60% at low temperatures and low CO concentrations, but at 2 vol. % CO, the N_2O selectivity in the homogeneous oxidation of HCN at 1123 K is only about 20%. This is of the same order of magnitude as for the heterogeneous oxidation of HCN over sulfated limestone in the presence of NO. Furthermore, the decomposition of N_2O over char and bed material is already fast in the bottom without limestone addition [30]. Consequently, limestone addition may not change the net formation of N_2O in the bottom part. The results in Fig. 5 show that an increase in temperature has the same effect as limestone addition. This indicates that the effect of limestone addition decreases with increasing temperature.

It is not known if HCN oxidation plays a role in formation of NO and N_2O in the upper part of the riser because the concentration is very low [29]. The low concentration of HCN is the net result of formation and destruction, and the formation rate may be high if the destruction rate is high, too. In the upper part of the riser, the concentration of solids and combustibles is low. Therefore, the heterogeneous reactions are less important than in the bottom, and HCN is partly oxidized homogeneously, as before limestone addition. Furthermore, the mean diameter of the particles in the riser is lower than in the bottom, and the degree of sulfation of is expected to be higher. The N_2O decomposition (equation R6) may thus not be important because the rate decreases with increasing degree of sulfation of the

limestone particles. If HCN is oxidized over sulfated limestone, significant amounts of N_2O are produced, enhanced by the higher NO concentration during limestone addition (Fig. 4). Whether HCN is oxidized over sulfated limestone or calcined limestone in the riser depends on the type of limestone and the Ca/S ratio. Limestone particles with a low sulfur capture capacity are typically less porous and exhibit pore plugging, making the CaO inside the shell of $CaSO_4$ inaccessible. Thus, the influence of limestone addition on the N_2O emission is expected to be smaller for limestones with a low sulfur capture capacity at a given Ca/S ratio, and this is confirmed by full-scale experiments [16]. Furthermore, if HCN does play a minor role in the upper part of the riser, and N_2O is formed mainly from char combustion, enhanced by the higher NO concentration [32], a minor influence of limestone addition on N_2O is also expected. Finally, Jensen et al. [5] showed that heterogeneous oxidation of HCN over char has similar NO and N_2O selectivities as over calcined limestone. In the cases with no influence of limestone on N_2O, it is possible that HCN is already oxidized by the heterogeneous path over char.

Conclusions

The following conclusions can be drawn from the present study:

1. With an inlet concentration of 400 ppmv HCN, significant amounts of N_2O are formed during HCN oxidation over calcined limestone at 1025 K in the presence of 500 ppmv NO and 1000–2000 ppmv O_2. The N_2O selectivity decreases with increasing O_2 concentration and temperature, but the NO selectivity shows the opposite trends and is 50–60% for O_2 concentrations above 5000 ppmv at 1123 K.
2. Parallel to the catalytic oxidation of HCN, a gas-solid reaction between HCN and CaO can take place, forming $CaCN_2$. The selectivities for NO and N_2O from oxidation of $CaCN_2$ under the present experimental conditions are 20–22% and 20–28%, respectively. The presence of NO in the gas enhances N_2O formation.
3. Sulfation of the limestone results in a lower catalytic activity for oxidizing HCN, a lower NO selectivity, and a higher N_2O selectivity. The catalytic activity of the sulfated limestone decreases with increasing SO_2 concentration to an asymptotic level. The N_2O selectivity from oxidizing HCN over sulfated limestone increased from about 10% to 22–28% in the presence of 430 ppmv NO.
4. For low-volatile fuels such as pet coke, limestone addition may result in a decrease in the NO emission. The explanation may be that calcined limestone catalyzes the reduction of NO by CO. For coals with a medium to high volatile content, two cases were identified: case 1, an increase in NO emission and a decrease in N_2O emission; case 2, an increase in NO emission and no effect on N_2O emission.
5. Case 1: This case was explained by the combined effect of limestone-catalyzed oxidation of HCN and NH_3 to NO and decomposition of N_2O. A mechanism proposed in the literature based on catalytic conversion of HCN to NH_3 with $CaCN_2$ as an intermediate was considered unlikely.
6. Case 2: This case was preferentially observed for large CFBCs where a significant part of the N_2O emitted is formed in the upper part of the riser. The relative importance of HCN and char oxidation is not clear, but HCN may be oxidized homogeneously or over sulfated limestone in the riser with a significant N_2O selectivity. N_2O formation from char combustion in the riser is enhanced by the higher NO concentration. These effects may balance a possible increased rate of N_2O decomposition over the limestone.

Acknowledgments

This work is part of the research program CHEC (Combustion and Harmful Emission Control) funded by the Danish Technical Research Council, Elsam (the Jutland-Funen Electricity Consortium), Elkraft (the Zealand Electricity Consortium), and the Danish and Nordic Energy Research Program.

REFERENCES

1. Rasmussen, I. and Clausen, J. C., in *Proceedings of the 13th International Conference on Fluidized-Bed Combustion* (K. J. Heinschel, Ed.), ASME, New York, 1995, pp. 557–563.
2. Jensen, A., "Nitrogen Chemistry in Fluidized Bed Combustion of Coal," Ph.D. Thesis, Department of Chemical Engineering, The Technical University of Denmark, Lyngby, 1996.
3. Lin, W., Johnsson, J. E., Dam-Johansen, K., and van den Bleek, C. M., *Fuel* 73:1202–1208 (1994).
4. Dam-Johansen, K. and Østergaard, K., *Chem. Eng. Sci.* 46:827–837 (1991).
5. Jensen, A., Johnsson, J. E., and Dam-Johansen, K., in *Proceedings of the 12th International Conference on Fluidized-Bed Combustion,* (L. Rubow and G. Commonwealth, Eds.), ASME, New York, 1993, pp. 447–454.
6. Shimizu, T. and Inagaki, M., *Energy Fuels* 7:648–654 (1993).
7. Shimizu, T., Tachiyama, Y., Fujita, D., Kumazawa, K., Wakayama, O., Ishizu, K., Kobayashi, S., Shikada, S., and Inagaki, M., *Energy Fuels* 6:753–757 (1992).
8. de Soete, G. G. and Nastoll, W., *Catalytic Nitrogen Chemistry on CaO and $CaCO_3$ at Fluidized-Bed Tem-*

perature Conditions, Institut Francais du Petrole, Rueil-Malmaison, Ref. 39362, 1991.
9. Shimizu, T., Ishizu, K., Kobayashi, S., Kimura, S., Shimizu, T., and Inagaki, M., *Energy Fuels* 7:645–647 (1993).
10. Dam-Johansen, K., Åmand, L. -E., and Leckner, B., *Fuel* 72:565–571 (1993).
11. Tsujimura, M., Furusawa, T., and Kunii, D., *J. Chem. Eng. Jpn* 16:132–136 (1983).
12. Åmand, L. -E., Leckner, B., and Dam-Johansen, K., *Fuel* 72:557–564 (1993).
13. Gavin, D. G., Powis, J., Laughlin, K., and McCaffrey, D. J. A., in *Proceedings from the International Conference on Coal Science,* (K. H. Michaelian, Ed.), 1993, pp. 561–564.
14. Leppälahti, J. and Kurkela, E., *Fuel* 70:491–497 (1991).
15. Bonn, B., Pelz, G., and Baumann, H., *Fuel* 74:165–171 (1995).
16. Leckner, B., Karlsson, M., Mjörnell, M., and Hagman, U., *J. Inst. Energy* 65:122–130 (1992).
17. Brown, R. A. and Muzio, L., in *Proceedings of the 11th International Conference on Fluidized-Bed Combustion,* (E. J. Anthony, Ed.), ASME, New York, 1991, pp. 719–724.
18. Boemer, A., Braun, A., and Renz, U., in *Proceedings of the 12th International Conference on Fluidized-Bed Combustion,* (L. Rubow and G. Commonwealth, Eds.), ASME, New York, 1993, pp. 585–598.
19. Lyngfelt, A. and Leckner, B., *Fuel* 72:1553–1561 (1993).
20. Collings, M. E. and Mann, M. D., *Energy Fuels* 8:1083–1094 (1994).
21. Hiltunen, M., Kilpinen, P., Hupa, M., and Lee, Y. Y., in *Proceedings of the 11th International Conference on Fluidized-Bed Combustion,* (E. J. Anthony, Ed.), ASME, New York, 1991, pp. 687–694.
22. Zhao, J., Grace, J. R., Lim, J. L., Brereton, C. M. H., and Legros, R., *Fuel* 73:1650–1657 (1994).
23. Moritomi, H., Suzuki, Y., Kido, N., and Ogisu, Y., in *Circulating Fluidized-Bed Technology III,* (P. Basu, M. Horio, and M. Hasatani, Eds.), Pergamon Press, Oxford, 1991, pp. 399–404.
24. Gavin, D. G. and Dorrington, M. A., *Fuel* 72:381–388 (1993).
25. Lyngfelt, A. and Leckner, B., *Chem. Eng. J.* 40:59–69 (1989).
26. Shimizu, T., Tachiyama, Y., Kuroda, A., and Inagaki, M., *Fuel* 71:841–844 (1992).
27. Lyngfelt, A., Bergqvist, K., Johnson, F., Åmand, L. -E., and Leckner, B., in *Gas Cleaning at High Temperatures,* (R. Clift and J. P. K. Seville, Eds.), Blackie Academic & Professional, Glasgow, 1993, pp. 470–491.
28. Hulgaard, T. and Dam-Johansen, K., *AIChE J.* 39:1342–1354 (1993).
29. Åmand, L. -E. "Nitrous Oxide Emission from Circulating Fluidized Bed Combustion," Ph.D. Thesis, Department of Energy Conversion, Chalmers University of Technology, Göteborg, 1994.
30. Johnsson, J. E., Åmand, L. -E., Dam-Johansen, K., and Leckner, B., 10:970–979 (1996) *Energy Fuels.*
31. Glarborg, P. and Miller, J. A., *Combust. Flame* 99:475–483 (1994).
32. Miettinen, H., Paulsson, M., and Strömberg, D., *Energy Fuels* 9:10–19 (1995).

Twenty-Sixth Symposium (International) on Combustion/The Combustion Institute, 1996/pp. 3343–3354

SCALING CHARACTERISTICS OF AERODYNAMICS, HEAT TRANSFER, AND POLLUTANT EMISSIONS IN INDUSTRIAL FLAMES

ROMAN WEBER
International Flame Research Foundation
P.O. Box 10 000, 1970 CA IJMUIDEN
The Netherlands

A review of the knowledge required for successful scaling of small-scale flames into industrial ones has been carried out from the point of view of fluid flow, heat transfer, and pollutant emissions. Constant velocity and constant residence time scaling criteria have been scrutinized for their applicability in engineering of gaseous, spray-oil, and pulverized coal flames. It has been demonstrated that both have limitations and, in particular when applying to two-phase combustion, there appear to be considerable difficulties in scaling of the interactions between the gaseous and solid (liquid) phases.

Specific considerations are given to scaling natural gas flames spanning the thermal input range of 7 kW to 14 MW. A methodology derived for scaling of the emission data with heat extraction has been used to quantify the spread in the NO_x correlation of Røkke et al. [60]. It has been concluded that to make the derived correlations applicable to industrial situations, the important effects of flue gas entrainment through the external (in-furnace) recirculation zone has to be included. In addition to the radiant fraction, another scaling parameter accounting for the radiation losses from the postflame region is needed. Rapidly developing new combustion technologies require scaling considerations on (1) flame–flame interactions and (2) steady and transient combustion of small quantities of fuel gas and air both injected into hot combustion products.

Introduction

In the process leading to improved burner designs, small- or semiindustrial-scale experiments play an important role in reducing overall development cost, increasing turnaround of burner concept validation tests, and providing detailed diagnostics to guide the burner concept evaluation. Results obtained on small-scale burners can be extrapolated to the full industrial-scale when scaling rules are used to account for the differences in thermal input range. At present, these scaling rules are not completely understood. A typical scenario often encountered is that a low NO_x burner, when installed in a furnace different from that on which it was originally tested, has produced unacceptable NO_x emissions. This is predominantly due to unforeseen alterations to either in-furnace fluid flow or heat transfer.

Objectives

The understanding of combustion chemistry including mechanisms of pollutant formation and destruction is the key factor in successful design of industrial-scale equipment. The knowledge of chemistry has increased substantially over the last two decades with respect to gaseous fuel combustion [1–4], pollutants [5,6], soot formation and destruction [7], reburning [8], SO_x formation and capture [9], and coal combustion [10]. On the basis of this knowledge, combustion engineers select design criteria appropriate for the particular process, among them stoichiometry, temperature regime, and residence time. Practical implementation of these criteria can be accomplished only by proper use of fluid mechanics, appropriate design of burner/furnace geometry, and control of heat transfer. While the first two control the mixing processes at both the micro- and macrolevels, and ultimately the local in-flame stoichiometries and residence time, the heat-transfer characteristics affect the overall temperature level. This paper reviews existing knowledge on how the design criteria and subsequent flame characteristics including emissions are altered while changing the burner thermal input (scale).

For the sake of clarity, the following arbitrary definition of scales, based on the thermal input, is introduced: laboratory-scale flames <300 kW_t; 300 kW_t <semiindustrial-scale flames <4 MW_t; full industrial-scale flames >4 MW_t.

Industrial Practices

Most combustion equipment manufacturers carry out the burner development work using semiindustrial-scale furnaces for testing prototype burners. Figure 1 shows a staged mixing burner, exemplifying

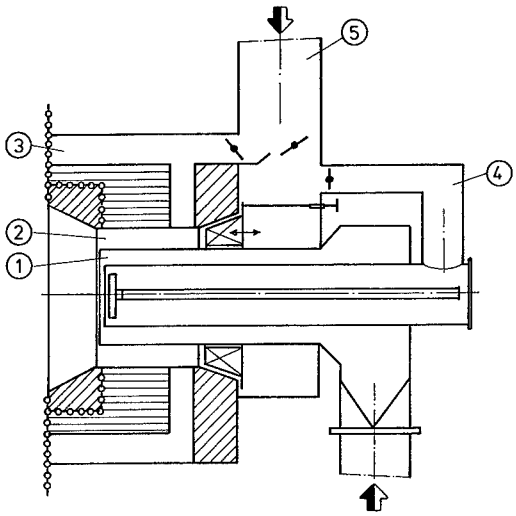

FIG. 1. Staged mixing burner for pulverized coal [1], (1) pulverized fuel with transport air; (2) secondary (swirled) combustion air; (3) tertiary air; (4) "bleeding" air; (5) total air supply.

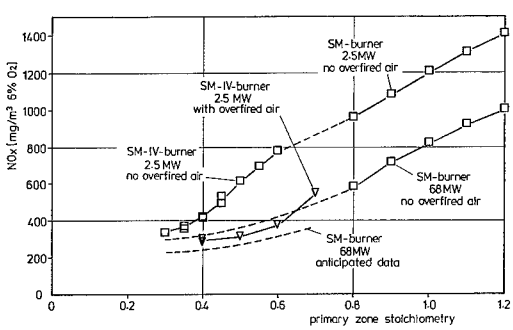

FIG. 2. Performance predictions for a new generation of staged mixing (SM) burners [12].

a family of low-NO_x externally air staged burners that were very popular in the mid eighties [11]. One of the main design parameters of the burner is the primary zone stoichiometry. Figure 2 shows the dependence of the NO_x emissions on this parameter for a 2.5-MW; version of the burner tested in the IFRF furnace No. 1, and emissions from a 680-MW_e boiler equipped with these burners of 68-MW_t thermal input [12]. The single burner tests were carried out under conditions of 0.1-MW/m^3 furnace firing density and 0.6-MW/m^3 flame firing density. The estimated residence times in the furnace and in the fuel-rich zone of the 2.5-MW_t flame were 6 s and 40 ms, respectively. The 68-MW_t burner was scaled geometrically from the 2.5-MW_t version, using the constant velocity principle, with some extra modifications to ensure that the primary zone stoichiometry of the full-scale burner corresponds to that of the prototype. For the full-scale burner, the residence time in the fuel-rich part of the flame is estimated to be 200 ms, while the residence time in the boiler is in the range of 1–3.5 s, depending on the positioning of the burner in the boiler. The boiler emission data collected under various operating conditions show substantially lower values (Fig. 2), which is attributed to the increased residence time in the fuel-rich part of the flame. Intensive testing of the staged mixing burner at the scale of 2.5 MW_t with and without overfired air has produced a new generation of the burner and its anticipated boiler performance [12], shown in Fig. 2. The previously established relationship between the single flame tests at 2.5-MW_t scale and the 640-MW_e boiler emissions serve as a scaling methodology for the new designs.

The three basic questions formulated by the combustion equipment manufacturers are

1. What is the minimum thermal input for the prototype combustion tests?
2. What scaling laws should be used on the prototype test results?
3. What would be the performance, of both the prototype and the final design, in furnaces/boilers of different shape and thermal characteristics?

Scaling Considerations

Scaling of combustion systems involves considerations on fluid flow, combustion, and heat transfer in the close vicinity of the burner and in the furnace. Theoretical considerations on scaling of combustion systems can be found in Spalding [13] and Beér and Chigier [14] who listed a large number of dimensionless groups derived using the fundamental differential equations for momentum, energy, and mass balance. Damköhler [15] was perhaps the first to formulate five dimensionless ratios for scaling chemical reactors. From the fluid dynamics perspective, scaling diffusion flames requires both kinematic and dynamic similarities to be maintained.

The main practical consequences of the theoretical analysis, based on the dimensionless groups [13–14], is that scaling of diffusion flames in enclosures by adhering strictly to the theoretical requirements is impossible. Maintaining even only the main dimensional group constant (e.g., Reynolds, Froude, and Damköhler numbers) leads to conflicting requirements. That is why in practice only a few of the scaling rules are obeyed, leading to so-called partial modeling or scaling [13]. Several methodologies of partial scaling were scrutinized by Beér and Chigier [14], Salvi and Payne [16], Lawn et al. [17], and more recently Smart et al. [18–20]. The two most frequently applied criteria for industrial flame scaling are the constant velocity and constant residence time

approaches (the constant Reynolds number criterion is seldom used since for industrial flames the Reynolds number typically exceeds 10^5).

Constant Velocity Scaling

The basic formula for the burner thermal input (Q) is as follows:

$$Q = K\rho_0 U_0 D_0^2 \tag{1}$$

where ρ_0, U_0, and D_0 relate to the inlet fluid density (typically combustion air density), characteristic burner (combustion air) velocity, and burner characteristic diameter (burner throat diameter); K stands for a proportionality constant. When a burner is scaled to a different thermal input using the constant velocity criterion (U_0 = const), the characteristic burner diameter can be evaluated easily

$$D_0 \propto Q^{0.5} \tag{2}$$

and so, if the geometrical similarity of the burner is maintained, the other burner dimensions can be calculated.

Constant Residence-Time Scaling

The principle of this scaling criteria is to maintain D_0/U_0 ratio constant while changing the burner thermal input. The ratio represents the inertial timescale of the flow, often called the convective timescale. At high enough Reynolds numbers, all time measures in the flow, except those associated with the (final) molecular dissipation processes, are proportional to D_0/U_0. It has been demonstrated that for simple burners, the D_0/U_0 ratio represents the flame residence time. Recalling Eq. (1) and invoking the requirement of maintaining D_0/U_0 constant results in the relationship

$$D_0 \propto Q^{0.33} \tag{3}$$

In practice, burner manufacturers seldom use this approach since it leads to very low windbox pressure for small-scale burners and excessive pressures for full-scale burners [17].

Scale Effect on Mixing

Since pollutant formation and destruction rates are affected strongly by both macro- and micromixing, it is imperative to examine how the mixing characteristics vary while changing the burner scale (thermal input). Using the constant residence time scaling principle, the (large) macromixing timescale D_0/U_0 is automatically kept unaltered. Sadakata and Hirose [21] have argued that in the case of an isotropic turbulence, even the micromixing timescale is constant for the constant residence time principle. Smart et al. [18,19], using the approach of Hawthorne et al. [22], have postulated that, to the first order of accuracy, the fractional degree of macromixing, X_f, at any point downstream of the burner exit is proportional to the normalized distance x/D_0, where x stands for the distance from the burner exit. The corollary of this relationship is that "the flames of any scale, or flames of identical scale but scaled down using different scaling criteria should show identical degrees of reaction at identical values of x/D_0 if all the combustion and pollutant formation reactions are everywhere (in the flame) fast compared to the micro mixing rate" [18].

Fluid Flow Pattern of Single Flames of Gaseous Fuels

Simulating full industrial-scale flames in either semiindustrial-scale or laboratory-scale experiments with one of the previously mentioned criteria makes sense only if the overall flow pattern is preserved. Scaling of the overall flow pattern of turbulent jet flames is applied routinely in the industry [23]. In most industrial applications, the Reynolds number is sufficiently large and so is the Froude number (with the exception of some low-velocity burners). Maintaining these two numbers at high enough levels is usually sufficient. However, care must be taken in scaling jets in furnaces to account for the entrainment of (recirculated) combustion products. Here, the Thring and Newby [24] criterion invokes the requirement of constant confinement expressed as furnace-to-burner-diameter ratio (the necessary scaling formulae can be found in Beér [23]). For swirl stabilized flames, an extra requirement of maintaining both the type of inlet vortex and the inlet swirl number is needed [25–27].

Fluid mechanics of natural gas burners using a central natural gas nozzle with small holes and swirling or nonswirling annular combustion air was studied by Fricker and Leuckel [28], Salvi and Payne [16] and more recently in the Scaling 400 project [29–36]. Salvi and Payne [16], varied the fuel-to-air-momentum ratio in the range of 0.3–0.5 and the confinement (furnace over burner throat diameter) in the range of 8–13.4 for flames of 0.58 and 2.31 MW_t thermal input. The Scaling 400 study has spanned the thermal input range of 30 kW_t to 12 MW_t. The experiments positioned along the line of thought (Fig. 3) indicate the constant velocity scaling principle with identical furnace confinement (6.1). The burners (Fig. 4) had identical fuel-to-air-momentum ratio of 0.3 (to achieve the same momentum and velocity ratios, the size of the fuel jets was manipulated). In the 300-kW_t BERL experiments [32] and the 1.3-MW_t British Gas tests [36], the confinement was 12.5 and 3.3, respectively. The primary conclusions of all these studies are that, to achieve the flow pattern similarity,

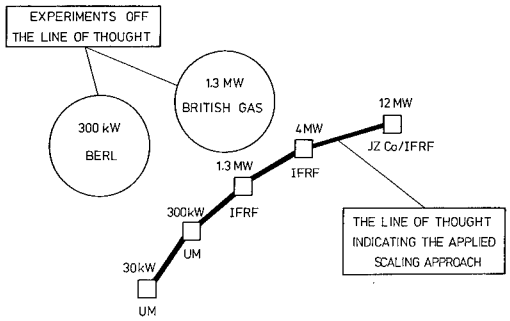

FIG. 3. Scaling 400 studies [29]; experiments along the line of thought indicate constant velocity (and simultaneously constant momentum) burner scaling while maintaining both confinement and thermal similarity; the experiments off the line of thought indicate variations in confinement and thermal similarity.

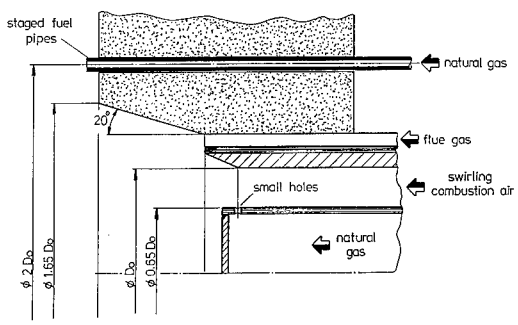

FIG. 4. Scaling 400 natural gas burner [29].

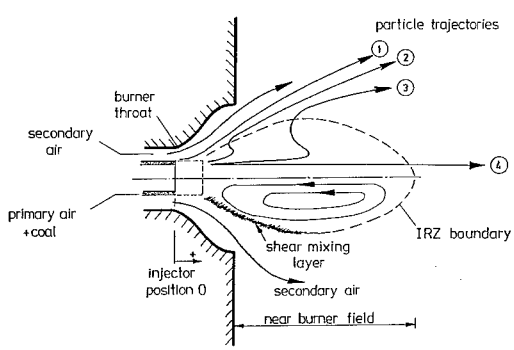

FIG. 5. Trajectories of coal particles in the aerodynamically air-staged burner [15].

- The fuel-to-air-momentum ratio must be maintained.
- The geometrical burner similarity should be maintained (small departures are acceptable).
- The effect of the confinement is secondary for confinements larger than 3.
- The laboratory-scale burners, with the burner characteristic diameter smaller than 5 cm, should decrease the inlet swirl by 20–30%.

Fluid mechanics of a central natural gas jet behind a circular bluff body is perhaps even more complex than that of swirl-stabilized flames described earlier. Although industrial interest in solving the problem certainly exists, so far most of the work has been done in small laboratory-scale (7–15 kW) flames [37,38]. Chen et al. [39] have identified the vortex strength and fuel-jet momentum flux as flame length scaling parameters. It would be informative to scale the small laboratory burner of Schefer et al. [37] to thermal inputs of 0.5 MW_t or perhaps even 1.5 MW_t using these scaling criteria. The conventional constant momentum ratio approach (combined with geometrical similarity), when applied to scaling this burner, has resulted in significantly dissimilar flames of 1.5-MW_t thermal input [40].

Fluid Flow Pattern of Single Flames of Oil and Pulverized Coal

Achieving the correct fuel stream momentum with respect to air momentum, while scaling flames of heavy fuel oil, is much more difficult. That is mainly because oil atomizer design produces a certain droplet size distribution that does not allow for an easy adjustment of the spray momentum. An excellent example of the effect of droplet size distribution on ignition pattern of industrial heavy fuel oil burner can be found in Lawn et al. [17]. Although there is a wealth of literature on oil atomization [41–42], little has been done on the development of the methodology for tailoring the spray properties to the burner fluid dynamics while scaling burners. This is clearly a gray area of industrial atomization. The experimental philosophy of Yule and Bolado [43], who used a parametric atomizer allowing for deconvolution of the effects of initial momentum, velocity, and droplet size distribution on spray laboratory-scale flames, should be applied to deriving the required scaling laws for industrial atomizers.

One of the possible methods of NO_x reduction with pulverized coal firing through swirl stabilized burners, is based on promoting penetration of the coal jet into the swirl-induced internal recirculation zone (IRZ) [44,45]. The degree of NO_x reduction is strongly dependent on the success in promoting coal devolatilization inside the depleted oxygen zone of the IRZ. The burner designer manipulates the interaction between the solid and gaseous phases promoting trajectories three and four, as shown in Fig. 5. The simplest method of accomplishing this is by insertion of the fuel-injector inside the burner quarl. Smart and Morgan [20] have examined how the flame characteristic, including NO_x emissions, vary with the insertion distance for both constant

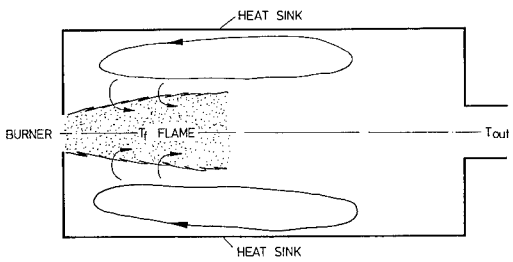

FIG. 6. Furnace-enclosed flame entraining recirculated combustion products.

residence time and constant velocity versions of the aerodynamically air-staged burner. Thus, one of the main scaling parameters for such burner design is the penetration distance of coal particles. In laboratory-scale experiments, the degree of penetration (penetration distance divided by the length of the IRZ) is substantially longer than in semiindustrial-scale experiments. This feature is certainly visible when comparing the 150-kW_t flames of both Abbas et al. [46] and Costa et al. [47] with the 2.5-MW_t flames of Smart et al. [18–20] (although different burners were used). This disparity can be overcome if the coal is pulverized finer for the small-scale experiments or even micronized if the thermal input is lower than 50 kW_t. For standard particle size distribution, small flames cannot practically be stabilized without a supporting fuel [48].

Heat Transfer

In the flame zone, where intensive combustion takes place, the rate of combustion determines the (peak) temperatures, which are altered by the flame stretch and radiation. In the postflame zone, where the release of chemical enthalpy has largely ceased, the rate with which the combustion product's temperature decreases is determined (mainly) by radiation and convection losses.

In the mid seventies and eighties, scaling of radiative characteristics of laminar and turbulent free flames was a subject of intensive research. Simple and useful correlations were derived for buoyancy-dominated turbulent [49] and laminar flames [50,51]. Radiation losses affect the NO_x emissions, and a single scaling parameter—radiant fraction—is used in scaling free jet flames. The work of Buriko and Kuznetsov [52], Turns and Myhr [53], Faeth et al. [54], and Delichatsios et al. [55,56] have provided quantification to this effect for several fuels of different sooting tendencies. For flames in furnaces with heat sinks present, the primary thermal similarity criterion is to achieve identical furnace exit temperatures in the small- and large-scale experiments. Since the heat losses increase with decreasing the flame (combustor) size, this requires manipulations to the furnace wall temperature and positioning of the heat sinks. Theoretically, the radiant fraction similarity parameter, developed originally for free flames, can be expanded further to account for the radiation exchange with walls and heat sinks.

However, in industrial furnaces where combustion products are recirculated from the postflame zone back to the flame roots (by momentum-driven recirculation zones), an additional radiation scaling parameter is needed. This parameter should account for the energy extracted from the postflame zone, altering the temperature of the combustion products. This will be demonstrated using a system consisting of a single flame positioned in a furnace equipped with a heat sink (Fig. 6). The energy balance for the flame reads

$$H_{in} + mc_p(T_{out} - T_0)\,\alpha + H_{abs} = H_{rad} + mc_p(T_f - T_0)(1 + \alpha) \quad (4)$$

where H_{in}, H_{abs}, and H_{rad} stand for burner thermal input, radiant energy absorbed by the flame, and radiant energy emitted by the flame, respectively. T_f, T_{out}, and T_0 are flame temperature, furnace exit temperature, and reference temperature, respectively, while c_p is the mean specific heat at constant pressure. The parameter α is defined as a ratio of the entrained fluid to the inlet flow rate (m). The preceding equation can be rearranged easily into a dimensionless form:

$$1 + \alpha\frac{T_{out} - T_0}{T_{af} - T_0} = X + (1 + \alpha)\frac{T_f - T_0}{T_{af} - T_0} \quad (5)$$

where X and T_{af} are the radiant fraction and adiabatic flame temperature, respectively. Eq. (5) can be combined with the overall energy balance for the whole furnace,

$$H_{in}(1 - X - Y) = mc_p(T_{out} - T_0) \quad (6)$$

with Y being the fraction of the total thermal input extracted in the postflame zone by radiation and convection. Combining Eqs. (5) and (6) gives a relationship for estimating the flame temperature, T_f,

$$1 - X - \frac{\alpha}{1 + \alpha}Y = \frac{T_f - T_0}{T_{af} - T_0} \quad (7)$$

Eq. (7) is a very useful expression for analyzing the effect of heat transfer (radiation) on the flame temperature and NO_x emissions. It shows that for free flames ($\alpha = 0$), the radiant fraction can be used as a single scaling parameter, which for nonsooting gaseous flames is in the range of 0.03–0.1. For sooty flames, the range increases to 0.1–0.2, while in the extreme case of buoyancy-controlled propane flames/it can be as high as 0.24 (see Ref. 49). In industrial applications, the term $\alpha Y/(1 + \alpha)$ is important, since Y can be as high as 0.5–0.6, while the entrainment parameter α can take values up to 2.

TABLE 1
Scaling characteristics of Flames 1 and 2 (Ref. 57).

Parameter	Flame 1 refractory lined furnace	Flame 2 water-cooled furnace
Thermal input	316	312
Furnace exit temperature (°C)	1113	935
NO_x (ppm, 3% O_2)	49	34
X (radiant fraction)	0.03	0.033
Heat extraction ($X + Y$)	0.325	0.49
Y	0.295	0.457
$\alpha Y/(1 + \alpha)$	0.164	0.196

Table 1 illustrates the point further, showing characteristics of flames issued from the same burner into furnaces configured either out of refractory lined segments or out of water-cooled panels. The dominant effect of the second term is clearly demonstrated. The earlier simple analysis can be further expanded to relate the Y parameter to the heat sink temperature and its positioning with the respect to the flame. It is possible that further refining of the energy analysis to thin layers (shear layers) where NO is formed may lead to powerful scaling laws.

Emission data of the Scaling 400 flames are shown in Figs. 7a and 7b, with the latter applicable to scaling NO_x emissions of gas-fired furnaces with the overall heat extraction ($X + Y$). In Fig. 7b, the emission data obtained under conditions of maintaining the burner-to-furnace-diameter ratio (the line of thought experiments of Fig. 3) have been plotted using solid symbols, while the open symbols refer to the 300-kW BERL experiments where the furnace is oversized. Although this type of information is certainly industrially valuable, there is a need to refine this information further to deconvolute the effects of X, Y, and α. Furthermore, systematic studies on the effect of altering the heat-extraction profile (repositioning of the heat sink with respect to the flame) are needed.

Scaling of Nitric Oxide Emissions of Single Hydrocarbon Flames

The emission data for nominal (design) load flames of the Scaling 400 flames are plotted in Fig. 7a as a function of thermal input ($Q^{0.5}$ scale is used since the burners were scaled using a constant velocity principle; Q stands for burner thermal input) and flame residence time (linear scale). The baseline points (marked 1–5) correspond to ambient combustion air temperature and 50% heat extraction. Figure 7b allows rescaling of the emission data to other furnace thermal conditions (see earlier section). The accuracy of the NO_x emission data and the thermal input values is better than 5%, while the residence time estimates are likely to be within ±10%. The emissions of the small-scale flames (30 kW and 300 kW) are substantially lower than the semiindustrial- and industrial-scale flames.

Røkke et al. [60] have studied nitric oxide emissions from buoyancy-dominated hydrocarbon turbulent jet flames. Their measurements, comprising methane, propane, and natural gas flames, were supported with a flamelet model that identified separate oxygen-consumption and fuel-consumption zones. The study has resulted in a simple scaling correlation

$$\frac{EI_{NO_x}\rho_0 u_0}{d_0} \approx 44Fr^{0.6} \approx 11\,\frac{u_0^{1.2}}{d_0^{0.6}} \qquad (8)$$

where ρ_0 is fuel density, u_0 is fuel exit velocity, and d_0 stands for the fuel (hole) exit diameter. In the preceding equation, EI_{NO_x} is the emission index, and Fr is the Froude number. The correlation and its comparison with numerous emission data are shown in Fig. 8, which is practically a replica of Fig. 4 of Ref. 60. It is remarkable that such a correlation is valid over the Froude number range up to 10^6 approaching momentum-dominated conditions. It is fair to say that the derived correlation features a relatively wide deviation from the measured data for any particular value of Froude number. It will be shown later that further improvements can be made if one accounts for radiation losses of the flames.

It is instructive to examine how the emission data of the Scaling 400 study on confined flames of relatively insignificant radiant fraction (X) and the overall heat extraction ($X + Y$) of the order of 0.4–0.7 conform to the correlation of Røkke et al. [60]. To this end, Fig. 9 is produced, containing emissions of the nominal Scaling 400 flames (marked with numbers 1–5), as well as a number of turndown conditions. The Froude number is calculated using the fuel gas velocity at the single gas hole and the hole diameter (Fig. 4). The natural gas flame data of Al-Fawaz et al. [67] have also been included. Figure 9, which shows how to scale the emissions with the heat extraction, contains emission data for natural gas

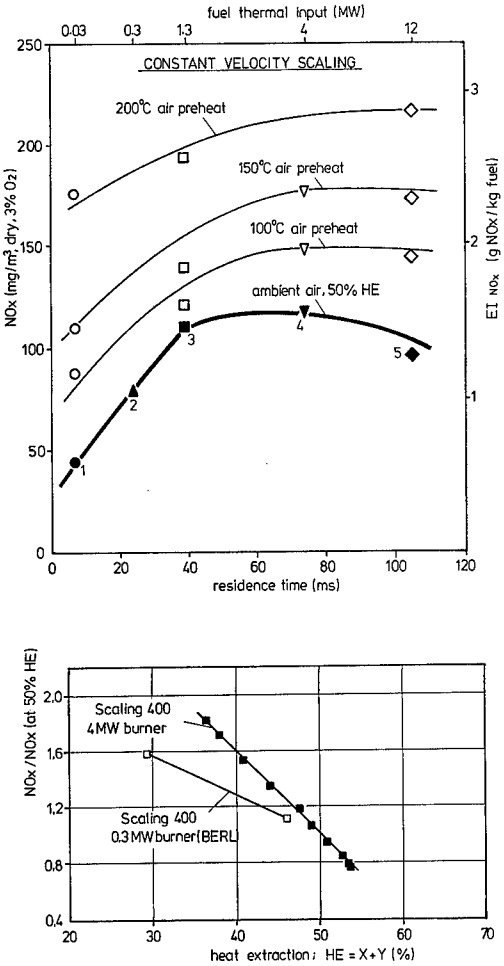

FIG. 7. (a) NO_x emissions of (Scaling 400) natural gas flames. Closed symbols, baseline (high NO_x) flames with 50% heat extraction; open symbols, baseline (high NO_x) flames with 50% heat extraction; preheated combustion air: (1) 30 kW; natural gas: CH_4 93.0%, C_2H_6 <3%, C_3H_8 <1%. (2) 300 kW; natural gas: CH_4 93.0%, C_2H_6 <3%, C_3H_8 <1%. (3) 1.3 MW; natural gas: CH_4 90.0%, C_2H_6 3.6%, C_3H_8 0.7%. (4) 4 MW; natural gas: CH_4 90.0%, C_2H_6 3.6%, C_3H_8 0.7%. (5) 12 MW; natural gas: CH_4 90.1%, C_2H_6 5.5%, C_3H_8 1.0%. (b) NO_x emission of (Scaling 400) natural gas flames—effect of overall heat extraction; solid symbols [58], open symbols [32,57].

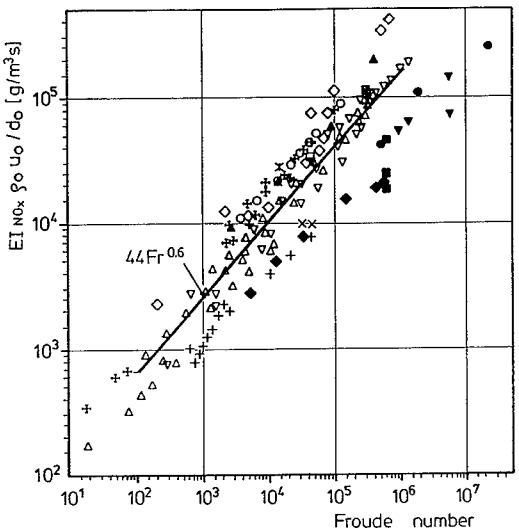

FIG. 8. Correlation of the emission index according to Eq. (8) [60]. ×, C_3H_8 Buriko and Kuznetsov [52]; □ C_3H_8 Takagi et al. [61]. ○, C_3H_8 Turns and Lovett [62]; ◇ C_3H_8 Turns and Myhr [53]. +, C_3H_8 Røkke et al. [63]; △ C_3H_8, Røkke et al. [60]. +, CH_4 Røkke et al. [60]; ▽ CH_4 Turns and Myhr [53]. ×, CH_4 Chen and Driscoll [64]; ▲ C_2H_4 Turns and Myhr [53]. ▼, H_2 Chen and Driscoll [64]; • H_2 Lavoie and Schlader [65]. ■, H_2 Bilger and Beck [66].

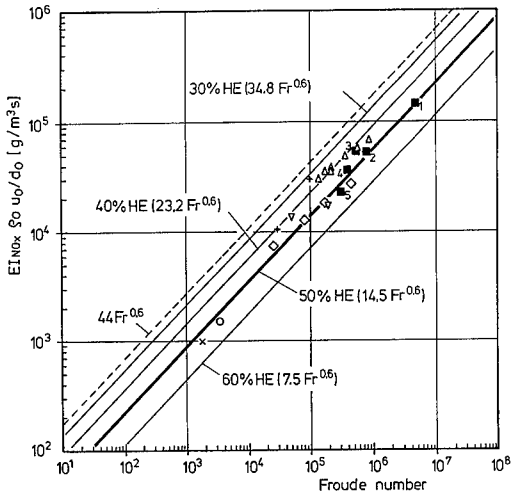

FIG. 9. Verification of Eq. (8) using Scaling 400 flame data. ■, 1,2,3,4,5; baseline flames, see Fig. 7; ▽, turndown flames of 300 kW experiments [35]; △, turndown flames of 1.3 MW experiments [34]; +, turndown flames of 4 MW experiments [33]; ◇, turndown flames of 12 MW experiments [30]; ×, natural gas flames (burner A) of Al-Fawaz et al. [67]; ○, natural gas flames (burner B) of Al-Fawaz et al. [67]; -----, correlation of Røkke et al. [60].

flames spanning the thermal input range of 30 kW to 14 MW. These data come from the semiindustrial Scaling 400 burners operated with fuel velocity in the range of 40–170 m/s and combustion air velocity in the range of 9–38 m/s. Thus, the correlation has been derived from the flame data of air-to-fuel-gas-velocity ratio up to 0.225 (see also Tomeczek et al. [68]). Certainly the correlation is encouraging, and

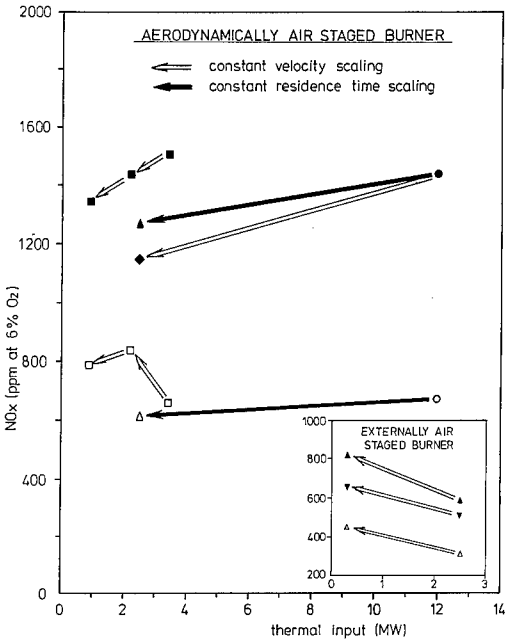

FIG. 10. Scaling of pulverized coal flames. Solid symbols, high-NO_x flames; open symbols, low-NO_x (staged) flames. *Aerodynamically air-staged burner.* ●,○-hvBb Göttelborn coal, 1.8% N, 36.2% volatiles [69]; ▲-hvBb Göttelborn coal, 1.43% N, 39% volatiles [70]; ■,□-mvB Coal Valley coal, 0.85% N, 32% volatiles [18,71]; ◆-hvBb Göttelborn coal, 1.3% N, 37% volatiles [72]. *Externally air-staged burner.* ▲-hvBb Göttelborn coal, fine coal particles [73]; ▼-hvBb Göttelborn coal, coarse coal particles [73]; △-hvBb Göttelborn coal, fine and coarse coal particles [73].

further work on deconvoluting the heat-transfer (losses) effects and jet entrainment effects should follow. It is expected that the effect of preheating the combustion air can also be incorporated.

Scaling of Nitric Oxide Emissions of Pulverized Coal Flames

Figure 10 shows a summary of experiments on pulverized coal flame scaling. The graph contains emission data of both the aerodynamically air-staged burner and the externally air-staged burner. Most of the emission data are from burners scaled using the constant velocity principle; only two cases are shown where the constant residence time scaling approach is used. A substantial amount of work is needed to derive appropriate correlations for scaling these emission data.

Scaling Correlations Needed for the Immersing New Technologies

The preceding sections have highlighted difficulties in relating small-scale experiments to industrial

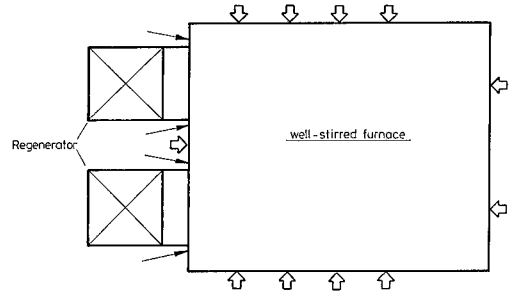

FIG. 11. Advanced fuel direct injection (FDI) system for low-NO_x combustion of natural gas with substantial fuel savings [79]. The arrows indicate descrete injections of natural gas and combustion air.

applications. Most of our knowledge on flame scaling is relevant to standard high-NO_x flames. Relevant information is scarce on low-NO_x designs. Furthermore, the existing knowledge applies to single flames only, while for most of industrial applications, rows of burners are common. Little is known about flame–flame interactions and related scaling relations.

New technologies for achieving ultralow NO_x emissions with natural gas firing are based on entraining flue gas into the fuel jet before combustion. Examples are the internal flue gas recirculation burner of John Zink Co. [74], Callidus Technologies [75], StAR II burner [76], or Eclipse/Altex prototype burner [77]. Today, many furnaces are equipped with heat-recovery systems allowing for preheating of combustion air and substantial fuel savings. Further progress in heat recovery and materials will certainly allow for operating furnaces with the combustion air temperature close to the furnace exit temperature. This opens up a completely new technological opportunity of designing the future furnaces as well-stirred reactors [78,79] with perhaps discrete injections of fuel gas and combustion air (Fig. 11). Before ignition takes place, both the fuel gas and combustion air streams entrain the in-furnace recirculating gases, which just promotes the self-induced flue gas recirculation effects. The final result is likely to be an extremely (energy) efficient system with low-NO_x emissions [80].

While engineering work has already been progressing toward development of such systems, the fundamental combustion community so far has done very little to provide the adequate scientific insight. The scaling relations related to steady and transient combustion of small quantities of fuel gas and air both injected into (hot) combustion products are needed. Fundamentals of natural gas combustion including nitrogen oxides and carbon monoxide formation and destruction mechanisms in combustion products containing oxygen are required [81].

Conclusions

A review of the knowledge required for scaling of small-scale flames into industrial ones has been carried out from the point of view of fluid flow, heat transfer, and pollutant emissions. Constant velocity and constant residence time scaling criteria have been scrutinized for their applicability in engineering of gaseous, spray-oil, and pulverized coal flames. It has been demonstrated that both have limitations and in particular when applying to two-phase combustion, there appear considerable difficulties in scaling of the interactions between the gaseous and solid (liquid) phases.

Correlations derived by Røkke et al. [60] for scaling of NO_x emissions of buoyancy-controlled hydrocarbon flames have been scrutinized against emission data of natural gas flames generated within the Scaling 400 project, spanning the thermal input range of $30kW_t$ to $12\ MW_t$. When the velocity at the single hole in the natural gas injector of the Scaling 400 burner was used to calculate the correlation parameters used by Røkke et al. [60], the flame data became related. A methodology developed within the Scaling 400 study to scale the emission data with heat extraction has been used to quantify the spread in the NO_x-emission correlation of Røkke et al. [60]. To make the correlation applicable to industrial situations, the important effects of flue gas entrainment through the external (in-furnace) recirculation zone has to be included. In addition to the radiant fraction, an additional scaling parameter accounting for the radiation losses from the postflame region is needed.

While there is some understanding of how to scale standard (high-NO_x) flames, there is limited knowledge on scaling of low-NO_x designs. There is an urgent need to improve the understanding of flame–flame interactions and to derive corresponding scaling correlations with respect to heat transfer, fluid mechanics, and pollutant emissions. The rapidly developing technologies of NO_x reduction in high-temperature processes using significant air preheat requires the support of the combustion community. The scaling relations related to steady and transient combustion of small quantities of fuel gas and air both injected into (hot) combustion products are required.

Acknowledgments

I am grateful to all my colleagues of the IFRF who have reviewed and commented upon the text. The comments of D. J. Morgan, N. Lallemant, F. Breussin, and J. Dugué are highly appreciated.

REFERENCES

1. Gardiner, W. C. Jr., *Combustion Chemistry,* Spring Verlag, New York, 1984.
2. Frenklach, M., Wang., H., Bowman, C. T., Hanson, R. K., Smith, G. P., Golden, D. M., Gardiner, W. C., and Lissianski, V., "An Optimized Kinetic Model for Natural Gas Combustion," Work-in-Progress Poster Presented at Twenty-Fifth International Symposium on Combusation, Irvine, CA, 1994.
3. Warnatz, J., *Twenty-Fourth Symposium (International) on Combustion,* The Combustion Institute, Pittsburgh, 1992, p. 553.
4. Just, T., *Twenty-Fifth Symposium (International) on Combustion,* The Combustion Institute, Pittsburgh, 1994, p. 687.
5. Bowman, C. T., in *Fossil Fuel Combustion* (Bartok, W. and Sarofim, A. F., Eds.), Wiley, New York, 1991.
6. De Soete, G. G., "Fundamentals of NO_x and N_2O Formation and Destruction," Utilisation of Solid Fuels, September 18–22, 1989, IFRF, Regal Riverside Hotel, Hong Kong.
7. Howard, J. B., *Twenty-Third Symposium (International) on Combustion,* The Combustion Institute, Pittsburgh, 1990, p. 1107.
8. Kilpinen, P., Glarborg, P., and Hupa, M., *Ind. Eng. Chem. Res.* 31:1481 (1992).
9. Pershing, D. W., "SO_x Fundamentals," Utilisation of Solid Fuels, September 18–22, 1989, IFRF, Regal Riverside Hotel, Hong Kong.
10. Smoot, L. D., *Fundamentals of Coal Combustion for Clean and Efficient Use,* Elsevier Amsterdam, 1994.
11. Leikert, K. and Michelfelder, S., "Operating Experience and Field Data of a 700 MW Coal-Fired Utility Boiler with Retrofit Low NO_x Staged Mixing Burners." Joint EPA/EPRI Symposium on Stationary Combustion NO_x Control, Vol. 1, Denver, CO, October 1980.
12. Jochem, M., Schreier, W., and Thierbach, H., "Development of an Ultra Low NO_x Staged Mixing Burner for Pulverized Coal: Test Results from Semi-Industrial Scale Application to Full Scale," Proceedings of the 11th IFRF Members Conference, Noordwijkerhout, the Netherlands, 1995.
13. Spalding, D. B., *Ninth Symposium (International) on Combustion,* The Combustion Institute, Pittsburgh, 1962, p. 833.
14. Beér, J. M. and Chigier, N. A., *Combustion Aerodynamics,* Applied Science Publishers Ltd., London, 1972.
15. Damköhler, G., *Elektrochem* 42:846 (1936).
16. Salvi, G. and Payne, R., "Investigation into the Scaling of Combustion Systems," IFRF Doc. No. F 31/a/52, 1981.
17. Lawn, C. J., Cunningham, T. S., Street, P. J., Matthews, K. J., Sarjeant, M., and Godridge, A. M., in *Principles of Combustion Engineering for Boilers,* (Lawn, C. J., Ed.), Academic Press, New York, 1987.
18. Smart, J. P., "On the Effect of Burner Scale and Coal Quality on Low NO_x Burner Performance," Ph.D. Thesis, University of London, 1992.
19. Smart, J. P., van de Kamp, W. L., and Morgan, M. E., *Fuel* 70:1350 (1990).

20. Smart, J. P. and Morgan, D. J., *Combust. Sci. Technol.* 100:331 (1994).
21. Sadakata, M. and Hirose, Y., *Fuel* 73:1338 (1994).
22. Hawthorne, W. R., Wedell, D. S., and Hottel, H. C., *Third Symposium (International) on Combustion,* The Combustion Institute, Pittsburgh, 1949, p. 266.
23. Beér, J. M., *J. Inst. Fuel* 466 (1966).
24. Thring, M. W. and Newby, M. P., *Fourth Symposium (International) on Combustion,* The Combustion Institute, Pittsburgh, 1952, p. 789.
25. Chigier, N. A. and Beér, J. M., *ASME J. Basic Engineer.* 86D:788 (1994).
26. Wall, T. F., in *Principles of Combustion Engineering for Boilers* (Lawn, C. J., Ed.), Academic Press, New York, 1987.
27. Weber, R. and Dugué, J., *Prog. Energy Combust. Sci.* 18:349 (1992).
28. Fricker, N. and Leuckel, W., *J. Inst. Fuel* 49:152 (1976).
29. Weber, R., Driscoll, J. F., Dahm, W. J. A., and Waibel, R. T., "Scaling Characteristics of the Aerodynamics and Low NO_x Properties of Industrial Natural Gas Burners," The Scaling 400 Study, Part I: Test Plan, GRI—93/0227, 1993.
30. Weber, R., Sayre, A. N., Dugué, J., and Horsman, H., The Scaling 400 Study, Part II: The 12 MW Test Results, GRI—93/0079, 1993.
31. Driscoll, J. F., Dahm, W. J. A., and Wu, M.-S., The Scaling 400 Study, Part III: The 30 kW Test Results, GRI Report No. 389443-9, 1993.
32. Sayre, A., Lallemant, N., Dugué, J., and Weber, R., The Scaling 400 Study, Part IV: The 300 kW BERL Test Results, GRI-94/0186, 1994.
33. Bertolo, M., Sayre, A. N., Dugué, J., and Weber, R., The Scaling 400 Study, Part V: The 4 MW Test Results, GRI-94/0187, 1994.
34. Sayre, A., The Scaling 400 Study, Part VI: The 1.3 MW Test Results, IFRF Do. No. F 40/y/13, 1995.
35. Dahm, W. J. A., Driscoll, J. F., and Hsieh, A., The Scaling 400 Study, Part VII: The 300 kW Test Results, Report No. 389443-14, Department of Aerospace Engineering, The University of Michigan, 1995.
36. Rhine, J. M., Shepherd, K., Sherwood, G., Hargrave, G., and Graham, D., Report on British Gas/GRI Collaboration on Turbulent Combustion, October 1995.
37. Schefer, R. W., Namazian, M., and Kelly, J., *Combust. Sci. Technol.* 56:101 (1987).
38. Schefer, R. W., Namazian, M., and Kelly, J., *Combust. Sci. Technol.* 67:123 (1989).
39. Chen, R.-H., Driscoll, J. F., Kelly, J., Namazian, M., and Schefer, R. W., *Combust. Sci. Technol.* 71:197 (1990).
40. McKindley, K., "Summary of Experimental Results from the 1.5 MW Bluff-Body Burner," British Gas, Loughborough, UK, 1994.
41. Lefebvre, H. A., *Atomization and Sprays,* Hemisphere Publishing Co., New York, 1989.
42. Williams, A., *Combustion of Liquid Fuel Sprays,* Butterworth, London, 1990.
43. Yule, A. J. and Bolado, R., *Combust. Flame* 55:1 (1984).
44. Weber, R., Smart, J. P., and Phelan, W. J., "NO_x Reduction and Burnout Optimization Using Aerodynamic Air-Staging and Air-Staged Precombustors," IFRF Doc. No. F 037/a/16, (1987).
45. Smart, J. P. and Weber, R., *J. Inst. E.* 62:237 (1989).
46. Abbas, T., Costen, P., and Lockwood, F. C., *Combust. Flame* 91:346 (1992).
47. Costa, M., Costen, P., Lockwood, F. C., and Mahmud, T., *Twenty-Third Symposium (International) on Combustion,* The Combustion Institute, Pittsburgh, 1990, p. 973.
48. Milosavljevic, V. D., Taylor, A. M. K. P., and Whitelaw, J. H., *Twenty-Third Symposium (International) on Combustion,* The Combustion Institute, Pittsburgh, 1990, p. 957.
49. Markstein, G. H., *Sixteenth Symposium (International) on Combustion,* The Combustion Institute, Pittsburgh, 1976, p. 1407.
50. Markstein, G. H. and De Ris, J., *Twentieth Symposium (International) on Combustion,* The Combustion Institute, Pittsburgh, 1984, p. 1637.
51. Kent, J. H. and Wagner, H. G., *Twentieth Symposium (International) on Combustion,* The Combustion Institute, Pittsburgh, 1984, p. 1007.
52. Buriko, Y. Y. and Kuznetsov, V. R., *Combust. Explos. Shockwaves* 13:296 (1978).
53. Turns, S. T. and Myhr, F. H., *Combust. Flame* 87:319 (1991).
54. Faeth, G. M., Gore, J. P., Cheuch, S. G., and Jeng, S. M., *Annu. Rev. Numer. Fluid Mech. Heat Trans.* 1 (1986).
55. Delichatsios, M. A. and Orloff, L., *Twenty-Second Symposium (International) on Combustion,* The Combustion Institute, Pittsburgh, 1988, p. 1271.
56. Delichatsios, M. A., De Ris, J., and Orloff, L., *Twenty-Fourth Symposium (International) on Combustion,* The Combustion Institute, Pittsburgh, 1992, p. 1075.
57. Sayre, A., Lallemant, N., Dugué, J., and Weber, R., *Twenty-Fifth Symposium (International) on Combustion,* The Combustion Institute, Pittsburgh, 1994, p. 235.
58. Weber, R. et al., "Scaling Laws for Natural Gas Burners," Scaling 400 studies, in preparation, 1996.
59. Heap, M. P., Lowes, T. M., and Walmsley, R., *Fourteenth Symposium (International) on Combustion,* The Combustion Institute, Pittsburgh, 1972, p. 883.
60. Røkke, N. A., Hustad, J. E., Sønju, O. K., and Williams, F. A., *Twenty-Fourth Symposium (International) on Combustion,* The Combustion Institute, Pittsburgh, 1992, p. 385.
61. Takagi, T., Ogasawara, M., Fujii, K., and Daizo, M., *Fifteenth Symposium (International) on Combustion,* The Combustion Institute, Pittsburgh, 1990, p. 1051.
62. Turns, S. R. and Lovett, J. A., *Combust. Sci. Technol.* 66:233 (1989).
63. Røkke, N. A., Hustad, J. E., and Sønju, O. K., First

International Conference on Combustion Technologies for a Clean Environment, Vol. 1, Paper 9.3, Vilamoura, Portugal, 1991.
64. Chen, R. H. and Driscoll, J. F., *Twenty-Third Symposium (International) on Combustion,* The Combustion Institute, Pittsburgh, 1991, p. 281.
65. Lavoie, G. A. and Schlader, A. F., *Combust. Sci. Technol.* 8:215 (1974).
66. Bilger, R. W. and Beck, R. E., *Fifteenth Symposium (International) on Combustion,* The Combustion Institute, Pittsburgh, 1975, p. 541.
67. Al-Fawaz, A. D., Dearden, L. M., Hedley, J. T., Missaghi, M., Pourkashanian, M., Williams, A., and Yap, L. T., *Twenty-Fifth Symposium (International) on Combustion,* The Combustion Institute, Pittsburgh, 1994, p. 1027.
68. Tomeczek, J., Góral, J., and Gradoń, B., *Twenty-Fifth Symposium (International) on Combustion,* The Combustion Institute, Pittsburgh, 1994, p. 1035.
69. Woycenko, D. M., Smart, J. P., Morgan, D. J., Van de Kamp, W. L., and Ereaut, P.R., "Evaluation of a 12 MW_t Aerodynamically Air-Staged Burner." IFRF Doc. F37/y/33, 1994.
70. Woycenko, D. M. and Smart, J. P., "Evaluation of a 2.5 MW_t Constant Residence Time Scaled Version of a 12 MW_t Aerodynamically Air Staged Burner," IFRF Doc. F37/y/31, 1993.
71. Smart, J. P., Van de Kamp, W. L., and Morgan, M. E., "The Effect of Scale on the Performance of the Aerodynamically Air Staged Burner," IFRF Doc. F37/y/19, 1989.
72. Weber, R., Dugué, J., Sayre, A., and Visser, B. M., *Twenty-Fourth Symposium (International) on Combustion,* The Combustion Institute, Pittsburgh, 1992, p. 1373.
73. Spliethoff, H., Smart, J., Jochem, M., and Reuther, D., "NO_x-arme Feuerungen und ihre Auforderungen an die Kohle-Ausmahlung," VGB-TW 203, ISSN-Nr. 0937-0188, 1992.
74. Waibel, R. T., private communication; *Chem. Engineer.* January 1994, p. 31.
75. Martin, R. R., "The Effect of Various Operating Parameters on NO_x Formation for Internal Recirculation Burners," *1993 Fall International Symposium Impact of the Clean Air Amendment Act of 1990,* American Flame Research Committee, Tulsa, OK, October 1993, p. 4–21.
76. Syska, A., Benson, C., Beér, J., Toqan, M., Moreland, D., and Ruiz, R., "Low NO_x, High Performance Burner," The Future of Combustion in Industry: Efficiency and Environment. Proceedings of the 10th Members Conference, IFRF, Noordwijkerhout, The Netherlands, May 1992.
77. Gemmer, B., "High Temperature Low NO_x Burners," Proceedings of the 8th Topic Oriented Technical Meeting—TOTeM8, IFRF, Loughborough, UK, 1993.
78. Tanaka, R., "New Progress of Energy Saving Technology Towards the 21st Century, Frontier of Combustion & Heat Transfer Technology: Advanced Combustion Technology for Industry," Proceedings of the 11th Members Conference, IFRF, Noordwijkerhout, The Netherlands, May 1995.
79. Matsumato, M., Nakamachi, I., Yasuoka, S., Saiki, N., and Kaizumi, T., "Advanced Fuel Direct Injection—FDI System," Proceedings of the 11th Members Conference, IFRF, Noordwijkerhout, The Netherlands, May 1995.
80. Kremer, H., *Gaswärme Int.* 43:482 (1994).
81. Visser, B. M., "Combustion of Mixtures of Natural Gas, Air and Hot Flue Gas," Proceedings of the 11th Members Conference, IFRF, Noordwijkerhout, The Netherlands, May 1995.

COMMENTS

Loo T. Yap, The BOC Group Technical Center, USA. Earlier we have proposed [2] the use of NO-emissions scaling relationships derived for simple turbulent diffusion flames [1] for more complex (industrial) burners under certain circumstances. We substantiated this with experimental and computational studies of two geometrical burners differing by a factor of 4 (67 kW and 266 kW). It is rewarding to see from your work that the application of these scaling relationships may guide rationalization of emission trends for burners over a much larger scale than we have examined.

Your extension of these scaling relationships for heat losses using experimental results for natural gas, however, is questionable. Deriving the original correlation, many assumptions including fuel (propane!), flamelet existence, flamelet structure, turbulence-chemistry interaction, flame-volume, characteristic scalar-dissipation rates, global NO-formation rates, and flame-temperature behavior were made [1]. Despite uncertainties, an NO-scaling relationship was derived to *leading order.* It is not clear whether the characteristic temperature (and thus heat loss) is the leading factor explaining the scatter of NO data.

The indiscriminate reduction of the correlation coefficients using complex experimental burner data with heat losses, as proposed in your paper, does not lend insight into this issue. A re-derivation of the correlation with a heat-loss term could have.

REFERENCE

1. Rokke, N. A., Hustad, J. E., Sonju, O. K., and Williams, F. A., *Twenty-Fourth Symposium (International) on Combustion,* The Combustion Institute, Pittsburgh, 1992, pp. 385–393.

2. Al-Fawaz, A. D., Dearden, L. M., Hedley, J. T., Missaghi, M., Pourkashanian, M., Williams, A., Yap, T. L., *Twenty-Fifth Symposium (International) on Combustion,* The Combustion Institute, Pittsburgh, 1994, pp. 1027–1034.

Author's Reply. As it has been indicated in the paper, it is remarkable that the NO-emissions scaling relationship (Fig. 8) is valid over the Frounde number range up to 10^6 approaching momentum-dominated conditions. At the same time it is fair to say, that the derived correlation features a relatively wide deviation from the measured data for any value of Froude number. As long as the wide spread is there, this leading order relationship is just an academical formula practically inapplicable in engineering practices. For various burner designs, combustion engineers are required to give guarantees on NO emissions for any particular application (furnace). Therefore, this leading order relationship has to be first of all derived again for different fuels separately. Furthermore, the important effects of burner/furnace confinement (including the external recirculation zone effects), and of different thermal conditions, have to be deconvoluted [1].

In Fig. 9 the Scaling 400 data on natural gas flames are plotted. Since in all these experiments the natural gases fired were of relatively similar composition (see paper), the correlation $14.5\mathrm{Fr}^{0.6}$ corresponding to 50% heat extraction fits well the experimental data. However, as shown in Fig. 7b the NO emissions are strongly altered by the heat extraction, even when the fluid dynamics together with the characteristic scalar-dissipation rates remain unaltered. Fig. 9 is to show that alterations to furnace thermal conditions cause a relatively large shift of this leading order correlation. To my understanding Fig. 9 provides a considerable insight, since it demonstrates that the heat losses (heat extraction) cannot be neglected, as it has been previously claimed. However, I do not claim that these *ad hoc* introduced parallel lines plotted in Fig. 9, constitute the fundamentally correct way of accounting for the heat losses. I absolutely agree with your statement that a "rederivation of the correlation with a heat loss term" is required.

[1] My comments on the paper of Al-Fawaz, A. D. et al. *Twenty-Fifth Symposium (International) on Combustion,* The Combustion Institute, Pittsburgh, 1994, p. 1034.

Twenty-Sixth Symposium (International) on Combustion/The Combustion Institute, 1996/pp. 3355–3362

STUDIES OF HELMHOLTZ RESONANCE IN A SWIRL BURNER/FURNACE SYSTEM

D. FROUD, A. BEALE, T. O'DOHERTY AND N. SYRED
Cardiff School of Engineering P.O. Box 917
Cardiff CF2 1XH
Wales, UK

This paper describes and analyzes the combustion-excited Helmholtz resonance in a swirl burner/furnace system. Preliminary work showed the importance of variables such as air/fuel ratio, mode of fuel entry, and length of exhaust pipe attached to the exit of the furnace. Conditions were chosen (50% axial, 50% premixed natural gas and air, 600-mm-long exit pipe, air/fuel ratio = 1.53) that gave a clean, near sinusoidal pressure signal at the furnace exit. This signal was used as a trigger to enable phase-averaged axial and tangential velocities as well as temperatures to be taken throughout the furnace and into the exit pipe. The results show that a lifted flame core region exists over all of the oscillation cycle. Combustion excitation via the Rayleigh criteria comes via a periodic combustion wave of annular form located next to the furnace wall. The minimum pressure of the resonance causes a large inflow into the furnace with well-known swirl-type flow patterns, which extinguishes the annular wall flame. The central flame core boundary is located in a low-velocity region between the forward and reverse flow regions. Conversely, the peak resonant pressure virtually stops the inflow into the furnace from the burner and allows the annular wall flame to propagate backward into the furnace. Complex coherent structures in the tangential radial direction are formed close to the junction of the swirl burner and the furnace. The influence of the precessing vortex core (PVC) in the swirl burner exhaust in setting up the resonance seems to be small; however, it does appear to further excite the resonance to higher amplitudes when its frequency is close to that of the Helmholtz oscillation.

Introduction

As has been reported by many workers, swirl flows are widely used to stabilize high-intensity flames with a wide variety of fuels [1,2]. This paper is concerned with instabilities occurring in a common type of configuration where a swirl burner fires into a furnace; the configuration used here is based on a unit for the efficient combustion of low-calorific-value gases; however, geometrically analogous configurations are used in many process heaters and certain gas turbine combustors [1]. It has been shown previously that considerable excitation of resonances in swirl burner systems can occur via acoustic coupling with simple straight exhaust tubes [3]. Maximum resonant amplitude occurred when the predicted quarter wave oscillator frequency matched that of a well-known coherent structure occurring in swirling flows, the precessing vortex core (PVC) [1,3,4]. No detailed analysis of the underlying coupling mechanisms has been made to date. This paper is concerned with Helmholtz excitation of swirl burner/furnace systems, combustion excitation via the Rayleigh criteria, and any interactions/excitations that can occur with the PVC phenomenon.

Results presented here have been obtained primarily from a 100-kW scale model of a larger 2-MW system [4,5] to facilitate configuration changes. A particular case is chosen that gives a sharp, near sinusoidal, high-amplitude pressure wave in the exhaust pipe, and detailed phase-averaged velocity and fluctuating temperature measurements have been made throughout much of the unit where access for instrumentation can be gained.

Apparatus

This has been described elsewhere [4,5] and, in summary, consists of a simple design of swirl burner with two tangential inlets and a geometrical swirl number (S) of 1.5, Fig. 1. The 100-kW system used employs a simple unlined steel casing for the furnace to allow for simplicity of access. Natural gas was used as fuel, 50% introduced axially on the centerline and 50% premixed through the two tangential inlets. The exhaust nozzle was extended backward into the swirl chamber so that the flow had to pass radially through a small annular gap to prevent flashback. Oscillation frequencies and amplitudes were measured by water-cooled pressure transducers attached to the exit pipe of the furnace. Temperatures were measured by computer-compensated, small-diameter (~30 μm), coated thermocouples inserted into the flow at

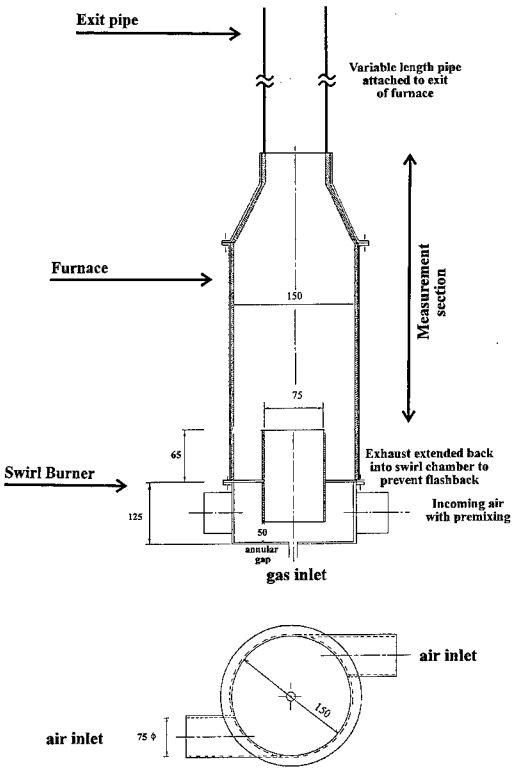

FIG. 1. Schematic of the 100-kW swirl burner.

appropriate points. A DANTEC LDA system was used in which the velocity measurements (or temperatures) could be overlaid and phase locked via a reference signal from the pressure transducer or thermocouple. The technique is derived directly from that used to characterize flows inside reciprocating engines [4]. All temperature measurements by thermocouple were compensated for radiative and convective losses.

Initial work [8] started by consideration of the effect of simply adding fixed sections of outlet pipe to the exhaust of the swirl burner/furnace system and investigating the resulting occurrence of resonance for a wide range of mixture ratios and modes of fuel entry. The effects so realized have been found to correspond to natural phenomena occurring in practical large-scale systems. This was then followed by detailed investigations of one particular resonant condition.

Results

Three modes of fuel injection into the swirl chamber were investigated: axial, tangential, and mixed 50% axial/premixed [8]. Highest amplitudes of oscillation were found with axial fuel entry and 50% axial premixed. A typical result, which has subsequently been analyzed in more detail, is shown in Fig. 2. For a constant fuel flow rate, the air flow rate is varied such that a range of mixture ratios is covered from fuel rich ($\varphi = 0.7$) to excess air ($\varphi = 2.2$). The frequency and relative amplitude for both the first and second harmonics are recorded, along with the following frequencies:

- The PVC frequency obtained from isothermal conditions in the swirl burner/furnace conditions; as is well-known, this is a near linear function of flowrate [1,4,5].
- The Helmholtz resonant frequency calculated by assuming the gases in the furnace volume act as the capacitance, and the flow oscillates in the neck of the exhaust. An average combustion temperature is assumed for the furnace with the methods described in Ref. 6 used for frequency calculations. A quarter wave organ pipe frequency has been similarly calculated [8] but is not reported here because its level does not correspond to measured frequencies.

Fig. 2 shows many interesting features:

- A high-amplitude, low-frequency resonance occurs for air-fuel ratios in the range of 1.2–1.75, the frequency of which is close to that of the predicted Helmholtz oscillation (40 Hz).

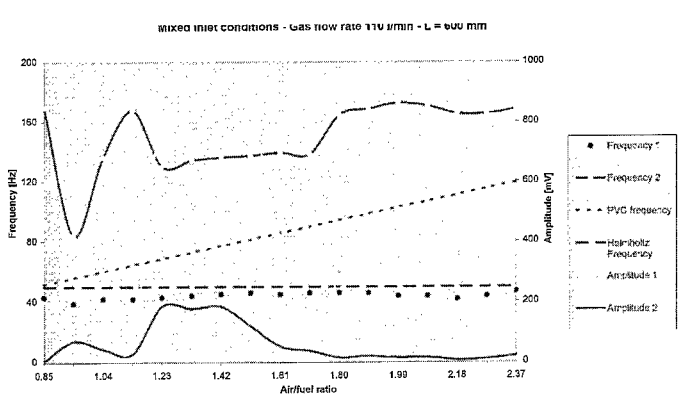

FIG. 2. Resonant state, 50% axial fuel entry, 50% premixed with natural gas and air, exit pipe length 600 mm.

- A second resonance of much reduced amplitude over the air-fuel ratio range between 1.2 and 1.75 with a frequency (130/140 Hz) some three times higher than that of the first resonance. The frequency varies quasi-linearly with air-fuel ratio for $1.2 < \varphi < 1.75$ and hence air flow rate as the natural gas flow rate is held constant. This appears to be a PVC structure induced by vortex breakdown in the exit of the furnace and is independent of the PVC formed in the exit of the swirl burner firing into the furnace [8].

Similar results have been achieved with axial fuel entry alone, different fuel flow rates, and variable furnace exit pipe lengths. Longer exit pipe lengths give sharper resonant peaks and much higher amplitudes of oscillation [8].

For all cases, combustion was not completed until the gases had entered the final pipe section attached to the furnace, as indicated by the high surface temperatures in this region. Combustion was always virtually 100% complete by the end of this pipe section. As will be shown later, the occurrence of the resonance causes considerable changes in flow structure to that normally measured under nonresonant conditions.

Because phase-averaging techniques were to be applied to characterize oscillatory velocity and temperature fields in the system, care was taken to choose a condition in which the most regular wave forms were found; this occurred with the conditions of Fig. 2. An air flow rate of 1600 L/min was chosen together with the stated natural gas flow rate of 110 L/min. A water-cooled pressure transducer was installed just above the outlet of the furnace to give a reference signal for the phase-averaging work; the characteristic frequency was 41 Hz. Fluctuating temperatures could only be measured in the furnace section (not in the attached pipe) because of the high velocities, pressure pulsations, and flow reversals. Phase-averaged tangential and axial velocities could be obtained in this section.

Phase-Averaged Temperature and Velocity Fields

Correlation experiments with two probes soon confirmed that the resonances in the furnace were, as expected, Helmholtz in nature, driving oscillations in the axial direction, at least in the wall region. Phase-averaged temperature fields obtained at four sections in the furnace/exhaust are shown in Figs. 3a, 4a, 5a, and 6a and correspond to phase shifts of 0°, 90°, 180°, and 270°. The 0° point corresponds to the point on the pressure wave when the signal gradient is at its maxima, and thus peak pressures in the exhaust correspond to the 90° results. Corresponding phase-averaged axial and tangential velocity fields are shown in Figs. 3b, 4b, 5b, 6b, 3c, 4c, 5c, and 6c. Detailed results are available in Ref. 8 for both velocities and temperatures over the range 0° to 360° in increments of 15°. The figures are arranged such that for each phase angle, the corresponding temperature, axial, and tangential velocity are together. The clearest description of the processes occurring in the furnace is obtained by examining the axial velocity contours.

At 0° phase angle, Fig. 3b, it is clear that flow is entering the furnace in a conical sheet surrounding a central large reverse flow/recirculation zone. Evidence of a corner eddy can be seen for $r/R_o > 0.8$ at the bottom of the figure where the swirl burner fires into the furnace. Tangential velocities are high throughout the chamber (Fig. 3c), typical Rankine distribution [1]. Near the swirl burner exit, near the centerline, a region of negative tangential velocity exists for $0 < r/R_o < 0.2$ and can only be caused by the presence of large coherent structures such as the PVC phenomena [1,4]. Because phase averaging was carried out at the frequency of the Helmholtz oscillation, it was not possible to resolve the higher frequency rotational velocity field associated with the PVC. This type of flow field is typical of many that have been reported previously [1]. The flame, as indicated by the temperature measurements, is unusual in that it is lifted and centrally located, forming a flame core (Fig. 3a). Comparison with Fig. 3b, the axial velocity field, indicates that this flame is stabilized in the low-velocity region between the forward and reverse flow regions and is fed by fuel from the axial inlet. Most of the fuel from the premixing appears to bypass the burning zone, carried in the high axial velocity regions. At this stage, the central flame located around the reverse flow zone feeds heat and active chemical species into the outer high-velocity region that receives premixed fuel and air via the tangential inlets; flow velocities and flame stretch are too high to allow ignition/flame propagation into this outer zone.

At a phase angle of 90°, considerable changes in the flow structure have occurred. The temperature field, Fig. 4a, shows that ignition has occurred in a thin annular zone near the wall at the end of the furnace because of flame propagation back from the exhaust tube fitted to the furnace. Maximum temperatures are of the order of 1050°C both in the central flame core region and in the wall zone. The central flame core region remains in virtually the same position with small changes in radius. The axial velocity field, Fig. 4b, shows that the cyclic pressure buildup in the furnace caused by the resonance has drastically reduced the flow into the furnace from the swirl burner, almost eliminating the strong reverse flow zone shown in Fig. 3b at 0° phase angle. The corner eddy region at the bottom has enlarged considerably, while the resonance also induces weak reverse flow (and hence combustion, Fig. 4a) in the wall region further up the furnace. Other areas of

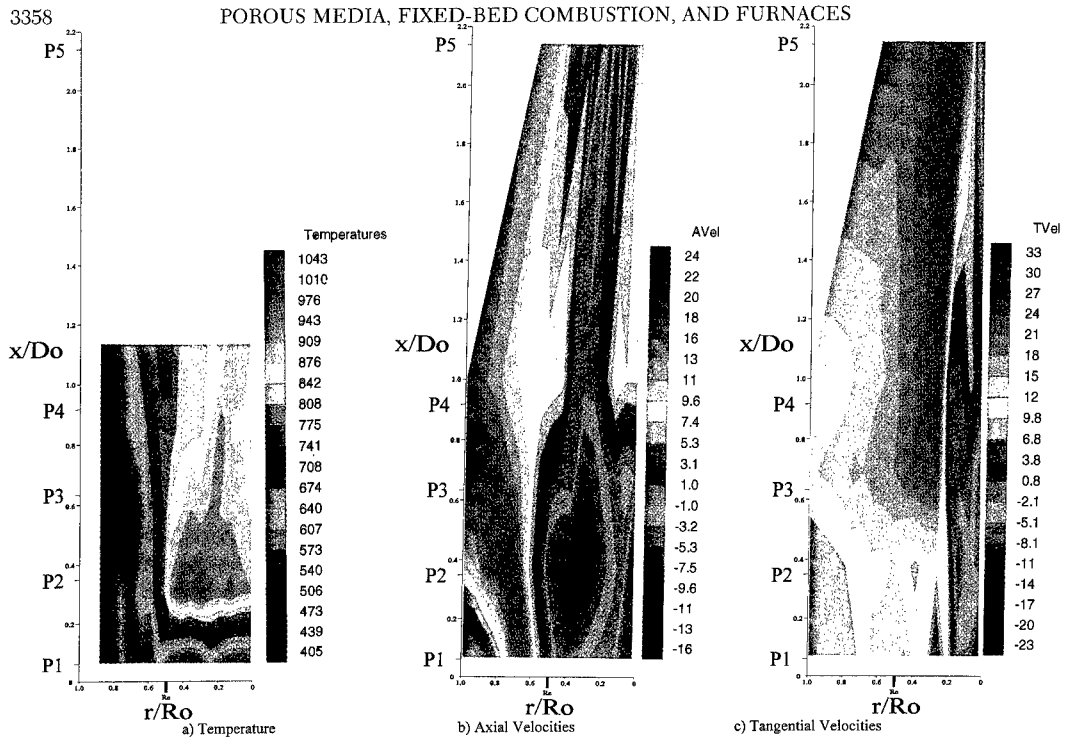

a) Temperature b) Axial Velocities c) Tangential Velocities

FIG. 3. Phase-averaged measurements taken at phase angle 0°.

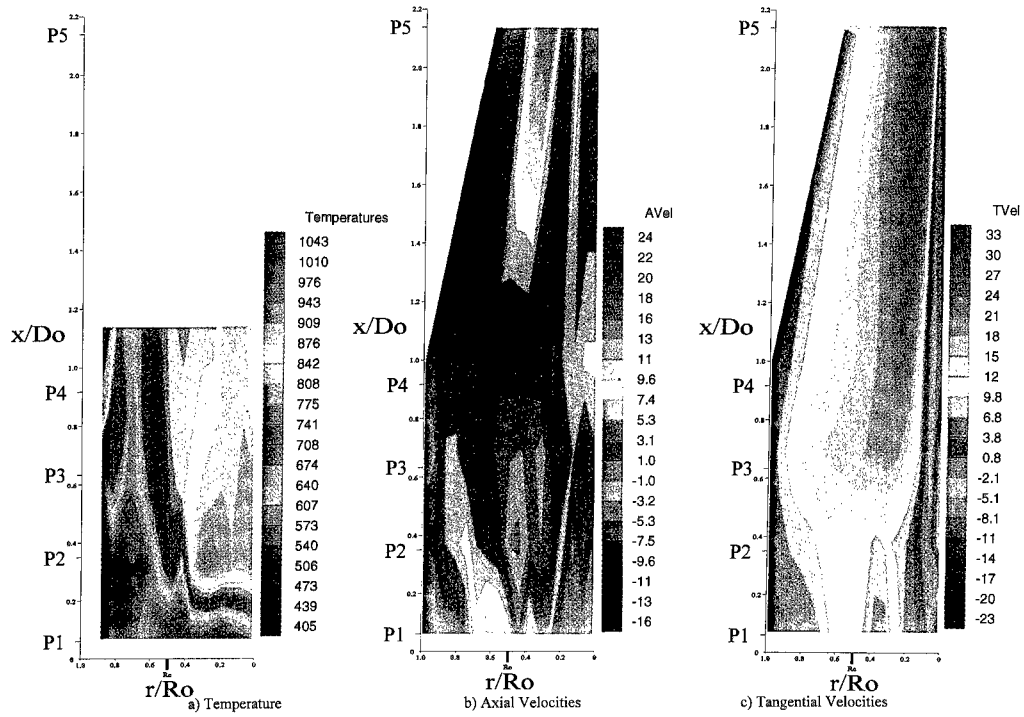

a) Temperature b) Axial Velocities c) Tangential Velocities

FIG. 4. Phase-averaged measurements taken at phase angle 90°.

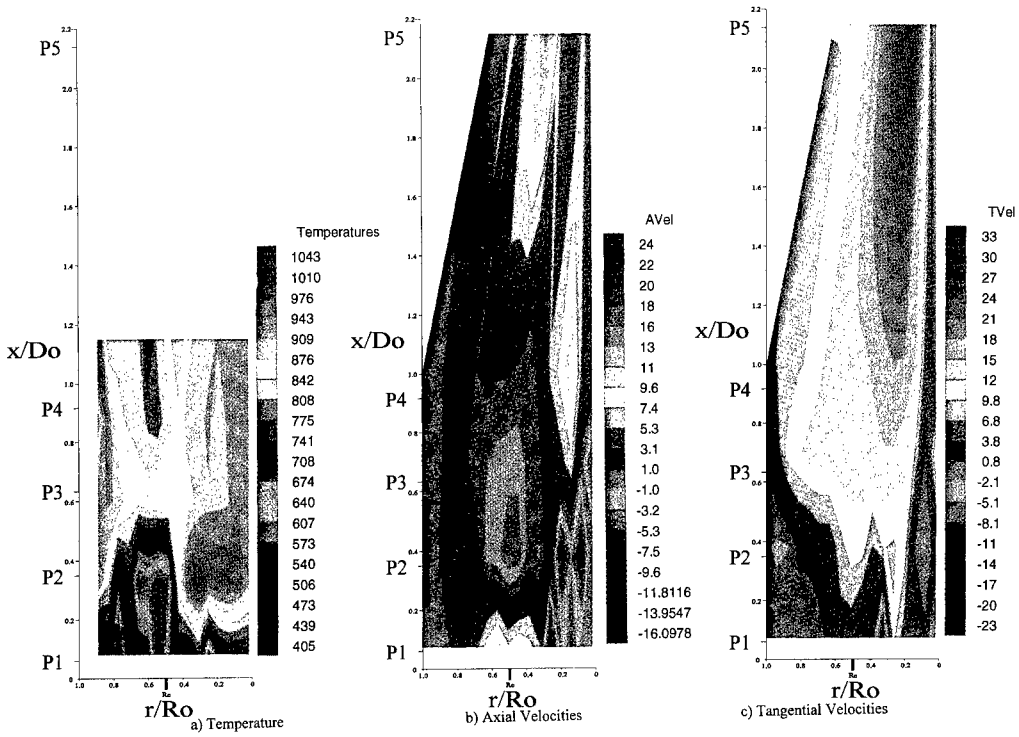

FIG. 5. Phase-averaged measurements taken at phase angle 180°.

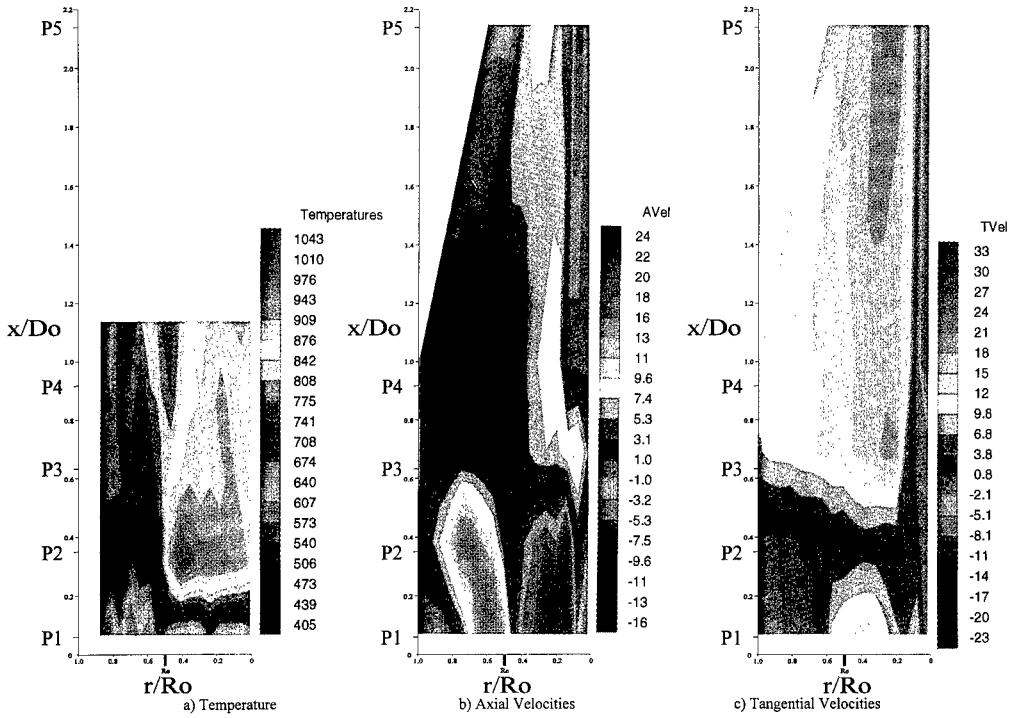

FIG. 6. Phase-averaged measurements taken at phase angle 270°.

reverse flow are also induced in the main body region of the furnace. Additionally, the tangential velocity field has weakened (Fig. 4c), in the central region and especially in the wall region. Vortex core precession is still evident on the centerline of the burner, to about one swirl burner exit diameter into the furnace, where a region of negative tangential velocity can be seen.

The effect continues at a phase angle of 180°, where the forward axial velocities have been further reduced (Fig. 5b). Reverse flow extends virtually along all of the wall region and over much of the central region of the furnace. Evidence of the return of a central reverse flow zone can be seen in the exit of the swirl burner, albeit in an annular form. The central flame core region, Fig. 5a, has now extended further down toward the swirl burner exit and widened near the top of the furnace, reflecting lower axial velocities. The outer annular flame next to the wall now extends nearly to the base of the furnace. Other results for different phase angles indicate that this annular flame extends to more than 50% of the furnace length for phase angles in the range $135° < \varphi < 225°$ [8]. For this phase angle, in the top and central sections of the furnace, the two flame regions have virtually joined together, while maximum temperature levels remain at about 1000°C. Clearly, this is the process that excites the resonance via the Rayleigh criteria [7] by adding heat close to the pressure peak, $\varphi = 90°$. The tangential velocity field, Fig. 5c, shows that intense swirl only remains in the top 60–70% of the furnace; at the exit of the swirl burner, maximum tangential velocities are only 25% of those at the end of the furnace. This reflects the severe restriction on the flow through the swirl burner caused by the pressure wave. In the center, there is still evidence of vortex core precession as shown by the negative tangential velocities. In the region $0.6 > r/R_o > 0.7$, and extending to about $0.5\ R_o$ downstream, a region of high negative tangential velocities also develops, again indicative of a large coherent structure. Detailed examination of other results showed this phenomenon occurred over a phase angle range of 150–270°, indicating that the phenomena takes some time to decay after its generation. No combustion appears to occur in this region (Fig. 5c). In the furnace exhaust, a small region of negative tangential velocity develops near the centerline, indicating vortex core precession.

At a phase angle of 270°, the outer wall combustion region has almost disappeared (Fig. 6a), just a trace appearing at the top of the furnace; the flame core has moved slightly downstream but is otherwise unchanged. Under the influence of the negative pressure induced by the resonance, the axial flow rapidly reestablishes itself in the furnace chamber (Fig. 6b) as does the central reverse flow zone; conversely, the region of reverse flow at the wall has moved upward to the furnace exit. The tangential velocity field, Fig. 6c, shows two main regions, one of residual swirl in the top half of the furnace and a bottom region developing in the lower 25% of the furnace. Negative tangential velocities have nearly disappeared in the swirl burner exit, indicating the elimination of vortex core precession; however, some occurs at the top of the furnace as with the 180° phase angle case, Fig. 6c. It is probable that this is the low amplitude PVC frequency (~140 Hz) picked up by the pressure transducer located just past the end of the furnace.

From Refs. 10 and 11, it is clear that the process is dominated by the system characteristic fill, mixing, and chemical kinetic times. The fill time is ~7 ms (obtained from dimensions and axial velocities, Figs. 6b and 3b) in the outer region close to the furnace wall. Total ignition-delay time appears to be of the order of 5 ms from comparison of Figs. 3a, 3b, 4a, and 4b and, as expected, is mainly dominated by mixing processes as the chemical ignition-delay time is only likely to be of the order ~1 to 1.5 ms [10]. There is a clear difference between this work and that of Refs. 10 and 11 in that the point of maximum energy release appears to occur at a phase angle of about 135°, some 45° after the peak pressure ($\varphi = 90°$), as opposed to some 25–45° before. This may be accounted for in the technique used to describe the heat-release rate, that is, temperature as opposed to OH^* chemiluminescence.

With no exhaust tube attached to the furnace, the Helmholtz oscillation virtually disappears and the flame structure changes to that described in Refs. 1 and 5, that is, an annular flame front anchored in and upstream of the exit of the swirl burner and surrounding a central reverse flow zone, with final burnout occurring well before the furnace exit. This contrasts with the very different combustion conditions described under resonant conditions.

Discussion

Helmholtz excitation of the swirl burner/furnace system is causing some unusual phenomena to occur. The regular pressure pulsations cause the flow into the furnace via the swirl burner to be interrupted regularly and virtually stopped, so that there are parallels with the operation of pulse combustors as described in Refs. 10 and 11. A clear difference is the occurrence of a central flame core throughout the cycle. Excitation via the Rayleigh criteria and combustion occurs from ignition and the intermittent combustion process in the annular wall flame occurring over a phase angle of 90°. Ignition in this region appears to occur via flame propagation from the exit pipe region, recirculation of heat and active chemical species from the central flame core, and velocity degradation/reversal in the wall region of the furnace, which allows the flame to propagate backward

through the fresh mixture toward the swirl burner. High levels of tangential velocity are recorded throughout the oscillation cycle at the top 60–70% of the furnace; in the lower part, complex coherent structures occur when the forward axial velocities are eliminated and little gas flows into the furnace, as indicated by the negative tangential velocities recorded. In the region where the swirl burner fires directly into the furnace, the lifted flame means that the entering flow is dominated by the isothermal swirling flow field. Reference to Fig. 2 indicates that the corresponding isothermal PVC frequency is of the order of 80 Hz for mean flow conditions. Because the flow rate into the burner varies considerably, in accord with the Helmholtz resonance, the PVC frequency will vary over the cycle from virtually 0 Hz (phase angle 180°) to probably more than 100 Hz (phase angle 0°). Thus, there may be a further coupling/excitation mechanism from the PVC. Ref. 8 shows that the highest amplitudes of the resonance are recorded for conditions where the Helmholtz frequency was close to the isothermal PVC frequency. Further resolution of these structures requires either flow visualization studies or more sophisticated phase-averaged measurements at different frequencies matching those of the PVC, including the measurement of radial velocities.

Conclusions

This paper has studied the driving of a Helmholtz resonance in a swirl burner/furnace system of practical design via natural gas combustion and excitation via the Rayleigh criteria. The Helmholtz resonance has been shown to be the dominant resonance over a wide range of mixture ratios, producing amplitudes nearly an order of magnitude higher than the second resonance, a PVC phenomenon. Parallels exist between this system and some pulse combustors in that some of the combustion process occurs in phase with the peak system pressure, although a major difference is that a lifted flame core exists on the central axis of the furnace throughout the oscillation cycle. The resonance causes a flow cycle into the furnace to develop in which the pressure minimum helps to suck a large mass of air and fuel into the furnace via the swirl burner, causing transient flow patterns in the furnace very similar to those recorded by other workers not using phase-averaging techniques (i.e., a central reverse flow zone and forward flow in an annular sheet). However, this flow pattern decays rapidly as the pressure wave builds up and ignition/combustion occurs in the outer annular wall layer. Eventually, a condition is reached where entry of air and fuel from the swirl burner into the furnace is virtually arrested and the annular wall flame extends to nearly the base of the furnace. Characteristic fill and ignition-delay times have been identified qualitatively. Extremely complex flow patterns develop in the base of the furnace over a phase angle range of 90° with evidence for the existence of large coherent structures. A PVC was detected in the exhaust contraction from the furnace to the final exit pipe, which did not appear to play a significant role in the generation of the resonance. A PVC also exists in the exit region of the swirl burner firing into the furnace. Because the flames were normally lifted from this region, this PVC frequency will be close to that for isothermal conditions. Evidence exists that coupling of this PVC frequency with that of the Helmholtz resonance can lead to substantial increase in the overall oscillation amplitude.

Nomenclature

D_o	diameter of the furnace, mm
PVC	precessing vortex core
r	radius, mm
R_e	exit radius of swirl burner, mm
R_o	radius of furnace attached to swirl burner, mm
S	geometric swirl number of burner (1.5)
T	temperature, °C
u	phase-averaged axial velocity, m/s
w	phase-averaged tangential velocity, m/s
X	axial distance downstream from the exit of the swirl burner firing into the furnace, mm
ϕ	phase angle relating the position on the pressure wave generated by the Helmholtz resonance, degrees; the 0° phase angle position corresponds to the position of maximum positive pressure gradient

REFERENCES

1. Gupta, A. K., Lilley, D. J., and Syred, N., *Swirl Flows*, Abacus Press, Tunbridge Wells, 1984.
2. Sayre, A., Lallemant, N., Dugué, J., and Weber, R., *Twenty-Fifth Symposium (International) on Combustion*, The Combustion Institute, Pittsburgh, 1994, pp. 235–242.
3. Syred, N., Hanby, V. I., and Gupta, A. K., *J. Institute Fuel* 46:402–407 (1973).

4. Froud, D., O'Doherty, T., and Syred N., *Combust. Flame* 100:407–412 (1995).
5. Claypole, T. C. and Syred, N., "Construction and Optimisation of a Furnace for the Economic Burning of Low Calorific Value Gases," EU Report No. EED-2-235-GB, published as EUR 10088 EN by the Commission of the European Communities, Brussels, 1985.
6. Putnam, A. A., *Combustion Driven Oscillations in Industry,* Elsevier, New York, 1971.
7. Rayleigh, Lord, *Proc. R. Society London Ser. A,* 93:148–157 (1916).
8. Froud, D., Ph.D. Thesis, University of Wales, 1995.
9. Dorrestein, W. R., *J. Institute Fuel* 48:387–392 (1968).
10. Keller, J. O., Bramlette, T. T., Westbrook, C. K., and Dec, J. E., *Combust. Flame* 79:151–161 (1990).
11. Keller, J. O., Barr, P. K., and Gemmen, R. S., *Combust. Flame* 99:29–42 (1994).

Twenty-Sixth Symposium (International) on Combustion/The Combustion Institute, 1996/pp. 3363–3368

THE EFFECT OF HEAT CONTENT AND COMPOSITION OF FUEL ON PULSE COMBUSTOR PERFORMANCE

A. KUSHARI, L. J. ROSEN, J. I. JAGODA AND B. T. ZINN
Laboratory for Pulse Combustion Processing
School of Aerospace Engineering
Georgia Institute of Technology
Atlanta, GA 30332-0150, USA

This paper reports partial results of an investigation into the use of pulse combustors to provide the heat required for the pyrolysis of organic wastes, such as black liquor, in fluidized beds. This process is economical only if the pyrolysis products, which are low in heat content but high in hydrogen concentration, can be used to fire the pulse combustor. This lead to a study of the effect of low heat content fuels with high hydrogen content on the operation of pulse combustors, the results of which are reported here. The performance of the pulse combustor was monitored by measuring sound pressure levels, heat release oscillations, frequencies of pulsations and the phase angle by which the heat release oscillations lead those of pressure. Sound pressure levels were found to be largely insensitive to heat content in fuels consisting only of methane and inert diluents. However, if the fuel contains hydrogen, the amplitude of the pulsations decreases as the heat content in the fuel is increased. This occurs because addition of hydrogen to the fuel accelerates the heat release during the cycle. In order to determine whether this early heat release is due to changes in the fluid mechanics, i.e., the mixing of reactants and ignition source in the combustor, or to the different kinetics of the combustion processes without and with hydrogen, a series of experiments was devised in which the composition of the fuel could be varied without changing the fluid mechanics in the pulse combustor. These tests clearly showed that the earlier heat release in the cycle, responsible for lower sound pressure levels in the pulse combustor, is caused by the faster burning rate of hydrogen.

Introduction

Pyrolysis for the treatment of organic wastes has been gaining increasing interest over recent years. One such application is the pyrolysis of black liquor, a byproduct of papermaking. Pyrolysis is an endothermic process. The heat of reaction is provided either by partial combustion of the waste or by heat transfer from an external combustion process. The pyrolysis of black liquor presents a particular challenge because it must occur at temperatures between 1000 and 1350 K. Below 1000 K the organics in the liquor are not completely pyrolized, while above 1350 K the salts in the liquor begin to form a smelt. In a recently proposed system [1], black liquor is pyrolized in a fluidized bed to which heat is added through a series of pulse combustor tail pipes submerged in the bed material. This system appears promising because of the relatively high heat transfer in pulse combustors [2] and in fluidized beds. Other advantages of pulse combustors are discussed elsewhere [3]. The above described process is, however, economically viable only if a part of the pyrolysis products can be used to fire the pulse combustors.

The performance of pulse combustors has been shown to depend critically upon the chemical composition of the fuel [4,5]. However, additional difficulties in the operation of pulse combustors with pyrolysis products may be caused by the low heat content of these fuels, typically 12 MJ/m^3 compared to 40 MJ/m^3 for natural gas. It is the goal of this study to investigate the effect of low heat content and relatively high hydrogen content of this fuel on the performance of pulse combustors.

Background

When a pulsed combustor operates at its limit cycle, the acoustic driving of the pulsations by the oscillatory combustion process exactly balances the acoustic losses due to flapper valves, acoustic radiation, and viscous effects. According to Rayleigh's criterion, driving occurs when the pressure and heat release fluctuations are in phase. Quantitatively, this balance between driving and damping at the limit cycle can be expressed as

$$\int_V \int_T P'(x, t)Q'(x, t)dtdV = \int_V \int_T \sum_i L_i(x, t)dtdV \quad (1)$$

where P' and Q' are the instantaneous pressure and heat release rates and L_i the instantaneous sum of

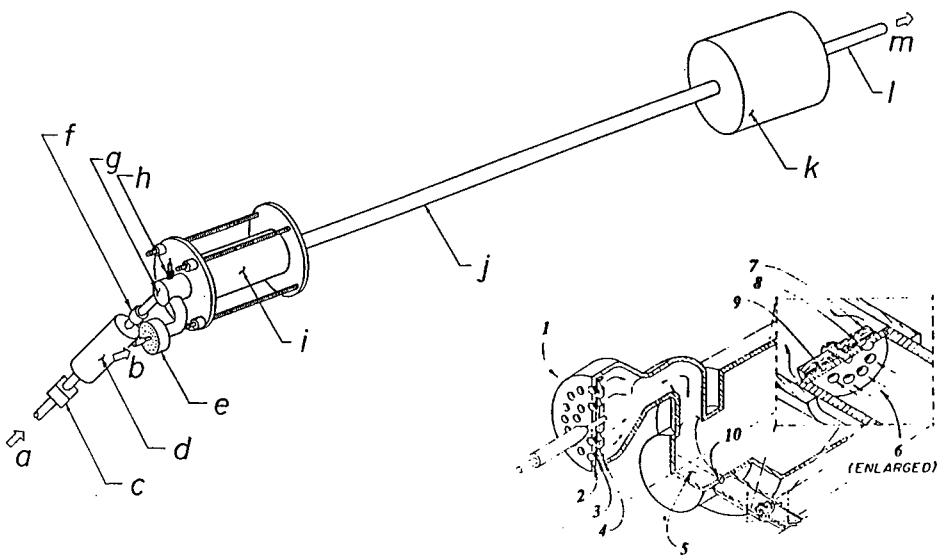

FIG. 1. Schematic of the pulse combustor; a, fuel supply; b, air inlet; c, fuel solenoid valve; d, fuel decoupler; e, air flapper valve; f, fuel flapper valve; g, mixing chamber; h, spark plug; i, combustion chamber; j, tail pipe, k, decoupler; l, vent pipe; m, exhaust. Cut away: 1, air valve; 2, front plate; 3, flapper; 4, back plate; 5, mixing chamber; 6, fuel valve; 7, back plate; 8, flapper; 9, front plate; 10, fuel orifice.

all losses. V is the volume of the combustor and T is the period of oscillation. Alternatively equation 1 can be written as

$$\boldsymbol{P} \cdot \boldsymbol{Q} \cdot \cos(\phi) = L \tag{2}$$

where $\boldsymbol{P}$ and $\boldsymbol{Q}$ are the pressure and heat release amplitudes, ϕ is the phase angle between them, and L is the sum of all losses during the cycle. Thus, if ϕ is less than 90°, the heat addition process will drive the pressure oscillations, otherwise it will damp. A less well known second part of Rayleigh's criterion states that the frequency of pulsations increases if the heat release oscillations lead those in pressure and vice versa [6].

Combustion processes are never spontaneous. Keller et al. [7] have identified three distinct processes in pulsed combustion that contribute to the total ignition delay time: (1) τ_{species}, the time required for air and fuel to mix, (2) τ_{mixing}, the time required for the incoming reactants to mix with the ignition source in the form of "hot products" remaining from the previous cycle, and (3) τ_{kinetic}, the post mixing chemical ignition time. The total ignition delay time, τ_{ignition}, is then given by

$$\tau_{\text{ignition}} = f(\tau_{\text{species}}, \tau_{\text{mixing}}, \tau_{\text{kinetic}}) \tag{3}$$

The processes inside the combustor are complex. It is, therefore, not possible to entirely decouple the above three "characteristic" times. But in general, an increase in any of these times will result in an increase in overall ignition delay times. Since the heat release generally leads the pressure fluctuations, a longer ignition delay time results in a smaller phase angle. Three physical factors affect the ignition delay time in a given combustor, the reactant flow rates which affect the mixing, and the temperature and fuel composition, which determine the chemical time.

Experimental Setup

A Helmholtz-type, nonpremixed, valved, pulsed combustor was chosen for this study since its operation has been extensively investigated at the Laboratory for Pulse Combustion Processing at Georgia Tech [8,9]. However, the reported results are applicable to many other types of pulse combustors whose operation is governed by similar physical principles.

The test combustor consists of a mixing chamber, a combustion chamber, a tail pipe, a decoupler, and a vent pipe (see Fig. 1). This figure also shows a cutaway view of the valve assembly and mixing chamber as an insert. Fuel and air enter sequentially at about 200 mm of water column and atmospheric pressure, respectively, through a pair of flapper valves, radially into the combustor. Ignition is achieved by activating the spark plug while sequentially introducing air and fuel. The ensuing combustion and expansion processes increase the pressure inside the combustor, which closes the flapper valves and expels hot combustion products through the tailpipe. Once the combustion process nears completion, the chamber

pressure starts to decrease. When the chamber pressure drops below the fuel line pressure, the fuel valve reopens, allowing fresh charges of fuel to enter the combustor. These mix with the air left from the previous cycle and are reignited by remaining pockets of burning gas, without the use of the spark plug. A little later during the cycle, the combustor pressure drops below atmospheric and the air valve reopens to admit a fresh charge of air. The rate of combustion now increases dramatically, causing the pressure in the combustor to rise and to close the valves. This results in a periodic process that can continue indefinitely without the use of a spark plug. The fuel air ratio is varied by adjusting the air flapper valve while the fuel valve remains fixed.

The effect of heat content and composition of the fuel upon pulse combustor performance was quantified by determining acoustic pressures and heat release rates in the pulse combustor. The amplitudes and frequencies of the pulsations were measured using a water-cooled piezoelectric transducer mounted on the wall of the combustion chamber. Global reaction, and, therefore, heat release rates were obtained by measuring C-C radiation through a quartz window in the upstream end of the pulse combustor using a photomultiplier fitted with the appropriate optical narrow-bandpass filter. Heat release and acoustic pressure signals were acquired using a computer-based data acquisition system running Labview. Fast Fourier Transforms (FFT) were performed on the raw data to obtain auto and cross spectra and, therefore, the phase angle between the pressure and heat release signals. Driving, as defined below, was calculated by integrating the product of the instantaneous pressure and heat release over one cycle using Simpson's rule [10]. Air and different fuel mixtures were measured upstream of the respective valves using calibrated flow meters, which were separated from the pulse combustor by decouplers.

Results and Discussion

The following three series of tests were carried out in order to be able to separate the effects of low heat content from those of the chemical make up of the fuel:

1. Burning methane diluted with carbon dioxide and helium to vary the heat content, keeping methane flow rate and fuel density constant
2. Burning methane-hydrogen mixtures diluted with carbon dioxide and helium to vary the heat content, keeping methane and hydrogen flow rates and fuel density constant
3. Burning various mixtures of methane and hydrogen diluted with carbon dioxide and helium; keeping power, fuel heat content, total fuel flow rate, and fuel density constant

Effect of Fuel Heat Content on Combustor Performance

The effects of heat content in the fuel upon the operation of the pulse combustor were studied. Two series of tests were carried out, one with a constant flow rate of methane of 2.35×10^{-4} m^3/s, the other with constant flow rates of methane at 1.9×10^{-4} m^3/s and hydrogen at 1.48×10^{-4} m^3/s. This corresponds to a total power input of 8.793 kW for both fuels. In the case of the methane-hydrogen mixture, 80% of the energy available in the fuel is supplied by the former. In both cases, various amounts of carbon dioxide and helium were added to the combustibles to reduce the heat content of the fuel. However, the proportions of diluents were carefully chosen to maintain flows of constant density, 0.6 kg/m^3 for pure methane and 0.45 kg/m^3 for the methane-hydrogen mixture. Air flow rates were also kept constant at 6.84×10^{-3} m^3/s for the former and 5.5×10^{-3} m^3/s for the latter. This means that the fuel-air ratios were maintained constant, although the fuel flow rates had to change when the heat contents of each of the fuels were varied. The heat content of the mixtures was varied from below that of pure methane (40 MJ/m^3) to that typical for black liquor pyrolysis products (12 MJ/m^3).

Figure 2 shows the variations of amplitude of the heat release and pressure fluctuations, their frequency, and the phase angle between them for methane and methane-hydrogen fuels. The pulse combustor operates well for both fuel types down to heat contents of 10–12 MJ/m^3. Operation with fuels of lower heat content requires a high fuel supply pressure, which no longer allows the flapper valve to close. As a result, the fuel enters the combustor throughout the cycle and the pulsations become very weak. The highest achievable heat content is higher for methane than for the methane-hydrogen mixture since hydrogen has a lower calorific value than methane.

There are some clear differences in the behavior of the pulse combustor when fired with the two fuels. For methane fuels, the sound pressure level and frequency of operation show very slight increases with heat content, especially for lower-calorific-value fuels. However, if 20% (by heating value) of the methane is replaced by an equivalent amount of hydrogen, the sound pressure level decreases with increasing heat content, while the pulse frequency first increases and then levels off, see Fig. 2a, b.

The explanation for this behavior can be found in the trends of phase angle and heat release fluctuations as a function of heat content in the fuel. The left-hand side of equation 2 represent the driving of the pressure pulsations by the heat release fluctuations. When this driving is balanced by the acoustic losses, represented by the right-hand side of the equation, the pulse combustor operates in its limit

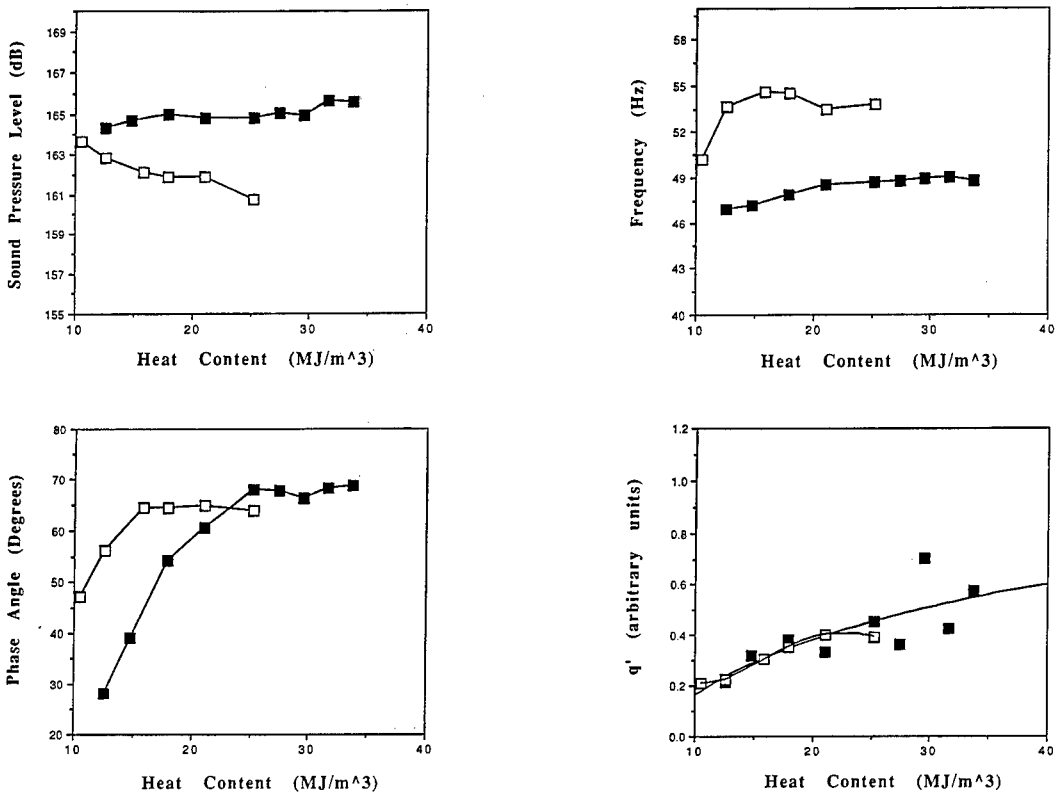

FIG. 2. (a), Dependence of sound pressure level on heat content of the fuel for (■) methane, and (□) methane-hydrogen-based fuels. (b), Dependence of frequency on heat content of the fuel for (■) methane, and (□) methane-hydrogen-based fuels. (c), Dependence of phase angle on heat content of the fuel for (■) methane, and (□) methane-hydrogen-based fuels. (d), Dependence of heat release amplitudes on heat content of the fuel for (■) methane, and (□) methane-hydrogen-based fuels.

cycle. If the magnitude of the heat release oscillations is increased, the driving process becomes stronger, causing an increase in acoustic pressure amplitudes. At the same time, the acoustic losses increase with increasing acoustic pressure amplitudes until the system operates in a new limit cycle with higher sound pressure level. On the other hand, if the phase angle, by which the fluctuations in heat release lead those in pressure, increases, the driving becomes weaker and the combustor operates at a lower sound pressure level. The experimental results presented in Fig. 2c, d show that the phase angle and heat release fluctuations increase with heat content for both types of fuel. This results in the competing effects discussed above. A careful inspection of Fig. 2c, d is necessary to determine which of these will dominate and under what circumstances.

The amplitudes of the heat release fluctuations increase at approximately the same rate for both types of fuels. However, the phase angle between heat release and pressure fluctuations at a given heat content are significantly larger for the hydrogen-containing fuels than for those with only methane. As a result, the driving force and, therefore, the pulsation amplitudes are smaller for hydrogen-containing fuels than for methane fuels with equal heat content.

According to Rayleigh's criterion, the larger phase angle for hydrogen-containing fuels is also responsible for the higher frequencies observed for these fuels. However, changes in temperature in the pulse combustor caused by the variation in air flow rate affect the speed of sound, and can therefore also lead to slight changes in the resonance frequency.

It is clear from the above discussion that the relative timing of the heat release with respect to the pressure cycle is critical for the operation of the pulse combustor. Since the oscillations in heat release lead those in pressure, a larger phase angle in Fig. 2c means an earlier heat release during the cycle. Thus, combustion occurs later in the cycle when the heat content in the fuel is reduced for both types of fuel. This may be due to less efficient mixing between the reactants and with the ignition sources caused by the presence of large quantities of

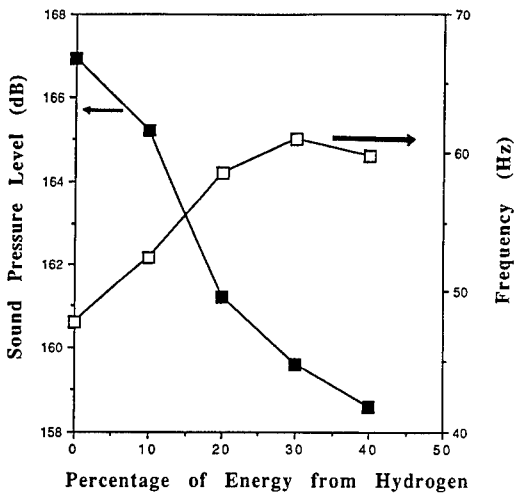

FIG. 3. Dependence of sound pressure level (■), and pulsation frequency (□), on hydrogen content (by percent of heat supplied) in the fuel.

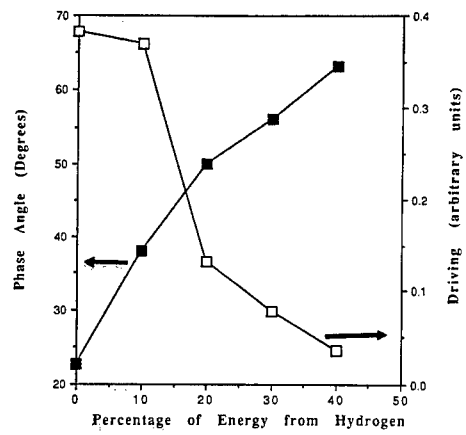

FIG. 4. Dependence of phase angle (■), and acoustic driving (□), on hydrogen content (by percent of heat supplied) in the fuel.

diluents, or to longer postmixing chemical ignition delay times caused by lower temperatures in the combustor. Furthermore, the fuel containing hydrogen ignites earlier during the cycle than the methane fuel because of the difference in combustion chemistry between methane and hydrogen, or the increased mixing, in the case of hydrogen fuels, because the lower heat content of hydrogen requires higher fuel flow rates for a given heat requirement. This, in turn, may lead to higher levels of turbulence, and thus more efficient mixing.

Separating the Effects of Chemistry from Those of Fluid Mechanics

In order to fully understand the above results, it must be possible to separate the effects of fluid mechanics from those of the chemistry. During previous investigations [4] of the effect of hydrogen in the fuel on the operation of pulse combustors, hydrogen was either added to or replaced parts of the methane flow. During all these tests, the flow rates as well as the composition of the fuel were changed. In the tests described below, judicious choices of diluents assured that fluid flow conditions remained constant even though the fuel composition was varied.

Different proportions of methane and hydrogen were mixed with carbon dioxide and helium to produce fuels of constant heat input per unit time (14.7 kW) and per unit volume of fuel (17.93 MJ/m^3), constant volume flow rate (8.17×10^{-4} m^3/s), constant density (0.45 kg/m^3) and, therefore, constant mass flow rate. In addition, the heat capacity of the fuel changed by less than 10%. The diffusivity of the fuel mixtures could not be kept constant. However, in the highly turbulent environment in the pulse combustor [11], turbulent mixing rather than diffusion dominates the transport processes. As a result, the fluid, mechanically controlled mixing remains essentially constant when the fuel composition is changed as long as the air flow rate remains constant. Any observed changes must, therefore, be entirely due to differences in chemical delay times for the different fuels.

Figure 3 shows the dependence of sound pressure level and frequency of pulsations upon hydrogen content in the fuel for an air flow rate of 6.3×10^{-3} m^3/s, similar to the air flow rates used in the above tests. The percentages of hydrogen in these figures refer to the fraction of total heat content of the fuel derived from hydrogen for the particular mixture. Clearly, the sound pressure level decreases while the frequency of pulsations increases as the hydrogen content in the fuel increases. The reason for this can be seen in Fig. 4. The phase angle by which the heat release leads pressure fluctuations increases with hydrogen content in the fuel, which causes the frequency of pulsation to rise. Also shown in Fig. 4 is the acoustic driving integrated over one cycle for various fuel compositions. It significantly decreases with increasing hydrogen content, primarily due to the increase in phase angle shown in Fig. 4. This results in the significant decrease in sound amplitude presented in Fig. 3. Comparing these results with those in Fig. 2 strongly suggests that the reduction in sound pressure level and frequency of pulsations observed in Fig. 2 are, indeed, primarily due to changes in combustion chemistry once hydrogen is introduced.

One additional observation of interest should be mentioned at this time. Table 1 shows the range of equivalence ratios over which pulsating operation could be sustained. Clearly, the addition of hydrogen

TABLE 1
Rich limits of operation of the pulse combustor firing fuels of different hydrogen contents (by percent of heat supplied) in the fuel

Percentage of hydrogen	Equivalence ratio at the rich limit
0	0.899
10	1.002
20	1.017
30	1.085
40	1.135

extends the rich limit of operation of the pulse combustor significantly. It has previously been shown [11] that fuel, which is supplied through a pressurized line, enters the pulse combustor much earlier in the cycle than fresh air. Furthermore, it was determined that the duration of the cycle is insufficient to permit complete combustion unless the fuel can burn immediately after entry, with air left over from the previous cycle. Thus, the combustor reaches a rich limit of operation near stoichiometric fuel and air flow rates when little air remains for the next cycle. During previous tests, this limit could be extended only if the duration of the cycle was extended by changing combustor geometry or by injecting the reactants earlier in the cycle by increasing their supply pressure. In the tests being reported here, this limit could be significantly extended by accelerating the combustion process through the addition of hydrogen to methane.

Conclusions

In summary, it was determined that changes in heat content do not have a marked effect on the sound pressure level in the pulse combustor as long as the only combustible in the fuel is methane. However, hydrogen in the fuel advances the timing of the heat release during the cycle. In agreement with Rayleigh's criterion, this leads to reduced driving, and thus lower amplitudes and increased frequency in the combustor. Hydrogen in the fuel also causes the decibel level in the combustor to decrease with increase in heat content. Tests in which the fluid mechanics in the combustor was kept constant while the composition of the fuel was changed have indicated that the changes in combustion chemistry rather than mixing rates are responsible for these observations. Finally, it was determined that while the addition of hydrogen to the methane fuel reduces the amplitude of the pulsations, the increase in combustion rate significantly extends the rich limit of operation of the pulse combustor by accelerating the combustion process.

Acknowledgment

This work is supported by the Department of Energy under Contract No. DE-FG04-93AL94649. Mr. Gideon Varga and Mr. Rick Balthaeser are the contract monitors.

REFERENCES

1. Mansour, M. N., Duria-Swamy, K., and Agha-Mohammadi, B., *Pulsed Combustion Process for Black Liquor Gasification,* Second Annual Report, DOE/CE/40893-T2, 1993.
2. Fedorov, B. N., *Juzherno—Fisicherkii Zhurnol* 32:167–180 (1977).
3. Zinn, B. T., "Pulsating Combustion," in *Advanced Combustion Methods,* (Weinberg, F. J., Ed.), Academic Press, London, 1986, pp. 113–181.
4. Jones, H. R. N. and Leng, J., *Combust. Flame* 99:404–412 (1994).
5. Keller, J. O. and Westbrook, C. K., *Twenty-First (International) Symposium on Combustion,* The Combustion Institute, Pittsburgh, 1986, pp. 547–555.
6. Lord Rayleigh, *The Theory of Sound,* Dover, New York, 1945, Vol. II, pp. 224–235.
7. Keller, J. O., Bramlette, T. T., Dec, J. E., and Westbrook, C. K., *Combust. Flame* 75:33–44 (1989).
8. Ku, S. H., Ph.D. Thesis, School of Aerospace Engineering, Georgia Institute of Technology, Atlanta, GA, August 1988.
9. Tang, Y. M., Waldherr, G., Jagoda, J. I., and Zinn, B. T., *Combust. Flame* 100:251–261 (1995).
10. Kreyszig, E., *Advanced Engineering Mathematics,* 5th ed., Wiley Eastern Ltd., New York, 1985.
11. Tang, J. M., Ku, S. H., Daniel, B. R., Jagoda, J. I., and Zinn, B. T., *Twenty-Third Symposium (International) on Combustion,* The Combustion Institute, Pittsburgh, 1990, pp. 1005–1010.

Twenty-Sixth Symposium (International) on Combustion/The Combustion Institute, 1996/pp. 3369–3375

STRUCTURES OF MULTIPLE COMBUSTION WAVES FORMED UNDER FILTRATION OF LEAN HYDROGEN-AIR MIXTURES IN A PACKED BED

A. V. SAVELIEV, LAWRENCE A. KENNEDY, A. A. FRIDMAN AND I. K. PURI

Department of Mechanical Engineering
University of Illinois at Chicago
Chicago, IL 60607-7022, USA

Combustion of lean hydrogen-air mixtures under filtration in an inert porous medium is studied experimentally. With the low hydrogen concentration (3–6%), superadiabatic wave propagation as a localized, stable temperature zone is observed with the combustion temperature reaching 800°C, which is much in excess of the adiabatic reaction temperature (300–500°C). The superadiabatic temperature rise due to effective heat regeneration in the system of "porous body-filtrating gas," results in complete combustion of even very lean reacting mixtures. It is found that with increasing hydrogen concentration, the localized waves become thermodiffusionally unstable, forming multidimensional cellular structures. Depending on experimental parameters, mainly the hydrogen concentration, two types of cellular structures are observed: three-dimensional spatial and planar. The cellular structures are characterized by partial combustion of hydrogen. This results in the formation of double wave structures, with the cellular structure followed by a stable or decaying superadiabatic wave. The formation of cellular structures is interpreted based on thermodiffusive instability of pore-level-driven combustion. A computational model incorporating detailed hydrogen-oxygen chemistry is used to analyze kinetic profiles over experimental temperature distributions.

Introduction

The use of hydrogen as a clean fuel offers significant environmental benefits, resulting in important CO and CO_2 emissions reduction. However, for conventional combustion systems, remaining NO_x emissions could be as high as in fossil fuel combustion. Pollution-free combustion is associated with hydrogen-lean flames, characterized by reduced temperatures and, hence, low thermal NO_x formation. Application of such a system is restricted by the ability to provide stable hydrogen flames over wide concentration limits.

The thermodiffusive instability, peculiar to low hydrogen concentration mixtures, is a widely observed phenomenon, resulting in unburned hydrogen emissions. This is the case of upward-propagating flames in tubes, when the lowest limit is close to 4% of hydrogen concentration, and cellular structures are formed [1]. Similar structures were studied in unconstrained and burner-stabilized hydrogen-air flames (e.g., Patnaik et al. [2,3]). For burner-stabilized flames it was found that the heat losses to the burner are the primary factor and that gravity plays only a secondary role in determining their structure and stability [3]. Comprehensive reviews of heat recirculation burners and lean hydrogen combustion are given in Refs. 4, 5.

The filtration combustion of air fuel mixtures with extensive heat exchange between the gas and the porous media is one of the possible ways to provide conditions for suppression of cellular instabilities. A low degree of thermal nonequilibrium between the solid and the gaseous phases corresponds to the low-velocity regime of filtration gas combustion, according to classification given by Babkin [6]. As was shown in earlier work [6–8], the combustion temperatures in low-velocity combustion waves propagating in the direction of gas filtration, can be significantly increased beyond the normal adiabatic temperatures due to internal heat regeneration in the porous bed system, leading to the ability to burn ultra-low heat content mixtures.

Superadiabatic or excess enthalpy flame temperatures occur whenever the heat is recirculated from hot products or the combustion zone to the unburned reactants, e.g., in so called heat recirculating burners [9]. Superadiabatic combustion in porous media is an internally organized process where the solid phase serves as an intermediate for heat accumulation and regeneration. General properties of filtration combustion waves, including thermal structure, mechanism, direction, and velocities of propagation were under experimental and theoretical consideration in the work of Babkin et al. [8], Zhdanok et al. [7], and others. Few studies, however, were devoted to the problems of stability and chemical structure of the waves.

Theoretical and experimental consideration of gas flow instability of low-velocity combustion waves was given by Vainshtein [10] and Minaev et al. [11]. It was shown, that the wave propagated in the direction

of filtration is hydrodynamically unstable if the reactor diameter exceeds a critical value. The instability was observed experimentally [11] as the deviation of the wave front from the plane normal to the gas flow direction.

It is widely recognized (e.g., see Takeno [12]) that extensive longitudinal heat transfer, high velocity of gas filtration, and strong nonstoichiometric compositions are associated with low combustion temperatures and wide zones of chemical reactions in the filtration gas combustion. This could lead to the peculiarities of combustion kinetic, resulting in incomplete, partial, and/or unstable combustion.

Existing models of thermal and kinetic flame structure in the porous media are based mainly on local volume-averaged treatment and well-mixed pore approximations. However, these approximations are no longer valid when the reaction front thickness approaches the pore diameter. Overall flame parameters, including kinetics, are to be greatly influenced by strong temperature and concentration gradients along the pore size. This important issue was addressed by Kaviany [13].

In the present work, the structures of combustion waves formed under filtration of hydrogen-lean mixtures with air are experimentally studied. Continuous superadiabatic or excess enthalpy waves, along with nonuniform cellular structures, were observed, depending on hydrogen concentration, flow characteristics, and parameters of the packed bed. A kinetic model was incorporated in order to analyze reaction-front structures and species distribution in the superadiabatic waves. The cellular flame structures are discussed in the frame of diffusion thermal instability of pore-size level combustion.

Experimental Apparatus

The experimental facility, designed to measure and characterized the combustion waves in a porous body under gas filtration are described in detail in our earlier study [7]. A combustion wave propagates in a vertical, 76-mm-diameter quartz tube, filled with a randomly packed bed of alumina particles. The heat insulation could be applied on either or both of the internal and external diameters of the combustion tube. To initiate the combustion wave an ignitor is located in the region where the gas flow enters the porous bed.

In the current experiments, the 5.6-mm and 3-mm solid alumina spheres were used as a packed bed material having a porosity of approximately 40%. The inner surface of the combustion tube was covered with a 3-mm layer of Kaowool insulation. Metered lean air H_2 mixtures, prepared by a gas supply system, were filtrated through the combustion tube at atmospheric pressure with flow rates from 3 to 12 m^3/h. High purity (99.995%) hydrogen was used.

Experiments were performed with the velocity of gas filtration in the range of 0.5–2 m/s. The hydrogen concentration was varied from 1 to 15% by volume. These experimental conditions correspond to a strong interphase heat exchange, permitting a one-temperature approximation model for the gas and solid.

The temperature distribution along the axis of the combustion tube was measured by an array of S-type thermocouples. Each fine gage thermocouple (130-μm wire diameter) was mounted in a 1.6-mm-diameter two-hole ceramic insulator, so that the junction remained completely covered. This provides temperature measurements very close to the solid phase temperatures. The latter was verified by inserting control thermocouples with the junctions mounted directly inside alumina pellets. Analog signals were digitized by National Instrument's AT-MIO-16 board. The real-time graphic presentation of temperature distribution and data storage was carried out by an IBM PC.

The combustion waves were initiated in a similar way for all the experiments conducted. Initially, the narrow zone of the ceramic bed was preheated by a gas combustion heater. Second, the standing wave of methane-air mixture combustion was initiated and maintained inside this zone during a fixed time interval. After formation of the initial thermal zone, the lean hydrogen-air mixture was filtrated through the porous bed.

Experimental Results

Consider the regimes of wave propagation observed with increasing hydrogen content in sets of experiments with the 5.6-mm alumina-packed bed and a constant filtration velocity of 1.3 m/s. Representative temperature profiles are presented in Fig. 1.

Under filtration of the reaction mixture through the high-temperature zone, the exothermic reaction of hydrogen oxidation occurs. However, in the limit of low hydrogen concentrations, the heat dissipation is not compensated by heat release and extinction of the combustion wave is observed (Fig. 1a).

As the hydrogen concentration is increased to over 4%, the heat release is sufficient to balance the energy loss, and a self-sustained superadiabatic wave (Fig. 1b) propagates in the porous bed. The energy, released in the reaction zone, is recovered by the porous body and then transferred to the unburned mixture entering the wave. Due to this heat recovery, the H_2-air mixture is preheated; this, coupled with the adiabatic temperature rise of the mixture (ΔT_a), results in a significantly higher maximum combustion temperature rise (ΔT_c) in the wave. In a transparent quartz tube, the combustion wave is observed as a highly luminescent zone, slowly

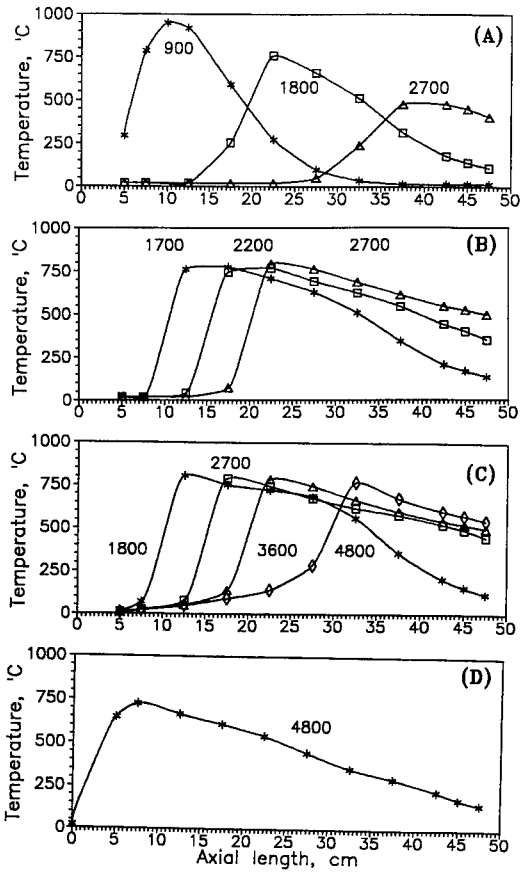

FIG. 1. Measured temperature profiles of combustion waves formed in the 5.6-mm packed bed with sequential increase of hydrogen concentration for a filtration velocity 1.3 m/s. (a) Decaying thermal wave, $[H_2] = 2.5\%$; (b) stable superadiabatic combustion wave, $[H_2] = 6.0\%$; (c) combustion wave with spatial cellular structure, $[H_2] = 6.8\%$; (d) two-dimensional cellular structure, $[H_2] = 9.0\%$. Numbers show propagation time in seconds.

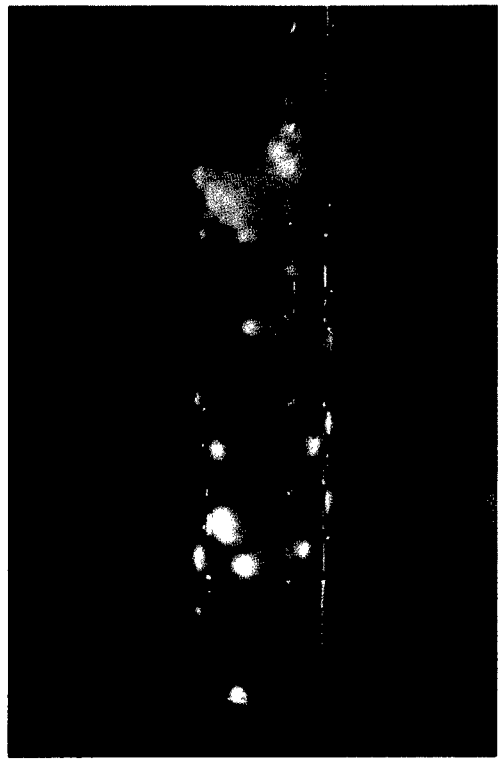

FIG. 2. Spatial cellular structure filling the tube behind the superadiabatic combustion wave, experimental conditions as in Fig. 1c.

traveling in the direction of the gas flow. The axial size of the wave is close to the tube diameter with the sharp front toward the filtering gas and a gradual front downstream.

The superadiabatic wave is stable with increase of hydrogen concentration only up to a certain limit (≈6%). Then, an instability occurs, first resulting in formation of hot spots on the upstream side of the combustion front. These spots could separate from the wave, but exist only in the short preheated zone preceding the wave.

Further increase of hydrogen concentration results in the formation of a cellular structure, filling the entire tube volume upstream of the propagating wave. The structure is visually observed as an array of localized hot spots irregularly positioned inside the porous bed (Fig. 2). Locations of the spots are fixed inside the bed and are often repeatable with the same experimental conditions. The luminous intensity of spots changes with time, and could be describe as twinkling. A momentary shut-off of the hydrogen supply will result in extinguishment of the hot spots, with the thermal wave remaining stable. Although the temperature in the cells is high, the average temperature profile (Fig. 1c) is changed only slightly. It is characterized by a slow increase of average temperature along the tube length before the wave, resulting from partial combustion of hydrogen in the cell structure. Reduction of hydrogen concentration in the cell structure leads to decay of amplitude of the superadiabatic wave and finally to its extinction. Thus, the cell structure, initiated by the traveling superadiabatic wave, is served further as an extinguisher of the primary wave.

The number of the cells grows with an increase of the hydrogen concentration. New cells are formed, with the old becoming brighter. However, when the hydrogen content was increased over 7%, the established cellular structure began to collapse. Cells moved upstream, localizing near the end of the ceramic body. As a result, a well-developed two-

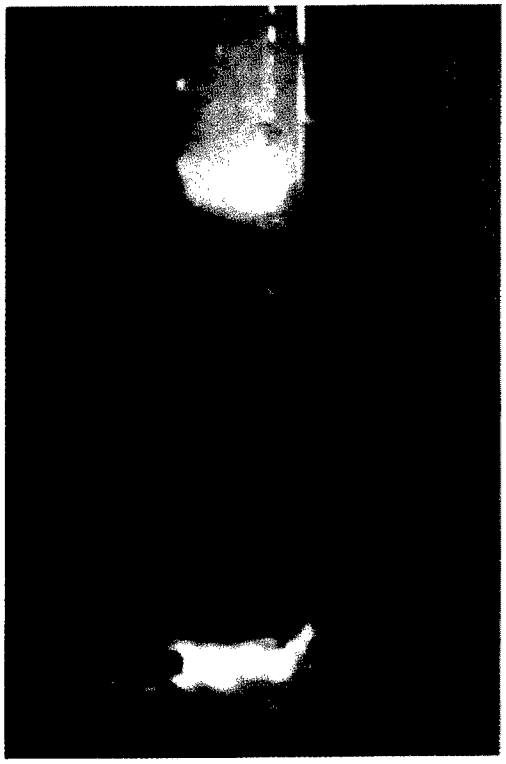

FIG. 3. Double wave formed by the planar cellular structure and a traveling superadiabatic wave, experimental conditions as in Fig. 4.

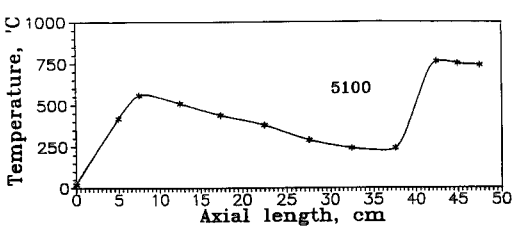

FIG. 4. Measured temperature profile of the double combustion wave structure formed in the 5.6-mm packed bed with a filtration velocity 1.7 m/s, $[H_2] = 9.5\%$. Number corresponds to propagation time in seconds.

dimensional structure was formed in the plane parallel to the upstream end of the packed bed. The high density of cells in the localized area led to the formation of a standing thermal wave. The temperature profile (Fig. 2d) shows that the temperature in the wave could be as high as 700°C.

The planar cellular structure was stable over the region of hydrogen concentrations. In some cases, the unburned hydrogen concentrations could be sufficiently high to support the superadiabatic wave, and a double wave structure was observed (Fig. 3).

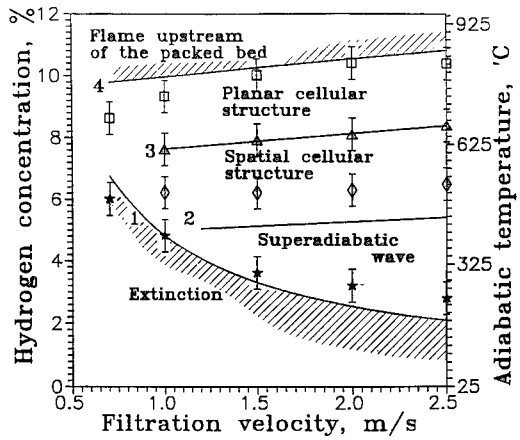

FIG. 5. Stability diagram for combustion of hydrogen-lean air mixtures under filtration in the 5.6-mm solid alumina packed bed. The point shows the experimental stability limits. The curves show the results of theoretical estimations: (1) corresponds to extinction limit (eq. 2), (2) refers to thermodiffusive stability limit (eq. 5), (3) and (4) correspond to the stability limits of the planar wave (eq. 7).

It consists of a standing planar cellular wave and superadiabatic wave slowly propagating upstream. The measured temperature profile for the double wave is represented in Fig. 4.

With the increase in hydrogen concentration to over 11%, the combustion zone traveled upstream and left the packed bed.

The described wave structures were observed with a wide range of experimental parameters. The stability diagram for 5.6-mm alumina spheres in the packed bed is presented in Fig. 5 as a function of filtration velocity and hydrogen concentration. The diagram contains areas of existence of the three structures observed: a stable superadiabatic wave, a spatial cellular structure with a decaying superadiabatic wave, and a planar cellular with a decaying or stable superadiabatic wave. Corresponding to Fig. 5, the main parameter governing the transition between the structures is the hydrogen content, while the filtration velocity is of secondary influence.

Discussion

The properties of the superadiabatic wave in the region of stable propagation are well predicted by theoretical considerations [6–8], based on an integral volume-averaged treatment of the porous media. If the radial heat losses are neglected and the one-temperature approximation is assumed valid, the parameters of the wave are related by the following simple equation resulting from an energy balance

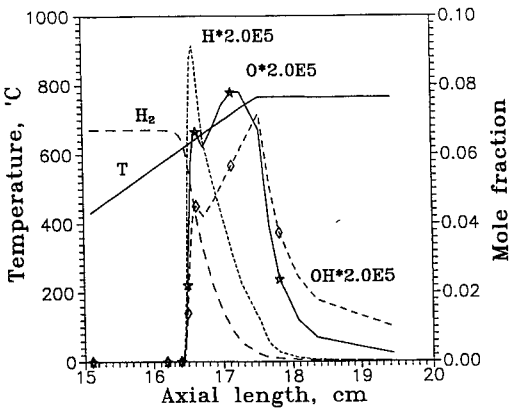

FIG. 6. Species profiles integrated over the experimental temperature profile for 5.6-mm alumina-packed bed and filtration velocity 1.3 m/s.

$$u/v_t = 1 - (\Delta T_a/\Delta T_c) \quad (1)$$

The integral balance can be extended to the case of lateral heat losses [5]

$$u/v_t = 1 - [(\Delta T_a/\Delta T_c)^2 - 4\beta\lambda_s/((c\rho)_g v)^2]^{1/2} \quad (2)$$

where β is the effective coefficient for heat exchange with surroundings.

The combustion temperature, T_c, used as a parameter in equations 1 and 2, is defined mainly by the chemical composition of the mixture. It grows only slightly with the increase of filtration velocity and adiabatic heat content because of the strong reaction rate temperature dependence. Variations of T_c within 15% are observed in the experiments conducted with 5.6-mm alumina-packed bed. A linear approximation of T_c obtained by fit of experimental data is used for the theoretical estimations below.

The experimental extinction limit is well described by equation 2 (Fig. 5, curve 1), with the assumption $u/v_t \to 1$. It means that the wave propagation is possible only when the adiabatic temperature and, hence, heating exceed the heat losses, and the expression under the square root in equation 2 remains positive:

$$\Delta T_a > 2(\beta\lambda_s)^{1/2}\, \Delta T_c/((c\rho)_g v) \quad (3)$$

The combustion temperature can be derived from integral propagation models [8], assuming a one-step chemical reaction with Arrhenius temperature dependence. However, the detailed understanding of combustion zone parameters requires modeling with full chemical kinetic.

In the one-temperature approximation, the kinetic equations can be integrated separately over the experimental temperature profile. This method was employed in the current study to analyze the reaction mechanism of lean hydrogen-air mixture combustion in the superadiabatic wave. The premixed hydrogen combustion is modeled employing the Sandia Chemkin-II [14] and premixed flame [11] codes, and by using the hydrogen chemistry reported in Ref. 16. Uniform radial distributions of temperature and velocity along with constant flow rate and isobaric conditions were assumed.

The flame structure is presented in Fig. 6 in terms of the profiles of the fuel (H_2) and radical species (H, O, and OH), and the experimental temperature profile. Overall, combustion is stable even though the radical concentrations are small (e.g., the peak OH level in Fig. 6 is 36 ppm). The low radical concentrations are due both to the low temperatures and ultra-lean conditions that require large diluent levels. Ordinarily, under these conditions, the rate of the critical chain terminating reaction $H + O_2 + M \to HO_2 + M$ dominates that of the chain branching step $H + O_2 \to O + OH$. However, the reaction zone broadening and recycling of thermal energy from the postcombustion region into the preheat region (through exchange of gas-phase heat with that in the porous media) ensure that sufficient chain branching occurs for stable flames to be established. Using the imposed temperature profiles, the calculations indicate that a peak heat release rate as high as $5.5 \cdot 10^7$ W/m^3 is possible in the reaction zone. For the calculations performed, the reaction zone thickness appears to be close to 1 cm, approaching the diameter of the packed bed particles with increase of hydrogen concentration.

Although the small thickness is not necessary to lead to two-dimensional instability of combustion front, it may serve as a secondary mechanism for development and stabilization of instabilities with wavelengths close to the porous diameter. At this point, the continuous media approximation is no longer valid and the pore-level combustion mechanism must be considered. For further analysis, we should refer to details of flow structure inside the packed bed.

The particle-based Reynolds number $Re = (vd/\nu)$ was varied from 100 to 1000 in these experiments, corresponding to irregular flow conditions with high vorticity and enhanced mixing inside the bed. The complex flow pattern inside the bed is divided into high velocity streams and wake zones. Characterized by low frequency of heat and mass exchange, well-mixed wake zones are the main structures capable of supporting combustion inside the pore, serving as flame holders. Location of combustion front inside the wake zone will result in an increase of viscosity, providing further conditions for extension and stabilization of zone.

Thermodiffusive stability of the combustion spot formed inside the porous bed can be explained by the following simplified analysis. Consider the spot as a viscous formation with an intensive heat and mass exchange in highly unsteady surrounding

streams. For formation and stability of the spot, the enthalpy flux from the spot should be smaller than enthalpy flux due to diffusion of fresh mixture. For the flows considered, the modified Reynolds analogies are valid [17], resulting in the following relation for heat and mass transfer between the combustion spot and the surrounding zone:

$$StPr^{2/3} = St_m Sc^{2/3} \quad (4)$$

Equation 4 gives the relation between the convection heat transfer coefficient h and the mass transfer coefficient h_m in the form:

$$Pr^{2/3}(h/(c\rho)_g v) = Sc^{2/3}(h_m/v) \quad (5)$$

The combustion spot is stable in the lean hydrogen-air mixture if the enthalpy flux from the combustion zone, proportional to $h\ \Delta T_c$, is smaller than enthalpy flux due to diffusion of hydrogen to the spot. The latter is proportional to mass flux h_m $[H_2]$, multiplied by combustion enthalpy ΔH_c.

Introducing the Lewis number ($Le = Pr/Sc$), the criterion for development of the instability is given by:

$$(\Delta T_a/\Delta T_c)Le^{2/3} \geq 1 \quad (6)$$

Equation 6 is represented in Fig. 5 ($Le^{2/3} = 2$) and is in good agreement with the experimental stability limit of a continuous superadiabatic wave.

Unlike the typical gaseous premixed flames, the ratio $\Delta T_a/\Delta T_c$ for filtration combustion is varied from $\Delta T_a/\Delta T_c < 1$, for superadiabatic waves, to $\Delta T_a/\Delta T_c > 1$, for waves propagating upward with the flow. According to the criterion of equation 6, mixtures characterized by $Le = 1$ (air mixtures with methane, acetylene) are always stable. Moreover, the combustion of mixtures with $Le > 1$ are stable up to the critical adiabatic temperature of the mixture, given by $\Delta T_a \approx (Le^{-2/3}\ \Delta T_c)$. For the case $\Delta T_a/\Delta T_c > 1$, the instability is suppressed by reverse front propagation.

Equation 6 is also useful for understanding some integral properties of cellular structures. First, with an increase of hydrogen concentration, spots were observed only in the narrow region preceding the superadiabatic wave; the required ΔT_c was reduced due to high temperatures. In the well-developed spatial structure, the linear rise of average temperature compensates the reduction of ΔT_a due to partial combustion of hydrogen.

The irregular packed bed is characterized by a distribution of properties, and more locations become available for formation of spots with the increase of ΔT_a. When a high density of the spots was reached, they began to interfere with each other, and the spatial cellular structure collapsed to a planar one. Establishment of the planar cellular structure was followed by the formation of a standing thermal wave. The gas mixture entering the bed was initially preheated by the narrow porous zone preceding the nonuniform combustion structure. From this viewpoint, the temperature distribution is analogous to the distribution in burner-stabilized flames [2]. High gas temperature in the combustion zone provides the conditions for a high concentration of spots, but the combustion is not complete. Note, that formal integration of the kinetic equations over the experimental temperature profile will result only in partial combustion of hydrogen.

Equations 1 and 2 permit the numerical description of the existence limits of the planar structure (Fig. 5, curves 3,4). According to equation 1, the flame will move upstream and leave the packed bed if the hydrogen concentration is sufficiently large, such that

$$[H_2] > (c\rho)_g\ \Delta T_c/(\Delta H_c \eta) \quad (7)$$

This estimate is in good agreement with the experimental limit (Fig. 5, curve 4).

Equation 7 can also be applied to describe the critical hydrogen concentration for the transfer between a spatial cellular structure and a planar one (Fig. 5, curve 3). Actually, this transfer occurs when the hydrogen concentration and adiabatic temperature are not yet sufficient to move all of the combustion zone upstream, but are already sufficient to pull the relatively cold and weak spatial cellular structure upstream. Using equation 7 in this case, the combustion temperature ΔT_c should be taken as an average temperature in a spatial cellular zone, and the adiabatic temperature corresponding to the portion of hydrogen burned in this zone. The best agreement with the experimental threshold requires $\eta = 0.4$, which means that about 40% of the hydrogen was burned in the cellular structure zone.

Conclusions

Combustion of lean hydrogen-air mixtures in an inert porous media was studied experimentally. Uniform superadiabatic and nonuniform cellular flame structures were observed for downstream-propagating waves, including double waves composed of both types of structures. The results are as follows:

1. Superadiabatic wave propagation as a localized, stable temperature zone is observed for the leanest mixtures burned. Hydrogen combustion is stable even for very lean mixtures with only 3% fuel. Due to the self-recuperation of the system, the temperature reached is much in excess (up to three times) of the adiabatic reaction temperature for unheated reactants; the superadiabatic waves are characterized by complete combustion and general properties similar to ones observed for other gaseous air-fuel mixtures reacting in an inert bed. The properties of superadiabatic waves

are well described by the integral volume-averaged treatment of combustion in porous media.

2. A computational model, incorporating detailed hydrogen-oxygen chemistry was used to analyze kinetic profiles over experimental temperature distributions. For calculations performed, reaction zone thickness appears to be close to 1 cm; this increases and approaches the diameter of the packed bed particles as the hydrogen concentration is increased. At this point, the continuous media approximation is no longer valid and a pore-level combustion mechanism is to be considered.
3. It was found that the superadiabatic wave becomes unstable with an increase of hydrogen concentration to 5–6%, forming multidimensional cellular structures. Two types of cellular structures were observed: three-dimensional and planar. According to experimental results, the transitions between the wave propagation regimes are controlled mainly by the hydrogen concentration, while the filtration velocity is of secondary influence. Cellular structures are characterized by partial combustion of hydrogen and permit sustained double-front flames for hydrogen concentration in the range from 8–10%.
4. The cell formation is analyzed as a thermodiffusive instability of pore-level-driven combustion. The criterion of instability is found as a relation between adiabatic temperature, combustion temperature, and Lewis number of the mixture. The predicted stability region is consistent with the above experimental limits.

Nomenclature

d	particle diameter
$(c\rho)$	thermal capacities
ΔH_c	enthalpy of hydrogen combustion
$[H_2]$	concentration of hydrogen
h	convection heat transfer coefficient
h_m	convection mass transfer coefficient
Le	Lewis number
Pr	Prandtl number
Re	Reynolds number
Sc	Schmidt number
Sh	Sherwood number
St	Stanton number
ΔT_a	adiabatic temperature rise $\Delta T_a = [H_2]\,\Delta H_c/(c\rho)_g$
ΔT_c	combustion temperature rise
v	gas mixture velocity
v_t	thermal wave velocity $v_t = v\,(c\rho)_g/(c\rho)_s$
u	combustion wave propagation velocity

Greek Symbols

β	effective coefficient for heat exchange with the surroundings
λ_s	effective thermal conductivity of the porous media
ν	kinematic viscosity
η	degree of combustion

Subscripts

a	adiabatic
c	combustion
g,s	gas, solid
t	thermal

REFERENCES

1. Lewis, B. and von Elbe, G., *Combustion Flames and Explosions of Gases,* Academic Press, New York, 1961, pp. 314–317.
2. Patnaik, G. and Kailasanath, K., *Combust. Flame* 99:247–253 (1994).
3. Patnaik, G. and Kailasanath, K., *Twenty-Third Symposium (International) on Combustion,* The Combustion Institute, Pittsburgh, 1991, p. 1641.
4. Weinberg, F., Proc. 3rd Internat. Conference on Combustion Technologies for a Clean Environment, Lisbon—Portugal (July 1995); also *Combust. Sci. Technol.* in press, 1996.
5. Weinberg, F., *Proc. Superadiabatic Combustion and Its Applications* (Zhdanok, S. A., Ed.), Belarus Academy of Sciences, Minsk, 1995, p. 1.
6. Babkin, V. S., *Pure Appl. Chem.* 65:335–344 (1993).
7. Zhdanok, S. A., Kennedy, L. A., and Koester, G., *Combust. Flame* 100:221–231 (1995).
8. Laevskii, Yu. M. and Babkin, V. S., in *Thermal Wave Propagation in Heterogeneous Media,* (Yu. S. Matros, Ed.), Nauka, Novosibirsk, 1988, p. 108.
9. Weinberg, F. J., *Nature* 233:239–241 (1971).
10. Minaev, S. S., Potytnyakov, S. I., and Babkin V. S., *Combust. Explos. Shock Waves* 30:306–310 (1994).
11. Vainshtein, P. B., *Combust. Explos. Shock Waves* 28:28–34 (1992).
12. Takeno, T., Sato, K., and Hase, K., *Eighteenth Symposium (International) on Combustion,* The Combustion Institute, Pittsburgh, 1981, pp. 465–471.
13. Sahraoui, M. and Kaviany, M., *Int. J. Heat Mass Transfer.* 37:2817 (1994).
14. Kee, R. J., Rupley, F. M., and Miller, J. A., Sandia Report SAND89-8009B UC-706, Sandia National Laboratories, Livermore, CA, 1989.
15. Kee, R. J., Grcar, J. F., Smooke, M. D., and Miller, J. A., Sandia Report SAND85-8240 UC-401, 1985. Sandia National Laboratories, Livermore, CA
16. Balakrishnan, G., Smooke, M. D., and Williams, F. A., *Combust. Flame* 102:329–340 (1995).
17. Chilton, T. H. and Colburn, A. P., *Ind. Eng. Chem.* 26:1183–1189 (1934).

Twenty-Sixth Symposium (International) on Combustion/The Combustion Institute, 1996/pp. 3377–3382

SUPERADIABATIC COMBUSTION WAVE IN A DILUTED METHANE-AIR MIXTURE UNDER FILTRATION IN A PACKED BED

SERGUEI I. FOUTKO, STANISLAV I. SHABUNYA, AND SERGUEI A. ZHDANOK
Chemical Physics Laboratory
Heat and Mass Transfer Institute
Minsk, Belarus

LAWRENCE A. KENNEDY
Department of Mechanical Engineering
University of Illinois at Chicago
Chicago, USA

The self-sustaining combustion wave, occurring when a methane-air mixture is filtered through a porous media, is examined theoretically in this paper. Such processes are characterized by an intense thermal interaction between the gas and the porous material. Due to the interfacial heat transfer, the solid phase is able to redistribute heat absorbed from reaction products to the unburned mixture. In the case of combustion waves cocurrent with the filtration flow, this results in peak temperatures exceeding the adiabatic one for the air-methane mixture. Theoretical treatment is conducted within a two-temperature model in which external heat losses are taken into account. The ignition temperature as the main parameter used in analytical solutions is determined for experimental conditions typical for methane-air mixtures burning under filtration in a packed bed. Analytical expressions predicting the combustion wave velocity and temperature distributions in the wave are derived. The results obtained are confirmed by numerical calculations and compared with related experimental data.

Introduction

In modern industrial processes dealing with organic fuels, heat-recuperation technologies are widely applied. These also play an important role in pollution control when mixtures with low calorific contents must be used. The great variety of possible configurations of such systems was extensively reviewed by Weinberg on the basis of the concept of excess enthalpy burning [1,2]. Another kind of system involves filtration combustion burners, where reactive gas mixtures flow through an initially preheated, inert, porous media resulting in self-sustaining combustion wave.

This approach has already proven to be efficient when used, for example, for the burning of organic pollutants in the exhaust air from automobile manufacturing factories [3], and as a successful application for the methanol-steam and the autothermic methane-steam reforming processes [4]. The most striking feature of such applications is the stable burning of organic mixtures with extremely low heat contents and a theoretical temperature rise across the flame as low as approximately 20 K (which is well below the normal flammability limits) [5]. This becomes possible because the energy released in the gas-phase combustion reaction is recirculated through the inert solid phase to the unburned mixture. Thus superadiabatic (i.e., exceeding the normal adiabatic) combustion temperatures can be attained.

As shown in Ref. 6, which is devoted to the theoretical treatment of the phenomena, the processes are characterized by an intense interfacial heat exchange between the gas and solid phases; this is intrinsic to the so-called *low velocity regime (LVR)*, according to the classification given in Ref. 7. In recent work [8,9], lean methane-air combustion waves cocurrent with the filtration flow were experimentally observed and some important relations for the governing parameters of the processes were elucidated. It was shown in these studies that the maximum temperature attained in the waves is defined only by an adiabatic temperature of a gas mixture and a "matching condition" between the combustion wave speed and that for the thermal wave propagation in the porous media:

$$T_{s,g}^{\max} = \frac{\Delta T_{ad}}{(1 - u_w/u_t)} \tag{1}$$

Thus, it becomes evident that accurate prediction of the combustion wave velocity u_w is crucial for obtaining desired temperature distributions or combustion velocity regimes in numerous practical

applications. Such an analytical prediction, considering the heterogeneity of the gas and solid temperature profiles in a porous media and the heat losses from the system to surroundings, has not been addressed in the pertinent literature. However, limiting cases are discussed in Ref. 6,10–12. The main objective of the present paper is to provide an adequate analytical prediction for the combustion wave velocity u_w defined by the governing filtration process parameters.

Analytical Model

The one-dimensional model chosen is a wave moving at a constant speed in an inert porous bed [9]. An air-fuel mixture flows through a porous media that has an externally heated, narrow zone of high temperature sufficient to initiate the combustion reaction. The reaction front width is assumed to be small in comparison with that of the preheat zone. The thermal conductivity of the porous media is considered to be large relative to that of the gas mixture. Other assumptions are that the energy exchange between the solid and the gas is proportional to the local temperature difference and the heat loss from the system occurs only through the porous media. The chemical kinetics is described by a one-step irreversible reaction:

$$CH_4 + 2O_2 + 7.524N_2 \rightarrow CO_2 + 2H_2O + 7.524N_2 + 847\text{kJ/mol}$$

with the reaction rate described by a first-order Arrhenius rate expression.

The set of equations describing the combustion waves in inert porous media, neglecting diffusion and thermal conductivity of the gas phase, has the form [13]:

$$(cp)_g \frac{\partial T_g}{\partial t} + u_g (cp)_g \frac{\partial T_g}{\partial x} = -\alpha(T_g - T_s) + QpW \quad (2)$$

$$(cp)_s \frac{\partial T_s}{\partial t} = \frac{\partial}{\partial x} \lambda_s \frac{\partial T_s}{\partial x} + \alpha(T_g - T_s) - \beta(T_s - T_0) \quad (3)$$

$$\frac{\partial A}{\partial t} + u_g \frac{\partial A}{\partial x} = -W \quad (4)$$

$$W = AKe^{-E/RT_g} \quad (5)$$

$$\lambda_s = \lambda_{ef} + \frac{32\sigma d_p \varepsilon T_s^3}{9(1-\varepsilon)} \quad (6)$$

where T_g, T_s are the solid and gas temperatures; $(cp)_s$, $(cp)_g$, their heat capacities; u_g the gas velocity; α the interfacial heat exchange coefficient; β the effective coefficient for heat losses from the system; T_0 the ambient temperature; Q the heat content of the reactive mixture; A the dimensionless concentration of fuel; ε the porosity, and λ_s the effective thermal conductivity of the porous media, which includes the influence of radiation, assuming an optically thick region around the high-temperature zone in the bed [14,15].

For a fully developed combustion wave propagating with a constant velocity, Eqs. (2) and (3) can be rewritten in a system of coordinates moving with the reaction zone, $\xi = x - u_w t$. Noting that $u_w \ll u_g$, these equations have the dimensionless form

$$\frac{d\tau}{d\zeta} = -(\tau - \theta) + \frac{\Delta T_{ad}}{\Delta T_{s,i}} \delta(\zeta) \quad (7)$$

$$-u \frac{d\theta}{d\zeta} = a \frac{d^2\theta}{d\zeta^2} + (\tau - \theta) - \frac{\beta\tau}{\alpha} \quad (8)$$

where dimensionless variables and parameters are

$$u_t = \frac{(cp)_g u_g}{(cp)_g + (cp)_s}, \qquad \Delta T_{ad} = \frac{Q}{c_g}$$

$$\tau = \frac{T_g - T_0}{T_{s,i} - T_0}, \qquad \Delta T_{s,i} = T_{s,i} - T_0$$

$$\theta = \frac{T_s - T_0}{T_{s,i} - T_0}, \qquad \zeta = \frac{\xi\alpha}{(cp)_g u_g}$$

$$u = \frac{u_w}{u_t}, \qquad a = \frac{\lambda_s \alpha}{((cp)_g u_g)^2} \quad (9)$$

In this paper, the reaction zone is assumed to be small in comparison with the preheat zone. The temperature of the gas can be considered to jump from $T_g(-0)$ to $T_g(+0)$, such that

$$T_g(+0) - T_g(-0) = \Delta T_{ad} \quad (10)$$

at the point where the temperature of the solid is equal to the ignition temperature, $T_{s,i}$. Hence, the reaction term in the Arrhenius expression can be replaced by an energy-release delta function [10]. This eliminates the need for the rate expression and divides the system into prereaction and postreaction zones.

The boundary conditions for Eqs. (7) and (8) are

$$\tau = \theta = 0, \qquad \zeta \rightarrow \pm\infty$$
$$\theta(+0) = 1 \quad \theta(-0) = 1$$
$$\theta'(-0) = \theta'(+0) \quad \tau(+0) - \tau(-0) = \frac{\Delta T_{ad}}{\Delta T_{s,i}} \quad (11)$$

To treat the system of Eqs. (7) and (8) with boundary conditions from Eq. (11), one need to find the solutions of the corresponding characteristic polynomial:

$$ak^3 + (a + u)k^2 + \left(u - 1 - \frac{\beta}{\alpha}\right)k - \frac{\beta}{\alpha} = 0 \tag{12}$$

It can be shown that Eq. (12) must have two negative roots, k_1 and k_2, and one positive root, k_3, to define the finite solutions of the system of Eqs. (7) and (8) with the boundary conditions from Eq. (11). Thus, the gas-phase and solid-phase temperature profiles are described by the following expressions:

$$\theta = e^{k_3\zeta} \tag{13}$$

and

$$\tau = \left(-uk_3 - ak_3^2 + \left(1 + \frac{\beta}{\alpha}\right)\right)e^{k_3\zeta} \tag{14}$$

for the domain where $\zeta < 0$ along with

$$\theta = \frac{k_2 - k_3}{k_2 - k_1}e^{k_1\zeta} + \frac{k_3 - k_1}{k_2 - k_1}e^{k_2\zeta} \tag{15}$$

and

$$\tau = \frac{k_2 - k_3}{k_2 - k_1}\left(-uk_1 - ak_1^2 + 1 + \frac{\beta}{\alpha}\right)e^{k_1\zeta} + \frac{k_3 - k_1}{k_2 - k_1}\left(-ak_2^2 - uk_2 + 1 + \frac{\beta}{\alpha}\right)e^{k_2\zeta} \tag{16}$$

for the region where $\zeta > 0$.

The solutions of Eq. (10), satisfying the boundary condition for the dimensionless gas temperature at the point $\zeta = 0$, have the form

$$k_3 = -\frac{1}{3}\left(1 + \frac{u}{a}\right) + \frac{1}{3}\left(\left(1 + \frac{u}{a}\right)^2 + \frac{3}{a}\left(1 - u + \frac{\beta}{\alpha} + \frac{\Delta T_{ad}}{\Delta T_{s,i}}\right)\right)^{1/2} \tag{17}$$

$$k_{1,2} = -\frac{1}{2}\left(1 + \frac{u}{a} + k_3\right) \pm \frac{1}{2}\left(\left(1 + \frac{u}{a} + k_3\right)^2 - \frac{4\beta}{\alpha a k_3}\right)^{1/2} \tag{18}$$

It should be noted that substituting Eq. (17) for k_3 in Eq. (12) defines the dimensionless combustion wave velocity, u, as an implicit function of the governing filtration process parameters

$$a, \quad \frac{\Delta T_{ad}}{\Delta T_{s,i}}, \quad \frac{\beta}{\alpha}$$

It is also of interest that, for the limiting case when $\alpha \to \infty$, Eqs. (12) and (17) give the velocity dependence obtained using the one-temperature approximation [7]:

$$u = 1 - \left(\left(\frac{\Delta T_{ad}}{\Delta T_{s,i}}\right)^2 - \frac{4\alpha\beta}{\alpha}\right)^{1/2} \tag{19}$$

To obtain the analytical prediction for the dimensionless combustion wave velocity u from Eqs. (12) and (17), two parameters, the ignition temperature $T_{s,i}$ and the effective coefficient for heat exchange with surrounding β, must be defined. The former may be estimated by considerating the temperature evolution of a gas element moving through the heated porous media in a self-sustaining combustion wave. Assuming a moderate heat exchange coefficient α, during the temperature evolution, there is a moment when the rate of heat release in the gas phase exceeds the rate of heat supply from the solid phase via the interfacial heat exchange mechanism. Following this point, the temperature increase for the gas element may be treated as a thermal explosion. Thus, one can directly apply the corresponding theory to determine the self-ignition threshold condition with the correction for fuel consumption and, consequently, obtain the induction time τ_{ind} for the reaction [16]:

$$\tau_{\text{ind}} = \frac{1}{K}\left(\frac{2\pi^2 R^2\, T_{s,i}^4}{\Delta T_{ad}^2\, E^2}\right)^{1/3} e^{E/RT_{s,i} - 1} \tag{20}$$

On the other hand, assuming that the reaction (fuel consumption) is almost completed in the distance of the order of the pore size (for a packed bed filled with spheres this is the diameter d of the spheres), we have $\tau_{\text{ind}} = d/u_{g,\text{pore}}$, where $u_{g,\text{pore}} = u_g/\varepsilon$ is a temperature-dependent averaged gas velocity in a pore. Finally, we can derive an approximation for the ignition temperature $T_{s,i}$ in the following implicit form:

$$\frac{V_e E/RT_{s,i} - 1}{(E/RT_{s,i})^{7/3}} = \left(\frac{\Delta T_{ad}^2\, R^5}{2\pi^2\, E^5}\right)^{1/3} \frac{d\varepsilon\, T_0 K}{u_{g,0}} \tag{21}$$

The effective coefficient for heat exchange with the surroundings β can be estimated assuming that the radiation losses play a dominant role. For a cylindrical geometry of the packed bed composed of a tube (with an internal diameter D) filled with solid spheres, this gives

$$\beta = \frac{4\sigma T_{s,\max}^4 \varepsilon' \varepsilon''}{D(T_{s,\max} - T_0)} \tag{22}$$

where ε' is an emissivity of the solid spheres and ε'' is a transmissivity factor for the tube material.

Numerical Solutions

To support and to test the analytical solutions obtained according to Eqs. (12) and (17), a computational procedure was performed using a full set of the basic Eqs. (2) through (4). These were calculated using the finite difference method. In the numerical calculation, the flame position is not specified beforehand but is decided as a result of the total energy balance in the combustion system. The boundary

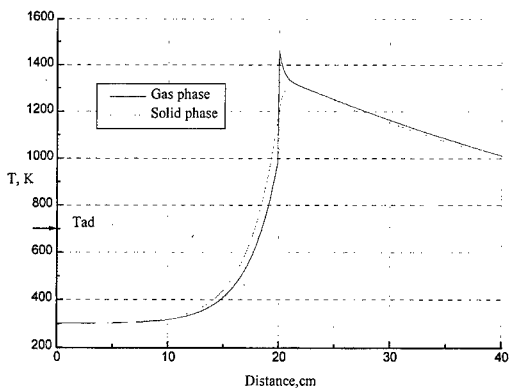

FIG. 1. Temperature profiles of a fully developed combustion wave (two-temperature analytical solution) in the case $\Phi = 0.17$, $u_g = 0.43$ m/s.

conditions for the computational procedure were set as follows:

$$T_g = T_s = T_0 \quad A = 1 \tag{23}$$

at the entrance, where the unburned mixture is flowing into the system, and

$$\partial T_g/\partial x = \partial T_s/\partial x = 0 \tag{24}$$

at the exit. To simulate the initiation of a combustion reaction, a high-temperature profile approximately 1200 K at the maximum and few centimeters in length was set in the solid phase as an initial condition. The calculation procedure was performed until a constant combustion wave velocity was obtained.

The size of the computational domain and all the values of the parameters used were chosen as close as possible to the conditions of the related experiments reported in Refs. 8 and 9. In these studies, a rather simple experimental facility was designed to measure the temperature- time history of lean methane-air combustion waves, cocurrent with filtration flow, propagating in a packed bed column of inert porous alumina. The test apparatus was a vertical quartz glass tube with internal diameter $D = 76$ mm and test section 1.3 m in length. The test section was filled with a randomly packed bed of solid alumina spheres (diameter $d = 5.6$ mm). The experimental apparatus included thermocouple temperature sensors and an electrical heater capable of initiating a combustion zone within the bed.

To simulate these experimental conditions, the layer formed by the solid alumina spheres was characterized as follows: $\varepsilon = 0.4$, $c_s = 1.3$ kJ/(kgK), $p_s = 2.5 \times 10^3$ kg/m^3, $\lambda_{ef} = 1.3$ W/(mK). The heat transfer coefficient, α, was estimated from the heat transfer around a sphere with a diameter $d = 5.6$ mm, which yielded (according to Ref. 17) α values in the range 6×10^4 to 8×10^4 W/(m^{3}K), depending on the superficial filtration velocity $u_{g,0} = 0.28$ to 0.43 m/s ($T_0 = 300$ K) for a methane-air mixture at the entrance in the packed bed. The equivalence ratios Φ for the mixture were varied from 0.17 to 0.5. Values of the frequency factor and the activation energy were chosen, according to Ref. 5, to be equal to $K = 2.6 \times 10^8$ s^{-1} and $E = 130$ kJ/mol, respectively.

Discussion

The analytical and numerical procedures described were applied to a number of experimental conditions revealing qualitatively similar results. Typical temperature profiles in gas and solid phases obtained from analytical solutions of Eqs. (12) and (17) for the experimental settings when $u_g = 0.43$ m/s and $\Phi = 0.17$ are shown in the Fig. 1. Here, the values of ignition temperature $T_{s,i}$ and effective coefficient for heat exchange with the surroundings β were $\Delta T_{s,i} = 850$ K and $\beta = 10^3$ W/(m^{3}K), respectively. These were obtained from Eqs. (21) and (22) with an emissivity $\varepsilon' = 0.45$ for solid alumina [14] and transmissivity factor $\varepsilon'' = 0.38$ for quartz glass [14]. It is interesting to note that the value of the ignition temperature, $\Delta T_{s,i}$, is almost independent of the equivalence ratio Φ in the region tested, $0.17 \leq \Phi \leq 0.5$, and rests within the temperature interval 850–950 K.

The corresponding numerical solution for the same experimental settings (and, accordingly, parameters used) is demonstrated in Fig. 2. Here one can see the propagation of a stable self-sustaining combustion wave with velocity $u_w = 1.7 \times 10^{-4}$ m/s. The temperature profiles are gradually approaching the fully developed state described by the analytical temperature distributions shown in Fig. 1. Further, as can be seen from the methane concentration distribution in the combustion wave in Fig. 2, (thin solid line), the small reaction zone assumption made previously is quite reasonable. Finally, it must be noted that the regimes under consideration now are essentially superadiabatic (i.e., maximum temperature in the wave exceeds the adiabatic one, which is marked by an arrow in Figs. 1 and 2).

All results obtained from analytical considerations and numerical calculations together with the corresponding experimental data [8,9] are presented in Fig. 3. As can be seen, there is good agreement between that predicted by Eqs. (12) and (17) and the experimental results.

Conclusions

Theoretical analysis of superadiabatic combustion wave propagation processes resulted in simple formulas for the combustion wave velocity and the temperature distribution in both gas and solid phases. A two-temperature analytical approximation and numerical solution of the problem were used to describe available experimental data. The influence of

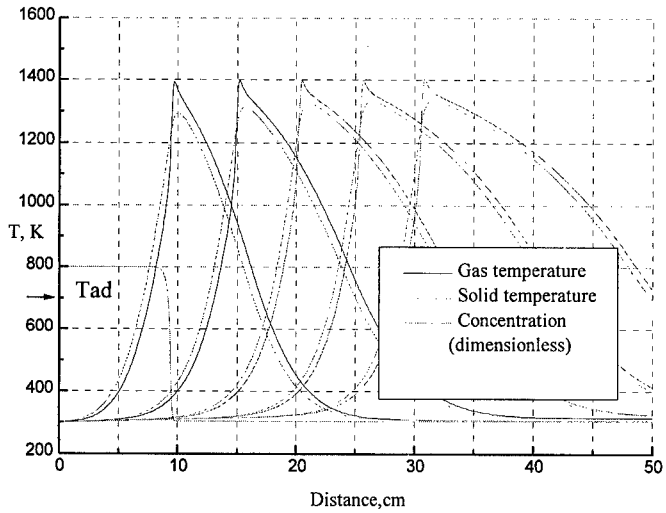

FIG. 2. Propagation of a stable, self-sustaining combustion wave in porous media (numerical calculations; time intervals 5 min between adjacent peaks) in the case $\Phi = 0.17$, $u_g = 0.43$ m/s, $u_w = 1.7 \times 10^{-4}$ m/s.

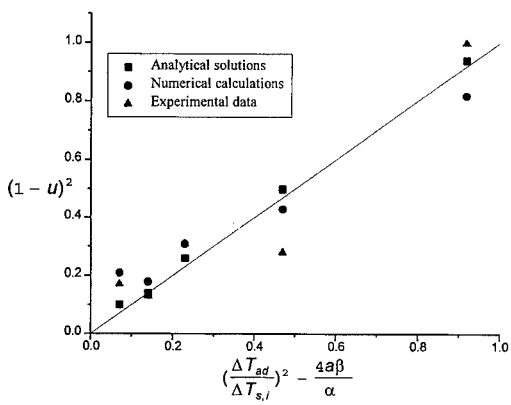

FIG. 3. Comparison of prediction of $u = u_w/u_t$, dimensionless wave speed, from two-temperature analytical theory, Eqs. (12) and (17), and results of numerical calculations with experimental data [8,9]. Solid line shows predictions from one-temperature approximation, Eq. (19) [9].

external heat losses was taken into account. One of the most important theory parameters, ignition temperature, was estimated using the theory of thermal explosion. Quantitative agreement of theoretical and experimental results demonstrates the possibility of using the developed approach for analysis of the combustion wave in porous media for technical applications.

Nomenclature

A	concentration of fuel, dimensionless
a	dimensionless $\lambda_s\alpha/((cp)_g u_g)^2$
(cp)	heat capacities, J/(m^{3}K)
E	activation energy, J/mol
K	frequency factor, s^{-1}
Q	heat of reaction, J/kg
R	gas constant, J/(molK)
T	temperature, K
ΔT_{ad}	adiabatic temperature rise, $\Delta T_{ad} = A_0 Q/(cp)_g$, K
d	diameter of the solid alumina spheres, m
D	internal diameter of a tube, m
u_g	gas mixture velocity, m/s
u_t	thermal wave velocity, $u_t = u_g(cp)_g/((cp)_g + (cp)_s)$, m/s
u	dimensionless velocity $u = u_w/u_t$
x	spatial distance, m

Greek Symbols

α	interfacial heat-exchange coefficient, W/(m^{3}K)
β	effective coefficient for heat exchange with surroundings, W/(m^{3}K)
λ_s	effective thermal conductivity of the porous media (including radiation), W/(mK)
ε	porosity, dimensionless
σ	Stephan's constant, W/(m^{2}K^4)
ε'	emissivity, dimensionless
ε''	transmissivity factor, dimensionless
Φ	equivalence ratio, dimensionless
τ_{ind}	induction time, s
θ	dimensionless solid temperature, $\theta = (T_s - T_0)/(T_{s,i} - T_0)$
τ	dimensionless gas temperature, $\tau = (T_g - T_0)/(T_{s,i} - T_0)$
ξ	spatial distance in moving coordinates, $\xi = x - u_w t$,m
ζ	dimensionless distance $\zeta = \alpha\xi/(cp)_g u_g$, m

Subscripts

g,s	gas, solid
i	ignition
o	ambient
w	wave
max	maximum temperature value

REFERENCES

1. Weinberg, F. J., *Nature* 233:239–241 (1971).
2. Weinberg, F. J., in *Advanced Combustion Methods* (F. J. Weinberg, ed.), Academic Press, London, 1986.
3. "A New Method of Destroying Organic Pollutants in Exhaust Air," Commercial report, ADTEC Co., Ltd., (1990).
4. Echigo, R. and Hanamura, K., in *Energy Conversion and Utilization with High Efficiency, Subarea D, Efficient Utilization of Energy,* pp. 57–62, September, 1993.
5. Hanamura, K., Echigo, R., and Zhdanok, S., *Int. J. Heat Mass Transfer* 13:3201–3209 (1993).
6. Babkin, V. S. and Laevskii, Y. M., in *Propagation of Heat Waves in Heterogeneous Media* (Y. S. Matros, ed.), Nauka, Novosibirsk, 1988, p. 108.
7. Babkin, V. S., *Pure Appl. Chem.* 65:335–344 (1993).
8. Koester, G. E., Kennedy, L. A., and Subramaniam, V. V., *Twenty-Fifth Symposium (International) on Combustion,* The Combustion Institute, Pittsburgh, 1994.
9. Zhdanok, S., Kennedy, L. A., and Koester, G., *Combust. Flame* 100:221–231 (1995).
10. Babkin, V. S. et al., *Combust. Explos. Shock Waves* 19:17–26 (1983).
11. Vortmeyer, D. and Jahnel, W., *Chem. Eng. Sci.* 8:1485–1496 (1972).
12. Gilles, E., *Chem. Eng. Sci.* 29:1211–1216 (1974).
13. Simon, B. and Vortmeyer, D., *Chem. Eng. Sci.* 1:109–114 (1978).
14. Siegel, R. and Howell J. R., *Thermal Radiation Heat Transfer,* McGraw-Hill, New York, 1972.
15. Yoshizava, Y., Sasaki H., and Echigo R., in *Proc. National Heat Transfer Conference,* Pittsburgh, 1987, pp. 1–5.
16. Frank-Kamenetzkii, D. A., *Diffuzia i Teploperedacha v Chimicheskoi Kinetike,* Nauka, Moscow, 1987, p. 349.
17. Kaviany, M., *Principles of Heat Transfer in Porous Media,* Springer-Verlag, New York, 1991, p. 626.

Twenty-Sixth Symposium (International) on Combustion/The Combustion Institute, 1996/pp. 3383–3389

MODELING OF PREMIXED GAS COMBUSTION IN POROUS MEDIA COMPOSED OF COARSE-SIZED PARTICLES: 1-D DESCRIPTION WITH DISCRETE SOLID PHASE

O. S. RABINOVICH, A. V. FEFELOV AND N. V. PAVLYUKEVICH
A. V. Luikov Heat and Mass Transfer Institute
Academy of Sciences of Belarus
15 P. Brovka Str., Minsk 220072, Belarus

A one-dimensional non-steady-state model of gas combustion in a porous medium, treated as a discrete structure, is proposed. Each element of this regular periodic structure consists of the three elements: a solid particle, a gas flow zone, and a gas stagnation zone. Combustion occurs in the flow zones; the solid particles and stagnation zones are chemically inert. Numerical simulation of the opposing waves of premixed methane-air combustion in the discrete-modeled porous medium reveals the pulsating nature of the process. The maximal temperature and burning rate in the combustion front as well as the velocity of its propagation are low in the regions of the gas flow zone, which are adjacent to the particles, and increase in the neighborhood of the stagnation zone. At the size of elementary cells greater than some critical value $d_{cr}^{(1)}$ (approximately 3 mm), the flame breaks into the high velocity regime of propagation in the neighborhood of the stagnation zone; the amplitude of pulsation of the combustion characteristics is increased considerably in this period. After crossing the threshold value $d_{cr}^{(1)}$, the high frequency oscillation (~100 Hz) of the position of combustion front and its temperature were found in a region of the flow zone adjacent to the stagnation zone. When the diameter of particles becomes greater than the second critical value $d_{cr}^{(2)}$, the flame propagates in the high velocity regime over all the regions of the flow zone; the amplitude of pulsation of combustion characteristics is reduced. The discrete model of gas combustion in a porous medium, composed of coarse-sized particles, leads to a qualitatively new result when the process under consideration is sensitive to high-temperature reactions in the gas phase, and the final composition of the gas mixture is of main practical interest.

Introduction

Investigations on gas combustion in porous media, the so called filtration gas combustion (FGC) have intensified during the last 10–15 years because of a number of specific features of the phenomenon that are important from the viewpoint of practical applications in power engineering, air purification and conditioning, and in flame-hazard prevention technique. Filtration gas combustion provides the advantages of lowering NO_x and CO emission [1,2], attaining superadiabatic combustion temperatures [3,4].

The basic results on premixed gas combustion in inert porous media were published in a series of papers by Babkin and coauthors [4–9]. Various steady-state combustion regimes determined by different physical mechanisms of chemical reaction transfer were studied.

Another branch of gas combustion in porous media, when a porous matrix influences the chemical kinetics of the process, is represented by catalytic combustion (see reviews in Refs. 10–11).

In all cases, the size of solid structural elements constituting the porous medium is one of the most important parameters determining the characteristics of combustion. When moving from small-sized to coarse-sized particles, the intensity of heat exchange between the gas and solid phases decreases. For the size of the structural elements of a porous medium exceeding the critical value d_{cr}, transition from the low-velocity regimes (LVR) of combustion front propagation (with the velocity $u \sim 10^{-4}$ m/s) to the high-velocity regimes (HVR, $u \sim 1$ m/s) is observed [6]. In the work by Shaulov [12], a wide range of experimental data on the limits of the high-velocity flame propagation regime in tubes and packed beds was analyzed.

The conventional theoretical description of gas combustion in porous media is based on the model of two mutually penetrating continua [8]. As first emphasized by Shahroui and Kaviany [13], continuum models are not adequate for many practical cases: the thickness of the preheating and reaction zones is often of the same order of magnitude (or even smaller) as the size of elements of a porous structure (i.e., the size of the solid particles in the case of a packed bed). Hence, the volume-averaged equations of the continuous model cannot be derived consistently from the pointwise conservation

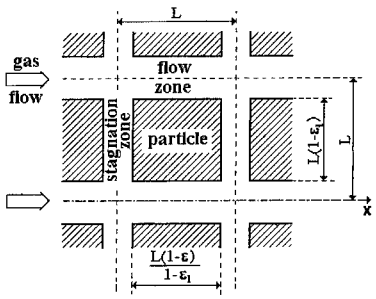

FIG. 1. Sketch of the model of a porous medium with discrete periodic structure.

equations for the two phases. As an example, for LVR of gas combustion in a porous medium (flame velocity $u \approx 1.5 \cdot 10^{-4}$ m/s and thermal diffusivity of the porous medium $a \approx 3 \cdot 10^{-7}$ m^2/s), the estimate of the characteristic length of the thermal zone in the combustion wave is $L_{\text{therm}} \approx a/u \approx 2 \cdot 10^{-3}$ m. It is obvious that a porous medium with a particle size larger than 10^{-3} m should be treated not as continuum but as a discrete structure to adequately describe combustion propagation in it.

In Ref. 13, the direct, two-dimensional pore-level model of premixed gas combustion was suggested and examined for a specific porous system with high porosity (0.8–0.9) and relatively small pore size ($1 \cdot 10^{-3}$ m). In fact, only steady-state combustion regimes were considered in this work when the gas flow rate was adjusted to achieve a situation with a standing combustion front. Neither low-velocity regimes nor transition to the high-velocity regimes was studied.

In the present work, a one-dimensional unsteady-state model of gas combustion in a porous medium, treated as a discrete structure, is suggested. This partially heuristic model reflects the main features of gas combustion front propagation in a porous medium with discrete structure and allows high-performance numerical simulation of the phenomenon for various combinations of the fuel concentration, gas flow rate, and the size of solid elements.

Description of the Model

The treatment of a porous medium as a discrete system is based on an experimentally proved concept of the existence of different hydrodynamic flow patterns in a porous medium under the conditions of gas blowing through it (Matros [14]). Two types of hydrodynamic zones in pores are observed, namely flow zones with jet-like gas flows and stagnation zones (i.e., gas interlayers between solid particles) where gas flow is absent. The total porosity of a porous medium ε is a sum of the flow zone porosity ε_1 and stagnation zone porosity ε_2: $\varepsilon = \varepsilon_1 + \varepsilon_2$. *In the proposed model,* the porous medium is regarded as a regular periodic structure composed of elementary cells, each of them consisting of a solid particle, a gas flow zone, and a gas stagnation zone (Fig. 1). The size of each zone of the porous structure is indicated in the same figure (the size of the elementary cell, L, is equal to the diameter of a real solid particle, d_p). The gas flow zones of all the elementary cells form the general continuous flow zone.

Relative values of the flow and stagnation zones were found experimentally in Ref. 14. As shown, the ratio $\varepsilon_2/\varepsilon$ depends mainly on the linear velocity of gas flow in a pore and on the gas viscosity, and is almost independent of the particle size. For air flow, $\varepsilon_2/\varepsilon \to 0.3$, when Darcy velocity < 0.5 m/s. The ratio $\varepsilon_2/\varepsilon = 0.3$ was used in our simulation, so that, at the total porosity $\varepsilon = 0.4$ which is common for packed beds, the porosity of the flow and stagnation zones was selected to be $\varepsilon_1 = 0.28$ and $\varepsilon_2 = 0.12$, respectively.

The one-dimensional approach used in the present work assumes that the main heat and mass transfer processes occur along the direction of gas flow and combustion front propagation. The opposing combustion waves (i.e., countercurrent ones with respect to the direction of gas flow) were considered. Gas combustion occurs only in the flow zone. Solid particles and stagnation zones are suggested to be chemically inert. Such a treatment of the stagnation zone is the simplest approach and can be justified as follows:

1. In the case of LVR (in the sense of the averaged velocity of the combustion front), the total amount of a gaseous fuel stored in the stagnation zones is negligible from the energy viewpoint as compared to the amount of the fuel delivered by the gas flow through the flow zone.
2. In the case of HVR, the propagation of a combustion front through the flow zone is weakly influenced by its environment.

The flow zone exchanges heat with neighboring solid particles and stagnation zones. The intensity of this heat transfer is determined by the conventional Nu-criterion correlation. In the solid particles and stagnation zones, only conductive heat transfer occurs. The effect of radiation heat transfer can be ignored when a low solid surface emissivity is proposed, as was done in Ref. 13.

Governing Equations

The energy, mass, and concentration conservation equations, as well as the state and kinetic equations for the flow zone are as follows:

$$c_g\rho_g\partial_t T_g = \partial_x(\lambda_g\partial_x T_g) - c_g\rho_g v\partial_x T_g + \hat{\alpha}_g(T_s - T_g) + QW\rho_g\zeta \quad (1)$$

$$\partial_t(\rho_g\zeta) = \partial_x(\rho_g D\partial_x\zeta) - \partial_x(\rho_g v\zeta) - \rho_g\zeta W \quad (2)$$

$$\partial_t\rho_g + \partial_x(\rho_g v) = 0 \quad (3)$$

$$\rho_g = PM/RT_g \quad (4)$$

$$W = k\exp(-E/RT_g) \quad (5)$$

Then the energy equations for the solid particle and stagnation zone can be written as follows:

$$c_s\rho_s\partial_t T_s = \partial_x(\lambda_s\partial_x T_s) + \hat{\alpha}_s(T_g - T_s) \quad (6)$$

$$c_g\rho_{g,st}\partial_t T_{st} = \partial_x(\lambda_{g,st}\partial_x T_{st}) + \hat{\alpha}_{st}(T_g - T_{st}) \quad (7)$$

The gas density in the stagnant zone is determined by a state equation similar to equation 4.

In the initial state of the process modeled, all the zones have the temperature of the incoming (cold) gas T_0, except for the right side of the porous sample ($x = L_E$), where the ignition temperature T_{ign} is sustained; in the flow zone, the initial concentration of the gaseous fuel (ζ_0) and the gas velocity (v_0) are equal to the relevant values at the gas entrance into the porous layer:

$$\underline{t = 0}: T_g = T_s = T_{st} = T_0, \zeta = \zeta_0$$

$$v = v_0 \ (0 \le x < L_E)$$

$$T_g = T_s = T_{ign} \ (x = L_E) \quad (8)$$

The set of the boundary conditions is presented below (after ignition, the adiabatic condition is developed at the boundary $x = L_E$):

$$\underline{x = 0}: \ T_g = T_s = T_0, \zeta = \zeta_0, v = v_0$$

$$\underline{x = L_E}: T_g = T_s = T_0 \ (t < t_{ign})$$

$$\partial_x T_g = \partial_x T_s = 0 \ (t > t_{ign}), \partial_x\zeta = 0 \quad (9)$$

The temperature profiles in a solid particle and in an adjacent stagnation zone should be matched in the temperature and heat flux quantities.

Heat and Mass Transfer Characteristics

The internal heat transfer coefficients $\hat{\alpha}_g$ and $\hat{\alpha}_s$, determining the heat transfer between the flow zone and a solid particle, are defined as follows:

$$\hat{\alpha}_g = \frac{\alpha S_p}{\varepsilon_1 L^3}\cdot\frac{1-\varepsilon_1}{1-\varepsilon}, \qquad \hat{\alpha}_s = \frac{\alpha S_p}{(1-\varepsilon)L^3} \quad (10)$$

The specific heat transfer coefficient α (related to the surface of a real particle) is calculated by the criterion formula [15]:

$$\alpha = \lambda_g Nu/L, \qquad \text{where } Nu = 2 + 1.1Re^{0.6}Pr^{1/3}$$

$$Re = \varepsilon_1 v\rho_g L/\mu, \qquad Pr = \mu c_g/\lambda_g$$

In the case of heat transfer between the flow and stagnation zones, the coefficient α is determined by the Nu = 2, as for the stationary gas layer in the stagnation zone.

The gas specific viscosity, heat conductivity, and diffusion coefficient are calculated using Sutherland's formulas [16]:

$$\mu = \mu_0 T_g^{3/2}/(T_g + C_\mu), \qquad \lambda_g = \lambda_0 T_g^{3/2}/(T_g + C_\lambda)$$

$$D = D_0 T^{5/2}(T_g + C_D)$$

The heat conductivity of a solid particle is considered to be constant.

Solution Method and Testing

The system of unsteady-state equations 1–7 was solved numerically by the implicit finite-difference scheme with iterations at every time step. Equations 6 and 7 were integrated by the through factorization method. The discrete nature of a porous medium is embodied in the step-function changes of the thermo-physical characteristics and internal heat transfer coefficients at the boundary between a solid particle and a stagnation zone. The time step as well as the nonuniform space grid were adapted to the rate of combustion front propagation and to the space variation of temperature and fields by a special procedure. The results of numerical simulation were tested with regard to choosing the space and time steps of integration.

Results and Discussion

The results of numerical simulation with the use of the proposed "discrete" model were compared with analogous results for the conventional two-phase continuous model. The corresponding continuous model was fitted to the discrete one in such a way that the averaged values of all the parameters in the two models were equal. The effective density and conductivity of the condensed phase in the continuous model were defined as

$$\tilde{\rho}_s = \rho_s(1-\varepsilon)/(1-\varepsilon_1),$$

$$\tilde{\lambda}_s = \lambda_g\lambda_s(1-\varepsilon_1)/(\lambda_g(1-\varepsilon) + \lambda_s\varepsilon_2)$$

Combustion of a stoichiometric methane-air mixture (a volume fraction of methane is 0.095) was considered. As Ref. in 13, the kinetic constant, activation energy, and heat of the one-step overall reaction were selected so that the calculated combustion temperature and the normal adiabatic flame velocity for the given gas mixture (in a plain medium) were equal to their experimental values: $k = 2.62\cdot 10^8$ 1/s, $E = 130$ KJ/mol, $Q = 4.387\cdot 10^7$ J/kg at $\Delta T_{ad} = 2008$ K, and $u_{norm} = 0.38$ m/s. Other parameters of the gas mixture were related to air. Parameters of the porous system correspond to a typical packed bed with the density of solid particles $\rho_s = 1200$ kg/m^3, the specific heat capacity $c_s = 1000$ J/(kg·K), and the heat conductivity $\lambda_s = 0.22$ W/(m·K).

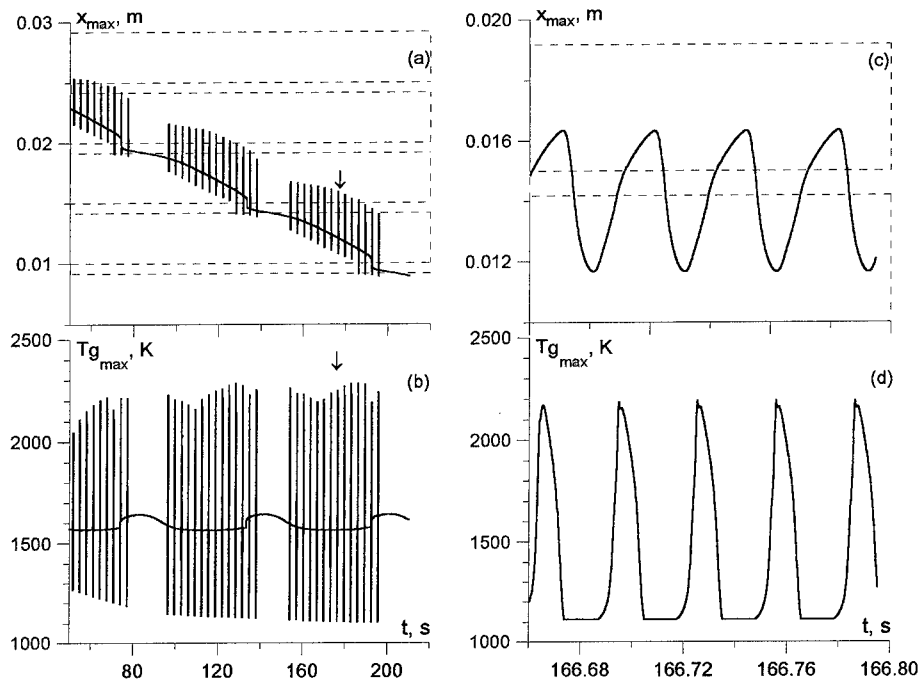

FIG. 2. Oscillations of the combustion front position, (a) and (c), and the maximum gas temperature, (b) and (d), in the discrete model; $d_p = 5$ mm, $v_0 = 0.1$ m/s. Vertical lines show the amplitude of the oscillations in the regions where oscillations occur; dotted lines indicate boundaries of solid particles; (c) and (d) represent the high-frequency sweep of the oscillations in the region shown by the arrows.

Nonflow System

First, consider the case when gas flow is absent. In this case, only high-velocity regimes may occur [4]. It is of interest to compare the calculated value of the critical size of an elementary cell, for which gas combustion in the nonflowing systems becomes possible, with the experimental data. Using the principle of equivalent heat losses, Shaulov [12] obtained the following relation between the critical diameter of a tube (d^t_{cr}) and the critical diameter of solid particles (d_{cr}): $d^t_{cr} = 0.36\, d_{cr}$. Based on the experimental value of the critical diameter for tubes ($\approx$3 mm), the critical diameter of the solid particle can be estimated as $\approx$8.3 mm. Our numerical simulation leads to a similar value for the continual and discrete models, $d_{cr} \approx 8$ mm.

Oscillatory Regimes of Flame Propagation at Low Gas Flow Rates

It must be emphasized that the present investigation is actually the first numerical simulation of FGC that takes into account the unsteady-state heat and mass transfer in the gas phase both for the discrete model and the continuous model.

One of the basic results obtained in the present work is the oscillatory instability of the combustion front propagation in both models. The instability is brought about by the slackening of the thermal interaction between the gas and solid phases when the particle diameter increases. The instability develops on the background of a rather wide preheating zone in the solid phase, as it occurs at a low gas flow rate.

The oscillation mechanism involves the following stages: (1) After the shift of the combustion front from its position, corresponding to the steady-state solution, to the side of the heated porous matrix, the flame starts to move in the opposite (to the gas flow) direction due to the heat conduction mechanism in the gas phase; (2) the combustion front accelerates and propagates at a higher velocity and temperature than those for the steady-state solution, so that the flame slips past the stationary position and moves until extinction occurs in the region where the porous matrix has a low temperature and where intense combustion is impossible; (3) after flame suppression, reignition occurs when the combustible gas mixture fills the previously heated channel of the flow zone.

In the acceleration period, the combustion front attains the velocity corresponding to HVR and a temperature close to or exceeding the adiabatic one.

For the gas flow rate $v_0 = 0.1$ m/s, the oscillations

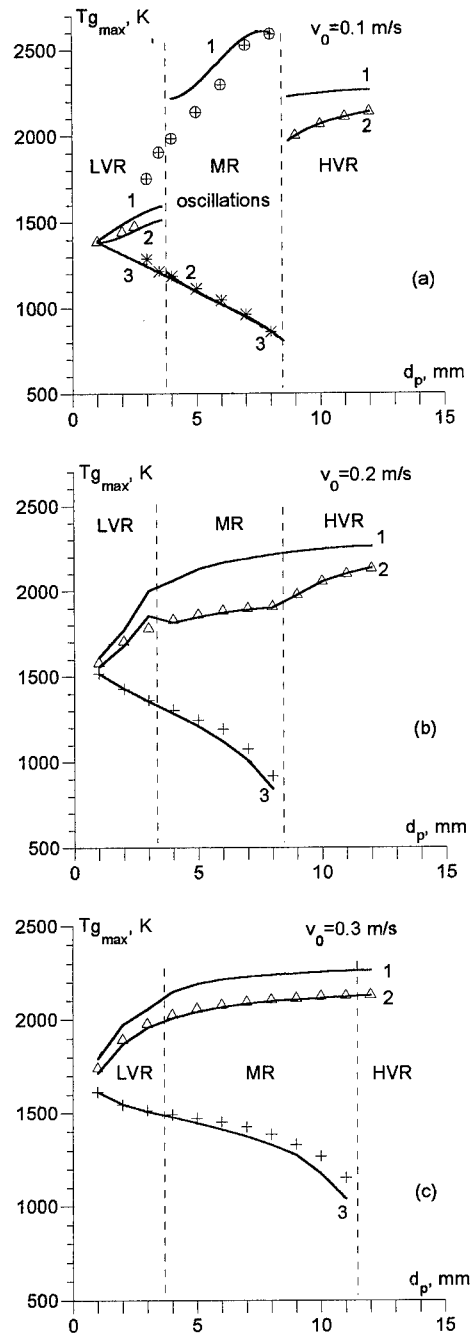

FIG. 3. Effect of the diameter of a solid particle, d_p, on the limits of pulsation (or oscillations) of the combustion wave temperature; 1, 2, the maximal and minimal values of $T_{g,max}$ in the discrete model; 3, $T_{s,max}$; symbols relate to the continuous model: Δ, the value of $T_{g,max}$ with no oscillations; $\oplus$, the maximum value of $T_{g,max}$ in oscillations; *, the minimal value of $T_{g,max}$ in oscillations; +, $T_{s,max}$.

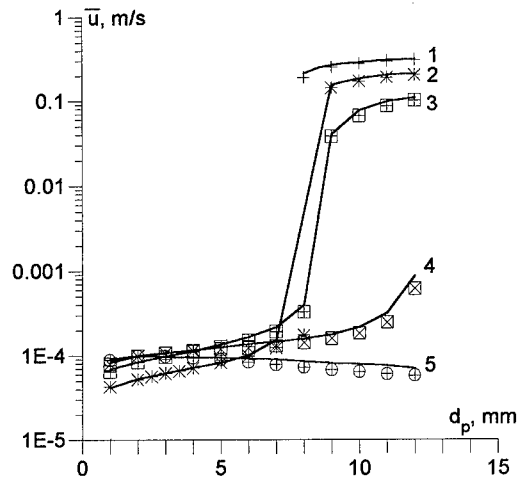

FIG. 4. Effect of the diameter of a solid particle, d_p on the mean combustion front velocity $\bar{u}$; the curves 1, 2, 3, 4, and 5 show $\bar{u}$ for the discrete model at the gas flow rate v_0 = 0, 0.1, 0.2, 0.3, and 0.4 m/s, respectively; the symbols indicate $\bar{u}$ calculated by the continuous model.

manifest themselves starting from the particle diameter ≈3.5 mm and last until the transition to the common high-velocity regime at $d_p > d_{cr} \approx 8.5$ mm. When the heat transfer between the flow and stagnation zones is ignored, the range of the particle diameters where the oscillations occur becomes much narrower. The oscillation frequency is of the order of 10–100 Hz and is determined by the time of convective filling of the preheating zone by the combustible gas mixture and by the induction time of ignition. When d_p tends to d_{cr}, the temperature of the heated condensed phase (in the wake of the combustion wave) decreases and the space amplitude of oscillations becomes so large that it exceeds the real length of the modeled porous sample.

These oscillations bear a resemblance to the pressure oscillations of similar frequency, which were observed in the experiments by Babkin on premixed gas combustion in closed vessels [6,7].

Peculiarities of FGC in the Discrete Model

Propagation of the opposing combustion wave in the discrete-modeled porous medium reveals its pulsating nature. The maximal temperature and burning rate in the combustion front and the velocity of its propagation are low in the regions of the gas flow zone adjacent to the particles, and increase in the neighborhood of the stagnation zone.

For small elementary cells ($L \leq 2$ mm), the pulsation is also small because of intense heat exchange between the solid and gas phases. The amplitude of pulsation of the maximum gas temperature does not exceed 200 K, and the order of magnitude of the

combustion front velocity remains that corresponding to LVR.

When the size of the elementary cells becomes larger than some critical value, $d_{cr}^{(1)}$ (approximately 3.0–3.5 mm), the flame breaks into the high velocity regime of propagation in the neighborhood of the stagnation zone. After reaching the next cold particle, the combustion front begins to move again with a low velocity. The maximum gas temperature rises greatly in the period of flame acceleration, and the temperature attains values close to the temperature of adiabatic gas combustion. Such a regime of combustion can be characterized as a mixed regime (MR). The mean front velocity for this regime is close to the analogous value for the continuous model because the front acceleration is changed by its strong retardation in the vicinity of cold particle upstream in the gas flow.

In the case of the low gas flow rate ($v_0 = 0.1$ m/s), the pulsations are superimposed on the high-frequency oscillation of the combustion front (Fig. 2). The periods of oscillatory propagation of the combustion front change to its translational movement after its mid-point passes the neighborhood of the stagnation zone.

When L becomes greater than the second critical value, $d_{cr}^{(2)}$, the flame propagates in HVR over all the regions of the flow zone. The interaction between the solid and gas phases becomes weaker and the amplitude of temperature and velocity pulsations decreases. The value of $d_{cr}^{(2)}$ depends on the gas flow rate and increases with increasing gas flow velocity.

Figure 3 exhibits the dependence of the limits of temperature pulsations in the combustion front on the variation of the cell size at different values of the gas flow rate. Increasing the gas flow rate leads to decreasing pulsation amplitude because the combustion temperature tends to the adiabatic value. The mean velocities of combustion front propagation are represented in Fig. 4. As would be expected, the transition to the fully developed HVR of the opposing combustion wave becomes impossible when the Darcy velocity of the gas exceeds the velocity of normal adiabatic flame propagation in a plain gas medium (as occurs at $v_0 = 0.4$ m/s).

Conclusions

The proposed unsteady-state model of premixed gas combustion in a porous medium with discrete structure provides such essential details of the process as a pulsation of physico-chemical parameters in the combustion front, its space oscillations, transition (under increasing particle size) from full LVR to the mixed regimes (MR) with the high front velocity in the vicinity of the stagnation zone, and then to the HVR throughout the whole porous sample.

Though the space pulsation of the combustion in real disordered porous systems should be masked, the temperature pulsations and oscillations must reveal themselves in the neighborhood of each solid particle. Whereas the mean velocities of the combustion front are similar for the discrete and continuous models, there are the regions of the combustion parameters where the effects associated with discreteness of a porous structure may essentially influence the concentrations of final products and be of great importance from the viewpoint of environmentally clean combustion.

Nomenclature

c	specific heat capacity
D	diffusion coefficient
d	particle diameter
E	activation energy
k	kinetic constant
L	size of an elementary cell
L_E	length of a porous sample
M	molecular mass
Nu	Nusselt number
P	pressure
R	universal gas constant
S	surface area
Q	reaction heat
T	local temperature
t	time
u	flame velocity
v	gas velocity
W	reaction rate
x	space coordinate
∂_t, ∂_x	partial derivatives with respect to t and x

Greek Symbols

α	internal heat transfer coefficient
ε	porosity
λ	heat conductivity
μ	viscosity
ρ	density
ξ	concentration

Subscripts

g	*gas*
st	*stagnation zone*
s	*solid phase*
ign	*ignition*
0	*initial conditions*

Acknowledgment

Financial support from the Fundamental Research Fund of the Republic of Belarus (grant T94-132) is gratefully acknowledged.

REFERENCES

1. Khinkis, M. J., Kunc, W., and Xiong, T.-Y., "Experimental Evaluation of a High-Efficiency Surface Combustor-Heater Concept With Low Pollutant Emissions," Presented at the American Flame Research Committee, International Symposium on Combustion in Industrial Furnaces and Boilers, Short Hills, New Jersey, Institute of Gas Technology, 1989.
2. O'Sullivan, J. B., and Khinkis, M. J., "Developments in Ultra-Low-Emission Natural Gas Combustion," Presented at the Vancouver Industrial Gas '90, Vancouver, British Columbia, Institute of Gas Technology, 1990.
3. Takeno, T., Sato, K., and Hase, K., *Eighteenth Symposium (International) on Combustion*, The Combustion Institute, Pittsburgh, 1981, p. 465.
4. Babkin, V. S. and Laevskii, Yu. M., *Fiz. Goren. Vzryva* 23(5):27–44 (1987) (in Russian). *Combust. Explos. Shock Waves* 23(5):531 (1987).
5. Babkin, V. S., Korzhavin, A. A., and Bunev, V. A., *Combust. Flame* 87:182–190 (1991).
6. Babkin, V. S., Bunev, V. A., and Korzhavin, A. A., in *Combustion of Gases and Natural Fuels*, (L. N. Stesik, Ed.), OIChF, Chernogolovka, 1980, p. 87 (in Russian).
7. Babkin, V. S., Bunev, V. A., et al., *Fiz. Goren. Vzryva* 21(5):17–22 (1985) (in Russian). *Combust. Explos. Shock Waves* 21(5):519 (1985).
8. Laevskii, Yu. M., Babkin, V. S., et al. *Fiz. Goren. Vzryva* 20(6):3–13 (1984) (in Russian).
9. Babkin, V. S., Drobyshevich, V. I., et al., *Doklady AN SSSR* 256(5):1157–1161 (1982) (in Russian).
10. Kiselev, O. V., Matros, Yu. Sh., and Chumakova, N. A., in *Propagation of Thermal Waves in Heterogeneous Media* (Yu. Sh. Matros, Ed.), Nauka, Novosibirsk, 1988, p. 145 (in Russian).
11. Kesselring, J. P., in *Advanced Combustion Method*, Academic Press, London, 1986, p. 237.
12. Shaulov, Yu. H., *Flame Propagation through Porous Media*, Azerbaijan Acad. of Sciences Publ., Baku, 1954 (in Russian).
13. Sahroui, M. and Kaviany, M., *Int. J. Heat Mass Transfer* 37(18):2817–2834 (1994).
14. Matros, Yu. Sh., *Non-Steady-State Processes in Catalytic Reactors*, Nauka, Novosibirsk, 1982 (in Russia).
15. Kaviany, M., *Principles of Heat Transfer in Porous Media*, Springer-Verlag, New York, 1991.
16. Bretshnaider, St., *The Properties of Gases and Liquids*, Khimia, Moscow-Leningrad, 1966 (in Russian).

INDEX OF AUTHORS AND DISCUSSORS

(**Bold face** numbers refer to papers' authors; other numbers refer to papers' discussors)

Abbas, T., **2241**, **2487**, **3041**
Abbud-Madrid, A., **1929**
Adomeit, G., **421**, **781**
Adriani, R., **2549**
Aftel, R., **1645**
Agafonov, G. L., **985**
Aharon, I., **1613**
Akamatsu, F., 1660, **1723**
Akanetuk, A. E. J., 619, 2064, 2132, 2238, 2266, 2502, 3110, **3137**, 3176, 3204, 3250
Aldén, M., **2787**
Aldredge, R. C., 395
Allen, M. G., **2779**, 2825, **2895**
Altenkirch, R. A., **1335**, **1477**
Åmand, L. E., **3253**
Ancia, R., **1009**
Anders, K., **1697**
Andersen, F. M. B., 2770
Anderson, W. R., 488, 982, **1043**, **1997**, 2074, 2124
Andresen, P., 153, **2589**, **2827**, **2949**
Antoranz, J. C., **1469**
Appel, J., **2387**
Araki, N., **3067**
Arellano, L., **2725**
Arena, U., **3243**
Arif, M., **497**
Arisawa, H., **791**
Aslam, T. D., **2981**
Assovskii, I. G., 1944, 2040
Astill, A. G., 1392, 2625
Atreya, A., **2181**, 2367
Axelbaum, R. L., **1137**, **1891**
Azuhata, S., **3189**

Babushok, V., **1377**
Bachmann, M., **2259**
Baer, D. S., **2851**
Bai, S., **3153**
Bailly, P., **923**
Balthasar, M., **2369**
Bar-Ziv, E., **3111**, 3187
Barbella, R., **2327**
Baritaud, T., 2556, 2603, **2627**, 2652
Barlow, R. S., 103, 346, 1168, 2169, **2191**, **2199**, 2213
Barnes, F. J., **589**
Bartenbach, B., **2311**
Bartenev, A. M., **2573**
Bassilakis, R., **2795**
Battin-Leclerc, F., **755**
Bauer, W., **2645**
Bäuerle, B., **2619**
Baum, H. R., **1453**, **1523**
Baumann, H., **3301**
Bauwens, L., 889, **2991**
Bazile, R., **105**
Beale, A., **3355**
Beatrice, C., **2517**
Beckstead, M. W., **1989**
Beeley, T., **3103**
Beér, J. M., **2295**
Behrendt, F., **1747**, **2619**
Belardini, P., **2517**
Bellan, J., 1619, 1628, 1661, **1713**, 1738, 2250, 2571, 2748
Benelli, G., 2748, 2755
Benish, T. G., **2319**
Berces, T., 550
Berg, P. A., **2133**
Bertagnolli, K. E., **1825**
Bertoli, C., **2517**
Beushausen, V., **2589**, **2827**
Bhattacharjee, S., **1335**, 1352, 1359, **1477**, 1502
Bilger, R. W., 65, 111, 1128
Blouquin, R., **1565**
Boccio, J. L., **2973**
Bockhorn, H., **807**, **2343**, **2369**, **2387**, **2431**
Boettner, J. C., **627**
Bolik, T., **1637**
Bolli, R., **2091**
Bollig, M., **729**, **2171**
Bonanno, A. S., **2795**
Bond, C., **2885**
Bond, T., **1771**
Bonn, B., **3301**
Booty, M. R., **891**
Borthwick, P., **1429**
Bossard, J. A., **1671**
Bourguignon, E., **447**
Bowman, C. T., **481**, 799, **2803**
Bozzelli, J. W., **633**, 648
Bradley, D., **915**, **2653**
Branch, M. C., **1929**
Brandt, M., **2741**
Bräumer, A., **2741**
Braun-Unkhoff, M., **659**
Bray, K. N. C., **1**, **259**
Brehm, J. A., **1875**
Brehob, E. G., **3169**
Bressloff, N. W., **2379**, 2523
Breussin, F., **211**

Brewster, M. Q., **2007**
Brezinsky, K., **1025**, **1805**, **1875**
Brill, T. B., **791**
Brillard, A., **3269**
Brindley, J., **891**
Brockhinke, A., **153**
Bromly, J. H., **589**
Brouwer, J., **2117**
Brown, M. J., **875**
Brown, R. C., **1909**
Brown, T. M., **1121**
Bruel, P., **923**
Brummund, U., **1687**
Bruno, C., 240, 363, 771, 1762, 1769, 1787, 2739, 2817, 2825
Bucher, P., **1899**
Buckley, S. G., **2455**
Buckmaster, J., **1143**, 2988
Bui, P. A., **1763**
Bui-Pham, M. N., **975**
Burgess, D. R. Jr., **1377**
Buschmann, A., **437**
Byrnes, M. A., **2241**

Cadman, P., 746, 789, 2523
Calcote, H. F., 1815, 2266
Calhoon, W. H. Jr., **59**
Callahan, C. V., **739**
Candel, S., **35**, **1079**, **1663**, **2041**, **2565**, 2809, 2817, 2893
Carlier, M., **747**
Carlson, J., **2421**
Castaldi, M. J., **693**
Castillo, J. L., **1469**
Cathonnet, M., **613**, **627**
Cavaliere, A., **2525**
Cernansky, N. P., **633**
Cessou, A., **1687**
Cha, M. S., **121**
Chagger, H. K., **1859**
Chaiken, R. F., **1571**, 1936, 2014, 2064, 3188
Champion, M., **923**
Chan, C. K., **2679**
Chang, A., **2091**
Chang, D. P. Y., **1953**
Chang, L. M., **2033**
Chang, W. C., **2207**, **2223**
Chao, Y. C., 120, 135, 355
Charalampopoulos, T. T., **1851**
Chauveau, C., **331**, **1259**
Cheatham, S., **1063**
Chelliah, H. K., **1395**
Chen, H., **651**
Chen, J., **1311**
Chen, J. H., **323**, **855**
Chen, J. Y., 56, **1771**, **2199**, **2207**, **2223**
Chen, Y. C., 34, **97**, 128, 404, 435, 1109, 1128, 2169, 2603
Cheng, R. K., 256
Cheng, T. C., **169**
Chernov, A., **1035**
Chesneau, X., **1259**
Chevalier, C., **773**
Chiga, M., **931**
Chigier, N., 1619, 1670, 1695, 1738, 2587
Chirone, R., **3243**
Chiu, H. H., **1653**
Cho, Y. D., **1723**
Choi, J. Y., 2883, **2925**, 2957
Choi, M. Y., 1199, **1243**, 1257, **2397**
Chomiak, J., **883**, **2557**
Chou, C. P., **1771**
Christo, F. C., **43**
Chung, S. H., **121**
Ciajolo, A., **2327**
Ciambelli, P., **1789**
Ciccarelli, G., **2973**
Coghe, A., **2549**
Cohen, Y., **659**
Colantonio, R. O., **1209**, **1219**
Collins, L. R., **315**
Colvin, M. E., **685**
Côme, G. M., **755**
Continillo, G., **907**, 1069, **1585**
Cook, C., **1645**
Corcione, F. E., **2533**, **2717**
Correa, S. M., **307**
Cossali, G. E., **2549**
Costen, P. G., **2241**, **2487**, **3041**
Cox, A., **2685**
Crelling, J., **3103**
Crescitelli, S., **1585**
Croiset, E., **3095**
Crosley, D. R., **959**, 973, 982, **1755**, 2006, **2133**
Crunelle, B., **967**
Cubuzio, L., 1420
Curran, H. J., **613**, **641**, 746, 780, **2669**, **2685**

Dagaut, P., **613**, **627**, 649, 666, 2676
Daily, J. W., 1242, 1815, 1908, **1929**
D'Alessio, A., **951**, 2292, 2301, 2325
Dally, B. B., 185, **2191**
Dam-Johansen, K., **2067**, 2124, **3335**
D'Amore, M., **1789**
D'Angelo, Y., **1739**
D'Anna, A., **2327**, **2517**
Daou, J., **1275**, 1628
Dasappa, S., 396, 1889, **2479**, 2493, 3083
Davidson, D. F., **481**, **799**
Davidson, J. E., **1989**
Davis, K. A., **3075**
Davis, N. T., **2819**, 2841
Davis, S. G., **1025**
De Joannon, M., **2525**
De Soete, G., **2487**
Dean, A. M., 2107
Del Giacomo, N., **2517**
Delabroy, O., **1663**

Delfosse, L., **3269**
Delichatsios, M. A., 1299, **1335**, 1352, 1435, 1452, 1485, 1493, **1495**, 1538, 2358, 2376
Dellinger, B., **497**
Desbordes, D., **3023**
Deschamps, B. M., **427**
Desgroux, P., **967**
Deshaies, B., **923**, **3023**
Deutschmann, O., **1747**
Devriendt, K., **1001**
Dewitt, W. A., **2679**
Diau, E. W. G., **2109**
Dibble, R. W., **1755**, **1771**, **2749**
Dietrich, D. L., 1619
Dimotakis, P. E., **2885**
Dinkelacker, F., 194, 281, 364, 411, **437**, 1119, 2572
Dixon-Lewis, G., 846
Domingo, P., **233**
Dopazo, C., 282
Dorofeev, S. B., **2965**
Doughty, A., 534, **589**, 658, 667, 2107
Drake, M. C., **347**, **2581**, 2635, 2834
Dreizin, E. L., 1907, **1919**
Drewes, V., **2597**
Driscoll, J. F., **129**, 248, **347**, 364, 387, 404, **2933**
Dryer, F. L., **739**, **1201**, **1209**, **1219**, 1241, **1899**, **1909**, **3059**
Du, D. X., **2359**
Du, J., **1137**
Duclos, J. M., **413**, **2627**
Duffy, B. L., **2099**
Dukhan, A., **3111**
Dunn-Rankin, D., 1612
Duplantier, S., **923**
Durox, D., **1311**
Dwyer, H. A., 1265, **1613**

Echekki, T., **323**, **855**
Echigo, R., **2709**
Eckbreth, A., 982, 2786, 2857
Efimenko, A. A., **2965**
Egolfopoulos, F. N., 479, **2885**
Ehrhardt, K. R., 2841
Eichholtz, M., **527**
Eickhoff, H., **2741**
Eigenbrod, C., 1207, **1235**, **1637**, 2739
Eigenmann, L., **2763**
Eisenberg, S., **2827**
ElKotb, M. M., **1937**, 2732
Endo, T., **2903**
Erm, A., **2161**
Essenhigh, R. H., 798, **3085**, 3118
Everest, D. A., **129**, **1161**, **1385**, 2394
Ezekoye, O. A., 913, 1308, **2661**, 2700

Faeth, G. M., **1593**
Fairweather, M., **365**
Fallon, G. S., **1395**
Fan, B. C., **3007**
Fansler, T. D., **2581**
Faravelli, T., **739**
Farrow, R. L., **975**
Fefelov, A. V., **3383**
Feikema, D. A., **129**
Fernandez-Pello, A. C., **1311**, **1361**, **1461**, **1505**
Ferreira, J. C., **2215**
Fiechtner, G. J., **2191**, **2199**
Fieweger, K., **781**
Figueira Da Silva, L. F., **3023**
Filla, M., **3295**
Fink, R., **2949**
Finlinson, J., 1824, 1833, 1979, 2014, **2025**
Flatness, S. A., **567**
Fleming, J. W., **1405**
Fletcher, D. F., **2191**
Fletcher, T. H., 3083, 3093, 3118, **3153**, **3161**, 3187
Flury, M., **2215**
Fomenko, I., **1961**
Fontijn, A., 534, 620
Fotache, C., 1770
Foumeny, E. A., **2241**
Fournet, R., **755**
Foutko, S. I., **3377**
Frank, P., **575**, **659**, **667**
French, D. T., **2581**
Frenklach, M., 701, **2285**, 2301, 2325, 2326
Fridman, A. A., **3369**
Frohn, A., **1697**
Frost, D. L., **1883**
Froud, D., **3355**
Früchtel, G., **75**, **195**
Fueyo, N., 48, 56, 74
Fujita, O., **1345**
Fujiwara, T., **2903**
Fujizaki, H., **3067**
Fukuchi, A., **1945**
Fureby, C., **241**
Furlong, E. R., **2851**
Furukawa, J., **405**, 444
Fusco, A., **2627**

Gaffuri, P., **739**, **2669**
Galiero, G., **1585**
Gallagher, N. B., **3197**
Gambi, G., **951**
Gann, R. G., 797, 1411, 1513, 1563
Gany, A., 1917, 1936
Ganz, B., **2763**
Gao, L. P., **1739**
Garcia-Ybarra, P. L., **1469**
Gardiner, W. Jr., 2115
Garo, J. P., **1461**
Garréton, D., **923**
Gaskell, P. H., **915**
Gasnot, L., **967**
Gass, J., **2215**
Gee, K. L., **283**
Gelfand, B. E., **2573**

Gerk, T. J., **1095**
Ghenaï, C., **331**
Ghoniem, A. F., 42, 194, 202, 248, 354, 862, 1102, 1530, **1531**, 2197, 2385, 2850
Gibbins, J., 1513, 3083, 3101, **3103**, 3134, 3143, 3160, 3167, 3188
Gilot, P., **3269**
Ginsberg, T., **2973**
Glarborg, P., **2067**, 2081
Glaser, K., **2487**
Glassman, I., 1435, 1451, **1875**, 1936
Glaude, P. A., **755**
Glumac, N. G., **1817**
Goel, S., **3127**, **3317**, 3334
Gökalp, I., **331**, 395, 412, **447**, 1207, 1217, 1233, **1259**, 2014
Goldfarb, I., **1557**
Goldshtein, V., **1557**
Golombok, M., 1619, **2653**, 2667
Gomez, A., **1739**
Gongwer, P. E., **791**
Goodwin, D. G., **1817**, 1832
Gore, J. P., **993**, **1453**, 2197, 2221
Goroshin, S., 1375, **1883**, **1961**
Goss, L. P., **145**
Gouldin, F. C., 379, **381**
Gran, I. R., **323**, **855**
Greenberg, J. B., **1705**
Greger, F., **3301**
Greul, U., **2231**
Griffin, D. W., **1291**
Griffiths, J. F., 753, 780, 2625, **2685**
Grinstein, F. F., **91**
Grotheer, H. H., **575**, **2405**, 2867
Guerre, S., **105**
Gülder, Ö. L., **427**, 2284, **2351**
Guo, F., **2251**
Gupta, A. K., 1619, **1645**, 1670, 2502
Gutheil, E., **83**, **1731**
Gutmark, E. J., **2471**, **2843**

Hadjiconstantinou, N., **2637**
Haggard, J. B. Jr., **1201**
Haile, E., **1663**
Hainsworth, D., **1859**
Halbgewachs, M. J., **2109**
Hall, M. J., **2613**
Halsbeck, J., **2091**
Hamins, A., 862, **1377**, 1411, **1413**, **1429**
Han, Z., **2717**
Hancock, R. D., **35**, **1087**
Hanson, R. K., **481**, **551**, **799**, **2851**, **2909**
Hanson-Parr, D. M., **1899**, **1981**, **2471**
Hantschk, C., **2835**
Harrington, J. E., **2133**
Harstad, K., **1713**
Hartick, J. W., **75**
Hartinger, K. T., **3301**
Hasegawa, T., **291**
Hassa, C., **2741**
Hassan, S., **2241**, **2487**
Hassel, E. P., **75**, **169**, **195**
Hayashi, S., **2155**, **2733**
Hayhurst, A. N., 3324, 3333
Haynes, B. S., **589**, 3101, **3119**
Heap, M. P., **2117**
Heberle, N. H., **1755**
Hecker, W. C., 1770, 2082, **2251**
Heckmann, E., **543**
Hein, K. R. G., **67**, **2231**
Held, T. J., **739**
Helenbrook, B. T., **815**
Hentschel, W., **2503**, 2547, **2589**, 2603, 2625
Herding, G., **2041**
Hermann, J., **2835**
Hertzberg, J., 1309
Hewson, J. C., **729**, **2171**
Heyl, A., **2369**
Heywood, J. B., 2625, **2637**, 2676
Hickman, S. R., **2007**
Hilka, M., 354
Hippler, H., **543**
Hirano, T., **405**, **1129**
Hirose, K., **2155**
Hisham, M. W. M., **641**
Ho, L., **2075**, **2125**
Hochgreb, S., **2645**, 2660
Hofbauer, H., **3325**
Hoffmann, A. B., **2295**
Hoffmann, J. G., **2709**
Hoffmann, S., 2748
Hofmann, D., **945**, 2818
Hollmann, C., **1731**
Holzäpfel, F., **187**
Homann, K. H., **2259**
Hönig, R., **2949**
Horii, T., **2903**
Horn, C., **575**
Howard, J. B., **711**, 2266, 2292, **2319**, 2367
Howard, S. L., **2033**
Hoyermann, K., **505**
Hsu, F. K., **2749**
Hsu, K. Y., **1087**
Hu, I., **307**
Huang, J., **693**, **2335**
Huertas, J. I., **1891**
Huh, H., **2933**
Hupa, M., **3317**, 3334
Hurt, R. H., **3075**, **3103**, 3118, 3144, **3169**
Hustad, J. E., 2502, 3082

I, W. K., **283**
Ibrahim, S. S., **365**
Ichinose, T., **3223**
Ikeda, E., **597**
Ilincic, N., **1997**
Ishizawa, S., **2605**
Ishizuka, S., **847**, **1129**

Ito, A., **1437**
Ito, K., **1189**, **1345**
Itoh, Y., **3213**

Jaggers, H., **365**
Jagoda, J. I., **3363**
Jang, W. K. I., **283**
Janicka, J., **75**, **169**, **195**
Jasuja, A. K., 2732, **2757**
Jeffries, J., 363, 982, 1824, 1833, **2133**, 2170, 2188
Jensen, A., **3335**
Jensen, K. A., **2397**
Jeung, I. S., **2925**, **2957**
Jiang, C. B., **1353**
Johnson, R. G., **891**
Johnsson, J. E., **3335**
Jones, A. D., **1953**
Jones, W. P., **275**
Joulain, P., **1311**
Joulin, G., **1565**
Ju, Y., 846, 873, **1283**
Jungfleisch, B., **2343**, **2387**
Jurng, J., 2188
Jursic, B. S., **651**
Just, T., **575**, 619, 701, 762, 2090, 2097, 2138

Kaaling, H., **2787**
Kadota, T., **1189**, **1251**, **1629**
Kailasanath, K., **91**, **899**, **1301**, 1530
Kakinuma, H., **397**
Kalghatgi, G. T., 128, 135, **2653**
Kamel, M. R., **2909**
Kandas, A., **3111**
Kaneko, S., **3223**
Kaneshige, M. J., **3015**
Kantorovich, I. I., **3111**
Kaplan, C. R., **1301**
Kappler, G., **2949**
Karagozian, A. R., **1095**, **2463**
Karatza, D., **2439**
Karl, A., **1697**
Karlsson, A., **2557**
Karpov, V., **249**
Kasahara, J., **2903**
Kashiwagi, T., **1345**, **1429**, 1502, 1512, 1521, 2430
Kato, I., **3067**
Kato, R., **2941**
Katsuki, M., **1723**
Katta, V. R., 1061, **1087**, **1151**, 1179, 1308, 1538
Kawashima, M., **1945**
Kee, R., 1753, 1881
Kelly, P., **1953**
Kemal, A., **2803**, 2841
Kendrick, D. W., **1079**
Kenedy, I. M., **1953**
Kennedy, L. A., **3369**, **3377**
Kern, R. D., **651**, 2310
Kettrup, A., **2859**
Khartchenko, S. S., **1845**
Khomik, S. V., **2573**
Kiefer, J. H., 587, **651**, 666, 683, 1032
Kikuchi, M., **1345**
Kilpinen, P., 3221, **3317**
Kim, H. K., **2181**
Kim, Y., 1685, 1703
Kimura, I., **2941**
King, M. K., **1227**, 1917, 2030
Kinoshita, S., **1103**
Kistler, J. S., **113**
Kitajima, A., **137**
Kjærgaard, K., **2067**
Klein, R., 411
Knapp, M., **2589**, **2827**
Knio, O. M., **203**
Knorre, V. G., **2303**
Knyazev, V. D., **513**
Kobayashi, H., **389**, **1369**, **3189**
Koch, R., **2763**
Koenig, M., **2613**
Koert, D. N., **633**
Kohl, S., **527**
Köhler, J., **2701**
Kohse Höinghaus, K., 48, 153, 982, 1824, 1832, 2284
Kolb, C. E., **1909**
Komiyama, M., **339**, **1103**
Kondoh, Y., **2139**
König, J., **1235**
Konishi, K., **1429**
Kono, M., **1189**, **1267**, **1637**
Konsur, B., **1291**
Kooker, D. E., **2033**
Koppe, S., **489**
Korobeinichev, O. P., **1035**, 1995, 2005
Koseki, H., **1445**
Koshland, C. P., **2049**, **2455**
Kostiuk, L. W., 379, **447**
Kotani, Y., **397**
Koutmos, P., **161**
Kowalewicz, A., 2515, 2587, 2643
Kozinski, J. A., **2495**
Kraft, M., **807**, **2431**
Krämer, H., **2741**
Kramlich, J. C., **567**
Krebs, W., 2385, **2763**
Kremer, H., **3309**
Kreutz, T. G., **113**
Krier, H., 1907
Kryuchkov, S. I., **2965**
Kumaran, S. S., **605**
Kushari, A., **3363**
Kusharin, A. Y., **985**
Kuzmin, A. I., **1845**
Kwan, K. C., **915**

Lacas, F., **1663**
Lachner, R., **2949**
Lafleur, A. L., **2319**
Lakkis, I., **1531**

Lancia, A., **2439**
Lange, M., 2809
Laskin, A., **669**
Lattimer, B. Y., **1541**
Laurent, T., **489**
Lavoie, G., 2635
Law, C. K., **113**, 355, **815**, **865**, **1025**, 1069, **1111**, **1867**, **1875**, **1919**, **2359**, **2413**
Leckner, B., 2470, **3231**, **3253**, 3334
Ledesma, E. B., **3205**
Lee, J., **3059**
Lee, J. G., **2771**
Lee, J. H. S., **1883**, **1961**
Lee, J. L., 1234
Lee, K. O., **1243**, **2397**
Lee, S., **2925**
Lee, S. W., **2725**
Lee, T. W., **455**
Lefebvre, A. H., **2757**
Leipertz, A., **945**, **2277**, **2869**
Lemire, G. W., **1043**
Lenoir, D., **2859**
Lenze, B., **187**
Leppard, W. R., **2669**
Leuckel, W., **187**, **2083**, **2311**
Levendis, Y. A., 2420, **2421**, 3135
Levinsky, H. B., **2147**
Li, C. Z., **2231**, **3205**, **3287**
Li, H. Z., **3007**
Li, S. C., **1017**
Lifshitz, A., 595, 620, **659**, **669**, 683, 692
Liggett, W., **1445**
Lin, C. L., **1653**
Lin, M. C., **521**, 550, 581, 595, 683, **2109**
Lindstedt, R. P., 701, **703**, 1033, 2350, 2367
Lingens, A., **1053**
Linteris, G. T., **1395**, **1421**
Lipatnikov, A., **249**
Litton, C. D., **1571**
Lockwood, F. C., **2241**, **2487**, **3041**
Löffler, G., **3325**
Löfström, C., **2787**
Long, M. B., **2161**
Longwell, J. P., **711**
Lottes, C. R., **1891**
Louw, R., **2405**
Lu, J., **3127**
Lucas, D., **2455**
Lucht, R. P., 973, **1087**, **1825**
Luczak, A., **2589**, **2827**
Ludwig, T., **1579**
Lunden, M. M., **3103**, **3169**
Lundgren, E., **241**
Luo, K. H., 1093
Luque, J., **959**
Lyngfelt, A., **3253**
Lyubovsky, M., **1779**

Ma, J., **3161**
Ma, M. C., **3119**
Maas, U., **83**
Macadam, S., **2295**
Mackie, J. C., **597**, 658, **3205**
Maffettone, P. L., **1585**
Magel, H. C., **67**, **2231**
Magnussen, B. F., 404, 411
Mahmud, T., **2241**
Makhviladze, G. M., **1549**
Makino, A., **1867**, 1889, **3067**
Mallet, C., **3095**
Maloney, D. J., **3169**, **3179**
Maly, P. M., **2075**, **2125**
Maly, R., **2597**, 2652, 2660, 2667, 2676, 2700, 2708
Man, C., **3103**
Mandin, P., **1311**
Mansour, M. S., **97**
Manz, P., **2589**
Marchese, A., 780, **1209**, **1219**, 1234
Margolis, S. B., **1969**
Marinov, N. M., **685**, **693**
Marquardt, M., **2343**, **2387**
Marra, F. S., **907**, 1530
Marran, D. F., **2161**
Marshall, P., **497**
Martel, C., **413**
Maruta, K., **389**, **1283**, **1369**
Masonjones, M., **823**
Masri, A. R., **43**, **49**, 111, 128, **2191**
Matalon, M., **1063**
Matsui, H., 504, **535**
Matsuo, A., **137**
Mauß, F., **2343**, **2369**
Mavridis, C., **161**
Mazziotti, G., **2533**
McDonell, V. G., **2725**
McGrattan, K. B., **1345**, **1523**
McIntosh, A. C., **891**, 2989
McLean, I. C., **875**
McLean, W. J., 2065
McManus, K. R., **2779**
Meagher, N. E., **1997**
Mebel, A. M., **521**, **2109**
Medvedev, S. P., **2573**
Megaridis, C. M., **1291**, 1309, 1619
Meier, W., 2154
Melius, C. F., **685**, **693**, **2109**
Mell, W. E., **1523**
Melton, L., **1413**
Méndez, F., **1797**
Menon, S., **59**, **299**
Mertens, J. D., **551**, 566, 611
Mescher, A. M., **3085**
Metcalfe, E., 666, 1428
Meyer, J., **1053**
Miccio, M., **3277**
Michael, J. V., 488, **605**
Michou, Y., **447**
Miller, F. J., **1327**

Miller, J. A., **461**, 1007, **2067**
Miller, J. H., **1181**
Miller, M. F., **2895**
Milosavljevic, I., **1515**, 2065, 3241
Min, K., **2637**
Minetti, R., **739**, **747**
Minutolo, P., **951**
Mitani, T., **2917**
Mitchell, R. E., **3137**, 3176
Mitrovic, A., **455**
Miyafuji, A., **339**
Miyasaka, K., **1505**
Miyoshi, A., **535**
Mizera, A., **1883**
Miziolek, A., **1377**
Mizomoto, M., **137**
Mizutani, Y., **1723**
Modiano, S. H., **2017**
Mohamed, C., **2685**
Mohammed, R. K., **2161**
Mokhov, A. V., **2147**, 2205
Mokrushin, V., **1035**
Möller, S. I., **241**
Molodetsky, I. E., **1919**
Mongia, R. K., **1771**, **2749**
Monkhouse, P., 2660, 3204, **3301**
Morhov, A., 1169
Morley, C., 648, 2700
Morris, C. I., **2909**
Moskaleva, L. V., **521**
Moss, J. B., **2379**
Most, J. M., **1311**
Mueller, C. J., **347**
Mukunda, H. S., 881, 1778, 1996, **2479**, 2883
Mullholland, G. W., **1445**, 2429
Musmarra, D., **2439**
Mwabe, P. O., **2447**

Nacke, F., **505**
Nagel, H., **2859**
Naik, P. D., **489**
Najm, H. N., **203**, 1159
Naruse, I., **3213**
Nassef, I., **1937**
Nau, M., **83**
Nayagam, V., **1201**, **1209**, **1219**
Neal, L. G., **2091**
Nebot, E. M., **43**
Neef, W., **83**
Neemann, K., **1053**
Nehse, M., **773**
Nelson, P. F., **2099**, **2231**, **3205**, **3287**
Neumeier, Y., **2811**
Nguyen, Q. V., 111, **357**, 444
Niazmand, H., **1613**
Niioka, T., **389**, **1189**, **1283**, **1369**, **2877**
Nishikado, K., **291**
Nishioka, M., **113**, **1071**, **2139**
Noble, A. R., **2133**
Noguchi, R. A., **1771**
Nomura, H., **1267**
Nooren, P. A., **177**
Norris, M. G., 2524, **2645**
Noto, T., **1377**
Numeier, Y., 2572

Obertacke, R., **2869**
O'Connor, J., 2723
Odeïde, A., **1259**
O'Doherty, T., **3355**
Ohtake, K., **3213**
Ohtomo, Y., **1369**
Oja, V., **1515**
Okamoto, K., **405**
Okasha, F., **3277**
Okuyama, Y., **1369**
Olson, S. L., **1345**, **1361**
Oran, E. S., **1301**, **2991**, **3033**
Orszag, S. A., **3059**
Osborne, R. J., **1121**

Palma, V., **1789**
Panagiotou, T., **2421**
Papailiou, D., **161**
Papas, P., **1405**
Parker, T. E., **2895**
Parr, T. P., **1899**, **1981**, **2471**, **2843**
Patel, N. M., **2479**
Patnaik, G., **899**
Patterson, P. M., **1859**
Paul, P. H., **357**
Paul, P. J., 396, **2479**
Paul, R. N., **259**
Pauwels, J. F., **967**
Pavlyukevich, N. V., **3383**
Peck, R. E., **1671**
Peeters, J., 626, 700, **1001**, 2065, 2145
Peeters, T. W. J., 81, **177**
Pepe, F., **2439**
Pershing, D. W., **2117**
Peters, N., 404, 420, **763**, 1077, 2403, 2556
Petersen, E. L., **481**, **799**
Peterson, T. W., **3197**
Pfahl, U., **781**
Pfefferle, L., 683, 1754, **1779**
Piana, J., **413**
Pigari, F., **211**
Pistone, L., 2493, 3300
Pitsch, H., **721**, **729**, **763**
Pitts, W. M., **1171**
Pitz, R. W., 445, 999, **1121**
Pitz, W. J., 232, 488, **633**, **641**, **685**, **693**, 780, 1016, **2669**, **2685**
Plessing, T., 2596
Poinsot, T., 74, **219**, 445, 2809, 2850, 2857
Polenov, A. N., **2573**
Pont, G., **2463**
Pope, S. B., **43**, **49**, 65, 248, 2213, 2221

Popov, O. E., **985**
Popp, P., **2693**
Pourkashanian, M., **1859**
Powers, J. M., 2015, 2988, 2998
Prasetyo, Y., **275**
Presser, C., **1413**, **1645**
Priddin, C. H., 74
Prieur, J., **427**
Pugmire, R. J., **3153**
Puri, I. K., **993**, **3369**

Rabinovich, O. S., **3383**
Rabitz, H., **1909**
Rachner, M., **2741**
Ragucci, R., **2525**
Rahman, M. S., **497**
Rahn, L. A., 2635
Ranzi, E., **739**
Rath, H. J., **1235**, **1267**, **1637**
Rawlins, W. T., **2895**
Reidick, A., **3309**
Reinelt, D., **1421**
Reitz, R. D., **2717**
Renard, P. H., **1079**
Renken, H., **1235**
Reuss, D. L., **347**
Reyes, C., **1953**
Ribaucour, M., **739**, **747**
Richard, J. R., **3095**
Richards, C. D., **1679**
Ridder, M., **2741**
Rist, D., **2949**
Roberts, J. P., **1549**
Roby, R. J., **1541**
Roekaerts, D., 82, **177**
Rogg, B., **1275**
Röhrig, M., **481**, **799**
Rolon, C., **2041**
Rolon, J. C., **1079**
Römming, H. J., **559**
Rosen, L. J., **1891**, **3363**
Rosner, D. E., 1815, 1832, 1842
Ross, H. D., **1301**, **1327**, 1359, 1459
Roth, N., **1697**
Roth, P., **583**, **621**, **1579**
Rouan, J. P., **3095**
Rubini, P. A., **2379**
Rudolph, V., **3261**
Ruediger, H., **2231**
Ruf, B., 1824
Rumminger, M. D., **1755**, 2154
Rybanin, S., **1487**

Saade, R., **2495**
Sacksteder, K., **1335**
Saito, K., **1437**
Sakai, Y., **847**, **931**
Sakak, A. S., **267**
Sala, M., 96, 2875
Salama, N., **1937**
Salatino, P., 3110, 3125, **3243**
Sampath, R., **3179**
Samuelsen, G. S., **2725**, **2819**
San Martin, J., **1469**
Sanders, J. P. H., 2221
Sankovitch, V., **1469**
Sanquer, S., **923**
Santavicca, D. A., **2771**
Sarig, N., **1705**
Sarofim, A. F., **823**, **2295**, **3111**, 3125, **3127**, 3221, **3317**, 3334
Sato, J., **1189**, **1267**, **1637**
Sato, K., **931**
Sausa, R. C., **1043**
Saveliev, A. V., **3369**
Sawchuk, R. A., **2351**
Sawyer, R. F., **2455**
Scacchi, G., **755**
Scalabrin, A., **3295**
Schadow, K. C., **2471**, **2843**
Schäfer, M., **2701**
Schäfer, T., **437**
Schauer, F. R., **1087**
Schaugg, J., **575**
Schiller, D. N., **1319**
Schlatter, M., **2215**
Schlüter, H., **2827**
Schmidt, R., **1747**, **2701**
Schmitt, F., **2369**
Schmoll, W. J., **145**
Schneider, A., **527**
Schnell, U., **67**, **2231**
Schofield, K., **1835**
Schraml, S., **2277**
Schreiber, I., **1557**
Schreiber, M., **267**, **1053**
Schulz, C., **2597**
Scott, M. J., **915**
Scouflaire, P., **2041**
Seeker, W. R., **2075**, **2125**
Segawa, D., **1251**, **1629**
Senba, M., **3067**
Senkan, S. M., **685**, **693**, **2335**
Serio, M. A., **2795**, **3145**
Seshadri, K., **729**, **763**, **831**, **1997**
Shabunya, S. I., **3377**
Shaddix, C. R., **1161**
Shamim, T., **2181**
Shandross, R. A., **711**
Sharifah, A. S. A. K., **2241**
Shaw, B. D., **1201**, **1613**
Sheinson, R. S., **1405**
Shepherd, I. G., 363, **373**, 435
Shepherd, J. E., **3015**
Sher, E., 2707
Shih, H. Y., **1353**
Shih, W. P., **2771**
Shiina, H., **535**

Shimada, M., **27**
Shimada, Y., **1621**
Shin, H. S., **1817**
Short, M., **891**
Shvartsberg, V., **1035**
Shy, S. S., **283**
Sichel, M., 2973, **3033**
Sick, V., **975**, **2597**, **2741**
Silverman, I., **1739**
Simmie, J. M., **613**, 753
Simonin, O., **923**
Singh, G., **1043**
Sinkovits, R. S., **91**, **899**
Sirignano, W. A., 1216, 1234, **1319**, 1612
Skaggs, R. R., **1181**
Skevis, G., **703**
Slagle, I. R., **513**
Smallwood, G. J., **427**
Smith, A. P., 2531
Smith, D. B., **875**
Smith, G. P., 566, **959**, **2133**, 2160
Smith, O. I., **2463**
Smith, P. J., **2117**
Smith, R. A., **2471**
Smith, T., **299**
Smith, W. W., **2795**
Smooke, M. D., **1121**, 1159, 1411, **1739**, **2161**, **2693**
Smoot, L. D., 1577, 2238, 3093, 3125, 3135, 3143, 3177
Smyth, K. C., **1161**, 1308, **1385**, 2169, 2284, 2341, 2394
Snelling, D. R., **427**, **2351**
Snyder, R., **2041**
Sochet, L. R., **739**, **747**
Solomon, P. R., **3145**
Solum, M. S., **3153**
Sommer, T., **621**
Soteriou, M., **1531**
Spliethoff, H., **2231**
Stairkovskii, A. Y., **2999**
Stanmore, B. R., **3269**
Stapf, D., **2083**
Steinberg, M., **1835**
Stepowski, D., **105**
Stewart, D. S., **2981**
Stöckelmann, E., **807**, **2431**
Stocker, D. P., **1361**
Stoliarov, S. I., **513**
Stouklov, I. G., **2909**
Stubington, J., 3250
Su, M. C., **605**
Subraminiam, S., **49**
Suh, J., **2181**
Sun, C. J., **1111**
Sung, C. J., **113**, **865**, **1111**, **2359**
Suntz, R., **2343**, **2387**
Suuberg, E. M., **1515**, 3094, 3102, 3125, 3160, 3195
Sweets, G., 2901
Syred, N., **3355**

Tacke, M. M., **75**, **169**, 194
Tada, S., **2709**
Tagawa, H., **2973**
Taghizadeh, K., **2319**
Takagi, T., **339**, **1103**
Takahashi, F., **145**, **1151**, 1179
Takemoto, Y., **1071**
Takeno, K., **3223**
Takeno, T., **27**, **993**, **1071**, **2139**
Takita, K., **2877**, 2939
Talbot, L., **2749**
Tamura, T., **389**
Tan, Y., **677**
Tanabe, M., **1235**, **1637**
Tang, L., **1335**
Taniguchi, M., **3189**
Tanke, D., **2303**
Tanoff, M. A., 281, 873, **1121**, 1411, **2161**
Taylor, P. H., **497**, 2420
Taylor, S. C., **875**
Telengator, A. M., **1969**, 1996
Temps, F., 1007, 2082
ter Meulen, H., 111, 2604, 2857, 2868
Terasaki, T., **2733**
Tesner, P. A., 2310
Theinel, Th., **2303**
Theisen, D., **2949**
Therssen, E., **747**
Thévenin, D., **1079**
Thibaut, D., **2565**
T'ien, J. S., **1353**
Timnat, Y. M., 1651
Tittmann, 1061
Togan, M., 2453, 3160
Tognott, L., 3101
Tokuda, K., **3223**
Tomboulides, A. G., **3059**
Tomita, E., **2749**
Tonello, N. A., **3033**
Tonfoni, C., **3295**
Toqan, M., 2302
Torero, J. L., **1361**
Tranter, R. S., **575**
Tregrossi, A., **2327**
Treviño, C., **1797**
Troe, J., **543**, 558, 582, 588, 640, 692, 1032
Trump, D. D., **145**
Tsang, W., **1377**
Tse, S. D., **1505**
Tseng, L. K., **993**
Tsuchiya, K., **535**
Tsue, M., **1251**, **1629**
Tsushima, S., **1723**

Ueda, T., **137**
Ujiie, Y., **1267**
Ulitsky, M., **315**
Umemura, A., **1621**
Upschulte, B. L., **2779**
Urban, D. L., **1361**

Vaccaro, S., **1789**
Vaglieco, B. M., **2533**
Valdati, B. A., **2161**
Valentino, G., **2717**
Van Kalmthout, E., **35**
Van Tiggelen, P. J., 626, **1009**, 1393
Van Tigglen, P., 479
Vander Wal, R. L., **2269**
Vanderhoff, J. A., 2015, **2017**
Vandooren, J., 719, **1009**
Vandsburger, U., **1541**
Vantelon, J. P., **1461**
Venkatesh, S., **1437**
Vernaglia, B. A., **3287**
Vervisch, L., **233**
Veynante, D., **35**, **413**, **1079**, **1663**
Vicenzi, E. P., **1899**
Vieille, B., **1259**
Viguier, C., **3023**
Violi, A., **2327**
Vlachos, D. G., 1070, **1754**, **1763**, 1778, 2292
Vogel, A., **1687**
Voisin, D., **613**
Vollmer, J. T., **527**
Volpp, H. R., **489**, 2138
Vortmeyer, D., **2835**
Vouros, P., **2421**

Wagner, H. Gg., **527**, **559**, **2303**
Walker, D. G., **365**
Walker, R. W., 639, **641**, 762, 780
Walther, D. C., **1361**
Wan, Y., 1685
Wang, H., **1025**, **2359**, **2413**
Warnatz, J., **83**, **773**, **1747**, **2619**
Warth, V., **755**
Wartha, C., **3325**
Wassenberg, H., **421**
Watt, M., **3153**
Webb, B. W., **3161**
Weber, R., **211**, **1143**, **1779**, **3343**
Wei, R., 648
Weinberg, F., **939**, 1241
Wendt, J. O. L., **2447**, **3197**
West, J., **1335**, **1477**
Westbrook, C., 632, **641**, **693**, 771, 1032, 2644, **2669**, **2685**
Westmoreland, P. R., 700, 1032, 1403, **1763**, 2301
Wichman, I. S., **1437**
Wiese, W., **2259**
Will, S., **2277**
Williams, A., **1859**
Williams, D. N., **2991**
Williams, F. A., 256, 265, **389**, **1017**, **1201**, 1643, 1927, **1969**, 2924, 2989
Williamson, J., **3103**
Willis, J. W., **2463**
Wilson, K. J., **2471**, **2843**
Winklhofer, E., 2284, **2541**, 2596
Winter, F., **3325**
Wintrich, F., **2869**
Wittig, S., 2731, **2763**
Woiki, D., **583**
Wolfrum, J., **437**, **489**, 2074, **2597**, 2834, 2866, **3301**
Woodruff, S. D., **3179**
Worlikar, A. S., **203**
Wornat, J., 2107
Wornat, M. J., **3075**, 3160, **3287**
Wouters, H. A., **177**

Xiao, K., 281
Xie, L., **2155**

Yakush, S. E., **1549**
Yamamoto, K., 135, **1129**
Yamamoto, Y., **3213**
Yamasaki, H., **1251**, **1629**
Yamashita, H., **27**, **1071**
Yan, H., **3261**
Yang, N. Y. C., **3075**, **3103**
Yao, J., **651**, **2981**
Yap, L. T., 3353
Ye, J., **1679**
Yeboah, Y. D., **3179**
Yeh, L. I., 1008
Yeo, J., **2653**
Yetter, R. A., **1899**, **1909**, **3059**
Yoon, Y., **1953**, **2957**
Yoshida, A., **397**, 411
Yoshida, H., **2709**
Yoshida, K., **1103**
Yoshida, M., **1283**
Yoshikawa, Y., **1103**
Yu, K. H., **2471**, **2843**
Yuasa, S., **1945**

Zahn, M., **2597**
Zamansky, V., 588, **2075**, 2090, 2097, 2124, **2125**, 2238
Zhang, C., **2181**
Zhang, D. K., **3261**
Zhang, Q., **651**
Zhang, X., **3111**
Zhang, Z., **1851**
Zhao, H., 2643
Zhao, Y., **3145**
Zhdanok, S. A., **3377**
Zheng, G., **2495**
Zheng, Q. P., 1651, **2757**
Zhou, C. Q., **2091**
Zhou, G., **883**
Zhou, W., **1909**
Zhou, X. C., **1453**
Zhu, D. L., **1111**, **2413**
Zimmermann, R., **2859**
Zimont, V., **249**, 274, 412
Zinn, B. T., **2811**, **3363**
Zinoviev, A., **1557**
Zondlo, J. W., **3179**

SUBJECT INDEX

01 Aerosols

Gas-Phase Combustion Synthesis of Aluminum Nitride Powder. R. L. Axelbaum, C. R. Lottes, J. I. Huertas, L. J. Rosen, 1891

01 Liquid

Droplet Size Distribution Effects in Spray Combustion. J. A. Bossard, R. E. Peck, 1671
Flame Propagation in Planar Droplet Arrays and Interaction Phenomena Between Neighboring Droplet Streams. N. Roth, A. Karl, K. Anders, A. Frohn, 1697
Experimental Study on High-Pressure Droplet Evaporation Using Microgravity Conditions. H. Nomura, Y. Ujiie, H. J. Rath, J. Sato, M. Kono, 1267
Effect of Liquid Drops on the Thermal Explosion of a Gas Mixture. V. Goldshtein, I. Goldfarb, A. Zinoviev, I. Shreiber, 1557
Burning Velocities in Fuel-Rich Aluminum Dust Clouds. S. Goroshin, I. Fomenko, J. H. S. Lee, 1961

02 Solid

Mechanisms Governing Trace Sodium Capture by Kaolinite in a Downflow Combustor. P. O. Mwabe, J. O. L. Wendt, 2447
Evolution of Particle Temperature and Internal Composition for Zirconium Burning in Air. I. E. Molodetsky, E. L. Dreizin, C. K. Law, 1919
Sodium Partitioning in a Pulverized Coal Combustion Environment. N. B. Gallagher, T. W. Peterson, J. O. L. Wendt, 3197
Conversion of Coal Tar to Soot During Coal Pyrolysis in a Post-Flame Environment. J. Ma, T. H. Fletcher, B. W. Webb, 3161
Transformations of Sludge Waste During Combustion in a Low-High-Low Temperature Reactor. J. A. Kozinski, R. Saade, G. Zheng, 2495
Burning Velocities in Fuel-Rich Aluminum Dust Clouds. S. Goroshin, I. Fomenko, J. H. S. Lee, 1961
The Behavior of Chromium in Laminar Hydrogen and Ethene Diffusion Flames. Y. Yoon, C. Reyes, A. D. Jones, P. Kelly, D. P. Y. Chang, I. M. Kennedy, 1953

02 Coal Combustion

(*Also see* Combustion in Practical Systems, Furnaces and Incinerators: Hetrogeneous Combustion, Dispersed Particles, Multiphase and Single Solid Particles)

Solid Fuel Utilization: From Coal to Biomass. F. C. Lockwood, 3041
Impact of Temperature and Fuel-Nitrogen Content on Fuel-Staged Combustion with Coal Pyrolysis Gas. U. Greul, H. Spliethoff, H.-C. Magel, U. Schnell, H. Ruediger, K. R. G. Hein, C.-Z. Li, P. F. Nelson, 2231
Control of NO_x Emissions by NO_x Recycle Approach. C. Q. Zhou, L. G. Neal, R. Bolli, J. Haslbeck, A. Chang, 2091
Surface Heterogeneity in the Formation and Decomposition of Carbon Surface Oxides. M. C. Ma, B. S. Haynes, 3119
Chemical Structure of Coal Tar During Devolatilization. M. Watt, T. H. Fletcher, S. Bai, M. S. Solum, R. J. Pugmire, 3153
Statistical Kinetics for Pulverized Coal Combustion. R. H. Hurt, M. M. Lunden, E. G. Brehob, D. J. Maloney, 3169
Fundamental Study on N_2O Formation/Decomposition Characteristics by Means of Low-Temperature Pulverized Coal Combustion. I. Naruse, Y. Yamamoto, Y. Itoh, K. Ohtake, 3213
The Role of Radiation Absorption in Defining Explosibility of Coal/Rock Dust Mixtures. C. D. Litton, R. F. Chaiken, 1571
The Impact of Fragmentation on Char Conversion During Pulverized Coal Combustion. R. E. Mitchell, A. E. Jacob Akanetuk, 3137
Laser Ignition and Flame Propagation of Pulverized Coal Dust Clouds. M. Taniguchi, H. Kobayashi, S. Azuhata, 3189
Sodium Partitioning in a Pulverized Coal Combustion Environment. N. B. Gallagher, T. W. Peterson, J. O. L. Wendt, 3197
Conversion of Coal Tar to Soot During Coal Pyrolysis in a Post-Flame Environment. J. Ma, T. H. Fletcher, B. W. Webb, 3161
The Fate of Fixed Carbon During the Fluidized-Bed Combustion of a Coal and Two Waste-Derived Fuels. U. Arena, R. Chirone, P. Salatino, 3243
Pollutant Formation During Coal Combustion in a CFB Test Furnace. A. Reidick, H. Kremer, 3309
Prediction of Coal-Water Slurry Dispersion in a Fluidized Bed Combustor. F. Okasha, M. Miccio, 3277
The Energy and Environmental Implications of Us-

ing Sewage Sludge as a Co-Fired Fuel Applied to Boilers. T. Abbas, P. Costen, G. De Soete, K. Glaser, S. Hassan, F. C. Lockwood, 2487
Single-Particle Combustion of Two Biomass Chars. M. J. Wornat, R. H. Hurt, K. A. Davis, N. Y. C. Yang, 3075
The Influence of Pressure on Char Combustion Kinetics. E. Croiset, C. Mallet, J.-P. Rouan, J.-R. Richard, 3095
Influence of Pressure on the Combustion Rate of Carbon. R. H. Essenhigh, A. M. Mescher, 3085
Transient High-Temperature Thermal Deactivation of Monomaceral-Rich Coal Chars. T. Beeley, J. Crelling, J. Gibbins, R. Hurt, M. Lunden, C. Man, J. Williamson, N. Yang, 3103
Propagation Limits of Dust/Air Flames Diluted by Additions of Inert Solid Particles. R. Blouquin, G. Joulin, 1565
A Transient Two-Dimensional Chemically Reactive Flow Model: Fuel Particle Combustion in a Nonquiescent Environment. J. Lee, A. G. Tomboulides, S. A. Orszag, R. A. Yetter, F. L. Dryer, 3059
Predicting the Near Burner Zone Flow Field and Chemistry of Swirl Stabilized Low-NO_x Flames of Pulverized Coal Using the RNG-k-ε, RSM, and k-ε Turbulence Models. F. Breussin, F. Pigari, R. Weber, 211
Flame Structure and Combustion Rate of Burning Graphite in the Stagnation Flow. A. Makino, I. Kato, M. Senba, H. Fujizaki, N. Araki, 3067
Fundamental Experiment on the Combustion of Coal–Water Mixture and Modeling of the Process. K. Takeno, K. Tokuda, T. Ichinose, S. Kaneko, 3223
Numerical Investigation on the Influence of Carbonaceous Particles on the Ignition Behavior of Methane/Air Mixtures. T. Ludwig, P. Roth, 1579
Characterization of Chaotic Dynamics in the Spontaneous Combustion of Coal Stockpiles. G. Continillo, G. Galiero, P. L. Maffettone, S. Crescitelli, 1585
Effects of CaO and Burnout on the Kinetics of NO Reduction by Beulah Zap Char. F. Guo, W. C. Hecker, 2251
An Experimental Study of the Release of Nitrogen from Coals Pyrolyzed in Fluidized-Bed Reactors. C.-Z. Li, P. F. Nelson, E. B. Ledesma, J. C. Mackie, 3205
Fragmentation of Small Coal Particles Under Fluidized-Bed Combustor Conditions. B. R. Stanmore, A. Brillard, P. Gilot, L. Delfosse, 3269
Coal Combustion and Gasification in a Compartmented, Fluidized-Bed Coal Gasifier. H. Yan, V. Rudolph, D.-K. Zhang, 3261
In Situ Alkali Concentration Measurements in a Pressurized, Fluidized-Bed Coal Combustor by Excimer Laser Induced Fragmentation Fluorescence. F. Greger, K. T. Hartinger, P. B. Monkhouse, J. Wolfrum, H. Baumann, B. Bonn, 3301
The Effects of Pyrolysis Temperature and Ion-Exchanged Metals on the Composition of Brown Coal Tars Produced in a Fluidized-Bed Reactor. B. A. Vernaglia, M. J. Wornat, C.-Z. Li, P. F. Nelson, 3287
A General Model for Devolatilization of Large Coal Particles. Y. Zhao, M. A. Serio, P. R. Solomon, 3145
Progress of Combustion in the Furnace of a Circulating Fluidized Bed Boiler. A. Lyngfelt, L.-E. Mand, B. Leckner, 3253

03 Combustion In Practical Systems

Measurements and Predictions of Nitric Oxide and Particulates Emissions from Heavy Fuel Oil Spray Flames. M. A. Byrnes, E. A. Foumeny, T. Mahmud, A. S. A. K Sharifah, T. Abbas, P. G. Costen, S. Hassan, F. C. Lockwood, 2241
Gas Phase Reactions of Hydrogen Peroxide and Hydrogen Peroxide/Methanol Mixtures with Air Pollutants. V. M. Zamansky, L. Ho, P. M. Maly, W. R. Seeker, 2125
Reburning Promoted by Nitrogen- and Sodium-Containing Compounds. V. M. Zamansky, L. Ho, P. M. Maly, W. R. Seeker, 2075
Modeling of Solid Particle Interaction in a High-Velocity, Hot Gas Stream. M. M. Elkotb, N. Salama, I. Nassef, 1937
High-Pressure Methane Oxidation Behind Reflected Shock Waves. E. L. Petersen, M. Röhrig, D. F. Davidson, R. K. Hanson, C. T. Bowman, 799

01 Diesel Engines

Modern Tools for Diesel Engine Combustion Investigation. W. Hentschel, 2503
Spectral Extinction Measurements of Spray Combustion in a Divided-Chamber Diesel Engine System. F. E. Corcione, G. Mazziotti, B. M. Vaglieco, 2533
Near-Field Entrainment in Unsteady Gas Jets and Diesel Sprays: A Comparative Study. R. Andriani, A. Coghe, G. E. Cossali, 2549
Interpretation of k-ε Computed Turbulence Length-Scale Predictions for Engine Flows. Z. Han, R. D. Reitz, F. E. Corcione, G. Valentino, 2717
Application of a Reduced Kinetic Model for Soot Formation and Burnout in Three-Dimensional Diesel Combustion Computations. P. Belardini, C. Bertoli, C. Beatrice, N. Del Giacomo, A. D'Anna, 2517
Analysis of Pyrolysis Process in Diesel-Like Combustion by Means of Laser-Induced Fluorescence. R. Ragucci, M. de Joannon, A. Cavaliere, 2525
An Experimental Database for Diesel Spray Combustion. E. Winklhofer, 2541
Chemical Kinetic Study of Dimethylether Oxidation in a Jet Stirred Reactor from 1 to 10 ATM: Ex-

periments and Kinetic Modeling. P. Dagaut, J.-C. Boettner, M. Cathonnet, 627
Self-Ignition of Diesel-Relevant Hydrocarbon-Air Mixtures Under Engine Conditions. U. Pfahl, K. Fieweger, G. Adomeit, 781
Flame Lift-off in Diesel Sprays. A. Karlsson, J. Chomiak, 2557

02 Furnaces and Incinerators

Solid Fuel Utilization: From Coal to Biomass. F. C. Lockwood, 3041
Mechanisms Governing Trace Sodium Capture by Kaolinite in a Downflow Combustor. P. O. Mwabe, J. O. L. Wendt, 2447
A Model for Prediction of Selective Noncatalytic Reduction of Nitrogen Oxides by Ammonia, Urea, and Cyanuric Acid with Mixing Limitations in the Presence of CO. J. Brouwer, M. P. Heap, D. W. Pershing, P. J. Smith, 2117
Control of NO_x Emissions by NO_x Recycle Approach. C. Q. Zhou, L. G. Neal, R. Bolli, J. Haslbeck, A. Chang, 2091
Gas Temperature Above a Porous Radiant Burner: Comparison of Measurements and Model Predictions. M. D. Rumminger, N. H. Heberle, R. W. Dibble, D. R. Crosley, 1755
A New Approach to Studying Pore Diffusivity During Char Combustion at FBC Conditions. S. Goel, A. F. Sarofim, J. Lu, 3127
Influence of Turbulent Mixing on the Pyrolysis of Chloroform Using Detailed Chemical Kinetics. M. Kraft, E. Stöckelmann, H. Bockhorn, 2431
Effects of External Acoustic Excitation on Enhanced Transport in a Resonant Incinerator. G. Pont, J. W. Willis, A. R. Karagozian, O. I. Smith, 2463
Compact Incinerator Afterburner Concept Based on Vortex Combustion. T. P. Parr, E. Gutmark, K. Wilson, D. M. Hanson-Parr, K. Yu, R. A. Smith, K. C. Schadow, 2471
Emissions of Nitrogen Oxides from Circulating Fluidized-Bed Combustors: Modeling Results Using Detailed Chemistry. S. Goel, A. Sarofim, P. Kilpinen, M. Hupa, 3317
The Energy and Environmental Implications of Using Sewage Sludge as a Co-Fired Fuel Applied to Boilers. T. Abbas, P. Costen, G. De Soete, K. Glaser, S. Hassan, F. C. Lockwood, 2487
Industrial Combustion Control Using UV Emission Tomography. A. Leipertz, R. Obertacke, F. Wintrich, 2869
Fundamental Experiment on the Combustion of Coal–Water Mixture and Modeling of the Process. K. Takeno, K. Tokuda, T. Ichinose, S. Kaneko, 3223
Studies of Helmholtz Resonance in a Swirl Burner/Furnace System. D. Froud, A. Beale, T. O'Doherty, N. Syred, 3355
The Effect of Heat Content and Composition of Fuel on Pulse Combustor Performance. A. Kushari, L. J. Rosen, J. I. Jagoda, B. T. Zinn, 3363
Adsorption of Metallic Mercury on Activated Carbon. D. Karatza, A. Lancia, D. Musmarra, F. Pepe, 2439

03 Liquid, Hybrid and Gas Rockets

Experimental Demonstration of Active Control of Combustion Instabilities Using Real-Time Modes Observation and Secondary Fuel Injection. Y. Neumeier, B. T. Zinn, 2811
Conditioned Dissipation and Average Consumption Maps in a Turbulent Nonpremixed Flame Using Planar Laser-Induced Fluorescence of O_2. S. Guerre, R. Bazile, D. Stepowski, 105
Flame Stabilization in Cryogenic Propellant Combustion. G. Herding, R. Snyder, P. Scouflaire, C. Rolon, S. Candel, 2041

04 MHD Power Generators

05 Ramjets and Augmentors

Real-Time Adaptive Feedback Control of Combustion Instability. A. Kemal, C. T. Bowman, 2803
Active Control of Liquid-Fueled Combustion Using Periodic Vortex-Droplet Interaction. K. H. Yu, T. P. Parr, K. J. Wilson, K. C. Schadow, E. J. Gutmark, 2843
Transient Simulation of Superdetonative Mode Initiation Process in SCRam-Accelerator. J.-Y. Choi, I.-S. Jeung, Y. Yoon, 2957

06 Solid Rockets

Oscillatory Combustion of Aluminized Composite Propellants. S. R. Hickman, M. Q. Brewster, 2007
Propellant Dark Zone Concentrations via Multichannel IR Absorption. S. H. Modiano, J. A. Vanderhoff, 2017
Laser Recoil Combustion Response of N5 Propellant from 1 to 9 Atmospheres. J. C. Finlinson, 2025
Evolution of Particle Temperature and Internal Composition for Zirconium Burning in Air. I. E. Molodetsky, E. L. Dreizin, C. K. Law, 1919

07 Spark Ignition Engines

Advanced Diagnostics for Minimizing Hydrocarbon Emissions from a Direct-Injection Gasoline Engine. M. C. Drake, D. T. French, T. D. Fansler, 2581
Relation Between Flame Propagation Characteristics and Hydrocarbon Emissions Under Lean Operating Conditions in Spark-Ignition Engines. N. Hadjiconstantinou, K. Min, J. B. Heywood, 2637
Heterogeneous/Homogeneous Reaction and Trans-

port Coupling During Flame-Wall Interaction. P. Popp, M. Smooke, M. Baum, 2693
Oxidation of Hydrocarbons from Lubricant Oil Layers in Spark-Ignition Engines. M. G. Norris, W. Bauer, S. Hochgreb, 2645
Polarization Separated Spatially Resolved Single Laser Shot Multispecies Analysis in the Combustion Chamber of a Realistic SI Engine with a Tunable KrF Excimer Laser. M. Knapp, A. Luczak, V. Beushausen, W. Hentschel, P. Manz, P. Andresen, 2589
Quantitative 2D Single–Shot Imaging of NO Concentrations and Temperatures in a Transparent SI Engine. C. Schulz, V. Sick, J. Wolfrum, V. Drewes, M. Zahn, R. Maly, 2597
Modeling Turbulent Combustion and Pollutant Formation in Stratified Charge SI Engines. T. A. Baritaud, J. M. Duclos, A. Fusco, 2627
Heat Release Rates Due to Autoignition, and Their Relationship to Knock Intensity in Spark Ignition Engines. D. Bradley, G. T. Kalghatgi, M. Golombok, J. Yeo, 2653
Heat Transfer Modeling During Knock and Flame Quenching in an Engine Chamber. O. A. Ezekoye, 2661
Time-Resolved Investigation of Hot Spots in the End Gas of an S. I. Engine by Means of 2-D Double-Pulse LIF of Formaldehyde. B. Bäuerle, J. Warnatz, F. Behrendt, 2619
Autoignition Chemistry in a Motored Engine: An Experimental and Kinetic Modeling Study. H. J. Curran, P. Gaffuri, W. J. Pitz, C. K. Westbrook, W. R. Leppard, 2669
1-D Simulation of a Spark Discharge in Air. M. Schäfer, R. Schmidt, J. Köhler, 2701
Experimental and Numerical Investigation of the Structure of Flames Under Engine Conditions. H. Wassenberg, G. Adomeit, 421
Surface Density Measurements of Turbulent Premixed Flames in a Spark-Ignition Engine and a Bunsen-Type Burner Using Planar Laser-Induced Fluorescence. B. M. Deschamps, G. J. Smallwood, J. Prieur, D. R. Snelling, Ö. L. Gülder, 427
An Experimental Study on Quenching Crevice Widths in the Combustion Chamber of a Spark-Ignition Engine. S. Ishizawa, 2605
A Fiber-Optic Probe to Measure Precombustion In-Cylinder Fuel-Air Ratio Fluctuations in Production Engines. M. J. Hall, M. Koenig, 2613
Extents of Alkane Combustion During Rapid Compression Leading to Single- and Two-Stage Ignition. A. Cox, J. F. Griffiths, C. Mohamed, H. Curran, W. J. Pitz, C. K. Westbrook, 2685

08 Turbine Combustors

Effect of Hardware Alignment on Fuel Distribution and Combustion Performance for a Production Engine Fuel-Injection Assembly. V. G. McDonell, L. Arellano, S. W. Lee, G. S. Samuelsen, 2725
The Effects of Fuel–Air Mixing on NO_x Formation in Non-Premixed Swirl Burners. T. Terasaki, S. Hayashi, 2733
A Numerical and Experimental Study of Fuel Evaporation and Mixing for Lean Premixed Combustion at High Pressure. M. Rachner, M. Brandt, H. Eickhoff, C. Hassa, A. Bräumer, H. Krämer, M. Ridder, V. Sick, 2741
Use of an Optical Probe for Time-Resolved *in Situ* Measurement of Local Air-to-Fuel Ratio and Extent of Fuel Mixing with Applications to Low NO_x Emissions in Premixed Gas Turbines. R. K. Mongia, E. Tomita, F. K. Hsu, L. Talbot, R. W. Dibble, 2749
Real-Time Adaptive Feedback Control of Combustion Instability. A. Kemal, C. T. Bowman, 2803
Experimental Demonstration of Active Control of Combustion Instabilities Using Real-Time Modes Observation and Secondary Fuel Injection. Y. Neumeier, B. T. Zinn, 2811
Optimization of Gas Turbine Combustor Performance Throughout the Duty Cycle. N. T. Davis, G. S. Samuelsen, 2819
Active Instability Control with Direct-Drive Servo Valves in Liquid-Fueled Combustion Systems. C. Hantschk, J. Hermann, D. Vortmeyer, 2835
Influence of Air and Fuel Flows on Gas Turbine Sprays at High Pressures. Q. P. Zheng, A. K. Jasuja, A. H. Lefebvre, 2757
A Simple Model of Ignition Modes of Dense Droplet Clouds. D. Thibaut, S. Candel, 2565
Self-Ignition of Hybrid (H_2 + Atomized Liquid Hydrocarbon Fuel + Gaseous Oxidizer) Mixtures at Engine Relevant Conditions. B. E. Gelfand, A. M. Bartenev, S. V. Khomik, S. P. Medvedev, A. N. Polenov, 2573
Stability and Emissions Characteristics of a Lean Premixed Gas Turbine Combustor. W.-P. Shih, J. G. Lee, D. A. Santavicca, 2771
Fluorescence Imaging of NO and O_2 in a Spray Flame Combustor at Elevated Pressures. B. L. Upschulte, M. G. Allen, K. R. McManus, 2779
Droplet Size Distribution Effects in Spray Combustion. J. A. Bossard, R. E. Peck, 1671
Catalytic Oxidation of Natural Gas Over Supported Platinum: Flow Reactor Experiments and Detailed Numerical Modeling. T. C. Bond, R. A. Noguchi, C.-P. Chou, R. K. Mongia, J.-Y. Chen, R. W. Dibble, 1771
A Study of Turbulent Diffusion Flames Formed by Planar Fuel Injection into the Wake Formation Region of a Slender Square Cylinder. P. Koutmos, C. Mavridis, D. Papailiou, 161
Visualization of Fuel Distribution in Premixed Ducts in a Low-Emission Gas Turbine Combustor Using Laser Techniques. C. Löfström, H. Kaaling, M. Aldén, 2787

Experimental and Numerical Study of a Premixed Flame Stabilized by a Rectangular Section Cylinder. P. Bailly, D. Garréton, O. Simonin, P. Bruel, M. Champion, B. Deshaies, S. Duplantier, S. Sanquer, 923
Fiber-Optic Sensors for Long-Wavelength Pyrometry and Thermometry in Gas Turbines. A. S. Bonanno, W. W. Smith, R. Bassilakis, M. A. Serio, 2795
Calculations of Turbulent Flames Using a PSR Microstructural Library. I. Z. Hu, S. M. Correa, 307

09 Fluidized Beds

Fundamental Study on N_2O Formation/Decomposition Characteristics by Means of Low-Temperature Pulverized Coal Combustion. I. Naruse, Y. Yamamoto, Y. Itoh, K. Ohtake, 3213
The Fate of Fixed Carbon During the Fluidized-Bed Combustion of a Coal and Two Waste-Derived Fuels. U. Arena, R. Chirone, P. Salatino, 3243
The Effect of the Bulk Equivalence Ratio on the PAH Emissions from the Combustion of PVC, Poly(styrene), and Poly(ethylene). T. Panagiotou, Y. A. Levendis, J. Carlson, P. Vouros, 2421
Fluidized Bed Combustion: Achievements and Problems. B. Leckner, 3231
The NO and N_2O Formation Mechanism During Devolatilization and Char Combustion Under Fluidized-Bed Conditions. F. Winter, C. Wartha, G. Läffler, H. Hofbauer, 3325
Pollutant Formation During Coal Combustion in a CFB Test Furnace. A. Reidick, H. Kremer, 3309
Scattering of Thermal Radiation in the Freeboard of a 1 MW_t Fluidized Bed Combustor with Coal and Limestone Feeding. M. Filla, A. Scalabrin, C. Tonfoni, 3295
Prediction of Coal-Water Slurry Dispersion in a Fluidized Bed Combustor. F. Okasha, M. Miccio, 3277
Structures of Multiple Combustion Waves Formed Under Filtration of Lean Hydrogen-Air Mixtures in a Packed Bed. A. V. Saveliev, L. A. Kennedy, A. A. Fridman, I. K. Puri, 3369
Coal Combustion and Gasification in a Compartmented, Fluidized-Bed Coal Gasifier. H. Yan, V. Rudolph, D.-K. Zhang, 3261
In Situ Alkali Concentration Measurements in a Pressurized, Fluidized-Bed Coal Combustor by Excimer Laser Induced Fragmentation Fluorescence. F. Greger, K. T. Hartinger, P. B. Monkhouse, J. Wolfrum, H. Baumann, B. Bonn, 3301
Nitrogen Chemistry in FBC with Limestone Addition. A. Jensen, J. E. Johnsson, K. Dam-Johansen, 3335
A General Model for Devolatilization of Large Coal Particles. Y. Zhao, M. A. Serio, P. R. Solomon, 3145
Progress of Combustion in the Furnace of a Circulating Fluidized Bed Boiler. A. Lyngfelt, L.-E. Émand, B. Leckner, 3253

Deflagration (*See* Flames)

04 Detonations

On the Evolution of Cellular Detonation. D. S. Stewart, T. D. Aslam, J. Yao, 2981
Detailed Structure and Propagation of Three-Dimensional Detonations. D. N. Williams, L. Bauwens, E. S. Oran, 2991
Onset of Oblique Detonation Waves: Comparison Between Experimental and Numerical Results for Hydrogen-Air Mixtures. C. Viguier, L. F. Figueira da Silva, D. Desbordes, B. Deshaies, 3023
Dimensional Analysis of the Effect of Flow Conditions on Shock-Induced Combustion. J.-Y. Choi, I.-S. Jeung, S. Lee, 2925
Transient Simulation of Superdetonative Mode Initiation Process in SCRam-Accelerator. J.-Y. Choi, I.-S. Jeung, Y. Yoon, 2957
Numerical Simulations of the Diffraction of Planar Detonations in H_2-O_2 Mixtures. N. A. Tonello, M. Sichel, E. S. Oran, 3033

01 Condensed-Phase

02 Gas-Phase

Unsteady Extinction Mechanisms of Diffusion Flames. F. Takahashi, V. R. Katta, 1151
Critical Conditions for Detonation Propagation Through Mixture with Decreasing Reaction Rate. S. I. Kryuchkov, S. B. Dorofeev, A. A. Efimenko, 2965
On the Evolution of Cellular Detonation. D. S. Stewart, T. D. Aslam, J. Yao, 2981
Experimental Observation of Unsteady H_2-O_2 Combustion Phenomena Around Hypersonic Projectiles Using a Multiframe Camera. J. Kasahara, T. Horii, T. Endo, T. Fujiwara, 2903
Detailed Structure and Propagation of Three-Dimensional Detonations. D. N. Williams, L. Bauwens, E. S. Oran, 2991
Oblique Detonation Stabilized on a Hypervelocity Projectile. M. J. Kaneshige, J. E. Shepherd, 3015
Onset of Oblique Detonation Waves: Comparison Between Experimental and Numerical Results for Hydrogen-Air Mixtures. C. Viguier, L. F. Figueira da Silva, D. Desbordes, B. Deshaies, 3023
PLIF Imaging of Hypersonic Reactive Flow Around Blunt Bodies. M. R. Kamel, C. I. Morris, I. G. Stouklov, R. K. Hanson, 2909
Dimensional Analysis of the Effect of Flow Conditions on Shock-Induced Combustion. J.-Y. Choi, I.-S. Jeung, S. Lee, 2925
Transient Simulation of Superdetonative Mode Ini-

tiation Process in SCRam-Accelerator. J.-Y. Choi, I.-S. Jeung, Y. Yoon, 2957
Numerical Simulations of the Diffraction of Planar Detonations in H_2-O_2 Mixtures. N. A. Tonello, M. Sichel, E. S. Oran, 3033

03 Failure

Oblique Detonation Stabilized on a Hypervelocity Projectile. M. J. Kaneshige, J. E. Shepherd, 3015

04 Initiation

The Influence of Initial Temperature on Flame Acceleration and Deflagration-to-Detonation Transition. G. Ciccarelli, J. L. Boccio, T. Ginsberg, H. Tagawa, 2973
Oblique Detonation Stabilized on a Hypervelocity Projectile. M. J. Kaneshige, J. E. Shepherd, 3015
Transient Simulation of Superdetonative Mode Initiation Process in SCRam-Accelerator. J.-Y. Choi, I.-S. Jeung, Y. Yoon, 2957
Deflagration-to-Detonation Transition in End Gases. C. K. Chan, W. A. Dewit, 2679

05 Limits

Critical Conditions for Detonation Propagation Through Mixture with Decreasing Reaction Rate. S. I. Kryuchkov, S. B. Dorofeev, A. A. Efimenko, 2965
Dimensional Analysis of the Effect of Flow Conditions on Shock-Induced Combustion. J.-Y. Choi, I.-S. Jeung, S. Lee, 2925

06 Multiphase

Detonation Supported by Combustible Dust Deposit. B.-C. Fan, H.-Z. Li, 3007

07 Structure

On the Evolution of Cellular Detonation. D. S. Stewart, T. D. Aslam, J. Yao, 2981
Detailed Structure and Propagation of Three-Dimensional Detonations. D. N. Williams, L. Bauwens, E. S. Oran, 2991
Dimensional Analysis of the Effect of Flow Conditions on Shock-Induced Combustion. J.-Y. Choi, I.-S. Jeung, S. Lee, 2925
Transient Simulation of Superdetonative Mode Initiation Process in SCRam-Accelerator. J.-Y. Choi, I.-S. Jeung, Y. Yoon, 2957

08 Theory

On the Evolution of Cellular Detonation. D. S. Stewart, T. D. Aslam, J. Yao, 2981
Detonation Supported by Combustible Dust Deposit. B.-C. Fan, H.-Z. Li, 3007
Dimensional Analysis of the Effect of Flow Conditions on Shock-Induced Combustion. J.-Y. Choi, I.-S. Jeung, S. Lee, 2925
Numerical Simulations of the Diffraction of Planar Detonations in H_2-O_2 Mixtures. N. A. Tonello, M. Sichel, E. S. Oran, 3033

09 Transition to Detonation

Critical Conditions for Detonation Propagation Through Mixture with Decreasing Reaction Rate. S. I. Kryuchkov, S. B. Dorofeev, A. A. Efimenko, 2965
The Influence of Initial Temperature on Flame Acceleration and Deflagration-to-Detonation Transition. G. Ciccarelli, J. L. Boccio, T. Ginsberg, H. Tagawa, 2973
Ignition and Detonation in N_2O-CO-H_2-He Mixtures. A. Y. Starikovskii, 2999
Onset of Oblique Detonation Waves: Comparison Between Experimental and Numerical Results for Hydrogen-Air Mixtures. C. Viguier, L. F. Figueira da Silva, D. Desbordes, B. Deshaies, 3023
Deflagration-to-Detonation Transition in End Gases. C. K. Chan, W. A. Dewit, 2679

(*Also see* Flames, DDT)

05 Diagnostic Methods

Modern Tools for Diesel Engine Combustion Investigation. W. Hentschel, 2503
Combustion Control Using a Multiplexed Diode-Laser Sensor System. E. R. Furlong, D. S. Baer, R. K. Hanson, 2851
Gas Property Effects on Droplet Atomization and Combustion in an Air-Assist Atomizer. R. Aftel, A. K. Gupta, C. Cook, C. Presser, 1645
Structure of an Acoustically Forced Turbulent Spray Flame. E. Haile, O. Delabroy, F. Lacas, D. Veynante, S. Candel, 1663
Investigation of Sooting in Normal-Gravity Droplet Combustion Using Light Extinction and Gravimetric Techniques. K.-O. Lee, K. A. Jensen, M. Y. Choi, 2397
The Effect of Changes in the Flame Structure on the Formation and Destruction of Soot and NO_x in Radiating Diffusion Flames. A. Atreya, C. Zhang, H. K. Kim, T. Shamim, J. Suh, 2181
Degenerate Four-Wave Mixing Measurements of Methyl Radical Distributions in Hydrocarbon Flames: Comparison with Model Predictions. R. L. Farrow, M. N. Bui-Pham, V. Sick, 975
Current State of Combustion Research in Microgravity. M. Kono, K. Ito, T. Niioka, T. Kadota, J. Sato, 1189
The Controlling Chemistry in Flame Generated

Surface Deposition of Na_2SO_4 and the Effects of Chlorine. M. Steinberg, K. Schofield, 1835
Contribution to the Analysis of Temporal and Spatial Structures Near the Lift-Off Region of a Turbulent Hydrogen Diffusion Flame. A. Brockhinke, P. Andresen, K. Kohse-Hšinghaus, 153
Polycyclic Aromatic Hydrocarbon and Soot Formation in Premixed Flames of CH_3Cl/CH_4 and CH_4. J. Huang, S. M. Senkan, 2335
Flamelet Behavior in a Turbulent Diffusion Flame Measured by Rayleigh Scattering Image Velocimetry. M. Komiyama, A. Miyafuji, T. Takagi, 339
Investigation of Sooting in Microgravity Droplet Combustion. M. Y. Choi, K.-O. Lee, 1243

01 CARS (Coherent Anti Stroke Raman Spectroscopy)

Effect of Temperature and Concentration Fluctuations on Radiative Heat Transfer in Turbulent Flames. W. Krebs, R. Koch, B. Ganz, L. Eigenmann, S. Wittig, 2763
Thermal Diffusion Effects and Vortex-Flame Interactions in Hydrogen Jet Diffusion Flames. R. D. Hancock, F. R. Schauer, R. P. Lucht, V. R. Katta, K. Y. Hsu, 1087
Temperature Profile Measurements in Stagnation-Flow, Diamond-Forming Flames Using Hydrogen CARS Spectroscopy. K. E. Bertagnolli, R. P. Lucht, 1825
Influence of Hydrogen Addition to Fuel on Temperature Field and Soot Formation in Diffusion Flames. Ö. L. Gülder, D. R. Snelling, R. A. Sawchuk, 2351
Flame Surface Density and Burning Rate in Premixed Turbulent Flames. I. G. Shepherd, 373
Two-Dimensional Mathematical Modeling of Laminar, Premixed, Methane-Air Combustion on an Experimental Slot Burner. D. Bradley, P. H. Gaskell, K. C. Kwan, M. J. Scott, 915
Flame Structure and Combustion Rate of Burning Graphite in the Stagnation Flow. A. Makino, I. Kato, M. Senba, H. Fujizaki, N. Araki, 3067

02 Chromatographic

The Effects of Pyrolysis Temperature and Ion-Exchanged Metals on the Composition of Brown Coal Tars Produced in a Fluidized-Bed Reactor. B. A. Vernaglia, M. J. Wornat, C.-Z. Li, P. F. Nelson, 3287

03 Fluorescence

Advanced Diagnostics for Minimizing Hydrocarbon Emissions from a Direct-Injection Gasoline Engine. M. C. Drake, D. T. French, T. D. Fansler, 2581
Quantitative 2D Single–Shot Imaging of NO Concentrations and Temperatures in a Transparent SI Engine. C. Schulz, V. Sick, J. Wolfrum, V. Drewes, M. Zahn, R. Maly, 2597
Analysis of Pyrolysis Process in Diesel-Like Combustion by Means of Laser-Induced Fluorescence. R. Ragucci, M. de Joannon, A. Cavaliere, 2525
Time-Resolved Investigation of Hot Spots in the End Gas of an S. I. Engine by Means of 2-D Double-Pulse LIF of Formaldehyde. B. Bäuerle, J. Warnatz, F. Behrendt, 2619
Effect of Hardware Alignment on Fuel Distribution and Combustion Performance for a Production Engine Fuel-Injection Assembly. V. G. McDonell, L. Arellano, S. W. Lee, G. S. Samuelsen, 2725
Stability and Emissions Characteristics of a Lean Premixed Gas Turbine Combustor. W.-P. Shih, J. G. Lee, D. A. Santavicca, 2771
Fluorescence Imaging of NO and O_2 in a Spray Flame Combustor at Elevated Pressures. B. L. Upschulte, M. G. Allen, K. R. McManus, 2779
PLIF Imaging Measurements of a Co-axial Rocket Injector Spray at Elevated Pressure. U. Brummund, A. Cessou, A. Vogel, 1687
Computational and Experimental Study of NO in an Axisymmetric Laminar Diffusion Flame. M. D. Smooke, A. Ern, M. A. Tanoff, B. A. Valdati, R. K. Mohammed, D. F. Marran, M. B. Long, 2161
Quantitative Two-Photon Laser-Induced Fluorescence Imaging of CO in Flickering CH_4/Air Diffusion Flames. D. A. Everest, C. R. Shaddix, K. C. Smyth, 1161
CH_3 Detection in Flames Using Photodissociation-Induced Fluorescence. P. Desgroux, L. Gasnot, B. Crunelle, J. F. Pauwels, 967
Characterization of Spherical Hydrocarbon Fuel Flames: Laser Diagnosis of the Chemical Structure Through the OH Radical. J. Känig, C. Eigenbrod, M. Tanabe, H. Renken, H. J. Rath, 1235
Structure of a Non-Premixed Flame Interacting with Counterrotating Vortices. D. Thévenin, J. C. Rolon, P. H. Renard, D. W. Kendrick, D. Veynante, S. Candel, 1079
Solid Propellant Diffusion Flame Structure. T. P. Parr, D. M. Hanson-Parr, 1981
Gas Temperature Above a Porous Radiant Burner: Comparison of Measurements and Model Predictions. M. D. Rumminger, N. H. Heberle, R. W. Dibble, D. R. Crosley, 1755
Flame Structure Measurement of Single, Isolated Aluminum Particles Burning in Air. P. Bucher, R. A. Yetter, F. L. Dryer, T. P. Parr, D. M. Hanson-Parr, E. P. Vicenzi, 1899
The Effect of Temperature on Soot Inception in Premixed Ethylene Flames. A. Ciajolo, A. D'Anna, R. Barbella, A. Tregrossi, A. Violi, 2327
Compact Incinerator Afterburner Concept Based on Vortex Combustion. T. P. Parr, E. Gutmark, K. Wilson, D. M. Hanson-Parr, K. Yu, R. A. Smith, K. C. Schadow, 2471

The Time Evolution of a Vortex-Flame Interaction Observed via Planar Imaging of CH and OH. Q.-V. Nguyen, P. H. Paul, 357

Surface Density Measurements of Turbulent Premixed Flames in a Spark-Ignition Engine and a Bunsen-Type Burner Using Planar Laser-Induced Fluorescence. B. M. Deschamps, G. J. Smallwood, J. Prieur, D. R. Snelling, Ö. L. Gülder, 427

Measurement of the Instantaneous Detailed Flalme Structure in Turbulent Premixed Combustion. A. Buschmann, F. Dinkelacker, T. Schäfer. M. Schäfer, J. Wolfrum, 437

Conditioned Dissipation and Average Consumption Maps in a Turbulent Nonpremixed Flame Using Planar Laser-Induced Fluorescence of O_2. S. Guerre, R. Bazile, D. Stepowski, 105

Visualization of Fuel Distribution in Premixed Ducts in a Low-Emission Gas Turbine Combustor Using Laser Techniques. C. Läfsträm, H. Kaaling, M. Aldén, 2787

On the Use of Light Sheet Methods in the Presence of Refraction by Flames. F. Weinberg, 939

A Real-Time Monitor for Toxic Metal Emissions from Combustion Systems. S. G. Buckley, C. P. Koshland, R. F. Sawyer, D. Lucas, 2455

In Situ Alkali Concentration Measurements in a Pressurized, Fluidized-Bed Coal Combustor by Excimer Laser Induced Fragmentation Fluorescence. F. Greger, K. T. Hartinger, P. B. Monkhouse, J. Wolfrum, H. Baumann, B. Bonn, 3301

Experimental Investigation of a SCRAMJET Model Combustor with Injection Through a Swept Ramp Using Laser-Induced Fluorescence with Tunable Excimer Lasers. R. Hänig, D. Theisen, R. Fink, R. Lachner, G. Kappler, D. Rist, P. Andresen, 2949

04 Laser

Advanced Diagnostics for Minimizing Hydrocarbon Emissions from a Direct-Injection Gasoline Engine. M. C. Drake, D. T. French, T. D. Fansler, 2581

Quantitative 2D Single–Shot Imaging of NO Concentrations and Temperatures in a Transparent SI Engine. C. Schulz, V. Sick, J. Wolfrum, V. Drewes, M. Zahn, R. Maly, 2597

Near-Field Entrainment in Unsteady Gas Jets and Diesel Sprays: A Comparative Study. R. Andriani, A. Coghe, G. E. Cossali, 2549

Time-Resolved Investigation of Hot Spots in the End Gas of an S. I. Engine by Means of 2-D Double-Pulse LIF of Formaldehyde. B. Bäuerle, J. Warnatz, F. Behrendt, 2619

Effect of Hardware Alignment on Fuel Distribution and Combustion Performance for a Production Engine Fuel-Injection Assembly. V. G. McDonell, L. Arellano, S. W. Lee, G. S. Samuelsen, 2725

Use of an Optical Probe for Time-Resolved *in Situ* Measurement of Local Air-to-Fuel Ratio and Extent of Fuel Mixing with Applications to Low NO_x Emissions in Premixed Gas Turbines. R. K. Mongia, E. Tomita, F. K. Hsu, L. Talbot, R. W. Dibble, 2749

Spatially Selective Chemistry Control in an Oil-Burning Furnace: A New Method to Reduce NO_x Emissions Developed Through Combined Three-Dimensional Laser Diagnostics. A. Luczak, S. Eisenberg, M. Knapp, H. Schlüter, V. Beushausen, Peter Andresen, 2827

Combustion Control Using a Multiplexed Diode-Laser Sensor System. E. R. Furlong, D. S. Baer, R. K. Hanson, 2851

On-line Emission Control of Combustion Processes by Laser-Induced Resonance-Enhanced Multi-Photon Ionization/Mass Spectrometry. R. Zimmermann, D. Lenior, A. Kettrup, H. Nagel, U. Boesl, 2859

PLIF Imaging Measurements of a Co-axial Rocket Injector Spray at Elevated Pressure. U. Brummund, A. Cessou, A. Vogel, 1687

Measurement of the Rate Coefficient of $H + O_2 + M \rightarrow HO_2 + M$ for $M = Ar$ and N_2 at High Pressures. D. F. Davidson, E. L. Petersen, M. Röhrig, R. K. Hanson, C. T. Bowman, 481

A Shock Tube Study of $H + HNCO \rightarrow H_2 + NCO$ and the Thermal Decomposition of NCO. J. D. Mertens, R. K. Hanson, 551

The Ignition and Oxidation of Allene and Propyne: Experiments and Kinetic Modeling. H. Curran, J. M. Simmie, P. Dagaut, D. Voisin, M. Cathonnet, 613

A LIF and CARS Study of the Effects of Upstream Heat Loss on NO Formation from Laminar Premixed Burner-Stabilized Natural-Gas/Air Flames. A. V. Mokhov, H. B. Levinsky, 2147

Degenerate Four-Wave Mixing Measurements of Methyl Radical Distributions in Hydrocarbon Flames: Comparison with Model Predictions. R. L. Farrow, M. N. Bui-Pham, V. Sick, 975

Characterization of Spherical Hydrocarbon Fuel Flames: Laser Diagnosis of the Chemical Structure Through the OH Radical. J. König, C. Eigenbrod, M. Tanabe, H. Renken, H. J. Rath, 1235

The Effect of CF_3I Compared to CF_3Br on OH· and Soot Concentrations in Co-Flowing Propane/Air Diffusion Flames. K. C. Smyth, D. A. Everest, 1385

The Sensitive Structure of Partially Premixed Methane-Air vs. Air Counterflow Flames. M. A. Tanoff, M. D. Smooke, R. J. Osborne, T. M. Brown, R. W. Pitz, 1121

The Controlling Chemistry in Flame Generated Surface Deposition of Na_2SO_4 and the Effects of Chlorine. M. Steinberg, K. Schofield, 1835

Measurements and Prediction of Air Entrainment

Rates of Pool Fires. X. C. Zhou, J. P. Gore, H. R. Baum, 1453
Observation of Sooting Behavior in an Emulsion Droplet Flame by Planar Laser Light Scattering in Microgravity. M. Tsue, D. Segawa, T. Kadota, H. Yamasaki, 1251
The Time Evolution of a Vortex-Flame Interaction Observed via Planar Imaging of CH and OH. Q.-V. Nguyen, P. H. Paul, 357
Turbulence Characteristics Within the Local Reaction Zone of a High-Intensity Turbulent Premixed Flame. J. Furukawa, K. Okamoto, T. Hirano, 405
Measurement of the Instantaneous Detailed Flame Structure in Turbulent Premixed Combustion. A. Buschmann, F. Dinkelacker, T. Schäfer, M. Schäfer, J. Wolfrum, 437
Analysis of Turbulence-Chemistry Interaction with Respect to NO Formation in Turbulent, Nonpremixed Hydrogen-Air Flames. M. Schlatter, J. C. Ferreira, M. Flury, J. Gass, 2215
Oxygen Atom Concentrations and NO Production Rates in a Turbulent H_2/N_2 Jet Flame. R. S. Barlow, G. J. Fiechtner, J.-Y. Chen, 2199
A Study of Turbulent Diffusion Flames Formed by Planar Fuel Injection into the Wake Formation Region of a Slender Square Cylinder. P. Koutmos, C. Mavridis, D. Papailiou, 161
Turbulent Length Scales in a Swirling Flame. G. Früchtel, E. P. Hassel, J. Janicka, 195
Experimental and Numerical Study of a Premixed Flame Stabilized by a Rectangular Section Cylinder. P. Bailly, D. Garréton, O. Simonin, P. Bruel, M. Champion, B. Deshaies, S. Duplantier, S. Sanquer, 923
High-Pressure Methane Oxidation Behind Reflected Shock Waves. E. L. Petersen, M. Röhrig, D. F. Davidson, R. K. Hanson, C. T. Bowman, 799
Tunable Diode Laser Absorption Measurements of Carbon Monoxide and Temperature in a Time-Varying, Methane/Air, Non-Premixed Flame. R. R. Skaggs, J. H. Miller, 1181
On the Use of Light Sheet Methods in the Presence of Refraction by Flames. F. Weinberg, 939
Assessment of Soot Volume Fractions from Laser-Induced Incandescence by Comparison with Extinction Measurements in Laminar, Premixed, Flat Flames. J. Appel, M. Marquardt, H. Bockhorn, B. Jungfleisch, R. Suntz, 2387
Study of Swirling Recirculating Hydrogen Diffusion Flame Using UV Raman Spectroscopy. M. M. Tacke, T. C. Cheng, E. P. Hassel, J. Janicka, 169
Measurements of the Detailed Flame Structure in Turbulent H_2–Ar Jet Diffusion Flames with Line-Raman/Rayleigh/LIPF-OH Technique. Y.-C. Chen, M. S. Mansour, 97
A Real-Time Monitor for Toxic Metal Emissions from Combustion Systems. S. G. Buckley, C. P. Koshland, R. F. Sawyer, D. Lucas, 2455
Experimental Investigation of a SCRAMJET Model Combustor with Injection Through a Swept Ramp Using Laser-Induced Fluorescence with Tunable Excimer Lasers. R. Hönig, D. Theisen, R. Fink, R. Lachner, G. Kappler, D. Rist, P. Andresen, 2949
Quantitative CH Determinations in Low-Pressure Flames. J. Luque, G. P. Smith, D. R. Crosley, 959

05 Photographic

Influence of Air and Fuel Flows on Gas Turbine Sprays at High Pressures. Q. P. Zheng, A. K. Jasuja, A. H. Lefebvre, 2757
On the Use of Light Sheet Methods in the Presence of Refraction by Flames. F. Weinberg, 939

06 Probes

Relation Between Flame Propagation Characteristics and Hydrocarbon Emissions Under Lean Operating Conditions in Spark-Ignition Engines. N. Hadjiconstantinou, K. Min, J. B. Heywood, 2637
Hydrogen–Oxygen Flame Doped with Trimethyl Phosphate, Its Structure, and Trimethyl Phosphate Destruction Chemistry. O. Korobeinichev, V. Shvartsberg, A. Chernov, V. Mokrushin, 1035
Quenching of Reaction in Gas-Sampling Probes to Measure Scramjet Engine Performance. T. Mitani, 2917
Turbulence Characteristics Within the Local Reaction Zone of a High-Intensity Turbulent Premixed Flame. J. Furukawa, K. Okamoto, T. Hirano, 405
A Simplified Phenomenological Model for Soot Growth Based on Plug Flow Reactor Experiments. B. Bartenbach, W. Leuckel, 2311

07 Radiometric

Fiber-Optic Sensors for Long-Wavelength Pyrometry and Thermometry in Gas Turbines. A. S. Bonanno, W. W. Smith, R. Bassilakis, M. A. Serio, 2795

08 Pyrometric

Thin-Filament Pyrometry in Flickering Laminar Diffusion Flames. W. M. Pitts, 1171
Evolution of Particle Temperature and Internal Composition for Zirconium Burning in Air. I. E. Molodetsky, E. L. Dreizin, C. K. Law, 1919
Fiber-Optic Sensors for Long-Wavelength Pyrometry and Thermometry in Gas Turbines. A. S. Bonanno, W. W. Smith, R. Bassilakis, M. A. Serio, 2795

09 Spectroscopic

Polarization Separated Spatially Resolved Single Laser Shot Multispecies Analysis in the Combustion Chamber of a Realistic SI Engine with a Tunable KrF Excimer Laser. M. Knapp, A. Luczak, V. Beu-

shausen, W. Hentschel, P. Manz, P. Andresen, 2589
Spectral Extinction Measurements of Spray Combustion in a Divided-Chamber Diesel Engine System. F. E. Corcione, G. Mazziotti, B. M. Vaglieco, 2533
Combustion Control Using a Multiplexed Diode-Laser Sensor System. E. R. Furlong, D. S. Baer, R. K. Hanson, 2851
On-line Emission Control of Combustion Processes by Laser-Induced Resonance-Enhanced Multi-Photon Ionization/Mass Spectrometry. R. Zimmermann, D. Lenior, A. Kettrup, H. Nagel, U. Boesl, 2859
Effect of Temperature and Concentration Fluctuations on Radiative Heat Transfer in Turbulent Flames. W. Krebs, R. Koch, B. Ganz, L. Eigenmann, S. Wittig, 2763
The Ignition and Oxidation of Allene and Propyne: Experiments and Kinetic Modeling. H. Curran, J. M. Simmie, P. Dagaut, D. Voisin, M. Cathonnet, 613
Degenerate Four-Wave Mixing Measurements of Methyl Radical Distributions in Hydrocrobon Flames: Comparison with Model Predictions. R. L. Farrow, M. N. Bui-Pham, V. Sick, 975
Observations of H_2O Formation in the Supersonic Combustion of H_2 by High-Enthalpy Air. M. F. Miller, W. T. Rawlins, M. G. Allen, T. E. Parker, 2895
Propellant Dark Zone Concentrations via Multichannel IR Absorption. S. H. Modiano, J. A. Vanderhoff, 2017
Oblique Detonation Stabilized on a Hypervelocity Projectile. M. J. Kaneshige, J. E. Shepherd, 3015
Flame Structure Measurement of Single, Isolated Aluminum Particles Burning in Air. P. Bucher, R. A. Yetter, F. L. Dryer, T. P. Parr, D. M. Hanson-Parr, E. P. Vicenzi, 1899
Combustion-Like Pyrolysis of Organic Polymers: Species and Kinetic Details by *T*-Jump/FTIR Spectroscopy. T. B. Brill, H. Arisawa, P. E. Gongwer, 791
Industrial Combustion Control Using UV Emission Tomography. A. Leipertz, R. Obertacke, F. Wintrich, 2869
Interaction of Turbulence and Radiation in Confined Diffusion Flames. J. W. Hartick, M. Tacke, G. Früchtel, E. P. Hassel, J. Janicka, 75
A Fiber-Optic Probe to Measure Precombustion In-Cylinder Fuel-Air Ratio Fluctuations in Production Engines. M. J. Hall, M. Koenig, 2613
Temperature Field Measurements in a Sooting Flame by Filtered Rayleigh Scattering (FRS). D. Hofmann, A. Leipertz, 945
The Optical Band Gap Model in the Interpretation of the UV-Visible Absorption Spectra of Rich Premixed Flames. P. Minutolo, G. Gambi, A. D'Alessio, 951
Study of Swirling Recirculating Hydrogen Diffusion Flame Using UV Raman Spectroscopy. M. M. Tacke, T. C. Cheng, E. P. Hassel, J. Janicka, 169

06 Electrical Properties of Flames

01 Electrons

02 Ions

PAH and Aromers: Precursors of Fullerenes and Soot. M. Bachmann, W. Wiese, K.-H. Homann, 2259

Engine Knock (*See* Combustion in Practical Systems, SI Engines)

07 Experimental Methods

The Effect of Changes in the Flame Structure on the Formation and Destruction of Soot and NO_x in Radiating Diffusion Flames. A. Atreya, C. Zhang, H. K. Kim, T. Shamim, J. Suh, 2181
Droplet Combustion Experiments in Spacelab. D. L. Dietrich, J. B. Haggard, Jr., F. L. Dryer, V. Nayagam, B. D. Shaw, F. A. Williams, 1201
Experimentally Measured Burning Rates of Premixed Turbulent Flames. E. Bourguignon, L. W. Kostiuk, Y. Michou, I. Gokalp, 447

01 Burners

The Effects of Fuel–Air Mixing on NO_x Formation in Non-Premixed Swirl Burners. T. Terasaki, S. Hayashi, 2733
Real-Time Adaptive Feedback Control of Combustion Instability. A. Kemal, C. T. Bowman, 2803
Impact of Temperature and Fuel-Nitrogen Content on Fuel-Staged Combustion with Coal Pyrolysis Gas. U. Greul, H. Spliethoff, H.-C. Magel, U. Schnell, H. Ruediger, K. R. G. Hein, C.-Z. Li, P. F. Nelson, 2231
Quantitative Two-Photon Laser-Induced Fluorescence Imaging of CO in Flickering CH_4/Air Diffusion Flames. D. A. Everest, C. R. Shaddix, K. C. Smyth, 1161
Structure of a Non-Premixed Flame Interacting with Counterrotating Vortices. D. Thévenin, J. C. Rolon, P. H. Renard, D. W. Kendrick, D. Veynante, S. Candel, 1079
Hydrogen–Oxygen Flame Doped with Trimethyl Phosphate, Its Structure, and Trimethyl Phosphate Destruction Chemistry. O. Korobeinichev, V. Shvartsberg, A. Chernov, V. Mokrushin, 1035
Gas-Phase Combustion Synthesis of Aluminum Nitride Powder. R. L. Axelbaum, C. R. Lottes, J. I. Huertas, L. J. Rosen, 1891
Propellant Dark Zone Concentrations via Multi-

channel IR Absorption. S. H. Modiano, J. A. Vanderhoff, 2017
Flame Surface Density and Burning Rate in Premixed Turbulent Flames. I. G. Shepherd, 373
Burning Velocity of Turbulent Premixed Flames in a High-Pressure Environment. H. Kobayashi, T. Tumura, K. Maruta, T. Niioka, F. A. Williams, 389
Study of Premixed Turbulent Combustion Including Landau-Darrieus Instability Effects. R. N. Paul, K. N. C. Bray, 259
Turbulence Characteristics Within the Local Reaction Zone of a High-Intensity Turbulent Premixed Flame. J. Furukawa, K. Okamoto, T. Hirano, 405
Two-Dimensional Mathematical Modeling of Laminar, Premixed, Methane-Air Combustion on an Experimental Slot Burner. D. Bradley, P. H. Gaskell, K. C. Kwan, M. J. Scott, 915
Highly Turbulent Premixed Flames Stabilized in a Co-Axial Jet Flame Burner. T.-W. Lee, A. Mitrovic, 455
Studies of Helmholtz Resonance in a Swirl Burner/Furnace System. D. Froud, A. Beale, T. O'Doherty, N. Syred, 3355

02 Combustion Bombs

Markstein Lengths of CO/H_2/Air Flames, Using Expanding Spherical Flames. M. J. Brown, I. C. McLean, D. B. Smith, S. C. Taylor, 875

03 Explosion Vessels

Turbulent Premixed Flame Propagation in a Cylindrical Vessel. M. Fairweather, S. S. Ibrahim, H. Jaggers, D. G. Walker, 365

04 Plug Flow Reactors

Direct Measurement of the Reaction Pair C_6H_5NO $\int$ C_6H_5 + NO by a Combined Shock Tube and Flow Reactor Approach. C. Horn, P. Frank, R. S. Tranter, J. Schaugg, H.-H. Grotheer, T. Just, 575
Experimental and Computational Investigation of Concentration Profiles of C_1-C_4 Hydrocarbon Radicals and Molecules in Low-Pressure C_2H_2/O/H Atomic Flames at 600 K. J. Peeters, K. Devriendt, 1001
Chemical Kinetic Modeling of High-Pressure Propane Oxidation and Comparison to Experimental Results. D. N. Koert, W. J. Pitz, J. W. Bozzelli, N. P. Cernansky, 633
Experimental Data and Kinetic Modeling of Primary Reference Fuel Mixtures. C. V. Callahan, T. J. Held, F. L. Dryer, R. Minetti, M. Ribaucour, L. R. Sochet, T. Faravelli, P. Gaffuri, E. Ranzi, 739
Pressure Effects on the Thermal de-NO_x Process. K. Kjærgaard, P. Glarborg, K. Dam-Johansen, J. A. Miller, 2067
Flow Reactor Studies and Testing of Comprehensive Mechanisms for NO_x Reburning. D. Stapf, W. Leuckel, 2083
A Simplified Phenomenological Model for Soot Growth Based on Plug Flow Reactor Experiments. B. Bartenbach, W. Leuckel, 2311

05 Shock Tubes

Measurement of the Rate Coefficient of H + O_2 + M $\rightarrow$ HO_2 + M for M = Ar and N_2 at High Pressures. D. F. Davidson, E. L. Petersen, M. Röhrig, R. K. Hanson, C. T. Bowman, 481
A Shock Tube Study of H + HNCO $\rightarrow$ H_2 + NCO and the Thermal Decomposition of NCO. J. D. Mertens, R. K. Hanson, 551
Direct Measurement of the Reaction Pair C_6H_5NO $\int$ C_6H_5 + NO by a Combined Shock Tube and Flow Reactor Approach. C. Horn, P. Frank, R. S. Tranter, J. Schaugg, H.-H. Grotheer, T. Just, 575
A Kinetic Study of the Oxidation of Acetonitrile: A Model for NO Formation from Fuel-Bound Nitrogen. E. Ikeda, J. C. Mackie, 597
The Ignition and Oxidation of Allene and Propyne: Experiments and Kinetic Modeling. H. Curran, J. M. Simmie, P. Dagaut, D. Voisin, M. Cathonnet, 613
Thermal Decomposition of Benzonitrile: A Combined Single-Pulse Shock Tube-ARAS Investigation. A. Lifshitz, Y. Cohen, M. Braun-Unkhoff, P. Frank, 659
Dissociation and Chain Reaction in the Pyrolysis of Pyrazine. J. H. Kiefer, Q. Zhang, R. D. Kern, H. Chen, J. Yao, B. S. Jursic, 651
Self-Ignition of Diesel-Relevant Hydrocarbon-Air Mixtures Under Engine Conditions. U. Pfahl, K. Fieweger, G. Adomeit, 781
A Kinetic Study of the Reactions of $NH(X^3\Sigma^-)$ with O_2 and NO in the Temperature Range from 1200 to 2200 K. H.-J. Römming, H. Gg. Wagner, 559
Observations of H_2O Formation in the Supersonic Combustion of H_2 by High-Enthalpy Air. M. F. Miller, W. T. Rawlins, M. G. Allen, T. E. Parker, 2895
Detonation Supported by Combustible Dust Deposit. B.-C. Fan, H.-Z. Li, 3007
PLIF Imaging of Hypersonic Reactive Flow Around Blunt Bodies. M. R. Kamel, C. I. Morris, I. G. Stouklov, R. K. Hanson, 2909
Soot Formation in the Pyrolysis of Benzene/Acetylene and Acetylene/Hydrogen Mixtures at High Carbon Concentrations. V. G. Knorre, D. Tanke, TH. Thienel, H. Gg. Wagner, 2303
Thermal Decomposition of C_2H_5I. S. S. Kumaran, M.-C. Su, K. P. Lim, J. V. Michael, 605
High-Pressure Methane Oxidation Behind Reflected Shock Waves. E. L. Petersen, M. Röhrig, D. F. Davidson, R. K. Hanson, C. T. Bowman, 799

06 Stirred Reactors

Dissociation and Chain Reaction in the Pyrolysis of Pyrazine. J. H. Kiefer, Q. Zhang, R. D. Kern, H. Chen, J. Yao, B. S. Jursic, 651
Chemical Kinetic Study of Dimethylether Oxidation in a Jet Stirred Reactor from 1 to 10 ATM: Experiments and Kinetic Modeling. P. Dagaut, J.-C. Boettner, M. Cathonnet, 627

07 Microgravity

Gravitational Effects on Sooting Diffusion Flames. C. R. Kaplan, E. S. Oran, K. Kailasanath, H. D. Ross, 1301
Current State of Combustion Research in Microgravity. M. Kono, K. Ito, T. Niioka, T. Kadota, J. Sato, 1189
Characterization of Spherical Hydrocarbon Fuel Flames: Laser Diagnosis of the Chemical Structure Through the OH Radical. J. König, C. Eigenbrod, M. Tanabe, H. Renken, H. J. Rath, 1235
Droplet Combustion Experiments in Spacelab. D. L. Dietrich, J. B. Haggard, Jr., F. L. Dryer, V. Nayagam, B. D. Shaw, F. A. Williams, 1201
High-Pressure Droplet Burning Experiments in Microgravity. B. Vieille, C. Chauveau, X. Chesneau, A. Odeïde, I. Gökalp, 1259
Experimental Study on High-Pressure Droplet Evaporation Using Microgravity Conditions. H. Nomura, Y. Ujiie, H. J. Rath, J. Sato, M. Kono, 1267
Experimental Study on Methane-Air Premixed Flame Extinction at Small Stretch Rates in Microgravity. K. Maruta, M. Yoshida, Y. Ju, T. Niioka, 1283
Microgravity Combustion of Methanol and Methanol/Water Droplets: Drop Tower Experiments and Model Predictions. A. J. Marchese, F. L. Dryer, R. Colantonio, V. Nayagam, 1209
An Unsteady-State Analysis of Porous Sphere and Droplet Fuel Combustion Under Microgravity Conditions. M. K. King, 1227
Opposed-Flow Flame Spread Across *n*-Propanol Pools. D. N. Schiller, W. A. Sirignano, 1319
Detailed Experiments of Flame Spread Across Deep Butanol Pools. H. D. Ross, F. J. Miller, 1327
Soot-Field Structure in Laminar Soot-Emitting Microgravity Nonpremixed Flames. C. M. Megaridis, D. W. Griffin, B. Konsur, 1291
Observation of Sooting Behavior in an Emulsion Droplet Flame by Planar Laser Light Scattering in Microgravity. M. Tsue, D. Segawa, T. Kadota, H. Yamasaki, 1251
Model Calculation of Steady Upward Flame Spread Over a Thin Solid in Reduced Gravity. C.-B. Jiang, J. S. T'ien, H.-Y. Shih, 1353
Quiescent Flame Spread Over Thick Fuels in Microgravity. J. West, L. Tang, R. A. Altenkirch, S. Bhattacharjee, K. Sacksteder, M. A. Delichatsios, 1335
Effects of Slow Wind on Localized Radiative Ignition and Transition to Flame Spread in Microgravity. T. Kashiwagi, K. B. McGrattan, S. L. Olson, O. Fujita, M. Kikuchi, K. Ito, 1345
An Experimental Study on Particle-Cloud Flames in Microgravity Field. Y. Okuyama, Y. Ohtomo, K. Maruta, H. Kobayashi, T. Niioka, 1369
Hydroxyl Radical Chemiluminescence Imaging and the Structure of Microgravity Droplet Flames. A. J. Marchese, F. L. Dryer, V. Nayagam, R. Colantonio, 1219
Influence of Gravity on the Propagation of Intially Spherical Flames. J. Daou, B. Rogg, 1275
Investigation of Sooting in Microgravity Droplet Combustion. M. Y. Choi, K.-O. Lee, 1243
Small-Scale Smoldering Combustion Experiments in Microgravity. D. P. Stocker, S. L. Olson, D. L. Urban, J. L. Torero, D. C. Walther, A. C. Fernandez-Pello, 1361

08 Explosions

Numerical Simulations of the Diffraction of Planar Detonations in H_2-O_2 Mixtures. N. A. Tonello, M. Sichel, E. S. Oran, 3033

01 Adiabatic and Nonadiabatic

02 Industrial

03 Inhibition

The Role of Radiation Absorption in Defining Explosibility of Coal/Rock Dust Mixtures. C. D. Litton, R. F. Chaiken, 1571

04 Limits

The Phenomena of Flame Propagation in a Rotating Tube. Y. Sakai, S. Ishizuka, 847
The Role of Radiation Absorption in Defining Explosibility of Coal/Rock Dust Mixtures. C. D. Litton, R. F. Chaiken, 1571

05 Safety

Burning Regimes for the Finite-Duration Releases of Fuel Gases. G. Makhviladze, J. P. Roberts, S. Yakush, 1549
Effect of Liquid Drops on the Thermal Explosion of a Gas Mixture. V. Goldshtein, I. Goldfarb, A. Zinoviev, I. Shreiber, 1557
The Role of Radiation Absorption in Defining Explosibility of Coal/Rock Dust Mixtures. C. D. Litton, R. F. Chaiken, 1571
Turbulent Premixed Flame Propagation in a Cylin-

drical Vessel. M. Fairweather, S. S. Ibrahim, H. Jaggers, D. G. Walker, 365
Deflagration-to-Detonation Transition in End Gases. C. K. Chan, W. A. Dewit, 2679

06 Theory

Detonation Supported by Combustible Dust Deposit. B.-C. Fan, H.-Z. Li, 3007
The Role of Radiation Absorption in Defining Explosibility of Coal/Rock Dust Mixtures. C. D. Litton, R. F. Chaiken, 1571
Turbulent Premixed Flame Propagation in a Cylindrical Vessel. M. Fairweather, S. S. Ibrahim, H. Jaggers, D. G. Walker, 365

07 Venting

Flame Propagation Along 90-Degree Bend in an Open Duct. K. Sato, Y. Sakai, M. Chiga, 931

09 Fire

Current State of Combustion Research in Microgravity. M. Kono, K. Ito, T. Niioka, T. Kadota, J. Sato, 1189
Global Properties of Gaseous Pool Fires. A. Hamins, K. Konishi, P. Borthwick, T. Kashiwagi, 1429
Detailed Experiments of Flame Spread Across Deep Butanol Pools. H. D. Ross, F. J. Miller, 1327
Two-Regime Global Kinetics of Cellulose Pyrolysis: The Role of Tar Evaporation. E. M. Suuberg, I. Milosavljevic, V. Oja, 1515
Numerical Simulation of Combustion in Fire Plumes. W. E. Mell, K. B. McGrattan, H. R. Baum, 1523
Creeping Flame Spread: Energy Balance and Application to Practical Materials. M. A. Delichatsios, 1495
Effects of Slow Wind on Localized Radiative Ignition and Transition to Flame Spread in Microgravity. T. Kashiwagi, K. B. McGrattan, S. L. Olson, O. Fujita, M. Kikuchi, K. Ito, 1345
The Transport of Carbon Monoxide from a Burning Compartment Located on the Side of a Hallway. B. Y. Lattimer, U. Vandsburger, R. J. Roby, 1541
Flame Base Structure of Small-Scale Pool Fires. S. Venkatesh, A. Ito, K. Saito, I. S. Wichman, 1437

01 Buoyant Flames and Wakes

Thin-Filament Pyrometry in Flickering Laminar Diffusion Flames. W. M. Pitts, 1171
Global Properties of Gaseous Pool Fires. A. Hamins, K. Konishi, P. Borthwick, T. Kashiwagi, 1429
Measurements and Prediction of Air Entrainment Rates of Pool Fires. X. C. Zhou, J. P. Gore, H. R Baum, 1453
Influence of Gravity and Pressure on Pool Fire-Type Diffusion Flames. J.-M. Most, P. Mandin, J. Chen, P. Joulain, D. Durox, A. C. Fernandez–Pello, 1311
Detailed Experiments of Flame Spread Across Deep Butanol Pools. H. D. Ross, F. J. Miller, 1327
Numerical Simulation of Combustion in Fire Plumes. W. E. Mell, K. B. McGrattan, H. R. Baum, 1523
Numerical Simulation of the Dynamics of Large Fire Plumes and the Phenomenon of Puffing. A. F. Ghoniem, I. Lakkis, M. Soteriou, 1531
Model Calculation of Steady Upward Flame Spread Over a Thin Solid in Reduced Gravity. C.-B.Jiang, J. S. T'ien, H.-Y. Shih, 1353
Flame Base Structure of Small-Scale Pool Fires. S. Venkatesh, A. Ito, K. Saito, I. S. Wichman, 1437

02 Fire Dynamics

Chemical Effects of CF_3H in Extinguishing Counterflow CO/Air/H_2 Diffusion Flames. G. S. Fallon, H. K. Chelliah, G. T. Linteris, 1395
Global Properties of Gaseous Pool Fires. A. Hamins, K. Konishi, P. Borthwick, T. Kashiwagi, 1429
Influence of Gravity and Pressure on Pool Fire-Type Diffusion Flames. J.-M. Most, P. Mandin, J. Chen, P. Joulain, D. Durox, A. C. Fernandez–Pello, 1311
Controlling Mechanisms in the Transition from Smoldering to Flaming of Flexible Polyurethane Foam. S. D. Tse, A. C. Fernandez–Pello, K. Miyasaka, 1505
Numerical Simulation of Combustion in Fire Plumes. W. E. Mell, K. B. McGrattan, H. R. Baum, 1523
Numerical Simulation of the Dynamics of Large Fire Plumes and the Phenomenon of Puffing. A. F. Ghoniem, I. Lakkis, M. Soteriou, 1531
Determination of the Spread Rate in Opposed-Flow Flame Spread Over Thick Solid Fuels in the Thermal Regime. S. Bhattacharjee, J. West, R. A. Altenkirch, 1477
Quiescent Flame Spread Over Thick Fuels in Microgravity. J. West, L. Tang, R. A. Altenkirch, S. Bhattacharjee, K. Sacksteder, M. A. Delichatsios, 1335
The Transport of Carbon Monoxide from a Burning Compartment Located on the Side of a Hallway. B. Y. Lattimer, U. Vandsburger, R. J. Roby, 1541

03 Flame Spread

Study of the Thermocapillary Layer Preceding Slow Steadily-Spreading Flames Over Liquid Fuels. P. L. Garcia-Ybarra, J. L. Castillo, J. C. Antoranz, V. Sankovitch, J. San Martin, 1469
Opposed-Flow Flame Spread Across *n*-Propanol Pools. D. N. Schiller, W. A. Sirignano, 1319
Detailed Experiments of Flame Spread Across Deep Butanol Pools. H. D. Ross, F. J. Miller, 1327
Creeping Flame Spread: Energy Balance and Ap-

plication to Practical Materials. M. A. Delichatsios, 1495
Model Calculation of Steady Upward Flame Spread Over a Thin Solid in Reduced Gravity. C.-B.Jiang, J. S. T'ien, H.-Y. Shih, 1353
Determination of the Spread Rate in Opposed-Flow Flame Spread Over Thick Solid Fuels in the Thermal Regime. S. Bhattacharjee, J. West, R. A. Altenkirch, 1477
The Dependence of the Flame Spread Rate Over Solid Fuel on Damkšhler Number and Heat Loss. S. Rybanin, 1487
Quiescent Flame Spread Over Thick Fuels in Microgravity. J. West, L. Tang, R. A. Altenkirch, S. Bhattacharjee, K. Sacksteder, M. A. Delichatsios, 1335
Effects of Slow Wind on Localized Radiative Ignition and Transition to Flame Spread in Microgravity. T. Kashiwagi, K. B. McGrattan, S. L. Olson, O. Fujita, M. Kikuchi, K. Ito, 1345
The Transport of Carbon Monoxide from a Burning Compartment Located on the Side of a Hallway. B. Y. Lattimer, U. Vandsburger, R. J. Roby, 1541

04 Safety

Suppression of a Baffle-Stabilized Spray Flame by Halogenated Agents. A. Hamins, C. Presser, L. Melton, 1413
Extinction Mechanisms of Near-Limit Premixed Flames and Extended Limits of Flammability. C. J. Sung, C. K. Law, 865
Ignition and Combustion of Bulk Titanium and Magnesium at Normal and Reduced Gravity. A. Abbud-Madrid, M. C. Branch, J. W. Daily, 1929
Global Properties of Gaseous Pool Fires. A. Hamins, K. Konishi, P. Borthwick, T. Kashiwagi, 1429
Opposed-Flow Flame Spread Across *n*-Propanol Pools. D. N. Schiller, W. A. Sirignano, 1319
Burning Regimes for the Finite-Duration Releases of Fuel Gases. G. Makhviladze, J. P. Roberts, S. Yakush, 1549
Controlling Mechanisms in the Transition from Smoldering to Flaming of Flexible Polyurethane Foam. S. D. Tse, A. C. Fernandez–Pello, K. Miyasaka, 1505
Creeping Flame Spread: Energy Balance and Application to Practical Materials. M. A. Delichatsios, 1495
Determination of the Spread Rate in Opposed-Flow Flame Spread Over Thick Solid Fuels in the Thermal Regime. S. Bhattacharjee, J. West, R. A. Altenkirch, 1477
Quiescent Flame Spread Over Thick Fuels in Microgravity. J. West, L. Tang, R. A. Altenkirch, S. Bhattacharjee, K. Sacksteder, M. A. Delichatsios, 1335
Effect of the Fuel Boiling Point on the Boilover Burning of Liquid Fuels Spilled on Water. J. P. Garo, J. P. Vantelon, A. C. Fernandez-Pello, 1461
Small-Scale Smoldering Combustion Experiments in Microgravity. D. P. Stocker, S. L. Olson, D. L. Urban, J. L. Torero, D. C. Walther, A. C. Fernandez-Pello, 1361

05 Smoldering

Controlling Mechanisms in the Transition from Smoldering to Flaming of Flexible Polyurethane Foam. S. D. Tse, A. C. Fernandez–Pello, K. Miyasaka, 1505
Small-Scale Smoldering Combustion Experiments in Microgravity. D. P. Stocker, S. L. Olson, D. L. Urban, J. L. Torero, D. C. Walther, A. C. Fernandez-Pello, 1361

06 Radiation

10 Flames

The Challenge of Turbulent Combustion. K. N. C. Bray, 1
Theroy and Modeling in Combustion Chemistry. J. A. Miller, 461
Using Direct Numerical Simulations to Understand Premixed Turbulent Combustion. T. Poinsot, 219
Solid Fuel Utilization: From Coal to Biomass. F. C. Lockwood, 3041
Anomalous Group Combustion of Premixed Clusters. H. H. Chiu, C. L. Lin, 1653
Experimental and Modeling Investigation of Aromatic and Polycyclic Aromatic Hydrocarbon Formation in a Premixed Ethylene Flame. M. J. Castaldi, N. M. Marinov, C. F. Melius, J. Huang, S. M. Senkan, W. J. Pitz, C. K. Westbrook, 693
Current State of Combustion Research in Microgravity. M. Kono, K. Ito, T. Niioka, T. Kadota, J. Sato, 1189
Suppression of a Baffle-Stabilized Spray Flame by Halogenated Agents. A. Hamins, C. Presser. L. Melton, 1413
Experimental Study of the Inhibition of Premixed and Diffusion Flames by Iron Pentacarbonyl. D. Reinelt, G.T. Linteris, 1421
Polydispersity and Reaction Zone Structure in Partially Premixed Spray Flames. J.B. Greenberg, N. Sarig, 1705
A Numerical Study of Large Amplitude Baroclinic Instabilities of Flames. J. Chomiak, G. Zhou, 883
Spatial and Temporal Dynamics of Flamelets in Turbulent Premixed Flames. C. Ghenaï, C. Chauveau, I. Gškalp, 331
Triple Flames and Partially Premixed Combustion in Autoignition of Non-Premixed Turbulent Mixtures. P. Domingo, L. Vervisch, 233
Probability Density Function Modeling of Premixed

Turbulent Opposed Jet Flames. W. P. Jones, Y. Prasetyo, 275
The Energy and Environmental Implications of Using Sewage Sludge as a Co-Fired Fuel Applied to Boilers. T. Abbas, P. Costen, G. De Soete, K. Glaser, S. Hassan, F. C. Lockwood, 2487
The Optical Band Gap Model in the Interpretation of the UV-Visible Absorption Spectra of Rich Premixed Flames. P. Minutolo, G. Gambi, A. D'Alessio, 951
Experimental Investigation of the Flame Structure and Extinction of Turbulent Counterflow Non-Premixed Flames. A. Kitajima, T. Ueda, A. Matsuo, M. Mizomoto, 137
Computational and Experimental Investigation of a Turbulent Non-Premixed Methane Flame. M. Nau, W. Neef, U. Maas, E. Gutheil, J. Warnatz, 83

01 Burning Velocity

Kinetic Modeling of the Oxidation of Large Aliphatic Hydrocarbons. M. Nehse, J. Warnatz, C. Chevalier, 773
Laminar Flame Speeds and Oxidation Kinetics of Benzene-Air and Toluene-Air Flames. S. G. Davis, H. Wang, K. Brezinsky, C. K. Law, 1025
Multistep Asymptotic Analyses of Flame Structures. K. Seshadri, 831
Experimental Study of the Inhibition of Premixed and Diffusion Flames by Iron Pentacarbonyl. D. Reinelt, G. T. Linteris, 1421
An Experimental Study on Particle-Cloud Flames in Microgravity Field. Y. Okuyama, Y. Ohtomo, K. Maruta, H. Kobayashi, T. Niioka, 1369
Laser Ignition and Flame Propagation of Pulverized Coal Dust Clouds. M. Taniguchi, H. Kobayashi, S. Azuhata, 3189
Combustion Intensity and Burning Rate Integral of Premixed Flames. F. C. Gouldin, 381
Burning Velocity of Turbulent Premixed Flames in a High-Pressure Environment. H. Kobayashi, T. Tamura, K. Maruta, T. Niioka, F. A. Williams, 389
A Test of an Engineering Model of Premixed Turbulent Combustion. V. Karpov, A. Lipatnikov, V. Zimont, 249
Mixing and Chemical Reaction in an Idealized Swirl Chamber. O. M. Knio, A. S. Worlikar, H. N. Najm, 203
Burning Velocities in Fuel-Rich Aluminum Dust Clouds. S. Goroshin, I. Fomenko, J. H. S. Lee, 1961
Three-Dimensional Spatial Flamelet Statistics for Premixed Turbulent Combustion Modeling. S. S. Shy, R. H. Jang, W. K. I, K. L. Gee, 283
Model Simulations of Freely Propagating Turbulent Premixed Flames. T. Smith, S. Menon, 299
Negative Flame Speed in an Unsteady 2-D Premixed Flame: A Computational Study. I. R. Gran, T. Echekki, J. H. Chen, 323

02 Cool

Comparison of Oxidation and Autoignition of the Two Primary Reference Fuels by Rapid Compression. R. Minetti, M. Carlier, M. Ribaucour, E. Therssen, L. R. Sochet, 747

03 Deflagration to Detonation Transition (DDT)

Time-Resolved Investigation of Hot Spots in the End Gas of an S. I. Engine by Means of 2-D Double-Pulse LIF of Formaldehyde. B. Bäuerle, J. Warnatz, F. Behrendt, 2619
Critical Conditions for Detonation Propagation Through Mixture with Decreasing Reaction Rate. S. I. Kryuchkov, S. B. Dorofeev, A. A. Efimenko, 2965
The Influence of Initial Temperature on Flame Acceleration and Deflagration-to-Detonation Transition. G. Ciccarelli, J. L. Boccio, T. Ginsberg, H. Tagawa, 2973
Ignition and Detonation in N_2O-CO-H_2-He Mixtures. A. Y. Starikovskii, 2999
Oblique Detonation Stabilized on a Hypervelocity Projectile. M. J. Kaneshige, J. E. Shepherd, 3015
Deflagration-to-Detonation Transition in End Gases. C. K. Chan, W. A. Dewit, 2679

04 Diffusion

Anomalous Group Combustion of Premixed Clusters. H. H. Chiu, C. L. Lin, 1653
Modeling of Turbulent Spray Diffusion Flames Including Detailed Chemistry. C. Hollmann, E. Gutheil, 1731
Computational and Experimental Study of NO in an Axisymmetric Laminar Diffusion Flame. M. D. Smooke, A. Ern, M. A. Tanoff, B. A. Valdati, R. K. Mohammed, D. F. Marran, M. B. Long, 2161
Instability of Diffusion Flames. A. Lingens, K. Neemann, J. Meyer, M. Schreiber, 1053
Heat Loss and Lewis Number Effects on the Onset of Oscillations in Diffusion Flames. S. Cheatham, M. Matalon, 1063
Effects of Multi-Dimensionality on a Diffusion Flame. M. Nishioka, Y. Takemoto, H. Yamashita, T. Takeno, 1071
Quantitative Two-Photon Laser-Induced Fluorescence Imaging of CO in Flickering CH_4/Air Diffusion Flames. D. A. Everest, C. R. Shaddix, K. C. Smyth, 1161
Thin-Filament Pyrometry in Flickering Laminar Diffusion Flames. W. M. Pitts, 1171
Characterization of Spherical Hydrocarbon Fuel Flames: Laser Diagnosis of the Chemical Struc-

ture Through the OH Radical. J. König, C. Eigenbrod, M. Tanabe, H. Renken, H. J. Rath, 1235
Droplet Combustion Experiments in Spacelab. D. L. Dietrich, J. B. Haggard, Jr., F. L. Dryer, V. Nayagam, B. D. Shaw, F. A. Williams, 1201
Structure of a Non-Premixed Flame Interacting with Counterrotating Vortices. D. Thévenin, J. C. Rolon, P. H. Renard, D. W. Kendrick, D. Veynate, S. Candel, 1079
Thermal Diffusion Effects and Vortex-Flame Interactions in Hydrogen Jet Diffusion Flames. R. D. Hancock, F. R. Schauer, R. P. Lucht, V. R. Katta, K. Y. Hsu
Microgravity Combustion of Methanol and Methanol/Water Droplets: Drop Tower Experiments and Model Predictions. A. J. Marchese, F. L. Dryer, R. Colantonio, V. Nayagam, 1209
An Unsteady-State Analysis of Porous Sphere and Droplet Fuel Combustion Under Microgravity Conditions. M. K. King, 1227
The Effect of CF_3I Compared to CF_3Br on OH· and Soot Concentrations in Co-Flowing Propane/Air Diffusion Flames. K. C. Smyth, D. A. Everest, 1385
Chemical Effects of CF_3H in Extinguishing Counterflow CO/Air/H_2 Diffusion Flames. G. S. Fallon, H. K. Chelliah, G. T. Linteris, 1395
Extinction of Non-Premixed Methane- and Propane-Air Counterflow Flames Inhibited with CF_4, CF_3H and CF_3Br. P. Papas, J. W. Fleming, R. S. Sheinson, 1405
The Effects of Flame Structure on Extinction of CH_4–O_2–N_2 Diffusion Flames. J. Du, R. L. Axelbaum, 1137
Shock Wave Interaction with a Fast Convection-Reaction Driven Flame. R. G. Johnson, M. R. Booty, M. Short, A. C. McIntosh, J. Brindley, 891
Ignition Delay Associated with a Strained Fuel Strip. T. J. Gerk, A. R. Karagozian, 1095
Studies on Strained Non-Premixed Flames Affected by Flame Curvature and Preferential Diffusion. T. Takagi, Y. Yoshikawa, K. Yoshida, M. Komiyama, S. Kinoshita, 1103
Response of Counterflow Premixed and Diffusion Flames to Strain Rate Variations at Reduced and Elevated Pressures. C. J. Sun, C. J. Sung, D. L. Zhu, C. K Law, 1111
Solid Propellant Diffusion Flame Structure. T. P. Parr, D. M. Hanson-Parr, 1981
Gas-Phase Combustion Synthesis of Aluminum Nitride Powder. R. L. Axelbaum, C. R. Lottes, J. I. Huertas, L. J. Rosen, 1891
Numerical Simulation of a Counterflow Diffusion Flame in Supersonic Airflow. K. Takita, T. Niioka, 2877
The Influence of Initial Temperature on Flame Acceleration and Deflagration-to-Detonation Transition. G. Ciccarelli, J. L. Boccio, T. Ginsberg, H. Tagawa, 2973
Shock-Wave-Enhancement of the Mixing and the Stability Limits of Supersonic Hydrogen-Air Jet Flames. H. Huh, J. F. Driscoll, 2933
Ignition and Combustion of Bulk Titanium and Magnesium at Normal and Reduced Gravity. A. Abbud-Madrid, M. C. Branch, J. W. Daily, 1929
Combustion Characteristics of Mg-CO_2 Counterflow Diffusion Flames. A. Fukuchi, M. Kawashima, S. Yuasa, 1945
Influence of Gravity and Pressure on Pool Fire-Type Diffusion Flames. J.-M. Most, P. Mandin, J. Chen, P. Joulain, D. Durox, A. C. Fernandez–Pello, 1311
Experiments and Numerical Simulation on Soot Formation in Opposed-Jet Ethylene Diffusion Flames. H. Wang, D. X. Du, C. J. Sung, C. K. Law, 2359
Determination of the Spread Rate in Opposed-Flow Flame Spread Over Thick Solid Fuels in the Thermal Regime. S. Bhattacharjee, J. West, R. A. Altenkirch, 1477
The Dependence of the Flame Spread Rate Over Solid Fuel on Damkšhler Number and Heat Loss. S. Rybanin, 1487
Quiescent Flame Spread Over Thick Fuels in Microgravity. J. West, L. Tang, R. A. Altenkirch, S. Bhattacharjee, K. Sacksteder, M. A. Delichatsios, 1335
Triple Flames and Partially Premixed Combustion in Autoignition of Non-Premixed Turbulent Mixtures. P. Domingo, L. Vervisch, 233
Conditioned Dissipation and Average Consumption Maps in a Turbulent Nonpremixed Flame Using Planar Laser-Induced Fluorescence of O_2. S. Guerre, R. Bazile, D. Stepowski, 105
Direct Numerical Simulation Analysis of Flame Surface Density Equation in Non-Premixed Turbulent Combustion. E. Van Kalmthout, D. Veynante, S. Candel, 35
Subgrid Mixing and Molecular Transport Modeling in a Reacting Shear Layer. S. Menon, W. H. Calhoon, Jr., 59
An Integrated PDF/Neural Network Approach for Simulating Turbulent Reacting Systems. F. C. Christo, A. R. Masri, E. M. Nebot, S. B. Pope, 43
A Mixing Model to Improve the PDF Simulation of Turbulent Diffusion Flames. A. R. Masri, S. Subramaniam, S. B. Pope, 49
Extinction of Counterflow Diffusion Flames Under Velocity Oscillations. J. S. Kistler, C. J. Sung, T. G. Kreutz, C. K. Law, M. Nishioka, 113
Characteristics of Lifted Flames in Nonpremixed Turbulent Confined Jets. M. S. Cha, S. H. Chung, 121
A Numerical Study on Flame Stability at the Transition Point of Jet Diffusion Flames. H. Yamashita, M. Shimada, T. Takeno, 27
Images of the Strained Flammable Layer Used to Study the Liftoff of Turbulent Jet Flames. D. A. Everest, D. A. Feikema, J. F. Driscoll, 129

Flamelet and PDF Modeling of CO and NO_x Emissions from a Turbulent, Methane Hydrogen Jet Nonpremixed Flame. J.-Y. Chen, W.-C. Chang, 2207
Analysis of Turbulence-Chemistry Interaction with Respect to NO Formation in Turbulent, Nonpremixed Hydrogen-Air Flames. M. Schlatter, J. C. Ferreira, M. Flury, J. Gass, 2215
Measurements of NO in Turbulent Non-Premixed Flames Stabilized on a Bluff Body. B. B. Dally, A. R. Masri, R. S. Barlow, G. J. Fiechtner, D. F. Fletcher, 2191
Simulation of a Bluff-Body-Stabilized Diffusion Flame Using Second-Moment Closure and Monte Carlo Methods. H. A. Wouters, P. A. Nooren, T. W. J. Peeters, D. Roekaerts, 177
Exothermicity and Three-Dimensional Effects in Unsteady Propane Square Jets. F. F. Grinstein, K. Kailasanath, 91
Turbulent Length Scales in a Swirling Flame. G. Früchtel, E. P. Hassel, J. Janicka, 195
Mixing and Chemical Reaction in an Idealized Swirl Chamber. O. M. Knio, A. S. Worlikar, H. N. Najm, 203
Reduced *n*-Heptane Mechanism for Non-Premixed Combustion with Emphasis on Pollutant-Relevant Intermediate Species. M. Bollig, H. Pitsch, J. C. Hewson, K. Seshadri, 729
Edge-Flame-Holding. J. Buckmaster, R. Weber, 1143
Hydroxyl Radical Chemiluminescence Imaging and the Structure of Microgravity Droplet Flames. A. J. Marchese, F. L. Dryer, V. Nayagam, R. Colantonio, 1219
Calculations of Turbulent Flames Using a PSR Microstructural Library. I. Z. Hu, S. M. Correa, 307
Experimental Investigation of the Flame Structure and Extinction of Turbulent Counterflow Non-Premixed Flames. A. Kitajima, T. Ueda, A. Matsuo, M. Mizomoto, 137
Impact of Mixing Model on Predicted NO Formation in a Nonpremixed, Partially Stirred Reactor. W.-C. Chang, J.-Y. Chen, 2223
Vortex-Flame Interactions and Extinction in Turbulent Jet Diffusion Flames. F. Takahashi, W. J. Schmoll, D. D. Trump, L. P. Goss, 145
Study of Swirling Recirculating Hydrogen Diffusion Flame Using UV Raman Spectroscopy. M. M. Tacke, T. C. Cheng, E. P. Hassel, J. Janicka, 169
Flamelet Behavior in a Turbulent Diffusion Flame Measured by Rayleigh Scattering Image Velocimetry. M. Komiyama, A. Miyafuji, T. Takagi, 339
Measurements of the Detailed Flame Structure in Turbulent H_2–Ar Jet Diffusion Flames with Line-Raman/Rayleigh/LIPF-OH Technique. Y.-C. Chen, M. S. Mansour, 97
Computational and Experimental Investigation of a Turbulent Non-Premixed Methane Flame. M. Nau, W. Neef, U. Maas, E. Gutheil, J. Warnatz, 83
Reduced Mechanisms for NO_x Emissions from Hydrocarbon Diffusion Flames. J. C. Hewson, M. Bolling, 2171
The Formation of SiO_2 from Hexamethyldisiloxane Combustion in Counterflow Methane-Air Flames. H. K. Chagger, D. Hainsworth, P. M. Patterson, M. Pourkashanian, A. Williams, 1859

05 Extinction

Heat Loss and Lewis Number Effects on the Onset of Oscillations in Diffusion Flames. S. Cheatham, M. Matalon, 1063
Droplet Combustion Experiments in Spacelab. D. L. Dietrich, J. B. Haggard, Jr., F. L. Dryer, V. Nayagam, B. D. Shaw, F. A. Williams, 1201
Experimental Study on Methane-Air Premixed Flame Extinction at Small Stretch Rates in Microgravity. K. Maruta, M. Yoshlda, Y. Ju, T. Niioka, 1283
Suppression of a Baffle-Stabilized Spray Flame by Halogenated Agents. A. Hamins, C. Presser, L. Melton, 1413
Chemical Effects of CF_3H in Extinguishing Counterflow CO/Air/H_2 Diffusion Flames. G. S. Fallon, H. K. Chelliah, G. T. Linteris, 1395
Extinction of Non-Premixed Methane- and Propane-Air Counterflow Flames Inhibited with CF_4, CF_3H and CF_3Br. P. Papas, J. W. Fleming, R. S. Sheinson, 1405
The Mechanism of Mutual Annihilation of Stoichiometric Premixed Methane-Air Flames. T. Echekki, J. H. Chen, I. Gran, 855
Extinction Mechanisms of Near-Limit Premixed Flames and Extended Limits of Flammability. C. J. Sung, C. K. Law, 865
The Effects of Flame Structure on Extinction of CH_4–O_2–N_2 Diffusion Flames. J. Du, R. L. Axelbaum, 1137
Experimental Study of the Inhibition of Premixed and Diffusion Flames by Iron Pentacarbonyl. D. Reinelt, G. T. Linteris, 1421
Shock Wave Interaction with a Fast Convection-Reaction Driven Flame. R. G. Johnson, M. R. Booty, M. Short, A. C. McIntosh, J. Brindley, 891
Studies on Strained Non-Premixed Flames Affected by Flame Curvature and Preferential Diffusion. T. Takagi, Y. Yoshikawa, K. Yoshida, M. Komiyama, S. Kinoshita, 1103
Numerical Simulation of a Counterflow Diffusion Flame in Supersonic Airflow. K. Takita, T. Niioka, 2877
Quiescent Flame Spread Over Thick Fuels in Microgravity. J. West, L. Tang, R. A. Altenkirch, S. Bhattacharjee, K. Sacksteder, M. A. Delichatsios, 1335
Effects of Unsteady Stretch on the Strength of a

Freely-Propagating Flame Wrinkled by a Vortex. C. J. Mueller, J. F. Driscoll, D. L. Reuss, M. C. Drake, 347
Extinction of Turbulent Premixed Flames by Small-Scale Turbulence at Kolmogorov-Microscale. A. Yoshida, H. Kakinuma, Y. Kotani, 397
Extinction of Counterflow Diffusion Flames Under Velocity Oscillations. J. S. Kistler, C. J. Sung, T. G. Kreutz, C. K. Law, M. Nishioka, 113
Characteristics of Lifted Flames in Nonpremixed Turbulent Confined Jets. M. S. Cha, S. H. Chung, 121
A Numerical Study on Flame Stability at the Transition Point of Jet Diffusion Flames. H. Yamashita, M. Shimada, T. Takeno, 27
Images of the Strained Flammable Layer Used to Study the Liftoff of Turbulent Jet Flames. D. A. Everest, D. A. Feikema, J. F. Driscoll, 129
Influence of Gravity on the Propagation of Initially Spherical Flames. J. Daou, B. Rogg, 1275
Experimental Investigation of the Flame Structure and Extinction of Turbulent Counterflow Non-Premixed Flames. A. Kitajima, T. Ueda, A. Matsuo, M. Mizomoto, 137
Vortex-Flame Interactions and Extinction in Turbulent Jet Diffusion Flames. F. Takahashi, W. J. Schmoll, D. D. Trump, L. P. Goss, 145
Flamelet Behavior in a Turbulent Diffusion Flame Measured by Rayleigh Scattering Image Velocimetry. M. Komiyama, A. Miyafuji, T. Takagi, 339

06 Holding

Effects of External Acoustic Excitation on Enhanced Transport in a Resonant Incinerator. G. Pont, J. W. Willis, A. R. Karagozian, O. I. Smith, 2463
Flame Lift-off in Diesel Sprays. A. Karlsson, J. Chomiak, 2557
Edge-Flame-Holding. J. Buckmaster, R. Weber, 1143
Flame Stabilization in Cryogenic Propellant Combustion. G. Herding, R. Snyder, P. Scouflaire, C. Rolon, S. Candel, 2041
Numerical Simulation of Flame-Stabilization and Combustion Promotion by Plasma Jets in Supersonic Air Streams. R. Kato, I. Kimura, 2941

07 Inhibition

The Effect of CF_3I Compared to CF_3Br on OH· and Soot Concentrations in Co-Flowing Propane/Air Diffusion Flames. K. C. Smyth, D. A. Everest, 1385
Extinction of Non-Premixed Methane- and Propane-Air Counterflow Flames Inhibited with CF_4, CF_3H and CF_3Br. P. Papas, J. W. Fleming, R. S. Sheinson, 1405
Experimental Study of the Inhibition of Premixed and Diffusion Flames by Iron Pentacarbonyl. D. Reinelt, G. T. Linteris, 1421

08 Laminar

Numerical and Asymptotic Studies of the Structure of Premixed *iso*-Octane Flames. H. Pitsch, N. Peters, K. Seshadri, 763
Laminar Flame Speeds and Oxidation Kinetics of Benzene-Air and Toluene-Air Flames. S. G. Davis, H. Wang, K. Brezinsky, C. K. Law, 1025
Experimental and Modeling Investigation of Aromatic and Polycyclic Aromatic Hydrocarbon Formation in a Premixed Ethylene Flame. M. J. Castaldi, N. M. Marinov, C. F. Melius, J. Huang, S. M. Senkan, W. J. Pitz, C. K. Westbrook, 693
Benzene Formation Chemistry in Premixed 1,3-Butadiene Flames. R. P. Lindstedt, G. Skevis, 703
Computational and Experimental Study of NO in an Axisymmetric Laminar Diffusion Flame. M. D. Smooke, A. Ern, M. A. Tanoff, B. A. Valdati, R. K. Mohammed, D. F. Marran, M. B. Long, 2161
Behavior of Key Reactions on NO Formation in Methane-Air Flames. M. Nishioka, Y. Kondoh, T. Takeno, 2139
Gravitational Effects on Sooting Diffusion Flames. C. R. Kaplan, E. S. Oran, K. Kailasanath, H. D. Ross, 1301
Effects of Multi-Dimensionality on a Diffusion Flame. M. Nishioka, Y. Takemoto, H. Yamashita, T. Takeno, 1071
Thin-Filament Pyrometry in Flickering Laminar Diffusion Flames. W. M. Pitts, 1171
Unsteady Extinction Mechanisms of Diffusion Flames. F. Takahashi, V. R. Katta, 1151
Acetylene and Ethylene Mole Fractions in Methane/Air Partially Premixed Flames. L.-K. Tseng, J. P. Gore, I. K. Puri, T. Takeno, 993
A LIF and CARS Study of the Effects of Upstream Heat Loss on NO Formation from Laminar Premixed Burner-Stabilized Natural-Gas/Air Flames. A. V. Mokhov, H. B. Levinsky, 2147
CH_3 Detection in Flames Using Photodissociation-Induced Fluorescence. P. Desgroux, L. Gasnot, B. Crunelle, J. F. Pauwels, 967
Degenerate Four-Wave Mixing Measurements of Methyl Radical Distributions in Hydrocarbon Flames: Comparison with Model Predictions. R. L. Farrow, M. N. Bui-Pham, V. Sick, 975
Droplet Combustion Experiments in Spacelab. D. L. Dietrich, J. B. Haggard, Jr., F. L. Dryer, V. Nayagam, B. D. Shaw, F. A. Williams, 1201
The Phenomena of Flame Propagation in a Rotating Tube. Y. Sakai, S. Ishizuka, 847
Thermal Diffusion Effects and Vortex-Flame Interactions in Hydrogen Jet Diffusion Flames. R. D. Hancock, F. R. Schauer, R. P. Lucht, V. R. Katta, K. Y. Hsu, 1087
Effects of Pressure Diffusion on the Characteristics

of Tubular Flames. K. Yamamoto, T. Hirano, S. Ishizuka, 1129
Experimental Study on Methane-Air Premixed Flame Extinction at Small Stretch Rates in Microgravity. K. Maruta, M. Yoshida, Y. Ju, T. Niioka, 1283
Microgravity Combustion of Methanol and Methanol/Water Droplets: Drop Tower Experiments and Model Predictions. A. J. Marchese, F. L. Dryer, R. Colantonio, V. Nayagam, 1209
An Unsteady-State Analysis of Porous Sphere and Droplet Fuel Combustion Under Microgravity Conditions. M. K. King, 1227
Extinction of Non-Premixed Methane- and Propane-Air Counterflow Flames Inhibited with CF_4, CF_3H and CF_3Br. P. Papas, J. W. Fleming, R. S. Sheinson, 1405
Multistep Asymptotic Analyses of Flame Structures. K. Seshadri, 831
Effect of Halogenated Flame Inhibitors on C_1-C_2 Organic Flames. T. Noto, V. Babushok, D. R. Burgess, Jr., A. Hamins, W. Tsang, A. Miziolek, 1377
The Mechanism of Mutual Annihilation of Stoichiometric Premixed Methane-Air Flames. T. Echekki, J. H. Chen, I. Gran, 855
Extinction Mechanisms of Near-Limit Premixed Flames and Extended Limits of Flammability. C. J. Sung, C. K. Law, 865
The Effects of Flame Structure on Extinction of CH_4–O_2–N_2 Diffusion Flames. J. Du, R. L. Axelbaum, 1137
Shock Wave Interaction with a Fast Convection-Reaction Driven Flame. R. G. Johnson, M. R. Booty, M. Short, A. C. McIntosh, J. Brindley, 891
Hydrogen–Oxygen Flame Doped with Trimethyl Phosphate, Its Structure, and Trimethyl Phosphate Destruction Chemistry. O. Korobeinichev, V. Shvartsberg, A. Chernov, V. Mokrushin, 1035
Ignition Delay Associated with a Strained Fuel Strip. T. J. Gerk, A. R. Karagozian, 1095
The Sensitive Structure of Partially Premixed Methane-Air vs. Air Counterflow Flames. M. A. Tanoff, M. D. Smooke, R. J. Osborne, T. M. Brown, R. W. Pitz, 1121
Studies on Strained Non-Premixed Flames Affected by Flame Curvature and Preferential Diffusion. T. Takagi, Y. Yoshikawa, K. Yoshida, M. Komiyama, S. Kinoshita, 1103
Response of Counterflow Premixed and Diffusion Flames to Strain Rate Variations at Reduced and Elevated Pressures. C. J. Sun, C. J. Sung, D. L. Zhu, C. K. Law, 1111
Experimental and Numerical Studies of Two-Stage Methanol Flames. S. C. Li, F. A. Williams, 1017
Combustion of Porous Energetic Materials in the Merged-Flame Regime. S. B. Margolis, F. A. Williams, A. M. Telengator, 1969
Solid Propellant Diffusion Flame Structure. T. P. Parr, D. M. Hanson-Parr, 1981
A Three-Phase Model of HMX Combustion. J. E. Davidson, M. W. Beckstead, 1989
Simplified Chemical-Kinetic Mechanisms for Characterizing the Structure of the Dark Zones of Double Base and Nitramine Propellants. N. Ilincic, W. R. Anderson, K. Seshadri, N. E. Meagher, 1997
A Numerical Study of Large Amplitude Baroclinic Instabilities of Flames. J. Chomiak, G. Zhou, 883
A New Time-Dependent, Three-Dimensional Flame Model for Laminar Flames. G. Patnaik, K. Kailasanath, R. S. Sinkovits, 899
Numerical Study of Premixed Laminar Flame Propagation in a Closed Tube with a Full Navier-Stokes Approach. F. S. Marra, G. Continillo, 907
Diamond Thin Film Deposition in Low-Pressure Premixed Flames. D. G. Goodwin, N. G. Glumac, H. S. Shin, 1817
Combustion Characteristics of Mg-CO_2 Counterflow Diffusion Flames. A. Fukuchi, M. Kawashima, S. Yuasa, 1945
Opposed-Flow Flame Spread Across *n*-Propanol Pools. D. N. Schiller, W. A. Sirignano, 1319
PAH and Aromers: Precursors of Fullerenes and Soot. M. Bachmann, W. Wiese, K.-H. Homann, 2259
Influence of Hydrogen Addition to Fuel on Temperature Field and Soot Formation in Diffusion Flames. Ö. L. Gülder, D. R. Snelling, R. A. Sawchuk, 2351
Flamelet Modeling of Soot Formation in Laminar Ethyne/Air-Diffusion Flames. M. Balthasar, A. Heyl, F. Mau§, F. Schmitt, H. Bockhorn, 2369
The Time Evolution of a Vortex-Flame Interaction Observed via Planar Imaging of CH and OH. Q.-V. Nguyen, P. H. Paul, 357
Combustion Intensity and Burning Rate Integral of Premixed Flames. F. C. Gouldin, 381
Two-Dimensional Mathematical Modeling of Laminar, Premixed, Methane-Air Combustion on an Experimental Slot Burner. D. Bradley, P. H. Gaskell, K. C. Kwan, M. J. Scott, 915
Tunable Diode Laser Absorption Measurements of Carbon Monoxide and Temperature in a Time-Varying, Methane/Air, Non-Premixed Flame. R. R. Skaggs, J. H. Miller, 1181
Initiation of Laminar Flames in Near-Limit $H_2/O_2/H_2O$ Mixtures. A. Y. Kusharin, O. E. Popov, G. L. Agafonov, 985
Hydroxyl Radical Chemiluminescence Imaging and the Structure of Microgravity Droplet Flames. A. J. Marchese, F. L. Dryer, V. Nayagam, R. Colantonio, 1219
Influence of Gravity on the Propagation of Initially Spherical Flames. J. Daou, B. Rogg, 1275
On the Use of Light Sheet Methods in the Presence of Refraction by Flames. F. Weinberg, 939
Polycyclic Aromatic Hydrocarbon and Soot Forma-

tion in Premixed Flames of CH_3Cl/CH_4 and CH_4. J. Huang, S. M. Senkan, 2335
Quantitative Comparison of Detailed Numerical Computations and Experiments in Counterflow Spray Diffusion Flames. L. P. Gao, Y. D'Angelo, I. Silverman, A. Gomez, M. D. Smooke, 1739

09 Limits

Experimental Study on Methane-Air Premixed Flame Extinction at Small Stretch Rates in Microgravity. K. Maruta, M. Yoshida, Y. Ju, T. Niioka, 1283
Shock-Wave-Enhancement of the Mixing and the Stability Limits of Supersonic Hydrogen-Air Jet Flames. H. Huh, J. F. Driscoll, 2933
Laser Ignition and Flame Propagation of Pulverized Coal Dust Clouds. M. Taniguchi, H. Kobayashi, S. Azuhata, 3189
Propagation Limits of Dust/Air Flames Diluted by Additions of Inert Solid Particles. R. Blouquin, G. Joulin, 1565
Initiation of Laminar Flames in Near-Limit $H_2/O_2/H_2O$ Mixtures. A. Y. Kusharin, O. E. Popov, G. L. Agafonov, 985
Analytical Study on Flame Stabilization in Reciprocating Combustion in Porous Media with High Thermal Conductivity. J. G. Hoffmann, R. Echigo, S. Tada, H. Yoshida, 2709

10 Premixed

Use of an Optical Probe for Time-Resolved *in Situ* Measurement of Local Air-to-Fuel Ratio and Extent of Fuel Mixing with Applications to Low NO_x Emissions in Premixed Gas Turbines. R. K. Mongia, E. Tomita, F. K. Hsu, L. Talbot, R. W. Dibble, 2749
Anomalous Group Combustion of Premixed Clusters. H. H. Chiu, C. L. Lin, 1653
Destruction of Benzene in High-Temperature Flames: Chemistry of Benzene and Phenol. R. A. Shandross, J. P. Longwell, J. B. Howard, 711
Numerical and Asymptotic Studies of the Structure of Premixed *iso*-Octane Flames. H. Pitsch, N. Peters, K. Seshadri, 763
Laminar Flame Speeds and Oxidation Kinetics of Benzene-Air and Toluene-Air Flames. S. G. Davis, H. Wang, K. Brezinsky, C. K. Law, 1025
Experimental and Modeling Investigation of Aromatic and Polycyclic Aromatic Hydrocarbon Formation in a Premixed Ethylene Flame. M. J. Castaldi, N. M. Marinov, C. F. Melius, J. Huang, S. M. Senkan, W. J. Pitz, C. K. Westbrook, 693
Degenerate Four-Wave Mixing Measurements of Methyl Radical Distributions in Hydrocarbon Flames: Comparison with Model Predictions. R. L. Farrow, M. N. Bui-Pham, V. Sick, 975
Molecular Beam Mass Spectrometric and Modeling Studies of Neat and NH_3-Doped Low-Pressure $H_2/N_2O/Ar$ Flames: Formation and Consumption of NO. R. C. Sausa, G. Singh, G. W. Lemire, W. R. Anderson, 1043
The Phenomena of Flame Propagation in a Rotating Tube. Y. Sakai, S. Ishizuka, 847
Effects of Pressure Diffusion on the Characteristics of Tubular Flames. K. Yamamoto, T. Hirano, S. Ishizuka, 1129
Experimental Study on Methane-Air Premixed Flame Extinction at Small Stretch Rates in Microgravity. K. Maruta, M. Yoshida, Y. Ju, T. Niioka, 1283
The Mechanism of Mutual Annihilation of Stoichiometric Premixed Methane-Air Flames. T. Echekki, J. H. Chen, I. Gran, 855
Extinction Mechanisms of Near-Limit Premixed Flames and Extended Limits of Flammability. C. J. Sung, C. K. Law, 865
Hydrogen–Oxygen Flame Doped with Trimethyl Phosphate, Its Structure, and Trimethyl Phosphate Destruction Chemistry. O. Korobeinichev, V. Shvartsberg, A. Chernov, V. Mokrushin, 1035
Response of Counterflow Premixed and Diffusion Flames to Strain Rate Variations at Reduced and Elevated Pressures. C. J. Sun, C. J. Sung, D. L. Zhu, C. K Law, 1111
A Numerical Study of Large Amplitude Baroclinic Instabilities of Flames. J. Chomiak, G. Zhou, 883
A New Time-Dependent, Three-Dimensional Flame Model for Laminar Flames. G. Patnaik, K. Kailasanath, R. S. Sinkovits, 899
Numerical Study of Premixed Laminar Flame Propagation in a Closed Tube with a Full Navier-Stokes Approach. F. S. Marra, G. Continillo, 907
Homogeneous Ignition of Hydrogen-Air Mixtures Over Platinum. P.-A. Bui, D. G. Vlachos, P. R. Westmoreland, 1763
Effects of External Acoustic Excitation on Enhanced Transport in a Resonant Incinerator. G. Pont, J. W. Willis, A. R. Karagozian, O. I. Smith, 2463
Triple Flames and Partially Premixed Combustion in Autoignition of Non-Premixed Turbulent Mixtures. P. Domingo, L. Vervisch, 233
Large Eddy Simulation of Unsteady Combustion. S. I. Mšller, E. Lundgren, C. Fureby, 241
Effects of Unsteady Stretch on the Strength of a Freely-Propagating Flame Wrinkled by a Vortex. C. J. Mueller, J. F. Driscoll, D. L. Reuss, M. C. Drake, 347
The Time Evolution of a Vortex-Flame Interaction Observed via Planar Imaging of CH and OH. Q.-V. Nguyen, P. H. Paul, 357
Flame Surface Density and Burning Rate in Premixed Turbulent Flames. I. G. Shepherd, 373
Combustion Intensity and Burning Rate Integral of Premixed Flames. F. C. Gouldin, 381
Burning Velocity of Turbulent Premixed Flames in

a High-Pressure Environment. H. Kobayashi, T. Tamura, K. Maruta, T. Niioka, F. A. Williams, 389
Study of Premixed Turbulent Combustion Including Landau-Darrieus Instability Effects. R. N. Paul, K. N. C. Bray, 259
Extinction of Turbulent Premixed Flames by Small-Scale Turbulence at Kolmogorov-Microscale. A. Yoshida, H. Kakinuma, Y. Kotani, 397
Probability Density Function Modeling of Premixed Turbulent Opposed Jet Flames. W. P. Jones, Y. Prasetyo, 275
Computation of Premixed Turbulent Combustion Using the Probability Density Function Approach. A. Sadat Sakak, M. Schreiber, 267
Experimental Analysis of Flame Surface Density Models for Premixed Turbulent Combustion. D. Veynante, J. Piana, J. M. Duclos, C. Martel, 413
Experimental and Numerical Investigation of the Structure of Flames Under Engine Conditions. H. Wassenberg, G. Adomeit, 421
Surface Density Measurements of Turbulent Premixed Flames in a Spark-Ignition Engine and a Bunsen-Type Burner Using Planar Laser-Induced Fluorescence. B. M. Deschamps, G. J. Smallwood, J. Prieur, D. R. Snelling, Ö. L. Gülder, 427
Measurement of the Instantaneous Detailed Flame Structure in Turbulent Premixed Combustion. A. Buschmann, F. Dinkelacker, T. Schäfer, M. Schäfer, J. Wolfrum, 437
Mixing and Chemical Reaction in an Idealized Swirl Chamber. O. M. Knio, A. S. Worlikar, H. N. Najm, 203
Experimental and Numerical Study of a Premixed Flame Stabilized by a Rectangular Section Cylinder. P. Bailly, D. Garréton, O. Simonin, P. Bruel, M. Champion, B. Deshaies, S. Duplantier, S. Sanquer, 923
Modeling of Premixed Gas Combustion in Porous Media Composed of Coarse-Sized Particles: 1-D Description with Discrete Solid Phase. O. S. Rabinovich, A. V. Fefelov, N. V. Pavlyukevich, 3383
Assessment of Soot Volume Fractions from Laser-Induced Incandescence by Comparison with Extinction Measurements in Laminar, Premixed, Flat Flames. J. Appel, M. Marquardt, H. Bockhorn, B. Jungfleisch, R. Suntz, 2387
The Optical Band Gap Model in the Interpretation of the UV-Visible Absorption Spectra of Rich Premixed Flames. P. Minutolo, G. Gambi, A. D'Alessio, 951
Polycyclic Aromatic Hydrocarbon and Soot Formation in Premixed Flames of CH_3Cl/CH_4 and CH_4. J. Huang, S. M. Senkan, 2335
Experimentally Measured Burning Rates of Premixed Turbulent Flames. E. Bourguignon, L. W. Kostiuk, Y. Michou, I. Gokalp, 447
Highly Turbulent Premixed Flames Stabilized in a Co-Axial Jet Flame Burner. T.-W. Lee, A. Mitrovic, 455
Three-Dimensional Spatial Flamelet Statistics for Premixed Turbulent Combustion Modeling. S. S. Shy, R. H. Jang, W. K. I, K. L. Gee, 283
Effect of Density Ratio on Flame Propagation Along a Vortex Tube. T. Hasegawa, K. Nishikado, 291
Model Simulations of Freely Propagating Turbulent Premixed Flames. T. Smith, S. Menon, 299
Calculations of Turbulent Flames Using a PSR Microstructural Library. I. Z. Hu, S. M. Correa, 307
Studies of Helmholtz Resonance in a Swirl Burner/Furnace System. D. Froud, A. Beale, T. O'Doherty, N. Syred, 3355
Spectral Model of Premixed Flame Propagation. L. R. Collins, M. Ulitsky, 315
Negative Flame Speed in an Unsteady 2-D Premixed Flame: A Computational Study. I. R. Gran, T. Echekki, J. H. Chen, 323
Analytical Study on Flame Stabilization in Reciprocating Combustion in Porous Media with High Thermal Conductivity. J. G. Hoffmann, R. Echigo, S. Tada, H. Yoshida, 2709
Quantitative CH Determinations in Low-Pressure Flames. J. Luque, G. P. Smith, D. R. Crosley, 959

11 Quenching

Heterogeneous/Homogeneous Reaction and Transport Coupling During Flame-Wall Interaction. P. Popp, M. Smooke, M. Baum, 2693
Heat Transfer Modeling During Knock and Flame Quenching in an Engine Chamber. O. A. Ezekoye, 2661
The Mechanism of Mutual Annihilation of Stoichiometric Premixed Methane-Air Flames. T. Echekki, J. H. Chen, I. Gran, 855
Model Calculation of Steady Upward Flame Spread Over a Thin Solid in Reduced Gravity. C.-B. Jiang, J. S. T'ien, H.-Y. Shih, 1353
The Time Evolution of a Vortex-Flame Interaction Observed via Planar Imaging of CH and OH. Q.-V. Nguyen, P. H. Paul, 357
An Experimental Study on Quenching Crevice Widths in the Combustion Chamber of a Spark-Ignition Engine. S. Ishizawa, 2605
Experimentally Measured Burning Rates of Premixed Turbulent Flames. E. Bourguignon, L. W. Kostiuk, Y. Michou, I. Gokalp, 447

12 Stretch

Markstein Lengths of CO/H_2/Air Flames, Using Expanding Spherical Flames. M. J. Brown, I. C. McLean, D. B. Smith, S. C. Taylor, 875
Structure of a Non-Premixed Flame Interacting with Counterrotating Vortices. D. Thévenin, J. C. Rolon, P. H. Renard, D. W. Kendrick, D. Veynante, S. Candel, 1079

Effects of Pressure Diffusion on the Characteristics of Tubular Flames. K. Yamamoto, T. Hirano, S. Ishizuka, 1129
Experimental Study on Methane-Air Premixed Flame Extinction at Small Stretch Rates in Microgravity. K. Maruta, M. Yoshida, Y. Ju, T. Niioka, 1283
Extinction Mechanisms of Near-Limit Premixed Flames and Extended Limits of Flammability. C. J. Sung, C. K. Law, 865
Shock Wave Interaction with a Fast Convection-Reaction Driven Flame. R. G. Johnson, M. R. Booty, M. Short, A. C. McIntosh, J. Brindley, 891
Ignition Delay Associated with a Strained Fuel Strip. T. J. Gerk, A. R. Karagozian, 1095
Studies on Strained Non-Premixed Flames Affected by Flame Curvature and Preferential Diffusion. T. Takagi, Y. Yoshikawa, K. Yoshida, M. Komiyama, S. Kinoshita, 1103
Response of Counterflow Premixed and Diffusion Flames to Strain Rate Variations at Reduced and Elevated Pressures. C. J. Sun, C. J. Sung, D. L. Zhu, C. K Law, 1111
Numerical Simulation of a Counterflow Diffusion Flame in Supersonic Airflow. K. Takita, T. Niioka, 2877
Effects of Unsteady Stretch on the Strength of a Freely-Propagating Flame Wrinkled by a Vortex. C. J. Mueller, J. F. Driscoll, D. L. Reuss, M. C. Drake, 347
A Test of an Engineering Model of Premixed Turbulent Combustion. V. Karpov, A. Lipatnikov, V. Zimont, 249
Extinction of Turbulent Premixed Flames by Small-Scale Turbulence at Kolmogorov-Microscale. A. Yoshida, H. Kakinuma, Y. Kotani, 397
Extinction of Counterflow Diffusion Flames Under Velocity Oscillations. J. S. Kistler, C. J. Sung, T. G. Kreutz, C. K. Law, M. Nishioka, 113
Two-Dimensional Mathematical Modeling of Laminar, Premixed, Methane-Air Combustion on an Experimental Slot Burner. D. Bradley, P. H. Gaskell, K. C. Kwan, M. J. Scott, 915
Influence of Gravity on the Propagation of Initially Spherical Flames. J. Daou, B. Rogg, 1275
Three-Dimensional Spatial Flamelet Statistics for Premixed Turbulent Combustion Modeling. S. S. Shy, R. H. Jang, W. K. I, K. L. Gee, 283
Negative Flame Speed in an Unsteady 2-D Premixed Flame: A Computational Study. I. R. Gran, T. Echekki, J. H. Chen, 323
Vortex-Flame Interactions and Extinction in Turbulent Jet Diffusion Flames. F. Takahashi, W. J. Schmoll, D. D. Trump, L. P. Goss, 145
Flamelet Behavior in a Turbulent Diffusion Flame Measured by Rayleigh Scattering Image Velocimetry. M. Komiyama, A. Miyafuji, T. Takagi, 339

13 Structure

Experimental Study of the Structure of Rich Ethane Flames. R. Ancia, J. Vandooren, P. J. Van Tiggelen, 1009
Instability of Diffusion Flames. A. Lingens, K. Neemann, J. Meyer, M. Schreiber, 1053
Effects of Multi-Dimensionality on a Diffusion Flame. M. Nishioka, Y. Takemoto, H. Yamashita, T. Takeno, 1071
Characterization of Spherical Hydrocarbon Fuel Flames: Laser Diagnosis of the Chemical Structure Through the OH Radical. J. König, C. Eigenbrod, M. Tanabe, H. Renken, H. J. Rath, 1235
Structure of a Non-Premixed Flame Interacting with Counterrotating Vortices. D. Thévenin, J. C. Rolon, P. H. Renard, D. W. Kendrick, D. Veynante, S. Candel, 1079
Thermal Diffusion Effects and Vortex-Flame Interactions in Hydrogen Jet Diffusion Flames. R. D. Hancock, F. R. Schauer, R. P. Lucht, V. R. Katta, K. Y. Hsu, 1087
Effects of Pressure Diffusion on the Characteristics of Tubular Flames. K. Yamamoto, T. Hirano, S. Ishizuka, 1129
Multistep Asymptotic Analyses of Flame Structures. K. Seshadri, 831
The Mechanism of Mutual Annihilation of Stoichiometric Premixed Methane-Air Flames. T. Echekki, J. H. Chen, I. Gran, 855
The Effects of Flame Structure on Extinction of CH_4–O_2–N_2 Diffusion Flames. J. Du, R. L. Axelbaum, 1137
Shock Wave Interaction with a Fast Convection-Reaction Driven Flame. R. G. Johnson, M. R. Booty, M. Short, A. C. McIntosh, J. Brindley, 891
Hydrogen–Oxygen Flame Doped with Trimethyl Phosphate, Its Structure, and Trimethyl Phosphate Destruction Chemistry. O. Korobeinichev, V. Shvartsberg, A. Chernov, V. Mokrushin, 1035
The Sensitive Structure of Partially Premixed Methane-Air vs. Air Counterflow Flames. M. A. Tanoff, M. D. Smooke, R. J. Osborne, T. M. Brown, R. W. Pitz, 1121
Studies on Strained Non-Premixed Flames Affected by Flame Curvature and Preferential Diffusion. T. Takagi, Y. Yoshikawa, K. Yoshida, M. Komiyama, S. Kinoshita, 1103
Solid Propellant Diffusion Flame Structure. T. P. Parr, D. M. Hanson-Parr, 1981
A Numerical Study of Large Amplitude Baroclinic Instabilities of Flames. J. Chomiak, G. Zhou, 883
A New Time-Dependent, Three-Dimensional Flame Model for Laminar Flames. G. Patnaik, K. Kailasanath, R. S. Sinkovits, 899
Shock-Wave-Enhancement of the Mixing and the Stability Limits of Supersonic Hydrogen-Air Jet Flames. H. Huh, J. F. Driscoll, 2933
Flame Structure Measurement of Single, Isolated

Aluminum Particles Burning in Air. P. Bucher, R. A. Yetter, F. L. Dryer, T. P. Parr, D. M. Hanson-Parr, E. P. Vicenzi, 1899
Compact Incinerator Afterburner Concept Based on Vortex Combustion. T. P. Parr, E. Gutmark, K. Wilson, D. M. Hanson-Parr, K. Yu, R. A. Smith, K. C. Schadow, 2471
Experimental and Numerical Investigation of the Structure of Flames Under Engine Conditions. H. Wassenberg, G. Adomeit, 421
Surface Density Measurements of Turbulent Premixed Flames in a Spark-Ignition Engine and a Bunsen-Type Burner Using Planar Laser-Induced Fluorescence. B. M. Deschamps, G. J. Smallwood, J. Prieur, D. R. Snelling, Ö. L. Gülder, 427
Measurement of the Instantaneous Detailed Flame Structure in Turbulent Premixed Combustion. A. Buschmann, F. Dinkelacker, T. Schäfer, M. Schäfer, J. Wolfrum, 437
Contribution to the Analysis of Temporal and Spatial Structures Near the Lift-Off Region of a Turbulent Hydrogen Diffusion Flame. A. Brockhinke, P. Andresen, K. Kohse-Häinghaus, 153
Two-Dimensional Mathematical Modeling of Laminar, Premixed, Methane-Air Combustion on an Experimental Slot Burner. D. Bradley, P. H. Gaskell, K. C. Kwan, M. J. Scott, 915
Three-Dimensional Spatial Flamelet Statistics for Premixed Turbulent Combustion Modeling. S. S. Shy, R. H. Jang, W. K. I, K. L. Gee, 283
Model Simulations of Freely Propagating Turbulent Premixed Flames. T. Smith, S. Menon, 299
Negative Flame Speed in an Unsteady 2-D Premixed Flame: A Computational Study. I. R. Gran, T. Echekki, J. H. Chen, 323
Vortex-Flame Interactions and Extinction in Turbulent Jet Diffusion Flames. F. Takahashi, W. J. Schmoll, D. D. Trump, L. P. Goss, 145
Flame Stabilization in Cryogenic Propellant Combustion. G. Herding, R. Snyder, P. Scouflaire, C. Rolon, S. Candel, 2041

14 Theory

Heat Loss and Lewis Number Effects on the Onset of Oscillations in Diffusion Flames. S. Cheatham, M. Matalon, 1063
Effects of Pressure Diffusion on the Characteristics of Tubular Flames. K. Yamamoto, T. Hirano, S. Ishizuka, 1129
A Numerical Study of Large Amplitude Baroclinic Instabilities of Flames. J. Chomiak, G. Zhou, 883
Homogeneous Ignition of Hydrogen-Air Mixtures Over Platinum. P.-A. Bui, D. G. Vlachos, P. R. Westmoreland, 1763
Opposed-Flow Flame Spread Across *n*-Propanol Pools. D. N. Schiller, W. A. Sirignano, 1319
Large Eddy Simulation of Unsteady Combustion. S. I. Möller, E. Lundgren, C. Fureby, 241
Probability Density Function Modeling of Premixed Turbulent Opposed Jet Flames. W. P. Jones, Y. Prasetyo, 275
Interaction of Turbulence and Radiation in Confined Diffusion Flames. J. W. Hartick, M. Tacke, G. Früchtel, E. P. Hassel, J. Janicka, 75
Propagation Limits of Dust/Air Flames Diluted by Additions of Inert Solid Particles. R. Blouquin, G. Joulin, 1565
Edge-Flame-Holding. J. Buckmaster, R. Weber, 1143
Modeling of Premixed Gas Combustion in Porous Media Composed of Coarse-Sized Particles: 1-D Description with Discrete Solid Phase. O. S. Rabinovich, A. V. Fefelov, N. V. Pavlyukevich, 3383
A Broader Definition of Symmetry Number and its Application to a Kinetic Model Describing Polyarene Growth. M. C. Masonjones, A. F. Sarofim, 823

15 Turbulent

The Challenge of Turbulent Combustion. K. N. C. Bray, 1
Using Direct Numerical Simulations to Understand Premixed Turbulent Combustion. T. Poinsot, 219
Modeling Turbulent Combustion and Pollutant Formation in Stratified Charge SI Engines. T. A. Baritaud, J. M. Duclos, A. Fusco, 2627
Use of an Optical Probe for Time-Resolved *in Situ* Measurement of Local Air-to-Fuel Ratio and Extent of Fuel Mixing with Applications to Low NO_x Emissions in Premixed Gas Turbines. R. K. Mongia, E. Tomita, F. K. Hsu, L. Talbot, R. W. Dibble, 2749
Effect of Temperature and Concentration Fluctuations on Radiative Heat Transfer in Turbulent Flames. W. Krebs, R. Koch, B. Ganz, L. Eigenmann, S. Wittig, 2763
Structure of an Acoustically Forced Turbulent Spray Flame. E. Haile, O. Delabroy, F. Lacas, D. Veynante, S. Candel, 1663
Modeling of Turbulent Spray Diffusion Flames Including Detailed Chemistry. C. Hollmann, E. Gutheil, 1731
NO_x Formation in Turbulent Lean-Premixed Combustion with Minimum Heat Losses. L. Xie, S. Hayashi, K. Hirose, 2155
The Phenomena of Flame Propagation in a Rotating Tube. Y. Sakai, S. Ishizuka, 847
The Influence of Initial Temperature on Flame Acceleration and Deflagration-to-Detonation Transition. G. Ciccarelli, J. L. Boccio, T. Ginsberg, H. Tagawa, 2973
Spatial and Temporal Dynamics of Flamelets in Turbulent Premixed Flames. C. Ghenaï, C. Chauveau, I. Gökalp, 331

Triple Flames and Partially Premixed Combustion in Autoignition of Non-Premixed Turbulent Mixtures. P. Domingo, L. Vervisch, 233
Large Eddy Simulation of Unsteady Combustion. S. I. Möller, E. Lundgren, C. Fureby, 241
Effects of Unsteady Stretch on the Strength of a Freely-Propagating Flame Wrinkled by a Vortex. C. J. Mueller, J. F. Driscoll, D. L. Reuss, M. C. Drake, 347
Flame Surface Density and Burning Rate in Premixed Turbulent Flames. I. G. Shepherd, 373
Combustion Intensity and Burning Rate Integral of Premixed Flames. F. C. Gouldin, 381
Burning Velocity of Turbulent Premixed Flames in a High-Pressure Environment. H. Kobayashi, T. Tamura, K. Maruta, T. Niioka, F. A. Williams, 389
A Test of an Engineering Model of Premixed Turbulent Combustion. V. Karpov, A. Lipatnikov, V. Zimont, 249
Study of Premixed Turbulent Combustion Including Landau-Darrieus Instability Effects. R. N. Paul, K. N. C. Bray, 259
Extinction of Turbulent Premixed Flames by Small-Scale Turbulence at Kolmogorov-Microscale. A. Yoshida, H. Kakinuma, Y. Kotani, 397
Turbulence Characteristics Within the Local Reaction Zone of a High-Intensity Turbulent Premixed Flame. J. Furukawa, K. Okamoto, T. Hirano, 405
Probability Density Function Modeling of Premixed Turbulent Opposed Jet Flames. W. P. Jones, Y. Prasetyo, 275
Computation of Premixed Turbulent Combustion Using the Probability Density Function Approach. A. Sadat Sakak, M. Schreiber, 267
Experimental Analysis of Flame Surface Density Models for Premixed Turbulent Combustion. D. Veynante, J. Piana, J. M. Duclos, C. Martel, 413
Experimental and Numerical Investigation of the Structure of Flames Under Engine Conditions. H. Wassenberg, G. Adomeit, 421
Surface Density Measurements of Turbulent Premixed Flames in a Spark-Ignition Engine and a Bunsen-Type Burner Using Planar Laser-Induced Fluorescence. B. M. Deschamps, G. J. Smallwood, J. Prieur, D. R. Snelling, Ö. L. Gülder, 427
Measurement of the Instantaneous Detailed Flame Structure in Turbulent Premixed Combustion. A. Buschmann, F. Dinkelacker, T. Schäfer, M. Schäfer, J. Wolfrum, 437
Conditioned Dissipation and Average Consumption Maps in a Turbulent Nonpremixed Flame Using Planar Laser-Induced Fluorescence of O_2. S. Guerre, R. Bazile, D. Stepowski, 105
Direct Numerical Simulation Analysis of Flame Surface Density Equation in Non-Premixed Turbulent Combustion. E. Van Kalmthout, D. Veynante, S. Candel, 35
Subgrid Mixing and Molecular Transport Modeling in a Reacting Shear Layer. S. Menon, W. H. Calhoon, Jr., 59
An Integrated PDF/Neural Network Approach for Simulating Turbulent Reacting Systems. F. C. Christo, A. R. Masri, E. M. Nebot, S. B. Pope, 43
A Mixing Model to Improve the PDF Simulation of Turbulent Diffusion Flames. A. R. Masri, S. Subramaniam, S. B. Pope, 49
Contribution to the Analysis of Temporal and Spatial Structures Near the Lift-Off Region of a Turbulent Hydrogen Diffusion Flame. A. Brockhinke, P. Andresen, K. Kohse-Höinghaus, 153
A Numerical Study on Flame Stability at the Transition Point of Jet Diffusion Flames. H. Yamashita, M. Shimada, T. Takeno, 27
Images of the Strained Flammable Layer Used to Study the Liftoff of Turbulent Jet Flames. D. A. Everest, D. A. Feikema, J. F. Driscoll, 129
Flamelet and PDF Modeling of CO and NO_x Emissions from a Turbulent, Methane Hydrogen Jet Nonpremixed Flame. J.-Y. Chen, W.-C. Chang, 2207
Simulation of Detailed Chemistry in a Turbulent Combustor Flow. H. C. Magel, U. Schnell, K. R. G. Hein, 67
Analysis of Turbulence-Chemistry Interaction with Respect to NO Formation in Turbulent, Nonpremixed Hydrogen-Air Flames. M. Schlatter, J. C. Ferreira, M. Flury, J. Gass, 2215
Measurements of NO in Turbulent Non-Premixed Flames Stabilized on a Bluff Body. B. B. Dally, A. R. Masri, R. S. Barlow, G. J. Fiechtner, D. F. Fletcher, 2191
Oxygen Atom Concentrations and NO Production Rates in a Turbulent H_2/N_2 Jet Flame. R. S. Barlow, G. J. Fiechtner, J.-Y. Chen, 2199
CFD Prediction of Coupled Radiation Heat Transfer and Soot Production in Turbulent Flames. N. W. Bressloff, J. B. Moss, P. A. Rubini, 2379
A Study of Turbulent Diffusion Flames Formed by Planar Fuel Injection into the Wake Formation Region of a Slender Square Cylinder. P. Koutmos, C. Mavridis, D. Papailiou, 161
Simulation of a Bluff-Body-Stabilized Diffusion Flame Using Second-Moment Closure and Monte Carlo Methods. H. A. Wouters, P. A. Nooren, T. W. J. Peeters, D. Roekaerts, 177
Interaction of Turbulence and Radiation in Confined Diffusion Flames. J. W. Hartick, M. Tacke, G. Früchtel, E. P. Hassel, J. Janicka, 75
Exothermicity and Three-Dimensional Effects in Unsteady Propane Square Jets. F. F. Grinstein, K. Kailasanath, 91
Turbulent Length Scales in a Swirling Flame. G. Früchtel, E. P. Hassel, J. Janicka, 195
Experimental and Numerical Study of a Premixed Flame Stabilized by a Rectangular Section Cylinder. P. Bailly, D. Garréton, O. Simonin, P. Bruel,

M. Champion, B. Deshaies, S. Duplantier, S. Sanquer, 923
On the Use of Light Sheet Methods in the Presence of Refraction by Flames. F. Weinberg, 939
Experimentally Measured Burning Rates of Premixed Turbulent Flames. E. Bourguignon, L. W. Kostiuk, Y. Michou, I. Gokalp, 447
Highly Turbulent Premixed Flames Stabilized in a Co-Axial Jet Flame Burner. T.-W. Lee, A. Mitrovic, 455
Three-Dimensional Spatial Flamelet Statistics for Premixed Turbulent Combustion Modeling. S. S. Shy, R. H. Jang, W. K. I, K. L. Gee, 283
Effect of Density Ratio on Flame Propagation Along a Vortex Tube. T. Hasegawa, K. Nishikado, 291
Model Simulations of Freely Propagating Turbulent Premixed Flames. T. Smith, S. Menon, 299
Calculations of Turbulent Flames Using a PSR Microstructural Library. I. Z. Hu, S. M. Correa, 307
Spectral Model of Premixed Flame Propagation. L. R. Collins, M. Ulitsky, 315
Negative Flame Speed in an Unsteady 2-D Premixed Flame: A Computational Study. I. R. Gran, T. Echekki, J. H. Chen, 323
Experimental Investigation of the Flame Structure and Extinction of Turbulent Counterflow Non-Premixed Flames. A. Kitajima, T. Ueda, A. Matsuo, M. Mizomoto, 137
Impact of Mixing Model on Predicted NO Formation in a Nonpremixed, Partially Stirred Reactor. W.-C. Chang, J.-Y. Chen, 2223
Vortex-Flame Interactions and Extinction in Turbulent Jet Diffusion Flames. F. Takahashi, W. J. Schmoll, D. D. Trump, L. P. Goss, 145
Study of Swirling Recirculating Hydrogen Diffusion Flame Using UV Raman Spectroscopy. M. M. Tacke, T. C. Cheng, E. P. Hassel, J. Janicka, 169
Analysis of Wet Co Oxidation Under Turbulent Non-Premixed Conditions Using a PDF Method and Detailed Chemical Kinetics. M. Kraft, E. Stöckelmann, H. Bockhorn, 807
Flamelet Behavior in a Turbulent Diffusion Flame Measured by Rayleigh Scattering Image Velocimetry. M. Komiyama, A. Miyafuji, T. Takagi, 339
Measurements of the Detailed Flame Structure in Turbulent H_2–Ar Jet Diffusion Flames with Line-Raman/Rayleigh/LIPF-OH Technique. Y.-C. Chen, M. S. Mansour, 97
Computational and Experimental Investigation of a Turbulent Non-Premixed Methane Flame. M. Nau, W. Neef, U. Maas, E. Gutheil, J. Warnatz, 83

11 Fluid Dynamics

The Challenge of Turbulent Combustion. K. N. C. Bray, 1
Spray Combustion Phenomena. G. M. Faeth, 1593
Using Direct Numerical Simulations to Understand Premixed Turbulent Combustion. T. Poinsot, 219
Interpretation of k-ε Computed Turbulence Length-Scale Predictions for Engine Flows. Z. Han, R. D. Reitz, F. E. Corcione, G. Valentino, 2717
PLIF Imaging Measurements of a Co-axial Rocket Injector Spray at Elevated Pressure. U. Brummund, A. Cessou, A. Vogel, 1687
Impacts and Control of Air Toxics from Combustion. C. P. Koshland, 2049
Numerical Simulation of Combustion in Fire Plumes. W. E. Mell, K. B. McGrattan, H. R. Baum, 1523

01 Atomization of Liquids

Spray Combustion Phenomena. G. M. Faeth, 1593
Active Control of Liquid-Fueled Combustion Using Periodic Vortex-Droplet Interaction. K. H. Yu, T. P. Parr, K. J. Wilson, K. C. Schadow, E. J. Gutmark, 2843
Influence of Air and Fuel Flows on Gas Turbine Sprays at High Pressures. Q. P. Zheng, A. K. Jasuja, A. H. Lefebvre, 2757
Self-Ignition of Hybrid (H_2 + Atomized Liquid Hydrocarbon Fuel + Gaseous Oxidizer) Mixtures at Engine Relevant Conditions. B. E. Gelfand, A. M. Bartenev, S. V. Khomik, S. P. Medvedev, A. N. Polenov, 2573
Gas Property Effects on Droplet Atomization and Combustion in an Air-Assist Atomizer. R. Aftel, A. K. Gupta, C. Cook, C. Presser, 1645
Droplet Size Distribution Effects in Spray Combustion. J. A. Bossard, R. E. Peck, 1671
Flame Stabilization in Cryogenic Propellant Combustion. G. Herding, R. Snyder, P. Scouflaire, C. Rolon, S. Candel, 2041
Effect of the Fuel Boiling Point on the Boilover Burning of Liquid Fuels Spilled on Water. J. P. Garo, J. P. Vantelon, A. C. Fernandez-Pello, 1461

02 Blast Waves

1-D Simulation of a Spark Discharge in Air. M. Schäfer, R. Schmidt, J. Köhler, 2701

03 Boundary Layer Phenomena

The Controlling Chemistry in Flame Generated Surface Deposition of Na_2SO_4 and the Effects of Chlorine. M. Steinberg, K. Schofield, 1835
Detonation Supported by Combustible Dust Deposit. B.-C. Fan, H.-Z. Li, 3007
Study of the Thermocapillary Layer Preceding Slow Steadily-Spreading Flames Over Liquid Fuels. P. L. Garcia-Ybarra, J. L. Castillo, J. C. Antoranz, V. Sankovitch, J. San Martin, 1469
A Transient Two-Dimensional Chemically Reactive Flow Model: Fuel Particle Combustion in a Non-

quiescent Environment. J. Lee, A. G. Tomboulides, S. A. Orszag, R. A. Yetter, F. L. Dryer, 3059
Flame Structure and Combustion Rate of Burning Graphite in the Stagnation Flow. A. Makino, I. Kato, M. Senba, H. Fujizaki, N. Araki, 3067
Ignition of Catalytic Reactions in a Vertical Wall Immersed in a Combustible Gas. C. Treviño, F. Méndez, 1797

04 Jets

Near-Field Entrainment in Unsteady Gas Jets and Diesel Sprays: A Comparative Study. R. Andriani, A. Coghe, G. E. Cossali, 2549
Droplet and Vapor Transport in a Turbulent Jet. J. Ye, C. D. Richards, 1679
Impacts and Control of Air Toxics from Combustion. C. P. Koshland, 2049
Numerical Simulation of Combustion in Fire Plumes. W. E. Mell, K. B. McGrattan, H. R. Baum, 1523
Instability of Diffusion Flames. A. Lingens, K. Neemann, J. Meyer, M. Schreiber, 1053
Quantitative Two-Photon Laser-Induced Fluorescence Imaging of CO in Flickering CH_4/Air Diffusion Flames. D. A. Everest, C. R. Shaddix, K. C. Smyth, 1161
Prediction of Coal-Water Slurry Dispersion in a Fluidized Bed Combustor. F. Okasha, M. Miccio, 3277
Characteristics of Lifted Flames in Nonpremixed Turbulent Confined Jets. M. S. Cha, S. H. Chung, 121
A Numerical Study on Flame Stability at the Transition Point of Jet Diffusion Flames. H. Yamashita, M. Shimada, T. Takeno, 27
Images of the Strained Flammable Layer Used to Study the Liftoff of Turbulent Jet Flames. D. A. Everest, D. A. Feikema, J. F. Driscoll, 129
Simulation of a Bluff-Body-Stabilized Diffusion Flame Using Second-Moment Closure and Monte Carlo Methods. H. A. Wouters, P. A. Nooren, T. W. J. Peeters, D. Roekaerts, 177
Exothermicity and Three-Dimensional Effects in Unsteady Propane Square Jets. F. F. Grinstein, K. Kailasanath, 91
Turbulent Length Scales in a Swirling Flame. G. Früchtel, E. P. Hassel, J. Janicka, 195

05 Mixing

Near-Field Entrainment in Unsteady Gas Jets and Diesel Sprays: A Comparative Study. R. Andriani, A. Coghe, G. E. Cossali, 2549
Effect of Hardware Alignment on Fuel Distribution and Combustion Performance for a Production Engine Fuel-Injection Assembly. V. G. McDonell, L. Arellano, S. W. Lee, G. S. Samuelsen, 2725
The Effects of Fuel–Air Mixing on NO_x Formation in Non-Premixed Swirl Burners. T. Terasaki, S. Hayashi, 2733
A Numerical and Experimental Study of Fuel Evaporation and Mixing for Lean Premixed Combustion at High Pressure. M. Rachner, M. Brandt, H. Eickhoff, C. Hassa, A. Bräumer, H. Krämer, M. Ridder, V. Sick, 2741
Use of an Optical Probe for Time-Resolved *in Situ* Measurement of Local Air-to-Fuel Ratio and Extent of Fuel Mixing with Applications to Low NO_x Emissions in Premixed Gas Turbines. R. K. Mongia, E. Tomita, F. K. Hsu, L. Talbot, R. W. Dibble, 2749
Active Control of Liquid-Fueled Combustion Using Periodic Vortex-Droplet Interaction. K. H. Yu, T. P. Parr, K. J. Wilson, K. C. Schadow, E. J. Gutmark, 2843
Droplet and Vapor Transport in a Turbulent Jet. J. Ye, C. D. Richards, 1679
Chemical Effects of CF_3H in Extinguishing Counterflow CO/Air/H_2 Diffusion Flames. G. S. Fallon, H. K. Chelliah, G. T. Linteris, 1395
Observations of H_2O Formation in the Supersonic Combustion of H_2 by High-Enthalpy Air. M. F. Miller, W. T. Rawlins, M. G. Allen, T. E. Parker, 2895
Measurements and Prediction of Air Entrainment Rates of Pool Fires. X. C. Zhou, J. P. Gore, H. R Baum, 1453
Influence of Turbulent Mixing on the Pyrolysis of Chloroform Using Detailed Chemical Kinetics. M. Kraft, E. Stöckelmann, H. Bockhorn, 2431
Compact Incinerator Afterburner Concept Based on Vortex Combustion. T. P. Parr, E. Gutmark, K. Wilson, D. M. Hanson-Parr, K. Yu, R. A. Smith, K. C. Schadow, 2471
Conditioned Dissipation and Average Consumption Maps in a Turbulent Nonpremixed Flame Using Planar Laser-Induced Fluorescence of O_2. S. Guerre, R. Bazile, D. Stepowski, 105
Direct Numerical Simulation Analysis of Flame Surface Density Equation in Non-Premixed Turbulent Combustion. E. Van Kalmthout, D. Veynante, S. Candel, 35
Subgrid Mixing and Molecular Transport Modeling in a Reacting Shear Layer. S. Menon, W. H. Calhoon, Jr., 59
Characteristics of Lifted Flames in Nonpremixed Turbulent Confined Jets. M. S. Cha, S. H. Chung, 121
Images of the Strained Flammable Layer Used to Study the Liftoff of Turbulent Jet Flames. D. A. Everest, D. A. Feikema, J. F. Driscoll, 129
Simulation of a Bluff-Body-Stabilized Diffusion Flame Using Second-Moment Closure and Monte Carlo Methods. H. A. Wouters, P. A. Nooren, T. W. J. Peeters, D. Roekaerts, 177
Mixing and Chemical Reaction in an Idealized Swirl

Chamber. O. M. Knio, A. S. Worlikar, H. N. Najm, 203

06 Nozzle Flow

An Experimental Database for Diesel Spray Combustion. E. Winklhofer, 2541

07 Particle Trajectories

Modeling of Turbulent Spray Diffusion Flames Including Detailed Chemistry. C. Hollmann, E. Gutheil, 1731

08 Plumes

Numerical Simulation of Combustion in Fire Plumes. W. E. Mell, K. B. McGrattan, H. R. Baum, 1523
Numerical Simulation of the Dynamics of Large Fire Plumes and the Phenomenon of Puffing. A. F. Ghoniem, I. Lakkis, M. Soteriou, 1531
Influence of Gravity on the Propagation of Initially Spherical Flames. J. Daou, B. Rogg, 1275

09 Supersonic Flow

Numerical Simulation of a Counterflow Diffusion Flame in Supersonic Airflow. K. Takita, T. Niioka, 2877
On Strained Flames with Hypergolic Reactants: The $H_2/NO/F_2$ System in High-Speed, Supersonic and Subsonic Mixing-Layer Combustion. F. N. Egolfopoulos, P. E. Dimotakis, C. Bond, 2885
Observations of H_2O Formation in the Supersonic Combustion of H_2 by High-Enthalpy Air. M. F. Miller, W. T. Rawlins, M. G. Allen, T. E. Parker, 2895
Experimental Observation of Unsteady H_2-O_2 Combustion Phenomena Around Hypersonic Projectiles Using a Multiframe Camera. J. Kasahara, T. Horii, T. Endo, T. Fujiwara, 2903
Onset of Oblique Detonation Waves: Comparison Between Experimental and Numerical Results for Hydrogen-Air Mixtures. C. Viguier, L. F. Figueira da Silva, D. Desbordes, B. Deshaies, 3023
PLIF Imaging of Hypersonic Reactive Flow Around Blunt Bodies. M. R. Kamel, C. I. Morris, I. G. Stouklov, R. K. Hanson, 2909
Quenching of Reaction in Gas-Sampling Probes to Measure Scramjet Engine Performance. T. Mitani, 2917
Shock-Wave-Enhancement of the Mixing and the Stability Limits of Supersonic Hydrogen-Air Jet Flames. H. Huh, J. F. Driscoll, 2933
Numerical Simulation of Flame-Stabilization and Combustion Promotion by Plasma Jets in Supersonic Air Streams. R. Kato, I. Kimura, 2941
Experimental Investigation of a SCRAMJET Model Combustor with Injection Through a Swept Ramp Using Laser-Induced Fluorescence with Tunable Excimer Lasers. R. Hšnig, D. Theisen, R. Fink, R. Lachner, G. Kappler, D. Rist, P. Andresen, 2949

10 Others

Numerical Study of Premixed Laminar Flame Propagation in a Closed Tube with a Full Navier-Stokes Approach. F. S. Marra, G. Continillo, 907
Swirl-Induced Intermittency: A Novel Effect Modifying the Turbulence Structure of Swirling Free Jets. F. Holzäpfel, B. Lenze, W. Leuckel, 187
Flame Propagation Along 90-Degree Bend in an Open Duct. K. Sato, Y. Sakai, M. Chiga, 931

Fluidized Bed Combustion (*See* Combustion in Practical Systems, Furnaces and Incinerators: Heterogeneous Combustion, Dispersed Particles)

12 Heat Transfer

1-D Simulation of a Spark Discharge in Air. M. Schäfer, R. Schmidt, J. Köhler, 2701
The Influence of Pressure on Char Combustion Kinetics. E. Croiset, C. Mallet, J.-P. Rouan, J.-R. Richard, 3095
Analytical Study on Flame Stabilization in Reciprocating Combustion in Porous Media with High Thermal Conductivity. J. G. Hoffmann, R. Echigo, S. Tada, H. Yoshida, 2709

01 Conduction

Effect of the Fuel Boiling Point on the Boilover Burning of Liquid Fuels Spilled on Water. J. P. Garo, J. P. Vantelon, A. C. Fernandez-Pello, 1461

02 Convection

Heat Transfer Modeling During Knock and Flame Quenching in an Engine Chamber. O. A. Ezekoye, 2661
Convective Ignition of a Granular Solid Propellant Bed: Influence of Propellant Composition. D. E. Kooker, S. L. Howard, L.-M. Chang, 2033

03 Radiation

Effect of Temperature and Concentration Fluctuations on Radiative Heat Transfer in Turbulent Flames. W. Krebs, R. Koch, B. Ganz, L. Eigenmann, S. Wittig, 2763
Gas Temperature Above a Porous Radiant Burner: Comparison of Measurements and Model Predictions. M. D. Rumminger, N. H. Heberle, R. W. Dibble, D. R. Crosley, 1755
Model Calculation of Steady Upward Flame Spread

Over a Thin Solid in Reduced Gravity. C.-B. Jiang, J. S. T'ien, H.-Y. Shih, 1353
Measurements of Coal Particle Shape, Mass, and Temperature Histories: Impact of Particle Irregularity on Temperature Predictions and Measurements. R. Sampath, Y. D. Yeboah, D. J. Maloney, S. Woodruff, J. W. Zondlo, 3179
Scattering of Thermal Radiation in the Freeboard of a 1 MW_t Fluidized Bed Combustor with Coal and Limestone Feeding. M. Filla, A. Scalabrin, C. Tonfoni, 3295
CFD Prediction of Coupled Radiation Heat Transfer and Soot Production in Turbulent Flames. N. W. Bressloff, J. B. Moss, P. A. Rubini, 2379
Interaction of Turbulence and Radiation in Confined Diffusion Flames. J. W. Hartick, M. Tacke, G. Früchtel, E. P. Hassel, J. Janicka, 75
Propagation Limits of Dust/Air Flames Diluted by Additions of Inert Solid Particles. R. Blouquin, G. Joulin, 1565
Initiation of Laminar Flames in Near-Limit $H_2/O_2/H_2O$ Mixtures. A. Y. Kusharin, O. E. Popov, G. L. Agafonov, 985

13 Heterogeneous Combustion

Anomalous Group Combustion of Premixed Clusters. H. H. Chiu, C. L. Lin, 1653
Measurements and Predictions of Nitric Oxide and Particulates Emissions from Heavy Fuel Oil Spray Flames. M. A. Byrnes, E. A. Foumeny, T. Mahmud, A. S. A. K Sharifah, T. Abbas, P. G. Costen, S. Hassan, F. C. Lockwood, 2241
Current State of Combustion Research in Microgravity. M. Kono, K. Ito, T. Niioka, T. Kadota, J. Sato, 1189
Polydispersity and Reaction Zone Structure in Partially Premixed Spray Flames. J. B. Greenberg, N. Sarig, 1705
Gas-Phase Combustion Synthesis of Materials. K. Brezinsky, 1805
Pulsating Instability in the Nonadiabatic Heterogeneous SHS Flame: Theory and Experimental Comparisons. A. Makino, C. K. Law, 1867
Supercritical Combustion Synthesis of Titanium Nitride. K. Brezinsky, J. A. Brehm, C. K. Law, I. Glassman, 1875
Flame Structure Measurement of Single, Isolated Aluminum Particles Burning in Air. P. Bucher, R. A. Yetter, F. L. Dryer, T. P. Parr, D. M. Hanson-Parr, E. P. Vicenzi, 1899
A Comprehensive Physical and Numerical Model of Boron Particle Ignition. W. Zhou, R. A. Yetter, F. L. Dryer, H. Rabitz, R. C. Brown, C. E. Kolb, 1909
Combustion Characteristics of Mg-CO_2 Counterflow Diffusion Flames. A. Fukuchi, M. Kawashima, S. Yuasa, 1945
Two-Regime Global Kinetics of Cellulose Pyrolysis: The Role of Tar Evaporation. E. M. Suuberg, I. Milosavljevic, V. Oja, 1515
Surface Heterogeneity in the Formation and Decomposition of Carbon Surface Oxides. M. C. Ma, B. S. Haynes, 3119
Statistical Kinetics for Pulverized Coal Combustion. R. H. Hurt, M. M. Lunden, E. G. Brehob, D. J. Maloney, 3169
Fundamental Study on N_2O Formation/Decomposition Characteristics by Means of Low-Temperature Pulverized Coal Combustion. I. Naruse, Y. Yamamoto, Y. Itoh, K. Ohtake, 3213
Emissions of Nitrogen Oxides from Circulating Fluidized-Bed Combustors: Modeling Results Using Detailed Chemistry. S. Goel, A. Sarofim, P. Kilpinen, M. Hupa, 3317
Single-Particle Combustion of Two Biomass Chars. M. J. Wornat, R. H. Hurt, K. A. Davis, N. Y. C. Yang, 3075
Flame Structure and Combustion Rate of Burning Graphite in the Stagnation Flow. A. Makino, I. Kato, M. Senba, H. Fujizaki, N. Araki, 3067
Coal Combustion and Gasification in a Compartmented, Fluidized-Bed Coal Gasifier. H. Yan, V. Rudolph, D.-K. Zhang, 3261

01 Catalytic Combustion

Heterogeneous/Homogeneous Reaction and Transport Coupling During Flame-Wall Interaction. P. Popp, M. Smooke, M. Baum, 2693
Numerical Modeling of Catalytic Ignition. O. Deutschmann, R. Schmidt, F. Behrendt, J. Warnatz, 1747
Gas Temperature Above a Porous Radiant Burner: Comparison of Measurements and Model Predictions. M. D. Rumminger, N. H. Heberle, R. W. Dibble, D. R. Crosley, 1755
Homogeneous Ignition of Hydrogen-Air Mixtures Over Platinum. P.-A. Bui, D. G. Vlachos, P. R. Westmoreland, 1763
Catalytic Oxidation of Natural Gas Over Supported Platinum: Flow Reactor Experiments and Detailed Numerical Modeling. T. C. Bond, R. A. Noguchi, C.-P. Chou, R. K. Mongia, J.-Y. Chen, R. W. Dibble, 1771
Pd on Low-Surface-Area α-Alumina System: Is Metallic Pd Active for Methane Combustion? M. Lyubovsky, R. Weber, L. Pfefferle, 1779
Catalytic Combustion of Carbon Particulate at High Values of the Carbon/Catalyst Mass Ratio. P. Ciambelli, M. D'Amore, V. Palma, S. Vaccaro, 1789
Ciambelli, M. D'Amore, V. Palma, S. Vaccaro
A Transient Two-Dimensional Chemically Reactive Flow Model: Fuel Particle Combustion in a Nonquiescent Environment. J. Lee, A. G. Tomboulides, S. A. Orszag, R. A. Yetter, F. L. Dryer, 3059
Ignition of Catalytic Reactions in a Vertical Wall Im-

mersed in a Combustible Gas. C. Treviño, F. Méndez, 1797

02 Dispersed Particles

Pd on Low-Surface-Area α-Alumina System: Is Metallic Pd Active for Methane Combustion? M. Lyubovsky, R. Weber, L. Pfefferle, 1779
Evolution of Particle Temperature and Internal Composition for Zirconium Burning in Air. I. E. Molodetsky, E. L. Dreizin, C. K. Law, 1919
An Experimental Study on Particle-Cloud Flames in Microgravity Field. Y. Okuyama, Y. Ohtomo, K. Maruta, H. Kobayashi, T. Niioka, 1369
Laser Ignition and Flame Propagation of Pulverized Coal Dust Clouds. M. Taniguchi, H. Kobayashi, S. Azuhata, 3189
Sodium Partitioning in a Pulverized Coal Combustion Environment. N. B. Gallagher, T. W. Peterson, J. O. L. Wendt, 3197
The Fate of Fixed Carbon During the Fluidized-Bed Combustion of a Coal and Two Waste-Derived Fuels. U. Arena, R. Chirone, P. Salatino, 3243
The Effect of the Bulk Equivalence Ratio on the PAH Emissions from the Combustion of PVC, Poly(styrene), and Poly(ethylene). T. Panagiotou, Y. A. Levendis, J. Carlson, P. Vouros, 2421
Fluidized Bed Combustion: Achievements and Problems. B. Leckner, 3231
Propagation Limits of Dust/Air Flames Diluted by Additions of Inert Solid Particles. R. Blouquin, G. Joulin, 1565
Burning Velocities in Fuel-Rich Aluminum Dust Clouds. S. Goroshin, I. Fomenko, J. H. S. Lee, 1961
Modeling of Premixed Gas Combustion in Porous Media Composed of Coarse-Sized Particles: 1-D Description with Discrete Solid Phase. O. S. Rabinovich, A. V. Fefelov, N. V. Pavlyukevich, 3383

03 Multiphase

Surface Tension Influences on Methanol Droplet Vaporization in the Presence of Water. H. A. Dwyer, I. Aharon, B. D. Shaw, H. Niazmand, 1613
Droplet and Vapor Transport in a Turbulent Jet. J. Ye, C. D. Richards, 1679
Combustion of Porous Energetic Materials in the Merged-Flame Regime. S. B. Margolis, F. A. Williams, A. M. Telengator, 1969
Prediction of Coal-Water Slurry Dispersion in a Fluidized Bed Combustor. F. Okasha, M. Miccio, 3277
Transformations of Sludge Waste During Combustion in a Low-High-Low Temperature Reactor. J. A. Kozinski, R. Saade, G. Zheng, 2495
Fundamental Experiment on the Combustion of Coal–Water Mixture and Modeling of the Process. K. Takeno, K. Tokuda, T. Ichinose, S. Kaneko, 3223
Numerical Investigation on the Influence of Carbonaceous Particles on the Ignition Behavior of Methane/Air Mixtures. T. Ludwig, P. Roth, 1579
Measurement of the Local Group Combustion Number of Droplet Clusters in a Premixed Spray Stream. F. Akamatsu, Y. Mizutani, M. Katsuki, S. Tsushima, Y. D. Cho, 1723
Structures of Multiple Combustion Waves Formed Under Filtration of Lean Hydrogen-Air Mixtures in a Packed Bed. A. V. Saveliev, L. A. Kennedy, A. A. Fridman, I. K. Puri, 3369
Superadiabatic Combustion Wave in a Diluted Methane-Air Mixture Under Filtration in a Packed Bed. S. I. Foutko, S. I. Shabunya, S. A. Zhdanok, L. A. Kennedy, 3377

04 Single Droplet

Spontaneous Ignition of Liquid Droplets from a View of Non-Homogeneous Mixture Formation and Transient Chemical Reactions. M. Tanabe, T. Bolik, C. Eigenbrod, H. J. Rath, J. Sato, M. Kono, 1637
Surface Tension Influences on Methanol Droplet Vaporization in the Presence of Water. H. A. Dwyer, I. Aharon, B. D. Shaw, H. Niazmand, 1613
Characteristics of Supercritical Droplet Gasification. A. Umemura, Y. Shimada, 1621
Investigation of Sooting in Normal-Gravity Droplet Combustion Using Light Extinction and Gravimetric Techniques. K.-O. Lee, K. A. Jensen, M. Y. Choi, 2397
Heat Loss and Lewis Number Effects on the Onset of Oscillations in Diffusion Flames. S. Cheatham, M. Matalon, 1063
Droplet Combustion Experiments in Spacelab. D. L. Dietrich, J. B. Haggard, Jr., F. L. Dryer, V. Nayagam, B. D. Shaw, F. A. Williams, 1201
High-Pressure Droplet Burning Experiments in Microgravity. B. Vieille, C. Chauveau, X. Chesneau, A. Odeïde, I. Gökalp, 1259
Experimental Study on High-Pressure Droplet Evaporation Using Microgravity Conditions. H. Nomura, Y. Ujiie, H. J. Rath, J. Sato, M. Kono, 1267
Microgravity Combustion of Methanol and Methanol/Water Droplets: Drop Tower Experiments and Model Predictions. A. J. Marchese, F. L. Dryer, R. Colantonio, V. Nayagam, 1209
An Unsteady-State Anaylsis of Porous Sphere and Droplet Fuel Combustion Under Microgravity Conditions. M. K. King, 1227
Observation of Sooting Behavior in an Emulsion Droplet Flame by Planar Laser Light Scattering in Microgravity. M. Tsue, D. Segawa, T. Kadota, H. Yamasaki, 1251
Effect of Liquid Drops on the Thermal Explosion of

a Gas Mixture. V. Goldshtein, I. Goldfarb, A. Zinoviev, I. Shreiber, 1557
Effects of Ambient Water in the Combustion Enhancement of Heavily Chlorinated Hydrocarbons: Studies on Droplet Burning. H. Wang, D. L. Zhu, Y. Saso, C. K. Law, 2413
Hydroxyl Radical Chemiluminescence Imaging and the Structure of Microgravity Droplet Flames. A. J. Marchese, F. L. Dryer, V. Nayagam, R. Colantonio, 1219
Statistical Analysis on Onset of Microexplosion for an Emulsion Droplet. M. Tsue, H. Yamasaki, T. Kadota, D. Segawa, 1629
Investigation of Sooting in Microgravity Droplet Combustion. M. Y. Choi, K.-O. Lee, 1243
Combustion Studies on Concentrated Distillery Effluents. N. M. Patel, P. J. Paul, H. S. Mukunda, S. Dasappa, 2479

05 Single Solid Particle

Flame Structure Measurement of Single, Isolated Aluminum Particles Burning in Air. P. Bucher, R. A. Yetter, F. L. Dryer, T. P. Parr, D. M. Hanson-Parr, E. P. Vicenzi, 1899
A Comprehensive Physical and Numerical Model of Boron Particle Ignition. W. Zhou, R. A. Yetter, F. L. Dryer, H. Rabitz, R. C. Brown, C. E. Kolb, 1909
Evolution of Particle Temperature and Internal Composition for Zirconium Burning in Air. I. E. Molodetsky, E. L. Dreizin, C. K. Law, 1919
Ignition and Combustion of Bulk Titanium and Magnesium at Normal and Reduced Gravity. A. Abbud-Madrid, M. C. Branch, J. W. Daily, 1929
Modeling of Solid Particle Interaction in a High-Velocity, Hot Gas Stream. M. M. Elkotb, N. Salama, I. Nassef, 1937
Structural Changes of Char Particles During Chemically Controlled Oxidation. X. Zhang, A. Dukhan, I. I. Kantorovich, E. Bar-Ziv, A. Kandas, A. F. Sarofim, 3111
A New Approach to Studying Pore Diffusivity During Char Combustion at FBC Conditions. S. Goel, A. F. Sarofim, J. Lu, 3127
Measurements of Coal Particle Shape, Mass, and Temperature Histories: Impact of Particle Irregularity on Temperature Predictions and Measurements. R. Sampath, Y. D. Yeboah, D. J. Maloney, S. Woodruff, J. W. Zondlo, 3179
The Impact of Fragmentation on Char Conversion During Pulverized Coal Combustion. R. E. Mitchell, A. E. Jacob Akanetuk, 3137
The NO and N_2O Formation Mechanism During Devolatilization and Char Combustion Under Fluidized-Bed Conditions. F. Winter, C. Wartha, G. Löffler, H. Hofbauer, 3325
Single-Particle Combustion of Two Biomass Chars. M. J. Wornat, R. H. Hurt, K. A. Davis, N. Y. C. Yang, 3075
Influence of Pressure on the Combustion Rate of Carbon. R. H. Essenhigh, A. M. Mescher, 3085
A Transient Two-Dimensional Chemically Reactive Flow Model: Fuel Particle Combustion in a Nonquiescent Environment. J. Lee, A. G. Tomboulides, S. A. Orszag, R. A. Yetter, F. L. Dryer, 3059
Combustion Studies on Concentrated Distillery Effluents. N. M. Patel, P. J. Paul, H. S. Mukunda, S. Dasappa, 2479
A General Model for Devolatilization of Large Coal Particles. Y. Zhao, M. A. Serio, P. R. Solomon, 3145

06 Solid Propellants

Combustion of Porous Energetic Materials in the Merged-Flame Regime. S. B. Margolis, F. A. Williams, A. M. Telengator, 1969
Solid Propellant Diffusion Flame Structure. T. P. Parr, D. M. Hanson-Parr, 1981
A Three-Phase Model of HMX Combustion. J. E. Davidson, M. W. Beckstead, 1989
Simplified Chemical-Kinetic Mechanisms for Characterizing the Structure of the Dark Zones of Double Base and Nitramine Propellants. N. Ilincic, W. R. Anderson, K. Seshadri, N. E. Meagher, 1997
Oscillatory Combustion of Aluminized Composite Propellants. S. R. Hickman, M. Q. Brewster, 2007
Propellant Dark Zone Concentrations via Multichannel IR Absorption. S. H. Modiano, J. A. Vanderhoff, 2017
Laser Recoil Combustion Response of N5 Propellant from 1 to 9 Atmospheres. J. C. Finlinson, 2025
Convective Ignition of a Granular Solid Propellant Bed: Influence of Propellant Composition. D. E. Kooker, S. L. Howard, L.-M. Chang, 2033
A Comprehensive Physical and Numerical Model of Boron Particle Ignition. W. Zhou, R. A. Yetter, F. L. Dryer, H. Rabitz, R. C. Brown, C. E. Kolb, 1909
Combustion-Like Pyrolysis of Organic Polymers: Species and Kinetic Details by *T*-Jump/FTIR Spectroscopy. T. B. Brill, H. Arisawa, P. E. Gongwer, 791

07 Solid-Solid

Metal-Sulfur Combustion. S. Goroshin, A. Mizera, D. L. Frost, J. H. S. Lee, 1883

08 Sprays

Spray Combustion Phenomena. G. M. Faeth, 1593
Spectral Extinction Measurements of Spray Combustion in a Divided-Chamber Diesel Engine Sys-

tem. F. E. Corcione, G. Mazziotti, B. M. Vaglieco, 2533
Near-Field Entrainment in Unsteady Gas Jets and Diesel Sprays: A Comparative Study. R. Andriani, A. Coghe, G. E. Cossali, 2549
Effect of Hardware Alignment on Fuel Distribution and Combustion Performance for a Production Engine Fuel-Injection Assembly. V. G. McDonell, L. Arellano, S. W. Lee, G. S. Samuelsen, 2725
A Numerical and Experimental Study of Fuel Evaporation and Mixing for Lean Premixed Combustion at High Pressure. M. Rachner, M. Brandt, H. Eickhoff, C. Hassa, A. Bräumer, H. Krämer, M. Ridder, V. Sick, 2741
Active Control of Liquid-Fueled Combustion Using Periodic Vortex-Droplet Interaction. K. H. Yu, T. P. Parr, K. J. Wilson, K. C. Schadow, E. J. Gutmark, 2843
Influence of Air and Fuel Flows on Gas Turbine Sprays at High Pressures. Q. P. Zheng, A. K. Jasuja, A. H. Lefebvre, 2757
A Simple Model of Ignition Modes of Dense Droplet Clouds. D. Thibaut, S. Candel, 2565
Fluorescence Imaging of NO and O_2 in a Spray Flame Combustor at Elevated Pressures. B. L. Upschulte, M. G. Allen, K. R. McManus, 2779
Gas Property Effects on Droplet Atomization and Combustion in an Air-Assist Atomizer. R. Aftel, A. K. Gupta, C. Cook, C. Presser, 1645
Anomalous Group Combustion of Premixed Clusters. H. H. Chiu, C. L. Lin, 1653
Characteristics of Supercritical Droplet Gasification. A. Umemura, Y. Shimada, 1621
Structure of an Acoustically Forced Turbulent Spray Flame. E. Haile, O. Delabroy, F. Lacas, D. Veynante, S. Candel, 1663
Droplet Size Distribution Effects in Spray Combustion. J. A. Bossard, R. E. Peck, 1671
Droplet and Vapor Transport in a Turbulent Jet. J. Ye, C. D. Richards, 1679
Modeling of Turbulent Spray Diffusion Flames Including Detailed Chemistry. C. Hollmann, E. Gutheil, 1731
Flame Propagation in Planar Droplet Arrays and Interaction Phenomena Between Neighboring Droplet Streams. N. Roth, A. Karl, K. Anders, A. Frohn, 1697
Investigation of Sooting in Normal-Gravity Droplet Combustion Using Light Extinction and Gravimetric Techniques. K.-O. Lee, K. A. Jensen, M. Y. Choi, 2397
An Experimental Database for Diesel Spray Combustion. E. Winklhofer, 2541
High-Pressure Droplet Burning Experiments in Microgravity. B. Vieille, C. Chauveau, X. Chesneau, A. Odeïde, I. Gökalp, 1259
Polydispersity and Reaction Zone Structure in Partially Premixed Spray Flames. J. B. Greenberg, N. Sarig, 1705
Experimental and Numerical Studies of Two-Stage Methanol Flames. S. C. Li, F. A. Williams, 1017
An Experimental Study on Particle-Cloud Flames in Microgravity Field. Y. Okuyama, Y. Ohtomo, K. Maruta, H. Kobayashi, T. Niioka, 1369
Flame Lift-off in Diesel Sprays. A. Karlsson, J. Chomiak, 2557
Electrostatic Dispersion and Evaporation of Clusters of Drops of High-Energy Fuel for Soot Control. J. Bellan, K. Harstad, 1713
Measurement of the Local Group Combustion Number of Droplet Clusters in a Premixed Spray Stream. F. Akamatsu, Y. Mizutani, M. Katsuki, S. Tsushima, Y. D. Cho, 1723
Quantitative Comparison of Detailed Numerical Computations and Experiments in Counterflow Spray Diffusion Flames. L. P. Gao, Y. D'Angelo, I. Silverman, A. Gomez, M. D. Smooke, 1739

14 Ignition

Autoignition Chemistry in a Motored Engine: An Experimental and Kinetic Modeling Study. H. J. Curran, P. Gaffuri, W. J. Pitz, C. K. Westbrook, W. R. Leppard, 2669
Kinetic Modeling of the Oxidation of Large Aliphatic Hydrocarbons. M. Nehse, J. Warnatz, C. Chevalier, 773
Self-Ignition of Diesel-Relevant Hydrocarbon-Air Mixtures Under Engine Conditions. U. Pfahl, K. Fieweger, G. Adomeit, 781
Numerical Modeling of Catalytic Ignition. O. Deutschmann, R. Schmidt, F. Behrendt, J. Warnatz, 1747
Homogeneous Ignition of Hydrogen-Air Mixtures Over Platinum. P.-A. Bui, D. G. Vlachos, P. R. Westmoreland, 1763
Laser Ignition and Flame Propagation of Pulverized Coal Dust Clouds. M. Taniguchi, H. Kobayashi, S. Azuhata, 3189
Triple Flames and Partially Premixed Combustion in Autoignition of Non-Premixed Turbulent Mixtures. P. Domingo, L. Vervisch, 233
Detailed Kinetic Reaction Mechanism for Ignition and Oxidation of α-Methylnaphthalene. H. Pitsch, 721
Ignition of Hydrogen and Oxygen in Counterflow at High Pressures. B. T. Helenbrook, C. K. Law, 815
Numerical Investigation on the Influence of Carbonaceous Particles on the Ignition Behavior of Methane/Air Mixtures. T. Ludwig, P. Roth, 1579
Ignition of Catalytic Reactions in a Vertical Wall Immersed in a Combustible Gas. C. Treviño, F. Méndez, 1797

01 Delay

Spontaneous Ignition of Liquid Droplets from a View of Non-Homogeneous Mixture Formation

and Transient Chemical Reactions. M. Tanabe, T. Bolik, C. Eigenbrod, H. J. Rath, J. Sato, M. Kono, 1637
A Simple Model of Ignition Modes of Dense Droplet Clouds. D. Thibaut, S. Candel, 2565
Self-Ignition of Hybrid (H_2 + Atomized Liquid Hydrocarbon Fuel + Gaseous Oxidizer) Mixtures at Engine Relevant Conditions. B. E. Gelfand, A. M. Bartenev, S. V. Khomik, S. P. Medvedev, A. N. Polenov, 2573
Dissociation and Chain Reaction in the Pyrolysis of Pyrazine. J. H. Kiefer, Q. Zhang, R. D. Kern, H. Chen, J. Yao, B. S. Jursic, 651
Comparison of Oxidation and Autoignition of the Two Primary Reference Fuels by Rapid Compression. R. Minetti, M. Carlier, M. Ribaucour, E. Therssen, L. R. Sochet, 747
Kinetic Modeling of the Oxidation of Large Aliphatic Hydrocarbons. M. Nehse, J. Warnatz, C. Chevalier, 773
Self-Ignition of Diesel-Relevant Hydrocarbon-Air Mixtures Under Engine Conditions. U. Pfahl, K. Fieweger, G. Adomeit, 781
Effect of Halogenated Flame Inhibitors on C_1-C_2 Organic Flames. T. Noto, V. Babushok, D. R. Burgess, Jr., A. Hamins, W. Tsang, A. Miziolek, 1377
Convective Ignition of a Granular Solid Propellant Bed: Influence of Propellant Composition. D. E. Kooker, S. L. Howard, L.-M. Chang, 2033
Ignition and Detonation in N_2O-CO-H_2-He Mixtures. A. Y. Starikovskii, 2999
Modeling of Solid Particle Interaction in a High-Velocity, Hot Gas Stream. M. M. Elkotb, N. Salama, I. Nassef, 1937
Extents of Alkane Combustion During Rapid Compression Leading to Single- and Two-Stage Ignition. A. Cox, J. F. Griffiths, C. Mohamed, H. Curran, W. J. Pitz, C. K. Westbrook, 2685
High-Pressure Methane Oxidation Behind Reflected Shock Waves. E. L. Petersen, M. Rŝhrig, D. F. Davidson, R. K. Hanson, C. T. Bowman, 799
Combustion Studies on Concentrated Distillery Effluents. N. M. Patel, P. J. Paul, H. S. Mukunda, S. Dasappa, 2479

02 Energy Requirements

Metal-Sulfur Combustion. S. Goroshin, A. Mizera, D. L. Frost, J. H. S. Lee, 1883
Influence of Pressure on the Combustion Rate of Carbon. R. H. Essenhigh, A. M. Mescher, 3085

03 Gases

15 Inhibition

Experimental Study of the Inhibition of Premixed and Diffusion Flames by Iron Pentacarbonyl. D. Reinelt, G. T. Linteris, 1421

01 Heterogeneous

02 Homogeneous

Chemical Effects of CF_3H in Extinguishing Counterflow CO/Air/H_2 Diffusion Flames. G. S. Fallon, H. K. Chelliah, G. T. Linteris, 1395
Effect of Halogenated Flame Inhibitors on C_1-C_2 Organic Flames. T. Noto, V. Babushok, D. R. Burgess, Jr., A. Hamins, W. Tsang, A. Miziolek, 1377
The NO and N_2O Formation Mechanism During Devolatilization and Char Combustion Under Fluidized-Bed Conditions. F. Winter, C. Wartha, G. Löffler, H. Hofbauer, 3325

16 Instability

Real-Time Adaptive Feedback Control of Combustion Instability. A. Kemal, C. T. Bowman, 2803
Experimental Demonstration of Active Control of Combustion Instabilities Using Real-Time Modes Observation and Secondary Fuel Injection. Y. Neumeier, B. T. Zinn, 2811
Active Instability Control with Direct-Drive Servo Valves in Liquid-Fueled Combustion Systems. C. Hantschk, J. Hermann, D. Vortmeyer, 2835
Stability and Emissions Characteristics of a Lean Premixed Gas Turbine Combustor. W.-P. Shih, J. G. Lee, D. A. Santavicca, 2771
Pulsating Instability in the Nonadiabatic Heterogeneous SHS Flame: Theory and Experimental Comparisons. A. Makino, C. K. Law, 1867
Analytical Study on Flame Stabilization in Reciprocating Combustion in Porous Media with High Thermal Conductivity. J. G. Hoffmann, R. Echigo, S. Tada, H. Yoshida, 2709

01 Acoustic

Active Instability Control with Direct-Drive Servo Valves in Liquid-Fueled Combustion Systems. C. Hantschk, J. Hermann, D. Vortmeyer, 2835
Active Control of Liquid-Fueled Combustion Using Periodic Vortex-Droplet Interaction. K. H. Yu, T. P. Parr, K. J. Wilson, K. C. Schadow, E. J. Gutmark, 2843
Structure of an Acoustically Forced Turbulent Spray Flame. E. Haile, O. Delabroy, F. Lacas, D. Veynante, S. Candel, 1663
Effects of External Acoustic Excitation on Enhanced Transport in a Resonant Incinerator. G. Pont, J. W. Willis, A. R. Karagozian, O. I. Smith, 2463
Studies of Helmholtz Resonance in a Swirl Burner/Furnace System. D. Froud, A. Beale, T. O'Doherty, N. Syred, 3355
The Effect of Heat Content and Composition of Fuel on Pulse Combustor Performance. A. Kushari, L. J. Rosen, J. I. Jagoda, B. T. Zinn, 3363

02 Fluid Dynamics

Instability of Diffusion Flames. A. Lingens, K. Neemann, J. Meyer, M. Schreiber, 1053
Numerical Study of Premixed Laminar Flame Propagation in a Closed Tube with a Full Navier-Stokes Approach. F. S. Marra, G. Cotinillo, 907
On Strained Flames with Hypergolic Reactants: The $H_2/NO/F_2$ System in High-Speed, Supersonic and Subsonic Mixing-Layer Combustion. F. N. Egolfopoulos, P. E. Dimotakis, C. Bond, 2885
Burning Velocity of Turbulent Premixed Flames in a High-Pressure Environment. H. Kobayashi, T. Tamura, K. Maruta, T. Niioka, F. A. Williams, 389
Study of Premixed Turbulent Combustion Including Landau-Darrieus Instability Effects. R. N. Paul, K. N. C. Bray, 259
Exothermicity and Three-Dimensional Effects in Unsteady Propane Square Jets. F. F. Grinstein, K. Kailasanath, 91
Swirl-Induced Intermittency: A Novel Effect Modifying the Turbulence Structure of Swirling Free Jets. F. HolzŠpfel, B. Lenze, W. Leuckel, 187
Influence of Gravity on the Propagation of Initially Spherical Flames. J. Daou, B. Rogg, 1275
Studies of Helmholtz Resonance in a Swirl Burner/Furnace System. D. Froud, A. Beale, T. O'Doherty, N. Syred, 3355

03 Nonlinear

Experimental Demonstration of Active Control of Combustion Instabilities Using Real-Time Modes Observation and Secondary Fuel Injection. Y. Neumeier, B. T. Zinn, 2811
Homogeneous Ignition of Hydrogen-Air Mixtures Over Platinum. P.-A. Bui, D. G. Vlachos, P. R. Westmoreland, 1763
Characterization of Chaotic Dynamics in the Spontaneous Combustion of Coal Stockpiles. G. Continillo, G. Galiero, P. L. Maffettone, S. Crescitelli, 1585

04 Others

Active Instability Control with Direct-Drive Servo Valves in Liquid-Fueled Combustion Systems. C. Hantschk, J. Hermann, D. Vortmeyer, 2835
Heat Loss and Lewis Number Effects on the Onset of Oscillations in Diffusion Flames. S. Cheatham, M. Matalon, 1063
A New Time-Dependent, Three-Dimensional Flame Model for Laminar Flames. G. Patnaik, K. Kailasanath, R. S. Sinkovits, 899
Oscillatory Combustion of Aluminized Composite Propellants. S. R. Hickman, M. Q. Brewster, 2007
Characterization of Chaotic Dynamics in the Spontaneous Combustion of Coal Stockpiles. G. Continillo, G. Galiero, P. L. Maffettone, S. Crescitelli, 1585
Structures of Multiple Combustion Waves Formed Under Filtration of Lean Hydrogen-Air Mixtures in a Packed Bed. A. V. Saveliev, L. A. Kennedy, A. A. Fridman, I. K. Puri, 3369

17 Kinetics

Theory and Modeling in Combustion Chemistry. J. A. Miller, 461
The Mutually Sensitised Oxidation of Ethylene and NO: An Experimental and Kinetic Modeling Study. A. Doughty, F. J. Barnes, J. H. Bromly, B. S. Haynes, 589
A Kinetic Study of the Oxidation of Acetonitrile: A Model for NO Formation from Fuel-Bound Nitrogen. E. Ikeda, J. C. Mackie, 597
Kinetic and Mechanistic Studies of the Reaction of Hydroxyl Radicals with Acetaldehyde Over an Extended Temperature Range. P. H. Taylor, M. S. Rahman, M. Arif, B. Dellinger, P. Marshall, 497
The Reactions of $O(^3P)$ Atoms with Aromatic Hydrocarbons with Unsaturated Side Chains. M. Eichholtz, S. Kohl, A. Schneider, J.-T. Vollmer, H.Gg. Wagner, 527
Elementary Reactions of the Methoxymethyl Radical in the Gas Phase: CH_3OCH_3 + F, CH_2OCH_3 + CH_2OCH_3, CH_2OCH_3 + O_2, and CH_2OCH_3 + O. K. Hoyermann, F. Nacke, 505
Gas Phase Reactions of Hydrogen Peroxide and Hydrogen Peroxide/Methanol Mixtures with Air Pollutants. V. M. Zamansky, L. Ho, P. M. Maly, W. R. Seeker, 2125
Chemical Kinetic Modeling of High-Pressure Propane Oxidation and Comparison to Experimental Results. D. N. Koert, W. J. Pitz, J. W. Bozzelli, N. P. Cernansky, 633
Self-Ignition of Diesel-Relevant Hydrocarbon-Air Mixtures Under Engine Conditions. U. Pfahl, K. Fieweger, G. Adomeit, 781
Reaction Mechanisms in Aromatic Hydrocarbon Formation Involving the C_5H_5 Cyclopentadienyl Moiety. C. F. Melius, M. E. Colvin, N. M. Marinov, W. J. Pitz, S. M. Senkan, 685
Experimental and Modeling Investigation of Aromatic and Polycyclic Aromatic Hydrocarbon Formation in a Premixed Ethylene Flame. M. J. Castaldi, N. M. Marinov, C. F. Melius, J. Huang, S. M. Senkan, W. J. Pitz, C. K. Westbrook, 693
The Reaction of Phenoxy Radicals with Mono-Chlorobenzene and Its Meaning for Gas-Phase Dioxin Formation in Incineration. H.-H. Grotheer, R. Louw, 2405
Reburning Promoted by Nitrogen- and Sodium-Containing Compounds. V. M. Zamansky, L. Ho, P. M. Maly, W. R. Seeker, 2075
Flow Reactor Studies and Testing of Comprehensive

Mechanisms for NO_x Reburning. D. Stapf, W. Leuckel, 2083
The Effect of Changes in the Flame Structure on the Formation and Destruction of Soot and NO_x in Radiating Diffusion Flames. A. Atreya, C. Zhang, H. K. Kim, T. Shamim, J. Suh, 2181
Molecular Beam Mass Spectrometric and Modeling Studies of Neat and NH_3-Doped Low-Pressure $H_2/N_2O/Ar$ Flames: Formation and Consumption of NO. R. C. Sausa, G. Singh, G. W. Lemire, W. R. Anderson, 1043
A New Approach to Studying Pore Diffusivity During Char Combustion at FBC Conditions. S. Goel, A. F. Sarofim, J. Lu, 3127
Reduced *n*-Heptane Mechanism for Non-Premixed Combustion with Emphasis on Pollutant-Relevant Intermediate Species. M. Bollig, H. Pitsch, J. C. Hewson, K. Seshadri, 729
Kinetics of the Reaction of Vinyl Radicals With Acetylene. V. D. Knyazev, S. I. Stoliarov, I. R. Slagle, 513
Absolute Reactive Cross Sections for the Reaction $OH + CO \rightarrow H + CO_2$. S. Koppe, T. Laurent, H.-R. Volpp, J. Wolfrum, P. D. Naik, 489
Ignition of Hydrogen and Oxygen in Counterflow at High Pressures. B. T. Helenbrook, C. K. Law, 815

01 Elementary Reactions

Measurement of the Rate Coefficient of $H + O_2 + M \rightarrow HO_2 + M$ for M = Ar and N_2 at High Pressures. D. F. Davidson, E. L. Petersen, M. Röhrig, R. K. Hanson, C. T. Bowman, 481
A Shock Tube Study of $H + HNCO \rightarrow H_2 + NCO$ and the Thermal Decomposition of NCO. J. D. Mertens, R. K. Hanson, 551
Direct Measurement of the Reaction Pair $C_6H_5NO \int C_6H_5 + NO$ by a Combined Shock Tube and Flow Reactor Approach. C. Horn, P. Frank, R. S. Tranter, J. Schaugg, H.-H. Grotheer, T. Just, 575
A Shock Tube Study of the Reaction of S–Atoms with NO. D. Woiki, P. Roth, 583
A Kinetic Study of the Oxidation of Acetonitrile: A Model for NO Formation from Fuel-Bound Nitrogen. E. Ikeda, J. C. Mackie, 597
Kinetic and Mechanistic Studies of the Reaction of Hydroxyl Radicals with Acetaldehyde Over an Extended Temperature Range. P. H. Taylor, M. S. Rahman, M. Arif, B. Dellinger, P. Marshall, 497
The Reactions of $O(^3P)$ Atoms with Aromatic Hydrocarbons with Unsaturated Side Chains. M. Eichholtz, S. Kohl, A. Schneider, J.-T. Vollmer, H.Gg. Wagner, 527
High-Temperature Reactions and Thermodynamic Properties of Phenyl Radicals. E. Heckmann, H. Hippler, J. Troe, 543
Elementary Reactions of the Methoxymethyl Radical in the Gas Phase: $CH_3OCH_3 + F$, $CH_2OCH_3 + CH_2OCH_3$, $CH_2OCH_3 + O_2$, and $CH_2OCH_3 + O$. K. Hoyermann, F. Nacke, 505
Experimental and Computational Investigation of Concentration Profiles of C_1-C_4 Hydrocarbon Radicals and Molecules in Low-Pressure $C_2H_2/O/H$ Atomic Flames at 600 K. J. Peeters, K. Devriendt, 1001
Experimental Study of the Structure of Rich Ethane Flames. R. Ancia, J. Vandooren, P. J. Van Tiggelen, 1009
Destruction of Benzene in High-Temperature Flames: Chemistry of Benzene and Phenol. R. A. Shandross, J. P. Longwell, J. B. Howard, 711
Dissociation and Chain Reaction in the Pyrolysis of Pyrazine. J. H. Keifer, Q. Zhang, R. D. Kern, H. Chen, J. Yao, B. S. Jursic, 651
Thermal Reduction of NO by NH_3: Kinetic Modeling of the $NH_2 + NO$ Product Branching Ratio. M. J. Halbgewachs, E. W. G. Diau, A. M. Mebel, M. C. Lin, C. F. Melius, 2109
An Intermediate Temperature Modeling Study of the Combustion of Neopentane. H. J. Curran, W. J. Pitz, C. K. Westbrook, M. W. M. Hisham, R. W. Walker, 641
Computer-Aided Design of Gas-Phase Oxidation Mechanisms–Application to the Modeling of *n*-Heptane and Iso-Octane Oxidation. G. M. Côme, V. Warth, P. A. Glaude, R. Fournet, F. Battin-Leclerc, G. Scacchi, 755
Kinetic Modeling of the Oxidation of Large Aliphatic Hydrocarbons. M. Nehse, J. Warnatz, C. Chevalier, 773
Laminar Flame Speeds and Oxidation Kinetics of Benzene-Air and Toluene-Air Flames. S. G. Davis, H. Wang, K. Brezinsky, C. K. Law, 1025
Reaction Mechanisms in Aromatic Hydrocarbon Formation Involving the C_5H_5 Cyclopentadienyl Moiety. C. F. Melius, M. E. Colvin, N. M. Marinov, W. J. Pitz, S. M. Senkan, 685
The $CH_3 + C_5H_5$ Reaction: A Potential Source of Benzene at High Temperatures. L. V. Moskaleva, A. M. Mebel, M. C. Lin, 521
The Reaction of Phenoxy Radicals with Mono-Chlorobenzene and Its Meaning for Gas-Phase Dioxin Formation in Incineration. H.-H. Grotheer, R. Louw, 2405
A Kinetic Study of the Reactions of $NH(X^3\Sigma^-)$ with O_2 and NO in the Temperature Range from 1200 to 2200 K. H.-J. Römming, H. Gg. Wagner, 559
Measurement of the Branching Ratio of NCO + NO into N_2O at 1100–1400 K. S. A. Flatness, J. C. Kramlich, 567
The Effects of Flame Structure on Extinction of CH_4–O_2–N_2 Diffusion Flames. J. Du, R. L. Axelbaum, 1137
Numerical Modeling of Catalytic Ignition. O. Deutschmann, R. Schmidt, F. Behrendt, J. Warnatz, 1747
Pd on Low-Surface-Area α-Alumina System: Is Me-

tallic Pd Active for Methane Combustion? M. Lyubovsky, R. Weber, L. Pfefferle, 1779
Ignition and Detonation in N_2O-CO-H_2-He Mixtures. A. Y. Starikovskii, 2999
Emissions of Nitrogen Oxides from Circulating Fluidized-Bed Combustors: Modeling Results Using Detailed Chemistry. S. Goel, A. Sarofim, P. Kilpinen, M. Hupa, 3317
The Influence of Pressure on Char Combustion Kinetics. E. Croiset, C. Mallet, J.-P. Rouan, J.-R. Richard, 3095
Thermal Decomposition of C_2H_5I. S. S. Kumaran, M.-C. Su, K. P. Lim, J. V. Michael, 605
Kinetics and Mechanism of the Reaction of $S(^3P)$ with O_2. A. Miyoshi, H. Shiina, K. Tsuchiya, H. Matsui, 535
Kinetics of the Reaction of Vinyl Radicals With Acetylene. V. D. Knyazev, S. I. Stoliarov, I. R. Slagle, 513
Absolute Reactive Cross Sections for the Reaction $OH + CO \rightarrow H + CO_2$. S. Koppe, T. Laurent, H.-R. Volpp, J. Wolfrum, P. D. Naik, 489

02 Heat Release Rates

Heterogeneous/Homogeneous Reaction and Transport Coupling During Flame-Wall Interaction. P. Popp, M. Smooke, M. Baum, 2693

03 Ionic Reactions

04 Modeling

Application of a Reduced Kinetic Model for Soot Formation and Burnout in Three-Dimensional Diesel Combustion Computations. P. Belardini, C. Bertoli, C. Beatrice, N. Del Giacomo, A. D'Anna, 2517
Autoignition Chemistry in a Motored Engine: An Experimental and Kinetic Modeling Study. H. J. Curran, P. Gaffuri, W. J. Pitz, C. K. Westbrook, W. R. Leppard, 2669
A Shock Tube Study of $H + HNCO \rightarrow H_2 + NCO$ and the Thermal Decomposition of NCO. J. D. Mertens, R. K. Hanson, 551
The Mutually Sensitised Oxidation of Ethylene and NO: An Experimental and Kinetic Modeling Study. A. Doughty, F. J. Barnes, J. H. Bromly, B. S. Haynes, 589
A Kinetic Study of the Oxidation of Acetonitrile: A Model for NO Formation from Fuel-Bound Nitrogen. E. Ikeda, J. C. Mackie, 597
Kinetic and Mechanistic Studies of the Reaction of Hydroxyl Radicals with Acetaldehyde Over an Extended Temperature Range. P. H. Taylor, M. S. Rahman, M. Arif, B. Dellinger, P. Marshall, 497
Experimental and Computational Investigation of Concentration Profiles of C_1-C_4 Hydrocarbon Radicals and Molecules in Low-Pressure C_2H_2/O/H Atomic Flames at 600 K. J. Peeters, K. Devriendt, 1001
Destruction of Benzene in High-Temperature Flames: Chemistry of Benzene and Phenol. R. A. Shandross, J. P. Longwell, J. B. Howard, 711
The Ignition and Oxidation of Allene and Propyne: Experiments and Kinetic Modeling. H. Curran, J. M. Simmie, P. Dagaut, D. Voisin, M. Cathonnet, 613
The Formation of C_2 During High-Temperature Pyrolysis of Fullerene C_{70}. T. Sommer, P. Roth, 621
Thermal Decomposition of Benzonitrile: A Combined Single-Pulse Shock Tube-ARAS Investigation. A. Lifshitz, Y. Cohen, M. Braun-Unkhoff, P. Frank, 659
Dissociation and Chain Reaction in the Pyrolysis of Pyrazine. J. H. Kiefer, Q. Zhang, R. D. Kern, H. Chen, J. Yao, B. S. Jursic, 651
Thermal Reduction of NO by NH_3: Kinetic Modeling of the NH_2 + NO Product Branching Ratio. M. J. Halbgewachs, E. W. G. Diau, A. M. Mebel, M. C. Lin, C. F. Melius, 2109
Chemical Kinetic Study of Dimethylether Oxidation in a Jet Stirred Reactor from 1 to 10 ATM: Experiments and Kinetic Modeling. P. Dagaut, J.-C. Boettner, M. Cathonnet, 627
An Intermediate Temperature Modeling Study of the Combustion of Neopentane. H. J. Curran, W. J. Pitz, C. K. Westbrook, M. W. M. Hisham, R. W. Walker, 641
Chemical Kinetic Modeling of High-Pressure Propane Oxidation and Comparison to Experimental Results. D. N. Koert, W. J. Pitz, J. W. Bozzelli, N. P. Cernansky, 633
Experimental Data and Kinetic Modeling of Primary Reference Fuel Mixtures. C. V. Callahan, T. J. Held, F. L. Dryer, R. Minetti, M. Ribaucour, L. R. Sochet, T. Faravelli, P. Gaffuri, E. Ranzi, 739
Computer-Aided Design of Gas-Phase Oxidation MechanismsÑApplication to the Modeling of *n*-Heptane and Iso-Octane Oxidation. G. M. Côme, V. Warth, P. A. Glaude, R. Fournet, F. Battin-Leclerc, G. Scacchi, 755
Kinetic Modeling of the Oxidation of Large Aliphatic Hydrocarbons. M. Nehse, J. Warnatz, C. Chevalier, 773
Laminar Flame Speeds and Oxidation Kinetics of Benzene-Air and Toluene-Air Flames. S. G. Davis, H. Wang, K. Brezinsky, C. K. Law, 1025
A Detailed Comprehensive Kinetic Model for Benzene Oxidation Using the Recent Kinetic Results. Y. Tan, P. Frank, 677
Experimental and Modeling Investigation of Aromatic and Polycyclic Aromatic Hydrocarbon Formation in a Premixed Ethylene Flame. M. J. Castaldi, N. M. Marinov, C. F. Melius, J. Huang, S. M. Senkan, W. J. Pitz, C. K. Westbrook, 693
Benzene Formation Chemistry in Premixed 1,3-Butadiene Flames. R. P. Lindstedt, G. Skevis, 703

Pressure Effects on the Thermal de-NO_x Process. K. Kjærgaard, P. Glarborg, K. Dam-Johansen, J. A. Miller, 2067
Reburning Promoted by Nitrogen- and Sodium-Containing Compounds. V. M. Zamansky, L. Ho, P. M. Maly, W. R. Seeker, 2075
A Model for Prediction of Selective Noncatalytic Reduction of Nitrogen Oxides by Ammonia, Urea, and Cyanuric Acid with Mixing Limitations in the Presence of CO. J. Brouwer, M. P. Heap, D. W. Pershing, P. J. Smith, 2117
Flow Reactor Studies and Testing of Comprehensive Mechanisms for NO_x Reburning. D. Stapf, W. Leuckel, 2083
Isotopic Labeling Studies of the Selective Non-Catalytic Reduction of NO with NH_3. B. L. Duffy, P. F. Nelson, 2099
Evidence for a New NO Production Mechanism in Flames. J. E. Harrington, G. P. Smith, P. A. Berg, A. R. Noble, J. B. Jeffries, D. R. Crosley, 2133
Acetylene and Ethylene Mole Fractions in Methane/Air Partially Premixed Flames. L.-K. Tseng, J. P. Gore, I. K. Puri, T. Takeno, 993
Effect of Halogenated Flame Inhibitors on C_1-C_2 Organic Flames. T. Noto, V. Babushok, D. R. Burgess, Jr., A. Hamins, W. Tsang, A. Miziolek, 1377
A Three-Phase Model of HMX Combustion. J. E. Davidson, M. W. Beckstead, 1989
Catalytic Oxidation of Natural Gas Over Supported Platinum: Flow Reactor Experiments and Detailed Numerical Modeling. T. C. Bond, R. A. Noguchi, C.-P. Chou, R. K. Mongia, J.-Y. Chen, R. W. Dibble, 1771
Catalytic Combustion of Carbon Particulate at High Values of the Carbon/Catalyst Mass Ratio. P. Ciambelli, M. D'Amore, V. Palma, S. Vaccaro, 1789
C_2H_2 and PAH as Soot Growth Reactants in Premixed C_2H_4-Air Flames. T. G. Benish, A. L. Lafleur, K. Taghizadeh, J. B. Howard, 2319
Experiments and Numerical Simulation on Soot Formation in Opposed-Jet Ethylene Diffusion Flames. H. Wang, D. X. Du, C. J. Sung, C. K. Law, 2359
Surface Heterogeneity in the Formation and Decomposition of Carbon Surface Oxides. M. C. Ma, B. S. Haynes, 3119
Effects of Ambient Water in the Combustion Enhancement of Heavily Chlorinated Hydrocarbons: Studies on Droplet Burning. H. Wang, D. L. Zhu, Y. Saso, C. K. Law, 2413
An Integrated PDF/Neural Network Approach for Simulating Turbulent Reacting Systems. F. C. Christo, A. R. Masri, E. M. Nebot, S. B. Pope, 43
Flamelet and PDF Modeling of CO and NO_x Emissions from a Turbulent, Methane Hydrogen Jet Nonpremixed Flame. J.-Y. Chen, W.-C. Chang, 2207
Extents of Alkane Combustion During Rapid Compression Leading to Single- and Two-Stage Ignition. A. Cox, J. F. Griffiths, C. Mohamed, H. Curran, W. J. Pitz, C. K. Westbrook, 2685
Thermal Decomposition of Benzene. Single-Pulse Shock-Tube Investigation. A. Laskin, A. Lifshitz, 669
High-Pressure Methane Oxidation Behind Reflected Shock Waves. E. L. Petersen, M. Röhrig, D. F. Davidson, R. K. Hanson, C. T. Bowman, 799
Detailed Kinetic Reaction Mechanism for Ignition and Oxidation of α-Methylnaphthalene. H. Pitsch, 721
Hydroxyl Radical Chemiluminescence Imaging and the Structure of Microgravity Droplet Flames. A. J. Marchese, F. L. Dryer, V. Nayagam, R. Colantonio, 1219
A Broader Definition of Symmetry Number and Its Application to a Kinetic Model Describing Polyarene Growth. M. C. Masonjones, A. F. Sarofim, 823
Structures of Multiple Combustion Waves Formed Under Filtration of Lean Hydrogen-Air Mixtures in a Packed Bed. A. V. Saveliev, L. A. Kennedy, A. A. Fridman, I. K. Puri, 3369
Reduced Mechanisms for NO_x Emissions from Hydrocarbon Diffusion Flames. J. C. Hewson, M. Bolling, 2171
Quantitative CH Determinations in Low-Pressure Flames. J. Luque, G. P. Smith, D. R. Crosley, 959
The Formation of SiO_2 from Hexamethyldisiloxane Combustion in Counterflow Methane-Air Flames. H. K. Chagger, D. Hainsworth, P. M. Patterson, M. Pourkashanian, A. Williams, 1859

05 Overall Rates

The Formation of C_2 During High-Temperature Pyrolysis of Fullerene C_{70}. T. Sommer, P. Roth, 621
A Model for Prediction of Selective Noncatalytic Reduction of Nitrogen Oxides by Ammonia, Urea, and Cyanuric Acid with Mixing Limitations in the Presence of CO. J. Brouwer, M. P. Heap, D. W. Pershing, P. J. Smith, 2117
A Kinetic Study of the Reactions of $NH(X^3\Sigma^-)$ with O_2 and NO in the Temperature Range from 1200 to 2200 K. H.-J. Römming, H. Gg. Wagner, 559
Pd on Low-Surface-Area α-Alumina System: Is Metallic Pd Active for Methane Combustion? M. Lyubovsky, R. Weber, L. Pfefferle, 1779
The Impact of Fragmentation on Char Conversion During Pulverized Coal Combustion. R. E. Mitchell, A. E. Jacob Akanetuk, 3137
Combustion-Like Pyrolysis of Organic Polymers: Species and Kinetic Details by *T*-Jump/FTIR Spectroscopy. T. B. Brill, H. Arisawa, P. E. Gongwer, 791
Single-Particle Combustion of Two Biomass Chars. M. J. Wornat, R. H. Hurt, K. A. Davis, N. Y. C. Yang, 3075

The Influence of Pressure on Char Combustion Kinetics. E. Croiset, C. Mallet, J.-P. Rouan, J.-R. Richard, 3095
Influence of Pressure on the Combustion Rate of Carbon. R. H. Essenhigh, A. M. Mescher, 3085
Thermal Decomposition of Benzene. Single-Pulse Shock-Tube Investigation. A. Laskin, A. Lifshitz, 669
A General Model for Devolatilization of Large Coal Particles. Y. Zhao, M. A. Serio, P. R. Solomon, 3145

18 Modeling and Scaling

The Challenge of Turbulent Combustion. K. N. C. Bray, 1
Using Direct Numerical Simulations to Understand Premixed Turbulent Combustion. T. Poinsot, 219
Solid Fuel Utilization: From Coal to Biomass. F. C. Lockwood, 3041
Interpretation of k-ε Computed Turbulence Length-Scale Predictions for Engine Flows. Z. Han, R. D. Reitz, F. E. Corcione, G. Valentino, 2717
Measurements and Predictions of Nitric Oxide and Particulates Emissions from Heavy Fuel Oil Spray Flames. M. A. Byrnes, E. A. Foumeny, T. Mahmud, A. S. A. K Sharifah, T. Abbas, P. G. Costen, S. Hassan, F. C. Lockwood, 2241
Catalytic Oxidation of Natural Gas Over Supported Platinum: Flow Reactor Experiments and Detailed Numerical Modeling. T. C. Bond, R. A. Noguchi, C.-P. Chou, R. K. Mongia, J.-Y. Chen, R. W. Dibble, 1771
Modeling of Solid Particle Interaction in a High-Velocity, Hot Gas Stream. M. M. Elkotb, N. Salama, I. Nassef, 1937
Subgrid Mixing and Molecular Transport Modeling in a Reacting Shear Layer. S. Menon, W. H. Calhoon, Jr., 59
A Transient Two-Dimensional Chemically Reactive Flow Model: Fuel Particle Combustion in a Nonquiescent Environment. J. Lee, A. G. Tomboulides, S. A. Orszag, R. A. Yetter, F. L. Dryer, 3059
Predicting the Near-Burner-Zone Flow Field and Chemistry of Swirl-Stabilized Low-NO_x Flames of Pulverized Coal Using the RNG-k-ε, RSM, and k-ε Turbulence Models. F. Breussin, F. Pigari, R. Weber, 211
Model Simulations of Freely Propagating Turbulent Premixed Flames. T. Smith, S. Menon, 299
Combustion Studies on Concentrated Distillery Effluents. N. M. Patel, P. J. Paul, H. S. Mukunda, S. Dasappa, 2479

01 Empirical

A Model for Prediction of Selective Noncatalytic Reduction of Nitrogen Oxides by Ammonia, Urea, and Cyanuric Acid with Mixing Limitations in the Presence of CO. J. Brouwer, M. P. Heap, D. W. Pershing, P. J. Smith, 2117
Study of Premixed Turbulent Combustion Including Landau-Darrieus Instability Effects. R. N. Paul, K. N. C. Bray, 259
Turbulent Length Scales in a Swirling Flame. G. Früchtel, E. P. Hassel, J. Janicka, 195
A Simplified Phenomenological Model for Soot Growth Based on Plug Flow Reactor Experiments. B. Bartenbach, W. Leuckel, 2311

02 Fundamental

Surface Tension Influences on Methanol Droplet Vaporization in the Presence of Water. H. A. Dwyer, I. Aharon, B. D. Shaw, H. Niazmand, 1613
Numerical and Asymptotic Studies of the Structure of Premixed *iso*-Octane Flames. H. Pitsch, N. Peters, K. Seshadri, 763
Gravitational Effects on Sooting Diffusion Flames. C. R. Kaplan, E. S. Oran, K. Kailasanath, H. D. Ross, 1301
Markstein Lengths of CO/H_2/Air Flames, Using Expanding Spherical Flames. M. J. Brown, I. C. McLean, D. B. Smith, S. C. Taylor, 875
The Sensitive Structure of Partially Premixed Methane-Air vs. Air Counterflow Flames. M. A. Tanoff, M. D. Smooke, R. J. Osborne, T. M. Brown, R. W. Pitz, 1121
Combustion of Porous Energetic Materials in the Merged-Flame Regime. S. B. Margolis, F. A. Williams, A. M. Telengator, 1969
Diamond Thin Film Deposition in Low-Pressure Premixed Flames. D. G. Goodwin, N. G. Glumac, H. S. Shin, 1817
Quenching of Reaction in Gas-Sampling Probes to Measure Scramjet Engine Performance. T. Mitani, 2917
A Comprehensive Physical and Numerical Model of Boron Particle Ignition. W. Zhou, R. A. Yetter, F. L. Dryer, H. Rabitz, R. C. Brown, C. E. Kolb, 1909
Measurements and Prediction of Air Entrainment Rates of Pool Fires. X. C. Zhou, J. P. Gore, H. R Baum, 1453
On Surface Growth Mechanism of Soot Particles. M. Frenklach, 2285
Flamelet Modeling of Soot Formation in Laminar Ethyne/Air-Diffusion Flames. M. Balthasar, A. Heyl, F. Mauß, F. Schmitt, H. Bockhorn, 2369
Effect of Liquid Drops on the Thermal Explosion of a Gas Mixture. V. Goldshtein, I. Goldfarb, A. Zinoviev, I. Shreiber, 1557
A New Approach to Studying Pore Diffusivity During Char Combustion at FBC Conditions. S. Goel, A. F. Sarofim, J. Lu, 3127
The Impact of Fragmentation on Char Conversion During Pulverized Coal Combustion. R. E. Mitchell, A. E. Jacob Akanetuk, 3137

Prediction of Coal-Water Slurry Dispersion in a Fluidized Bed Combustor. F. Okasha, M. Miccio, 3277
Experimental Analysis of Flame Surface Density Models for Premixed Turbulent Combustion. D. Veynante, J. Piana, J. M. Duclos, C. Martel, 413
Direct Numerical Simulation Analysis of Flame Surface Density Equation in Non-Premixed Turbulent Combustion. E. Van Kalmthout, D. Veynante, S. Candel, 35
An Integrated PDF/Neural Network Approach for Simulating Turbulent Reacting Systems. F. C. Christo, A. R. Masri, E. M. Nebot, S. B. Pope, 43
A Mixing Model to Improve the PDF Simulation of Turbulent Diffusion Flames. A. R. Masri, S. Subramaniam, S. B. Pope, 49
Flamelet and PDF Modeling of CO and NO_x Emissions from a Turbulent, Methane Hydrogen Jet Nonpremixed Flame. J.-Y. Chen, W.-C. Chang, 2207
Simulation of Detailed Chemistry in a Turbulent Combustor Flow. H. C. Magel, U. Schnell, K. R. G. Hein, 67
CFD Prediction of Coupled Radiation Heat Transfer and Soot Production in Turbulent Flames. N. W. Bressloff, J. B. Moss, P. A. Rubini, 2379
A Study of Turbulent Diffusion Flames Formed by Planar Fuel Injection into the Wake Formation Region of a Slender Square Cylinder. P. Koutmos, C. Mavridis, D. Papailiou, 161
Swirl-Induced Intermittency: A Novel Effect Modifying the Turbulence Structure of Swirling Free Jets. F. Holzäpfel, B. Lenze, W. Leuckel, 187
Edge-Flame-Holding. J. Buckmaster. R. Weber, 1143
Modeling of Premixed Gas Combustion in Porous Media Composed of Coarse-Sized Particles: 1-D Description with Discrete Solid Phase. O. S. Rabinovich, A. V. Fefelov, N. V. Pavlyukevich, 3383
A Broader Definition of Symmetry Number and its Application to a Kinetic Model Describing Polyarene Growth. M. C. Masonjones, A. F. Sarofim, 823
Impact of Mixing Model on Predicted NO Formation in a Nonpremixed, Partially Stirred Reactor. W.-C. Chang, J.-Y. Chen, 2223
Quantitative Comparison of Detailed Numerical Computations and Experiments in Counterflow Spray Diffusion Flames. L. P. Gao, Y. D'Angelo, I. Silverman, A. Gomez, M. D. Smooke, 1739
Superadiabatic Combustion Wave in a Diluted Methane-Air Mixture Under Filtration in a Packed Bed. S. I. Foutko, S. I. Shabunya, S. A. Zhdanok, L. A. Kennedy, 3377

03 Others

Modeling Turbulent Combustion and Pollutant Formation in Stratified Charge SI Engines. T. A. Baritaud, J. M. Duclos, A. Fusco, 2627
1-D Simulation of a Spark Discharge in Air. M. Schäfer, R. Schmidt, J. Kšhler, 2701
A Numerical and Experimental Study of Fuel Evaporation and Mixing for Lean Premixed Combustion at High Pressure. M. Rachner, M. Brandt, H. Eickhoff, C. Hassa, A. Bräumer, H. Krämer, M. Ridder, V. Sick, 2741
Emissions of Nitrogen Oxides from Circulating Fluidized-Bed Combustors: Modeling Results Using Detailed Chemistry. S. Goel, A. Sarofim, P. Kilpinen, M. Hupa, 3317
A Test of an Engineering Model of Premixed Turbulent Combustion. V. Karpov, A. Lipatnikov, V. Zimont, 249
Characterization of Chaotic Dynamics in the Spontaneous Combustion of Coal Stockpiles. G. Continillo, G. Galiero, P. L. Maffettone, S. Crescitelli, 1585

19 Oxidation (*Also see* Kinetics)

Oxidation of Hydrocarbons from Lubricant Oil Layers in Spark-Ignition Engines. M. G. Norris, W. Bauer, S. Hochgreb, 2645
The Reactions of $O(^3P)$ Atoms with Aromatic Hydrocarbons with Unsaturated Side Chains. M. Eichholtz, S. Kohl, A. Schneider, J.-T. Vollmer, H.Gg. Wagner, 527
An Intermediate Temperature Modeling Study of the Combustion of Neopentane. H. J. Curran, W. J. Pitz, C. K. Westbrook, M. W. M. Hisham, R. W. Walker, 641
Chemical Kinetic Modeling of High-Pressure Propane Oxidation and Comparison to Experimental Results. D. N. Koert, W. J. Pitz, J. W. Bozzelli, N. P. Cernansky, 633
Computer-Aided Design of Gas-Phase Oxidation Mechanisms–Application to the Modeling of *n*-Heptane and Iso-Octane Oxidation. G. M. Côme, V. Warth, P. A. Glaude, R. Fournet, F. Battin-Leclerc, G. Scacchi, 755
Extents of Alkane Combustion During Rapid Compression Leading to Single- and Two-Stage Ignition. A. Cox, J. F. Griffiths, C. Mohamed, H. Curran, W. J. Pitz, C. K. Westbrook, 2685
Analysis of Wet Co Oxidation Under Turbulent Non-Premixed Conditions Using a PDF Method and Detailed Chemical Kinetics. M. Kraft, E. Stöckelmann, H. Bockhorn, 807

20 Phase Changes

Gas-Phase Combustion Synthesis of Aluminum Nitride Powder. R. L. Axelbaum, C. R. Lottes, J. I. Huertas, L. J. Rosen, 1891
Combustion Characteristics of Mg-CO_2 Counterflow Diffusion Flames. A. Fukuchi, M. Kawashima, S. Yuasa, 1945
Statistical Analysis on Onset of Microexplosion for

an Emulsion Droplet. M. Tsue, H. Yamasaki, T. Kadota, D. Segawa, 1629

01 Condensation

Surface Tension Influences on Methanol Droplet Vaporization in the Presence of Water. H. A. Dwyer, I. Aharon, B. D. Shaw, H. Niazmand, 1613
The Controlling Chemistry in Flame Generated Surface Deposition of Na_2SO_4 and the Effects of Chlorine. M. Steinberg, K. Schofield, 1835
A Mathematical Model of Laser-Induced Synthesis of Ultrafine SiC Powders. S. S. Khartchenko, A. I. Kuzmin, 1845

02 Evaporation

Spray Combustion Phenomena. G. M. Faeth, 1593
A Numerical and Experimental Study of Fuel Evaporation and Mixing for Lean Premixed Combustion at High Pressure. M. Rachner, M. Brandt, H. Eickhoff, C. Hassa, A. Bräumer, H. Krämer, M. Ridder, V. Sick, 2741
Surface Tension Influences on Methanol Droplet Vaporization in the Presence of Water. H. A. Dwyer, I. Aharon, B. D. Shaw, H. Niazmand, 1613
Flame Propagation in Planar Droplet Arrays and Interaction Phenomena Between Neighboring Droplet Streams. N. Roth, A. Karl, K. Anders, A. Frohn, 1697
Experimental Study on High-Pressure Droplet Evaporation Using Microgravity Conditions. H. Nomura, Y. Ujiie, H. J. Rath, J. Sato, M. Kono, 1267
Effect of Liquid Drops on the Thermal Explosion of a Gas Mixture. V. Goldshtein, I. Goldfarb, A. Zinoviev, I. Shreiber, 1557
Two-Regime Global Kinetics of Cellulose Pyrolysis: The Role of Tar Evaporation. E. M. Suuberg, I. Milosavljevic, V. Oja, 1515
Visualization of Fuel Distribution in Premixed Ducts in a Low-Emission Gas Turbine Combustor Using Laser Techniques. C. Löfström, H. Kaaling, M. Aldén, 2787
Effect of the Fuel Boiling Point on the Boilover Burning of Liquid Fuels Spilled on Water. J. P. Garo, J. P. Vantelon, A. C. Fernandez-Pello, 1461

03 Nucleation

Effect of the Fuel Boiling Point on the Boilover Burning of Liquid Fuels Spilled on Water. J. P. Garo, J. P. Vantelon, A. C. Fernandez-Pello, 1461

21 Pollutants

Solid Fuel Utilization: From Coal to Biomass. F. C. Lockwood, 3041
Modern Tools for Diesel Engine Combustion Investigation. W. Hentschel, 2503
Measurements and Predictions of Nitric Oxide and Particulates Emissions from Heavy Fuel Oil Spray Flames. M. A. Byrnes, E. A. Foumeny, T. Mahmud, A. S. A. K Sharifah, T. Abbas, P. G. Costen, S. Hassan, F. C. Lockwood, 2241
Kinetic and Mechanistic Studies of the Reaction of Hydroxyl Radicals with Acetaldehyde Over an Extended Temperature Range. P. H. Taylor, M. S. Rahman, M. Arif, B. Dellinger, P. Marshall, 497
Comparison of Oxidation and Autoignition of the Two Primary Reference Fuels by Rapid Compression. R. Minetti, M. Carlier, M. Ribaucour, E. Therssen, L. R. Sochet, 747
The Reaction of Phenoxy Radicals with Mono-Chlorobenzene and Its Meaning for Gas-Phase Dioxin Formation in Incineration. H.-H. Grotheer, R. Louw, 2405
Control of NO_x Emissions by NO_x Recycle Approach. C. Q. Zhou, L. G. Neal, R. Bolli, J. Haslbeck, A. Chang, 2091
The Effect of Changes in the Flame Structure on the Formation and Destruction of Soot and NO_x in Radiating Diffusion Flames. A. Atreya, C. Zhang, H. K. Kim, T. Shamim, J. Suh, 2181
Re-Initiation of Soot Surface Growth in Premixed Counterflow Flames. M. Marquardt, F. Mauß, B. Jungfleisch, R. Suntz, H. Bockhorn, 2343
Compact Incinerator Afterburner Concept Based on Vortex Combustion. T. P. Parr, E. Gutmark, K. Wilson, D. M. Hanson-Parr, K. Yu, R. A. Smith, K. C. Schadow, 2471
Reduced *n*-Heptane Mechanism for Non-Premixed Combustion with Emphasis on Pollutant-Relevant Intermediate Species. M. Bollig, H. Pitsch, J. C. Hewson, K. Seshadri, 729
An Experimental Study of the Release of Nitrogen from Coals Pyrolyzed in Fluidized-Bed Reactors. C.-Z. Li, P. F. Nelson, E. B. Ledesma, J. C. Mackie, 3205
Adsorption of Metallic Mercury on Activated Carbon. D. Karatza, A. Lancia, D. Musmarra, F. Pepe, 2439

01 HC (Hydrocarbons) and CO

Advanced Diagnostics for Minimizing Hydrocarbon Emissions from a Direct-Injection Gasoline Engine. M. C. Drake, D. T. French, T. D. Fansler, 2581
Relation Between Flame Propagation Characteristics and Hydrocarbon Emissions Under Lean Operating Conditions in Spark-Ignition Engines. N. Hadjiconstantinou, K. Min, J. B. Heywood, 2637
Oxidation of Hydrocarbons from Lubricant Oil Layers in Spark-Ignition Engines. M. G. Norris, W. Bauer, S. Hochgreb, 2645
Modeling Turbulent Combustion and Pollutant For-

mation in Stratified Charge SI Engines. T. A. Baritaud, J. M. Duclos, A. Fusco, 2627
Optimization of Gas Turbine Combustor Performance Throughout the Duty Cycle. N. T. Davis, G. S. Samuelsen, 2819
Destruction of Benzene in High-Temperature Flames: Chemistry of Benzene and Phenol. R. A. Shandross, J. P. Longwell, J. B. Howard, 711
Gas Phase Reactions of Hydrogen Peroxide and Hydrogen Peroxide/Methanol Mixtures with Air Pollutants. V. M. Zamansky, L. Ho, P. M. Maly, W. R. Seeker, 2125
Chemical Kinetic Study of Dimethylether Oxidation in a Jet Stirred Reactor from 1 to 10 ATM: Experiments and Kinetic Modeling. P. Dagaut, J.-C. Boettner, M. Cathonnet, 627
Quantitative Two-Photon Laser-Induced Fluorescence Imaging of CO in Flickering CH_4/Air Diffusion Flames. D. A. Everest, C. R. Shaddix, K. C. Smyth, 1161
Pollutant Formation During Coal Combustion in a CFB Test Furnace. A. Reidick, H. Kremer, 3309
An Experimental Study on Quenching Crevice Widths in the Combustion Chamber of a Spark-Ignition Engine. S. Ishizawa, 2605
Tunable Diode Laser Absorption Measurements of Carbon Monoxide and Temperature in a Time-Varying, Methane/Air, Non-Premixed Flame. R. R. Skaggs, J. H. Miller, 1181
Analysis of Wet Co Oxidation Under Turbulent Non-Premixed Conditions Using a PDF Method and Detailed Chemical Kinetics. M. Kraft, E. Stöckelmann, H. Bockhorn, 807
Reduced Mechanisms for NO_x Emissions from Hydrocarbon Diffusion Flames. J. C. Hewson, M. Bolling, 2171

02 NO_x

Theory and Modeling in Combustion Chemistry. J. A. Miller, 461
Polarization Separated Spatially Resolved Single Laser Shot Multispecies Analysis in the Combustion Chamber of a Realistic SI Engine with a Tunable KrF Excimer Laser. M. Knapp, A. Luczak, V. Beushausen, W. Hentschel, P. Manz, P. Andresen, 2589
Quantitative 2D Single–Shot Imaging of NO Concentrations and Temperatures in a Transparent SI Engine. C. Schulz, V. Sick, J. Wolfrum, V. Drewes, M. Zahn, R. Maly, 2597
Modeling Turbulent Combustion and Pollutant Formation in Stratified Charge SI Engines. T. A. Baritaud, J. M. Duclos, A. Fusco, 2627
The Effects of Fuel–Air Mixing on NO_x Formation in Non-Premixed Swirl Burners. T. Terasaki, S. Hayashi, 2733
Optimization of Gas Turbine Combustor Performance Throughout the Duty Cycle. N. T. Davis, G. S. Samuelsen, 2819
Fluorescence Imaging of NO and O_2 in a Spray Flame Combustor at Elevated Pressures. B. L. Upschulte, M. G. Allen, K. R. McManus, 2779
A Shock Tube Study of the Reaction of S–Atoms with NO. D. Woiki, P. Roth, 583
A Kinetic Study of the Oxidation of Acetonitrile: A Model for NO Formation from Fuel-Bound Nitrogen. E. Ikeda, J. C. Mackie, 597
Gas Phase Reactions of Hydrogen Peroxide and Hydrogen Peroxide/Methanol Mixtures with Air Pollutants. V. M. Zamansky, L. Ho, P. M. Maly, W. R. Seeker, 2125
Impact of Temperature and Fuel-Nitrogen Content on Fuel-Staged Combustion with Coal Pyrolysis Gas. U. Greul, H. Spliethoff, H.-C. Magel, U. Schnell, H. Ruediger, K. R. G. Hein, C.-Z. Li, P. F. Nelson, 2231
Thermal Reduction of NO by NH_3: Kinetic Modeling of the NH_2 + NO Product Branching Ratio. M. J. Halbgewachs, E. W. G. Diau, A. M. Mebel, M. C. Lin, C. F. Melius, 2109
Pressure Effects on the Thermal de-NO_x Process. K. Kjærgaard, P. Glarborg, K. Dam-Johansen, J. A. Miller, 2067
Reburning Promoted by Nitrogen- and Sodium-Containing Compounds. V. M. Zamansky, L. Ho, P. M. Maly, W. R. Seeker, 2075
Flow Reactor Studies and Testing of Comprehensive Mechanisms for NO_x Reburning. D. Stapf, W. Leuckel, 2083
Control of NO_x Emissions by NO_x Recycle Approach. C. Q. Zhou, L. G. Neal, R. Bolli, J. Haslbeck, A. Chang, 2091
Isotopic Labeling Studies of the Selective Non-Catalytic Reduction of NO with NH_3. B. L. Duffy, P. F. Nelson, 2099
Computational and Experimental Study of NO in an Axisymmetric Laminar Diffusion Flame. M. D. Smooke, A. Ern, M. A. Tanoff, B. A. Valdati, R. K. Mohammed, D. F. Marran, M. B. Long, 2161
Behavior of Key Reactions on NO Formation in Methane-Air Flames. M. Nishioka, Y. Kondoh, T. Takeno, 2139
NO_x Formation in Turbulent Lean-Premixed Combustion with Minimum Heat Losses. L. Xie, S. Hayashi, K. Hirose, 2155
Evidence for a New NO Production Mechanism in Flames. J. E. Harrington, G. P. Smith, P. A. Berg, A. R. Noble, J. B. Jeffries, D. R. Crosley, 2133
A Kinetic Study of the Reactions of $NH(X^3\Sigma^-)$ with O_2 and NO in the Temperature Range from 1200 to 2200 K. H.-J. Römming, H.Gg. Wagner, 559
Measurement of the Branching Ratio of NCO + NO into N_2O at 1100–1400 K. S. A. Flatness, J. C. Kramlich, 567
Effects of Multi-Dimensionality on a Diffusion

Flame. M. Nishioka, Y. Takemoto, H. Yamashita, T. Takeno, 1071
A LIF and CARS Study of the Effects of Upstream Heat Loss on NO Formation from Laminar Premixed Burner-Stabilized Natural-Gas/Air Flames. A. V. Mokhov, H. B. Levinsky, 2147
Molecular Beam Mass Spectrometric and Modeling Studies of Neat and NH_3-Doped Low-Pressure $H_2/N_2O/Ar$ Flames: Formation and Consumption of NO. R. C. Sausa, G. Singh, G. W. Lemire, W. R. Anderson, 1043
The Sensitive Structure of Partially Premixed Methane-Air vs. Air Counterflow Flames. M. A. Tanoff, M. D. Smooke, R. J. Osborne, T. M. Brown, R. W. Pitz, 1121
Chemical Structure of Coal Tar During Devolatilization. M. Watt, T. H. Fletcher, S. Bai, M. S. Solum, R. J. Pugmire, 3153
Fundamental Study on N_2O Formation/Decomposition Characteristics by Means of Low-Temperature Pulverized Coal Combustion. I. Naruse, Y. Yamamoto, Y. Itoh, K. Ohtake, 3213
Fluidized Bed Combustion: Achievements and Problems. B. Leckner, 3231
Emissions of Nitrogen Oxides from Circulating Fluidized-Bed Combustors: Modeling Results Using Detailed Chemistry. S. Goel, A. Sarofim, P. Kilpinen, M. Hupa, 3317
The NO and N_2O Formation Mechanism During Devolatilization and Char Combustion Under Fluidized-Bed Conditions. F. Winter, C. Wartha, G. Löffler, H. Hofbauer, 3325
Pollutant Formation During Coal Combustion in a CFB Test Furnace. A. Reidick, H. Kremer, 3309
The Energy and Environmental Implications of Using Sewage Sludge as a Co-Fired Fuel Applied to Boilers. T. Abbas, P. Costen, G. De Soete, K. Glaser, S. Hassan, F. C. Lockwood, 2487
Industrial Combustion Control Using UV Emission Tomography. A. Leipertz, R. Obertacke, F. Wintrich, 2869
Flamelet and PDF Modeling of CO and NO_x Emissions from a Turbulent, Methane Hydrogen Jet Nonpremixed Flame. J.-Y. Chen, W.-C. Chang, 2207
Simulation of Detailed Chemistry in a Turbulent Combustor Flow. H. C. Magel, U. Schnell, K. R. G. Hein, 67
Analysis of Turbulence-Chemistry Interaction with Respect to NO Formation in Turbulent, Nonpremixed Hydrogen-Air Flames. M. Schlatter, J. C. Ferreira, M. Flury, J. Gass, 2215
Measurements of NO in Turbulent Non-Premixed Flames Stabilized on a Bluff Body. B. B. Dally, A. R. Masri, R. S. Barlow, G. J. Fiechtner, D. F. Fletcher, 2191
Oxygen Atom Concentrations and NO Production Rates in a Turbulent H_2/N_2 Jet Flame. R. S. Barlow, G. J. Fiechtner, J.-Y. Chen, 2199
Effects of CaO and Burnout on the Kinetics of NO Reduction by Beulah Zap Char. F. Guo, W. C. Hecker, 2251
Impact of Mixing Model on Predicted NO Formation in a Nonpremixed, Partially Stirred Reactor. W.-C. Chang, J.-Y. Chen, 2223
An Experimental Study of the Release of Nitrogen from Coals Pyrolyzed in Fluidized-Bed Reactors. C.-Z. Li, P. F. Nelson, E. B. Ledesma, J. C. Mackie, 3205
Nitrogen Chemistry in FBC with Limestone Addition. A. Jensen, J. E. Johnsson, K. Dam-Johansen, 3335
Quantitative CH Determinations in Low-Pressure Flames. J. Luque, G. P. Smith, D. R. Crosley, 959

03 Odors

04 PAH (Polycyclic Aromatic Hydrocarbons)

Analysis of Pyrolysis Process in Diesel-Like Combustion by Means of Laser-Induced Fluorescence. R. Ragucci, M. de Joannon, A. Cavaliere, 2525
On-line Emission Control of Combustion Processes by Laser-Induced Resonance-Enhanced Multi-Photon Ionization/Mass Spectrometry. R. Zimmermann, D. Lenior, A. Kettrup, H. Nagel, U. Boesl, 2859
Reaction Mechanisms in Aromatic Hydrocarbon Formation Involving the C_5H_5 Cyclopentadienyl Moiety. C. F. Melius, M. E. Colvin, N. M. Marinov, W. J. Pitz, S. M. Senkan, 685
Benzene Formation Chemistry in Premixed 1,3-Butadiene Flames. R. P. Lindstedt, G. Skevis, 703
PAH and Aromers: Precursors of Fullerenes and Soot. M. Bachmann, W. Wiese, K.-H. Homann, 2259
Soot Surface Growth by Polycyclic Aromatic Hydrocarbon and Acetylene Addition. S. Macadam, A. B. Hoffmann, J. M. Beér, A. F. Sarofim, 2295
C_2H_2 and PAH as Soot Growth Reactants in Premixed C_2H_4-Air Flames. T. G. Benish, A. L. Lafleur, K. Taghizadeh, J. B. Howard, 2319
The Effect of Temperature on Soot Inception in Premixed Ethylene Flames. A. Ciajolo, A. D'Anna, R. Barbella, A. Tregrossi, A. Violi, 2327
The Effect of the Bulk Equivalence Ratio on the PAH Emissions from the Combustion of PVC, Poly(styrene), and Poly(ethylene). T. Panagiotou, Y. A. Levendis, J. Carlson, P. Vouros, 2421
Soot Precursor Material: Visualization via Simultaneous LIF-LII and Characterization via TEM. R. L. Vander Wal, 2269
Polycyclic Aromatic Hydrocarbon and Soot Formation in Premixed Flames of CH_3Cl/CH_4 and CH_4. J. Huang, S. M. Senkan, 2335
The Effects of Pyrolysis Temperature and Ion-Exchanged Metals on the Composition of Brown Coal Tars Produced in a Fluidized-Bed Reactor.

B. A. Vernaglia, M. J. Wornat, C.-Z. Li, P. F. Nelson, 3287

05 Particles (Also see Aerosols)

Mechanisms Governing Trace Sodium Capture by Kaolinite in a Downflow Combustor. P. O. Mwabe, J. O. L. Wendt, 2447
The Effect of Pool Diameter on the Properties of Smoke Produced by Crude Oil Fires. G. Mulholland, W. Liggett, H. Koseki, 1445
Re-Initiation of Soot Surface Growth in Premixed Counterflow Flames. M. Marquardt, F. Mauß, B. Jungfleisch, R. Suntz, H. Bockhorn, 2343
The Fate of Fixed Carbon During the Fluidized-Bed Combustion of a Coal and Two Waste-Derived Fuels. U. Arena, R. Chirone, P. Salatino, 3243
Soot Precursor Material: Visualization via Simultaneous LIF-LII and Characterization via TEM. R. L. Vander Wal, 2269

06 Soot (Also see Soot)

Application of a Reduced Kinetic Model for Soot Formation and Burnout in Three-Dimensional Diesel Combustion Computations. P. Belardini, C. Bertoli, C. Beatrice, N. Del Giacomo, A. D'Anna, 2517
The Effect of CF_3I Compared to CF_3Br on OH· and Soot Concentrations in Co-Flowing Propane/Air Diffusion Flames. K. C. Smyth, D. A. Everest, 1385
The Effect of Pool Diameter on the Properties of Smoke Produced by Crude Oil Fires. G. Mulholland, W. Liggett, H. Koseki, 1445
Soot Surface Growth by Polycyclic Aromatic Hydrocarbon and Acetylene Addition. S. Macadam, A. B. Hoffmann, J. M. Beér, A. F. Sarofim, 2295
Soot Formation in the Pyrolysis of Benzene/Acetylene and Acetylene/Hydrogen Mixtures at High Carbon Concentrations. V. G. Knorre, D. Tanke, TH. Thienel, H. Gg. Wagner, 2303
The Effect of Temperature on Soot Inception in Premixed Ethylene Flames. A. Ciajolo, A. D'Anna, R. Barbella, A. Tregrossi, A. Violi, 2327
Influence of Hydrogen Addition to Fuel on Temperature Field and Soot Formation in Diffusion Flames. Ö. L. Gülder, D. R. Snelling, R. A. Sawchuk, 2351
Comprehensive Two-Dimensional Soot Diagnostics Based on Laser-Induced Incandescence (LII). S. Will, S. Schraml, A. Leipertz, 2277
Experiments and Numerical Simulation on Soot Formation in Opposed-Jet Ethylene Diffusion Flames. H. Wang, D. X. Du, C. J. Sung, C. K. Law, 2359
Soot-Field Structure in Laminar Soot-Emitting Microgravity Nonpremixed Flames. C. M. Megaridis, D. W. Griffin, B. Konsur, 1291
Conversion of Coal Tar to Soot During Coal Pyrolysis in a Post-Flame Environment. J. Ma, T. H. Fletcher, B. W. Webb, 3161
Assessment of Soot Volume Fractions from Laser-Induced Incandescence by Comparison with Extinction Measurements in Laminar, Premixed, Flat Flames. J. Appel, M. Marquardt, H. Bockhorn, B. Jungfleisch, R. Suntz, 2387

07 SO_x

A Shock Tube Study of the Reaction of S–Atoms with NO. D. Woiki, P. Roth, 583
Gas Phase Reactions of Hydrogen Peroxide and Hydrogen Peroxide/Methanol Mixtures with Air Pollutants. V. M. Zamansky, L. Ho, P. M. Maly, W. R. Seeker, 2125
Control of NO_x Emissions by NO_x Recycle Approach. C. Q. Zhou, L. G. Neal, R. Bolli, J. Haslbeck, A. Chang, 2091
Fluidized Bed Combustion: Achievements and Problems. B. Leckner, 3231
Pollutant Formation During Coal Combustion in a CFB Test Furnace. A. Reidick, H. Kremer, 3309

08 Metals

Mechanisms Governing Trace Sodium Capture by Kaolinite in a Downflow Combustor. P. O. Mwabe, J. O. L. Wendt, 2447
Combustion Characteristics of Mg-CO_2 Counterflow Diffusion Flames. A. Fukuchi, M. Kawashima, S. Yuasa, 1945
Sodium Partitioning in a Pulverized Coal Combustion Environment. N. B. Gallagher, T. W. Peterson, J. O. L. Wendt, 3197
The Energy and Environmental Implications of Using Sewage Sludge as a Co-Fired Fuel Applied to Boilers. T. Abbas, P. Costen, G. De Soete, K. Glaser, S. Hassan, F. C. Lockwood, 2487
Transformations of Sludge Waste During Combustion in a Low-High-Low Temperature Reactor. J. A. Kozinski, R. Saade, G. Zheng, 2495
The Behavior of Chromium in Laminar Hydrogen and Ethene Diffusion Flames. Y. Yoon, C. Reyes, A. D. Jones, P. Kelly, D. P. Y. Chang, I. M. Kennedy, 1953
A Real-Time Monitor for Toxic Metal Emissions from Combustion Systems. S. G. Buckley, C. P. Koshland, R. F. Sawyer, D. Lucas, 2455
Adsorption of Metallic Mercury on Activated Carbon. D. Karatza, A. Lancia, D. Musmarra, F. Pepe, 2439

09 Chlor- and Chlor-fluro carbons

On-line Emission Control of Combustion Processes by Laser-Induced Resonance-Enhanced Multi-Photon Ionization/Mass Spectrometry. R. Zim-

mermann, D. Lenior, A. Kettrup, H. Nagel, U. Boesl, 2859
The Reaction of Phenoxy Radicals with Mono-Chlorobenzene and Its Meaning for Gas-Phase Dioxin Formation in Incineration. H.-H. Grotheer, R. Louw, 2405
Influence of Turbulent Mixing on the Pyrolysis of Chloroform Using Detailed Chemical Kinetics. M. Kraft, E. Stöckelmann, H. Bockhorn, 2431
Effects of Ambient Water in the Combustion Enhancement of Heavily Chlorinated Hydrocarbons: Studies on Droplet Burning. H. Wang, D. L. Zhu, Y. Saso, C. K. Law, 2413
Thermal Decomposition of C_2H_5I. S. S. Kumaran, M.-C. Su, K. P. Lim, J. V. Michael, 605

10 Others

Pollutant Formation During Coal Combustion in a CFB Test Furnace. A. Reidick, H. Kremer, 3309

22 Propagation Rates

Unsteady Extinction Mechanisms of Diffusion Flames. F. Takahashi, V. R. Katta, 1151
Combustion of Porous Energetic Materials in the Merged-Flame Regime. S. B. Margolis, F. A. Williams, A. M. Telengator, 1969
Pulsating Instability in the Nonadiabatic Heterogeneous SHS Flame: Theory and Experimental Comparisons. A. Makino, C. K. Law, 1867

01 Detonations

Time-Resolved Investigation of Hot Spots in the End Gas of an S. I. Engine by Means of 2-D Double-Pulse LIF of Formaldehyde. B. Bäuerle, J. Warnatz, F. Behrendt, 2619
Critical Conditions for Detonation Propagation Through Mixture with Decreasing Reaction Rate. S. I. Kryuchkov, S. B. Dorofeev, A. A. Efimenko, 2965

02 Laminar Flames

Markstein Lengths of CO/H_2/Air Flames, Using Expanding Spherical Flames. M. J. Brown, I. C. McLean, D. B. Smith, S. C. Taylor, 875
The Phenomena of Flame Propagation in a Rotating Tube. Y. Sakai, S. Ishizuka, 847
Multistep Asymptotic Analyses of Flame Structures. K. Seshadri, 831
Determination of the Spread Rate in Opposed-Flow Flame Spread Over Thick Solid Fuels in the Thermal Regime. S. Bhattacharjee, J. West, R. A. Altenkirch, 1477
The Dependence of the Flame Spread Rate Over Solid Fuel on Damköhler Number and Heat Loss. S. Rybanin, 1487
Turbulent Premixed Flame Propagation in a Cylindrical Vessel. M. Fairweather, S. S. Ibrahim, H. Jaggers, D. G. Walker, 365
Mixing and Chemical Reaction in an Idealized Swirl Chamber. O. M. Knio, A. S. Worlikar, H. N. Najm, 203
Edge-Flame-Holding. J. Buckmaster, R. Weber, 1143
Burning Velocities in Fuel-Rich Aluminum Dust Clouds. S. Goroshin, I. Fomenko, J. H. S. Lee, 1961
Flame Propagation Along 90-Degree Bend in an Open Duct. K. Sato, Y. Sakai, M. Chiga, 931
Assessment of Soot Volume Fractions from Laser-Induced Incandescence by Comparison with Extinction Measurements in Laminar, Premixed, Flat Flames. J. Appel, M. Marquardt, H. Bockhorn, B. Jungfleisch, R. Suntz, 2387

03 Liquids

Flame Propagation in Planar Droplet Arrays and Interaction Phenomena Between Neighboring Droplet Streams. N. Roth, A. Karl, K. Anders, A. Frohn, 1697
Study of the Thermocapillary Layer Preceding Slow Steadily Spreading Flames Over Liquid Fuels. P. L. Garcia-Ybarra, J. L. Castillo, J. C. Antoranz, V. Sankovitch, J. San Martin, 1469
Opposed-Flow Flame Spread Across *n*-Propanol Pools. D. N. Schiller, W. A. Sirignano, 1319

04 Solids

Pulsating Instability in the Nonadiabatic Heterogeneous SHS Flame: Theory and Experimental Comparisons. A. Makino, C. K. Law, 1867
Metal-Sulfur Combustion. S. Goroshin, A. Mizera, D. L. Frost, J. H. S. Lee, 1883
Oscillatory Combustion of Aluminized Composite Propellants. S. R. Hickman, M. Q. Brewster, 2007
Ignition and Combustion of Bulk Titanium and Magnesium at Normal and Reduced Gravity. A. Abbud-Madrid, M. C. Branch, J. W. Daily, 1929

05 Turbulent Flames

The Challenge of Turbulent Combustion. K. N. C. Bray, 1
Using Dorect Numerical Simulation to Understand Premixed Turbulent Combustion. T. Poinsot, 219
Relation Between Flame Propagation Characteristics and Hydrocarbon Emissions Under Lean Operating Conditions in Spark-Ignition Engines. N. Hadjiconstantinou, K. Min, J. B. Heywood, 2637
An Experimental Database for Diesel Spray Combustion. E. Winklhofer, 2541
Turbulent Premixed Flame Propagation in a Cylin-

drical Vessel. M. Fairweather, S. S. Ibrahim, H. Jaggers, D. G. Walker, 365
Flame Surface Density and Burning Rate in Premixed Turbulent Flames. I. G. Shepherd, 373
A Test of an Engineering Model of Premixed Turbulent Combustion. V. Karpov, A. Lipatnikov, V. Zimont, 249
Contribution to the Analysis of Temporal and Spatial Structures Near the Lift-Off Region of a Turbulent Hydrogen Diffusion Flame. A. Brockhinke, P. Andresen, K. Kohse-Hšinghaus, 153
Flame Propagation Along 90-Degree Bend in an Open Duct. K. Sato, Y. Sakai, M. Chiga, 931
Experimentally Measured Burning Rates of Premixed Turbulent Flames. E. Bourguignon, L. W. Kostiuk, Y. Michou, I. Gokalp, 447
Effect of Density Ratio on Flame Propagation Along a Vortex Tube. T. Hasegawa, K. Nishikado, 291
Spectral Model of Premixed Flame Propagation. L. R. Collins, M. Ulitsky, 315

23 Property Measurements

Combustion Control Using a Multiplexed Diode-Laser Sensor System. E. R. Furlong, D. S. Baer, R. K. Hanson, 2851

01 Composition

Polarization Separated Spatially Resolved Single Laser Shot Multispecies Analysis in the Combustion Chamber of a Realistic SI Engine with a Tunable KrF Excimer Laser. M. Knapp, A. Luczak, V. Beushausen, W. Hentschel, P. Manz, P. Andresen, 2589
Spatially Selective Chemistry Control in an Oil-Burning Furnace: A New Method to Reduce NO_x Emissions Developed Through Combined Three-Dimensional Laser Diagnostics. A. Luczak, S. Eisenberg, M. Knapp, H. Schlüter, V. Beushausen, Peter Andresen, 2827
Computational and Experimental Study of NO in an Axisymmetric Laminar Diffusion Flame. M. D. Smooke, A. Ern, M. A. Tanoff, B. A. Valdati, R. K. Mohammed, D. F. Marran, M. B. Long, 2161
Acetylene and Ethylene Mole Fractions in Methane/Air Partially Premixed Flames. L.-K. Tseng, J. P. Gore, I. K. Puri, T. Takeno, 993
Quenching of Reaction in Gas-Sampling Probes to Measure Scramjet Engine Performance. T. Mitani, 2917
C_2H_2 and PAH as Soot Growth Reactants in Premixed C_2H_4-Air Flames. T. G. Benish, A. L. Lafleur, K. Taghizadeh, J. B. Howard, 2319
Oxygen Atom Concentrations and NO Production Rates in a Turbulent H_2/N_2 Jet Flame. R. S. Barlow, G. J. Fiechtner, J.-Y. Chen, 2199

02 Electric Properties (Also see Electric Properties of Flames*)*

03 Species Identification

Heterogeneous/Homogeneous Reaction and Transport Coupling During Flame-Wall Interaction. P. Popp, M. Smooke, M. Baum, 2693
On-line Emission Control of Combustion Processes by Laser-Induced Resonance-Enhanced Multi-Photon Ionization/Mass Spectrometry. R. Zimmermann, D. Lenior, A. Kettrup, H. Nagel, U. Boesl, 2859
Fluorescence Imaging of NO and O_2 in a Spray Flame Combustor at Elevated Pressures. B. L. Upschulte, M. G. Allen, K. R. McManus, 2779
CH_3 Detection in Flames Using Photodissociation-Induced Fluorescence. P. Desgroux, L. Gasnot, B. Crunelle, J. F. Pauwels, 967
C_2H_2 and PAH as Soot Growth Reactants in Premixed C_2H_4-Air Flames. T. G. Benish, A. L. Lafleur, K. Taghizadeh, J. B. Howard, 2319
Industrial Combustion Control Using UV Emission Tomography. A. Leipertz, R. Obertacke, F. Wintrich, 2869
The Effects of Pyrolysis Temperature and Ion-Exchanged Metals on the Composition of Brown Coal Tars Produced in a Fluidized-Bed Reactor. B. A. Vernaglia, M. J. Wornat, C.-Z. Li, P. F. Nelson, 3287
Experimental Investigation of a SCRAMJET Model Combustor with Injection Through a Swept Ramp Using Laser-Induced Fluorescence with Tunable Excimer Lasers. R. Hänig, D. Theisen, R. Fink, R. Lachner, G. Kappler, D. Rist, P. Andresen, 2949

04 Spectra

05 Temperature

Spatially Selective Chemistry Control in an Oil-Burning Furnace: A New Method to Reduce NO_x Emissions Developed Through Combined Three-Dimensional Laser Diagnostics. A. Luczak, S. Eisenberg, M. Knapp, H. Schlüter, V. Beushausen, Peter Andresen, 2827
Combustion Control Using a Multiplexed Diode-Laser Sensor System. E. R. Furlong, D. S. Baer, R. K. Hanson, 2851
Temperature Profile Measurements in Stagnation-Flow, Diamond-Forming Flames Using Hydrogen CARS Spectroscopy. K. E. Bertagnolli, R. P. Lucht, 1825
Gas Temperature Above a Porous Radiant Burner: Comparison of Measurements and Model Predictions. M. D. Rumminger, N. H. Heberle, R. W. Dibble, D. R. Crosley, 1755
Convective Ignition of a Granular Solid Propellant

Bed: Influence of Propellant Composition. D. E. Kooker, S. L. Howard, L.-M. Chang, 2033
Measurements of Coal Particle Shape, Mass, and Temperature Histories: Impact of Particle Irregularity on Temperature Predictions and Measurements. R. Sampath, Y. D. Yeboah, D. J. Maloney, S. Woodruff, J. W. Zondlo, 3179
Industrial Combustion Control Using UV Emission Tomography. A. Leipertz, R. Obertacke, F. Wintrich, 2869
Flame Structure and Combustion Rate of Burning Graphite in the Stagnation Flow. A. Makino, I. Kato, M. Senba, H. Fujizaki, N. Araki, 3067
Temperature Field Measurements in a Sooting Flame by Filtered Rayleigh Scattering (FRS). D. Hofmann, A. Leipertz, 945

06 Velocity: Pressure: Flow Direction

Interpretation of k-ε Computed Turbulence Length-Scale Predictions for Engine Flows. Z. Han, R. D. Reitz, F. E. Corcione, G. Valentino, 2717
Spatially Selective Chemistry Control in an Oil-Burning Furnace: A New Method to Reduce NO_x Emissions Developed Through Combined Three-Dimensional Laser Diagnostics. A. Luczak, S. Eisenberg, M. Knapp, H. Schlüter, V. Beushausen, Peter Andresen, 2827
Extinction of Non-Premixed Methane- and Propane-Air Counterflow Flames Inhibited with CF_4, CF_3H and CF_3Br. P. Papas, J. W. Fleming, R. S. Sheinson, 1405
Experimental Analysis of Flame Surface Density Models for Premixed Turbulent Combustion. D. Veynante, J. Piana, J. M. Duclos, C. Martel, 413
Swirl-Induced Intermittency: A Novel Effect Modifying the Turbulence Structure of Swirling Free Jets. F. Holzäpfel, B. Lenze, W. Leuckel, 187
Flame Propagation Along 90-Degree Bend in an Open Duct. K. Sato, Y. Sakai, M. Chiga, 931

07 Others

Comprehensive Two-Dimensional Soot Diagnostics Based on Laser-Induced Incandescence (LII). S. Will, S. Schraml, A. Leipertz, 2277
Two-Regime Global Kinetics of Cellulose Pyrolysis: The Role of Tar Evaporation. E. M. Suuberg, I. Milosavljevic, V. Oja, 1515
A New Approach to Studying Pore Diffusivity During Char Combustion at FBC Conditions. S. Goel, A. F. Sarofim, J. Lu, 3127
Measurements of Coal Particle Shape, Mass, and Temperature Histories: Impact of Particle Irregularity on Temperature Predictions and Measurements. R. Sampath, Y. D. Yeboah, D. J. Maloney, S. Woodruff, J. W. Zondlo, 3179
Experimental Analysis of Flame Surface Density Models for Premixed Turbulent Combustion. D. Veynante, J. Piana, J. M. Duclos, C. Martel, 413

Pyrolsis (*See* Thermal Decomposition)

24 Reaction Mechanisms

Theroy and Modeling in Combustion Chemistry. J. A. Miller, 461
Autoignition Chemistry in a Motored Engine: An Experimental and Kinetic Modeling Study. H. J. Curran, P. Gaffuri, W. J. Pitz, C. K. Westbrook, W. R. Leppard, 2669
The Reactions of $O(^3P)$ Atoms with Aromatic Hydrocarbons with Unsaturated Side Chains. M. Eichholtz, S. Kohl, A. Schneider, J.-T. Vollmer, H.Gg. Wagner, 527
High-Temperature Reactions and Thermodynamic Properties of Phenyl Radicals. E. Heckmann, H. Hippler, J. Troe, 543
Destruction of Benzene in High-Temperature Flames: Chemistry of Benzene and Phenol. R. A. Shandross, J. P. Longwell, J. B. Howard, 711
Thermal Decomposition of Benzonitrile: A Combined Single-Pulse Shock Tube-ARAS Investigation. A. Lifshitz, Y. Cohen, M. Braun-Unkhoff, P. Frank, 659
Dissociation and Chain Reaction in the Pyrolysis of Pyrazine. J. H. Kiefer, Q. Zhang, R. D. Kern, H. Chen, J. Yao, B. S. Jursic, 651
Chemical Kinetic Study of Dimethylether Oxidation in a Jet Stirred Reactor from 1 to 10 ATM: Experiments and Kinetic Modeling. P. Dagaut, J.-C. Boettner, M. Cathonnet, 627
An Intermediate Temperature Modeling Study of the Combustion of Neopentane. H. J. Curran, W. J. Pitz, C. K. Westbrook, M. W. M. Hisham, R. W. Walker, 641
Chemical Kinetic Modeling of High-Pressure Propane Oxidation and Comparison to Experimental Results. D. N. Koert, W. J. Pitz, J. W. Bozzelli, N. P. Cernansky, 633
Experimental Data and Kinetic Modeling of Primary Reference Fuel Mixtures. C.V. Callahan, T. J. Held, F. L. Dryer, R. Minetti, M. Ribaucour, L. R. Sochet, T. Faravelli, P. Gaffuri, E. Ranzi, 739
Comparison of Oxidation and Autoignition of the Two Primary Reference Fuels by Rapid Compression. R. Minetti, M. Carlier, M. Ribaucour, E. Therssen, L. R. Sochet, 747
Flow Reactor Studies and Testing of Comprehensive Mechanisms for NO_x Reburning. D. Stapf, W. Leuckel, 2083
Isotopic Labeling Studies of the Selective Non-Catalytic Reduction of NO with NH_3. B. L. Duffy, P. F. Nelson, 2099
Catalytic Oxidation of Natural Gas Over Supported Platinum: Flow Reactor Experiments and Detailed Numerical Modeling. T. C. Bond, R. A. No-

guchi, C.-P. Chou, R. K. Mongia, J.-Y. Chen, R. W. Dibble, 1771
On Surface Growth Mechanism of Soot Particles. M. Frenklach, 2285
Two-Regime Global Kinetics of Cellulose Pyrolysis: The Role of Tar Evaporation. E. M. Suuberg, I. Milosavljevic, V. Oja, 1515
Combustion-Like Pyrolysis of Organic Polymers: Species and Kinetic Details by *T*-Jump/FTIR Spectroscopy. T. B. Brill, H. Arisawa, P. E. Gongwer, 791
Detailed Kinetic Reaction Mechanism for Ignition and Oxidation of α-Methylnaphthalene. H. Pitsch, 721
Reduced *n*-Heptane Mechanism for Non-Premixed Combustion with Emphasis on Pollutant-Relevant Intermediate Species. M. Bollig, H. Pitsch, J. C. Hewson, K. Seshadri, 729

01 Identification of Intermediates and Products

Experimental and Computational Investigation of Concentration Profiles of C_1-C_4 Hydrocarbon Radicals and Molecules in Low-Pressure C_2H_2/O/H Atomic Flames at 600 K. J. Peeters, K. Devriendt, 1001
The Formation of C_2 During High-Temperature Pyrolysis of Fullerene C_{70}. T. Sommer, P. Roth, 621
Comparison of Oxidation and Autoignition of the Two Primary Reference Fuels by Rapid Compression. R. Minetti, M. Carlier, M. Ribaucour, E. Therssen, L. R. Sochet, 747
Computer-Aided Design of Gas-Phase Oxidation Mechanisms–Application to the Modeling of *n*-Heptane and Iso-Octane Oxidation. G. M. Côme, V. Warth, P. A. Glaude, R. Fournet, F. Battin-Leclerc, G. Scacchi, 755
Benzene Formation Chemistry in Premixed 1,3-Butadiene Flames. R. P. Lindstedt, G. Skevis, 703
The CH_3 + C_5H_5 Reaction: A Potential Source of Benzene at High Temperatures. L. V. Moskaleva, A. M. Mebel, M. C. Lin, 521
Measurement of the Branching Ratio of NCO + NO into N_2O at 1100–1400 K. S. A. Flatness, J. C. Kramlich, 567
Thermal Decomposition of Benzene. Single-Pulse Shock-Tube Investigation. A. Laskin, A. Lifshitz, 669
Experimental Investigation of a SCRAMJET Model Combustor with Injection Through a Swept Ramp Using Laser-Induced Fluorescence with Tunable Excimer Lasers. R. Hönig, D. Theisen, R. Fink, R. Lachner, G. Kappler, D. Rist, P. Andresen, 2949

02 Reaction Pathways

Experimental and Computational Investigation of Concentration Profiles of C_1-C_4 Hydrocarbon Radicals and Molecules in Low-Pressure C_2H_2/O/H Atomic Flames at 600 K. J. Peeters, K. Devriendt, 1001
The Formation of C_2 During High-Temperature Pyrolysis of Fullerene C_{70}. T. Sommer, P. Roth, 621
Reaction Mechanisms in Aromatic Hydrocarbon Formation Involving the C_5H_5 Cyclopentadienyl Moiety. C. F. Melius, M. E. Colvin, N. M. Marinov, W. J. Pitz, S. M. Senkan, 685
Benzene Formation Chemistry in Premixed 1,3-Butadiene Flames. R. P. Lindstedt, G. Skevis, 703
Behavior of Key Reactions on NO Formation in Methane-Air Flames. M. Nishioka, Y. Kondoh, T. Takeno, 2139
A Kinetic Study of the Reactions of $NH(X^3\Sigma^-)$ with O_2 and NO in the Temperature Range from 1200 to 2200 K. H.-J. Römming, H.Gg. Wagner, 559
Acetylene and Ethylene Mole Fractions in Methane/Air Partially Premixed Flames. L.-K. Tseng, J. P. Gore, I. K. Puri, T. Takeno, 993
Ignition and Detonation in N_2O-CO-H_2-He Mixtures. A. Y. Starikovskii, 2999
PAH and Aromers: Precursors of Fullerenes and Soot. M. Bachmann, W. Wiese, K.-H. Homann, 2259
The NO and N_2O Formation Mechanism During Devolatilization and Char Combustion Under Fluidized-Bed Conditions. F. Winter, C. Wartha, G. Löffler, H. Hofbauer, 3325
Thermal Decomposition of Benzene. Single-Pulse Shock-Tube Investigation. A. Laskin, A. Lifshitz, 669
Detailed Kinetic Reaction Mechanism for Ignition and Oxidation of α-Methylnaphthalene. H. Pitsch, 721
A Broader Definition of Symmetry Number and its Application to a Kinetic Model Describing Polyarene Growth. M. C. Masonjones, A. F. Sarofim, 823

25 Review Papers

The Challenge of Turbulent Combustion. K. N. C. Bray, 1
Theroy and Modeling in Combustion Chemistry. J. A. Miller, 461
Spray Combustion Phenomena. G. M. Faeth, 1593
Using Direct Numerical Simulations to Understand Premixed Turbulent Combustion. T. Poinsot, 219
Solid Fuel Utilization: From Coal to Biomass. F. C. Lockwood, 3041
Modern Tools for Diesel Engine Combustion Investigation. W. Hentschel, 2503
Impacts and Control of Air Toxics from Combustion. C. P. Koshland, 2049
Current State of Combustion Research in Microgravity. M. Kono, K. Ito, T. Niioka, T. Kadota, J. Sato, 1189

Multistep Asymptotic Analyses of Flame Structures. K. Seshadri, 831
Gas-Phase Combustion Synthesis of Materials. K. Brezinsky, 1805
Fluidized Bed Combustion: Achievements and Problems. B. Leckner, 3231
Scaling of Characteristics of Aerodynamics, Heat Transfer, and Pollutant Emissions in Industrial Flames. R. Weber, 3343

Safety (*See* Fire, Safety; Explosion, Safety)

26 Soot

Analysis of Pyrolysis Process in Diesel-Like Combustion by Means of Laser-Induced Fluorescence. R. Ragucci, M. de Joannon, A. Cavaliere, 2525
The Effect of Changes in the Flame Structure on the Formation and Destruction of Soot and NO_x in Radiating Diffusion Flames. A. Atreya, C. Zhang, H. K. Kim, T. Shamim, J. Suh, 2181
Gravitational Effects on Sooting Diffusion Flames. C. R. Kaplan, E. S. Oran, K. Kailasanath, H. D. Ross, 1301
The Effect of Pool Diameter on the Properties of Smoke Produced by Crude Oil Fires. G. Mulholland, W. Liggett, H. Koseki, 1445
Re-Initiation of Soot Surface Growth in Premixed Counterflow Flames. M. Marquardt, F. Mauß, B. Jungfleisch, R. Suntz, H. Bockhorn, 2343
C_2H_2 and PAH as Soot Growth Reactants in Premixed C_2H_4-Air Flames. T. G. Benish, A. L. Lafleur, K. Taghizadeh, J. B. Howard, 2319
Comprehensive Two-Dimensional Soot Diagnostics Based on Laser-Induced Incandescence (LII). S. Will, S. Schraml, A. Leipertz, 2277
Soot-Field Structure in Laminar Soot-Emitting Microgravity Nonpremixed Flames. C. M. Megaridis, D. W. Griffin, B. Konsur, 1291
Flamelet Modeling of Soot Formation in Laminar Ethyne/Air-Diffusion Flames. M. Balthasar, A. Heyl, F. Mauß, F. Schmitt, H. Bockhorn, 2369
CFD Prediction of Coupled Radiation Heat Transfer and Soot Production in Turbulent Flames. N. W. Bressloff, J. B. Moss, P. A. Rubini, 2379
Temperature Field Measurements in a Sooting Flame by Filtered Rayleigh Scattering (FRS). D. Hofmann, A. Leipertz, 945
Assessment of Soot Volume Fractions from Laser-Induced Incandescence by Comparison with Extinction Measurements in Laminar, Premixed, Flat Flames. J. Appel, M. Marquardt, H. Bockhorn, B. Jungfleisch, R. Suntz, 2387
The Optical Band Gap Model in the Interpretation of the UV-Visible Absorption Spectra of Rich Premixed Flames. P. Minutolo, G. Gambi, A. D'Alessio, 951
Polycyclic Aromatic Hydrocarbon and Soot Formation in Premixed Flames of CH_3Cl/CH_4 and CH_4. J. Huang, S. M. Senkan, 2335
Investigation of Sooting in Microgravity Droplet Combustion. M. Y. Choi, K.-O. Lee, 1243

01 Control

Comprehensive Two-Dimensional Soot Diagnostics Based on Laser-Induced Incandescence (LII). S. Will, S. Schraml, A. Leipertz, 2277

02 Formation

Spectral Extinction Measurements of Spray Combustion in a Divided-Chamber Diesel Engine System. F. E. Corcione, G. Mazziotti, B. M. Vaglieco, 2533
Application of a Reduced Kinetic Model for Soot Formation and Burnout in Three-Dimensional Diesel Combustion Computations. P. Belardini, C. Bertoli, C. Beatrice, N. Del Giacomo, A. D'Anna, 2517
Investigation of Sooting in Normal-Gravity Droplet Combustion Using Light Extinction and Gravimetric Techniques. K.-O. Lee, K. A. Jensen, M. Y. Choi, 2397
Acetylene and Ethylene Mole Fractions in Methane/Air Partially Premixed Flames. L.-K. Tseng, J. P. Gore, I. K. Puri, T. Takeno, 993
The Effect of CF_3I Compared to CF_3Br on OH· and Soot Concentrations in Co-Flowing Propane/Air Diffusion Flames. K. C. Smyth, D. A. Everest, 1385
The Effect of Pool Diameter on the Properties of Smoke Produced by Crude Oil Fires. G. Mulholland, W. Liggett, H. Koseki, 1445
On Surface Growth Mechanism of Soot Particles. M. Frenklach, 2285
Soot Surface Growth by Polycyclic Aromatic Hydrocarbon and Acetylene Addition. S. Macadam, A. B. Hoffmann, J. M. Beér, A. F. Sarofim, 2295
Soot Formation in the Pyrolysis of Benzene/Acetylene and Acetylene/Hydrogen Mixtures at High Carbon Concentrations. V. G. Knorre, D. Tanke, TH. Thienel, H.Gg. Wagner, 2303
Re-Initiation of Soot Surface Growth in Premixed Counterflow Flames. M. Marquardt, F. Mauß, B. Jungfleisch, R. Suntz, H. Bockhorn, 2343
The Effect of Temperature on Soot Inception in Premixed Ethylene Flames. A. Ciajolo, A. D'Anna, R. Barbella, A. Tregrossi, A. Violi, 2327
Influence of Hydrogen Addition to Fuel on Temperature Field and Soot Formation in Diffusion Flames. Ö. L. Gülder, D. R. Snelling, R. A. Sawchuk, 2351
Comprehensive Two-Dimensional Soot Diagnostics Based on Laser-Induced Incandescence (LII). S. Will, S. Schraml, A. Leipertz, 2277
Experiments and Numerical Simulation on Soot

Formation in Opposed-Jet Ethylene Diffusion Flames. H. Wang, D. X. Du, C. J. Sung, C. K. Law, 2359
Soot-Field Structure in Laminar Soot-Emitting Microgravity Nonpremixed Flames. C. M. Megaridis, D. W. Griffin, B. Konsur, 1291
Observation of Sooting Behavior in an Emulsion Droplet Flame by Planar Laser Light Scattering in Microgravity. M. Tsue, D. Segawa, T. Kadota, H. Yamasaki, 1251
Conversion of Coal Tar to Soot During Coal Pyrolysis in a Post-Flame Environment. J. Ma, T. H. Fletcher, B. W. Webb, 3161
A Simplified Phenomenological Model for Soot Growth Based on Plug Flow Reactor Experiments. B. Bartenbach, W. Leuckel, 2311
Soot Precursor Material: Visualization via Simultaneous LIF-LII and Characterization via TEM. R. L. Vander Wal, 2269

03 Morphology

The Effect of Pool Diameter on the Properties of Smoke Produced by Crude Oil Fires. G. Mulholland, W. Liggett, H. Koseki, 1445
On Surface Growth Mechanism of Soot Particles. M. Frenklach, 2285
Soot Precursor Material: Visualization via Simultaneous LIF-LII and Characterization via TEM. R. L. Vander Wal, 2269
Controlled Combustion Synthesis of Nanosized Iron Oxide Aggregates. Z. Zhang, T. T. Charalampopoulos, 1851

04 Oxidation

Application of a Reduced Kinetic Model for Soot Formation and Burnout in Three-Dimensional Diesel Combustion Computations. P. Belardini, C. Bertoli, C. Beatrice, N. Del Giacomo, A. D'Anna, 2517
Catalytic Combustion of Carbon Particulate at High Values of the Carbon/Catalyst Mass Ratio. P. Ciambelli, M. D'Amore, V. Palma, S. Vaccaro, 1789
Re-Initiation of Soot Surface Growth in Premixed Counterflow Flames. M. Marquardt, F. Mauß, B. Jungfleisch, R. Suntz, H. Bockhorn, 2343
Numerical Investigation on the Influence of Carbonaceous Particles on the Ignition Behavior of Methane/Air Mixtures. T. Ludwig, P. Roth, 1579

05 Precursors

Experimental Study of the Structure of Rich Ethane Flames. R. Ancia, J. Vandooren, P. J. Van Tiggelen, 1009
The CH_3 + C_5H_5 Reaction: A Potential Source of Benzene at High Temperatures. L. V. Moskaleva, A. M. Mebel, M. C. Lin, 521
On Surface Growth Mechanism of Soot Particles. M. Frenklach, 2285
The Effect of Temperature on Soot Inception in Premixed Ethylene Flames. A. Ciajolo, A. D'Anna, R. Barbella, A. Tregrossi, A. Violi, 2327
A Broader Definition of Symmetry Number and its Application to a Kinetic Model Describing Polyarene Growth. M. C. Masonjones, A. F. Sarofim, 823
The Optical Band Gap Model in the Interpretation of the UV-Visible Absorption Spectra of Rich Premixed Flames. P. Minutolo, G. Gambi, A. D'Alessio, 951
Soot Precursor Material: Visualization via Simultaneous LIF-LII and Characterization via TEM. R. L. Vander Wal, 2269

27 Thermal Decomposition

Dissociation and Chain Reaction in the Pyrolysis of Pyrazine. J. H. Kiefer, Q. Zhang, R. D. Kern, H. Chen, J. Yao, B. S. Jursic, 651
Influence of Turbulent Mixing on the Pyrolysis of Chloroform Using Detailed Chemical Kinetics. M. Kraft, E. Stöckelmann, H. Bockhorn, 2431
An Experimental Study of the Release of Nitrogen from Coals Pyrolyzed in Fluidized-Bed Reactors. C.-Z. Li, P. F. Nelson, E. B. Ledesma, J. C. Mackie, 3205
The Effects of Pyrolysis Temperature and Ion-Exchanged Metals on the Composition of Brown Coal Tars Produced in a Fluidized-Bed Reactor. B. A. Vernaglia, M. J. Wornat, C.-Z. Li, P. F. Nelson, 3287

01 Gas

A Shock Tube Study of H + HNCO → H_2 + NCO and the Thermal Decomposition of NCO. J. D. Mertens, R. K. Hanson, 551
Direct Measurement of the Reaction Pair C_6H_5NO ∫ C_6H_5 + NO by a Combined Shock Tube and Flow Reactor Approach. C. Horn, P. Frank, R. S. Tranter, J. Schaugg, H.-H. Grotheer, T. Just, 575
High-Temperature Reactions and Thermodynamic Properties of Phenyl Radicals. E. Heckmann, H. Hippler, J. Troe, 543
The Formation of C_2 During High-Temperature Pyrolysis of Fullerene C_{70}. T. Sommer, P. Roth, 621
Thermal Decomposition of C_2H_5I. S. S. Kumaran, M.-C. Su, K. P. Lim, J. V. Michael, 605
Thermal Decomposition of Benzene. Single-Pulse Shock-Tube Investigation. A. Laskin, A. Lifshitz, 669
A Simplified Phenomenological Model for Soot Growth Based on Plug Flow Reactor Experiments. B. Bartenbach, W. Leuckel, 2311

02 Liquid

Analysis of Pyrolysis Process in Diesel-Like Combustion by Means of Laser-Induced Fluorescence. R. Ragucci, M. de Joannon, A. Cavaliere, 2525
Spatially Selective Chemistry Control in an Oil-Burning Furnace: A New Method to Reduce NO_x Emissions Developed Through Combined Three-Dimensional Laser Diagnostics. A. Luczak, S. Eisenberg, M. Knapp, H. Schlüter, V. Beushausen, Peter Andresen, 2827

03 Solid

Convective Ignition of a Granular Solid Propellant Bed: Influence of Propellant Composition. D. E. Kooker, S. L. Howard, L.-M. Chang, 2033
Chemical Structure of Coal Tar During Devolatilization. M. Watt, T. H. Fletcher, S. Bai, M. S. Solum, R. J. Pugmire, 3153
An Experimental Study on Particle-Cloud Flames in Microgravity Field. Y. Okuyama, Y. Ohtomo, K. Maruta, H. Kobayashi, T. Niioka, 1369
Conversion of Coal Tar to Soot During Coal Pyrolysis in a Post-Flame Environment. J. Ma, T. H. Fletcher, B. W. Webb, 3161
Combustion-Like Pyrolysis of Organic Polymers: Species and Kinetic Details by *T*-Jump/FTIR Spectroscopy. T. B. Brill, H. Arisawa, P. E. Gongwer, 791
Transformations of Sludge Waste During Combustion in a Low-High-Low Temperature Reactor. J. A. Kozinski, R. Saade, G. Zheng, 2495
Fundamental Experiment on the Combustion of Coal–Water Mixture and Modeling of the Process. K. Takeno, K. Tokuda, T. Ichinose, S. Kaneko, 3223

28 Thermochemistry and Thermodynamics

Direct Measurement of the Reaction Pair $C_6H_5NO \int C_6H_5 + NO$ by a Combined Shock Tube and Flow Reactor Approach. C. Horn, P. Frank, R. S. Tranter, J. Schaugg, H.-H. Grotheer, T. Just, 575
High-Temperature Reactions and Thermodynamic Properties of Phenyl Radicals. E. Heckmann, H. Hippler, J. Troe, 543

29 Transport Properties

Thermal Diffusion Effects and Vortex-Flame Interactions in Hydrogen Jet Diffusion Flames. R. D. Hancock, F. R. Schauer, R. P. Lucht, V. R. Katta, K. Y. Hsu, 1087
Measurements of Coal Particle Shape, Mass, and Temperature Histories: Impact of Particle Irregularity on Temperature Predictions and Measurements. R. Sampath, Y. D. Yeboah, D. J. Maloney, S. Woodruff, J. W. Zondlo, 3179
Swirl-Induced Intermittency: A Novel Effect Modifying the Turbulence Structure of Swirling Free Jets. F. Holzäpfel, B. Lenze, W. Leuckel, 187

01 Diffusion

Oxidation of Hydrocarbons from Lubricant Oil Layers in Spark-Ignition Engines. M. G. Norris, W. Bauer, S. Hochgreb, 2645
Numerical Modeling of Catalytic Ignition. O. Deutschmann, R. Schmidt, F. Behrendt, J. Warnatz, 1747
Transformations of Sludge Waste During Combustion in a Low-High-Low Temperature Reactor. J. A. Kozinski, R. Saade, G. Zheng, 2495

02 Thermal Conductivity

03 Thermal Diffusion

04 Viscosity

Exothermicity and Three-Dimensional Effects in Unsteady Propane Square Jets. F. F. Grinstein, K. Kailasanath, 91

30 Combustion Synthesis

Diamond Thin Film Deposition in Low-Pressure Premixed Flames. D. G. Goodwin, N. G. Glumac, H. S. Shin, 1817
Temperature Profile Measurements in Stagnation-Flow, Diamond-Forming Flames Using Hydrogen CARS Spectroscopy. K. E. Bertagnolli, R. P. Lucht, 1825
The Controlling Chemistry in Flame Generated Surface Deposition of Na_2SO_4 and the Effects of Chlorine. M. Steinberg, K. Schofield, 1835
A Mathematical Model of Laser-Induced Synthesis of Ultrafine SiC Powders. S. S. Khartchenko, A. I. Kuzmin, 1845
Gas-Phase Combustion Synthesis of Materials. K. Brezinsky, 1805
Pulsating Instability in the Nonadiabatic Heterogeneous SHS Flame: Theory and Experimental Comparisons. A. Makino, C. K. Law, 1867
Supercritical Combustion Synthesis of Titanium Nitride. K. Brezinsky, J. A. Brehm, C. K. Law, I. Glassman, 1875
Metal-Sulfur Combustion. S. Goroshin, A. Mizera, D. L. Frost, J. H. S. Lee, 1883
Gas-Phase Combustion Synthesis of Aluminum Nitride Powder. R. L. Axelbaum, C. R. Lottes, J. I. Huertas, L. J. Rosen, 1891
Controlled Combustion Synthesis of Nanosized Iron Oxide Aggregates. Z. Zhang, T. T. Charalampopoulos, 1851
The Formation of SiO_2 from Hexamethyldisiloxane Combustion in Counterflow Methane-Air Flames. H. K. Chagger, D. Hainsworth, P. M. Patterson, M. Pourkashanian, A. Williams, 1859